

ECSMGE 24

Lisbon, Portugal

Geotechnical Engineering Challenges to Meet Current and Emerging Needs of Society

Les Défis de la Géotechnique pour Répondre aux Besoins Actuels et Émergents de la Société

Proceedings of the
XVIII European Conference on
Soil Mechanics and Geotechnical Engineering

Comptes Rendus du
XVIIIème Congrès Européen de
Mécanique des Sols et de la Géotechnique

Lisbon, 26-30 August 2024

Editors
Nuno Guerra, Manuel Matos Fernandes, Cristiana Ferreira, António Gomes Correia, Alexandre Pinto, Pedro Sêco e Pinto

Sociedade Portuguesa de Geotecnia
SIMSG ISSMGE
CRC Press Taylor & Francis Group
www.ecsmge-2024.com

GEOTECHNICAL ENGINEERING CHALLENGES TO MEET CURRENT AND EMERGING NEEDS OF SOCIETY

'Geotechnical Engineering Challenges to Meet Current and Emerging Needs of Society' includes the papers presented at the XVIII European Conference on Soil Mechanics and Geotechnical Engineering (Lisbon, Portugal, August 26 to 30th, 2024). The papers aim to contribute to a better understanding of problems and solutions of geotechnical nature, as well as to a more adequate management of natural resources. Case studies are included to better disseminate the success and failure of Geotechnical Engineering practice. The peer-reviewed articles of these proceedings address the six main topics:

- New developments on structural design
- Geohazards
- Risk analysis and safety evaluation
- Current and new construction methods
- Environment, water, and energy
- Future city world vision

With contributions from academic researchers and industry practitioners from Europe and abroad, this collection of conference articles features an interesting and wide-ranging combination of innovation, emerging technologies and case histories, and will be of interest to academics and professionals in Soil Mechanics and Geotechnical Engineering.

PROCEEDINGS OF THE XVIII EUROPEAN CONFERENCE ON SOIL MECHANICS AND GEOTECHNICAL ENGINEERING, 26–30 AUGUST 2024, LISBON, PORTUGAL

COMPTES RENDUS DU XVIIIÈME CONGRÈS EUROPÉEN DE MÉCANIQUE DES SOLS ET DE LA GÉOTECHNIQUE, 26-30 AOÛT 2024, LISBONNE, PORTUGAL

Geotechnical Engineering Challenges to Meet Current and Emerging Needs of Society

Les Défis de la Géotechnique pour Répondre aux Besoins Actuels et Émergents de la Société

Edited by

Nuno Guerra

NOVA University of Lisbon, Portugal

Manuel Matos Fernandes

University of Porto, Portugal

Cristiana Ferreira

University of Porto, Portugal

António Gomes Correia

University of Minho, Portugal

Alexandre Pinto

President of the Portuguese Geotechnical Society, Portugal

Pedro Sêco e Pinto

President of the Scientific Committee of ECSMGE 2024



CRC Press
Taylor & Francis Group
Boca Raton London New York Leiden

CRC Press is an imprint of the
Taylor & Francis Group, an **informa** business

A BALKEMA BOOK

Designed cover: Maria Brito and Leading

First published 2025
by CRC Press/Balkema
4 Park Square, Milton Park, Abingdon, Oxon, OX14 4RN

and by CRC Press/Balkema
2385 NW Executive Center Drive, Suite 320, Boca Raton FL 33431

CRC Press/Balkema is an imprint of the Taylor & Francis Group, an informa business

© 2025 selection and editorial matter, Nuno Guerra, Manuel Matos Fernandes, Cristiana Ferreira, António Gomes Correia, Alexandre Pinto and Pedro Sêco e Pinto; individual chapters, the contributors

Typeset by Integra Software Services Pvt. Ltd., Pondicherry, India

The right of Nuno Guerra, Manuel Matos Fernandes, Cristiana Ferreira, António Gomes Correia, Alexandre Pinto and Pedro Sêco e Pinto to be identified as the authors of the editorial material, and of the authors for their individual chapters, has been asserted in accordance with sections 77 and 78 of the Copyright, Designs and Patents Act 1988.

The Open Access version of this book, available at www.taylorfrancis.com, has been made available under a Creative Commons Attribution-Non Commercial-No Derivatives (CC-BY-NC-ND) 4.0 license.

Although all care is taken to ensure integrity and the quality of this publication and the information herein, no responsibility is assumed by the publishers nor the author for any damage to the property or persons as a result of operation or use of this publication and/or the information contained herein.

British Library Cataloguing-in-Publication Data
A catalogue record for this book is available from the British Library

Library of Congress Cataloging-in-Publication Data
A catalog record has been requested for this book

ISBN: 978-1-032-54816-6 (hbk)
ISBN: 978-1-003-43174-9 (ebk)
DOI: 10.1201/9781003431749

Proceedings of the XVIII ECSMGE 2024
GEOTECHNICAL ENGINEERING CHALLENGES
TO MEET CURRENT AND EMERGING NEEDS OF SOCIETY
© 2024 the Authors
ISBN 978-1-032-54816-6
Open Access: www.taylorfrancis.com, CC BY-NC-ND 4.0 license

ECSMGE 24
XVIII EUROPEAN CONFERENCE ON SOIL MECHANICS AND GEOTECHNICAL ENGINEERING

Contents

Preface xlv

Acknowledgements xlvii

Editor Biographies xlix

Advisory Committee
Comité Consultatif li

Scientific Committee
Comité Scientifique liii

Organizing Committee
Comité d'Organization lv

Board of Reviewers
Comité de Révision lvii

KEYNOTE LECTURES
Conférences Principales

On the interdependency between geotechnical and structural design 3
M. Topolnicki

Geotechnical aspects of February 6, 2023 Kahramanmaraş-Türkiye earthquake sequence 25
K.O. Cetin, E. Cakir, A. Elsaid, F. Cuceoglu, B. Soylemez, S. Ocak & B.U. Ayhan

Risk analysis and mitigation in geotechnical engineering – Lessons learned from the collapse of the historical archive in Cologne due to underground construction 45
C. Moormann & M.J.P. Effenberger

How AI and IoT are transforming geotechnical site monitoring and construction 72
A. Gomes Correia & E. Gastine

Soil reinforcement based on bio-geo-chemical processes: from laboratory insights to field applications 84
L. Laloui, D. Terzis, R. Harran, J. Bosch, A. Elmaloglou, S. ten Bosch, M. Buyuklu & Z.N. Sahlab

3D planning in the Lisbon of the future: requirement or necessity? 96
C. Pinto

STATE-OF-THE-ART REPORTS
Rapports sur l'état de l'art

Recent trends in monitoring tunnelling-induced displacements of structures 113
E. Bilotta

High-speed rail earthworks design developments and innovative trials – building Britain's technical legacy 127
G. Katsigiannis

Exploring rate and temperature effects on residual strength. Review and implications for a landslide case study 137
N.M. Pinyol, L.M. Garcia, A. Lloret & M. Alvarado

Specificities of floating offshore wind turbines for risk and safety evaluation of anchoring systems 154
B. Cerfontaine, S.M. Gourvenec & D.J. White

Basal-reinforced pile-supported embankments, dealing with risks and safety during design and construction 167
S.J.M. van Eekelen, P.G. van Duijnen & T. Schweckendiek

Tremie Concrete for special geotechnical works – a story about performance and sustainability 178
K. Beckhaus

Cutoffs in dams: Overview and recent developments 187
G. Pereira

Sustainability report of the European large geotechnical institutes platform 197
A. Marin, T.L. Christiansen, T.R. Smaavik, C. Carlsson, Y. Rogbeck, B. Žlender, T. Bračko, A. Insana & J. Machacek

10 years of carbon calculator use: what have we learned for the future? 204
A. Ottaviani, D. de Melo, L. Bruni, R. Gupta & C. Nelsen

The Cube system - a new diaphragm wall technique for future cities 210
F.-W. Gerressen

Thermal behaviour of soils: studies and applications in current energetic and climatic contexts 218
A. Vieira

Conference Forum Lectures - Challenges of underground space in the cities of the future
Conférences du Forum du Congrès - Les défis de l'espace en sous-sol dans les villes du futur

Unearthing the urban future: the evolving role of tunnel and underground structures in modern cities 231
A. Cornaro

Underground and beyond: The road to resilience 235
A.N.P. Lamas

Underground space: Opportunity or a non sense option? 241
P.R. Silva

Heritage Time Capsule Project Lectures
Conférences sur le Projet Heritage Time Capsule

The Heritage Time Capsule project and the Portuguese geotechnical history 247
J. Mateus de Brito

HTC - Creating and discovering the ISSMGE Heritage Time Capsule 262
S. Pathmanandavel, E. Bilotta, C.J. MacRobert & C. Chung

PAPERS
Articles

A - New developments on structural design
A - Nouveaux développements en matière de conception structurelle

Incorporating site variability into LRFD design of piles 273
M.Y. Abu-Farsakh & M. H. Rahman

Evaluation of design methods for geosynthetic-reinforced pile-supported embankments based on case studies 278
M.Y. Abu-Farsakh & M. Izadifar

Development of CPT-V_s correlations for soft quaternary clays of Szeged city Hungary 282
A. Al-Azazmeh & A. Mahler

Method for determining soil mechanical parameters from in-situ test data on the base of real nonlinear soil deformation 286
A.A. Alekhin, A.Zh. Zhussupbekov & G.A. Zhairbaeva

An experimental study of failure mechanisms developed in rock masses under circular footing 291
A. Alencar, C. Sánchez-Barberán, R. Galindo, M. Muñiz-Menéndez & A. Viana da Fonseca

A comparative discussion on soil arching evolution in CPS and GRPS embankments 295
M. Almasraf, A. Salimnezhad, B.E. Kelek, O. Cinininoglu & S. F. Cinicioglu

A modified Rowe cell with bender elements for dynamic testing of soils and interfaces 301
A. Almukashfi, R. Castellanza, A. Gomes Correia, M. Arroyo, C. Zuretti, D. Bendea & I.D. Moldovan

Renforcement par inclusions rigides: évaluation du transfert de charge au sein d'une plateforme granulaire renforcée ou non par des géosynthétiques 305
A.M. Alzate, B. Simon, C. Terqueux, L. Briançon & P. Villard

Prediction of uplift and compression bearing capacity of screw piles in saturated sand 311
D.K. Andreasen, A.K. Koteras & L. B. Ibsen

Evaluating the reliability of existing methods for predicting installation torque of screw piles in saturated sand: A comparative study 315
D.K. Andreasen, L.B. Ibsen & A. K. Koteras

1-D intrinsic compression curves for settlement analysis of soft clays 320
C. Athanasiu, A.B. Tsegaye, E.R. Sørlie & K.E.L. Johnsen

Numerical modelling of rigid inclusion reinforced road platform, under surface loading and mobile loading 326
T. Badinier, N. Ouechten, T. Dubreucq & L. Thorel

Centrifuge modelling of tapered wall jacked into dense sand 330
L. Bałachowski, W.F. Kabeta, L. Thorel, M. Blanc & T. Dubreucq

Effects of non-linear response of shallow foundations on transmission tower serviceability 334
P. Barbieri, T. Newson, M.Y. Xiao & H. P. Hong

Automating stability analysis using BIM-FEA-Integration 338
J. Beck, H. Jürgens & S. Henke

Micropile bearing capacity analysis using fiber optic technology 342
R. Bednarek & A. Jaroszek

Cross analysis between different evaluation methods of small strain moduli in clays and marls of Parisian subsoil 346
N. Berthoz, N. Dufour, A. Rallu, Y. Aslan & D. Branque

Settlement analysis for a nuclear plant design 352
M. Blanckaert, B. Pelletier, S. Depinois & M. T. Hoang

A critical review of field testing of helical steel piles 356
P.J. Bourne-Webb, T.M. Bodas Freitas, P. Marques & E. Godinho

Modelling the interaction of an underground structure with the soil in a megalopolis 361
I. Boyko, V. Nosenko & O. Lytvyn

Machine learning to improve the ground model for road settlement prediction 365
M. Brček, J. Panuška & M. Kopecký

Automatic parameter calibration of advanced constitutive soil models and application to a boundary value problem 369
F. Brosz, J. Machaček & H. Zachert

Mechanical features of stabilized soils with low cement content 375
M.A. Castaneda-Lopez, T. Lenoir, L. Thorel & J.-P. Sanfratello

Application of optimization algorithms in geotechnical engineering as decision-making support tool 380
K. Cerek, E. Hadjiloo & J. Grabe

Performance-based interaction domains for pile groups 384
R. Cesaro, R. Di Laora, C. Iodice & A. Mandolini

Rheological study of soil-cement-GGBFS mixture 390
S. Choudhary, P.K. Meena, A. Kumawat & L. Borana

Influence of volumetric boundary conditions on the water-retention behaviour of reconstituted and intact clay shales 395
F. Christ & A.A. Lavasan

Definition and analysis of ground surface vibration curves induced by railway traffic 400
A. Colaço, R. Gomes & E. Fortunato

Integrating cluster-based knowledge for local undrained shear strength prediction 404
S. Collico, G. Spagnoli, A. Fraccica & E. Romero

Back-analysis of deep excavations supported by strutted retaining walls 410
V.I. Cordoni, L. Gelonch, B. Solà, C. de Santos & A. Ledesma

Correlations between SPT and DPSH results based in energy measurements 414
N. Cruz, J. Cruz, C. Rodrigues, L. Fagundes & C. Chaquisse

Hydric and mechanical properties assessment of basalts from Madeira island, Portugal 418
N. Cueto, J.F. Vieira de Sousa, J.P.S. Perneta, R. Meza & M. L. Pereira

Analysis of the feasibility of applying reinforcement for laying direct foundations 424
M.C.C.S. da Silva & P.C. de A. Maia

Rate-dependent confined crushing in granular media 428
S.K. Das

Slog: an open geotechnical software 433
J. de Sauvage

A semi-analytical model for axial soil-pile interaction in generalized inhomogeneous soils 438
A. Della Corte, O. Orakci, A. Tsikas, S. François & G. Anoyatis

Integrating MT-InSAR and conventional monitoring with numerical analysis for tunnel excavations: A case study 444
G. Della Ragione, E. Bilotta, Di Mariano & A. Gens

A t-z approach for the design of axially loaded piles in consolidating soil 448
A.E. Detlefsen, A. Franza & K.K. Sørensen

Port silo foundations on piles under vertical cyclic stresses 452
P. Dogaru & R. Ciortan

Effect of strain-softening and strength anisotropy on the undrained resistance of deeply embedded pile/pipe section 456
Y.P. Dong

Improvement of tubular piles by effective closure 462
M. Doubrovsky & V. Dubravina

Mechanical characterization of a saturated marine clay for pavement design and performance 468
J.H.C. Everton & S. Erlingsson

Integrating local data into geotechnical design through a predictive probabilistic approach 474
A. Finiasz, J. Hassaoui, C. Jacquard & E. de Rocquigny

Impact of the testing methods on physical properties of high plastic clay 478
J. Frankovská, M. Brček & J. Brčeková

Reinforced soil technique for temporary slope stabilisation in loose saturated ground 482
G.R. French & S.D. Thomas

Creative approaches for enhancing excavation shoring efficiency through diaphragm wall prestressing techniques 488
M.C. Frydrych

Limit equilibrium solution for lateral pile capacity in cohesive soil 492
T. Gans-Or & S. Pinkert

Effect of microplastics on swelling behaviour of geosynthetic clay liners (GCLs) 497
Y. Gao, R.K. Rowe & A. El-Zein

The behaviour of piles in unsaturated expansive clays under cyclic lateral loading 503
T.A.V. Gaspar, R.A. Murison, S.W. Jacobsz, G. Heymann & A.S. Osman

Undrained triaxial test stress path shape as an indicator of sample quality 507
V. Gjelsvik & K. Kahrs

Cohesive soil behavior under cyclic loading in undrained conditions 511
A. Głuchowski & W. Sas

Numerical simulation of pore water pressure evolution beneath a raft foundation during a river flooding 515
E.P. Graterol, J.G. Gutiérrez-Ch, L. Mediero & S. Senent

Evaluation train induced ground vibration boom with Vibtrain 520
A. Håård, J.A.T. Johansson, K. Viking & S. Larsson

On the thermal failure of sand-clay mixture 524
A. Hamidi, A. Shirasb & S. Tourchi

Soil-structure interaction of two different configurations of a cut and cover tunnel 528
A.M. Hasan, B.J. Shwan & O.Q. Aziz

Dynamic pull-out tests to characterize the earthquake behavior of soil-nailed walls 532
G. Hawwa, J. de Sauvage, P. Joffrin, Y. Fargier & J.P. Rajot

Use of BIM methodology in Geotechnical Projects – Construction of underground reservoirs 538
A. Henriques, N. Silva & M. Lopes

Evaluation of some "similar" dissipation tests 542
E. Imre, L. Bates & D. Marchetti

A closed-form equation for the failure locus of pile groups subjected to generalized loading conditions 548
M. Iovino, C. Iodice, R. Di Laora, L. de Sanctis & A. Mandolini

Cyclic properties of sand-clay mixtures at low confining stresses 554
V. Jagodnik, D. Marušić, J. Peranić, M. Vivoda Prodan, Ž. Arbanas & D. Katalinić

Measuring the undrained shear strength of very soft, clay-rich sediments 560
L. Jaksic, M. Konstadinou, A. Talmon, T. van Kessel & E. Meshkati

Settlement evaluation of reinforced embankment over a soft subgrade: Numerical modelling with different soil models based on a full-scale study 564
B. Janevski, J.Br. Papić, A. Skejić & A. Turalić

A study on ultimate vertical bearing capacity of spread foundations of sand-clay two layers ground 568
K. Kaneda & S. Ohtsuka

Numerical modelling of soil-pile interaction in a subsiding soil 572
J.G. Kania, L.L.C.G. de Sousa, O. Hededal & K.K. Sørensen

Nonlinear numerical analysis of foundations on basis of plate load test results 576
Y. Kirichek & O. Tregub

Multidisciplinary design optimisation of vibro stone columns and dynamic replacement 582
B. Knabe, C. Tinat & M. Rosenberg

On the use of compliance correction for performing truly constant volume cyclic direct simple shear tests on sands 588
M. Konstadinou & A. Bezuijen

Effects of physical characteristics on the shear behaviour of Foulum glaciofluvial sand 592
J.Z. Krabbe, K.K. Sørensen & M.R. Lodahl

An advanced method to predict umbrella arch behaviour in soft ground tunnelling 596
S. Kuder, J. Klopčič, B. Pulko & J. Logar

Repeated LWD test to assess the stiffness properties of clayey soil 600
D. Kuttah

Some applications of interaction domains to pile foundations design 606
A. Lambrughi, A. Chiarelli, M. Orlandini & A. Mandolini

Discrete modelling of stress relaxation in crushable sands based on fracture theory 610
J. Lei, M. Arroyo, M.O. Ciantia & N. Zhang

Assessing tunnel-structure interaction effects in London Clay 614
J. Liu, A. Tsiampousi, A. Ruiz López & D.M.G. Taborda

Centrifuge modelling of sand and sawdust embankments on peat for sustainable infrastructure development 618
M. Long, L. von der Tann, S. Ritter, P. Paniagua, M. Dahl, M. Konstantinou & C. Cengiz

Interpretation of pressuremeter tests in clays with non-linear elastic behaviour 622
A. Lopes dos Santos, T. Nader & J. Habert

Soil-pile interaction mechanisms under compressive service load 628
J.C. Lourenço & J.A. Santos

Seismic stability of gravity retaining walls: reliability assessment and web application 633
Z. Luo, B.M. Das & K. Sobhan

Direct design method of shallow foundation based on in situ tests results, application to dynamic cone penetrometer 637
T.A. Luong, P. Reiffsteck, F. Szymkiewicz & M. Benz-Navarrete

Key concepts in soil mechanics: simple hands-on and team-based strategies to promote active learning 641
J. Macedo & M. Pinho-Lopes

Concrete arches and reinforced soil: a sustainable alternative structure for road bridges 647
K. Malekmohammadi, A. Moncada & I.P. Damians

Analytical method to check the uplift of a jet-grouting plug 651
A.B. Martínez-Bacas

Parameter identification for constitutive models based on pressuremeter test 656
I. Marzouk, F. Tschuchnigg, H.F. Schweiger & N. Hödlmoser

Advanced numerical modelling using the Hardening Soil Small Strain material model for sensitive excavations adjacent to a metro station 660
C. Merino, J. González & A. Prados

Axial behaviour of displacement pile groups in sand based on model tests in a calibration chamber 664
F. Mitlmeier & Ch. Moormann

Terramesh: Solutions for great heights. Design and durability 670
L. Molano, D. García, D.C. Freitas, G.M. Torres & M. Jimenez

Assessment of the degree of saturation in sands by bender element testing 674
F. Molina-Gómez, A. Viana da Fonseca, C. Ferreira & G. Cascante

Characterization of intermediate soils by innovative in-situ testing procedures using Medusa DMT 679
P. Monaco, S. Amoroso, A. Chiaradonna, D. Marchetti, T.M.H. Le & J.-S. L'Heureux

Performance of cantilever sheet pile walls in sensitive clays: Case study Campus Ullevål 683
E. Monsås, S. Oberhollenzer, E.J. Lande & M. Løyland

Morphological characterization of grain-scale sphericity using 2D x-ray microtomography images 689
T.K. Moura, L.C.S.M. Ozelim, G.M. Alelvan, T.D. Rosa & M.D.T. Casagrande

Accuracy of in-situ assessment of soil density and moisture content using the non-nuclear method 693
J. Neves, C. Lopes & C. Silva

Analysis and modelling of Resonant Column test results on reconstituted specimens of a saturated pyroclastic soil 697
G. Nicodemo, N. Poursalimi, V. Foresta & S. Ferlisi

Accumulated axial strains for bentonite sand mixture due to cyclic loading with low confining pressures 701
T. Nishimura

PIV analysis of ground during horizontal pile loading by centrifuge tests 705
M. Odagiri, T. Takatoshi & Y. Asaka

Correlating q_{net} to E_{ur} of Paleogene clays of high plasticity 711
N. Okkels, L. Bødker & T. Thorsen

High embankments on soft soils – geotechnical design based on field monitoring and back analysis, Romania, Sebeș-Turda motorway 715
A.C. Olteanu, T. Malancu & C. Tomsa

Assessing the impact of correlated geotechnical properties on the behaviour of retaining structures 719
E. Panagiotis, I. Rocchi & V. Zania

A new approach for evaluation of remoulded shear strength in clays using the cone penetration test 723
P. Paniagua, P.W. Mayne, B. Di Buò & S.S. Agaiby

Alert soil mechanics instructors of the main unsaturated soil issues: What and how to teach when experts disagree 727
M. Pantazidou, S. Houston, J. McCartney, A. Tarantino & M. Bardanis

From EN 1998-5:2004 to prEN 1998-5:2023: Has the calculation of earth pressures improved or deteriorated? 733
L. Pantelidis

Influence of carbonate content on the shear strength of a beach sand from the northeastern coast of Brazil 739
K. Polemis Júnior, A.S. Moura, C.U.V. Verissimo, F.C. Silva Filho, D.A. Nascimento, R.A. Cordeiro Silva & D.R. de Lima

Soil plugging in small diameter tube samplers in silty soils 745
E. Pöyry, M.S. Farhadi, M. Haikola, T.T. Länsivaara

A glimpse into the future of site supervision: Data collection during pile installation at the Amaliahaven construction site 750
J. Putteman, P.S.F. Le Lan, C.J.F. van Marrewijk, T. Jottier, J.N. Bruens, A.A. Roubos & M. van der Pol

Influence of the subgrade geomechanical classification on the short term and long-term performance of a railway track 755
A. Ramos, A. Gomes Correia & R. Calçada

Prediction of resilient modulus of unsaturated soils considering inter-particle suction bonding 761
A. Rana, A. Azizi, A. Kumar, M. Lloret-Cabot & D.G. Toll

Evolution of shallow foundation load test from static to cyclic loading 765
P. Reiffsteck, F. Szymkiewicz, C. Minatchy, T. Sanagawa & D. Yokoyama

A novel undrained saturation method for triaxial testing of cohesive specimens 769
A. Rismanchian & A. Tavallali

Large scale direct shear tests on rockfill 63/180mm 773
J. Rocha, P. Mengé & M. Muñiz-Menéndez

Numerical modelling of unsaturated bentonite subjected to different hydro-mechanical stress paths 777
C.E. Rodríguez, A. Gens, R. Vasconcelos & J. Vaunat

Bi-directional testing of bored piles in chalk 783
M. Roed, J.S. Steenfelt & O. Hededal

Monitoring pile construction impact near sheet pile quay walls: Some remarks 789
P. Ruggeri, M. Senigagliesi, P. Alesiani & V.M.E. Fruzzetti

Applying machine learning to the development of surrogate models for shafts in clay 795
A. Ruiz López, D.M.G. Taborda, A. Tsiampousi, A.M.G. Pedro & S. Hardy

Field investigations of combined raft-pile foundation with adjustable interaction between the raft and the piles 799
O. Samorodov, S. Tabachnikov, O. Dytiuk, O. Krotov, Y. Vynnykov, Y. Kirichek & V. Shapoval

Seismic and load inclination factors for estimating the bearing capacity of strip footings 805
T. Santana, N. Guerra, A. Antão & M. Vicente da Silva

Conception d'un remblai avec prise en compte de la succion d'un sol non saturé pour justifier la stabilité 809
V. Savatier, C. Nogue Sanchez, D. Mahmutovic & O. Denk

Shear and creep behaviour of frozen granular soils under compressive and tensile loading 815
U. Schindler, S. Chrisopoulos, S. Vogt & R. Cudmani

Influence of installation effects on the performance of laterally loaded pile groups 821
T. Schlager, C. Moormann & H. Schiewe

Correlating CPTu to G_0 in high plasticity Paleogene clays 827
E. Skouboe, K.H. Lundvig & N. Okkels

Numerical investigation on attenuation response of machine foundation under horizontal excitation 831
A. Singh, P. Ghosh & S. Surapreddi

Evaluation full-scale mooring pile load test Rotterdam 837
J.J.M. Sluis, H.J. Lengkeek & A.A. Roubos

Compressibility characteristics and hydraulic conductivity of slurry clays using large diameter Rowe cell 843
K. Soe, M. Swamynaidu & A. Tyagi

Application of the new Brazilian pavement design method (MeDiNa) in the design of flexible pavement structures using fine-grained tropical soils 849
M.A.S. Sousa, R.Q. Coutinho, L.M.G. Motta & C.D. Castro

Combined pile-raft and raft foundation modelling and design for three distinct office buildings in Lisbon, Portugal 855
A. Sousa, A. Pinto & N. Silva

Advanced constitutive model parameter determination, optimisation and selection using a database of triaxial tests and machine learning tools 861
M.T. Stals, K. Siderius & R.B.J. Brinkgreve

Effective strength parameters of Danish clay tills - revisited 865
J.O. Steensen-Bach, J.S. Steenfelt & O. Hededal

Digital geotechnical information management in a life cycle perspective 871
M. Svensson & O. Friberg

Behaviour of continuous flight auger piles in homometric and carbonated sands 875
F. Szymkiewicz, L. Makki, S. Fanelli, C. Minatchy, F. Guirado & J. Habert

Static load tests on raft on rigid inclusions 881
F. Szymkiewicz, C. Bohn, L. Briançon, S. Lambert, P. Garnier & L. Carpinteiro

Simplified methodology to evaluate the stability of a group of isolated caisson-type maritime infrastructures 885
D. Tarragó & A. Gens

Viscous resistance of clay soil under kinematic shear 889
A.Z. Ter-Martirosyan & L.Yu. Ermoshina

Applications of PS suspension logging test in port infrastructures 893
A. Tijera, E. Asanza & R. Ruiz

On the modelling of state and history dependency of small strain stiffness of soils with application to 1D settlement analysis 897
A.B. Tsegaye & J.-S. L'Heureux

The influence of clay and silt content on reducing stiffness of soil in a small range of strains 903
W. Tymiński, T. Kiełczewski & P. Stajszczak

Geotechnical and structural design of primary support for shaft and tunnelling construction works at Santos station-Lisbon subway - a 3D FE modelling approach 907
M. Unas, S. Ferreira, F. Bernardo, R. Pistone, R. Pina & A. Tavares

Static load tests on energy piles: Effects of thermal cycles 913
R. Vasilescu, F. Szymkiewicz, C. Minatchy, F. Guirado, V.T. Nguyen, A.M. Tang & J.M. Pereira

Uncovering soft soils with 3D Empirical Bayesian Kriging: A case study on cone penetration test data 917
J. Viegas, A. Gallardo, A.C. Costa & R. Marinaro

Mechanical behaviour of geosynthetic sheets used to reinforce load transfer mattresses in the case of embankments on soft soils reinforced by rigid inclusions 923
P. Villard

Assessment of shear wave velocity variation in compacted soil using pulse transmission techniques 927
C. Walker & A. Heitor

Mechanical and physicochemical study of a cemented sand exposed to wetting and drying cycles 931
A. Wassermann, A. Abdallah, O. Cuisinier, C. Diliberto & J.-M. Mechling

Application of the isotache law and the power creep law on prediction of long-term consolidation behaviour 935
Y. Watabe & Y. Miyata

The impact of small strain stiffness parameters on geotechnical numerical modelling - a case study in Budapest, Hungary 939
Á. Wolf, K. Ficzek & Zs. Szilvágyi

Numerical study of ground movements induced by traditional foundation underpinning 945
J. Woodcock, A. Fasano & A. Nikolic

Comparison of Markov Chain Monte Carlo and Sequential Monte Carlo inference techniques for calibrating soil parameters in a braced excavation 949
N. Yang, T. Le & L.T. Nguyen

Simulation of sand-fines mixtures behaviour based on bounding surface plasticity and equivalent void ratio 955
F.H. Yeh, L.F. Prada-Sarmiento, M. Tafili, D. Sarkar, T. Wichtmann & L. Ge

Load bearing mechanism of screw piles under compressive loading in clayey soil 961
P. Zahedi & D. Igoe

Simplified finite element modeling of TBM tunneling 967
H. Zaiter, H. Mroueh & E. Bourgeois

Determining the modulus of subgrade reaction for piled raft foundations by numerical modelling 971
B. Zarazvand & J. Frankovska

Examining the behavior of laterally loaded large-diameter monopiles using coupled FDM-DEM simulations 975
Z. Zhang, Z.-T. Zhang, X.-D. Zhang, W. Wang, G.-M. Yu & Z.-Q. Zhang

Research on macro-meso relationship of geological materials based on Discrete Element Method: Review and prospect 979
M. Zhou, Q. Zhang & R. Ding

Numerical simulations of soil tests emulating ground behaviour beneath super-tall building foundations 983
Y. Zhou & T. Kiriyama

Challenges in characterisation of natural sands with fines 989
H. Zhou & S. Sharma

Smart foundations for undermined and seismically affected territories 995
A. Zhussupbekov, B. Bazarov, A. Sarsembayeva, A. Omarov, S. Mussakhanova & D. Mukhanov

Method for triaxial experiments for unconventional strain paths and back-calculation using Neohypoplasticity 1001
J. Zürn, L. Mugele & H.H. Stutz

Creep of organic soils due to small load increments 1005
C. Zwanenburg, B. Wittekoek & M. Konstadinou

B - Geohazards
B - Géorisques

Discharge flow rate under sheet piles, a prediction model 1013
A. Ahangar Asr, A. Johari & A. A. Javadi

Contract for the stabilization of the north cliff in Azenhas do Mar 1017
S. Almeida & M. Pereira

Overcoming geotechnical challenges to maximise re-use of an existing brownfield site for use as a rail test track 1023
P. Anning, J.K. Thillainadarajah & A. Kushwaha

Ravines in collapsible soils of Luanda, Angola: forms of erosion – state of the art 1027
F.M. António, F.A.B. Bonito & A.A.R.C.A. Benta

Reliability analysis of a Po River embankment affected by underseepage 1033
I. Bertolini, M. Marchi, L. Tonni & G. Gottardi

Concept for sustainable lab and in-situ research on earthquake induced geohazards 1038
J. Bojadjieva, V. Sheshov, K. Edip, T. Kitanovski, D. Ivanovski, I. Gjorgjeska & A. Bogdanovic

Seabed and sub-seabed boulders as an engineering hazard in the marine environment; a risk mitigation strategy for subsea cables 1042
L.J. Burley, E. Tataki, H.M. Taylor, V. Terente & N. Dyer

The Tonbridge to Hastings undrained earthwork and modernisation programme and engineering research (THUMPER) 1048
D. Butcher, S. Fielder, S Holt & T. Hunt

Centrifuge tests on the uplift and deformation patterns of clay cover layers in deltas 1052
C. Cengiz, M.A. Cabrera, B. Wittekoek, M. Fransen, L. Wopereis & C. Zwanenburg

UAS thermal imagers for monitoring and analysing landslide in a mudstone area 1056
H.-W. Chen, C.Y. Chen & Y.Y. Liu

Evaluating the interface shear strength of geocomposite drain and HDPE geomembrane layers in landfill cover systems 1062
F. Chihi & G. Varga

A simplified procedure for FE analysis of an earth dam under seismic loading 1066
A. Choudhury, P. Ghosh & S.K. Mishra

Change of soil permeability during and after soil liquefaction 1072
M.-C. Chu, C.-C. Tsai, Y.-C. Kao, Y.-X. Liu & C.-Y. Jou

Strength and rainfall-induced erosion resistance of bio-cemented soil slopes 1076
R. Devrani, P. Vangla & S. Sharma

Evaluating undrained shear strength and sensitivity in soft sensitive clay using piezocone and field vane tests 1080
B. Di Buò, P.W. Mayne, P. Paniagua & S.S. Agaiby

Numerical analysis of an unstable slope 1086
A. Di Mariano, J. Serna-Garcia, Y.F. Vargas-Alzate & A. Gens

Monitoring the hydro-mechanical effects of vegetation cover on shallow landslide triggering: Preliminary results from a case study in western Norway 1090
A. DiBiagio, V. Capobianco, A. Oen & L.M. Tallaksen

Slope stabilization at Régua-Ferrão section of the Douro railway line 1094
C.M. Dinis & A.M. Pereira

Resonant column round-robin testing 1100
N. Dufour, H. Calissano, L. Batilliot, I. Rogoff, C. Simon, A. Disantantonio, T. Lando & E. Bourguignon

Experimental investigation of influence of soil plasticity on compression characteristics and creep behaviour of clayey soils 1104
M.N. Duy & J. Jerman

Nonlinear finite element analyses of earthquake effects in slopes 1109
A. Eikebrokk & A.M. Kaynia

Appraisal of various measures for liquefaction flowslide mitigation in a mild sloping ground 1113
M.H. Fansuri, M. Chang, R.R. Rayhansyah, H.J. Lin, T.C. Upomo & R. Kusumawardani

Coastal cliff stabilization and access stair reconstruction at Peneco beach, Algarve, Portugal 1119
C. Fartaria, A. Pinto, J. Dinis, P. Nunes & M. Silva

A design procedure for high energy rockfall barriers 1123
D. García, L.Molano, G. Torres & D. Freitas

Calibration of soil water retention parameters based on field measurements 1127
T.A.V. Gaspar, S. Pradhan, A.S. Osman & D.G. Toll

Use of Bayesian Kriging to develop new soil property maps for Quito, Ecuador 1131
C.E.L. Gilder, M.M. Othman, C. Zapata, E.A. Holcombe, R. De Risi, F. De Luca & P.J. Vardanega

Liquefaction resistance of carbonate sands from cone penetration tests 1136
D. Giretti & V. Fioravante

2D Seismic response analyses from 3rd Level Seismic Microzonation in the Southern Italy: Approaches and applications 1142
S. Grasso, M.R. Massimino & M.S.V. Sammito

Slope stability modelling of urbanisation scenarios for communities in north Quito, Ecuador 1146
R. Hen-Jones, C. Zapata, E. Jiménez, E.A. Holcombe & P.J. Vardanega

Forensic investigation of quick clay landslide released by construction work at Asak, Norway 1150
H. Heyerdahl, Å.M.W. Amdal, R. Frauenfelder, K. Sverdrup-Thygeson & A.O.K. Lysdahl

Vulnerability assessment of buildings to landslides: application to Swiss case studies 1154
E.P. Howald, L. Francone & D. Martinelli

Fire-induced changes in the geotechnical properties of a volcanic soil 1160
L. Iervolino, D. Peduto & V. Foresta

Remote sensing techniques for soil-structure interaction health monitoring 1166
D. Infante, S. Moretti, M. Zimbardo & A. Scotto di Santolo

Slope failures risk acceptance in the construction of roads on the clayey mine spoil dump, Czech Republic 1170
J. Jurko & N. Droniuc

Local site response analyses based on field measurements compared to vs30 site-condition and geologic and topographic constraints 1174
O. Kegyes-Brassai, G. Kovacs, T. Toth, B. Labar & A. Wolf

A geotechnical and geophysical characterization of the influence of seasonal variation on railway embankments 1179
Q. Khan, S. Donohue, A. Trafford, B. Dashwood & J.E. Chambers

Laboratory assessment of shear strength parameters in sandy soil by lime permeation method and sensitivity analysis from Doi Chang case study 1183
A. Koirala & S. Soralump

Numerical and experimental evidence of the impact of soil nonlinearity on the response of an SSI system 1188
M. Koronides, S. Kontoe, L. Zdravković, D.M. Potts, A. Vratsikidis, D. Pitilakis & A. Anastasiadis

Particle size distribution induced fabric effects on the onset and post liquefaction behaviours of soils 1194
J. Leak & D. Barreto

On the liquefaction induced pore water pressure ratio underneath existing buildings 1199
S. Lirer, F. Valtucci, P. Bonassisa, L. Mele & A. Flora

Disintegration of natural granite residual soil and the geohazard implication 1205
X.Y. Liu, Y. Miao, X.W. Zhang, G. Wang & H.D. Gao

Endangered historic sites: The case study of Santa Croce in Ravenna (Italy) 1209
M. Marchi, I. Bertolini & G. Gottardi

Coastal erosion process at Calhetas parish, São Miguel island, Azores 1214
F. Marques, A.M. Malheiro, P. Amaral, A. Santos & L. Cunha

Prediction program for slow moving landslides 1218
R. Marte & H. Ramoser

Mapping and monitoring tailings storage facilities with muography 1224
M.A. McLean, F. Scutti, R. Seikel, S. Krishnan, C. Webster, S. Collins, S. Palanisamy, P.H. Panchal, J. Donovan, A.R. Duffy, C. Goss & A.N. Christensen

Liquefaction resistance of TP-Lisbon sand: A comparison between cyclic triaxial and cyclic direct simple shear tests 1228
F. Molina-Gómez, A. Viana da Fonseca, C. Ferreira & B. Caicedo

Geotechnical interventions to mitigate the geomorphological risk of the access road to Ribeira Quente parish - Azores archipelago 1232
L. Moniz, P. Amaral, A.M. Malheiro, F. Marques & A. Santos

Effect of bentonite permeation on the fabric and strength of Ottawa Sand 1236
D. Mourtada & G.A. Jaoude

Mapping the 3D effect for slope stability analyses of quick clay slopes 1241
S.S. Nagula, L. Rødvand, H.P. Jostad & S. Degago

Analysis of rock slope failures. Case studies on Romanian mountain roads 1245
A.-Cs Nagy, C. Bruchental, D.M. Paşca, V.-S. Fărcaş, D.-V. Moldovan & L.-E. Moldovan

Geotechnical seismic site characterization of deep alluvial sand sites in the South Iceland Lowland 1249
E.A. Olafsdottir, S. Erlingsson & B. Bessason

Numerical modelling of the seismic site effects in Lisbon: role of buried and surficial morphology 1255
L. Oliveira, R.C. Gomes, S. Amoroso, A. Pagliaroli & P. Teves-Costa

Expansive and collapsible soil behaviour under the Revised Soil Classification System 1259
R. Ortiz-Hernández & E. Rojas-González

Rockburst conditions prediction based on a decision tree algorithm 1265
D. Owusu-Ansah, J. Tinoco, J. Matos & F. Lohrasb

Combining slope satellite image analysis and artificial intelligence algorithms for highway service level assessment 1269
D. Owusu-Ansah, J. Tinoco, J. Matos & R. Cabral

Stabilization of excavation slopes between km 0+000 and km 2+000 of the EN337, in the municipality of Vouzela 1273
F. Paulino, E. Fernandes & A. Dinis

ReSist - A municipal policy to increase awareness on seismic risk 1277
C. Pinto, M.A. Ferreira, C. Almeida, M. Inácio, P. Pacheco, C. Pousada, C.S. Ferreira & A. Ferreira

The Citizens Observatories as a tool to manage geohazards. Lisbon Multihazards CO case study 1283
C. Pinto, A. Frias, P. Leonardo, C.S. Oliveira, M. Inácio, R. Carrilho Gomes & M. Ferreira

An early warning procedure based on coupling short-time weather forecasting and numerical slope analysis 1287
M. Pirone, G. Forte, A. Santo, G. Urciuoli & L. Picarelli

Ground investigation methods used in high-speed railway for mitigation of dissolution features risk in chalk 1291
S. Pryce, M. Black, H. Saroglou, G. Katsigiannis & S. Muniyasamy

Sensitivity analysis of the effects of liquefiable soil deposits on differential settlement of buildings by numerical modelling 1297
J. Quintero, M. Millen & A. Viana da Fonseca

A new, durable micropile for the foundation of rockfall protection structures 1301
M.J. Rebhan, H.-P. Daxer, R. Marte, M. Schuch & S.L. Burtscher

Landslide susceptibility map of the southern slope of the municipality of Odivelas using the AHP method 1305
A.J. Roque & M.J. Coelho

Numerical and theoretical investigation on the triggering mechanisms of rainfall-induced landslides 1311
G.M. Rotisciani, A. Desideri & A. Amorosi

Innovations in liquefaction mitigation: Modelling the mechanical cyclic behavior of biocemented soils 1315
Z.N. Sahlab, D. Terzis & L. Laloui

Performance design of shallow foundations interacting with liquefiable soils 1319
I. Sarao Mannelli, V. Minardi, G. Canetta & B. Becci

Effects of temperature, pore fluid composition and rate of shearing on the residual shear strength of soils 1325
G. Scaringi, O.P. Dhakal & M. Loche

Sand stabilization with colloidal silica for protection from liquefaction caused by dynamic loads 1330
R.F. Sharafutdinov, D.P. Kuznetsova, V.S. Morozov & Y.I. Stolyarov

Landslide monitoring: comparative analysis of long-term automated systems in Brazil and the UK 1335
A. Silva, C. Levesque, B. Norberto, S. Holloway & D. Fornelli

Assessment of geotechnical properties using optimisation methods 1341
M. Stãnciucu & I. Mircea

Comparative assessment of liquefaction susceptibility of unconsolidated deposits 1346
M. Stãnciucu & I. Dogaru

Liquefaction risk assessment of airport infrastructure using geological data and remote sensing techniques 1350
M. Taftsoglou, S. Valkaniotis, G. Papathanassiou & S. Argyroudis

Sand boil observations and geotechnical characterization of river embankments for the development of a backward erosion piping database 1356
L. Tonni, M. Marchi, I. Bertolini, A. Bassi & A. Rosso

Thermo-hydro-mechanical analysis of soil strata suffered from desiccation cracking 1362
S. Tourchi, M. Jabbarzadeh & H. Sadeghi

Prediction of water content under climatic actions. A method based on spectral analysis and soil transfer functions 1368
Y.F. Vargas-Alzate, J. Vaunat, A.M. Zapata-Franco & A. Di Mariano

Managing uncertainties in the geotechnical design of climate change resilient infrastructures 1373
P. Vitale & Z.Q. Liu

Shear strength of sand under different range of confining stresses using various shearing devices 1377
M. Vivoda Prodan, J. Peranić, V. Jagodnik, D. Marušić, D. Štiberc, N. Kamenar & Ž. Arbanas

Simulation of responses of a Tender Net Foundation on silty ground subjected to consecutive earthquakes 1383
H. Vo-Cong, K. Takeuchi, Y. Tomono & T. Matsumoto

Enhancing landslide anomaly detection in aerial imagery through pre-processing and GANomaly deployment 1389
C.H. Wang, K.C. Lo, C.Y. Hu & P.H. Wang

Development and experimental calibrations of a multifunction slope monitoring device - Smart Pole 1394
C.H. Wang, S.Y. Jeng, B.J. Hou & Y.T. Hu

The A83 Loch Shira landslide, Scotland 1398
M.G. Winter, T. Waaser & G. Fiddes

Back analysis of flexible barrier response following an open hillslope landslide impact at Pa Mei, Hong Kong 1402
E.K.L. Wong, J.W.C. Lau, J.-W. He, Z.-H. Zhou & S.L. Chan

Technical aspects and remediation work for hazardous landslides: Tskneti example, Georgia 1408
T. Yildiz, D. Kuparadze & D. Pataridze

Towards improved earthquake preparedness: Site effects considering multiple seismic zones 1412
A.M. Zapata-Franco, Y.F. Vargas-Alzate, J. Vaunat & A. Di Mariano

C - Risk analysis and safety evaluation
C - Analyse des risques et évaluation de la sécurité

FEM parametric analyses of the seismic behaviour of tunnel-soil-overstructure systems 1421
G. Abate & M.R. Massimino

A novel framework to evaluate the influence of seismic performance of geotechnical systems on the resilience of road networks 1425
C. Amendola, R. Conti, P. Zimmaro, M. Marinelli, L. Pariota, L. Di Costanzo & F. de Silva

Experimental landfill of filtered iron ore flotation tailings at Minas-Rio system 1430
D.G. Amorim, L.F. Silva, F.F. Rezende, T.A. Nicoli, U. Albino, F. Saliba & R.C. Silva

Monitoring and analyzing vibrations from tunnel boring machine in urban areas 1434
Y. Aslan, A. Rallu, D. Branque, N. Berthoz, C. Chatzigogos & T. Makrypidi

Evaluation of slope safety during pile driving in clay 1440
Y. Attari, E. Sørlie, H.P. Jostad & G.R. Eiksund

Effect of increased vertical stress on the state of grains in tailings 1444
S. Aulestia, V. Wiklund, M. Dossey, R. Knutsson & J. Laue

Spatial vulnerability of levees to cascading hazards 1448
M. Bačić, N. Rossi, L. Librić & M.S. Kovačević

Insights from the implementation of levelAMS, a geotechnical asset management software, on Brisa's network 1452
J. Barros, M. Pinheiro, M. Cruz, I. Gonzalez & T. Miranda

Distributed strain, settlement and temperature sensing in geotechnical earth embankments 1457
Ł. Bednarski, T. Howiacki, R. Sieńko & K. Zuziak

Effect of suction and preparation method on the compressibility of Stava silty tailings 1463
G. Bella, D. Czerski, S. Ghezzi, M. Giani, M. Lüscher & C. Ambrosi

Extension of the Lisbon subway between Santos station and the Terminal of the Cais do Sodré station - assessment of excavation induced damage in buildings 1469
F. Bernardo, S. Ferreira, R. Pistone, R. Pina & A. Tavares

Eurocode 7 – Second Generation: Retaining structures – Looking beyond the partial factors for safety in design 1475
W. Bogusz

Excavation and tunnelling impact on existing structures in the context of the second generation Eurocodes 1481
W. Bogusz

Pile response to the effect of basement construction in soft clay 1485
T. Boonyarak, A.Y. Aung & Z.Z. Aye

Assessment of displacements and deformation mechanisms in a rockfill dam: case study of Cerro da Mina reservoir 1491
L. Bottaro, G. Tavares, M. Oliveira & A. Rodrigues

Eurocode 7 – second generation reinforced fill structures 1497
G. Bräu & N. Denies

The implications of poor leadership on geotechnical risk 1503
C.A. Bridges

Designing a pre-load embankment for the construction of a stage over a sanitary landfill founded in soft soils 1507
A. Brito & J. Carreto

Eurocode 7 – second generation - numerical methods 1513
S. Burlon, H. Walter & C.C. Smith

Tensile strength of rocks: Comparison of different testing methods 1517
J. Castro, J. Justo, M.H. Olson & M. Miranda

Probability-based hybrid landslide assessment system integrating landslide susceptibility and numerical modeling 1521
Y.-H. Chen & K.-W. Liao

Large-scale soil investigations for greenfield railways using airborne geoscanning: A case study from Mato Grosso, Brazil 1527
C.W. Christensen, B.R. Bloss, A.A. Silva, E.J. Harrison, M.S. Gomes & R.W.M. Ferraz

The use of dynamic load tests for execution control of driven precast piles in logistic warehouses 1531
J. Costa, J.M. Díaz & J.C. Sanchez

Review of SPT-undrained shear strength correlation for UK soil deposits 1535
J.J. Crispin, C.E.L. Gilder & P.J. Vardanega

Why geotechnical engineering isn't ready yet for machine learning? 1539
T. Daktera & L. Janodet

Geotechnical parameters estimation in iron ore tailings piles via Bayesian models 1543
B.M. de Lacerda, R. Chammas, T.C.O. Fonseca & T.B. dos Santos

Interactive three-dimensional management of data from technological control of stacks and dams – case study 1547
B.M. de Lacerda, S.C. Chammas, W. Silva & V. Rezende

A method for the prediction of greenfield 3D settlement troughs around deep excavations 1551
M. De Luca, G. Russo, M.V. Nicotera & I. Esposito

Monitoring of soil deformations induced by deep mixing using an FME-based data analysis tool 1555
F. Deckner, V. Enbom, A. Kriege, K. Borgström & T. Forsberg

Calibration of a numerical model for the investigation of piled rafts under dynamic loading 1560
Y. Degu, O. Reul, A. Worku & F. Tschuchnigg

Eurocode 7 – Second generation. Design of ground improvement works 1566
N. Denies, C. Bohn, P. Pandrea, M. Topolnicki, C. Plomteux & K. Trybocka

Estimation of permeability coefficient using machine learning algorithms on the example of AdaBoost and Artificial Neural Network algorithms 1572
J. Dzięcioł & W. Sas

Probabilistic stability assessment of deforested steep slopes using 3D finite element method 1578
A. Ebener & K. Lesny

Development of database of monitoring results for retaining walls of deep excavations 1584
A. Ene, I. Ciocaniu, D. Marcu & H. Popa

Eurocode 7 – Second generation: determination of representative values 1588
J. Estaire, J. Sorgatz & T. Orr

Behaviour of stabilizing piles arranged with different layouts 1594
L. Fantera, S. Lirer, A. Desideri & S. Rampello

Safety assessment of a gravity dam using a hydromechanical model: fracture propagation at the dam/foundation interface 1600
M.L.B. Farinha, N.M. Azevedo & S. Oliveira

Analysis of subsidence problems on a highway section in Valencia (Spain) with the help of satellite radar interferometry 1606
A. Fernández Eusebio, J. Moreno Robles, F. Pardo de Santayana, D. Mora Cejudo, A. Parrilla Alcaide, D. Carrasco Díaz, A. Mendizabal, J. Duro, D. Monells & R. Iglesias

Characterization of a highway reinforced earth wall pathology with the help of a terrestrial laser scanner model, analyses of the causes and proposal of remediation measures 1612
A. Fernández Eusebio, J. Moreno Robles, F. Pardo de Santayana, D. Mora Cejudo & A. Parrilla Alcaide

Comparison between biocementation and a traditional cover solution to avoid ravines in slopes caused by water flow 1618
R. Fernández Rodríguez & R. Cardoso

Risk analysis of decommissioning design of tailings dams 1622
J.S. Figueira, C. Mata, G. Tavares, A. Brito, J. Marcelino & L. Caldeira

Comparison of floating and end-bearing pile wall barriers for tunnelling in layered soil 1626
A. Franza

A holistic risk sensitivity analytical approach for assessing flood protection infrastructure 1630
H.K. Fung & V. Nyambayo

Eurocode 7 – second generation - ground model 1636
H. Garin, M. Baldwin, P. Reiffsteck, K-J. van der Made & R. Wudtke

Influence of lateral stress on soil-structure interface tests in a hollow cylinder apparatus 1640
S. Gehring, H.H. Stutz, T. Lohrmann & Ph. Förschler

Numerical investigation of the interaction between existing tunnels and driven pile installation 1644
L. Hai, P. Yensri, A. Faramarzi & N. Metje

Earth mounds construction in York's Norman castles: Implications for current performance and protection 1650
A. Heitor, P. Winslow, E. Yenne, C. MacRae & S. Gandolfi

Seismic response of the Kathmandu basin from 3D physics-based numerical simulations 1655
V.M. Hernández-Aguirre & R. Rupakhety

Revisit a landslide in Boulder clay at Selset, Yorkshire: Insights from probabilistic analysis 1659
W. Huang, S. Bulolo, W. Zhang & M. Zhang

Flash floods in Lisbon – Local scale mitigation and adaptation measures 1665
M. Inácio, C. Pinto, C. Almeida, P. Leonardo & M. Morais

Climate change impacts on safety of levees: A Review 1669
J.K. Janga, K.R. Reddy & J. Schulenberg

Evaluation of unsaturated slope stability under rainfall infiltration based on experimental and numerical modeling 1675
J. Josifovski & B. Susinov

Impact of a spacing reduction in a fall cone test 1679
R. Khalili, C. Jommi & W.T. Sołowski

Probabilistic analysis for the design of a Vienna metro shaft using Monte Carlo simulation 1685
O. Kichaieva & D. Adam

Effect of flood duration on levee stability 1689
E. Koch & R.P. Ray

Deformations assessment of phosphogypsum waste heap in Wiślinka after 15 years of its reclamation 1693
A.P. Korzec & W. Świdziński

Representative values of geotechnical parameters derived from dynamic penetration test 1699
E. Kucova & M. Kuvik

3-D geotechnical modelling contributing to the risk management in a road construction project - a case study 1703
R. Kudou-Wada, K. Takahashi, C. Konishi, R. Ito & K. Sakurai

Evaluation of the reliability of pressuremeter tests using a multi-criteria analysis 1707
L. Lachérade, A. Marache, A. Denis, I. Halfon, J. Rohmer, L. Closset & F. Quesnel

Finite element modelling of a tailings dam using the Clay and Sand Model 1712
A. Laera, V.H. Miranda, R.J N. Azeiteiro, T. Bui, S. Brasile & R.B.J. Brinkgreve

Brief insights: In-situ permeability test in weathered and poorly-graded rockfill 1718
C. Laina-Gómez, D. Escudero-Merino & E. Asanza-Izquierdo

Eurocode 7 – Second generation: rock engineering 1724
L. Lamas, J. Estaire, J.P. Harrison, N. Maca, P. Pinto & H. Walter

Analysis and simulation of a rainfall-induced landslide on Enna Area (Italy) 1730
V. Lentini, K. Pinargote & F. Castelli

Eurocode 7 – second generation – spread foundations 1734
K. Lesny & T. Orr

A new interpretation method of rapid pile load testing: verification through comparison with static load test 1740
S. Lin, S. Kamei, I. Yamamoto, K. Watanabe, T. Matsumoto & N. Shkodrani

Various approaches to derive state of tailings materials on the basis of shear wave velocity measurement 1746
M.J. Lipiński, M. Wdowska & I. Puspitaningrum

Analysis of risk associated with failures of tailings storage facility 1752
Z.Q. Liu, S.S. Nagula, L. Piciullo & S. Lacasse

Hydro-Mechanical response of a shale subjected to gas transport in the context of radioactive waste disposal 1756
Q. Llabjani, A. Ferrari, L. Laloui & P. Marschall

Relevance of correlation length in geotechnical engineering 1760
M. Lloret-Cabot, K. Zhang, W. Zhang & D. Toll

Challenges in the geotechnical characterisation of bauxite tailings (Red Mud) 1764
I. Lopes, M. Garcia & G. Tavares

Assessment of shear stiffness and damping variations in undrained cyclic triaxial tests of iron ore tailings 1770
J.C. Lourenço, D.L.D. Camacho & P.A.L.F. Coelho

Eurocode 7 – Second generation: anchors, rock bolts and soil nailed structures 1774
N. Maca

Failure in cohesive soil due to hydraulically induced fractures 1780
H. Machacek, B. Odenwald & K.J. Witt

Mine tailings properties and its hypoplastic predictions 1786
H.R. Manaviparast, T. Miranda, G. Medicus & N. Cristelo

The use of physically based methods to locate the in-site surveys in areas prone to rapid landslides 1790
M.C. Mandaglio, N. Moraci & M. Ciurleo

A comparative study of European and Japanese pile design codes based on a test site data 1795
K. Mandal, S. Lin, G. Belokas, N. Shkodrani & T. Matsumoto

Control of technological processes during underground construction in the historical centre of megacities in weak soils using interactive geotechnical monitoring 1801
R.A. Mangushev, A.I. Osokin & I.P. Diakonov

Structural health monitoring and inspection of dams based on Unmanned Aerial Vehicles photogrammetry with image 3D reconstruction 1807
J. Marcelino, J. Manso, D. Leite, N.C. Marques & O. Freire

The use of vane shear tests in granular materials for shear strength measurement 1811
J. Meng & J. Laue

Practical application of non-linear dynamic soil-structure interaction analysis. Case study in the Groningen field, The Netherlands 1815
C. Merino & J.M. Torres

Influence of permeability on the behaviour of tailings storage facilities by hydromechanical numerical analysis 1821
C. Midão, A. Viana da Fonseca & S. Rios

Establishing the geotechnical category through analysis of difficult soils - a proposed procedure 1825
E. Milutinovici, G. Dragomir & D. Mihailescu

Numerical assessment of the ongoing settlements of the western tower of Terreiro do Paço, in Lisbon, Portugal 1829
L. Miranda & J. Carreto

An energetic approach to the soil mechanical behaviour description in a zero-dimensional formulation 1835
A. Yu. Mirnyy

Eurocode 7 – second generation – piled foundations 1840
Ch. Moormann & S. Burlon

Evaluation of seismic-induced crest settlement of earth dams 1846
A. Nardo, G. Biondi & E. Cascone

Slope failure cause evaluation based on earthworks management and meteorological conditions analyses 1852
T.Q. Nguyen, D.B. Van, M.V. Nguyen, N.A. Do, P. Osinski & E. Koda

Effect of variability parameters on 3D probabilistic slope stability prediction 1856
E.A. Oguz & T.M.H. Le

Application of the slurry deposition method to the reconstitution of samples of wolframite ore tailings 1860
J.P. Oliveira, P. Coelho & L. Araújo Santos

The use of InSAR to analyse ground displacement: the case study of Póvoa de Santa Iria industrial area 1864
M. Ormeche, R.C. Gomes & A.P. Falcão

Rehabilitation of overpass at Ch.19.978 of Fier-Vlora high-way. Influence of time of consolidation in the performance of the overpass structure 1869
E. Paçi, N. Shkodrani & A. Dervishaj

Geotechnical pathologies of Spanish historical monuments adjacent to natural slopes. Case histories 1875
F. Pardo de Santayana, J. González-Gallego & J.A. Díez

Slope instability risk assessment along the Almada municipality coastline, Portugal 1881
F. Paulino, E. Fernandes, A. Dinis, A. Aires & A. Godinho

Strength resistance of sea dikes to increased wave overtopping due to the rise in sea levels 1886
M. Pohl, T. Nuber & J. Moreno

Seepage in a flood protection dam – first centrifuge test results 1890
G. Portmann, A. Arnold, Y. Zhang & A. Askarinejad

Internal erosion initiation in gap-graded soils: A 3D microstructure assessment using convolutional autoencoders 1896
J. Qi, N. Yousefpour, G. Narsilio & M. Pouragha

Geotechnical conditions of "Debelo brdo" tunnel construction on the highway E-80: Nis-Merdare-Pristina ("Peace Highway") 1901
D. Rakic, I.B. Ikodinovic, R. Lapcevic & D. Lukic

Geotechnical structures stability: ULS calculations using the finite element method 1905
D. Remaud & E. Bourgeois

Iron tailings reclamation: Geotechnical analysis during emerged and submerged excavations 1909
L. Rezende, M. Ehrlich & A. Oliveira

Accuracy of machine learning techniques in forecasting tunnelling-induced soil settlements with limited data 1915
T. Richa, J.M. Pereira, L.-M. Guayacan-Carrillo, G. Chapron & F. Lanquette

Centrifuge model tests to evaluate the stability of embankments in hydrodynamic conditions 1920
S. Rios, A. Viana da Fonseca, L. Ribeiro, C. Cengiz & S.J.M. van Eekelen

Distributed fibre optic sensing of stabilised soil 1924
S. Ritter, E.S. Rørvik, H.J. Meland, S. Hov & P. Paniagua

Use of steel piles in the de-characterization process of tailings dams in Brazil 1929
R.F. Rodrigues, A.N. Milagres, M.M.M. Fontes, M.R. Petronilho, B.C. Novais & G. Hurtado

Influence of the procedure for determining the characteristic values of strength parameters on the probability of failure of unsupported cuts 1935
F.P.S. Rogério, N.M.C. Guerra, A.N. Antão, M. Vicente da Silva & M. Matos Fernandes

Exploring soil mechanics laboratory tests: accuracy, discrepancies, and implications 1941
J. Rohac

Assessment of seismic ground amplification at the Chieti courthouse site 1946
N. Salvatore, A. Pagliaroli, F. Di Buccio, A. Pizzi & S. Amoroso

EUROCODE 7 – Second generation - Interplay with Eurocode 8: Implications for ground investigation 1950
G. Scarpelli, L. Callisto & S. Foti

Influence of pore fluid composition on shear strength of reconstituted normally consolidated kaolinite 1954
M. Schröder & J. Grabe

Groundwater statistics in the second-generation Eurocode 7 1958
T. Schweckendiek, J. Estaire & A.J. Bond

Analysis of the soil-structure interaction of a high-rise building near sensitive infrastructures 1964
M. Seip, M. Hassan, S. Leppla & A. Norkus

Performance of state parameter for undrained shear behaviour 1970
S.U.U.S. Shah & A. Ahmad

Seismic bearing capacity of shallow foundations on soil reinforced by rigid inclusions 1974
Y. Shen, J. Pérez-Herreros, F. Cuira, S. Burlon & J-F. Semblat

Influence of spatial variability of strength on bearing capacity for unsaturated soil 1980
B.J. Shwan

Prediction of load transfer curves in pile groups executed in profiles of granular soils from field test measurements 1984
D.F. Silva & A.S. Moura

Automated monitoring for effective implementation of observational method in an urban excavation in Lisbon, Portugal 1988
A. Silva, C. Levesque, C. Martins & R. Tomásio

Comparison of collapse loads obtained in 2D and 3D slope stability limit analysis 1992
W.T. Sołowski, L.-A. Marchadour & L.A. Ikonen

Optimal pavement design using the failure probability 1996
R. Varga, P. Jelušič, T. Bračko, B. Macuh & B. Žlender

Cathédrale de Beauvais: les accidents structurels des XIIIe et XVIe siècles eurent-ils une origine géotechnique? Partie 1: Contexte historique et naturel 2002
J.D. Vernhes, P. Renault & Y. Zotna

Cathédrale de Beauvais: les accidents structurels des XIIIe et XVIe siècles eurent-ils une origine géotechnique? Partie 2: Accidents structurels et rôle de la géotechnique 2008
J.D. Vernhes, P. Renault & Y. Zotna

Interpretation of large diameter preliminary pile tests in Ampthill Clay, West Walton and Oxford Clay formations for Thame Valley viaduct 2013
S. Vitorino & H. Yeow

Surface roughness evolution of EPDM and its impact on the long-term sealant performance of gasketed joints of segmental shield tunnels 2019
J.C. Xie & X. Huang

Prediction of the displacement field induced by the excavation of very shallow and large tunnels: A case study 2025
W. Yang, D. Boldini & D. Zhang

Evaluation of the induced axial force behaviour for bored tunnel construction adjacent to existing long piles 2031
P. Yensri, A. Faramarzi & N. Metje

Application of numerical modelling in Next Generation of Eurocode 7 2037
H.C. Yeow & G. Katsigiannis

Analysis of pore characteristics of natural structured clay applying the combination of SEM and MIP 2043
X.W. Zhang, G. Wang & X.Y. Liu

Case study on interpretation of cone penetration tests in sandy soil layers 2047
Y. Zhang, X. Ma, C. Ji, X. Zhang, W. Li & M Yang

Small- and full-scale test programme on uplift induced slope failure 2052
C. Zwanenburg, A.R. Koelewijn, B.J. van der Kolk, U. Förster, M. Post & H.T.J. de Bruijn

D - Current and new construction methods
D - Méthodes de construction actuelles et nouvelles

Improvement of local soils by adding marble powder 2059
O. Aiche, A. Medjnoun, R. Bahar & M. Khiatine

Design, construction and monitoring phases of a diaphragm wall shoring application near the Golden Horn 2063
Ö. Akçakal, C. Acar, M.N. Velioğlu & O. Sevim

Physical, geometrical and chemical characterisation of incinerator bottom ash towards its use as recycled aggregate 2067
F. Almeida, J.R. Carneiro & M.L. Lopes

Design and execution of retaining-walls using the reinforced jet-grouting technique 2071
J.L. Arcos, X. Beal, R. Gil, J.M. Dimas & M. Segovia

Pile driveability predictions of open ended tubular piles in sand using the Unified Method 2076
K. Argyroulis, J. Putteman, K. Gavin & A.A. Roubos

Experimental study of geotextiles effects on bearing capacity of a non-lateritic tropical soil 2081
M.G. Avelar, P.C. Rodrigues & H.N. Pitanga

Enzymatically mediated precipitation of calcium phosphate compounds: a promising approach for sustainable soil enhancement 2085
M. Avramenko, K. Nakashima, C. Takano & S. Kawasaki

Activating decarbonisation in the piling supply chain 2089
C.A. Barker & J. Ly

Use of the Brazilian test and frost sensitivity test for determining the aptitude for earthworks of difficult soils stabilized by special lime-based binder 2093
L. Batali, G. Andrieş & C. Grégoire

The effect of the anisotropic state of stress on the normal force in a deep tunnel preliminary deformable lining 2097
L. Batocchioni, S. Miliziano & V. Rodrìguez González

Lot 2: Lisbon Metro extension between Santos station and the terminal of Cais do Sodré station. Geological and geotechnical model and parameterisation 2101
J. Bento, S. Ferreira, D. Teles Fortes, R. Pistone, N. Cruz, J. Cruz, A. Tavares & R. Pina

In situ and laboratory investigation of dynamic performance of a cement-stabilised Chalk trial embankment 2107
O. Boumendjel-Game, M. Vowles, M. Fleetwood, H. Saroglou & G. Katsigiannis

Secant piles pit enclosure made with deep soil mixing columns and CFA piles 2113
A. Boureanu, D. Ciumeică, A. Măgureanu & L. Sata

Foundation solutions near Trancão river, in Lisbon 2117
I. Braz, A. Pinto, C. Simões, T. Gomes & C. Caxias

Earth retaining solutions and facades underpinning, for the refurbishment an historic building, in Lisbon 2123
I. Braz, A. Pinto, D. Henriques & R. Santos

The use of foam glass for a lightweight fill and highway foundation on soft soil conditions 2127
J.W.R. Brouwer & C.R. van Laerhoven

Sensitivity analysis of load transfer curves in case of rigid inclusions 2132
P. Burtin & J. Racinais

Benefits of finite element method analysis to the design of the Saint Maur Créteil caverns metro station 2138
M. Cahn, N. Simon, N.H. Nguyen, S. Burlon, E. Talut & J. Subervie

Fiber optic sensors in geotechnical works - a review 2144
P. Caldas & M.L. Laranjo

Biocementation treatment of a Portuguese motorway slope to prevent ravine formation 2148
R. Cardoso, M. Oliveira, M. Cruz, I. Gonzalez, A.T. Rodrigues, B. Anjos, L. Sapin & A. Esnault-Fillet

Load-penetration response of a site-won soil reinforced with natural fibres. Application for unpaved roads 2152
D.M. Carlos, J. Macedo & M. Pinho-Lopes

Assessment of stiffness parameters of stone columns 2158
E. Carvajal Díaz, P. Ruiz-Terán, J. Castro & M. Miranda

A case study of offshore stone columns by the novel S-Alpha Dive system: San Ignacio bridge in Bilbao 2164
E. Carvajal Díaz & P. Ruiz-Terán

Numerical analyses of the optimum length of stone columns and their encasements 2168
J. Castro, M. Miranda, A. Márquez, J. Fernández-Ruiz & S. Melentijevic

End bearing of large diameter piles in sand during driving 2172
D. Cathie, S. Raymackers, T. Vergote, G. Haine, J. Saraiva & A. Burgraeve

Degradation mechanisms of the hydro-mechanical behaviour of a lime-treated clay exposed to wetting and drying cycles 2178
N. Chabrat, G. Russo, E. Vitale, O. Cuisinier & F. Masrouri

Deformation characteristics of existing three-line tunnels with connected aisle induced by three-line mechanized tunnels under-crossing 2183
J.Q. Chang, D.M. Zhang, H.W. Huang & M. Thewes

Fluid rheology and its implications for flow and cuttings transport in horizontal directional drilling (HDD) bores 2189
S.P.C. Che, C.O. Menkiti & S.A. Jefferis

Enhancing soil-cement mixture's performance with GGBS 2195
S. Choudhary, K. Meena, M. Kumar & L. Borana

Consolidating existing road structures using self-drilling bars 2199
I.A. Ciocaniu, A.C. Onescu, S. Manea & P. Uta

Geotechnical works for an underground electric power station, in Bucharest 2203
D. Ciumeică, A-E. Popa, L. Sata & S. Manea

Compressibility transition between a marine onshore clay to artificial carbonate silt soil behaviour 2207
A. Conrado-Palafox, T. Newson & A. Ahmed

Development and laboratory testing of a low-cost wireless in-place inclinometer prototype 2212
R. Correia dos Santos & J. Marcelino

Earth retaining structures in the form of diaphragm walls and their application in *Liberdade* underground station 2218
C.H. da Costa, A.T. Rodrigues, M. Fernandes & J.L. Arcos

Shear wave velocity and permeability evolution of MICP-treated carbonate bearing sand 2223
G. Das, S. Joshi, M. Judge, F. McDermott, M. Long & S. Donohue

The practice of testing ground nails 2227
M. de Carvalho

Studying impact of reclamation technique on vibrocompaction performance 2231
A. Debaize, T. Pille & K. Dedecker

Site tests on retaining systems and uplift anchors of Nordhavnstunnel in Denmark 2235
B. Demir, C. Bauduin, M. Palaiologou, J.D. Christensen, S. Yding & S.K. Tomac

Acceleration of embankment construction on soft soils of Salamanga using wick drains and counterweight fills 2241
H. Dete & C. Quadros

The sustainable future of vertical drains 2245
J.W. Dijkstra & R. Bodamer

Giant shear box tests on recycled 6F5 for tracked plant platforms 2249
S. Divall, M.C.R. Davies, S.E. Stallebrass, J. Mahony, S. Quintavalle, J. Bowen-Bravery, T. Johnson-Watts & R. Mulligan

Forensic evaluation of gabion walls 2254
M. Duffy-Turner, M.G. Winter, I.M. Nettleton & P. Liew

Numerical modelling of suction bucket foundations subjected to axial loading 2258
E. Eleftheriou & D.M.G. Taborda

Discrete element modelling of centrifuge experiments on pile jacking 2262
A. Ezzeddine, B. Cazacliu, P. Richard, R. Artoni & L. Thorel

Mechanical behavior of Ypresian plastic clays 2266
S. Fanelli, L. Makki, E. Bourgeois, F. Szymkiewicz & P. Reiffsteck

Lisbon new circular Metro underground line: Centenary buildings underpinning 2270
C. Fartaria, A. Henriques, C. Martins, A. Pinto & R. Tomásio

Execution and quality control applied on the construction of soil-cement embankments 2274
E. Fernandes, P. Antunes, J.P. Simões, J. Ramalho & B. Monteiro

Solutions of excavations and peripherical earth retaining walls in dense urban area 2278
L. Fernandes & R. Justiniano

Effects of soil improvement on the axial load capacity of drilled displacement piles – a CPT based case history analysis 2282
G. Figueroa Palacios & A. Lemnitzer

Use of a natural inorganic binder to improve the mechanical properties of mining tailings 2288
M.M.M. Fontes, M.D. de O. Corrêa, A.M. Santos, A.B.S.P. de Paiva & G.M. de D. Vieira

The influence of partial saturation on the engineering properties of a metakaolin-improved sand 2292
A. Fraccica, E. Romero, M. Arroyo & G. Spagnoli

Muck identification and anomaly detection in earth pressure balance shield based on multi-task deep learning 2296
L. Fu, D.M. Zhang, H.W. Huang, A.G. Cohn & Z.Q. Liu

Reconstitution of samples for the study of mechanical behaviour of sulphide-rich soils 2300
N. Garcia, P. Gunnvard, Q. Jia & J. Laue

A case study on energy-based evaluation of deep vibro compaction method 2304
A. Gokalp, A. Dinc, S. Adatepe & R. Düzceer

Performance evaluation of CDC compaction for warehouses: a case study of European projects 2309
C. Guglielmelli & J.W. Dijkstra

Artificial Ground Freezing for underground excavation: a coupled modelling approach supporting tunnelling design 2313
G. Guida, F.Casini, A. Restaini & A. Celot

Innovative and sustainable geosynthetic solutions in the field of bridge abutment construction 2317
H. Hangen & O. Detert

Consequences of geometrical imperfections for deep dry mixing columns in a deep excavation pit 2323
M.K. Haugen, M.Kahlström, P.A. Mortensen, K.M. Kjærstad & Y. Pan

Deep excavation solutions for the construction of a logistic park in Loures (Lisbon) 2327
A. Henriques, R. Tomásio, F. Ramalho & J. Dias

Management of the dynamic performance of earthworks for High-Speed Rail 2331
A. Hope, O. Boumendjel-Game, H. Wood, H. Saroglou, G. Katsigiannis, S. Butler & J. Dudfield

Enhanced ductility and energy absorption of coal wash-rubber crumb mixtures for track substructure 2337
H. Hunt, B. Indraratna & Y. Qi

Exploring the use of fine surplus silica sand in low CO_2 emission earth construction 2341
A. Iravanian, A. Wayu, H. Gustavsson & L. Korkiala-Tanttu

Framework for evaluating scour risk and optimising scour mitigation 2346
J. Irvine, I. Torres & M. Divilly

Field tests on vertical and horizontal resistance of steel sheet piles installed by the Press-in with Auger 2352
Y. Ishihara, K. Okada, M. Eguchi, A. Mori & T. Miyanohara

Case history of installation and static vertical load testing on piles executed by the rotary cutting press-in in Amsterdam 2358
Y. Ishihara, K. Okada, Y. Toda & Y. Kitano

Construction method and methodology for the optimization of panels overlap in cut-off walls in Santa Maria Dam, Sinaloa 2364
E. Jiménez Ontiveros, F.J. Blanco Blanco & V.H. Olivera Luis

Soil improvement methods in the Mediterranean railway corridor, Pulpí – Vera stretch, Almería 2368
E. Jiménez Ontiveros, L.M. de la Rosa Domínguez, D. Martínez Sánchez & J. Lavado Rodríguez

Solution of excavation and peripheral earth retaining walls near sensitive structures – O'Living Development, Lisbon 2372
R. Justiniano & A. Pinto

Deep and complex excavation in an urban environment in Miraflores, Oeiras 2376
R. Justiniano & A. Pinto

Performance investigation of a newly proposed drainable pipe fitting 2380
K. Kawai, K. Nakashima, K. Maeda & S. Fukatsu

Use of CO_2-induced siderite and dolomite with nanoclay for soil improvement 2384
H.A. Keykha, M. Mavroulidou & H. Mohamadzadeh Romiani

Staged construction of surcharged embankments over peat for a national road in Co. Donegal, Ireland 2388
P. Kissane, F.J. Buggy, G. Ward, B.A. McCabe, F. Fattahi Masrour & F. Towey

New concept of drilling auger for displacement pile installation 2394
A. Krasiński

Comparative trials of geosynthetic materials in the base of road pavement on the section of the Central Ring Road in the Moscow Region 2400
A. Kuznetsova

Degradation of expanded clay strength after creep tests 2405
C.B. Laskowski, J. Estaire & E. Roces

On the ground settlements observed during execution of jet grouting columns in urban area adjacent to a historic building 2409
J. Logar, B. Pulko, J. Smolar & K. Oštir

Precision measurements constrain the implementation of more accurate testing in earthworks quality assurance 2413
B.G. Look

Ground improvement solutions at the plot 14 of the Northern Lisbon logistic platform 2417
M. Lopes, A. Pinto, A.L. Gonçalves & J. Moreno

The foundations of the Rhine bridge Hard-Fussach (Austria) 2421
F. Lopez & E. Steinlechner

Role of tunnel ground loss on the mitigating effect of pile-wall barriers 2426
N. Losacco

Sand-rubber mixtures as vibration dampening foundation materials: scaled physical model studies 2430
B.R. Madhusudhan

Performance assessment of a combined foundation system of end-bearing and floating piles in a challenging soil profile 2434
A. Magdy, M. Shahien, M. El Sawwaf & A. Nasr

Study of the behaviour of treated load transfer platform on rigid inclusions 2440
J. Mannah, C. Chalak, H. Farhat, L. Briançon, S. Grange, K. Varain, D. Dias & T. Lenoir

Comparison of the effects of different additives on the improvement of physical and mechanical properties of clayey soil 2445
N. Marinković, E. Zlatanović, Z. Bonić, N. Romić, D. Cvetković & B. Stanković

Lisbon new circular metro line: interconnection section between new line and existing terminus 2451
P. Marques, C. Martins, C. Fartaria, R. Tomásio & A. Pinto

Application of Machine Learning algorithms to drilling data for deep foundations and soil treatments 2456
E. Martínez García, M. García Alberti & A.A. Arcos Álvarez

Lisbon new circular Metro line: Buildings underpinning 2460
C. Martins, C. Fartaria, R. Tomásio & A. Pinto

Effect of the binder content in a soft stabilized soil unreinforced and reinforced subjected to cyclic loading – energy evaluation 2464
L.A. Martins, A.A.S. Correia, P.J. Venda Oliveira & L.J. Lemos

Underpinning and strengthening of an existing port infrastructure to allow 8m depth dredging for the installation of a high-capacity vessel synchrolift 2468
P. Matias Ramos & L. Esteves

Effects of sheet pile driving on soil density within soil exchange drillings 2474
U. Matthiesen & M.Pohl

Use of xanthan gum produced by a bacteria to reduce the soil permeability 2478
A. Mendonça, P.J. Venda Oliveira, P. Morais & A.P. Chung

Experimental study on strength and deformation properties of treated clay soils under triaxial and oedometric conditions 2482
J. Milosevic, S. Zivaljevic & T. Santana

Assessment of the bearing capacity of bored piles with Expander Body technology using pressuremeter test-based methods 2486
F.F. Monteiro, A.S. Oliveira, R.P. Cunha, M.F.P. Aguiar, C.M. Silva & P.J.R. Albuquerque

Influence of temperature on strut loads in braced excavations 2492
P.-A. Mortensen & T. Sandane

Development of a pioneering foundation system for a 225 000 m^3 LNG storage tank in Canada by using driven closed-ended steel piles non-connected to the concrete slab (rigid inclusions) 2496
J. Munoz-Castelblanco, N. Lafreme, Z. Gilbert, P. Moine & L. Boutillon

Soil biocementation using the carbonic anhydrase metabolic pathway 2502
W. Mwandira, M. Mavroulidou, M.J. Gunn & D. Purchase

Brief report on the construction of the Liberdade/São Bento Station of circular line G (Pink Line) of the Porto Metro 2507
V. Nascimento, S. Mateus & I. Coelho

Finite element analyses of slurry trench stability and deformations – back-calculation of field tests in soft clay 2511
E. Nilsen, K. Karlsrud & E.J. Lande

The role of nano-materials and nanotechnology as a high-tech technology in geotechnical engineering 2515
H. Niroumand & L. Balachowski

Investigations of material discharge caused by groundwater flow during the installation of bored piles 2519
H. Nissen, C. Fierenkothen, E. Dornecker & M. Herten

Industrial warehouse retaining walls and pavements strengthening at Quinta do Adarse, Alverca, Portugal 2524
T.M.L. Paludeto, M. Lopes & A. Pinto

Application of Cutter Soil Mixing technology in retaining walls 2528
A. Peixoto & P. Gomes

The description of underground works evolution in Hospital Santo António station (Porto Metro) 2534
A. Pereira, T. Azeredo, A. Carvalheira & I. Coelho

Influence of curing under stress on the geotechnical behavior of a treated silty soil 2538
L. Pigeot, N. Dufour, A. Soive, H. Calissano, L. Batilliot, F. Dermenonville & A. Loukili

Ground improvement and special foundations at North Lisbon Logistic Platform, plot 1, Portugal 2543
A. Pinto, M. Lopes, P. Marques, A.L. Gonçalves, A. Perez, J. Moreno & J. Moreno

Special foundations at the cycle-pedestrian bridge over the Trancão river, Portugal 2547
A. Pinto, A. Rodrigues, P. Santos & C. Caxias

Stabilization of the access platform to an electrical substation: diagnosis, design and site works follow-up 2551
G. Pisco, N. Nogueira, S. Pinto & A. Carvalheira

Consideration of the variable contact geometry between the drum and the soil surface in vibratory roller compaction 2555
J. Pistrol, M. Hager, D. Adam & F. Kopf

Circular diaphragm wall for a deep shaft 2559
C. Radu, D. Ciumeică, A. Boureanu & L. Sata

Deep foundation system of the Promenada Mall extension in Bucharest, Romania 2563
C. Radu, C. Năstase, T. Matei, P. Danilov, I. Buzilă, M. Popa, O. Chițu & R. Geanguș

Analysis and re-sloping for slope stabilization in São José neighbourhood, João Pessoa, Paraíba, Brazil - case study 2567
A.V.F.S. Ramos, G.K.S. Simões & F.L. Soares

Numerical modelling of shafts – comparison between SBE and EBS construction methods 2573
L.M. Repsold, A.M.G. Pedro & J. Almeida e Sousa

Cost effective & sustainable solutions for embankments on soft soils - performance review of geocells in embankment 2577
K.A. Ria Zamara, J. Kawalec & M. Wayne

Geotechnical challenges of excavating the deepest metro station in Lisbon - Estrela station 2581
V. Ribeiro, J.E. Simões, J.C. Andrade, N. Vaz, P. Araújo & O. Marques

From design to the construction – the case of the track tunnels T33 and T34 between Rato and Santos of the future circular line of Lisbon metro 2585
V. Ribeiro, J.C. Andrade, J. Simões, O. Marques, P. Araújo & N. Vaz

Erosion testing on sloped ground treated with enzyme-induced carbonate precipitation 2589
L. Rivera & P. Bandini

Ground improvement between stone columns: a performance study on various soil types using in-situ testing 2593
L. Roldan, M. Sottile, A.O. Sfriso & J. Rola

Rough pile stereolithography for centrifuge modelling 2599
G. Sabaliauskaite, S. Divall, A.M. McNamara, S.E. Stallebrass & R.N. Taylor

Performance of segmental driven geothermal energy piles subjected to impact and bending loads 2603
H. Sadeghi & R.M. Singh

Influence of soil constitutive models on settlement prediction of urban tunnelling 2607
B. Salehi & B.S. Muntau

Pressure cell results for a ballasted railway track section tested in the CEDEX Track Box 2613
M. Santana, S. Merino & J. Estaire

Foundation piles and submerged wall of berths 6, 7 and 8 at the Port of Maputo 2617
J. Santos & L. Tomás

The threaded displacement piling system technical and economical efficiency leading to sustainable foundations solutions 2621
L. Sata & S. Manea

Large-scale test on basal steel-reinforced piled embankments 2625
M. Schneider, M. Hell, P. Pandrea, B. Wittekoek, S.J.M. van Eekelen, M. Topolnicki, K. Makowska, R. Sieńko & H. Zachert

The pile inspector, a new quality tool to read pile base enlargement of bored piles 2631
N. Schneider, O. Stahlhut & P. Lenz

Highrise building NION with a combined pile-barrette-raft foundation 2637
M. Seip, S. Fischer & R. Katzenbach

Deep excavation solutions in an urban environment - Distrikt residential project, Lisbon 2642
J. Silva, I. Braz & A. Pinto

Excavation, earth retaining solutions and facades underpinning of a historic building in Estoril, Portugal 2648
J. Silva, C. Martins & A. Pinto

Behavior of geocell reinforced sandy soils under static load 2654
M.C. Simsek & N. Huvaj

Evaluating the effects of a deep excavation on monumental buildings: MarmorKirken station in Copenhagen 2658
F.M. Soccodato & G. Tropeano

Prediction model for strength of cement-stabilized clays for in-situ soil mixing using artificial neural network 2662
M. Swamynaidu & A. Tyagi

Setup and calibration of piles with FBG strain sensors in a geotechnical centrifuge 2667
C. Tang, A.M. Marshall, C.M. Heron, A. Franza & J. Xu

Finite element simulation of biocement precipitation in soils 2671
V.S. Terra, F.M.F. Simões & R. Cardoso

Design and modelling for groundwater engineering and control 2675
S.D. Thomas, G. French, J. Watson & B. Casal

Square shallow foundation on four rigid inclusions subjected to uncentered vertical load: Centrifuge modelling 2681
L. Thorel, M. Blanc, A. Neel, A. Jagu, Ph. Audrain, P. Gaudicheau & S. Lerat

Mechanical properties of a gravel soil injected with a polyurethane binder 2685
G. Tintelnot & G. Spagnoli

Excavation, retaining wall and deep foundations solutions for an office building at Alcântara – Lisbon 2689
R. Tomásio, F. Veloso & N. Rosa

Analysis of the influence in soil permeability, with the use of high-density drilling fluids applied in the internal edge of drilling rows 2695
A.H.P. Toyoshima, C.C. Soares, G.C. Alvarez & G.C.L.R. Costa

De-construction as part of life cycle management 2699
A. Tuomela, J. Majava, T. Luukkonen & P. Leviäkangas

3D small-scale tests on steel-reinforced piled embankments 2703
S.J.M. van Eekelen, M. Schneider, B. Wittekoek, M. Hell, P. Pandrea, P. Schauber, M. Topolnicki, K. Makowska, K. Zdanowicz, R. Sieńko & H. Zachert

Groundwater in geosynthetics-reinforced pile-supported embankments, 3D Experiments 2709
S.J.M. van Eekelen, B. Wittekoek, R.A. Zwaan, A. Bezuijen & A. Nancey

Effect of the variable discharge capacity of prefabricated vertical drains on the behaviour of an embankment built on soft soils 2715
P.J. Venda Oliveira

Research on the formation mechanism and application of curtain for ground drilling grouting in water-rich sand layer 2721
X.S. Wang, Z.S. Yao, C.X. Rong, X.J. Wang & B. Tang

The geotechnical works for the construction of the Travis Brow link road, Stockport, UK 2727
A. Willoner & L. Allievi

Forensic examination of gravity block walls 2731
M.G. Winter, M. Duffy-Turner, I.M. Nettleton & P. Liew

Experimental and numerical study on the compaction of granular soils by vibrations 2735
M. Wotzlaw, D. Aubram & F. Rackwitz

Interpretation of ion exchange in soil-bentonite mixtures 2739
R. Yu, A. Takai, T. Kato & T. Katsumi

A review of DFOS sensors installation methods for curved surfaces in tunnels 2745
S.Q. Zhang, K. Zhang & Z.L. Li

E - Environment, water and energy
E - Environnement, eau et énergie

Concrete piles with lowest carbon emissions and optimised environmental impact 2751
K.A. Abushama, W. Hawkins, L. Pelecanos & T. Ibell

Long-term horizontal cyclic loading model test results of monopile for offshore wind turbines 2755
C.T. Akdag & F. Rackwitz

Machine learning to expedite concept monopile design 2760
J.S. Alexander, R.M. Buckley & S.A. Whyte

Raising the standard of flood protection in Hull: the Humber Hull Frontages flood defence scheme 2764
L. Allievi & A. Willoner

Influence of spatial variability of ground conditions on energy pile thermal yield 2768
Q.I. Alqawasmeh, G.A. Narsilio & M.J. Kreitmair

Are construction errors in the placement of ground heat exchanging loops in energy piles important to consider? 2772
Q.I. Alqawasmeh, G.A. Narsilio & N. Makasis

Improving the remoulded shear strength of a quick clay using biochar 2777
E.W. Ånes, J.I. Loshelder, S. Hov, P. Paniagua & S. Ritter

Utilisation of geological surplus masses in landfill cover: percolation results from pilot test 2783
E.W. Ånes, S. Ritter, T. Pabst, A.C. Stridal, N.G. Nilsen, K. Hovland & G. Okkenhaug

Effect of setback distance of leachate recirculation systems on the slope stability of bioreactor landfills 2788
L.S. Avinash & A. Mishra

Effect of saline water on the strength behavior of beach sand from northeastern Brazil coastline 2793
G.F. Azevedo, A.S. Moura, F.C.S. Filho, R.F. Leme, D.R.L. Gonçalves & R.P. Cunha

Experimental assessment of adsorbed water for geomechanical applications 2797
S. Babiy, A. Tuttolomondo & L. Laloui

Investigating foundation damping for OWTs using small strain hardening model calibrated with element scale tests 2801
M. Barzan, S. Kasyap & D. Igoe

Generalized P-y curves for monopile design using the PISA methodology 2805
L. Berenguer Todo Bom

Evaluation of the geomechanical properties of lime-treated silt samples extracted from an experimental levee 6 years after construction 2810
F. Bertola, F. Klotz, P. Gerard & B. François

Solving challenges of operational areas for renewable energy infrastructure 2816
M. Beußе & L. Vollmert

Physical models of mechanical root-soil interaction 2821
A. Boiero, M. Arroyo & E. Romero

Revisiting the effect of coefficient of thermal expansion in energy pile-soil interactions 2827
T.M. Bodas Freitas, P.J. Bourne-Webb, M. Fernandes & D. Sterpi

Back-analysis of a small-scale (1g) energy pile test using the finite element method 2832
P.J. Bourne-Webb, T.M. Bodas Freitas & D. Abrantes

Climate change impacts on geotechnical infrastructure 2838
C.A. Bridges

Site selection and early-stage design of trenchless submarine cable landings 2842
L.J. Burley, V.A. Terente, H.K. Waterston, H.J.B. Bryan & D. Hinxman

Different jacket foundation installation methods for three offshore substations 2848
A. Cardoso, J. Leplat, N. Van Damme & S. Raymackers

Soil treatment solutions for the construction of steel storage tanks: Design and behaviour 2852
E. Carvajal Diaz, P. Barros & P.Matos

Effect of the concentration of the activator on the mechanical properties of the geopolymer stabilized soil 2858
D. Chami, A. Cuccurullo & P. Gerard

Improving mechanical performance of soil-bentonite by slag cement addition 2862
J. Chen, Y. Masaki, A. Takai, T. Kato & T. Katsumi

Applying electrokinetic technology coupled with enzyme-induced carbonate precipitation treatment to Cu- and Pb-contaminated loess remediation 2866
W.C. Cheng, L. Wang, Z.F. Xue & M.M. Rahman

Waste valorisation in landfill barriers: Opportunities and challenges 2870
F. Chihi & G. Varga

Simulation of pile installation in chalk: Discrete and continuum approaches 2876
M.O. Ciantia, J. Zheng, M. Previtali & J.A. Knappett

Initial design and testing of a new site investigation tool for the direct determination of *p-y* soil reaction curves: ROBOCONE 2880
J. Creasey, A.E. Hajjar, A.T. Conn, E. Ibraim, A.H. Bateman, G. Mylonakis, G. Martin, A. Diambra, K. Wen, B.P.J. Cerfontaine, S.M. Gourvenec, D.J. White, D. Igoe & S.S. Kasyap

Effects of stabilization on the behaviour of Finnish sensitive soils 2884
M. Di Sante, G. Di Luigi, I. Bellezza, F. Mazzieri, E. Fratalocchi, B. Di Buò & T. Länsivaara

Class A predictions for centrifuge modelling of uplift induced instabilities of river embankments 2889
E. Dodaro, G. Gottardi, M. Pirone, C. Mancuso, R. Ventini, D. Giretti, C.G. Gragnano, V. Fioravante, F. Zarattini & F. Gabrieli

Design and construction carbon reductions for HS2 station road network rail overbridge with polymer geogrid reinforced soil wall abutments and wingwalls on shallow foundations 2895
C. Doulala-Rigby, M. Dalwadi, J. Belton, M. Duffy-Turner, R. Blackmore, G. Katsigiannis & H.M.B. Al-Hashemi

A laboratory study of freeze-thaw effects on hydraulic conductivity of kaolin-sand mixtures 2901
S. Feng, E. Ibraim & P.J. Vardanega

Sustainable erosion control in geotechnical structures – case study 2905
A. Ferreira, J. Sousa, J. Dias & A. Neves

Enhancement of soil mechanical properties with biopolymers 2909
N. Fradj, I. Kádár, K. Kopecskó & A. Németh

Experimental study on the elasticity modulus of RCA-RTW mixtures 2915
K. Gabryś & W. Sas

The impact of geotechnical spatial variability on the installation of suction caisson anchors 2921
E. Gallagher, S. Buykx, C. Reale & D. Igoe

Insight into modelling offshore monopiles via 3D finite element analyses 2925
D. Gaudio, A.B. Batilas, L.M. Lapastoure, A. Loukas, J. Lee, T. Joseph & I. Thusyanthan

Technical solutions for reducing CO_2 footprint in MSE wall constructions 2931
A. Grandclerc & T. Joussellin

Why natural log of soil permeability is a linear function of void ratio for 0-400μm soils having a sandy-silty-clayey matrix? 2935
J.C. Gress, M. Ferreira & J.M. Cuinet

Theoretical assessment of the advective-diffusive transport of contaminants through landfill composite liners 2939
N. Guarena, A. Dominijanni & M. Manassero

The effect of soil type on the temperature-dependent strength parameters 2945
M. Guner, S. Polat, U.C. Erginag, O. Cinicioglu, M. Sutman & A. Hashemi

Preliminary study of the influence of marble dust on clayey soils improvement depending on the characteristics of the natural soil 2950
E. Gutierrez, J.L. Pastor, M. Cano, A. Santos & T. Hino

The use of LCA in a slope stability study for a quay rehabilitation assessment 2955
E. Hafstad, G. Waldheim, A.B. Lundberg & S. Larsson

Large-scale soil bio-cementation: insights into homogeneity, quality control, and waste handling 2960
R. Harran, D. Terzis, M. Büyüklü & L. Laloui

Thermal soil properties as a basis for design of underground high voltage cables 2964
K. Hendler, C. Meier, S. Kleiber, J. Stegner, C. Drefke & C. Boley

Validation of the applicability of the PS logger borehole probe for diverse geotechnical scenarios 2970
R.M. Hen-Jones, P. Worthington, G. Comber, S. Garantini & P.J. Vardanega

Impact of soil parameters on cyclic pull-out capacity of offshore screw anchors 2974
C.F. Ho, A.P. Dyson & A. Tolooiyan

Improving soil dry compaction by adding granular material 2978
Y. Hocini, A. Medjnoun & R. Bahar

Moisture content distribution in a dike cross-section – A case study of a geophysical investigation 2982
Zs. Illés, G. Nagy, L. Nagy & A. Kovács

Using grain size distribution to estimate permeability 2987
E. Imre, Á. Bálint, D.Q. Houng, L. López, Cs. Kollár, L. Répássy, D.K. Mwinken, Zs. Illés, M. Datcheva, W. Baille, D. Barreto, J. Leak & S. Feng

The potential use of shallow geothermal systems to urban acclimatization – how to evaluate and how to implement? 2991
M. Inácio, C. Pinto, A. Vieira & I. Moitinho de Almeida

Behaviour of model pipe piles jacked in calcarenite 2995
M. Jafari, H. Gharsallaoui & A. Holeyman

Les tunnels de drainage de Lisbonne: Enjeux et spécificités 3001
C. Jassionnesse, G. Euzen & F. Rocha

Jet grouting experience in river borne materials (RBM) 3007
A.C. Joshi, Arvind & V.A. Sawant

Accelerated implicit cyclic loading with the hypoplastic sand 3011
T. Kadlíček & D. Mašín

Discrete element modelling of axial load testing on piles under the influence of ageing 3015
S.S. Kasyap, M.B. Mohammed & D. Igoe

The effect of polypropylene fibre content on the mechanical properties of mass-stabilised soils 3020
L.C. Kelly, S.B. Mickovski & A. Gonzalez-Ollauri

3D and 1D modelling of monitored monopiles located in the Belgian North Sea 3024
A. Kheffache, B. Stuyts, C.Sastre Jurado, W. Weitjens & C. Devriendt

The permeability characteristics of compacted recycled materials for landfill barriers in Norway 3030
T. Kim, E.W.Ånes, G.W. Åsli, Y. Suzuki & S. Ritter

Identifying porosity distribution and swell anisotropy of laboratory sedimented high plasticity clay through NMR imaging 3034
E.M. Kinslev, I. Rocchi & L.T.P. Meireles

Study on carbon-neutral ground improvement using recycled concrete fines 3038
T. Kono, S. Nishiie & M. Sugimoto

Formulation of a practical multi-surface plasticity model for sands 3042
D. Konstantinidis, H.J. Burd & C.M. Martin

Adaptation of a constitutive model for sand to account for non-plastic fines 3046
D. Konstantinidis, C.M. Martin & H.J. Burd

Reclamation of former brown coal mines: determining shear strength 3050
J. Kostal & P. Cernoch

Thermal activation of sewers and embedding in a heating-cooling network 3054
T. Kugler & Ch. Moormann

Accelerated stabilization of municipal solid waste in bioreactor landfills 3060
G. Kumar, K.R. Reddy & J.K. Janga

Basic characteristics of environment-friendly soil-cement material with added biochar 3066
Y. Kurimoto & Y. Asaka

Prediction of short piles response to lateral monotonic load in dense sand at Blessington 3070
L.-M. Lapastoure & D. Igoe

Microbial biopolymer-based soil treatment (BPST) effectiveness on the soil hydraulic erosion reduction assessed via laboratory to field scale methods 3074
S. Lee, I. Chang, M. Lee, Y.M- Kwon & G.C- Cho

Modelling hysteretic damping of soils for monopiles 3078
A.R. Leon Bal, M. Jafari, L.A. Berenguer Todo Bom & M. Goodarzi

Analysis of different temporary anchor points for construction of 380 kV high-voltage transmission masts 3082
S. Leppla, J.C. Paninski & R. Freund

Geotechnical characterization of a test site in Zeebrugge for large scale tests of monopiles in the framework of the SAGE-SAND project 3088
N. Letizia, G Anoyatis, L. Simonin, H. Rattez, F. Collin, S. François, H. Claes & J. Soete

A novel mechanical energy storage solution using underground CO_2 hydrate capsules 3094
O. Lev Yehudi, A. Franza, N. von Solms & A. Klar

Three-dimensional characterization of non-uniform deformation in drying fine sediments: An x-ray CT study 3100
L. Li & B. Zhao

Axial resistance of piles during driving in chalk 3104
T. Liu, R.M. Buckley, B.W. Byrne, S. Kontoe, R.J. Jardine, K. Vinck & R.A. McAdam

The contribution of ductile cast-iron piles to a more sustainable deep foundations industry 3109
F. Lopez & E. Steinlechner

3D Thermo-mechanical analysis of a real-world thermally activated piled foundation 3113
A. Lupattelli & D. Salciarini

Soil stabilization with plastic waste and sisal fibres 3118
R. Luzia, D. Gardete, D. Monteiro & M. Sousa

Geomechanical evaluation of analogs of reservoirs for geological storage of CO_2 3123
D. Manzanal, C.B. Laskowski, M. Cortés, P. Vidal, C.B. Laskowski, M. Cortés, P. Vidal & J. Allard

Testing methodologies to evaluate waste-based liners 3129
L. Marchiori, M.V. Morais, A. Albuquerque, L. Andrade Pais & V. Cavaleiro

Numerical analysis of monopiles supporting offshore wind turbines exposed to scour and cyclic loading 3133
C. Menéndez-Vicente & S. López-Querol

Physical modelling of the behaviour of buried gas pipe under surface loading 3137
A. Mertz, C. Dano, F. Emeriault, O. Jenck, C. Fernandez, A. Lebrun & M. Polo

Bervie Braes at 10 years: critical review of the effectiveness of slope stabilisation measures 3141
S.B. Mickovski

Experimental tests to evaluate skirt penetration resistance in scour protection for offshore foundations 3145
M. Miranda, J. Castro, E. Varela, M. Jahanshahinowkandeh, J. Sarmiento & R. Guanche

Impact of transport distance in life cycle assessments of geosynthetic reinforced soil walls 3149
A. Moncada, S. Olivella, I.P. Damians & R.J. Bathurst

An introduction to shared anchor in weak rock for floating systems 3153
L. Montalti, F. Moreno & V. Terente

Ballast degradation under different cycles and rotational speeds in micro-Deval equipment 3159
N.S. Montero-Cubillo, J. Estaire & E. Marull

Influence of different seasonal snow cover on thermal regime of the ground 3165
Z. Motamedi, H. Mattsson, J. Laue, S. Knutsson & J. Casselgren

COOP Project: Energy piles under combined loading 3171
H. Mroueh, T. Badinier, M. Blanc, T. Dubreucq, J. de Sauvage, F. Szymkiewicz, J.-M. Pereira, A.-M. Tang & R. Vasilescu

Back-analysis of a full-scale dyke stress test with advanced models for soft soils 3176
S. Muraro, C. Chao, L. Su & C. Jommi

Type-curves to assess seepage under sheet-piles for dewatering geotechnical works in limited 2D geometries 3182
S. Navarro Carrasco, J.A. Jiménez-Valera & I. Alhama Manteca

Producing pore pressure due to heat for bentonite-sand mixture with difference dry densities 3186
T. Nishimura

Database of measured shear wave velocity profiles for Icelandic soil sites 3190
E.A. Olafsdottir, S. Erlingsson & B. Bessason

Assessment of soil constitutive models to predict the response of offshore wind turbines subjected to lateral cyclic loads 3194
O. Orakci, G. Anoyatis, S. François, S. Chow & Y. Tian

Lignin used as stabilizer in an expansive unsaturated soil 3198
S. Orlandi, D. Manzanal, C. Laskowski, L.G. Libardi & L. Oldecop

Application of a new real-time analysis of the size distribution of rock fragments 3202
J. Ortuta & V. Greif

Laboratory testing and numerical modelling of seepage in building materials 3206
M. Pap, A. Mahler, Zs. Illés & S.G. Nehme

Assessment of waste dump affected area and its stability analysis for sustainable utilization of land and waste materials - a case study from the Sisdol dumpsite, Nepal 3212
D.R. Pathak & M. Rijal

Groundwater control during metro construction in urban areas – the Cityringen experience 3218
E. Paulatto, L.M. Markussen, J. Damgaard, F. Petrella & J. Flink

Recycled red mud as an useful geotechnical material 3224
P. Pavšič, M. Đurić, M. Košir, A. Mauko Pranjić, A. Mladenovič, P. Oprčkal, S. Seršen & V. Zalar Serjun

Carbon management in geotechnical engineering solutions 3228
O.J. Perttu, S.H. Vicente, M.S. Löfman, T. Dettenborn, J. Forsman & T. Teittinen

Sustainability assessment of a geotechnical site investigation in Holocene deposits: A case study from northern Germany 3233
W.T. Pfeiffer, U. Matthiesen & M. Pohl

A coupled thermo-hydro-mechanical hypoplastic model for fine-grained soils accounting small strain effects 3237
M. Pico & D. Mašín

Temporary cofferdam at Caniçada Dam, Portugal 3243
A. Pinto, L. Caldeira, F. Cerqueira, N. Plasencia & F. Gomes

A model-scale test setup development to monitor temperature and moisture content variations around energy piles 3247
S. Polat, U.C. Erginag, M. Guner, O. Cinicioglu & M. Sutman

On the influence of jack-up footprints on the dynamic behaviour of offshore foundations 3251
T. Pucker

A novel framework for modeling the vegetation and atmosphere effect on the behaviour of infrastructure embankments 3255
V. Pujević & L. Zdravković

Hydraulic properties of general-shape monodisperse granular materials: An insight from pore-network perspective 3261
J. Qi, W. Fei & G. Narsilio

Hydraulic conductivity of bentonite amended flyash liners for MSW landfills 3265
K.V.N.S. Raviteja, J.K. Janga & K.R. Reddy

A 4D investigation of model pile installation 3270
T. Riccio, M.O. Ciantia, M. Previtali, M.J. Brown & L. Csetenyi

New electric powered drill rig to meet sustainable geotechnique 3274
M. Rispal, C. Jacquard, G. de Oliveira Souza & P. Reiffsteck

Thermal characterization of Aveiro soil for multiscale building energy simulation using shallow geothermal system 3278
R.B. Roka, A. Vieira, A. Figueiredo & C. Cardoso

Environmental life cycle assessment of ground reinforcement using rigid inclusions 3284
M. Saadé & E. Antoinet

Centrifuge modelling of hollow heated piles in saturated sand 3288
G. Sabaliauskaite, S.E. Stallebrass, A.M. McNamara, R.N. Taylor, S. Divall & J.P. Panchal

Effects of AM fungi on root biomechanical properties 3293
T. Sakolpanya, V. Kamchoom, X.W. Chen & A.K. Leung

Review on carbon footprint in deep foundations: Case study for helical piles in Brasília, DF 3297
B. Sandoval & R.P. Cunha

Evaluation of frost heaving in frozen foundation layers due to the transfer of water in a gaseous state 3303
A. Sarsembayeva, Ph.E.F. Collins & S. Mussakhanova

Compression characteristics of compacted sand-bentonite mixtures with and without saturation 3307
S. Sato, T. Nishimura & K. Nakai

Effect of rainwater infiltration from pavement surface on base course bearing capacity 3311
K. Sato, T. Fujikawa, C. Koga & Y. Isobe

Influence of grille spacing on the uplift behaviour of steel grillages for OHLs 3316
C.J. Shepherd, M. Brown, C. Davidson, C.T.S. Beckett & S. Flint

The SOURCE project: Quantifying and reducing the uncertainties associated with in situ stiffness measurements 3321
N.S. Shinde, R.M. Buckley & L.P. Rieman

The environmental advantage of bi-directional pile testing related to traditional top-down testing 3325
A. Silva, M. England & M. Profittlich

Portugal first HVAC submarine power transmission cable - from engineering to construction 3329
R. Silvano, V. Terente, L. Burley, R. Francos, A. Santos & M. Conceição

Residues' physical identification for soil-waste materials 3335
A. Studart, L. Marchiori, A. Albuquerque, V. Cavaleiro, L. Andrade Pais, M.E.G. Boscov & I. Strozberg

One dimensional static and dynamic compression behaviour of foam glass aggregate 3339
J. Szendefy & W.S. Mustafa

Impact of stiffness properties and overconsolidation on the lateral behaviour of monopile foundations in clay deposits 3345
D.M.G. Taborda, A. Tsiampousi & K. Georgiadis

Numerical modelling of the long-term cyclic ratcheting of monopile foundations under lateral loading 3349
P. Tantivangphaisal, D.M.G. Taborda & S. Kontoe

A bibliometric analysis on geotechnical research trends in floating offshore wind energy 3353
A.D. Tasbasi, Y.C. Ceylan, N. Huvaj & A. Osman

Pisão dam. Multi-purpose hydraulic scheme of Crato - Portugal. Issues involving the natural materials availability 3357
G. Tavares, S. Oliveira, H. Lopes, J. Camões Lourenço & N. Rodrigues

Numerical evaluation of the long-term performance of energy piles in hot-dominated climates 3361
S. ten Bosch, E. Ravera & L. Laloui

Strength, microstructural, and leaching characteristics of phosphogypsum-fly ash mixtures 3365
Y. Thakur, A. Tyagi & S. Sarkar

Advances in groundwater recharge during construction dewatering 3369
S.D. Thomas, J. Watson & G.R. French

Flood and drought mitigation using stormwater attenuation and enhanced infiltration systems 3375
S.D. Thomas, G.R. French, J.A. O'Meara, M.P. Dale & B. Casal

Integration of ground energy systems for low-carbon heating and cooling of buildings 3381
S.D. Thomas, A. Vieira, C. Pinto & J. Lapa

Finite element modelling of wave loading on a multi-layered gassy soil seabed using complex number theory 3387
S.D. Thomas

A study of soil contamination by residues of single-use face masks 3392
V.A. Thomassen, R.M. Singh & R. Cardoso

Influence of culverts on frost depth in embankments: A field study 3396
K. Tommik, S. Knutsson & J. Laue

Triaxial cyclic behaviour of calcareous sand for offshore energy applications 3400
N. Ullah, J. Andries, G. Anoyatis, S. François, Y. Tian & S.H. Chow

Experimental study on the hydraulic behaviour of compacted soil mixtures in river embankments 3406
R. Ventini, M. Pirone & C. Mancuso

Viscoplasticity and large strain consolidation modelling with converging isotaches 3410
T.A. Vergote & Y. Devrieze

Effects of sustained loads on geogrid pullout behaviour embedded in a recycled construction and demolition waste 3416
C.S. Vieira & P.M. Pereira

Effect of cyclic loading stress level and amplitude on the behaviour of a soft soil chemically stabilized unreinforced and fibre-reinforced 3422
J. Villarroel-Ortega, A.A.S. Correia, P.J. Venda Oliveira & L. Leal Lemos

Parametric study of stability in landfills due to changes in waste composition 3428
H. Vučenović, K. Herceg, D. Domitrović & Ž. Veinović

Critical state behaviour of anthropogenic clay in a direct simple shear test 3432
N.S. Walrave, C. Zwanenburg & I.E. van Gelder

Numerical investigation on induced liquefaction during monopile installation by vibratory driving in a 1G scale test 3436
T. Wehbe, G. Anoyatis, H. Rattez & S. François

Seabed and sub-seabed boulders as an engineering hazard in the marine environment; methods of detection and quantification 3440
M.J. Wetton, D.P. Vaughan & N. Dyer

The potential of energy micropiles as energy geostructures 3446
M.F. Yozy Kepdib, J.A. Facciorusso, C. Madiai & R.M. Singh

Effect of the acetylation on the water resistance of biopolymer stabilised soil 3450
X. Yu, S.J. Armistead, J. McGregor, N. Martsinovich & C.C. Smith

Mechanical characteristics of non-cohesive soil improved by fibre and cement addition 3455
K. Zabielska-Adamska, P. Dobrzycki & M. Wasil

Evaluation of PFOS contamination in aquifers under single lined landfills 3459
L. Zhao, R.K. Rowe & A. El-Zein

Effect of saturation conditions on thermal properties of sands 3465
Z. Zhou, A. Diambra & T. Liu

Validation of a sulfide soil landfill numerical model 3470
A. Ziagharib, C. Maurice, Q. Jia, J. Laue & J. Macsik

F - Future city world vision
F - Vision mondiale de la ville du future

Reinforcement of a coarse granular aggregate with microgrids: Influence on packing 3477
R. Anjos, M. Pinho-Lopes & W. Powrie

State of the art on the recovery of mechanical energy in the city. The role of seismic metamaterials 3483
S. Brûlé, S. Guenneau & S. Enoch

Data analysis in geotechnics – an approach to the construction of an urban tunnel 3487
A. de Vilhena Costa, I. Coelho & A. Gomes Correia

Geotechnical works impacting existing railway infrastructure – French practice in railway safety measures 3491
A. Guimond-Barrett, R. English-Martin, C. Czabanski, F. Chille & T. Kaira

Towards an open geotechnical data platform in France 3497
I. Halfon & M. Beaufils

The application of Digital Twins and the Internet of Things to assess the metro dynamic effects on historical buildings 3503
I. Kaliukh, O. Trofymchuk, Y. Berchun, V. Berchun, Y. Melashenko, Y. Pavliuk, Y. Slyusarenko, V. Shokarev, V. Tytarenko, N. Kosheleva, Y. Ischenko, A. Shokarev, V. Shuminskiy, V. Siedin & V. Kovba

Digital transformation in geotechnical engineering 3507
A. Măgureanu & L. Sata

The integration of the underground space in the planning policies for Lisbon in the future 3511
C. Pinto, P. Leonardo, M. Inácio, A. Frias & I.M. Almeida

Challenges in assessing the hydrogeological impact of underground structures in urban renewal projects 3515
R. Ramos, F.T. Jeremias & L. Caldeira

Experiences with using parametric 3D modelling in geotechnical engineering 3521
M. Rømoen, M. Kahlström, D. Ryghseter & N.B. Hansen

Insights on drop mass systems to predict pile compressive resistance from dynamic load test energy measurements 3525
J.A. Santos & J. Viegas

A geotechnologist network 3530
S.D. Thomas & K.G. Higgins

Author index 3535

Proceedings of the XVIII ECSMGE 2024
GEOTECHNICAL ENGINEERING CHALLENGES
TO MEET CURRENT AND EMERGING NEEDS OF SOCIETY
© 2024 the Authors
ISBN 978-1-032-54816-6
Open Access: www.taylorfrancis.com, CC BY-NC-ND 4.0 license

ECSMGE 24
XVIII EUROPEAN CONFERENCE
ON SOIL MECHANICS AND
GEOTECHNICAL ENGINEERING

Preface

The ISSMGE European Region and the Portuguese Geotechnical Society (SPG) are pleased to welcome you to the XVIII European Conference on Soil Mechanics and Geotechnical Engineering in Lisbon, Portugal, on the 26th to the 30th of August 2024.

The geotechnical challenges that the world faces are getting increasingly complex and interrelated. To develop a renewed commitment with the engineering core values and ethics in this time of rapid and defying changes, the theme of the Conference is: "Geotechnical Engineering challenges to meet current and emerging needs of society". Considering this framework, the topics of the conference are:

A - New developments on structural design.

B – Geohazards.

C - Risk analysis and safety evaluation.

D - Current and new construction methods.

E - Environment, water and energy.

F - Future city world vision.

After the pandemic period, the aim of the conference is to share in person knowledge and experience with our colleagues and strengthen the relationship between members of the geotechnical community, emphasizing the important contribution of the geotechnical engineering to solve the current and emerging society needs.

We hope that this conference exceeds your expectations with very interesting lectures, papers, posters, exhibitions and technical visits.

We gratefully thank all the speakers, authors, reviewers, supporting committees, members of ISSMGE technical committees, chairs of sessions, exhibitors, institutional partners, as well as all other participants making this conference outstanding.

We hope you have a pleasant stay in Portugal and look forward to seeing you again.

Lisbon, August 2024

Lyesse Laloui,
ISSMGE Vice-President for Europe

Alexandre Pinto,
Chairman of the Organizing Committee of the XVIII ECSMGE 2024

Proceedings of the XVIII ECSMGE 2024
GEOTECHNICAL ENGINEERING CHALLENGES
TO MEET CURRENT AND EMERGING NEEDS OF SOCIETY
© 2024 the Authors
ISBN 978-1-032-54816-6
Open Access: www.taylorfrancis.com, CC BY-NC-ND 4.0 license

ECSMGE 24
XVIII EUROPEAN CONFERENCE
ON SOIL MECHANICS AND
GEOTECHNICAL ENGINEERING

Acknowledgements

The Portuguese Geotechnical Society (SPG) gratefully acknowledges the important support to the XVIII ECSMGE, Lisbon, 2024, from all the Conference Partner companies.

The Portuguese Geotechnical Society also acknowledges the enthusiasm and support of the members of the Advisory Committee, the Scientific Committee and the Organizing Committee of the XVIII ECSMGE, as well as the strong participation of the Board of Reviewers that contributed to the high scientific quality of the proceedings.

The Portuguese Geotechnical Society acknowledges the important role of the authors, keynote lecturers, SOA, Forum and HTC lecturers, chairpersons, and all the persons and entities that contributed to the success of the XVIII ECSMGE.

The editors thank Mr. Manuel Carvalho and Miss Maria João Carvalho for their meticulous and comprehensive efforts in proofreading and formatting the text. Their dedication has contributed to the high quality and readiness for publication of these proceedings.

The editors extend their appreciation to Leading and in particular to Maria Brito, for her expertise in crafting the captivating graphical design of the book cover.

Proceedings of the XVIII ECSMGE 2024
GEOTECHNICAL ENGINEERING CHALLENGES
TO MEET CURRENT AND EMERGING NEEDS OF SOCIETY
© 2024 the Authors
ISBN 978-1-032-54816-6
Open Access: www.taylorfrancis.com, CC BY-NC-ND 4.0 license

ECSMGE 24
XVIII EUROPEAN CONFERENCE
ON SOIL MECHANICS AND
GEOTECHNICAL ENGINEERING

Editor Biographies

Nuno Guerra is Associate Professor at NOVA School of Science and Technology, where he lectures undergraduate, master and postgraduate courses in the fields of Soil Mechanics and Geotechnical Engineering, in the Civil Engineering Department. His research interests are the study of the collapse of geotechnical structures, geotechnical design considering the variability of soil properties, soil-structure interaction and the performance of retaining structures. He was Vice-President of the Portuguese Geotechnical Society (2012-2016), member of several Organizing and Scientific Committees of national conferences and Geotechnical Engineer and Consultant. He was (2004-2008) and is now (from 2016) member of the Board of the journal "Geotecnia" published by SPG, ABMS and SEMSIG. He is author of 75 papers published in national and international journals and in the proceedings of national and international conferences.

Manuel Matos Fernandes is Professor of Soil Mechanics and Geotechnical Engineering at the Faculty of Engineering of the University of Porto. His main research areas concern numerical modelling of geotechnical works, deep urban excavations and the history of Construction. He was editor of the journals Geotecnia (2000-04) and Soils & Rocks (2012-16) and President of the Portuguese Geotechnical Society (2016-20). He is author of textbooks on Soil Mechanics and Geotechnical Engineering published in Portugal and internationally. From 1991 to 2012, he co-organized the series International Workshops on Applications of Computational Mechanics in Geotechnical Engineering and co-edited its proceedings (6). In 2013 he was awarded with the Prize in Pedagogic Excellency at his university.

Cristiana Ferreira is Assistant Professor in the Department of Civil Engineering at the Faculty of Engineering of the University of Porto and an integrated member of CONSTRUCT (Institute of R&D in Structures and Construction). Her research is mainly focused on laboratory and field soil characterisation, wave-based non-destructive testing, seismic and static liquefaction characterisation and mitigation, and the mechanics of non-textbook geomaterials. She has 3 published books as editor, 32 papers in peer-reviewed scientific journals and more than 50 papers in conference proceedings.

António Gomes Correia is professor and researcher at the Institute for Sustainability and Innovation in Structural Engineering (ISISE) of University of Minho. His activities involve research, teaching and consulting in the general field of geotechnical and transportation engineering for 44 years. He has been a keynote speaker and member of the organising/technical committees for many well established international conferences. He is a co-founder of the International Society for Intelligent Construction (ISIC) as well as has founded the conference series on Transportation Geotechnics. He is also one of founding editors for the international journal "Transportation Geotechnics" (from 2014), as well as for "Transportation Engineering" (from 2020), both published by Elsevier. He is also editor of the journal "Geotecnia" (from 2016) published by SPG, ABMS and SEMSIG. He is an author/coauthor of 190 scholarly publication indexed in SCOPUS.

Alexandre Pinto is founder and technical manager of JETsj Geotecnia Lda. and invited Professor at Instituto Superior Técnico (IST) of Technical University of Lisbon. His activities involve consulting and teaching in the general field of geotechnical engineering for 30 years. He is an author/coauthor of 120 technical papers. He has been a keynote speaker and member of the organising/technical committees for several conferences. He was Vice President of Portuguese Geotechnical Society from 2016 to 2020 and is President from 2020 to 2024.

Pedro Sêco e Pinto was a Full Professor of Geotechnical Engineering at Coimbra University. He is a member of European Union Academy of Sciences, a Fellow of Portuguese Institute of Engineers and a former Director of Research of National Laboratory of Civil Engineer (LNEC). He was ISSMGE Board Member, Immediate Past President, ISSMGE President and ISSMGE Vice President. He was Chairman of ISSMGE TC "Earthquake Geotechnical Engineering". He presented 350 State-of-the Art Lectures in 80 countries. He was an Editorial in Chief of 2 International Journals and he is member of 7 Editorial Boards. He has been a member of Advisory Committee of 100 International Conferences. He worked as World Bank Consulting and United Nations Consulting. He worked on 450 major projects in Dams, Power plants, Bridges, Special Foundations, Tunnels, Highways, Landslides, Dykes, Airports and Quay Walls, in 23 countries. He is author or co-author of 500 Technical and Scientific Reports and 180 papers for Conferences and Journals and contributed for 13 Books. He received more than 50 International Awards.

Proceedings of the XVIII ECSMGE 2024
GEOTECHNICAL ENGINEERING CHALLENGES
TO MEET CURRENT AND EMERGING NEEDS OF SOCIETY
© 2024 the Authors
ISBN 978-1-032-54816-6
Open Access: www.taylorfrancis.com, CC BY-NC-ND 4.0 license

ECSMGE 24
XVIII EUROPEAN CONFERENCE
ON SOIL MECHANICS AND
GEOTECHNICAL ENGINEERING

Advisory Committee
Comité Consultatif

Lyesse Laloui - Vice-President of the ISSMGE for Europe 2022-2026 (Chairman)
Marc Ballouz - President of the ISSMGE 2022-2026
Laura Caldeira - President of LNEC, Lisbon
Eduardo Fortunato - Member of the Conference Organizing Committee
Mario Manassero - Vice-President of the ISSMGE for Europe 2017-2022
Charles Ng - Immediate Past-President of the ISSMGE 2017-2022
Haraldur Sigursteinsson - Chair of the XVII Conference Organizing Committee
Neil Taylor - Secretary General of the ISSMGE

Proceedings of the XVIII ECSMGE 2024
GEOTECHNICAL ENGINEERING CHALLENGES
TO MEET CURRENT AND EMERGING NEEDS OF SOCIETY
© 2024 the Authors
ISBN 978-1-032-54816-6
Open Access: www.taylorfrancis.com, CC BY-NC-ND 4.0 license

ECSMGE 24
XVIII EUROPEAN CONFERENCE
ON SOIL MECHANICS AND
GEOTECHNICAL ENGINEERING

Scientific Committee
Comité Scientifique

Pedro Sêco e Pinto - Past-President of the ISSMGE 2005-2009 (Chairman)
Michael Bardanis (Greece)
Kaspars Bondars (Latvia)
Loretta Batali (Romania)
Rasin Duzceer (Turkey)
Liudas Furmonavicius (Lithuania)
Jana Frankovska (Czech & Slovak)
Vyacheslav Ilychev (Russia)
David Igoe (Ireland)
Yuriy Kirichek (Ukraine)
Omar Kutsnashvili (Georgia)
Lehar Letsaar (Estonia)
Dimitrios Loukidis (Cyprus)
Andras Mahler (Hungary)
Leo Matesic (Croatia)
Manuel Matos Fernandes (Portugal)
Christian Moormann (Germany)
Trude Orbech (Norway)
Ervin Paci (Albania)
Jovan Papic (Republic of North Macedonia)
Sebastiano Rampello (Italy)
Fernando Pardo Santayana (Spain)
Helmut Schweiger (Austria)
Klaas Siderius (The Netherlands)
Haraldur Sigursteinsson (Iceland)
Wojciech Solowski (Finland)
Suzana Svetličič (Slovenia)
Dimitrios Terzis (Switzerland)
David Toll (UK)
Andry Totsev (Bulgaria)
Tamara Ulasik (Belarus)
Nicolas Utter (France)
Monika de Vos (Belgium)
Mirjana Vukicevic (Serbia)
Katarzyna Zabielska (Polland)
Sabid Zekan (Bosnia & Herzegovina)

Proceedings of the XVIII ECSMGE 2024
GEOTECHNICAL ENGINEERING CHALLENGES
TO MEET CURRENT AND EMERGING NEEDS OF SOCIETY
© 2024 the Authors
ISBN 978-1-032-54816-6
Open Access: www.taylorfrancis.com, CC BY-NC-ND 4.0 license

ECSMGE 24
XVIII EUROPEAN CONFERENCE ON SOIL MECHANICS AND GEOTECHNICAL ENGINEERING

Organizing Committee
Comité d'Organization

Alexandre Pinto - (Chairman)
José Mateus de Brito (HTCP)
Ana Cardoso (IP)
António Cristovão (Keller)
António Gomes Correia (UM)
Cristiana Ferreira (FEUP)
Isabel Fernandes (FCUL, SPG)
Eduardo Fortunato (LNEC, SPG)
António Viana da Fonseca (FEUP)
Nuno Guerra (FCTUNL)
José Neves (ISTUL, SPG)
Paulo da Venda Oliveira (FCTUC)
Nadir Plasencia (EDP)
Cláudia Pinto (CML)
Paulo Ramos (Teixeira Duarte)
Edmundo Vieira Simões (Mota-Engil)
Marcelino Mateus da Silva (LNEC)
Castorina Vieira (FEUP, SPG)

Proceedings of the XVIII ECSMGE 2024
GEOTECHNICAL ENGINEERING CHALLENGES
TO MEET CURRENT AND EMERGING NEEDS OF SOCIETY
© 2024 the Authors
ISBN 978-1-032-54816-6
Open Access: www.taylorfrancis.com, CC BY-NC-ND 4.0 license

ECSMGE 24
XVIII EUROPEAN CONFERENCE
ON SOIL MECHANICS AND
GEOTECHNICAL ENGINEERING

Board of Reviewers
Comité de Révision

Pascal Aguado
Jorge Almeida e Sousa
Sara Amoroso
Armando Antão
José Luis Arcos
Gustavo Armijo
Marcos Arroyo
Enrique Asanza-Izquierdo
Michael Bardanis
Daniel Barreto
Loretta Batali
Fátima Batista
Mickaël Beaufils
Georgios Belokas
Robert Bendzovski
Judith Bernis
Adam Bezuijen
Emilio Bilotta
Dominique Blanc
Witold Bogusz
Daniela Boldini
Malek Bouazza
Emmanuel Bourgeois
Peter John Bourne-Webb
Rossella Bovolenta
Ilknur Bozbey
Maria Luísa Braga Farinha
Denis Branque
M. Fraser Bransby
Sandro Brasile
Gerhard Bräu
Sylvie Bretelle
Laurent Briancon
Kevin Briggs
Ronald Brinkgreve
Andrea Brito
Mike Brown
Sebastien Burlon
Martin Cahn
Laura Caldeira
Michele Calvello
José Cândido Freitas
Herminia Cano
Giuseppe Cardile
Rafaela Cardoso
Joana Carreto
Rui Carrilho Gomes
Mariana de Carvalho
Jorge Castro
Daniele Cazzuffi
Ricky Chan
Feyza Cinicioglu
Ozer Cinicioglu
Adrian Ciutina
Paulo Coelho
Simonetta Cola
Aires Colaço
Nilo Consoli
António Alberto Correia
Roberto Coutinho
Nuno Cristelo
António Cristovão
Nuno Cruz
Roberto Cudmani
Olivier Cuisinier
Marco D'Ignazio
Anna D'Onofrio
Paulo da Venda Oliveira
Dimitrios Daskalopoulos
Samson Degago
Hans Dete
Oliver Detert
Gonçalo Diniz Vieira
Andrea Dominijanni
George Dounias
José Echave
José Estaire
Settimio Ferlisi
Isabel Fernandes
Cristiana Ferreira
Fernanda Bessa Ferreira
Alessandro Flora

Maxime Fonty
Daniele Fornelli
Eduardo Fortunato
Jana Frankovska
Teresa Freitas
Liudas Furmonavicius
Andrea Galli
George Gazetas
Antonio Gens
Hubert Godin
Alp Gokalp
António Gomes Correia
Arjan Grashuis
Alex Greeuw
Pedro Guedes de Melo
Nuno Guerra
Bruno Guimarães Delgado
Kazimierz Gwizdała
Koen Haelterman
Amir Hamidi
Ellen Haugen
Kilic Havvanur
Ana Heitor
Flip Hoefsloot
Robert Hofmann
Wengui Huang
Nejan Huvaj
David Igoe
Patrick Ijnsen
Chiara Iodice
Anooshesh Iravanian
Richard Jardine
Orianne Jenck
Celeste Jorge
Josif Josifovski
Takeshi Katsumi
Satoru Kawasaki
Amir Kaynia
Yuriy Kirichek
Jonathan Knappett
Edina Koch
Stavroula Kontoe
Adam Krasinski
Ozaydin Kutay
Jean-Sébastien L'Heureux
Luís Lamas
Jan Laue
Luís Leal Lemos
Lehar Leetsaar
José Leitão Borges
Valentina Lentini
Kerstin Lesny
Zili Li
Stefania Lirer
Tingfa Liu
Monica Lofman
Isabel Lopes
Alexandre Lopes Dos Santos
Mafalda Lopes Laranjo
Freddy Lopez
Dimitrios Loukidis
João Lourenço
Giulia Lugli
António M G Pedro
Natalia Maca
András Mahler
Maria Clorinda Mandaglio
Alessandro Mandolini
João Manso
Diego Manzanal
João Marcelino
Lígia Martins
Leo Matesic
José António Mateus de Brito
Paulo Matias Ramos
Manuel Matos Fernandes
Svetlana Melentijevic
António Mendonça
Maria Migliazza
Krunoslav Minažek
Tiago Miranda
Fausto Molina-Gómez
Nuno Monteiro Azevedo
Nicola Moraci
Sravan Muguda-Viswanath
Mauro Muniz Menendez
José Muralha
Peter Nagy
Nicolas Nayrand
Ian Nettleton
José Neves
Ilies Nicoleta
Tomoyoshi Nishimura
Simon Oberhollenzer
Shulyatyev Oleg
Trude Orbech
Trevor Orr
Anatolii Osokin
Ervin Paci
André Paixão
Marina Pantazidou
Jovan Papic
Fernando Pardo
Manuel Parente
António Paula
Skevi Perdikou
Carlos Pereira
Sabrina Perlo

Alexandros Petalas
Margarida Pinho Lopes
Alexandre Pinto
Paulo Pinto
Pedro Pinto
Marianna Pirone
Nadir Plasência
A.B. Ponomaryov
João Portugal
Martin Preene
Ivan Puig Damians
José Quintanilha de Menezes
Jérôme Racinais
Frank Rackwitz
Ana Ramos
Sebastiano Rampello
Nuno Raposo
Sylvie Raymackers
Marlee Reed
David Reid
Philippe Reiffsteck
Mohammad Rezania
Sara Rios
Carlos Rodrigues
Luís Rodrigues de Sousa Miranda
António Roque
Agustin Ruiz Lopez
Gianpiero Russo
César Sagaseta
Maha Saleh
Teresa Santana
Luís Santos
Ricardo Neves Correia Santos
Harry Saroglou
Ernestos Sarris
Assel Sarsembayeva
Giuseppe Scarpelli
Felix Schroeder
Timo Schweckendiek
Helmut F. Schweiger
João Serra
A. V. Shaposhnikov
A. G. Shashkin
Brian Sheil
Daichao Sheng
Jinquan Shi
Klaas Siderius
Lucia Simeoni
Neil Smith
Ecidineia Soares
Wojciech Solowski
Julia Sorgatz
Giovanni Spagnoli
Ruud Steenbrink
Vetle Stene
Hans Henning Stutz
Bruno Stuyts
Waldemar Swidzinski
Zsolt Szilvagyi
David Taborda
Stephen Thomas
Luc Thorel
Joaquim Tinoco
David Toll
Laura Tonni
António Topa Gomes
Michał Topolnicki
José Manuel Torres Serrano
Andrey Totsev
José Filinto Trigo
Giuseppe Tropeano
Anne Tuomela
Nicolas Utter
K Van Dalen
Kristof Van Royen
José Nuno Varandas
Paul J. Vardanega
Roberto Vassallo
Thomas Vergote
Jean-David Vernhes
António Viana da Fonseca
Ana Vieira
Castorina Vieira
Giulia Viggiani
Claudia Vitone
Bas Vos
Mirjana Vukićević
Goran Vukotic
Phil Watson
Mike Winter
Ákos Wolf
Hoe Yeow
Xinyuan Yu
Yeliz Yukselen
Katarzyna Zabielska-Adamska
Lidija Zdravkovic
Sabid Zekan
Maurizio Ziccarelli
Cor Zwanenburg

Keynote Lectures
Conférences Principales

Proceedings of the XVIII ECSMGE 2024
GEOTECHNICAL ENGINEERING CHALLENGES
TO MEET CURRENT AND EMERGING NEEDS OF SOCIETY
© 2024 the Authors
ISBN 978-1-032-54816-6
DOI 10.1201/9781003431749-1
Open Access: www.taylorfrancis.com, CC BY-NC-ND 4.0 license

ECSMGE 24
XVIII EUROPEAN CONFERENCE ON SOIL MECHANICS AND GEOTECHNICAL ENGINEERING

Keynote Lecture

On the interdependency between geotechnical and structural design

Sur l'interdépendance entre le dimensionnement géotechnique et le dimensionnement structurelle

M. Topolnicki*
Keller Polska Sp. z o.o., Gdańsk, Poland
**michal.topolnicki@keller.com*

ABSTRACT: Civil engineering structures are designed with consideration for the interaction between the structure and the ground. This interaction can be complex and is taken into account to varying degrees in the geotechnical and structural designs, which are interdependent. Demanding projects increasingly require the integration of geotechnical and structural design. However, current practice typically separates these two areas and assigns them to different design teams. Effective collaboration between geotechnical and structural engineers is therefore essential to optimise structural and geotechnical designs. A well-designed geotechnical solution, carefully selected to utilise a better foundation technique or alternative ground improvement system, can provide significant benefits. These benefits may include lower construction costs, shorter construction times, reduced CO_2 emissions, or the elimination of specific technical risks. Appropriate modifications to the structural design can also enable the implementation of a new geotechnical solution that may not have been feasible otherwise. This can result in similar advantages. The process of collaboration and arriving at final combined solutions using advanced design tools, as well as the benefits achieved, are illustrated and discussed through completed project examples. The selection of projects was based on the distinct responsibilities of geotechnical and structural engineers in developing the implemented foundation solution. Improved understanding between geotechnical and structural designers can be achieved through a better knowledge of each other's discipline.

RÉSUMÉ: Les ouvrages de génie civil sont conçus en tenant compte de l'interaction entre la structure et le sol. Cette interaction peut être complexe et est prise en compte à des degrés divers dans les conceptions géotechniques et structurelles, qui sont interdépendantes. Les projets exigeants nécessitent de plus en plus l'intégration de la conception géotechnique et structurelle. Cependant, la pratique actuelle sépare généralement ces deux domaines et les confie à des équipes de conception différentes. Une collaboration efficace entre les ingénieurs géotechniques et structurels est donc essentielle pour optimiser ces deux aspects. Une solution géotechnique bien conçue, soigneusement choisie pour utiliser une meilleure technique de fondation ou un système alternatif d'amélioration du sol, peut apporter des avantages significatifs. Il peut s'agir de coûts de construction moins élevés, de délais de construction plus courts, d'une réduction des émissions de CO_2 ou de l'élimination de risques techniques spécifiques. Des modifications appropriées de la conception structurelle peuvent également permettre la mise en œuvre d'une nouvelle solution géotechnique qui n'aurait pas été possible autrement, et des avantages similaires peuvent en résulter. Le processus de collaboration et l'élaboration de solutions combinées finales à l'aide d'outils de conception avancés, ainsi que les avantages obtenus, sont illustrés et discutés à l'aide d'exemples de projets réalisés. La sélection des projets a été basée sur les responsabilités distinctes des ingénieurs en géotechnique et en structure dans le développement de la solution de fondation mise en œuvre. Une meilleure compréhension entre les concepteurs géotechniques et structurels peut être obtenue grâce à une meilleure connaissance de la discipline de l'autre.

Keywords: Geotechnical design; structural design; foundation; optimisation; collaboration.

1 INTRODUCTION

From the perspective of 50 years, which happens to correspond to my professional career, I have witnessed the growing role of geotechnics in civil engineering. Although the foundations of structures have always been important, there have been and continue to be major changes in foundation engineering, triggered by new trends in construction and developments in geotechnics. We are building in ever more challenging conditions, for example in densely built-up areas, on very weak or degraded soils, and next to or even under

existing buildings. Structures are becoming more sophisticated and more daring and need to be built faster. New foundation techniques have been introduced, and those already in use have been significantly improved, opening up new possibilities that were not available before.

These changes have had a significant impact on structural and geotechnical design and have led to an increase in specialisation. In addition, the rapid development of engineering methods and the availability of advanced computational software have placed analyses, that not long ago required the work of large design teams, within the reach of small but professional practices.

My eminent teacher at university used to say that "civil engineering structures are not built in the air" to emphasise the point that structural design should not be carried out in isolation from geotechnical design. At present, the interdependence between structural and geotechnical design seems self-evident and the need for effective collaboration between engineers of both disciplines needs no justification. However, in day-to-day engineering practice, different situations arise which impact upon this ideal. The reality depends on the size and importance of the project, the risks involved, the staffing and capabilities of the smaller or larger design offices, and the applicable legal regime governing the whole construction process, the way investments are made, tenders and contracts are managed, works are insured and so on, which can vary even within the European Union. For these reasons, many readers of this paper will undoubtedly have their own experiences and opinions as to what this cooperation looks like in reality and whether it delivers the expected results. Such a broad picture would also be more objective than my limited experience. Nevertheless, this paper can be seen as an introduction to a broader discussion on this important topic.

The following sections present experiences and results of practical design collaboration between geotechnical engineers and structural engineers on challenging structures where the original foundation system had to be modified to meet the expectations of the clients and the general contractors responsible for the structural works. The selection of projects was based on the distinct responsibilities of geotechnical and structural engineers in developing the implemented foundation solution. The five selected examples include the following:

Case 1 – design of a modern sustainable office building, illustrating the involvement of a geotechnical engineer to optimise the foundation design in terms of construction cost and reduction of CO_2 emissions, subject to demanding verification and approval by the structural engineer;

Case 2 – geotechnical design for a large silo, developed in collaboration between geotechnical and structural engineers to find a better solution that reduced settlement and mitigated risk compared to the original foundation design, without increasing construction costs;

Case 3 – foundation design of a road bridge in very difficult conditions due to the presence of soft soils and groundwater under high artesian pressure, leading to the use of spread foundations on improved ground, which became possible after the bridge structure was modified by the structural engineer;

Case 4 – design of retaining systems for long and deep excavations for access ramps to an under-river tunnel, involving a major change in construction method, illustrating the geotechnical contractor's assumption of a leading role and design responsibility for these works and the tunnel designer's support in this regard;

Case 5 – design and execution of ground improvement works for the foundation of a football stadium by a geotechnical contractor in a situation where the structural design had not been completed, including the impact of late client led changes in relation to the stadium structure.

So, taking each case in turn.

2 CASE 1 - SUSTAINABLE OFFICE BUILDING

The building incorporates state-of-the-art technology for sustainable utility management and air quality control, including an anti-pandemic system, and has been awarded a BREEAM Excellent rating. With a height of 55m and a length of 120m, the building has a terraced layout and houses a two-storey underground car park with 218 spaces (Figure 1a).

The alternative foundation solution for this building, developed by a geotechnical contractor and ultimately adopted for construction, uses a perimeter diaphragm wall, CFA piles, and foundation slab as an integrated support system (Figure 1b). It represents a significantly optimised solution compared to the original design developed by the structural engineer, not only in terms of reducing the cost of the geotechnical works, but also in terms of reducing the carbon footprint. However, the client's agreement to implement the alternative solution was subject to the approval of the structural engineer. The structural engineer required a calculation to demonstrate that the optimised foundation system would not cause greater settlement than the original design and would meet the load bearing capacity requirements of the code.

In the subsoil, below the level of the foundation slab, the following soil layers with a slope of

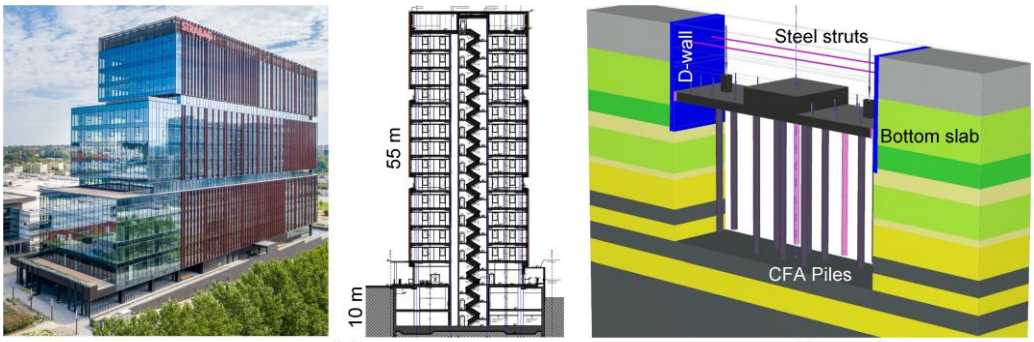

Figure 1. (a) Modern 13-storey office building (courtesy of Ghelamco); (b) The integrated foundation system consisting of perimeter diaphragm wall, CFA piles, and a bottom slab.

approximately 1:10 occur: organic silt, up to 3m thick, over a length of about 30% of the longitudinal cross-section of the building; medium sand, up to 3m thick, over a length of about 20%; sandy clay, 1 to 4m thick, over a length of about 50%; and below this, coarse sand, 4 to 7m thick, underlain by alternating layers of clay and sand. Groundwater is present at a depth of about 5m below the bottom of the excavation and poses no threat to the works. Under these ground conditions, the foundation of the heavy building required deep foundations and the support of the approximately 10m deep excavation with diaphragm walls and temporary struts.

The original foundation design included a 0.6m thick and 13 to 16.5m deep diaphragm wall around the entire 302.5m perimeter of the building, used as a shoring system to protect the excavation and as a permanent outer wall for the underground part of the building (Figure 2a). The foundation slab was supported by 186 CFA piles of 0.8m diameter and 21m average length, consisting of a 12m pile section below the bottom of the foundation slab and a 9m upper section, designed to carry 100% of the applied loading. The design assumed that the piles would be installed from ground level due to the dense pattern of cross struts in the excavation, which prevented the piling rig from working inside the pit. This required the upper part of the piles to be trimmed and the cutting debris to be removed.

The alternative solution was to combine the diaphragm wall, CFA piles, and foundation slab as bearing elements of an integrated support system. This allowed the number of piles to be reduced to 119 while increasing their length by 3 and 4m, shortening the diaphragm wall by an average of 2.5m and reducing the thickness of the foundation slab from 1.0 to 0.9m, locally, from the original 1.9 to 1.35m (Figure 2b).

It was crucial for the project that the geotechnical engineer carried out advanced calculations to confirm that the alternative solution could be implemented without compromising the design originally adopted by the structural engineer. For this task, two three-dimensional FEM models with generalised ground conditions were created in PLAXIS 3D to analyse 8.4m wide transverse sections S1 and S2 of the foundation slab (Figure 3a), which pass through heavily and moderately loaded parts of the building (Figure 2). The calculation results showed that the expected settlements of the foundation slab for the integrated support system were even lower than for the original design, which assumed that the full acting load would be carried by a relatively large number of piles, without considering the slab interaction (Figures 3b and 3c, respectively). The load-settlement curves of the CFA piles, both individually and in groups, were also carefully examined to verify the shaft and base resistances and to determine their ultimate load bearing capacity. Based on the positive results of these analyses, the alternative foundation design was subsequently approved by the structural engineer.

In order to optimise the thickness of the foundation slab and design its reinforcement, the geotechnical engineer developed a map of equivalent stiffnesses of the subsoil based on the calculated settlements and stresses under the slab in the two representative sections S1 and S2 (Figure 4a). As shown in Figure 4b, very similar settlements were obtained in the equivalent stiffness calculation, allowing the use of Autodesk ROBOT software to determine the final geometry and reinforcement of the foundation slab.

By implementing an optimised foundation solution for the building, developed by the geotechnical contractor, a significant reduction in the carbon footprint of the foundation works was also achieved. It is worth noting that the installation of the CFA piles, used an innovative solution to limit concreting to the effective length of the pile, further reducing the amount of concrete used on site. This involved the use of a bentonite slurry to ensure the stability of the borehole along the unconcreted length of the top of the pile as the auger was pulled out of the ground. A detailed summary of the carbon footprint reductions achieved is presented in Table 1.

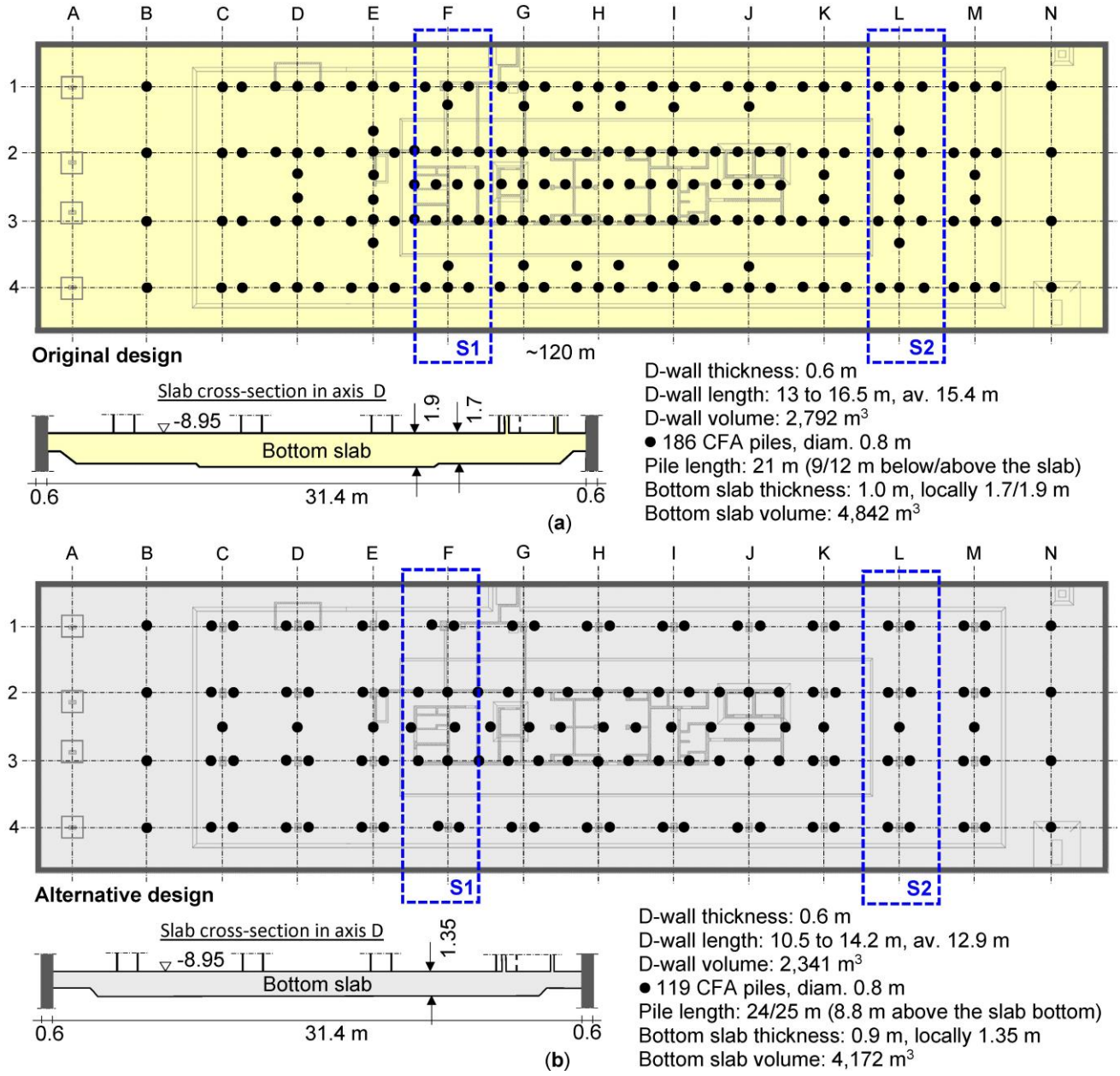

Figure 2. (a) Structural engineer's design with diaphragm wall around the perimeter and CFA piles taking the full applied load; (b) Geotechnical engineer's integrated design using perimeter diaphragm wall, CFA piles, and foundation slab.

Table 1. Concrete consumption and carbon footprint comparison of the two design solutions.

Element	Original design	Alternative design
Diaphragm wall:		
- concrete volume	2792 m^3	2341 m^3
- CO_2 emission	1300 ton	1100 ton
CFA piles:		
- concrete volume	1944 m^3	942 m^3
- CO_2 emission	748 ton	370 ton
Foundation slab:		
- concrete volume	4842 m^3	4172 m^3
- CO_2 emission	2400 ton	2100 ton
Sum CO_2 emission	4448 ton	3570 ton
Sum CO_2 emission in [%]	100%	80%

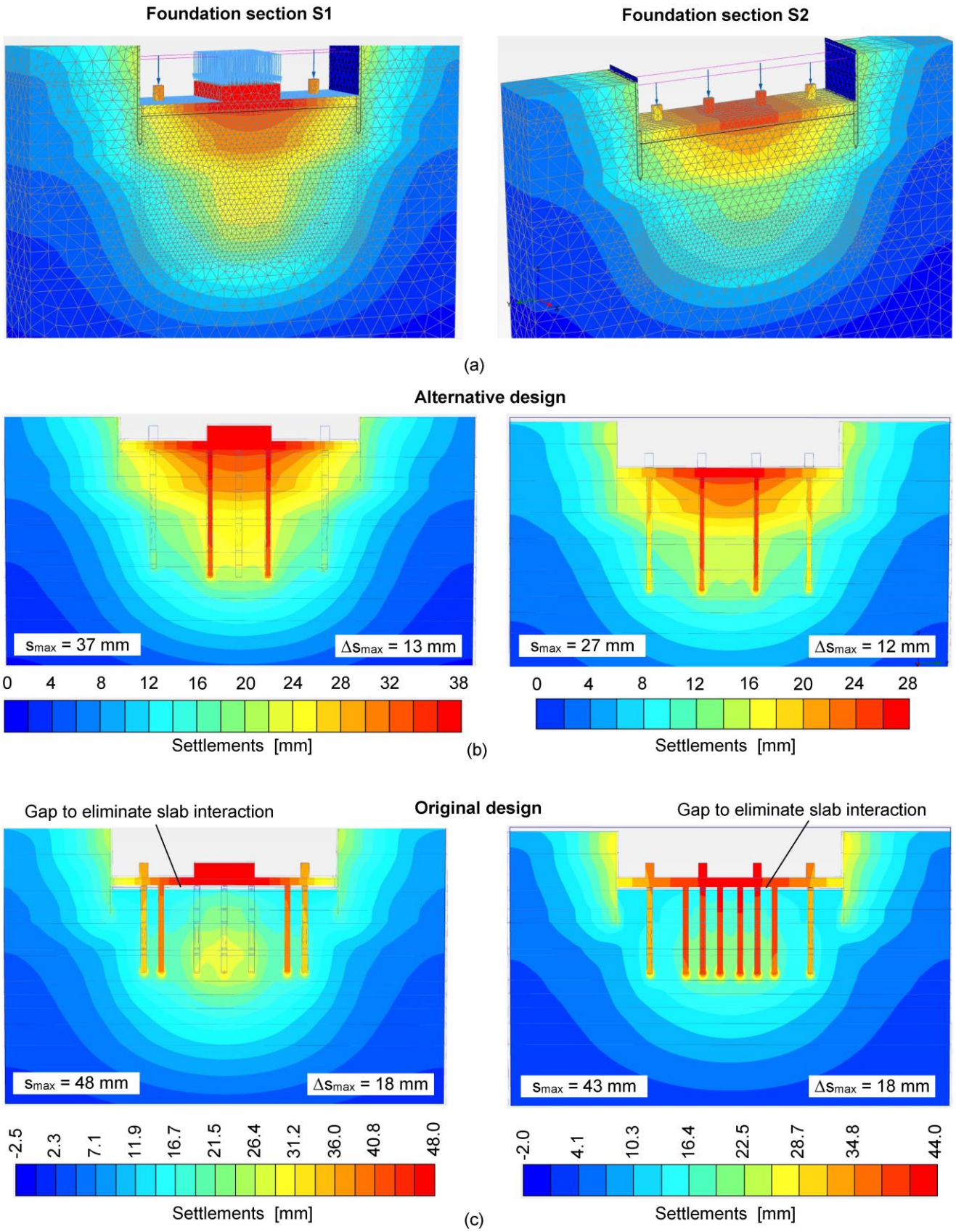

Figure 3. FEM analyses carried out by the geotechnical designer: (a) PLAXIS 3D models of heavily and moderately loaded foundation sections S1 and S2; (b) predicted settlements for the integrated foundation system, consisting of perimeter diaphragm wall, piles, and bottom slab; (c) settlements calculated for the original piling design without the load bearing contribution of the foundation slab.

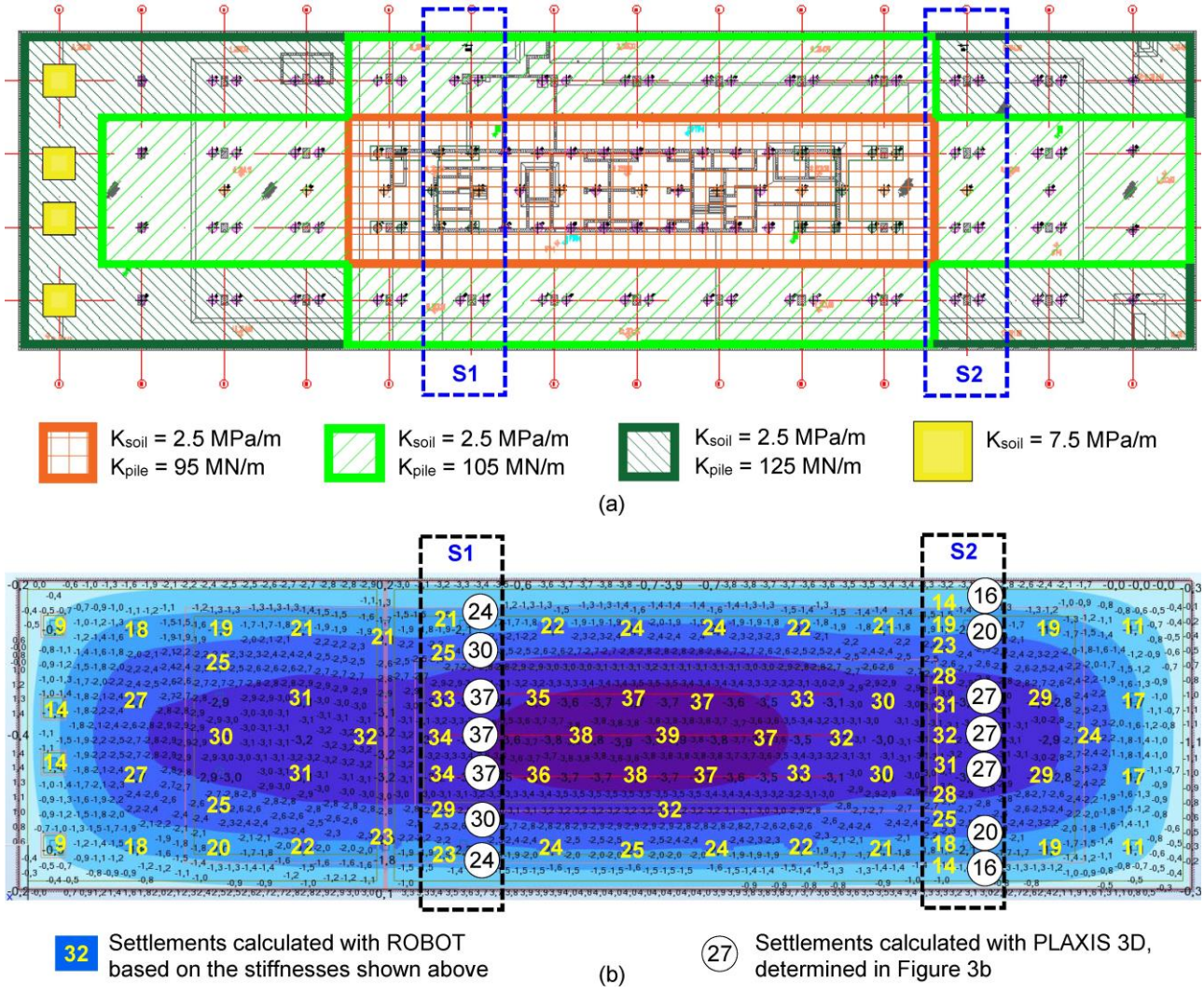

Figure 4. (a) Equivalent stiffness of the subsoil under the foundation slab; (b) Comparison of settlements determined by FEM calculations for sections S1 and S2 with settlements calculated using Autodesk ROBOT for the entire slab based on the equivalent stiffnesses shown in part (a).

3 CASE 2 - LARGE CLINKER SILO

This example illustrates the very close and effective collaboration between silo designers working on behalf of the client and engineers employed by the geotechnical contractor, which ultimately resulted in a very robust foundation support system being adopted.

The silo, with a capacity of approximately 120,000 tonnes of clinker, has a diameter of 55m and a total height of about 65m. The reinforced concrete walls rest on a ring foundation, initially 4.5m wide and 1.2m thick. At the bottom of the silo are three belt conveyor channels, 5.3m wide and 5m high. The relevant characteristic load combinations for the geotechnical design are cases A and B, as defined in Figure 5. The maximum bottom pressure inside the silo reaches 510kPa.

The ground conditions at the silo site are complex with a predominance of cohesive soils of varying thickness and consistency (Figure 6). Based on soil investigations, comprising borings and CPT and DMT tests, the following soil layers have been identified: 1 – a heterogeneous manmade fill with 1 to 3m thickness, 2 – medium dense ($q_c < 12.5$MPa) to dense ($q_c > 12.5$MPa) sands with thickness of 2 to 5m, 3 – sandy clay with soft ($q_c < 2$MPa) to stiff ($q_c = 2$ to 3MPa) consistency and thickness of about 2m, 4 – silt with soft ($q_c < 2$MPa) to hard ($q_c > 5$MPa) consistency and 4 to 5m thick, 5 – silty clay, stiff ($q_c = 2$ to 4MPa) and very stiff ($q_c = 4$ to 6MPa), with thickness of 2 to 10m, 6 – high plasticity clay, very stiff ($q_c = 4$ to 6MPa) and 4 to 6m thick, 7 – limestone rubble filled with sandy/silty clay, with $q_c = 4$ to 40MPa and thickness of 1 to 5m, 8 – limestone rock with a weathered upper zone that has some karst voids filled

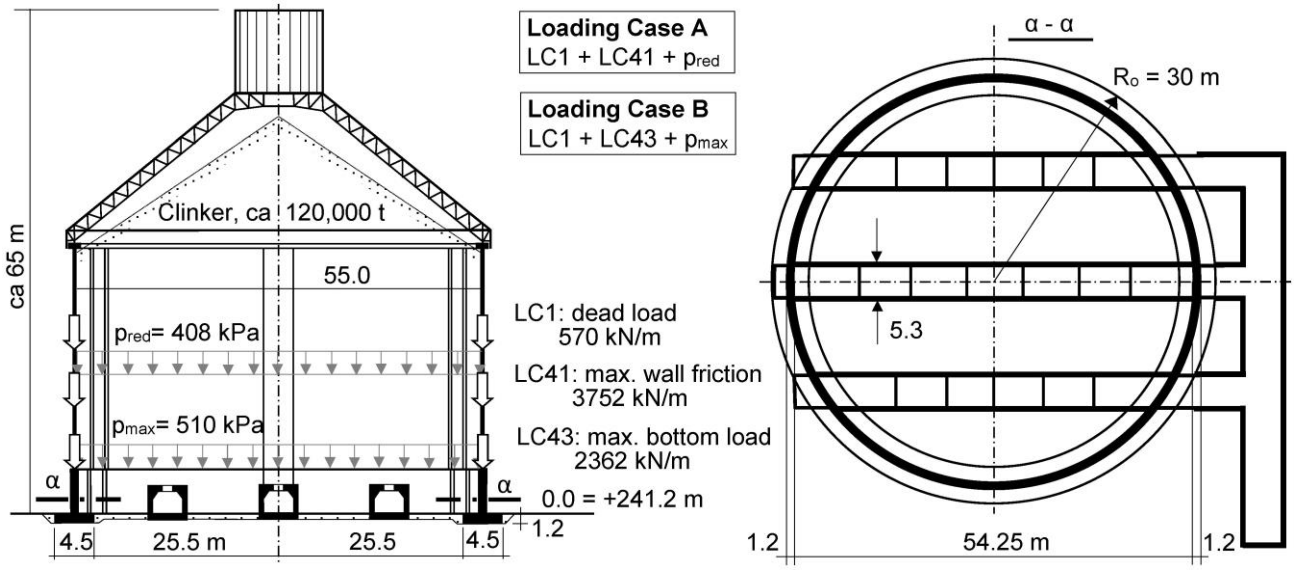

Figure 5. Basic geometry of the silo and two loading cases used for the geotechnical design (characteristic loads).

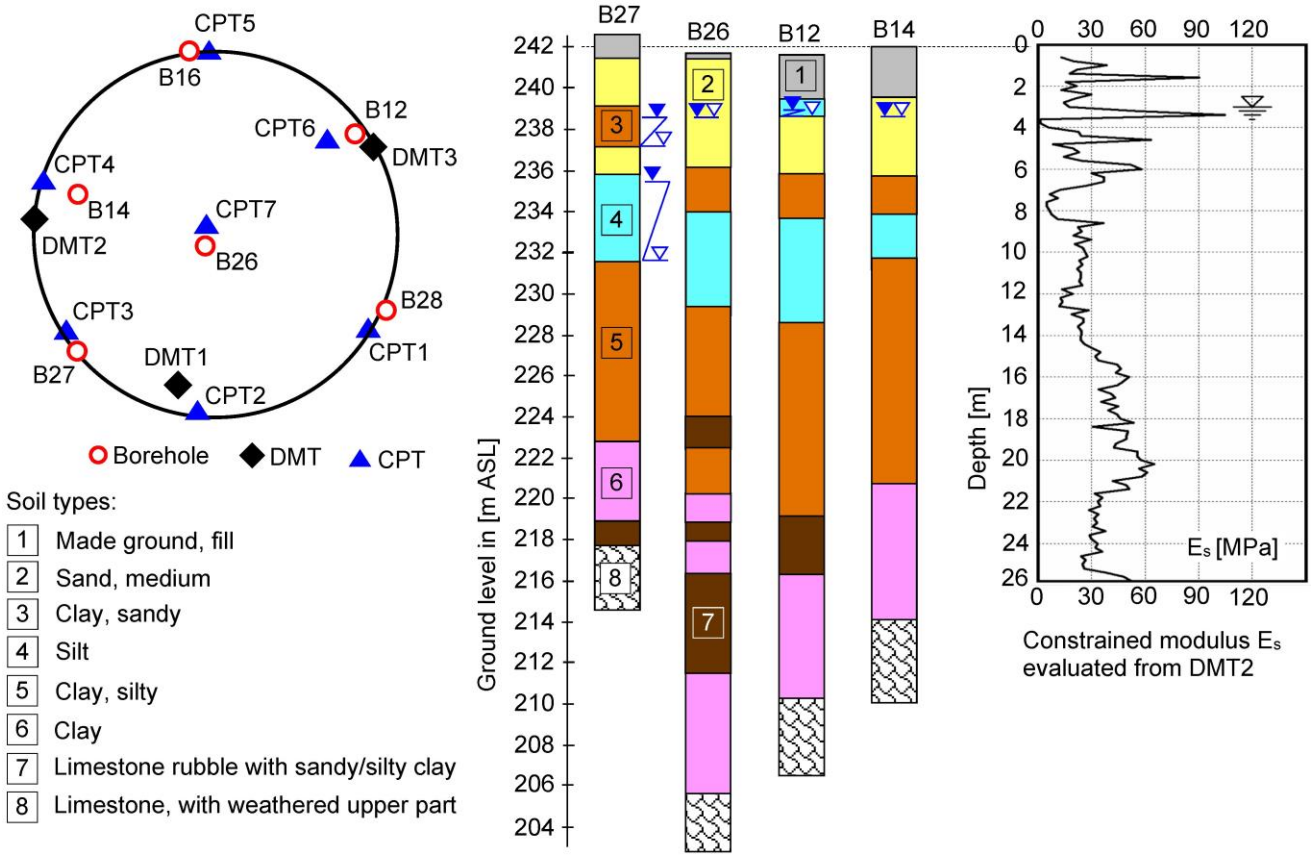

Figure 6. Location and sample results of soil investigations at the silo construction site.

with weathered materials, occurring at the depth of 24 to 35m below ground surface. The groundwater is approximately 3m below the surface.

Given the highly variable nature of the subsoil and the high loads, the first consideration was to support the silo ring foundation and the conveying channels on 180 and 76 CFA piles, respectively. These piles would be long enough to penetrate the limestone and carry the full applied load (Figure 7a). Although this solution was feasible in principle, it was difficult to accurately determine the pile length necessary to achieve the required bearing capacity and the safety margin required by the piling standard. In particular, there was uncertainty in determining the relevant strength parameters for the limestone rubble layer (7) and the weathered limestone rock (8). In addition, the much higher settlement of the silo floor compared to the ring foundation resulted in severe bending of the

piles and torsion of the ring, both of which could lead to overstressing of the piles.

These risks led the designers to consider the piled raft concept for the ring foundation and the use of gravel columns inside the silo (Figure 7b). The number of CFA piles was increased from 180 to 270 and their length was reduced to about 20m by embedding the pile bases in layers (5) and (6). By shortening the piles, the settlement of the ring foundation was increased, allowing the foundation to absorb part of the applied load. The upper zone of the soil immediately below the base of the ring, within a 6m wide perimeter strip, was to be additionally compacted to a depth of 2 to 3m. The gravel columns, 0.6m in diameter and up to 15m long, were introduced to improve the ground and equalise its stiffness within the silo floor, resulting in a reduction of total and differential settlements within the treatment zone. This solution was thoroughly checked by the structural engineer and the geotechnical engineer through independent analyses using 2D and 3D numerical models created in PLAXIS. These studies showed that with a calculated ring foundation settlement of 60 to 80mm, the piles would carry approximately 90% and the ring foundation base approximately 10% of the applied load. However, horizontal pile displacements of between 30 and 40mm and relatively large channel settlements of between 200 and 340mm were still predicted (Figure 8), making their design much more complex.

Taking into account the shortcomings of the two foundation solutions mentioned above, the geotechnical engineer proposed supporting the ring foundation and the conveying channels on 110 barrettes of 2.5×0.8m cross-section, constructed using slurry wall technology and a classic grab (Figure 9). The main arguments in favour of this solution were to increase the load bearing capacity of the supporting elements and to reduce their bending compared to the piles, thus reducing the torsion of the ring foundation. Preliminary calculations for this variant, carried out in PLAXIS 3D Foundation, for fixed barrettes with lengths of 22m below the ring foundation and 20m below the channels, showed promising results and improved the foundation system for the silo. After further consultation with the structural engineer, it was decided that the proposed solution was acceptable, provided that the length of the barrettes was more closely matched to the ground conditions to reduce possible differential settlements. On this basis, after additional SPT tests were carried out to more accurately determine the position and mechanical parameters of layers (7) and (8), the barrettes lengths shown in Figures 10a,b were finally adopted. Plane strain and three-dimensional FEM analyses (the latter for selected silo sectors with an opening angle of 15° to capture the influence of silo wall stiffness) showed that the expected settlements of the ring foundation were between 31 and 51mm (Figures 10b,c), which met the design requirements. The stiffer and less flexible barrettes carry almost the full applied load, and their horizontal displacement is about 10 times less than that of the piles (Figure 10d).

Additional plane strain FEM calculations were carried out to determine settlements of the conveying channels and to assess the increase in vertical stress acting on them due to the greater displacement of the ground relative to the channels supported on barrettes (Figures 11a,b,c). Only the critical loading case B was considered in these analyses. Two loading schemes, both involving a two-stage calculation sequence, were considered to estimate the upper and lower limits of the stress increase. In scheme 1, a uniform pressure of 510kPa was applied to the channels and to the silo floor at the foundation level (Figure 11d). This assumption implies that no friction on the vertical channel walls is taken into account. In scheme 2, the same pressure of 510kPa was applied throughout the silo floor at the level of the top of the channels, together with the assumption that the substitute 'soil' between the channels has zero volume weight and a high internal friction angle of 40 degrees (Figure 11e). This implies that the full friction on the vertical channel walls is included. The resulting channel displacements obtained for schemes 1 and 2 were then applied as the prescribed displacements in the second stage of both calculations. This procedure was repeated separately for each channel and the resulting vertical stress was determined. Based on these analyses, it was recommended that an increased channel load pressure of 10 to 15% be used for their structural design.

In summary, the risks associated with the foundation system were significantly reduced by the use of barrettes. A detailed comparison of the second and third foundation design concepts is shown in Table 2. The costs of both variants were the same. The successful operation of the silo has demonstrated that the chosen foundation system with barrettes has fulfilled its task.

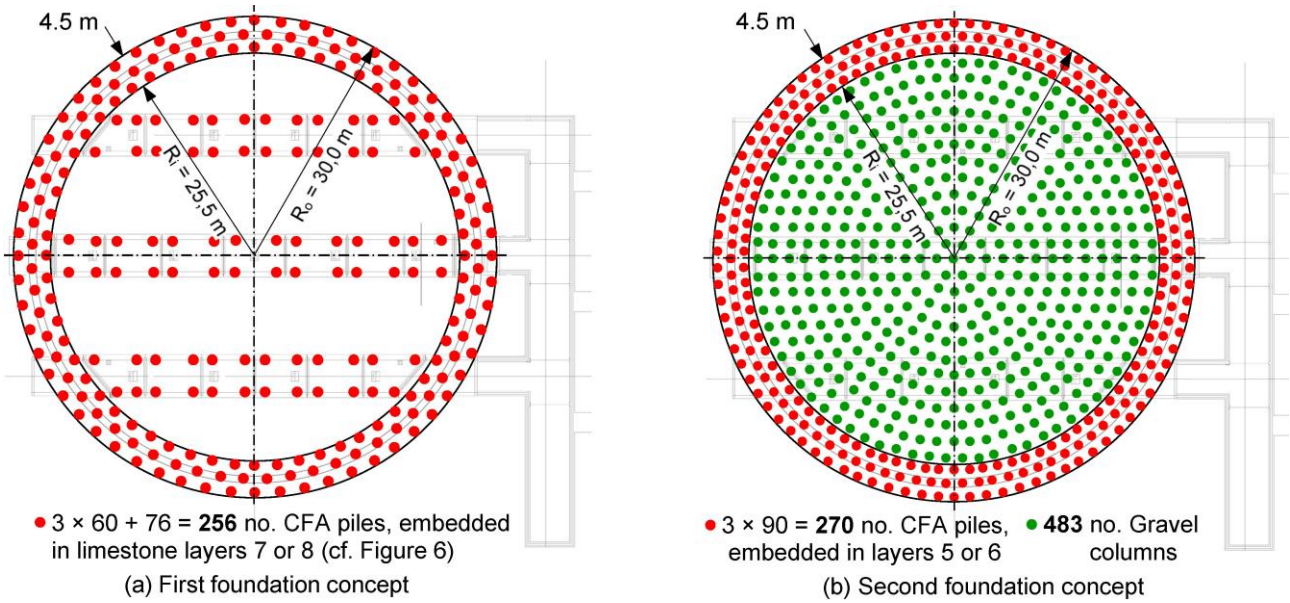

Figure 7. The first and second design concepts for the silo ring foundation and belt conveyor channels.

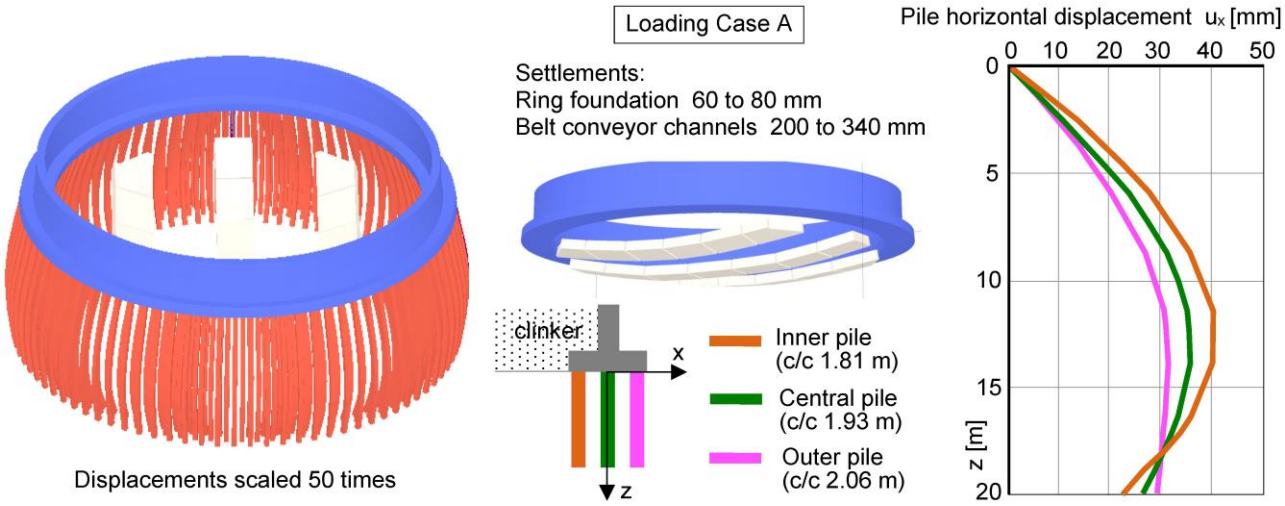

Figure 8. Selected results of the FEM analyses for the second design concept.

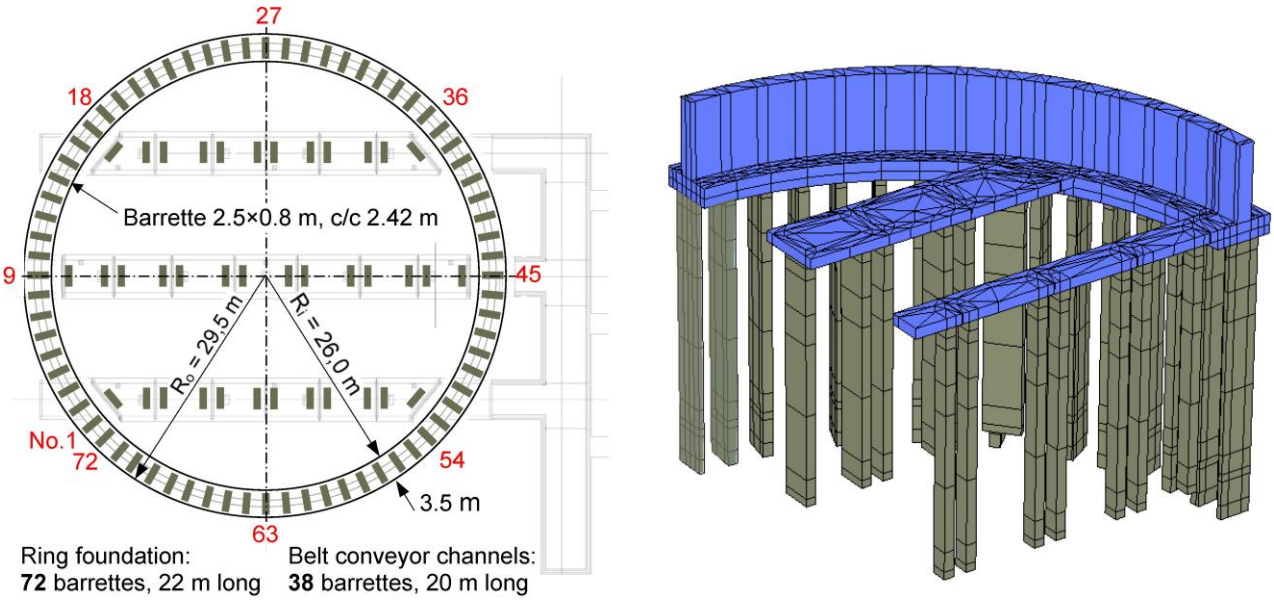

Figure 9. Third design concept with a total of 110 barrettes and provisional barrette lengths of 22 and 20 meters.

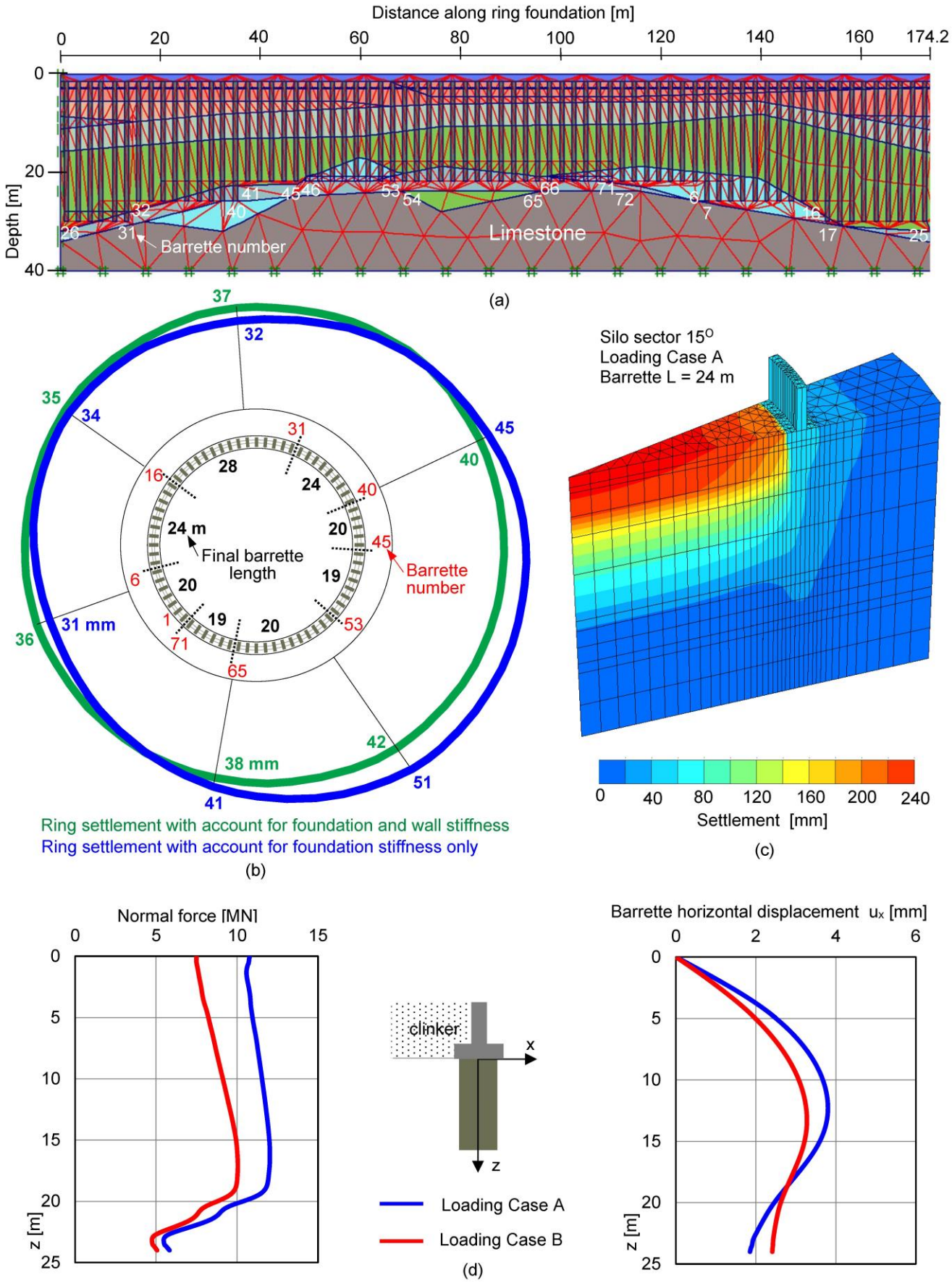

Figure 10. Third design concept, adopted for construction: (a) final adjustment of the barrette lengths under the ring foundation to 19, 20, 24 and 28 m; (b) Settlement of the ring foundation for Loading Case A; (c)-(d) example calculation results for a 24 m long barrette and Loading Case A.

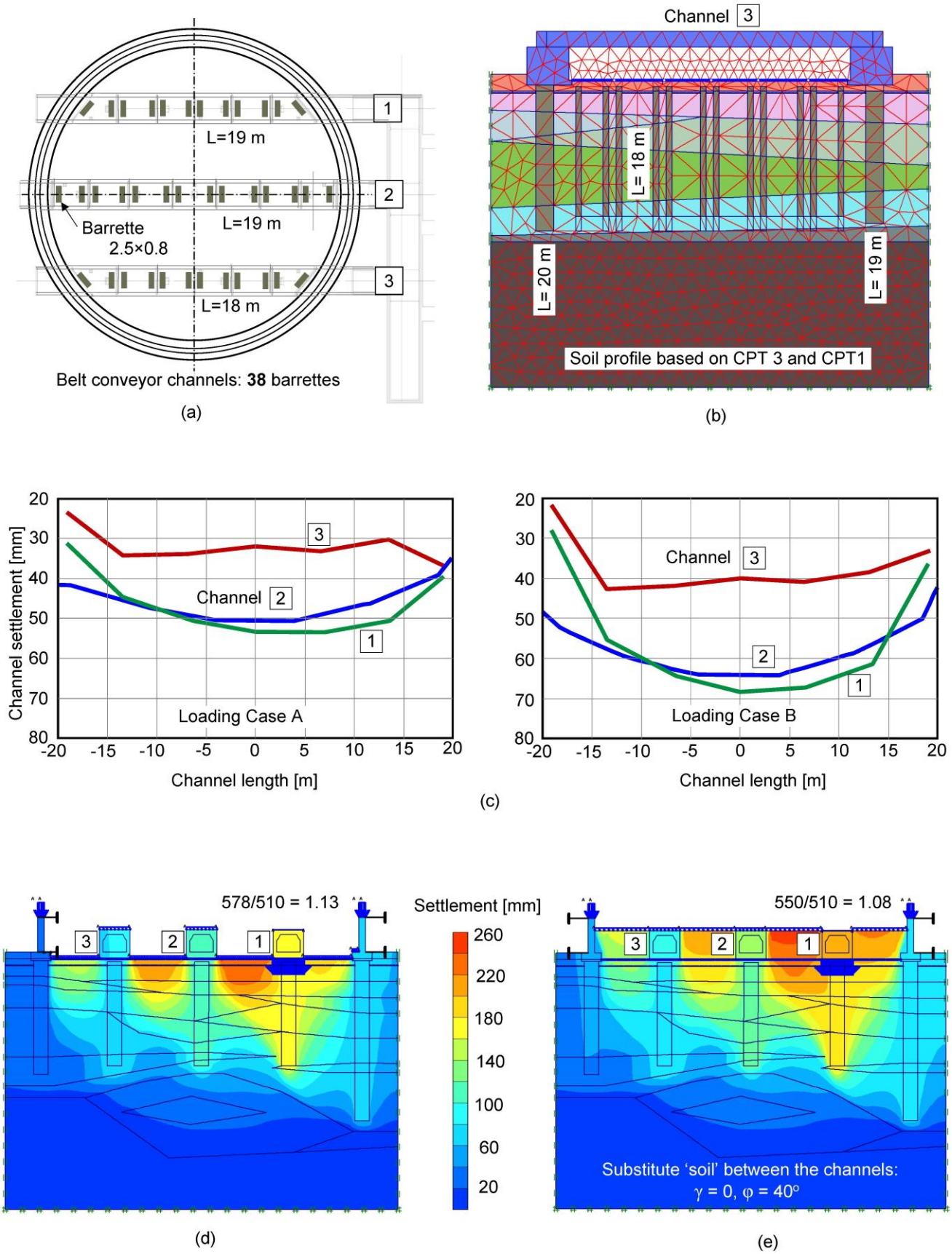

Figure 11. Foundation design for belt conveyor channels: (a) arrangement and final lengths of the barrettes; (b-c) plane strain FEM model and calculated settlements of three channels for loading cases A and B; (d, e) evaluation of the increase in load pressure acting on a conveying channel no. 1 for calculation schemes 1 (d) and 2 (e).

Table 2. Comparison of two foundation design concepts.

Characteristics	Pile-raft and gravel columns	Barrettes
Settlement [mm]: - ring foundation - conv. channels	 60 to 80 200 to 340	 30 to 50 30 to 70
Horizontal displ. of ring supporting elements [mm]	pile 30 to 40	barrette 3 to 4
Duration of geot. works [days]	75	60
Foundation cost	same	
Width of ring foundation [m]	4.5	3.5 (260 m^3 less)

4 CASE 3 - ROAD BRIDGE

The bridge crosses a local road and a river valley. The valley is filled with Quaternary fluvial sediments in the form of peat and gyttjas, highly compressible and up to 11m thick, underlain by silty clays and silts of medium stiff to stiff consistency. Beneath are fine and medium sands, with medium to dense compaction. Shallow groundwater is locally present at depths of 0.5 to 1.5m, depending on river level fluctuations. The main aquifer is located in sandy soils at a depth of 15 to 25m. It is artesian and high flowing, with the water table stabilising at about 6m above ground level. Under these conditions, the geotechnical challenge was not only the low strength and deformation parameters of the organic and cohesive soils, but also the risk of possible uncontrolled artesian water outflows mobilised when penetrating through the confining soil layers.

Such situations actually happened in the past. In the early 1990's, during the drilling of a well about 1.2km from the bridge site, an intense flow of artesian groundwater occurred, washing away large amounts of fine soil. The surrounding area began to settle, threatening the stability of a neighbouring house. In another case, the collapse of a single-family house under construction some 25km away, but only 100m from the same river, was also reported as the result of a sinkhole that was triggered during well drilling (Damicz et al., 2007). Similar cases in different locations include bridge foundations and are therefore particularly relevant. Wojtasik and Różański (2011) describe a significant disruption caused by intensive seepage of artesian groundwater stabilised at 3.5m above the working level, resulting from the driving of 17m long precast concrete piles that penetrated the confining soil layers. The repairs caused a 6-month delay and the additional costs exceeded the planned cost of the foundation work. Świeca and Walczak (2007) reported hydraulic failure during the construction of bridge piers. In this case, loosening of the subsoil due to artesian outflow created a stability risk for the bridge's spread foundations.

The geometry of the bridge spans was dictated by the requirement to provide a passage for large wild animals under the structure, close to the river with a width of at least 100m, not including the river, and with a minimum 5m height. The design used at the tender stage was a three-span cable-stayed (extra-dosed) prestressed concrete bridge with spans of 60, 120 and 60m (Figure 12a). The bridge is 30m wide and has a pair of two-lane carriageways with emergency lanes on a 4m high single box structure. The deck structure is suspended from two 23m high V-shaped steel pylons. The abutments for the outer (ballast) spans are founded outside the marshy area. The approach embankments on either side of the bridge are approximately 9m high.

The bridge foundations are supported on precast concrete piles with a cross-section of 0.4×0.4m. The length of the piles is determined by the required bearing capacity and extends down to the bearing sands with artesian groundwater. The foundations are monolithic reinforced concrete slabs, 2.1 to 3.9m high, in the shape of an octagon inscribed in a 24.6×24.8m rectangle, which form the top of 133 piles under each pylon. The lengths of the piles are 30m and 33m. The foundations of the abutments are monolithic reinforced concrete slabs measuring 1.8×10.4×31m, each supported by 118 piles 14 to 17m long. To mitigate the risk of uncontrolled artesian water seepage, the designer recommended special precautions, including the installation of dewatering wells to reduce artesian water pressure and the use of special expansion seals consisting of bentonite tape fixed in grooves around the perimeter of the piles. It was also recommended that appropriate field tests be carried out prior to installation of the production piles.

The appointed general contractor was aware of the geotechnical challenges of the tender design and undertook extensive studies to find a less risky alternative. These studies eventually led to the design of a single-span tied-arch bridge with a span of 120m, shown in Figure 12b. The superstructure consists of two steel arches with lateral bracing. The deck acts as a tie beam and includes a reinforced concrete slab integrated with the steel deck. The suspension system consists of prestressed hangers arranged in a diagonal network. The frame structure of the western abutment accommodates the local road which passes underneath the new main road. Compared to the tender design, the structure of the single-span bridge is significantly

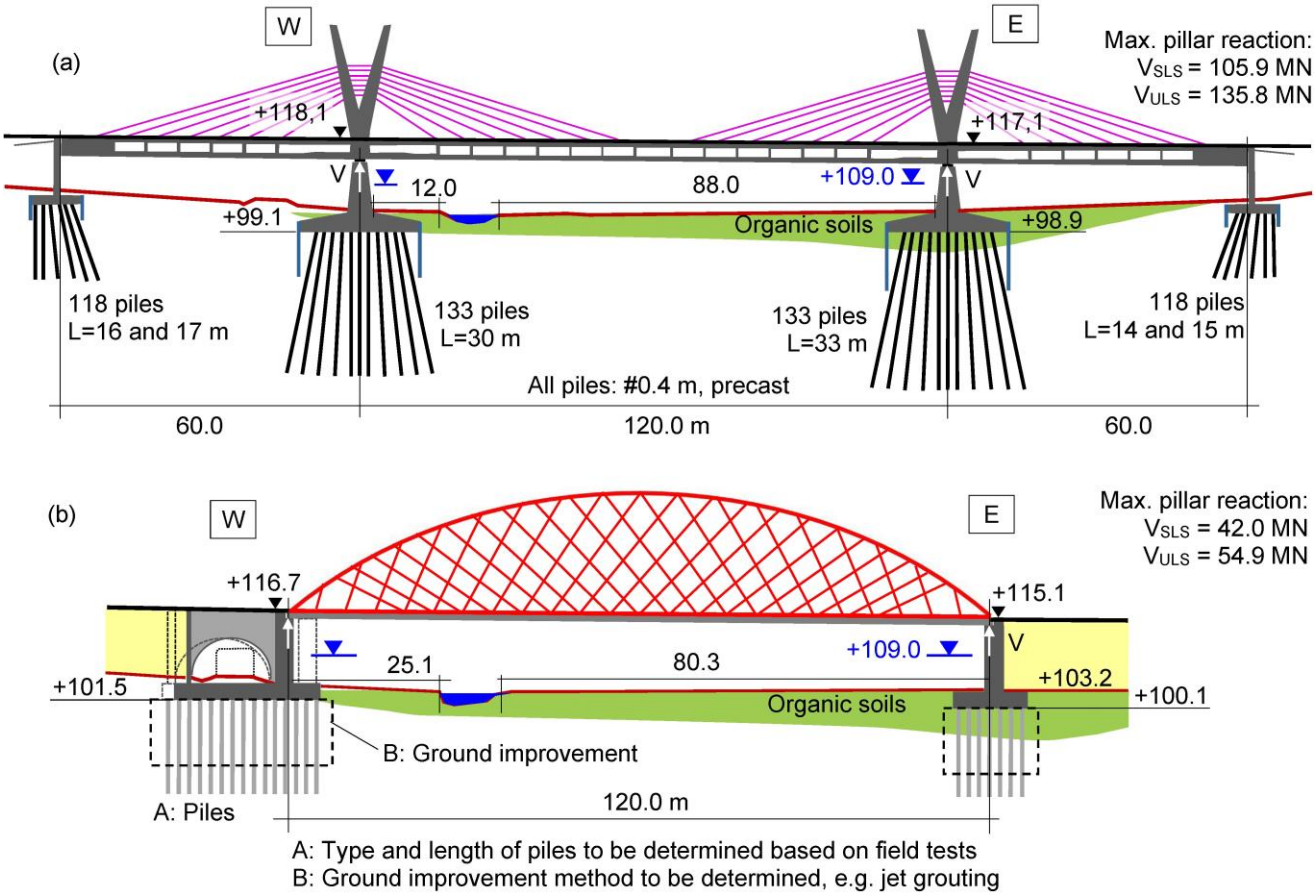

Figure 12. (a) Bridge design at tender stage, comprising a three-span extradosed structure; (b) Alternative bridge design proposed by the structural engineer working for the appointed general contractor, with two foundation concepts.

lighter, resulting in a 60% reduction in the maximum pillar reaction force, which was one of the main objectives of the alternative design (cf. Figures 12a,b).

Based on the advice of geotechnical experts, two foundation systems were considered for the arched bridge. These were the use of piles (option A) or spread foundations on improved ground (option B). In the case of piles, it was assumed that shorter piles would be used, which would not penetrate the water-bearing sands. It was recommended that field tests should be carried out with different types of piles to assess the load bearing capacity that could be achieved. Option B was considered to be the most rational method of foundation for the bridge abutments due to the relatively low ground pressures under the foundation slabs and the lack of interference with the artesian layer. The possibility of using jet grouting technology for the required ground improvement was raised, but no detailed design was subsequently developed.

At this stage, the appointed geotechnical contractor proposed the use of wet deep soil mixing (DSM) instead of jet grouting and prepared the design. The adopted ground improvement scheme included 2.4m diameter and 9.5m and 15m long DSM columns on the west and east sides, respectively (Figure 13). The design column lengths were chosen to ensure that a sufficiently thick layer of clay would remain beneath the ground improvement zone to prevent seepage of artesian water during the soil mixing operations. The design decision to leave a minimum distance of 2m from the sand layer was a difficult choice between mitigating potential hydraulic piping and leaving a layer of plastic clay that could be too thick, which would contribute to increased settlement of the abutments. Additional soil investigations were also recommended prior to column installation to map the actual thickness of the clayey deposits beneath both abutments, which were slightly displaced compared to the tender design. On the east side, organic soil replacement by dredging and high-pressure water jetting was also assumed to help achieve the required compressive strength of the soilmix material.

Two FEM models were created in PLAXIS for each side of the bridge, including the areas where ground improvement was required under the approach embankments. In this way, a coherent foundation system was designed for the entire structure. The

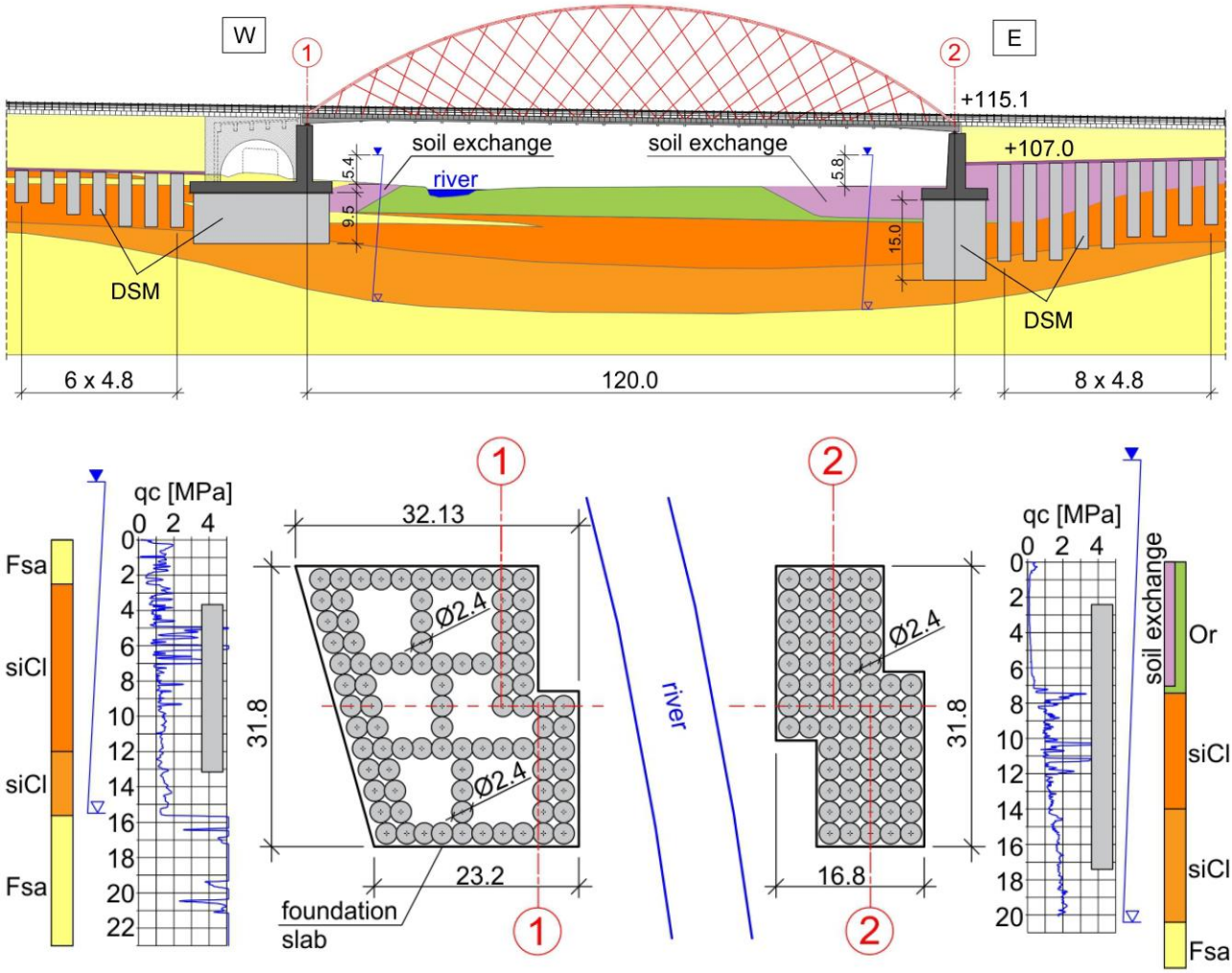

Figure 13. The geotechnical contractor's design for the arched bridge foundation using wet soil mixing (DSM).

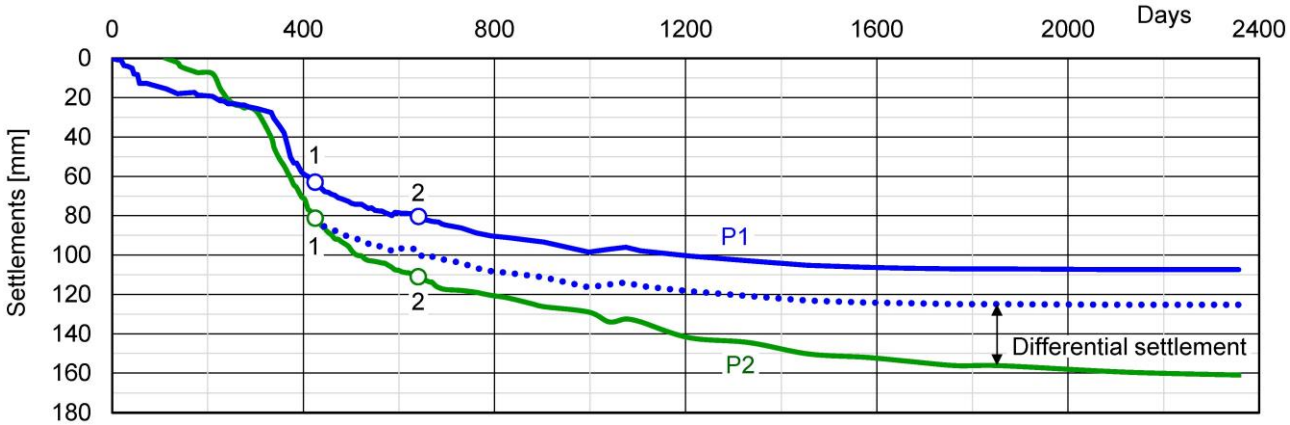

Figure 14. Observed mean settlement of the foundations of the western (P1) and eastern (P2) pillars: 1 - asphalt layers laid, earthworks completed; 2 - start of bridge operation.

calculations showed that for the most critical load combinations, the maximum design stress in the soilmix column was 804kPa, resulting in a required characteristic compressive strength of 1.42MPa. In order to provide a higher level of safety, a conservative 2MPa minimum and 3MPa average soilmix compressive strength was specified in the design. Monitoring of the bridge pillars over a period of almost six and a half years has shown that the foundation method used has met the design expectations (Figure 14). The differential settlement between the two pillars is less than 40mm and well within the design limit of 60mm.

This case illustrates a situation where a change in bridge type by the bridge designer to a lighter and less

settlement sensitive single-span structure enabled the geotechnical engineer to design and implement an innovative foundation solution for the bridge abutments that would not otherwise have been possible. To the best of the author's knowledge, this is the first time in Europe that a bridge of such a long span has been founded on improved ground using the deep wet soil mixing technique (Mitrosz and Skóra, 2021).

5 CASE 4 - EXCAVATIONS FOR TUNNEL ACCESS RAMPS

The project involved the construction of two large excavations for tunnel access ramps on either side of the river, 750m and 340m long on the west and east side respectively, and up to circa 22m deep (Figure 15). The ground comprised alternating marine and alluvial deposits of medium-dense to dense sands and soft organic silts to a depth of about 24m below ground level (GL), and then underlying silty clay and sand layers. The low-permeable silty clay layer could not be used as a natural cut-off barrier for the deepest parts of the pits because it would be unstable and heave during excavation. The groundwater in the area of the tunnel is mostly confined and stabilises at a depth of about 1m below the GL, corresponding to +0.5m above sea level (ASL). The tunnel structure had to be protected against a maximum water level of +2.5m ASL during normal operation, which represents the extreme flood level. During construction, two design water levels of +0.5m and +1.5m ASL were also used in the analyses.

The original design for the construction and protection of the excavations included permanent and temporary diaphragm walls and a 1.5m thick bottom plug anchored by micropiles, constructed using underwater concrete technology (Figure 16). In the deepest parts (cross-section C), a 1m thick jet grouted (soilcrete) sealing slab was planned below the pit bottom to facilitate initial lowering of the groundwater level for the installation of temporary struts required to ensure wall stability when the final excavation depth was reached. The challenges of delivering the works for this design included:

- the difficulty of removing soil from the excavation supported by closely spaced transverse struts (the same limitation applies to the lowering and lifting of large TBM components);
- the need to use heavy, long-reach excavation equipment working close to the pit edge, imposing high additional loads on the diaphragm walls;
- the need to install a water management system to fill and dewater the excavation and to construct settling ponds that take up working space;
- the accumulation of dusty sediments at the bottom of the pit, making underwater concreting difficult and risky, especially at greater depths;
- achieving a watertight joint between the concrete plug and the diaphragm wall;
- ensuring continuity of the underwater concrete over large areas of the excavation bottom;
- the difficulty of installing micropiles from floating pontoons or an auxiliary platform in long pits with closely spaced transverse struts mounted just above the water surface and to great depths, up to circa 54m;
- the long duration of the associated works.

Based on its own design analyses, the geotechnical contractor proposed to move from working underwater to a dry operation to cut construction time, mitigate risks, and reduce costs. The alternative design included

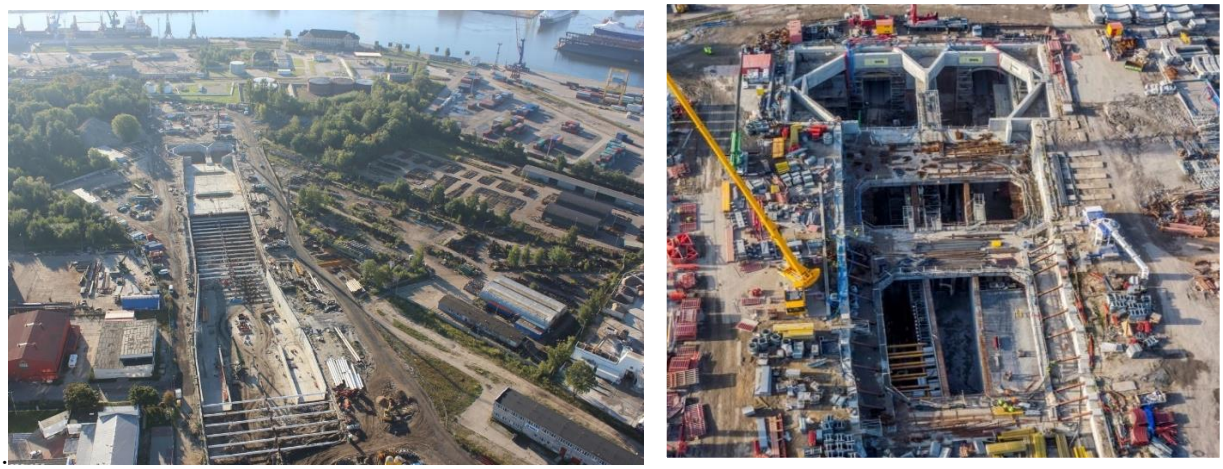

(a) *(b)*

Figure 15. (a) Construction of the west access ramp to the under-river tunnel; (b) TBM launching shaft on the east side.

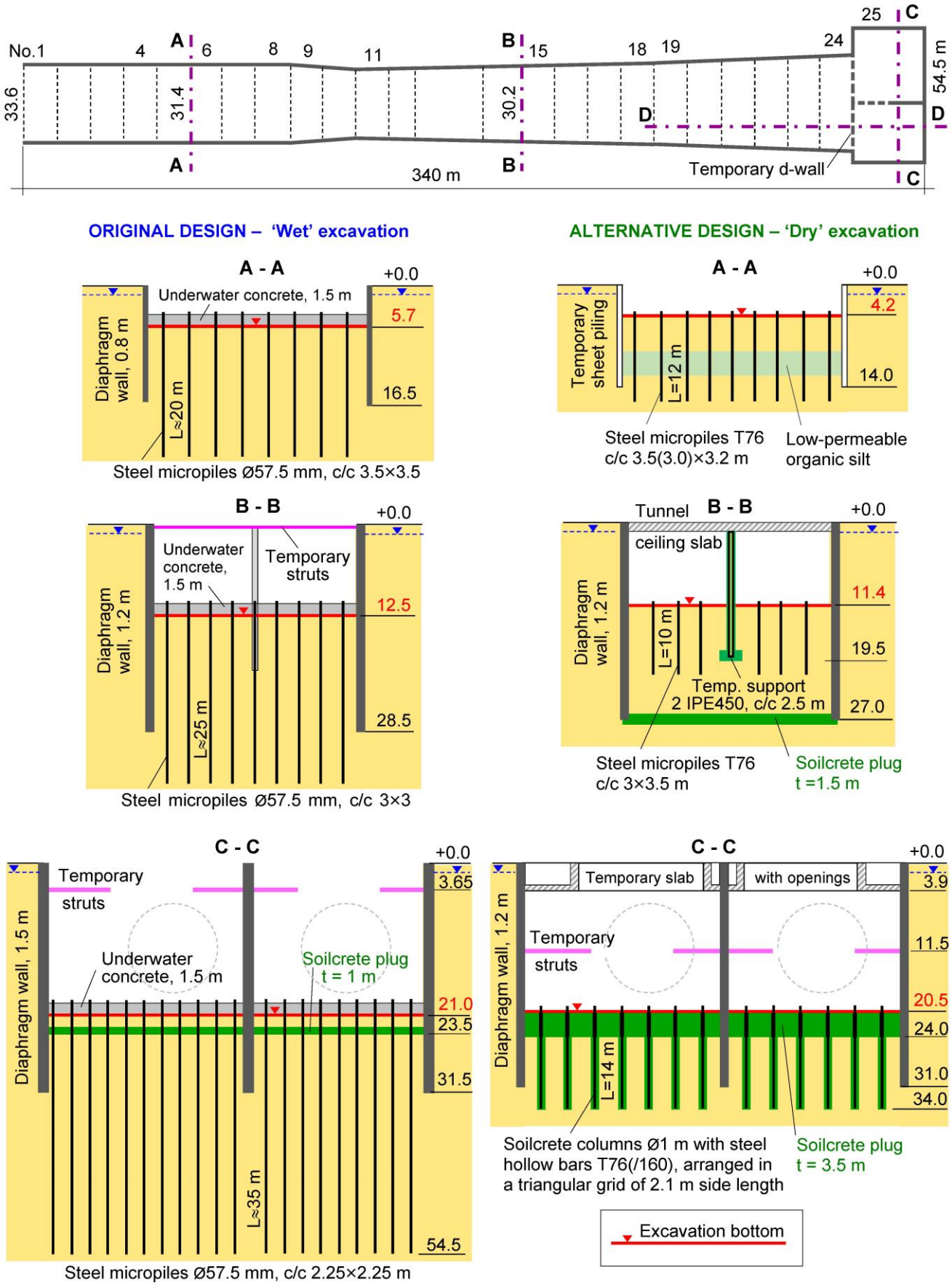

Figure 16. Comparison of the original design assuming 'wet' excavation with the geotechnical contractor's alternative design assuming 'dry' excavation for three cross-sections on the east side.

three main solutions, which are shown in Figure 16 in comparison with the original design.

For the shallow excavation areas, represented by cross-section A, conventional temporary sheet piling was selected as the most economical shoring system. The sheet piling crosses the low permeable organic silt layer, which forms a natural sealing barrier. The uplift resistance of the concrete slab at the bottom was provided by micropiles consisting of 76mm diameter hollow steel bars.

In the central parts of the excavations, represented by cross-section B, a 1 to 1.5m thick soilcrete plug, depending on the actual excavation depth, was designed to create a horizontal cut-off barrier between the walls. The plug is placed at a depth that ensures its stability against uplift by the dead weight of the overlying soil. These sections also include an anchored foundation slab with relatively short steel micropiles.

As the ramps near the TBM launching and receiving shafts, the construction method changes again to include a thicker soilcrete plug just below the foundation slab which is anchored into the soilcrete columns using hollow steel bars (cross-section C). The anchoring bars were installed centrally in 1m diameter soilcrete columns, constructed as part of a single production cycle together with the plug columns that were 3.1m in diameter and 3 or 3.5m in length (Figure 17a). Along the plug section the steel bar diameter was increased to 160mm with factory grouted corrugated sheathing. The anchoring elements were positioned in a grid of equilateral triangles with a c/c spacing of 2.1m or 2.25m, adapted to the basic arrangement of the columns forming the horizontal plug. Due to simultaneous execution of the anchoring elements and plug columns, the monolithic connections between the two elements were improved and thus the required rigidness and water tightness of the whole system protecting the excavation bottom was ensured.

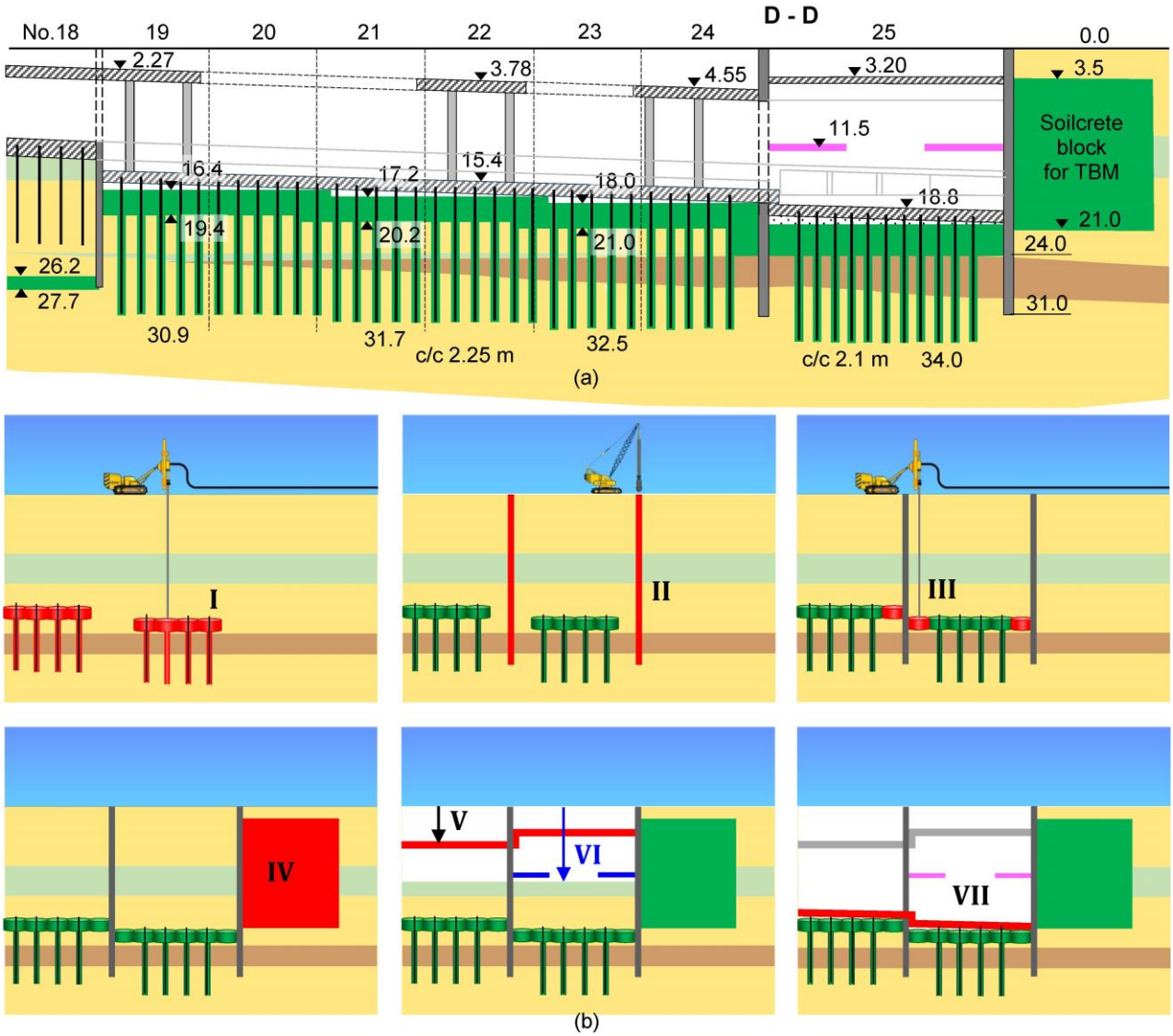

Figure 17. (a) Longitudinal section through the deepest parts of the east tunnel ramp; (b) Phasing of construction works.

The thickness and length of the diaphragm walls were also optimised. Particular attention was paid to the impact of phasing the work, including (Figure 17b):

Phase I – Execution of 1m diameter soilcrete columns, over-reamed at the top to 3.1m diameter to form a sealing plug, leaving an open strip along the planned diaphragm walls, followed by installation of anchoring bars in fresh soilcrete, disconnecting at specified depths and pulling top bar sections;

Phase II – Construction of permanent and temporary diaphragm walls, allowing simultaneous work on several phases;

Phase III – Installation of soilcrete plug columns along diaphragm walls to complete horizontal sealing.

Phase IV – Construction of soilcrete blocks in front of the launching and receiving shafts, stabilising the TBM at the start and end of the shield drilling operation;

Phase V – Primary excavation and construction of a reinforced concrete top slab with openings;

Phase VI – Continuation of excavation to the required depth allowing installation of temporary steel struts inside the launching and receiving shafts;

Phase VII – Final excavation and construction of the bottom slabs, anchored to steel micropiles, followed by dismantling of the temporary struts.

The alternative design helped to make the works much safer and more controllable and was approved for implementation by the tunnel designer and the public client. The geotechnical contractor took the lead and design responsibility for this part of the tunnel works. All designs were checked using different numerical models, as shown in Figure 18a, and the displacements expected from each approach were similar, giving confidence in the solution adopted. Collaboration with the tunnel designers was very efficient and enabled expectations to be met. For example, the structural engineers designed sophisticated concrete slabs with large openings for the launching and receiving shafts, which contributed significantly to limiting wall displacements while allowing convenient excavation and assembly/disassembly of the TBM (Figure 18b).

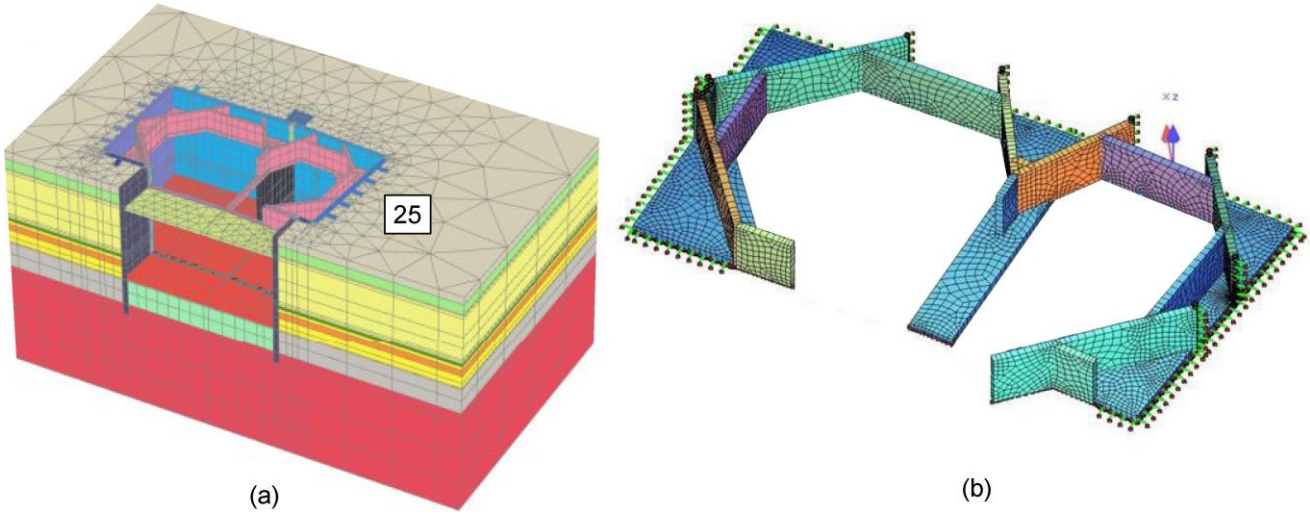

Figure 18. (a) Numerical model of the launching shaft in PLAXIS 3D; (b) Structural engineer's design of the supporting concrete slab at the top of the launching shaft.

6 CASE 5 - FOOTBALL STADIUM

The construction of a stadium for the European Football Championships, which was carried out under great time pressure and therefore split into two separate phases of (1) site preparation and ground improvement and (2) stadium construction, is an example of insufficient co-operation between different contractors and design teams, resulting in the implementation of ad hoc measures to limit potential adverse impacts.

A view of the 41,620-seat stadium, which has an elliptical shape and dimensions of 236×203×45m, is shown in Figure 19a. The architectural concept and initial structural design raised the stadium above the flat, waterlogged site. It was assumed that about 60% of the stadium foundations, supporting the north, east and south stands (Figure 19b), would be founded on a ring embankment approximately 8m high from the original ground level and 55 to 65m wide at the base (Figure 19c). In the western section, the structure of the stands and stadium facilities is supported on a slab and footings founded at various depths, between 2.5 and 4.5m below groundwater level. The roof of the stadium is supported by 82 truss girders spaced 8m apart, transferring a vertical load of approximately 1,800kN and a horizontal load of approximately 700kN to the foundations.

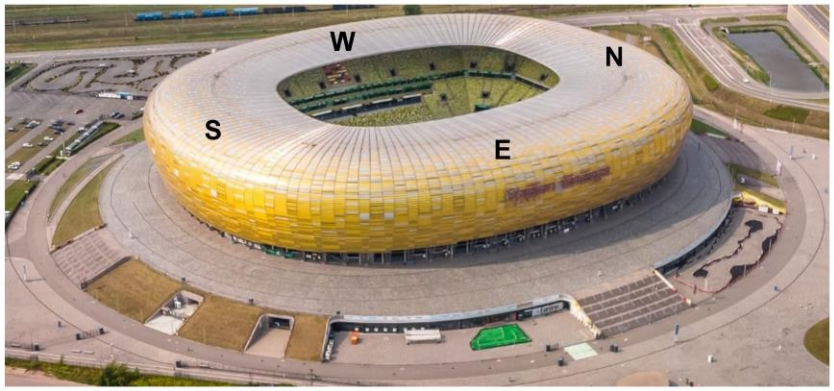

(a)

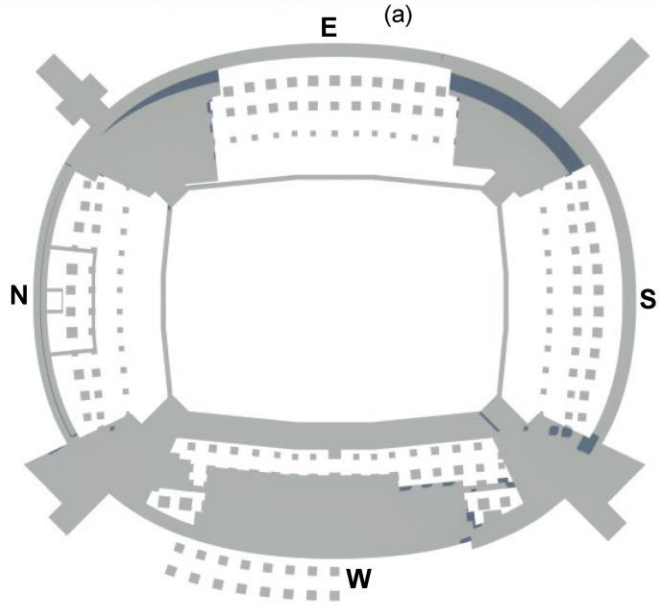

(b)

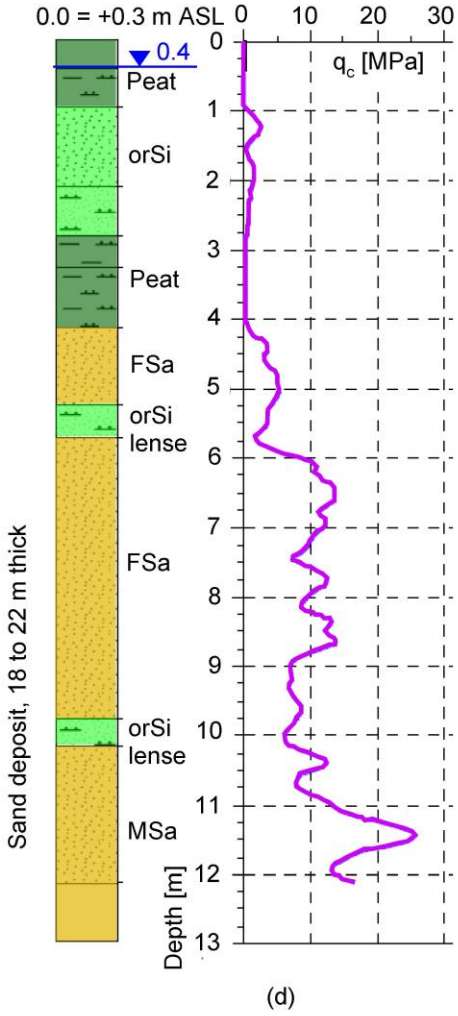

(d)

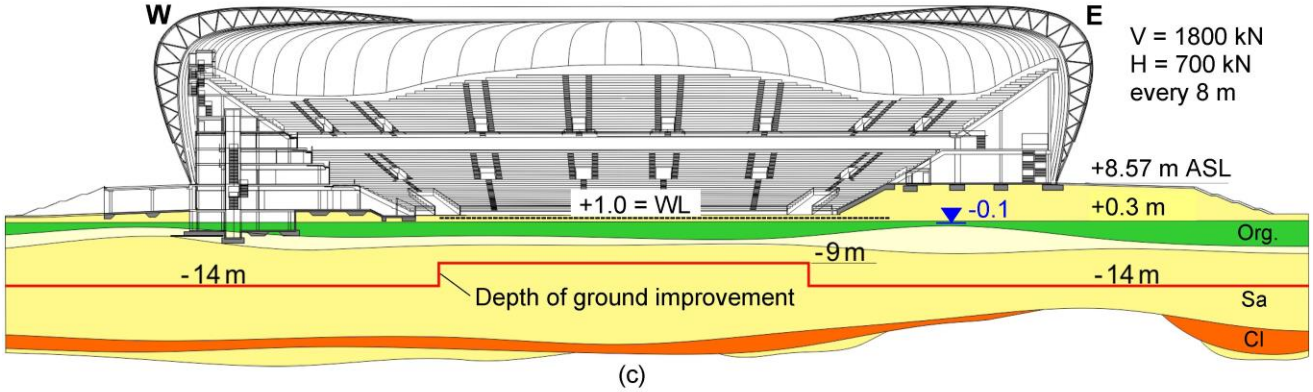

(c)

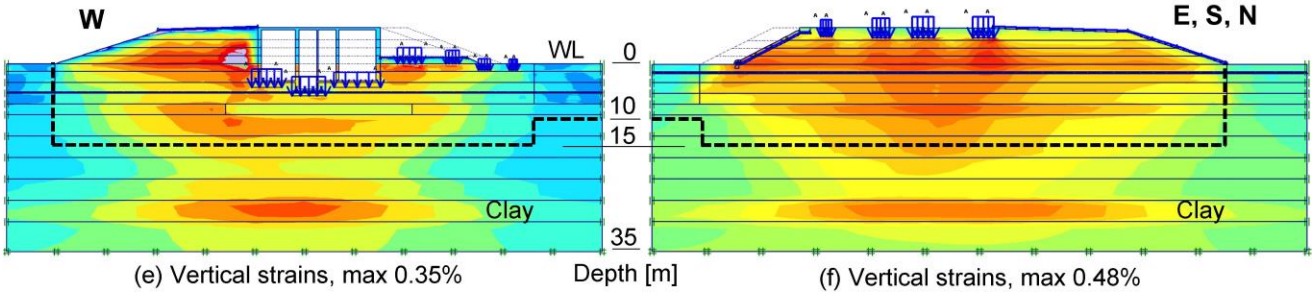

(e) Vertical strains, max 0.35%

(f) Vertical strains, max 0.48%

Figure 19. (a) Completed stadium; (b) initial layout of pad and slab foundations; (c) Stadium cross-section in W- E direction; (d) ground conditions (example CPT profile); (e, f) Calculated distribution of vertical strains in the subsoil.

The construction site was a flat former estuary, crossed by numerous drainage ditches, with groundwater at a depth of about 0.4m. At the surface there were organic soils from 1 to about 5.5m thick, underlain by fine and medium sands of varying density and thickness of about 18 to 22m, containing lenses of organic silt. Beneath the sands was a layer of clay from 1.5 to 6m thick, underlain by medium sands and gravels and, at a depth of 32m, also lignite. An example of a CPT sounding is shown in Figure 19d.

The first phase of work consisted of replacing the organic soils with natural aggregate and compacting the backfill and soil beneath the replacement zone. The contract was awarded to a general earthworks contractor who engaged a geotechnical contractor to carry out the deep compaction work. The planned volume of soil replacement to be carried out using conventional excavators and without lowering the groundwater level was about 324,000m^3, the volume of backfill to the working level at +1m ASL was approximately 412,000m^3, and the volume of soil to be treated by vibro compaction (VC) to a depth of 15m below the ring embankment and 10m below the pitch was about 1.27 million m^3.

At this stage of the design, the structure of the stadium was only known in outline. For this reason, the structural designers formulated only general criteria for the required ground improvement, which was to meet the condition of a CPT tip resistance of at least 15MPa within the compacted zone. It was assumed that the foundation pressures would not exceed 300kPa, and that the total and differential settlements of adjacent footings should be limited to values of 30 and 10mm respectively. It was also assumed that the entire ring embankment would be constructed first, and that the consolidation period of the subsoil prior to the construction of the stadium foundations would be between 4 and 6 months. In the area of the western stand, the plan was to remove part of the embankment after the preloading phase, while maintaining safe slopes, and then to construct the deeper foundations by locally lowering the ground-water table.

A detailed ground improvement design was prepared by the geotechnical contractor. The calculations carried out to verify the settlement of the embankment and the stadium foundations showed that the design assumptions could be met by adhering to the planned consolidation period of the subsoil under the embankment, even taking into account the settlement mobilised in the clay layer below the improvement zone (Figures 19e and f).

However, soil compaction using deep vibrators in a triangular grid of 3m proved more difficult than expected. The reason for the unsatisfactory compaction within the soil replacement zone and immediately below, as shown in Figure 20a, was: an excessive content of fine fractions within the backfill, caused by inaccurate excavation carried out in continuous 24h/7d operation; the low quality of the backfill material, which was difficult to obtain in large quantities, and in a short time; and the decreasing efficiency of the VC process at shallow depths. Attempts to reduce the spacing between compaction points and to use more powerful vibrators were also unsuccessful. Under these conditions, the geotechnical contractor added dynamic compaction (DC), carried out from an elevated working level at +2m ASL, with the aim of compacting the soil to a depth of -4 m BSL. Sixteen tonne pounders with a 2×2m base were used, dropped from a height of 19m for the primary and secondary compaction points, arranged in a 7.5×7.5m square grid, and from a height of 10m for the final ironing phase, carried out at intermediate points. The average compaction energy was 550kJ/m^3, and the average aggregate consumption was 6 to 8m^3/point. The use of DC proved to be very successful, as confirmed by the results of the control CPTs shown in Figure 20a. The first phase of work was completed with the handover of the ground prepared for further construction works, and the site levelled and compacted by vibratory rollers at +1m ASL.

For the geotechnical contractor responsible for the ground improvement, the task seemed to be complete. However, this was not quite the case, as the design team undertaking the second phase of work introduced significant changes to the stadium structure that were accepted by the investor. In order to shorten construction time and reduce costs, parts of the ring embankment under the north, east and south stands were replaced by a single-storey reinforced concrete structure (Figure 20b), and on the east side, outside the stands, the embankment was replaced by a new facility providing additional rental space (Figure 20c). As a result, the structure was planned to be built first, with the remaining embankment sections around the perimeter of the stadium built at the end of the works. This also meant that the original plan to consolidate the subsoil under the weight of the ring embankments prior to stadium construction had to be abandoned.

The decisions described were made without consulting the geotechnical contractor. It was assumed that the bearing capacity of the improved ground would be sufficient because the reduced total weight of the structure would result in lower foundation pressures than originally anticipated. However, subsequent check analyses carried out (this time) with the involvement of the ground improvement designers revealed that once the target embankment was in place, and without the planned consolidation of the subsoil,

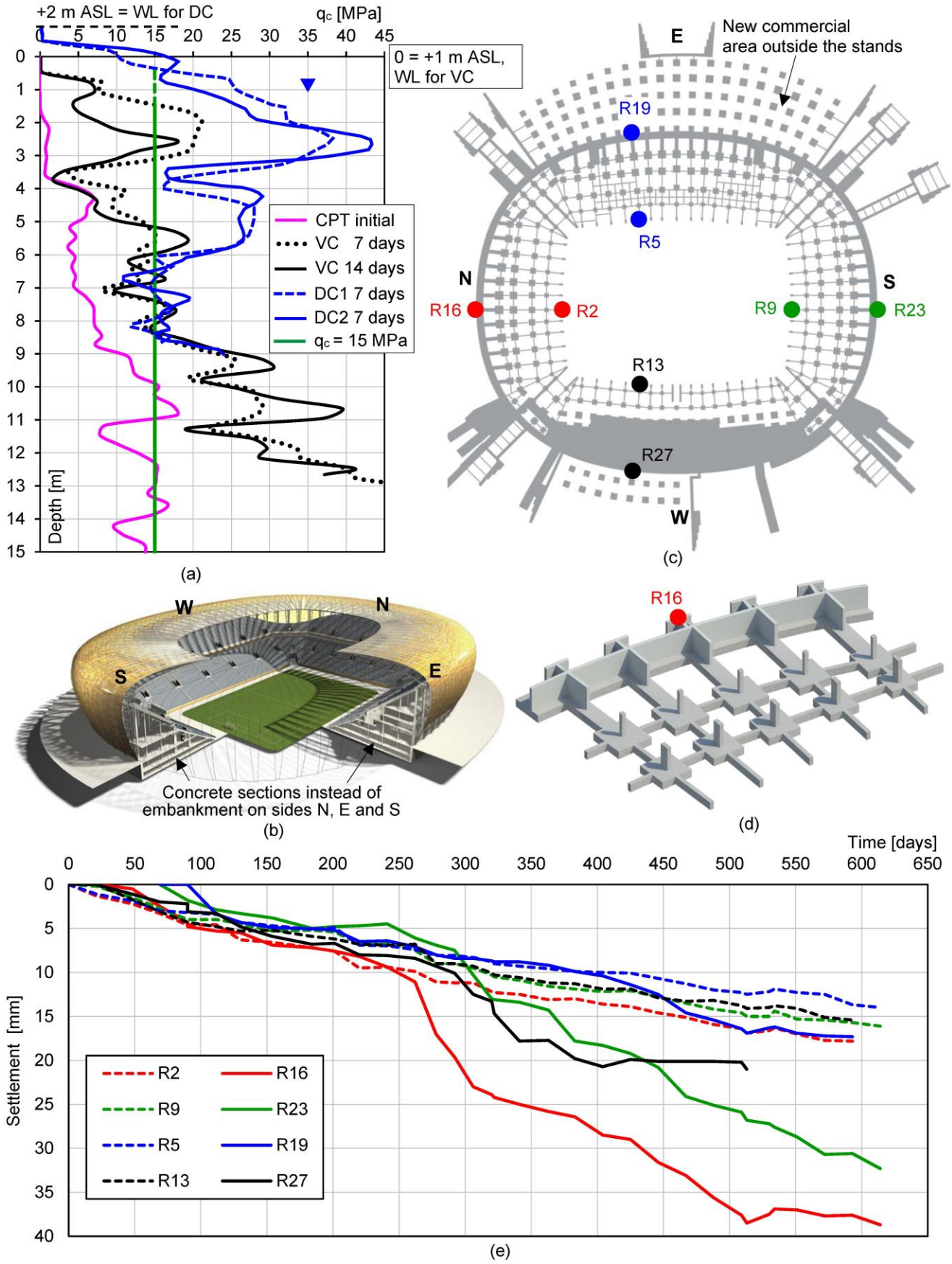

Figure 20. (a) Initial and control CPT tests in relation to the acceptance criterion (VC - Vibro Compaction, DC - Dynamic Compaction); (b) Location of selected control survey points; (c) Modified stadium structure, with concrete sections instead of the embankment; (d) Foundation pads with interconnecting beams; (e) Observed settlement at selected survey points.

there was a risk of excessive differential settlement of the footings and bending of the perimeter foundation supporting the roof truss girders. A stiffening of the entire foundation system was therefore recommended and implemented, consisting of reinforced concrete beams connecting the individual footings, and transverse walls in the plane of the truss girders along the perimeter strip foundation (Figure 20d).

The described intervention in the design of the foundations was essentially the only action that could be taken due to the timing of the construction work that had already begun. The stiffening of the foundation system proved to be necessary and effective, as confirmed by the settlements measured at the survey points shown in Figure 20c. By comparing the settlements on the north (point R16) and south (R23) sides, where the embankment was constructed, with those on the west (R27) and east (R19) sides, where there was no embankment, the impact of the embankment construction on the foundation settlement can be assessed, causing additional displacement of the order of 20mm. The maximum settlement recorded was approximately 38mm, slightly above the design limit, but the differential settlements between adjacent foundations were not exceeded. This case study illustrates that the separation of construction and design into two phases, with the geotechnical part separated from the structural part, carries the risk of overlooking important design assumptions which, if not addressed, could have led to undesirable and serious deformations in the structure and the potential need for significant remedial work.

7 CONCLUSIONS

An attempt has been made to illustrate the relationship between geotechnical and structural design using examples from five projects involving different structures and cases of collaboration between engineers from both disciplines. The projects discussed were carried out in Poland, taking into account national building regulations and practices. They include foundation designs adapted to the soil and groundwater conditions and to the sensitivity of the structures to deformation. An important criterion for the selection of projects was also the consideration of the changing role of structural and geotechnical engineers and their responsibility for the final foundation solution. Detailed comparisons of the original and implemented foundation designs show the benefits achieved. These included not only lower construction costs and shorter construction times, but also reduced CO_2 emissions and the elimination of specific technical risks. Appropriate modifications to the structural design of a bridge also enabled the implementation of a novel foundation solution that would not otherwise have been possible.

The practice of civil engineering design has become increasingly specialised. This includes foundation design and has been driven by the observed and continuous development of foundation techniques and execution capabilities, as well as the use of specialised engineering software for geotechnical design. Experience has also played an important role, as geotechnics is known to be both a science and an art. In this context, geotechnical engineers are usually better prepared than general structural engineers to select the most appropriate foundation solution, taking into account various design criteria. It is therefore becoming increasingly important for the two disciplines to work together. To enable effective collaboration, it is advisable for geotechnical engineers to develop their professional skills in structural design. Similarly, structural engineers should improve their geotechnical knowledge. A better mutual understanding between the two disciplines will help to achieve beneficial results in the future, comparable to the examples presented.

ACKNOWLEDGMENTS

I would like to thank my colleagues at Keller Polska: Dr R. Buca, D. Dymek, Ł. Dziadoń, J. Głowacka, P. Kwaśniewski, M. Marciniak, O. Mitrosz, J. Figiel-Najduk, T. Skóra, S. Sławik, Dr G. Sołtys, Dr J. Świniański, and A. Zachodni for their contributions to the development of alternative design solutions presented in this paper, as well as Prof. J. Biliszczuk, Prof. K. Gwizdała, Cz. Hodurek, T. Kołakowski, W. Kosecki, K. Topolewicz, Ch. Wentz, Dr R. Wojdak and Prof. K. Żółtowski for their kind cooperation.

REFERENCES

Damicz, J., Srokosz, P., Bartoszewicz, A., Lossman, W. (2007). Degradation of subsoil caused by well drilling (in Polish), In: *Proceedings Conf. on Construction Failures*, Międzyzdroje, Poland.

Mitrosz, O., Skóra, T. (2021). Floating foundation of road bridge abutments on soilmix columns and observed performance, In: *Proceedings Conf. Deep Mixing 2021 – Best Practice and Legacy,* pp. 336-344, Gdańsk, Poland. Available at: www.dfi.org.

Świeca, M., Walczak, K. (2007). Hydraulic failure during bridge construction (in Polish), In: *Proceedings Conf. on Construction Failures*, Międzyzdroje, Poland.

Wojtasik, A., Różański, M. (2011). Failure of bridge foundation in complex soil and water conditions (in Polish), *J. Bridges*, *Materials and Technologies*, 4/2011.

Proceedings of the XVIII ECSMGE 2024
GEOTECHNICAL ENGINEERING CHALLENGES
TO MEET CURRENT AND EMERGING NEEDS OF SOCIETY
© 2024 the Authors
ISBN 978-1-032-54816-6
DOI 10.1201/9781003431749-2
Open Access: www.taylorfrancis.com, CC BY-NC-ND 4.0 license

ECSMGE 24
XVIII EUROPEAN CONFERENCE ON SOIL MECHANICS AND GEOTECHNICAL ENGINEERING

Keynote Lecture

Geotechnical aspects of February 6, 2023 Kahramanmaraş-Türkiye earthquake sequence

Aspects géotechniques de la séquence sismique du 6 Février 2023 à Kahramanmaraş, Turquie

K.O. Cetin*, E. Cakir, A. Elsaid, F. Cuceoglu, B. Soylemez, S. Ocak
Department of Civil Engineering, Middle East Technical University, Ankara, Türkiye

B.U. Ayhan
Department of Civil Engineering, Istanbul Bilgi University, Istanbul, Türkiye

**ocetin@metu.edu.tr; kemalondercetin@gmail.com*

ABSTRACT: The earthquakes that occurred in Pazarcık and Ekinözü-Kahramanmaraş on February 6, 2023, had a profound impact southeastern Türkiye and northwestern Syria. With moment magnitudes of M7.8 and M7.6, these earthquakes, ruptured multiple fault segments within a span of 9 hours, presenting an unexpected scenario for seismic hazard assessments. During the Pazarcık event, the peak ground acceleration levels, corresponding to DD-1 (with a 2475-year return period) and DD-2 (with a 475-year return period) design levels as defined in the Turkish Building Earthquake Code, were exceeded at 5 and 22 strong ground motion stations, respectively. Ground motion prediction equations (GMPEs) underpredicted the recorded PGA levels at stations within 70 km from the fault rupture, particularly for the Pazarcık earthquake. Seismic soil liquefaction emerged as a significant geohazard, notably observed in Gölbaşı-Adıyaman and İskenderun-Hatay regions. The significant shaking triggered more than 3,000 landslides and rock falls, resulting in casualties. Damage to infrastructure was substantial, with 7 bridges sustaining significant damage, two of which were attributed to the liquefaction of foundation soils. Lifelines suffered significant damage due to fault rupture, liquefaction, and permanent ground deformations. Similarly, port facilities in İskenderun reported severe damage due to liquefaction and post-earthquake fires. Although all 140 dams in the influence region preserved their water retention capabilities, the reservoir levels at two of them had to be lowered as part of emergency response actions. While there was a partial collapse in a stone-paved railway tunnel serving the Gölbaşı-Malatya line, no major damage was reported at tunnel structures. Retaining structures, predominantly stone walls, incurred damages, whereas reinforced earth walls displayed greater resilience. The collapse or heavy damage to over 650,000 residential units was the major cause of over 55,000 casualties.

RÉSUMÉ: Les tremblements de terre qui ont eu lieu à Pazarcık et Ekinözü-Kahramanmaraş le 6 février 2023 ont eu un impact profond sur le sud-est de la Turquie et le nord-ouest de la Syrie. Avec des magnitudes de moment de M7.8 et M7.6, ces tremblements de terre ont rompu plusieurs segments de failles dans un intervalle de 9 heures, présentant un scénario inattendu pour les évaluations des risques sismiques. Lors de l'événement de Pazarcık, les niveaux d'accélération maximale du sol, correspondant aux niveaux de conception DD-1 (avec une période de retour de 2475 ans) et DD-2 (avec une période de retour de 475 ans) tels que définis dans le Code de construction parasismique turc, ont été dépassés à 5 et 22 stations de mouvement du sol, respectivement. Les équations de prédiction du mouvement du sol (GMPEs) ont sous-estimé les niveaux de PGA enregistrés dans les stations situées à moins de 70 km de la rupture de la faille, en particulier pour le séisme de Pazarcık. La liquéfaction sismique des sols est apparue comme un géo- risque significatif, notamment observé dans les régions de Gölbaşı-Adıyaman et d'Iskenderun-Hatay. La secousse significative a déclenché plus de 3 000 glissements de terrain et chutes de rochers, entraînant des pertes en vies humaines. Les dommages aux infrastructures ont été importants, avec 7 ponts subissant des dommages significatifs, dont deux ont été attribués à la liquéfaction des sols de fondation. Les lignes de vie ont subi d'importants dommages en raison de la rupture de la faille, de la liquéfaction et des déformations permanentes du sol. De même, les installations portuaires d'Iskenderun ont signalé des dommages graves dus à la liquéfaction et aux incendies post-sismiques. Bien que les 140 barrages de la région d'influence aient préservé leurs capacités de rétention d'eau, les niveaux des réservoirs de deux d'entre eux ont dû être abaissés dans le cadre des mesures d'intervention d'urgence. Alors qu'il y a eu un effondrement partiel dans un tunnel ferroviaire pavé de pierre desservant la ligne Gölbaşı-Malatya, aucun dommage majeur n'a été signalé aux structures de tunnel. Les structures de soutènement, principalement des murs de pierre, ont subi des dommages, tandis que les murs de terre renforcés ont fait preuve d'une plus grande résilience. L'effondrement ou les dommages graves à plus de 650 000 unités résidentielles ont été la principale cause de plus de 55 000 décès.

Keywords: Kahramanmaraş earthquakes; geotechnics; geohazards; liquefaction; dams; bridges; retaining structures; ports.

1 INTRODUCTION

On February 6, 2023, at 04:17 local time, a seismic event with a moment magnitude of M7.8 occurred along the East Anatolian Fault (EAF). This earthquake originated at a focal depth of 8.6 km, with its epicenter located in the Pazarcık district of Kahramanmaraş province in Türkiye. As shown in Figure 1, epicenter of the event lies approximately 40 km northwest of Gaziantep metropolitan city, and about 33 km southeast of Kahramanmaraş, precisely at coordinates 37.288°N, 37.043°E (Cetin et al., 2023). During the Pazarcık earthquake, a fault rupture zone stretching 190 km in length and 25 km in width, oriented in a northeast-southwest direction, was mapped (USGS, 2023a). Remarkably, merely eleven minutes after the main shock, another earthquake with M6.7 occurred in the same region.

At 13:24 local time, 9 hours after the Pazarcık event, another major earthquake shook the region, registering a moment magnitude of M7.6. This subsequent seismic event had a focal depth of 7.0 km, with its epicenter located in Ekinözü, Elbistan district of Kahramanmaraş province. The epicenter of the event is shown in Figure 1, approximately 98 km northwest of Adıyaman, and 62 km northeast of Kahramanmaraş, situated at 38.089°N, 37.239°E (Cetin et al., 2023). The Ekinözü-Elbistan earthquake shares the same left-lateral strike-slip mechanism as the Pazarcık event, rupturing a fault zone spanning approximately 120 km in length and 18 km in width, primarily oriented in an east-west direction (USGS, 2023b). Key attributes of these earthquakes, including their moment magnitudes, focal depths, and mechanisms, are detailed in Table 1 (Cetin et al., 2023; Cetin and Ilgac, 2023), as documented by various national and international organizations.

Table 1. Some characteristics of Pazarcık and Elbistan earthquakes.

Institution	Magnitude, M		Depth (km)		Focal Mechanism	
	Pazarcık	Elbistan	Pazarcık	Elbistan	Pazarcık	Elbistan
AFAD[1]	7.7	7.6	8.6	7		
KOERI[2]	7.7	7.6	10	10		
USGS[3]	7.8	7.5	17.9	10		
EMSC[4]	7.7	7.5	10	10		

[1] Turkish Prime Ministry-Disaster and Emergency Management Presidency
[2] Kandilli Observatory and Earthquake Research Institute
[3] United States Geological Survey
[4] European Mediterranean Seismological Centre

In addition to the Pazarcık and Ekinözü events, an independent earthquake struck the Yayladağı district in Hatay province on February 20, 2023, registering a magnitude of 6.3 with a focal depth of 21.73 km. This event occurred approximately 135 km south of the Pazarcık earthquake epicenter and 225 km south of the epicenter of Ekinözü earthquake. Following the earthquake sequence, over 11,000 aftershocks were recorded in the region until the end of March 2023. The intense shaking and resultant damage affected numerous provinces, including the cities of Adana, Adıyaman, Diyarbakir, Elazig, Malatya, Gaziantep, Hatay, Kahramanmaraş, Şanlıurfa, Kilis, and Osmaniye, which collectively house a population of over 15 million. The earthquake sequence resulted in more than 60,000 casualties and caused the destruction of over 650,000 residential units jointly in Türkiye and Syria (Cetin et al., 2023; Cetin and Ilgac, 2023).

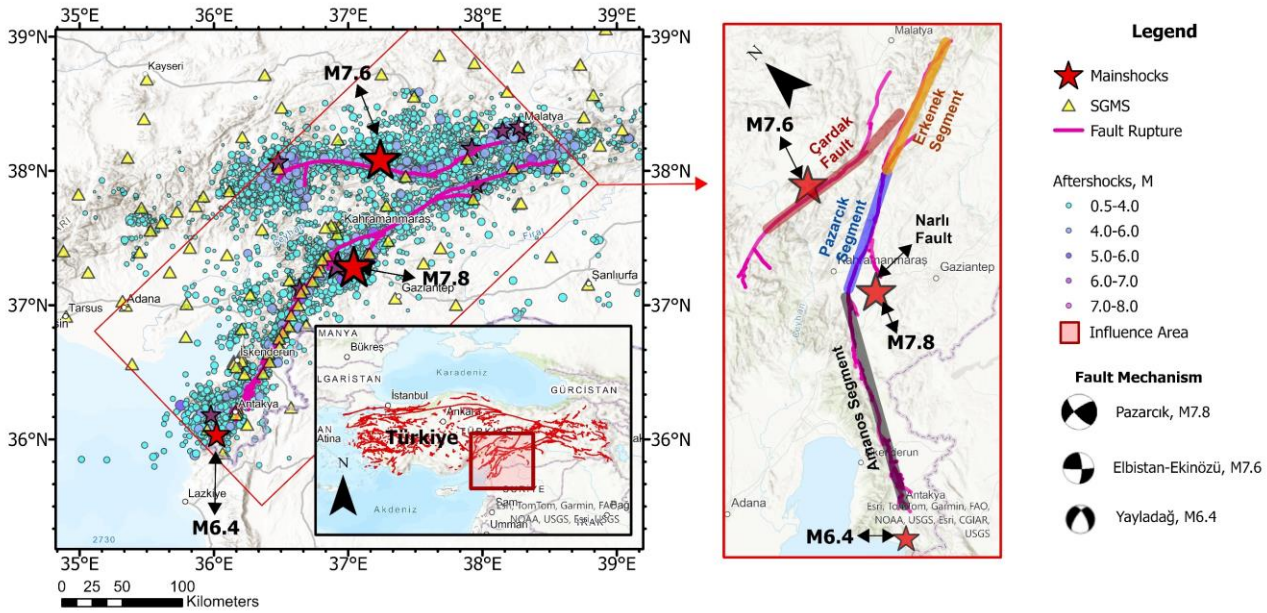

Figure 1. The map of the region, showing the East Anatolian Fault zone, the epicenters of the main- and aftershocks.

The events triggered a wide range of geohazards, including:

A. Soil liquefaction and -induced ground failures, resulting in excessive settlements, lateral spreads and global or local bearing capacity shear failures at or around various structure foundations. More specially they were mapped at:
   a. free field sites,
   b. residential structures,
   c. harbors/ports,
   d. embankments/dams,
   e. bridges/viaducts,
   f. airports.
B. Landslides and Rockfalls,
C. Permanent displacements/deformations due to factors other than soil liquefaction, including fault offset and strong ground shaking, and their effects on:
   a. retaining structures
   b. embankments / earthfill and rockfill dams.

This manuscript summarizes the findings of earthquake and geotechnical engineering reconnaissance field studies performed immediately after the earthquakes, along with their preliminary evaluation results. It presents the geotechnical assessment of residential structures, bridges, hydraulic structures (dams), airports, and retaining structures. Before the discussion of induced geohazards, a brief discussion on fault rupture mechanisms and strong ground motion characteristics will be presented next.

2 FAULT RUPTURE MECHANISMS AND STRONG GROUND MOTION CHARACTERISTICS

Turkiye, located at the convergence point of the Eurasian, African, and Arabian plates, encompasses a significant portion of the Anatolian block. It is surrounded by prominent geological features: the North Anatolian Fault (NAF) to the north, the East Anatolian Fault (EAF) to the east, the Hellenic and Cyprus subduction zones to the south, and an extension regime to the west. The Anatolian block displays a counterclockwise rotation and westward translation in relation to the three surrounding plates (Cetin et al., 2023; Cetin and Ilgac, 2023). The East Anatolian Fault Zone (EAFZ), spanning 450 km from Karlıova-Bingöl to Hatay, is characterized by a northeast-trending left-lateral strike-slip fault system. This zone serves as a significant plate boundary, with the Arabian Plate shifting approximately 10-11 mm northeastward annually, compressing the Anatolian Plate (Cetin et al., 2023).

Seismic activity in the Eastern Mediterranean region, particularly affected by the recent earthquake sequence, is intricately linked to the dynamic interactions among the Arabian, African, and Anatolian plates. In the east, the Arabian Plate collides with the Eurasian Plate, while to the west, the convergence of the African and Anatolian plates brings them close together (McKenzie, 1972). Since the Late Cretaceous period, there has been a gradual convergence between the Eurasian Plate and the Arabian and African plates, predominantly occurring in a north-south direction. This prolonged convergence ultimately led to the closure of the Tethys Ocean, which once separated the Arabian and African plates from the Eurasian plate (Kavuzlu, 2006).

The collision between the Arabian Plate and the Anatolian Plate, occurring along the Bitlis-Zagros Thrust Belt, has been a significant geological process shaping the Anatolia region since the Middle-Late Miocene period (Gülen et al., 1987; Arpat and Şaroğlu, 1975). This ongoing continent to continent collusion and convergence have resulted in the shortening and thickening of the Anatolian block, which is positioned between the Eurasian and Arabian-African plates. Beginning in the Late Miocene-Pliocene period, the Anatolian block, unable to accommodate the compression and deformation, began to undergo lateral translation westward due to the effects of the strike-slip North Anatolian and East Anatolian Faults (Kavuzlu, 2006).

During the collision between the Arabian and the Anatolian Plates, the Arabian Plate separated from the African Plate along the North-South Dead Sea Transform Fault, propelled by the Arabian Plate's faster northward movement compared to Africa Continent (Gülen et al., 1987).

In line with the outlined translational plate boundaries and tectonic context, the moment tensor solution for the Pazarcık earthquake indicates motion along a nearly vertical fault plane, trending northeast-southwest, predominantly left-lateral strike-slip motion. Originating on the Narlı Fault to the south, the Pazarcık earthquake fault rupture propagated bilaterally along the East Anatolian Fault zone, rupturing the Pazarcık and Erkenek fault segments to the northeast and the Amanos segment to the southwest. The distribution of aftershocks linked to this earthquake suggests a unique example of a complex rupture pattern, with the rupture terminating in Hatay to the south and in Doğanyol by the Pütürge segment to the north. Mapping of fault offsets reveals a range of 3-7 meters, while the rupture length surpassed 300 kilometers. Additionally, as noted earlier, a M6.8 aftershock occurred just west of the the

Pazarcık earthquake's epicenter, rupturing the Salçagöz Fault (Cetin et al., 2023).

The Ekinözü earthquake, representing a notable occurrence of short-term seismic triggering, triggered along the Çardak-Sürgü Fault segment, exhibiting predominantly left-lateral strike-slip motion similar to the Pazarcık event. Initiating on the east-west trending Çardak Fault, which extends further south in the west, the Ekinözü event progressed eastward over the northeast-southwest trending Doğanşehir fault zone towards the city of Malatya. Estimated to span approximately 160 km in total rupture length, the earthquake resulted in fault offsets ranging from 2 to 8 meters (Cetin and Ilgac, 2023).

These seismic events were monitored by the Disaster and Emergency Management Presidency (AFAD) stations located throughout the region. AFAD operates a network of 1548 strong ground motion stations (SGMSs) spanning the entire country. During the Pazarcık earthquake, 379 of these stations were activated. Notably, the maximum peak ground accelerations (PGA) were recorded in Hatay-Antakya, aligning with reports of more severe structural damage. Specifically, at SGMS station #3126, PGA levels peaked at 1.23 g in the north-south direction and 1.04 g in the east-west direction. According to the Turkish Building Earthquake Code (TBEC-18), the design basis seismic scenarios for return periods of 2475 and 475 years are referred to as DD-1 and DD-2 levels, respectively. During the Pazarcık event, the DD-1 and DD-2 design basis PGA values were surpassed at 5 and 22 SGMSs, respectively, as shown in Figure 2. This figure illustrates the interevent residuals, representing the difference between the recorded and design basis PGA intensities, plotted against the Joyner and Boore (1988) distance (R_{jb}).

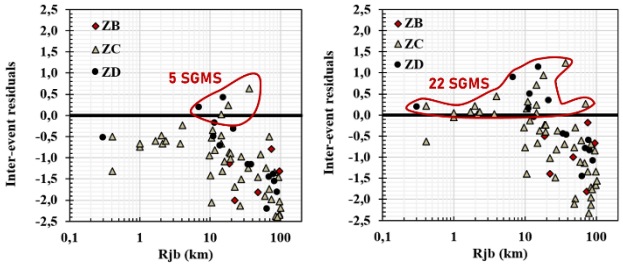

a) DD-1 **b)** DD-2

Figure 2. Variability in PGA residuals with TBEC-18.

Similarly, the Ekinözü event was monitored by 387 SGMS stations. Among these, the maximum PGA values were recorded at Kahramanmaraş-Göksun Station #4612. Here, the PGA levels peaked at 0.65 g in the north-south direction and 0.53 g in the east-west direction.

Figure 3 illustrates the attenuation of the recorded PGA intensities with R_{jb} for both seismic events. It is noteworthy that in close proximity to the fault rupture, recorded ground motions exhibit higher intensity levels compared to the median values estimated by NGA West 2 ground motion predictions equations (GMPEs), as discussed in Cetin et al., 2024a. However, beyond a distance of 70 km from the fault rupture, recorded PGA levels attenuated more rapidly, suggesting that GMPEs overestimated these PGA intensities.

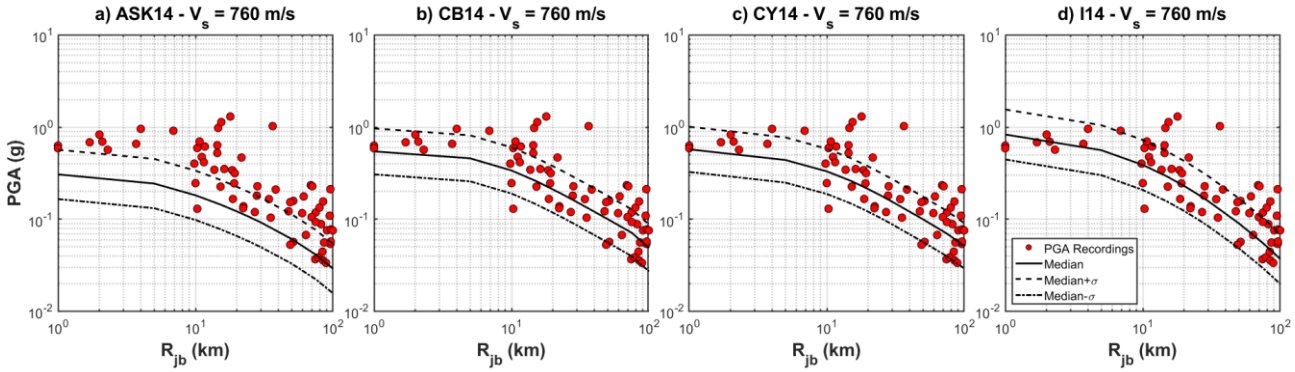

Figure 3. Joyner and Boore distance attenuation of the recorded PGAs as compared with the NGA West-2 GMPEs of Abrahamson et al. (2014)-ASK14, Campell and Bozorgnia (2014)-CB14, Chiou and Youngs (2014)-CY14 and Idriss (2014)-I14 for the Pazarcık earthquake (adapted from Cakir and Cetin, 2024).

In addition to R_{jb} distances, variations in the intensity, duration, and frequency characteristics of strong ground motion records (SGMR) were observed to be influenced by factors such as site conditions and orientation, and rupture velocity (Wu et al., 2023; Abdelmeguid et al., 2023; Ren et al., 2024). Figure 4 demonstrates significant variations in these characteristics within a short distance span in Hatay metropolitan city, as observed at SGMSs #3123, 3124, 3125, and 3126, located within a few kilometers of each other. Detailed discussions on these variabilities and their underlying reasons were thoroughly addressed in Alsaid and Cetin (2023) and Cetin and Alsaid (2023) and will not be reiterated here.

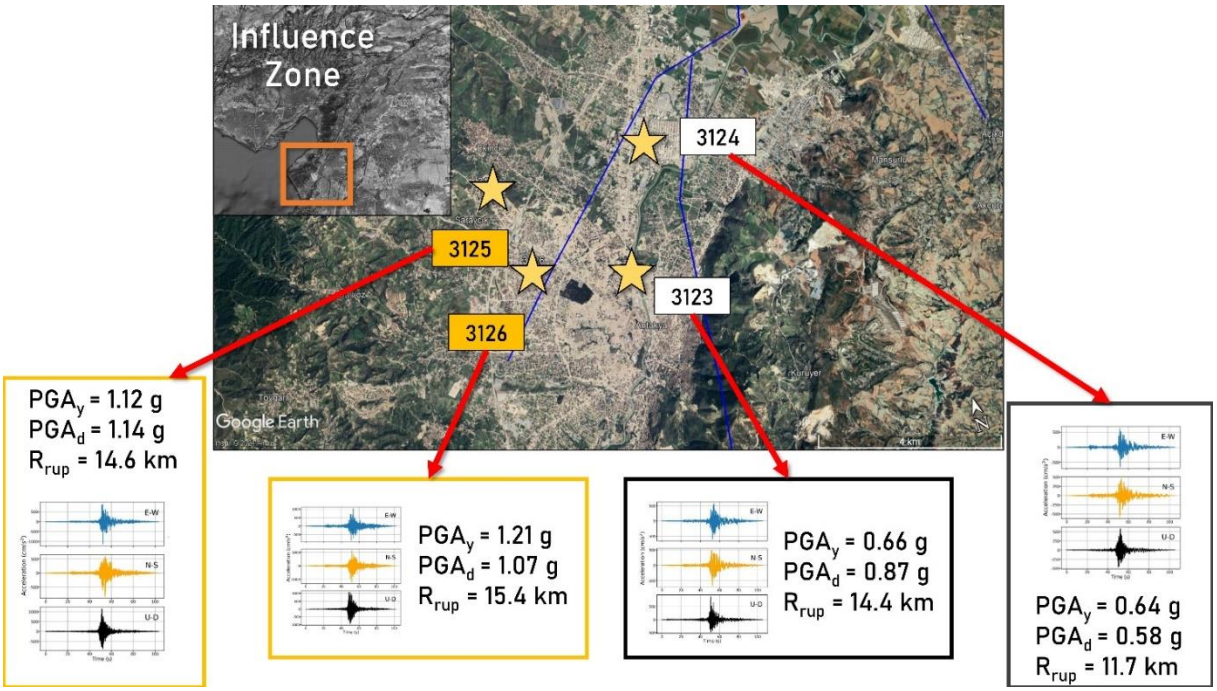

Figure 4. SGMS records in Hatay-Antakya during the Pazarcık event.

In summary, both the Pazarcık and Ekinözü earthquakes occurred within an unusually short timeframe of only 9 hours. This rapid succession of two significant seismic events with large magnitudes was not accounted for in the scenarios outlined in seismic hazard assessments. Moreover, the joint ruptures of three segments during the Pazarcık event, and two segments during the Ekinözü event, were deemed as scenarios with either zero or very low probability in seismic source characterization studies. Therefore, their larger-than-expected moment magnitudes and occurrence within such brief periods classified these earthquakes as unexpected, rare events from both seismological and engineering perspectives.

Moreover, site-specific factors such as soil conditions, basin effects, and the fault rupture propagation characteristics, including its directivity (forward vs. backward) and velocity (sub vs. super shear), contributed to significant variability in the observed characteristics of strong ground motion records. This variability was evident in the wide range of scatter observed in strong ground motion record characteristics, which consequently resulted in widely variable and scattered levels of structural damage.

Finally, it's noteworthy that the median predictions of the Next Generation Attenuation, West 2 (NGA West-2) GMPEs consistently underestimated PGA intensities at R_{jb} distances shorter than 70 km. However, beyond the 70 km mark, the recorded intensities exhibited a faster attenuation with distance, compared to the median intensities predicted by the GMPEs.

3 GEOHAZARDS FOLLOWING THE KAHRAMANMARAŞ EARTHQUAKE SEQUENCE

3.1 Seismic soil liquefaction

Following the Kahramanmaraş earthquake sequence, seismically induced soil liquefaction emerged as a significant contributor to damages observed in both natural and built environments. Reconnaissance field investigations were promptly conducted to gather time-sensitive perishable data and assess the extent of destruction in the aftermath of the earthquakes. Sites displaying visible signs of seismic soil liquefaction, including soil ejecta and pronounced foundation and ground deformations such as excessive settlements and lateral spreads, were systematically identified and documented.

The initial phase of reconnaissance efforts to document liquefied sites began on the third day following the earthquakes and continued for over two months. Numerous national and international research teams, including the teams from Geotechnical Extreme Events Reconnaissance Association (GEER) and Earthquake Engineering Research Institute (EERI), participated in these surveys, leading to the compilation of data on a digital platform named SiteEye (Saha Gözü in Turkish), which is accessible at www.sahagozu.com.

A total of 428 liquefaction case histories were documented from various sources, including studies by Cetin and Ilgac (2023), Cetin et al. (2024a; 2024b; 2024c, 2024d) and Moug et al. (2023). The locations

of these liquefaction occurrences are depicted in Figure 5. These sites were categorized into six geographical regions labeled L1 through L6, as illustrated in the same figure.

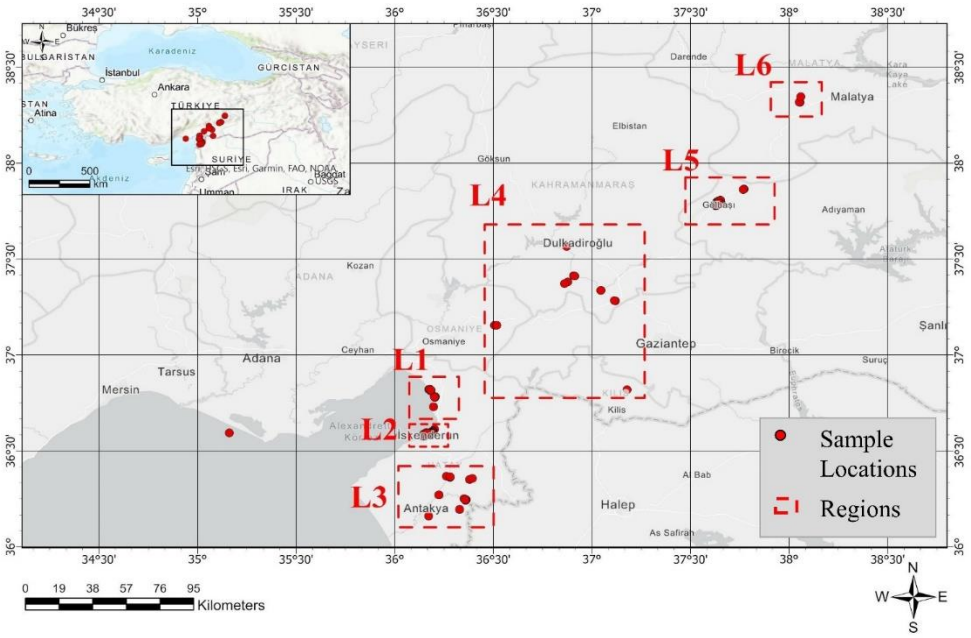

Figure 5. Map of liquefaction case history sites after Cetin et al. (2024b).

When collecting surface soil ejecta from liquefaction sites, particular emphasis was placed on obtaining representative soil samples. To accomplish this, when possible, a continuous sampling method was employed by vertically inserting a tube into the ejecta cone. This technique was chosen to address concerns regarding possible segregation or layering within the ejecta material. Additionally, efforts were undertaken to track the trajectory of the surface ejecta and determine its source, thereby verifying that it accurately represented the liquefied soil layer. This verification was crucial to ensure that the material was not transported to the ground surface due to excessive pore water pressure-induced flow. Whenever possible, existing borelogs were used to support this validation process. However, in cases where site-specific borelog data was unavailable, linking the characteristics of the ejecta soil sample directly to potential liquefied soil layers posed a challenge.

After labeling, ejecta samples were transported to the Middle East Technical University (METU), Soil Mechanics Laboratory. They underwent a 24-hour period of oven drying. Subsequently, a representative portion of the dried sample was immersed in a sodium hexametaphosphate solution (5 ml/1000 g) overnight to facilitate the separation of soil particles. Following this, wet sieving was conducted to isolate and collect the finer portion (< 0.074 mm) of the specimen. The fines portion was then stored in large bottles for further grain size assessments. Coarser portions remaining after wet sieving underwent a second round of oven drying before being subjected to dry sieving. These procedures adhere to the standards outlined by ASTM International, specifically ASTM D6913 (2017) and ASTM D7928 (2016). The Atterberg limits of the retrieved samples were estimated according to ASTM D4318 (2010). Laboratory test results will be presented separately for each ejecta region.

Figures 6a and 6b present the grain size distribution curves of the soil ejecta alongside the liquefaction susceptibility bounds outlined by Tschuida (1970). A complete presentation of the soil ejecta sites, grain size and consistency characteristics of these soil ejecta sites is presented in Cetin et al. (2024b) and will not be repeated herein due to page limitations. For instance, the sample retrieved from the Çay neighborhood in İskenderun-Hatay, with ID #38 exhibits fines and silt contents of 18.4% and 15%, respectively (see Figure 6a). Notably, apart from specimen ID #45, which displays a gravel content of 45%, all grain size distribution curves of the ejecta material fall within the bounds of the "susceptible to liquefaction region" as defined by Tsuchida (1970). Conversely, concerning the samples retrieved from the Adıyaman-Gölbaşı region, a significant number of ejecta grain size distribution curves lie outside the liquefaction susceptibility limits established by Tsuchida (1970), primarily due to their elevated fines content. Among the 31 specimens analyzed, hydrometer tests were conducted on 6 to estimate their clay contents. These

tests revealed clay contents ranging from 13% to 20%, as illustrated in Figure 6b. Most of the CL type soil ejecta are retrieved from Gölbaşı-Adıyaman region. The liquid limits of these samples vary in between 32 and 38%. Their plasticity index values are estimated to be in the range of 16 to 23%. Unexpectedly, two ejecta samples with plasticity indices higher than 30% are retrieved from Hatay Airport, one of which is classified as high plasticity clay (CH).

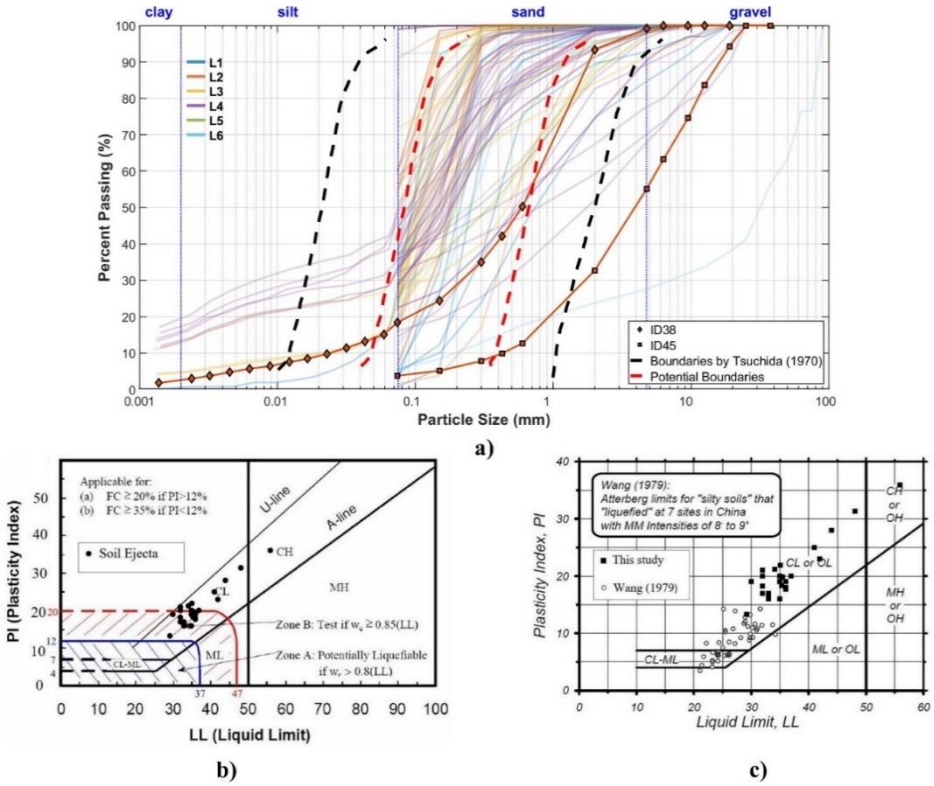

Figure 6. a) Grain size distribution of all samples indicated in Figure 5 b) susceptibility analysis followed by Seed et al. (2003), and c) susceptibility analysis followed by Wang (1979).

The consistency limits of the ejecta samples are shown on the Seed et al. (2003) liquefaction susceptibility chart, as depicted in Figure 6c. Most of the ejecta samples are situated within the "Zone B: Testing Recommended" region of the chart. However, notably, 12 out of 74 samples fall beyond the susceptibility region delineated by the Seed et al. chart. Subsequently, the laboratory test results are collectively presented alongside the Wang (1979) data, which were compiled from samples of liquefied "silty soil" layers at 7 sites in China. Figure 6d provides a comparative view of the overall database on the plasticity chart, indicating that clayey soils are susceptible to liquefaction and capable of producing ejecta under significant cyclic loading intensity and duration. It is imperative to note that additional detailed site investigations and laboratory testing programs are being conducted to scrutinize the liquefaction (cyclic) responses of fine-grained soils liquefied during the Türkiye-Kahramanmaraş Earthquake sequence.

Following a general introduction to the characteristics of the soil ejecta samples, a more in-depth discussion will be provided by grouping them under various headings. These headings will cover soil liquefaction manifestations in different contexts, including those observed in free fields and in the vicinity of building foundations, dams, bridges, ports and harbors, and airports.

3.1.1 Free field liquefaction sites

Following the Kahramanmaraş Earthquake sequence, soil ejecta samples were collected from more than 200 locations, predominantly concentrated along the İskenderun coastal region, Demirköprü, and Kumlu regions in Hatay city. Adiditonally, soil ejecta was manifested in Gölbaşı town in Adıyaman city, along with instances in Türkoğlu and Emiroğlu in Kahramanmaraş metropolitan city. Figure 7 presents images from free-field ejecta sites, with their corresponding locations indicated in Figure 5.



Figure 7. Free-field soil ejecta sites at a) Payaş Dörtyol-Hatay coastal line, b) A Port facility in İskenderun, c) İskenderun-Hatay, d) Demirköprü-Hatay, e) Emiroğlu-Kahramanmaraş, f, g, h, and j) Gölbaşı-Adıyaman after Kahramanmaraş Earthquakes.

3.1.2 Liquefaction around building foundations

In the districts of Savaş and Çay in İskenderun-Hatay, as well as in Gölbaşı town in Adıyaman city, the geological, geotechnical, and hydrogeological conditions played a role in the favor of triggering soil liquefaction. These areas are characterized by loose and soft alluvial and marsh sediments, shallow groundwater levels, and strong shaking intensities and durations. Consequently, substantial bearing capacity failures of building foundations, accompanied by excessive settlements, and lateral translations, occurred. In Gölbaşı, the most severely affected area was primarily situated north of Atatürk Boulevard on the Gaziantep-Malatya highway, particularly near the lake, where loose or soft alluvial sediments are thicker. The reduction in bearing capacity due to liquefaction and cyclic mobility led to settlements ranging from 10 to 90 cm, as depicted in Figure 8a.

In İskenderun, numerous residential building foundations in Çay district experienced settlements induced by liquefaction and bearing failures. The settlements of foundations varied from 3 to 17 cm in the Savaş Neighborhood and reached approximately 42 cm in the Çay Neighborhood. Moreover, differential settlements of up to 30 cm were observed, resulting in the tilting of buildings, as depicted in Figure 8b.



Figure 8. Liquefaction-induced settlement observed at a) Gölbaşı-Adıyaman, and b) İskenderun-Hatay.

3.1.3 Ports/Harbors

Soil liquefaction caused significant damage on port facilities along the Mediterranean coast in İskenderun-Hatay. The liquefaction manifestations were widespread at various locations, including the public beach and shoreline of Dörtyol municipality, several ports within the İskenderun Bay area, and regions of İskenderun Customs and Fishery Port. Pictures taken at these sites are shown in Figure 9. Vertical and lateral displacements and deformations were also evident and mapped near areas with sand ejecta, likely caused by the lateral spreading of quay walls. In more intricate facilities, such as ports, cranes, and weighbridges were surveyed to be tilted or overturned due to liquefaction-induced bearing capacity failures and ground deformations.



Figure 9. Liquefaction-induced deformations at port facilities in, b) A Port facility in İskenderun, c) Fishery Warf, d, e, and f) İskenderun State Harbor.

3.1.4 Dams

The Kahramanmaraş Earthquakes significantly affected 140 dams in the region, with the majority located within a 50 km radius from the fault rupture. Fortunately, these dams retained their water-retaining capabilities, and no instances of uncontrolled water release were reported. However, as part of emergency response measures, the water levels at two earthfill dams, namely Sultansuyu and Arıklıkaş, were gradually lowered in a controlled manner due to extensive permanent deformations (1-2 m) occurring at the dam bodies (Cetin et al., 2024d). Additionally, surface manifestations of liquefaction were observed at these dams, possibly attributed to the inadequate compaction of the filter material layers, as illustrated in Figure 10. A detailed discussion of the deformations mapped at these dams will be presented in Section 3.3.



Figure 10. Surface manifestation of liquefaction observed at a) Sultansuyu Dam and b) Arıklıkaş Dam.

3.1.5 Bridges

Reconnaissance surveys indicated damage to a total of 7 bridges (Caner et al., 2023). Among these, two failures were attributed to soil liquefaction: Demirköprü and Karasu Bridges. Demirköprü Bridge, located in Hatay-Demirköprü, was surveyed by the reconnaissance team from the Middle East Technical University. Detailed field surveys were conducted to map the intricate patterns of displacements, deformations, and surface manifestations of soil liquefaction. All observable displacements and manifestations, including soil ejecta, excessive settlements, and lateral spreads, were accurately located. Figures 11a-c show the two most eastern spans of the bridge, along with the rotational failure observed in the south-east abutment. Notably, in Figure 11b, the reinforced concrete bored piles in the east abutment tilted 20° towards the Asi River, accompanied by settlements reaching as high as 1.0 to 1.5 m at the abutment embankment, as shown in Figure 7c. Figure 11d displays the widespread sandy ejecta and volcanoes induced by liquefaction mapped at the site. Six samples were collected from the ejecta soil, with a focus on obtaining representative soil samples. The retrieved ejecta samples were classified as non-plastic silty sand (SM) with an average 25% fines content (Ocak and Cetin, 2024). Liquefaction susceptibility analysis was conducted following the method proposed by Seed et al. (2003), and Figure 11e indicates that, except for a few data points (less than 5% of available data points), the majority of fine-grained soils are classified as not susceptible, confirming the selection of the suspected critical soil layer as the silty sand (Unit 2, SM) layer.

The second bridge affected by liquefaction-induced ground deformations is the Karasu Bridge, situated over the Karasu River. Both the eastern and western approach embankments exhibited significant differential settlements, ranging between 40-45 cm and 50-55 cm, respectively (see Figure 12c). Moreover, lateral spreading, exceeding 150 cm, was observed within the influence zone of bridge piers and foundations (see Figure 12a-b). The approach embankments of the bridge are underlain by layers of low to high plasticity stiff clay and liquefaction-susceptible clayey and silty medium dense sand units. Specifically, non-plastic silty sands with fines contents ranging from 21% to 42% were identified as the liquefaction suspect soil units during the Pazarcık earthquake. Figure 12d provides a comparative display of the grain size distribution curves of these non-plastic SM samples, alongside the liquefaction susceptibility bounds proposed by Tschuida (1970). It is noteworthy that the grain size distribution curves consistently fall within the recommended susceptible soils range. To evaluate the susceptibility of fully saturated fine-grained soils and their mixtures to liquefaction, assessments were conducted utilizing Atterberg limits and referencing the chart suggested by Seed et al. (2003). As depicted in Figure 12e, fully saturated soils falling within Zone A or B were deemed susceptible to liquefaction, in accordance with the procedure outlined by Seed et al. (2003).

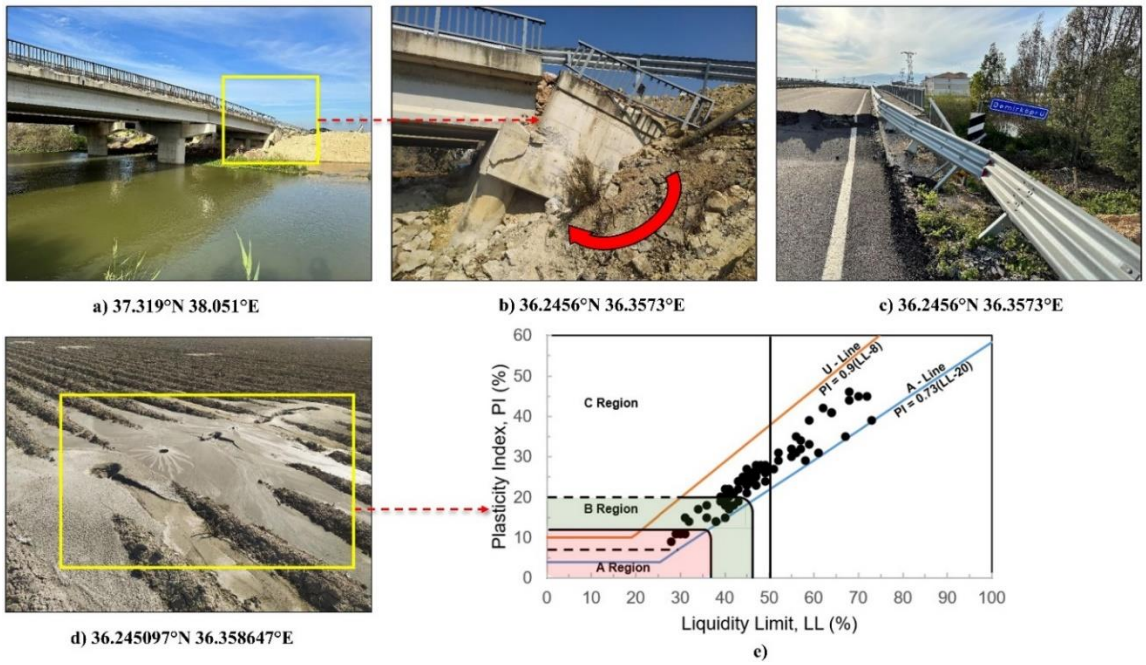

Figure 11. Site investigation at Demirköprü Bridge: a) General overview of the bridge, b) rotational failure at eastern span of the bridge due to seismic soil liquefaction, c) soil ejecta in the vicinity of the bridge, and d) liquefaction susceptibility analysis followed by Seed et al. (2003).

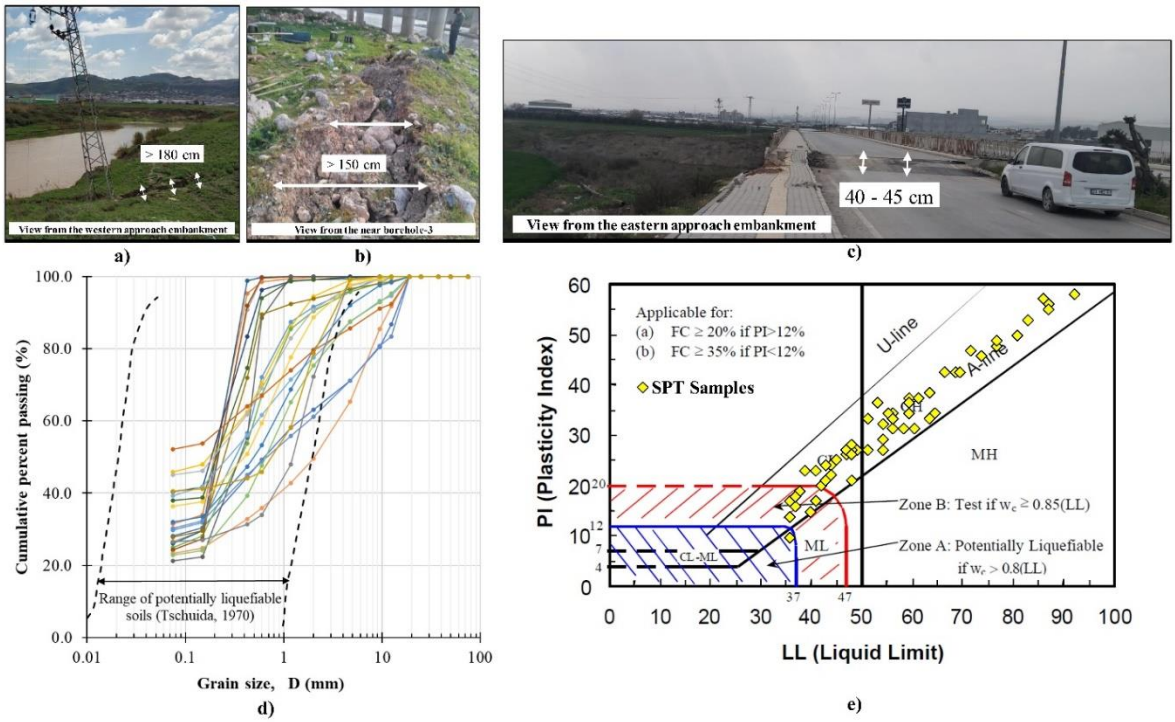

Figure 12. Site investigation at Karasu Bridge: a, b) lateral spreading nearby bridge piers, differential settlements on approach embankments) soil ejecta in the vicinity of the bridge, d) particle size distribution curves for non-plastic silty sands with susceptibility bounds proposed by Tschuida (1970) and e) liquefaction susceptibility analysis followed by Seed et al. (2003).

3.1.6 Airports

A total of 11 airports are present in the earthquake region, as depicted in Figure 13a, and all, except one, performed well despite the high levels of shaking. Unfortunately, the Hatay Airport runway sustained damage attributed to fault displacements and soil liquefaction, as illustrated in Figure 13b-c and 13e-f. Excessive settlement and lateral spreading were documented on airport runway due to reconsolidation and volumetric compaction after liquefaction. As expected, no damage was reported in airport structures such as terminal buildings, where ground improvement and deep foundation design solutions were implemented (see Figure 13d). Five samples were retrieved from these locations, classified as clayey sand (SC), and low to high plasticity clays (CL or CH). Further analyses regarding liquefaction triggering and liquefaction-induced settlements are discussed in Cetin et al. (2024e).

3.1.7 Liquefaction-induced lateral spreading and inundation

Liquefaction-induced lateral spreading and inundation were observed in several regions, notably along the shorelines of Gölbaşı Lake in Adıyaman, and İskenderun Bay in Hatay. A vivid example was documented at the old Gölbaşı Vocational School, situated on the southern shores of Gölbaşı Lake, as shown in Figure 14. The lateral displacements and settlements were clearly evident on the cobblestone-paved yard of the school, as illustrated in the same figure. The total lateral displacements exceeded five meters.

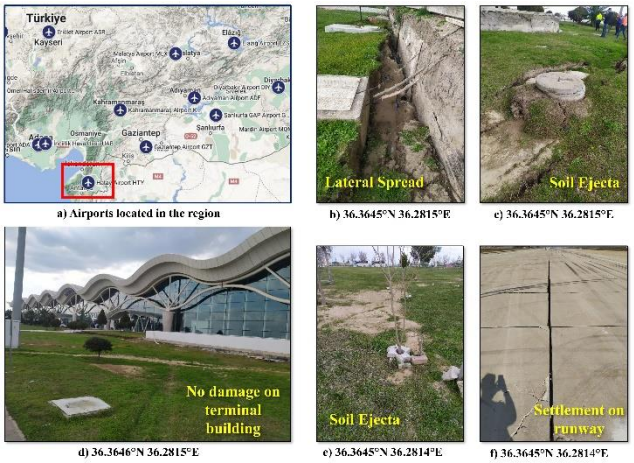

Figure 13. Site photos taken at the Hatay Airport.

In the İskenderun district, lateral deformations were mapped along the ports and shoreline. At certain locations, approximate lateral deformations and vertical deformations were measured as 90 cm and 60 cm, respectively. Some of these lateral spreading sites are shown in Figure 15.

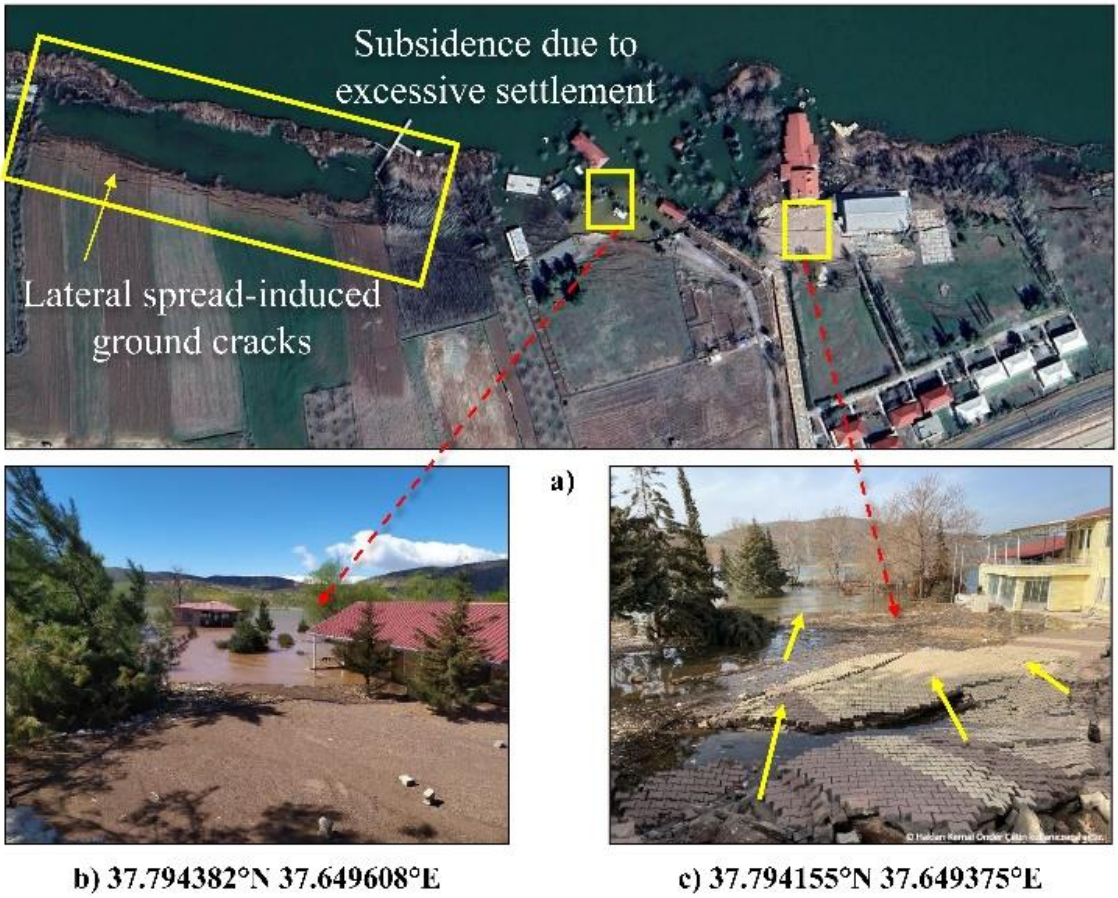

Figure 14. Lateral spreading and subsidence observed in Gölbaşı-Adıyaman adapted from Cetin et al. (2024c).



Figure 15. Lateral spreading observed at Hatay-İskenderun.

3.2 Landslides and rockfalls

Gorum et al. (2023) conducted an extensive evaluation using satellite and aerial imagery to assess the earthquake-affected area, complementing remote observations with field investigations. As depicted in Figure 11, a total of 3673 coseismic landslides

associated with this event were mapped, marking it as the largest compilation of coseismic landslides from a single seismic event in Türkiye. Over 90% of these mapped landslides occurred within a 20-km-wide zone along the fault rupture.

Global observations suggest that coseismic landslides could be triggered in the far field with peak ground acceleration (PGA) values as low as 0.02–0.08 g (Jibson and Harp, 2016), although most occur at higher levels of shaking. Typically, about 90% of landslides occur where PGA exceeds 0.12 g (Tanyas and Lombardo, 2019). Consistently with available literature, the locations of documented coseismic landslides were observed to fall within regions shaken by PGA levels exceeding 0.12 g.

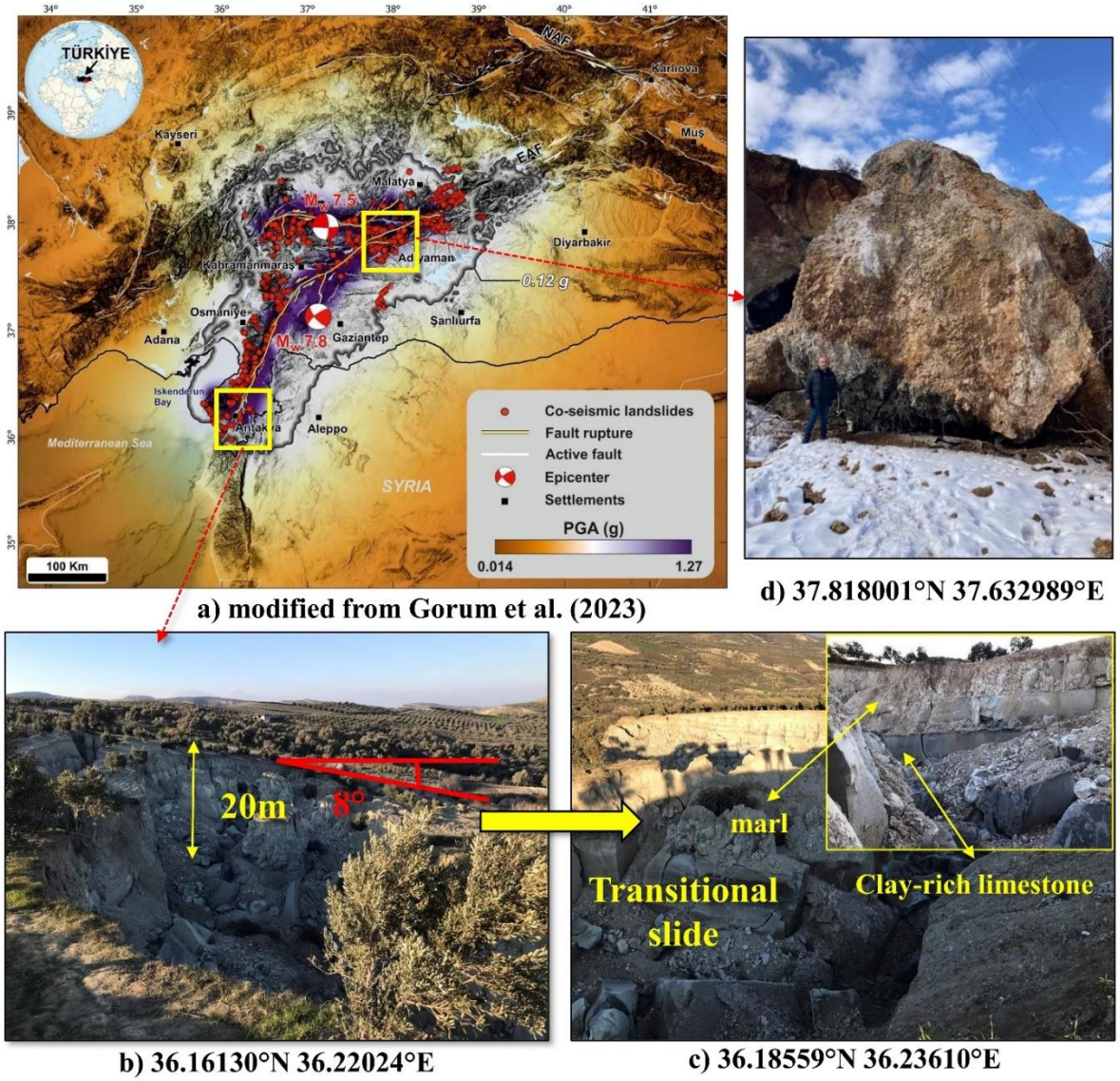

Figure 16. a) Spatial distribution of coseismic landslides overlain by the Kahramanmaraş Earthquakes fault rupture and PGA recordings for M>5.5 modified from Gorum et al. (2023), b, c) representation of transitional slide documented in Tepehan Village, and d) rockfalls reported in Gölbaşı.

In Tepehan village, a significant landslide event took place, characterized as a transitional slide with an area of approximately 1.3 km^2, as shown in Figure 16b and 16c. The slope gradient measured at the site was 8°. The sliding mass primarily consisted of marl and clay-rich limestone, exacerbated by significant rainfall in the area. The failure thickness measured 20 m, with the sliding basal surface identified as the upper bedding surface of a clay-rich limestone unit interbedded with marl, exhibiting intense weathering in the upper parts (Sümer et al., 2023). Additionally, rockfalls occurred across the entire area, with bedrock rotational landslides predominantly observed in the north.

In Adıyaman-Gölbaşı, particularly in the Karamağara locality, large block rockfalls were

documented, as depicted in Figure 16d. The name "Karamağara" translates to "black cavern" in English, indicating its formation through the karstification of limestone units in the region. Following the seismic events, these rockfalls nearly obstructed the entrance to the cavern and blocked the village road adjacent to it for two days, temporarily impeding access to villages located to the north.

3.3 Permanent ground/soil displacements/deformations

In this section, permanent ground displacements resulting from fault offset will be discussed. Additionally, the displacements and deformations surveyed at retaining structures, as well as earthfill, and rockfill dams and embankments, will be presented.

3.3.1 Fault offset

Immediately after the earthquakes, deformation zones and offset features were documented, along with numerous instances of surface ruptures. These displacements were also revealed by Sentinel-2 deformation analyses, conducted by COMET, as illustrated in Figure 17a. Figure 17b-f presents some examples of these instances for the Pazarcık and Elbistan events. During the Pazarcık event, the fault rupture extended over 400 km, with offsets reaching up to 7.2 meters (Kurcer et al., 2023; Cetin and Ilgac, 2023). Unfortunately, during the Pazarcık event, the fault rupture intersected the axis of the Erkenek Dam, resulting in a 3.4 m left lateral offset on the dam body as shown in Figure 17b (Cetin et al., 2024d). In contrast, the Ekinözü event was characterized by a fault rupture of 160 km, with offsets reaching up to 8.8 meters (Parlak et al., 2023).

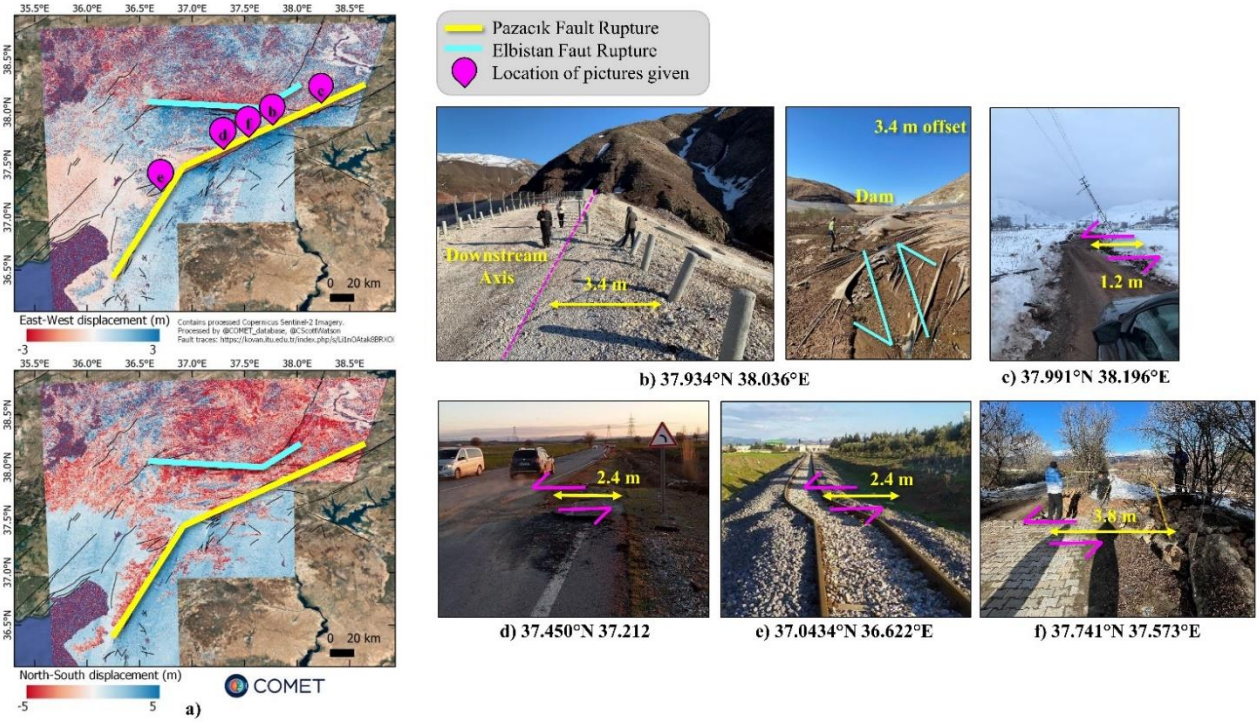

Figure 17. a) Sentinel-2 deformation analyses provided by COMET after Cetin and Ilgac (2023), b) fault offsets mapped b) across the Erkenek Dam, in c) Çelikhan, d) Pazarcık, e) Islahiye, and f) Balkar.

3.3.2 Retaining structures

Many retaining structures were reported to have failed, with failures primarily concentrated on stone gravity-type walls, as depicted in Figure 18a. Additionally, some failures of reinforced concrete walls were attributed to seismic soil liquefaction, as seen in Figure 18b. Conversely, well-designed and constructed anchored, reinforced, piled, or stabilized walls exhibited better performance under high seismicity, as illustrated in Figure 18c-d.

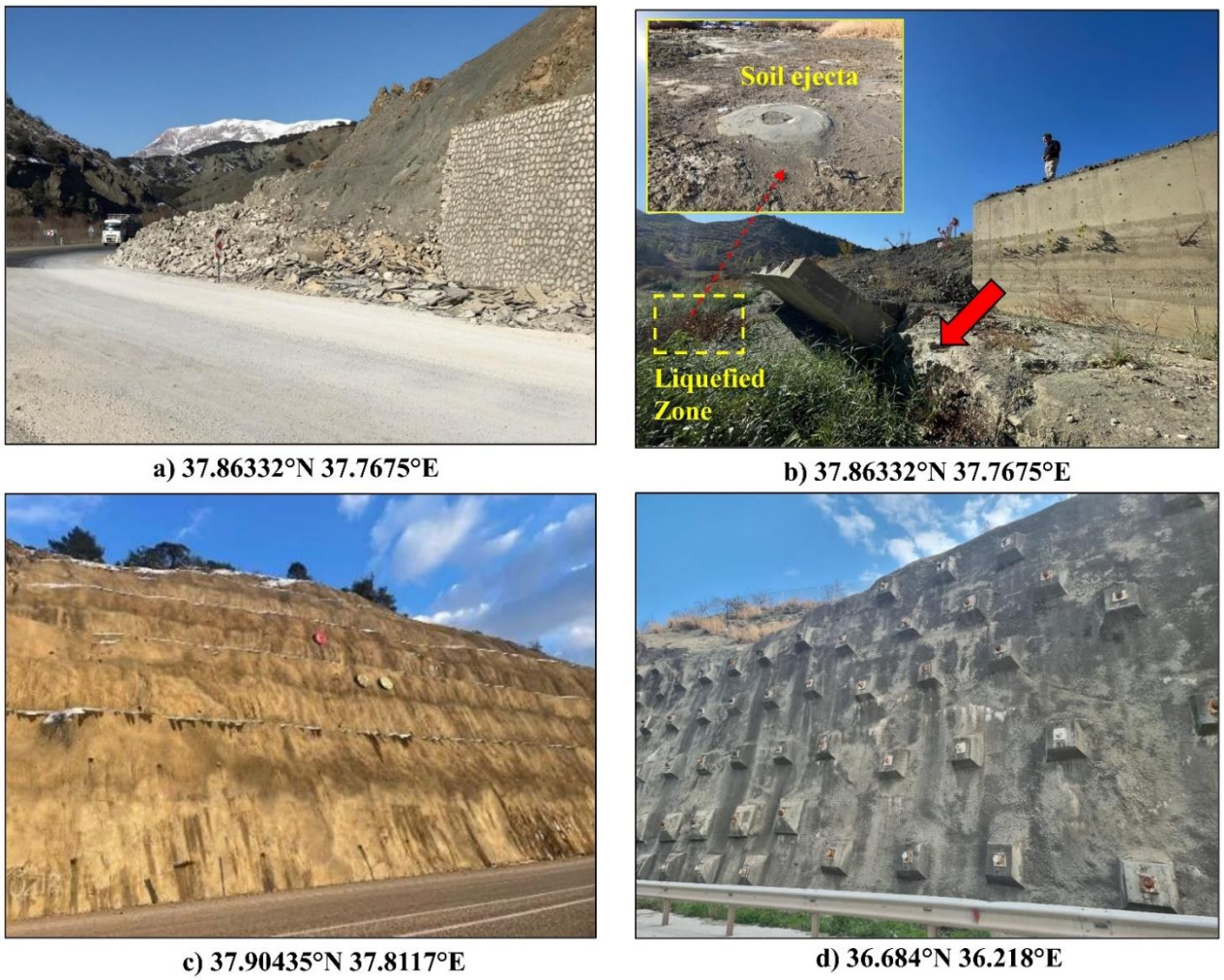

Figure 18. Retaining wall performance after the Kahramanmaraş Earthquakes: a) Stonewall, b) Cantilever, c, and d) anchored walls.

3.3.3 Earth embankments/earthfill-rockfill dams

Over 140 water retention structures in the earthquake-affected area experienced high ground shaking, with most dams falling within the high-intensity shaking zone. The observed levels of damage is illusrated in Figure 19 using a color-coded permanent displacement scale, where yellow and green indicate "no permanent displacements" and "50 cm permanent displacements," respectively. In the figure, square, diamond, and filled circles represent concrete, rockfill, and earthfill dams, respectively. Despite high intensity shaking levels, all dams successfully continued their water retention functions without significant damage. Notably, high-capacity dams such as Atatürk, Keban, Berke, Sır, Karakaya, and Birecik did not experience permanent deformation or displacements. However, some earthfill and rockfill dams were observed to have been more severely affected as compared to concrete dams.

As part of emergency response measures, controlled lowering of water levels occurred at two dams: Sultansuyu and Arıklıkaş. Deformations at these dams primarily are reported as longitudinal cracks extending parallel to the crest, accompanied by lateral translations and settlements. These permanent deformations were associated with inadequate compaction the interface plane in between clay-core and filter materials. Their magnitudes were also evaluated to be correlated with the intensity of shaking. More specifically, they were observed to increase with decreasing R_{jb} distances. Despite permanent displacements reaching 1-2 meters in earth-fill dams, they have managed to retain water, and the absence of permanent deformations on downstream slopes and auxiliary structures is noteworthy. Figure 20 illustrates the dams experiencing permanent displacements at their crests exceeding one meter after the Kahramanmaraş Earthquake sequence.

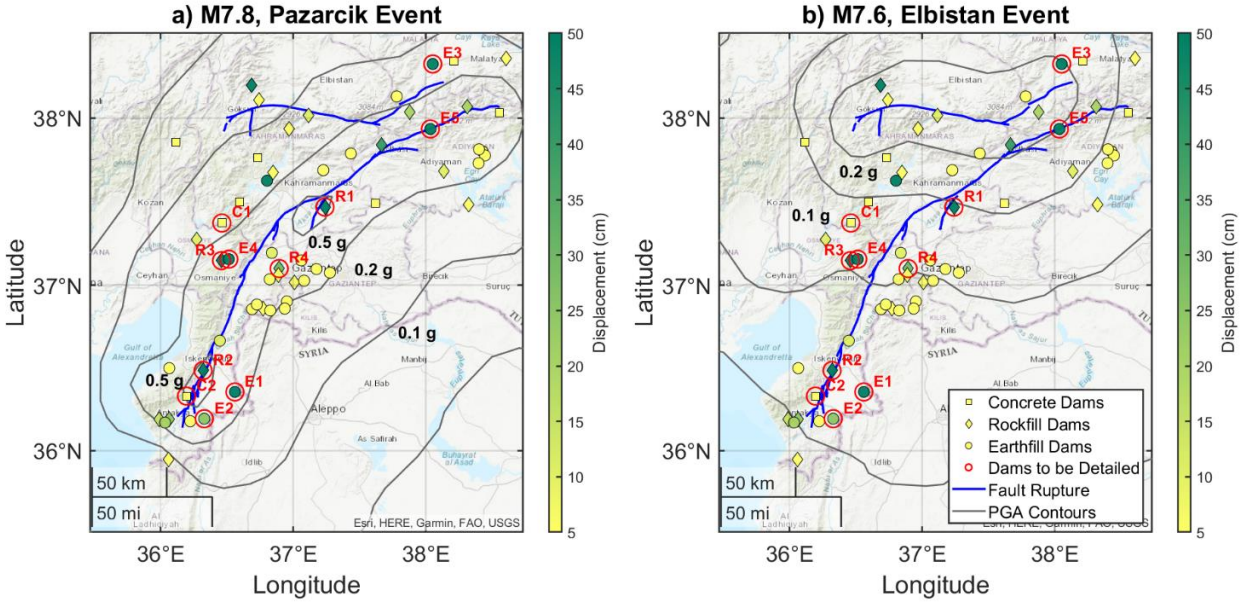

Figure 19. Spatial distribution of dams located within the R_{jb} distance of 50 km for both a) Pazarcık and b) Ekinözü-Elbistan Earthquakes and representation of documented lateral displacements after Cetin et al. (2024d).



Figure 20. Some examples of permanent ground deformations documented at earthfill dams, a) Reyhanli Dam, b) Ariklikas Dam and c) Sultansuyu Dam.

4 LESSONS LEARNED

The February 6, 2023 Kahramanmaraş Earthquake sequence yielded valuable and unique lessons for the earthquake and geotechnical engineering community, particulary in the following areas:

A. Seismic Hazard Assessment:

- Source Characterization: The sequence highlighted the importance of considering the possibility of multiple fault segments rupturing within a short timeframe, which may not have been adequately accounted for in seismic hazard assessments.
- Ground Motion Prediction Equations (GMPEs): It revealed discrepancies between the predicted and recorded ground motion intensities, especially in proximity to the fault rupture, emphasizing the need for improved GMPEs.

B. Geohazards:

- Fault Displacements: The earthquake sequence demonstrated significant fault displacements, underscoring the need for robust structural design and planning in seismically active regions.
- Seismic Soil Liquefaction: Instances of liquefaction-induced bearing capacity failures and ground deformations highlighted the vulnerability of structures built on liquefiable soils.
- Landslides and Rockfalls: The widespread occurrence of landslides and rockfalls emphasized the need for comprehensive slope stability assessments and mitigation measures.
- Strong Ground Shaking-Induced Soil Deformations: Observations of soil deformations in various infrastructure elements, including residential building foundations, retaining

structures, harbors and ports, dams, and airports, emphasized the importance of considering site-specific soil conditions and ground response characteristics in engineering designs and construction practices.

More specifically, the important observations, findings and lessons regarding **earthquake engineering** are detailed as follows:

i) The M7.8 Pazarcık-Kahramanmaraş earthquake was triggered due to the joint rupture of the Narlı, Pazarcık, and Erkenek fault segments along the East Anatolian Fault Zone. Similarly, 9 hours after this event, the Ekinözü earthquake hit the region with the combined rupture of the Çardak, Sürgü, and Doğanşehir fault segments again along the East Anatolian Fault Zone. This unexpected combination of multiple fault segment ruptures in both events, along with the occurrence of two design basis level seismic events within a period of 9 hours, were not fully considered in either deterministic or probabilistic seismic hazard assessment scenarios prior to these events. Multiple segment fault rupture scenarios should be given more consideration in seismic source characterization. Recent events have revealed that they might be more likely and frequent than we have considered them to be. Also, the occurrence of consecutive earthquake events in short periods and affecting the same region needs to be better assessed by the engineering community, with possible implications in earthquake design codes.

ii) The directivity and speed of fault rupture can significantly impact the ground shaking characteristics, including their intensity, duration, and frequency content. Hence, it is timely to seek better ways to represent directivity and fault rupture velocity effects on SGMR characteristics, with possible implications for earthquake design codes.

iii) The earthquake shaking duration should be incorporated as a design parameter. Seismic hazard maps for shaking durations, similar to those prepared for peak ground acceleration (PGA) or spectral acceleration, need to be developed. This will provide engineers and planners with a more comprehensive understanding of the seismic hazard and enable them to design structures that are resilient to the duration as well as the intensity of ground shaking.

iv) Further damaging effects of aftershocks on already damaged structures should be considered as part of design-basis scenarios, especially for critical infrastructure such as hospitals, bridges, ports, harbors, airports, and dams. These structures may need to provide uninterrupted service after a major earthquake, and accounting for the potential impact of aftershocks is crucial for ensuring their resilience and functionality. This consideration should be integrated into the design and planning processes to enhance the overall earthquake resilience of critical infrastructure systems.

v) Probabilistic fault rupture hazard assessments should be mandated for critical structures, including bridges, tunnels, and pipeline systems, located on active faults. By conducting these assessments, engineers and decision-makers can better understand the potential risks posed by fault rupture events and develop appropriate mitigation measures to enhance the resilience of critical infrastructure. This proactive approach can help ensure the safety and functionality of essential structures in the event of future earthquakes, ultimately reducing the overall impact on communities and infrastructure systems.

Similarly, important observations, findings and lessons involving **geotechnical engineering** are detailed as follows:

i) Seismic soil liquefaction is identified as a major cause of damage after the earthquake sequence. The lessons learned from previous earthquake events, such as the 1964 Alaska and Niigata earthquakes, have led to the implementation of additional preventive measures to mitigate liquefaction-induced failures in regions prone to seismic activity. For example, in California, USA, seismic demand corresponding to a 2475-year return period is now utilized for liquefaction triggering estimations in the design of residential buildings. This approach reflects a more comprehensive understanding of the potential risks associated with liquefaction and allows for more robust design solutions to be implemented. Therefore, adopting seismic demands corresponding to return periods longer than 475 years, preferably 2475 years, is recommended for liquefaction triggering evaluations in order to enhance the resilience of infrastructure and minimize the impact of liquefaction-induced damage.

ii) Under intense ground shakings characterized by peak ground acceleration (PGA) exceeding 0.4 g and long durations associated with moment magnitudes (M) greater than 7.0, significant reductions in both the strength and stiffness of fully saturated soft clays are observed. This phenomenon is particularly pronounced in sensitive clays with cone penetration resistance (q_c) less than 1 MPa or Standard Penetration Test (SPT) N_{60} values less than 7 blows per 30 cm. Engineering specifications should include a comprehensive discussion on the softening behavior of soft clays under cyclic loading conditions. Additionally, provisions should be made to address the potential need for mitigation measures to ensure the stability and performance of structures founded on such soils during seismic events.

iii) A guideline for calculating the bearing capacity of soils susceptible to strength and stiffness loss under cyclic loading is essential for ensuring the stability and performance of structures founded on such soils during seismic events. The guideline should offer a systematic approach for engineers to assess the bearing capacity of soils susceptible to strength and stiffness loss under cyclic loading, thereby enhancing the resilience of structures to seismic hazards.

iv) Due to excessive displacements and deformations observed on their approach embankments, despite the absence of structural damage on some critical viaducts (e.g.: Ataturk-Turgut Ozal and Başpınar Viaducts in Nurdagı-Gaziantep), they could not provide full service after the events. Approach embankments should receive equal attention to the structural elements of viaducts or bridges, therefore careful consideration is required in terms of material selection, compaction procedures, or the need for ground improvements.

v) The geometric and geotechnical properties of basins in urban areas should be evaluated, and seismic demand analyses should be performed for sites classified as ZD and ZE, according to TBEC-18 (equivalent to NEHRP site classes D and E).

vi) Deterministic landslide triggering maps should be developed for scenario earthquakes, and probabilistic seismic landslide hazard maps should be developed compatible with PSHA. These will enable to identify structures and settlements which could be affected by seismically triggered landslides and tockfalls.

vii) Stone gravity walls should be avoided as a retaining structure in hisgh seismicity areas. Instead, well-designed and constructed reinforced earth walls should be preferred.

viii) The filter materials in earthfill and rockfill dams typically consist of liquefiable sand and gravel. In adequate compaction of these materials lead to liquefaction and concentrated displacements at the filter interfaces.

5 SUMMMARY AND CONCLUSION

The earthquakes that struck Pazarcık and Ekinözü-Kahramanmaraş on February 6, 2023, along the East Anatolian Fault Zone (EAFZ), resulted in significant life losses and widespread destruction spanning a significant geographical area covering southeastern Turkiye and northwestern Syria. Among over 55,000 casualties, 92 were attributed to landslides and rockfalls. Unfortunately, the majority of casualties resulted from mass collapse and severe damage to residential buildings. Over 650,000 residential structures experienced mass collapse or severe damage during the earthquakes and became uninhabitable.

Peak Ground Accelerations (PGAs) recorded at distances from the fault exceeded anticipated levels, surpassing those specified in the Turkish Building Earthquake Code. In the field of Geotechnical Engineering, numerous case studies emerged, particularly in the regions of Adıyaman-Gölbaşı and Hatay-İskenderun, where soil liquefaction was predominantly observed.

Critical engineering structures such as bridges, viaducts, and tunnels generally performed well and continued service with limited interventions. A partial collapse in a railway tunnel was reported along with 7 bridges experienced moderate to heavy damage. Two of these bridge foundations suffered from liquefaction-induced deformations. In the earthquake-affected region, there are a total of 11 airports, and except the Hatay airport, the rest provided uninterrupted service despite the intense levels of shaking. The runway of Hatay Airport suffered damage due to fault movements and soil liquefaction, impacting its serviceability. The damage distributions spreading across a wide range were observed in retaining structures. While stone gravity walls were observed to suffer from ground displacements more frequent than reinforced concrete retaining systems, reinforced earthfill walls performed exceptionally well even after being subjected to intense shaking levels exceeding 0.5 g. All hydraulic structures maintained their water retention capabilities. Two of the 140 dams in the region, namely Sultansuyu and Arıklıkaş dams, suffered from permanent crest displacements mapped to be in the range of 1 to 2 meters. As part of emergency response measures, the reservoir levels at these were lowered in a controlled manner.

The earthquake sequence yielded valuable and unique lessons for the earthquake and geotechnical engineering community, particulary in the areas of seismology and seismic hazard assessment, more specifically in seismic source characterization and ground motion prediction models. Additionally, it provided case histories and lessons involving geohazards such as fault displacements, seismic soil liquefaction, landslides and rockfalls, permanent ground deformations.

REFERENCES

Abdelmeguid, M., Zhao, C., Yalcinkaya, E. et al. (2023). Dynamics of episodic supershear in the 2023 M7.8 Kahramanmaraş/Pazarcık earthquake, revealed by near-field records and computational modeling. *Commun Earth Environ* 4, 456. https://doi.org/10.1038/s43247-023-01131-7.

Abrahamson N. A., Silva W. J., and Kamai R., (2014). Summary of the ASK14 Ground motion relation for active crustal regions. *Earthquake Spectra*, 30, 1025–1057. https://doi.org/10.1193/070913eqs198m.

Alsaid, A., and Cetin. K. O. (2023). Duration Characteristics of Strong Ground Motions Recorded during the 6 February 2023 M7.8 Pazarcık, Kahramanmaraş, Türkiye Earthquake. Seismological Letter, 95(2A), 720-729. https://doi.org/10.1785/0220230300.

Arpat, E., Şaroglu, F., (1975). Türkiye'deki bazi onemli genç tektonik olaylar (Some important young tectonic events in Turkiye). *Türkiye Jeoloji Kurumu Bülteni (Turkiye Geological Society Bulletin),* 18, 91-110 (In Turkish).

Cakir E., and Cetin K. O. (2024). Liquefaction triggering and induced ground deformations at metallurgical facility in Dörtyol-Hatay after the February 6 Kahramanmaraş earthquake sequence. *Soil Dynamics and Earthquake Engineering*, 178, 108465, https://doi.org/10.1016/j.soildyn.2024.108465.

Campbell K. W., and Bozorgnia Y. (2014). NGA-West2 Ground Motion Model for the Average Horizontal Components of PGA, PGV, and 5% Damped Linear Acceleration Response Spectra. *Earthquake Spectra*. 30(3):1087-1115. doi:10.1193/062913EQS175M.

Cetin, K. O., and Ilgac, M., (2023). Reconnaissance Report on February 6, 2023 Kahramanmaraş-Pazarcık (Mw=7.7) and Elbistan (Mw=7.6) Earthquakes. *Türkiye Earthquake Recconaissance and Research Alliance*. Doi: 10.13140/RG.2.2.15569.61283/1.

Cetin, K. O. and Alsaid, A., (2023). Intensity and Durational Characteristics of Seismograms Recorded during the February 6, 2023, M7.8 Türkiye Kahramanmaraş Pazarcık Earthquake. *9th Geotechnical Symposium*, Istanbul, Türkiye, 22-24 November, Doi: 10.5505/2023geoteknik.SS-13.

Cetin, K. O, Ilgac, M., Can, G., and Cakir, E. (2023). Preliminary Reconnaissance Report on February 6, 2023, Pazarcık Mw=7.7 and Elbistan Mw=7.6, Kahramanmaraş-Türkiye Earthquakes. *Middle East Technical University Earthquake Engineering Research Center (METU EERC) Report No: METU/EERC 2023-01.* doi: 10.13140/RG.2.2.32975.97446.

Cetin. K. O., Alsaid, A., and Ozacar, A. A. (2024a). Intensitycharacteristics of Seismogramsrecorded During the February 6, 2023, M7.8 Türkiye Kahramanmaraş Pazarcık earthquake, *Turkish Journal of Civil Engineering,* under review.

Cetin, K. O., Soylemez, B., Guzel, H., and Cakir, E., (2024b). Soil Liquefaction Sites Following the February 6, 2023, Kahramanmaraş-Türkiye Earthquake Sequence., *Bulletin of Earthquake Engineering*, https://doi.org/10.1007/s10518-024-01875-3.

Cetin, K. O., Moug, D., Soylemez, B., Ayhan, B. U., Zarzour, M., Al-Suhaily, A., Akil, B., Unutmaz, B., Firat, S., Tekin, E., Cakir, E., Frost, D., Macedo, J., Bray, J., Moss, R., Bassal, P., Gurbuz, A., Isik, N. S., Akin, M., Sahin, A., and Duman, E. (2024c). Ground Failures and Foundation Performances in Adıyaman-Gölbaşı. *Earthquake Spectra*, under review.

Cetin, K. O., Cuceoglu, F., Ayhan, B. U. Yildirim, S., Aydin, S., Demirdogen, S., Er, Y., Gurbuz, A., and Moss, R. (2024d). Performance of Hydraulic Structures during February 6, 2023, Kahramanmaraş-Türkiye Earthquake Sequence. *Earthquake Spectra*, under review.

Cetin, K. O, Cakir, E., Eyigun, Y., and Gokceoglu, C. (2024e). Soil Liquefaction Manifestation at Hatay Airport after the February 2023 Türkiye Earthquake Sequence. *Earthquake Spectra*, under review.

Cetin, K. O., Ayhan, B. U., Cuceoglu, F., and Yildirim, S., (2023f). Performance of Reyhanlı Dam During February 6, 2023 Kahramanmaraş-Türkiye Earthquake Sequence. *Soil Dynamics and Earthquake Engineering*, under review.

Chiou B. S.-J., and Youngs R. R., (2014). Update of the Chiou and Youngs NGA model for the average horizontal component of peak ground motion and response spectra, *Earthquake Spectra* 30, 1117–1153. https://doi.org/10.1193/072813eqs219m.

COMET (Centre for the Observation and Modelling of Earthquakes, Volcanoes, and Tectonics, 2023; courtesy of Lazecky, M., Maghsoudi, Y., Watson, S., Wright, T., Elliott, J., Hooper, A., and Weiss, J; method from Lazecky et al., 2020).

Cornell, C. A. (1968). Engineering Seismic Risk Analysis. *Bulletin of the Seismological Society of America*,58(5), 1583-1606.

Gorum, T., Tanyas, H., Karabacak, F., Yilmaz, A., Girgin, S., Allstadt, K. E., Suzen, M. L. and Burgi, P. (2023). Preliminary Documentation of coseismic ground failure triggered by the February 6, 2023 Türkiye Earthquake Sequence. *Engineering Geology*, 327, 107315. https://doi.org/10.1016/j.enggeo.2023.107315.

Gülen, L., Barka, A., Toksöz, M.N., (1987). Kıtaların çarpışması ile ilgili kompleks deformasyon: Maraş üçlü eklemi ve çevre yapıları (Complex deformation related to the collision of continents: Maras triple joint and surrounding structures). *Yerbilimleri (Geosciences).* 14, 319-336 (In Turkish).

Idriss I. M. (2014). An NGA-West2 Empirical Model for Estimating the Horizontal Spectral Values Generated by Shallow Crustal Earthquakes. *Earthquake Spectra*. 30(3):1155-1177. doi:10.1193/070613EQS195M.

Jibson, R. W., Harp, E. W. (2016). Ground motions at the outermost limits of seismically triggered landslides. *Bull. Seismol. Soc. Am.* 106, 708–719. https://doi.org/10.1785/0120150141.

Joyner, W. B., and D. M. Boore. (1988). Measurement, Characterization, and Prediction of Strong Ground Motion. *Earthquake Engineering and Soil Dynamics II*—Recent Advances in Ground-Motion Evaluation 43-102.

Kavuzlu, M., (2006). Altınözü (Antakya) ve yakın civarının tektono-stratigrafisi (Tectono-stratigraphy of Altinozu (Antakya) and its immediate surroundings). *Master Thesis, Cukurova University Graduate School of Science*, (In Turkish).

Kürçer, A., H. Elmacı, E. Özdemir, C. Güven, T. Güler, İ. Avcu, Ş. Olgun, H. O. Avcı, H. Aydoğan, A. A. Yüce,

F. E. Çetin, A. Ayrancı, Z. Akyol, Ö. A. Soykasap, G. Altuntaş, U. Demirörs, O. Karayazı, A. Bayrak, and S. Özalp. (2023). 06 Şubat 2023 Pazarcık (Kahramanmaraş) Depremi (Mw 7,7) Saha Gözlemleri ve Değerlendirmeler. *MTA Genel Müdürlüğü, Rapor No: 14138, 187 s*., Ankara. Accessed August 20, 2023. https://www.mta.gov.tr/v3.0/bilgi-merkezi/2023-maras-depremi-raporlari.

McKenzie, D.P., (1972). Active tectonics of the Mediterranean region. *Roy Ast Soc Geophys J*. 30 (2), 109-185.

Ocak, S. and Cetin, K. O (2024). Liquefaction-induced Failure of Demirköprü Bridge Pile Foundation and Retaining System Following the February 6 Kahramanmaraş Earthquake Sequence, *Journal of Earthquake Engineering,* under review.

Parlak, O., A. Yavuzoğlu, A. Bayrak, O. Karayazı, and Ş. Olgun. (2023). 06 Şubat 2023 Elbistan (Kahramanmaraş) Depremi (Mw 7,6) Saha Gözlemleri ve Değerlendirmeler. *MTA Genel Müdürlüğü, Rapor No: 14139, 99s*., Ankara. Accessed August 20, 2023. https://www.mta.gov.tr/v3.0/bilgi-merkezi/2023-maras-depremi-raporlari.

Ren, C, Wang, Z, Taymaz, T., Hu, N., Luo, H, Zhao, Z., Yue, H, Song, X, Shen, Z, Xu, H, Geng, J., Zhang, W., Wang, T, Ge, Z., Irmak, T. S., Erman, C., Zhou, Y., Li, Z, Xu, H., Cao, B., and Ding, X. (2024). Supershear triggering and cascading fault ruptures of the 2023 Kahramanmaraş, Türkiye earthquake doublet. Science, 383, 305-311. DOI: 10.1126/science.adi1519.

Seed, R B., Cetin, K.O., Moss, R.E.S., Kammerer, A., Wu, J., Pestana, J., Riemer, M., Sancio, R.B., Bray, J.D., Kayen, R.E., and Faris, A. (2003). Recent advances in soil liquefaction engineering: a unified and consistent framework. *Keynote presentation, 26th Annual ASCE Los Angeles Geotechnical Spring Seminar*, Long Beach, CA.

Sümer, O., Drahor, M., Ongar, A., Tepe, C., Duman, A., (2023). Geoscientific report of field studies after February 6, 2023 Mw=7.7 Pazarcık, Mw=7.6 Elbistan (Kahramanmaras) and February 20, 2023 Mw=6.4 Defne (Hatay) earthquakes (In Turkish), p. 66.

Tanyas¸, H., and Lombardo, L., (2019). Variation in landslide-affected area under the control of ground motion and topography. Eng. Geol. 260 https://doi.org/10.1016/j.enggeo.2019.105229.

Tsuchida H (1970) Prediction and countermeasure against the liquefaction in sand deposits. *Abstract of the Seminar in the Port and Harbor Research Institute* (in Japanese)

Turkish Building Earthquake Code (2018). T. C. Resmi Gazete.

USGS, 2023a. M 7.8-Pazarcik earthquake, Kahramanmaras earthquake sequence. https://earthquake.usgs.gov/earthquakes/eventpage/us6000jllz/executive. [accessed 3 December 2023].

USGS, 2023b. M 7.5-Elbistan earthquake, Kahramanmaras earthquake sequence. https://earthquake.usgs.gov/earthquakes/eventpage/us6000jlqa/executive [accessed 3 December 2023].

Wang, W (1979) Some findings in soil liquefaction *Water Conservancy and Hydroelectric Power Scientific Research Institute*, Beijing, China.

Wu, F., Xie, J., An, Z., Lyu, C., Taymaz, T., Irmak, T., S., Li, X., Wen, Z., and Zhou, B. (2023). Pulse-like ground motion observed during the 6 February 2023 Mw7.8 Pazarcık Earthquake (Kahramanmaraş, SE Türkiye) *Earthquake Science*, 36(2023), 328-339. https://doi.org/10.1016/j.eqs.2023.05.005.

Proceedings of the XVIII ECSMGE 2024
GEOTECHNICAL ENGINEERING CHALLENGES
TO MEET CURRENT AND EMERGING NEEDS OF SOCIETY
© 2024 the Authors
ISBN 978-1-032-54816-6
DOI 10.1201/9781003431749-3
Open Access: www.taylorfrancis.com, CC BY-NC-ND 4.0 license

ECSMGE 24
XVIII EUROPEAN CONFERENCE ON SOIL MECHANICS AND GEOTECHNICAL ENGINEERING

Keynote Lecture

Risk analysis and mitigation in geotechnical engineering – Lessons learned from the collapse of the historical archive in Cologne due to underground construction

Analyse et atténuation des risques dans l'ingénierie géotechnique - Enseignements tirés de l'effondrement des archives historiques à Cologne causé par une construction souterraine

C. Moormann*
University of Stuttgart, Institute of Geotechnical Engineering, Stuttgart, Germany
MGC · Prof. Moormann Geotechnik Consult, Stuttgart · Cologne · Munich, Germany

M.J.P. Effenberger
University of Stuttgart, Institute of Geotechnical Engineering, Stuttgart, Germany

**christian.moormann@igs.uni-stuttgart.de*

ABSTRACT: In the field of geotechnical engineering, risks that materialise can have a significant impact on the serviceability and stability of a geotechnical structure, as well as its construction timeline. Additionally, these risks can potentially affect the surrounding environment. Those risks arise not alone from variable and complex characteristics of the subsoil and groundwater, as well as from design and modelling of the soil-structure interaction, but also from execution process. Hence, risk management must identify various sources of risk and conduct risk analyses to assess the probability and consequences of undesirable events. Risk control and mitigation measures should cover all stages of ground investigation, geotechnical interpretation, design and construction. These aspects are explored and reflected on the collapse of the Historical Archive of the city of Cologne as an example. On March 3rd, 2009, the collapse of the archive and adjacent buildings occurred during the construction of the new North-South metro line. This incident caused significant damage to the city of Cologne, but also affected the underground construction sector in general. With a total damage sum of around 1.2 billion euros, it stands as the most severe accident on a German construction site to date. The investigation of the damage evidence was a technically challenging task that lasted more than twelve years. It involved numerous steps, including the construction of a 34 m deep investigation shaft. Based on these experiences the consequences for the independent checking of design and execution, for the quality assurance of underground works and their supervision, but also the need for a risk prevention based on communication and partnership between all parties involved in the construction process is reflected.

RÉSUMÉ: Dans le domaine de l'ingénierie géotechnique, les risques qui se matérialisent peuvent avoir un impact significatif sur l'aptitude au service et la stabilité d'une structure géotechnique, ainsi que sur le calendrier de sa construction. En outre, ces risques peuvent potentiellement affecter le milieu environnant. Ces risques découlent non seulement des caractéristiques variables et complexes du sous-sol et des eaux souterraines, ainsi que de la conception et de la modélisation de l'interaction sol-structure, mais aussi du processus d'exécution. Par conséquent, la gestion des risques doit identifier les différentes sources de risques et mener des analyses de risques pour évaluer la probabilité et les conséquences d'événements indésirables. Les mesures de contrôle et d'atténuation des risques doivent couvrir toutes les étapes de l'étude du sol, de l'interprétation géotechnique, de la conception et de la construction. Ces aspects seront explorés et réfléchis à partir de l'exemple de l'effondrement des archives historiques de la ville de Cologne. Le 3 mars 2009, l'effondrement des archives et des bâtiments adjacents s'est produit pendant la construction de la nouvelle ligne de métro Nord-Sud. Cet incident a causé des dommages importants à la ville de Cologne, mais a également affecté le secteur de la construction souterraine en général. Avec un montant total de dommages d'environ 1,2 milliard d'euros, il s'agit de l'accident le plus grave survenu sur un chantier allemand à ce jour. L'enquête sur les dommages a été une tâche techniquement difficile qui a duré plus de douze ans. Elle a comporté de nombreuses étapes, dont la construction d'un puits d'investigation de 34 mètres de profondeur. Sur la base de ces expériences, les conséquences pour le contrôle indépendant de la conception et de l'exécution, pour l'assurance qualité des travaux souterrains et leur supervision, mais aussi la nécessité d'une prévention des risques basée sur la communication et le partenariat entre toutes les parties impliquées dans le processus de construction seront reflétées.

Keywords: Risk analysis; reliability; geotechnical engineering; collapse; risk mitigation.

1 INTRODUCTION

Dealing with uncertainties and risks is an omnipresent task in structural and geotechnical engineering. The key features distinguishing geotechnical and structural engineering are the natural origin of the ground and the lack of sufficient data to characterize the ground using the more familiar frequentist interpretation of probability (Chwala et al., 2022). Therefore, especially for the design of geotechnical structures an appropriate consideration of uncertainties and risks is essential for all engineering stages - from soil investigation, field and laboratory testing, specification of subsoil models and evaluation of soil/ rock properties to calculation with adequate empirical, analytical or numerical models, execution and supervision. The motivation to elaborate risk management and assessment is first and foremost the avoidance of danger to people and property but unquestionable also the elimination of financial and societal consequences a severe failure like the collapse of the historical archive in Cologne considered later can produce. Baecher (2023) discusses four case studies of large infrastructure projects from several continents, stressing remaining challenges of uncertainty quantification and interpretation in practice. Uncertainty in geotechnical engineering has several sources, and its quantification is difficult (Phoon et al., 2022), making risk analysis a complicated task. In geotechnical engineering the risk is related to a probability of failure or the probability of a specific event occurring and its consequence. A risk becomes unacceptable once the probability of failure or the probability of an event occurring and its consequence (directly on human and properties, but also financial or societal) becomes too large. Therefore, geotechnical engineers exert high efforts to estimate probabilities of failure of structures, i.e. their reliability, as accurately as possible using various different techniques (Baecher & Christian, 2003; Ang & Tang, 2007).

Reliability assessment of structures is regulated in ISO 2364, but Phoon et al. (2019) opt for an increased use of reliability-based methods over the conventional deterministic approaches since these are insensitive to variable data.

Ebner & Lesny (2022) investigated the opinion of the engineering practice in view of the second generation of Eurocode 7, where reliability-based design principles are increasingly adapted. The assessment of their survey revealed that one of the major limitations of the application of reliability-based design are perceived to be insufficient data, lack of acceptance and insufficient knowledge. Both, Ebner & Lesny (2022) and Baecher (2023) argue for an increased integration of statistical methods in engineering education.

Chwala et al. (2022) published a recent and detailed state-of-the-art report about risk and reliability in geotechnical engineering. Literature and international standards propose several techniques and guidelines for proper risk assessment, but in practice, risk analysis can lack the precision and unconditional consistency required to avoid disastrous accidents in geotechnical engineering.

The present paper documents some basic considerations on risk management (Section 2) and risk assessment (Section 3) in geotechnical design and on related uncertainty-informed decision making (Section 4) before two examples of back-analysis of failed structures, i.e. so-called forensic analyses, are presented (Section 5). Finally, the aspects of risk assessment are explored and reflected on the collapse of the Historical Archive of the city of Cologne as an dramatic case study (Section 6). On March 3rd, 2009, the collapse of the archive and adjacent buildings occurred during the construction of the new North-South metro line. With a total damage sum of around 1.2 billion euros, it stands as the most severe accident on a German construction site to date. The investigation of the damage evidence was technically a very challenging task that lasted more than twelve years. It involved numerous steps, including the construction of a 34 m deep investigation shaft. The concept for the investigations as well as the identified cause for the damage will be presented. Based on these experience consequences for the independent checking of design and execution, for the quality assurance of underground works and their supervision, but also the need for a risk prevention based on communication and partnership between all parties involved in the construction process is reflected (Section 7).

2 RISK MANAGEMENT

A general and practical guideline for risk management is specified by ISO 31000, which provides the principles and frameworks risk management should adhere to. In some countries, the corresponding national geotechnical societies have published their own technical guidelines, like Phoon et al. (2022), Spross et al. (2017) or van Staveren (2013) which do not deviate substantially from the principles of ISO 31000. According to ISO 31000, the key aspect of risk management is the iterative and systematic application of principles in the scope of value creation and protection. This circular process is illustrated in Figure 1.

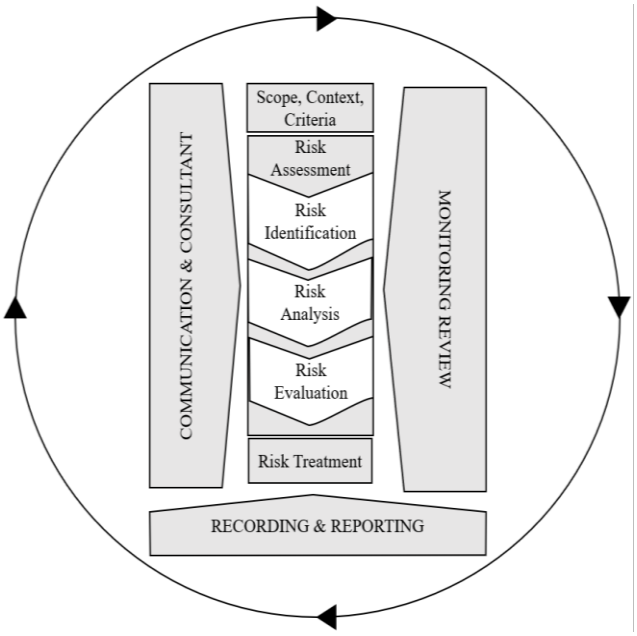

Figure 1. Process of risk management according to ISO 31000, Fig. 4.

The heart of this procedure is the assessment of risks, which is discussed in IEC/ISO 31010 in a general, non-subject-related way. All of these techniques and procedures are supposed to support the decision-making process, in a qualitative or quantitative approach.

2.1 Qualitative approaches

Qualitative approaches generally rank risks systematically, based on their probability of occurrence and their consequence. This is usually done in the early stages of a project, with few project specific data available. Key element is to try to estimate the probability of occurrence and the risk's consequence subjectively. A simple tool is the design of a risk matrix (Fig. 2), also called ´traffic-light matrix´ where identified risks are listed and compared based on their magnitude (Lacasse et al., 2019).

Engineering judgement plays a large role in risk management, assessment and decision making. Nevertheless, Baecher (2023) stresses the importance of "putting numbers on engineering judgement". It is argued that human judgment is flawed and biased, thus subjective estimates should be carefully reviewed.

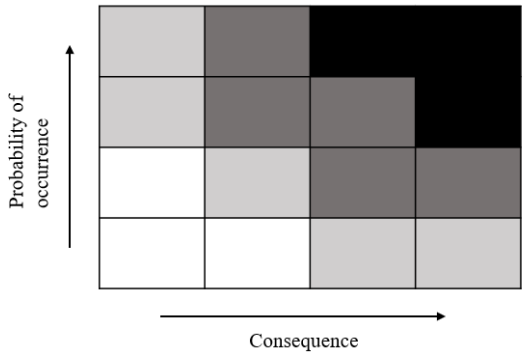

Figure 2. Qualitative 4x4 Risk Matrix.

2.2 Quantitative Approaches

As already mentioned, risk is defined as the probability of occurrence multiplied with its consequence. This common risk definition is flawed, since it accounts for low-probability/high-consequence risks equally as for high-probability/low-consequence risks. Depending on the project stakeholders, risk consequence must be defined differently (Baecher 2003). Quantitative risk management approaches aim to analyse these expected consequences based on known values. A common tool is to build a risk register. There, all risks are listed with their corresponding expected consequence and possibly other important information for the case of the risk occurring. Risk consequence is not trivial to estimate and is often known by a range in terms of cost. In that case, the expected consequence is usually calculated applying Monte-Carlo simulation to obtain the expected consequence distribution (NAP, 2018). A common and effective tool for risk management in a qualitative and/or quantitative manner is the analysis of event trees or logic trees. They provide an intuitive way of illustrating the progress of events. Here, "problems are decomposed into tractably small pieces and then brought back together to shed light on the prospect of system failures." (Baecher 2003). Event trees are similar to fault trees but fault trees start at the systems failure, leading back to an initial state.

Starting from an "initiating event", in the first level there is either a "success state" or a "failure state", both having a specific probability of occurrence. An event tree can have several levels or branches. This structure enables the assessment of different events occurring for complicated systems. An example of an event tree can be found in Figure 3. These risks and their probability of occurrence are usually depicted annualized. Event trees can become complex fast, with hundreds of events and branches. In reality, the probability of an event occurring is only for the simplest cases a constant value, but a function of several different parameters. For example, the grout anchor failure is dependent on its load. Event tree structure simplifies if the tree is regarded as a "model

of a physical system". This entails that only physical states are supposed to be modelled as events in the tree and other "states of nature" should be incorporated in the reliability analysis of the event governing the branch probability. Another option is to model states of nature within a logic tree, preceding event trees corresponding to a system. It is important to analyse geotechnical risks on the equal time axis, especially concerning natural hazards. At the end of an event tree branch one can accommodate a consequence tree, which is different type of event tree that models the failure state in more detail. To summarize, Logic trees can be utilized to model state of natures, event trees single system response and consequence trees the failure states (Baecher & Christian, 2003).

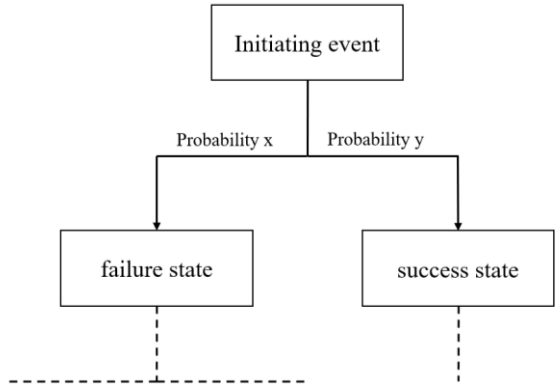

Figure 3. Event tree (simplified) according to Baecher (2003).

3 RISK ASSESSMENT

3.1 Uncertainty in geotechnical engineering

Risk Assessment is closely related to quantifying and estimating uncertainties and unknowns. Uncertainties are often separated in two categories, aleatoric and epistemic uncertainty.

Aleatoric uncertainty or random uncertainty is associated with processes whose variability comes from „a property of nature – independent of anyone's knowledge about it". Examples for these kinds of processes are more general dice throws or coin tosses i.e. repeatable experiments. In geotechnical engineering of soil properties are treated as aleatoric. Aleatoric uncertainties are per definition unpredictable and random, only natural hazard frequencies or spatial variations their relative frequencies of occurrence can be observed (Baecher & Christian, 2003).

Epistemic uncertainty stems from the engineering problem, that all models are imperfect, and cannot simulate completely accurate the conditions of real-world problems. Thus, epistemic uncertainty is characterised by *„imperfect knowledge"*, also *„knowledge based"* (Ang & Tang, 2008). Examples for these kinds of games uncertainties are card, or more geotechnically related model uncertainty or parameter transition uncertainty. Epistemic uncertainty is generally more subjective, meaning it is expressed less by frequencies but by the "*strength of belief"* in the truth or falsity of an event (Baecher and Christian, 2003).

Baecher and Christian (2003) advertise a slightly different naming and classification of uncertainty, which is more intuitive to the general engineer but does not differ substantially from the elaborations above. The authors discuss three categories of uncertainty:

- Natural variability
- Knowledge uncertainty
- Decision Model uncertainty

Thus, natural variability is a naturally random process approximated by statistical simplifications and knowledge uncertainty generally can be a lack of information. Underneath Decision Model uncertainty, the authors summarize other important sources like operational uncertainty, revolving around construction and human factors, or decision uncertainty which captures further construction management aspects of a problem like time preferences.

3.1.1 Spatial variability

The spatial variability of natural soil deposits was already recognised by Terzaghi (Wu, 2011). Currently, many research activities are devoted to the calculation of failure probabilities of complex systems using elaborate calculational models. Earlier publications like Duncan (2000) provide simple estimations, more applicable in a practical environment but less on complicated problems. Spatial variability is generally allocated to the 'natural variability' class of uncertainty. It means that observable geotechnical parameters are variable to different degrees in space, depending on their deposition and geological properties. Huber (2013) and Sudret & Der Kiureghian (2000) provide detailed reviews about how spatial variability can be treated in geotechnical engineering. In the following, common approaches to tackle special variability are elaborated in a simplified fashion.

A common way of describing spatial variability in subsoil is by applying random field theory. There are several ways of defining a random field (Liu et al., 2019), whereby in geotechnical engineering Gaussian random fields are mostly applied. Taking the measurements, the characterisation of spatial variability is carried out by separating the residual variation from a trend within the spatially varying soil property. The residual variation should be similar from the

different locations to be considered homogeneous. The random fields correlation properties are described by a correlation matrix, which is computed with an autocorrelation function. The autocorrelation function is supposed to approximate the statistical relationship of the spatially varying soil property in space. This implies that if data is plenty, a statistical analysis can be performed to determine the autocorrelation function by regression analysis. Common choices are exponential, second-order autoregressive or Gaussian usually calculated based on the scale of fluctuation (Li & Li, 2021).

Ching et al. (2023) investigated the two current trends of modelling spatial variability, sparse Bayesian learning and Gaussian process regression. They report the conclusion that Gaussian processes outperform sparse Bayesian learning in the case of 2D and 3D CPT measurements, and the other way around for 1D CPT measurements.

Random fields can also be utilized for reliability assessment using the Random Finite-Element Method. This numerical Monte-Carlo based approach computes the factor of safety of the system based on the statistical definition of the random field properties using Finite-Element analysis. Depending on the used techniques the calculated factors of safety can deviate substantially, compared to the 5% characteristic value specified by Eurocode 7 (Hicks, 2023). For more details and practical illustrations, the reader is referred to the works of Arnold (2016) and Varkey (2020). Liu et al. (2019) provides a general review about the advances in Gaussian random field generation.

3.1.2 Model uncertainty

Model uncertainty belongs to the class of knowledge- or epistemic uncertainty. It reflects the deviation between a prediction made by a model and measured behaviour. Model uncertainty influences the probability of failure strongly, which is why it should be accounted for (Phoon et al., 2022). ISO 2394 mentions a model factor, which is the ratio between the measured and predicted quantity. Zhang et al. (2015) introduced a technique based on two calculational models, one a numerical simulation, the other a mobilized strength model, calculating the top wall deflection of a cantilever retaining wall. The approach involves splitting the model factor into several different components. Their introduced correction factor splits into systematic and residual component. With the correction factor, first the model factor of the numerical model is determined, second the model factor of the analytical model is evaluated.

Bayesian methods can also be applied for determining the model uncertainty (Zhang et al., 2009) within that framework the model uncertainty is quantified by assuming a normally distributed model error with a mean value and standard deviation. Bayes Theorem is used to update these quantities accordingly. The procedure is illustrated with data of centrifuge modelled slopes to calculate the model uncertainty of common analytical methods for slope stability assessment.

3.1.3 Human factors

Sowers (1993) performed a comprehensive analysis of over 500 case studies of reported civil engineering failures. The author identifies three main causes of failure: absence, ignorance, and rejection of current technologies. Absence of knowledge or current technology denotes the cause of 12 % of failures. This includes lack of data, i.e. the magnitude of a 1000 year return period extreme weather event. It is argued that "blindly" relying on an estimation, based on the observed time period is ignorance or rejection. Ignorance is encountered by the author often in shape of a "know-it-all" attitude of engineers, who are often not properly qualified or experienced enough for specialized and complex problems. This cause is linked to 33 % of failures. Over 55 % of failures are classified in the rejection category, which includes several different aspects. The major ones that lead to rejection are faulty communications, pressures on the engineer like time, economical or ecological constraints. Thus, 88 % of failures can be appointed to human error. Some of the proposed mitigating measures are persisting engineering education, recognition of limitations and "resisting the unbalanced pressures that thwart good engineering" (Sowers, 1993).

Bea (2006) extends this discussion by reflecting the advances made in the field of quantifying uncertainty due to natural variation or model uncertainty even though these sources account for only 12 % of failures compared to the 88% influenced by human errors. The author introduced a framework that aims to include human, organisational, and knowledge related factors with existing reliability-based techniques. Different methods are proposed: proactive, reactive, and interactive. Each approach is linked to a different time where measurements are taken to either decrease the likelihood of failure occurring, adhere failure prevention based on analysis of near failure conditions, or intervening with proper management whilst failure builds up and thereby preventing its occurrence (i.e. the observational method, further discussed in section Decision Making). An example of an initial design for an offshore platform in mudslide prone territory is provided, where the probability of failure is evaluated based on intrinsic uncertainty (here, natural variation of the soil and analytical model

uncertainty), and based on extrinsic factors – probability of failure given a mudslide. The total probability of failure is strongly governed by the extrinsic probability failure, implying a short life time of 25-30 years of the structure. Overall, the author encourages the application of the outlined approaches like the use of the observational method for amending quality and reliability in geotechnical projects (Bea, 2006).

3.2 Reliability assessment

In geotechnical engineering, risk is defined as the product of probability of occurrence and the consequence, where the consequence is often defined in terms of financial cost but can take different shapes depending on the geotechnical structure and the failure mode (Einstein & Baecher, 2023).

The aim of geotechnical reliability analysis is the estimation of a probability of failure. ISO 2394 provides general guidance not limited to geotechnical engineering, Hereby ISO 2394 distinguishes between risk-informed and reliability-based approaches, where the difference lies in the incorporation of the consequences of failure.

3.3 Probability of failure

For the evaluation of the probability of failure, a performance function *g(x)* needs to be defined in dependence of a single parameter (random variable) *x* or a parameter vector $\bar{x}$. The performance function $g(\bar{x})$ indicates the failure domain of the system response if $g(\bar{x}) < 0$. If $g(\bar{x}) > 0$, the system would be in the safe domain (Fig. 4).

The parameters or random variables are described based on their statistical distribution (i.e. mean value and standard deviation for a normal distribution). For the calculation of the probability of failure, the joint probability density function $j(\bar{x})$ is needed, the mathematical formulation is defined as,

$$P_f = \int \dots \int_{g(x)<0} j(\bar{x}) d\bar{x} \qquad (1)$$

where the performance function is integrated with respect to each random variable. Depending on the system and the performance function, the integral usually is not solved analytically, but by simulation.

Another common method in geotechnical engineering is to express the reliability in terms of the reliability index β. If the performance function $g(\bar{x})$ is linear and the random variables are normally distributed,

$$P_f = \Phi(-\beta) \qquad (2)$$

with β being the ratio between mean μ_g and standard deviation σ_g of the performance function $g(\bar{x})$ and Φ being the standard normal cumulative distribution function. Here, a larger reliability index, results in a smaller probability of failure (Ji and Cao, 2023).

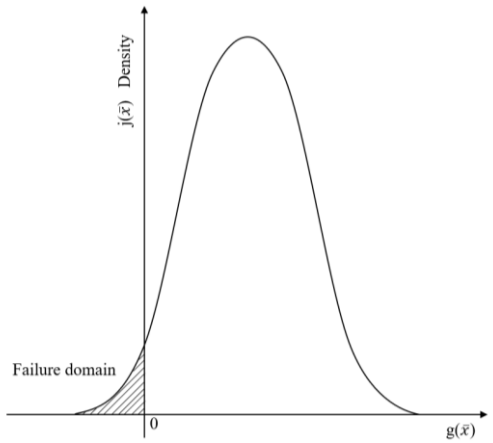

Figure 4. Illustration of the failure domain of a performance function.

The concept of a factor of safety is for many engineers that are not familiar with probabilistic methods more intuitive and the reliability index β can also be expressed in dependence of a calculated factor of safety *F*,

$$\beta = \frac{\mathrm{E}[F]-1.0}{\sigma[F]} \qquad (3)$$

with, *E[F]* being the expected value (or mean) of the factor of safety *F* and *σ[F]* being the standard deviation of the factor of safety (Christian et al., 1994). The formulation of the reliability index β enabled different analytical solutions that are capable of estimating the systems probability of failure, like the First-Order-Reliability-Method (FORM) or the First-Order-Second-Moment (FOSM) which are only discussed conceptually and simplified in this article.

Assuming the statistical distributions of necessary input parameters are known, to calculate the reliability index defined in Eq. 3, the expected value of the performance function (in this case the factor of safety formulation) and its standard deviation are necessary for evaluation. Based on a Taylor series approximation and assuming no correlation of the variables, the standard deviation is

$$\sigma[F] \approx \sum_{i=1}^{k} \left(\frac{\partial g}{x_i} \cdot \sigma_{x_i} \right) \qquad (4)$$

FOSM approximates the second moment of the performance function, using the second moments (standard deviations) of the variables with a first order truncated Taylor series. One limitation is, that the shape of the distribution of the performance function must be known for the calculation of reliability index

and/or probability of failure. A second limitation lies in implicitly assuming constant derivatives over the entire performance function domain using the Taylor approximation, (Baecher & Christian, 2003; (Christian et al., 1994). Further illustrations and more details are elaborated by Duncan (2000).

The FORM estimate eliminates the need of knowing the shape of the performance function. FORM lacks accuracy with increased non-linearity of the performance function. Then more orders of the Taylor approximation can be included into the formulation, making it more complicated but a more accurate linearization. The concept of FORM based on Hasofer & Lind (1974) is to first transform the correlated variables into uncorrelated Gaussian Space with the Rosenblatt transformation. In Gaussian space the joint probability density is supposed to be maximised with regard to the largest area in the failure domain. This corresponds to the minimum distance from the origin to the so-called design point. Thus, the FORM procedure is an optimization problem to find the minimum distance of the design point, which also corresponds to the definition of the reliability index β, which is often done using the Rackwitz-Fiessler iteration sequence. With the reliability index, the probability of failure can be estimated (Bucher. 2009).

FORM is one of the most common tools for reliability assessment in civil engineering, with various literature available. The implementation of FORM can be done in several different computational frameworks. For more details the reader is referred to the original source (Hasofer & Lind, 1974) or works published by Bucher (2009), Baecher & Christian (2003) or Ji & Cao (2023).

Another common approach to reliability assessment is by simulation applying Monte-Carlo analysis. There, the shape of the performance function does not need to be known and it does not need to be linear. Monte-Carlo involves solving the performance function for a large amount of simulations, depending on the accuracy required. The probability of failure can be expressed as,

$$P_f \approx \frac{1}{m}\sum_{i=1}^{m} I(g(\bar{x}^{(i)}) \quad (5)$$

with $I(g(\bar{x}^{(i)}))$ being an indicator function. Its result is either 0 if $g(\bar{x}^{(i)}) > 0$ (safe domain) or 1 if $g(\bar{x}^{(i)}) < 0$ (unsafe domain) for one sample i of $\bar{x}$. The "confidence" in the estimate of P_f becomes larger for a larger number of simulations m. The variance of the failure estimate is expressed as,

$$\sigma_{P_f}^2 = \sqrt{\frac{P_f}{m}} \quad (6)$$

For an infinite amount of simulations, the probability of failure would become exact. Especially the evaluation of low failure probabilities becomes computationally expensive and inefficient, which is why often more elaborate sampling techniques are employed like importance sampling, directional sampling, subset simulation, etc. (Bucher, 2009; Phoon et al., 2022).

Beer et al. (2013) discuss further on numerical reliability assessment techniques such as interval modeling, fuzzy modeling, Monte-Carlo simulations, and the idea of imprecise probabilities.

3.4 Metamodelling

The idea of applying surrogate-metamodeling and other machine learning techniques has gained popularity in recent developments revolving around reliability assessment of geotechnical structures. The motivation lies in the substitution of complex (numerical) formulation with an approximation of less computational cost. The combination of a metamodel with advanced sampling strategies enables the computation of low failure probabilities. One common technique is the Kriging approach, that has its origin in geostatistics for modeling spatial variability of soil properties. Zhang et al. (2011) define a Kriging model with Gaussian correlation and calibrate this model based on N simulations of a numerical model. This is performed by a maximum likelihood estimate, which is defined as a multivariate normal distribution based on the assumption that the N simulations can be modelled as a Gaussian random field. Once the model is calibrated, the performance function is evaluated for additional predictions. This is illustrated for a pile capacity model, a single foundation in layered soil and a slope in layered soil. The authors use the FORM approach for further reliability analysis.

Another application is described by van den Eijnden et al., (2022), where a metamodel is formulated using Gaussian processes, capable of updating the reliability of a river dyke. For the reliability analysis an active-kriging based Monte-Carlo simulation algorithm is proposed, that learns two Gaussian processes - one for prediction, one for classification - based on convergence criteria. The second metamodel is needed to classify the parameter space into separate domains depending on whether a converging solution can be found. This step is important to incorporate survival data i.e. a state of the construction process, where the numerical model calculated failure, but it did not occur in reality. This procedure is separately treated by van der Krogt et al. (2021).

Ordinary Kriging and Gaussian processes are often used and they are quite similar, in procedure and results. One of the main differences can be on how inferences are performed, either based on Maximum likelihood or variography, even though the results are nearly identical (Christianson et al., 2023).

Teixeira et al. (2021) provide a recent review about metamodeling approaches for reliability analyses. They compare the four most common techniques, response surfaces, polynomial chaos expansions, support vector machines and Kriging models. The Kriging model can be described as robust and versatile compared to the aforementioned methods, also being the only one capable of handling strongly non-linear performance functions. Nevertheless, the authors stress the necessity for hierarchical techniques for selection of the modelling approach and its assumptions.

3.5 Bayesian modelling

Bayesian approaches are also a trending field in geotechnical reliability analysis, since they offer the opportunity to draw inferences with a comparably scarce data basis. Based on this inference, uncertainty can be comfortably quantified. Various type of data can be used, completely depending on the statistical model that is defined. In geotechnical engineering, measurement data is frequently used for reliability updating.

One similar application is described by Jiang et al. (2018, 2022) and Geyer et al., (2021), where Bayesian techniques are used to update spatially varying soil parameters, described by random fields using field measurements. De Wolff et al. (2021) propose a Bayesian approach to update the retaining wall performance of deep excavation, using real-time measurement data. Hereby, wall-deflection measurements, obtained through the observational method, are used to update the model parameters of a spring model for computation of wall deflection. Baecher (2017) argues, that Bayesian methodology enables quantitative data analysis with regard to the observational method instead of the qualitative assessment. The author advocates these approaches to permit the observational method a computable interpretation, making stronger use of data and allowing distinct inference.

3.6 Consequence

The consequence in risk analysis is usually expressed in terms of cost, number of fatalities or a combination of both. Therefore, a common way of depicting risk is via probability-consequence charts or frequency-number (*FN*) charts. Figure 5 shows a *FN* Chart for the tolerable risk of different guidelines according to Lacasse et al. (2019) for dams, slopes or in a more general context. The Hong Kong guideline (Mak, 2006) is one of the most frequently used criterions. Even though the lines provide a clear distinction, the difference between acceptable and unacceptable risk is in practice less abrupt but more fluent. For cases where the fatality is larger than 1,000, a detailed assessment is recommended. Furthermore, it is suggested to define ALARP zones (´As Low As Reasonably Possible´), where the risk cannot be decreased without taking excessive and unreasonable measures. These could be generally implemented for low probability-high consequence risks, or for a number of fatalities > 1,000 (Lacasse et al. 2019; Mak, 2006).

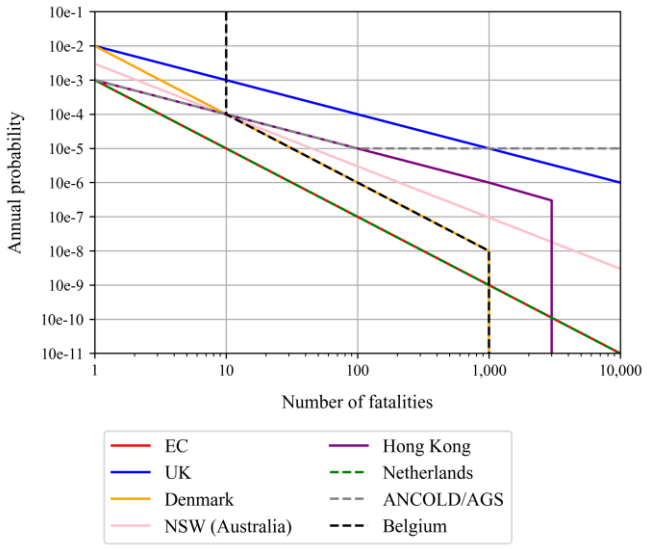

Figure 5. combined FN Chart of different guidelines for slopes, dams and general acceptance according to Lacasse et al. (2019).

4 DECISION-MAKING

Burland (1987) proposed the ´soil mechanic triangle´, later renamed the ´geotechnical triangle´, where he combines the fundamentals of geotechnical engineering, reflecting the views of Terzaghi, Casagrande and Peck, with one of its original purposes of guiding the development of soil mechanic courses. Phoon et al. (2022) extended the triangle by incorporating further sources of uncertainty associated with the main three elements in geotechnical engineering (Fig. 6):

- ground profile
- soil behaviour
- idealised model

All of the assumptions revolving around these key elements are to some extent uncertain, which is why one aims to quantify these uncertainties in the scope of

decision-making and risk management (Phoon et al., 2022). The extended triangle lists techniques and other points of attention to support the decision-making in geotechnical engineering projects.

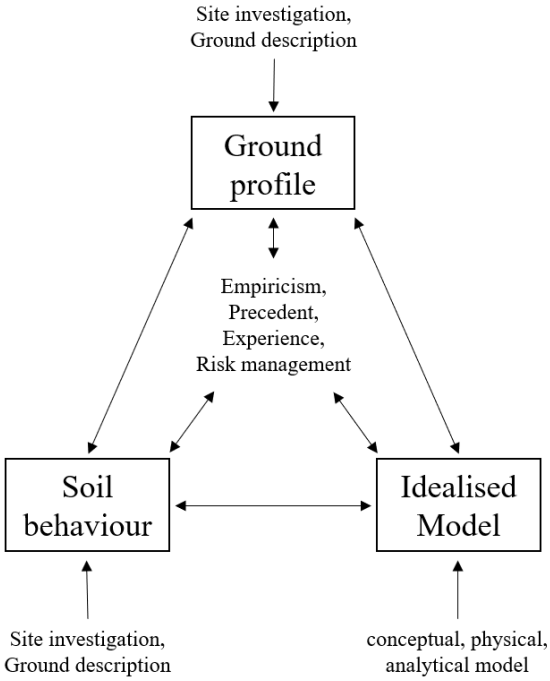

Figure 6. Geotechnical triangle according to (Phoon et al., 2022) and (Burland, 1987).

Phoon et al. (2022) list a large number of tools to quantify uncertainty of various sources and complexities. All of these approaches and numerical methods in general are supposed to aid the engineer to perform uncertainty-informed decision making, stressing the need for uncertainty quantification.

One of the earlier, non-calculational tools for uncertainty assessment is the widely applied observational method. It was first introduced by Terzaghi as "learn-as-you-go" and later backed-up by Peck (1969). It is a common technique in geotechnical engineering supporting risk management and decision-making. The key concept is to propose a design based on the available information at that time whose resulting magnitude can be measured on site. Next, a field measurement concept is introduced, aiming to measure quantities that can be related to the initial design assumptions and reduce uncertainty about site conditions. Based on the measurements, the uncertainty about site conditions decreases and the initially proposed design can be adapted as necessary (Wu, 2011).

Wu (2011) discusses the successful application of the observational method based on several case studies of embankment construction. The applications are versatile, i.e. the improved estimate of highly sensitive model input parameters or Bayesian updating of the material properties of a Finite-Element model.

The observational method is an intrinsically Bayesian concept, which optimally can be coupled. Bayesian thinking and Bayesian analysis enables a quantitative evaluation of the observational method (Baecher, 2017).

Einstein & Baecher (2023) elaborate on Bayesian ways to support decision-making. They provide two examples of large-scale tunnelling projects, the Gotthard-Basis-Tunnel and the Brightwater Conveyance Tunnel Seattle. For the Gotthard-Basis-Tunnel Bayesian methods where applied in combination with the observational method to predict the tunnelling cost and schedule, applying the Decision Aids for Tunnelling computational tool. This is achieved by updating the lithology section-wise using geological data, boring information, etc.

5 FORENSIC ANALYSES

In literature there are several examples focussing on the back-analysis of failed structures, called forensic analyses. In the following, two examples are illustrated.

5.1 Slope collapse in Taiwan

In the year 2010 a landslide occurred on Taiwan's' Freeway No. 3, north of Taipei (Fig. 7). As cause of failure Wang et al. (2013) reported a worsened shear strength of the soil and degenerating anchors.

They obtained this conclusion by conducting a Bayesian probabilistic analysis to calculate the soil shear strength (friction angle) and the ground anchor forces. The adjacent rock stratigraphy exhibits dipped slopes with an inclination of 10° to 30°, thus the slope was highly prone to sliding on a rock surface to begin with (Wang et al., 2013).



Figure 7. Landslide 2010 on Freeway 3 in Taiwan, (source: https://www.nasc.gov.tw).

For Bayesian analysis in geotechnical engineering there are generally no closed form solutions available since the formulated likelihood functions are not conjugate with the prior distributions. Therefore, Wang et al. (2013) utilized a Markov Chain Monte Carlo algorithm called Metropolis-Hastings to calculate the posterior distribution (probability distribution for a given data set) with defined lognormal prior distributions and likelihood function. The likelihood function connects a factor of safety formulation based on a slip surface limit equilibrium formulation with an error term. The study reports only the lognormal marginal distributions and not the joint distribution or the posterior predictive function. The authors focus on an illustrating the comparison of a Maximum Likelihood analysis compared to the full Bayesian approach. Nevertheless, the benefits of performing a statistical analysis of this case study are laid out, since the results aid in interpreting the cause of failure, governing the decision making for the remediation. Based on this collapse, the authors stress the importance of anchor maintenance.

5.2 Levee failure in Breitenhagen

Kool et al. (2019) describe a comprehensive forensic analysis of the Breitenhagen levee breach (Fig. 8). In 2013 the rivers Elbe and Saale in Germany exhibited high water levels which was partly a cause for the breach of a levee located close to the confluence of both rivers, in proximity to the village Breitenhagen.



Figure 8. Levee failure at Breitenhagen, aerial view (source: Kool et al. 2019).

The forensic analysis was conducted non-probabilistic. Therefore, the likelihood of occurrence was estimated subjectively, which is concluded not to be the optimal way of assessment. Furthermore, it is claimed that the results were majorly influenced by the lower bound soil parameters, especially a low cohesion, which had to be estimated based on Dutch and German codes. Nevertheless, the authors provide a detailed framework for the forensic analysis of levee failures. It involves the definition of an initial model based on the available data and modelling boundary conditions to justify the model choice. Based on elaborate sensitivity analysis the model input parameters are systematically varied as scenarios. The evaluation of the scenarios allows insight to identify the most likely scenario corresponding with the failure condition. Kool et al. (2021) extend this study with the incorporation of a Bayesian approach for the back-analysis. The authors use FORM for the reliability assessment, and can reach via the Bayesian method a more objective estimate of the most likely scenario matching the failure.

6 CASE STUDY: COLLAPSE OF THE HISTORICAL ARCHIVE IN COLOGNE

On March 3rd, 2009 the Historical Archive of the City of Cologne, Germany, and adjacent residential buildings collapsed (Figs. 9 and 13). These buildings were located at the square ´Waidmarkt´ in the immediate neighbourhood to the deep excavation ´GWB´ which was part of the construction work for a new 4.3 km long north-south underground line in Cologne. At the time of the accident the final excavation level had just been reached around 26.6 m below ground level. The collapse was a dramatic loss for Cologne's urban society but has also a severe impact on other underground and infrastructure construction activities. With a damage amount evaluated to around 1.2 billion euros it was the most serious accident on a German construction site to date.

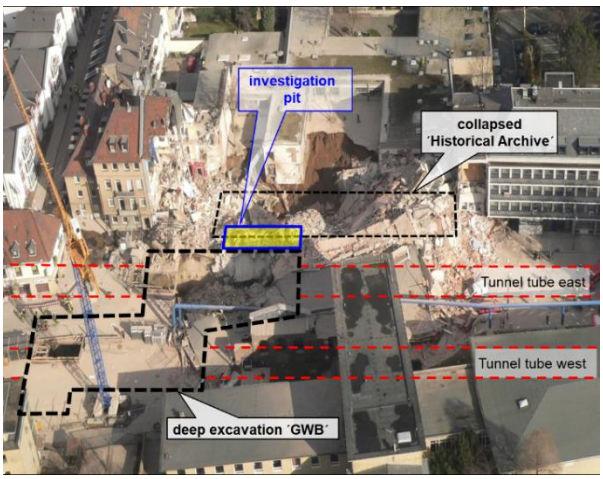

Figure 9. Aerial view of the collapsed Historical Archive and neighbouring residential buildings on Cologne's Waid-markt immediately after the accident on March 3rd, 2009.

After phases of immediate stabilisation, salvage and an initial survey, the cause of the damage was clearly clarified through a technically highly demanding investigation of evidence lasting more than twelve years, during which, among others, a 34 m deep

inspection shaft was executed in direct neighbourhood to the potentially damaged diaphragm wall of the deep excavation ´GWB´. As the measures for the conservation of evidence and for the investigation of the cause of damage were concluded and based on that a settlement between employer and construction joint venture was reached in 2020, it is possible to report on the measures and the identified cause of damage.

6.1 Deep excavation ´GWB´

The excavation pit ´GWB´ was constructed with diaphragm walls with wall thicknesses of 1.0 m and 1.5 m. With regard to the stabilisation against hydraulic ground failure the diaphragm walls were embedded up to 45 m below ground level, i.e. a lower wall edge of 2.8 m above sea level (a.s.l.) in the corner areas and 6.25 m a.s.l. on the long sides of the walls considering the higher hydraulic gradients resulting from the spatial inflow at the corners of the excavation (Aulbach & Ziegler, 2013).

The retaining walls were anchored in the upper part and braced by two reinforced concrete slabs constructed during excavation at 10.0 m (37.8 m a.s.l.) and 17.3 m (30.5 m a.s.l.) below ground level (Fig. 10a).

The dewatering in the ´GWB´ pit was carried out via wells arranged in the footprint of the excavation pit and filtered in the quaternary and/or tertiary, which led to a lowering of the free groundwater level in the quaternary and a (partial) relaxation of the tertiary aquifer. Within the diaphragm wall enclosure the groundwater level in the quaternary layers was lowered by open dewatering.

Overall, the realised excavation corresponds to the in the past often successfully realized concept of a "tertiary excavation pit" with water-pressure-retaining walls embedded into the tertiary in conjunction with an internal tertiary dewatering system to relieve the hydraulic head in the Tertiary below the excavation bottom. The relief of the tertiary hydraulic head is essential to ensure the hydraulic stability of the excavation base and to minimise upward flows in the earth resistance area of the retaining walls.

6.2 Subsoil conditions

The subsoil conditions at the ´Waidmarkt´ site are illustrated for a east-west section in Figure 10. Below street level and up to 6 m thick fillings Pleistocene terrace deposits (Quaternary) down to a depth of around 14 m a.s.l. which consist of terrace gravels and sands of the Rhine of varying grain size and composition, into which cohesive, slightly silty secondary sediments and isolated cohesive layers of decimetre thickness can be incorporated in some areas.

a) Before collapse

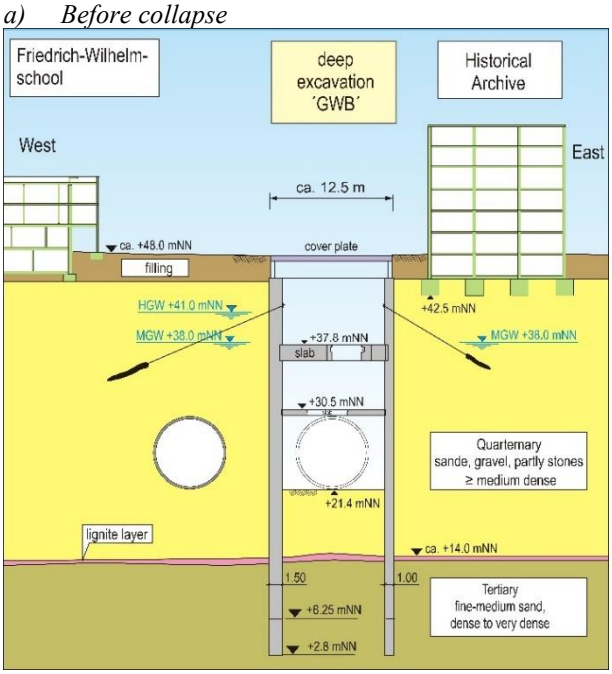

b) After collapse

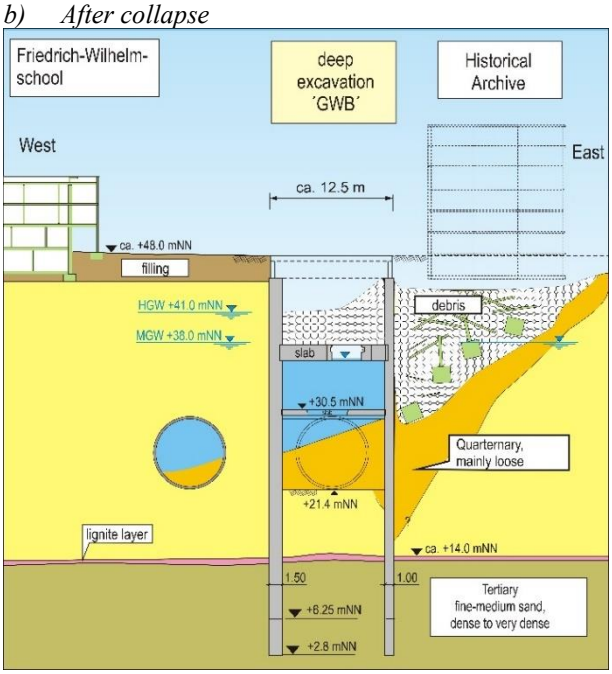

Figure 10. East-west section through the deep excavation ´GWB´ with neighbouring buildings and subsoil situation (position of section corresponds to section 1-1 in Fig. 11).

Separated from the terrace body by a thin layer of tertiary fine sand, the surface of an Oligocene lignite layer is reached at approx. 14.0 m a.s.l. which was explored in predominantly continuous thicknesses of 0.7 m to 1.8 m, but is also exposed locally.

The lignite is underlain by tertiary dense to very dense fine-medium sands which were exposed as a largely uniform layer with a thickness of approx. 48 m down to a depth of -35 m a.s.l. Due to their high uniformity ($C_U \leq 2$) and their mica content, the water-filled tertiary sands can be easily hydraulically

mobilised what must be considered for dewatering, drilling works etc.

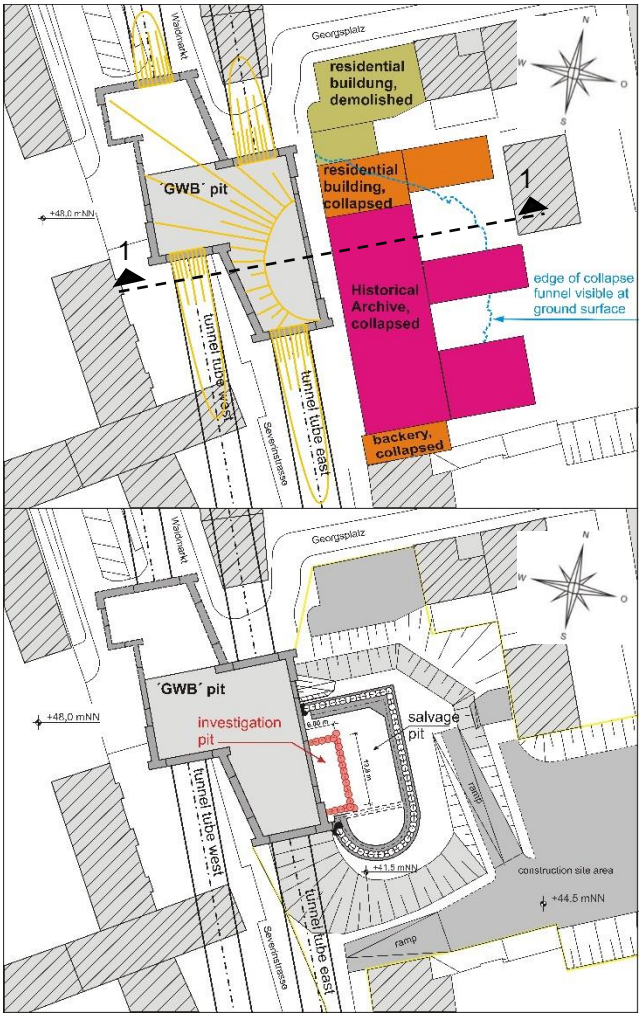

Figure 11. Site plan of the deep excavation ´GWB´ at ´Waidmarkt´ square in Cologne, a) at the time of the collapse with existing buildings and upper edge of the failure funnel, b) with salvage pit and investigation pit after the accident during salvage and preservation of evidence.

Concerning the groundwater situation, two aquifers have to be considered, a quaternary and a tertiary aquifer. The local hydrogeological conditions at the ´Waidmarkt´square are strongly influenced by the river Rhine and its water levels, both in terms of groundwater levels and the direction of groundwater flow. The groundwater levels in the Quaternary follow the water levels of the Rhine, which is located approx. 400 m east from ´Waidmarkt´, with a slight attenuation and generally fluctuate between approx. 36.5 and 40 m a.s.l.; at high tide whereat water levels of 41.5 m a.s.l. and more are reached in exceptional cases. The groundwater levels in the tertiary aquifer are at around 36 to 39 m a.s.l. and also follow the changes in the Rhine level with slight attenuation.

6.3 Execution of the deep excavation

The diaphragm wall was already constructed in 2005 using the conventional two-phase method. As joint system lost flat steel profiles were used which had a smooth surface on the side of the subsequent panel. When excavating the neighbouring panel, the tool used for cleaning the joint and removing concrete that has flowed in behind the joint profiles was therefore not guided by the joint construction. In fact, the cleaning of the diaphragm wall joints resp. stop ends was only partially successful, so that in the course of the excavation leaks occurred in several places at the joints, which required sealing measures to stop local water inflow.

An analysis of the execution records of the diaphragm wall carried out after the accident shows that obstacles were encountered during the production of panels #10 and #11 (Fig. 12) of the eastern diaphragm wall. During the construction of bite #10.3, obstacles were encountered at a depth of approx. 25 m (21.8-22.8 m a.s.l.) which made the use of a chisel necessary. The problems were even more severe during the following construction of the neighbouring panel #11, which was planned as a 3.4 m wide single bite closing panel being the last panel to be executed for the whole ´GWB´ pit. Massive obstructions were encountered in this panel at a depth of approx. 23 m (23.2-22.8 m a.s.l.), which caused a damage to the grab shells used. This obstruction could not be removed even with the use of chisels. In consequence, the grab shell was changed from 3.4 m to 2.8 m wide and the excavation of panel #11 was continued to the final level. An evaluation of the recorded concrete consumption shows a lower additional consumption for panel #11 compared to the theoretical concrete consumption than for the other panels. It was not possible to precisely analyse the increase or decrease in concrete consumption over the height due to the small number of measuring points; however, a decrease in concrete consumption up to the height of the obstacles encountered is recognisable.

With regard to the quality assurance and records of the diaphragm wall construction, further anomalies were identified, e.g. identical logs of the verticality measurements of panels #5 and #11 as well as missing acceptance records of the reinforcement cages and indications of missing shear reinforcement which had to be added on site in the course of coupling the reinforcement cage sections over the open trench.

After excavation of the ´GWB´ pit to the lower edge of the cover plate (Fig. 10a) and construction of the cover plate at street level, excavation was interrupted for tunnelling with TBMs passing in 2007 the non-excavated pit during the shield drive for the

construction of the eastern and western tunnel tubes, before further excavation below the cover plate was continued applying a top/down method in 2008.

Parallel to the further excavation, dewatering was carried out in the excavation pit, initially with four discharging wells (B1 to B4) and four relief wells (E1 to E4) connecting the tertiary with the quaternary aquifers (Fig. 12). As it was not possible to achieve with these wells a groundwater drawdown corresponding to the excavation progress and, in particular, the necessary relief of the hydraulic head in the tertiary aquifer three further discharging wells and a total of 19 additional wells were successively installed (Fig. 12). The recorded water extraction rates show that despite the roughly constant water level differences between the outside and inside water levels over a longer period of time, a significant increase in the extraction rate from around 115 l/s (corresponding to 414 m³/h) to around 180 l/s (648 m³/h) and a maximum of >200 l/s (720 m³/h) was recorded at the beginning of December 2008 in connection with the commissioning of additional wells. These pumping rates were significantly higher than the expected water extraction rates.

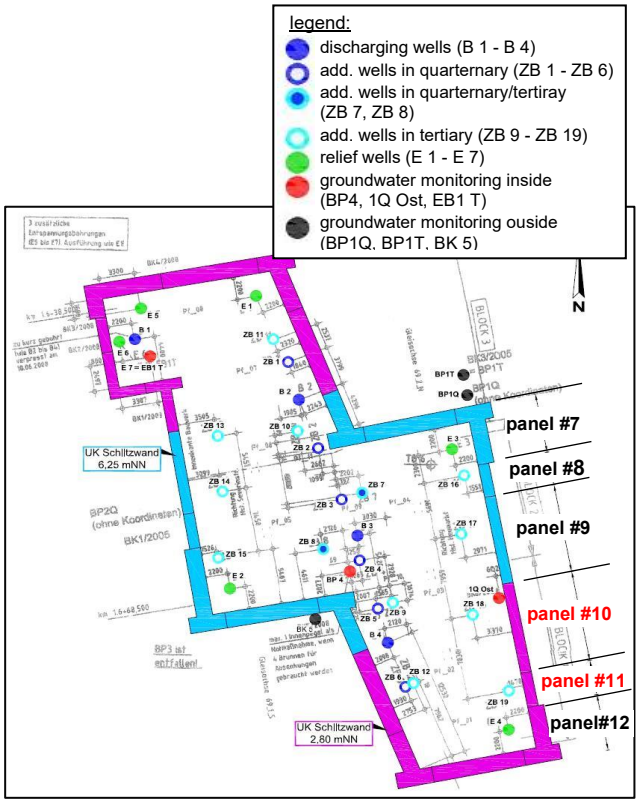

Figure 12. Ground plan of the excavation pit ´GWB´ with groundwater discharching and relief wells; status before collapse in March 2009.

At the time of the accident in March 2009, the ´GWB´ pit had largely been excavated to the final excavation level: while the reinforcement of the floor slab had already been laid on the clean layer in the western section, the excavation of the last 0.3 m for the construction of the final subgrade was carried out in the eastern section, starting from the rough subgrade. At midday on March 3rd, 2009, work began on the construction of a pump sump for water collection below the planned final excavation level in order to control water ingress from the diaphragm wall in the area of the joint between panels #10 and #11 (positon of panels marked in Fig. 12).

6.4 Collapse of March 3rd, 2009

On March 3rd, 2009, at 13:58 pm, an accident occurred in the deep excavation ´GWB´ during which about 5,000 m³ of sand and gravel flowed into the excavation pit, causing the collapse of the adjacent ´Historical Archive´ of the City of Cologne, a massive 7-storey reinforced concrete skeleton building, immediately adjacent to the excavation pit to the east, as well as of parts of the adjacent multi-storey residential buildings on both sides (Fig. 11a). The spread foundation of the Historical Archive, consisting of single and strip foundations founded in the quaternary sands and gravels, sank into the ground (Fig. 10b); foundations were later recovered from a depth of up to 20 m below ground level. This sudden “loss of foundation” caused the building to tilt towards the street, then to completely collapse, thereby partly falling into the excavation pit, breaking through its covering (Figs. 9, 13). The soil inflow at the lowest level of the excavation pit resulted in the formation of a cone of debris up to 7 m high consisting of quaternary sands and gravels, the foothills of which reached into the four tunnel tubes (Fig. 11a) and whose greatest height was directly in front of the eastern diaphragm wall (Fig. 10 b and 11b). Although the workers fleeing from the final excavation level of the ´GWB´ pit who had noticed a rapidly increasing water and then soil ingress during final excavation and construction of the pump sump in front of the eastern diaphragm wall, warned the visitors to the Historical Archive and the residents of the neighbouring residential buildings of the impending accident at the proverbial last minute, two young residents tragically died in the subsequent collapse of the residential buildings. At that moment, around 30 linear kilometres of archives from 1,200 years of Cologne´s city and regional history, the city's memory that has grown over the centuries, seemed to have been destroyed within seconds and lost forever.

6.5 Immediate stabilisation measures

On the evening of March 3rd and on March 4th, 2009, initial inspections of the damaged area and immediate measures to stabilise the excavation were carried out

by placing around 1,600 m³ of concrete on the base of the excavation (´ballast concrete´) via the northern staircase and on March 8th, 2009, an inspection of the tunnel tubes was carried out in order to decide on further safety measures to avert danger. This was followed by the demolition of the neighbouring residential buildings being at risk of collapse. In addition, a comprehensive monitoring programme was installed for the excavation pit and on the existing buildings and continuously adapted in order to detect any further risk to stability at an early stage.



Figure 13. Salvaging the archives from the rubble of the collapsed Historical Archive at Waidmarkt, looking west with the eastern diaphragm wall of the ´GWB´ pit.

In an initial salvage phase, the fire brigade and the Governmental disaster relief organization carefully removed the huge cone of rubble and debris under the protection of a temporary lightweight hall erected over the excavation pit (Fig. 13) and handed over the archive material that came to light to archivists and many volunteers. In the east of the ´GWB´ pit, in the area of the collapse funnel recognisable here by its tearing edge (see Fig. 11a), the debris from the historical archive was removed to just above the mean groundwater level, i.e. around 9 m below street level. In this way, by September 2009, 85 % of the archive material had already been recovered, albeit mostly severely damaged. The recovered relics were initially stored temporarily in almost 20 asylum archives throughout Germany. Damp archive materials were partially freeze-dried to prevent mould growth.

6.6 Deep excavation for salvage

After salvaging the rubble and archival material down to the mean groundwater level (38 m a.s.l.), investigations carried out up to that point revealed that further rubble from the Historical Archive had ´slipped´ down to a depth of around 20 m below ground level (28 m a.s.l.) in a comparatively narrow collapse funnel. For the City of Cologne, the obligation towards its own historical heritage and to the various lenders of archive items made it necessary to take all reasonable measures to salvage these archival materials buried below the groundwater level, so that a so-called ´salvage excavation pit´ was planned and realised for this purpose.



Figure 14. Salvage pit (in the foreground) in front of the eastern diaphragm wall of the ´GWB´ pit.

Based on a conceptual study, the excavation pit was constructed in the form shown in Figures 14 and 15 with ground plan dimensions of around 16.5 m by max. 30 m and a rounded section (´apse´) in the south, as a particularly large amount of archival material was suspected here. The excavation pit thus enclosed significant areas of the explored excavation funnel. The construction pit was secured on three sides by a secant bored pile wall (pile diameter D = 1.2 m, pile length 29.5 m) and braced against the eastern diaphragm wall by a circumferential reinforced concrete beam with three tubular steel struts and a reinforced concrete strut which were pre-stressed by hydraulic presses.

An additional 24 micro-piles which together with the bored pile wall formed a type of pile-trestle construction were installed at the eastern wall of the salvage pit in order to transfer the strut forces into the ground with minimal deformation. The horizontal loads were thus transferred from the west side of the ´GWB´ pit via the concrete slabs and the damaged eastern diaphragm wall into the salvage pit. The connection of the bored pile walls to the diaphragm wall of the ´GWB´ pit was realized with ground freezing after an initial stabilisation using foam injections proved to be insufficient. The rubble and archives were excavated under water. Possible horizontal displacements of the eastern diaphragm wall of the ´GWB´ pit at the level of the upper concrete slabs had to be limited to 2 mm to 3 mm at maximum. Construction of the salvage pit began in spring 2010.

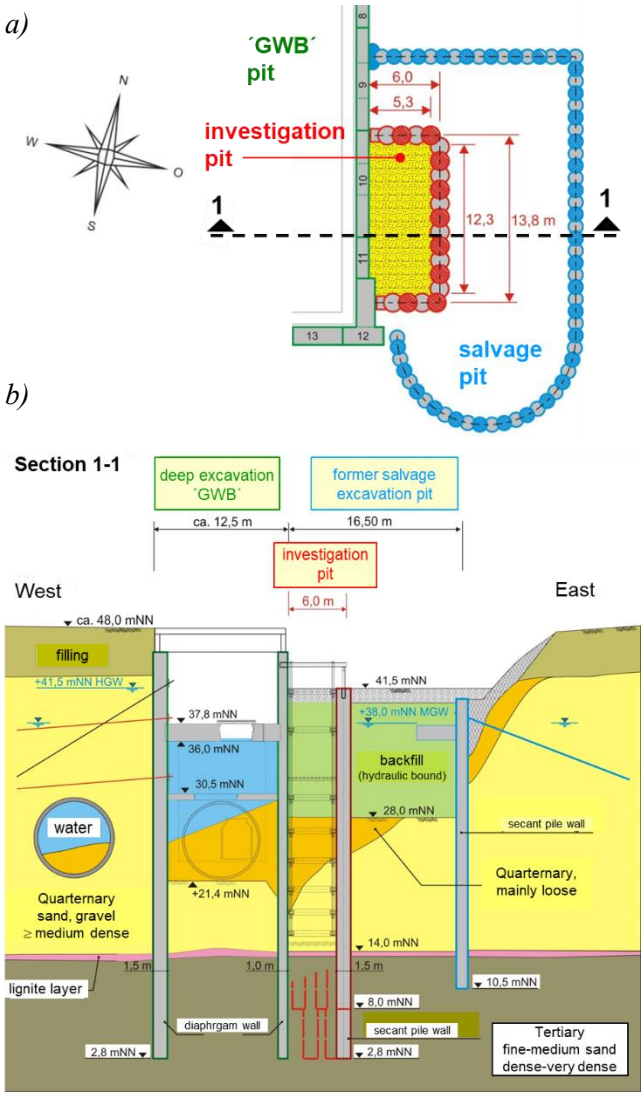

Figure 15. Salvage pit and inspection pit to the east of the ´GWB´ pit: a) ground plan, b) cross-section 1-1.

Due to some difficulties in the construction process and due to unexpectedly large and difficult to salvage foundation bodies weighing up to 30 t, the salvage of the archival material was completed just in summer 2011. The area covered with archival material ended above the predicted depth of 28 m a.s.l. Nevertheless, excavation was carried out to this depth and the remaining debris in the excavation pit was removed to ensure a clear construction area for the subsequent investigation pit. This work and the subsequent collection of evidence within the salvage pit by the court-appointed expert and the experts from the public prosecutor's office lasted until spring 2012, after which the salvage pit was backfilled with a flowable, hydraulically bound material and the temporary struts were removed. During this process, a pre-stressed reinforced concrete structure was installed in the salvage pit at the level of the upper concrete slab of the ´GWB´ pit to provide low-deformation support for the eastern diaphragm wall, taking into account the requirements of the subsequent inspection pit (Fig. 18).

6.7 Investigation of the cause of damage

The clarification of the cause of the damage was the subject of technically extremely demanding and extensive investigations, which - interrupted by construction measures to create the necessary boundary conditions for the preservation of evidence - lasted from 2009 to 2020. In addition to the investigations by the public prosecutor's office in Cologne, evidence on the cause and avoidability of the collapse was collected in an independent preservation of evidence procedure initiated by the owner immediately after the accident. Prof. Dr.-Ing. H.-G. Kempfert, Hamburg, was appointed by the Cologne Regional Court as geotechnical expert in the independent evidence proceedings.

From the outset, two possible scenarios were analysed in parallel with regard to the cause of the collapse of the ´Historical Archive´ building:

- "Suspected area of diaphragm wall quality" with horizontal soil ingress, for example through a void area in the diaphragm wall;
- "Suspected area of vent formation" with vertical soil ingress into the excavation pit through its base, for example through breakthroughs in the lignite layer.

6.7.1 Indirect investigations

Immediately after the collapse subsoil investigations were carried out to clarify the subsoil conditions and to examine the stability of the excavation pit and of the surrounding buildings including several public secondary schools. These investigations already formed a dense grid, which was supplemented with further investigations by the expert in the court evidence from 2009 to the beginning of 2010. Further investigation campaigns followed, including investigations requested by the parties involved in the preservation of evidence process. The scope of the exploration finally realised (Fig. 16), including a total of 113 core drillings, 260 heavy dynamic probing tests (DPH), 186 borehole dynamic probing tests (BDP) and 18 cone penetration tests (CPT), was so intensive that further condensation of the grid was no longer technically reasonable, particularly in the vicinity of the eastern diaphragm wall. In addition, extensive laboratory tests were carried out also. These investigations made it possible to identify the centre of the damage to a tightly confined area in the vicinity of panel #11 in the eastern part of the diaphragm wall of the ´GBW´ pit.

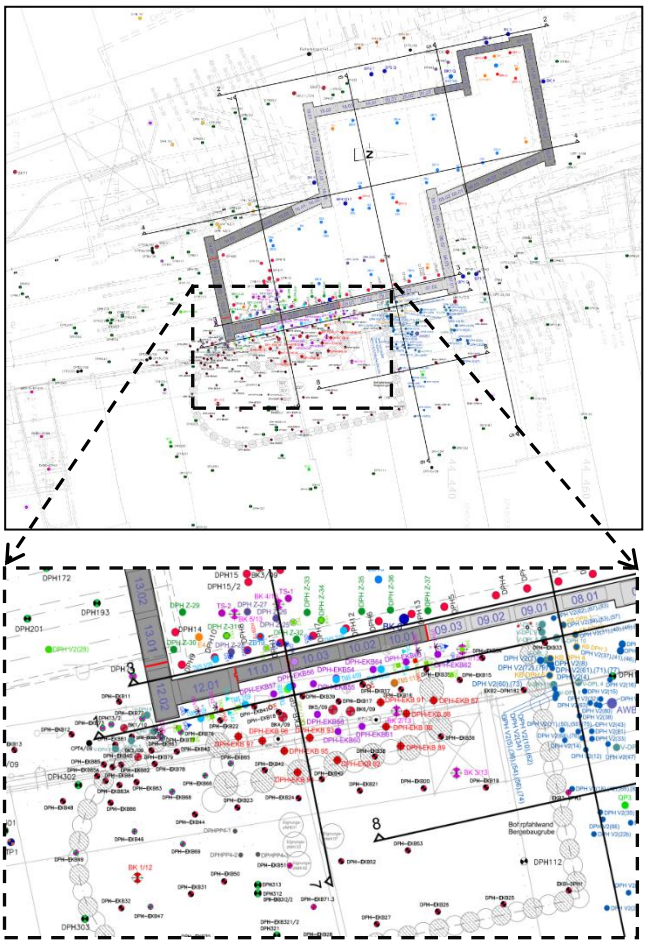

Figure 16. Ground plan: Soil investigation focusing on the south-eastern corner of the ´GWB´ pit.

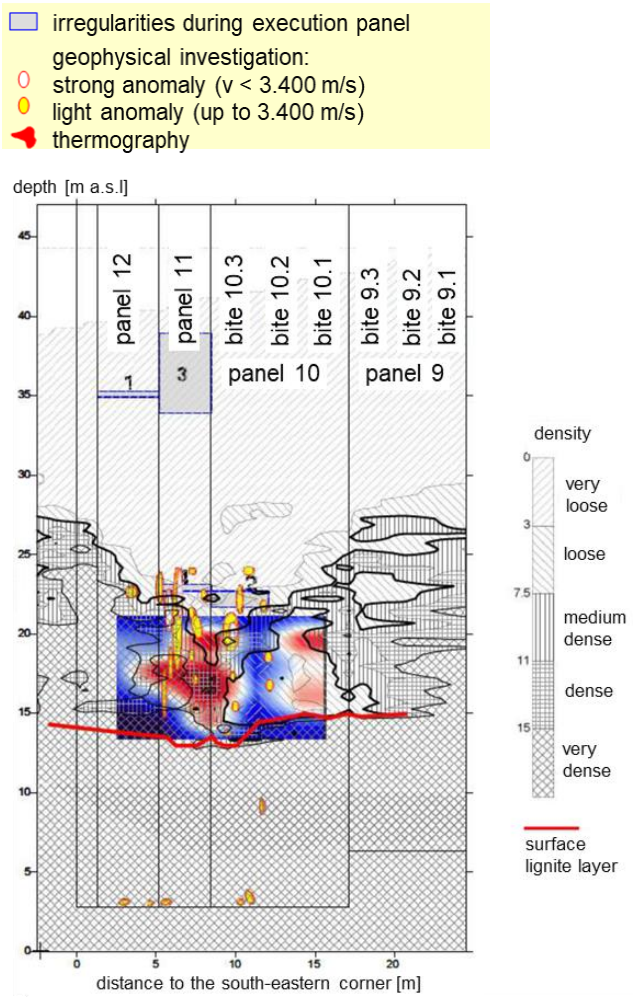

Figure 17. View of the eastern diaphragm wall of the ´GWB´ pit (looking west) with comilation of the results of all indirect exploration measures (source: expert report by Prof. Kempfert (2011-2020), modified).

The core drillings being modified to monitoring wells were used by the court-appointed expert to investigate the integrity of the eastern diaphragm wall of the ´GWB´ excavation pit by applying indirect methods. In particular, seismic cross-hole tomography was successfully used to check the presence, quality and integrity of the diaphragm wall panels. The planned geometric embedment of the diaphragm wall panels could be verified, but at the same time, in the area of the joint between the adjacent panels #10 and #11 at a depth of approx. 16 m to 23 m a.s.l., i.e. between the final excavation level down to the quaternary base, significantly reduced local wave velocities were clearly recognisable identifying anomalies (Fig. 17).

Supplementary thermographic investigations in the form of fibre-optical temperature measurements in combination with the heating method (heat pulse method) showed clear and significant temperature anomalies in the groundwater flow and thus clear indications of hydraulic pathways in the area of the joint between the diaphragm wall panels #10 and #11 in a depth range of approx. 13 m to 20 m a.s.l. (Fig. 17). However, there were no indications for a vertical flow around the base of the diaphragm wall.

In accordance with the anomalies identified during the construction of diaphragm wall panel #11 (see section 6.3), the results of the investigation gave rise to the suspicion that the accident was probably due to one - or possibly several - defects in the joint area of the eastern diaphragm wall, in particular in the joint area between panels #10 and #11 at a level between the final excavation level and the lignite layer (Fig. 17), while a hydraulic ground failure was largely ruled out as the cause of the failure and an erosion ground failure due to a thin vent appeared unlikely even as a (co-) cause of the damage event (Sieler et al. 2012).

6.7.2 Investigation pit: concept

While the numerous indirect investigations had already provided reliable indications of the cause of the damage related to "Suspected area of diaphragm wall quality", a direct visual inspection of the suspected areas was required to dispel the last possible doubts regarding the cause of the damage.

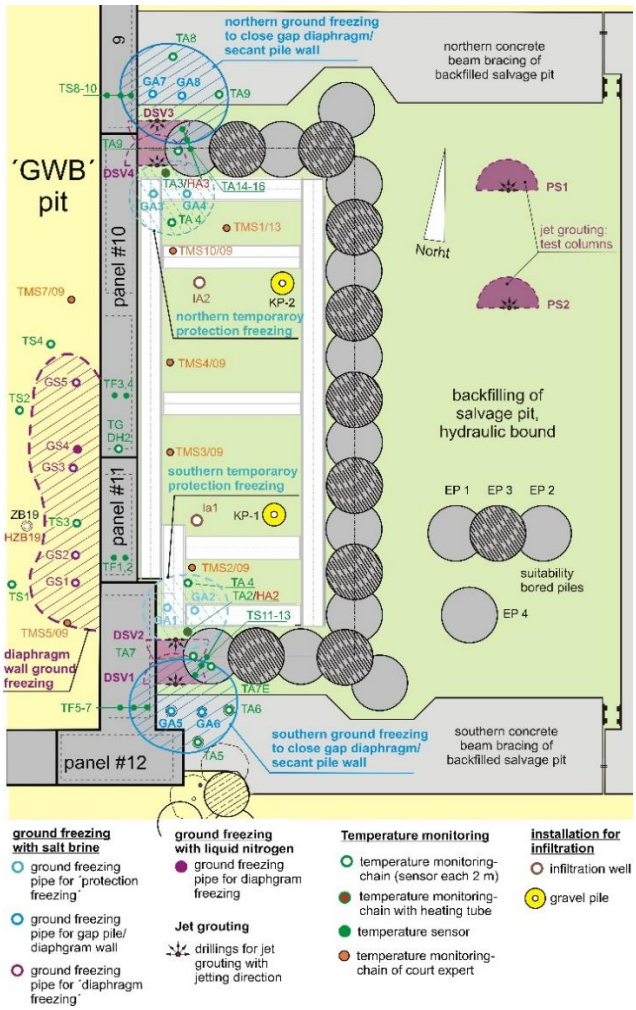

Figure 18. Ground plan of the investigation pit with secant bored pile wall and connecting construction to the diaphragm wall of the ´GWB´ pit plus ground freezing for the diaphragm wall.

In this regard, the construction of an inspection pit inside the ´GWB´ pit (as part of the recovery of the excavation pit) and the construction of an external excavation pit were discussed as alternatives. After the decision on the recovery concept was delayed, the Cologne Regional Court ordered the construction of an external investigation pit in December 2010 in accordance with the specifications of the court-appointed expert. This investigation pit, located in the centre of the collapse funnel in front of the diaphragm wall panels #10, #11 and #12 of ´GWB´ pit, had comparatively small ground plan dimensions of around 6.0 m x 13.8 m (axial dimensions) or 5.3 m x 12.3 m (clear internal dimensions, see Figs. 11b and 15) and was intended to allow inspection of both the diaphragm wall and - layer by layer - the subsoil conditions down to the surface of the lignite layer, which was expected at 14.0 m to 14.8 m a.s.l. in the construction area of the investigation pit, i.e. at a depth of 34 m below street level resp. 27.5 m below working level. The investigation pit was designed for underwater excavation and inspection by divers. In a second stage, it was considered as a supplementary option, and this was also taken into account in the planning and design of the pit, to deballast the inspection pit using compressed air. However, the use of compressed air was considered optional and made dependent on the findings obtained during the underwater exploration. The design of the investigation pit is reported in detail in Moormann et al. (2014). The main elements are presented hereinafter.

6.7.3 Investigation pit: Retaining wall

The investigation pit enclosure was constructed on three sides as a secant bored pile wall with large diameter bored piles (D = 1.50 m) (Fig. 17). The pile base level was initially planned uniformly at 2.8 m a.s.l., corresponding to the depth of the diaphragm wall of the ´GWB´ pit. The planned pile length was therefore almost 40 m. The piles had to be executed fully cased while maintaining a water load inside the casing to be controlled depending on the quaternary groundwater level and a sufficient advanced penetration of the casing below borehole level in order to minimise construction-related loosening, particularly with regard to the sensible evidence situation. Under the special requirements, test piles were initially executed in order to test suitability of the execution process. Despite the use of a powerful rotary drilling rig (´BG 40´), the first test pile could unexpectedly not be drilled down to its final depth at the end of 2012, as after drilling through the lignite layer it was not possible to drive the casing into the tertiary sands with the required forward penetration. As a result of the execution of further test piles, various optimisation approaches were identified, in particular a reduction in the statically required embedment depth of the secondary piles by 5.2 m to 8.0 m a.s.l. (see Fig. 15), the use of a separate hydraulic unit ('PowerPack') for the casing oscillator ('Leffer 2000'), with which the casing could be torqued independently of the excavation process and kept in continuous oscillation, as well as soil replacement ahead of the actual pile drilling (backfilling with 0/32 mm gravel sand) in the area of the hydraulically bound backfill material of the ´salvage pit´ (28.5 m to 41 m a.s.l.), with which the influence of abrasion in the binder-stabilised sands of the backfill could be minimised. In addition, a method called ´gravel shuttling´ was developed to reduce casing friction: After the lignite layer had been passed with the casing, the borehole was backfilled with gravel (8/16 mm) to a height of approx. 3 m, the casing was then initially pulled back to 0.5 m below the gravel filling level and the drilling process was then continued with advance casing to the final depth.

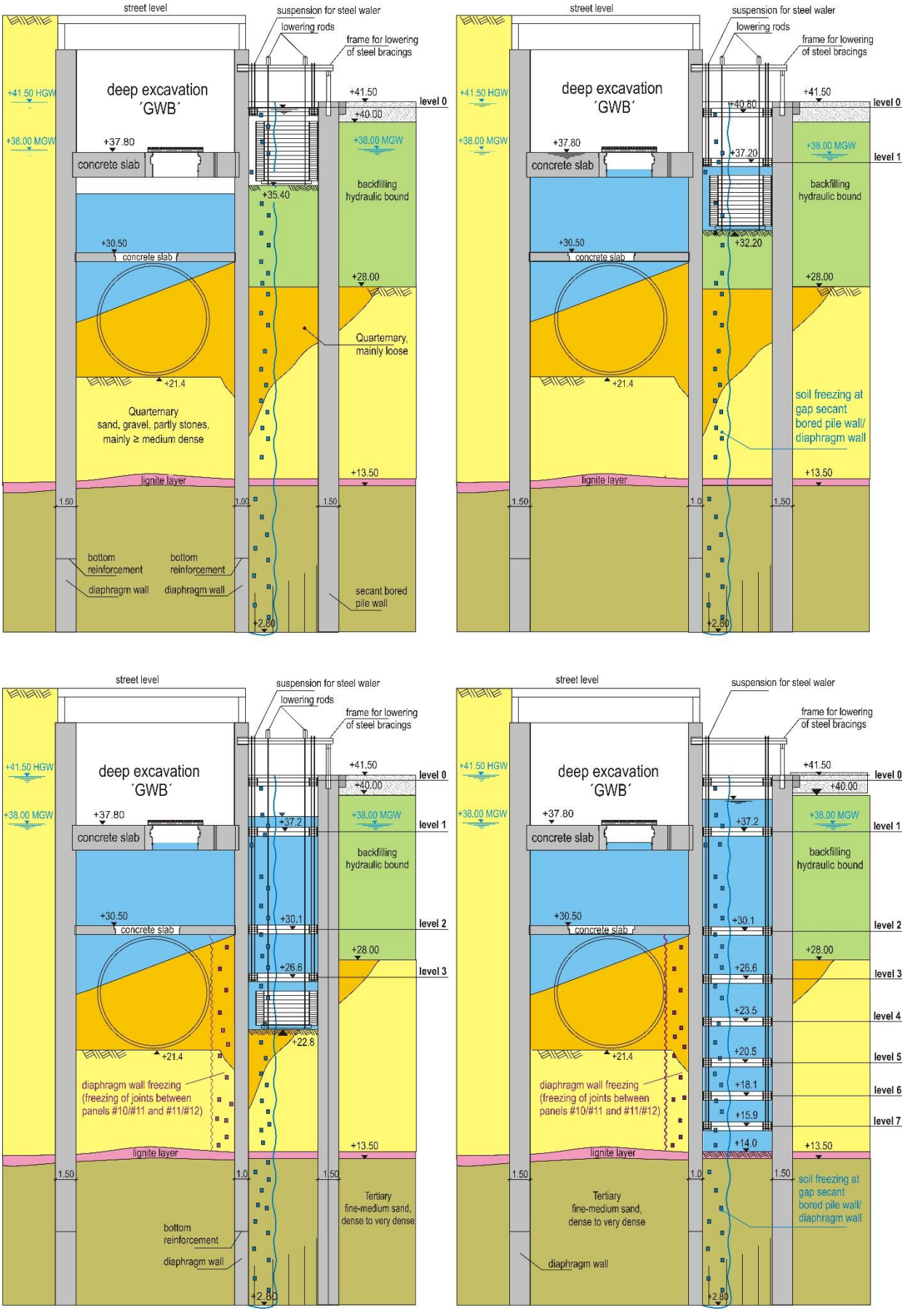

Figure 19. Construction sequence of the inspection pit (west-east section, selected stages).

A multi-stage construction was chosen for the mechanical and hydraulically sealed connection of the secant pile wall of the inspection pit to the diaphragm wall of the ´GWB´ pit with jet grouting as the main element (Fig. 18). As a preliminary step, a temporary ´protection freezing´ was realised inside the inspection pit. Under its protection, it was possible to grout the soil body, which would later be in contact with the free groundwater in the connection area, using the jet grouting method without having to worry about any impact on the soil situation inside the inspection pit. As a fall-back level and to seal the gap below the excavation level, a further ground freezing, the so-called ´connection freezing´, was realized on the outer side of the gap and operated for the construction period. The shielding and connection freezing were both carried out using the salt brine freezing method.

6.7.4 Investigation pit: Inner bracing system

The investigation pit was braced by steel bracing frames in a total of eight levels (Figs. 18 and 19). This bracing solution ensured that the eastern diaphragm wall of the ´GWB´ pit was supported almost over its entire surface, thus ensuring that the earth pressure effects on the diaphragm wall from the east remained as unchanged as possible and were distributed almost evenly, so that overall the boundary conditions of the stable initial situation of the ´GWB´ pit were not significantly changed and at the same time the diaphragm wall could be safely supported even in the event of larger defects. Due to the cramped conditions in the investigation pit and the fact that the bracing had to be installed under water, a concept was developed in which the pre-assembled steel frames for all eight bracing levels were lifted into the investigation pit after an initial excavation phase (35.4 m a.s.l.) and then lowered as a 'package' following the excavation using hydraulic devices, whereby the topmost frames were successively fixed in place (Fig. 19). The dead weight of the prefabricated, horizontally telescopable frames made of sectional steel was between 17.5 t and 27.5 t per bracing layer.

6.7.5 Investigation pit: Freezing of the eastern diaphragm wall

To stabilise the diaphragm wall joints, a frozen ground body was arranged on the inside of ´GWB´ pit, i.e. to the west of the eastern diaphragm wall, within the soil volume deposited in this area ('cone of debris') in the course of the accident and in the quaternary sands and gravels between the former final excavation level in the ´GWB´ pit (21.8 m a.s.l.) and the lignite layer in the area of the two diaphragm wall joints of panels #10 and #11 and of panels #11 and #12 to be inspected (Figs. 18 and 19). This so-called 'diaphragm wall freezing' served to stabilise the soil in the diaphragm wall joints as well as the soil behind them and at the same time to hydraulically seal possible defects in the diaphragm wall, whereby the planning of this freezing measure was based on an assumed defect geometry.

Four brine freezing pipes (GS1 to GS3 and GS5) and a nitrogen lance (GS4) were installed for the diaphragm wall freezing (Fig. 18), whereby the latter could be used to generate increased heat extraction locally and in defined depth sections that could be varied by moving the feed pipes if the exploration work required this, for example when faults were encountered, which was almost always the case during the execution. The freezing area extended from approx. +28 m a.s.l., i.e. the surface of the debris cone reaching just below the lower concrete slab bracing, to the surface of the lignite at approx. 14.0 m a.s.l., so that this frozen soil body had a height of approx. 14 m.

6.7.6 Investigation pit: Underwater excavation

The excavation of the investigation pit was carried out under water and, due to the dimensions of the ground plan and the multi-layer bracing, in very confined conditions using a suction pump. The suction pump, which was suspended from an excavator and lowered into the working areas defined by the bracing frames, was guided underwater at the current excavation level by a diver of the court-appointed expert.

The excavation was carried out in layers of 0.50 m increments from the relevant level of 28 m a.s.l. to the surface of the lignite layer. In the vicinity of the diaphragm wall, the excavation was carried out particularly carefully, if necessary by manually loosening and conveying the soil to the suction pump. Holding points were provided at several levels to secure the diaphragm wall and the base of the excavation pit. The mixture conveyed by the suction pump was channelled through a desanding/separation system to separate the soil material from the process water. The excavated material was laid out field by field, addressed in terms of engineering geology and geotechnics and anthropogenic finds which were of particular importance with regard to the demarcation of the collapse funnel and which were identified (e.g. with regard to their possible origin from the historical archives) and mapped. Furthermore, extensive soil mechanical and mineralogical analyses were regularly carried out on soil samples taken.

Particular challenges for the securing and exploration of evidence arose when diaphragm wall defects and their filling were encountered, as a joint filling frozen by the aforementioned ´diaphragm wall freezing´ gradually thaws in direct contact with the 'free' water of the inspection pit and therefore only has

a very limited ´service life´. This service life, which defined the time window available to the expert´s divers for the collection of evidence and for the installation of appropriate mechanical protection, depended on the respective boundary conditions (geometry, water temperature, etc.). Temporary (air-filled pressure cushions) and permanent mechanical securing systems (including mortar-filled ´Bullflex´ cushions and securing plates) had to be developed with which defects could be sealed after the preservation of evidence. After the installation of a suitable cavity-filling mechanical system, stationary conditions were again established with regard to the freezing, also depending on the boundary conditions. The concept had to be further developed in the detected open void area (see section 6.7.8) and additional horizontal freezing lances and protection by steel tubes had to be installed underwater in layers in the void area what proved to be time-consuming.

The excavation and exploration of evidence in the inspection pit began in January 2014 and was completed in July 2020 with the excavation of the surface of the lignite. All of the work had to be carried out by divers at increasingly great depths, which was a key boundary condition.

a)

b)

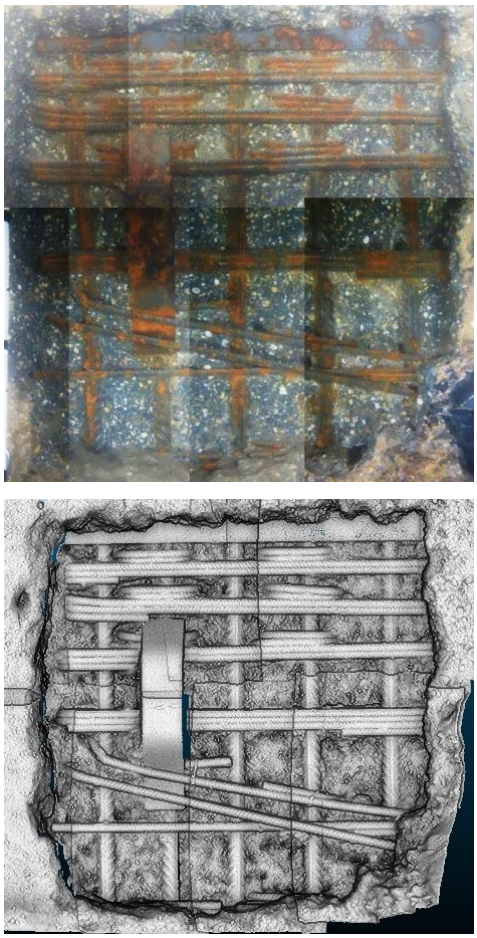

Figure 20. Exemplary image of a reinforcement window in the diaphragm wall panel #10.1, a) photographic, b) with underwater laser scan.

6.7.7 Collection of evidence: Approach

During the successive excavation of the investigation pit, not only the detailed documentation of the excavated soil material was carried out as described, but also a comprehensive survey of the diaphragm wall surface. The underwater recording consisted of several elements that were applied in each 0.5 m excavation step: In addition to an initial video recording by the diver´s helmet camera, a) a recording with a high-resolution video, b) a recording with an underwater laser scanner and c) a manual-electronic measurement of the geometry of the diaphragm wall surface (only in the case of anomalies) were carried out geometrically referenced by a guide construction. In addition, the diaphragm wall surface was recorded with a sonar device. As a result of these recordings, the expert and his divers were able to provide a complete graphic-visual and photogrammetric documentation of the diaphragm wall surface down to a depth of 34 m below street level in outstanding quality. The underwater laser scanner obtained from the United States proved to be particularly efficient (Fig. 20).

The area of the joints between panels #10 and #11 as well as between panels #11 and #12 was examined with particular care. When joint fillings and defects were encountered, the joint or void material was completely collected in special trays and the joint/ defect geometry was documented using the afore-mentioned methods and with the additional use of smaller GoPro cameras for the interior and flanks of the joints/defects.

In selected sub-areas, in particular in the overlapping area of the reinforcement cages of the diaphragm wall panels "reinforcement windows" were exposed in order to check the position and dimensions of the reinforcement cages and the possible absence of reinforcing bars (Fig. 20).

6.7.8 Collection of evidence: Findings

In the course of the exploration of evidence carried out in this way, in the area of the joint between panels #10 #11, from a depth of approx. 25.2 m a.s.l. on, concrete increasing in width by depth was detected, which extended from panel #10 into panel #11 (Fig. 22) and reached a width of around 600 mm at a depth of approx. 23.0 m a.s.l. A large natural boulder was encountered beneath this concrete from panel #10 at a depth of 22.1-21.4 m a.s.l. and thus directly at or below the final excavation level in the ´GWB´ excavation pit to the south of the panels #10/#11 joint, i.e. in the cross-sectional area of panel #11 (Figs. 21a and 22).

a)

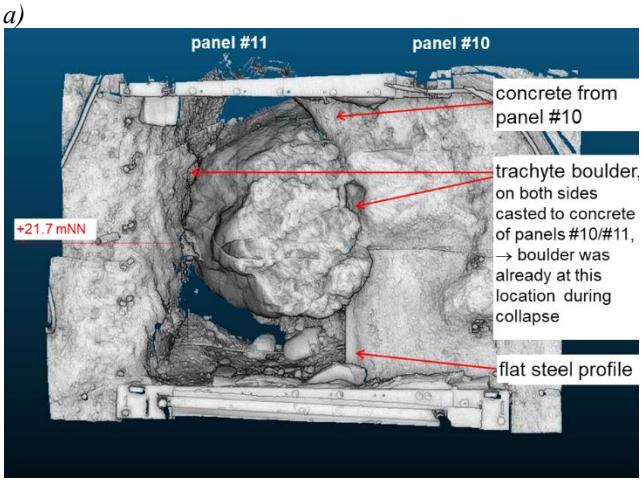

b)

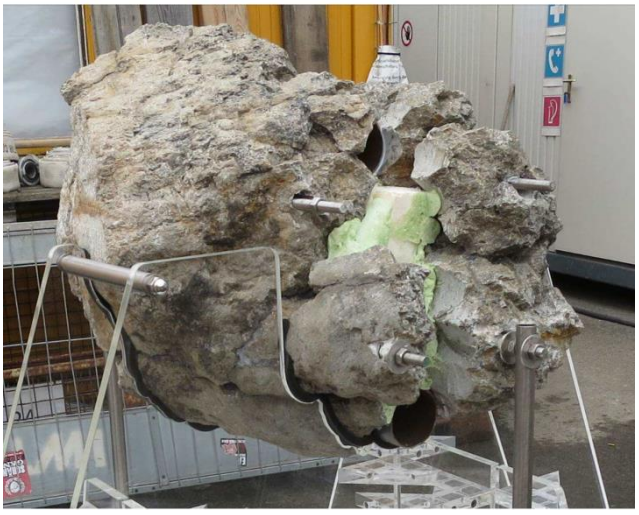

Figure 21. Natural boulder (trachyte) from the joint Lamellen 10/11, a) underwater laser scan in situ, b) recovered and assembled block (basis: Kempfert (2011-2022), reworked).

The trachyte boulder with a diameter of around 600 mm and a length of around 1.20 m was first extensively documented in situ. It was then divided into two half-shells with the help of guided overcut horizontal drillings, which were carried out with an underwater drilling template approximately in the centre of the block, and recovered from the joint using anchors. In dry conditions, the boulder was re-assembled and examined (Fig. 21b). Traces of the teeth of diaphragm wall grabs were found on both the northern and southern sides of the boulder; traces from the reinforcement cage of panel #11 were also found on the southern side. These traces prove that the natural boulder was already in the position encountered during the exploration of the evidence when panel #11 was executed (Fig. 23). In conjunction with the triangularly growing concrete from panel #10 found above it, it can be concluded that the natural boulder was encountered in the course of the execution of panel #10 and was displaced into the ground section of the later panel #11 during the attempt to salvage it, without the salvage being successful (Fig. 23). During the construction of panel #11, the boulder was then not removed from under the overlying concrete; after the change to the 2.4 m wide grab shells, the teeth of the diaphragm wall grab merely "scraped" along the natural boulder (Fig. 23).

Under the trachyte boulder, a continuously open void up to 600 mm wide and filled with quaternary material was encountered in the further excavation over the depth, which, although only explored up to the surface of the lignite, is expected to be in fact open to the lower edge of the diaphragm wall.

Based on the distribution of anthropogenic findings, colour changes of the in-situ soil material and other indicators such as the erosion/ presence of the filter cake in the joint surfaces, it was possible to identify and to prove that the base of the "moving" masses (collapse funnel) in the void lies at a level of around 18.7m a.s.l. In consequence it can be concluded that the area of the void through which around 5,000 m³ of quaternary material flowed in the course of the accident is only around 2.3 m high and about 600 mm wide and therefore has an area of only approx. 1.5 m² in total.

Based on an independent evaluation of the laser scan images taken by the expert Prof. Kempfert and his divers in the inspection pit, Figure 22 shows the area around the joint between panels #10 and #11 with the "open" void area filled with quaternary sands and gravels from 21.7 m a.s.l. downwards, the trachyte boulder above it and the triangle shaped concrete that flowed in behind the flat steel profile (stop end) when panel #10 was poured and which was not removed in the course of the excavation of panel #11.

At the time the damage occurred on March 3rd, 2009, the excavation level in the ´GWB´ pit in front of panels #10 and #11 was around 22.0 m a.s.l.; the planned final excavation level would have been 21.7 m a.s.l.

The discovery of the natural boulder in the northern area of panel #11 and the open void below it, filled with quaternary material and 450 mm to 640 mm wide in the further course, as well as the successful demarcation of that part of the void area that was passed by the granular-fluid mixture during the accident, provide a clear and forensic clarification of the cause of the damage. Despite this the layer-by-layer excavation and exploration of evidence in the inspection pit was continued down to the depth of the surface of the lignite layer at approx. 14.0 m a.s.l.

In a final step, the lignite was also exposed in sections using a specially manufactured excavation box using the caisson method in order to verify that the

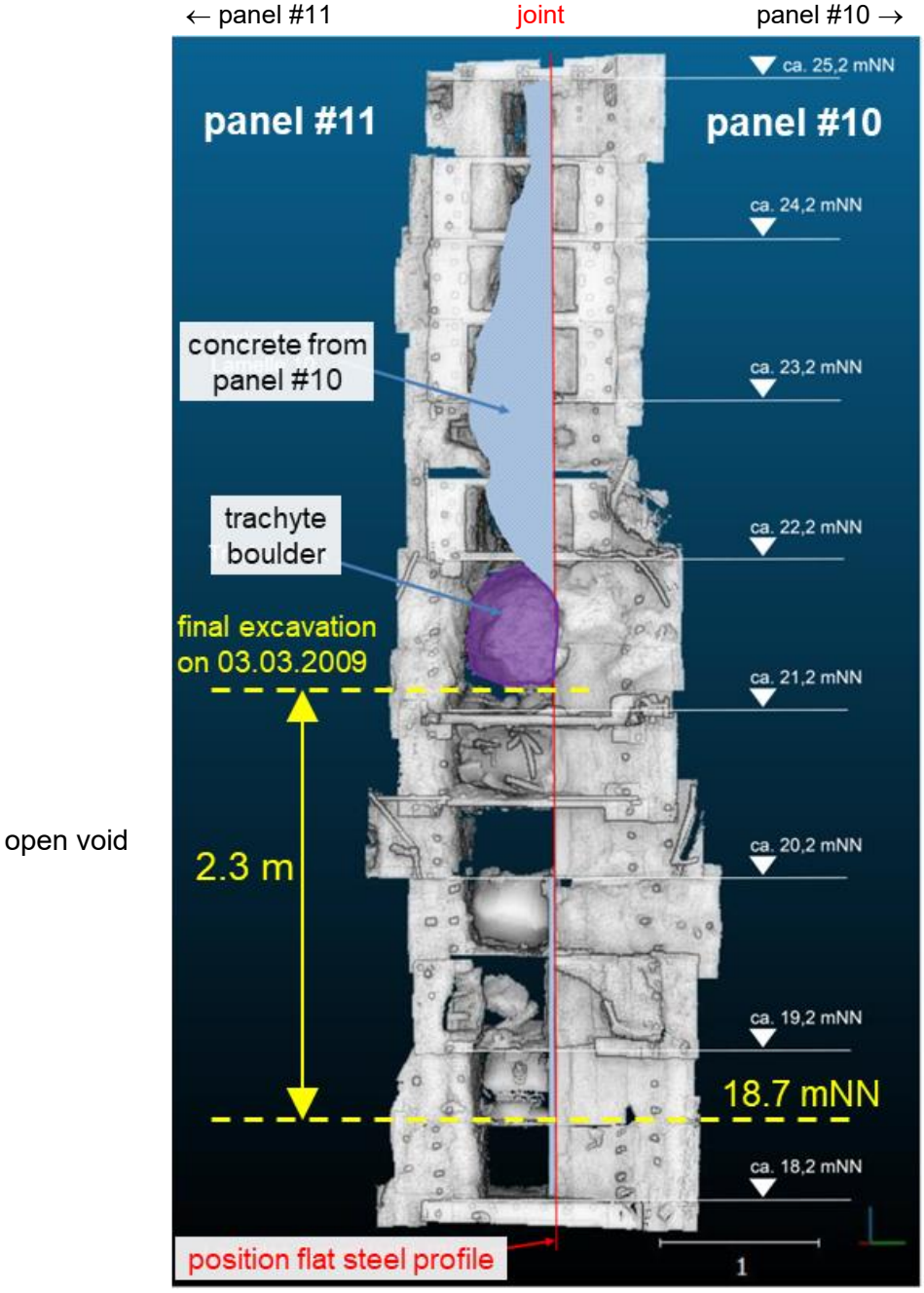

Figure 22. Compiled visualisaiton of the explored situation in the joint area of the diaphragm wall panels #10/#11 (evaluation of the underwater laser scans based on Kempfert (2011-2022)).

lignite layer in the ground plan of the inspection pit was intact and without defects. This additional proof was provided in 2020. This meant that the thesis of a suspected area of "vent formation" with a vertical material entry through the base of excavation could be definitively and legally ruled out in the sense of a ´counter-evidence´.

The results of the very demanding investigation of evidence were documented by Prof Kempfert in several expert reports (Kempfert, 2011-2020).

6.8 Cause of the collapse

As a result of the highly complex preservation of evidence procedure and investigations it was possible to clarify the cause of the damage clearly and beyond doubt. As a result of the investigations carried out from 2009 to 2020, the accident on March 3rd, 2009 can be attributed solely, i.e. mono-causally, to a defect that remained in the joint area between two panels during the construction of the diaphragm wall. In the area of the joint between the panels #10 and #11 an approxi-

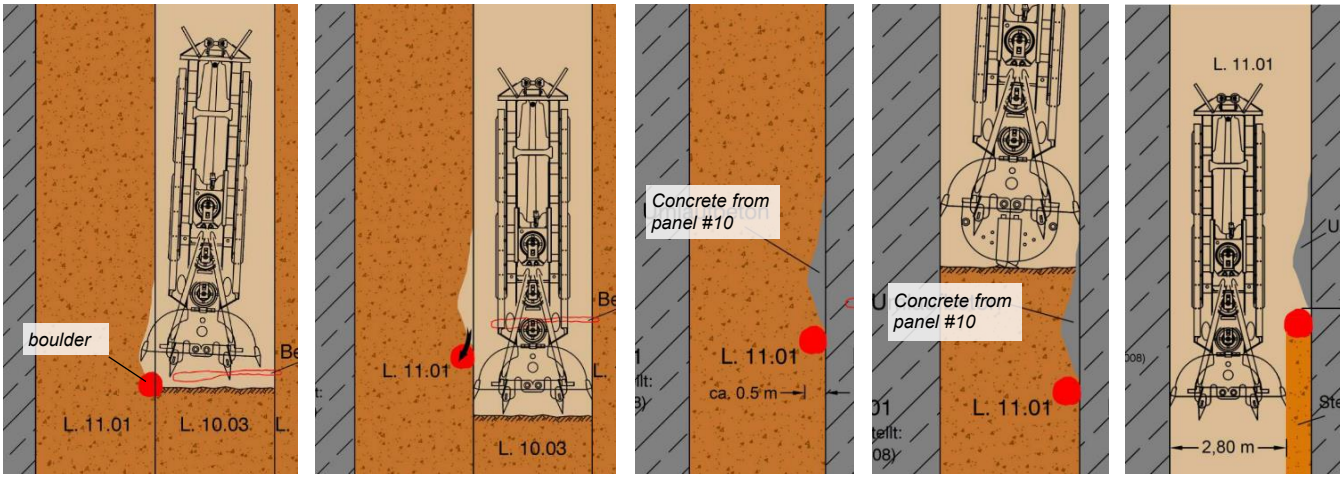

Figure 23. Construction sequence of the panels #10 and #11 of the eastern diaphragm wall with the natural boulder (trachyte, marked in red) encountered during execution of both panels.

mately 600 mm wide void was found below approx. 21.7 m a.s.l., i.e. at about the level of the final excavation of the ´GWB´ pit downwards. This defect results from the fact that the existing soil material in this area had not been excavated and replaced by concrete during the construction of diaphragm panel #11. A triangular wedge of concrete, which protruded into the cross area of panel #11 (Figs. 22 and 23), had not been removed in the course of the excavation of panel #11 and was therefore the initial of this defect. The triangle-shaped concrete originates from previous execution of adjacent panel #10: during excavation of this panel the trachyte boulder was hit in the southern outer edge of the panel´s cross section and trials to catch and remove the boulder creates a void in the area of the adjacent panel 11 which was poured by concrete which flowed behind the flat steel profile that was used as joint resp. stop end element (Fig. 23).

As a result of the challenging investigation of the evidence, it was proven that during the accident on March 3rd, 2009 around 5,000 m³ of quaternary material flowed through the void in the depth section between 21.2 m a.s.l. and about 18.7 m a.s.l., which led to the collapse of the historical archive, literally as the ground was removed from under the foundations. It can be assumed that this void in panel #11 continues below the section through which the granular-fluid mixture flow passed to the lower edge of the diaphragm wall.

The cause of the damage can therefore be traced back to an execution issue respectively to the fact that suitable countermeasures were not taken in response to the difficulties encountered during the execution of panel #11 of the diaphragm wall in 2005. The obstacles encountered during excavation of this panel and the failure to remove these obstacles, finally the change of the grab shells from 3.40 m to 2.80 m wide for excavation of the 3.4 m wide, single bite panel #11 were an unambiguous evidence that the panel #11 was not executed in a regular way and that from the depth where the grab shells were changed most probably a 600 mm wide void filled with quaternary sand and gravels was left.

Technically, it would have been possible to reliably seal the remaining defect in panel #11, for example with one or two columns executed using the jet grouting method.

Against the background of these results of the investigation of the evidence, the City of Cologne and the construction JV, which still assumed an alternative course of events, reached an out-of-court agreement in a moderated procedure to settle the financial loss incurred by the City of Cologne and concluded finally on a settlement in June 2020. According to this settlement the construction JV paid 600 million euros in damages to the City of Cologne and committed themselves to reconstruct the damaged ´GWB´ excavation pit and to finalize this structure at its own expense and under its own responsibility.

Currently it is expected that the very challenging reconstruction activities will last until about 2032, what means that it will have taken nearly 25 years from the occurrence of the damage to its removal and to the moment the first metro train will have run through the ´GWB´ underground structure at the ´Waidmarkt.

7 CONLUSIONS

7.1 Dealing with serious damage cases

The accident at the deep excavation pit for the ´GWB´ structure at ´Waidmarkt´ in Cologne on March 3rd, 2009 was a dramatic case of damage with far-reaching

consequences for the city of Cologne, in particular due to the collapse of the adjacent historical archive, for the north-south metro project and local residents, but also for all those involved in the project. Contrary to the expectations of many of those involved, the cause of the damage was clearly and unequivocally clarified in an unprecedented process of preserving evidence in terms of complexity, technical challenges and scope, but also in terms of duration and effort. All of the independently obtained evidence from the indirect and direct investigations form a complete and consistent overall picture. The only cause was a 0.6 m wide void in a diaphragm wall panel located just at resp. below the excavation pit´s final excavation level, which was a consequence of an execution error. The fact that it was possible to identify and document this mono-causal cause of damage in an extremely challenging environment in such a clear and qualified manner, and thus in a way that would stand up in court, is first and foremost the merit of the court-appointed expert witness, Prof. Dr H.-G. Kempfert and his team, who led the evidence proceedings through all the technical difficulties with great commitment and professional expertise.

The technical challenges that arose during the underwater preservation of evidence in an up to 34 m deep excavation pit next to a damaged diaphragm wall was a daily companion for all those involved in the realisation and creation of the structural condition for the investigation over years. New solutions and prototype-like concepts had to be developed, tested and implemented for many tasks relating to the preservation of evidence and the realisation of the construction work. The successful realisation of the investigation of the evidence and the clear clarification of the cause of the damage were the prerequisites for ending the evidentiary proceedings with an out-of-court settlement between the parties involved, thus avoiding a lengthy legal dispute.

Nevertheless, the fact that more than 15 years have passed since the damage occurred should be motivation for further considerations regarding the prevention and handling of (major) damage cases in ground engineering.

The example of the Waidmarkt accident shows that it is often not possible to quickly clarify the cause of the damage, as extensive and time-consuming investigations of the subsoil situation and the structural conditions, which are initially not accessible to direct inspection, especially in underground construction, are required. Promising approaches for alternative concepts for dealing with damage events and for accelerating following procedures e.g. by combining measures for investigation and reconstruction are documented in international context for other major damages, such as the Nicoll Highway Collapse in Singapore (Whittle & Davies, 2006).

7.2 Risk prevention and mitigation

Risk prevention and risk mitigation are even more important tasks than dealing with damage cases as these are the only tools to avoid collapses and damages.

Based on experiences from damages consequences for the independent checking of design and execution, for the quality assurance of underground works and their supervision, but also the need for a risk prevention based on communication and partnership between all parties involved in the construction process needs to be discussed and implemented especially but not solely for major projects.

Besides measures and approaches for risk management and assessment during design, as discussed in sections 2 to 4 of the present paper the successful realisation of geotechnical structures in engineering practice requests the following additional measures especially related to checking and quality assurance:

1. An independent structural *and* geotechnical checking is essential and must include both,
   a. the checking of the design and all verifications and
   b. the supervision and monitoring of the execution.
2. For all stages of soil investigation, design, execution, checking and supervision geotechnical expertise and experience is required; therefore it is mandatory to involve an independent geotechnical checking engineer at least for structures of the Geotechncial Category 3 according to EN 1997-1.
3. The (independent) supervision of execution of special geotechnical works like e.g. piling, diaphragm walls, ground improvement and injections has to be carried out by qualified and experienced experts on site.
4. A risk prevention in partnership needs to be established and practiced in all phases of planning and realisation. In this context a regular communication on technical level between client, contractors, designers and the independent checking engineer is essential. Such a regular communication, e.g. organisationally to be implemented by jour fixes, allows also to identify and discuss any irregularities and anomalies occurred during execution.

All of the above measures are relevant and needs to be established but especially a regular technical communication between all parties is considered to be an essential tool for risk prevention and mitigation during the execution.

In this regard the presented case study of the collapse of the ´Historical Archive´ at the Waidmarkt in the city of Cologne is an example where irregularities during execution of the diaphragm wall were observed and documented but were subsequently not pursued further neither internally inside the construction companies nor in communication with the owner´s independent supervision and by the owner itself. As shown in section 3.1.3 of this paper human factors have been identified as main cause for failure on site and one of the major impacts are faulty communications as well as pressures on the involved people like time, economical or ecological constraints. In this regard, an open-minded communication focused on technical aspects and a partnership-based approach are considered to be effective mitigating measures for risks in geotechnical engineering and execution.

REFERENCES

Ang, A.H.S, Tang, W.H. (2006): Probability concepts in engineering: Emphasis on applications to civil and environmental engineering. 2nd ed., J. Wiley & Sons, 432 pp.

Arnold, P. (2016) Probabilistic modelling of un saturated slope stability accounting for hetero-geneity. Ph.D. thesis, University of Manchester, Faculty of Engineering and Physical Scienes.

Aulbach, B.; Ziegler, M. 2013. Ermittlung der Error-derlichen Einbindetiefe von Baugrubenwänden bei Gefährdung durch hydraulischen Grund-bruch. In: 9. Österreichische Geotechniktagung, 2013, Tagungsbeiträge, Österreichischer Ingenieur- und Architekten-Verein, Wien (Hrsg.), 149-160 (in German).

Bea, R. (2006): Reliability and human factors in geotechnical engineering. J. of Geotech. And Geoenviron. Eng. Vol. 132, Issue 5, 631-643. https://doi.org/10.1061/(ASCE)1090-0241(2006)132:5(631).

Baecher, G.B., Christian, J.T., (2003): Reliability and statistics in geotechnical engineering. 1st ed., J. Wiley & Sons, 618 pp.

Baecher, G.B. (2023): 2021 Terzaghi Lecture: Geo-technical systems, uncertainty, and risk. Journal of Geotechnical and Geoenvironmental Engineering, Vol 149, Issue 3. https://doi.org/10.1061/jggefk.gteng-10201.

Baecher, G.B. (2017): Bayesian thinking in geotechnics, Geo-Risk 2017, 19 pp. https://doi.org/10.1061/9780784480694.001.

Beer, M., Zhang, Y., Quek, S. T., Phoon, K.K. (2013): Reliability analysis with scarce information: Comparing alternative approaches in a geotechnical engineering context. Structural Safety, Vol 41, 1-10. https://doi.org/10.1016/j.strusafe.2012.10.003.

Bucher, C. (2009): Computational analysis of randomness in structural mechanics. Structures and Infrastructures Book Series, Vol. 3, 248 pp. https://doi.org/10.1201/9780203876534.

Burland, J.B. (1987): The teaching of soil mechanics – A personal view, Nash lecture. Proc. 9th ECSMGE, Dublin, Vol. 3, 1427-1447.

Ching, J., Yoshida, I., Phoon, K.-K. (2023): Comparison of trend models for geotechnical spatial variability: Sparse Bayesian Learning vs. Gaussian Process Regression. Gondwana Research, Vol. 123, 174-183. https://doi.org/10.1016/j.gr.2022.07.011.

Christian, J.T., Ladd, C.C., Baecher, G.B. (1994): Reliability applied to slope stability analysis. J. of Geotech. Eng., Vol. 120, Issue 12. https://doi.org/10.1016/0148-9062(95)92555-V.

Christianson, R.B., Pollyea, R.M., Gramacy, R.B. (2023): Traditional kriging versus modern Gaussian processes for large-scale mining data. Statistical Analysis and Data Mining: The ASA Data Science Journal, Vol. 16, Issue 5, 488-506. https://doi.org/10.1002/sam.11635.

Chwala, M., Phoon, K.-K., Uzielli, M., Zhang, J., Zhang, L., Ching, J. (2022): Time capsule for geotechnical risk and reliability. Georisk: Assess-ment and Management of Risk for Engineered Systems and Geohazards, 17:3, 439-466. https://doi.org/10.1080/17499518.2022.2136717.

de Wolf, W.J., Korff, M., van Seters, A., van Daalen; J.H. (2021): Bayesian Inference for deep excavations. Geotechnical Aspects of Underground Construction in Soft Ground – Proc. of the 10th Int. Sym. on Geotech. Aspects of Underground Construction in Soft Ground, IS-CAMBRIDGE 2022, 529-535. https://doi.org/10.1201/9780429321559-69.

Duncan, J.M. (2000): Factors of safety and reliability in geotechnical engineering. J. of Geotech. and Geoenvironmental Eng., Vol. 126, Issue 4. https://doi.org/10.1061/(asce)1090-0241(2000)126:4(307).

Ebener, A., Lesny, K. (2022): A Review on the current use of RBD in geotechnical design practice in view of the next Eurocode Proc. 8th Int. Symp. On Geotechnical Safety and Risk (ISGSR 2022), Newcastle, Austria, Eds. J. Hunag et al., Research Publishing, Singapore, 903-908. https://doi.org/10.3850/978-981-18-5182-7_00-18-001.xml.

Einstein, H.H., Baecher, G.B. (2023): Decision making in rock engineering and engineering geology. GeoStrata Magazine Archive, Vol. 27, Issue 1. https://doi.org/10.1061/geosek.0000466.

Geyer, S., Papaioannou, I., Straub, D. (2021): Bayesian analysis of hierarchical random field for material modelling. Probabilistic Engineering Mechanics, Vol. 66(10), 103167. https://doi.org/10.1016/j.probengmech.2021.103167.

Hasofer, A.M., Lind, N.C. (1974): Exact and invariant second-moment code format. J. of the Engineering Mechanics Division, Vol. 100, Issue 1.

https://doi.org/10.1061/jmcea3.0001848.
Hicks, M.A. (2023): Slope reliability assessments for linear infrastructures. In: K.K. Phoon, T. Shuku, J. Ching (Eds.), Uncertainty, Modelling, and Decision Making in Geotechnics, 1st ed., CRC Press 457-472. https://doi.org/10.1201/9781003333586-19.
Huber, M. (2013): Soil variability and its consequences in geotechnical engineering. Ph.D. Thesis, University of Stuttgart, Institute for Geotechnical Engineering, Vol. 69.
International Organization for Standardization. (2018): *Risk Management Guidelines*. ISO Standard No. 31000:2018. https://www.iso.org/standard/65694.html.
International Organization for Standardization. (2019): *Risk management – Risk assessment techniques*. ISO Standard No. 31010:2019. https://www.iso.org/standard/72140.html.
International Organization for Standardization. (2015): *General principles on reliability for structures*. ISO Standard No. 2394:2015. https://www.iso.org/standard/58036.html.
Ji, J., Cao, Z., (2023): Geotechnical reliability analysis for practice. In: K. K. Phoon, T. Shuku, J. Ching (Eds.), Uncertainty, Modelling, and Decision Making in Geotechnics, 1st ed., CRC Press, 219-245. https://doi.org/10.1201/9781003333586-8.
Jiang, S.-H., Papaioannou, I., Straub, D. (2018): Bayesian updating of slope reliability in spatially variable soils with in-situ measurements. Engineering Geology, Vol. 239, 310-320. https://doi.org/10.1016/j.enggeo.2018.03.021.
Jiang, S.-H., Wang, L., Ouyang, S., Huang, J., Liu, Y. (2022): A comparative study of Bayesian inverse analyses of spatially varying soil parameters for slope reliability updating. Georisk: Assessment and Management of Risk for Engineered Systems and Geohazards, 16:4, 746-765 https://doi.org/10.1080/17499518.2021.2010098.
Kempfert, H.-G. (2011-2020): Beweisverfahren KVB und Stadt Köln ./. Arge Nord-Süd Stadtbahn Köln, Los Süd u.a. (Einsturz des Historischen Archivs der Stadt Köln). Landgericht Köln 5 OH 1/10. Sachverständigengutachten Teil I bis X, (in German, not published).
Kool, J.J., Kanning, W., Jommi, C., Jonkman, S.N. (2019): Forensic analysis of Levee Failures: The Breitenhagen case. Int. J. of Geoengineering Case Histories, 5 Issue 2, 70-92. https://doi.org/10.1080/17499518.2020.1815213.
Kool, J.J., Kanning, W., Jommi, C., Jonkman, S.N. (2021): A Bayesian hindcasting method of levee failures applied to the Breitenhagen slope failure. Georisk: Assessment and Management of Risk for Engineered Systems and Geohazards, 15(4), 299-316 https://doi.org/10.1080/17499518.2020.1815213.
Lacasse, S., Nadim, F., Liu, Z.Q, Eidsvig, U.K., Le, T.M.H, Lin, C.G. (2019): Risk assessment and dams – Recent developments and applications. Proc. of the XVII ECSMGE-2019, Geotechnical Engineering foundation of the future, Reykjavik. http://doi.org/10.32075/17ECSMGE-2019-1110.
Li, J., Li, X., (2021): Spatial Variability. In: W. Cui, S. Fu, Z. Hu (Eds.), Encyclopedia of Ocean Engineering, 1st ed., Springer Nature Singapore, pp. 9. https://doi.org/10.1007/978-981-10-6963-5.
Liu, Y., Li, J., Sun, S., Yu, B., (2019) Advances in Gaussian random field generation: a review. Computational Geosciences, Vol. 23, 1011-1047. https://doi.org/10.1007/s10596-019-09867-y.
Mak, L.M. (2006): Geotechnical standards in Hong Kong. ACESS Workshop on Harmonization of Design Codes in Asian Region. https://doi.org/10.1142/9789812772480_0014.
Moormann, Ch., Sieler, U., Schwarze, J., Kahlen, G. (2014): Herstellung der 34 m tiefen Besichtigungs-baugrube am Waidmarkt in Köln – Spezialtiefbau unter besonderen Anforderungen. Vorträge zum 10. Hans Lorenz Symposium 2014 an der TU Berlin, Veröffentlichungen des Grundbauinstitutes der Technischen Universität Berlin, Vol. Nr. 64, 139-163 https://doi.org/10.13140/2.1.1992.4804.
National Academy of Sciences. (2018): Guidelines for managing geotechnical risks in design–build projects. Cooperative Research Program, 80 pp. https://doi.org/10.17226/25262.
Peck, R.B. (1969): Advantages and Limitations of the observational method in applied soil mechanics – 9th Rankine Lecture. Géotechnique, 19(2), 171-187. https://doi.org/10.1680/geot.1969.19.2.171.
Phoon, K.-K. Ching, J., Wang, Y. (2019): Managing risk in geotechnical engineering – From data to digitalization. Proc. 7th Int. Symp. on Geotechnical Safety and Risk (ISGSR 2019), Eds: J. Ching, D.-Q. Li and J. Zhang, Research Publishing, Singapore, 13-34. https://doi.org/10.3850/978-981-11-2725-0-sl-cd.
Phoon, K.-K., Cao, Z., Ji, J., Leung, Y.F., Najjar S., Shuku, T., Tang, C., Yin, Z.-Y., Ikumasa, Y., Ching, J. (2022): Geotechnical uncertainty, modelling, and decision making. Soils and Foundations, Vol. 62, Issue 5. https://doi.org/10.1016/j.sandf.2022.101189.
Sowers, G. (1993): Human factor in civil and geotechnical engineering failures. J. Geotech. Eng., Vol. 119, Issue 2, 238-256.
Spross, J., Olsson, L., Stille, H. (2018): The Swedish Geotechnical Society's methodology for risk management: a tool for engineers in their everyday work. Georisk: Assessment and Management of Risk for Engineered Systems and Geohazards, 12:3, 183-189. https://doi.org/10.1080/17499518.2017.1416643.
Sudret, B., Der Kiureghian, A. (2000): Stochastic Finite Element methods and reliability – A State-of-the-Art Report. Department of Civil & Environmental Eng., University of California, Berkeley, Rep. No. UCB/SEMM-2000/08.
Teixeira, R., Nogal, M., O'Connor, A. (2021): Adaptive approaches in metamodel-based reliability analysis: A review. Structural Safety, Vol. 89, 102019. https://doi.org/10.1016/j.strusafe.2020.102019.

van den Eijnden, A.P., Schweckendiek, T., Hicks, M.A. (2022): Metamodelling for geotechnical reliability analysis with noisy and incomplete models. Georisk: Assessment and Management of Risk for Engineered Systems and Geohazards, 16(3), 518-535. https://doi.org/10.1080/17499518.2021.1952611.

van der Krogt, M.G., Schweckendiek, T., Kok, M. (2021): Improving dike reliability estimates by incorporating construction survival. Engineering Geology, Vol. 280, 105397. https://doi.org/10.1016/j.enggeo.2020.105937.

van Staveren, M.T. (2013): Geotechnics on the move: guidance for a risk-driven way of working. Georisk: Assessment and Management of Risk for Engineered Systems and Geohazards, 7(3), 225-236. https://doi.org/10.1080/17499518.2013.803370.

Varkey, D. (2020): Geotechnical uncertainties and reliability-based assessments of dykes. Ph.D. Thesis, Delft University of Technology.

Wang, L., Hwang, J.H., Luo, Z., Juang, C.H., Xiao, J. (2013): Probabilistic back analysis of slope failure – A case study in Taiwan. Computers and Geotechnics, Vol. 51, 12-23. https://doi.org/10.1016/j.compgeo.2013.01.008.

Whittle, A.J., Davies, R.V. (2006): Nicoll Highway Collapse: Evaluation of geotechnical factors affecting design of excavation support system. Proc. Int. Conf. on Deep Excavations, Singapore.

Wu, T.H. (2011): 2008 Peck Lecture - The Observational Method: Case history and models. J. of Geotech. and Geoenvironmental Eng., Vol. 137, Issue 10. https://doi.org/10.1061/(asce)gt.1943-5606.0000509.

Zhang, D., Phoon, K.-K., Huang, H.W., Hu, Q. (2015): Characterization of model uncertainty for cantilever deflections in undrained clay. J. of Geotech. and Geoenvironmental Eng., Vol. 141(1). https://doi.org/10.1061/(asce)gt.1943-5606.0001205.

Zhang, J., Zhang, L.M., Tang, W.H. (2009): Bayesian framework for characterizing geotechnical model uncertainty. J. of Geotech. and Geoenvironmental Eng., Vol 135, Issue 7. https://doi.org/10.1061/(asce)gt.1943-5606.0000018.

Zhang, J., Zhang, L.M., Tang, W.H. (2011): Kriging numerical models for geotechnical reliability analysis. Soils and Foundations, Vol. 51(6), 1169-1177. https://doi.org/10.3208/sandf.51.1169.

Proceedings of the XVIII ECSMGE 2024
GEOTECHNICAL ENGINEERING CHALLENGES
TO MEET CURRENT AND EMERGING NEEDS OF SOCIETY
© 2024 the Authors
ISBN 978-1-032-54816-6
DOI 10.1201/9781003431749-4
Open Access: www.taylorfrancis.com, CC BY-NC-ND 4.0 license

ECSMGE 24
XVIII EUROPEAN CONFERENCE ON SOIL MECHANICS AND GEOTECHNICAL ENGINEERING

Keynote Lecture

How AI and IoT are transforming geotechnical site monitoring and construction

Comment l'IA et l'IdO transforment la surveillance des sites géotechniques et la construction

A. Gomes Correia*
Department of Civil Engineering, ISISE, University of Minho, Guimarães, Portugal

E. Gastine
Europe itmsol, Paris, France

**agc@civil.uminho.pt*

ABSTRACT: Artificial intelligence (AI) and internet of things (IoT) are the most transforming advancements in geotechnical site monitoring and construction. Indeed, the increasing integration of AI and IoT devices and technologies into construction processes have enhanced construction management as a benefit from real-time feedback that provides early warning systems, facilitating timely interventions and ensuring construction site safety, as well as structural health monitoring of built environment. This presentation will start summarising the state of the art of these advancements in geotechnical works. Two field works in Portugal, one on infrastructure earthworks and another on a metro line in an area of dense urbanisation with new and old buildings, including historical monuments, involving trenches, load transfer platform solutions and main station, serve to demonstrate the benefits of applying these developments in comparison to traditional management techniques.

RÉSUMÉ: L'intelligence artificielle (IA) et l'internet des objets (IdO) sont les technologies les plus transformatrices en matière de surveillance des sites géotechniques et de construction. En effet, l'intégration croissante des dispositifs et des technologies de l'IA et de l'IdO dans les processus de construction a amélioré la gestion de la construction grâce à un retour d'information en temps réel qui fournit des systèmes d'alerte anticipés, facilitant les interventions en temps réel et garantissant la sécurité du site de construction, ainsi que la surveillance de l'état structurel de l'environnement bâti. Cette présentation commencera par résumer l'état de l'art de ces avancées dans les travaux géotechniques. Deux chantiers au Portugal, l'un sur des travaux de terrassement d'infrastructures et l'autre sur une ligne de métro dans une zone d'urbanisation dense avec des bâtiments neufs et anciens, y compris des monuments historiques, impliquant des tranchées, des solutions de plate-forme de transfert de charge et la station principale, servent à démontrer les avantages de l'application de ces développements par rapport aux techniques de gestion traditionnelles.

Keywords: Artificial intelligence; internet of things; monitoring; earthworks; metro line.

1 INTRODUCTION

The Internet of Things (IoT) and Artificial Intelligence (AI) technologies offer immense potential for revolutionizing geotechnical monitoring, enhancing efficiency, accuracy, and safety across construction projects. By coupling IoT sensors with AI algorithms, geotechnical monitoring systems can collect vast amounts of data in real-time, enabling proactive decision-making, allowing to implement timely interventions and preventive measures to mitigate risks (Tan et al., 2022). In this context, A/D converters play a crucial role in this coupling by digitizing analogue signals from sensors, thus enabling the processing and analysis of data by AI algorithms. These converters bridge the gap between the physical world of sensor measurements and the digital facilitating the seamless operation of IoT-based monitoring systems. These systems exhibit the ability to detect structural impacts, monitor buildings through tilt sensors, and issue alerts upon surpassing predefined thresholds. Moreover, IoT generates novel datasets, revolutionizing risk assessment, design, construction, and maintenance practices (Kumar et al.,

2023). Furthermore, AI algorithms analyse the data collected by IoT sensors to identify patterns, anomalies, and trends indicative of potential hazards, construction deficiencies or structural weaknesses. Machine learning techniques, such as neural networks or decision trees, among others, can learn from historical data to predict future events or assess the health status of the structural elements (Singh and Tyagi, 2023; Zhang et al., 2023). This predictive capability enhances the effectiveness of Early Warning Systems (EWS), enabling proactive measures to prevent catastrophic events (Kumar et al., 2023).

These developments that have emerged over the last decade are now maturing, offering significant advancements in construction site monitoring. These advancements primarily benefit from three key technologies: IoT, the availability of low-power, long-distance communication protocols, and the development of AI methods. These technological achievements enable the acquisition, transmission, and synthesis of geometric and structural geotechnical data, which are crucial for monitoring and mitigating risks on construction sites, especially in underground environments.

However, the integration of IoT, A/D converters and AI also presents challenges, including data privacy concerns, cybersecurity risks, and the need for interoperability among heterogeneous sensor networks (Liang et al., 2024). Addressing these challenges requires robust data governance frameworks, encryption protocols, and standardized communication protocols to ensure the reliability, security, and scalability of integrated geotechnical monitoring systems.

In this paper, we begin with this concise overview, underscoring the advantages of integrating IoT, A/D converters, and AI in geotechnical construction. Subsequently, we delve into a detailed exploration of emerging communication tools, web monitoring platforms, and AI applications. These considerations are contextualised within two field projects conducted in Portugal: one centred on transport infrastructure earthworks, and the other on a metro line located in an area marked by dense urbanization and a blend of new and historic structures, including monuments. The analysis underscores the superiority of these cutting-edge technologies when compared to conventional approaches and technologies.

2 EMERGING COMMUNICATION

Recent advances in geotechnical and structural monitoring are primarily linked to the emergence of wireless data transmission methods that are compatible with the scale of construction sites and make it possible to solve the recurring problem of powering sensors on these sites.

2.1 LoRaWAN radio networks

LoRaWAN (Long Range Wide Area Network) radio networks have gained significant attention in recent years for their ability to provide long-range, low-power communication suitable for various IoT applications, including geotechnical monitoring in construction projects. These networks operate on radio bands, offering excellent coverage even in challenging environments like urban areas or underground construction sites (Raza et al., 2017; Shanmuga Sundaram et al., 2020; Centenaro et al., 2016).

The LoRaWAN was developed in 2015 by the LoRa Alliance following research conducted from 2009 onwards in Grenoble, France (LoRa Alliance, 2024).

The LoRaWAN radio protocol has found unexpected applications in construction projects. Its key characteristics include the utilization of free and Europe-approved frequency bands, capable of transmitting data up to one kilometer in urban environments and up to 10 kilometers in open fields. Moreover, the protocol consumes minimal energy, and its limitations are compatible with geotechnical instrumentation, as geotechnical measurements are relatively low-frequency and require minimal digital space.

The LoRaWAN protocol enables the transmission of information from autonomous battery-powered sensors dispersed across the entire surface area of a construction site via radio, covering distances typical of extensive worksites for several years.

Deploying LoRaWAN networks necessitates the installation of fixed gateways and antennas to provide coverage for construction sites. This network of gateways must be managed by a "network core" linked to a supervision platform. This platform is essential for configuring the radio communication network, managing communications, and decrypting information received from the sensors.

LoRaWAN technology is not the sole low-power radio technology making strides in the construction sector; it is one of the LPWAN (Low Power Wide Area Network) communication technologies fueling the advancement of the IoT. Other promising communication protocols, such as LTE-M or NB-IoT, which utilise telephone operator infrastructures, are also emerging (Bajic et al., 2023; Malik et al., 2020; Rastogi et al., 2022). However, their adoption is

currently limited by the availability of sensors compatible with these protocols.

2.2 Cellular communication and 5G

Significant advancements have been achieved in cellular communication technologies, facilitating their deployment in the niche yet rapidly expanding field of surveillance, which demands handling large data streams (such as acoustic measurements, vibration monitoring, real-time scanner tracking, video image analysis, etc.).

Particularly noteworthy progress has been made in managing cybersecurity risks associated with communication lines, eliminating coverage gaps, and optimizing communication throughput. It is worth noting that the advent of 5G communications, with their capacity for handling vast amounts of data, paves the way for numerous applications, albeit raising concerns regarding the sustainability of the volumes of data transmitted, analyzed, and stored.

3 WEB MONITORING PLATFORMS AND AI

Downstream, handling increasingly large data flows from construction sites has become feasible only with the emergence of robust, secure platforms capable of storing this data in data lakes. These platforms offer user-friendly, real-time internet access to pertinent, verified, translated, and summarized information for remote users with diverse needs.

The development of hosting platforms accessible in Software as a Service (SaaS) mode on trusted European clouds has facilitated high-speed access to technical information streams on all construction sites. This is done in compliance with cybersecurity and sovereignty requirements mandated by the General Data Protection Regulation (GDPR) and forthcoming AI Act regulations (CoC, 2020; CISPE, 2021).

One of the most promising aspects of these ongoing developments is the ability to train artificial intelligence models using the vast quantities of data collected from construction sites. These models can then operate in real-time to enhance the value of the gathered information. AI can now be leveraged for trend forecasting, expert filtering, and advanced alarms, offering powerful tools for engineers (Zhang et al., 2023).

Furthermore, AI has potential offline applications, particularly in information synthesis and construction design.

Again, it is crucial to emphasize the ethical and environmental implications of AI usage (Liang et al., 2024). The storage and processing of vast amounts of information for AI model creation require significant energy consumption, contributing to companies' carbon footprints and potentially hindering efforts to combat climate change. The benefits of AI usage must be balanced against the carbon cost of its production.

Moreover, significant ethical risks may arise during the development of AI models. The AI Act provides valuable clarification by categorizing applications into four distinct risk levels (unacceptable, high, low, minimal), thereby enabling the responsible use of AI models with minimal ethical risks in the construction sector (Taddeo and Floridi, 2018).

4 APPLICATION TO EARTHWORKS – CASE STUDY

Earthwork processes often encounter significant uncertainties, requiring flexibility from planning and management teams to address unforeseen events like severe weather or equipment failures. Successful solutions for these challenges relies heavily on the expertise of the teams involved. However, since this expertise is not always readily available, decision support systems become invaluable. These systems not only compile and organize knowledge and experience from past projects but also foster collaboration across different specialties and teams throughout all phases of construction projects, aligning with modern concepts like Construction 4.0 and Building Information Modeling (Han et al., 2022).

In the context of earthworks, decision support systems serve various purposes, from predicting material behavior and equipment productivity to monitoring equipment positioning and optimizing resource allocation (Gomes Correia et al., 2013; Gomes Correia, 2018; Marques et al., 2008; Parente et al., 2015, 2016, 2018). These systems leverage on technologies such as artificial intelligence, simulation, and optimization algorithms, to tackle different problems and objectives (Choi and Han, 2023).

To illustrate the effectiveness of these systems, a real case study from Portugal involving road construction is presented (Neves et al., 2024). This study aimed to optimize resource allocation across multiple construction and excavation fronts, minimizing costs and project duration through multi-objective optimization (Jaafar and El-Halawani, 2022).

4.1 Technologies

In the specific case of earthworks, decision support is generally sought in order to predict (e.g., behavior of geomaterials, slope safety, equipment productivity as a function of working conditions), monitor (e.g.,

position of transport equipment, downtime, mechanical breakdowns), and/or optimize (e.g., distribution of geomaterial volume between excavation and embankment fronts, minimization of transport distances, optimal allocation of mechanical resources).

Based on technologies such as artificial intelligence, simulation, optimization algorithms, and sensing, these systems can be divided according to the methodology adopted and the objectives of decision support.

On the one hand, there is planning support, typically based on forecasting or robust optimization systems, which aim to create robust plans that not only encompass the predictable work to be carried out, but also include contingency plans for potential disruptive situations. On the other hand, there is construction support, focused on monitoring and reactive optimization systems, which advocate maximum flexibility in adjusting the initial plan in response to more volatile environments or the possibility of unforeseen occurrences.

Figure 1 shows the workflow of the optimization system paired with IoT system for earthworks projects. In the following subsection, it is presented an illustrative example of the potential of this type of systems in planning and construction phases, respectively, adopting as reference a real case study associated with the earthwork phases of a road construction project in Portugal. The project consisted of 24 embankment construction fronts, fed by 15 excavation fronts. The total volume of processed geomaterial was approximately 1,500,000 m³ over an approximate extension of 20 km of highway, with the average estimated duration of the work being approximately 6 months. The equipment fleet consisted of a total of 6 compactors, 14 spreading equipment, 29 excavators, and 39 geomaterial transport trucks.

For this application, a simulation of conditions close to real was carried out, using only the aforementioned available resources to develop the work according to the practices already commonly used in the industry. The adopted methodology described in Neves et al. (2024) was based on the work developed by Correia and Magnan (2012), Parente et al. (2018, 2022), aiming to find optimal solutions for the allocation of equipment fleet by work fronts and over time, simultaneously minimizing costs and work execution duration (multi-objective optimization).

4.2 Application to planning/design

As previously mentioned, the aim of this simulation was to showcase the potential of integrating these technologies for optimal equipment fleet allocation. Given the dynamic nature of the problem, with multiple work fronts such as excavations/ cuts and embankments progressing simultaneously, the solution must also be dynamic. This means that as teams complete work on one front, they need to transition to another, considering factors like varying transport distances, types of geomaterials, and available space. To achieve these objectives, the system requires input on available mechanical resources, including compactors, spreaders (e.g., bulldozers, graders), excavators, and transport trucks, along with specifications for each. Additionally, information on the work to be carried out, such as excavation and embankment fronts, their locations, types, volumes of associated geomaterials, and maximum number of active equipment, is needed. With access to this data, the optimization algorithm, based on a non-dominated sorting genetic algorithm II (NSGA-II) (Deb et al., 2002), seeks the best resource allocation solution throughout the project.

The multi-objective optimization process encompasses multiple stages. These range from the choice of the optimal distribution of geomaterial volumes between fronts, while minimizing transportation distances (which can alternatively be defined by the user based on project requirements), to the optimal allocation of all available equipment over time throughout the workfronts, adopting a scheduling methodology that defines where each equipment should be and for how long, resulting in the minimization of global execution costs and duration. The process takes approximately 3 hours in a conventional laptop (in this case, Intel i7-10750H 2.60GHz, with16GB RAM and running Windows 11) and presents solutions in a Pareto format. Each point on the Pareto front represents an equipment allocation, evaluated based on duration and cost (Figure 2). These solutions offer optimal trade-offs between time and cost, allowing flexibility in decision-making.

Results can be accessed in various formats, such as spreadsheets or maps, enabling visualization of equipment allocation for each work phase. This facilitates analysis of different scenarios and selection of the best option based on time, cost, and allocation details provided for each solution.

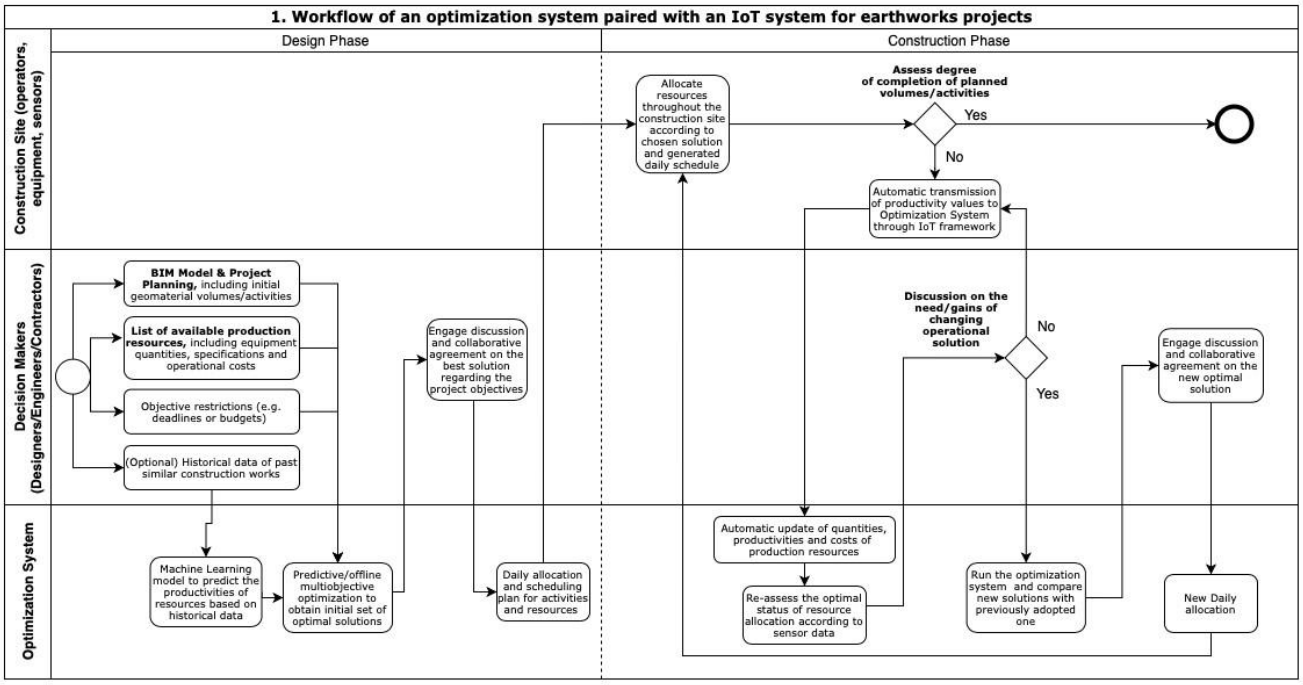

Figure 1. Workflow of the optimization system paired with IoT system for earthworks projects.

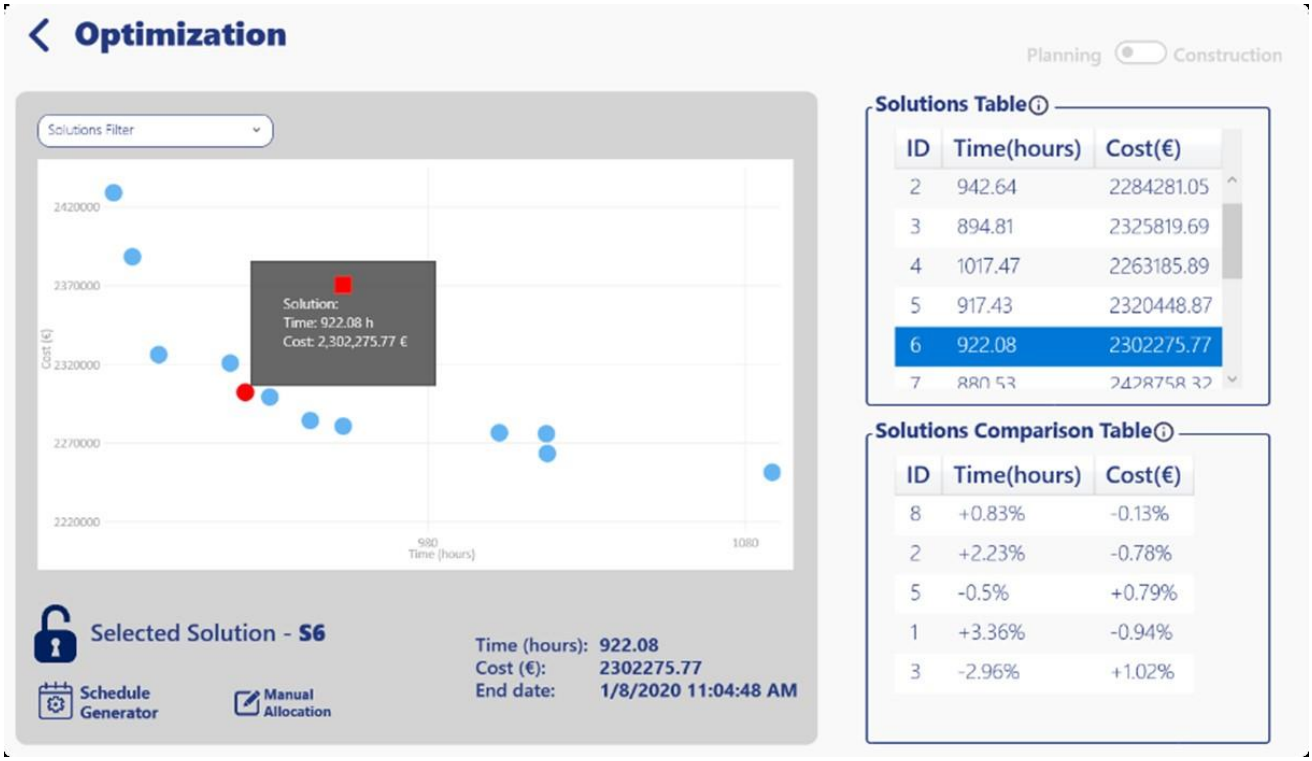

Figure 2. Pareto front solutions output from the planning/design phase of the system.

4.3 Application to construction phase

This simulation incorporates GPS positioning sensors in transport trucks during construction, enabling productivity assessment based on cycle counts within specified periods. This system also infers excavation and compaction team efficiency during loading and unloading cycles. These assessments are conducted with minimal intervention, as GPS is only installed on the transport trucks. Initially, productivity measurements are indicative, assuming trucks are fully loaded. However, these values are adjusted monthly based on topographic measurements at each work front. These measurements, part of regular quality control processes, provide accurate volumes of

excavated and embanked geomaterials, allowing for comparison with system estimates.

To address variations between actual and estimated volumes, a corrective factor, 'k', is applied to truck productivity. This factor is proportional to the ratio of actual volumes measured topographically to those estimated by the system. The system operates in monitoring and control mode from the beginning of the construction phase. A control dashboard offers real-time project progress monitoring, productivity tracking at each work front, and live transport equipment location updates (Figure 3). It also issues notifications for potential issues and provides access to activity history and project parameters.

In case of project changes, such as equipment breakdowns or alterations to material types, the system recalculates costs and duration for subsequent phases. Users can choose to accept revised forecasts or request resource reallocation to optimize work efficiency.

During re-optimization, a third minimization objective, Re-Allocation Disruption (RAD), considers the cost of reallocating equipment between work fronts. RAD minimizes disruptions caused by equipment changes, optimizing the reorganization process. In both planning/design and construction phases, the system not only allocates resources but also selects the optimal fleet, ensuring efficient resource utilization. Nomenclature for solutions in re-optimization facilitates tracking of adjustments throughout the project. The system maintains a descriptive database of project development, enabling future analyses and applications of artificial intelligence for knowledge extraction. It can also illustrate the normal operation of the control dashboard, offering a comprehensive overview of project status, productivity metrics by work front, real-time transport equipment tracking via map visualization, and notifications for potential issues. This dashboard also provides access to activity history and project parameter editing functions.

In the event of re-optimization, the system generates a new set of solutions, with each solution evaluated based on minimization objectives, once again presented in Pareto format. The system adjusts solutions dynamically, accounting for changes in project conditions and constraints.

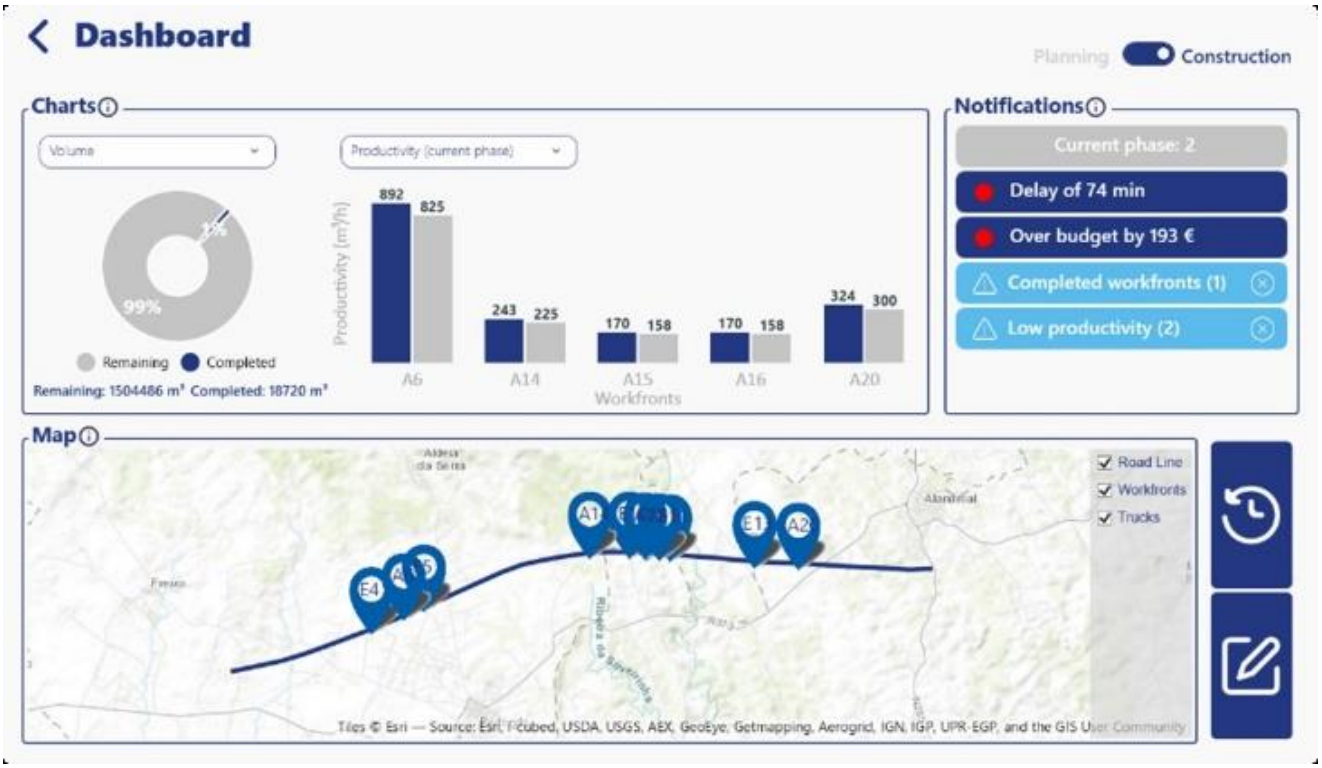

Figure 3. Monitoring and control dashboard for the conducted construction simulation.

Figure 4 displays the allocation adjustments resulting from re-optimization. Each solution corresponds to a specific equipment allocation, evaluated by associated duration and cost metrics. The system also evaluates the Re-Allocation Disruption (RAD) associated with each solution, providing additional decision support for users.

4.4 Intelligent compaction

The concept of Industry 4.0 (i4.0) offers new opportunities for intelligent optimization of

compaction operations (Parente et al., 2018; Gomes Correia, 2018). By leveraging smart sensors and real-time monitoring, i4.0 enables the creation of virtual models to simulate compaction processes and continuously assess geomaterial properties. Machine learning algorithms enhance predictive capabilities and facilitate classification of geomaterials based on their properties, leading to improved compaction quality.

Figure 5 illustrate the most representative tools of i4.0 applied in intelligent compaction (Gomes Correia, 2018).

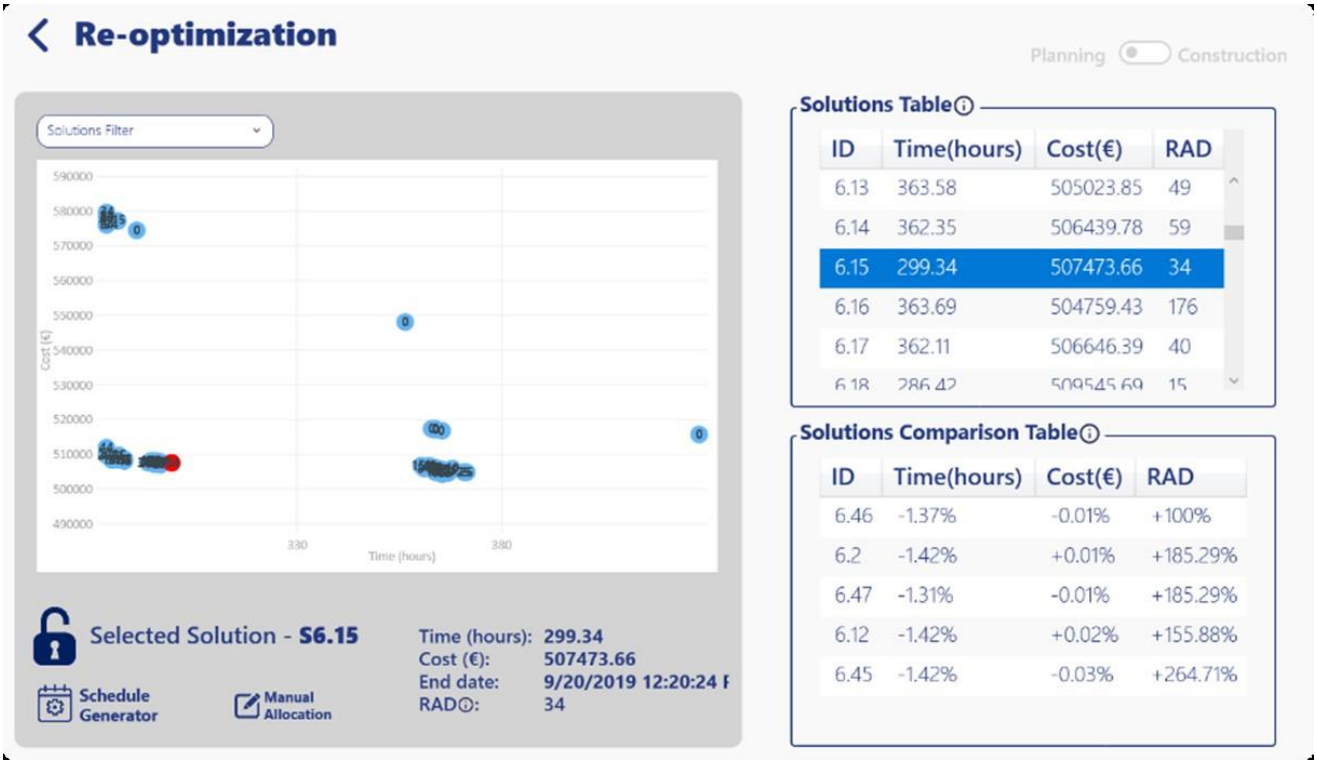

Figure 4. Pareto front solutions output of adjustments that arise from the re-optimization process.

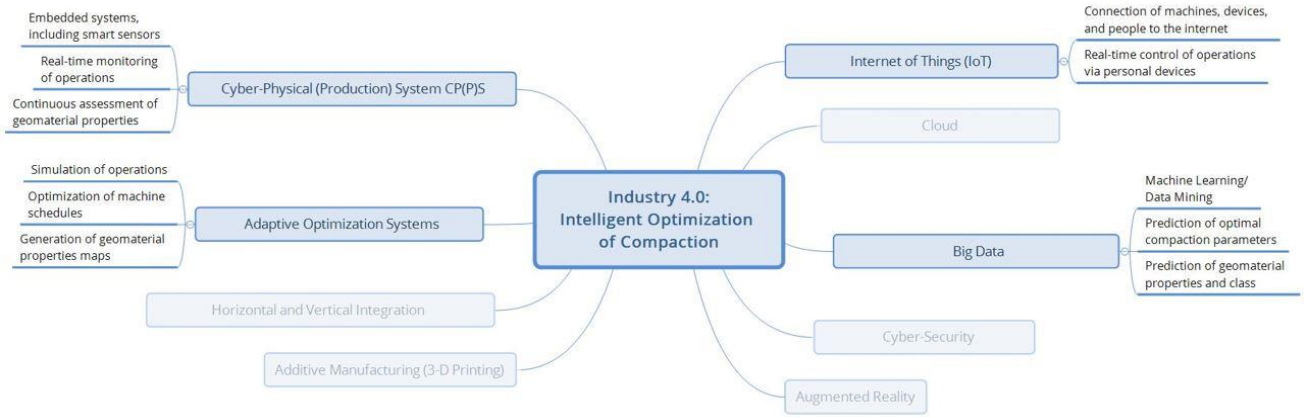

Figure 5. Industry 4.0 technologies applied to intelligent optimization of compaction.

Indeed, this approach can provide an agile and autonomous decision-making facing the challenges posed by dynamic and unpredictable environments, such as those encountered in compaction operations. To achieve this, it prioritises the utilisation of technologies like smart sensors for real-time monitoring of the compaction process. This enables the creation of a virtual representation of physical compactors within a simulation model and facilitates continuous assessment of geomaterial properties and continuous compaction control. Indeed, unlike traditional methods that may only sample certain areas, these technologies can monitor and assess the entirety of the compacted area in real-time.

On one hand, this forms the foundation for real-time scheduling and optimization of compactor tasks,

while simultaneously processing the feedback data from the geomaterial. On the other hand, this data can also be subjected to machine learning and data mining algorithms. These techniques not only enable the prediction of optimal compactors parameters but also allow for the continuous compaction control and classification of geomaterials based on their properties, the so-called intelligent compaction (IC). This offers opportunities for further enhancement and refinement of the compaction process and deliver quality control parameters that can be directly compared with design parameters (Tatsuoka and Gomes Correia, 2018; Gomes Correia and Ramos, 2022).

Furthermore, this entire process is underpinned by the connectivity of compactors, devices, and personnel to the internet, aligning with the principles of the Internet of Things (IoT). This connectivity fosters transparency, enhances communication, and facilitates real-time control of operations from any location worldwide with internet access, using personal communication devices such as smartphones.

In summary, intelligent compaction emerges as a pivotal technology, particularly during the construction phase, facilitating automated functions such as perception, analysis, decision-making, and execution (Xu et al., 2022). This technology holds significant importance in global engineering construction endeavours. At its core, intelligent compaction plays a crucial role in accurately perceiving compaction quality information, involving dynamic solutions to the interaction between rigid cylinders and elastic half-spaces (Paulmichl et al., 2022). However, there remains a need for further exploration to meet the precision requirements of quality control and dynamic solutions in this area. In this context, the integration of intelligent compaction within the previously discussed optimization framework holds significant promise for enhancing the efficiency and effectiveness of earthwork projects. It will improve project management by enabling proactive decision-making based on accurate and up-to-date information. For instance, the optimization system can dynamically adjust compactor routes and operating parameters in response to variations in soil type, conditions, or unexpected obstacles encountered during construction. By analysing compaction data in real-time, the system can identify areas of suboptimal compaction and allocate resources accordingly to ensure uniform compaction, thereby ensuring consistent compaction levels and meeting specified engineering design criteria across the entirety of the construction site.

5 APPLICATION TO AN URBAN METRO LINE – CASE STUDY

The Lisbon metro construction site, spanning between Santos and Cais do Sodre stations, serves as an intriguing showcase for the utilization of these technologies. This multifaceted construction project faces numerous challenges, including the construction of a sizable station on the urban side of the Santos hill, the excavation of a traditional tunnel within Lisbon's historic district, the creation of a trench in a densely populated urban area adjacent to sensitive buildings, the building underpinning through which the line passes, and the seamless integration with the operational station at Cais do Sodre. More detailed information is available at Martins et al. (2024).

Addressing these diverse challenges necessitated the implementation of an advanced monitoring system comprising robotic measurements, IoT sensors, a web platform, and real-time processing leveraging artificial intelligence. Figure 6 identify the monitoring devices (liquid level sensor and extensometer) for the specific case of underpinning building, solution adopted to facilitate the deactivation of the foundation piles of existing buildings within the tunnel projection area and to start excavation for the construction of the tunnel structure, part of Lisbon Metro line - new circular line.

5.1 Database process

The ARGOS platform was selected to centralize, store in Software as a Service (SaaS) mode, and manage monitoring data for the entire site during the extension of the works. The measurements encompass a wide range of data types, including manual and automatic topographic measurements, convergence measurements, borehole extensometer measurements, stress measurements, crack openings, altimetric liquid level monitoring, piezometric measurements, inclinometric measurements, and automatic high-end vibration measurements.



Figure 6. Lisbon Metro line new circular line: Underpinning building - Monitoring devices.

5.2 Monitoring data management and visualisation

All data are securely stored on a hyper-secure, trusted European cloud that complies with GDPR as well as European requirements regarding artificial intelligence. These data are accessible in real-time through a responsive web interface, presented in various formats such as plans, multi-layer GIS interfaces, dynamic maps, 3D views, dashboards, graphs, and reports.

5.2.1 Sensors technologies, wireless, communication protocols, cloud platform

The extensive coverage of the site, combined with the high number of sensors and measurement frequencies, along with the presence of various challenging traffic lanes, necessitated the adoption of automated measurements for the robotic theodolites, vibration sensors, and geotechnical and structural IoT sensors.

To ensure comprehensive coverage, both above and below ground, a network of radio bases was deployed across the entire site. Managed by the ARGOS core network, this radio network facilitates the secure and encrypted transmission of field data back to the central system.

5.2.2 Prediction models and anomaly detection

All raw data are securely transmitted to the cloud-based database where they undergo real-time processing to generate actionable information for the users.

Raw measurements may not always be immediately usable due to various reasons. These could include the need for transformation of electrical data for comprehension, presence of statistical errors such as artifacts or parasites, or excessively high data flow rates that are impractical for direct analysis by engineers. For instance, in the field of vibration monitoring, each instrument may generate thousands of measurements per second, which must be condensed into manageable indicators for site monitoring purposes.

In addressing these challenges, the monitoring platform assumes a critical role in real-time data processing. It employs mathematical, statistical, and logical algorithms, as well as artificial intelligence models, to perform tasks such as summarizing data, reducing noise, and making real-time forecasts based on historical data. For example, artificial intelligence algorithms can be trained to recognize and eliminate erroneous topographical data, enhancing the reliability of the information delivered and fortifying the overall robustness of the monitoring system. This sophisticated tool leverages the expertise of topographic engineers to ensure the integrity and accuracy of the monitoring data.

5.2.3 Alerts and actions

Once processed, the availability of reliable real-time measurements forms the cornerstone of effective site risk management. Customized detection thresholds are established for each sensor, triggering advanced alarms instantly upon their surpassing. These alarms are configured with various levels of sensitivity, conditional triggers, differentiated responses based on thresholds, schedules, and alarm groupings, among other details tailored to the site's configuration and

management requirements. Table 1 illustrates the criteria for alerts, references, and alarms utilized for monitoring settlements in column 10 (Figure 6) of the building during load transfer operations as part of the underpinning process. These settlements are associated with the load step values applied by the jacking.

Table 1. Lisbon Metro line new circular line: Underpinning building - Monitoring thresholds for column 10.

Column	Estimated Load (kN)	Load step	Load (kN)	Settlement measured in Liquid Level Sensors (mm)		
				Alert	Reference	Alarm
10	3362	10%	336	0,4	0,5	0,6
		20%	672	0,7	0,8	1,1
		30%	1008	1,0	1,2	1,6
		40%	1344	1,4	1,7	2,3
		50%	1680	1,8	2,2	2,9
		60%	2016	2,1	2,5	3,4
		70%	2353	2,5	3,0	4,1
		80%	2689	2,8	3,4	4,5
		90%	3025	3,1	3,7	5,0
		100%	3362	3,5	4,2	5,7

The alarms activated by the ARGOS platform are integrated into a comprehensive action plan detailing proactive and corrective measures to be taken when thresholds are breached. Upon activation, the ARGOS software promptly dispatches notifications in real time to designated stakeholders, providing details of the triggered alarm, the observed value, and the timestamp of the occurrence.

This proactive approach enables the site management team to swiftly intervene and mitigate any potential risks that could jeopardize the safety of personnel or structures within the construction site perimeter.

6 CONCLUSIONS

The integration of IoT and AI technologies in geotechnical engineering has led to the development of advanced Early Warning Systems (EWS) capable of real-time communication of critical events. These technologies facilitate efficient monitoring through reliable connections between sensors, control units and communication methods. Challenges include scalability, sustainability, and security. Best practices involve integrating AI-powered systems that can collect vast amounts of data in real-time and analyse it to provide actionable insights. By analysing trends and correlations in the data, AI models can forecast potential incidents and trigger early warning systems, allowing for proactive intervention and risk mitigation measures.

Earthwork construction projects often face uncertainties, requiring flexibility from planning and management teams to handle unforeseen events like weather changes or equipment failures. Decision support systems play a vital role by compiling past knowledge and facilitating collaboration among teams, aligning with modern construction principles like Construction 4.0 and Building Information Modelling (BIM). These systems utilize technologies like artificial intelligence and optimization algorithms to predict, monitor, and optimize earthwork processes.

A case study from a road construction project in Portugal illustrates how these systems optimize equipment fleet allocation, considering factors like cost, duration, and resource availability. In planning, the system creates robust plans with contingency measures, while during construction, it monitors productivity and adapts to disruptions. Historical data from projects enable future analysis and knowledge extraction, contributing to continuous improvement in earthwork construction.

In this context, intelligent compaction, as part of earthworks, leverages IoT and AI technologies to enhance the efficiency and effectiveness of soil compaction processes. Furthermore, the application of the previous optimization systems for earthworks, allows for informed decision-making by dynamically adjusting compaction equipment deployment and work schedules based on compaction performance. Smart sensors allow monitor compaction in real-time, providing data for optimization of the compaction. AI algorithms analyse this data to predict optimal parameters of the interaction roller-soil, and classify soil types, improving compaction quality and allowing assessment of design parameters. IoT connectivity enables remote monitoring and control, enhancing transparency and communication throughout all the earthwork process.

A second case study involving a metro construction site in Lisbon, illustrates also the use IoT and AI. In this case, the data, securely stored on a trusted European cloud complying with GDPR and AI regulations, are made accessible in real-time via a responsive web interface, offering various formats like plans, GIS interfaces, dynamic maps, and dashboards. To cover the extensive site and high sensor count, automated measurements using robotic theodolites, vibration sensors, and IoT sensors were deployed, managed by the ARGOS core network. Raw measurements undergo real-time processing to produce actionable insights, overcoming challenges like data transformation and high flow rates. A monitoring platform employs AI to enhance data reliability, recognizing and eliminating errors. Customized thresholds trigger advanced alarms,

enabling proactive risk management. Notifications alert stakeholders to potential risks, ensuring swift intervention to maintain site safety.

As a concluding note, the couple of IoT and AI technologies presents unparalleled prospects for transforming geotechnical construction and management methodologies. This synergy heralds the era of safer and more resilient project developments, delivering substantial advantages for all the players across the design, construction, and maintenance sectors, ultimately enhancing societal well-being.

ACKNOWLEDGEMENTS

The authors conceived and wrote the paper, but they incorporated figures and drawings from collaborative work of colleagues of the team, duly cited in the paper. Regarding the earthwork topic, developed applied research based on Manuel Parent's PhD thesis, conducted in 2015, under the supervision of the first author, has been instrumental. Additionally, the collaborative efforts within the framework of intelligent compaction, including the International Society for Intelligent Compaction (ISIC), as well as the Technical Committee 202 "Transportation Geotechnics" of the International Society for Soil Mechanics and Geotechnical Engineering (ISSMGE), and its counterpart in Portugal, CPGT of the Geotechnical Portuguese Society (SPG), are also acknowledged.

Additionally, the first author acknowledge FCT / MCTES through national funds (PIDDAC), allocated to the R&D Unit Institute for Sustainability and Innovation in Structural Engineering (ISISE) under reference UIDB / 04029/2020, project UID/QUI/00686/2020 of CQ, and the Associate Laboratory Advanced Production and Intelligent Systems ARISE under reference LA/P/0112/2020.

The authors are also grateful to Lisbon Metro (Metropolitano de Lisboa) for the permission to use technical information, as well as to the contractor's consortium (Mota Engil, Spie Batignolles and Itmsol) and to the designer's team (COBA and JETsj Geotecnia).

REFERENCES

Bajic, E., Mekki, K. and Rup, C. (2023). LTE-M communication for low-powered IIoT: An experimental performance study. *17th International Conference on Mobile Ubiquitous Computing, Systems, Services and Technologies*, UBICOMM 2023, Sep 2023, Porto, Portugal. Available at: https://hal.science/hal-04222955, accessed: 01/04/2024.

Centenaro, M., Vangelista, L., Zanella, A. and Zorzi, M. (2016). Long-range communications in unlicensed bands: the rising stars in the IoT and smart city scenarios. IEEE Wireless Communications, 23 (5): 60-67. https://doi.org/10.1109/MWC.2016.7721743.

Choi, G. and Han, S. (2023). Reinforcement learning-based dynamic planning of cut and fill operations for earthwork optimization. *Automation in Construction*, 156. https://doi.org/10.1016/ j.autcon.2023.105111.

CISPE (2021). Data Protection Code of Conduct for Cloud Infrastructure Service Providers, available at: https://www.edpb.europa.eu/system/files/2023-03/2021_cispe_cloud_iaas_data_protection_code_of_conduct_-_gdpr_compliance_0.pdf, accessed: 01/04/2024.

CoC (2020). EU Data Protection Code of Conduct for Cloud Service Providers, December 2020, available at: https://eucoc.cloud, accessed: 01/04/2024.

Correia, A. G. and Magnan, J-P. (2012). Trends and challenges in earthworks for transportation infrastructures. Advances in Transportation Geotechnics II (Seiichi Miura et al., eds.). *Proceedings of the 2nd International Conference on Transportation Geotechnics*, Hokkaido , Japan, ICTG 2012, pp. 1 – 12. Taylor and Francis – Balkema. https://doi.org/10.1201/b12754.

Deb, K., Pratap, A., Agarwal, S. and Meyarivan, T. (2002). A fast and elitist multiobjective genetic algorithm: NSGA-II. *IEEE Trans Evol Comput*, 6, pp. 182–197.

Gomes Correia, A. (2018). Extended 2nd Proctor Lecture: Compaction improvements from an Industry 4.0 perspective. *40 Years of Roller Integrated Continuous Compaction Control (CCC) - Anniversary Symposium*, by Adam, D., & Larsson, S. (Eds.). November 29th, 2018 - Symposium Proceedings. Mitteilungen des Institutes für Geotechnik. http://hdl.handle.net/20.500.12708/24485.

Gomes Correia, A. and Ramos, A. (2022). A geomechanics classification for the rating of railroad subgrade performance. *Railway Engineering Science*, 30 (3): 323 – 359. http://doi.org/10.1007/s40534-021-00260-z.

Gomes Correia, A., Cortez, P., Tinoco, J. and Marques, R. (2013). Artificial intelligence applications in transportation geotechnics. *Geotechnical and Geological Engineering*, Springer, 31(3): 861-879. http://doi.org/ 10.1007/s10706-012-9585-3.

Han, T., Ma, T., Fang, Z., Zhang, Y. and Han, C. (2022). A BIM-IoT and intelligent compaction integrated framework for advanced road compaction quality monitoring and management. *Computers and Electrical Engineering*, 100. https://doi.org/10.1016/j.compeleceng.2022. 107981.

Jaafar, K. and El-Halawani, L.I. (2022). Simulation-based multi-objective optimization model for machinery allocation in shallow foundation. *International Journal of Construction Management*, 22 (15): 2845 – 2854. ttps://doi.org/10.1080/15623599.2020.1827693.

Kumar, G.S.A., Roy, A., Singh, R., Gehlot, A., Iqbal, M.I. and Akram, S.V. (2023). A comprehensive approach to real-time site monitoring and risk assessment in

construction settings using Internet of Things and artificial intelligence. *SSRG International Journal of Electrical and Electronics Engineering*, 10 (8): 112 – 126. https://doi.org/10.14445/23488379/IJEEE-V10I8P111.

Liang, C-J., Le, T-H, Ham, Y., Mantha, B.R.K., Cheng, M. H. and Lin, J.J. (2024). Ethics of artificial intelligence and robotics in the architecture, engineering, and construction industry. *Automation in Construction*, 162. https://doi.org/10.1016/j.autcon.2024.105369.

LoRa Alliance (2024). Available at: https://lora-alliance.org/, accessed: 01/04/2024.

Malik, H., Alam, M.M., Kuusik, A., Le Moullec, Y. and Pärand, S. (2020). Narrowband Internet of Things (NB-IoT) for industrial automation. *Wireless Automation as an Enabler for the Next Industrial Revolution* (eds M.A. Imran, S. Hussain and Q.H. Abbasi). https://doi.org/ 10.1002/9781119552635.ch4.

Marques, R., Gomes Correia, A. and Cortez, P. (2008). Data mining applied to compaction of geomaterials. Eight International *Conference on the Bearing Capacity of Roads, Railways and Airfields*, Champaign, Illinois, USA.

Martins, C., Fartaria, C., Tomásio, R. and Pinto, A. (2024). Lisbon new circular Metro underground line: Buildings underpinning. Proceedings of the *XVIII ECSMGE 2024*, Lisbon, Portugal. CRC (in press).

Neves, J., Moutinho, J., Freire, A.C., Paixão, A., Monteiro, B., Parente, M. and Gomes Correia, A. (2024). A geotecnia na transição eco-digital das infraestruturas de transporte (Geotechnics in the eco-digital transition of transport infrastructures). *Geotecnia*, Número Extra (2024): 41-78. https://doi.org/ 10.14195/2184-8394_extra2024_1_3 (in Portuguese).

Parente, M., Correia, A.G. and Cortez, P. (2016). Metaheuristics, Data mining and geographic information systems for earthworks equipment allocation. *Procedia Engineering*, 143: 506 – 513. https://doi.org/10.1016/j.proeng.2016. 06.064.

Parente, M., Cortez, P. and Gomes Correia, A. (2015). An evolutionary multi-objective optimization system for earthworks. *Expert Systems with Applications*, 42 (19): 6674–6685. http://doi.org/10.1016/j.eswa.2015.04.051.

Parente, M., Gomes Correia, A., Figueira, G. and Mehrsai, A. (2018). Towards improving earthworks production from an Industry 4.0 perspective: the role of remote information technologies and dynamic optimization techniques. *Proceedings of 7th Transport Research Arena (TRA 2018)*, Vienna, Austria.

Parente, M., Amândio, A., Moutinho, J. and Gomes Correia, A. (2022). Digital twin optimization framework for earthworks production optimization and management. *Proceedings of the 11th International Conference on the Bearing Capacity of Roads, Railways and Airfields* (BCRRA2022), Trondheim, Norway.

Paulmichl, I. Adam, C. and Adam, D. (2022). A numerical study on the response of the oscillation roller-Soil interaction system. *Advanced Structured Materials*, 156, pp. 161 - 172, http://doi.org/10.1007/978-3-030-79325-8_14).

Rastogi, E., Kumar Maheshwari, M., Roy, A., Saxena, N. and Ryeol Shin, D. (2022). Energy efficiency analysis of narrowband Internet of Things with auxiliary active cycles for small data transmission. *Trans Emerging Tel Tech*., 33(1):e4376. https://doi.org/ 10.1002/ett.4376.

Raza, U., Kulkarni, P. and Sooriyabandara, M. (2017). Low power wide area networks: An overview. *IEEE Communications Surveys & Tutorials*, 19 (2): 855-873, https://doi.org/10.1109/COMST.2017. 2652320.

Shanmuga Sundaram, J. P., Du, W. and Z. Zhao (2020). A survey on LoRa networking: Research problems, current solutions, and open issues. *IEEE Communications Surveys & Tutorials*, 22 (1): 371-388, doi: 10.1109/COMST.2019.2949598.

Singh, R. and Tyagi, V. (2023). Innovative applications of IoT in civil engineering: Enhancing efficiency and sustainability. *3rd International Conference on Advancement in Electronics and Communication Engineering,* AECE 2023: 1028 – 1031. https://doi.org/10.1109/AECE59614. 2023.10428145.

Taddeo, M., and Floridi, L. (2018). How AI can be a force for good. *Science*, 361(6404): 751-752. https://doi.org/ 10.1126/science.aat59.

Tan, J., Sha, X., Lu, T. and Dai, B. (2022). A short survey on future research of AI and IoT technologies. *2022 International Wireless Communications and Mobile Computing*, IWCMC 2022: 190 – 195. http://doi.org/10.1109/ IWCMC55113.2022.9825425.

Tatsuoka, F. and Gomes Correia, A. (2018). Importance of controlling the degree of saturation in soil compaction linked to soil structure design. *Transportation Geotechnics*, 17(Part B): 3-23. https://doi.org/10.1016/ j.trgeo.2018.06.004.

Xu, G., Chang, G.K., Wang, D., Correia A.G. and Nazarian, S. (2022). The pioneer of intelligent construction—An overview of the development of intelligent compaction. *Journal of Road Engineering*, 2 (4): 348 – 356. https://doi.org/10.1016/j.jreng.2022.12.001.

Zhang, W., Pradhan, B., Stuyts, B. and Xu, C. (2023). Application of artificial intelligence in geotechnical and geohazard investigations. *Geological Journal*, 58 (6): 2187 – 2194. https://doi.org/10.1002/gj.4779.

Proceedings of the XVIII ECSMGE 2024
GEOTECHNICAL ENGINEERING CHALLENGES
TO MEET CURRENT AND EMERGING NEEDS OF SOCIETY
© 2024 the Authors
ISBN 978-1-032-54816-6
DOI 10.1201/9781003431749-5
Open Access: www.taylorfrancis.com, CC BY-NC-ND 4.0 license

ECSMGE 24
XVIII EUROPEAN CONFERENCE ON SOIL MECHANICS AND GEOTECHNICAL ENGINEERING

Keynote Lecture

Soil reinforcement based on bio-geo-chemical processes: from laboratory insights to field applications

Renforcement des sols basé sur des processus biogéochimiques: des observations en laboratoire aux applications sur le terrain

L. Laloui*, D. Terzis, R. Harran, J. Bosch, A. Elmaloglou, S. ten Bosch, M. Buyuklu, Z.N. Sahlab
Soil Mechanics Laboratory, Swiss Federal Institute of Technology, EPFL, Lausanne. Switzerland

**lyesse.laloui@epfl.ch*

ABSTRACT: Addressing the pressing need for sustainable and efficient engineering solutions as an alternative to traditional chemical synthesis, this paper highlights the emergence of bio-geotechnical engineering, specifically focusing on Microbially Induced Calcite Precipitation (MICP). MICP presents itself as a promising and sustainable approach to soil stabilization, mitigating environmental concerns linked with cement-based products. Through harnessing microorganisms present in soil and groundwater, MICP not only enhances soil mechanical properties but also contributes to geohazard mitigation. This comprehensive paper spans MICP studies, ranging from microscopic characterizations to lab-scale testing and large-scale applications, showcasing its adaptability and versatility. It delves into the bio-chemo-mechanical principles of MICP, emphasizing the increasing interest and expanding research within the field. The discussion extends to advancements in modeling tools, crucial for evaluating and optimizing MICP processes. These innovations play a pivotal role in bridging the gap between theoretical research and practical applications, guiding the design of MICP for real-world scenarios. Furthermore, the paper stresses the necessity of shifting focus towards MICP application at natural sites, highlighting its potential to become a standard in sustainable geotechnical engineering. The call for more attention to practical implementations reinforces the paper's contribution to advancing MICP as a viable and eco-friendly alternative in the field.

RÉSUMÉ: Répondant à la nécessité pressante de solutions d'ingénierie durables et efficaces en tant qu'alternative à la synthèse chimique traditionnelle, cet article met en lumière l'émergence du génie bio-géotechnique, se concentrant spécifiquement sur la Précipitation de Calcite Induite par les Micro-organismes (MICP). Le MICP se présente comme une approche prometteuse et durable pour la stabilisation des sols, atténuant les préoccupations environnementales liées aux produits à base de ciment. En exploitant les micro-organismes présents dans le sol et les eaux souterraines, le MICP améliore non seulement les propriétés mécaniques du sol mais contribue également à la mitigation des risques géotechniques. Cet article couvre les études sur le MICP, allant des caractérisations microscopiques aux tests à l'échelle laboratoire et aux applications à grande échelle, mettant en avant son adaptabilité et sa polyvalence. Il explore les principes bio-chimiques-mécaniques du MICP, soulignant l'intérêt croissant et l'expansion de la recherche dans ce domaine. La discussion s'étend aux progrès des outils de modélisation, cruciaux pour évaluer et optimiser les processus du MICP. Ces innovations jouent un rôle clé dans le comblement de l'écart entre la recherche théorique et les applications pratiques, guidant la conception du MICP pour des scénarios du monde réel. De plus, l'article souligne la nécessité de déplacer l'attention vers l'application du MICP sur des sites naturels, mettant en avant son potentiel pour devenir une norme dans le génie géotechnique durable. L'appel à accorder davantage d'attention aux mises en œuvre pratiques renforce la contribution de l'article à faire progresser le MICP en tant qu'alternative viable et respectueuse de l'environnement dans le domaine.

Keywords: Sustainable geotechnical engineering; bio-geotechnics; microbially induced calcite precipitation; soil stabilization.

1 INTRODUCTION

The geotechnical market is rapidly expanding in response to a growing global population and increasing urbanization rates. This growth compels the industry to explore new land sites that often have poor soil quality and are more exposed to geohazards, necessitating stabilization. As a result, the soil stabilization market is expected to grow to become a

$ 33.3 billion industry by 2025 (IndustryARC, 2021) in response to these challenges.

Traditional soil stabilization methods have predominantly depended on cement grouting. However, in light of escalating environmental challenges and increasing awareness of the substantial impact of cement-based products on the ongoing climate crisis, there is an expanding legislation framework advocating for the adoption of more environmentally sustainable techniques (ENVI, 2020).

Bio-geotechnical strategies, which replicate natural forms, processes, and systems, are at the forefront of alternative soil improvement methods. These strategies leverage nature's time-tested designs and innovations to create environmentally friendly solutions. A notable example is Microbially Induced Calcite Precipitation (MICP) which uses soil and groundwater microorganisms, to control the rate and intensity of calcite mineralization. This biocementation process forms a natural binder that stabilizes the soil and improves its mechanical properties, offering a sustainable alternative for soil stabilization and geohazard mitigation (Dejong et al., 2013; Terzis and Laloui, 2019a; Harran et al., 2023a).

This paper delves into the fundamentals of Microbially Induced Calcite Precipitation (MICP), encompassing the current research landscape and its bio-geo-chemo-mechanical principles. It thoroughly examines the core concepts of the process and their implications across various scales of study addressing how these principles are tackled both experimentally and through modelling. These scales range from microscopic characterization to lab-scale mechanical testing, extending to large-scale applications and pilot projects.

2 STATE OF THE RESEARCH IN THE FIELD

As Figure 1 illustrates, there has been a notable surge in publications delving into the fundamentals and applications of MICP, highlighting the growing interest in the field. These articles focus on using MICP to catalyze the bio-chemical reactions of calcite mineralization using both local and introduced microorganisms, enabling mineralization within practical engineering timescales. The comprehensive review of this interdisciplinary body of research includes those by Terzis and Laloui (2019a) and Harran et al. (2023a), which highlight the wide array of biological, chemical, and mechanical factors involved as well as the global efforts to establish representative models and upscale the technology. The reviews also detail the influence of several factors, such as the physical properties of soils, and the type and concentration of bacteria and reagent solutions, on the efficacy of the MICP process. Furthermore, they discuss how these variables can be tailored to suit a diverse range of uses such as:

- Soil strengthening
- Leakage control
- Slope stabilization
- Liquefaction mitigation
- Fugitive dust control
- Erosion control
- Land reclamation

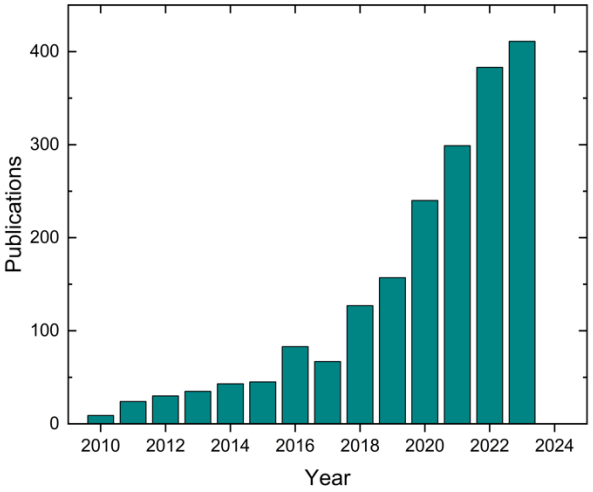

Figure 1. Number of published research articles tackling MICP per year (Scopus).

The large number of applications demonstrates the versatility and adaptability of MICP in practical applications.

3 MICP BIO-CHEMICAL PROCESSES

To consider the MICP process, a good understanding of the underlying chemical reactions is essential. Calcite mineralization can be achieved through multiple bio-chemical pathways including sulfate reduction, denitrification, and ureolysis. The latter is particularly efficient for most geotechnical applications and has consequently been the subject of extensive study. This process involves the hydrolysis of urea Eq. (1), that is catalyzed through the urease enzyme. This reaction produces ammonium ions, which increase the pH, and carbonate ions. In the presence of a natural or introduced calcium source, the alkaline environment favors the precipitation and formation of calcite Eq. (2). The urease enzyme significantly accelerates this process making it feasible in an engineering timeframe.

$$CO(NH_2)_2 + 2H_2O \xrightarrow{urease} 2NH_4^+ + CO_3^{2-} \quad (1)$$

$$Ca^{2+} + CO_3^{2-} \rightarrow CaCO_3 \downarrow \quad (2)$$

Although multiple bacteria strains can produce the urease enzyme, *S. pasteurii* has been the most abundantly researched due to its activity in temperature and pH ranges that align with typical geotechnical project sites. Enzymatically Induced Calcium Carbonate Precipitation (EICP) is another approach which involves the ex-situ extraction of urease, which is then introduced directly into the soil. This technique facilitates the catalyzation of the reaction while circumventing the need to introduce live bacteria into the soil, offering a different approach to soil stabilization and mineralization (Terzis and Laloui, 2019b).

A significant drawback of the ureolysis process is the production of ammonium as a byproduct, which poses risks of groundwater and soil contamination. However, new techniques such as chemically induced calcite precipitation (Park et al., 2020) and ex-situ MICP (Terzis and Laloui, 2021) have been developed to mitigates the risk of ammonium contamination.

4 A MULTI-PHYSICAL, MULTI-SCALE PROCESS

4.1 Microscopic processes

A comprehensive investigation of the mechanical properties of biocemented soils begins with an analysis of the microscopic mechanisms that govern the macroscopic behavior. Central to these investigations is identifying of the soil's microstructural properties and the transport processes that occur during biocementation.

One of the most important microstructural properties is the different forms calcite can take as it precipitates in the soil. Precipitated calcite can create active bonds in the form of interparticle bonds, passive bonds by coating the grain surfaces, and filling the pore space. Each of these forms, shown in Figure 2, uniquely contributes to the mechanical response of biocemented soils, highlighting their importance in understanding and optimizing soil stabilization processes.

Advancements in imaging techniques through Scanning Electron Microscopy (SEM) and X-Ray micro-Computed Tomography (micro-CT) have allowed us to gain deeper insights into the particle-level interactions in biocemented soils. These techniques can provide a detailed 3D reconstruction of the soil's micro-structure as well as quantitative analysis of the calcite distribution in the soil and the different forms it takes. Terzis and Laloui (2018) reconstructed a 3D micro-CT scan of a biocemented sample, successfully identifying the different solid components, sand grains and calcite, as well as outlining the pore spaces as shown in Figure 3

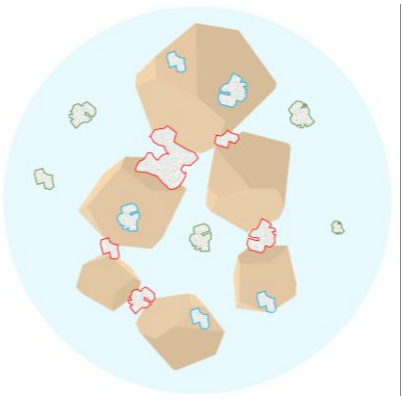

Figure 2. Schematic of precipitated calcite in the soil as: inter-particle bonds (red), grain coating (blue), and filling the pore space (green).

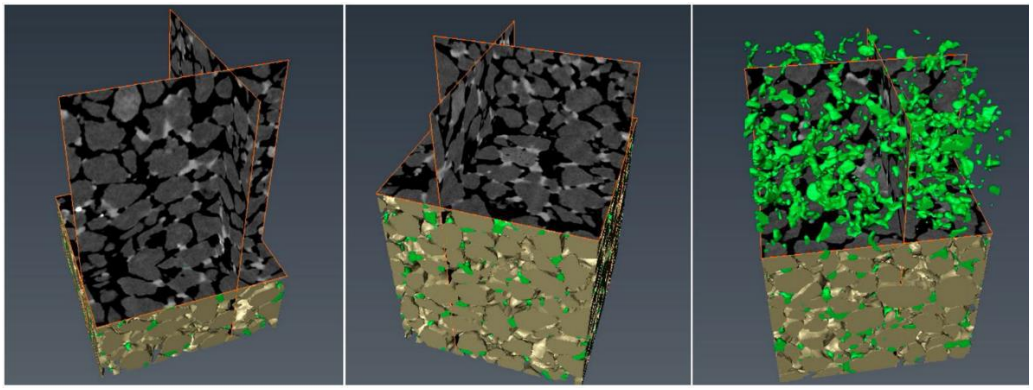

Figure 3. 3D volume reconstruction of a bio-cemented sand sample, with a horizontal section of $1.5\ mm^2$*, obtained through micro-CT scans: sand grains in brown calcite bonds in green (as shown in (Terzis and Laloui, 2018)).*

Through advanced image analysis techniques, these 3D reconstructions were used to accurately estimate the number of active bonds in the scanned samples, shown in Figure 4 producing a range between $75 - 84\%$ depending on the soil gradation and other microscopic soil properties (Terzis and Laloui, 2018, 2019b).

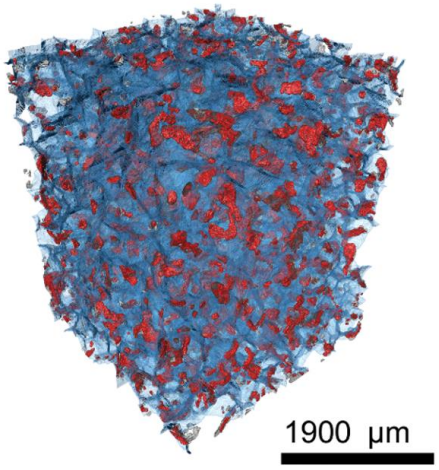

Figure 4. 3D view of active bonds (red) and spline lines (blue) in a bio-cemented sand (Terzis and Laloui, 2018).

More recently, Roy et al. (2023) were able to thoroughly analyze the contact and pore networks of biocemented sands using similar 3D micro-CT scans gaining a deeper understanding of the flow within the pore networks and the resulting calcite precipitation. Their findings particularly highlight the pivotal role of the initial microstructure in influencing these processes.

Fluid flow during the MICP process as well as after cementation is also thoroughly investigated through the use of microfluidic chips. These physical models allow the simulation of flow channels or porous geomaterials with varying properties. They particularly facilitate continuous microscopic observations, making it possible to track the evolution of calcite formation and the influence of micro-parameter at all stages of the MICP process. Elmaloglou et al. (2020, 2022) used a meter-long chip with varying pore-size distributions to track the formation of calcite crystals, following their evolution at different treatment stages with time-lapse microscopy, which helped quantify calcite formation and repartition (Figure 5).

These microscopic insights are pivotal to unraveling the primary mechanisms governing the MICP process, laying a crucial foundation for formulating reactive transport models that simulate the precipitation process. Additionally, they are essential in developing representative mechanical models that accurately incorporate the distinct contributions of the various forms of precipitated calcite.

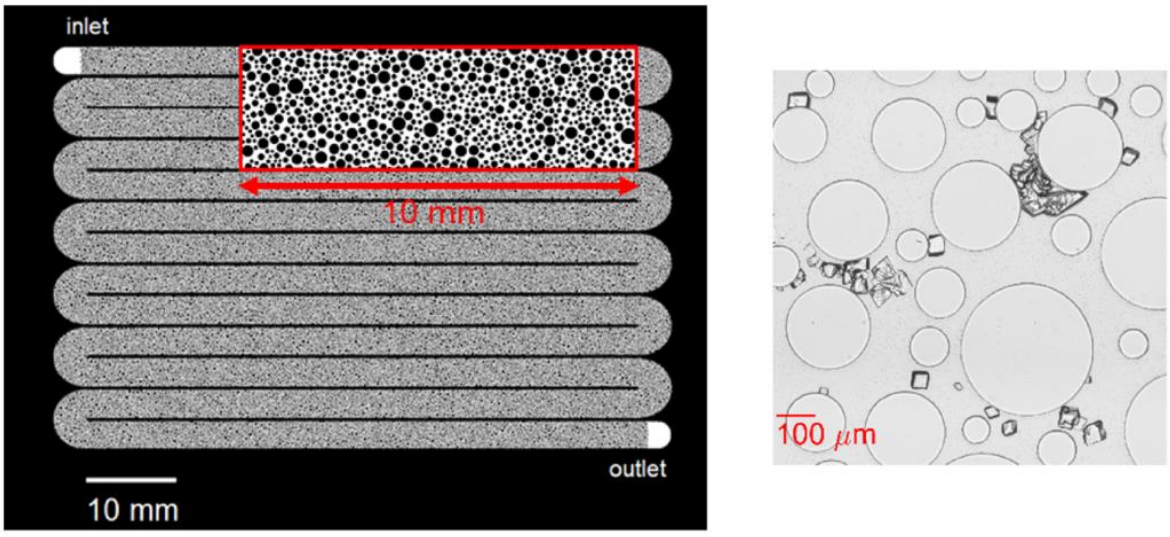

Figure 5. Microfluidic chip of a heterogeneous porous medium (adapted from Elmaloglou et al. (2022)).

4.2 Meso-scale mechanical performance and modeling

Although microscopic tests provide valuable information about the behavior of biocemented soils, laboratory tests at the representative elementary volume scale remain essential to characterize these soils for practical applications.

Biocemented soils, while sharing certain similarities with soils treated using traditional grouting materials, exhibit unique complexities in their characterization. This uniqueness is largely due to the

multiphysical processes involved in their formation. A primary distinction lies in the binder distribution within the soil. Traditional cementation methods involve mixing cement uniformly with soil, resulting in a homogeneous distribution. In contrast, MICP employs less invasive injection techniques, which can lead to a heterogeneous distribution of calcite. This variability often translates into distinct mechanical behaviors when compared to their traditionally cemented counterparts.

These complexities underline the necessity of establishing specific, representative metrics for analyzing and comparing biocemented soil samples. The gravimetric calcite content is a commonly used metric since it can be easily determined from laboratory and field samples through methods like acid digestion. However, it is important to note that it can only provide a global indication of the calcite content in the sample and does not fully distinguish the calcite distribution, causing two samples with identical calcite mass content to exhibit different mechanical properties. Despite this limitation, gravimetric calcite content remains a crucial and practical metric for estimating the behavior of biocemented soil samples.

The impact of various bio-chemical and mechanical factors on mechanical performance, as depicted in Figure 6, has been assessed through standardized geomechanical tests. Terzis et al. (2016) used triaxial tests to explore the effects of different treatment protocols on the chemical reaction efficiency and mechanical performance. They observed that a pulse injection scheme achieved a reaction efficiency – defined as the ratio of effluent to injected calcium ions – of over 80% when a longer reaction time was allowed between pulses, as shown in Figure 7. Conversely, with a recirculation injection protocol, reaction efficiency improved as the reagents were circulated through the sample for extended periods. These results provide valuable insights for the design and execution of field-scale treatment protocols. Such insights are crucial in facilitating the broader adoption and practical application of this technique, as they help optimize the treatment process for enhanced efficiency and effectiveness.

Moreover, the study found that the mechanical performance of the treated samples also showed significant improvement. With a calcite content of around 8.5%, there were notable increases in both the shear strength angle and apparent cohesion, underlining the effectiveness of the treatment protocols in enhancing the soil's structural integrity.

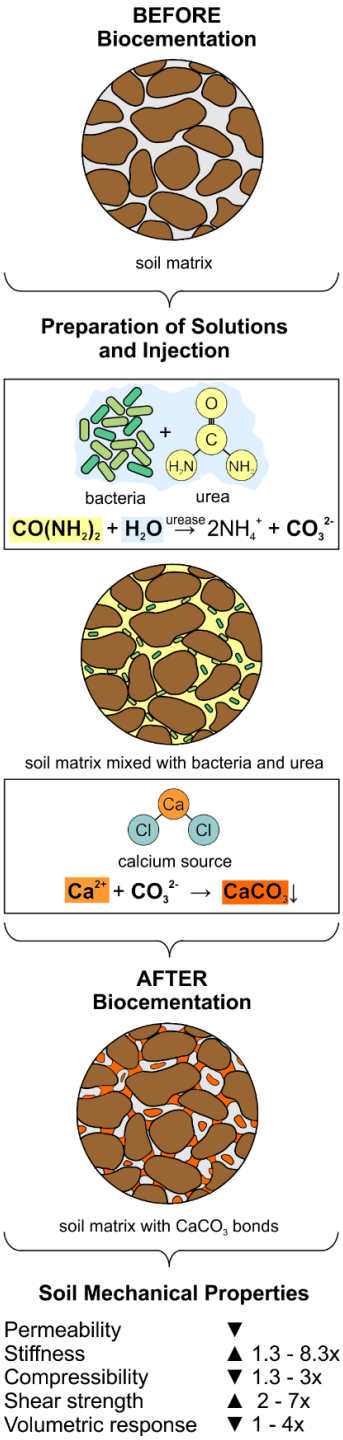

Figure 6. Schematic view of the biocementation process and its effects on soil properties.

In their 2019 study, Terzis and Laloui expanded their investigation to include additional bio-chemical factors, such as applying a novel freeze-dried bacteria powder, and examining its impact alongside soil gradation on mechanical performance. They conducted multiple unconfined compression tests on fine, medium, and coarse sand samples with varying calcite contents, the results of which are depicted in Figure 8. The figure reveals that fine sand exhibited significantly lower strength at comparable calcite

contents than medium sand. This observation was further supported by triaxial tests on these sands, shown in Figure 9. While an improvement in strength was evident in both fine and medium sands compared to their untreated counterparts, the medium sand showed a substantially larger enhancement in strength at each level of confining pressure (Terzis and Laloui, 2019b).

Recent research by Harran et al. (2022) investigated the deformability characteristics of bio-cemented sands, particularly focusing on how these properties change over time and under varying stress conditions. A key observation from these studies is the notable reduction in deformability attributed to biocementation. When subjected to sustained loading, biocemented samples observed smaller axial strains as demonstrated in Figure 10(a). Additionally, the study revealed that samples with higher calcite content demonstrated significantly reduced axial deformations when subjected to uniaxial loading. Samples with a calcite content of around 5% exhibited approximately four times less axial strain than compared to their untreated state, as illustrated in Figure 10 (b).

The experimental findings accumulated thus far serve as a vital foundation for developing and validating multi-physical models, which are indispensable for designing and optimizing of practical applications. The four principal physical processes of MICP — biological, chemical, hydraulic, and mechanical — are intricately interconnected, as depicted in Figure 11. Fauriel and Laloui (2011, 2012a, 2012b) used these interconnections to develop a comprehensive bio-chemo-hydro-mechanical model that successfully captured both calcite distribution and the resulting mechanical performance. Building upon this groundwork, Bosch et al. (2024) recently introduced an advanced fully coupled model that incorporates elasto-plasticity. The model could fully simulate the treatment process and the mechanical response of a shallow foundation making it particularly suited for practical applications.

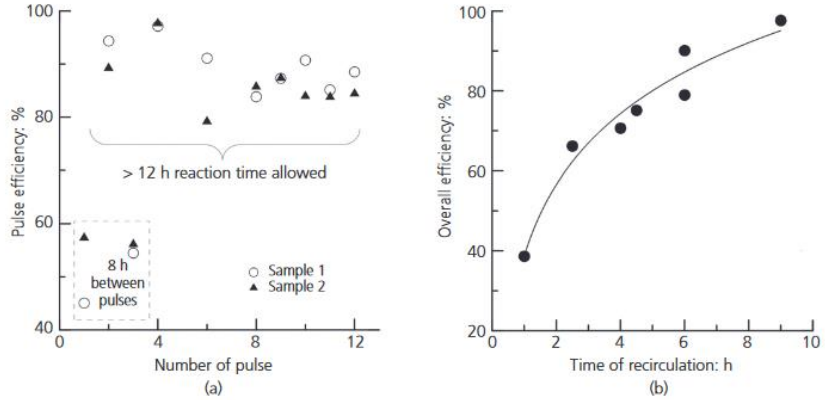

Figure 7. (a) reaction efficiency for samples treated using pulse injections, (b) reaction efficiency for samples treated using recirculation (as shown in (Terzis et al., 2016)).

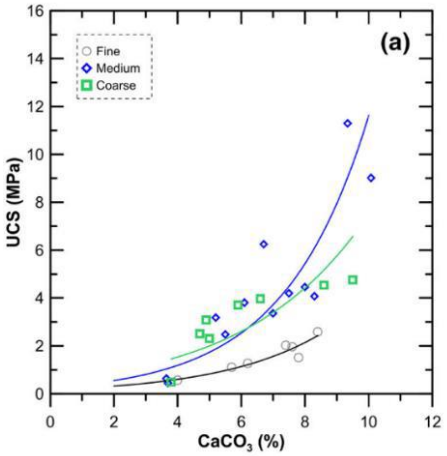

Figure 8. Unconfined compression strength for fine, medium and coarse sand (as shown in (Terzis and Laloui, 2019b).

Modeling approaches can also be tailored to concentrate specifically on the mechanical performance of biocemented soils. This for, of modeling involves developing advanced constitutive models capable of replicating the soil's mechanical behavior given a specific calcite content. A notable example is the Advanced Constitutive Model for Environmental Geomechanics – Biochemistry (ACMEG-B), which was introduced by Fauriel (2012). This model, building on the ACMEG framework originally developed by Laloui and François (2009), incorporates the impact of calcite through parameters related to densification and bonding. Such an approach allows the model to accurately reflect the distinct mechanical performance of biocemented soils under various loading conditions, as illustrated by Figure 12.

4.3 Large scale applications

Transitioning insights from micro and meso-scale studies to field applications represents a critical advancement in incorporating MICP into standard industrial practices. MICP stands out as an environmentally conscious soil improvement technique and boasts distinct advantages over traditional methods. As illustrated in Figure 13, a key benefit is the superior penetrability of bio-cementation solutions. The relatively small dimensions of microorganisms, typically ranging from 0.5-1 μm in diameter and 2-5 μm in length, allow for enhanced permeation within the pores and microfractures of porous media, a stark contrast to the larger particles of traditional cement. This characteristic, combined with the low viscosity of the treatment solutions, facilitates effective permeation grouting at lower injection pressures compared to the high-pressure fluid mixing required in traditional grouting methods. This approach lowers energy consumption and reduces operational costs, as it can be achieved with standardized equipment. Combining these benefits, with the mechanical improvements that are comparable to traditional cement reinforcement establishes MICP as a serious alternative to traditional grouting methods. The application range of biocementation compared with various treatment methods is shown in Figure 14.

To demonstrate the applicability of biocementation for field applications, the technique was used, alongside traditional stabilization techniques, to stabilize a slope encompassing approximately 3000 m3 of earth mass, shown in Figure 15. The bio-cementation treatment involved 51 injection boreholes, each 4.5 m deep, targeting the failure slip surface Despite the natural terrain's low permeability, local fissures facilitated the rapid dispersion of the reactants. Bio-cementation's efficiency was evaluated using a comprehensive assessment which included laboratory tests, in-situ monitoring, microstructural inspections, and aerial surveillance post-stabilization. This holistic assessment revealed that the bio-stabilized zone experienced slower displacement rates than compared to the rest of the slope, demonstrating biocementation's potential in real-world conditions.

More recently, Harran et al. (2023b) made significant progress in upscaling biocementation in a novel large-scale experimental basin ($8\,m \times 10\,m \times 2.5m$), shown in Figure 16. The concrete basin is equipped with drainage at the bottom to avoid the accumulation of reagents that produces unrealistic precipitation patterns that are normally observable at the bottom and edges of other large-scale basins. In this unique setup, various MICP techniques and injection protocols were tested to optimize the MICP process.

The tests were accompanied by a comprehensive monitoring and assessment campaign that included both field scale and laboratory tests. In the field, an extensive dynamic penetrometer campaign evaluated the spatial distribution of calcite and the resulting increase in mechanical performance.

Additionally, chemical monitoring of both injected and effluent solutions was conducted to track reagent consumption and evaluate MICP efficiency. In the lab, mechanical performance was assessed using unconfined compression tests and microscopic observations to view the changes at the pore level.

Buyuklu et al. (2023) later used the same basin to investigate the impact of various injection techniques and protocols on the spatial distribution of calcite.

The resulting cemented sand columns shown are shown in Figure 17. The tests used a similar comprehensive testing campaign using dynamic penetrometer measurements and triaxial tests as well as laboratory calcite content measurement.

Building on these insights Ten Bosch et al. (2022) developed a representative reactive transport model, capturing the calcite precipitation patterns from these experiments as shown in Figure 18.

This advancement in modeling tools is crucial for guiding MICP's design and optimization for practical applications. It equips practitioners with invaluable knowledge and empirical data, bridging the gap between theoretical research and real-world implementation, and underscores the growing maturity of MICP as a viable solution in geotechnical engineering.

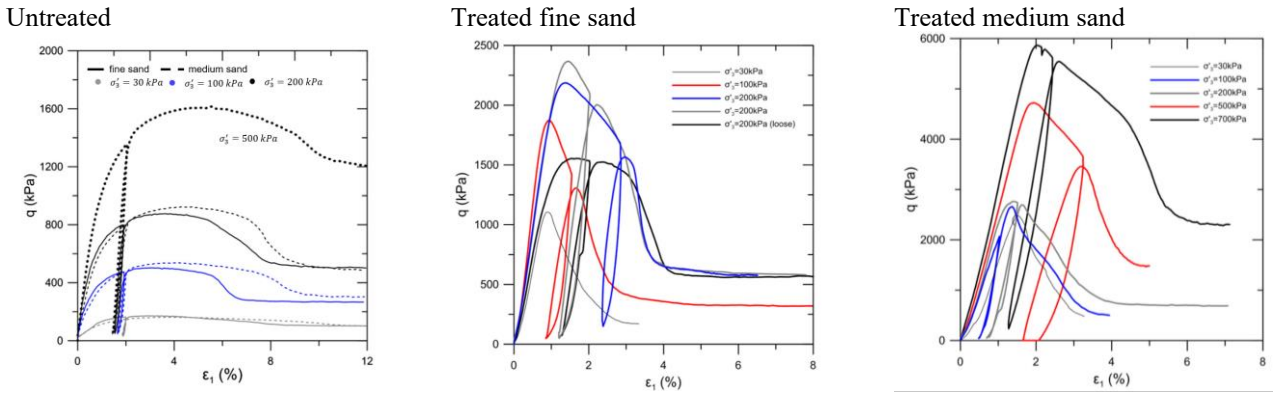

Figure 9. Drained triaxial test for untreated and treated fine and medium sands (as shown in (Terzis and Laloui, 2019b).

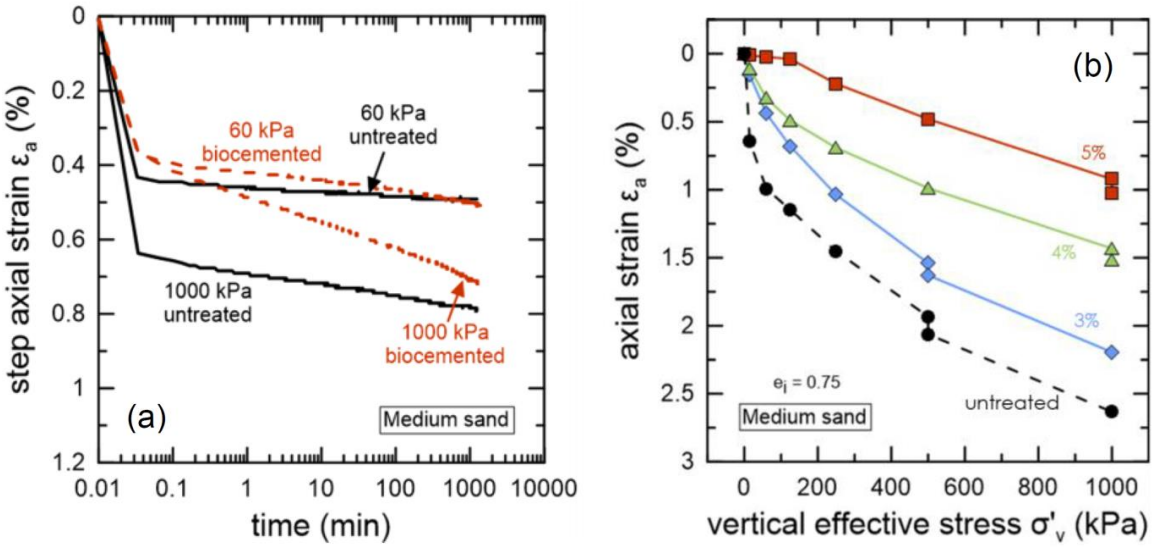

Figure 10. (a) time dependent compressibility of biocemented medium sand, (b) stress dependent compressibility of a bio-cemented medium sand (Harran et al., 2022).

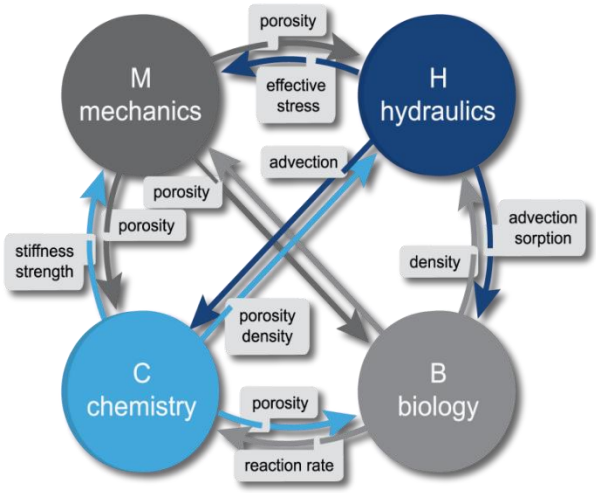

Figure 11. Process coupling in multi-physical models (as shown in (Fauriel and Laloui, 2012b)).

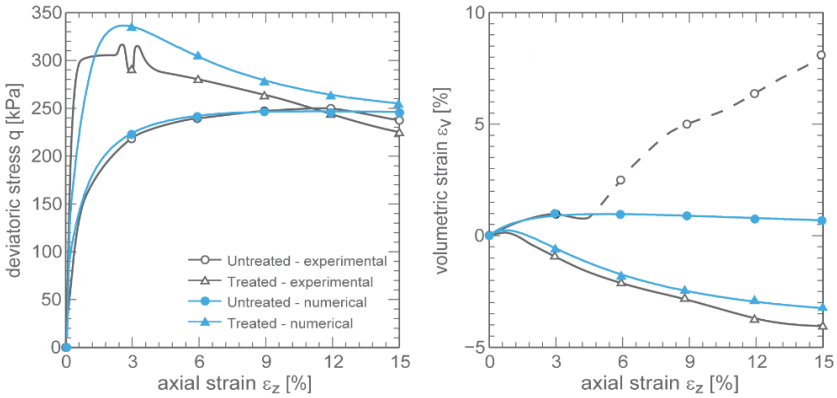

Figure 12. ACMEG-B model performance for a drained triaxial test (as shown in (Fauriel and Laloui, 2012b)).

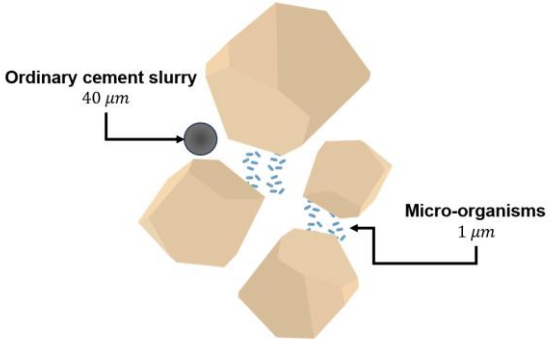

Figure 13. Size comparison between biocementation micro-organisms and traditional grouting materials.

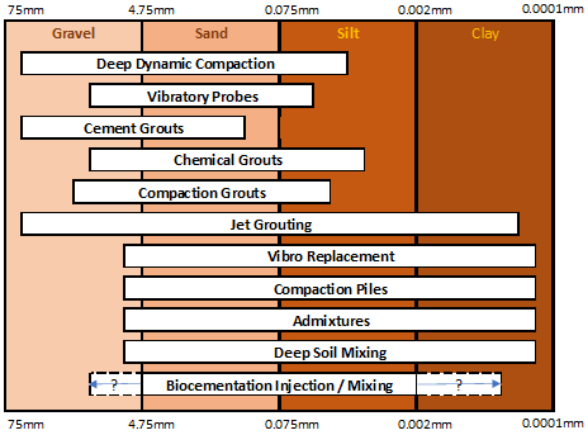

Figure 14. Application range of biocementation in different soil types and comparison with the limits of various treatment methods.

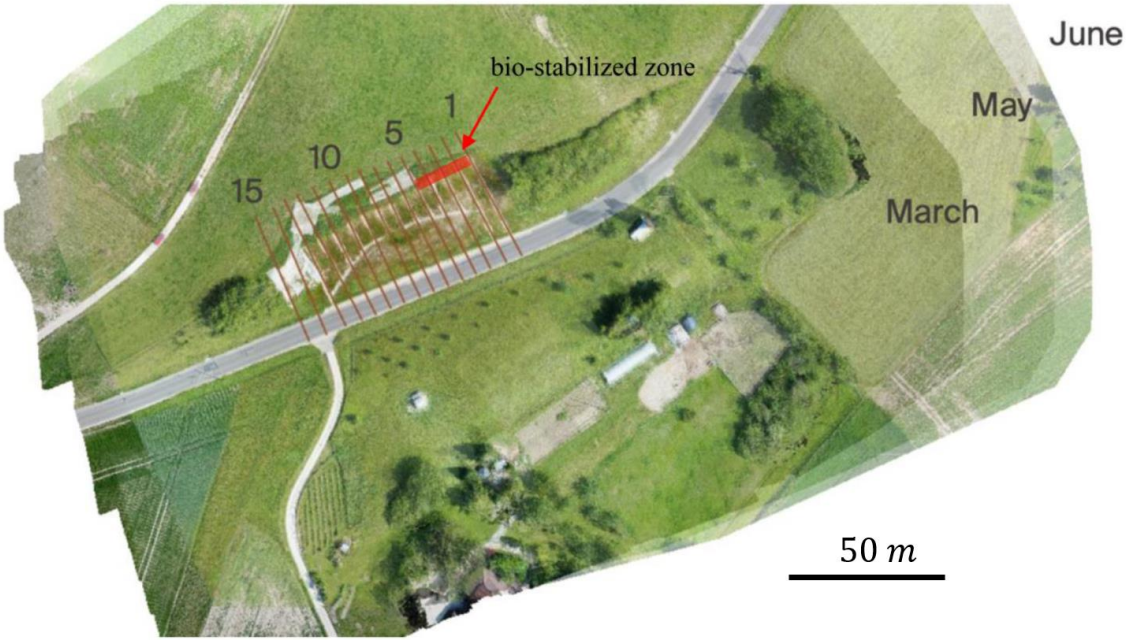

Figure 15. Aerial image of the slope and the bio-stabilized zone (as shown in (Terzis et al., 2020)).



Figure 16. Large-scale experimental basin used for biocementation upscaling (as shown in (Harran et al., 2023b)).



Figure 17. Improved sand columns following various injection techniques in the experiment of Buyuklu et al. (2023).

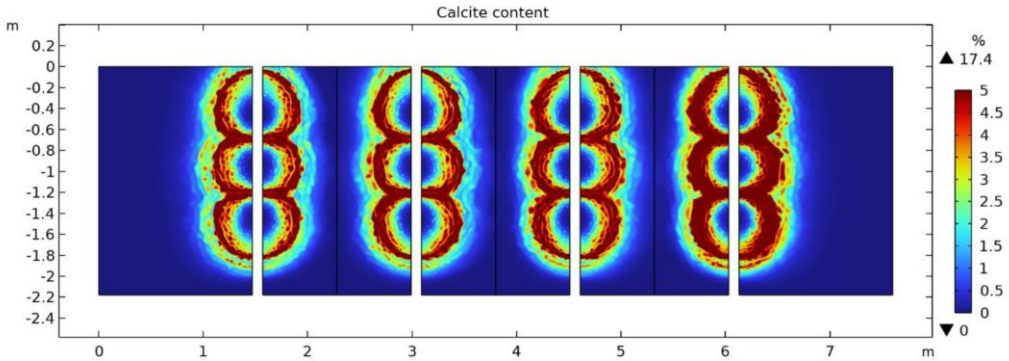

Figure 18. Longitudinal cross section of calcite content obtained from 3D simulations of the experimental basin (as shown in (Ten Bosch et al., 2022)).

5 CONCLUSION AND FUTURE PERSPECTIVES

In conclusion, the comprehensive exploration of biocemented soils across various scales has significantly advanced our understanding of their mechanical properties. The intricate interplay of the bio-chemo-hydro-mechanical properties in biocemented sands has been elucidated, showcasing their potential for a wide range of geotechnical applications. This detailed understanding is critical in evaluating the potential of biocemented soils to withstand and adapt to various environmental conditions, making them a viable solution for geotechnical challenges.

The journey from laboratory-scale experiments to large-scale applications marks a pivotal moment for the field of biocementation. Recent advancements have successfully bridged the gap between small-scale controlled environments and real-world scenarios. These large-scale trials have been instrumental in replicating the complexities of natural sites, thereby providing a more realistic assessment of the potential and limitations of biocementation techniques.

The insights from the laboratory and large-scale experiments have led to the introduction of robust modeling tools that enable better evaluation and optimization of biocementation, allowing for more precise predictions and efficient designs. They facilitate the simulation of various scenarios, including different soil types and environmental conditions, thus enhancing the adaptability of biocementation techniques. This modeling capability is crucial for practitioners, offering a reliable means to predict outcomes and tailor approaches to specific site conditions.

Future work in biocementation is poised to expand its applications and focus on implementation in natural sites. Continued research and development are needed to refine techniques, enhance efficiency, and reduce costs, making biocementation more accessible and feasible for widespread use. The potential for this technology to contribute to sustainable development and environmental conservation is immense, particularly in the context of mitigating geohazards and enhancing soil stability. As we move forward, the integration of biocementation into standard geotechnical practice is not just a possibility but an impending reality, paving the way for more sustainable and resilient infrastructural development.

ACKNOWLEDGEMENTS

The authors wish to thank the European Research Council (ERC) for the financial support under the European Union's Horizon 2020 research and innovation program (Grant Agreement No.: 788587). This work was also supported by the Swiss State Secretariat for Education, Research and Innovation (SERI) under contract number 23.00426.

REFERENCES

Bosch, J.A., Terzis, D., Laloui, L. (2024). A bio-chemo-hydro-mechanical model of transport, strength and deformation for bio-cementation applications. Acta Geotech. https://doi.org/10.1007/s11440-023-02172-0.

Buyuklu, M., Terzis, D., Laloui, L. (2023). On the Effect of Injection Parameters and Techniques Towards Achieving Homogenous Soil Bio-Improvement: Insights From A Large-Scale Experiment | 9th Geotechnical Symposium. Presented at the 9th Geotechnical Symposium, Istanbul, Istanbul, Turkey. https://doi.org/10.5505/2023geoteknik.SS-07.

Dejong, J.T., Soga, K., Kavazanjian, E., Burns, S., Van Paassen, L.A., AL Qabany, A., Aydilek, A., Bang, S.S., Burbank, M., Caslake, L.F., Chen, C.Y., Cheng, X., Chu, J., Ciurli, S., Esnault-Filet, A., Fauriel, S., Hamdan, N., Hata, T., Inagaki, Y., Jefferis, S., Kuo, M., Laloui, L., Larrahondo, J., Manning, D.A.C., Martinez, B., Montoya, B.M., Nelson, D.C., Palomino, A., Renforth, P., Santamarina, J.C., Seagren, E.A., Tanyu, B., Tsesarsky, M., Weaver, T. (2013). Biogeochemical processes and geotechnical applications: Progress, opportunities and challenges. Geotechnique 63, 287–301. https://doi.org/10.1680/geot.SIP13.P.017.

Elmaloglou, A., Terzis, D., De Anna, P., Laloui, L. (2022). Microfluidic study in a meter-long reactive path reveals how the medium's structural heterogeneity shapes MICP-induced biocementation. Sci Rep 12, 19553. https://doi.org/10.1038/s41598-022-24124-6.

Elmaloglou, A., Terzis, D., De Anna, P., Laloui, L., Mahé, S., Miele, F. (2020). Microfluidic-Based Study on the Activation and Evolution of Calcite Bio-Mineralization for Geotechnical Applications 74–82. https://doi.org/10.1061/9780784482834.009.

ENVI, C. on the E.P.H. and F.S., 2020. Draft motion for a resolution on EU Strategy on adaptation to climate change.

Fauriel, S. (2012). Multiphysical Modelling of Soils with a Focus on Microbially Induced Calcite Precipitation. EPFL.

Fauriel, S., Laloui, L. (2012a). A Bio-Hydro-Mechanical Model for Propagation of Biogrout in Soils 4041–4048. https://doi.org/10.1061/41165(397)413.

Fauriel, S., Laloui, L. (2012b). A bio-chemo-hydro-mechanical model for microbially induced calcite precipitation in soils. Computers and Geotechnics 46, 104–120. https://doi.org/10.1016/j.compgeo.2012.05.017.

Fauriel, S., Laloui, L. (2011). Modelling of biogrout propagation in soils. Presented at the Computational Geomechanics, COMGEO II - Proceedings of the 2nd International Symposium on Computational Geomechanics, pp. 578–586.

Harran, R., Terzis, D., Laloui, L. (2023a). Mechanics, Modeling, and Upscaling of Biocemented Soils: A Review of Breakthroughs and Challenges. International Journal of Geomechanics 23, 03123004. https://doi.org/10.1061/IJGNAI.GMENG-8446.

Harran, R., Terzis, D., Laloui, L. (2023b). Addressing the challenges of homogeneity, quality control and waste handling in soil bio-cementation: A large-scale experiment. Soils and Foundations 63, 101332. https://doi.org/10.1016/j.sandf.2023.101332.

Harran, R., Terzis, D., Laloui, L. (2022). Characterizing the Deformation Evolution with Stress and Time of Biocemented Sands. Journal of Geotechnical and Geoenvironmental Engineering 148, 04022074. https://doi.org/10.1061/(ASCE)GT.1943-5606.0002871.

IndustryARC (2021). Soil Stabilization Market Share, Size and Industry Growth Analysis 2020- 2025.

Laloui, L., François, B. (2009). ACMEG-T: Soil Thermoplasticity Model. J. Eng. Mech. 135, 932–944. https://doi.org/10.1061/(ASCE)EM.1943-7889.0000011.

Park, S.-S., Le, T.-T., Nong, Z., Moon, H.-D., Lee, D.-E. (2020). Chemically Induced Calcium Carbonate Precipitation for Improving Strength of Sand. Journal of Materials in Civil Engineering 32, 04020238. https://doi.org/10.1061/(ASCE)MT.1943-5533.0003318.

Roy, N., Frost, J.D., Terzis, D. (2023). 3-D contact and pore network analysis of MICP cemented sands. Granular Matter 25, 62. https://doi.org/10.1007/s10035-023-01347-6.

ten Bosch, S., Bosch, J., Terzis, D., Laloui, L., 2022. Multiphysical numerical modelling of an MICP upscaling experiment with ex-situ hydrolysis. ISSMGE. https://doi.org/10.53243/ICEG2023-442.

Terzis, D., Bernier-Latmani, R., Laloui, L. (2016). Fabric characteristics and mechanical response of bio-improved sand to various treatment conditions. Géotechnique Letters 6, 50–57. https://doi.org/10.1680/jgele.15.00134.

Terzis, D., Laloui, L. (2021). Method and system for producing a carbonate-containing species-rich, nitrogen-containing species-free solution. WO2021234434.

Terzis, D., Laloui, L. (2019a). A decade of progress and turning points in the understanding of bio-improved soils: A review. Geomechanics for Energy and the Environment 19, 100116. https://doi.org/10.1016/j.gete.2019.03.001.

Terzis, D., Laloui, L. (2019b). Cell-free soil bio-cementation with strength, dilatancy and fabric characterization. Acta Geotech. 14, 639–656. https://doi.org/10.1007/s11440-019-00764-3.

Terzis, D., Laloui, L. (2018). 3-D micro-architecture and mechanical response of soil cemented via microbial-induced calcite precipitation. Sci Rep 8, 1416. https://doi.org/10.1038/s41598-018-19895-w.

Terzis, D., Laloui, L., Dornberger, S., Harran, R. (2020). A Full-Scale Application of Slope Stabilization via Calcite Bio-Mineralization Followed by Long-Term GIS Surveillance. Presented at the Geo-Congress 2020, American Society of Civil Engineers, pp. 65–73. https://doi.org/10.1061/9780784482834.008.

Proceedings of the XVIII ECSMGE 2024
GEOTECHNICAL ENGINEERING CHALLENGES
TO MEET CURRENT AND EMERGING NEEDS OF SOCIETY
© 2024 the Authors
ISBN 978-1-032-54816-6
DOI 10.1201/9781003431749-6
Open Access: www.taylorfrancis.com, CC BY-NC-ND 4.0 license

ECSMGE 24
XVIII EUROPEAN CONFERENCE ON SOIL MECHANICS AND GEOTECHNICAL ENGINEERING

Keynote Lecture

3D planning in the Lisbon of the future: requirement or necessity?

La planification en 3D dans la Lisbonne du future: exigence ou nécessité?

C. Pinto*
Lisbon Municipality, Lisbon, Portugal
**claudia.pinto@cm-lisboa.pt*

ABSTRACT: Current cities already use part of their underground space for several uses, such as the water supply systems, sewage and communication networks, heavy mobility solutions as the subway, highway tunnels, and also parking; however, these interventions are not carried out in an integrated manner, sometimes leading to constraints, especially in terms of impact on the natural resources with significant consequences on the surface level. Therefore, it is necessary to envision future cities as contributing to the implementation of sustainable development goals, which, in our understanding, requires the integration of the subsurface into planning and management strategies that are crucial to address contemporary environmental and social challenges. To implement this strategy, it is essential to involve several stakeholders, including local governments, communities, private companies, technical experts, and real estate, to ensure that the solutions are viable from a technical and economic point of view and benefit the city.

RÉSUMÉ: Aujourd'hui, les villes utilisent déjà une partie de leur espace souterrain à des fins diverses, telles que l'approvisionnement en eau, les réseaux d'assainissement et de communication, les solutions de mobilité lourde comme le métro, les tunnels routiers ou encore les parkings; cependant, ces interventions ne sont pas réalisées de manière intégrée, ce qui entraîne parfois des contraintes, notamment en termes d'impact sur les ressources naturelles, avec des conséquences importantes au niveau de la surface. Il est donc nécessaire d'envisager les villes du futur comme contribuant à la mise en œuvre des objectifs de développement durable, ce qui nécessite selon nous l'intégration du sous-sol dans les stratégies de planification et de gestion qui sont cruciales pour répondre aux défis environnementaux et sociaux contemporains. Pour mettre en œuvre cette stratégie, il est essentiel d'impliquer plusieurs parties prenantes, notamment les gouvernements locaux, les communautés, les entreprises privées, les experts techniques et le secteur immobilier, afin de s'assurer que les solutions sont viables d'un point de vue technique et économique et qu'elles profitent à la ville dans son ensemble.

Keywords: Underground use; planning strategy; impact mitigation; integrated sustainability solutions; society engagement.

1 INTRODUCTION

In the 20th century there was a population increase and its concentration in urban areas, leading to the need for new buildings and infrastructures to improve people's living conditions (Almeida *et al.*, 2008). In Lisbon the need for space led to the occupation of sensitive areas with less favourable geotechnical characteristics, reflected in increased construction costs.

Technological development allows for construction in height and depth; however, it requires specific geotechnical knowledge, usually obtained through geotechnical survey campaigns and *in situ* and laboratory testing (Almeida *et. al*, 2008; 2010).

The increase in projects for the construction of underground structures, with a strong geotechnical component, sometimes with serious implications for surrounding buildings, led the Lisbon Municipality to establish rules determining that excavation and foundation works could only be carried out by specialized companies and technicians (Pinto, 2020).

This municipal document was the basis for standardizing excavation work in urban areas, defining a set of rules for geotechnical projects. (Pinto, 2020).

Based on the municipal regulations and in close collaboration with the Engineers Portuguese Order, the Geotechnical Specialisation Commission developed some recommendations for the excavation design, implemented in 1991.

The final version of this work, entitled "*Recommendations for geotechnical surveys to support the design of foundations and excavation of current buildings*", was presented in 2003 and defined

the procedures to be considered in the reconnaissance of sites, the requirements for the geotechnical project, execution phases and the monitoring and observation of the soil's behaviour during the construction (Pinto, 2020).

For decades, site investigation campaigns and projects produced a large amount of data that has been collected and integrated into databases, enabling the implementation of a geoscientific information system with a special focus on the elaboration of the Lisbon geotechnical mapping (Almeida *et al.*, 2008; 2010; Matildes *et al*, 2010; Pinto, 2020; Pinto *et al.*, 2023a; 2023b).

In addition, a survey and design of a database for underground occupation have been carried out, and the survey of basements in some areas of the city has now been completed (Pinto *et al.*, 2020).

This paper will present the ongoing projects in Lisbon Municipality. This information has a high potential for 3D planning and management in future cities and should be considered fundamental for projects optimization, cost reduction, and decision support.

2 CONTEXT INFORMATION

2.1 Lisbon geological setting

Lisbon geology is well documented in several studies developed since the 19th century; however, the most detailed geological mapping for Lisbon city, was produced by Fernando Moitinho de Almeida in 1986, at a scale of 1:10.000. The author introduces an innovation using in addition to the classic stratigraphic criterion the representation of alluvial cover and man-made deposits (not always differentiated), using information from geotechnical boreholes and excavations, which gives the geological map a geotechnical component (Moitinho de Almeida, 1986). Including depth information made it possible to define the geological structures present and the thickness of the surficial deposits (Moitinho de Almeida, 1986).

According to Pais *et al.* (2006), Lisbon city presents different subsurface geological formations, from the Cretaceous to Miocene periods, which are covered by Holocene materials (alluvium fills), as a result of the installation of a fluvial network (Figure 1).

Except for the Lisbon Volcanic Complex (CVL), formed by effusive and explosive episodes, which resulted in basaltic rocks and interspersed deposits of ash and pyroclasts, the Lisbon subsurface consists of sedimentary formations, including cretaceous limestones and the clays and conglomerate rocks from the Benfica Complex.

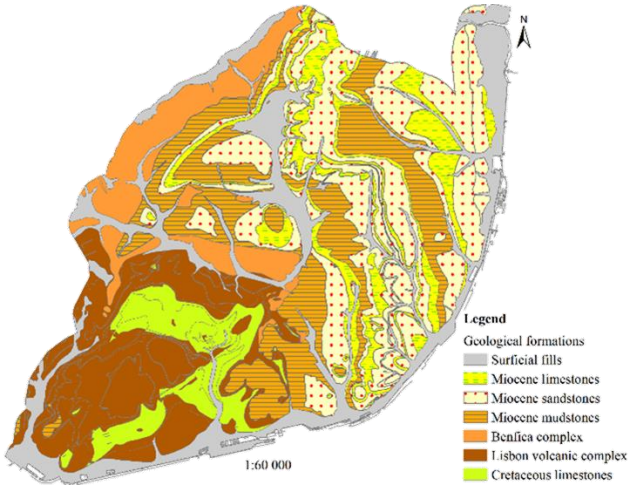

Figure 1. Simplified geological map (adapted from Pais et al., 2006).

The Miocene series comprises 15 stratigraphic units characterized by clayey, sandy, and silty soils, carbonate sandstones and limestones. All these units present significant lateral and vertical facies variations, reflecting the alternance of sea and continental environments (Almeida, 1991; Pais *et al.*, 2006).

The surficial fills include the alluvial deposits associated with the Tagus River and those from its subsidiary watercourses (Ribeira de Alcântara, Benfica, Campo Grande, Vale do Pereiro, Arroios, Chelas).

2.2 Lisbon masterplan

Territorial management instruments are regulatory and establish the land use regime, defining territorial occupation models and the organisation of urban networks and systems in a bi-dimensional representation. They also aim to articulate the sectoral policies established in the national and regional instruments with local development strategies (Pinto, 2020).

Although these instruments define the land use models, they do not consider the underground occupation carried out without any strategic planning. (Pinto, 2020).

Lisbon Master Plan (CML, 2012) is a policy instrument that seeks to define strategic guidelines for the development of Lisbon city. It was approved in August 2012, and for the first time, incorporates a set of natural and man-made risks mapping, such as landslides susceptibility, seismic hazard (Figure 2), flooding vulnerability, and the impact of direct tidal effect in the riverfront area.

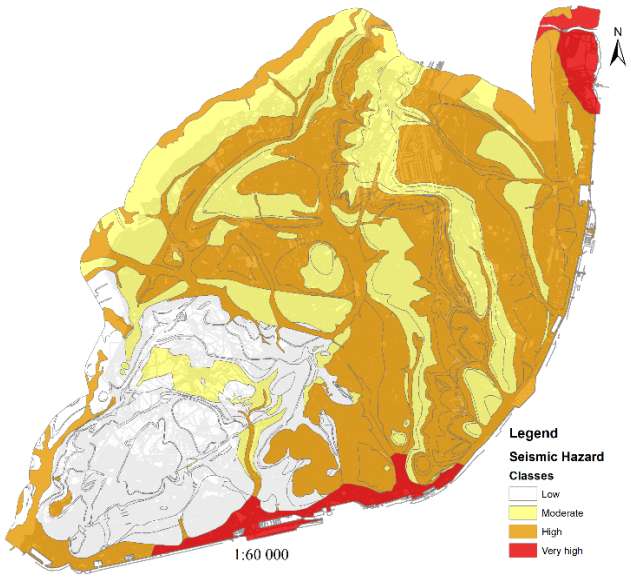

Figure 2. Seismic hazard map. Lisbon Master Plan.

In addition to the graphic elements, some rules have been defined for the intervention/occupation in the most vulnerable zones. As an example, in areas of high and very high seismic hazard, it is necessary to deliver geological, hydrogeological, and geotechnical studies to define technical solutions compatible with the characteristics of the territory and to implement, at the same time, mitigation measures (CML, 2012).

The Lisbon Master Plan's bi-dimensional approach is clearly insufficient to overview all the variables at stake (Pinto, 2020).

In the author's opinion, the definition of planning policies for the cities of the future should be based on a 3D approach, considering both surface development models and underground occupation, integrating city demands with sustainable use of existing resources.

Geology and geotechnics are essential disciplines for the development of a sustainable underground occupation policy. However, solutions should consider different variables, which requires detailed knowledge of geological and geotechnical characteristics as well as the existing structures and infrastructures that converge on them.

It is also urgent to consider that the engineering solutions could be compatible with local resources, such as groundwater, but considering them as an opportunity and not a constraint.

Several projects managed by the author have been implemented in Lisbon Municipality to help achieve this goal.

3 ONGOING PROJECTS

3.1 GeoSIG Project

The Municipality of Lisbon has an important collection of geological and geotechnical data obtained through numerous campaigns carried out over the last few decades.

This data is a valuable resource and, when properly organised, provides highly applicable information in many areas of urban planning and management. However, the value of this information depends on the standardisation of the source data, its constant updating, its availability, and the existence of metadata to assess its origin and quality (Pinto, 2020).

Based on the above assumptions, over the last few years Lisbon Municipality has sought to develop data structures supported by management systems, with the aim of restructuring the processes of entering and updating existing data and enabling not only the data's logical storage but also its effective management, aiming at the production of the necessary outputs.

As a result of the evolution of computer technology, new storage technologies were developed that made it possible to effectively manage the large volume of data obtained from geotechnical surveys (Almeida *et al.*, 2003; Culshaw *et al.*, 2006; Almeida, 2011; Silva, 2015; Pinto, 2020).

The spread of GIS has boosted new tools for analysing and spatially visualising data, making it possible to produce geological/geotechnical thematic mapping, on common computers, at low cost (Silva, 2015). The interpolation tools associated with these systems allow for 3D modelling, which optimises mapping production (Zuquette & Gandolfi, 2004; Silva, 2015; Pinto, 2020).

Through a project financed by the FEDER (LISBOA-01-0527-FEDER-000894), the GeoSIG application was developed. The app has a web interface but a restricted access (Figure 3). That condition was imposed by the companies that provides the data; however, the municipality uses this information to support decision-making and municipality initiatives and intends to provide some thematic analyses based on borehole data that will be part of the geotechnical map (Pinto, 2020). In general terms the users of the GeoSIG app can:

- Georeference boreholes and other *in situ* testing.
- Upload data resulting from a campaign.
- Visualize the distribution of sampling in Lisbon area.
- Filling data into alphanumeric tables.
- Produce thematic analyses.
- Download the geological report.

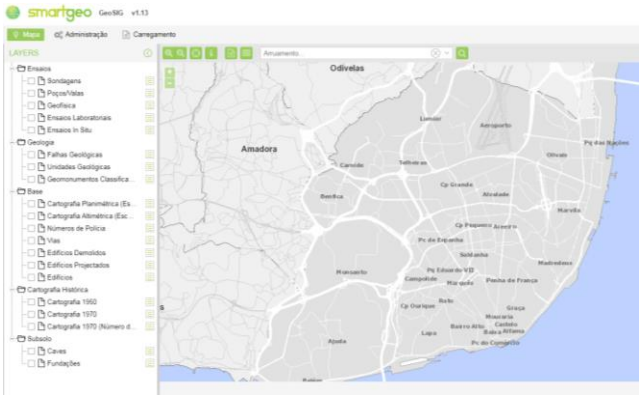

Figure 3. Main interface of the GeoSIG platform.

This platform integrates more than 13.000 boreholes distributed heterogeneously throughout the municipality area (Figure 4). The user can access data related to the lithology, the water level, SPT values, recovery rates, laboratory tests, and other relevant information associated with each borehole.

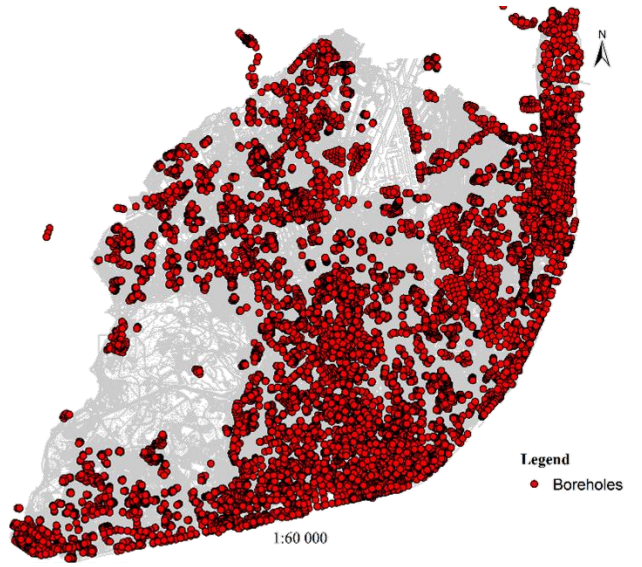

Figure 4. Distribution of boreholes in Lisbon city (Source: GeoSIG).

The GeoSIG database is intended to provide macro-scale analysis and outputs, so a local study is still required for projects in a specific area.

The analysis and modelling of lithology, lithostratigraphy, soils resistance (through SPT) and water levels allow the production of information suitable for urban planning (Pinto *et al.*, 2023). They can also be used to perform more specific studies, such as seismic microzonation based on geotechnical data (Oliveira *et al.*, 2019), enabling several actors, including designers, planners and others, to assess the constraints and estimate the order of magnitude of the costs for carrying out a particular geotechnical project, making it possible to optimise projects from an early stage (Gonçalves *et al.*, 2017; Pinto, 2020).

3.1.1 Case study 1: thickness of the coverage deposits

Due to its heavily urbanised landscape, non-natural processes such as excavations and landfill deposits often change the terrain morphology. Nowadays, the exact location of these exploitations is unknown.

In addition these materials have also resulted from the extensive mining industry, which had an essential role in the reconstruction of Lisbon after the earthquake of 1755, related to the extraction of limestones, basalts, sandstones and mudstones in ancient quarries (Pinto, 2005; Cunha *et al.*, 2017).

Through geological campaigns performed in Lisbon, several anthropogenic deposits, highly heterogeneous in nature, extension, and thickness, were intersected (Pinto, 2020).

To perform a detailed subsurface dynamic analysis aiming at the location of ancient quarries and their landfill material thickness, cartographic and topographic information dating from 1911, 1950, 1970, 2012 was used to create digital terrain models, which allowed the terrain morphology changes to be identified and the volume of landfill materials to be obtained (Figures 5).

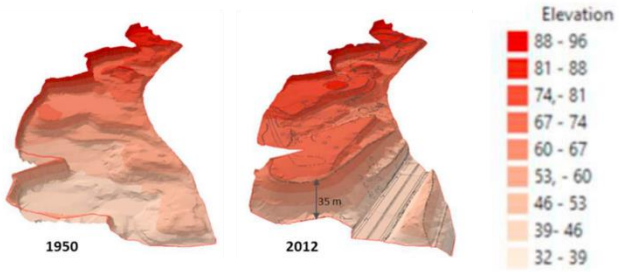

Figure 5. 3D model of a quarry in 1950 and 2012.

The analysis shows that the area contains several landfill deposits, particularly in the NW part of the quarry, where the deposits reach 35m in thickness.

Other studies have used several sets of aerial photographs with stereoscopic coverage (Vasconcelos, 2011).

A map representing the landfill and excavation areas and indicating their thickness, whenever possible, has been created to compile the information obtained from these studies.

3.1.2 Case study 2: thickness of alluvium fills

Alluvial deposits are related to the ancient watercourses and the deposits from the Tagus River. Their composition reflects the erosion of the bedrock or, when close to the Tagus River, presents sandy and muddy layers.

Gravitational deposits, or colluvium fills, are found at the base of some outcrops. They are essentially

made up of disaggregated materials and are generally small in thickness (Pinto *et al.*, 2012).

The lithologies and thicknesses of alluvium fills are highly variable, ranging from centimetres to 40 metres in the riverside area (Lopes, 2001). Tagus River alluvium has been recognised in countless boreholes, particularly those that resulted from the interventions made by the Administration of the Port of Lisbon and the construction of the "*25 de Abril Bridge*". According to this data, the alluvium reaches a thickness of around 58 metres in the area of the Tagus River embankment (Zbyszewsky, 1963).

The GeoSIG database assessed the thickness of alluvium fills in Lisbon Downtown. The borehole data were interpolated using the IDW (inverse distance weight) interpolator (Pinto, 2020).

The main alluvium thickness is related to the ancient water lines, such as *Ribeira de Arroios*, *Vale do Pereiro and Esteiro da Baixa* and the Tagus alluvium (Figure 6).



Figure 6. Thickness of alluvial deposits (Lisbon Downtown).

The high thickness of these materials could constrain urban occupation because they have unsatisfactory resistance and high deformability.

Geotechnical survey campaigns are demanded to characterise the soils' properties to evaluate the project conditions in an early stage. Poor recognition could have implications during the construction phase, increasing the risk already inherent to the geological uncertainty associated with engineering works and the cost of construction (Almeida *et al.*, 2008; Pinto, 2020).

3.1.3 Case study 3: groundwater level position

Most of the requests in urban areas aim to improve population living conditions and accessibility. In consolidated areas, these improvements are the construction of basements for space optimisation.

These underground structures directly impact the water table and, in some cases, the piezometric level, especially in situations where they have a significant volume, such as underground parking, and tunnels related with mobility solutions ou water supply, which can intersect free or confined aquifer layers (Pinto, 2020).

When affecting shallower flows, the hydrogeological regime tends to adapt, and as the formations are more decompressed at the top, this readaptation is favoured. However, when the impact is developed at deeper flows layers and exhibits significant dimensions, the barrier effect may have long-term effects as the ability to adapt will be less and slower.

In either situation, the consequence is a decrease in the foundation elements' resistance capacity and impulses in adjacent buildings' buried structures (Almeida, 2003).

The impact on the evolution of the water table must be recognised at the design stage to allow the adoption of solutions that are both feasible for their intended purposes and mitigate the impact on the surroundings, which can increase construction costs (Pinto, 2020).

In 2012 some rules were implemented by the author in the Lisbon Master Plan, consisting of the presentation of hydrogeological studies for areas affected by land development operations, demanding the determination of hydrogeological characterisation parameters for local contexts. This obligation applies to wetland areas, those with a high to very high flooding vulnerability, and areas subject to direct tidal effect, according to articles nr. 13 and 22 of the Masterplan regulation.

Some analyses were carried out in some areas of Lisbon city as proof of concept. As performed to the assessment of the thickness of the coverage deposits, the water level data were also interpolated using IDW, aiming to generate groundwater surfaces (Figure 7).

This information allows Lisbon Municipality to optimise water use for different purposes, essentially to promote sustainable use of undergorund resources in a climate change context (Pinto, 2020).

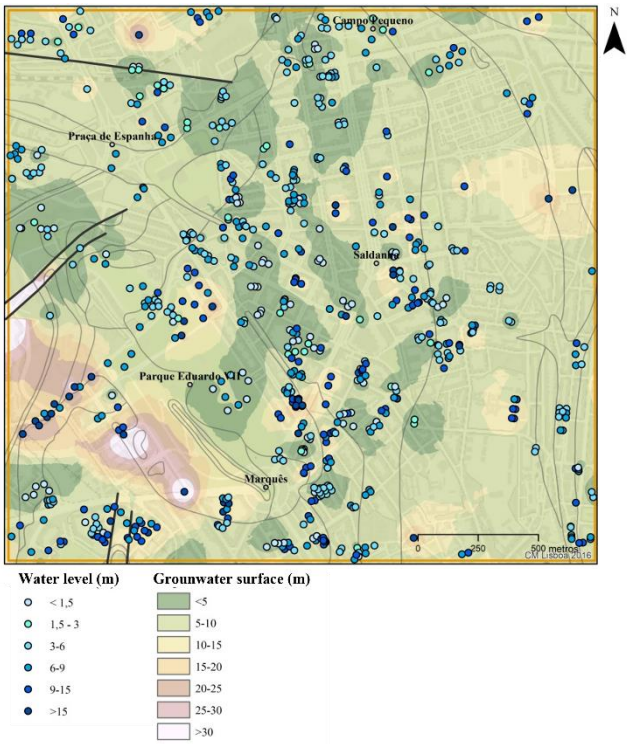

Figure 7. Water level position and surfaces (Avenidas Novas area).

Points of different intensities represented the water level according to depth, and polygons reflected the water surface, defining depth classes.

In general, the water table is located between 5 and 10m, which is also related to the geological formation's permeability (Pinto, 2020).

Knowledge of this variable allows assessment of potential impacts on buildings since water percolation affects mechanical behaviour. Discontinuities in rocks allow water percolation to deeper levels, promoting erosion phenomena. In soils, the circulation of water can cause the dragging of the smallest materials, leading to internal erosion phenomena and the subsidence of surface structures, often at the level of the road network.

Rising water levels can result in settlement and uplift phenomena, which also impact structures and infrastructures (Pinto, 2020).

Assessing flooding risk in urban environments can also be emphasized because the probability of flooding will be heightened in areas with flat and a surface water table.

3.2 ModSub 3D Project

In addition to geological, geotechnical, and hydrogeological characteristics, proper subsurface planning requires knowing the location, characteristics, geometry, and deployment levels of buried structures and infrastructures, such as water pipes, sewage systems, gas lines, electrical and communication cables, tunnels, basements, and parking.

Accurate information enables more efficient planning and execution of underground construction projects. It prevents accidental damages during excavation or construction activities, which sometimes cause service disruptions and high repair costs. It also allows for avoiding last-minute adjustments or delays due to unexpected conditions during excavation.

From a sustainable perspective, this information helps assess the environmental impact of excavation and construction on groundwater flow, considering the possibility of reusing the resource for other purposes (Pinto, 2020).

The strategy defined by Lisbon Municipality to address the identification and representation of basements in buildings, parking, and tunnels was based on the development of a tool called ModSub 3D, built on ESRI software, in particular ArcGIS Pro.

Besides the general characteristics of those elements, the database model incorporates tables for the edition of attributes related to:

- Foundations – geometry, type of foundation and deployment levels;
- Building basements – geometry, partial or fully buried, primary use, existing pumping and deployment levels (Figure 8);
- Retaining walls – excavation method, retaining wall type and deployment levels;
- Tunnels – The section type, primary use, excavation and containment methods, base and top elevation and pumping.

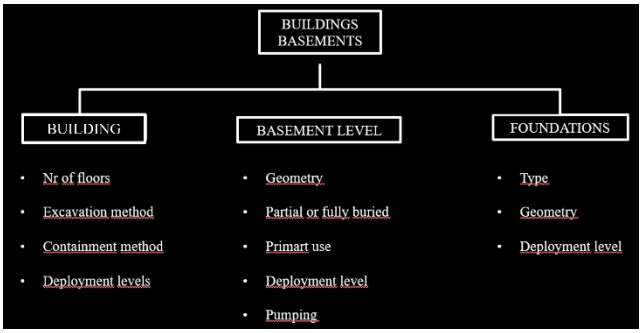

Figure 8. Database scheme: building basements (ModSub 3d).

To optimise the fulfilment of the attributes and help the user during the process, a series of guided steps and a pre-configured workflow were designed using the ArcGIS *Tasks* tool (Figure 9).

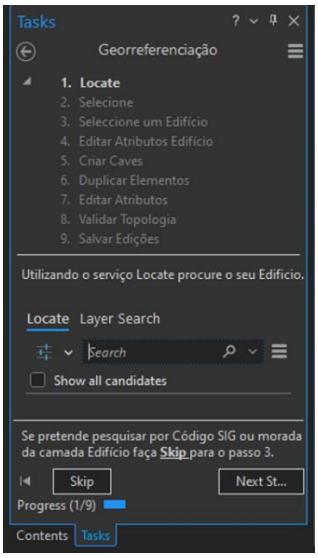

Figure 9. Example of a screen from the Tasks tool showing the workflow related with the georeferencing process.

Nowadays, 8.900 buildings in specific parts of the city (Parque das Nações, Baixa Pombalina, Benfica) have been analysed and integrated into the ModSub 3D app. Figure 10 presents an example of an area where information about building basements has already been uploaded. The polygons with the geometry of the buried elements are shown in yellow.

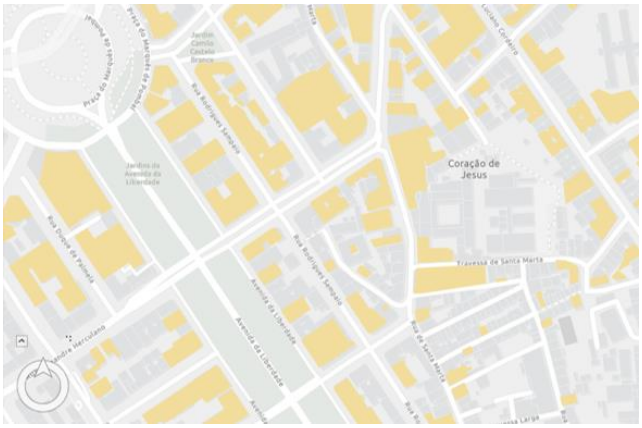

Figure 10. Building basements in Avenida da Liberdade.

This information enables a more detailed understanding of subsurface occupation, which should serve as the basis for planning interventions and defining integrated strategies for the city's development.

At a more specific level, will allow for assessing the impact of underground construction on the local hydrogeological regime (Pinto, 2020).

Developing 3D models for the surface and subsurface occupation is a goal. A few exercises have been performed resulting in general models, such as the one in Figure 11.



Figure 11. Representation of a three-dimension model (Parque das Nações); in green and grey we see the surface occupation and in brown the building basements.

BIM (Building Information Modeling) models have revolutionized 3D representation. The process involves creating and managing digital representations of places' physical and functional characteristics.

These digital models are used throughout the building's lifecycle, from initial planning and construction to operation and maintenance. BIM allows architects, engineers, and construction professionals to collaborate more effectively, analyze potential issues before construction begins, and streamline the overall building process. It can also enhance sustainability efforts and improve facility management.

Although this technology is widely applied in construction management, its future use on the scale of underground planning in cities should be considered and in the figure 12 is presented the use of BIM to manage the Lisbon Drainage Master Plan (Gomes *et al.,* 2023).

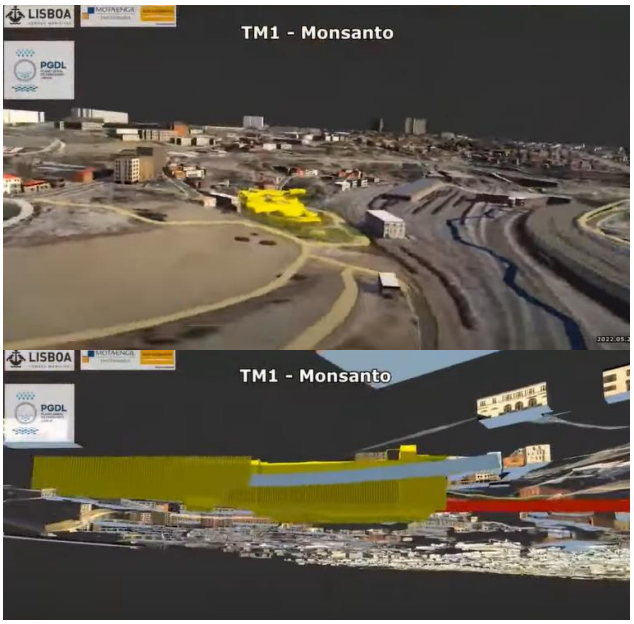

Figure 12. Image of the BIM model used for the Lisbon Drainage Master Plan (source: municipality services).

3.3 LisbonSlides Project

A map of susceptibility to mass movements was provided in Lisbon's Master Plan. The map results from a physical model drawn up by the Faculty of Sciences, University of Lisbon (Vasconcelos, 2011), that took into account the geological, geotechnical and hydrogeological data available in Lisbon Municipality databases, resulting in the identification of moderate to very high susceptibility areas (Figure 13).

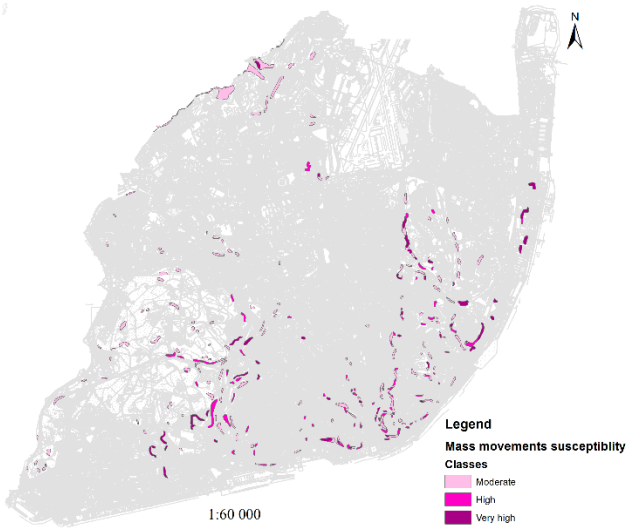

Figure 13. Mass Movements Susceptibility Map. Lisbon Master Plan.

The results show that the susceptibility areas are related with natural slopes, retaining walls, and buildings.

3.3.1 Case study: Rua Damasceno Monteiro

On the 27th of February, 2017, a support wall collapsed. The movement affected several buildings in Rua Damasceno Monteiro (Figure 14).

The intervention involved the construction of a retaining wall, the structural recovery of the affected buildings, and the relocation of the affected populations. The intervention cost was ten times higher than reinforcing the retaining wall.

This example shows that mass movements, especially related to built structures, should be managed through a proactive approach rather than a reactive one.



Figure 14. Set of photos of the mass movement occurred in Rua Damasceno Monteiro (source: municipality services).

3.3.2 Implementation of a managing strategy

The municipality hired specialised companies to survey all the situations identified on the map. The work involved visiting the sites and filling out a database with various parameters.

Regarding the prioritisation of interventions and implementation of a mitigation strategy by the municipality services, the final results were presented considering the need for an intervention or monitorisation.

Additionally, each type of result was requested to be classified into three classes: A, B, or C. Depending on the class, the intervention or monitoring procedure was required within a maximum period of 1, 3, or 5 years (Figure 15).

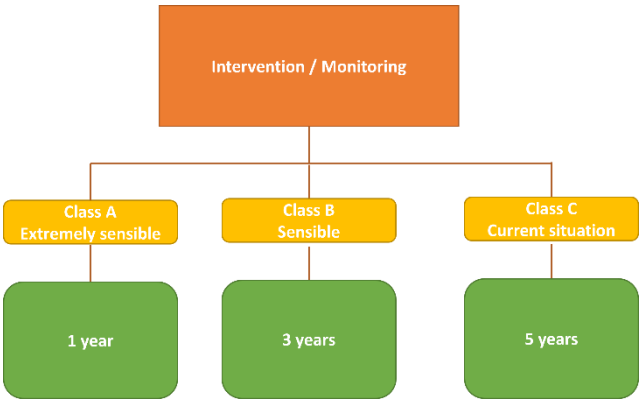

Figure 15. Diagram with the management model implemented for mass movement susceptibility.

The situations that didn‘t present any evidence were removed from the initial list.

In summary, the work carried out allowed for the identification of the following situations:

- 64 buildings needing urgent intervention – class A;
- 74 buildings needing intervention – class B;
- 101 buildings needing intervention – class C;
- 54 buildings needing monitorisation – class A;
- 203 buildings needing monitorisation – class B;
- 991 buildings needing monitorisation – class C;
- 560 buildings removed from the list;
- 26 retaining walls needing urgent intervention – class A;
- 49 retaining walls needing intervention – class B;
- 77 retaining walls needing intervention – class C;
- 40 retaining walls needing monitorisation – class A;
- 95 retaining walls needing monitorisation – class B;
- 354 retaining walls needing monitorisation – class C;
- 123 retaining walls removed from the list;
- 25 natural slopes needing urgent intervention – class A;
- 24 natural slopes needing intervention – class B;
- 20 natural slopes needing intervention – class C;
- 22 natural slopes needing monitorisation – class A;
- 31 natural slopes needing monitorisation – class B;
- 172 natural slopes needing monitorisation – class C;
- 30 natural slopes removed from the list.

Not all situations identified are the responsibility of the municipal services, as many of the sites are privately owned. Tables 1 and 2 summarise the situations for which Lisbon Municipality is responsible.

Table 1. Municipality and co-ownership buildings.

	Co-Ownership	**Municipality property**
Intervention – Class A	0	6
Intervention – Class B	1	8
Intervention – Class C	0	19
Monitorisation – Class A	3	3
Monitorisation – Class A	2	13
Monitorisation – Class A	10	55
Removed from the list	20	46

Table 2. Municipality retaining walls and natural slopes.

	Retaining walls	**Natural slopes**
Intervention – Class A	5	16
Intervention – Class B	21	13
Intervention – Class C	30	10

This approach allows the municipality's services to better manage this situation and affect the budget needed for each project. Several of these interventions have already been executed.

3.4 GeoSustained Project

GeoSustained is an ongoing research project financed by the Portuguese Foundation for Science and Technology (PTDC/ECI-CON/1866/2021).

Several actions aim to assess the use of geothermal solutions for building and infrastructure acclimatization (Inácio *et al.*, 2023), which would make cities more sustainable and resilient to climate change.

Lisbon Municipality is a partner in the consortium, involved in implementing the mandatory elements for installing the system and disseminating the solution's potential among private and public entities and real estate agents.

LNEC coordinates the project, and in addition to Lisbon Municipality, the consortium includes the University of Aveiro and the Lisbon Energy Agency - Lisboa E-Nova.

Two actions were defined to achieve this goal. The first consists of defining the best practices for implementing shallow geothermal solutions in urban environments; the second is developing a workflow guide with the necessary information to implement the system's municipal licensing procedure.

Besides these actions, and considering decision-support, Lisbon Municipality intends to develop a dynamic map to identify the shallow geothermal systems in Lisbon (Inácio *et al.*, 2023). The purpose is to support the preliminary assessment of the viability of shallow geothermal systems for new buildings, challenging project developers and planners to consider using this clean energy resource in their projects.

Three boreholes were made in different locations within the municipality territory to collect samples from the Lisbon's geological formations (Figure 16).

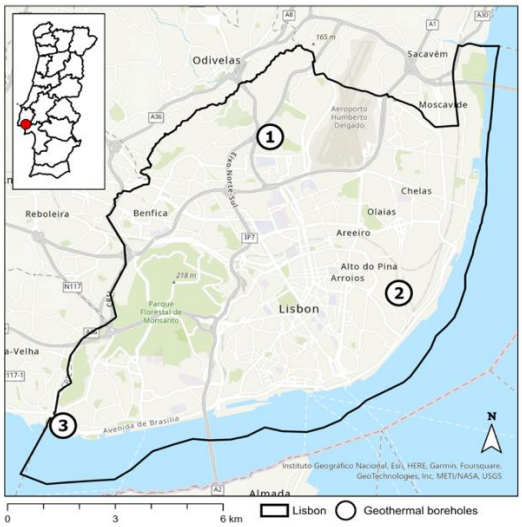

Figure 16. Location of the 3 boreholes performed in the framework of GeoSustained Project.

Undeformed samples were also collected at these sites. Laboratory tests are being performed to determine these formations' thermal and thermomechanical characteristics. In addition, temperature and thermal conductivity measuring sensors were installed along the drilled depths (every 5 m) to detect seasonal and in-depth temperature variations (Inácio *et al*.,2023).

3.4.1 Geothermal systems concept

From 15-20 meters depth onwards, the subsurface temperature is not dependent on seasonal variations in air temperature but rather on the heat flux from the earth's and the geological, hydrogeological, and geothermal characteristics of the bedrock (Ramalho *et al.*, 2013).

Very low-enthalpy or surface geothermal systems are renewable energy systems that use the Earth's natural heat to warm and cool buildings and other structures, such as roads and tunnels. They are an efficient and clean technology (excluding pumps), contributing to reducing carbon footprint.

In terms of concept, they are heat exchange systems that use the ground, aquifers, or effluents as a medium of exchange (Lapa, 2024).

This is achieved by placing geothermal probes (primary circuit) in vertical boreholes, horizontal planes, or buried structural elements such as piles, walls, or slabs, which are thermally activated and transmit the ground temperature to a geothermal heat pump.

Thermal distribution can also follow central heating systems; however, geothermal systems with thermally activated building structures (Figure 17) are the most efficient as they use the thermal mass of these structure elements (Lapa, 2024).

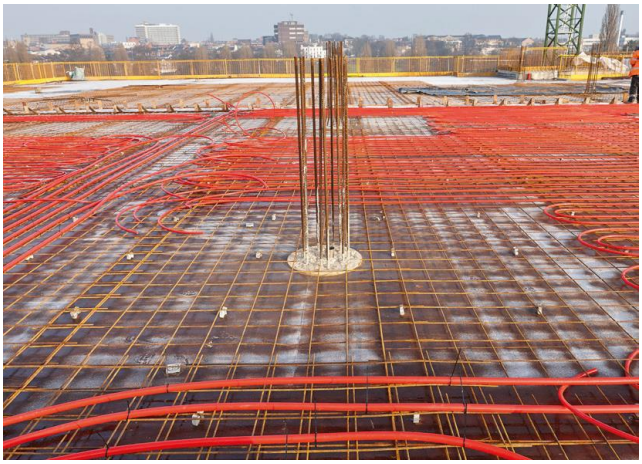

Figure 17. Thermally activated ground slab (Lapa, 2024).

The various combinations of thermal sources, such as soil (geothermal probes or heat exchangers in

structural elements), air (cooling towers), water (using sewage networks or pools), and sun (solar panels and photovoltaics), represent an opportunity to improve the efficiency and sustainability of geothermal systems. Connecting different systems is the starting point for applications in residential buildings, increasing the interest of property owners in finding efficient solutions based on renewable energy sources. Research on the complementarity of these solutions has led to more competitive prices for equipment and materials (Lapa, 2024).

3.4.2 Advantages of using geothermal systems to buildings acclimatization in urban areas

Geothermal systems offer three advantages: energy savings, thermal comfort, and environmental sustainability.

The systems have low maintenance requirements and a long lifespan, resulting in energy savings. This, combined with reducing carbon emissions and dependence on fossil fuels, leads to greater environmental sustainability. Additionally, they promote greater thermal comfort by maintaining a constant temperature regardless of external weather conditions (Lapa, 2024).

Geothermal systems have a higher initial cost (around 15%), than traditional HVAC systems but offer long-term returns. The return on investment for school facilities can be realized in 5 to 6 years, while for residential buildings, it may take between 10 to 15 years.

The work carried out under GeoSustained Project can be extrapolated to other municipalities.

Lisbon is a pilot city for defining the best approaches to increasing the use of geothermal energy in Portugal. This approach is aligned with the best practices ongoing in other European countries.

4 SUSTAINABLE DEVELOPMENT GOALS

The 2030 Agenda for Sustainable Development defines a strategy with 17 main goals that all countries must implement (Figure 18).

In the framework of this paper, and regarding Lisbon Municipality strategy, the sustainable goals that could be achieved are nr. 7, 9, 11 and 13 (United Nations, 2015).



Figure 18. Sustainable development goals. (United Nations, 2015).

4.1.1 Goal 7: Ensure access to affordable, reliable, sustainable, and modern energy for all.

GeoSustained Project is an excellent example of promoting new technologies that use clean energy sources, such as low-enthalpy geothermal, ensuring access to information and good practices for project developers.

4.1.2 Goal 9: Build resilient infrastructure, promote inclusive and sustainable industrialization and foster innovation

The reuse of excavation materials, the storage and reuse of groundwater exploited during the excavation, and the use of underground heat for urban climatization could constitute a sustainable and resilient infrastructure. The necessary knowledge was obtained from the data collected in the geological/geotechnical prospecting campaigns carried out in Lisbon and compiled in different databases in the GeoSIG, ModSub 3D and GeoSustained Projects framework.

4.1.3 Goal 11: Make cities and human settlements inclusive, safe, resilient, and sustainable

The proactive approach used to manage natural risk and climate change presented in GeoSIG, ModSub 3D, LisbonSlides, and GeoSustained contributes to achieving this goal. Geological, geotechnical, and hydrogeological data permit the territory manager and the designer to address different situations as constraints or resources.

The action lines of the various projects result in policies and plans based on the necessary knowledge to be able to develop and implement mitigation and adaptation measures to the impacts resulting from natural and climatic phenomena at various scales: a more local scale with the adoption of specific

measures for the territory's vulnerability and a more holistic and integrated vision aiming at risk management and planning.

4.1.4 Goal 13: Take urgent action to combat climate change and its impacts

The GeoSIG project contributes to the knowledge of natural resources such as groundwater. A proper planning and integrated management of urban operations will allow reusing groundwater for other purposes. This action will promote the reduction of the impact of climate change, specifically water scarcity.

Through the GeoSustained Project, Lisbon Municipality intends to integrate climate change measures into local policies and strategies for urban planning. Shallow geothermal energy is a clean energy that enables the reduction of greenhouse gas emissions and the carbon footprint. Built awareness through stakeholders' education will increase the capacity to implement mitigation and adaptation measures.

5 FINAL CONSIDERATIONS

Urban development strongly pressures natural resources, especially in densely urbanised areas. The needs for housing, commercial and service areas, the underground occupation for parking, mobility systems and urban infrastructure networks could cause problems such as soil and groundwater contamination and create barriers to groundwater flow with significant impacts on the surface (Figure 19).

Geological features are rarely an impediment to urban development. Still, they can condition it through questions related to urban design and construction costs (Marker, 2009), making it imperative that decisions regarding development in large cities should be based on guidelines to promote sustainability and resilience.

Territorial management instruments must incorporate the mapping that supports the regulations seeking to adapt planning to the physical reality of the territory, optimising the use and occupation of the land to the nature of the geological substrate, safeguard the preservation of natural resources and values, and promote the quality of life and safety of the population, considering economic, political, and social factors.

This study has shown that underground space can and should be integrated into urban planning policies, not only from the perspective of mitigating the impact of natural risks but also in defining the best locations for certain urban operations, allowing for cost savings and new projects optimisation. The correct use of underground space, particularly its natural resources, will also help to boost the city's resilience in future scenarios, such as water scarcity.

This work reinforces the role of the municipality as a land manager, which is responsible for providing essential information on land constraints, providing decision-makers with the means to support their decisions, municipal technicians with information to help analyse projects, and developers with information on the constraints and costs associated with urban operations.

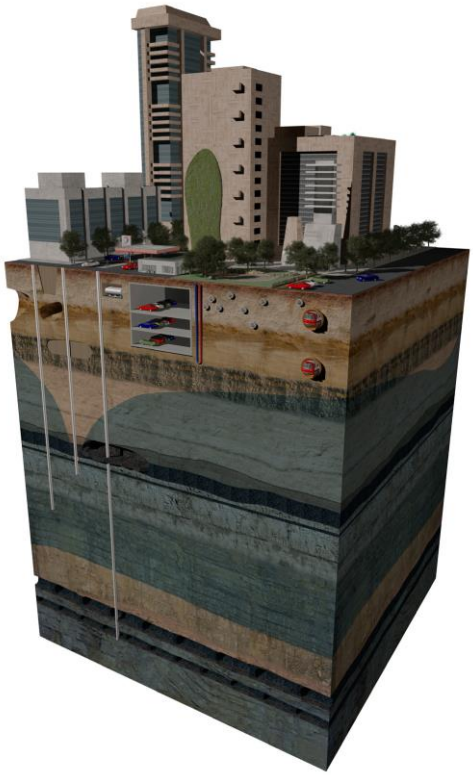

Figure 29. Conceptual model - Underground occupation in urban areas (parking, mobility network and urban infrastructures).

3D planning in the Lisbon of the future: requirement or necessity?

It can be both. A necessity if future societies aim to be environmentally, politically, economically, and socially sustainable, and it may have to be achieved through a requirement.

ACKNOWLEDGEMENTS

The author would like to thank to the Foundation for Science and Technology for the funding obtained through the GeoSIG LISBOA-01-0527-FEDER-000894) and the GeoSustained Projects (PTDC/ECI-COM/1866/2021).

REFERENCES

Almeida, I.M. (1991). *Caraterísticas Geotécnicas dos Solos de Lisboa.* Tese de Doutoramento. Faculdade de Ciências - Universidade de Lisboa, Lisboa. 485 pp.

Almeida, I.M., Marques, F.M.S.F. e Almeida, G.B. (2003). Spatial geotechnical database for planning and design in the Lisbon area (Portugal). In: *Iu, V.P., Lamas, L.N.; Li, Y-P (eds). Proceedings of the 9th International Conference Enhancement Promot Comput. Methods Eng. Science*. A. A. Balkema, Macao, China, 25-28 November 2003. pp. 509-514.

Almeida, I.M.; Almeida, G.; Lopes, I. e Pinto, C. (2008). Subsurface 3D Engineering Geological Mapping Using a Geotechnical Database, In: *Proceedings of the 3rd International Conference on Site Characterization*. Taipei, Taiwan. No. A03-076. pp 789-792. ISBN 978-0-415-46936-4.

Almeida, I.M, Matildes, R., Taborda, R., Carreira, D., Pinto, C. e Jeremias, F.T. (2010). GeoSIS_Lx a Geoscientific Information System for Lisbon Geotechnical Data Management. In: *Williams et al. (eds). Proceedings of the IAEG 2010 Congress - Geologically Active*. Taylor & Francis Group, London, England. pp. 1611-1618. ISBN 978-0-415-60034-7.

Almeida, I.M. (2011). *Geologia urbana, cartografia geotécnica e bases de dados. Megacidades. O nosso futuro global*. Geonovas. 23 e 24: 93-94.

CML (2012). Plano Diretor Municipal de Lisboa. Available at: www.lisboa.pt/cidade/urbanismo/planeamento-urbano/plano-diretor-municipal, accessed 25/02/2024.

Culshaw, M.G.; Jackson, I. e Giles, J.R.A. (2006). The provision of digital spatial data for engineering geologists. *Bulletin of Engineering Geology and the Environment*. 65 (2): 185-194.

Cunha, J.; Gonçalves, L.M.S.; Aguilera, F.; Roldan, P.A.; Pinto, C. (2017). *Subsurface dynamic evaluation to identify old quarries in urban áreas: Lisbon city case study.* In: Urban Subsurface Planning and Management Week. SUB-URBAN 2017, 13-16 march 2017, Bucharest, Romania, Procedia Engineering 209: 195-201.

Gomes, T., Morais, M. (2023). PGDL – Integração SIG-BIM para uma visão 360º do Plano Geral de Drenagem de Lisboa. Encontro de Utilizadores ESRI 2023. Centro de Congressos de Lisboa, Lisboa, Portugal. Outubro 2023.

Gonçalves, L. M. S., Pinto, C.; Seabra, A.L.; Pais, P. (2017) *The importance of connecting decision makers and urban planners with subsurface specialists for a sustainable city development: The COST TU1206 SUB-URBAN Lisbon Workshop contributes*, Final Conference COST TU1206 - SUBURBAN 2017 Conference, Bucarest, Romenia, March 13-16.

Inácio, M., Pinto, C., Vieira, A., Almeida, I. M., Ferreira, A., Leonardo, P. and Frias, A. (2023). Contribuição da geologia na localização dos furos geotérmicos do Projeto GeoSustained, In: *Atas do 18º Congresso Nacional de Geotecnia (18CNG)*, Évora, Portugal, pp 331-340 (Geology's contribution to the location of geothermal boreholes of GeoSustained Project in Portuguese).

Lapa, J. (2024). Geotermia superficial na climatização de edifícios. Webinar: A aplicação de sistemas geotérmicos em contexto urbano. Ordem dos Engenheiros, 21 de março de 2024, online.

Lopes, I.M.F. (2001). *Avaliação das condições geológicas e geotécnicas para a caraterização do risco sísmico. Aplicação à Colina do Castelo de São Jorge*. Tese de Mestrado em Geotecnia. Faculdade de Ciências – Universidade de Lisboa. 294 pp.

Marker, B R. 2009. Geology of megacities and urban areas. in Engineering Geology for Tomorrow's Cities. Culshaw, M G, Reeves, H J, Jefferson, I, and Spink, T W (editors). Engineering Geology Special Publications **22**. (Bath, UK: Geological Society of London.), pp. 33-48.

Matildes, R., Pinto, C.; Taborda, R., Almeida, I.M. e Jeremias, F.T. (2010). 3D geological model of Lisbon. In: *Williams et al. (eds). Proceedings of the IAEG 2010 Congress - Geologically Active*. Taylor & Francis Group, London, England. pp. 2201-2208. ISBN 978-0-415-60034-7.

Moitinho de Almeida, F. (1986). Notícia Explicativa e 4 Folhas da Carta Geológica do concelho de Lisboa, na escala 1:10 000. Serviços Geológicos de Portugal.

Oliveira, L., Teves-Costa, P., Pinto, C., Gomes, R.C., Almeida, I.M., Ferreira, C., Pereira, T. and Sotto-Mayor, M. (2019). Microzonagem sísmica baseada em dados de sondagens geotécnicas: aplicação a Lisboa. 11.º Congresso Nacional de Sismologia e Engenharia Sísmica. Lisbon, Portugal. (Seismic microzonation based on geotechnical data: application to Lisbon in Portuguese).

Pais, J.; Moniz, C.; Cabal, J.; Cardoso, J.L.; Legoinha, P.; Machado, S.; Morais, M.A., Lourenço, C.; Ribeiro, M.L.; Henriques, P.; Falé, P. (2006). Notícia Explicativa e 2.ª Edição da Folha 34-D (Lisboa). Carta Geológica de Portugal, na escala 1:50 000. Instituto Nacional de Engenharia, Tecnologia e Inovação. Lisboa. 74 pp.

Pinto, M.J. (2005). *Levantamento cartográfico de locais de pedreiras no concelho de Lisboa*. 5º volume da Coleção de Estudos Urbanos – Lisboa XXI. Câmara Municipal de Lisboa, Lisboa. 159 pp.

Pinto, C. e Almeida, I (2012a). O desenvolvimento do modelo de dados relacional associado à Carta Geotécnica de Lisboa. *Atas do 13º Congresso Nacional de Geotecnia: Pensar e construir com a natureza – Uma visão para a Engenharia.* Laboratório Nacional de Engenharia Civil, Lisboa. 17-20 Abril 2012.

Pinto, C. (2020) *Modelação de dados geológicos e geotécnicos visando a produção de cartografia geotécnica em áreas urbanas – Aplicação a Lisboa.* Tese de Doutoramento. Faculdade de Ciências da Universidade de Lisboa. Available at: http://hdl.handle.net/10451/50398, accessed: 12/03/2024.

Pinto, C. Inácio, M., Almeida, I.M., Taborda, R., Leonardo, P. and Frias, A. (2023a). O sistema de informação geocientífica GeoSIG e a sua aplicação no planeamento

urbano da cidade de Lisboa, In: Atas do 18º Congresso Nacional de Geotecnia (18CNG), Évora, Portugal, pp 291-300 (The GeoSIG geoscientific information system and its application to urban planning in the city of Lisbon in Portuguese).

Pinto, C., Moitinho de Almeida, I., Taborda, R. (2023b). Cartografia geotécnica em áreas urbanas. In: Resumos do XI Congresso Nacional de Geologia, Coimbra, Portugal, 17 a 19 julho 2023.

Ramalho, E.C., Marrero-Diaz, R., Carvalho, M., Ramada, A., Pinto, C. (2010). Alfama springs, Lisbon, Portugal: Cultural geoheritage throughout the centuries. *Geoheritage*. 12.

Culshaw, M.G.; Jackson, I. e Giles, J.R.A. (2006). The provision of digital spatial data for engineering geologists. *Bulletin of Engineering Geology and the Environment*. 65 (2): 185-194.

Silva, A.M.P. (2015). *Caraterização geológica e geotécnica da área compreendida entre o Lumiar e Olival de Basto*. Dissertação apresentada à Universidade de Lisboa para obtenção do grau de Mestre em Geologia Aplicada – Especialização em Geologia de Engenharia. Lisboa, 185 pp.

United Nations (2015). Transforming our world: the 2030 Agenda for Sustainable Development. United Nations General Assembly, New York, UK. Available at: https://sdgs.un.org/2030agenda, accessed: 05/02/2023.

Vasconcelos, M.A.D.F. (2011). *Cartografia de Suscetibilidade à Ocorrência de Movimentos de Vertente em contexto urbano: o Concelho de Lisboa.* Tese de Mestrado em Geologia do Ambiente, Riscos Geológicos e Ordenamento do Território. Faculdade de Ciências – Universidade de Lisboa, Lisboa. 212 pp.

Zbyszewsky, G. (1963). Notícia Explicativa da Folha 4 – Lisboa, da Carta Geológica de Portugal, à escala 1:50.000. Serviços Geológicos de Portugal. Lisboa. 93 pp.

Zuquette, L.V.; Gandolfi, N. (2004). *Cartografia Geotécnica*. Oficina de Textos. Brasil, 189 pp.

State-of-the-art Reports
Rapports sur l'état de l'art

Proceedings of the XVIII ECSMGE 2024
GEOTECHNICAL ENGINEERING CHALLENGES
TO MEET CURRENT AND EMERGING NEEDS OF SOCIETY
© 2024 the Authors
ISBN 978-1-032-54816-6
DOI 10.1201/9781003431749-7
Open Access: www.taylorfrancis.com, CC BY-NC-ND 4.0 license

ECSMGE 24
XVIII EUROPEAN CONFERENCE ON SOIL MECHANICS AND GEOTECHNICAL ENGINEERING

State-of-the-art Report

Recent trends in monitoring tunnelling-induced displacements of structures

Tendances récentes en matière de surveillance des déplacements induits par le creusement des tunnels sur les structures

E. Bilotta*
University of Napoli Federico II, Naples, Italy
**emilio.bilotta@unina.it*

ABSTRACT: Monitoring and control of tunnelling induced displacements in urban areas are a matter of primary importance to minimise excavation risks and enhance project acceptance. For this purpose, suitable and reliable monitoring techniques are routinely adopted in underground construction. Fast progresses in sensor technology have boosted the development of innovative monitoring for tunnel projects through prototypes and field trials. The latter have been generally carried out in conjunction with the routine conventional monitoring, allowing for comparison and validation. Consequently, a wide interested has been generated around some innovative techniques that permit real-time control of induced strain of structures (e.g. fibre optics), allow for historical movements trends (e.g. InSAR), and may provide cost-effective additional information (e.g. LiDAR and photogrammetry). At the same time, resolution, power supply and communication potential of conventional measuring techniques for displacement monitoring have largely improved in recent years. This paper reviews the state-of-art of monitoring the displacements induced by tunnel construction and explores the current trends in developments of innovative sensing techniques.

RÉSUMÉ: La surveillance et le contrôle des déplacements induits par le creusement des tunnels dans les zones urbaines sont d'une importance primordiale pour minimiser les risques liés à l'excavation et améliorer l'acceptation du projet. À cette fin, des techniques de surveillance appropriées et fiables sont régulièrement adoptées dans les constructions souterraines. Les progrès rapides de la technologie des capteurs ont stimulé le développement d'une surveillance innovante pour les projets de tunnels à travers des prototypes et des essais sur le terrain. Ces derniers ont généralement été associés à la surveillance conventionnelle de routine, ce qui a permis de les comparer et de les valider. Par conséquent, un grand intérêt a été suscité par certaines techniques innovantes qui permettent un contrôle en temps réel de la déformation induite des structures (par exemple, la fibre optique), permettent de suivre les tendances historiques des mouvements (par exemple, l'InSAR), et peuvent fournir des informations supplémentaires rentables (par exemple, LiDAR et photogrammétrie). Dans le même temps, la résolution, l'alimentation électrique et le potentiel de communication des techniques de mesure conventionnelles pour la surveillance des déplacements se sont largement améliorés ces dernières années. Cet article passe en revue l'état de l'art en matière de surveillance des déplacements induits par la construction de tunnels et explore les tendances actuelles en matière de développement des techniques de surveillance innovantes.

Keywords: Tunnelling; monitoring; structures; displacements; innovation.

1 INTRODUCTION

Tunnel construction in the built environment requires careful control of induced displacements through suitable and reliable monitoring techniques (Mair, 2008). In the last decade, innovative monitoring systems have attracted wide interest and they have been progressively applied in tunnel projects in addition to conventional sensing. Nonetheless, conventional monitoring techniques have been not discontinued and their resolution, power supply and communication potential have largely improved in recent years (Ma et al., 2021). Nowadays monitoring tunnel construction provides a large volume of data to be processed, to alert of potential risk and trigger immediate corrective actions (Meyer et al., 2013; Gonzalez-Arteaga et al., 2020). Further, gathered data can feed existing digital twins of the construction process (Boje et al., 2020; Pan and Zhang, 2021), thus expanding the potential use of sensing techniques to "performance monitoring" in the whole tunnel life-cycle (Soga et al., 2019).

Starting from the state-of-art of techniques for monitoring displacements induced by tunnel construction on adjacent buildings, this paper explores the current trends in the development of innovative sensing technologies, focusing on the results of pilot applications that have proven their reliability and potential to enhance the whole structures' life-cycle.

2 MONITORING IN TUNNEL PROJECTS

In tunnel engineering, displacements need to be measured inside the tunnel cavity, for safety reasons and to ensure that the tunnel deformation falls within prescribed limits that guarantee its stability in both the short- and the long-term (e.g. convergence, extrusion, lining deflection), as well as above the tunnel to control induced ground and building movements (Figure 1). Deformation of the lining structures and tilt of buildings also require to be measured. The emphasis of structural health monitoring in tunnelling has traditionally been put on displacements (Brownjohn, 2007), and more recently on strain.

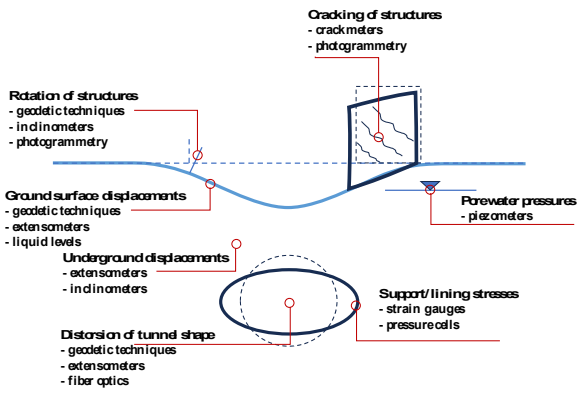

Figure 1. Tunnel construction and associated monitoring (modified from Hoult and Soga, 2014).

An overview of currently adopted measurement techniques for displacement, rotation and strain is shown in Table 1, with an indication of their range, resolution, and accuracy (BTS/ICE, 2004; ITA-AITES, 2011; Hoult and Soga, 2014; Morino et al., 2023).

Digital optical levelling is routinely performed to measure with high accuracy vertical movements on staffs and pins. *Laser distance meters* are also used for automatic and continuous measurement of convergence of the tunnel section, with accuracy up to ± 0.5 mm. *Total stations* (either manually or automatically operated) are primarily used to measure tunnel lining inflection and tunnelling-induced building deformation with an accuracy of ± 1 mm, or ± 2 mm if reflector-less (Hoult and Soga, 2014).

Laser scanner technology is also widely used in tunnelling since it enables a distributed assessment of convergence and deformation of the tunnel cavity as well as displacements of aboveground structures. Compared to point measurements, such as those operated by total stations, laser scanners can detect up to 2 million points per second, thus generating large point cloud data sets (cf. § 3.3). Light-Detection-And-Ranging (*LiDAR*) technology, adopted by high-resolution terrestrial laser scanners, is suitable to detect movements inside the tunnel with good accuracy (about ± 1.5 mm) since it does not require external lighting and it is robust in wet environments containing air particulate. Using the latest technology and in the most favorable conditions displacements may be detected with an accuracy up to ± 0.5 mm (Walton et al., 2018).

Global Navigation Satellite Systems (GNSS), providing signals from space that transmit positioning and timing data to receivers on Earth, allow the height of a point above sea level (orthometric height) to be measured with an accuracy of 10 mm without conventional levelling (Meyer et al., 2005). Hence, they are suitable for monitoring "visible" building displacements (i.e. along the line of sight to at least five orbiting GNSS satellites). Currently, by installing a network of high-frequency receiving antennas and adopting the best-performing Real-Time Kinematic (RTK) positioning technique (Odolinski and Teunissen, 2020), an accuracy of about ± 1 mm may be achieved on quasi-static structural displacements, compared to Precise Point Positioning technique (PPP, Zumberge et al., 1997), that reaches about ± 5 mm (Qu et al., 2022).

Satellite constellations equipped with SAR, Synthetic Aperture Radars, permit radar images of the Earth surface to be acquired, providing information on the distance between the radar and the reflecting point (Cumming and Wong, 2005). Interferometric analysis of phase differences between two images (InSAR) allows the ground elevation to be measured with high accuracy (Digital Elevation Model, DEM), while movements of points on the ground surface can be detected by Differential Interferometry (DInSAR), as it will be discussed in § 3.2. For instance, the *Persistent Scatterer SAR Interferometry* (PS-InSAR) is suitable for measuring deformations in urban areas and its use to detect displacements induced by tunnelling on buildings has increased recently, achieving millimetric accuracy. Terrestrial applications of SAR interferometry have been also developed, where the antennas move on a track in front of the object, rather than along the satellite orbit.

Table 1 also provides information on the accuracy of *hydrostatic levelling systems* for measuring vertical displacements through pressure head changes with respect to a reference tank, of *inclinometers*, using

biaxial servo-accelerometers or MEMS for monitoring horizontal ground displacements at depth, through *inclinometers*, and *borehole extensometers* for monitoring displacements in the ground. Structural tilt is measured by means of electrolevels, servo-accelerometer or MEMS sensors (*tiltmeters*).

Changes of crack width in structures undergoing movements are locally monitored by installing on their surface *wire extensometers* or *crackmeters* (for smaller measurement base). *Photogrammetry* is increasingly being used for crack detection (Stent et al., 2016), as discussed in § 3.3.

Monitoring structural strain is very important to control the performance of both the supporting tunnel lining and the tunnelling-affected nearby structures and buildings, either directly or through stresses that can be derived. Although structural strains can be computed from measured displacements, it is common to measure them directly, by using dedicated sensors. The most used are *electrical strain gauges*, either measuring change of electrical resistance due to strain (*resistive type*) or measuring change of vibration frequency of a metallic wire upon stretching (*vibrating wire type*). The latter are widely used in tunnel monitoring since they are cheap, high reliable and durable (Morino et al., 2023). Alternatively, *fibre optic* strain gauges have been increasingly used in the last decades (Moss and Matthews, 1995; Soga and Schooling, 2016; Floris et al., 2021), and they are becoming more common in tunnelling, as discussed in § 3.1.

Table 1. Features of monitoring techniques/sensors.

	device	range	resolution	accuracy
displacement and rotation	Digital optical levels	distance up to 30 m	0.1 - 0.01 mm	± 0.3 mm/km
	Laser distance meters	distance up to 150 m	0.1 mm	up to ± 0.5 mm
	Total stations	distance up to 1 km	0.1 mm	up to ± (0.6 mm+ $10^{-6}\times$ dist. in mm) up to ± 0.1mm diff disp.
	Laser scanner	distance up to 30 m	variable	up to ± 1.5 mm up to ± 8 arcseconds
	GPS/GNSS	distance up to 15 km	variable	± 5 mm in plan ± 10 mm in height
	PS-InSAR	any	variable	± 1 mm/year
	Hydrostatic levelling	up to 100 mm	0.01 mm	up to ± 0.1 mm
	Inclinometer	± 53°from vertical	0.04 mm/m	± 0.2 mm/m
	Tiltmeter	50 to 175 mm/m	0.05 to 0.3 mm/m	± 0.1 mm/m
	Wire extensometer	meters	0.01 mm	± 1 mm
	Crackmeter	up to 150 mm	0.01 mm	up to ± 0.01 mm
	Borehole extensometer	up to 200 mm	up to 0.01 mm	up to ± 0.1 mm
strain	Electrical strain gauges	vib. wires: up to 0.3%	0.5 to 1 $\mu\varepsilon$	vibrating wires: up to ± 1 $\mu\varepsilon$
	Fibre-optic strain gauges	up to 1%	up to 1 $\mu\varepsilon$	up to ± 10 $\mu\varepsilon$

3 EMERGING TECHNOLOGIES

Most of the well-established "conventional" geodetic techniques to monitor tunnelling induced displacements, namely digital optical levels and automatic total stations, share the common feature to achieve accurate measurements with relatively few data collection and processing. On the other hand, these measurements are spatially discontinuous. For this reason, in some cases critical mechanisms can be hard to reveal. Emerging techniques, such as laser scan or photogrammetry, and at a larger scale SAR differential interferometry, provide clouds of point measurements, that may be processed to obtain distributed information about change of surface conditions, hence continuous displacement profiles and deformation patterns. Fibre-optic sensing also results in distributed or quasi-distributed strain measurements over long distances. All these "emerging" techniques produce data of high resolution and large spatial coverage at relatively low cost at the field scale. Over the past decade, they have undergone significant validation in pilot applications that hint at a step change in tunnelling-induced displacement and strain monitoring.

3.1 Fibre-optics sensors

An optical fibre is a cylindrical structure that transmits light along its axis and is essentially made of three coaxial parts (Figure 2): a photosensitive core that carries the light, usually made of pure silicon dioxide (SiO_2) glass, a surrounding cladding made of glass with a lower refractive index (by means of a different level of impurities), a buffer coating outside, made of acrylate or polyamide, that protects the brittle fibre. Due to the core higher refractive index (RI), compared to the cladding, the light travelling in the core is reflected at the core-cladding interface. Single- or multi-mode fibres differ each other for the number of potential paths that light can take, depending on the size and refracting index variation in the core. Since propagation at higher modes decreases the signal-to-noise ratio (Nöther, 2010), single-mode fibres are generally preferred for long distances. In addition to glass fibres, polymer optical fibres (POFs) are also available, where the core is commonly made with polymethyl methacrylate (acrylic glass). However, POFs have very high attenuation compared to silica, which results in very low transmission distances.

Optical reflectometry techniques are useful to characterize optical fibres, in the time (Optical Time Domain Reflectometry, OTDR), coherence (Optical Coherence Domain Reflectometry, OCDR) and frequency domain (Optical Frequency Domain Reflectometry, OFDR).

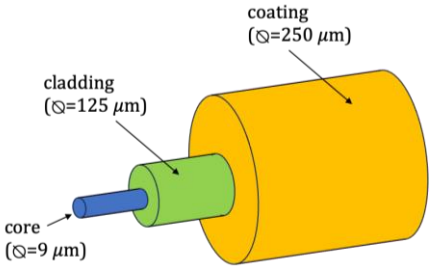

Figure 2. Structure of a single-mode optical fibre.

By using a visible laser propagating along the fibre core, Hill et al. (1978) created a periodic structure (grating) in the core with an increased refractive index, which generates a wavelength-specific dielectric Bragg mirror. The possibility to scan over the signals returned by the gratings kick-started the use of communication optical fibres as testing sensors to measure strain or temperature that, affecting their central wavelength, modify their ability to reflect and transmit light. Meltz et al. (1989) engraved the first Fibre Bragg Grating (FBG) sensor in the core of a germanosilicate optical fibre exposed to an interference pattern of ultraviolet laser light with a specific wavelength (Figure 3a). Since then, several different techniques were developed to permit the multiplexing of many FBG sensors along a single fibre (Davis and Kersey, 1997), hence their use in many structural sensing applications. Optical frequency domain reflectometry (OFDR) can nowadays be used to measure the wavelength of light reflected form thousands of low reflectivity Bragg gratings, distributed along single-mode fibres (Childers et al., 2001), allowing for quasi-distributed FBG (DFBG) technology (Vlachopoulos, 2023).

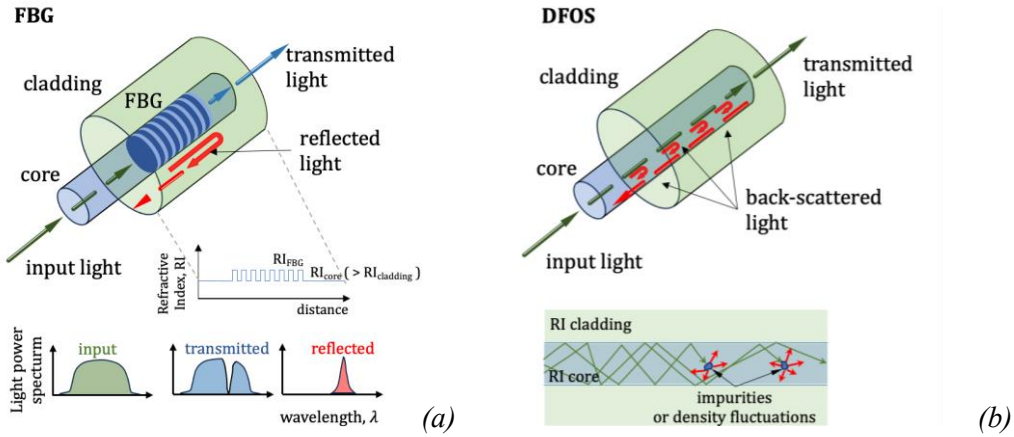

Figure 3. (a) FBG structure; (b) backscattered light along an optical fibre (modified after Kechavarzi et al., 2016 and Chai et al., 2019).

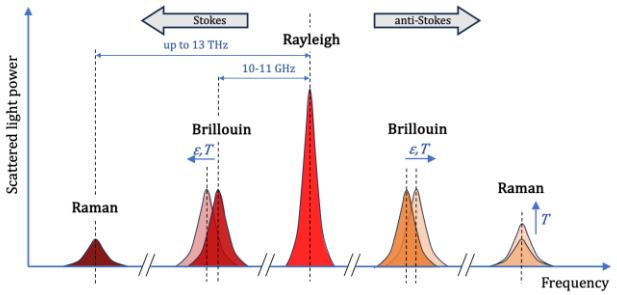

Figure 4. Backscattered light power spectra. ε, strain; T, temperature (modified from Kechavarzi et al., 2016).

Optical Backscatter Reflectometer (OBR), based on OFDR, uses light backscatter caused by random fluctuations in the refractive index profile along the fibre for the same purposes (Güemes et al., 2010). In fact, such perturbations, caused by the interaction of photons with impurities or density fluctuation within the fibre's core, behave like weak natural gratings engraved all along the fibre length (Figure 3b). Three types of light scattering exist: the linear Rayleigh scattering, where the backscattered light has the same frequency as the transmitted light; the non-linear Brillouin scattering, that produces a shift in frequency of the backscattered light; the Raman scattering, that produces new photons with lower (Stokes-component) or higher (Anti-Stokes component) energy (Figure 4). Distributed fibre optic sensing technique (DFOS) takes advantage of the influence of strain and temperature change on the fibre refractive index, hence on the properties of the backscattered light.

The Rayleigh backscatter undergoes a shift in the local spectral frequency and a time shift, produced by the cumulative changes in the refractive index. Such spectral and temporal shifts can be measured by performing a cross-correlation on the backscattered light signals in the time-domain (OTDR) or in the frequency-domain (OFDR), and scaled to return distributed temperature or strain measurements (Güemes et al., 2010).

The frequency of the Brillouin peak, ν_b, is directly proportional to the acoustic velocity and refractive index and it shifts linearly with changes in longitudinal

strain and temperature in the fibre core (Soga, 2014; Kechavarzi et al. 2016):

$$\Delta\nu_b = C_\varepsilon \cdot \Delta\varepsilon + C_T \cdot \Delta T \quad (1)$$

C_ε and C_T slightly vary around values of 500 MHz/% and 1 MHz/◦C, respectively, for standard telecommunication single mode fibres and at the operating wavelength of 1550 nm as used with Brillouin OTDR. Their value can be obtained by accurate calibration. Since the distance where the scattered light is generated can be calculated from the time interval between the launch of the pulsed light and the arrival of the backscattered light, once the fibre refractive index is known, the distribution of strain along the fibre can be obtained.

Another sensing method called Brillouin Optical Time Domain Analysis (BOTDA) can be used, that generally achieve larger accuracy. However, since it requires analysing the power difference between a pulse (pump) light and a continuous (probe) light sent in opposite direction from the two ends of the fibre, to stimulate the Brillouin scattering, it is unsuitable in case of fibre breakage during installation and monitoring (Soga and Luo, 2018).

For both FBG and DFOS the characteristics of FO measurements depend on the analyser (Table 2).

Table 2. Typical features of FO analysers (Vlachopoulos, 2023).

technique	FBG	DFBG	BOTDR/ BOTDA	Rayleigh OFDR
max sensing length	> 1000 m	< 50 m	> 1000 m	< 40 m
repeatability	± 0.1-10 με	± 1 με	± 1 με	± 5 με
spatial resolution	0.10 m	~ 6 mm	0.1-1 m	0.65 mm
max number of measurement points	10-20	> 1000	> 1000	> 1000
sensing range	± 17500 με	± 30000 με	± 30000 με	± 30000 με
acquisition frequency	< 1000 Hz	< 250 Hz	< 1 Hz	< 60 Hz
unit price (approx. EUR)	15k-120k	> 60k	90k-250k	50k-150k
sensor price (approx. EUR)	~ 250 – 1000 per sensor	~ 250 – 5000 per sensor	0.10 per m of fibre	0.10 per m of fibre

An application of FBG to monitor the displacements induced to two heritage buildings by the excavation of a new tunnel for Bank Station Capacity Upgrade (BSCU) is described by Acikgoz et al. (2021, 2022).

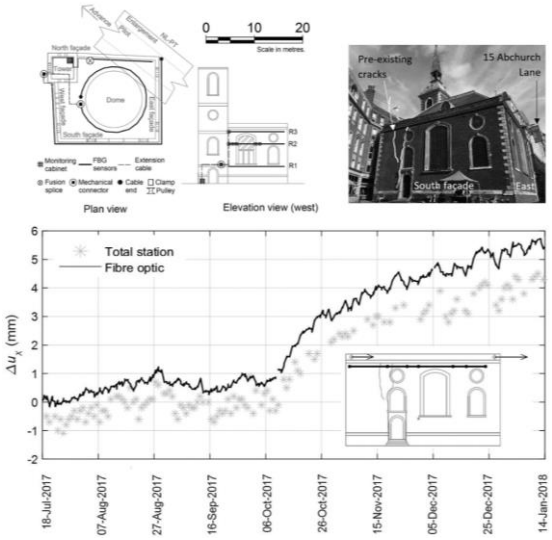

Figure 5. Monitoring St Mary Abchurch during BSCU: validation of FBG measurements against total station (modified after Acikgoz et al., 2021, 2022).

Figure 5 summarises the instrumentation installed on the masonry façades and dome of St. Mary Abchurch, including levelling targets, prisms and FBG optical fibres. The strains measured by FBGs deployed along the South façade of the church were integrated to obtain the relative horizontal displacements between the top corners of the façade, to be compared with displacements measured by a total station on a series of prisms. The time series plotted in Figure 5 along a period of about 6 months, corresponding to the pilot tunnel excavation and the enlargement, show the same trends in both datasets. The observed 1 to 2 mm differences were explained by the different locations of the prisms and fibre-optic sensors. Since the FBG data were validated by conventional measurements, fibre optic monitoring was continued after construction to measure the long-term effects on the church. Strain measurements confirmed that the consolidation-induced movements generally had a negligible effect on most of the structure. However, they produced an unexpected increase of the major pre-existing cracks in the South façade. This justifies careful crack detection and long-term monitoring of heritage buildings adjacent to tunnel excavation.

Kechavarzi et al. (2016) describe three case studies of pilot application of DFOS to monitor the deformation of existing tunnels due to adjacent tunnelling: an old-brick tunnel at the Thameslink King's Cross station in London (Mohamad et al., 2010), a cast-iron Royal Mail tunnel at the Liverpool Street Crossrail station in London (Gue et al., 2015), and a segmental bolted tunnel lining of the Singapore MRT Circle Line 3 (Mohamad et al., 2012). In the earliest case, dating back to 2005, in addition to conventional monitoring of displacements induced by

the underpassing new tunnel in the existing old-brick tunnel, two innovative systems were used: displacement measurements by digital camera imaging (cf. § 3.3) and DFOS (Alhaddad et al., 2014). The DFOS measurements using BOTDR allowed to identify localized high strains in the masonry and to detect the associated cracking.

Two examples of tunnel lining monitoring with DFOS to measure the strains arising during construction, using BOTDR, and check the design assumptions are also given by Kechavarzi et al. (2016): the National Grid London Power Tunnel, where DFOS were embedded in the pre-cast SFR concrete lining segments, and a SCL tunnel for Crossrail Liverpool Street station. In the latter, DFOS were embedded to monitor the strain change in the lining in correspondence of the opening of a cross-passage (breakout and excavation).

It is also worth mentioning the long-term structural health monitoring of an existing concrete-lined tunnel facility at CERN (Geneva; Switzerland), where Brillouin optical time domain analysis (BOTDA) allowed detecting strain changes that did not exceed 20 με (Di Murro et al., 2016).

The application of DFOS to measure tunnelling induced ground horizontal strains and displacements has been tested in field trials by Klar et al. (2014), that deployed a shallow fibre optic sensing cable (0.5 m deep) at two sites: during the TBM excavation of a 3 m-diameter, 18 m-deep tunnel, and for pipe-jacking a 1 m-diameter, 6 m-deep water main. Measurements were taken using two different optical technologies, the Brillouin OTDA (with accuracy of 5 με) and the back scattered Rayleigh reflectometry (with accuracy <1 με). The fiber optic readings allowed accurate measurements, providing information about volume loss, trough width (position of the inflection point) and ratio between trough length and width. The comparison between the measurements obtained by the two different technologies demonstrated an excellent agreement, although the Rayleigh reflectometry would be a better candidate to obtain the trough length, thanks to its higher spatial resolution. An investigation at laboratory scale on the performance of Rayleigh reflectometry to monitor soil horizontal strain induced by deep underground movements – involving comparison with Particle Image Velocimetry and numerical Finite Element back-analysis – has been recently carried out by Della Ragione et al. (2023a).

3.2 Differential SAR interferometry

Interferometric Synthetic Aperture Radar (InSAR) uses the phase difference between two high-resolution radar images to extract information about topography within a specific area. A Synthetic Aperture Radar (SAR) is a side-looking imaging radar system that exploits the Doppler effect (i.e. the change of frequency wave perceived by an observer moving relative to the source of the wave) due to the motion of the receiving antenna, to synthesize a much larger aperture. This improves the azimuth resolution, otherwise limited by the ratio between the antenna size and the range, or distance to the target (r_o in Figure 6). Airborne and spaceborne (satellite) SAR systems allow retrieving a large amount of information on the Earth's topography. As mentioned in § 2, Differential InSAR (DInSAR) can be used to detect the displacement occurring between two subsequent images. However, to discriminate from measurement the effect of atmospheric changes in the same time interval, suitable procedures are required. Since the early 2000's, many techniques have been proposed.

In this framework, Persistent Scatterers Interferometry (PSI) aims at identifying targets on the Earth surface that have a stable phase in time (persistent). These targets (PS) are characterized by high reflectivity and often correspond to point-wise scatterers.

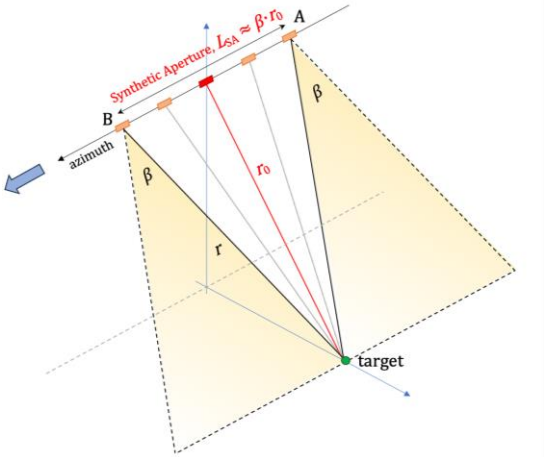

Figure 6. SAR schematic (modified after Meyer, 2019).

The first PSI technique is the pioneering Permanent Scatterers approach (PSInSAR®) proposed by Ferretti et al. (2000, 2001), later extended to include in the analysis less bright Distributed Scatterers (Ferretti et al., 2011). The Small BAseline Subset (SBAS) technique (Berardino et al, 2002), developed immediately after PSInSAR®, is one of the most extensively used. Several other PSI techniques have been developed, as Hooper et al. (2004) or Perissin and Wang (2012): a careful review is provided by Crosetto et al. (2016). Since brighter pixels are characterized by high signal-to-noise ratio, all the mentioned methods achieve improved measurement accuracy.

Once targets are selected, their movement along the sensor-to-target direction (or Line of Sight, LoS) can be detected from the phase variation between two SAR acquisitions. This requires that an accurate Digital Elevation Model is available, and the corresponding phase variation removed, that the geometrical decorrelation, resulting from two distinct viewing geometries is purged, and that the so-called residual topographic error (the difference between the true elevation of the PS centre and that resulting from DEM) is accounted for. Finally, several algorithms have been proposed to estimate and filter out from the interferograms the atmospheric phase component (e.g., Zebker et al., 1997; Ding et al. 2008; Perissin et al. 2011).

The lack or low density of Permanent Scatterers, occurring mostly in non-urban areas, can be partially addressed by using X-band (frequency from 8 to 12 GHz, wavelength, $\lambda = 25$ to 37.5 mm) very high-resolution SAR data — e.g. from TerraSAR-X or COSMO-SkyMed constellations— in comparison to C-band (4 to 8 GHz, 37.5 to 75 mm) — e.g. from Envisat or Sentinel constellations. In addition, artificial Corner Reflectors (CRs) can be deployed on site, that result in good interferometric phases to derive the displacement with higher accuracy. Under optimal conditions (high quality PSs and minimum atmospheric effects) sub-millimetre accuracy was obtained in PSInSAR time series (Ferretti et al. 2007).

However, two limitations of DInSAR and PSI must be mentioned: the one-dimensional nature of measurements (along the LoS) and the "*wrapped phase*" ambiguity. The former implies that only one component of the target displacement is directly measured: its projection into the LoS direction. When ascending and descending SAR data are available, they can be independently processed to calculate vertical and East-to-West horizontal components, hence partially addressing the issue. Different methods have been proposed to derive 3D deformation from DInSAR (Hu et al, 2014), either by combining different datasets, or by making use of auxiliary GNSS, or by making assumptions, the latter being the most widely adopted. On the other hand, wrapped phase limits the ability of PSI to measure "fast" (compared to the satellite revisit time) or, equivalently, "large" displacements. When the differential displacement over the revisit time is larger than $\lambda/4$ – corresponding to the limit "wrapping" value of phase, π – the phase information would be affected by phase cycle loss, hence the actual displacement would be underestimated and difficult to be retrieved unambiguously. Despite several research efforts this issue does not seem completely solved. Wu et al. (2022) have recently proposed a method for phase unwrapping suitable for displacement monitoring in urban areas.

A review of the use of InSAR to displacement monitoring in geotechnical engineering has been carried out by Shimizu (2022). A few applications to monitor tunnelling induced displacements have been carried out in the last decade. Barla et al. (2016) performed a multi temporal-InSAR analysis on Cosmo SkyMed SAR images in both the ascending and descending direction. The measured displacements agree well with the conventional survey (robotic total station and GNSS). In urban area, a series of works dealing with the use of InSAR data in post-tunnelling damage assessment procedures were carried out by Milillo et al. (2018), Giardina et al. (2019) and Macchiarulo et al. (2021). These papers focus on the construction of Crossrail tunnels in London (UK) showing how multi-temporal InSAR was used to assess the extent of damage to over 800 affected buildings. Applications in the urban area of Naples (Italy) have been carried out by Santangelo et al. (2021) and Della Ragione et al. (2023), the latter aimed to get a "remote" assessment of volume loss.

Recently, Di Mariano et al. (2024) have compared the ground movements measured with conventional optical survey nearby Fonerìa station during tunnel construction for a branch of metro Line 9 (now Line 10 South) in the city of Barcelona (Spain) with those measured by PSInSAR® analyses of TerraSAR-X images. Figure 7 shows a comparison between the two data sets in transverse section, in approximately greenfield conditions. A large scatter can be seen in the PSInSAR® measured settlement that were fitted by a Gaussian curve. Nevertheless, fitting curves corresponding to the conventional monitoring (highly correlated) and to the InSAR monitoring are very close to one another and result in similar values of volume loss and inflection point distance. In the same figure a comparison between the InSAR profile of the tunnelling-induced settlement of a monitored building block and the corresponding readings from the total station survey indicates that both trend and magnitude are very close. In fact, the higher "visibility" of PSs on the building roof likely improved the quality of the backscattered radar signal, hence the measurements.

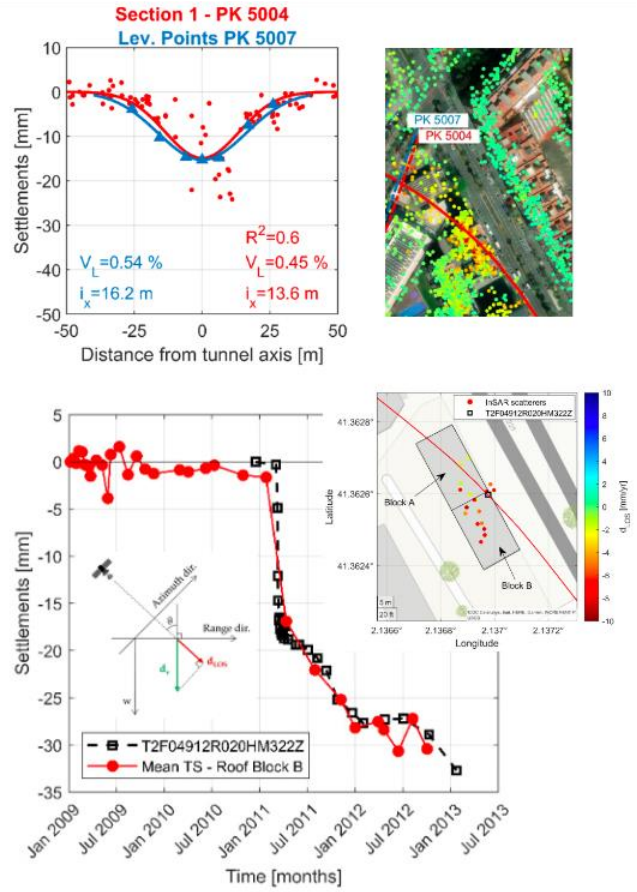

Figure 7. Barcelona Metro Line 10: comparison between conventional monitoring and PSInSAR® (modified after Della Ragione, 2024; Di Mariano et al., 2024).

This allowed to validate PSInSAR® monitoring, showing how it can be used after tunnel construction to expand the existing dataset from conventional survey and to control reliably the evolution of displacements in the long-term.

Serrano-Juan et al. (2016, 2017) carried out an application of both satellite and ground-based InSAR (GB-SAR, or Terrestrial In-SAR) in a construction site affected by underground works in Barcelona, in addition to conventional levelling, highlighting that besides accurate displacement measurements, the GB-SAR automation allows for high-density temporal coverage and concluding that the combined use of different techniques may result in a deeper understanding of the impact of subsidence on nearby buildings. A review of GB-InSAR for deformation monitoring is made by Monserrat et al. (2014).

3.3 From range sensing to range imaging sensing

As mentioned in § 2, among range sensing techniques, high-precision terrestrial laser scanning (TLS) can capture spatial coordinates of a target with sub-millimetric accuracy. Typically, several laser beams are used to scan the objects, producing a point cloud that is used to construct a detailed model. This technique is suitable to measure ground and structure deformation in contactless mode and in a wide range of environmental conditions, including low-light underground excavations. Deformation monitoring is carried out using change detection methods to track the target position or shape change at different epochs. Different detection methods can be adopted: point-to-point, line-to-line and surface-to-surface: an exhaustive review has been done by Shen et al. (2023).

The current practice for engineering applications focuses mainly on point-based methods since they generally achieve the required accuracy. In the framework of monitoring, these methods need to consider that since distinct scans cannot be identical, it is not possible to sample the same point in two different acquisitions. Therefore a "deformation monitoring block" should be identified and used for tracking. The *Fitting method* and the *Geometric Centre method* are suitable to carry out coordinate calculations of the target thus identified, the former often involving regular shape targets (even artificial), the latter suitable to process more irregular shapes. Alternatively, *Cloud-to-Cloud comparison* (C2C, Girardeau-Montaut et al., 2005) can be carried out. The simplest application of C2C is the *Nearest Point method*, that finds the closest corresponding points in clouds from two subsequent epochs and assumes their distance as relative displacement. If a model surface can be interpolated among the cloud points, the method evolves in a *Cloud-to-Model method* (C2M), where the detection of displacement is based on the distance between cloud points and the reference model surface, along the normal direction to the surface. A further evolution is the *Multiscale Model-to-Model Cloud Comparison*, M3C2 (Lague et al, 2013). The large amounts of data that is produced by point-based approaches can be overcome by feature-based approaches, that involve line or surface fittings on the features extracted from the point-cloud. However, within the framework of terrestrial laser scanning there is still a need for further research about line-based and surface-based deformation monitoring (Shen et al., 2023). In tunnel monitoring, TLS has been generally applied for deformation monitoring during the operational phase, in terms of profile and section deformation, clearance inspection and crack detection.

For the case of St. Mary Abchurch described above (Acikgoz et al. 2022, Pascariello et al. 2023a, b), TLS was successfully employed to monitor displacements of the building façades. Changes in the bottom elevation of the parapet wall were detected using the Piecewise Alignment Method, PAM (Teza et al., 2007) and M3C2 (Lague et al., 2013). The point clouds (Figure 8) were post-processed to determine the

tunnelling-induced displacements. The figure presents a comparison between a near-continuous profile of vertical displacements along the South façade, calculated using the PAM method from changes between the point cloud obtained on March 23rd, 2017 (before tunnelling) and January 16th, 2018 (after the tunnel face completely passed the building) and the corresponding socket displacements.

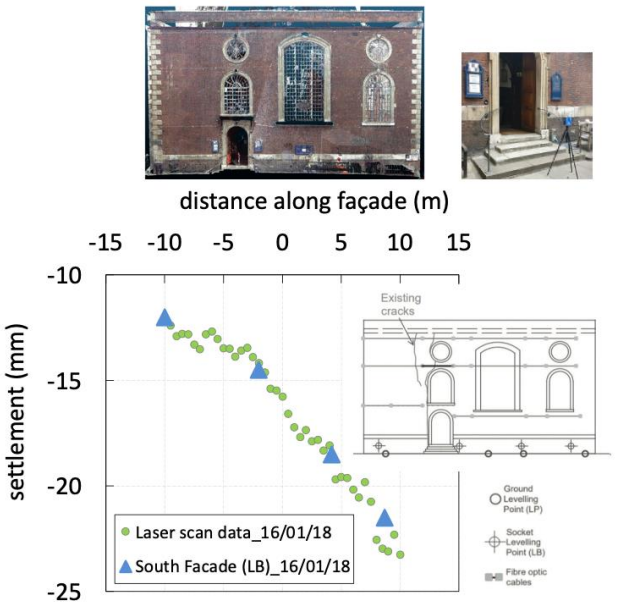

Figure 8. Monitoring St Mary Abchurch during BSCU: South façade point cloud; TLS derived displacements compared to socket settlements (Pascariello et al., 2023a, b).

The agreement between the two data sets is very good. However, the laser scan continuous profile additionally reveals a change of gradient above the doorway, corresponding to the pre-existing crack. Therefore, the profile obtained from levelling is not due to a gradual façade hogging but produced by a local relative rotation between the two edges of the pre-existing crack. This confirmed the measurements of FBG sensors (see Figure 5), indicating that the crack further opened during tunnel construction.

Nowadays, digital photography has reached a technological level that it can potentially replace more traditional and expensive surveying technologies (Soga and Schooling, 2016). Similarly to LiDAR scanners, time-of-flight (ToF) cameras can be employed for ranging, where the entire "scene" is captured with a single light pulse, rather than point-by-point with a rotating laser beam (as in LiDAR scanners). This class of imaging techniques, able to measure the distance of points as a function of time travel of a particular wave emitted from the sensor and bounced back from an object surface, allows to perform a so called "*range imaging sensing*".

Advances in digital imaging quality enable the use of different types of sensors for non-contact range sensing that can create 3D point clouds based on multiple overlapping of 2D images (Soga et al., 2019). Lighting is of course a crucial issue to be carefully addressed. In proper light conditions, even consumer-grade digital cameras can be successfully used to produce a point cloud by taking multiple overlapping 2D images of a scene and applying photogrammetry or by employing Structure-from-Motion (SfM) technique to extract a 3D model from a series of images taken from different viewpoints (Schonberger and Frahm, 2016). A system which can detect visual changes on concrete tunnel linings, such as cracks and leakage, has been recently developed by Stent et al. (2016).

Photogrammetry involves processing images to obtain geometric and physical information about the photographed objects: details on its industrial applications can be found in Luhmann (2010). In civil engineering, both aerial and close-range image capturing are carried out for monitoring purpose. However, in underground engineering, the former is less usual due to the complex construction environment, although it is receiving increasing interest. Close-range photogrammetry and DIC (Digital Image Correlation) or PIV (Particle Image Velocimetry; Stanier et al., 2016) have received more attention in the last fifteen years for the periodical inspection of existing tunnels (Attard et al., 2018).

An interesting application of close-range photogrammetry to monitor the structural displacements induced by tunnelling is reported by Alhaddad et al. (2018) for a case study at Moorgate station in London, as part of the construction of the Elizabeth line. A new connection tunnel was built to link the new station to the existing platform tunnels. This required a new stair adit tunnel (5.2 m wide SCL inclined tunnel with varying heights) to be constructed upwards, directly beneath an existing escalator tunnel (D = 4.3 m, cast-iron segmental lining). Tight limits to the escalator deformation were set, hence continuous monitoring was needed during construction. Three digital single lens reflex cameras (with 55 mm focal length) were installed to monitor three separate spaces of the escalator, in addition to conventional monitoring with total stations. The cameras were set to take images every 5 minutes. Up to 18 targets were installed in each monitored section of the escalator tunnel. Each camera was equipped with a tiltmeter, allowing monitoring target settlements relative to the camera, and a retro target, needed for a direct comparison with less frequent total station measurements. This comparison showed a good match between photogrammetry and total station monitored settlements (Figure 9). The Authors showed that with

photogrammetric monitoring a sub-millimetric accuracy of measurements can be reached, compared to millimetric accuracy of automatic total stations, at a much lower cost of the equipment. Moreover, the DIC system's high precision (i.e. random difference between multiple measurements of an unchanged value) enabled measuring the escalator curvatures over very short chords, that are highly sensitive to noise.

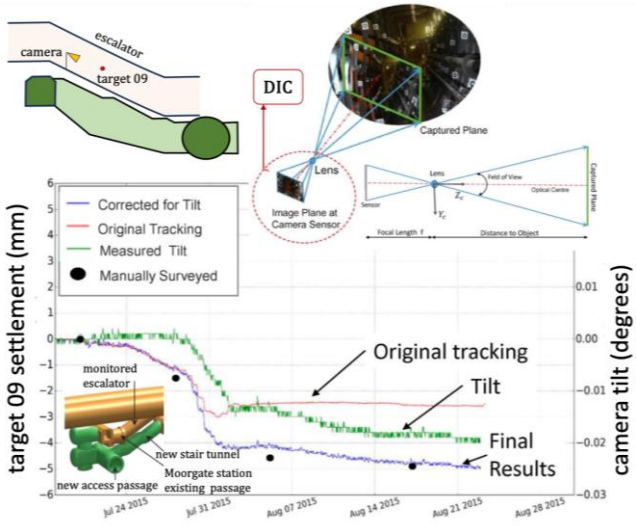

Figure 9. DIC system compared to total station results at Moorgate station (modified after Alhaddad et al. 2018).

Recently, Dalgic et al. (2023) described an experimental campaign aimed at measuring the response of two-storey masonry buildings to foundation settlement profiles mimicking those induced by tunnelling. In the experiments, synchronized video cameras and 2D DIC were used as the primary measurement system for crack detection and to estimate the crack size and length. The photogrammetry was complemented by secondary measurement systems consisting of displacement transducers (LVDTs) and FBG fibre-optic strain gauges to capture the deformed shapes of the structures. The comparative analysis of the collected data sets demonstrated their consistency.

3.4 Wireless Sensor Network (WSN)

On-site cables connecting sensors in large construction sites can be difficult to handle and to protect from possible damages, due to the extensive works that characterise those sites. For this reason, wireless technology has been increasingly applied in tunnel projects in the last decades to avoid deploying too many transmission cables. For instance, Bilotta & Russo (2013) used wireless data loggers to gather frequency measurements from vibrating wire strain gauges embedded in precast reinforced concrete segments for tunnel lining, thus monitoring their structural behaviour throughout the entire life cycle: from the production phase, during installation and in the long term. Since then, technological improvements permitted to reduce the size of the sensors and their power consumption while the development of new communication protocols allowed larger distance to be covered. Many "established" sensors listed in Table 1 have been innovated in recent years to improve their resolution, to reduce power consumption and to enable them to be integrated in a network, thanks to wireless communication. Micro-electromechanical system (MEMS) sensors combine mechanical and electronic modules, allowing for both sensing and data processing and transmission in a very small space. Due their high resolution, low power consumption, easy deployment in large number, and high potential for integration in a wireless network, they have been increasingly applied during underground construction in the last years, as pilot Wireless Sensor Networks (Soga and Schooling, 2016). However, expert knowledge is needed to reliably set up the wireless network environment and the interoperability of different WSN is very limited. Therefore, their use in construction projects remains limited, primarily by the contractors' perception of a lower reliability compared to a wired system, that is not compensated enough in terms of structural safety by the MEMS high sensing accuracy (Ma et al., 2021). To boost their acceptance, guidelines for the application of WSN to civil infrastructures have been developed by the Cambridge Centre for Smart Infrastructure and Construction (Rodenas-Herráiz et al., 2016).

4 CONCLUSIONS

The main features of both established and emerging technologies to monitor tunnelling-induced displacements and strains have been discussed in the paper. Future trends for structural health monitoring during tunnel construction should be identified in the perspective of an ideal extension of the use of sensors to monitor the performance of structures in their whole life cycle. This includes not only the construction process, but also the use, service, and dismantling of structures.

The increasing use of the emerging sensing technologies presented in the paper (Fibre-optic sensors, InSAR based techniques, imaging and photogrammetry, WSN) to monitor the effects on existing structures and infrastructures of adjacent tunnelling and underground construction can provide evidence of their ability to secure high safety levels, thus making the way to life-cycle structural "performance" monitoring. However, potential

obstacles to their wider adoption should be overcome. For instance, optical fibres take time to install, which may discourage their use, also in view of their mechanical vulnerability. Therefore, a technological breakthrough is needed to make fibre-optic sensors more robust and easier to install. On the other hand, the use of photogrammetry and range imaging will advance more through improved lighting (which is a major problem in underground environment) than through upgraded equipment.

Monitoring technologies will also be enhanced by advances in algorithms. It is the case of PS-InSAR: PSI algorithms should be improved to reduce the errors due to wrapped phase that affect measurements. Although the current space agency plans to expand the number of SAR missions in the future suggest an increasing use of InSAR monitoring, PSI experts and professionals in charge of interpreting and using PSI results, such as geotechnical engineers, should intensify their collaboration to improve the usability of this technique for monitoring tunnelling-induced displacements on structures.

Overall, the combined adoption of various sensors, as shown in some of the examples in this paper, can better exploit the advantages of each technique, thus helping to capture more accurately both the current state of the structure and its evolution.

Finally, the integration of distributed sensors into wireless systems and the development of increasingly intelligent high-precision micro-sensors (such as MEMS) hint at the possibility of developing machine-learning-based algorithms to increase the accuracy of target identification and of training artificial neural networks to process data sets.

ACKNOWLEDGEMENTS

The Author wishes to acknowledge the collaborative research projects with Cambridge CSIC and UPC-BarcelonaTech that provided some of the results presented in this paper, and the many colleagues that shared their experience on emerging monitoring technologies. He also warmly acknowledges the unvaluable contribution of former and current research students to those projects.

REFERENCES

Acikgoz, S., Fidler, P.R.A., Pascariello, M.N., Kechavarzi, C., Bilotta, E., DeJong M.J., Mair, R.J. (2021) A Fibre-optic Strain Measurement System to Monitor the Impact of Tunnelling on Nearby Heritage Masonry Buildings, *Int. J. of Architectural Heritage* http://doi.org/10.1080/15583058.2021.1884318.

Acikgoz, S., Luciano, A., Dewhirst, M., DeJong, M.J. Mair, R. (2022) Innovative monitoring of a heritage building during nearby tunnelling in London Clay, *Géotechnique*, http://doi.org/10.1680/jgeot.19.P.243.

Alhaddad, M., Dewhirst, M., Soga, K., Devriendt, M. (2018) A new photogrammetric system for high-precision monitoring of tunnel deformations, *Proc. ICE - Transport*, 172(2), pp. 81-93. Thomas Telford Ltd, http://doi.org/10.1680/jtran.18.00001.

Alhaddad, M., Wilcock, M., Bevan, H., Gue, C., Elshafie, M., Soga, K., Devriendt, M., Waterfall, P., Wright, P. (2014) Multi suite monitoring of an existing cast iron tunnel subjected to tunnelling induced ground movements, *Geo-Shanghai 2014*, China, pp. 357-361.

Attard, L., Debono, C.J., Valentino, G., Di Castro, M. (2018) Tunnel inspection using photogrammetric techniques and image processing: A review, *ISPRS J. Photogramm. Remote Sens.*, 144, pp. 180–188, http://doi.org/10.1016/j.isprsjprs.2018.07.010.

Barla, G., Tamburini, A., Del Conte, S., Giannico, C. (2016) InSAR monitoring of tunnel induced ground movements, *Geomechanics Tunnelling*, 9(1), pp. 15-22, http://doi.org/10.1002/geot.201500052.

Berardino, P., Fornaro, G., Lanari, R., Sansosti, E. (2002) A new algorithm for surface deformation monitoring based on small baseline differential SAR interferograms, *IEEE TGRS* 40(11), pp. 2375-2383, http://doi.org/10.1109/TGRS.2002.803792.

Bilotta, E., Russo, G. (2013) Internal forces arising in the segmental lining of an earth pressure balance-bored tunnel. *ASCE J Geotechnical and Geoenvironmental Engineering*, 139(10), pp. 1765-178, http://doi.org/10.1061/(ASCE)GT.1943-5606.0000906.

Boje, C., Guerriero, A., Kubicki, S., Rezgui, Y. (2020) Towards a semantic Construction Digital Twin: Directions for future research. *Autom. Constr.* 114, 103179, https://doi.org/10.1016/j.autcon.2020.103179.

Brownjohn J.M.W. (2007) Structural health monitoring of civil infrastructure. *Phil. Trans. Royal Soc. A: Math., Physical and Engineering Sciences*, 365(1851), pp. 589 - 622, http://doi.org/10.1098/rsta.2006.1925.

BTS/ICE (2004). *Tunnel lining design guide*. The British Tunnelling Society and The Institution of Civil Engineers Default Book Series. January 2004, http://doi.org/10.1680/tldg.29866.

Chai, Q., Luo, Y., Ren, J., Zhang, J.Z., Yang, J., Yuan, L., Peng, G.-D. (2019) Review on fiber-optic sensing in health monitoring of power grids, *Opt. Eng.* 58(7), 072007, http://doi.org/10.1117/1.OE.58.7.072007.

Childers, B.A., Froggatt, M.E, Allison, S.G., Moore, T.C., Hare, D.A., Batten, C.F., Jegley, D.C. (2001) Use of 3000 Bragg grating strain sensors distributed on four eight-meter optical fibers during static load tests of a composite structure. In: *Proceedings of the SPIE Conference*, 4332, pp. 133-142, San Diego, CA, https://doi.org/10.1117/12.429650.

Crosetto, M., Monserrat, O., Cuevas-González, M., Devanthéry, N., Crippa, B. (2016) Persistent Scatterer In-

terferometry: A review, *ISPRS Journal of Photogrammetry and Remote Sensing*, 115, pp. 78-89, http://doi.org/10.1016/j.isprsjprs.2015.10.011.

Cumming, I.G., Wong, F.H., (2005) *Digital Processing of Synthetic Aperture Radar Data*, Norwood, MA, Artech House, Inc.

Dalgic, K.D., Gulen, B., Liu, Y., Acikgoz, S., Burd, H., Marasli, M., Ilki, A. (2023) Masonry buildings subjected to settlements: Half-scale testing, detailed measurements, and insights into behaviour. *Engineering Structures*, 278, art. no. 115233, http://doi.org/10.1016/j.engstruct.2022.115233

Davis, M.A., Kersey, A.D. (1997) Fiber Bragg grating sensors for infrastructure sensing, In: *Proc. Optical Fiber Communication Conference*, Dallas (USA), 177-178, https://doi.org/10.1109/OFC.1997.719799.

Della Ragione, G. (2024) *An integrated approach for assessing the impact of tunnel excavations in urban areas*, PhD Thesis, Univ of Napoli Federico II, Italy.

Della Ragione, G., Abadie, C.N., Xu, X., da Silva Burke, T.S., Moeller, T., Bilotta, E. (2023a) Fibre optic sensing for strain field measurement in geotechnical laboratory experiments, *Géotechnique Letters* http://doi.org/10.1680/jgele-2023-048.

Della Ragione, G., Rocca, A., Perissin, D., Bilotta, E. (2023b) Volume Loss Assessment with MT-InSAR during Tunnel Construction in the City of Naples (Italy), *Remote Sensing*, 15(10), art. no. 2555, http://doi.org/10.3390/rs15102555.

Di Mariano, A., Gens, A., Della Ragione, G., Bilotta, E., Sanchez, J., Royo, B., Cespa, S. (2024) Case study of soil-structure interaction during tunnelling for Barcelona Metro: a comparison between conventional and innovative displacement measurements, *Proc. 11th Int. Symp. Geotech. Aspects of Underg. Constr. in Soft Ground*, 2024 Macao SAR, China.

Di Murro, V., Pelecanos, L., Soga, K., Kechavarzi, C., Morton, R. F. (2016) Distributed fibre optic long-term monitoring of concrete-lined tunnel section TT10 at CERN, In: *Proc. International Conference on Smart Infrastructure and Construction*, Cambridge, UK http://doi.org/10.1680/tfitsi.61279.027.

Ding, X.L., Li, Z.W., Zhu, J.J., Feng, G.C., Long, J.P. (2008) Atmospheric Effects on InSAR Measurements and Their Mitigation, *Sensors*, 8, 5426-5448. http://doi.org/10.3390/s8095426.

Ferretti, A., Fumagalli, A., Novali, F., Prati, C., Rocca, F., Rucci, A., (2011) A new algorithm for processing interferometric data-stacks: SqueeSAR, *IEEE Transactions on Geoscience and Remote Sensing,* 49(9), 3460–3470 http://doi.org/10.1109/TGRS.2011.2124465.

Ferretti, A., Prati, C., Rocca, F. (2000) Nonlinear subsidence rate estimation using permanent scatterers in differential SAR interferometry, *IEEE TGRS,* 38(5), 2202-2212, http://doi.org/10.1109/36.868878.

Ferretti, A., Prati, C., Rocca, F. (2001) Permanent scatterers in SAR interferometry, *IEEE TGRS*, 39(1), 8–20, http://doi.org/10.1109/36.898661.

Ferretti, A., Savio, G., Barzaghi, R., Borghi, A., Musazzi, S., Novali, F., Prati, C., Rocca, F. (2007) Submillimeter accuracy of InSAR time series: experimental validation. *IEEE TGRS,* 45(5), 1142–1153, http://doi.org/10.1109/TGRS.2007.894440.

Floris I., Adam J.M., Calderón P.A., Sales S. (2021) Fiber Optic Shape Sensors: A comprehensive review, *Optics and Lasers in Engineering*, 139, 106508, http://doi.org/10.1016/j.optlaseng.2020.106508.

Giardina, G., Milillo, P., Dejong, M.J., Perissin, D., Milillo, G. (2019) Evaluation of InSAR monitoring data for post-tunnelling settlement damage assessment. *Struct. Control and Health Monit.*, 26(2), e2285.1-19, https://doi.org/10.1002/stc.2285.

Girardeau-Montaut, D., Roux, M., Marc, R., Thibault, G. (2005) Change detection on points cloud data acquired with a ground laser scanner. *International Archives of Photogrammetry, Remote Sensing and Spatial Information Sciences* 36 (Part 3), 30–35.

González-Arteaga, J., Alonso, J., Moya, M., Merlo, O., Navarro, V., Yustres, A. (2020) Long-term monitoring of the distribution of a building's settlements: Sectorization and study of the underlying factors. *Eng. Struct*. 205, 110111, http://doi.org/10.1016/j.engstruct.2019.110111.

Gue, C.Y., Wilcock, M., Alhaddad, M., Elshafie, M., Soga, K. Mair, R.J. (2015), The monitoring of an existing cast iron tunnel with distributed fibre optic sensing (DFOS), *J. Civ. Struct. Health. Monit.*, (5) pp. 573-586. https://doi.org/10.1007/s13349-015-0109-8.

Güemes, A., Fernández-López, A., Soller, B. (2010) Optical fiber distributed sensing- physical principles and applications, *Structural Health Monitoring* 9(3), pp. 233– 245, https://doi.org/10.1177/1475921710365263.

Hill, K.O., Fujii, Y., Johnson, D.C., Kawasaki, B.S. (1978), Photosensitivity in optical fiber waveguides: Application to reflection filter fabrication, *Appl. Phys. Lett.* 32 (10) 647–649, https://doi.org/10.1063/1.89881.

Hooper, A., Zebker, H., Segall, P., Kampes, B. (2004) A new method for measuring deformation on volcanoes and other natural terrains using InSAR persistent scatterers, *Geophys. Res. Lett.* 31 (23), https://doi.org/10.1029/2004GL021737.

Hoult, N.A., Soga, K. (2014) Sensing solutions for assessing and monitoring tunnels. In: *Woodhead Publishing Series in Electronic and Optical Materials*, *Sensor Technologies for Civil Infrastructures* (Wang et al.eds), Woodhead Publishing, 56, pp. 309-346, http://doi.org/10.1533/9781782422433.2.309.

Hu, J., Li, Z.W., Ding, X.L., Zhu, J.J., Zhang, L., Sun, Q., (2014) Resolving three-dimensional surface displacements from InSAR measurements: a review, *Earth Sci. Rev.* 133, 1–17. https://doi.org/10.1016/j.earscirev.2014.02.005.

ITA-AITES WG2-Research (2011) *Monitoring and Control in Tunnel Construction*. ITA report n°009.

Kechavarzi, C., Soga, K., de Battista, N., Pelecanos, L., Elshafie, M., Mair, R.J. (2016) *Distributed Optical Fibre Sensing for Monitoring Civil Infrastructure - A*

Practical Guide, ICE Publishing, 192 pp. http://doi.org/10.1680/dfossmci.60555.

Klar, A., Dromy, I., Linker, R. (2014) Monitoring tunneling induced ground displacements using distributed fiber-optic sensing, *Tunnelling and Underground Space Technology*, 40, pp. 141-150, http://doi.org/10.1016/j.tust.2013.09.011.

Lague, D., Brodu, N., Leroux, J. (2013) Accurate 3D comparison of complex topography with terrestrial laser scanner: Application to the Rangitikei canyon (NZ), *ISPRS J. of Phot. Rem. Sens.*, 82, pp. 10-26, http://doi.org/10.1016/j.isprsjprs.2013.04.009.

Luhmann, T. (2010) Close range photogrammetry for industrial applications, *ISPRS J. Photogramm. Remote Sens.* 65 (6), pp. 558–569, http://doi.org/10.1016/j.isprsjprs.2010.06.003.

Ma, E., Lai, J., Wang, L., Wang, L., Xu, S., Li, C., Guo, C. (2021) Review of cutting-edge sensing technologies for urban underground construction, *Measurement*, 167, https://doi.org/10.1016/j.measurement.2020.108289.

Macchiarulo, V., Milillo, P., DeJong, M.J., Gonzáles Martí, J., Sánchez, J., Giardina, G. (2021) Integrated InSAR monitoring and structural assessment of tunnelling-induced building deformations, *Structural Control and Health Monitoring,* 28(9), e2781, http://doi.org/10.1002/stc.2781.

Mair, R.J. (2008) Tunnelling and geotechnics: New horizons. *Geotechnique*, 58 (9), pp. 695-736

Meltz, G., Morey, W. W., Glenn, W. H. (1989) Formation of Bragg gratings in optical fibers by a transverse holographic method, *Opt. Lett.* 14, pp. 823-825, https://doi.org/10.1364/OL.14.000823.

Meyer, C., Cucino, P., Eccher, G., Ulrich, D. (2013) The Florence high-speed railway hub: 4D monitoring - Innovations in data acquisition and data management for tunnelling projects in sensitive urban areas. In: *Proc. of* WTC 2013, Geneva (Switzerland), pp. 1403–1410.

Meyer, F. (2019) Spaceborne Synthetic Aperture Radar – Principles, Data Access, and Basic Processing Techniques, In: *SAR Handbook: Comprehensive Methodologies for Forest Monitoring and Biomass Estimation* (Flores et al. eds). NASA. http://doi.org/10.25966/ez4f-mg98.

Meyer, T.H., Roman, D.R., Zilkoski, D.B. (2005) What does height really mean? Part IV: GPS Heighting. *Surv. & Land Information Science*, 66(3), pp. 165-183, https://opencommons.uconn.edu/nrme_articles/5.

Milillo, P., Giardina, G., DeJong, M.J., Perissin, D., Milillo, G. (2018) Multi-Temporal InSAR Structural Damage Assessment: The London Crossrail Case Study, *Remote Sens*., 10(2), 287, http://doi.org/10.3390/rs10020287.

Mohamad, H., Bennet, P.J., Soga, K., Mair, R.J., Bowers, K. (2010) Behaviour of an old masonry tunnel due to tunnelling-induced ground settlement. *Géotechnique* 60(12): 927-938, https://doi.org/10.1680/geot.8.P.074.

Mohamad, H., Soga, K., Bennet, P.J., Mair, R.J., Lim, C.S. (2012) Monitoring twin tunnel interaction using distributed optical fiber strain measurements. *ASCE J. Geotech. Geoenv. Engineering*, 138(8), pp. 957-967, https://doi.org/10.1061/(ASCE)GT.1943-5606.0000656.

Monserrat, O., Crosetto, M., Luzi, G. (2014) A review of ground-based SAR interferometry for deformation measurement, *ISPRS Journal of Photogrammetry and Remote Sensing*, 93, pp. 40-48, http://doi.org/10.1016/j.isprsjprs.2014.04.001.

Morino A., Balestrieri A., Carrieri G., Martino M., Pezzetti G. (2023) Monitoring. In: *Handbook on Tunnels and Underground Works* (Bilotta E. et al. eds.), 2 (5), SIG - Società Italiana Gallerie, CRC Press.

Moss, R. M., Matthews, S. L. (1995) In-service structural monitoring—a state of the art review, *Struct. Eng*. 73, 23–31.

Nöther, N. (2010) *Distributed Fiber Sensors in River Embankments: Advancing and Implementing the Brillouin Optical Frequency Domain Analysis*, PhD Thesis, Technical University of Berlin (Germany).

Odolinski, R., Teunissen, P.J. (2020) Best integer equivariant estimation: Performance analysis using real data collected by low-cost, single-and dual-frequency, multi-GNSS receivers for short-to long-baseline RTK positioning. *J. Geod*., 94, pp. 1–17 https://doi.org/10.1007/s00190-020-01423-2.

Pan, Y., Zhang, L. (2021) Roles of artificial intelligence in construction engineering and management: A critical review and future trends, *Autom. Constr*., 122, 103517, https://doi.org/10.1016/j.autcon.2020.103517.

Pascariello, M.N., Bilotta, E., Acikgoz, S., Schooling J., Mair, R. (2023a) Innovative monitoring and advanced numerical modelling of a heritage masonry building affected by urban tunnelling, *Gallerie e grandi opere sotterranee*, 147, pp. 9-19.

Pascariello, M.N., Luciano, A., Bilotta, E., Acikgoz, S., Mair, R. (2023b) Numerical modelling of the response of two heritage masonry buildings to nearby tunnelling. *Tunnelling and Underground Space Technology*, 131, art. no. 104845, http://doi.org/10.1016/j.tust.2022.104845.

Perissin, D., Wang, T., (2012) Repeat-pass SAR interferometry with partially coherent targets, *IEEE TGRS*, 50 (1), 271–280. http://doi.org/10.1109/TGRS.2011.2160644.

Perissin, D., Wang, Z., Wang, T. (2011) The SARPROZ InSAR tool for urban subsidence/manmade structure stability monitoring in China. In: *Proc. 34th Int. Symp. Remote Sensing of the Environment (ISRSE)*, Sydney (Australia).

Qu, X., Shu, B., Ding, X., Lu, Y., Li, G., Wang, L. (2022) Experimental Study of Accuracy of High-Rate GNSS in Context of Structural Health Monitoring, *Rem. Sens.* 14(19), 4989, https://doi.org/10.3390/rs14194989.

Rodenas-Herráiz, D., Soga, K., Fidler, P., de Battista, N. (2016) *Wireless sensor networks for civil infrastructure monitoring—a best practice guide*, ICE Publishing, London, UK.

Santangelo, V., Bilotta, E., Di Martire, D., Ramondini, M., Russo, G. (2021) An application of A-DInSAR for monitoring tunnelling-induced displacements in urban area. The case study of the Naples Metro Line 6 stretch

Mergellina-Chiaia. *Gallerie e grandi opere sotterranee*, 139, pp. 9-16.

Schonberger, J. L. Frahm, J.-M. (2016) Structure-from-Motion Revisited, In: *Proc. 2016 IEEE Conference on Computer Vision and Pattern Recognition (CVPR)*, pp. 4104–4113, IEEE. http://doi.org/10.1109/CVPR.2016.445.

Serrano-Juan, A., Pujades, E., Vázquez-Suñè, E., Crosetto, M., Cuevas-González, M. (2017) Leveling vs. InSAR in urban underground construction monitoring: Pros and cons. Case of La Sagrera railway station (Barcelona, Spain), *Engineering Geology*, 218, pp. 1-11, http://doi.org/10.1016/j.enggeo.2016.12.016.

Serrano-Juan, A., Vázquez-Suñè, E., Monserrat, O., Crosetto, M., Hoffmann, C., Ledesma, A., Criollo, R., Pujades, E., Velasco, V., Garcia-Gil, A., Alcaraz, M. (2016) GB-SAR interferometry displacement measurements during dewatering in construction works. Case of La Sagrera railway station in Barcelona, Spain, *Eng. Geol.*, 205, pp. 104 - 115, http://doi.org/10.1016/j.enggeo.2016.02.014.

Shen, N., Wang, B., Ma, H., Zhao, X., Zhou, Y., Zhang, Zh., Xu, J. (2023) A review of terrestrial laser scanning (TLS)-based technologies for deformation monitoring in engineering, *Measurement*, 223, 113684, http://doi.org/10.1016/j.measurement.2023.113684.

Shimizu, N. (2022) Application of satellite technology (GPS and SAR) for monitoring ground surface displacements in rock and geotechnical engineering, In: *Proc. 20th ICSMGE*– Rahman and Jaksa (Eds). AGS, Sydney, Australia, pp. 597-616.

Soga, K. (2014) Understanding the real performance of geotechnical structures using an innovative fibre optic distributed strain measurement technology. *Rivista Italiana di Geotecnica*, 4, 7-48. https://associazionegeotecnica.it/wp-content/uploads/2017/05/rig_4_2014_soga-.pdf.

Soga, K., Schooling, J. (2016) Infrastructure sensing, *Interface Focus* 6, 20160023, http://doi.org/10.1098/rsfs.2016.0023.

Soga, K., Luo, L. (2018) Distributed fiber optics sensors for civil engineering infrastructure sensing, *J. Struct. Integrity and Maintenance*, 3(1), pp. 1-21, http://doi.org/10.1080/24705314.2018.1426138.

Soga, K., Ewais, A., Fern, J., Park, J. (2019) Advances in Geotechnical Sensors and Monitoring. In: *Geotechnical Fundamentals for Addressing New World Challenges* (Lu & Mitchell eds). Springer Series in Geomechanics and Geoengineering. http://doi.org/10.1007/978-3-030-06249-1_2.

Stanier, S.A., Blaber, J., Take, W.A., White, D.J. (2016) Improved image-based deformation measurement for geotechnical applications. *Can. Geotech. J.* 53(5), pp. 727–739, https://doi.org/10.1139/cgj-2015-0253.

Stent, S., Gherardi, R., Stenger, B., Soga, K., Cipolla, R. (2016) Visual change detection on tunnel linings. *Machine Vision and Applications* 27, 319–330. http://doi.org/10.1007/s00138-014-0648-8.

Teza, G., Calgaro, A., Zaltron, N., Genevois, R. (2007) Terrestrial laser scanner to detect landslide displacement fields: a new approach. *Int. Journal of Remote Sensing* 28(16), pp. 3425-3446, http://doi.org/10.1080/01431160601024234.

Vlachopoulos, N. (2023) The use of fiber optics for ground and tunnel support monitoring – Two decades of lessons learned, In: *Proc. WTC 2023*, pp. 2336-2344, http://doi.org/10.1201/9781003348030-281.

Walton, G., Diederichs, M.S., Weinhardt, K., Delaloye, D., Lato, M.J., Punkkinen, A. (2018) Change detection in drill and blast tunnels from point cloud data, *Int. J. of Rock Mechanics and Mining Sciences*, 105, pp. 172–181, http://doi.org/10.1016/j.ijrmms.2018.03.004.

Wu, S., Zhang, B., Ding, X.L., Shahzad, N., Zhang, L., Lu, Z. (2022) A hybrid method for MT-InSAR phase unwrapping for deformation monitoring in urban areas, *International Journal of Applied Earth Observation and Geoinformation*, 112, 102963, http://doi.org/10.1016/j.jag.2022.102963.

Zebker, H.A., Rosen, P.A., Hensley, S. (1997) Atmospheric effects in interferometric synthetic aperture radar surface deformation and topographic maps, *J. Geophys. Res. Solid Earth*, 102(B4), pp. 7547–7563, https://doi.org/10.1029/96JB03804.

Zumberge, J.F., Heflin, M.B., Jefferson, D.C., Watkins, M.M., Webb, F.H. (1997) Precise point positioning for the efficient and robust analysis of GPS data from large networks. *J. of Geoph. Res. Solid Earth,* 102(B3), pp. 5005-5018, http://doi.org/10.1029/96JB03860.

.

Proceedings of the XVIII ECSMGE 2024
GEOTECHNICAL ENGINEERING CHALLENGES
TO MEET CURRENT AND EMERGING NEEDS OF SOCIETY
© 2024 the Authors
ISBN 978-1-032-54816-6
DOI 10.1201/9781003431749-8
Open Access: www.taylorfrancis.com, CC BY-NC-ND 4.0 license

ECSMGE 24
XVIII EUROPEAN CONFERENCE ON SOIL MECHANICS AND GEOTECHNICAL ENGINEERING

State-of-the-art Report

High-speed rail earthworks design developments and innovative trials – building Britain's technical legacy

Travaux de terrassement pour un train à grande vitesse, development de conception et essais innovants - construire l'héritage technique de la Grande-Bretagne

G. Katsigiannis*
Ferrovial Construction, London, UK
**georgios.katsigiannis@ekfb.com*

ABSTRACT: Selection of appropriate engineering mitigations for Britain's new high speed rail line HS2 earthworks to ensure compliance with track slab performance criteria reflective of the railway's high operating speed represents a major technical challenge which is exacerbated by the challenging ground conditions encountered in the central section (Contract C23) of Phase One. High plasticity over-consolidated clays and extremely weak and weathered mudstones are prone to large magnitude and long duration movements due to loading or unloading. To overcome the technical challenges associated with uncertainty in predicting long-term ground behaviour and ensuring subgrade performance with limited previous case studies on ground formations that had not been extensively studied, the C23 team developed and implemented collaboratively with the Client a number of large-scale innovative Earthworks trials to increase confidence in heave and settlement predictions, pursue significant design efficiencies, validate the geotechnical performance of engineering fill materials and maximise the material re-use of the site won soils. This paper provides an overview of some of these large-scale earthwork trials and the design and construction lessons learnt describing how the C23 team set new standards of practice for the industry while building a strong technical legacy which will be passed on to future infrastructure projects in the UK and abroad.

RÉSUMÉ: La sélection des mesures d'atténuation technique appropriées pour les travaux de terrassement de la nouvelle ligne ferroviaire à grande vitesse britannique HS2, afin d'assurer la conformité aux critères de performance de la dalles de la voie ferrée reflétant la grande vitesse operationelle du chemin de fer, représente un défi technique majeur qui est exacerbé par les conditions de sol difficiles rencontrées dans la section centrale (contrat C23) de la première phase. Les argiles sur-consolidées à haute plasticité et les mudstones extrêmement faibles et altérés sont sujets à des mouvements de grande magnitude et de longue durée dus au chargement ou au déchargement. Pour surmonter les difficultés techniques liées à l'incertitude dans la prédiction du comportement du sol à long terme et assurer la performance de la plate-forme avec des études de cas antérieures limitées sur des formations géologiques qui n'avaient pas été étudiées de manière approfondie, l'équipe C23 a développé et mis en œuvre en collaboration avec le client un certain nombre d'essais de terrassement innovants à grande échelle pour accroitre la confiance dans les prédictions de soulèvement et de tassement, poursuivre des efficacités de conception significatives, valider la performance géotechnique des matériaux de remblai d'ingénierie et maximiser la réutilisation des matériaux des sols gagnés sur le site. Cet article donne un aperçu de certains cas de ces essais de terrassement à grande échelle et des leçons tirées de la conception et de la construction, décrivant comment l'équipe C23 a établi de nouvelles normes de pratique pour l'industrie tout en construisant un solide héritage technique qui sera transmis aux futurs projets d'infrastructure au Royaume-Uni et à l'étranger.

Keywords: Earthworks; high-speed rail; heave, settlement; materials; lime.

1 INTRODUCTION

1.1 The HS2 project

In January 2012, the UK Government announced its intention to proceed with a new high-speed railway line (HS2) and published the preferred line of the route from London to the West Midlands as the first phase (Phase 1) of a national high-speed rail network. Phase 1 involves the construction of a new railway line of approximately 230 km in length between London and the West Midlands. For construction purposes, the

overall route was subdivided into three Delivery Areas:

- Southern
- Central
- Northern

The delivery areas were further subdivided into seven areas, each representing a main works civils contract (MWCC).

1.2 The C23 Project

EKFB, a joint venture that brings together international expertise from four leading civil engineering construction companies: Eiffage, Kier, Ferrovial Construction and BAM Nuttall, have been appointed by HS2 Ltd to deliver Civil Engineering works across an 80km section of the new high speed rail link between the Chiltern Tunnel and Long Itchington Wood. The C23 project represents the biggest single geotechnical contract ever awarded in the UK and the scope includes 45 high-speed rail (mainline) embankments and 30 cuttings, 15 viaducts, over 5 km of green (cut and cover) tunnels, 22km of road diversions and 81 overbridges. The earthworks operations include over 30 million cubic metres of excavation.

The Arcadis, Setec, Cowi Design Joint Venture (ASC) has been appointed by EKFB to provide detailed design services for the civil engineering assets with additional support being provided by TYPSA, ARUP and WSP.

1.3 Technical challenges

What differentiates HS2 from other earthworks projects in the UK is the tight end product performance criteria for the high-speed rail earthworks assets required to be achieved over the design life of 120 years, reflective of the selection of slab track system and the high operating speed of the rail line. The minimal operational maintenance of the slab track means that it cannot accommodate as much movement as a ballasted track, and therefore any movement of the supporting platform must be kept within specified limits to maintain the safe operation of the railway. Hence, strict post track slab installation heave and settlement performance criteria are imposed by the HS2 Technical Standards - Earthworks to ensure the required geometrical accuracy and stability of the track. Selection of appropriate engineering measures to achieve compliance with the HS2 performance requirements, represents a major technical challenge for the project and has been the key focus area of the geotechnical design teams.

This technical challenge is exacerbated by the particularly challenging, uncertain, and variable ground conditions encountered across the length of the C23 contract. Over-consolidated and high plasticity clays such as the Gault, Ampthill, Kimmeridge and Clay formations and weak mudstones such as the Lias Group Whitby, Dyrham and Charmouth formations are particularly prone to large magnitude and long duration ground movements due to loading or unloading, resulting from variable soil stiffness and low soil permeability.

The severity of impact on the track system combined with the uncertainty presented by the prevailing ground conditions create specific ground risks within the C23 Project area, the key earthworks risks identified by HS2 as the project developed included deep cutting heave, embankment settlement and dynamic amplification.

Overall, the biggest and most pressing challenge for EKFB and ASC has been to identify, specify and build appropriate earthworks design measures to effectively mitigate these technical risks whilst at the same time ensuring that the carbon footprint and the impact on the environment are minimised.

At an early stage in the development of the Scheme Design HS2 and EKFB agreed that investing in a series of earthworks trails during the design stage would enable greater understanding of some of the specific performance characteristics of some of the key strata. This approach reduced uncertainty and enabled efficient solutions to be incorporated into the design. The key to receiving the Client's support for these early trials was to demonstrate their potential to enable cost efficiencies into the design by reducing uncertainty.

2 SETTLEMENT

2.1 Predicting settlement

In saturated clay soils of low permeability, the loading due to embankment weight initially results in an immediate settlement and the development of excess pore pressure. This is followed by time dependent consolidation settlement.

The prediction of settlement and comparison against acceptability criteria for the project requires an estimation of both the magnitude of total potential settlement and the time period over which that settlement will occur. Settlement is calculated considering 3 components: immediate (i.e. undrained, elastic or instantaneous), consolidation (i.e. primary, time dependent) and secondary (i.e. creep). Total long-term settlement is the sum of the three components although secondary creep settlement is often assumed to be negligible in over-consolidated clays.

2.2 Settlement criteria

The HS2 Technical Standard - Earthworks (HS2, 2019a), defines "earthworks settlement" as *the permanent downward displacement of the earthwork due to static effects (such as consolidation) and any accumulated effects of dynamic loading.* The following sources of settlement were addressed by the design: a) settlements within embankment materials; and b) settlements in natural soils below embankments, including secondary consolidation.

The total settlement limit value to be satisfied by design is 60mm for *long* (i.e. more than 800m long earthwork asset without a discontinuity) high-speed line embankments and 30mm for *short* high-speed line embankments. This further drops to 15mm for the areas within 150m of switches and crossings (S&Cs). The design also needs to satisfy the 1:1000 maximum longitudinal distortion criterion when assessed over less than 15m reducing to 1:2000 when assessed over 120m and 1:1000 maximum transverse distortion to the alignment. The above limit values are to be applied from the time of installation of slab track and for a design life of 120 years.

Several typical mitigations for earthworks settlement are suggested by the HS2 Technical Standards with the ones listed below selected by the C23 JV:

- Excavate and replace (E&R): where the unsuitable material is at shallow depth, and groundwater conditions are favourable to open excavation.
- Consolidation by temporary surcharge: accelerate consolidation of compressible soils.
- Consolidation with band drains: in association with surcharging to reduce time to achieve consolidation.
- Hold period: a duration of time within the MWCC contract where the majority of settlement is allowed to occur prior to track construction. Surcharging and band drains may be used to accelerate settlement and reduce the duration of the hold period.
- Piled foundation with load transfer platform: soft, compressible soil that cannot be improved by other methods, and deep E&R is impractical.

Moreover, for earthworks where the predicted ground movements approach the limits specified in Technical Standards, in-ground instrumentation (e.g. extensometers, piezometers) needs to be installed as appropriate to monitor the ground movements and changes in the porewater pressures during and following construction, in order to verify the predicted magnitude, timescale and rate of ground movement. Where instrumentation is needed to monitor settlement, both internal settlements within newly constructed embankments and settlements of natural ground beneath embankments is monitored.

2.3 Scheme design

The design of HS2 requires a relatively low alignment but visual and noise mitigation creates a need for large scale landscape bunds associated with many of the mainline embankments. Thus, while the mainline may only be typically 8 to 10m above existing ground level, in some cases the total embankment loading applied by the earthworks may be the result of up to 15m of fill placed over a footprint up to 100m wide.

Stage 1 Scheme design indicated that predicted settlement under these large embankment loadings could be significant with deformation possibly extending to notable depth, particularly within the Charmouth Mudstone formation. This resulted in extensive settlement mitigation measures being proposed under the mainline embankments, in the form of pressure relief drains (PRDs), which accelerate consolidation by providing shorter path for excess pore water pressures to dissipate, and piled load transfer platforms (PLTPs), which reduce settlement by transferring the load to deeper more competent strata. The majority of settlement mitigations were concentrated on viaduct transitions where HS2 longitudinal distortion criteria are particularly onerous when combined with construction programme constraints. The total proposed design mitigations across the 45 mainline embankments included up to 95,000 PRDs and over 4,000 reinforced concrete piles. Requiring over 5,000m^3 virgin sand aggregate and 22,000m^3 of concrete including 3,250 tonnes of reinforcement, these were costly and carbon intensive settlement mitigation solutions.

2.4 Settlement trials

2.4.1 Trials scope and objectives

To mitigate uncertainty and assess the actual settlements that will occur with depth (magnitude, depth of influence, consolidation and immediate settlement, duration of settlement), embankment settlement trials were carried out inform detailed design and support the design optimisations. Two trial embankment monitoring sites were identified (see Figure 1) in the northern section of C23. These are referred to as Boddington Settlement Trial 1 and 2. The embankments were formed from material excavated from the adjacent cutting trial and were located within the footprint of future landscape earthworks to minimise double handling. The embankments loading induced settlement of the

underlying soils which was monitored using several different techniques.

The purpose of the trials was to provide data on the settlement and corresponding stiffness and consolidation characteristics of the underlying soils. In order to measure this, shape arrays were installed in shallow trenches below the embankments. In addition, further instrumentation, comprising load cells, extensometers, and piezometers, were installed below Settlement Trial 2.

2.4.2 Settlement trials location

Settlement trials 1 and 2 are located 7.5 km approximately southeast of Southam and 14 km north of Banbury, on the outskirts of Wormleighton Village, Warwickshire.



Figure 1. Settlement Trials aerial view.

2.4.3 Ground conditions

The published geological map for the area shows the site located on solid geology of the Charmouth Mudstone Formation of the Lias Group, with no overlying superficial deposits. However, the ground investigation data records show locally Head is present within the footprint of the embankments. The Charmouth Mudstone Formation comprises grey mudstone with sporadic thin bands and nodules of occasionally shelly limestone. The Charmouth Mudstone Formation typically reaches thicknesses of 100 m to 150 m.

Based on the ground investigation information, the Charmouth Mudstone formation is inferred to have a highly weathered thickness of about 10 m. The formation has been distinguished in two facies: CHAM-C Z described as firm to very stiff slightly sandy slightly gravely CLAY; and CHAM-MDST extremely weak becoming weak with depth, thinly laminated/bedded dark grey slightly calcareous to calcareous MUDSTONE. Locally at settlement trial 2 at the sides of the stockpile, HEAD deposits of variable thickness from 0.3 m to 0.85 m, overlies Charmouth Mudstone Formation. This formation comprises generally very soft to stiff slightly sandy slightly gravelly CLAY.

2.4.4 Trial embankments construction

Prior to instrumentation installation and embankment construction the site was cleared of ecology and archaeology, temporary drainage was installed and the upper 300 to 400 mm of topsoil and soft subsoil was removed. For Settlement Trial 1, the construction started on 23rd of July 2019 and took about 2 months to reach the full height of the embankment. The geometrical characteristics of the first trial embankment are as follows:

- Embankment width at the base: 70 m
- Crest maximum width: 30 m
- Side slopes: 1V to 2.5H
- Embankment height: 8 m
- Embankment length: 170 m

For Settlement Trial 2, the construction started on 05th of November 2020 and took about 1 month to reach maximum embankment height of 8m. The geometrical characteristics of the second trial embankment are as follows:

- Embankment width at the base: 95 m
- Crest maximum width: 55 m
- Side slopes: 1V to 2.5H
- Embankment height: 8 m
- Embankment length: 150 m

2.4.5 Testing, results and analysis

The values measured by the total earth pressure cells installed below the trial were compared to the construction history which allowed an estimate of the bulk density of the fill to be made which was used to estimate the loading imposed on the underlying strata by both embankments.

Installation and performance of the magnetic extensometers was largely successful. When plotted, the extensometer results suggested, as might be expected, that the elastic settlement ceased shortly after the completion of the embankment. For Settlement Trial 1, the settlement at the end of construction was 55mm, compared to the observed settlement below Settlement Trial 2 of 40mm at the same point in time.

The Asaoka (Asaoka, 1978) method was used to interpret and extrapolate settlement observations for both Settlement Trials. The observed settlement during Settlement Trial 1 was plotted using four different time intervals, Δt (10, 25, 50 and 100 days) and the total settlement was estimated to be around 85mm.

It was concluded that the drainage paths are shorter than might be assumed from the ground investigation infromation, possibly suggesting that the discontinuities within the weathered and unweathered Charmouth Mudstone act as drains. If the ground

model is forced to fit the initial drainage scenario, with longer drainage paths, then the values of the coefficient of consolidation (cv) needed to provide a match to the settlement data are significantly larger than the values measured from oedometer tests. Based on the above, the drainage path length was assumed to be 4.8m which would give a height of the assumed compressible layer of 4.8m for one way drainage and 9.6m for two-way drainage. Using these lengths, the cv was estimated to be 1.3m^2 per year for one-way drainage and 1.8m^2 per year for two-way drainage.

The observed settlement during Settlement Trial 2 was plotted using the same time intervals (10, 25, 50 and 100 days) and the total settlement was estimated to be around 96mm. Drainage path lengths of 3.1 and 6.2m or one and two-way drainage were adopted while two way drainage into the underlying limestone was also checked. Using these lengths, the cv was estimated to be 1.0m^2 per year for one-way drainage and 1.3m^2 per year for two-way drainage.

While consolidation was still ongoing at slower rate when the embankments were decommisioned to allow for construction of the permanent works to proceed, the extensometers showed that 65% of the settlement occurs in the weaker soils between ground level and 2.5m. These soils will likely be dug out and replaced (E&R mitigation) during the HS2 permanent embankments construction. In addition, only 4% of the total movement was measured in extensometers installed below 15m which enabled the designers to succefully establish the zone of influence of the embankment loading.

Several vibrating wire piezometers were installed to monitor pore water pressure at different depths below Settlement Trial 2. The smoothed data from these plots allowed the excess pore water pressures to be calculated and plotted with time. Upper piezometers, installed from 10 to 20m depth, showed, as expected, that the excess pore water pressures increased at the end of loading and decreased through the monitoring period.

2.5 Settlement design efficiencies

Based on the observations from both Settlement Trials, the settlement analyses were refined in the detailed design, supported also by information from the targeted ground investigation and laboratory soil testing results within the high-risk areas of the C23 embankments and transitions zones to viaducts. The horizontal permeability was assumed to be greater than the vertical permeability due to conditions such as particle orientation, fissures and jointing in the rock due to geological processes and the possible presence of silt partings while a moderate increase in soil stiffness values for Charmouth Mudstone was also confirmed. The implementation of the findings in the detailed design of the permanent embankments eventually resulted in the elimination of 3,070 load transfer platform piles (59km total piling length) and removal of over 80,000 PRDs (640km total vertical drain length) as part of the settlement mitigations. This contributed to approximately 20,000 tC02 emissions savings including material embodied carbon and emissions related to transportation and construction works.

3 HEAVE

3.1 Predicting heave

The HS2 Phase 1 alignment creates the requirement for several deep (up to 30m) cuttings within the C23 area which will be underlain by high plasticity over consolidated clay and mudstone deposits. Since the early stages of the scheme design, there has been an appreciation of the level of risk associated with heave occurring at the base of such excavations with magnitudes and time to completion which could cause unacceptable deformations in the sensitive HS2 track slab.

During the excavation of a cutting, many tonnes of soil are removed and the ground below the formation level experiences a reduction in vertical stress which causes the ground to relax or rebound; this upward expansive movement is defined as heave (Butler et al., 2020).

Heave has been observed in over-consolidated high plasticity clay soils across the UK and is expected to occur in deep cuttings excavated in Gault, West Walton, and Oxford Clay formations and in mudstone and clay geological formations of the Lias Group of Jurassic age. The heave movement is anticipated to comprise of two main components:

- Immediate heave due to vertical unloading (elastic confining stress relaxation)
- Plastic and time dependent heave which is assumed to be the inverse of a consolidation settlement mechanism.

The time-dependent component is the main concern as it has the potential to extend well into the operational phase of HS2. It was recognised at an early stage that there were limited case studies of the heave phenomenon in the strata present in the C23 project area and that this created significant uncertainty in predicting long-term ground behaviour. The predicted heave behaviour largely depends on the soil stiffness; stress history and locked in horizontal stresses; and the soil permeability which are parameters notoriously

hard to confidently measure even with advanced laboratory or in-situ soil tests.

Initial analysis undertaken at concept stage suggested that cuttings greater than 12m depth in the high plasticity clay strata likely to be encountered by the HS2 could exhibit significant long-term heave and thus present a risk of long-term deformation.

3.2 Heave criteria

The HS2 Technical Standard for Earthworks (HS2, 2019a), defines "earthworks heave" as *the permanent upward displacement of the earthwork due to static effects, including hydraulic uplift.*

The total heave limit value to be satisfied by design is 60mm for *long* high-speed line cuttings and 15mm for *short* cuttings. This further drops to 10mm for the areas within 150m of S&Cs. The design also needs to satisfy the 1:1000 maximum longitudinal distortion criterion when assessed over less than 15m reducing to 1:2000 when assessed over 120m and 1:1000 maximum transverse distortion to the alignment. The above limit values are to be applied from the time of installation of slab track and for a design life of 120 years.

3.3 Scheme design

During scheme design, heave was assessed by ASC DJV, and numerical analyses were undertaken. Based on these studies, 6 deep mainline cuttings were identified as high-risk where the predicted long-term heave movements exceeded the HS2 Technical Standards limits and hence provision for robust heavily engineered mitigation was considered necessary. Following optioneering studies, a piled supported 1m thick reinforced concrete slab was selected as the most appropriate heave mitigation. Within the 6 identified cuttings of concern the total proposed mitigation slabs encompassed over 2.3km of the route and incorporated over 640 tension piles. Requiring a total of 37,800m3 concrete and 5,700 tonnes of reinforcement, this was a costly and carbon intensive heave mitigation solution.

3.4 Heave trial

3.4.1 Trial scope and objectives

Due to uncertainty in predicting long-term ground behaviour, particularly estimating magnitude, and duration of deep cutting heave below formation level during 120 years of operation, it was proposed to undertake a heavily monitored trial cutting to inform the understanding of the heave. The aim of the heave trial cutting was to provide an increased level of certainty in the estimation of heave that could be incoperated into the detailed design of the earthworks to enable the optimisations of mitigation measures for the potentially heaving cuttings.

A combination of in-ground magnetic extensometers and inclinometers, and surface topographical targets were specified to record ground movements. Vibrating wire piezometers were specified to record changes in pore pressures. Generally, the design of the extensometers and piezometers considered the depth of influence of anticipated ground movement due to stress relief while the inclinometers were installed in lower and mid-upper slope. Moreover, a weather station was installed to allow seasonal trends to be investigated.

3.4.2 Trial location

The site selected for the trial was located 7.5 km approximately southeast of Southam and 14 km north of Banbury, on the outskirts of Wormleighton Village, Warwickshire. The topography of the site is characterised by the rolling hills of the area and was constructed on the HS2 line of route and will ultimately form the northern-most 300m of the approximatley 2 km long Boddington Cutting.



Figure 2. Heave Trial aerial view.

3.4.3 Ground conditions

The site is underlain by the Charmouth Mudstone formation of varying weathering grades with minor head deposit in the vicinity of the transition to the Oxford Canal South Embankment. The formation typically comprises grey mudstone with sporadic thin bands and nodules of occasionally shelly limestone. A potentially continuous limestone band was identified in the ground investigation that had the potential to impact the observed response to excavation.

3.4.4 Heave trial construction

The cutting slopes were designed at an angle of 1V:4H with a platform width of approximately 17m and a maximum depth of about 15m to closely resemble the geometry of the permanent works. The total projected volume to be excavated, based on the trial cutting geometry, was 271,000 m^3. It was intended to undertake the excavation in one phase but due to

adverse weather conditions and flooding events, the construction programme was carried out in 3 phases. After the clearing of ecology and archaeology, the construction of access routes and drainage, and the installation and baselining of instrumentation bulk earthworks commenced in August 2019, but the works were hampered by inclement weather throughout October culminating in a significant rainfall event at the end of the month. At the beginning of December 2019, EKFB were able to drain and recommence works on the site and the final excavation level was reached on the northern part of the cutting with approximately 2.50m of excavation remained on the southern part (volume excavated up to end of December 2019 was 257,500 m3 with 13,500 m3 left to excavate). Continuing restrictions due to weather and then the Covid-19 pandemic resulted in the final excavation works only re-starting in June 2020 with the final level of excavation reached at the end of July 2020.



Figure 3. Heave Trial at formation level.

3.4.5 Testing, results and analysis

Monitoring periods have been defined to ensure the ground response was recorded over the relevant periods.

- Monitoring Period 1 (pre-excavation): the period prior to the excavation, after installation of the in-ground monitoring instruments. This period was used to establish stable readings and set a baseline for each instrument.
- Monitoring Period 2 (excavation): the period from start of the excavations works, until the bottom of the excavation profile (formation level of the cutting) is reached. This period was originally specified to last 3 months in the design but actually lasted for approximately 1 year between August 2019 and July 2020 and has been sub-divided into 3 phases.
- Monitoring Period 3 (post excavation): the period from reaching final excavation profile to the decommissioning of the trial and commencement of the main works for the Boddington Cutting and Oxford Canal South Embankment. Monitoring over this period was critical, as the response of the trial cutting to unloading was expected to occur mainly on this period, and results from this monitoring would allow to confirm design assumptions and so possibly impact the specified heave mitigations for the permanent works. This period lasted for approximately 2.5-3 years from summer 2020 until early 2023.

The results from the Heave Trial indicated that the mechanism of heave movement in the base of the excavation is a distributed movement over a significant depth which can be attributed to swelling due to stress relief due to the excavation of the cutting. This occurred as both immediate (during excavation) and long-term swelling with a maximum value being recorded at the deepest part of the cutting.

The conclusion was that a maximum movement of 30-50mm occurred in the deepest parts of the cutting. The immediate heave was estimated at approximately 30% of the total observed movement (i.e. 10-15mm) which is distributed over a shallower depth than the longer term swelling. The magnitude of ground movement reduces with depth, with the proportion of immediate to long-term reducing as well. Negligible movement was considered to be occurring 35m below the base of the cutting. The swelling in the upper 2.5m was estimated to have reached 95% of the predicted total at after 2.5 to 3 years. The period to reach 95% of the predicted movement reduces with depth, reaching 1-1.5 years 25 m below the base of the cutting. A forward projection was undertaken for the surface monitoring points and upper most magnets located along the centreline of the cutting which indicated that there was a further 5-15mm of movement still to occur albeit at a very slow rate. This residual movement (which was below the HS2 Technical Standards total heave limit) was expected to be concentrated over the upper 2.5m located directly below the base of the cutting.

The trial also provided valuable lessons in relation to the installation and commissioning of the instruments and subsequent monitoring phases. The most prominent issue was the result of the flooding of the excavation during the works and the subsequent build-up of debris in several of the magnet extensometer monitoring ducts. The flooding also caused delays in the construction programme, resulting in 3 phases of excavation instead of the single, continuous phase of excavation specified as part of the design. There were also lessons learnt associated with the survey control and impact to the measurements due the casing reductions required during excavation.

In additon to heave, a second mechanism of ground movement occurred during the trial. This was a downslope ratcheting mechanism attributed to the

seasonal drying and wetting in the near surface (1-2m bgl). A seasonal fluctuation of up to 10mm was recorded in the vertical inclinometers installed in the upper clay slope with approximately 50% being irrecoverable. This movement was comparable with observations in other cut slopes and is indicative of the "Vadose Zone" effects that are identifed as risks in the HS2 Technical Standard for Earthworks (2019a).

3.5 Heave design efficiencies

The Heave Trial observations indicated that the total measured heave was about half the original cautious prediction, and the rate of the movement was faster than the initially estimated rate. This greater certainty in the heave mechanism reduced the uncertainty and enabled a reduction in conservatism to be fed into the detailed design of the earthworks. The soil stiffness and anisotropic permeability values were refined supplemented also by information from the targeted ground investigation and laboratory soil testing results within the high-risk areas of the C23 deep cuttings.

The concentration of the observed residual movements over the upper 2.5m below the base of the trial cutting provided the sufficient evidence to the designers so that the heave of the permanent deep cuttings to be mitigated with a combination of 2-3m E&R with well graded Class 1 material (which in many cases were also required to satisfy the static and dynamic subgrade performance requirements) and a Hold Period ranging from 9 months to 22 months. This represented a more cost-efficient response to the remaining residual heave risk and resulted in the removal of all 6 areas of pile slabs in the detailed design eliminating the need for 37,000 m^3 of concrete and 5,700 tonnes of steel reinforcement and contributing to approximately 70,000 tC02 emissions savings including material embodied carbon and emissions related to transportation and construction works.

4 PERFORMANCE OF EARTHWORK MATERIALS

4.1 Earthworks scale

C23 is the single largest earthworks contract ever awarded in the UK requiring about 30,000,000 m^3 engineering fill materials for high-speed line (mainline) embankments, highway earthworks and landscape (environmental) bunds. This large volume of material is being sourced from the C23 cutting and green tunnel excavations and needs to be properly handled and transported in line with the EKFB's complex and sophisticated mass haul plan representing a significant planning and operations challenge.

4.2 Embankment requirements

HS2 mainline Upper Embankment Fill (UEF) and Lower Embankment Fill (LEF) consist of either structured chalk, stabilised chalk, stabilised glacial till or granular fill e.g., Class 1A1, 1B1, 1C1, 9G, 9J or 9K (HS2 SCEW 600, 2019b). Cohesive soils (Class 2) with high sulphate contents are not suitable for reuse as mainline or highway embankment fill due to risk of swelling while low to intermediate plasticity cohesive soils (LL <50%) with low sulphate content are suitable for reuse as mainline embankment fill after stabilisation. High plasticity cohesive soils (LL>65% and PI>40%) are Class 4 (HS2 SCEW 600, 2019b).

In addition to the material and compaction requirements of the mainline fill, there are static and dynamic stiffness performance criteria required for the constructed earth structure i.e. Modulus of Deformation based on EV2 measurement and dynamic performance based on Raleigh Wave Velocity criteria.

In order to secure the C23 mass haul plan baseline and introduce further carbon and cost efficiencies by maximising site won material re-use, EKFB in collaboration with ASC and HS2, planned and executed a number of large-scale earthwork material trials utilising materials and construction techniques proposed for the main works. The aim of these trials was particularly to confirm the suitability of a number of earthworks materials for high-speed rail UEF, LEF and E&R (i.e. foundation treatment).

4.2.1 Trial scope and objectives

The earthwork material trials were planned based on the availability of an area of land, the published geology, the underlying ground conditions, and the likely nature of locally available fill. The objectives of the trials included the review of suitable improvement options (e.g. stabilisation) for re-use of any excavated materials for embankment fill; determination of in situ Modulus of Deformation (EV2) and dynamic performance parameters; verification of the foundation conditions; earthworks control and verification to validate performance of earthworks during construction; and review of SCEW 600 contract specific Tables 6/1 and Table 1/5 requirements.

As mentioned before, many of the C23 embankments are built with Glacial Till stabilised with lime to increase its strength, density, stiffness, and shear wave velocity. A 3m height embankment trial was carried out in Newton Purcell area with lime stabilised locally sourced Glacial Till, obtained from a borrow pit excavated adjacent to the trial embankment.

The Glacial Till was encountered below the glaciofluvial deposits and was described to comprise firm, becoming stiff, grey to dark grey, slightly gravelly to gravelly clay. The gravel comprised limestone, flint, and mudstone, suggesting that the till is derived from local and distant rocks.

The design geometry of the embankment, which was governed by the surface geophysics testing requirements, comprised of target height of 3.5m, including 16 layers of 200-250 mm compacted thickness; and total length of 60m and width 20m including 2 testing areas 30m x 20m. For the construction of the embankment, the material was improved using binder contents of 1%, 1.5%, 2%, and 2.5% and produced the stiff to very stiff material generally seen throughout the trial. After adding lime, the Glacial Till classifies as 9J lime stabilised cohesive material.

4.2.2 Testing results

Strength/stiffness tests (UCS, triaxial, CBR, shear box) and the classification tests (particle density, pulverisation, calcium carbonate content, PSD) were conducted and samples were tested for optimum moisture content using modified (4.5kg hammer) and standard (2.5kg hammer) proctor tests and also for the natural moisture content tests.

Plate Load Tests were performed for measuring the EV2 of the material and Light Weight Deflectometer (LWD) for measuring the bearing capacity (deflection) of the subgrade/subsoils. The HS2 Technical Standard (2019a) requires minimum EV2 values of 45MPa – 60MPa and a maximum EV2 value of 500 MPa to be measured. For the measurement of EV2, the French standard procedure was specified which uses a 600 mm diameter plate and has an approximate depth of influence of 1.2m. The results showed that EV2 values remain mainly within the same range of 60-200 MPa and very small increases were observed as the embankment height was ascending. No significant differences were observed between the two test areas for each layer.

There was also an opportunity for the Continuous compaction control (CCC) to be tested in Newton Purcell trial. CCC is a roller integrated compaction measurement method for dynamically excited rollers, which allows for the compaction success to be continuously measured online. During the trial, the optimum number of compaction passes were assessed in line with the specification for the fill material and an optimized compaction rate was applied in the remainder of the embankment construction after the assessment.

Upon assessment of the trial results and considering the compaction and static performance requirements, an 1.5% minimum lime content was recommended by the DJV for HS2 permanent embankment fill. Minimum dry density of 94% and Maximum Air Voids of 5% were proposed as appropriate acceptance criteria for the 1.5% lime stabilised material.

Moreover, surface wave geophysical tests, namely MASW and CSW, were undertaken while rotary open hole boreholes were drilled through the completed trial embankment to a depth of 15m below formation level, to undertake downhole and crosshole seismic testing through the embankment fill and foundation strata to validate the inverted values of shear wave velocity from MASW/CSW surveys. The results from both the surface wave and intrusive geophysical methods succesfully confirmed exceedance of the shear wave velocity design assumption of 250m/s for the stabilised fill material for all minimum binder contents tested as part of this trial.

4.2.3 Material efficiencies

Overall, the earthworks materials trials successfully enabled the re-use of site won materials as engineering fill for mainline embankments and E&R. They also successfuly demonstrated the potential to reduce the minimum (lime) binder content from 2.5% to 1.5% while also satisfying the materials performance criteria, EKFB were able to eliminate up to 30,000 tonnes of lime for C23 permanent works, securing significant cost savings and over 50,000 tC02e reduction.

5 CONCLUSIONS

The planning and execution of the settlement and heave earthwork trials in advance of detailed design enabled the C23 teams to refine design parameters and incoperate significant cost efficiencies into the design by reducing or eliminating heavily engineered heave and settlement mitigations. The greater certainty as a result of these trials also enabled a reduction in the risk provision reduired for the project as it moved into construction. Ongoing construction stage monitoring installed in the permanent HS2 earthwork assets will further validate the information gathered from the field trials, in relation to settlement and heave in these challenging ground conditions and should enable further risk reduction and potential efficency in terms of the active managment of hold periods within the construction programme.

The C23 heave and settlement trials are amongst very few large-scale, instrumented earthwork trials carried out in the UK and will provide valuable

information for the design of similar earthworks in the future.

Moreover, a large number of site won materials trials succesfully confirmed the improved performance through stabilisation and the suitability as engineering fill for permament works securing EKFB‘s mass haul plan but also introducing efficiencies by reducing the total volume of lime binder required in C23 embankments by 40%.



Figure 4. Lime Stabilised Glacial Till Trial in Newton Purcell,

Further earthworks design and material re-use efficiency opportunities have already been mapped out and are being pursued at the late stages of the detailed design, with particular focus on the remaining carbon hot spots.

EKFB technical teams working collaboratively with the DJV and the Client are delivering technical excellence while building a lasting technical and sustainability legacy that will be passed on to future earthworks projects in the UK and abroad.

ACKNOWLEDGEMENTS

The author would like to thank his colleagues from HS2 Ltd, EKFB JV and ASC DJV involved in the planning and design of the earthworks trials, the execution of works and the interpretation of the results and implementation of the findings in the detailed design of the C23 permanent earthworks. An acknowledgement is also due to the HS2 and EKFB Project and Risk Management teams that recongnised the value that the early implementation of those proposed trials represented.

REFERENCES

Asaoka, A. (1978). Observational procedure of settlement prediction. Soils and Foundations, Journal of the Soils and Foundations Engineering, 18(4), 87-101.

Butler, S., Hope, A., Madinier, B., & Zilles, A, (2021). Ground Heave in Deep Cuttings: Evolution from Generic to Specific Models to Enable Refinement of a Risk Management Strategy. ICE Publication High Speed Two (HS2): Infrastructure Design and Construction (Volume1), 2021. https://doi.org/10.1680/hs2.65765.371.

HS2 (2019a). Technical Standard – Earthworks.

HS2 (2019b). Specification for Civil Engineering Works (SCEW) 600 series - Earthworks.

Proceedings of the XVIII ECSMGE 2024
GEOTECHNICAL ENGINEERING CHALLENGES
TO MEET CURRENT AND EMERGING NEEDS OF SOCIETY
© 2024 the Authors
ISBN 978-1-032-54816-6
DOI 10.1201/9781003431749-9
Open Access: www.taylorfrancis.com, CC BY-NC-ND 4.0 license

ECSMGE 24
XVIII EUROPEAN CONFERENCE ON SOIL MECHANICS AND GEOTECHNICAL ENGINEERING

State-of-the-art Report

Exploring rate and temperature effects on residual strength. Review and implications for a landslide case study

Exploration des effets de la vitesse et de la température sur la résistance résiduelle. Examen et implications pour une étude de cas de glissement de terrain

N.M. Pinyol
Department of Civil and Environmental Engineering, Universitat Politècnica de Catalunya, Barcelona, Spain
CIMNE, Centre Internacional de Mètodes Numèrics a l'Enginyeria, Barcelona, Spain

L.M. Garcia, A. Lloret, M. Alvarado
Department of Civil and Environmental Engineering, Universitat Politècnica de Catalunya, Barcelona, Spain

**nuria.pinyol@upc.edu*

ABSTRACT: A large landslide immediate to a reservoir, identified in 2006, is the guiding case to discuss its triggering, namely a consequence of fast reservoir drawdown, and its post-failure response. The reactivation of the landslide, twelve years later, allowed the validation of some hypotheses assumed in the first study (2012). The risk of landslide acceleration, for a constant residual friction and an assumed thermal pressurization of the sliding surface, was not realistic since the landslide never accelerated. In recent years, efforts have been addressed to gain further knowledge by developing advanced numerical tools and a better understanding of clay shear strength. The paper presents the developments achieved. The results of a comprehensive experimental program to investigate the effect of shear strain rate and temperature are presented for a variety of soil types. The expected landslide response under rapid drawdown conditions was simulated by a material point method-based numerical tool that handles, in a dynamic formulation, large displacements and soil /rock materials characterized by temperature, strain rate, and strain softening dependence. The risk of landslide acceleration, predicted in the 2012 analysis looks, at present, as a remote event.

RÉSUMÉ: Un important glissement de terrain à proximité immédiate d'un réservoir, identifié en 2006, est le cas directeur pour discuter de son déclenchement, à savoir une conséquence de l'abaissement rapide du réservoir, et de sa réponse après la rupture. La réactivation du glissement de terrain, douze ans plus tard, a permis de valider certaines hypothèses retenues dans la première étude (2012). Le risque d'accélération du glissement de terrain, pour un frottement résiduel constant et une pressurisation thermique supposée de la surface de glissement, n'était pas réaliste puisque le glissement de terrain ne s'est jamais accéléré. Au cours des dernières années, des efforts ont été déployés pour acquérir de nouvelles connaissances en développant des outils numériques avancés et une meilleure compréhension de la résistance au cisaillement de l'argile. Le document présente les développements réalisés. Les résultats d'un programme expérimental complet visant à étudier l'effet de la vitesse de déformation et de la température de cisaillement sont présentés pour une variété de types de sols. L'avenir attendu des glissements de terrain dans des conditions de rabattement rapide a été simulé par un outil numérique basé sur la méthode des points de matériau qui traite, dans une formulation dynamique, les grands déplacements et les matériaux sol/roche caractérisés par la température, la vitesse de déformation et la dépendance à l'adoucissement de la déformation. Le risque d'accélération des glissements de terrain, prédit dans l'analyse de 2012, semble, à l'heure actuelle, être un événement lointain.

Keywords: Landslide; residual strength; strain-rate and temperature effects; drawdown; case history.

1 INTRODUCTION

1.1 Background to a reactivated landslide

The detection of a 2 km long crack parallel to a reservoir in 2006 in the north of Spain led to the geological and geotechnical identification of a landslide. The work carried out during 3 years included: (a) interpretation of air photo, field mapping, 16 borehole logs; (b) installation of monitoring systems and their interpretation; (c) laboratory tests for the characterization of the materials involved; (d) back-analysis of slope stability to determine possible

causes; (e) the study of the stability of the landslide in future situations of exploitation of the reservoir; and (d) the assessment of the risk of acceleration. The case was described in Pinyol *et al.* (2012).

The observed crack delimited the crest of a reactivated ancient compound translational landslide of 40 million m^3. Figure 1 shows three representative profiles showing the geology, the position of the boreholes, and the position of the landslide sliding surface estimated in 2009.

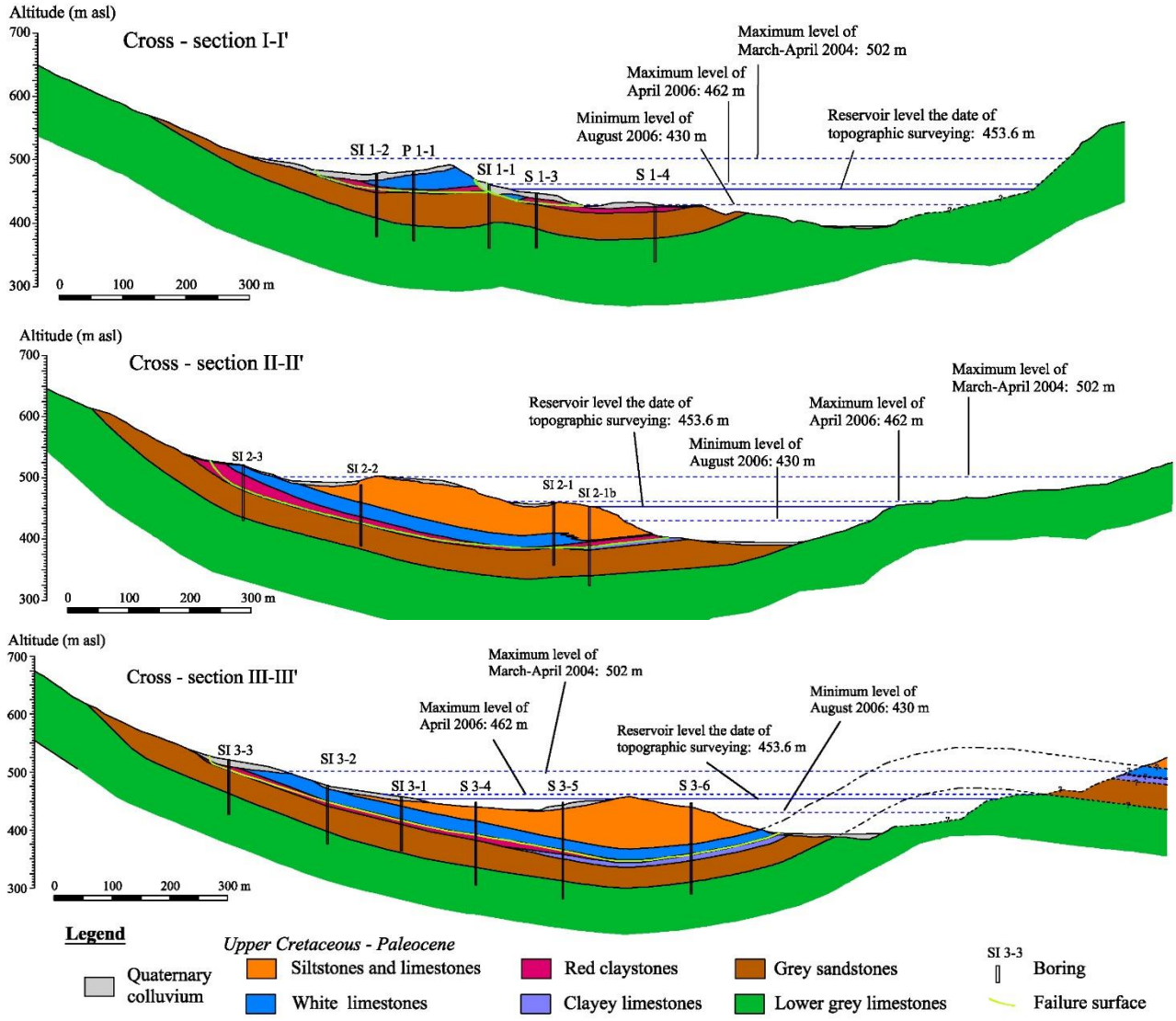

Figure 1. Geological cross-section. Same legend for all of them (Pinyol et al., 2012).

According to the conclusions of the geological and geomorphological work, the rupture surface was located in a Garumnian claystone layer (LL=45%; PI=23%, %<2μm=30%), interstratified between rock units. However, the slide movement, recorded by inclinometers after their installation in 2006, for three years, between the time of inclinometer installation after the identification of the landslide (2006) and the completion of the initial study (2009), did not allow us to confirm precisely the position of the slip surface. The clay was analysed in the laboratory using conventional identification tests and mechanical and hydraulic experiments (ring shear test and permeability test).

The stability of the landslide, affected by rainfall and the level of the reservoir submerging the toe of the slope was evaluated. With this purpose, the distribution of the water pressure into the slope was calculated using a flow-deformation coupled calculation model using the finite element-based code (Code_Bright, 2024). The changes in water level that occurred in 2002-2009, as well as the average rainfall, were introduced as boundary conditions to estimate properly the pore water pressure distribution. The

model followed the approach presented in Pinyol *et al.* (2008).

The results of this analysis, in terms of pore water pressures, were validated with pressure records provided by vibrating wire piezometers installed in the claystone layer and the limestone and sandstone layers above and below the claystone.

The stability analysis performed, by means of a limit equilibrium method, considering the water pressure distribution previously calculated by the coupled hydro-mechanical calculation, showed that the conditions considered, in terms of geometry, the variation of reservoir levels, and the available shear strength at the failure surface consistent with laboratory shear tests, could justify the rupture observed in 2006.

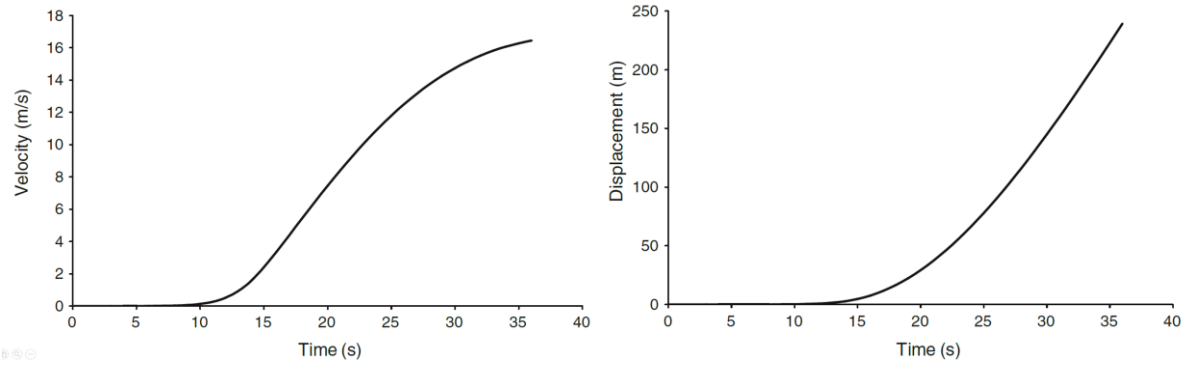

(a) *(b)*

Figure 2. Calculated evolution of the sliding velocity and run out, considering thermo-hydro-mechanical coupled effects (Pinyol et al., 2012).

The stability analysis concluded that slope stability was lost when the water pressure along the sliding surface, located in a layer of clay of low permeability, was significantly higher than the value corresponding to the reservoir level. This situation occurred when the reservoir level dropped during 2005 and 2006 after a long period of high levels at relatively high velocity (up to 25 cm/day).

The expected evolution of the landslide was evaluated in 2012, having in mind the risk of acceleration and the potential effect of a tsunami as occurred in the well-known case of Vajont landslide (Italy, 1996) (Alonso & Pinyol, 2010). The analysis of the acceleration risk, described in Pinyol *et al.* (2012), introduced the possible generation of pore pressures inside the basal shearing band of the sliding surface due to the heat generated by frictional work that, in turn, leads to an increase in interstitial pressure and, consequently, a reduction of available shear strength. The phenomenon of temperature increase during fast shearing has been recently measured in Kohler *et al.* (2023) in a ring shear apparatus.

This analysis was carried out with the tools available at the time, following the approach presented in Pinyol & Alonso (2010), also applied in the case of Vajont landslide. Other contributions addressed also this problem (Vardoulakis, 2002).

The modelling work performed indicated that the unstable slope could accelerate, by heat-induced pore water pressurization, and reach a maximum velocity of 16 m/s and a displacement of hundreds of meters (Figure 2). This estimation was not realistic since the landslide never accelerated. However, in the case of Vajont landslide, during the three years previous to the catastrophic acceleration, the landslide exhibited accumulated displacements whose rate could be correlated with the reservoir elevation history and accumulated rainfall. Therefore, even though we could not provide a consistent explanation of the causes of the landslide motion without an abrupt acceleration, the risk of acceleration was accepted as possible.

1.2 Twelve years later

At present, the landslide remains active and, as occurred during the dry period between 2004 and 2006, the recent drought in north-east Spain in 2021-2023 forced the reduction of the reservoir elevation to very low levels (Figure 3). This drawdown was preceded by 7 years in which the reservoir remained at high elevation. The consequence was a reactivation of the landslide. Fortunately, since 2009 the landslide has been instrumented with inclinometers and piezometers and valuable information is available.

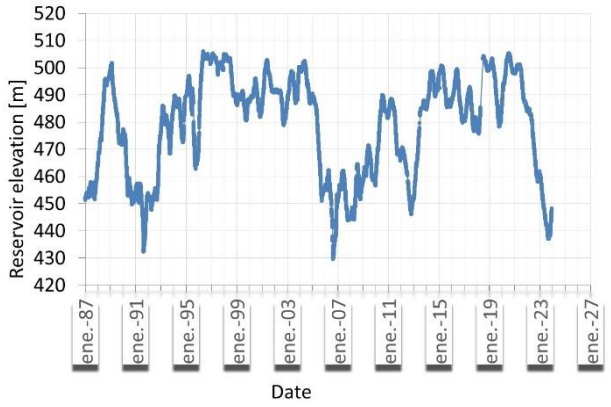

Figure 3. Reservoir level in time.

Again, the instability observed by accumulated displacements of the landslides, triggered by the drawdown, did not induce its abrupt acceleration predicted by the thermally-induced pore water pressurization.

During these twelve years, our effort has been addressed to gain further insight into the response of the landslide behaviour and the factors affecting its velocity, as well as its modelling through recently developed tools. With this aim, advances in numerical developments and the characterization of the soil of the sliding surface have been carried out.

1.2.1 Advanced modelling

The methodology presented by Pinyol et al. (2012) exhibited some limitations, especially regarding the definition of landslide geometry. The geometry had to be simplified and pre-defined by interacting wedges. In addition, the shear bands, where the thermal coupling may develop, had to be also imposed "a priori". At that time, no more sophisticated numerical tools allowing the simulation of thermally-induced accelerated landslides were available, to the knowledge of the authors. With the aim of overcoming such limitations, the thermal, mechanical, and hydraulically governing equations were implemented in numerical software suitable to model large displacements and deformations. The material point method (MPM) (Sulsky *et al*., 1994) was selected. This method can deal with large deformations and avoid the problems of mesh distortion associated with standard finite element methods thanks to two spatial discretizations: an Eulerian computational mesh, where the equations are solved and cover the whole domain, and Lagrangian material points that are used to discretise the mass of materials as well as to store all the relevant data (properties, independent and state variables) (Zhang *et al.,* 2017; Fern *et al.*, 2019). The material points can move during the calculation throughout the computational mesh according to the computed results (Figure 4).

The modelling of thermally-induced pressurization due to the dissipation in heat of the frictional work generated in shear bands required a new approach to avoid the pathological dependence on the computational mesh that appears when using the standard formulation. This limitation was solved by defining embedded numerical shear bands that develop as a result of the computed shear strains. In these embedded shear bands, the frictional work is computed. The thickness of the embedded joints, representing the thickness of the actual shear bands developed in the field, is imposed as an input parameter and does not depend on the size of the computational mesh. All the details of the developments for the MPM-based modelling of thermally accelerated landslides are presented in Pinyol *et al.* (2018).

The advances in numerical development consist of an MPM-based software able to introduce the thermo-hydro-mechanical couplings in the post-failure behaviour of landslides. In addition, this generalized numerical tool allows the implementation of additional improvements (i.e. non-constant properties, more advanced constitutive models, unsaturated conditions, and additional boundary conditions).

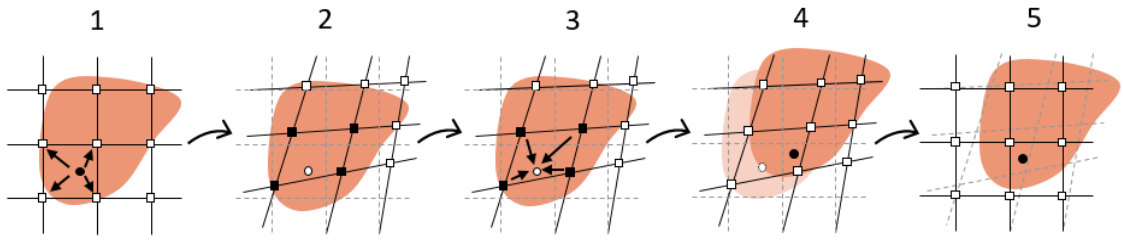

Figure 4. MPM discretization scheme and computational cycle: (1-2) all the physical properties of the continuum are transferred from MPs to the mesh nodes where governing equations are solved (lagrangian phase); (3-4) solutions are mapped back from nodes of the deformed mesh to MPs and their positions are updated (convective phase); (5) nodal displacements are discarded and the computational mesh is reset to the initial configuration (Di Carluccio, 2021).

1.2.2 An insight into shearing strength

Regarding the observed slow motion, the focus has been recently addressed to evaluate in more detail the nature of shear strength, which is a key factor controlling the behaviour of landslide velocity. The soil strength is far from being a constant property. For a given soil and pore fluid, it depends on stress state, pore pressure, accumulated strain, and strain rate (all of them are variables that may change during the landslide motion), as well as aging. Several contributions to these topics can be found in the literature.

In first-time failures, the available strength in shearing bands varies from peak to residual values when shearing strains accumulate, especially in soils with significant clay content (Lupini *et al*., 1981; Skempton, 1985; Stark & Eid, 1997). Residual strength controls the behaviour of ancient or reactivated landslides. In the first estimation of stability, a constant residual shear strength is adopted for the sliding surface. However, for more advanced analysis of the evolution of creeping slides, eventually evolving towards a rapid failure, such a simple assumption prevents a proper understanding of the observed behaviour.

One phenomenon invoked to explain the slow motion of landslides is the rate-hardening of shear strength of shear bands (a concept equivalent to viscous resisting forces). The increment of the strength with the shear rate can prevent the acceleration. Once a landslide becomes unstable, because of a non-equilibrated balance between acting and resisting forces, and accelerates, the increment of the strength (or viscous forces) with shearing velocity may lead to reducing the acceleration and, eventually, to a situation of constant creeping velocity even if the intensity of the triggering factors is maintained in time. Viscous resistant forces, proportional to the shearing rate, were considered by Angeli *et al.* (1996) and Corominas *et al.* (2005) to analyse the response of creeping landslides. Other approaches include the rate effect on the frictional angle (Bowden and Tabor, 1964; Mitchell, 1976; Rice & Ruina, 1983; Davis *et al.,* 1993; Wedage *et al.,* 1998b). Seguí *et al.* (2020) included also the strain rate effect on the friction angle in the energy-based approach, combined with thermal interaction due to frictional work.

From an extensive account of experimental work available in the literature (Tika *et al*., 1996; Saito et al., 2006; Scaringi & di Maio, 2016; Scaringi *et al*., 2018; Wang *et al*., 2020; Ma *et al*., 2021, Kohler et al., 2023) it is observed that the effect on the residual strength of varying the shearing velocity depends on the properties of the tested material and the range of the applied velocities. The effects observed can be positive, neutral, or negative, in the sense that increasing the shear rate, leads to a larger (positive) or smaller (negative) value of the residual strength, compared with the strength measured at very small deformation rates. Sometimes, no effect is observed (neutral).

In this paper, the effect of the shear strain rate on the residual strength is evaluated for different types of soils including the clay of the landslide discussed here. In case of a positive strength effect for the clay of the landslide analysed, this phenomenon may explain the slow velocity observed, because it could prevent its frictional heating-induced acceleration. These ideas were evaluated for planar and compound landslide by Alonso *et al*. (2016) and by Seguí *et al.* (2020).

Another factor affecting the variation of the available shear strength on the sliding surface discussed and evaluated in this paper is the temperature. Seguí & Veveakis (2021) evaluate a real case with the previously developed mathematical model and provide measurements of the temperature inside of the shear band.

Temperature increments induced by the frictional work, which may induce excess pore water pressure, as discussed before, may also affect the intrinsic friction. In addition, the temperature may be due to external factors. In the case of active landslides, the temperature on the sliding surface can be affected by atmospheric conditions, and its changes may become more relevant due to climate change. A few studies on this topic are available in the literature, although the interest in evaluating the effect of temperature on the strength of soils has grown in recent years.

The effect of the temperature on residual shear strength is evaluated by Bucher (1975), Shibasaki & Yamasaki (2010); Yavari *et al.* (2016); Shibasaki *et al.* (2017); and Loche & Scaringi (2023). Bucher (1975) concluded that the temperature effect was not relevant in two low-plasticity soils for temperatures ranging from 10 ◦C to 60 ◦C. The effect was observed more relevant in Shibasaki & Yamasaki (2010), who tested smectite-rich soil. They concluded that the tested soils exhibited less strength at a lower temperature under slow shearing velocities. This research was complemented by Shibasaki *et al.* (2017) where soils with different smectite content were sheared at different velocities (ranging from 0.0025 to 5 mm/min) at temperatures from 6 ◦C to 29 ◦C and normal stresses of 50, 100, 150, and 200 kPa. They concluded that the strength of smectite-bearing soils reduces at lower temperatures under relatively slow shearing rates (< 0.1 mm/min) whereas the effect is opposite under relatively high shearing rates (> around 0.1–0.5 mm/min): the soil strengthened when

temperature decreases. Soils without smectite content exhibited a slight weakening due to heating (and strengthening at cooling) at the whole range of shearing rates (0.0025–0.5 mm/min) applied.

Loche & Scarinigi (2023) evaluated the effect of temperature on two pure clays (ca-bentonite and kaolin) until temperature of 55ºC and shear rates of 0.018-44.5 mm/min. They conclude that the effect of the temperature depends on the type of clay, and, furthermore, the magnitude and sign of the temperature effect change with the rate of shearing. In the interpretation of the results, they incorporate the heating-induced swelling and contraction upon cooling.

To evaluate the effect of the temperature of the clay of the landslide analysed here, velocity- and temperature-controlled shearing tests were carried out. With the aim of getting a better understanding of the observed results, a systematic and consistent program of ring shear tests on samples of different soils characterized by different plasticity and grain size distribution was carried out.

1.3 Outline of the remainder of the paper

According to the above introduction, this paper first presents the main conclusions of the landslide analysis presented in Pinyol *et al.* (2012), and a discussion comparing the back-analysis, hypothesis, and prediction carried out at that time with the new field data.

A second section is addressed to show experimental data on the effect of the shearing rate and temperature on the residual strength.

Third, the landslide motion is evaluated by numerical modelling including internally-generated increments of temperature and potential pressurization of water. A sensitivity analysis is performed to evaluate the effect of some hypothesis and properties to prevent thermal acceleration, among them, the shear-rate hardening or temperature, based on the experimental data.

A section with conclusions and ongoing and future works closes the paper.

2 UPDATED ANALYSIS OF THE LANDSLIDE STABILITY

During the operation of the reservoir from 2009 until the present (2023), the landslide was monitored by means of manual inclinometers (some of them installed in newly excavated boreholes located close to the previous ones Figure 1), piezometers and surface displacements using geodesy, and INSAR technique.

2.1 Verification of the sliding surface position

It would have been desirable to verify the precise position of the sliding surface by means of inclinometric records. However, this was not possible because during the period analyzed before the publication of the 2012 paper, the inclinometers installed after the detection of the landslide did not provide relevant movement, except for inclinometer 3.1, located in the central part of profile III (Figure 1), in which 6 mm of accumulated displacement was recorded between December 2006 and December 2009.

The new inclinometric measurements made it possible to validate the position of the slip surface proposed in 2009 (Figure 1) which was considered in the stability analysis. The inclinometer measurements are not included here due to the limited space. Table 1 shows the depths of the sliding surface estimated in 2009, and the depth according to the more recent data. It should be noted that the estimated position of the rupture surface, according to geological studies and the interpretation of the shear surface in the borehole cores, fits well with inclinometer measurements. The only relevant difference is in the sliding surface position at the top of Profile II (SI 2-1). In this case, several shear surfaces were identified, and the position of the sliding surface selected for the calculations was the bottom of the clay layer and, it actually appears, according to the inclinometers, at the top.

The differences detected in the geometry and position of the landslide surface in the previous studies are not considered relevant in terms of the conclusion reached regarding the slope stability analyses.

Table 1. Estimated position and measurement of the sliding surface at the position of inclinometers.

Profile	Inclino-meter	Estimated depth in 2009 [m]	Average depth according to the relative motions observed in the inclinometers [m]
I	SI 1-1	4 and 14	7
	SI 1-2	25	22
II	SI 2-1	74	67
	SI 2-2	60	55
	SI 2-3	37	15
III	SI 3-1	41	40
	SI 3-2	28	24
	SI 3-3	17	10

2.2 Response of landslide to reservoir elevation

Slope stability analyses indicated that the slope is stable under the hypothesis of a hydrostatic pressure distribution inside the slope at the reservoir elevation. The safety factors obtained by limit equilibrium are relatively high as shown in Figure 5.

As verified by Pinyol *et al.* (2012), the lowering of the reservoir level is a cause of slope instability, especially when the drawdown reaches a high velocity and occurs after long periods in which the reservoir level is maintained at high levels. In this case, pore pressures in the clay are high and in equilibrium with the reservoir level. This situation explains the failure observed in 2006 due to the intense drawdown (Figure 3) and the lack of any symptoms of instability in the summers of 1991 and 2012. In addition, other factors such as the direct contribution of rainfall or the underground water supply from the upper part of the hillside can also increase the pressure and promote instability.

The more recent drawdown, initiated in the summer 2021, reached the lowest level in the summer 2023, (Figure 3), and triggered the instability of the landslide. According to INSAR measurements, displacements between November 2022 and August 2023, in the upper area of the slide between the position of profile I and II (Figure 1), were maximum and reached up to 40 mm, which corresponds to an average sliding speed of 4.5 mm/month.

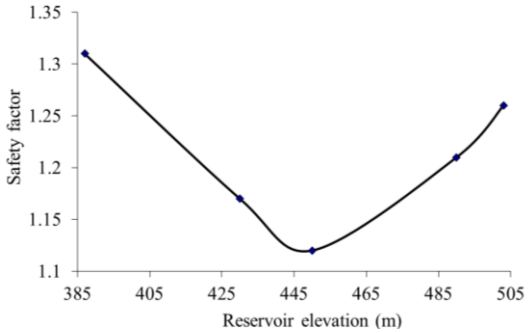

Figure 5. Safety factors calculated by limit equilibrium under a hydrostatic pressure distribution corresponding to a given reservoir level (Profile II).

According to the piezometer installed in SI 2-2 inside of the clay layer, the pore water pressure remained relatively high during the last drawdown (2022-2023), indicating that the process of dissipation of water pressure is slower than the drawdown velocity. On the contrary, the pressure registered in the deepest sensor, inside of the rock unit, follows the level of the reservoir almost immediately. It was also observed, between 2006 and 2009, that the pressure of the limestone and sandstone strata, above and below the clay layer, is mainly controlled by the level of the reservoir at low elevations, an indicator of its high permeability.

The accumulated excess pore water pressure on the clay layer was significantly high when the water level of the reservoir dropped from 480 to 440 m in 2022. It should be noted that drawdowns in the range of relativelly low elevations (lower than 500 m.a.s.l.) lead to the accumulation of excess water pressures larger than a drawdown, of the same magnitude, between higher reservoir elevations. The reason is that the stress relief due to changes in the total stress, because of the removal of the water weight induces a water pressure discharge and, therefore, an instantaneous reduction in pore water pressure. This effect is greater at higher reservoir levels where the loss of total stress directly affects the submerged area. Drops in water level from low levels only affect the area near the foot of the slide, and therefore, the pressure accumulated in upper zones inside of the slope does not reduce instantaneously due to the stress relief and must be dissipated by flow, which takes time.

3 TESTED MATERIALS AND EXPERIMENTAL PROGRAM

Six different types of soils were tested to evaluate the effect of the shear rate and temperature (Figure 6). The clay corresponds to the material where the sliding surface of the landslide was localized. These materials were selected to have a wide range of soils in terms of physical properties and mineralogical composition. Figure 7 and Figure 8 show their grain size distributions and plasticity.



Figure 6. Tested materials.

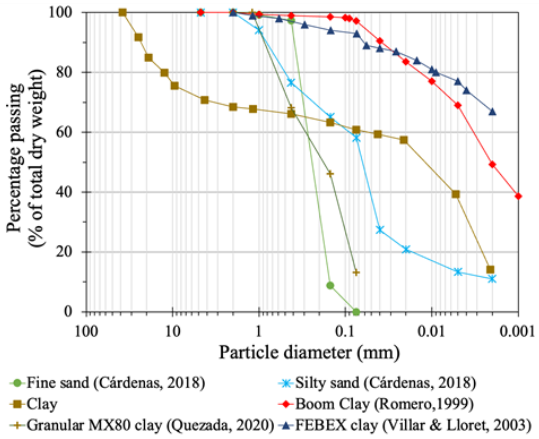

Figure 7. Grain size distribution of tested materials.

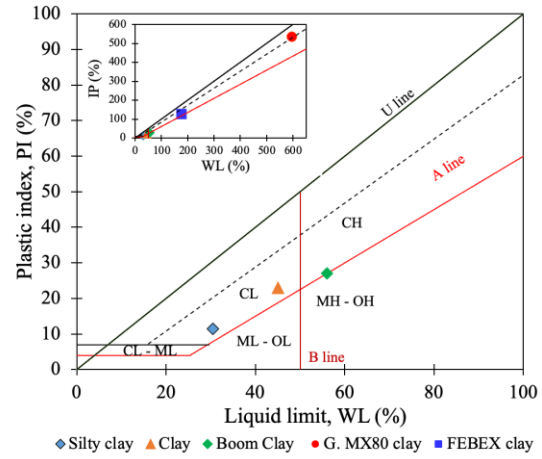

Figure 8. Plasticity chart of tested clayey materials.

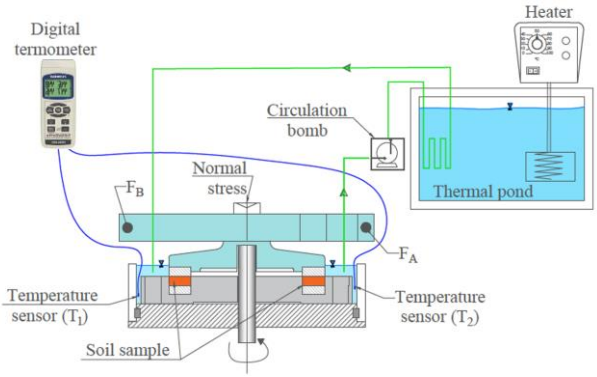

Figure 9. Control temperature system in the Bromhead shearing cell.

Shear tests at different shearing velocities and temperatures were carried out in a modified Bromhead ring shear equipment (Bromhead, 1979). The temperature conditions of the test specimens were controlled by cooling or heating water within the thermal bath surrounding the cell (Figure 9). The soil temperature is assumed to be equal to the bath water due to the high thermal conductivity of metal surrounding the soil and the slow rate of temperature changes.

The specimens were manufactured with the fraction of the remolded soils that pass through an ASTM#40 sieve (0.425 mm). Their initial water contents were small and corresponded to their hygroscopic conditions prevailing in the laboratory (T≈20 ºC, RH=60%). The powder obtained was placed carefully inside the shearing cell and compacted using a controlled displacement press machine at a relatively low velocity until reaching 10 MPa of normal stress. In the case of the bentonite samples, Boom, G.MX80, and FEBEX clay, the normal stress increased to a small value to maintain a relatively low density and reduce the swelling during subsequent wetting.

The tests at constant temperature and increasing shear velocity were carried out at dry conditions to reduce the wall friction that is generated in saturated specimens while the soil samples are extruded from the shearing zone during the test. The leakage of the material is a limitation of the shear box because of the gap between the fixed upper part and the rotating lower part. To prevent the leakage of soil, the gap can be sealed as discussed in Kohler et al. (2023). However, testing dry samples also avoids the effects of the generation of excess pore water pressure due to the contraction or dilation of the sample during shearing and to the temperature increasing by friction, especially at relatively large velocities. The combined effects make it difficult to isolate the effect of the shearing rate.

However, it should be noted that the residual strength measured includes the effect of suction on the strength (Lai *et al.,* 2010; Merchan *et al*., 2011; Hu *et al.,* 2018; Hoyos *et al*., 2020), which is expected to be substantially higher than the strain rate effect.

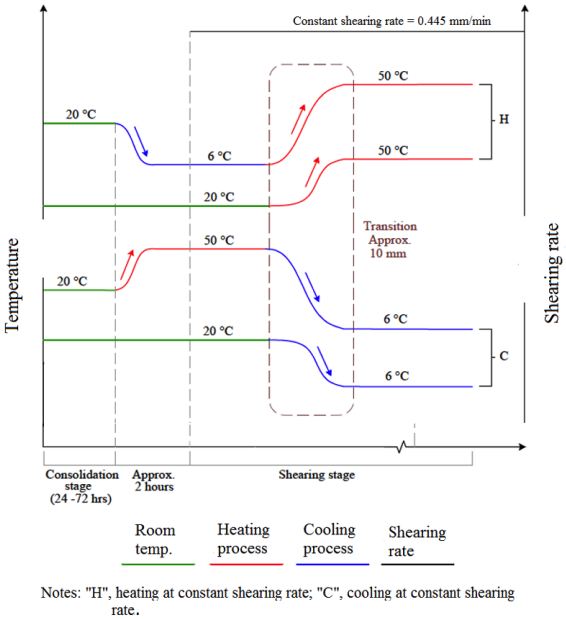

Notes: "H", heating at constant shearing rate; "C", cooling at constant shearing rate.

Figure 10. Schematic experiment stages for shearing rate and temperature-controlled tests (García et al. 2023).

Two tests were carried out for each material at two normal stresses (100 kPa and 200 kPa). The shearing stage under constant normal stress starts with a slow velocity (v_0^l) of 0.089 mm/min until the soil reaches residual conditions. Later on, 4 velocity steps were applied in the following ascending order: 0.445, 2.226, 11.13, and 45 mm/min. They range between moderate to rapid landslide according to Varnes classification (Hungr *et al.,* 2014).

In the case of temperature-controlled tests at constant shearing velocity, after compaction of the dry samples in the shearing cell, all the samples were loaded to the target normal stress of 100 kPa, a value that remained constant during the shearing test. Subsequently, the samples were saturated in the shear box by immersion at room temperature (≈20 ºC). The tests were carried out at 0.445 mm/min. From the initial condition of room temperature (≈20 ºC), temperature changes ranging between 6ºC to 50 ºC were applied. The transient period of temperature before equilibrium lasted approximately thirty minutes. Figure 10 shows schematically the stages applied in the temperature-controlled tests.

4 SHEAR RATE EFFECTS

Figure 11 shows the results for the Garumnian landslide clay. The large values obtained, compared with the 12º measured in the saturated direct shear test, is a consequence of the well-known effect of suction on the strength. For the range of applied shearing velocities the frictional angle increased up to 2º.

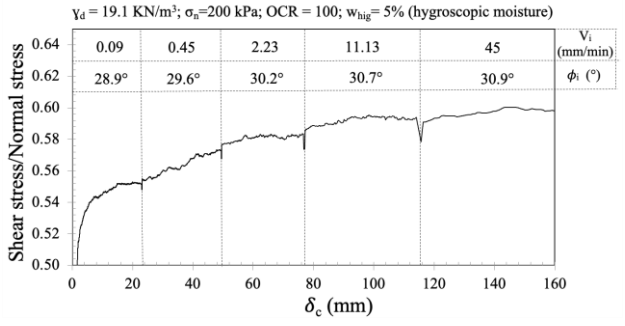

Figure 11. Ratio between residual shear strength (τ) and normal stress (σ_n) in ring shear tests at different shearing velocities on remolded samples of the clay of the landslides at hygroscopic humidity.

Figure 11 shows the results in terms of residual strength obtained at different shearing velocities normalized by the value obtained at slow (minimum) velocity applied at the beginning of the test for all the materials. During some tests, it was observed some dispersion in the shear stress/displacement relationship. The criteria to define the residual strength for each displacement rate was selected to be the minimum strength after the measured first maximum (peak) strength. The effect of normal stress is not discussed here. In general, all materials experienced a positive rate effect (strengthening behaviour), except for the silty clay that, in three tests described a negative rate effect.

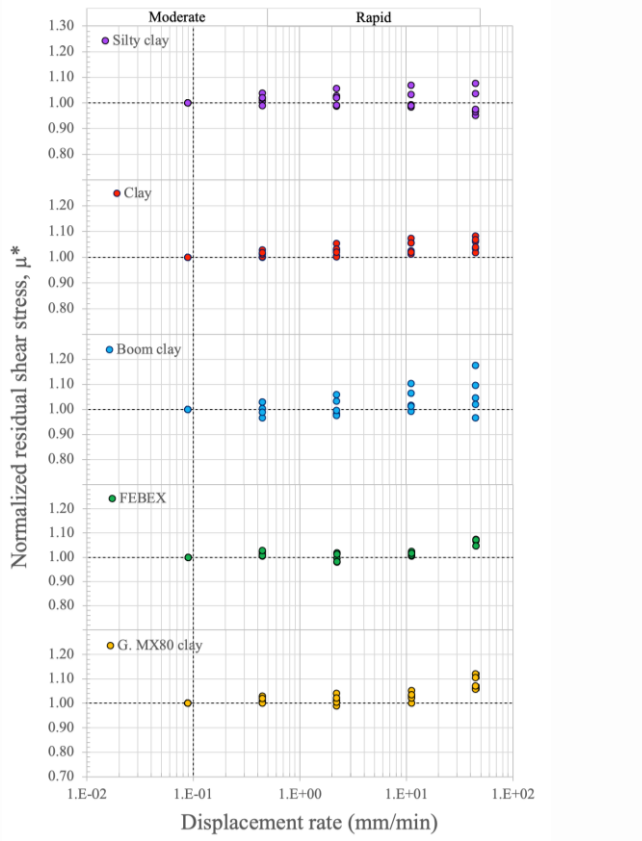

Figure 12. Normalized residual shear stress variation with the displacement rate measured in ring shear tests.

5 TEMPERATURE EFFECTS

The temperature effect was evaluated in 67 samples of the one-component soil-type. Temperature steps of increasing and decreasing the temperature in the range of 6ºC and 50ºC were applied.

Figure 13(a) shows one of the experimental results for the cooling test on the landslide clay sample. Initially, the temperature is equal to 51ºC and at a certain time during shearing, it is reduced to 6ºC. To show the temperature evolution without oscillations, the measured temperature is fitted by an exponential function in terms of accumulated displacement. At the beginning of the test at a constant temperature, the remolded sample exhibits a softening response. Initially τ increases linearly up to a peak value and, afterward, the shearing strength reduces gradually with the accumulated displacement increment towards a

residual value. The applied step of temperature induces a transient regime and a subsequent steady-state stabilization.

Figure 13(b) shows the response of a Boom clay sample subjected to heating (from 5ºC to 51ºC).

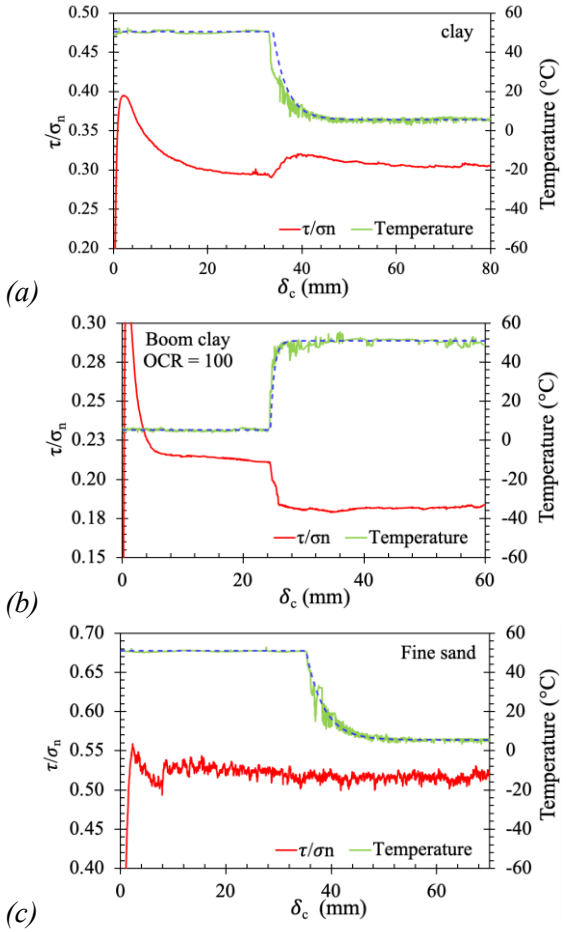

Figure 13. Normalized shear strength (τ/σ_n) and measured and fitted temperature during shearing displacement (u) at the constant shearing rate of 0.445 mm/min and normal stress of 100 kPa for (a) the clay of the landslide; (b) Boom clay; (c) Fine sand. (García et al. 2023).

Again, an initial softening response is observed, as well as the instantaneous change of the strength with the temperature change.

In both clays, increments of temperature in the range evaluated indicate that an increase in temperature leads to a decrease in strength, and an equal and opposite trend is observed when temperature decreases. A cooling-hardening and heating-softening is observed.

The response due to temperature changes was similar in FEBEX clay. Samples of G. MX80 exhibit a behaviour that does not follow the general trends observed in the rest of the samples. G. MX80 samples continuously expanded during shearing, which was not observed in the rest of the tests. In the case of fine sand samples, the effect was almost negligible (Figure 13(c)).

The temperature effect is plotted by transforming all the values of the friction coefficients into their equivalent friction angle. It is convenient to plot the increment of the friction angle measured in each test when a controlled change of temperature is applied. The slope, $\Delta\phi/\Delta T$, for each soil (Figure 14) increases from an essentially zero slope (Castelldefels sand) to a higher slope when fine's content and plasticity increase (except for G. MX80 samples) for the evaluated temperature range (from 6ºC to 55ºC and from 55ºC to 6ºC).

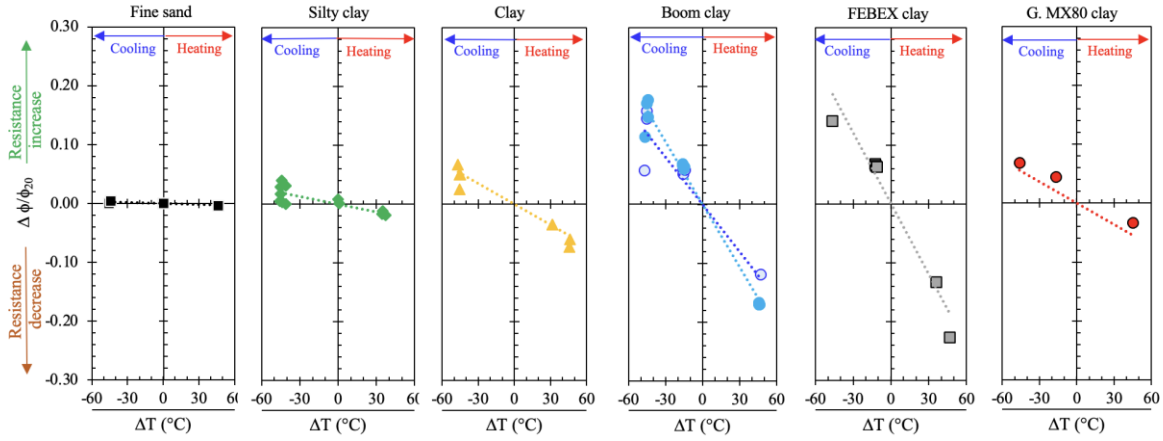

Figure 14. Effect of temperature variation (ΔT) on the residual friction angle variation ($\Delta\phi$) of the basic soils measured at a constant shearing rate of 0.445 mm/min. Experimental values and trend line (García et al. 2023). ϕ_{20} is the residual friction angle for a temperature of 20ºC.

6 MODELING LANDSLIDE RUN-OUT INCLUDING THERMAL AND STRAIN RATE EFFECTS WITH MPM

6.1 Features included in the MPM modelling and its effects

The analysis presented by Pinyol *et al.* (2012) evaluated the run-out including the thermal acceleration of the landslides with a simple geometry of two blocks (Figure 15) obtaining the run-out indicated in Figure 2. The modelling in MPM allowed us to introduce: (a) a more realistic cross- section (Figure 16) without predefining the basal sliding surface and internal shearing planes; (b) modelling of the rock stratum above the clay layer whose elastoplastic properties follow a strain-softening Mohr-Coulomb model; (c) incorporation of water as an incompressible (high volumetric stiffness) material and no shearing strength.

These modifications added to the initial modelling some features that contributed to preventing the acceleration of the landslide because of different causes:

(a) The basal landslide failure, which is part of the solution, follows the counter-slope that the clay layer exhibits at the lower part of the landslide because of the syncline. It helps to stabilize the unstable mass, unlike the planar shearing surface pre-defined in the two-block model.

(b) The advance of the landslide motion requires the generation of shear localization bands inside of the mobilized mass, a necessary result to get a movement kinematically admissible. These shearing planes can be observed in Figure 17. The resistance provided by these shearing surfaces plans, developing in a strain softening material, was not included in the first analysis.

(c) The weight and inertia of the reservoir water, incorporated in the MPM, oppose the movement and tend to reduce its velocity.

However, these additional considerations included in the MPM calculation cannot prevent the acceleration of the landslide.

The resulting run-out and velocity are shown in Figure 17 in terms of displacements and, in Figure 18, in terms of velocity versus displacements. The initially predicted maximum velocity of 16 m/s reduces to 12 m/s in the new calculation and the unstable mass stops after 120 m of run-out. This is smaller than the distance predicted previously.

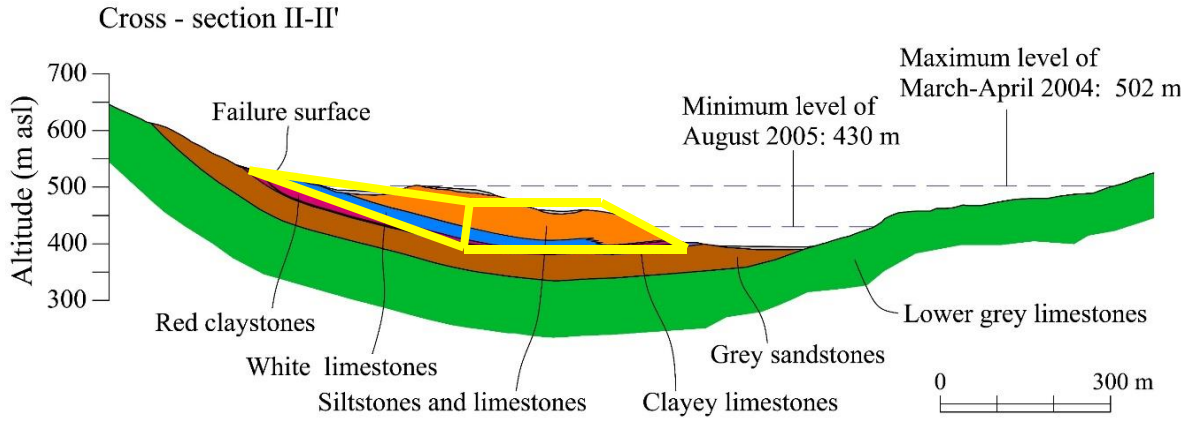

Figure 15. Two-block geometry for simplified analysis of the thermal acceleration of the landslide.

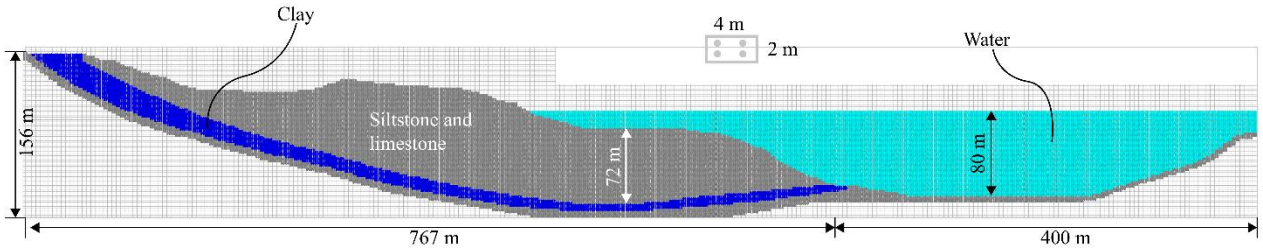

Figure 16. MPM discretization of the landslide: computational mesh and material points.

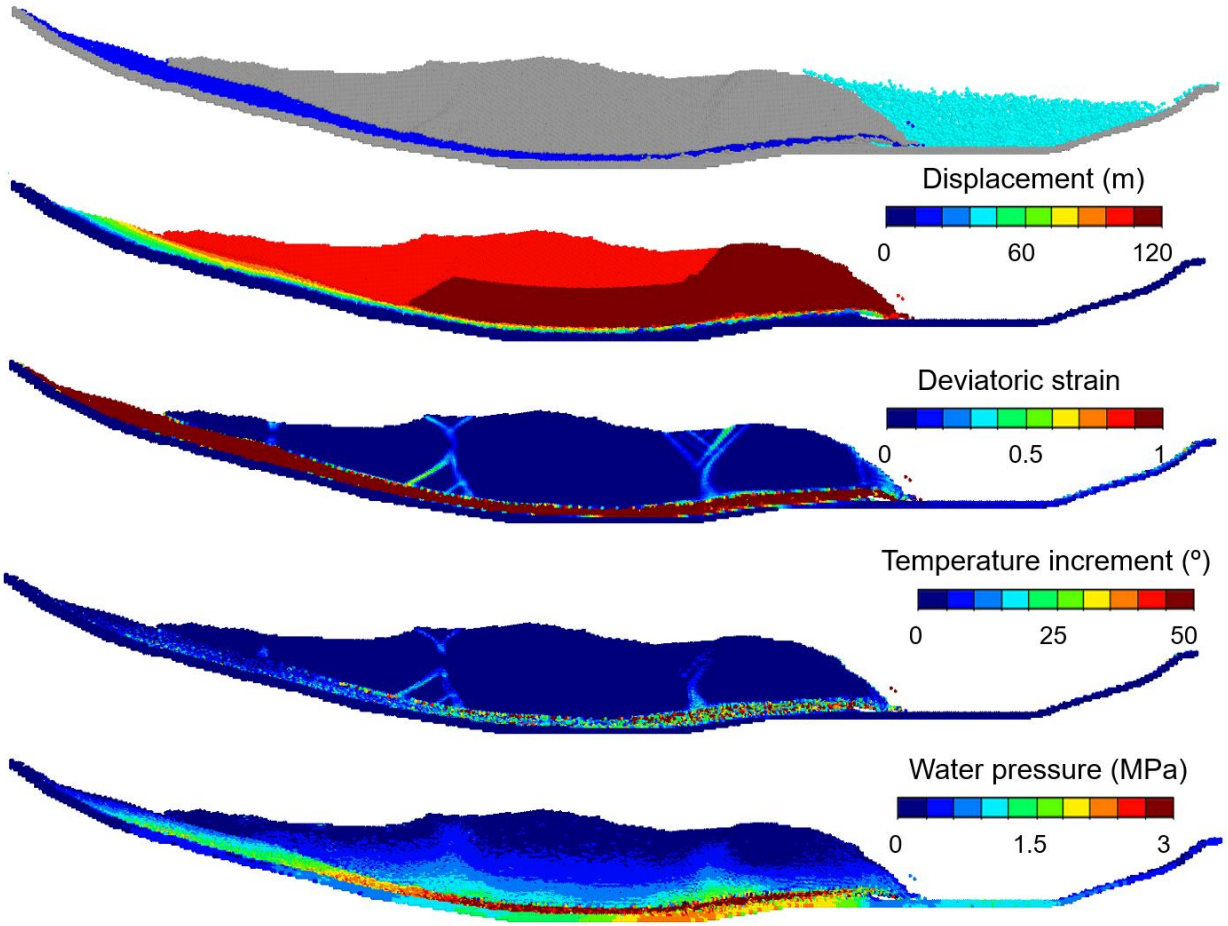

Figure 17. MPM results considering first estimation of parameters, without including shear rate effects.

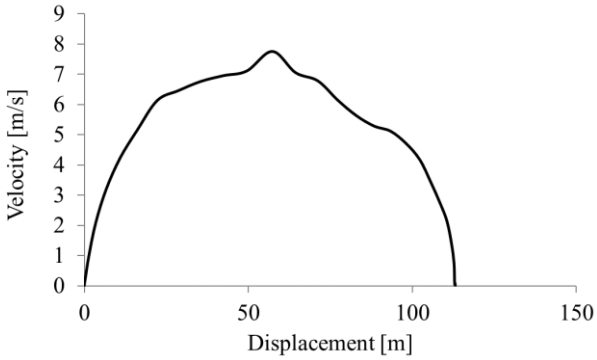

Figure 18. Displacement and velocity of the toe of the landslide calculated by MPM considering the first estimation of parameters and without including shear rate effects.

Figure 17 shows also the temperature increments and pore water pressure generated due to thermal effects. Note that increments of temperature are also observed in the mobilized rock along the generated shearing plans and not only in the basal shearing band. However, the subsequent induced excess pore water pressures are not so significant as those observed in the clay layer due to its dissipation during the motion because of the high permeability of the rock (10-6 m/s, 5 orders of magnitude larger than the permeability of the clay).

6.2 Review of some properties and shear strain effects

The MPM-based model of the landslide including thermal effects also predicted a large acceleration not observed in the field even if considering additional factors. The previously presented MPM results came from a pessimist estimation, considering the selected values of relevant parameters that favour the acceleration of the landslide due to thermal effects. The permeability value was selected as $5 \cdot 10^{-11}$ m/s, being the value measured in the laboratory, despite knowing that in the field the permeability is usually higher. A larger value, around 10^{-10} – 10^{-8} m/s, may be likely a good estimation of the field permeability. A larger permeability allows a larger dissipation of the thermal pressurization of pore water, generated during the motion, and reduces the thermally-induced acceleration.

The thickness of the basal shear band was assigned to be 5 mm. As discussed in Pinyol *et al.* (2012), it is difficult to estimate accurately the thickness of the

shearing band, even if recovered samples are examined. A larger value could have been considered.

On the other hand, to incorporate the strain-rate effects, hardening of the frictional angle is implemented in the MPM code by means of the following general equation, which also includes strain softening:

$$\phi' = \phi'_{res} + \left(\phi'_{peak} - \phi'_{res}\right) e^{-\eta \varepsilon_d^p} + \bar{\phi}' \left(1 - e^{-\alpha \dot{\varepsilon}_d^p}\right) \quad (1)$$

where, ϕ'_{peak} and ϕ'_{res} are the maximum and minimum effective friction angles associated with shearing at a slow strain rate, η is a model parameter that controls the loss of strength from the peak to residual friction at slow rates, $\bar{\phi}'$ is the maximum increment of the effective friction angle due to rate effects, and α is the parameter controlling the rate strain effects. ε_d^p is the deviatoric plastic strain and $\dot{\varepsilon}_d^p$ is the deviatoric plastic strain rate.

The selected law (Ec. 1) is expressed in terms of deformation because constitutive models are implemented in terms of deformation and stress. However, the laboratory experiments provide the strength variation in terms of shearing displacements. To correlate deformations and relative displacements, the thickness of the shear band should be estimated.

Considering these aspects, an updated case is simulated, if compared with the previous MPM model, in which the clay permeability is assumed equal to 10^{-8} m/s and the thickness of the shear band equal to 200 mm.

In addition, the strain-rate hardening law (Eq. (1)) is calibrated, inspired by the velocity-controlled ring shear test carried out on the clay samples of the landslide presented above. The maximum increment of friction angle with the shear strain is assumed to be equal to $\bar{\phi}'$=2º. $\phi'_{res}$is equal to 11.5º, and no strain softening is included. Figure 20 shows the friction angle evolution with the rate of shear strain. The value of $\alpha=10^{-7}$ 1/s has been selected. The residual friction angle varies from a minimum value, 11.5º, for shear strain rates smaller than 10^{-9} s^{-1}, to a maximum value of 13.5º when the strain rate reaches values of 10^{-6} s^{-1} (approximately). This range of shear strains corresponds to $1.2 \cdot 10^{-5}$ mm/min (= 0.5 mm/month) and $1.2 \cdot 10^{-2}$ mm/min (= 518 mm/month) for the assumed shear band thickness value of 200 mm. This threshold covers the measured velocities in the landslide, around 10 mm/month (= $2.3 \cdot 10^{-4}$ mm/min).

The shear strain rate-dependent law of friction angle introduced into the calculations has been inspired by laboratory results. However, one should be aware of the limitations of the available experimental data. Unfortunately, the increase in resistance is obtained for a range of speeds in the order of 1 mm/min (= 43200 mm/month), much higher than the speeds recorded in the field.

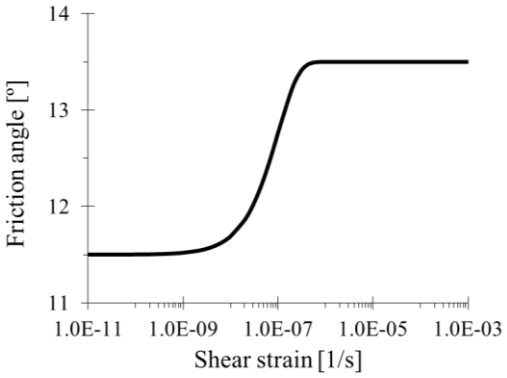

Figure 19. Shear strain-dependent friction angle considered in MPM calculation.

The results obtained by MPM calculation models are presented below. Different cases are distinguished to highlight the effect of the phenomena considered: thermal interaction and shear strain rate hardening (Table 2). Case 1 is the same as the case presented above, but with a shear band thickness of 200 mm instead of 5 mm. Case 2 includes, with respect to Case 1, the positive effect of the shear strain rate. In Case 3, the thermal interaction and shear strain rate effects are disabled in the code. Finally, in Case 4, shear strain rate hardening is included, but the possibility of thermal interaction is nullified.

Figure 21 shows the evolution of the movement in terms of displacement and velocity of a material point located in the landslide toe for Case 1. The maximum velocity achieved is reduced with respect to the MPM results previously obtained. This is explained because in Case 1 a thicker shear band is considered. The significant velocities and displacements calculated for Case 1 were not observed in the field.

Strain rate hardening leads to completely different results (Case 2) (Figure 21). The increased strength prevents the acceleration of the slide. Thermal effects, although activated in Case 2, do not lead to the accumulation of relevant excess pore pressures to induce a loss of clay shear strength. This can be seen in Figure 22, which shows the evolution of the excess pore pressure calculated at three points inside the clay layer for Cases 1 and 2. In Case 1, pressure increase of the order of MPa leads to a sharp drop in frictional resistance (Figure 22(a)). However, in Case 2, the pressure does not exceed a few kPa (Figure 22(b)), irrelevant values compared to the effective stresses applied along the sliding surface located at a depth of several tens of meters in the central part.

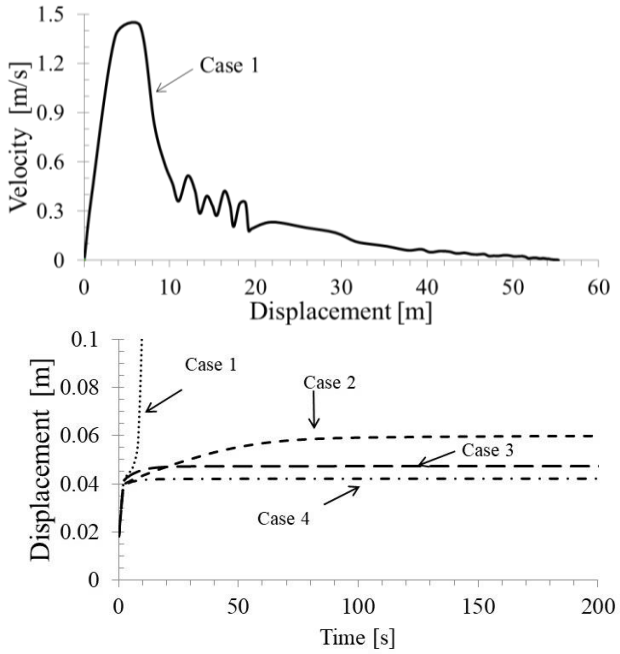

Figure 20. Velocity and displacement of the toe of the landslide, calculated by MPM for different cases (Alvarado et al. 2019).

Table 2. Cases analysed in MP and incorporated effects.

Case	THM	Strain rate hardening
Case 1	Yes	No
Case 2	Yes	Yes
Case 3	No	No
Case 4	No	Yes

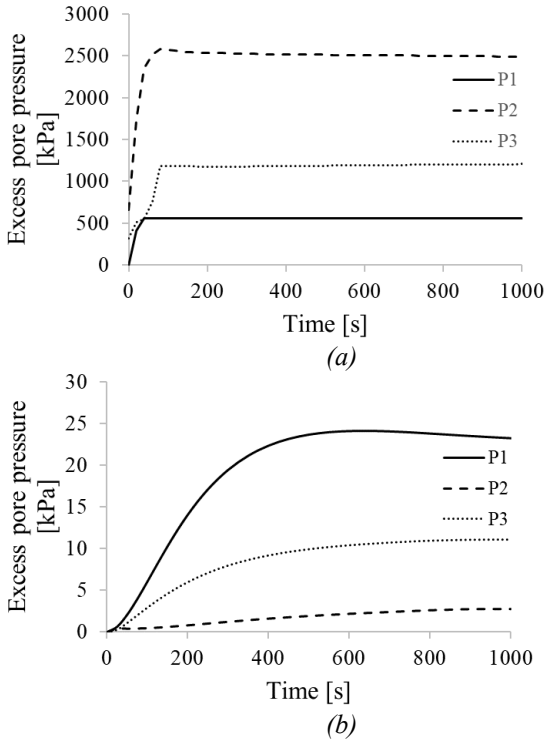

Figure 21. MPM calculated excess pore pressure in materials points P1, P2, and P3. (a) Case 1; (b) Case 2 (Alvarado et al. 2019).

According to these results, the shear strain rate hardening can prevent the acceleration of the landslide. The motion stops after a displacement of 6 cm. A new equilibrium position is restored. The thermal-hydro-mechanical effects are not developed in Case 2. The behavior observed in this case (Case 2) is similar to the behaviour obtained in Cases 3 and 4 in which heat generation by frictional work is disabled. As expected, the displacement is the smallest one in Case 4.

7 CONCLUSIONS

The paper describes the research work developed to estimate the risk of acceleration of a large landslide affected by reservoir level variations and, in particular, by a rapid drawdown scenario. The reported results cover almost 20 years. The landslide was reactivated twice in this period, in both cases as a consequence of a rapid drawdown (2006 and 2023). The working methodology departed from previous standard practice, largely based on the calculation of safety factors. The described approach followed two lines of thought: (a) the application of a calculation procedure (MPM) capable of dealing with large displacements, in a dynamic formulation of the problem; and (b) a review of phenomena controlling shear strength, namely strain rate effects and temperature.

A comprehensive set of shearing tests at controlled strain rate and temperature shows that friction increases when the shearing rate increases and decreases when temperature increases. The strain rate effect contributes to stabilizing (in the sense of avoiding the acceleration) a creeping landslide. Increasing temperature leads to a decrease in residual friction, an effect progressively more pronounced when soil plasticity increases.

Temperature changes have two different effects on soil strength: (a) an 'intrinsic' effect that may be conceptually understood as a modification of the soil skeleton, and (b) an induced effect, especially in saturated (clay) soils, because temperature dilates the water and, in impervious soils, it will induce pore water pressure increments, a reduction in effective stress, and a decrease of shear strength. This phenomenon and its effects on landslide mobility were explored in the previous contribution mentioned in the paper. Note that the two mentioned effects of temperature, intrinsic and water pressurization, go in the same direction, namely increasing the risk of acceleration.

The reported experimental findings go in parallel with the application of the results to modelling the expected behaviour of the landslide. The initial MPM

calculation procedure was upgraded to include the favourable effect of strain rate and the thermally-induced pore pater pressurization of the sliding surface material as a result of the frictional work and its dissipation in temperature increase.

The results of sensitivity analysis that combines the opposite effects of thermal pressurization and shearing rate show that the risk of a fast acceleration of the landslide is small provided its creeping velocity remains below a critical value. Further research is needed to incorporate strain rate, intrinsic temperature, and thermal pore water pressurization effect into the computational model.

8 ACKNOWLEDGEMENTS

Acknowledge the support of Ministeri de Ciència i Innovació (MICIN), Agencia Estatal de Investigación (AEI) and el Fons Europeu de Desenvolupament Regional (FEDER) in the framework of the research project PID2022-141429OB-I00. The first author, Associate Professor Serra Húnter, gratefully acknowledges the funding from the Departament de Recerca and Universitats de la Generalitat de Catalunya.

REFERENCES

Alonso, E.E., and Pinyol, N.M. (2010). Criteria for rapid sliding I. A review of Vaiont case. *Engineering Geology*, 114 (3–4): 198–210. https://doi.org/10.1016/j.enggeo.2010.04.018.

Alonso, E.E., Zervos, A., and Pinyol, N.M. (2016). Thermo-poro-mechanical analysis of landslides: from creeping behaviour to catastrophic failure. *Géootechnique,* 66 (3): 202–219. https://doi.org/10.1680/jgeot.15.LM.006.

Alvarado, M., Pinyol, N.M. and Alonso, E.E. (2019). Landslide motion assessment including rate effects and thermal interactions: revisiting the Canelles landslide. *Canadian Geotechnical Journal*, 56 (9): 1338–1350. https://doi.org/10.1139/cgj-2018-0779.

Angeli, M.-G., Gasparetto, P., Menotti, R.M., Pasuto, A. and Silvano, S. (1996). A visco-plastic model for slope analysis applied to a mudslide in Cortina d'Ampezzo, Italy. *Quarterly Journal of Engineering Geology and Hydrogeology*, 29 (3): 233-240. https://doi.org/10.1144/GSL.QJEGH.1996.029.P3.06.

Bowden, F.P. and Tabor, D. (1964). Friction and Lubrication of Solids, Part II. Oxford University Press, London.

Bromhead, E., (1979). A simple ring shear apparatus. *Ground Eng.* 12 (5): 40–44.

Bucher, F. (1975). *Die Restscherfestigkeit natürlicher Bo ̈den, ihre Einflussgro ̈ssen und Beziehungen als Ergebnis experimenteller Untersuchungen*. PhD thesis, ETH Zurich. https://www.research-collection.ethz.ch/handle/20.500.11850/135170.

Cárdenas Díaz, O. E., 2018. Estudio del comportamiento de colapso en arenas arcillosas bajo un estado generalizado de tensiones. PhD thesis. Universitat Politècnica de Catalunya (UPC). http://hdl.handle.net/10803/663332.

Corominas, J., Moya, J., Ledesma, A., Lloret, A., and Gili, J.A. (2005). Prediction of ground displacements and velocities from groundwater level changes at the Vallcebre landslide (Eastern Pyrenees, Spain). *Landslides*, 2 (2): 83-96. https://doi.org/10.1007/s10346-005-0049-1.

Code_Bright (2024). https://deca.upc.edu/en/projects/code_bright/code_bright.

Davis, R.O., Desai, C.S. and Smith, N.R. (1993). Stability of motions of translational landslides. *Journal of Geotechnical Engineering*, 119 (3): 420‑432. doi:10.1061/(ASCE)0733-410(1993)119:3(420).

Di Carluccio, G. (2021). Dynamic large deformation modelling of soils including static liquefaction. *PhD thesis,* Universitat Politècnica de Catalunya. http://hdl.handle.net/10803/675540.

Fern, J., Rohe, A. and Soga, E.A. (2019). *The Material Point Method for Geotechnical Engineering: a Practical Guide*. CRC Press. https://doi.org/10.1201/9780429028090.

Hoyos, L.R., Yepes, J.E., Velosa, C.L. and Puppala, A.J. (2020). Unsaturated shear strength of compacted clayey soil via suction-controlled ring shear testing. In: *E3S Web of Conferences, vol. 195. EDP Sciences*, p. 03024. https://doi.org/10.1051/e3sconf/ 202019503024.

Hungr, O., Leroueil, S. and Picarelli, L. (2014). The Varnes classification of landslide types, an update. *Landslides,* 11: 167–194. https://doi.org/10.1007/s10346-013-0436-y.

Hu, W., Scaringi, G., Xu, Q., Van Asch, T.W., Huang, R. and Han, W. (2018). Suction and rate-dependent behaviour of a shear-zone soil from a landslide in a gently-inclined mudstone-sandstone sequence in the Sichuan basin, China. *Engineering Geology*, 237: 1–11. https://doi.org/10.1016/j.enggeo.2018.02.005.

Kohler, M., Hottiger, S., and Puzrin, A.M. (2023). Rate, Water Pressure, and Temperature Effects in Landslide Shear Zones. *Journal of Geophysical Research: Earth Surface*, 128 (9). https://doi.org/10.1029/2023JF007220.

Lai, X., Wang, S., Qin, H. and Liu, X. (2010). Unsaturated creep tests and empirical models for sliding zone soils of Qianjiangping landslide in the Three Gorges. *J. Rock Mech. Geotech. Eng.* 2 (2): 149–154. https://doi.org/10.3724/SP.J.1235.2010.00149.

Lupini, J.F., Skinner, A.E. and Vaughan, P.R. (1981). The drained residual strength of cohesive soils. *Géotechnique,* 31 (2): 181-213. https://doi.org/10.1680/geot.1981.31.2.181.

Garcia, L.M., Pinyol, N.M., Lloret, A. and Soncco, E.A. (2023). Influence of temperature on residual strength of clayey soils. *Engineering Geology*. (323), 107220. https://doi.org/10.1016/j.enggeo.2023.107220.

Loche, M. and Scaringi, G. (2023). Temperature and shear-rate effects in two pure clays: Possible implications for

clay landslides. *Results in Engineering*, 20, 101647. https://doi.org/10.1016/j.rineng.2023.101647.

Ma, J., Zhao, X., Li, S. and Duan, Z., (2021). Effects of high shearing rates on the shear behavior of saturated loess using ring shear tests. *Geofluids*, 1-12. https://doi.org/10.1155/2021/6527788.

Merchan, V., Romero, E. and Vaunat, J. (2011). An adapted ring shear apparatus for testing partly saturated soils in the high suction range. *Geotech. Test. J.*, 34 (5): 433–444. https://doi.org/10.1520/GTJ103638.

Mitchell, J.K. (1976). *Fundamentals of Soil Behaviour*. John Wiley & Sons, New York, USA.

Pinyol, N.M., Alonso, E.E. and Olivella, S. (2008). Rapid drawdown in slopes and embankments. *Water Resources Research* 44, W00D03. Special issues on: Hydrology and mechanical coupling in earth sciences and engineering: interdisciplinary perspectives. https://doi.org/10.1029/2007WR006525.

Pinyol, N.M. and Alonso, E.E. (2010). Criteria for rapid sliding II. Thermo-hydro-mechanical and scale effect in Vaiont case. *Engineering Geology*, 114 (3–4): 211–227. https://doi.org/10.1016/j.enggeo.2010.04.017.

Pinyol, N.M., Alonso, E.E., Corominas, J. and Moya, J. (2012). Canelles landslide: modelling rapid drawdown and fast potential sliding. *Landslides*, 9(1): 33–51. https://doi.org/10.1007/s10346-011-0264-x.

Pinyol, N.M., Alvarado, M., Alonso, E.E. and Zabala, F. (2018). Thermal effects in landslide mobility. *Geotechnique*, 68 (6): 528–546. https://doi.org/10.1680/jgeot.17.P.054.

Quezada, C., 2020. Hydro-mechanical characterisation of a mixture of sand/bentonite (80/20). *Master Thesis*. UPC. http://hdl.handle.net/2117/342956.

Rice, J.L. and Ruina, A.L. (1983). Stability of steady frictional slipping. *J. Appl. Mech*., 50: 343-349.

Romero, E., Gens, A., Lloret, A., 1999. Water permeability, water retention and microstructure of unsaturated compacted Boom clay. *Engineering Geology*, 54 (1-2): 117-127. https://doi.org/10.1016/S0013-7952(99)00067-8.

Seguí, C., Rattez, H. and Veveakis, M., (2020). On the stability of deep-seated landslides. The cases of Vaiont (Italy) and Shuping (Three Gorges Dam, China). *J. Geophys. Res. Earth Surf.,* 125, e2019JF005203. https://doi.org/10.1029/2019JF005203.

Seguí, C. and Veveakis, M. (2021). Continuous assessment of landslides by measuring their basal temperature. *Landslides*, 18 (May): 3953–3961. https://doi.org/10.1007/s10346-021-01762-x.

Skempton, A.W. (1985). Residual strength of clays in landslides, folded strata and the laboratory. *Géotechnique*, 35 (1): 3–18. https://doi.org/10.1680/geot.1985.35.1.3.

Stark, T.D. and Eid, H.T. (1997). Slope stability analyses in stiff fissured clays. *J. Geotech. Geoenviron.,* 123 (4): 335–343. https://doi.org/10.1061/(ASCE)1090-0241(1997)123:4(335).

Saito R, Fukuoka, H. and Sassa K. (2006). Experimental Study on the Rate Effect on the Shear Strength. In: *Disaster Mitigation of Debris Flows, Slope Failures and Landslides*. Tokyo, Japan; 421-427.

Scaringi, G. and di Maio, C. (2016). Influence of Displacement Rate on Residual Shear Strength of Clays. *Procedia Earth and Planetary Science*., 16: 137-145 https://doi.org/10.1016/j.proeps.2016.10.015.

Scaringi, G., Hu, W., Xu, Q. and Huang, R. (2018). Shear-rate-dependent behavior of clayey bi-material interfaces at landslide stress levels. *Geophysical Research Letters*, 45, 766–777. https://doi.org/10.1002/2017GL076214.

Shibasaki, T. and Yamasaki, T. (2010). Experimental investigation on temperature effect on residual strength characteristics of soils. [in Japanese]. *J. Jpn. Landslide Soc*., 47 (5): 255–264. https://doi.org/10.3313/jls.47.255.

Shibasaki, T., Matsuura, S. and Hasegawa, Y. (2017). Temperature-dependent residual shear strength characteristics of smectite-bearing landslide soils. *J. Geophys. Res. Solid Earth* 122 (2): 1449–1469. https://doi.org/10.1002/2016JB013241.

Sulsky, D., Chen, Z. and Schreyer, H. L. (1994). A particle method for history-dependent materials. *Computer Methods in Applied Mechanics and Engineering*, 118 (1–2): 179–196. https://doi: 10.1016/0045-7825(94)90112-0.

Sulsky, D. and Kaul, A. (2004). Implicit dynamics in the material-point method. *Computer Methods in Applied Mechanics and Engineering*, 193 (12–14): 1137–1170. https://doi.org/10.1016/j.cma.2003.12.011.

Tika, T.E., Vaughan, P.R. and Lemos, L.J.L. (1996). Fast shearing of pre-existing shear zones in soil. *Géotechnique*, 46 (2): 197-233. https://doi.org/10.1680/geot.1996.46.2.197.

Wang, L., Han, J., Liu, S. and Yin, X., (2020). Variation in shearing rate effect on residual strength of slip zone soils due to test conditions. *Geotech. Geol. Eng.,* 38 (3): 2773–2785 . https://doi.org/10.1007/s10706-020-01186-9.

Wedage, A.M.P., Morgenstern, N.R. and Chand, D.H. (1998). A strain rate dependent constitutive model for clays at residual strength. *Can. Geotech. J*., 35, 284-298. https://doi.org/10.1139/cgj-35-2-284.

Vardoulakis, I. (2002). Dynamic thermo-poro-mechanical analysis of catastrophic landslides. *Géotechnique*, 52 (3): 157–171. https://doi.org/10.1680/geot.2002.52.3.157.

Veveakis, E., Vardoulakis, I. and Di Toro, T. (2007). Thermoporomechanics of creeping landslides: The 1963 Vaiont slide, northern Italy. *Journal of Geophysical Research*, 112 (F3), F03026. https://doi.org/10.1029/2006JF000702.

Villar, M.V. and Lloret, A., (2003). Características THM de la bentonita extraída del desmantelamiento FEBEX. In: *V Jornadas de Investigación y Desarrollo Tecnológico en Gestión de Residuos Radiactivos.* Empresa Nacional de Residuos Radioactivos, ENRESA, pp. 203–216.

Yavari, N., Tang, A.M., Pereira, J.M. and Hassen, G. (2016). Effect of temperature on the shear strength of soils and the soil–structure interface. *Canadian Geotechnical Journal*, 53 (7):1186–1194. https://doi.org/10.1139/cgj-2015-0355.

Zhang, X., Chen, Z. and Liu, Y. (2017). The Material Point Method. A Continuum-Based Particle Method. *Elsevier and Tsinghua University Press*. doi.org/10.1016/B978-0-12-407716-4.00003-X.

Proceedings of the XVIII ECSMGE 2024
GEOTECHNICAL ENGINEERING CHALLENGES
TO MEET CURRENT AND EMERGING NEEDS OF SOCIETY
© 2024 the Authors
ISBN 978-1-032-54816-6
DOI 10.1201/9781003431749-10
Open Access: www.taylorfrancis.com, CC BY-NC-ND 4.0 license

ECSMGE 24
XVIII EUROPEAN CONFERENCE ON SOIL MECHANICS AND GEOTECHNICAL ENGINEERING

State-of-the-art Report

Specificities of floating offshore wind turbines for risk and safety evaluation of anchoring systems

Spécificités des éoliennes flottantes pour l'évaluation du risque et de la sécurité de leurs systems d'ancrages

B. Cerfontaine*, S.M. Gourvenec, D.J. White
University of Southampton, Southampton, UK

**b.cerfontaine@soton.ac.uk*

ABSTRACT: Floating offshore wind turbines (FWT) are still in their infancy and represent only 0.2% of currently installed commercial offshore wind capacity (193 MW of 65 GW) but will be critical to achieve net-zero objectives by 2050. The design of mooring systems and anchors for FWTs relies heavily on established Oil and Gas (O&G) practice, although governed by different design requirements. Reassessment and refinement of anchor system design methods and practices is necessary, recognising the different risks from FWT failure and the imperative for mass-production within the next 25 years. This paper identifies first the main differences between floating O&G and FWT and the associated geotechnical challenges and risks; then four key developments relevant to industry needs are selected and the solutions to reduce risk and uncertainty are then detailed: (i) Shared anchors; (ii) Farm-wide reliability assessment; (iii) Whole-life geotechnical design; and (iv) Screw pile installation. These examples show how physical, numerical and theoretical modelling can compensate for the current lack of FWT field experience to reduce design risk and raise project viability. Finally, technical project-wide risk is put into perspective by a comparison with the planet-wide risk resulting from delayed offshore wind farm installation.

RÉSUMÉ: Les éoliennes flottantes en mer (EFM) ne représentent que 0,2% de la capacité éolienne offshore commerciale disponible (193 MW sur 65 GW), mais seront essentielles pour atteindre les objectifs de zéro émission nette d'ici 2050. Une réévaluation et un raffinement des méthodes de conception des systèmes d'amarrage et des ancres pour les EFM, basée sur les pratiques et l'expérience de l'industrie pétrolière, sont nécessaires pour prendre en compte leurs spécificités (e.g. conséquences limitées d'une défaillance) et la nécessité de les produire en masse dans les 25 prochaines années. Cet article identifie les principales différences entre les technologies flottantes pétrolières et éoliennes, ainsi que les défis et les risques géotechniques associés. Quatre développements clés pertinents pour l'industrie sont ensuite sélectionnés, et les solutions pour réduire les risques et les incertitudes sont ensuite détaillées: (i) Ancres partagées; (ii) Évaluation de la fiabilité à l'échelle du parc; (iii) Conception géotechnique tout au long de la vie; et (iv) Installation de pieux vissés. Ces exemples montrent comment la modélisation physique, numérique et théorique peut compenser le manque d'expérience de terrain avec les EFM afin de réduire les risques de conception et d'accroître la viabilité des projets. Enfin, le risque technique à l'échelle du projet est mis en perspective avec le risque planétaire résultant du retard de l'installation de parcs éoliens offshore.

Keywords: Offshore geotechnics; anchoring; risk and reliability; physical modelling; numerical modelling.

1 INTRODUCTION

1.1 Decarbonisation and offshore wind

Weaning society off fossil energy sources is an urgent challenge to limit the impact of future climate change (IPCC, 2021). Among the multiple solutions that must be deployed, the development of offshore wind energy sources is key to achieve climate neutrality, i.e. 'net zero', across Europe and worldwide. The Global Offshore Wind Energy Compact (IRENA et al., 2021) sets a global ambition of 380 GW of offshore wind capacity by 2030 and 2000 GW by 2050 to meet the aims of the Paris Agreement.

Europe and the UK have led in offshore wind installation over the last twenty years, almost entirely in shallow waters where bottom-fixed foundations, such as monopiles, are cost-effective. However, Floating Wind Turbines (FWT) are needed to unlock more than 70% of the offshore wind potential in the European Economic Area, where floating structures are required in water deeper than 50 m (International Energy Agency, 2019). FWT will also unlock areas

further away from shore, where stronger and more consistent winds can be harnessed to generate more energy. The pace and scale of necessary offshore wind development, in conjunction with the development of new technologies introduces new geotechnical risk and safety challenges to be evaluated and overcome.

1.2 Floating offshore wind

Floating offshore wind is a nascent technology, comprising < 0.2% of total global offshore wind capacity at the close of 2023 (GWEC, 2022). Currently, only four commercial floating offshore wind farms, totalling 24 FWTs, have been installed – all across Europe, located in Scotland (Hywind Scotland – 30 MW, Kincardine 50MW), Norway (Hywind Tampen – 88MW) and Portugal (WindFloat Atlantic – 25MW). The high scenario 2050 projections for UK offshore wind alone involve between 5,000 and 20,000 FWTs, which must be built in the next two decades (Putuhena et al., 2023). By comparison, there are currently 25 floating Oil & Gas (O&G) production facilities operating in the North Sea and East Atlantic (Gourvenec et al., 2022) – a population that will soon be eclipsed by floating offshore wind platforms.

Multiple concepts of FWT platforms exist and are still under development (Figure 1), but all need at least three mooring lines to stabilise and maintain the platform in position. Catenary mooring, formed of heavy metal chains, are the currently favoured configuration, but taut and semi-taut mooring concepts are under development for FWTs.

Mooring lines are anchored to the seabed by a diverse range of anchor technologies (Cerfontaine et al., 2023b), many of which have been used for decades for O&G platforms. However, the scale and pace of FWT development will put the existing supply chain under considerable strain, from vessel availability (site investigation and installation) to lab testing facilities, raw materials and anchor manufacture capability. Therefore, a reassessment of anchor design and the associated risk, built on previous O&G experience, is necessary to reflect specificities of FWT and unlock their large-scale deployment.

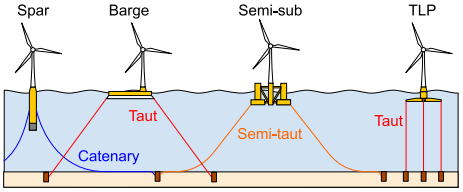

Figure 1. Different types of floating offshore wind platforms (Spar, Barge, Semi-submersible and Tension Leg Platform) and mooring systems (Catenary, Semi-taut and Taut). Various mooring systems are suitable for different platforms with exception of TLP. Drawing not to scale.

1.3 Risk and reliability evidence from O&G

The O&G industry has operated floating structures of comparable size to a floating wind turbine for around 50 years (Randolph et al., 2011; Ronalds, 2005). Ship-shaped, spar-shaped or semi-submersible floating O&G production systems are typically moored by 6-12 mooring lines designed for an operating life of 20-30 years, and have been used across a range of water depths to more than 3000 m (e.g. Moore et al., 2017).

The population of floating O&G platforms is relatively small, compared with the >3000 fixed platforms installed in the Gulf of Mexico, which provide a statistically-significant population to assess their reliability. However, recent pan-industry projects have examined the reliability of floating O&G platform moorings and anchors (Horte et al., 2017), based on failure data from operating facilities and from probabilistic analysis using existing design methods.

A mooring system reliability of 2×10^{-4}/annum is often targeted, although this is linked to the consequences of failure associated with the release of hydrocarbons (Goodwin et al., 2000). For the mooring lines, observed failures lead to an estimated average failure rate of 3×10^{-3}/annum (Ma et al., 2013). For the anchoring system, designed to a target 4×10^{-4}/annum (Gilbert et al., 2005), there are insufficient case studies of failures to develop a corresponding average observed failure rate. This suggests an inconsistency between design practice for moorings lines and anchors since the anchors are in practice more reliable than mooring lines, which represent the station-keeping 'weak link'.

Insights from these experiences can provide lessons learnt for FWT and have 3 key implications:

1. Current design practice for anchors is leading to a higher anchor reliability than the attached mooring line based on target reliabilities and practical observations.
2. Adjusted design approaches for FWT need to be calibrated against different target reliability, because failure consequences of FWT do no entail the same environmental and human risk.
3. 'Unrecognised' components of anchor capacity (such as consolidation-driven whole-life response, or inertial effects for very fast loading), which require quantification and adoption in design methods.

1.4 Reliability-based design for FWT

Reliability-based design optimisation of offshore renewable energy structures (Clark et al., 2018) can contribute to the reduction in design conservatism and cost, adapted to the specificities of FWT detailed in the next section. Probabilistic approaches for the design of

bottom-fixed offshore wind turbines have been introduced (Charlton et al., 2022; Shittu et al., 2021; Zhang et al., 2023), but fewer studies exist for FWT (Devin et al., 2021; Hallowell et al., 2018).

While thousands of bottom-fixed structures have already been installed and provide a statistically-significant population to assess existing design practice, the several tens of installed FWT provide only limited ability to assess their reliability (Kolios et al., 2009; Li et al., 2022) and identifying critical modes of failure. This is even more prevalent for anchors, although advances in anchoring design will be supported by a rapid growth in performance data as new FWTs are deployed. For example, at a nominal failure rate of 2×10^{-4}/annum, across a population of 10,000 FWTs, each with 3 mooring lines and anchors, 6 failures per year might be expected.

Geotechnical aspects are often neglected or oversimplified in reliability-based approaches, due to the inherently high geotechnical uncertainties, either epistemic (i.e., uncertainty on predictive models) or aleatoric (i.e., uncertainty on design variables). It is more complex to measure, quantify and predict soil properties and soil-foundation responses, than for human-made materials or structures.

The goal of this Paper is to review geotechnical challenges and risks induced by the specificities of FWT, and to demonstrate how physical, numerical and theoretical approaches can be leveraged to reduce both epistemic and aleatoric uncertainty, by identifying new modes of failure, by developing new predictive models or by enhancing soil characterisation.

2 SPECIFICITIES OF FLOATING OFFSHORE WIND

In the following section, the specific challenges and opportunities of FWT are detailed, and compared with current floating O&G (Figure 2) and bottom-fixed wind practice. The consequences for the anchor design and risk analysis are highlighted in each case.

2.1 Generalities

Consequence of failure: Failure of a FWT represents only a minimal risk to human life or the environment, as structures are uncrewed and do not lead to hydrocarbon release, unlike hydrocarbon drilling or production platforms. Without these hazards, a higher probability of failure (i.e. lower reliability) may be acceptable and need only be weighed against economic considerations.

How deep is deep? Bottom-fixed O&G have been built up to 535m water depth (Petronius Platform), while bottom-fixed wind becomes impractical and uneconomical beyond 60m water depth. This is due partly to technical consideration, e.g. the need to limit riser movement for O&G (Randolph et al., 2011), and partly to different business models, which makes gigantic fixed structures unaffordable for wind.

Development size: While O&G platforms are built across a limited number of isolated sites, tens of thousands of FWT will be built in farms of hundreds of structures, over hundreds or thousands of km^2.

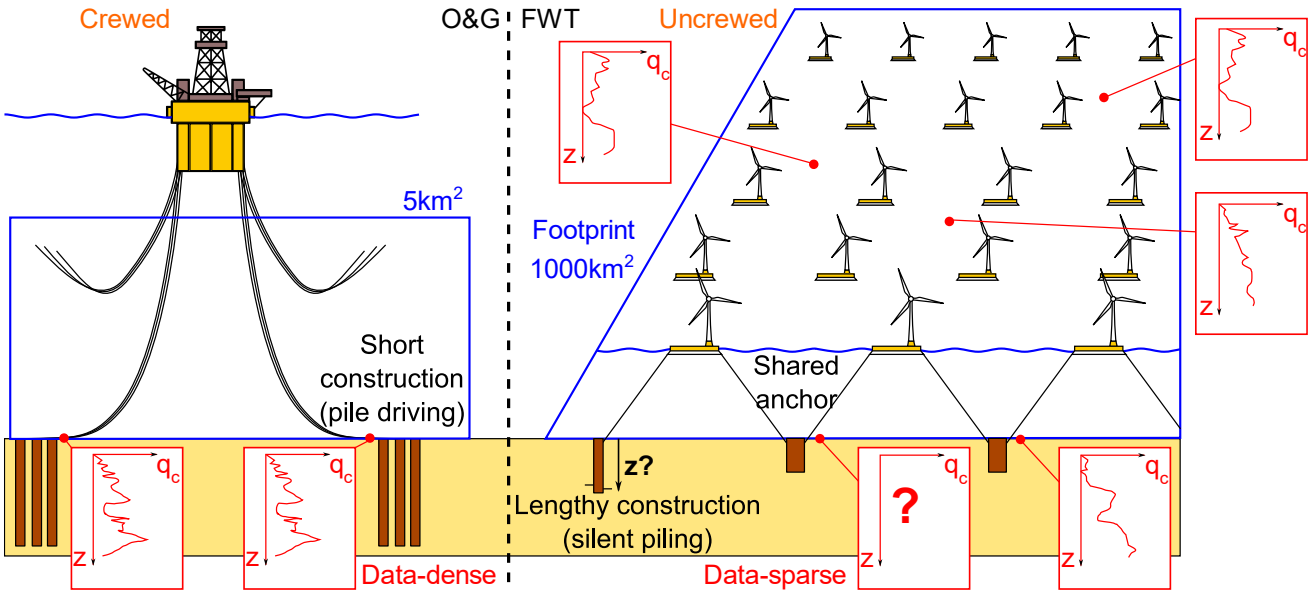

Figure 2. Comparison of floating Oil and Gas (O&G) and Floating Wind Turbine (FWT) farm.

The scale and pace of this deployment will put additional constraints on the supply chain. The industry has to move from the O&G template of bespoke anchor design and production to mass-production, which requires greater understanding of anchor and mooring performance and enhanced guidelines for engineers.

2.2 New technologies

Reducing size of mooring line systems: New technologies offer potential to increase efficiency of mooring lines and anchors. Efficiency in mooring lines can be achieved by (i) reducing the number of lines, at the expense of a lower system resilience (Fontana et al., 2018); and (ii) reducing the length of lines with taut or semi-taut synthetic mooring configurations. The latter solution improves platform compliance in relatively shallow water, reduces steel consumption and FWT footprint. However, those two solutions impose greater magnitude of loads and greater vertical uplift component of loads to anchors increasing the challenge of geotechnical anchor design (Huang et al., 2020), even if load-reduction devices can mitigate load increase (e.g. Festa et al., 2024).

Reducing number of anchors: The number of anchors required across a FWT farm can be reduced by linking multiple lines from different FWT to a common "shared" anchor (Fontana et al., 2018). This can reduce the number of anchors by up to 60%, but also introduces complexity of loading onto the anchor, which could be detrimental to its cyclic performance (Herduin, 2019) and induce strength degradation risk in the longer term.

Silent anchor installation: New environmental restrictions aim at reducing underwater noise, which makes pile driving either impossible or more expensive. This has led to development of new installation methods, such as vibro-piling (Kementzetzidis et al., 2022), or new anchor types, such as screw piles (Cerfontaine et al., 2022). Existing uncertainties due to the lack of field experience are being progressively reduced through field, laboratory and numerical studies.

2.3 New ground modelling approaches

Different sizes: The design of floating wind farms face greater uncertainties in ground conditions than O&G or even bottom-fixed wind farms, due to their scale and the need for at least 3 anchors per turbine. For example, the recently-installed Seagreen wind farm located offshore Scotland covers an area comparable to the city of Lisbon, extending from the Vasco de Gama bridge out to the Atlantic Ocean (Figure 3). By comparison, the footprint of a single O&G platform or development is a few 100s of m^2 to a few km^2 (Randolph et al., 2011).

Uncertainties in ground conditions increase risk in both predicting installation refusal and holding capacity of anchors. Ground conditions can vary considerably across a site and a thorough soil investigation at all potential anchor points, including along the installation path for drag anchors, may be too expensive and time consuming (Jenner et al., 2002).

Site investigation approach: Early assessments of the right strategy for site investigation across offshore wind farms advocated for greater geophysical-geotechnical data integration to estimate engineering parameters, to reduce uncertainties in ground models (Sauvin et al., 2019; Vardy et al., 2017) and to speed up the site investigation process. Developing anchor technologies and design methods resilient to uncertainties in ground conditions is a key pathway to reduce the risk.

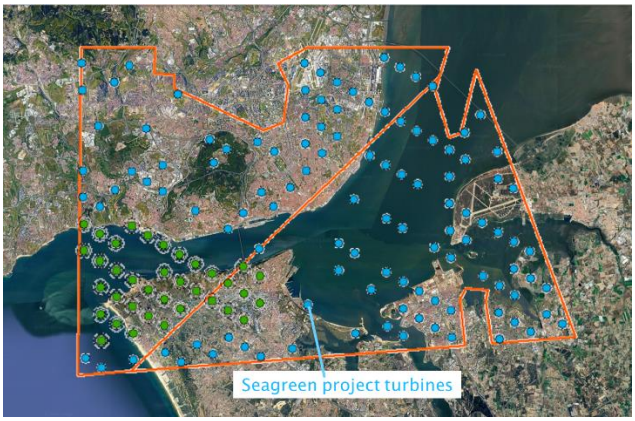

Figure 3. Footprint of a typical offshore wind farm (Seagreen).

Farm-wide assessment: Another consequence of the large population of structures in a wind farm is that the design must consider the likelihood of multiple failures. Although a design storm event may impose the same sea state throughout a farm, this will not exert the same maximum load on all turbines. Assessments of reliability therefore are more realistically performed considering the full farm-wide population.

2.4 New design philosophies

Traditional geotechnical design of anchors compares the maximum peak static load sustained by the anchor to its minimum drained or undrained capacity. Reduced soil strength due to cyclic loading from wave and wind effects on the soil properties, is typically considered by a quasi-static approach, and is accounted for by a degradation factor on the static properties (Jostad et al., 2014).

Whole-life design: A more realistic and less conservative design approach should account for the through-life variation in soil strength, by capturing the complex, physical mechanisms taking place into the soil, beyond the drained/undrained dichotomy. For instance, consolidation episodes (pore water pressure dissipation) in between storm events (pore water pressure accumulation) lead to soft clay densification and to a progressive increase of its undrained strength with time (Laham et al., 2021). This effect is encapsulated into a "whole-life geotechnical design" philosophy and has implications for anchor design, life extension and decommissioning (Gourvenec, 2022).

Rate effects: Loads induced by wind and wave action usually have a period ranging from 5s to 15s. At this loading rate, some anchor will experience partial drainage (Cerfontaine et al., 2023b), which can unlock significant temporary uplift resistance when compared to a purely drained loading, as demonstrated for plates (Chow et al., 2020) and suction caissons (Cerfontaine et al., 2016). In addition, FWT systems are dynamic in essence, and the highest loads often happen at a fast loading rate, e.g. due to mooring line snatch loading. Considering inertial effects into the ground can also unlock additional anchor resistance (Kwa et al., 2021).

3 KEY FOCUS TOPICS

To illustrate how the aforementioned challenges are being addressed, four key focus topics have been selected for more detailed discussion, as topics of high importance for the industry. These are (i) Shared anchors, (ii) Farm-wide design for reliability and risk, (iii) Whole-life geotechnical design approach, and (iv) Installation of screw piles. It is shown below how adequate physical, numerical and theoretical modelling can reveal new modes of failure and eventually reduce their associated design risk.

3.1 Shared anchors

Shared anchors can experience a reduction in peak lateral load between 30% and 50% (Fontana et al., 2018; Pillai et al., 2022) with respect to unidirectionally loaded anchors, as mooring lines are pulling in opposite directions, as shown in Figure 4. However, the angle of the resulting load to the horizontal direction is always greater than the angle of the mooring line itself, as horizontal components of each line oppose each other, but vertical components add up. This effect will be reinforced for taut mooring lines, which should become more common with the development of synthetic mooring systems but can also be true for catenary mooring lines if the anchor padeye is below ground level.

Pile type anchors are the most adapted to anchor sharing, due to their vertical symmetry (Cerfontaine et al., 2023), but can be vulnerable to cyclic inclined loading. Indeed, it was shown by Huang et al. (2020) that such loading had a positive impact on the lateral resistance, but a detrimental impact on the vertical resistance. The risk associated with shared anchors is increased by the lack of data and prior experience with this technology. A single commercial floating wind farm (Hywind Tampen) is secured by shared anchors and has been fully in operation since the summer 2023. Observations from real-life case studies should give more confidence in their use in the future.

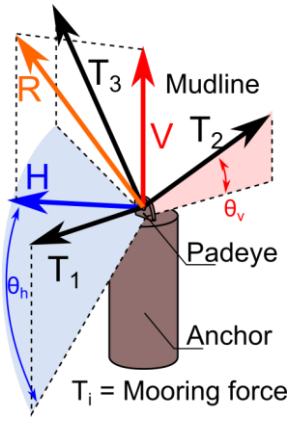

Figure 4. Simplified representation on the loads applied to a shared anchor by three mooring lines (Ti=1,2,3), vertical (V) and horizontal (H) components of the resulting load (R), θ_v is the inclination of any force to the horizontal direction, θ_h is the position of the resulting load in plane with respect to a reference direction.

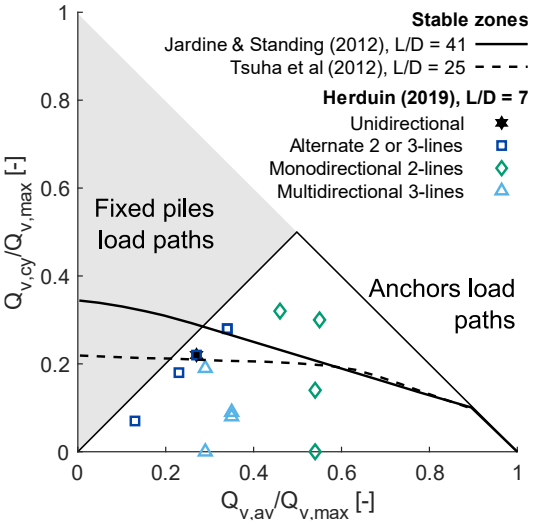

Figure 5. Stability diagrams for piles cyclically loaded axially, after (Herduin, 2019; Jardine et al., 2012; Tsuha et al., 2012). Dots indicate loading configurations that led to failure of the anchor, from Herduin (2019). Mooring lines were inclined of 40° to the horizontal. ($Q_{v,av}$, $Q_{v,cy}$, $Q_{v,mon}$) are the average and cyclic applied vertical loads, and monotonic vertical resistance of the pile.

The epistemic uncertainty associated with the behaviour of shared anchors can be reduced by careful experiments, such as centrifuge testing. The most comprehensive set of tests was undertaken by Herduin (2019) on relatively short and rigid piles for mooring lines inclined of 40° to the horizontal and embedded in sand. However, no framework for shared anchor design exists to date.

Results can be represented by using the stability diagram framework, which depicts stable combinations of purely vertical average and cyclic amplitude loads normalised by the maximum vertical resistance, e.g. the combinations that lead to a vertical displacement lower than 0.1D after 1000 cycles. For comparison, stable zones identified by previous researchers are depicted in Figure 5, (Jardine et al., 2012; Tsuha et al., 2012), for relatively long piles with L/D in the range 25-41.

Results from centrifuge tests of an anchor under shared loading conditions (Herduin 2019) were analysed in the stability diagram framework, by considering the projected vertical components of the applied load. Each test also had a horizontal component, which was either fixed in direction (unidirectional, $\theta_h = cst$), took different discrete directions (alternate, $\theta_h = \theta_{h1}$ or θ_{h2}), had a narrow range of variation (monodirectional $15° < \theta_h < 75°$) or was changing continuously in multiple directions (multidirectional $0° < \theta_h < 360°$). The most detrimental loading paths were those involving large variation in the horizontal load components, as they led to an unstable response for vertical loads much lower than previously identified for purely vertical loading. However, mooring lines in the research were inclined of 40° to the horizontal, representative of mooring systems for wave energy converters. More research is needed to cover lower mooring line angles ($\theta_v < 20°$), more representative of realistic conditions for floating wind turbines.

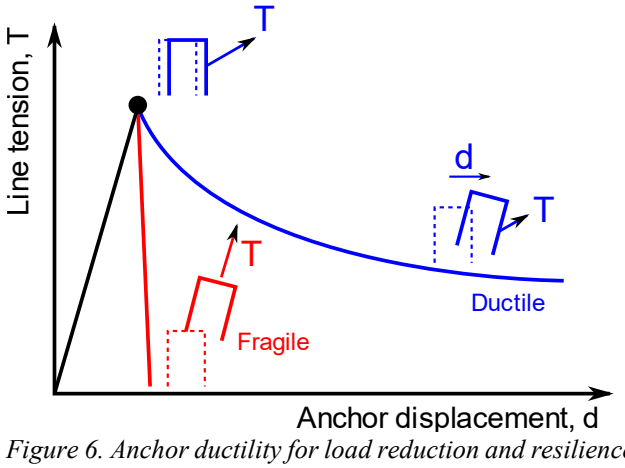

Figure 6. Anchor ductility for load reduction and resilience.

A higher reliability and resilience can be unlocked by using anchoring technologies with enhanced resilience and ductility, as shown in Figure 6. While vertical anchor resistance is often fragile and drops fast post-peak (e.g. for a pile), lateral resistance is more ductile and exhibits residual resistance. Therefore, a "failed" anchor laterally loaded can still mobilise some resistance, while the induced anchor movement can reduce the load applied by the mooring line (reduced pre-tension for taut mooring lines).

This resilience can be particularly critical for shared anchors, where the failure of one anchor or mooring line can lead to a cascading effect and progressive failure of more anchors, thus reducing the reliability of the system with respect to a non-shared configuration (Hallowell et al., 2018).

3.2 Farm-wide design for reliability and risk

The difference in failure consequences for FWT compared to O&G structures justifies a revisiting of load and resistance partial factors where these have been inherited from O&G design practice and should prompt wider adoption of probabilistic methods to meet a target reliability identify the optimum design approach from both a cost and safety perspective.

A benefit of assessing design reliability using a probabilistic approach is that uncertainties and variations can be readily incorporated allowing their effect on reliability to be quantified. For example, as well as the natural temporal variations in annual maximum storm intensity, it is also possible to allow for the uncertainty in designed capacity across the multiple structures in a wind farm, as well as temporal variations in geotechnical properties due to whole life effects (see Section 3.3).

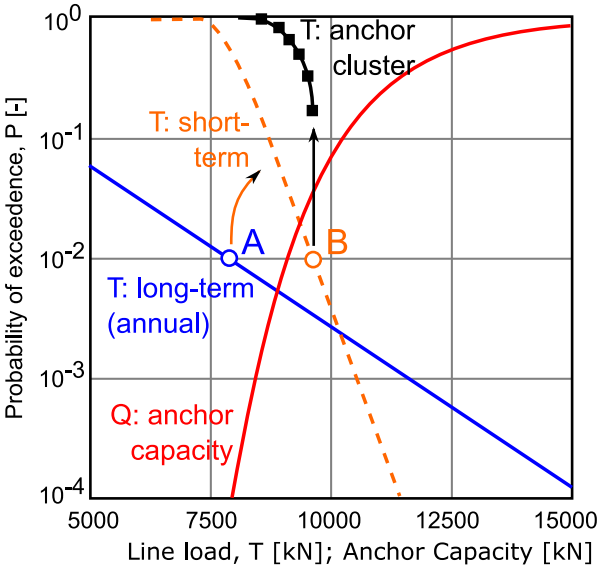

Figure 7. Wind farm-wide load (T) and resistance (Q) variations, based on analysis in Stanisic et al. (2019).

This farm-wide approach is illustrated here by considering a farm-wide analysis of mooring line loads and anchor resistances during a design event. Figure 7 illustrates the complexity of assessing farm-wide uncertainty in load and resistance for a wind farm comprising many turbines, each with multiple mooring lines and anchors. This example is based on the floating system reported by Stanisic et al. (2019), which analysed a floating barge structure stabilised by four clusters of 6 mooring lines and anchors.

Considering first the design loading actions, the characteristic annual maximum mooring line load – termed the most probable maximum, MPM, Stanisic et al. (2018) is assigned a distribution, usually developed from time domain simulations, which is referred to as the long term variability (blue solid curve in Figure 7). In this example, the distribution of the MPM mooring load for multiple floating units in the same sea state for which the long term MPM is T = 7800 kN, and has a 1% chance of annual exceedence (P = 0.01, point A).

If the same floating unit is exposed to a given sea state for different periods of time, or on different occasions, the actual maximum load will differ – this is referred to as short term variablity. The short term variability associated with a long-term (annual) maximum marked as A (P = 0.01) is shown as the orange dashed curve in Figure 7. Due to this short term variability, given the occurance of a sea state that causes A (P = 0.01), there is a 1% probability (P = 0.01) of T = 9600 kN. That is, among an array of 100 floating units, for a long term MPM of 7800 kN, one unit would be expected to see 9600 kN. This defines the variation in loads across an array of floating units when the farm is subjected to the same sea state. It therefore controls the potential for multiple failures.

In addition, there is a further variability to consider within the maximum loads among multiple anchors in the same cluster of mooring lines/anchors. In Figure 7, Point B shows an illustrative MPM anchor load from short and long term variablity. The neighbouring anchors in the 6-anchor cluster are exposed to loads that are lower, but within 11% of this maximum (as indicated by the black markers). This in-cluster variation in loading influences the potential for a single line failure to cascade into a full loss of station-keeping (Stanisic et al., 2019).

The geotechnical anchor capacity is always uncertain due to (i) uncertainty in the ground properties and (ii) uncertainty in the model used to assess the anchor capacity from the ground properties, and is represented by a fragility curve in reliability-based design. In Figure 7 an example fragility curve is shown (Q, red solid line in), which is based on the typical uncertainty in foundation capacity envelopes presented by Shen et al., (2023) using random fields analysis. Their analyses capture the variation in capacity for a foundation placed at random locations on ground with known mean and coefficient of variation in undrained shear strength.

Usually the long term and short term variabilities are combined in the assessment of a design load distribution (e.g. Stanisic et al. 2019). However, it is useful to decouple these effects for farm-wide design because this allows the farm-scale spatial variation in loading to be estimated. This can be achieved by sampling the design loads across the array using the short term variability superimposed on a single representative case from the long term variability.

When combined with the spatial variability in geotechnical capacity, this approach allows the probability of failure of multiple structures within a farm to be quantified, incorporating the correlation between the design loads and resistances across different turbines within a farm.

3.3 Whole-life geotechnical design approach

Accumulated soft soil strength degradation, i.e. softening, over the life of an offshore foundation or anchor is typically captured by so called ‘SN’ curves, to account for the reduced strength (S) due to undrained cyclic loading over a number of cycles (N) for the design life (Andersen, 2015). However, in reality, stormy weather periods (high load amplitude), typically winters, alternate with quiet weather periods (low load amplitude), during which accumulated pore water pressures, that have led to softening, dissipate, leading to a recovery and even enhancement of the soil strength in normally and lightly overconsolidated clays (Gourvenec, 2020, 2022; Kwa et al., 2023c). Therefore, considering only strength degradation in soft soils is often overly conservative.

The “whole-life” geotechnical design approach applied to soft soils explicitly includes the effect of consolidation periods throughout the life of an anchor or foundation. The approach is exemplified in Figure 8, which represents the theoretical state of a representative soil element close to an anchor over 3 years of operation, divided in 3 winters and 3 summers. Significant storms are assumed to occur during winter time, and lead to the accumulation of pore water pressure (u, in Figure 8b) and a reduction in the current undrained strength (s_u, in Figure 8b).

Each storm takes place in undrained conditions, hence at constant void ratio, depicted by a horizontal line in Figure 8a. Dissipation of pore water pressure and subsequent consolidation occur in between storm events and mostly during summer time, leading to a soil densification (reduction in e in Figure 8a).

The time necessary to fully dissipate pore water pressures depends on material, geometric properties and load applied (Kwa et al., 2023b), so the consolidation process is not complete after every summer, but the undrained strength still progressively increases beyond its initial value ($\Delta s_u > 0$ in Figure 8b). Similarly, the potential rise in s_u depends on the initial over-consolidation ratio of the soil (Gourvenec et al., 2014).

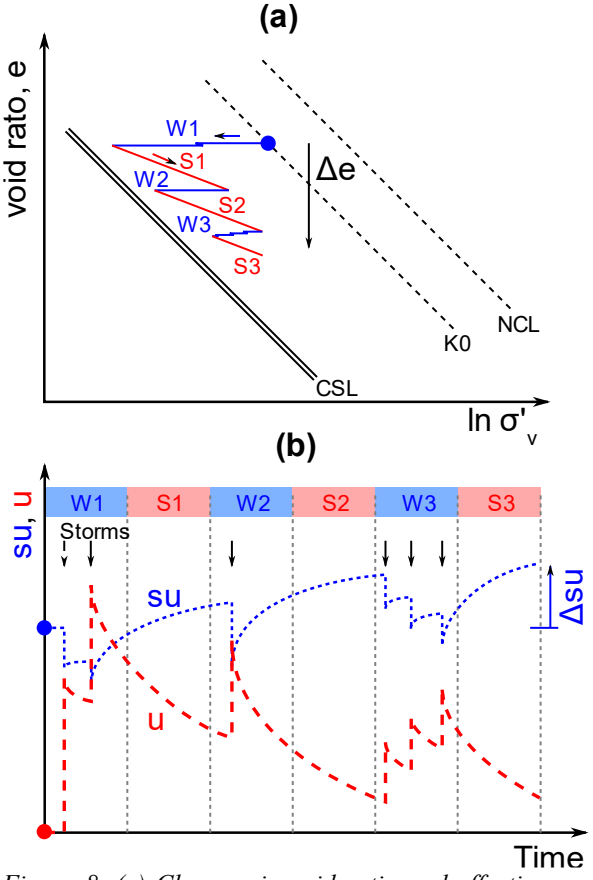

Figure 8. (a) Changes in void ratio and effective vertical stress of an element of soil close to an anchor due to episodes of cyclic loading during winters (W) and summer (S) periods. (b) Change in pore water pressure (u) and mobilizable undrained strength in the soil element (su) with time. Schematic representation of whole-life effect, not to scale. Based on (Laham et al., 2021).

The whole-life approach illustrates that the drained/undrained dichotomy is insufficient for modern design. It is possible to unlock additional anchor resistance, if a more complex physics is taken into account, and if probabilistic design is adopted, as the soil strength increase depends on its loading history. 10,000 3-year long histories representative of a wave energy converter attached to a plate anchor have been considered in combination with an anchor macro-element, capable of tracking average undrained strength degradation and pore water pressure dissipation (Kwa et al. 2023a). The anchor diameter necessary to limit the probability of failure to 10^{-3} was extrapolated from those results and ranges between 5 and 6m across different coefficients of consolidation (Figure 9). By comparison, a diameter of 7.5m would have been necessary if only undrained strength degradation had been considered, without any consolidation.

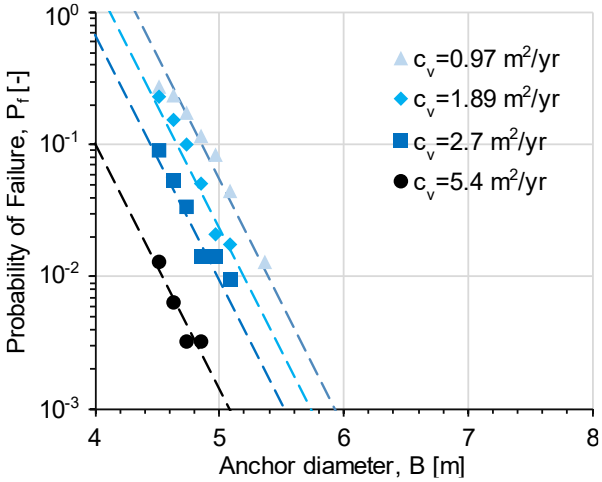

Figure 9. Probability of failures for a given anchor diameters as a function of the coefficient of consolidation (c_v), calculated based on 10,000 load history simulations, (Kwa et al., 2023).

A similar approach has been adopted coupling the anchor macro model with hydrodynamic mooring line analyses for floating wind, predicting minimum plate anchor areas of half that from traditional design by considering whole-life soil response and load reduction devices (Kwa et al., 2023a).

3.4 Installation of screw piles

Screw piles are composed of one or several helices attached to a steel shaft (see Figure 10), which are very efficient to sustain axial uplift loading and can be "silently" installed by applying axial force and torque at their head to screw them into the ground (Cerfontaine et al., 2023a). Screw piles have been widely used onshore, but their use offshore requires a significant upscaling in their dimensions and the development of bespoke installation tools (Cerfontaine et al., 2020).



Figure 10. Sketch of a screw pile (rotated 90°). D_h and p_h are the helix diameter and pitch and D_s is the shaft diameter.

So far, the risk of refusal during installation due to insufficient force and torque capabilities has impeded their adoption, despite a continuously growing interest. Indeed, the magnitude of the vertical reaction (crowd) force required to install large-scale screw piles according to onshore guidelines ranges from 10-20MN, which cannot be sustained by current installation vessels. Those guidelines require a pitch-matched installation, which means that the helix will advance axially by one helix pitch per rotation of the helix, and is often referred to as perfect installation.

Geotechnical centrifuge modelling and DEM simulations were used to prove the feasibility of large screw pile installation in sand (Cerfontaine et al., 2021) with limited reaction force, thus reducing the perceived installation risk. It was shown that a change in installation parameter (AR = advancement ratio) below the range allowed by the design guidelines ($0.8 \leq AR \leq 1.2$), could lead to a significant reduction in the measured crowd force (Figure 11). The AR is the ratio of the vertical displacement of the pile for each pile revolution. It is equal to 1 in pitch-matched conditions and lower than 1 during overflighting.

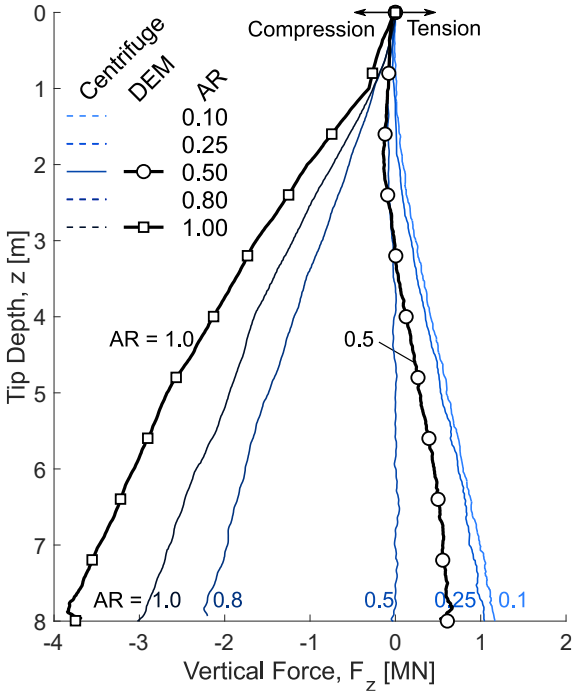

Figure 11. Vertical (crowd) force measured in centrifuge and DEM modelling of single-helix screw pile installation in a medium-dense sand at fixed ARs. AR = advancement ratio, = 1 for pitch-matched and <1 for overflighted piles. After Cerfontaine et al. (2021).

The overflighting physical mechanism was revealed by DEM simulations. During pile overflighting, the helix edge picks up some soil and forces it to move upwards, which is constrained by the existing soil acting as a non-linear spring. The resistance of the upper soil to this imposed movement creates a reaction force acting on the helix and oriented downwards. The lower the imposed AR, the more the resulting force is reduced, and a tensile force was eventually measured. This means that the pile pulls itself into the ground. It was also shown that the tensile resistance was enhanced by the installation, which created some preloading of the ground.

The installation in the field is not AR-controlled as per the experiment, but is undertaken at constant resulting force. The sum of reaction forces acting on the shaft, helix and tip is equal to the screw pile and installation tool weight. The AR of a given pile would then vary during installation to adapt to ground conditions, with a lower AR expected in a denser sand. A pile could then overcome undetected harder soil layers, which de-risks the installation, though some research on overflighting in clay and boulder effects still has to be undertaken. A significant torque still has to be provided during installation, which can reach tens of MNm, but was deemed less of an issue than the required reaction force by contractors.

The powerful combination of physical and numerical modelling, enabled a mechanism-based theoretical framework to be developed, leading to further pile geometry optimisation to further reduce installation requirements and reduce risk (Cerfontaine et al., 2022).

4 RISK – A WIDER PERSPECTIVE

4.1 Project-wide and planet-wide perspectives

It is useful to close this review of risk and safety evaluation of floating offshore wind by considering the wider risk perspective, including the impact of climate change (Figure 12).

So far, this paper has focused on a *project-wide* (or company-wide) perspective, which considers the risk and safety associated with company personnel and the general public who are exposed directly to hazards during the project operations. The environmental impact assessment, or other activities required to meet regulatory requirements, widen this scope by ensuring that nearby ecosystems remain safe from harm.

On the other hand, the perspective that an individual may have, or that society collectively has is called here a *planet-wide* perspective. It is not unique, as different social groups, nationalities and regional populations will have varying views on the relative importance of wider risks. However, there is an international consensus that global warming must be kept below 1.5° and we must develop offshore

renewable energy sources to reach carbon neutrality by 2050. Therefore, the *planet-wide* perspective on offshore renewables includes the climate-related risk from *not* developing a project – or delaying the construction and development process – as well as the risks associated with going ahead (Figure 12).

Any delay to the growth of offshore renewable energy (ORE) raises the risk of not reaching climate neutrality by 2050 and causes harm through the climate impacts from that prolonged fossil fuel use. This harm reaches the same individuals as the project-based risk field of view, but it also has the potential to affect the entire global population, due to the distributed impact of carbon emissions.

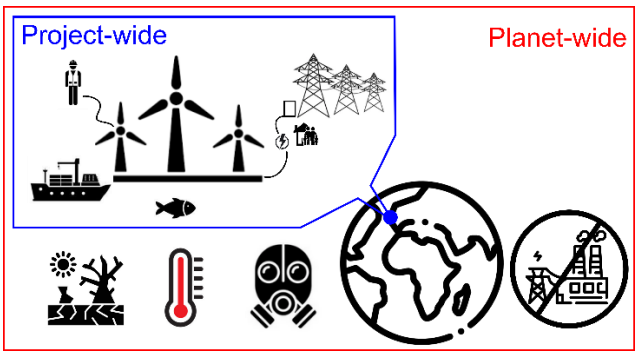

Figure 12. Risk views: project-wide vs planet-wide.

4.2 Human risk linked to carbon emissions

The consequences on human health (heat/cold, air pollution, loss of habitable areas…) of carbon emissions occur through the many cascading impacts outlined in the major national and international reports produced by organisations such as the Intergovernmental Panel on Climate Change (IPCC).

The simplest approach to quantify these *planet-wide* impacts so they can be weighed against *project-wide* risks, is to use the mortality cost of carbon. That is, the estimated cost, in human lives, per unit of additional carbon emissions. Bressler (2021) describe an analysis of more than 100 studies into the human risk from climate change across a wide range of impact. It is concluded that 4,400 tonnes of carbon emitted in 2020 is expected to cause one excess (i.e. additional) death during the period 2020-2100.

4.3 *Planet-wide* human risk linked to Offshore Renewable Energy

Using the metrics from Section 4.2, it is simple to assess the difference in human risk from the *project-wide* and *planet-wide* perspectives given in Figure 12. For instance, It was estimated by The Crown Estate (2022) that an additional 17Mt of CO_2 would have been produced in 2022 if the 45 TWh offshore wind energy had been produced by fossil fuel-based energy. Therefore, each TWh of UK offshore wind currently saves 86.5 lives globally over this century. The 2022 UK offshore wind production will have saved 3900 lives by 2100 and these outcomes will grow and accumulate with each future year of offshore wind production.

The same logic can be applied to a future offshore wind farm that is currently being proposed and designed. A 2 GW capacity floating wind farm operating at a typical capacity factor of 50% will produce 260 TWh of electricity over a 30-year operating life. Based on the fossil fuel abatement and carbon mortality rates above, this wind farm will save 22,700 lives that would otherwise be lost as excess deaths due to climate change impacts from fossil fuel burning.

This saving of $>10^4$ lives by mitigating climate risk far exceeds the human risk seen in the *project-wide* perspective. Figures for industrial injuries and deaths show that the wind, solar and nuclear industries are safer than coal and fossil fuel production, on a global average, although high regional variations are present. The wind power industry has a death rate estimated to be 0.04 deaths/TWh production (Ritchie, 2020), or 10 deaths over the operating life of a 2 GW wind farm.

These simplified comparisons illustrate the increasing importance of a holistic perspective on risk, and the need for carbon and risk literacy among practising engineers. A holistic perspective, understood and acknowledged by all stakeholders, will ensure that the planning and development of energy systems including ORE will maximise the societal benefits and minimise overall human risk, not only the risk to those directly involved in projects.

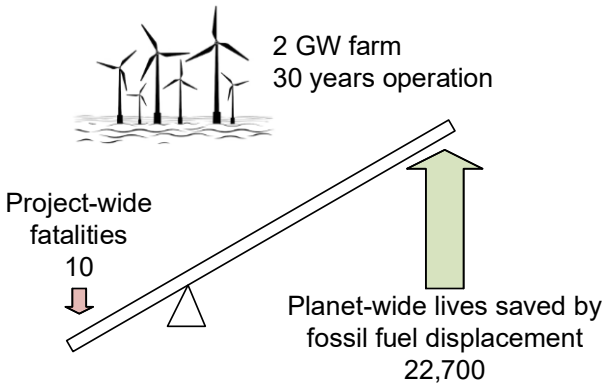

Figure 13. Human mortality from an offshore wind farm.

5 CONCLUSIONS

The design of floating offshore wind turbines (FWT) has so far been based on the experience accumulated by the Oil and Gas (O&G) industry. However, the scale and pace of floating offshore wind developments

to reach net-zero by 2050 is such that new design practices, technologies and guidelines must be developed to better suit FWT specificities and reduce their associated risk. By comparison with O&G, floating wind farms extend over a much greater area, are expected to be more than 100 times more numerous and their failure have a much lower impact.

Among various enhancement possibilities, two new design approaches (e.g. "whole-life" design or farm-scale reliability assessment) and two new technologies (e.g. shared anchors or "silently" installed screw piles) were discussed in this paper. The perceived risk associated to each innovation is magnified by the lack of field experience, which does not allow for a real-life estimation of their reliability. In each case, it is shown how physical, numerical and theoretical modelling can be combined to identify to new failure modes or provide sound evidence to reduce their associated risk.

Finally, it is argued that the *project-wide* risk related to those innovations should be put into perspective with the *planet-wide* risk associated with the delayed operation of new offshore wind units and prolonged operation of fossil-fuel energy systems. A holistic approach is necessary to encompass risk at different scales and maximise the benefits to society at wide.

ACKNOWLEDGEMENTS

This project received funding from the European Union's Horizon 2020 research and innovation programme under the Marie Sklodowska-Curie grant agreement no. 753156. This research was partly funded by the EPSRC (SEAMLESS project) through the Supergen Flexible Fund award. This study forms part of the activities of the Royal Academy of Engineering Chair in Emerging Technologies Centre of Excellence for Intelligent & Resilient Ocean Engineering (IROE) at the University of Southampton. Susan Gourvenec is supported by the Royal Academy of Engineering through the Chairs in Emerging Technology scheme. David White is supported by the EPSRC Offshore Renewable Energy Supergen Hub (EPSRC grant EP/Y016297/1).

REFERENCES

Andersen, K. H. (2015). Cyclic soil parameters for offshore foundation design. In V. Meyer (Ed.), *Frontiers in Offshore Geotechnics III*.

Bressler, R. D. (2021). The mortality cost of carbon. *Nature Communications*, *12*(1), 1–12. https://doi.org/10.1038/s41467-021-24487-w.

Cerfontaine, B., Brown, M. J. J., Davidson, C., Sharif, Y. U., Huisman, M., & Ottolini, M. (2022). Optimised screw pile design for offshore jacket foundations in medium-dense sand. *Geotechnique Letters*, *12*(2), 1–13. https://doi.org/10.1680/jgele.21.00105.

Cerfontaine, B., Brown, M. J., Knappett, J. A., Davidson, C., Sharif, Y. U., Huisman, M., Ottolini, M., & Ball, J. D. (2023a). Control of screw pile installation to optimise performance for offshore energy applications. *Geotechnique*, *73*(3). https://doi.org/10.1680/jgeot.21.00118.

Cerfontaine, B., Ciantia, M., Brown, M. J., & Sharif, Y. U. (2021). DEM study of particle scale and penetration rate on the installation mechanisms of screw piles in sand. *Computers and Geotechnics*, *139*(11), 104380. https://doi.org/10.1016/j.compgeo.2021.104380.

Cerfontaine, B., Collin, F., & Charlier, R. (2016). Numerical modelling of transient cyclic vertical loading of suction caissons in sand. *Geotechnique*, *66*(2), 121–136. https://doi.org/10.1680/jgeot.15.P.061.

Cerfontaine, B., Knappett, J. A., Brown, M. J., Davidson, C., & Sharif, Y. (2020). Optimised design of screw anchors in tension in sand for renewable energy applications. *Ocean Engineering*, *217*(12), 10801. https://doi.org/10.1016/j.oceaneng.2020.108010.

Cerfontaine, B., White, D., Kwa, K., Gourvenec, S., Knappett, J., & Brown, M. (2023b). Anchor geotechnics for floating offshore wind : Current technologies and future innovations. *Ocean Engineering*, *279*(March), 114327. https://doi.org/10.1016/j.oceaneng.2023.114327.

Charlton, T. S., & Rouainia, M. (2022). Geotechnical fragility analysis of monopile foundations for offshore wind turbines in extreme storms. *Renewable Energy*, *182*, 1126–1140. https://doi.org/10.1016/j.renene.2021.10.092.

Chow, S. H., Diambra, A., O'Loughlin, C. D., Gaudin, C., & Randolph, M. F. (2020). Consolidation effects on monotonic and cyclic capacity of plate anchors in sand. *Geotechnique*, *70*(8), 720–731. https://doi.org/10.1680/jgeot.19.TI.017.

Clark, C. E., & DuPont, B. (2018). Reliability-based design optimization in offshore renewable energy systems. *Renewable and Sustainable Energy Reviews*, *97*(January), 390–400. https://doi.org/10.1016/j.rser.2018.08.030.

Devin, M. C., DuPont, B. L., Hallowell, S. T., & Arwade, S. R. (2021). Optimizing the Cost and Reliability of Shared Anchors in an Array of Floating Offshore Wind Turbines. *ASCE-ASME Journal of Risk and Uncertainty in Engineering Systems, Part B: Mechanical Engineering*, *7*(4), 1–10. https://doi.org/10.1115/1.4051163.

Festa, O., Gourvenec, S., & Sobey, A. (2024). Comparative analysis of load reduction device stiffness curves for floating offshore wind moorings. *Ocean Engineering*, *298*(September 2023), 117266. https://doi.org/10.1016/j.oceaneng.2024.117266.

Fontana, C. M., Hallowell, S. T., Arwade, S. R., DeGroot, D. J., Landon, M. E., Aubeny, C. P., Diaz, B., Myers, A. T., & Ozmutlu, S. (2018). Multiline anchor force dynamics in floating offshore wind turbines. *Wind*

Energy, *21*(11), 1177–1190. https://doi.org/10.1002/we.2222.

Gilbert, R. B., Choi, Y. J., Dangayach, S., & Najjar, S. S. (2005). Reliability-based design considerations for deepwater mooring system foundations. *Frontiers in Offshore Geotechnics, ISFOG 2005 - Proceedings of the 1st International Symposium on Frontiers in Offshore Geotechnics*, 317–323. https://doi.org/10.1201/noe0415390637.ch29.

Goodwin, P., Ahilan, R. V., Kavanagh, K., & Connaire, A. (2000). Integrated mooring and riser design: target reliabilities and safety factors. *Conference on Offshore Mechanics and Arctic Engineering*.

Gourvenec, S. (2020). Whole-Life Geotechnical Design: What Is It? What's It For? So What? And What Next? In B. Gilbert & P. Jeanjean (Eds.), *Proceedings of the Fourth International Symposium on Frontiers in Offshore Geotechnics*.

Gourvenec, S. (2022). Whole Life Design: Theory and Applications of This New Approach to Offshore Geotechnics. *Indian Geotechnical Journal*, *52*(5), 1129–1154. https://doi.org/10.1007/s40098-022-00627-x.

Gourvenec, S. M., Vulpe, C., & Murthy, T. G. (2014). A method for predicting the consolidated undrained bearing capacity of shallow foundations. *Geotechnique*, *64*(3), 215–225. https://doi.org/10.1680/geot.13.P.101.

Gourvenec, S., Sturt, F., Reid, E., & Trigos, F. (2022). Global assessment of historical, current and forecast ocean energy infrastructure: Implications for marine space planning, sustainable design and end-of-engineered-life management. *Renewable and Sustainable Energy Reviews*, *154*, 111794. https://doi.org/10.1016/j.rser.2021.111794.

GWEC. (2022). *Global Wind Report*. https://gwec.net/global-wind-report-2022/.

Hallowell, S. T., Arwade, S. R., Fontana, C. M., DeGroot, D. J., Aubeny, C. P., Diaz, B. D., Myers, A. T., & Landon, M. E. (2018). System reliability of floating offshore wind farms with multiline anchors. *Ocean Engineering*, *160*(October 2017), 94–104. https://doi.org/10.1016/j.oceaneng.2018.04.046.

Herduin, M. (2019). *Multi-directional loading on shared anchors for offshore renewable energy: definition and preliinary investigation into soil behaviour and anchor performance* (Issue June). University of Western Australia.

Horte, T., Okkenhaug, S., & Paulshus, O. (2017). Structural Reliability Analysis for Mooring Lines in Ultimate and Accidental Limit State. *Proc. Offshore Technology Conference*.

Huang, T., O loughlin, C., Gaudin, C., Tian, Y., & Lu, T. (2020). Drained response of rigid piles in sand under an inclined tensile load. *Geotechnique Letters*, *10*(1), 30–37. https://doi.org/10.1680/jgele.19.00028.

International Energy Agency. (2019). *Offshore Wind Outlook 2019*.

IPCC. (2021). *Climate Change 2021: The Physical Science Basis. Contribution of Working Group I to the Sixth Assessment Report of the Intergovernmental Panel on Climate Change* (A. Masson-Delmotte, V., P. Zhai, S. L. Pirani, C. Connors, S. Péan, et al. (eds.)). Cambridge University Press. https://doi.org/10.1017/9781009157896.

IRENA, & GWEC. (2021). *A next Decade Action Agenda to advance SDG7 on sustainable energy for all, in line with the goals of the Paris Agreement on Climate Chang*. https://www.un.org/sites/un2.un.org/files/2021/09/irena_and_gwec_offshore_wind_energy_compact_-_final_1.pdf.

Jardine, R. J., & Standing, J. R. (2012). Field axial cyclic loading experiments on piles driven in sand. *Soils and Foundations*, *52*(4), 723–736. https://doi.org/10.1016/j.sandf.2012.07.012.

Jenner, C., Finch, M., Finlayson, K., & Harker, G. (2002). Optimising integrated site investigations for offshore wind farm projects. *Proc. SUT Conference on Offshore Site Investigation and Geotechnics.*

Jostad, H. P., Grimstad, G., Andersen, K. H., Saue, M., Shin, Y., & You, D. (2014). A FE procedure for foundation design of offshore structures - Applied to study a potential OWT monopile foundation in the Korean Western Sea. *Geotechnical Engineering*, *45*(4), 63–72.

Kementzetzidis, E., Pisanò, F., Tsouvalas, A., Elkadi, A. S. K., & Metrikine, A. V. (2022). Gentle Driving of Piles at a sandy site combining axial and torsional vibrations: installation tests. *(Submitted for Publication in) Ocean Engineering*.

Kolios, A., Brennan, F., Group, N. A., Building, W., & Kingdom, U. (2009). Reliability Based Design of Novel Offshore Structures. *3rd International Conference on Integrity, Reliability and Failure*, *July*, 20–24.

Kwa, K. A., Festa, O., White, D. J., Gourvenec, S., & Sobey, A. (2023a). Design benefits for plate anchors for floating offshore wind through coupling floater, mooring and geotechnical responses. *Proceedings of the 9th International SUT OSIG Conference "Innovative Geotechnologies for Energy Transition."*

Kwa, K. A., Weymouth, G. D., White, D. J., & Martin, C. M. (2021). Analysis of the added mass term in soil bearing capacity problems. *Geotechnique Letters*, *11*(1), 80–87. https://doi.org/10.1680/jgele.20.00097.

Kwa, K. A., & White, D. J. (2023b). Numerical modelling of plate anchors under sustained load: The enhancement of capacity from consolidation. *Computers and Geotechnics*, *158*(October 2022), 105367. https://doi.org/10.1016/j.compgeo.2023.105367.

Kwa, K. A., White, D. J., Tosdevin, T., Jin, S., & Greaves, D. (2023c). Whole-life modelling of anchor capacity for floating systems: The RSN–CSI approach. *Applied Ocean Research*, *138*(March), 103671. https://doi.org/10.1016/j.apor.2023.103671.

Laham, N. I., Kwa, K. A., White, D. J., & Gourvenec, S. M. (2021). Episodic simple shear tests to measure strength changes for whole-life geotechnical design. *Geotechnique Letters*, *11*(1), 103–111. https://doi.org/10.1680/jgele.20.00124.

Li, H., & Guedes Soares, C. (2022). Assessment of failure rates and reliability of floating offshore wind turbines. *Reliability Engineering and System Safety*, *228*(August). https://doi.org/10.1016/j.ress.2022.108777.

Ma, K., Energy, C., Company, T., Duggal, A., Smedley, P., & Exploration, B. P. (2013). A Historical Review on Integrity Issues of Permanent Mooring Systems. *Proceedings of the Offshore Technology Conference*, *3*.

Moore, B., Easton, A., Cabrera, J., Webb, C., & George, B. (2017). Stones Development: Turritella FPSO-Design and Fabrication of the World's Deepest Producing Unit. *Offshore Technology Conference*.

Pillai, A. C., Gordelier, T. J., Thies, P. R., Dormenval, C., Wray, B., & Parkinson, R. (2022). Anchor loads for shallow water mooring of a 15 MW floating wind turbine — Part I : Chain catenary moorings for single and shared anchor scenarios. *Ocean Engineering*, *May*, 111816. https://doi.org/10.1016/j.oceaneng.2022.111816.

Putuhena, H., White, D., Gourvenec, S., & Sturt, F. (2023). Finding space for offshore wind to support net zero : A methodology to assess spatial constraints and future scenarios , illustrated by a UK case study. *Renewable and Sustainable Energy Reviews*, *182*(April), 113358. https://doi.org/10.1016/j.rser.2023.113358.

Randolph, M., & Gourvenec, S. (2011). Offshore Geotechnical Engineering. In *Offshore Geotechnical Engineering* (First). Spon Press. https://doi.org/10.1201/9781315272474.

Ritchie. (2020). *What are the safest and cleanest sources of energy?* OurWorldInData.Org. https://ourworldindata.org/safest-sources-of-energy

Ronalds, B. F. (2005). Applicability ranges for offshore oil and gas production facilities. *Marine Structures*, *18*(3), 251–263. https://doi.org/10.1016/j.marstruc.2005.06.001.

Sauvin, G., Vanneste, M., Vardy, M. E., Klinkvort, R. T., & Forsberg, C. F. (2019). Machine Learning and Quantitative Ground Models for Improving Offshore Wind Site Characterization. *Proceedings of the Offshore Technology Conference*. https://doi.org/https://doi.org/10.4043/29351-MS.

Shen, Z., Pan, Q., Chian, S. C., Gourvenec, S., & Tian, Y. (2023). Probabilistic failure envelopes of strip foundations on soils with non-stationary characteristics of undrained shear strength. *Geotechnique*, *73*(8), 716–735. https://doi.org/10.1680/jgeot.21.00169.

Shittu, A. A., Mehmanparast, A., Hart, P., & Kolios, A. (2021). Comparative study between S-N and fracture mechanics approach on reliability assessment of offshore wind turbine jacket foundations. *Reliability Engineering and System Safety*, *215*(April), 107838. https://doi.org/10.1016/j.ress.2021.107838.

Stanisic, D., Efthymiou, M., Kimiaei, M., & Zhao, W. (2018). Design loads and long term distribution of mooring line response of a large weathervaning vessel in a tropical cyclone environment. *Marine Structures*, *61*(March), 361–380. https://doi.org/10.1016/j.marstruc.2018.06.004.

Stanisic, D., Efthymiou, M., White, D. J., & Kimiaei, M. (2019). Reliability of mooring lines and piles for a permanently manned vessel in a tropical cyclone environment. *Applied Ocean Research*, *82*(June 2018), 430–446. https://doi.org/10.1016/j.apor.2018.10.019.

The Crown Estate. (2022). *Offshore wind report 2022*. https://www.thecrownestate.co.uk/our-business/marine/offshore-wind.

Tsuha, C. H. C., Foray, P. Y., Jardine, R. J., Yang, Z. X., Silva, M., & Rimoy, S. (2012). Behaviour of displacement piles in sand under cyclic axial loading. *Soils and Foundations*, *52*(3), 393–410. https://doi.org/10.1016/j.sandf.2012.05.002.

Vardy, M., Oppenheimer, M., Dubash, N. K., O'Reilly, J., & Jamieson, D. (2017). The intergovernmental panel on climate change: challenges and opportunities. *Annual Review of Environment and Resources*, *42*(55–75).

Zhang, Z., Wang, T., Chen, Z., & Zhang, J. (2023). Reliability analysis for monopile foundation of offshore wind turbine considering correlated wind and waves and spatially varying soils. *Ocean Engineering*, *286*(P2), 115594. https://doi.org/10.1016/j.oceaneng.2023.115594.

Proceedings of the XVIII ECSMGE 2024
GEOTECHNICAL ENGINEERING CHALLENGES
TO MEET CURRENT AND EMERGING NEEDS OF SOCIETY
© 2024 the Authors
ISBN 978-1-032-54816-6
DOI 10.1201/9781003431749-11
Open Access: www.taylorfrancis.com, CC BY-NC-ND 4.0 license

ECSMGE 24
XVIII EUROPEAN CONFERENCE ON SOIL MECHANICS AND GEOTECHNICAL ENGINEERING

State-of-the-art Report

Basal-reinforced pile-supported embankments, dealing with risks and safety during design and construction

Remblais renforcés sur inclusions rigides, prise en compte des risques et de la sécurité lors de la conception et la construction

S.J.M. van Eekelen*
Deltares, Delft, Netherlands

P.G. van Duijnen
Geotec Solutions, Culemborg, Netherlands

T. Schweckendiek
Deltares, Delft, Netherlands

**suzanne.vaneekelen@deltares.nl*

ABSTRACT: For the safe and cost-effective design and construction of geosynthetic-reinforced pile-supported (GRPS) embankments, four components are essential: (1) A well-validated design model that closely aligns with measurements, (2) A model factor that transforms the results of this design model into 'characteristic' values, ensuring that the results of the model are on the safe side in over 99.7% of the cases, (3) A set of partial factors, calibrated in such a way that the required safety level is achieved and (4) Experience and lessons learned. This paper guides the reader along these four components. The paper shows that the Concentric Arches model offers the closest match to measurements and explains the determination of the model factor and the set of partial factors, as conducted for the design guideline for GRPS embankments CUR226. The paper concludes with some examples of lessons learned from cases involving failures or near-failures.

RÉSUMÉ: Pour une conception et une construction sûres et économiques des remblais renforcés par géosynthétiques sur inclusions rigides (GRPS), quatre éléments sont essentiels: (1) un modèle de conception bien validé qui correspond étroitement aux mesures, (2) un facteur de modèle qui transforme les résultats du dimensionnement en valeurs "caractéristiques", garantissant que les résultats du modèle sont du côté de la sécurité dans plus de 99. 7% des cas, (3) un ensemble de facteurs partiels, calibrés de manière à atteindre le niveau de sécurité requis et (4) l'expérience et les enseignements tirés. Cette publication guide le lecteur le long de ces quatre composantes. Il montre que le modèle des arcs concentriques est celui qui correspond le mieux aux mesures et explique la détermination du facteur de modèle et de l'ensemble des facteurs partiels, comme cela a été fait pour le guide de conception des remblais du GRPS CUR226. L'article se termine par quelques exemples de leçons tirées de cas d'ouvrages défaillants ou proche de la rupture.

Keywords: State of the art; safety and risk analyses; geosynthetic-reinforced pile-supported embankments; lessons learned.

1 GEOSYNTHETIC-REINFORCED PILED EMBANKMENTS, RISKS AND SAFETY

The construction of geotechnical infrastructure often faces challenges associated with soft soils with low strength and high compressibility. Risks include bearing failure, excessive settlement, and slope instability. Furthermore, time and cost are also key elements in the design and construction phases.

To address these concerns and risks, geosynthetic - reinforced pile-supported (GRPS) are a practical and cost-effective solution. They find frequent application in supporting roads, highways, railways, storage tanks, industrial areas, and even buildings. GRPS embankments are quick to build, settlement-free and they cause no damage to nearby sensitive constructions due to horizontal soil deformations. Van Eekelen and Han (2020) published a state-of-the art review of the technology.

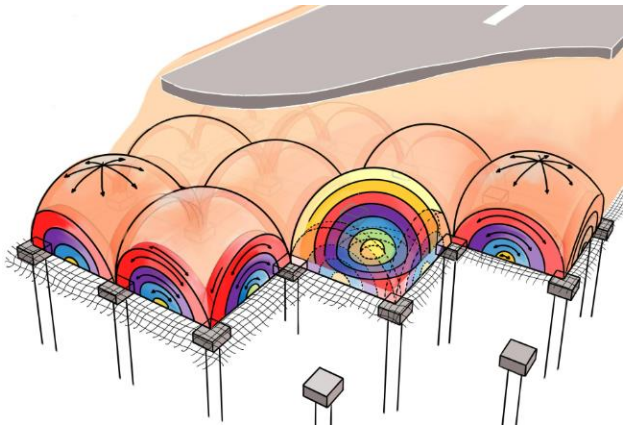

Figure 1. A geosynthetic-reinforced pile-supported embankment. Design methods employ soil arching, as depicted through the Concentric Arches (CA) model of van Eekelen et al. (2013 and 2015). The largest principal forces follow the curves of the hemispheres and 2D arches.

A GRPS embankment includes (Figure 1):

- Piles with or sometimes without pile caps.
- Basal reinforcement, in most cases a geosynthetic reinforcement (GR), positioned at the embankment's base.
- The embankment itself, with the bottom layer (the 'mattress') made of high-quality frictional material, like sand or crushed aggregate (crushed rock or crushed recycled construction material). In some regions, alternatives like high-quality laterite are used.

For the safe and cost-effective design and construction of GRPS embankments, four components are essential:

1. **A well-validated design model (Section 2):** An accurate model that precisely predicts the tensile strain in the GR. This means that the stress distribution, GR forces and deformations are also known.
2. **A model factor (Section 4):** The model factor transforms the calculated GR strain into a 'characteristic' value, ensuring that the calculated GR strain is on the safe side in more than 99% of the cases.
3. **Partial factors (Section 5):** A set of partial factors for load and material properties, to meet the required safety level. The Eurocode gives reliability indices β for this purpose.
4. **Experience and lessons learned (Section 6).**

This paper guides the reader through these four components.

2 VALIDATION OF DESIGN METHODS FOR GRPS EMBANKMENTS

The three main European design methods for GRPS embankments are:

The Concentric Arches (CA) model of van Eekelen et al., (2013, 2015, adopted in the Dutch CUR226, 2016, see Figure 1);

The model of Zaeske (2001), adopted in the German EBGEO, (2011);

The model of Hewlett and Randolph (1988) adopted in both the French ASIRI (2012) and the British Standard (BS8006, 2010).

These models calculate the GR tensile strain and the corresponding GR tensile force. During designing, it should be checked that the design value of the GR tensile force $T_{s;d}$ is smaller than the design value of the long-term GR tensile strength $T_{r;d}$.

We prefer a model that predicts measurements as accurately as possible. Safety will be addressed later and discussed in the next sections.

Figure 2 compares the three European models with 115 measurements from various sources. No model factor or partial factors were applied in these calculations. The figure shows that the Concentric Arches model on matches the measurements best. Although its standard deviation is smaller than for the other models, it remains considerable. Because of its best match with the measurements, the CA model was adopted in CUR226 (2016). Therefore, this paper focuses on the determination of the model factor for the CA model and the partial load- and material factors for CUR226.

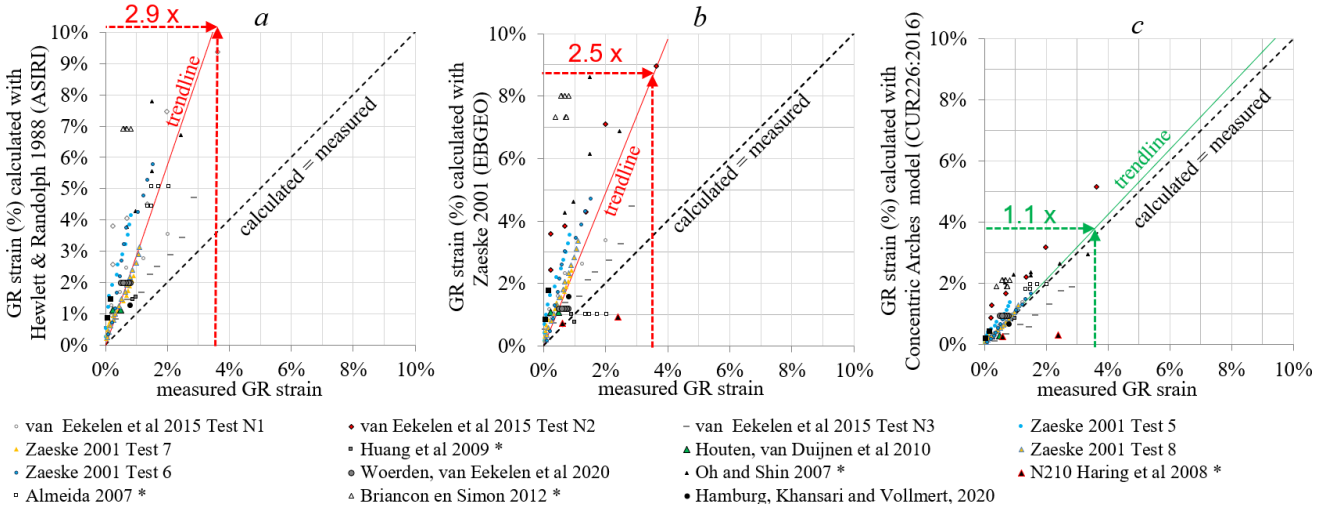

*Figure 2. Comparison of calculations and measurements in field projects and series of experiments. Figure modified after van Eekelen et al., 2015. Calculations were conducted using (a) The soil arching model of Hewlett and Randolph (1988) and uniform load distribution, as adopted in ASIRI (2012), with subsoil support**; (b) Zaeske's soil arching model (2001) and triangular load distribution, as adopted in EBGEO (2011); (c) The Concentric Arches (CA) model for the soil arching (van Eekelen et al., 2013, 2015) and inverse-triangular or uniform load distribution, depending on the subgrade reaction, as adopted in CUR226 (2016).*

***The soil arching model of Hewlett and Randolph (1988) and uniform load distribution was also adopted in BS8006 (2010), but BS88006 does not include subsoil support. This results in higher calculated values and less match with the measurements than in this graph (a).*

3 THE FOUR REFERENCE CASES FOR THE MONTE CARLO ANALYSES

Van Duijnen et al. (2015) presented Monte Carlo (MC) analyses conducted for calibrating both the model factor for the CA model, and the partial factors for CUR226 (2016). This section provides the starting points for these MC analyses. The results of the MC analyses will be presented in Section 4 (model factor) and Section 5 (partial factors).

3.1 Four cases: geometry and soil properties

Table 5 details the four cases that were examined in the MC analyses. Case 3 represents a typical Dutch piled embankment. Cases 1, 2 and 4 are exceptional situations, representing the extremes of the design method.

Table 1. Details of the four cases for the MC analyses.

	Case	1	2	3	4
Pile spacing s_x and s_y	(m)	3.25	1.75	2.25	2.25
Embankment height H	(m)	10	1.5	3.5	3.5
Width square pile cap a	(m)	1.25	0.40	0.75	0.75
Fill friction angle φ	(deg)	35	45	45	35
Surcharge traffic load p	(kN/m^2)	20	50	20	20

In all four cases, the fill unit weight was 19 kN/m^3. The piles, arranged in a square pattern, had square pile caps. The calculations were conducted for a subgrade reaction modulus k of 0 and 100 kN/m^3. Van Duijnen et al. (2015) demonstrated non-square pile arrangements ($s_x \neq s_y$) only slightly affected the resulting values of β.

3.2 Variation coefficients for geometry and embankment fill

Table 2 lists the variation coefficients applied in the calibration study for both geometry and fill and soil properties. These values were determined as follows:

The values for the pile centre-to-centre distance were determined by analysing the measured pile positions in a railway project in Houten in the Netherlands (van Duijnen et al., 2010).

Table 2. Variation coefficients V for soil properties and geometry in the calibration study.

Property	V
Centre-to-centre pile spacing s_x and s_y	0.10 m
Embankment height H	0.05 m
Fill friction angle φ	0.10
Unit weight of the fill γ	0.05
Subgrade reaction modulus k	0.25

The values for the fill and soil properties were default values for common soil types, as recommended in the national annex of EC7.

The student-T distribution for the 95% value was used for the probability distribution of fill and soil, as illustrated in Figure 3 and Figure 4.

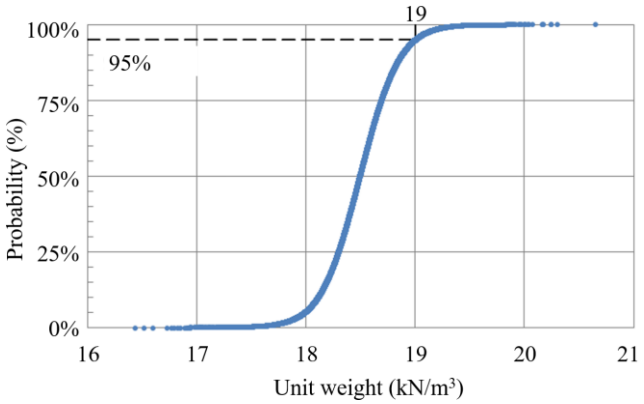

Figure 3. Relationship between the characteristic value of the unit weight γ of the fill (19 kN/m³) and the student-T distribution used in the MC analyses.

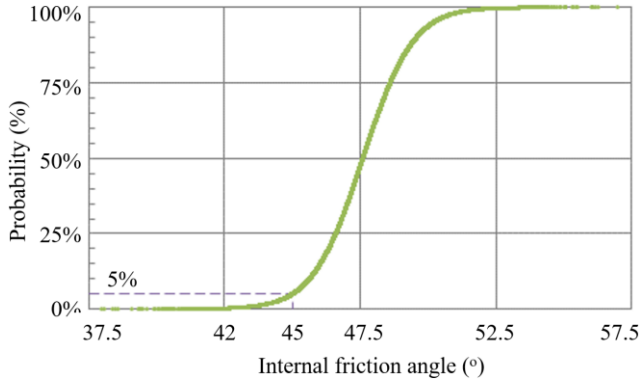

Figure 4. Relationship between the characteristic value of the fill friction angle (45°) and the student-T distribution used in the MC analyses.

3.3 Geosynthetic Reinforcement (GR) properties and variation coefficients

The tensile strength on the label of a GR role represents the short-term strength of the GR leaving the factory. Suppliers of geosynthetic reinforcement (GR) must test the short-term tensile strength for each production batch. Batches are approved only if all tensile strength results exceed the short-term strength indicated on the label.

The strength reduces in time, due to environmental factors, installation damage, and material behaviour (creep, relaxation). The long-term strength is the tensile strength at the end of the lifetime (100 years). This long-term strength was used for the present calibration study, although this resulted in an underestimation of the lifetime reliability.

In the MC analysis, the variation coefficient of 0.05 was applied for the tensile strength. This is a slightly conservative estimate, as the variations provided by the suppliers are somewhat lower.

The GR axial stiffness was chosen at 22 times the design value of the long-term tensile strength, with a variation coefficient of 0.1, resulting in the combinations of long-term tensile strenth and stiffness given in Figure 5. Note that this way to determine the GR axial stiffness differs from design practice, where it is calculated from the short-term strength, using isochronous curves (CUR226; 2016).

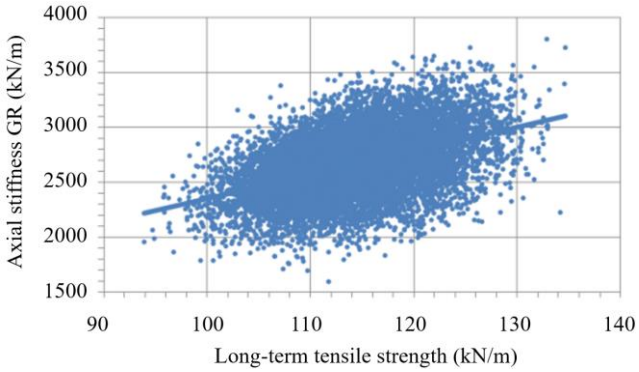

Figure 5. Scatter plot of the applied combinations of long-term tensile strength and axial stiffness of the GR in the MC analyses.

3.4 Surcharge traffic load: reduction of target reliability index β

Eurocode EC1-4 gives characteristic traffic loads. With their current insights, the authors would create a stochastic model for traffic load, with a variation coefficient of 0.14. This was not done at the time. Instead, the loads applied in the calibrations were nominal values from EC1-4. Since the uncertainty in the load had already been accounted for in these nominal values, the target reliability index β was reduced, as further detailed in Section 5.3.

4 CALIBRATION OF THE MODEL FACTOR

4.1 Statistical analysis

Figure 6 shows the ratio between the measured GR strains r_e (experimental value) and calculated GR strains r_t (theoretical value) for the 115 tests of Figure 2. For 22 of the 115 measurements, we find $r_e/r_t > 1.0$, meaning that the calculation under-predicted the measurement. So, these 22 were predictions on the unsafe side. The remaining 115 calculated values matched or exceeded the measured values ($r_e/r_t \leq 1.0$). NEN-EN 1990 (2011, Eurocode 0, annex D) recommends determining the model factor using the mean model error factor (correction factor) $b = r_e/r_t$, which is 0.727 with a variation coefficient about 0.702 for the 115 measurements considered. The distribution is assumed lognormal.

Table 3 lists the model error statistics for different subsets of data, with an increasing maximum subgrade reaction modulus. Soft soil areas are most relevant for

the safety analyses of GRPS embankments. Therefore, we focus on the 22 data sets with k ≤ 236 kN/m^3. Figure 7 shows these 22 data sets.

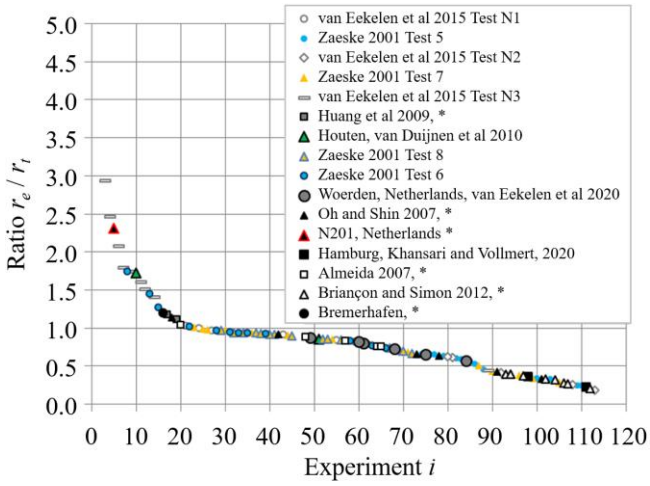

*Figure 6. Ratio of measured GR strain (r_e) and calculated GR strain (r_t), in descending order. Two results (values 5-8) are beyond the displayed scale. The symbol * in the legend refers to references given in Van Eekelen et al., 2015. The data in the figure is the same as in Figure 2c but presented differently.*

Table 3. Mean value model error factor $b = r_e/r_t$ and its variation coefficient, based on subsets of the 115 considered measurements, with different maximum subgrade reaction moduli k.

Subgrade reaction modulus k (kN/m^3)	Number of data sets N	Mean correction factor $b = r_e/r_t$	Coefficient of variation V
0	11	0.833	0.163
≤ 158	17	0.806	0.246
≤ 236	**22**	**0.775**	**0.306**
≤ 480	46	0.679	0.857
≤ 1200	54	0.700	0.868
≤ 3138	115	0.727	0.702

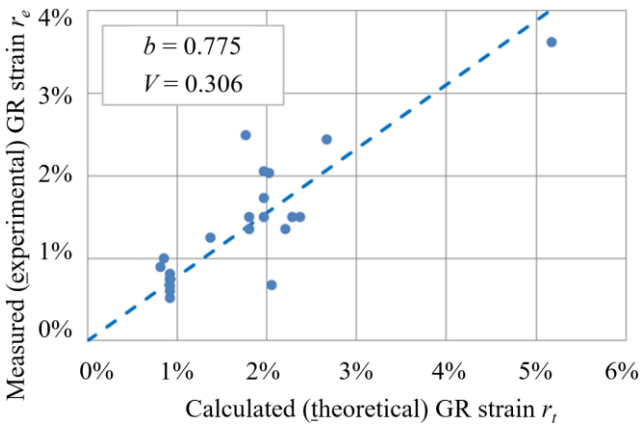

Figure 7. Measured versus calculated GR strain for the 22 data points of Figure 6 with subgrade reaction modulus k ≤ 236 kN/m^3.

4.2 Determination of the model factor

The model factor was determined for the SLS, as follows. First, the GR strain was calculated for case 3 in the SLS (no partial factors), using the Concentric Arches (CA) model. The resulting maximum GR strain was about 2.7%.

Then, an MC analysis was conducted. For each draw, the GR strain, calculated with the CA model, was multiplied with a factor b, whose value was determined using the above determined mean value for b of 0.775 and its variation coefficient of 0.306.

Figure 8 shows a detail of the result of the MC analysis of case 3. From this result, we determine the GR strain for the SLS target reliability index, which is 2.8, corresponding with the target probability of failure is 0.24% (≅ 5% · 5%, $P_f = \Phi(-2.8)$). The figure shows that the GR strain for 0.24% failure is about 3.60%.

The model factor was calculated with:

$$\gamma_{model} = \frac{\varepsilon(P_{f=0.24\%})}{\varepsilon_t} = \frac{3.6}{2.7} \approx 1.4 \qquad (1)$$

If the GR strain is calculated using the CA model in CUR226, using characteristic input values, and the calculated GR strain is multiplied with the model factor γ_{model}, then, the resulting calculated GR strain exceeds the measured GR strain in 100% - 0.24% = 99.76% of the cases. In other words, reality is worse than the calculation in 0.24% of the cases in the SLS (β = 2.8). Van Duijnen et al. (2015) conducted this analysis for all four cases, and further elaborated on this model factor determination.

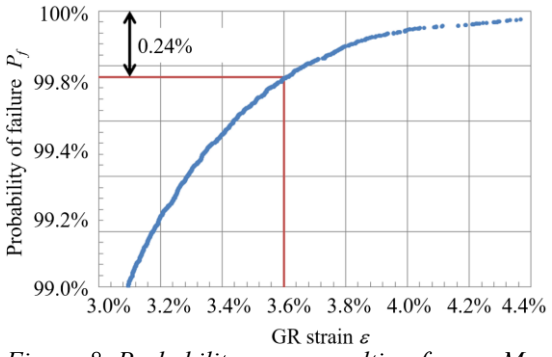

Figure 8. Probability curve resulting from a Monte Carlo analysis in SLS (all partial factors = 1.0) for case 3, to determine the model factor for the Concentric Arches model.

5 CALIBRATION OF THE PARTIAL FACTORS

5.1 Introduction

An advantage of using partial material- and load factors is that it allows for taking into account the influence of uncertainty in input parameters.

Van Duijnen et al. (2015) calibrated a set of partial material and load factors for CUR226 (2016). They demonstrated that using these factors ensures meeting the reliability indices β as required by NEN-EN 1990 (2011, Eurocode 0). This section summarizes the calibration of the partial factors for CUR226 (2016).

To the best of the knowledge of the authors, CUR226 (2016) was the first to base these factors for a GRPS embankment on statistical analyses, utilizing measurement data and probabilistic analyses.

5.2 Failure mechanisms and target probability of failure

Table 4 gives the target reliability index β, and the corresponding probability of failure P_f, for the three reliability classes (RC), as recommended by Eurocode 0 EN 1990 for new structures. In Section 5.3, we will adjust these values to account for the fully probabilistic treatment of resistance, while using the design values of the surcharge load (i.e. already including a safety margin). As previously mentioned, the authors would not adopt this approach today. Instead, they would create a stochastic model for traffic load and keep the same values of β.

Table 4. Required reliability classes (RC) and the corresponding probability of failure P_f for new GRPS embankments. From Eurocode 0 EN 1990.

Reliability index β / Prob. of failure during lifetime P_f		Service function (selection and experience of the authors)	Design service life (years)
RC 1	3.3 /4.8·10^{-4}	Roads, greenhouses	50
RC 2	3.8 / 7.2·10^{-5}	Abutments viaducts/bridges	50 to 100
RC 3	4.3 / 8.5·10^{-6}	Railways, important bridges	50 to 100

For CUR226, these target values were interpreted to apply to the entire structural system, comprising various failure mechanisms. Figure 9 shows a simplified fault tree, with the most relevant failure mechanisms for a GRPS embankment.

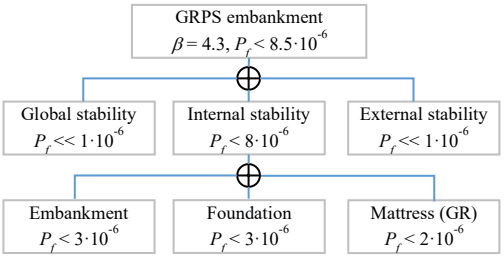

Figure 9. Fault tree with the most relevant failure mechanisms for a GRPS embankment (RC3).

The system's failure probability depends on how individual failure mechanisms interact. For example, if the reinforcement ruptures or the bearing capacity is lost, the entire system may fail. In such cases, the upper limit of the system failure probability is the sum of individual failure mechanisms (an OR-gate ⊕).

We assigned target probabilities of failure to individual failure mechanisms based on their role in the system, as defined in the fault tree (Schweckendiek et al., 2012). When designing, the assignment of target probabilities of failure is somewhat arbitrary, as long as the required system target reliability is achieved. It is economic to assign higher target values to failure mechanisms with costly mitigation. For CUR226 (2016), we defined fault trees for the three reliability classes and used them in the Monte Carlo (MC) analysis.

Notice that defining target reliability values based on system reliability considerations, as common for flood defences in the Netherlands (Schweckendiek et al., 2013), leads to stricter target values compared to the commonly used approach in the Eurocodes context, which is assigning the target reliability values stated in EN 1990 directly to individual failure modes and structural members. In that sense, the calibration presented here is slightly conservative.

5.3 Reduction target reliability index β to account for using design values of traffic load

Unfortunately, no appropriate statistical model was available for explicit uncertainty of the traffic load. As mentioned in Sections 3.4 and 5.2, EC1-4 gives characteristic nominal values of the traffic loads. Since the uncertainty in the load has already been accounted for in these nominal values, we reduced the target reliability index β using a standardized influence coefficient $\alpha_R = 0.8$ for the resistance as suggested by ISO 2394.

$$\beta_{T|s_d} = \Phi(-\alpha_R \beta_T) = \Phi(-0.8\beta_T) \qquad (2)$$

Table 5 presents the resulting target reliability indices in de ultimate limit state (ULS) for the three reliability classes with and without surcharge load.

Table 5. Target reliability index for the ULS.

	RC 1	RC 2	RC 3
Without surcharge load β_T [1]	3.5	4.0	4.6
Conditional target reliability index $\beta_{T\,|Sd}$ using the design/characteristic value of the surcharge load [2]	2.8	3.2	3.7

[1] *These values for ‚no traffic' are higher than the Eurocode values, this is the result of the fault space allocation in the fault tree of Figure 9.*
[2] *These values for ‚traffic' were determined from the fault tree of Figure 9 and then reduced using equation (2).*

5.4 Calibration of the Partial Factors

The calibration of the partial factors was done for the four reference cases of Section 3. The partial factors for RC1 and RC2 were determined iteratively, as shown in the flow chart in Figure 10.

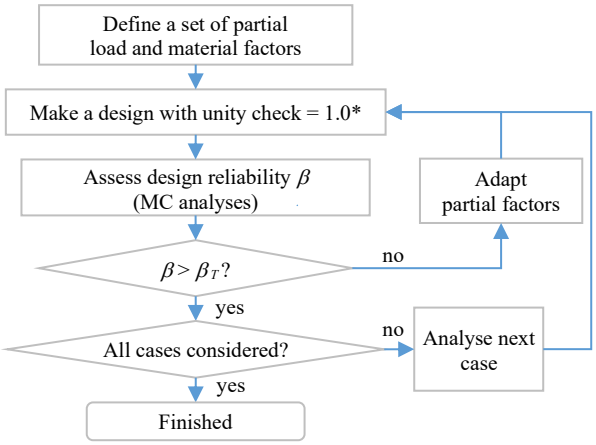

*Figure 10. Flow chart of the calibration workflow for the determination of a set of partial factors that ensures compliance with the target reliability for all four test cases. *Unity check = 1.0 means: design value of the GR tensile strength = design value of the tensile force.*

Back in 2015 however, it was unrealistic to conduct the eighty million calculations necessary for an MC analysis for RC3. Therefore, the approach of Figure 10 was altered, with the purpose of producing Figure 11. Instead of making a design with unity check = 1.0, MC analyses were conducted for various chosen values of tensile strength. Each MC analysis resulted in one dot in Figure 11. For case 3, all necessary calculations were conducted, while for the other cases, the lines were extrapolated as shown in Figure 11.

5.5 Results

Table 6 presents the partial factors that meet the required reliability for all cases without overdesigning the construction.

Table 6. Resulting partial material- and load factors and the model factor. These were adopted in CUR226 (2016).

	SLS	ULS		
Partial factor		**RC1**	**RC2**	**RC3**
Angle of internal friction	1.00	1.05	1.10	1.15
Unit weight	1.00	0.95	0.90	0.85
Tensile strength GR	1.00	1.30	1.35	1.45
Axial stiffness GR	1.00	1.00	1.00	1.00
Subgrade reaction modulus	1.00	1.30	1.30	1.30
Surcharge load	1.00	1.05	1.10	1.20
Model factor	1.40	1.40	1.40	1.40

Van Eekelen and Vollmert (2018) compared the safety levels achieved by the safety approaches of EBGEO (Lastfall 1) and CUR226 (RC1 and RC3, Table 6). They concluded that the safety level of EBGEO exceeds that of CUR226 in most cases. This suggests that there is room for optimization on the German side, as CUR226 meets the reliability requirements of Eurocode 0 EN 1990.

Figure 11 presents the calculated relation between the characteristic (95%) long-term tensile strength and the calculated reliability index β (the dots) for the four reference cases of Table 1. The figure was produced using the partial factors of RC3, as explained in the previous section.

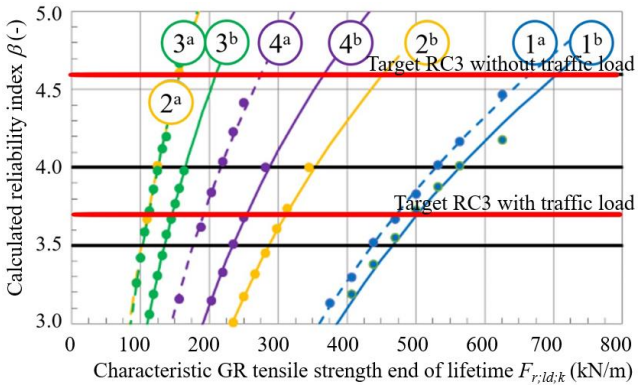

Figure 11. Reliability indices β, calculated using MC analyses with the RC3 partial factors of Table 6, for the four cases of Table 1, (a) without surcharge load and (b) with surcharge load. Subgrade reaction modulus k = 0 kN/m³.

The figure shows for example the following:

- For a thick embankment (case 1), the reliability index β is much less sensitive for the GR tensile strength than for thin embankments (case 2).
- Traffic loading affects the reliability of a thick embankment much less than for a thin embankment (1a and 1b of the thick embankment of case 1, are positioned close to each other, while there is a large distance between 2a and 2b, that belong to the thin embankment of case 2).
- The influence coefficient for the surcharge load ($\alpha_R = 0.8$) may be overestimated for GRPS embankments, reducing the target β_T too much

in certain cases. Let us consider case 1, without surcharge load (1a). For the target β_T without surcharge load for RC3 (4.6, see Table 5), Figure 11 gives an required tensile strength of about 650 kN/m. However, for the case with surcharge load (case 1b, and β_T=3.7, see Table 5), Figure 11 gives a required tensile strength of about 500 kN/m. It is evident that it is not logical to require less tensile strength for the case with surcharge load. So, the target reliability index β_T for the cases with surcharge load (denoted as $\beta_{T|s_d}$) should be considered as a lower limit. Therefore, the results in Figure 11 were assessed using engineering judgement, to finalize the final decisions on the partial factors for surcharge load.

Table 7 shows the calculated reliability indeces β for the four cases for the serviceability limit state (SLS) and the three reliability classes (RC1, RC2 and RC3) in the ultimate limit state (ULS). The table was made using the procedure of Figure 10.

The table illustrates that it was not possible to find a set of partial factors that exactly match the required reliability for all cases. The red-coloured italicised values in Table 7 are slightly below the target reliability index. The situation without surcharge load is not realistic for practical designs, and therefore these relatively low values were accepted.

Table 7. Calculated reliability index β.

	Without surcharge load				With surcharge load			
	SLS	**RC1**	**RC2**	**RC3[1]**	**SLS**	**RC1**	**RC2**	**RC3[1]**
Target β	2.8	3.5	4.0	4.6	2.8	2.8	3.2	3.7
Case								
1	2.82	3.56	4.05		2.81	3.58	4.02	
2	*2.67*	*3.31*	*3.67*		2.63	3.28	3.65	
3	2.78	3.50	3.98	4.75	2.76	3.49	3.95	4.31
4	*2.72*	*3.42*	*3.84*		2.70	3.38	3.80	

[1]*Due to time limitations, not all cases were analysed in RC3 because at least eighty million calculations were required for these RC3 cases.*

6 EXPERIENCE, CHALLENGES AND LESSONS LEARNED[1]

The preceding sections looked at the safety philosophy of GRPS embankments. Combining the well-validated CA model with the explained model factor and partial factors, makes it possible to create a safe and cost-effective design.

GRPS embankments are increasingly being constructed worldwide, and in most cases, perform excellently. They show minimal to no settlement and deformations. As a result, minimal maintenance is required, saving both costs and hindrance. However, occasionally, failures or near-failures occur before, during or after the construction of the GRPS embankment. Piles may lose their bearing capacity, and sometimes the GR ruptures or a significant instability occurs. This section addresses some of those cases of failures or near-failures. The purpose of this section is to be educational.

6.1 Case 1 – GR rupture

Case 1 in Figure 12 shows a road that was excavated after the rupture of a significant portion of the GR. In this case, the GR strength was found to be insufficient. The authors speculate that three factors may have contributed to this failure.

1. The embankment height was insufficient, measuring less than the 66% of the net diagonal spacing between the piles, which is the minimum embankment height required by CUR226. Van Eekelen and Han (2020) list minimum height requirements from various standards or guidelines. Most require more height than CUR226. In the past, insufficient embankment height has been identified as a contribution factor to failures. In the 1980s, attempts to reduce the load on the geosynthetic by decreasing the embankment height proved counterproductive. The soil arching became less efficient, and the structure became more susceptible to local loads. It was later understood that sufficient embankment height is crucial for proper soil arching development. Gue and Tan (2015), for example, described an example of 'punching through the embankment like 'mushrooms' and studied the case with numerical analyses. They attributed the mushroom problem to ineffective soil arching due to unsuitable fill and a large pile spacing relative to the fill height.

[1] *Chapter 6 provides narratives of failure cases on the brink of collapse or cases of failure. The authors have carefully crafter their words to investigate the causes of the damages, approaching the subject with both care and respect. It is acknowledged that the authors may nog possess full or accurate information about certain details, potentially leading ot incorrect conclusions. In an effort to shield the privacy of those involved, some details have been altered or stories combined. Furthermore, this section will never achieve completeness. The goal of this passage is to facilitate learning.*



Figure 12. Case 1. Ruptured GR in a GRPS embankment.

2. The GRPS embankment was designed using FEM only, raising the risk of overlooking numerical calculation errors and resulting in under-design. It is advisable to employ a well-validated analytical model in addition to the numerical model.
3. Finally, the geosynthetics were applied directly on top of piles caps with relatively sharp edges, despite attempts during construction to smoothen them. The geosynthetics were not protected with a protection layer of sand or for example a nonwoven between pile cap and reinforcement.

6.2 Case 2 – Pile rupture

In case 2, nearly all piles ruptured due to a change in the construction sequence.

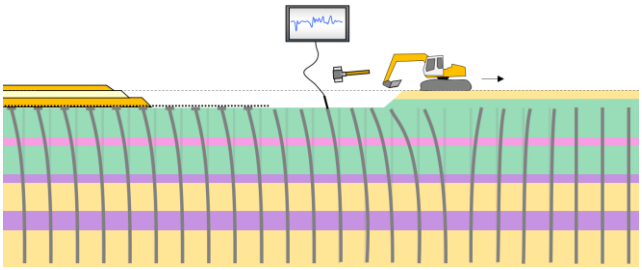

Figure 13. Case 2. The GRPS embankment was designed with the assumption that excavation would take place first. The deformations in the figures were based on FEM calculations but exaggerated.

A highway had to be constructed on a thick layer of peat and organic clay. The piles had to be installed up to 2.0 m below ground level. The top two meters, were excavated to install the pile caps and the reinforced mattress.

The designers had anticipated installing the piles after excavation. Expecting limited bending moments, the piles were lightly reinforced and prestressed. This provided a significant cost saving due to the large quantity of piles.

However, the decision was made to change the construction sequence. The piles were first driven up to 2 m below the ground surface, followed by excavation using a relatively lightweight excavator.

The piles found themselves between the excavated area on one side and the yet-to-be-excavated soil with the excavator on the other side. As the excavator continued working, all the piles bent first in one direction and then in the other direction, breaking one by one, as shown in Figure 13.

It is particularly bitter that, in this case, all piles underwent acoustic testing to assess their condition. However, the cracks visible in the measurement charts went unnoticed until after the completion of the full embankment.

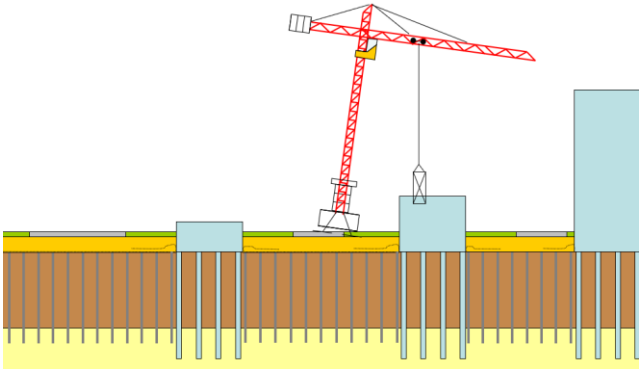

Figure 14. Case 3. Residential area. The GRPS embankment was not designed for the crane loading during the apartment construction.

6.3 Case 3 - Overloading

In case 3, a residential area was built, with the surrounding infrastructure, such as roads and green spaces, founded on GRPS embankments. The GRPS embankments were constructed first, followed by the construction of the apartments. Heavy cranes were employed for apartment construction. Unfortunately, during the design phase, the anticipated crane loads were underestimated, resulting in severe damage to the GRPS embankments.

6.4 Cases 4 and 5 – Loss of subsoil support

In the 2010s, some failures were related to the use of a design method that did not anticipate the decrease in and loss of subsoil support. Cases 4 and 5 are examples that experienced excessive post-construction deformations due to this reason. In both cases, the columns or piles stayed intact.

Case 4 (Camp and Siegel, 2006), located in coastal South Carolina, involved a road on a GRPS embankment, constructed on reclaimed marshland with 6.5 m of svery soft highly plastic clay. Shortly after completion, the GRPS embankment developed an irregular surface with humps at the column locations and depressions in the areas between the

column locations. The differential deformation was so significant that the road had to be closed almost immediately after completion.

In this case, the design method implicitly assumed a lifelong subsoil support, resulting in the use of three layers of PP geogrid with a total tensile strenth of 20 kN/m, significantly less than the current European guidelines require. Subsoil settlement caused overloading of the GR, leading to further loading of the subsoil and excessive deformations.

Additionally, the low embankment height (1.1 m) compared to the pile spacing (centre-to-centre 2.5 m) contributed to the issues.

Case 5 was a residential area in Europe, founded on a GRPS embankment, installed on a 10 m soft soil layer. Again, subsoil settlement overloaded the GR, causing rupture and transferring most of the load to the soft subsoil, resulting in substantial differential settlement. The area experienced widespread cracking and deformation of the buildings and other structures soon after construction. As a consequence, many of the houses became uninhabitable and substantial portions of the site had to be demolished.

Cases 4 and 5 had been designed in using the same design method that does not anticipate the decrease in and loss of subsoil support. Nowadays, most well-validated design methods can include the consequences of settling subsoil.

6.5 Cases 6 and 7 – Adjacent fills

The site of case 6 site faced poor accessibility due to soft soil. To enhance accessibility, a geotextile was installed before the construction phase began. The geotextile extended beyond the embankment and was left in place.

Later, a heap of fill was placed adjacent to the embankment, causing significant horizontal ground deformation. This resulted in the displacement of the edge pile row from beneath the mattress. Case 7 also suffered from damage to an adjacent fill, except that there was no geotextile underneath.

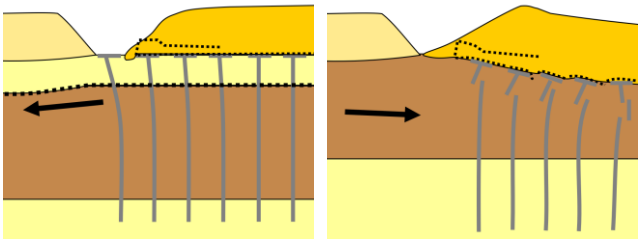

Figure 15. Cases 6 and 7. Fill adjacent to GRPS embankment. Left: with a left-in-place geotextile underneath. Right: without.

6.6 Recommendations

The following recommendations were based on the above listed, and other personal experiences:

- Use one widely accepted design guideline or standard that uses a well-validated analytical method to design the GR. Do not combine partial factors from different guidelines.
- In addition to the analytical design method, use numerical analyses to determine the pile bending moments and check for excessive deformations or instability. Switch on secondary effects.
- Be sure to include the various construction and loading phases in the design calculations. Stick to the plan or make additional calculations.
- Be sure to account for future reduction in subsoil support, which often occurs due to consolidation under the weight of the working platform, erosion, or groundwater changes.
- Be sure to meet boundary conditions, like the minimum embankment height, given by the design guidelines. Keep within the geometries for which the calculation rules were validated.
- Be sure to calculate with correct values for the long-term GR characteristic strength, including strength decreases due to factors such as installation damage, UV light exposure, the environmental conditions it encounters, and time-dependent behaviour, such as creep or relaxation. In the Netherlands, a Code for Design Parameters of Geosynthetic Reinforcement (2023) has recently been published for this purpose, encompassing all existing requirements for determining the design parameters of geosynthetic reinforcement, including end-of-lifetime tensile strength and GR stiffness. Additionally, the Code clarifies requirements where necessary.
- Never hesitate to seek a review of your design.

REFERENCES

Almeida, M.S.S., Ehrlich, M., Spotti, A.P., Marques, M.E.S., 2007. Embankment supported on piles with biaxial geogrids. Geotech. Eng., 160(4), 185-192.

ASIRI (2012). *Recommendations for the design, construction and control of rigid inclusions ground improvements* (The French version is of 2012, The English version is of 2013).

Briançon, L., Simon, B., 2012. Performance of Pile-Supported Embankment over Soft Soil: Full-Scale Experiment, *J. Geotechn. Geoenviron.* Eng. 2012.138:551-561.

BS8006 (2010). *Code of practice for strengthened/reinforced soils and other fills*. British Standards Institution, UK.

Camp., W.M. and Siegel, T.C. (2006). Failure of a column-supported embankment over soft ground. *4th Int. Conf. on Soft Soils*, Vancouver, B.C., USA.

CUR226 (2016). See Van Eekelen & Brugman (2016).

EBGEO (2011). *Recommendations for Design and Analysis for Earth Structures using Geosynthetic Reinforcements*. German Geotechnical Society (German version is of 2010, English version if 2011).

Gue, S.S., Tan, Y.C. (2015). Failures of Ground Improvement Works in Soft Ground. Chapter 3 in: *Ground Improvement Case Histories: Embankments with Special Reference to Consolidation and Other Physical methods*. Elsevier Geo-Engineering book series. DOI: 10.1016/S1571-9960(05)80026-6.

Haring, W., Profittlich, M., Hangen, H. (2008). Reconstruction of the national road N210 Bergambacht to Krimpen a.d. IJssel, NL: design approach, construction experiences and measurement results. In: Proceedings 4th European Geosynthetics Conference, September 2008, Edinburgh, UK.

Hewlett, W.J. and Randolph, M.F. (1988). Analysis of piled embankments. *Ground Engineering*, 21(3): 12-18.

Huang, J., Han, J., Oztoprak, S., 2009. Coupled Mechanical and Hydraulic Modeling of Geosynthetic-Reinforced Column-Supported Embankments. J. Geotech. Geoenviron. Eng. 2009.135:1011-1021.

Khansari, A. and Vollmert, L., (2020). Load transfer and deformation of geogrid-reinforced piled embankments: field measurement. *Geosynth. Int.* 27 (3) 332-341. DOI: 10.1680/jgein.19.00002

NEN 1990: NEN-EN 1990+A1+A1/C2 (nl). *Basis of structural design,* ICS 91.010.30; 91.080.01, (December 2011, Eurocode 0).

Oh, Y.I., Shin, E.C., 2007. Reinforced and arching effect of geogrid-reinforced and pile-supported embankment on marine soft ground. Marine Georesources and Geotechnology, 25, 97-118.

Schweckendiek, T., Vrouwenvelder, A.C.W.M., Calle, E.O.F., Jongejan, R.B., Kanning, W. (2013): *Partial Factors for Flood Defences in the Netherlands. Modern Geotechnical Codes of Practice – Development and Calibration*, Fenton, G.A. et al. (eds.). Special Geotechnical Publication. Taylor & Francis.

van Duijnen, P.G., van Eekelen, S.J.M. and van der Stoel, A.E.C. (2010). Monitoring of a Railway Piled Embankment. *Proc. 9ICG*, Brazil, 1461-1464.

van Duijnen, P.G., Schweckendiek, T., Calle, E.O.F., van Eekelen, S.J.M. (2015). Calibration of Partial Factors for Basal Reinforced Piled Embankments. *Proc. Geotechnical Safety and Risk V*, Rotterdam, Netherlands. DOI: 10.3233/978-1-61499-580-7-431.

van Eekelen, S.J.M., Bezuijen, A. and van Tol, A.F. (2013). An analytical model for arching in piled embankments. *Geotext. & Geomembr*. 39: 78-102. DOI: 10.1016/j.geotexmem.2013.07.005.

van Eekelen, S.J.M., Bezuijen, A. and Van Tol, A.F. (2015). Validation of analytical models for the design of basal reinforced piled embankments. *Geotext. & Geomembr*, 43(1): 56 - 81. DOI: 10.1016/j.geotexmem.2014.10.002.

van Eekelen, S.J.M. and Brugman, M.H.A., Eds. (2016). *Design Guideline Basal Reinforced Piled Embankments* (CUR226). CRC Press, Delft, Netherlands.

van Eekelen, S.J.M. and Vollmert, L. (2018). The design guideline basal reinforced piled embankments; The Dutch CUR226:2016 and the German EBGEO:2010; A comparison of design models and safety approaches. *Proc. 11ICG*, Seoul, Rep. of South-Korea.

van Eekelen, S.J.M. and Han, J. (2020). Geosynthetic-reinforced pile-supported embankments: state of the art. *Geosynth. Int*., 27 (2) 112-141. DOI: 10.1680/jgein.20.00005.

van Eekelen, S.J.M., Venmans, A.A.M., Bezuijen, A., van Tol, A.F. (2020). Long term measurements in the Woerden geosynthetic-reinforced pile-supported embankment. *Geosynth. Int.* 27 (2), 142-156 DOI: 10.1680/jgein.17.00022.

van Eekelen, S.J.M, Schneider, M., Hell, M., Wittekoek, B., Makowska, K., Zdanowicz, K., Pandrea, P., Sieńko, R., Schauber, P., Topolnicki, M., Zachert, H. (2024). 3D small-scale tests on steel-reinforced piled embankments. *Proc. ECSMGE24*, Lisbon, Portugal.

Voorschrift Ontwerpparameters Geokunststof-wapening. (2023). (Code for design parameters of geosynthetic reinforcement). Committee of the Dutch Ministry of Public Works (Rijkswaterstaat) and the Dutch railway authority (ProRail). Downloadable for free at: https://ngo.nl/publicaties/ (in Dutch).

Zaeske, D., 2001. *Zur Wirkungsweise von unbewehrten und bewehrten mineralischen Tragschichten über pfahlartigen Gründungselementen.* PhD Thesis. Schriftenreihe Geotechnik, Uni Kassel, Heft 10, February 2001 (in German).

Proceedings of the XVIII ECSMGE 2024
GEOTECHNICAL ENGINEERING CHALLENGES
TO MEET CURRENT AND EMERGING NEEDS OF SOCIETY
© 2024 the Authors
ISBN 978-1-032-54816-6
DOI 10.1201/9781003431749-12
Open Access: www.taylorfrancis.com, CC BY-NC-ND 4.0 license

ECSMGE 24
XVIII EUROPEAN CONFERENCE ON SOIL MECHANICS AND GEOTECHNICAL ENGINEERING

State-of-the-art Report

Tremie Concrete for special geotechnical works – a story about performance and sustainability

Tremie Concrete pour travaux géotechniques spéciaux – une histoire de performance et de durabilité

K. Beckhaus*
BAUER Spezialtiefbau GmbH, Schrobenhausen, Germany
**Karsten.Beckhaus@bauer.de*

ABSTRACT: Five decades ago, when the first standards on concrete were written, concrete technology was relatively simple. Modern "high-performance" concrete is far more complex. Specifying the essential criteria for successful placement of concrete in submerged conditions using tremies at depths in excess of 100 m is a major challenge. A joint task group of EFFC and DFI (European Federation of Foundation Contractors and Deep Foundations Institute) has brought together a broad church of industry experts to find a common understanding on this topic. The group is presently updating the 2nd edition of the EFFC/DFI Guide to Tremie Guide for Deep Foundations, and edition 3 will be released by the end of 2024. It will also highlight the need for sustainability, to which the Tremie Guide contributes with its performance-based concept to design concrete, giving all options to materialize a lower-carbon concrete without diminishing quality aspects. Future approaches may be founded on lessons learned from numerical modelling which is a key to better understanding the complex interactions governing concrete flow mechanisms. The task group continues its work to validate simulations to justify new requirements, e.g., a reduction in workability retention for long pours. It is hoped that the recommendations in the Tremie Guide will become contractually binding norms to make them broadly applied in practice, resulting in a higher quality reliability in quality and optimised sustainability.

RÉSUMÉ: Lorsqu'il y a plus de 50 ans les premières normes sur le béton et le béton trempé ont été rédigées, la technologie du béton était assez simple. Le béton moderne est beaucoup plus complexe, ce qui permettrait de le qualifier également de béton « à hautes performances ». Préciser les critères nécessaires à une mise en place réussie du béton en conditions immergées dans les fondations actuelles, qui peuvent dépasser des profondeurs de 100 m, est un défi. Un groupe de travail conjoint de l'EFFC et de la DFI (Fédération européenne des entrepreneurs en fondations et Deep Foundation Institute) a réuni des experts du secteur mais également des consultants pour trouver une compréhension commune sur des sujets connexes. Le groupe met actuellement à jour la 2e édition du Guide to Tremie Guide for Deep Foundations, et l'édition 3 sera publiée d'ici fin 2024. Elle mettra également en lumière le besoin de durabilité, auquel le Guide Tremie contribue avec son concept basé sur la performance. Concevoir du béton, en offrant toutes les options pour matérialiser un béton bas carbone sans diminuer les aspects qualitatifs. Les approches futures pourraient s'appuyer sur les enseignements tirés de la modélisation numérique, clé pour mieux comprendre les interactions complexes régissant les mécanismes d'écoulement concrets. Le groupe de travail poursuit ses travaux pour valider les simulations afin de justifier de nouvelles exigences, par ex. concernant une rétention d'ouvrabilité réduite pour de longues heures de mise en place du béton. À terme, les réglementations révisées sur le béton seront fusionnées dans des normes pertinentes et contractuellement contraignantes pour les rendre largement appliquées dans la pratique, pour une plus grande fiabilité de qualité et pour optimiser la durabilité de la construction.

Keywords: Fresh concrete; performance; quality; sustainability.

1 HISTORY

The very first meeting of the EFFC/DFI Concrete Task Group (CTG) took place on 23rd of January 2014 in Amsterdam. It was initially set up by the European Federation of Foundation Contractors (EFFC) that had discussed, in their annual general meeting in October 2013, the quality of geotechnical works in the light of concrete quality. It was decided that a broad group of experts should discuss the lack of suitable test methods and sufficient testing of relevant properties of fresh concrete for placement in deep foundations and

provide a state-of-the-art report. The CTG, presently comprising 15 full members, has been working in a very trustful and target-oriented atmosphere for more than 10 years. With a constant overall target to reduce defects in deep foundations, see Figure 1, caused directly by inadequate workability or stability of concrete, or indirectly by a lack of consideration of related parameters effecting the flow of concrete and/or proper filling of the excavation.

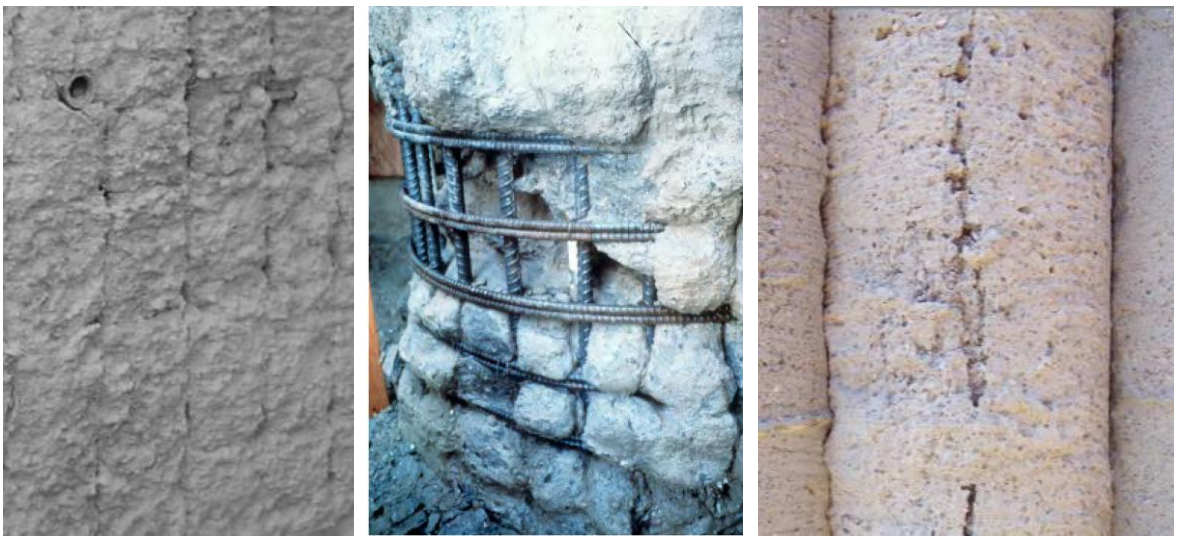

Figure1. Imperfections in deep foundations.

The CTG decided from the very start to invite consultants to join the group to bring their technical views on these complex and exclusively quality-related topics. A group of corresponding members, consulting the group and reviewing status papers and drafts, was also established as well as a group of academics to give scientific advice.

The major focus has always been on the specification and testing of fresh concrete as the core of a "Tremie Guide". It was intended to use the Australian tremie handbook [CIA Z17, 2012] as a start-off, which was created in the same sense to give updated recommendations better suited for modern tremie concrete. Given the fact that the CTG chairman was also a member of the Australian working group it was guaranteed that all relevant information beyond the published recommended practice was considered in its entirety.

The basic scope and structure of the "EFFC/DFI Guide to Tremie Concrete for Deep Foundations" (Tremie Guide) set out in the 1st Edition (2016) was repeated in the 2nd Edition (2018) and will remain the same for the 3rd edition. To the core of the fresh concrete specification and testing, other topics were added including design, execution, and the need or benefit of monitoring the quality by non-destructive test method. The 1st edition also contained recommendations on support fluids. The task of supporting open boreholes and trenches using support fluids is a complex subject which cannot be adequately covered in a simple sub-section. A separate support fluid task group was therefore established, and a guide was issued in 2019. This group is currently working on the 2nd edition, implementing lessons learned from a field research study that is ongoing. That same approach had been applied for the evolution of the Tremie Guide.

Based on a comprehensive study of international standards and literature the CTG acknowledged the demand for a detailed test program for fresh concrete properties. By that time, colleagues representing the Deep Foundation Institute from America joined the Group. Meetings attended by up to 20 full members took place in European cities, as well as the USA.

A big step forward occurred when approximately €150,000 was received from industry sponsors. The money was used to carry out an extensive test program in the laboratory and in the field, in Europe and the USA. This was contributed to by specialist contractors opening their construction sites for a detailed investigation of the concrete used. Researchers from the Technical University in Munich and from the Missouri University of Science and Technology collected data for multiple concrete mixes, reflecting also their technical boundary conditions of application, for later interpretation and assessment of results, with the main findings merged into the 2nd Edition 2 of the Tremie Guide.

Finally, it was already decided for the preparation of the 2nd Edition to add a chapter on Numerical Modelling Methods for backing up the Group's understanding of tremie flow and cross-checking

reasonable conclusions regarding flow mechanisms within an excavation during casting. A sub-group with mainly academics was established and worked separately on what computer programs can and cannot prove without exceeding their limited capabilities to deliver reliable simulations.

After the 2nd Edition had been released – again for free download from the homepages at effc.org and dfi.org – the Group was silent for a period of 4 years until it met again during the DFI/EFFC Conference on Deep Foundations and Ground Improvement in Berlin in May 2022. It was decided to produce a 3rd Edition, in order to: -

- emphasise the need to reduce greenhouse gas emissions,
- strengthen the recommendations regarding acceptance criteria with respect to testing,
- add new findings from numerical modelling,
- update individual sections where users had asked for clarifications.

2 THE TREMIE GUIDE EDITION 3

As the name suggests, the Guide to Tremie Concrete for Deep Foundations is limited to the application of the "tremie method" to install cast-in-situ elements like bored piles, diaphragm walls or elements, for which a typical set-up is shown in Figure 2. The Guide defines the tremie method as follows:

„*Concrete pouring method by use of a tremie pipe in order to prevent the concrete from segregation or contamination by the fluid inside the excavation, where the tremie pipe – after the initial placement – remains immersed in previously poured, workable concrete until the completion of the concreting process*".

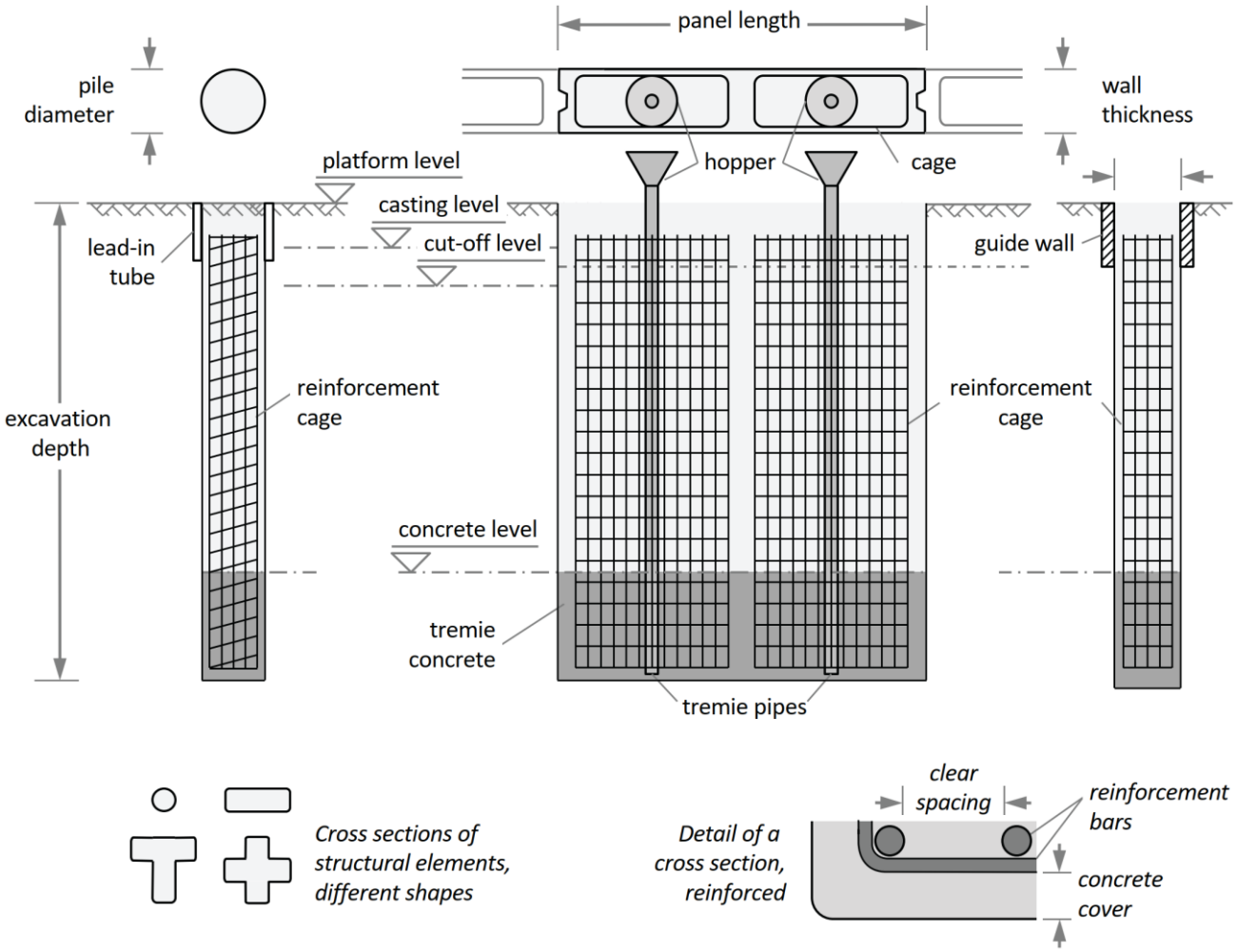

Figure 2. Examples of deep foundations.

Anyone working in the deep foundations sector will know that concrete and additive technology continually advances and becomes ever more complex. When normative regulations were established decades ago, a blend of Portland cement and aggregates mixed with enough, but not too much water framed the boundaries of concrete technology. Bored Piles or Diaphragm Walls had not been 100 m

deep, or even deeper, at that time. Concrete technology advanced drastically at the same time, as the deep foundation industry expanded the boundaries. However, test methods have not evolved at the same rate. That means in turn, that a single test for the concrete‘s consistency, like a slump test, is no longer sufficient to test fresh concrete for geotechnical works with much higher requirements on workability than decades ago.

The water to cement ratio as one of the main factors to control strength and other physical properties after hardening, remains the prevailing parameter in concrete mix design. In order to meet execution demands, both sufficient workability and stability of the fresh concrete are the essential pre-condition to ensure a complete filling, and a full integrity of the completed works. The focus of the Tremie Guide!

2.1 General

The background has been presented by the history of the Concrete Task Group founded to reduce defects in deep foundations.

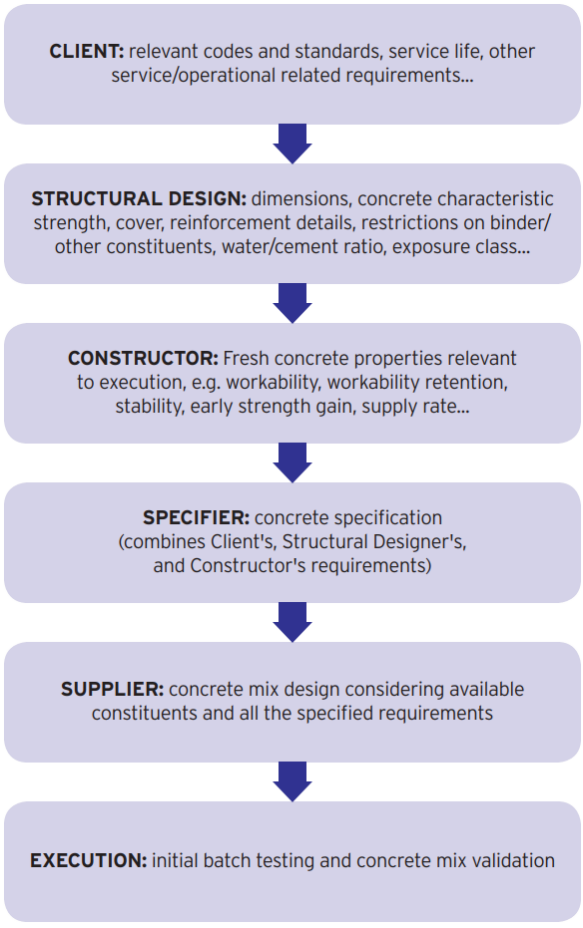

Figure 3. Typical evolution of concrete mixes.

The primary purpose of the Guide to Tremie Concrete for Deep Foundations (Tremie Guide) is to give guidance on fresh concrete characterisation with respect to its performance, the concrete mix design process, and the methods used to test the fresh concrete. The principles of this Guide apply to tremie concrete for deep foundations but may also be applied for other forms of deep foundations (e.g., continuous flight auger piling).

Figure 3 summarises how the demanding and often conflicting requirements should be considered throughout the development of a concrete mix. The Guide highlights the important areas that require careful consideration in order to minimise the potential risks, including the appropriate structural detailing and the use of state-of-the-art execution methods.

It is strongly believed, and that’s why the Tremie Guide is addressing all stakeholders, that getting the mix right can only be achieved via a joint approach between the Constructor, the Structural Designer, and the Concrete Supplier.

2.2 Design considerations impacting concrete flow

The structural design of deep foundations is a specialist subject requiring both structural and geotechnical input, as it must also consider the conditions for the execution of the deep foundation works. However, within the context of the Tremie Guide, the recommendations are limited mainly to the detailing of the reinforcement cages.

It is obvious that the reinforcement bars, in their longitudinal (usually vertical) and transversal combined configuration present a considerable obstruction to flow. The main criteria to obey are subsequently enough clear space for the concrete to flow through „windows“, and the concrete cover to allow complete filling of the excavation and embedment of the reinforcement. It should be recognised that the required minimum cover for execution $c_{min,execution}$ for ensuring concrete placement is independent from the structural need for a minimum cover to ensure bond or durability. The designer should consider specifying a minimum clear spacing and a nominal cover respecting both demands.

Figure 4 summarises these main recommendations, which are explained in more detail in the Tremie Guide. It should also be noted that for the concrete placement in deep foundations a larger clear distance in relation to the maximum grain size of concrete aggregate D_{max} is needed to avoid blocking, and that for practicable reasons the outer dimensions of the cage need to include a tolerance, Δd_c for its installation into the excavation with a nominal dimension equal to that of the excavation tool.

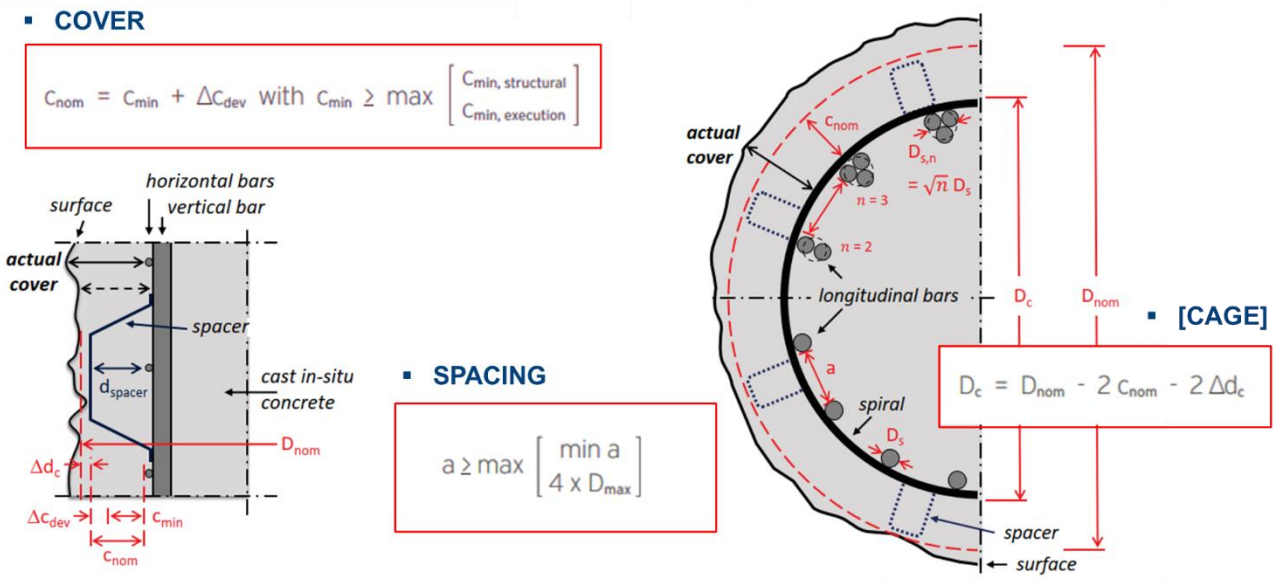

Figure 4. Considerations for detailing a reinforcement cage in deep foundations (also applicable to rectangular).

2.3 Properties of tremie concrete

It has already been explained that a principal task for the CTG has been to consider modern concrete technology. There was a consensus to focus on the right performance of fresh concrete, driven by the rheology of the bulk concrete mix, but also – on a microscale – of the paste where inter-particle mechanisms and chemical actions become relevant. In this context, the principle – normative – requirements for self-levelling, self-compacting by gravity, and filling the excavation, are all governed by the concrete's workability characteristics. Stability characteristics must avoid the negative effects of segregation, bleeding or filtration. A sufficient control of stiffening (with time) is a matter of workability retention.

Figure 5 explains Tremie Concrete performance in simple rheology terms, and gives evidence why Tremie Concrete should not be mistaken with a self-compacting or self-consolidating concrete, often referred to as ‚SCC'. In comparison to normal concrete that is vibrated to overcome the yield value to initiate flow, Tremie Concrete and SCC both have a much lower yield and a much lower viscosity, which is the resistance to flow, once started. However, Tremie Concrete does need a significantly higher yield than SCC mainly in order to control stability e.g., avoid segregation over often long workability retention times, achieved by retarding admixtures (that are seldom used for SCC). At the same time, the viscosity of Tremie Concrete is significantly lower than for SCC, mainly to ease distribution and to limit the time to empty a truck i.e., to reduce total pouring times, which in turn limits the time for any segregation to occur.

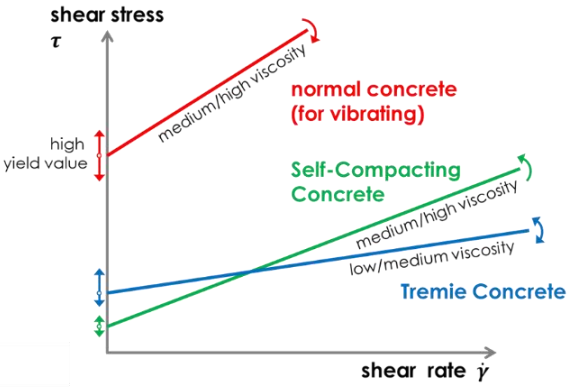

Figure 5. Qualitative comparison of rheology for different types of concrete.

2.4 Concrete mix design

The right concrete mix design has to be based on a good general knowledge of concrete technology. The section just highlights typical steps in developing a concrete mix design for deep foundations and assumes that suppliers have a sufficient range of established concrete mix designs. However, as the Tremie Guide also presents non-normative test methods to better characterise fresh Tremie Concrete, additional considerations on mix design, constituents, and proportioning might be useful also for concrete technology generalists.

2.5 Specifying and testing of concrete, and quality control of concrete production

In this central section of the Tremie Guide, "A New Approach to Specifying Fresh Concrete" is presented.

As indicated in the sections above, fresh tremie concrete cannot be described by a single measure of consistence (workability) only. As stated in the Guide,

the consistence of a concrete is the best characterisation for its ability to fill the excavation and to "squeeze" through openings in the reinforcement cage. However, more characterisation, and testing, is needed to ensure good performance.

The EFFC/DFI research program has clearly revealed that for fresh Tremie Concrete, the Slump Flow (SF) test is much more sensitive than the widely used slump or flow table tests. Figure 6 comprises a preferred range for a SF target value to be specified as recommended in the 2nd Edition of the Guide that will be narrowed down to a default value for typical applications in the 3rd Edition.

In combination with the Slump Flow test, it is literally no extra effort to also get an indication of the concrete's viscosity and stability, two more important characteristics. As the test equipment for this "triple test" is the standard slump test equipment, as shown in Figure 7, plus a stopwatch, there should be no issue at all to implement such testing on a regular basis i.e., also on site for standard acceptance testing if specified.

In fact, the Slump Flow test not only shows the initial workability but also, by repeated testing, its development over time. The workability retention test validates the end of workability that occurs after placement, see Figure 8.

In the context of necessary workability retention, the decisive question to answer is, how long the concrete load is being moved or displaced before finally cast. This could happen, for example for the first load, before the pour is completed. And Numerical Modelling can help to better understand dependencies, as explained in section 2.9.

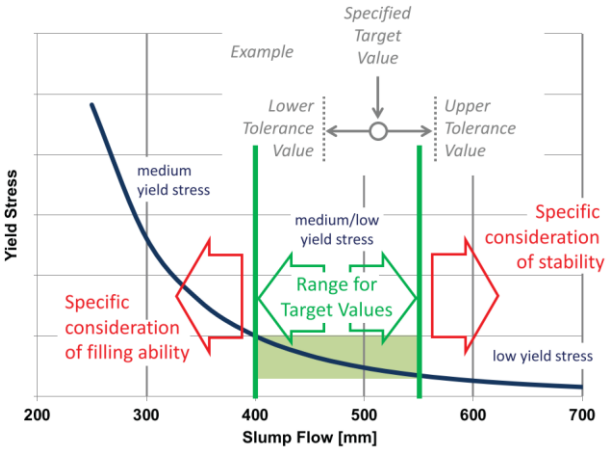

Figure 6. Slump Flow curve related to yield stress and recommended range for tremie concrete (Figure 11, ed 2).

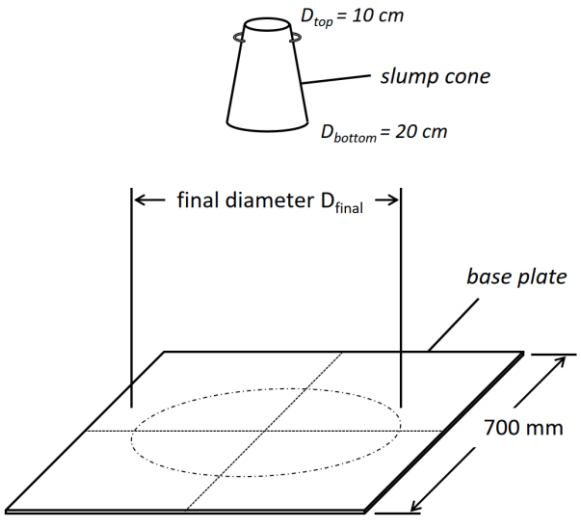

Figure 7. Test equipment for combined slump flow, slump flow velocity and VSI test.

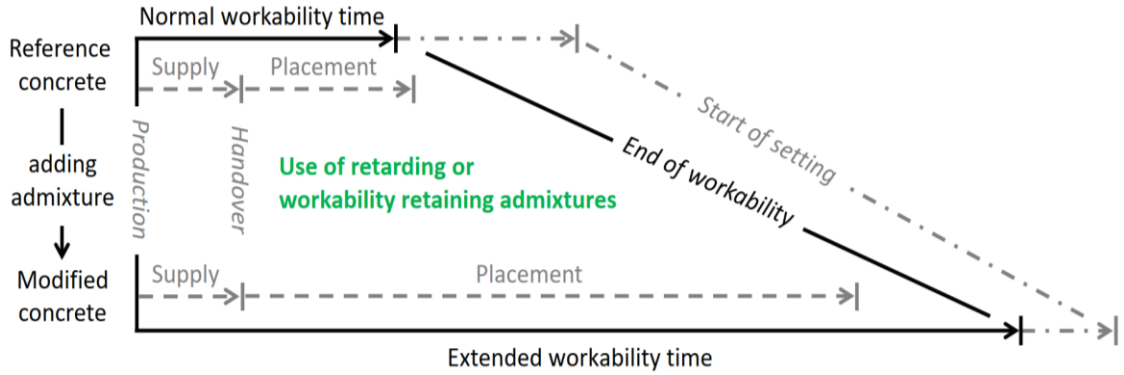

Figure 8. Extension of workability time.

2.6 Execution

Techniques and methods used prior to concreting and for the actual tremie pouring operation are clearly within the scope and responsibility of the specialist contractor. However, a quality control inspection & test plan may vary according to country or region. As European, American and International Standards and Codes of Practice vary, the Guide limits its recommendations to what is considered good practice, without scrutinising individual state-of-the-art practices. Execution parameters contribute greatly to a successful concrete placement and will have influence on the final distribution of concrete in a completed element.

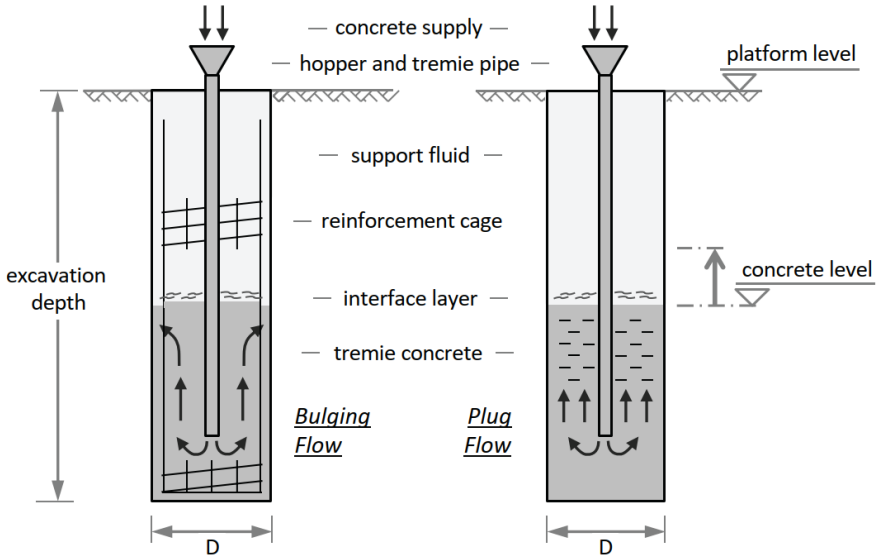

Figure 9. Schematic of bulging and plug flow.

Consensus in the Group was built on a principle of understanding concrete flow mechanisms. Based on experience and observations on many tremie concrete pours, and backed up by numerical modelling, there are two extremes of how fresh concrete displaces earlier poured concrete and distributes through an excavation. Figure 9 shows, in a simplified schematic, the bulging flow path in the case of maximum friction at the outsides of the excavation e.g., by a reinforcement cage, and the plug flow in case of literally no friction restricting the flow at the outside.

The most critical step in the tremie concreting process is attributed to the initial placement. The first batch or batches of concrete have to be continuously poured until a safe embedment of the open tremie pipe is achieved, by a concrete level in the excavation affecting an outside pressure at the outlet (equal to the inside hydrostatic pressure in the tremie pipe (levelled after the dynamic flow downwards), high enough to let the concrete level in the tremie pipe above the outside concrete level. This stage is shown in the centre of Figure 10. Other relevant parameters are discussed in detail in the Tremie Guide.

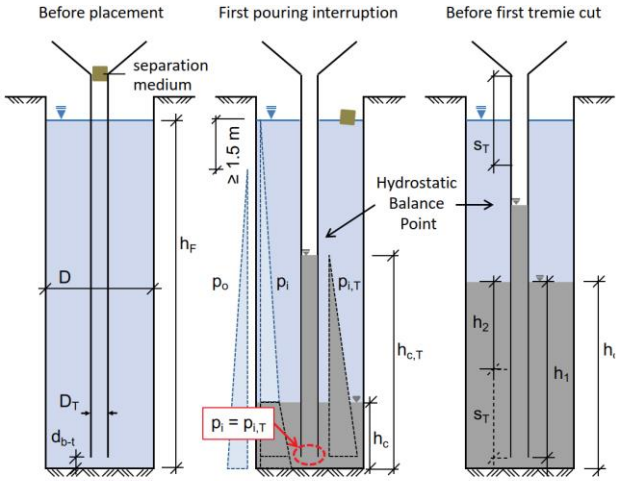

Where:

h_F	Fluid level in excavation
D_T	Diameter of tremie pipe
D	Dimension (diameter or thickness) of excavation
d_{b-t}	Distance from bottom of excavation to tremie pipe outlet
h_c	Concrete level in excavation
$h_{c,T}$	Concrete level in tremie pipe (= hydrostatic balance point)
h_1/h_2	Embedment of tremie pipe before (1) / after (2) tremie pipe cut
s_T	Section length of tremie pipe section to cut, with: $h_2 \geq 3$ m [10ft]
p_o/p_i	Hydrostatic pressure outside (o) / inside (i) of excavation
$p_{i,T}$	Hydrostatic pressure inside the tremie pipe

Figure 10. Phases in the tremie pour sequence.

2.7 Full scale trials

This brief section in the Tremie Guide emphasises the potential of full-scale trials to identify problematic conditions and address these before commencement of the permanent works. These might not be obvious before starting a new project. The extent and scope should be proportionate to the project size.

The components to be tested should be selected from a review of:

- the design and detailing,
- the fresh concrete performance,
- the constructor's placement methods, overall experience and capability, and
- the experience in the given ground properties.

Any extra time and costs needed for such trials must be recognised by the client at an early stage and specified in detail in the tender documents. In any event, it is recommended to perform on-site conformity testing to verify or allow adaption of the concrete mix design usually developed in the supplier's laboratory.

2.8 Quality control of completed works

It is essential that the Constructor complies with relevant standards for quality assurance and control, and that the production process is supervised and undertaken by competent persons with suitable training, qualifications and experience.

Some imperfections of the hardened concrete of the deep foundation element are possible even though good practice construction methods were applied by the Constructor. Quality control requirements for the completed works should therefore make allowance for acceptance of some imperfections where these are not significant with regard to the structural performance and durability of the completed works. To support efficient and consistent inspection and acceptance, acceptable imperfections should be clearly identified in work procedures and inspection and test requirements. Optional non-destructive testing methods might assist, and their use should be planned upfront in detail. To give one example with relevance to execution: testing pipes are usually pre-installed in the excavation by attaching them to the reinforcement cage, and their configuration must obey the same rules as for the reinforcement bars to ensure the required clear spacing for concrete flow.

2.9 Numerical modelling of concrete flow

This section is the most dynamic regarding reaction on consideration of the latest developments. To cope with the new knowledge generated at a scientific level, it requires time to publish the validated results.

A 4th Edition of the Tremie Guide is planned which will present further modelling results once completed. This will allow a better understanding of concrete flow mechanisms and the sensitivity to changes in various parameters such as concrete rheology, clear spacing, cover thickness, volume and height of the open excavation to be filled.

It should be noted that numerical modelling is used to understand principal interrelations resulting in flow patterns. It has not been, and will not be, intended to use a numerical model as a realistic digital twin. To do so, the methods would need to allow realistic simulations not only of bulk flow but also for stability issues like concrete segregation which in turn would affect the workability and filling ability of the fresh concrete in a real and usually very complex situation.

3 FUTURE

A key objective of the CTG was to translate the Tremie Guide's approach to applying the performance concept to the design and testing of tremie concrete into standards. A significant step has been to move away from a descriptive minimum cement content, which is required in the older generation execution standards for Bored Piles and Diaphragm Walls (EN 1536 and EN 1538) in Europe. New, performance-related, but also more specific regulations not only improve the quality of completed works, but also make it possible to improve sustainability by reducing cement and thus the carbon footprint of foundations.

In favour of a clear assignment of concrete topics to the relevant European standard EN 206 on Concrete – Specification, performance, production and conformity, concrete related regulations were copied and pasted from the standards for the execution of special geotechnical works (EN 1536, EN 1538, EN 12699 and EN 14199) without any harmonisation, let alone a revision of the content in the context of modern concrete technology and modern execution aspects.

Subject to the formal approval of CEN, Figure 11 shows the relationship between the future EN 206-3 and the relevant execution standards for concrete placement. For bored piles and diaphragm walls produced in accordance with EN 1536 and EN 1538, tremie concrete is standardised due to the applied excavation method, amongst others.

It should also be noted that EN 206 defines tasks for the specifier, the producer and user in its parts -1 and -3 which are relevant for concrete in general and for tremie concrete in particular. This establishes the mutual endeavour of all parties involved to work together, as is also defined in the scope and purpose of the Tremie Guide. The right concrete will never be a

product that is blindly taken off the shelf in future either. But the new EN 206-3 paves the way for specifying and testing the required performance in the respective area of application more precisely. Engineering assessment and concrete-technology expertise remain essential.

EN 206-3 not only opens up the standard for plastic concrete to cover applications that may go beyond load-bearing structures, but also prescribes the Slump Flow test method for tremie concrete as the future main criterion. The relevant clause states that "Tremie concrete shall be specified by slump flow, by a target value, based on a detailed engineering assessment." The standard allows to choose the actual target value from the range from 400 to 550 mm or to set to 450 mm, with a maximum tolerance of +/- 50 mm, as recommended in the Tremie Guide.

Regarding all three main characteristics of fresh concrete (workability, workability retention and stability), EN 206-3 refers to normative and non-normative test methods based on the Tremie Guide, which are described in an informative annex. This informative annex will become superfluous once the same test methods have become normative. Standardisation within the EN-12350 series for fresh concrete test methods has been applied for at corresponding task group under the umbrella of CEN/TC 104 for Concrete and Related Products.

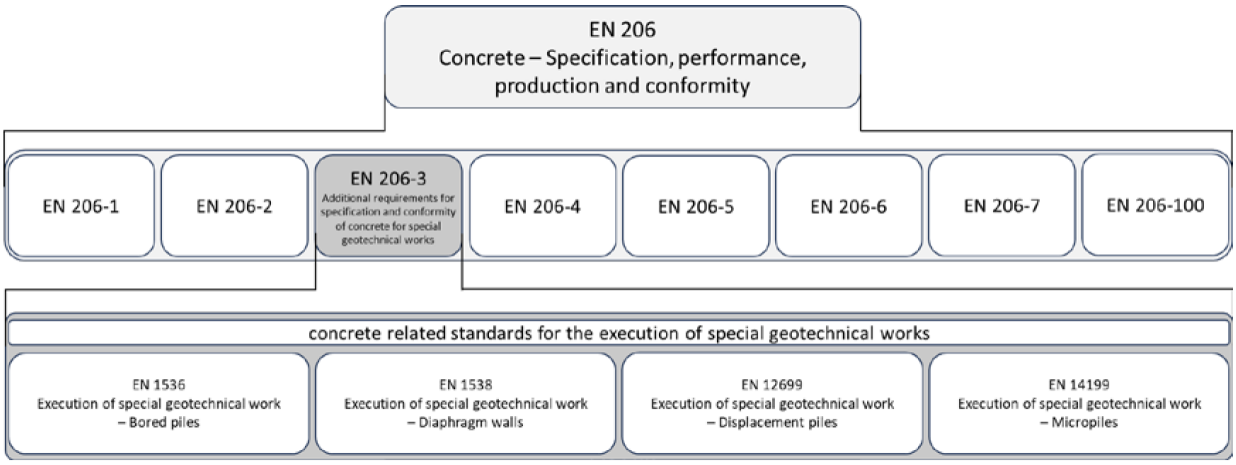

Figure 11. Relationship between EN 206-3 and concrete related standards for the execution of special geotechnical works.

4 CONCLUSIONS

Up to date, in a 10-year period, the joint EFFC/DFI Concrete Task Group has made great efforts to establish a Guide to Tremie Concrete for Deep Foundations in its 3rd Edition to be published shortly. A 4th Edition is already in preparation, which will incorporate the last validated findings from Numerical Modelling.

Already from the 1st Edition in 2016, the Guide has focused on improving the quality throughout the whole process of in-situ casting of deep foundations. To do so, the Guide has always been intended as a practical addition to existing standards, not a substitute. Project specifications, standards and codes should always take precedence.

However, the Guide assists individuals and corporations involved in the procurement, design, and construction of bored piles and diaphragm walls including Owners/Clients, Designers, General Contractors and Specialist Contractors.

ACKNOWLEDGEMENTS

The author is grateful for the continuous and extraordinary support provided by the members of the EFFC/DFI Concrete Task Group and wishes to express his sincere thanks to all experts and sponsors who have contributed to the Tremie Guides.

REFERENCES

CIA Z 17 (2012). Recommended Practice, Tremie Concrete for Deep Foundations, Concrete Institute of Australia.

EFFC/DFI (2018, 2024). Guide to Tremie Concrete for Deep Foundations, European Federation of Foundation Contractors and Deep Foundation Institute, draft for 3rd Edition from 2024, based on 2nd Edition from 2018.

Proceedings of the XVIII ECSMGE 2024
GEOTECHNICAL ENGINEERING CHALLENGES
TO MEET CURRENT AND EMERGING NEEDS OF SOCIETY
© 2024 the Authors
ISBN 978-1-032-54816-6
DOI 10.1201/9781003431749-13
Open Access: www.taylorfrancis.com, CC BY-NC-ND 4.0 license

ECSMGE 24
XVIII EUROPEAN CONFERENCE ON SOIL MECHANICS AND GEOTECHNICAL ENGINEERING

State-of-the-art Report

Cutoffs in dams: Overview and recent developments

Les parois étanches dans les barrages: Aperçu et développements

G. Pereira*
Soletanche Bachy, Rueil Malmaison, France
**gustavo.pereira@soletanche-bachy.com*

ABSTRACT: The purpose of dams is to retain water or, in the case of tailings dams, to retain saturated materials. In most cases, the body of a well-performing dam can be considered impervious; however, seepage through the foundation depends on the geological conditions and is often excessive. This seepage is usually controlled by grout curtains, cutoffs, or a combination of both. Illustrated by recent case studies, this paper will present and discuss cutoffs and their recent technological developments: different construction techniques and materials constituting the cutoffs; excavation equipment; and the monitoring technologies used during and after excavation to ensure the quality of the final product. The challenges of new-build construction and of dam repair will also be addressed.

RÉSUMÉ: Les barrages ont pour but de retenir l'eau ou, dans le cas des barrages à stériles, de retenir des matières saturées. Dans la plupart des cas, le corps d'un barrage en bon état peut être considéré comme étant imperméable ; cependant, les infiltrations à travers les fondations dépendent des conditions géologiques et sont souvent excessives. Ces infiltrations sont généralement contrôlées par des rideaux d'injections, des coupures étanches ou par une combinaison des deux. Illustré par des études de cas récentes, cet article présentera et discutera les coupures étanches et leurs développements technologiques récents : différentes techniques de construction et matériaux constituant les coupures ; équipement d'excavation ; et les technologies de contrôle utilisées pendant et après l'excavation pour s'assurer de la qualité du produit final. Les particularités associées à la construction de barrages neufs et à la réparation des existants seront également abordés.

Keywords: Dam, cutoff, dam remediation.

1 INTRODUCTION

Following very intense development in the 20th century, and in particular until the 1970s, dam construction has slowed significantly in recent decades. The reasons for this slowdown are multiple; nevertheless, dams remain today fundamental infrastructures for irrigation, human consumption, power generation, energy storage and flood control, among others.

In the near future, at the same time that energy consumption will maintain its upward trend, worldwide population will keep increasing and climate change will compound the effects of water scarcity and floods, the installed storage capacity worldwide will dwindle (due to sedimentation of reservoirs), and dams built in the mid-20th century will be many decades old. For these reasons, dam construction and remediation initiatives are likely to increase, globally as a whole if not in every country. Due to the relevance of dams, this paper aims to present developments that may be used in the future, both for new build and remediation projects. So as to accomplish their general role of storing water, dams need to be as watertight as possible. Dams rely on the use of practically impervious materials to ensure that minimal seepage occurs through the body of the dam (be it concrete, low permeability backfill, synthetic membranes, asphalt, or others).

Seepage through the foundation, however, depends above all on the hydraulic conductivity of the *in situ* geological formations, which can vary greatly depending on its nature (e.g. alluvium, rock) and state (fine or coarse alluvium; fractured or massive rock; etc.), but is frequently incompatible with the dam's intended purpose and needs to be controlled. This is commonly achieved by grouting and/or cutoffs. It should also be noted that, besides limiting the amount of seepage through the foundation and hence the loss of water in the dam, grout curtains and cutoffs play a key role in the stability of the dam by limiting downstream uplift pressures.

A cutoff is formed by impervious elements installed in the ground up to an impervious stratum. It

requires the removal (or at least restructuration) of the *in situ* material during its installation. This is contrary to grouting, which materializes a barrier by filling the voids of the foundation material. This paper will only address the specific case of grouting when it is performed in conjunction with cutoffs.

The subject of cutoffs is vast, be it in terms of construction techniques, materials, or other aspects. This paper does not intend to perform an exhaustive review of the subject; instead, its focus will be on interesting recent developments and techniques, as well as less common aspects of construction and design. A more exhaustive review, albeit one with less updated information and references, can be found in ICOLD (2018).

2 CONSTRUCTION METHODS

Cutoffs can be broadly divided into positive cutoffs and semi-positive cutoffs (ICOLD, 2005). Positive cutoffs are those in which the *in situ* ground is excavated to allow the installation of an engineered material. This is the case of diaphragms and secant-pile cutoffs, among others. Positive cutoffs can be further sub-divided into single-stage cutoffs, in which the fluid used to stabilise the trench will harden and serve as the permanent cutoff material (in the case of a cemente-bentonite slurry wall), and two-stage cutoffs, in which the drilling fluid will be displaced by the final material (usually a tremied concrete formulation).

Semi-positive cutoffs are those where the original soil is mixed in place with a binder. This is, for example, the case of soil mixing and jet grouting.

2.1 Diaphragms

Diaphragms are a type of positive cutoff that includes soil-bentonite walls, cement-bentonite walls and concrete diaphragm walls (plastic or conventional concrete). Soil-bentonite walls, excavated with backhoe or similar, are common in America as a cost-effective method for shallow cutoffs; these will not be addressed in this paper.

The other types of wall use the diaphragm wall technique, developed since the 1950s, in which alternate primary panels are installed followed by secondary panels, and the interface between both is ensured by different types of joints (which will be adressed in chapter 2.3). The excavation equipment has evolved continuously, from rope grabs to the efficient and powerful hydraulic grabs still used today for excavation of soil and soft rocks. Depths over 125 m can be attained, with thicknesses up to 2000 mm.

Arguably the single most important diaphragm wall development for cutoffs was the development of the hydromill (Hydrofraise) by Soletanche in the 1970s, for it allowed the excavation of much stronger rocks. Hydromills have since been continuously developed, namely in terms of capacity and precision.

Roller bits have been used in hydromills for hard rock excavation (Figure 1), being clearly superior to standard cutting teeth when rock UCS (unconfined compressive strenght) exceeds 100 MPa. The drilling progresses as the roller bits locally punch through and crunch the rock; in order to do so, the bits need to mobilize significant vertical reaction force.



Figure 1. Roller bits for hard rock excavation.

A substantial innovation in this context is the Gripper Hydrofraise, patented by Soletanche Bachy. The advance rate of the drilling equipment is proportional to the vertical force that can be exerthed on the cutting tool; this force, however, was generally limited by the reaction provided by the weight of the hydromill, which is pendular (i.e. hangs from the carrier). The Gripper Hydrofraise does not suffer from this limitation: through the hydraulicaly operated Gripper pads in its anchor module, it will react laterally against the excavated ground (see Figure 2, on the left). This allows it to mobilize friction on the excavated ground, and therefore to apply additional force when the drilling module is jacked against the drilling face (see Figure 2, on the right).

Depending on the Gripper Hydrofraise model, up to 2000 kN of pull-down force can be deployed. At the same time, the tools and carriers are prepared to exceed depths of 200 m. The Grippers have the added benefits of stabilizing the cutting tool and reducing vibration levels during excavation, minimizing wear and tear. The conjunction of Gripper Hydrofraise and roller bits has allowed viable penetration into rocks with UCS up to 300 MPa in the ongoing NSC105 project in Singapore.

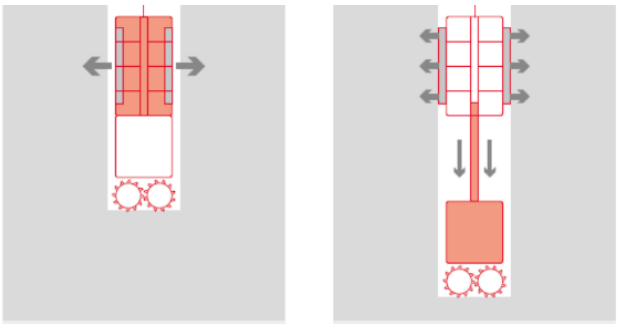

Figure 2. Gripper Hydrofraise operating principle: gripping stage (left) and drilling stage (right).

Compact rigs have also been developed in recent years, based on the need for high-capacity equipment capable of working in constrained spaces. This allows for example its use inside dam galleries (figure 3), something that would not be possible with standard hydromill equipment. In the case of the Subansiri project in India (Mallet et al., 2019), the Hydrofraise rigs operated inside 7x7 m^2 galleries located at different platform levels and had frequently to be hoisted from one platform to the other.

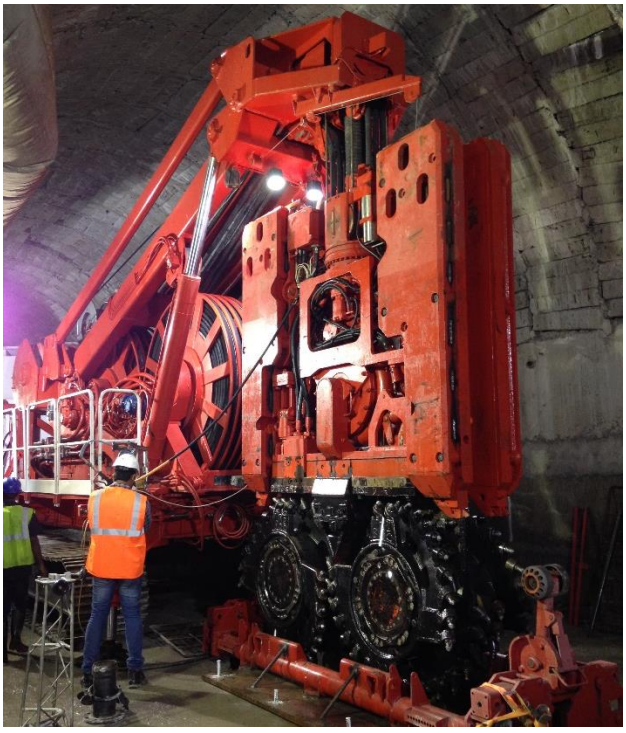

Figure 3. Compact Hydrofraise equipment operating inside a gallery in Subansiri dam.

Another development of the compact Hydrofraise that will further increase its capabilities for use in dams is the adoption of a detachable powerpack: besides further reducing the size of the rig, it simplifies operations and ventilation requirements while working inside galleries by eliminating a source of exhaust gases. Another development still is the adoption of Grippers in these compact machines, further optimizing rock excavation.

2.2 Piles

In order to form a seepage barrier, circular piles will need to overlap, forming what is commonly known as secant piles. Alternate primary piles are installed and, following some days of curing, secondary piles will be installed in between them. Pile cutoffs will intrinsically possess more interfaces between overlapping elements than is the case for diaphragms, and as such are more prone to defects in these areas. Depths in excess of 100 m can be attained; however, the production of a conventional Kelly-bar rig installing drilled shafts at large depths does not compare favourably to the production of hydromills or of RCD (reverse circulation drilling) piling equipment.

A recent example of piling cutoff in difficult conditions is the remediation works in Boone dam in the USA (Barredo et al., 2021). In this project, the karstic limestone exhibited marked pinnacles that risked triggering unacceptable deviations, if conventional piles or diaphragm walls were to be used: the drilling tool would touch the hard pinnacle rock and, instead of penetrating the limestone, would slide along the pinnacle feature. The chosen solution was to use directional drilling (capable to actively correct deviations, but limited to small diameters unsuitable for cutoff implementation) to drill a 196 mm pilot borehole. Then, an RCD equipment (Wirth 818 from HMH) drilled the final 1270 mm pile coaxially with the pilot borehole, using a stinger inserted into the borehole as a guide (Figure 4). Piles up to 55 m in depth were installed, with deviations below 0.25 %.



Figure 4. RCD hard rock drilling tool with protruding stinger used in Boone dam remediation.

Another interesting solution to a specific problem was developed by Trevi for the Arapuni remediation project in New Zealand (Wharmby et al., 2007). In this remediation project, 400 mm piles at 350 mm centres were installed up to a depth of almost 90 m with an RCD tricone. Such a small overlap up to such a large depth was only possible with a specific, custom-built guide (Figure 5, from Wharmby et al., 2007), that would slide through the previously excavated pile to guide the drilling of the next pile. This solution required, of course, a sufficiently stable ground to allow safe operation of the guide-tool combo.



Figure 5. RCD tricone drilling tool with guide (left) and overlapping drillholes in the Arapuni dam remediation.

2.3 Soil mixing

Amongst the various methods used for soil mixing, possibly the most useful development for cutoffs concern CSM (cutter soil mixing), as well as the patented Trenchmix method. Like other soil mixing techniques, these systems are suited to soils (overburden, residual soil) and cannot be used in hard ground.

Cutter soil mixing can be considered a derivative of hydromill technology, hence constructing rectangular panels in depth (thicknesses up to 1200 mm and depth, depending on carrier, up to 35 m). Panels are built side by side, with sufficient overlap between them to ensure continuity of the cutoff. Figure 6 shows the CSM tool from Bauer.

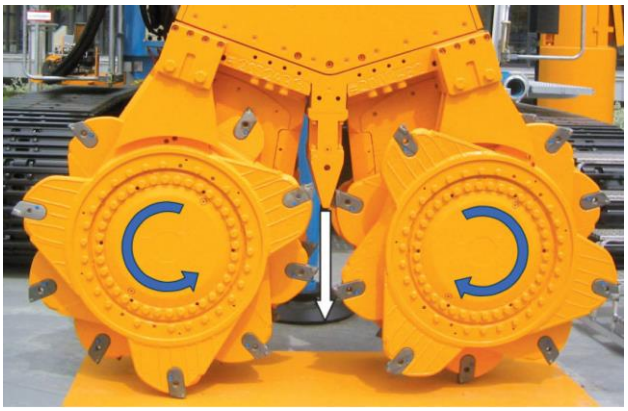

Figure 6. CSM operating principle indicating slurry flow (in white) and cutter drum rotation directions (in blue).

Trenchmix is a patented technique by Soletanche Bachy, consisting of a trencher capable of producing continuous cutoffs in a very efficient and rapid way (Figure 7). Thicknesses are limited to 500 mm, while depths depend on the size and power of the equipment, but cannot reasonably exceed 30 m. This technique has proven to be very effective in dyke remediation, for example in the Rhyne valley.



Figure 7. Operating Trenchmix equipment in a dyke remediation project.

2.4 Jet grouting

Jet grouting consists of cutting the soil with high velocity jet of fluid(s), and mixing the eroded soil with a self-hardening grout, to form columns and other structures in the ground. The classification of jet grouting into single, double or triple jet grouting pertains to the fluids being used (Figure 8).



Figure 8. From left to right: single, double and triple jet grouting.

An innovative development of jet grouting for cutoffs is the E-JET Elliptical Jet patented by Trevi (Leoni and Pianezze, 2017), as the system allows to optimize the shape of the jetted element. By carefully managing the rotation speed of the monitor, an approximation of a rectangular shape can be obtained (Figure 9 and Figure 10, from Trevi and Soilmec) leading to savings in time and materials. Panel sizes are heavily dependent on geology (overburden or residual soil), while depths up to 100 m can realistically be reached.

On another note, jet grouting advances have focused on the sustainable construction and on minimising environmental impact. For example, several case histories of reuse of jet grouting spoil have

been identified. Depending on the techniques, water consumption can be reduced, evacuation of cuttings can be limited, and cement consumption can equally be reduced.

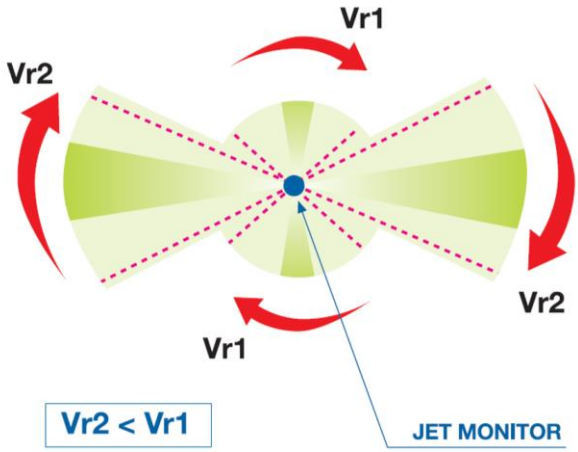

Figure 9. E-JET operating principle.



Figure 10. Excavated E-JET panels.

2.5 Cutoffs complemented by grouting

As noted previously, grouting is addressed in this document only for cases where it serves as complement to a cutoff.

The first case relates to the continuation of a cutoff by a grout curtain. This may be the case when the cutoff will be limited to a certain depth of overburden soil, whereas grouting will be applied to the fissured rock mass below. In this case, much care is to be taken in overlapping both solutions. A typical method is to install the cutoff and then to drill through it to instal a grout curtain on the same axis of the cutoff, and to thoroughly grout the contact between the cutoff and the grout curtain.

The other case concerns mostly the execution of the cutoff itself: in cases when the ground is extremely pervious, drilling fluid for diaphragm wall or piling will be lost into the ground, making excavation impossible. In this case, prior grouting will limit the loss of drilling fluid, as well as having a beneficial effect on the stability of the materials adjoining the excavation.

3 MATERIALS

The following sub-chapters will focus on the main attributes of the different types of cutoff materials.

In the case of positive cutoffs, these materials will range from cement-bentonite mixtures, to plastic concrete, to conventional concrete. The properties of each mixture will be tailored according to the project's requirements.

In the case of semi-positive cutoffs, the *in situ* soil plays a large role in the final parameters of the treated ground. For example, it is well known that soil mixing or jet grouting of granular soils leads to higher strength and stiffness than in fine grained soils.

3.1 Permeability

The first criterion for the material in a cutoff is its imperviousness, on which will depend the barrier's performance. Considering the cutoff material in itself, very low permeabilities are to be expected. For example, for plastic concrete, permeabilities in the order of 10^{-10} to 10^{-11} m/s are typical. This permeability will be increased by the presence of discontinuities, either those introduced by unwanted defects, or those associated with the construction methods, in particular joints between discrete cutoff elements.

Vidil (2018) indicates the following equivalent permeabilities for dwalls, accounting for the use of several types of joints (see Table 1).

Table 1. Estimates of equivalent diaphragm wall permeability, for different types of joints (adapted from Vidil, 2018)

Type of joint	Permeability (m/s)
Stop end tubes	10^{-8}
CWS	10^{-10} to 10^{-9}
"Dry" joint	10^{-8}
Milling	10^{-10} to 10^{-9}
Milling + joint sealant	10^{-10} to 10^{-9}

The well-known CWS (Complete Water Stop, Figure 11), patented by Bachy in 1982 and subsequently adopted at a global scale, represents a marked improvement compared to the previously used stop end tubes. However, for several reasons it is not practical to use a CWS joint beyond 60 m in depth. Milled joints (Figure 12) implemented with hydromills

can, on the contrary, be implemented to the bottom of the excavation.

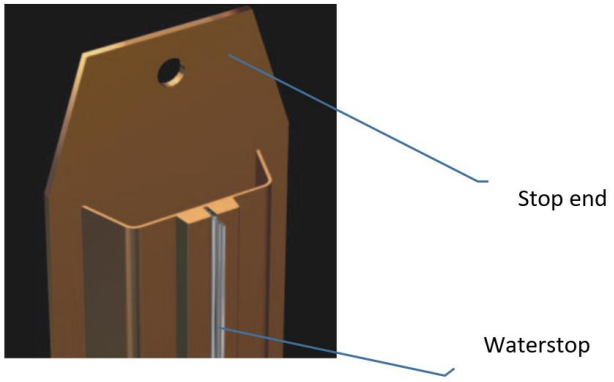

Figure 11. CWS joint complete with waterbar.

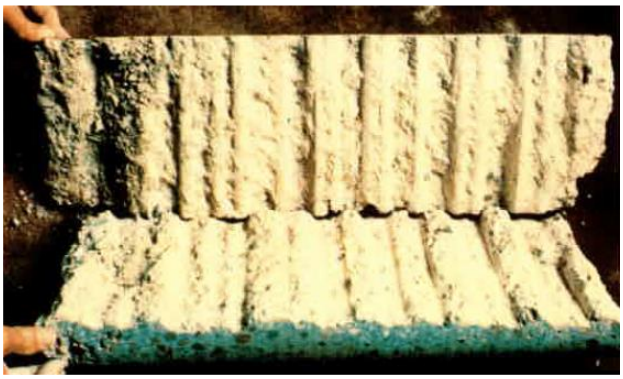

Figure 12. Milled concrete in a hydromill joint.

Another innovative development (Mosser and Monleau, 2020) concerns the inclusion of a hydroswelling joint sealant in conjunction with a milled joint. The patented system requires an auxiliary steel cage to keep the join sealant in place (Figure 13) and also the installation of sacrificial hydraulic jacks in depth; these hydraulic jacks will be pressurized just after concreting the panel and will push the joint sealant against the previously cast panels on either side of the newly cast panel. The system has been successfully implemented in cutoffs in Chile and an improvement of the permeability coefficients indicated in Table 1 is expected with additional return of experience.

In the case of secant pile walls, it is reasonable to assume similar permeabilities to those indicated for milled joints in diaphragm walls. In the case of soil mixing and jet grouting, realistic permeabilities, obtained from return of experience, are in the order of 10^{-7} m/s to 10^{-8} m/s.

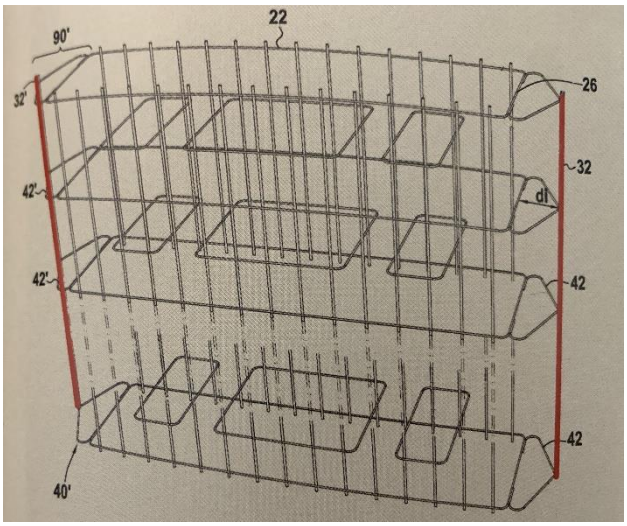

Figure 13. Hydroswelling joint sealant and milled joint: sealant location and auxiliary support cage.

3.2 Strength and stiffness

An equally relevant criterion concerns the stiffness and the strength of the cutoff material. It is advisable that the material has low stiffness, i.e. a matching stiffness to that of the ground on which it is installed (say a cutoff material no more than 5 times stiffer than the ground), so as to minimize stress concentrations on the barrier.

On the other hand, the material needs to be strong enough to resist the loads imposed on the cutoff, the largest of which are often the differential hydraulic pressures acting on both upstream and downstream faces (see Figure 14), which induce substantial bending and shear stresses on the wall. In the case of seismic regions, the kinematic interaction of the cutoff with the adjoining ground may also govern the design, by imposing shear and bending on the cutoff (see Figure 15).

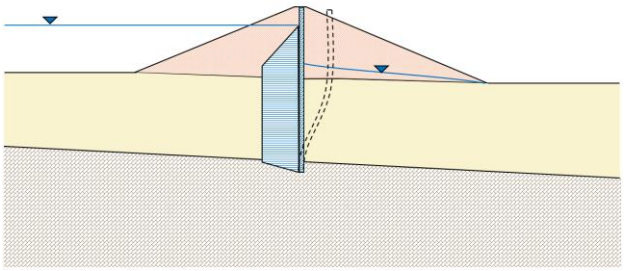

Figure 14. Exaggerated deformed shape of cutoff under differential hydraulic pressures.

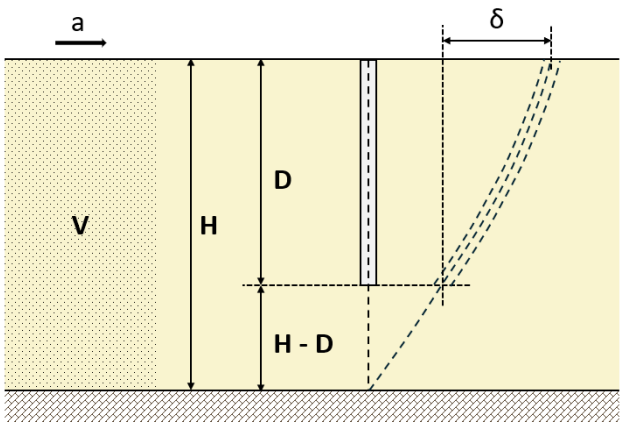

Figure 15. Exaggerated deformed shape of cutoff under seismic conditions - case of homogeneous ground underlain by bedrock (adapted from Soulomiac, 1986).

The significance of ductility (the capacity of the material to accumulate extensive plastic deformation) should also be noted, as the aforementioned load cases are likely to induce more or less localized yield zones. Similarly, it is important to assess the strength and ductility of the material under realistic confinement pressures: cutoff walls being frequently very deep, the confining pressures will increase considerably in depth. Hence the interest in establishing triaxial testing programs by specialized laboratories to assess and adjust the mixes. For all these reasons, plastic concrete formulations and cement-bentonite mixes have been used more and more frequently. Ongoing studies, by a joint working group of the German associations DWA, HTG and DGGT, are expected to provide guidance and objective design criteria on these materials (Beckhaus et al., 2023).

The same comments apply to soil mixing and jet grouting, which typically have strength similar to those of plastic concrete (UCS < 10 MPa, in general), with the caveat that soil mixing and jet grouting, contrary to plastic concrete, are not industrial man-made products and show much larger variability than batching plant mixes: the stiffness and ductility of these materials is very dependent on the ground type and should be assessed carefully. A final remark, valid for cement-bentonite slurry, plastic concrete, soil mixing or jet-grouting materials, concerns the slower increase in strength of these materials as they harden, when compared to the behaviour of conventional concrete. As such, it is nowadays broadly accepted to measure strength at 56 days or 90 days in the case of the former materials, instead of the 28 days commonly used for the latter.

Regarding conventional concrete (with strengths above 20 MPa), either as plain concrete or with reinforcement, its use has diminished greatly, namely due to cost and to the aspects detailed above. To be noted that reinforcement cages add further cost and installation complexity but provide a degree of ductility that plain concrete would not possess and may be required, depending on the load cases.

Finally, readers are invited to peruse the guides developed jointly by the European Federation of Foundation Contractors and by the Deep Foundations Institute of the USA: the first guide concerns tremie concrete for deep foundations (EFFC/DFI, 2018), while the second guide addresses support fluids for deep foundations (EFFC/DFI, 2019). Both documents are applicable to diaphragm wall or piling cutoffs, in large part if not in full.

3.3 Sustainability

In terms of environmental impact and carbon emissions in particular, most of the emissions in an infrastructure project are usually linked to the fabrication of construction materials, and not to installation processes. In the case of cutoffs, as in other geotechnical works, carbon emissions are mostly due to cement and may be reduced with selection of appropriate alternatives, such as furnace slag, fly ash or other alternative binders.

Figure 16 below (with data from Soletanche Bachy's EXEGY low carbon concrete) provides indicative values for scope 3 carbon emissions for plastic concrete (kg CO2 eq/m^3), depending on the type of binder used. It can be observed that: if the project's requirements can be met with alternative binders, if these are readily available and if the associated cost is compatible with the project, very important reductions in carbon emissions can be obtained. The internal laboratory of a specialized geotechnical contractor will be able to establish the viability of such alternatives.

Target compressive resistance (in MPa)	0,5	1	2	5	10
CEM I	280	337	394	490	547
CEM II	279	328	427	476	541
CEM III/A	127	141	151	218	268
CEM III/B Low Carbon	111	121	129	182	222
CEM III/C Very Low Carbon	74	81	92	121	152
Slagsol 95/5 Ultra Low Carbon	60	64	73	93	106

Figure 16. Indicative values of carbon footprint of plastic concrete (kg CO2 eq/m3) for different types of binder.

4 MONITORING AND CONTROL

The continuity of the cutoff is fundamental to ensure adequate performance of the dam's foundation, since a small opening between adjacent cutoff elements

increases the equivalent permeability of the wall by many times. As such, knowledge of the real location of the discrete elements forming the cutoff is necessary to ensure continuity.

This chapter will differentiate between monitoring of construction, performed during installation of the cutoff, and quality control verification, performed following partial or full installation of the cutoff element.

4.1 Monitoring during installation

Monitoring of the drilling tool location during installation is arguably more valuable because of the possibility, depending on the cutoff method being used, to retrieve part or all of the deviation. Hydromills and in particular Hydrofraise monitoring devices have been able to reliably locate the drilling tool in real time in xx, yy and zz directions, but also in terms of the twist of the tool (rotation around zz). The operator can then trim the tool's trajectory, by independently adjusting the torque of both motors and by actioning guiding jacks on the tool's frame (Figure 17). Verticality tolerances of < 0.25% are nowadays common, but have frequently been bettered, even at large depth, especially in homogeneous ground conditions. It should be noted that the more advanced hydraulic grabs can also adjust their positioning via guiding plates, albeit with more limited correction capability and with achievable verticality tolerances in the order of 0.5%.



Figure 17. Command panel of Gripper Hydrofraise. At the centre of the touch screen, the real time position of the tool (in vertical planes xz and yz) is depicted in green, while the deviation limits are represented in grey.

Directional drilling can, by definition, correct deviations, and therefore to achieve negligible tolerances; however, the maximum diameter of commonly available tools is small, around 300 mm, and not suitable for cutoff piling works (exception made for pilot holes for guiding other tools, as presented before). Other piling techniques are not able to significantly redress deviations.

Jet grouting and soil mixing techniques are also not able to correct deviations, with the exception of CSM which, being related to hydromill tools, has some ability to do so. However, both jet grouting and soil mixing equipment are fitted with sensors to measure deviations in depth. Finally, while verticality tolerances are higher for these methods (in the order of 1%), it should be noted that both techniques are used for relatively shallow cutoff depths, and that deviation control is therefore less critical.

Regarding the particular case of Trenchmix, the fact that the tool has a comparatively high deviation tolerances (< 3%) and cannot readily correct any deviation are not problematic, because the cutoff is continuous, without overlap of discrete elements.

4.2 Post-installation control

In the case of two-stage post-concreted cutoffs (e.g. concrete diaphragm walls and piles), location in depth can be verified by several methods. Indirectly it can be verified through geophysics, before concreting, for example via ultrasonic echo-detection (with the well-known Koden system from Koden Electronics) or by sonar calipering (the SONICaliper system from Fugro Loadtest). Typically, the geophysical readings from all the cutoff discrete elements will be assembled on a 3D visualisation software and compared with the drilling tool's on-board results, to ensure that overlap is obtained throughout the cutoff.

These techniques cannot be used for single-stage methods like slurry walls, soil mixing and jet-grouting. However, an interesting alternative technique can be used to estimate the diameter of jet grout columns. The Cyljet (proprietary technique from Sixense) is based on the spatial variability of electrical resistivity, and it requires the installation of a non-metallic tube inside the columns, into which electrodes are introduced at regular intervals. By analysing the differences in potential generated by an induced electrical current, it is possible to estimate the geometry of the jetted column.

Direct verification via coring (Figure 18) can also be used for assessing positioning but, due to its inherent cost, is more useful for inspecting the cutoff material and the interfaces between discrete cutoff elements, both inside the borehole (via CCTV or OPTV Optical Televiewer, Figure 19) and with analysis of the extracted core. It is worth mentioning that the use of a pigment in the concrete of either secondary or primary elements is very helpful in identifying and analysing the interfaces. Finally, coring boreholes can be used to directly assess

performance of the cutoff via stable water level tests or falling head tests.



Figure 18. Coring of interface between two adjacent castings (note pigmented concrete of secondary piles).

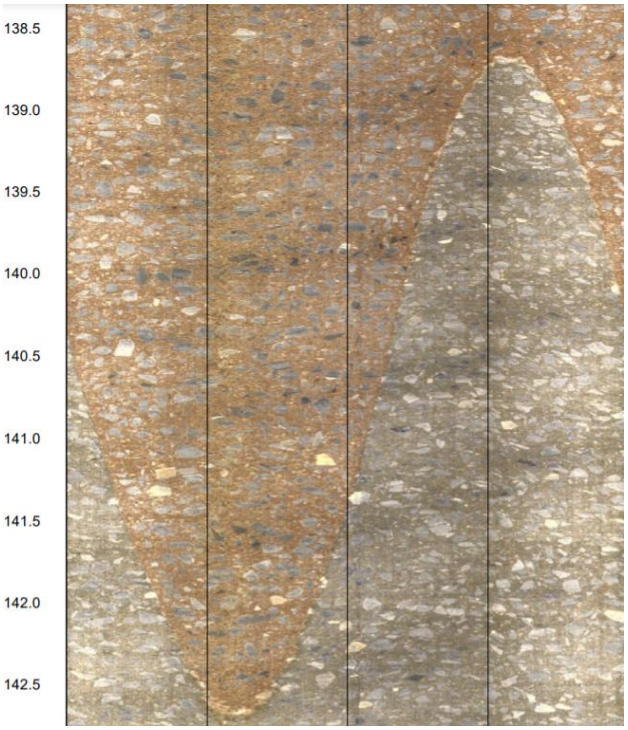

Figure 19. OPTV 360-degree image of a cutoff borehole (note pigmented concrete of secondary piles).

5 NEW BUILDS VS REPAIR

The case of new build is, by definition, less constrained than the case of dam repairs. Although limitations do exist in such cases, for example with cutoffs being built in valleys with often steep slopes, difficult accesses, and restricted space, at least the structure of the dam is not built yet.

Remediation works, on the other hand, are often very constrained; in terms of planning and logistics, but also because of the possible impacts on the existing dam, which sometimes continues operating with full reservoirs. The works are to be monitored so that strict limits are not exceeded, for example in terms of vibration levels or inclinometric or topographical displacement readings. Furthermore, evaluating the dams' stability during all stages of the cutoff works is often required, sometimes involving complex geomechanical modelling.

One such example of the type of analysis to be carried out is depicted in Figure 20. A remediation project where a cutoff was to be installed at the downstream toe of an embankment dam was value-engineered with a cement-bentonite cutoff. This cement-bentonite slurry wall was to be excavated with hydraulic grabs, deploying a construction sequence such that considerable lengths of trench would be left open for some time, with cutoff material in fresh or not fully hardened states.

This required an analysis of the excavation stability, but also of the global stability of the embankment, as the critical failure surfaces often extended well beyond the dam toe (these problems being intrinsically tridimensional, they are better addressed resorting to 3D numerical models).

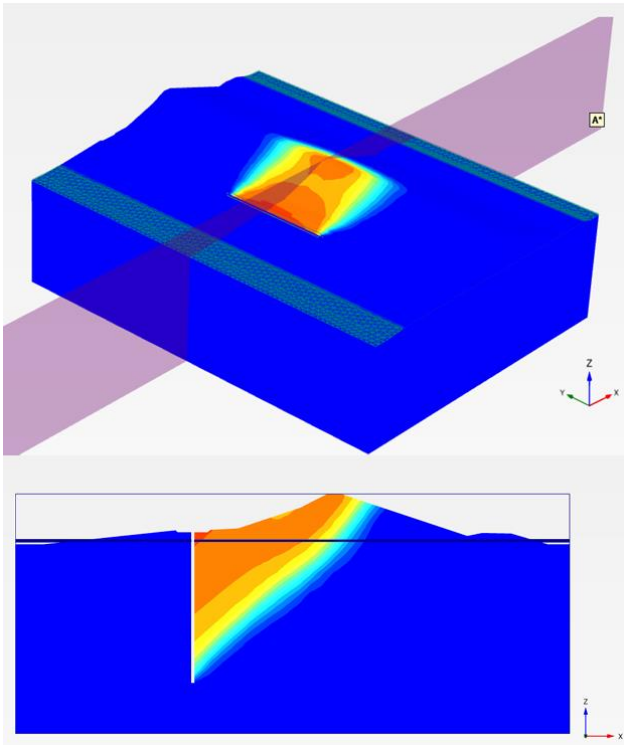

Figure 20. 3D FEM stability assessment of a dam during cutoff excavation: displacement contours associated with mobilization of a failure surface: 3D view (top) and 2D section through the middle of the failure surface (bottom).

Besides stability analysis, other fundamental axis are the development of the cement-bentonite mixes, in order to render its rheology predictable and reliable, and the fine tuning of construction sequences so that the required safety factors are met for all the load scenarios.

6 FUTURE DEVELOPMENTS

It is not possible to avoid mentioning the spectacularly fast development of machine learning and other AI techniques.

While construction equipment has been equipped with a multitude of sensors for decades, and that real time data transfers from drilling rigs to and from cloud storage has been done for several years now, these new techniques seem very promising in terms of making the most of the vast amounts of data being generated.

These will be important not only in terms of production (e.g. fine tuning of excavation rates), or quality control (e.g. articulation with BIM models), but also in the development of new technical solutions.

7 CONCLUSIONS

In view of the maintenance requirements of existing dams, and of the likelihood of an increase in dam construction to deal with the cumulative effects of diminishing storage, growing water scarcity, and increasing energy demands, growth of dam-related work is foreseeable in the upcoming years. The construction of cutoffs, which are a fundamental part of many dams, both for seepage control and for uplift pressure reduction, should similarly experience growth.

The techniques presented in this paper, while not all groundbreaking, show a track record of continuous and sustained development by the profession, with marked improvements in the applicability, efficiency and quality of the works that can be built. The efforts on sustainability and the need for limitation of carbon emissions are highlighted by the search for alternative binders. A full range of methods is available to improve and verify the quality of cutoffs, serving the needs of a wide range of dam projects, from the simplest and shallowest green field cutoff to the deepest and most challenging remediation project.

Future developments are likely to continue to focus on the axis above, but the accelerating developments of machine learning and other AI techniques should bring valuable insights into the large amounts of data that construction sites and equipment now generate.

REFERENCES

Barredo, V. et al. (2021). Construction Techniques and Challenges during the Cutoff Wall Installation at TVA Boone Dam Remediation Project, In: *Safety, Security, and Emergency Response in the 21st Century - USSD 2021 Annual Conference*, Virtual Conference, USA, pp. 1-13.

Beckhaus, K., Kayser, J., Kleist, F., Quarg-Vonscheidt, J., Alós Shepherd, D. (2023). Design concept for sustainable cut-off walls made of highly deformable filling materials, In: *Role of Dams and Reservoirs in a Successful Energy Transition - 12th ICOLD European Club Symposium,* Interlaken, Switzerland, pp. 641-650.

EFFC/DFI (2018). Joint EFFC/DFI Concrete Task Group - Guide to Tremie Concrete for Deep Foundations 2nd Edition, EFFC and DFI.

EFFC/DFI (2019). Joint EFFC/DFI Support Fluids Task Group - Guide to Support Fluids for Deep Foundations 1st Edition, EFFC and DFI.

ICOLD (2005). Dam Foundations, Bulletin 129 1st Edition, ICOLD, France.

ICOLD (2018). Cutoffs for Dams, Bulletin 150 1st Edition, CRC Press/Balkema, The Netherlands.

Leoni, F. M., Pianezze G. (2017). Elliptical Jet Grouting: An Innovative, Viable, and Effective Solution: The Example of the Bottom Plugs for the SELA Projects in New Orleans, LA, In: *Grouting 2017, the Fifth International Conference on Grouting*, Honolulu, Hawai, pp. 11-20.

Mallet, S., Arunachalam, S., Abinader, A. (2019). Une hydrofraise compacte sur le plus grand barrage d'Inde; A compact Hydrofraise on the largest dam in India, *Travaux*, no. 953, pp. 44-49 (in French).

Mosser, J. F., Monleau, S. (2020). Joints hydrogonflants pour parois moulées; Hydro-swelling joint sealants for diaphragm walls, *Travaux*, no. 957, pp. 41-47 (in French).

Souloumiac, R. (1986). Méthode simplifiée de calcul des pieux en zones sismiques; Simplified calculation method for piles in seismic zones. *Annales de l'institut technique du bâtiment et des travaux publics*, no. 441, pp. 61-87 (in French).

Vidil, P (2018). Recommended junctions between diaphragm wall panels for deep excavations, In: *DFI 2018 - International Conference on Deep Foundations and Ground Improvement,* Rome, Italy, pp. 389-398.

Wharmby, N., Lucchi, M., Newson, T., Amos, P. (2007). Arapuni dam foundation enhancement works, In: *Common ground - proceedings of the 10th Australia New Zealand Conference on Geomechanics*, Brisbane, Australia, pp. 330-335.

Proceedings of the XVIII ECSMGE 2024
GEOTECHNICAL ENGINEERING CHALLENGES
TO MEET CURRENT AND EMERGING NEEDS OF SOCIETY
© 2024 the Authors
ISBN 978-1-032-54816-6
DOI 10.1201/9781003431749-14
Open Access: www.taylorfrancis.com, CC BY-NC-ND 4.0 license

ECSMGE 24
XVIII EUROPEAN CONFERENCE ON SOIL MECHANICS AND GEOTECHNICAL ENGINEERING

State-of-the-art Report

Sustainability report of the European large geotechnical institutes platform

Rapport sur la durabilité du groupement européen des grands instituts de géotechnique

A. Marin
ETH Zurich, Zurich, Switzerland

B. Žlender, T. Bračko
University of Maribor, Maribor, Slovenia

T.L. Christiansen*, T.R. Smaavik
Norwegian Geotechnical Institute, Oslo, Norway

A. Insana
Politecnico di Torino, Torino, Italy

C. Carlsson, Y. Rogbeck
Swedish Geotechnical Institute, Linköping, Sweden

J. Machacek
Technical University of Darmstadt, Darmstadt, Germany

**thea.lind.christiansen@ngi.no*

ABSTRACT: The European Large Geotechnical Institutes Platform (ELGIP) is a group of 15 leading research organizations in geotechnical engineering that aims to promote internationally the profession and its societal relevance. One of ELGIP's objectives is to drive sustainability in geotechnical engineering and establish a common platform for sustainable practices and knowledge transfer across national borders in Europe through its working group on Sustainability. This paper summarizes the latest efforts of ELGIP's Sustainability working group (WGS), with contributions from ten national organizations in Europe. The current practice in geotechnical engineering is evaluated both qualitatively, by highlighting selected projects with significant components related to sustainability within WGS, and quantitatively, by presenting the level of involvement of the partner institutes in relation to each specific sustainable development goal (SDG) of UN's 2030 Agenda. Finally, general recommendations with respect to the future development of current practice are made based on the outcome of the evaluation. The paper demonstrates the important role that geotechnical engineering can play in achieving sustainable development goals.

RÉSUMÉ: Le Groupement Européen des Grands Instituts de Géotechnique (ELGIP) comprend 15 organismes de recherche dans l'ingénierie géotechnique et vise à élever au niveau international la profession et sa pertinence sociétale. L'un des objectifs de l'ELGIP est de promouvoir le développement durable dans l'ingénierie géotechnique et d'établir une plateforme commune pour les pratiques durables et le transfert de connaissances au-delà des frontières nationales en Europe par son groupe de travail sur la durabilité. Ce document résume les derniers efforts du groupe de travail avec des contributions de dix organismes nationaux en Europe. La pratique actuelle de l'ingénierie géotechnique est évaluée qualitativement, en mettant en évidence projets sélectionnés avec des composantes significatives liées à la durabilité au sein de ces organisations, et quantitativement, en présentant le niveau d'implication des instituts partenaires par rapport à chaque objectif de développement durable (ODD) de l'Agenda 2030 de l'ONU. Enfin, des recommandations générales concernant le développement futur des pratiques actuelles sont formulées sur la base des résultats de l'évaluation. Le document démontre le rôle important que l'ingénierie géotechnique peut jouer dans la réalisation des objectifs de développement durable.

Keywords: Geotechnical engineering; research; sustainability; knowledge transfer; collaboration.

1 INTRODUCTION

The evolution of society in relation to the sustainable development goals (SDGs) set by UN's 2030 Agenda for Sustainable Development (UN, 2015) is a very complex process easily affected by factors such as lagging policy making and implementation, or concurring crises. Rather than being independent, such factors tend to cascade and produce cumulative effects and chain reactions, given their origin in the interlaced environmental, economic, and social threads of the society. Typical examples for the past decade are the

COVID-19 pandemic or the armed conflicts, which, beyond the tremendous death tolls, cascaded in food shortage, job losses, supply chain issues, increasing energy costs, or inflation, just to mention some of their global and local effects.

Unfortunately, UN's evaluation of the current global state of progress towards the SDGs of the 2030 Agenda indicates a rather slow implementation and even regression in some specific areas, caused mainly by such interdependent crises experienced in the past years. Consequently, the fundamental questions that need a timely answer are "Where are we now?" and "Where are we heading?". Sharply defined answers to these questions can identify necessary steps required to achieve the desired progress on the path towards a more sustainable future, as shown by the Global Sustainability Report 2023 (Miranda et al., 2023).

Experience has shown that sustainable progress is impossible while focusing only on specific areas of interest. The compounded risks affecting the various interlaced threads of the society call for a holistic approach in evaluating the current state and planning mitigation and development strategies. Collective effort at all levels is essential, along with a clear path of knowledge transfer between society and decision-makers.

In this context, the role of research cannot be overstated, as it has the potential to provide valuable insights and guidance in decision-making processes to achieve the SDGs. Catalysed by the complex interplay of the compounded risks projected on interdependent societal layers, the research interest related to UN's SDGs has advanced significantly in the past decade, and an exponentially increasing number of relevant scientific contributions has been generated (Figure 1).

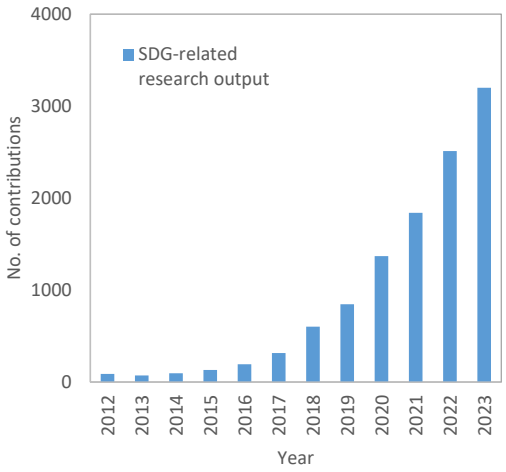

Figure 1. Scientific output relevant to the SDGs generated in the past decade (SCOPUS, 2024).

According to SCOPUS the contributions cover 27 different fields of interest, out of which social sciences, environmental science, and engineering are the most relevant ones, collectively attracting a total number of contributions comparable to the other fields cumulated.

Geotechnical engineering, as part of the broader engineering area and with ramifications in environmental sciences, has the potential to contribute significantly to the advancement of UN's Sustainability Agenda. The current paper provides a summary of the sustainability status in geotechnical engineering research reported by members of ELGIP, with the intent to encourage further development in this direction, catalyse the knowledge transfer from ELGIP to the decision-makers, and accelerate the achievement of the relevant SDGs.

2 METHODOLOGY

The results presented herein were obtained by processing the answers provided by the members of the Working Group Sustainability (WGS) of ELGIP to three main questions: (i) "What is the current strategy or policy for sustainable development in your organisation?" (ii) "How do you work towards specific sustainable development goals (SDGs) from a geotechnical perspective?" (iii) "What is the ongoing and recently finished work of relevance to sustainability?" The detailed input can be found in the recently published report of ELGIP (Christiansen et al., 2023).

Out of the 15 ELGIP members, 10 organisations from 10 European countries (Figure 2) are part of WGS and provided input on their current strategies and policies for sustainable development, and their specific activities and projects towards achieving sustainability goals from a geotechnical perspective. These organisations are Spanish National Public Works Research Centre (CEDEX), Czech Technical University in Prague (CTU), Swiss Federal Institute of Technology in Zürich (ETHZ), Norwegian Geotechnical Institute (NGI), Polish Geological Institute (PGI), Politecnico di Torino (PoliTo), Swedish Geotechnical Institute (SGI), Technical University of Darmstadt (TUDa), Université Gustave Eiffel (UGE), and University of Maribor (UM).

Initially, a qualitative evaluation of the activities of WGS members is conducted. The main relevant topics are identified using approximately 60 recent projects provided by each institute and classified in relation to sustainable development. Subsequently, most significant projects (Table 1) are briefly described to

showcase their relevance to sustainability. Moreover, the leading areas of interest for future development of geotechnical engineering within the framework of sustainability are identified and briefly discussed.

In the next step, the activity is evaluated quantitatively by roughly assessing the level of involvement in relation to the SDGs. The assessment is performed by determining the number of institutes of WGS actively working towards each SDG. The quantitative evaluation is put into perspective using the global level of achievement of the SDGs estimated by averaging the realisation of the specific targets presented by Miranda et al. (2023) for each SDG in UN's Global Sustainability Report 2023.



Figure 2. European countries represented in the WGS of ELGIP.

3 RESULTS

3.1 Qualitative evaluation of current activities in relation to sustainability

The qualitative evaluation revealed four topics in which WGS members are involved: (1) climate change, (2) environmental impact of (geo)structures, (3) circularity and reuse of geomaterials and (4) social sustainability (Table 1). In terms of SDGs, the most relevant ones, attracting most of the activity in geotechnical engineering are:

- SDG-7 - Ensure access to affordable, reliable, sustainable, and modern energy for all
- SDG-9 - Build resilient infrastructure, promote inclusive and sustainable industrialization and foster innovation
- SDG-11 - Make cities and human settlements inclusive, safe, resilient, and sustainable
- SDG-12 - Ensure sustainable consumption and production patterns

Further SDGs were reported by the WGS members covering almost the entire spectrum of goals, with the exception of Poverty Eradication (SDG-1), Zero Hunger (SDG-2) and Peace, Justice and Strong Institutions (SDG-16). The apparent irrelevance of these goals to geotechnical engineering could be explained by a rather strict interpretation of their definitions by the WGS members. Given the interdependent nature of SDGs, geotechnical engineering makes indirect contributions to these seemingly unrelated goals by addressing societal needs relevant to SDGs 7, 9, 11 and 12 with effective solutions.

Moreover, less technical goals such as gender equality (SDG-5), decent work and growth (SDG-8), and reduced inequalities (SDG-10) are, on the one hand, an essential part of the intramural organisational strategies of the institutes often including established and dedicated internal strategic-operational units. On the other hand, these aspects can be found in the implementation of the various projects, in which the institutes are involved.

As an example, project GEOLAB (GEOLAB, 2021), involving 11 experimental installations from nine European countries with the purpose of addressing challenges faced by the Critical Infrastructure of Europe (relevant to SDGs 7, 9, 11, 12), is committed in its implementation to SDGs 5, 8 and 10. More specifically, the project contributes to the reduction of inequalities between potential researcher groups with unequal financial and technical means (SDG-10) by offering free access to experimental infrastructure. Besides the essential role of scientific merit and relevance of the intended research, the free access is granted by taking into account the participation of female (SDG-5) and early stage (SDG-8) researchers, which tend to be under-represented in such projects. Moreover, the specific composition of the management team and international advisory board of GEOLAB was set-up to meet minimum criteria related to gender balance.

Further on, the activity of WGS members related to ongoing and recently completed projects relevant to sustainability is briefly summarized to offer a clearer overview of the specific actions currently driving the progress towards the SDGs at the European level. Table 1 provides a summary of some major projects mentioned by the WGS, categorized by topics.

Table 1. Collaborative European projects relevant to sustainability divided into topics.

Topic	Projects
Climate change	GEOLAB (GEOLAB, 2021)
Environmental impact of (geo)structures	SENSE-ACT (SENSE, 2023)
Circularity and reuse of geomaterials	ARV (ARV, 2022), URGE (URBACT, 2022), CINDERELA (CINDERELA, 2018)
Social sustainability	FP3-IAMRAIL (Europe's Rail, 2022) RID (RID, 2023) REMEDY (Langford et al., 2021) 2015 Gorkha Earthquake Relief (Amdal et al., 2018)

For topic (1) climate change, most projects listed by WGS members focus on three main sub-topics: (i) identification/detection/assessment, mapping and visualisation, (ii) prevention, and (iii) mitigation/adaption strategies against natural hazards (e.g. landslides, flooding) associated with climate change (Insana et al., 2021).

In terms of collaborative involvement at European level on this topic, the already mentioned project GEOLAB (ongoing) (GEOLAB, 2021) stands out as a one-stop-shop of high-end physical research infrastructure. The aim of the project is to address challenges associated with climate change faced by the critical infrastructure of Europe by facilitating ground-breaking research and innovation through experimental testing. In this sense, a wide spectrum of problems related to climate change, which do not focus necessarily on one of the sub-topics mentioned above, are investigated. Furthermore, geotechnical institutes from France, Italy, Norway, and Sweden are involved on a relatively independent basis with the topic of nature-based solutions (NBS) in relation to coastal geotechnical infrastructure, river dykes, large embankments, land use and land cover. The use of NBS for both prevention and mitigation/adaption strategies against the impact of climate change is explored in the relevant projects.

Within topic (2) environmental impact of (geo)structures, more than 20 ongoing or recently finished projects were indicated by the WGS members, dealing with subjects such as: life-cycle assessment (LCA) and eco-geo-analysis tools for geotechnical structures, management of tailings storage, construction on contaminated soils, design methods achieving the reduction of carbon footprint of (geo)structures without compromising safety, geospatial tools for site optimization and environmental impact reduction, thermal energy, and geo-structures. The high number of nationally funded projects is an indication of the strong interest of local decision-makers in the various applications of this topic in relation to geotechnical engineering.

A notable example of collaborative involvement in this topic is the project SENSE-ACT (ongoing) (SENSE, 2023), which involves 14 partners from 10 countries (four of which are outside Europe). The main objective of the project is to demonstrate reliable and cost-efficient CO2 storage solutions using ground surface deformation detection combined with geomechanical modelling and inversion to provide information on pressure distribution and hydraulic behaviour of storage sites.

Topic (3) circularity and reuse of geomaterials includes projects mostly concentrated around three sub-topics: (i) re-use and life-cycle extension of existing structures, (ii) circularity of materials and (iii) management of waste and earth materials. In this area of interest, multiple projects stand out by their large-scale collective effort at European level.

Project ARV (ongoing) (ARV, 2022) involves 35 partners from eight European countries and aims at implementing six large-scale demonstration projects of climate positive circular communities and subsequently developing guidelines and a policy framework for future energy-efficient, circular, and digital solutions in the construction industry.

Project URGE (recently finished) (URBACT, 2022) involved nine European cities, which committed to exchange knowledge and experience, while implementing integrated urban policies focused on circularity in the construction tasks. Similarly, project CINDERELA (recently finished) (CINDERELA, 2018) involved 13 partners from seven countries and aimed at developing and demonstrating a new business model for companies in setting up successful circular economy business cases based on waste-to-resource opportunities. The project provided full-service assistance in terms of know-how for manufacturing and application of secondary raw materials in buildings and civil engineering works.

The last topic identified during the qualitative evaluation of the activity of WGS members is (4) social sustainability, with subtopics such as sustainable communities and infrastructure, or improved living conditions. One of the main projects reported here is FP3-IAM4RAIL (ongoing) (Europe's Rail, 2022), involving 94 partners at European level. The project aims to provide innovative technical requirements, methods, and solutions to minimise lifecycle costs and extend service life while meeting safety requirements and improving the reliability, and capacity of the railroad system. As expected for such a

large project, its impact extends beyond the topic of social sustainability. An interesting aspect investigated is the use of alternative materials in the railway track section, a typical application of the topic related to circularity and reuse of materials mentioned before.

Further projects worth mentioning in this topic are: (i) the earthquake relief project (finished) (Amdal et al., 2018) supported by FORUT, NGI and Engineers Without Borders in Norway, providing geotechnical assistance for the reconstruction of primary schools in the areas affected by the 2015 earthquake from Gorkha (M7.8) in Nepal; (ii) the RID project (ongoing) (RID, 2023) aiming at developing safe infrastructure by up-to-date guidelines for investigation and selection of soil improvement solutions for national roads and motorways in Poland; (iii) the REMEDY (recently finished) project (Langford et al., 2021) aiming at reducing the risk of damage to neighbouring structures caused by groundworks during and after execution of a project.

The qualitative evaluation of the current activities of WGS members provided the opportunity to explore some of the main directions for future development in geotechnical engineering in relation to sustainability. In this context, the first identified area of interest is circularity. The circular use of materials and structural elements (e.g. existing foundations) is already engaging the geotechnical community and is expected to generate even more interest while new methods for reusing, recycling and repurposing of construction materials are being developed.

A further area of interest is the use life-cycle assessment (LCA) in geotechnical design. This is already established in general product development, where the evaluation of environmental impact and costs are done using LCA. Nevertheless, this concept has not been extensively addressed and used in geotechnical engineering. The implementation of an LCA-based perspective is expected to optimize geotechnical design and increase its sustainability levels.

Energy optimization is a further area of interest expected to gain more traction in the years to come, considering the intensive use of energy in geotechnical works and the potential of improving associated processes in terms of energetic efficiency. In addition to sustainability concerns, the recent European energy crisis resulting from the conflict between Russia and Ukraine underscores the critical importance of efficient energy use across all sectors.

Sustainability assessments are expected to become more important in the decades to come. With the second generation of Eurocodes to be published and implemented at national level roughly by the end of 2027, sustainability will be one of the elements that must be considered during design of geotechnical structures. New methods will be required to evaluate projects from another perspective, by taking into account factors such as impact on environment and economy, equality and social justice.

Finally, yet importantly, nature-based solutions (NBS) emerged as a further area of interest for future developments on geotechnical engineering. On the backdrop of sustainability enhancement of geotechnical structures provided by the second generation of EC7, the use of renewable resources, environmentally friendly materials calls for implementation of NBS for a wide range of problems. Already attracting attention in countries with extensive coastal exposure (France, Italy, Norway, Sweden), where the effects of erosion processes can be mitigated using NBS, the topic is expected to become more relevant in further areas of geotechnical engineering.

As briefly mentioned before, the identified areas of interest for future development overlap with the general rules, measures and strategies for sustainability that will be included in the second generation of Eurocodes relevant to geotechnical engineering. This is a clear confirmation of the significance of sustainability at European level, and an indication of the ongoing common efforts of the relevant national institutions to promote this aspect in geotechnical engineering.

3.2 Quantitative evaluation of current activities in relation to sustainability

The results of the qualitative evaluation presented in the previous section demonstrate that the WGS members generally have holistic strategies in terms of sustainability, contributing with their activities and organisational strategies to the entire spectrum of SDGs. However, the focus of this paper is more on the activities of the WGS members and their specific projects with outcomes influencing the local, national and global achievement of the most relevant sustainability goals.

On average, each WGS member reported most of their projects as relevant to five out of the 17 SDGs of the 2030 Agenda, indicating a high level of commitment to sustainability, which goes beyond the sphere of science and technology. Figure 3 shows the distribution of the cumulated self-assessed activity of WGS members along the entire range of SDGs. As mentioned in the previous section, the current activity is mostly concentrated on topics such as affordable and clean energy (SDG-7), industry, innovation and infrastructure (SDG-9), sustainable cities and communities (SDG-11), and responsible consumption and production (SDG-12). The emphasis on the

specific SDGs is not a surprise, considering the specific character of applications of geotechnical engineering. Nevertheless, it is still unclear to what extent this is caused by a spatial variation of focus and development among European countries and how much it originates from a rather subjective interpretation of the SDG definitions.

In addition to the activity distribution, Figure 3 displays the estimated level of achievement for each SDG. On average, the current global progress towards all SDGs rates at 2.8 out of 5, which means that the current state is far from the final target. Generally, the influence of the recent crises such as the COVID-19 pandemic, the sharp increase of cost-of-living, armed conflicts and natural disasters can be clearly seen in the relatively low level of achievement combined with significant recessive trends outlined in the UN report.

Interestingly, SDG 9 related to industry, innovation, and infrastructure, which displays the highest level of achievement, is the same goal that attracts most activities and projects of WGS members (i.e. all participating institutes have reported project with outcomes contributing to this goal). In this context, a correlation can be seen between increased activity of relevant stakeholders, such as the geotechnical institutes in this case, and an increased level of achievement. The high number of projects also confirms the increased research and development spending from the part of the decision-makers acknowledged by Miranda et al. (2023).

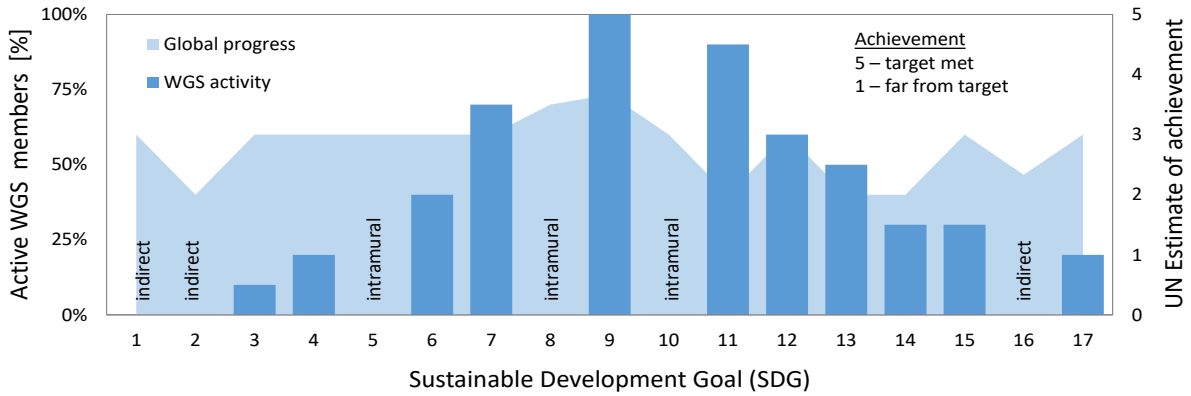

Figure 3. Involvement of WGS members in SDGs and UN estimated achievement according to Miranda et al. (2023).

4 CONCLUSIONS AND RECOMMENDATIONS

In the assessment of the sustainability status of ELGIP approximately 60 projects from 10 European geotechnical institutes were analysed. The assessment included a qualitative and quantitative evaluation of the activities of the institutes in relation to sustainability.

The qualitative evaluation of the projects indicates that geotechnical engineering can play a significant role in sustainable development. The four main sustainability-related topics identified in the assessment include projects with direct relevance to 14 out of the 17 SDGs of UN's 2030 Agenda for Sustainable Development. Nevertheless, the number of institutes participating in the evaluation is a strong limitation of the results presented herein. Consequently, more data with a higher level of granularity is required to prove clearly that the wide range of SDGs to which WGS members contribute is the result of the spatial variation of focus and development among European countries and not just a consequence of the subjectivity of the institutes while interpreting the description of the goals.

Various institutions may hold different perspectives regarding their contributions to SDGs. The self-assessed extent of the contributions strongly depends on the acquaintance with a goal definition: a cursory understanding of the goal might lead to a more reduced self-assessed contribution, whereas a more thorough one could yield a different conclusion. This complexity is a challenge in assessing an institution's impact on the SDGs solely through their self-reported alignment with specific goals.

Furthermore, the qualitative evaluation revealed the importance of pursuing less technical SDGs in the definition, organisation, and implementation of projects (e.g. gender balance targets, social inclusion measures). In this way, sustainability levels can be improved irrespective of the size and technical scope of the project.

Although not specifically analysed in this paper, the intramural adoption of a sustainability perspective at the organisational level of the institutes is a further important contribution towards a more sustainable community and has the potential to add the same perspective to the activities of researchers steering them towards more sustainability-oriented topics.

The quantitative evaluation of the projects confirms the holistic approach of the WGS members towards sustainability. Nevertheless, the limited amount of data collected and compiled in the assessment represents a limitation of the general applicability of the results, as already mentioned in the case of the qualitative analysis.

The correlation observed between the concentrated activity of the institutes towards SDGs 7, 9, 11 and 12, and the increased level of global achievement reported by Miranda et al. (2023) demonstrates the positive effect of collective effort. Moreover, broadly defined collaborative projects have the potential to contribute to multiple SDGs and to attract more funding. In this context, collaboration proves to be the key to a successful sustainable approach, and it is highly recommended in future projects, considering that sustainability-related challenges are global rather than national.

Finally, yet importantly, the results showed that increased research and development spending generates a greater number of projects in a specific area of interest, and consequently leads to a higher level of achievement of relevant SDGs. In this sense, reinforcing cross-network dissemination between research institutes, decision makers, funding agencies, businesses, and society is highly recommended. This can be done both nationally, in the case of individual WGS members, and internationally at European level, in the case of the entire ELGIP consortium, by using simple tools such as regular sustainability status reports as a basis for dialogue.

REFERENCES

Amdal, Å. M. W., Høydal, Ø. A. and Ødegaard, T. (2018). Field work in Dolakha District, FORUT Report, Gjøvik, Norge.

ARV (2022). ARV – Climate Positive Circular Communities, [online] Available at: https://greendeal-arv.eu/, accessed: 14/03/2024.

Christiansen, T. L., Smaavik, T. R. et al. (2023). Sustainability Status Report. Working Group Sustainability (WGS), European Large Geotechnical Institutes Platform (ELGIP).

CINDERELA (2018). CINDERELA – New Circular Economy Business Model for More Sustainable Urban Construction, [online] Available at: https://www.cinderela.eu/, accessed: 14/03/2024.

Europe's Rail (2022). FP3-IAM4RAIL – Holistic and Integrated Asset Management for Europe's Rail System, [online] Available at: https://projects.rail-research.europa.eu/eurail-fp3/, accessed: 17/03/2024.

GEOLAB (2021). GEOLAB – Science for enhancing Europe's Critical Infrastructure, [online] Available at: https://project-geolab.eu, accessed: 14/03/2024.

Insana, A., Beroya-Eitner, M. A., Barla, M., Zachert, H., Žlender, B., van Marle, M., Kalsnes, B., Bračko, T., Pereira, C., Prodan, I., Szymkiewicz, F. and Löfroth, H. (2021) Climate Change Adaptation of Geo-Structures in Europe: Emerging Issues and Future Steps, *Geosciences,* 11(12), pp. 488, https://doi.org/10.3390/geosciences11120488.

Langford, J., Lande, E. J., Sandane, T., Kahlstrøm, M., Nadim, F., Norén-Cosgriff, K., Piciullo, L., Ritter, S., Hauser, C., Lysdahl, A., Attari, Y. and Formreide, R. (2021) BegrensSkade II – REMEDY – Risk Reduction of Groundwork Damage: An Overview, In: *IOP Conference Series: Earth and Environmental Science, Volume 710*, Helsinki, Finland. http://doi.org/10.1088/1755-1315/710/1/012058

Miranda, J. J., Scholz, I., Agard, J., Al-Ghanim, K., Bobylev, S. N., Dube, O. P., Hathie, I., Kanie, N., Madise, N. J., Malekpour, S., Montoya, J. C., Pan, J., Persson, Å., Sagar, A., Shackell, N. (2023). Global Sustainable Development Report 2023: Times of crisis, times of change: Science for accelerating transformations to sustainable development, United Nations, New York, USA.

RID (2023). RID – Road Innovation Development, Issue 2D, [online] Available at: https://www.gov.pl/web/ncbr-en/rid/, accessed: 17/03/2024.

SENSE (2023). SENSE - Assuring integrity of CO2 storage sites through ground surface monitoring, [online] Available at: https://www.sense-act.eu/, accessed: 14/03/2024.

UN (2015). 2030 Agenda for Sustainable Development. United Nations, New York, USA. Available at: https://www.un.org/sustainabledevelopment/development-agenda/. accessed: 18/03/2024.

URBACT (2022). URGE – Circular building cities, [online] Available at: https://urbact.eu/networks/urge, accessed: 17/03/2024.

Proceedings of the XVIII ECSMGE 2024
GEOTECHNICAL ENGINEERING CHALLENGES
TO MEET CURRENT AND EMERGING NEEDS OF SOCIETY
© 2024 the Authors
ISBN 978-1-032-54816-6
DOI 10.1201/9781003431749-15
Open Access: www.taylorfrancis.com, CC BY-NC-ND 4.0 license

ECSMGE 24
XVIII EUROPEAN CONFERENCE ON SOIL MECHANICS AND GEOTECHNICAL ENGINEERING

State-of-the-art Report

10 years of carbon calculator use: what have we learned for the future?

10 ans d'utilisation des calculateurs carbone: qu'avons-nous appris pour l'avenir?

A. Ottaviani*
Soletanche Bachy, Rueil-Malmaison, France

D. de Melo
Univ.of California, Davis, United States

L. Bruni
Injectosond Italia - S.R.L, Arenzano, Italy

R. Gupta
Freeport-McMoran, Phoenix, Arizona, United States

C. Nelsen
Delve Underground, Washington D. C., United States

**ayelen.ottaviani@sf-group.com*

ABSTRACT: Correct measurement of emissions from the geotechnical industry has been a challenge for the last 10 years and remains a key process to achieving the environmental transition objectives towards 2050. In this context, there have been multiple calculation tools developed in Europe, coming from different actors, such as contractors, consultants, federations, and associations. In view of their importance and multiplicity, it is essential to evaluate their use, reliability, and effectiveness for a correct orientation of future efforts. This study aims to analyse the use of European calculators in a practical way at the local and project level, as well as their reference position worldwide. The role of the calculators coming from geotechnical associations and federations as regulators and guarantors of transparency in the sector has been another important axis of evaluation. And finally, the complexity and the level of detail required in the indicators of the tools to achieve the highest possible utilization and support of the commercial departments in a project bidding phase were compared.

RÉSUMÉ: La mesure correcte des émissions de l'industrie géotechnique a été un défi au cours des dix dernières années et reste un processus clé pour atteindre les objectifs de la transition environnementale à l'horizon 2050. Dans ce contexte, de nombreux outils de calcul ont été développés en Europe, provenant de différents acteurs, tels que des entrepreneurs, des consultants, des fédérations et des associations. Compte tenu de leur importance et de leur multiplicité, il est essentiel d'évaluer leur utilisation, leur fiabilité et leur efficacité afin d'orienter correctement les efforts futurs. Cette étude vise à analyser l'utilisation des calculateurs européens de manière pratique au niveau local et au niveau des projets, ainsi que leur position de référence au niveau mondial. Le rôle des calculateurs provenant des associations et fédérations géotechniques en tant que régulateurs et garants de la transparence dans le secteur a été un autre axe d'évaluation important. Enfin, la complexité et le niveau de détail requis dans les indicateurs des outils pour obtenir la meilleure utilisation possible et le meilleur soutien des départements commerciaux dans la phase de soumission d'un projet ont été comparés.

Keywords: Life cycle assessment; carbon footprint; calculator; environmental product declaration.

1 INTRODUCTION

Over the past 10 years, it has become evident that the building and construction sector plays a crucial role in global energy consumption and carbon emissions. In 2021, the building and construction sector alone was responsible for 37% of global energy and process-related carbon dioxide (CO2) emissions, with carbon emissions from building operations reaching a unprecedented high of 10 GtCO2, and those related to

materials production (e.g. concrete, steel, aluminium, glass and bricks) contributing an additional 3.6 GtCO2.

The European context of regulations and directives on sustainable development and energy efficiency of buildings (RE2020, CSRD, Tertiary Decree, European Taxonomy, etc.) is getting stronger and stronger and is pushing companies in the building sector to better measure the emissions released during the manufacturing, transport, construction, and end-of-life phases of all built infrastructures. But this momentum is even more driven by the expectations of clients and investors, who already at the project bidding stage are particularly interested in knowing the environmental impact of their future projects.

Geotechnical engineering projects play a large role in the civil infrastructure system, making substantial contributions to the construction sector in terms of energy and resource consumption. As such, practitioners can apply sustainability as a design criterion and to value that effort by presenting emission calculations and comparisons to clients. To accomplish this, several tools have been developed over the past decade that quantify embodied carbon through environmental product declarations (EPDs) or life cycle assessments (LCAs).

The European Federation of Foundation Contractors (EFFC) and the Deep Foundation Institute (DFI) developed one of the first tools to calculate the embodied carbon of geotechnical construction projects, the EFFC/DFI Carbon Calculator, a decade ago.

However, other tools have been used for some time in the market, such as (EC3, eTool, ECOM, SimaPro, e-CO2ncerned). A comparative review of these tools and their use over the last decade was conducted to understand the differences in scope, calculation methods and applicability to the industry. The market reaction to the use of the EFFC-DFI calculator by commercial teams has been analysed to understand the necessary improvements to be made to the tool.

2 ENVIRONMENTAL IMPACT QUANTIFICATION METHODS

Numerous methodologies are available for evaluating environmental impacts, each serving distinct purposes.

Among the most used approaches are life cycle assessment, carbon footprinting, and environmental product declarations. Although these methods share certain similarities, each has distinct characteristics and adheres to different standards.

2.1 Life cycle assessment

Life cycle assessment (LCA) is a systematic analytical framework to evaluate the environmental impacts of a product or system over its entire life cycle. Several organizations have created standards to define the perimeter, processes and principles of the calculations, however, the most recognized procedures are included in the ISO14000 standards. It is primarily concerned with the process-based methodology, which is usually defined in four phases: goal and scope definition, life cycle inventory (LCI), life cycle impact assessment (LCIA), and interpretation (ISO 2006).

The scoping phase of an LCA is often described as "cradle-to-grave" (A-C), which includes impacts from the raw material extraction phase to the end of the useful life of the product or system, or "cradle-to-gate", which only includes impacts up to the last stage of the manufacturing process before the product passes through the site (A1-A3).

The LCI quantifies the relevant environmental flows of inputs (e.g. raw materials, water and energy resources) and outputs (e.g. emissions to air, water and soil and waste generation) of the system. Then, in the LC phase, the environmental flows contained in the LCI are translated into environmental and human health impact indicators. A LCI and an LCIA can be compiled in a spreadsheet or in a specific computer program, as explained later in this document.

2.2 Carbon footprint

Carbon footprinting (CF) and LCA are related but distinct methods for assessing the environmental impact of a product or system. Although CF applies life cycle principles and accounting methods, it is based on a single impact category: GHG emissions related to climate change, often quantified as GWP. LCAs, on the other hand, evaluate other environmental impacts, such as energy use, water consumption and air pollution (Motta 2022).

As with LCA, several standards exist to standardize CF procedures for both corporate and product analysis. The Greenhouse Gas Protocol Corporate Standard (GHG Protocol) is the most widely used international emissions accounting standard and has served as the basis for most other standards, including those developed by ISO.

2.3 Environmental product declaration

An EPD is a verified and registered document that conveys information on the life-cycle environmental impact of a product adhering to standards like ISO 21930 and EN 15804 for the building and construction

sector (EN 2012; ISO 2017). These provide a valuable open data source for comprehensive LCAs.

3 EXISTING TOOLS: PHASE 1

In the first stage of the study, five carbon calculation tools from organizations, associations and external suppliers were compared. A summary of these is presented in Table 1.

Table 1. Summary table of major characteristics of the carbon calculation tools.

Tool	EC3	eTool	Embodied Carbon Estimator (ECOM)	SimaPro	EFFC DFI Carbon Calculator
Organization	Building Transparency	Cerclos	Structural Engineering Institute	Pre Sustainability	EFFC-DFI
Activity Sector	Building	Building	Structural Engineering	Several	Geotechnical Engineering
Geographic Regions	Global	Global	North America	Global	Global*
Standard	ISO 21930 EN 15804	ISO 14040/44,27001, 21930 EN 15978, 15804 PAS 2080	EN15978	ISO 14040/44	ISO 14067 PAS 2050:2011
Impact Categories	GWP**	GWP **	GWP	GWP **	GWP
LCA Scope	A1-A3	A-C	A1-A3	A-C	A-B, C2
LCIA Method	Various***	CML	CML	Various***	Assigned Factors***
BIM Plug-In	✓	✓	×	×	×
Cost	Free	600-7,500 USD/yr (based on features)	Free	2,600-7,275 EUR/yr (based on features)	Free

3.1 Embodied carbon in construction calculator (EC3)

EC3 is a web-based tool developed by Building Transparency, a nonprofit organization, that allows users to determine the embodied carbon of building materials and structures based on third-party verified EPDs.

An important characteristic of this tool is the life cycle scope included in the GWP calculation, considering a 'cradle-to-gate' life cycle.

Two of the most notable advantages of this tool are that it is free and user-friendly. The interface makes it extremely easy for inexperienced users. It also takes into account uncertainties, providing more realistic ranges of GWP than if a single, deterministic value were given. However, the scope of the tool is more oriented to superstructures, which may limit its applicability to other types of projects.

3.2 ETool

ETool, a web-based application developed by Cerclos, serves as a tool for evaluating the environmental impacts of projects and identifying areas for improvement. eTool offers templates for building components, energy, and water use. Users have the flexibility to choose from these templates or create their own to determine GHG emissions. This tool provides a financial cost analysis, combining environmental impact assessment with financial analysis.

eTool offers robust functionality for the environmental and financial assessment of projects, but can be difficult to understand for users unfamiliar with sustainability assessment and life-cycle analysis.

eTool focuses on building and construction projects, which restricts its applicability and the quality of data related to other sectors.

3.3 ECOM - Embodied Carbon Order of Magnitude

Embodied Carbon Order of Magnitude (ECOM) is a web-based estimator developed by the Structural Engineering Institute (SEI) that allows users to determine approximate embodied carbon of material products, assembling of framing, or entire structural frame. This tool relies on data sourced from publicly available EPDs.

The interface is easy to comprehend and does not require significant research prior to use. However, users are limited to a small selection of material types and strengths and cannot model life cycle stages beyond material production. Consequently, results may not provide a comprehensive assessment of the total environmental impacts associated with structural projects.

3.4 SimaPro

SimaPro is a software and web-based tool developed by PRe-Sustainability widely used for sustainability reporting, carbon, environmental, social and water footprinting, biodiversity assessments, and sustainable product design.This tool allows users to model LCAs of products, processes, and systems, as well as auxiliary products within a life cycle chain.

SimaPro houses an extensive database of LCI data, which can be used in a wide range of industries and sectors.

SimaPro offers tools to generate comprehensive reports and visualizations of calculated impacts. While SimaPro is a powerful and multidisciplinary tool for performing LCA, it has some potential drawbacks, such as cost and complexity.

3.5 EFFC-DFI Carbon calculator

The EFFC-DFI Carbon Calculator is an Excel-based tool dedicated to calculating embodied carbon of foundations and other geotechnical systems. The calculator accounts for several emission sources within the embodied carbon calculation, including material manufacturing, material transportation, energy consumption, people's transport, equipment transportation, equipment manufacturing, waster transportation, and waste management.

The EFFC-DFI calculator requires a series of inputs for each emission source category. For instance, in material manufacturing, users are prompted to specify material type, quantity, and additional information like cement type and steel shape.

These details enhance the accuracy of embodied carbon estimates, recognizing that emission factors differ based on these aspects.

It is important to highlight that this tool assigns recommended emission factors from different databases for each input, although users have the option to utilize country specific databases for materials (France, United Kingdom, and United States) and electricity grids, following ISO 14067 and PAS 2050:2011 standards.

Moreover, users can create subprojects, allowing them to compute the carbon footprint of specific project segments. These can be consolidated to model the embodied carbon of an entire project. Results can be generated for subprojects, projects, and comparisons between multiple projects. The calculator automatically creates pie and bar charts of results, providing a visual representation of the data.

5 EXISTING TOOLS: PHASE 2

In phase 2 of the study, we have incorporated a look at possible internal tools developed by construction companies, which are not accessible to the public, but are used in the bidding stage, and what impact they may have with those already studied.

The French global Group VINCI has been taken as an example, with implementation in more than 120 countries around the world, and with a specific business line of foundations. The Group has developed the e-CO2ncerned calculator, which includes a specific development for geotechnical activities.

E-CO2ncerned is a Carbon Footprint tool common to all VINCI entities that allows both to calculate the greenhouse gas (GHG) emissions of a project and to compare the GHG emissions of several variants. It is Carbon Footprint® certified by the Bilan Carbone Association and ADEME. The calculator started as an Excel file, which was later moved to a web development. The calculator counts emissions with a VCA approach, from "cradle-to-grave".

The emission factors (EF) used in e-CO2ncerned come from different databases: ADEME (Environmental and Energy Maitrise Agency) carbon database, EcoInvent database, Environmental and Health Declaration Sheets (FDES) from INIES, and VINCI Group internal data.

The web interface used is one of the advantages of the tool, as well as the reports that are automatically

obtained at the end of the project, which allow to compare a base solution with an alternative in a quick way and with appropriate graphics.

Likewise, the possibility of incorporating in the analysis other stages of the project that are not specific to geotechnical engineering, according to user comments, has allowed to analyze the integrity of the project and shows the client a general and wide vision of the project.

However, being an internal calculator, at a tender stage, it has been impossible for the client to compare the environmental impacts with those of other competitors' tenders.

Feedback from users has shown a lack of confidence on the part of clients in the emissions factors used, due to their internal origin.

6 COMPARISON BETWEEN TOOLS

To date, the EFFC-DFI Carbon Calculator is the only tool specifically designed to model environmental impacts of geotechnical projects. Other internal calculators for individual companies, such as the e-CO2ncerned calculator, have geotechnical modules.

In contrast, tools like EC3 and eTool primarily target the building sector, while SimaPro offers broader applicability across various industries.

While it is possible to adapt these tools for geotechnical projects, doing so requires extensive data manipulation to align inputs with the specific requirements of each calculator.

The EC3 calculator, on the other hand, allows users to specify certain material characteristics, but this is dependent on EPD availabilities. Other more comprehensive tools, such as SimaPro, allow users to incorporate specific elements, such as aggregates, based on available LCI datasets, leaving the practitioner to correctly manipulate inputs to model different concrete contributions.

The e-CO2ncerned calculator is limited to a list of materials, with specific strengths, which could be limiting in case of adding a new material.

Another point of comparison is ease of use. Although tools like SimaPro offer more flexibility in modeling processes and scopes, this introduces a further level of complexity. This could add a barrier for new users. In contrast, the EFFC-DFI Carbon Calculator streamlines much of the user activity required in other tools, making it more accessible and efficient to implement. However, this comes with some trade-offs, as users are limited to a predefined set of materials, energy, and transportation options based on the emission factor database.

A comparative study of a point project has been carried out with the EFFC and e-CO2ncerned calculators, presenting base solution and alternative solution data, and analyzing the feedback obtained by the client. A summary of these is presented in Table 2.

The base solution presented included: Sheet Piles Anchors; Soil improvement, RC, Earthworks, Dredging, Pavement, and utilities.

Alternative solution: Slurry wall, Starsol Piles, Anchors, Soil improvement, RC, Earthworks, Dredging, Pavement, and utilities.

Table 2. Total emissions expressed in (TCO2eq).

Tool	Emissions basic solution	Emissions alternative solution
EFFC-DFI	4518	2716
e-CO2ncerned	3700	2900

The differences in emissions are mainly based on the EFFC-DFI concept of ratios versus a detailed approach in the e-CO2ncerned calculator, based on power and equipment usage.

From an action analysis point of view, it was concluded that detailed energy consumption analyses can be useful to understand future actions to be implemented by the company on that topic, such as Scope 1 and 2 emission reduction trajectories. However, in the overall view of a project, and for the practical purposes of showing general data to a client, the ratios are sufficient, since in both cases it is noted that the impact due to materials accounts for about 70% of emissions, and at a tender stage, and when comparing with an alternative design, it is the overall data that is of commercial interest.

To further improve its usefulness, the EFFC-DFI Carbon Calculator could consider expanding its database to include additional input streams, which would allow more diverse processes and systems to be modeled.

7 CONCLUSIONS

Four tools were analyzed in phase 1, in addition to the EFFC-DFI carbon calculator, to understand their scopes of application, standards and characterization factors, calculation methodologies, etc.

Then in phase 2 the EFFC-DFI calculator has been compared with a company internal calculator to understand the commercial impact and customer requirements in Europe.

Based on this study, the following conclusions can be drawn:

- To date, the EFFC-DFI Carbon Calculator is the only tool specifically designed to model the

environmental impacts of geotechnical projects, with a focus on deep foundations.

- eTool, and SimaPro stand out for their ability to perform comprehensive LCA, as opposed to other that are limited to CF assessments. These tools enable users to evaluate multiple environmental impact categories concurrently, allowing for a more holistic analysis that ensures design changes do not inadvertently shift environmental burdens from one category to another.
- From a commercial aspect, the automatic report produced by the e-CO2ncerned calculator makes it easier for commercial teams to sell and compare an alternative solution with a base solution. The EFFC-DFI carbon calculator could improve this aspect and provide a commercial report in Word format.
- The EFFC-DFI Carbon Calculator could be enhanced by expanding its database to encompass additional input flows. This would broaden the range of applications and adaptability to meet specific project needs.
- In most of the applied projects, the EFFC-DFI calculator generates more confidence in the customers than the internal calculators of the companies, because it comes from a neutral organization. One way to further improve the future positioning of the calculator in the market is to obtain new external certifications.

In the context of geotechnical engineering projects, the EFFC-DFI carbon calculator stands out as the most suitable and user-friendly option. By incorporating the recommendations made here, this tool could be further enhanced for improved applicability.

ACKNOWLEDGEMENTS

The authors would like to thank the Deep Foundation Institute (DFI), the European Federation of Foundation Contractors (EFFC), and the American Society of Civil Engineers (ASCE) Geo-Institute (GI) for their support of this effort.

REFERENCES

BSI Standards Publication (2023). PAS 2050:2011 Specification for the Assessment of the Life Cycle Greenhouse Gas Emissions of Goods and Services, Https://Www.En-Standard.Eu. Accessed September 4, 2023. https://www.en-standard.eu/pas-2050-2011-specification-for-the-assessment-of-the-life-cycle-greenhouse-gas-emissions-of-goods-and-services/.

ISO (2022). ISO 14067:2018. Greenhouse gases. Carbon footprint of products. Available at: https://www.iso.org/standard/71206.html.

ISO (2022). ISO 14064-1:2018. Greenhouse gases
Part 1: Specification with guidance at the organization level for quantification and reporting of greenhouse gas emissions and removals. Available at: https://www.iso.org/standard/66453.html.

Motta, Wladmir H. 2022. Carbon Footprint as a First Step Towards LCA Usage. In Towards a Sustainable Future - Life Cycle Management: Challenges and Prospects, edited by Zbigniew Stanislaw Klos, Joanna Kalkowska, and Jędrzej Kasprzak, Springer International Publishing, Cham, Switzerland, pp. 265–75. https://doi.org/10.1007/978-3-030-77127-0_24.

U.S. Green Building Council (2012) EN 15804—2012 Sustainability of Construction Works, Environmental Product Declarations, Core Rules for the Product Category of Construction Products. Available at: https://www.usgbc.org/resources/en-15804%E2%80%942012-sustainability-construction-works-environmental-product-declarations-core-ru, accessed: 26/10/2023.

Proceedings of the XVIII ECSMGE 2024
GEOTECHNICAL ENGINEERING CHALLENGES
TO MEET CURRENT AND EMERGING NEEDS OF SOCIETY
© 2024 the Authors
ISBN 978-1-032-54816-6
DOI 10.1201/9781003431749-16
Open Access: www.taylorfrancis.com, CC BY-NC-ND 4.0 license

ECSMGE 24
XVIII EUROPEAN CONFERENCE ON SOIL MECHANICS AND GEOTECHNICAL ENGINEERING

State-of-the-art Report

The Cube system - a new diaphragm wall technique for future cities

Le système Cube - une nouvelle technique de paroi moulée pour les villes du futur

F.-W. Gerressen*
BAUER Maschinen GmbH, Schrobenhausen, Germany
**Franz-Werner.Gerressen@bauer.de*

ABSTRACT: Diaphragm wall technique is usually used to construct structural elements in the ground, commonly used for retaining systems, permanent foundation elements or deep ground-water barriers, named Cut-Off-Walls (COW). It can be anticipated that global urbanization and increasing demands on environmental considerations will need to be accommodated in underground space in the future. These trends show an increasing requirement for diaphragm walling in even more complex conditions, especially in inner-city applications with limited space. Therefore, there is the demand to minimize the size of equipment to accommodate such projects. Following this demand, a new trench cutter system, the so-called CUBE System, was recently developed. The complete trench cutter system has been fit into container size dimensions so that it can work in very limited space conditions. In addition, complex conditions in terms of space limitations require specifically adapted solutions for slurry, spoil, reinforcement and concrete handling and the related logistics to ensure smooth production. Due to the limited space requirements, the impact on the surrounding environment is limited. As the system is electric driven, an additional reduction of carbon footprint can be expected. First tests of the system have been carried out and the results will be shared. The paper will explain the construction process and the specific challenges and experiences made for these extreme conditions.

RÉSUMÉ: La technique de la paroi moulée est généralement utilisée pour construire des éléments structurels dans le sol. Elle est généralement dédiée à des systèmes de soutènement, des éléments de fondation permanents ou des barrières de retenue des eaux souterraines profondes appelées "cut-off walls" (COW). Les tendances et projections mondiales nous démontrent un besoin croissant en termes de demandes de projets de productions de parois moulées et ce dans des conditions encore plus complexes en particulier concernant les applications en zones urbaines aux espaces limités. En conséquence de quoi il existe une demande de réduction drastique de la taille des équipements dédiés afin de pouvoir réaliser les travaux. Afin de répondre à cette demande, un nouveau système de création de parois-moulées appelé « CUBE System » a été récemment mis au point. Le système complet a été adapté aux dimensions de containers afin de pouvoir travailler dans des espaces très limités. En outre, les conditions complexes en termes de limitation de l'espace nécessitent des solutions spécifiquement adaptées pour la manutention des boues, des déblais, des armatures, du béton ainsi que pour la logistique connexe afin de garantir une production sans heurts. En raison de cette demande de réduction d'espace, l'impact sur l'environnement est limité étant donné que le système fonctionne à l'électricité. Nous pouvons donc nous attendre à une réduction supplémentaire de l'empreinte carbone. Les premiers essais du système ont déjà été effectués et les résultats pourront être communiqués. L'article expliquera le processus de construction, les défis spécifiques ainsi que les retours d'expériences faits dans ces conditions extrêmes.

Keywords: Diaphragm wall; trench cutter; cube system.

1 INTRODUCTION

Urbanization trends showed an increasing population in recent years. Hand in hand the number of peoples living in cities is growing subsequently. To date, over 50% (around 4 billion people) of the world's population already lives in cities and urban areas. The expand of the cities calls for new infrastructure like new underground metro lines, water systems, logistic centres, underground parking and much more. This and rising prices in cities ask for solutions for future projects. Further, the demand for more resources and existing structures in the urban areas request

technology, which can deal with great depths and challenging soil conditions.

Equipment suppliers facing challenges with competing trends of developing small equipment for inner city jobsites but also provide solutions for increasing depths. The challenge to develop machines with low emissions and solutions to reduce impact on daily lives sets restriction to fundamentally rethink methods and processes. In addition, the developments must be more and more powerful, to meet tight schedules and therefore are able to carry out cost effective projects.

One chance to confront these trends is the diaphragm wall method. It combines many features like the ability to be used in various soil and rock conditions with high performance or the possibility to use it in inner-city regions.

1.1 The history of diaphragm wall technique

Searching in the history of the diaphragm wall technique, one can find a first patent which was approved back in 1912 by a company called “Carl Brand” in Germany. This is based on the experiences for the use of clay slurries and it’s stabilizing effect in uncased boreholes. Another patent was approved in the US by Ranney back in 1936. Both patents were almost forgotten before the method really started. A kind of revival and the real start could be seen in the late 1940’s and early 1950’s. Several publications discussed the thixotropic fluids and were patented by Hans Lorenz 1950/51. Also, Christian Veder received an Austrian Patent in 1950 for a methodology of installing water tide walls by using contiguous, uncased boreholes, stabilized by slurry and concreting after excavation. As well company “ICOS” applied for patents on slurry wall constructions by the end of 1940’s in Italy. First full-scale projects have been finally carried out by ICOS for the Metro in Milan e.g., in 1956. With the success of the projects the interest in this technology increases. In addition, with expiring patents, several international construction companies, mainly in Europe and Japan, started to develop additional and alternative equipment for the purpose of installing Diaphragm walls (Gerressen, 2019).

1.2 Equipment history

1.2.1 The grab

To install the first rectangular diaphragm wall panels, ICOS designed a first special grab/clamshell, named crocodiles (Figure 1), which can be seen as the predecessor of today’s grab/clamshell technology.

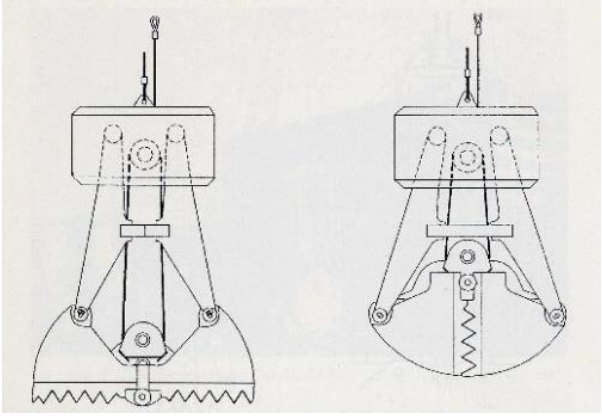

Figure 1. Wire rope grab (ICOS 1960).

A mechanically operated wire rope grab was used as the first type of excavating tool. The closing mechanism is actuated by a pulley block system inside the grab body, whilst the opening of the jaws is actuated by the weight of the block sliding on guides. The grabbing capacity of the initial generations of grabs was limited. The development of heavy-duty crawler cranes with two hydraulically operated winches made it possible to build grabs with jaw widths up to 4.5 m and a weight of over 15 tons. The excavation capacity of the grab system could therefore be increased significantly (Figure 2).

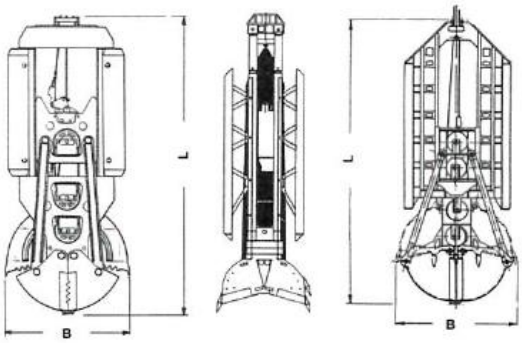

Figure 2. Wire rope grabs, Casagrande (left), Bauer (middle), Leffer (right).

Over recent years, the mechanically operated wire rope grab has been improved by replacing the pulley block system with hydraulically operated rams. Now, with both closing and opening of the jaws being actuated by hydraulic rams, the output capacity has increased significantly. Because of their heavy weight, these types of grabs do not need to be operated in a freefall mode. Hydraulic hoses and electric cables can, therefore, follow the grab into the trench without difficulty. The electric cables attached to the grab also allow the installation of inclinometers, and if necessary, deviations can be corrected by hydraulically operated steering plates as shown in Figure 3.



Figure 3. Hydraulic grab with steering plates.

The grab excavation technology is a widely used and common system. There are, however, some limitations in the system:

- The excavation output reduces with increasing trench depth because of the intermittent excavation process.
- It is difficult to excavate hard soil formations.
- For deep walls it is difficult to construct a sufficient joint system.

The introduction and development of the hydraulic trench cutter system made it possible to overcome these problems and it opened new horizons for the use of the diaphragm wall technique (Gerressen, 2019).

1.2.2 The cutter

In 1962, a kind of suction cutter unit was launched in Germany, which can be seen as one of the predecessors of today's cutter/hydro-fraise technology. Also, two Japanese companies (Tone Boring and Okumura Corporation) developed in the early 1960's a new reverse circulation concept for rectangular panels. While Tone Boring cutting blades rotated around vertical axes, Okumura used two cutting wheels, driven by a chain, and rotating around horizontal axes. The idea of a hydraulically driven cutter was introduced in Europe around 1975 by the French company Soletanche with the brand name "Hydrofraise". The arrival of the cutter technology in Europe prompted other companies to greater activities during the 1980's. Casagrande of Italy brought a system with a chain drive, like Okumura. In 1984 Bauer in Germany brought their system of trench cutter BC on the market. The BC system was designed from the beginning to penetrate rock layers. The cutter wheels are driven by vertically mounted high speed hydraulic motors. A special gear system converts the high-speed rotation of the hydraulic motors into slower rotation of the cutter wheels. With this system, the torque on the wheels can be increased in comparison to other design concepts. The torque of the cutter wheels combined with the weight of the cutter is strong enough to cut into hard soils, crush stones up to a certain grade and overcut into the concrete of adjacent panels. An overview of the various concept is shown in Figure 4.

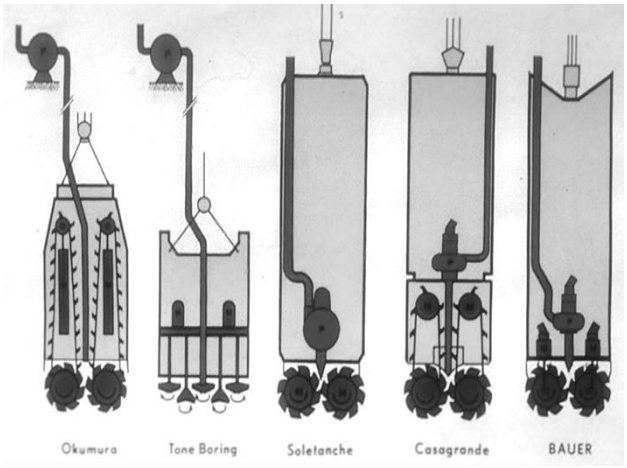

Figure 4. Cutter development.

The trench cutter itself is a reverse circulation excavation tool (Figure 5).

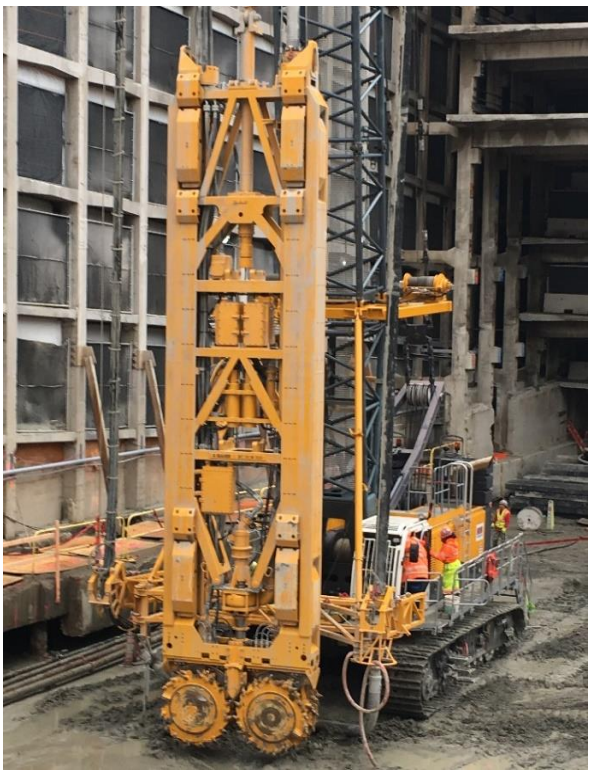

Figure 5. Trench Cutter.

It consists of a heavy steel frame with two drive gears attached to its bottom end, which rotates in opposite direction around the horizontal axis. Cutter wheels are mounted onto the drive gears.

As they rotate, the soil beneath the cutter wheels is continuously broken up, removed, mixed with the bentonite slurry in the trench and moved towards the opening of the suction box of the pump. A centrifugal pump located right above the cutter wheels conveys the slurry via a hose system up to a desanding plant.

Then the slurry loaded with soil and rock particles is cleaned and returned into the trench.

The torque of the cutter wheels combined with the weight of the cutter is strong enough to cut into hard soils, crush stones up to a certain grade and overcut into the concrete of adjacent panels.

Depending on the soil, different types of cutter wheel configurations and teeth can be deployed, ranging from aggressive teeth for cutting fine-grained soil to percussive teeth for crushing boulders. Cutter wheels may conveniently be changed to suit different types of rock.

2 WHERE WE ARE TODAY

2.1 Construction sequence

The working steps usually follow a pre-defined sequence. The main steps are shown in Figure 6. After a pre-excavation, which is necessary to allow starting the suction pump installed in the cutter frame, the excavation of a primary panel starts. Most common is to install multiple bite primaries as shown in Figure 6.

After finishing several primary panels, the installation of secondary, single bite panels takes place while overcutting the adjacent primary panels. The Overcut Joint System is a well proven way for the installation of diaphragm walls using the trench cutter system. In confined conditions the use of special auxiliary equipment (e.g., for installation of reinforcement cages) might become necessary. During excavation the open trench is stabilized by supporting fluid.

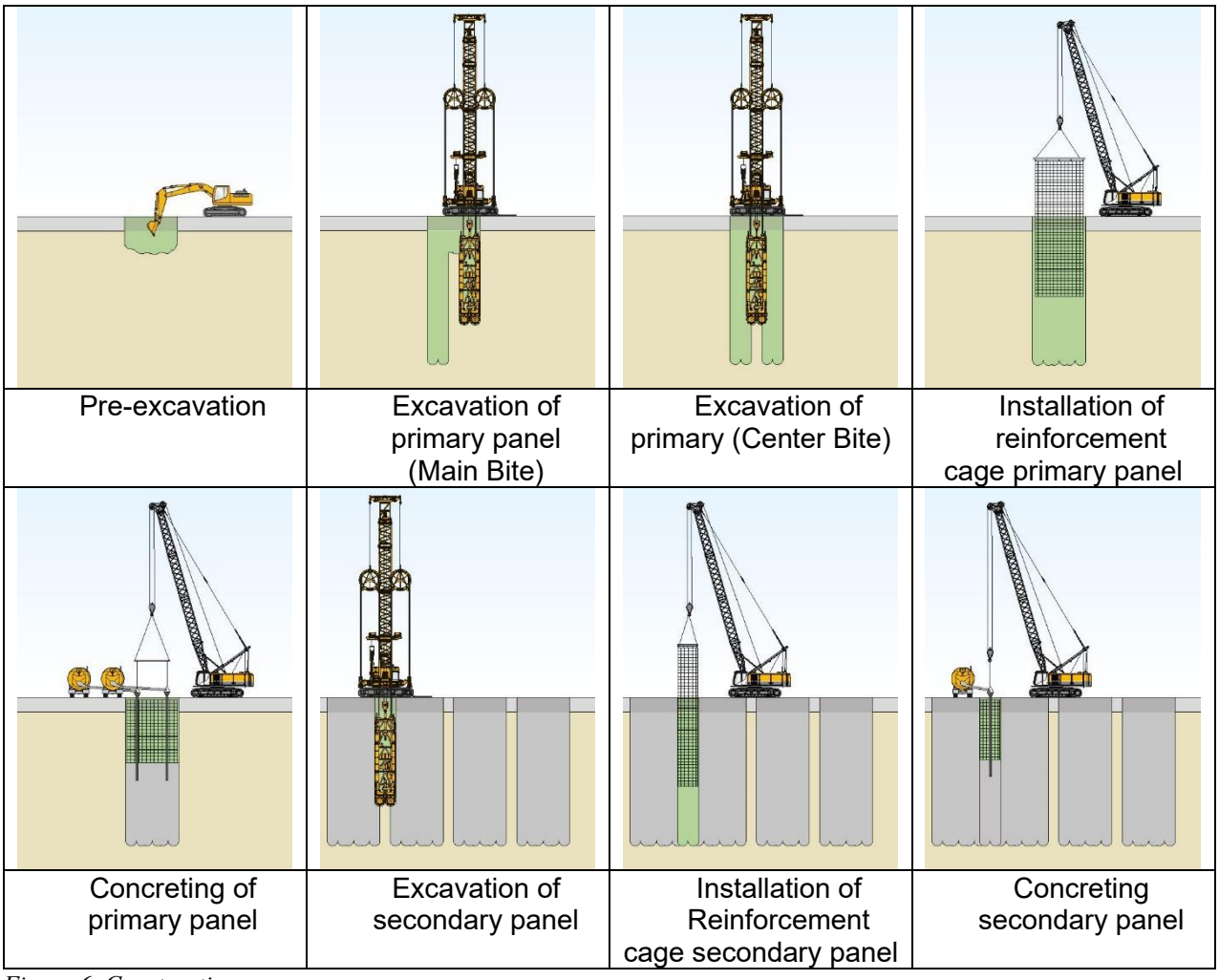

Figure 6. Construction sequence.

2.2 Site set-up and logistics

For diaphragm walling, the handling of the slurry is crucial and compared to other methods, a more complex site set-up becomes necessary.

Beside the cutter and its base carrier, other equipment such as desanding plant, mixing plant, different pumps and storage of the slurry requires space. Further access areas, for the supply of reinforcement cages, concrete and the transport of the excavated material are needed as well as storage of spare parts etc.

As the technique possesses many advantages, the demand to use it also in limited site conditions already led to a special carrier of reduced height, for so called low-headroom applications.

2.3 Development of equipment

Currently it is possible to monitor two different trends in the development of the equipment. On the one hand, it shall be possible to reach greater depth (Figure 7) and higher performance.



Figure 7. Cutter system for great depth up to 250 m.

On the other hand, small and confined situations require small flexible equipment (Figure 8) with low emissions (Gerressen and Blatt, 2020). Especially inner-city jobsites set challenges with the demand to new infrastructure. Over the years different contrary developments to satisfy demands took place. But all these developments had in common that it was possible to identify the diaphragm walling equipment. A completely new approach to widen the range of application is the so-called CUBE system, shown in Figure 9. The system is the next step in the miniaturization of the diaphragm wall technique.



Figure 8. Low-headroom cutter system.

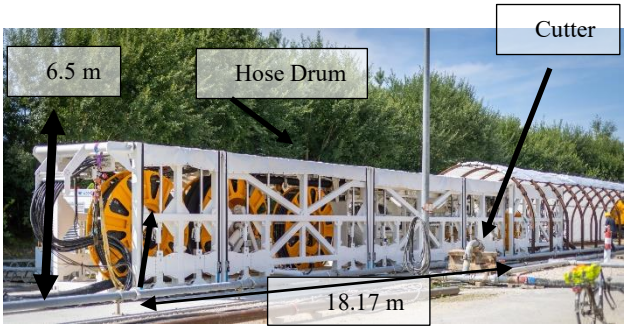

Figure 9. CUBE-System.

2.4 Aim of the system

The aim of the system is to provide additional possibilities. For example, it is possible to create walls out of underground structure, such as metro stations or tunnels. This new flexibility widens the range of possibilities during the planning stage of new infrastructure (for example underground car parking's, water reservoirs, storage areas, etc.). Currently new planned projects often cannot be planned and executed where it would be needed, as existing structures set restrictions. So, in some cases projects are not even started because of lack of technical solutions or enormous efforts in case of execution. In those cases, compromises must be made, e.g., find new not ideally locations, postpone or even cancel projects. With compromises always come additional costs over the lifetime of such a project.

Underground use of space is an important topic in that regard. If cities want to remain cultural, social, and economic centres, they will have to build as compactly as possible within the currently available space. The use of underground spaces as an extension of the urban public domain is an important part of this. But there is one major problem: much of the available space is already taken up by above-ground structures and traditional construction methods becomes increasingly difficult to justify. Now, in a

"Future City world Vision", the system allows planning of underground structures exactly where it is needed in conjunction with minimum impact on the environment above ground level. This creates new options and solutions for planers and urban development with an opportunity to explore the cities underground space better and safely. Due to its flexible application possibilities, great things can be created below ground, while life on the surface goes about its usual business. Execution of D-Wall out of a tunnel as shown in Figure 10 is one of the options. The depth of the tunnel is flexible and can be adjusted to the existing structures. To avoid additional works like e.g., groundwater lowering, it is recommended to have the tunnel above groundwater level.

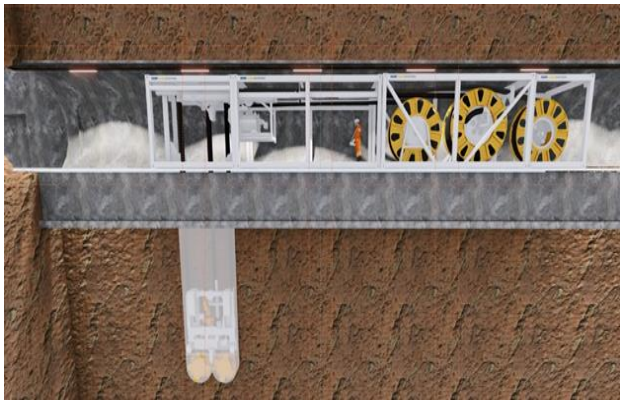

Figure 10. Cube system working in tunnel.



Figure 11. Cube system in very tight spaces.

An alternative of course is to use the system in very tight space conditions keeping e.g. the traffic alive, as shown in Figure 11.

3 THE CUBE SYSTEM

As the ones who have shaped the cutter technology in special foundation engineering, we thought it is time to redefine industry boundaries once again by the development of the BAUER Cube System. As the name indicates, the components are aligned in high cube container. The dimensions of the system can be seen in Figure 11. Within 4 high cube container it contains all known components of a diaphragm wall cutter. As displayed in Figure 12, panels with a length of 2400 mm and widths of up to 1000 mm are possible. To fit the cutter into the containers, it needs to be separated into two pieces. The first container accommodates the cutter head, where the cutter wheels and gearboxes are mounted. Within the second container the pumping unit is placed. To start the cutting process, this unit needs to be placed over the cutter head. For that a pre-excavation of only 1.5 m is necessary to lower the first part and therefore enable the second unit to move over. After both parts are connected, the cutter unit can work. The working principle is identical to standard trench cutting systems.

Because of the containerized dimensions, the need of heavy transports becomes irrelevant, which makes the system flexible and easy to transport. By connecting the containers with so-called quick ties, a fast and uncomplicated assembling can be ensured.

On both sides of the containers, passages make it possible to walk through (see Figure 12 at the right). This is an important factor to meet the safety standards for first aid access and material transport within a tunnel. Further it guarantees a safe environment for service tasks, such as teeth change on the wheels.

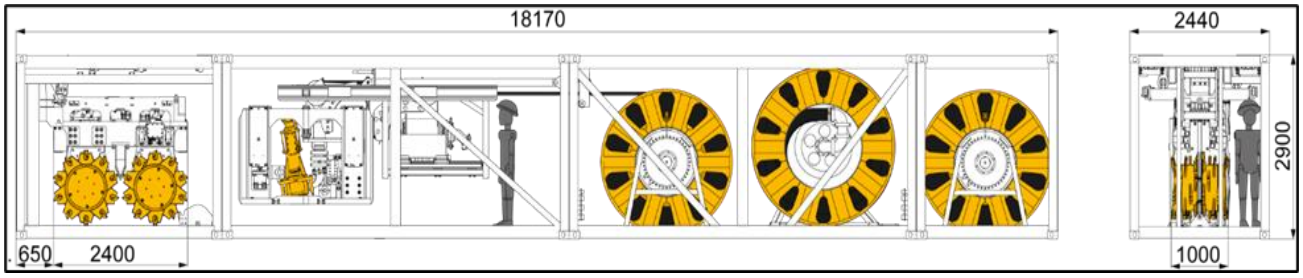

Figure 12. CUBE system - dimensions in mm.

3.1 Test site

In order to understand the processes and restrictions as well as to get a feeling for very confined conditions, a test was carried out first. Scope of the test was the construction of 7 single bite panels. Therefore, a complete jobsite set-up was assembled (Figure 13). In addition, a working platform, which included the rail system was constructed. Further a tunnel was simulated to work within height and width restrictions.

In total, five primary and two secondary panels were executed, whereby one primary was constructed to the maximum depth of 40 m. This is the actual maximum depth capability of the CUBE System. All other panels had a depth of 15 m. All panels were concreted using a concrete pump. Different reinforcement cages were tested. Further different equipment tests were carried out as well.

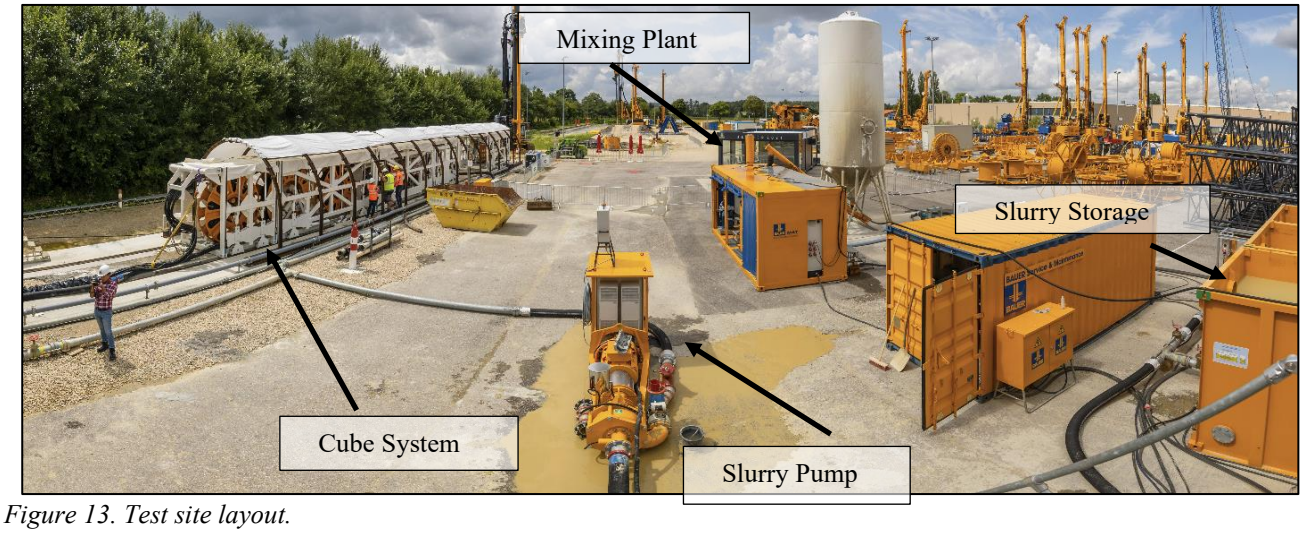

Figure 13. Test site layout.

As the cutter system is not mounted on a carrier with tracks, a new idea for the movement of the system was developed. The movement now is generated by a clamping device and by hydraulic cylinders, as shown in Figure 14. The device clamps hereby on a rail system and a cylinder push or pull the system in the desired direction. In the meantime, the opposite clamping device moves into position and ensures a continuous movement. Using this system, the CUBE system can move at a speed of 1.2 m/min.



Figure 14. Clamping device.

Like any other cutter system, a pre-excavation is required. The system can work with a reduced pre-excavation depth of 1.5 m, which can be carried out by a small excavator also within confined conditions.

The cutting process itself is not different compared to standard equipment. The loosened material is transported via the stabilizing fluid to a desanding plant. Here the solids are separated from the liquid medium, which is afterwards ready for reuse. Cutting performances on the test site were comparable with performances on sites with similar ground conditions.



Figure 15. Reinforcement and concreting container.

Although the cutting process is quite like the standard procedure, reinforcing and concreting are a bit more challenging due to the very limited height restrictions. Therefore, two different types of reinforcement cages were tested to assess the handling and installation during the construction within a tunnel. Each segment of the cages had a height of 1.85 m and were transported to an independent container. This container (Figure 15) contains all handling devices for the installation of the reinforcement cages and tremie pipes. Thus, it is also responsible for the concreting process.

During the test, it was found that the use of prefabricated cages in conjunction with the use of Lenton couplers as shown in Figure 16 was the most favourable solution for practical application. The connection time of two segments was approx. 15 min.



Figure 16. Cage coupling.

A concrete pump (Figure 17) supplied the concrete through the simulated tunnel to the trench (Gerressen et al, 2022).



Figure 17. Concrete supply via concrete pump.

4 CONCLUSION

With an increasing number of people moving into urban and inner-city areas, the demand for new infrastructure will also soar in the future. Existing buildings and structures as well as high prices for areal spread, set restrictions and for these new infrastructure facilities. In addition, environmental aspects will become more important and will raise the question for new strategies. The impact of these demands will further influence for the construction process and the design of equipment.

The importance to provide solutions for confined space jobsites with challenging soil conditions already rises difficulties for logistics, storage, and methods, as well as equipment to solve the restrictions. Today, suppliers already provide compact machines of high performance.

The CUBE System with its new design, new thinking of system and its reduced dimensions will make numerous projects possible, which lack of solutions until today.

The test proofed the functionality of the system and therefore provides opportunities for projects which had never been thought before.

With this, the system can become part of the “Future City world Vision”.

REFERENCES

Gerressen, F.-W.; (2019) Diaphragm Walls – From the past to the future, SEFE 9 –, São Paulo, Brazil, June 2019.

Gerressen, F.-W.; Blatt, A. (2020). Confined space and inner-city projects – future challenge and opportunity for diaphragm walling, 10th Anniversary Conference on Deep Foundation Technologies for Infrastructure Development in India, November 2020

Gerressen, F.W. Blatt, A., Weixler, L. (2022) The miniaturization of diaphragm wall technique – the Cube system, 47th Annual Conference on Deep Foundations, USA, October 2022

Proceedings of the XVIII ECSMGE 2024
GEOTECHNICAL ENGINEERING CHALLENGES
TO MEET CURRENT AND EMERGING NEEDS OF SOCIETY
© 2024 the Authors
ISBN 978-1-032-54816-6
DOI 10.1201/9781003431749-17
Open Access: www.taylorfrancis.com, CC BY-NC-ND 4.0 license

ECSMGE 24
XVIII EUROPEAN CONFERENCE ON SOIL MECHANICS AND GEOTECHNICAL ENGINEERING

State-of-the-art Report

Thermal behaviour of soils: studies and applications in current energetic and climatic contexts

Comportement thermique des sols: études et applications dans les contextes énergétiques et climatiques actuels

A. Vieira*
LNEC (National Laboratory for Civil Engineering), Lisbon, Portugal
**avieira@lnec.pt*

ABSTRACT: The study of the thermal behaviour of soils dates back several decades, often associated with its strain rate dependency. More recently with the diversification of soil use, such as in the exploitation of shallow geothermal systems and other applications, this study has gained renewed interest and an enlarged scope. Moreover, in the current climatic context, both the different amplitudes of thermal cycles and the expressive, sometimes sudden, variations in water table levels, especially at geological shallower levels, are likely to impact the performance of structures and infrastructure. The assessment of the sustainability of soil use as a resource and its structural study must be based on an adequate knowledge of its behaviour from a multiphysical perspective, where thermal, mechanical, and hydraulic processes interact. A phenomenological description of the thermal behaviour of soils is presented in an integrated view, considering experimental and numerical characterization, aiming a proper planning and a sustainable use, furthermore with reference to ongoing studies on the geological formations of the city of Lisbon.

RÉSUMÉ: L'étude du comportement thermique des sols remonte à plusieurs décennies, souvent associée à leur comportement visqueux. Avec la diversification de l'utilisation des sols, comme dans l'exploitation des systèmes géothermiques et d'autres applications, cette étude a connu un regain d'intérêt. De plus, dans le contexte climatique actuel, les amplitudes variables des cycles thermiques et les variations importantes, parfois soudaines, du niveau de la nappe phréatique, en particulier dans les niveaux géologiques peu profonds, sont susceptibles d'avoir un impact sur les performances des structures et des infrastructures. Tant l'évaluation de la durabilité de l'utilisation des sols en tant que ressource que leur étude structurelle doivent être basées sur une connaissance adéquate de leur comportement d'un point de vue multiphysique, où les processus thermiques, mécaniques et hydrauliques interagissent. Une description phénoménologique du comportement thermique des sols est présentée dans une vision intégrée, s'appuyant sur une caractérisation mathématique et expérimentale, visant une planification appropriée et une utilisation durable, en référence aux études en cours sur les formations géologiques de la ville de Lisbonne.

Keywords: Soil thermal behavior; shallow geothermal systems; sustainability; urban planning.

1 INTRODUCTION

From a Soil Mechanics and Geotechnics perspective, the thermal study of soil has evolved significantly, not only in its phenomenological description and constitutive analysis but also in its scope and approach, over the last few decades. Particularly regarded as a construction material, foundation, and support for civil engineering works, its value as a resource in the energy context becomes apparent, especially it what concerns to the exploitation of shallow geothermal systems, among other applications. Consequently, the importance of this study for the performance and safety of constructions, infrastructure and geotechnical structures, is now expanding, especially at the urban level, to the issues of planning and sustainable management, which also impact, in different ways, directly or indirectly, with the former. Thus, from the point of view of Geotechnical Engineering and Environmental Geotechnics, the thermal study of soil, its understanding, characterization, modelling and approaches, have become more complex, sometimes substantially, at a time when the study of georesources off the planet has already begun (Delage et al., 2023).

The study of soil behaviour should be considered in a multiphysical perspective, in which mechanical, thermal, hydraulic, and sometimes chemical and electrical processes interact in a non-trivial way. For example, in the case of shallow geothermal systems, and more specifically, in energy geostructures, there is an interaction between them and the surrounding ground, due to the heat exchange over the seasonal heating and cooling cycles, which causes stresses and strains both in the soil and in the geostructure that must be properly considered in design. This interaction is dependent on many factors and its evaluation remains a topic of research. In turn, thermal actions in the soil can induce changes in the pore water pressures. Additionally, the existence of water flows through the soil can also induce heat transport by convection and advection, depending on the grain size of the soil and the flow velocity, with consequent coupled effects. Upstream of these interactions, and determining their occurrence, the process of heat transfer by conduction between the soil and the shallow geothermal system determines its sizing and energy efficiency alongside the evolution of temperature distribution in the soil over time.

Involving higher temperature ranges than those generally associated with the operation of shallow geothermal systems, the thermal behaviour of soils and rocks assumes particular relevance in cases of radioactive waste disposal, in slope sliding and instability processes, in landslides on faults (where the heat produced by friction, leading to water expansion can cause thermoplastic collapse of the soil skeleton, in addition to the direct and significant impact on the mechanical properties of the solid skeleton) (Cecinato and Zervos, 2012, Alonso et al., 2015), among other examples.

The phenomenological, instrumental (laboratory and field), constitutive and numerical study of the thermal behaviour of soils (and other geomaterials), a relatively recent field of research, is of scientific relevance to society, at a time when the effects of climate change and the search for renewable energy sources, promoting the reduction of CO_2 emissions, are at the centre of society's concerns. It is believed that the progressive increase in temperature and extreme events, where, for example, long periods of drought (with drying and increased cracking of surface soils) interspersed with short periods of extreme precipitation, is liable to create conditions for the occurrence of collapse processes and large deformations. Additionally, the predicted increase in the amplitude, number and duration of heat waves, as is expected, for example, in Iberian Peninsula Mediterranean region, which is considered a climate change hotspot (Soares et al., 2024), might induce changes in soil state conditions and properties, particularly impacting the most superficial soil geological deposits. These effects will pose increasing challenges to the functionality and safety of current and future engineering works.

In the contexts of the most recent use of soil as a resource, namely for shallow geothermal applications, including district heating and cooling (DHC) and thermal storage, in the perspective of more efficient energy use, sustainability planning, and under circular economy scope, a proper thermal characterization of soil is essential. It is intended to allow the geothermal potential to be assessed, the sizing of air conditioning systems, the optimization of their performance and the evaluation of interferences, also enabling the proper geotechnical and structural design of structures and infrastructure. Thermal tests in soils and rocks and the knowledge of temperature distribution at depth, new numerical and geospatial modelling techniques and tools, advanced instrumentation using next-generation sensors, data processing, machine learning and process optimization, are of particular relevance here. These and other tools aim at a more precise and integrated characterization of the soil, which will contribute to the development and promotion of a more sustainable future.

From the point of view of both Soil Mechanics and Environmental Geotechnics, the consideration of temperature dimension in the behaviour and characterization of soils is crucial for a comprehensive understanding of the performance of civil engineering constructions and the assessment of their impact on the surrounding environment, especially in urban areas.

2 THERMAL BEHAVIOUR

In 1943, Terzaghi established a mathematical comparison between the consolidation process in soils and other processes, such as heat diffusion and the propagation of electric current in solids. The heat diffusion equation, also known as the heat equation, describes the rate of change of temperature in a material as a function of its position and time. In a homogeneous and isotropic medium without external heat sources, it takes the following form:

$$\frac{\partial T}{\partial t} = -\alpha . \nabla^2 T \qquad (1)$$

where T is the temperature at a specific point and time and α is the thermal diffusivity (thermal diffusion coefficient), which depends on the thermal conductivity λ, density ρ and specific heat capacity c ($\alpha = \lambda/(\rho . c)$).

Mitchell (1993) established a series of parallels between the different flows that can occur through soil and their respective governing laws: fluid (Darcy's law), electric (Ohm's law), chemical (Flick's law), and thermal (Fourier's law), contextualizing their importance and noting that all these physical processes interfere in geotechnical problems through direct or coupled processes.

Regarding heat conduction, Fourier's Law establishes that:

$$q = -\lambda . \nabla T \quad (2)$$

where q is the thermal flux vector.

Heat transfer in soils involves various mechanisms, as identified by De Vries (1958) and Farouki (1981), mainly conditioned by the soil's degree of saturation and particle size distribution, being thermal conduction the predominant process. These seminal works describe the fundamentals of heat transfer in soils. In his monography Farouki (1981) provided a comprehensive analysis of this physical process, particularly focusing on the description of different methods to evaluate thermal properties, from which thermal conductivity is the most relevant, and how they are influenced by different factors, considering soil´s multiphase composition. It is worth mentioning that thermal conduction is also clearly the dominant process in the case of energy geostructures (Brandl, 2006). The degree of saturation is the parameter that most influences thermal conductivity, it can vary by about an order of magnitude between fully saturated and unsaturated conditions. Other factors such as porosity, particle shape, mineral composition, among others, might also significantly influence this property.

More recently, with a special focus on of shallow geothermal systems, the thermal characterization of soils has sparked renewed interest in the field of engineering, driving a series of fundamental and applied studies in this area, especially due to its influence on the design and performance of these systems and other applications.

The evaluation of thermal conductivity, which quantifies the ability of materials to conduct heat, can be done empirically through direct correlation of data compiled in different lithological units, semi-empirically through the application of mathematical relationships involving the conductivity and volumetric fractions of the different soil phases, among other parameters, and through field or laboratory measurements (Vieira et al., 2017). As for experimental measurements, Enhanced Thermal Response Tests, deserve special mention, as they allow distributed determination of thermal properties, along the depth and thus along the different soil and rock layers. These field tests, by taking into account the specific conditions of a particular site (stress state, water level depth and possible water flows), eliminate the inherent difficulties of laboratory sampling and specific limitations of transient and steady-state conditions tests (analytical approximations, testing times, thermal losses, among others).

Low et al. (2015) published a compilation of conductivity measurements through laboratory and in situ tests, which showed that in situ measurements consistently reveal higher values. Possible explanations for these discrepancies include hypotheses of sample disturbance, alteration of their stress state (effect of confinement stress) and migration and/or loss of water within the sample. The effect of the confining stress was confirmed by Maranha and Vieira (2018) through numerical analysis by FEM in an assemblage of quartz spheres in void, considering different spatial arrangements. An increase in the applied isotropic stress level resulted in higher thermal conductivity due to the increase in contact area caused by the thermal expansion of the spheres. These results were in agreement with the analytical expression proposed by Sakatani et al. (2017). In-depth study of conductivity has been carried out through analysis of thermal tests in transient conditions by Aljundi et al. (2024) using a high-precision probe. In addition to variations in state parameters, the influence of control parameters (temperature and test duration) was analysed. The effect of heterogeneity was minimized by conducting systematic tests on the same sample. This study also involved the evaluation of thermal conductance at the contact surface between the thermal probe and the soil sample and its relevance for the numerical reproduction of the tests and in the conductivity evaluation. Overall, the importance of state parameters was confirmed, and regarding test control parameters, the significant influence of temperature (eventually due to the increased particles contact area due to thermal expansion of soil particles) and test duration was observed (Figure 1). In the case of dry soil, it was shown that the standard test duration of 100 s is not sufficient to eliminate the boundary effect of the probe.

The determination of thermal parameters can also be done through inversion techniques using field measurements, thus eliminating the difficulties of evaluating thermal conductivity and volumetric heat capacity across heterogeneous soils (Romio et al., 2019; Li et al., 2022).

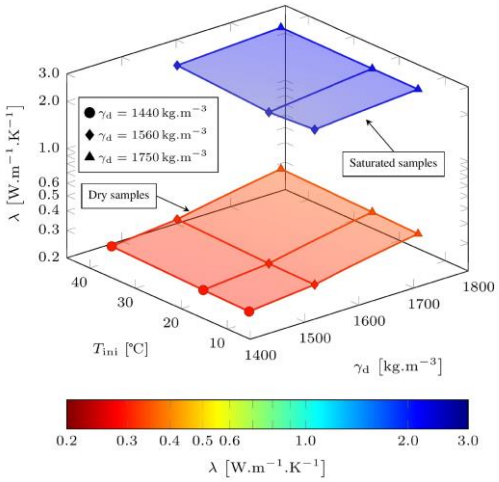

Figure 1. Thermal conductivity measurements (effect of saturation, density and temperature) (Aljundi et al., 2024).

Recent works highlight the potential of these techniques. Figure 2 shows schematically the proposal of Li et al. (2022), based on the inlet and outlet temperature data recorded in borehole heat energy storage (BTES) and soil temperature, which through a modified duct thermal energy storage method and an iterative procedure allow the progressive correction of initially adopted parameters, consequently enabling the optimization of the performance of the system. This method was verified with operational data based on long-term monitoring conducted in a large-scale BTES project in Chifeng, China.

The increasing installation of shallow geothermal systems and the recognition of their great potential have resulted in growing research, also making available a considerable amount of data across a range of environments and operational conditions, contributing to expanding knowledge in this field, allowing for a greater understanding of the parameters and factors which influence thermal parameters, their determination and the importance of their proper evaluation.

Soil thermal conductivity depends on state parameters and its determination, in what concerns to laboratory evaluations, as occurs in geotechnical parameters, depends on the quality of sampling, among other factors that might modify the structure and composition of the soil (such as stress and strain dependence), the direction (due to anisotropy) and type of test. Thermal characterization is already an integral part of soil studies and will continue to play a crucial role as increasingly complex environmental challenges are faced, involving a multidisciplinary approach. It is import to pursuit the development of advanced techniques and methods to characterize soil thermal properties.

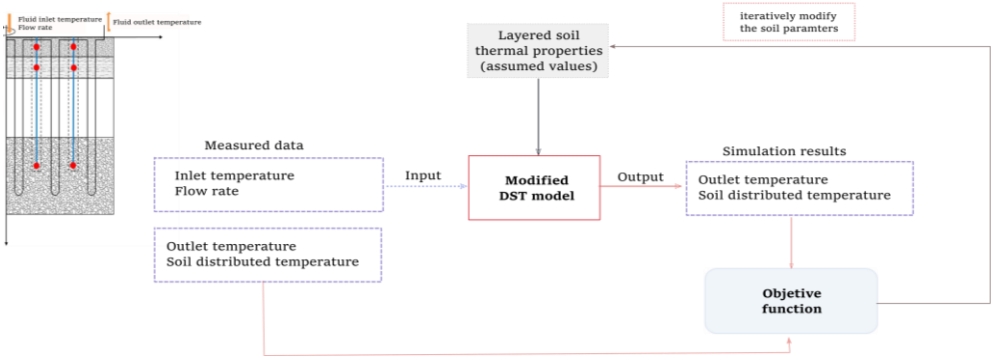

Figure 2. Parameter estimation method (adapted from Li et al., 2022).

3 THERMOMECHANICAL BEHAVIOUR

The temperature variation is directly related to the kinetic energy of molecules, inducing consequent mechanical effects in a system. Temperature changes generate volume variations and/or alterations of pressure in the pores of soils. A first insight into the parameters that influence the soil response to a temperature rate can be obtained for the problem involving a saturated soil element under isotropic conditions. In this case, the analytical solution for the rate of volumetric deformation induced by temperature rate is:

$$\dot{\varepsilon_v} = -\beta \dot{T} \quad (3)$$

Under these conditions, it is possible to determine the coefficient of volumetric thermal expansion and the rate of variation of interstitial pressure for any drainage condition, respectively, β and $\dot{u}$. These quantities depend on the coefficients of volumetric thermal expansion of the solid particle β_g and water β_w, on the volumetric elasticity moduli of the solid skeleton and Biot's modulus, K e K_f, respectively, on the porosity n ($K_f = K_w/n$, where K_w is the volumetric compressibility modulus of water) and on the rate of flow per unit volume that enters or leaves the soil voids, $\dot{\zeta}$, according to:

$$\beta = \frac{[K+(1-n)K_f]\beta_{g+K_f}\left(n\beta_w - \frac{\dot{\zeta}}{T}\right)}{K+K_f}\,\dot{T} \qquad (4)$$

$$\dot{u} = K.K_f\,\frac{[n(\beta_w-\beta_g)]-\frac{\dot{\zeta}}{T}}{K+K_f}\,\dot{T} \qquad (5)$$

In fully drained conditions $K_f = 0$ or if $\beta_w = \beta_g$, no interstitial pressures develop, otherwise (under undrained or partially drained conditions), there is a change in water pressures in the pores. The tendency is such that with an increase in temperature, as the coefficient of expansion of water is greater than that of solid particles, the solid skeleton restricts expansion and the pressure in the pores increases, consequently reducing effective stress (and strength). The opposite occurs when the temperature decreases. Understanding how these variables interact is essential to understand the mechanical processes caused by thermal actions, for example, for assessing thermo-mechanical effects in energy structures.

However, the effect of temperature is more complex, because soil behaviour is essentially irreversible. As referred by Leroueil and Marques (1996), temperature has two major effects on soils: thermal expansion of soil particles and pore water, and thermally induced modification of strength at the contacts between particles. In other words, temperature induces elastic and plastic effects.

Mitchell (1993) explained the combined effect of these phenomena on the temperature-volume-effective stress behaviour of soils in both drained and undrained conditions, based on thermal tests in isotropic conditions in a normally consolidated saturated illite under a temperature loading cycle (an initial increase from 18.9 to 60.8ºC followed by cooling to 18.9ºC) under a constant isotropic total stress of 200 kPa. These tests allowed the observation of irreversible volumetric deformation, known as thermal compaction and the induction of residual pressure under undrained conditions. This contractant behaviour may be explained by compressive plastic strains caused by heating, due to a decrease in the soil's yield strength which supersedes the thermal elastic dilation. According to Mitchell, these effects must be taken into account, both in the field and in the laboratory.

It was observed, for subsequent thermal cycles of loading and unloading, of the same amplitude, that the behaviour observed is similar to that of secondary compression reloading, that is the irreversible deformation tend to disappear.

However, for overconsolidated soils, the situation is more complicated, and soils, during heating in drained conditions, can initially exhibit a dilatant behaviour as a result of the prevailing influence of elastic effects, followed, for higher temperatures, by volume reduction caused by thermoplastic strains. The results obtained by Hueckel and Baldi (1990) in natural Pasquasia clay clearly show the effect of the thermal loading history on the volumetric behaviour during heating. Qualitatively similar results were obtained by Cekerevac and Laloui (2004), which once more demonstrated the influence of stress history on thermal behaviour. They also analysed the response to thermal loading and unloading cycles. Again, with the consideration of thermal cycles, processes become considerably more complex. The effect of thermal compaction for lower OCR values is evident, although the cause of the high inelastic deformations observed for higher OCRs in cooling cycles is not as clear. In subsequent cycles, the behaviour tends to be essentially elastic.

Also for tests under isotropic conditions, Sultan (1997) investigated experimentally the effects of the thermal loading rate on the contraction curve, with results showing a very significant effect of the cooling rate, with a decrease in thermal expansion as the discharge (cooling) rate decreased. Conversely, Cui et al. (2000) drew attention to the likelihood of results showing expansion during cooling.

For non-isotropic stress states, the thermal influence processes become even more complex. Leroueil and Marques (1996) merit special mention for their work analysing the effect of temperature and viscosity, under different conditions, from a critical state perspective. They observed a decrease in the preconsolidation stress and in the yield surface with increasing temperature (similar to what happens with decreasing strain rate), as well as an increase in compressibility. Regarding the critical state friction angle, the results are contradictory. Laloui et al. (2014) also provided a very comprehensive and detailed compilation of the main aspects observed in the thermohydromechanical behaviour of soils, in the context of shallow geothermal applications, emphasizing the difficulty regarding some behavioural trends for non-isotropic conditions.

These briefly described aspects are largely based on laboratory characterization. This has been done mainly through traditional Soil Mechanics testing equipment properly adapted for testing under non-isothermal conditions.

Significant progress has been made in constitutive modelling with proposals for advanced models that increasingly accurately reproduce observed behaviours. A thorough review of the main constitutive models for soils was compiled by Christodoulides et al. (2020), categorizing thermal models into thermoelastic, thermoelastoplastic, and

thermoviscoplastic. Thermoelastic models encompass analytical solutions and stress-strain-temperature elastic relationships. Different types of elastic models extended to non-isothermal conditions can be found in the literature, such as extensions for isotropic elasticity, which can be categorized as linear thermoelasticity, thermohypoelasticity and thermohyperelasticity.

In thermoplasticity, irreversible deformations can be induced by non-uniform temperature fields, which is compliant with the systematic experimental evidence showing the occurrence of plastic strains caused by thermal loading. This type of models includes analytical solutions, models with critical state structure involving temperature dependence in the hardening law, thermoplastic models with multi-mechanisms - involving isotropic and deviatoric thermoplastic deformations - and others. In thermo-viscoplastic models, rate dependency, one of the most relevant features of soil behaviour, is considered to overcome limitations of thermoelastoplastic models.

The subloading concept due to Hashiguchi was also used to reproduce the influence of non-isothermal conditions on the stress-strain-time behaviour of soils. A version of the viscoplastic subloading soil model proposed by Maranha et al. (2016), restricted to isotropic stress and strain conditions, was extended to non-isothermal conditions by Maranha et al. (2017), introducing temperature dependence of the size of the yield surface and the position of the centre of homothety. The first version of the model allowed for the capture of the large volumetric expansion strains observed in highly over-consolidated clays by Cekerevac and Laloui (2004) in the initial stages of heating tests. These strains were considered irreversible and the corresponding coefficient of thermal expansion variable and much larger than that directly resulting from the constituent minerals of the soil's solid phase. In order to reproduce these trend, it was necessary to assume that the previous unloading stress (necessary to obtain the over-consolidated state) was fast enough so that creep was still occurring at the beginning of the heating stage. However, this change was not sufficient to reproduce the behaviour of the subsequent unloading cycles (cooling). Thus an improved version of this model, introducing temperature dependence motion to the centre of homothety, was presented in Maranha et al. (2018). Using this model, a very good adjustment of the three heating and cooling tests presented in Cekerevac and Laloui (2004), considering the variability between the three soil samples and the same material model constants for all, was achieved (Figure 3).

The extension of this thermoviscoplastic model for generalized stress states is under development. This study will be supported by new tests in a triaxial chamber adapted for non-isothermal conditions for Lisbon soils under the scope of Project Geosustained (PTDC/ECI-CON/1866/2021). Isotropic stress thermal cycles at different strain will be carried out in order to obtain the evolution of thermal expansion for different soils and gather additional information to support the above referenced model assumptions and obtain data for parameter calibration. Thermal tests in axisymmetric stress conditions will also be carried out.

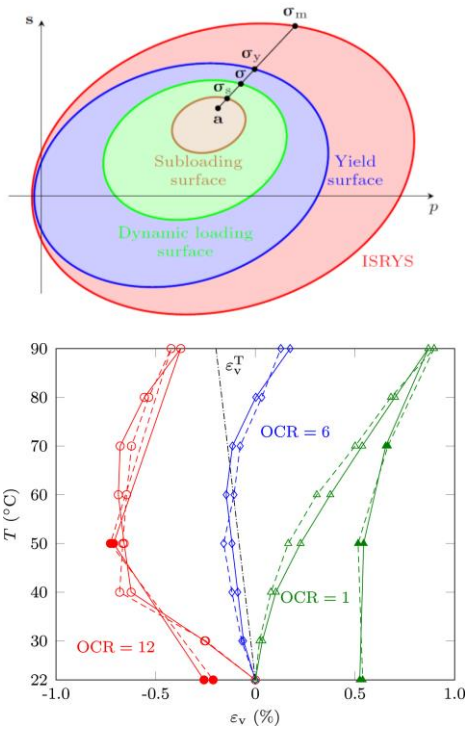

Figure 3. Surfaces of original model (top figure) (Maranha et al., 2016) and numerical reproduction of experimental thermal tests of Cekerevac and Laloui (2004) (dashed lines) (Maranha et al., 2018).

Alongside developments in mathematical and computational reproduction of the thermo-hydromechanical behaviour of soils, especially in the context of shallow geothermal applications, advances in deformation measurement systems in laboratory and field settings (in terms of quality and volume of data), notably high-precision stereophotogrammetry, and genetic algorithm techniques for model calibration, and other technological advancements, will continue to allow further progress in the study of the thermohydromechanical behaviour of soils.

The compilation above presented, mainly focused on geothermal systems, did not made reference to partially saturated states, anisotropy, localization of deformation, spatial variability, dissection and fissuring, which all affect soil thermomechanical. It is believed that some of these aspects will become increasingly relevant in future climatic contexts.

4 PLANNING AND SUSTAINABILITY

The utilization of surface soil layers as a renewable and stable thermal energy resource and reservoir through shallow geothermal systems, here with a special focus on closed-loop systems and ground source heat coupled systems, including district heating and cooling (DHC) and thermal storage, has been changing the paradigm of soil study, utilization, planning and management in a more interdisciplinary perspective. Shallow geothermal energy is a promising low-carbon source to meet the heating and cooling demands of buildings and infrastructure. In this context, new solutions are emerging with the aim of harnessing thermal energy from the soil across various climatic conditions. For instance, capturing energy released in industrial settings for later use in space heating, domestic hot water systems, and other applications. Overall, a seasonal balance between heating and cooling is sought to avoid introducing changes in soil temperature fields and thus potential undesirable effects.

In this context, it is worth mentioning the approach of Walch et al. (2022), proposing a rational utilization methodology of the resource, taking into account the geothermal potential for the use of Ground Source Heat Pumps (GSHPs), defining this potential as the one that ensures seasonal regeneration of soil energy exchanges through re-injection of excess heat from space cooling. The goal is to estimate the usable energy to meet the energy demand of buildings at the regional scale, calculated for both direct heat exchange and urban DHC systems under different scenarios of climate change and market penetration levels of cooling systems.

Accounting for the seasonal regeneration of GSHP systems required matching the geothermal technical potential with the energy needs of buildings. This study involved not only mapping potential installations near buildings but also the one of DHC, noting that while individual GSHPs are directly connected to nearby buildings, DHC permits the transportation of heat between areas with high geothermal potential to areas with high energy demand. The methodology includes three phases (Figure 4): the first involves geospatial processing to match potential GSHP systems to building energy demands, the second analytical modelling to quantify the technical potential of heat exchange for GSHP systems, and the third analysis to optimize the location of the technical potential between individual GSHP systems and DHC. Applications were carried out by Walch et al. (2022) in Swiss cities (Geneva and Lausanne), where heating needs prevail but is foreseeing a significant increase in cooling demand. The results indicated that individual GSHPs could cover up to 63% of cooling demand and 55% of heating demand by 2050. With the use of DHC, these values increase to 87% and 85%, respectively

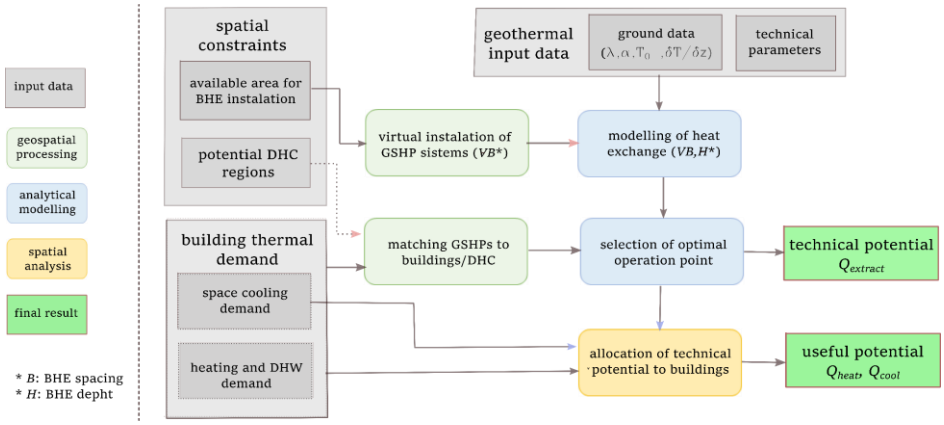

Figure 4. Three stages workflow for modelling the technical potential of GSHP and the useful potential for heat and cooling supply (adapted from Walch et al., 2022).

A rational and structured management at the urban level, as above proposed, always has at its basis an adequate thermal characterization of the soil. A similar approach, adapted to different climatic contexts where cooling needs prevail, emerges as a promising path for planning these systems. Thermal conductivity (and specific heat) geospatial mapping serve as the initial basis for the systems sizing, design and energy efficiency evaluation. In the absence of this information, thermal conductivity can be estimated from direct correlations with the lithological type. Dalla Santa et al. (2020) recently published a comprehensive compilation of thermal conductivity range values based on measurement results in different lithologies, which served as the basis for the initial estimation of this property for the geological formations in the city of Lisbon (Figure 5). This proposal was complemented with estimates based on

mineralogical composition and geotechnical parameters. This work is being complemented based on geotechnical information (derived from a large database of boreholes in the city available on GIS platforms available from the Lisbon Municipal Council), and also, with a higher level of detail and precision, with laboratory measurement data on undisturbed samples. This will entail characterization at three scales (city, site, and sample) which will be systematically updated. In a subsequent stage, based on the characterization of the soil at depth, sustainability analyses will be conducted for different types of buildings, taking into account the city' climate in climatic scenarios where cooling needs predominate, as is typical of Mediterranean climates.

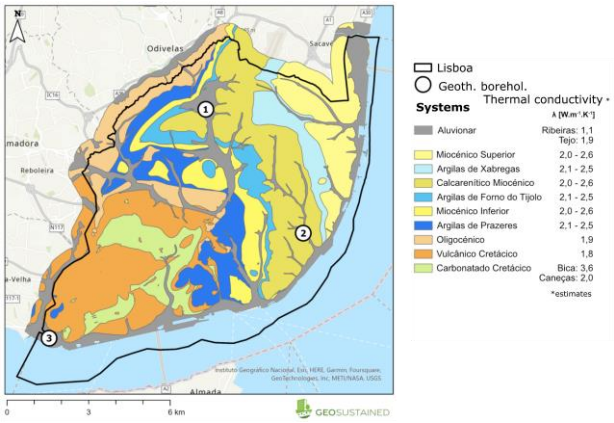

Figure 5. First estimate of Lisbon geological systems thermal conductivity (Inácio et al., 2023).

Soil temperature at a given location and its evolution at depth is also essential elements for the sizing and planning of geothermal systems. In general, the temperature at a particular location equals the average annual temperature at that location. However, in urban areas due to subsurface occupation and a variety of structural alterations and neighbourhood and boundary effects, ground temperature field can be altered. In addition to the study mentioned above for the city of Lisbon, continuous temperature recording is being carried out with fibre optic sensors in different locations of the city up to a depth of 120 m. Similar records exist at the University of Aveiro Campus since 2019, where temperature evolution is monitored in 15 research boreholes, placed around a shallow geothermal system integrating composed of 43 BHEs, with a 10-minute interval. This study aims to assess the long-term influence of a geothermal system operation on ground temperature.

Results of temperature profiles in this system are shown in Vieira et al. (2024), where are depicted monthly minimum and maximum average temperatures at various boreholes along with initial temperature profiles, numerically obtained based on laboratory conductivity results. Also concerning this system, heat maps of two research boreholes over a monitoring period of about 4 years (with some recording interruptions them during the pandemic period) are analysed. The processing of the large amount of data registered in this system is ongoing through correlation studies, incorporating factors such as: distance to the BHE, effects of facade orientation (solar exposure), and atmospheric temperature (via data from a nearby weather station). An increase in temperature has been observed, especially in the shallower depths, which is consistent with a rise in temperature in the city of Aveiro (both average and extreme) in the years under consideration.

When it comes to shallow geothermal systems, it is also of special relevance to promote the study and quantify the environmental impacts of their construction and operation, using appropriate metrics, in order to adequately assess the potential benefits of these systems. With this purpose, the Life Cycle Assessment (LCA) method, as defined by ISO 14040, which involves the compilation and evaluation of the inputs, outputs, and potential environmental impacts of a product system throughout its life cycle and enables accounting environmental impacts for any product, can be particularly suitable for these studies. It encompasses various life phases, beginning with raw material extraction and production, through operation, and concluding with end-of-life phases (e.g., disposal or landfill). This type of evaluation was carried out for a university building located in northern Portugal by Aljundi (2004), where an integrated analysis of the building energy simulation (BEM) with EnergyPlus tool and that of the installed geothermal system, was conducted based on appropriate soil characterization and local meteorological conditions. The BHE system was integrated in the BEM using the g-function models. The building model was calibrated using monitored temperature data recorded inside two rooms using temperature sensors and the primary energy needs for heating and cooling were assessed and compared with the design values. The effect of varying ground thermal conductivity was analysed in terms of system sizing for different scenarios. The sustainability analysis of the shallow geothermal system was conducted considering environmental and economic aspects using LCA methodology. A sensitivity analysis was performed to show the influence of soil thermal conductivity on BHE system sizing and, therefore, on its life cycle environmental impacts, and comparisons were made for different climatic contexts (different Portuguese cities) where the energy needs differ from that of the base case study. Moreover, the effect of the renewable energy share in electricity production on the environmental

impact of the operation of the system was studied. Overall, this study revealed the efficiency of the system in terms of energy and environmental aspects, with thermal conductivity being a critical aspect in energy simulation and in the quantification of environmental indicators.

The increasing urbanization and climate change will continue to promote the development of innovative solutions for energy and environmental management. The use of soil as a thermal reservoir emerges as a promising alternative to largely meet the heating and cooling needs in large urban centres, promoting decarbonization and improving the quality of life in cities. This utilization should be based on adequate soil knowledge, thus allowing appropriate management of this resource to avoid undesirable consequences, such as significant changes in soil temperature fields, which, besides affecting system performance over time, can have various impacts (from reducing the energy performance, to altering soil mechanical properties and, eventually, interfere with the surrounding biological environment).

5 FINAL REMARKS AND PERSPECTIVES

The relevance and scope of thermal soil study have evolved considerably in recent decades, from understanding the mechanisms of heat transfer, with the proposal of semi-empirical relationships taking into account the multiphase constitution of soil to estimate thermal properties, to significant advances in understanding the phenomenology of its multiphysical behaviour (thermohydromechanical), supported by laboratory tests under non-isothermal conditions, case studies of geotechnical works and structures, and the development of advanced constitutive models, to the issues related to the direct use of superficial geological layers as thermal reservoirs. Challenges stemming from increasing urbanization and climate change will continue to drive innovative solutions for energy management and environmental protection. Proper analysis of these solutions requires a multidisciplinary approach, with planning topics emerging as crucial. In this regard, geospatial mapping of soil thermal properties, the provision of adequate information for the design of each system with increasing discretization at the local and district levels, and the use of specific methodologies to assist in decision-making regarding strategic areas for the systems installation aiming at optimizing their performance, are essential.

It is particularly significant to analyse the temperature field alteration due to the exploitation of shallow geothermal systems at local and district-levels, both in the medium and in the long terms. For this purpose, monitoring and data analysis considering interferences, boundary effects, hydrogeological conditions, and climatic variations, will increasingly allow a better understanding of the possible induced alterations in soil deposits and their causes.

Regarding thermohydromechanical behavior, there is a mature understanding of the subject although doubts persist in some observed trends, both in isotropic stress states and generalized ones. Accounting for these effects must be considered in energy geostructures. Thermoplastic soil behaviour, which includes aspects of thermal compaction and consideration of strain rate in non-isothermal behaviour, should continue to receive attention, both in fundamental and applied research contexts. It is anticipated that the increasing frequency, amplitude and duration of heat waves and of long periods of drought alternated with intense rainfall, enhancing collapse phenomena large deformations and slope stability, is liable to progressively affect the performance of geotechnical structures and infrastructure, and it is essential to model these effects.

For considering these and other aspects, other approaches may be necessary, taking into account partial saturation and discontinuous medium analyses. Collaboration among different areas of knowledge, related to Civil Engineering, Geology, Environmental Engineering, Mechanical Engineering, Climatology and Land Use Planning, is essential for the success of this research. Integrating different perspectives and using advanced computational tools is NECES for the development of accurate and reliable models that allow for the optimization of soil utilization as a geothermal resource. The study of soil thermal behaviour is an ever-evolving research domain that demands thorough consideration in tackling the challenges of contemporary society.

ACKNOWLEDGEMENTS

The author acknowledges the Portuguese Foundation for Science and Technology support under Project GeoSustained (PTDC/ECI-CON/1866/2021).

REFERENCES

Aljundi, K. (2024). *Sustainability of efficient solutions in shallow geothermal systems. Case study in Aveiro University.* PhD Thesis, Lisbon University.

Aljundi K., Pereira C., Vieira A. et al. (2024). Test conditions influence on thermal conductivity and contact conductance of sand at transient state, *Soils and Foundations*, 64 (1), 101405. https://doi.org/10.1016/j.sandf.2023.101405.

Alonso E.E., Zervos A. and Pinyol N.M. (2015). Thermo-poro-mechanical analysis of landslides: From creeping behaviour to catastrophic failure. *Géotechnique*, 66, pp. 202–219. https://doi.org/10.1680/jgeot.15.LM.006.

Brandl H. (2006). Energy foundations and other thermo-active ground structures. *Géotechnique*, 56(2), pp. 81–122. https://doi.org/10.1680/geot.2006.56.2.81.

Cecinato F. and Zervos A. (2012). Influence of thermomechanics in the catastrophic collapse of planar landslides. *Can. Geotech. J.* 49, pp. 207–225. https://doi.org/10.1139/t11-095.

Cekerevac C. and Laloui L. (2004). Experimental study of thermal effects on the mechanical behaviour of a clay. *Int. J. Numer. Anal. Methods Geomech* 28(3), pp. 209–228. https://doi.org/10.1002/nag.332.

Cui Y., Sultan N. and Delage, P. (2000). A thermomechanical model for saturated clays. *Can. Geotech. J*. 37, pp. 607-620. https://doi.org/10.1139/t99-111.

Christodoulides P., Vieira A., Lenart S. et al. (2020). Revewing the modeling aspects and practices of shallow geothermal energy systems. *Energies* 13, 4273. https://doi.org//10.3390/en10122044.

Dalla Santa G., Galgaro A., Sassi R. et al. (2020). An updated ground thermal properties database for GSHP applications. *Geothermics*, 85, 101758. https://doi.org/10.1016/j.geothermics.2019.101758.

Delage P., Caicedo B., Golombek M- et al. (2023) Investigating the Martian soil at the InSight landing site. *Soils and* Rocks, 28(3), *Special Issue: Deformation Characteristics of Geomaterials: Honorary & Special Lecture*, S. Rios, A. Viana da Fonseca and C. Ferreira (eds.). https://doi.org/10.28927/SR.2024.005023.

De Vries D.A. (1958). Simultaneous transfer of heat and moisture in porous media. *Trans. Am. Geophys. Union*, *39*, pp. 909–916.

Farouki, O.T. (1981). *Thermal Properties of Soils*. U.S. Army Corps of Engineers, Cold Regions Research and Engineering Laboratory.

Hueckel T. and Baldi G. (1990). Thermoplasticity of saturated clays: Experimental constitutive study. *J. Geotech. Engrg*., 112 (2), https://doi.org/10.1061/(ASCE)07339410(1990)116:12(1778).

Inacio M., Pinto C., Vieira A. et al. (2023). Contribution of geology to the location of geothermal cores for the geosustained project. *Proceed. of the 18th National Geotecnical* Congress, Évora, Portugal. (in Portuguese)

Laloui L., Olgun C.G., Sutman M., McCartney J.S. et al. (2014). Issues involved with thermoactive geotechnical systems: Characterization of thermomechanical soil behavior and soil-structure interface behavior. *J. Deep Found. Inst.*, 8, pp. 108–112.

Leroueil S. and Marques M. (1996). *Measuring and Modelling Time Dependent Soil Behaviour*; T. Sheahan & V. Kaliaki. ASCE, New York.

Li P, Guo F., Yang X. (2022). An inversion method to estimate the thermal properties of heterogeneous soil for a large-scale borehole thermal energy storage system. *Energy and Buildings*, 263, 112045. https://doi.org/10.1016/j.enbuild.2022.11204.

Low J., Loveridge F. and Powrie W. (2015) A comparison of laboratory and in situ methods to determine soil thermal conductivity for energy foundations and ground heat exchanger applications. *Acta Geotech.* 10, 209-218.

Maranha, J. R., Pereira C. and Vieira A. (2016). A viscoplastic subloading soil model for rate-dependent cyclic anisotropic structured behaviour. *Int. J. Numer. Anal. Methods Geomech*. 40(11), pp. 1531–1555, https://doi.org/10.1002/nag.2494.

Maranha, J. R., C. Pereira, and A. Vieira (2017). Thermoviscoplastic subloading soil model for isotropic stress and strain conditions. In A. Ferrari and L. Laloui (Eds.), *Advances in Laboratory Testing and Modelling of Soils and Shales* (ATMSS), pp. 479–485. Cham: Springer International Publishing.

Maranha J. R., Pereira, C. and Vieira A. (2018). Improved subloading thermo-viscoplastic model for soil under strictly isotropic conditions. *Geomech. Energy Environ*, 14, pp. 38-47. https://doi.org/10.1016/j.gete.2018.01.002.

Maranha J.R. and Vieira A. (2018). Stress dependency of the thermal conductivity of a regular arrangement of spheres in a vacuum. *Proceedings 9th Eur. Conf. Numer. Methods Geotech. Eng.* (NUMGE 2018), Matos Fernades (eds.), Taylor and Francis, Porto, Portugal

Mitchell, J. K. (1993). *Fundamentals of soil behavior*, 2nd Ed., John Wiley & Sons, New York.

Romio l.C., Roberti D.R., Buligon L. et al. (2019). A Numerical Model to Estimate the Soil Thermal Conductivity Using Field Experimental Data. *Appl. Sci.,* 9, 4799; https://doi.org/10.3390/app9224799.

Sakatani N., Ogawa K, Lijima Y et al. (2017) Thermal conductivity model for powdered materials under vacuum based on experimental studies. *AIP Advances* 7, 015310, https://doi.org/10.1063/1.4975153.

Soares P., Johannsen F., Lima D. et al. (2024). High-resolution downscaling of CMIP6 Earth system and global climate models using deep learning for Iberia. *Geosci. Model Dev.*, 17(1), 229–259, https://doi.org/10.5194/gmd-17-229-2024.

Sultan, N. (1997). *Étude du Comportement Thermo-Méchanique de Lárgile de Boom: Expériences et Modélisation.* Ph.D. Thesis, Ecole Nationale des Ponts et Chaussés.

Terzaghi, K. (1943). *Theoretical Soil Mechanics.* John Wiley & Sons.

Vieira A., Alberdi-Pagola M., Christodoulides P. et al. (2017). Characterisation of ground thermal and thermo-mechanical behaviour for shallow geothermal energy applications. *Energies*, 10, 2044, https://doi.org/10.3390/en10122044.

Vieira A., Aljundi K., Antunes A. et al. (2024). Analysis of ground temperature measurement data. Impact of the operation of a shallow geothermal system. (*8th Portuguese-Spanish Geotechnical Day*) (in portuguese).

Walch A., Li X., Chambers J. et al. (2022). Shallow geothermal energy potential for heating and cooling of buildings with regeneration under climate change scenarios. *Energy* 244 123086. https://doi.org/10.1016/j.energy.2021.123086.

Conference Forum Lectures - Challenges of underground space in the cities of the future

Conférences du Forum du Congrès - Les défis de l'espace en sous-sol dans les villes du futur

Proceedings of the XVIII ECSMGE 2024
GEOTECHNICAL ENGINEERING CHALLENGES
TO MEET CURRENT AND EMERGING NEEDS OF SOCIETY
© 2024 the Authors
ISBN 978-1-032-54816-6
DOI 10.1201/9781003431749-18
Open Access: www.taylorfrancis.com, CC BY-NC-ND 4.0 license

ECSMGE 24
XVIII EUROPEAN CONFERENCE ON SOIL MECHANICS AND GEOTECHNICAL ENGINEERING

Conference Forum Lecture

Unearthing the urban future: the evolving role of tunnel and underground structures in modern cities

Déterrer l'avenir urbain: le rôle évolutif des tunnels et des structures souterraines dans les villes modernes

A. Cornaro*
ETH, Amberg Engineering Zurich, Switzerland
**acornaro@ethz.ch*

ABSTRACT: In the pursuit of maintaining and enhancing the livability of our cities, the utilization of both open and subterranean spaces is becoming increasingly crucial. This paper explores the imperative for multidimensional urban planning and infrastructure development, highlighting the rising significance of underground spaces. Addressing the escalating demands for housing, office space, infrastructure, and open areas within urban environments, the author underscores the necessity for strategic allocation of both surface and subsurface resources. International case studies of innovative underground developments are examined, showcasing multifaceted projects that ingeniously leverage subterranean space to meet diverse urban needs. This paper elucidates the pivotal role that tunnel and underground structures will play in shaping the future of modern cities, advocating for a forward-thinking approach to urban planning that embraces the full spectrum of spatial possibilities.

RÉSUMÉ: Dans la quête du maintien et de l'amélioration de la qualité de vie de nos villes, l'utilisation des espaces ouverts et souterrains devient de plus en plus cruciale. Cet article explore l'impératif d'une planification urbaine multidimensionnelle et du développement des infrastructures, en soulignant l'importance croissante des espaces souterrains. Répondant à la demande croissante de logements, d'espaces de bureau, d'infrastructures et d'espaces ouverts dans les environnements urbains, l'auteur souligne la nécessité d'une allocation stratégique des ressources de surface et souterraines. Des études de cas internationales de développements souterrains innovants sont examinées, présentant des projets à multiples facettes qui exploitent ingénieusement l'espace souterrain pour répondre à divers besoins urbains. Cet article élucide le rôle central que les tunnels et les structures souterraines joueront dans l'avenir des villes modernes, en plaidant pour une approche avant-gardiste de la planification urbaine qui embrasse tout le spectre des possibilités spatiales.

Keywords: Underground structures; urban planning.

1 INTRODUCTION

Cities are dynamic ecosystems where space is both scarce and precious. As urban populations surge and demands for housing, office space, infrastructure, and open areas escalate, urban planners face the daunting challenge of accommodating these needs within limited surface areas.

In response, the exploration of subterranean spaces has gained traction, offering a solution to the spatial conundrum. This article navigates through the labyrinth of urban planning, shedding light on the pivotal role that underground spaces play in shaping the future of modern cities

1.1 The necessity for multidimensional urban planning

To comprehend the significance of underground spaces, one must first acknowledge the multidimensional nature of urban planning (Admiraal and Cornaro, 2021).

Han Admiraal and Antonia Cornaro have extensively studied the intricate dynamics of urban spaces, emphasizing the need for holistic approaches that transcend traditional surface-level planning. Urban environments are not merely two-dimensional; they encompass layers of infrastructure, utilities, and potential living, recreational, social, and working spaces that extend beneath the surface. Neglecting this

vertical dimension leads to underutilization of valuable resources and exacerbates urban congestion and environmental strain.

As cities evolve, so must their planning strategies. Traditional urban planning often prioritizes surface developments, neglecting the vast potential that lies beneath. However, as populations burgeon and land becomes scarcer, this approach is no longer tenable. Shana Debrock, an advocate for subterranean urbanism, argues that the future of urban development hinges on embracing the full spectrum of spatial possibilities, including underground spaces (Debrok, 2021).

By adopting a multidimensional perspective, cities can optimize their limited land resources and foster sustainable growth.

1.2 Utilizing underground spaces to meet urban needs

The utilization of underground spaces presents a myriad of opportunities to address the diverse needs of urban populations. From housing and transportation to recreation and commerce, subterranean developments offer versatile solutions that complement surface-level infrastructure. ITACUS, the ITA's committee of Underground Space, dedicated to exploring the potential of underground spaces, emphasizes the importance of reimagining urban landscapes to encompass both horizontal and vertical dimensions.

2 CASE STUDIES

Several case studies from around the globe illustrate the innovative ways in which cities are harnessing underground spaces to alleviate urban pressures. Some examples are outlined below.

2.1 Hong Kong cavern development plan

Hong Kong, a city known for its dense urban fabric, faces significant challenges in meeting the demands for housing and infrastructure. To address this, the Hong Kong government has embarked on ambitious cavern development plans. (Ho, Wong, 2016)

By excavating vast underground caverns beneath the city, Hong Kong aims to create additional space for facilities such as transportation hubs, utilities, and storage. These caverns not only optimize land use but also enhance urban resilience by providing critical infrastructure protected from external threats such as typhoons and land scarcity.

They complement the inner-city urban underground uses and underground pedestrian networks.

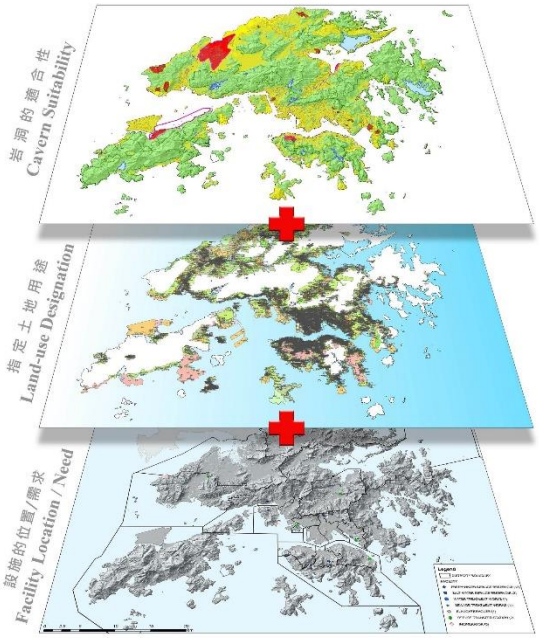

Figure 1. A task under the Study on Long-term Strategy for Cavern Development, CEDD.

2.2 Singapore: creating spaces for growing needs

The Urban Redevelopment Authority (URA) of Singapore emphasizes the significant role of underground spaces in creating a sustainable and resilient city of the future.

It highlights the importance of utilizing underground spaces for various purposes, including infrastructure, utilities, and transportation, to optimize land use and address the challenges of limited surface space in urban environments. By incorporating underground developments into urban planning strategies, Singapore aims to maximize the efficiency and functionality of its cityscape while enhancing the quality of life for its residents.

This underscores the URA's commitment to embracing innovative solutions and leveraging all available spatial possibilities to create a more livable and sustainable urban environment.

Singapore's Jurong Rock Caverns: In Singapore, the Jurong Rock Caverns project exemplifies how subterranean spaces can be leveraged for strategic storage and industrial purposes. Situated beneath Jurong Island, the caverns provide secure storage for liquid hydrocarbons, freeing up valuable surface land for other developments.

This innovative use of underground space not only enhances Singapore's energy security but also demonstrates the potential of subterranean solutions to address pressing urban challenges.

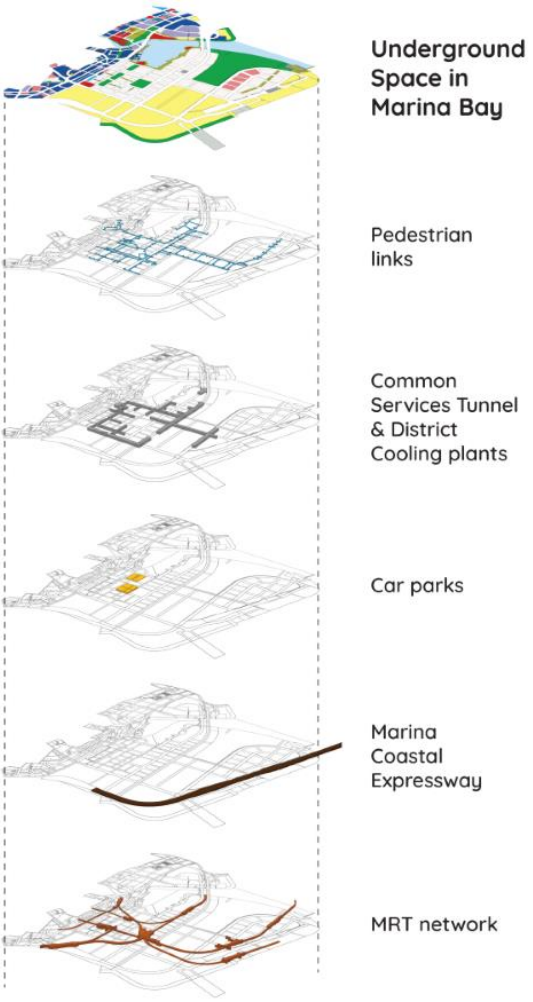

Figure 2. Spatial layering approach, Singapore, URA (2024).

2.3 London's subterranean infrastructure

London, a city with centuries of urban development, is increasingly looking underground to expand its infrastructure network.

From Crossrail, Europe's largest construction project, to the Thames Tideway Tunnel, which aims to alleviate pressure on the city's aging sewer system, London is harnessing subterranean spaces to enhance connectivity and resilience. These projects demonstrate London's commitment to integrated urban planning that encompasses both surface and subsurface realms.

A station schematic of Crossrail can be viewed below in figure 3. The Elizabeth line station at Canary Wharf is situated beneath a five-story mixed-use complex called Crossrail Place, which features a public rooftop garden. The station is so spacious that it could accommodate the entirety of Canary Wharf's iconic skyscraper, One Canada Square, laid horizontally within its confines.

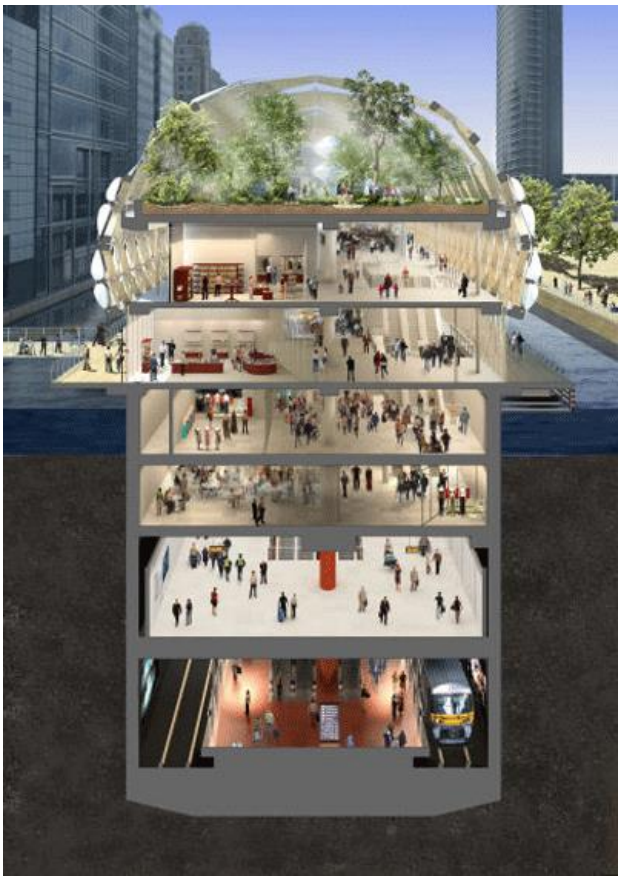

Figure 3. Station schematic of Canary Wharf, Crossrail.

An initiative that was co-launched by ITACUS, the ITA Committee of Underground Space through its National Action Think Deep Programme (NATDP) is the Think Tank *Think Deep UK,* a group of built environment experts committed to creating resilient, sustainable and liveable cities through smart use of underground space. Its mission is (1) to promote an awareness of the value of underground assets and to create a policy framework that can enable their fair use. (2) To inform and guide the general public, decision makers, politicians and professionals how the use of urban underground space can create better cities with socio-economic benefits for society. (3) To encourage thinking deeply when making decisions and planning for the future of our cities.

Such groups and initiatives help improve and broaden public opinion on the topic and are the basis of future policy shaping the future of cities.

2.4 Flanders region Urban Underground Space (UUS) plan

In the Flanders region of Belgium, the Urban Underground Space (UUS) Plan seeks to optimize the use of underground spaces for a variety of purposes, including parking, utilities, and recreational facilities.

By integrating underground developments into urban planning processes, Flanders aims to alleviate

surface congestion and enhance the quality of urban life. This comprehensive approach to underground space management serves as a model for sustainable urban development in densely populated regions.

2.5 Switzerland's national strategy on the underground

Switzerland, known for its engineering prowess, has developed a national strategy to maximize the potential of underground spaces. Recognizing the need for coordinated planning and management, Switzerland's strategy emphasizes the importance of integrating underground developments into broader urban planning frameworks.

From transportation tunnels to underground energy provision to underground research facilities, Switzerland's approach underscores the versatility and resilience of subterranean solutions in shaping the future of urban environments.(Swisstopo, 2023).

3 CHALLENGES AND OPPORTUNITIES

Despite the immense potential of underground spaces, their integration into urban planning poses unique challenges. Technical feasibility, cost considerations, and regulatory frameworks often impede the realization of subterranean projects. Moreover, public perception and safety concerns can hinder public acceptance of underground developments. However, as demonstrated by successful case studies and ongoing research initiatives, these challenges are by far not insurmountable.

The various cited case studies from around the world illustrate innovative approaches to utilizing underground spaces in urban environments and how they can benefit society overall.

4 CONCLUSION

In the pursuit of sustainable urban development, the utilization of underground spaces is no longer a mere novelty but a necessity. As cities grapple with escalating urban pressures, embracing multidimensional planning approaches that encompass both surface and subsurface realms is imperative.

The case studies highlight the diverse approaches cities are taking to address urban pressures and create more sustainable, resilient, and livable urban environments through the strategic use of underground spaces. By harnessing the full spectrum of spatial possibilities, cities can unlock new avenues for growth, innovation, and livability. As Antonia Cornaro and Han Admiraal assert, the future of urbanism lies beneath our feet, waiting to be unearthed (Admiraal and Cornaro, 2016).

REFERENCES

Admiraal, H. and Cornaro, A. (2016). Tunnelling and Underground Space Technology - Why underground space should be included in urban planning policy – And how this will enhance an urban underground future. *Tunnelling and Underground Space Technology*, 55, (May): 214-220 doi.org/10.1016/j.tust.2015.11.013.

Admiraal, H., and Cornaro, A. (2021*).* Une approche de planification multidimensionnelle (MDPA)— Vers une nouvelle justification de la planification et de la visualisation des espaces souterrains dans le cadre du métabolisme urbain. 14. *Proceedings of AFTES 2021.*

URA (2024). Creating Spaces for Our Growing Needs. Urban Redevelopment Authority.

Debrok, S. (2021). The onset of underground urban planning in Flanders, *IOP Conference Series: Earth and Environmental Science,* 703: 012012, https://iopscience.iop.org/article/10.1088/1755-1315/703/1/012012/pdf.

Ho, T., and Wong, J.C.F. (2016). Strategic use of rock caverns and underground space for sustainable urban development of Hong Kong. *Procedia Engineering,* 165: 705-716 doi.org/10.1016/j.proeng.2016.11.768.

Swisstopo (2023) Switzerland's New Strategy for the Sustainable Use of the Subsurface, https://www.admin.ch/gov/de/start/dokumentation/medienmitteilungen.msg-id-92770.html.

Proceedings of the XVIII ECSMGE 2024
GEOTECHNICAL ENGINEERING CHALLENGES
TO MEET CURRENT AND EMERGING NEEDS OF SOCIETY
© 2024 the Authors
ISBN 978-1-032-54816-6
DOI 10.1201/9781003431749-19
Open Access: www.taylorfrancis.com, CC BY-NC-ND 4.0 license

ECSMGE 24
XVIII EUROPEAN CONFERENCE ON SOIL MECHANICS AND GEOTECHNICAL ENGINEERING

Conference Forum Lecture

Underground and beyond: The road to resilience

Souterrain et au-delà: En route pour la résilience

A.N.P. Lamas*
Amberg Engineering , Brussels, Belgium
**plamas@ambergengineering.com*

ABSTRACT: Cities currently house more than half of the world's population, and by 2050, this number is expected to rise dramatically. With increasing urbanization, cities face significant challenges, including the need for sufficient and appropriate infrastructure, particularly transportation infrastructure. Besides, public owners are taking the environmental impact of their projects more and more seriously, and as a result, both designers and contractors need to tackle this arising concern and find solutions to increase resiliency of their projects. In this context, tunnelling offers an underground alternative to standard surface transport networks , providing new space in saturated areas and opening the door to exploring more resilient and sustainable ways of urbanism. Designing a new path into this transformation will however imply a social mindset change. Advanced construction techniques help minimize surface disturbance and habitat disruption. Real-time monitoring systems together with artificial intelligence and predictive analytics are being used to optimize maintenance schedules and detect potential issues before they escalate. A new construction era begins and possibilities offered by the underground are yet to be rediscovered.

RÉSUMÉ: Plus de la moitié de la population mondiale habite à ce jour dans des villes et on attend cette chiffre d'augmenter énormément d'ici 2050. Avec l'urbanisation croissante, les villes sont confrontées à des défis importants, notamment la nécessité de disposer d'infrastructures suffisantes et appropriées, en particulier dans le domaine des transports. En outre, les institutions publics prennent de plus en plus au sérieux l'impact environnemental de leurs projets et, par conséquent, les concepteurs et les entrepreneurs doivent s'attaquer à cette préoccupation croissante et trouver des solutions pour accroître la résilience de leurs projets. Dans ce contexte, les tunnels offrent une alternative souterraine aux réseaux de transport de surface, fournissant des nouveaux espaces dans les zones saturées et en ouvrant la voie à l'exploration des modes d'urbanisme plus résilients et durables. La conception d'une nouvelle voie vers cette transformation impliquera toutefois une évolution de mentalité à niveau social. Des nouvelles techniques de construction permettent ces jours de minimiser les perturbations de la surface et de la population. Des systèmes de suivi en temps réel, associés à l'intelligence artificielle et à l'analyse prédictive, sont utilisés pour optimiser les plannings de maintenance et détecter les problèmes potentiels avant qu'ils ne s'aggravent. Une nouvelle ère de construction commence et les possibilités offertes par le sous-sol restent à redécouvrir.

Keywords: Tunnel; resilience; innovation , mindset.

1 INTRODUCTION

The development of new infrastructure in today's global context is faced with several challenges, particularly when it comes to ensuring resilience of new infrastructure. In addition, the modern urban environment is characterized by a heavily constrained network, presenting many restrictions for transportation development, such as space limitations, conglomeration of existing structures, surface traffic, and disturbances to the everyday life of the city's residents. Underground infrastructure can be seen as a perfect alternative solution for both of these problems.

This article aims to explore possibilities within the underground space. On one hand, underground infrastructure provides various opportunities for sustainable practices, taking advantage of self-sustaining energy sources through geothermic activation and exploring innovative construction methods to reduce the carbon footprint. On the other hand, it allows for efficient use of surface space, promoting social cohesion and civic engagement.

Regulatory and policy context transformation required to transition to this new way of imagining infrastructure development are also discussed in the following chapters.

2 NEW CHAPTER IN INFRASTRUCTURE DEVELOPMENT

The engineering private sector is just beginning to accept the challenge of participating in this new commitment, enhancing infrastructure resiliency. Environmental considerations are now central to tunnelling projects. The main challenge consists of identifying the hazards that could jeopardize the durability of the project soon enough to be able to confront them.

Once the target has been outpointed, expert collaboration and rigorous study of the case in its context will allow us to seize the opportunity to change the industry pattern and develop our project within a sustainable frame.

Embracing a circular economy approach promotes the reuse, recycling, and repurposing of materials to reduce the overall environmental footprint of the project. Exploring possibilities of the underground space is set to be the new path to ensure liveability in urban environments as we know them.

2.1 New initiatives and criteria assessment

Improving energy efficiency is the key to building resilience. Such a goal can only be achieved in the context of a supporting policy framework. Creating fair green certifications and transparent labelling, incentivizing data-driven design tools, or promoting investments in recycled, reused, and bio-based materials are some of the initiatives that can help promote such a scenario.

Once the framework is constructed, third-party verification of work site processes and emissions shall guarantee sustainability compliance during construction. Regulatory measures regarding the design and conception of the infrastructure will ensure long-term compliance for the remaining infrastructure's lifespan.

2.1.1 Updating sustainability assessment

Every construction project counts with several indicators that can be assessed from a sustainability perspective. Such indicators have traditionally had an importance regarding the general overview of the construction project.

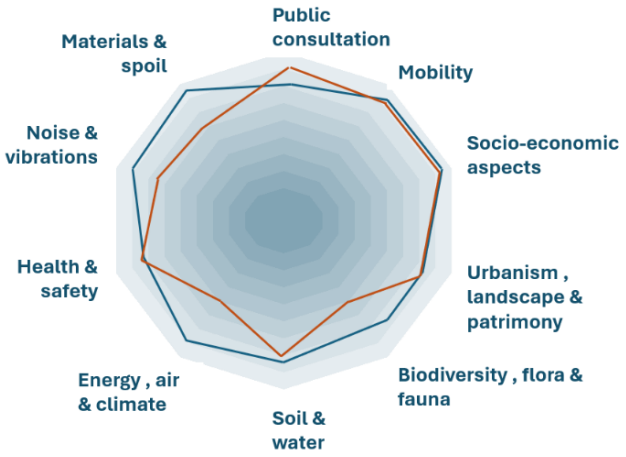

Figure 1. Sustainability indicators relative weight drift between standard (orange) and resilient (blue) metro projects decision-making.

However, since public policies are drifting to adapt to new resilience requirements relative weight or such indicators also ought to be reconsidered, as illustrated in Figure 1.

Standardizing requirements from a policy perspective is essential. To evaluate a project's sustainability performance, it is necessary to define adequate criteria based on the following facts:

- Quantifiable factors;
- Qualitatively ascertainable criteria;
- Regulated framework;
- Resilience requirements for infrastructure included in tender specifications.

2.2 Mindset & policy change

In order to fully implement the initiatives discussed in chapter §2.1, a change in mindset is required to encourage a policy transition. Currently, decision makers in the construction industry are typically manufacturers, owners, and developers. However, we are advocating for a shift in mentality so that governments take on the responsibility of promoting resilience and become the key decision makers when it comes to construction projects. This can be achieved by regulating the construction framework. Once this shift is accomplished, designers will guide policy makers in implementing a new, more resilient approach to construction.

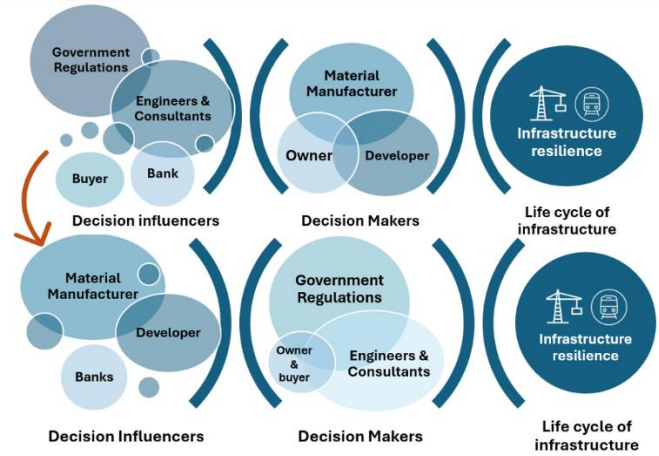

Figure 2. Shift in decision-making intervenors on infrastructure life cycle

In this reinvented scenario, new responsibilities shall be assumed by the designers:

- Design for longer life
- Increase research and education in decarbonisation strategies
- Digitalization of design to ensure optimization from a very early stage of the project (BIM)
- Design based in local materials reuse (ie. muck treatment for concrete production)
- Closed collaboration with manufacturers to enhance the use of circular materials
- Improve management of on-site construction with circular design
- Design for disassembly and re-use when possible (reuse of TBMs and construction facilities)

3 EXPLORING UNDERGROUND POTENTIAL

3.1 Geothermic activation of metro network

Geothermic activation of underground infrastructure is imagined as a shortcut to ensure self-sustainability of new metro networks.

Feasibility studies for geothermic activation of subway projects involve the following steps:

- Identification of the horizontal and vertical alignment of the layout;
- Definition of existing solutions;
- Division of the line into homogeneous sections in geological and hydrogeological terms;
- Application of geothermic abacuses to each homogeneous section identified to evaluate the winter and summer geothermal potential and the total thermal power that can be exchanged with the ground;
- Identification of receptors;
- Assessment of the economic, regulatory and technical framework;
- Definition of the studies to be carried out in the subsequent phases of the project and planning.

Amberg Engineering has explored methodology together with GEOEG for Brussels Metro and also with NGE for L15 Grand Paris.

3.1.1 Grand Paris Ligne 15

In the context of the opportunity study, an assessment of L15O geothermal retaining walls and tunnel potential has been conducted. Results show that a geothermal activation of the line would make it possible to mobilize the following powers below:

Table 1. Table of exchangeable power results for L15O

Season	Tunnel	Stations	Total
Summer	2,57 MWh	0,99 MWh	3,56 MWh
Winter	5,43 MWh	0,82 MWh	6,25MWh

A preliminary analysis of potential energy needs per station was equally drafted. It should be noted that the energy demand for cooling in the anticipated scenario is greater than the demand for heating, due to the permanent need for cooling the technical rooms.

The requirements per station would therefore be:

Table 2. Table of exchangeable power results for L15O

In winter	In summer	All the year
162 kWh / station	376 kWh / station	376 kWh / technical rooms

The conclusion withdrawn is that activation of the retaining walls alone is enough to cover the stations' heating and cooling needs all over the year. The technical rooms could be cooled all year round.

However, the risk of using the system continuously in a single mode (cooling) is to lead to an annual thermal drift with a decrease in thermal performance over time (heat saturation of the ground). A further study on this particular issue was to be pursued.

3.1.2 Metro Nord Brussels

A similar study was conducted on Metro Brussels, including in this case geothermic activation of the station slabs. Results showed that power mobilized would suffice to provide energy for the stations and energy-efficient housing within a 100m radio from the metro stations.

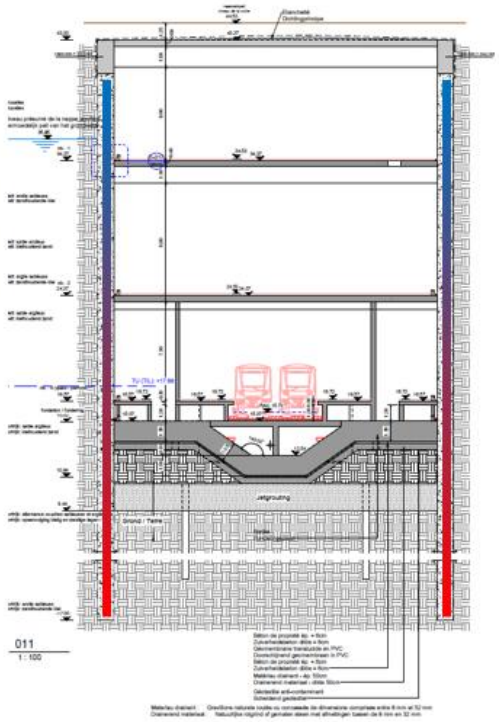

Figure 3. Geothermic activation of Metro Nord Bruxelles station.

3.2 Innovation for resilience

3.2.1 Materials

It is well known that most current construction materials rely on energy-intensive, mineral-based extractive processes which cause deleterious environmental impacts all through the life span of the material. Concrete and cement by themselves are responsible of ~1.5% of global CO2 emissions. Besides, the 'take-make-waste' model still governs current material production practices. This means that most construction materials become waste once their lifespan is completed.

Aiming for decarbonising materials at a global scale in the construction sector imposes a mindset change to unblock resistance, and for that purpose, policymakers must engage actors across the value chain.

Investment on further materials investigation shall be a first priority goal for actors within the material production chain. Recent studies have found that the inclusion of limestone fines in a CEM I and GGBS ternary system improved material efficiency, demonstrating that the limestone fines could be used as a replacement for both the CEM I and GGBS portions of the blend. This results in concrete with both a lower embodied carbon and a reduced use of GGBS, whilst producing an equivalent performance.

Action still needs to be taken by policymakers in order to implement a regulatory framework that can impose new carbon print limitations on construction materials. A restrictive policy change regarding construction materials would trigger increased investment in alternative solutions. In this regard, the UK has just set a European example with the update of the standard BS 8500:2023, which incorporates the use of multi-component cements. This update allows for a reduction in the proportion of Portland cement used for a given volume, thereby reducing the embodied carbon in the concrete produced.

3.2.2 Artificial Intelligence

In recent times, the quest for innovative ways to reduce carbon footprint has led to increased exploration of out-of-the-box thinking. Every effort counts towards achieving the goal of resilience and given the point at which we stand today, conventional approaches may no longer suffice. It is, therefore, imperative to explore creative solutions and rethink our development approach. How can IA help geotechnical engineers in achieving this objective? Some of the possibilities that can be developed through this new powerful tool might be:

- Increasing efficiency through a faster data analysis;
- Reducing material consumption by ensuring a more accurate design ;
- Increasing safety by granting a more controlled construction environment.

Digitalizing the entire project lifecycle will make data-driven decisions easier and faster.

Furthermore, IA , as a data-based tool, will allow us to improve the calibration of geotechnical models by using historical data combined with real-time backanalysis. This methodology will rapidly compare monitoring data (such as topography, inclinometers, piezometers, etc.) with geotechnical information from surveys, which had previously been introduced in a digital twin (numerical models). This cross-check of geotechnical data will provide a more accurate representation of the real soil behaviour.

Relying on such a data platform may allow us to eventually optimise construction projects by reducing geotechnical uncertainties for a more suitable design.

Besides, new machine learning algorithms analyse excavation data in real-time, optimizing tunnelling strategies and minimizing wear on equipment. AI-driven predictive analytics can optimize TBM performance and prevent potential operational disruptions. This ensures not only greater efficiency but also extends the operational lifespan of the machinery.

The integration of machine learning into geotechnical engineering represents a significant challenge but may open a whole world of possibilities regarding efficiency and safety during construction.

Undoubtedly, systematic analysis of the context constraints and requirements, followed by a well-planned implementation of novel strategies like IA, will be key steps for the industry to take towards a more efficient, and therefore more sustainable future in construction.

3.3 Reconsidering underground space

3.3.1 Madrid's reconditioning

M30 road is an urban motorway that with a total length of 32.5km and three lanes per direction, circles the central districts of Madrid.

As it passes through Las Ventas, M30 alignment, dating from the late 70's, had not being conceived underground despite running below the surface level.

However, recently approved urban proposal foresees transitioning this stretch from an Open Cut to a Cut & Cover solution, allowing to create a green recreative area above the current traffic lanes. This measure will not only entail covering M30 roadways with a green refreshing carpet but will also decrease sound disturbances due to heavy traffic in the area.

Besides, the new park will enhance communication between neighbouring districts that where at the moment split apart by the urban motorway, transforming urban fabric perspectives.



Figure 4. Current situation at Las Ventas bridge, Madrid.



Figure 5. Foreseen urban action Las Ventas bridge, Madrid.

Being able to recover a damaged urban framework in such a way that it allows to rebrand a neighbourhoods character, revitalizing its surroundings proves the real impact of exploring new underground opportunities.

This being said , truth is underground works initiatives are too often burdened by high cost estimations expectations, from a policy making perspective. However , mixed solutions such as Cut&Covers might arise great opportunities to relieve urban pressure within rather affordable budgets. Counting on creative technical teams supporting policy decision making should allow to explore alternative ways of reinventing saturated metropolitan areas.

4 CONCLUSIONS

Underground infrastructure innovation and development open up the possibility of exploring the urban fabric in ways that were just not technologically possible years ago.

Imagining the possibilities of creating a self-sufficient underground space and building the tools to explore it and take the most out of it defies the traditional concept of geotechnical and tunnelling engineering as we knew it.

Achieving a better balance between infrastructure development and resilience is nonetheless, a major task. Taking up this challenge has yet become our responsibility as a generation, making the assignment both appealing and demanding. Engaging ourselves as engineers in this urgent request implies committing to the responsibility of changing direction. We have it still in our hands to take action and make it happen.

REFERENCES

El Economista. (2023).Underground Works on M-30 at Ventas beginning by the end of the year https://www.eleconomista.es.

European Union (2023). *The green deal industrial plan*, Speeding up the contribution of Europe's innovative clean tech industries to net-zero..Luxembourg.

GEOEG. (2020). Bruxelles Métro Nord: activation thermique des tunnels *Analyse d'opportunité*. Brussels Métro Nord - GEOEG.

GEOEG. (2023). Ligne 15 Ouest du Grand Paris Express *Analyse d'opportunité*. Grand Paris Express, Ligne 15 Ouest - GEOEG.

German Tunnelling Committee (ITA-AITES) (2023). Sustainability in Underground Construction Basics, Boundary Conditions and Objectives *DAUB-Working Group*, Deutscher Ausschuss für unterirdisches Bauen e. V. (DAUB).

MPA The Concrete Center (2023). *BS 8500-1:2023 Concrete* – Complementary British Standard to BS EN 206 – Part 1: Method of specifying and guidance for the specifier, from Concrete Futures, spring 2023.

MPA The concrete center (2023). *BS 8500-2:2023 Concrete* – Complementary British Standard to BS EN 206 – Part 2: Specification for constituent materials and concrete, from Concrete Futures, spring 2023.

United Nations Environment Programme. (2022). *Global Status Report for Buildings and Construction: Towards a Zero-emission*, Efficient and Resilient Buildings and Construction Sector..Nairobi.

United Nations Environment Programme. (2023). *Building Materials and the Climate*: Constructing a New Future. Nairobi.

Proceedings of the XVIII ECSMGE 2024
GEOTECHNICAL ENGINEERING CHALLENGES
TO MEET CURRENT AND EMERGING NEEDS OF SOCIETY
© 2024 the Authors
ISBN 978-1-032-54816-6
DOI 10.1201/9781003431749-20
Open Access: www.taylorfrancis.com, CC BY-NC-ND 4.0 license

ECSMGE 24
XVIII EUROPEAN CONFERENCE ON SOIL MECHANICS AND GEOTECHNICAL ENGINEERING

Conference Forum Lecture

Underground space: Opportunity or a non sense option?

L'espace souterrain: Opportunité ou option insensée?

P.R. Silva*
Saraiva+Associados, Lisbon, Portugal
**prsilva@msa.com.pt*

ABSTRACT: The growth of the world population and its movement to cities in search of better opportunities will continue to place urban infrastructures and the needs for housing, equipment and services under great pressure. This growing demand, which is expected to continue, poses major challenges to city management. The topic does not end with the issue of available space, but nowadays it is mainly focused on sustainability issues. For example, the costs associated with mobility (time and pollution) and the provision of services (operation and maintenance of urban services) place available space under great scrutiny. For architects, among other professionals, urban planning and design, the design of different uses and buildings, must take in to account the dimension of the lifestyle it provides. Architecture as an art of creating the physical space where human activity takes place has to consider which spaces are best for each use, associating this placement in the territory with a way of life, providing private space and public space in a desirable balance for the development of a plural and happy society. This consideration of spaces for different uses has meant that, over time, the underground space has been used to house some of the activities. This allocation has been variable, but population growth and the need to make the best and most efficient use of available space opens up new perspectives.

RÉSUMÉ: La croissance de la population mondiale et son déplacement vers les villes à la recherche de meilleures opportunités continueront de mettre les infrastructures urbaines et les besoins en logements, équipements et services sous forte pression. Cette demande croissante, qui devrait se poursuivre, pose des défis majeurs à la gestion de la ville. Le sujet ne se limite pas à la question de l'espace disponible, mais il se concentre aujourd'hui principalement sur les questions de durabilité. Par exemple, les coûts associés à la mobilité (temps et pollution) et à la fourniture de services (exploitation et entretien des services urbains) soumettent l'espace disponible à un examen minutieux. Pour les architectes, entre autres professionnels, l'urbanisme et le design, la conception des différents usages et des bâtiments, doivent prendre en compte la dimension du style de vie qu'ils offrent. L'architecture en tant qu'art de créer l'espace physique où se déroule l'activité humaine doit considérer quels espaces sont les meilleurs pour chaque usage, en associant cet emplacement sur le territoire à un mode de vie, en fournissant un espace privé et un espace public dans un équilibre souhaitable pour le développement d'une société plurielle et heureuse. Cette considération des espaces pour différents usages a fait qu'au fil du temps, l'espace souterrain a été utilisé pour abriter certaines activités. Cette répartition a été variable, mais la croissance démographique et la nécessité d'utiliser au mieux et le plus efficacement l'espace disponible ouvrent de nouvelles perspectives.

Keywords: Underground construction; sustainability; lifestyle; architecture.

1 INTRODUCTION

The growth of the world population has caused enormous pressure on cities, the main centers of economic activity and which offer more opportunities for work, quality of life and leisure (Figure 1).

Cities have been the great catalysts for development, with a great concentration of economic activities, namely services, industry and leisure, with the consequent increase in those who want to live there, resulting in a clear need for housing and education, health, culture, among others.

This fact has caused great pressure on land use in areas where there are cities, with enormous environmental impacts and infrastructure costs associated with these expansions.

The cost of expanding construction horizontally, especially with regard to the maintenance and exploitation of urban and transport infrastructures, has put pressure on construction to be carried out vertically in many circumstances, often densifying low-density spaces that are already in place. infrastructure and which are demolished.

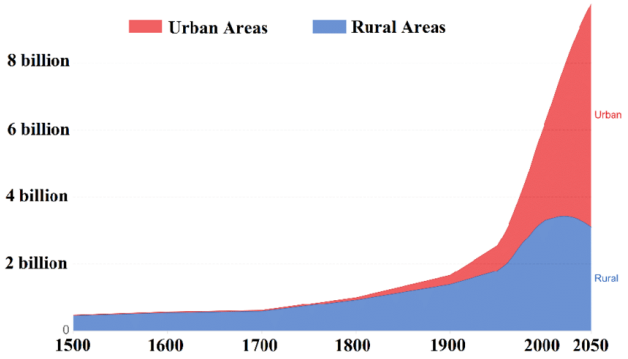

Figure 1. Urban vs Rural areas; Source: Research Gate.

2 OVERVIEW OF UNDERGROUND CITIES

This densification is, from a certain point of view, a sustainable response, maximizing resources, saving infrastructure and also minimizing mobility needs.

The exponential increase in the built space of cities, and the consequent competition between uses, led to the set of urban infrastructures that support their functioning occupying "non-useful" territory, that is, the underground.

Along with the increase in population, the development of economic activity has systematically changed production models, consumption continues to increase as well as emissions.

These new lifestyles have caused profound changes in natural balances and put biodiversity and, above all, the planet's biocapacity under great pressure, which will certainly lead us, if drastic changes are not introduced in the way we use the planet, to a collapse.

The increase in the area occupied by cities and the degradation of the global state of the planet are two facts that are intrinsically linked.

Although architecture and urban design, an activity of architects and which we develop at S+A, cannot in themselves solve this problem, they can, as instruments for creating the physical space where we live, be agents of change, inducing changes in styles of life.

Man has always sought shelter and with the evolution of his needs, he has gone from simple protection from the elements, and defense against predatory animals, to a broader search for comfortable living spaces.

The shelter always had a connection with "under the roof", and in some cases it was even "under the ground".

On the other hand, our desire to be outdoors, with natural light, factors that influence the entire natural environment and in some way our well-being, lead to the outdoor space also being designed.

Over time, the occupation of underground soil has had different reasons, such as Cappadocia in Turkey (Figure 2), Pilsen in the Czech Republic, or Naours in France.

Some of these spaces continue to be incorporated into our activities, especially as tourist attractions that provide "experiences", an aspect that is important to consider in land use competition and that in many circumstances can have major impacts on the functioning of cities.

The search for "shelter", which has become home, continues to be a very relevant factor today and not just due to climatic factors.

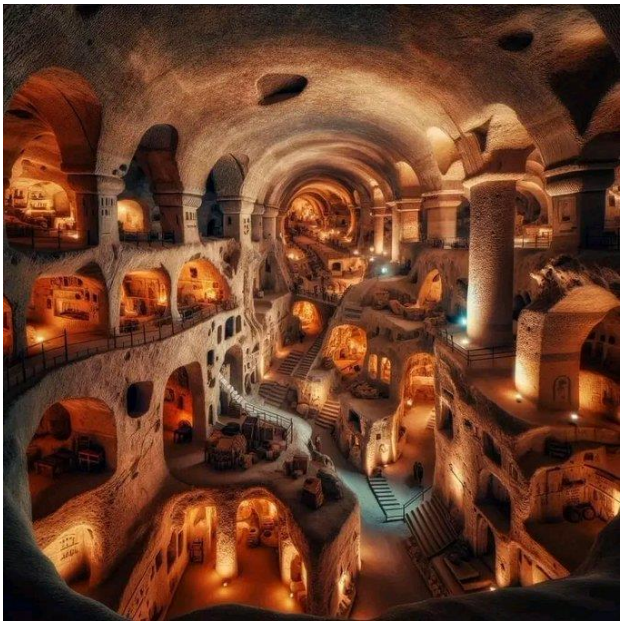

Figure 2. Derinkuyu, Turkey – Underground city; Source: Reddit.

The increase in living conditions was, and continues to be, a challenge, as well as finding new answers to the comfort needs that new lifestyles demand.

Society is evolving and ways of living are changing, looking for new models of organizing spaces, whether built or outdoors, an aspect that has proven to be extremely important for the quality of life required in the days of today.

This factor of the need of free space for everyone to enjoy outdoor living puts even more pressure on the city's land.

Our projects can respond to the most challenging programs, whether through the composition of construction elements or with new design solutions. Throughout our professional practice, we have seen programmatic responses to the most varied challenges, namely new use programs, climate protection, minimization of energy and water consumption,

comfort requirements, spaces adapted to different lifestyles.

These are new responses to the "shelter" that has become "home", in the current conditions of society, and which obviously takes different forms in different geographies.

However, we continue to observe several phenomena that continue to put pressure on the city's spaces and are causing significant changes in built spaces.

3 NON SENSE OPTION?

But in essence, we can summarize the situation as a new "shelter" and protection from the "weather". Shelter in the current context, that is, protected spaces for all the activities that society develops, has different characteristics and responds in many cases to the stimuli of new lifestyles.

In the case of "weather" protection, we are not only talking about effective protection from the weather and the climatic factors of each location, but we must include "sheltering the planet from the weather", that is, actively contributing to reductions in consumption and emissions in all possible components and, at the same time, ensure the increase in biodiversity by freeing up space on the surface to house new green spaces and also not occupying new natural territories with construction.

Underground construction has arisen for various reasons, but initially due to a lack of available space to expand the supply, namely commerce and leisure.

It is also worth noting that in some geographies, planned activities and uses cannot be carried out outdoors for a large part of the year, nor is there natural light. In these cases, why not?



Figure 3. Montreal Underground city; Source: Guide to Underground City.

Even without considering climatic conditions of extreme temperatures or lack of daylight, some of the activities are already, and some always have been, carried out in many enclosed spaces, without natural light, such as theater or cinema, and can clearly be transferred for buried spaces, leaving surface spaces free for housing or office uses, uses where natural light is clearly more valued.

There are already several examples of shopping centers, multifunctional spaces and also plans to expand the city into underground spaces.

We can point to Montreal, Singapore, and Helsinki as examples (Figures 3, 4 and 5).



Figure 4. Singapore Underground plan; Source: Ziptopia.

These are expansions of cities that take advantage of existing structures or that plan new areas for expansion and rehabilitation with very different programs and uses.

These are ambitious examples, which are important to evaluate not only from the perspective of efficiency and soil optimization, which is important and economically very relevant, but fundamental from the perspective of protecting the planet and the quality of life of all inhabitants.

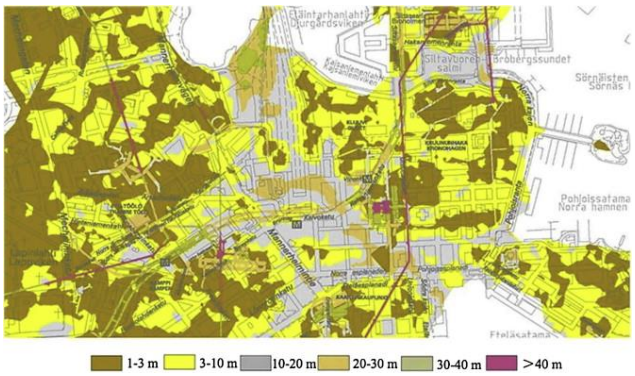

Figure 5. Helsinki Underground plan; Source: Science Direct.

When occupying the underground areas, it will be important to assess under which circumstances the infrastructure will be more efficient in terms of air conditioning or energy consumption.

But also, what uses are appropriate: commerce? hotels? culture? leisure?

It seems clear that some activities that take place in enclosed spaces can be transferred underground, freeing up surface territory, but other aspects, some already described above, must be taken in to account. Especially regarding habitability and the need for each use.

One of the situations that will be important to present in this short note is the case of underground projects that are developed to offer a different "experience" of life.

In recent decades, there has been an increased demand for lifestyles that are very focused on distinctive factors.

The underground has also been the target of proposals for highly spectacular projects, where the challenges are enormous, namely how natural light enters, or what type of infrastructure will need to be installed.

We can point out two cases, one in Mexico City, with the Underground Scraper (instead of skyscrapers) or the recent proposal from NEOM, a KSA PIF, The Aquellum (Figure 6), a vision of a digital underground community on a mountain next to the Gulf of Aqaba.

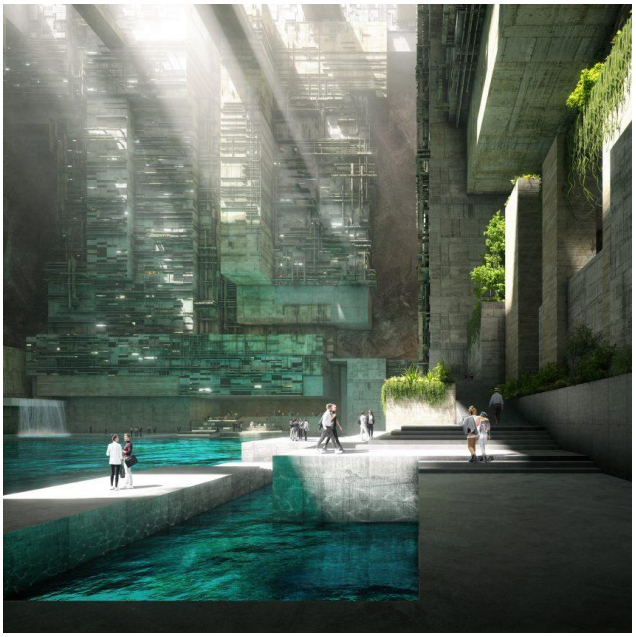

Figure 6. NEOM – Aquellum – Source: NEOM.

4 FINAL REMARKS

are proposals with enormous challenges for all project areas, particularly geotechnical. Not only because of much more construction underground, but because the volume of built elements that will overlap in this space can grow a lot, making the integration of all systems and technical requirements much more demanding.

There are also major challenges to technology, such as how to bring natural light underground?

The world continues to pose challenges to the creators of built space and to all the technical disciplines that contribute to these creations.

The need for shelter from the elements will continue, but now with new ingredients that we have to incorporate into projects, ensuring a unique quality, as should be the objective of each and every construction project.

REFERENCES

Guide to Underground City (2024). Tourism Montreal, Available at: https://www.mtl.org/en/experience/guide-underground-city-shopping, accessed: 20/04/2024.

NEOM (2024). Available at: https://www.neom.com/en-us/regions/aquellum, accessed: 15/04/2024.

Research Gate (2021). Challenges and New Research Directions to the Development of Smart Cities: Systems-of-Systems Perspective, Available at: https://www.researchgate.net/figure/Urban-and-rural-areas-population-1500-2050-2_fig1_349817516, accessed: 22/04/2024.

Science Direct (2016). Development for urban underground space in Helsinki. Available at: https://www.sciencedirect.com/science/article/pii/S1876610216307834, accessed: 30/04/2024.

Ziptopia (2025). These 8 Hidden Underground Cities Are Groundbreaking (Literally), Available at: https://www.zipcar.com/ziptopia/future-city/eight-hidden-underground-cities, accessed: 30/04/2024.

Heritage Time Capsule Project Lectures
Conférences sur le Projet Heritage Time Capsule

Proceedings of the XVIII ECSMGE 2024
GEOTECHNICAL ENGINEERING CHALLENGES
TO MEET CURRENT AND EMERGING NEEDS OF SOCIETY
© 2024 the Authors
ISBN 978-1-032-54816-6
DOI 10.1201/9781003431749-21
Open Access: www.taylorfrancis.com, CC BY-NC-ND 4.0 license

ECSMGE 24
XVIII EUROPEAN CONFERENCE ON SOIL MECHANICS AND GEOTECHNICAL ENGINEERING

Heritage Time Capsule Project Lecture

The Heritage Time Capsule project and the Portuguese geotechnical history

Le projet Heritage Time Capsule et l'histoire géotechnique Portugaise

J. Mateus de Brito*
Consulting Engineer, Ex-TPF/Cenor, Lisbon, Portugal
**jmateusdebrito@gmail.com*

ABSTRACT: Within the scope of the Heritage Time Capsule (HTC) project, launched by the International Society of Soil Mechanics and Geotechnical Engineering (ISSMGE), the Portuguese Geotechnical Society (SPG) has been developing actions related to the History of Geotechnics in Portugal. The objectives of the project, the actions already carried out and the main aspects of the contribution given by SPG are described. The most relevant aspects of the development of geotechnics in Portugal and main large projects in the last 70 years are briefly presented. Main large geotechnical engineering projects underway and those planned are also briefly presented.

RÉSUMÉ: Dans le cadre du projet Héritage Time Capsule (HTC), lancé par la Société Internationale de Mécanique des Sols et d'Ingénierie Géotechnique (ISSMGE), la Société Géotechnique Portugaise (SPG) a développé des actions liées à l'histoire de la géotechnique au Portugal. Les objectifs du projet et les actions déjà réalisées ainsi que les principaux aspects de la contribution apportée par SPG sont décrits. Les aspects les plus importants du développement de la géotechnique au Portugal et les principaux grands projets des 70 dernières années sont brièvement présentées. Les principaux grands projets d'ingénierie géotechnique en cours et ceux prévus pour le futur sont également brièvement présentés.

Keywords: Portuguese geotechnical history; portuguese geotechnical works; Heritage Time Capsule project.

1 PORTUGUESE NATIONAL SOCIETY

SPG was formally created in 1972, although in reality it began in 1951, the year in which the Portuguese Society of Soil Mechanics (SPMS) was created (Nascimento, 1990), developing its activity within the scope of the Soil Mechanics Commission of the Portuguese Engineers' Order (OE), which was led by Professor Manuel Rocha (Figure 1). In 1952, this Commission promoted, a course on Soil Mechanics of great impact on the national technical environment. It was this course that definitively established Soil Mechanics in Portugal.

The Commission of OE became independent in 1960 and joined the ISSMFE in the same year. In 1966, coinciding with the holding in Lisbon of the First International Congress of Rock Mechanics (Figure 1), became part of the International Society of Rock Mechanics - ISRM (SPG, 2021). With this, also in Portugal, rock mechanics was established as an independent discipline, within the scope of geotechnical engineering. At that congress, around 800 people participated and around 250 works were presented, many of exceptional interest. Manuel Rocha was elected President for the period 1966-1970 and the secretariat of ISRM was installed at Laboratório Nacional de Engenharia Civil (LNEC), where it remains until today.

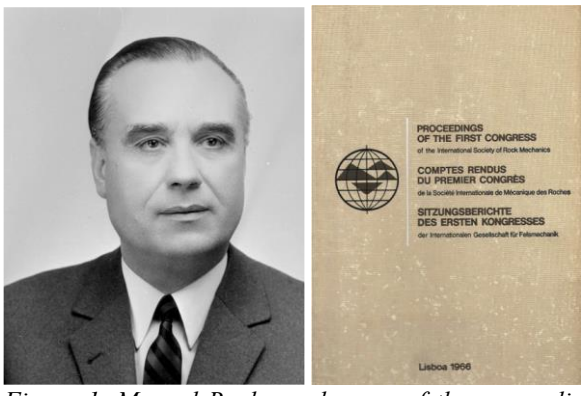

Figure 1. Manuel Rocha and cover of the proceedings of the First International Congress of Rock Mechanics.

Since then, the SPMS became member and represents in Portugal the International Association for Engineering Geology and the Environment - IAEG (1972), the International Tunnelling Association - ITA (1980), and the International Geosynthetics Society - IGS (2001).

SPG launched the first issue of Geotecnia Journal in June-July 1971 (Figure 2), with José Folque as director, and the president of SPMS, Úlpio Nascimento, as editor (Figure 3). The publication of Geotecnia journal has been a regular activity of SPG. Currently, the journal is published by SPG with the collaboration of the Brazilian Association of Soil Mechanics and Geotechnical Engineering (ABMS) and the Spanish Society of Soil Mechanics and Geotechnical Engineering (SEMSIG). The journal is published quarterly.

In 2007, Solos e Rochas Brasilian Journal, that was first released in 1978, acquired the status of an international journal, being, since then, published in english, by ABMS and SPG under the title Soils and Rocks (Figure 2). This journal is published quarterly.



Figure 2. Covers of the first issue of Geotecnia Journal (June-July 1971) and of Volume 30, N. 1 January-April 2007, first issue of Soil and Rocks Journal.



Figure 3. José Folque (left) and Úlpio Nascimento (right).

SPG awards four prizes:

- Manuel Rocha Award, established in 2003, with the aim of rewarding research works at the doctoral level; the prize is awarded every four years;
- SPG Award/Young Geotechnicians Award/José Folque Award, since 1984-1985 biennium, with the aim of encouraging research within the scope of postgraduate activities at master's level;
- Geotecnia Journal Award/Úlpio Nascimento Award, since 1986-1987 biennium, with the aim of reward the article with the greatest technical and scientific interest published in the journal;
- Ricardo Esquível Teixeira Duarte Award, established in 2017, with the aim of distinguishing the authors of design solutions for geotechnical works or projects with a relevant geotechnical component, already completed (every two years).

In 1984 the Manuel Rocha Lecture was established by SPG and the Association of Geotechnicians Former Students of Universidade Nova de Lisboa (UNL). It is held annually at the Calouste Gulbenkian Foundation headquarters, with geotechnical guest speakers of recognized merit, alternately Portuguese and foreign. Forty lectures have already been presented to date.

Manuel Rocha was one of the pioneers of geotechnics in Portugal and he is considered the most illustrious Portuguese geotechnician. He was the driving force behind rock mechanics studies and one of the greatest international researchers in this field. He was director of LNEC between 1954 and 1974, date in which he took up the position of Minister of Public Works.

Under the auspices of SPG, in addition to the First International Congress of Rock Mechanics, the main international conferences held in Portugal were:

- 7th Congress of IAEG, at LNEC (1994);
- 11th Congress of ISRM at LNEC (1996);
- 3rd International Congress of Environmental Geotechnics at LNEC (1998);
- 2nd Internacional Conference of Earthquake Geotechnical Engineering, at LNEC (1999).

It is worth noting that Ricardo Oliveira was elected IAEG Vice-President for Europe in 1986 and IAEG President (1990-1994). It is also worth noting the election of Pedro Sêco e Pinto for ISSMGE Vice-President for Europe (2001-2005) and ISSMGE President (2005-2009).

SPG also collaborates with ABMS in the organization of the Victor de Mello Lecture, that was established in 2008. It takes place every two years, alternating in Portugal and Brazil, and is preferably given during the Luso-Brazilian Geotechnical Congresses. Eight lectures have been presented to date.

2 THE HERITAGE TIME CAPSULE PROJECT

In 2021, ISSMGE launched a project with the objective to collect the main milestones of the contribution of geotechnics to the development of each country at national level and around the world, creating an HTC, and invited the Member Societies to give their contribution. SPG accepted the challenge and considered this to be a unique opportunity to publicize the achievements and current state of Portuguese geotechnical engineering, as well as to foresee and prepare the future, thus filling the existing gap in the systematization of knowledge in these areas. Beyond this first phase, concerning contributions, three more phases have emerged as explained by Pathmanandavel et al (2024) in this European Conference.

3 SPG CONTRIBUTION TO HTC

SPG defined the following objectives for its contribution to the HTC project: (i) disseminate the cultural, scientific and technological heritage, showing what is important in the history of Portuguese geotechnics, thus catalyzing the interest of geotechnicians, especially the youngest, and contributing to eliminating the gap between the industry and academia; (ii) highlight, alongside the development of Portuguese geotechnics, the role of civil engineering and the country's social, economic and political development; (iii) present the most suggestive cases of geotechnical works, which highlight, through the corresponding solutions, the development and characterization of each of the stages of scientific knowledge and construction techniques; iv) highlight successes and show failures of the past.

SPG primarily developed the following topics as the basis of the Portuguese contribution:

- Pillars of Portuguese geotechnics;
- Relevant Portuguese geotechnical works, in the country and abroad;
- History of geotechnics in Portugal.

The following pillars were considered as representative of national geotechnical engineering activity:

- Geotechnical associations, events, and publications: evolution of geotechnical associations, main Portuguese geotechnical events and international geotechnical events that took place in Portugal;
- Geotechnical consultancy companies: history and main achievements of the main consultancy companies of the past and present;
- Geotechnical works contractors: history and main achievements of the main contractors of the past and the present.

For the relevant geotechnical works, the presentation of the information was made in detailed sheets, prepared by the design and construction companies.

For the history of geotechnics in Portugal it was considered that this could not be presented without mentioning civil engineering and social, economic and political development in Portugal and abroad. Therefore, alongside the evolution of geotechnics, it was considered relevant to mention the most striking aspects of the evolution of civil engineering and to introduce some events that determined the development of Portugal and some relevant international references. The geotechnical works, were chosen due to their geological and geotechnical conditions, reflecting relevant and innovative aspects. The history of geotechnics covers the period from the mid-17th century to the beginning of the third decade of the 21st century, having been divided into relevant time periods. A recent paper from the author, related to Portuguese Geotechnical History, was published in Geotecnia Journal (Mateus de Brito, 2024).

The documents produced by SPG are hosted in the websites https://spgeotecnia.pt and https://www.issmge.org/the-society/time-capsule.

4 DEVELOPMENT PATH OF GEOTECHNICAL ENGINEERING IN PORTUGAL (1950-2020)

4.1 1950s. The foundation of LNEC and the beginning of the maturity period of Portuguese engineering

During this decade, the execution of public works had a significant increase in Portugal, namely large hydraulic projects to produce electricity and for irrigation and water supply. The elaboration and execution of plans for these uses were extended to overseas provinces. The implementation of the electrification program was a success, showing significant results in a considerably short period of time. Existing hydroelectric companies played a decisive role. Portuguese concrete dam engineering entered a period of maturity that allowed it to design and build large concrete dams, which marked a remarkable development. Sixteen concrete dams were completed, representing the largest number of these dams built in a decade in Portugal.

In the field of civil engineering research and particularly in geotechnics, a decisive step was taken with the constitution of LNEC at the end of 1946, as part of a movement to create the so-called State Laboratories, which emerged in the post-war period in many European countries, with direct responsibility for promoting research applied to European reconstruction activities (Maranha das Neves, 2008).

In this decade, it is fair to highlight the pioneering role of Facudade de Engenharia da Universidade do Porto (FEUP), in launching the Stability Studies Seminar, that began in April 1952, involving not only structural materials, but also Soil Mechanics. It should also be mentionid, in the 1955/56 academic year, the study plan for the Civil Engineering courses at Instituto Superior Técnico (IST) and FEUP, that began to include a semester-long subject on Soil Mechanics.

Until the end of the 1950s, studies and projects were carried out by public bodies, without specific geotechnical training, based essentially on the experience of the engineers involved, and using national and foreign consultants. The first private engineering consultancy company, Hidrotécnica Portuguesa, was founded in 1957, initially dedicated to the study and design of hydraulic works.

The main drivers of change in the 1950s were:

- Notable increase in the construction of dams for the production of electrical energy;
- Development of an ambitious Alentejo Irrigation Plan;
- Creation of a course in Soil Mechanics at IST and FEUP (1955);
- Creation of the first large consultancy company (1957);
- Construction of Paradela dam (112 m), first rockfill CFRD dam in the country, tallest in the world of its type (1958);
- Launch of Lisbon Metro (ML) with two lines, built from 1955 to 1958.

Of the geotechnical works carried out in this decade stands out, for its symbolism, the Cabril dam (Figure 4), completed in 1954, still the tallest Portuguese dam, that is recognized as having marked the development of the double-curvature vault type dams of its time. The dam has a maximum height of 132 m above the foundation and a crest length of 290 m. It is one of the greatest achievements of national engineering and marked the time as particularly notable for the technical level of Portuguese engineering (Xerez, 1954). It marked the transition between the collaboration given by eminent foreign technicians and the total intervention and responsibility of Portuguese technicians.

4.2 1960s. Emergence of large engineering consultancy companies

In this decade there was an endogenization of technology, which led the national engineering sector to develop capacities to design all types of large works built by Portuguese people, in the country and abroad, resulting in a remarkable period of execution of major engineering works, involving the construction of several sections of highway in the regions of Lisbon and Oporto, vital for the development of the country, and several dams throughout the territory, promoting the development of construction techniques and the growth in the number of specialized engineers, who contributed to the construction of these works in Portugal and later abroad.

In this period, LNEC assumed a fundamental role in Soil Mechanics, Rock Mechanics, and Engineering Geology research, carried out by its technicians.

New design and consultancy companies emerged, such as Coba (1962), Profabril (1963), Hidroprojecto (1966) and Consulmar (1970), all of them integrating geotechnical specialists, who would also play a decisive role in the development of the Portuguese geotechnical market.

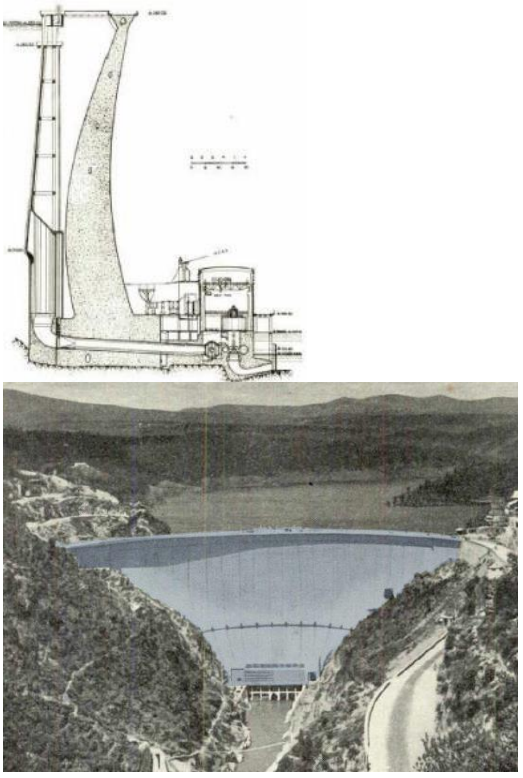

Figure 4. Transversal section and downstream view of Cabril dam, in June 1954 (Xerez, 1954).

With the inauguration of the then-named Ponte Salazar (currently 25 de Abril bridge), on August 6, 1961, connecting Lisbon to the Setúbal peninsula, Portugal got the longest suspension bridge span in Europe. Among the innovations in the construction of this bridge are the foundations of the towers of the two pillars on the river, made up of large concrete blocks with plan dimensions of 40 m x 23 m, built using the so-called open caisson method with air domes, achieving a depth of 79 m at the foundation of the south tower.

The main drivers of change in the 1960s were:

- Industrialization of basic sectors of the Portuguese economy;
- Creation of the LNEC Geotechnical Department (1961);
- Holding of the First ISRM Congress, at LNEC (1966);
- Establishment of Engineering Geology as an autonomous science (mid-1960s);
- Construction of 25 de Abril bridge;
- First sections of highway in Lisbon and Oporto regions;
- Emergence of large engineering consultancy companies;
- Development of diaphragm wall and anchoring technologies and widespread of its use in urban excavations;
- Universal acceptance of the concept of Geotechnics.

The most relevant achievement of the decade was the construction of dry docks of the Lisnave Naval Shipyard in Almada, that opened in 1967 and quickly gained a foothold in shipbuilding and repair, to such an extent that the docking capacity was expanded to receive oil tankers from new generation then planned, with ships up to 1 000 000 ton. With the expansion with dock 13 (Figure 5), the largest dry dock in the world at the time (320 m x 97 m), built between 1969 and 1971, Lisnave became considered one of the best ship repair yards in Europe and an international reference in the sector. The local geotechnical conditions are very favorable, as, at the level of the foundations of the walls and bottom slabs of the dock, there are very dense Miocene sandy clays, whose average permeability coefficient made it possible for the adoption of very economical structural solutions, with drained bottom slabs supported directly on the ground.

4.3 1970s. Democracy and turn to Europe. Start of soil and rock mechanics teaching at universities

Following the revolution of 1974, which established a democratic regime in Portugal, major changes took place in the Portuguese business sector, namely at the construction sector, with some consulting and construction companies going into irreversible decline and others entering a restructuring phase. Most of the economy sectors were nationalized. The independency of African territories under Portuguese administration (Angola, Mozambique, Guinea Bissau, Cape Verde and S. Tomé and Príncipe) took place in 1975, which made most of the technicians who worked there to return to Portugal mainland, contributing to increase the staff of various official bodies, consultants, and contractors.

At the end of the decade, due to the economic growth and following the trend in the previous years in the developed countries, multiplication of large urban excavations started, not only for metro lines or other transportation works, but also for underground car parking of new buildings or under public spaces.

In 1975, specialization courses and, after, postgraduate courses in geotechnics, were created at the newly created UNL. In 1980, master degrees were created at the same university.

The main drivers of change in geotechnics in the 1970s were:

- Development of computers and the advent of the finite element method;
- Creation of Postgraduate Courses in Geotechnics at UNL (1975/76);
- Evolutionary trend towards the construction of embankment dams with zoned profiles with chimney filter;
- Significant increase in the use of soil treatment processes;
- Consolidation of important slopes of railway Lisbon-Oporto in Santarém (1970);
- Pioneer temporary tangent piles with 4 levels of anchors support wall of ML Alameda Station (1974);
- Beginning of the construction of Sines Port, one of the most relevant works of Portuguese engineering (1973).

In this decade the most relevant entreprise was the construction of Cahora Bassa hydroelectic schema, in Mozambique, completed in 1974. It comprises a concrete arch dam, 164 m high, that creates the second largest artificial lake in Southern Africa. The concrete vault dam has appurtenant works designed for a peak flow of 12,600 m^3/s and an underground

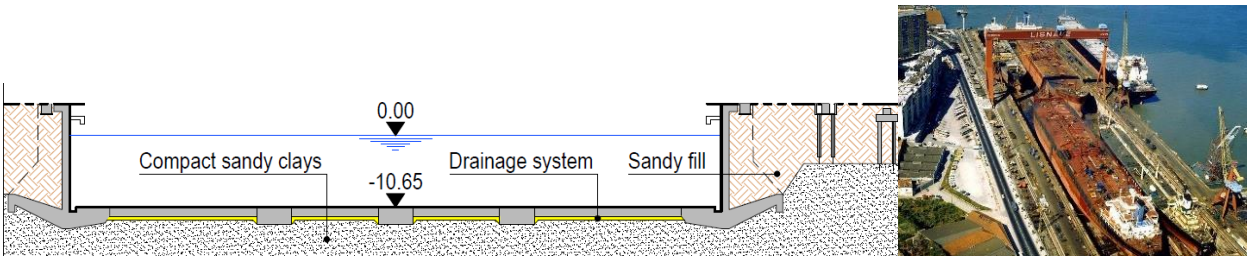

Figure 5. Transversal section and aerial view of Lisnave dock 13.

power plant on the south bank of the Zambezi River with five groups of 415 MW each (Figure 6). The rock mass at the site is made up of granitoid gneiss with excellent mechanical qualities, which, due to the existence of some lamprophyric and gabbric veins, posed some design and execution problems. This dam was a testimony of Portuguese engineering capacity to design the installation of high-power hydroelectric schemas.

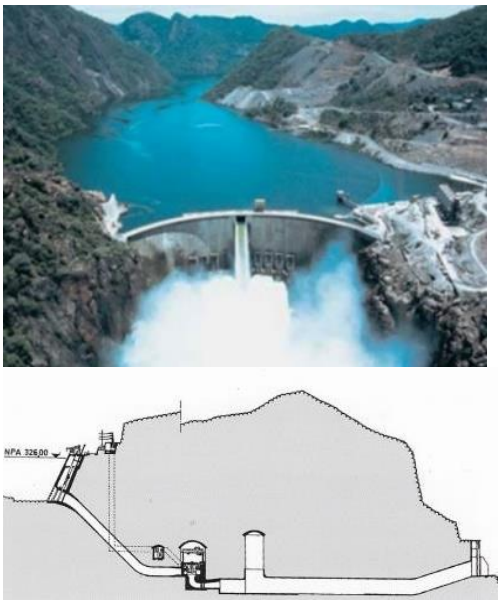

Figure 6. Downstream aerial view of Cabora Bassa Dam at maximum flood discharge and longitudinal section of the power plant and hydraulic circuit (Cruz et al, 2007).

4.4 1980s. Emergence of community funds. Generalized teaching of geotechnics in universities

With the first years of the 80s, the economic cycle reversed itself again and the construction market suffered major impact. The deterioration in demand and the worsening of the economic and financial situation created a situation without parallel since the 1974-75 recession.

In 1985, Portugal joined the European Economic Community (EEC), which would play a fundamental and decisive role in the country's economic development, with an obvious repercussion on the development of geotechnics.

The last years of this decade witnesed the dynamism of civil construction works, namely in the road, airport, river, and maritime areas, which resulted from importing of technologies already widely applied in other countries, but which led to the modernization of the construction industry, development of technological means and training of specialized technicians.

In the decade there was a widespread progress in the teaching of geotechnics at universities and began the creation of teaching teams with adequate geotechnical training and a doctorate degree in the country.

During the 1970s, rockfill, a very abundant material in the country, was not used either in dams or in roads or airports embankments, due to the lack of knowledge on the mechanical behavior of these materials, as well as of adequate construction techniques. So, in the 1980s, LNEC began an ambitious research project on rockfill, which covered the theoretical and experimental aspects of the rockfill mechanics, with the Beliche dam becoming a case study around which all the research was developed. The materials to be used in the dam were tested with equipment designed and built at LNEC. This set of studies contributed to placing Portugal and LNEC in a leading position in the field of rockfill use in various types of infrastructure (Maranha das Neves, 2008).

The main drivers of change in geotechnics in the 1980s were:

- Portugal's accession to the EEC;
- Beginning of the development of the research area in universities;
- Creation of Masters in Soil Mechanics and Engineering Geology;
- Research project on rockfill at LNEC;
- Start of copper production in Somincor mines (1988);
- Development of the nailed wall technique;
- Development of excavation support with diaphragm walls using a hydromill;
- Emergence of major environmental concerns.

The construction of the Beliche dam was completed in 1986. It consists of a zoned

embankment, with well graded schist and greywacke rockfill shells and a clayey core, of weathered schist, upstream and downstream chimney filters with double layers of coarse filter and fine filter (Figure 7). It was the first dam of this type to be built in Portugal. The foundation consists of schist and graywacke.

4.5 1990s. Great public works development

The 1990s were a very intense period of construction in Portugal, largely resulting from the availability of European Community funds within the scope of various development support programs resulting from Portugal's integration into the EEC. The many millions of euros allocated to Portugal were a strong driver of the country's economy, reflected in many areas, especially in road infrastructure, in water

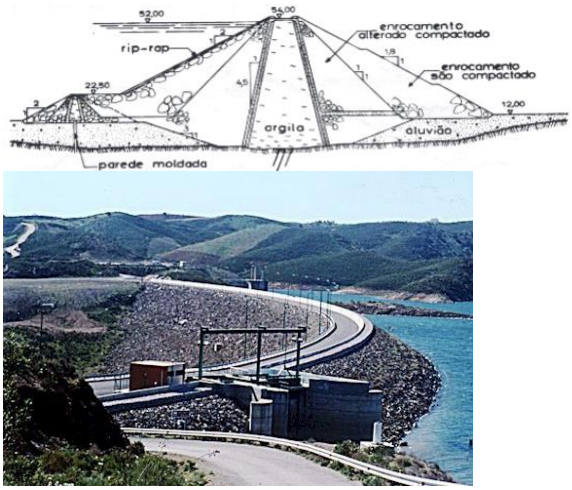

Figure 7. Cross section and vew of Beliche dam.

supply, both for consumption and irrigation, in the production of hydroelectric power and in environmental domain.

In the teaching of geotechnics, the trends of the previous decade were consolidated with a progress in research and significant increase in the number of doctorates reaching an international quality level.

In urban planning, the Expo'98 complex stands out in the northeast zone of Lisbon, with major works being carried out (Figure 8). It is considered one of the largest infrastructure projects at national and even European level. Located in the alluvial zone of the Tagus River, where the muddy alluvium reaches maximum depths of around 25 m, these works constituted a notable engineering achievement, with a strong geotechnical component, whose completion represented an enormous technical challenge.

At Madeira Island a new road network was built over a period of around 15 years, starting in 1989, which greatly improved the connections between Funchal and other main cities on the island. This was the most important investment in the history of Madeira, exceeding 2 000 M€.

The main drivers of change in geotechnics in the 1990s were:

- Publication of the Dam Safety Regulations (1990);
- Development of rockfill dam construction;
- Explosion of Portuguese road construction;
- Construction of long-span road bridges;



Figure 8. Expo'98 aerial view.

- Construction of large-section road tunnels;
- Construction of new ML lines;
- Bologna Declaration (1999).

The most relevant road work carried out in this decade was the Vasco da Gama bridge, over the Tagus River, in Lisbon, inaugurated in 1998. It is one of the largest national infrastructure projects and the second longest bridge in Europe, contributing decisively to the development of national road accessibility, with relevance to the Lisbon metropolitan area. The cost was around 1 000 M€. This road complex comprises a bridge, several viaducts and access roads, totaling 18 200 m, of which 12 340 m are on bridge and viaducts. The bridge and access viaducts cross the Tagus River alluvial valley (Figure 9), which, in this area, reaches a width of more than 12 km and a maximum thickness of around 80 m (Seco e Pinto & Oliveira, 1998). The main bridge, crossing the north channel, is a cable-stayed structure 826 m long and with a free span of 420 m between towers. The towers of the central span, 148 m high, rest on massive headers on 2.2 m diameter bored piles built under large cofferdams.

Another achievement that must be mentioned is the construction of the Al Whada dam, in Morocco, aimed to control flooding, irrigation, water supply and production of hydroelectric energy, located in an high seismic risk area. It is a zoned earth dam with 1 600 m long and with a maximum height above the foundation of 88 m. The volume of excavations was 13,8 Mm^3 and the volume of earthfill was 26.4 Mm^3.

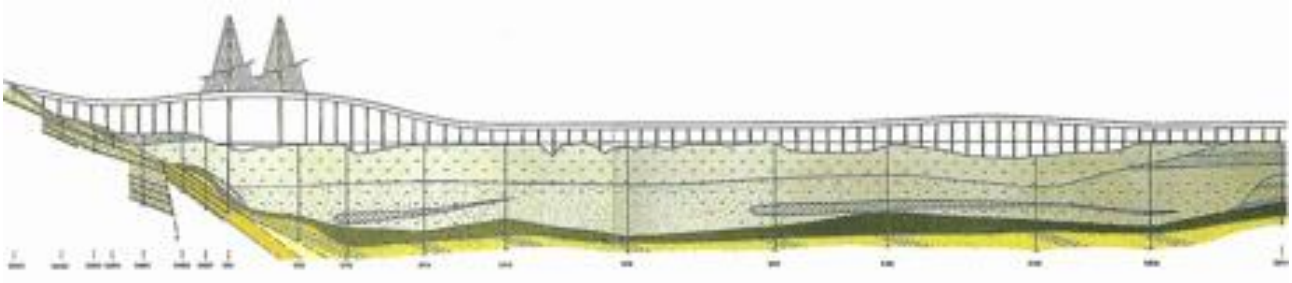

Figure 9. Geologic longitudinal section of west zone of Vasco da Gama bridge (Portuguese Engineers' Order, 2003).

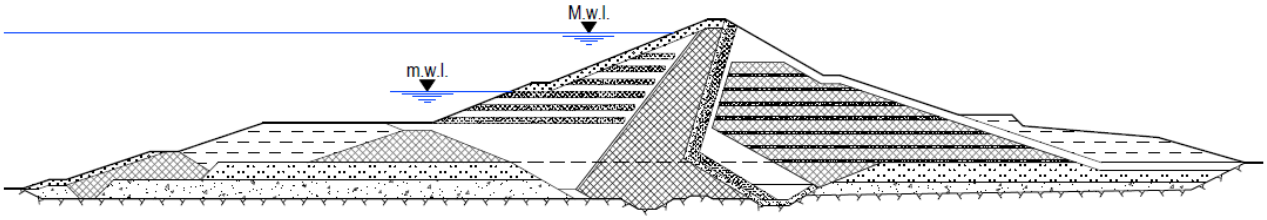

Figure 10. Transversal section of Al Whada dam, Morocco (Mineiro, 1991).

The foundation is constituted by marls interspersed with sandstones, with the riverbed being filled with coarse and fine alluvium (Figure 10).

The design of the dam, the configuration and layout of the spillway, the restitution channel, and the energy dissipation pit, were strongly conditioned by the very adverse geological and geotechnical conditions of the foundation, where the existence of expansive marls interlayered with rigid sandstone banks, dictated the positioning of the dam's main hydraulic works (Mineiro, 1991). It is the second largest dam in Africa, after the Aswan dam, and the largest in Morocco.

4.6 2000s. Increase in the internationalization of Portuguese engineering. Maturity of teaching and research in geotechnics

At the beginning of the century, teaching and research in geotechnics reached maturity. New university campuses or new university buildings were opened at the beginning of the decade, creating better conditions for teaching and research, and strengthening laboratory capacity.

From 2004 onwards the instability of the internal market and the retraction of national investment severely affected the construction and consultancy companies that had to extend their activities abroad.

Only at the end of the decade the government decided to give greater impetus to public works, having granted a significant part of large projects to the private sector, with a strong social impact on the country. Concession groups were created, called Public Private Partnerships (PPP), which developed global projects covering the design, financing, construction, and exploration components, with six PPP sub-concessions being created for highways.

The main drivers of change in geotechnics in the 2000s were:

- Significant progress in research in geotechnics applied to civil engineering in the field of theory, materials characterization and innovation of construction technologies;
- Large volume of highway construction throughout the Continent and Madeira Island, which included the construction of numerous bridges, tunnels, embankment and slope stabilization works;
- Expansion of ML and beginning of construction of Oporto subway (MP);
- Strong decline in investment since 2004, which severely affected companies in the consultancy sector;
- Increase in work carried out by Portuguese design companies to external markets.

Of the ML works, it is worth highlighting the completion, in 2007, of the Terreiro do Paço Station, adjacent to Tagus River. The station structure corresponds to a large reinforced concrete box, built from the ground surface, 140 m long and 24 m width in the wide zone (Figure 11). The soils are predominantly clayey-silty alluvium, ranging from very soft silt to sand with a very significant predominance of clean sand at the base of the alluvium. Underlying the alluvium, slightly below the base of the station bottom slab, occur Miocene formations, composed of very stiff clays. The retaining structures consist of alternated reinforced concrete and bentonite-cement piles 1,50 m in diameter. For the temporary shoring system, five levels of pairs of horizontal struts were used, between the longitudinal faces of the retaining structures, consisting of tubular steel profiles (ϕ711 mm) with an

average horizontal spacing of 3.5 m. The struts were heavily prestressed during installation, with a uniform prestress of 3 500 kN per strut, introduced by 4 hydraulic jacks. This system was complemented, in the wide area of the station, with a 3 m thick jet grouting slab, between the depths of 18 and 21 m placed between the existing tunnel, previously filled with poor concrete, and the retaining structures. The excavation was carried out in 5 phases, until reaching a depth of 26.5 m (Matos Fernandes, 2010, Mateus de Brito, 2020).

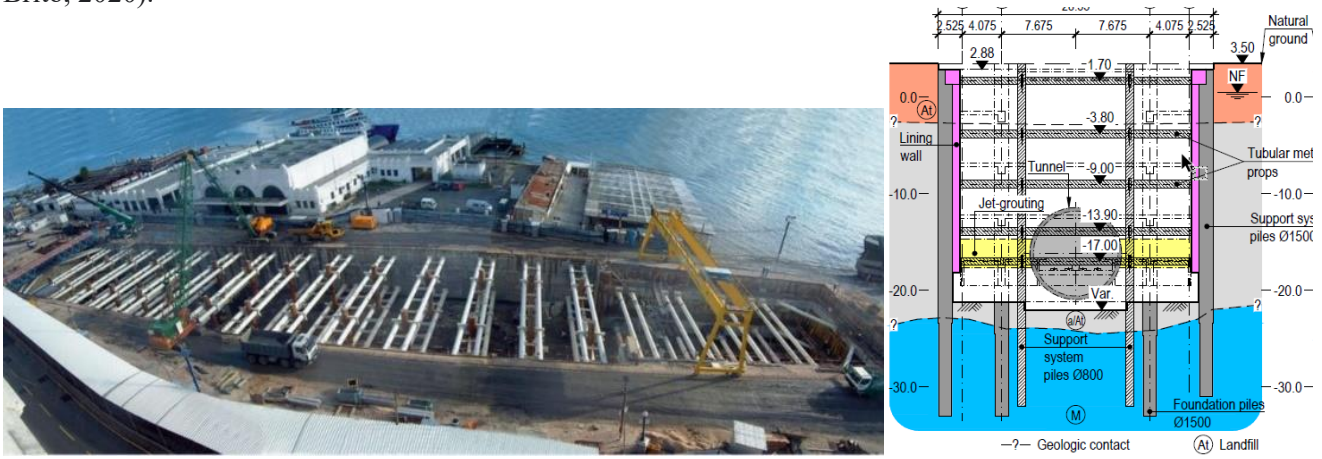

Figure 11. View of Terreiro do Paço Station during construction and cross section of the wide area of the station after completion of the last excavation phase (Mateus de Brito & Matos Fernandes, 2014).

Regarding university education, there were serious difficulties that affected the quality of geotechnical training and led to a reduction in the number of civil engineering students with this training, as well as the teaching staff necessary to provide it. Between 2010 and 2014, there was an abrupt reduction of the number of students placed in civil engineering courses, because of the crisis. After 2015 the number stabilized at around 400 students, about half the number of students placed in the precedent decade. Although there has been a tendency towards an increase in interest in civil engineering training, it appears that the number of students placed in universities will not guarantee an adequate response to the needs and the challenges that the country is currently going through.

The main drivers of change in geotechnics in the 2010s were:

- Significant reduction in public investment;
- Search for consultancy and construction companies to increase their activity abroad;
- Completion of important geotechnical works abroad, designed and built by Portuguese engineering companies;
- Increase in the number of PhDs in geotechnics in Portuguese universities;
- Significant reduction in the number of students in civil engineering;
- Entry into force of Eurocodes (2019);
- Power reinforcements in existing dams; the most important (732 MW) was in Venda Nova dam (2017);
- Conclusion of important new hydroelectric dams.

4.7 2010s. Retraction of public investment

As a result of the financial crisis that began in 2008, there was a significant retraction in public investment from 2010 onwards, which led the government to suspend some infrastructure projects, with consultancy and construction companies being forced to increase its activity in foreign markets in Africa, Asia, and Latin America, namely in Angola, Mozambique, Algeria, and Brazil.

In 2018 the Place des Martyres Station was inaugurated, the most important underground station on the Algiers metro, located at a square with the same name, in the central area of the city, at the base of the Kasbah and near Algiers' harbor. Highly important archaeological findings located in the whole square area rendered the initial excavation cut and cover method impracticable and led to the development of an alternative solution consisting of an underground excavation. It comprises a gallery with unusual large dimensions, with a maximum span of 26 m, height of 19 m, and maximum depth of 35 m, corresponding to an excavation cross section of 397 m^2 and a length of 144 m (Figure 12). Most of the underground works were done in moderately to slightly weathered sericitic schist. In the area, an alluvial layer and landfills were identified with a significant thickness, about 7 m and groundwater level located in the base of the fill layers with in-depth water percolation in the most fractured zones of the rock mass (Conceição et al, 2012).

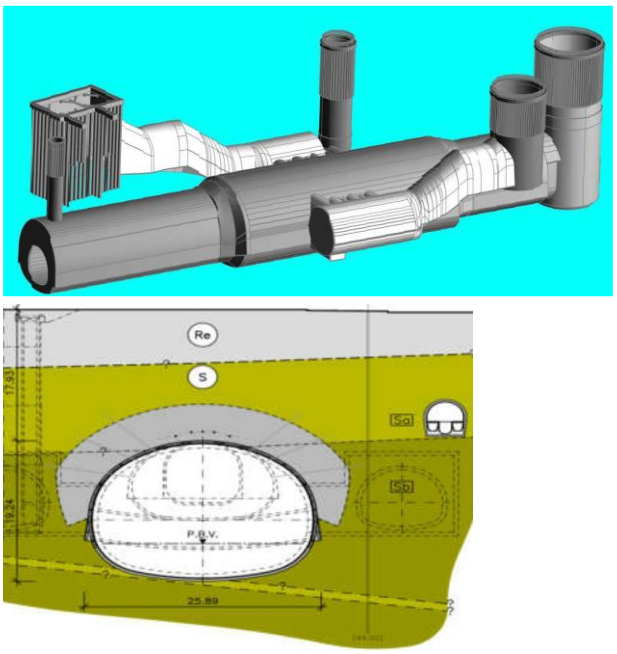

Figure 12. 3D view and cross section of the Place des Martyres Station in Alger (Conceição et al, 2012).

4.8 2020s. Large public investment in railways and renewable energies

In the beginning of this decade some important achievements were completed, and others are ongoing. Most of these achievements are financed by the Recovery and Resilience Plan (2021-2028), integrated at NextGenerationEU, that is the EU's 800 000 M€ temporary recovery instrument to support the economic recovery from the coronavirus pandemic and build a greener, more digital and more resilient future.

One of the largest initiatives in the history of Portuguese hydroelectric energy sector, the Alto Tâmega Electric Production System, was completed in 2023, with an investment of more than 1 500 M€. It is a complex formed by three dams and three hydroelectric plants: Alto Tâmega, Daivões and Gouvães. It stands out for its great reversibility capacity, with a total installed power of 1 158 MW, of which 880 MW are reversible. The Alto Tâmega dam reservoir has a total area of 466 ha for a storage volume of 56.2 Mm^3. The plant has two groups installed with a total power of 160 MW. It is a double-curved vault with a height of 104.5 m, a crest length of 335 m and 220 000 m^3 of concrete volume. It is founded on a phyllitic-grauvachic formation, made up of mica schists with interstratifications of dark carbonaceous schists, with stiffness at the bottom of the valley of 23 to 30 GPa and on the slopes of 7 to 22 GPa (Figure 13).

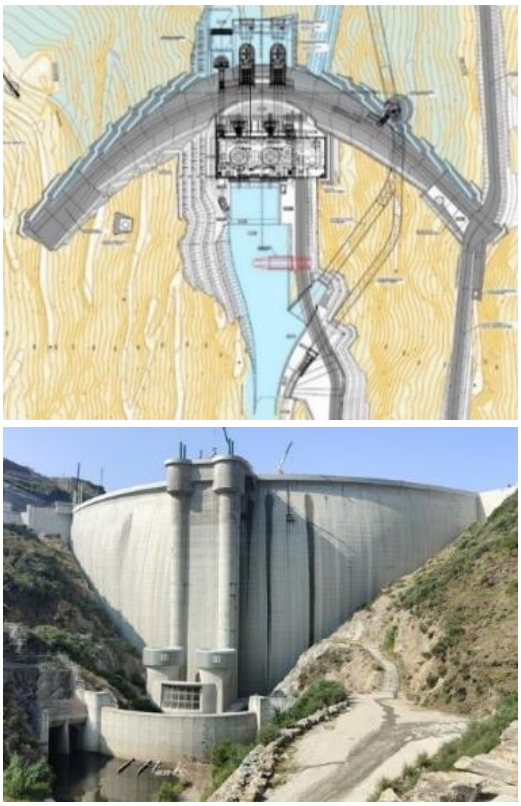

Figure 13. Plan and upstream view of Alto Tâmega dam.

Concerning railway lines, is planned in this decade, a global investment of 2 700 M€ both for the construction of new railway lines, covering a length of 214 km, and for the modernization of existing lines, covering around 900 km. In 2024, the first phase of the railway line between Évora and Elvas was completed, integrated into the future Southern International Corridor, linking Sines to Elvas near the Spanish border. This new section, with 80 km, is the first high-speed connection in Portugal, for passengers and goods, with an investment of 442 M€.

This new railway platform will constitute the largest railway line built in over a century in Portugal and is one of the largest railway works carried out in recent years. It is the first new railway infrastructure built to meet the criteria to be considered a high-speed line, having a maximum circulation speed equal to or greater than 250 km/h, for passengers, and 120 km/h, for goods. It was built on a single electrified track ballasted in Iberian gauge (1,668 m), but on a platform for double track and with the installation of multipurpose sleepers, to facilitate a future migration to European gauge (1,435 m) (Figure 14). It has around 30 bridges and viaducts and 89 km of new rail, resulting in an excavation volume of 7.1 Mm^3 and of earthfills of 5.9 Mm^3.



Figure 14. New HSRL linking Évora to Elvas.

In mid-2024 the first section of the new Lisbon-Oporto high speed railway line will be awarded, covering a length of 290 km. It has a design speed of 300 km/h and a journey time of 1h15. It will be carried out in 3 phases. Phase 1, that comprises the section between Oporto and Soure, is an investment of around 3 000 M€ and is expected to be concluded in 2028. Phase 2, between Soure and Carregado, has an estimated investment of 1 900 M€ and should be completed by 2030. Phase 3, between Carregado and Lisbon, has a small impact on travel time, so it should only be built later (see Figure 21). The first route corresponds to 71 km between Oporto and Oiã, including the construction of a new road-rail bridge, with two decks, over the Douro River, a new underground station in Santo Ovídio (Gaia), a twin-tube tunnel of around 6 km, that ran underground in the municipality of Gaia, five single-tube tunnels, as well as 15 double-track bridges and two single-track bridges.

Also ML will make important investments in this decade. The extension of the Yellow and Green Lines, already under construction, is an important upgrade to ML network with 2 km of track and 2 new stations. By creating a new connection between two existing lines, this project will form a circle line which will enhance the usability of public transportation services in the city centre (Figure 15). Construction works started in 2021 and passenger services are planned to start in 2025. The total cost is 331.4 M€.

Another important ML project, which began in 2024 and will end in 2027, is the expansion of the Red Line between S. Sebastião and Alcântara serving the western part of the city of Lisbon (Figure 15). It will have 4 new stations and around 4 km of track. The total cost is 405.4 M€.

The ML network will continue to expand in this decade, through a light surface metro system, which will serve the municipalities of Loures and Odivelas, with the connection to the rest of the network made through an interface in the existing Odivelas station, on the Yellow Line. It is called the Violet Line and will have a total of 17 stations and is approximately 13 km long, predominantly on the surface (8.6 km), but also with sections in trenches (0.4 km), viaducts (0.4 km) and tunnels (four tunnels with a total length of 3.7 km) as well as 3 underground stations and 2 trench stations (Figure 15). The project represents an investment of 527.3 M€, and the work should be completed in 2028.



Figure 15. Future Lisbon Metro network.

With regard to MP, the six lines in operation will be upgraded by the end of 2024 with the Pink Line (Casa da Música-São Bento), and the extension of the Yellow Line (Santo Ovídio-Vila d'Este), whose construction began in 2021 (Figure 16). The Pink Line extension is in tunnel through the central axis of the city of Oporto, with an approximate length of 3.1 km, and includes the construction of 4 new stations. The cost is 333 M€. It will improve access to central areas of the city with important business, residential and health facilities. The extension of Yellow Line has a length of about 3,15 km and 3 stations.

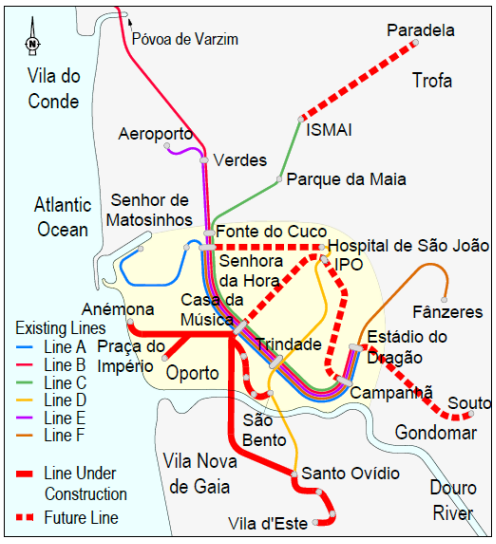

Figure 16. Future Oporto Metro network.

Another line, the Rubi Line of MP, whose construction began in the first half of 2024, will connect Casa da Música and Santo Ovídio (Figure 16) with a length of 6.3 km, including 8 stations and 2 tunnels. It includes the construction of a new crossing over the Douro River, the Ferreirinha bridge (Figure 17). The construction of this new line costs 435 M€.

MP will have in the future four more new lines, planned to be built by 2030. These lines will have a total length of 37 km and 38 stations, with a cost of around 1 000 M€ (Figure 16).



Figure 17. Porto Metro network. 3D view of Ferreirinha bridge.

The other very important transport infrastructure, planned to start in 2024, is the new Lisbon International Airport. It will be the biggest public project since the Vasco de Gama bridge and will put an end to a discussion that has been going on since the end of the 1960s. This airport has great probability to be located at Alcochete. In the first phase, planned to be concluded in 2030, the solution will involve a dual airport, with the current Lisbon airport. The new airport will have only one runway with a cost of 3 200 M€. Figure 18 shows the location foreseen for the new airport and the new highway and railway accesses.

For highway and railway accesses to the airport, is necessary to build a third crossing over the Tagus River, between Chelas (Lisbon) and Barreiro (Setúbal), that should be completed by the end of 2030 (Figure 18). The crossing will have a length of 13 km and the bridge will have a length of 7 200 m. The deck of the bridge will have two lanes for high-speed railway, two for conventional railway, and two side lanes with three lanes each for road traffic. The estimated cost in 2008 was around 1 800 M€.

The Lisbon General Drainage Plan, whose construction began in 2019 and is expected to be completed in 2030, is intended to significantly reduce flooding in critical locations of Lisbon, and the consequent social and economic costs, preparing the city for extreme events caused by climate change. The work includes tunnels between Monsanto and Santa Apolónia (4.6 km) and between Chelas and Beato (1 km) with an internal diameter of 5.5 m. The tunnels are being executed by a tunneling boring machine that has around 130 m long, 6.41 m

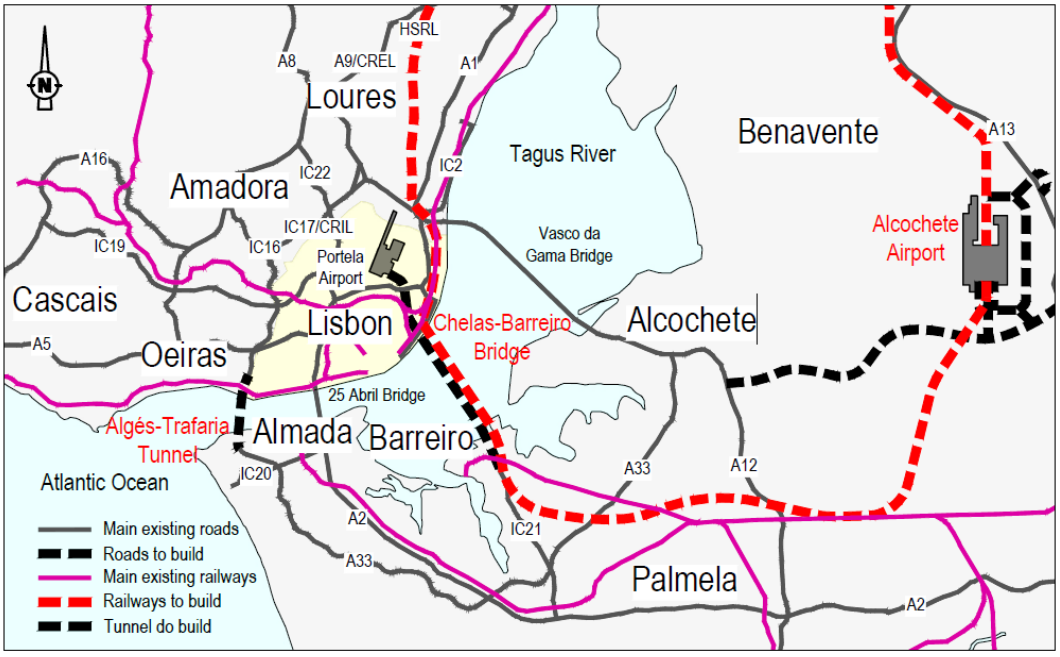

Figure 18. Location of future Alcochete airport and road and raiway accessabilities.



Figure 19. View of the cutting head of TBM and north portal of Monsanto-Santa Apolónia tunnel.

external diameter and a cutting head that weighs 70 ton, and which will advance around 10 m per day (Figure 19).

The Port of Sines has an important volume of containerized cargo movement. In 2022, Sines Terminal XXI had an additional 204 m of mooring quay, corresponding to Phase 3A (see Figure 23). In 2023, an increase in the embankment area (Phase 3B) was built, providing 1 150 m of docks, which allows it to simultaneously operate three mega-carriers of 330 m each. By 2025, additional quays and embankments will be built, and the same will happen by 2027 (Figure 23). Lastly, Terminal XXI will have a 1 950 m quay front, 60 ha of embankments and 19 super post Panamax quay gantries, suitable for simultaneously operating four of the largest ships currently in commercial operation, measuring 400 m in length overall. Capacity will then be 4.1 MTEU/year (TEU=20-foot containers), almost double the 2.3 MTEU in 2021.

The adopted quay solution consists of a reinforced concrete beam slab, over five alignments of piles. The piles are made of reinforced concrete with metallic pipe formwork, with a length of about 25 m, a penetration into the rocky substrate of 4.00 m, and a 1.30 m diameter. For the execution of the piles was used an equipment positioned on vessels (Figure 20).

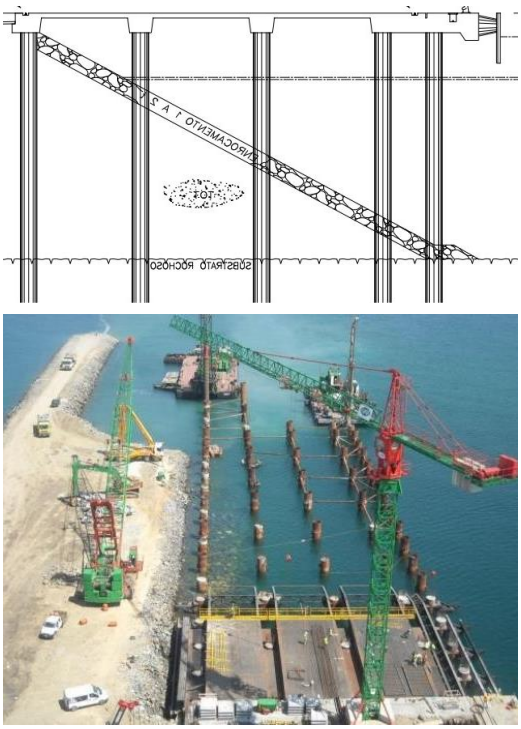

Figure 20. Transversal section ot the adopted solution for the quay and view of piles execution of the phase 2 of Terminal XXI (Linhares, 2012).

5 FUTURE MAIN GEOTECHNICAL ENGINEERING PROJECTS IN PORTUGAL

The main projects with a significant geotechnical component that are expected to be carried out in the decades ahead will be mainly in the areas of transport infrastructure (mainly railways, maritime and port), energy production (reversibility of existing dams, eolic onshore and offshore, geothermal, lithium mining explorations), environmental industry (soil decontamination) and those resulting from climate change resilience projects (protection and support works in coastal and underwater areas, stabilization of landslides and drainage works to control floods).

In the future, it is expected that the most relevant achievement will be the extensions of the HSRL. Firstly Lisbon-Oporto will extend to Vigo and another line will be built to Badajoz, which would allow the connection between Lisbon and Madrid in 3 hours. Later, 2 new lines are expected to be constructed: Aveiro-Salamanca and Évora-Faro-Seville (Figure 21).



Figure 21. Future HSRL network.

By the middle of the century probably the fourth Tagus crossing will link Algés to Trafaria and will close the Lisbon's outer circular roadway (Figure 18).

Due to safety, environmental and cost reasons the TBM tunnel is the more favorable solution. The tunnel will cross the alluvium formations and will have 5 km long with an inner diameter of 14,20 m, that allow two traffic galleries with three lanes each (Pompeu-Santos, 2022).

Another future relevant work will be the new Vasco da Gama container terminal (Figure 23), whose project foresees an installed capacity of around 3.5 MTEU, with a 1 375 m quay front, allowing simultaneous operation of three additional ships with 400 m long. It will involve an investment of around 640 M€. This terminal is fundamental for the expansion of the port of Sines and will allow it to be on par with large European ports, such as Rotterdam (Netherlands) and Antwerp (Belgium).

Portugal is one of the most promising European countries where lithium resources exist with high potential for use and could thus make an important contribution to the development and expansion of new non-polluting technologies. Therefore, the implementation of the exploration of lithium mines in the country is a project of high national, European, and global interest, contributing to meet the enormous demand for this metal in which Europe is lacking and dependent on other countries.

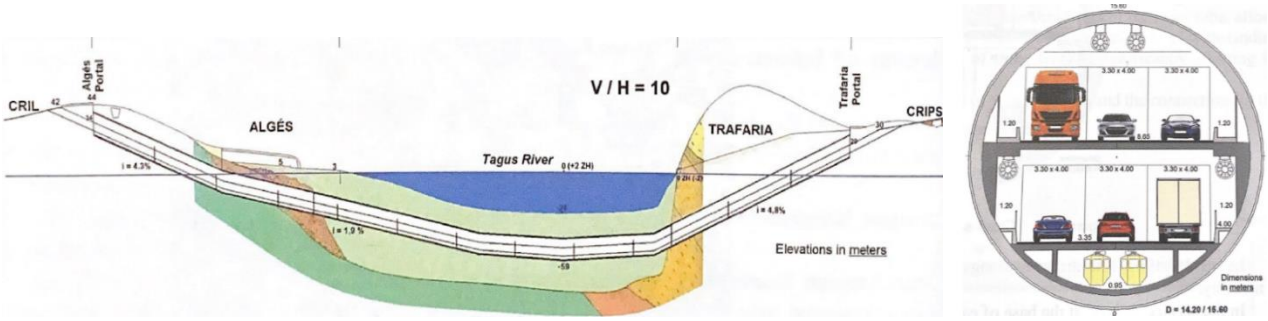

Figure 22. Longitudinal section of the proposed TBM tunnel for Algés-Trafaria crossing. Lay-out of traffic galleries of the tunnel with three lanes each (Pompeu-Santos,2022).

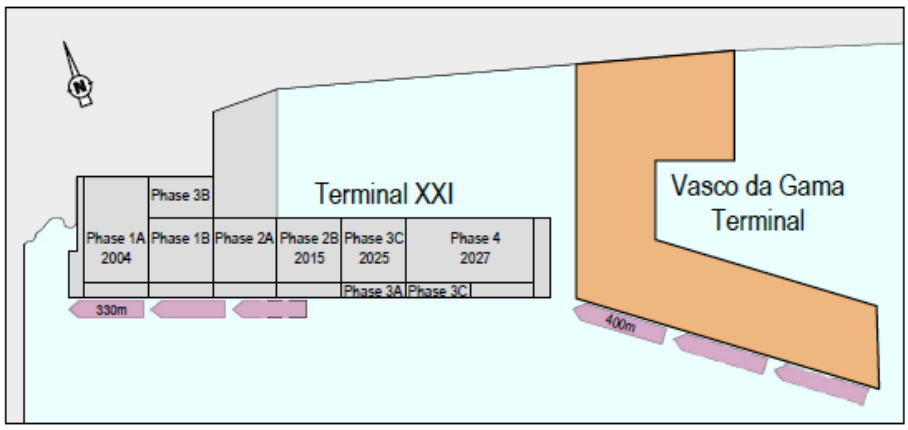

Figure 23. Construction phasing of Terminal XX1 and future Vasco da Gama Terminal.

6 CLOSING FINAL REMARKS

The challenge launched by ISSMGE, through the HTC project, was a unique opportunity to publicize the main achievements and the current state of Portuguese geotechnical engineering. Reflection work was carried out by SPG on the development trajectory of national geotechnics over the last 100 years, from the first steps taken in 1920s, through the period of the 1950s/1960s, in which was created a geotechnical community in the country, until the first years of the 2020s.

Over the last 100 years, Portugal has progressed from an underdeveloped country to a country that today has almost all the characteristics of developed countries. Therefore, to make the history of the development of geotechnics, it was necessary to succinctly address the role of civil engineering, from which geotechnical engineering emanates, in the social, economic, and political development of the country. The projects included in this paper are indicative of the infrastructure works that took place in Portugal which are characterized by having conditioning geological conditions and relevant geotechnical features, resulting in innovative aspects of design and execution, which are certainly a reference for the practice of geotechnical engineering. For these projects, that marked their time, Portuguese geotechnical engineers provided important to crucial input for the design and construction.

For geotechnical related activities we need more individuals with appropriate qualification and experience. The world is changing very fast and we have to renovate the geotechnical competences and to create new disciplines and new approaches. In Portugal we have an excellent level of knowledge and qualifications among young people who attend our engineering universities, but we need to significantly increase the number of candidates for civil engineering courses to increase significantly to guarantee an adequate response to the needs of our society and the fulfillment of the challenges that the country will experience. We have to make geotechnical engineering more attractive for young people.

REFERENCES

Conceição, M., Baião, C., Santos, A., Oliva, R., Cruz, F. and Prado, R. (2012). Algiers Metro. Extensiom A Line–Place Emir Abdelkader-Place Des Martyres. General conception of underground stations (in Portuguese). *13º Congresso Nacional de Geotecnia.* Lisboa.

Cruz, A. A., Mineiro, A. J. C. and Coutinho, J. A. (2007). *António de Carvalho Quintela. Professor, Engineer and Researcher* (in Portuguese). Associação Portuguesa dos Recursos Hídricos.

Linhares, M. P. C. (2012). *Tecnology and management of port works structures* (in Portuguese). Master thesis. Instituto Superior de Engenharia do Porto.

Maranha das Neves, E. (2008). *Brief reflections on engineering*. Jubilation Lesson (in Portuguese). 16th December. IST. Lisboa.

Mateus de Brito, J. and Matos Fernandes, M. (2014). Terreiro do Paço Station of Lisbon Metro. *Túneis em Portugal.* CPT. SPG. LNEC.

Mateus de Brito, J. (2020). Judgement in geotechnical engineering practice. 37th Manuel Rocha Lesson. *Soils and Rocks*, *44 (2)*, 1-26. https://doi.org/10.28927/SR.2021.063821.

Mateus de Brito, J. (2024). The Time Capsule Project and Portuguese Geotechnical History (in Portuguese). *Geotecnia, Extra Volume*, 125-161. https://doi.org/10.14195/2184-8394_extra2024_1 _6.

Matos Fernandes, M. (2010). Deep urban excavations in Portugal: practice, design, research, and perspectives. 23th Manuel Rocha Lesson. *Soils and Rocks, 33 (3)*, 115–142. https://doi.org/10.28927/SR.333115.

Mineiro. A. J. C. (1991). Design of embankment dams. New security criteria656 (in Portuguese). 6th Manuel Rocha Lesson. *Geotecnia 62*, 5-71. https://doi.org/10.14195/2184-8394_62.

Nascimento, U. (1990). Contribution to the geotechnics history in Portugal (in Portuguese). *Geotecnia 58*, 3-16. Conference given in the Engineers' Order in 17/11/1987. https://doi.org/10.14195/2184-8394_58_1.

Portuguese Engineers' Order (2003). *One hundred Portuguese engineering works in the world in the 20th Century* (in Portuguese).

Pompeu-Santos, S. (2022). *Innovation in TBM traffic tunnels*. CRC Press.

Pathmanandavel, S., Billota, E., MacRobert, C. J. and Chung, C. (2024). Creating and discovering the ISSMGE Heritage Time Capsule. *18th European Conference of Soil Mechanics and Geotechnical Engineeering.* Lisbon.

Seco e Pinto, P. S. and Oliveira, R. (1998). A recent difficult foundation problem. The case of new Tejo Bridge". *4th International Conference on Case Histories and Geotechnical Engineering*, St. Louis. Special Lecture.

SPG (2021). About the Portuguese Geotechnical Society. Accessed 15 March 2024, in the website https://www.spgeotecnia.pt/pages/1.

Xerez, C. (1954). The Cabril development (in Portuguese). *Revista Técnica 243*.

Proceedings of the XVIII ECSMGE 2024
GEOTECHNICAL ENGINEERING CHALLENGES
TO MEET CURRENT AND EMERGING NEEDS OF SOCIETY
© 2024 the Authors
ISBN 978-1-032-54816-6
DOI 10.1201/9781003431749-22
Open Access: www.taylorfrancis.com, CC BY-NC-ND 4.0 license

ECSMGE 24
XVIII EUROPEAN CONFERENCE ON SOIL MECHANICS AND GEOTECHNICAL ENGINEERING

Heritage Time Capsule Project Lecture

HTC - Creating and discovering the ISSMGE Heritage Time Capsule

Création et découverte de la capsule temporelle du patrimoine de l'ISSMGE

S. Pathmanandavel*
ISSMGE HTC Lead, Sydney, Australia

E. Bilotta
University of Napoli Federico II, Naples, Italy

C.J. MacRobert
Stellenbosch University. Cape Town, South Africa

C. Chung
AGL Consulting, Dublin, Ireland

**sukumar.pathmanandavel@gmail.com*

ABSTRACT: The ISSMGE Heritage Time Capsule (HTC) project will launch key initiatives in 2024 to actively engage with the individual members of the International Society for Soil Mechanics and Geotechnical Engineering (ISSMGE). A significant initiative is the design and launch of a new website, dedicated for the HTC project to present, online, in a useful and engaging way, the diverse contributions made to the HTC. These contributions are from ISSMGE Member Societies, Past Presidents, Technical Committees, Corporate Associates, Key Persons, and other Board Level Representatives, and include video recordings, commented slide presentations, text documents and articles. Furthermore, this paper describes the HTC discoverer program, where individual members can provide their reports on HTC contribution(s) of their choice, for review and hosting on the HTC website. Plans for HTC discovery sessions in 2024 on areas of specific interest to ISSMGE regions are also included in the paper. The focus of this paper is the need and opportunity for discovery, the planned discovery process, and the anticipated outcomes of the discovery phase. The discovery phase bridges the contributions received from 2022 to 2024, to the display and sealing of a physical time capsule in 2026 at the 21st ICSMGE in Vienna, Austria, and the final phase of the HTC project reflecting on the needs of geotechnical engineering in the next 100 years.

RÉSUMÉ: Le projet ISSMGE Heritage Time Capsule (HTC) lancera des initiatives clés en 2024 pour s'engager activement avec les membres individuels de l'ISSMGE. Une initiative importante est la conception et le lancement d'un nouveau site web, dédié au projet HTC, pour présenter en ligne, de manière utile et attrayante, les diverses contributions apportées à la HTC. Ces contributions proviennent des sociétés membres de l'ISSMGE, des anciens présidents, des comités techniques, des entreprises associées, des personnes clés et d'autres représentants du conseil d'administration, et comprennent des enregistrements vidéo, des présentations de diapositives commentées, des documents textuels et des articles. En outre, ce document décrit le programme de découverte HTC, dans le cadre duquel les membres individuels peuvent fournir leurs rapports sur les contributions HTC de leur choix, qui seront examinés et déposés sur le site web HTC. Les plans pour les sessions de découverte HTC en 2024 sur des domaines d'intérêt spécifique pour les régions ISSMGE sont également inclus dans le document. Le présent document met l'accent sur la nécessité et l'opportunité de la découverte, sur le processus de découverte prévu et sur les résultats escomptés de la phase de découverte. La phase de découverte fait le lien entre les contributions reçues entre 2022 et 2024, l'exposition et le scellement d'une capsule temporelle physique en 2026 lors de la 21e édition de l'ICSMGE à Vienne, en Autriche, et la phase finale du projet HTC qui réfléchit aux besoins de l'ingénierie géotechnique au cours des 100 prochaines années.

Keywords: Time capsule; ISSMGE; geotechnical engineering; individual members; discoverer program.

1 INTRODUCTION

Prompted by the approach of the centenary in 2036 of the 1st International Conference on Soil Mechanics and Foundation Engineering held at Harvard University, the first author, initiated a conversation in October 2019 with the ISSMGE Board (2017-2022) about the desirability of a time capsule project for the ISSMGE. In March 2020, the ISSMGE Board approved the formation of a 16-person committee, led by the first author, to proceed with a scoping study.

Generally, the intent is for the contents of a time capsule to be closed then opened and viewed (i.e., discovered) in say, 100 years or a longer period. Therefore, understandably, the main questions raised by those outside the Heritage Time Capsule (HTC) team at the beginning of this project were: How long should the time capsule be kept sealed? How will it be protected over that time? What technologies need to be incorporated to enable future generations to understand its contents? The HTC design team considered however that there were other aspects of the time capsule that needed to be first addressed.

Indeed, it rapidly became clear that there was not a common understanding of the material to be placed in the time capsule. Across geographies, there is a significant diversity of knowledge and practice, and in application of technology, for instance there is the often-quoted aspect of increasing distance with time between theory and practice in geotechnical engineering. In addition to all this, "geotechnical engineering challenges to meet current and emerging needs of society", this conference's slogan, suggests there is unlikely to be a universal understanding and acceptance of what needs to be placed in a time capsule.

The HTC team was excited by the possible benefits of a visible and accessible fusion of material from disparate sources to the advancement of geotechnical engineering. It was essential therefore that as many people as possible, at all levels of the ISSMGE community, participate and contribute to the time capsule, for the contents in the time capsule to be a reasonable reflection of geotechnical practice globally. Capturing diversity in an effective and transparent manner was paramount. Technology enabled the creation of a webpage platform within the ISSMGE website, to hold and host information and make it widely accessible. Figure 1 presents an extract from one such Member Society contribution.

The HTC team soon realised a few further steps were required to convert information into knowledge and collective insight. Four clearly defined and separate phases have emerged, these being

- Phase 1 - Contributions
- Phase 2 - Discovery
- Phase 3 - Time Capsule
- Phase 4 - 100 years on

In 2024, the HTC projet is transitioning from Phase 1 - Contributions to Phase 2 - Discovery, and this is the opportunity for ISSMGE individual members to make a mark in the HTC project.

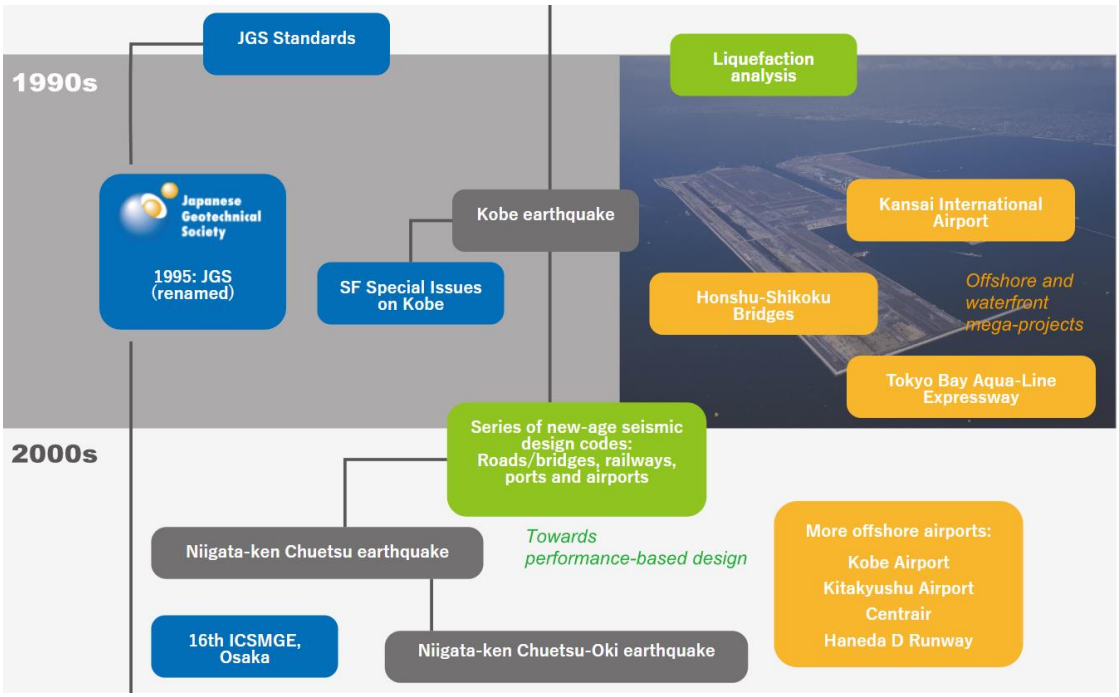

Figure 1. An extract of contribution in the form of a dynamic HTML format for browsing on screen, Japanese Geotechnical Society.

2 HTC PROJECT OVERVIEW

The idea of the time capsule is not new in the ISSMGE, and a physical object (in the form of a blue barrel) to be filled with contents, made its public appearance in 2013 at the quadrennial ISSMGE conference (18th ICSMGE in Paris). Jean-Louis Briaud (President 2009 - 2013) noted in his 45th Progress Report (2013) the following in relation to the time capsule, "*While the final decision is still in the air, here is what we have in mind. Each society would have the opportunity to place one small item in a barrel size container which would be the time capsule. This time capsule would be kept in a secure place and opened in 150 years* ". It is fitting that the curent President Marc Ballouz, who as Chair of the ISSMGE Public Relations Committee (2009 - 2013), championed the idea of a time capsule, is now acting with the ISSMGE Board, to direct the HTC team to bring to a successful conclusion a vision aired over a decade ago. A conclusion that would not have been possible without the leadership of President Charles Ng between 2017 and 2022 (see Figure 2).



Figure 2. Passing of the Presidential Gavel at the 20th ICSMGE, Sydney, Australia. (from ISSMGE Website).

Table 1 shows how in 2020, the HTC design team started work on creating an online repository (virtual time capsule) for the 21,000 or so individual members of the ISSMGE to access and get to know where geotechnical engineering's origins were, what and who guided its development, and the paths followed in

Table 1. Project progress overview & timeline.

Year	Project progress and timeline
2020	• Scoping of the project by a 16-person project committee, and formation of a design team • Work started on creating an online repository (virtual time capsule), hosted in the ISSMGE website, (https://www.issmge.org/), under the Society tab
2021	• Communications sent to and followed by online meetings with Member Societies, Technical Committees, Past Presidents, and Corporate Associates
2022	• Contributions received in the lead up to and following the 20th ICSMGE, Sydney • Launch of the time capsule project in a plenary session at the 20th ICSMGE, Sydney • Renaming of the project to Heritage Time Capsule (HTC)
2023	• A project update was provided in "ISSMGE Heritage Time Capsule – 3 Years on" (2023) • Construction started on the dedicated website for HTC, under a subdomain of issmge.org • Contributions added from ISSMGE Bulletin archives • HTC sessions held in Asia (17th ARC, Astana, Kazakhstan) and Australasia (14th ANZ, Cairns, Australia)
2024 (plan)	• Young Member Presidential Group (YMPG) help to prepare an initial stock of discoverer reports • Dedicated HTC website launch scheduled for the HTC session in GeoShanghai 2024 conference (Shanghai, China), at the end of May • Discoverer program to be announced, post launch of the dedicated HTC website • HTC sessions to be held in Africa, Europe and South America, and HTC follow up sessions to be held in Asia, and Australasia
2025 (plan)	• Work to be undertaken on the physical time capsule (Phase 3), and Phase 4 - 100 years on • Further HTC follow up sessions to be held
2026 (plan)	• Unveiling and sealing of the physical time capsule at the 21st ICSMGE in Vienna, Austria • Presenting the results of the HTC sessions on region specific issues

the various regions of the world, pitfalls and successes, and the philosophies in practice in many of its technical subdisciplines. Table 1 also shows progress from the start of the project and the planned timeline to the next quadrennial international conference in 2026 (21st ICSMGE in Vienna, Austria). The HTC project logo, developed in 2021, highlights the importance of the past, present and future in the HTC project (Figure 3).

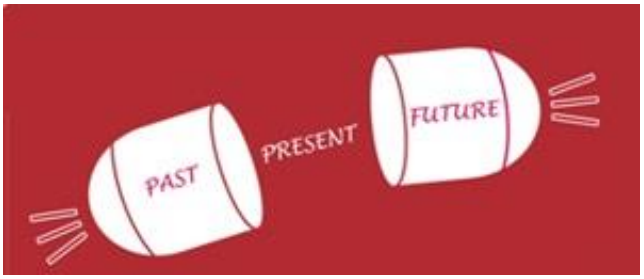

Figure 3. The HTC project logo.

The first step in this journey, Phase 1 - Contributions, started in the lead up to the 20th ICSMGE (Sydney, 2022). Contributions were invited from those related to the ISSMGE, including Member Societies, Technical Committees, Corporate Associates, Past Presidents & Key Persons, Vice Presidents, and Board level Committees. The material received includes video recordings, commented slide presentations, text documents and articles, all held online. Contributions on behalf of some of the past presidents were made by nominated champions. Table 2 shows the status of responses (as of February 2024).

Received material are presently hosted in the ISSMGE website, (https://www.issmge.org/the-society/time-capsule), and will be moved in 2024 to a dedicated website under a subdomain of issmge.org.

Table 2. Status of responses as of February 2024.

ISSMGE Category	Responses held from	Comments
Past Presidents	12 no.	
Member Societies (MSs)	56 no.	Further submissions in 2024 are invited from MSs, TCs, and CAs. These can be new or additions / amendments to existing material.
Technical Committees (TCs)	18 no.	
Corporate Associates (CAs)	5 no.	

Phase 2 - Discovery, is a pivotal element of the HTC project, in which the opportunity is provided for ISSMGE individual members to shine a spotlight on the HTC contribution(s) of their choice, and earn their individual place as discoverers in the HTC website. Also in Phase 2, there are the HTC discovery sessions, hosted at the ISSMGE Regional Conferences, and follow up HTC sessions held under the auspices of Member Societies, to address region-specific issues.

HTC sessions are planned to be held at the 2024 ISSMGE Regional Conferences, being, the European XVIII ECSMGE (Lisbon, Portugal), the African 18th ARCSMGE (Algiers, Algeria) and the Panamerican XVII PCSMGE (La Serena, Chile). Further, in 2024, follow up HTC sessions are planned, for the Asia region at GeoShanghai 2024 (Shanghai, China), and for the Australasia region, at local events of the Australian Geomechanics Society (AGS) and the New Zealand Geotechnical Society (NZGS). ISSMGE individual members are encouraged to participate and contribute at these HTC sessions.

The ISSMGE Board has also set the HTC team the challenging task of what to place in long term storage in a physical time capsule, for the benefit of geotechnical engineers many generations hence. This is tackled in Phase 3 - Time Capsule, with the physical time capsule to be unveiled (and sealed) at the 21st ICSMGE to be held in Vienna, 2026.

Throughout all this, the HTC team had in mind, what is the practical value, now and for the immediate future, for the geotechnical community? In Phase 4 of the project, 100 years on, with the benefit of experience and knowledge from Phases 1, 2 and 3, the ISSMGE global cohort will be further engaged to examine how we think and act as a community of practice, and the need to recalibrate ourselves.

While 100 years might seem a very long time to look ahead, we do have the benefit of records of what has happened in geotechnical engineering over the past 100 years, aided in some small way by the work of the HTC project. Furthermore, in practice, there should be no issue with teams of individual members who wish to work on shorter time periods (e.g. 20 years, 50 years). Projection and imagining into the future can prompt us to consider what other fields of engineering and other related fields (e.g. project management) are working on, and accepting what we now hold to be essential and or important may not necessarily be that way in the future.

3 HTC WEBSITE DESIGN & ARCHITECTURE

The dedicated HTC website, under a subdomain of issmge.org, is scheduled for launch at the HTC session in GeoShanghai 2024 conference (Shanghai, China) at the end of May. This website aims to present different types of material to the visitor in a useful and engaging way. Of particular note is the contributions section that displays a gallery of about 30 randomly selected

contributions. Each time the home page loads, different contributions appear in a different order. Visitors are also provided with the option to navigate through the different types of contributions through button links at the top of the gallery. The home page also contains a prominent search form, where contributions can be searched based on keywords. Results are returned based on title, content, specifically assigned tags and categories.

The top row of the home page displays the upcoming HTC sessions in the ISSMGE regions of Africa, Asia, Australasia, Europe, North America and South America. The top bar of the HTC Website contains the main content structure navigation options of the website, which are: *What is the HTC?*, *Contributions*, *Discovery*, *News*, *Contact*, and *Search* tabs. In the coming months, two additional tabs will be shown, being *Time Capsule*, and *100 years on*. These relate respectively to the display and sealing of a physical time capsule in 2026 at the 21st ICSMGE in Vienna, Austria, and the final phase of the HTC project reflecting on the needs of geotechnical engineering in the next 100 years.

The home page also features prominently discoverers' reports and items relating to the HTC, and blogs submitted by individuals. Scrolling features are enabled, to facilitate quick access to reports, news items and blogs. Furthermore social sharing buttons have been added so users can share contributions and discoverer reports on social media.

4 THE DISCOVERER PROGRAM

An essential requirement for the discovery process is the engagement of the individual members. As mentioned before, engagement by as many of the individual members of the ISSMGE is a much-desired aim of the HTC team. Hence, considerable attention was paid to the development and launch of a HTC discoverer program.

At the time of the launch of the ISSMGE Time Capsule project at the Sydney international conference in 2022, four individual members tested the initial discoverer concept, and their discoverer reports now form part of the HTC project. These discoverer reports are presently hosted in the ISSMGE website, (https://www.issmge.org/the-society/time-capsule). Table 3 shows the names the four early discoverers, the Member Societies they are affiliated with, and the HTC contributions that were the subject of their discoveries. Dr Peter Day, Chair of the ISSMGE Corporate Associates Presidential Group (CAPG), provided valuable help by reviewing the early discoverer reports, and suggesting ways in which future requests for discoverer reports could be framed.

Table 3. Early discoverers.

Name, Member Society	Reported Contributions
Asal Bidarmaghz, Australian Geomechanics Society	• Austrian Geotechnical Society • French Committee for Soil Mechanics and Geotechnics • TC103 on Numerical Methods in Geomechanics
Choo Siung Chung, Malaysian Geotechnical Society	• Le Comité Français de Mécanique des Sols et de Géotechnique • Hellenic Society of Soil Mechanics and Geotechnical Engineering • Canadian Geotechnical Society
Monica Löfman, Finnish Geotechnical Society	• Macedonian Association for Geotechnics • TC101 Laboratory Testing
Sonia H. M. Marques, Sociedade Portuguesa de Geotecnia	• Sociedad Colombiana de Geotecnia • Canadian Geotechnical Society • TC304 Risk

The HTC Team has now sought the assistance of the Young Member Presidential Group (YMPG) Core Team (Figure 4), to create additional discoverer reports prior to the launch of the HTC website. YMPG carries out activities that help ISSMGE engage with the next generation of geotechnical engineers. These activities are aimed at encouraging collaboration and communication among young members. YMPG has liaison members in over 40 of the 90 Member Societies, and over 1,100 corresponding members.

Two of the Core Team members, Bridget Lokoe and Judy Eid, are leading the work of coordinating the preparation of discoverer reports by members of the YMPG liaison.



Figure 4. Members of the YMPG Core Team 2022-2024.

The HTC team expects the uploading to the website of the discoverer reports created by the YMPG liaisons to inspire the individual members of the ISSMGE to create a larger number of discoverer reports. These discoverer reports will be uploaded for display on the HTC website, and for sharing on social media. The HTC team believes the creation and sharing of many discoverer reports, in all regions of the ISSMGE, will both increase awareness of the HTC website, as well as help to increase the visibility of the geotechnical engineering profession and its contribution to the wellbeing and security of society.

Multiple discoverers can make discoveries of any one particular HTC material (or part thereof), as long as the work of the discoverer reports is unique. Discoverer reports may also be prepared by small teams or groups of individual members, provided a lead discoverer is appointed for the contribution. Figure 5 outlines the steps applicable to the discoverer reports.

Invitation to the ISSMGE individual members to submit discoverer reports will be announced in 2024, post launch of the dedicated HTC website at the GeoShanghai 2024 conference, at the end of May.

Each discoverer will prepare a brief report for storing and sharing on the HTC website. The emphasis of the report is to shine a spotlight on the chosen HTC contribution(s) or parts thereof and bring the HTC contributions to the reader's attention. The discoverer's report can be a brief note, video, audio, or other forms able to be stored and displayed online. Following are the nominal guidelines in terms of length, and while brevity is valued, greater lengths will be considered on their merit.

- Word document - up to 1,000 words,
- Video - up to 3 min length
- PowerPoint presentation - up to 8 slides

A discoverer is required to be an individual member of the ISSMGE. The discoverer's report should:

- State, in the beginning, the Member Society the discoverer is affiliated with,
- Identify, in the beginning, which HTC contributions i.e. Member Societies, Technical Committees, Past Presidents, etc., that are selected for the discoverer report,
- Be complete and self-contained, and presented in a suitable fashion for review,
- Carefully identify which parts of the discoverer report are drawn from the HTC contributions, and what parts are their own insights, thoughts and comments, and,
- Not include material external to the HTC contributions that may be subject to copyright or other restrictions from publication.

Figure 5. Steps applicable to discoverer reports.

5 HTC DISCOVERY SESSIONS

The discovery sessions are organised along regional lines, reflecting the makeup of the ISSMGE Board. The regional Vice Presidents are representatives of their region; hence they can act on behalf of their Member Societies and guide them along a theme that is most reflective of the present needs of the regions.

Thus, Australasia region's theme is geo-education, reflecting the interest in the region on the operation of systems and mechanisms (including university education) that can have an impact on geotechnical engineering capability and capacity to respond to current and future needs. Figure 6 provides an illustrative overview of the HTC sessions carried out and planned for the Australasia region.

In Asia, the HTC project has provided the opportunity to discuss measures that can be undertaken to increase collaboration between Member Societies, both across the region, as well with Member Societies in the other regions. The HTC themes for Africa, Europe and North and South America regions are at various stages of development. The HTC Africa team, with representatives from six Member Societies, and liaising with the other Member Societies in the African region, is working on the launch of a 1-hour plenary HTC session at the 18th ARCSMGE, Algiers, Algeria.

The following individual members are leading the development of regional HTC sessions:

- Africa - Akua Asantewaa Akosah-Yentumi
- Asia - Mingliang Zhou
- Australasia - Golnaz Alipour
- Europe - Pedro Pinto, ISSMGE past President (2005 - 2009)
- Pan-American - Hugo Acosta Martinez

HTC discovery sessions provide for leadership opportunities for the emerging cohort of individual members to challenge established wisdom, and in turn obtain increased knowledge about the ISSMGE and the current and diverse conditions that are in operation in their region. As much as possible, the HTC sessions are to be reported, either in the ISSMGE Bulletin or in a relevant Journal(s) of the region. The HTC session on geo-education at the ANZ2023, Cairns, Australia last year has been comprehensively reported in the paper, "ISSMGE HTC project session at 14th ANZ conference on geomechanics" (2023).

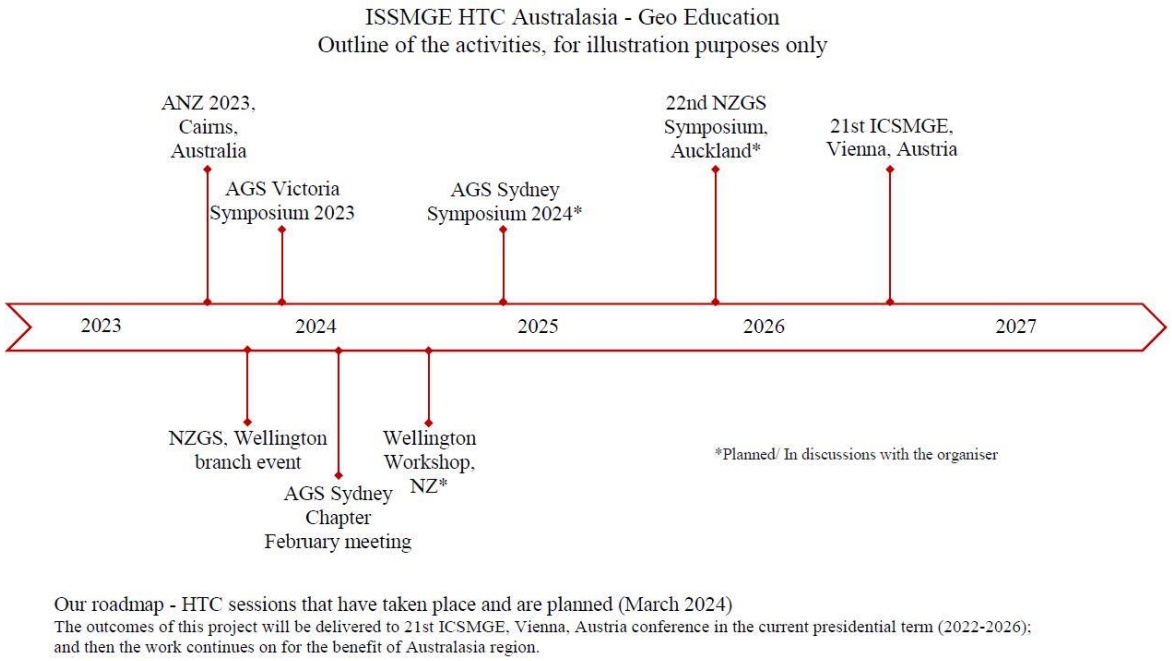

Figure 6. Geo-Education Australasia road map, updated March 2024 (from HTC Australasia team).

6 THE OUTCOMES OF DISCOVERY

The discovery phase is designed as a pivotal point in the HTC project, providing input to the subsequent two phases, Phase 3 - Time Capsule and Phase 4 - 100 years on. If, as the HTC team hopes, sufficiently large numbers of individual members become engaged in the discovery process, either as discoverers or as participants in the HTC discovery sessions, or both, there is an increased likelihood of a more widely shared understanding of the HTC project and a perspective of geotechnical engineering that is more aware and understanding of the diversity in geotechnical engineering among the individual members. Thus, the ground would have been well prepared for in-depth and informed discussions in 2025 and 2026 about what aspects of our current and past practice we want to share with generations hence in the time capsule (Phase 3).

Additionally, those individual members involved and engaged in Phases 1 and 2 may be able to better represent at all levels, and across geographies, thoughts and aspirations about the future of geotechnical engineering, and what the profession might or should look like in 100 years on (Phase 4). Figure 7 points to a possible future imagined.

Imagine the next 100 years

In 'discovering' contributions made, the HTC team has been very much impressed and moved by the wholehearted dedication of so many of our individual members at all levels in collaborating and contributing to the advancement of the geotechnical engineering community and profession. ISSMGE has played a vital role in leading and encouraging this work.

The HTC team could imagine, aided by the outcomes of the work of the HTC project, and led by the ISSMGE, there could be an interest by many in the geotechnical community, in charting out a path or paths for the overall advancement of geotechnical engineering in the successive decades to come, not only in the various technical streams, but also in terms of benefit to society, such as disaster mitigation, climate change, energy, reuse, productivity and the various challenges that cities and less populated areas face. Such forward planning may help increase the visibility of geotechnical engineering in society, and help achieve earlier and more effective feedback loops of our activities.

Figure 7. A possible future imagined.

7 CONCLUSIONS

The paper has illustrated the initiatives launched to create an ISSMGE Heritage Time Capsule (HTC) that aim to actively engage with the Member Societies and individual members of the ISSMGE. Among these are the design and the scheduled launch of a new dedicated website, under a subdomain of issmge.org, at the HTC session at GeoShanghai 2024 conference (Shanghai, China), at the end of May, and the engagement of individual members for discovery, bridging the contributions received, to the display and sealing of a physical time capsule at the 21st ICSMGE in Vienna and to the final phase of the HTC project, reflecting on the needs of geotechnical engineering in the next 100 years.

The success of the HTC project, and achieving its important aspirations now largely depends on what individual members can and should do in respect of the HTC project. A reasonably broad and deep working space has been provided by the HTC project for the individual members of the ISSMGE to feel that they all are included in this project and that they can contribute to their own level of interest.

An action taken to become a discoverer can provide benefits to the individual in terms of knowledge gained through studying HTC contributions, and individual profile recognised through hosting of the discoverer report in the HTC website and the potential to share the discoverer reports on social media. The results of the discovery sessions across the six regions of the ISSMGE have the possibility to create clarity of action plan for future for the geotechnical community, and to help improve effectiveness of geotechnical engineering for future generations.

Let's imagine, together, the coming 100 years.

ACKNOWLEDGEMENTS

The authors gratefully acknowledge the Presidents and the ISSMGE Boards of 2017-2022 and 2022- 2026, for their approval and support for this project. We thank immediate past President Charles Ng for his support for the time capsule project, and to President Marc Ballouz for his insight that a dedicated website was required the HTC project, and his vision for a physical time capsule to be opened in 100 years.

The authors are also very grateful for the Member Societies, Technical Committees, Corporate Associates, Past Presidents and Key persons, Champions for Past Presidents, Vice Presidents, and Board level Committees for their commitment to the project and for their contributions. Special thanks are due to Pedro Pinto, Roger Frank, Harry Poulos, Peter Day and Pierre Delage, who have provided their valuable time helping the HTC team with this project.

We thank the four early discoverers for their willingness to trial the discoverer program. The Young Members Presidential Group (YMPG) has been invaluable in helping to carry out many key actions of the HTC project. The ISSMGE IT team (ARGO – E Group) led by Kostis Tsantilas, has demonstrated that they are highly committed to making viewer experience a priority in the development of the time capsule webpage, and now the design and construction of the dedicated HTC website, and we thank them for their great support.

Finally, the authors thank all the members of the HTC team who are working hard on many fronts and actions to advance the HTC project, and we highly value their inputs and comments on this paper at its various stages of preparation.

REFERENCES

Briaud, J.L. President 1370 days report (2013), ISSMGE Bulletin: Volume 7, Issue 4, Page 16, July 2013 https://www.issmge.org/publications/issmge-bulletin/vol-7-issue-4-july-2013.

ISSMGE Heritage Time Capsule – 3 Years on (2023), ISSMGE Bulletin, Volume 17, Issue 2, April 2023 (https://www.issmge.org/publications/issmge-bulletin/vol-17-issue-2-april-2023).

ISSMGE HTC project session at 14th ANZ Conference on Geomechanics (2023), *Australian Geomechanics,* Vol 58: No 4, pp 10-17, December 2023.

A - New developments on structural design
A - Nouveaux développements en matière de conception structurelle

Proceedings of the XVIII ECSMGE 2024
GEOTECHNICAL ENGINEERING CHALLENGES
TO MEET CURRENT AND EMERGING NEEDS OF SOCIETY
© 2024 the Authors
ISBN 978-1-032-54816-6
DOI 10.1201/9781003431749-23
Open Access: www.taylorfrancis.com, CC BY-NC-ND 4.0 license

ECSMGE 24
XVIII EUROPEAN CONFERENCE ON SOIL MECHANICS AND GEOTECHNICAL ENGINEERING

Incorporating site variability into LRFD design of piles

Intégration de la variabilité du site dans la conception LRFD des pieux

M.Y. Abu-Farsakh*
Louisiana Transportation Research Center, Louisiana State University, Baton Rouge, USA
M.H. Rahman
HVJ Associates, Dallas, TX, USA
**cefars@lsu.edu*

ABSTRACT: The properties of geotechnical materials are inherently variable due to many uncertainty sources including spatial variability, measurement error, statistical error, and model bias. This study focused on evaluating the site variability from cone penetration tests (CPT), and its implementation into the Load and Resistance Factor Design (LRFD) of pile foundations. For this purpose, data from six project sites with multi CPT tests performed at different locations were collected. The spatial variability of CPT data for each site was evaluated using the semi-variogram. The coefficient of variation due to spatial variability ($COV_{R,spatial}$) was determined for each site. The total coefficient of variation ($COV_{R,total}$) for each site was then estimated from $COV_{R,}$spatial and the method coefficient of variation ($COV_{R,method}$), which were then used to calibrate the resistance factors ($\phi_{spatial}$, ϕ_{total}) for application to LRFD design of piles. The results of this study demonstrated the significance of incorporating site variability into LRFD design of piles. For sites with lower site variability than the design method (i.e., $COV_{R,spatial} < COV_{R,method}$), the value of the $COV_{R,total}$ will be decreased, and hence the resistance factors ($\phi_{spatial}$ or ϕ_{total}) will be increased (credit), and vice versa.

RÉSUMÉ: Les propriétés des matériaux géotechniques sont intrinsèquement variables en raison de nombreuses sources d'incertitude, notamment la variabilité spatiale, l'erreur de mesure, l'erreur statistique et le biais du modèle. Cette étude s'est concentrée sur l'évaluation de la variabilité du site à partir des essais de pénétration du cône (CPT) et sur sa mise en œuvre dans la conception des facteurs de charge et de résistance (LRFD) des fondations sur pieux. À cette fin, des données provenant de six sites de projet avec des tests multi-CPT effectués à différents endroits ont été collectées. La variabilité spatiale des données CPT pour chaque site a été évaluée à l'aide du semi-variogramme. Le coefficient de variation dû à la variabilité spatiale ($COV_{R,spatial}$) a été déterminé pour chaque site. Le coefficient de variation total ($COV_{R,\ total}$) pour chaque site a ensuite été estimé à partir du COV_R, spatial et du coefficient de variation de la méthode ($COV_{R,\ méthode}$), qui ont ensuite été utilisés pour calibrer les facteurs de résistance ($\phi_{spatial}$, ϕ_{total}) pour application au LRFD conception de pieux. Les résultats de cette étude ont démontré l'importance d'intégrer la variabilité du site dans la conception des pieux LRFD. Pour les sites avec une variabilité de site inférieure à celle de la méthode de conception (c.-à-d. $COV_{R,spatial} < COV_{R,méthode}$), la valeur du $COV_{R,total}$ sera diminuée et, par conséquent, les facteurs de résistance ($\phi_{spatial}$ ou ϕ_{total}) seront augmentés (crédit), et vice versa.

Keywords: Site variability; pile foundation; CPT; resistance factor.

1 INTRODUCTION

All natural soil deposits are highly variable in their properties and are rarely homogeneous. These properties vary inherently from point to point horizontally and vertically due to several reasons including the depositional environment, the degree of weathering, and the physical environment (Elkateb et al. 2003, Lumb 1974). Variability of geotechnical soil properties is a complex phenomenon that results from many disparate sources of uncertainties. The four primary sources of geotechnical uncertainty that affect the soil behavior are the spatial variability of soil deposit, the random measurement errors, statistical error, and the model bias.

Lacasse and Nadim (1996) showed that the geotechnical parameters had variability in both horizontal and vertical directions with a greater inclination to be similar to the closely neighboring. McVay et al. (2009) conducted a study to evaluate the resistance factors (ϕ) for the Load and Resistance Factor Design (LRFD) of piles that incorporates the effect the spatial variability of local soil strength. Faraone (2014) presented a methodology that incorporates the framework of reliability-based design, while accounting for the site specific spatial variability, which is applicable to several deep foundation design practices (like pile foundations).

2 EVALUATING AND INCORPORATING SITE VARIABILITY INTO LRFD

In order to define the spatial variability from the measured data, it requires engineers to determine the correlation between data pairs that are separated by different distances using different parameters. One of the main parameters that is used to measure the site variability is known as the semi-variogram, γ(h), which can be defined as the distance range, a, that defines the end of correlation between data pairs as:

$$\gamma(h)=\frac{1}{2n_h}\sum (q_i - q_j)^2 \quad (1)$$

where q_i and q_j are data pairings (separated by distance h), and n_h is total number of data pairs.

Several theoretical models are available to predict the spatial covariance function, such as spherical, exponential, Gaussian, and circular. The most widely used amongst these models is the spherical model.

The ranges obtained from semi-variogram analyses are used to determine the reduction factor, α (McVay et al., 2009), which will be applied to calculate the spatial coefficient of variation $COV_{R,spacial}$ as a function of the coefficient of variation, COV_q, of the field measurements and/or laboratory results (e.g., CPT_{-qt}, SPT-N, S_u) using the following equation:

$$COV_{R,spatial} = \sqrt{\alpha}\, COV_q \quad (2)$$

For application to pile foundation design, the generalized expression for COV_R can be given as follows (McVay et al. 2009):

$$COV_{R,\,spatial} = \frac{\sigma_R}{R_n} = \frac{\sqrt{\pi^2 D^2 \sum_{j=1}^{n_L} L_{Lj}^2 \alpha_{Lj} \sigma_{Lj}^2 + \sigma_{EB}^2}}{\pi D \sum_{j=1}^{n_L} L_{Lj} m_{Lj} + m_{EB}} \quad (3)$$

where D is diameter of pile; L_{Lj} are length intervals of shaft; m_{Lj} are expected values of fs_{Lj} in each layer; m_{EB} is expected value of end bearing resistance; α_{Lj} is α for each layer calculated following McVay et al. (2009) approach; σ_{Lj2} is the variance in q for each layer; and σ_{EB2} is the variance in end bearing resistance.

In equation 3, the reduction factor, α is a function of (L/a_v, D/a_h), where a_v and a_h are the correlation ranges in both the vertical and horizontal directions, respectively; and L and D are the pile length and pile diameter, respectively.

Once the value of COV_R is defined, the resistance factor, ϕ, for pile design according to LRFD method can be calculated using the following modified first order second moment method (MFOSM) calibration equation proposed by McVay et al. (2009):

$$\phi = \frac{\lambda_R\left(\gamma_D \frac{Q_D}{Q_L} + \gamma_L\right)\sqrt{\frac{1+COV_Q^2}{1+COV_R^2}}}{\left(\lambda_{QD}\frac{Q_D}{Q_L} + \lambda_{QL}\right)\exp\left(\beta_T\sqrt{\ln\left(1+COV_R^2\right)\left(1+COV_Q^2\right)}\right)} \quad (4)$$

where λ_R is the resistance bias factor; Q_D and Q_L are the dead load and live load, respectively; β_T is the target reliability index; γ_D and γ_L are the load factors for dead load and live load, respectively; λ_{QD} and λ_{QL} are the load bias factors (mean ratio of measured over predicted value) for the dead load and live load, respectively. COV_{QD} and COV_{QL} are the coefficient of variation values for the dead load and live load, respectively. The Q_D/Q_L is the dead load to live load ratio, which is assumed to be 3 in this study.

The value of resistance bias factor, λ_R, is calculated as:

$$\lambda_R = \frac{\sum \lambda_{Ri}}{N} \quad (5)$$

where λ_{Ri} is the resistance bias factor for each site and N is the number of sites.

The coefficient of variation of the random loads, COV_Q, was introduced by McVay et al. (2009) using the following equation:

$$COV_Q = \sqrt{\frac{\frac{Q_D^2}{Q_L^2}\lambda_{QD}^2 COV_{QD}^2 + \lambda_{QL}^2 COV_{QL}^2}{\frac{Q_D^2}{Q_L^2}\lambda_{QD}^2 + 2\frac{Q_D}{Q_L}\lambda_{QD}\lambda_{QL} + \lambda_{QL}^2}} \quad (6)$$

where COV_{QD} and COV_{QL} are the coefficient of variation values for the dead load and live load, respectively.

2.1 Description of CPT Sites and subsurface soil characterization

Six sites in Louisiana with many CPT tests performed at each site were used to evaluate the effect of site variability on LRFD design of piles. These sites are: Metairie site with 14 CPT tests performed at different locations down to 36.6 m; Accelerated Loading Facility (ALF) site with 10 CPT tests performed at different locations down to 15.2 m; Bayou Lacassine site with 10 CPT tests performed at different locations down to 22.9 m; US90 & LA85 site with 22 CPT tests performed at different locations down to 27.4 m; Hammond site with 7 CPT tests performed at different locations; and LA1 site with 22 CPT tests performed at different locations down to 22.9 m. Figure 1 presents the CPT locations for LA 1 site.

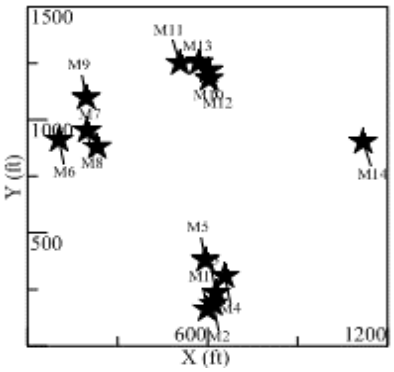

Figure 1. Plan view of CPT locations for Metairie site.

The subsurface soil conditions for the six sites were characterized using the results of CPT tests, as well as, the soil borings and associated laboratory tests. As an example, the profile of soil type for Metairie site, results of SPT tests and undrained shear strength, S_u, and the profiles of average corrected tip resistance per foot, for all the CPTs, are presented in Figure 2.

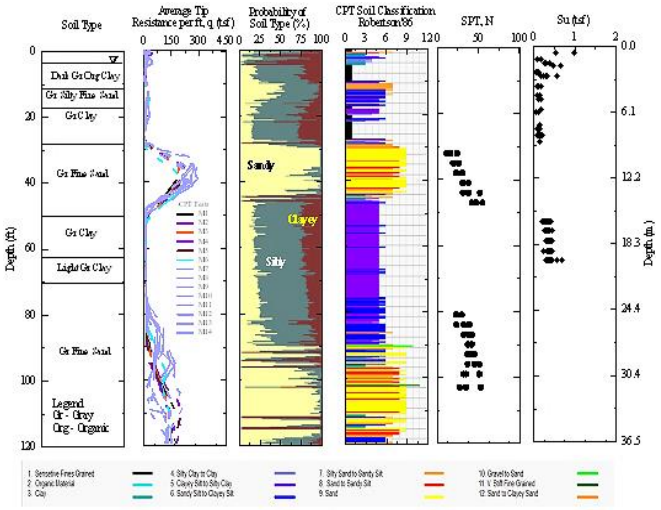

Figure 2. Soil boring and CPT soil classification at Metairie site.

The coefficient of variation (COV) of the corrected cone tip resistance, q_t, was calculated for each site. The profiles of CPT tests were used to classify the subsurface soil using the probabilistic region "soil behavior" estimation method (Zhang and Tumay 1999) as shown in Figure 2. In addition, the CPT soil classification proposed by Robertson (1990) was adopted in this study to define the soil layering. For Metairie site, six soil layers were identified for analysis: 0.0 - 8.5 m, 8.5 - 12.2 m, 12.2 - 15.2 m, 15.2 - 23.8 m, 23.8 - 33.8 m, and 33.8 - 36.6 m.

3 RESULTS AND ANALYSES

3.1 Site variability from CPT data and LCPC Pile-CPT method

To investigate the site variability from CPT data and its effect on the LRFD design of piles using the LCPC pile-CPT design method, the CPT data (q_t) collected from the six project sites was evaluated separately per site. In order to investigate the effect of site variability for each site using the geo-statistics tools, all the collected data for each site should be first transferred to stationary data without any trend, which is necessary to perform the semi-variogram analyses. Data transformation from nonstationary to stationary data was performed for all six sites.

Experimental variogram analyses were performed using the JeoStat software for each soil layer of the six sites. The resulted experimental semi-variograms for four soil layers at Metairie site are presented in Figure 3. Variability analyses for this site were done in the vertical direction only, and the horizontal semi-variograms were not included due to long spacing between the CPT points. The spherical model was adopted here to fit the model's semi-variogram with the experimental semi-variogram data to define the vertical correlation range, a_v, for each soil layer.

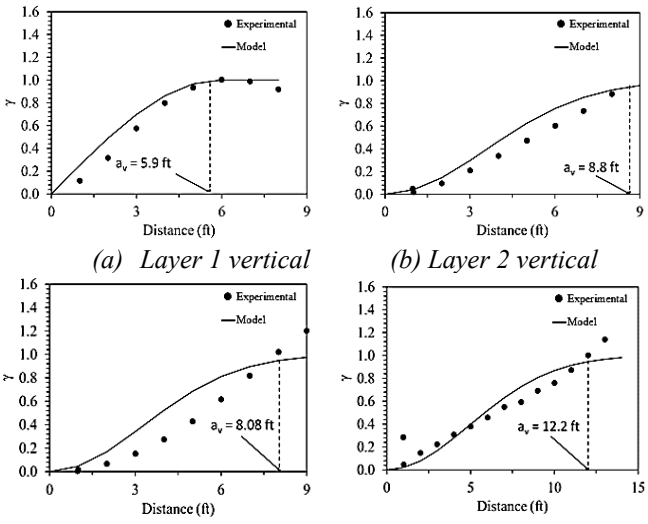

(a) Layer 1 vertical *(b) Layer 2 vertical*

(c) Layer 3 vertical *(d) Layer 4 vertical*

Figure 3. The experimental and spherical semi-variogram models for four soil layers at Metairie site.

The statistical data and the correlation length values, a_v, determined by the semi-variograms were used to calculate the LRFD resistance factors, ϕ, for the six sites as shown in Table 1. Equation (3) was used to evaluate $COV_{R,spatial}$, while equation (6) was used to calculate COV_Q. The layer's mean, m, and standard deviation, σ, were calculated from the CPT- q_t data

(using the JeoStat software). The resistance factor considering spatial variability, $\phi_{spatial}$, for each site was then evaluated using equation (4). Following the procedure proposed by Elkateb et al. (2003), the values of $COV_{R,spatial}$ for Metairie, ALF, Bayou Lacassine, US90 & LA85, Hammond, and LA1 sites were calculated as 0.20, 0.11, 0.08, 0.09, 0.16 and 0.10, respectively. The corresponding LRFD resistance factors based on spatial variability, $\phi_{spatial}$, are 0.77, 0.93, 0.98, 0.95, 0.85 and 0.95 for Metairie, ALF, Bayou Lacassine, US90 & LA85, Hammond, and LA1 sites, respectively. These resistance factors were calculated using the $COV_{R,spatial}$ only. The LRFD resistance factors was also calculated using the design method resistance coefficient of variation, $COV_{R,method}$, which is equal to 0.31 for LCPC pile-CPT design method (Amirmojahedi and Abu-Farsakh, 2019). The corresponding method's resistance factor, ϕ_{method}, for LCPC design method equals 0.61 based on Amirmojahedi and Abu-Farsakh (2019) study, which is the same for all sites. In evaluating ϕ_{method}, no consideration was given to site variability, although variability between the different sites in Louisiana were indirectly included in the calibration of ϕ_{method}. In this study, the authors recommend to incorporate both the $COV_{R,spatial}$ and the $COV_{R,method}$ in the LRFD calibration of resistance factor, ϕ_{total}, using the following proposed equation:

$$COV_{R,total} = \frac{c1 \times COV_{R,spatial} + c2 \times COV_{R,method}}{c1+c2} \quad (7)$$

where c1 and c2 are weighted coefficients for the spatial site variability and design method variability, respectively, which can be evaluated based on engineering judgment of the specific site variability. In this study, the authors assumed c1 = c2 = 0.5, since both variabilities are of close importance.

Table 1. Calibrated resistance factors, ϕ, for LCPC Pile-CPT design method.

Parameters	Metairie	ALF	BL	US90	Hammond	LA1
$COV_{R,spatial}$	0.20	0.11	0.08	0.09	0.16	0.1
$COV_{R,method}$ (LCPC)	0.31					
$COV_{R,total}$	0.255	0.21	0.195	0.20	0.235	0.205
COV_Q^2	0.011					
$\phi_{spatial}$	0.76	0.91	0.96	0.94	0.83	0.93
ϕ_{method} (LCPC)	0.61					
ϕ_{total}	0.67	0.74	0.77	0.76	0.70	0.75

Table 1 presents the $COV_{R,spatial}$, $COV_{R,total}$ and ϕ_{total} for different sites. It can be seen that the values of ϕ_{total} are different for the different sites, basically based on the variability on the $COV_{R,spatial}$ of the site. The relatively high site variability of Metairie site resulted on lower resistance factor, ϕ_{total} = 0.67, than the other sites; while the low site variability of Bayou Lacassine site resulted on higher resistance factor, ϕ_{total} = 0.77, than the other sites.

4 CONCLUSIONS

This study investigated the effect of site variability on the geotechnical properties from site exploration, and its implementation into LRFD design of pile foundations. Based on the findings of this study, the following conclusions can be made:

- Spatial site variability can be evaluated from site exploration involved multi CPT tests performed at different locations within the same site.
- The effect of site variability can be implemented into LRFD design of pile foundations through evaluating the spatial and total coefficients of variation ($COV_{R,spatial}$, $COV_{R,total}$) of the site using the semi-variogram approach, which can be used to calibrate the resistance factor ($\phi_{spatial}$ or ϕ_{total}) for the specific site using Equation (4).
- The values of $COV_{R,spatial}$ for all six sites are lower than $COV_{R,method}$. In $COV_{R,method}$, no consideration is given to the specific site variability, although variability between different sites in Louisiana were indirectly included in the LCPC method.
- For sites with lower site variability than the variability of design method (i.e., $COV_{R,spatial} < COV_{R,method}$), the total coefficient of variation ($COV_{R,total}$) decreases and the corresponding resistance factor ($\phi_{spatial}$ or ϕ_{total}) increases, and vice versa; hence giving a credit to low variability sites as compared to high variability sites in terms of increasing either $\phi_{spatial}$ or ϕ_{total}, for use in the design of pile foundations.

ACKNOWLEDGEMENT

This research project is funded by the Louisiana Transportation Research Center (Project No. 16-6GT) and the Louisiana Department of Transportation and Development (Project No. DOTLT1000112).

REFERENCES

Amirmojahedi, M. 2020. *Estimation of the Axial and Lateral Capacity of Driven Piles from the Results of Cone Penetration Test and Finite Element Analysis*. Ph.D. Dissertation, Louisiana State University, Baton Rouge, LA, 323 p.

Elkateb, T., Chalaturnyk, R., and Robertson, P. K. 2003. An Overview of Soil Heterogeneity: Quantification and

Implications on Geotechnical Field Problems. *Canadian Geotechnical Journal*, 40, pp. 1–15. https://doi.org/10.1139/t02-090.

Faraone, M.A. 2014. *Geostatistical analysis for reliability based design of foundations*. PhD dissertation, University of Florida, 172 p.

McVay, M., Klammler, H., Bloomquist, D., Otero, J., and Faraone, M. 2009. Modifications of LRFD Resistance Factors Based on Site Variability. FDOT Report BD545-76. Tallahassee, FL: Florida Department of Transportation, 123 p.

Lacasse, S. and Nadim, F. 1996. Uncertainties in Characterizing Soil Properties. In Uncertainty in the Geological Environment: From Theory to Practice, C. D. Shackleford, P. P. Nelson, and M. J. S. Roth (eds.), *Geotechnical Special Publication 58*, pp. 49–75. New York: ASCE.

Lumb, P. 1974. *Application of Statistics in Soil Mechanics*. In Soil Mechanics – New Horizons, I. K. Lee (ed.), pp. 44–111. New York: Elsevier.

Zhang, Z., and M.T. Tumay (1999). Statistical to Fuzzy Approach toward CPT Soil Classification. *Journal of Geotechnical and Geoenvironmental Engineering*, 125(3), 179–186. https://doi.org/10.1061/(ASCE)1090-0241(1999)125:3(179).

Proceedings of the XVIII ECSMGE 2024
GEOTECHNICAL ENGINEERING CHALLENGES
TO MEET CURRENT AND EMERGING NEEDS OF SOCIETY
© 2024 the Authors
ISBN 978-1-032-54816-6
DOI 10.1201/9781003431749-24
Open Access: www.taylorfrancis.com, CC BY-NC-ND 4.0 license

ECSMGE 24
XVIII EUROPEAN CONFERENCE ON SOIL MECHANICS AND GEOTECHNICAL ENGINEERING

Evaluation of design methods for geosynthetic-reinforced pile-supported embankments based on case studies

Évaluation des méthodes de conception des remblais sur pieux renforcés par des géosynthétiques sur la base d'études de cas

M.Y. Abu-Farsakh*
Louisiana Transportation Research Center, Louisiana State University, Baton Rouge, LA, USA

M. Izadifar
Department of Civil & Environmental Engineering, Louisiana State University, Baton Rouge, LA, USA

**cefars@lsu.edu*

ABSTRACT: This paper evaluates the performance of several empirical geosynthetic-reinforced pile-supported (GRPS) embankment design methods, which include the BS8006, Nordic, EBGEO, FHWA, and CUR226 methods. Assessment of these GRPS design methods was performed using three field case studies using four criteria: the efficacy, stress concentration ratio, maximum differential settlement, and maximum reinforcement. The results show that the performance of GRPS design methods varies from case to case and depends on the criterion considered. For efficacy criterion, the field measurements are closer to Nordic and EBGEO than the other methods. For SCR criterion, the field measurements are closer to BS8006 than the other methods, and to finite element models (FEM) in two cases. However, for the maximum tension and differential settlements criteria, the field measurements are much closer to CUR226, EBGEO, and FEMs.

RÉSUMÉ: Cet article évalue les performances de plusieurs méthodes empiriques de conception de remblai sur pieux renforcés de géosynthétiques (GRPS), notamment les méthodes BS8006, Nordic, EBGEO, FHWA et CUR226. L'évaluation de ces méthodes de conception GRPS a été réalisée à l'aide de trois études de cas sur le terrain en utilisant quatre critères: l'efficacité, le rapport de concentration des contraintes, le tassement différentiel maximal et le renforcement maximal. Les résultats montrent que les performances des méthodes de conception GRPS varient d'un cas à l'autre et dépendent du critère considéré. Pour le critère d'efficacité, les mesures de terrain sont plus proches de Nordic et EBGEO que des autres méthodes. Pour le critère SCR, les mesures de terrain sont plus proches de la BS8006 que des autres méthodes, et des modèles éléments finis (FEM) dans deux cas. Cependant, pour les critères de tension maximale et de tassements différentiels, les mesures sur le terrain sont beaucoup plus proches de CUR226, EBGEO et FEM.

Keywords: Geosynthetics; load transfer platform; piles; embankments.

1 INTRODUCTION

The construction of road embankments on soft soils often faces potential challenges such as bearing capacity failure, slope failure, lateral sliding, and excessive differential settlement. An effective solution is to use geosynthetic-reinforced pile-supported (GRPS) embankments. The inclusion of a load transfer platform (LTP) allows for effective redistribution of stresses onto the pile caps, which leads to smaller differential settlement. The load transfer from embankment load to pile caps takes place due to three factors: soil arching, development of geosynthetic tension, and soil-geosynthetics interaction. To fully understand the mechanisms of GRPS embankments, many studies had been carried out including full-scale field testing (e.g., Lu et al., 2020), experimental studies (e.g., Rue et al., 2016), and theoretical analyses (e.g., McGuire et al., 2020).

Several analytical methods were developed in literature to evaluate the vertical load distribution on the pile caps and soft soil surface in GRPS embankments. Hewlett and Randolph (1988) developed a semi-spherical arching model to characterize the load transfer mechanism based on 3D model tests. However, this method does not consider the effect of geosynthetic reinforcement. Low et al. (1994) improved the Hewlett and Randolph method by including the body force in a plain-strain differential equation. The BS8006 (2010) design method used the Hewlett and Randolph (1988) method to calculate the vertical load distribution. The EBGEO (2011) adopted Kempfert method (2004), which is based on laboratory modeling of piled-embankment systems. Combining

the EBGEO (2011) and Hewlett and Randolph (1988) methods and based on laboratory observations, Van Eekelen et al. (2013) proposed a new model with concentric arches and hemispheres for analyzing the arching effect. Lee et al. (2020) proposed an inverse-triangular shape distribution for the vertical load on top of soft soil and a uniform distribution for stiff soil, which is compatible with Van Eekelen's concentric arches model. Filz and Smith (2006) derived the vertical stress distribution on embankment based on the generalized form of Terzaghi's method. Filz et al. (2019) added the following refinements to Terzaghi's method: limiting vertical shearing of embankment to the part of the embankment below the critical height, separating the embankment into two layers based on the location of the LTP, and considering different piles arrangements. The Filz and Smith (2006) method has been adopted in the FHWA.

2 BRIEF REVIEW OF DESIGN METHODS

In this study, five design methods were selected for comparison and evaluation using field measurements. These methods include the British method (BS8006), German method (EBGEO), Nordic method (NGG 2005), Netherland CUR226 (2016) method (2016), and FHWA method (Schaefer et al., 2017).

The main assumptions in British (BS8006) method are that the soil arching between two adjacent piles is developed in a hemispherical shape, and the soil failure occurs either at the crown of the arch or at the pile cap, as shown in Figure 1. Several equations are proposed to calculate the arching efficacy, maximum tension in geosynthetics, and maximum differential settlement between the mid-span of two piles and pile cap. The BS8006 method recommends a maximum strain of 6% for design.

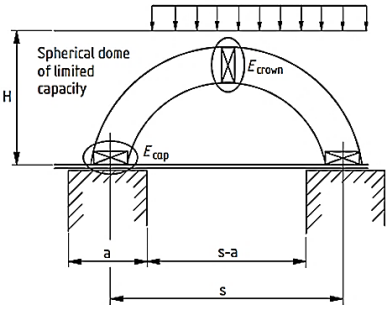

Figure 1. Arching mechanism and critical failure locations for BS8006 method (2016).

In German EBGEO method, the multi-arching theory is used as shown in Figure 2. The model is based on the lower bound theorem of plasticity as well as experimental observations of stress directions in the arch. The subsoil support is considered when determining the reinforcement tension. The vertical stresses on the pile cap and subgrade soil are assumed to be uniformly distributed. The membrane theory is used to calculate the tensile force in geosynthetic reinforcement. The maximum strain can be estimated using design charts provided in the EBGEO design code. No equation provided to estimate the differential settlement between the pile cap and mid-span of subgrade soil in this method. Hence the BS8006 equation is used to calculate the differential settlement.

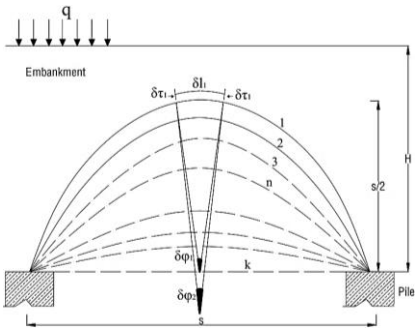

Figure 2. Multi-arching theory by Kempfert et al. (2004).

In CUR226 method, a concentric arches model are adopted for GRPS embankments (Kempfert et al., 2004) based on observations of stress formation and distribution in laboratory testing. The concentric-arch model is solved using the limit equilibrium approach. A schematic drawing of the concentric arches model is shown in Figure 3. The vertical load is divided into three parts: load on pile cap, load on geosynthetic square area, and load on geosynthetic strips generated from 2D arches. A relationship equation was proposed between the three components. Once the vertical stress distribution is determined, the reinforcement tension can be calculated. The distribution of vertical load along the geosynthetic layers can be assumed either uniform or inverse triangular.

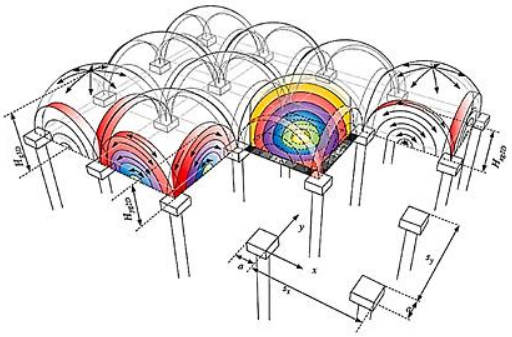

Figure 3. Concentric arches by Van Eekelen et al. (2013).

In FHWA design method, the pile type, spacing, diameter, and length will be first determined based on service limit state and ultimate limit state. An equation is provided to calculate the critical height of embankment, which is important to determine the

stress distribution. The method adopts the load-displacement compatibility method proposed by Filz and Smith (2006) to estimate the vertical load on top of pile cap and geosynthetics. The vertical load is divided into four components: average vertical stress acting down on top of geosynthetics in the area underlain by pile, average vertical stress acting down on top of geosynthetics in the area underlain by soil, average vertical stress acting on bottom of geosynthetics in the area underlain by pile, and average vertical stress acting on bottom of geosynthetics in the area underlain by soil. The vertical equilibrium of system is then satisfied.

In Nordic design method (NGG 2005), the load carried by reinforcement will be first calculated based on the assumption of a soil wedge. By assuming the vertical stress on top of subgrade is uniform, the vertical stress can then be calculated. An equation is proposed to calculate the tension in reinforcements. The maximum differential settlement is calculated using the same equation in BS8006 method.

3 FINITE ELEMENT MODEL (FEM)

A 2D and 3D FEMs were developed for GRPS embankments using PLAXIS2D & 3D softwares. The Mohr-Coulomb (MC) model was used for cohesionless soil layers and embankment fill, and the modified Cam Clay model was used for cohesive soils. The granular material in LTP was modeled using the Hardening Soil model. The piles were simulated using linear elastic model. In this study, the equivalent stiffness method was adopted to simulate the piles in the 2D FE model, in which pile spacing and diameter remain unchanged while the piles' stiffness and permeability of surrounding soil are adjusted. The interface between geosynthetics and geomaterials, and between piles and surrounding soils were modeled using interface elements and MC frictional model.

Four criteria were adopted in this study to evaluate the performance of GRPS embankments: efficacy, stress concentration ratio, maximum differential settlement, and maximum tension in geosynthetic reinforcement. Definition of these criteria can be found in Izadifar et al. (2023).

4 EVALUATING OF DESIGN METHODS

The five GRPS embankment design methods were evaluated using three case studies and the results of FE analysis. The first case study was presented by Liu et al. (2007) for the 18 ft. high GRPS embankment located in Shanghai, China. The second case was conducted by Briançon and Simon (2012) on a 16 ft. high full-scale experiment within the French national research project located northeast Paris. The third case was presented by Huang et al. (2009) for a 5.9 ft. height GRPS embankment constructed in northeast of Helsinki, Finland.

Figure 4 presents the comparison between the field measurements, FE results, and estimations from the GRPS design methods based on the four different criteria.

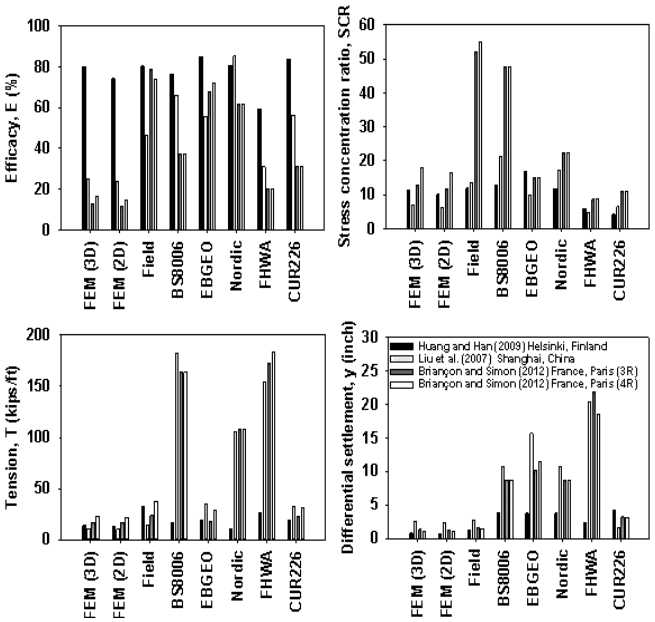

Figure 4. Performance evaluation of GRPS design methods based on field measurements.

It can be seen that the performance of each GRPS design method varies for different case studies and different criteria. In general, all the design methods tend to overestimate the four design criteria, sometimes by a very large amount. For example, the BS8006, Nordic, and CUR226 methods overestimate the tension by about 10, 6, and 2 times, respectively, for the Shanghai case. On the contrary, the FE results provide close agreement with the field measurements in most scenarios except for the efficacy and SCR values of the Paris case. Comparing the 2D and 3D FE results showed that the 3D provides closer results to field measurements. However, the difference between the 2D and 3D for the different criteria are low.

For the GRPS design methods, however, the accuracy of each design method is highly dependent on the case study and the criterion of interest. For efficacy criterion, the field measurements are closer to Nordic and EBGEO than the other methods. For SCR criterion, the field measurements are closer to BS8006 than the other methods, and to FEM in two cases. However, for the maximum tension and differential settlements criteria, the field measurements are much closer to CUR226, EBGEO, and FEMs.

5 CONCLUSIONS

- The performance of GRPS design methods varies from case to case and depends on the criterion considered due to assumed arching model.
- The 2D and 3D FEMs provide close agreement with field measurements in most scenarios except for the efficacy and SCR values of the Paris case.
- For efficacy criterion, the field measurements are closer to Nordic and EBGEO than the other methods.
- For SCR criterion, the field measurements are closer to BS8006 than the other methods, and to FEM in two cases.
- For the maximum tension and differential settlements criteria, the field measurements are much closer to CUR226, EBGEO, and FEMs.

ACKNOWLEDGEMENTS

This research is funded by the Louisiana Transportation Research Center (Project No. 20-2GT) and the Louisiana Department of Transportation and Development (Project No. DOTLT1000337).

REFERENCES

Briançon, L. and Simon, B. (2012). Performance of Pile-Supported Embankment over Soft Soil: Full-Scale Experiment. Journal of Geotechnical and Geoenvironmental Engineering, Vol. 138, pp.551–561. https://doi.org/10.1061/GT.1943-5606.0000561.

BS8006-1. (2010). Code of Practice for Strengthened/ reinforced Soils and Other Fills. British Standards Institution BSI, London, UK, 250 p.

CUR226. (2016). Design Guideline Basal Reinforced Piled Embankments. In: Design Guideline Basal Reinforced Piled Embankments. CRC press, 156 p.

EBGEO. (2011). Recommendations for Design and Analysis of Earth Structures Using Geosynthetic Reinforcements. Digital in English. German geotechnical society. https://DOI:10.1002/9783433600931.

Filz, G.M. and Smith, M.E. (2006). Design of Bridging Layers in Geosynthetic-Reinforced Column-Supported Embankments. Report No.VTRC 06-CR12, Virginia Transportation Research Council, Charlottesville, Virginia, 2006, 48 p.

Filz, G.M., Sloan, J.A., McGuire, M.P., Smith, M., and Collin, J. (2019). Settlement and Vertical Load Transfer in Column-Supported Embankments. Journal of Geotechnical and Geoenvironmental Engineering,. https://doi.org/10.1061/(ASCE)GT.1943-5606.0002130.

Hewlett, W.J., and Randolph, M.F. (1988). Analysis of Piled Embankments. Ground Engineering, Vol. 21(3), pp. 12–18.

Huang, J., J. Han, and S. Oztoprak. (2009). Coupled Mechanical and Hydraulic Modeling of Geosynthetic-Reinforced Column-Supported Embankments. Journal of Geotechnical and Geoenvironmental Engineering, Vol. 135(8), pp. 1011-1021. https://doi.org/10.1061/GT.1943-5606.0000026.

Izadifar, M., Luo, N., Abu-Farsakh, M. Y., and Chem, S. (2023) Performance Evaluation of Design Methods for Geosynthetic-Reinforced Pile-Supported Embankments. Journal of Transportation Research Record, Vol. 2677 (11). https://doi.org/10.1177/03611981231165994.

Kempfert, H.G., Gobel, C., Alexiew, D., and Heitz, C. (2004). German Recommendations for Soil Reinforcement above Pile-Elements. In: EUROGeo3, Third Geosynthetic Conference, Munchen, Vol. 1, pp. 279–283.

Lee, T., Van Eekelen, S.J., and Jung, Y.H. (2020). Numerical Verification of the Concentric Arches Model for Geosynthetic-reinforced Pile-supported Embankments: Applicability and Limitations. Canadian Geotechnical Journal, Vol. 58(3), pp. 441-454. https://doi.org/10.1139/cgj-2019-0625.

Liu, H. L., Ng, C. W., and Fei, K. (2007). Performance of a Geogrid-reinforced and Pile-supported Highway Embankment over Soft Clay: Case Study. Journal of Geotechnical and Geoenvironmental Engineering, 133: 1483-1493. https://doi.org/10.10611090-0241(2007)133:12(1483).

Low, B.K., Tang, S.K., and Choa, V. (1994). Arching in Piled Embankments. Journal of Geotechnical Engineering, Vol. 120, pp. 1917–1938. https://doi.org/10.1061/0733-9410(1994)120:11(1917).

Lu, W., Miao, L., Wang, F., Zhang, J., Zhang, Y., and Wang, H. (2020). A Case Study on Geogrid-Reinforced and Pile-Supported Widened Highway Embankment. Geosynthetics International, Vol. 27, pp. 261-274. https://doi.org/10.1680/jgein.19.00024.

McGuire, M., Sloan, J., and Filz, G. (2020). Effectiveness of Geosynthetic Reinforcement for Load Transfer in Column-supported Embankments. Geosynthetics International, Vol. 27, pp. 200–218. https://doi.org/10.1680/jgein.19.00012.

NGG (Nordic Geosynthetic Group). (2005). Nordic Guidelines for Reinforced Soils and Fills.

Rui, R., Van Tol, F., Xia, X.L., Van Eekelen, S., Hu, G., and Xia, Y.Y. (2016). Evolution of Soil Arching; 2D DEM Simulations. Computers and Geotechnics, Vol. 73, pp.199–209. https://doi.org/10.1016/j.compgeo.2015.12.006.

Schaefer, V. R., Berg, R. R., Collin, J. G., Christopher, B. R., DiMaggio, J. A., Filz, G. M., and Ayala, D. (2016). Ground Improvement Methods–Reference Manual Vols. I and II. FHWA-NHI-16-027 and FHWA-NHI-16-028.

Van Eekelen, S.J.M., Bezuijen, A., and Van Tol, A.F. (2013). An Analytical Model for Arching in Piled Embankments. Geotextiles and Geomembranes, Vol. 39: pp. 78–102. https://doi.org/10.1016/j.geotexmem.2013.07.005.

Proceedings of the XVIII ECSMGE 2024
GEOTECHNICAL ENGINEERING CHALLENGES
TO MEET CURRENT AND EMERGING NEEDS OF SOCIETY
© 2024 the Authors
ISBN 978-1-032-54816-6
DOI 10.1201/9781003431749-25
Open Access: www.taylorfrancis.com, CC BY-NC-ND 4.0 license

ECSMGE 24
XVIII EUROPEAN CONFERENCE ON SOIL MECHANICS AND GEOTECHNICAL ENGINEERING

Development of CPT-V_s correlations for soft quaternary clays of Szeged city Hungary

Développement de corrélations CPT-V_s pour les argiles molles du quaternaire ville de Szeged Hongrie

A. Al-Azazmeh*
BME University of Science and Technology, Budapest, Hungary

A. Mahler
Budapest University of Technology and Economics, Budapest, Hungary

**azazmeh9999@edu.bme.hu*

ABSTRACT: The role of small-strain parameters of soils in contemporary engineering geology is significant. Empirical correlations for shear-wave velocity (V_s) at Szeged city in the Southern Great Plain region of Hungary were assessed using research measurements of seismic piezocone test (SCPTu) and multichannel analysis of surface waves (MASW) results that were collected. In general, numerous existing cone penetration tests (CPT) -V_s or CPTu-V_s correlations for soils have been examined. Five indices were used in the assessment, including the ratio of the estimated to measured V_s values, the root mean square error (RMSE), the ranking index (RI), the ranking distance (RD), and the Variable Coefficient (CVK). Afterward, new empirical correlations for Szeged were formulated, and their performance was evaluated by comparing the predicted and measured values of V_s. This correlation offers a method to estimate V_s (shear wave velocity) from CPT data tailored to Szeged city's clay-like dilative soils, as per the Robertson 2016 chart. This recommendation constitutes a valuable contribution to the practice of geologists and engineers not only in Szeged city but also in other similar depositional environments in Hungary.

RÉSUMÉ: Les paramètres de faible déformation des sols jouent un rôle crucial en géologie technique contemporaine. À Szeged, dans la région sud de la Grande Plaine de Hongrie, des corrélations empiriques pour la vitesse des ondes de cisaillement (V_s) ont été évaluées à partir de mesures de tests sismiques au piézocône (SCPTu) et d'une analyse multicanal des ondes de surface (MASW). Les nouvelles corrélations formulées pour Szeged offrent une méthode précise pour estimer V_s à partir des données CPT, adaptées aux sols dilatés argileux de la région, en se conformant au graphique Robertson 2016. Cette recommandation est une contribution précieuse pour les géologues et ingénieurs, tant à Szeged que dans d'autres environnements similaires en Hongrie.

Keywords: In situ testing; shear wave velocity; cone penetration test; empirical correlation.

1 INTRODUCTION

V_s is a measure of the speed at which shear waves propagate through a soil medium. It is typically expressed in meters per second (m/s) or kilometers per second (km/s). The shear wave velocity is directly related to the shear modulus (G_{max}) of the soil, which is a measure of its stiffness or resistance to deformation under shear stress (Steve Kramer 1996).

To obtain V_s measurements, both in situ and laboratory tests can be performed. In situ tests involve the use of specialized equipment to generate and measure seismic waves directly in the ground. Common in situ tests for V_s measurement include the seismic cone penetration test (SCPT), seismic refraction, and downhole testing.

This paper seeks to identify the best empirical correlations for estimating shear wave velocity in different soil types in Szeged city Figure 1. using data from the Cone Penetration Test. Reliable data will be collected from reputable ground investigation firms. By applying empirical correlations, shear wave velocity will be calculated, and statistical and graphical analyses will be performed to compare the calculated and measured values.

These analyses will guide us in determining the most accurate correlations for each soil type. The study outcomes will yield valuable insights for estimating shear wave velocity in different Hungarian soils in Szeged city.

A comprehensive understanding of the soil behavior and its variability with depth is crucial for

reliable- seismic hazard assessment and design of resilient structures.



Figure 1. Map of Szeged city Hungary.

2 SITE DESCRIPTION AND DATA SOURCES

Situated in the Pannonian Basin above the Algyő High, the city of Szeged showcases sedimentary formations from the Neogene and Quaternary periods. The Neogene period (gyalog L. 2016) left behind marine sediments, while the Quaternary period witnessed the influence of glacial and alluvial deposits that have shaped the landscape.

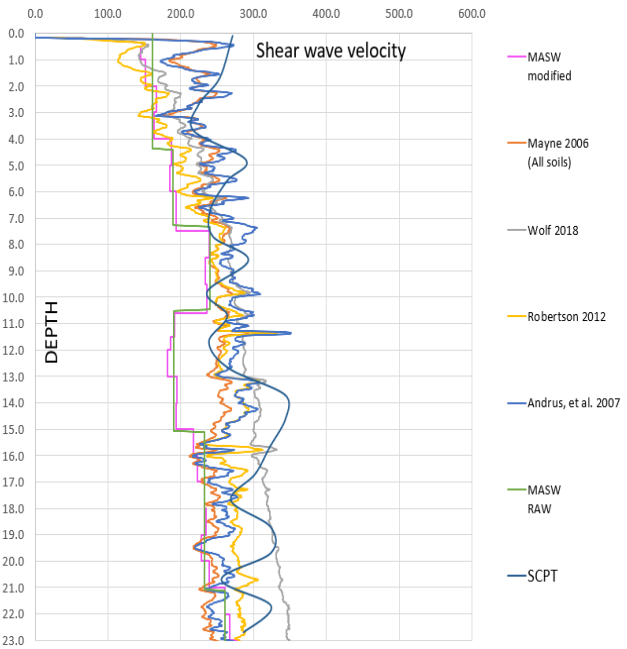

Figure 2. Seismic data (MASW&SCPT) measured in Szeged city.

The first step involves collecting site data including cone penetration tests (CPTs), seismic measurements (MASW or SCPT), and boreholes. Mapping helps identify relevant CPTs for assessment. Two MASW and one SCPT measurements, along with eleven CPTu measurements, were chosen for the study.

Considering that MASW data typically provides average shear wave velocities for a zone spanning several meters, whereas CPTu soundings offer data points at much finer intervals (typically every 1-2 cm), methods for alignment and averaging are employed. This may involve averaging CPTu data points across the depth intervals covered by MASW measurements or averaging MASW readings themselves Figure 2. Furthermore, integrating MASW and CPTu data is pursued to obtain a comprehensive understanding of subsurface conditions. MASW data offers insights into the overall shear wave velocity profile, while CPTu data provides detailed information on soil properties and stratigraphy at specific depths.

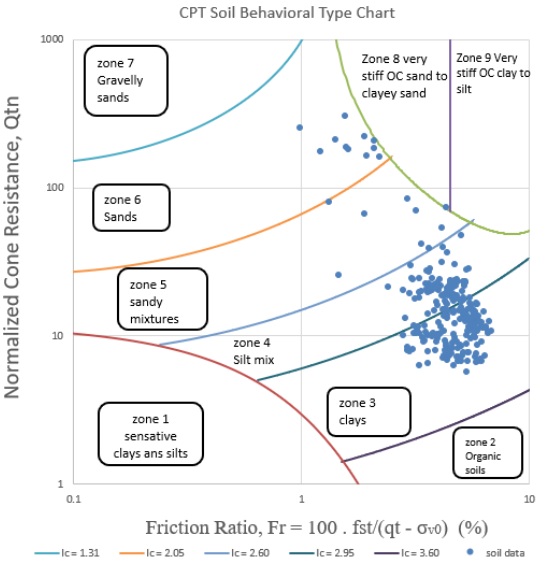

Figure 3. Soil Behavioural Type (SBT_n) Chart (Robertson 2009) for normalized Cone Penetration Test (CPT) results.

The soils collected in this study primarily demonstrate clay-like behavior meaning They possess high plasticity, low permeability, and are prone to volume changes known as shrinkage and swelling in response to moisture fluctuations. they exhibit high cohesion and low shear strength, rendering them susceptible to deformations and stability concerns, and as depicted in Robertson's (2009) soil behavioral type (SBT) chart Figure 3.

Over 40 V_s-CPT correlations were assessed for this study Table 1 Figure 2 displays the primary correlations that were evaluated.

Table 1. Previously suggested correlations between Vs and CPT or CPTU data for various soil classifications.

Correlations		Soil	Notes
(Mayne 2006)	$V_S = 118.8\ log\ f_s + 18.5$	Sands, clays, and organic plastic clays	fs is the sleeve friction in kPa
(Andrus, et al. 2007)	$V_S = 2.62 \cdot {q_t}^{0.395} \cdot {I_c}^{0.912} \cdot z^{0.124} \cdot SF^a$	Combined Holocene–Pleistocene soils	SF is a scaling factor that depends on soil deposit age, a = 0.88–0.92 for Holocene-age sites, z is depth in m a = 1.11–1.12 for Pleistocene sites
(Wolf 2018)	$V_S = 11.97 \cdot {q_t}^{0.262} \cdot {I_c}^{0.709} \cdot z^{0.107}$	All soils	q_t is the total cone tip resistance, I_c is the soil behavior type categorization index
(Cai, Puppala and Liu 2014)	$V_S = 7.954 \cdot {q_t}^{0.403}$	Soft clays	R^2 value of 0.631.
(Robertson and Cabal 2012)	$V_{S1} = (10^{0.55Ic+1.68} \cdot q_{c1N})^{0.5}$	All soils	q_{c1N} Truly normalized (i.e. dimensionless) cone penetration resistance corrected for overburden stress.

3 METHODOLOGY

In the assessment of correlations, the Root Mean Square Error (RMSE) Eq.1 is commonly used to measure the accuracy by comparing predicted values from the correlation with the actual measured values. The correlation with the lowest RMSE value is considered the most effective in providing accurate predictions. Consequently, RMSE serves as a valuable tool in identifying correlations that offer precise estimations for the studied outcome variable (Ziegler 2016) (Kuhn and Johnson 2013):

$$RMSE = \sqrt{\frac{1}{N} \sum_{i=1}^{N} (V_{s,measured} - V_{s,calculated})^2} \quad (1)$$

To achieve this optimization, the RMSE was minimized by adjusting the multipliers (factors) of the input parameters for each correlation tested. Robertson 2012& Wolf 2018 (All soils) correlation were selected as the model equation to generate the proposed correlations:

$$V_S = (\sigma v`/P_a)^{0.25} \cdot (10^{a\,Ic+b} \cdot q_{c1N})^c \quad (2)$$

$$V_S = a \cdot {q_t}^b \cdot {I_c}^c \cdot z^d \quad (3)$$

Where P_a is the atmospheric pressure, and q_{c1N} the Truly normalized cone tip resistance, truly normalized (i.e., dimensionless) cone penetration resistance corrected for overburden stress (qc1N) and I_c (soil behavior type index) parameters in these correlations contributes to a better prediction of vs and help reflects the geological site characteristics in reality.

4 RESULTS

Through the optimization process, notable improvements were obtained in the model equation for the studied categories.

All soils: based on the (253) data pairs the recommended best-fit equation for predicting vs in m/s is:

$$V_S = (\sigma v`/P_a)^{0.25} \cdot (10^{0.398Ic+3.65} \cdot q_{c1N})^{0.387} \quad (4)$$

$$V_S = 3.94 \cdot {q_t}^{0.397} \cdot {I_c}^{0.827} \cdot z^{0.066} \quad (5)$$

Where σv` is the effective overburden stress, Figure 4 shows the proposed correlation (eq.4) for all soils compared to the original one, most of the predicted values of V_s are within 20% of the measured V_s, and noticeable improvement in RMSE.

Quaternary -Age Soils: Based on the quaternary data pairs, the recommended best-fit equation for predicting V_s in m/s is:

$$V_S = (\sigma v`/P_a)^{0.25} \cdot (10^{0.372Ic+4.08} \cdot q_{c1N})^{0.368} \quad (6)$$

Tertiary-Age soils: For predicting V_s in m/s, the recommended equation in case any tertiary soils found in higher depths is:

$$V_S = (\sigma v`/P_a)^{0.25} \cdot (10^{0.545Ic+2.1} \cdot q_{c1N})^{0.47} \quad (7)$$

In the scatter plots, Figure 5 illustrate the performance of the proposed Equation 4. The arrangement of these data points reflects the level of agreement or correlation between the estimated and

measured values. The data points tend to cluster closely around a straight line, suggesting a more accurate estimation of Vs. However, it is expected to observe some scattering due to measurement errors and inherent variability in soil properties.

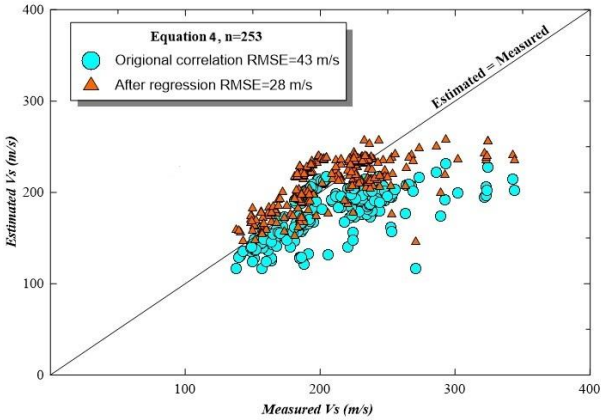

Figure 4 The proposed correlation (eq.4) for all soils compared to the original one.

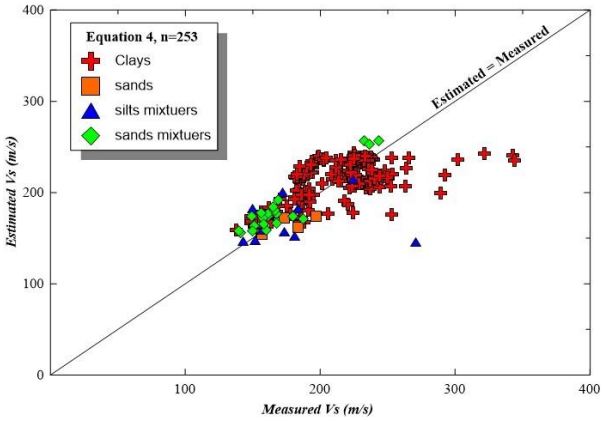

Figure 5. The proposed correlation (eq.4) for all data points showing all 4 soil types.

5 CONCLUSION AND RECOMMENDATION

In a comprehensive study conducted in Szeged city, correlations between shear wave velocity (V_s) and cone penetration test (CPT) results were investigated. Reliable Data were collected, resulting in 253 data pairs. Statistical analysis was performed using key parameters (K and RMSE) to identify suitable correlations for Szeged city soil types.

The study found that correlations proposed by (Robertson and Cabal 2012) and (Wolf 2018) provided accurate predictions for shear wave velocity across different soil categories. The derived equation also performed well. For Quaternary and tertiary age soils, Robertson (2012) and Wolf Akos (2018) correlations were recommended.

The findings emphasize the need for region-specific correlations due to the influence of soil formation and geological settings. It is crucial to involve expert engineers and conduct site-specific testing, as there is no direct relationship between CPT and Vs. Caution should be exercised when using empirical correlations, considering available data, uncertainties, and applying them within calibrated conditions.

REFERENCES

Andrus, R.D., N.P. Mohanan, P. Piratheepan, B.S. Ellis, and T. L. Holzer (2007). Predicting shear-wave velocity from cone penetration resistance. *Proceedings of the 4th International Conference on Earthquake Geotechnical Engineering*, Paper No. 1454.

Cai, G., A.J. Puppala, and S. Liu (2014). Characterization on the correlation between shear wave velocity and piezocone tip resistance of Jiangsu clays. *Engineering Geology*, 171, March 2014: 96-103. https://doi.org/10.1016/j.enggeo.2013.12.012.

Gyalog, L., Maros, G., Pelikan, P. (2016). *Budapest geoguid*. budapest: Hungarian Institute Of Geology And Geophysics.

Kramer. S. (1996). *Geotechnical Earthquake Engineering*. Prentice-Hall, New Jersey.

Kuhn, M. and Johnson, K. (2013). *Applied predictive modeling*. https://doi.org/10.1007/978-1-4614-6849-3.

Mayne, P.W. (2006). Undisturbed sand strength from seismic cone tests. *Geomechanics and Geoengineering.* Vol. 1: 239-257. https://doi.org/10.1080/17486020601035657.

Robertson, P.K., and K.L. Cabal. (2012). *Guide to Cone Penetration Testing.*

Wolf, Á. (2018). *Modeling and Development of Infrastructure Systems*.

Ziegler, A. (2016). *An Introduction to Statistical Learning with Applications.* R. G. James, D. Witten, T. Hastie, and R. Tibshirani (2013). Berlin: Springer. 440 pages, https://doi.org/10.1002/bimj.201500224.

Proceedings of the XVIII ECSMGE 2024
GEOTECHNICAL ENGINEERING CHALLENGES
TO MEET CURRENT AND EMERGING NEEDS OF SOCIETY
© 2024 the Authors
ISBN 978-1-032-54816-6
DOI 10.1201/9781003431749-26
Open Access: www.taylorfrancis.com, CC BY-NC-ND 4.0 license

ECSMGE 24
XVIII EUROPEAN CONFERENCE ON SOIL MECHANICS AND GEOTECHNICAL ENGINEERING

Method for determining soil mechanical parameters from in-situ test data on the base of real nonlinear soil deformation

Méthode de détermination des paramètres mécaniques du sol à partir de données d'essais in situ sur la base d'une déformation non linéaire réelle du sol

A.A. Alekhin
Ural State University of Railway Transport, Ekaterinburg, Russia

A.Zh. Zhussupbekov
L.N. Gumilyov Eurasian National University, Astana, Kazakhstan/Moscow State University of Civil Engineering, Moscow, Russia

G.A. Zhairbaeva
L.N. Gumilyov Eurasian National University, Astana, Kazakhstan

**Gulnaz.W@mail.ru*

ABSTRACT: The physical nonlinearity of soil deformation distinguishes it from the deformation of structural materials, as the stiffness characteristics of soil depend on the stress-strain state. Therefore, determining the mechanical parameters of soils requires considering the in-situ stress conditions. This article presents an in-situ method for determining these parameters for a phenomenological physically nonlinear soil model. The method also allows for determining the characteristics of an elastic-plastic model with the Coulomb flow condition. The use of this method for designing foundations on non-rocky soils (sand, clay) can significantly reduce costs while ensuring reliability. The method is based on special procedures for solving inverse nonlinear problems through numerical simulation of soil deformation under static loading. It also takes into account the geometric nonlinear factor of comparability of one-dimensional and angular deformations in non-rocky soils. The core idea of the method is to minimize the deviations between actual soil deformations from in-situ tests and numerically simulated deformations using a verified physically nonlinear soil model. The application of this method in the design of a spread-slab foundation for a high-rise residential building in Ekaterinburg (Russia) resulted in a one million USA dollars cost reduction while maintaining the necessary foundation reliability. This was achieved by using a physical and mathematical soil model that accurately represents the nonlinear deformation behavior of the soil and incorporates the actual values of soil mechanical parameters. The article includes the algorithm of the method and provides examples of its practical application in the design of real projects.

RÉSUMÉ: La non-linéarité physique de la déformation du sol la distingue de la déformation des matériaux structurels, car les caractéristiques de rigidité du sol dépendent de l'état de contrainte et de déformation. Par conséquent, la détermination des paramètres mécaniques des sols nécessite la prise en compte des conditions de contrainte in situ. Cet article présente une méthode in situ pour déterminer ces paramètres pour un modèle phénoménologique de sol physiquement non linéaire. La méthode permet également de déterminer les caractéristiques d'un modèle élastique-plastique avec la condition d'écoulement de Coulomb. L'utilisation de cette méthode pour la conception de fondations sur des sols non rocheux (sable, argile) peut réduire considérablement les coûts tout en garantissant la fiabilité. La méthode est basée sur des procédures spéciales de résolution de problèmes non linéaires inverses par simulation numérique de la déformation du sol sous charge statique. Elle prend également en compte le facteur géométrique non linéaire de comparabilité des déformations unidimensionnelles et angulaires dans les sols non rocheux. L'idée centrale de la méthode est de minimiser les écarts entre les déformations réelles du sol provenant d'essais in situ et les déformations simulées numériquement à l'aide d'un modèle de sol physiquement non linéaire vérifié. L'application de cette méthode à la conception d'une fondation à dalle étalée pour un immeuble résidentiel de grande hauteur à Ekaterinbourg (Russie) a permis de réduire les coûts d'un million de dollars américains tout en maintenant la fiabilité nécessaire de la fondation. Ce résultat a été obtenu grâce à l'utilisation d'un modèle physique et mathématique du sol qui a permis d'obtenir des résultats précis.

Keywords: Soil; non-linearity; characteristics; method; practical use.

1 INTRODUCTION

Soil base is a basic, often the most pliable, load-bearing element of the building. Not being, as a rule, constructive element of the building (except maybe artificially created reinforced soil massifs (geomassifs) soil base takes on entire load from building, affecting operational and strength parameters of the building. This situation certainly determining the mechanical parameters of a physically nonlinear soil from in-situ tests because laboratory tests for these purposes are complex and on various reasons their results are unreliable. In the 1940s Russian scientist Botkin experimentally determinated and investigated physically nonlinear type of deformation of non-rocky soils (clays and sands) (Botkin, 1940); later this feature of nonrocky soils was confirmed by other geotechnicians (Alekhin, 2015, 2022), (Malyshev, 1994). (Mirsayapov, 2011), (Lushnikov, 2019), (Zhussupbekov, 2023). Currently researches on various aspects of this fundamental reality are being actively and successfully developed. One of the most important aspect is development of the methods for determining design parameters of nonlinear soil models from in-situ test data including geometric nonlinearity as well as soil rheological properties. If the question of geometric nonlinearity, which importance for soil deformation has not yet been fully elucidated, is solved rather simply, mainly by a small adjustment of formulas for relative strains, while very complex but important investigations of rheological properties simultaneously with physical nonlinearity are now carried out at number of laboratories: perhaps an effective in-situ method will allow for rheological theory to be corrected taking into account initial stress state in soils; perhaps an application of this method will also may help to assess more accurately geometric nonlinearity influence, for example, at designing neighbouring buildings. Thus, the validity to solve problem of using in-situ test data was predetermined both by unique physical properties of non-rocky soil itself as specific kind of solid medium with specific internal bonds and by the presence of the initial stress state of the soil (both of them are inevitably destroyed when taking soil samples). To solve this problem reliable authentic for soil deformation the soil physical-mathematical model with complex nonlinear dependencies is needed. At present Botkin's model is the only systematically and consistently verified model, including its practical application. Moreover, for nowadays this is the only soil model with complex nonlinear dependencies for which it was possible to develop a convenient method for determining true values of design mechanical parameters from in-situ test data that much increase reliability and accuracy of geotechnical design (Bodkin, 1940). General principles of the proposed method, particular in solving the revers unstable problems can be applied for determining mechanical parameters of other types of physically nonlinear models. Below algorithm for the determination of mechanical parameters of physically nonlinear soil model in relation to the Botkin's model is presented. As for the way of derivation of constitutive relations for the Botkin's model as well as the formula of less general physically linear Young-Hook's model, they are referred to the, so called, phenomenological form obtained as a result of approximation of data of actual and presentable in general parameters of the stress-strain state (SSS) of mechanical tests on deformation. Phenomenological difference between physically linear and physically nonlinear (Botkin, 1994) deformation types of a solid medium is shown at Figure 1: this figure graphically and with the help of formulas explains the fundamental difference between the deformation of artificial (essentially manmade) materials with dense and strong, and therefore most often elastic bonds between particles (structural materials) and the deformation of naturally formed solid medium with movable in that or in some other degree connections between their particles (non-rocky soils). Naturally such a great fundamental difference in the deformation of two types of solid substance could be ignored by scientists.

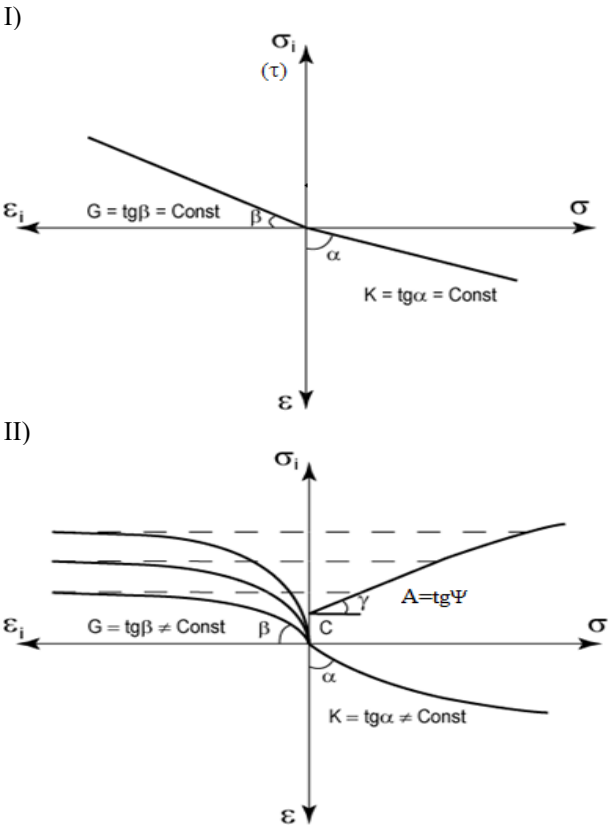

Figure 1. Types of deformation.

I) physically linear type of deformation (solid materials and rocks) II): physically nonlinear type of deformation (non-rocky soils: sands and clays); K and G – bulk modulus and shear modulus respectively; σ and ε – first invariants of the stress and strain tensors (bulk deformation); σ_i and ε_i – second invariants of the stress and strain deviators shape deformation).

Type I Inauthentic for the soil (phisically linear) [First investigator R. Hooke, 17-th century]

Type II Authentic for the soil (phisically nonlinear) [First investigator – A. Botkin, 20-th century]

I) Characteristics of Rigidity: E = const; ν = const → K = E/(1-2ν) = const; G = 0.5E/(1+ν) = const

II) Characteristics of Rigidity: $K = \sigma^{1-\alpha}/A_0 \neq$ const; $G = (\sigma_u - \sigma_i)/B = (A\sigma + C)/(B + \varepsilon_i) \neq$const ($\sigma_u = A\sigma+C$ – Soil strength condition according Mises and Botkin) → $E3KG/(K+ G) \neq$ const; $\nu= 0.5(K-2G)/(K+G) \neq$ const

2 METHODOLOGY

From the formulas shown in the Figure1 it follows that in contrast to the invariance of Young's modulus E with respect to the stress-strain state (SSS) for structural materials and rocks (I type of deformation) for non-rocky soils (II type of deformation) this value under called "modulus of deformation" is different at different points of soil base since form and magnitude of the reactive forces produced in the soil mass by external load are complex (see, for example, Figure 2).

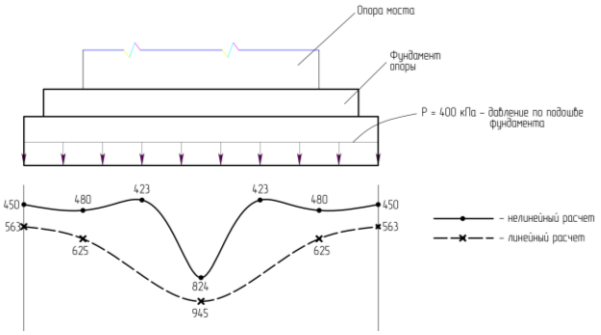

Figure 2. Distribution of reactive forces under foundation.

Thus, the value E (modulus of deformation) is physical and mathematical analogue of the Young's modulus from phenomenological Hooke's theory-model), and cannot be technologically acceptable stiffness characteristic (or parameter) for non-rocky soils because it cannot be determined at each point of soil base for a spatial assessment of its stiffness. However, when using the nonlinear phenomenological Botkin's theory-model in design the problem of determining real stiffness of soil base at each point is easily solved. To do this it is necessary to obtain from in-situ tests data meanings of mechanical parameters of Botkin's soil model (A, B, C, A_0, α), which along with meanings of stress-strain parameters (σ and ε_i) determine values of non-rocky soil stiffness characteristics (K and G) that should be used in design. The algorithm for determining actual (with index «f» of parameters A_f, B_f, C_f, $A_{f\,0}$, α_f) is given below: index «m» denotes numerically simulated values, for example, settlements at i-th load stage S_{mi}, while stage S_{fi} are corresponding values from in-situ test data.

Set of required parameters: $z_k = \{A_f, B_f, C_f, A_{0f}\, \alpha_f\}$.

a)

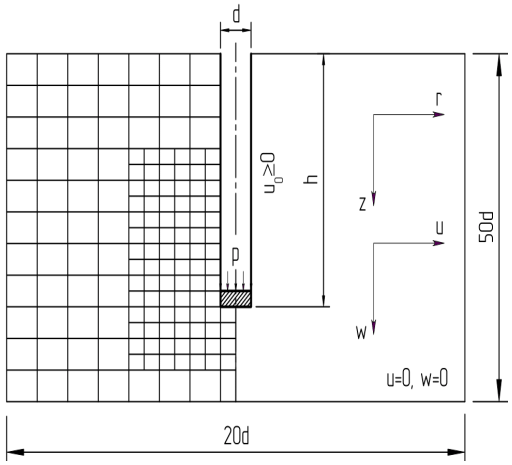

b)

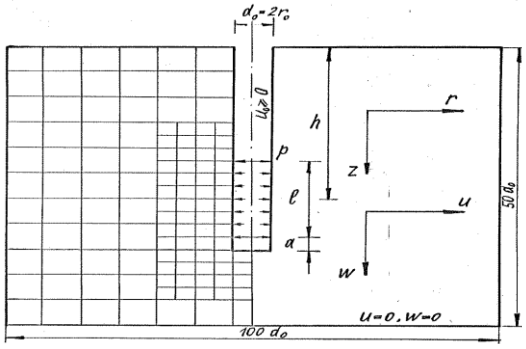

Figure 3. Test type, a) Rigid circle plate; b) Radial pressuremeter.

Algorithm for determining actual values of soil mechanical parameters:

1. Determination of the parameter

$$B_f = \frac{B_m \sum S_{fi}}{S_m} \qquad (1)$$

(formula is obtained from linear dependence of soil settlement on parameter B (Alekhin, 2015, 2022), with use of Least squares method for statistical processing of relationships between experimental results and corresponding results of numerical modeling):

$$S = \sqrt{3}B/2 \int_0^1 y_z d_z \qquad (2)$$

2. Determination of the parameter A_f by search method through frictional angle parameter φ with its technically sensitive step 1^0 using formula of (Malyshev,1994):

$$A = \frac{\sqrt{2(3+\mu^2)\sin\varphi}}{3+\mu\sin\varphi} \quad (3)$$

3. Determination of the parameter C_f by Tikhonov's procedure (Malyshev,1994) (Zhusupbekov, 2023) for solving unstable inverse problems, the essence of which consists in minimizing the deviation between actual physical measurements of any parameter (for example, soil settlements S_{fi}) and their numerically simulated values S_{mi} with using stable direct solution and verified physical and mathematical soil model:

$$min\sum\left(S_{fi} - S_{mi}\right)^2 \quad (4)$$

Also were used program ALEXANDER (Alekhin, 2015) to solve the direct boundary value stable problems and program FLEXIPLEX (Alekhin A. 2022) to search the global minimum of function (4);

4. Determination of the parameter α_f by Tikhonov's procedure with programs ALEXANDER and FLEXIPLEX;

5. Determination of the parameter A_{0f} by Tikhonov's procedure with programs ALEXANDER (Alekhin, 2015), (Zhussupbekov, Sarsembayeva and Alibekova, 2023) and FLEXIPLEX

For determining parameters A_{0f} and α_f can be used programm FLEXIPLEX for search global minimum on two parameters.

In the case of using an elastic-plastic soil model, for example with a limiting surface determined by the soil strength criterion according to Coulomb-Mohr version, the actual values of limiting surface parameters can be obtained from Malyshev relations (Malyshev,1994): (Formula 3,5)

$$C = \frac{\sqrt{2(3+\mu^2)\cos\varphi}}{3+\mu\sin\varphi}\, c \quad (5)$$

Where φ and c are soil strength parameters on Coulomb's version of soil strength, μ – Lode parameter. These formulas made it possible to use the simplest minimization procedure with single result being obtained by looking over different values of angle φ.

3 CONCLUSION

Using physically nonlinear Botkin's model several geotechnical objects were designed and built in Ekaterinburg, namely: strip foundations of 6-storey neighboring buildings instead of pile foundations, retaining wall close to 9-storey building and spread-slab foundation of 35-storey high-rise building (see Figure 4a and Figure 4b). In all these cases Botkin's soil model with design parameters values from in-situ test data were used for design of foundations. At all cases the cost of geotechnical constrictions was about $1 million less than the cost in original project on the base of Hooke's linear theory and with significant increase in reliability of the design solution on the base of true soil model: for example, in the case of 35-storey high-rise building, on eluvial hard silty-argillaceous loam and sandy loam, actual settlements differ from design one for about 25%, that is, discrepancy coincides with discrepancy due to replacing in design real soil by ideal continuous medium.

a)

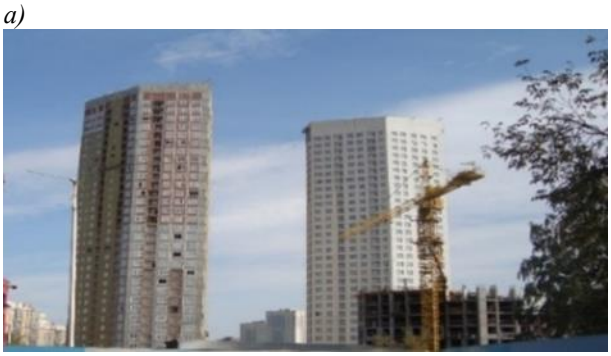

b)

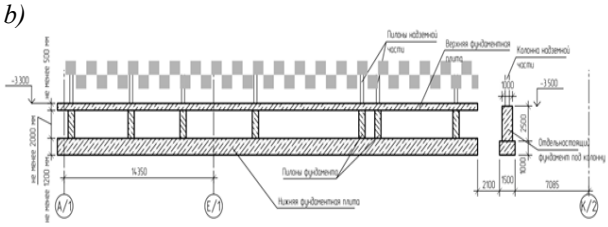

Figure 4. a) High-rise buildings in Ekaterinburg city: left building on the spread slab foundation is $1 cheaper than others of the same kind; b) Cross section of spread slab foundation.

REFERENCES

Alekhin A. 2015. Substantiation of the method of determination of nonlinear soil model parameters from in-situ test data. Ekaterinburg: UralNIIproject.

Alekhin A. 2022. Algorithm for determining the mechanical parameters of soils for the nonlinear Botkin model from results of in-situ tests. Novocherkassk: LIK.

Botkin A. I., 1940. "On strength of bulk solids and brittle materials", Izvestiya VNII gidrotehniki, vol. 26, pp. 205-236

Botkin A. 1994.On the strength of bulk and brittle materials. Moscow: RIIG.

Zhussupbekov, A., Sarsembayeva, A., Alibekova, N. 2023 Preliminary Assessment of the Bearing Capacity of Soils Using a Geotechnical Database *Lecture Notes in*

Networks and Systems, 2023, 574 LNNS, pp. 3065–3074
DOI: 10.1007/978-3-031-21432-5_338

Zhussupbekov, A.Z., Kemerbayeva, A., Iskakova, T., Yeleusinova, A.E., Morev, I.O. 2023. Application of information modeling technology in geotechnics, Proceedings of the 17th Asian Regional Conference on Soil Mechanics and Geotechnical Engineering. Smart Geotechnics for Smart Societies. Astana, Kazakhstan, pp. 2310–2317
DOI:10.1201/9781003299127-356

Malyshev V. 1994. Strength of soils and stability of soil bases of the structures. Moscow: Stroyizdat.

Mirsayapov IT 2011.Calculation model of long-term nonlinear deformation of clayey soils under complex stress state

Lushnikov, V., Zhussupbekov, A., Omarov, A., Tanyrbergenova, G. 2019. Hypotheses of the Tilting of Nevyansk Tower. Sustainable Civil Infrastructures, 2019, pp. 242–248.
DOI 10.1007/978-3-030-01923-5_17

Proceedings of the XVIII ECSMGE 2024
GEOTECHNICAL ENGINEERING CHALLENGES
TO MEET CURRENT AND EMERGING NEEDS OF SOCIETY
© 2024 the Authors
ISBN 978-1-032-54816-6
DOI 10.1201/9781003431749-27
Open Access: www.taylorfrancis.com, CC BY-NC-ND 4.0 license

ECSMGE 24
XVIII EUROPEAN CONFERENCE ON SOIL MECHANICS AND GEOTECHNICAL ENGINEERING

An experimental study of failure mechanisms developed in rock masses under circular footing

Étude expérimentale des mécanismes de rupture développés dans les massifs rocheux sous semelle circulaire

A. Alencar*, C. Sánchez-Barberán
Universidad Politécnica de Madrid, Madrid, Spain

R. Galindo
Universidad Politécnica de Madrid, Madrid, Spain
CONSTRUCT-GEO, Faculdade de Engenharia da Universidade do Porto (FEUP), Porto, Portugal

M. Muñiz-Menéndez
Laboratorio de Geotecnia-CEDEX, Madrid, Spain

A. Viana da Fonseca
CONSTRUCT-GEO, Faculdade de Engenharia da Universidade do Porto (FEUP), Universidade do Porto, Porto, Portugal

ana.sdealencar@upm.es

ABSTRACT: The study of the bearing capacity of shallow foundation on rock mass is a topic that still have many parts to be studied, due to the particularities of each rock mass (discontinuities, anisotropy...). The present paper presents how the discontinuities, even being distanced from the foundation, affect the ultimate load and the failure mode. It is highlight that the definition the failure type is very important to limit the area of influence of each foundation, checking that it does not destabilize other nearby structures. According to the numerical calculations, it is estimated that in cases of circular footings the size of the breaking wedge is much smaller, than in the cases of strip foundation. In the laboratory, initially several tests are carried out to characterize the material; subsequently, three tests are performed that simulate superficial footings on rock mass with a horizontal discontinuity (at the block bottom). Different geometric configurations (block size and footing width) and boundary condition (in one case the bottom of the block is free to move and in the others are fixed) are adopted in order to see how the ultimate load and the form of failure change. It is observed that the ultimate load is highly influenced by the presence and the resistance of discontinuities, also that the failure mode changes in function of the boundary conditions. The results obtained in laboratory tests are also compared with the analytical solution for shallow foundation on anisotropic discontinuous rock mass. The laboratory tests were performed in sandstone, from Burgos, Spain.

RÉSUMÉ: La capacité portante des fondations superficielles sur massif rocheux est un sujet qui comporte encore de nombreuses parties à étudier, en raison des particularités de chaque massif rocheux (discontinuités, anisotropie...). Le présent article analyse comment la présence de discontinuités, même si elles sont éloignées de la fondation, modifie la charge ultime et le mode de rupture. Il est important de souligner que définir le type de rupture est très important pour limiter la zone d'influence de chaque fondation, en vérifiant qu'elle ne déstabilise pas les autres structures. Selon les calculs numériques, on estime que dans le cas de fondations circulaires, la taille du coin de rupture est beaucoup plus petite que dans le cas de fondations filantes. En laboratoire, plusieurs tests sont réalisés dans un premier temps pour caractériser le matériau; ensuite, trois essais sont réalisés qui simulent des semelles superficielles sur un massif rocheux présentant une discontinuité horizontale (le fond du bloc). Différentes configurations géométriques (taille des blocs et largeur des fondations superficielles) et conditions limites (dans un cas le bas du bloc est libre de mouvement et dans les autres il est fixe) sont adoptées afin de voir comment la charge ultime et la forme de rupture changent. On observe que la charge ultime est très influencée par la présence et la résistance des discontinuités, et que le mode de rupture change en fonction des conditions limites. Les résultats obtenus lors des tests en laboratoire sont également comparés à la solution analytique pour fondation superficielle sur massif rocheux discontinu anisotrope. Les tests en laboratoire ont été réalisés dans du grès provenant de Burgos, en Espagne.

Keywords: Circular footing; laboratory model test; rock mass; failure mechanism; splitting.

1 INTRODUCTION

The analytical solution for a shallow foundation on rock mass (Serrano et al., 2000), just as the classic failure wedges (Terzaghi, 1943, Prandtl, 1920) are developed considering strip footing. More recently, some numerical studies analyzed the bearing capacity and the failure wedge of circular footing.

Clausen (2013) proposed a series of charts with a coefficient, that multiplied by the uniaxial compressive strength for intact rock mass (UCS), allows an estimation of the bearing capacity of a circular footing.

Melentijevic et al. (2019) compared the wedge obtained with plane-strain and axisymmetric conditions, simulating a strip and a circular footing. According to the results, the area affected by the failure wedge in the case of circular footing is much less than in the case of strip foundation.

Alencar et al. (2019) developed a shape coefficient that allows conversion of the bearing capacity obtained by the analytical solution (Serrano et al., 2000) strip foundation in the value of the bearing capacity for a circular footing. This coefficient also can be used with the analytical solution proposed by Serrano et al. (2016) for shallow foundation on anisotropic discontinuous rock mass.

In the present paper, an experimental study is carried out, trying to simulate a shallow foundation on rock mass. The failure load and mechanism obtained are analyzed. With rock mass, no similar study was found. However, with soils some experiments have been performed like Chi and Lin (2020) who studied the bearing capacity of footing on one or two-layered soil; Hassani et al. (2023) analyzed the behavior of strip foundations with inclined loading on a soil-reinforced with geogrid.

2 CHARACTERIZATION AND METHODOLOGY

The studied rock was a Lower Cretaceous (Weald facies) medium grain quartzarenite from Burgos, Spain. This rock shows beige tone with veining in form of pinkish and orange stains. Table 1 presents a summary of the parameters obtained in the laboratory test carried out.

The sandstone used in the laboratory test shows a transversely isotropic foliation, so as that the anisotropy does not interfere with the results all samples were taken perpendicular to the Z direction.

Table 1. Sandstone properties obtained in laboratory tests.

Sandstone properties		Number of test	Values	
			Avg	SD**
Density (kg/m^3)		10	2133	30
Direct tensile strength (MPa)*		11	0.57	0.17
Uniaxial compression strength (MPa)*		7	22.1	1.0
Young's modulus (GPa)*		7	1.8	0.2
Poisson's Ratio		7	0.21	0.06
P-wave velocity (m/s)	X (β = 90º)	10	1563	187
	Y (β = 90º)	10	1672	213
	Z (β = 0º)	10	1362	202

** Perpendicular to Z direction.*
*** Standard deviation*

The blocks are from outcrops in the surface and show a GSI that can be considered equal to 100. The typical value of the parameter m_i for sandstone is 19 (Hoek et al., 1998).

In order to simulate different foundation configurations 3 blocks were tested varying the boundary conditions (Table 2 and Figure 1). In all cases the foundation is located in the center of the block; laterals boundaries are free, none lateral confinement was applied; to simulated an infinite block the base of block 2 was glued on fine steel plate, and the base of block 3 was glued on perfect rigid steel plate. The blocks were attached in the plates using the same glue applied in the direct tensile test (epoxy adhesive EA 9483).

Table 2. Blocks geometry.

Block	Dimension (cm)	Foundation diameter (*B*) (cm)	Base condition
1	15x15x15	3.8	Free
2	20x20x20	3.8	Fix*
3	20x20x20	2.0	Fix

** The block broke when it was detached from the support.*

3 RESULTS AND COMMENTS

In the case of block 1, all boundaries were free to move, and the failure load was 84.1 MPa. Before the failure in the lateral surface vertical cracks appeared. The block is broken into three parts, more the splitting wedge (Figure 2).

Block 2 was glued in a thin plate, being the ultimate load 100.6 MPa. The failure occurred in a fragile way; one-half of the block detached from the plate - breaking the block into two parts and the splitting wedge (Figure 3).

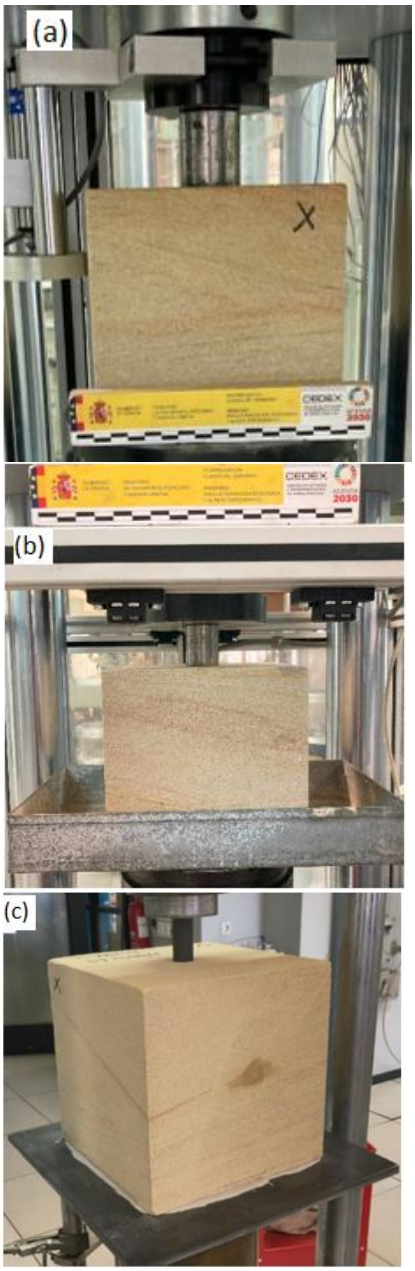

Figure 1. Blocks: (a) 1; (b) 2; (c) 3.

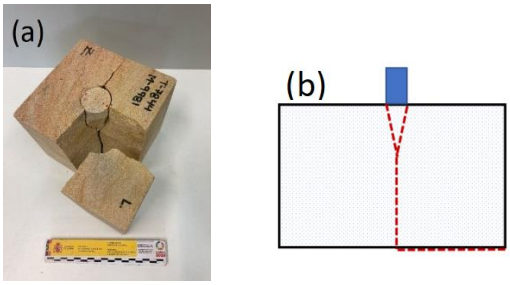

Figure 2. Block 1. (a) After failure. (b) Failure scheme.

The block 3 was attached in a perfect rigid steel plate (1 cm of thickness), the failure load was 185.0 MPa. In that case, as the block could not be detached from the plate, a horizontal and a vertical crack was formed, breaking the block into two parts; in a certain way detaching it from the plate (Figure 4).



Figure 3. Block 2 after failure.



Figure 4. Block 3 after failure.

According to the method proposed by Clausen (2013) - for circular footing, without influence of the boundary conditions and assuming that the rock mass is homogeneous and isotropic - the bearing capacity of the rock in this study is about 475 MPa, once the GSI is 100, $m_i = 19$ and UCS = 22.1 MPa.

Using the analytical solution for anisotropic discontinuous rock mass (Serrano et al., 2016) jointly with the shape coefficient proposed by Alencar et al. (2019), it can be estimated the bearing capacity considering a horizontal discontinuity. The horizontal discontinuity represents the bottom of the blocks in the laboratory test. How can be observed in the results shows in Table 3 the values obtained in laboratory test are of the same order of magnitude as to estimate by the theory that is dependent on the discontinuity strength; remarking the influence of the discontinuities in the failure load.

Table 3. Bearing capacity estimated by Serrano et al. (2016) jointly with the coefficient proposed by Alencar et al. (2019).

Boundary condition		**Bearing Capacity (MPa)**
Internal friction angle of the discontinuity	10º	50
	20º	77
	30º	106
Without discontinuity		402

However, the theoretical solution implies the worse location of the horizontal discontinuity, while in the laboratory test it is between 4 and 10 times the width of the foundation. The great difference with the analytical solution in isotropic rock mass highlights the influence of the discontinuity resistance; while the different location of the lower contour in relation to the dimension of the experimental footing clearly indicates that the position is influential much more than expected, even at 10 the width of the foundation.

4 CONCLUSION

As expected in a case with high GSI, the ultimate bearing load is much higher than the UCS. However, it is important to highlight that although the spacing between the discontinuities (simulated) is much greater than the size of the foundation, still influences the failure load. Being the failure load obtained much less than estimated using the Clausen (2013) method or Serrano et al. (2000) that do not consider the presence of a discontinuity.

However, the results obtained in the experimental test are coherent to estimate using the method proposed by Serrano et al. (2016) for anisotropic discontinuous rock mass, jointly with the coefficient proposed by Alencar et al. (2019).

It was observed, that without lateral confinement, it is very difficult to achieve the formation of the theoretical failure wedges, occurring in the three cases the splitting.

As future work, this study can be extended by performing more tests with different geometric configurations - with the aim of knowing how the presence of a discontinuity, even distanced from the foundation, changes the ultimate bearing capacity and the manner of the failure.

ACKNOWLEDGEMENTS

The research described in this paper was financially supported by the European Union-NextGenerationEU - UP2021-035.

It has also been partially funded by the project “Neural networks and optimization techniques for the safe design and maintenance of transportation infrastructures: geotechnics of volcanic rocks and slope stability, IA-PYROSLOPE (PID2022-139202OB-I00)” of the Ministry of Education and Science.

The cooperation between the University of Porto and the Tecnical University of Madrid (UPM) is supported by the mobility program of the Universidad Politécnica de Madrid collaboration with Banco Santander (VMOVILIDAD23RAGA).

This work was also part of the research activities of CONSTRUCT (Institute of R&D in Structures and Construction), supported by national funds through FCT/MCTES (PIDDAC), with base funding UIDB/04708/2020.

REFERENCES

Alencar, A.S., Galindo, R., Melentijevic, S. (2019). Bearing capacity of foundation on rock mass depending on footing shape and interface roughness. *Geomech. Eng*., 18, 391–406.

Chi, C.-M.; Lin, Z.-S. (2020). The Bearing Capacity Evaluations of a Spread Footing on Single Thick Stratum or Two-Layered Cohesive Soils. *J. Mar. Sci. Eng*., 8, 853. https://doi.org/10.3390/jmse8110853.

Clausen, J. (2013). Bearing capacity of circular footings on a Hoek–Brown material. . *Int J Rock Mech Min Sci*. 57. 34–41. https://doi.org/10.1016/j.ijrmms.2012.08.004.

Hassani, M., Shokri, M., Ghanbari, A. (2023) Laboratory Study of the Behavior of Geogrid-Reinforced Strip Foundations with Inclined Loading. *Geotech Geol Eng* 41, 3335–3347. https://doi.org/10.1007/s10706-023-02458-w.

Hoek, E., Marinos, P., Benissi, M. (1998). Applicability of the Geological Strength Index (GSI) Classification for very weak and sheared rock masses. The case of the Athens Schist Formation. *Bul Eng Geo Env*. 57. 151-160. https://doi.org/10.1007/s100640050031.

Melentijevic, S., Alencar, A., Galindo, R. (2019). Failure mechanisms developed in rock masses under circular footing. *Proceedings of the XVII ECSMGE-2019*. https://doi.org/10.32075/17ECSMGE-2019-0537.

Prandtl, L. (1920). *Über die Härte plastischer Körper. Nachr. Ges*. Wiss. Goettingen, Math.-Phys. Kl., 74–85.

Serrano, A., Olalla, C., González, J. (2000) Ultimate bearing capacity of rock masses based on the modified Hoek–Brown criterion. *Int J Rock Mech Min Sci*, V 37-6, 1013-1018, https://doi.org/10.1016/S1365-1609(00)00028-9.

Serrano, A., Olalla, C., Galindo, R. A. (2016). Ultimate bearing capacity of an anisotropic discontinuous rock mass based on the modified Hoek–Brown criterion. *Int J Rock Mech Min Sci*, V 83, 24-40, https://doi.org/10.1016/j.ijrmms.2015.12.014.

Terzaghi, K. (1943). *Theoretical soil mechanics*. 5th ed., John Wiley & Sons Inc., N. Y.,N.Y.

Proceedings of the XVIII ECSMGE 2024
GEOTECHNICAL ENGINEERING CHALLENGES
TO MEET CURRENT AND EMERGING NEEDS OF SOCIETY
© 2024 the Authors
ISBN 978-1-032-54816-6
DOI 10.1201/9781003431749-28
Open Access: www.taylorfrancis.com, CC BY-NC-ND 4.0 license

ECSMGE 24
XVIII EUROPEAN CONFERENCE ON SOIL MECHANICS AND GEOTECHNICAL ENGINEERING

A comparative discussion on soil arching evolution in CPS and GRPS embankments

Une discussion comparative sur l'évolution de l'effet de voûte du sol dans les remblais en CPS et GRPS

M. Almasraf, A. Salimnezhad
Department of Civil Engineering, Ozyegin University, Istanbul, Turkey

B.E. Kelek, O. Cinininoglu
Department of Civil Engineering, Bogazici University, Istanbul, Turkey

S.F. Cinicioglu*
Department of Civil Engineering, Ozyegin University, Istanbul, Turkey

**feyza.cinicioglu@ozyegin.edu.tr*

ABSTRACT: The behavior and design of piled embankments constructed on soft soils are significantly influenced by soil arching, characterized by the redistribution of stresses between the yielding mass and the surrounding nonyielding soil. On the other hand, lateral spreading action within the embankment acts as an important factor in the load distribution mechanism. Considering the lateral deformations and principal stress directions, this study investigated arching evolution in CPS and GRPS embankments under self-weight using FEM analyses in 2D and 3D. A series of numerical models were employed to examine the impact of geometry parameters such as embankment height and center-to-center pile spacing on arching evolution. The lateral earth pressure coefficients and horizontal deformations inside the fill were observed to understand the arching mechanism and pile efficacy.

RÉSUMÉ: Le comportement et la conception des remblais sur pieux construits sur des sols mous sont significativement influencés par l'effet de voûte du sol, caractérisé par la redistribution des contraintes entre la masse déformable et le sol non déformable environnant. D'autre part, l'action de propagation latérale à l'intérieur du remblai constitue un facteur important dans le mécanisme de distribution des charges. En tenant compte des déformations latérales et des directions des contraintes principales, cette étude a examiné l'évolution de l'effet de voûte dans les remblais en CPS et GRPS sous l'effet de leur propre poids, en utilisant des analyses par la méthode des éléments finis en 2D et 3D. Une série de modèles numériques a été utilisée pour examiner l'impact de paramètres géométriques tels que la hauteur du remblai et l'espacement entre les pieux centre-à-centre sur l'évolution de l'effet de voûte. Les coefficients de pression latérale du sol et les déformations horizontales à l'intérieur du remblai ont été observés afin de comprendre le mécanisme de voûte et l'efficacité des pieux.

Keywords: Soil arching; CPS and GRPS embankments; lateral earth pressure coefficient; principal stress directions; Geogrid.

1 INTRODUCTION

Modern societies depend exceedingly on transportation systems, which cover extensive distances and demand specific considerations in their design. In geotechnical engineering, the interaction between soil and structures is an important aspect when designing transportation infrastructure like embankments, tunnels, and pipelines.

Embankments, frequently constructed in lowland areas with soft and alluvial soils, are particularly prone to significant settlements and deformations. Overcoming these challenges typically involves employing two common approaches. The first approach utilizes controlled stage construction techniques (Indraratna et al., 2005; Oztoprak and Cinicioğlu, 2005; Oser and Cinicioglu, 2017). The second method involves embedding piles into the ground beneath the embankment (Han and Gabr, 2002; Kelesoglu and Cinicioğlu, 2010). The latter approach is known for promoting soil arching, a phenomenon that has received increasing academic attention in recent years.

The economic and optimal use of piles beneath embankments to enhance soil arching has been investigated in numerous studies. However, the stability and durability of the load transfer mechanism resulting from arching are still subjects of ongoing

research, necessitating further investigation (Van Eekelen et al., 2013).

Embankments that are supported by high modulus columns (piles) are commonly known as "conventional pile-supported (CPS) embankments." Compared to the traditional staged construction method, CPS embankments are more efficient by significantly reducing expected settlement and shortening the construction period (Mesri et al., 1994; Fagundes et al., 2017). Moreover, CPS embankments can effectively prevent local failure and deformations (Van Eekelen et al., 2020).

The arching mechanism plays a crucial role in governing the CPS embankments' behavior, controlling the stress distribution between the soil and structural elements with different rigidities. Soil arching occurs due to the relative displacement of piles and soil.

Geosynthetic-reinforced pile-supported (GRPS) embankments were developed as an improvement to the CPS embankments (Van Eekelen and Han, 2020; Van Eekelen et al., 2020). Geosynthetic reinforcements create resistance to the lateral spreading of the fill. Geosynthetic reinforcements are laid in the granular fill as a load transfer platform on top of the piles. Thus, geosynthetic reinforcements support the arching mechanism in the soil by providing more efficient and stable load transfer to the piles. Likewise, when the GRPS embankments are preferred, the need for large pile caps is reduced, and the pile spacing can be increased (Van Eekelen et al., 2013; Van Eekelen et al., 2020).

In the CPS embankments, arching is the only mechanism that reduces the share of the fill load borne by the subsoil between the piles. However, in GRPS embankments, the loads from the fill located under the arched zone are transferred to the piles through geosynthetic reinforcement (Van Eekelen and Han, 2020).

Following the model proposed by Hewlett and Randolph (1988), the lateral earth pressure coefficient (K) in the arched zone between two piles can be classified into three states. These K values represent the active, passive, and at-rest conditions for points on the pile, under the arch crown, and above the arch, respectively. Observing how K values change both horizontally and vertically within the fill could be used as an indication of the arching evolution.

This study analyzes the potential relationships between the pile spacing, presence of geogrid reinforcement, embankment height, lateral fill displacement, piles' deflection, lateral earth pressure coefficient values, and arching evolution through 2D and 3D Finite Element analyses. Eighteen Plaxis 2D and three 3D model tests for various embankment heights and pile spacings were conducted for this purpose, and the results are presented in this paper.

2 MAIN FEATURES OF THE PARAMETRICAL ANALYSES

The conventional pile-supported (CPS) embankments under self-weight in a plane strain 2D and 3D conditions were modeled using the finite element method (FEM) based software Plaxis. The soil profile of Stanstead Abbots (Willow Plantation or Harlow) was selected as a well-documented case history to represent the soft ground over which the embankment will be constructed (Oztoprak and Cinicioglu, 2007; Hird et al., 1995). The soil stratigraphy and geotechnical properties of Stanstead Abbotts are presented in Figure 1 and Table 1, respectively. The groundwater table is located at a depth of 1.5 m beneath the ground surface. To focus on the arching behavior, the embankment's shoulder slopes were defined as 1:3 (V: H) to prevent potential slope instability.

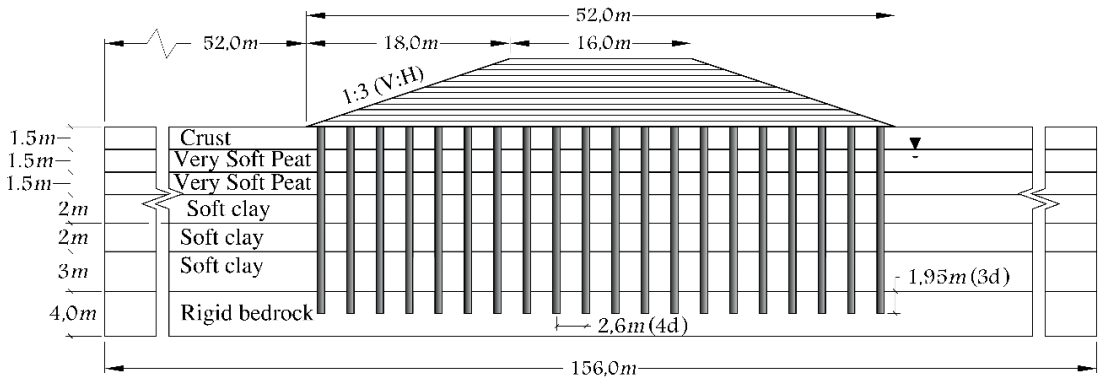

Figure 1. Studied embankment model.

Table 1. Material parameters for the piled embankment.

Material	Soil Model	Unit weight		Poisson's ratio	Permeability	Void ratio	Adopted from Hird et al., 1993		
		γ_{unsat} kN/m^3	γ_{sat} kN/m^3	ν_{ur}	$k_x=k_y$ m/s	e_0	λ^*	κ^*	ϕ (°)
Crust	Soft Soil	13	16	0.15	2.5×10^{-5}	0.8	0.060	0.009	29
Very soft peat		7.4	11.4	0.15	2.5×10^{-5}	7.3	0.147	0.006	34
Very soft peat		7.4	11.4	0.15	2.5×10^{-5}	8.2	0.179	0.020	34
Soft clay		13.2	16.2	0.15	2.5×10^{-10}	1.5	0.163	0.015	28
Soft clay		13.2	16.2	0.15	2.5×10^{-10}	1.45	0.158	0.013	28
Soft clay		13.2	16.2	0.15	2.5×10^{-10}	1.4	0.060	0.009	28
Embankment fill	Hardening Soil	16	19	0.2	4×10^{-5}	0.5	E_{50}^{ref} kN/m^2	E_{oed}^{ref} kN/m^2	E_{ur}^{ref} kN/m^2
							25×10^3	25×10^3	75×10^3
Bedrock	Mohr-Coulomb	27	30	0.3	-	0.5	E'_{ref} kN/m^2	-	-
							4.9×10^6		
Pile	Linear Elastic	24	24	0.3	-	-	30×10^6	-	-

The behavior of the soft ground beneath the embankment was modeled using the soft soil model with undrained loading stages followed by the consolidation stages in between.

Three different heights (6, 8, and 10m) were considered to analyze the behavior of the GRPS and CPS piled embankments resting on the considered soil profile. The staged construction technique was adopted, and layer placement thicknesses were chosen as 0.5m each. After completion of fill construction, excess pore water pressure was allowed to dissipate during the final consolidation phase.

A reduction factor (R_{inter}) of $2/3\phi$ was applied to the shear strength parameter of the soil surrounding the piles. The soil profile ends with a bedrock layer at the bottom. Piles of 13.45 meters were embedded for a depth of 3d into the bedrock. The pile diameters (d) were taken as 0.65m across all models. The center-to-center spacing of the piles varied as 4d, 5d, and 6d. Also, three CPS models with a pile spacing of 5d and the rectangular pile arrangement were analyzed in 3D.

The CPS 2D FEM models were analyzed after being reinforced with two layers of geogrid located at 0.35m and 0.7m over the pile heads. The geogrid layer is defined as an elastic material with isotropic properties and a stiffness (EA) equal to 1500 kN/m.

3 RESULTS

Figure 2 displays the variation in K values against the fill height through a vertical cross-section from the top to the bottom of the fill centerline for GRPS and CPS models. There are two main ranges for the K value along the cross-section: compression ($K_p<K<K_0$) and relaxation ($K_a<K<K_0$) zones.

The compression zone is a key indicator of arching and mobilized shear strength. The thickness of the compression region increases with the increase of pile spacing. However, the strongest part of the formed arches is located where the K value is closest to K_p = 3, indicating the greatest compression of the soil grains.

The lateral spreading of the embankment from the centerline towards the toes leads to the formation of a region with the K value ranging from K_a to K_0 (relaxation zone). Inspecting the thickness of the relaxation zone in the GRPS models with geogrid shows that the thickness is smaller for the geogrid-reinforced models compared to the models with no geogrid. This observation supports the idea that the lateral spreading of the embankment could be the reason for the formation of the relaxation zone. The presence of the geogrid layers limits the horizontal deformation, and as a result, the thickness of the relaxation zone will be reduced, too. It means that the thickness or height of the passive zone would also be greater for the GRPS models.

Previous studies using trapdoor models or specific embankment sections have shown that, due to the rigidity of the side walls or boundaries, the K values through the same vertical cross-section start from K_0 and reach K_p in the arching zone (Meena et al., 2020). This behavior is due to the limited horizontal deformation of soil in models with rigid side boundaries. In contrast, modeling the full-size embankment allows for lateral spreading of the fill from the centerline towards the sides, resulting in the formation of the active zone under the crest.

Figure 3 illustrates the lateral earth pressure values (K) variation along a vertical cross-section (at the centerline) in the 6m high embankment with the pile

spacings of 4d, 5d, and 6d. Also, in the left part of Figure 3, the principal stress direction is shown through the half-body of the fill. The rotation of the principal stresses is an indication of arching.

For the GRPS models, the arch height, which was calculated based on the direction of the principal stresses, is as follows: for all fill heights with the 4d pile spacing, the arch height is 1.9m. In models with the 5d and 6d pile spacing, the arch height range is 2.45m- 2.25m and 3.m-2.65m for the fill heights of 4m, 5m, and 6m, respectively.

In the case of CPS models, for all fill heights with the 4d pile spacing, the arch height is 1.7m. In models with the 5d pile spacing, the arch height range is 2.3m-1.85m and 2.7m-2.4m for the fill heights of 4m, 5m, and 6m, respectively. It is obvious that in both GRPS and CPS models with a pile spacing of 4d, the arch height is not sensitive to changes in fill height.

It should be noted that arch heights are always smaller than the compression zone thickness. The results indicated that, for both CPS and GRPS models, only a K value greater than 0.95 leads to the formation of an arch within the compression zone.

Figure 4 presents the difference between the pile head deflection for the GRPS and CPS embankments with 6, 8, and 10 m heights and different pile spacings of 4d, 5d, and 6d. It could be seen that there is a considerable difference between the maximum pile deflection of GRPS and CPS models. The difference between the deflection of the CPS and GRPS embankment models is more prominent when the center-to-center spacing between the piles increases from 4d (2.6m) to 6d (3.9m).

The horizontal deformation of the 10mH-6d GRPS and CPS embankment models at the bottom of the fill is demonstrated in Figure 5. The maximum horizontal displacement for the CPS model is 15.6cm at 18 m from the centerline, and the value decreases to 11.67cm at 21m for the GRPS model.

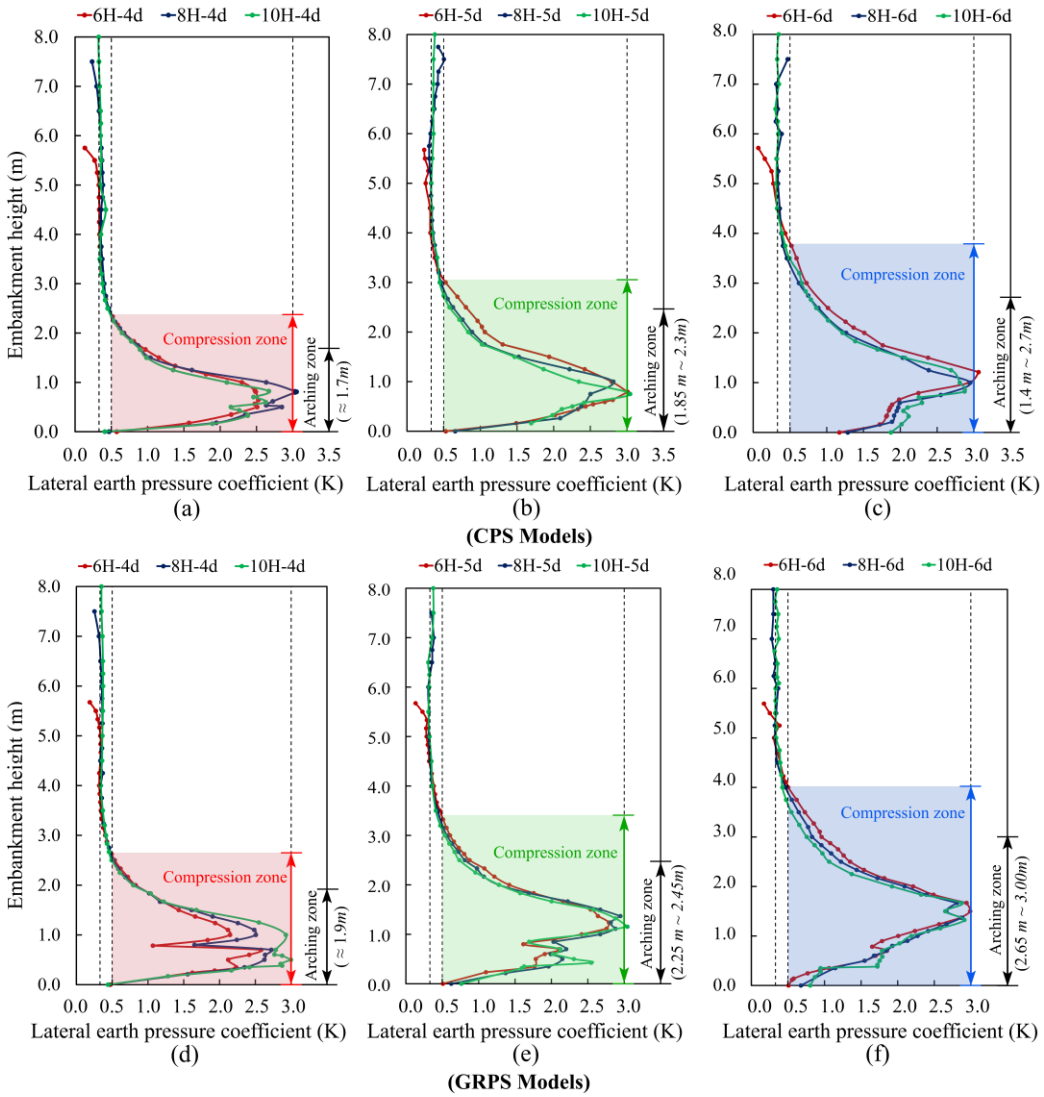

Figure 2. Lateral earth pressure at the vertical centerline of CPS and GRPS embankments.

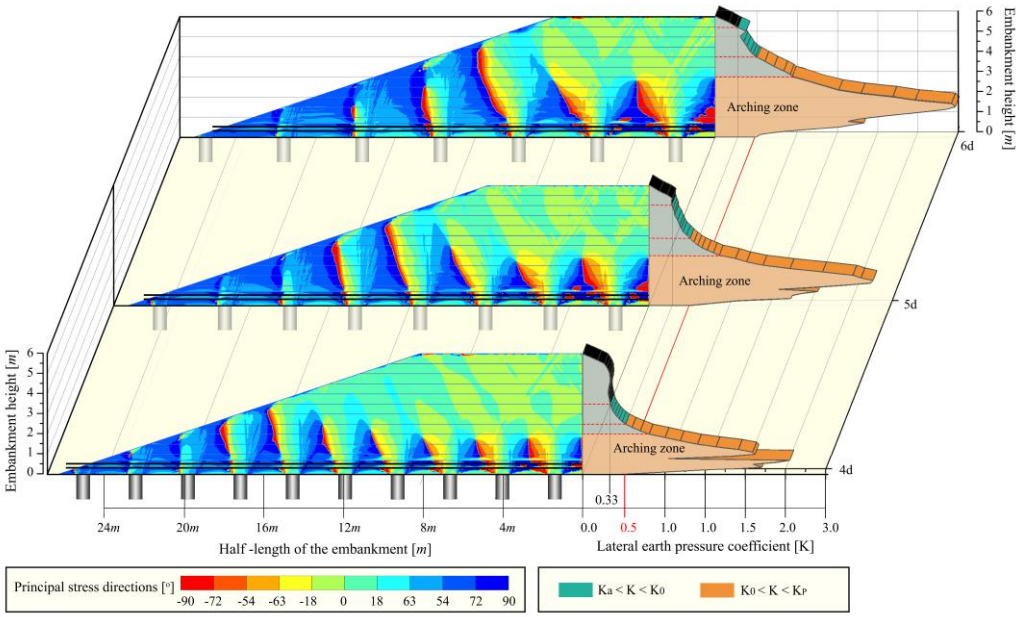

Figure 3. Relationship between principal stress directions and K values for 6m high embankment.

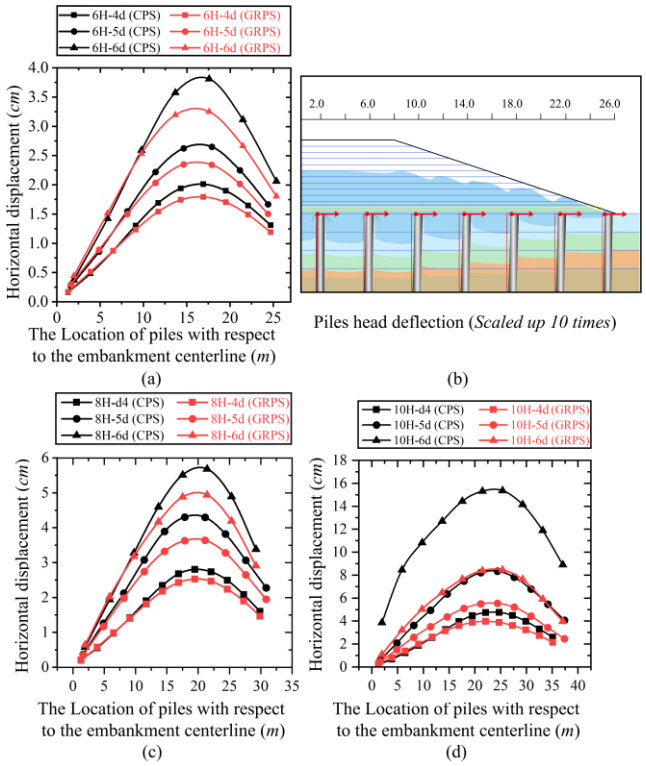

Figure 4. Piles' head deflection for CPS and GRPS models.

Figure 6 shows the pile efficacy (E) for all CPS and GRPS models versus the height of the embankment (H) and center-to-center pile spacing (s). Pile efficacy can be defined as the ratio of the loads carried by the piles to the total load of the embankment calculated as $E = P/s\gamma H$ (P is the total load carried by the pile). It is obvious that the pile efficacy for the geogrid-reinforced models improves in comparison with the models with no geogrid. For example, for the 4d pile spacing in all heights, there is an almost 10% improvement in the pile efficacy values. Moreover, the efficacy of 3D models with 5d pile spacing is greater than that of GRPS and CPS 2D models' efficacy. In the case of 3D models, the efficacy is raised by increasing the fill height. The results for GRPS models showed that the efficacy increases with a decrease in pile spacing.

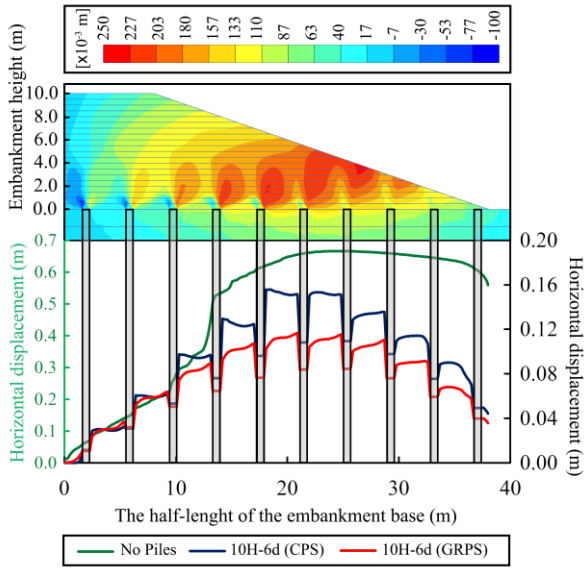

Figure 5. Horizontal displacement of GRPS and CPS embankments' base for 10mH-6d model versus non-piled embankment.

4 CONCLUSIONS

The effects of varying parameters, such as pile spacing and embankment height, on the arching evolution were studied through numerical analysis of CPS and GRPS

embankment models. The study yields the following conclusions:

The use of geogrid reinforcement decreased the piles' deflection and the horizontal displacement of the embankment.

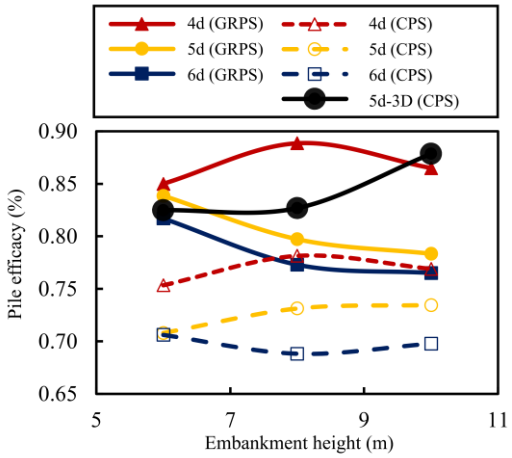

Figure 6. Pile efficacy of GRPS and CPS models.

Geogrid reinforcement increased the thickness of the compression zone and improved the load transfer mechanism to piles. For both CPS and GRPS models, only a K value greater than 0.95 leads to the formation of an arch within the compression zone.

The efficacy of CPS and GRPS increases with a decrease in pile spacing.

ACKNOWLEDGEMENTS

The authors would like to thank the Scientific and Research Council of Turkey (TUBITAK) for supporting this study with project number 122M040.

REFERENCES

Fagundes, D. F., Almeida, M. S., Thorel, L., and Blanc, M. (2017). Load transfer mechanism and deformation of reinforced piled embankments. *Geotextiles and Geomembranes*, 45(2), 1-10. https://doi.org/10.1016/j.geotexmem.2016.11.002.

Han, J., and Gabr, M. A. (2002). Numerical analysis of geosynthetic-reinforced and pile-supported earth platforms over soft soil. *Journal of geotechnical and geoenvironmental engineering*, 128(1), 44-53. https://doi.org/10.1061/(ASCE)1090-0241(2002)128:1(44).

Hewlett, W. J., and Randolph, M. F. (1988). Analysis of piled embankments. In *International journal of rock mechanics and mining sciences and geomechanics abstracts* (Vol. 25, No. 6, pp. 297-298). Elsevier Science. https://doi.org/10.1016/0148-9062(88)91283-1.

Hird, C. C., (1993). *Numerical Modelling of the Willow Plantation Embankment (Stanstead Abbotts)*. Research Report No: DCSE/93/G/1, University of Sheffield, UK.

Hird, C. C., Pyrah, I. C., Russell, D., and Cinicioglu, F. J. C. G. J. (1995). Modelling the effect of vertical drains in two-dimensional finite element analyses of embankments on soft ground. *Canadian Geotechnical Journal*, 32(5), 795-807. https://doi.org/10.1139/t95-077.

Indraratna, B., Sathananthan, I., Bamunawita, C., and Balasubramaniam, A. S. (2005). Theoretical and numerical perspectives and field observations for the design and performance evaluation of embankments constructed on soft marine clay. In *Elsevier geo-engineering book series* (Vol. 3, pp. 51-89). Elsevier. https://doi.org/10.1016/S1571-9960(05)80005-9.

Kelesoglu, M. K., and Cinicioglu, S. F. (2010). Free-field measurements to disclose lateral reaction mechanism of piles subjected to soil movements. *Journal of geotechnical and geoenvironmental engineering*, 136(2), 331-343. https://doi.org/10.1061/(ASCE)GT.1943-5606.0000217

Meena, N. K., Nimbalkar, S., Fatahi, B., and Yang, G. (2020). Effects of soil arching on behavior of pile-supported railway embankment: 2D FEM approach. *Computers and Geotechnics*, 123, 103601. https://doi.org/10.1016/j.compgeo.2020.103601.

Mesri, G., Lo, D. O. K., and Feng, T. W. (1994, January). Settlement of embankments on soft clays. In *Proceedings of the Conference on Vertical and Horizontal Deformations of Foundations and Embankments*. Part 2 (of 2) (pp. 8-56). Publ by ASCE.

Oztoprak, S., and Cinicioglu, S. F. (2005). Soil behaviour through field instrumentation. *Canadian geotechnical journal*, 42(2), 475-490. https://doi.org/10.1139/t04-121.

Oztoprak, S., and Cinicioglu, S. F. (2007). Looking into an appropriate methodology for the embankment design and construction on soft soils. *Lowland Technology International*, 9(2, Dec), 21-28.

Oser, C., and Cinicioglu, S. F. (2017). Embankment Design Method Combining Limit-State Approach with Stress-Path Application. *International Journal of Geomechanics*, 17(4), 04016101. https://doi.org/10.1061/(ASCE)GM.1943-5622.0000796.

Van Eekelen, S. J. M., Bezuijen, A., and Van Tol, A. F. (2013). An analytical model for arching in piled embankments. *Geotextiles and Geomembranes*, 39, 78-102. https://doi.org/10.1016/j.geotexmem.2013.07.005.

Van Eekelen, S. J. M., and Han, J. (2020). Geosynthetic-reinforced pile-supported embankments: state of the art. *Geosynthetics International*, 27(2), 112-141. https://doi.org/10.1680/jgein.20.00005.

Van Eekelen, S. J. M., Venmans, A. A. M., Bezuijen, A., & Van Tol, A. F. (2020). Long term measurements in the Woerden geosynthetic-reinforced pile-supported embankment. *Geosynthetics International*, 27(2), 142-156. https://doi.org/10.1680/jgein.17.00022.

Proceedings of the XVIII ECSMGE 2024
GEOTECHNICAL ENGINEERING CHALLENGES
TO MEET CURRENT AND EMERGING NEEDS OF SOCIETY
© 2024 the Authors
ISBN 978-1-032-54816-6
DOI 10.1201/9781003431749-29
Open Access: www.taylorfrancis.com, CC BY-NC-ND 4.0 license

ECSMGE 24
XVIII EUROPEAN CONFERENCE ON SOIL MECHANICS AND GEOTECHNICAL ENGINEERING

A modified Rowe cell with bender elements for dynamic testing of soils and interfaces

Une cellule Rowe modifié avec des capteurs piézoélectriques pour des essais dynamique des sols et des interfaces

A. Almukashfi
ISISE, Universidade do Minho, Guimarães, Portugal

R. Castellanza
Department of Earth and Environmental Sciences (DISAT), University of Milano-Bicocca, Milan, Italy

A. Gomes Correia
ISISE, Universidade do Minho, Guimarães, Portugal

M. Arroyo
Department of Geotechnical Engineering and Geosciences, UPC, Barcelona, Spain

C. Zuretti
Zuretti Luigi srl; Mesenzana (VA), Italy

D. Bendea, I.D. Moldovan*
Faculty of Engineering, Lusófona University, Lisbon, Portugal/CERIS, IST, UL, Lisbon, Portugal
**dragos.moldovan@ulusofona.pt*

ABSTRACT: The expansion of construction projects in seismic regions with poor soil conditions and the vast legal and financial implications of faulty geotechnical information have led stakeholders to call for faster, cheaper and more reliable characterization of geomaterials under dynamic conditions. A popular approach to dynamic testing of geomaterials involves piezoelectric transducers called bender elements. Despite their widespread use, bender element measurements are still hampered by considerable uncertainty in the interpretation of the output signal. Aspects such as wave directivity, apparatus-induced size effects, and boundary reflectivity are still poorly understood and accounted for. This communication presents a modified Rowe cell apparatus, designed to obtain experimental data to better understand these effects. Besides offering all advantages of a conventional Rowe cell (controllable state conditions, hydraulic loading), the device is fitted with bender elements, and features a larger diameter (200mm), adjustable height (20-100mm) and controllable boundary conditions (rigid, semi-rigid or flexible). The cell offers eight insertion slots where bender elements can be housed with distinct orientations. The bender elements operate in echo mode as the insertion slots are located on the same side of the sample. A reliability study of the new Rowe cell is presented, along with some illustrative examples of its potential use.

RÉSUMÉ: L'expansion des projets de construction dans des régions sismiques présentant des sols de mauvaise qualité et les vastes implications juridiques et financières d'informations géotechniques erronées ont conduit les parties concernées à appeler à une caractérisation plus rapide, moins coûteuse et plus fiable des géomatériaux dans des conditions dynamiques. Une approche populaire de l'essai dynamique des géomatériaux fait appel à des capteurs piézoélectriques appelés «bender elements». Malgré leur utilisation répandue, les mesures par des capteurs piézoélectriques sont encore pénalisées par une incertitude considérable dans l'interprétation du signal de sortie. Des aspects tels que la trajectoire des ondes, les effets de taille induits par les appareils et la réflectivité aux limites sont encore méconnus et pris en compte.Cette communication présente une nouvelle cellule Rowe, conçu pour obtenir des données expérimentales permettant de mieux comprendre ces effets. Outre les avantages d'une cellule Rowe conventionnelle (conditions d'état contrôlées, chargement hydraulique), l'appareil est équipé de capteurs piézoélectriques et présente un plus grand diamètre (200 mm), une hauteur réglable (20-100 mm) et des conditions aux limites contrôlées (rigide, semi-rigide ou flexible). La cellule offre huit emplacements d'insertion dans lesquels des capteurs piézoélectriques peuvent être logés avec des orientations particulières. Les capteurs piézoélectriques fonctionnent en mode écho car les emplacements d'insertion sont situées du même côté de l'échantillon. Une étude de fiabilité de la nouvelle cellule Rowe est présentée, accompagnée de quelques exemples illustrant son utilisation potentielle.

Keywords: Small strain shear modulus; bender element; modified Rowe cell; dynamic interface.

1 INTRODUCTION

Bender elements (BEs) are piezoelectric transducers used for the experimental identification of small strain shear moduli (G_0) of geomaterials. A typical BE setup consists of two BEs: a transmitter that is excited by a voltage (input signal) and vibrates laterally to generate a shear wave, and a receiver that reads the arrival of that wave at another point of the geomaterial (output signal). The travelling time of the shear wave gives its velocity, from which the shear modulus can be obtained. Despite their widespread use, the precision, reproducibility, and robustness of G_0 measurements obtained with BEs are still largely open to debate. The main questions are related to the identification of wave travel time, for which a variety of time and frequency domain techniques exist, but no clear consensus has emerged (e.g. Arroyo et al. 2010, Yang & Gu, 2013).

A key component of BE test uncertainty is model error (Arroyo et al. 2006). The elastodynamic model underlying most current interpretation methods is that of a plane wave propagating between source and receiver. Using this simple model, a variety of relevant wave-propagation phenomena like near-field effects (Lee & Santamarina, 2005), sample boundary effects (Moldovan & Correia, 2021) or particle scattering (Yang & Gu, 2013) become noise. Those noises are strongly dependent on the source-to-receiver distance, sample dimensions, or particle diameter.

A modified Rowe cell fitted with multi-directional BEs was designed and manufactured to better understand such issues. As opposed to oedometers, Rowe cells offer drainage control, measure the pore water pressure, and are less prone to environmental perturbations as they use hydraulic loading systems. An adaptation of a Rowe cell to allow for the insertion of BEs was reported by Ngoc et al (2019). The benders were installed in the tip-to-tip configuration, which hinders some of the mechanical systems of the cell, like the pressurized membrane at the top of the sample. In the present work, the transmitter and receiver BEs are installed only in the bottom pedestal of the apparatus and measure the rebounds of the wave from the top boundary. The top platen can be rigid or flexible. The rebound measurement is a relatively new concept in BE experiments and proven particularly convenient in the context of Rowe measurements. The following sections present a brief description of the modified Rowe cell and its measurements.

2 DESIGN AND CONSTRUCTION

The prototype design is based on a conventional Rowe cell, modified to enable the flexible definition of the sample's geometry, fitting of BEs, and multiple types of boundary conditions. The diameter of the sample is set to 200 mm and its height can be varied between 40 and 200 mm. A drainage line enables the pore water pressure measurement. Additionally, a displacement transducer (LVDT) is incorporated for the accurate measurement of the vertical strain (Figure 1).

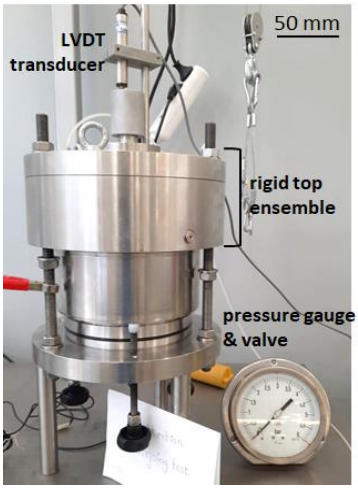

Figure 1. General view of the modified Rowe cell.

The bottom pedestal is designed to hold up to eight BEs in different positions. These were selected using numerical models (Moldovan & Cismasiu 2018) to enable both off-centre and off-plane locations of the BEs (Figure 2). The distance between a transmitter inserted in the center of the pedestal, and the receiver ranges between 30 mm (B4) and 70 mm (B1) with 10 mm increments. Slot C4 is an exception, its distance to the transmitter being $30\sqrt{2}$ mm.

The installation and removal of the BEs from the pedestal are simplified by specially designed bender capsules and screws. On the internal walls of the slots, O-rings are inserted, to fix the BEs and stop leakage when a test is performed on a saturated sample. The slots that are not hosting BEs are filled with metallic plugs.

Transmitter and receiver BEs may be installed in the same plane or out of plane. The coplanar setup is aimed at minimizing the content of compression waves in the output signal. Conversely, the non-coplanar setup is aimed at accommodating both (direct) compression waves and (reflected) shear waves in the same output signal.

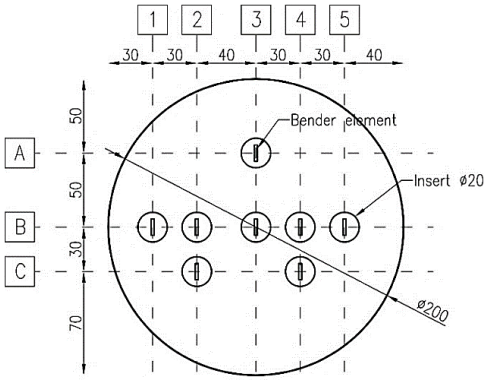

Figure 2. Insertion slots of BEs in the bottom pedestal.

On the opposite side of the sample, various boundary conditions may be applied, including rigid (steel, aluminum, plexiglass) or fluid-pressurized flexible membrane. The rigid setups (Figure 3) are designed to maximize boundary reflections, enabling the best possible echo reading of the shear wave signal for the correct assessment of G0. The rigid plates are actuated by a piston capable of applying up to 70 MPa of pressure to the geomaterial.

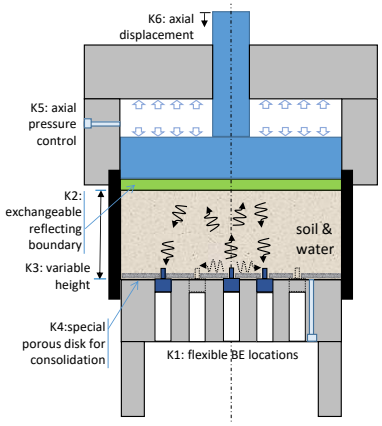

Figure 3. Rigid top boundary configuration.

The flexible setup (Figure 4) uses a pressurized membrane to apply the confining pressure to the geomaterial. The setup is designed to replicate the flexible boundary conditions that occur in triaxial pressure chambers, enabling the quantification of the wave energy that is lost at the sample-apparatus interface. As opposed to the rigid setup, the objective of flexible setups is to maximize the energy radiated from the sample (boundary losses).

3 RELIABILITY AND VALIDATION

An extensive set of experiments was performed to validate the BE results obtained with the new Rowe cell against other results available in the literature, and to assess their reproducibility (consistency of repeated measurements).

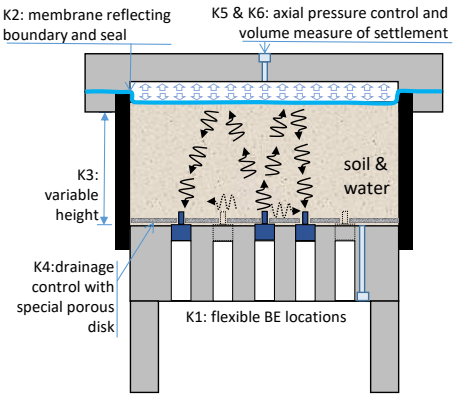

Figure 4. Flexible top boundary configuration.

The experiments were conducted on dry samples of the Toyoura sand benchmark (Yamashita et al., 2009) and performed using a sample height of 60 mm. Toyoura sand is rounded and uniformly graded, with almost no particles with a diameter below 75 µm (Sieve No. 200). The sand has a mean particle diameter D_{50} of 0.15 mm and a uniformity coefficient C_u of 1.43. One BE receiver was used, located 30 mm away from the transmitter BE in a non-coplanar setup (Figure 5). The experiment is conducted using a rigid boundary. The applied vertical pressure is 200kPa. While various void ratios were tested, the results presented below were obtained for e=0.85.

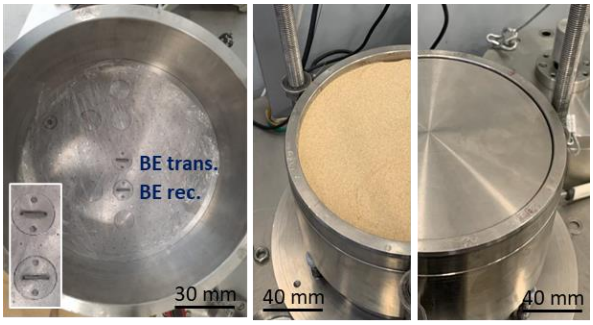

Figure 5. BEs, sample preparation, and rigid top platen.

To assess the reliability of the G_0 measurements in the echo mode, the tests were repeated 10 times in full, i.e. the sample was removed from the modified Rowe cell, dried and set up again. The correlations between the output signals obtained on these tests varied between 0.762 and 0.997, with most results above 0.850, indicating strong correlation. The error bands of the output signals for all experiments are presented in Figure 6. The signals obtained in the 10 experiments are consistent until the arrival of the shear waves and less so after that, as the higher attenuation and complexity affecting reflection patterns compromise the consistency of the plots. The validation of the modified Rowe cell measurements is based on the comparison of the shear moduli obtained with six interpretation techniques (first break, first bump, zero-

crossing, peak-to-peak, cross-correlation, and cross-spectrum) and for three void ratios, with those reported by an international parallel test (Yamashita, et al. 2009). The average shear moduli obtained in the modified Rowe cell on 10 repeated experiments are around the median values of the shear moduli reported by the parallel test (Figure 7), indicating that the measurements are consistent with established practice.

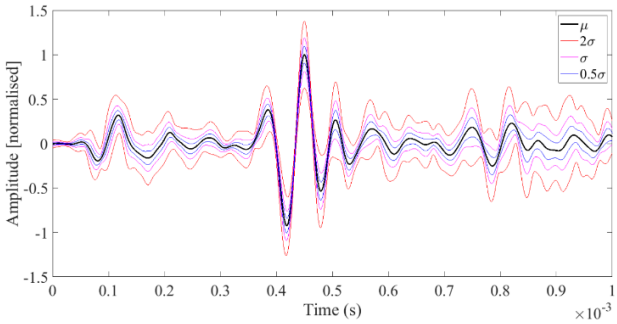

Figure 6. Average and error bands of output signals.

The results are relatively compact, with standard deviations below 4% of the average value, which means that approximately 95% of the readings are anticipated to fall within 8% of the average value.

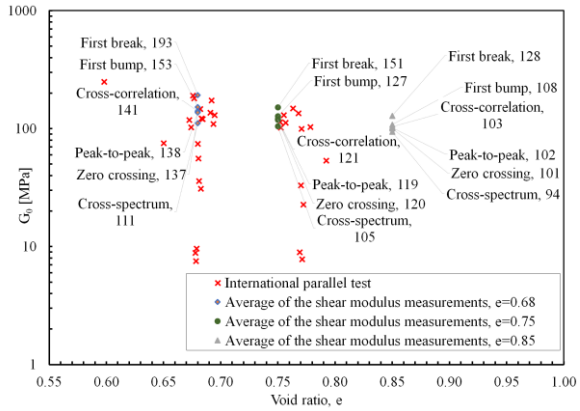

Figure 7. Shear moduli obtained with the modified Rowe cell (using rigid top boundary), in the context of the international parallel test.

4 CONCLUSIONS

A new, modified Rowe cell with flexible geometry was designed to be fitted with BEs. The BE locations and orientations are flexible, enabling the observation of multiple shear and compression waves with a single receiver. Besides offering the same level of control as a regular Rowe cell, the new device can be fitted with different boundary conditions on the plate with no BEs. Rigid boundary conditions can be used to maximize the wave reflections and support a clear reading of the shear modulus in the echo mode, while flexible boundaries can be used to assess boundary losses in conditions similar to those in the triaxial test. The readings obtained with the new device are robust and match those reported in literature benchmarks.

ACKNOWLEDGEMENTS

This research is supported by Fundação para a Ciência e Tecnologia through projects PTDC/EAM-GTC/29923/2017, 2022.06879.PTDC, UIDB/04625/2020, and UIDB/04029/2020.

REFERENCES

Arroyo, M., Muir Wood, D., Greening, P.D., Medina, L. and Rio, J. (2006). Effects of sample size on bender-based axial G0 measurements. *Géotechnique,* 56(1): 39-52. https://doi.org/10.1680/geot.2006.56.1.39.

Arroyo, M., Pineda, J.A. and Romero, E. (2010). Shear wave measurements using bender elements in argillaceous rocks. *Geotechnical Testing Journal,* 33: 1-10. https://doi.org/10.1520/GTJ102872.

Lee, J.-S. and Santamarina, J. (2005). Bender elements: performance and signal interpretation. *Journal of Geotechnical and Geoenvironmental Engineering,* 131(9): 1063–1070. https://doi.org/10.1061/(ASCE)1090-0241(2005)131:9(1063).

Moldovan, I.D. and Cismasiu, I. (2018). FreeHyTE: a hybrid-Trefftz finite element platform. *Advances in Engineering Software,* 121: 98-119. https://doi.org/10.1016/j.advengsoft.2018.03.014.

Moldovan, I.D. and Correia, A.G. (2021). Optimisation of receiver's location in bender element experiments using computational wave filtration. *Soil Dynamics and Earthquake Engineering,* 143: 106591. https://doi.org/10.1016/j.soildyn.2021.106591.

Ngoc, T., Fatahi, B. and Khabbaz, H. (2019). Impacts of drying-wetting and loading-unloading cycles on small strain shear modulus of unsaturated soils. *International Journal of Geomechanics,* 19(8): 04019090.https://doi.org/10.1061/(ASCE)GM.1943-5622.0001463.

Yamashita, S., Kawaguchi, T., Nakata, Y., Fujiwara, T. and Shibuya, S. (2009). Interpretation of international Parallel Test on the Measurement of Gmax Using Bender Elements. *Soils and Foundations,* 49(4): 631-650. https://doi.org/10.3208/sandf.49.631.

Yang, J. and Gu, X. Q. (2013). Shear stiffness of granular material at small strains: does it depend on grain size? *Géotechnique,* 63(2): 165-179. https://doi.org/10.1680/geot.11.P.083.

Proceedings of the XVIII ECSMGE 2024
GEOTECHNICAL ENGINEERING CHALLENGES
TO MEET CURRENT AND EMERGING NEEDS OF SOCIETY
© 2024 the Authors
ISBN 978-1-032-54816-6
DOI 10.1201/9781003431749-30
Open Access: www.taylorfrancis.com, CC BY-NC-ND 4.0 license

ECSMGE 24
XVIII EUROPEAN CONFERENCE ON SOIL MECHANICS AND GEOTECHNICAL ENGINEERING

Renforcement par inclusions rigides: évaluation du transfert de charge au sein d'une plateforme granulaire renforcée ou non par des géosynthétiques

Soil reinforced by rigid inclusions: evaluation of the load transfer within the granular platform reinforced or not by geosynthetics

A.M. Alzate*, B. Simon
Terrasol, Paris, France

C. Terqueux
Menard, Orsay, France

L. Briançon
INSA Lyon, Lyon, France

P. Villard
3SR/CNRS UMR 552/University Grenoble Alpes, Grenoble, France

**anamaria.alzate@setec.com*

RESUME: Cet article s'inscrit dans le cadre du projet national français ASIRI+ (2019 - 2024) qui est une extension du projet ASIRI (2005-2012) et qui vise à fournir des recommandations pour la conception d'un renforcement par inclusions rigides. Le premier objectif de l'article est d'améliorer les méthodes analytiques d'ASIRI (2012) pour la conception de plateformes de transfert de charge dans le cas des semelles sur inclusions rigides, en utilisant des calculs par éléments finis en 3D. Le deuxième objectif est de comparer différentes méthodes de dimensionnement de renforcement par géosynthétiques afin de développer et de valider un modèle analytique. Trois méthodes sont étudiées: la méthode Concentric Arches (CA), une méthode d'éléments discrets en 3D (DEM), et un modèle biphasique simplifié (Taspie+).

ABSTRACT: This article is part of the French national project ASIRI+ (2019 - 2024), an extension of the ASIRI project (2005-2012), aiming to provide recommendations for the design of a soil reinforced by rigid inclusions. The first objective of the article is to improve the analytical methods of ASIRI (2012) for the design of load transfer platforms in the case of shallow foundations on rigid inclusions, using 3D finite element calculations. The second objective is to compare different methods for the design of geosynthetic reinforcement in order to develop and validate an analytical design model. Three methods are studied: the concentric arches method (CA), a 3D discrete element method (DEM), and a simplified biphasic model (Taspie+).

Keywords: Geosynthetics; rigid inclusions; concentric arches; load transfer platforms; shallow foundations.

1 INTRODUCTION

Le renforcement par inclusions rigides est un procédé qui s'est largement répandu en France ces trente dernières années. Les recommandations ASIRI (2012) ont détaillé des méthodes simplifiées pour la définition de la charge limite pouvant être reprise par le matelas de répartition. Ces méthodes sont largement éprouvées pour la définition de la charge limite lorsque le mécanisme de poinçonnement du matelas peut se développer « librement » (calculs en zone courante pour une maille infinie avec une épaisseur de matelas et un entraxe entre les inclusions suffisant). En revanche, les méthodes proposées peuvent s'avérer conservatives dans le cas particulier des semelles sur inclusions et dans le cas des remblais ne permettent pas d'évaluer le transfert de charge dans le matelas en présence des géosynthétiques.

Cet article a pour objectif de définir quelques pistes d'amélioration des méthodes simplifiées afin de d'évaluer le transfert de charge dans le cas d'un matelas de répartition, avec ou sans géosynthétiques, sous une semelle (§2) ou sous un remblai (§3).

2 SEMELLE SUR INCLUSIONS RIGIDES

2.1 Règles simplifiées d'ASIRI

Suivant les règles ASIRI (2012), la contrainte limite de poinçonnement dans le matelas $q_p^+(P)$ est déterminée en partie courante suivant le mécanisme de Prandtl à partir de la formule ci-dessous (avec q_s^+ la contrainte dans le sol à la base du matelas à la rupture et N_q facteur de portance) ; la contribution du poids et de la cohésion sont négligés:

$$q_p^+(P) = N_q q_s^+ \qquad (1)$$

La formule ci-dessous suppose implicitement un développement « libre » d'un mécanisme de poinçonnement au sein du matelas (épaisseur et entraxe suffisants). Dans le cas d'une semelle sur IR, la résistance au poinçonnement du matelas peut être affectée défavorablement par l'effet de bord (Figure 1).

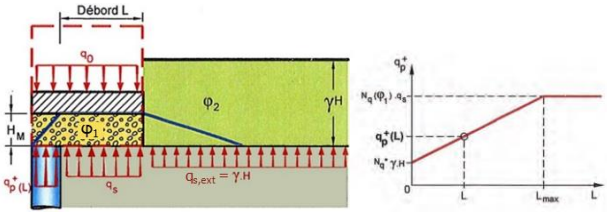

Figure 1. Prise en compte du débord L [ASIRI, 2012].

ASIRI (2012) propose une approche simplifiée consistant à interpoler entre la contrainte de référence $q_p^+(P)$ correspondant au débord L_{max} (obtenue avec un facteur de portance N_q de l'ordre de 30 à 50) et la contrainte $q_p^+(0)$ correspondant à un débord nul (obtenue avec une borne inférieure du facteur de portance noté N_q^*, de l'ordre de 10 à 30). La contrainte résultante notée $q_p^+(L)$ est définie comme suit:

$$q_p^+(L) = q_p^+(0) + \frac{L}{L_{max}}\left(q_p^+(P) - q_p^+(0)\right) \qquad (2)$$

avec : $q_p^+(0) = N_q^* q_{s,ext}$

L_{max} : largeur du mécanisme de Prandtl.

Cette approche est complétée par des règles empiriques pour prendre en compte la position des inclusions dans la semelle. En particulier, pour une inclusion située dans le coin on a:

$$q_{p,a}^+ = \frac{7}{12} q_p^+(P) + \frac{5}{12} q_p^+(L) \qquad (3)$$

Enfin, à titre de comparaison, on peut définir un facteur de portance équivalent avec effet de bord noté « $N_{q,eq}$ » en posant : $N_{q,eq} = q_{p,a}^+ / q_s$ où q_s est défini tel que $q_0^* = \alpha \times q_{p,a}^+ + (1-\alpha) \times q_s$, α étant le taux de substitution et q_0* la contrainte moyenne à la base du matelas. Afin d'illustrer la démarche, on étudie le cas d'une semelle carrée sur quatre inclusions de diamètre B suivant les données du Tableau 1. Le Tableau 2 présente les résultats obtenus pour L = 0,6 m, q_0^* = 100 kPa.

Tableau 1. Paramètres de calcul.

$B_{semelle}$ [m]	B [m]	φ_1 [°]	φ_2 [°]	α [%]	$q_{s,ext}$ [kPa]
2,21	0,34	38	30	7,4	10

Tableau 2. Résultats – ASIRI (2012).

N_q [-]	N_q* [-]	L_{max} [m]	$q_p^+(0)$ [kPa]	$q_p^+(P)$ [kPa]	$q_p^+(L)$ [kPa]	$q_{p,a}^+$ [kPa]	$N_{q,eq}$ [-]
49	26	2,4	260	1084	465	826	19

2.2 Comparaison à un traitement numérique en éléments finis 3D

Le facteur $N_{q,eq}$ obtenu avec les règles simplifiées ASIRI (2012) est comparé à celui obtenu via un modèle aux éléments finis 3D. On reprend la configuration décrite dans le Tableau 1 et on étudie un quart de modèle par symétrie (voir Figure 2). Une étude paramétrique est réalisée en faisant varier le rapport entre le débord L et le diamètre de l'inclusion B ($0 \le L/B \le 1{,}75$), le rapport entre la hauteur H du matelas et B (H/B = 1,5 et H/B = 1,0) et le rapport des contraintes de confinement à l'extérieur et l'intérieur de la semelle ($q_{s,ext}/q_s$ = 0,25, $q_{s,ext}/q_s$ = 0,33 et $q_{s,ext}/q_s$ = 0,50).

La rupture du matelas est supposée atteinte pour un déplacement imposé u_z fonction du diamètre B de l'inclusion (avec u_z = B/10 et u_z = B/5). On définit ainsi le facteur de portance équivalent $N_{q,eq} = q_p^{max}/q_s$ avec q_p^{max} la contrainte de rupture et q_s la contrainte verticale sous le matelas à l'intérieur de la semelle.

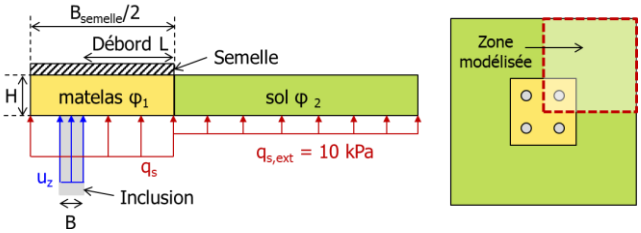

Figure 2. Modèle 3D (coupe et vue en plan).

La Figure 3 et la Figure 4 présentent l'évolution de $N_{q,eq}$ en fonction de L/B comparé aux résultats obtenus avec les méthodes analytiques ASIRI (2012).

On peut voir que le facteur de portance équivalent obtenu est 1,5 à 4 fois supérieur au facteur ASIRI avec effets de bord et dans certains cas dépasse le facteur de portance ASIRI sans effets de bord (N_q =49 pour φ_1 = 38°).

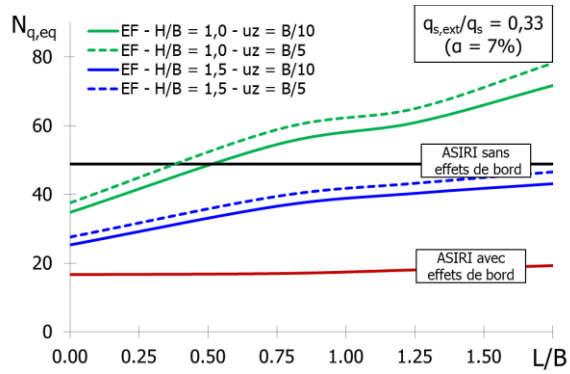

Figure 3. Facteur de portance équivalent fonction de L/B pour différentes valeurs de H/B ($q_{s,ext}/q_s$ fixé = 0,33).

La Figure 3 montre que plus le rapport H/B est faible plus $N_{q,eq}$ est élevé ce qui traduit l'effet bénéfique lié à la présence de la semelle qui bloque le développement du mécanisme de rupture. On peut voir également que la pente des courbes est plus élevée pour H/B =1 que pour H/B =1,5.

La Figure 4 montre que l'augmentation de q_s a pour effet d'augmenter l'ordonnée à l'origine des courbes en conservant la même pente qui est fonction du rapport H/B. Enfin, on note que le critère de rupture imposée (u_z = B/10 ou u_z = B/5) a un faible un impact sur les résultats.

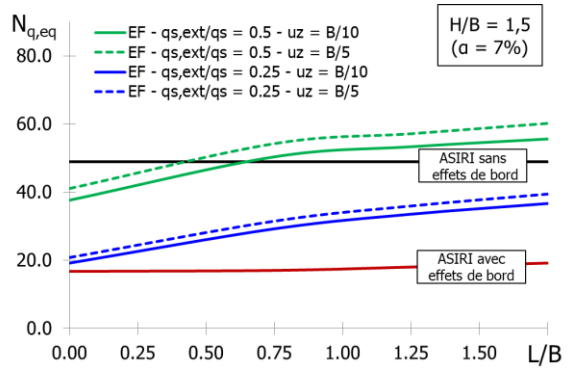

Figure 4. Facteur de portance équivalent fonction de L/B pour différentes valeurs de $q_{s,ext}/q_s$ (H/B fixé = 1,5)

3 REMBLAI SUR INCLUSIONS RIGIDES AVEC MATELAS RENFORCE OU ON PAR GEOSYNTHETIQUES

3.1 Description des méthodes

3.1.1 Méthode DEM

L'étude menée avec la méthode DEM (Tran et al., 2019 et Tran et al., 2021) est utilisée comme point de comparaison pour évaluer les méthodes analytiques en présence de géosynthétiques.

Dans la méthode des éléments discrets 3D (DEM) des particules élémentaires sont utilisées pour simuler la microstructure des matériaux granulaires, et une méthode couplée éléments discrets - éléments finis (DEM - FEM) permet de décrire le comportement du géosynthétique et son interaction avec le matériau granulaire.

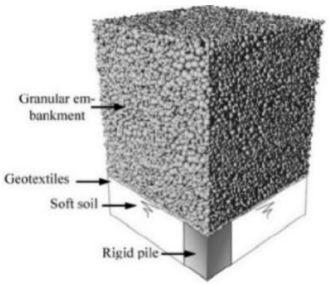

Figure 5. Méthode DEM [Villard et al., 2024].

3.1.2 Arches concentriques (CA)

La méthode arches concentriques (CA) décrite Figure 6, est une méthode de conception de renforcement par géosynthétiques développé par S. Van Eekelen qui est couramment utilisée, et présentée dans le CUR 226 néerlandais (2016). Cette méthode de dimensionnement se base sur un calcul en deux étapes. La première étape permet de définir la part de charge transmise par effet de cisaillement (A, B et C) et la deuxième étape décrit le comportement (force de traction et déformation maximum) du géosynthétique sous la charge résiduelle (B+C).

Une feuille de calcul a été développée par S. Van Eekelen afin de faciliter le calcul de ces deux étapes. Celle-ci a été utilisée afin de comparer les différentes méthodes.

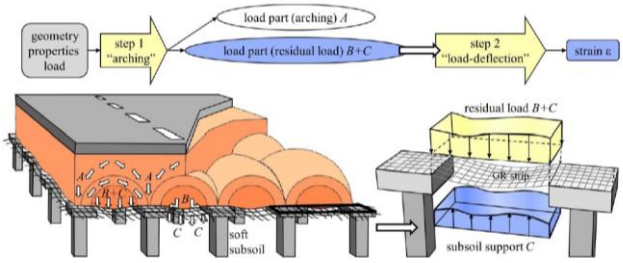

Figure 6. Méthode CA [Van Eekelen, 2016].

3.1.3 Modèle Taspie+

Le modèle Taspie+ (Cuira & Simon, 2009) est un modèle biphasique simplifié suivant les règles d'ASIRI qui a pour objet l'étude d'une cellule élémentaire centrée sur une inclusion soumise à un chargement vertical (voir Figure 7). La prise en compte des géosynthétiques est réalisée en ajoutant dans les équations du modèle, à la hauteur du géosynthétique, la relation entre le déplacement de ce dernier et la charge qu'il peut transférer à ses extrémités.

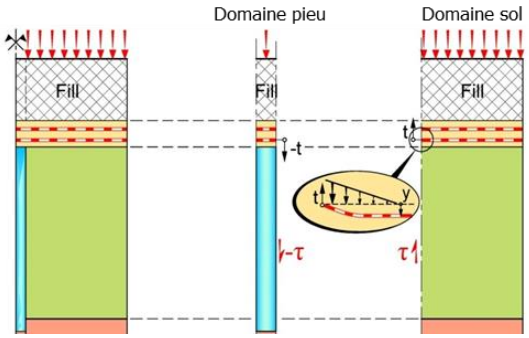

Figure 7. Modèle Taspie+ [Simon et al., 2014].

Cette relation est déduite du comportement des bandes reliant les têtes d'inclusion, selon les côtés des mailles. Ces bandes sont supposées soumises à une pression différentielle p distribuée selon un profil triangulaire inverse (voir Figure 8). L'équilibre élastique de la bande est étudié en grandes déformations (avec prise en compte des effets de second ordre) et sa résolution permet d'établir une relation non linéaire directe entre la pression p et la flèche Δy qui en résulte.

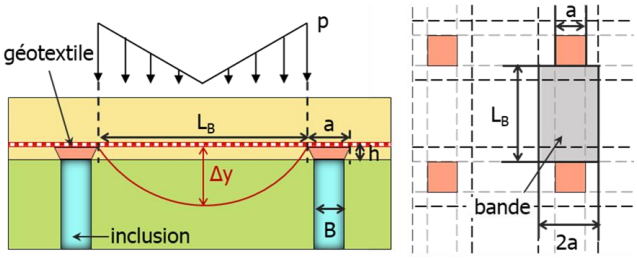

Figure 8. Bande soumise à un profil triangulaire inverse.

3.2 Comparaisons

3.2.1 Configurations étudiées

On reprend les configurations de l'étude DEM servant de référence (Tran et al., 2021), soit :

- Inclusions carrées de 0,6 m de côté ;
- Maille carrée de 3,0 m x 3,0 m ;
- Trois hauteurs de matelas : H = 0,75 m, H = 1,5 m et H = 3 m ;
- Géosynthétique bidirectionnel de raideur J = 3000 kN/m.

Différentes valeurs du module du sol entourant les inclusions sont étudiées, comprises entre 0,01 à 1 MPa.

Pour le matelas, deux densités enveloppes et compatibles avec les caractéristiques microscopiques du modèle DEM sont étudiées, voir Tableau 3. Ces dernières sont utilisées directement dans la méthode CA en considérant l'angle de frottement résiduel. L'utilisation du modèle Taspie+ nécessite la définition préalable du module de déformation du matelas compatible avec les paramètres microscopiques et macroscopiques du modèle DEM. On se base pour cela sur les simulations numériques d'essais triaxiaux effectuées sur des échantillons de matelas en utilisant le modèle DEM (Tran et al., 2019), afin de calibrer une loi contrainte-déformation. Cette démarche a permis de déterminer un module du matelas en fonction de la contrainte verticale σ'_v comme suit (voir Tableau 4):

$$E_{50} = E_{50}^{ref} \left(\frac{\sigma'_v}{p_{ref}}\right)^m \quad (4)$$

Tableau 3. Paramètres macroscopiques matelas- DEM/CA

Densité	φ'_{pic} [°]	$\varphi'_{res.}$ [°]	γ_d [kN/m^3]
Lâche	34	26	14.40
Dense	46	26	16.20

Tableau 4. Paramètres matelas –Taspie+.

Densité	$E_{50,ref}$ [MN/m^2]	p_{ref} [kPa]	ν [-]	m [-]	γ_d [kN/m^3]
Lâche	2,10	100	0,3	0,24	14.40
Dense	3,50	100	0,3	0,15	16.20

3.2.2 Efficacité sans géosynthétiques

L'efficacité est définie comme le rapport de l'effort en tête des inclusions rigides sur l'effort total de la maille. La Figure 9 présente l'efficacité sans prise en compte les géosynthétiques pour les modèles DEM et Taspie+. Pour les deux modèles, on observe une augmentation de l'efficacité lorsque le module du sol diminue. Avec le modèle DEM, on atteint un pic au-delà duquel le matelas plastifie, entraînant une diminution de l'efficacité. En revanche, avec le modèle Taspie+, ce pic n'est pas visible, car le matelas se comporte de manière élastique. Des vérifications de non-poinçonnement du matelas sont effectuées ultérieurement, conformément aux considérations décrites dans le §2.

De plus, on peut noter que dans le cas d'un matelas lâche, les courbes sont comparables pour des modules de sol supérieurs à 0,2 MPa, avant la rupture du matelas. En revanche, dans le cas d'un matelas dense, le modèle Taspie+ sous-estime l'efficacité. Cette observation s'explique par le fait que dans le modèle Taspie+, le transfert des charges au niveau du matelas s'effectue par cisaillement vertical, plafonné à $k\tan\delta \times \sigma'_v$. Le facteur $k\tan\delta$ est un paramètre empirique qui représente le produit d'un frottement $\tan\delta$ par un coefficient de butée k (tel que $\sigma'_N = k\,\sigma'_v$). Dans la pratique, le facteur $k\tan\delta$ est plafonné forfaitairement à 1 indépendamment de la densité du matelas. Les comparaisons avec la méthode DEM inciteraient ici à adapter la valeur de $k\tan\delta$ à la densité du matelas.

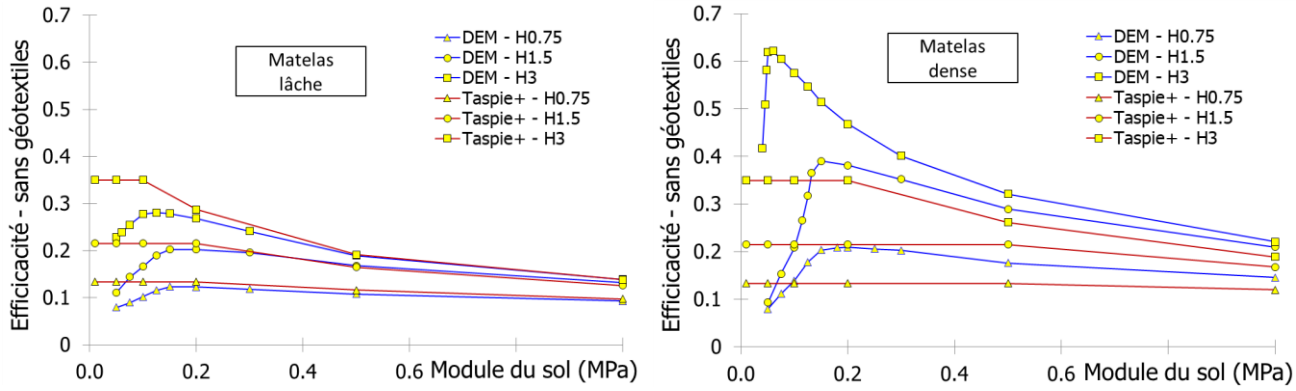

Figure 9. Comparaison DEM/Taspie – Efficacité sans géosynthétiques.

3.2.3 Efficacité avec géosynthétiques

La Figure 11 et la Figure 12 présentent la comparaison, entre les différentes méthodes, de l'efficacité avec prise en compte des géosynthétiques.

Les résultats obtenus avec Taspie+ montrent une évolution similaire à ceux obtenus par la méthode DEM. Pour les matelas de type lâche, l'accord est satisfaisant. En revanche, pour les matelas de type dense les résultats se placent du côté de la sécurité. L'adaptation de la distribution de la pression différentielle selon un profil triangulaire inverse s'appliquant seulement à une fraction de la demi-maille (profil tronqué) pourrait conduire à un meilleur accord pour des matelas denses (Figure 10). En effet, à résultante de pression p constante, ceci a pour conséquence de diminuer la flèche Δy du géosynthétique et donc de rigidifier l'ensemble (avec une traction associée dans le géosynthétique également plus faible). La mise en place d'un profil de ce type est en accord avec les observations réalisées dans les modèles DEM qui montrent que la distribution de la pression suit une fonction polynomiale du troisième degré (Villard et al., 2024). Cette fonction peut être simplifiée suivant le profil Figure 10.

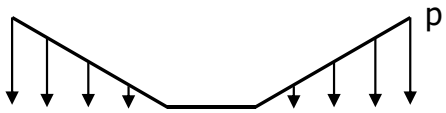

Figure 10. Profil triangulaire inverse « tronqué ».

Les résultats obtenus avec la méthode CA montrent que celle-ci surestime la part de charge A, donc l'efficacité, pour les matelas de type lâche et sous-estime légèrement l'efficacité dans le cas des matelas denses de forte hauteur (H = 1,5 m et H = 3,0 m). Mais pour le cas H = 0,75 m l'accord est satisfaisant.

3.2.4 Tassements en surface avec géosynthétiques

La Figure 13 présente le tassement en surface avec prise en compte des géosynthétiques pour le modèle DEM et le modèle Taspie+. Les résultats sont comparables entre les deux modèles. Pour les matelas de type dense, les tassements sont surestimés avec la méthode Taspie+ ce qui corrobore les observations réalisées sur l'efficacité du report de charge §3.2.3. Pour les matelas de type mou les résultats sont comparables, excepté pour des fortes épaisseurs de matelas où le calcul Taspie+ semble sous-estimer les tassements.

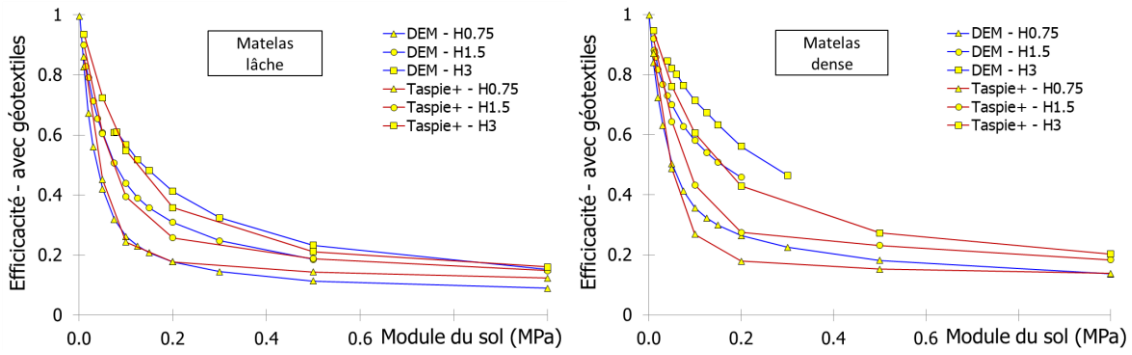

Figure 11. Comparaison DEM/Taspie – Efficacité.

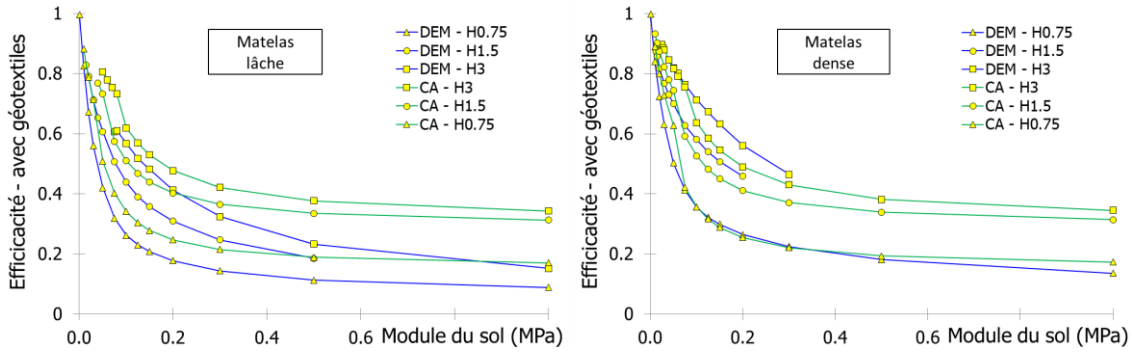

Figure 12. Comparaison DEM/CA – Efficacité.

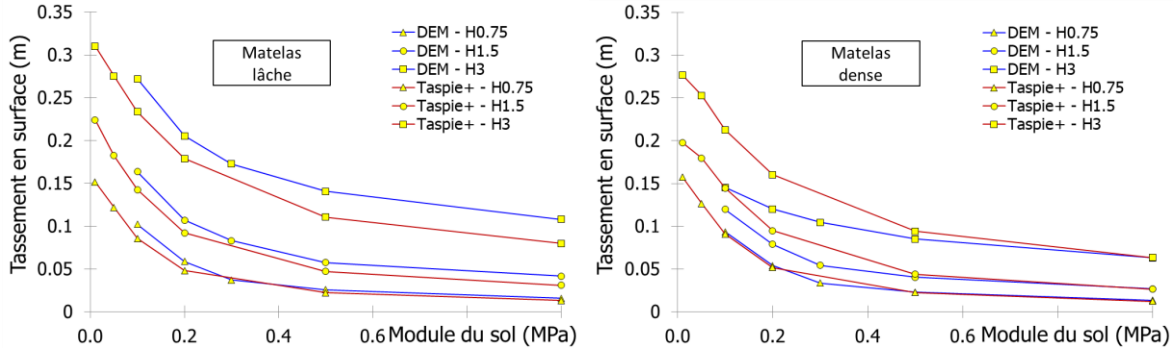

Figure 13. Comparaison DEM/Taspie – Tassements.

4 CONCLUSIONS

Pour le cas d'une semelle sur inclusions, les résultats montrent que les règles ASIRI (2012) sous-estiment la charge limite d'un facteur variant entre 1,5 et 3. Des abaques basés sur des calculs numériques peuvent être proposés pour la nouvelle version des recommandations qui sera éditée à la fin du projet ASIRI+.

Pour le cas d'un remblai sur inclusions, les comparaisons entre les modèles DEM et Taspie+ ont montré que les résultats obtenus évoluent de manière comparable en termes d'efficacité et de tassements. Pour les matelas de type lâche l'accord est bon. Pour les matelas de type dense les résultats se placent du côté de la sécurité. Une amélioration du modèle Taspie+ pourrait consister à adapter, selon la densité du matelas, la valeur du frottement limite $k\tan\delta \times \sigma'v$ ainsi que la distribution de la pression différentielle (suivant un profil triangulaire inverse tronqué). Néanmoins, en pratique, l'utilisation d'un profil non tronqué s'avère sécuritaire pour le dimensionnement. En ce qui concerne les comparaisons entre les modèles CA et DEM, la méthode CA n'a pas montré une bonne cohérence des résultats d'efficacité avec la méthode DEM dans le cas d'un sol lâche. Cependant, elle montre un bon calage avec le type de sol dense, plus particulièrement pour un remblai de hauteur 0,75m, et se place du côté de la sécurité pour les deux autres hauteurs de remblai.

REFERENCES

ASIRI (2012). Recommandations pour la conception, le calcul, l'exécution et le contrôle des ouvrages sur sols améliorés par inclusions rigides verticales, IREX-Presses des Ponts, Paris, France.

Cuira, F. & Simon, B. (2009). Deux outils simples pour traiter des interactions complexes d'un massif renforcé par inclusions rigides, 17th ICSMGE, Alexandria, 1163-1166.

CUR 226 (2016) Design Guideline Basal Reinforced Piled Embankments, SBRCURnet, Delft, Pays-Bas.

Simon, B., Briançon L., Auray G. (2014) Pile-Supported Embankment over Soft Soil for South Europe Atlantic High Speed Line, 10th ICG, Berlin.

Tran, Q.A., Villard, P., Dias, D. (2019). Discrete and continuum numerical modeling of soil arching between piles. *International Journal of Geo-mechanics*.19(2). https://doi:10.1061/(ASCE)GM.1943-5622.0001341

Tran, Q. A., Villard, P., Dias, D. (2021). Geosynthetic reinforced piled embankment modeling using discrete and continuum approaches. Geotextiles and Geomembranes, 49(1), 243-256. https://doi.org/10.1016/j.geotexmem.2020.10.026

Van Eekelen, S.J.M. (2016). The 2016-update of the Dutch Design Guideline for Basal Reinforced Piled Embankments. *Procedia engineering*, *143*, 582-589.

Villard, P. (2024). Mechanical behaviour of geosynthetic sheets used to reinforce load transfer mattresses in the case of embankments on soft soils reinforced by rigid inclusions. ECSMGE 2024

Proceedings of the XVIII ECSMGE 2024
GEOTECHNICAL ENGINEERING CHALLENGES
TO MEET CURRENT AND EMERGING NEEDS OF SOCIETY
© 2024 the Authors
ISBN 978-1-032-54816-6
DOI 10.1201/9781003431749-31
Open Access: www.taylorfrancis.com, CC BY-NC-ND 4.0 license

ECSMGE 24
XVIII EUROPEAN CONFERENCE ON SOIL MECHANICS AND GEOTECHNICAL ENGINEERING

Prediction of uplift and compression bearing capacity of screw piles in saturated sand

Prévision de la capacité de charge en compression et en soulèvement des pieux vissés dans le sable saturé

D.K. Andreasen*, A.K. Koteras, L.B. Ibsen
Aalborg University, Aalborg, Denmark

**dka@build.aau.dk*

ABSTRACT: Accurate determination of bearing capacity for screw piles remains an unresolved challenge. Previous research has predominantly concentrated on uplift capacity equations for helical anchors, with limited focus on compression capacity. This study aims to assess and adapt existing methodologies for determining the bearing capacity of screw piles, accounting for the distinct geometrical features, and applying them to both uplift and compression capacities. Additionally, Cone Penetration Test (CPT)-based methods are investigated for their applicability in this context. The research methodology entails reviewing current bearing capacity determination methods, modifying them to accommodate the unique screw pile geometry, and analysing CPT-based approaches. Static load tests are conducted at Aalborg University's laboratory to obtain reference static bearing capacities. Comparisons are drawn between the outcomes of the adapted earth pressure theory-based and CPT-based methods and the lab-obtained static bearing capacities. The results indicate that the existing framework is inadequate and unreliable for determining the uplift and compression bearing capacity of the screw piles investigated. The study highlights the necessity for further research and development of novel methodologies to enhance the accuracy of screw pile bearing capacity predictions.

RÉSUMÉ: La détermination précise de la capacité portante des pieux vissés reste un défi non résolu. Les recherches antérieures se sont principalement concentrées sur les équations de capacité de soulèvement pour les ancrages hélicoïdaux, avec une attention limitée à la capacité de compression. Cette étude vise à évaluer et à adapter les méthodologies existantes pour déterminer la capacité portante des pieux vissés, en tenant compte des caractéristiques géométriques distinctes, et à les appliquer aux capacités de soulèvement et de compression. En outre, les méthodes basées sur le test de pénétration du cône (CPT) sont étudiées pour leur applicabilité dans ce contexte. La méthodologie de recherche comprend l'examen des méthodes actuelles de détermination de la capacité portante, leur modification pour tenir compte de la géométrie unique des pieux vissés, et l'analyse des approches basées sur le CPT. Des essais de charge statique sont effectués au laboratoire de l'Université d'Aalborg pour obtenir des capacités portantes statiques de référence. Des comparaisons sont établies entre les résultats des méthodes adaptées basées sur la théorie de la pression des terres et basées sur les CPT, et les capacités de charge statique obtenues en laboratoire. Les résultats indiquent que le cadre existant est inadéquat et peu fiable pour déterminer la capacité portante de soulèvement et de compression des pieux vissés étudiés. L'étude souligne la nécessité de poursuivre les recherches et de développer de nouvelles méthodologies pour améliorer la précision des prévisions de capacité portante des pieux vissés.

Keywords: Screw piles; analytical methods; CPT-based methods; experiments.

1 INTRODUCTION

Screw piles have historically been used for sustaining tension loads with minimal focus on the compressive bearing capacity. To introduce screw piles into the housing market, it is a necessity to study their behaviour under compressive loading. Screw piles are steel piles with different configurations with varying diameters of hollow, tubular shaft and thread sizes. The screw piles studied in this paper are illustrated in Figure 1. The threads are welded on with a constant pitch. Furthermore, the threads are continuous and therefore a special case of previously studied helical piles (Das and Shukla, 2013). The study of bearing capacities in this paper is based on experiments performed at Aalborg University 'Sand Box' with the dimensions of 4.4 x 2.5 x 3.2 meters and a hydraulic multi-purpose robot.

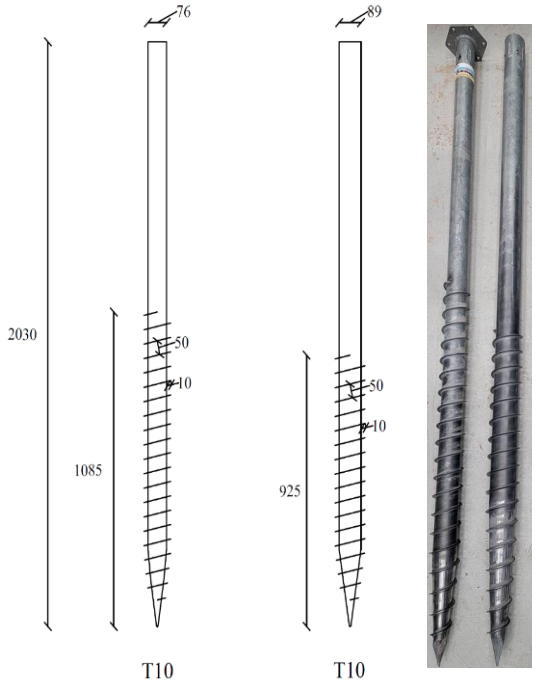

Figure 1. Screw piles used at Aalborg University with geometries in [mm] on the left.

2 EXPERIMENTS

The experimental procedure is separated into different steps which are described in the following subsections. The experiments are carried out in saturated silica sand where Aalborg Sand No. 1 is used with parameters listed in (Nielsen and Nielsen, 2018).

2.1 Soil preparation

For testing the soil in the 'Sand Box' the soil must be able to be returned to initial conditions, this is achieved by liquefaction using pumps to generate a water gradient sufficient to subdue the generated stresses through compaction of the soil. Subsequently the soil is vibrated in a pattern to achieve uniform soil conditions which is ensured by performing small cone penetration tests (CPT's) and to minimize the boundary effects which arise from vibrating the soil.

2.2 Cone penetration test

To verify the uniformity of the soil conditions, before performing the installation and testing of the screw piles, six CPT's are conducted at six different positions in the 'Sand Box'.

2.3 Installation

The installation is controlled to ensure reliable and reproducible results. Furthermore, to minimize soil disturbance the screw pile is installed with a rate of one pitch per rotation which equivalently was used in previous studies of screw piles (Ghaly and Hanna, 1991).

2.4 Static load testing

The method for determining bearing capacities is carried out using a displacement-controlled static load test performed with a hydraulic piston.

2.4.1 Tensile load test

The pile is subjected to a tensile load, during the test load and displacements are measured. Failure during the tensile load test is determined as the point at which a sudden drop in the exerted tensile load occurs. This is equivalent to the maximum tensile load during the test.

2.4.2 Compression load test

The compression load test is started, and the load and displacement are measured, the displacement-controlled test is loaded until 100 mm with unloading at 50 mm. The compressive bearing capacity is determined at 50 mm and D/10 of displacement based on experience from load-displacement curves.

2.5 Extent of experiments

In this paper, the results of 6 tensile tests and 28 compressive tests are studied. Two different pile configurations are illustrated in Figure 1 and the geometrical sizes are given in Table 1.

Table 1. Geometrical sizes of studied screw piles.

Pile Name	Diameter [mm]	Thread size [mm]	Pitch [mm]
D76T10	76	10	50
D89T10	89	10	50

The tests were carried out in different relative densities varying from 41% to 97%.

3 METHODS

Different methods for determining the uplift and compressive static bearing capacities are investigated and adapted to the geometry of the screw piles shown in Figure 1. The bearing capacities are studied by two solution approaches, both analytical methods and CPT-based methods.

3.1 Analytical methods

In this paper, two analytical methods are investigated. Firstly, the Mitsch and Clemence method (M&C method) is studied which is based on the failure

mechanism of cylindrical shear (Mitsch and Clemence, 1985). Originally this method was developed for predicting the uplift capacity of helical anchors however, it is modified to account for compressive loading by introducing the bearing capacity factor instead of the uplift capacity factor (Mohajerani, Bosnjak and Bromwich, 2016). The other analytical method studied is a further development of the Mitsch and Clemence cylindrical shear method where Perko's method is derived from soil pressures and static solution, unlike Mitsch and Clemence theory, which is based on failure lines and a kinematic solution (Perko, 2009). The main factors studied by Mitsch and Clemence are the coefficient of lateral earth pressure and friction angle, where Perko's method is more focused on the ultimate bearing pressure and soil shear strength (Perko, 2009) (Mitsch and Clemence, 1985).

3.2 CPT-based methods

Similarly, to analytical methods, different CPT-based methods have been studied. In this paper, four different methods have been investigated. Firstly, the LCPC method which is calibrated for drilled, driven, and cast screw piles which are reliable for complex layered soils. However, this is not considered as a stand-alone method consequently supplementary for analytical methods (Perko, 2009). Secondly, the ICP-05 method which is developed for large-diameter driven tubular piles in very dense sands, is common in offshore structures. The failure is studied as local shear failure using the Coulomb criterion (Jardine, Merritt and Schroeder, 2015). The NGI-05 method is developed for driven piles in sandy soils and uses empirical factors to determine the ultimate skin friction. Furthermore, a triangular distribution of soil pressures with depth, and homogeneous soil deposits is assumed (Clausen, Aas and Karlsrud, 2005). The last CPT-based method studied is the UWA-05 method which similarly to the other methods are developed for driven piles. However, the UWA-05 method is based on siliceous sands and the pile having a large diameter (Lehane, Schneider and Xu, 2007).

3.3 Adaptations

The adaptations of the methods are mainly based on geometrical differences. The LCPC method is similarly to the analytical methods adapted primarily to the geometrical part. However, the other CPT-based methods do not have the same degrees of freedom and thereby the geometrical difference is not capable of being captured. Furthermore, the CPT-based methods are developed for driven piles which differs significantly from the installation procedure of the screw piles studied in this paper and therefor is suspected to yield unfavourable results. Thereby the screw piles are assumed to be tubular and hollow piles for the CPT-based methods.

4 RESULTS

Based on the adaptation of the analytical and CPT-based methods the uplift and compressive static bearing capacities are determined. To quantify the precision of these models a percentage level of exceedance (PLE) has been chosen to represent the credibility of the studied methods, which is determined by Equation (1).

$$PLE = \left(\frac{Q_{theory} - Q_{measured}}{Q_{measured}}\right) \cdot 100 \qquad (1)$$

where Q_{theory} (kN) is the calculated bearing capacity based on the methods, $Q_{measured}$ is the measured bearing capacity that is derived from the static tests. Based on all the experiments the percentage level of exceedance has been calculated and shown in Figure 2 for tensile bearing capacity and Figure 3 for compressive bearing capacity.

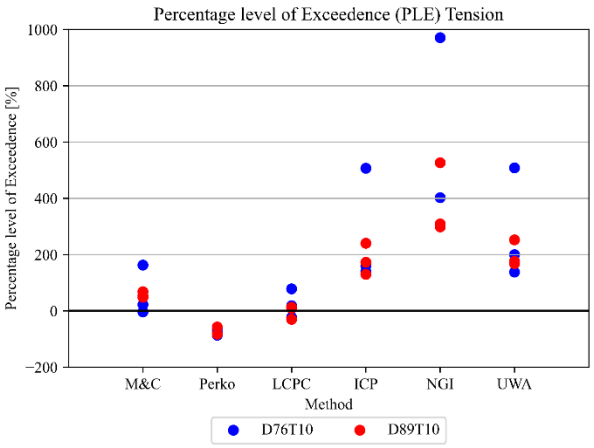

Figure 2. Percentage level of exceedance from tensile tests. Red indicates the results for the D89T10 pile, and blue indicates the results for the D76T10 pile.

5 CONCLUSION

Based on the results shown in Figure 2 and 3 it can be concluded that the current framework is inadequate for reliably predicting the bearing capacity of the screw pile configurations studied at Aalborg University. In compression, the variation in predictions is significant, which indicates the reliability of the results is low however, the Perko method indicates the lowest deviation of results, which is indicative that it consistently predicts wrong. For tensile bearing

capacities, it is shown that most of the CPT-based methods overpredict the uplift capacity significantly, whereas the NGI-05 method, in the worst case, has a percentage level of exceedance of 970%. However, the Perko method shows relatively low scatter, which indicates that this is the most consistent method for both uplift and compression. Furthermore, most methods underpredicts the compressive bearing capacity and over predicts the uplift bearing capacity. In conclusion the current framework is not sufficient to determine the bearing capacities of the screw piles used at Aalborg University and thereby, further adaptations or developments are required.

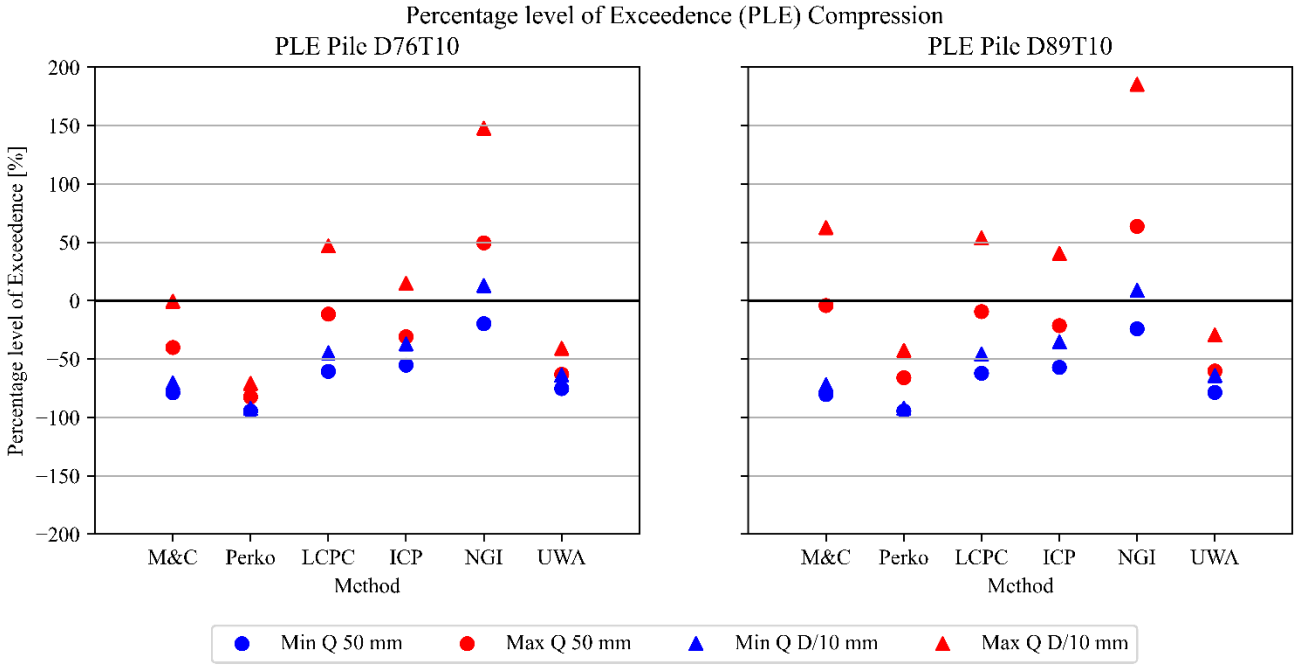

Figure 3. Percentage level of exceedance from compression tests. Red indicates the maximum value of PLE and blue indicates the minimum value of PLE. Triangles and circles indicate the two different definitions of failure at D/10 mm and 50 mm respectively.

REFERENCES

Clausen, C.J.F., Aas, P.M. and Karlsrud, K. (2005). Bearing Capacity of Driven Piles in Sand, the NGI Approach. https://doi.org/10.1201/NOE0415390637.

Das B. M. and Shukla. S. K. (2013). *Earth Anchors*, 2nd ed., J. Ross Publishing, Inc.

Ghaly, A. and Hanna, A. (1991), Experimental and theoretical studies on installation torque of screw anchors, In: Canadian Geotechnical Journal, Volume (28) Number 3. https://doi.org/10.1139/t91-046.

Jardine, R.J., Merritt, A.S. and Schroeder, F.C. (2015), The ICP Design Method and Application to a North Sea Offshore Wind Farm. IFCEE 2015. https://doi.org/10.1061/9780784479087.025.

Lehane, B.M., Schneider, J.A. and Xu, X. (2007). Development of the UWA-05 Design Method for Open and Closed Ended Driven Piles in Siliceous Sand. In: GeoDenver 2007 – Contemporary Issues in Deep Foundations. https://doi.org/10.1061/40902(221)12.

Mitsch M. P. and Clemence S. P. (1985), The Uplift Capacity of Helix Anchors in Sand , American Society of Civil Engineers (ASCE), pp. 26-47.

Mohajerani A., Bosnjak D. and Bromwich D. (2016), Analysis and design methods of screw piles: A review. In: The Japanese Geotechnical Society (Soils and Foundations), Volume (56), pp 115-128. https://doi.org/10.1016/j.sandf.2016.01.009.

Nielsen, S. D., and Nielsen, B. N. (2018). Data report on Baskarp Sand No. 15: 2018 Delivery, 1st ed Aalborg Universitet, Institut for Byggeri og Anlæg. DCE Technical reports No. 256.

Perko, H.A. (2009). Helical Piles: A Practical Guide To Design and Installation, 1st ed., Wiley, https://doi.org/10.1002/9780470549063.

Proceedings of the XVIII ECSMGE 2024
GEOTECHNICAL ENGINEERING CHALLENGES
TO MEET CURRENT AND EMERGING NEEDS OF SOCIETY
© 2024 the Authors
ISBN 978-1-032-54816-6
DOI 10.1201/9781003431749-32
Open Access: www.taylorfrancis.com, CC BY-NC-ND 4.0 license

ECSMGE 24
XVIII EUROPEAN CONFERENCE ON SOIL MECHANICS AND GEOTECHNICAL ENGINEERING

Evaluating the reliability of existing methods for predicting installation torque of screw piles in saturated sand: A comparative study

Évaluation de la fiabilité des méthodes existantes pour prédire le couple d'installation des pieux à vis dans le sable saturé: Une étude comparative

D.K. Andreasen*, L.B. Ibsen, A.K. Koteras
Aalborg University, Aalborg, Denmark

**dka@build.aau.dk*

ABSTRACT: Screw piles have been the subject of extensive research, with various methodologies proposed to predict installation torque from earth pressure theory-based and Cone Penetration Test (CPT)-based perspectives. Accurate prediction of installation torque is crucial for determining the required equipment, assessing the suitability of screw piles as a foundation solution, and ensuring that the pile material does not yield under the installation torque necessary for a specific installation depth. This study aims to modify existing methods and adapt them to the unique geometry of the screw piles investigated at Aalborg University. The methodologies compared in this study are based on experiments in saturated sand carried out at the laboratories at Aalborg University. The results indicate that earth pressure theory-based approaches provide more consistent outcomes, while CPT-based methods exhibit greater scatter. Consequently, it is concluded that current methods for predicting installation torque are unreliable, necessitating further research.

RÉSUMÉ: Les pieux vissés ont fait l'objet de recherches approfondies, avec diverses méthodologies proposées pour prédire le couple d'installation à partir de la théorie de la pression terrestre et de l'essai de pénétration au cône (CPT). Une prédiction précise du couple d'installation est cruciale pour déterminer l'équipement nécessaire, évaluer l'adéquation des pieux vissés en tant que solution de fondation et s'assurer que le matériau du pieu ne cède pas sous le couple d'installation nécessaire pour une profondeur d'installation spécifique. Cette étude vise à modifier les méthodes existantes et à les adapter à la géométrie unique des pieux vissés étudiés à l'Université d'Aalborg. Les méthodologies comparées dans cette étude sont basées sur des expériences dans du sable saturé réalisées dans les laboratoires de l'Université d'Aalborg. Les résultats indiquent que les approches basées sur la théorie de la pression des terres fournissent des résultats plus cohérents, tandis que les méthodes basées sur les CPT présentent une plus grande dispersion. Par conséquent, il est conclu que les méthodes actuelles de prévision du couple d'installation ne sont pas fiables et qu'il est nécessaire de poursuivre les recherches.

Keywords: Screw piles; earth pressure; CPT; experiments.

1 INTRODUCTION

The common practice for installing piles in soil, is driving piles or bored piles however, for screw piles the installation procedure is different since it is being inserted into the ground by rotation and in some cases exerted an axial force. Due to the difference in installation methods, it is essential to understand the effects of rotating the pile down into the soil and how to minimize the soil disturbance during installation. Here (Ghaly and Hanna, 1991) suggested an installation rate of one pitch per rotation, which is an indication of the influence of the pile geometry on the disturbance of the soil. This effect is similar to that experienced through boring holes.

Prediction of installation torque is a necessity for ensuring a safe and reliable installation of screw piles in different soil conditions. This paper seeks to compare existing methods for predicting the installation torque based on full-scale laboratory testing in the 'Sand Box' at Aalborg University. The test setup is 4.4 x 2.5 meters and 3.2 meters in depth.

2 EXPERIMENTS

The full-scale laboratory test conducted in this study is performed on six different pile geometries, where a principle sketch is illustrated in Figure 1.

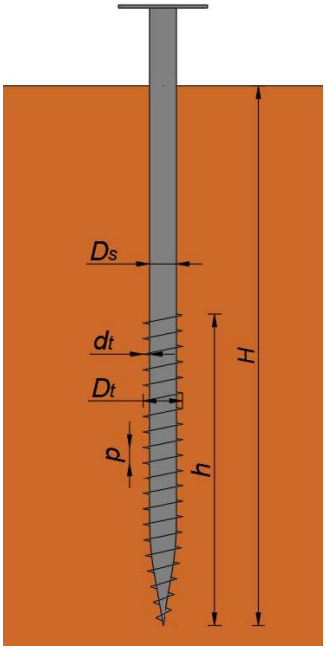

Figure 1. Principle sketch of screw piles used at Aalborg University.

For all piles, the installation depth, *H*, is kept constant at 1.7 meters and the pitch, *p*, for all pile configurations are the same, 50 millimetres and the thickness, *t*, of the steel is 5 millimetres and finally, the threaded length, *h,* is 1 meter. The geometrical sizes of the screw piles are listed in Table 1. The naming of the piles is based on the diameter, D, and the thread size, T.

Table 1. Geometrical sizes of studied screw piles.

Pile Name	D_s [mm]	d_t [mm]	D_t [mm]
D76T10	76	10	96
D76T20	76	20	116
D89T10	89	10	109
D89T20	89	20	129
D115T20	115	20	155
D140T20	140	20	180

2.1 Preparation of the Sand Box

Before installation of the screw piles, the test set-up must be prepared for desired soil state. This is carried out by liquefying the soil and reverting it back to the loosest state, which subsequently is vibrated to the desired soil state. The vibration of the saturated sand is carried out in a manner to minimise boundary effects and obtaining relative densities of approximately 50%, 70% and 85%. The soil state is investigated with small cone penetration tests (CPTs), where six CPTs, at different locations in the Sand Box, are performed to study the uniformity of the prepared saturated sand.

2.2 Installation

The screw piles are installed at the desired positions by applying torque with a steady rate of one pitch per rotation minimising the soil disturbance (Ghaly and Hanna, 1991). During installation, the installation torque and depth are measured with a torque measurement device and LiDAR measurements. The output of the installation is an installation curve, which is illustrated in Figure 2 for a D89T10 pile.

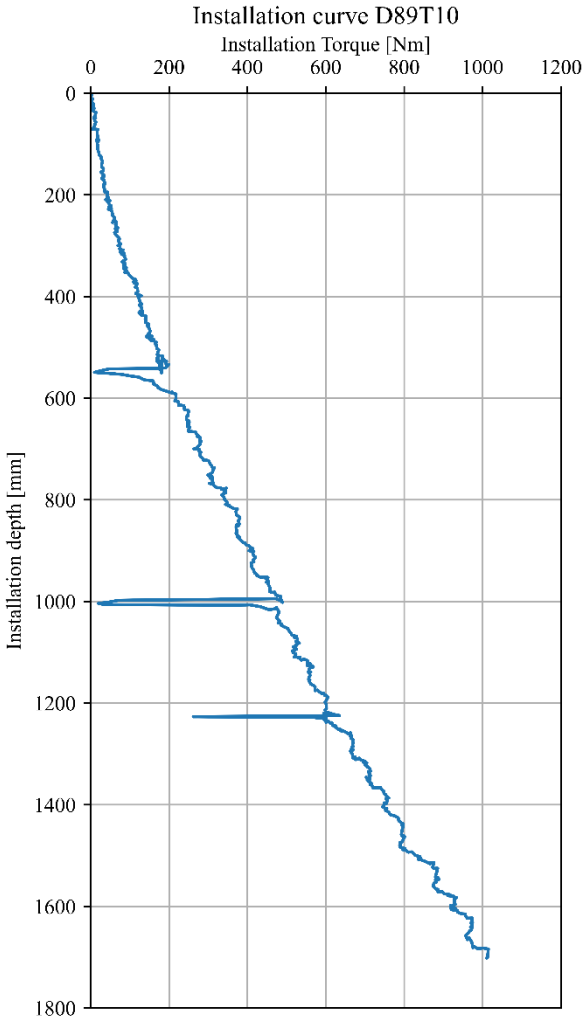

Figure 2. Example of installation curve of a D89T10 pile.

The installation torque, which is determined from the installation curve, is taken as the mean torque over the last rotation, which alleviates some of the uncertainty associated with the measurement, such as observing a spike in the torque.

2.3 Extend of experiments

In this paper, a sample size of 64 piles is studied however, some are regarded as outliers and thereby neglected when evaluating the studied methods. Three piles were omitted due to the following reasons:

- Unexpected low torque measurements, the measuring device failed.
- Abrupt change in installation speed and, thereby greater disturbance of soil

Thereby, the sample size was reduced to 61 piles.

3 METHODS

Predicting the installation torque is evaluated based on different methods where two different approaches are studied, earth pressure-based methods and CPT-based methods, respectively. The older methods were based on earth pressure theory, whereas newer studies have been based on CPT measurements. The following methods have been adapted in accordance with the screw pile geometries illustrated in Figure 1 and listed in Table 1.

3.1 Earth pressure-based methods

Two earth pressure-based methods are investigated. The original approach defined by Ghaly and Hanna was based on a single-pitch helical pile and is a summation of resisting torque contributions from the earth pressure which occur during installation (Ghaly and Hanna, 1991). Later the Ghaly and Hanna method was modified by Sakr with the same considerations with respect to torque contributions of earth pressures occurring during installation (Sakr, 2015). The difference between the two methods lies in the stress analysis where Ghaly and Hanna use total stresses and Sakr studies effective stresses.

3.2 CPT-based methods

Newer approaches are based on utilization of CPT measurements where three different CPT-based methods are studied in this paper. Tsuha and Aoki proposed a model for deep helical piles in sand based on the assumption that the installation torque consists of a resisting moment acting on each helix in conjunction with a moment acting on the shaft (Tsuha and Aoki, 2010). Further development of Tsuha and Aoki's method was done by Gavin who correlated both contributions of the installation torque to CPT measurements and thereby it will be the Gavin method which will be evaluated (Gavin et al., 2013). The prediction of installation torque was further investigated by Al-Baghadi. Initially, the method was modelled for straight shafted piles with two contributions to the installation torque from the shaft and the base of the pile. Later the model was expanded to govern single helix piles with an additional contribution from the helix (Al-Baghadi et al., 2017). Lastly Davidson altered some of the contributions from (Al-Baghadi et al., 2017) and introduced an additional contribution from a helix angle (Davidson et al., 2018).

3.3 Adaptations

The adaptations of the methods are mainly based on geometrical differences since they were developed for single helix piles, thereby the contribution from each helix is summed excluding the first and last helix which will have contributions from the base and leading edge.

4 RESULTS

Based on the adaptation of the earth pressure and CPT-based methods installation torque is calculated. The predicted installation torque based on the described methods is compared to the measured torque. To evaluate the method's accuracy and reliability the predicted torque is plotted against the measured torque and results for all the methods are illustrated in Figure 3. Here it is shown the method proposed by Gavin significantly overpredicts the installation torque and shows great scatter at higher values of the installation torque. For quantifying the reliability and accuracy of the methods linear regression has been performed on all methods with the intersection being zero due to no torque should be predicted when no installation torque is being measured the results of the linear regression are listed in Table 2.

Table 2. Results of linear regression for all methods.

Method	Regression fit slope	R^2
Ghaly and Hanna	0.607	0.946
Sakr	2.567	0.898
Gavin	8.998	0.887
Al-Baghadi	1.809	0.882
Davidson	2.052	0.883

For an ideal fit, the regression fit slope should be equal to 1 which indicates that the methods predict the experimental measurements. The Ghaly and Hanna method has the highest R^2-value which stipulates that the reliability of the earth pressure-based method is a more consistent predictor of the installation torque for the screw piles studied at Aalborg University. Generally, the earth pressure-based methods indicate that they are more consistent in comparison to the CPT-based methods.

To compare and evaluate the two different methodologies one method has been chosen to represent the different approaches. For the earth

pressure-based methods, Ghaly and Hanna are chosen due to the higher R^2-value however, the slope is below 1 which indicates that it underpredicts the installation torque. Contrary to the earth pressure-based method the CPT-based methods overpredicts the installation torque since all slopes are above one, the chosen representative method for CPT-based methods is Davidson. The two representative methods are illustrated in Figure 4 where the regression line and ideal line are added Here it becomes apparent that the Ghaly and Hanna method is the most accurate and consistent method. This is attributed to the theoretical approach from the earth pressure theory and is furthermore, better at predicting installation torque at greater torque measurements where Davidson method shows greater scatter which is further indicated by the lower R^2-value.

5 CONCLUSION

Based on the results depicted in Figure 3-4 and the results from the linear regression listed in Table 2 it can be concluded that existing methods accuracy of predicting the installation torque is inadequate, however, the method shows consistent results which is indicated by the R^2-value. Thereby, the reliability in terms of consistency of existing methods are acceptable. Regarding the overall reliability of existing methods further studies are necessary to achieve a sufficient and adequate method for predicting installation torque for the screw piles studied at Aalborg University.

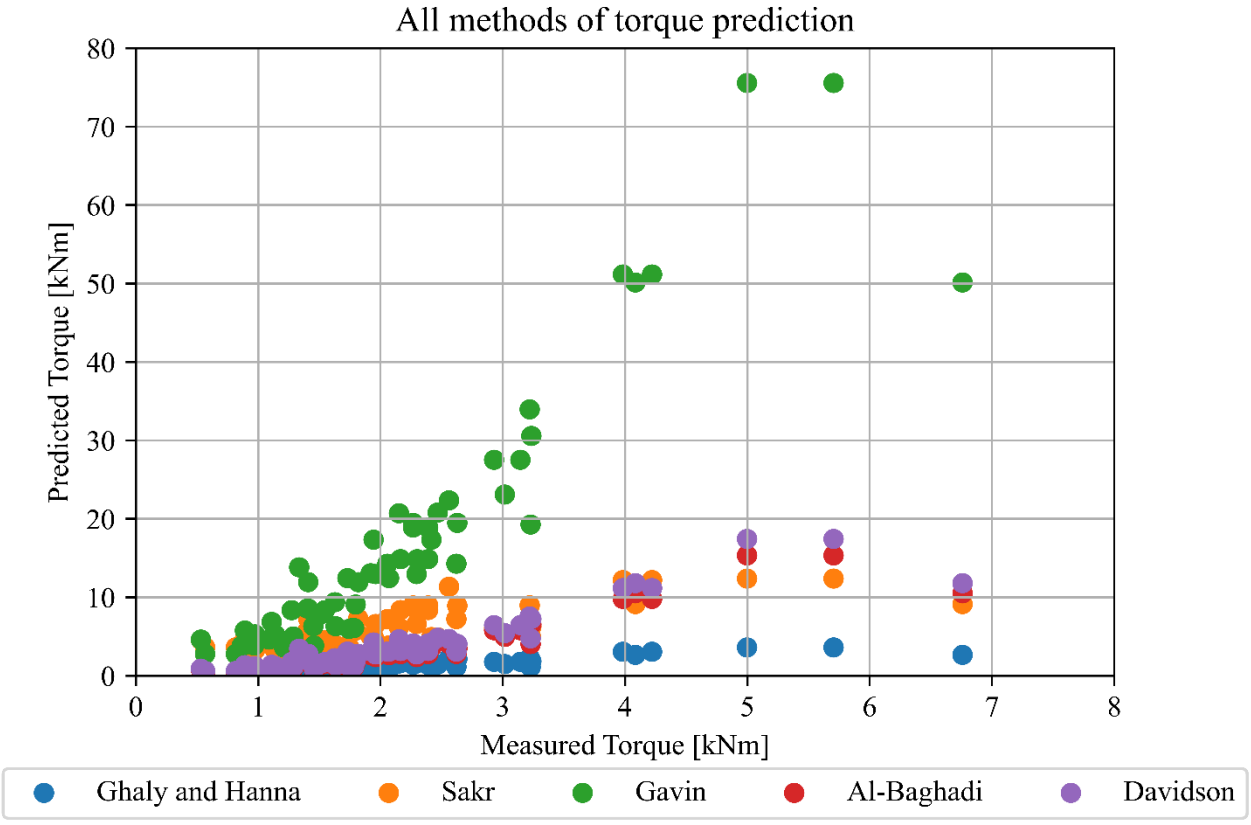

Figure 3. All methods illustrated with predicted and measured torque.

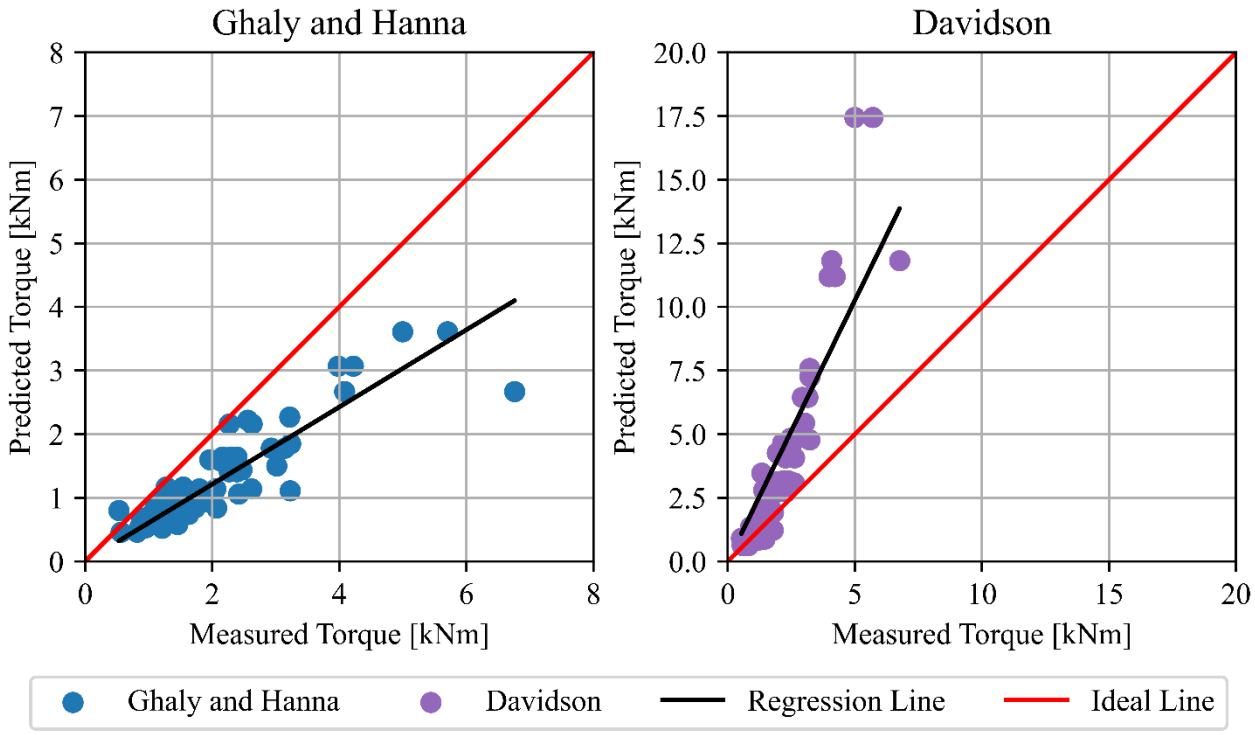

Figure 4. Chosen methods illustrated with predicted and measured torque.

REFERENCES

Al-Baghadi T., Davidson C., Brown M., Knappett J., Brennan A., Augarde C.E., Coombs W.M., Wang L., Richards D. and Blake A. (2017). CPT based design procedure for installation torque prediction for screw piles installed in sand. In: Proceedings of the 8th international conference on offshore site investigation & geotechnics (SUT OSIG), Vol 1. Londan: Society for Underwater Technology (SUT). pp. 346-353. https://doi.org/10.3723/OSIG17.346.

Davidson C. Al-Baghdadi T. Brown M. Brennan A. Knappett J. Augarde C. Coombs W. Wang L. Richards D. Blake A. Ball J. (2018). A modified CPT based installation torque prediction for large screw piles in sand. In: Proceedings of the 4th international symposium on cone penetration testing. CRC Press. 21–22 June 2018. Delft. The Netherlands. pp. 255–261.

Gavin K. Doherty P. Spagnoli G. (2013). Prediction ofthe installation torque resistance of large diameter helical piles in dense sand. In: Lutenegger A. Proceedings of 1st international geotechnical symposium of helical foundations. Amherst. pp. 578–585.

Ghaly, A. and Hanna, A. (1991), Experimental and theoretical studies on installation torque of screw anchors, In: *Canadian Geotechnical Journal*, Volume (28) Number 3. https://doi.org/10.1139/t91-046.

Sakr M. (2014). Retracted: relationship between installation torque and axial capacities of helical piles in cohesionless soils. J Perform Constr Facil 29(6):04014173. https://doi.org/10.1061/(ASCE)CF.1943-5509.0000621.

Tsuha C.H.C., Aoki N. (2010). Relationship between installation torque and uplift capacity of deep helical piles in sand. Can Geotech J 47(6):635–647. https://doi.org/10.1139/T09-128.

Proceedings of the XVIII ECSMGE 2024
GEOTECHNICAL ENGINEERING CHALLENGES
TO MEET CURRENT AND EMERGING NEEDS OF SOCIETY
© 2024 the Authors
ISBN 978-1-032-54816-6
DOI 10.1201/9781003431749-33
Open Access: www.taylorfrancis.com, CC BY-NC-ND 4.0 license

ECSMGE 24
XVIII EUROPEAN CONFERENCE ON SOIL MECHANICS AND GEOTECHNICAL ENGINEERING

1-D intrinsic compression curves for settlement analysis of soft clays

Courbes de compression monodimensionnelles intrinsèques pour l'analyse de tassements d'argiles mous

C. Athanasiu
Multiconsult Norge AS, Oslo, Norway

A.B. Tsegaye*
Norwegian Geotechnical Institute, formerly Multiconsult, Trondheim, Norway

E.R. Sørlie
Multiconsult Norge AS, Oslo, Norway

K.E.L. Johnsen
Løvlien Georåd AS, formerly Multiconsult ASA

**anteneh.biru.tsegaye@ngi.no*

ABSTRACT: Settlements in soils occur due to changes in effective stress (instant settlements) and creep in time during and after application of the effective stress changes (delayed settlements). In soft clays, the delayed settlement can be significant and must be accounted for. This paper presents a settlement analysis method that accounts for both instant and delayed components. Relations between accumulated creep strain, apparent age of the soil layer and the pre-consolidation stress due to creep are established as 1-D Intrinsic Compression Curves (1-D ICC). The paper describes the parameters used with the 1-D ICC method and how they can be determined from the constant rate of strain (CRS) oedometer tests including a creep phase. The construction and the use of 1-D ICC method to model the settlement development with time during and after consolidation process are also presented.

RÉSUMÉ: Les tassements du sol se produisent en raison de changements dans la contrainte effective (tassements instantanées) et de fluage, en temps, pendant et après l'application des changements de contrainte effective (tassements retardés). Dans les argiles molles, les tassements retardés peuvent être importants et doivent être pris en compte. L'article présente une méthode d'analyse des tassements qui prend en compte à la fois les composantes instantanées et retardés. Les relations entre la déformation de fluage accumulée, l'âge apparent de la couche de sol et la contrainte apparente de pré-consolidation due au fluage sont établies sous forme de Courbes de Compression Intrinsèques en problème monodimensionnel, CCI 1-D. L'article décrit les paramètres utilisés avec la méthode CCI 1-D et comment la méthode peuvent être utilisée pour modéliser le développement des tassements dans le temps.

Keywords: Oedometer tests; instant and delayed strains; embankment settlements.

1 INTRODUCTION

Bjerrum (1967) postulated the concept of instant, $\Delta\varepsilon_i$, and delayed, $\Delta\varepsilon_d$, compression strain due an increase in effective vertical stress, $\Delta\sigma'_v$, and due to creep in a period, Δt, under constant effective stress, respectively, Figure 1.

Based on results from oedometer tests conducted with different periods of time to creep under constant effective stress after consolidation, Bjerrum postulated that lines with equal creep rate, isotaches, are parallel with the Instant 1-D compression line, Figure 2.

The isotache concept and the insight into the creep behaviour of soils have been accumulated in time over many decennia (Den Haan, 2007).

The aim of the paper is to present a simplified method for calculating settlements of soft clays accounting for instant and delayed (creep) compression strains.

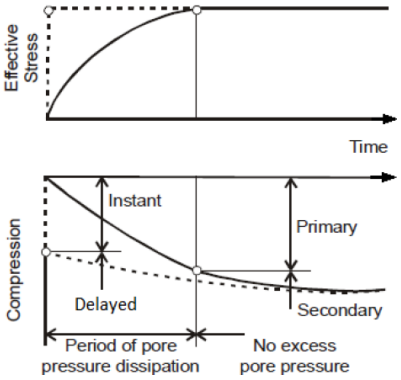

Figure 1. Instant and delayed compression (Bjerrum, 1967).

The method is based on a simplified formulation of tangent creep resistance as a function of apparent age and on an intrinsic compression curve of accumulated delayed strain, ε_c, vs. age of the clay deposit, t_a.

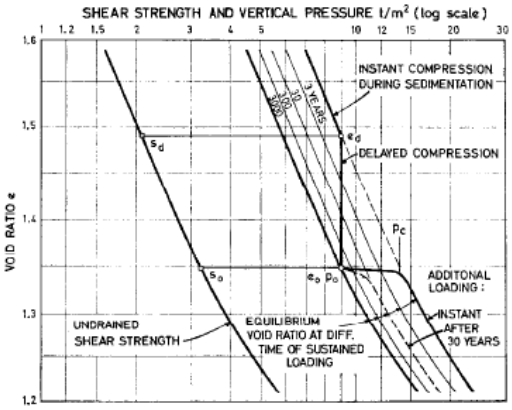

Figure 2. e-log σ'_v diagram showing isotaches (Bjerrum, 1967).

2 INSTANT AND DELAYED COMPRESSION STRAINS

The calculation of compression strains (settlements) due to an increase in effective stress from σ'_1 to $\sigma'_2 = \sigma'_1 + \Delta\sigma'$ in a period of time from t_1 to $t_2 = t_1 + \Delta t$ can be performed separately for instant and creep part, if the stress and time increments, $\Delta\sigma'$ and Δt are small enough to neglect the parameter variation with stress and time.

The delayed (creep) strain increment due to a time interval from t_1 to t_2 can be expressed as:

$$\Delta\varepsilon_{del} = \mu^* \cdot ln\left(\frac{t_2}{t_1}\right) = \frac{1}{r_s} \cdot ln\left(\frac{t_2}{t_1}\right) = \frac{C_\alpha}{(1+e_o)} log\left(\frac{t_2}{t_1}\right) \quad (1)$$

where e_o is the void ratio, and μ^*, r_s, and C_α are tangent creep parameters (for a time interval, Δt_a, from $t_1 = t_a$ to $t_2 = t_a + \Delta t_a$).

The increment of instant strain due to an increment of effective stress from σ'_1 to σ'_2 is calculated as: for $\sigma'_1 < p'_c < \sigma'_2$:

$$\Delta\varepsilon_{inst} = \kappa'^* \cdot ln\left(\frac{p'_c}{\sigma'_1}\right) + \lambda^* \cdot ln\left(\frac{\sigma'_2}{p'_c}\right) \quad (2)$$

The parameters $\kappa'^* = \frac{C'_s}{(1+e_o)\ln 10} = \frac{1}{m'_{OC}}$ refer to instant (without creep) compression within the over consolidation (OC) stress range in contrast to $\kappa^* = \frac{C_s}{(1+e_o)\ln 10} = \frac{1}{m_{OC}}$ which refer to total, instant including creep compression (as measured in oedometer tests) in the same, OC range.

By equating creep strain with plastic strain in normal consolidation range, (Leroueil et al., 1985), found that the ratio of the effective stresses, σ'_1 and σ'_2, at the same strain, measured in two oedometer tests with the same soil and initial state performed with two different strain rates, $\dot{\varepsilon}_1$ *and* $\dot{\varepsilon}_2$, are related by:

$$\frac{\sigma'_1}{\sigma'_2} = \left(\frac{\dot{\varepsilon}_2}{\dot{\varepsilon}_1}\right)^B, \; B = \frac{C_\alpha}{C_c} = \frac{\mu^*}{\lambda^*} = \frac{m_{NC}}{r_s} \cdot \quad (3)$$

Consequently, in the NC range, the rate parameter, B, is related to C_α and C_c as given in Eq. (3), and is found to depend on the type of clay (Mesri and Godlewski, 1977; Leroueil et al., 1985). The Eq. (3) is based on Janbu's definition of constrained modulus in NC range (Janbu, 1963), where σ'_r is the reference stress.

Following the Eq. (3), a relation can be obtained between creep and compression parameters in NC range:

$$\mu^*_{NC} = \frac{B}{M/\sigma'} = \frac{B}{m_{NC}} \quad (4)$$

in which M is the compression tangent constrained modulus and σ' is the applied effective stress in NC range.

Laboratory tests show that the isotaches corresponding to a constant ratio t_{ai}/t_{ai-1} are not equidistant but are narrower as the apparent age increases and, consequently, that the creep rate decays more than linear with log of time, Figure 3.

Figure 3a presents the results from special compression tests with four 125 mm long, sub-elements connected in series by (Mesri and Feng, 1986 and Mesri et al., 1995). Leroueil et al. (1986) and Leroueil and Marques (1996) reinterpreted the results to define the compression curves of each sub-element subjected to consolidation under a pressure increment from 97 to 138 kPa, followed by creep phase at constant stress of 138 kPa. Also drawn on the figure is a fictitious isotaches assuming B= 0.03 for St-Hilaire

clay. The set of isotaches coincides very well with the observed behaviour. The blue points in Figure 3b are constructed as follows. The void ratio at the intersection between an isotache and the vertical line corresponding to constant stress of 138 kPa in Figure 3a is plotted against the strain rate of this isotache (the lower horizontal axis). The plot e vs. strain rate shows that the isotaches are not equidistant (Δe from 10^{-8} to 10^{-9} min^{-1} is less than Δe from 10^{-5} to 10^{-6} min^{-1}).

In our opinion the compression curves of the four sub-elements in Figure 3 include both instant and delayed compression strains (Hypothesis B). The monitored strain rates match the set of isotaches and prove that the clay behaviour is strain rate dependent during primary consolidation.

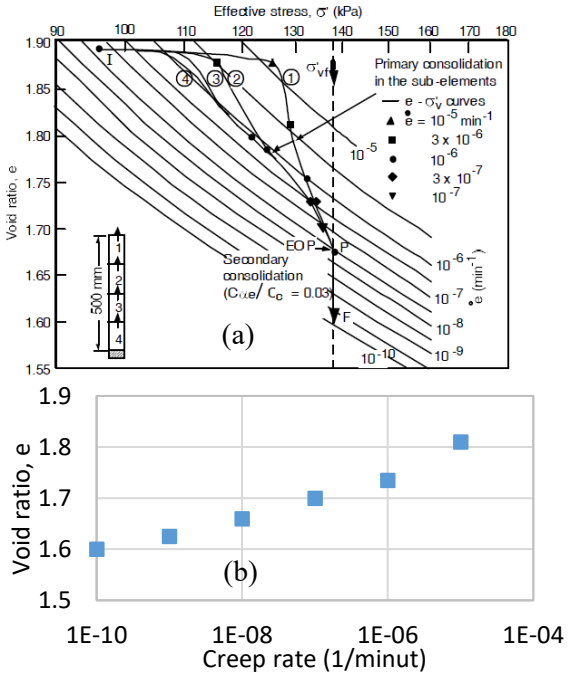

Figure 3. a) Consolidation of Saint-Hilaire clay; from Mesri et al. (1995); from Leroueil (2006) b) Void ratio versus creep rate from the data in figure (a).

Further arguments for hypothesis B may be found in Degago et al. (2011).

The results shown in Figure 3a are used to obtain a picture of distance between two consecutive isotaches in log scale as a function of creep rate. As the isotaches represent lines of equal creep rate and, at the same time, lines of equal creep time, the relation between creep rate and time is found from the definition of creep rate:

$$\dot{\varepsilon}_c = \frac{\mu^*}{t} \qquad (5)$$

If creep parameter, μ*, is independent on time, the isotaches are equidistant. The blue point curve, constructed as void ratio distance between two consecutive log cycle creep rates (10^{-5} 1/min, 10^{-6} 1/min, and so on) at stress 138 kPa, shows, however, that the isotaches are not equidistant, indicating a non-linear creep parameter.

The non-linearity of creep parameter has been discussed by many researchers, e.g., (Watabe et al., 2012, Karim and Lo, 2020, Yuan et al., 2015), (Vergote et al., 2021). Based on several CRS oedometer tests including creep phases under constant stress, the following expression is proposed for creep parameter as a function of time:

$$\mu^* = \frac{\mu^*_{NC}}{[1+\alpha \cdot ln\left(\frac{t}{t_{inst}}\right)]} \qquad (6)$$

where α is empirical factor determined experimentally. t_{inst} is the time corresponding to virgin (instant) compression line along which only instant strains are developed as a function of applied effective stress (no creep strains.) A value of 1 second is assumed for t_{inst}.

Using Eqs. (5) and (6) we obtain the differential equation for the accumulated creep strain rate at the time t:

$$d\varepsilon_c = \mu^* \cdot \frac{dt}{t} = \frac{dx}{r_{sNC} \cdot x \cdot [1+\alpha \cdot ln(x)]} \qquad (7)$$

with $x = t/t_{inst}$. The differential equation (7) is integrated to obtain the accumulated creep strain at age, t_a, under constant effective stress, p'_0:

$$\varepsilon_c = \frac{1}{D} ln\,[1 + \alpha \cdot ln\,(\frac{t_a}{t_{inst}}] \qquad (8)$$

where $D = r_{sNC} \cdot \alpha$

From Eq. (8) we can obtain a relation between the apparent age, t_a, and the accumulated creep strain, ε_c, as:

$$t_a = t_{inst} \cdot exp\,\{\frac{1}{\alpha} \cdot [exp(D \cdot \varepsilon_c) - 1]\} \qquad (9)$$

If accumulated creep strain is equated to plastic strain, the intrinsic relation between over-consolidation ratio and age is obtained as:

$$\frac{p'_c}{p'_o} = [1 + \alpha \cdot ln\left(\frac{t_a}{t_{inst}}\right)]^A \qquad (10)$$

with $A = \frac{1}{D \cdot (\lambda^* - \kappa'^*)}$.

The pre-consolidation pressure, p'_c, is defined by the intersection between unloading-reloading line (with slope κ'^*) from p'_0, ε_0 and instant compression line (slope λ^*) in contrast to the apparent, oedometer pre-consolidation stress, p'_{ca}, defined at the intersection between unloading-reloading line (slope

κ^*, without delayed strains) from p'_0, ε_0 and oedometer isotach (slope λ^*), as seen in Figure 4.

To verify the validity of the proposed formulation for creep parameter, an attempt is made to model experimental results of normalized pre-consolidation (p'_{ca}/p'_{c0}) where p'_{c0} is the apparent pre-consolidation stress at a strain rate of 10^{-7} 1/s, as a function of creep rate, Figure 5. The blue line depicts the relationship predicted based on Eq.(6). As seen from Figure 5, the agreement of prediction to measurements is encouraging. Similar good agreement is shown in Figure 6 for Osaka Bay clays.

Experimental results show also that r_s is low when creep is measured at effective stress, $\sigma' \geq p'_{ca}$, and r_s increases gradually as the ratio σ'/p'_{ca} decreases, (e.g., Christensen, 1985). This is since the age of the clay and, consequently, r_s, increases as σ'/p'_{ca} decreases.

Using the proposed formulation of creep parameter, Eq.(6), and combining Eqs.(8)-(10), the relation between μ^* (or r_s) and σ'/p'_{ca} is obtained as follows:

$$\mu^* = \frac{1}{r_s} = \mu^*_{NC} \cdot \left(\frac{\sigma'}{p'_{ca}}\right)^{1/A} \qquad (11)$$

The results of creep oedometer tests on Bangkok clay, showing measured r_s vs. σ'/p'_{ca} and the relation predicted by Eq. (11) are shown in Figure 7.

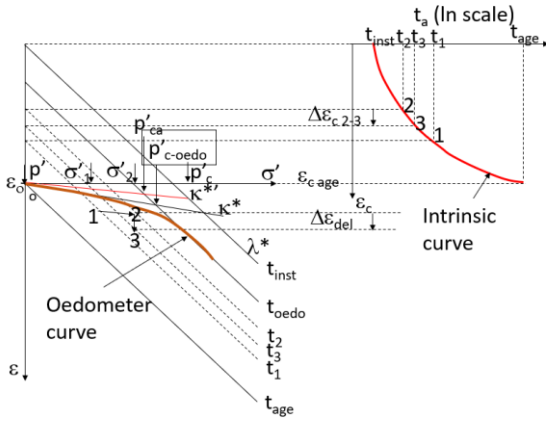

Figure 4. Intrinsic creep strain curve: ε_c vs. ln (t_a).

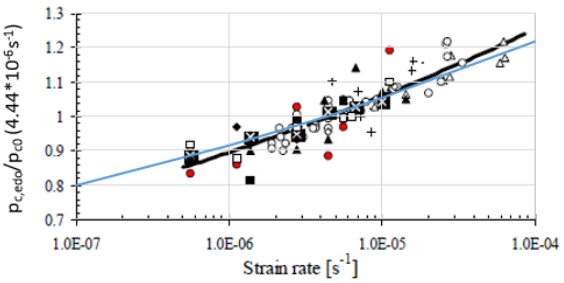

Figure 5. Normalized pre-consolidation vs. strain rate at a strain of 10% for finish clays, from (Leroueil et al., 1985). Blue line prediction uses Eq.(6) and α=0.005, λ=0.35, k*'=0.002 and r_{sNC}=44.*

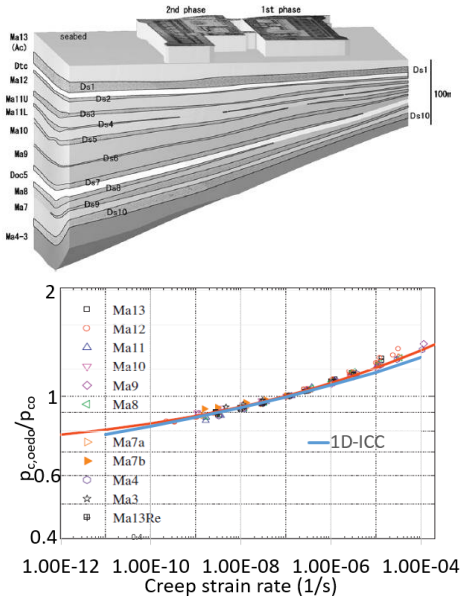

Figure 6. a. Stratigraphy model of Kansay International Airport; b. p'_{ca}/p'_{c0}-log $\dot{\varepsilon}_c$ relationship for clays at Osaka Bay (red curve – proposed trend line, (Watabe et al., 2012), blue curve predicted by Eq. (6)). ($\alpha = 0.1$; $\lambda^* = 0.3$; $\kappa^{*\prime} = 0.002$; $r_{sNC} = 47$).

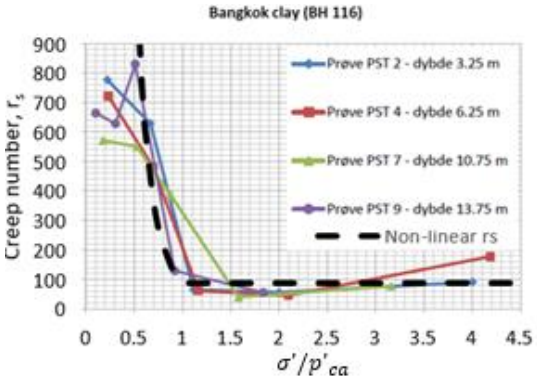

Figure 7. Variation of r_s with σ'/p'_{ca} (Athanasiu, 2012).

3 SOFT CLAY BEHAVIOR UNDER LOADING AND INTRINSIC CURVES

Experimental results reveal that creep rate decreases with time (Figure 3 and Figure 7) and that stress-strain curves obtained in oedometer tests depend on the rate of strain at which the test is performed (Figure 5 and Figure 6)

The accumulated creep strain during consolidation in geological time can be described by an intrinsic relation (1-D Intrinsic Compression Curve) between accumulated creep strain and apparent age of the deposit, ε_c vs. t_a, Eq. (8) as shown in Figure 4.

The 1-D ICC is the "fingerprint" of the creep geological history of the clay deposit.

The strain changes due to changes in stress and time can be calculated using the frame of 1-D ICC as follows.

Let the point 1 in Figure 4 describe the stress-strain-age (σ'_1, ε_{c1}, p'_{c1} and t_1) conditions before a new load change is applied. If the effective stress is increased from σ'_1 to σ'_2, the apparent age will be changed from t_1 to $t_2 < t_1$ (the clay becomes "younger" and with a lower accumulated creep strain). The increment of instant strain, $\Delta\varepsilon_{inst}$, is calculated using Eq.(2).

The preconsolidation stress remains unchanged, $p'_{c2} = p'_{c1}$ if $\sigma'_2 < p'_{c1}$ but must be updated, $p'_{c2} = \sigma'_2$ if $\sigma'_2 > p'_{c1}$.

The accumulated creep strain, is then calculated as plastic strain:

$$\varepsilon_{c,2} = (\lambda^* - \kappa'^*) \cdot \frac{p'_{c,2}}{\sigma'_2} \qquad (12)$$

and the apparent age t_2 is calculated using Eq.(9). Let the time required by consolidation process to increase effective stress from σ'_1 to σ'_2 be Δt . The change in delayed strain due to Δt is equal to the increase in intrinsic accumulated strain from ε_{c2} to ε_{c3} where ε_{c3} corresponds to the apparent age in point 3 ($t_3 = t_2 + \Delta t$) and can be calculated using Eq.(8). The change in delayed strain is then calculated as:

$$\Delta\varepsilon_{del} = \varepsilon_{c,3} - \varepsilon_{c,2} \qquad (13)$$

The pre-consolidation stress at point 3 must now be updated due to age changing to t_3 using Eq.(9) to obtain p'_{c3}/σ'_3, ($\sigma'_3 = \sigma'_2$) as a function of t_3.

The procedure described above can be repeated for all steps of a consolidation process, where in each step the stress-strain-age state of point 1 is updated from the stage at point 3 in previous step.

4 CALIBRATION OF PARAMETERS USING THE CREEP PART OF OEDOMETER TEST

During the creep part of the oedometer test the effective stress is, theoretically, kept constant. Care must be taken to align the measured time, t_m, with the apparent age time, t_a: at the start of the creep test, t_a is equal to t_{oedo}, Figure 8.

The calibration requires two sets of simple iterations, one for compression indices, (λ* or m_{NC}, κ* and κ*') and one for creep parameters (B or r_{sNC} and α). The accuracy of the geological age of a clay deposit depends on how well the geological history of the deposit is known. In addition, it is assumed that pre-consolidation pressure is induced exclusively by creep, i.e., the clay is NC, aged clay.

The comparison between measured and computed accumulated strains are shown in Figure 9.

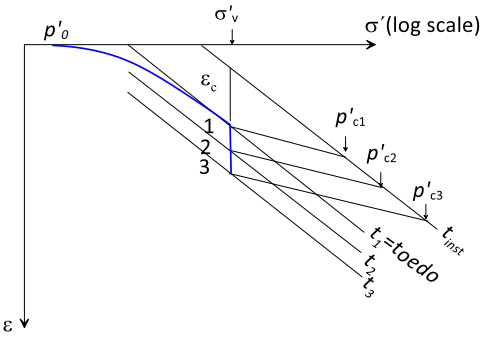

Figure 8. Creep test part starts on t_{oedo} line.

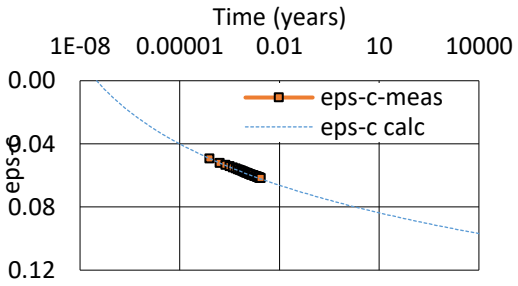

Figure 9. Comparison of measured and computed creep strains during creep part of the test.

5 BACK-CALCULATION OF OEDOMETER TEST

Next the calibration of 1-D ICC method is illsustrated using incremental oedometer loading (IL) test results of samples taken from the well-known Väsby test fill, Sweden.

The Väsby test fill (Chang, 1981), consists soft sediments of glacial and post-glacial origin.

Figure 10 presents the results of incremental loading (IL) oedometer test on sample taken with 200 mm Laval sampler from 4.2 m depth (Leroueil et al., 1985, Degago and Grimstad, 2016).

The consolidation and creep settlement parameters resulted from matching the oedometer curve with the back-calculated curve in Figure 10, are presented in Table 1.

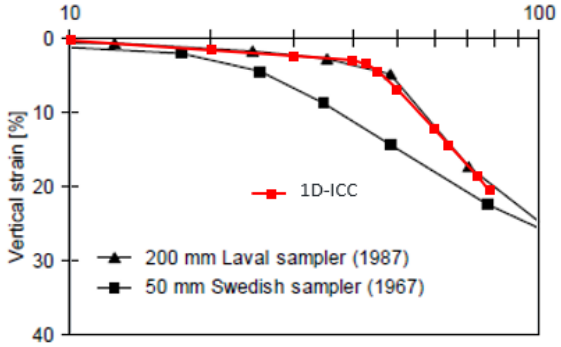

Figure 10. Calibration of incremental oedometer test results on samples taken at 4.2 m from Väsby field depth using two different samplers, data from (Leroueil and Kabbaj, 1987).

Table 1. Calibrated parameters.

Parameter	Units	Value
κ^*	-	0.1
λ^*	-	0.3
κ'^*	-	0.02
B	-	0.06
α	-	0.06
t_{age}	years	1000
p'_{ca}	kPa	44.9
$p'_{c\text{-}oedo}$	kPa	50
p'_0	kPa	30

6 CONCLUSIONS

A time resistance formulation is proposed to describe the variation of creep parameter, μ^*, with apparent age of a clay sediment.

Experimental results are compared to those predicted by the proposed formulation and the comparison shows fair good agreement.

The paper defines an intrinsic compression curve of accumulated creep strain of a clay layer effectively supporting the overburden pressure throughout the age of the deposit. This is used as a framework to calculate instant and delayed strains caused by steps of effective stress and time increments.

ACKNOWLEDGEMENTS

The authors are indebted to their colleagues, particularly to Anders Bye and Joar Spencer Gloppestad for fruitfull discussions regarding the consequences of delayed strains on settlements of offshore structures.

The contribution from workshops organized at Norwegian University of Science and Technology, NTNU, on creep settlements are also gratefully aknowledged.

REFERENCES

Athanasiu, C. (2012). Experience on calculating consolidation and creep deformations. Advanced models with applications to embankments. PLAXIS Course, NTNU, Trondheim.

Bjerrum, L. (1967). Engineering geology of Norwegian Normally-consolidated marine clays as related to settlements of buildings. *Géotechnique* 17 (2): 83-118.

Chang, C. E. H. (1981). Long term consolidation beneath the test fills at Vasby, Sweden. SGI Repport No 13.

Christensen, S. (1985). Creep tests in oedometer, Eberg clay, SINTEF Division of Geotechnical Engineering.

Degago, S. and Grimstad, G. (2016). Evaluation of soil parameters for creep calculations of field cases. *Proc. of the 17th Nordic Geotechnical Meeting*. Reykjavik, Island.

Degago, S. A., Grimstad, G., Jostad, H. P., Nordal, S. and Olsson, M. (2011). Use and misuse of the isotache concept with respect to creep hypotheses A and B. *Géotechnique* 61(10): 897-908.DOI: 0.1680/geot.9.P.112.

Den Haan, E. (2007). A history of the development of Isotache models. DOI:10.13140/ RG.2.2.32972.13441.

Janbu, N. (1963). Soil compressibility as determined by oedometer and triaxial tests. *Proc. 3rd Eur. Conf. Soil Mech*., Weisbaden.

Karim, M. R. and Lo, S. C. R. (2020). Non-linearity of creep coefficient. *Geotechnical Research* 7(2):90–95.DOI: https://doi.org/10.1680/jgere.19.00018.

Leroueil, S. (2006). The isotache approach. Where are we 50 years after its development by Professor Suklje? Suklje Memorial Lecture.

Leroueil, S. and Kabbaj, M. (1987). Discussion of 'Settlement analysis of embankments on soft clays' by Mesri & Choi. *ASCE* 113(9): 1067-1070.

Leroueil, S., Kabbaj, M., Tavenas, F. and Bouchard, R. (1985). Stress–strain–strain rate relation for the compressibility of sensitive natural clays. *Géotechnique*35(2):159-180. DOI:10.1680/geot. 1985.35.2.159.

Leroueil, S. and Marques, M. E. S. (1996). Importance of Strain Rate and Temperature Effects in Geotechnical Engineering.

Mesri, G. and Feng, T. W. (1986). Stress-strain-strain rate relation for the compressibility of sensitive natural clays. Discussion. *Géotechnique* 36(2): 283–290.

Mesri, G., Feng, T. W. and Shahien, M. (1995). Compressibility parameters during primary consolidation. *Proceedings, International Symposium on Compression and Consolidation of Clayey Soils*, Hiroshima, Japan.

Mesri, G. and Godlewski, P. M. (1977). Time and stress-compressibility interrelationship. *ASCE J Geotech Eng Div* 103(5): 417-430.

Vergote, T. A., Leung, C. F. and Chian, S. C. (2021). Elastoviscoplastic modelling with distorted isotaches and swelling for constant strain rate and incremental loading. *International Journal for Numerical and Analytical Methods in Geomechanics* 45(13).DOI: 10.1002/nag.3248.

Watabe, Y., Udaka, K., Nakatani, Y. and Leroueil, S. (2012). Long-term consolidation behavior interpreted with isotache concept for worldwide clays. *Soils and Foundations* 52(3): 449-464.DOI: https://doi.org/10.1016/j.sandf.2012.05.005.

Yuan, Y., Whittle, A. J. and Nash, D. F. T. (2015). Model for Predicting and Controlling Creep Settlements with Surcharge Loading. *Deformations Characteristics of Geomaterials*: 931–938.DOI: doi:10.3233/978-1-61499-601-9-931.

Proceedings of the XVIII ECSMGE 2024
GEOTECHNICAL ENGINEERING CHALLENGES
TO MEET CURRENT AND EMERGING NEEDS OF SOCIETY
© 2024 the Authors
ISBN 978-1-032-54816-6
DOI 10.1201/9781003431749-34
Open Access: www.taylorfrancis.com, CC BY-NC-ND 4.0 license

ECSMGE 24
XVIII EUROPEAN CONFERENCE ON SOIL MECHANICS AND GEOTECHNICAL ENGINEERING

Numerical modelling of rigid inclusion reinforced road platform, under surface loading and mobile loading

Modélisation numérique d'une plateforme de chaussée renforcée par inclusion rigide soumis à des charge de surface et des charge mobile

T. Badinier*, N. Ouechten
Univ Gustave Eiffel, GERS-SRO, Marne-la-Vallée, France

T. Dubreucq, L. Thorel
Univ Gustave Eiffel, GERS-CG, Bouguenais, France

**Thibault.badinier@univ-eiffel.fr*

ABSTRACT: In the context of the French National Project ASIRI+, the behaviour of rigid inclusion systems with thin platforms has been studied using physical centrifuge models. These systems are particularly useful in cases of road construction on soft soil subjected to significant settlement, or for studying the behaviour of rigid inclusion systems during construction phases. However, these systems differ from classic reinforcement systems with rigid inclusions due to the specificity of the loading. Indeed, on linear infrastructure or circulating platforms, the loadings are limited to small areas, potentially loading only one inclusion at a time and failing to generate a beneficial arching effect. Moreover, these loadings are usually moving over time, which modify load transfer and repartition in the rigid inclusions. To complement the centrifuge model study, we propose a numerical study in this paper to compare results and help analyse the behaviour of these systems. We first discuss the model fitting on the centrifuge results, followed by a parametric study to analyse the effect of key parameters on load transfer and failure mechanisms. Lastly, we developed a model representing the behaviour of these structures under mobile loading. This allowed us to study the evolution of the load transfer mechanism and the elastic-plastic behaviour of the load transfer platform under several loading cycles.

RÉSUMÉ: Dans le cadre du Projet National ASIRI+ (France), le comportement d'un système de renforcement de sol par inclusion rides avec une plateforme de transfert de charge mince a été étudié à l'aide d'un modèle réduit centrifugé. De tels systèmes de renforcement de sol sont particulièrement intéressants pour la construction de routes sur des sols meubles subissant d'importants tassements ou pour l'étude des phases de construction. Cependant, de tels systèmes diffèrent des systèmes classiques de renforcement par inclusion rigide par la spécificité de leur chargement. En effet, sur les infrastructures linéaires ou les plateformes de circulation, les charges sont limitées à des zones restreintes, et ne sollicitent parfois qu'une seule inclusion en même temps, ne créant pas les effets d'arche de report de charge. De plus, ces charges sont généralement mobiles, ce qui modifie la répartition des charges dans les inclusions. Pour compléter l'étude sur modèle réduit centrifugé, il est proposé une étude numérique dans le but de confronter les résultats et d'analyser le comportement du système. Ainsi, dans cet article est présenté le travail de calage du modèle numérique sur les résultats expérimentaux, puis une étude paramétrique sur quelques paramètres clés dans le but d'analyser leurs influences sur les mécanismes de report de charge et de rupture. Enfin, un modèle représentant le comportement de la structure soumise à un chargement mobile est présenté. Il permet d'étudier la variation des effets de transfert de charge et le comportement élastoplastique de la plateforme sous l'influence de plusieurs cycles de chargement.

Keywords: Rigid inclusions; numerical modelling; mobile loading.

1 INTRODUCTION

The rigid inclusion system aims to create a composite soil by including a network of rigid elements (similar to micro-piles) inside the soft soil layer. Such systems are created in order to support buildings and construction in areas of soft soil that are subject to potential high settlement (ASIRI, 2012). In the process, a Load Transfer Platform (LTP) is constructed on top of the composite soil with a granular material. The behaviour of such a system results in an unequal sharing of the surface load between the soil and rigid inclusions. Indeed, the differential settlement between the soft soils and the rigid inclusions creates specific force chains between the granular elements, focusing the load on the rigid inclusions. This effect is known as the arching effect and can be represented in Figure 1.

In 2019, the French National Project was launched with the aim of developing rigid inclusion systems

and improving the comprehension of their behaviour. Among the project's works, we focus here on the understanding of rigid inclusion systems under mobile load solicitation. Indeed, the rigid inclusion reinforcement process can be used for circulation platform reinforcement, for example. In such cases, the loads are constituted by trucks or machinery. These conditions might also occur during the construction stage (compaction of the load transfer platform). Therefore, the loads are restricted to a small area and are not always on top of an inclusion or covering several inclusions. Such loading cases do not correspond to classical rigid inclusion cases and cannot generate an arching effect.

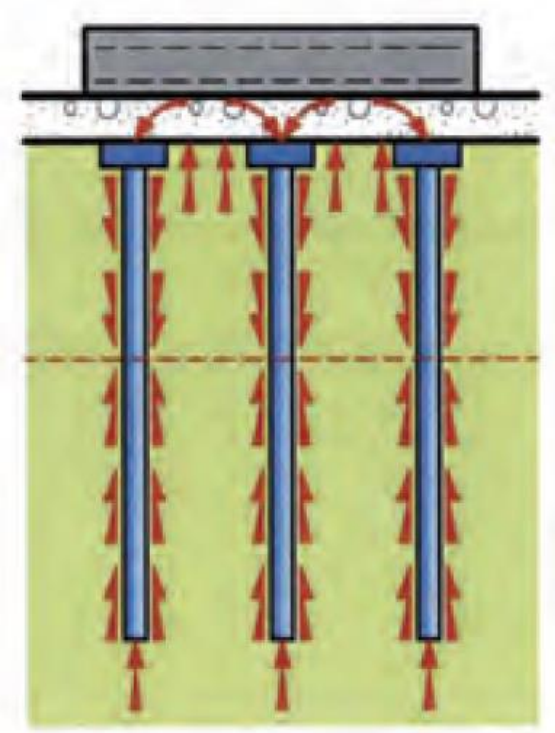

Figure 1. Behaviour of rigid inclusion system (ASIRI, 2012)

2 CENTRIFUGE AND NUMERICAL MODELING

In order to address such loading cases, several models have been studied using a centrifuge test device at the University Gustave Eiffel in Nantes (Corte 1984). The test program consisted of 15 test configurations. A slab was loaded on top of a soil model reinforced by rigid inclusions (Dubreucq et al., 2023). We focus here on two of these configurations: one where the slab was placed on top of an inclusion, and one where the slab was placed between two inclusions (see Figure 2 and Table 1)

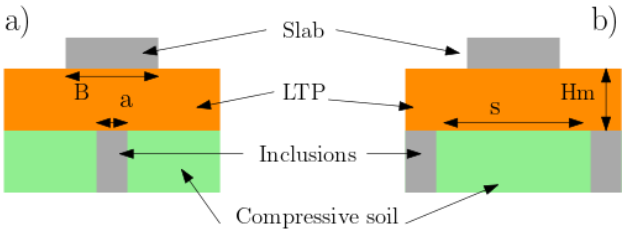

Figure 2. Studied cases a) and b).

Table 1. Model size parameters at prototype scale.

S	a	B	Hm
100 cm	10 cm	30 cm	60 cm

The numerical model is built using the FEM software CESAR LCPC (Humber et al. 2005) at prototype scale. The model is not representative of realistic dimensions, but is designed to explore and understand the behaviour of the system. The model is represented in 2D, with aluminium slab and inclusion. The compressive soil is modelled by expanded polystyrene as it represents an equivalent soil. The LTP is modelled by dense Hostun sand.

The numerical model was built according to the presented geometry. The material parameters were selected as follows: linear elastic for the aluminium elements, perfectly plastic Mohr-Coulomb for the LTP, and hardening Von Mises model for the equivalent soft soil. The parameters of the models were fitted on two preliminary tests of slab only on sand and only on soft soil. The parameters are listed in table 2, and fitting results are presented in Figure 3.

Table 2. Models parameters.

	Aluminium	Sand	Soft soil
$\boldsymbol{\rho}$	2700 kg/m^3	1650 kg/m^3	15 kg/m^3
$\boldsymbol{E}$	62 GPa	5	0.8MPa
$\boldsymbol{\nu}$	0.24	0.25	0.01
$\boldsymbol{\phi}$	-	36°	-
$\boldsymbol{c}$	-	3 kPa	-
$\boldsymbol{\psi}$	-	23°	-
$\boldsymbol{K_{VM}}$	-	-	30 kPa
$\boldsymbol{H_{VM}}$	-	-	230 kPa/def

Based on the initial models, a second model was built with a mobile load. It represents a rolling load placed on top of the LTP and displaced from one side to another for multiple loading cycles. The mobile load is set to represent a service load at a fraction of the ultimate load determined from previous computations.

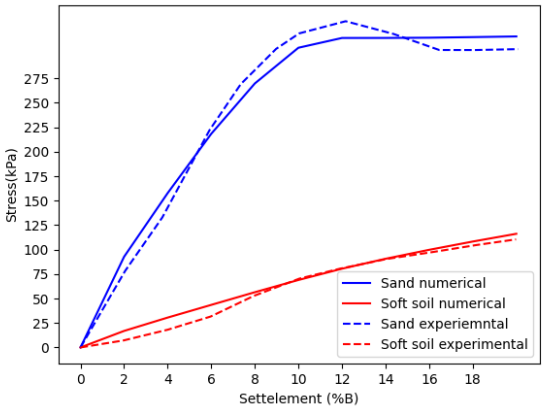

Figure 3. Results of fitting models.

3 RESULTS OF NUMERIALC MODELS

The results of experimental models are not presented in detail in this work.

3.1 First models

The results of models a) and b) are presented in Figures 4 and 5.

Figure 4 presents the shearing band pattern computed for both models. The patterns are the same as those obtained with experimental models.

Figure 5 presents the load-displacement results for both models and both experimental and numerical models. We observe a very good agreement between numerical and experimental results. Moreover, we can observe that the overall behaviour of the system is similar regardless of the position of the slab. We have confirmed this observation with complementary studies with intermediate positions of the slab (not presented here).

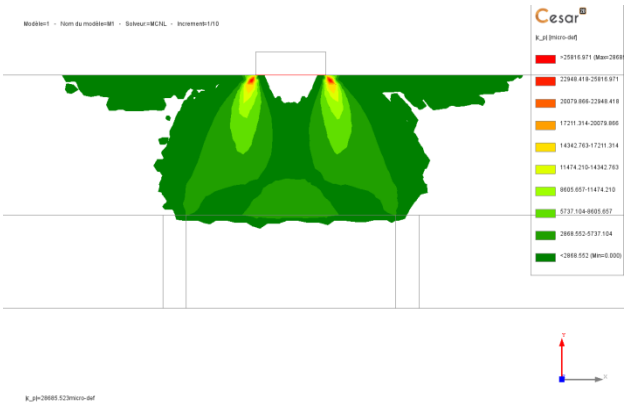

Figure 4. Shearing band patterns on cases b).

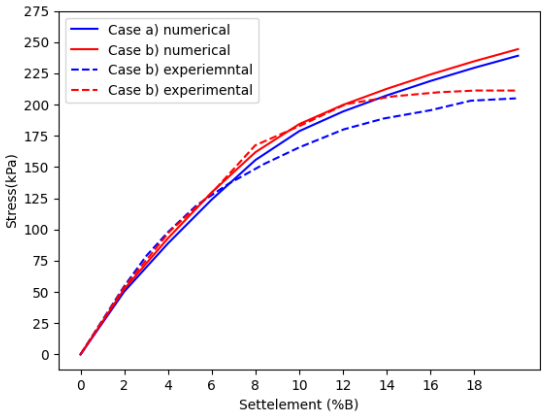

Figure 5. Results for case a) and b).

3.2 Mobile load models

Some results of the mobile loading models are shown on Figure 6. These figures represent the vertical stress at the interface between LTP and composite soil. This figure clearly shows that the arching effect causes the stress to be much more important on top of the inclusion. The weight load of the LTP is focused on the inclusion, and the soft soil is less loaded. However, after the first loading cycle, we observe that the arching effect was destroyed by the mobile loading. Indeed, the load on top of the inclusion is almost null and the load is now sheared onto the top of the soft soil.

This phenomenon can be explained as the mobile loading is not wide enough to transfer its load to the inclusion regardless of its position. Therefore, while between two inclusions, it generates plastic strain, forcing the mechanical interaction between the LTP and soft soil. Mechanically, this results in an unloading of the inclusions.

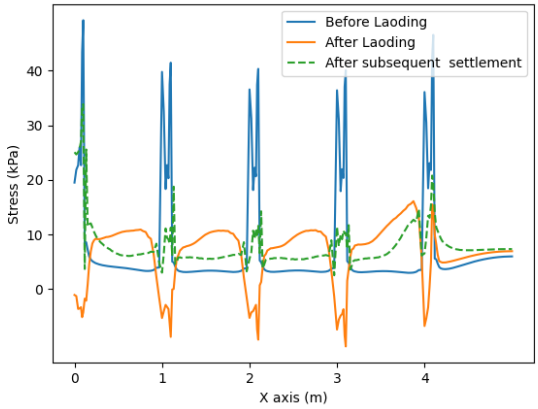

Figure 6. Vertical stress on surface between LTP and composite soil.

3.3 Subsequent settlement

As this phenomenon could be damaging to the arching effect and final behavior of the system, we studied the effect of subsequent settlement. Indeed, we postulate that such behavior will mostly occur during the construction phase of the LTP compaction. Moreover, as it overloads the soft soil, this phenomenon will result in subsequent and continuous settlement of the soft soil, regenerating the arching effect.

This hypothesis was tested by imposing a second settlement phase after the loading cycles. This results in the development of a new arching effect, as shown in Figure 6.

4 CONCLUSION

In this paper, we have presented part of the numerical work prepared in parallel with experimental modelling conducted in the scope of the French National Project ASIRI+. The goal of this work is to model and observe the behaviour of a rigid inclusion system subjected to small slab loading and mobile loading, with a thin load transfer platform. In such cases, the arching effect will not appear as the loading zone is too small to interact with more than one inclusion. Therefore, the resistance of the system should be studied with care. We present numerical modelling which shows good agreement with the experimental results and promising potential. In a second model, we expose the behaviour of a similar system subjected to mobile loading. The mobile loading applied on the LTP disturbs the chain forces in the granular layer and disrupts the pre-existing arching effect in the LTP, which may have an influence on the final behaviour of the system. However, subsequent settlement may regenerate the arching effect.

ACKNOWLEDGEMENTS

The work presented in this article is based on the master thesis of Nizar Ouchten. It is part of the French National Project ASIRI+, and is self-funded by the University Gustave Eiffel.

REFERENCES

ASIRI, (2012), Recommendations for the design, construction and control of rigid inclusion ground improvements, Presse des Ponts et Chaussée

Corte, J. F. (1984). The LCPC centrifuge., Symposium on recent advances in geotechnical centrifuge modeling https://escholarship.org/uc/item/73k7s64v

Dubreucq, T., Thorel, L. , Jagu, A., Neel, A., Lerat, S., Gaudicheau, P., and Audrain P. (2022) Remblais de faible épaisseur Essais 2D en centrifugeuse, research repport, ASIRI+ Project.

Humbert, P., Dubouchet, A., Fezans, G., Remaud, D. (2005). Cesar-lcpc, un progiciel de calcul dédié au génie civil. Bulletin des laboratoires des ponts et chaussées 256, 7–37.

Proceedings of the XVIII ECSMGE 2024
GEOTECHNICAL ENGINEERING CHALLENGES
TO MEET CURRENT AND EMERGING NEEDS OF SOCIETY
© 2024 the Authors
ISBN 978-1-032-54816-6
DOI 10.1201/9781003431749-35
Open Access: www.taylorfrancis.com, CC BY-NC-ND 4.0 license

ECSMGE 24
XVIII EUROPEAN CONFERENCE ON SOIL MECHANICS AND GEOTECHNICAL ENGINEERING

Centrifuge modelling of tapered wall jacked into dense sand

Modélisation physique d'une parois conique fonçée dans du sable dense

L. Bałachowski*, W.F. Kabeta
Faculty of Civil and Environmental Engineering, Gdańsk University of Technology, Poland

L. Thorel, M. Blanc, T. Dubreucq
Université Gustave Eiffel, Nantes' Campus, GERS-CG, Bouguenais, France

**lech.balachowski@pg.edu.pl*

ABSTRACT: A series of static penetration tests of trapezoidal walls in dense Fontainebleau sand were performed in the geotechnical centrifuge at Gustave Eiffel University. The models of wall with three different shapes (straight profile with thickness D=16mm, 0.75 degree and 1.5 degree of taper angle) but with the same volume were used. The soil mass was instrumented with five stress cells located at two levels at 2D, 4D and 6D distance from the wall axis to follow the stress state changes during the model penetration. Moreover, three pressure sensors were integrated on the model surface to track the changes of normal stress during the continuous penetration of the wall. Thus for the three walls of different geometry the evolution of the following variables is considered during monotonic penetration of the wall: 1) total vertical force; 2) horizontal stresses in the soil mass; 3) normal stresses on the wall surface.

RÉSUMÉ: Une série de pénétrations statiques d'une paroi dans du sable de Fontainebleau dense est effectuée dans la centrifugeuse géotechnique de l'Université Gustave Eiffel. Le volume de chaque paroi est identique mais leur profile varie: rectangle d'épaisseur D=16mm ou trapèze d'angle 0.75° ou 1.5°. Pour suivre l'évolution des contraintes pendant le fonçage continu du modèle, le massif du sol est instrumenté: cinq capteurs de contrainte distribués à deux niveaux à la distance de 2D, 4D et 6D de l'axe de paroi. Trois capteurs de contrainte sont de plus intégrés dans la paroi afin de mesurer la contrainte normale lors du fonçage de la paroi, dont l'effort vertical de fonçage est enregistré. Ainsi pour les 3 géométries, on compare pendant le fonçage, l'évolution: 1) des efforts de fonçage; 2) des contraintes horizontales dans le massif; 3) des contraintes normales à la paroi.

Keywords: Installation effects; dense sand; pushed-in piles.

1 INTRODUCTION

The installation of displacement piles induces significant changes of displacement, strain, and stress fields in the surrounding soil. These effects are considered in the physical modelling of tapered piles/trapezoidal walls in centrifuge in the present study. The testing program includes the installation of pushed-in continuous walls with observation of displacement patterns and stress evolution in the vicinity of the model. In addition, the tapered piles are installed in-flight by driving and pushed-in mode to evaluate their bearing capacity. Some studies on interface friction are also planned within this project (Foray et al., 1998; Bałachowski, 2006). This paper focuses on the installation of tapered walls with stress evolution in the soil mass and on the model surface.

Tapered piles are characterized by a gradually decreasing cross section with depth. Timber piles are traditional examples of such structures (Christin et al., 2013). Nowadays, concrete precast or cast-in place piles (Khan et al., 2008; Lee et al., 2009), steel or composite tapered piles are also applied (Sakr et al., 2004). They can be also used for densification of sandy subsoil (Zil'berberg & Sherstnev, 1990; Stuedlein et al., 2016).

2 PHYSICAL MODEL SETUP

In the range of Geolab (2021) European project, a series of centrifuge tests was performed at Gustave Eiffel University (Nantes, France) in the GERS-CG lab (Gers-CG, 2023). This geo-centrifuge (Thorel, 2022) has a radius of 5.5m and a total mass of 2tons can be embarked in the swinging basket.

2.1 Soil mass preparation and instrumentation

Prior to each test, the homogeneous soil mass was prepared using sand raining technique to achieve designed relative density 0.68 and the dry bulk density of 1620 kg/m^3 measured with boxes disposed at the bottom of the container. Uniform Fontainebleau quartz

sand (NE34) with d_{50}=0.206 mm was used with parameters described in (Andria-Ntoanina et al., 2010; Beroya-Eitner et al., 2022). The container with a transparent glass (Figure 1) and inside dimensions of 800×450 mm enables visual observation of soil behaviour during wall installation.

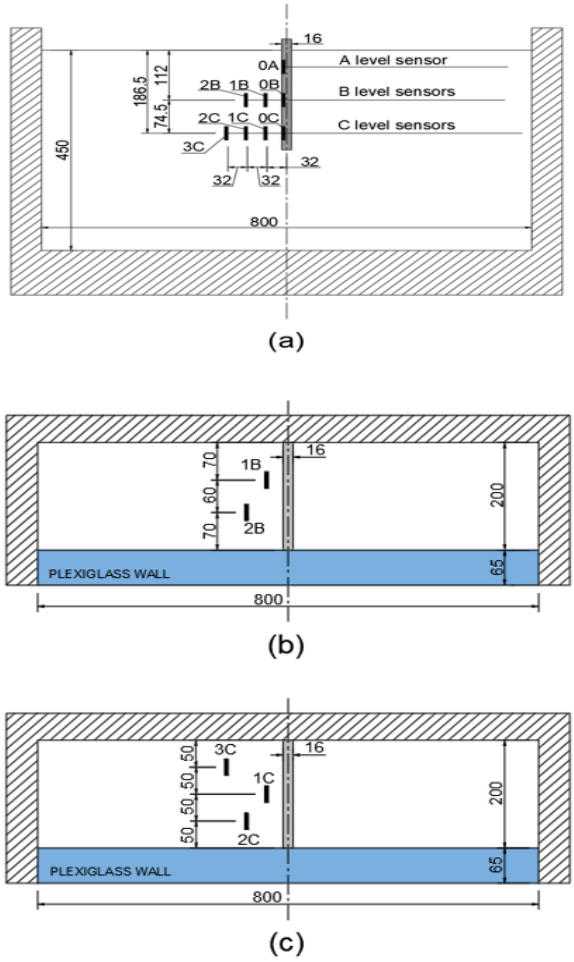

Figure 1. Centrifuge model setup and soil instrumentation: (a) vertical cross-section, (b) B level horizontal cross-section, (c) C level horizontal cross-section. (All dimensions in [mm]).

Kyowa small-sized soil pressure transducers having an outer diameter of 30 mm and a pressure-sensing surface diameter of 23 mm were used. Five sensors where placed in the soil mass at two levels (Figure 1b, 1c). Additional three sensors were fixed on the model surface (Figure 2). All transducers were calibrated in centrifuge under loading-unloading cycles induced by the increased gravity.

2.2 Model walls

Three model walls were used: straight wall (denoted as 'S') with 0° taper angle, tapered wall with 0.75° taper angle (denoted as 'T1') and wall with 1.5° taper angle (denoted as 'T2'), see Figure 2a-c. Each model was equipped with three normal stress sensors fixed on its surface (Figure 2d). The model wall was fitted to the container width of 20 cm to reduce any gap in the contact wall-glass. At final embedment only a few sand grains were trapped between the model and transparent wall.

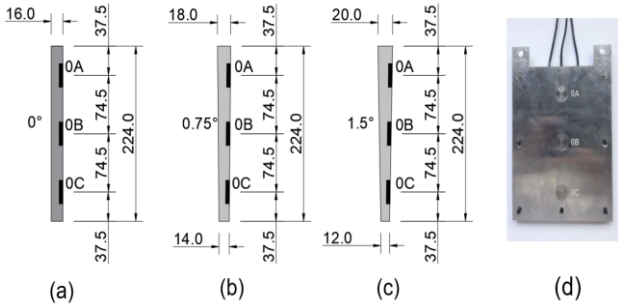

Figure 2. Instrumented models with a taper angle of: (a) 0° (standard S wall), (b) 0.75° (T1), (c) 1.5° (T2) and (d) model wall – front view.

2.3 Test execution

Three monotonic pushed-in tests with tapered walls were completed on single series. The centrifuge operated at an acceleration level of 25g. In each test, the wall was pushed into the subsoil with 0.1 mm/s rate to the depth of 224 mm, which gives the wall slenderness 14.

3 RESULTS

3.1 Total force mobilization

The mobilization of axial force during wall installation is given (Figure 3) for each wall type. It can be noticed that the total force required for monotonic installation of the wall was slightly lower for the models with higher taper angles compared to the straight profile. At final embedment the penetration force for T2 (respectively T1) constitutes only about 0.75 (resp. 0.9) of corresponding axial force for straight wall.

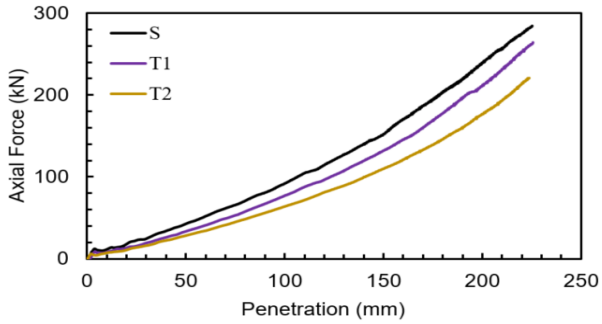

Figure 3. Axial force mobilized during wall installation (model scale).

3.2 Horizontal stress in the soil mass

The horizontal stress development (at fixed altitude) in the soil mass during installation of the wall is shown in Figure 4. A distinct peak in horizontal stress was observed in the soil mass just before the wall base has passed the level of the stress cell. This tendency can be noticed for the sensors in upper (B) and lower (C) levels. Once the wall base has moved below the position of the stress cells, a continuous decrease in normal stress was observed for the straight wall model. In contrast for tapered models the stress cells at the upper level exhibit further slight re-mobilization of horizontal stress, especially for the wall with higher taper angle. The maximum value of horizontal stress gradually decreases with distance from the wall. For the stress sensors placed at a given distance to the wall the highest maximum horizontal stress is noticed for the straight wall.

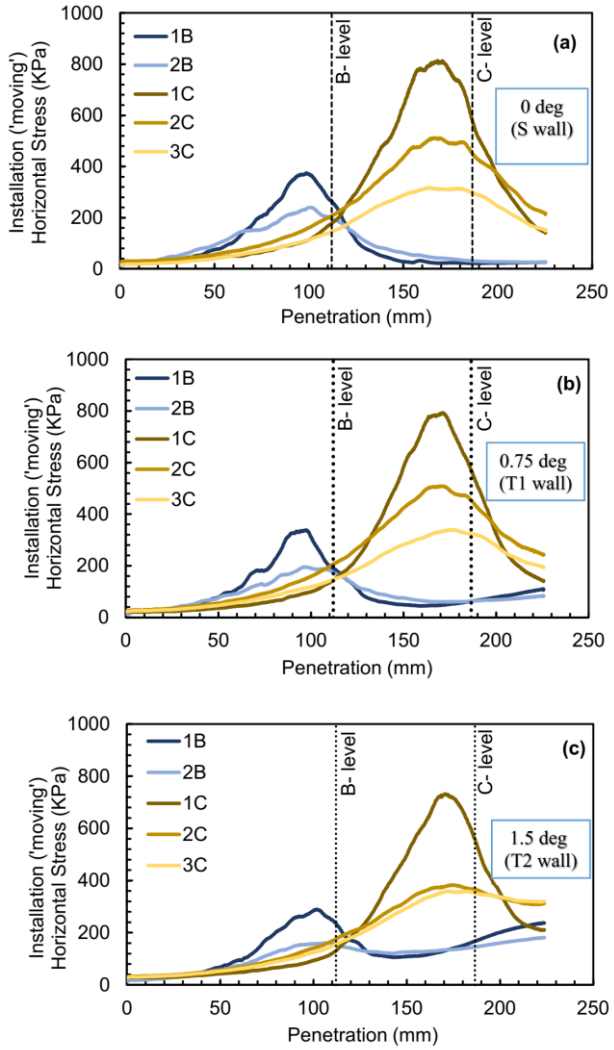

Figure 4. Stress distribution in the soil mass during wall installation (a) standard (S), (b) tapered (T1), and (c) tapered (T2).

3.3 Normal stress at the wall interface

The mobilization of normal stress at three positions (moving downwards) during tapered wall pushed-in is given in Figure 5. The observed maximum normal stress on the wall increases with the taper angle. At final stage of penetration, a sharp increase of normal stress is observed near the base due to mobilization of base resistance. One should also notice that the normal stress sensors on the tapered wall capture not only horizontal stress component but the vertical one as well. The latter can considerably influence the recorded values especially in case of the stress cell located in the vicinity of the base.

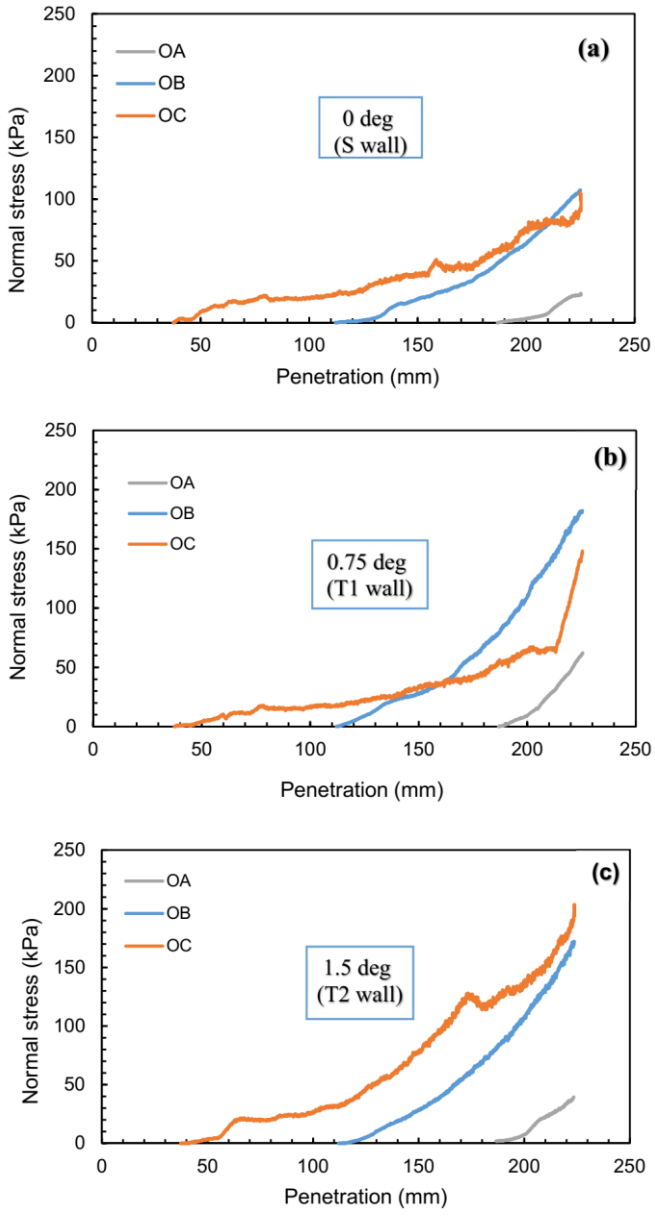

Figure 5. Normal stress mobilization on the wall during installation (a) standard (S), (b) tapered (T1), and (c) tapered (T2).

4 CONCLUSIONS

The installation of the continuous wall induces modifications in horizontal stress in the soil mass, normal stress at the model interface, and reduced axial force necessary for the penetration of tapered walls. The lateral stress modification in the vicinity of models is a function of taper angle. While the highest level of horizontal stress in the soil mass is observed for the straight wall, the normal stress on the wall surface is the largest for the model with the highest taper angle. The maximum horizontal stress in the soil mass for T1 and T2 wall is about 0.95 and 0.8 of the corresponding stress for the straight wall. However, at the end of installation both horizontal and normal stresses are significantly higher for tapered walls than for the standard one. The resulting installation effort is the lowest for T2 wall as higher shaft friction of tapered walls does not compensate the lower contribution of the wall base. The test results on walls can be qualitatively applied to describe the behaviour of tapered pile models.

ACKNOWLEDGEMENTS

This project has received funding from the European Union's Horizon 2020 research and innovation programme under Grant Agreement No. 101006512.

REFERENCES

Andria-Ntoanina, I., Canou, J., & Dupla, J. (2010). Caractérisation mécanique du sable de Fontainebleau NE34 à l'appareil triaxial sous cisaillement monotone. *Laboratoire Navier–Géotechnique. CERMES, ENPC/LCPC*.

Bałachowski, L. (2006). Scale effect in shaft friction from the direct shear interface tests. *Archives of Civil and Mechanical Engineering*, *6*(3), 13–28. https://doi.org/10.1016/S1644-9665(12)60238-6.

Beroya-Eitner, M. A., Machaček, J., Viggiani, G., Dastider, A. G., Thorel, L., Korre, E., Agalianos, A., Jafarian, Y., Zwanenburg, C., Lenart, S., Wang, H., Zachert, H., & Stanier, S. (2022). *GEOLAB Material Properties Database* (1.0) [dataset]. Zenodo. https://doi.org/10.5281/ZENODO.7462287

Christin, J., Le Kouby, A., Reiffsteck, P., & Rocher-Lacoste, F. (2013). Essais de chargement statique de pieux en bois instrumentés avec des extensomètres amovibles. *Proceedings of 18th International Conference on Soil Mechanics and Geotechnical Engineering, Paris: challenges and innovations in geotechnics, Volume 1.*

Foray P., Bałachowski L., Raoult G. (1998). Scale effect in lateral friction. *Proceedings of International Conference Centrifuge'98*, Tokyo, pp.211-216.

Geolab. (2021). *Geolab – Science for enhancing Europe's Critical Infrastructure*. https://project-geolab.eu/.

Gers-CG. (2023). *Centrif-UGE*. https://cg.univ-gustave-eiffel.fr/en/translate-to-english-equipements/translate-to-english-centrif-uge.

Khan, M. K., El Naggar, M. H., & Elkasabgy, M. (2008). Compression testing and analysis of drilled concrete tapered piles in cohesive-frictional soil. *Canadian Geotechnical Journal*, *45*(3), 377–392. https://doi.org/10.1139/T07-107.

Lee, J., Paik, K., Kim, D., & Hwang, S. (2009). Estimation of Axial Load Capacity for Bored Tapered Piles Using CPT Results in Sand. *Journal of Geotechnical and Geoenvironmental Engineering*, *135*(9), Article 9. https://doi.org/10.1061/(ASCE)GT.1943-5606.0000036.

Sakr, M., EL Naggar, M. H. E., & Nehdi, M. (2004). Load transfer of fibre-reinforced polymer (FRP) composite tapered piles in dense sand. *Canadian Geotechnical Journal*, *41*(1), Article 1. https://doi.org/10.1139/t03-067.

Stuedlein, A. W., Gianella, T. N., & Canivan, G. (2016). Densification of Granular Soils Using Conventional and Drained Timber Displacement Piles. *Journal of Geotechnical and Geoenvironmental Engineering*, *142*(12), Article 12. https://doi.org/10.1061/(ASCE)GT.1943-5606.0001554.

Thorel, L. (2022). Physical Modelling Facilities: From Galileo to 3D Printing. *Proceedings of 10th ICPMG Int. Conf. on Physical Modelling in Geotechnics*, 64–72. https://www.issmge.org/uploads/publications/53/115/P00503.pdf.

Zil'berberg, S. D., & Sherstnev, A. D. (1990). Construction of compaction tapered pile foundations (from the experience of the "Vladspetsstroi" trust). *Soil Mechanics and Foundation Engineering*, *27*(3), Article 3. https://doi.org/10.1007/BF02306664.

Proceedings of the XVIII ECSMGE 2024
GEOTECHNICAL ENGINEERING CHALLENGES
TO MEET CURRENT AND EMERGING NEEDS OF SOCIETY
© 2024 the Authors
ISBN 978-1-032-54816-6
DOI 10.1201/9781003431749-36
Open Access: www.taylorfrancis.com, CC BY-NC-ND 4.0 license

ECSMGE 24
XVIII EUROPEAN CONFERENCE ON SOIL MECHANICS AND GEOTECHNICAL ENGINEERING

Effects of non-linear response of shallow foundations on transmission tower serviceability

Effets de la réponse non linéaire des fondations superficielles sur l'aptitude au service des pylônes de transmission

P. Barbieri*, T. Newson, M.Y. Xiao, H.P. Hong
Department of Civil Engineering, Western Ontario University, Spencer Engineering, London, Canada
**pbarbie2@uwo.ca*

ABSTRACT: Electrical transmission tower design has been a key global topic driving the development of reliability analysis of foundations since the 1980s. Many reliability-based ultimate limit state design methods for shallow foundations can be traced to seminal work conducted in the 1980s by EPRI. However, current design simplifies the foundation behaviour to be equivalent to a perfectly pinned or fixed point which does not allow proper consideration of serviceability conditions. This paper presents a simplified assessment of the soil-structure interaction of a transmission tower to better understand the effect of the non-linear behaviour of the foundation on the structural response and elucidate whether it is relevant.

RÉSUMÉ: Depuis les années 1980, la conception des pylônes de transmission électrique est un sujet mondial clé qui a conduit au développement de l'analyse de fiabilité des fondations. De nombreuses méthodes de conception de l'état limite ultime basées sur la fiabilité pour les fondations peu profondes peuvent être attribuées aux travaux fondamentaux menés dans les années 1980 par l'EPRI. Cependant, la conception actuelle simplifie le comportement de la fondation pour qu'il soit équivalent à un point parfaitement chevillé ou fixe, ce qui ne permet pas de prendre correctement en compte les conditions de service. Cet article présente une évaluation simplifiée de l'interaction sol-structure d'une tour de transmission afin de mieux comprendre l'effet du comportement non linéaire de la fondation sur la réponse structurelle et d'élucider si elle est pertinente.

Keywords: Foundation; transmission line; non-linear; serviceability.

1 INTRODUCTION

The determination of serviceability limit states in foundation design depends on the intended purpose of the structure being supported. This limit state may not reflect an intrinsic limit of the foundation itself, but rather a situation for which the foundation movement hinders the ability of the superstructure to deliver the desired service. The same foundation, subjected to similar levels of loading, may have different serviceability limit states depending on it being used to support a building, bridge, or other structure. Even within similar transmission structures, the same foundation can have different serviceability limits.

Currently, transmission tower design guidelines in Canada and the U.S. do not recommend specific serviceability limits for the design of foundations or transmission towers. However, standards from other countries address this issue. For example, the Chinese standard DL/T741-2001 (NDRC 2001) specifies limits for tolerable levels of inclination for pole towers. It also specifies limits at which corrective measures should be taken. Majcherczyk and Niedbalski (2017) indicate that a similar standard exists in Poland. BN-90/9056-01 specifies that the deviation from the vertical of the transmission pylon peak, standing without conductors, is H/300, where H is the height of the structure.

The analysis of the response of transmission towers to wind loads, whether in scaled models, finite element models or considering field conditions, is usually limited to the structure itself. However, few authors have investigated the behaviour of the foundations. (Savory et.al. 1998, 2008) measured the force applied in the foundations by placing strain gages in all the tower feet directly above the foundation. The structure was a 44 m tall transmission tower located in Dorset (England) between 1995 and 1999. Along with the strains, the wind speed at 10 m height was also recorded. The results showed that foundation load is proportional to the square of the wind speed, with measured loads below ultimate limit state loads specified by code, with a code overprediction of 14%.

Structural analysis of transmission towers subjected to wind loads does not consider the

foundation stiffness and displacement. This omission can have significant consequences given the non-linear behaviour of the structure. This paper uses a simplified foundation model and assesses the effect on the structural response compared to the typical fixed supports. The objective is to better understand how to define a serviceability limit state for the foundations.

2 METHODOLOGY

2.1 Wind load

The wind load is modelled based on the combination of a mean wind speed and a turbulent wind component. For synoptic winds, the mean wind speed is considered constant at any given height. Variation with height is controlled by a power law wind profile with an exponential coefficient of 1/7, with the wind speed at 10 m height above the ground surface used as a reference value. The turbulent flow around the mean wind speed is modelled as a Gaussian random process based on the Kaimal spectrum and the Davenport coherence model (Simiu and Scanlan 1996), and simulated using the spectral representation method (SRM) (Shinozuka and Jan 1972). The wind speed is transformed into loads following CSA 60826-10 (2019) guidelines.

In this study, a 46.9 m tall transmission tower with adjacent spans of cables is considered. The investigation is carried out based on a location in Ottawa (Canada), and the corresponding 10-minute mean wind speed at 10 m height with a return period of 10, 25, 100 and 500 years equals 22.81, 24.07, 25.94 and 28.09 m/s respectively, which is adopted to generate the wind speed field for later analysis.

2.2 Structural model

A finite element model of the structure developed in ANSYS Multiphysics 18.0 (ANSYS 2014) was used for the analysis. The model was employed by (Mara and Hong 2013) considering rigid foundations. Each tower member is modelled using three 2-node BEAM188 beam elements, with 6 degrees of freedom at each node. The material nonlinearity in the tower member is included by using a bilinear hysteretic model. Each span of cables consists of 2 conduct lines and 1 ground line with a span length of 488 m. Each cable within a span is modelled using thirty 2-node link elements with only axial loading capacity. The ends of the tower-line system are connected to springs that represent the stiffness of the remote towers and cables. The details of the geometric variables and material properties of the tower and cables can be found in Yang and Hong (2016). The structural model includes the effects of the geometric non-linearity using a large-deformation analysis.

2.3 Reaction loads

Figure 1 shows the vertical, longitudinal, and horizontal components of the reaction loads in the foundations of the lattice transmission tower for the 500-year event. The reactions include the effects of the dead load (45 kN), which accounts for the offset between the uplift and compression directions. The main effect of the wind load relates to the axial components required to balance the overturning moment, with the mean value of the horizontal components being less than 10%.

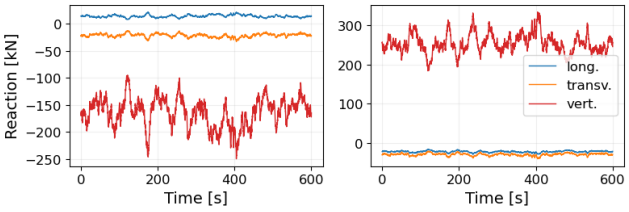

Figure 1. Transmission tower reactions to the 500-year event.

Table 1 shows the temporal mean value and standard deviation of the reaction loads due to the wind alone for different return periods (TR). The horizontal component is generally below 10% of the vertical components, with the significance reducing as the return period increases. It can also be seen that the variation around the mean value, indicated by the standard deviation, is relatively constrained as well.

Table 1. Reaction load mean (standard deviations) in kN.

TR [yr]	Vertical	Long.	Trans.
10	138.2 (17.0)	12.1 (1.5)	16.7 (2.1)
25	153.9 (19.0)	13.5 (1.7)	18.6 (2.3)
100	178.7 (22.4)	15.8 (2.0)	21.6 (2.7)
500	209.5 (26.6)	18.5 (2.4)	25.4 (3.2)

2.4 Foundation design

Following the ASCE (2020) guidelines, foundations were designed for the 100-year event. Uplift capacity was computed using the Meyerhof and Adams (1968) method with a safety factor of 1.5 in a uniform stratigraphy with a loose Hostun sand. The required design parameters are provided by Schanz et al. (1999): friction angle at failure $\varphi_p = 34º$, dilatancy angle at failure $\psi_p = 0º$, a reference stiffness modulus $E_{50}^{ref} = 20\,MPa$, a stress dependency power $m = 0.65$, an unloading reloading Poisson ratio $\nu_{ur} = 0.2$, a reference Young modulus for unloading and

reloading $E_{ur}^{ref}/E_{50}^{ref} = 3.0$. A unit weight $\gamma_s = 19\,kN/m^3$ is adopted. The IEC 60826 (2003) and CIGRE (2002) design guidelines are concerned only with the ultimate limit state, and thus, do not consider the foundation stiffness or force-displacement behaviour. Two circular chimney shallow foundation designs are adopted, a "deep" foundation with an embedment depth (D) of 2.00 m and a width (B) of 0.75 m, and a "shallow" foundation with D of 1.25 m and B 1.75 m. In both cases, foundation and column thicknesses of 30 cm were adopted. According to current design guidelines, these foundations are equivalent to each other (with a safety factor slightly above 1.5).

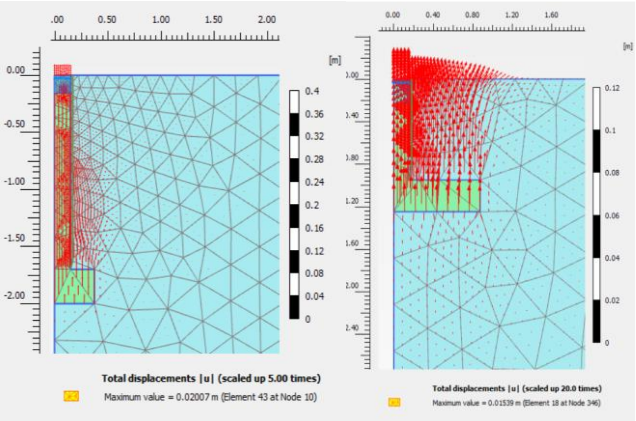

Figure 2. Displacement field at pull-out failure for the "deep" (left) and "shallow" (right) foundations.

2.5 Load tests

Axisymmetric PLAXIS (Bentley 2020) finite element models of the foundations were developed to analyse the response when subjected to different levels of excitation. The Hostun sand is modelled using the Hardening Soil model, an associated elasto-plastic model that combines the Mohr-Coulomb failure surface with an elliptical cap and has a stress-dependent stiffness that distinguish between virgin and un/reloading. Concrete is modelled as an elastic material. Interface elements were included between the column and the soil, so no shear transfer took place. The models were loaded statically first to the dead load level, and then subjected to load cycles corresponding to the 100/500-year events, to determine the foundation stiffness. This stiffness is then used in the structural model to determine the transmission tower responses. Figure 2 shows the displacement (velocity vector) field at pull-out failure for the two foundations with D/B of 2.7 and 0.7 respectively. A clear difference in the behaviour can be seen, where the deep foundation mechanism is far more localized around the foundation (base/column), whereas the shallow foundation mechanism extends to the free surface with an apparently outward-curving edge (related to the angle of dilation of the sand).

3 RESULTS

3.1 Soil-structure interaction

Figure 3 show the response of the foundations when subjected to loads alternating between pull-out and compression cycles corresponding to repeated 100 (blue) and 500-year (red) design storms. The design loads, corresponding to the 100-year event, are shown as dashed grey lines. A clear difference in the behaviour of both foundations is seen. Wide hysteresis loops with increasing permanent deformations characterize the response of the "deep" foundation, while very narrow hysteresis loops are seen for the "shallow" foundation. This is due to the failure mechanisms observed in Figure 2 and reflected in the pull-out and compression test also shown in Figure 3. A common feature of both foundations is that the initial loading is always less stiff than the unload-reload behaviour. This can be in part explained by the high $E_{ur}^{ref}/E_{50}^{ref} = 3.0$ used for the Hostun sand.

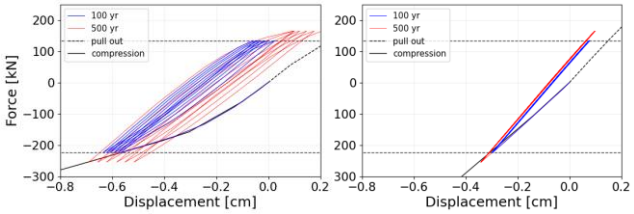

Figure 3. D/B of 2.7 (left) and 0.7 (right) foundations subjected to 100 and 500-year events.

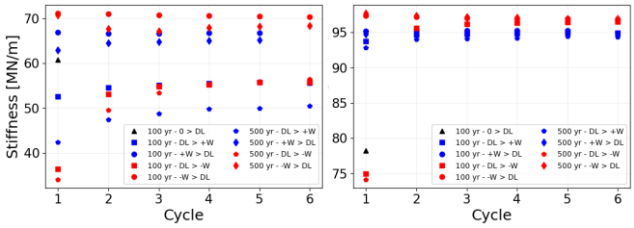

Figure 4. D/B of 2.7 (left) and 0.7 (right) foundations secant stiffness for 100-year and 500-year events.

The hysteresis loops in Figure 3 are transformed into a secant stiffness to represent loading or unloading behaviour, in the compressive and pull-out directions. The resulting secant stiffnesses are presented in Figure 4. After the first load cycle, the stiffness stabilizes. The "shallow" foundation has a more uniform stiffness across load levels (100 or 500-year) for loading or unloading. The latter is reflected in the narrower hysteresis loops shown in Figure 3. The deep foundation exhibits a markedly different behaviour under loading or unloading, with a stiffer unloading,

explained by the wider hysteresis loops. Interestingly, whether the loading is in the compressive or pull-out direction, there is no significant change in stiffness. Based on the results, a 60 MN/m stiffness is used for the "deep" case & 95 MN/m for the "shallow" case in the structural model.

Table 2. Transmission tower peak displacements [m].

TR [yr]	Fixed	Deep	Shallow
10	0.1379	0.1760	0.1616
25	0.1543	0.1969	0.1808
100	0.1804	0.2303	0.2113
500	0.2131	0.2723	0.2496

Table 3. Natural frequencies [Hz].

Mode	Fixed	Deep	Shallow
Transverse	1.155	1.033	1.074
Longitudinal	1.219	1.074	1.121
Vertical	1.555	1.555	1.555

The effect of the foundation stiffness can be seen in the transverse and longitudinal natural frequencies of the structure. As Table 3 shows, the vertical stiffness of the foundation affects the overall horizontal stiffness of the structure, with a more flexible foundation inducing a more flexible (lower natural frequency) structure. Therefore, models that consider fixed foundations tend to over-estimate the stiffness and natural frequency of the structure.

4 CONCLUSIONS

It is well-known from theoretical approaches that foundation geometry affects stiffness and non-linear behaviour under repeated load cycles. However, the absence of a proper quantification precluded the estimation of its significance in terms of the SLS. Our analysis has shown that it plays a crucial role in the response of transmission towers to wind loads. This has so far been ignored by design standards. The comparison of different foundation geometries (that from a design point of view are equivalent) shows that the dissimilar responses can affect the SLS and the long-term response after many load-cycles associated with significant weather events. Thus, the structural serviceability cannot be effectively studied without the foundation component, and the foundation serviceability limit is a function of its stiffness and non-linear response to load cycles. This preliminary numerical analysis demonstrates the problem. Further calibration using model testing in a centrifuge and available full-scale test results is required to refine the design approach to be calibrated.

REFERENCES

NDRC (2001). DL/T741-2001 Operating code for overhead transmission line, China.

Majcherczyk T., Niedbalski, Z. (2017). The influence of underground coal mining on an overhead high-voltage power line, *Technical Transactions*, Vol (114), pp. 87-100, https://doi.org/10.4467/2353737XCT.17.034.6345.

Savory, E., Parke, G., Disney, P., Toy, N., Zeinoddini, M. (1998). Field measurements of wind-induced trans. tower found. loads, *Wind & Structures*. http://dx.doi.org/10.12989/was.1998.1.2.183.

Savory, E., Savory, G., Disney, P., Toy, N. (2008). Wind-induced transmission tower foundation loads: A field study-design code comparison, *Jour. of Wind Eng & Ind Aero*, Vol (96) pp. 1103-1110, https://doi.org/10.1016/j.jweia.2007.06.033.

Simiu, E., Scanlan, R. H. (1996). *Wind effects on structures: fundamentals and applications to design,* John Wiley New York, U.S.. https://doi.org/10.1002/9781119375890.

Shinozuka, M., Jan, C. M. (1972). Digital simulation of random processes and its applications, *Journal of Sound and Vibration*. Vol (25), pp. 111-128, https://doi.org/10.1016/0022-460X(72)90600-1.

CSA (2019). CAN/CSA-C22.3 No. 60826-10 Design criteria of overhead transmission lines, Canadian Standards Association, Toronto, Canada.

Yang, S. C., Hong, H. P., (2016). Nonlinear inelastic responses of trans. tower-line system under downburst, *Eng Struct.* Vol (123), pp. 490-500, https://doi.org/10.1016/j.engstruct.2016.05.047.

ANSYS Inc. (2007). ANSYS® Multiphysics (v 9.0).

Mara, T. G., Hong. H. P. (2013) Effect of wind direction on the response and capacity surface of a trans. tower. *Eng Struct*. Vol (57) pp. 493-501, http://dx.doi.org/10.1016/j.engstruct.2013.10.004.

ASCE (2020). No. 74 Guidelines for Electrical Transmission Line Structural Loading, Third Edition, American Society of Civil Engineers, Reston, Virginia.

Meyerhof, G. G., Adams, J. I. (1968). The ultimate uplift capacity of foundations. *Canadian Geotechnical Journal.* Vol (5), pp. 225-244, https://doi.org/10.1139/t68-024.

Schanz, T., Vermeer, P. A., Bonnier, P. G. (1999) The hardening soil model: Formulation and verification. *Beyond 2000 in Computational Geotechnics*. pp. 281-296, http://dx.doi.org/10.1201/9781315138206-27.

International Electrotechnical Commission (2003) IEC 60826 Design criteria of overhead transmission lines, HIS, Switzerland.

CIGRE (2002) Working Group 22.07 - Foundations The design of transmission line support foundations - an overview, Paris, France.

Proceedings of the XVIII ECSMGE 2024
GEOTECHNICAL ENGINEERING CHALLENGES
TO MEET CURRENT AND EMERGING NEEDS OF SOCIETY
© 2024 the Authors
ISBN 978-1-032-54816-6
DOI 10.1201/9781003431749-37
Open Access: www.taylorfrancis.com, CC BY-NC-ND 4.0 license

ECSMGE 24
XVIII EUROPEAN CONFERENCE ON SOIL MECHANICS AND GEOTECHNICAL ENGINEERING

Automating stability analysis using BIM-FEA-Integration

L'automation d'analyse de la stabilité employant l'intégration du BIM envers la FEA

J. Beck*, H. Jürgens, S. Henke
Helmut-Schmidt-University, Hamburg, Germany
**beckjo@hsu-hh.de*

ABSTRACT: This paper examines chances and frontiers of BIM-to-FEA integration for geotechnical projects using a real-world excavation pit project underscoring its practical applicability. A BIM model is first created, which includes the urban context, the subsoil, the excavation pit, and the building to be erected. Elements relevant to the numerical model are identified, pre-processed and transferred to the FEA software leveraging an interactive automation routine. After the calculations and stability analysis, the results are back-transferred to the BIM model, which triggers an update routine for geometries and properties of the BIM model's objects enabled by their parametric definition. It is demonstrated that 2D numerical models can be derived from a complex BIM model. Strict adherence to the model structure and the establishment of appropriate modelling rules are prerequisites for this. The approach allows real-time interaction between BIM and FEA with automatic compliance of the stability. The developed automation process shows potential for efficiency gains, particularly in variational analyses and supports version control and data consistency.

RÉSUMÉ: Ce papier étudie les opportunités et les frontières pour l'intégration du BIM envers la FEM dans les projets géotechniques, en utilisant une fouille réelle, ce qui souligne l'applicabilité pratique. En premier lieu, une modèle BIM est créé, qui inclut le contexte urbain, le sous-sol, la fouille et le bâtiment à construire. Les éléments qui sont nécessaires au modèle numérique sont identifiés, prétraités et transférés au logiciel de FEM pour être tirés d'une routine de l'automation interactive. Après avoir effectué les calculs et l'analyse de la stabilité, les résultats sont transférés de retour au modèle BIM, que déclenché la routine de mise à jour pour les géométries et les attributs des objets du modèle BIM, causée par leurs définitions paramétriques. Il est démontré que les modèles numériques bidimensionnels peuvent être dérivés d'un modèle BIM complexe. L'adhérence élevée à la structure du modèle et l'établissement des règles appropriées pour la modélisation sont un prérequis pour ceci. L'approche permet d'interagir de temps réel entre le BIM et la FEM avec la conformité automatique de la stabilité. Le process d'automation qui est développé dans ce papier permet aux les gains efficients, notamment pour l'analyse variationnelle, et avalise le contrôle de version et la consistance de data.

Keywords: BIM; FEA; automation; integration; analysis.

1 INTRODUCTION

Building Information Modelling (BIM) exerts significant influence on the digitization of the AEC sector. Its model and data centric approach is increasingly adopted in geotechnical projects. In current practice, geotechnical design analysis is usually performed in separate, disconnected models. BIM models as well as analysis models frequently change during early project stages due to information gain and design changes. Such changes in one domain could potentially affect the validity of other domains models. After each change, the validity should be checked and evaluated. Due to the data isolation in the traditional process of design analysis, the evaluation and adjustments have to be done manually, which is flexible, but laborious and error prone.

To address these shortcomings a fully automated workflow integrating BIM and Finite Element Analysis (FEA) for stability analysis is proposed.

2 METHODOLOGY

The proposed process consists of the following steps: (I) Create a highly parametric BIM model, (II) extract and evaluate parameters needed for design analysis from the BIM model, (III) create two-dimensional (2D) FE model and calculate, (IV) dimensional optimisation, here using the Differential Evolution Algorithm (V) update BIM models using calculation results. Between each step, a version-controlled JSON-file is created, which is then used to trigger the next step and to evaluate, if a modification in one model affects the other one.

The implementation uses *Seequent Leapfrog Works, Autodesk Revit* and *Robert McNeel & Associates Rhino.Inside* for creating and managing the BIM models and *Bentley PLAXIS 2D (Version 2023-2)* for the numerical analysis. A python-webserver is used for data processing and transferring.

The developed process is validated and evaluated using a slightly adapted real world case study. The investigated excavation pit is located in an urban area in northern Germany and has been numerically investigated in (Jürgens & Henke, 2022). The therein listed numerical parameters are also used in the present study.

3 IMPLEMENTATION AND CASE STUDY

3.1 Parametric BIM models

In parametric modelling, in contrast to direct modelling, geometries are described by parameters and constraints. Editing such parameters results in an accordingly updated geometry. BIM authoring tools usually differ between components and a project layer, whereby the components tend to be more parametric.

The model granularity and the parametric logic needs to be set up in a way, that the results from the numerical calculation can update the BIM model. For example, if a calculation objective is to optimize the length of each diaphragm wall lamella, the lamellas need to be modelled individually and their geometric extents shall be driven by a corresponding length parameter.

The BIM models for the present case study are introduced in (Beck & Henke, 2023b) and are further developed for this contribution. Figure 1 shows a 3D view of selected coordinated BIM models.

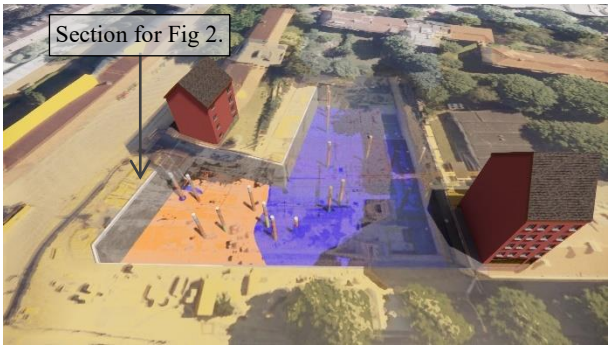

Figure 1. 3D view of coordinated BIM models.

3.2 Data extraction and evaluation

The derivation of the plain strain 2D FE model follows the approach introduced in (Beck & Henke, 2023a). Given the problem definition, which is the stability analysis of a diaphragm wall here, the BIM models and other data sources are queried for relevant content. It is differentiated between elements, that are represented in the numerical model by one-dimensional elements (anchors, wall, etc.) and two-dimensional elements (soils) as well as boundary conditions and material properties. This is made possible by the underpinned semantic model and a rule-based system that evaluates how each element is represented in the FE domain. This approach allows the integration of additional expert knowledge with little effort.

In the following, selected major steps in the developed process are outlined. Whilst many optional parameters can be set, the necessary inputs for the automation are location and type of analysis to conduct. A plane cutting the diaphragm wall perpendicularly at the point to be calculated is created. The resulting polylines of this plane's intersection with the 3D meshes that represent the soil volumes in the BIM model require further processing, as they cannot be directly used for meshing due to tiny segments and angles as well as small gaps between adjacent polylines. Besides that, they do not consider the construction sequence and the limited model area in the numerical domain. To address this issue, Boolean operations and topologically aware simplification techniques are applied as described in (Beck & Henke, 2023a). Figure 2 a) shows an exemplary cross-section through the subsoil model and the diaphragm wall with projected anchors. The width of the section used for the numerical analysis is 90 m, the depth is 50 m. Before the simplification, 19 closed polylines with 4983 control points are present in this area, of which 2593 are unique, meaning no other point is at that location. These polylines are not suited for mesh creation, due to small segments, small angles and little gaps between adjacent regions. After simplification, 17 polylines with 108 points (38 unique) remain. These can be then be used for mesh creation, see Figure 2 b). Multiple evaluation metrices and simplification algorithms ensure good mesh quality. The displayed mesh quality is calculated as ratio of the radius of outer to inner circle of a triangle, normalized to an equilateral triangle resulting in a minimal value of 0.19. The information for material creation in the 2D model is collected from the derived object and adjacent objects in the BIM model, e.g. for calculating anchor distance, as well as from external data sources where geometrical and non-geometrical information are considered. Throughout the whole process the relationships between the objects in the BIM model and its derived counterparts in the numerical model are maintained.

All information required for creating the numerical model is merged in one structured, human- and

machine-readable text file using the JSON-format. This file is updated periodically and after certain events and is version controlled. If changes are found and a calculation in this scope already exists, the calculation is not compliant with the BIM model anymore and has to be recalculated. This information is displayed in a project dashboard, where all calculations are listed and managed. Depending on the number of numerical simulations and their computation times it might not be sensible to trigger a recalculation on changes instantly. The proposed procedure allows to evaluate changes prior to recalculation, so if only minor changes occur, a recalculation can be omitted. The file and the update scripts are designed to minimize the effort in recalculations, e.g. if no discretized geometry is changed, no meshing procedure is conducted.

a) Cross section from the BIM model at the point of interest, with diaphragm wall and projected achors

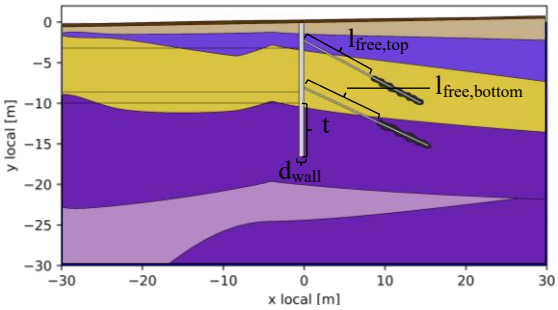

b) Optimized geometry and resulting mesh quality in the FE model

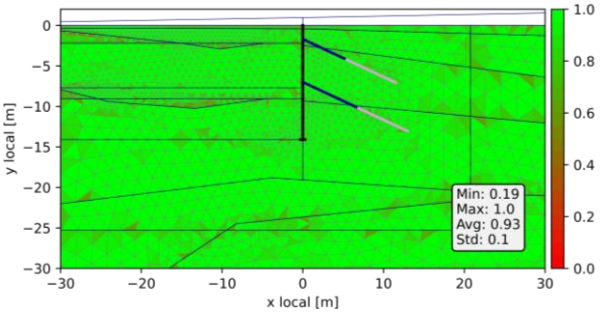

c) Incremental strains $\Delta\gamma_s$ after strength reduction and optimization

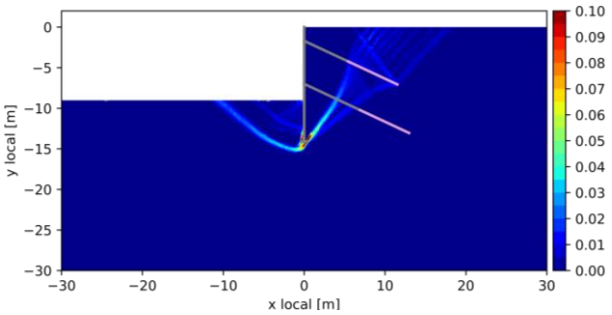

Figure 2. Processing and calculation of an exemplary cross-section

3.3 FE model creation and stability analysis

The named JSON-data is used to trigger the model creation routines which utilize the API provided by the used numerical software. The model creation follows these main steps: (I) Create materials, (II) create geometries, (III) assign materials to the geometry, (IV) generate mesh, (V) create construction sequence via calculation phases, (VI) assign hydraulic / thermal flow conditions. After the model has been created and calculated, strength reduction method for the surrounded soil is conducted and the resulted Factor of Safety (FoS) is stored. The implementation allows for real time interaction between the used programs, for example if the wall thickness needs to be adjusted, the corresponding parameter can be set in the BIM authoring tool and the corresponding parameters in the numerical model are updated immediately.

The soil parameters for the numerical model were realistically determined within the context of an inverse parameter calibration based on inclinometer measurements (Jürgens & Henke, 2022). As a constitutive model, the Hardening Soil Small model is employed, considering hardening plasticity and small strain stiffness. The information on the material parameters used for the soils, the diaphragm wall and the tie-back can be found in (Jürgens & Henke, 2022). The dimensions of the structures for the investigated excavation pit are based on preceding calculations using the limit equilibrium method (LEM) using BLUM's method. Due to the advantages of FEA compared to LEM, such as near-realistic constitutive models and soil-structure interaction behavior, system reserves are probably available. Therefore, the stochastic optimization algorithm, Differential Evolution (DE), originally proposed by (Storn & Price, 1997), is used. The statically required embedment depth t, the free anchor length of the two tiebacks l_{free} and the diaphragm wall width d_{wall} are optimized by creating a population with $n = 4$ adjustable parameters that is iteratively improved on the basis of evolutionary processes. Minimizing the FoS as a result of the strength reduction method serves as the objective function for DE. Therefore, it has to be noted, that this procedure does not find an economic solution. For the optimization process, the dimension of vectors used in DE D is set to 5, from which the population size $m = D \cdot n = 5 \cdot 4 = 20$ is calculated. The implementation of DE for the numerical model is done using the *scipy* library with Python.

Figure 2 c) displays the results of the strength reduction method for the optimized condition in the form of incremental strains for the section highlighted in Figure 1. After a total of 320 calculations, respectively 16 iterations, the following optimized

parameters for the dimension of the excavation pit wall are obtained $t_{\mathrm{DE}} = 4.17$ m, $l_{\mathrm{free,top,DE}} = 8.40$ m, $l_{\mathrm{free,bottom,DE}} = 8.24$ m, $d_{\mathrm{wall,DE}} = 0.69$ m with an minimized Factor of Safety $FoS = 1.18$. Table 1 compares this solution with the initial configuration and indicates optimization potential; see Section 4 for a discussion of practical applicability.

Table 1. Parameters before and after optimization.

	Before Optimization	**After Optimization**
t [m]	6.70	4.17
$l_{\mathrm{free,top}}$ [m]	9.60	8.40
$l_{\mathrm{free,bottom}}$ [m]	10.40	8.24
d_{wall} [m]	0.60	0.69
FoS [-]	1.66	1.18

3.4 Update of BIM models

A routine to analyse the calculation results is triggered, when a new version of the output files created by the numerical software is saved. In addition to default ones, results based on the problem definition are parsed and stored in a separate JSON-file. This file is also version controlled as descried above. If changes are detected, a routine updating the BIM models starts.

In the present case study, the main optimized parameters, that are transferred back to the BIM model, are the anchor lengths as well as the width and the embedment depth of the diaphragm wall. As the corresponding BIM objects are modelled parametrically, only the belonging parameters need to be set and the geometries and derived evaluations update automatically. It is also documented how a parameter is set – either as a result from a changed calculation or another way, e.g. manually. As a result, a re-calculation of the model directly after it has been calculated is avoided. Additional results, such as the FoS, displacements and moment distributions can be set directly assigned to BIM models or by reference, which is preferable for bigger datasets.

4 CONCLUSION AND OUTLOOK

A conceptual BIM-FEA-Integration framework based on commonly used software tools was introduced. It allows for fully automated derivation of 2D-FE models, their calculation and the update of the parametric BIM models based on simulation results and dimensional optimization. The consistency between the numerical models with the BIM models is continuously verified, which is enabled by version-controlled text files that are used to transfer data between process sections. The conducted case study shows that the developed procedure is robust and that complex site conditions can be adequately considered. The conducted stability analysis using strength reduction method proved suitable as a possible method for optimizing design relevant geometric parameters. The used geometry evaluation metrics and simplification techniques and metrices are going to be published separately.

Future endeavors shall strive to more standardization which is supposed to increase efficiency gains and reduce entry thresholds for practitioners. Investigations on the suitability of different optimization techniques and objectives and considering more parameters are also promising to increase the practical applicability. If a single objective optimization technique is applied for real world problems, it is feasible to use an economic evaluation as the objective function instead of the FoS and use the FoS as a constraint.

ACKNOWLEDGEMENTS

The authors are grateful for the project data provided by the Central Technical Division of Ed. Züblin AG and Züblin Spezialtiefbau GmbH.

REFERENCES

Beck, J. & Henke, S. (2023a) „A novel approach towards automated derivation of two-dimensional, numerical models from geotechnical building information models (BIM)“, *Proceedings 10th NUMGE 2023.* London. doi: 10.53243/NUMGE2023-28.

Beck, J. & Henke, S. (2023b) „Investigation on knowledge-based BIM-FEM-Integration using an inner-city excavation pit“, p. 118–123, http://www.dggt.de/images/fstg2023-01, in German.

Jürgens, H. & Henke, S. (2022) „ Investigations into the design of excavation pits using the finite element method“, *Numerische Methoden in der Geotechnik.* Hamburg, 12.-13.09.2022, in German.

Storn, R. & Price, K. (1997) „Differential Evolution – A Simple and Efficient Heuristic for global Optimization over Continuous Spaces“, *Journal of Global Optimization*, 11(4), p. 341–359, doi: 10.1023/A:1008202821328.

Proceedings of the XVIII ECSMGE 2024
GEOTECHNICAL ENGINEERING CHALLENGES
TO MEET CURRENT AND EMERGING NEEDS OF SOCIETY
© 2024 the Authors
ISBN 978-1-032-54816-6
DOI 10.1201/9781003431749-38
Open Access: www.taylorfrancis.com, CC BY-NC-ND 4.0 license

ECSMGE 24
XVIII EUROPEAN CONFERENCE ON SOIL MECHANICS AND GEOTECHNICAL ENGINEERING

Micropile bearing capacity analysis using fiber optic technology

Analyse de la capacité portante des micropieux en utilisant la technologie de la fibre optique

R. Bednarek*
West Pomeranian University of Technology in Szczecin, Szczecin, Poland

A. Jaroszek
Design and construction studio A-Plus, Szczecin, Poland

**bednarek@zut.edu.pl*

ABSTRACT: This paper discusses the bearing capacity of micropiles and the performance of shortening pile measurement using fiber optic technology. Results from a static pile load test on a micropile are presented, along with an analysis of the shortening of the pile shaft based on data obtained from fiber optic measurements. An optical fiber, placed at the center of the micropile, was used to measure deformations along the entire length of the pile. The test involved a 6-meter-long micropile and was conducted until failure. Successive load stages enabled the analysis of the behavior of the entire micropile shaft under load. The ground conditions facilitated the interaction of the pile side with the soil from the surface. The test was conducted on a micropile using rock bolting technology with ARCO steel pipes, which serve as the reinforcement of the micropile. A fiber optic sensor was placed inside the pipe (bar).

RÉSUMÉ: Cet article traite de la capacité portante des micropieux et de la performance de la mesure du raccourcissement des pieux en utilisant la technologie de la fibre optique. Les résultats d'un essai de charge statique sur un micropieu sont présentés, accompagnés d'une analyse du raccourcissement du fût du pieu basée sur les données obtenues par des mesures à fibre optique. Une fibre optique, placée au centre du micropieu, a été utilisée pour mesurer les déformations sur toute la longueur du pieu. L'essai a impliqué un micropieu de 6 mètres de long et a été mené jusqu'à la rupture. Les étapes de charge successives ont permis d'analyser le comportement de l'ensemble du fût du micropieu sous charge. Les conditions du sol ont facilité l'interaction du côté du pieu avec le sol depuis la surface. L'essai a été réalisé sur un micropieu utilisant la technologie de boulonnage de roche avec des tuyaux en acier ARCO, qui servent de renforcement au micropieu. Un capteur à fibre optique a été placé à l'intérieur du tuyau (barre).

Keywords: Mikropile; distributed fiber optic sensing; geotechnical load tests; soil mechanics.

1 INTRODUCTION

The primary characteristic of the micropile installation technique is its effectiveness in high-resistance soils, including rocky terrains, as well as in areas with limited overhead space and uneven surfaces (FHWA, 2005). In this context, tip resistance is often overlooked, with a predominant emphasis on load transfer through skin friction (Allen et al., 2004). Choi & Cho (2010) observed that the injection of neat cement grout can potentially enhance the load capacity of micropiles by over 100% in both soil and rock environments.

For the tested micropile, the ARCO steel pipe anchoring technology was employed. The advantage of this method lies in the integration of corrugated pipes with the ground through a mixture of grout and sand, similar to the reinforcement in concrete structures, thereby ensuring protection against external factors.

Additionally, some researchers (Finno et al., 2002; Holman & Barkauskas, 2007) have highlighted the potential for relative displacement between the steel casing and the neat cement grout. However, the use of stronger grouts and corrugated pipes, as in this study, can mitigate this issue. Żarkiewicz (2023) observed a significant impact of the simultaneous mobilization of skin resistance and resistance under the pile base near its base in his studies, which may also be relevant for loaded micropiles. While the application of micropiles in various solutions is not novel, their comprehensive examination and analysis, particularly in terms of interaction with the ground, are relatively scarce, similar to the situation with the larger market for

standard piles, where despite greater accessibility, research is also limited.

In recent years, the use of distributed fiber optic monitoring systems has significantly increased in geotechnical applications. These systems provide the advantage of offering distributed strain and temperature measurements with high accuracy along the entire length of the structure, without any data gaps (Monsberger 2020). Ouyang (2015) and Schilder (2013) have utilized fiber optic instrumentation to monitor load tests, focusing respectively on a large diameter pile in London and on reinforced concrete piles. Esmaeili (2013) presented a case study on the use of micropiles for reinforcing high railway embankments, while Glisic (2002) discussed the application of fiber optic sensors in monitoring pile behavior during axial compression, pullout, and flexure tests.

The primary objective of this study is to introduce a fiber-optic approach to micropiles, to assess their performance in sand-fine gravel soil, and subsequently to determine the causes of the loss of bearing capacity of the tested micropile. Figure 1 presents the schematic and a view of the conducted load test.

2 EXPERIMENTAL SETUP

The micropile used in this study is a result of employing self-drilling anchors, with a diameter of approximately 16 cm and a length of 6 meters. It is drilled by rotation using an R51 steel pipe equipped with a disposable drill bit tip. This pipe is inserted using a drilling machine specifically designed for this task. The choice of drilling fluid, either water-cement or water, depends on the soil type. Upon completion of the drilling process, a substantial injection of water-cement mixture is conducted. The bar, serving as the reinforcement for the perforated micropile, eliminates the need for additional reinforcement insertion. The continuous threading ensures excellent adhesion of the cement mortar.

In addition to the previously described setup, a linear fiber-optic strain sensor, EpsilonRebar, supplied by shmsystem.pl, was installed inside the micropile's steel pipe reinforcement.

The use of a pure water-cement grout facilitated the easy installation of the sensor within the central part of the micropile. EpsilonRebar is capable of providing accurate strain and crack measurements over its entire length.

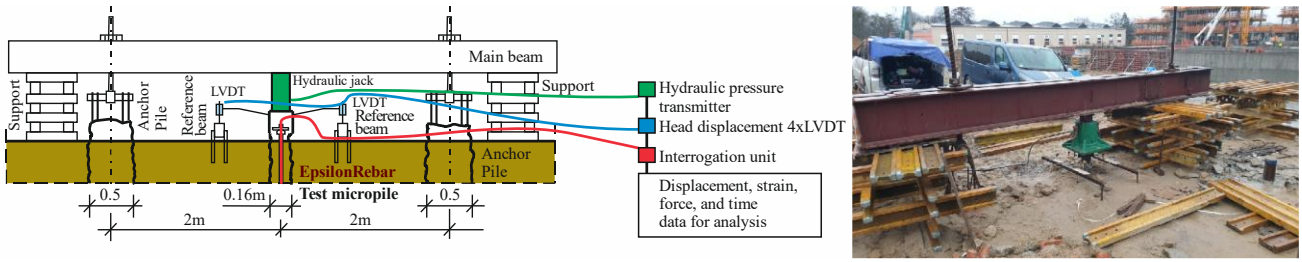

Figure 1. Schematic of the load test and photograph of the test setup.

It is designed as a composite rebar, available in any diameter, with a standard diameter of Ø5 mm. This sensor is suitable for direct embedding into newly-designed structures (such as concrete or soil) or for installation within existing structures (for example, inside grooves in concrete or on the surface of pipelines).

EpsilonRebar's resistance to mechanical loads and environmental conditions makes it ideal for in-situ applications in construction sites or existing infrastructure. The sensor's specifications include a strain measurement resolution of 1.0 με, a strain measurement range of ±2 %, an operating temperature range from -20 to +100 °C, and it is made of glass fiber and epoxide. The sensor utilizes scattering techniques such as Rayleigh, Brillouin, or Raman for its measurements.

3 RESULTS AND ANALYSES

The load test was conducted according to the scheme presented in Figure 2.

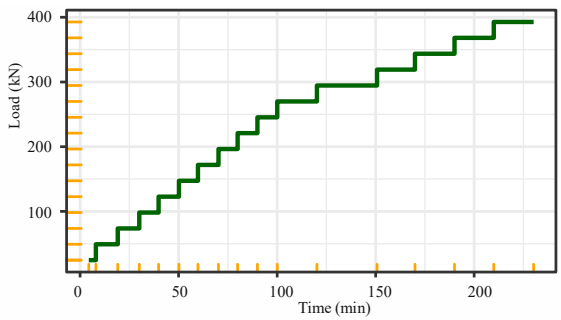

Figure 2. Variation of load over time (hydraulic pressure change of 0.5 MPa).

The study was carried out in 17 stages of loading, with the assumption that the test would continue until

the micropile failed. During the test, efforts were made to maintain the condition that the transition to the next loading stage would occur when, after 10 minutes, the average settlement recorded by the displacement sensors at the micropile head was less than 0.05 mm. After 100 minutes, particularly beyond the applied force of 270 kN, stabilization occurred over a period longer than 10 minutes for each load stage.

The displacement of the micropile head is presented in Figure 3 for successive loading stages. The last six stages required stabilization periods longer than 10 minutes. In the final stage, the micropile failed.

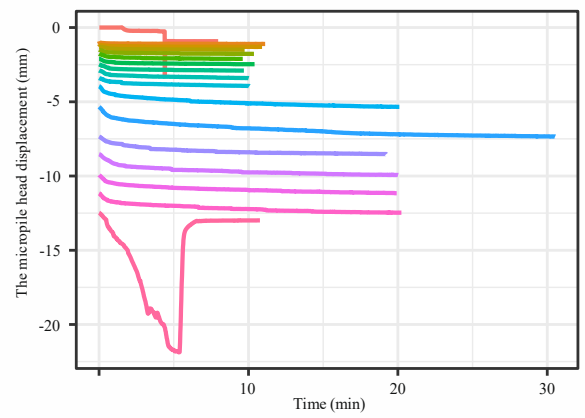

Figure 3. The displacement of the micropile head.

This figure (Figure 4) illustrates the continuous displacement of the micropile head, plotted against the backdrop of the total shaft shortening over time.

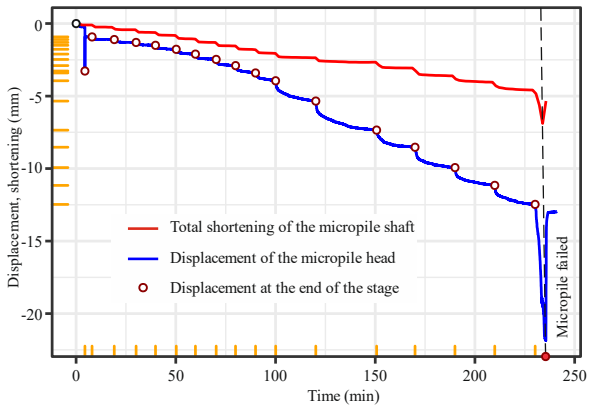

Figure 4. Continuous displacement of the micropile head with total shaft shortening over time and end-of-stage head displacements.

Additionally, it highlights the final displacements of the micropile head at the end of each loading stage, providing a comprehensive view of the micropile's behavior under progressive loading conditions.

Next figure (Figure 5) depicts the correlation between the shortening of the micropile shaft and its depth along the entire length of the micropile, as measured by the high-precision fiber-optic sensor EpsilonRebar. The results, showcasing measurements with an accuracy of 1 cm, are presented for the first ten loading stages, during which the micropile quickly stabilized under the applied load. This detailed analysis illustrates the variations in shaft shortening with depth at each stage, providing crucial insights into the initial structural behavior of the micropile under varying loading conditions.

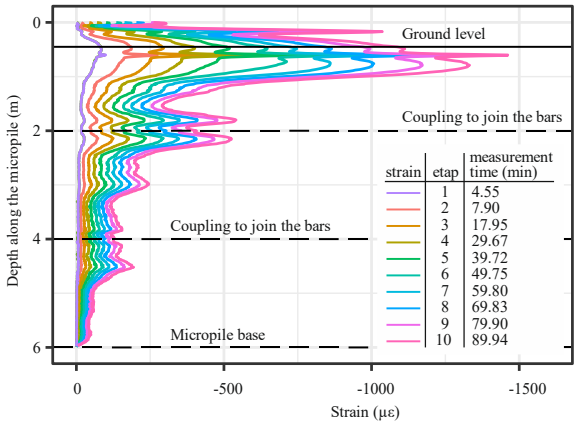

Figure 5. Relationship between the micropile shaft shortening and depth for the first ten loading stages.

Continuing the analysis, the subsequent Figure 6 extends our understanding to the later phases of the load testing.

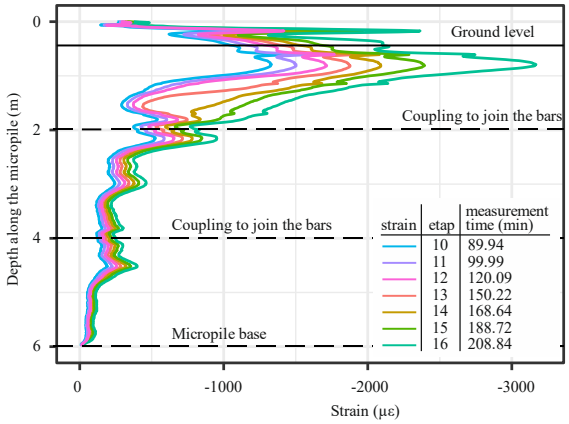

Figure 6. Relationship between the micropile shaft shortening and depth for the next six loading stages.

In this chart (Figure 6), the horizontal axis has been rescaled to twice its original size for clarity. It presents the behavior of the micropile during the following six stages of loading, further elucidating the structural response under increased stress.

The last chart, Figure 7, illustrates the final 5 minutes of the test, during which the micropile shaft failed, rather than a loss of bearing capacity in the soil substrate. This crucial phase highlights the structural

limits of the micropile under extreme loading conditions. The determination of the shaft's failure was made possible through the use of a fiber-optic sensor, which unequivocally allowed for the assessment of the nature of the damage.

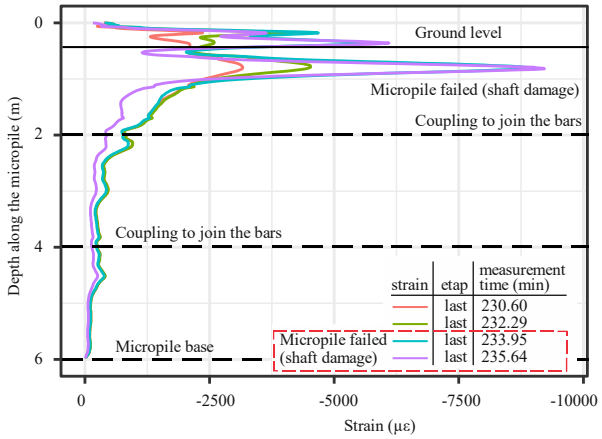

Figure 7. The final 5 minutes leading to micropile shaft failure.

4 CONCLUSIONS AND ACKNOWLEDGEMENTS

This project was an intriguing endeavor that served as a test of our capabilities and prepared us for significantly larger tasks. It required the coordination of numerous variables within a constrained timeframe. Breaking away from conventional solutions and adopting an unconventional approach allowed for the application of one of the most interesting solutions currently available for monitoring piles along their entire length. This solution is not only simple to install but also provides a vast amount of data for analysis. Future plans include correlating the obtained results with theoretical and semi-empirical analyses of the micropile-soil interaction. Further field studies of this nature are also planned.

The project, which involves the micropile tests at the designated test site, is funded privately as part of a collaborative initiative aimed at employing micropiles in regional investments.

REFERENCES

Allen, C., Jesús, G., Donald, B., & Tom, A. (2004). *Micropiles: recente advances and future trends*. In Proc. of the Current Practices and Future Trends in Deep Foundations (pp. 140-415), Los Angeles. ASCE Geotechnical Special Publication. https://doi.org/doi:10.1061/40743(142)9.

Choi, C., & Cho, S.D. (2010). *Field verification study for micropile load capacity*. In Proc. of the 10th International Workshop on Micropiles (pp. 1-10), Washington, DC.

Esmaeili, M.H., Nik, M.G., & Khayyer, F. (2013). *Experimental and Numerical Study of Micropiles to Reinforce High Railway Embankments*. Int. J. Geomech., 13, 729-744. https://doi.org/10.1061/(ASCE)GM.1943-5622.0000280.

Finno, R.J., Scherer, S.D., Paineau, B., & Roboski, J. (2002). *Load transfer characteristics of micropiles in dolomite*. In Proc. of the Deep Foundations 2002: An International Perspective on Theory, Design, Construction, and Performance (pp. 1038-1053), Orlando. ASCE. http://dx.doi.org/10.1061/40601(256)73.

FHWA NHI-05-039. (2005). *Micropile design and construcion*. Federal Highway Administration, U. S. Department of Transportation, Washington, DC.

Glisic, B., Inaudi, D., & Nan, C. (2002). *Pile Monitoring with Fiber Optic Sensors During Axial Compression, Pullout, and Flexure Tests*. Transportation Research Record, 1808, 11 - 20. https://doi.org/10.3141/1808-02

Holman, T.P., & Barkauskas, B.D. (2007). *Mechanics of micropile performance from instrumented load tests*. In Proc. of 7th FMGM 2007: (pp. 1-14). Boston: ASCE. http://dx.doi.org/10.1061/ 40940(307)8.

Ouyang, Y., Broadbent, K.A., Bell, A., Pelecanos, L., & Soga, K. (2015). *The use of fibre optic instrumentation to monitor the O-Cell load test on a single working pile in London*. https://doi.org/10.1680/ECSMGE.60678.VOL2.08.

Monsberger, C.M., Lienhart, W. & Hayden, M. (2020). *Distributed fiber optic sensing along driven ductile piles: Design, sensor installation and monitoring benefits*. J Civil Struct Health Monit 10, 627–637. https://doi.org/10.1007/s13349-020-00406-3.

Schilder, C., Kohlhoff, H., Hofmann, D., Basedau, F., Habel, W.R., Baessler, M., Niederleithinger, E., Georgi, S., & Herten, M. (2013). *Static and dynamic pile testing of reinforced concrete piles with structure integrated fibre optic strain sensors*. Other Conferences. https://doi.org/10.1117/12.2026813.

Żarkiewicz, K. (2023). *The Analysis of Pile Skin and Base Resistances Interaction Based on Static Pile Load Test in Experimental Research*. Architecture, Civil Engineering, Environment. 16. 141-150. https://doi.org/10.2478/acee-2023-0041.

Proceedings of the XVIII ECSMGE 2024
GEOTECHNICAL ENGINEERING CHALLENGES
TO MEET CURRENT AND EMERGING NEEDS OF SOCIETY
© 2024 the Authors
ISBN 978-1-032-54816-6
DOI 10.1201/9781003431749-39
Open Access: www.taylorfrancis.com, CC BY-NC-ND 4.0 license

ECSMGE 24
XVIII EUROPEAN CONFERENCE ON SOIL MECHANICS AND GEOTECHNICAL ENGINEERING

Cross analysis between different evaluation methods of small strain moduli in clays and marls of Parisian subsoil

Analyse croisée entre différentes méthodes d'évaluation des modules en petites déformations dans les argiles et marnes du bassin Parisien

N. Berthoz*
Centre for Tunnel Studies (CETU), Bron, France

N. Dufour
GéoCoD, Cerema, Aix-en-Provence, France

A. Rallu, Y. Aslan, D. Branque
University of Lyon, ENTPE, LTDS - UMR CNRS 5513, Vaulx-en-Velin, France

**Nicolas.berthoz@developpement-durable.gouv.fr*

ABSTRACT: The design of geotechnical structures requires an accurate assessment of the strain moduli of the grounds. Experience shows that these depend on the range of strain considered. In particular, for dynamic problems (e.g. vibrations induced by the excavation of a tunnel), the maximum shear modulus G_{max} has to be estimated. To contribute to this topic, the results of surface wave measurements under ambient noise (H/V method), cross-hole tests, resonant column tests and pressuremeters tests performed in various clay and marl formations in the Paris subsoil are presented. The analysis concerns the relationship between these different types of measurements and their comparison with data in the literature.

RÉSUMÉ: La conception des ouvrages géotechniques nécessite une évaluation précise des modules de déformation des terrains. L'expérience montre que ceux-ci dépendent de la gamme de déformation considérée. En particulier, pour les problèmes dynamiques (par exemple les vibrations induites par le creusement d'un tunnel), le module de cisaillement maximal G_{max} doit être estimé. Pour contribuer à cette problématique, les résultats de mesures d'ondes de surface sous bruit ambiant (méthode H/V), d'essais cross-hole, d'essais à la colonne résonnante et d'essais pressiométriques réalisés dans différentes formations argileuses et marneuses du sous-sol parisien sont présentés. L'analyse porte sur la relation entre ces différents types de mesures et leur comparaison avec les données de la littérature.

Keywords: Shear modulus; strain level; in-situ wave velocities; resonant column.

1 INTRODUCTION

In geotechnical engineering, predicting the movements of a soil subjected to external mechanical action requires knowledge of its stiffness. However, it is well known that the soil stiffness is not intrinsic to the material. Under a given stress condition (e.g. a fixed mean pressure), soils and weak rocks have a stiffness that decreases as the amplitude of their strain increases. In parallel, numerous experimental observations from laboratory tests have shown that the stiffness of these materials changes very little for strain levels below 10^{-5} (*e.g.* Clayton and Heymman, 2001; Vardanega and Bolton, 2013). For these very low strain levels, it is therefore possible to define a reference shear modulus (G_{max}). Knowledge of G_{max}, combined with data quantifying the degradation of the shear modulus G as a function of strain, is then required to predict ground displacements in geotechnical design.

In practice, there are several experimental methods for determining G_{max} (*e.g.* Atkinson, 2000; Clayton, 2011). On the one hand, in situ geophysical methods are based on the measurement of the propagation velocity of surface or volume seismic waves. For these methods, the value of G_{max} is generally derived from the measurement of the shear wave velocity (V_s) in the ground, using the relationship $G_{max} = \rho.V_s^2$ (with ρ the soil mass density). On the other hand, laboratory methods performed on cored or reconstituted soil samples placed in a triaxial cell are based either on the measurement of the shear wave propagation velocity (bender element testing) or on the measurement of the local or global strain of the sample under controlled mechanical stress (resonant column). It should be noted that cross-analyses of results obtained by these

different methods tend to show that G_{max} values measured in situ are generally higher than those measured in the laboratory (*e.g.* Stokoe et *al.*, 1994).

Although laboratory methods have the disadvantage of using small soil samples that may have been disturbed during drilling and sampling, they have allowed us to demonstrate the influence of various parameters on G_{max}. On the basis of these laboratory tests, several authors have shown the dependence of G_{max} to various parameters as the mean effective pressure (p'), the void index (e), the degree of consolidation (OCR), the plastic index (PI) or the loading path. Several semi-empirical formulations relating G_{max} to these different parameters have been proposed (*e.g.* Hardin and Black, 1968; Hardin and Blandford, 1989; Viggiani and Atkinson, 1995).

Laboratory tests (resonant column, precision triaxial test) also have the great advantage of allowing the reduction in secant shear modulus G as a function of strain (γ) to be quantified over a relatively wide range of strains (*e.g.* from 10^{-5} to 10^{-2} for the resonant column). Thus, by considering a hyperbolic relationship between shear stress and strain (e.g. Duncan and Chang, 1970), several authors (e.g. Hardin and Drnevich, 1972; Vucetic and Dobry, 1991; Santos and Gomes Correia, 2001; Darendeli, 2001) have shown that it is possible to express the reduction in material stiffness as a function of strain in terms of a hyperbolic relationship between G/G_{max} and γ/γ_r of the following general form:

$$\frac{G}{G_{max}} = \frac{1}{1+(\gamma/\gamma_r)^{\alpha}} \qquad (1)$$

where γ_r represents the reference shear strain and α is referred to the curvature parameter.

The aim of this paper is to contribute to this problem by taking advantage of a major measurement campaign carried out as part of the E-Pilot research project, dedicated to the study of vibrations induced by tunnel boring machines. Pressuremeter tests, cross-hole tests, surface wave measurements under ambient noise (H/V method) and resonant column tests were carried out in various clay and marl formations in the Paris subsoil. The analysis concerns the relationship between these different types of measurements and their comparison with data in the literature.

2 EXPERIMENTAL SITE DESCRIPTION

2.1 Geological context

The study site is located in the city of Wissous, in the southern suburbs of Paris. It is located on a plateau (Orly plateau) with a succession of subhorizontal clay-limestone and marl formations.

A T6-116 survey (116 mm diameter double tube core barrel), 39.5 m deep, referenced SC08198, was drilled on site in December 2022. This hole revealed the stratigraphic succession described in Figure 1 with, from bottom to top, the Masses and marls of gypsum (Lower Ludian, -38 My), the Suproagypseous marls of Argenteuil and Pantin, the Green clays, the Brie and Sannois limestones, and the quaternary plateau silts.

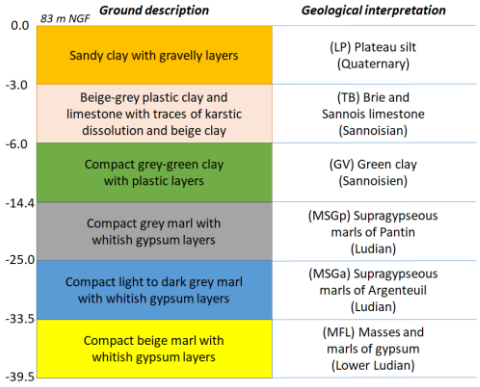

Figure 1. Geological profile (scale not observed). 83 NGF correspond to the surface of the work site.

2.2 Geotechnical characteristics

Table 1 summarises the main state parameters of these different formations: wet mass density ρ, dry mass density ρ_d, water content w, voids index e, degree of saturation Sr, blue-value VBS, plasticity index PI, fine content FC and over-consolidation ratio OCR.

Table 1. Geotechnical characteristics of the grounds.

	LP	TB	GV	MSGp	MSGa	MFL
State parameters						
ρ (kg/m³)	1980	1990	1950	1930	1980	1810
ρ_d (kg/m³)	1660	1640	1560	1530	1600	1380
w (%)	20	21	25	26	23	31
e (-)	0.58	0.61	0.70	0.73	0.65	0.92
Sr (%)	--	93	97	97	97	92
VBS (-)	3	2	6	2	5	3
PI (-)	12	19	33	28	37	45
OCR (-)	1	1	2	1	1.5	1
FC (%)	80	56	97	86	97	87
Mechanical parameters						
E_M (MPa)	8	23	13	43	45	180
p_l^* (MPa)	0.8	2.1	1.1	3.2	3.1	5.8
c' (kPa)	5	15	20	30	30	60
φ' (°)	28	32	15	25	20	35

These were measured in the laboratory on samples taken from the aforementioned core hole, and consolidated by other measurements taken from other surveys carried out in the same geological context.

Pressiometric caracteristics (geometrical means of Ménard moduli E_M and limit pressure p_l^*) and plastic parameters (effective cohesion c' and friction angle φ') are also given in Table 1. These values are deducted of all the tests made for the construction of line 18 metro on the Orly plateau. Note in particular that these values are consistent with the results of the two pressiometric boreholes made in the study site.

3 MEASUREMENTS OF V_S PERFORMED

Three types of measurements of the shear wave velocities V_s have been performed on the study site to assess the maximum shear modulus G_{max}: in-situ cross-hole test, in-situ ambient noise measurements (H/V method), laboratory tests on resonant column apparatus.

3.1 Cross-hole measurements

Measurements of shear wave velocity V_s were carried out between two boreholes 12 m apart, 80 mm in diameter, lined with PVC pipe and sealed to the ground. The signals obtained were of good quality and interpreted in accordance with ASTM D4428.

Significant contrasts appear between the different layers of soil, with little dispersion by layer. The geometric means of V_s by layers are: 353 m/s in LP, 448 m/s in TB, 200 m/s in GV, 423 m/s in MSGp and 471 m/s in MSGa.

It should be noted that the measurements taken beyond a depth of 26 m correspond to oblique paths between the transmitter (maintained at a depth of 26 m) and the receiver of variable depth. The wave speeds measured in the MFL formation are therefore underestimated. The corrected value considering the oblique path is equal to 750 m/s.

3.2 Ambient noise measurements (H/V)

The H/V method is a geophysical method used to analyse the structure of the subsurface. Its primary purpose is to investigate parameters such as the depth to bedrock then, through inversion processes, the shear wave velocity of soil layers. This method entails the comparison of the amplitude of horizontal ground motion (H) with the amplitude of vertical ground motion (V) across various frequencies. During in-situ monitoring, five 3D geophones (TROMINO from the Moho brand) are positioned at 10-meter intervals on the ground surface. These geophones feature three highly sensitive orthogonal acquisition channels with high resolution and a precision of 10^{-7} mm/s. Placed on the natural surface of the ground, 3 m above the worksite platform, measurements were conducted for 30 minutes under ambient noise, without specific mechanical excitation. Considering the superficial layer's depth 6 m (cross hole test), calculations were performed for a frequency range of 0.5-20 Hz.

H/V curves are calculated simultaneously from all sensors using Geopsy software (Figure 2a) and from each sensor using Grilla software (example of one sensor is given in Figure 2b). These profiles are almost identical, showing a similar response of all the sensors.

Classifying H/V peaks as of geological or non-geological origin involves examining the corresponding spectra. A geological peak is characterized by a maximum in the X and Y directions (blue and green) and a minimum in the Z direction (pink), forming an eye shape (Figure 2c). Consequently, based on this criterion, three peaks of stratigraphic origin are identified: $f_3(2.1Hz)$, $f_2(8\ Hz)$ and $f_1(14\ Hz)$.

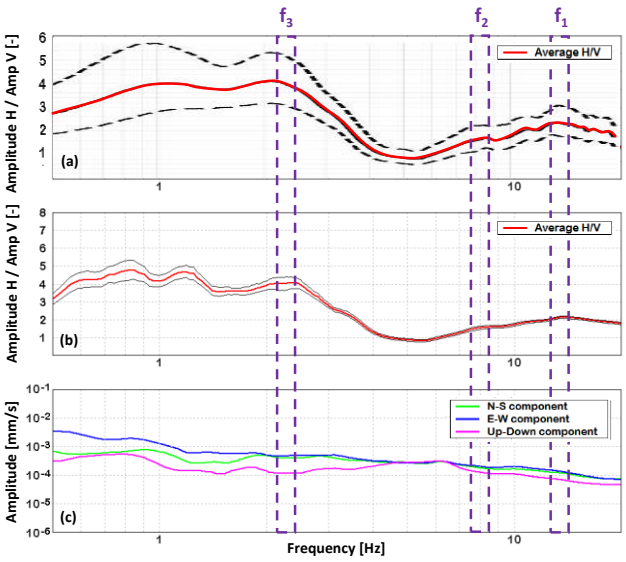

Figure 2. Visualization of (a) Global spectrum amplitude ratio H/V across all sensors, (b) Individual spectrum amplitude ratio H/V from a single sensor, and (c) Spectrum amplitude by direction from the single sensor.

Based on these three peaks, the first three geological layers can be identified. Constraints are required in the inversion process of H/V peaks, either on depth or shear wave velocity. For the upper layer, a depth constraint is specified as $H_1 = 6$ m. Although the resonance equation layer $\frac{V_S}{4H} = f$ cannot be applied in multilayer scenarios, it can serve as a preliminary approximation. Consequently, the shear wave velocity V_S of the resonating layer is estimated as $V_{s1} \approx 4\,H_1\,f_1 \approx 4 \times\ 6\ \text{m} \times 14\ \text{Hz}\ \approx\ 340\ \text{m/s}$.

The second layer, characterized by the frequency $f_2(8\,Hz)$, underwent analysis using a trial-and-error method in Grilla software to achieve the best fit of the H/V Spectral Ratio at this specific frequency. This analysis shows the existence of a layer with a shear wave velocity V_{s2}= 450 m/s situated at depths between 6 and 9 m below the worksite platform (77 to 80 m NGF). Similarly, the third layer, identified with a shear wave velocity V_{s3} of 130 m/s (Figure 4), is located at depths between 6 and 12 m (71 to 77 m NGF).

3.3 Fixed-base resonant column measurements

Five resonant column tests were carried out in the laboratory, one in each of the present layers, with the exception of the LP. These tests, conducted in accordance with ASTM-D4015-15, were carried out on specimens 50 mm in diameter and 100 mm high, loaded in torsion.

The samples, which were nearly saturated in their natural state, were resaturated by applying an internal back-pressure. The Biot coefficients obtained were greater than 0.93. The tests were carried out at confining pressures equal to the geostatic mean effective stress at the depth of each sample.

The shear wave velocities measured for each test, in function of the distortion are presented in Figure 3.

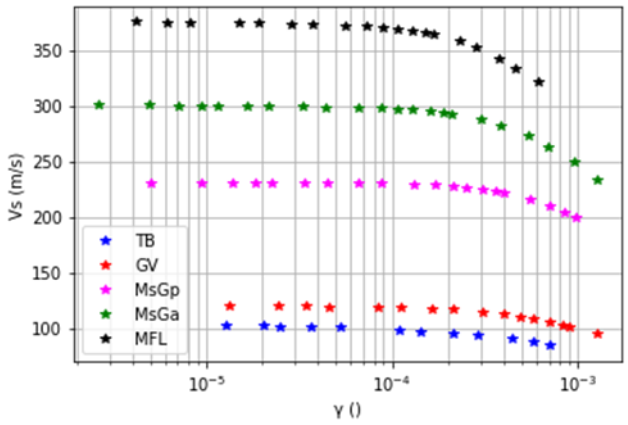

Figure 3. Results of the resonant column tests.

4 CROSS ANALYSIS OF THE MEASUREMENTS OF G_{MAX}

Figure 4 summarises the shear wave velocities measured on cross-hole tests, resonant column tests (values for a distortion of 10^{-5}) and estimated by H/V approach.

Firstly, Figure 4 illustrates that employing measurements under ambient noise using the H/V approach enables estimation of shear wave properties up to a depth of approximately 15 m. It is crucial to note that achieving these results relies on the engineer possessing prior knowledge of local stratigraphy. This understanding is essential to initiate the trial-and-error approach with certain constraints, such as the layer thickness in our case.

Figure 4 shows a good agreement between the Vs measured in situ using the cross-hole tests and those derived from the H/V method, particularly for the top two layers. It illustrates also that the V_s measured at the laboratory scale (resonant column tests) are 1.5 to 4 times lower than in-situ (cross-hole tests).

The maximum shear moduli ($G_{max} = \rho.V_s^2$) calculated in each layer by the two methods are summarised in Table 2. In this table, the geometric means of the V_s measured per layer presented in Figure 3 are used, together with the wet densities given in Table 1. The large difference between the V_s values obtained from the different types of measurements is further increased by squaring them.

Table 2. G_{max} deduced from shear wave velocities.

G_{max} (MPa)	LP	TB	GV	MSGp	MSGa	MFL
Measurements						
Resonant Column	-	22	29	105	182	260
Cross Hole	248	425	78	352	404	1018
Estimation by empirical formula						
Carlton & Pestana (2016) $G_{max\text{-}lab}$	--	110	170	184	289	163
Reiffsteck et al. (2022) $G_{max\text{-}insitu}$	96	340	93	452	474	867

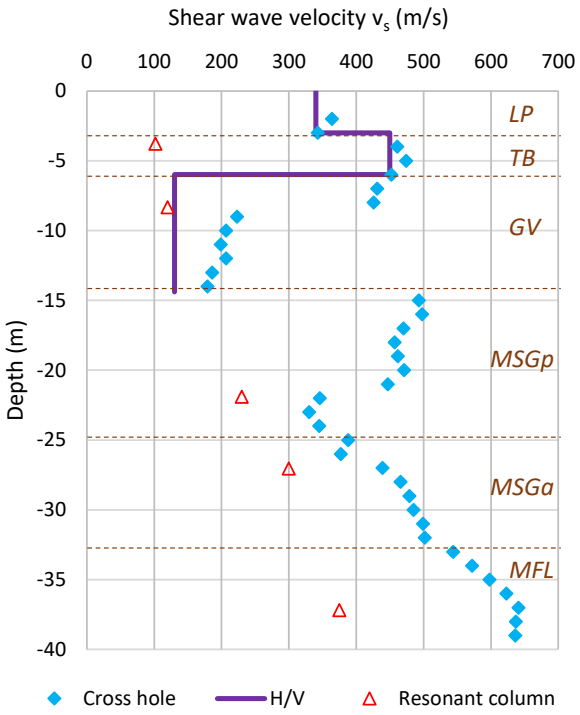

Figure 4. Shear wave velocities measurements.

To go deeper on comparison between in-situ and laboratory shear moduli, the summary provided by Carlton & Pestana (2016), which includes the large-scale test campaign carried out in the USA in the 1990s as part of the ROSRINE project, is used. All the experimental results considered by the authors are shown in blue in Figure 5. These points mixed tests on 331 different soils (sands or clays of different countries), reconstituted or "undisturbed". Our measurements are added in red on this figure.

According to this summary, the moduli measured in the laboratory are lower than those measured in situ (cross-hole). However, the difference observed here appears to be very large, particularly for TB and MFL. The low moduli measured in the laboratory are probably related to sample disturbance during coring or sample preparation (Stokoe *et al*. (1994), cited by Cami (2017)).

By calibration on 1680 laboratory measurements, Carlton & Pestana (2016) propose an estimate of the laboratory measured shear moduli $G_{max,lab}$ as a function of the void index e, the average effective stress p', the over-consolidation ratio OCR, the plasticity index PI and the fine content FC of the soil. In the case of fine soils (FC > 30%), this equation applies:

$$G_{max,lab}(\text{MPa}) = 0.1 * 790.2 * e^{-1.309} * p'^{0.465} * OCR^{2.022*(IP/100)^{1.933}} * (FC/100 + 1)^{-0.124} \quad (2)$$

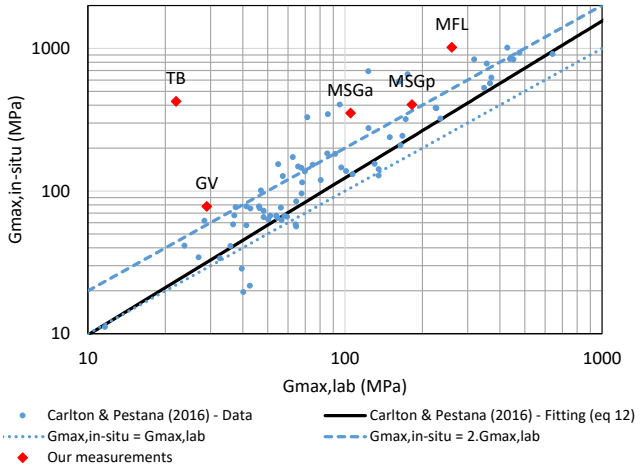

Figure 5. Ratio between the shear moduli measured in-situ and in laboratory.

The moduli measured (Table 2) appear to be 3 to 5 times lower than estimated in the TB and GV. As a result, it seems that the resonance column tests carried out on the most superficial are not very representative of the real shear strain moduli. However, the samples taken appeared to be little disturbed. Multiply systematically the type of tests and consolidate their consistency with empirical expressions would therefore appear to be a good principle to adopt in projects.

Pressuremeter tests were also carried out on the site studied. The pressuremeter moduli measured E_M are summarised in Table 1. These moduli correspond to large distortion ranges (10^{-2} to 10^{-1}), greater than those discussed previously. However, Reiffsteck et *al* (2022) proposed a correlation between G_{max} and E_M on the basis of 750 couples of [E_M; V_s] deduced from 26 different sites (Equation 3):

$$G_{max} = \rho . V_s^2 = \rho . (a . E_M{}^b)^2 \quad (3)$$

where the coefficients (a; b) depend on the type of soil. For clays (LP and GV formations can be considered belong to this category here), this pair is (a = 98; b = 0.29). For marls (TB, MSGa, MSGp, MFL), the values are (189; 0.25).

The calculated moduli are summarised in Table 2. They appear to be in fairly good agreement with the results of the cross-hole test, which supports the expression proposed by Reiffsteck et *al* (2022).

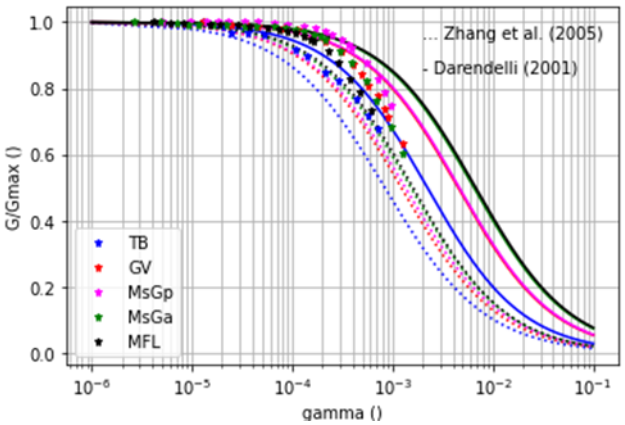

Figure 6. Decrease of the normalised shear modulus with the shear strain magnitude.

5 EVOLUTION OF THE SHEAR MODULUS WITH SHEAR STRAIN

The resonant column tests carried out enable the evolution of the shear modulus with the amplitude of the distortion to be quantified. The curves obtained of normalised shear modulus G/G_{max} are shown in Figure 6 (colored stars). Normalized shear modulus is the current shear modulus G divided by G_{max} obtained in laboratory with a resonant column apparatus.

Experimental results are compared to empirical relationships (solid and dotted lines) that have been proposed in the literature for clay, under the Eq. 1.

Darendeli (2001) and Zhang et *al.* (2005) proposes the expression of γ_r and α given in Eq. 5 and 6

respectively, where p' is the confining pressure and Pa the atmospheric pressure:

$$\alpha = 0{,}919 \qquad (5)$$
$$\gamma_r = \left(0.0352 + 0.00101\, I_p . OCR^{0.325}\right). p'^{0.348}$$

$$\alpha = 0.0021\, PI + 0.834 \quad ; \quad \gamma_r = \left(0.0749 + 0.0011\, I_p\right). \left(p'/Pa\right)^{0.316 \exp\left(-0.0142\, I_p\right)} \qquad (6)$$

These curves are presented in Figure 6: markers and lines in blue correspond to TB, in red to GV, in pink to MsGp, in green to MsGa and in black to MFL. These two types of empirical relationship frame the measured curves.

6 CONCLUSIONS

Analysis of the different methods of measuring G_{max} in the laboratory and *in situ*, and comparison with the literature, mainly show that:

- the cross-hole tests provide reference values for G_{max} to evaluate the vibratory phenomena associated with TBM excavation because they affect a volume of soil representative of the problem studied;
- the H/V method under ambient noise allows to recover V_s values close to those measured by the cross-hole tests, on condition to have a prior knowledge of the stratigraphy in order to constrain the inversion process;
- laboratory measurements using a resonance column give G_{max} values 2 to 4 times lower than those measured in situ (cross hole), in line with observations in the literature;
- the decrease of the normalised modulus G/G_{max} with the distortion observed in the laboratory appears to be little affected by any disturbance of the sample due to the sampling.

ACKNOWLEDGEMENTS

The authors thank the Société du Grand Paris, Arcadis, Vinci Construction and Me2i for the data acquisition, C. Gaillard (CETU), H. Calissano, L. Batilliot and M. Vanwolleghem (Cerema) for their contributions to this study, and French national research agency (ANR) in the project E-PILOT (ANR-21-CE22-0011).

REFERENCES

Atkinson, J. H. (2000). *Non-linear soil stiffness in routine design.* Géotechnique, 50(5), pp 487–508.

Cami, K. (2017). *Imagerie du module de cisaillement in situ du sol par méthodes d'ondes de surface et essais géotechniques: caractérisation des petites aux grandes déformations,* PhD, Univ. Paris-Est.

Carlton, B.D., Pestana, J.M. (2016). *A unified model for estimating the in-situ small strain shear modulus of clays, silts, sands and gravels,* Soil dynamic and Earth Engineering, 88, 345-355, doi:10.1016/j.soildyn.2016.01.019.

Clayton, C. R. I., Heymann, G. (2001). *Stiffness of geomaterials at very small strains*. Géotechnique, 51(3), 245–255, doi:10.1680/geot.2001.51.3.245.

Clayton, C.R.I. (2011). *Stiffness at small strain: research and practice,* Géotechnique, 61(1), pp.5-37, doi:10.1680/geot.2011.61.1.5

Darendeli, M. B. (2001). *Development of a new family of normalized modulus reduction and material damping curves.* Ph.D. thesis, Univ. of Texas.

Duncan, J. M., Chang, C.-Y. (1970). *Nonlinear analysis of stress and strain in soils*. J. Soil. Mech. and Found. Div., 96(5), 1629–1653, doi:10.1061/JSFEAQ.0001458.

Hardin, B. O., Black, W. (1968). *Vibration modulus of normally consolidated clay*. Journal of Soil Mechanics and Foundation Div., 94(2), 353–369, doi:10.1061/JSFEAQ.0001100.

Hardin, B. O., Blandford, G. E. (1989). *Elasticity of particulate materials*. J.G.E., 115(6), 788–805, doi:10.1061/(ASCE)0733-9410(1989)115:6(788).

Hardin, B. O., Drnevich, V. P. (1972). *Shear modulus and damping in soils: Design equations and curves*. J. Soil Mech. and Found. Div., 98(7), 667–691, doi:10.1061/JSFEAQ.0001760.

Reiffsteck P., Jacquard C., Jandel E., Petitjean E., Benoit J. (2022). *Prediction of Shear Wave Velocity Vs from PMT*, ISSMGE, Sydney.

Santos, J.V., Gomes Correia, A, (2001). *Reference threshold shear strain of soil. Its application to obtain an unique strain-dependent shear modulus curve for soil*. ICSMGE, Istanbul.

Stokoe, K.H.II, Wright, S., Bay J.A., Roesset J.M. (1994). *Characterization of geotechnical sites by SASW method*. Geophys charact. of sites, New Delhi: Oxford & IBH Publish Pvt Ltd, pp. 15-25.

Vardanega, P.J., Bolton, M.D. (2013). *Stiffness of Clays and Silts: Normalizing Shear Modulus and Shear Strain*. J. Geotech. & Geoenv Eng, 139(9), doi:10.1061/(ASCE)GT.1943-5606.0000887.

Viggiani, G., Atkinson, J.H. (1995). *Interpretation of bender element tests*. Géotechnique 45(1), 149-154, doi:10.1680/geot.1995.45.1.149.

Vucetic, M., Dobry, R. (1991). *Effect of soil plasticity on cyclic response*. J. Geo. Eng, 117(1), 89–107, doi:10.1061/(ASCE)0733-9410(1991)117:1(89).

Zhang, J., Andrus, R.D., Juang, C.H. (2005) *Normalized shear modulus and material damping ratio relationships*, J.G.G.E., 131, 453–464, doi:10.1061/(ASCE)1090-0241(2005)131:4(453).

Proceedings of the XVIII ECSMGE 2024
GEOTECHNICAL ENGINEERING CHALLENGES
TO MEET CURRENT AND EMERGING NEEDS OF SOCIETY
© 2024 the Authors
ISBN 978-1-032-54816-6
DOI 10.1201/9781003431749-40
Open Access: www.taylorfrancis.com, CC BY-NC-ND 4.0 license

ECSMGE 24
XVIII EUROPEAN CONFERENCE ON SOIL MECHANICS AND GEOTECHNICAL ENGINEERING

Settlement analysis for a nuclear plant design

Etude de tassement pour le design d'une centrale nucléaire

M. Blanckaert*, B. Pelletier, S. Depinois
EDF TEGG, Aix en Provence, France

M.T. Hoang
Terrasol, Paris, France

**margaux.blanckaert@edf.fr*

ABSTRACT: Nuclear plants are very heavy and sensitive structures, therefore very interesting to study in geotechnics. When the site contains soft soil layers, settlements can be significant, and foundation adaptation may be required. Since standard methods are not fit for such high displacements and low tolerances, sophisticated settlement studies are carried out to ensure feasibility. First, adequate geotechnical soil investigations have to be carried out in order to evaluate soil behavior and particularly to estimate their stiffnesses accurately. Once in-situ and laboratory tests have been cross-analysed, soil moduli are derived for the correct range of strains. For new projects on existing sites, the choice of soil moduli is often guided by a back analysis carried out on the nearby operating plant. The complexity might lead to build a 3D model to assess the settlements, taking into account various elements (dewatering, sequence of construction, different backfill areas, etc.). Both drained and undrained (with consolidation) situations are considered. Non-linear behaviour is also assessed for sensitivity calculations. The results are to be used in the different aspects of the design with regards to the tolerances (raft design, thresholds against flooding levels, joints between buildings, pipe displacements, etc.). The article presents the calibration of the settlement model using in-situ data as well as the back-experience from the monitoring on the current plant nearby and give an overview for the use of the results.

RÉSUMÉ: Les centrales nucléaires sont des infrastructures sensibles apportant une charge importante au sol, ce qui rend leur étude géotechnique très intéressante. Lorsque le sol est compressible, les tassements peuvent être significatifs et les systèmes de fondations doivent être adaptées en conséquence. Ainsi, des études de tassements détaillées sont menées afin d'assurer la faisabilité de construction de tels ouvrages. Tout d'abord, des investigations géotechniques sont réalisées afin d'établir un modèle géotechnique. Pour cela, une analyse croisée est réalisée entre les essais de laboratoire et les reconnaissances in-situ. Les modules de sol sont ensuite adaptés aux gammes de déformations apportées par le projet. Pour les nouveaux projets sur les sites existants, le choix des modules est également conditionné par une analyse en retour des déplacements de la centrale en activité. Dans le cadre de notre étude, un modèle 3D a été réalisé afin d'estimer les tassements sous un projet de centrale nucléaire. Des comportements linéaires et non linéaires ont été considérés avec des calculs drainés et en consolidation. Les résultats peuvent être utilisés pour différents éléments de design (radier, joints entre galeries ou bâtiments, etc.) en prenant en considération les tolérances adéquates pour traduire la variabilité des terrains et du phasage de construction par exemple.

Keywords: Settlement analysis; nuclear plant; finite elements analysis.

1 INTRODUCTION

A nuclear plant as built in the 20th century weights several hundred thousand tons, inducing average stresses under the rafts of 200 to 500 kPa. New models in current projects around the world are more powerful, have more features, therefore get larger and heavier (exceeding half a million tons, and inducing average stresses up to 700 kPa). Before the construction of a new nuclear plant, a settlement study is thus essential to ensure an adequate design.

A geotechnical soil model has to be built based on in-situ investigations and laboratory tests. Depending on the soil and the loads expected to be brought by the project, geotechnical moduli have to be adapted to fit the range of strains the soil will experience. In our study, the fitting is based on the back-experience from the monitoring on the current plant nearby, with a nonlinear elastic model derived from pressuremeter data as developped in the ARSCOP project (Hoang et al. 2020). This model already allowed the reproduction of many sets of settlement data: nuclear power plants, high-rise towers in the district of La Défense (Paris, France) and pre-loading embankments at Calais, France.

In our study, two different geotechnical models have been built: one to validate the soil moduli under the existing power plant, and a second one for the new plant, based on the first model but with a strain adaptation because of the greater loads of the future buildings (therefore inducing more strain).

2 SETTLEMENT STUDY FOR THE EXISTING NUCLEAR PLANT

In our study, the geotechnical model has been built with the analysis of the extensive in-situ and laboraty tests and an adaption to strains ranges.

2.1 Nonlinear elastic model from pressuremeter

In the framework of the French national project ARSCOP devoted to the development of the pressuremeter test, a total review of the settlement calculation has been initiated. The aim of this project is to develop a unified calculation approach of shallow foundations and rafts settlements.

In this framework, in order to have a good estimate of settlement under spread foundations, a calculation method has been developed to combine the variation of the deformation modulus according to the strain range and take advantage of short calculation time of analytical methods. This method is based on decay curves, allowing moduli to vary according to the strain range. The aim is to provide the load-settlement curve of any spread foundation up to a load close to 50% of its bearing capacity. For higher loads, the time effects should be considered, and the elasticity theory is not appropriate. The deformation modulus is assessed by considering Menard pressuremeter modulus (Ménard and Rousseau, 1962) for high strain level (10^{-2} to 10^{-1}).

The ground under the spread foundation is divided into various sublayers where E can vary according to the strain level:

$$\frac{E}{E_M} = k(\varepsilon) = \frac{k_0}{1 + \varepsilon/\varepsilon_0}$$

where E_M is the Menard pressuremeter modulus and k_0 and ε_0 depending on the soil type from the Ménard α parameter, as described in (Hoang et al. 2020):

- Type 1: sands and gravels (α=1/3) k_0=6,67 and ε_0=0,005
- Type 2: dense sands and gravels (α=1/2), k_0=4,5 and ε_0=0,008
- Type 3: overconsolidated clays (α=2/3), k_0=3,20 and ε_0=0,014

2.2 Geotechnical model

The existing nuclear plant has been monitored with displacement sensors, during both construction and operation of the buildings. It is a very good way to evaluate repartition of settlements in different soil layers to calibrate the geotechnical model and check its consistency.

Predictive calculations at the time gave greater settlements than the observations show. The available documents suggest that strain corrections were not properly applied and might have led to this overestimation. ARSCOP curves have been used to calibrate soil moduli for the current plant with regards to the calculated strain range. Pressuremeter modulus can be used directly with a non-linear elastic model to match the measurements. Corrected moduli were 3 or 4 higher than E_M, depending on the soil type.

The modulus obtained for each layer shows a relative homogeneity, therefore a linear elastic soil model with one single equivalent modulus per layer is deemed sufficient in our study (Figure 1).

2.3 Modelization

An axisymetrical Plaxis 2D model has been implemented with the calibrated soil moduli. A realistic construction sequence has been set, including excavations, dewatering, backfilling, and loading of the buildings. Drained and undrained behaviors have been computed for 2 soil laws: an elastic and Hardening Soil Model (HSM).

Drained behavior has been firstly implemented to assess the maximum settlement. Undrained

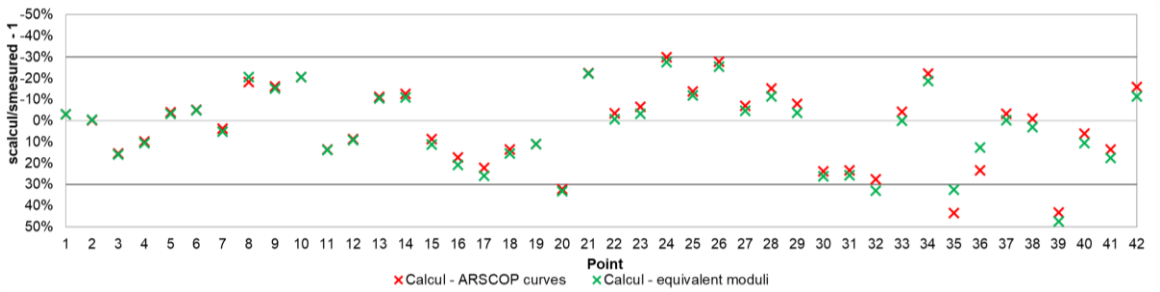

Figure 1. Comparison of measured and back-calculated settlement for the current plant (the ordinate is the discrepancy between calculation and observation, the x-axis represents the various monitoring points all over the existing plant).

calculation was considered to evaluate the impact of the excess pore pressure in deep layers, due to the additional building loads. During the loading, an insignificant increase of excess pore is observed under the plant and dissipated at the end of construction (Figure 2). Therefore, drained and undrained simulations get similar settlement during the loading, and then equal settlements at the end (no more excess pore pressure). After the construction, settlement observations showed no evolution, which correlates with the absence of consolidation or creep of any kind. Excess pore pressure calculations were therefore consistent with settlement observations.

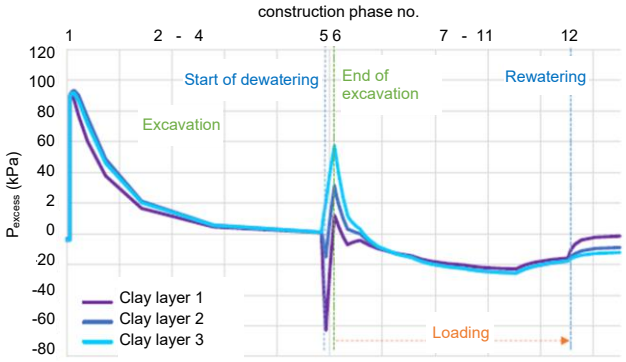

Figure 2. Estimation of the generation of excess pore pressure in deeper layers under the existing nuclear plant.

Linear and HSM calculations were done, both for the drained and undrained cases, to evaluate if there were discrepancies that would invalidate the previous estimation that a linear model with a single modulus for each layer was sufficient to accurately reproduce the expected settlements (as long as it is carefully calibrated). Settlement results are similar and consistent with observations (Figure 3). It does not however mean that the additional loads only solicited the soil in the elastic domain (small deformations) since the choice of the moduli has been made with (secant moduli). The computed strains are also within the estimated range, ensuring consistency of the calculation.

The geotechnical model for the existing plant is therefore validated since calculations and observations give similar results. Moduli can be used with a reassessment for the adequate strain ranges for the future nuclear plant.

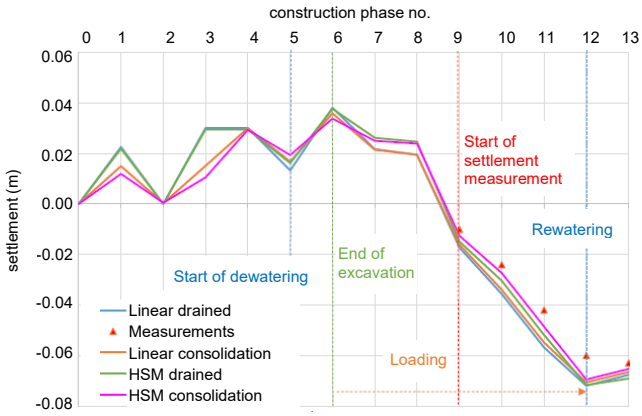

Figure 3. Comparison between settlement calculations and observations for the existing nuclear plant.

3 SETTLEMENT STUDY FOR THE NEW NUCLEAR PLANT

3.1 Geotechnical model

The same process is considered for the new plant to be built nearby (with a stratigraphy not significantly different) using the same pressuremeter modulus, and approximately 50% higher loads induced on the soil. Therefore, degradation is applied on soil moduli with the adequate range of strain.

Moduli for the new nuclear plant are approximately 20% smaller than the corrected moduli used for the existing nuclear plant, resulting in stronger degradations (

Figure 4).

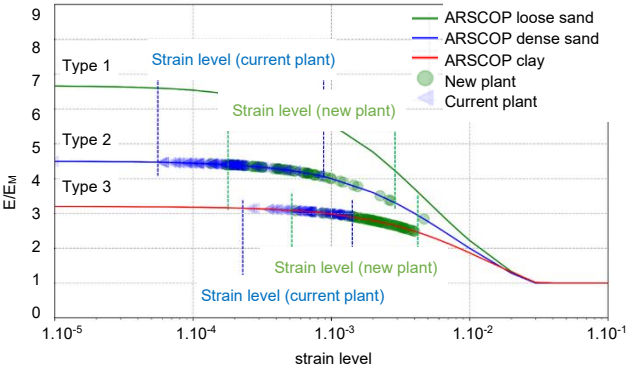

Figure 4. Variation of modulus with strain levels on the current and new plants – ARSCOP curves.

3.2 Modelization

Once soil moduli have been calibrated, a Plaxis 3D model has been built to evaluate the plant settlements (Figure 5). Most of the buildings were implemented as rigid elements except for the bigger and heavier ones - to assess raft deformations.

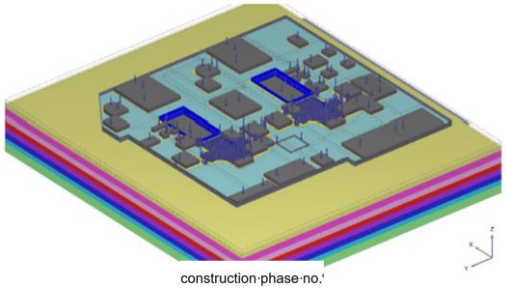

Figure 5. Plaxis 3D model for the future nuclear plant.

The same type of calculations as for the existing nuclear plant have been implemented: linear and HSM soil laws for drained and undrained behaviors.

The consolidation calculation shows greater excess pore pressure during construction (Figure 6 phases 14 to 21 - 200 kPa, compared to Figure 2 phases 6 to 11 - 20 kPa on the existing plant). It is due to the greater loads. It explains that the undrained model (orange line in Figure 7) induces less settlement than the drained model (blue line in Figure 7): excess pore pressure is significant during loading and does not allow immediate settlement.

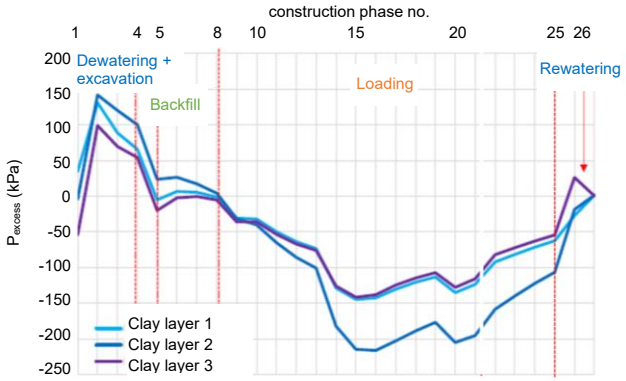

Figure 6. Estimation of the generation of excess pore pressure in deeper layers under the future nuclear plant.

However, excess pore pressures are dissipated at the end of the loading because the construction time is longer than it was for the existing nuclear plant. Therefore, drained and undrained calculation give similar final settlement (Figure 7).

Linear and HSM (drained and undrained) calculations were also done to evaluate if there were any nonlinear behavior in soil layers. Both soil laws give similar final settlement results (Figure 7), demonstrating that the soil still globally works in the estimated strain ranges.

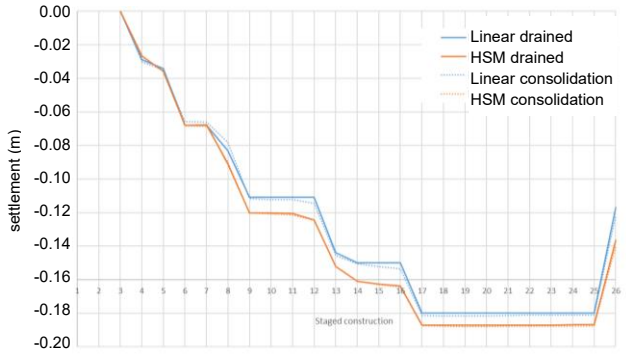

Figure 7. Comparison between linear and HSM calculation – settlement of HR centre.

The difference between phases 25 and 26 (corresponding to the rewatering at the end of the earthworks) lies in the way the reloading modulus is estimated in both behavior laws (all the calibration is done on first loading moduli).

The 3D-settlement model allows to extract the settlement at any point and any phase. It is then possible to evaluate differential settlements along structures like the various embedded galleries (example in Figure 8). Those are essential for calibrating adequate rebars and joints.

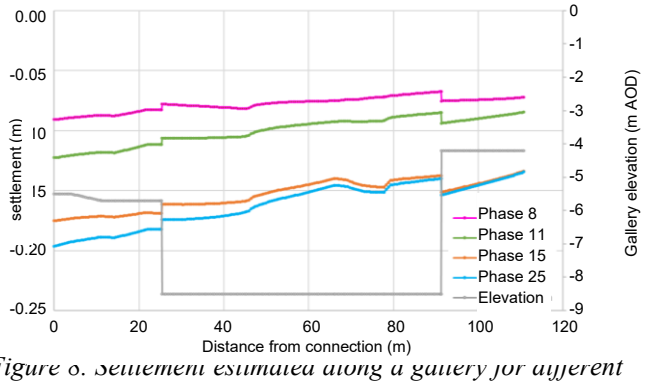

Figure 8. Settlement estimated along a gallery for different phases against its elevation profile (in grey).

4 CONCLUSION

An adapted geotechnical model is essential to predict and understand settlement under buildings. In order to evaluate the settlement of a future nuclear plant and give adequate settlement values for the design, detailled settlement studies are done. They are based on a geotechnical model calibrated on extensive in-situ and laboratory tests data. Depending on the range of strains, the moduli can be corrected with ARCSCOP cuves. It has been tested and compared with existing plant monitoring data on the same site. Settlement observations and calculations are consistant thanks to the calibration done on the moduli. For the future project, since the loads are greater, the moduli should however be adapted with the strains. It can lead to realistic settlement values for the future design.

REFERENCES

Menard, L., Rousseau, J. (1962). L'évaluation des tassements. Tendances nouvelles. Sols Soils No. 1, pp. 13-20, Paris.

Hoang M.T. & al. 2020. Vers une approche de calcul unifiée du tassement des semelles et des radiers, JNGG2020.

Proceedings of the XVIII ECSMGE 2024
GEOTECHNICAL ENGINEERING CHALLENGES
TO MEET CURRENT AND EMERGING NEEDS OF SOCIETY
© 2024 the Authors
ISBN 978-1-032-54816-6
DOI 10.1201/9781003431749-41
Open Access: www.taylorfrancis.com, CC BY-NC-ND 4.0 license

ECSMGE 24
XVIII EUROPEAN CONFERENCE ON SOIL MECHANICS AND GEOTECHNICAL ENGINEERING

A critical review of field testing of helical steel piles

Un examen critique des essais sur le terrain de pieux hélicoïdaux

P.J. Bourne-Webb*, T.M. Bodas Freitas
CERIS, Instituto Superior Técnico, ULisboa, Lisbon, Portugal

P. Marques, E. Godinho
Helica, Tomar, Portugal

**peter.bourne-webb@tecnico.ulisboa.pt*

ABSTRACT: In this paper, an initial appraisal of the existing body of knowledge contained in the records of full-scale axial maintained load tests on helical steel piles (HSP) is presented. There are numerous case studies on full-scale testing of HSP which cover a variety of configurations (no. helices, helix spacing, depth of installation, etc.), ground conditions, testing procedures and definitions of failure. This data base is being critically reviewed by the authors and in this paper, the procedures employed in the review are outlined and illustrated through a selection of the case studies. The review involved examining the time-displacement and time-load data (when available), to confirm the reliability of the test stages from a given test and then applying a uniform failure condition across all studies. It is shown that the short loading stage durations employed in most studies (so-called quick test) and not imposing a creep criterion, especially in the latter stages of the test, means that the ultimate capacity is often overstated. This revised and updated database will be used to critically appraise resistance calculation methods used in practice and develop reliability-based design procedures for HSP that are compatible with Eurocode 7.

RÉSUMÉ: Dans cet article, une première évaluation de l'ensemble des connaissances contenues dans les enregistrements d'essais de charge axiale maintenue à grande échelle sur des pieux en acier hélicoïdaux (HSP) est présentée. Il existe de nombreuses études de cas sur les essais à grande échelle de HSP qui couvrent une variété de configurations (nombre d'hélices, espacement des hélices, profondeur d'installation, etc.), conditions de terrain, procédures d'essai et définitions de défaillance. Cette base de données est en cours d'examen critique par les auteurs et dans cet article, les procédures employées dans l'examen sont décrites et illustrées à travers une sélection d'études de cas. L'examen impliquait d'examiner les données de déplacement temporel et de charge temporelle (lorsqu'elles étaient disponibles), afin de confirmer la fiabilité des étapes de test à partir d'un test donné, puis d'appliquer une condition de défaillance uniforme dans toutes les études. Il est montré que les courtes durées d'étapes de chargement employées dans la plupart des études (essai dit rapide) et n'imposant pas de critère de fluage, en particulier dans les dernières étapes de l'essai, font que la capacité ultime est souvent surestimée. Cette base de données révisée et mise à jour sera utilisée pour évaluer de manière critique les méthodes de calcul de résistance utilisées dans la pratique et développer des procédures de conception basées sur la fiabilité pour les HSP qui sont compatibles avec l'Eurocode 7.

Keywords: Helical piles; field tests; design; safety.

1 INTRODUCTION

Helical steel piles (HSP) in various configurations have been used since the 19th century when Mitchell (1848) proposed their use in providing secure ship mooring and for the foundations of near-shore structures such as lighthouses and piers. For this study, HSP are considered to be a foundation element comprising a central, small diameter shaft of variable length with one or more sections of helix located at intervals along the shaft, from the tip. The helices may have differing diameter but typically are 3 to 5 times the diameter of the shaft and spaced 3 helix diameters apart. This latter ensures a so-called individual helix failure mechanism (Perko, 2009) by minimising interference between the respective failure mechanisms.

Since the 1960s and more-so, the 1980s until the present day, there has been an effort to provide a greater scientific understanding of the mechanisms of load-transfer of HSP, and how e.g. the ultimate resistance might vary from experience and design methods drawn from conventional piles. In reviewing these studies, it became apparent that while testing procedures were broadly similar, i.e. use the so-called "quick test", ASTM (2020): a) often load control was poor and not held within acceptable tolerances of the target value, b) it is not reported if the ASTM

recommended consideration of creep was made, to ensure the final load step(s) were stable, and c) a variety of definitions of failure have been employed including maximum attained load or the load associated with a settlement of 10%D, amongst others. It was felt that the former could lead to overstatement of pile resistance, while the latter makes the comparison of results between themselves and in relation to analytical calculation methods, and assessment of their reliability rather difficult. Therefore, it was decided to revisit the body-of-knowledge associated with HSP load testing that is available in the literature. In the following, the methodology adopted in reviewing the HSP database is outlined, along with some examples of its application to selected case studies and how the updating of the database will proceed.

2 METHODOLOGY

In order to uniformize the results of the various HSP load testing studies; first, where possible, the stability of the loading increments and the stability of the settlement versus time were assessed to ensure that each load stage was stable and secondly, a consistent definition for the ultimate resistance of each HSP was applied.

Loading stability was assessed visually for the most part. Figure 1 illustrates poor load control where variations of 20 to 50 kN (3 to 5% of the applied load) occurred. Typically, for the load range of this test, the limit on load variation would be 5 kN (<1 %), ICE (2007). When the load drops off in this manner there is no reliable definition of the load being maintained in a particular load stage, and e.g., the displacement rate will be artificially slowed by the reducing load.

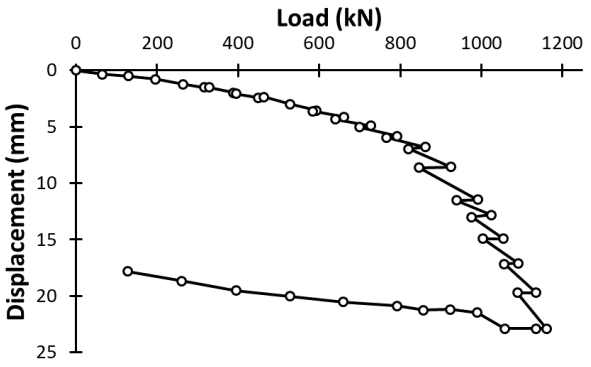

Figure 1. Example of poor load control, from Tappenden (2007).

A simplified version of the approach suggested by England (1992) has been implemented to assess the settlement vs. time, with the time-displacement data fitted with a simgle hyperbolic function to extrapolate and assess whether the recorded settlement was likely to have reached a stable (asymtotic) value at infinite-time. Eqtn. 1 describes this function (shown schematically in Figure 2(a)), where t is the elapsed time during the load stage and s, the increment in displacement in the same period while m and c are the slope and intercept values. The inverse of m, yields the asymptotic value for the displacement as t → ∞.

$$\frac{t}{s} = m.t + c \qquad (1)$$

Likewise, following Fleming (1992) but again using a single hyperbolic function, as per Chin (1972), the load-displacement response was extrapolated and used to derive the ultimate resistance. Only data from stable load stages as defined above, was taken forward into this stage. A single function was used on the basis that most of the load resistance derives from the helix(es) and it was also assumed that the elastic shortening on most HSP would be only a few-mm and could be ignored. Eqtn. 2 describes the hyperbolic function used to extrapolate the load-displacement response where N is the applied load and the other parameters were defined for Eqtn. 1 (Figure 2(a)).

$$\frac{s}{N} = m.s + c \qquad (2)$$

In this case, the inverse of m, yields the asymptotic value for the load, R_∞ as s → ∞.

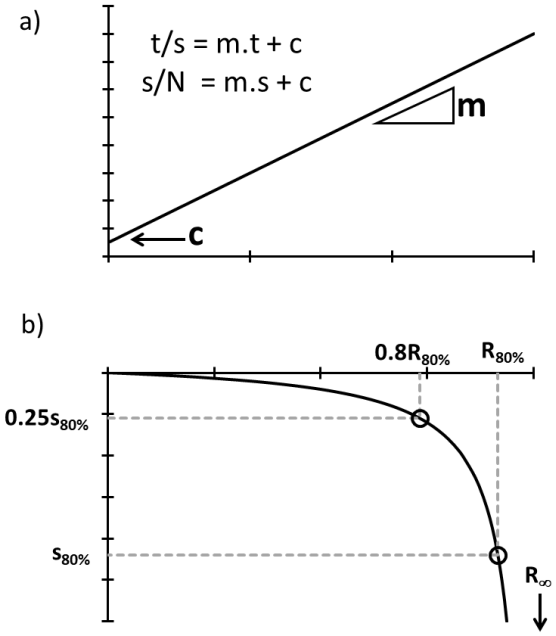

Figure 2. Schematic representation of hyperbolic functions (Equations 1 & 2) and Brinch-Hansen 80% failure criteria.

After some deliberation over the various failure criteria that have been proposed, e.g., as outlined in Fellenius (1980), it was decided that two values would be derived to represent the ultimate resistance, $R_{u,m}$: one based on Brinch-Hansen's 80% criterion (see Fgure 2(b)) which defines the ultimate resistance, $R_{80\%}$ as the load that gives four times the displacement generated by a load at $0.8R_{80\%}$ (Fellenius, 1980) and the asymtotic load obtained from Eqtn. 2. The ratio of $R_{80\%}$ to R_{∞} is about 90±2 %. It is considered that $R_{80\%}$ ensures that a more uniform and comparable state of mobilisation (approching a plunging failure) between case staudies and would be used for the assessment of design methodologies, while R_{∞} will be used in the assessment of analytical calculation models which imply full mobilisation of the pile resistance.

Rather than using the test data directly, Eqtn. 2 was used to derive $R_{80\%}$ and its associated setttlement, $s_{80\%}$ using Eqtns 3 and 4 (see Appendix 1),

$$R_{80\%} = {}^{11}/_{12\mathrm{m}} \qquad (3)$$

$$s_{80\%} = {}^{11c}/_{m} \qquad (4)$$

In some case studies, the test piles were provided with internal sensors, to allow the load-transfer from the pile to the ground to be assessed. Where available, this data has been reassessed and equivalent values for associated resistance parameters (α^* and β^* along the shaft and inter-helix cylinder) and end-bearing capacity factors, N_c^* or N_q^* as appropriate for total and effective stress analysis, were determined. These values are then to be used for comparison with values from analytical solutions. This aspect of the test database will not be discussed here.

3 CRITIQUE OF CASE STUDIES

3.1 Time-extrapolation

The method described above is illustrated here based on the results for tests on HSP in clay reported by Zhang (1999). The compression test shown here was undertaken on a 5.18 m long pile with a 219 mm diam. shaft and 3 no., 356 mm diam. helices, spaced at 1.5 helix diameters. Eleven stages of loading were applied and within each stage, the loads generally varied by less than about ±2 kN (1%).

This is one of the few cases where the author states that creep was considered. However, it is apparent that whatever consideration was made, creep rates were very high from early on when compared to e.g., the 0.25 mm/hr limit referenced by ASTM (2020) or the 0.1 mm/20 min in ISO (2018), for maintained load testing, Figure 3.

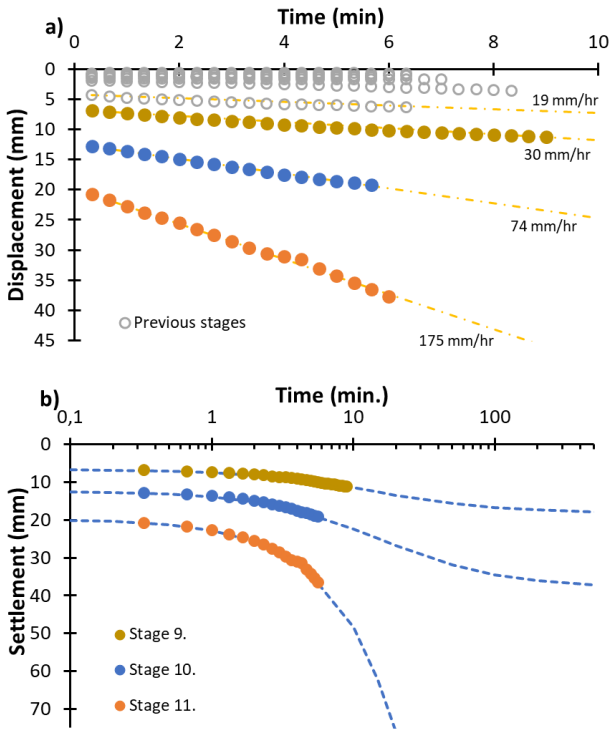

Figure 3. Time extrapolation of load test settlement data.

In Figure 3(a), the settlement rates for the last three stages are examined in more detail. Settlement rates towards the end of each, were in excess of 20 mm/hr. The time-extrapolation of the data from each stage is shown in Figure 3(b) where it can be seen that Stages 9 and 10 are predicted to reach a stable value at ∞-time, while Stage 11 is heading towards a plunging failure. In this example, the stage durations were systematically less than 10 minutes and therefore there is some uncertainty in the extrapolation to ∞-time, especially in the latter stages of the test. It is recommended that loading stages should last at least 30 minutes and/or until the creep rate is less than 0.1 mm/20 min. to increase data reliability.

3.2 Interpretation of ultimate load resistance

In the same example, based on the above, the last stage of the test was deemed to be unstable and therefore should not be considered, i.e., failure occurs at a load between that in Stages 10 and 11 (172 – 177 kN). The failure load reported by Zhang was 180 kN – the load mobilised in Stage 11, as pile settlements reached 10% of the helix diameter (36 mm).

The test stages deemed stable were then treated using the load extrapolation to ∞-displacement, described above. The result of this assesment is shown in Figure 4(a) which illusrates how it is only the last

few stages where the effect is significant and how the resulting collapse load can be affected. Figure 4(b) shows the resulting hyperbolic interploation through the treated load-displacement data, along with the failure loads, R_{∞} = 177 kN and $R_{80\%}$ = 162 kN. In this example, the difference with respect to the ultimate resistance quoted by Zhang (1999) is less than 5% but with this revision, it is clear that the result is based on stable data.

Figure 5 further illustrates the impact of this reappraisal by comparing the revised results of three tests: *A1 C Long* has already been presented, *A2 C Short* is the same as A1 but with a shorter embedment of 3.1 m, and *A3 C Long* has only two helices with a spacing of 3 helix diameters but is otherwise the same as A1. In all cases, someof the later load stages did not trend to a stable displacement-time response and the revised load-displacement curves led to a reduction in the inferred ultimate resistance, of up to 15% in the case of A2.

4 FINAL COMMENTS

The purpose of the work presented was to a) develop a sense of the quality and robustness of the field test data relating to HSP that had been published previously and b) reform the data base on the basis of tests that can be demonstrated to be well-controlled and then presented in a uniformized manner to aid further interpretation. This evaluation has also informed the testing specification that will be employed for field testing undertaken as part of the project HELIPORT.

Given the cost of undertaking field load tests on piles (generally), it is imperative that good control of the process is maintained to ensure the data produced are of the best quality and the investment is not wasted. Clear load control (ICE, 2007) and creep (ASTM, 2020) criteria should be specified and checked, and loading stages should be of sufficient length to ensure that it can be verified reliably that the pile settlement will stabilise – from this assessment the load should be held 30 minutes and/or until the creep condition (e.g. 0.1 mm/20 min.) is met.

ACKNOWLEDGEMENTS

The work presented was financed by the Fundação para a Ciência e a Tecnologia (FCT), Portugal, via the project HELIPORT doi. 10.54499/2022.08947.PTDC and UIDB/04625/2020. The authors would like to express their gratitude to the funding institution. Thanks also to Prof. Chalaturnyk of the University of Alberta for providing the original data files of Zhang (1999).

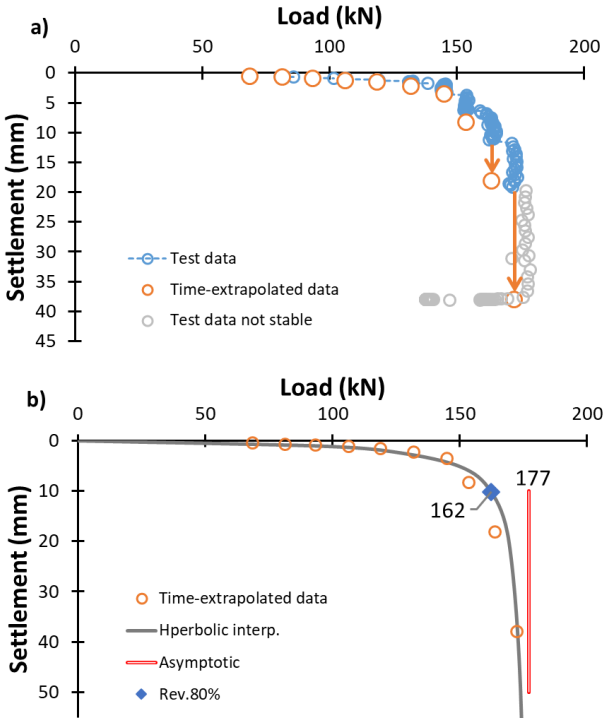

Figure 4. Load-displacement response and failure.

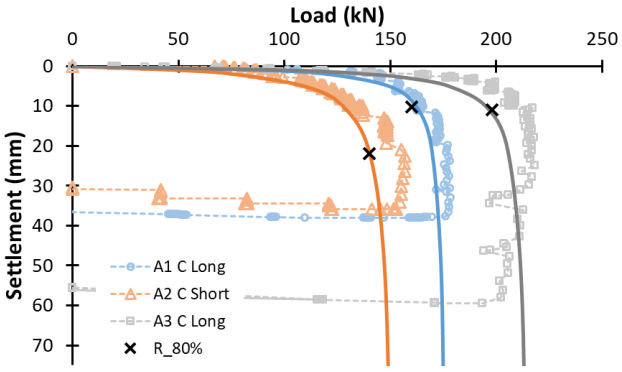

Figure 5. Impact of time & displacement extrapolation on inferred ultimate resistance.

REFERENCES

ASTM (2020). D1143/D1143M-20: Standard Test Methods for Deep Foundation Elements Under Static Axial Compressive Load, ASTM, https://doi.org/10.1520/D1143_D1143M-20.

Chin, F.K. (1972). Inverse slope as predictor for ultimate bearing capacity of piles. *Proc. 3rd Southeast Asian Conference of Soil Engineering*, Hong Kong, pp. 83–91.

England, M. (1992). Pile settlement behaviour: An accurate model, in: *Application of Stress-Wave Theory to Piles*. Routledge.

Fellenius, B.H. (1980). The analysis of results from routine pile load tests. *Ground Engineering* 19–31. https://cdn.ca.emap.com/wp-content/uploads/sites/13/1980/09/GE-Sept-1980-

The-analysis-of-results-from-routine-pile-load-tests.pdf (accessed: 27/02/2024).
Fleming, W.G.K. (1992). A new method for single pile settlement prediction and analysis. *Géotechnique* 42(3), 411–425. https://doi.org/10.1680/geot.1992.42.3.411.
ICE (2007). SPERWall Pile testing, in: *Specification for Piling and Embedded Retaining Walls*. Thomas Telford, pp. 99–110
ISO (2018). 22477-1 Pile load test by static axially loaded compression.
Mitchell, A. (1848). On submarine foundations; particularly the screw pile and moorings. *Minutes of the Proc. of the Inst. of Civil Engineers* 7, 108–132. https://doi.org/10.1680/imotp.1848.24220.

APPENDIX 1.

Derivation of Brinch-Hansen 80% failure criteria parameters from hyperbolic function:

$$R_{80\%} = \frac{s_{80\%}}{m.s_{80\%}+c} \qquad [1.1]$$

$$0.8R_{80\%} = \frac{0.25s_{80\%}}{m.0.25s_{80\%}+c} \qquad [1.2]$$

Solving simultaneously,

$$\frac{\cancel{s_{80\%}}}{ms_{80\%}+c} = 1{,}25\left[\frac{0.25\cancel{s_{80\%}}}{m0.25s_{80\%}+c}\right]$$

$$0.25ms_{80\%} + c = 1.25(0.25)m.s_{80\%} + c$$

$$\big(1 - 1.25(0.25)\big)c = (1.25(0.25) - 0.25)ms_{80\%}$$

$$\Rightarrow s_{80\%} = {}^{11c}/_{m} \qquad [1.3]$$

Substituting into [1.1],

$$R_{80\%} = \frac{{}^{11c}/_{m}}{m.\left({}^{11c}/_{m}\right)+c}$$

$$\Rightarrow R_{80\%} = {}^{11}/_{12m} \qquad [1.4]$$

Perko H.A., (2009). *Helical piles: a practical guide to design and installation*. J. Wiley, Hoboken, N.J.
Tappenden, K.M. (2007). Predicting the Axial Capacity of Screw Piles Installed in Western Canadian Soils (Master thesis). University of Alberta, Edmonton, Canada. https://era.library.ualberta.ca/items/dc5fb64d-c916-4a58-8607-a2eb59231262/view/884f0e87-2ef0-443e-b593-6962f59a82f8/4008200.pdf (accessed: 27/02/2024).
Zhang, D.J.Y. (1999). Predicting Capacity of Helical Screw Piles in Alberta Soils (Master thesis). University of Alberta, Edmonton, Canada. https://era.library.ualberta.ca/items/77edf5ee-1e61-4227-b841-b79384dd1055 (accessed: 06/11/2023).

Proceedings of the XVIII ECSMGE 2024
GEOTECHNICAL ENGINEERING CHALLENGES
TO MEET CURRENT AND EMERGING NEEDS OF SOCIETY
© 2024 the Authors
ISBN 978-1-032-54816-6
DOI 10.1201/9781003431749-42
Open Access: www.taylorfrancis.com, CC BY-NC-ND 4.0 license

ECSMGE 24
XVIII EUROPEAN CONFERENCE ON SOIL MECHANICS AND GEOTECHNICAL ENGINEERING

Modelling the interaction of an underground structure with the soil in a megalopolis

Modélisation de l'interaction d'une structure souterraine avec le sol dans une mégapole

I. Boyko, V. Nosenko*, O. Lytvyn
Kyiv national university construction and architecture, Kyiv, Ukraine
v.s.nosenko@gmail.com

ABSTRACT: The paper presents an assessment of the interaction of the elements of the "soil-tunnel" system under conditions of changes in the stiffness of the structure when soil parameters change. The study was carried out using numerical modelling and field tests with cyclic loads typical for such structures. In megacities, large-diameter underground tunnels are being constructed; they are several kilometres long and pass-through soils with different properties. An example of such a facility is the construction of a 3.6 m diameter tunnel in Kyiv with a length of about 10 km. Its depth varies from 5 to 90 m. In some parts of the tunnel, due to long-standing erosion processes, the semi-hard clay surrounding the tunnel is replaced by much weaker flowable sandy loam, so there is a need to strengthen the weak foundation. To evaluate the effectiveness of different options for strengthening the foundation, field tests were carried out by injecting polymer mortars into the soil in different volumes and over different areas, followed by cyclic load tests. During the test of the weak base in its natural state, vertical displacements of 3.7 cm were recorded. These displacements are 2 times higher than in semi-hard clay. The volume of mortar used for the reinforced foundation was justified so that the displacements did not exceed the permissible operational requirements. Subsequently, numerical modelling of the interaction of natural and reinforced foundations with an underground structure at different stages of its life cycle was carried out in a physically nonlinear formulation.

RÉSUMÉ: L'article présente une évaluation de l'interaction des éléments du système "environnement du sol-tunnel" dans des conditions de changement de la rigidité de la structure lorsque les paramètres du sol changent. L'étude a été réalisée à l'aide d'une modélisation numérique et d'essais sur le terrain avec des charges cycliques typiques pour de telles structures. Dans les mégapoles, des tunnels souterrains de grand diamètre sont construits; ils mesurent plusieurs kilomètres de long et traversent des sols aux propriétés différentes. Un exemple de ce type d'installation est la construction d'un tunnel de 3,6 m de diamètre à Kiev, d'une longueur d'environ 10 km. Dans certaines parties du tunnel, en raison de processus d'érosion de longue date, l'argile semi-dure entourant le tunnel est remplacée par un limon sableux fluide beaucoup plus faible, d'où la nécessité de renforcer les fondations fragiles. Pour évaluer l'efficacité des différentes options de renforcement de la fondation, des essais sur le terrain ont été réalisés en injectant des mortiers polymères dans le sol en différents volumes et sur différentes zones, suivis d'essais de charge cyclique. Lors de l'essai de la base faible dans son état naturel, des déplacements verticaux de 3,7 cm ont été enregistrés. Ces déplacements sont 2 fois plus élevés que dans l'argile semi-dure. Le volume de mortier utilisé pour la fondation renforcée a été justifié de manière à ce que les déplacements ne dépassent pas les exigences opérationnelles admissibles. Par la suite, la modélisation numérique de l'interaction des fondations naturelles et renforcées avec une structure souterraine à différents stades de son cycle de vie a été réalisée dans une formulation physiquement non linéaire.

Keywords: Underground structure; numerical modelling.

1 INTRODUCTION

Modern cities face many complex geotechnical challenges. It is necessary to solve the issues of deep pits, design and construction of foundations of high-rise buildings under loads of various types in different geological conditions, taking account the presence of existing buildings when laying underground structures, and much more. The problem of insufficient territory in large cities is solved by using underground space (Broere, 2016). The work of many geotechnics shows the level of complexity and relevance of issues related to the use of underground space for the construction of buried engineering structures, such as subway tunnels in the historic environment (Burghignoli et al. 2013). The peculiarities of designing and experimental research of tunnel-type structures are devoted to the works of many scientists (Mair, 2008). The downside of human activity in cities is the pollution of the territory and the

need to solve geo-environmental problems associated with the transport of household waste. For this purpose, large-diameter collectors are constructed, which are tunnels designed to transport household wastewater to the place of its treatment. These tunnels are several kilometers long and run through soils with different properties. The design and construction of such structures requires an integrated approach, including: initial analysis of the topographic and geological situation, surveys along the route of the structure, specification of soil parameters depending on the calculation methods used to assess the interaction between the soil environment and the structure, selection of construction technology, assessment of changes in soil parameters on the stress-strain state of the tunnel structures, improvement of soil properties in certain sections of the tunnel.

2 INTERACTION OF AN UNDERGROUND STRUCTURE WITH THE SOIL

The main purpose of this paper is to evaluate the interaction of the elements of the "soil environment-tunnel" system under conditions of changes in structural stiffness and soil parameters. The research was carried out both by means of numerical modelling and by conducting field tests of the tunnel elements with cyclic loads.

2.1 Tunnel construction

An example of such a complex geotechnical facility is the construction of a tunnel for a new main city sewer in Kyiv, which is about 10 km long. Its depth varies from 5 m to almost 90 m. The tunnel consists of an outer lining of 8 precast concrete segments forming a circle and an inner lining of reinforced concrete cylindrical fragments with a protective polymer coating inside. The tunnel for installing the collector was constructed using a 3,600 mm diameter tunnel boring machine with sectional installation of the outer segments to the ground and their wedging, after which the secondary lining was installed in the inner space of the primary lining, and the space between them was injected with cement mortar. In certain sections of the tunnel, temporary soil freezing, temporary water lowering and protective screens made of walls in the ground were used to protect it from the effects of active groundwater movement. At the stage of operation, the tunnel is a cylindrical structure with an internal diameter of 2760 mm. During operation, the internal walls of the tunnel structure are subjected to cyclic loading due to daily changes in its operation mode. The minimum pressure at the bottom of the collector is 10 kPa, and the maximum pressure is up to 30 kPa. The outer casing of the collector is under ground pressure, which varies depending on the depth of the deposit from 90 kPa to 450 kPa.

2.2 Geological conditions

For the vast majority of the tunnel's length, the geotechnical profile around the tunnel is represented by semi-hard, sometimes stiff, marl clay, which has the following physical and mechanical properties: density $\rho \approx 1.9$ t/m^3, cohesion c=70...95 kPa, friction angle $\varphi \approx 12°$, and modulus of deformation E≈35 MPa. This soil has low permeability properties, which provides additional protection for the tunnel. However, in some sections of the tunnel route, due to long-standing erosion and siltation processes, there is no clay, and the environment around the tunnel is represented by weak plastic sandy loam and flowable sandy loam. The main physical and mechanical properties of these sandy loams are: density $\rho \approx 1.8$ t/m^3, cohesion c≈10 kPa, friction angle $\varphi \approx 18°$ and modulus of deformation E≈6 MPa. These characteristics were further verified by testing the weak soil with a pressiometer.

2.3 Changes in soil properties

In order to avoid uneven deformations of more than 10 mm per 1 m of the buried structure length in areas with a sharp change in geological structure, it was proposed to strengthen weak sandy loam soils by injecting solutions into the soil. The following were considered as possible alternatives for injection: silicate, cement and cement-polymer mortars of different water-cement ratios (time to reach design strength is more than 1 day) and, as an alternative, rapidly hardening two-component polymer mortars (time to reach design strength is 15-20 minutes).

Analysing the possible technologies for strengthening the soil base, we can note the advantages and disadvantages of each. Cementation is a technology that can be used for most soils, but the disadvantage is that it takes several days to gain strength and has an average cost among other technologies. Silicification is used for hard sands and sandy loams, but is ineffective for water-saturated soils, which in this case are the main ones on the site of the buried structure. Silicification has the lowest cost per 1 m^3 of treated base compared to other technologies. When using polymer mixtures, the advantage is that in order to strengthen the soil base under existing buried structures, it is necessary to make technological holes for injectors of the smallest size (20 mm in diameter), while for other technologies the holes have a diameter of 50 mm. Another advantage of polymeric solutions is their fast curing

(up to 30 minutes) and, as a result, the ability to ensure a fast pace of work. The disadvantage is the highest cost among other technologies. Based on the technical and economic comparisons and taking into account the factor of rapid gain of the required strength and formation of bonds with the surrounding soil, injections using a two-component polymer solution were chosen as the main option. An important aspect of the injection technology is the possible heterogeneity of the artificially fixed soil mass and, as a result, the need to select injection modes to obtain the required deformation parameters of the fixed mass. To select the injection modes and predict the deformations of the consolidated soil base, a series of field studies of the technology with different injection modes and subsequent testing of the base by loading the tunnel segments were carried out at the experimental sites in real soil conditions.

2.4 Full-scale testing of tunnel segments

By applying a series of gradually increasing loads to the tunnel fragments placed in the soil, a series of field tests of the soil base in its natural state were carried out and vertical displacements were recorded, which in the range of operating pressures ranged from 16 mm to 37 mm for weak sandy loam soils, respectively (Figure 1). These displacements are significantly higher than those recorded for the areas where the subsoil was made up of semi-hard clays. After that, a series of experimental injections of polymeric mortar into weak sandy loam soils was performed to select the mode of supply and volume of such mortar so that the reinforced base had deformation characteristics close to semi-hard clay. For the reinforced base, vertical deformations ranging from 8 mm to 21 mm were obtained after the initial loading. This is 2 times less than for the unfixed base, but more than for the neighbouring areas with semi-hard clays. The reinforced base was reloaded, which corresponds to the operating mode of the reservoir with cyclic loads. After reloading, the deformations ranged from 5 mm to 11 mm. Such deformation values ensure compliance with the requirements for the allowable difference in deformation for neighbouring parts of the collector located in different soil conditions.

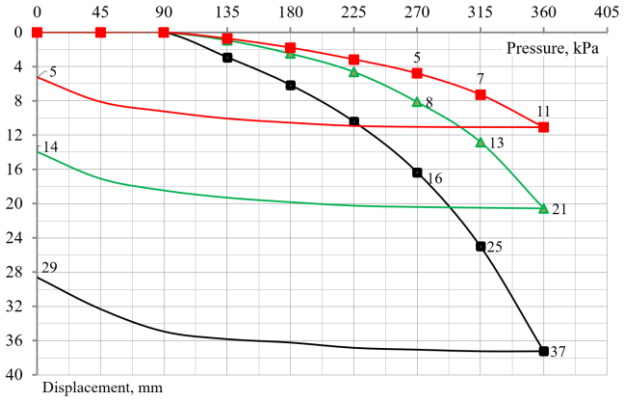

Figure 1. Dependence of displacements of the experimental tunnel section on the pressure on it at different properties of the base soil.

2.5 Numerical modelling of tunnel-soil interaction

To evaluate the effectiveness of various reinforcement options, numerical simulations of the stress-strain state of the soil medium-tunnel system at different stages of its life cycle were performed in a physically nonlinear formulation.

The soil model used in the numerical simulation allows to take into account changes in the deformation parameters of soils depending on the level of applied stresses and to describe the deformation processes of dispersed soils under complex loading/unloading trajectories.

To obtain correct results of numerical simulation, it is necessary to identify the model parameters in advance on the basis of laboratory soil tests or previously conducted field experiments.

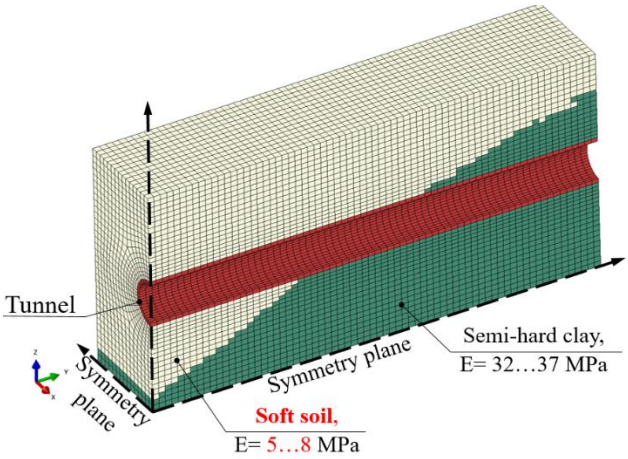

Figure 2. Finite element model of the "soil environment - tunnel" system.

.

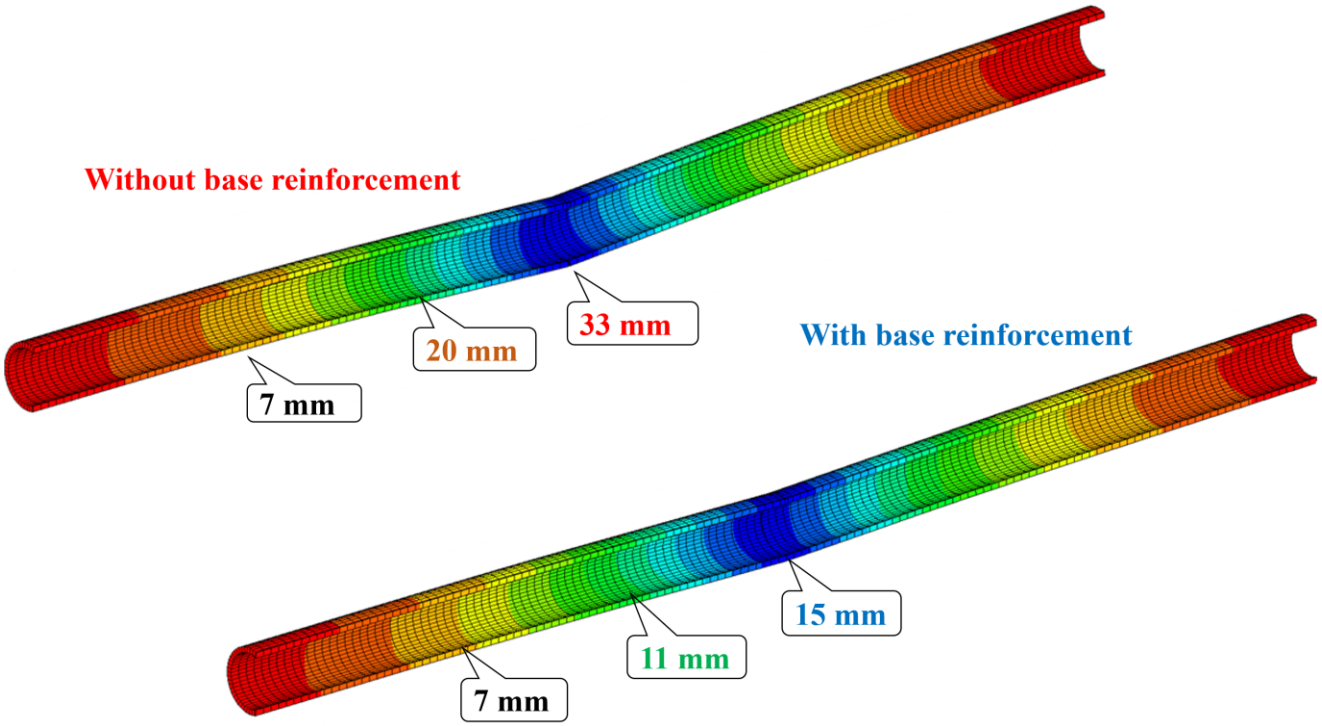

Figure 3. Comparison of displacements of the tunnel section obtained by numerical simulation for the variant without and with strengthening of the weak soil base.

According to the numerical modelling data, at the maximum pressure from the tunnel structures to the base during the operation of the reinforced base, the displacement reached to 13 mm, and the data of measurements of the structure displacement in the field experiment at the same pressure showed 11 mm.

The discrepancy between the numerical modelling and field experiments was up to 25% in the direction of overestimation of deformations in the modelling.

Three-dimensional numerical modelling of the tunnel-soil interaction in the transition zone from semi-hard clay to weak soils for two scenarios: the first, when the tunnel base was natural, and the second, with reinforced injection, showed a possible maximum difference in their displacements of 33 mm and 15 mm, respectively. Numerical modelling of the entire tunnel section in the zone of weak soils allowed us to select the effective number of weak base strengthening zones and the volume of polymeric mortar to strengthen and stabilize the weak soil and ensure safe operation of the tunnel.

3 CONCLUSIONS

The experimental results showed a decrease in the deformation of the fixed base under cyclic loads by up to 2 times compared to the unfastened base. On the basis of test injections with different volume of polymer mixture is established that in these soil conditions, the deformation of the fixed base depends on the injection mode and its volume.

A set of measures, including full-scale field tests and numerical modelling of the interaction between the foundation and the underground structure with the identification of foundation parameters, allowed us to substantiate an effective technology for strengthening a weak soil foundation and now we have experience of its safe operation. In the future, it is planned to extend this approach to the design of underground structures for sheltering people and energy facilities in Ukraine.

REFERENCES

Broere, W. (2016) Urban Underground Space: Solving the Problems of Today's Cities. *Tunnelling and Underground Space Technology*, 55, 245-248. https://doi.org/10.1016/j.tust.2015.11.012.

Burghignoli A., Callisto L., Rampello S., Soccodato F.M., Viggiani G.M.B. (2013) The crossing of the historical centre of Rome by the new underground Line C: A study of soil-structure interaction for historical building, In: Geotechnics and Heritage, 1st ed., Publisher, CRC Press, GB, London, pp. 97-136 https://doi.org/10.1201/b14965.

Mair R. (2008) Tunnelling and geotechnics: new horizons. *Géotechnique*, 58, 695-736. https://doi.org/10.1680/geot.2008.58.9.695.

Proceedings of the XVIII ECSMGE 2024
GEOTECHNICAL ENGINEERING CHALLENGES
TO MEET CURRENT AND EMERGING NEEDS OF SOCIETY
© 2024 the Authors
ISBN 978-1-032-54816-6
DOI 10.1201/9781003431749-43
Open Access: www.taylorfrancis.com, CC BY-NC-ND 4.0 license

ECSMGE 24
XVIII EUROPEAN CONFERENCE ON SOIL MECHANICS AND GEOTECHNICAL ENGINEERING

Machine learning to improve the ground model for road settlement prediction

Apprentissage automatique pour améliorer le modèle de sol pour la prévision des tassements routiers

M. Brček*
Department of Geotechnics, Faculty of Civil Engineering, Slovak University of Technology in Bratislava, Slovakia

J. Panuška
PanGEO s.r.o., Zvolen, Slovakia

M. Kopecký
Department of Geotechnics, Faculty of Civil Engineering, Slovak University of Technology in Bratislava, Slovakia

**martin.brcek@stuba.sk*

ABSTRACT: The article discuss data processing and development of predictive ground model on the basis of data from extensive engineering geological survey. Basic model inputs are spatial coordinates (X, Y, elevation). Ground model with assigned soil groups, deformation properties and ground water level is created with input of spatial coordinates. Basic statistical and machine learning algorithms (regression, classification, clustering) were used in Python script to develop predictive ground model. Predictions are compared with the ground model developed by engineering geologist. ground model was used to calculate the settlement of the embankment subgrade in the highway route D1 for international and domestic transport.

RÉSUMÉ: L'article traite du traitement des données et du développement d'un modèle prédictif du sol sur la base de données provenant d'une étude géologique approfondie. Les entrées de base du modèle sont les coordonnées spatiales (X, Y, élévation). Le modèle de sol avec les groupes de sols assignés, les propriétés de déformation et le niveau de la nappe phréatique est créé à partir des coordonnées spatiales. Des algorithmes statistiques de base et d'apprentissage automatique (régression, classification, regroupement) ont été utilisés dans un script Python pour développer un modèle de sol prédictif. Les prédictions sont comparées au modèle de sol développé par l'ingénieur géologue. Les résultats montrent une grande précision de prédiction avec une erreur acceptable, mais avec une plus grande efficacité si l'apprentissage automatique est utilisé. Les profils géologiques d'ingénierie obtenus ont été utilisés pour calculer le tassement de la plate-forme de remblai sur le tracé de l'autoroute.

Keywords: Ground model; data processing; settlement; machine learning.

1 INTRODUCTION

Application of machine learning algorithms is on the rise in geotechnical engineering. This is due to the huge amount of data produced (laboratory measurements, geological survey, in-situ testing etc.) and due to empirical nature of the profession. Machine learning was used to predict small strain shear modulus (Cruz, Santos, & Cruz, 2013), predict slope movements (Yang, Yin, & Liu, 2019) and liquefaction potential (Goh & Goh, 2007), (Samui & Sitharam, 2011). Additionally, there are articles that discuss the classification of subsoil or the mapping of some geological features (Šapina, 2016), (Zhou & Wu, 1994), (Tsiaousi, Travasarou, Drosos, Ugalde, & Chacko, 2018). The development of ground models through machine learning is somewhat comparable with geostatistical algorithms such as Kriging (Cressie, 1990).

In this study, machine learning is utilized to develop ground model for calculating settlement in a large infrastructural project (highway of length 15 km). The automatically generated ground model for settlement analysis must include deformation properties (oedometric modulus E_{oed}) of various soil groups. Oedometric moduli were assigned to different soil groups based on soil type and its physical state (consistency or density). Settlement calculations were

automatically performed in 111 ground profiles obtained solely by inputting spatial coordinates X, Y, Z.

2 METHODOLOGY

A dedicated application was developed to process and analyse the available data and create an engineering geological model with the settlement calculation. This application incorporates a suite of interconnected machine learning and neural network algorithms.

2.1 Material

Engineering geological data from bore logs are crucial for learning phase of model development. Following data were used for analysis:

- Text documentation of realized and archive boreholes
- Spatial coordinates of boreholes (*X, Y*) and their elevation *Z* (m a.s.l.)
- Ground water level
- Atterberg limits, grain size distribution curves, oedometric moduli

Visual Basic for Applications was used to extract:

- Borehole name
- Soil class USCS (American Society for Testing and Materials, 2017)
- Depth boundaries of single layer
- Soil consistency (set as lower consistency) → description (keyword) "soft to stiff " or "stiff to soft" → resultant consistency soft with symbol T
- Soil was set to organic (symbol O) in case of organic matter (keywords: detrit, rotten wood, wood, plants)
- Homogenized soil group f [CH-CV-CE, MH-MV-ME, CE, ML-MI], fs [CS, MS, SC, SM], fg [CG, MG, GC, GM], g [GF, GP, GW], s [SF, SP, SW], r [soft rocks], OR, Y
- origin/genesis of soil: quaternary sediment D (deluvial), F (fluvial) and Neogene sediments N (Figure 1)
- spatial coordinates of borehole X, Y, Z
- ground water level

A total of 444 boreholes were processed with 3558 soil layers. Laboratory tests, Atterberg limits (liquid and plasticity limit), percentage of fines, and grain size distribution curves were used to develop quasi homogenous soil groups. In total, 1071 samples were processed, with 109 oedometric moduli.

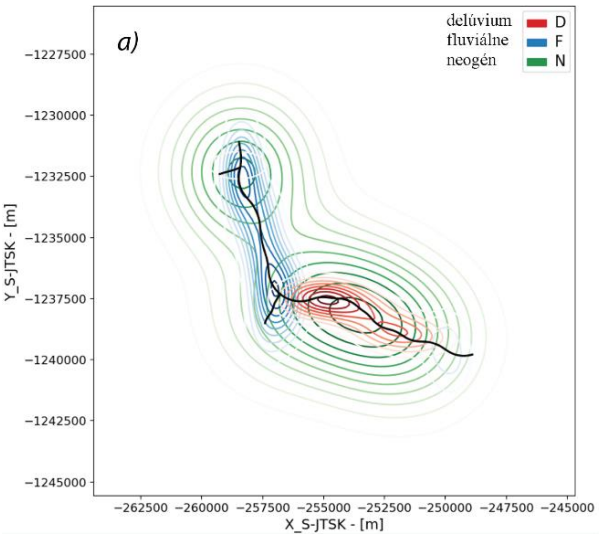

Figure 1. Distribution of soils in the highway route D1.

2.2 Methods of machine learning

Methods of supervised learning and unsupervised learning were employed to predict ground model including ground water level. The K-means clustering (KMC) algorithm was utilized to identify critical quasi-homogeneous sections along the highway route. The algorithm's inputs consist of the spatial coordinates of terrain surface & elevation and oedometric modulus. An elbow diagram was used to determine the optimal number of clusters, which was found to be 9 in this study.

The accuracy of the model is calculated as follows:

$$ACCURACY=TP/(TP+FP) \quad (1)$$

where *TP* is number of correctly assigned data points, *FP* is number of misclassified points.

2.3 Prediction of ground water level

Ground water level was predicted by deep feed forward artificial neural network (ANN). Algorithm inputs are spatial coordinates of terrain surface & elevation. For training, 75% of the total 405 groundwater level data points were used, while 25% were used for model validation.

2.4 Prediction of soil genesis

The Random Forest (RF) algorithm was trained for the classification task. Inputs for classification included the elevation, and the depth of the center of the homogeneous layer from the surface, in addition to spatial coordinates. Each borehole was subdivided into elements with thickness of 0.1 m (oversampling). The model consists of 10 decision trees, with equal weights for single classes and entropy as the optimization criterion. The number of data points for each genesis

are shown in Table 1. Overall, 65% of the data were used for learning, and 35% for testing. The accuracy of the model (Table 1) shown very good prediction of soil genesis.

Table 1. Number of inputs for model with soil genesis.

Soil genesis	km 0.0-6.0	Accuracy of model (%)
F - fluvial	8700	98.92
N-neogene	3860	96.29
D-deluvium	590	97.61
Overall	*13 150*	*98.09*

A different procedure was utilized to predict soil consistency. The Support Vector Machine (SVM) algorithm with bootstrap aggregation and One vs. One classification strategy was employed. Input parameters consisted of the same parameters as in previous models, supplemented by inputs for genesis and soil consistency. Furthermore, no subdivision was applied to soil layers (no oversampling of elements with thickness of 0.1 m). A regularization parameter C=50, with equal weights for classes, and 200 sub-models were used

Oedometric modulus and unit weights were assigned to soils based on their consistency, soil group, genesis, and highway part A – F.

3 RESULTS

3.1 Identification of homogenous units on highway route and prediction of groundwater level

The highway route, with 9 classes identified by K-means clustering (KMC) and resultant 6 quasi homogenous parts are depicted in Figure 2. These six quasi-homogeneous parts, labeled A – F, were identified across two sections of the highway route. The first part, A – C, predominantly consists of fluvial sediments, while the second part, D – F, is mostly characterized by deluvial sediments.

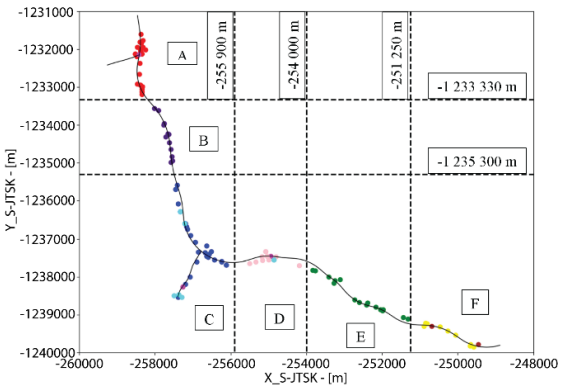

Figure 2. Result of KMC clustering algorithm.

Only results from part one are presented in this paper.

The maximum error between predicted and measured water level is 7.24 m, with an average error of 1.99 m.

3.2 Comparison of ground models of homogenous units on highway route

Differences in depths of observed parameters between machine created ground models (ML) and ground models developed by engineering geologist (EG) are shown in Figure 3. Differences were found in determining the depth of the surface cover (f/fs), thickness of gravelly (gZ, gK) sediments, depositional depth of the Neogene sediments (N), and groundwater level (HPV). The depth difference in estimating soil layers or groundwater levels is generally up to 2.0 meters. The largest error, 3.5 m can be found in the estimation of Neogene depth in profile km 13.550. The errors in profile km 8.475 are interesting due to the fact that no learning points were provided in this section (there are only cuts in this part and no embankments, thus no need for settlement calculation). The model was not trained within a radius of 1.0 km from this point; however, the error is only slightly above 2.0 meters. The ground models are developed for settlement analysis, thus, the comparison of settlement in chosen profiles is of interest.

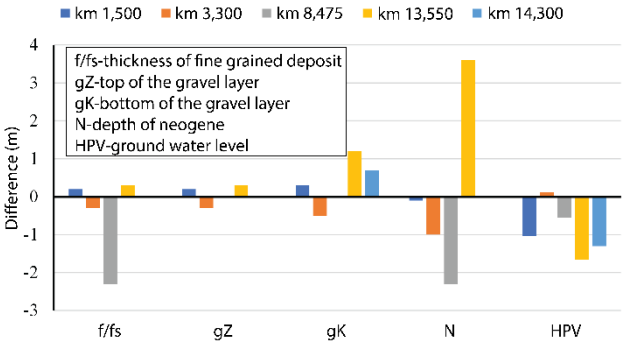

Figure 3. Comparison of profiles created by ML algorithm and human made (EG).

3.3 Comparison of measured and predicted settlements

Calculated settlements for ground models developed by machine and by hand are summarized in Table 2. A difference of up to 10% is considered very good and appears promising for the analysis. The comparison of predicted and measured settlements (by horizontal inclinometers) is presented in Table 2 and Figure 4. The maximum difference is slightly above 20%. It must be noted that such difference could be caused not only by the misprediction of ground model but also by the use of a simple analytical calculation model for

ground settlement analysis. Finally, a difference of 20% is considered acceptable, particularly if the model is intended for preliminary quantitative analysis.

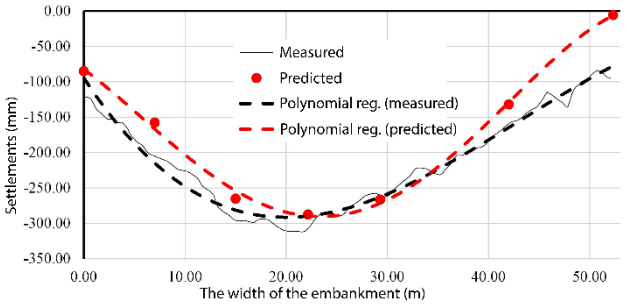

Figure 4. Comparison of calculated and measured settlements, HINK-17, km 6.416.

Bigger differences are only observed at the endpoints, where the measurements are affected by the design of the end of the guide casing embedded and the works in its vicinity.

Table 2. Comparison of calculated settlements for ground models developed by machine (ML) with Horizontal Inclinometer Measurements (HINK).

	HINK	**ML**
Section	Settlements (mm)	
km 1.500	106.14	126.72
km 2.081	123.44	113.20
km 6.416	292.64	287.48
km 6.653	270.96	257.58

4 CONCLUSIONS

This paper was focused on a real case of application of artificial intelligence in construction practice.

To determine ground settlement, it was necessary to create a spatial engineering geological ground model of the motorway section D1 Budimír-Bidovce, which included information about groundwater, soil horizons, and their geotechnical characteristics.

The presented predictive model can deliver robust and fast ground model development used for quantitative analysis of soil conditions at given site. The effectiveness of used approach was demonstrated on example of settlement analysis. Calculation of 111 settlement profiles takes only tens of minutes. The increase in robustness of the presented approach is enhanced by combining it with Building Information Modeling (BIM) and Geographic Information System (GIS) tools.

ACKNOWLEDGEMENTS

The authors are grateful for the financial support provided by Grant Agency of the Ministry of Education, Science, Research and Sport of the Slovak Republic. The project presented in this article is supported by grant project VEGA-1/0745/21.

REFERENCES

American Society for Testing and Materials. (2017). ASTM D2487-17. Standard Practice for Classification of Soils for Engineering Purposes (Unified Soil Classification System). West Conshohocken, PA, 2017: ASTM International.

Cressie, N. (1990). The Origins of Kriging. Mathematical Geology, 239-252. https://doi.org/10.1007/BF00889887

Cruz, M., Santos, J. M., & Cruz, N. (2013). Estimating the Maximum Shear Modulus with Neural Networks. Recent Trends in Applied Artificial Intelligence, Amsterdam, Netherlands, 684-693.

Goh, A., & Goh, S. (2007). Support vector machines: Thier use in geotechnical engineering as illsutrated using seismic liquefaction data. Computers and Geotechnics, 34, 410-421. https://doi.org/10.1016/j.compgeo.2007.06.001

Samui, P., & Sitharam, T. (2011). Machine learning modelling for predicting soil liquefaction susceptibility. Natural Hazards and Earth System Sciences, 11, 1-9. https://doi.org/10.5194/nhess-11-1-2011

Šapina, M. (2016). A Comparison of Artificial Neural Networks and Ordinary Kriging depth maps of the Lower and Upper Pannonian stage border in the Bjelovar Subdepression, Northern Croatia. The Mining - Geology - Petroleum Engineering Bulletin, 75-86.

Tsiaousi, D., Travasarou, T., Drosos, V., Ugalde, J., & Chacko, J. (2018). Machine Learning Applications for Site Characterization Based on CPT Data. Geotechnical Earthquake Engineering and Soil Dynamics, COnference, Austin, Texas, V, 461-472.

Yang, B., Yin, K., Lacasse, S. & Liu, Z. (2019). Time series analysis and long short-term memory neural network to predict landslide displacement. Landslides, 16 (4), pp. 677-694. DOI 10.1007/s10346-018-01127-x

Zhou, Y., & Wu, X. (1994). Use of Neural Networks in the Analysis and Interpretation of Site Investigation Data. Computers and Geotechnics, 16 (2), 105-122. https://doi.org/10.1016/0266-352X(94)90017-5

Proceedings of the XVIII ECSMGE 2024
GEOTECHNICAL ENGINEERING CHALLENGES
TO MEET CURRENT AND EMERGING NEEDS OF SOCIETY
© 2024 the Authors
ISBN 978-1-032-54816-6
DOI 10.1201/9781003431749-44
Open Access: www.taylorfrancis.com, CC BY-NC-ND 4.0 license

ECSMGE 24
XVIII EUROPEAN CONFERENCE ON SOIL MECHANICS AND GEOTECHNICAL ENGINEERING

Automatic parameter calibration of advanced constitutive soil models and application to a boundary value problem

Calibration automatique des paramètres des modèles constitutifs avancés du sol et application à un problème de valeur limite

F. Brosz*, J. Machaček, H. Zachert
Department of Civil and Environmental Engineering, Institute of Geotechnics, Technical University of Darmstadt, Darmstadt, Germany

**frederik.brosz@tu-darmstadt.de*

ABSTRACT: Simulating the nonlinear and anelastic behaviour of soils under monotonic and cyclic loading requires advanced constitutive models. Determining the parameters of these models is often time-consuming and requires a high level of expertise. Automatic calibration can help to simplify and speed up the calibration process and increase the accessibility of advanced soil models to less experienced users. In this paper, the automatic parameter calibration of the parameters for monotonic and cyclic loading is presented for Hypoplasticity with Intergranular Strain and SANISAND. The calibration is performed based on the results of drained and undrained monotonic triaxial tests, oedometric compression tests and undrained cyclic triaxial tests on sand. A thorough comparison of simulations with a manual calibration and the experimental data is presented. Hints on the transfer to a boundary value problem and on the robustness of the automatically calibrated parameters are given. It is shown that the automatic parameter calibration improves the accuracy of the constitutive model predictions.

RÉSUMÉ: La simulation du comportement non linéaire et anélastique des sols soumis à des charges monotones et cycliques nécessite des modèles constitutifs avancés. La détermination des paramètres de ces modèles prend souvent beaucoup de temps et nécessite un haut niveau d'expertise. L'étalonnage automatique peut contribuer à simplifier et à accélérer le processus d'étalonnage et à rendre les modèles de sol avancés plus accessibles aux utilisateurs moins expérimentés. Dans cet article, la calibration automatique des paramètres pour les charges monotones et cycliques est présentée pour Hypoplasticity with Intergranular Strain et SANISAND. L'étalonnage est effectué sur la base des résultats d'essais triaxiaux monotones drainés et non drainés, d'essais de compression oedométrique et d'essais triaxiaux cycliques non drainés sur le sable. Une comparaison approfondie des simulations avec une calibration manuelle et les données expérimentales est présentée. Des indications sur le transfert à un problème de valeur limite et sur la robustesse des paramètres calibrés automatiquement sont données. Il est démontré que le calibrage automatique des paramètres améliore la précision des prédictions du modèle constitutif.

Keywords: Constitutive model; automatic parameter calibration; monotonic and cyclic triaxial tests; heuristic optimization algorithms.

1 INTRODUCTION

Calibrating the parameters of soil constitutive models manually remains a complex and time-intensive task which requires a deep understanding of the model's features. Frequently, the model's parameters cannot be determined based on specific experiments or empirical relations. Instead, iterative adjustment of the parameters by back-calculating results from laboratory tests is often required. Throughout this process, the parameters undergo continuous refinement until a satisfactory agreement between the simulation and experimental data is reached. Thereby, the effort typically concentrates on refining one parameter, keeping the others fixed. Existing calibration software such as Ex-Calibre (Kadlíček et al., 2018) or GA-cal (Mendez et al., 2021) is limited to monotonic loading. The Automatic Calibration Tool numgeo-ACT was developed to simplify and speed up the calibration process for monotonic (Machaček et al., 2022) and cyclic loading (Brosz et al. 2023, Machaček and Staubach, 2023). In this work, the performance of numgeo-ACT is demonstrated by the calibration of a hypoplastic model (von Wolffersdorff, 1996) with Intergranular Strain extension (IGS) (Niemunis and Herle, 1997) and SANISAND-04 (Dafalias and Manzari, 2004). The results of the automatic parameter calibration are compared to the results of a manual

calibration (Wichtmann et al., 2019). The paper is structured as follows. Section 2 explains the automatic calibration software numgeo-ACT. Section 3 presents the setup used for the automatic parameter calibration while the results of the automatic parameter calibration and the comparison with a manual calibration are given in Section 4. Some hints on the transfer to a boundary value problem and on the robustness of the automatically calibrated parameters are given in Section 5.

2 NUMGEO-ACT

Numgeo-ACT[1] (Machaček et al., 2022) offers the possibility to automatically calibrate a large number of advanced constitutive soil models by using the freely accessible FE software numgeo (www.numgeo.de, Machaček and Staubach, 2021). The basis for the automatic calibration is a database containing all tests for the material to be calibrated (e.g. oedometric compression tests, monotonic/cyclic drained/undrained triaxial tests or simple shear tests). At the beginning of the calibration process, single element test simulations (1 finite element with one integration point) of all experiments stored in the database are performed with numgeo using an estimated set of parameters. The results of the simulations are then analysed and compared with the results of the experiments. A Fréchet distance measure (Eiter and Mannila, 1994) is used to calculate the discrepancy between simulation and experiment. To ensure that all variables have the same influence on the optimisation process, a comparison is made in scaled stress and strain planes according to the procedure documented in Machaček et al. (2022).

3 EXAMPLE CALIBRATION FOR KARLSRUHE FINE SAND

The experimental basis for the automatic parameter calibration (AC) is the database of Karlsruhe fine sand by Wichtmann and Triantafyllidis (2016a and 2016b). The parameters of the hypoplastic model $h_s, n, \alpha, \beta, e_{i0}, e_{c0}$ and e_{d0} and the parameters of the Intergranular Strain m_T, m_R, R, β_R and χ were calibrated simultaneously based on two oedometric compression tests, five drained and three undrained monotonic triaxial tests as well as six undrained cyclic triaxial tests. The critical friction angle was set to $\varphi_c = 33.1°$ according to Wichtmann et al. (2019) and was kept fixed during the optimisation process. For SANISAND-04, the parameters of the critical state λ, ξ, e_0, M_e und M_c were set according to Wichtmann et al. (2019) and a variation during the optimization of ± 5 % (Parameter λ, ξ and e_0) and ± 3 % (Parameter M_e and M_c) in relation to the initial value was allowed. The other parameters $G_0, m, h_0, \nu, n_b, n_d, A_0, c_h, z_{max}$ and c_z were optimized within the limits given in Table 2. Due to the limitations of the SANISAND-04 model in capturing the elasto-plastic response under constant-η loading (Taiebat and Dafalias, 2007), the oedometric compression tests were not included in the calibration. The results of the automatic parameter calibration are compared to a manual calibration with excellent simulation results (MC) presented by Wichtmann et al. (2019) on the same sand. It is worth mentioning that the experimental tests used in the MC differ slightly from the experimental tests used in the AC. In this work, the same numerical platform and implementation was used for AC and the back-calculations with the MC.

4 RESULTS & COMPARISON WITH MANUAL CALIBRATION

4.1 Hypoplasticity with IGS extension

The parameters calibrated by AC are presented in Table 1 together with the corresponding upper and lower parameter bounds for the hypoplastic model with IGS extension. A comparison of the results of the AC (red curves) with the results of the MC (blue curves) is given for the monotonic tests in Figure 1 and for the undrained cyclic triaxial tests in Figure 2. The initial stiffness and the deviatoric peak stresses of the drained monotonic triaxial tests are captured well by the AC and the MC, while the predictions of both approaches for the dilatancy behaviour deviate partly from the experimental results (Figure 1, upper row). The predictions of the undrained monotonic triaxial tests and the oedometric compression tests are in good agreement with the experimental data (Figure 1, lower row).

The comparison of the AC with the MC is given for the undrained cyclic triaxial tests in Figure 2 for the $p - q$ plane (p: mean effective stress, q: deviatoric stress). Again, AC and MC lead to very similar results.

Compared to the experiments, both approaches predict a too contractive behaviour during the first cycle, while all further cycles agree better with the experiments. The predictions of both approaches do not reach zero mean effective stress, instead the simulations end up in a lens-shape behaviour (a known shortcoming of the hypoplastic model with IGS). The

[1] https://github.com/j-machacek/ numgeo-ACT

prediction of the decrease of mean effective stress simulated with the parameters of the AC lead to a better agreement with the experimental results of the tests no. 1 and 5 reaching smaller mean effective stress for the same number of loading cycles (Figure 2). This shows that numgeo-ACT is able to find parameters which predict the cyclic loading slightly better than the MC. Given the models capabilities, both approaches predict the experimental data sufficiently well under monotonic and cyclic loading.

Table 1. Results of the automatic parameter calibration (AC), best fit parameters for the hypoplastic model with IGS extension with corresponding bounds.

Parameter	best fit value	Lower bound	Upper bound
φ_c / rad	0.578	-	-
h_s / GPa	17.5	0.001	45
n / -	0.21	0.1	0.5
e_{d0} / -	0.615	0.609	0.745
e_{c0} / -	1.091	1.049	1.166
e_{i0} / e_{c0} / -	1.11	1.05	1.30
α / -	0.17	0	0.5
β / -	2.91	0.1	6
m_T / -	1.1	1.1	10
m_R / -	5.7	2	10
R / -	2.47E-04	1.0E-04	2.5E-04
β_R / -	0.30	0.05	1.4
χ / -	0.86	0.4	7

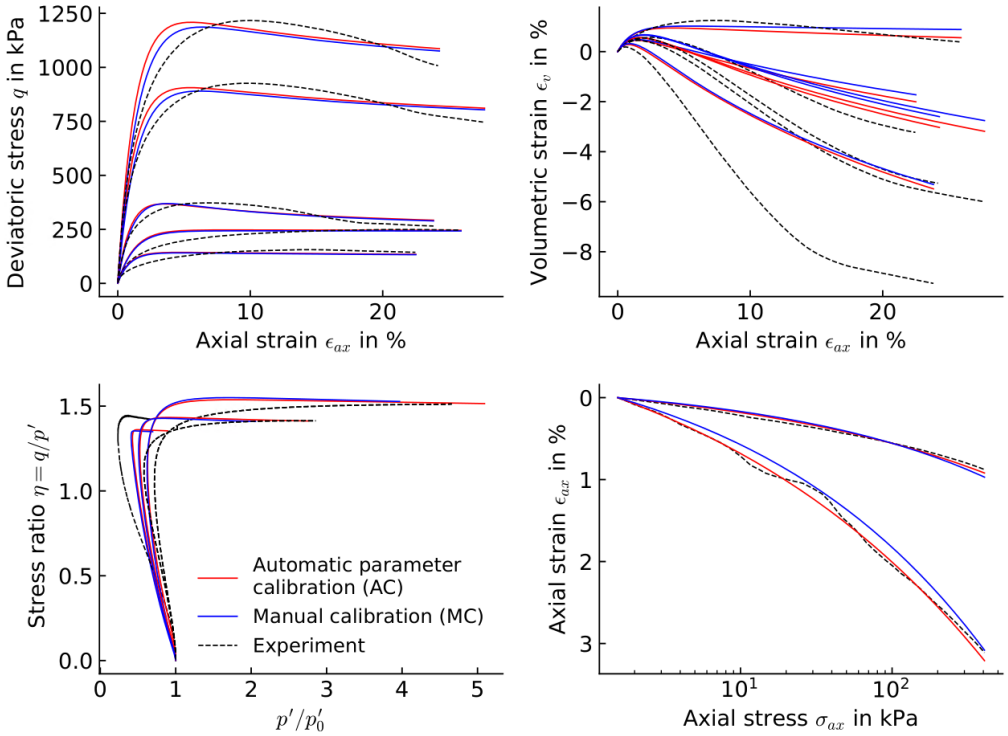

Figure 1. Comparison of the results of the automatic parameter calibration (AC, red curves) with the results of the manual calibration (MC, blue curves) for Hypoplasticity with IGS for drained monotonic triaxial tests (upper row), undrained monotonic triaxial tests (lower row, left) and oedometric compression tests (lower row, right).

4.2 SANISAND-04

The parameters for the SANISAND-04 model obtained by AC are presented in Table 2 together with the corresponding upper and lower parameter bounds. A comparison between the AC and the MC is presented for the monotonic tests in Figure 3 and for the cyclic tests by means of the excess pore water pressure in Figure 4.

As noticed for the hypoplastic model with IGS extension (Section 4.1), the predictions with AC are in very good agreement with the MC for SANISAND-04 for monotonic loading (Figure 3). Comparing the results of the cyclic tests, it is evident that the predictions of the AC for the trend of pore water pressure are in better agreement with the experiments than those of the MC.

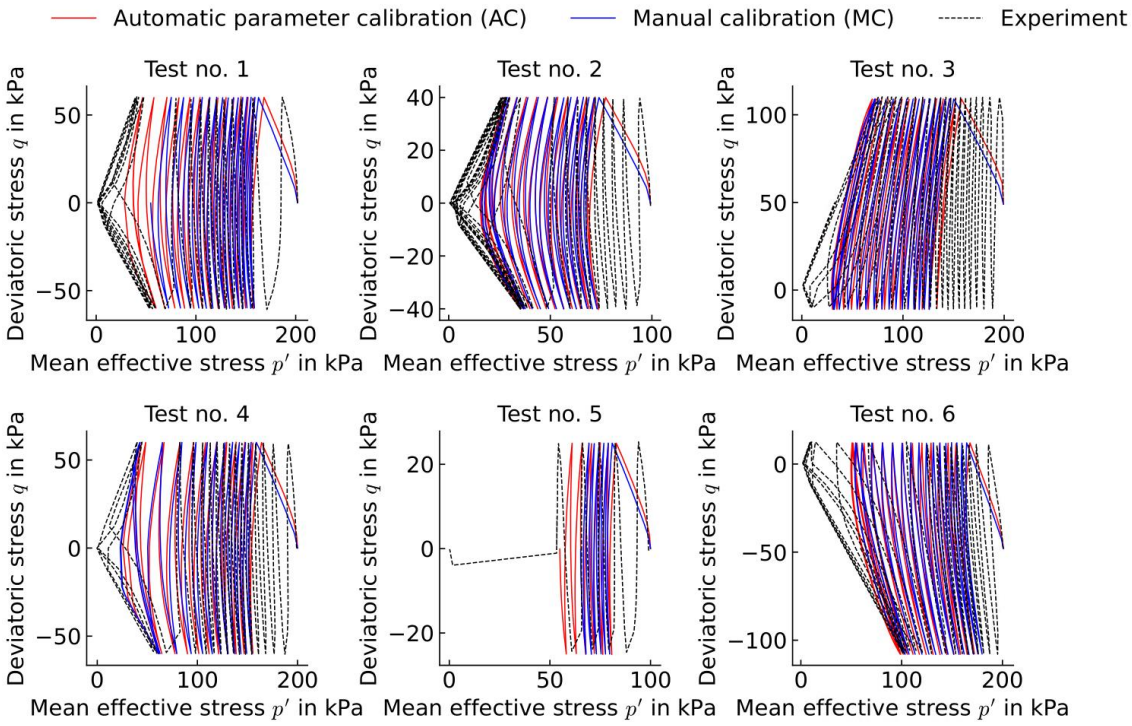

Figure 2. Comparison of the results of the automatic parameter calibration (AC, red curves) with the results of the manual calibration (MC, blue curves) for Hypoplasticity with IGS for undrained cyclic triaxial tests.

The MC predicts a too rapid increase of the porewater pressure compared to the experiments. Both approaches AC and MC reach zero effective stress in five out of 6 experiments.

5 ROBUSTNESS

The reproductability of the automatic parameter calibration was shown by Machaček et al. (2022). The robustness of automatically calibrated parameters in the application is shown using a boundary value problem of an earthquake-prone embankment which is based on centrifuge tests with Nevada sand by Muraleetharan et al. (2004). For the automatic parameter calibration of Nevada sand, four drained monotonic triaxial tests with constant mean effective stress, four undrained monotonic triaxial tests, two isotropic compression tests and two undrained cyclic triaxial tests were considered. For the SANISAND-04 model, the results are provided in Machaček and Staubach (2023).

6 SUMMARY AND CONCLUSION

The automatic parameter calibration software numgeo-ACT was developed to calibrate advanced constitutive soil models for monotonic and cyclic loading. Its performance was demonstrated by the parameter calibration for a hypoplastic model with Intergranular Strain and for SANISAND-04. The parameters for monotonic and cyclic loading were calibrated simultaneously based on two oedometric compression tests, five drained monotonic triaxial tests, three undrained monotonic triaxial tests and six undrained cyclic triaxial tests on soil samples of Karlsruhe fine sand.

Table 2. Results of the automatic parameter calibration (AC), best fit parameters for SANISAND-04 with corresponding bounds.

Para-meter	Best fit value	Lower bound	Upper bound
G_0 / kPa	66.1	50	200
υ / -	0.03	0.001	0.1
M_c / -	1.34	1.295	1.375
M_e / -	0.93	0.896	0.952
λ_c / -	0.121	0.116	0.128
e_0 / -	1.100	1.048	1.158
ξ / -	0.204	0.195	0.215
m / -	0.026	0.005	0.05
h_0 / -	16.9	1	20
c_h / -	0.73	0.3	1.1
n_b / -	1.1	0.6	2.5
A_0 / -	1.05	0.2	1.4
n_d / -	2.26	0.5	4
z_{max} / -	12.5	1	60
c_z / -	315	50	10000

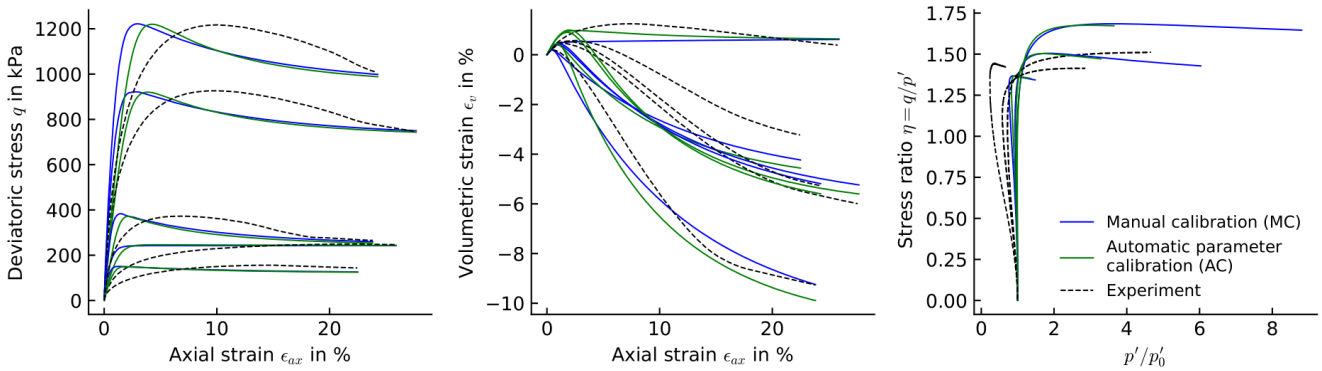

Figure 3. Comparison of the results of the automatic parameter calibration (AC, green curves) with the results of the manual calibration (MC, blue curves) for SANISAND-04 for drained monotonic triaxial tests (left and centre) and undrained monotonic triaxial tests (right).

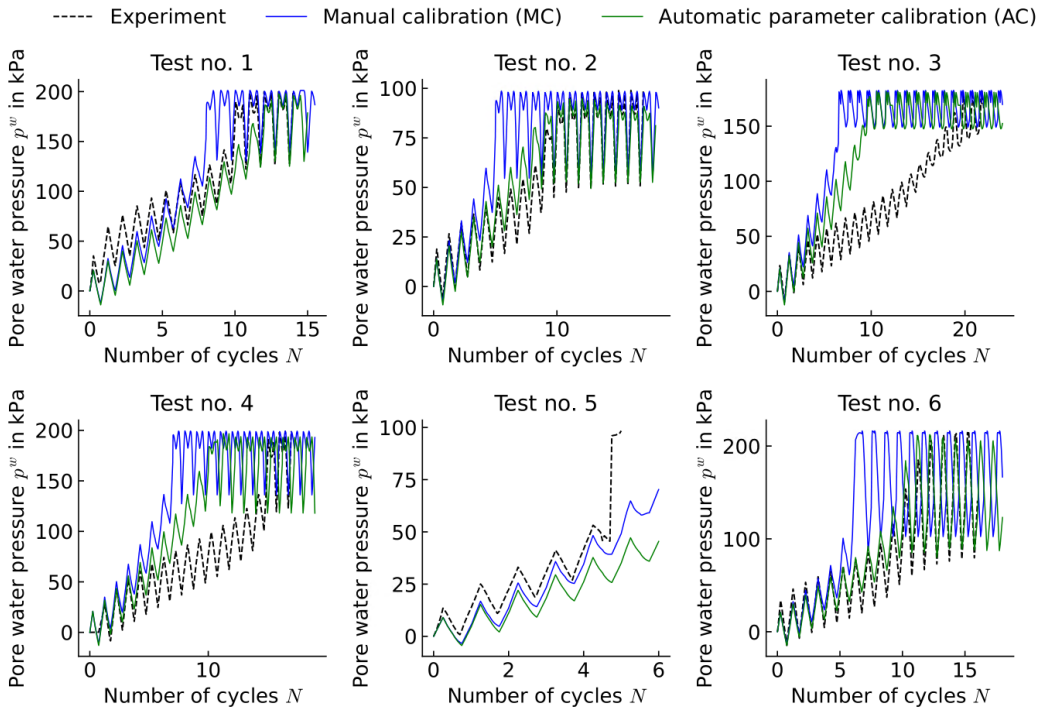

Figure 4. Comparison of the results of the automatic parameter calibration (AC, green curves) with the results of the manual calibration (MC, blue curves) for SANISAND-04 for undrained cyclic triaxial tests.

The results of the automatic parameter calibration were then compared to the results of a manual calibration from Wichtmann et al. Both approaches lead to very similar results and fit the experimental data of the monotonic and cyclic tests quite well. The automatically calibrated parameters give slightly better predictions of the pore water pressure build-up of the undrained cyclic triaxial tests. numgeo-ACT has proven to be an efficient and reliable tool to derive parameter sets for advanced constitutive soil models and allows for an optimised simulation of soil behaviour under monotonic and cyclic loading (Machaček et al., 2022, 2023 and Brosz et al., 2023).

7 REFERENCES

Brosz, F., Machaček, J. and Zachert, H. (2023). Automatic parameter calibration of two sophisticated soil models based on monotonic and cyclic tests on sand. 10th European conference on numerical methods in geotechnical engineering, Proceedings 10th NUMGE 2023, Imp. College London. https://doi.org/10.53243/NUMGE2023-415.

Dafalias, Y.F. and Manzari, M.T. (2004). Simple plasticity sand model accounting for fabric change effects. *Journal of engineering mechanics,* 130(6):. 622–634.

Eiter, T. and Mannila, H. (1994). Computing discrete fréchet distance. Tech. Rep. CD-TR 94/64, TU Vienna, Austria.

Kadlíček T., Janda T., Sejnoha M. (2018). Automatic online calibration software EXCALIBRE. 24th international conference engineering mechanics 2018, pp 353–356. https://doi.org/10.21495/91-8-353.

Machaček, J. and Staubach, P. (2021). A finite-element program for the simulation of hydro-mechanically coupled geotechnical processes. German society for Geotechnics e.V. Würzburg.

Machaček, J., Staubach, P., Tavera, C.E.G, Wichtmann, T. and Zachert, H. (2022). On the automatic parameter calibration of a hypoplastic soil model. *Acta Geotechnica*, 17(11): 5253–5273. https://doi.org/10.1007/s11440-022-01669-4.

Machaček, J., Siegel, S., Staubach, P. and Zachert, H. (2023). Automatic Parameter Calibration of Two Advanced Constitutive Models. Challenges and Innovations in Geomechanics, vol. 288, M. Barla, A. Di Donna, D. Sterpi, and A. Insana, Eds. Cham: Springer International Publishing, pp. 110–117. https://doi.org/10.1007/978-3-031-12851-6_14.

Machaček, J. and Staubach, P. (2023). Entwicklungen in der numerischen Modellierung geotechnischer Randwertprobleme. *Bautechnik*, vol. 100(9): 1–12, 2023. https://doi.org/10.1002/bate.202300060.

Mendez, F.J., Pasculli, A., Mendez, M.A.; Sciarra, N. (2021). Calibration of a hypoplastic model using genetic algorithms. *Acta Geotechnica*, 16, 2031-2047. https://doi.org/10.1007/s11440-020-01135-z.

Muraleetharan, K., Deshpande, S., Adalier, K. (2004). Dynamic deformations in sand embankments: centrifuge modelling and blind, fully coupled analyses. *Canadian geotechnical journal*, 41: 48-69.

Niemunis, A. and Herle, I. (1997). Hypoplastic model for cohesionless soils with elastic strain range. Mechanics of cohesive-frictional materials, 2(4): 279–299.

Taiebat, M. and Dafalias, Y.F. (2007). SANISAND: Simple anisotropic sand plasticity model. *Numerical and analytical methods in geomechanics*, 32(8): 915-948. https://doi.org/10.1002/nag.651.

von Wolffersdorff, P.-A. (1996). A hypoplastic relation for granular materials with a predefined limit state surface. *Mechanics of cohesive-frictional materials*, 3(3):. 251–271.

Wichtmann, T. and Triantafyllidis, T. (2016a). An experimental database for the development, calibration and verification of constitutive models for sand with focus to cyclic loading: part I—tests with monotonic loading and stress cycles. *Acta Geotechnica*, 11(4): 739–761. https://doi.org/10.1007/s11440-015-0402-z.

Wichtmann, T. and Triantafyllidis, T. (2016b). An experimental database for the development, calibration and verification of constitutive models for sand with focus to cyclic loading: part II—tests with strain cycles and combined loading. *Acta Geotechnica*, 11(4): 763–774. https://doi.org/10.1007/s11440-015-0412-x.

Wichtmann, T., Fuentes and W., Triantafyllidis, T. (2019). Inspection of three sophisticated constitutive models based on monotonic and cyclic tests on fine sand: Hypoplasticity vs. Sanisand vs. ISA. *Soil dynamics and earthquake engineering*, 124:172-183. https://doi.org/10.1016/j.soildyn.2019.05.001.

Proceedings of the XVIII ECSMGE 2024
GEOTECHNICAL ENGINEERING CHALLENGES
TO MEET CURRENT AND EMERGING NEEDS OF SOCIETY
© 2024 the Authors
ISBN 978-1-032-54816-6
DOI 10.1201/9781003431749-45
Open Access: www.taylorfrancis.com, CC BY-NC-ND 4.0 license

ECSMGE 24
XVIII EUROPEAN CONFERENCE ON SOIL MECHANICS AND GEOTECHNICAL ENGINEERING

Mechanical features of stabilized soils with low cement content

Caractéristiques mécaniques des sols faiblement traités au ciment

M.A. Castaneda-Lopez*, T. Lenoir, L. Thorel
Université Gustave Eiffel, Bouguenais, France

J.-P. Sanfratello
Colas SA, Magny-les-Hameaux, France

**mario-alexander.castaneda-lopez@univ-eiffel.fr*

ABSTRACT: Soil chemical stabilization with cement is a common technique to enhance the engineering and mechanical properties of in situ soils according to stress rates imposed by civil engineering projects. Usually, moderate quantities of cement are used, around 5 to 10% of the dry material. However, cement manufacturing is one of the biggest sources of greenhouse gas emissions, specifically carbon dioxide. For this reason, reducing cement content by a few percent in geotechnical structures built with cement stabilized soils (CSS) has a high environmental interest, particularly in view of the involved volumes of material. This work aims to contribute to a better understanding of the mechanical characteristics of stabilized soils with low cement contents. First, the mechanical behavior of a soil treated with 3% cement was studied for several curing times. Next, measured fracture parameters were correlated. Finally, these measurements were used to characterize the Mohr-Coulomb (MC) failure criterion. Results showed a high correlation between compressive and MC parameters. An alternative method for estimating MC parameters for CSS based on tensile and compressive properties was successfully checked. The proposed approach can be used to determine design parameters for geotechnical structures.

RÉSUMÉ: Dans les projets de Génie Civil, le traitement des sols au ciment est une technique courante pour améliorer les propriétés techniques et mécaniques des sols en place. En général, les quantités de ciment utilisé sont modérées, de l'ordre de 5 et 10 % du matériau sec. Toutefois, la fabrication du ciment est l'une des sources d'émission les plus importantes de gaz à effet de serre et en particulier de dioxyde de carbone. C'est pourquoi, réduire de quelques pourcent la teneur de ciment dans les structures géotechniques réalisées avec des sols traités présente un intérêt environnemental certain, notamment en raison des volumes de matériau impliqué. Ce travail vise à contribuer à une meilleure compréhension des caractéristiques mécaniques des sols faiblement traités. Pour commencer, le comportement mécanique d'un sol traité avec 3% de ciment a été étudié pour plusieurs temps de cure. Ensuite, les liens entre les différents paramètres de rupture mesurés ont été établis par corrélation. Enfin, ces mesures ont permis de caractériser le critère de rupture de Mohr-Coulomb. Les résultats ont montré une forte corrélation entre les paramètres de compression et les paramètres de MC. Une méthode alternative d'estimation des paramètres MC pour le CSS basée sur les propriétés de traction et de compression a été vérifiée avec succès. L'approche proposée peut être mise en œuvre pour obtenir les paramètres de dimensionnement des structures géotechniques.

Keywords: Cement-stabilized soils; earthworks, correlation analysis, Mohr-Coulomb.

1 INTRODUCTION

Cement stabilization of soils is a common technique to enhance the engineering and mechanical properties of in situ soils according to stress rates imposed by civil engineering projects (Correia et al., 2019; Preteseille & Lenoir, 2016). Use of cement-stabilized soils (CSS) cover a wide range of civil engineering applications such as embankments, foundations, slope protection, pavements and rail construction (Consoli et al., 2007; Diambra et al., 2018).

CSS constitute an intermediate class of geomaterials whose mechanical behavior is at the boundary between soil and rock mechanics (Lenoir et al., 2021; Schnaid et al., 2001). Compressive and tensile strength are widely employed as indicators of stabilization. Whereas compressive strength is linked to granular packing and bonding compounds, tensile strength is more related to the amount of cementitious compounds (Consoli et al., 2001). However, these characteristics represent a defined state of stresses and don't necessarily match with the service state of stresses of structures.

It is generally accepted that the failure mode of CSS can be represented with the Mohr-Coulomb (MC) criterion (Schnaid et al., 2001). Use of compressive and tensile properties to determine MC parameters for design purposes is related in literature (Lenoir et al.,

2021; Piratheepan et al., 2012; Sivakugan et al., 2014). Using direct and indirect measurements, the present work investigates the shear strength of a low-cement treated clayey soil.

2 MATERIALS AND METHODS

2.1 Materials

2.1.1 Soil

Studied material (A) was collected from the covering soil of an aggregate quarry at Soignies, Belgium (50° 34' 25.759'' N, 4° 2' 16.476'' E). The grain size curve is shown in Figure 1.

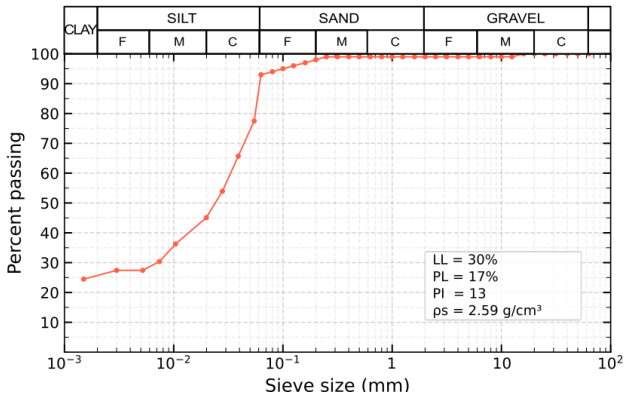

Figure 1. Particle-size distribution. F: fine, M: medium, C: coarse. PL: plastic limit, LL: liquid limit, PI: plastic index and ρ_s specific mass.

The soil is classified as A-6 (11), CL and A2 following the AASHTO (M 145-91), USCS (ASTM D2487-17) and GTR (NF P11-300) classification systems. The clay activity (A) is low A = PI/clay content = 0.29, which suggest a not significant swelling potential. Natural moisture content is below the PI (liquidity index < 0).

2.1.2 Soil treatment

Soil was treated with 3% of Portland-limestone cement (weight of dry material) CEM II/A-LL 42.5 R (NF EN 197-1). Main constituents of the binder are clinker (80-94%) and limestone (6-20%). The Optimum Moisture Content (OMC) and Maximum Dry Density (MDD) were determined following the standard Proctor compaction tests (NF P94-093): OMC = 15.5%, MDD = 1.79 g/cm^3. Reference values for sample preparation are 96% of MDD at OMC.

Samples were tested after several curing times (CT): 7, 28, 90, 180 and 360 days. For curing, samples were stored in a room with temperature controlled at 20 °C in plastic bags to keep constant moisture content.

2.2 Experiments

Experimental program is summarized in Table 1. For Unconfined Compression Strength test (UCS), Direct Tensile Strength test (DTS) and Indirect Tensile Strength test (ITS), tests are carried out on a Zwick/Roell Z150 press. Crosshead speed was 0.1 mm/min for UCS and DTS and 0.3 mm/min for ITS.

2.2.1 UCS

Tests followed the standard EN 13286-41:2021. Principle of testing is presented in Figure 2 (a). The maximum load registered, corresponding to the failure load, is equal to the UCS. Due to it is a compressive load, its value is positive.

2.2.2 DTS

Tests followed the standard EN 13286-40. As vertical load is a traction load, its value is negative (Figure 2 (b)). Minimal value corresponds to the DTS.

2.2.3 ITS

Tests followed the standard NF EN 13286-42. Principle of test is displayed in Figure 2 (c). Analytical solution of stresses at the center of the specimen during ITS test is used to construct the stress tensor (Piratheepan et al., 2012; Preteseille et al., 2014; Thompson, 1966).

2.2.4 Direct Shear test (DS)

Tests were carried out in a machine Sheartest VJT following the standard NF EN ISO 17892-10. Shear rate was 0.12 mm/min. The contact area used to calculate the normal (σ) and shear stress (τ) is corrected following the procedure proposed by (Skuodis & Tamošiūnas, 2014). Levels of normal stress varied between 2 and 250 kPa.

Table 1. Experimental program.

Test	Standard	D (mm)	H (mm)	CT (days)	Number of Samples	Number of Samples, total
UCS	EN 13286-41:2021	100	200		3	15
DTS	NF EN 13286-40	100	200	7, 28, 90,	3	15
ITS	NF EN 13286-42	100	100	180, 360	4	19
DS	NF EN ISO 17892-10	60	35		15	75

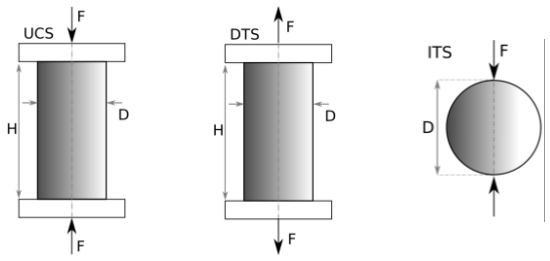

(a) (b) (c)

Figure 2. Characteristics of mechanical tests employed: (a) UCS, (b) DTS, (c) ITS.

3 RESULTS AND DISCUSSION

For UCS, DTS and ITS, mean values and standard deviation (SD) are presented in

Table 3. For DS, conventional linear regressions parameters c (cohesion) and φ (friction angle) corresponding to the MC criteria are presented for each CT with the coefficient of determination, R^2. R^2 is higher than 0.93 for 3 out of 5 CT studied, which suggest the suitability of this model to represent the failure characteristics of the studied material.

Linear regressions are used to represent UCS, DTS, ITS and cohesion as a function of CT (Xuan et al., 2012) following the eq. (1). Results, shown in

Table 3, reveal a good agreement between traction gain and CT. For UCS and c, unexpectedly, a poor correlation with CT is identified, with higher values for CT = 90 days. For φ, regressions also revealed a poor correlation (R^2=0.15).

$$y = a\,log_{10}(CT) + b \qquad (1)$$

Table 2. Regression models for experimental results.

Test	a	b	R^2
UCS (MPa)	0.338	1.281	0.403
DTS (MPa)	0.077	0.053	0.840
ITS (MPa)	0.063	0.074	0.842
c (MPa)	0.050	0.238	0.473

A comprehensive correlation between studied parameters was done (Figure 3). Results agree with the linear correlation between $Log_{10}CT$ and the tensile strength enhancement (Table 2).

DTS and ITS are highly correlated ($R_{DTS\text{-}ITS}$ = 1.00). The ratio DTS/ITS is 1.04±0.09. For practical purposes this ratio is assumed as 0.8 (SETRA & LCPC, 2000). A moderate correlation is also identified between UCS and MC parameters ($R_{UCS\text{-}c}$ = 0.73 and $R_{UCS\text{-}\phi}$ = 0.66). Correlation between the tensile strength (either DTS or ITS) and the MC parameters are moderated, with higher coefficients for cohesion ($R_{DTS\text{-}c}$ = 0.39, $R_{ITS\text{-}c}$ = 0.43).

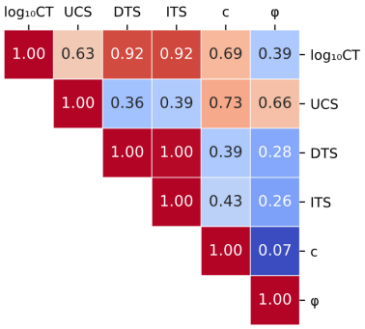

Figure 3. Correlation matrix of the dataset

Mean results after 7 days of cure are displayed in a $\{\sigma - \tau\}$ space in Figure 4. Here, principal stresses in the failure, i.e., the couple (σ_3, σ_1), are used to represent Mohr semi-circles for UCS $(0, UCS)$, DTS $(DTS, 0)$ and ITS $(ITS, -3ITS)$ (Jaeger et al., 2007). Direct shear results are depicted as both the couple (σ, τ) of individual tests (scatterplot) and the MC envelope (linear regression).

Results suggests a link between MC envelope and UCS and ITS values for a given CT as reported in the literature (Piratheepan et al., 2012). This approach states that the envelope of Mohr-Coulomb's failure corresponds to the tangent to the ITS and UCS semi-circles. Mathematically, it relies on either UCS or ITS, and the ratio $\xi = ITS/UCS$. This ratio varies within quite a narrow range 0.10 ± 0.02.

In Table 4, this approach is applied to the experimental dataset for a given CT and compared to the measured values from DS test. Results are in good agreement. When comparing the ratio between estimated and measured values, it varies between 0.84 and 1.22 with a mean of 1.07 for c and between 0.77 and 1.40 with a mean of 1.03 for φ.

It is interesting to remark that φ_ξ is close to a constant value (49.4±5.5°), which suggest that CT doesn't have effect on friction angle.

Table 3. Experimental results. Max and min values in bold

CT (days)	UCS (MPa)		DTS (MPa)		ITS (MPa)		DS		
	Mean	SD	Mean	SD	Mean	SD	c (MPa)	φ (°)	R^2
7	**1.53**	0.05	**0.13**	0.02	**0.14**	0.02	**0.24**	50.2	0.942
28	1.65	0.15	0.15	0.01	0.15	0.01	0.35	**36.3**	0.568
90	**2.41**	0.01	0.18	0.03	0.18	0.01	**0.37**	55.9	0.933
180	1.77	0.11	**0.26**	0.07	**0.23**	0.01	0.33	41.7	0.485
360	2.11	0.02	0.25	0.04	0.22	0.03	0.34	**62.0**	0.936

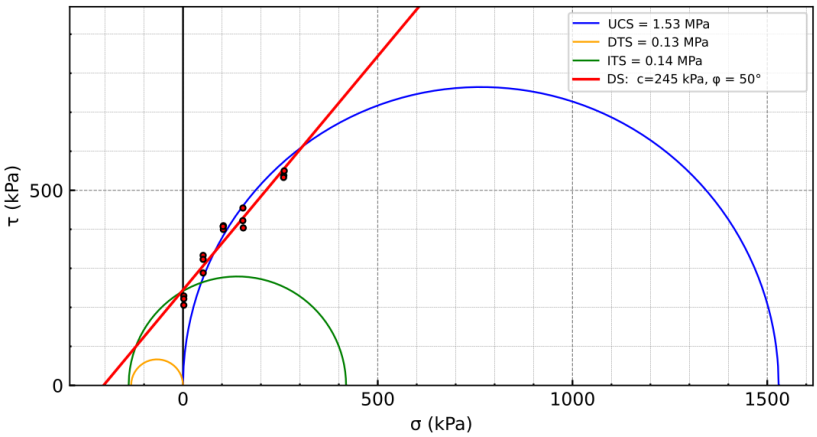

Figure 4. Mean results after 7 days of cure. UCS (blue), DTS (orange), ITS (green) and Direct shear (red).

Table 4. Measured (c, φ) and estimated (c_ξ, φ_ξ) MC param.

CT (days)	ξ	Estimated		$\frac{c_\xi}{c}$	$\frac{\varphi_\xi}{\varphi}$
		c_ξ kPa)	φ_ξ (°)		
7	0.09	271.0	51.0	1.11	1.02
28	0.09	293.4	50.9	0.84	1.40
90	0.07	368.8	56.0	0.99	1.00
180	0.13	402.9	41.0	1.22	0.98
360	0.10	405.0	48.0	1.18	0.77

4 CONCLUSIONS

This work shows that tensile properties are linearly correlated with curing time. Moreover, DTS≈ITS and DTS exhibit higher SD. The ITS/UCS ratio is 0.10.

For a given curing time, a good relationship is identified between UCS and MC parameters. The alternative method for estimating MC parameters for CSS based on ITS and UCS is successfully checked. Friction angle seems to be independent from CT.

ACKNOWLEDGEMENTS

The authors would like to thank the Gustave Eiffel University, Materials and Infrastructures Department (MAST) for the technical support and laboratory facilities to carry out this research.

REFERENCES

Consoli, N. C., Foppa, D., Festugato, L., & Heineck, K. S. (2007). Key Parameters for Strength Control of Artificially Cemented Soils. *Journal of Geotechnical and Geoenvironmental Engineering*, *133*(2), 197–205. https://doi.org/10.1061/(asce)1090-0241(2007)133:2(197).

Consoli, N. C., Prietto, P. D. M., Carraro, J. A. H., & Heineck, K. S. (2001). Behavior of Compacted Soil-Fly Ash-Carbide Lime Mixtures. *Journal of Geotechnical and Geoenvironmental Engineering*, *127*(9), 774–782. https://doi.org/10.1061/(ASCE)1090-0241(2001)127:9(774).

Correia, A. A. S., Venda Oliveira, P. J., & Lemos, L. J. L. (2019). Strength assessment of chemically stabilised soft soils. *Proceedings of the Institution of Civil Engineers: Geotechnical Engineering*, *172*(3), 218–227. https://doi.org/10.1680/jgeen.17.00011.

Diambra, A., Festugato, L., Ibraim, E., Peccin da Silva, A., & Consoli, N. C. (2018). Modelling tensile/compressive strength ratio of artificially cemented clean sand. *Soils and Foundations*, *58*(1), 199–211. https://doi.org/10.1016/j.sandf.2017.11.011.

Jaeger, J. C., Cook, N. G. W., & Zimmerman, R. (2007). *Fundamentals of Rock Mechanics* (4th ed.). Blackwell.

Lenoir, T., Dubreucq, T., Lambert, T., & Killinger, D. (2021). Safety factor calculation of a road structure with cement-modified loess as subgrade. *Transportation Geotechnics*, *30*(May), 100604. https://doi.org/10.1016/j.trgeo.2021.100604.

Piratheepan, J., Gnanendran, C. T., & Arulrajah, A. (2012). Determination of c and φ from IDT and Unconfined Compression Testing and Numerical Analysis. *Journal of Materials in Civil Engineering*, *24*(9), 1153–1164. https://doi.org/10.1061/(asce)mt.1943-5533.0000493.

Preteseille, M., & Lenoir, T. (2016). Mechanical Fatigue of a Stabilized/Treated Soil Tested with Uniaxial and Biaxial Flexural Tests. *Transportation Research Procedia*, *14*(December), 1923–1929. https://doi.org/10.1016/j.trpro.2016.05.159.

Preteseille, M., Lenoir, T., Gennesseaux, E., & Hornych, P. (2014). Structural test at the laboratory scale for the utilization of stabilized fine-grained soils in the subgrades of High Speed Rail infrastructures: Analytical and numerical aspects. *Construction and Building Materials*, *61*, 164–171. https://doi.org/10.1016/j.conbuildmat.2014.02.069.

Schnaid, F., Prietto, P. D. M., & Consoli, N. C. (2001). Characterization of Cemented Sand in Triaxial Compression. *Journal of Geotechnical and Geoenvironmental Engineering*, *127*(10), 857–868. https://doi.org/10.1061/(ASCE)1090-0241(2001)127:10(857).

SETRA, & LCPC. (2000). *Réalisation des remblais et des*

couches de forme (GTR) (Cerema (ed.); 2nd ed.).

Sivakugan, N., Das, B. M., Lovisa, J., & Patra, C. R. (2014). Determination of c and Φ of rocks from indirect tensile strength and uniaxial compression tests. *International Journal of Geotechnical Engineering*, *8*(1), 59–65. https://doi.org/10.1179/1938636213Z.00000000053.

Skuodis, Š., & Tamošiūnas, T. (2014). Direct Shear Tests with Evaluation of Variable Shearing Area. *Mokslas – Lietuvos Ateitis*, *6*(5), 499–503. https://doi.org/10.3846/mla.2014.692.

Thompson, M. R. (1966). *Split Tensile Strength of Lime-Stabilized Soils*. 69–82. https://trid.trb.org/view/121697

Xuan, D. X., Houben, L. J. M., Molenaar, A. A. A., & Shui, Z. H. (2012). Mechanical properties of cement-treated aggregate material – A review. *Materials & Design*, *33*(1), 496–502. https://doi.org/10.1016/j.matdes.2011.04.055.

Proceedings of the XVIII ECSMGE 2024
GEOTECHNICAL ENGINEERING CHALLENGES
TO MEET CURRENT AND EMERGING NEEDS OF SOCIETY
© 2024 the Authors
ISBN 978-1-032-54816-6
DOI 10.1201/9781003431749-46
Open Access: www.taylorfrancis.com, CC BY-NC-ND 4.0 license

ECSMGE 24
XVIII EUROPEAN CONFERENCE ON SOIL MECHANICS AND GEOTECHNICAL ENGINEERING

Application of optimization algorithms in geotechnical engineering as decision-making support tool

Application des algorithmes d'optimisation en génie géotechnique comme outil de soutien à la prise de décision

K. Cerek*, E. Hadjiloo, J. Grabe
Hamburg University of Technology, Hamburg, Germany
**kacper.cerek@tuhh.de*

ABSTRACT: This paper advocates for climate-responsive optimization in civil engineering, leveraging the NSGA-II algorithm. Conducting an in-depth study on a dike structure, the integration of pymoo with Plaxis 2023.2 via Python emerges as a potent decision support tool. Employing a plane strain approach with 15-noded triangular elements, the numerical model undergoes SRFEA for stability assessment. Three objectives, material demand (f1), LC2 exploitation (f2), and LC3 exploitation (f3), are systematically minimized by NSGA-II. Results, depicted in a Pareto surface, spotlight a wider spread for material demand, emphasizing its variability. Findings underscore the pivotal role of multi-objective algorithms in guiding sustainable civil engineering decisions amid climate change challenges.

RÉSUMÉ: Cet article plaide en faveur de l'optimisation adaptative au climat dans le génie civil, en exploitant l'algorithme NSGA-II. En menant une étude approfondie sur une structure de digue, l'intégration de pymoo avec Plaxis 2023.2 via Python émerge comme un puissant outil de soutien à la décision. En utilisant une approche de contrainte simple avec des éléments triangulaires à 15 nœuds, le modèle numérique fait l'objet d'une analyse de stabilité par SRFEA. Trois objectifs, la demande de matériaux (f1), l'exploitation LC2 (f2) et l'exploitation LC3 (f3), sont systématiquement minimisés par NSGA-II. Les résultats, représentés dans une surface de Pareto, mettent en lumière une plus grande variabilité de la demande de matériaux. Les conclusions soulignent le rôle central des algorithmes multi-objectifs dans la conduite de décisions durables en génie civil face aux défis du changement climatique.

Keywords: SRFEA; Multi-objective evolutionary algorithm; NSGA-II; decision support tool; dikes.

1 INTRODUCTION

The impact of climate change is compelling the civil engineering sector to prioritize the optimization of constructed structures. Geotechnical engineering frequently encounters the challenge of designing structures that must satisfy diverse objectives. The decision-making process regarding which solution to adopt for the final design is often intricate and far from straightforward.

This study is dedicated to present the advantages of employing a multi-objective evolutionary algorithm, NSGA-II, for the purpose of identifying trade-offs among various objectives. To achieve this, an extensive investigation of a dike structure has been undertaken in this paper, with the aim of discovering the most optimal solutions for three distinct objective functions.

2 GENERAL INFORMATION

2.1 Decision-making support tool

The following study presents implementation of a decision-making support tool, which enables users to make more reasonable and more optimal decisions considering their geotechnical problem. The presented routine incorporates multi-objective optimization framework *pymoo* (Blank and Deb, 2020) and integrates it via Python programming language (Van Rossum and Drake, 2009) with FEM-software Plaxis 2023.2 (Plaxis, 2023).

This paper implements the multi-objective Nondominated Sorting Genetic Algorithm (NSGA-II) from Deb et al. (2002), which offers an elitist-preserving approach. The NSGA-II combines a random parent population with its offspring in order to find a set of trade-offs which are represented by a Pereto-front, or a Pareto-surface, if there are more than two objectives defined. The algorithm has been succefully applied for solving multi-objective

geotechnical problems, e.g. Cerek and Grabe (2023), Cerek et al. (2023) and Das et al. (2016).

The self-programmed Python code triggers the FEM-simulations which deliver searched results. The outcomes are then evaluated by NSGA-II algorithm and the process repeats itself until predefined termination criteria are met. More to selection process of optimal solutions and set up of the algorithm can be found in Cerek and Grabe (2023) and Cerek et al. (2023). Once a set of trade-offs are found, the algorithm stops and a pareto-surface is displayed, where a user may find the problem's optimal solutions for defined objectives. Based on that, a fully aware decision might be made taken all important objectives into account.

Table 1. Soil parameters applied in FEM-model.

	Unit	Clay 1	Clay 2	Sand 1	Sand 2
γ_{unsat} (unsaturated unit weight)	(kN/m³)	16.0	15.0	18.0	19.0
γ_{sat} (saturated unit weight)	(kN/m³)	16.0	15.0	20.0	21.0
E' (Young´s modulus)	(MN/m²)	2.5	2.0	20.0	40.0
ν' (Poisson's ratio)	(-)	0.3	0.3	0.2	0.2
c' (effective cohesion)	(kN/m²)	10.0	10.0	0.1	0.1
s_u (undrained shear strength)	(kN/m²)	25.0	20.0	-	-
φ'* (effective friction angle)	(°)	17.5	17.5	30.0	35.0
ψ' (dilatancy angle)	(°)	0.0	0.0	5.0	5.0
$k_{x/y}$ (horizontal/vertical permeability)	(m/s)	$1.0E^{-9}$	$1.0E^{-10}$	$1.0E^{-4}$	$1.0E^{-4}$

* For undrained conditions, effective friction angle $\varphi' = 0.0°$

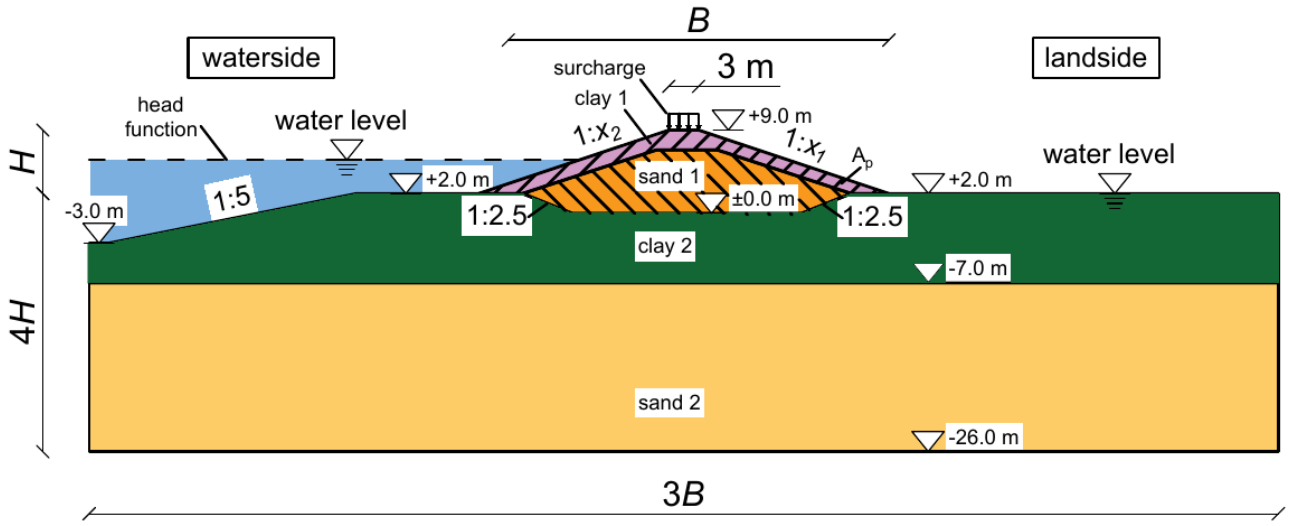

Figure 1. Model geometry.

2.2 Strength reduction finite element analysis (SRFEA)

In this research, all numerical simulations were performed using the commercial displacement-based finite element software Plaxis 2023.1 (Plaxis, 2023). The SRFEA was employed, which provides a Factor of Safety (*FoS*). The soil strength parameters were reduced until structural collapse was observed. Equation 1 outlines the formulation of *FoS*, with c', φ', and s_u representing the effective cohesion, effective friction angle, and undrained shear strength, respectively. The safety factors were not incorporated in our simulations, and all values represent characteristic data. Additionally, it's worth noting that, in the case of undrained shear strength, we solely applied a straightforward reduction of s_u.

$$FoS = \frac{\tan \varphi'}{\tan \varphi'_{mob}} = \frac{c'}{c'_{mob}} = \frac{s_u}{s_{u,mob}} \qquad (1)$$

3 NUMERICS

3.1 Numerical model

The finite element model employs a plane strain approach, employing 15-noded triangular elements. To ensure a dependable Factor of Safety (FoS), we meticulously refined the mesh by opting for a relative element size of 0.015. The total count of finite elements fluctuates based on individual model setups. In the interest of computational efficiency, we employed a coarser mesh for the lower soil layer without compromising model accuracy. Conversely, the mesh along the dike crest underwent refinement to accommodate the application of a line load.

In the scope of this study, we adopted a Mohr-Coulomb failure criterion. The model encompassed four distinct soil layers. It should be pointed out that fine-grained soil layers are modelled for undrained conditions, since quick loading rate is occuring within the simulation. The soil properties, as detailed in Table 1, and the model geometry, including the soil layers, are visually represented in Figure 1.

3.2 Model geometry

The selection of dimensions for the numerical model was guided by the recommendations provided by Mestat et al. (2004). These recommendations are based on correlations between the height of the dike H and the overall model depth, as well as between the width of the dike B and the total model width. The geometric configuration of the system is further characterized by two parametric variables, denoted as x_1 and x_2, which represent the horizontal components of the slope.

3.3 Calculation phases and loads

The model comprises four consecutive calculation phases. The initial phase, referred to as LC0, utilizes gravity loading to establish initial stresses. Subsequently, a plastic Nil-step phase (LC1) is executed, followed by a fully coupled flow-deformation analysis phase (LC2). In LC2, a head function is applied to the water level on the waterside of the dike. In the subsequent plastic calculation phase (LC3), a uniformly distributed surcharge load of 10.0 kN/m² is applied to the dike crest. Both LC2 and LC3 are followed by a safety analysis that incorporates SRFEA, as described in Section 2.2 of this paper.

Throughout all phases, the water level on the landside remains constant. In contrast, on the opposite side, it is initially set at +2.0 m. During the transient calculation phase, the water level progressively rises in a linear fashion up to +5.0 m. The critical load cases are indicated in Figure 1.

4 OPTIMIZATION PROBLEM

4.1 Problem definition

4.1.1 Variables

The geometry of the numerical model is parametrised by the horizontal components of the slope, as mentioned in Section 3.2. The lower boundaries x_l and upper boundaries x_u are given by Equations 2-3. The rounding of variables during the optimization process was set to two decimal places.

$$x_l = \{1.5; 1.5\} = \{x_{1,min}; x_{2,min}\} \quad (2)$$

$$x_u = \{4.5; 4.5\} = \{x_{1,max}; x_{2,max}\} \quad (3)$$

4.1.2 Objectives

This study delves into the intricacies of an optimization problem characterized by three semi-independent objectives, each represented by specific objective functions: f_1, f_2, and f_3 as detailed in Equations 4-6. Over successive algorithm generations, all objective functions are systematically minimized. Function f_1 pertains to the material demand A_p that is expresses by cross-sectional area. Both functions f_2 and f_3 are formulated as reciprocals of their respective FoS obtained from calculation phase LC2 or LC3.

$$f_1 = A_p \quad (4)$$

$$f_2 = \frac{1}{FoS_{LC2}} \quad (5)$$

$$f_3 = \frac{1}{FoS_{LC3}} \quad (6)$$

Consequently, optimization is performed for both horizontal components of the slope on the landside and waterside. This optimization is carried out with regard to minimizing material demand and ensuring a satisfactory factor of safety, both during the coupled flow-deformation analysis phase (LC2) and the plastic calculation phase (LC3).

5 STUDIES

This paper focuses on the multi-objective optimization of a dike structure using the NSGA-II algorithm. The algorithm, with an initial population of 100, was employed for this purpose. The termination criterion for design space tolerance was set to two decimal places, checked every second iteration to ensure a diverse range of outcomes.

Figure 2 depicts the results obtained from the optimization process. It is evident that the spread of solutions for the objective f_1 (material demand) is notably wider compared to f_2 and f_3. The Pareto surface

aids the decision-making process for the final design by offering an overview of possibilities.

The variables resulting from the optimization process are illustrated in Figure 3. It can be concluded that, for the selected objectives corresponding to defined load cases, a design with a steeper slope on the waterside is preferable, as the spread of solutions for this side is smaller. Conversely, results for the landside slope vary between the lower and upper boundaries.

Table 2 provides exemplary results for variables and objectives resulting from the optimization process (Sol1, Sol2), as well as for a traditional design (Sol3). It is crucial to emphasize that the difference in material demand between the presented solutions Sol1 and Sol2 is nearly 90%. This implies that choosing a design with a smoother landside slope would lead to a substantial increase in costs, CO2 footprint, and construction time. It should also be mentioned that the traditional design Sol3 would collapse under the applied surcharge load in LC3, even though it has flatter slopes and requires about 85% more material than Sol1.

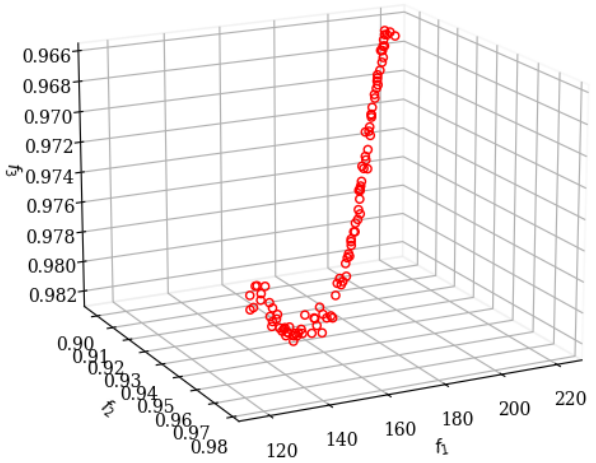

Figure 2. Pareto surface illustrating the optimization of three-objectives problem: f_1 – material demand; f_2 – exploitation for LC2; f_3 – exploitation for LC3.

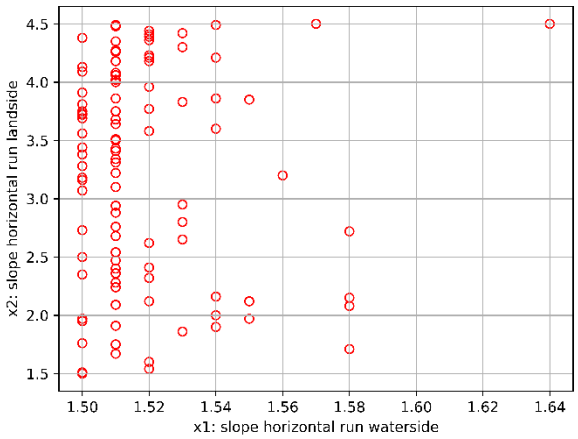

Figure 3. Results illustrating the optimization process variables x_1 and x_2 (horizontal components of the slope).

Table 2. Exemplary results of optimization process

	x_1	x_2	f_1	f_2	f_3
Sol1	1.50	1.51	117.65	0.98	0.98
Sol2	1.64	4.50	221.47	0.90	0.97
Sol3	3.00	3.00	216.60	0.95	>1.00

6 CONCLUSIONS

The study presented in this paper demonstrates that the application of multi-objective algorithms in the design process enhances problem understanding and provides a diverse set of solutions, which can be evaluated based on predefined objectives. The proposed routine, incorporating Finite Element Method (FEM) simulation and optimization techniques, has proven to be a valuable decision support tool in the design process, especially when dealing with numerous objectives that are challenging for classical human evaluation.

The adoption of this approach empowers engineers to make informed decisions, contributing to the creation of more sustainable structures. Consequently, it aids in the reduction and deceleration of climate changes caused by the civil engineering industry.

REFERENCES

Blank, J., Deb, K. (2020): Pymoo: Multi-Objective Optimization in Python. In IEEE Access 8, pp. 89497–89509. DOI: 10.1109/ACCESS.2020.2990567.

Cerek, K., Grabe, J. (2023): Numerical simulation and optimization of dike geometry using multi-objective evolutionary algorithm NSGA-II. In ISSMGE. DOI: 10.53243/NUMGE2023-80.

Cerek, K., Hadjiloo, E., Grabe, J. (2023): Sustainable dike adaptation measures using finite element method and optimization algorithm NSGA-II. (manuscript accepted). In GEOTEC Hanoi 2023.

Das, M.R., Purohit, S., Das, S.K. (2016): Multi-objective Optimization of Reinforced Cement Concrete Retaining Wall. In Indian Geotech J 46 (4), pp. 354–368. DOI: 10.1007/s40098-015-0178-y.

Deb, K., Pratap, A., Agarwal, S., Meyarivan, T. (2002): A fast and elitist multiobjective genetic algorithm: NSGA-II. In IEEE Trans. Evol. Computat. 6 (2), pp. 182–197. DOI: 10.1109/4235.996017.

Mestat, Ph., Bourgeois, E., Riou, Y. (2004): Numerical modelling of embankments and underground works. In Computers and Geotechnics 31 (3), pp. 227–236. DOI: 10.1016/j.compgeo.2004.01.003.

PLAXIS (2023): PLAXIS 2D 2023.1 Reference Manual. Edited by Bentley.

Van Rossum, G., Drake, F. L. (2009): Python 3 Reference Manual.: CA: CreateSpace.

Proceedings of the XVIII ECSMGE 2024
GEOTECHNICAL ENGINEERING CHALLENGES
TO MEET CURRENT AND EMERGING NEEDS OF SOCIETY
© 2024 the Authors
ISBN 978-1-032-54816-6
DOI 10.1201/9781003431749-47
Open Access: www.taylorfrancis.com, CC BY-NC-ND 4.0 license

ECSMGE 24
XVIII EUROPEAN CONFERENCE ON SOIL MECHANICS AND GEOTECHNICAL ENGINEERING

Performance-based interaction domains for pile groups

Domaines d'interaction basés sur les performances pour les groupes de pieux

R. Cesaro*, R. Di Laora, C. Iodice, A. Mandolini

Department of Engineering, Università della Campania "Luigi Vanvitelli", Aversa, Italy

**raffaele.cesaro@unicampania.it*

ABSTRACT: In many engineering problems the design of piles is ruled by a threshold acceptable value of absolute and differential settlements as well as rotations under working loads. To verify that settlements and rotations of a piled foundation, under some combined axial load-moment action, do not exceed acceptable values, the construction of 'performance-based' interaction domain would be a useful design tool. To this end, the response of pile groups subjected to combined actions including vertical load, Q, and moment components along x and y axes, M_x and M_y, is first investigated by means of a simple ad-hoc numerical code, fixing the settlement and/or rotation to a given threshold value. Closed-form expressions for the performance-based interaction domains in the Q-M_x-M_y space are then obtained by matching the numerical results. Due to the limited number of parameters involved, which are already required in routine design, the proposed domains can be easily employed for the design of pile groups.

RÉSUMÉ: Dans de nombreux problèmes d'ingénierie, la conception des pieux est déterminée par une valeur seuil acceptable des tassements absolus et différentiels, ainsi que des rotations sous des charges de travail. Pour vérifier que les tassements et les rotations d'une fondation sur pieux, soumise à une action combinée de charge axiale et de moment, ne dépassent pas les valeurs acceptables, la construction d'un domaine d'interaction "basé sur la performance" serait un outil de conception utile. À cette fin, la réponse de groupes de pieux soumis à des actions combinées, comprenant une charge verticale, Q, et des composantes de moment le long des axes x et y, M_x et M_y, est d'abord étudiée au moyen d'un code numérique simple ad hoc, en fixant le tassement ou la rotation à une valeur seuil donnée. Des expressions analytiques pour les domaines d'interaction basés sur la performance dans l'espace Q-M_x-M_y sont ensuite obtenues en mettant en correspondance les résultats numériques. En raison du nombre limité de paramètres impliqués, qui sont déjà nécessaires dans la conception courante, les domaines proposés peuvent être facilement utilisés dans la conception courante de groupes de pieux.

Keywords: Pile groups; eccentric loading; performance-based design; analytical solution.

1 INTRODUCTION

Piled foundations are designed to ensure an adequate safety margin against failure (Ultimate Limit State, ULS) and a satisfactory behaviour in terms of settlements and rotations under working loads (Serviceability Limit State, SLS). However, in many engineering problems the design is ruled by SLS checks, i.e., by some threshold values of settlements and/or rotation which must not be exceeded. The example of a wind turbine is paradigmatic in this sense, given that the foundation is generally designed not to exceed a rotation of 0.5° to guarantee that it is tolerated by the structure without loss of serviceability during the entire lifespan. In light of the above, employing interaction domains fixing acceptable values of settlements and/or rotations would facilitate the assessment of SLS requirements. While expressions for failure envelopes of pile groups under combined loads have been proposed by recent works (Di Laora et al., 2019 and 2022; Iovino et al., 2021; Sakellariadis and Anastasopoulos 2022; Cesaro et al., 2024), there are still no solutions available for performance-based interaction diagrams. To fill this lack, a simple numerical approach is first proposed to investigate the response of pile groups subjected to a vertical load, Q, and to an external moment vector inclined by the angle α_M with respect to the y axis (with M_x and M_y moment components along x and y axes, Figure 1), fixing settlements or rotations to a given value. Using the results obtained with the code as benchmarks, closed-form solutions for performance-based interaction diagrams are thereby provided which allow to assess all the combinations of loads leading to a specific value of displacement of the pile group. Note that the horizontal load component has been disregarded; this simplification is consistent with the design of tall structures (such as wind turbines or bridge piers) since, from an engineering viewpoint, in this case the horizontal load is usually negligible

compared to the vertical eccentric component. The proposed simple formulae are found to be in remarkable agreement with the more rigorous solution, and therefore represent a useful practical tool for the design of pile groups.

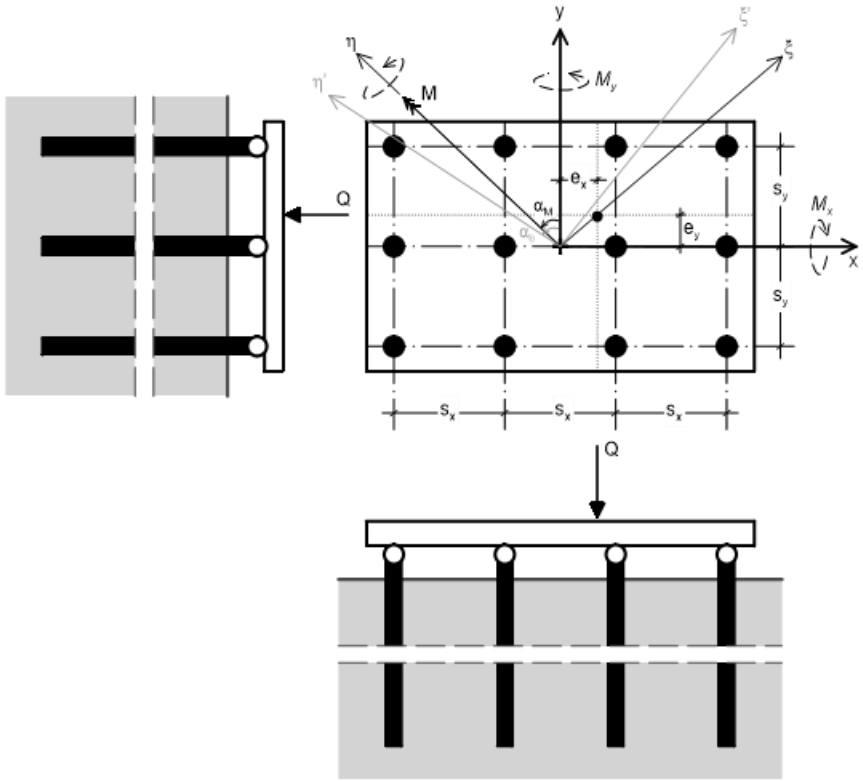

Figure 1. Pile group subjected to a vertical eccentric load (e_x and e_y, s_x and s_y are the eccentricities and the pile spacings along x and y axes, respectively).

2 NUMERICAL CODE

The numerical procedure to compute pile group settlement and rotation under an arbitrary load path and hence obtain the performance-based interaction diagrams, is detailed in the ensuing.

The following simplified assumptions have been made (Mandolini and Viggiani, 1997):

(a) Piles are modelled as uniaxial elements, characterized by a failure load in compression (N_u) and in uplift ($-S_u$), and by an elastic stiffness (k_s). The single pile load-settlement curve is described employing a hyperbolic relationship as suggested by Chin (1972) and the non-linearity is simulated using a stepwise linear incremental procedure;

(b) Piles heads are connected through a rigid free-standing cap having infinite strength;

(c) To account for pile group effects, interaction factors are used superimposing the effect of any pair of piles in the group (Poulos, 1968; Randolph and Wroth, 1979). Pile-to-pile interaction affects only the elastic component of the pile settlement because the non-linearity is essentially concentrated at the pile-soil interface (Randolph, 1994; Kanellopoulos and Gazetas, 2020).

As concerns the elastic axial stiffness, the adoption of a unique value for both compression and uplift is acceptable from an engineering standpoint since in many applications the base contribution is a small percentage of the total stiffness (Randolph and Wroth, 1978) and can thus be neglected. It should be pointed out that the numerical procedure can be employed by adopting a different load-settlement law to reproduce the load-settlement response of the single pile; likewise, the interaction coefficients can be evaluated by using one of the expressions and/or approaches available in literature. In this work the interaction coefficients, α_{ij}, are calculated using the approximated expression proposed by Randolph and Wroth (1979):

$$\alpha_{ij} = \frac{\ln(r_m/s_{ij})}{\ln(r_m/r)} \quad (1)$$

where s_{ij} is the distance between the piles i and j, r is the radius of pile j and r_m is the "magic radius", i.e., the distance at which the deformative field associated to

pile j displacement, and measured from its axis, is assumed to be negligible:

$$r_m = \left\{0.25 + [2.5\rho(1-\nu_s) - 0.25]\frac{G_L}{G_b}\right\} L \quad (2)$$

In the above equation L is the pile length; G_L and G_b are the soil shear moduli at the depth L and underneath pile base, respectively; ν_s is the Poisson's coefficient of the soil; ρ is a parameter depending on the soil homogeneity (equal to 1 for a homogeneous medium and to 0.5 for a "Gibson-type" soil), defined as $G_{L/2}/G_L$, where $G_{L/2}$ is the soil shear modulus at the depth $L/2$. As shown by Mylonakis and Gazetas (1998), for a floating pile the magic radius can be estimated as:

$$r_m \approx \chi_1\chi_2 L(1-\nu_s)\text{u} \quad (3)$$

where $\chi_1\chi_2$ is equal to 2.5 for an homogeneous halfsapce and 1 for a Gibson soil on rigid bedrock at depth 2.5L.

The elastic settlement, w_i, of a pile in the group of n piles, is given by:

$$w_i = \sum_{j=1}^{n} \frac{1}{k_{sj}} P_j \alpha_{ij} \quad (4)$$

Note that, the hypothesis (a) and (c) assure that the interaction factors do not vary with the load level. To account for pile non-linear behaviour under its own load, assuming Chin's hyperbole as the load-settlement curve for the single pile, the tangent compliance to be employed in the stepwise linear incremental procedure is given by:

$$\frac{dw_i}{dP_i} = \frac{1}{k_{si}\left(1-\frac{P_i}{P_{iU}}\right)^2} \quad (5)$$

where P_i and P_{iU} are respectively the load acting on pile i and its axial capacity in compression (N_u) or in uplift ($-S_u$) depending on the sign of P_i. This means that for $i=j$ the right-hand side of eq. (4) must be multiplied by the following factor:

$$\alpha_\psi = \frac{1}{\left(1-\frac{P_i}{P_{iU}}\right)^2} \quad (6)$$

For any (Q, M) pair applied to the pile group, the distribution of the axial loads at the head of each pile as well as the displacement components of the rigid raft must satisfy the following compatibility and equilibrium equations:

$$w_i = w_0 + \theta_x y_i + \theta_y x_i \quad (7a)$$

$$\sum_{i=1}^{n} P_i = Q \quad (7b)$$

$$\sum_{i=1}^{n} P_i x_i = M_y \quad (7c)$$

$$\sum_{i=1}^{n} P_i y_i = M_x \quad (7d)$$

where w_0 is the settlement of the cap evaluated at the origin of the reference system, θ_x and θ_y, are the rotations of the cap about x and y axis, respectively. Note that Equation (7a) must be written for each of the n piles.

The construction of the performance-based interaction domains corresponding to fixed values of the vertical settlement is shown in Figure 2 for a 3×4 pile group. With reference to loading paths in which a vertical eccentric load increases at constant eccentricity, M/sQ, with α_M = 0, the points of the domain are obtained by deriving Q (and, consequently, M) corresponding to a given w/d (e.g., 2, 5, 10%) in the load-settlement curves (Figure 2a) calculated by the above-described numerical procedure. From Figure 2b it is possible to notice that the perfomance-based domains are superimposed to the theoretical failure surface (Di Laora et al., 2019; Cesaro et al., 2024) until the selected w/d is reached (i.e., $w/d \leq 2\%$ if the performance diagram is calculated for w/d = 2%). It follows that these domains contract only on the side of positive Q, that is in the same direction of the considered w/d.

Likewise, it is possible to derive the domains limiting the rotation, θ, to a given value. The procedure can be applied by simultaneously setting θ and w/d (Figure 5). It should be observed that, contrary to the case of fixing w/d, choosing θ as performance parameter corresponds to a symmetric contraction of the domain along the M axis - a consequence of adopting the same curve for both positive and negative values of the rotation.

3 SIMPLIFIED FORMULATION

To provide an easy-to-use tool to estimate the performance-based interaction domains, simplified formulae are proposed.

If the performance parameter is the vertical displacement, the interaction domain can be approximated with the following expression:

$$\sqrt{\left(\frac{M_x}{M_{xu}}\right)^2 + \left(\frac{M_y}{M_{yu}}\right)^2} = \frac{4[\lambda_w Q(Q_c+Q_t) - Q^2 - \lambda_w^2 Q_c Q_t]}{\lambda_w^2 (Q_c - Q_t)^2} \quad (8)$$

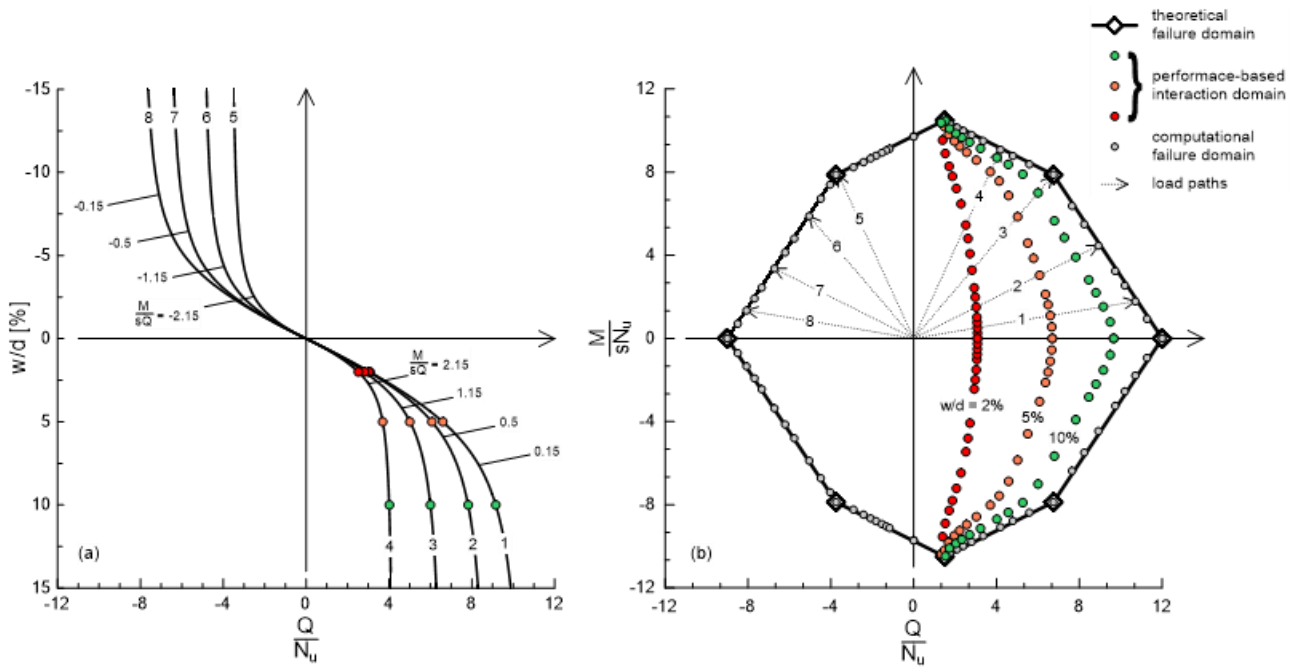

Figure 2. Load-settlement curves for a 3×4 pile group with applied vertical eccentric loads (Su/Nu = 3/4, s/d = 3, r_m/d=40, $k_s d/Nu$=80, α_M = 0, where d is the pile diameter) (a) and dimensionless interaction domains in the Q-M plane (b).

where Q_c and Q_t are the axial capacities of the group in compression and in uplift, M_{xu} and M_{yu} are the maximum ultimate moment capacities of the group around x and y axes and λ_w is the ratio between the vertical load corresponding to the fixed value of the vertical displacement and Q_c (or Q_t). M_{xu} and M_{yu} can be calculated from the failure domain, and for a value of α_M not corresponding to a vertex of the domain, a linear interpolation between two consecutive vertexes of the M_x-M_y failure locus is needed (Cesaro et al. 2024). The group vertical settlement taking into account the pile-to-pile interaction and the non-linearity of the single pile behaviour can be estimated as:

$$w = \frac{\lambda_w Q_u}{n k_s}\left[R_s + \frac{1}{(1-\lambda_w)} - 1\right] \qquad (9)$$

where R_s is the amplification factor for group settlement:

$$R_s = \sum_{i=1}^{n}\sum_{j=1}^{n}\alpha_{ij}/n \qquad (10)$$

Thus λ_w may be easily calculated as:

$$\lambda_w = \frac{1+\frac{K_v w}{Q_u} - \sqrt{1+\frac{K_v w}{Q_u}\left(\frac{4}{R_s}+\frac{K_v w}{Q_u}-2\right)}}{2\left(1-\frac{1}{R_s}\right)} \qquad (11)$$

where K_v (= nk_s/R_s) is the elastic vertical stiffness of the group. Taking r_m = $2L(1\text{-}\nu_s)$ and ν_s = 0.3, it is possible to investigate the influence of the pile slenderness ratio L/d and normalized pile spacing s/d, on the parameter R_S (Figure 3). It follows that R_S can be estimated as:

$$\frac{R_S}{n} = 0.9exp\left(-0.5\sqrt{\frac{ns}{L}}\right) \qquad (12)$$

where $R_G = R_S/n$ is the group reduction factor.

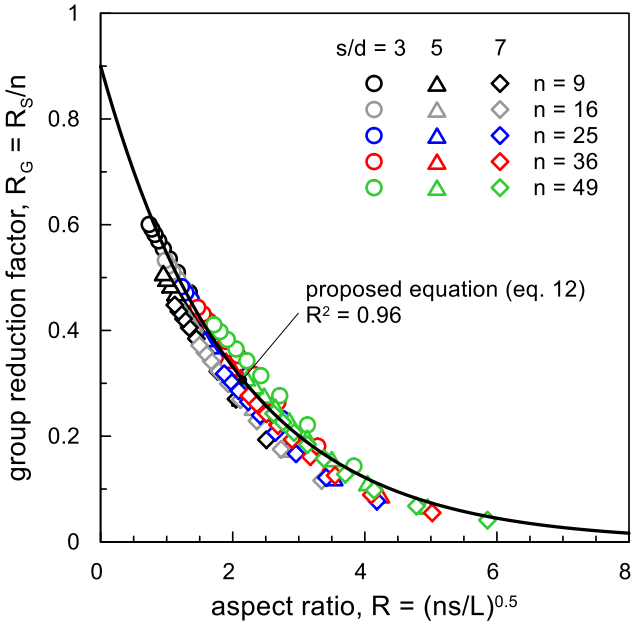

Figure 3. Group reduction factors.

Note that, Equations 9 and 12 allow to simply derive the pile group load-settlement curve under vertical centered load.

On the other hand, if the maximum cap rotation is the chosen performance parameter, the interaction domain can be estimated with the following expression:

$$\sqrt{\left(\frac{M_x}{\lambda_{\theta x} M_{xu}}\right)^2 + \left(\frac{M_y}{\lambda_{\theta y} M_{yu}}\right)^2} = \frac{4[\lambda_\theta^{0.5} Q(Q_c+Q_t) - Q^2 - \lambda_\theta Q_c Q_t]}{\lambda_\theta (Q_c - Q_t)^2} \quad (13)$$

where λ_θ is the ratio between the resultant moment corresponding to the fixed value of the rotation and M_u.

The cap rotation, taking into account the pile-to-pile interaction and the non-linearity of the single pile behaviour, can be estimated as:

$$\theta = \frac{\lambda_\theta M_u}{K_\theta (1-\lambda_\theta)} \quad (14)$$

then λ_θ is given by:

$$\lambda_\theta = \frac{\theta K_\theta}{M_u + \theta K_\theta} \quad (15)$$

where K_θ is the elastic rotational stiffness of the group, depending on the axis orientation about which the group capacity assessment is required (Figure 1):

$$K_\theta = \frac{n}{\sum_{i=1}^{n} \frac{\sum_{j=1}^{n} \xi_j' \alpha_{ij}}{\xi_i' k_s \sum_{z=1}^{n} \xi_z'^2}} \quad (16)$$

in which

$$\xi_i' = x_i \cos(\alpha_\theta) - y_i sin(\alpha_\theta) \quad (17)$$

It should be pointed out that for a given resultant moment acting on pile group around a generic axis η, the maximum cap rotation could occurs about a different axis η', i.e., $\alpha_M \neq \alpha_\theta$ (Figure 1). However, it can be observed that for a square group of identical piles the difference between α_M and α_θ is always negligible from an engineering viewpoint, thus the evaluation of the group capacity can be carried out in the same direction as the resultant moment vector.

As in the previous case, it is possible to define the group rotational stiffness as the ratio between the elastic rotational stiffness of the group in absence of interaction ($k_s \Sigma \xi_i'^2$) and the group rotational amplification factor $R_{S\theta}$, that can be estimate through the following expression (Figure 4):

$$R_{S\theta} = 0.4\left[n^{-1.45}\left(\frac{L}{s}\right)^{0.4}\right]^{-0.45} \quad (18)$$

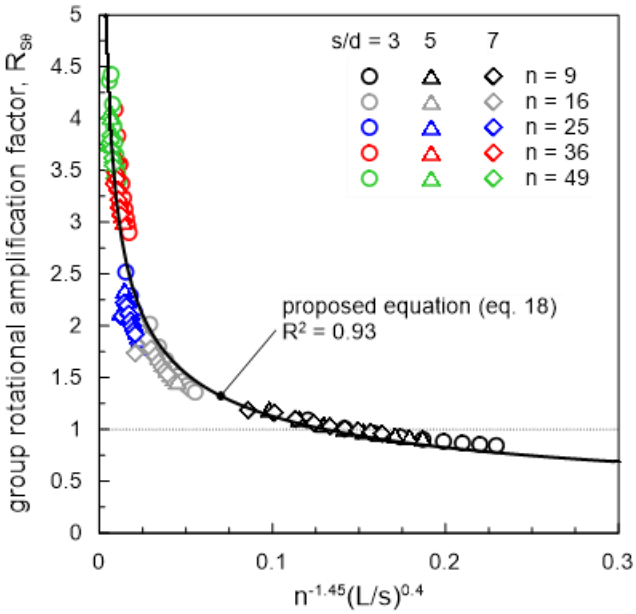

Figure 4. Group rotational amplification factor.

The domain derived by fixing both the performance parameters can be easily computed intersecting Equations (8) and (13) obtaining a very satisfactory match with the numerical results (Figure 5).

4 CONCLUSIONS

A simple numerical code to derive performance-based interaction domains is proposed based on the procedure presented in an early work by Mandolini and Viggiani (1997). This involved the selection of the load-settlement curve for the single pile and the possibility to account for the pile-to-pile interaction which is considered to affect only the elastic component of the single pile settlement. After calculating the load-displacement curves for different loading paths involving vertical eccentric loads applied to the pile group, the construction of the performance-based interaction domains is carried out by fixing settlement and/or rotation to a threshold value and deriving the corresponding load from the above curves. Simple formulae to employ in routine design are also provided taking into account the non-linear behaviour of the single pile and the pile-to-pile interaction. The results obtained employing the proposed formulae match very satisfactorily those derived with the numerical procedure. It is worth of note that the procedures and formulations presented have general validity since the results are depending on the input data. The proposed domains are straightforward design tool enabling to simultaneously

carry out SLS checks for all load combinations necessitating only the capacity and stiffness of the single pile as ingredients, thus avoiding complex finite element modelling of the whole foundation.

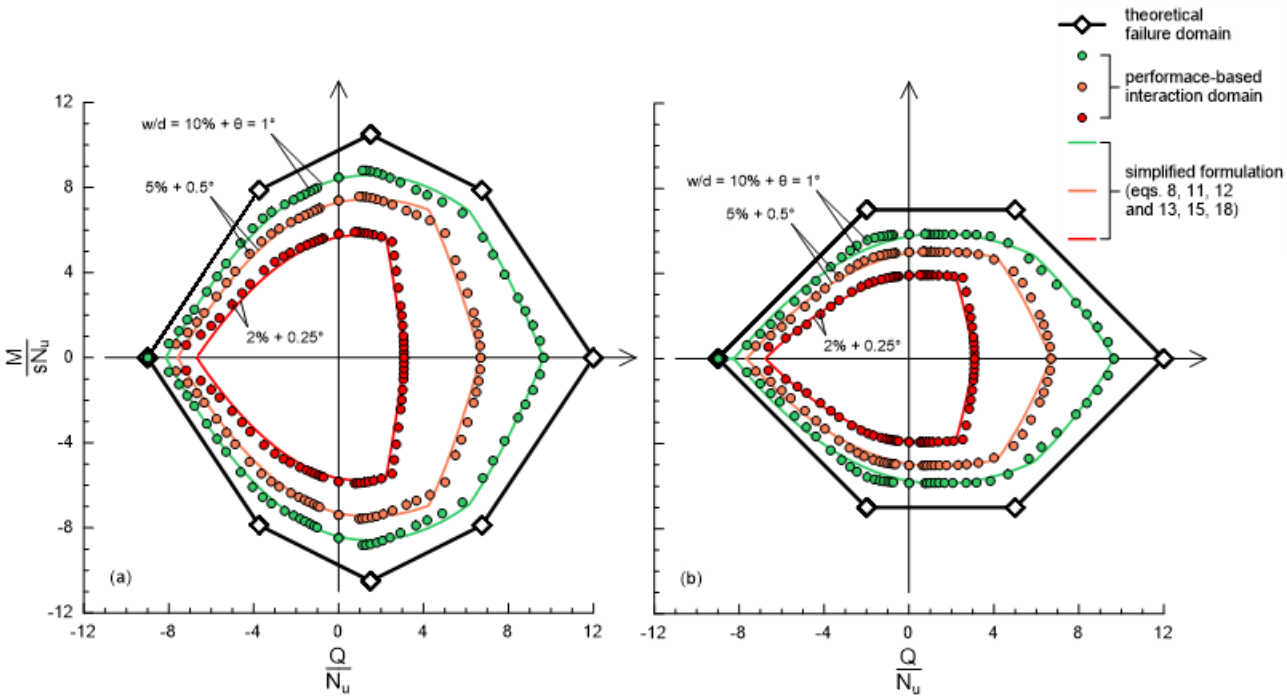

Figure 5. Dimensionless interaction domains in the Q-M plane for a 3×4 piles group (Su/Nu = 3/4, s/d = 3, r_m/d=40, k_sd/Nu=80): α_M = 0° (a); α_M = 90° (b).

REFERENCES

Chin, F. K. (1972). The inverse slope as a prediction of ultimate bearing capacity of piles. *Proceedings of the 3rd SEACSE*, Hong Kong, pp. 83-91.

Cesaro, R., Di Laora, R., Iodice, C. and Mandolini, A. (2024). Interaction domains for capacity- and performance-based design of pile groups. *Acta Geotechnica.* https://doi.org/10.1007/s11440-023-02168-w.

Di Laora, R., de Sanctis, L. and Aversa, S. (2019). Bearing capacity of pile groups under vertical eccentric load. *Acta Geotechnica*. 14 (1), 193–205. https://doi.org/10.1007/s11440-018-0646-5.

Di Laora, R., Iodice, C. and Mandolini, A. (2022). A closed-form solution for the failure interaction diagrams of pile groups subjected to inclined eccentric load. *Acta Geotechnica*, 17(8), 3633-3646. https://doi.org/10.1007/s11440-021-01439-8.

Iovino, M., de Sanctis, L., Maiorano, R.M.S. and Aversa, S. (2021). Failure envelopes of pile groups under inclined eccentric load. *Géotechnique Letters*, 11(4), 247-253. https://doi.org/10.1680/jgele.21.00059.

Kanellopoulos, K. and Gazetas, G. (2020). Vertical static and dynamic pile-to-pile interaction in non-linear soil. *Géotechnique* 70(2), 432–4. https://doi.org/10.1680/jgeot.18.P.303.

Mandolini, A. and Viggiani, C. (1997). Settlement of piled foundations. *Géotechnique*, 47(3), 791-816. https://doi.org/10.1680/geot.1997.47.4.791.

Mylonakis, G. and Gazetas, G. (1998). Settlement and additional forces of grouped piles in layered soil. *Géotechnique*, 48(1),55–72. https://doi.org/10.1680/geot.1998.48.1.55.

Poulos, H. G. (1968). Analysis of the settlement of pile groups. *Géotechnique*, 18, 449-471. https://doi.org/10.1680/geot.1968.18.4.449.

Randolph, M. F. and Wroth, C. P. (1978). Analysis of deformations of vertically loaded piles. *J. Geotech. Engng Div., ASCE*, 104, GT12, 1465-1488. https://doi.org/10.1061/AJGEB6.0000729.

Randolph, M. F. and Wroth, C. P. (1979). Analysis of vertical deformation of pile groups. *Géotechnique,* 29(4), 423-439. https://doi.org/10.1680/geot.1979.29.4.423.

Randolph, M. F. (1994). Design methods for pile groups and piled rafts. *Proceedings 13th ICSMFE*, New Delhi, vol. 5, pp. 61-82.

Sakellariadis L. and Anastasopoulos, I. (2022). On the mechanisms governing the response of pile groups under combined VHM loading. *Géotechnique*. https://doi.org/10.1680/jgeot.21.00236.

Proceedings of the XVIII ECSMGE 2024
GEOTECHNICAL ENGINEERING CHALLENGES
TO MEET CURRENT AND EMERGING NEEDS OF SOCIETY
© 2024 the Authors
ISBN 978-1-032-54816-6
DOI 10.1201/9781003431749-48
Open Access: www.taylorfrancis.com, CC BY-NC-ND 4.0 license

ECSMGE 24
XVIII EUROPEAN CONFERENCE ON SOIL MECHANICS AND GEOTECHNICAL ENGINEERING

Rheological study of soil-cement-GGBFS mixture

Etude rhéologique du mélange sol-ciment-GGBFS

S. Choudhary, P.K. Meena, A. Kumawat, L. Borana*
Indian Institute of Technology Indore, India

**lalitborana@iiti.ac.in*

ABSTRACT: The rheological parameters of the soils and soil-cement mixtures, such as storage modulus, loss modulus, viscosity, flow points, shear stress, yield stress, and many more, are being studied to examine and understand the response of the soil microstructure subjected to external stress. In this study, a stress-controlled rotational rheometer is used on several test specimens of clay soil mixed with Ordinary Portland Cement (OPC) and Ground Granulated Blast Furnace Slag (GGBFS). The soil specimens underwent shear deformations at the rate of 0.01% to 100% using a 50 mm diameter measuring shaft at various time intervals during the Amplitude Sweep Test (AST). AST was performed to investigate the viscoelastic properties of the soil paste having OPC (15% by weight of dry soil) and different proportions of GGBFS (0%, 20%, 30%, and 40% by dry weight of OPC). The obtained test results showed that, when the strain rate was low, storage modulus (G') exceeded loss modulus (G") for all the samples (15%C-0%G, 15%C-20%G, 15%C-30%G, 15%C-40%G). Notably, the sample with 20% GGBFS replacement (15%C-20%G) exhibited the highest G' value among all compositions, which indicates that the 20% GGBFS replacement sample deforms and returns to its original state more quickly than the other samples.

RÉSUMÉ: Les paramètres rhéologiques des sols et des mélanges sol-ciment tels que le module de stockage, le module de perte, la viscosité, les points d'écoulement, la contrainte de cisaillement, la limite d'élasticité et bien d'autres sont étudiés pour examiner et comprendre la réponse de la microstructure du sol soumise à des contraintes externes. Dans cette étude, un rhéomètre rotatif à contrainte contrôlée est utilisé sur plusieurs éprouvettes de sol argileux mélangées à du ciment Portland ordinaire (OPC) et à du laitier de haut fourneau granulé broyé (GGBFS). Les échantillons de sol ont subi des déformations par cisaillement à un taux de 0,01% à 100% à l'aide d'un arbre de mesure de 50 mm de diamètre à différents intervalles de temps au cours du test de balayage d'amplitude (AST). L'AST a été réalisée pour étudier les propriétés viscoélastiques de la pâte de sol contenant de l'OPC (15% en poids de sol sec) et différentes proportions de GGBFS (0%, 20%, 30% et 40% en poids sec d'OPC). Les résultats des tests obtenus ont montré que, lorsque la vitesse de déformation était faible, le module de conservation (G') dépassait le module de perte (G") pour tous les échantillons (15%C-0%G, 15%C-20%G, 15%C-30%G, 15%C-40%G). Notamment, l'échantillon avec 20% de remplacement de GGBFS (15% C-20% G) présentait la valeur G' la plus élevée parmi toutes les compositions, ce qui indique que l'échantillon de remplacement de 20% de GGBFS se déforme et revient à son état d'origine plus rapidement que les autres échantillons.

Keywords: Amplitude sweep test (AST); ground granulated blast furnace slag (GGBFS); loss modulus (G"); rheometer; storage modulus (G').

1 INTRODUCTION

At present, the extensive production of industrial wastes such as fly ash, ground granulated blast furnace slag (GGBFS), silica fumes, and more presents a major global concern due to its significant environmental, social, and economic implications. As industries continue to expand and manufacturing processes intensify, the need to dispose of the generated wastes also intensifies significantly (Buddhdev and Timani, 2021). Ground Granulated Blast Furnace Slag (GGBFS) is one of such industrial by-products of steel industries that are produced in millions of tonnes globally, including India. GGBFS is a well-known Supplementary Cementitious Material (SCM) that possesses pozzolanic and latent hydraulic properties, and it is used to partially replace Ordinary Portland Cement (OPC) to a certain extent depending on applicability. Over the past few decades, OPC has been widely employed in the stabilization of soft clay soils. The soil-cement mixtures, comprising soil, cement, and water, exhibit qualities like better strength gain, reduced permeability, compressibility, improved durability, etc., that make them suitable for a variety of applications, ranging from road construction to foundation stabilization (Choudhary et al., 2023). However, the use of OPC raises notable environmental concerns due to the carbon dioxide (CO_2) emissions generated in its manufacturing process. OPC is directly accountable for approximately 5% of artificial CO_2 emissions, with 1 tonne of cement production yielding 800 kg of CO_2 (Damtoft et al., 2008; Gartner,

2004). In recent years, researchers and engineers have explored the incorporation of SCMs like ground granulated blast furnace slag (GGBFS) to enhance the performance of soil-cement blends further. GGBFS undergoes a strong reaction with calcium hydroxide, a by-product of cement hydration, resulting in the production of additional cementitious compounds like calcium silicate hydrate (CSH) and calcium aluminate hydrate (CAH) (Yi et al., 2015).

In the current scenario, most of the SCMs have been under-utilized except for Fly Ash (FA). FA has been widely employed to enhance the mechanical properties of fine-grained soils, such as maximum dry density, swelling, optimum moisture content, consistency limits (Barman and Dash, 2022), shear strength, compressibility (Singh et al., 2021a, 2021b) and many more. However, there is very limited information available in the research studies regarding the utilization of GGBFS in geotechnical engineering. D.D. Higgins et al. (1998) studied the possible utilization of GGBFS to improve the strength of lime-stabilised clay soils. The authors conducted experimental tests on different lime/slag ratios on two different clay soils, Kaolinite and Kimmeridge Clay. From this study, it was found that with an increase in the curing period, the strength of the clay-lime-GGBFS mixture also increased significantly for both the above-mentioned soils. It was also found that GGBFS alone has no effect on the strength enhancement of the soils and it requires an activator like lime, cement, etc. to provide significant strength. Yi et al. (2015) used Carbide-slag (CS) activated GGBFS for the stabilization of soft clay soils. The investigation focused on exploring the strength gained behaviour of soft clay soils when added with CS-GGBFS at varying proportions by performing a series of UCS tests. The results revealed that maximum unconfined compressive strength gain was observed for an optimum CS content of 4-6% in the soil-CS-GGBFS mixture. The UCS values were almost twice for CS-GGBFS stabilized soft soils in comparison to cement-treated soft soils.

Some researchers have conducted comprehensive investigations, including rheological evaluations, to investigate as well as understand the possible advantages and limitations related to the usage of GGBFS in soil-cement mixtures. Rheology, the study of the flow and deformation of materials, provides insights into the material's behaviour under external stress conditions. Amplitude sweep test (AST) in rheology is often employed to investigate the viscoelastic properties of materials, including soil-cement mix. AST involves applying oscillatory shear stress or strain to a material and observing its response over a range of amplitudes while maintaining a constant frequency. By varying the level of oscillatory amplitudes, the material's viscoelastic properties can be assessed by measuring its storage modulus, loss modulus, and yield stress as a function of the applied stress. The storage modulus (G') reflects the material's elastic or 'solid-like' behavior, while the loss modulus (G") represents its viscous or 'liquid-like' behavior. Yield stress, on the other hand, marks the transition from a solid-like to a fluid-like state, crucial for understanding flow initiation under stress. A few researchers used rheology to investigate different characteristics of virgin clay soils and clay combined with various additives. Celik and Akcuru (2020) investigated the use of Bottom Ash (BA) as a mineral component in permeation grouts made of cement. This study tested 28 various mix proportions with six different BA contents and four different water contents using a number of analytical and experimental procedures. According to the findings, there was no noticeable change in yield stress values for any water-to-binder (w/b) ratio when BA was substituted. The substitution of BA had some minor effects on yield stress; nonetheless, for all combinations, there was a noticeable downward trend in yield stress values as the w/b ratio increased. Wang et al. (2021) examined how temperature and hydration time affect the rheological characteristics of Ordinary Portland Cement (OPC) slurries, particularly emphasizing the simulation of high-temperature conditions in a laboratory setting. Portland cement PO42.5 samples with water-to-cement ratios (W/Cs) spanning from 0.5 to 2.0 were prepared for the rotational viscometer. The research also explored the rheological models and the laws governing the observed changes in rheological parameters for cement slurries exhibiting different degrees of hydration across varying temperatures ranging from 30°C to 80°C. Newton, Bingham, and power law models were applied to fit the rheological test data, and a mathematical analytical expression was introduced for the fitted curve. It is worth noting that GGBFS can augment the engineering properties of clay soil when used as a partial replacement for OPC in soil-cement mixtures. However, there is limited information available regarding the rheology of GGBFS-mixed soil-cement combinations.

In this study, rheological parameters like viscosity, yield stress, and flow behaviour index are investigated to understand the rheological characteristics of GGBFS-mixed soil-cement mixtures. Rheology is conducted at different time intervals with various GGBFS proportions as replacements for OPC.

2 MATERIALS AND METHODOLOGY

2.1 Materials

Clay soil used in this study was collected from a test site in IIT Indore, Madhya Pradesh, India. OPC and GGBFS were obtained through collaboration with industrial partners. Figure 1 illustrates the particle size distribution (PSD) curve of the soil. In accordance with the Unified Soil Classification System (USCS), adopted from ASTM D-2487-98, the soil is categorized as highly compressible clayey soil. The index properties of the clay soil are listed in Table 1.

Table 1. Index properties of clay soil.

Property	Value
Natural water content (%)	14.50
Optimum moisture content (%)	28.5
Liquid limit (%)	79.20
Plastic limit (%)	35.62
Specific gravity	2.70
Shrinkage limit (%)	11.35
Maximum dry unit weight (kN/m^3)	1.44
USCS soil classification	CH

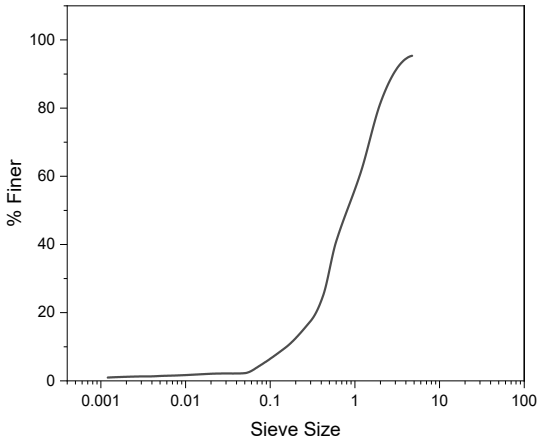

Figure 1. Particle size distribution (PSD) curve of clay soil.

For preparing the test samples, fine clay soil (passing through 600 microns) was mixed with 15% OPC (by dry weight of soil), and three different percentages of 20%, 30%, and 40% of GGBFS were used to replace OPC in the same soil-cement mixture. The soil-OPC-GGBFS mixture was thoroughly mixed for 15 minutes using a mechanical mixer. To maintain consistency and provide sufficient hydration opportunities, the water was added as 1.5 times the liquid limit of clay soil (Choudhary et al., 2023). After the mixing, the slurry sample prepared was kept for 60 minutes in a bowl to provide appropriate time for the hydration process (Buddhdev and Timani, 2021). The bowl was covered with a moisture-retaining film for this entire time to prevent any moisture loss. The different proportions of clay soil, OPC, and GGBFS taken for the testing sample preparation are shown in Table 2.

Table 2. Different proportions of the mix used for this experimental study.

Soil (g)	OPC (By weight of soil) (%)	GGBFS Replacement (By weight of OPC) (%)	Final amount (Soil+ OPC+ GGBFS) (g)
300	15%	0%	300+45
		20%	300+36+9
		30%	300+31.5+13.5
		40%	300+27+18

2.2 Testing procedure

The Amplitude Sweep Test (AST) was performed to study the response of the soil-OPC and soil-OPC-GGBFS mixture under the application of external stresses. To ascertain the rheological characteristics of the sample, Anton Paar-Modular Compact Rheometer (MCR) 102 with a 50mm diameter parallel plate measuring shaft is employed. Table 3 illustrates the configurational setup for AST with controlled shear deformation (CSD) referred from previous studies (Khaidapova et al., 2018).

Table 3. Configuration setup of conducted Amplitude Sweep Test (AST).

Parameters	Corresponding values
Plate distance	D= 2mm
Shear deformation	γ= 0.01% to 100%
Number of Measuring points	25 points
Angular frequency	0.5 Hz ($\omega = \pi$ s-1)
Duration of experiments	15 min

A small quantity of 15-20 grams of the prepared sample is carefully placed on the rheometer's fixed measuring plate. A normal force of FN = 12N was applied during the test to maintain an undisturbed quasi-elastic soil structure after lowering the top measuring plate up to the required measuring gap of 2 mm. For the given soil-OPC-GGBFS mixture, the test samples underwent six tests performed at 20-minute intervals, starting from 60 minutes post mixing process, to observe the variations of different

rheological properties like G', G" with respect to shear strain.

3 RESULTS AND DISCUSSION

3.1 G'/G" vs. shear strain

The amplitude sweep test demonstrates the relationship between various rheological properties, including the loss modulus (G"), storage modulus (G'), flow point, and yield point, as shown in Figure 2. It exhibits three distinct phases. Phase 1: In this phase, both the loss modulus (G") and storage modulus (G') are parallel, indicating the elastic behavior of the sample. This means that the material primarily stores and releases energy when subjected to deformation, and it quickly returns to its original shape once the deformation is removed. Phase 2: The point where G' and G" become equal signifies the transition from elastic to Newtonian behavior of the sample. Phase 3: The final phase indicates that the bonding between sample particles is breaking down, and the viscous characteristics start to dominate. In this phase, G" (loss modulus) has a higher value than G' (storage modulus). It represents the material's tendency to flow and deform readily, with less ability to return to its original shape after deformation.

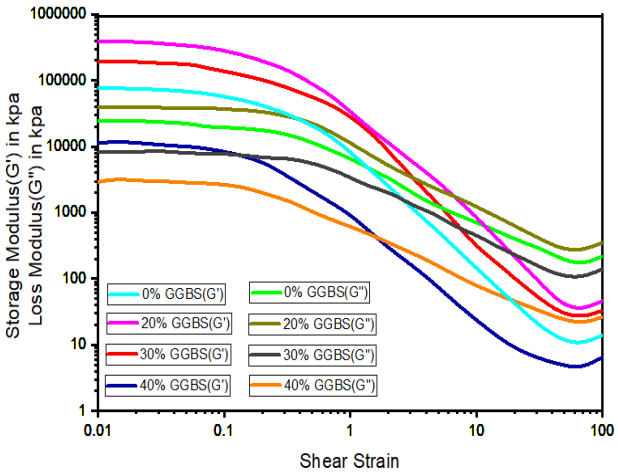

Figure 2. Amplitude sweep test data for clay soil with 15% OPC and 0%, 20%, 30%, and 40% GGBFS replacement.

As shown in Figure 2, the major focus of AST was to examine the viscoelastic behaviour of samples with 15% OPC sample with different percentages of GGBFS replacement (0%, 20%, 30%, 40%). From the results, it can be observed that when the shear strain was low, G' exceeded G" for all the samples (15C, 15%C-20%G, 15%C-30%G, and 15%C-40%G). Notably, the sample with 20% GGBFS replacement (15%C-20%G) exhibited the highest G' value among all compositions. This indicates that the 20% GGBFS replacement sample primarily stores and releases energy when subjected to deformation and returns to its original shape more quickly than the other samples. As the applied shear strain increased, G" surpassed G', and the samples began to exhibit fluid-like behavior. The point at which this transition from elastic to viscous behavior occurs, represented by the intersection of G" and G', is indicated as the flow point. In Figure 2, the order in which the flow point was reached for the compositions is as follows: 15%C < 15%C-40%G < 15%C-30%G < 15%C-20%G. It implies that the sample with 20% GGBFS replacement has the least tendency to behave like a fluid compared to the other samples, as it reached the flow point later.

3.2 Flow points

Figure 3 illustrates the relationship between flow point values with respect to varying GGBFS replacement in soil when mixed with OPC. Li et al. (2018) presented a distinct relationship between the packing density and the rheological properties. It states that, as the packing density decreases leads to the requirement of higher water content and lower workability. The angular particles in the GGBFS form a framework in the packing system and reduce the packing density of the soil sample. From Figure 3, it is evident that when 20% of GGBFS is used to replace OPC in the mixture, the material becomes fluid enough to flow (the flow point tends to increase). However, further increment in the GGBFS content increases the viscosity and reduces the flow point of the composite mixture.

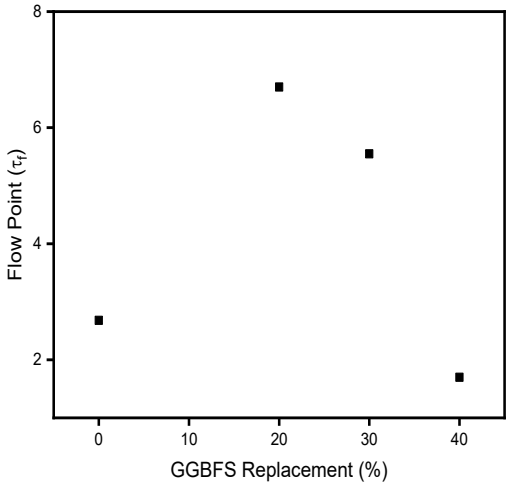

Figure 3. Variation of flow point with the addition of OPC with different GGBFS replacement ratios.

4 CONCLUSIONS

This study investigates the influence of various GGBFS ratios on the rheological parameters of clay soil blended with OPC. A set of experimental tests conducted through the Amplitude Sweep Test explores the deformation behavior. The conclusions drawn from the experimental findings are as follows:

i. It has been observed that adding GGBFS with OPC has a considerable impact on the stiffness, structural stability, and shear behaviour of re-constituted soil because the reaction happening between OPC and GGBFS makes very good bonding with soil particles.
ii. The increase in GGBFS replacement raises the flow point, loss modulus, and storage modulus, which indicates that the soil stability and strength have increased due to good soil particle interlocking.
iii. With an increase in GGBFS content, the viscosity of the Soil-OPC-GGBFS mixture also increases, which increases the flow point values. This increased viscosity has the consequence of decreasing the mixture's inclination to flow and disperse.

It is to be noted that the current study mainly focussed on the deformation behaviour of the soil-OPC-GGBFS mixture for a certain proportion. However, there are many aspects of this study, such as dynamic mechanical analysis, time-dependent deformation behaviour, optimization of GGBFS content at different moisture content, in-depth microstructural analyses, and long-term durability of GGBFS-blended soil-cement mixtures under diverse environmental conditions to better understand the impact of GGBFS on the soil-cement mixtures.

REFERENCES

ASTM Committee D-18 on, Rock, 2017. Anonymous. 1998. ASTM D-2487-98 Standard practice for classification of soils for engineering purposes. American Society for Testing and Materials, USA. i.

Barman, D., Dash, S.K., 2022. Stabilization of expansive soils using chemical additives: A review. J. Rock Mech. Geotech. Eng. 14, 1319–1342. https://doi.org/10.1016/j.jrmge.2022.02.011.

Buddhdev, B.G., Timani, K.L., 2021. Critical Review for Utilization of Blast Furnace Slag in Geotechnical Application, in: Latha Gali, M., Raghuveer Rao, P. (Eds.), Problematic Soils and Geoenvironmental Concerns. Springer Singapore, Singapore, pp. 87–98.

Celik, F., Akcuru, O., 2020. Rheological and workability effects of bottom ash usage as a mineral additive on the cement based permeation grouting method. Constr. Build. Mater. 263, 120186. https://doi.org/10.1016/j.conbuildmat.2020.120186.

Choudhary, S., Singh, M.J., Borana, L., 2023. Time-dependent settlement behaviour of clayey soil treated with deep cement mixed column. Smart Geotech. Smart Soc. 752–757. https://doi.org/10.1201/9781003299127-100.

D.D. Higgins, J.M.K. and S.W., n.d. Soil Stabilization using Lime-Activated Ground Granulated Blast Furnace Slag. ACI Symp. Publ. 178. https://doi.org/10.14359/6023.

Damtoft, J.S., Lukasik, J., Herfort, D., Sorrentino, D., Gartner, E.M., 2008. Sustainable development and climate change initiatives. Cem. Concr. Res. 38, 115–127. https://doi.org/10.1016/j.cemconres.2007.09.008.

Gartner, E., 2004. Industrially interesting approaches to "low-CO2" cements. Cem. Concr. Res. 34, 1489–1498. https://doi.org/10.1016/j.cemconres.2004.01.021.

Khaidapova, D.D., Klyueva, V. V., Skvortsova, E.B., Abrosimov, K.N., 2018. Rheological Properties and Tomographically Determined Pore Space of Undisturbed Samples of Typical Chernozems and Soddy-Podzolic Soils. Eurasian Soil Sci. 51, 1191–1199. https://doi.org/10.1134/S106422931810006X.

Li, D., Wang, D., Ren, C., Rui, Y., 2018. Investigation of rheological properties of fresh cement paste containing ultrafine circulating fluidized bed fly ash. Constr. Build. Mater. 188, 1007–1013. https://doi.org/10.1016/j.conbuildmat.2018.07.186.

Singh, M.J., Borana, L., Weiqiang, F., Xu, D.-S., 2021a. Long-Term Swelling Characteristics of Montmorillonite Clay with and without Fly Ash: Wetting–Drying Cycle Influence in 1D Oedometer Condition. J. Test. Eval. 51. https://doi.org/10.1520/JTE20210248.

Singh, M.J., Feng, W., Xu, D.-S., Borana, L., 2021b. Experimental Investigation of Long-Term Behaviour of Fly Ash Blended Indian Black Cotton Soil, in: Civil Infrastructures Confronting Severe Weathers and Climate Changes Conference. Springer, pp. 14–22. https://doi.org/10.1007/978-3-030-79647-1_2.

Wang, M., Zhu, Z., Liu, R., Li, S., Zhang, C., Liu, Y., Zhang, L., Bai, J., 2021. Influence of extreme high-temperature environment and hydration time on the rheology of cement slurry. Constr. Build. Mater. 295, 123684. https://doi.org/10.1016/j.conbuildmat.2021.123684.

Yi, Y., Gu, L., Liu, S., Puppala, A.J., 2015. Carbide slag-activated ground granulated blastfurnace slag for soft clay stabilization. Can. Geotech. J. 52, 656–663. https://doi.org/10.1139/cgj-2014-0007.

Proceedings of the XVIII ECSMGE 2024
GEOTECHNICAL ENGINEERING CHALLENGES
TO MEET CURRENT AND EMERGING NEEDS OF SOCIETY
© 2024 the Authors
ISBN 978-1-032-54816-6
DOI 10.1201/9781003431749-49
Open Access: www.taylorfrancis.com, CC BY-NC-ND 4.0 license

ECSMGE 24
XVIII EUROPEAN CONFERENCE ON SOIL MECHANICS AND GEOTECHNICAL ENGINEERING

Influence of volumetric boundary conditions on the water-retention behaviour of reconstituted and intact clay shales

Influence des conditions limites volumétriques sur le comportement de rétention d'eau des schistes argileux reconstitués et intacts

F. Christ
Ruhr-University Bochum, Chair of Foundation Engineering, Soil and Rock Mechanics, Bochum, Germany
A.A. Lavasan*
University of Luxembourg, Laboratory of Computational Soil Mechanics and Foundation Eng., Luxembourg
**arash.lavasan@uni.lu*

ABSTRACT: Tunnelling in swellable soils is a challenging procedure with high risk of damage into the tunnel structure. To minimize the risk of damage to the tunnel support, a rigid or ductile principle of tunnel structure design are often applied to hinder or tolerate deformation in the ground upon swelling, respectively. Considering the coupled interactions between tunnel structure and the swelling rock, prediction of hydration process in swelling clay shales requires investigation of the water retention behaviour of shale under different tunnelling relevant boundary conditions. In this study, the main focus lies on the volumetric boundary conditions. For this purpose, the soil-water retention curves (SWCCs) of both intact and reconstituted Opalinus clay shale (OPA) were determined experimentally. This was carried out for each of the two materials under constant volume conditions in microcells, representing stiff tunnel lining, as well as without volumetric constraints, representing unsupported tunnels, where the intermediate states (deformation tolerant tunnel linings) can be fairly defined through interpolated. In contrast to bentonite that exhibits a noticeable influence of the volumetric boundary conditions, experiments on Opalinus indicated a rather smaller or eventually no influence in case of intact and reconstituted OPA, respectively. This phenomenon is believed to be attributed to mineralogy and fabric of samples.

RÉSUMÉ: Le creusement de tunnels dans des sols gonflants est une procédure difficile qui présente un risque élevé d'endommagement de la structure du tunnel. Pour minimiser le risque d'endommagement du support du tunnel, un principe rigide ou ductile de conception de la structure du tunnel est souvent appliqué pour entraver ou tolérer la déformation du sol en cas de gonflement, respectivement. Compte tenu des interactions couplées entre la structure du tunnel et la roche gonflante, la prédiction du processus d'hydratation dans les schistes argileux gonflants nécessite l'étude du comportement de rétention d'eau du schiste dans différentes conditions limites pertinentes pour le tunnel. Dans cette étude, l'accent est mis sur les conditions limites volumétriques. À cette fin, les courbes de rétention d'eau dans le sol (SWCC) des schistes argileux d'Opalinus (OPA) intacts et reconstitués ont été déterminées expérimentalement. Cette opération a été réalisée pour chacun des deux matériaux dans des conditions de volume constant dans des microcellules, représentant un revêtement de tunnel rigide, ainsi que sans contraintes volumétriques, représentant des tunnels non soutenus, où les états intermédiaires (revêtements de tunnel tolérants à la déformation) peuvent être assez bien définis par interpolation. Contrairement à la bentonite qui présente une influence notable des conditions limites volumétriques, les expériences sur l'Opalinus ont indiqué une influence plutôt faible, voire nulle, dans le cas de l'OPA intacte et de l'OPA reconstituée, respectivement. Ce phénomène serait attribué à la minéralogie et à la composition des échantillons.

Keywords: Swelling shale; soil-water retention behaviour; volumetric constraints.

1 INTRODUCTION

Underground construction in shales is of special interest not only because shales are considered as host rock for nuclear waste repository, but also several passageways as well as utility tunnels have been excavated in swellable clay shales. To assess the swelling evolution in shales, it is essential to properly evaluate the mechanical as well as hydraulic behaviours such as soil-water retention characteristics of the shale. However, the literature shows that the mechanical boundaries can dramatically impact the hydraulic behaviour as of Bentonite is a specific type of smectic clay. To address this phenomenon for tunnelling application, the new Belchen highway tunnel (Ziegler et al., 2022a) was chosen as the case study and the influence of tunneling-relevant boundary conditions on the SWCC of Opalinus clay shale which was the host rock in this project, was studied.

2 MATERIAL AND METHODS

This section gives a brief overview of the material studied, the sample preparation and the methods used to determine the water retention behaviour.

2.1 Material tested

Opalinus Clay (OPA) is a marine clay shale that was formed during the Jurassic period. The material consists of various types of facies, which are determined by the quantity of quartz, carbonates, and clay minerals. The studied OPA originates from the construction site of the new Belchen highway tunnel in the Jura Mountains in Northern Switzerland, which connects Basel and Lucern. Mineralogical studies revealed a composition that closely resembled the shaly facies of OPA at Mont Terri Underground Research Laboratory (Ziegler et al., 2022b).

The material was tested as intact rock, as well as in a reconstituted state as compacted powder. For the intact samples, the drilling cores were carved to a diameter of 3 cm on the lathe and then cut to a height of 8 mm using a diamond band saw. For the reconstituted samples, intact material was first ground to less than 0.25 mm grain size and then compacted to a dry density of 2.0 g/cm³.

2.2 Soil-water characteristic curve

In this study, a total of four soil-water characteristic curves (SWCCs) for intact OPA and compacted OPA powder (each 2 samples) at an initial dry density ρ_d of 2.0 g/cm^3 were determined. In each case, one sample was used for SWCC at constant volume and one for free swelling conditions. Starting point for determined SWCCs were the preserved in-situ water content and suction of the intact OPA, and the hygroscopic water content of OPA powder and its resulting suction after compaction. From this state, the samples were both saturated and dried. These two states were selected as initial states as they are relevant most of geotechnical applications. The in-situ water content and the corresponding suction of the intact material form the initial state for the practical background of this study, i.e. swelling during mechanised tunnelling. The hygroscopic water content and the corresponding suction in the compacted state of the OPA powder are in turn the starting point for all experimental hydro-mechanical tests in the main project. Initial conditions are summarized in Table 1. Two values are given for intact OPA, as the initial states differ slightly for the two different volumetric boundary conditions. To ensure constant volume conditions, samples were installed in microcells as proposed by Seiphoori et al. (2014).

Since the vapor equilibrium technique (Delage et al. (1998), VET) is appropriate to use in combination with microcells, this experimental method was used in this study to determine SWCCs. By doing so, the suction range between 3 and 350 MPa was covered.

Samples for constant volume conditions were prepared according to Section 2.2. For free swelling conditions, compacts of powder or shards of intact OPA were directly stored in small plastic containers in desiccators. These desiccators contain oversaturated salt solutions in order to expose the samples to a defined suction. Nevertheless, the final suction of the samples was measured with a chilled mirror hygrometer (CMH). The void ratio needed to determine the degree of saturation (S_r) for the free swelling SWCC was determined via immersion weighing in paraffin oil (Christ et al., 2022). Experimental data was fitted with the van Genuchten equation (van Genuchten (1980), Equation 1):

$$\theta = \theta_r + \frac{\theta_s - \theta_r}{[1+(\alpha\psi)^n]^m} \quad (1)$$

where Θ is the volumetric water content, Θ_r the residual volumetric water content, Θ_s the saturated volumetric water content, m, n, α are soil/fitting parameters and ψ the total suction.

The air-entry value (AEV) was determined according to the commonly used graphical construction method (Pasha et al., 2016), where the AEV is defined as the intersection of the tangent through the inflection point of the SWCC and the horizontal line of S_r=1. Here, this exact value was explicitly calculated corresponding to Soltani et al. (2021) via the first and second derivatives.

Table 1. Initial parameters of intact and reconstituted samples.

		Intact	Reconstituted
ψ_{init}	[MPa]	60-65	68
S_r	[%]	63-67	18

Another method to obtain information about the water retention behaviour of a soil is to derive it from the pore size distribution using MIP. The method associates the mercury intrusion with the drying path of a SWCC by considering the mercury intrusion at a given pressure p to be the same as the air intrusion at a matric suction ψ_m (Ferrari and Romero, 2019).

3 RESULTS AND DISCUSSION

Soil water characteristic curves (SWCCs) of compacted OPA powder and intact OPA for free swelling and volume constant conditions are shown in

Figures 1 and 2, respectively. Fitting curves were obtained by the least square method using the van Genuchten equation (Eq. 1), leaving out residual and saturated volumetric water contents or rather degrees of saturation. Fitting parameters are summarised in Table 2. It should be noted that these are not classic SWCCs, where a material is installed as a slurry and then dried (initial drying), rehydrated (main wetting) and dried again (main drying). The focus of the SWCCs in this study is on the initial state, which results from the in-situ state (intact material) or the initial state of all experimental tests in this study (powder).

Table 2. Van Genuchten fitting parameters and AEV of determined SWCCs in this study.

		Reconstituted		**Intact**
		free	VC	combined
n	[-]	1.503	1.558	2.132
m	[-]	0.335	0.358	0.452
α	[1/MPa]	0.290	0.211	0.019
ψ_{AEV}	[MPa]	1.49	2.07	26.34

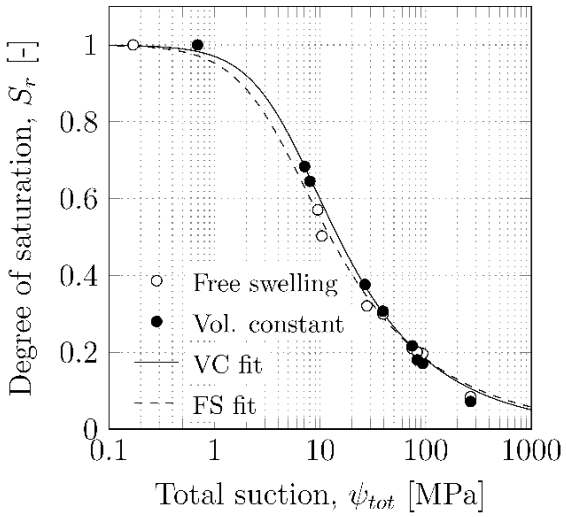

Figure 1. Soil-water characteristic curves of reconstituted OPA – experimental data and van Genuchten fit.

The derivation of the matric suction—saturation relationship should be limited to the low-suction range, in which capillarity dominates the water retention properties (Romero et al., 1999).

For OPA powder, the initial state corresponds to a suction of 68 MPa at a degree of saturation of 18%. A minor difference between volume constant and free swelling boundary conditions can be observed in the wetting branch. No difference can be seen in the drying branch, which is due to the fact that the applied volumetric boundary conditions are irrelevant for drying and the associated potential shrinkage of the sample. Microcells for the preservation of volume-constant boundary conditions were introduced in Seiphoori et al. (2014) as part of investigations into the water retention behaviour of compacted bentonite in the context of radioactive disposal.

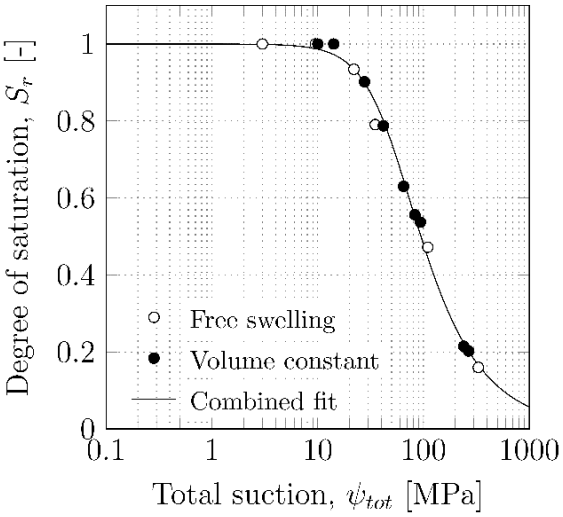

Figure 2. Soil-water characteristic curve of intact OPA – experimental data and van Genuchten fit.

In this study, a more evident influence of the volumetric boundary conditions on water absorption during hydration was observed. It was argued that further hydration is inhibited by the prevention of continued subdivision of the clay particles by the constant-volume boundary conditions, which in turn prevents further water absorption on and between the clay particles. In the present study, the SWCC of compacted OPA powder at constant volume boundary conditions shows a slightly higher degree of saturation at the same total suction than the SWCC without volumetric constraints. A look at the underlying data shows that this difference is due to the prevented expansion of the material. The water content is almost the same in both cases at the same total suction. With free swelling, however, the void ratio increases steadily as total suction decreases, whereas it remains the same for the constant-volume SWCC. The fact that the influences of the volumetric boundary conditions are not as pronounced in this case as in the study by Seiphoori et al. (2014) can be attributed to the mineralogy of the two materials analysed. While Seiphoori et al. (2014) investigated MX-80 bentonite, which has a smectite content of 85%, OPA consists of only 11-16% illite/smectite mixed layer minerals. Smectites are the clay minerals with the highest water absorption capacity. As a result, MX-80 has a significantly higher swelling capacity and therefore reacts more sensitive to restrictions in volumetric swelling. In view of the fact that the different volumetric boundary conditions for determining the SWCC were taken into account in order to consider the tunnelling relevant volumetric boundary conditions of

rigid lining, *no lining* and *deformation-tolerant lining*, it can be concluded that a combined SWCC is sufficiently accurate given the minor deviations observed.

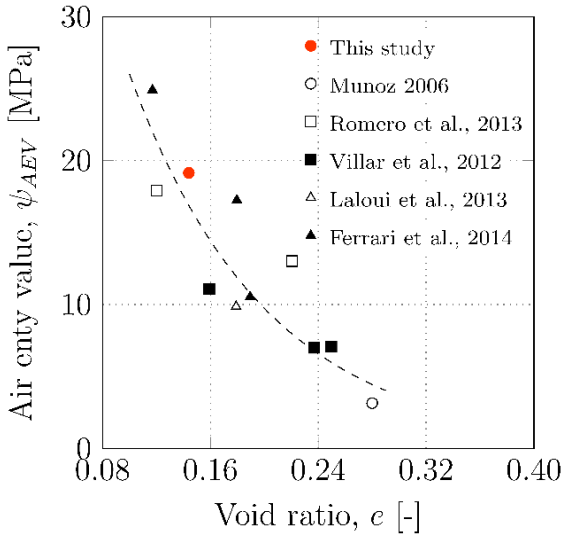

Figure 3. Air-entry value over void ratio from Ferrari et al. (2014) complemented with data from this study.

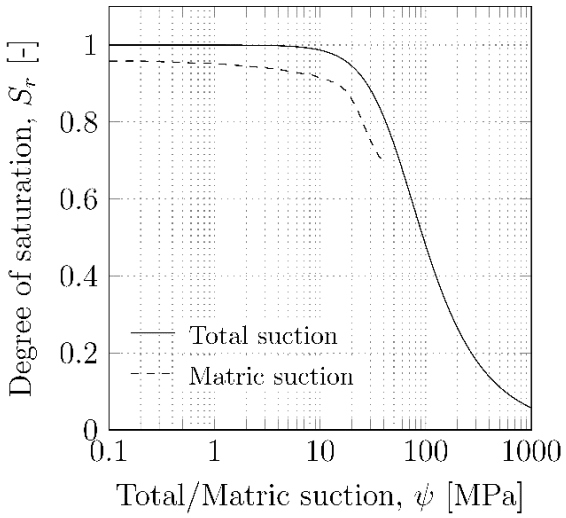

Figure 4. Separate consideration of matric and total suction in the context of the SWCC of intact OPA.

The initial state of intact OPA samples was at a total suction ψ_{tot} between 60 and 65 MPa and corresponding degrees of saturation between 63 and 67%. Experimental data of the SWCCs in Figure 2 show no difference for both volumetric boundary conditions considered. The points all appear to lie on the same scanning curve. Thus, no distinction was made in the fitting between the two different boundary conditions and all points were merged to derive a single combined parameter set. The fact that there is no recognisable difference between free and constant-volume swelling for the intact OPA in the SWCC can be attributed to a further point in addition to the influence of mineralogy already mentioned above. Diagenesis and the resulting structure play the decisive role here. As shown in Christ et al. (2023), the structure of the intact material acts as an additional attractive force and further reduces the swelling capacity. As OPA is ground, the swelling pressure and the water uptake capacity according to Enslin-Neff increase significantly. Both increase more with increasing grinding fineness. Due to the once again lower swelling capacity of the intact OPA compared to the OPA powder, the volumetric boundary conditions no longer play a significant role in the determination of the SWCC. An influence can no longer be identified from the data.

Air-entry values (AEVs) determined according to Equ. 1 are also summarised in Table 2. From a physical point of view, the AEVs are not actual air entry values, as they were determined using the wetting path and not the drying path. Nevertheless, they are considered here as characteristical values of a SWCC. It is noticeable that the AEV of the intact material is more than ten times the AEV of the powder. The magnitude of AEVs depend on different factors, like the density, grain size-distribution or aggregation (Nishimura et al., 2012), and thus factors that influence the size of the pore diameters. The smaller the pore diameter, the greater the suction required for air to penetrate into the pore space and thus to bring the sample into an unsaturated state. Due to the higher dry density of the intact material (ρ_d=2.3 g/cm³) compared to the compacted powder (ρ_d=2.0 g/cm³), the observed difference is plausible. This is also confirmed by the pore-size distribution of the two materials. The peak of the pores and thus the most common pore diameter is 300 nm for the powder, whereas it is only 10 nm for the intact OPA. Ferrari et al. (2014) summarised data from various studies on the water retention behaviour of intact OPA. The yielded exponential fit is plotted with available data from the literature in Figure 3. The AEV from this study shows very good agreement with the data and the corresponding exponential fit. Note: The value in Figure 3 from this study differs from the value in Table 2 because it is based on the definition of the AEV in Ferrari et al. (2014). There, the AEV is the suction that correlates to a degree of saturation of 95% in the SWCC. As mentioned before, the SWCC can also be derived from the MIP data. Thereby, pressure that must be applied to penetrate mercury into the pores of the sample is converted to a matric suction. Figure 4 shows both SWCCs for the intact material, the van Genuchten fit of the total suction and MIP data of the matric suction. The two curves fit together very well. The bend in the two courses runs almost parallel. Due to the upper limit of the MIP, the SWCC of the matric suction ends at approx. 40 MPa.

The difference between the two curves is due to the osmotic suction of the sample or rather the pore fluid. Ferrari et al. (2014) showed with a separate determination of the osmotic suction of OPA with the contact and non-contact filter paper method that this matches quantitatively well. In the current study, the proportion of osmotic suction decreases slightly as the degree of saturation increases, from 18.8 MPa at S_r=75% over 16.8 MPa at S_r=80% and 14.2 MPa at S_r =85% to 13.5 MPa at S_r =90%. This is attributable to the fact that the sample is saturated via the vapour phase, which lowers the ion concentration in the pore fluid and. thus the osmotic suction.

4 CONCLUSIONS

In this study, the soil water retention behaviour of intact and powder compacted Opalinus clay has been assessed in free and constrained volume conditions. The experimental results indicated no significant influence of volumetric boundary conditions on the SWCC of OPA. The air-entry value obtained form current experiments was found to be consistent with other measurements in the literature. Finally, the MIP-driven SWCC of the matric suction showed the same trend as the SWCC of total suction.

ACKNOWLEDGEMENTS

The financial supports provided by University of Luxembourg and by DFG through Collaborative Research Centre SFB-837 (A5) are appreciated.

REFERENCES

Christ, F., Lieske, W., Herz, C., and Wichtmann, T. (2022). Evaluation of the Penetration Behavior of Viscous Fluids into Porous Media in the Context of Volume Determination. *Geotechnical Testing Journal*, 45(4). http://doi.org/10.1520/GTJ20210213.

Christ, F., Lieske, W., Lavasan, A. A., Bakker, E., and Wichtmann, T. (2023). Impact of Reconstitution on the Hydro-Mechanical Behaviour of Opalinus Clay Shale. Under review at *Engineering Geology*.

Delage, P., Howat, M., and Cui, Y. (1998). The relationship between suction and swelling properties in a heavily compacted unsaturated clay. *Engineering Geology*, 50(1-2):31–48. https://doi.org/10.1016/S0013-7952(97)00083-5.

Ferrari, A., Favero, V., Marschall, P., and Laloui, L. (2014). Experimental analysis of the water retention behaviour of shales. *International Journal of Rock Mechanics and Mining Sciences*, 72(2):61–70. https://doi.org/10.1016/j.ijrmms.2014.08.011.

Ferrari, A. and Romero, E. M. (2019). Thermo–Hydro–Mechanical Testing of Shales. In: Dewers, T., Heath, J., and Sanchez, M., editors, *Shale*, Geophysical Monograph Series, pages 83–97. https://doi.org/10.1002/9781119066699.ch6.

Nishimura, T., Koseki, J., and Rahardjo, H. (2012). Determination of Air-Entry Value for Different Compacted Unsaturated Soil. In: *2nd International Conference on Transportation Geotechnics (ICTG)*, Hokkaido, Japan, pages 604–609.

Pasha, A. Y., Khoshghalb, A., and Khalili, N. (2016). Pitfalls in Interpretation of Gravimetric Water Content–Based Soil-Water Characteristic Curve for Deformable Porous Media. *International Journal of Geomechanics*, 16(6). https://doi.org/10.1061/(ASCE)GM.1943-5622.0000570.

Romero, E., Gens, A., and Lloret, A. (1999). Water permeability, water retention and microstructure of unsaturated compacted Boom clay. *Engineering Geology*, 54(1-2):117–127. https://doi.org/10.1016/S0013-7952(99)00067-8.

Seiphoori, A., Ferrari, A., and Laloui, L. (2014). Water retention behaviour and microstructural evolution of MX-80 bentonite during wetting and drying cycles. *Géotechnique*, 64(9):721–734. https://doi.org/10.1680/geot.14.P.017.

Soltani, A., Azimi, M., Boroomandnia, A., and O'Kelly, B. C. (2021). An objective framework for determination of the air-entry value from the soil–water characteristic curve. *Results in Engineering*, 12:100298. https://doi.org/10.1016/j.rineng.2021.100298.

Van Genuchten, M.T. (1980) A Closed Form Equation for Predicting the Hydraulic Conductivity of Unsaturated Soils. Soil Science Society of America Journal, 44, 892-898.

Ziegler, M., Lavasan, A.A., and Loew, S. (2022a). Stress evolution around a TBM tunnel in swelling clay shale over four years after excavation. *Tunnelling and Underground Space Technology,* 128,104649. https://doi.org/10.1016/j.tust.2022.104649.

Ziegler, M., Brixel, B., Lavasan, A.A., Christ, F., and Loew, S. (2022b). Investigations in the new TBM-excavated Belchen highway tunnel: Summary and conclusions. *ENSI Research and Experience 2021*. (ENSI-AN-11284):342–358.

Proceedings of the XVIII ECSMGE 2024
GEOTECHNICAL ENGINEERING CHALLENGES
TO MEET CURRENT AND EMERGING NEEDS OF SOCIETY
© 2024 the Authors
ISBN 978-1-032-54816-6
DOI 10.1201/9781003431749-50
Open Access: www.taylorfrancis.com, CC BY-NC-ND 4.0 license

ECSMGE 24
XVIII EUROPEAN CONFERENCE ON SOIL MECHANICS AND GEOTECHNICAL ENGINEERING

Definition and analysis of ground surface vibration curves induced by railway traffic

Définition et analyse des courbes d'atténuation des vibrations induites par le trafic ferroviaire.

A. Colaço
CONSTRUCT-FEUP, University of Porto

R. Gomes
Faculty of Engineering, University of Porto

E. Fortunato*
National Laboratory for Civil Engineering (LNEC)

**efortunato@lnec.pt*

ABSTRACT: Prediction and control of ground-borne noise and vibrations are amongst the largest environmental challenges for railway exploitation in urban areas. Empirical methods based on attenuation curves, similar to those presented by the Federal Transit Administration (FTA) and the Federal Railroad Administration (FRA), could be extremely versatile for a first estimative of the vibration levels at the ground surface. Despite the value of the presented curves, these have a generalist character, not allowing to attend to the particular and specific scenarios. Furthermore, both railway technology and construction techniques adopted in other regions of the world are quite distinct from USA reality giving rise to poor predictions when applied in distinct contexts. In this way, advanced numerical modelling is a reliable alternative, allowing incorporation of the geological and geotechnical profile, type and geometric configuration of the railway track and railway vehicle specific to each case under study and, therefore, achieving a more elaborate level of detail in the analysis. On this work, a 2.5D FEM-PML (Finite Element Method – Perfectly Matched Layer) numerical approach is used to compute the ground surface vibration curves for different scenarios. From the results obtained, it is possible to state that, even being a conservative approach in some of the scenarios under consideration, the application of the empirical methodology proposed by FTA/FRA should be considered only as a first indicator, and it is recommended that more detailed analyses be performed in situations that require a higher control of the permitted vibration levels.

RÉSUMÉ: La prévision et le contrôle du bruit et des vibrations transmis au sol constituent l'un des plus grands défis environnementaux de l'exploitation ferroviaire en zone urbaine. Des méthodes empiriques basées sur des courbes d'atténuation, similaires à celles présentées par la *Federal Transit Administration* (FTA) et par la *Federal Railroad Administration* (FRA) pourraient être extrêmement polyvalentes pour une première estimation des niveaux de vibration à la surface du sol. Malgré la valeur des courbes présentées, celles-ci ont un caractère généraliste, ne permettant pas de s'intéresser à des scénarios particuliers et spécifiques. En outre, la technologie ferroviaire et les techniques de construction adoptées dans d'autres régions du monde sont assez différentes de la réalité américaine, ce qui donne lieu à prévisions inadéquates lorsqu'elles sont appliquées dans des contextes distincts. De cette manière, la modélisation numérique avancée constitue une alternative fiable, permettant d'incorporer le profil géologique et géotechnique, le type et la configuration géométrique de la voie ferrée et du véhicule ferroviaire spécifique à chaque cas étudié et, par conséquent, d'atteindre un niveau de détail plus élaboré dans l'analyse. Dans ce travail, une approche numérique 2,5D FEM-PML (*Finite Element Method – Perfectly Matched Layer*) est utilisée pour calculer les courbes d'atténuation des vibrations pour différents scénarios. À partir des résultats obtenus, il est possible d'affirmer que, même s'il s'agit d'une approche conservatrice dans certains des scénarios considérés, l'application de la méthodologie empirique proposée par FTA/FRA doit être considérée uniquement comme un premier indicateur, étant recommandé d'effectuer davantage analyses détaillées dans des situations qui nécessitent un contrôle plus élevé des niveaux de vibration autorisés.

Keywords: Railway traffic; vibrations; numerical modelling; attenuation curves.

1 INTRODUCTION

Based on experimental data, the Federal Transit Administration (FTA) and the Federal Railroad Administration (FRA) proposed a general vibration assessment method. The main principle of such methodology consists in the evaluation of vibration attenuation curves, defined through the maximum value of the running RMS (root-mean-square) of the vertical velocity as a function of the distance to the railway infrastructure, which are subsequently corrected to meet the presence of buildings and taking into account their specificity (Quagliata, 2018) (Hanson et al., 2012).

The ground surface vibration curves were derived from the statistical treatment of experimental results. The consideration of such curves to specific scenarios should be adapted employing adjustment factors, also of an empirical nature. These are given as single values to add to the base level preconized by the reference curves.

Despite the value of the presented curves, and as can be understood, the empirical curves reported have a generalist character, not allowing to attend to the particular and specific scenarios, as discussed in Sadeghi et al. (2019). In this way, advanced numerical modelling is a reliable alternative, allowing incorporate the geological and geotechnical profile, type and geometric configuration of the railway track and railway vehicle specific to each case under study and, therefore, achieving a more elaborate level of detail in the analysis.

2 NUMERICAL MODEL

Alternatively, to the solutions reported previously, ground surface vibration curves can be evaluated through advanced numerical modelling, being subsequently corrected to meet the dynamics of the existing buildings in the vicinity of the railway infrastructure. For this purpose, a validated numerical approach is used to model the train-track-(tunnel)-ground system (Lopes et al., 2016).

This approach corresponds to a sub-structured methodology, where the modelling domain is divided into a 'stationary' component, composed by the track-(tunnel)-ground system, and a 'moving' component (train), where a 2D vehicle model is adopted and only vertical excitation is considered. The interaction between both is established by coupling the vehicle contact points with the remaining system. The basic formulation of the interaction scheme is summarised in Figure 1.

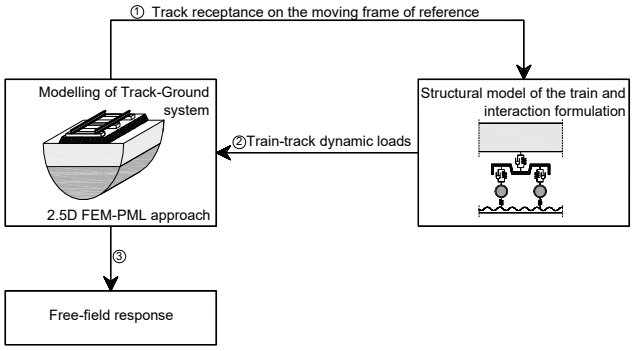

Figure 1. Representative scheme of the numerical modelling approach.

In terms of the track-(tunnel)-ground simulation, a 2.5D FEM-PML model is used. This formulation assumes a linear elastic behaviour of the different components and an infinite structure and invariable properties (geometrical and mechanical) in the direction of development of the track. Assuming these conditions, the three-dimensional solution of the problem is found through a 2.5D procedure based on the finite elements approach, where the analysis are carried out in the wavenumber/frequency domain. For its application, all the variables, i.e., loads (action) and displacements (response), are transformed to the wavenumber/frequency domain by means of a double Fourier transform, associated with the direction along the track and with time. Transformed quantities are functions of the Fourier images of x (longitudinal coordinate) and t (time), defined as wavenumber (k1) and frequency (ω). Moreover, a topic of particular relevance is the formulation of special procedures to treat the boundary effects inherent to the truncation of the domain associated with the finite element discretization. In order to avoid this spurious reflection of waves, a 2.5D PML approach is adopted. Full details about the mathematical formulation of the 2.5D FEM-PML model can be found in Lopes et al. (2014).

From this numerical approach, it is possible to compute vibration levels along the surface of the ground that are used to define the ground surface vibration curves.

3 PARAMETRIC STUDIES

3.1 General description

The numerical investigations in this study are based on the geometric and geomechanical properties illustrated in Figure 2. As can be seen, the scenario of analysis corresponds to a slab track in a tunnel.

To decrease computational effort, symmetry was used to reduce the modelling domain to half of its dimensions.

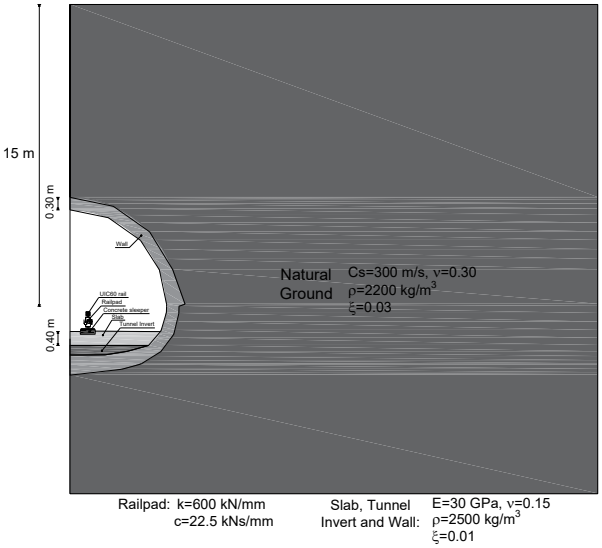

Figure 2. Geometry and properties of the track-tunnel-ground system.

Regarding rolling stock, the passage of the Alfa-Pendular vehicle is considered. The geometric properties and weight per axle can be found in dos Santos et al. (2016).

The train-track interaction is essential in problems involving the generation of vibrations. In the present work, the dynamic interaction mechanism is provided by the rail unevenness and the synthetic unevenness profile is generated according to the FRA proposal (Hanson et al., 2012).

The parametric studies consider two different train speeds (100 km/h and 200 km/h) and two different rail unevenness classes. At this respect, a distinction is made between the curves evaluated for a track in perfect conditions (Class 6 of the FRA classification) and a track in a not so good condition (according to Class 3 in the FRA classification).

3.2 Results and discussion

As initially stated, the numerical model 2.5D FEM-PML is applied for the prediction of vibration levels at the ground surface. In this way, Figure 3 presents the vertical vibration velocity for an observation point located at the ground surface, on the symmetry plane and considering the following variables: train speed equal to 200 km/h and maintenance Class 3. The ground surface vibration curves are defined through the maximum value of the running RMS (red line in Figure 3) of the vertical velocity as a function of the distance to the track.

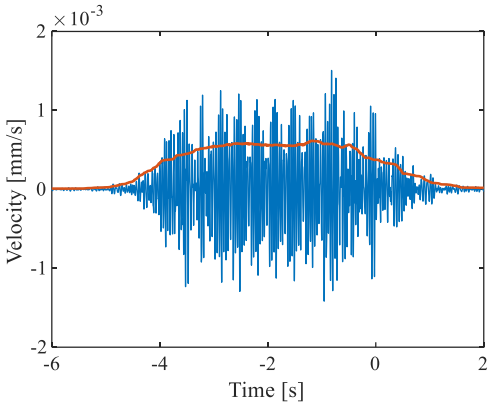

Figure 3. Vertical vibration velocity for an observation point located at the ground surface, on the symmetry plane.

Figure 4 presents the comparison between the vibration attenuation curves evaluated through the numerical approach and the attenuation curves proposed by FTA for the different scenarios under analysis.

The FTA curves correspond to those defined for Rapid Transit and Light Rail Vehicles and it was assumed two adjustment factors: i) speed factor ($20\log(\text{speed}/\text{speed}_{ref})$, speed_{ref}=50 mph); ii) track quality factor (0 dB for Class 6; +10 dB for Class 3).

As can be seen from Figure 4, and as expected, the vibration levels increase with the train speed and the degradation of the track quality. These general trends are also verified from FTA proposal through the adjustment factors adopted.

A comparison between numerical and empirical results allows to identify, for the conditions admitted, maximum deviations around 8 dB, indicating a significant difference. For some cases, the FTA curves underestimate the vibrations levels.

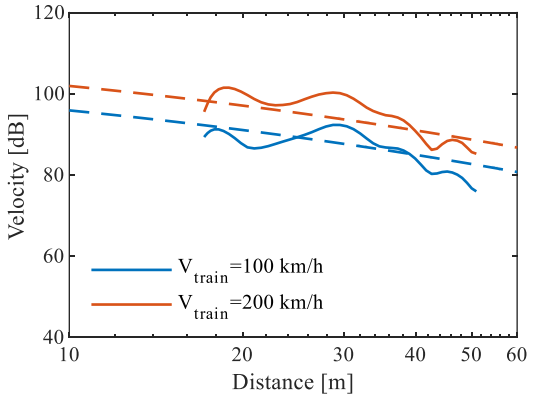

a)

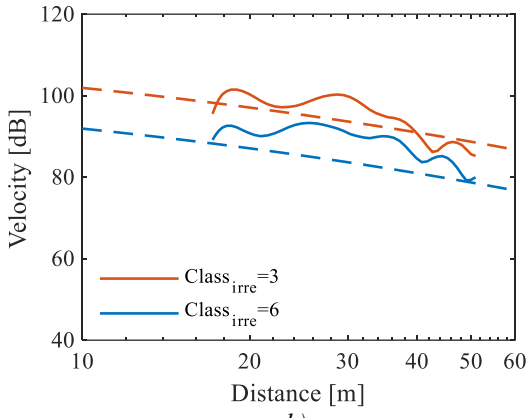

b)

Figure 4. Ground surface vibration curves (dB ref. 10^{-8} m/s): a) influence of the train speed; b) influence of the track condition (solid line – numerical result; dash line: FTA proposal).

4 CONCLUSIONS

Based on the results obtained from the parametric studies conducted, it can be concluded that the application of the empirical methodology proposed by FTA should be regarded as an initial indicator. It is advisable to perform more detailed analyses in situations that require stricter control of allowed vibration levels.

ACKNOWLEDGEMENTS

This work is financially supported by: Base Funding - UIDB/04708/2020 with DOI 10.54499/UIDB/04708/2020 and Programmatic Funding - UIDP/04708/2020 with DOI 10.54499/UIDP/04708/2020 of the CONSTRUCT - Instituto de I&D em Estruturas e Construções - funded by national funds through the FCT/MCTES (PIDDAC); by national funds through the FCT/MCTES (PIDDAC), under the project PTDC/ECI-EGC/3352/2021 – IntRAIL – Intelligent prediction tool for ground-borne noise and vibrations induced by railway traffic; Individual Grant No. 2022.11639.BD; CEECIND (Scientific Employment Stimulus - 5th Edition) provided by FCT (https://doi.org/10.54499/2022.00898.CEECIND/CP1733/CT0005). Part of the work was conducted in the framework of the TC202 National Committee of the Portuguese Geotechnical Society (SPG) "Transportation Geotechnics," in association with the International Society for Soil Mechanics and Geotechnical Engineering (ISSMGE-TC202).



REFERENCES

Dos Santos, N. C., A. Colaço, P. Alves Costa, and R. Calçada (2016). Experimental analysis of track-ground vibrations on a stretch of the Portuguese railway network, *Soil Dynamics and Earthquake Engineering*, 90: 358-80. http://doi.org/10.1016/j.soildyn.2016.09.003

Hanson, C. E., J. C. Ross, and D.A. Towers (2012). High-Speed Ground Transportation Noise and Vibration Impact Assessment. Federal Railroad Administration - Department of Transportation, Office of Railroad Policy and Development. Washington DC.

Lopes, P., P. Alves Costa, M. Ferraz, R. Calçada, and A. Silva Cardoso (2014). Numerical modeling of vibrations induced by railway traffic in tunnels: From the source to the nearby buildings, *Soil Dynamics and Earthquake Engineering*, 61-62: 269-85. http://doi.org/10.1016/j.soildyn.2014.02.013.

Lopes, P., J. Fernández Ruiz, P. Alves Costa, L. Medina Rodríguez, and A. Silva Cardoso (2016). Vibrations inside buildings due to subway railway traffic. Experimental validation of a comprehensive prediction model, *Science of The Total Environment*, 568: 1333-43. http://doi.org/10.1016/j.scitotenv.2015.11.016.

Quagliata, A. (2018). Transit Noise and Vibration Impact Assessment Manual. Office of Planning and Environment Federal Transit Administration - Department of Transportation. Washington DC.

Sadeghi, J., M. H. Esmaeili, and M. Akbari (2019). Reliability of FTA general vibration assessment model in prediction of subway induced ground borne vibrations, *Soil Dynamics and Earthquake Engineering*, 117: 300-11. http://doi.org/10.1016/j.soildyn.2018.11.002.

Proceedings of the XVIII ECSMGE 2024
GEOTECHNICAL ENGINEERING CHALLENGES
TO MEET CURRENT AND EMERGING NEEDS OF SOCIETY
© 2024 the Authors
ISBN 978-1-032-54816-6
DOI 10.1201/9781003431749-51
Open Access: www.taylorfrancis.com, CC BY-NC-ND 4.0 license

ECSMGE 24
XVIII EUROPEAN CONFERENCE ON SOIL MECHANICS AND GEOTECHNICAL ENGINEERING

Integrating cluster-based knowledge for local undrained shear strength prediction

Intégration de connaissances basées sur les clusters pour la prédiction locale de la résistance au cisaillement non drainé

S. Collico
DMT GmbH & Co. KG, Essen, Germany

G. Spagnoli*
Sweco, Essen, Germany

A. Fraccica
Istituto Superiore per la Protezione e la Ricerca Ambientale (ISPRA), Rome, Italy

E. Romero
Universität Politecnica de Catalunya (UPC), Barcelona, Spain

**giovanni.spagnoli@sweco-gmbh.de*

ABSTRACT: The prediction of local (i.e., site-specific) undrained shear strength from soil properties (e.g., water content, Plasticity index, Liquid Limit) is a cost-effective solution to preliminary assess the proper foundation type at a project site. Nevertheless, the local dataset is often incomplete and sparse to infer robust prediction of local strength parameters. To bypass such inconvenience, global or soil-type correlations might be employed to predict undrained shear strength from local soil properties measurements. However, by doing so two main drawbacks can arise: a great uncertainty is introduced for prediction of undrained shear strength due to the large number of soil types the global database is usually composed. Secondly, a problem of pertinence might arise when soil type-specific correlations are employed. In this study the local predictions of undrained shear strength are estimated integrating clustered global information through a Bayesian formulation, which allow to assess the problem of local dataset incompleteness. The methodology is shown by making use of an already compiled and published database.

RÉSUMÉ: La prédiction de la résistance au cisaillement non drainée locale (c'est-à-dire spécifique au site) à partir des propriétés du sol (par exemple, la teneur en eau, l'indice de plasticité, la limite de liquidité) est une solution rentable pour évaluer préliminairement le type de fondation approprié sur un site de projet. Néanmoins, l'ensemble de données locales est souvent incomplet et clairsemé pour déduire une prédiction robuste des paramètres de résistance locaux. Pour éviter de tels inconvénients, des corrélations globales ou par type de sol pourraient être utilisées pour prédire la résistance au cisaillement non drainé à partir de mesures locales des propriétés du sol. Cependant, ce faisant, deux inconvénients principaux peuvent survenir: premièrement, une grande incertitude est introduite pour la prévision de la résistance au cisaillement non drainé en raison du grand nombre de types de sols qui composent habituellement la base de données mondiale. Deuxièmement, un problème de pertinence pourrait surgir lorsque des corrélations spécifiques au type de sol sont utilisées. Dans cette étude, les prédictions locales de la résistance au cisaillement non drainé sont estimées en intégrant des informations globales groupées via une formulation bayésienne, ce qui permet d'évaluer le problème de l'incomplétude des ensembles de données locaux. La méthodologie est présentée en utilisant une base de données déjà compilée et publiée.

Keywords: Undrained shear strength; local dataset; global dataset; Bayesian; cluster-based.

1 INTRODUCTION

At a project site local (i.e., site-specific) geotechnical data are often incomplete and sparse. A typical scenario is the one where the amount of soil properties and Atterberg limits measurements exceed the number of undrained shear strength observations. It is then common practice to compute a weighted average of undrained shear strength measurements with direct and indirect estimates of it. However, the indirect estimates of undrained shear strength might carry large systematic uncertainties when global correlation are used (Collico and Arroyo, 2023; Ching and Phoon, 2019). On the other hand, when soil type-specific correlations are applied a problem of pertinence might arise. To assess such issues, Bayesian methodologies

have been proposed to assess and reduce systematic uncertainties by sequentially updating local information with global and regional measurements (Zhang et al., 2004; Wang and Cao, 2013; Wang et al. 2010). Despite being efficient, these approaches would require the complete set of independent variables to first construct and further validate correlations.

More recently Ching and Phoon (2019) and Wu et al. (2022) developed an efficient and elegant hybrid Bayesian methodology to assess uncertainty of local data and account for global geotechnical information. In this context, it might be pertinent to wonder whether global information or filtered ones according to some criterion should be considered for local undrained shear strength updating. This seems particularly relevant when incomplete and scarce information are available at the project site. A first approach would be to filter global information according to the same soil-types identified at the project site. Nevertheless, by filtering the database according to the same textural soil classification might not represent an optimal criterion. If a soil type classification problem based on some in-situ test is considered, it is thought that the geological textural classification might not be an exhaustive indicator of soil (Collico et al., 2023).

As alternative to filtering, unsupervised data-driven approaches, such as cluster-based solutions can be applied. In particular, cluster-based solution appropriately calibrated by engineers' interpretation and experience might provide an efficient way of data subdivision to allocate soil-similarity (Collico et al. 2024). Aware of that, in this study, the hybrid workflow proposed by Ching and Phoon (2019) is developed and extended to account for global cluster-based information and allocate data site similar for local undrained shear strength updating. The approach is demonstrated making use of already compiled and published databases such as CLAY/10/7490 (Ching et al., 2014) and S-CLAY/7/168 (D'Ignazio et al., 2016).

2 GLOBAL DATABASE DESCRIPTION

Let denoted as Y_g datapoints from global database here represenetd by four geotechnical parameters such as that: Y_g = [Y_{g1}=LL; Y_{g2}=PL; Y_{g3}=PI; Y_{g4}= w; Y_{g5}=Su/σ'_{v0}], with LL=liquid Limit, PL=Plastic Limit, PI=plasticity Index, w=water content and Su/σ'_{v0}=normalized undrained shear strength.

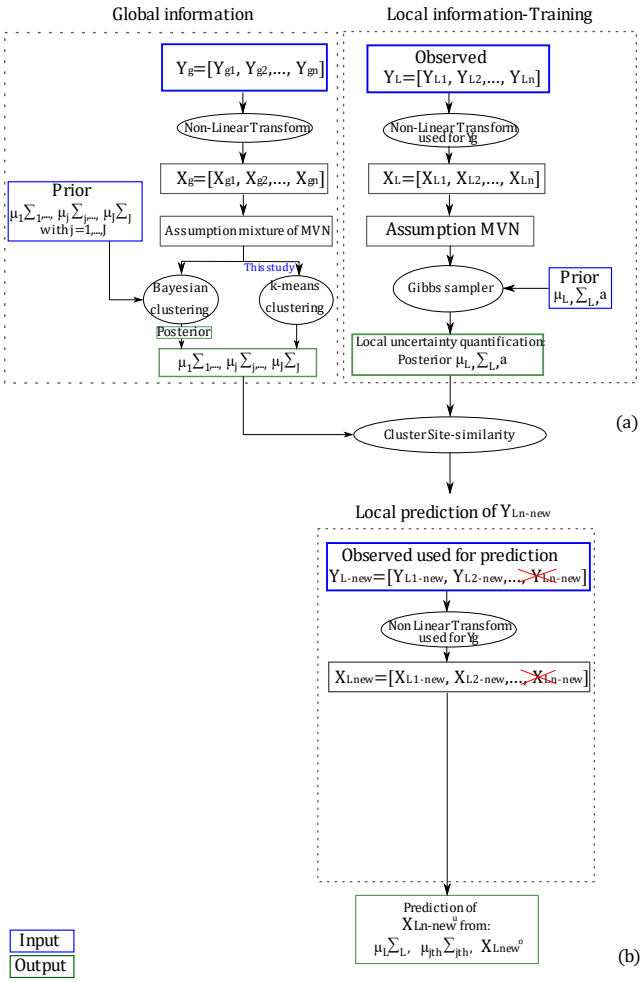

Figure 1. Workflow of methodology employed in this study.

2.1 Probabilistic model for Global information

The proposed method requires the definition of a global (i.e., no-local) multivariate Probability Density Function (PDF). Such no-local PDF is of mainly importance when scarce and incomplete X_L information is available at a project site.

To construct a valid multivariate normal distribution, the variables Y_g (non-normal distributed) (Figure 1) needs to be transformed into normally distributed ones X_g. This is accomplished through a non-linear transform (see Ching and Phoon, 2014). It is then assumed a linear dependence among X_g variables such that their probability density can be described by a $n-th$ dimensional Gaussian Mixture Model which reads:

$$f(X_g|\Theta) = \sum_{j=1}^{J} \pi_j f(X_g|\mu_j, \sum_j) \qquad (1)$$

with $f(X_g|\mu_j, \sum_j)$ denoting the j-th multivariate normal component (i.e., j-th cluster) with mean μ_j, covariance $\sum_j$ and weight π_j. J is the number of Gaussian mixture components and Θ vector containing

all Gaussian Mixture parameters (i.e., means, Covariances and weights). For J=1 eq. (1) recovers the definition of multivariate normal distribution. In this study the global datapoints are modelled by eq. (1) through the k-Means algorithm. Nevertheless, a Bayesian Mixture formulation could be also applied instead of eq. (1) allowing to infer prior knowledge about clusters depending on local dataset information.

2.2 Probabilistic model for Local dataset

Let consider the local dataset reported in Table 1 for a the Norwegian site of Drammen (D'Ignazio et al., 2016) as example. Table 1 represents an optimistic scenario at a project-site. A more realistic situation is the one where 60% of datapoints in Table 1 are missing. Let denote as X_{L^u} the missing entries and as X_{L^o} the observed datapoints of X_L. In such a case, great uncertainty would characterize local PDF parameters, making Bayesian inference necessary.

To construct a valid local PDF, the datapoints Y_L are transformed into X_L by considering the same non-linear transform coefficients employed for Y_g (Figure 1a). After transformation, the local datapoints X_L are assumed to be distributed according to a multivariate normal distribution as:

$$f(X_L|\mu_L, \sum_L) = mvn(X_L|\mu_L, \sum_L) \quad (2)$$

with $\mu_L, \sum_L$ mean and covariance matrix of local PDF.

2.3 Bayesian formulation for incomplete datasets

To assess the local data incompleteness the Bayesian formulation proposed by Ching and Phoon, (2019) is employed. We here recall only the main steps of the methodology.

As a first step, the prior knowledge of the unknown random variables has to be defined (Figure 1a). Therefore, the prior knowledge of μ_L, $\sum_L$ and hyperparameters a for $\sum_L$ parametrization, need to be elicited. Having denote as $f(\mu_L)$ and $f(\sum_L)$ the prior density distribution of μ_L and $\sum_L$, their conjugate form is assumed since enable exact sampling. The prior knowledge of μ_L is taken as a normal multivariate distribution, while $\sum_L$ is modelled as the inverse Wishart distribution such as:

$$f(\mu_L) = mvn\,(\mu_L|\mu_0, C_0) \quad (3)$$

$$f(\sum_L) = IW\,(\sum_L|\sum_0, v) \quad (4)$$

Table 1. Local observation for a Norway Site (Drammen).

Depth	LL (%) (Y_{L1})	PL (Y_{L2})	PI (Y_{L3})	w (%) (Y_{L4})	Su/σ'_{v0} (Y_{L5})
Training Y_L					
5.21	58.72	10.34	0.80	65.47	0.189
6.16	65.58	18.82	0.81	65.58	0.164
7.14	75.2	20.56	0.78	56.15	0.148
7.45	88.51	18.73	0.73	65.25	0.141
7.50	88	18	0.73	65	0.245
7.80	60	29	0.89	52	0.322
8.48	75.84	15.3	0.76	61.65	0.210
9.04	78.22	19.1	0.76	58.22	0.133
9.25	33	23	1.12	32	0.157
9.42	92.23	20.35	0.72	64.08	0.186
11.93	40.16	8.75	0.89	27.60	0.0872
13.00	25	3	0.96	26	0.178
Testing Y_L					
4.01	39.28	9.74	0.90	30.68	0.181
13.04	25	3	0.96	25.7	0.119
17.39	23.3	2.73	0.97	17.2	0.122

The mean μ_0 is taken as zero mean vector of $nx1$ dimension, while the prior covariance matrix C_0 (nxn) is taken to be a diagonal matrix with very large diagonal elements (i.e., 104), such that $f(\mu_L)$ tend to be uninformative. Concerning $f(\sum_L)$ the inverse-Wishart distribution is assumed with scale matrix $\sum_0$ and degree of freedom $v = n + 1$. To make $f(\sum_L)$ noninformative a heirarchical form can be applied (Huang and Wand 2013; Ching and Phoon 2019):

$$f(\sum_L|a) = IW\,(\sum_L|\sum_0, v) \quad (5)$$

$$f(a_i) = IG(a_i|\alpha, \beta) \quad (6)$$

where $(a = [a_1, \ldots, a_n])$ are the random hyperparameters required for $\sum_L$ parametrization. The prior of each hyperparameters $f(a_i)$ is assumed an inverse gamma distribution with scale and shape parameters α, β. In this study α, β are taken as 0.5 and 10^{-4} respectively such that a non-informative linear dependence and variance is assumed (Wu et al., 2022).

2.4 Local posterior inference

The Posterior inference of the local unknown random variables (μ_L, $\sum_L, a$) is derived through the Gibbs sampler (GS) (Geman and Geman, 1984), which decompose the unknown random parameters into groups to randomly sample each group conditional on the remaining ones. This allows to sequentially draw T times the unknown random variables, to final generate (T-t_b) random samples of μ_L, $\sum_L$ and a, which are asymptotically distributed as the target posterior distribution. t_b is defined as burning period (i.e., the

number of generated samples to be discard for posterior inference). It worth noticing that, when missing information characterize the local dataset, by partitioning local mean and covariance matrix accordingly, the Bayesian formulation allow to draw T samples of missing datapoints X_{L^u} conditional to the observed X_{L^o} ones (see Ching and Phoon, 2019 and Wu et al., 2022).

2.5 Local prediction integrating cluster-based information

When the local training dataset is scarce and incomplete, the statistical uncertainty of local PDF parameters $(\mu_L, \sum_L, a, X_{L^u})$ can be significant, propagating into local soil parameters prediction, here denoted as X_{L-new}. In this case, it is reasonable to rely on global information, which are statistically more robust. Nevertheless, global databases might be composed of too different soil-types leading to a too generic prediction of local soil parameters. In this context, the clustering approach previously described in section 2.2 might come in help since enable to filter global information "similar" to the local site of interest. The data similarity between each t-th local samples, generated during the Gibbs sampler, and the j-th global cluster is quantified as follows:

$$p(\mu_{L,t}|\mu_{gj}, \sum_{gj}) = \frac{\pi_j f(\mu_{L,t}|\mu_{gj}, \sum_{gj})}{\sum_{j=1}^{J} \pi_j f(\mu_{L,t}|\mu_{gj}, \sum_{gj})} \quad (7)$$

with:

$$f(\mu_{L,t}|\mu_{gj}, \sum_{gj}) = \left|\sum_{gj}\right|^{-1/2} \cdot (2\pi)^{-n/2} \cdot \exp\left(\left[-0.5(\mu_L - \mu_{gj})^T \sum_{gj}^{-1} (\mu_L - \mu_{gj})\right]\right. \quad (8)$$

and π_j weigth of the j-th Gaussian mixture component.

Once site similarity of the t-th sample is assessed, prediction of X_{L-new} can be inferred according to the hybrid method proposed by Ching and Phoon (2019) as:

$$f(X_{L-new-t}|hb) = f\left(X_{L-new}|\mu_{gj}, \sum_{gj}\right) \cdot f(X_{L-new}|\mu_L, \sum_L) \quad (8a)$$

$$f(X_{L-new-t}|hb) = \sum_{t=tb+1}^{T} w_t \cdot f\left(X_{L-new-t}|\mu_{hb,t}, \sum_{hb,t}\right) \quad (8b)$$

with $\mu_{gj}, \sum_{gj}$, mean and covariance matrix of the most similar j-th global cluster, $\mu_{hb,t}, \sum_{hb,t}$ mean and covariance matrix of the hybrid multivariate distribution given by product of $f(X_{L-new}|\mu_{gj}, \sum_{gj})$ and $f(X_{L-new}|\mu_L, \sum_L)$ and w_t is the weight of each condition density distribution $f(X_{L-new-t}|hb)$.

3 CASE STUDY

To capture the benefit of cluster-based information on local prediction, the Norway site, Drammen (Table 1), extracted from D'Ignazio et al. (2016) is considered. The local dataset is subdivided into training (to derive posterior estimated of local PDF parameters) and testing. Four case scenarios are exploited:

- Only 40% of datapoints of Table 1 is considered available for training, while the remaining 60% is considered missing. We denote such scenario as Incomplete case;
- All the datapoints of Table 1 are considered for training. Such case is denotated as Complete scenario.
- For both Complete and Incomplete scenarios, global information employed in eq. (8) is subdivided in one (no-cluster scenario) and two clusters (cluster-based scenario) for a total of four different cases (i.e., Incomplete no-cluster, Incomplete cluster-based, Complete no-cluster, Complete cluster-based). It is worth noticing that for illustration purposed optimal data subdivision (criterion such as BIC) is not considered.

For local X_{L-new} prediction, we will assume that all information (LL, PL, PI, $w = Y_{L-new^o}$) will be available except for Su/σ'_{v0}, which is here taken as variable of interest to be predicted (i.e., $Su/\sigma'_{v0} = Y_{L-new^u}$).

4 RESULTS

As a first step both local and global datapoints are transformed from Y into X domain (Figure 2a and Figure 2b). As a second step global information are subdivided according to the number of clusters selected (i.e., one and two in this study). The k-means algorithm is used as illustrative example. Figure 2c reports the global database subdivision re-transformed in the original Y space when two clusters are selected.

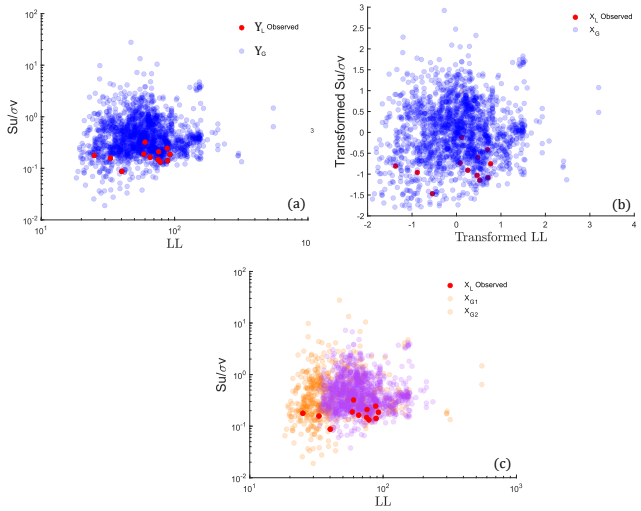

Figure 2. Global and local Normalised undrained shear strength and Liquid Limit datapoints: a) in the original Y space. b) in the X space. c) subdivided according to two clusters after k-NN algorithm.

As a third step the Gibbs sampler is run to compute posterior estimates of local PDF parameters (μ_L, $\sum_L$, a) and (μ_L, $\sum_L$, a, $X_L{}^u$) for the Complete and Incomplete case scenarios respectively. These posterior estimates are then employed to further generate X_{L-new} to be converted into the original Y space. It is worth noticing that at this stage no testing datapoints have been used. The generated samples X_{L-new} would then represent soil parameter prediction if no additional information at the site is acquired.

As an example, Figure 3 reports the generated (T-t_b) samples of local undrained shear strength and LL according to the four scenarios considered. It can be observed that by considering the Complete scenario, no major difference subsists between generated samples of no-cluster (Figure 3a) and cluster-based (Figure 3b) cases. This does not come as surprise since a not clean separation among clusters subsists. When 40% of datapoints are considered for training (Incomplete scenario), generated samples start to converge to global datapoints scatter independently whether one or two cluster are considered (Figure 3c, Figure 3d respectively).

When additional local information becomes available (i.e., testing datapoints), the local undrained shear strength $Y_{L-new}{}^u$ can then be predicted from the observed testing datapoints $Y_{L-new}{}^o$ and trained PDF parameters μ_L, $\sum_L$, a, for the four scenarios. It can be observed that when the training is performed using the complete local dataset a better prediction of undrained shear strength in terms of accuracy and precision is obtained.

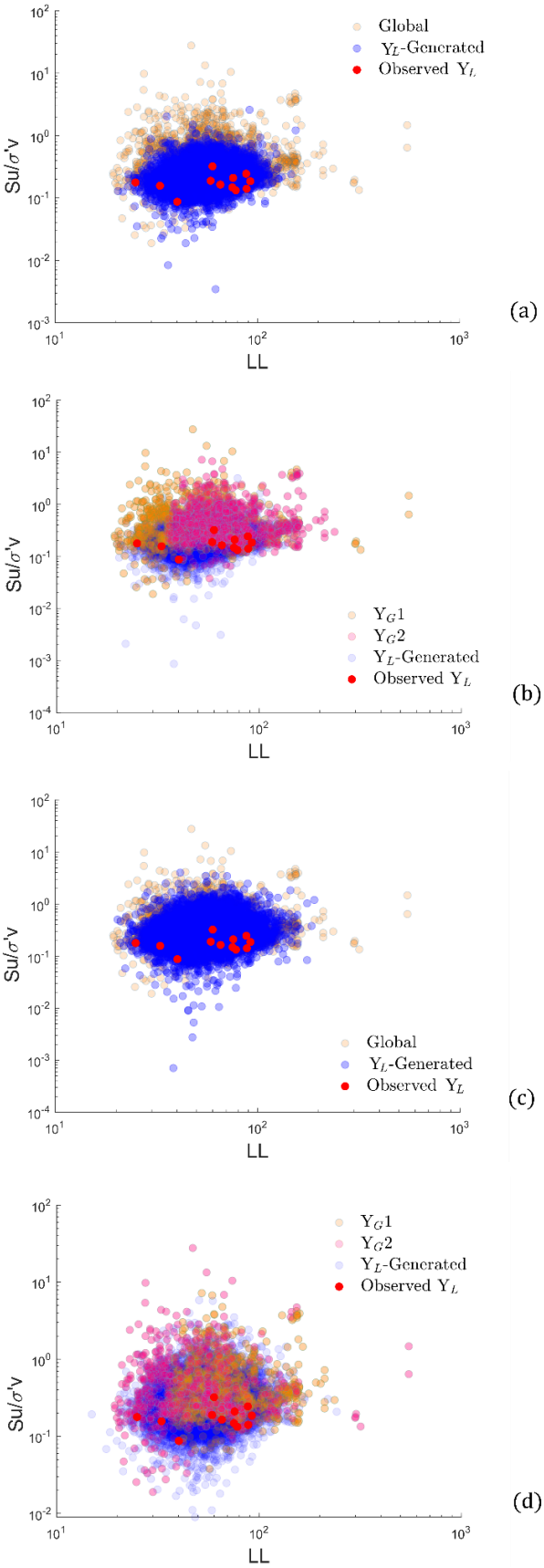

Figure 3. Generated $Y_{L\text{-}new}$ samples for: a) Complete no-cluster scenario. b) Complete cluster-based scenario. c) Incomplete no-cluster scenario. d) Incomplete cluster-based scanrio.

The accuracy seems to slightly increase for both Complete and Incomplete scenarios when clustering approach is employed. Nevertheless, such difference is negligible since the two clusters introduced according to the k-means approach are not characterized by major difference in terms of Pearson correlation and Covariance.

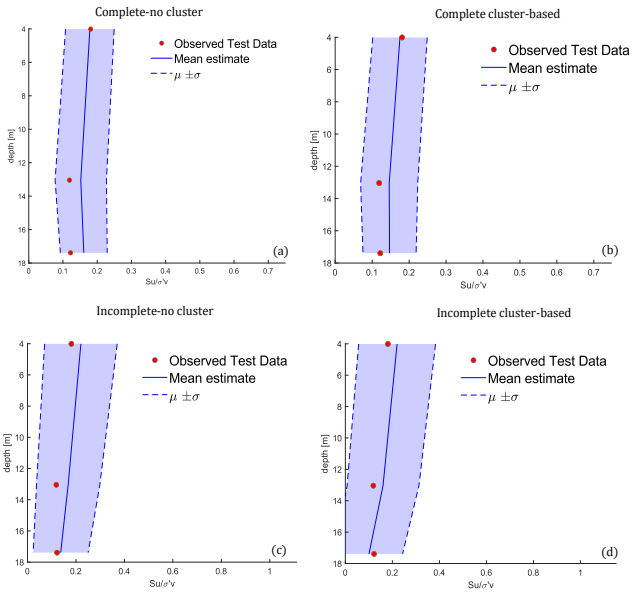

Figure 4. Predicted Su/σ'_{v0} for: a) Complete no-cluster scenario. b) Complete cluster-based scenario. c) Incomplete no-cluster scenario. d) Incomplete cluster-based scanrio.

5 CONCLUSIONS

This paper propose a Bayesian formulation (implementing and extending the formulation by Ching and Phoon (2019)) to integrate cluster-based global knowledge for local undrained shear strength prediction, and assess the challenge of local database incompletness. The work hihglight how cluster-based knowledge might slighlty increase accuracy of local undrained shear strength prediction. Neverthless, the work hihglights how cluster-based solution should be integrated with reason within the described Bayesian formulation. To do so, the approach proposed could provide more significance improvement to local undrained shear strength prediction when a Bayesian Mixture formulation is employed for global dataset manipulation. This would allow to account for more insightful information based on local dataset structure and enegineering experience.

REFERENCES

Ching, J. and Phoon, K.K. (2019) Constructing site-specific multivariate probability distribution model using Bayesian machine learning. *Journal of Engineering Mechanics*, 145 (1). https://doi.org/10.1061/(asce)em.1943-7889.0001537.

Ching, J., Phoon, K.K. and Chen, C.H. (2014) Modeling piezocone cone penetration (CPTU) parameters of clays as a multivariate normal distribution. *Canadian Geotechnical Journal*, 51(1), https://doi.org/10.1139/cgj-2012-0259.

Collico, S. and Arroyo, M. (2023) Bayesian mixture analysis of a global database to improve unit weight prediction from CPTu. *Engineering Geology*, 327, pp. 107353. https://doi.org/10.1016/j.enggeo.2023.107353.

Collico, S., Arroyo, M. and Devincenzi, M. (2024) A simple approach to probabilistic CPTu-based geotechnical stratigraphic profiling. *Computers and Geotechnics*, 165, pp. 105905. 10.1016/j.compgeo.2023.105905.

Tan, S.A. and Länsivaara, T.T. (2016) Correlations for undrained shear strength of Finnish soft clays. *Canadian Geotechnical Journal*, 53 (10), pp. 1628–45. https://doi.org/10.1139/cgj-2016-0037.

Geman, S. and Geman, D. (1984) Stochastic relaxation, Gibbs distributions, and the Bayesian restoration of images. *IEEE Transactions on Pattern Analysis and Machine Intelligence*, 6, pp. 721–41.

Huang, A. and Wand, M. P. (2013) Simple marginally noninformative prior distributions for covariance matrices. *Bayesian Analysis*, 8 (2), pp. 439–52. https://doi.org/10.1214/13-BA815.

Wang, T. Au, S.K. and Cao, Z. (2010) Bayesian approach for probabilistic characterization of sand friction angles. *Engineering Geology*, 114 (3–4), pp. 354–363, https://doi.org/10.1016/j.enggeo.2010.05.013.

Wang, Y. and Cao, Z. (2013) Probabilistic characterization of Young's modulus of soil using equivalent samples. *Engineering Geology*, 159, pp. 106–118. https://doi.org/10.1016/j.enggeo.2013.03.017.

Wu, S., Ching, J. and Phoon, K.K. (2022) Quasi-site-specific soil property prediction using a cluster-based hierarchical Bayesian model. *Structural Safety*, 99, pp. 102253. https://doi.org/10.1016/j.strusafe.2022.102253.

Zhang, L., Tang, W.H., Zhang, L. and Zheng, J. (2004) Reducing uncertainty of prediction from empirical correlations. *Journal of Geotechnical and Geoenvironmental Engineering*, 130 (5), https://doi.org/10.1061/(ASCE)1090-0241(2004)130:5(526).

Proceedings of the XVIII ECSMGE 2024
GEOTECHNICAL ENGINEERING CHALLENGES
TO MEET CURRENT AND EMERGING NEEDS OF SOCIETY
© 2024 the Authors
ISBN 978-1-032-54816-6
DOI 10.1201/9781003431749-52
Open Access: www.taylorfrancis.com, CC BY-NC-ND 4.0 license

ECSMGE 24
XVIII EUROPEAN CONFERENCE ON SOIL MECHANICS AND GEOTECHNICAL ENGINEERING

Back-analysis of deep excavations supported by strutted retaining walls

Rétro-analyse d'excavations profondes soutenues par des murs étayés

V.I. Cordoni
Universitat Politècnica de Catalunya-BarcelonaTech, Barcelona, Spain

L. Gelonch, B. Solà, C. de Santos
SAALG Geomechanics, Barcelona, Spain

A. Ledesma*
Universitat Politècnica de Catalunya-BarcelonaTech, CIMNE, Barcelona, Spain

**alberto.ledesma@upc.edu*

ABSTRACT: Design of deep excavations involves the definition of the retaining walls and struts to support earth pressures. Despite the experience and the procedures available to estimate the forces acting on the struts, their prediction is still difficult and comparison between field measurements and numerical simulations suggest that there are many factors not taken into account in the routine calculations. This paper presents a software (DAARWIN) that can be used to manage field data and to perform backanalysis in an automatic manner to predict soil parameters. It is a cloud based platform combined with the Plaxis Finite Element code, that uses genetic algorithms to solve the backanalysis. This software has been applied to the identification of soil parameters and strut loads in a real case involving a deep excavation from Toulouse Metro in France.

RÉSUMÉ: La conception d'excavations profondes implique la définition des murs de soutènement et des entretoises pour supporter les pressions des terres. Malgré l'expérience et les procédures disponibles pour estimer les forces agissant sur les entretoises, leur prédiction reste difficile et la comparaison entre les mesures sur le terrain et les simulations numériques suggère que de nombreux facteurs ne sont pas pris en compte dans les calculs de routine. Cet article présente un logiciel (DAARWIN) qui peut être utilisé pour gérer les données de terrain et effectuer une rétro-analyse de manière automatique pour prédire les paramètres du sol. Il s'agit d'une plate-forme basée sur le cloud combinée au code Plaxis Finite Element, qui utilise des algorithmes génétiques pour résoudre la rétro-analyse. Ce logiciel a été appliqué à l'identification des paramètres du sol et des charges des entretoises dans un cas réel impliquant une excavation profonde du métro de Toulouse en France.

Keywords: Backanalysis; optimization; deep excavation; retaining walls; strut loads.

1 INTRODUCION

Deep excavations using diaphragm walls usually include the installation of struts to temporarily ensure their stability. Traditional and empirical procedures to design diaphragm walls are not accurate when estimating strut forces as they oversimplify the earth-pressure distribution. Moreover, even when a "beam-on-spring" approach is used for wall design (a popular procedure among practising engineers), the strut loads may be underpredicted , due to soil arching effects and stress redistribution (Karlsrud & Andresen, 2005). This is a classical soil-structure interaction problem in which both soil and concrete stiffness play a fundamental role. Despite the huge development of numerical codes for geotechnical design, the working load supported by the struts is difficult to predict and a conservative approach is usually proposed (Goh et al., 2017, Zhang et al., 2019). In fact, in reported cases where the loads in the struts were monitored, their values were not totally consistent with the calculated ones (Moormann, 2002; Finno et al., 2002; Houhou et al., 2019). Several factors have been described to explain the differences between measured and computed strut loads, as installation effects, stiffness of the wales, temperature changes and pre-stressing (Moorman, 2002). This is why the observational method has been a valuable methodology to control excavation works and therefore, monitoring has become an essential task. Within this context the interpretation of field instrumentation in actual excavations can be enhanced if a numerical geotechnical model is used.

In this regard, geotechnical backanalysis can be a powerful tool to compare field measurements with predictions of the model. Backanalysis in Geotechnics is useful to calibrate soil constitutive models from

laboratory tests, but also to identify soil properties from field measurements. Some of the Finite Element programmes for geotechnical design developed so far include a backanalysis feature (Levasseur et al., 2008; Hashash et al., 2010; de Santos, 2015). The software DAARWIN (SAALG, 2023), coupled with Plaxis, performs backanalysis in a systematic manner and is able to manage the information provided by an initial design and by field data.

This paper presents an application of DAARWIN to a well documented case study, the Saint-Agne Metro Station, located in Line B of the Toulouse Metro, France, (Houhou et al., 2019), and focusses on the estimation of the struts loads.

Based on the information from this project, a numerical model has been built using finite elements in Plaxis 2D and Plaxis 3D, subsequently the influence of the loads produced by the struts was analyzed. The backanalysis of the measurements obtained during the excavation process improved the characterization of the soil layers and was useful to analyze the loads of the struts.

2 BACKANALYSIS USING DAARWIN

Backanalysis is also referred as "inverse problem", that is, estimating the parameters of a soil constitutive model from field measurements. An "objective function" is defined, which depends on the differences between measurements obtained through instrumentation and values calculated through a conceptual model. The solution to the identification problem is obtained by searching for the minimum of the objective function, for which optimization algorithms are used (Levasseur et al., 2008; Hashash et al, 2010; de Santos, 2015).

Traditionally, the backanalysis methodology was carried out manually, however, numerical techniques allow to perform that task in an automatic manner. Thus, backanalysis can be used in a systematic way to continuously analyze field data from monitoring and to assess the validity of the assumptions made during the design stage (Ledesma and Romero, 1997). That fills the gap between models from the design phase and measurements during construction and helps in the interpretation of the field instrumentation, reducing uncertainty.

The software DAARWIN is in fact a cloud-based platform based on machine learning algorithms (genetic algorithms) that integrates the management of field data from monitoring with numerical analyses using Plaxis code, and is able to identify parameters of geotechnical constitutive models by comparing measurements with finite element calculations. All the analyses in DAARWIN are performed using a parallel high-performance cloud-computing architecture running 200 server instances per backanalysis. The software was developed by a start-up company from a University research work (SAALG, 2023). A complete description of the methodology can be found in de Santos (2015).

3 DESCRIPTION OF THE CASE STUDY

The Saint-Agne station is located on the new Line B of the Toulouse Metro, France. This station is a 55.2 m × 17.15 m rectangular deep excavation, described in detail in Vanoudheusden et al. (2005), Zghondi et al. (2009), and Houhou et al. (2019). The retaining structure consists of a diaphragm wall cast in situ with a thickness of 1.0 m and reaching a depth of 20.65 m. During excavation to a depth of 17.2 m, the retaining walls were supported at the top by partial slabs and diagonal beams and at depth by 2 or 3 levels of temporary steel struts. Figure 1 shows a typical section of the diaphragm wall.

The excavation area was monitored in two sections. Each section included an inclinometer on the diaphragm wall and 4 vibrating wire strain gauges installed at each strut level with an automatic data acquisition system. Maximum measured horizontal displacement was about 9.7 mm at inclinometer 1. Construction activities included staged lowering of the water table, excavation and shoring. In each stage, the water table was first lowered to 1m below the bottom of the next excavation stage, then the soil was removed and the props were installed 0.4–0.5 m above the bottom of the excavation. This procedure was carried out for each phase until reaching the end of the excavation.

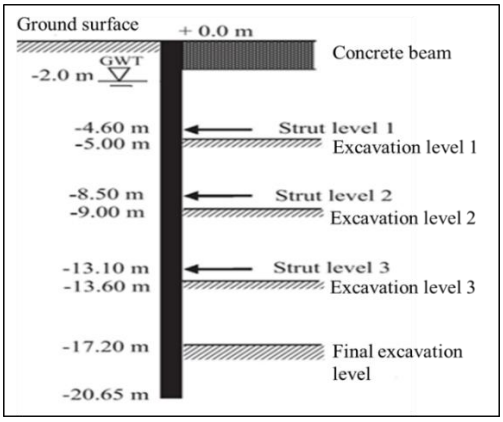

Figure 1. Typical wall cross-section (modified from Hohou, 2019).

The soil profile with the main geotechnical parameters initially provided is shown in Table 1,

adapted from Houhou et al. (2019), where a 3D simulation using code FLAC and the elastic-Mohr Coulomb model was presented. Here, code Plaxis 2D and 3D was used, with the Hardening Soil model with small strains as constitutive law, and an automatic backanalysis was carried out to better match the field instrumentation.

4 BACKANALYSES PERFORMED

A sensitivity analysis was carried out first, in order to detect the parameters that have more influence on the variables measured. This is a standard first step in DAARWIN (Cordoni, 2023). Once the parameters controlling the problem were detected, it was possible to define the conditions for the backanalysis (parameters to identify and range of the values in the search space). This is the case presented in this paper.

The most significant layers, in terms of influence on the measured displacements were identified as layers 4, 7, 8 and 9 (see Table 1), and the main parameters to identify were E_{50}, E_{ur} for those layers. To simplify the analyses, the following relations were adopted: $E_{oed}=E_{50}$ and $G_o=2.6\ E_{50}$. The rest of the parameters were fixed and based on the information provided (Table 1). Note that in excavation problems, the unloading-reloading modulus, E_{ur}, plays an important role when predicting displacements. The values identified in the backanalysis were, for the sandy clays (layer 4), E_{50}=50 MPa, E_{ur}=200 MPa; for the fine to medium sands (layer 7), E_{50}=60 MPa, E_{ur}=220 MPa; for the sandy clays (layer 8), E_{50}=210 MPa, E_{ur}= 540 MPa; and for the clays (layer 9), E_{50}=270 MPa, E_{ur}=1010 MPa. These values obtained are consistent with the geological and geotechnical information available. In particular the high modulus of the lower clays corresponds to the type of material involved (a molasse). Figure 2 shows the comparison between the measured horizontal displacements and the computed ones using those parameters.

5 STRUT LOADS

The loads of the struts were obtained from the numerical analyses. In the papers describing the case, an efficiency factor of 0.5 was defined to account for the difference between the theoretical load obtained in the calculations and the measured value (Houhou et al., 2019). That is, the measured load was half of the theoretical load computed from the shortening of the struts obtained considering the horizontal displacement in the inclinometers at the level of the strut. This is in fact a reduction of the theoretical strut stiffness by a factor of 2, which may be due to the stiffness of the connection between the struts and the wall.

When using the backanalysis procedure, the strut loads were more consistent with the measured values and an efficiency coefficient was not required. However, it was noticed that wall dis-placements are not very sensitive to the strut stiffness beyond a minimum value. In fact, multiplying or dividing the current strut stiffness by a factor of 3 had little influence on wall displacements. That explains the difficulty in determining numerically the force at the struts. Figure 3 shows the measured and computed strut loads. Note that differences can be as high as 1000 kN, which points out the difficulty in matching strut loads.

6 CONCLUSIONS

The paper presents an application of the software DAARWIN to a real case involving a strutted deep excavation. That software is able to manage field data and to perform backanalyses in an automatic manner, which can be very useful in geotechnical design and construction and particularly when combined with the observational method.

Table 1. Main initial parameters of the soil layers: natural specific weight, permeability, earth pressure coefficient, Poisson's ratio, cohesion, friction angle, dilatancy angle, Young modulus (after Houhou et al., 2019).

Layer	Depth(m)	γ(kN/m^3)	K(m/s)	K_o	ν	c'(kPa)	φ'(°)	ψ(°)	E(MPa)
1. Fill	0-1.2	20	$6\cdot10^{-4}$	0.5	0.3	0	25	0	66-78
2. Clays	1.2-2.8	22	$1\cdot10^{-9}$	1.6	0.3	80	33	0	78-94
3. Clay sands	2.8-5.2	21	$1\cdot10^{-7}$	1.6	0.3	52	37	3	94-117
4. Sandy clays	5.2-7.6	22	$5\cdot10^{-8}$	1.6	0.3	84	32	0	117-141
5. Fine to medium sands	7.6-8.6	21	$1\cdot10^{-6}$	1.6	0.3	0	36	5	141-151
6. Sandy clays	8.6-10.2	22	$5\cdot10^{-8}$	1.6	0.3	84	32	0	151-167
7. Fine to medium sands	10.2-12.7	21	$1\cdot10^{-6}$	1.6	0.3	0	36	5	167-191
8. Sandy clays	12.7-21	22	$5\cdot10^{-8}$	1.6	0.3	84	32	0	191-274
9. Clays	>21	22	$1\cdot10^{-9}$	1.6	0.3	80	33	0	274-360

Regarding wall displacements, they are well reproduced using backanalyzed parameters, however, measured strut loads are still difficult to simulate, because they are less sensitive to global wall displacements.

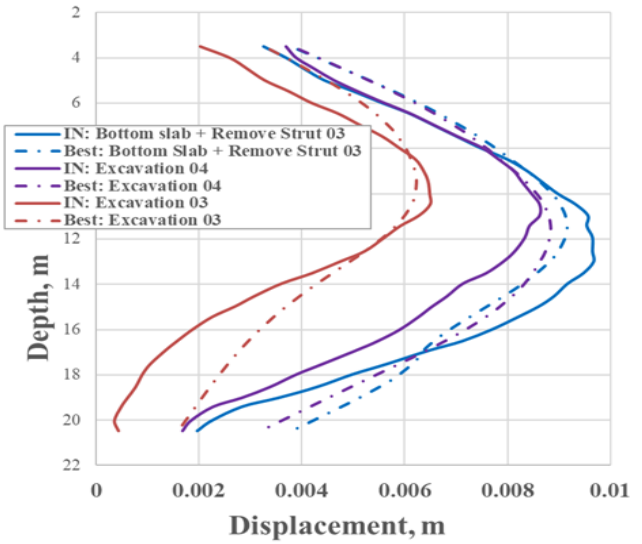

Figure 2. Measured and computed wall displacements.

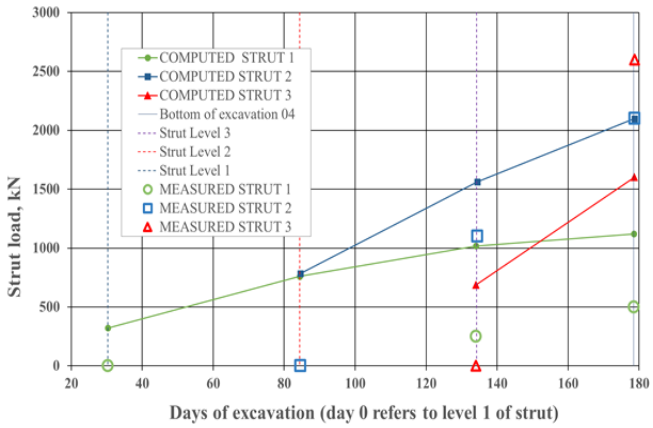

Figure 3. Measured and computed strut loads.

ACKNOWLEDGEMENTS

The financial support to SAALG from the European Union through the European Innovation Council, Project GEORGIA 190151860, is gratefully acknowledged.

REFERENCES

Cordoni. (2023). *Análisis inverso del comportamiento de los puntales en excavaciones entibadas.* Master Thesis. UPC - BarcelonaTech.

de Santos, C. (2015). *Backanalysis Methodology Based on Multiple Optimization Techniques for Geotechnical Problems.* UPC - BarcelonaTech, PhD Thesis. http://doi.org/10.5821/dissertation-2117-96016.

Finno, R.J., Bryson, S., Calvello, M. (2002). Performance of stiff support system in soft clay. *J. of Geotechnical and Geoenvironmental Engng.,* 128(8), pp. 660-671. https//doi.org/10.1061/(ASCE)1090-0241(2002)128:8(660).

Goh, A.T.C., Zhang, F., Zhang, W., Chew, O.Y.S. (2017). Assessment of strut forces for braced excavation in clays from numerical analysis and field measurements. *Computers and Geotechnics,* 86, pp. 141-149. http://dx.doi.org/10.1016/j.compgeo.2017.01.012.

Hashash, Y.M.A., Levasseur, S., Osouli, A., Finno, R., Malecot, Y. (2010). Comparison of two inverse analysis techniques for learning deep excavation response. *Computers and Geotechnics*, 37, pp. 323-333 https//doi.org/10.1016/j.compgeo.2009.11.005.

Houhou, M.N., Emeriault, F., Belounar, A. (2019). Three-dimensional numerical back-analysis of a monitored deep excavation retained by strutted diaphragm walls. *Tunneling and Underground Space Technology*, 83, pp. 153-164. http://doi.org/10.1016/j.tust.2018.09.013.

Karlsrud, K., Andresen, L. (2005). Loads on braced excavations in soft clay. *Int. Journal of Geomechanics,* 5(2), pp- 107-113. http://doi.org/ 10.1061/(ASCE)1532-3641(2005)5:2(107).

Ledesma, A. and Romero, E. (1997). Systematic backnalysis in tunnel excavation problems as a monitoring technique. *14th Int. Conf. on Soil Mechanics and Foundation Engineering*, Hamburg, 1425-1428.

Levasseur, S., Malecot, Y., Boulon, M., Flavigny, E. (2008). Soil parameter identification using genetic algorithm. *Int. J. Numerical and Analytical Methods in Geomechanics*, 32(2), pp. 189-213. http://doi.org/ 10.1002/nag.614g.

Moormann, Ch. (2002). In-situ monitoring and analysis of braced excavations with irregular shape. *Geotechnical aspects of Underground Construction in Soft Ground.* IS Toulouse'02*, pp. 523-528.*

SAALG Geomechanics (2023). Description of DAARWIN software, its features and capabilities. Available at: https://www.saalg.com/product (accessed 10/10/2023).

Vanoudheusden, E., Petit, G., Robert, J., Emeriault, F., Kastner, R. (2005).Comportement d'une paroi moulée en site urbain: Modélisations et mesures. *16th Int. Conf. on Soil Mechanics and Geotechnical Engineering*, Osaka, pp. 1141-1145. http://doi.org/10.3233/978-1-61499-656-9-1141.

Zghondi, J., Emeriault, F., Kastner, R. (2009).Multi-criteria procedure for the back-analysis of multi-supported retaining walls. *Geotechnical Aspects of Underground Construction in Soft Ground*, IS Shanghai'08, pp. 207 - 213.

Zhang, W., Hou, Z., Goh, A.T.C., Zhang, R. (2019). Estimation of strut forces for braced excavation in granular soils from numerical analysis and case histories. *Computers and Geotechnics*, 106, pp. 286-295. http://doi.org/10.1016/j.compgeo.2018.11.006.

Proceedings of the XVIII ECSMGE 2024
GEOTECHNICAL ENGINEERING CHALLENGES
TO MEET CURRENT AND EMERGING NEEDS OF SOCIETY
© 2024 the Authors
ISBN 978-1-032-54816-6
DOI 10.1201/9781003431749-53
Open Access: www.taylorfrancis.com, CC BY-NC-ND 4.0 license

ECSMGE 24
XVIII EUROPEAN CONFERENCE ON SOIL MECHANICS AND GEOTECHNICAL ENGINEERING

Correlations between SPT and DPSH results based in energy measurements

Corrélations entre les résultats SPT et DPSH basées sur des mesures d'énergie

N. Cruz
MOTA-ENGIL/University of Aveiro, Porto, Portugal

J. Cruz*
MOTA-ENGIL, Porto, Portugal

C. Rodrigues, L. Fagundes
Polytechnic Institute of Guarda, Guarda, Portugal

C. Chaquisse
University of Aveiro, Aveiro, Portugal

**jorge.cruz@mota-engil.pt*

ABSTRACT: Dynamic probing tests, namely in the case of the super-heavy version, are commonly used in geotechnical investigations, particularly in heterogeneous soils, stiff soils, compacted to very compacted soils and in decomposed rock. The more usual approaches to obtain the subsequent geotechnical parameters consists in transforming the N_{20} DPSH results in equivalent N_{SPT} and use the correlations established with this latter. However, the usual correlations used in our days are based in the concept of corrected SPT values, namely N_{60} and $(N_1)_{60}$, which creates an important limitation to its use in DPSH results. A research work consisting in pairs of SPT and DPSH tests executed side by side with the same equipment (hammer, anvil, rods, etc.), both instrumented with energy measurements obtained from the SPT Analyzer (PDI), was performed in the Institute Polytechnic of Guarda (IPG, Portugal) experimental site. The obtained results revealed differences between the Energy Transfer Ratios (ETR) of DPSH and SPT tests, which seems to be related with the different penetration devices (SPT sampler and DPSH cone). Departing from that it was possible to compare both the test results (N_{SPT} and N_{20}) and the respective corrected values, N_{60} or $(N_1)_{60}$. Presentation and discussion of results will be presented in the paper herein.

RÉSUMÉ: Les essais de sondage dynamique, notamment dans le cas de la version super-lourd, sont couramment utilisés dans les investigations géotechniques, notamment dans les sols hétérogènes, les sols raides, les sols compactés à très compactés et dans les roches décomposées. Les approches les plus usuelles pour obtenir les paramètres géotechniques ultérieurs consistent à transformer les résultats N_{20} DPSH en équivalent N_{SPT} et à utiliser les corrélations établies avec ce dernier. Cependant, les corrélations habituelles utilisées de nos jours reposent sur le concept de valeurs SPT corrigées, à savoir N_{60} et $(N_1)_{60}$, ce qui crée une limitation importante à son utilisation dans les résultats DPSH. Un travail de recherche consistant en des paires d'essais SPT et DPSH exécutés côte à côte avec le même équipement (mouton, enclume, tiges, etc.), tous deux instrumentés avec des mesures d'énergie obtenues à partir de l'analyseur SPT (PDI), a été réalisé dans le laboratoire expérimental site de le Institut Polytechnique de Guarda (IPG, Portugal). Les résultats obtenus ont révélé des différences entre les taux de transfert d'énergie (ETR) des tests DPSH et SPT, qui semblent être liées aux différents dispositifs de pénétration (échantillonneur SPT et cône DPSH). À partir de là, il a été possible de comparer à la fois les résultats des tests (N_{SPT} et N_{20}) et les valeurs corrigées respectives, N_{60} ou $(N_1)_{60}$. La présentation et la discussion des résultats seront présentées dans le document ci-dessous.

Keywords: SPT; DPSH; penetration resistance; energy transfer ratios; energy efficiency.

1 INTRODUCTION

Dynamic penetration tests are widely used in the geotechnical characterization of soil massifs, especially in heterogeneous, stiff/dense/compacted soils and decomposed rock, where static penetration is seriously limited. Among these, the Standard Penetration Test (SPT) is undoubtedly the more popular and common in-situ geotechnical test used worldwide, which gives it an important advantage for a successful applicability in a wide range of geo-materials. On the other hand, dynamic probing tests

have the great advantage of characterizing soil profiles continuously, especially in terms of strength (ISSMFE-TC16, 1989). Within this group of tests, Dynamic Probing Super-Heavy test (DPSH) is very similar to SPT in what concerns the mode of penetration and potential energy, thus very easy to be compared with, giving access to the available SPT correlations.

Both SPT and DPSH tests consist in the blow count needed for the penetration of a standard element by means of an impact produced by a hammer falling from a certain height. The hammer and falling weight are similar in these two tests, thus generating the same potential energy, while the main difference is related with the equipment that firstly penetrates the soil, namely a SPT 45 cm normalized sampler and a DPSH cone with diameter similar to the SPT sampler. Furthermore, SPT tests are performed inside a borehole previously drilled until the depth of each test (typically performed every 1.0-1.5 m), while DPSH is penetrated directly from the surface without need of a borehole, thus generating continuous profiles. The results of both tests correspond to the number of blows to penetrate a length of 30 cm (N_{SPT}) and 20 cm (N_{20}), respectively representing SPT and DPSH tests.

Given the similarity between both tests, it is of great practical interest to obtain DPSH normalized parameters identical to the SPT, opening an access to the most updated SPT correlations.

The International Geotechnical Society (ISSMFE, 1989) has established a reference value of 60% of the theoretical free fall of 474 J, E_{60}, for comparisons among tests performed by different equipment. The corresponding N value is designated as N_{60} and can be obtained from Eq. 1 as:

$$N_{60} = N \frac{E}{E_{60}} \quad (1)$$

where N corresponds to the energy E, which has to be known. The energy is to be obtained below the driving head (ISSMFE, 1989).

The more recent procedures and available correlations from SPT results, require the SPT normalized parameters, N_{60} and $(N_1)_{60}$ (Robertson et al., 1983, Seed et al., 1985, Skempton, 1986), represented by the Eq. 1 to Eq. 4. Thus, DPSH results should be represented by similar parameters. In the following sections an experimental frame performed in the Institute Polytechnic of Guarda (IPG), Portugal, experimental site under this subject is presented and discussed. The N_{60} and $(N_1)_{60}$ parameters are defined by the following equations:

$$N_{60} = C_E * C_R * C_B * C_S * N_{SPT} \quad (2)$$

$$C_E = \frac{ER_r}{60} \quad (3)$$

$$ER_r = \left(\frac{E_R}{E_P}\right) * 100 \quad (4)$$

$$(N_1)_{60} = C_N * N_{60} \quad (5)$$

where C_E represents the correction factor related with the energy transmitted to the rods, C_R and C_B the corrections related with the length of the rods and the diameter of the borehole, C_S the correction factor related with the liner, C_N the correction factor related with the overburden stress in granular soils, ER_r the energy ratio transferred to the rods, E_R the energy effectively transferred to the rods and E_P the potential energy of the hammer falling from a specific height.

More detailed information on the SPT normalized parameters can be easily found in the referenced bibliography.

2 EXPERIMENTAL WORK

The experimental frame related with this work was performed in the IPG experimental site, which has been used in the several studies related with in-situ tests in residual soils. The local geology corresponds to the residual soils, which are the result of the chemical weathering of Guarda granitic formation where the experimental site is located. Detailed information can be found in several available publications (e.g. Ávila Martins et al., 1963; Rodrigues, 2003; Cruz, 2010).

The experimental frame consisted in the execution of pairs of DPSH/SPT tests performed side by side, following the procedures recommended in Eurocode 7-Geotechnical design, part 3. A PDI SPT Analyzer equipment (1999) was used to measure the energy delivered to the rods of each DPSH and SPT blow and both tests were performed with the same equipment characterized by a 63.5 kgf hammer falling from 0.75 m height, which correspond to 476.3 J. The same rods were used in the execution of both tests, bore holes were performed without introducing casing and liners were not used in the SPT sampler. The blow frequency was the same in both tests (23 to 25 blows per minute). For comparing purposes, the number of blows considered in each test were taken at similar depths and the DPSH number of blows (N_{20}) was transformed (N_{30}), multiplying the earlier by 1.5, in order to have comparable lengths of determination.

After the execution of tests, the obtained field results were object of statistical treatment to analyse the energy efficiency and then globally compared in what concerns to the energy efficiency, field results at

the same depth ranges and normalized parameters. The normalized SPT parameters followed the current procedures (expressed by eq. 1 to 3), while for DPSH similar correction factors were applied except for the borehole diameter correction, which was discarded since the test is not executed inside a borehole.

The granitic residual massif under study consistently reveals an increase of the penetration resistance with depth, which is well represented both by SPT and DPSH tests, although with different evolution rates (Figure 1).

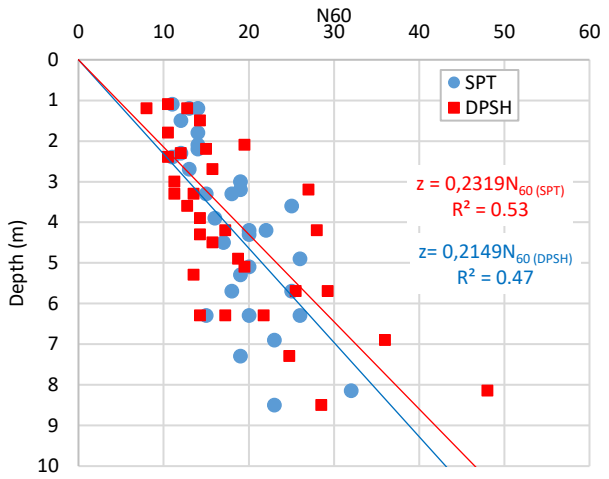

Figure 1. Evolution of penetration resistance with depth in the SPT and DPSH tests.

Compairing directly the global results of N_{20} with N_{SPT}, obtained at equivalent depths, it becomes obvious the (expected) lower blowcount of N_{20} (Figure 2), which is naturally justified by the different lenghts of penetration.

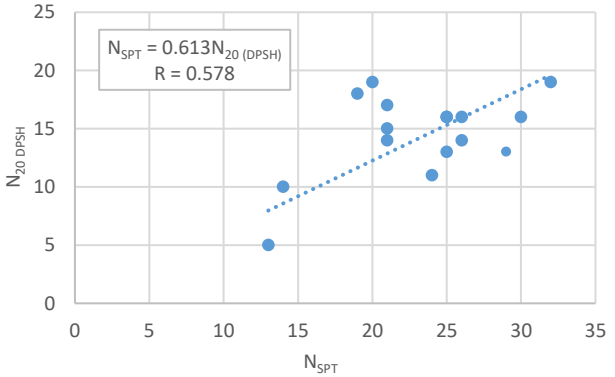

Figure 2. Relation between the penetration resistance N_{SPT} and N_{20}.

On the other hand, the experimental transmitted energy (ETR) results measured by the SPT Analyzer reveal that the delivered energy is not the same in each test (Figure 3), which can only be adressed to the different tip equipments (SPT sampler and DPSH cone) since all the other equipments are the same. In fact, the superficial contact area of the DPSH conic tip with the ground is constant the whole test (155.0 cm^2), while the area of SPT sampler varies according to a penetration length of 15 to 45 cm with internal and external contact with the ground (405.3 cm^2 a 1215.8 cm^2). The normalization of ETR by the N_{30} and N_{SPT} values seem to produce a more robust correlation between both tests (Figure 4).

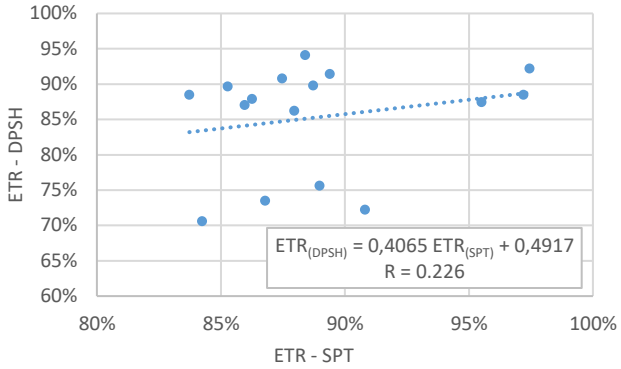

Figure 3. Relation between transmitted energy (ETR) in SPT and DPSH tests.

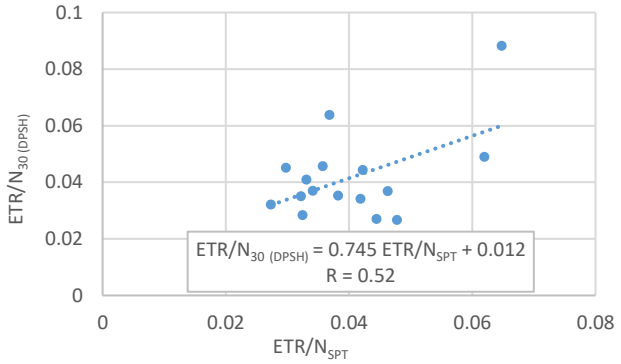

Figure 4. Relation between the ETR/N_{SPT} of SPT and ETR/N_{30} of DPSH tests.

The different obtained delivered energies seem to be related with the differences of contact areas, suggesting that higher contact generate a more efficient form to transfer to the soil the available energy generated by each blow. Figure 5 represents the mean ETRs obtained in the first, second and third 15 cm penetration phases of SPT tests and seems to corroborate the previous explanation, since the contact area of the SPT sampler with the soil is increasing with penetration.

As consequence, the comparison of normalized parameters instead of the simple blowcounts of each test is much more reliable, which is clearly proved by the diagram of Figure 6. Being so, if all the correction factors are applied, the normalized parameters obtained by both tests are equivalent, thus the available modes of correlation for SPT tests can be equally applied to DPSH tests. In the case of DPSH the C_B

factor (related with the diameter of borehole) should be considered equal to 1, while the remaining are applied as in the case of the SPT test.

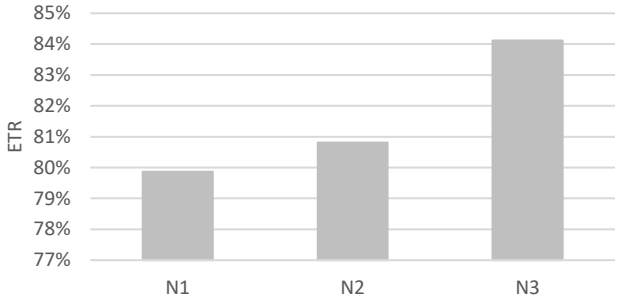

Figure 5. Evolution of ETR in the SPT tests.

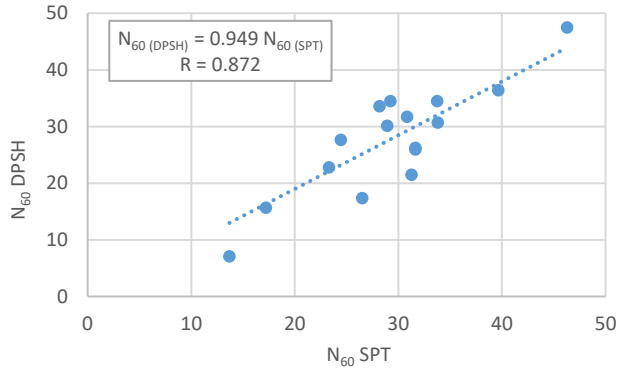

Figure 6. Relation between the N_{60} of SPT and $(N_{30})_{60}$ of DPSH tests.

3 CONCLUSIONS

The experimental frame presented herein clearly revealed that the energy efficiency is higher in the case of the SPT test than in the case of DPSH, which seems to be related with the higher contact area of the SPT sampler with the soil compared with the DPSH cone-soil contact. The higher the contact area the higher the energy efficiency. The comparison between normalized blow counts showed that the ratio between test results is basically equivalent. As consequence of the present findings, if the field work is performed with hammers of known (measured, calibrated) energy efficiencies (as it should) it is possible to obtain DPSH normalized parameters (considering C_B =1) that can be used in the current correlations settled for SPT tests. Naturally, this is a limited experience within certains strength and depth ranges, as well as in very specific geologic environment, and so the study should be enlarged to other geo-materials with other strengths and different test depths to validate this conclusions. For the time being, local calibration with 1 or 2 pairs of SPT-DPSH tests will allow to evaluate the sustainability of the findings presented herein.

REFERENCES

Cruz, N. (2010). *Modelling geomechanics of residual soils by DMT tests*. PhD thesis, Porto University. http://web.archive.org/web/20190326185829/https://nbdfcruz.wordpress.com/phd/.

ISSMFE (1989). Report of the ISSMFE - Technical Committee on Penetration Testing of Soils - TC 16 with Reference Test Procedures: CPT - SPT - DP - WST, ISSN 0281-7578.

Martins, J. A., Medeiros, A. C., Pilar, L., Ferro M. N. and Mesquita, L. P. (1963). Geological Map of Portugal, Folha 18-C – Guarda, 1st Edition.

PDI (1999). SPT ANALYZER - SPT Users Manual. Pile Dynamics Inc. Ohio, 30 p.

Robertson, P.K., Campanella, R.G. & Wightman, A. (1983). SPT-CPT Correlations. *ASCE Journal of Geotechnical Engineering*, 109(11): 1449-1459. https://doi.org/10.1061/(ASCE)0733-9410(1983)109:11(1449).

Rodrigues, C.M.G. (2003). *Geotechnical characterization and geomechanic behaviour study of a saprolitic granite soils from Guarda*. PhD thesis, Coimbra University, Portugal (in Portuguese).

Seed, H. B., Tokimatsu, K., Harder, L. F., & Chung, R. M. (1985). The Influence of SPT Procedures in Soil Liquefaction Resistance Evaluations. Journal of Geotechnical Engineering, ASCE, 111 (12), 1425-1445. https://doi.org/10.1061/(ASCE)0733-9410(1985)111:12(1425).

Skempton, A.W. (1986). Standard Penetration Test Procedures and the Effects in Sands of Overburden Pressure, Relative Density, Particle Size, Ageing and Overconsolidation. *Géotechnique,* 36(3): 425-447. doi: 10.1680/geot.1986.36.3.425.

Proceedings of the XVIII ECSMGE 2024
GEOTECHNICAL ENGINEERING CHALLENGES
TO MEET CURRENT AND EMERGING NEEDS OF SOCIETY
© 2024 the Authors
ISBN 978-1-032-54816-6
DOI 10.1201/9781003431749-54
Open Access: www.taylorfrancis.com, CC BY-NC-ND 4.0 license

ECSMGE 24
XVIII EUROPEAN CONFERENCE ON SOIL MECHANICS AND GEOTECHNICAL ENGINEERING

Hydric and mechanical properties assessment of basalts from Madeira island, Portugal

Évaluation des propriétés hydriques et mécaniques des basaltes de l'île de Madère, Portugal

N. Cueto*
University of Alicante, Alicante, Spain
Laboratório Regional de Engenharia Civil, Madeira Island, Portugal

J.F. Vieira de Sousa, J.P.S. Perneta
Laboratório Regional de Engenharia Civil, Madeira Island, Portugal

R. Meza
GIS4tech, Spin-Off of University of Granada, Granada, Spain

M.L. Pereira
Instituto de Investigação em Vulcanologia e Avaliação de Riscos, Universidade dos Açores, Ponta Delgada, Portugal

nora.cueto@ua.es

ABSTRACT: This investigation explores the influence of physical properties on capillarity and uniaxial compressive strength from 56 specimens of basalts from Madeira Island, Portugal. Three well differentiated basalt types belonging to the Upper (massive and vesicular basalt) and the Middle (altered massive basalt) Volcanics Complexes were studied. Water absorption coefficient by capillarity and uniaxial compressive strength were assessed as a function of real and apparent densities, total and open porosities, water absorption at atmospheric pressure and unit weight applying simple and multiple linear regressions to obtain reliable prediction models. Water absorption coefficient by capillarity equations show high correlation coefficients ($R > 0.98$). The proposed best equation is expressed as a function of water absorption at atmospheric pressure and apparent density. Meanwhile, the best fit for uniaxial compressive strength, given by apparent density, open porosity, and unit weight has a moderate correlation. While apparent density has a predominant statistical weight in the prediction of uniaxial compressive strength, open porosity has a minor contribution. Unsupervised clustering processes using principal component analysis identifies three well differentiated groups whose inner cohesion is intimately related to open porosity (very low to high porosity), pore size and type (fine intercrystalline and large vesicular pore type, respectively) and the natural weathering degree of basalts. Some results obtained in this research could be used as indicator parameters in geotechnical classifications to assist with fast decisions when using basalts as building materials or as a foundation in civil engineering construction.

RÉSUMÉ: Cette étude explore l'influence des propriétés physiques sur la capillarité et la résistance à la compression uniaxiale de 56 éprouvettes de basaltes de l'île de Madère. Trois faciès bien différenciés appartenant au Complexes Volcaniques Supérieur et Moyen ont été étudiés. Le coefficient d'absorption d'eau par capillarité et la résistance en compression uniaxiale ont été comparés et liés aux masses volumiques réelles et apparentes, aux porosités totales et ouvertes, à l'absorption d'eau à la pression atmosphérique et au poids unitaire en appliquant une analyse statistique avancée. Le coefficient d'absorption d'eau par capillarité obtenu par des modèles de régression linéaire simple et multiple montrent des coefficients de corrélation élevés ($R > 0,98$; respectivement). La meilleure équation proposée est exprimée en fonction de la masse volumique apparente et de la porosité ouverte. Le meilleur ajustement pour la résistance à la compression uniaxiale, donné par la masse volumique apparente et la porosité ouverte, présente une corrélation modérée, où la masse volumique apparente avait un poids statistique prédominant dans la prédiction de cette variable, avec une contribution mineure de la porosité ouverte. L'analyse non supervisée de groupes identifie trois groupes bien différenciés dont la cohésion interne est intimement liée à la porosité ouverte à la taille, au type de pores et au degré d'altération naturelle des basaltes. Certains résultats obtenus pourraient être utilisés comme paramètres indicateurs dans les classifications géotechniques pour permettre une prise de décision rapide dans l'utilisation des basaltes comme matériaux de construction ou comme fondations pour les constructions de génie civil.

Keywords: Volcanic rocks; multivariate analysis; spontaneous imbibition; petrophysical properties; building rock.

1 INTRODUCTION

Research on the physico-mechanical properties of basalts is currently booming due to their potential use as reservoirs for hydrogen (Yaseri et al., 2023) and CO_2 (Iglauer and Al-Yaseri, 2021) storage in the accelerating race to find solutions for energy transition and climate change mitigation.

In Madeira Island, basalt studies are more focused on its use as a foundation material in civil engineering works, on its performance in slope stability for risk assessment, and on its use as an ornamental and building stone, both in new construction and in the conservation and restoration of the regional architectural heritage (Sempere-Valverde et al., 2023, Alves et al., 2019, Maia and Aslani, 2016, Lourenço et al., 2010). While physical (e.g. density, porosity, etc.) and mechanical (e.g. uniaxial compressive strength, elastic modulus, indirect tensile strength, point load index, etc.) properties of basalts are widely assessed worldwide (Pereira et al., 2021, and references therein), research on water transport mechanisms remains scarce.

Basalts used as building stones and with a pore size distribution ranging from 0.1 μm to 10 μm (within the medium range of capillary active pore size) are found to be more prone to deterioration due to the physico-chemical processes induced by both water sorption and solutes' transport (Çelik and Kaçmaz, 2016). Moreover, basalts exhibit variations in their resistance due to material weathering, as showed by numerical evaluations on slope stability (Silva et al., 2023). Both erosion processes and changes in the hydraulic conditions of basaltic grounds due to water level variations are suggested as causes of such deterioration. From our own field experiences, we recognise that episodic slope collapses are either caused by torrential rains or stagnant water. In the latter, fluid movements are induced first by permeability and then by capillarity. Thus, the existence of a parameter that relates fluid transport integrated with other geoengineering properties is of foremost importance to better develop prevention plans and minimise geological hazards.

To address this problem, water transport in volcanic rocks has started to be considered in an internal database that has been developed by Laboratório Regional de Engenharia Civil (LREC) since 2012 (Vieira de Sousa et al., 2012) and is currently expanding to cover more territory of Madeira Island and incorporate parameters of critical importance in predicting both hydric and mechanical properties. In fact, capillarity and permeability have proved to be indicators of susceptibility to deterioration and possible collapse of volcanic rocks (Cueto et al., 2018, Perneta and Vieira de Sousa, 2023).

Therefore, the main objective of the present study is to determine the influence of physical properties on capillarity and uniaxial compressive strength. For this purpose, the results will be analysed by applying multivariate statistics and empirical equations will be provided to estimate these parameters. Final considerations will be addressed in the context of the application of these parameters as accurate indicators within geoengineering properties.

2 MATERIALS AND SAMPLING

2.1 Geographical and geological setting

The Madeira Island is the largest and most populated of the homologous Archipelago and is located in the eastern sector of the North Atlantic ocean, between latitudes 32º 38' N and 32º 52' N. It corresponds to a volcanic edifice (1861 m above sea level) that has been originated by a hot spot. Madeira Island comprises three main volcanostratigraphic terms: (a) Lower Volcanic Complex (CVI. > 5.57 My); (b) Middle Volcanic Complex (CVM. 5.57 - 1.8 My); and (c) Upper Volcanic Complex (CVS. 1.8 - 0.007 My) (Ramalho et al., 2015, Brum da Silveira et al., 2010), with alkali olivine basalts being an important rock material in this island (Hughes and Brown,1972).

2.2 Basalts

Three massive, one vesicular and one altered massive basalt samples were selected to carry out this study, from which 56 specimens in total were extracted. Massive basalts were quarried in São Vicente (Bc-SV) and São Martinho, Funchal (Bc-SA, Bc-SB), and the vesicular basalt sample (Bv-SV) was cored in São Vicente. Both belong to the Funchal Unit, CVS. The altered massive basalt (Bca-E) was obtained in Encumeada, Ribeira Brava, in the geological context of CVM, Penha d'Águia Unit.

At mesoscale, massive basalts are dark grey in colour and show almost no signs of weathering. In the Bc-SV sample, a very isolated vesicular porosity type can be seen (2.62 ± 1.80 mm). The Bc-SA and Bc-SB samples show a vesicular porosity type smaller than those observed in Bc-SV (0.88 ± 0.36 mm, 0.79 ± 0.24; respectively), but also isolated, and widely dispersed throughout the samples. In both samples, discontinuity surfaces are observed with increasing depth. These are fissures and, less frequently, stylotites-like discontinuities, with a very fine aperture (~1 mm), open or partially cemented by a whitish mineral. In sample Bc-SA the fissure density increases significantly compared to sample Bc-SB.

In vesicular basalts, macroporosity extends over 30-40% of the sample, has no preferential organisation and has a size variation in the range of 1.5 mm to 6 mm.

The altered compact basalt sample, Bca-E, is generally grey in colour, with some brownish areas. It has about 10% vesicular porosity and, in some specimens, this macroporosity is partially cemented by a whitish mineral. Isolated and narrow-opening fissures are present. The matrix of Bca-E is more porous than the rest of the studied basalts, probably and partly due to the natural weathering of the rock mass (W_2 in accordance with ISRM (1981)).

Bc-SV, Bv-SV and Bca-E samples were collected from outcrops, meanwhile Bc-SB and Bc-SA samples were obtained from a borehole drilled at depths of ~20 m to 35 m.

3 METHODS

The cylindrical specimens were cut according to the specifications of each test standard, i.e. h/d=1 (~70 mm). The number of specimens tested in each experiment, as well as the porous facies classification based on Anon. (1979), are stated in Table 1.

Petrophysical properties, namely real, ρ_r, and apparent, ρ_b, densities and total, p, and open, p_o, porosities were determined following the NP EN 1936 (2008) standard. Water absorption at atmospheric pressure, A_b, and water absorption coefficient by capillarity, C, were respectively carried out in accordance with NP EN 13755 (2008) and NP EN 1925 (2000) standards. The studies of spontaneous imbibition of water were completed with the analysis of capillary curves based on the SF model of Hall and Hoff (2021). To obtain the mechanical properties, tests have only been carried out to determine the uniaxial compressive strength, σ_c, according to NP EN 1926 (2008). The unit weight, γ_d, was obtained through the relation of total weight of oven-dried specimen and total volume of the specimen.

The descriptive and multivariate statistical analyses of the results were carried out using IBM SPSS Statistics 25.0.0 as in Cueto (2020), namely scatter diagram analysis, multiple linear regressions (LR), principal component analysis (PCA), and hierarchical cluster analysis (CA). Unsupervised cluster analysis using simplified PCA variables was performed employing the K-Nearest Neighbours algorithm from the scikit-learn Python 3 library (Jupyter Notebook 6.5.2).

4 RESULTS AND DISCUSSION

Table 1 shows the physical and mechanical properties results of the studied basalts, classified accordingly to Anon. (1979) as (i) very low - low porous, (ii) medium porous, and (iii) medium - high porous type. This grouping is exactly coincident with the massive, vesicular, and altered massive facies, respectively.

All multivariate analyses, whether dependent (LR) or interdependent (PCA and CA), prove that p_o is one of the main controlling factors in both hydric and mechanical properties. The higher the p_o, the higher the C and A_b, and the lower the σ_c. Empirical equations presented in Table 2 reveal that C can be predicted with high precision from Eq. 1. LR identified the variables A_b ($\beta = 0.999$) and ρ_b ($\beta = 0.019$) as significant predictors of C. This model is highly significant ($p < 0.001$; $R = 0.98$), however, among equations 1 to 4, Eq. 2 and Eq. 4 are the most efficient ones, because only one parameter is needed to estimate C and the models remain highly significant. This finding is reasonable since A_b and p_o are related through the saturation coefficient (Benavente, 2002). Equations 5 to 7 for estimating σ_c found, on the other hand, have moderate correlation coefficients (Table 2). The simplest (Eq. 7) predicts σ_c from ρ_b and maintains almost the same p (< 0.001) and R (~0.81) values.

The capillarity analysis shows two pore families controlling the water movement in Bv-SV. Large vesicular pores are well interconnected through the fine intercrystalline matrix porosity, extending and enhancing capillary suction. Despite this, the C results are lower than expected. This could be because the macropores size distribution is skewed towards values greater than 1.5 mm, which is the smallest size measured in this sample. Additionally, vesicles were detected overlapping each other, leading to an increase in the size of the macropores in their confluence zone. It has been verified experimentally that the mass of the water column is conditioned by the maximum pore size for capillary mobility. Jurin's Law for a wetting liquid supports this, as the capillary height for a pore radius of 1 mm is 1.5 mm. This suggests that gravity forces would be the primary mechanism in this situation and that fluid movement by capillarity would be insignificant (Hall and Hoff, 2021, Benavente, 2002).

Figure 1 displays the outcomes derived from unsupervised cluster analysis simplifying the PCA variables to assess the data quality from the categorization of rock facies. This process discriminated the three well-differentiated studied petrological varieties.

Table 1. Physico-mechanical properties of the studied basalts. Mean, standard deviation (SD), minimum (Min.) and maximum (Max.) values of real, ρ_r, and apparent, ρ_b, density; total, p, and open, p_o, porosity; water absorption at atmospheric pressure, A_b, water absorption coefficient by capillarity, C, unit weight, γ_d, and uniaxial compressive strength, σ_c. Upper, CVS, and Middle, CVM, Volcanic Complex; number of specimens tested, Nº.

Basalt Type			ρ_r (kg/m^3)	ρ_b (kg/m^3)	p (%)	p_o (%)	A_b (%)	C ((g/m^2)/s$^{0.5}$)	γ_d (kN/m^3)	σ_c (MPa)
CVS	Massive (Very low – low porous)	Nº	39	39	39	39	33	21	39	39
		Mean	3065	2955	4.0	0.8	0.4	0.4	28.8	214.3
		SD	56	50	2.6	0.9	0.3	0.3	0.5	54.2
		Min.	2973	2805	0.9	0.0	0.0	0.1	27.2	103.0
		Max.	3167	3007	9.4	2.6	0.8	1.2	29.6	322.4
	Vesicular (Medium porous)	Nº	7	7	7	7	-	7	7	-
		Mean	3146	2383	24.2	5.0	-	2.1	22.3	-
		SD	27	121	4.2	1.1	-	0.5	1.4	-
		Min.	3100	2175	20.1	4.1	-	1.7	20.0	-
		Max.	3174	2491	31.4	7.1	-	3.1	23.5	-
CVM	Altered (Medium – high porous)	Nº	10	10	10	10	10	-	10	10
		Mean	2971	2580	12.6	10.0	4.2	-	25.3	109.9
		SD	77	248	7.2	6.9	3.0	-	2.4	52.5
		Min.	2893	2220	4.1	1.8	0.8	-	21.8	55.6
		Max.	3162	2893	23.4	20.4	9.0	-	28.4	212.5

Massive facies dominate the leftmost part in Figure 1, whereas vesicular facies is concentrated in the upper-right area. In the lower-right corner are grouped altered massive basalts.

Certain specimens of this last facies, however, are more related to massive facies due to their prominent physical properties as ρ_r and ρ_b. As a result, they are assigned to a zone closer to the massive facies group.

Nonetheless, the classification does not fall much short because it places these specimens outside of the massive facies' high point concentration and, in some cases, relatively near to the altered massive facies. Consequently, the specimens labelled in Figure 1 might be considered transitional since they fall between two facies.

These findings suggest that the inner cohesion of basalts facies is intimately related to open porosity (very low to high porosity), pore size and type (fine intercrystalline and large vesicular pore type, respectively), and the natural weathering degree of basalts (Table 1).

CA, performed with the shortest distance method (nearest neighbour) using the Euclidean distance as a measure of dissimilarity between specimens, aids unsupervised cluster analysis by identifying the three clearly distinguished facies.

These results underline the fact that if an unsupervised classification algorithm can perform a classification process with an extremely high level of accuracy, how much more could a supervised classification algorithm do with a large number of specimens? It may not only be able to categorise, but it may also be able to detect samples or specimens that lie between two facies and create additional sorts of inputs depending on the training data if properly labelled. This would shorten the time and cost of laboratory work, accelerate the generation of results, and help in making informed decisions.

Table 2. Logarithmic expressions of capillary absorption coefficient, C ((g/m^2)/s$^{0.5}$), and uniaxial compressive strength, σ_c (MPa), as a function of physical properties: water absorption at atmospheric pressure, A_b (%), apparent density, ρ_b (kg/m^3), open porosity, p_o (%), unit weight, γ_d (kN/m^3). R, multiple correlation coefficient.

Eq.	Logarithmic expressions	R
1	$LogC = -2.781 + 0.990 \cdot LogA_b + 0.867 \cdot Log\rho_b$	0.9828
2	$LogC = 0.213 + 0.974 \cdot LogA_b$	0.9827
3	$LogC = -2.179 + 0.611 \cdot Log\rho_b + 0.658 \cdot Logp_o$	0.9668
4	$LogC = -0.086 + 0.629 \cdot Logp_o$	0.9665
5	$Log\sigma_C = -27.767 + 12.240 \cdot Log\rho_b - 0.042 \cdot Logp_o - 8.510 \cdot \gamma_d$	0.8214
6	$Log\sigma_C = -12.736 + 4.333 \cdot Log\gamma_d - 0.026 \cdot Logp_o$	0.8147
7	$Log\sigma_C = -14.330 + 4.795 \cdot Log\rho_b$	0.8107

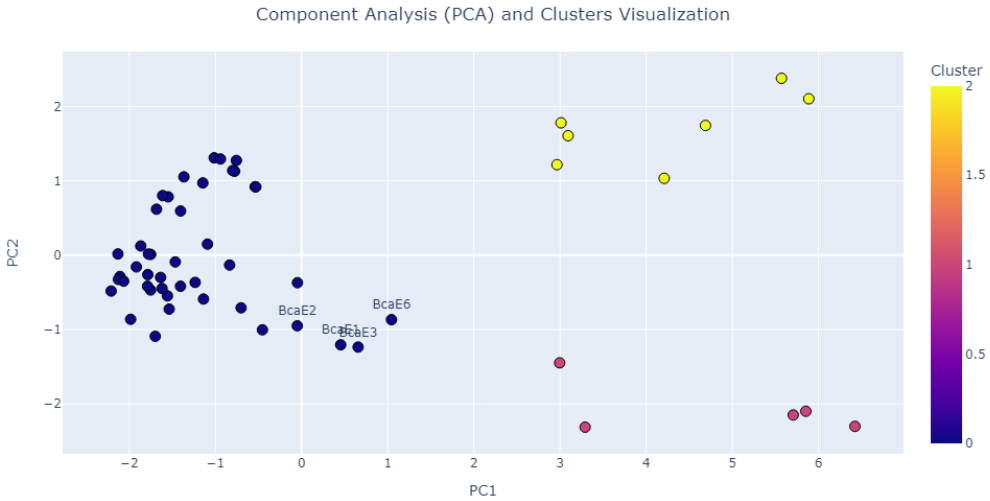

Figure 1. PCA and clusters visualization obtained from unsupervised cluster analysis. Massive (blue), vesicular (yellow) and altered massive (pink) basalt specimens. The labelled specimens belong to the altered massive facies, yet they exhibit prominent physical properties (i.e. ρ_r, ρ_b) similar to massive facies.

5 CONCLUSIONS

This investigation contributes to a better understanding of the physical properties influence on hydric and mechanical properties of basalts from Madeira Island, applying multivariate statistical analyses, and provides valuable insights for their application in geoengineering projects.

The equations developed in this study for water absorption coefficient by capillarity and uniaxial compressive strength can be used as reliable prediction models and can assist in assessing their suitability as construction and building materials, and for improving known classifications in civil engineering projects.

Unsupervised clustering processes using principal component analysis classified the basalts into three well-differentiated groups based on open porosity, pore size and type, and the natural weathering degree of basalts. This finding suggests that this approach can be used to guide the selection of specific types of basalts for different applications, considering their intrinsic controlling factors. In addition, this process can be further enhanced with the use of supervised classification algorithms for categorising samples accurately and identifying transitional specimens between facies into larger petrophysical databases, leading to more efficient and cost-effective laboratory work, faster generation of results, and better-informed decision-making.

Future works for gaining deeper understanding of water movement in vesicular basalts will be conducted, expanding the number of samples to be tested and conducting further microscopic analysis or employing advanced imaging techniques to identify and quantify the actual pore structure. This will provide a more comprehensive interpretation of the pore size distribution and its impact on sorption mechanisms.

ACKNOWLEDGEMENTS

The authors are grateful for the financial support provided by the European Union - Next Generation EU, by the Spanish Ministry of Universities, the University of Alicante (project reference: MARSALAS22-09), and the fellowship from “la Caixa” Foundation (ID 100010434) with the code LCF/BQ/DR22/11950029. The authors would also like to thank Dr. Christophe Ortiz and Prof. Carla Gonçalves, and Engs. Darren and Helen Gruett, for their valuable help in revising and editing respectively the French and the English texts.

REFERENCES

Alves, R., Faria, P., Brás, A. (2019). Brita Lavada - An eco-efficient decorative mortar from Madeira Island, *Journal of Building Engineering*, 24, 100756. https://doi.org/10.1016/j.jobe.2019.100756.

Anon. (1979). Classification of rocks and soils for engineering geological mapping part I: Rock and soil materials, *Bulletin of the International Association of Engineering Geology*, 19, 364-371. https://doi.org/10.1007/BF02600503.

Benavente, D. (2002). *Modelización y estimación de la durabilidad de materiales pétreos porosos frente a la*

cristalización de sales, Ph.D. Thesis, University of Alicante, Spain.

Brum da Silveira, A., Madeira, J., Ramalho, R., Fonseca, P., Prada, S. (2010). *Carta Geológica (folhas A e B) e Notícia Explicativa da Carta Geológica da Ilha da Madeira na Escala de 1:50000*, Secretaria Regional do Ambiente e Recursos Naturais, Governo da Região Autónoma da Madeira e Universidade da Madeira, Funchal, Portugal.

Çelik, M. Y., Kaçmaz, A. U. (2016). The investigation of static and dynamic capillary by water absorption in porous building stones under normal and salty water conditions, *Environmental Earth Sciences*, 75, 307. https://doi.org/10.1007/s12665-015-5132-x.

Cueto, N. (2020). *Major controlling factors on fluid transport properties in complex marine and freshwater carbonate rocks: An integrated experimental and theoretical study on the relation between permeability and capillarity*, Ph.D. Thesis, University of Alicante, Spain.

Cueto, N., Vieira de Sousa, J. F., Fernandes, C., Benavente, D., Urbani, F., Meza, R., Fernandes, É., García-del-Cura, M. A. (2018). Water transport in lapilli tuff from Madeira Island, Portugal: implications on degradation mechanisms and durability, In: *16CNG - 16º Congresso Nacional de Geotecnia*, Açores, Portugal, 12 p.

Hall, C., Hoff, W. D. (2021). *Water Transport in Brick, Stone and Concrete*, 3rd ed., CRC Press, London. https://doi.org/10.1201/9780429352744.

Hughes, D. J., Brown, G. C. (1972). Basalts from Madeira: A Petrochemical contribution to the genesis of oceanic alkali rock series, *Contributions to Mineralogy and Petrology*, 37, 91-109. https://doi.org/10.1007/BF00371069.

Iglauer, S., Al-Yaseri, A. (2021). Improving basalt wettability to de-risk CO_2 geo-storage in basaltic formations, *Advances in Geo-Energy Research*, 5, 3, 347-350. doi: 10.46690/ager.2021.03.09.

ISRM (1981). Basic geotechnical description of rock masses, *International Journal of Rock Mechanics and Mining Sciences*, 18, 85-110.

Lourenço, J. C., Brito, J. M., Santos, J., Rosa, S. P. P., Rodrigues, V. C., Oliva, R. (2010). Geotechnical characterization of volcanic rocks and soils of Madeira Island, In: *ISRM International Workshop on Rock Mechanics and Geoengineering in Volcanic Environments*, Puerto de la Cruz, Spain.

Maia, L., Aslani, F. (2016). Modulus of elasticity of concretes produced with basaltic aggregate, *Computers and Concrete*, 17, 1, 129-140. http://dx.doi.org/10.12989/cac.2016.17.1.129.

NP EN 13755 (2008). Natural stone test methods. Determination of water absorption at atmospheric pressure, European Committee for Standardization, Brussels, Belgium.

NP EN 1925 (2000). Natural stone test method. Determination of water absorption coefficient by capillarity, European Committee for Standardization, Brussels, Belgium.

NP EN 1926 (2008). Natural stone test method. Determination of uniaxial compressive strength, European Committee for Standardization, Brussels, Belgium.

NP EN 1936 (2008). Natural stone test method. Determination of real density and apparent density and of total and open porosity, European Committee for Standardization, Brussels, Belgium.

Pereira, M. L., da Silva, P. F., Fernandes, I., Chastre, C. (2021). Characterization and correlation of engineering properties of basalts, *Bulletin of Engineering Geology and the Environment*, 80, 2889-2910. https://doi.org/10.1007/s10064-021-02107-7.

Perneta, J. P. S., Vieira de Sousa, J. F. (2023). Volcanic rocks from Madeira Island, Portugal. A contribution to its characterization, In: *18CNG - 18º Congresso Nacional de Geotecnia*, Évora, Portugal, 1387-1396.

Ramalho, R. S., Brum da Silveira, A., Fonseca, P. E., Madeira, J., Cosca, M., Cachão, M., Fonseca, M. M., Prada, S. N. (2015). The emergence of volcanic oceanic islands on a slow-moving plate: The example of Madeira Island, NE Atlantic, *Geochemistry, Geophysics, Geosystems*, 16, 2, 522-537. https://doi.org/10.1002/2014GC005657.

Sempere-Valverde, J., Ramalhosa, P., Chebaane, S., Espinosa, F., Gama Monteiro, J., Bernal-Ibáñez, A., Cacabelos, E., Gestoso, I., Guerra-García, J. M., Canning-Clode, J. (2023). Location and building material determine fouling assemblages within marinas: A case study in Madeira Island (NE Atlantic, Portugal), *Marine Pollution Bulletin*, 187, 114522. https://doi.org/10.1016/j.marpolbul.2022.114522.

Silva, E. C., Barros, M. J. S., Barros, J. G., Simões, D. H. A., Barros, L. A. M. (2023). Geological and geotechnical studies for slope stability analysis in the interior of Maranhão: Proposal for slope conformation in the city of Açailândia/MA - MA 125, In: *18CNG - 18º Congresso Nacional de Geotecnia*, Évora, Portugal, 1117-1126.

Vieira de Sousa, J. F., Sousa, D. M. F., Oropeza, C. R. (2012). Geotechnical characterization of volcanic rock materials of Madeira Island, In: *13CNG - 13º Congresso Nacional de Geotecnia*, Lisboa, Portugal.

Yaseri, A., Esteban, L., Giwelli, A., Sarout, J., Sarmadivaleh, M., Kanakiya, S., Adam, L. (2023). Potential of hydrogen underground storage in volcanic reservoirs of Australia: is it worth looking into? In: *AHRC2023 - Australian Hydrogen Research Conference*, Canberra, Australia. https://doi.org/10.2139/ssrn.4483701.

Proceedings of the XVIII ECSMGE 2024
GEOTECHNICAL ENGINEERING CHALLENGES
TO MEET CURRENT AND EMERGING NEEDS OF SOCIETY
© 2024 the Authors
ISBN 978-1-032-54816-6
DOI 10.1201/9781003431749-55
Open Access: www.taylorfrancis.com, CC BY-NC-ND 4.0 license

ECSMGE 24
XVIII EUROPEAN CONFERENCE ON SOIL MECHANICS AND GEOTECHNICAL ENGINEERING

Analysis of the feasibility of applying reinforcement for laying direct foundations

Analyse de la faisabilité de l'application de renforcements pour la pose de fondations directes

M.C.C.S. da Silva*, P.C. de A. Maia
Universidade Estadual do Norte Fluminense Darcy Ribeiro, Campos dos Goytacazes, Brasil
cmariacarollina@gmail.com

ABSTRACT: With urban expansion, the need to build in massifs with low support capacity and high deformability is increasingly common. A solution to this geotechnical problem is soil manipulation to improve its performance. In this sense, geosynthetics have been playing a prominent role in replacing conventional reinforcement solutions. The bibliography shows that the use of these materials, particularly in the case of shallow foundations, increases the load capacity and decreases the magnitude of settlements. The present study aims to analyze the technical feasibility of applying reinforcement for laying shallow foundations, with emphasis on the use of geosynthetics, as well as the parameters with the greatest influence on increasing the load capacity and reducing the magnitude of the settlement of the soil- reinforcement. The main parameters studied include: the characteristics of the foundation mass and the reinforcement, the geometry of the foundation and the nature of the loading. From an analytical model, variations of these parameters were simulated, within an acceptable range, seeking to estimate the load capacity based on Terzaghi's theory. In addition, a sensitivity analysis was carried out using the First-Order Second-Moment. The results make possible to determine under what conditions of stiffness of the foundation and reinforcement the execution of the technique is safely efficient. According to the analysis of the data in reduced models, it can be stated that the reinforcement ensured greater stability, enabling the construction in soils of low resistance.

RÉSUMÉ: Avec l'expansion urbaine, la nécessité de construire dans des massifs à faible capacité de support et à forte déformabilité est de plus en plus courante. Une solution à ce problème géotechnique est la manipulation du sol pour améliorer ses performances. En ce sens, les géosynthétiques jouent un rôle de premier plan en remplacement des solutions de renforcement conventionnelles. La bibliographie montre que l'utilisation de ces matériaux, notamment dans le cas de fondations peu profondes, augmente la capacité de charge et diminue l'ampleur des tassements. La présente étude vise à analyser la faisabilité technique de l'application de renforcements pour la pose de fondations superficielles, en mettant l'accent sur l'utilisation de géosynthétiques, ainsi que les paramètres ayant la plus grande influence sur l'augmentation de la capacité de charge et la réduction de l'ampleur du tassement du sol. renforcement. Les principaux paramètres étudiés comprennent : les caractéristiques du massif de la fondation et du ferraillage, la géométrie de la fondation et la nature du chargement. A partir d'un modèle analytique, les variations de ces paramètres ont été simulées, dans une plage acceptable, en cherchant à estimer la capacité de charge selon la théorie de Terzaghi. De plus, une analyse de sensibilité a été réalisée en utilisant le Second-Moment du Premier Ordre. Les résultats permettent de déterminer dans quelles conditions de rigidité de la fondation et du renforcement l'exécution de la technique est efficace en toute sécurité. Selon l'analyse des données en modèles réduits, on peut affirmer que le renforcement a assuré une plus grande stabilité, permettant la construction dans des sols de faible résistance.

Keywords: Reinforcement; shallow foundation; geosynthetic.

1 INTRODUCTION

Currently, with urban expansion, it is very common to build in masses that have low support capacity and high deformability. The solution to this geotechnical problem is the use of techniques to improve the performance of the mass.

Conventional treatment methods range from replacing part of the weak soil with a suitably thick layer of stronger granular fill, increasing the size of the foundation base, or a combination of the two methods, for example. However, a more economical alternative is the use of geosynthetics to reinforce the soil.

In the soil-structure-geosynthetic interaction mechanism, the synthetic material, which deforms according to the structure's request, adds a portion of tensile strength to the soil due to the friction developed. Particularly, in the case of shallow foundations laid on masses with low load capacity and high compressibility, the introduction of geosynthetics

provides an increase in support capacity and a significant reduction in settlements.

2 OBJECTIVES

The main objective of the article is to define the stiffness conditions of the mass and reinforcement in which the application of the technique, in the case of direct foundations, is efficient with safety and economy.

3 METHODOLOGY

The concept of soil reinforcement was initially published by Vidal (1969) and was consolidated in the pioneering work of Binquet and Lee (1975a, 1975b) with an evaluation of the behavior of sand mass reinforced with metal strips. Over time, with new requirements and technologies in relation to material, shapes and sizes, metallic strips were replaced by geosynthetics.

The Figure 1 below shows the configuration and parameters of a foundation reinforced with geosynthetic. The main parameters studied include depth of the first reinforcement layer (u), geosynthetic width (b), number of reinforcements (N), spacing between layers (h) and total reinforcement thickness (d).

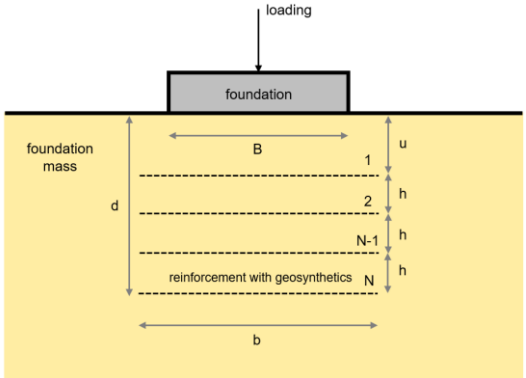

Figure 1. Configuration and parameters of a foundation reinforced with geosynthetic.Source: Adapted from Corrêa, 2021.

The performance of the reinforcement element, in this case, the geosynthetic element, is related to its sizing and the specification of the values of its relevant properties. In the case of reinforcing a shallow foundation, the following properties are worth highlighting: the tensile strength, the deformation at failure, the tensile stiffness modulus and creep behavior, as well as the adhesion and the friction angle of the soil-soil interface. geosynthetic.

The methodology for calculating the load capacity was defined based on the bibliography, considering the models proposed by Sharma et al. (2009). Initially, it was considered that the reinforced mass behaves similarly to a foundation on a mass with two types of soil.

Figure 2 presents the schematic section of a shallow foundation placed on soil.

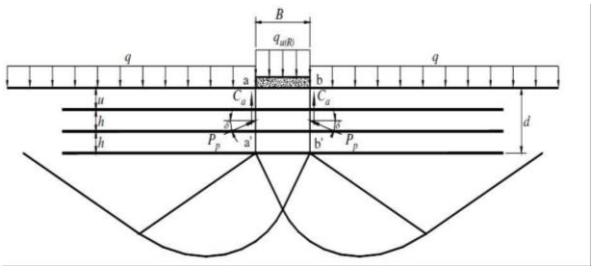

Figure 2. Similar failure in foundations laid on solid ground with two types of soil. Source: Sharma et al., 2009.

The failure mechanism is characterized by punching in the reinforcement layer followed by general shear failure in the unreinforced mass.

$$q_r = q_0 + \frac{2(C_a + P_p sen\delta_p)}{B} - \gamma_t d + \Delta q_t \quad (1)$$

where, q_r is the load capacity of the reinforced soil, q_0 is the load capacity of the unreinforced soil, C_a is the adhesion force, P_p is the force resulting from the passive thrust of the soil, δ_p is the angle of the passive force with the horizontal, which can be adopted as $0{,}5\varphi_r$, where φ_r is the angle of friction of the soil used as reinforcement, B is the width of the foundation, , γ_t is the specific weight of the layer of reinforced soil, d is the thickness of the layer reinforced and Δq_t is the increase in load due to the tension in the reinforcement.

The load capacity of a shallow square foundation on reinforced soil is then determined by the equation:

$$q_r = q_0 + \frac{4c_a d}{B} + 2\gamma_t d^2\left(1 + {}^{2D}/_{d}\right)\frac{K_s tan\varphi_r}{B} + \frac{4\sum_{i=1}^{N} T_i tan\delta_p}{B} - \gamma_t d \quad (2)$$

where, K_s is the punching thrust coefficient, T_i is the tensile force in the synthetic material and N is the number of reinforcement layers.

It is worth mentioning that, for this estimate, the traction of a geogrid of the Fortrac model, from Huesker, was considered, which has a traction resistance of up to 2500kN/m.

The punching thrust coefficient was obtained using the abacus proposed by Chen (2007), which relates K_s as a function of the friction angle.

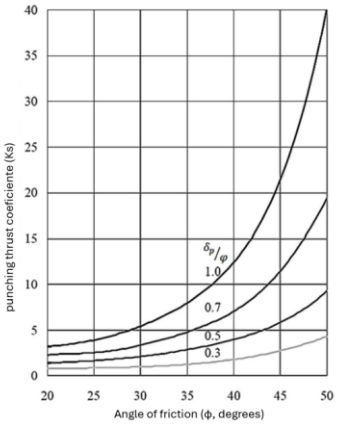

Figure 3. Punching thrust coefficient as a function of friction angle. Source: Adapted from Chen, 2007.

For the acceptability criterion of probabilistic analysis, the Brazilian standard does not specify numerically. The bibliography shows model evaluation criteria regarding the reliability index and probability of rupture. The tables below show the relationships found.

Table 1. Risk acceptability scale using the MIL – STD – 882 standard. Source: Adapted from Clemens (1983) adapted by Aoki (2011).

β	Occurrence	Recurrence Time	Frequency	Risk Level	Prob. Level	p_f
-7,94	Certainty	1 day	All day		1	1,00
0,00	50% probability	2 days	Every 2 days		2	0,50
0,52	frequent	1 week	Every week	A	$3x10^{-1}$	0,30
1,88	likely	1 month	Every month	B	$3x10^{-2}$	0,03
2,75	Occasional	1 year	Every year	C	$3x10^{-3}$	0,003
3,43	Remote	10 years	Every decade	D	$3x10^{-4}$	0,0003
4,01	Very remote	100 years	Every century	E	$3x10^{-5}$	0,00003
4,53	Unlikely	1000 years	Every millennium		$3x10^{-6}$	0,000003
7,27	Never	5,47E+12	Age of the Universe		0	1,83E-13

Table 2. Reliability assessment considering a useful life of 50 years according to the ELT 1110-2-547 standard. Source: Adapted from U.S. Army Corps of Engineers (1997).

Expected performance level	β	Probability of ruin
High	5,0	0,0000003
Good	4,0	0,00003
Above average	3,0	0,001
Below average	2,5	0,006
Low	2,0	0,023
Unsatisfactory	1,5	0,07
Risky	1,0	0,16

4 RESULTS AND DISCUSSION

In this sense, the first considering a medium-sized building, with an allowable load capacity $qadm = 200kPa$ and a 1 meter square footing and the other considering a large building, with a permissible load capacity $qadm = 500kPa$ and a 3 meter square footing.

It is worth mentioning that, for both cases, a rigid, square foundation was considered, based on a sand mass, reinforced with a geogrid. In the applied method, the input data are the average values and variances of the soil parameters, the geometric characteristics of the foundation, and the estimated values of the other soil parameters necessary for the deterministic analysis.

Therefore, the thickness of the minimum reinforcement layer was 0.5m and the maximum was 3m, varying from 0.5m to 0.5m. In addition, the base width (B) and specific weight (γ) were also considered.

From this, the First Order Second Moment method is applied, verifying the effect of varying the number of layers (N) and the thickness of the reinforced layer (d) on the probability of rupture and the reliability index.

The analysis considers that the foundation mass can be sand that is not very compact and moderately compact.

Some considerations are made in the literature about the massive configuration for this case. It was observed that the load capacity of the soil suffers an insignificant increase for conditions with more than six layers of reinforcement, a result confirmed by Das (1989) and Omar et al. (1993), which was also observed in this work.

Considering a soft mass, for the situation in question, the best reinforcement contribution occurs when the number of layers is equal to 2. From the graph below, it is also possible to see that the increase in the number of layers after this number, has not a significant effect.

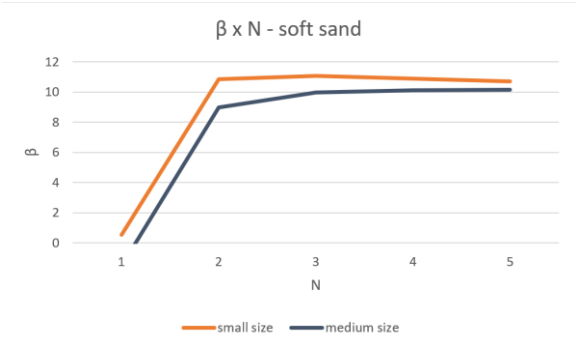

Figure 4. Behavior of the foundation mass vs. reliability index considering a soft mass in a small building and medium-sized building.

There is a consensus in the literature that the reinforcement length should be around 5B and the ideal number of layers is normally limited to up to 5. For higher numbers of layers, it has been demonstrated in the literature that there is no significant gain in capacity of the soil, only generating an increase in costs for the enterprise.

For the mass and reinforcement configurations considered in this analysis, it was possible to notice that, for all types of soil considered, and for the two loading conditions, when the number of layers is above

3, no significant increases in the index were generated. of reliability.

The graphs below show the behavior of the number of reinforcements for a less compact massif, a significant increase in the reliability index can be seen when including reinforcement (with just one layer).

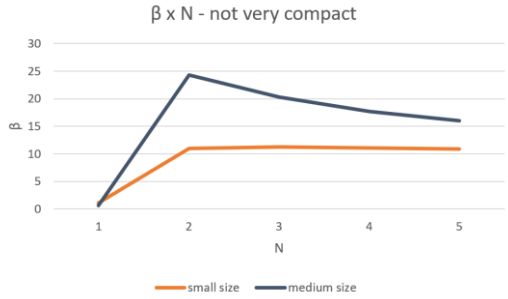

Figure 5. Behavior of the foundation mass vs. reliability index considering a less compact mass in a small building and a medium-sized building.

Furthermore, tests also demonstrated that for reinforcement to be efficient, the last layer must never be located at a depth greater than 2B. In this analysis, the depth of the reinforcement layer thickness reached 3 meters in both cases. Thus, it is possible to see graphically that, when a small building is considered, and therefore, the foundation is 1 meter wide, when the reinforcement exceeds 2 meters in thickness, there is no major influence on the reliability index.

The graphs below show the relationship between the reliability index and depth for the types of soil considered.

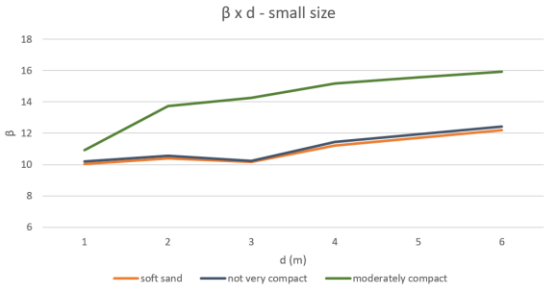

Figure 6. Behavior of the foundation mass vs. reliability index for a small building of a soft sand, not very compact and moderately compact.

The literature also shows that for direct foundations based on clay soils, Shin et al. (1993) and Omar et al. (1993) concluded that a good depth for the first layer of reinforcement is 0.4B, regardless of the anchorage length. The ideal length for anchoring was defined within the range of 4.5B to 5B. According to the authors, to influence the improvement of load capacity, the number of layers of reinforcement must be limited to 5, in addition the first layer of reinforcement must not be located at depths greater than 1.8B.

5 CONCLUSIONS

According to the analysis carried out, it is possible to state that the reinforcement substantially increases the load capacity and reduces the magnitude of settlements, allowing better behavior of the foundation from the point of view of resistance and deformability. The results suggest that the effectiveness of reinforcement is greater in masses with low support capacity.

However, increasing the number of reinforcement layers and the thickness of that layer beyond a specific number, 3 layers and 2.5m, does not produce a significant increase in load capacity.

REFERENCES

Binquet, Jean; Lee, Kenneth L. (1975a). Bearing capacity tests on reinforced earth slabs. *Journal of the geotechnical Engineering Division, v. 101, n. 12*, p. 1241-1255, https://doi.org/10.1061/AJGEB6.0000219.

Binquet, Jean; Lee, Kenneth L. (1975b). Bearing capacity analysis of reinforced earth slabs. *Journal of the geotechnical Engineering Division, v. 101, n. 12*, p. 1257-1276, https://doi.org/10.1061/AJGEB6.0000220.

Chen, Q. (2007). *An experimental study on characteristics and behavior of reinforced soil foundation*. PhD dissertation, Louisiana State University, Baton Rouge, USA, p. 368,

Corrêa, B. R. F. (2021). *Assessment of soil-structure-geosynthetic interaction in shallow foundations reinforced with geogrid.* Masters dissertation. LECIV-UENF. p. 88.t

Das, B. M.; Omar, M. T. (1994). The effects of foundation width on model tests for the bearing capacity of sand with geogrid reinforcement. *Geotechnical and Geological Engineering*, *12*, 3, p. 133 – 141, https://doi.org/10.1007/BF00429771.

Omar, M. T., Das, B. M., Puri, V. K., & Yen, S. C. (1993). Ultimate bearing capacity of shallow foundations on sand with geogrid reinforcement. *Canadian geotechnical journal*, 30(3), 545-549, https://doi.org/10.1139/t93-046.

Omar, M. T., Das, B. M., Yen, S. C., Puri, V. K., & Cook, E. E. (1993). Ultimate bearing capacity of rectangular foundations on geogrid-reinforced sand. *Geotechnical Testing Journal, 16(2),* 246-252, https://doi.org/10.1520/GTJ10041J.

Sharma, R., Chen, Q., Abu-Farsakh, M., & Yoon, S. (2009). Analytical modeling of geogrid reinforced soil foundation. *Geotextiles and Geomembranes, 27(1)*, 63-72, https://doi.org/10.1016/j.geotexmem.2008.07.002.

Vidal, Henri. *The principle of reinforced earth.* Highway research record, n. 282, 1969.

Proceedings of the XVIII ECSMGE 2024
GEOTECHNICAL ENGINEERING CHALLENGES
TO MEET CURRENT AND EMERGING NEEDS OF SOCIETY
© 2024 the Authors
ISBN 978-1-032-54816-6
DOI 10.1201/9781003431749-56
Open Access: www.taylorfrancis.com, CC BY-NC-ND 4.0 license

ECSMGE 24
XVIII EUROPEAN CONFERENCE ON SOIL MECHANICS AND GEOTECHNICAL ENGINEERING

Rate-dependent confined crushing in granular media

Écrasement confiné dépendant du taux dans les milieux granulaires

S.K. Das*
NIT Rourkela, Rourkela, Odisha, India
**dassoukat@nitrkl.ac.in*

ABSTRACT: Does granular material show strain rate-dependent response, especially with quasi-static loading conditions? The answer is both yes and no since it depends on various factors like particle shape, size and crushability. Such time-dependent behaviour in granular materials is extremely important in various industries where both particle crushing and loading rates are combined. The focus of the research has been to numerically exploit the strain rate effects at the grain scale level and link it with macroscopic response while simultaneously taking into account the evolution of particle size distribution during the fragmentation process. The numerical simulation of one-dimensional (1D) compression shows quasi-static loading, which presumably produces a rate-independent response, and can demonstrate significant rate-dependent features during particle crushing. The variation in the contact force distribution within the granular assembly at different loading rates, dictates the stress response and the crushing events. Relatively low strain rate compression favours homogeneous crushing involving a large number of particles that consequently reduces the strength via fragment rearrangement. Conversely, a high strain rate promotes localized crushing within fewer particles, and thus strain hardening is observed.

RÉSUMÉ: Les matériaux granulaires montrent-ils une réponse dépendante du taux de déformation, en particulier dans des conditions de chargement quasi-statiques ? La réponse est à la fois oui et non, car cela dépend de divers facteurs tels que la forme, la taille et la broyabilité des particules. Ce comportement dépendant du temps dans les matériaux granulaires est extrêmement important dans diverses industries où la fragmentation des particules et les taux de chargement sont combinés. L'objectif de la recherche a été d'exploiter numériquement les effets du taux de déformation au niveau de la granulométrie et de les relier à la réponse macroscopique tout en tenant compte simultanément de l'évolution de la distribution de taille des particules pendant le processus de fragmentation. La simulation numérique de la compression unidimensionnelle (1D) montre un chargement quasi-statique, qui produit vraisemblablement une réponse indépendante du taux, et peut présenter des caractéristiques significatives dépendantes du taux pendant le broyage des particules. La variation de la distribution des forces de contact au sein de l'assemblage granulaire à différentes vitesses de chargement dicte la réponse au stress et les événements de broyage. Une compression à faible taux de déformation favorise un broyage homogène impliquant un grand nombre de particules, ce qui réduit par conséquent la résistance via le réarrangement des fragments. En revanche, un taux de déformation élevé favorise un broyage localisé dans moins de particules, et donc un durcissement par déformation est observé.

Keywords: Crushable; granular; rate-dependent; DEM; quasi-static.

1 INTRODUCTION

Strain rate plays a major role in determining the time-dependent responses (creep, stress relaxation, delayed plasticity, etc.) of geomaterials (Karimpour and Lade, 2013; Lade and Karimpour, 2010). Contrary to the popular belief that time dependency is prevalent among the cohesive geomaterials (clay, rock and concrete) only, a list of laboratory experiments has confirmed that significant time effects are observed in granular soils as well (Augustesen et al., 2004; Kongkitkul et al., 2008).

The importance of rate-dependent behaviour in granular materials has been recognized since the mid of the 20th century. Initially, the primary focus was limited to the overall macroscopic strength-stiffness gain with increasing strain rate (Casagrande and Shannon, 1948; Lee et al., 1969). However, researchers have recently paid greater attention towards understanding the micromechanical attributes behind the macroscopic rate dependency of granular materials.

Crushability is considered to be the primary grain-scale parameter that controls the rate-dependent response in granular materials (Augustesen et al., 2004). Researchers surmise that during rate-dependent loading, stress waves traverse through the grain contacts leading to individual grain reorienting itself to accomplish a new equilibrium position. The time difference between such processes (wave propagation

and post-crushing rearrangement) leads to rate-dependent material response (di Prisco and Imposimato, 1996).

In order to explore the causes of crushing and to track the mechanism inside the sample during rate-dependent breakage, advanced experimental procedures such as X-rays, CT scans, etc. are being used nowadays (Andò et al., 2013; Mahbub and Haque, 2016; Parab et al., 2014). However, some crucial micromechanical parameters that control the variables influencing the breakage of particles and the inherent time dependency are still hard to achieve. The essence of the present work revolves around the micromechanical understanding of the interaction between time dependency and particle breakage. Various micro-micro-scale parameters such as stress-strain profile, contact force distribution, spatial contact force and particle size distribution are analyzed in order to explain the time-dependent behaviour of the crushable granular materials.

2 MODELLING SCHEME

In a crushable granular assembly, the micromechanical processes associated with strain rate-dependent fragmentation cannot be assessed through conventional geotechnical experiments. In addition, it is hard to distinguish the effects of post-fragmented particles on the rate-dependent response during progressive loading. To cope up with such experimental limitations, strain rate-dependent loading and grain crushing are simulated numerically using discrete element modelling (DEM). Besides studying the micro-processes, DEM simulation also helps to overcome the limitation of laboratory experiments by mimicking test conditions where grain breakage is restrained.

2.1 Model geometry and applied strain rate

In the present study, one-dimensional (1D) compression (oedometric compression) (Figure 1a) on a granular assembly consisting of particles with a diameter ranging between 1 mm to 3 mm, is simulated using 2D DEM using Particle flow code (PFC-5, Itasca) (Itasca, 2015). At the first stage of modelling, the program generates a square box filled with 1932 disc-shaped circular particles (Figure 1a). The initial width of the box is 0.15 m, and the height is 0.15 m. The particles are generated randomly without allowing any overlap with a near-uniform grain size distribution (*gsd*) having d_{50} of 2 mm and initial porosity of 20%. Uniform *gsd* is chosen because it is well known that such an assembly is prone to crushing as compared to an assembly with a wide range of particles due to a reduced cushioning effect (Ben-Nun et al., 2010; Karimpour and Lade, 2010).

Two different monotonic strain rates (0.2/s and 20/s) corresponding to a high and a low strain rate are adopted. The strain rates are chosen such that during the analyses the samples remain in the quasistatic regime which is checked by measuring the inertial number at different strain levels (Figure 1b). The lateral movement of the horizontal walls is restricted to ensure 1D compression. To eliminate any boundary effect-induced stress anisotropy, the specimen dimensions and the size of the particles are chosen such that the scale ratio, which is the ratio of the side of the specimen to the mean particle diameter d_{50} comes out as $\geq$ 25 for all the analyses (Cheng et al., 2017).

2.2 Material parameter and breakage model

The selected material parameters, listed in Table 1, are chosen such that the macroscopic and microscopic responses of the granular assembly resemble the experimentally observed behaviour of coarse sand.

Table 1. DEM model input parameters.

Parameter	Value
The density of the	2650
Particle diameter (d) (m)	0.001 - 0.003
Initial porosity (n_0)	0.2
The initial number of	1932
Normal and shear stiffness	1×10^9
Inter-particle friction	0.6
Largest grain diameter	0.003
Weibull modulus (m)	4.0
Material tensile stress	14.5

The present study has followed the updated replacement method described by Ben-Nun and Einav (Ben-Nun and Einav, 2008). Here, a critical force is calculated based on the assigned Brazilian breakage criterion and compared against the acting normal forces at any instant of time. Once the average contact normal force on a grain exceeds the threshold breakage force, the particle is deleted and replaced by a set of smaller particles (Figure 1c). The fragmented particle volume (area in case of 2D) is increased quickly to regain the original volume of the mother particle to ensure the conservation of mass (Figure 1d).

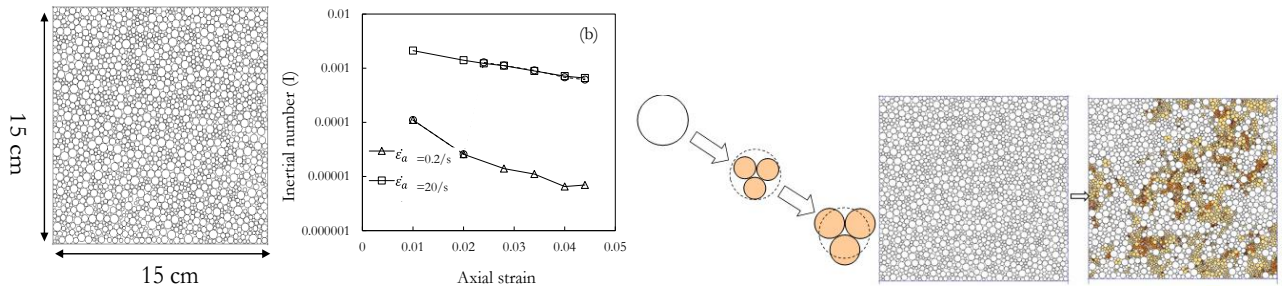

(a) (b)

Figure 1. (a) Initial sample. (b) Inertial number profile (c) Post-crushing replacement of smaller particles (d) intact sample to Crushed sample.

3 RESULTS AND DISCUSSIONS

3.1 Stress-strain response

Axial stress-strain responses under one-dimensional compression at strain rates $\dot{\varepsilon}_a$=0.2/s & 20/s are depicted in Figure 2 for both non-crushable and crushable granular groupings. Simulations proceeded until around 5% strain due to increasing computational demands at higher strain levels due to excessive crushing. Typically, axial stress rises with strain in granular samples during confined 1D compression without a clear differentiation between elastic and plastic changes. Crushable granular materials largely reflect this but with sporadic fluctuations because of pronounced crushing incidents. For non-crushable granules (Figure 2a), stress ascends more swiftly during high strain rate compression.

At lower rates ($\dot{\varepsilon}_a$=0.2/s), compression occurs with minimal strength gain until 1.5% axial strain. However, by 4%-5% axial strain, both strain rate responses align in stress magnitude. Stresses in crushable samples deviate consistently throughout (Figure 2b). The high strain rate response in crushable specimens follows the non-crushable sample response until 3% axial strain, then strengthens. Conversely, the crushable specimen under a low strain rate softens post 3.5% axial strain compared to its non-crushable counterpart. A consolidated stress-strain outcome is shown in Figure 2c, highlighting these observations. The deviations between crushable and non-crushable responses stem from rate-dependent particle crushing.

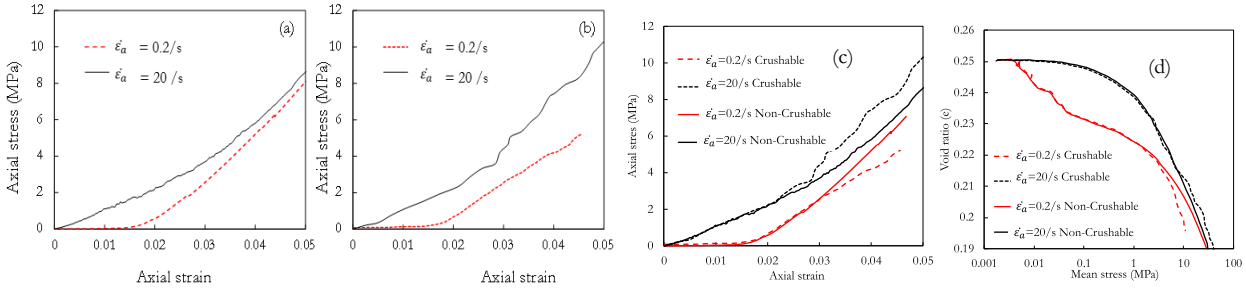

Figure 2. Axial stress vs. axial strain response for (a) non-crushable and (b) crushable granular materials; (c) combined axial stress-axial strain (d) combined void ratio-mean stress response for crushable and non-crushable granular material.

Thermodynamically, if fragmentation prevails, energy dispersed through compression decreases, leading to hardening (Wu et al., 2016). Yet, current simulations suggest strain rates can alter this behaviour by affecting the overall crushing in the sample. The sample can show hardening or softening in stress-strain behaviour (Figure 2c) and dilation or compression in volumetric behaviour (Figure 2d) due to the combined effect of rate and crushing.

3.2 Crushing response

To track the development of crushing influenced by different strain rates, gsds are plotted in Figure 3a, corresponding to different strain levels for two strain rate scenarios. Plotting gsds is a conventional way to quantify the amount of crushing in a sample before and after a compression test. The gsds at a low strain (2%) are almost mirror images of the initial gsd regardless of the strain rate settings because of the absence of any crushing. As loading progresses, higher crushing is observed under a slow strain rate i.e. $\dot{\varepsilon}_a$=0.2/s, whereas it remains visibly less for the high strain rate case. This

illustrates a pattern: a faster loading rate results in lesser crushing and vice versa.

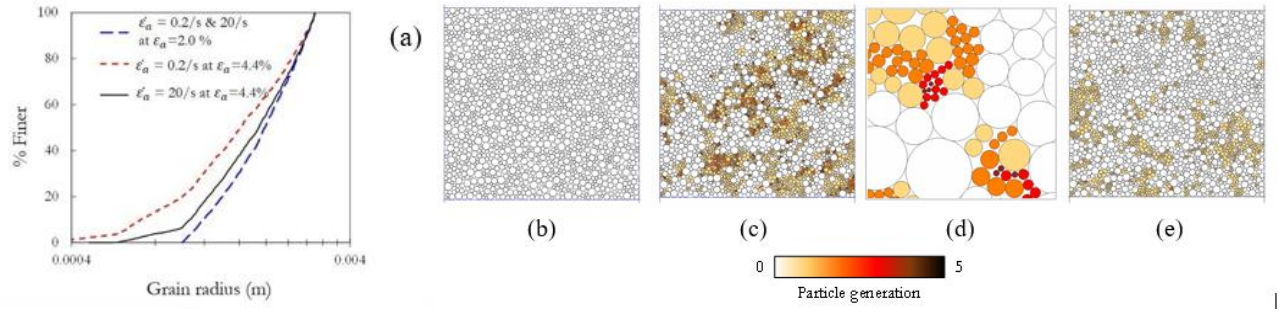

Figure 3. (a) Evolution of grain size distribution at two strain levels 0.02 and 0.044. Evolving crushing topology (b) initial state, at strain 2% for $(\dot{\varepsilon}_a = 0.2/s)$ *and* $(\dot{\varepsilon}_a = 20/s)$ *(c) advanced stage at strain 4.4% for* $(\dot{\varepsilon}_a = 0.2/s)$ *(d) Up to fourth generation of particles in the zoomed figure* $(\dot{\varepsilon}_a = 0.2/s)$ *(e) at strain 5.0% for* $(\dot{\varepsilon}_a = 20/s)$.

Images of the crushed DEM samples under both low and high strain rates are depicted in Figure 3(b-e). Notable variations in crushing progression between the two strain rate scenarios are evident as loading advances (4.4% strain). With faster loading, crushing has primarily yielded the initial particle generation (Figure 3e), while at a slower rate, crushing has progressed up to its fourth cycle (Figure 3c-d).

3.3 Contact force distribution

In order to explore the micromechanics behind such time-dependency along with crushing, contact force distribution is traced at different stages of loading (Figure 4). The non-crushable samples with different loading rates give a similar response when the loading reaches an advanced stage (strain 4.4%, Figure 4a) which indicates granular materials are less sensitive to time-dependent loading, especially at the quasi-static regime. Hence, the axial stress difference also reduces (Figure 2a). However, the responses are dissimilar in the case of the crushable granular samples (Figure 4b) since both the samples, have different rates of compression, and possess different numbers of particles due to crushing.

In the simulations, the prescribed breakage criterion is controlled by the average normal contact force on particles. Increased modal contact force density, as seen in Figure 4a, implies more uniform crushing in low strain rate samples, unlike the high rate sample where the wider contact force distribution suggests that less number of particles are carrying the majority of the load. Therefore, the overall force is distributed among a larger number of particles for low rate sample and hence a softening is observed in the macroscopic stress-strain profile.

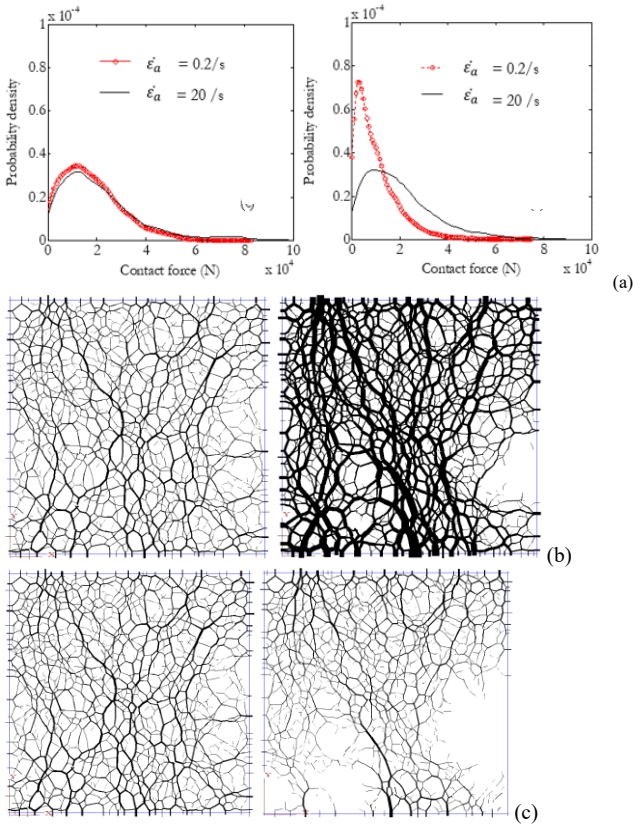

Figure 4. Contact force distribution at strain level 0.044 for non-crushable (left) and crushable sample (right) Force chain at 2% strain for (b) $(\dot{\varepsilon}_a = 0.2/s)$ *(c)*$(\dot{\varepsilon}_a = 20/s)$*; at stress level 581 kPa for (a)* $(\dot{\varepsilon}_a = 0.2/s)$ *(b)* $(\dot{\varepsilon}_a = 20/s)$.

Figure 4b-c reveals force chain distributions in granular assemblies at the same axial strains and stress levels respectively. At 2% axial strain, high strain rate samples exhibit thicker contact forces than their slower counterparts (Figure 4b). At a uniform 581 kPa stress, force chains are homogeneously distributed in low rate samples unlike the high rate sample where the same stress is heterogeneously distributed around the boundaries of the sample (Figure 4c). Slow strain rate samples allow more particle interactions, leading to homogeneous contact force distribution resulting in

extensive crushing, followed by strength reduction. In high-strain rate samples, localized crushing results in material densification and hardening.

4 CONCLUSIONS

The present study offers a vivid picture of the rate-dependent response of granular material using DEM. It shows the micromechanical insights of the crushable and non-crushable granular assemblies while subjected to strain rate-dependent loading. The following conclusions can be drawn from the present investigation.

For non-crushable granular materials, the strain rate sensitivity is pronounced in the low strain level, whereas, at the higher strain it attains the same stress irrespective of the rate of loading.

In the case of crushable granular materials subjected to slow strain rate compression, a large number of particles undergo crushing, since homogeneous contacts between the particles are established. Crushing increases the number of contacts which consequently reduces the mean contact force in the sample. Hence, the overall strength is reduced.

On the contrary, the high-rate sample gains strength because of localized crushing-induced material densification around the sample boundaries followed by sample hardening.

REFERENCES

Andò, E., Viggiani, G., Hall, S.A., Desrues, J., 2013. Experimental micro-mechanics of granular media studied by x-ray tomography: recent results and challenges. Géotechnique Letters 3, 142–146. https://doi.org/10.1680/geolett.13.00036.

Augustesen, A., Liingaard, M., Lade, P.V.P. V, Asce, M., 2004. Evaluation of time-dependent behavior of soils. International Journal of Geomechanics 4, 137–156. https://doi.org/10.1061/ASCÊ1532-3641'2004'4:3'137'.

Ben-Nun, O., Einav, I., 2008. A refined DEM study of grain size reduction in uniaxial compression, in: 12th International Conference of International Association for Computer Methods and Advances in Geomechanics (IACMAG). Goa,India, pp. 702–708.

Ben-Nun, O., Einav, I., Tordesillas, A., 2010. Force Attractor in Confined Comminution of Granular Materials. Phys Rev Lett 104, 108001. https://doi.org/10.1103/PhysRevLett.104.108001.

Casagrande, A., Shannon, W.L., 1948. Strength of soils under dynamic loads. Proceedings of the American Society of Civil Engineers 74, 591–608.

Cheng, H., Shuku, T., Thoeni, K., Yamamoto, H., 2017. Calibration of micromechanical parameters for DEM simulations by using the particle filter. EPJ Web Conf 140, 12011. https://doi.org/10.1051/epjconf/201714012011.

di Prisco, C., Imposimato, S., 1996. Time dependent mechanical behaviour of loose sands. Mechanics of Cohesive-frictional Materials 1, 45–73. https://doi.org/10.1002/(SICI)1099-1484(199601)1:1<45::AID-CFM3>3.0.CO;2-O.

Itasca, P.-5, 2015. Itasca Consulting Group Inc.

Karimpour, H., Lade, P. V, 2013. Creep behavior in Virginia Beach sand. Canadian Geotechnical Journal 1178, 1159–1178. https://doi.org/10.1139/cgj-2012-0467.

Karimpour, H., Lade, P. V, 2010. Time effects relate to crushing in sand. Journal of Geotechnical and Geoenvironmental Engineeringnical 136, 1209–1219. https://doi.org/10.1061/ASCÊGT.1943-5606.0000335.

Kongkitkul, W., Tatsuoka, F., Duttine, A., Kawabe, S., Enomoto, T., Di Benedetto, H., 2008. Modelling and simulation of rate-dependent stress-strain behaviour of granular materials in shear. Soils and Foundations 48, 175–194. https://doi.org/10.3208/sandf.48.175.

Lade, P. V, Karimpour, H., 2010. Static fatigue controls particle crushing and time effects in granular materials. Soils and Foundations 50, 573–583. https://doi.org/https://doi.org/10.3208/sandf.50.573.

Lee, K.L., Seed, H.B., Dunlop, P., 1969. Effect of Transient Loading on the Strength of Sand, in: Proceedings of the 7th International Conference on Soil Mechanics and Foun- Dation Engineering. Mexico City, Mexico, pp. 239–247.

Mahbub, A. al, Haque, A., 2016. X-ray computed tomography imaging of the microstructure of sand particles subjected to high pressure one-dimensional compression. Materials 9, 7–15. https://doi.org/10.3390/ma9110890.

Parab, N.D., Claus, B., Hudspeth, M.C., Black, J.T., Mondal, A., Sun, J., Fezzaa, K., Xiao, X., Luo, S.N., Chen, W., 2014. Experimental assessment of fracture of individual sand particles at different loading rates. Int J Impact Eng 68, 8–14. https://doi.org/10.1016/j.ijimpeng.2014.01.003.

Wu, Y., Yamamoto, H., Izumi, A., 2016. Experimental investigation on crushing of granular material in one-dimensional test. Periodica Polytechnica Civil Engineering 60, 27–36. https://doi.org/10.3311/PPci.8028.

Proceedings of the XVIII ECSMGE 2024
GEOTECHNICAL ENGINEERING CHALLENGES
TO MEET CURRENT AND EMERGING NEEDS OF SOCIETY
© 2024 the Authors
ISBN 978-1-032-54816-6
DOI 10.1201/9781003431749-57
Open Access: www.taylorfrancis.com, CC BY-NC-ND 4.0 license

ECSMGE 24
XVIII EUROPEAN CONFERENCE ON SOIL MECHANICS AND GEOTECHNICAL ENGINEERING

Slog: an open geotechnical software

Slog: un logiciel libre pour le calcul géotechnique

J. de Sauvage*
Université Gustave Eiffel, Bron, France
**jean.de-sauvage@univ-eiffel.fr*

ABSTRACT: In the era of complex numerical modelling, the geotechnical engineering practice always resort to simpler numerical tools, exhibiting the key phenomena. Such software is important for teaching since it allows to better understand the principles underlying the design of structures. They are also important for expertise or research on the one hand because they are easy to use and on the other hand because they establish a clear link between the assumptions made and the results. Most of this software is distributed under proprietary licenses, generating a "black box" effect and offering little flexibility to take a particular situation into consideration. From a teaching point of view, it is often useful to consider aberrant hypotheses in order to show their consequences. The Gustave Eiffel University is therefore developing geotechnical calculation software, entitled Slog. Open access and developed with Python, a widely used language, this software aims to federate a community of user-contributors, particularly among geotechnical teachers and students. In order to be able to easily compare different potential structures on the same site or, conversely, to be able to assess the relevance of a structure in different sites, the user is led to independently define the ground model and the anthropogenic actions. The intersection between both is carried out automatically, allowing the user to easily modify the properties of one or the other automatically. This flexible and scalable process is useful for teaching. The detailed example of the study of the stability of reinforced soils is presented here.

RÉSUMÉ: À l'ère de la modélisation numérique complexe, la pratique de l'ingénierie géotechnique recourt toujours à des outils numériques plus simples, mettant en évidence les phénomènes clés. De tels logiciels sont importants pour l'enseignement puisqu'ils permettent de mieux comprendre les principes sous-tendant le dimensionnement des ouvrages géotechniques. Ils sont également importants pour l'expertise ou la recherche d'une part parce qu'ils sont faciles à utiliser et d'autre part parce qu'ils établissent un lien clair entre les hypothèses formulées et les résultats. La plupart de ces logiciels sont distribués sous licences propriétaires, générant un effet de « boîte noire » et offrant peu de flexibilité pour prendre en compte une situation particulière. D'un point de vue pédagogique, il est souvent utile de considérer des hypothèses aberrantes afin d'en montrer les conséquences. L'Université Gustave Eiffel développe ainsi un logiciel de calcul géotechnique, intitulé Slog. En libre accès et développé avec Python, langage très utilisé, ce logiciel a pour vocation de fédérer une communauté d'utilisateurs-contributeurs, notamment parmi les enseignants et étudiants géotechniques. Afin de pouvoir comparer facilement différentes structures potentielles sur un même site ou, à l'inverse, pouvoir évaluer la pertinence d'un ouvrage dans différents sites, l'utilisateur est amené à définir indépendamment le modèle de sol et les actions anthropiques. L'intersection entre les deux s'effectue automatiquement, permettant à l'utilisateur de modifier facilement et automatiquement les propriétés de l'un ou de l'autre. Ce processus flexible et évolutif est utile pour l'enseignement. L'exemple détaillé de l'étude de la stabilité des sols renforcés est présenté ici.

Keywords: Geotechnical software; open access; teaching modelling.

1 INTRODUCTION

Complex numerical modeling, specifically by finite elements, is today widely developed in geotechnical engineering, integrating the most complex constitutive laws and, when used correctly, produce predictions in accordance with field observations (El Arja, 2020). However, in engineering practice, geotechnical calculation still uses simplified tools exhibiting the key phenomena. As an example, the c-phi reduction method makes it possible to determine the safety factor of a slope but, in practice, most studies are carried out using traditional tools considering a bundle of potential failure surfaces and evaluating, for each of them, the ratio between motor and resistant efforts (Pilot, 1966).

Such software is important for teaching since it allows a better understanding of the principles underlying the design of structures. With some commercial finite element software students can have the impression that "you just have to press a button". However, it would be simplistic to locate the sole interest of simplified digital tools there. They are also important for expertise or research on the one hand

because they are easy to use and on the other hand because they establish a clear link between the calculation hypotheses retained and the results produced. The goal here is not to condemn this or that calculation method but to emphasize the usefulness for the geotechnical engineer of having access to all the calculation hypotheses and being able to modify them as he wishes, avoiding the "black box" effect. Open software provides the flexibility to take into consideration a particular situation. From an educational point of view, it also makes it possible to integrate aberrant assumptions into the calculation in order to show their consequences. Open software dedicated to geotechnical engineering can be found but they are generally devoted to one specific application. One can think for example about geotecha (https://github.com/rtrwalker/geotecha) for the consolidation of soft soils or PyGeo (https://github.com/CalvinNeo/PyGeo) for the recognition of structural surfaces.

Université Gustave Eiffel is therefore developing geotechnical calculation software, entitled Slog, freely distributed through its GitHub platform (https://github.com/Ifsttar/Slog). Developed using Python, a widely used programming language, this software aims to bring together a large community of user-contributors, particularly among geotechnical teachers and students. Accessible to the greatest number of people through the use of Python, Slog aims to respond to the difficulties of geotechnical engineers by taking into account the specificities of this domain.

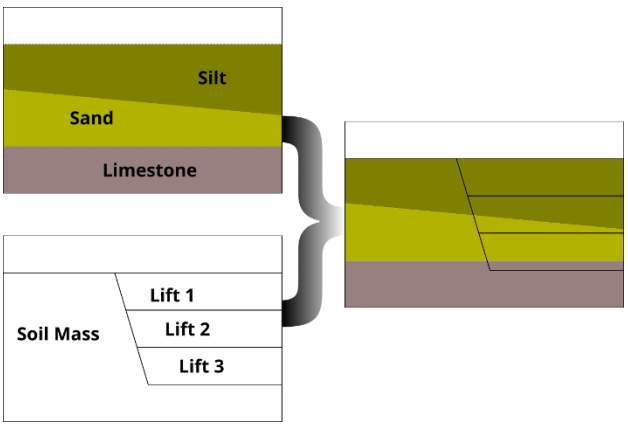

Figure 1. Domains considered for the study of a soil-nailed wall (top left: geology, bottom left: anthropogenic actions, right: intersection.

In order to be able to easily compare different potential geotechnical assets on the same site or, conversely, to be able to evaluate the relevance of an asset in different sites, the user is led to independently define a "geology" (partition of the space in blocks of soil) and an "asset" (set of anthropogenic actions). The intersection between "geology" and "asset" is made automatically, allowing the user to easily modify the properties of one or the other automatically. This flexible process proves useful on an educational level. A detailed example is presented here: the study of the stability of soil-nailed wall. This example is deliberately simplistic to make the screen output easier to read. In practice, a large number of slices must be considered and, depending on the method chosen (Fellenius, Bishop, perturbations, etc.) the geometry of the failure surface must be adapted.

2 DESCRIBING THE TERRAIN

One of the specificities of geotechnical engineering is to be placed in a merely known environment: the soil in place. This particularity leads to the definition of a terrain model, based on the study of geological maps, on the analysis of geotechnical surveys and laboratory tests as well as on extrapolations. During a project, the terrain model can therefore evolve according to new investigations and the revision of some assumptions. At the same time, the project itself may have to evolve between the different study phases. Where most software requires defining *ab initio* a domain divided into homogeneous zones, Slog suggests defining two distinct domains, one representing the terrain model (constituted of „Faciès" objects) and the other representing the anthropogenic actions, *i.e.* the building project. The software itself generates a unique domain for the study by realizing the intersection of the two domains thus defined by the user.

As an example, let us consider a soil-nailed wall excavation project in a layered soil (See Figure 1). The user first defines a Geology consisting of a layer of Silt above a layer of Sand, itself above a layer of Limestone. Secondly, the user defines the domains linked to anthropogenic action: a "Soil Mass" domain corresponding to the part of the soil that the project plans to leave in place and three domains "Lift1", "Lift2" and "Lift3 » corresponding to successive excavation lifts. The software then generates by automatic intersection the division of the space usable for the calculations. The automatic intersection algorithm is taken from (Foster et al., 2019).

If additional tests carried out during the design study indicate that the sand layer actually has a higher modulus than the initial estimate, the user can simply modify the Geology and the terrain model automatically inherits the new properties. In the same way, if during the project, it is decided to review the dip of the sand/silt interface, this can be done on the Geology and the calculation of the intersection with the Anthropic Action immediately gives a new terrain model for the calculation. Note that, when constructing

a Geology, Slog determines if all the facies constitute a partition of space, that is to say that they cover all the points of the calculation domain on the one hand and that they do not overlap each other. If this condition is not met, an error message is returned.

The Object Oriented programming implemented in Slog allows all the elements of a class to inherit the properties of this class (see Figure 2). In particular, the Geology facies like the anthropogenic geometry elements all inherit from the Polygon class. The latter are therefore the boundaries of the different geotechnical elements and the fact that they share properties facilitates the calculation of their intersection but above all allows them to be defined according to a similar procedure (list of vertices given in the trigonometric direction). This procedure facilitates interfacing between Slog and software such as GMSH (Geuzaine and Remacle, 2009), an open access mesher. Although the calculations carried out in Slog do not *a priori* require a mesh, the GMSH geometry module is very useful for generating geometries.

The Class Diagram presented in Figure 2 also allows to understand the overall structure of the terrain model. What has been presented so far actually constitutes a given configuration of the project. In particular, the division presented in Figure 1 assumes that 3 excavation lifts have been carried out but nothing prevents a subsequent configuration from including an additional lift or an embankment at the wall tip. A project is therefore a list of Configurations. Finally, for each Configuration, a set of structural elements (Geotextiles, nails, walls, etc.) are superimposed on the terrain which must also interface with the terrain model.

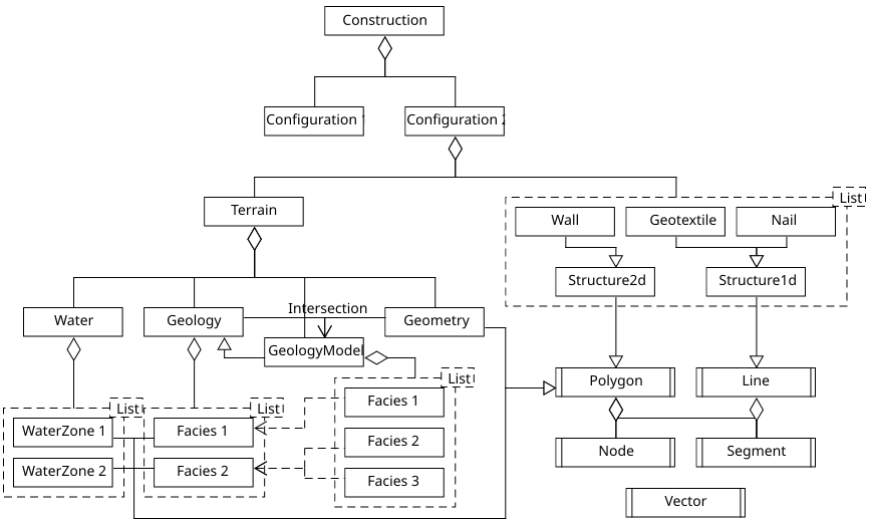

Figure 2. Slog structuring class diagram.

3 MANAGING STRUCTURAL ELEMENTS

Here we call structural elements the anthropogenic elements that can be taken into account in the calculation. We can thus think of nails, reinforcements or geotextiles in the case of reinforced soil support but more generally, these structural elements include diaphragm walls, sheet piles or even gravity walls. We could also think of injected soil elements but the strong proximity between "2d Structure" type objects and "Facies" type objects allows the user, depending on the needs of his calculation, to decide if he prefers represent jet grouting as a structural element or an element of Geology.

Note at this point that the current version of Slog is purely two-dimensional. A three-dimensional version is expected to be developed but has not yet been developed and, in engineering practice, many calculations are carried out in 2D. Thus, the truly linear elements (nails, anchors, etc.) and the surface elements (geotextiles, sheet piles, etc.) are both represented by linear elements. Unlike most geotechnical software, the structural elements being defined in parallel with the terrain model, they have no impact on the Geology and the Facies crossed remain continuous. In order to separate the upstream soil and the downstream soil of a sheet pile for example, it is necessary to translate this separation into "Anthropogenic actions". Through the intersection of Geology and Anthropogenic Actions, this discontinuity will then be apparent in the domain study. From an educational point of view, this choice makes it possible to impose on the user a reflection on the nature of the structural elements that he introduces.

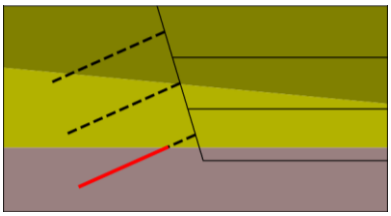

Figure 3. Addition of Nail objects and highlighting of intersection between the nails and the limestone (red).

In Figure 3 the example of the excavation presented above is completed by nails. The Polygon intersection function allows, in this case, to automatically determine the intersection between the nails and the Limestone layer. In practice, *nail3.intersect_polygon(limestone)* returns the list of intersections between nail 3 and the limestone layer. This list can contain several elements (if the limestone layer is concave) but it can also be empty (for example, if the nails were horizontal in our example). In any case, the following bit of code can be applied:

```
> for elem in clou3.intersect_polygon(limestone):
>     elem.ConstituveLaw = FZhao_limestone_grout
```

By having defined *FZhao_limestone_grout* as the law of Frank and Zhao (Frank and Zhao, 1982) with parameters corresponding to the interface between limestone and grout, these two lines of code make it possible to attribute the correct mechanical characteristics to this interface and without worrying about whether this interface actually exists. This robustness makes it possible to easily modify the geometry chosen for the project. Indeed, if we ultimately decide to consider horizontal nails, it is not necessary to redefine all of the interfaces.

4 CALCULATIONS METHOD

4.1 Choice of a failure surface and determination of safety factor

In order to determine the stability of the soil-nailed wall studied, we first choose a failure surface. On Figure 4, the example of logarithmic spirals is given but Slog includes also circles and slip lines. Currently, the definition of failure surfaces is not implemented in classes with dedicated methods and it only relies on functions defined in a separate modulus, called *slog_calculations.py*.

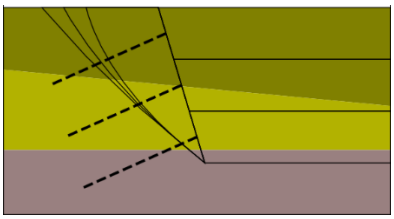

Figure 4. Computation of three logarithmic spiral failure surfaces.

In order to use the slice method, the failing block is subdivided into slices. This is enabled by the polygon intersection functions of Slog. Note that the slices thus created, inheriting from the Polygon class, are intrinsically equipped with the *self.area* method allowing the calculation of their surface and therefore their weight. On Figure 5, a slice intercepts different Facies and the calculation of its weight is easily done by subdividing it into the intersections with these different Facies.

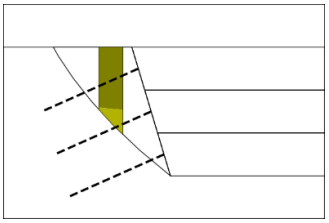

Figure 4. top left, choice of a rupture surface and slice zones; top right, automatic creation of the slices used for the stability calculation; bottom, intersection with nail.

In order to apply the slice method, it is essential to determine the resisting forces along the failure surface at the base of each slice. This requires the knowledge of the length of the slice basis as well as the maximal friction which can be mobilised on this basis. Here the basis is defined as the intersection between the failure line, the slice and the Facies *sand*. Therefore it inherits parameters from the Facies *sand* and, among them, the friction angle ϕ. This process is implemented in the function *sliceResistance* in the package *slog_calculations.slope_stability.*

In the case of nailing, specific stabilizing forces linked to the presence of nails must be added to the friction forces. To do this, it is necessary to determine the position of the intersection between the failure surface and the nails. This is, once again, done easily through the intersection method.

Once this point has been determined, the stabilizing force to be included in the slope stability calculation is computed using the intersection between the nail and the stable soil mass since the intersection inherits from its „parents“.

4.2 Modelling the nails

One way to determine these stabilizing forces is to integrate the equation of the beams along the nail taking into account the movement of the failing block and the friction at the interface between the nail and the different Facies it crosses (Delmas et al, 1986). To do this, it is necessary to implement a finite difference type calculation along this nail, which must therefore be discretized. The discretization of the nail is easily done using the linspace tool from the numpy library. As mentioned in section 3, Nail type objects have a method allowing them to define their interface with Facies. Each element of the discretized nail can therefore be assigned to a given interface and thus be provided with a friction model (e.g. Frank and Zhao law).

4.3 Encapsulation of calculation methods

Currently, the only calculation available in Slog is the slope stability (with or without nails) and it is not implemented in an Object Oriented way. Before including new calculations, the developers focus on the transition from functions packages to method libraries. However, the example of soil-nailed walls hereby presented aims at illustrating the powerfulness of the Object Oriented description of the Geology and the Geometry.

5 CONCLUSIONS

The Slog software, built in the form of a Python library offers a structure that is both robust and easy to use, allowing on the one hand the use of existing geometric libraries and on the other hand the creation of numerous calculation models. Development under a free license also allows the free use of the code by students, teachers and professionals alike, allowing everyone to have access to the entire calculation code and therefore to understand and question the assumptions underlying the results obtained. However, the „black box“ effect of geotechnical softwares can only be removed if the open source code is accompanied by a clear theroritical manuel. A significant effort has still to be carried out regarding this point.

Finally, open development should allow the creation of various modules but also the federation of a community of user-contributors around tools such as a forum. Apart from the educational interest of this software, Slog can then become a medium for disseminating research results. One of the main specificities of geotechnical calculation is based on the definition of the terrain model and close attention will be paid to this by developers.

ACKNOWLEDGEMENTS

The development of Slog was made possible by the work of Jad Sadek, as part of a mission from the Junior-Enterprise X-Projets. Through his availability, his alertness and his rigor, he made it possible to set the heart of the terrain model system.

REFERENCES

Delmas, P., Cartier, G. and Abdelhedi, A. (1986) ‘Une nouvelle méthode de dimensionnement du clouage des pentes: programme Prosper’, *Bulletin de liaison des Laboratoires des Ponts et Chaussées*, (141).

El Arja, H. (2020) Contribution à la modélisation numérique des excavations profondes. Université Paris Est. PhD thesis

Foster, E.L., Hormann, K. and Popa, R.T. (2019) ‘Clipping simple polygons with degenerate intersections’, Computers & Graphics: X, 2, p. 100007. https://doi.org/10.1016/j.cagx.2019.100007.

Frank, R. and Zhao, S.R. (1982) ‘Estimation par les paramètres pressiométriques de l’enfoncement sous charge axiale de pieux forés dans des sols fins’, Bulletin de liaison des Laboratoires des Ponts et Chaussées, (119).

Geuzaine, C. and Remacle, J.-F. (2009) ‘Gmsh : a three-dimensionnal finite element mesh generator with built-in pre- and post-processing facilities.’, International Journal for Numerical Methods in Engineering, 79(11), 1309–1331. https://doi.org/10.1002/nme.2579

Pilot, G. (1966) ‘Calcul de la stabilité des pentes. Utilisation de l’ordinateur CAE 510 du laboratoire central programmes 1.1 et 1.2’, Bulletin de liaison des Laboratoires des Ponts et Chaussées, 22, 4–1.

Proceedings of the XVIII ECSMGE 2024
GEOTECHNICAL ENGINEERING CHALLENGES
TO MEET CURRENT AND EMERGING NEEDS OF SOCIETY
© 2024 the Authors
ISBN 978-1-032-54816-6
DOI 10.1201/9781003431749-58
Open Access: www.taylorfrancis.com, CC BY-NC-ND 4.0 license

ECSMGE 24
XVIII EUROPEAN CONFERENCE ON SOIL MECHANICS AND GEOTECHNICAL ENGINEERING

A semi-analytical model for axial soil-pile interaction in generalized inhomogeneous soils

Un modèle semi-analytique pour l'interaction axiale sol-pieu dans des sols inhomogènes généralisés

A. Della Corte
KU Leuven, Bruges, Belgium

O. Orakci
KU Leuven, Bruges, Belgium / The University of Melbourne, Melbourne, Australia

A. Tsikas
Quantum Neural Technologies QNT, Athens, Greece

S. François
KU Leuven, Leuven, Belgium

G. Anoyatis*
KU Leuven, Bruges, Belgium

**george.anoyatis@kuleuven.be*

ABSTRACT: The seminal work of Nogami & Novak in 1976 for the harmonic response of end-bearing piles in homogeneous soil strata, is extended in this study to generate a benchmark semi-analytical model for piles in vertically inhomogeneous soils. Following the classical dynamic model and previous work to treat soil inhomogeneity under static axial loads, the pile is modelled as a rod, and the soil as an approximate continuum of the Tajimi type. The approximation resides in reducing the number of the elastodynamic equations which govern the soil motion to one, which satisfies the equilibrium in the vertical direction, by eliminating certain stresses and displacements in the soil. This is based on the physically motivated assumption that the vertical normal and shear stresses in the soil are essentially controlled exclusively by the vertical component of the soil displacement, for the axisymmetric problem at hand. Soil inhomogeneity is introduced via a generalized power law variation of the soil shear modulus with depth. The proposed generalized formulation can treat any type of soil inhomogeneity by employing in the solution pertinent shape functions to capture the soil modes, which satisfy the boundary conditions of the pile-soil system. The solution is expressed in terms of series and includes: (i) displacements and stress fields in the soil and along the pile-soil interface; (ii) displacements and normal stresses along the pile length, and (iii) dynamic pile head stiffness and damping.

RÉSUMÉ: Le travail fondateur de Nogami et Novak en 1976 sur la réponse harmonique des pieux d'appui en sol homogène est étendu dans cette étude pour générer un modèle semi-analytique de référence pour les pieux dans les sols verticalement inhomogènes. En suivant le modèle dynamique classique et les travaux précédents sur le traitement de l'inhomogénéité du sol sous des charges axiales statiques, le pieu est modélisé comme une tige et le sol comme un continuum approximatif de type Tajimi. L'approximation réside dans la réduction du nombre d'équations élastodynamiques qui régissent le mouvement du sol à une seule, qui satisfait à l'équilibre dans la direction verticale, en éliminant certaines contraintes et déplacements dans le sol. Cela repose sur l'hypothèse physiquement motivée selon laquelle les contraintes normales et de cisaillement verticales dans le sol sont essentiellement contrôlées exclusivement par la composante verticale du déplacement du sol, pour le problème axisymétrique en question. L'inhomogénéité du sol est introduite par le biais d'une variation généralisée de la loi de puissance du module de cisaillement du sol avec la profondeur. La formulation généralisée proposée peut traiter tout type d'inhomogénéité du sol en utilisant, dans la solution, des fonctions de forme pertinentes pour capturer les modes du sol, qui satisfont aux conditions aux limites du système pieu-sol. La solution est exprimée en termes de séries et comprend: (i) les champs de déplacement et les champs de contrainte dans le sol et le long de l'interface pieu-sol; (ii) les déplacements et les contraintes normales le long de la longueur du pieu, et (iii) la rigidité et l'amortissement dynamiques de la tête de pieu.

Keywords: Complex dynamic pile stiffness; analytical model; generalized soil inhomogeneity; soil-pile interaction.

1 INTRODUCTION

The consideration of dynamic soil-structure interaction (SSI) is crucial to evaluate the seismic vulnerability of structures. It is well known that the assumption of a fixed-base condition at the foundation level causes an underestimation of the natural period of superstructures (Mylonakis and Gazetas, 2000). During the last decades, a variety of methods of various levels of accuracy and sophistication have been developed to take into account the effect of the foundation (e.g., Veletsos and Meek, 1974; Gazetas, 1984; Maravas et al., 2014; Anoyatis and Lemnitzer, 2017b; 2023; Cui et al., 2022). On one hand, powerful finite element commercial software can handle a variety of complex soil–pile configurations, such tools can be computationally expensive. On the other hand, analytical models provide a cost-effective alternative solution for soil–pile interaction analysis and allow engineers to test different design scenarios and optimize the pile and superstructure for given soil conditions. For dynamic analyses in particular, analytical models are further free of the selection of appropriate mesh size and absorbing boundaries (e.g. viscous boundaries, infinite elements, boundary elements) to control radiation conditions and avoid spurious reflections. The proposed solution models the pile as a rod, following the classical strength-of-materials solution, and assumes perfect bonding at the soil-pile interface. The soil is modelled as an approximate continuum of the 'Tajimi' type, applied by Novak and Nogami to piles in homogeneous soils under axial and lateral inertial loading (Nogami and Novak, 1976; Novak and Nogami, 1977). Such models reduce the number of dependent variables by eliminating certain stresses and displacements in governing elastodynamic equations.

Key to the Tajimi approach in axial mode is the physically motivated assumption that the vertical normal, σ_z, and vertical shear stresses, τ_{rz}, in the soil, are controlled solely by the vertical displacement u_z (Mylonakis, 2001; Anoyatis and Mylonakis, 2012; Anoyatis et al., 2013, 2019, 2023). The influence of radial displacement is neglected by Nogami and Novak, 1976 and is considered to be vanishingly small by Mylonakis, 2001. This reduces the two equations of classical axisymmetric elasticity to one. The solution derived in this work extends the study of Anoyatis et al., 2023 to treat any type of soil inhomogeneity, applying pertinent mathematical techniques.

The soil-pile system response is expressed in terms of a generalized Fourier series of eigenfunctions (soil modes) along the vertical coordinate. The soil modes are obtained by employing appropriate shape functions to tackle soil inhomogeneity. Apart from its intrinsic theoretical interest, the proposed model has distinct advantages over other simple analytical models, e.g., Winkler-type solutions, (Novak, 1974; Scott, 1981; Anoyatis and Lemnitzer, 2017a) and more advanced models (e.g., Anoyatis et al., 2019, 2023) as it tackles any type of soil inhomogeneity in the vertical direction, consider the continuity of the medium in the vertical direction, and is free of empirical constants. The predictive power of the model is verified against the recent work of Anoyatis et al., 2023 for given types of inhomogeneity.

2 SOIL-PILE SYSTEM

The problem investigated in this study is depicted in Figure 1: A single, solid vertical pile of length L and circular cross section of diameter d is embedded in an inhomogeneous soil layer that rests on a rigid rock. The pile is subjected to an axial harmonic force of amplitude P and cyclic frequency ω, that is $P\,e^{i\omega t}$.

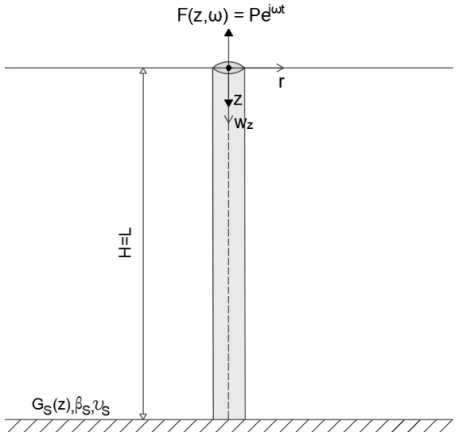

Figure 1. Problem under investigation.

The pile is modelled as an elastic rod of Young's Modulus E_p and mass density ρ_p. The soil layer is characterized by its soil mass density ρ_s, Poisson's ratio ν_s, and hysteretic material damping β_s. Soil inhomogeneity is considered through a depth-dependent complex-valued shear modulus $G_s^* = G_s(z)(1 + 2i\beta_s)$. The variation of soil shear modulus with depth is expressed by a power law function:

$$G_s^* = G_{sH}^* \left[b + (1-b)\left(\frac{z}{H}\right) \right]^n \qquad (1)$$

In Equation (1), z is the vertical coordinate, n and b are dimensionless inhomogeneity parameters. b links the stiffness at the surface of the layer G_{s0} to the stiffness at its base G_{sH}, that is, $b = (G_{s0}/G_{sH})^{1/n}$.

3 SOIL ANALYSIS

The equilibrium of vertical forces acting on a soil element in axisymmetric conditions in cylindrical coordinates yields the governing differential equation:

$$\frac{\partial(\tau\, r)}{\partial r} + r\,\frac{\partial \sigma}{\partial z} + r\,\rho_s\,\frac{\partial^2 u}{\partial t^2} = 0 \tag{2}$$

where $u = u_z(r,z,\omega)$ is the vertical displacement, $\tau = \tau_{rz}(r,z,t)$ and $\sigma = \sigma_z(r,z,t)$ are the vertical soil shear and normal stresses. The first and the second terms represent axisymmetric shearing and compression stresses, respectively, while the third term accounts for the development of inertial force due to vertical oscillations. The stress-displacement relations for axisymmetric deformations in a Tajimi - type continuum are written as in Nogami and Novak, 1976; Anoyatis et al., 2023:

$$\sigma \approx -\eta_s^2\, G_s^*\,\frac{\partial u}{\partial z} \tag{3a}$$

and

$$\tau \approx -G_s^*\,\frac{\partial u}{\partial r} \tag{3b}$$

where $\eta_s^2 = 2(1-\nu_s)/(1-2\nu_s)$ is a compressibility parameter related to the Tajimi approximation, as discussed in the earlier works of Mylonakis, 2001 and Anoyatis et al., 2019. Substituting Equations (3) into Equation (2), and considering harmonic displacement $u = u(r,z,\omega)e^{i\omega t}$ the equilibrium equation is rewritten in terms of soil displacements as:

$$\frac{1}{r}\frac{\partial}{\partial r}\left(r\frac{\partial u}{\partial r}\right) + \eta_s^2\frac{\partial}{\partial z}\left[\frac{G_s^*(z)}{G_{sH}^*}\frac{\partial u}{\partial z}\right] + \left(\frac{\omega}{V_{sH}^*}\right)^2 u = 0 \tag{4}$$

where $V_{sH}^* = V_{sH}\sqrt{1+2i\beta_s}$ is the complex shear wave velocity in the soil at depth $z = H$.

The solution to Equation (4) can be expressed as the product of the solutions of the two ordinary differential equations that arise from the application of the method of separation of variables:

$$R'' + \frac{1}{r}R' - q^2 R = 0 \tag{5a}$$

and

$$(\bar{G}_s\Phi)' + \lambda\bar{G}_s\Phi + \left(\frac{\omega}{V_{pH}^*}\right)^2\Phi = 0 \tag{5b}$$

where $\bar{G}_s = G_s^*(z)/G_{sH}^*$ expresses in a dimensionless form the profile of soil stiffness and V_{pH}^* is the complex propagation velocity of P-waves in the soil medium at depth $z = H$. q and λ are variables that emerge from the application of the method of separation of variables, and they are linked through the compressibility coefficient as $q = \eta_s\sqrt{\lambda}$. The general solution to Equation (5a) has been obtained in the past work of (Mylonakis, 2001). Equation (5b) is a general Sturm-Liouville equation and $\Phi = \Phi(z,\omega)$ are the associated soil modes, the solution of which has been found in the recent work of (Anoyatis et al., 2023) for two patterns of soil inhomogeneity $n = 1$ (linear) and $n = 2$ (parabolic). The solution derived in this paper can treat any type of inhomogeneity. The technique used to find the soil modes will be shown in detail in Section 3.1.

Displacements and shear stresses in the soil are expressed in terms of generalized Fourier series as:

$$u = \sum_{m=1}^{\infty} B_m\, K_0(q_m r)\, \Phi_m \tag{6}$$

and

$$\tau = \sum_{m=1}^{\infty} G_s^*\, B_m\, q_m\, K_1(q_m r)\, \Phi_m \tag{7}$$

where B_m are Fourier coefficients, and K_0 and K_1 are the modified Bessel functions of the second kind, zero and first order, respectively.

3.1 Soil modes

Equation (5b) can be solved by expressing the soil modes $\Phi = \Phi(z,\omega)$ in terms of a Fourier series as:

$$\Phi_m(z,\omega) = \sum_{j=1}^{\infty} S_j(\omega)\,\Psi_j(z) \tag{8}$$

in which S_j are the Fourier coefficients to be determined, and $\Psi_j(z)$ is a shape function of the form $cos(\alpha_j z)$ in which $\alpha_j = (\pi/2H)(2j-1)$.

Fundamental to this analysis, is the orthogonality identity of the shape functions:

$$\int_0^H \Psi_j\,\Psi_k\,dz = 0,\ j \neq k \tag{9}$$

Substituting Equation (8) into Equation (5b), making use of Equation (9) and, using the concept of the weak formulation, yields the following equation:

$$\sum_{j=1}^{\infty} S_j^m \int_0^H \bar{G}_s\,\Psi_j'\,\Psi_k'\,dz - \sum_{j=1}^{\infty} S_j^m\,\lambda_m \int_0^H \bar{G}_s\,\Psi_j\,\Psi_k\,dz - \left(\frac{\omega}{V_{pH}^*}\right)^2 S_k^m \int_0^H \Psi_k^2\,dz = 0 \tag{10}$$

The eigenvalues, λ_m, and the corresponding eigenvectors, S_j^m, depend on the frequency and can be obtained by solving the system of equations which emerges from Equation (10), ω time. The real and the imaginary part of the first soil mode at $\omega = 0$, $\omega = 0.5\,\omega_1$, $\omega = \omega_1$ for a damped soil medium ($\beta_s = 0.05$), $b = 0.25$ and $n = 1$ are illustrated in Figure 2, using $N = 50$ modes. Each mode is normalised by its value at $z = 0$.

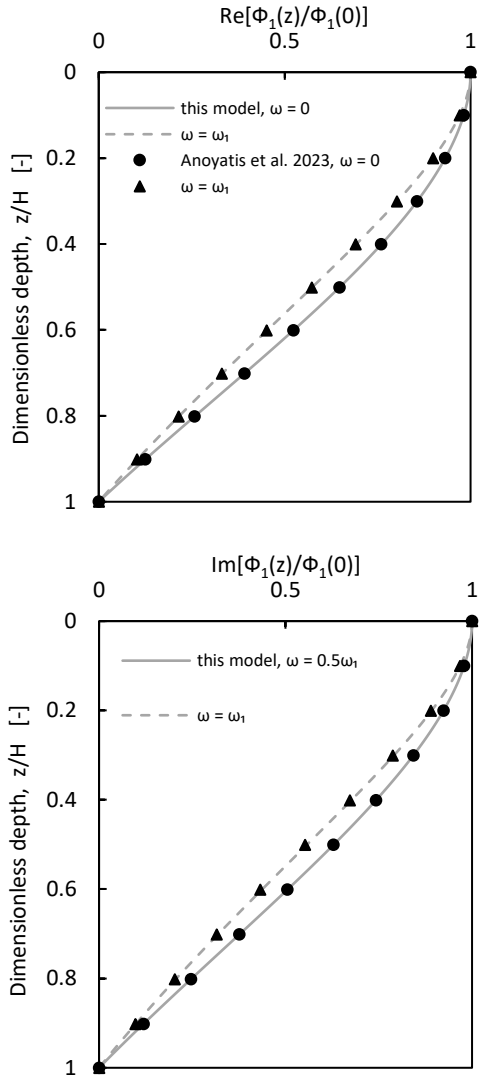

Figure 2. Real and imaginary parts of the first soil mode. Comparison with the closed form solution of Anoyatis et al., 2023.

Figure 3 shows the derivative of the first soil mode, $\Phi_1'(z,\omega)$, which has been normalised respect to its value at $z = H$. The dynamic effect on the soil mode can be clearly seen at the resonance frequency ($\omega = \omega_1$). Evidently, the results obtained by using the approximate proposed model with the semi closed-form solution developed by Anoyatis et al., (2023) are in excellent agreement.

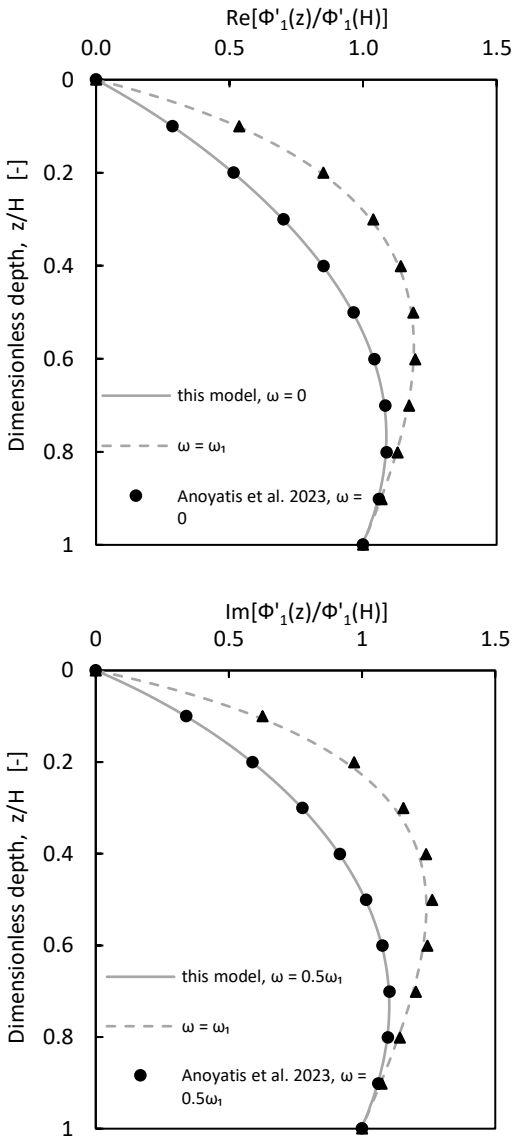

Figure 3. Real and imaginary parts of the derivative of the first soil mode. Comparison with the closed form solution of Anoyatis et al., 2023.

4 SOIL-PILE INTERACTION ANALYSIS

The equilibrium of vertical forces acting on a pile segment yields the equation of the pile motion.

$$-E_p A_p \frac{\partial^2 w}{\partial z^2} + \pi d \tau_0 - \omega^2 \tilde{m}_p w = F \qquad (11)$$

where A_p is the pile cross sectional area, $\tilde{m}_p = \rho_p\, A_p$ is the pile material density, and $\tau_0 = \tau(r = d/2, z, \omega)$ is the vertical shear stress at the soil-pile interface. $F = F(z,\omega)$ can be expanded in Fourier series as:

$$F(z,\omega) = \sum_{m=1}^{\infty} f_m\, G_s^*\, \Phi_m(z,\omega) \qquad (12)$$

where the coefficients f_m are obtained by applying the orthogonality of the soil modes:

$$f_m = \int_0^H F(z,\omega)\,\Phi_m\,dz \,/ \int_0^H G_s^*\Phi_m^2\,dz \quad (13)$$

Substituting Equations (6), (7) and (12) into Equation (11), considering perfect bonding at the soil-pile interface and utilizing the weak form, yields the following equation which allows the evaluations of the coupled B_m Fourier coefficients:

$$E_pA_p\sum_{m=1}^{\infty}B_m\,K_0(s_m)\int_0^H\Phi_m'\Phi_k'\,dz\;+ \\ 2\pi\,s_k\,B_k\,K_1(s_k)\int_0^H G_s^*\Phi_k^2\,dz\;- \\ \omega^2\,\tilde{m}_p\sum_{m=1}^{\infty}B_m\,K_0(s_m)\int_0^H\Phi_m\Phi_k\,dz \\ = P\,\Phi_k(0) \quad (14)$$

where $s_m = q_m d/2$ is a dimensionless parameter.

The pile response w is given by the following expression:

$$w(z,\omega) = \sum_{m=1}^{\infty}B_m\,K_0(s_m)\,\Phi_m(z,\omega) \quad (15)$$

5 PILE STIFFNESS AND DAMPING

The pile head stiffness is defined as the ratio of the force P acting on the pile head over the corresponding displacement:

$$K^* = P\Big/\sum_{m=1}^{N}B_m\,K_o(s_m)\,\Phi_m(z,\omega) \quad (16)$$

where $K^* = K^*(\omega)$ is a complex-valued stiffness. The real part represents the dynamic stiffness, and the ratio of the imaginary part over twice its real part, the damping ratio $\zeta(\omega) = Im[K^*(\omega)]/2Re[K^*(\omega)]$.

Results of the normalised dynamic pile head stiffness with normalised excitation frequency, for two values of E_p/E_{sH}, for a pile slenderness ratio $L/d = 25$, and for three types of inhomogeneity i.e., $n = 0.5$; $n = 1$, and $n = 2$ are shown in Figure 4. The soil has a stiffness ratio between the surface and the bottom $b = 0.25$ (Eq. (1)), damping ratio $\beta_s = 0.05$ and Poisson's ratio $\nu_s = 0.4$. The values for the pile-soil material density ratios are $\rho_p/\rho_s = 1.25$ for $E_p/E_{sH} = 100$ and $\rho_p/\rho_s = 1.5$ for $E_p/E_{sH} = 1000$. The number of modes used is 50.

The proposed predictions are compared against results from the work of Anoyatis et al., 2023. It is shown that the models are in perfect agreement. Some general trends are observed: for frequencies below the resonance, the dynamic stiffness decreases monotonically with frequency. Such attenuation is stronger for stiffer soils, i.e., $E_p/E_{sH} = 100$. At resonance, a drop in stiffness is observed. Beyond the resonance, the stiffness increases. For $n = 0.5$ the values of the dynamic pile stiffness are higher than the case of $n = 1$ and 2 since the corresponding soils are stiffer. As a consequence, the resonance is reached at higher values of excitation frequency.

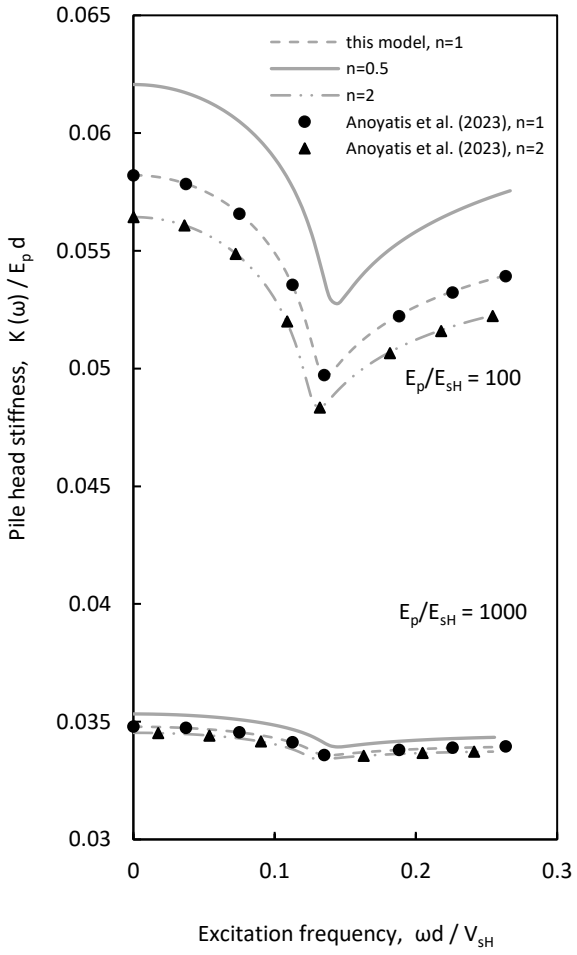

Figure 4. Variation of normalized dynamic pile head stiffness with normalized excitation frequency, for different types of soil inhomogeneity. Comparison with results from Anoyatis et al., 2023.

Figure 5 plots the variation of the pile head damping $\zeta(\omega)$ with the dimensionless frequency ω/ω_1 for $n = 0.5$ and for selected values of pile slenderness ratios. For all cases examined, the damping is practically unaffected by frequency in the low-frequency range. In the vicinity of the first resonance, it exhibits a jump, marking the emergence

of travelling waves in the medium, and thus radiation damping.

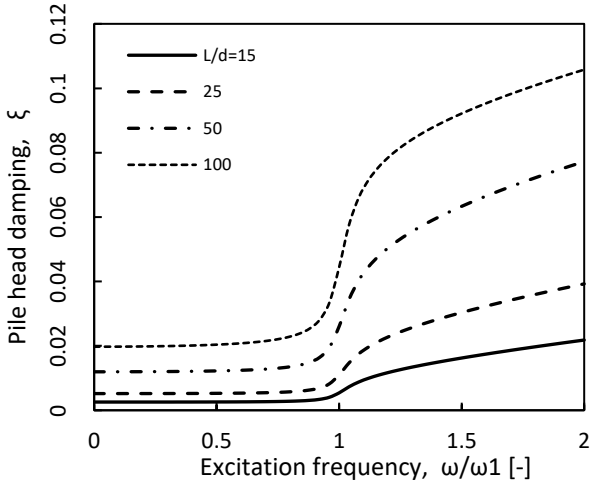

Figure 5. Variation of damping ξ with excitation frequency ω/ω_1. $n = 0.5, b = 0.25,\ \beta_s = 0.05,\ \nu_s = 0.4, E_p/E_{sH} = 1000,\ \rho_p/\rho_s = 1.5$.

6 CONCLUSIONS

A novel semi-analytical solution is derived for the analysis of end-bearing piles that are embedded in a generalized vertically inhomogeneous soil stratum over a rigid base that is subjected to an axial harmonic force. The proposed approximate-continuum solution uses pertinent trigonometric functions to approximate the actual shape functions. This approach is shown to generate results that are in perfect agreement with results obtained from the more rigorous model developed by Anoyatis et al, 2023, limited to specific types of soil inhomogeneity, linear and parabolic variation of the soil stiffness with the depth. The proposed model, with minor modifications, could further take into account transient loads and generate time histories of the pile response, displacement and stress fields.

The Python scripts and data of this study will be made openly available on the KU Leuven webpage titled 'Soil–Structure Interaction Toolkit', at the URL: https://bwk.kuleuven.be/projects/SSItk/, which aims to host scripts and data for a wide range of commonly met soil-pile interaction problems.

ACKNOWLEDGEMENTS

The research proposed in this paper was supported by KU Leuven through the project "ATHENA Analytical & programming efficiency in geoTecHnical ENgineering Applications" (C24E/22/009), KU Leuven Internal Funds. The authors are grateful for this support.

REFERENCES

Anoyatis G., and Mylonakis G. (2012). Dynamic Winkler modulus for axially loaded piles, *Geotechnique,* 62(6):521-536. doi.org/10.1680/geot.11.P.052.

Anoyatis G., Di Laora R., Mylonakis G. (2013). Axial kinematic response of end-bearing piles to P waves, *Int J Numer Anal Methods Geomech,* 37(17):2877-2896. doi.org/10.1002/nag.2166.

Anoyatis G., and Lemnitzer A. (2017a). Dynamic pile impedances for laterally–loaded piles using improved Tajimi and Winkler formulations. *Soil Dynamics and Earthquake Engineering*, 92, 279-297. doi.org/10.1016/j.soildyn.2016.09.020.

Anoyatis G., and Lemnitzer A. (2017b). Kinematic Winkler modulus for laterally-loaded piles. *Soils and Foundations*, 57(3), 453-471. doi.org/10.1016/j.sandf.2017.05.011.

Anoyatis G., Mylonakis G., Tsikas, A. (2019). An analytical continuum model for axially loaded end-bearing piles in inhomogeneous soil, *Int J Numer Anal Methods Geomech*. 43(6):1162-1183. doi.org/10.1002/nag.2886.

Anoyatis G., François S., Orakci O., Tsikas A. (2023). Soil-pile interaction in vertical vibration in inhomogeneous soils. *Earthquake Engng Struct Dyn,* 1-20. doi.org/10.1002/eqe.3968.

Cui C., Meng K., Xu C., Wang B., (2022). Vertical vibration of a floating pile considering the incomplete bonding effect of the pile-soil interface. *Computers and Geotechnics, (Vol. 150).* https://doi.org/10.1016/j.compgeo.2022.104894.

Gazetas G., (1984). Seismic response of end-bearing single piles. *Int J Soil Dynam Earthq Eng;3(No. 2):82-93.*

Maravas A., Mylonakis G., Karabalis D. L. (2014). Simplified discrete systems for dynamic analysis of structures on footings and piles. S*oil Dynamics and Earthquake Engineering, (Vol. 61-62).*

Mylonakis G., and Gazetas G. (2000) Seismic soil-structure interaction: beneficial or detrimental? *J Earthq Eng.;4(3):277-301.*

Mylonakis G., (2001). Winkler modulus for axially loaded piles. *Géotechnique*, 51(5), 455-461. doi.org/10.1680/geot.2001.51.5.455.

Novak M., (1974). Dynamic stiffness and damping of piles. *Canadian Geotechnical Journal,* 11(4):574-598. doi.org/10.1139/t74-059.

Nogami T., and Novak M. (1976). Soil-pile interaction in vertical vibration, *Earthquake Engineering & Structural Dynamics*, 4(3):277-293. doi.org/10.1002/eqe.4290040308.

Novak M., and Nogami, T. (1977). Soil-pile interaction in horizontal vibration. *Earthquake Engineering & Structural Dynamics*, 5(3), 263-281. doi.org/10.1002/eqe.4290050305.

Scott R. F. (1981). Foundation analysis. *Prentice Hall.*

Veletsos A.S. and Meek J.W. (1974). Dynamic Behaviour of Building-Foundation Systems. *Earthq. Eng. Struct. Dyn. 3*, 121–138.

Proceedings of the XVIII ECSMGE 2024
GEOTECHNICAL ENGINEERING CHALLENGES
TO MEET CURRENT AND EMERGING NEEDS OF SOCIETY
© 2024 the Authors
ISBN 978-1-032-54816-6
DOI 10.1201/9781003431749-59
Open Access: www.taylorfrancis.com, CC BY-NC-ND 4.0 license

ECSMGE 24
XVIII EUROPEAN CONFERENCE ON SOIL MECHANICS AND GEOTECHNICAL ENGINEERING

Integrating MT-InSAR and conventional monitoring with numerical analysis for tunnel excavations: A case study

Intégration de la surveillance MT-InSAR et conventionnelle avec l'analyse numérique pour l'excavation des tunnels: Un cas d'étude

G. Della Ragione, E. Bilotta*
University of Napoli Federico II, Naples, Italy

Di Mariano, A. Gens
Universitat Politècnica de Catalunya, BarcelonaTech, Barcelona, Spain

**emilio.bilotta@unina.it*

ABSTRACT: Multi Temporal Interferometric Synthetic Aperture Radar (MT-InSAR) is a remote sensing technique used for monitoring surface deformations with high precision and spatial resolution. This study aims to evaluate the effectiveness of this technique for tunnelling monitoring by complementing data gathered by conventional optical monitoring and comparing the resulting dataset with FE numerical analysis using Plaxis3D software. The comparison generally reveals good agreement, indicating the potential of MT-InSAR for monitoring tunnelling-induced displacements. The integration of MT-InSAR with conventional monitoring and numerical analysis can provide a comprehensive understanding of the behaviour of the ground during the excavation process, contributing to the development of efficient and safe tunnelling practices.

RÉSUMÉ: Le radar interférométrique à synthèse d'ouverture multitemporelle (MT-InSAR) est une technique de télédétection utilisée pour surveiller les déformations de surface avec une précision et une résolution spatiale élevées. Cette étude vise à évaluer l'efficacité de cette technique pour la surveillance du creusement des tunnels en complétant les données recueillies par le contrôle optique conventionnel et en comparant l'ensemble des données obtenues avec l'analyse numérique par éléments finis à l'aide du logiciel Plaxis3D. La comparaison révèle généralement une bonne concordance, ce qui indique le potentiel de la technique MT-InSAR pour la surveillance des déplacements induits par le creusement de tunnels. L'intégration de MT-InSAR à la surveillance conventionnelle et à l'analyse numérique peut fournir une compréhension complète du comportement du sol pendant le processus d'excavation, contribuant ainsi au développement de pratiques de creusement de tunnels efficaces et sûres.

Keywords: Tunnelling; MT-InSAR; finite element; displacements; monitoring.

1 INTRODUCTION

The excavation of large diameter tunnels in urban areas may represent a potential risk for existing buildings, particularly in complex geological conditions and in densely exploited underground space. Monitoring tunnelling induced displacement during construction is therefore required to ensure the structural health of the above buildings and nearby infrastructures and to guarantee their serviceability levels. Datasets gathered from monitoring can be used to validate the numerical analysis of complex soil-structure interactions during tunnelling, thus enabling a better support to corrective measures during construction.

Nowadays, in addition to conventional optical prisms and levelling devices, buildings' movements can be monitored by processing data from synthetic aperture radar (SAR) satellites. The ability of radar satellites to measure the field of displacements induced by tunnel excavations in urban areas has quickly improved in the last decade (Perissin et al., 2012; Barla et al. 2016; Milillo et al, 2018; Giardina et al., 2018). High-resolution SAR satellites, such as the COSMO-SkyMed (CSK) or TerraSAR-X constellations, have been launched and new and more advanced ones are going to be. At the same time, data processing techniques have been implemented in research and commercial platforms and the use of Multi-Temporal Interferometric Synthetic Aperture Radar (MT-InSAR) technique for structural health monitoring of buildings and infrastructures has emerged (Ferretti et al., 2011; Caprino et al., 2023).

In this paper, ground and buildings movements measured by MT- InSAR analyses of satellite images recorded during tunnel construction for a branch of metro Line 9 (now Line 10 south) in the city of

Barcelona (Spain) are used to complement data gathered by conventional optical monitoring and compared with the results of Finite Element analysis of the effects of tunnelling on a residential building in the area. This allows to discuss the potential and limitations of MT-InSAR to provide additional information for the verification and validation of numerical models in urban tunnel construction.

2 CASE STUDY

2.1 Ground conditions and works

The paper refers to the case study of a mechanised tunnel excavation in the city of Barcelona. The excavation, belonging to the Line 9 (L9) project, was executed with a 12.06 m diameter Earth Pressure Balance (EPB) Tunnel Boring machine (TBM) and was part of the L9 branch connecting Barcelona to its port logistics activities zone. Tunnelling, in this area, started from Foneria station and was headed towards Ildefons Cerdà station (from the left to the right in Figure 1), about 700 m apart from the first one. The tunnel alignment crosses a densely urbanised area with a cover to diameter ratio, C/D, in the range 2.5-3.0. The geological profile along the alignment (Figure 1) involved Quaternary soft alluvial and detrital deposits (QM, QS and QR), overlaying Miocene hard formations (M1U and M2L) consisting of siltstone and argillite. The water table is located in the alluvial deposits at a depth of about 8 m from the ground surface and at 22-28 m above the tunnel crown.

The first 100 m or so of the excavation were quite challenging due to the presence of mixed ground conditions at the tunnel face, including a thin layer of highly permeable gravels at the tunnel crown. This contingency caused loss of pressure in the EPB cutter head and, as a result, some overexcavation was experimented just before the boring machine approached a well monitored 10-storey residential framed building (Figure 1) having a 2-level underground parking garage. Below the building, tunnelling became even more difficult because the alignment curves (radius of curvature of 300 m) right where the building south façade is located (Figure 1). The challenging tunnelling conditions led to volume losses in the range 0.5-1.0% that gave rise to significant ground movements. As the EPB machine moved towards the north façade of the building (from Block B towards Block A in Figure 2b), the mixed ground conditions at the tunnel face gradually changed to approximately uniform conditions with the harder Miocene materials occupying nearly the whole excavation section. Also, the tunnel depth slowly increased contributing to lower observed volume losses.

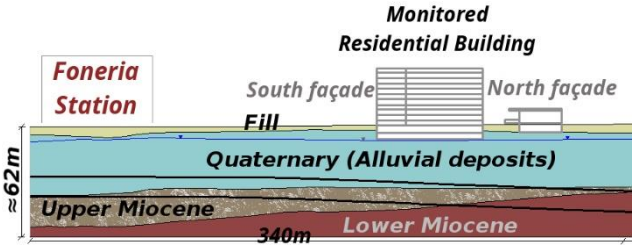

Figure 1. Geological profile in the area of study.

2.2 Monitoring

A comprehensive instrumentation system was set up to monitor tunnelling operations. Manual and automatic instruments were used to measure surface and subsurface ground movements (Figure 2a), as well as 3D movements of the framed building and its basement (Di Mariano et al., 2021).

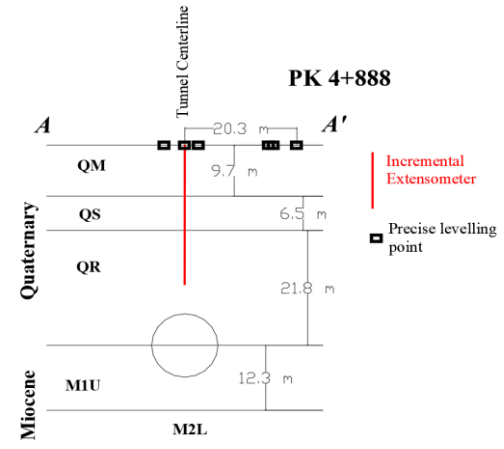

(a)

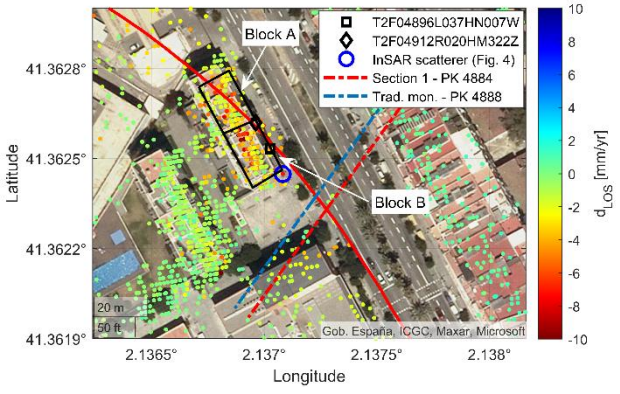

(b)

Figure 2. (a) Conventional monitoring at PK4888; (b) InSAR scatterers, selected monitoring sections and LPs.

To complement the database of measurements taken with conventional monitoring, for the purpose of this work MT-InSAR data were also used (Figure 2b). 32 SAR images were acquired by the TerraSAR-X full archive in Stripmap mode in an ascending path

direction, from January 7th 2009 to October 2nd 2012, and processed by TRE-Altamira by SqueeSAR®, an advanced algorithm for surface displacement detection developed by Ferretti et al. (2011). Further details on the methodology can be found in Di Mariano et al. (2024).

3 NUMERICAL MODELLING

To study the complex Soil Structure Interaction (SSI) phenomenon produced by tunnelling below the monitored residential building, fully coupled 3D numerical analyses were carried out with the commercial Finite Element (FE) code PLAXIS 3D. For simplicity purposes, a geological profile with horizontal stratigraphic layers was considered (Figure 3). The numerical model reproduces the tunnel curved alignment, the operating parameters of the EPB boring machine and the installation of the lining. It also reproduces the conicity of the shield, the weight of the back-up trailer and the eccentric position of the lining with respect to the EPB shield. The model replicates the excavation process with a step-by-step procedure that allows to consider the segments width. Nevertheless, the segmentation of the lining in the tunnel transverse direction is not considered.

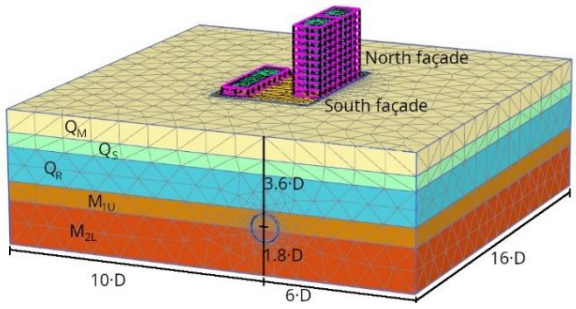

Figure 3. FE model (D = tunnel diameter).

A non-linear type of the hyperbolic constitutive model, formulated in the frame of friction hardening plasticity, was used to represent the behaviour of all ground materials. The model considers the nonlinear ground stiffness decay as shear strains increase. On the other hand, linear-elastic laws were assumed for all structural elements, which were far from failure conditions.

Table 1. Soil parameters.

	(kN/m³)	c' (kPa)	,	$E_{50,ref}$ (MPa)	$E_{ur,ref}$ (MPa)	$E_{oed,ref}$ (MPa)	m	K (m/s)
Q_M	17	0	29	16	48	12	0.9	5e-4
Q_S	19.6	0	34	11	33	10	0.65	4e-4
Q_R	21	1	30	15	46	10	0.6	1e-5
M_{1U}	21	1	36	46	180	25	0.8	2e-5
M_{2L}	22.5	10	33	278	833	100	0.9	1e-7

The main geomechanical parameters used in the analysis reported in this paper are shown in Table 1. They were inferred from both laboratory and in situ investigations. A few attempts have been made to adjust the initial estimate of soil stiffness parameters to adequately reproduce the ground movements observed along the line, also considering the effect of contingency ground treatments that were undertaken during the underpassing of the residential building in the model.

4 RESULTS

Figure 4 shows a comparison between the settlement time history evaluated by processing SAR images of the scatterer, circled in blue in Figure 2, and the corresponding settlement calculated by FEA. In the same figure the settlement profile of the close LP T2F4896L037HN007W has also been added for further comparison. Overall, the numerical results match well both InSAR and optical levelling data.

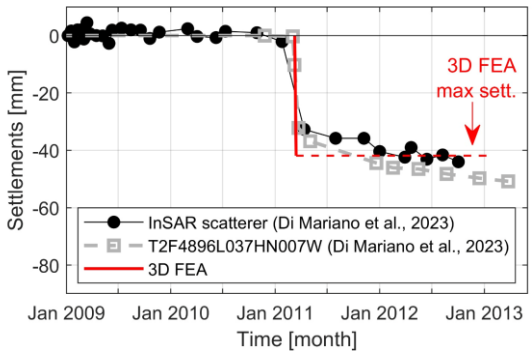

Figure 4. Time series comparison between InSAR scatterer, levelling point and corresponding FEA output.

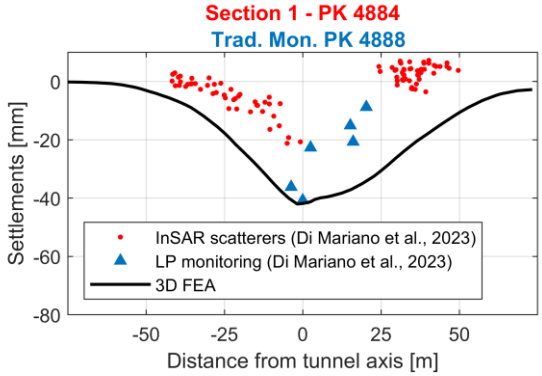

Figure 5. Settlement trough: satellite data (InSAR), conventional optical levelling (LP) and FEA results.

In Figure 5 the displacement of Permanent Scatterers and Levelling Points after the full passage of the TBM across the transverse section at PK4888 are compared with the computed settlement profile. The PS displacements along the satellite LoS, gathered

in a 10 m wide band across the section, were projected along the vertical direction, assuming that the ground displacements due to tunnelling were predominantly vertical. This assumption may lead to an acceptable error, lower than 5% on the maximum settlement (Della Ragione et al., 2023). The levelling points (same Figure 5) also confirm that such error is not large.

The FE calculated profile matches only two LP measurements, while it generally overestimates the overall settlement trough that, despite the scatter of the MT-InSAR data, emerges clearly from both sets of measurements. Further inspection is needed to understand such discrepancy and validate the model.

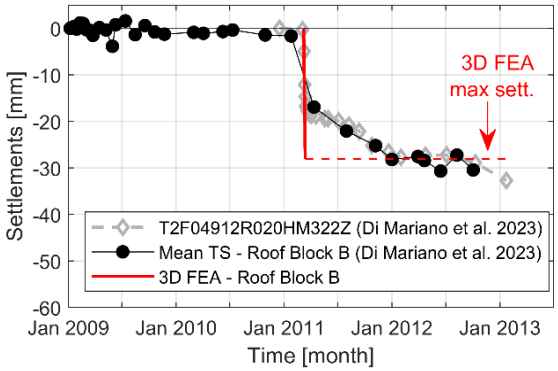

Figure 6. Block B roof displacement (InSAR, LP, FEA).

Finally, in Figure 6 the time histories of displacement of the PSs that belong to the roof of Block B is averaged and compared both with that of the prism T2F04912R020HM322Z, on the same building roof, and with the corresponding numerical calculation. A good matching can be appreciated in this case.

5 CONCLUSIONS

The paper compares the movement monitored by processing SAR images collected by the satellite TSX1 (TerraSAR-X) during the construction of Line 9 of Barcelona metro with the numerical results of the construction process obtained with the commercial code Plaxis3D. Data gathered during construction by conventional optical monitoring are also shown. The comparison indicates the potential of MT-InSAR to monitor the effects of tunnel excavation in urban areas. Even though MT-InSAR cannot substitute terrestrial measurements, since the latter provides a reliable benchmark for the former, it can indeed complement optical monitoring as a mean to verify and validate numerical modelling. This is possible due to the large amount of data than can be retrieved by processing images even long after the work completion.

ACKNOWLEDGEMENTS

SAR images were processed by TRE-Altamira as part of a research agreement with Barcelona TECH (UPC). The authors are grateful to the company and in particular to Dr Jordi Sanchez, Dr Beatriz Royo and Dr Stefano Cespa for their support. The optical survey data were kindly provided by Infraestructures de la Generalitat de Catalunya, S.A.U.

REFERENCES

Barla, G., Tamburini, A., Del Conte, S., Giannico, C. (2016) InSAR monitoring of tunnel induced ground movements. Geomech. Tunn. 2016(9) 15–22. https://doi.org/10.1002/geot.201500052.

Caprino A., Bonaldo G., Lorenzoni F., da Porto F. (2023) Application of Multi-Temporal InSAR (MT-InSAR) for structural monitoring: the case study of Scrovegni Chapel in Padova, Procedia Structural Integrity, 1578-1585.

Della Ragione G., Rocca A., Perissin D., Bilotta E. (2023) Volume Loss Assessment with MT-InSAR during Tunnel Construction in the City of Naples (Italy). Remote Sens. 2023, 15, 2555. https://doi.org/10.3390/rs15102555.

Di Mariano, A., Franza, A., Limatola, V., Gens, A., Bilotta, E. (2021). Building Response to Line 9 EPB Tunnelling in Barcelona. A Case Study. In: Challenges and Innovations in Geomechanics. IACMAG 2021. Lecture Notes in Civil Engineering, vol 126. Springer, Cham. https://doi.org/10.1007/978-3-030-64518-2_21.

Di Mariano, A., Gens, A., Della Ragione, G., Bilotta, E., Sanchez, J., Royo, B., Cespa, S. (2024). Case study of soil-structure interaction during tunnelling for Barcelona Metro: a comparison between conventional and innovative displacement measurements. Proc. 11th Int. Symp. Geotech. Aspects of Underg. Constr. in Soft Ground, 2024 Macao SAR, China.

Ferretti A., Fumagalli A., Novali F., Prati C., Rocca F. and Rucci A. (2011) A New Algorithm for Processing Interferometric Data-Stacks: SqueeSAR, in IEEE Transactions on Geoscience and Remote Sensing, 49(9), 3460-3470. 10.1109/TGRS.2011.2124465.

Giardina, G., Milillo, P., DeJong, M.J., Perissin, D., Milillo, G. (2018) Evaluation of InSAR monitor-ing data for post-tunnelling settlement damage assessment. Struct. Control. Health Monit. 2018, 26, e2285.

Milillo, P., Giardina, G., DeJong, M.J., Perissin, D., Milillo, G. (2018) Multi-temporal InSAR struc-tural damage assessment: The London Crossrail case study. Remote Sens. 2018, 10, 287. https://doi.org/10.3390/rs10020287.

Perissin, D., Wang, Z., Lin, H. (2012) Shanghai subway tunnels and highways monitoring through Cosmo-SkyMed Persistent Scatterers. ISPRS J. Photogramm. Remote Sens. 2012, 73, 58–67.

Proceedings of the XVIII ECSMGE 2024
GEOTECHNICAL ENGINEERING CHALLENGES
TO MEET CURRENT AND EMERGING NEEDS OF SOCIETY
© 2024 the Authors
ISBN 978-1-032-54816-6
DOI 10.1201/9781003431749-60
Open Access: www.taylorfrancis.com, CC BY-NC-ND 4.0 license

ECSMGE 24
XVIII EUROPEAN CONFERENCE ON SOIL MECHANICS AND GEOTECHNICAL ENGINEERING

A t-z approach for the design of axially loaded piles in consolidating soil

Une approche t-z pour la conception de pieux chargés axialement dans un sol consolidant

A.E. Detlefsen, A. Franza*, K.K. Sørensen
Aarhus University, Aarhus, Denmark

*anfr@cae.au.dk

ABSTRACT: This paper presents a t-z model for the analysis of vertically loaded single piles in consolidating soil, using a beam on hyperbolic vertical springs whose tangent stiffness is a function of the normalised mobilised stress in the soil (affected by the consolidation-induced increase in effective stresses) and load history (accounting for loading, unloading and reversed loading). The validation is carried out with published experimental and analytical results. Next, a parametric study illustrates, for floating and end-bearing piles, the temporal evolution of settlement and neutral plane, considering with a simplified approach both displacements and non-displacement piles. Contrarily to end-bearing foundations, the neutral plane location of floating piles is sensitive to the temporal evolution of excess pore water pressure; thus, for the analysis of floating piles, t-z springs with a constitutive law dependent on effective stress should be adopted.

RÉSUMÉ: Cet article présente un modèle t-z pour l'analyse de pieux simples chargés verticalement dans un sol consolidant, utilisant une poutre sur des ressorts verticaux hyperboliques dont la raideur tangente est une fonction de la contrainte mobilisée normalisée dans le sol (affectée par l'augmentation induite par la consolidation des contraintes effectives) et de l'historique de charge (tenant compte des phases de chargement, de déchargement et de chargement inversé). La validation est réalisée avec des résultats expérimentaux et analytiques publiés. Une étude paramétrique illustre, pour les pieux flottants et les pieux en butée, l'évolution temporelle du tassement et du plan neutre, en considérant, avec une approche simplifiée, à la fois les pieux à déplacement et les pieux sans déplacement. Contrairement aux fondations en butée, la localisation du plan neutre des pieux flottants est sensible à l'évolution temporelle de la pression interstitielle excessive; ainsi, pour l'analyse des pieux flottants, des ressorts t-z avec une loi constitutive dépendant de la contrainte effective devraient être adoptés.

Keywords: Consolidation; pile; settlement; t-z curve; neutral axis.

1 INTRODUCTION

When piles are affected by a combination of external loads and consolidation processes, performance-based design requires the estimate of settlements. Despite numerical modelling capabilities (Russo et al., 2020; Liang et al., 2023), practitioners mostly rely on simplified load capacity assessments (e.g. Danish National Annex to Eurocode 7; EN 1997-1 DK NA:2007) or neutral plane-based approaches to assess the effects of consolidating soil (Fellenius, 2023). However, these simplified methods have limitations. This paper presents an analytical model for the soil-pile interaction suitable for serviceability assessments.

2 INTERACTION MODEL

The proposed soil-pile interaction model is a beam on nonlinear t-z springs whose behaviour is affected by the consolidation. Namely, this model is based on a two-stage analysis method (i.e. consolidation-induced greenfield settlements used as input for the interaction analysis), Terzaghi's 1D consolidation theory for non-uniform initial excess pore water pressure distributions (Lovisa et al., 2010), the Euler-Bernoulli beam theory for the pile, nonlinear t-z springs (distributed along the shaft and base of the pile) as a ground model.

For the t-z springs, the approach of Chen et al. (2009) is adopted. The initial stiffness K_0 is estimated according to Randolph & Wroth (1978), if not stated otherwise, with base $K_{0,b} = \frac{d_p E_{s,0}}{1-\nu_s^2}$ and shaft per running meter $K_{0,s} = \frac{\pi E_{s,0}}{(1+\nu_s)\ln(2\, r_m/d_p)}$, where $E_{s,0}$= initial Young's modulus, ν_s = soil Poisson's ratio, r_m = magic radius, d_p = pile diameter. According to the Duncan hyperbolic stiffness degradation, the tangent stiffness for further loading or reverse loading is $K_{tan} = (1 - F_m/F_u)^2 K_0$, where F_m is the mobilised force at the spring, F_u is the ultimate

spring force obtained by integrating the failure shaft friction τ_f or base pressure q_f, whereas $K_{tan} = K_0$ in the case of unloading (i.e. spring reaction F_m attains the largest, in magnitude, positive or negative force mobilised at the spring). If not stated otherwise, the beta-method model is used to estimate $\tau_f = \beta\sigma'_v$ and $q_f = N_q\sigma'_v$ from the vertical effective stress σ'_v, obtained from the consolidation analysis. The model neglects effective stress variation at the soil-pile interface induced by local soil shearing in the near-pile soil region; therefore, the interaction and consolidation analyses are uncoupled (Kim et al., 2011). The self-weight of the pile is disregarded in this paper, although it can be included. The solution is solved using the Finite Element Method in incremental steps. For further details refer to Detlefsen (2023).

3 RESULTS

3.1 Validation

The model predictions are compared, with analytical and centrifuge results of a pile in consolidating soil for the two scenarios illustrated in Figure 1.

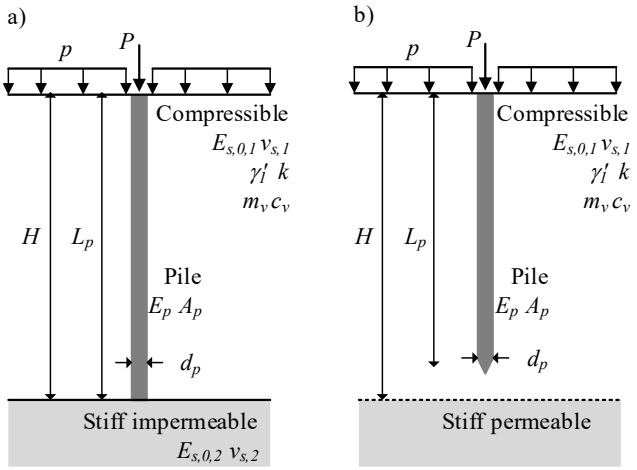

Figure 1. Modelled pile and ground conditions for a) end-bearing pile, and b) floating pile.

First, the model is validated against results obtained by Chen et al. (2009) using a similar analytical formulation for an end-bearing pile in consolidating soil and one-way drainage towards the surface (impermeable stiff bottom layer at the pile base). Figure 1a displays the problem geometry and parameters. The pile has length L_p = 10 m (equal to the consolidating layer thickness H), diameter d_p = 0.5 m, Young's modulus E_p = 20 GPa, and head load P. The compressible layer has γ' = 10 kN/m^3, $\beta = K\tan\phi'$ = 0.3. For the base layer, $E_{s,0,2}$ = 500 MPa, $\nu_{s,2}$ = 0.3, and ultimate base pressure q_f = 4.6 MPa. Surcharge pressure is set to p = 150 kPa. For direct comparison, along the shaft the initial tangent stiffness of the nonlinear springs $K_{0,s}$ is set to match the values adopted by Chen et al. (2009), associated with a displacement of 0.5 mm at $\tau_{f,0}$, which for r_m =17.5 m is associated with a gradient $E_{s,0,1}/z = 10.5$ MPa/m according to Randolph & Wroth's expression. Chen et al. (2009) adopted a 1D non-linear consolidation method, in which the coefficient of consolidation, c_v, and the coefficient of compressibility, m_v, are varying during consolidation. However, in this paper, Terzaghi's one-dimensional consolidation theory is adopted using m_v = 10^{-4} m^2/kN and c_v = 0.1644 m^2/day.

Figure 2 shows the response of the unloaded pile, in terms of mobilised shaft friction and axial force along the pile, for an average degree of consolidation $U_{v,avg}$ = 0.5 and 1. Also, Figure 2a reports ultimate shaft friction profiles τ_f during consolidation, as affected by excess pore water pressure dissipation and the impermeable bottom boundary. An excellent agreement with benchmark results is seen in Figure 2. Similarly, there is agreement with Chen et al. (2009) for the case of the loaded pile with P of 200 kN (Detlefsen 2023), which led to a downward shift in the neutral plane due to the external head load from a depth of 9 m to 8.5 m.

Second, the centrifuge test results from Lam et al. (2009) are simulated. As shown in Figure 1b, the experiment modelled a floating pile in consolidating clay under two-way drainage conditions (with the clay layer located between two coarse-grained layers); the base distance from the bottom coarse-grained layer is one diameter. The model pile was installed at 1 g; then, the model was spun up to 60 g for 16 hours, until an average degree of consolidation of 90% was reached. The tubular aluminium pile (E_p = 70 GPa, outer diameter d_p = 1.2 m, length L_p = 16.8 m) was embedded in fully saturated clay (height H = 18 m; pre-consolidation pressure of 80 kPa before centrifuge testing; effective unit weight γ' = 6.3 kN/m^3; water table at the clay surface) and having on both sides dense Leighton Buzzard 100/170 sand layers. The top sand layer had a unit weight γ_{dry} = 15 kN/m^3 and a thickness of 3 m, giving a surcharge load p = 45 kPa. In the analytical model, it is assumed for the clayed layer $E_{s,0,1}$ = 2.76 MPa, Poisson's ratio $\nu_{s,1}$ = 0.35, β = 0.3, N_q = 10.7, and r_m = 27.1 m. From back-analysis, using the method suggested by Lovisa et al. (2010), the coefficient of consolidation c_v = 0.0433 m^2/day and m_v = 3.64 10^{-4} m^2/kN were estimated from measured subsurface excess pore water pressures and greenfield surface settlements, respectively (Detlefsen, 2023).

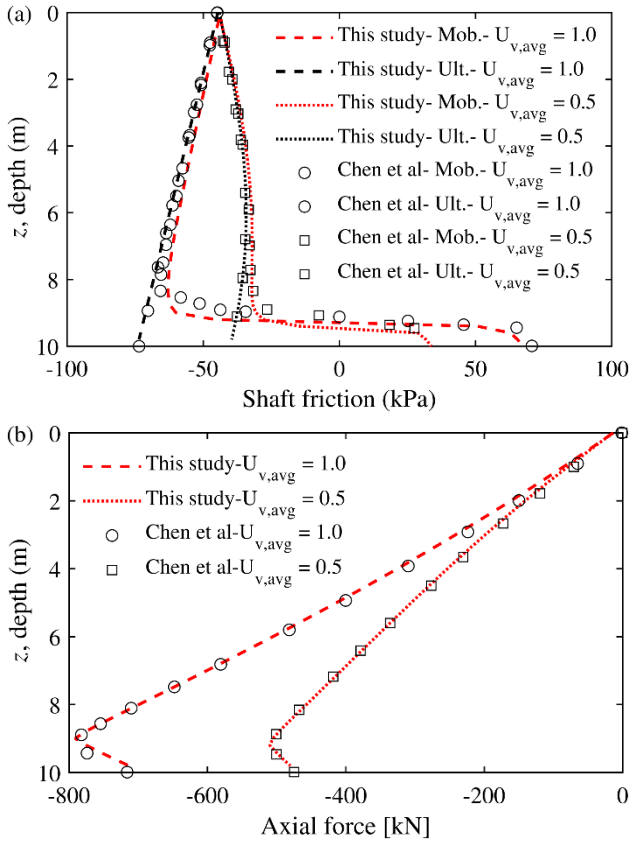

Figure 2. Comparison with analytical results for an unloaded pile: (a) shaft friction; (b) axial force.

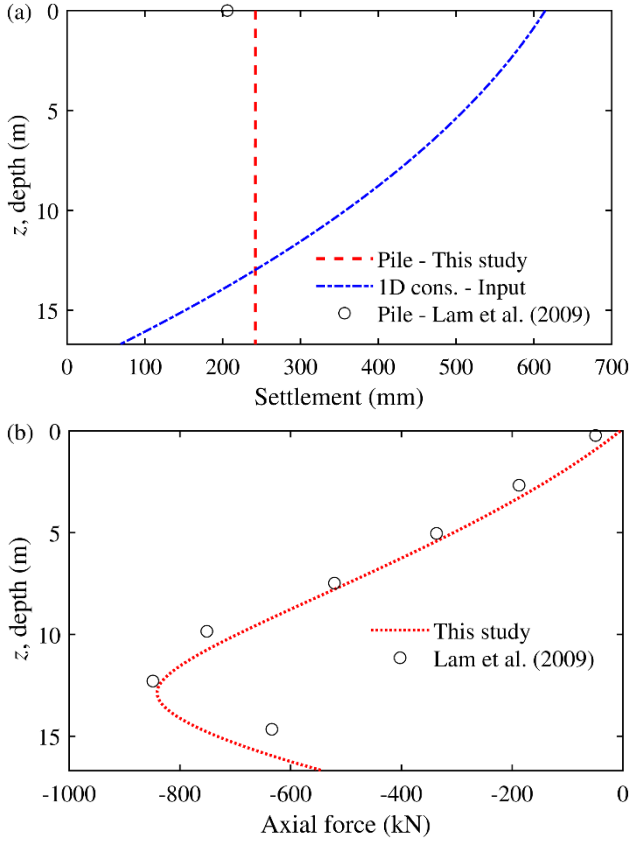

Figure 3. Comparison with centrifuge test results: (a) axial force; (b) greenfield and pile settlements.

Figure 3 compares prototype experimental and analytical results at 90% average degree of consolidation of. Despite a slight overestimation of the consolidation-induced settlement of the pile (predicted settlement of 242 mm instead of 206 mm, due to the stiffening effect of the base coarse-grained layer which was neglected), the predicted axial force profile is in satisfactory agreement with the experimental data. The axial force profiles show there is agreement between the experimental and analytical neutral planes, being at a depth of approximately 0.75 L_p.

3.2 Sensitivity study

A parametric study of the neutral plane depth and consolidation-induced settlements is carried out. The considered case study generalises the prototype experimental scenario in Figure 1b for head load P of 0 (for unloaded piles) or 1000 kN (for loaded piles).

Two different head load histories prior to consolidation and application of service loads are considered for displacement and non-displacement piles respectively. This is done to approximately take the effect of residual stresses and unloading stiffness along displacement piles into account, which will differ from ground stiffness and stress distributions of bored piles. Prior to the surcharge application p, (i) "non-displacement" piles have the head load P monotonically applied; (ii) "displacement piles" were subjected first to a head load of 99% the load capacity, then unloaded, and finally reloaded to the target P. During the consolidation, the head load P is kept constant. For both head loading and consolidation, the load transfer of the t-z springs is described by K_{tan}, as previously detailed. Results are normalised as for Kog (2016): the depth of the neutral plane is divided by the pile length giving $\psi = z_{np}/L_P$, while the normalised settlement of the pile head is $\Delta = \Delta_p E_p A_p/(p\, H^3)$.

Figure 4 displays the results for unloaded piles ($P = 0$) with a length $L_P = 0.4\, H$ to $1.4H$, where H is the thickness of the consolidating layer. The embedment L_P/H is found to impact the temporal evolution of the neutral plane depth ψ of floating piles ($L_P/H < 1.0$), whereas ψ is not affected by the time factor T_v for end-bearing piles ($L_P/H \geq 1.0$). This trend of ψ is also notable in Figure 5 which compares the neutral plane depth ψ of loaded piles when having an embedment for floating $L_P/H = 0.8$ and end-bearing $L_P/H = 1.2$. Thus, it is important to model the soil-pile interaction for floating piles in consolidating soil.

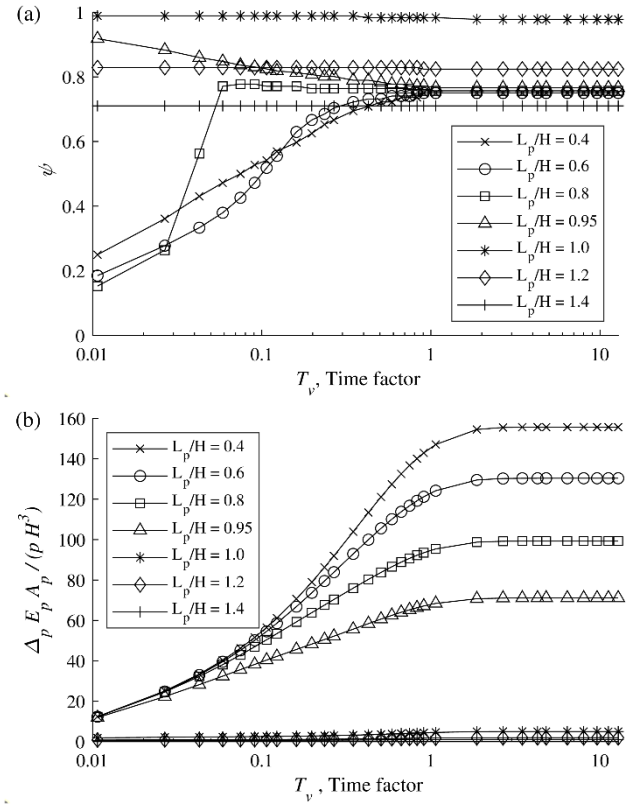

Figure 4. Settlement response of unloaded non-displacement piles against time factor with varying embedment depth: (a) neutral plane depth and (b) normalised settlements.

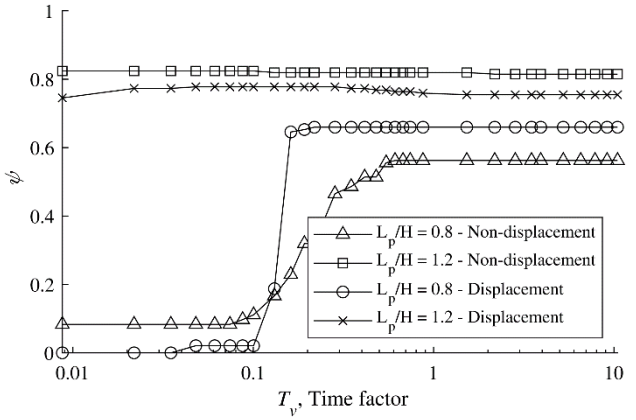

Figure 5. Normalised neutral plane depth of loaded (P = 1000 kN) displacement and non-displacement piles with varying embedment length.

4 CONCLUSIONS

This paper presents a beam on hyperbolic t-z springs model for the time-dependent stress analysis of unloaded and loaded piles in consolidating soil. A parametric study illustrated the importance of modelling the excess pore water pressure dissipation and installation in the case of floating piles.

Future work will address a consistent stiffness formation in terms of effective stresses.

REFERENCES

Chen, R., Zhou, W. and Chen, Y. (2009). Influences of soil consolidation and pile load on the development of negative skin friction of a pile. *Computers and Geotechnics*, 36(8): 1265–1271. DOI:10.1016/j.compgeo.2009.05.011.

Detlefsen, A. E. (2023). An effective stress nonlinear model for the analysis of axially loaded single piles in consolidating soil. *MSc thesis*, Aarhus University, Aarhus, Denmark.

Fellenius, B. H. (2023). Basics of foundation design–a textbook. Electronic Edition. https://www.fellenius.net/papers.

Kim, H.-J. and Mission, J.L.C. (2011). Development of negative skin friction on single piles: uncoupled analysis based on nonlinear consolidation theory with finite strain and the load-transfer method. Canadian Geotechnical Journal, 48(6): 905–914. DOI:10.1139/t11-004.

Kog, Y.C. (2016). Axially loaded piles in conso- lidating layered soil. *International Journal of Geomechanics*, 16 (1): 905–914. DOI:10.1061/(ASCE)GM.1943-5622.0000523.

Lam, S., Ng, C.W., Leung, C. F. and Chan, S. (2009). Centrifuge and numerical modeling of axial load effects on piles in consolidating ground. *Canadian Geotechnical Journal*, 46(1): 10–24. DOI:10.1139/T08-095.

Liang, R., Yin, Z.Y., Yin, J.H. and Wu, P. C. (2023). Numerical analysis of time-dependent negative skin friction on pile in soft soils. *Computers and Geotechnics*, 155, 105218. DOI:10.1016/j.compgeo.2022.105218.

Lovisa, J., Read, W. and Sivakugan, N. (2010). Consolidation behavior of soils subjected to asymmetric initial excess pore pressure distributions. *International Journal of Geomechanics*, 10(5): 181–189. DOI:10.1061/(ASCE)GM.1943-5622.0000143.

Randolph, M. F. and Wroth, C. P. (1978). Analysis of deformation of vertically loaded piles. *Journal of the geotechnical engineering division*, 104(12): 1465–1488. DOI:10.1061/AJGEB6.0000729.

Russo, G., Di Girolamo, L. and Marone, G. (2020). BEM and FEM Approaches to the Analysis of Negative Skin Friction on Piles. *Geotechnical Engineering Journal of the SEAGS & AGSSEA*: 51(2). http://seags.ait.asia/journals/2020/51-2.

Proceedings of the XVIII ECSMGE 2024
GEOTECHNICAL ENGINEERING CHALLENGES
TO MEET CURRENT AND EMERGING NEEDS OF SOCIETY
© 2024 the Authors
ISBN 978-1-032-54816-6
DOI 10.1201/9781003431749-61
Open Access: www.taylorfrancis.com, CC BY-NC-ND 4.0 license

ECSMGE 24
XVIII EUROPEAN CONFERENCE ON SOIL MECHANICS AND GEOTECHNICAL ENGINEERING

Port silo foundations on piles under vertical cyclic stresses

Fondations de silos portuaires sur pieux soumis à des contraintes cycliques verticales

P. Dogaru
General Construct Grup Srl, Constanta, Romania

R. Ciortan*
Technical Sciences Academy of Romania, Bucharest, Romania

**ciortanromeo@yahoo.com*

ABSTRACT: A particular category of structures relating to port operations is represented by the metal silo buildings in which bulk goods, especially grain, are handled and stored. The proper foundation solution for silo bins in Constanta port (Romania) is based on concrete bored piles to undertake the high loads and transfer them to the soil. A particularity of the port infrastructure consists of weak soil layers regarding bearing capacity. This aspect, alongside the cyclical nature of the loading/unloading activity, leads to a different approach to determining the bearing capacity of a bored pile within the indirect foundation system of the steel silo bin. The highly demanding nature of the cyclic actions mentioned above (10-12 annual load-unload cycles), along with the over-unitary value of the ratio between the live and dead loads, promotes a complex approach regarding the bearing capacity of the piles. Moreover, the studies and calculations have indicated that the cumulative residual pile settlement (after in-situ analysis of several loading-unloading cycles) is a critical factor in considering the bearing capacity of the bored pile. Consequently, considering some technological constraints, the bearing capacity of a pile against vertical loads is approx. 20% lower for cyclic loads rather than static loads, which is essential when designing infrastructure solutions.

RÉSUMÉ: Une catégorie particulière de structures liées aux d'exploitation portuaires est représentée par les silos métalliques dans lesquels les marchandises en vrac, en particulier les céréales, sont manipulées et stockées. La solution de fondation appropriée pour les silos du port de Constanta (Roumanie) est basée sur des pieux forés en béton pour supporter les charges élevées et les transférer au sol. L'une des particularités de l'infrastructure portuaire réside dans la faiblesse des couches de sol en termes de capacité portante. Cet aspect, ainsi que la nature cyclique de l'activité de chargement/déchargement, conduit à une approche différente pour déterminer la capacité portante d'un pieu foré dans le système de fondation indirecte du silo en acier. La nature très exigeante des actions cycliques mentionnées ci-dessus (10-12 cycles annuels de chargement et de déchargement), ainsi que la valeur sur-unitaire du rapport entre les charges vives et les charges permanents, favorisent une approche complexe en ce qui concerne la capacité portante des pieux. En outre, les études et les calculs ont indiqué que le tassement résiduel cumulatif du pieu (après l'analyse in situ de plusieurs cycles de chargement et de déchargement) est un facteur critique dans l'examen de la capacité portante du pieu foré. Par conséquent, compte tenu de certaines contraintes technologiques, la capacité portante d'un pieu contre des charges verticales est inférieure d'environ 20 % pour des charges cycliques plutôt que statiques, ce qui est essentiel lors de la conception de solutions d'infrastructure.

1 INTRODUCTION

Silo bin storage foundations are usually based on piles because of the high loads to be transferred to the soil and the existence of weak layers on site in terms of bearing capacity (e.g., the nature of the fills used in the process of widening/forming harbour berths). Cyclic loading imposed by the silo functioning is probably the most complex mode of foundation soil loading, and modelling such loading requires analysis of both the soil-structure interaction and the cyclic loading-unloading behaviour of the soil.

Moreover, given the highly particular character of these bulk storage facilities (in this case study - grain) by using metal cells made of thin-walled sheets and profiles (working with active compression zones) in conjunction with a poorly load-bearing infrastructure, the identification of structural design solutions by considering the dynamic character of long-term operation becomes very complex and complicated.

2 CASE STUDY

The present study analyses the results of cyclic loading-unloading tests, through 8 cycles, on test bored piles realized on the site of berth 80 in the port of Constanta, during the development of a grain terminal with a capacity of approximately 198,900

tonnes was built (see Figure 1). The grain storage silo consists of:

- a group of 4 cells with a capacity of 10,000 tonnes;
- a group of 8 cells with a capacity of 10,000 tonnes;
- a group of 6 cells with a capacity of 10 900 tonnes;
- a group of 6 cells with a capacity of 2 250 tonnes;

Using the full-scale working model (test bored pile) results, a comparative analysis of the influence of cyclic loading in determining the final value of the ultimate vertical load-carrying capacity of a concrete bored friction pile at the studied site was performed.



Figure 1. Grain terminal at berth 80 - port of Constanta.

An essential condition for the safe operation of the grain terminal's service technology was the limitation of differential settlement between the structures supporting its specific equipment. In this respect, the differential settlement that may occur between the pile groups of the grain silo infrastructure and the metal towers supporting the cargo elevators was also considered.

The geotechnical investigation for the construction located behind the 80 berths, Port Constanta South, was done by drilling six geotechnical boreholes 42.00m deep. To complete the information on the last intercepted layer, three of the drilled holes were continued to a depth of 42.00 m.

To simplify the sequence of the intercepted strata, they have been grouped into three lithological complexes, resulting in the following synthetic lithological column of the site:

- C1 (at depths of 0.00 - 11.80 m). - the complex formed by anthropogenic fill (predominantly composed of cohesive strata): clay, dusty clay, sandy clay, clayey dust; weakly cohesive strata: clayey sand, dusty sand, clayey sandy dust and non-cohesive strata: fine sand - large, with small gravel. All this succession of strata contains boulders and limestone blocks. At the top of drill holes F1, F2, F3, and F6, iron ore deposits from the deposition of ore over time have been traced over a variable thickness of 0.10 to 0.80 m;
- C2 (at depths of 9.40 - 35.80 m). - The intermediate complex is composed of an alternation of cohesive strata (clay, greasy clay, dusty clay, sandy clay, clayey dust), weak cohesive strata (clayey sand, dusty sand, sandy clay dust) and non-cohesive strata (fine sand, fine - medium sand, coarse sand, granular-pebble gravel. All this sequence of strata contains concretions and limestone - boulder elements);
- C3 (at depths of 30.80 - 42.00 m). - lower complex, is composed of an alternation of chalky clay / chalky, whitish dusty clay with concretions and limestone boulders. Drilling was stopped in this complex without crossing it (at depths of 40.00 - 42.00 m).

To determine by testing the ultimate compressive load-bearing capacity of the test pile, three thresholds (values) of vertical load force, 7000 kN, 8500 kN and 10,000 kN, respectively, were considered for analysis. The aim was to identify the maximum compressive bearing capacity of the pile by referring to the value of the recorded and especially to the cumulative values of the residual settlements of the loading-unloading cycles considered. The pile cumulative settlement value during the cyclic test thus becomes the determining factor in the evaluation of the vertical bearing capacity, also taking into account that in the group behaviour of the piles, this value increases considerably and can lead to differential settlement of the grain cells's foundations in the studied site.

3 RESULTS

Considering the results of the cyclic compression tests carried out on the test piles, the following aspects were highlighted, as follows:

- For a loading force value of 7000 KN, the resulting value of the residual settlement after the eight load-unload cycles is about 2mm. After the first two load-unload cycles, the value of the residual settlement was stabilised below 1mm for each cycle, which leads to the hypothesis of an "elastic" response of the foundation soil.
- For a loading force value of 8500 KN, the resulting value of the residual settlement after the eight load-unload cycles is about 32mm. After the first five load-unload cycles, the value of the residual settlement was stabilised below

2mm for each cycle with a discharging character.

- For a loading force value of 10,000 KN, the resultant value of the residual settlement after the eight load-unload cycles is about 112mm.

After the first four load-unload cycles, the residual settlement had a constant character and a value of approx. 7 mm for each cycle.

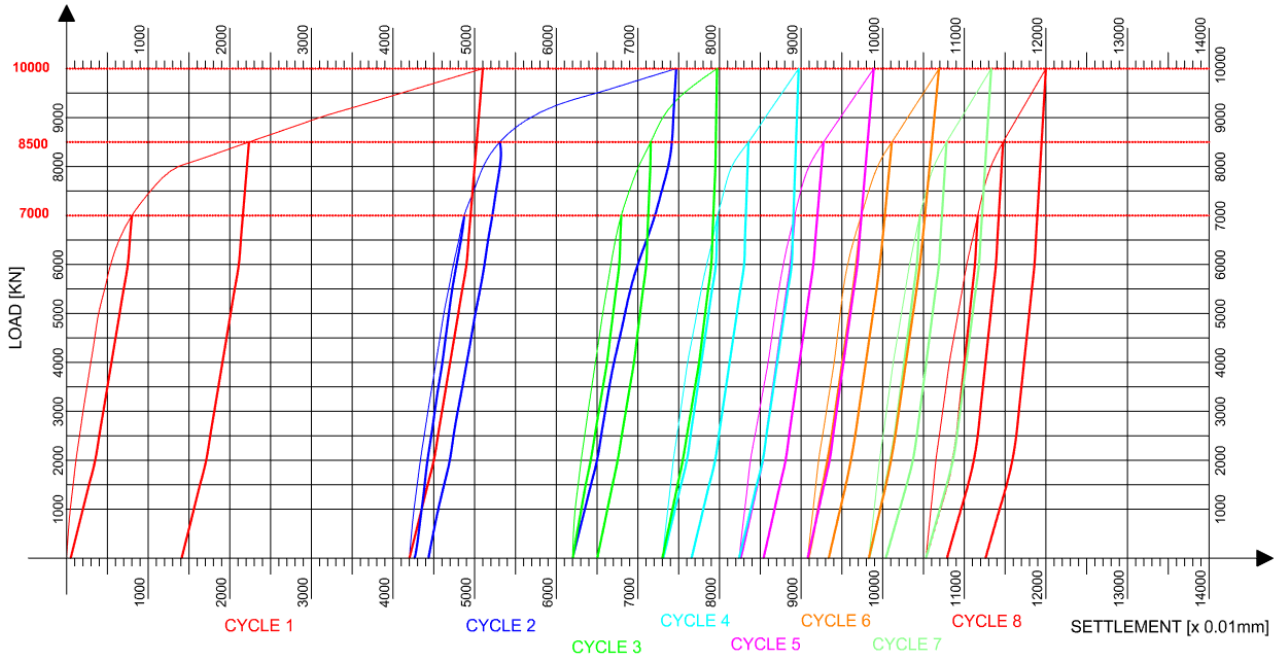

Figure 2. Load-settlement curves (8 cyclic compression tests of Pile P.I3) for the loads of: 7000kN;8500kN;10000kN.

Also, from the graphical analysis shown below in Figure 3÷5, it can be seen that if the loading load decreases to 7000 kN, the deformation is much smaller, having an almost linear character during the load-unload cycles.

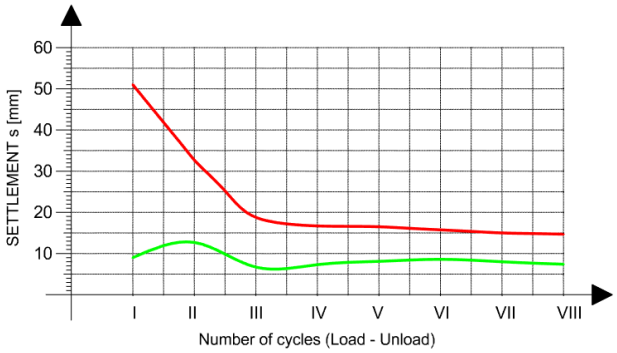

Figure 3. Load-settlement curves (8 cyclic compression tests of Pile P.I3) for the load of 10000kN.

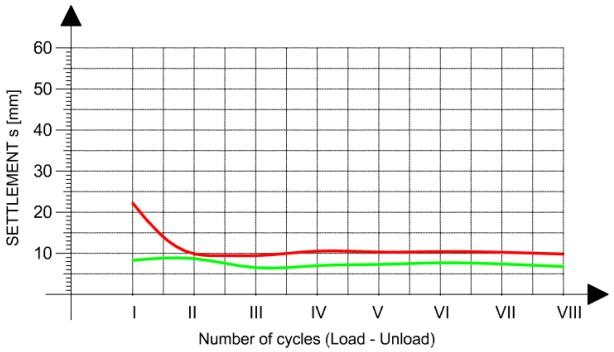

Figure 4. Load-settlement curves (8 cyclic compression tests of Pile P.I3) for the load of 8500kN.

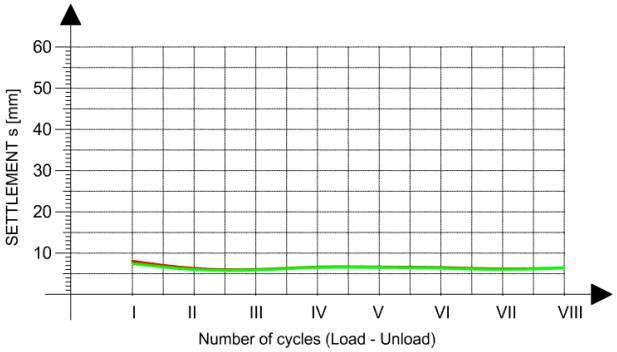

Figure 5. Load-settlement curves (8 cyclic compression tests of Pile P.I3) for the load of 7000kN.

The ratio between maximum settlement (load sequence) and its specific return (unload sequence) shows that it is higher at 10000 kN load, decreases at 8500 kN load and becomes unity at 7000 kN load (Figure 6).

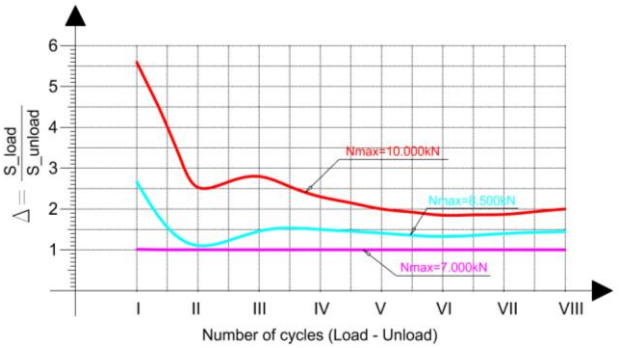

Figure 6. Ratio of maximum load-unload settlement registered values.

The cumulative size of the residual settlement increases with the number of loads, but it can be seen that this evolution is zero for the 7000 kN load (Figure 7).

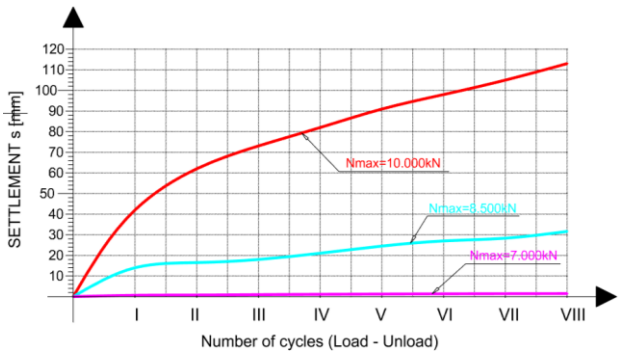

Figure 7. Cumulative residual settlement diagram for 8 load-unload cycles.

4 CONCLUSIONS

In the case of friction piles, the effect of cyclic loads must be considered as the cumulative residual settlement occurs, thus exceeding the permissible values and those required by the operation of technological equipment.

For the above, determining the bearing capacity of a friction pile should be conditional on the acceptable value of the resultant residual settlement (by summation) over the loading-unloading cycles considered in the test phase of the test piles. Thus, the cumulative residual pile settlement (after analysis of the loading-unloading cycles considered) should be considered as a determining factor that provides the bearing capacity of the pile.

Consequently, the specific nature of the foundation soil in port areas, which consists of fills, then sands and clay formations, and at-depth limestone in various states of degradation, requires that in the case of grain terminals, the foundation piles should be checked for cyclic actions given the variability of live load. The studies and calculations have shown that in the field conditions in the port of Constanta, considering some technological constraints, the design bearing capacity of piles at vertical loads is approx. 20% lower for cyclic loads than for static loads, which is essential to consider when designing infrastructure solutions.

REFERENCES

Dogaru, P., Ciortan, R., Tsitas, G. (2016) Foundation solutions for grain warehouses in the Port of Constanta" at the 13th National Conference on Geotechnics and Foundations - Cluj - Napoca / Romania, pp 349-356.

Dogaru, P., Krkljus, D., Vlăescu, D. (2019). Proper infrastructure design at high verticals loads, nearby waterfront structures, published în Ovidius University Annals Constantza (OUAC) - Series Civil Engineering, Year XXI, Issue XXI http://revista-constructii.univ-ovidius.ro/doc/editii/2019.pdf.

Dogaru, P., Krkljus D., Ghencea, A., Tudose, C., Didă, L. (2019). The new grain terminal at berth 80, Constanta South Port – the challenges and outlook of a great project, published în Romanian AICPS journal Review 3-4/2019. http://www.aicps.ro/revista/aicps-review-3-4-2019/content#page/n59/mode/2up.

Dogaru, P., Ciortan, R. (2021). The behaviour of piles under the effect of vertical cyclic actions, at the 14th National Conference on Geotechnics and Foundations - Bucharest, 2-3 June. 2021.

Dogaru, P. (2022). Modern approaches for advanced calculation of port foundations on piles under cyclic loading, PhD Thesis. https://www.univ-ovidius.ro/sustinerea-publica-a-tezelor-de-doctorat/3250-domeniul-inginerie-civila-si-instalatii-abordari-moderne-pentru-calculul-avansat-privind-fundatiile-portuare-pe-piloti-la-solicitari-ciclice.

Proceedings of the XVIII ECSMGE 2024
GEOTECHNICAL ENGINEERING CHALLENGES
TO MEET CURRENT AND EMERGING NEEDS OF SOCIETY
© 2024 the Authors
ISBN 978-1-032-54816-6
DOI 10.1201/9781003431749-62
Open Access: www.taylorfrancis.com, CC BY-NC-ND 4.0 license

ECSMGE 24
XVIII EUROPEAN CONFERENCE ON SOIL MECHANICS AND GEOTECHNICAL ENGINEERING

Effect of strain-softening and strength anisotropy on the undrained resistance of deeply embedded pile/pipe section

Effets de l'adoucissement mécanique et de l'anisotropie sur la résistance non drainée des fondations profondes

Y.P. Dong*
Technical University of Denmark, Copenhagen, Denmark
**yuedo@dtu.dk*

ABSTRACT: The bearing capacity of soils is critical for the design and analysis of foundations. The classical solutions derived from methods of characteristics and bound theories are based on the rigid plasticity and associated flow rule, which may not be realistic for natural soils. The undrained shear strength of soft clays exhibits strain-softening and anisotropic behavior in the lab tests, which creates complexity to choose appropriate strength parameters in conventional design process. In addition, the stress-strain characters are non-associative and path dependent, which also affects the bearing capacity of soils. This paper investigates one classical stability problem (i.e. deeply-embedded pile/pipe section) using the finite element analysis and MIT-E3 soil model, and demonstrates the effects of strain-softening and strength anisotropy on the undrained resistance of soils. The computed results are compared with analytical solutions and finite element limit analysis. These findings have strong practical implications to predict the bearing capacity of foundations and interpret insitu tests.

RÉSUMÉ: La capacité portante des sols est essentielle pour la conception et l'analyse des fondations. Les solutions classiques, dérivées de la méthode des caractéristiques et des théorèmes de l'analyse limite, reposent sur la loi d'écoulement associée au comportement rigide-plastique, qui peut ne pas être réaliste pour les sols naturels. La résistance au cisaillement non drainée des argiles molles présente un adoucissement et un comportement anisotrope lors des essais effectués en laboratoire, rendant le choix de paramètres de résistance adaptés complexe au cours du processus de conception. De plus, les caractéristiques contraintes-déformations sont non-associatives et dépendent du chemin suivi, ce qui affecte également la capacité portante des sols. Cet article examine un problème classique de stabilité (c. -à-d. section de pieux/pieux tubulaires profondément encastrés) utilisant l'analyse par éléments finis et le modèle de sol MIT-E3, et démontrant les effets de l'adoucissement mécanique et de l'anisotropie sur la résistance non drainée des sols. Les résultats calculés sont comparés aux solutions analytiques et à l'analyse des limites par éléments finis. Ces découvertes ont d'importantes répercussions pratiques pour prédire la capacité portante des fondations et interpréter les tests in situ.

Keywords: Bearing capacity of soils; strain-softening; strength anisotropy.

1 INTRODUCTION

A class of solutions in soil mechanics are based on the rigid plasticity and associated flow rule, such as bearing capacity of rigid footings obtained from methods of characteristics and bound theorems (Terzaghi 1943), and lateral resistance of deep buried pile section (Randolph and Houlsby 1984). They have provided sound theoretical basis in many geotechnical problems such as design of foundations, and interpretation of strength parameters from insitu penetration tests. However, real soil behavior is not rigid plastic and associative as observed in the lab tests, and exhibits complex features including (i) anisotropic strain-stress-strength relation, (ii) non-associated flow rule, (iii) stress-induced dilations, (iv) strain hardening/softening, and (v) rate-dependency. This implies that the results and conclusions based on the classical plasticity theories may have limitations in practical applications.

For cohesive soils, the limiting capacity of foundations is normally derived based on the undrained assumption with isotropic strength properties such as Tresca or Von Mises criteria. However, natural clays generally exhibit strength anisotropy resulting from preferred direction in one-dimensional deposition (Ladd 1991; Whittle 1993). Figure 1(a) clearly demonstrates significant undrained shear strength anisotropy of K_0-normally consolidated soft clays from the results of standard laboratory triaxial compression (CK_0UC), extension (CK_0UE), and direct simple shear (CK_0DSS) tests. This indicates that soils at different region of the slope in Figure 1(b) may not reach failure states simultaneously, leading to

progressive failure mechanisms. Furthermore, the mobilized shear resistance in each mode of failure depends on the shear strain level in the soil.

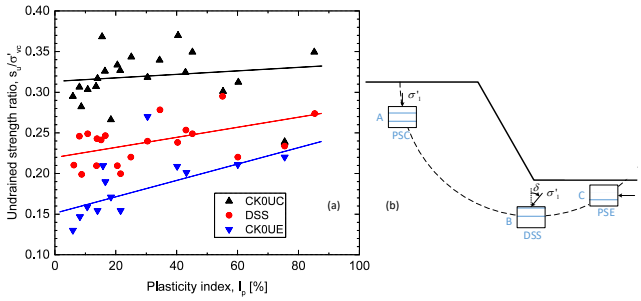

Figure 1. Undrained strength anisotropy (a) from CK0U and DSS tests on normally consolidated clays and silts, and (b) related shear modes on failure surface (Ladd 1991).

This paper investigates one classical undrained stability problems (i.e. deeply embedded pile/pipe section) using finite element analysis and the MIT-E3 model (Whittle and Kavvadas 1994), to highlight important effects of strain-softening and strength anisotropy on the undrained bearing capacity of non-associated clays. The computed results are compared with those from bound theories and finite element limit analysis.

2 DESCRIPTION OF THE MIT-E3 MODEL

The MIT-E3 model was developed to describe the rate-independent behavior of overconsolidated clays under cyclic loading, based on the observation of experimental data. The formulation of the MIT-E3 model was described in Whittle and Kavvadas (1994). In general, the model formulation comprises four components: (1) an elastoplastic model for normally consolidated clay including anisotropic and strain-softening behaviour; (2) nonlinear para-elastic equations to describe the small strain nonlinearity and hysteretic response in unloading and reloading; (3) bounding surface plasticity for irrecoverable, anisotropic and path dependent behaviour of overconsolidated clays, and (4) non-associated flow rules. Extensive comparisons with measured data from undrained shear tests performed in different modes (e.g. triaxial, plane strain, and simple shear) of shearing show that the model gives excellent predictions of conditions at maximum shear stress and describes accurately the nonlinear shear stress-strain behaviour (Whittle 1993; Whittle et al. 1994).

The model was implemented into Abaqus™ through a user-specified subroutine (UMAT) using an automatic explicit substepping algorithm with error controls, and details of the integration and verification were described in Dong (2023).

2.1 Plane strain tests

The soil behaviour in plane strain conditions are relevant to some typical geotechnical problems in practice, and are particularly focused in this paper. Figure 2 shows the computed effective stress paths and stress-strain response for the K_0- normally consolidated undrained plane strain compression (PSK_0UC) and extension (PSK_0UE) tests for Boston Blue Clay (BBC).

The normalized peak shear strength in compression mode, $s_{u,PSC}/\sigma'_{vp} = 0.344$, occurs at small strain level $\varepsilon_a = 0.2\%$, and the post-peak strain-softening effect is significant. While in the extension mode, a smaller shear strength $s_{u,PSE}/\sigma'_{vp} = 0.187$ is mobilized at larger strain level $\varepsilon_a > 3\%$, and no strain-softening effect is shown. These test results clearly demonstrate complex soil behavior that is strain-softening, anisotropic, and stress-path dependent.

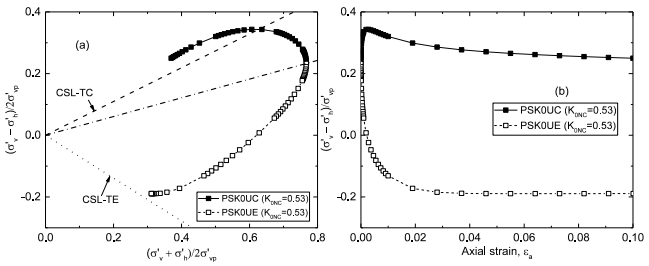

Figure 2. Simulated results of PSK0UC and PSK0UE tests of BBC from the MIT-E3 model.

2.2 Direct simple shear test

Figure 3 shows the computed effective stress paths and shear stress-strain behaviour of the K_0-normally consolidated undrained direct simple shear tests (CK_0DSS) for BBC with two different K_{0NC} values. The produced results are consistent with the previous plane strain compression/extension tests.

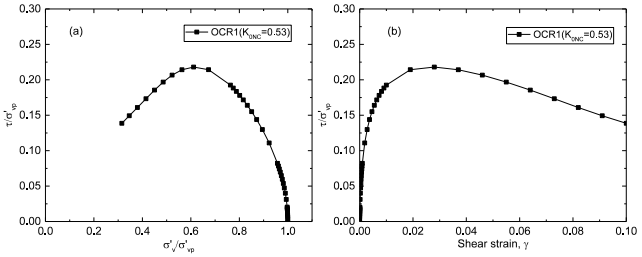

Figure 3. Simulated results of CK0DSS tests of BBC from the MIT-E3 model.

2.3 Directional shear cell test

The directional shear cell (DSC) was developed to investigate the soil behaviour under controlled rotation of principle stress directions (Arthur and Menzies

1972; Sture et al. 1987). Normal and shear stresses can be applied independently on four sides of the plane-strain device, thus achieving rotation of major principal stress direction in the plane of loading from plane-strain compression through maximum shear to extension. In the tests, soil specimens are sheared by imposing principal stress increments oriented at angle, δ, to the original direction of deposition. Figure 4 shows the computed stress paths from the DSC tests on the K_0 -normally consolidated BBC in the depositional plane, and clearly demonstrates that the undrained shear strength are affected by the loading directions and principle stress rotations. The undrained strength can be well represented by the elliptic envelope proposed by Davis and Christian (1971), which will be described in the next section. Figure 4 presents coresponding incremental shear stress-strain response in the depositional plane, and clearly demonstrates variation of mobilised shear strength with the strain under different loading directions.

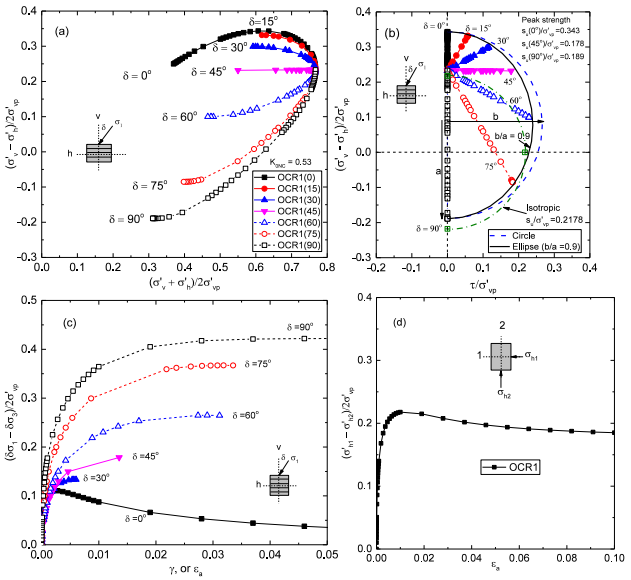

Figure 4. Simulated results of CK0DSC tests of BBC from the MIT-E3 model.

3 ANISOTROPIC STRENGTH ENVELOPE OF K0-CONSOLIDTED CLAY IN PLANE STRAIN CONDITIONS

The anisotropic strength function by Davis and Christian (1971) is well suited to the undrained strength envelope of K_0-consolidated soft clays, which can be expressed as an elliptical strength envelope in the deviatoric shear stress space $\left[\left(\sigma_x-\sigma_y\right)/2,\tau_{xy}\right]$, using eq. (1),

$$F=\left(\frac{q_{xy}-h}{a}\right)^2+\left(\frac{\tau_{xy}}{b}\right)^2-1=0$$
$$q_{xy}=\left(\sigma_y-\sigma_x\right)/2;h=\left(s_{u,0^\circ}-s_{u,90^\circ}\right)/2 \quad (1)$$
$$a=\left(s_{u,0^\circ}+s_{u,90^\circ}\right)/2;b=\frac{a\times s_{u,45^\circ}}{\sqrt{s_{u,0^\circ}\times s_{u,90^\circ}}}$$

where σ_x,σ_y and τ_{xy} are the normal and shear stresses in the x,y plane; q_{xy} is the average deviator normal stress, representing strength; h represents centre of the ellipse; $s_{u,0^\circ}$, $s_{u,45^\circ}$ and $s_{u,90^\circ}$ are the undrained shear strengths at $\delta=0^\circ,45^\circ$, and 90° for compression, respectively; and a,b are parameters to determine the size of the ellipse.

This anisotropic strength criterion can represent the undrained strength envelope of K_0 -normally consolidated BBC in the directional shear cell (DSC) tests, with parameters $b/a=0.9$. Figure 4 also includes the strength envelope and undrained shear stress-strain path in the horizontal bedding plane which is isotropic, with the undrained shear strength $s_{u,iso}/\sigma'_{vp}=0.2178$.

Ukritchon (1998) implemented this anisotropic strength criteria into the finite element limit analysis (Sloan 2013), and provided the upper and lower bound solutions for several plane-strain stability problems (e.g. strip footing, pile section, slope stability, and braced excavation). These solutions can be used to compare the results from finite element analyses using the MIT-E3 model.

4 RESISTANCE OF DEEPLY-EMBEDDED PILE/PIPE SECTION

4.1 Finite element model

The undrained resistance of deeply-embedded pile/pipe section in homogeneous clay (Randolph and Houlsby 1984), is conducted to investigate the effect of strain-softening and strength anisotropy. It also has practical significance to derive the limiting pressure on laterally loaded vertical piles and vertically loaded horizontal pipes embedded in deep cohesive soils, as well as interpretation of T-Bar penetration tests. The geometry and mesh of this analysis is shown in Figure 5, and plane strain condition is assumed considering that the pile/pipe is long. Quadratic elements (CPE6MPH: A 6-node modified quadratic plane strain triangle, pore pressure, hybrid, linear pressure, hourglass control) are used in the analysis for more accurate results in undrained condition. The ground is set as weightless in K_0 -normally consolidated state

(with the initial stress condition $\sigma'_{v0} = 100kPa, K_{0NC} = 0.53$, $OCR = 1$), and zero initial pore water pressure. However, the loading is applied in both isotropic bedding plane and anisotropic depositional plane.

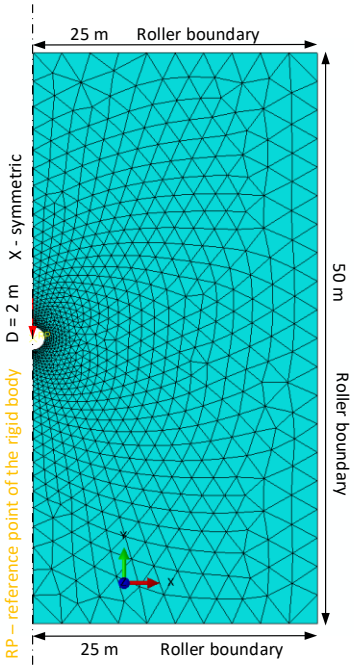

Figure 5. Finite element model.

4.2 Available solutions

Randolph and Houlsby (1984) derived analytical lower and upper bound solutions for the lateral resistance in isotropic soils by the method of characteristics. The limiting pressure factor N_p is reported in eq. (2),

$$N_p = \frac{P}{s_u D} = \pi + 2\Delta + \cos\left(\frac{\pi}{4} - \frac{\Delta}{4}\right)\left(\sqrt{2} + \sin\left(\frac{\pi}{4} - \frac{\Delta}{4}\right)\right) \quad (2)$$

where P is the applied lateral load, D is the diameter of the section, s_u is the undrained shear strength of the clay, $\sin\Delta = f_s / s_u$ is the interface roughness ratio (0 for perfectly smooth, 1 for perfectly rough), f_s is the limiting shear stress at the interface.

Ukritchon (1998) studied this problem in both isotropic and anisotropic soils using the finite element limit analysis and the anisotropic criterion by Davis and Christian (1971). The isotropic case is the same as the lateral loading of vertical pile section in Randolph and Houlsby (1984), whereas the anisotropic case is more related to the vertically loaded pipe section in deep soils and the T-bar penetration tests in geotechnical site investigation (Stewart and Randolph 1994). For anisotropic soils, the limiting pressure is defined in eq. (3) using the modified factor N'_p and the average strength $s_{u,avg}$,

$$\frac{P}{D} = N'_p s_{u,avg} = N'_p \frac{\left(s_{u,0^\circ} + s_{u,90^\circ}\right)}{2} \quad (3)$$

Randolph and Houlsby (1984) applied a uniform shear stress on the soil-pile interface to consider the friction on the pile, and the shear stress is equal to the undrained shear strength of the soil. However, this assumption may not be realistic in real situations where slippage and separation between the soil and pile can occur. To consider this effect, the interface is represented by contact pairs with Lagrangian algorithm, and the slip limit is specified by the peak undrained shear strength of the soil. For the analyses in the isotropic bedding plane, the slip limit is equal to the isotropic shear strength $s_{u,iso}$, whereas for the analyses in the anisotropic depositional plane, the slip limit is equal to the average strength $s_{u,avg}$. The obtained bearing capacity factor is smaller than the analytical solution from limit analysis.

4.3 Computed results

Figure 6 shows the normalised load-displacement response (in terms of $N_p \sim s/B$) from the MIT-E3 model in the isotropic bedding plane and anisotropic depositional plane. The peak bearing capacity factors in both cases fall below those from Davis and Christian (1971) and Ukritchon (1998), for both smooth and rough soil/pile interface. These results clearly demonstrate that the bearing capacity will be reduced on the clay with strain-softening behaviour, and the decrease is affected by the level of strain-softening.

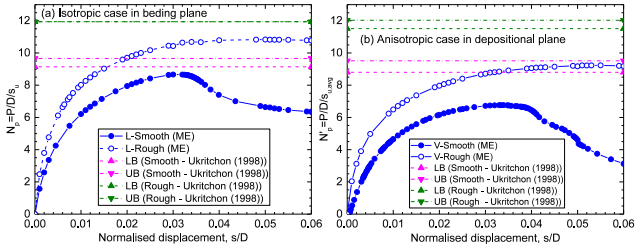

Figure 6. Normalised load-displacement response of deeply embedded rigid pile section in (a) the isotropic bedding plane, and (b) anisotropic depositional plane from the MIT-E3 model.

To diagnose the mechanism of strain-softening, Figure 7 shows the transformed horizontal shear stress (q_h / σ'_{vp}) and strain (ε_h) distribution in the soil around the pile at the peak resistance, for the smooth case. It can be seen that the shear stress in the elements with peak shear strain is below the peak shear strength of

the soil, indicating post-peak strain-softening. In contrast, the shear strain on the right side of the pile is so small that the peak shear strength of soils is not fully mobilised yet.

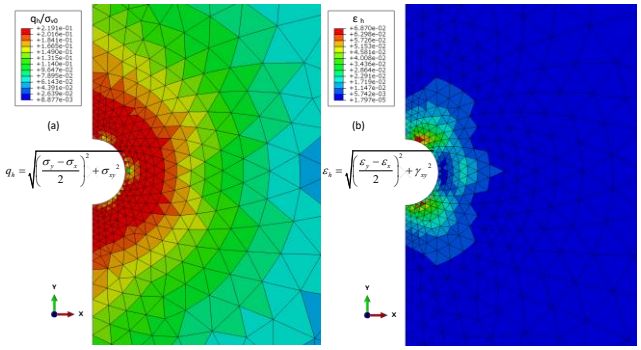

Figure 7. Distribution of transformed shear stress and strain in the soil around the rigid pile section with smooth interface in the isotropic bedding plane at the peak load from the MIT-E3 model.

For anisotropic soils, the computed resistance factor N'_p is much smaller than the analytical solution from Ukritchon (1998), based on the average peak strength ratio $s_{u,avg}/\sigma'_{vp} = 0.265$, and also smaller than the previous isotropic cases. This is mainly caused by the strain-softening and strength anisotropy of the soils, as discussed in the previous section. Figure 4 shows that the peak undrained strength is not mobilised at the same strain level for different shear directions, and the compressive strength starts to decrease at relatively small strain before other shear strength modes are reached. Figure 8(a) shows the normalised strength (f) distribution around the pipe at the peak resistance for the smooth case, and it can be seen that the soil strength is not fully mobilised in a large area around the pile. Figure 8(b) shows the direction of major principal stress (δ) indicating shearing modes of the soil, which can explain the complex effect of strength anisotropy at different shearing modes and strain level.

Similar effect of strength anisotropy was also reported in Randolph and Andersen (2006), where an anisotropic soil model was used in the finite element analysis. These results clearly imply that (i) the computed resistance will be over-estimated in natural soils with strain-softening behaviour using analytical solution from rigid plasticity, (ii) the interpreted soil strength from T-bar tests will be under-estimated in anisotropic soils with strain-softening behaviour, and (iii) it may be difficult to select appropriate average strength values in conventional stability analysis.

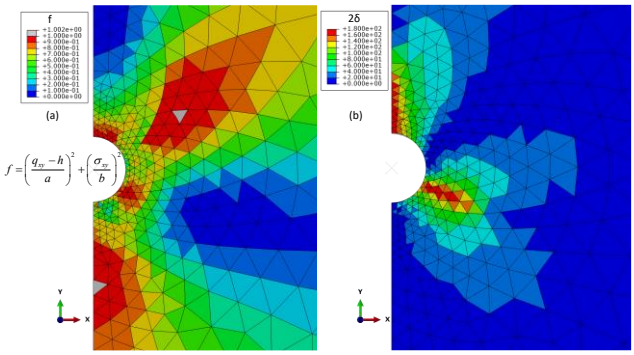

Figure 8. Distribution of normalised shear strength and principal stress direction in the soil around the rigid pipe section with smooth interface in the anisotropic depositional plane at the peak load from the MIT-E3 model.

5 CONCLUSIONS

The deeply-embeded pile/pipe section analysis has been investigated using finite element analyses and the MIT-E3 model, to demonstrate the effects of strain-softening and strength anisotropy on the undrained bearing capacity of non-associated clay. General conclusions are drawn for future applications:

- The undrained bearing capacity derived from the rigid plasticity and associated flow rule may have limitations in practical applications for natural soils with strain-softening and strength anisotropy behavior. Finite element analysis with realistic soil models can be useful to evaluate the bearing capacity of soils more accurately.
- The strain-softening behavior will reduce the undrained bearing capacity factor based on the peak strength, and the reduction depends on the degree of softening in the stress-strain path. This is because the peak strength is not mobilized simultaneously at all points in the soil due to the non-uniform strain distribution in the soil, and in some elements the peak strength is mobilized before the peak load is reached and the strength in those elements decreases while other elements are mobilizing the peak strength.
- The effect of strength anisotropy on the bearing capacity is more complex because the peak shear strength depends on different shearing modes and strain levels in the analysis. Selection of appropriate undrained strength parameters remains challenging in conventional stability analyses, and advanced finite element

analysis with anisotropic soil models can be a good option.

ACKNOWLEDGEMENTS

This research is an extension of previous collaborations with Prof. Andrew J. Whittle and late Prof. Scott W. Sloan. Prof Guy T. Houlsby is also acknowledged for discussion on bearing capacity problems.

REFERENCES

Arthur, J. R. F., and Menzies, B. K. (1972). "Inherent anisotropy in a sand." *Géotechnique*, 22(1), 115–128.

Davis, E. H., and Christian, J. T. (1971). "Bearing Capacity of Anisotropic Cohesive Soil." *Journal of the Soil Mechanics and Foundations Division*, 97(5), 753–769.

Dong, Y. (2023). "Performance of explicit substepping integration scheme for complex constitutive models in finite element analysis." *Computers and Geotechnics*, 162, 105629.

Ladd, C. C. (1991). "Stability Evaluation during Staged Construction." *Journal of Geotechnical Engineering*, 117(4), 540–615.

Randolph, M. F., and Andersen, K. H. (2006). "Numerical Simulation of T-Bar Penetration in Soft Clay." *International Journal of Geomechanics*, 6(6), 411–420.

Randolph, M. F., and Houlsby, G. T. (1984). "The limiting pressure on a circular pile loaded laterally in cohesive soil." *Géotechnique*, 34(4), 613–623.

Sloan, S. W. (2013). "Geotechnical stability analysis." *Géotechnique*, 63(7), 531–571.

Stewart, D. P., and Randolph, M. F. (1994). "T-Bar Penetration Testing in Soft Clay." *Journal of Geotechnical Engineering - ASCE*, 120(12), 2230–2235.

Sture, S., Budiman, J. S., Ontuna, A. K., and Ko, H. Y. (1987). "Directional Shear Cell Experiments on a Dry Cohesionless Soil." *Geotechnical Testing Journal*, 10(2), 71–79.

Terzaghi, K. (1943). *Theoretical Soil Mechanics*. John Wiley & Sons, Inc.

Ukritchon, B. (1998). "Application of numerical limit analyses for undrained stability problems in clay." MIT.

Whittle, A. J. (1993). "Evaluation of a constitutive model for overconsolidated clays." *Géotechnique*, 43(2), 289–313.

Whittle, A. J., Degroot, D. J., Ladd, C. C., and Tian-Ho, S. (1994). "Model prediction of anisotropic behavior of Boston blue clay." *Journal of Geotechnical Engineering*, 120(2), 199–224.

Whittle, A. J., and Kavvadas, M. J. (1994). "Formulation of MIT-E3 constitutive model for overconsolidated clays." *Journal of Geotechnical Engineering*, 120(1), 173–198.

Proceedings of the XVIII ECSMGE 2024
GEOTECHNICAL ENGINEERING CHALLENGES
TO MEET CURRENT AND EMERGING NEEDS OF SOCIETY
© 2024 the Authors
ISBN 978-1-032-54816-6
DOI 10.1201/9781003431749-63
Open Access: www.taylorfrancis.com, CC BY-NC-ND 4.0 license

ECSMGE 24
XVIII EUROPEAN CONFERENCE ON SOIL MECHANICS AND GEOTECHNICAL ENGINEERING

Improvement of tubular piles by effective closure

Amélioration des pieux tubulaires par une fermeture efficace

M. Doubrovsky*, V. Dubravina
Odesa National Maritime University, Odesa, Ukraine
**m.doubrovsky@gmail.com*

ABSTRACT: Important problem of the piled structures design is ensuring of reasonable cost of piling. It can be provided by shortening either of piles length or the number of pipes in the pile foundation (keeping another pile's dimensions and material properties without changes). Both such approaches should provide a required bearing capacity of the pile foundation (axial compressing loads are considered). These results may be achieved if each short-cut pile is improved and bears the same loading as a pile of normal (initially designed) length or if each pile of normal length is improved and bears larger axial force in comparison with its initially designed capacity. The aim of the presented study was to clarify some possibilities to improve the pipe pile's bearing capacity using an internal rigid diaphragm (closure) placed inside the pile's shaft. It increases the bearing capacity of the tubular pile due to additional soil reaction inside the shaft (it was confirmed by known on-site measurements). Laboratory research aiming to study the mentioned effect was produced with the pipe pile's model pressed into sandy soil. These tests allowed us to clarify conditions of soil plagues formation at the pile's tip and under the diaphragm as well as their interaction. Also, some conclusions and recommendations were made clarifying the diaphragm's positive contribution to pile bearing capacity, the effect of the closure's location along the pipe shaft (distance from the tip), and the influence of the diaphragm's design (shape, etc.).

RÉSUMÉ: Le problème important de la conception des structures sur pieux est de garantir un coût de pieux raisonnable. Cela peut être obtenu en raccourcissant soit la longueur des pieux, soit le nombre de tuyaux dans la fondation sur pieux (en gardant les dimensions et les propriétés matérielles d'un autre pieu sans modifications). Ces deux approches doivent fournir une capacité portante requise de la fondation sur pieux (les charges de compression axiales sont prises en compte). Ces résultats peuvent être obtenus si chaque pieu raccourci est amélioré et supporte la même charge qu'un pieu de longueur normale (initialement conçue) ou si chaque pieu de longueur normale est amélioré et supporte une force axiale plus grande par rapport à sa capacité initialement conçue. Le but de l'étude présentée était de clarifier certaines possibilités pour améliorer la capacité portante du pieu tubulaire en utilisant un diaphragme rigide interne (fermeture) placé à l'intérieur du fût du pieu. Cela augmente la capacité portante du pieu tubulaire en raison d'une réaction supplémentaire du sol à l'intérieur du puits (cela a été confirmé par des mesures connues sur site). Des recherches en laboratoire visant à étudier l'effet mentionné ont été réalisées avec le modèle du pieu enfoncé dans un sol sableux. Ces essais ont permis de préciser les conditions de formation des invasions de sol en pointe de pieu et sous le diaphragme ainsi que leur interaction. En outre, certaines conclusions et recommandations ont été formulées clarifiant la contribution positive du diaphragme à la capacité portante du pieu, l'effet de l'emplacement de la fermeture le long du fût du tuyau (distance de la pointe) et l'influence de la conception du diaphragme (forme, etc.).

Keywords: Tubular pile; bearing capacity; internal diaphragm.

1 INTRODUCTION

Modern marine transportation and offshore structures such as deep-water port berths, oil and gas platforms, raid and offshore fixed single point moorings, submerged stores, and others often include steel tubular piles of essential length (80-100 m and more) as main bearing elements. Such tubular piles should provide high bearing capacity in case of external axial loads application (Doubrovsky et al., 2018, Tomlinson and Woodward, 2008, Randolph et al., 1991).

Besides, piling works may provoke some environmental problems connected with the hammer's operation (noise, vibration, dynamic action, carbon footprint, etc.). One of the ways to reduce environmental hazards during pipe pile driving is decreasing piling work volume. It can be provided by shortening either of pile's length (i.e. depth of driving) or the number of pipes in the pile foundation (keeping another pile's dimensions and material properties without changes). Both such approaches should provide a required bearing capacity of the pile foundation despite the short-cut piles or fewer piles number (axial compressing loads are considered).

These results may be achieved if each short-cut pile is improved and bears the same loading as a pile of normal (initially designed) length or if each pile of normal length is improved and bears larger axial force in comparison with its initially designed capacity.

So, the study aimed to clarify some possibilities to improve the pipe pile's bearing capacity using an internal rigid diaphragm (closure) placed inside the pile's shaft. This innovation increases the bearing capacity of the tubular pile due to additional soil reaction inside the shaft as has been confirmed by known on-site measurements (Tomlinson and Woodward, 2008) and our previous physical modeling (Doubrovsky et al., 2022).

As in many cases, large diameter tubular piles of shelf structures are installed without plugging effect or with partial plugging (Randolph et al., 1991, White et al., 2010, Gudavalli et al. 2013, Lehane and Gavin, 2004), the approach based on the use of the closure of the pile's shaft looks rather attractive for deep water port, marine, and offshore engineering. So, it needs detailed consideration and study aiming to determine the method's peculiarity, an appropriate sphere of application, details of diaphragm design, and its proper location along the pile's shaft.

2 APPLICATION OF INTERNAL DIAPHRAGM IN STEEL TUBULAR PILES

Recommended technology to install the internal diaphragm was described (perhaps first) in Tomlinson and Woodward, 2008. A hole is necessary for the diaphragm to release water pressure in the soil plug and to allow the expulsion of silt. Stresses on the underside of the diaphragm are high during driving and radial stiffeners are needed.

According to Tomlinson and Woodward, 2008, the minimum depth above the pile toe for locating the diaphragm is the penetration below the sea bed required for fixity against lateral loading. There are formulas in some norms allowing the determination of the fixity's depth depending on soil properties and the pile's bending rigidity; roughly this depth may be determined in the interval of (5-7) d. However, further penetration is necessary to form the soil plug under the diaphragm by compacting the soil within the plug and developing the necessary base resistance. Thus, mentioned authors considered two locations for two soil plugs formation during the tubular pile driving: at the open end of the pile and under the internal diaphragm.

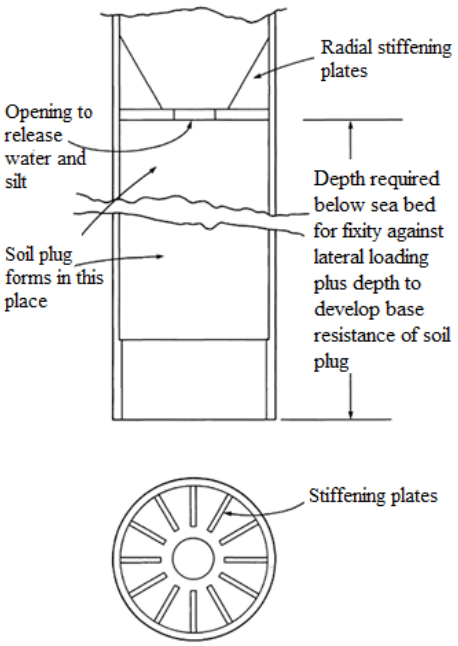

Figure 1. Steel tubular pile with the diaphragm.

As an example of the diaphragm's practical application, we may refer to the piling works at the Hadera coal unloading terminal near Haifa (Tomlinson and Woodward, 2008). Open-end piles 1424- and 1524-mm OD were proposed but initial trial driving showed that very deep penetrations, as much as 70m below sea bed in calcareous sands, would be needed to develop the required axial resistance. The blow count diagram showed quite low resistance at 36m below the sea bed. Trials were then made of the diaphragm method. A diaphragm with a 600 mm hole giving 83% closure of the cross-section was inserted 20m above the toe. This increased the driving resistance at 39m below the sea bed and another trial with a 300 mm hole (95% closure) gave a higher resistance at 37m. It was supposed that such improvement of piles bearing capacity was stipulated by soil plug formation below the mentioned diaphragms.

3 LABORATORY MODEL TESTING

Regarding that obvious effect (an increase of the pile's bearing capacity) has been achieved by the use of the rigid diaphragm, we intended to study the peculiarities of the considered approach by providing model static tests in laboratory conditions. We aimed to obtain parameters describing the considered pile driving process – both qualitative (related to the process in general) and quantitative (characteristic for the applied model pile-soil system) ones.

As to the method of pile installation, we suppose that traditional approaches (use of impact hammer or vibro hammer) are not reliable enough to provide safety of the rigid diaphragm fixed by welding inside

the pile's shaft and interacting with soil under the diaphragm. In order to avoid dynamic actions upon the diaphragm during pile penetration we prefer to consider a safer but more effective method of pressing load application (jacking) (White et al, 2010).

To clarify the above-mentioned items related to the tubular pile with an internal diaphragm, we fulfilled a series of experimental studies in the Geotechnical Laboratory of the Department "Sea, River Ports and Waterways" at Odessa National Maritime University (Odessa, Ukraine).

For pile testing, we used a soil box of dimensions: width of 600 mm, length of 750 mm, and depth of 1100 mm (Figure 2). For the model of the tubular open-end pile, we apply steel pipe d=50 mm external diameter, wall pipe thickness 1 mm, l=800 mm length. To drive the pipe into fine sand mechanical jack has been applied.

For experimental studies we used fine sand with the following characteristics: internal friction angle 33^0; density 14.5 kN/m^3; void ratio 0.71; moisture 0.07%; Young modulus 16 MPa, Poisson's ratio 0.3.

The first series of the experiment aimed to determine conditions of the soil plug formation at the tip of the open-end pile model. A detailed description of this study was presented in (Doubrovsky et al., 2022).

The second series of the experiment was devoted to clarification of the role and contribution of the internal diaphragm. For the model pile the diaphragm was produced as a circular steel plate (4 mm thickness), with its diameter corresponding to the inner diameter of the pile.

The internal diaphragm was fixed at several positions by changing the distance from the tip of the model pile: 0 (closed-end); 3d; 6d; 9d (total length of the pile was equal to 16d). As it is demonstrated by the diagrams presented in Figure 3, the application of the internal diaphragm provides increasing open-end pile bearing capacity. The degree of such an increase depends on the diaphragm location. For the considered options of the diaphragm fixing point, the minimum increment of the open-end pile bearing capacity relates to the 3d distance between the diaphragm and the pile tip, and the maximal increment is measured at the 9d distance.

Perhaps mentioned circumstances may be commented by the following way. The upper plug under the diaphragm may be formed if there is a proper base reaction developed inside the shaft. Such a situation may occur if the upper plug (being in the process of formation) meets the already-formed lower plug. The last transfers additional pressure to the soil under the toe and provokes an additional base reaction.

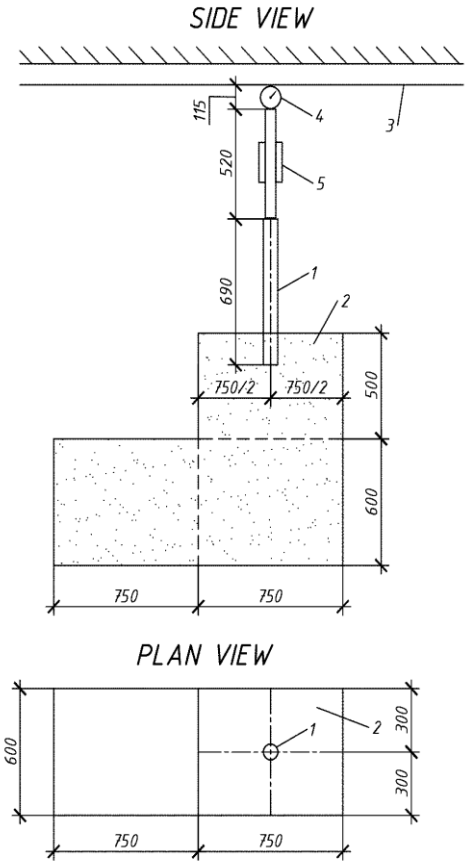

Figure 2. Scheme of the experiment: 1 – pile model; 2 – sandbox; 3 – bearing beam; 4 – force gauge (dynamometer); 5 – jack loading system (telescopic) (all sizes in millimeters).

Thus, the additional external force acts on the plug and increases soil density in it. In fact, after that stage, two plugs are combined and work as one large plug between the diaphragm and the pile's toe. The creation of the mentioned large plug and its effective contribution to the pile bearing capacity may be provided only in case of the "right" location of the diaphragm (not too low and not too high). For our model tests the maximal bearing capacity of the open-ended pile was measured in the case of the 9d distance of the diaphragm from the pile tip.

It may be explained, particularly, by the fact that for the considered test conditions, approximate driving depth t= (4-5)d at the initial stage of pile installation is needed to dense soil due to the development of the friction forces inside the pile's shaft and to form a lower soil plug at the pile tip. If then to apply similar consideration for the follow-on stage of the driving process – compaction of the soil under the diaphragm due to the similar friction forces, required penetration depth for this stage to form the upper plug may be of similar value (4-5) d.

So the total distance between the pile toe and the diaphragm may be considered as the sum of these two parts of the penetration depth, i.e., approx. (8-10) d. Such location of the diaphragm may be optimal to form two plugs consecutively and to combine them in one large plug.

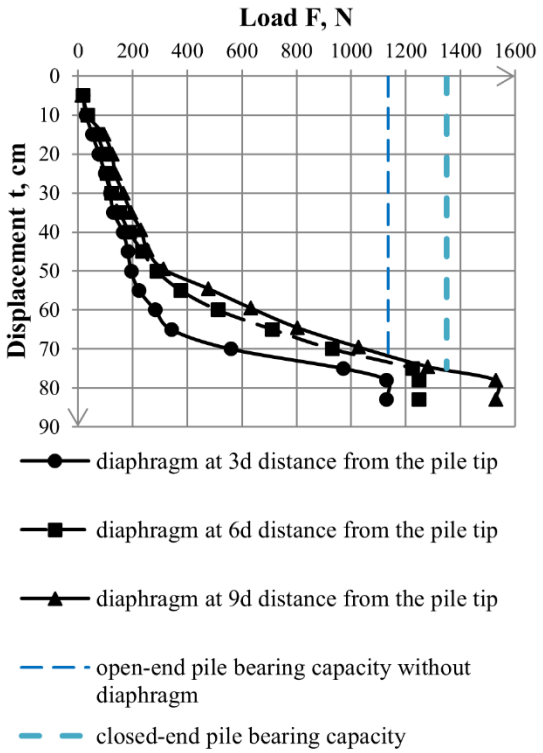

Figure 3. Dependencies between vertical axial load upon the model open-end pile and its displacements.

Regarding quantitative parameters of open-end pile bearing capacity (Figure 3), we would like to note that due to the diaphragm's contribution, pile bearing capacity may be increased (in our tests up to 15-20%). Another effect consists in the possibility to decrease pile driving depth (10-15%). Mentioned figures should be considered concerning possible experimental errors stipulated by differences in the reproducibility of the model ground preparation as well as measurement inaccuracy (about 10% in total).

For the conditions of our laboratory model testing (skipping the details of intermediate conversions and calculations), it was determined that the related prototype is a tubular pile of diameter 1.0 m driven up to 10 m into similar sandy soil. Its bearing capacity (sum of the toe and shaft bearing capacities) is 1723 kN. For comparison: the calculated value of the prototype bearing capacity according to the recommendation of the related Ukrainian code occurred to be 2020 kN (some 15% difference). Also, for plugging effect assessment we have to consider scale effects stipulated by the influence of internal pile diameter. This aspect is subject to a study for further investigations.

4 VARIATION OF INTERNAL DIAPHRAGM DESIGN

To assess the effectiveness of various forms of the pile's closure, we considered 3 types of diaphragm: flat, conical (in 3 variants, differing in the angle of the cone), and cylindrical (Figure 4, dimensions in mm).

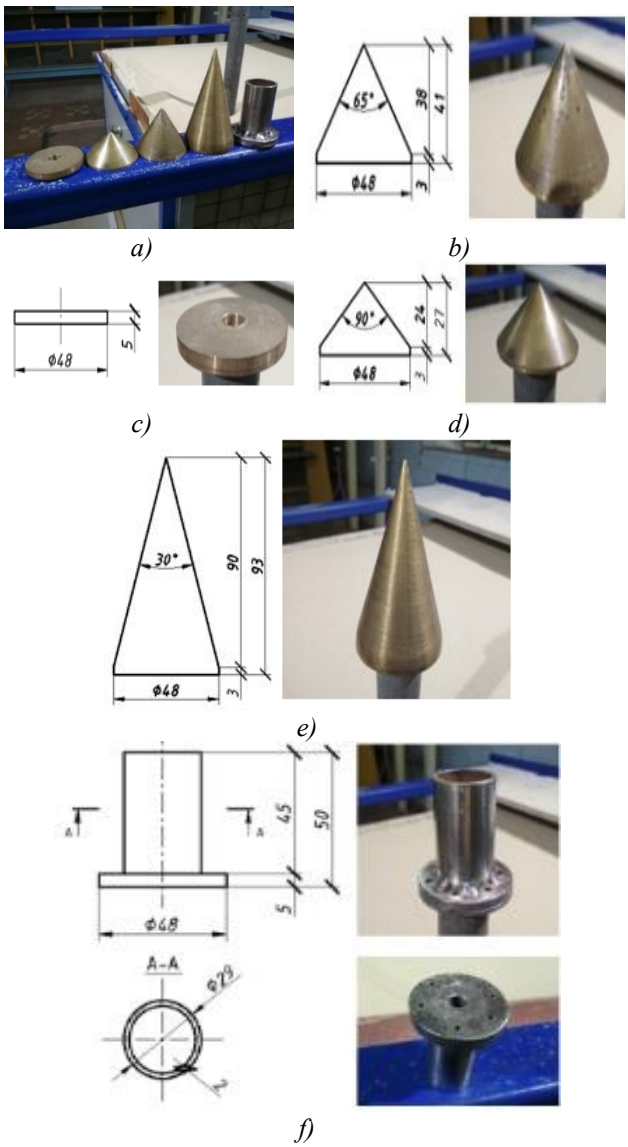

Figure 4. Details of the experimental pile (sizes in mm): a – closures of different shapes applied in the experiment; b – conic closure 65^0; c - flat closure; d – conic closure 90^0; e - conic closure 30^0; f - cylindric closure.

The driving of the model pile was carried out until the pile reached its bearing capacity, i.e. until the moment when the movements of the pile increased without an increase in the external load.

Of the three considered conical diaphragm options (with a cone angle of 30^0, 65^0, and 90^0), the best result was obtained for a pile's closure with an angle of 65^0.

A comparison of load-displacement dependencies for piles with different types of the diaphragm is shown in Figure 5. The last shows that the cylindrical diaphragm occurred to be the most effective and the flat closure was least effective.

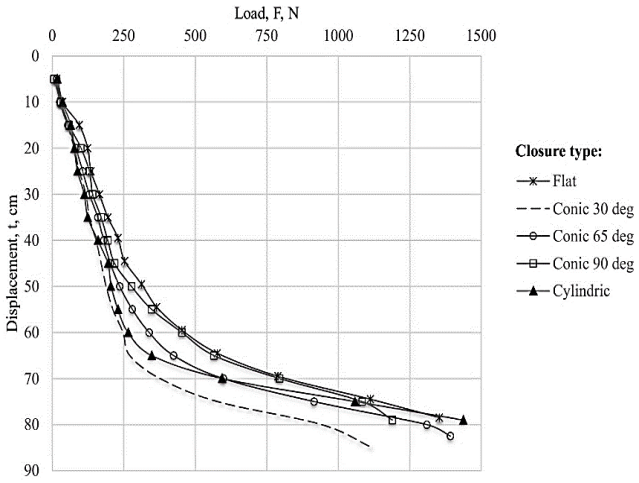

Figure 5. Dependencies between vertical axial load upon the model pile and its displacements for closure of different shapes located at 9d distance from the tip.

A comparison of the work of the model pipe pile in two extreme cases (with an open and closed-end) and in the cases of the diaphragm of effective shape (cylindrical and conical with a cone angle of 65^0) is presented in Figure 6.

To analyze the influence of the location of the closure on the bearing capacity of the pile, the experimental dependence of the resistance of the soil to pile driving N (equivalent to the vertical load on the pile) on the depth D of the cylinder diaphragm location is of interest. Figure 7 shows an example of such a relationship, summarizing the data we obtained in the experiments.

According to this diagram, by choosing in advance the location of the closure, it is possible at the initial stage to facilitate the pile driving compared to the pile with a closed-end, and at the final stage of pile installation, it is possible to approximate the value of the bearing capacity of the pile with closure to the parameters of the pile with a closed end. This ability to regulate the resistance to pile driving is important for the optimal and economical choice of technological equipment when installing the pile foundation of the structure.

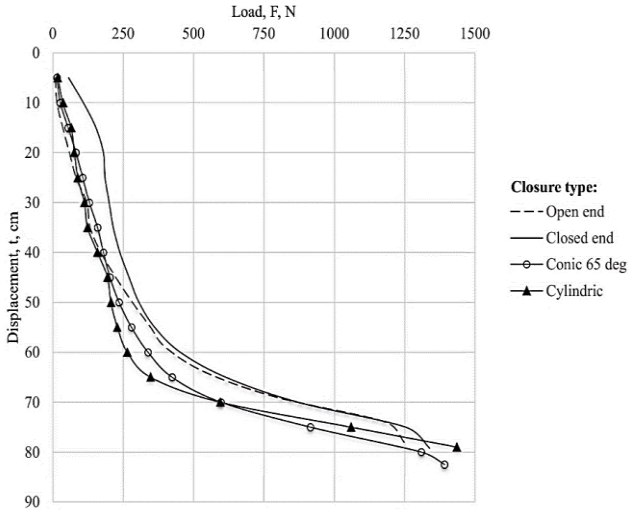

Figure 6. Dependencies between vertical axial load upon the model pile and its displacements for the absence of the closure (open and closed ends) and for the presence of the closure (conic and cylindric) located at 9d distance from the tip.

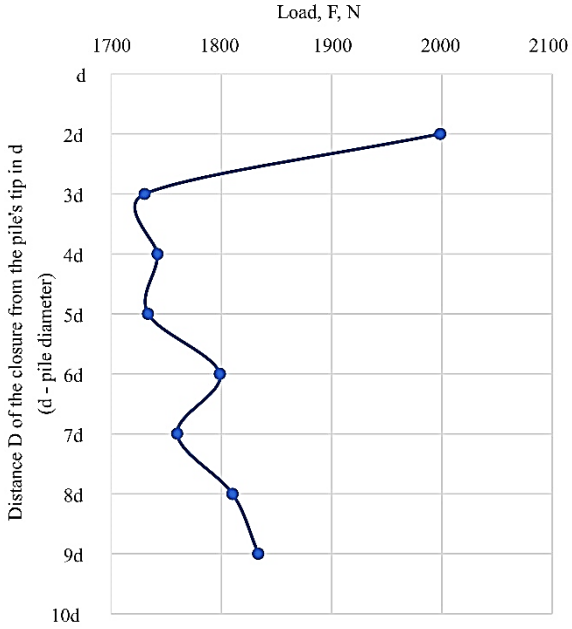

Figure 7. Dependencies between vertical axial load upon the model pile and cylindrical closure's location (distance from the tip D).

Obtained experimental dependencies (Figures 5 and 6) can be analytically described by approximating functions with good correlation indexes similarly to the method proposed earlier (Doubrovsky et al., 2022). For data interpreted in Figure 7 another approach should be worked out in the further numerical analysis.

5 CONCLUSIONS

As obtained from the presented initial series of our experimental studies, a rigid diaphragm inside the tubular open-end pile may be a useful element for increasing the pile's bearing capacity.

Consecutive formation of two soil plugs (the lower one formed just at the pile tip and then the upper one formed under the diaphragm) leading to their partial or full integration is most effective when the optimal location of the diaphragm inside the pile shaft is provided. From the point of view of pile bearing capacity under axial compressive load and for the considered experimental conditions, such proper distance between the pile tip and internal diaphragm occurred to be around 9d (d – pile diameter).

Improvement of the pile effectiveness determined by experimental modeling for the above-mentioned pile-soil conditions provides 15-20% increase of the bearing capacity or a 10-15% reduction of the driving depth.

An interesting possibility of regulating the value of the bearing capacity of the pile by changing the position of the diaphragm along the pile's shaft is brought out. Such an approach can be effective if the open-ended tubular pile does not provide the required bearing capacity of the pile, and the closed-end pile results in excessive bearing capacity or causes the use of too-powerful and expensive pile-driving equipment. The use of a pile with a closure leads to an intermediate option between piles with an open and closed-end, which allows for optimization of the design of the pile foundation of the structure and reduces the cost of piling work.

Another important effect of increasing the bearing capacity of a tubular pile through the use of an internal diaphragm is to reduce the volume of piling and accordingly to decrease noise, vibration, dynamic action, carbon footprint, etc., providing the improvement of the environmental situation at the construction site.

ACKNOWLEDGMENT

The authors would like to express gratitude to colleagues from the Geotechnical Laboratory of the Department "Sea, River Ports and Waterways" at Odessa National Maritime University for their valuable support and assistance in model test arrangement and fulfillment.

This study was supported at the Technion by a fellowship from the Lady Davis Foundation.

REFERENCES

Doubrovsky M., Gerashchenko A., Dobrov I., Dubrovska O. (2018) Innovative Design and Technology Solutions for Development of Port and Offshore Pressed-in Piled Structures, *Proc. of the First International Conference on Press-in Engineering*, Kochi, Japan, pp. 91-99.

Doubrovsky M., Kusik L., Dubravina V. (2022) Bearing Capacity of Tubular Piles: Technological Improvements and Model Testing. In: Zhu HH., Garg A., Zhussupbekov A., Su LJ. (eds) Advances in Geoengineering along the Belt and Road. BRWSG 2021. Lecture Notes in Civil Engineering, vol 230. Springer, Singapore. https://doi.org/10.1007/978-981-16-9963-4_11.

Gudavalli S.R., Safaqah O., Seo H. (2013) Effect of soil plugging on Axial Capacity of Open-Ended Pipe Piles in Sands. *Proceedings of the 18-th International Conference on Soil Mechanics and Geotechnical Engineering*, Paris, France, pp. 1487-1490.

Lehane, B. M. and Gavin, K. G. (2004) Discussion of "Determination of bearing capacity of open-ended piles in sand". Journal of Geotechnical and Geoenvironmental Engineering, 130 (6), pp. 656 – 658. https://doi.org/10.1061/(ASCE)1090-0241(2004)130:6(656.2).

Randolph, M.F., Leong, E.C. and Houlsby, G.T. (1991) One-dimensional analysis of soil plugs in pipe piles, *Geotechnique*, 41 (4), pp. 587-598 https://doi.org/10.1680/geot.1991.41.4.587.

Tomlinson M. and Woodward J. (2008) *Pile design and Construction Practice*, Fifth edition, Taylor & Francis, N.Y.

White, D.J., Deeks, A.D. and Ishihara, Y. (2010) Novel piling: axial and rotary jacking, *Proc. of the 11th International Conference on Geotechnical Challenges in Urban Regeneration*, London, UK, CD, 24 p.

Gudavalli S.R., Safaqah O., Seo H. (2013) Effect of soil plugging on Axial Capacity of Open-Ended Pipe Piles in Sands. *Proceedings of the 18-th International Conference on Soil Mechanics and Geotechnical Engineering*, Paris, France, pp. 1487-1490.

Proceedings of the XVIII ECSMGE 2024
GEOTECHNICAL ENGINEERING CHALLENGES
TO MEET CURRENT AND EMERGING NEEDS OF SOCIETY
© 2024 the Authors
ISBN 978-1-032-54816-6
DOI 10.1201/9781003431749-64
Open Access: www.taylorfrancis.com, CC BY-NC-ND 4.0 license

ECSMGE 24
XVIII EUROPEAN CONFERENCE ON SOIL MECHANICS AND GEOTECHNICAL ENGINEERING

Mechanical characterization of a saturated marine clay for pavement design and performance

Caractérisation mécanique d'une argile marine saturée pour la conception et la performance des chaussées

J.H.C. Everton*
Royal Institute of Technology KTH, Stockholm, Sweden
The Swedish Road and Transport Research Institute VTI, Linköping, Sweden

S. Erlingsson
The Swedish Road and Transport Research Institute VTI, Linköping, Sweden
University of Iceland, Reykjavik, Iceland

**jose.everton@vti.se*

ABSTRACT: The study investigates the resilient behaviour of a fully saturated marine clay, crucial for pavement design amidst concerns of rising groundwater levels affecting pavement structures. Traditional testing standards do not address saturated conditions, prompting a new approach. Undisturbed marine clay samples were collected in the Onsøy area, Norway and underwent Repeated Load Triaxial (RLT) tests to determine their resilient modulus (M_R). The study outlines sample preparation, consolidation and finally RLT test procedures. Results revealed low M_R values, indicating the soft nature of the Onsøy clay. Two distinct test procedures yielded contrasting stress dependency patterns, raising concerns regarding the accurate representation of the material's mechanical behaviour. Factors such as overburden stress, load repetition, pore water pressure and sample quality were explored. Sustained overburden stresses led to a stiffer response and higher sensitivity to shearing. Increased load repetitions stiffened the material further. Finally, an analysis of samples' disturbance was used to differentiate the two test procedures, showing that conducting RLT tests in a fully saturated sample without overburden stress produced poor-quality samples. The study's significance lies in characterizing a saturated material using non-standardized testing methods, offering insights into pavement design considerations.

RÉSUMÉ: L'étude se concentre sur le comportement résilient d'une argile marine entièrement saturée, qui est essentiel pour la conception des chaussées afin de faire face à l'augmentation du niveau des eaux souterraines. Les essais traditionnels ne prennent pas en compte les conditions de saturation, d'où la nécessité d'une nouvelle approche. Des échantillons d'argile marine ont été prélevés en Norvège et soumis à des essais triaxiaux à charge répétée (RLT) pour déterminer leur module de résilience (M_R). Les résultats ont révélé une faible résilience, indiquant la nature molle de l'argile. Deux procédures d'essai différentes ont donné des modèles de comportement mécanique contrastés, ce qui soulève des inquiétudes quant à leur représentation exacte. Les facteurs tels que la surcharge, la répétition de la charge et la qualité de l'échantillon ont été étudiés, montrant que des contraintes soutenues et des répétitions de charge plus élevées renforcent la rigidité du matériau. Une analyse de la perturbation des échantillons a été utilisée pour différencier les procédures d'essai, indiquant que la réalisation d'essais RLT dans un échantillon entièrement saturé sans contrainte de surcharge produit un échantillon de mauvaise qualité. Cette étude est importante pour mieux comprendre les considérations relatives à la conception des chaussées en caractérisant les matériaux saturés à l'aide de méthodes d'essai non normalisées.

Keywords: Subgrades; soft clay; resilient modulus; permanent deformation; repeated load triaxial test.

1 BACKGROUND

The stiffness of fine-grained subgrades is highly sensitive to the moisture content (Blackmore et al. 2020), hence impervious surfacing combined with proper drainage systems are important for the overall performance of a pavement structure (Charlier et al. 2009). For the same reason, the pavement's unbounded layers are in an unsaturated condition most of the time (Salour and Erlingsson 2013). However, depending on the terrain topography, parts of the pavement structure could be periodically exposed to the groundwater table (GWT), especially its subgrade, also known as the formation level.

Seasonal GWT variation is a common phenomenon, and some studies predict that sea level rise associated with more precipitation can cause a permanent increase in GWT, thus affecting the

formation layer in low-lying terrains (Chen and Wang 2023). Therefore, characterizing the resilient modulus (M_R) of subgrade materials in saturated conditions is important for pavement design and performance.

Existing M_R testing standards are not designed to evaluate saturated subgrades, thus a new test procedure was trialled for characterizing the M_R of a material on such condition. Undisturbed block samples of marine clay were collected in Norway and transported to Sweden where Repeated Load Triaxial (RLT) tests were conducted to characterize their M_R.

2 METHODOLOGY

2.1 Sampling

The material was sampled in the Onsøy area, located in southeastern Norway bordering the Oslo fjord. Undisturbed block samples were retrieved from 3 to 5 meters below ground level (bgl) using a Sherbrooke block sampler. The samples were about 25 cm high by 18 cm diameter, and after retrieval, they were involved in plastic foil and protected inside a 20 cm diameter plastic tube to minimize travel disturbances.

2.2 Material characteristics

The Onsøy substrata consists of a deposition area originating from rapid marine clay deposition from the last deglaciation phase followed by a gradual sedimentation process after the uplift of the region above sea level (Gundersen et al. 2019). The GWT is located at 1 m bgl and a medium to high plasticity dark grey silty clay is found between the dry crust (≤ 1 m bgl) and the bedrock (at 8 to 40 m bgl). Therefore, the block samples collected for this study are all in a saturated condition. Table 1 summarises the index properties of the material and Equations 1-2 are the best estimate for the effective, σ'_{v0}, and apparent preconsolidation, σ'_p, stresses as reported in Gundersen et al. (2019):

$$\sigma'_{v0} = 5.01 \cdot (z - 1) + 17.5, \quad 1 \leq z \leq 9 \qquad (1)$$

$$\sigma'_p = 6.9 \cdot (z + 4.54), \quad 3 \leq z \leq 20 \qquad (2)$$

where z is the depth in meters.

Table 1. Material index properties.

γ_s (kN/m^3)	a (kPa)	ϕ'_{cv} (°)	s_{uC} (kPa)	I_p (%)	w_s (%)
27.1	5	30	15.8	44	70

In Table 1, γ_s is the unit weight of solids, a is attraction, ϕ'_{cv} is the friction angle, s_{uC} is the undrained shear strength in triaxial compression, I_p is the plasticity index and w_s is the gravimetric moisture content.

2.3 Specimen preparation

The undisturbed block samples were trimmed down to 10 cm diameter and sliced down to 20 cm high. Following the trimming process, the sample was placed on a pedestal, where a flushed porous stone and water-soaked filter paper were resting.

Thereafter, water-soaked filter paper strips were placed around the sample, in a bid to accelerate the consolidation of the specimen, as the water flow would be both axial and radial in the sample. Subsequentially, a second water-soaked filter paper, a flushed porous stone and a top cap connected to the backpressure were placed above the sample, and a latex membrane was fitted around it with the aid of a membrane stretcher. Finally, a set of 3 LVDTs spaced at 120° were installed in the third mid-height of the sample to measure deformation during the RLT test. Figure 1 shows the aforementioned steps.



Figure 1. Specimen preparation steps.

The coefficient of earth pressure at rest k_0 of the material is 0.6 (Gundersen et al. 2019) and thus the horizontal in-situ stress is given by $\sigma_{3\text{-ref}} = k_0$ x σ'_{v0}. Table 2 summarises the effective in-situ stress as well as the initial void ratio e_0 before the consolidation.

Table 2. Reference stresses at retrieved depth and OCR.

Sample ID	Depth (m)	σ'_{v0} (kPa)	σ_{3-ref} (kPa)	Void ratio e_0 (-)
S1	4.85	36.8	22.1	1.87
S2	4.33	34.2	20.5	1.87
S3	3.83	31.7	19.0	1.87

2.4 Consolidation

Samples were flushed via the top cap, keeping the drainage valve open throughout. The flushing consisted of a saturation ramp where both backpressure u_{bkp} and cell pressure σ_3 were increased at the same rate, keeping a net confining pressure σ_{3net} = σ_3 - u_{bkp} of 10 kPa, until u_{bkp} reached 190 kPa.

The consolidation phase was initiated after a Skempton B-value higher than 0.95 was obtained. Thereafter, an anisotropic consolidation phase was started by simultaneously increasing σ_{3net} at 1.5 kPa/min and the deviatoric stress σ_d at 0.5 kPa/min to reestablish field stress levels. The consolidation was complete when the backvolume change flattened out, which took over 16 hours. A complete description of the method can be found in NGTS (2016).

2.5 Repeated load triaxial test

The testing procedures described in AASHTO T:307 (AASHTO 2003) and NCHRP 1-28A (NCHRP 2003) for characterising the resilient properties of subgrades are not designed for testing fully saturated samples or soft materials. For the latter, it was verified that the shear stresses proposed in those procedures would be higher than the shear strength of the clay used in this study, which would lead to premature failure during cyclic loading. Whereas, for the former, changing confining stresses rapidly in between stress paths, as in the NCHRP 1-28A procedure, does not accord with the consolidation stresses in a fully saturated and quite impermeable material such as clay, where such changes demand a lengthy stress equalization period.

Hence, two sets of stress paths were trialled instead. The first followed the same principle as in AASHTO T:307 (Table 3), consisting of three loading sequences going from a higher to a lower σ_3, containing five stress paths (100 cycles each) at increasing stress ratios while keeping a small static stress. It should be noted that the loading sequences started with the confining stress according to the one applied in the consolidation phase ($\sigma_{3\text{-ref}} = k_0 \times \sigma'_{v0}$), and that the static stress was only a fraction of the deviatoric stress imposed during the consolidation phase, as indeed is adopted in AASHTO T:307.

Table 3. M_R for sat. samples – test procedure 1 (S1 and S2).

Load. Seq.	Confining pressure (kPa)	Static stress (kPa)	Stress ratio (σ_1/σ_3) per stress path				
			1	2	3	4	5
1	σ_{3-ref}	10% $\cdot \sigma_{d-max}$	1.3	1.4	1.5	1.6	1.7
2	$0.75 \cdot \sigma_{3-ref}$		1.4	1.5	1.6	1.7	1.8
3	$0.5 \cdot \sigma_{3-ref}$		1.6	1.8	2.1	2.3	2.6

As the RLT test in test procedure 1 was conducted under stress relaxation, i.e. lower effective stress than the yielded at the consolidation phase, another testing procedure was developed, consisting of a RLT test conducted with the same overburden stress imposed in the k_0-consolidation. It included three loading sequences with σ'_v targeting 0.7, 1 and 1.3 times σ'_{v0}. Those figures would reflect the effect of constructing in cut, on-grade or in fill section. Each load sequence was divided into three stress paths (100 cycles each) whose vertical stresses reflect the typical stresses induced by traffic load on the top of the subgrade. Table 4 summarises the procedure and Figure 2 illustrates it.

Table 4. M_R for sat. samples – test procedure 2 (S3).

L. Seq	Confining pressure (kPa)	Static stress (kPa)	Stress ratio (σ_1/σ_3)		
			1	2	3
1	$0.7 \cdot \sigma_{3-ref}$	$0.7 \cdot (\sigma'_{v0} - \sigma_{3-ref})$	2.1	2.2	2.3
2	σ_{3-ref}	$\sigma'_{v0} - \sigma_{3-ref}$			
3	$1.3 \cdot \sigma_{3-ref}$	$1.3 \cdot (\sigma'_{v0} - \sigma_{3-ref})$			

2.6 Response modelling

The test results were modelled using the Universal Model for M_R (Equation 3) (AASHTO 2008) to obtain material parameters that can be used to calculate the subgrade's M_R at different sets of stresses from the combination of overburden and traffic-induced stresses:

$$M_R = k_1 \cdot \left(\frac{\theta}{p_a}\right)^{k_2} \cdot \left(\frac{\tau_{oct}}{p_a} + 1\right)^{k_3} \quad (3)$$

where k_1, k_2 and k_3 are material parameters, θ is the bulk stress (kPa), τ_{oct} is the octahedral stress (kPa) and p_a is a reference pressure considered 100 kPa.

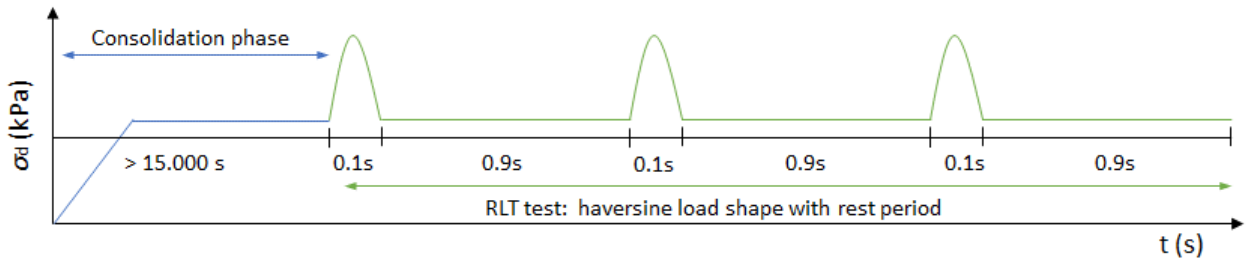

Figure 2. Schematic of RLT test on saturated S3.

3 RESULTS AND DISCUSSION

The best fit M_R prediction model was calculated and is presented in Table 5 along with the predicted M_R for stresses likely to be experienced on the top of the subgrade. Such stresses were calculated based on a typical road structure in Norway (Statens vegvesen 2013) of 1.5 m in thickness, given the adoption of a frost protection layer. Therefore, it resulted in θ = 44 kPa and τ_{oct} = 6.5 kPa, for a σ_3 = 10 kPa.

The $M_{R\text{-predicted}}$ for the Onsøy clay turned out to be in the low range, varying from 8 to 17 MPa, according to the different procedures employed for conducting the RLT test. These figures are in line with expected results for soft clays (Simonsen et al. 2002), however, the procedures yield quite different stress dependency patterns, which raises questions about which best represents the material's behaviour.

Table 5. Universal model best-fit parameters and stiffness.

Sample	k_1 (-)	k_2 (-)	k_3 (-)	R^2 (-)	$M_{R\text{-predicted}}$ (MPa)
S1	494	0.753	-13.532	.963	11.5
S2	232	0.442	-12.017	.930	7.7
S3	23 046	3.362	-34.316	.996	16.6

3.1 Effect of overburden stress

Samples 2 and 3 were subjected to a k_0-consolidation, but the cyclic loading phase differed as seen in Table 3 and Table 4, especially regarding the static stress or overburden. When the static stresses were sustained throughout the RLT test (S3), the material showed a stiffer response and a higher sensitivity to shearing, as can be seen in Figure 3.

3.2 Effect of load repetition

S3 was also subjected to a second RLT test where the same stress paths as in Table 4 were employed, however, 10 000 cyclic loads (N) per stress path were applied, instead of one hundred. Such test is usually performed to obtain the permanent deformation (PD) properties of the material; however, the focus was assessing the impact of load repetition on the M_R.

The average resilient strain from the last five cycles of each stress path was used for calculating the M_R in both tests whether N was 100 or 10 000. Figure 4 demonstrates the stiffening process that occurred when the sample was subjected to a higher number of load repetitions.

3.3 Effect of pore water pressure

The stress applied during consolidation targeted effective stresses by maintaining a constant backpressure, thus already subtracting pore water pressure (PwP). However, under cyclic loading, an excess PwP is generated. For the condition where the overburden was maintained throughout the cyclic phase, as in S3, the excess PwP was only about 2 kPa, in contrast to the condition where the overburden was removed, as in S1 and S2, where the excess PwP was about 4 kPa (Figure 5).

This is explained by the fact that in S1 and S2 a higher dynamic stress was imposed for a lower static stress, as can be inferred from Table 3, whereas in S3 a higher static and lower cyclic stress was imposed (Table 4), which is consistent with the estimates for the subgrade level.

Although the difference in excess PwP is minimal, the combination of higher excess PwP and higher cyclic stress results in more axial strain (Zhang et al. 2020), which may explain the lower stiffness observed for S1 and S2 compared to S3.

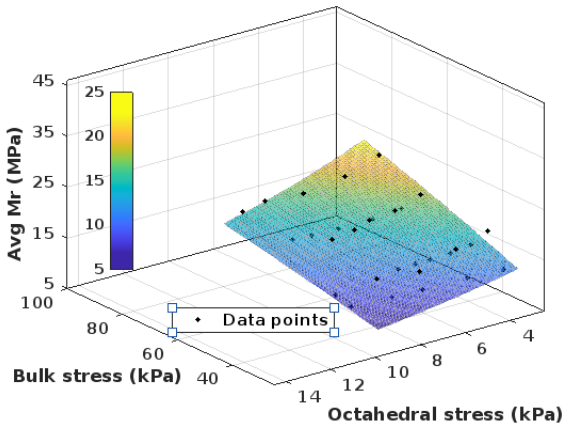

a)

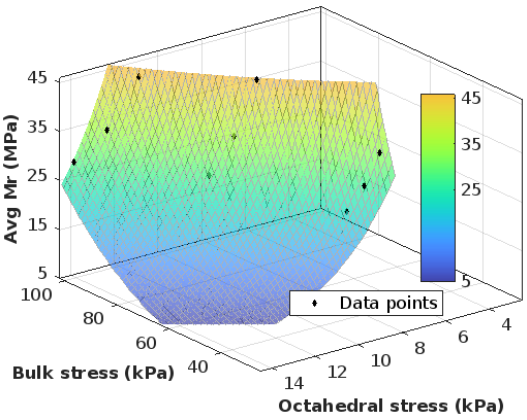

b)

Figure 3. Predicted M_R a) S1 and S2 b) S3.

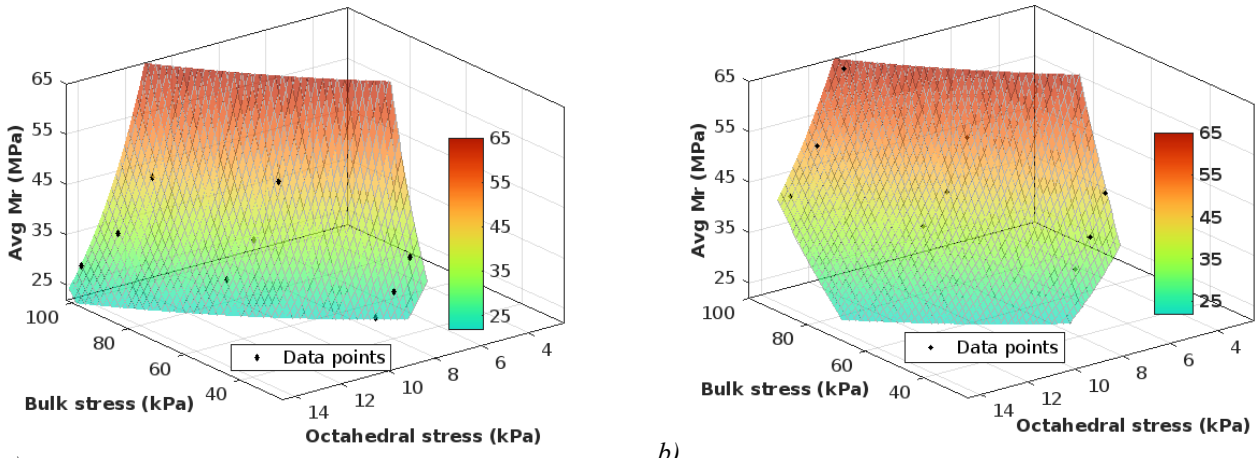

Figure 4. Predicted M_R a) S3 | N:100 b) S2 | N: 10 000.

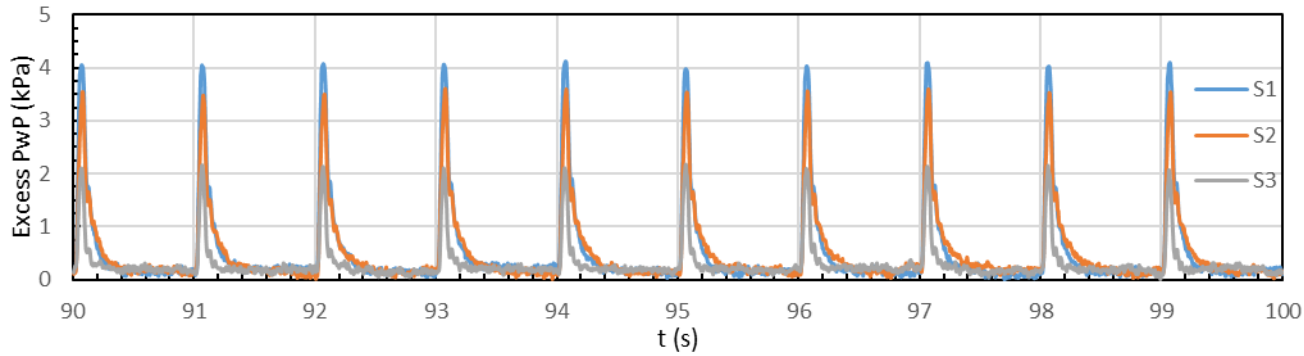

Figure 5. Excess PwP measured in the last stress path of the M_R test.

3.4 Effect of sample disturbance

The samples quality was assessed in terms of their normalized change in void ratio $\Delta e/e_i$ using the criteria for sample disturbance proposed by Lunne et al. (2006), where changes above 0.07 indicated poor to very poor sample quality. The $\Delta e/e_i$ for S1 and S2 was 0.117 and 0.137, respectively, whereas for S3 was 0.063. The hypothesis is that the stress relaxation observed in the test procedure 1 promoted such disturbance.

One of the effects of sample disturbance is the break of cementation bonds between particles that results in lower shear strength at small strains (<3-4%) (Lunne et al. 2006). As the traffic-induced stesses are rather low at the subrade depth (> 1.5m), they generate small strains and thus, the lower strenght caused by the sample disturance might explain the lower stiffness measured for S1 and S2 in comparison with S3.

4 CONCLUSIONS

Undisturbed samples of a marine clay were collected in the surrounding area of the Oslo fjord in Norway and had their resilient behaviour characterized in the laboratory via RLT tests, conducted on fully saturated samples. As this condition deviates from standard practice for characterizing the M_R, two procedures were trialled and evaluated in this study. Their differences concern the overburden stress and the confining stress path at subsequent load sequences.

Both procedures yielded low M_R values, confirming the soft behaviour of the Onsøy clay. Nevertheless, the test procedure 2 (with overburden) produced a stiffer response. The results were further discussed in terms of sample disturbance and the procedure 1 (without overburden) resulted in a poor-quality sample, which might explain the lower stiffness obtained when using such procedure. Furthermore, the material showed a stiffening behaviour as an effect of load repetition. The results are limited to one material in fully saturated conditions, but it can offer a better understanding of its behaviour for pavement design purposes. Future studies will concentrate on testing other soils as well as testing in unsaturated conditions.

ACKNOWLEDGEMENTS

This research is funded by the Swedish Transport Agency. The authors are grateful to the Norwegian

Public Roads Administration for providing the samples and discussing the testing method.

REFERENCES

AASHTO. 2003. Standard Method of Test for Determining the Resilient Modulus of Soils and Aggregate Materials: AASHTO Designation T 307-99 (2003). AASHTO, Washington, DC.

AASHTO. 2008. Mechanistic-Empirical Pavement Design Guide - A Manual of Practice (Interim Edition). American Association of State Highway and Transportation Officials (AASHTO), Washington, DC.

Blackmore, L., Clayton, C.R.I., Powrie, W., Priest, J.A., and Otter, L. 2020. Saturation and its effect on the resilient modulus of a pavement formation material. Géotechnique, **70**(4): 292–302. doi:10.1680/jgeot.18.P.053.

Charlier, R., Hornych, P., Sršen, M., Hermansson, Å., Bjarnason, G., Erlingsson, S., and Pavšič, P. 2009. Water Influence on Bearing Capacity and Pavement Performance: Field Observations. *In* Water in Road Structures. *Edited by* A. Dawson. Springer Netherlands, Dordrecht. pp. 175–192.

Chen, X., and Wang, H. 2023. Impact of sea level rise on asphalt pavement responses considering seasonal groundwater and moisture gradient in subgrade. Transportation Geotechnics, **40**: 100992. doi:10.1016/j.trgeo.2023.100992.

Gundersen, A.S., Hansen, R.C., Lunne, T., L'Heureux, J.-S., and O. Strandvik, S. 2019. Characterization and engineering properties of the NGTS Onsøy soft clay site. AIMS Geosciences, **5**(3): 665–703. doi:10.3934/geosci.2019.3.665.

Lunne, T., Berre, T., Andersen, K.H., Strandvik, S., and Sjursen, M. 2006. Effects of sample disturbance and consolidation procedures on measured shear strength of soft marine Norwegian clays. Canadian Geotechnical Journal, **43**(7): 726–750. doi:10.1139/t06-040.

NCHRP. 2003. Harmonized test methods for laboratory determination of resilient modulus for flexible pavement design. Washington, DC.

NGTS. 2016. Laboratory procedures and standards for the NGTS project. Report No. 20160154-02-R.

Salour, F., and Erlingsson, S. 2013. Moisture-Sensitive and Stress-Dependent Behavior of Unbound Pavement Materials from in Situ Falling Weight Deflectometer Tests. Transportation Research Record: Journal of the Transportation Research Board, **2335**(1): 121–129. doi:10.3141/2335-13.

Simonsen, E., Janoo, V.C., and Isacsson, U. 2002. Resilient Properties of Unbound Road Materials during Seasonal Frost Conditions. Journal of Cold Regions Engineering, **16**(1): 28–50. doi:10.1061/(ASCE)0887-381X(2002)16:1(28).

Statens vegvesen. 2013. Vegbygging: høringsutgave, Håndbok 018 (In Norwegian). Statens vegvesen.

Zhang, Z., Chen, Y., Ye, G., Xiang, P., Xiao, Y., and Wang, Q. 2020. Empirical Method for Evaluating Resilient Modulus of Saturated Silty Clay under Cyclic Loading. Advances in Civil Engineering, **2020**: 1–12. doi:10.1155/2020/8846895.

Proceedings of the XVIII ECSMGE 2024
GEOTECHNICAL ENGINEERING CHALLENGES
TO MEET CURRENT AND EMERGING NEEDS OF SOCIETY
© 2024 the Authors
ISBN 978-1-032-54816-6
DOI 10.1201/9781003431749-65
Open Access: www.taylorfrancis.com, CC BY-NC-ND 4.0 license

ECSMGE 24
XVIII EUROPEAN CONFERENCE ON SOIL MECHANICS AND GEOTECHNICAL ENGINEERING

Integrating local data into geotechnical design through a predictive probabilistic approach

Comment une approche probabiliste permet d'intégrer les données locales dans la conception géotechnique

A. Finiasz*, J. Hassaoui, C. Jacquard
Fondasol, Avignon, France

E. de Rocquigny
Operation Data, Paris, France

**arnaud.finiasz@groupefondasol.com*

ABSTRACT: Site investigation and assessment of the soil and rock characteristics are essential parts of the geotechnical design process. These characteristics can be assessed from a variety of in situ tests. In France, the Ménard pressuremeter test is widely used. This in-situ testing method is used to determine the stress-strain relationship of the tested soil and to evaluate, among others, the Ménard limit pressure (p_{lM}) which is used to calculate the bearing capacity of a foundation. In this paper, we show how different predictive models can be used to infer a distribution, with depth, of the p_{lM} parameter for a new construction project, based on the historical data available in the vicinity. We then demonstrate how this information is used throughout the process of site investigations and geotechnical design. Before the site investigations, this approach allows for a preliminary overview of the mechanical characteristics of the soils, and for better targeted field investigations. This method is then used in the interpretative report, to ensure better reliability of the geotechnical design and construction recommendations.

RÉSUMÉ: Les reconnaissances géotechniques et les essais visant à caractériser les sols et les roches sont le fondement de toute conception géotechnique. Si cette caractérisation peut s'obtenir par une variété d'essais in situ, en France, on a largement recours au pressiomètre Ménard. Cette méthode d'essai permet de tracer une courbe contrainte-déformation du sol testé et d'en déduire, entre autres, la pression limite (p_{lM}) qui est utilisée pour la justification en portance des fondations. Dans cet article, nous montrons comment différents modèles prédictifs peuvent être utilisés pour établir la distribution, en fonction de la profondeur, de la pression limite p_{lM} au droit d'un projet de construction, à partir des données historiques disponibles à proximité. On montre ensuite comment cette information peut être exploitée dans la définition d'une campagne de reconnaissance et dans les études géotechniques. Avant toute reconnaissance, cette information donne une première image des caractéristiques mécaniques des sols, et permet d'établir un programme optimisé. Cette approche est ensuite exploitée lors de l'établissement du rapport d'étude et permet de fiabiliser la conception géotechnique et les préconisations relatives aux travaux.

Keywords: Probabilistic modelling; pressuremeter test; foundation design; indicator kriging.

1 INTRODUCTION

Building a ground model for geotechnical design starts by assessing available knowledge for the project site and its surroundings. Through site visit and desk study, a preliminary ground model can be established which forms the basis for planning field and laboratory tests.

Among the abundant data that is available to the geotechnical engineer, results from previous site investigation at the studied site or in the vicinity constitute a prime source of information. However, parsing through numerous site investigation reports is time consuming and building an unbiased and comprehensive synthesis is difficult. No one can check dozens of borehole logs and remember every bit of information.

We believed that a comprehensive synthesis of previous site investigations, in the form of a preliminary ground model, would help our engineers build optimised site investigation programs, targeted at verifying and updating the anticipated model.

It is with that goal in mind that Fondasol started a few years ago to work on two distinct projects: the first consisted in structuring the factual data from past site investigations, and second consisted in testing with our data scientists the various geostatistical algorithms available in the literature to build a predictive ground model from the structured data.

2 BUILDING A PRELIMINARY GROUND MODEL FROM HISTORICAL DATA

In France, the most common in-situ test is the Menard pressuremeter, which provides a stiffness modulus E_M used in settlements calculations and a measure of ground resistance through the limit pressure P_{IM} which can be used to estimate the bearing capacity of a foundation. As a prebored in-situ test, the geological nature of the soil is also provided on the borehole logs.

Being the most abundant test in our database, and the one that our engineers are the most familiar with, it is the one we decided to use to build the preliminary ground model. However, the methods exposed here could easily be applied to other in-situ tests where ground strength is measured at regular intervals with depth, such as SPT tests.

2.1 The first attempts

The first algorithms that we experimented with were aimed at predicting the most likely soil conditions at a given point in space. We naturally looked at kriging and its variants, but we faced multiple challenges mostly due to the nature of the data. We tried 2D kriging by layers of different thicknesses, 2D kriging of derived values (such as foundation depth for a given structure), 3D kriging, but results were not easy to read and the level of uncertainty of the results was even harder to display.

A deeper shortcoming of those classical geostatistical approaches stems for the fact that predicting the most likely outcome is of lesser importance than the distribution of likely values, much like when presenting the range of values obtained by in-situ tests in a given soil layer. A naïve way to do so is by representing a distribution of values equated to the mere histogram of empirical data in a given soil layer (example in Figure 1).

One limitation of such a simple sample by soil layer, is that the distribution will not display the natural tendency of soil characteristics improving with depth (at least for sedimentary soils), which will also tend to widen the distribution in case of thick layers.

Estimating the increment of soil characteristics with depth can easily be achieved with a simple linear regression and can then be supplemented by calculating a lower bound (or upper bound) line for a given risk, as suggested by Baguelin et al., 2000. Such representation is oriented towards determining characteristic values with depth but requires a strict classification of test results by homogenous layers beforehand, as well as assuming a linearly increasing characteristic, both of which can stand short of the empirical evidence.

To give a global overview of soil conditions on a site, in the form of a preliminary ground model eschewing the limitations of the aforementioned methods of kriging, sampling or linear regression, we have experimented more elaborate distributional models. They involve a mixture of non-parametric and parametric statistical models inferring how the distribution of the limit pressure evolves with depth.

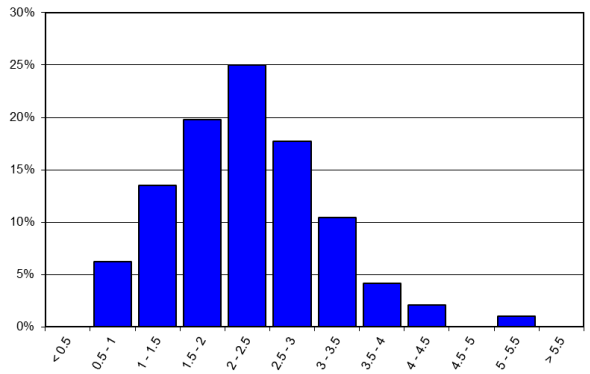

Figure 1. Histogram of the limit pressure (in MPa) in the Cretaceous White Chalk for a site west of Paris (Limay).

2.2 The current iteration

The models we are currently using infer 4 curves with depth corresponding to the following empirical quantiles: Q10, Q25, Q75 and Q90. These curves then determine 3 surfaces (as can be seen in figure 2):

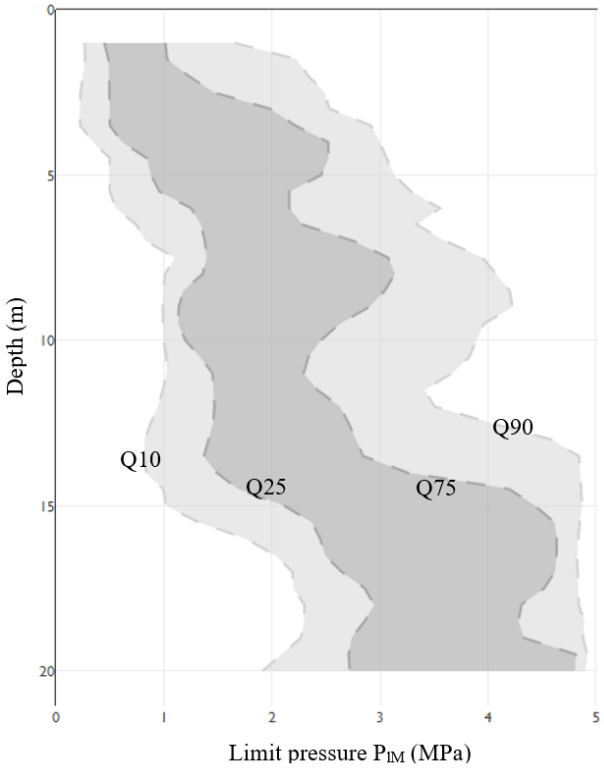

Figure 2. Example of the distributional model of the limit pressure with depth for a site north of Paris (Aubervilliers).

- A central zone corresponding to the two middle quartiles, where most likely values can be found (used for example when calculating the sleeve friction contribution to a pile's bearing capacity).
- A lower bound zone, between Q10 and Q25 where characteristic values are likely to be selected, say for shallow foundation design.
- An upper bound zone, between Q75 and Q90, for situations where higher values need to be considered, for example when assessing the drivability of a pile through a compact layer.

2.3 Constructing the distributional model

To help building the distributional model, the geotechnical engineer is presented with all the available boreholes from the database within a selected search radius. He must then exclude inappropriate boreholes based on geological and topographical criteria. As exposed in 2.4, this is very important to ensure a reliable distribution.

Typically, when studying a site in an alluvial plain, boreholes on the slopes rising towards the surrounding plateau have to be retreated even if they are fairly close to the site. This is, for example, shown in figure 3 where boreholes too close to the river or too high in altitude (to the north) are excluded.

Different distributions are then modelled at regular depth intervals from the selected boreholes including smoothing with depth as necessary and a weighing of distance.

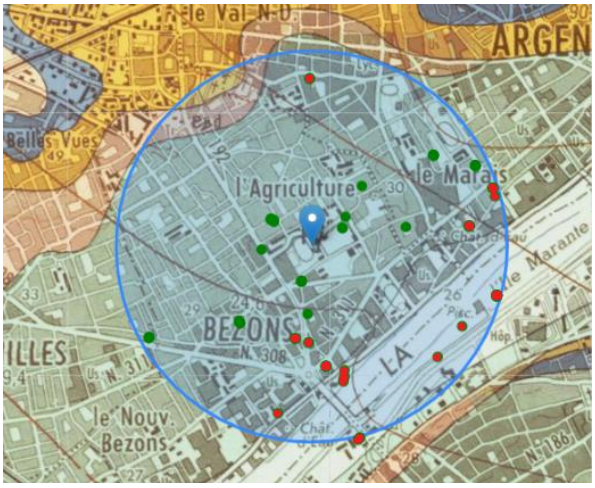

Figure 3. Example of borehole selection based on the geological and topographical context.

2.4 Adjusting the parameters

In order to measure the influence of the different parameters on the quality of the model, benchmarking was carried out through a leave one out process. The test samples consisted of groups of boreholes (corresponding typically to 1 or 2 site investigation reports) and the learning sample included all other boreholes in the vicinity.

Figure 4 shows an example of the fitting that was obtained for one of the test samples. This helped us adjust the model, with an essential part depending on a meaningful selection of the boreholes.

This is why we have kept the geotechnical engineer at the centre of the selection process, providing him with different visualisations of the geological data from boreholes to facilitate the selection and help identify outliers (for example due to improper positioning in the database). In the process of moderating boreholes, the engineer's judgement is very important to avoid excluding boreholes that could dutifully point out a geological anomaly.

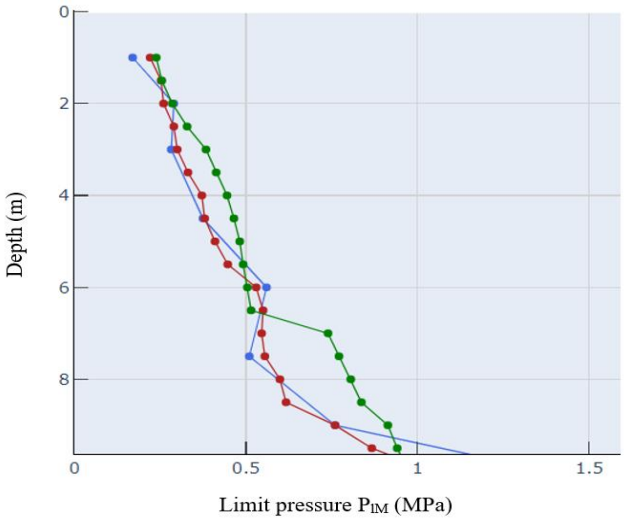

Figure 4. Test sample Q25 (blue) compared to the predicted Q25 based on surrounding boreholes (red = current algorithm, green = indicator kriging).

3 USING THE PREDICTED GROUND MODEL IN GEOTECHNICAL DESIGN

3.1 Preparing site investigations

The level of information provided by the preliminary ground model can be used by the geotechnical engineer to tailor an adapted site investigation program. We believe that the seasoned incorporation of surrounding data, instead of building a ground model exclusively from the ad hoc boreholes, is a crucial improvement in the realm of building risk mitigation.

This should also allow for more targetted investigations, and, depending on the uncertainties that need to be adressed, possibly modulating boreholes according to where it is most valuable to secure a reliable inital ground model.

3.2 Preliminary design

Our first example is a preliminary report for the reconstruction of a hotel in Nantes. Drilling even one borehole was extremely difficult due to the existing building occupying the whole lot and the density of underground pipes and cables in the adjacent streets.

It was decided to base the preliminary report solely on the predicted ground model and to postpone the site investigations to after the existing building was taken down. Figure 5 shows the predicted ground model constructed using the data from 11 boreholes and more than 200 pressuremeter tests.

Based on the predictive ground model, it was estimated that the new building would be supported by piled foundations, of approximately 13 to 15m in length and a preliminary estimate of their bearing capacity was provided. When the site investigations were carried out for the detailed design, this preliminary design proved to be conservative, with the bedrock encountered around a depth of 9.5m, allowing for slightly shorter piles.

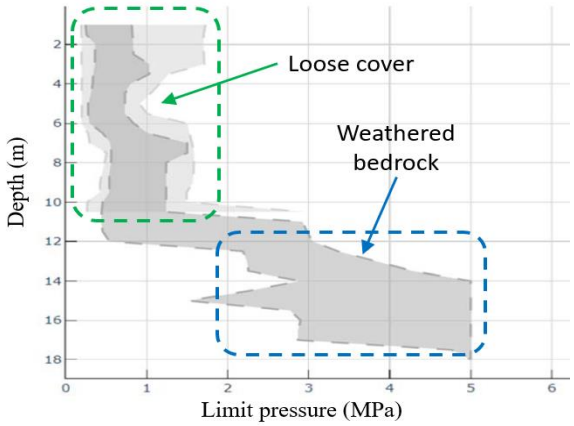

Figure 5. Distribution of P_{IM} with depth and its interpretation for the Nantes project.

3.3 Interpretative report

When comes the time to establish the final ground model for the geotechnical design, care should be taken to not give too much importance to the investigations carried out on the site and balance it with the data provided by the predictive model. With a limited number of boreholes, it is difficult to capture the variability of the soil conditions in full.

When the predictive model is based on abundant and reliable data, the point of the site investigation is to confirm or adjust the model. In this regard, the probable credibility of the site investigation results should be examined in reference to the predictive model.

Figure 6 shows the results of a single borehole conducted at a construction site in a sugar refinery north-east of Reims compared to the probabilistic P_{IM} distribution which was constructed using data from 35 boreholes in the immediate vicinity. We can see that the test results are totaly within the range of what was expected, and the design values have therefore been selected by the engineer based on the predictive model, roughly following the Q25 curve which seemed appropriate for piled foundations, and more reliable than using the test results of a single borehole.

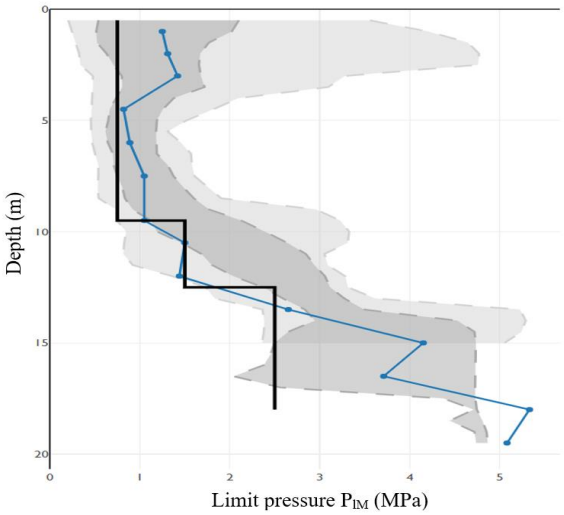

Figure 6. Predictive model from an interpretative report with field tests results in blue and design values in black.

4 FINAL WORDS

We believe that the use of historical data in geotechnical engineering supported by geostatistical algorithms will rapidly become the norm. It should, at first, allow for optimised site investigations with a reduced environmental footprint. But the final goal should be to optimise the construction itself, with a better estimate of the design's level of safety.

REFERENCES

Baguelin, F. and Kovarik, J.B. (2000). Une méthode de détermination des valeurs caractéristiques des paramètres géotechniques. *Revue Française de Géotechnique*, 93, 35-41. https://doi.org/10.1051/geotech/2000093035.

Marache, A., Breysse, D., Piette, C. and Thierry, P. (2009). Geotechnical modeling at the city scale using statistical and geostatistical tools: The Pessac case (France). *Engineering Geology*, 107 (3-4), 67-76. https://doi.org/10.1016/j.enggeo.2009.04.003.

Wang, Y., Huang, K. and Cao, Z. (2013). Probabilistic identification of underground soil stratification using cone penetration tests. *Canadian Geotechnical Journal*, 50 (7), 766-776. https://doi.org/10.1139/cgj-2013-0004.

Proceedings of the XVIII ECSMGE 2024
GEOTECHNICAL ENGINEERING CHALLENGES
TO MEET CURRENT AND EMERGING NEEDS OF SOCIETY
© 2024 the Authors
ISBN 978-1-032-54816-6
DOI 10.1201/9781003431749-66
Open Access: www.taylorfrancis.com, CC BY-NC-ND 4.0 license

ECSMGE 24
XVIII EUROPEAN CONFERENCE ON SOIL MECHANICS AND GEOTECHNICAL ENGINEERING

Impact of the testing methods on physical properties of high plastic clay

Impact des méthodes d'essai sur les propriétés physiques de l'argile à haute plasticité

J. Frankovská*, M. Brček
Department of Geotechnics, Faculty of Civil Engineering, Slovak University of Technology in Bratislava, Slovakia

J. Brčeková
Department of Geology of Mineral Deposits, Faculty of Natural Sciences, Comenius University, Slovakia

jana.frankovska@stuba.sk

ABSTRACT: Geotechnical properties vary locally, and there are uncertainties in the parameter interpretation and in determining characteristic and representative values for geotechnical design. The impact of the testing methods on the intrinsic properties of high plastic clays is analysed in the paper. The laboratory tests for determining the liquid and plastic limits are by far the most widely used index tests and are often adopted to assess the mechanical behaviour of clay. The laboratory investigation results for determining liquid limits using the fall-cone method and method based on Casagrande-type devices were analysed. The density of the soil particles was determined by the pycnometer method by fluid displacement and the pycnometer method by gas displacement. Helium was used as the measurement gas. Test samples of fine-grained soils were taken on five bentonite deposits in the Western Carpathians, Slovakia. Chemical analyses confirmed geotechnical evaluations of fine-grained soil properties. Tests were performed on 15 samples of very high plastic and extremely high plastic clays. Significant differences were observed based on the laboratory method used.

RÉSUMÉ: Les propriétés géotechniques d'une formation varient localement et il existe des incertitudes dans l'interprétation des différents paramètres et dans la détermination des valeurs caractéristiques et représentatives nécessaires pour le dimensionnement géotechnique. L'impact des méthodes d'essai sur les propriétés intrinsèques des argiles à haute plasticité est analysé dans cet article. Les essais de laboratoire pour déterminer les limites de liquidité et de plasticité sont de loin les essais indicateurs les plus utilisés et sont souvent adoptés pour évaluer le comportement mécanique de l'argile. Les résultats des recherches en laboratoire pour déterminer les limites de liquidité en utilisant la méthode du pénétromètre a cône et la méthode basée sur les dispositifs de type Casagrande ont été analysés. La masse des grains a été déterminée par la méthode du pycnomètre par déplacement de fluide et la méthode du pycnomètre par déplacement de gaz. L'hélium a été utilisé comme gaz de mesure. En outre, des échantillons de sols fins ont été prélevés sur six gisements de bentonite dans les Carpates occidentales, en Slovaquie. Des tests ont été effectués sur 15 échantillons d'argile à plasticité très élevée et extrêmement élevée. Les évaluations des propriétés géotechniques des sols fins ont été confirmées par des analyses chimiques. Des différences significatives ont été observées en fonction de la méthode de laboratoire utilisée.

Keywords: Bentonite; particle density; gas pycnometer; fluid pycnometer; fall-cone method.

1 INTRODUCTION

Bentonite is a rock formed by the intense alteration of volcanic material. It consists mainly of clay minerals belonging to the smectite group, which are hydrated aluminium silicates containing Fe and Mg and Na or Ca. Bentonite has strong colloidal properties, and its volume increases severalfold in contact with water. The special properties of bentonite, such as high plasticity, swelling, water adsorption, viscosity and thixotropy, make it a valuable material for various uses and applications. Due to its viscosity and plasticity, bentonite is used in geotechnical engineering (e.g. diaphragm walls, grouting admixtures) and other areas of civil engineering, e.g. in Portland cement and mortars.

Bentonite is an important mineral raw material whose worldwide production is steadily increasing. The Slovak Republic is one of the major producers of bentonite in the world. Over the last 10-15 years, several bentonite deposits have been opened in Slovakia, most of which have yet to be explored and documented in detail. To better exploit bentonite from individual deposits in Slovakia, it is necessary to

determine the fundamental physical properties of bentonite and other material characteristics that predetermine its use in various sectors of the economy. In this study, we focused on testing the density of bentonite solid particles and plasticity by two different methods to determine an efficient method for its laboratory determination.

All tested samples were obtained from five significant deposits on the SW edge of the Kremnické vrchy Mts., Western Carpathians (Figure 1). The bentonite deposits are described by Gorniak et al., 2017; Baláž and Kúšik 2015, and the mineralogical and chemical characteristics of bentonites are discussed by Osacký et al. (2019).

2 METHODOLOGY

Two different methods were used to determine density (bulk density). Gay-Lussac pycnometer with water and a gas (helium) pycnometer (type ULTRAPYC 1200e, Quan-tachrome Instrument, method according to ASTM D6093-97:2011 and EN ISO 17892-3 were compared.

2.1 Material

For testing, bentonite samples (Table 1) were collected, and all were classified as clays with extremely high plasticity.

Table 1. Identification of bentonite samples for testing.

Locality (number of samples)	Specimen labelling
Lutila (4)	LUI-1, LUI-2, LUI-3, LUI-4
Kopernica (2)	KOP-2, KOP-3
Stará Kremnička (4)	STK-1, STK III-1, STK III-2, STK III-3
Jelšový Potok (3)	JP-1, JP-2, JP-3
Bartošova Lehôtka (2)	BL II-1, BL II-2

2.2 Testing methods for density determination

Laboratory testing of solids density was performed using the pycnometric liquid injection method and the gas injection method. All 50 ml liquid pycnometers (Gay Lussac shape) with a ground neck and a ground stopper with a longitudinal capillary orifice (m1) were calibrated at least three times prior to testing to ensure that the measured values of the pycnometer volume (V) did not differ by more than 0.010 cm^3.

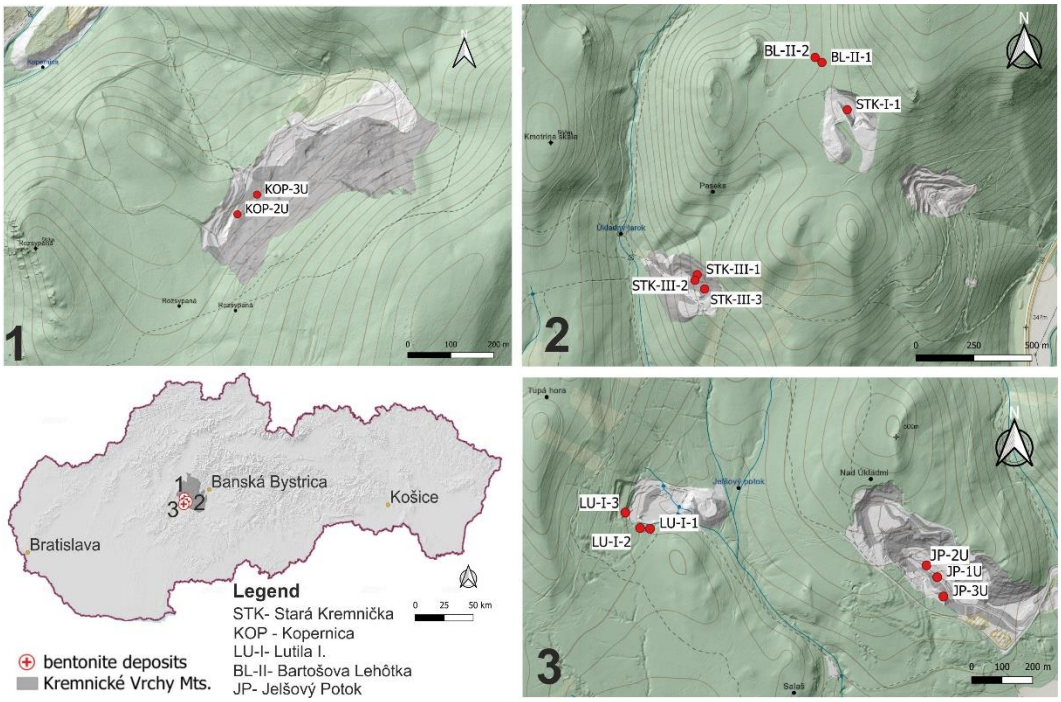

Figure 1. Deposits of bentonites in Kremnické vrchy Mts., Western Carpathians.

The test procedure consisted of several successive steps. The specific gravity (ρ_s) of the bentonite sample tested was calculated from the data obtained. Two identical samples were always tested in parallel.

The second method used (the gas injection method) is based on Archimedes' principle of fluid (gas) motion and the technique of gas expansion (Boyle's law). Gas can be considered an ideal displacement agent because it penetrates the smallest pores, thus ensuring maximum accuracy. For this study, helium was used.

A fully automatic Quantachrome Ultrapyc 1200e (accuracy < ±0.03%, measurement repeatability < ±0.015% was used as the measuring instrument.

2.3 Testing methods for plasticity determination

The basic test for the plasticity of clay characterisation is the liquid limit determination. Two laboratory methods for determining liquid limits were used: the fall-cone method and the method based on Casagrande-type devices according to EN ISO 17892-12.

3 RESULTS

Density values (ρ_s) of bentonite in the 2.46-2.73 g/cm^3 range were measured by the liquid injection method. From the graphical representation of the measured data (Figure 2), two groups with different densities can be distinguished. The more abundant cluster (about 75%) of the samples takes values in the range 2.61-2.73 g/cm^3. The second part of the samples (STK-1, STKIII-3, BLII-1, BLII-2) concentrates in the density range from 2.46 to 2.49 g/cm^3. Although not as pronounced, a similar pattern is evident in the data determined by the gas pycnometer method (Figure 3). Density values (ρ_t) were measured in the 2.36-2.53 g/cm^3 range. This is consistent with the montmorillonite content (Table 2). It ranges from 18.7% to 31% in the lower density samples. The montmorillonite content ranges from 64.5 to 76.6% in the higher density samples. For individual bentonite samples, the coefficient of variation ranged from 0.0037 to 0.0269%, and the standard deviation of volume ranged from 0.0027 to 0.02%. The determined volumes were in the range of values 2.1007 - 3.6997 cm^3. The weights of the specimens ranged from 5.0857 to 9.0561 g, corresponding to an optimally filled cuvette, i.e. 75% of its volume. The results from the measurements in the gas pycnometer show that the measured density values are consistently lower than those from the measurements in the liquid pycnometer. A statistical method comparison shows that they differ by 5-7% (Figure 2 and Figure 3).

Chemical analyses confirmed geotechnical evaluations of fine-grained soils properties. The montmorillonite content of the tested samples is presented in table 2. Bentonites could be divided into two groups: a small amount of montmorillonite (BL II 1, BL II 2, STK 1, STK III-3) and a high amount of montmorillonite (JP-1, JP-2, JP-3, KOP-2, KOP-3, LUI-1, LUI-4, LUI-3 KOP-3, LUI-1, LUI-4, LUI-3, LUI-2, STK III-1, STK III-2).

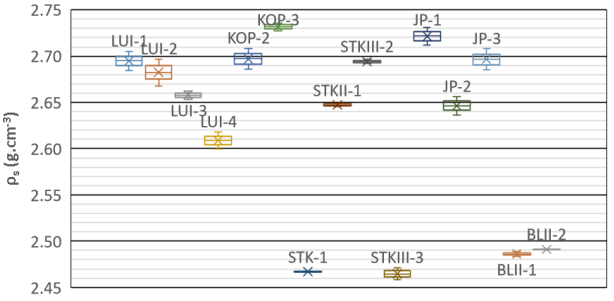

Figure 2. Density of solid particles by the liquid pycnometer method.

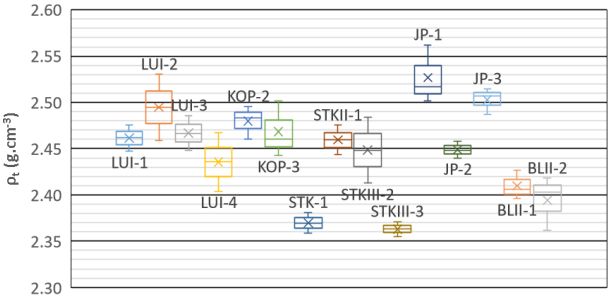

Figure 3. Density of solid particles by the gas pycnometer method.

Table 2. Montmorillonite content of the tested samples.

Sample	Montmorillonite (%)
STK 1, STK III-3	27,4 – 31,1
BL II 1, BL II 2	18,7 – 27,7
JP-1, JP-2, JP-3, KOP-2,	71,6 – 75,6
KOP-3, LUI-1, LUI-4, LUI-3,	74,0 – 76,6
LUI-2, STK III-1, STK III-2	64,5 – 68,4

The reliability or accuracy of density measurements using a pycnometer with a control fluid may be limited due to random or systematic errors. In particular, errors occurring during heating (boiling) of the pycnometer, when escaping air bubbles, may entrain soil particles, or in extreme cases, cause the soil to splash (overflow) through the neck of the pycnometer. Another possible error occurs when refilling the pycnometer with control fluid when the excess fluid should flow out through the capillary after the plug is inserted. A small air bubble may remain under the stopper or in the capillary, causing an underestimation of the measured density. Conversely, insufficient moisture removal from the pycnometer's surface will lead to an overestimation of the true density.

Density determination with a gas pycnometer allows high accuracy to be achieved because the measurement is fast and automatic. However, even with this method, some factors can negatively affect the test result. These include, in particular, uncontrolled variations in the temperature of the instrument during the measurement process,

contamination of the sample (e.g. by moisture), contamination of the cuvette or other parts of the pycnometer, and heating of the cuvette caused by prolonged use. Also, the petrophysical characteristics of the rock, in particular the structure of the rock pores (blind pores), may prevent the process of replacing the air with the gas (helium) used and thus overestimation of the sample volume and determination of a lower density (Viana et al., 2002). Considering the latter, the slight decrease in the measured density may be mainly due to the presence of air and moisture trapped in fine bentonite pores smaller than 100 ηm (Ondrášik & Kopecký, 2014).

The liquid limits of tested samples determined by the Casagrande method were 100% to 124%. The values of liquid limits determined by 80g/30° cone ranged from 90% to 114% (Figure 4).

These values confirmed the hypothesis that significant differences in the liquid limit values determined by the Casagrande apparatus and the fall cone for high plastic clays exist.

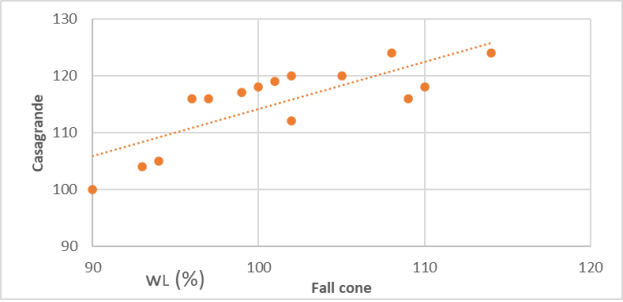

Figure 4. The liquid limits by the Casagrande and Fall cone method.

4 CONCLUSIONS

In this study, the results of the measurements of the density of solid particles according to EN ISO 17892-3 and the liquid limit according to EN ISO 17892-12 are presented. Fifteen bentonite samples were collected from mining deposits on the SW edge of the Kremnické vrchy Mts., Western Carpathians. The bentonite samples were tested by: the pycnometric liquid injection method (ρ_s) and the pycnometric gas injection method (ρ_t). The comparison between them showed a close 5-7% difference.

Determination of the density of solid particles with a gaseous pycnometer offers the advantages of a simple, fast, and, above all, fully automated instrument. Although experiments on bentonite samples have shown high accuracy, care must also be taken to investigate the influence of various service and material factors that may affect the density determination.

For high plastic clay specimens, significant differences in the liquid limit values determined by the Casagrande apparatus and the fall cone were determined.

ACKNOWLEDGEMENTS

The authors are grateful for the financial support the Grant Agency of the Ministry of Education, Science, Research and Sport of the Slovak Republic provides. Grant project APVV-20-0175 supports the project presented in this article.

REFERENCES

Baláž, P. & Kušík, D. (2015): *Slovak Minerals Yearbook 2015*. State Geological Institute of Dionyz Stur, Bratislava, ISBN: 978-80-8174-021-3.

EN ISO 17892-3: 2015 Geotechnical investigation and testing. Laboratory testing of soil. Part 3: Determination of particle density.

EN ISO 17892-12: 2018 Geotechnical investigation and testing. Laboratory testing of soil. Part 12: Determination of liquid and plastic limits.

Górniak K., Szydłak T., Gaweł A., Klimek A., Tomczyk A., Motyka J., Bahranowski K. (2017): Bentonite from the Central Slovakia Volcanic Field – A prospective raw material for Polish industry" *Mineralogia*, 48 (1-4), 23-38, DOI: 10.1515/mipo-2017-0009.

Ondrášik, M. & Kopecký, M., (2014): Rock pore structure as main reason of rock deterioration. In *Studia geotechnica et mechanica* Vol. 36, No. 1. pp. 79-88, Publisher: Wrocław University of Technology, Poland, DOI: 10.2478/sgem-2014-0010.

Osacký, M., Binčík, T., Paľo, T., Uhlík, P., Madejová, J., Czímerová, A. (2019): Mineralogical and physico–chemical properties of bentonites from the Jastrabá Formation (Kremnické vrchy Mts., Western Carpathians) *Geologica Carpathica*, 2019, 70 (5), 433–445, DOI: 10.2478/geoca-2019-0025.

Viana, M., Jouannin, P., Pontier, P., Chulia, D. (2002): About pycnometric density measurements. Talanta, 57 (3), 583-593, DOI: 10.1016/S0039-9140(02)00058-9.

Proceedings of the XVIII ECSMGE 2024
GEOTECHNICAL ENGINEERING CHALLENGES
TO MEET CURRENT AND EMERGING NEEDS OF SOCIETY
© 2024 the Authors
ISBN 978-1-032-54816-6
DOI 10.1201/9781003431749-67
Open Access: www.taylorfrancis.com, CC BY-NC-ND 4.0 license

ECSMGE 24
XVIII EUROPEAN CONFERENCE ON SOIL MECHANICS AND GEOTECHNICAL ENGINEERING

Reinforced soil technique for temporary slope stabilisation in loose saturated ground

Technique de sol renforcé pour la stabilisation temporaire des pentes dans un sol meuble et saturé

G.R. French, S.D. Thomas*
OGI Groundwater Specialists Ltd, Durham, UK

**stephen.thomas@ogi.co.uk*

ABSTRACT: During 2020, a method to provide stability to an initially unstable soil excavation was required in loose saturated soil. The initial slope angle was up to 45° to the horizontal, with saturated ground causing local slip failures and running sand into the excavation. The excavation was surrounded by existing sensitive infrastructure, so it was not feasible to construct shallow excavation slopes, nor feasible to use techniques such as soil nails or anchors. It was neither feasible to use a steel sheet pile wall nor a secant pile wall. To provide soil reinforcement to enhance slope stability, a system was designed that incorporated the construction of a highly permeable angular drainage stone channel along the toe of slope, combined with aggregated cemented angular stone "wedges" compacted orthogonally to the toe of the slope. This combined drainage and reinforced soil system met the economic budget for the client. To comply with Eurocode 7 design standards, including using appropriate partial safety factors on the soil parameters, a PLAXIS 3D analysis was undertaken to demonstrate stability under drained conditions. This ground stabilisation was successful, with stability maintained for the required two years until the infrastructure was ultimately constructed and backfilled.

RÉSUMÉ: Au cours de l'année 2020, une méthode permettant d'assurer la stabilité d'une excavation de sol initialement instable a été nécessaire dans un sol meuble et saturé. L'angle de pente initial était de 45° par rapport à l'horizontale, le sol saturé provoquant des ruptures de glissement locales et du sable coulant dans l'excavation. L'excavation était entourée d'infrastructures fragiles existantes, de sorte qu'il n'était pas possible de construire des pentes d'excavation peu profondes, ni d'utiliser des techniques telles que des clous à terre ou des ancrages. Il n'était pas possible d'utiliser un mur de palplanches en acier ni un mur de pieux sécants. Afin de renforcer le sol afin d'améliorer la stabilité de la pente, un système a été conçu qui incorporait la construction d'un canal de drainage angulaire en pierre très perméable le long du pied de la pente, combiné à des « coins » angulaires en pierre cimentée agrégés compactés orthogonalement au pied de la pente. Ce système combiné de drainage et de sol renforcé a permis de respecter le budget économique du client. Pour se conformer aux normes de conception de l'Eurocode 7, y compris l'utilisation de facteurs de sécurité partiels appropriés sur les paramètres du sol, une analyse 3D PLAXIS a été entreprise pour démontrer la stabilité dans des conditions drainées. Cette stabilisation du sol a été couronnée de succès, la stabilité ayant été maintenue pendant les deux années requises, jusqu'à ce que l'infrastructure soit finalement construite et remblayée.

Keywords: Soil reinforcement; drainage system; stabilising slopes.

1 INTRODUCTION

The upgrade of an energy infrastructure of national significance took place in the United Kingdom in 2020. Part of this upgrade programme required the construction of a temporary battered excavation to install buried pipework infrastructure. The excavation level varied between 76.46 m STN10 and 76.66 m STN10, where STN10 was the site-specific datum. This resulted in an excavation depth of circa 3m to 3.5 m bgl.

One side of the excavation had exposed vertical piles, with pile caps constructed above. On three sides of the excavation, the slopes were battered at slope angles varying between 30°-45° (Figure 1) and displayed soil instability. During an initial site visit, water ingress was observed seeping through the sides of the excavation, together with progressive slope failure in the form of running sand (Figure 2).

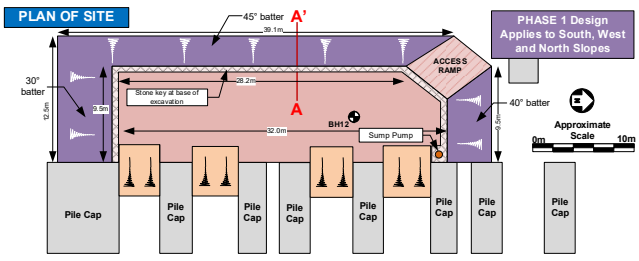

Figure 1. Site plan showing the layout of the excavation.



Figure 2. Excavation with unstable sloping sides.

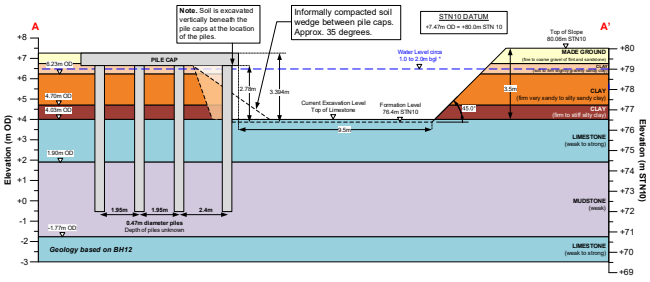

Figure 3. Conceptual model including the general excavation geometry.

As it was intended that infrastructure construction would only take 12 weeks during which undrained soil conditions were in place, the excavation had no slope reinforcement. However, due to a delay in construction programme, the excavation needed to remain open for up to two years longer than the anticipated 12 weeks, so resulting in drained (effective stress) conditions.

To provide stabilisation of the ground for a period of up to two years, the challenge to the civil engineers was to design a robust system to mitigate soil instability, including erosion protection. The constraints on any slope stabilisation were substantial, with traditional techniques such as sheet pile walls, king post walls, secant pile walls or soil anchors, excluded due to the potential impact on the surrounding sensitive infrastructure. This paper presents the design solution implemented by the civil engineers, together with the geotechnical modelling and analysis that was undertaken using PLAXIS 3D to support the design.

2 SITE CONDITIONS

The pipeline excavation had previously been constructed using battered slopes by a previous contractor. To the western, southern and northern sides of the excavation, there were slopes which were calculated to be in the range of 30° to 45°.

However, as a consequence of the high water-table, and steep slope angle, under drained soil conditions, the combination of the low drained shear strength and high groundwater seepage face resulted in local instability and running sand (Figure 2).

The geology on the site is characterised by predominantly superficial clay soils which overlay limestone and mudstone. The clay soils contain frequent lenses of sand and silt. The water level across the site is typically one metre below ground level. The geology with the construction detail overlaid is depicted in Figure 3. All elevations are presented relative to the site datum named STN10, where +7.47 m OD = 80.0 m STN10.

3 GEOTECHNICAL SOIL PARAMETERS

The geological sequence, as depicted in Figure 3, is summarised as follows:

Unit 0: MADE GROUND comprising gravel sized fragments of flint and sandstone.
Unit 1: Soft to firm slightly gravelly sandy CLAY.
Unit 2: Firm mottled very sandy to sandy silty CLAY.
Unit 3: Firm to Stiff dark grey silty CLAY.
Unit 4: Weak to strong dark grey LIMESTONE.
Unit 5: Extremely weak to weak thickly laminated grey MUDSTONE.

Derivation of geotechnical parameters for each unit are presented in the following sections. This derivation has required the incorporation of limited available site investigation, historical research, industry best practice, and authors' own judgement.

3.1 Unit 0: Made ground

Made Ground was described as fine to coarse gravel of flint and sandstone, from which it was considered appropriate to adopt drained parameters for this unit; with drained strength parameters presented in Table 1 used as inputs to the finite element analysis.

A conservative value of Young's Modulus has been selected (Table 1) based on a typical well-graded loose '*Sand/Gravel silty*' from Table 2 (Obrzud and Truty, 2010). Poisson's ratio was selected from a table of typical values for soils (Bowles, 1996).

Table 1. Geotechnical Characteristic Parameters – Unit 0 – Made Ground.

Parameter	Characteristic Value
Weight density, γ	17 kN/m^3
Angle of internal friction, φ	25.0°
Effective cohesion, c'	0.0 kPa
Young's Modulus, E'	7.0 MPa
Poisson's ratio, ν'	0.2

Table 2. Typical values of Young's Modulus for granular materials (MPa) (Obrzud and Truty, 2010).

USCS	Description	Loose	Medium	Dense
GW, SW	Gravels/Sand well-graded	30-80	80-160	160-320
GM, SM	Sand, uniform	10-30	30-50	50-80
GM, SM	Sand/Gravel silty	7-12	12-20	20-30

3.2 UNITS 1, 2 and 3 – Clay soils

The clay soils were broken down into three units based on the geological descriptions:

- UNIT 1: soft to firm dark brown slightly gravelly sandy Clay.
- UNIT 2: firm mottled orange and reddish brown very sandy to sandy silty Clay.
- UNIT 3: firm to stiff dark grey silty Clay

Weight density test data were not available for the natural clay soils, however a range between 17 kN/m^3 and 21 kN/m^3 was expected based on historical site investigation. Parameters in Table 2 have been selected based on this range and experience of working with similar soils.

Drained shear strength parameters for these units were selected on the basis that the excavation was expected to remain open for two further years. As shear strength data were not available to determine the drained strength parameters of the Clay, Plasticity Index (I_p) test data were used to determine undrained shear strength, together with equations outlined in British Standard: Code of Practice for Earth Retaining Systems (British Standard, 2015*,* Section 4.3.1.4).

Conservative values of Young's Modulus and Poisson's ratio were selected for each Clay unit using the typical values for soils (Bowles, 1996). Effective cohesion, *c'* is taken as 0.0 kPa as suggested in British Standard: Code of Practice for Earth Retaining Systems (British Standard, 2015)

A summary of the characteristic parameters used for each Clay unit for the slope stability analysis are presented within Table 3.

Table 3. Geotechnical Characteristic Parameters – Units 1, 2 and 3.

Parameter	Unit 1	Unit 2	Unit 3
Weight density, γ (kN/m³)	18	19	19
Angle of internal friction, φ'_{pk} (°)	21	21	21
Effective cohesion, c' (kPa)	0	0	0
Young's Modulus, E' (MPa)	2	5	7
Poisson's ratio, v'	0.2	0.2	0.2

3.3 Units 4 and 5 – Limestone and mudstone

Rock behaviour differs from soil as it is generally stiffer and stronger. A linear stress dependency, as obtained from the Mohr-Coulomb model is generally not sufficient. The Hoek-Brown failure criterion is a better non-linear approximation of the strength of rock, and accounts for several factors including strength, disturbance and weathered nature of the rock. Input parameters to PLAXIS 3D are as follows: Young's Modulus, E (kPa); Poisson's ratio, v (-); Uniaxial compressive strength (UCS) of intact rock, σ_{ci} (kPa); Intact rock parameter, m_i (-); Geological strength index, GSI (-) and Disturbance factor, D (-).

Borehole descriptions suggest the Limestone is medium strong and thinly to medium bedded. The Mudstone is described as extremely weak to weak and thickly laminated to medium bedded. The selection of Young's Modulus and Poisson's ratio (Table 4) is based on typical values of Young's Modulus available in the literature (Some Useful Numbers, 2016).

Table 4. Summary of Design Rock Parameters – Units 4, 5.

Parameters	Limestone Unit 4	Mudstone Unit 5
Young's modulus, E (kPa)	1.5 x 10^7	1.0 x 10^6
Poisson's ratio, v (-)	0.2	0.2
Uni-axial compressive strength of intact rock, σ_{ci} (kPa)	49,200	20,000
Intact rock parameter, m_i (-)	10	4
Geological strength index, GSI (-)	12	10
Disturbance factor, D (-)	0	0

4 GROUNDWATER

Groundwater was encountered in boreholes outside the excavation at levels of circa 1 m bgl, and observed seeping into the excavation up to circa 2 m above the toe of the slope. Approximately 30 m away from the excavation was an area of a previous excavation which had been backfilled with sand and gravel. This area became waterlogged due to the surrounding clayey soil having a much lower permeability, and acted as a hydraulic boundary which defined the position of the water table boundary condition at a distance of 30 m in the PLAXIS 3D finite element model (*PLAXIS 3D, 2019).*

5 DESIGN METHOD FOR SOIL STABILISATION USING SLOPE REINFORCEMENT

The excavation was surrounded by existing sensitive infrastructure, so it was not feasible to construct shallow excavation slopes, or feasible to use techniques such as soil nails or anchors. was neither feasible to use a steel sheet pile wall nor a secant pile wall. To provide soil reinforcement to enhance slope stability, a system was designed that incorporated the construction of a highly permeable angular drainage stone channel along the toe of slope, combined with

aggregated cemented angular stone "wedges" which are compacted orthogonally to the slope toe.
The construction sequence is as follows:

- Install a stabilising angular stone key at the toe of the slope (Figure 4) so groundwater can seep out of the batter without loss of soil fines.
- Sump pump residual water away from sump in the corner of the excavation.
- Install cemented aggregate wedges in the slope at spacings of 2.5 m. These wedges increase friction between the soil particles and prevent circular slip failure from occurring along the long west side of the excavation (Figures 4 and 5).
- Place angular stone onto the remaining exposed slope face, then push into the soil and compact with the bucket of the excavator. This will mitigate the surface erosion due to rainfall. Place the stone on exposed surfaces of the aggregate wedges to give a uniform appearance across the slope.
- Visually monitor the embankments during and after stabilisation works for any ground movement.
- Regularly refer to the Inspection, Testing and Monitoring (ITM) Plan, and to the staged sequence of installation.

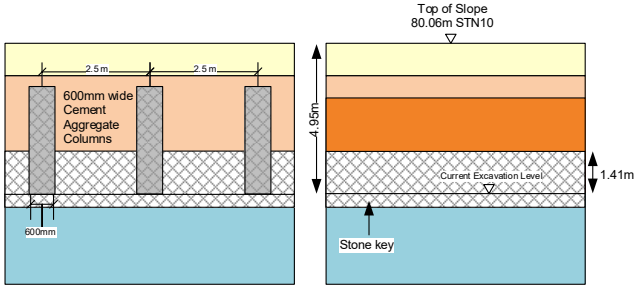

Figure 4. Inclined view of stone key aggregate wedges.

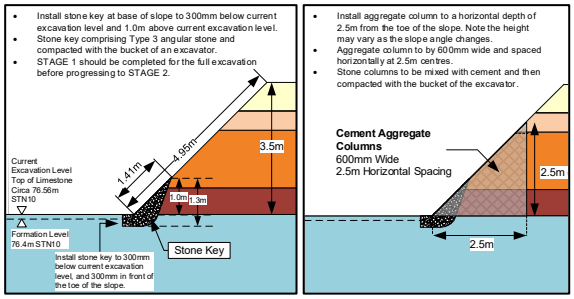

Figure 5. Sectional view of stone key aggregate wedges.

5.1 Unit 6: Compacted angular stone key used for drained reinforcement

The compacted angular stone key used MOT Type 3 (Figure 6) angular stone (SIMTEC Material Testing), with the weight density (Table 5), selected using a table of typical values (Some Useful Numbers, 2016).

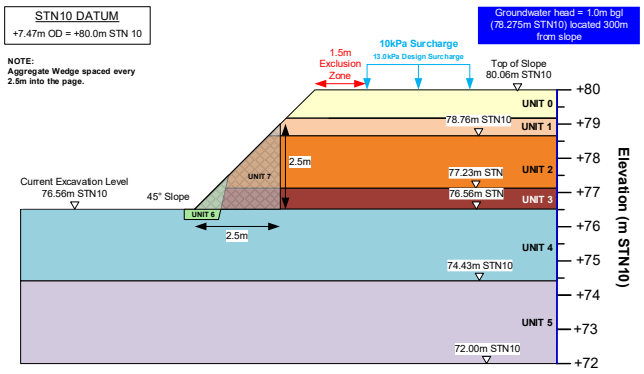

Figure 6. Conceptual model of the cemented angular stone soil reinforcement.

Table 5. Geotechnical Characteristic Parameters – Unit 6 Angular Stone Key.

Parameter	Unit 6
Weight density, γ (kN/m³)	19
Young's Modulus, E (MPa)	100
Contribution from particle angularity φ'_{ang} (°)	4
Contribution from the PSD, φ'_{PSD} (°)	4
Effective angle of shearing resistance, $\varphi'_{cv,k}$ (°)	38
Contribution from Dilatancy, φ'_{dil} (°)	6
Peak angle of internal friction, φ_{pk} (°)	44
Effective cohesion, c' (kPa)	0
Poisson's ratio, v'	0.2

Based on a gravel classification of 'GW - Medium Dense' Young's Modulus of compacted angular stone, was selected using values in Table 5. Shear strength was determined using the equations and tables presented in British Standard (British Standard, 2015) Section 4.3.1.3:

5.2 Unit 7 – Cemented aggregate wedge

Each aggregate wedge was constructed using angular stone mixed with cement. When cured, this resulted in a high strength similar to concrete.

Table 6 depicts the PLAXIS 3D Input parameters used based on typical properties of concrete available in the literature (Some Useful Numbers, 2016).

Table 6. Geotechnical Characteristic Parameters - Unit 7 Cemented Aggregate Wedge.

Parameter	Unit 7
Weight density, γ (kN/m³)	21.0
Young's Modulus, E (kPa)	1.0×10^6
Poisson's ratio, v'	0.2

Slope stability validation was conducted in accordance with Eurocode 7 (Eurocode, 2004 & 2009), utilising the 'Geotechnical Design by Calculation' method, undertaken using PLAXIS 3D Version 2019. PLAXIS 3D (*PLAXIS 3D,2019)* is a finite element software designed for three-dimensional analysis of deformation and stability in geotechnical engineering.

6 PLAXIS 3D SIMULATION OF DESIGN SOLUTION

PLAXIS 3D was used as the design tool to develop the proposed design solution. The software was used to check that the design provided sufficient ground resistance to prevent failure of the slopes under drained conditions. Partial factors of safety were utilised and the design adjusted (primarily the spacing of the cemented aggregate wedges) until the design complied with Eurocode requirements.

6.1 Partial factors of safety

The following partial factors of safety were selected in accordance with relevant design standards (British Standards, 2015).

- Partial factor, $\gamma_m = 1.25$ to reduce tan φ'_and c' for drained shear strength
- Partial factor, $\gamma_m = 1.40$ to reduce σ_{ci} for rock
- Load factor, $\gamma_L = 1.30$ to increase destabilizing actions of surcharge loading

As defined in Eurocode 7, non-factored parameters, are referred to as 'characteristic', with factored parameters used in calculations, referred to as 'design'.

6.2 Model geometry

The following geometry in Table 7 was adopted for input into the PLAXIS 3D Mathematical Model.

Table 7: Input Values to the Plaxis-3D model.

Input	Value
Existing excavation level	76.56m STN10
Top of existing batter	80.06m STN10
Slope angle	45°
Cemented aggregate wedge – width	0.6m
Cemented aggregate wedge – height	2.5m
Cemented aggregate wedge – horizontal length	2.5m
Model width (i.e. wedge horizontal spacing)	2.5m

6.3 Surcharge loading and exclusion zone

A characteristic surcharge of 10 kPa is applied to the top of the batter as required by Eurocode 7 (Eurocode, 2004). The surcharge load has been specified 1.5m from the crest of the batter, meaning that there must be a 1.5m exclusion zone to plant and machinery.

7 RESULTS OF SLOPE STABILITY FINITE ELEMENT ANALYSIS VALIDATION

Numerical modelling of the slope stabilisation using the cemented aggregate wedge approach was carried out using PLAXIS 3D, using input values of Table 7.

Due to the symmetry between each of the aggregate wedges, the domain of the PLAXIS model needed to be only 2.5 m wide. In the vertical dimension, the various geological units (Unit 0 to Unit 3) were input as horizontal layers. The slope angle was defined as 45°, with the 13 kPa design loading applied downwards outside the 1.5 m exclusion zone.

The compacted angular stone key (Unit 6) was simulated as an irregular shaped horizontal strip as outlined in Figure 4. The cemented aggregate stone wedge (Unit 7) was simulated as a 600mm wide triangular structure, 2.5 m deep in the centre of the model (Figure 4 and Figure 6).

Figure 7 and Figure 8 depict the contours of simulated soil displacement (i) based on the working design loads, and (ii) when loads increased until simulated failure is reached.

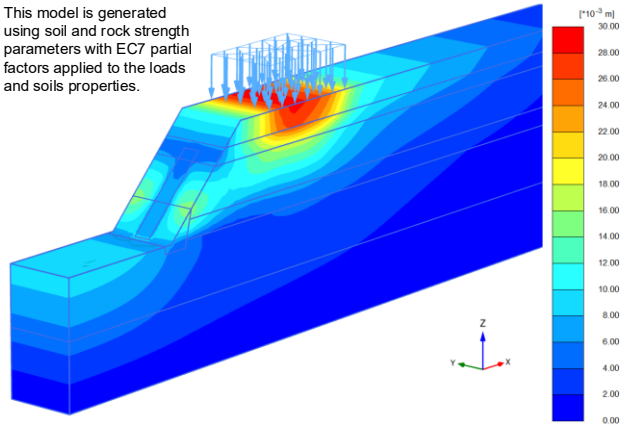

Figure 7. Displacement at working design load.

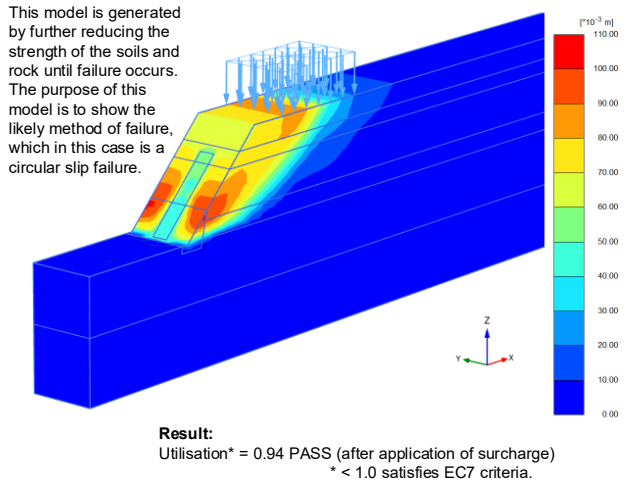

Figure 8. Displacement at model failure.

The PLAXIS 3D model evaluates the stabilizing design parameters required to produce sufficient forces to resist the destabilizing design actions just prior to model failure. The model then calculates the utilisation factor $\boldsymbol{U}$, from the equation $\boldsymbol{E_d / R_d}$ where:

$\boldsymbol{E_d}$ is the design value of the effect of destabilising actions, i.e. loads and stresses

$\boldsymbol{R_d}$ is the design value of the stabilising resistance to actions, i.e. the maximum load/stress that the structure can support before failure.

To demonstrate stability, Eurocode 7 requires the Utilisation, $\boldsymbol{U}$, to be less than 1.0. For the parameters and partial factors described in Table 7, PLAXIS calculates $\boldsymbol{U}$ **= 0.94**

8 CONSTRUCTION METHODOLOGY

The design process resulted in the completion of a series of critical documents required to ensure (i) the construction fulfils the design objectives to stabilise the excavation slopes for a period of at least two years, (ii) there is no collateral damage to surrounding infrastructure, and (iii) the construction is conducted to defined safety standards.

These critical documents included:

(a) Design Strategy document, including all relevant calculations
(b) Clear construction sequence drawings
(c) Design Risk Assessment (DRA)
(d) Inspection, Testing & Monitoring (ITM) Plan
(e) Signed design certificates
(f) Insurance certificates

All site personnel were required to be suitably trained, qualified and certificated to work on this sensitive site.

In summary, the construction proceeded safely with the excavation producing safe and stable exposed slopes for more than the two-year duration required.

9 CONCLUSIONS

An open cut temporary excavation was left open for longer than anticipated. This required the slopes to be stabilized due to the drained soils conditions that had developed, so causing the slopes to become unstable.

A unique slope stabilization solution was developed which comprised the installation of an angular stone key at the base of the slope (Figure 9), which helped to intercept groundwater and stabilize the top of the slope, together with cemented aggregate wedges installed within the slope to provide resistance to the overall soil mass (Figure 10).

The design solution was simulated in PLAXIS 3D with the utilization value, U, calculated as 0.94, demonstrating slope stability under Eurocode 7. Construction proceeded safely, with the excavation producing stable exposed slopes for longer than the two-year duration required.



Figure 9. Construction of angular stone key.



Figure. 10. Construction of aggregate wedge.

REFERENCES

Bowles, J. E. (1996) *Foundation Analysis and Design* 5th Edition', McGraw-Hill, New York, USA.

British Standard (2015). *'Code of Practice for Earth Retaining Structures'* Ref: BS 8002.

Eurocode 7 BS EN 1997-1:2004 *'Geotechnical Design Part 1 General Rules Feb 2009'.*

Eurocode 7 NA to BS EN 1997-1:2004, '*UK National Annex to Eurocode 7: Geotechnical Design – Part 1: General Rules'.*

Obrzud R. & Truty, A. (2010) *The Hardening Soil Model* – A Practical Guidebook Z soil. Ref: 100701 report, Date: 31.01.2012.

PLAXIS 3D (2019) Material Models Manual.

SIMTEC Material Testing, *'Gradation Analysis Test Report Type 3 Subbase'.*

Some Useful Numbers on the Engineering Properties of Materials' https:\\Useful-Numbers.pdf.

Proceedings of the XVIII ECSMGE 2024
GEOTECHNICAL ENGINEERING CHALLENGES
TO MEET CURRENT AND EMERGING NEEDS OF SOCIETY
© 2024 the Authors
ISBN 978-1-032-54816-6
DOI 10.1201/9781003431749-68
Open Access: www.taylorfrancis.com, CC BY-NC-ND 4.0 license

ECSMGE 24
XVIII EUROPEAN CONFERENCE ON SOIL MECHANICS AND GEOTECHNICAL ENGINEERING

Creative approaches for enhancing excavation shoring efficiency through diaphragm wall prestressing techniques

Approches créatives pour améliorer l'efficacité de l'étayage des fouilles grâce aux techniques de précontrainte des parois diaphragmatiques

M.C. Frydrych*
Warsaw University of Technology/Faculty of Civil Engineering, Warsaw, Poland
**mateusz.frydrych.dokt@pw.edu.pl*

ABSTRACT: Diaphragm walls are essential in geotechnical engineering for both retaining structures and deep foundations. However, modern projects encounter challenges in designing cross-sectional profiles precisely due to technical complexity. The growing demand for sustainable building materials further increases the difficulty of implementation. This paper proposes integrating prestressing technology to enhance diaphragm walls construction efficiency. Prestressed tendons are incorporated nonlinearly into the reinforcement structure, reducing bending moments, minimizing steel usage, and improving structural integrity. This unconventional concept, previously unexplored in scientific literature, represents a significant advancement. A dynamic numerical model is central to this research, enabling precise delineation of diaphragm wall cross-sections and meticulous analysis of displacements and forces under various scenarios. Advanced computational tools like the Sofistik application are utilized, with validation done using the Plaxis software. This unconventional approach has profound implications in geotechnical engineering, offering opportunities for optimization such as reduced material consumption, accelerated project completion, and cost savings. An exemplary application involves using diaphragm walls as cantilever structures spanning two underground floors, eliminating the need for additional support or ground anchorage. The presented approach can help the construction sector optimize costs while maintaining a sustainable approach.

RÉSUMÉ: L'utilisation généralisée des parois moulées en génie géotechnique présente des défis modernes en raison de spécifications complexes et de l'impératif de durabilité pour réduire les émissions de carbone. Une méthode novatrice est proposée ici pour optimiser la construction des murs de soutènement en utilisant la précontrainte. Cette approche intègre des tendons précontraints de manière non linéaire, réduisant les moments de flexion, minimisant l'usage de l'acier, réduisant les déplacements et améliorant l'intégrité structurelle. Cette méthodologie révolutionnaire, basée sur un modèle numérique dynamique précis, permet une analyse détaillée des déplacements et des forces transversales. La recherche, validée par des logiciels avancés comme Sofistik et Plaxis, offre des opportunités d'optimisation en réduisant la consommation de matériaux, en accélérant les projets et en économisant du temps et de l'argent. Une application remarquable est l'utilisation de murs diaphragmes en porte-à-faux pour couvrir deux étages souterrains, éliminant le besoin de supports supplémentaires. Cette approche novatrice améliore la faisabilité des projets pour les entrepreneurs et assure la prudence financière des investisseurs.

Keywords: Prestressed diaphragm walls; numerical analysis; Sofistik; innovation.

1 INTRODUCTION

Creative approaches to technology development have long been a focal point within both the scientific community and industry stakeholders interested in the subject. Notably, emerging optimal solutions increasingly prioritize ecological considerations and sustainable approaches within the construction sector. Is it feasible to introduce a new technology that aligns with contemporary expectations, while minimizing risks and enhancing cost efficiency? This article introduces the concept of prestressing the diaphragm wall used for excavation shoring, potentially obviating the need for one level of shoring strut or ground anchors. Furthermore, prestressing offers the potential to reduce the required amount of conventional reinforcement for the reinforced concrete section. The author emphasizes technological aspects such as project speed and the flexibility of action within the structure, ultimately optimizing both time and costs.

In many cases around the world, a conventional approach to constructing underground parts of buildings is being considered, usually using top&down or bottom-up methods. These methods require extra support like steel struts, strutted slabs, or ground anchors, leading to execution challenges such as slower excavation work with steel struts and the expense and feasibility issues with ground anchors.

In a typical approach beyond specific method to constructing underground parts of projects using diaphragm walls, the process generally involves the following phases:

- Constructing guide walls leading to the diaphragm walls.
- Excavating the trench in soil with bentonite slurry support.
- Placing a prefabricated reinforcement cage in the excavation filled with bentonite
- Pouring the diaphragm wall using the contractor method.
- After achieving adequate concrete strength, excavation of the pit can commence. Support is provided through steel struts or ground anchors, and these techniques can be combined based on stability needs and the number of underground levels.

2 INNOVATIVE PROPOSITION WITH EFFECTIVE RESULTS

This article presents an alternative approach to the implementation of underground parts of the investment, which may be attractive to the construction sector. This concept proposes placement prestressing system known in the bridge construction industry into the diaphragm wall, which, according to analyses, makes it possible to dispense with additional strutting, thus making it possible to build two underground storeys much faster and cheaper with the same level of safety. The use of prestressing in diaphragm walls reduces the use of steel and concrete and reduces the need for construction equipment due to the lack of the need to install steel struts or ground anchors. Thus, this type of approach can be environmentally friendly by reducing carbon footprint emissions, which is very important in today's approach to engineering (Pomponi and Stephan, 2021). Resigning from these elements may be invaluable from a logistic point of view, especially in densely built-up urban areas, where there are other buildings around the investment that cannot be disturbed by deep excavations (Łupieżowiec, 2021).

In the presented concept, optimization and an unconventional approach to constructing underground parts of projects involve incorporating a prestressing system with tendons within the reinforcement cage. These tendons, encased in plastic sheaths, are permanently attached to the cage and can be arranged linearly or nonlinearly as in bridge solutions, utilizing anchoring at the bottom of the reinforcement cage (Martí et al., 2013). The reinforcement cage with tendons can be placed in the excavation allowing them to be surrounded by concrete during pouring, effectively blocking tendon movement. This solution introduces a slight change to the technological process by placing modified reinforcement baskets in the bentonite:

- the prestressing cables are installed into the prepared reinforcement cage (which has been appropriately designed for the case of the pre-stressed diaphragm wall in question) in a dedicated system casing laid according to the detailed design, i.e., the geometry of the cables as well as the installation method and their length are designed according to the method proposed by the author.
- concreting then takes place as in the typical approach, with care being taken to ensure that the tremie pipes do not overwhelm the placed tendons.
- depending on the design assumptions, after the concrete obtains the required strength, the structure should be prestressed, after which further deepening of the excavation is possible.

Due to the possibility of non-linear arrangement of prestressing tendons, it is possible to obtain high efficiency of the prestressed cross-section. Concept of this method was presented in Figure 1.

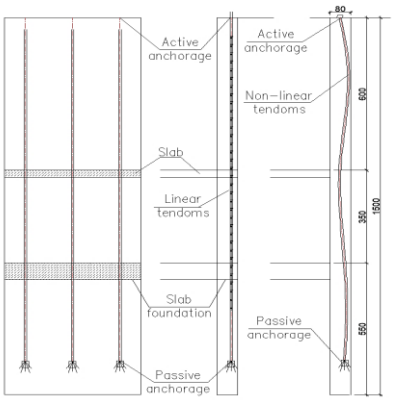

Figure 1. Cross sections of the method described for one section of the diaphragm wall with three prestressing tendons installed in linear proposition and non-liner proposition [own source].

3 NUMERICAL VALIDATION AND FEM RESULTS

To ensure the reasonableness of the obtained results in numerical analyses, it is necessary to pay attention to the quality of the input data (Michalak and Przybysz, 2021). In the case of structural prestressing, this is the value and impact of the prestressing force and the limits set by current design standards. Sofistik v2023 was chosen to analyse such an unconventional structural system using FEM, because this software

allows the analysis of prestressed structures loaded with soil pressure in one model, including the possibility of analysing multiple implementation phases, which is very beneficial in examining geotechnical issues. Thanks to the extensive reporting engine in the post-processor, it is possible to detect most numerical errors, which is extremely important in geotechnical issues, because the error in a given phase is transferred to the next ones and ultimately incorrect results are obtained. The idea of FEM operation is widely described in the literature and this article focuses on its application. In general computer calculations ultimately rely on these meticulous considerations (Kacprzyk and Rakowski, 2016): a) the idealization of the actual design, b) discretization of the issue, c) solution of optimal computer algorithms, d) verification and interpretation of results.

The obtained stresses from individual integrals of the stress field allow for the determination of internal forces and subsequent dimensioning. Due to the lack of dedicated software for this type of analysis, Sofistik was used - a comprehensive programming platform, which allowed the analysis of soil, reinforced concrete and prestressing issues in one model. The Sofistik model is run through a computational engine, and its outcomes are assessed using the WINGRAF module. In this module, it is possible to visualize the model geometry, given loads and results in the form of displacements and internal forces for individual phases, which is simplified in Figure 2.

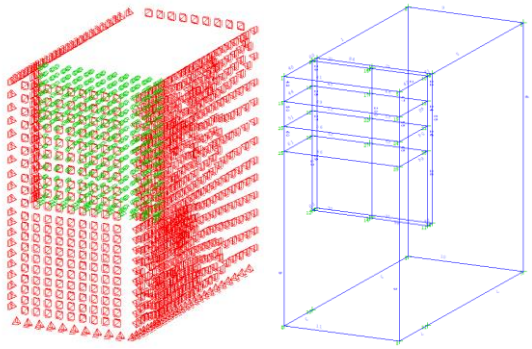

Figure 2. Geometry model result from Sofistik software with given boundary conditions in the form of an interface. This 3D model was created using solid elements [own source].

Before investigating the prestressed diaphragm wall method, the author created a diaphragm wall model for a simple cantilevered system using Sofistik and Plaxis software using Hardening Soil (Hs) model. Stress and displacement results from both programs were compared, revealing a convergence within 1.0 %. This agreement validated the accuracy of the diaphragm wall model in Sofistik without prestressing, confirming its suitability for analysing prestressed elements in the diaphragm wall (see Figure 3).

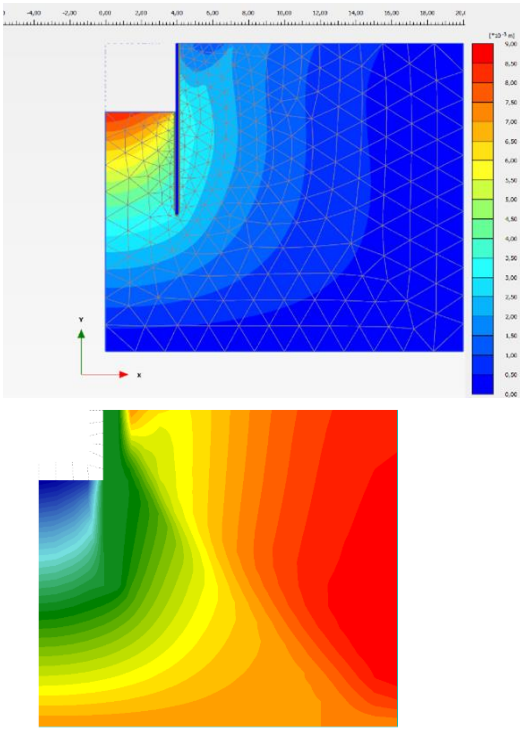

Figure 3. Presentation of validation results for vertical displacements in Plaxis and Sofistik software [own source].

After validating the numerical models in two software programs, the prestressing algorithm was developed for the diaphragm wall model. Aligning equations for reinforced concrete in soil with prestressing tendons posed a challenge, adapted to meet software and soil description Hs requirements. The algorithm enables input of prestressing force, tendon distribution, rheological coefficients, and tendon elongation study is presented in Figure 4. Results were visualized in Sofistik, allowing manual scaling for structural emphasis, useful for detecting irregularities in complex systems. This capability demonstrated the behaviour of the prestressed diaphragm wall in the soil body.

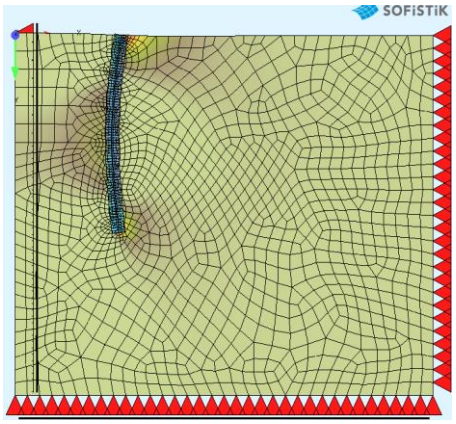

Figure 4. Operation of the prestressing algorithm with a linearly specified prestressing tendon located on the excavation side. Manually scale was used to present possibility of prestressing [own source].

Utilizing the provided model geometry and a developed prestressing algorithm, the author investigated the impact of incorporating prestressing tendons into the diaphragm wall cross-section. The goal was to confirm the viability of designing a diaphragm wall as an excavation enclosure reinforced with a prestressing system for two underground levels. The analysis demonstrated that prestressing significantly reduced horizontal displacements at the top for a 0.8 m thick wall exposed at 6.0 m. Without considering the prestressing system, constructing such a structure without additional reinforcement, like steel struts, would be unfeasible.

The final results for the final phase of the prestressed diaphragm wall based on optimized horizontal displacements and optimal, i.e. structure-safe, stresses are shown in Figure 5.

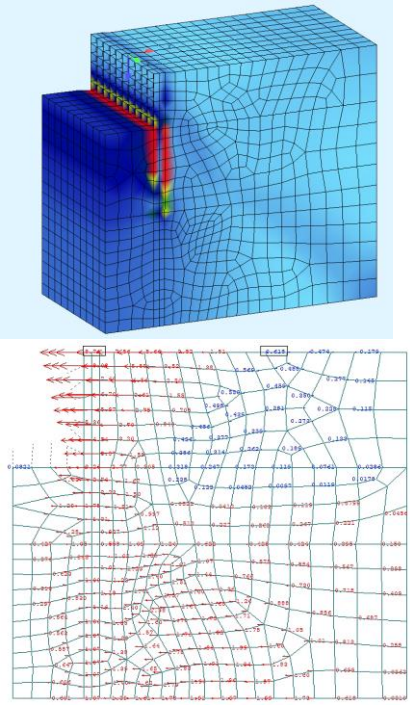

Figure 5. Presentation of the results of prestressing in a diaphragm wall as to stresses and horizontal displacements[own source].

The displacements of the cap of a diaphragm wall uncovered at 6.0 m with a thickness of 0.8 m are 16.2 mm without using additional expansion, which, given the assumed load of 5 kPa on the excavation surface, would make it impossible to design such a support. Uniform ground conditions were assumed in the form of sandy clay.

4 CONCLUSION

The article presents an unconventional approach to the design and implementation of diaphragm walls using prestressing. The open-source software Sofistik was used to develop this issue because there is no dedicated one. The model environment setting was checked with Plaxis. The results show many technological benefits such as:

- improved waterproofing of the enclosure, decreasing groundwater influx and enhancing watertightness.
- minimization or complete elimination of concrete tension, leading to reduced reinforcement in the concrete section.
- increased durability and reduced thickness of the excavation enclosure without compromising stiffness, allowing for more flexible building volume due to reduced enclosure thickness.
- decreased horizontal deformations of the excavation enclosure, ensuring safety for nearby structures.
- wider spacing between temporary excavation supports.

Future research will include detailed analyses considering various design situations using prestressing along with actual savings during construction. Eliminating one level steel struts or ground anchors is possible and can bring many benefits while maintaining the design assumptions.

REFERENCES

Bentley (2022). Plaxis 3D. Available at: https://www.bentley.com/software/plaxis-3d/, accessed: 20/03/2024.

Łupieżowiec M. (2021). Monitoring the Impact of the Large Building Investments on the Neighborhood. *Applied Sciences* vol. 11(14), 6537. https://doi.org/10.3390/app11146537.

Pomponi F., Stephan A. (2021). Water, energy, and carbon dioxide footprints of the construction sector: A case study on developed and developing economies, *Water Research*, vol. 194, 116935. https://doi.org/10.1016/j.watres.2021.116935.

Martí J., Gonzalez-Vidosa F., Yepes V., Alcalá J. (2013) Design of prestressed concrete precast road bridges with hybrid simulated annealing, *Engineering Structures*, 2013, Vol. 48, pp.342-352. https://doi.org/10.1016/j.engstruct.2012.09.014.

Michalak H., Przybysz P. (2021). The Use of 3D Numerical Modeling in Conceptual Design: A Case Study. *Energies*, Vol. 14(16), pp.1-21. https://doi.org/10.3390/en14165003.

Rakowski G., Kacprzyk Z. (2016). *Metoda Elementów Skonczonych w Mechanice Konstrukcji*, 3rd ed., Publishing House of the Warsaw University of Technology, Warsaw, Poland, pp. 5–432.

Sofistik (2023). Sofistik FEA 2023. Available at: https://docs.sofistik.com/2023/en/fea/index.html.

Proceedings of the XVIII ECSMGE 2024
GEOTECHNICAL ENGINEERING CHALLENGES
TO MEET CURRENT AND EMERGING NEEDS OF SOCIETY
© 2024 the Authors
ISBN 978-1-032-54816-6
DOI 10.1201/9781003431749-69
Open Access: www.taylorfrancis.com, CC BY-NC-ND 4.0 license

ECSMGE 24
XVIII EUROPEAN CONFERENCE ON SOIL MECHANICS AND GEOTECHNICAL ENGINEERING

Limit equilibrium solution for lateral pile capacity in cohesive soil

Solution d'équilibre limite pour la capacité latérale des pieux dans un sol cohésif

T. Gans-Or, S. Pinkert*
Ben-Gurion university of the Negev, Beer-Sheva, Israel
**pinkerts@bgu.ac.il*

ABSTRACT: This paper presents a limit equilibrium solution for the lateral pile capacity problem in cohesive soil. The solution is based on an implementation of the slice method, the mobilized strength concept, and optimization of slip surface geometries. This study shows an improvement in the inner slice forces inclination, which is inspired from previous upper-bound solution. The overall nature of the solution is of a lower-bound solution, as it satisfies full equilibrium and the concept of maximizing the applied load to failure. The obtained results show excellent agreement with the lower-bound solution for both cases of perfectly smooth and rough pile interfaces, and an overall good agreement to the entire range of soil-pile interface roughness. Based on this excellent agreement, further problems can be investigated using the developed limit equilibrium method.

RÉSUMÉ: Cet article présente une solution d'équilibre limite pour le problème de la capacité latérale des pieux dans un sol cohésif. La solution est basée sur la mise en œuvre de la méthode des tranches, le concept de force mobilisée et l'optimisation de la géométrie de la surface de glissement. Cette étude montre une amélioration de l'inclinaison des forces de la tranche intérieure, qui s'inspire des solutions précédentes de la limite supérieure. La nature globale de la solution est une solution de limite inférieure, car elle satisfait l'équilibre complet et le concept de maximisation de la charge appliquée jusqu'à la rupture. Les résultats obtenus montrent un excellent accord avec la solution de la limite inférieure pour les deux cas d'interfaces de pieux parfaitement lisses et rugueuses, et un bon accord général pour toute la gamme de rugosité de l'interface sol-pieu. Cet excellent accord peut servir de base à d'autres problèmes qui pourraient être étudiés à l'aide de la méthode d'équilibre limite développée.

Keywords: Lateral pile capacity; cohesive soils; mobilized strength; optimization; slice method.

1 INTRODUCTION

Lateral pile capacity is a key tool in geotechnical engineering, as piles are widely used to support moments and lateral forces. Lateral pile capacity estimation is traditionally expressed as a function of soil and pile properties multiplied by a resistance factor N (Broms, 1964). For cohesive soils, the lateral pile capacity, P_{ult}, is commonly described as:

$$P_{ult} = NS_uD \quad (1)$$

where S_u is the undrained shear strength and D is the pile diameter.

The lateral resistance factor of piles in cohesive soils has been evaluated by applying lower-bound (LB) and upper-bound (UB) plasticity theorems, which consider eligible stress fields and plastic work considerations, respectively (Yu, 2006). The exact solution for N is obtained when the LB and UB solutions converge. In these solutions, it has been shown that N is highly dependent on the soil-pile interface roughness, which can be described as αS_u where $0 \leq \alpha \leq 1$.

As of today, the exact solution for the resistance factor for the entire range of alpha is still inconclusive, except for a perfectly rough pile ($\alpha = 1$), where $N = 11.94$ was found to be the exact solution. In the case of a perfectly smooth pile ($\alpha = 0$) the highest LB solution is $N = 9.142$ (Randolph and Houlsby, 1984) and the lowest UB solution is $N = 9.2$ (Martin and Randolph, 2006). This paper presents the alternative of limit equilibrium (LE) solution for the lateral pile capacity problem.

2 IMPLEMENTING THE SLICE METHOD

Gans-Or and Pinkert (2023) suggested an alternative and novel approach for extracting the resistance factor,

using a modification of the slice method which is widely applied in slope stability calculations (for example: Fellenius 1936, Bishop 1955, Morgenstern and Price 1965, Spencer 1967). The slice method was chosen since it combines equilibrium principles and failure mechanisms. The soil shear strength is expressed using the mobilized strength, $S_{u,m} = S_u/Fs$, where $S_{u,m}$ is the mobilized undrained shear strength and Fs is a factor of safety. For any arbitrary potential failure slip surface, the pile capacity can be expressed as:

$$P_a = NS_{u,m}D \tag{2}$$

where P_a is the applied horizontal force per unit length. Unlike plasticity solutions that directly evaluate P_{ult}, the resistance factor N is calculated in terms of a general P_a and a Fs that is evaluated using a LE solution:

$$N = \frac{P_a Fs}{S_u D} \tag{3}$$

By minimizing the Fs, this work defines the resistance factor according to the maximal soil strength mobilization, which obtained along the most critical slip surface.

2.1 Numerical slice definition

For the LE solution, this work utilizes the slice method, in which the soil is subdivided into horizontal slices. To allow the investigation of numerous slip surfaces (as part of Fs minimization), the slices geometry is generalized in terms of numerical discretization, as described below.

Using polar coordinates, the area bounded by the slip surface is discretized into m slices, where each slice is tangentially incremented by $d\theta = \pi/m$. Figure 1 presents the general slice n, which is numerically described using (i, j, k) indices, where i is the slice radial index, j is the tangential index corresponding to i, and k is the tangential index corresponding to $i + 1$. A line stretching from (i, j) to $(i + 1, k)$ is located on the examined slip surface and is inclined in β_n. The arc extended from $(i, 1)$ to $(i + 1,1)$ is located on the soil-pile interface, and θ_i angle is at its middle.

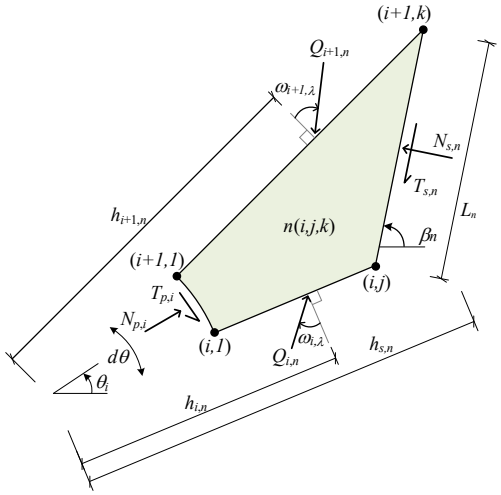

Figure 1. Horizontal Slice numerical definitions and applied forces.

2.2 External load discretization

The external load P_a is divided to each slice as the normal force $N_{p,i}$ and the mobilized shear (adhesion) force $T_{p,i}$ at the soil-pile interface. These forces satisfy equilibrium with P_a by:

$$\sum_{i=1}^{m} N_{p,i} \cos\theta_i + T_{p,i} \sin\theta_i = P_a \tag{4}$$

$$\sum_{i=1}^{m} N_{p,i} \sin\theta_i + T_{p,i} \cos\theta_i = 0 \tag{5}$$

Based on Gans-Or and Pinkert (2023), $T_{p,i}$ and $N_{p,i}$ are described as:

$$T_{p,i} = \alpha \frac{S_u}{Fs} R d\theta \tag{6}$$

$$N_{p,i} = \left(P - 2\alpha \frac{S_u}{Fs} R\right)\left(\frac{\pi}{4} - \frac{\theta_i}{2}\right) d\theta \tag{7}$$

2.3 Slice forces

There are several loads developed in response to external forces, as shown in Figure 1. $N_{s,n}$ represents the normal force and $T_{s,n}$ represents the mobilized shear force on the slice slip surface, given by:

$$T_{s,n} = \frac{S_u}{Fs} L_n \tag{8}$$

where L_n is the length of the slice slip surface. The interslice forces $Q_{i,n}$ and $Q_{i+1,n}$ which are located at distances $h_{i,n}$ and $h_{i+1,n}$ from the pile center, are inclined by ω_i and ω_{i+1}, respectively. Note that the interslice forces inclination ω is described by a general function, $f(\lambda, \theta_i)$, that will be described in Section 3.

2.4 Slice equilibrium

For any examined slip surface, all slices maintain both force and moment equilibriums. For forces equilibrium, the following regression rule was developed for each slice:

$$Q_{i+1,n} = Q_{i,n}\frac{sin(\beta_n-\theta_{r,i}+\omega_i)}{sin(\beta_n-\theta_{r,i+1}+\omega_i)} + \frac{N_{p,i}\,cos(\beta_n-\theta_i)-T_{s,n}-T_{p,i}\,sin(\beta_n-\theta_i)}{sin(\beta_n-\theta_{r,i+1}+\omega_i)} \quad (9)$$

For moments equilibrium, the following regression rule was developed for each slice:

$$Q_{i+1,n}h_{i+1,n} = Q_{i,n}h_{i,n}\frac{cos(\omega_i)}{cos(\omega_{i+1})} + \frac{N_{s,n}h_{s,n}\,cos(\beta_n-\theta_i)-T_{s,n}h_{s,n}\,sin(\beta_n-\theta_i)-T_{p,i}R}{cos(\omega_{i+1})} \quad (10)$$

where $h_{s,n}$ is the radial distance between the pile centre and the middle of L_n.

2.5 Factor of safety evaluation

Using these regression rules, two Fs values can be extracted for any slip surface; $F_{s,F}$ and $F_{s,M}$, representing Fs for global force equilibrium and moment equilibrium considerations, respectively:

$$F_{s,F} = S_u\frac{\sum_{i=1}^{m}\gamma_i\chi_i}{\sum_{i=1}^{m}\epsilon_i\chi_i-\eta(1+\zeta)} \quad (11)$$

$$F_{s,M} = S_u\frac{\sum_{i=1}^{m}\mu_i}{\sum_{i=1}^{m}\xi_i-2\eta H} \quad (12)$$

where η refers to the force and its location H at the extreme slices; $n(1,j,k)$ and $n(m,j,k)$. The other parameters in equations 12 and 13 are given by:

$$\chi_i = \frac{\prod_{z=i+1}^{m}sin(\beta_z-\theta_{r,z}+\omega_{z,\lambda})}{\prod_{z=i}^{m}sin(\beta_z-\theta_{r,z+1}+\omega_{z,\lambda})} \quad (13.1)$$

$$\zeta = \frac{\prod_{i=1}^{m}sin(\beta_i-\theta_{r,i}+\omega_{i,\lambda})}{\prod_{i=1}^{m}sin(\beta_i-\theta_{r,i+1}+\omega_{i,\lambda})} \quad (13.2)$$

$$\gamma_i = 2\alpha R d\theta\left[\begin{matrix}\left(\frac{\pi}{4}-\frac{\theta_i}{2}\right)cos(\beta_i-\theta_i)\\ +\frac{1}{2}sin(\beta_n-\theta_i)\end{matrix}\right] + L_i \quad (13.3)$$

$$\epsilon_i = P_a\left(\frac{\pi}{4}-\frac{\theta_i}{2}\right)d\theta\,cos(\beta_i-\theta_i) \quad (13.4)$$

$$\mu_i = \frac{L_i h_{s,i}\,sin(\beta_i-\theta_i)+\alpha R^2 d\theta}{cos(\omega_{m+1,\lambda})} \quad (13.5)$$

$$\xi_i = \frac{N_{s,i}h_{s,i}\,sin(\beta_i-\theta_i)}{cos(\omega_{m+1,\lambda})} \quad (13.6)$$

The Fs which satisfies all equilibrium requirements (both forces and moments) is achieved for a specific value of the constant λ that satisfies:

$$F_s = F_s(\lambda)|_{F_{s,F}(\lambda)=F_{s,M}(\lambda)} \quad (14)$$

2.6 Limit equilibrium solution

The LE solution presented in this work follows the nature of LB solution because:

1. Both LE and LB solutions satisfies full equilibrium, with a stress state that does not infer the (mobilized) failure criterion.
2. According to Eq. 3, Fs minimization correlates with P_a maximization, similarly to the efforts of LB solutions to maximize the P_{ult} value.

LE solution for the lateral pile resistance factor N yielded good agreement with traditional plasticity solution (Gans-Or and Pinkert, 2023). For the case of smooth soil-pile interface ($\alpha = 0$), the best LE solution was $N = 9.168$, which is margined by 0.3% to the best LB solution. For the case of rough soil-pile interface ($\alpha > 0$), an assumption for the boundary force η and its location H (Eq. 11 and 12) was made, and yet good agreements were found. Even though the LE solution corresponds to the LB nature, the geometry of the critical slip-surface (for each examined α) was found to be similar to UB solutions failure mechanisms.

Although the difference between LE solutions and LB solutions may seem negligible for practice use, it is of high academic interest to close this elusive gap. The process of improving the LE solution should focus on examining different inner slices forces inclinations functions (ω in Eq. 9 and 10), due to its high influence on N. Note that the motivation for improving these functions comes from the various existing slope stability slice methods which differ from each other by the inner slice's forces inclination assumptions (Duncan et al., 2014).

3 IMPROVEMENTS IN LATERAL PILE CAPACITY SOLUTION

The inclination function of ω was previously expressed in terms of a given linear shape function multiplied by a scalar (Gans-Or and Pinkert, 2023). In this work, a more adequate inner slice forces inclination function is suggested for improving the lateral pile capacity solution. The new function is inspired by previous UB failure mechanisms and the force distributions of Martin and Randolph (2006), by means of relating the ω distribution to a reference point located in a λR distance from the pile center

along the symmetricity axis. For example, Figure 2 shows a graphical implementation of the three cases of λ= 0.1, 0.5 and 0.9. For each λ value, a point in λR distance is set, from which a line (dashed) is stretched to the soil-pile interface, at a corresponding $\theta_{r,i} = \theta_i - d\theta/2$ angle. Then, the inner slice force inclination, ω_i, is perpendicular to this dashed line. Analytically, ω_i should satisfy:

$$\lambda = \frac{\sin \omega_i}{\cos(\omega_i - \theta_{r,i})} \quad (15)$$

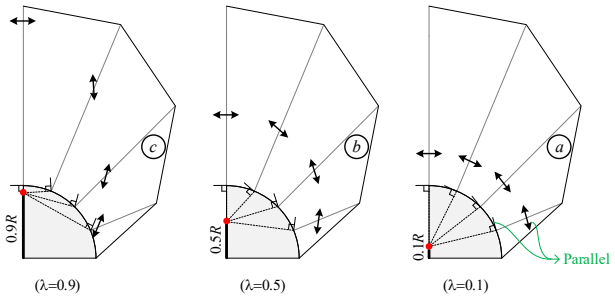

Figure 2. Graphical implementation of ω distribution according to a given λ.

As presented in equations 11 and 12, for each λ value any examined slip surface yields two independent safety factors: $F_{s,F}$ and $F_{s,M}$. Figure 3 presents a conceptual extraction of Fs that is based on Eq. 14. Then, by applying Eq. 3, the resistance factor of the soil can be extracted.

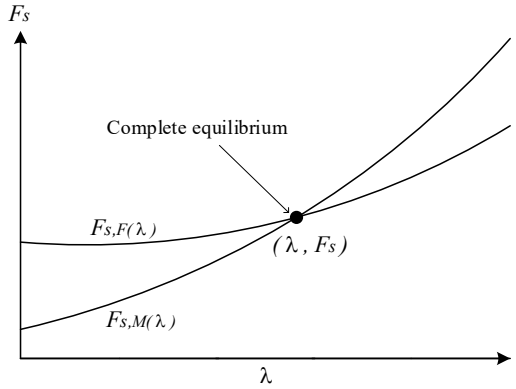

Figure 3. Conceptual extraction of Fs for any examined slip surface.

As shown in the Figure 2, λ variation changes the entire geometrical nature of the force distribution and inclination. For example, as λ decreases the inclination pattern is more circular, and as λ increases the inclination pattern is more elliptical.

An additional improvement in this work includes the Fs minimization process. The numerical search for the critical slip surface is a time-consuming task which requires an efficient optimization process in order to achieve sufficient convergence. In this work, a gradient descent process was implemented to improve the minimization efficiency, intended to decrease the total number of examined slip surfaces. This optimization method gradually converges into one single critical slip surface for a specific resolution (m and dr), as the critical slip surface was proved to be single solution problem (Gans-Or and Pinkert, 2023). The robustness of this Fs minimization process, is by its ability to examine any slip surface geometry without using pre-defined slip surface shape functions or shape assumptions.

4 RESULTS AND DISCUSSION

Table 1 presents LE solutions for lateral pile capacity in cohesive soil (N), for all soil-pile roughness α. For comparison, Table 1 also includes the LB solution (Randolph and Houlsby, 1984) and the previous LE solution (Gans-Or and Pinkert, 2023).

For the case of a perfectly smooth soil-pile interface ($\alpha = 0$), the optimal LE solution in this work is $N = 9.149$. This solution is almost identical to the best LB solution to date ($N = 9.142$) with a minor gap of 0.08%. For comparison, the previous LE solution had a 0.3% gap with the LB solution.

Table 1. Resistance factor results, compared to LB and previous LE solutions.

α	LB	LE (Previous work)		LE (current work)		
	N	N	Gap to LB	λ	N	Gap to LB
0	9.142	9.168	0.3%	0.51	9.149	0.08%
0.2	9.886	9.819	0.67%	0.44	9.83	0.56%
0.4	10.531	10.422	1%	0.39	10.466	0.62%
0.6	11.088	11.042	0.41%	0.33	11.052	0.32%
0.8	11.563	11.635	0.77%	0.27	11.584	0.18%
1	11.94	12.125	1.5%	0.22	12.09	1.2%

Among all N results shown in Table 1, the case of $\alpha = 0$ should be highlighted since no additional assumptions were made to the solution (regarding the forces at the slip surface boundaries). In this case, the LE solution is nearly identical to the LB solution, even though it was derived using a modification of the LE slice method. This fact illustrates the potential of using LE methods for other capacity problems.

For the entire range of rough soil-pile interfaces ($\alpha > 0$), the optimal LE solutions obtained using the inner slice inclination function (Eq. 15) resembled the LB solutions better than the previous LE solutions. For a rough soil-pile interface, where the exact plastic solution is $N = 11.94$, the best LE solution was found to

be $N = 12.09$, which results in an improvement of 0.3% over the previous LE solution. For $\alpha > 0$ cases, the gaps to LB solutions are mostly dependent on the assumptions made regarding the boundary forces (η) and their location (H), which could be addressed and modified in further research. Nonetheless, the LE solutions presented in this study were found with substantial agreement with LB solutions.

In addition to the resistance factor results, each α case is correlated to a single and unique critical slip surface geometry. The critical slip surfaces geometries are closely similar to the UB failure mechanisms. This fact reveals the potential of implementing LE methods for capacity problems, since these solutions combine both equilibrium considerations and failure mechanisms.

5 CONCLUSIONS

This paper presents an advanced limit equilibrium solution for the lateral pile capacity problem in cohesive soil. The limit equilibrium is solved based on the slice method, which is adequately adapted to the lateral pile problem using a polar coordinates system. By improving the pattern of the inter-forces inclination and by using an efficient optimization process, improved resistance factor values were obtained compared to previous lower bound results. The fact that the developed method both reaches a good agreement and follows the lower bound nature, shows the valuable potential for using this method in further investigations.

REFERENCES

Broms, B.B. (1964). Lateral resistance of piles in cohesionless soils. *J Soil Mech Found Div*, 90(3)123-156, https://doi.org/10.1061/JSFEAQ.0000614.

Bishop, A.W. (1955). The use of the slip circle in the stability analysis of slopes. *Géotechnique*, 5(1):7-17, https://doi.org/10.1680/geot.1955.5.1.7.

Duncan, J.M., Wright, S.G., and Brandon T.L. (2014). *Soil strength and slope stability*, 2nd ed., Wiley, New Jersey, USA.

Fellenius, W. (1936). Calculation of stability of earth dam. *International Commission on Large Dams of the World Power Conference.* 4:445-462.

Gans-Or, T. and Pinkert, S. (2023). Implementing the slice method to evaluate lateral pile capacity in cohesive soil. *International Journal for Numerical and Analytical Methods in Geomechanics*,2023;1-13. https://doi.org/10.1002/nag.3609.

Martin, C.M., and Randolph, M.F. (2006). Upper-bound analysis of lateral pile capacity in cohesive soil. *Géotechnique*, 56(2):141-145. https://doi.org/10.1680/geot.2006.56.2.141.

Morgenstern, N.R. and Price, V.E. (1965). The analysis of the stability of general slip surfaces. *Géotechnique*,15(1):79-93. https://doi.org/10.1680/geot.1965.15.1.79.

Randolph, M.F., and Houlsby, G.T. (1984). The limiting pressure on a circular pile loaded laterally in cohesive soil. *Géotechnique*, 34(4):613-623. https://doi.org/10.1680/geot.1984.34.4.613.

Spencer, E.A. (1967). A method of analysis of the stability of embankments assuming parallel inter-slice forces. *Géotechnique*, 17(1):11-26. https://doi.org/10.1680/geot.1967.17.1.11.

Yu, H.S. (2006). Plasticity and Geotechnics. *Springer*, 1st ed. https://doi.org/10.1007/978-0-387-33599-5.

Proceedings of the XVIII ECSMGE 2024
GEOTECHNICAL ENGINEERING CHALLENGES
TO MEET CURRENT AND EMERGING NEEDS OF SOCIETY
© 2024 the Authors
ISBN 978-1-032-54816-6
DOI 10.1201/9781003431749-70
Open Access: www.taylorfrancis.com, CC BY-NC-ND 4.0 license

ECSMGE 24
XVIII EUROPEAN CONFERENCE ON SOIL MECHANICS AND GEOTECHNICAL ENGINEERING

Effect of microplastics on swelling behaviour of geosynthetic clay liners (GCLs)

Les effets des microplastiques sur le gonflement des geosynthétiques bentonitiques (GSB)

Y. Gao
University of Sydney, Sydney, Australia

R.K. Rowe
Queen's University, Kingston, Ontario, Canada

A. El-Zein*
University of Sydney, Sydney, Australia

**abbas.elzein@sydney.edu.au*

ABSTRACT: Microplastics (MPs) are emerging persistent pollutants and landfills have been evidenced as one of the main sinks of MPs. Landfill-based lining systems are employed to prevent contaminated leachate from migrating to underlying aquifers. Geosynthetic clay liners (GCLs) composed of bentonite clay are widely used in lining systems due to their high swelling capacity and low hydraulic conductivity. However, bentonite clay is chemically reactive, and its engineering properties are significantly affected when exposed to ion-concentrated solutions. No studies have investigated the impacts of MPs on the engineering properties of GCLs despite the well documented presence of MPs in landfill leachate. In this paper, results of an experiment during which a GCL was exposed to spherical 1 μm polystyrene MPs in the laboratory are reported. The effects of the exposure on the swelling potential of the GCL and the interaction between MP and bentonite, using scanning electron microscopy (SEM), are discussed. Swelling index (SI) and oedometer swelling strain tests were conducted to characterize swelling behaviour. While the preliminary results reported here are limited to a single type, size and shape of MP, no evidence of an effect of polystyrene MPs on swelling of GCL's bentonite has been found.

RÉSUMÉ: Les microplastiques (MP) sont des polluants pérennes, et les centres de décharges de déchets (dépotoirs) ont été identifiées comme l'un des principaux sites de contamination par les MP. Des systèmes de revêtement, a la base des dépotoirs, sont utilisés pour empêcher le lixiviat contaminé de migrer vers les aquifères sous-jacents. Les revêtements à base de géosynthétiques bentonitiques (GSB) composés d'argile bentonite sont largement utilisés en raison de leur grande capacité de gonflement et de leur faible conductivité hydraulique. Cependant, l'argile bentonite est chimiquement réactive, et ses propriétés hydrauliques and mécaniques sont modifiées lorsqu'elle est exposée à des solutions concentrées en ions. Aucune étude n'a examiné les impacts des MP sur les propriétés des GSB malgré la présence bien documentée des MP dans le lixiviat des décharges. Dans cet article, les résultats de plusieurs essais de laboratoire en cours, durant lesquelles un GSB a été exposé à des MP de polystyrène sphérique de 1 μm de taille, sont rapportés. Les effets de MP sur le potentiel de gonflement du GSB et l'interaction entre le bentonite et les MP, par l'intermédiaire de microscopie électronique à balayage (MEB) sont discutés. Des tests d'indice de gonflement (SI) et de contrainte de gonflement à l'odomètre ont été réalisés pour caractériser le comportement de gonflement. Bien que les résultats préliminaires rapportés ici se limitent à un type, une forme et une taille de MP, aucune preuve d'un effet des MP en polystyrène sur le gonflement de la bentonite des GSB n'a été trouvée.

Keywords: Polystyrene microplastics; GCLs; swell; clay microstructure.

1 INTRODUCTION

The accumulation of plastic waste in the environment may pose a risk to human health and environmental sustainability. Weathering can accelerate the breakdown of large-sized plastics and generate tiny fragments smaller than 5 mm, termed microplastics (MPs) (Li et al., 2021). Microplastics have been categorised as a global emerging contaminant by the World Health Organization (Alan et al., 2022).

In the past few years, progressive efforts have been made to study MPs in terrestrial environments. Many studies have investigated the transport and retention of MPs in saturated porous media and explored the effects of co-contaminants on MP transport and vice versa (Li et al., 2021; Rong et al., 2022). A few studies

have reported changes in the properties of MP-contaminated soils. Microplastics may alter the pore structures of soil due to their small particle sizes and may influence soil properties. Jannesarahmadi et al. (2023) found that 30~200 μm polyethylene (PE) and polyvinylchloride (PVC) influence evaporation characteristics, porosity and water-retention of sand-bentonite mixtures. Yu et al. (2023) investigated the effects of MPs on the saturated hydraulic conductivity, water holding capacity and wet-aggregate size distribution of agricultural soils. They found no significant changes in these properties when soils were exposed to polyester and polypropylene (PP) at environmentally relevant MP concentrations. Wang et al. (2023) reported similar findings that small amounts of polyethylene (PE) MPs did not vastly alter water-holding capacity, whereas a high mass ratio can reduce it significantly.

The above studies have experimentally studied the properties of MP-contaminated soils by mixing soil samples with MP particles in the dry state. However, soils may be contaminated by hydration with MP-rich leachate, especially in landfills. Geosynthetic clay liners (GCLs) are used to prevent contaminated leachate from migrating to underlying aquifers. They need to be sufficiently hydrated by the subsoil and to achieve significant swelling, before exposure to leachate, in order to achieve the required low hydraulic conductivity. This is because bentonite is chemically reactive and premature exposure to leachate can inhibit its swelling potential (Tian et al., 2016). To the best of the authors' knowledge, no study has explored the effects of exposure to MPs on the swelling capacity of GCLs used in landfills. To address this gap, this study reports two sets of tests: swell index (SI) tests on sodium-bentonite extracted from the GCLs and oedometer swell strain tests of entire GCLs exposed to polystyrene MPs. In addition, scanning electron microscopy (SEM) tests on bentonite extracted from the GCL after the oedometer tests were carried out.

2 MATERIALS AND METHODS

2.1 Tested materials

An X2000 GCL with powdered sodium bentonite, manufactured by Geofabrics Australia was used in this study. The bentonite was sandwiched between a needle-punched nonwoven (NW) cover geotextile and a scrim-reinforced (woven + nonwoven, W/NW) carrier geotextile. The GCL samples were stored in a storage box at 20~25℃. The initial thickness of the GCL (including both bentonite and geotextiles) was approximately 10~11 mm, with an initial gravimetric water content of the bentonite of 9.7%. Other basic properties of the GCL are shown in Table 1.

Polystyrene microplastics (PSMP) were chosen as the MP in this study because of their reported presence in landfill leachates and wide availability (Kabir et al., 2023). PSMP with a mean diameter of 1 μm were purchased from Bioscientific Australia. This size was chosen on the assumption that the smaller the MP particle, the more likely it is to penetrate into the GCL. PSMP were provided in 100% dry powders and aqueous suspensions with 2.5% solids (w/v) concentration. The dry powders and aqueous suspensions were stored under 20~25℃ and 3~5℃, respectively. PSMP solutions used in swell index (SI) and oedometer swell strain tests were prepared by diluting the stock solution to target concentrations (e.g., 50 mg/L and 100 mg/L). While reported concentrations of MPs reported in studies of landfill leachate are generally much lower, many of these studies are limited to larger-sized MPs. The conservatively high concentrations of PSMP were chosen to increase the likelihood of detecting any effects on GCL swelling.

Table 1. X2000 GCL basic properties.

Properties	Value	Data source
Bentonite mass per unit area (g/m^2)	4250	Supplier
GCL total mass per unit area (g/m^2)	4900	Supplier
Hydraulic conductivity (m/s)	2.4×10^{-11}	Supplier
Swell index (mL/2g)	≥ 24	Supplier
Gravimetric water content as stored	9.3%	Measured by oven-dried method

2.2 Swell index (SI) test

Bentonite clay is the major component in engineering GCLs, contributing to their swelling and barrier performance. The swell index (SI) has been widely used to evaluate the swelling characteristics of bentonite used in GCLs. A series of SI tests were conducted in this study based on the ASTM D 5890 standard, modified to allow measurement of the effect of MPs. Four scenarios of bentonite exposed to MPs were considered, as shown in Table 2. In tests 1, 3 and 4, 2 g of bentonite powder extracted from GCLs was placed at the bottom of a 100 mL volumetric flask. Working solutions (i.e., distilled water and PSMP solutions) were slowly added to the flask along its sidewall to 100 mL. In test 2, 2 g of bentonite was mixed with 10 mg of PSMP dry powder, and the mixture was carefully poured into the bottom of the volumetric flask. Distilled water was slowly added to reach 100 mL. The swelling volume of bentonite was

monitored. Tests 1 and 2 were repeated to confirm the reliability of results. Given the unevenness of the swelling surface of the sample, two readings were taken in each case, corresponding to lowest and highest levels of the surface.

Table 2. Test plan for SI tests.

Test No.	Sample	Working Solution	PSMP /Bentonite Mass Ratio	Repeat Tests
1	2 g of bentonite	Distilled water	/	Yes
2	2 g of bentonite + 10 mg PSMP powder	Distilled water	1:200	Yes
3	2 g of bentonite	Distilled water with 100 mg/L PSMP	1:200	No
4	2 g of bentonite	Distilled water with 50 mg/L PSMP	1:400	No

2.3 Oedometer swell strain test

The GCL sheets were cut into 50 mm diameter specimens, and the initial height H_0 of specimens was measured by a vernier calliper. An oedometer test apparatus was employed to measure the vertical swell deformation ΔH, as shown in Figure 1. The apparatus consisted of a stainless steel oedometer cell (50 mm inner diameter and 53 mm height), a stainless-steel container and a dial gauge (25.4 mm capacity and 0.0254 mm (1 mil) graduation).

A GCL specimen, a quartz porous disc and a top cap were placed in the oedometer cell. Extra care was needed during the installation to minimise bentonite loss from the edge of the GCL specimen. No porous disc and filter paper were used between the bottom of the container and the GCL specimen to prevent MPs from being entrapped by instrument accessories during hydration. The top cap provided a 2 kPa seating pressure to simulate a near-free swell scenario.

Four types of permeating solutions, loosely approximating onsite scenarios of GCL hydration were considered: distilled water (baseline), PSMP in distilled water, $CaCl_2$, and PSMP in $CaCl_2$. The permeating solutions were added to the container once the dial gauge reading became stable after applying the seating pressure to the samples in the oedometer setup. The experimental procedures were based on the ASTM D 4546 standard. Dial gauge readings were recorded at eleven different time on the first day (i.e., 15 seconds, 30 seconds, 1 minute, 2 minutes, 4 minutes, 8 minutes, 15 minutes, 30 minutes, 1 hour, 2 hours, 3 hours), and then once a day (i.e., 24 hours, 48 hours, etc) until the swelling rate slowed down to less than 0.01 mm/hour. The swell strains at different time were calculated as $\Delta H/H_0 * 100\%$. Duplicate tests were conducted to assess the reliability of results. The different scenarios considered for this test are shown in Table 3.

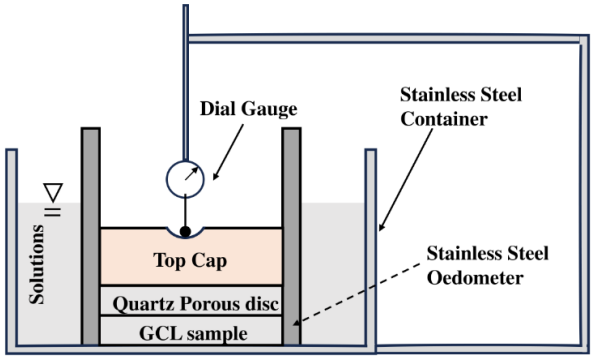

Figure 1. Oedometer test apparatus (not in scale).

Table 3. Test plan for oedometer swell strain tests.

Test No.	Specimen information		Permeating solution
	Initial thickness	Initial GCL mass	
1	10.7 mm	12.2 g	Distilled water
2	10.6 mm	12.5 g	Distilled water
3	10.8 mm	11.0 g	Distilled water with 100 mg/ L PSMP
4	10.5 mm	10.3 g	Distilled water with 100 mg/L PSMP
5	10.7 mm	11.3 g	10 mM $CaCl_2$
6	10.4 mm	11.5 g	10 mM $CaCl_2$
7	10.1 mm	11.5 g	10 mM $CaCl_2$ with 100 mg/L PSMP
8	10.2 mm	10.6 g	10 mM $CaCl_2$ with 100 mg/L PSMP

2.4 Scanning electron microscopy (SEM)

Scanning electron microscopy (SEM) imaging of bentonite specimens taken from the sample at the end of the oedometer swell strain tests was further conducted. The aim was to investigate any interactions between bentonite and PSMP, and any changes in the former as a result of exposure to the latter.

A Sigma VP HD (Zeiss) was used for high-resolution imaging. The oedometer-test GCL samples were freeze-dried under -50 °C vacuum conditions. Small amounts of bentonite were extracted from the edge and centre of the freeze-dried sample. In addition, a specimen was cut from the carrier geotextile by a pair of scissors. These specimens were glued on the SEM stub by a piece of carbon tape. Specimens on the stub were gold-coated to minimize charging effects on SEM imaging. This study used an EHT of 5kV and aperture of 30 μm.

3 RESULTS AND DISCUSSION

3.1 Swell index (SI) test

The results of the swell index (SI) test are shown in Figure 2. The ASTM D 5890 standard requires 16~24 hours before bentonite volume reading. In the experiments conducted here, it is found that around ten days are needed before swelling ceases.

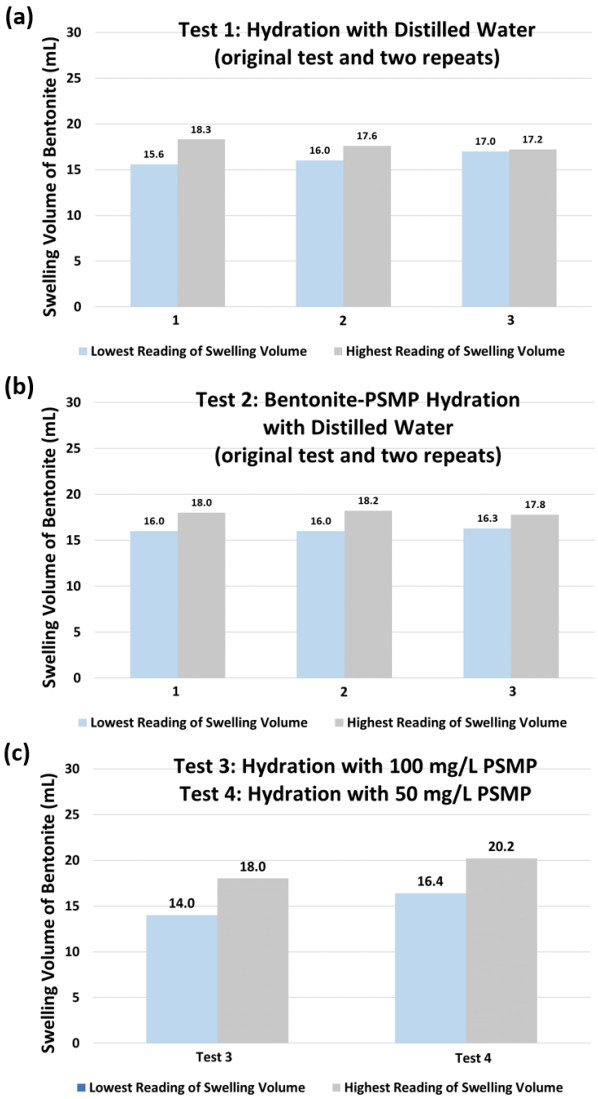

Figure 2. Swell index (SI) results (a) Test 1; (b) Test 2; (c) Tests 3 and 4.

Figures 2a and 2b confirm reasonable repeatability of the SI tests. The standard deviationsof the highest volume reading in the set tests 1 and 2 are 0.45 and 0.16 mL, respectively, and fall within the readability of the volumetric flask of 0.5 mL.

No differences can be found in the SI values between pure bentonite and bentonite-PSMP mixture hydrating with distilled water. The average of the highest volume readings in tests 1 and 2 are 17.7 mL and 18.0 mL, respectively. Hence, it appears that, for a mass ratio of PSMP to bentonite of up to 0.5%, the presence of PSMP does not affect the swell index of sodium bentonite. Tests 2 and 3 studied the SI of bentonite under the same mass ratio between bentonite and PSMP but in different PSMP-bentonite mixing conditions. No differences can be observed in the SI values in these two cases. The SI of bentonite in 100 mg/L PSMP solutions, based on lowest reading, is slightly smaller than that in 50 mg/L PSMP, as seen in Figure 2c, but more data is required before determining whether this difference is significant.

3.2 Oedometer swell strain test

Changes in the vertical swell strain of GCL specimens exposed to PSMP solutions are shown in Figure 3. The rate of swelling initially increases to 0.9 mm/hour then slowly declines after 4 minutes. The swell strains reported below correspond to the time t_{limit} at which swell rate first reaches 0.01 mm/hour. The value of t_{limit} was determined through interpolation. Table 4 and Figure 3 show generally good repeatability of experiments, with the possible exception of tests 7 and 8. The swell strain of GCL hydrating in 10 mM $CaCl_2$ with 100 mg/L PSMP are 34.8% and 39.7% in tests 7 and 8, respectively. In addition, in test 3, the rate of 0.01 mm/hour has been reached after 65 hours, compared to 35 hours in the repeated test 4.

As expected, samples exposed to $CaCl_2$ experienced reduced swelling (swell strains of 38.3% and 38.9% in tests 5 and 6, compared to 43.0% and 43.1% in tests 1 and 2). This is due to the increase in ion concentration in the pore water which inhibits osmotic swelling of Na-bentonite.

Table 4. Elapsed time and swell strain at 0.01 mm/hour swell rate of oedometer swell strain tests.

Test No.	Hydration solution	t_{limit} (hour)	Swell strain (%)
1	DW	83	43.0
2	DW (repeat)	95	43.1
3	PSMP 100 mg/L in DW	65	42.4
4	PSMP 100 mg/L in DW (repeat)	35	38.7
5	10 mM $CaCl_2$	51	38.3
6	10 mM $CaCl_2$ (repeat)	61	38.9
7	PSMP 100 mg/L in 10 mM $CaCl_2$	45	34.8
8	PSMP 100 mg/L in 10 mM $CaCl_2$ (repeat)	59	39.7

* DW is distilled water; t_{limit} is the time it takes to reach 0.01 mm/hour swell rate

The swell strains of tests 3 and 4 are 42.4% and 38.7%, respectively. A small decrease in the swell

strain is observed in GCL hydrated in distilled water with 100 mg/L PSMP compared to that in distilled water. In addition, a decrease in swell strain is found in test 7, compared to tests 4 and 5. However, no such decrease is recorded in repeat test 6 and, therefore, the results are inconclusive. Further tests are needed to identify any co-effects of PSMP and $CaCl_2$ on the swell characteristics of GCLs.

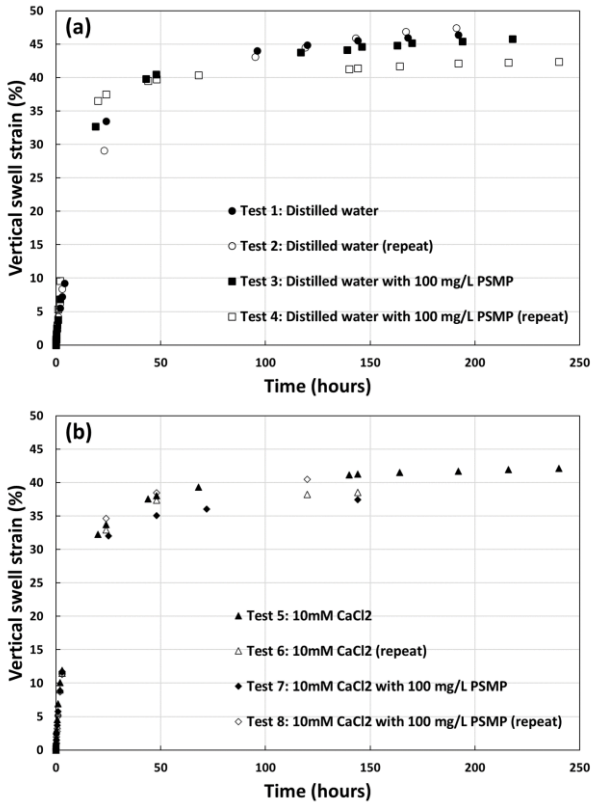

Figure 3. Oedometer swell strain test results (a) Tests 1-4 in distilled water with/without PSMP; (b) Tests 5-8 in 10 mM $CaCl_2$ with/without PSMP.

3.3 SEM of PSMP and clay microstructure

The morphology and size of PSMP are shown in Figure 4. The PSMP particles appear to be regular microspheres with 1 μm size as described by the supplier. The highly regular spherical shape of the particles makes it easier to distinguish them from bentonite and geotextiles in SEM images.

Figure 5 shows SEM images of GCL components of oedometer swell strain test 3. PSMP particles are observed on the bentonite specimen taken at the edge of GCL, as seen in Figure 5a. PSMP particles attach to the clay surface. Some large pores (around 1 μm in size) appear in the clay microstructure although it is unclear whether they are due to interaction with PSMP or handling of the specimen. Figure 5b shows that, on the carrier geotextile specimen, many PSMP particles aggregate and attach to the retained bentonite but not, it appears, to the geotextile itself, possibly indicating a preference for the clay. It is not clear whether this is accidental or indicates selective attachment to the bentonite. Finally, in Figure 5c, no PSMP can be seen on the bentonite extracted from the centre of GCL. It seems that the PSMP has not penetrated through the bentonite under the conditions of the test reported in this paper.

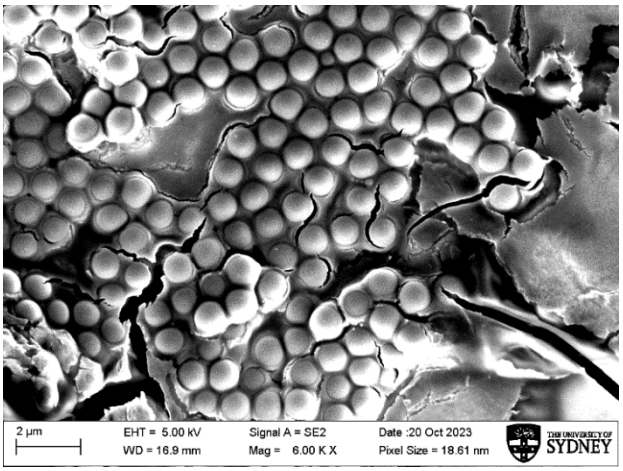

Figure 4. SEM image of PSMP.

4 CONCLUSIONS

This study investigated the effects of PSMP on the swelling characteristics of GCLs. The swelling behaviour has been quantified by the swell index and oedometer vertical strain tests. Small decreases in swelling of GCL exposed to 100 mg/L of 1 μm spherical PSMP, relative to control experiments, have been observed. However, further testing is required to establish whether these differences are significant or fall within the range of experimental variability. SEM imaging shows that individual PSMP are retained on the bentonite attached to the carrier geotextile during hydration.

The study has been limited to a single size, single type MP. Further tests are ongoing by the authors to evaluate the effects of higher ionic strength and PSMP concentrations of hydration solutions, as well as the effects of other types, sizes and concentrations of MPs.

ACKNOWLEDGEMENTS

The authors would like to acknowledge the assistance by the Sydney Microscopy & Microanalysis for using SEM. This research was supported by Australian Research Council (ARC) Discovery Grant DP220100218.

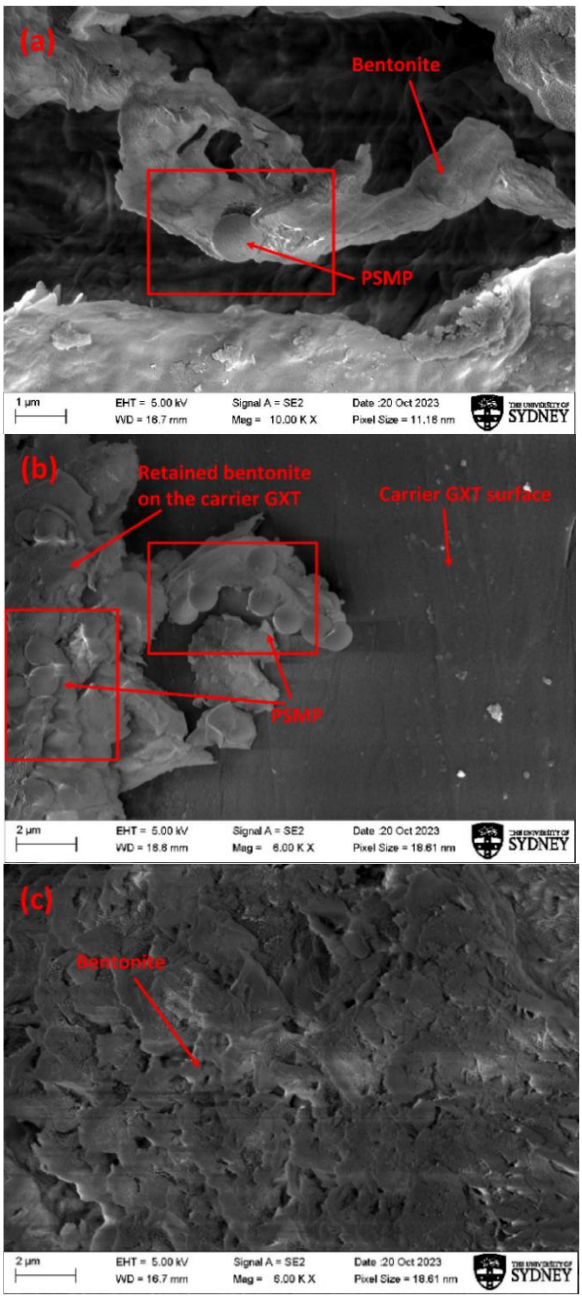

Figure 5. SEM images of the GCL specimen in test 3 (a) bentonite taken from the edge of GCL; (b) carrier geotextile (GXT) specimen with bentonite attached; (c) bentonite taken from the centre of GCL.

REFERENCES

Alan, B., Flemming, C., Todd, G., Bart, K., Shirley, P., Sandra, W., and Stephanie, W. (2022). Dietary and inhalation exposure to nano-and microplastic particles and potential implications for human health. *World Health Organization,Geneva, Switzerland, Licence: CC BYNC-SA 3.0 IGO.*

ASTM, D4546. (2021). Standard test methods for one-dimensional swell or collapse of soils. *ASTM International*.

ASTM, D5890. (2019). Standard test method for swell index of clay mineral component of geosynthetic clay liners. *ASTM International*.

Jannesarahmadi, S., Aminzadeh, M., Raga, R., and Shokri, N. (2023). Effects of microplastics on evaporation dynamics in porous media. *Chemosphere, 311*, 137023, DOI: https://doi.org/10.1016/j.chemosphere.2022.137023.

Kabir, M. S., Wang, H., Luster-Teasley, S., Zhang, L., and Zhao, R. (2023). Microplastics in landfill leachate: Sources, detection, occurrence, and removal. *Environmental Science and Ecotechnology*, 100256, DOI: https://doi.org/10.1016/j.ese.2023.100256.

Li, M., Zhang, X., Yi, K., He, L., Han, P., and Tong, M. (2021). Transport and deposition of microplastic particles in saturated porous media: Co-effects of clay particles and natural organic matter. *Environmental Pollution, 287*, 117585, DOI: https://doi.org/10.1016/j.envpol.2021.117585.

Rong, H., Li, M., He, L., Zhang, M., Hsieh, L., Wang, S., . . . and Tong, M. (2022). Transport and deposition behaviors of microplastics in porous media: Co-impacts of N fertilizers and humic acid. *Journal of hazardous materials, 426*, 127787, DOI: https://doi.org/10.1016/j.jhazmat.2021.127787.

Tian, K., Benson, C. H., and Likos, W. J. (2016). Hydraulic conductivity of geosynthetic clay liners to low-level radioactive waste leachate. *Journal of Geotechnical and Geoenvironmental Engineering, 142*(8), 04016037, DOI: https://doi.org/10.1061/(ASCE)GT.1943-5606.0001495.

Wang, Z., Li, W., Li, W., Yang, W., and Jing, S. (2023). Effects of microplastics on the water characteristic curve of soils with different textures. *Chemosphere, 317*, 137762, DOI: https://doi.org/10.1016/j.chemosphere.2023.137762.

Yu, Y., Battu, A. K., Varga, T., Denny, A. C., Zahid, T. M., Chowdhury, I., and Flury, M. (2023). Minimal Impacts of Microplastics on Soil Physical Properties under Environmentally Relevant Concentrations. *Environmental science & technology, 57*(13), 5296-5304, DOI: https://doi.org/10.1021/acs.est.2c09822.

Proceedings of the XVIII ECSMGE 2024
GEOTECHNICAL ENGINEERING CHALLENGES
TO MEET CURRENT AND EMERGING NEEDS OF SOCIETY
© 2024 the Authors
ISBN 978-1-032-54816-6
DOI 10.1201/9781003431749-71
Open Access: www.taylorfrancis.com, CC BY-NC-ND 4.0 license

ECSMGE 24
XVIII EUROPEAN CONFERENCE ON SOIL MECHANICS AND GEOTECHNICAL ENGINEERING

The behaviour of piles in unsaturated expansive clays under cyclic lateral loading

Le comportement des pieux dans les argiles expansives non saturées sous chargement latéral cyclique

T.A.V. Gaspar*
University of Sheffield, Department of Civil & Structural Engineering, Sheffield, United Kingdom

R.A. Murison, S.W. Jacobsz, G. Heymann
University of Pretoria, Department of Civil Engineering, Pretoria, South Africa

A.S. Osman
Durham University, Department of Engineering, Durham, United Kingdom

t.a.gaspar@sheffield.ac.uk

ABSTRACT: This article presents the results of full-scale testing of laterally loaded piles installed in an unsaturated expansive clay profile. For the pile tested under natural water content conditions, a distinctive accumulation of progressive displacement (or ratcheting) was observed in the direction of applied loading. This behaviour was attributed to the local yielding of the bonded/cemented material along soil fissures. In contrast, the 'wet' pile, tested after the clay profile was allowed to swell for a period of 6 months exhibited no ratcheting. Given that fissures would likely have swelled closed prior to testing of the 'wet' pile, local yielding of the bonded material along fissures due to applied loading would not have occurred, thereby limiting any ratcheting behaviour. Moreover, as the number of loading cycles increased, the 'dry' pile displayed an increased cycle stiffness. Given the local yielding that would have occurred during initial load cycles, it is postulated that this behaviour be ascribed to subsequent load cycles pushing intact masses of clay against one another at the fissure interfaces. Conversely, the 'wet' pile demonstrated slight reductions in cycle stiffness. Assuming constant water content conditions within the clay profile, this result is due to local reductions in void ratio behind the loaded pile, causing increases in saturation, thereby reducing soil suction and stiffness with increasing load cycles.

RÉSUMÉ: Cet article présente les résultats d'essais à grande échelle de pieux chargés latéralement installés dans un profil d'argile expansive non saturée. Pour le pieu testé dans des conditions naturelles de teneur en eau, une accumulation distincte de déplacement (ou de comportement de crantage) a été observée dans la direction de la charge appliquée. Ce comportement a été attribué au fléchissement local de matériau lié/cimenté à l'intérieur des fissures du sol desséché. En revanche, le pieu "humide", testé après que le profil d'argile ait été autorisé à gonfler pendant une période de 6 mois, n'a montré aucun comportement de crantage. Étant donné que les fissures auraient probablement gonflé et se seraient refermées avant le test du pieu "humide", le fléchissement local du matériau lié le long des fissures dû à la charge appliquée n'aurait pas eu lieu, limitant ainsi tout comportement de crantage. De plus, à mesure que le nombre de cycles de chargement augmentait, le pieu "sec" affichait une raideur cyclique accrue. Compte tenu du fléchissement local qui aurait eu lieu lors des cycles de charge initiaux, on postule que ce comportement est dû aux cycles de charge ultérieurs poussant des masses intactes d'argile les unes contre les autres. En revanche, le pieu "humide" a montré de légères réductions de la raideur cyclique. En supposant des conditions constantes de teneur en eau dans le profil d'argile, ce résultat est dû à des réductions locales du rapport de vide derrière le pieu chargé, entraînant une augmentation de la saturation, réduisant ainsi la succion du sol et la raideur avec l'augmentation des cycles de charge.

Keywords: Piles; expansive clays; unsaturated soils; lateral cyclic loading.

1 INTRODUCTION

Expansive, or swelling clays, pose significant challenges for engineers worldwide. These clays are typically characterised by their high plasticity, causing them to expand when wetted and shrink and crack when they dry. This differential movement can have substantial economic consequences for overlying or adjacent structures (Jones and Holtz, 1973). The volumetric behaviour of such clays becomes a particular challenge in the context of wind turbines, where strict tolerances for differential foundation movements are typically prescribed.

Additionally, in the case of piled foundations, prior research has indicated that the aforementioned volume changes are accompanied by variations in shaft capacity (Blight, 1984; Gaspar et al., 2023). To address these challenges, the WindAfrica research project (http://community.dur.ac.uk/wind.africa/) was initiated with the goal of developing practical guidelines for designing onshore wind turbine (piled) foundations in expansive soil conditions.

Previous publications on the WindAfrica project have presented i) the hydromechanical behaviour of expansive clays (Gaspar et al., 2022; Murison et al., 2023), ii) centrifuge modelling of piled foundations in expansive clays (Gaspar et al., 2023), iii) and the behaviour of a full-scale instrumented pile in response to soil swell (da Silva Burke et al., 2022). In this study, the behaviour of laterally loaded piles are presented.

2 METHODOLOGY

The large-scale testing described in this study took place adjacent to an existing bentonite mine near Vredefort, in the Free State Province of South Africa. A simplified borehole log, as well as plastic and liquid limits are presented in Figure 1. Tests were conducted on two separate areas at the site. The first set of tests was conducted on a 'dry' area, where the soil was kept at natural water content conditions. A second set of tests (referred to as the 'wet' tests) was conducted on a section of the site which was flooded for a period of 6 months after pile installation to allow swell to occur prior to testing. The two sections were sufficiently far apart to ensure that flooding of the 'wet' area did not influence the 'dry' area.

The test layout was identical for both the 'dry' and 'wet' tests, and has been illustrated in Figure 2. The setup consisted of two 600 mm diameter piles, at a 2 m centre-to-centre (c/c) spacing, embedded 6 m into the expansive clay profile. Cyclic lateral loading was applied to the pile heads under load control using a hydraulic jack. The point of load application was 500 mm above the natural ground level. Lateral displacements of the piles during loading were measured using linear variable differential transformers (LVDTs). To measure strain distributions along the length of the piles throughout testing, a combination of vibrating wire strain gauges (VWSGs) and fibre Bragg gratings (FBGs) were attached to the steel reinforcing. Detailed descriptions of the performance of these measurements have been provided by Murison et al. (2022).

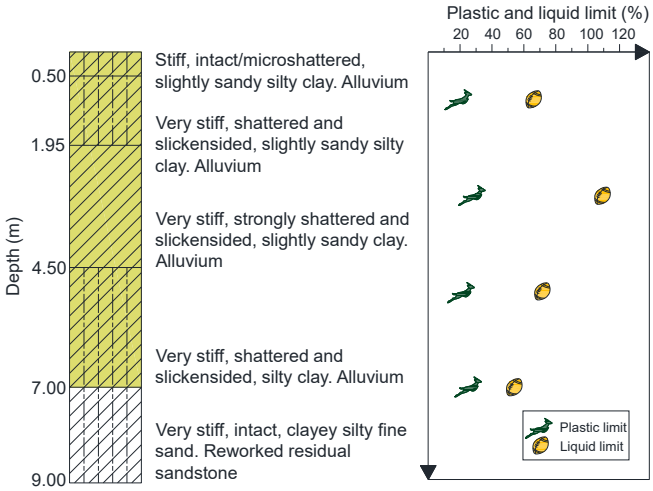

Figure 1. Simplified soil profile and plastic and liquid limits.

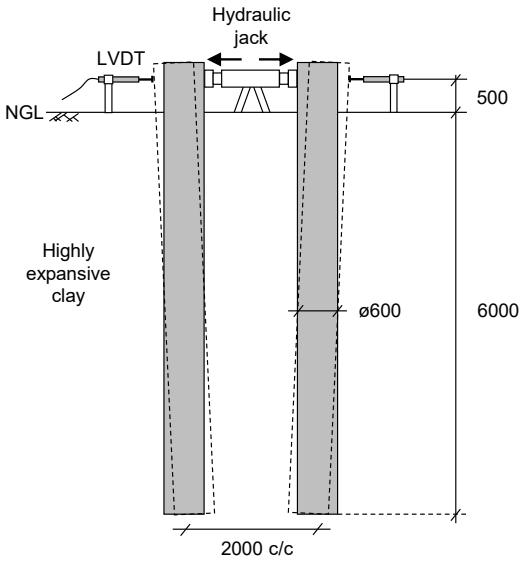

Figure 2. Free pile test layout.

3 RESULTS

The tests discussed in this paper involved the free ended piles which were subjected to 500 load cycles. The magnitude of applied lateral loads ranged from 10 – 110 kN. The results presented in Figure 3 indicate the applied load versus lateral displacement cycles for a 'dry' and 'wet' test. From this figure it can be seen that the pile tested under natural water content conditions (Figure 3a) illustrated an accumulated progressive displacement (or ratcheting behaviour) in the direction of the applied load. Given that the 'dry' test took place in a desiccated, highly fissured profile, this ratcheting behaviour is attributed to local yielding of the bonded/cemented material along the fissures.

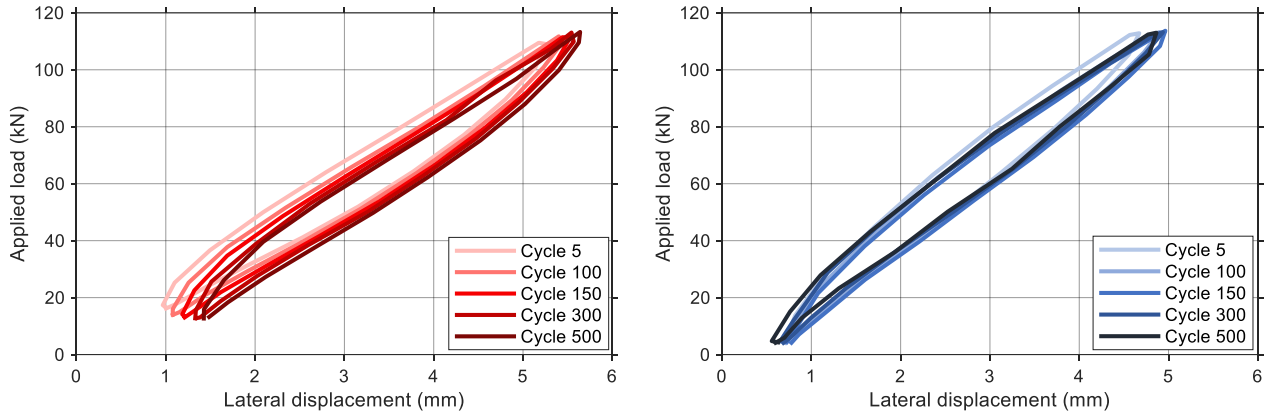

a) 'Dry' test *b) 'Wet' test*

Figure 3. Load-displacement curves for various cycles throughout lateral loading of free piles.

Conversely, Figure 3b) does not exhibit any ratcheting behaviour for the 'wet' pile, tested in the swelled profile. Given that any fissures within the expansive clay profile would likely have swelled closed during the wetting process, it can be appreciated that local yielding of the cemented material would not have occurred to the same extent during the testing of the 'wet' pile. Additionally, as highlighted by Gaspar and Jacobsz (2021), as an initially unsaturated soil is wetted up, the strain required to cause failure (i.e. ductility) increases, which further justifies the absence of local yielding during the 'wet' test.

For each load-unload cycle, an indication of the stiffness of the pile-soil system was given by the lateral cycle stiffness. The cycle stiffness was defined as the slope of a line connecting the peak and the trough of any given load-displacement cycle, as indicated in Figure 4.

The evolution of cycle stiffness throughout testing for both piles is presented in Figure 5. An initial observation from this result is that the 'wet' pile initially illustrates a higher stiffness than the 'dry' pile. An explanation for this result can be described by considering the underlying mechanisms at play throughout a swell process. As discussed by Gaspar et al. (2023) in describing the behaviour of centrifuge modelling of piled foundations in expansive clays, the initial portion of a swell process is governed by increases in lateral pressure against a pile shaft. Once swell magnitude exceeds some critical value, the effects of swell-induced softening within the clay tend to dominate the behaviour along the pile/soil interface. The higher initial stiffness for the 'wet' pile illustrated in Figure 5, suggests that for the testing conducted in this study, the increases in lateral pressure against the pile shaft were the dominant mechanism at the time of testing.

From Figure 5 it can also be seen that stiffness increased with cycle number for the 'dry' pile. As mentioned previously, the ratcheting behaviour observed for the 'dry' pile was attributed to local yielding of the cemented/bonded material along fissures. However, after such bonding was largely destroyed, intact masses of clay would have been pushed against each other at the fissure interfaces with continued loading, thereby producing the observed increases in cycle stiffness.

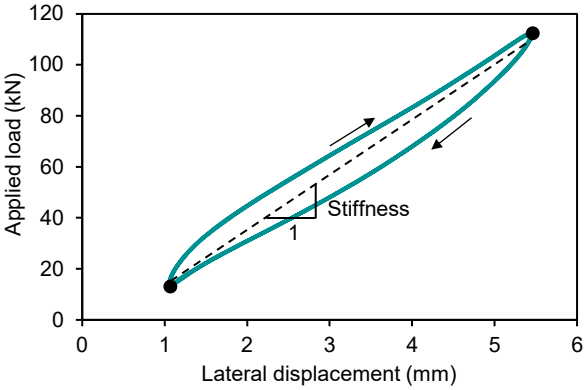

Figure 4. Definition of cycle stiffness.

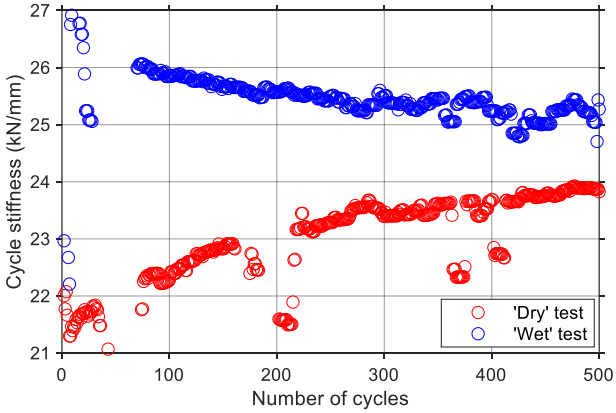

Figure 5. Cycle stiffness versus cycle number for piles in the 'dry' test and 'wet' test.

In contrast, changes in lateral stiffness for the 'wet' pile were comparatively less. However, the slight reductions can be described by considering the principles of unsaturated soil mechanics. Throughout the application of consecutive load cycles, local compaction would have occurred behind the pile. Assuming no changes in water content, this slight reduction in void ratio would have increased the degree of saturation, thus reducing the magnitude of soil suction and stiffness of the clay. Soil water retention curves (SWRCs) for soil sampled from this site (as discussed by Murison et al. (2023) and Eost et al. (2023)) illustrate that even slight increases in saturation can result in suction reductions of several megapascals.

4 CONCLUSIONS

This paper presents the results of full-scale testing of laterally loaded piles under 'dry' (natural water content) and 'wet' (flooded and allowed to swell for 6 months) conditions. Results from the study illustrate that for a pile tested under 'dry' conditions, an accumulation of displacement (or ratcheting behaviour) occurs in the direction of applied loading. This behaviour is attributed to the local yielding of the bonded/cemented material along desiccated soil fissures. Conversely, for the pile tested under 'wet' conditions, where such fissures would likely have swelled closed, no ratcheting is observed.

It was also found that with increased cycle number, increases in cycle stiffness were observed for the 'dry' pile. Given the local yielding occurring along fissures during initial load cycles, subsequent load applications would have resulted in intact masses of unsaturated clay being pushed against one another, providing the increased stiffness observed.

In contrast, the pile tested under 'wet' conditions showed slight decreases in cycle stiffness. The suggested explanation for this outcome is based on fundamental principles of unsaturated soil mechanics. During loading, local compaction behind the pile would have produced slight reductions in void ratio. Assuming constant water content conditions, this reduction would have increased the degree of saturation, reducing soil suction and thus stiffness within the expansive clay.

ACKNOWLEDGEMENTS

The authors would like to express their gratitude to the UK Engineering and Physical Sciences Research Council (EPSRC) Global Challenges Fund for the financial support under the WindAfrica project, Grant Ref: EP/P029434/1. The first 4 authors of this paper would also like to thank the Springboks for winning the Rugby World Cup the weekend this paper was completed!

REFERENCES

Blight, G.E. (1984). Power Station Foundations in Deep Expansive Soil. *1st International Conference on Case Histories in Geotechnical Engineering, Missouri*, 77–86.

da Silva Burke, T.S., Jacobsz, S.W., Elshafie, M.Z.E.B. and Osman, A.S. (2022). Measurement of pile uplift forces due to soil heave in expansive clays. *Canadian Geotechnical Journal*, 59(12): 2119–2134. https://doi.org/10.1139/cgj-2021-0079.

Eost, L., Gaspar, T.A.V. and Osman, A.S. (2023). Hydromechanical characterisation of a highly expansive clay. *E3S Web of Conferences,* 382: 09004, https://doi.org/10.1051/e3sconf/202338209004.

Gaspar, T.A.V., Jacobsz, S.W., Heymann, G., Toll, D.G., Gens, A. and Osman, A.S. (2022). The mechanical properties of a high plasticity expansive clay, *Engineering Geology,* 303: 106647. https://doi.org/10.1016/j.enggeo.2022.106647.

Gaspar, T.A.V., Jacobsz, S.W., Smit, G. and Osman A.S. (2023). Centrifuge modelling of piled foundations in swelling clays. *Canadian Geotechnical Journal* (ahead of print). https://doi.org/10.1139/cgj-2022-0449.

Gaspar, T.A.V. and Jacobsz, S.W. (2021). Brazilian Tensile Strength Test conducted on ductile unsaturated soil samples. *Geotechnical Testing Journal*, 44(3): 20190078. https://doi.org/10.1520/GTJ20190078.

Jones D.E. and Holtz W.G. (1973). Expansive soils – the hidden disaster. *Civil Engineering*, 43(8): 49–51.

Murison, R.A., Jacobsz, S.W., da Silva Burke, T.S., Gaspar, T.A.V. and Osman, A.S. (2022). Monitoring bending moment distributions in large-scale laterally loaded piles using fibre Bragg gratings and vibrating wire strain gauges. *10th International Conference on Physical Modelling in Geotechnics (ICPMG), Daejeon, Korea,* 346–349.

Murison, R.A., Jacobsz, S.W., Gaspar, T.A.V., da Silva Burke, T.S. and Osman, A.S. (2023). Drying and wetting soil-water retention behaviour of a highly expansive clay under varying initial density, *E3S Web of Conferences,* 382: 09005, https://doi.org/10.1051/e3sconf/202338209005.

Proceedings of the XVIII ECSMGE 2024
GEOTECHNICAL ENGINEERING CHALLENGES
TO MEET CURRENT AND EMERGING NEEDS OF SOCIETY
© 2024 the Authors
ISBN 978-1-032-54816-6
DOI 10.1201/9781003431749-72
Open Access: www.taylorfrancis.com, CC BY-NC-ND 4.0 license

ECSMGE 24
XVIII EUROPEAN CONFERENCE ON SOIL MECHANICS AND GEOTECHNICAL ENGINEERING

Undrained triaxial test stress path shape as an indicator of sample quality

Forme du chemin de contrainte d'essai triaxial non drainé comme indicateur de la qualité de l'échantillon

V. Gjelsvik*, K. Kahrs
Norwegian Geotechnical Institute (NGI), Trondheim, Norway

**vidar.gjelsvik@ngi.no*

ABSTRACT: When determining soil strength parameters from laboratory tests for use in geotechnical safety evaluations, knowing the quality of the test sample is important. The quality of a triaxial test sample is commonly assessed by evaluating Δe (the change in void ratio during consolidation to the initial in situ stress)/e_0 (the initial void ratio). However, the type of behaviour of a sample during advanced testing can also provide information about the sample quality. We have analysed the stress paths of 89 active and passive anisotropically consolidated undrained triaxial tests on high quality block samples of clay with regard to shape, average dilatancy, and strain at failure and visualized the results in plots of the normalized shear stress against the overconsolidation ratio. From those plots, typical regions where points with a certain stress path shape, average dilatancy, or strain at failure can be identified as well as outliers. Our analysis indicates that outliers typically are points with a lower sample quality.

RÉSUMÉ: La qualité d'un échantillon d'argile est très importante afin de bien évaluer les paramètres de résistance du sol à l'aide d'essais en laboratoire. La qualité d'un échantillon d'essai triaxial est généralement évaluée en analysant le changement de l'indice des vides (Δe) pendant la consolidation de l'échantillon par rapport à l'indice des vides initial (e_0). Cependant, le comportement du sol pendant l'essai triaxial peut également en dire long sur la qualité de l'échantillon. Dans ce papier nous avons analysé les chemins de contrainte de 89 essais triaxiaux actifs et passifs non drainés et consolidés anisotropiquement sur des échantillons de bloc d'argile de haute qualité. L'analyse compare les différents chemins de contrainte par rapport à leur forme, la dilatance moyenne de l'échantillon et la déformation à la rupture. Les résultats sont comparés et visualisés en utilisant la contrainte de cisaillement normalisée en fonction du degré de sur-consolidation. La méthode présentée dans ce papier permet d'identifier des valeurs aberrantes en comparant avec la forme des cheminements de contrainte, la dilatance moyenne ou la déformation à la rupture. Notre analyse indique que les valeurs aberrantes sont généralement des points avec une qualité d'échantillon inférieure.

Keywords: Triaxial test stress path; overconsolidation ratio; dilatancy; sample quality.

1 INTRODUCTION

When determining soil strength parameters from laboratory tests for use in geotechnical safety evaluations, knowing the quality of the sample is important. There are well-established methods for quantifying sample quality for advanced tests such as triaxial and oedometer tests (Lunne et al., 1997; Karlsrud and Hernandez-Martinez, 2013; Berre et al., 2022). However, the behaviour of a sample during advanced testing also provides information about sample quality (e.g. Paniagua et al., 2017). Strength parameters from triaxial tests are usually determined graphically from a stress path plot. In this project, we have analysed the stress paths of 89 anisotropically consolidated undrained active (CAUc) and passive triaxial (CAUe) tests performed on high quality block samples of clay with regard to shape, average dilatancy before failure, and strain at failure. This paper demonstrates typical signs of good sample quality and gives examples of the expected behaviour for clays with overconsolidation ratios (OCRs) between 1 and 6.

2 ASSESSMENT OF SAMPLE QUALITY

The quality of a triaxial test sample is commonly assessed according to the classification given in ISO standard 19901-8:2014. The classification is based on the ratio between the change in void ratio during consolidation of the sample to in situ stresses (Δe) and the initial void ratio (e_0) and was originally proposed by Lunne et al. (1997). The extended classification for OCRs between 1 and 6 proposed by the Norwegian Geotechnical Society (NGF, 2013) is presented in Table 1.

Table 1. Evaluation of sample quality (NGF, 2013).

OCR	$\Delta e/e_0$			
1 to 2	<0.04	0.04-0.07	0.07-0.14	>0.14
2 to 4	<0.03	0.03-0.05	0.05-0.10	>0.10
4 to 6	<0.02	0.02-0.035	0.035-0.07	>0.07
Quality	1	2	3	4

1 very good to excellent, 2 fair to good, 3 poor, 4 very poor

Earlier studies have shown that piston samples with excellent quality according to the $\Delta e/e_0$-criterion still could have considerable disturbance compared to block samples (Paniagua et al., 2017; L'Heureux et al., 2018), measured by the undrained shear resistance. Therefore, the authors believe that data presented in this article could be useful in the overall assessment of clay sample disturbance.

3 DATA

We have used data from anisotropically consolidated undrained active (CAUc) and passive (CAUe) triaxial tests performed on high quality (class 1 or class 2) Ø250 mm block samples of clay from NGI's GEODIP high quality database (NGI, 2018). All triaxial tests in the database are consolidated to the assumed in situ stress state before shearing. An overview of the test sites with the number of CAUc and CAUe tests used from each site is given in (NGI, 2018). Table 2 shows the range of basic parameters in the database.

Table 2 Range of basic properties

Parameter	**Range**
w (%)	25 – 55
γ_t (kN/m³)	17 – 20
Clay content (%)	20 – 60
I_p (%)	5 – 30
S_t	2 – 225
OCR	1.1 – 6.2

The triaxial test data is visualized below by means of a stress -strain plot where $t = \frac{\sigma_a - \sigma_r}{2}$ (Figure 1) and a MIT stress path plot, where $s' = \frac{\sigma_a' + \sigma_{r'}}{2}$ (Figure 2). The stresses are normalized by the assumed in situ effective vertical stress.

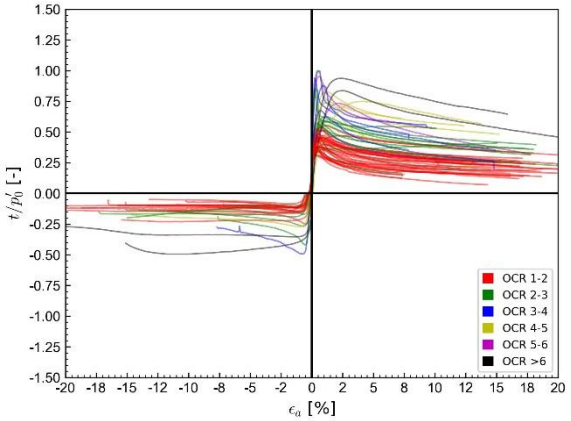

Figure 1. A normalized stress-strain plot visualizing the results from all active and passive triaxial tests.

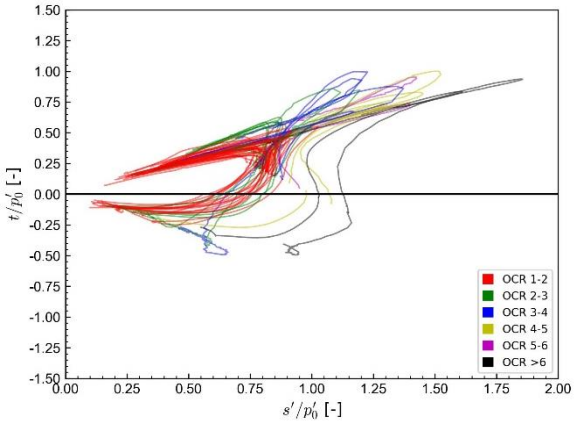

Figure 2. A normalized NGI/MIT stress path plot visualizing the results from all active and passive triaxial tests.

4 METHOD

4.1 Stress path shape

We have plotted the stress path of each active and passive triaxial test in a normalized MIT plot. The stress paths can be seen to group into four distinct types of shape according to the sample's dilative and contractive behaviour in shear just before and after failure: (1) a "contraction only" shape with a rounded turning point, (2) a "slight dilation, then contraction" shape with a sharp turning point either to the left or to the right of the zero dilatancy line (typically CAUc) or a loop to the left of the zero dilatancy line (typically CAUe), (3) a "dilation, then contraction" type with a looping turning point (pigs tail) to the right of the zero dilatancy line, and (4) a "dilation only" shape without a turning point. Our data does not contain any samples with stress path type 4.

Typical examples of shape types 1, 2, and 3 are given in Table 3. For each example, we have shown the stress path corresponding to zero dilatancy, which in an MIT plot is a straight line with gradient 3.

Table 3. Typical examples of stress path shape types 1-3.

Type	CAUC	CAUE
1	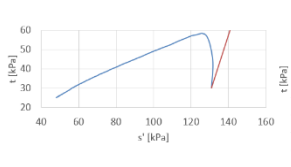	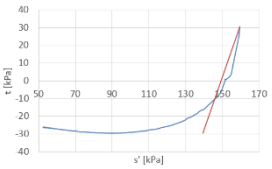
2	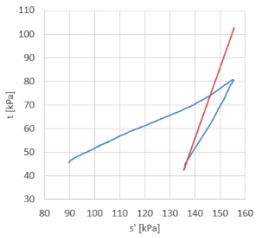	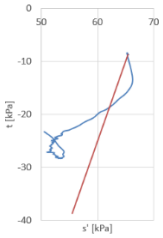
3	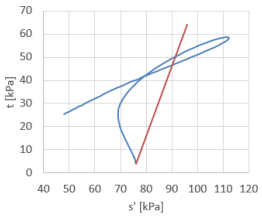	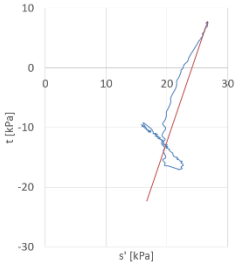

4.2 Average dilatancy

The average dilatancy is computed as the dilatancy between the initial stress state and the stress state at failure:

$$\overline{D} = \frac{\Delta\sigma'_m}{\Delta\sigma_d} = \frac{\sigma'_{m,f} - \sigma'_{m,0}}{\sigma_{d,f} - \sigma_{d,0}} \quad (1)$$

where σ_d (kPa) is the deviatoric stress and σ'_m (kPa) is the effective octahedral stress. For tests where failure occurs at an axial strain greater than 10%, the stress state at 10% axial strain is used. The average gradient from initial state to failure in the MIT-plot is:

$$\frac{\Delta t}{\Delta s'} = \frac{3}{1+6\overline{D}} \quad (2)$$

4.3 Axial strain at failure, maximum shear stress, and overconsolidation ratio

The axial strain at failure, the shear strength, and the overconsolidation ratio at the depth of the triaxial test sample are provided in the GEODIP database and used directly. For tests where failure occurs at an axial strain greater than 10%, an axial strain of 10% and a shear strength equal to the shear stress at 10% axial strain are used.

5 RESULTS

The results are shown in plots of the normalized shear strength c_u/p'_0 against the OCR where each data point corresponds to one of the 89 triaxial tests. The data point colours correspond to different stress path types (Figure 3), different ranges of average dilatancy (Figure 4), and different ranges of axial strain at failure (Figure 5).

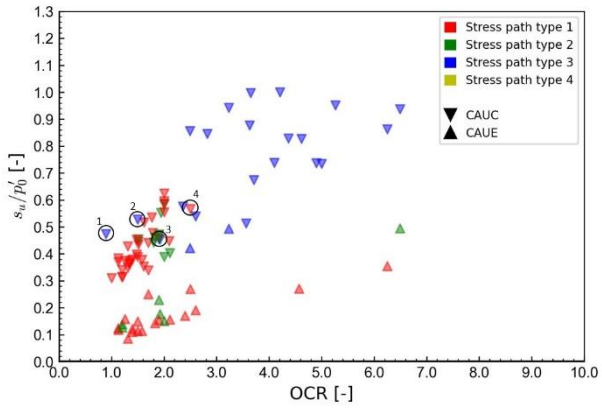

Figure 3. Normalized shear strength plotted against OCR. The data point colours correspond to stress path types 1-4.

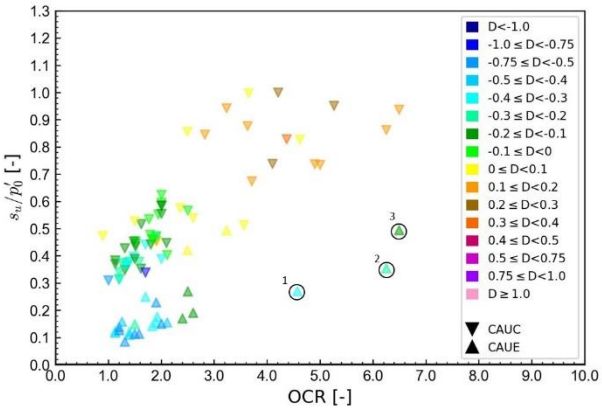

Figure 4. Normalized shear strength plotted against OCR. The data point colours correspond to different ranges of average dilatancy, $\overline{D}$.

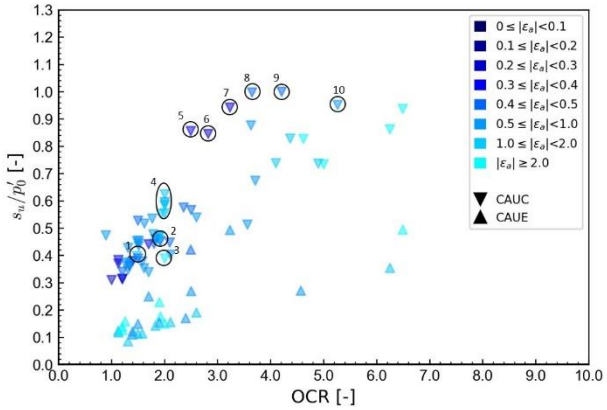

Figure 5. Normalized shear strength plotted against OCR. The data point colours correspond to different ranges of axial strain at failure.

6 DISCUSSION

For active triaxial tests, we see that stress path type 1 generally occurs for OCRs between 1 and 2, type 2 for OCRs around 2, and type 3 for OCRs larger than 2.5. For passive triaxial tests, there is no such pattern. We have marked four outliers in Figure 3. Outliers 1-3 are stress path type 3 samples that are very close to having stress path type 2 (very small loop). Outlier 4 is a stress path type 1 sample that dilates up to a shear stress of almost 50% of the maximum shear stress, so this sample is close to having stress path type 2.

In Figure 4, we see that for active triaxial tests there is a general trend of the average dilatancy increasing from large negative values (contraction) to large positive values (dilation) with increasing OCR and normalized shear strength. The results clearly demonstrate the mechanism behind the well-known stress history dependence, described in the SHANSEP procedure (Ladd and Foott, 1974). This OCR dependency can also be seen for passive triaxial tests, but only for OCR values less than 3.2. There are, however, few passive triaxial test samples with OCRs larger than 3.2. All three of those samples (marked 1, 2, and 3 in Figure 4) are of quality 2. More data is needed to conclude on whether those samples are outliers or whether there is more scatter in the CAUe data than in the CAUc data. The gradient, $\frac{\Delta t}{\Delta s'}$ ranges from about $-\frac{6}{7}$ for NC-clays to $+\frac{1}{1}$ for OC-clays, noting that also the initial stress state ranges from K_0' = 0,55 – 1,0 for NC- to OC-clays respectively.

In Figure 5, we see that for active triaxial tests there is a general trend of the axial strain at failure increasing with increasing OCR and normalized shear strength. For passive triaxial tests, there is a lot more scatter in the data, and no clear trend can be seen. In particular, there are many CAUe samples with low OCRs that fail at a high axial strain. We have marked ten outliers among the CAUc data points. Outliers 1, 2, and most of the test samples marked as outlier 4, which exhibit a higher axial strain at failure than what would be expected from the general trend in the data, are from sites Onsøy and Bothkennar. Those sites have high plasticity (I_p above 30%) relative to the other sites. Outliers 5-10, which exhibit a lower axial strain than expected, are from site Emmerstad. The clay from this site is probably cemented. Outlier 3 has a stress-strain curve that is known to be typical of samples that have been disturbed.

7 CONCLUSIONS

In this paper, we have provided three plots that visualize a high quality undrained triaxial test sample's typical behaviour in undrained shear with regard to the shape of the stress path, the average dilatancy, and the axial strain at failure. For active tests, regions where samples with a given overconsolidation ratio typically will plot can be identified. Outliers are typically samples of a lower quality or with material characteristics that differ from those of most of the other samples. To improve the plots' usefulness as a tool for visually assessing sample quality, it may be necessary to create separate plots for clays with different material characteristics. For passive tests, there is more scatter in the data, and more data with overconsolidation ratios larger than 3 is needed to conclude on whether similar regions can be identified here.

ACKNOWLEDGEMENTS

The project presented in this article was funded in part by the Norwegian Research Council through the Strategic Research Project SP8-GEODIP at NGI.

REFERENCES

Berre, T., Lunne, T., & L'Heureux, J. S. (2022). Quantification of sample disturbance for soft, lightly overconsolidated, sensitive clay samples. *Canadian Geotechnical Journal*, *59*(2), 300-303

Karlsrud, K. and Hernandez-Martinez,F. G. (2013). Strength and deformation properties of Norwegian clays from laboratory tests on high-quality block samples. *Can. Geotech. J.*, 50(12): 1273-1293. http://doi.org/10.1139/cgj-2013-0298

Lunne, T., Berre, T. and Strandvik, S. (1997). Sample disturbance effects in soft low plastic Norwegian clay. In: *Recent Developments in Soil and Pavement Mechanics*, Almeida (ed.), Balkema, Rotterdam, Netherlands, pp. 81-102.

NGF (2013). Melding 11 Veiledning for prøvetaking (Guidelines for sampling), Norsk Geoteknisk Forening. Oslo, Norway (in Norwegian).

NGI (2018). SP8 – Soil Parameters in Geotechnical Design (GEODIP). GEODIP's high-quality database: Clay, Norwegian Geotechnical Institute, Oslo, Norway, Rep. 20150030-02-R rev. 2.

Paniagua, P., L'Heureux, J.-S., Carroll, R., Kåsin, K. and Sjursen, M. (2017). Evaluation of sample disturbance of three Norwegian clays. In: *Proceedings of the 19th International Conference on Soil Mechanics and Geotechnical Engineering*, Seoul, South Korea, pp. 481-484.

Proceedings of the XVIII ECSMGE 2024
GEOTECHNICAL ENGINEERING CHALLENGES
TO MEET CURRENT AND EMERGING NEEDS OF SOCIETY
© 2024 the Authors
ISBN 978-1-032-54816-6
DOI 10.1201/9781003431749-73
Open Access: www.taylorfrancis.com, CC BY-NC-ND 4.0 license

ECSMGE 24
XVIII EUROPEAN CONFERENCE ON SOIL MECHANICS AND GEOTECHNICAL ENGINEERING

Cohesive soil behavior under cyclic loading in undrained conditions

Comportement des sols cohésifs sous chargement cyclique dans des conditions non drainées

A. Głuchowski*, W. Sas
Warsaw University of Life Sciences - SGGW, Warsaw, Poland
**andrzej_gluchowski@sggw.edu.pl*

ABSTRACT: This paper investigates the cyclic plastic creep phenomenon in cohesive soils during cyclic loading. Plastic creep, defined as the accumulation of excessive plastic strains under a medium stress state in constant stress or strain amplitude tests, is part of the shakedown theory for cohesive soils. Cyclic triaxial tests were conducted to understand the mechanisms, proposing a cyclic plastic creep mechanism. The soil response was analyzed based on pore pressure, stress paths, and plastic strain change, revealing that cyclic plastic creep takes the form of abation for cohesive soils in undrained conditions. In this phase, unlike in shakedown, where the accumulation of plastic strain to a steady-state value is observed, the sample experiences a decreasing plastic strain accumulation rate due to cyclic loading. Therefore, instead of the shakedown criterion, the abation slope is proposed as a form of soil behavior evaluation in long-term cyclic loading. These findings have implications for improving the design and performance of structures on cohesive soils, like foundations or embankments.

RÉSUMÉ: Cet article examine le phénomène de fluage plastique cyclique dans les sols cohésifs pendant le chargement cyclique. Le fluage plastique, défini comme l'accumulation de déformations plastiques excessives sous un état de contrainte moyenne dans des tests à amplitude constante de contrainte ou de déformation, fait partie de la théorie de la consolidation pour les sols cohésifs. Des essais triaxiaux cycliques ont été réalisés pour comprendre les mécanismes, proposant ainsi un mécanisme de fluage plastique cyclique. La réponse du sol a été analysée en se basant sur la pression interstitielle, les trajectoires de contrainte et le changement de déformation plastique, révélant que le fluage plastique cyclique prend la forme d'une abattement pour les sols cohésifs dans des conditions non drainées. À cette phase, contrairement à la consolidation, où l'accumulation de déformation plastique jusqu'à une valeur d'état stable est observée, l'échantillon connaît un taux d'accumulation de déformation plastique décroissant en raison du chargement cyclique. Par conséquent, au lieu du critère de consolidation, la pente d'abattement est proposée comme une forme d'évaluation du comportement du sol lors du chargement cyclique à long terme. Ces résultats ont des implications pour l'amélioration de la conception et des performances des structures sur des sols cohésifs, telles que les fondations ou les remblais.

Keywords: Cyclic loading; shakedown; cohesive soil; undrained conditions; cyclic plastic creep.

1 INTRODUCTION

Cohesive soils often constitutes a subgrade of constructions subjected to cyclic loading. The design process of foundations or earth structures founded on this soil type must include the most unfavourable situations which are undrained conditions.

Cohesive soils have low permeability and higher than non-cohesive soils compressibility and therefore this soil type accumulates greater deformation and fails at lower stress state (Toyota and Takada, 2021).

Cyclic loading may have different amplitude levels and what is more, the amplitude can vary with time. Within a span of service time, the structure can be subjected to repeated loading characterised by various stress amplitude, frequency and can be subjected to large number of cycles (Han et al., 2021).

The cohesive soils in undrained conditions typically exhibits increase in excess pore water pressure what brings the soil to and overconsolidated state (Han et al., 2021; Nie et al., 2023). The cohesive soil deformation is a result of stiffness degradation which proceeds with cycle numbers expressed by logarithmic relationship (Głuchowski and Sas, 2020).

Due to high deformability of cohesive soil in undrained conditions, the laboratory tests are focussing on the deformation characteristics and aims to deploy a empirical or constitutive models describing effect of cyclic loading (Chai et al., 2015; Feng et al.,

2021; Lei et al., 2020; Li and Selig, 1996; Sakai et al., 2003).

When the deformation during cyclic loading is analysed two strain categories can be distinguished: resilient strains ε_r and plastic strains ε_p. The cohesive soil deformation is generally explained within a framework of shakedown theory (Hu et al., 2012; Pasten et al., 2014; Qian et al., 2016; Xiao et al., 2018).

Based on this theory, the distorted response characteristics of coarse-grained materials can be classified into three categories: (i) plastic shakedown (Range A), (ii) plastic creep (Range B), and (iii) incremental collapse (Range C).

The Ranges of soil response indicates that some limits are existing within this framework when soil develops plastic deformation in certain range and magnitude. Range A – plastic shakedown occurs when the plastic strain rate decreases rapidly, Range B plastic creep occurs when plastic strain rate keeps decreasing or remains at a low level, Range C – where plastic strain rate decreases slowly or keeps increasing.

The strain accumulation models are based mostly on relationship to number of cycles as time equivalent (Fu et al., 2021; Guo et al., 2013; Zhou and Gong, 2001; Zhu et al., 2021). Such approach comes from Yasuhara et al. (Yasuhara et al., 1992) studies which indicated that clay behaviour under cyclic loading is similar to that under creep loading. This approach suits more for plastic strain development during cyclic loading. However, models which utilizes the relationship to number of cycles are empirical models which limits its applicability.

This article presents triaxial test results on cohesive soil with a mid-probe pore water pressure sensor for accurate measurement of Δu, examining the long-term response to cyclic loading.

2 MATERIAL AND METHODS

2.1 Material

In this study, sieve and aerometric (Bouyoucos method using a modification made by Casagrande) tests were conducted on cohesive soil. The test results are presented in Table 1. Soil employed in this study is commercially acquired kaolin KOM manufactured by Surmin-Kaolin (Nowogrodziec, Poland). The mineral composition provided by producer is: 51.5% SiO_2, 34.5% Al_2O_3, 0.63% K_2O, 0.54% TiO_2, 0.53% Fe_2O_3 as well as small quantities of Ca, Mg, Na and Mn oxides. The soil was composed of the silt fraction f_{Si} which constitutes 88% and the clay fraction f_{Cl} which constitutes 12% of the total soil mass. Additionally, test on the soil dynamic properties were conducted to establish the shear wave velocity V_S. Table 1 presents the results of physical and mechanical tests on cohesive soil.

Table 1. Index and mechanical properties of cohesive soil in this study.

Properties	Symbol	Value
Dry density	ρ_d ($g \cdot cm^{-3}$)	1.93
OMC	(%)	12.3
Liquid limit	w_l (%)	20.8
Plasticity limit	w_p (%)	40.2
Plasticity index	Ip (-)	19.4
Void ratio	e_0 (-)	0.410
S-wave velocity	V_s ($m \cdot s^{-1}$)	243.5
Shear modulus	G_0 (MPa)	130.0

2.2 Methods

Cyclic triaxial tests were performed using a triaxial apparatus on four soil samples, each of which having a diameter of 0.07 m and a height of 0.14 m. The soil samples were compacted using the Proctor method at OMC. Initial void ratio e_0 ranged from 0.37 to 0.41. The tests were performed at 1 Hz frequency for $2 \cdot 10^4$ cycles. The σ'_3 during tests was set to 45, 90, 135, 180 kPa represented by 1.1 to 1.4 abbreviation. The q_a – deviator stress amplitude ($q_a = 0.5(q_{max} - q_{min})$) was equal to ~21 kPa q_m deviator stress median ($q_m = 0.5(q_{max} + q_{min})$) was equal to ~32 kPa.

3 RESULTS

Cyclic triaxial test results in *q-p'* space are presented in Figure 1. The objective of this cyclic loading program was to investigate the loading effects at various confining pressure levels. Therefore, at higher σ'_3 values, different soil responses are observed. At σ'_3 = 45 kPa, the observed excess pore water pressure is lower than for Test 1.2 with σ'_3 = 90 kPa. The slope of the critical state line, M, is equal to 0.873 (for φ' = 22.4°), and the preconsolidation pressure σ_p equals 220 kPa (Proctor compaction effect); therefore, for Test 1.1 and 1.2, the stress path moves towards the deviator stress axis.

It's worth noting that the stress paths on the dry side, characteristic of overconsolidated soils, may intersect the yield surface above the critical state line. Therefore, in drained conditions, dilative plastic strains would be produced, and the yield surface may shrink. In undrained conditions, the stress paths stop before the aforementioned mechanism could occur. This effect is accompanied by high plastic strain accumulation, as seen in Figure 2. For Test 1.2, the specimen responds to cyclic loading with a higher *p'* decrease and lower ε_p accumulation. The soil response on the wet side shows the opposite response.

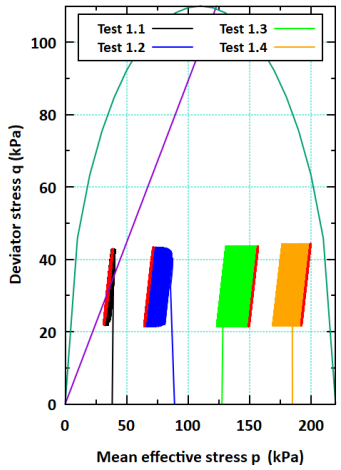

Figure 1. Cyclic triaxial test results –relationship between deviator stress q and mean effective stress p'. Res lines indicate last 4·10³ cycles.

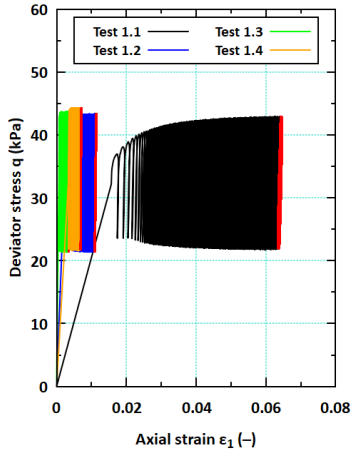

Figure 2. Deviator stress versus axial strain for cyclic triaxial test results in this study.

For tests 1.1 and 1.2, the stress paths move toward the deviator stress axis. For tests 1.3 and 1.4 the stress paths move in opposite direction. This means that in the case of tests 1.3 and 1.4, pore pressure is lower than at the beginning of the test.

The plastic strain development during cyclic loading shows that the most damaging effect is observed in the first cycle. In Figure 3a, Normalized accumulated plastic strain is presented. The plot shows how much of the plastic strain accumulated in the first cycle, $\varepsilon_{p,1}$, constitutes the total accumulated plastic strain after the Nth cycle, $\varepsilon_{p,N}$. After $2 \cdot 10^4$ cycles, $\varepsilon_{p,1}$ shear is between 19% to 50%, showing the significance of the first cycle on soil response. The plastic strain accumulated in the first loading cycle may have different origins. The technical issues of the contact surface between the pedestal and the top cap impact the test results. Therefore, in Figure 3b, the accumulated plastic strain is presented without accounting for the first cycle.

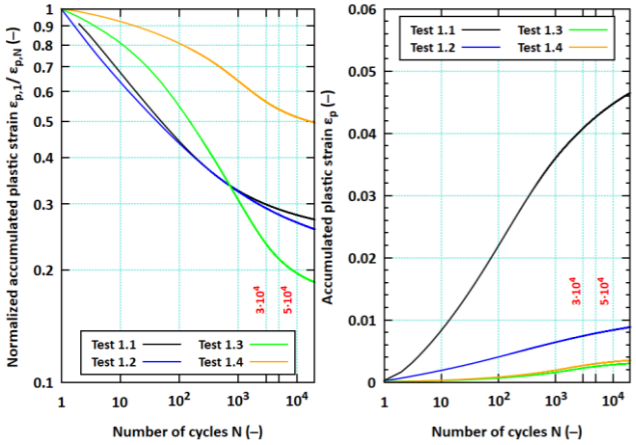

Figure 3. Plastic strain accumulation characteristics during cyclic loading in terms of normalized accumulated plastic strain (a) and accumulated plastic strain without first cycle.

Plastic strain accumulation characteristics indicates phenomena called *abation* which represents plastic strain increment $d\varepsilon_p$ in a constant, decreasing manner depicted by logarithmic law. Since the $d\varepsilon_p$ in *N+1* cycle is smaller than for *N*-th cycle, the tests results indicate that this rate of changes occurs in constant manner. In terms of shakedown theory abation can be compared to cyclic plastic creep. The shakedown criterion relays on accumulated plastic strain between $3 \cdot 10^4$ and $5 \cdot 10^4$ cycle. In the case of cohesive soil instead of this relationship, simple abation slope A_S can be used as soil behavior criterion as follows (1):

$$A_s = \varepsilon_p \cdot \log_N 10 \qquad (1)$$

Abation slope is empirical parameter and utilizes the classical strain accumulation models by referring to number of cycles relationship.

4 CONCLUSIONS

In conclusion, the cyclic loading program aimed to investigate soil responses at various confining pressure levels have shown different soil responses. The σ'_3 values, affected excess pore water pressure and stress paths evolution. The stress paths on the dry side may intersect the yield surface in drained conditions. In undrained conditions, stress paths stop possibly achieving yield surface, what is accompanied by high plastic strain accumulation. The soil behavior on the wet side exhibits the opposite trend. Additionally, the plastic strain development shows a significant impact in the first cycle, with the phenomenon of abation indicating plastic strain increment in a logarithmic decreasing manner. Introduced in this article, abation slope A_S, may become a crucial empirical parameter,

which can be used as a soil behavior criterion in cohesive soils under cyclic loading.

ACKNOWLEDGEMENTS

The work reported here was carried out within the Preludium project financed by National Science Centre, Poland (number 2016/23/N/ST10/02185). The authors wish to express its gratitude to the National Science Centre for its financial support.

REFERENCES

Chai, J.-C., Wu, H.-N., Xu, Y.-S., Zhang, D.-M., and Shen, S.-L. (2015). Evaluation of train-load-induced settlement in metro tunnels. *Proceedings of the ICE - Geotechnical Engineering*, 168(5): 396–406. https://doi.org/10.1680/geng.13.00159.

Feng, D., Zhu, X., Wang, J., Cai, Y., Guo, L., Du, Y., and Hu, X. (2021). The effects of cyclic loading on the reconsolidation behaviours of marine sedimentary clays under intermittent drainage conditions. *Soil Dynamics and Earthquake Engineering*, 141: 106510. https://doi.org/10.1016/j.soildyn.2020.106510.

Fu, Z., Wang, G., Song, W., Yu, Y., Wei, P., and Wu, T. (2021). Deformation Behavior of Saturated Soft Clay under Cyclic Loading with Principal Stress Rotation. *Applied Sciences*, 11(19): 8987. https://doi.org/10.3390/app11198987.

Głuchowski, A., and Sas, W. (2020). Long-Term Cyclic Loading Impact on the Creep Deformation Mechanism in Cohesive Materials. *Materials*, 13(17): 3907. https://doi.org/10.3390/ma13173907.

Guo, L., Wang, J., Cai, Y., Liu, H., Gao, Y., and Sun, H. (2013). Undrained deformation behavior of saturated soft clay under long-term cyclic loading. *Soil Dynamics and Earthquake Engineering*, 50: 28–37. https://doi.org/10.1016/j.soildyn.2013.01.029.

Han, J., Yin, Z.-Y., Dano, C., and Hicher, P.-Y. (2021). Cyclic and creep combination effects on the long-term undrained behavior of overconsolidated clay. *Acta Geotechnica*, 16(4): 1027–1041. https://doi.org/10.1007/s11440-020-01078-5.

Hu, C., Liu, H., and Huang, W. (2012). Anisotropic bounding-surface plasticity model for the cyclic shakedown and degradation of saturated clay. *Computers and Geotechnics*, 44: 34–47. https://doi.org/10.1016/j.compgeo.2012.03.009.

Lei, H., Liu, M., Feng, S., Liu, J., and Jiang, M. (2020). Cyclic Behavior of Tianjin Soft Clay under Intermittent Combined-Frequency Cyclic Loading. International *Journal of Geomechanics*, 20(10): 04020186. https://doi.org/10.1061/(ASCE)GM.1943-5622.0001805.

Li, D., and Selig, E. T. (1996). Cumulative Plastic Deformation for Fine-Grained Subgrade Soils. *Journal of Geotechnical Engineering*, 122(12): 1006–1013. https://doi.org/10.1061/(ASCE)0733-9410(1996)122:12(1006) .

Nie, G., Liu, Y., Liu, Z., Liang, Z., Xue, J., and Liang, Y. (2023). The Effects of Drainage Conditions on the Cyclic Deformation Characteristics of Over Consolidated Clayey Soil. International *Journal of Civil Engineering*, 21(4): 603–615. https://doi.org/10.1007/s40999-022-00787-0.

Pasten, C., Shin, H., and Santamarina, J. C. (2014). Long-Term Foundation Response to Repetitive Loading. *Journal of Geotechnical and Geoenvironmental Engineering*, 140(4): 04013036. https://doi.org/10.1061/(ASCE)GT.1943-5606.0001052.

Qian, J.-G., Wang, Y.-G., Yin, Z.-Y., and Huang, M.-S. (2016). Experimental identification of plastic shakedown behavior of saturated clay subjected to traffic loading with principal stress rotation. *Engineering Geology*, 214: 29–42. https://doi.org/10.1016/j.enggeo.2016.09.012.

Sakai, A., Samang, L., and Miura, N. (2003). Partially-Drained Cyclic Behavior and its Application to the Settlement of a low Embankment Road on Silty-Clay. *Soils and Foundations*, 43(1): 33–46. https://doi.org/10.3208/sandf.43.33.

Toyota, H., and Takada, S. (2021). Soil element assessment of cyclic-load-induced settlement considering combination of vertical, horizontal, and shear stresses in cohesive soil. *Soils and Foundations*, 61(3): 752–764. https://doi.org/10.1016/j.sandf.2021.02.007.

Xiao, Y., Zheng, K., Chen, L., and Mao, J. (2018). Shakedown analysis of cyclic plastic deformation characteristics of unbound granular materials under moving wheel loads. *Construction and Building Materials*, 167: 457–472. https://doi.org/10.1016/j.conbuildmat.2018.02.064.

Yasuhara, K., Hirao, K., and Hyde, A. F. L. (1992). Effects of Cyclic Loading on Undrained Strength and Compressibility of Clay. *Soils and Foundations*, 32(1): 100–116. https://doi.org/10.3208/sandf1972.32.100.

Zhou, J., and Gong, X. (2001). Strain degradation of saturated clay under cyclic loading. *Canadian Geotechnical Journal*, 38(1): 208–212. https://doi.org/10.1139/t00-062.

Zhu, W., Dai, G., and Gong, W. (2021). Study on Cyclic Cumulative Deformation Characteristics and the Equivalent Cyclic Creep Model of Soft Clay. *Mathematical Problems in Engineering*, 2021: 1–11. https://doi.org/10.1155/2021/5588494.

Proceedings of the XVIII ECSMGE 2024
GEOTECHNICAL ENGINEERING CHALLENGES
TO MEET CURRENT AND EMERGING NEEDS OF SOCIETY
© 2024 the Authors
ISBN 978-1-032-54816-6
DOI 10.1201/9781003431749-74
Open Access: www.taylorfrancis.com, CC BY-NC-ND 4.0 license

ECSMGE 24
XVIII EUROPEAN CONFERENCE ON SOIL MECHANICS AND GEOTECHNICAL ENGINEERING

Numerical simulation of pore water pressure evolution beneath a raft foundation during a river flooding

Simulation numérique de l'évolution de la pression interstitielle sous un radier lors d'une inondation

E.P. Graterol*, J.G. Gutiérrez-Ch, L. Mediero, S. Senent
E.T.S.I. de Caminos Canales y Puertos. Universidad Politécnica de Madrid, Madrid, Spain

**ep.graterol@alumnos.upm.es*

ABSTRACT: In the last decades, the rapid growth of population in urban areas has led to construction of buildings with several basement levels. Usually, many of these new structures are built below the water table and/or on floodplains. Under such conditions, if a river flooding occurs, seepage flow can mobilize pore water pressure in the soil. Therefore, upward pressures (called buoyant forces) acting on the raft foundation could be developed. Thus, the understanding of this behaviour is a key aspect for safety of such buildings. In this work, a numerical model is employed to assess the variation of pore water pressure beneath a raft foundation as a result of river flooding. The finite difference code FLAC2D is used, simulating a real flood in Pamplona (Spain) due to a fluvial overflow of the Arga River. Results suggest that numerical models can be employed to simulate the mobilized pore water pressure beneath a raft foundation caused by river flooding. In addition, despite being transitory, such natural hazard events can be critical for safety of buildings with basements. Results also show the relevance of the soil properties on the evolution of pore water pressure mobilized beneath raft foundations.

RÉSUMÉ: Au cours des dernières décennies, la croissance rapide de la population dans les zones urbaines a conduit à la construction de bâtiments à plusieurs niveaux de sous-sol. Habituellement, bon nombre de ces nouvelles structures sont construites sous la nappe phréatique et/ou sur des plaines inondables. Dans ces conditions, si une crue se produit, le débit d'infiltration augmente la pression interstitielle dans le sol et des pressions (appelées forces flottantes) agissant vers le haut sur le radier pourraient se développer. Ainsi, la compréhension de ce comportement est un aspect clé pour la sécurité de tels bâtiments. Dans ce travail, on utilise un modèle numérique pour évaluer la variation de la pression de l'eau interstitielle sous un radier lors d'une inondation. Pour ce faire, le logiciel de différences finies FLAC2D est utilisé, simulant une inondation réelle à Pampelune (Espagne) due au débordement de la rivière Arga. Les résultats suggèrent que des modèles numériques peuvent être utilisés pour mesurer la pression de l'eau interstitielle sous un radier tout en tenant compte des inondations fluviales, et que ces événements naturels, bien qu'étant transitoires, peuvent être critiques pour la sécurité des bâtiments avec sous-sol. Les résultats montrent également l'importance des propriétés du sol sur l'évolution de la pression interstitielle sous les radiers.

Keywords: Pore water pressure; raft foundation; river flooding; numerical simulation.

1 INTRODUCTION

Buildings with basement levels can be exposed to permanent or transitory hydrostatic pressures during its construction and service life (Ren et al., 2022). Permanent hydrostatic pressure occurs when the structure is partially or fully built below a constant water table. On the other hand, transitory hydrostatic pressure occurs when water table changes, due to either rainwater infiltration caused by an intense storm or river flooding (Chaudhary, 2012; Bikçe et al., 2018), being the latter of greater risk when the structure is located on a floodplain.

During river flooding, the infiltrated water will generate pore water pressures under the underground structure, which magnitude will depend on the water depth below the water table, the soil permeability, and the flood event duration. Thus, underground structures should be designed with enough uplift resistance and safety to support excess pore water pressures due to water table changes.

Although problems associated with water table changes are documented in many cities around the world (Bikçe et al., 2018), such an aspect is not currently considered as a crucial factor; however, this phenomenon should be considered in the design of future buildings, given the economic losses (i.e., building damages) associated with water table changes (Kreibich and Thieken, 2008). For that reason, recent works on this topic have been conducted (Alonso-Pollán et al., 2018; Zhang et al., 2019; Graterol et al., 2022), and some guidelines have been proposed.

Nevertheless, despite previous efforts, a more in-depth analysis of the impact of water table changes on building safety is still needed (Liu et al., 2023).

This paper provides a contribution that assess the influence of water table changes beneath the raft foundation of a building with one basement level and diaphragm walls. To that end (i) a real flood event registered in in the Arga River in Pamplona (Spain) is used; (ii) a building located on the Arga River floodplain in Pamplona is considered; and (iii) numerical models in FLAC2D to simulate the water table changes due to flooding are developed.

2 CASE STUDY AND DATA

2.1 Case study

The building to be analyzed herein is located in the city of Pamplona in central northern Spain. This city is crossed by the Arga River, with a catchment area of around 500 km^2 (Lompi et al., 2023). Over the years, Arga River fluvial floods have produced significant losses in some areas of Pamplona close to the river, such as the neighborhoods of Txantrea, San Jorge and Rochapea, the latter being one of the most affected during such natural hazard events (Munárriz, 2022). For this reason, this research analyses the effect of Arga River flooding on the pore water pressure mobilized beneath a raft foundation. To that end, a building located in the potential flooded zone in the Rochapea neighborhood is considered as an example (see Figure 1).

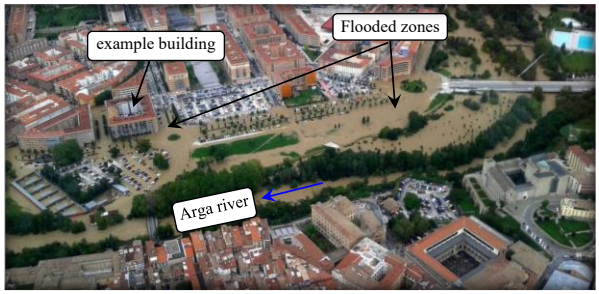

Figure 1. Rochapea neighborhood in the 9 June 2013 flood in Pamplona (Spain) (modified from Noticias de Navarra, 2022).

2.2 Data

According to the Spanish real-time SAIH system (Sistema Automático de Información Hidrológica, in Spanish), which provides real time data in the Ebro River Basin Authority, the Arga River suffered one of the most recent and highest floods on the 10th of December 2021, in which a maximum water depth of 4.8 meters was recorded in Pamplona. Accordingly, the water depth (h)–time (t) curve recorded for such event is employed in this work (see Figure 2). Such a curve is obtained from flood maps obtained for Rochapea neighborhood by Soriano et al. (2023) by using hydrodynamic simulation; note that, $t_{peak} = 9$ hours and $t_{end} = 22.2$ hours represent, respectively, the time in which the highest water depth is reached and the flood event duration. In this way, the impact of a real flood event (similar to the one illustrated in Figure 1) on an example building located in the potential flooded zone in the Rochapea neighborhood is simulated.

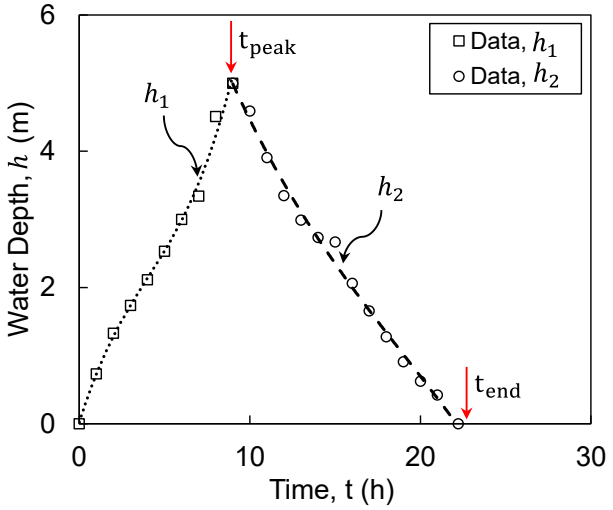

Figure 2. Water depth–time curve simulated for the 10th of December 2021 flood in Pamplona (Spain) (data from Soriano et al. 2023).

The fitted curve reported in Figure 2 is obtained from the following equations (h_1 and h_2) as a function of time (t), as:

$$h_1(t) = 8.228 \times 10^{-3}t^3 - 9.963 \times 10^{-2}t^2 + 7.959 \times 10^{-1}t + 2.094 \times 10^{-2} \quad (1)$$

$$h_2(t) = -7.460 \times 10^{-4}t^3 + 4.277 \times 10^{-2}t^2 - 1.138t + 12.31 \quad (2)$$

3 NUMERICAL MODEL

The numerical models of this work are developed through the Finite Difference Method and its implementation in FLAC2D (Itasca Consulting Group, 2016). Figure 3 shows the conceptual model of an example building located on Pamplona floodplain. Note that, the building has one basement level and diaphragm walls, that the raft foundation is placed on a clay layer, and that the ground profile (formed by a clay bottom layer and a sand upper layer) is hydraulically connected to the Arga River. On the

other hand, Figure 4 shows the associated numerical model developed in FLAC2D, which models only half of raft foundation ($L_r = 20$ m), given the structure symmetry. The total width of the model is $L = 50$ m, the thicknesses of the sand and clay layers are $h_s = 2.5$ m and $h_c = 15$ m, respectively, and the diaphragm wall length is $l = 7.5$ m.

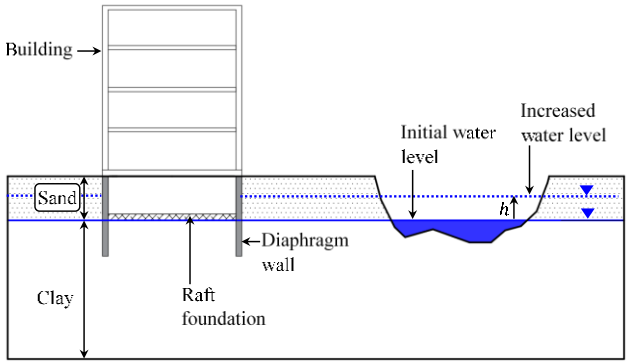

Figure 3. Conceptual model.

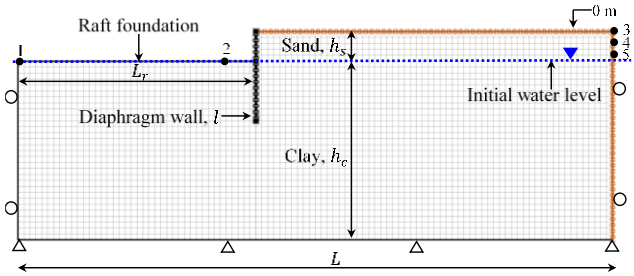

Figure 4. Set-up of the numerical model.

Table 1 lists the input geotechnical parameters used in the numerical models. Note that, reasonable values for sandy and clayey material from Zhang et al (2019) are employed. Regarding the boundary conditions (see Figure 4), the external boundaries are restraint except for the top boundary that remains free. Similarly, both vertical and horizontal movements of the diaphragm wall are restrained along its entire length, whereas the base that represent the raft foundation remains free.

At the beginning of the simulation (t = 0 hours), the initial water level is located at the bottom of the sand layer (i.e., 2.5 m below the ground surface); which is considered as the reference level ($h = 0$) for water level changes. Subsequently, the water level changes are attributed to the Arga River flooding, which is simulated through the variation of pore water pressure (U) applied on the boundary nodes (see brown points in Figure 4). During the duration time in which the water level is below the ground surface (i.e., $h < h_s$), only the pore water pressures at the right boundary of the model are modified. On the other hand, if the water level in the river rises and overflows onto the ground surface (i.e., $h \geq h_s$), pore water pressures at the top boundary of the model are applied. In each case, the values of U (with time) are computed as a function of the h values reported in Figure 2.

Table 1. Geotechnical parameters used in the numerical models (Zhang et al., 2019).

Property	Sand	Clay
Saturated density, ρ_{sat} (kg/m^3)	2020	2104
Young's modulus, E (MPa)	25	40
Poisson's ratio, ν	0.30	0.25
Permeability, k (m/s)	5.35x10^{-5}	7.11x10^{-7}

During the numerical simulation, the pore water pressures mobilized at the observation points (black points in Figure 4) are recorded. Such points correspond to: (i) the center of the raft foundation (point 1); (ii) near the corner of the raft foundation (point 2); and (iii) the right boundary of the model (points 3 to 5). The pore water pressures mobilized in points 3 to 5 correspond to the applied boundary condition based on the water depth–time curve obtained in the Arga River in Pamplona and shown in Figure 2, so they also serve as control points for the entry and exit flows of the model.

4 RESULTS

4.1 Pore water pressure response during the flood event in the Arga River in Pamplona

Figure 5 shows the pore water pressure (U) mobilized at the five observation points indicated in Figure 4; in particular, points located beneath the raft foundation (points 1 and 2: U_1 and U_2, respectively) and at the right boundary of the model (points 3 to 5: U_3 to U_5, respectively). As it can be seen, the U values recorded at the center and around the corner of the raft foundation are similar. For instance, for t < 9 h, U_1 and U_2 increase slowly because during this time the sand layer becomes progressively saturated only through the right boundary, with the rising of the water level. Once the water table reaches the ground surface (i.e, $h = h_s$), the entry of the water flow occurs not only through the right boundary but also through the ground surface. As a result, both U_1 and U_2 increase rapidly until reaching t_{peak}. Then, U_1 and U_2 decrease in a similar way to the curve obtained for the flood event until $t \cong 15$ h. Then, for t > 15 h, the rate of decrease of U_1 and U_2 is lower. This behavior might be attributed to the fact that the water table level drops below the ground surface for t > 14.5 h (note that $U_3 \cong 0$ for t > 14.5 h), so pore water pressure dissipation occurs only through the clay (i.e., through the most impermeable material). Finally, after the flood event end ($t > t_{end}$), pore water pressures

beneath the raft foundation continue to decrease, but at a very slow rate, until the initial water level is reached; however, this situation has not been obtained in the models developed herein due to the excessive computation time that is required. On the other hand, as expected, the U_3 to U_5 response is similar to the disturbance induced by the flood event shown in Figure 2.

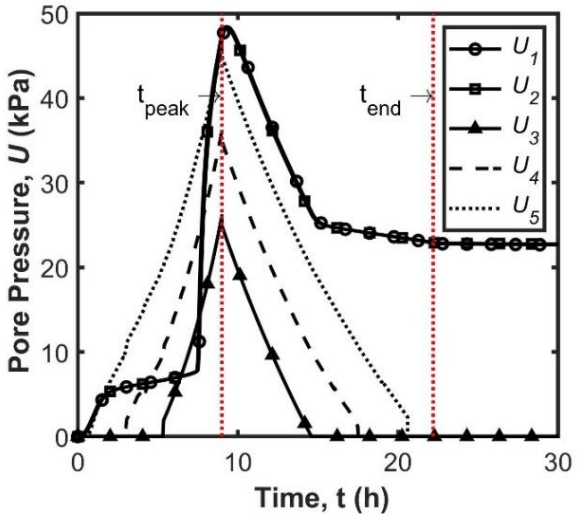

Figure 5. Pore pressure response for the flood depth–time curve presented in Figure 2, with the parameter values presented in Table 2.

4.2 Effect of soil permeability on the pore water pressure response

In this section, the effect of clay permeability on the pore water pressure response beneath the raft foundation (points 1 and 2: U_1 and U_2, respectively) is analyzed. Three different permeability values for the clay layer are considered ($k_1 = 7.11 \times 10^{-7}\, m/s$, $k_2 = 7.11 \times 10^{-8}\, m/s$ and $k_3 = 7.11 \times 10^{-9}\, m/s$). The sand layer permeability is kept constant as listed in Table 1. The selected permeability values for the clay layer are within the range of values suggested by Muzás (2007) for clayey materials.

As it can be observed in Figure 6, the decrease in the clay permeability affects not only the maximum pore water pressure mobilized beneath the raft foundation but also the time in which U starts to be mobilized and the corresponding time in which such maximum value is obtained. For example, note that U_1 and U_2 have a similar trend for the k_1 permeability value; however, for k_2 and k_3 values, U_2 starts to be mobilized before U_1, obtaining the maximum values later than in the models for k_1. Similarly, a decrease in clay permeability (from k_1 to k_3), reduces the mobilized pore water pressure beneath the raft foundation by approximately 5 times (see Figure 6).

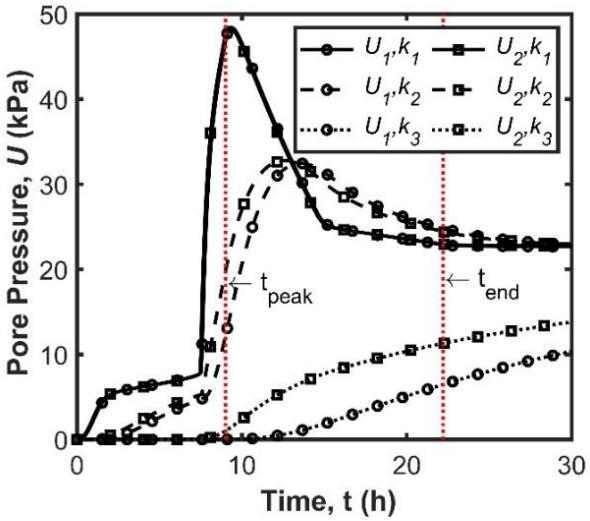

Figure 6. Effect of clay permeability on the pore pressure response for the flood depth–time curve presented in Figure 2.

5 CONCLUSIONS

In this work, the pore water pressure mobilized beneath a raft foundation of a building exposed to a real flood event was analyzed. The water depth–time curve obtained for the 10 December 2021 flood event in the Arga River in Pamplona (Spain) was used; an example building with one basement level in the Rochapea neighborhood (Pamplona) was considered; and numerical models incorporating representative geometric, geotechnical and hydraulic aspects of the analyzed problem were developed. The flooding event was induced in the numerical model as a boundary condition through pore water pressure computed from the water depth–time curve recorded during the flood event. In addition, the impact of soil permeability on the mobilized pore water pressure beneath the raft foundation was evaluated.

Numerical results show that, after the soil below the foundation is fully saturated, the pore water pressure mobilized beneath a raft foundation has a similar trend to the water depth–time curve. Furthermore, it is observed that a variation of the clay permeability has a great effect both on the pore water pressure mobilized beneath the raft foundation, and on the corresponding time in which such maximum value is reached. Finally, numerical results suggest that it is necessary to incorporate the possible effects that flooding events could generate during the building construction and its service life into the design of the raft foundation of buildings; in particular, to those buildings built in floodplains with water table close to the ground surface. Thus, such structures will be reasonably safe from flooding actions.

ACKNOWLEDGEMENTS

The first author is the recipient since 2022 of one Fellowship for PhD research provided by the José Entrecanales Ibarra Foundation. Also, this research was funded by the Spanish Ministry of Science and Innovation (Grant No. PID2019-108060RB-I00). The authors are grateful for the financial support provided by both institutions. Furthermore, the authors would like to thank the Spanish National Geographic Institute for kindly providing Digital Terrain Models of Pamplona (Spain) and the SAIH system of the River Ebro Basin Authority for providing streamflow data.

REFERENCES

Alonso-Pollán, J.A., Muñoz, L.M., Jimenez, R. (2018). Reliability analysis of constant total stress foundations subjected to water table fluctuations. *Numerical Methods in Geotechnical Engineering IX*, 1: 523-529.

Bikçe, M., Örnek, M., Faruk, O. (2018). The effect of buoyancy force on structural damage: A case study. *Engineering Failure Analysis,* 92: 553-565. https://doi.org/10.1016/j.engfailanal.2018.06.014

Chaudhary, M.T.A. (2012). Implications of rising groundwa-ter level on structural integrity of underground structures–in-vestigations and retrofit of a large building complex. *Structural Survey,* 30(2): 111-129. https://doi.org/10.1108/02630801211228725

Graterol, E.P., Gutiérrez-Ch, J.G., Mediero, L., Senent, S. (2022). Simulación numérica de las fuerzas de flotabilidad bajo losas de cimentación profundas, In: *XI Simposio Nacional de Ingeniería Geotécnica*, Mieres, Spain, pp. 263-270.

Itasca Consulting Group. (2016). FLAC, Version 8.0. User's Manual. Mineapolis, USA.

Kreibich, H., Thieken, A. (2008). Assessment of damage caused by high groundwater inundation. *Water Resources Research*, 44(9): W09409. https://doi.org/10.1029/2007WR006621

Liu, H., Sun, W., Zhang, Y., Zhang, W., Han, F., Su, W. (2023). Experimental analysis on the interaction between underground structures and sand layer underground wáter level change. *Underground Space*, 10: 15-36. https://doi.org/10.1016/j.undsp.2022.08.006

Lompi, M., Mediero, L., Soriando, E., Caporali, E. (2023). Climate change and hydrological dam safety: a stochastic methodology based on climate projections. *Hydrological Sciences Journal*, 68(6): 745-763. https://doi.org/10.1080/02626667.2023.2192873

Munárriz, M. (2022). Rochapea, guerra contra las inundaciones bajo el suelo. *Diario de Navarra.* [online] Available at: https://www.diariodenavarra.es/noticias/navarra/pamplona-comarca/2022/09/17/rochapea-guerra-inundaciones-el-suelo-541449-1002.html, accesed: 03/07/2023.

Muzás, F. (2007). *Mecánica del Suelo y Cimentaciones*, vol. 1. Fundación Escuela de la Edificación. Madrid, España.

Noticias de Navarra. (2022). Un nuevo colector en la Rochapea contra las inundaciones. *Noticias de Navarra.* [online] Available at: https://www.noticiasdenavarra.com/pamplona/2022/11/16/nuevo-colector-rochapea-inundaciones-6235544.html, accesed: 03/07/2023.

Ren, Z., Lu, Q., Liu, K., Ni, P., Mei, G. (2022). Model-scale tests to examine water pressures acting on potentially buoyant underground structures in clay strata. *Journal of Rock Mechanics and Geotechnical Engineering*, 14: 861-872. https://doi.org/10.1016/j.jrmge.2021.09.014

Soriano,E., Schröter, K., Ullrich, S., Paprotny, D., Bagli, S.,Santillán, D., Cueto-Felgueroso, L., Lompi, M., Mediero, L. (2023). Assessing the impact of climate change on fluvial flood losses in urban areas. The case study of Pamplona (Spain). Hydrological Sciences Journal. https://doi.org/10.1080/02626667.2023.2246452

Zhang, J., Cao, J., Mu L., Wang, L., Li, L. (2019). Buoyancy force acting on underground structures considering seepage of confined water. *Complexity*, 2019: 1-10. https://doi.org/10.1155/2019/7672930.

Proceedings of the XVIII ECSMGE 2024
GEOTECHNICAL ENGINEERING CHALLENGES
TO MEET CURRENT AND EMERGING NEEDS OF SOCIETY
© 2024 the Authors
ISBN 978-1-032-54816-6
DOI 10.1201/9781003431749-75
Open Access: www.taylorfrancis.com, CC BY-NC-ND 4.0 license

ECSMGE 24
XVIII EUROPEAN CONFERENCE ON SOIL MECHANICS AND GEOTECHNICAL ENGINEERING

Evaluation train induced ground vibration boom with Vibtrain

Évaluation du “boom des vibrations du sol” induit par les trains avec VibTrain

A. Håård
WSP, Stockholm, Sweden

J.A.T. Johansson*
Norwegian Geotechnical Institute, Oslo, Norway

K. Viking
Trafikverket, Stockholm, Sweden

S. Larsson
KTH, Stockholm, Sweden

**jjo@ngi.no*

ABSTRACT: The Swedish Transport Administration is planning new high-speed railway lines that will connect Stockholm, Gothenburg, and Malmö, with operating speeds from 250 to 320 km/h. However, at such high speeds in soft soil areas, can result in significant amplification of ground vibrations, a "ground vibration boom." This phenomenon was first observed in Sweden in 1997, leading to extensive research, during which the NGI developed the VibTrain tool for train-induced ground vibration analysis. There are still various challenges associated with train speeds exceeding 200 km/h on soft ground. To achieve optimized and sustainable ground improvement, a better understanding of its dynamic and cyclic behavior, as well as the validation of design tools and construction techniques, is needed. This paper presents a revival and re-evaluation of VibTrain for assessing the risk of the ground vibration boom for planning of new lines. The tool was compared with previous analyses of the Ledsgård case and extended with a parametric study of both the load model HSLM-A and ground improvement using lime cement stabilization. Additionally, VibTrain was compared with the results from Tyrens (2016) for the Järna location in East link. The analysis indicates that VibTrain is well-suited for initial assessments of the risk associated with the ground vibration boom. However, for the detailed design of soil improvement, more sophisticated calculation models are required. Results indicate importance of the train load description and of well characterized dynamic properties of track and subsoil. Validation of numerical models with field test at speeds above 300 km/h are recommended.

RÉSUMÉ: La Direction suédoise des transports prévoit de nouvelles lignes ferroviaires à grande vitesse reliant Stockholm, Göteborg et Malmö, avec des vitesses de 250 à 320 km/h. Cependant, à de telles vitesses dans des zones de sol mou, des vibrations importantes du sol, appelées "boom des vibrations du sol", peuvent se produire. Ce phénomène, observé en Suède en 1997, a conduit à des recherches approfondies. L'Institut norvégien de géotechnique a développé VibTrain, un outil d'analyse des vibrations du sol induites par les trains. Des défis subsistent pour les vitesses dépassant 200 km/h sur sol mou. Une compréhension approfondie du comportement dynamique et cyclique du sol, la validation des outils de conception et des techniques de construction sont nécessaires pour une amélioration optimisée et durable du sol. Cet article présente une réévaluation de VibTrain pour évaluer le risque du "boom des vibrations du sol" dans la planification des nouvelles lignes. L'outil a été comparé à des analyses antérieures et étendu avec une étude paramétrique de l'amélioration du sol par stabilisation au ciment de chaux. VibTrain a été comparé aux résultats de Tyrens (2016) pour l'emplacement de Järnaslätten dans l'Ostlänken. L'analyse suggère que VibTrain convient bien aux évaluations initiales du risque lié au "boom des vibrations du sol", mais des modèles de calcul plus sophistiqués sont nécessaires pour la conception détaillée de l'amélioration du sol en raison de divergences observées dans des conditions de sous-grade améliorées.

Keywords: Train vibrations; vibtrain; lime cement; train load model.

1 INTRODUCTION

The Swedish Transport Administration (STA) is planning for new railway lines with higher speeds (250–320 km/h) than the existing ones (maximum 200 km/h). The increased speed poses several technical challenges for the infrastructure design with respect to

soft soil settlement, ground vibrations and need for optimizing (Ekström & Hallingberg, 2012) the track design with respect to material use and CO2-footprint. One challenge is the so called ground vibration boom (Krylov, 2017), during which the train speed approaches the wave speed (critical speed) in the underlying track-foundation system. This phenomenon can cause significant train and ground vibrations and is essential to avoid (STA, 2023). It was observed when the X2000 train was introduced in late 1990s in Sweden with a new track at Ledsgård on very soft ground containing organic clay and vibration levels became 10 times larger than previously experienced (Madshus & Kaynia, 2000). Extensive underground reinforcement was necessary to increase the critical speed and reduce the track and ground vibrations (Holm et. al. 2002, Hall et. al. 2023). There is a need for better understanding of the long-term static and dynamic behaviour of lime cement stabilized subsoil to optimize the railway foundations, therefore STA have taken initiative to several related studies (e.g. Hall et. al. 2022). Here the Vibtrain software has been applied to study the effect on the critical speed of the train load model, and the subsoil lime cement reinforcement.

2 VIBTRAIN

Vibtrain was developed by NGI (Madshus Kaynia) to try to understand the first observations of the high speed phenomenon at Ledsgård in 1998. Vibtrain consists of a beam on a horizontally layered halfspace with the vertical train loads are modelled as moving point loads (Krylov). Stiffness matrices for the beam and are combined with ones for the half space (Kausell). Further details are given in Håård (2022) and Norén-Cosgriff (2017). The recompiled version of Vibtrain was satisfactorily verified by comparing with the earlier results (Madshus/Kaynia 2000).

3 EFFECT OF LOAD MODEL (HSLM-A)

The critical speed phenomenon was investigated in a parametric load study with the HSLM-A load model of the EN 1991-2, which has 10 train sets (A1-A10) with different lengths, axle loads and axle distances. The track and subgrade were modelled with the same parameter values as reported in Madshus & Kaynia (1999) for all train load models. Figure 1 shows the effect of load model on variation of the "critical speed". The variation depends on the on the match between the load frequency (ratio of train speed to the vehicle length, the boogie or the axle spacing) and the response frequency corresponding to the critical speed. It is important that the load model encompasses a range of frequencies as to detect the critical speed and the larges track deflection which is dependent on the specific numerical model and its input parameters.

For design and comparison of different remedial measures, where the critical speed is higher than the allowable train speed, it necessary to have some other criteria as allowable vibration or deflection level, e.g. in STA (2023) the requirement of a maximum deflection 2 mm is used.

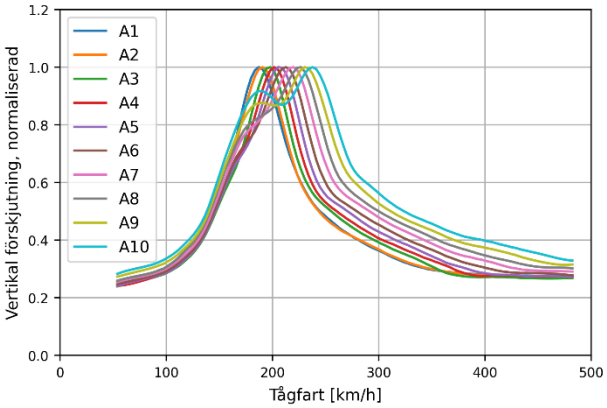

Figure 1. Effect of train load model on critical speed.

4 EFFECT OF LIME CEMENT REINFORCEMENT COMPARISON WITH FE-ANALYSIS

To study the effect on the critical speed of an increased subsoil stiffness in VibTrain, an equivalent modulus is used, assuming the entire soil mass has an homogenously increased stiffness, proportional to the reinforced volume fraction (η-factor) and the elastic modulus increase due to soil reinforcement (γ-factor) (Håård, 2022). We consider a specific case for the Järna plain some 50 km south-west of Stockholm (se also Müller et. al. 2020) with 2 m high embankment over soft clay. Three reinforcement cases were considered, 1) singular lime cement columns (LCC) 0.6m diameter and 20 m deep, placed in a regular grid with c-c distance of 1.1 m; 2) Two 10 m deep lime cement "walls" along the track, one beneath each rail, with 1.5 m separation in the transverse direction. The walls consist of overlapping columns with a c-c distance of 0.5m; and 3) a combination of the above singular columns and walls. The three cases have reinforcement volume fraction of 0.27, 0.21 and 0.46 respectively. Further details about incorporating design recommendations given by STA (2023) when establishing geometry, soil and lime cement properties are given in Håård (2022).

Below Vibtrain results are compared with the ones from the finite element software (ωFE-N) used in the design (Müller et. al. 2020). In ωFE-N the ground reinforcement is modelled explicitly as 3D columns inside the soil volume, thus smearing of properties is avoided. However, the ωFE-N uses Abaqus for creating geometries and the resulting stiffness matrices with millions of degrees of freedoms are solved in the frequency domain with a parallell computer at KTH to resulting in computing times of few seconds for one train passage.

Figure 2 shows for different train speeds "peak-to-peak" deflection, the sum of the maximum downward and upward deflection during the each train passage. The three subfigures clearly show the effect of reinforcement increasing the critical speed from some 300+ km/h for the unreinforced to over 400 km/h for the case with for case with most reinforcement. The results (not shown) indicate in general Vibtrain and ωFE-N have similar vibration frequencies, while Vibtrain gives larger deflections for most cases and train speeds. Possible reasons for discrepancy in deflection could be the simplified modelling of the embankment in Vibtrain and/or the use of first order tetrahedra elements in the FE-analysis. Such elements are known to give overly stiff response for nearly incompressible material such as clay (see e.g. Frâncu 2021, Hall 2022).

5 DISCUSSION

The difference in the numerical analysis methods indicate a difficulty in comparing different methods for evaluating the effects of and optimizing subsoil reinforcements. To evaluate the effect of reinforcement layouts, e.g. a percentage increase in critical speed or rather percentage decrease in deflection could be used for evaluating the effect of different reinforcement solutions (e.g. Müller et. al. 2020, Norén-Cosgriff 2019).

To optimize subsoil reinforcement extensive research is required both with respect to improve the evaluation of in-situ static, dynamic, and long-term properties of LCC, achieve desired field properties, and advance numerical modeling for specific column configurations. E.g. there is no standardized procedure for evaluating the in-situ stiffness of LCC (Helle et. al 2022, Dannewits 2005) and thus actual dynamic properties of lime cement reinforcement which can have substantial spatial variation (e.g. Larsson et. al. 2005) is difficult to characterize. E.g. there are very few reported studies of the dynamic interaction between track, soil and LCC in which individual columns are modelled (Müller et. al 2020). Therefore validation with field tests are vital to improve the tools used in railway design.

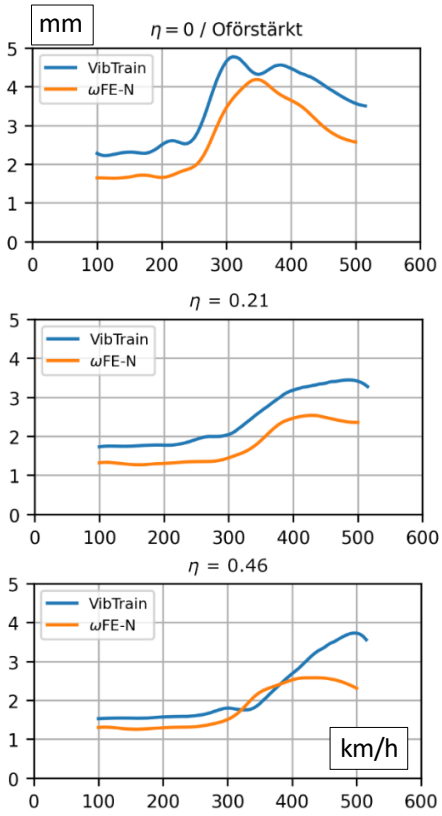

Figure 2. Maximum sum of downward and upward deflection "peak-to-peak" (mm) during the each train passage for different train speeds. Upper: unreinforced soil, Middle: case 2) walls along track, Lower: case 3) walls along track + singular columns.

6 CONCLUSIONS AND OUTLOOK

The study showed the recompiled 20+ year old VibTrain tool runs very fast on modern computers, yielding in about a minute, critical speed results consistent with original Ledsgård investigations.

Vibtrain can function as a fast calculation kernel in a screening tool for the highspeed phenomenon giving more detailed result then the simple shear wave speed criteria in the current STA regulations. However, detailed design of geotechnical remedial measures should be performed with more advanced tools which can account for more complicated soil and reinforcement geometry and bedrock depth variation.

In VibTrain, modeling geotechnical measures like soil reinforcement with lime-cement columns via the equivalent modulus method aligns with expected behavior, indicating that an increased equivalent modulus reduces displacement and raises the critical train speed.

Comparing Vibtrain results with ωFE-N (Ülker-Kaustell 2016) for the Ostlänken case, there is good agreement for unreinforced subsoil cases, but differences arise for reinforced subsoil due to inclusion of individual lime cement columns in the ωFE-N model and the use of the equivalent stiffness modulus in VibTrain.

The study shows the importance a realistic description of the track and subgrade properties and also the need for developing a load description capturing the main features of the planned train types for the new railways in Sweden.

In addition to the vertical load there is also need for a demand metric for irregular rail induced horizontal and vertical motions which can affect the long term behaviour of the track and subgrade response, and environmental vibrations.

Finally we emphasize the urgent need for new field tests ("Ledsgård 2.0") at speeds over 300 km/h for evaluating the accuracy of modern analysis tools and more importantly our geodynamical knowledge.

ACKNOWLEDGEMENTS

The authors are grateful for the financial support provided by the Swedish Transport Authority and to Ph.D. Mahir Ülker-Kaustell på Tyréns Sverige AB for sharing FE-results.

REFERENCES

Dannewitz, N. et al. (2005) «Seismic control method for deep stabilization». Swedish Deep Stabilization report No. 35. SGI. www.sgi.se/globalassets/publikationer/svensk-djupstabilisering/sd-ar35.pdf.

Ekström, J. & Hallingberg, A. (2012). 8 million meter deep stabilization for road on clay. Husbyggaren 3: 6–11, https://issuu.com/husbyggaren/docs/hb_3_2012_web.

Frâncu, M., Asgeirsson, A., Erleben, K., Rønnow, M. J. L. (2021). Locking-Proof Tetrahedra. ACM Transactions on Graphics, 40(2), http://doi.org/10.1145/3444949.

Hååard A. (2022) Train induced ground vibration analysis with VibTrain. https://urn.kb.se/resolve?urn=urn:nbn:se:kth:diva-315762.

Hall, L., Shih, J., Zangeneh, A., Pacoste, C. & Johansson, J. (2022). Design of Foundations for High-speed Railway Embankments. SBUF Rapport 13842. https://www.sbuf.se/projektresultat/projekt?id=137e3b15-0d51-4a5e-ac93-82d2e123452c.

Hall, L., Shih, J.-Y. Zangeneh, A. and Pacoste, C. (2023) "A methodology for control and design of required ground reinforcement measures regarding train-induced ground vibrations," Transportation Geotechnics, vol. 42, doi: 10.1016/j.trgeo.2023.101038.

Helle, T. E, et. al. (2022). Documenting strength and stiffness of ground-improved soils applying KlimaGrunns methodology. Geoteknikkdagen. https://www.vegvesen.no/contentassets/f64e1ebd4215429ba8c1f399d375e19b/artikkel_geoteknikkdagen-2022.pdf.

Holm, G., et. al. (2002). Mitigation of Track and Ground Vibrations by High Speed Trains at Ledsgård, Sweden. Swedish Deep Stabilization, report 10. SGI. https://sgi.se/globalassets/publikationer/svensk-djupstabilisering/sd-r10.pdf.

Krylov, V. V.,(2017) "Focusing of ground vibrations generated by high-speed trains travelling at trans-Rayleigh speeds," Soil Dynamics and Earthquake Engineering, vol. 100, pp. 389–395, doi: 10.1016/j.soildyn.2017.06.015.

Larsson, S., Stille, H. and Olsson, L., (2005) "On horizontal variability in lime-cement columns in deep mixing," Géotechnique, vol. 55, no. 1, pp. 33–44, doi: 10.1680/geot.2005.55.1.33.

Madshus, C. & Kaynia, A. (2000). High-speed Railway Lines on Soft Ground: Dynamic Behaviour at Critical Train Speed. Journal of Sound and Vibration 231(3): 689–701, doi: 10.1006/jsvi.1999.2647.

Müller, R., Mahir Ülker-Kaustell, M. and Hedenstedt, S., (2020) Dynamic analysis of of railway embankment on clay, Grundläggningsdagen.

Norén-Cosgriff, K., Dahl, B.M., Park, J., Kaynia, A.M. (2021). FE Modelling as a Design Tool for Mitigation Measures for Railway Vibrations. In: *Noise and Vibration Mitigation for Rail Transportation Systems. Notes on Numerical Fluid Mechanics and Multidisciplinary Design*, vol 150. Springer, Cham. Doi: 10.1007/978-3-030-70289-2_45.

Swedish Transport Administration, (2023) Requirements for and design of geotechnical structures, https://puben.trafikverket.se/dpub/visa-dokument/8c7297a7-b128-4552-b1af-7f16dea05ecf.

Proceedings of the XVIII ECSMGE 2024
GEOTECHNICAL ENGINEERING CHALLENGES
TO MEET CURRENT AND EMERGING NEEDS OF SOCIETY
© 2024 the Authors
ISBN 978-1-032-54816-6
DOI 10.1201/9781003431749-76
Open Access: www.taylorfrancis.com, CC BY-NC-ND 4.0 license

ECSMGE 24
XVIII EUROPEAN CONFERENCE ON SOIL MECHANICS AND GEOTECHNICAL ENGINEERING

On the thermal failure of sand-clay mixture

Sur la rupture thermique du mélange sable-argile

A. Hamidi, A. Shirasb
School of Engineering, Kharazmi University, Tehran, Iran

S. Tourchi*
Department of Civil and Environmental Engineering, University of Luxembourg, Luxembourg

**saeed.tourchi@uni.lu*

ABSTRACT: Failure conditions in soils at elevated temperatures appear to be highly dependent on stress and temperature history. Temperature-controlled triaxial tests were conducted to gain a deeper understanding of the effects of stress and temperature history on the undrained strength of sand-clay mixtures. Particular attention was paid to the thermal behaviour of the sand-bentonite material considerining the thermal curing time effects. A comprehensive experimental programme was conducted consisting of (i) isotropic drained heating followed by undrained triaxial compression at room temperature and elevated temperatures and (ii) an isotropic drained heating and cooling cycle followed by undrained triaxial compression. The results provide insights into a wide range of thermomechanical behaviours in clays. Data obtained at elevated temperatures were compared with those obtained from tests conducted at ambient temperatures. Based on these comparisons, the study presents and discusses the thermal effects on various behaviours. These include the influence of thermal history on shear strength, experimental evidence of the influence of temperature on pore pressure and the thermal effects on elastic modulus. In addition, the evolution of negative excess pore water pressure as a function of temperature is discussed.

RÉSUMÉ: Les conditions de défaillance des sols à des températures élevées semblent dépendre fortement de l'historique de contrainte et de température. Des tests triaxiaux à température contrôlée ont été effectués pour acquérir une compréhension plus approfondie des effets du stress et de l'historique de la température sur la résistance non drainée des mélanges de sable. Une attention particulière a été accordée au comportement thermique dépendant du temps du matériau de sable-bentonite. Un programme expérimental complet a été réalisé composé de (i) un chauffage drainé isotrope suivi d'une compression triaxiale non draine à la température ambiante et des températures élevées et (ii) un cycle de chauffage et de refroidissement drainé isotrope suivi par une compression triaxiale non draineuse. Les résultats fournissent un aperçu d'un large éventail de comportements thermomécaniques dans les argiles. Les données obtenues à des températures élevées ont été comparées à celles obtenues à partir de tests effectués à des températures ambiantes. Sur la base de ces comparaisons, l'étude présente et discute des effets thermiques sur divers comportements. Il s'agit notamment de l'influence de l'histoire thermique sur la résistance au cisaillement, des preuves expérimentales de l'influence de la température sur la pression des pores et des effets thermiques sur le module élastique. De plus, l'évolution de la pression négative de l'eau des pores en excès en fonction de la température est discutée.

Keywords: Temperature; sand-bentonite material; thermal history; triaxial tests; shear strength.

1 INTRODUCTION

A realistic and robust analysis of thermo-hydro-mechanical (THM) coupling phenomena relevant to sustainable subsurface activities, such as geothermal energy production, temporary or seasonal storage of hydrogen fuel, long-term storage of CO2 and radioactive waste, and natural risk analyses, needs to be generalized to include the response of soil to heating and the effect of temperature on soil mechanical properties. Heating can cause alterations in the mechanical characteristics of geomaterials due to various physical processes at the microstructural level. Several such processes and alterations have been reported in laboratory experiments and are believed to be crucial for analyzing these geo-systems (see, for example, Hueckel and Baldi 1990; Delage et al. 2000; Cekerevac and Laloui 2004). It should be noted that there is not sufficient experimental data on the temperature dependency of shear strength due to the insufficient attention to thermal curing and the applied temperature history before failure. The volumetric behaviour due to temperature changes strongly depended on the stress history or the overconsolidation ratio (OCR). The peculiarities of the mechanical response of soil to heating established in early experiments consist of a substantial thermoplastic contraction at high external effective stress or low OCR (close to normally consolidated conditions),

initial expansion followed by thermal contraction in slightly overconsolidated conditions, and thermal expansion at low external stress or high OCR, as well as the possibility of thermal failure during undrained heating under constant non-isotropic stress. Thermal failure refers to various soil failure conditions caused by elevated temperatures (Hueckel et al., 2009).

This contribution presents the principal results of an experimental investigation performed on saturated sand-clay mixtures to investigate the role of the thermomechanical loading history prior to undrained triaxial loading. Isotropic drained heating followed by undrained triaxial compression tests was performed at elevated temperatures to evaluate the role of thermal and mechanical soil history in reaching failure. Therefore, a new thermal triaxial device was developed for this purpose. The results were compared with the mechanical responses of the samples at the reference (ambient) temperature. The testing tools used, the experimental procedure employed, and the material studied are first described, and the results of the experimental campaign are presented and discussed afterwards.

2 MATERIALS AND METHODS

Clay and silica sand were mixed and compacted in eight equal layers in a cylindrical mould. The physical properties of these soils are presented in Table 1 (more details can be found in Shirasb et al. 2020). Undrained triaxial tests were carried out using a modified thermal triaxial cell with an electronic data logger system capable of measuring axial stress, axial strain, volume change, and excess pore water pressure. The triaxial cell was calibrated to handle pressures up to 2000 kPa and temperatures up to 90°C. Heating was induced by placing a spiral heater around the specimen. After preparing the samples, a back pressure of 700 kPa was applied until a Skempton B value of 0.95 during six days of saturation. The time required to complete the thermal consolidation tests was less than 40 h at all temperatures and confining pressures.

The thermal and mechanical histories of the soil appear to be crucial to understanding how the failure condition varies with temperature. Two cases with different stress histories were considered, as discussed below.

Case 1: Isotropic drained heating followed by undrained triaxial compression at elevated temperatures.

Case 2: Isotropic drained heating and cooling cycles, followed by undrained triaxial compression.

In the first set, sand-clay samples were consolidated for five days at constant temperatures of $20°C - 40°C - 60°C$ and $80°C$ under confining stresses of 100 kPa $-$ 500 kPa and 1000 kPa. After consolidation, the undrained shear load started at a rate of 0.2 mm/min. The loading continued up to the axial strain of about 20%. During shear loading, deviatoric stress, axial strain, and excess pore water pressure were measured using calibrated sensors and a data acquisition system. Thermal stress paths were applied to the samples in the second group of tests, and their behaviour was monitored. Two samples were heated from the reference temperature $20°C$ to $80°C$ under the confining pressure of 100 kPa for five days and 1 day. Subsequently, the temperature decreased to the reference value and sheared after thermal equilibrium in an undrained condition.

Table 1. Physical properties of the tested soils.

Property	**Sand**	**clay**	**1: 1 mixture**
Name (**USCS***)	SW	CH	CH
Clay (%)	0	68	34
Silt (%)	2	31	16.5
Sand 0.06-0.2 (mm)	23	1	12
Sand 0.2-1 (mm)	55	0	27.5
Sand (>1 mm)	20	0	10
LL (%)	–	179	83
PI (%)	NP	125	57
w_{opt} (%)	–	–	21.4
$\gamma_{d,\max}(\mathbf{kN/m^3})$	–	–	17.0

3 RESULTS AND DISCUSSION

For case 1, the samples consolidated at the reference temperature showed smaller shear strengths than those consolidated at higher temperatures, as shown in Figure 1a, 1c, and 1e. The behaviour trend for these samples was consistent with the thermal behaviour of the normally consolidated clays reported in other studies (Kuntiwattanakul *et al.* 1995; Tanaka *et al.* 1997; Abuel-Naga *et al.* 2006). The shear strength of the thermally consolidated samples was also increased with increasing the confining pressures, as shown in Figure 1c and 1e. Also, based on the results of the first Case, the samples consolidated at the reference temperature showed positive pore water pressure, whereas the thermally consolidated samples exhibited a different trend of behaviour (Figure 1b, 1d, and 1f).

The induced pore pressure in these samples decreased with increasing temperature. The pore pressure reached negative values for the samples consolidated at higher temperatures. For example, the samples consolidated at $80°C$ experienced negative pore pressure at all confining pressures; however, at the temperature of $60°C$ negative pore pressure was only observed in the tests with confining pressures of 100 kPa.

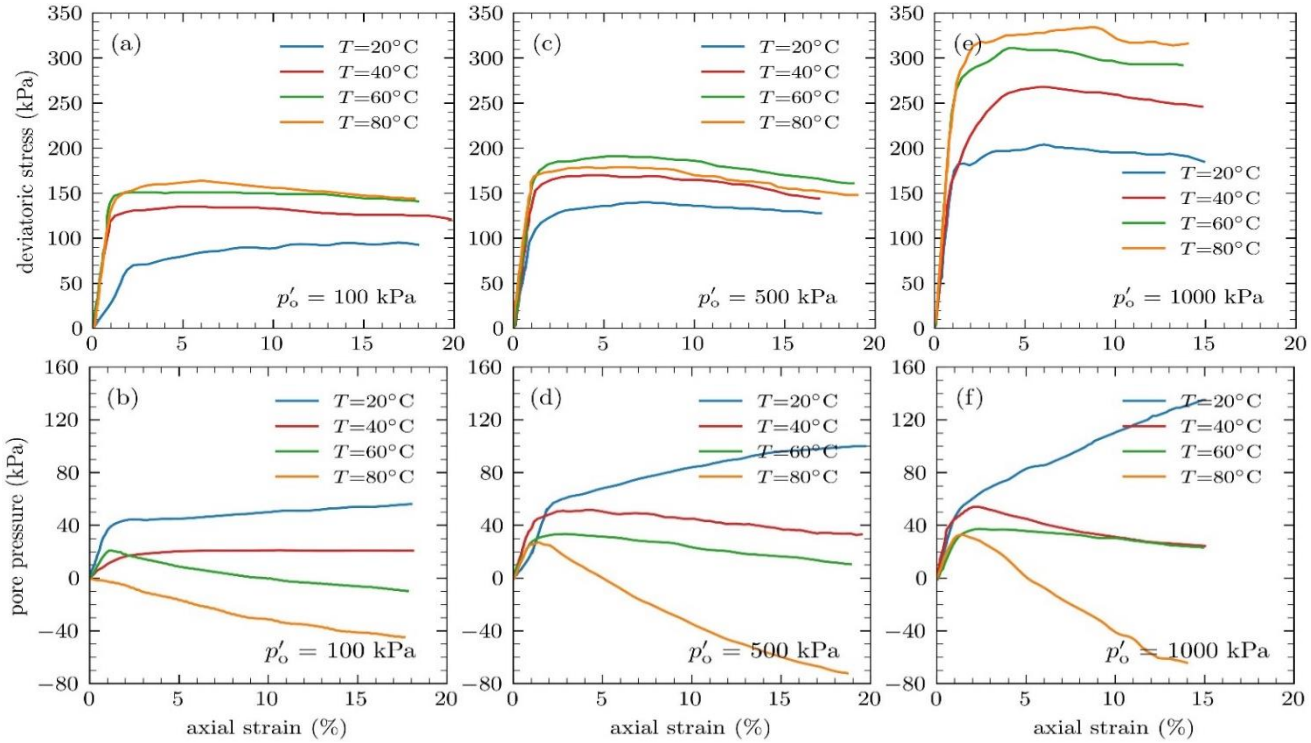

Figure 1. Results of undrained shear test on sand-clay mixture (Case 1).

The samples consolidated at 40°C did not show negative pore pressures for all confining pressures. The trend of excess variations in the pressure of the pore water at higher temperatures is similar to that of structured clays (Rios *et al.* 2014).

In Case 2, the shear strength and Skempton A coeffient were evaluated, the variation in shear strength with temperature is shown in Figure 2a, where the increase in peak shear strength during the thermal cycle is clearly identified. The sample with five days of thermal loading reached greater shear strength than the sample with one day of thermal loading. In case the samples are cooled again to reference temperature, the shear strength of the sample on day 5 of thermal loading is about 62% higher than the initial strength; however, the shear strength for the sample with one day of thermal loading increased by approximately 43%. Thermal consolidated samples also failed at the lower strain level and experienced softening behaviour, as shown in Figures 1c and 1e. The behaviour trend for the thermally cured samples was very similar to those for the structured or overconsolidated clays (Marques 1996).

Figure 2b shows the variations of Skempton's pore pressure coefficient, A (associated with the peak shear strength), with the temperature at the confining stress of 100 kPa. When the value of A is about 0.6 for the sample sheared at the reference temperature of 20°C, decreased to about zero for the sample consolidated for one day at 80°C and then was cooled to 20°C, or even to a negative value for the sample that was consolidated for five days at 80°C and was cooled back to the reference temperature.

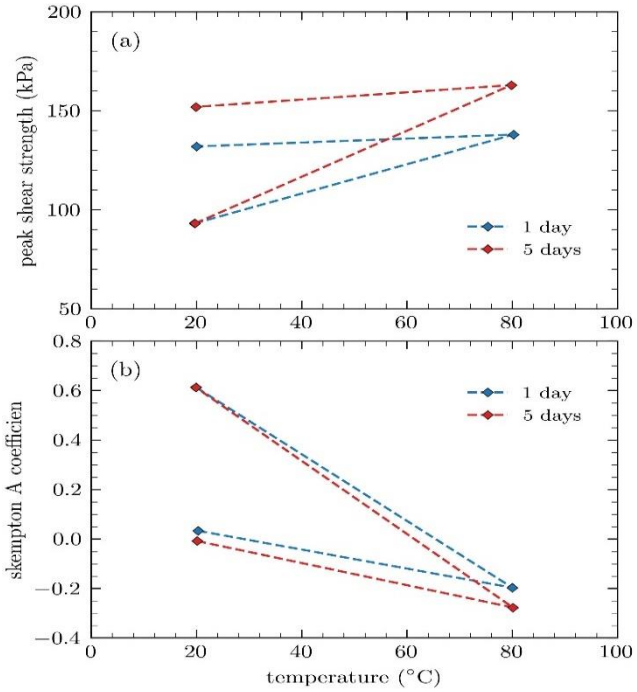

Figure 2. Variation of shear characteristics for the temperature cycle at the confining pressure of 100 *kPa: (a) Shear strength and (b) Skempton's A coefficient (Case 2).*

The effect of elevated temperature on the elastic modulus of samples in case 1 is presented in Figure 3. In this figure, the undrained secant modulus is calculated at 50% shear strength (E_{50}). The results

indicated that the elasticity modulus was higher in the specimens with longer consolidation time and higher temperatures than those tested at the reference temperature.

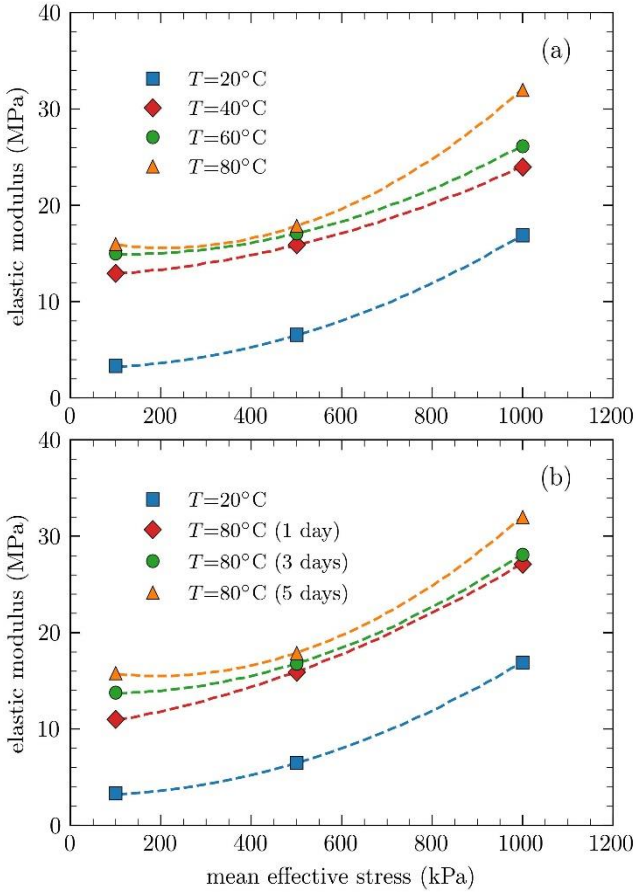

Figure 3. Effect of temperature and consolidation time on the secant modulus at half peak strength.

4 CONCLUSIONS

An experimental program was carried out in a new triaxial cell with a modified thermal triaxial cell to investigate some thermomechanical issues in sand-clay materials. The specimens were installed in thermal triaxial apparatus to experience an undrained triaxial stress path representative of the undrained strength. Two cases of different stress histories were performed. The higher the temperature and heating time, the stiffer and more brittle the triaxial response. The strains also obtained at peak stress decrease while there is a strong gain in peak stress. Increasing the thermal consolidation parameters (time and temperature) reduced pore pressure and transitioned from positive to negative values. The thermal cycle increased the shear strength and experienced a negative pore water pressure that exhibited a transition towards the quasi-structured behaviour.

ACKNOWLEDGEMENTS

The authors acknowledge the financial support provided by the European Commission through a Marie Curie Fellowship (Grant agreement ID: 101033084) awarded to Dr Saeed Tourchi (corresponding author).

REFERENCES

Abuel-Naga, HM, Bergado, DT, Ramana, GV, Grino, L, Rujivipat, P & Thet, Y (2006), 'Experimental evaluation of engineering behavior of soft Bangkok clay under elevated temperature', *Journal of Geotechnical and Geoenvironmental Engineering*,132(7),902–910, https://doi.org/10.1061/(ASCE)1090-0241(2006)132:7(902).

Cekerevac, C & Laloui, L 2004, 'Experimental study of thermal effects on the mechanical behaviour of a clay', *International Journal for Numerical and Analytical Methods in Geomechanics*,28(3),209–228, https://doi.org/10.1002/nag.332.

.Delage, P, Sultan, N & Cui, YJ 2000, 'On the thermal consolidation of Boom clay', *Canadian Geotechnical Journal*, 37(2), 343–354, https://doi.org/10.1139/t99-105.

Hueckel, T & Baldi, G 1990, 'Thermoplasticity of Saturated Clays - Experimental Constitutive Study', *Journal of Geotechnical Engineering-Asce*,116(12),1778–1796, https://doi.org/10.1061/(ASCE)0733-9410(1990)116:12(1778).

Hueckel, T, Francois, B & Laloui, L 2009, 'Explaining thermal failure in saturated clays', *Geotechnique*,59(3),197–212, https://doi.org/10.1680/geot.2009.59.3.197.

Kuntiwattanakul, P, Towhata, I, Ohishi, K & Seko, I 1995, 'Temperature Effects on Undrained Shear Characteristics of Clay', *Soils and Foundations*, 35(1),147–162, https://doi.org/10.3208/sandf1972.35.147.

Marques, MES 1996, 'Strain-rate and temperature effect on consolidation of natural clays', PhD Thesis, M. Sc. thesis, COPPE, Federal University of Rio de Janeiro, Brazil.

Rios, S, da Fonseca, AV & Baudet, BA 2014, 'On the shearing behaviour of an artificially cemented soil', *Acta Geotechnica*, 9(2), 215–226, https://doi.org/10.1007/s11440-013-0242-7.

Shirasb, A, Hamidi, A & Ahmadi, MM 2020, 'Consolidation characteristics of a thermally cured sand–bentonite mixture', *SN Applied Sciences*, 2(6), 1116, https://doi.org/10.1007/s42452-020-2932-8.

Tanaka, N, Graham, J & Crilly, T 1997, 'Stress-strain behaviour of reconstituted illitic clay at different temperatures', *Engineering Geology*, 47(4),339–350, https://doi.org/10.1016/S0013-7952(96)00113-5.

Proceedings of the XVIII ECSMGE 2024
GEOTECHNICAL ENGINEERING CHALLENGES
TO MEET CURRENT AND EMERGING NEEDS OF SOCIETY
© 2024 the Authors
ISBN 978-1-032-54816-6
DOI 10.1201/9781003431749-77
Open Access: www.taylorfrancis.com, CC BY-NC-ND 4.0 license

ECSMGE 24
XVIII EUROPEAN CONFERENCE ON SOIL MECHANICS AND GEOTECHNICAL ENGINEERING

Soil-structure interaction of two different configurations of a cut and cover tunnel

Interaction sol-structure de deux configurations différentes d'un tunnel en tranchée couverte

A.M. Hasan*
Civil Engineering Department, College of Engineering, Salahaddin University-Erbil, Erbil, Iraq

B.J. Shwan
Water Resources Engineering Department, College of Engineering, Salahaddin University-Erbil, Erbil, Iraq

O.Q. Aziz
Civil Engineering Department, College of Engineering, Salahaddin University-Erbil, Erbil, Iraq

ahmed.hasan@su.edu.krd

ABSTRACT: This paper investigates soil-structure interactions for a short/shallow cut and cover tunnel will be constructed in Erbil using Plaxis-2D software. In the analysis, different cross-sectional shapes, triangle cut and cover tunnel (TCCT) and horseshoe cut and cover tunnel (HCCT) shapes, were suggested. These two shapes were simulated for a tunnel having a total height of 5.2m, a width of 8m, and a 0.9m permanent lining. The maximum overburden soil above the tunnel's roof or crown was approximately 7.8m. The simulation of the interaction was performed between a coarse-grained soil and the 0.9m concrete lining. The soil parameters were selected under the worst case to provide the safest scenario. The simulation results showed that the horseshoe cross-sectional configuration produced less shear force and bending moment on different parts of the tunnel components, indicating that less concrete and steel bars could be used for the same cross-sectional area of the tunnel, resulting in reduced carbon dioxide emissions into the air.

RÉSUMÉ: Cet article étudie les interactions sol-structure pour un tunnel en tranchée couverte court/peu profond construit à Erbil à l'aide du logiciel Plaxis-2D. Lors de l'analyse, différentes formes de section transversale, en forme de triangle et de fer à cheval, ont été suggérées. Ces deux formes ont été simulées pour un tunnel ayant une hauteur totale de 5.2m, une largeur de 8m et un revêtement permanent de 0.9m. La hauteur maximale des morts-terrains au-dessus de la couronne du tunnel était d'environ 7.8m. La simulation de l'interaction a été réalisée entre un sol à gros grains entièrement saturé et le revêtement en béton de 0.9m. Les paramètres du sol ont été sélectionnés dans le pire des cas (conditions non drainées) afin de fournir le scénario le plus sûr. Les résultats de la simulation ont montré que la configuration transversale en fer à cheval produisait moins de force de cisaillement et de moment de flexion sur différentes parties des composants du tunnel, ce qui indique que moins de béton et de barres d'acier pourraient être utilisées pour la même section transversale du tunnel, ce qui entraînerait une réduction émissions de dioxyde de carbone dans l'air.

Keywords: Tunnel shape; soil-structure interaction; plaxis-2D; numerical analysis; shear force.

1 INTRODUCTION

The shape of the cross-section of an underground tunnel usually is a consequence of the proposed construction method, function of tunnel and geotechnical conditions (Nguyen et al., 2021). For a cut and cover construction method, tunnels are usually made with different cross-sectional shapes such as rectangular (Di et al., 2016), horseshoe (Abdellah et al., 2022) and arch shaped (Li et al., 2020). The influence of the cross-sectional tunnel shapes has been investigated by a number of researchers, for example, in terms of the stability of a shallow tunnel (Abdellah et al., 2022) and soil settlements under dynamic loads (Di et al., 2016). Triangle shaped tunnels have not been thoroughly studied in terms of the lining thickness and the distribution of the shear force and bending moment. Tunnel shape selection has a significant effect on the mechanical performance of the lining. Reasonable tunnel shapes minimize excessive bending moment on the lining under the self-weight of soil and surcharges. Thus, designing of tunnels requires shape optimization. Therefore, in this research, a comparative numerical study between triangle shaped and horseshoe shaped tunnel was performed using Plaxis 2D software to determine their

influences on the soil deformation around the tunnels and the distribution of the amount of the shear force and bending moment on the tunnel lining. In addition, a comparison was made in terms of the volume of the reinforced concrete per meter length in each shape to know which shape will use less reinforced concrete resulting in reduced carbon dioxide emissions into the atmosphere.

2 NUMERICAL MODELLING

2.1 Material parameters

Three materials were considered in the numerical analysis using Plaxis 2D: backfill soil, bed rock and reinforced concrete tunnel lining. The physical and geotechnical properties of the proposed soil backfill were determined in laboratory by Hasan et al. (2023) as shown in Table 1. From a site visit and visual inspection, the rock type was considered as weak and its properties were assumed shown in Table 1. The tunnel lining is made from reinforced concrete (RC). The input parameters of the RC lining are shown in in Table 2. Note that EA is Young's modulus times the area of the lining and EI is Young's modulus times the moment of inertia of the linings cross section, required parameters in the software.

2.2 Ground profile

The proposed cut and cover tunnel located in Erbil governorate. The total length of the tunnel is approximately 170 m with a width of 8 m. The maximum height of the soil over the roof/crown of the tunnel is approximately 7.8 m (see Figure 1). The tunnel is located in a valley, whose topography was surveyed. The client requested and emphasized the triangle shape of the tunnel having a cross sectional area of 38.25m^2 (see Figure 2). Therefore, a comparison was made to confirm to the client the lower cost of the horseshoe cross-sectional tunnel having an area of 27.2m^2 (see Figure 3) compared to the triangular one.

2.3 Finite element analysis

Plaxis 2D software was utilised to perform the numerical analysis because the cross-sectional dimensions are much smaller than the longitudinal length of the tunnel. Thus, plane-strain element type is used in the FE model for all materials. Figure 1 shows the mapped mesh of the 2D FE analysis for the worst case. The bedrock and tunnel lining were considered as linear elastic materials. However, the was soil modelled under Mohr-Coulomb failure criteria. The interface between the soil and the tunnel lining was also considered.

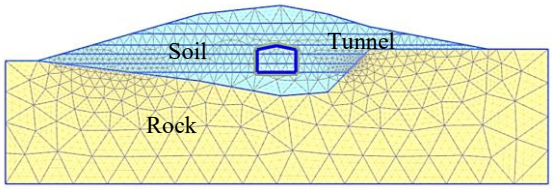

Figure 1. Meshed model for the worst scenario of the tunnel soil profile and construction phases.

Table 1. Physical and geotechnical properties of the used dense sand and rock in the numerical analysis.

Property	Soil	Rock
Void ratio, *e*	0.65	0.40
Dry unit weight, γ_d (kN/m^3)	16.2	21.0
Angle of internal friction, φ^o	40	25
Cohesion, c′ (kPa)	1	100
Young's Modulus, E′ (MPa)	52	200
Poisson's ratio, *v'*	0.4	0.15
Specific gravity, G_s	2.73	-
Degree of saturation, S_r (%)	78	-

Table 2. Tunnel lining numerical analysis parameter.

Parameters	RC lining
EA (kN/m)	18 000 000
EI (kN.m^2/m)	1 220 000
Thickness, d (cm)	90
Poisson's ratio, *v*'	0.15

3 NUMERICAL ANALYSIS RESULTS

3.1 Soil deformations above and around the tunnel

Figures 4 and 5 show the total soil deformation of TCCT and HCCT, respectively. Inspection of Figures 4 and 5 shows that the maximum amount of total deformation of the soil above the TCCT is much wider and has a different shape compared to the one of HCCT. This is also true in terms of the soil deformation distributed directly below the foundation of the TCCT. However, the soil deformation above and below the HCCT is uniformly distributed, confirming that the horseshoe shape gives an almost uniform and smooth soil stress distribution around the tunnel and thus uniform shear force (SF) and bending moments (BM). This in turn leads to usage of less lining thickness and reinforcement steel, as confirmed in the next subsection. In addition, this also proves that the different tunnel shapes induce different patterns of soil pressure, which in turns greatly influences the

structural design of tunnel members (i.e., soil-structure interaction).

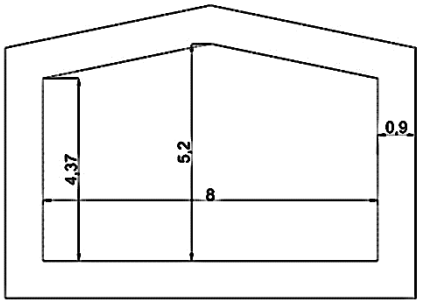

Figure 2. Triangle cross-section of the tunnel.

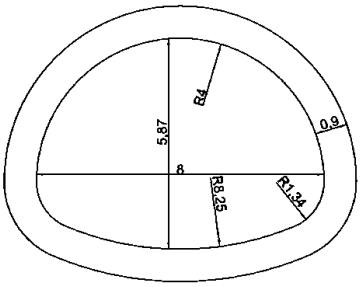

Figure 3. Horseshoe cross-section of the tunnel.

Inspection of Figures 4 and 5 also shows that the deformation in the rock is negligible (the boundary was covered by the blue colour), which only occurred in the soil.

3.2 Influence of tunnel shapes on the lining thickness

To investigate the effect of the tunnel shapes on the lining thickness, shear force (SF) and bending moment (BM) distributions on the roof/crown and footing/invert members of the TCCT and the HCCT are presented in Figure 6, respectively, from the output of Plaxis 2D. The numerical analysis output values of the SF and BM for both shapes are organized in Table 3. It can be noted from Table 3 and Figure 6 that the maximum SF on the roof of TCCT tripled compared to the SF on the crown of HCCT. In addition, the maximum SF on the footing of TCCT is 1.7 times greater than the SF on the invert of HCCT.

Inspection of Figure 6 and table 3 also shows that the BM on the roof and footing of TCCT is 1.1 and 1.37 times greater than BM on crown and invert of HCCT, respectively. From the numerical results in Table 3, it is observed that the SF on the tunnel members significantly changed compared to the slight change of the BM.

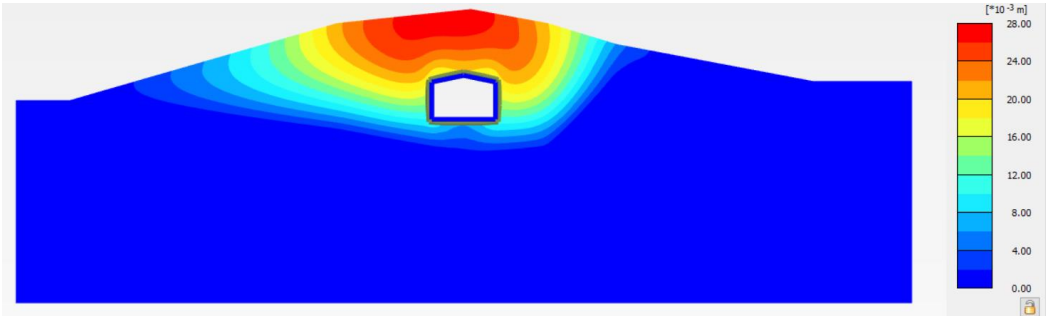

Figure 4. Total displacement of the soil and the rock around the TCCT.

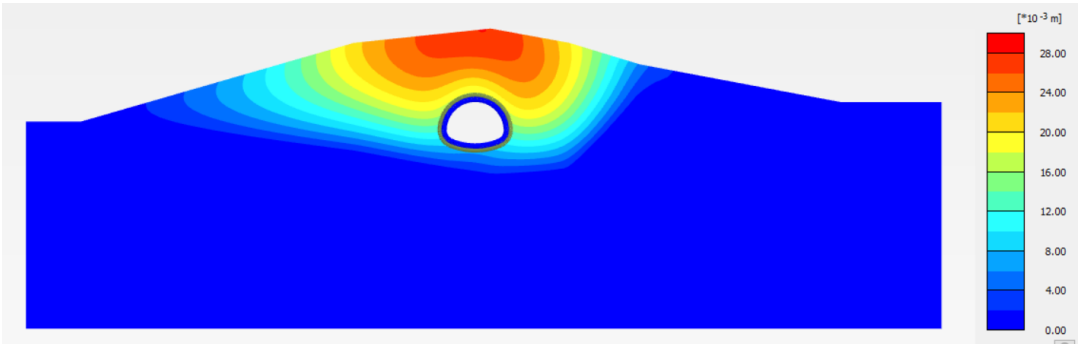

Figure 5. Total displacement of the soil and the rock around the HCCT.

It is obvious from the principles of structural engineering design that the change in the SF and BM greatly affects the lining thickness and the reinforcement steel, respectively. In the numerical analysis, the thickness of the lining in each shape and members (see Figures 2 and 3) of the tunnels was 90cm.This value was increased to 110cm and reduced to 40cm after structural design of the lining

of tunnels considering the SF on the roof and crown in TCCT and HCCT, respectively, see Table 4. The 90cm lining thickness was also increased to 140cm and reduced to 85cm in the footing and invert for the TCCT and HCCT, respectively. This significant change in the lining thickness greatly changes the cost per meter length of the cross-sectional area. The total extra cost per meter length of the cross-sectional area of RC lining is 2590.42 US$ (considering 140US$/m of RC) if the TCCT was used instead of HCCT. This is a huge difference in cost which can be induced by changing the tunnel's shape and thickness. Using HCCT not only reduces cost in the engineering projects but also reduces carbon dioxide emissions into the air when less reinforced concrete amounts are used.

4 CONCLUSIONS

Based on the numerical analyses, the following conclusions could be drawn:

1- It seems that the SF is much more sensitive than the BM when the shape of the tunnels is changed due to change in soil pressure distribution.
2- Due to cross-sectional shape change, a great reduction in tunnel thickness lining from 1100mm (roof) to 400mm (crown) occurred, which it is a great promising in minimizing amount of cement and carbon dioxide emissions into the atmosphre.

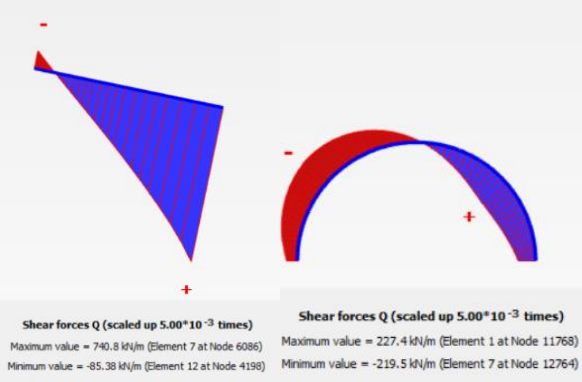

Figure 6. Shear force and bending moment diagrams of the roof right side of the TCCT and the crown of the HCCT.

Table 3. Shear force and bending moment numerical results.

Tunnel shape	Roof / Crown		Footing/Invert	
	SF	BM	SF	BM
	kN	kN.m	kN	kN.m
Triangle	704.8	-734.2	886.0	901.6
Horseshoe	227.4	-660.2	521.8	656.1

Table 4. Tunnel lining thickness based on the produced shear force on the members.

Item	Roof or Crown	Footing or Invert
	Thickness (mm)	Thickness (mm)
Triangle shape	1100	1400
Horseshoe shape	400	850
Extra lining Thickness	700	550
Total Extra cost (US$)/m	2590.42	

REFERENCES

Abdellah, W. R., Haridy, A. K. A., Mohamed, A. K., Kim, J. G., & Ali, M. A. M. (2022). Behaviour of Horseshoe-Shaped Tunnel Subjected to Different In Situ Stress Fields. *Applied Sciences (Switzerland)*, *12*(11). https://doi.org/10.3390/app12115399.

Di, H., Zhou, S., Xiao, J., Gong, Q., & Luo, Z. (2016). Investigation of the long-term settlement of a cut-and-cover metro tunnel in a soft deposit. *Engineering Geology*, *204*, 33–40. https://doi.org/10.1016/j.enggeo.2016.01.016.

Hasan, A., Hummadi, R., & Azeez, O. (2023). The performance of laterally loaded piles in layered sandy soils under variable degree of saturation. *E3S Web of Conferences*, *382*. https://doi.org/10.1051/e3sconf/202338207002.

Li, S., Han, G., Ho, I.-H., Ma, L., Wang, Q., & Yu, B. (2020). *Coupled Effect of Cross-Sectional Shape and Load Reduction on High-Filled Cut-and-Cover Tunnels Considering Soil-Structure Interaction*. https://doi.org/10.1061/(ASCE).

Nguyen, T. T., Do, N. A., Karasev, M. A., Kien, D. Van, & Dias, D. (2021). Influence of tunnel shape on tunnel lining behaviour. *Proceedings of the Institution of Civil Engineers: Geotechnical Engineering*, *174*(4), 355–371. https://doi.org/10.1680/jgeen.20.00057.

Proceedings of the XVIII ECSMGE 2024
GEOTECHNICAL ENGINEERING CHALLENGES
TO MEET CURRENT AND EMERGING NEEDS OF SOCIETY
© 2024 the Authors
ISBN 978-1-032-54816-6
DOI 10.1201/9781003431749-78
Open Access: www.taylorfrancis.com, CC BY-NC-ND 4.0 license

ECSMGE 24
XVIII EUROPEAN CONFERENCE ON SOIL MECHANICS AND GEOTECHNICAL ENGINEERING

Dynamic pull-out tests to characterize the earthquake behavior of soil-nailed walls

Clouage des sols: Comportement sous sollicitation sismique de l'interface sol-cloué

G. Hawwa*, J. de Sauvage, P. Joffrin, Y. Fargier, J.P. Rajot
Université Gustave Eiffel, Bron, France

**ghida.hawwa2@univ-eiffel.fr*

ABSTRACT: Soil-nailed walls are commonly used for their cost-effectiveness and ease of implementation. These structures have demonstrated remarkable seismic resilience, as evidenced by post-earthquake surveys following events like the Loma Prieta earthquake. Researchers have attributed their stability to the dynamic mobilization of friction at the soil-nail interface. However, designing soil-nailed walls to withstand seismic forces often results in increased stiffness, which can affect the transfer of motion to the structures they support. Improving the seismic design of these walls requires a closer examination of the local dynamic behavior at the soil-nail interface, a topic that has received limited attention in the existing literature. To address this gap, the RRO laboratory at Gustave Eiffel University has recently developed an innovative impulsive pullout testing device. This paper introduces the device, which is capable of applying static tension forces and a series of dynamic load pulses at the nail's head, reaching up to 50% of the applied force and operating at specified frequencies ranging from 0.1 to 5 Hz. In addition to traditional tension force and displacement measurements at the nail head, this device incorporates optical fiber technology to monitor micro strains along the entire length of the steel bar with millimeter longitudinal resolution. This new approach enables the comprehensive investigation of the local seismic behavior of the interface, with the goal of proposing an improved design model for soil-nailed walls.

RÉSUMÉ: Les murs en sol cloué sont couramment utilisés pour leur rentabilité et leur facilité de mise en œuvre. Ces ouvrages ont démontré une résilience sismique remarquable, comme en témoignent les enquêtes menées après des événements tels que le séisme de Loma Prieta. Les chercheurs ont attribué leur stabilité à la mobilisation dynamique du frottement à l'interface sol-clou. Cependant, le dimensionnement des murs en sol cloué sous sollicitations sismiques entraîne souvent une rigidité accrue, ce qui peut avoir un impact sur le transfert des mouvements aux structures qu'ils soutiennent. L'amélioration de ce dimensionnement nécessite un examen plus approfondi du comportement dynamique local à l'interface sol-clou, un sujet peu abordé dans la littérature existante. Pour combler cette lacune, le laboratoire RRO de l'Université Gustave Eiffel a récemment développé un nouvel appareil impulsif d'essais d'arrachement innovant. Cet article présente l'appareil, qui est capable d'appliquer des tensions statiques et une série d'impulsions de charge dynamique à la tête du clou, atteignant jusqu'à 50 % de la force appliquée et fonctionnant à des fréquences spécifiées allant de 0,1 à 5 Hz. Cette nouvelle approche permet d'effectuer une étude détaillée du comportement sismique local de l'interface, dans le but de proposer un modèle de dimensionnement amélioré pour les murs en sol cloué.

Keywords: Soil-nailed wall; pull out test; interface; seismic behavior.

1 INTRODUCTION

Soil reinforcement techniques, such as soil-nailed walls, originally introduced in France in 1972-1973 to support a railway platform in Versailles, have gained widespread use due to their ability to enhance soil stability and strength (Schlosser and Unterreiner, 1991). These walls offer several advantages, including lightweight equipment, adaptability to various site conditions, and efficiency in terms of time and cost. The core principle behind soil-nailed walls is the interaction between the soil inclusion and the surrounding soil. The resistance provided by soil nails is a result of the axial tension that develops within the nail due to the deformation of the soil mass around it (Schlosser and Unterreiner, 1991). Additionally, these structures have demonstrated their resilience during powerful ground motion events. A notable example is the 1989 Loma Prieta earthquake, that occurred at magnitude of 7.1 and was considered to be at that time the costliest single natural disaster in the United States' history, causing massive damage in various areas of San Francisco Bay. Nine soil-nailed walls were inspected post-earthquake, and despite their proximity to the earthquake's epicenter, these walls exhibited no signs of distress or deformation, in

contrast to other structures that sustained severe damage (Vucetic et al., 1998). Different methods have been employed to study the dynamic behavior of soil-nailed walls. These include centrifuge (Tufenkjian and Vucetic, 2000), 1g shaking table tests (Yazdandoust, 2017;Tabucanon et al., 1995; Xu et al., 2020), and numerical models. However, these studies primarily focus on assessing the global stability of the entire structure and do not account for localized deformations at the soil-nail junction. In contrast, static pull-out tests have proven effective in investigating the interaction and shear strength between the nail and the surrounding soil. These tests have explored various parameters, such as nail length, diameter, stiffness, and interface roughness (Tei and Milligan, 1998). The grouting pressure and saturation of soil influence was also investigated through laboratory pull-out tests (Su, 2006) on CDG (completely graded granite) classified as well graded, clayey gravelly silty sand frequently present at slopes in Hong Kong. Moreover, studies have delved into soil properties, including cohesion, friction angle, moisture content, and particle degradation (Shahraki Ghadimi *et al.*, 2017). Cyclic shear box tests, conducted by (Poulos, 1989) and (Tabucanon et al., 1995), have shed light on the degradation of skin friction in the interface under cyclic loads. Factors like the number of cycles, amplitude of displacements, roughness, and interface stiffness were considered in these studies, which revealed a reduction in shear stresses after a specific number of cycles. Furthermore, research by Zhou *et al.* examined the influence of particle shape in shear cyclic tests, demonstrating that particle breakage near the interface and soil densification contributed to an increased contact area between particles in the interface zone (Zhou *et al.*, 2020), resulting in a gradual increase in the interface friction angle. To further explore dynamic resistance at the interface, rapid pull-out tests were conducted by Tan et al. (2008) using an impulsive hammer with varying nail roughness and diameter. The tests showed that the pre-peak pullout response was stiffer and achieved higher peak pullout values with larger nail diameters, especially for rough-textured nails. Notably, the rate of loading had no effect in the case of smooth nails. However, it's worth noting that dynamic resistance at the interface, particularly for rough-textured nails, remains insufficiently understood. To address this knowledge gap, the GERS-RRO laboratory introduced an innovative dynamic pull-out device and combines it with optical fiber to monitor strain evolution and calibrate measurements. This device aims to provide essential experimental data on the characteristics of the soil-nail interface during dynamic loading, contributing to a deeper understanding of the behavior of soil-nailed walls.

2 THE DYNAMIC PULL-OUT DEVICE

2.1 Description of the device

An innovative equipment was developed to enable the application of dynamic, controlled, and predetermined tensile forces on reinforcement bars within geotechnical structures. This pull-out testing device may apply a dynamic tension force with specified frequency ranging from 0.1 to 5 Hz, corresponding to frequencies typically associated with moderate earthquakes.

The design of the equipment allows for the superimposition of vibrational pulses onto the static loading applied either in incremental steps or as a gradual slope.

The device consists of an actuator connected to a hydraulic circuit, that is controlled through programmable automaton. The device is designed to enable testing both in a laboratory setting and out in the field. For this purpose, the structure consists of components, each weighing less than 30 kilograms.

2.2 Components of the device

The five components of this device are shown in Figure1: a hydraulic pump of 700MPa maximum pressure equipped with an oil radiator, a hydraulic accumulator with a pressure regulator and a pressure gauge (manometer), a high-pressure controlled modulating solenoid valve, a programmable user interface for integrating the programmable logic controller (PLC), and finally, a 600kN hydraulic jack attached to the nail for imposing loading. These elements are designed for robustness, have undergone field testing, and can be transported individually by a single person.

2.3 Mode of operation

The system can operate in both manual and automatic modes. The automatic mode allows for the programming of test cycles by interacting with the programmable logic controller (PLC). The static load can be applied as load increments in traditional incremental loading pull-out tests (steps configuration), or during a linear increase of the tensile force (slope configuration).

The fundamental principle underlying the functionality of this device is to enable the simultaneous imposition of a specific dynamic pulse alongside a static tensile load of a predetermined magnitude. Similarly, in the slope configuration, the

linear increase of the tensile load can reach up to 350 kN, with the same duration.



Figure 1. Connection of the device in running order: (1) hydraulic pump, (2) hydraulic accumulator, (3) controlled solenoid valve, (4), programable automate (PLC).

The dynamic pulse generated during loading is defined by two key parameters:

- Period of pulse, which falls within a range of 100ms to 5000ms, corresponding to a frequency range of 0.1 to 5 Hz.
- Amplitude of tension pulse, ranging from 1% to 50% of the static tensile load.

These pulses are superimposed onto the ongoing static loading program. They are centered and their intensity oscillates by +/- the specified amplitude for the specified pulse duration.

3 EXPERIMENTAL TESTING AND ASSESMENT OF THE DEVICE

3.1 Experimental setup

Table 1.Specifications of used bar

Nominal diameter (mm)	Yield stress (N/mm²)	Yield load (kN)	Ultimate load (kN)	Area (mm²)	Weight (Kg/m)
32 mm	550	405	440	804	6.31

Initial tests were carried out to check and validate the accurate functioning of the apparatus, specifically concerning the generation of pulsed tensile forces applied to a steel bar in a controlled laboratory environment.

To achieve this, a steel bar (with specifications outlined in Table 1) was inserted into a hollow metallic tube, used as a reservoir for the sand to fill in. The tube is 2 m in length, and the internal diameter 150 mm (Figure 2).

The steel nail was centered in the tube with one of the ends securely affixed using a support plate and a nut, and glued with silicon to avoid leakage of the sand. In order to ensure the proper connections at the edges of the tube, and avoid inducing any parasite moments or bending when applying tension in the steel bar, the two edges of the tube were cut parallel with laser geometry control. In order to fill the sand, the tube was placed in a vertical position. Hostun sand HN31 with well-defined properties, such as maximum density of 1.62 g/cm3 (Zeybek, 2017) was used to fill the tube after the bar was installed.

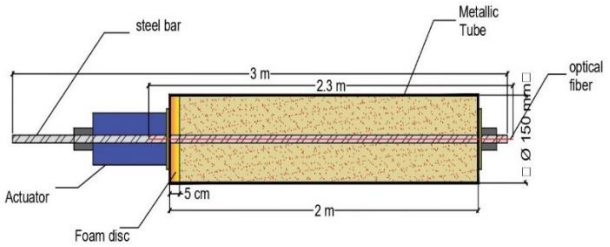

Figure 2. Illustration of the metallic tube used as sand reservoir setup.

With the nail placed prior to sand installation as well as a foam disc (0.95 L) of volume being used to ensure the centering of the bar, and as a stopper of the sand at the top edge of the tube, the total volume to be filled with sand thus is 32.86 liter. At the maximum density of sand, a mass of about 55kg of sand would be required to fill up the tube. The sand was filled along four levels, and a quarter was filled per once. Each insertion was followed by vibration of the metallic tube to ensure maximum density is attained. However, the remaining mass of non-filled sand was measured to 2.4 kg. This has affected the density assumed, and eventually the new value of the sand density in the tube is 1.54 kg\l, corresponding to a relative density of 79.1 %.

3.2 Monitoring and measurements

The nail's head is fitted with a load sensor, enabling direct measurement of applied tensile force, to be checked against the force generated by the dynamic machine. Additionally, the steel bar is equipped with an optical fiber that spans its entire length, in order to measure strain during the loading process. The tests also aimed to ensure accurate calibration of the strain measurements obtained through this optical fiber, through comparing the values to theatrically computed strains. The optical fiber employed, with a length of 2.3 m, is securely affixed within the grooves to the nail's surface. Measurements are taken at an acquisition frequency of 125Hz, with a discretization of 2.6mm between recording points along the fiber.

3.3 Testing procedure

In order to investigate the performance of the interface of soil and nail, both static and dynamic loads were

applied. The static tests were designed in two different configurations, using an incremental loading process performed over four stages at specified pressures of 10-100-140-213 bar, and another slope loading up till 213 bar. The employment of the dynamic loading however requires the definition of the properties of the dynamic pulse to be imposed as well as that for the static tension. An incremental loading process same as that used in static tests was also used.

The pulse applied was defined at 5% and 20% amplitude of the loading, with varying the chosen frequency between 2 ,4 and 5Hz. Each increment in loading was sustained for a period of 20 seconds/step, with always having the first step in only static (no pulse applied).

4 RESULTS AND DISCUSSION

The results represented in the following section correspond to dynamic test, pulse applied at 5Hz, with an amplitude of 20% of the static tension load. It is to be noted though that the same loading and strains profile was maintained at other frequencies of 2Hz and 4Hz. The color mapping represented in Figure 3, displays the strains record by the optical fiber through the loading procedure at every position along the nail. The horizontal strips marked in yellow frames the executed dynamic pulses. It can be observed that the dynamic pulse occurs at the same time along every position of the nail, which indicates that the load is being transmitted uniformly through the nail.

In order to verify the measurements of the optic fiber, the strains measured were compared to the strains calculated using Hook's law ($\sigma = E\varepsilon, \varepsilon = \frac{F}{AE}$), where E is modulus of the steel material, ε the strains in axial direction, F the force applied at the head of nail, and A the surface area of the nail cross section, assumed constant. Figure 4 depicts the comparison, highlighting the alignment between the computed strain values and those obtained from the optical fiber measurements at the end point of the fiber located in the actuator (nearest to the position of the load sensor). The following plot allows us to verify the compatibility of the loading sensor and optical fiber.

The values of the strains measured by the fiber are slightly smaller than those computed by Hook's law accounting only for the deformations induced by the tension applied at the head of the nail.

This indicates that the interface between soil and the nail experiences little friction that reduces the impact of the tension caused by the pull-out, and eventually the deformations.

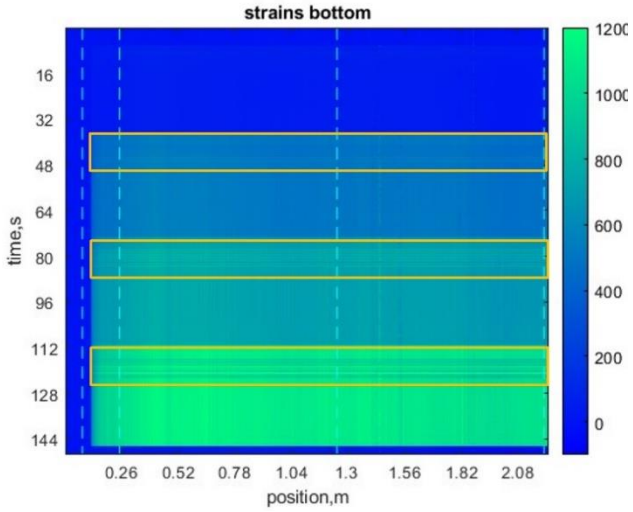

Figure 3. Color mapping representing the strains' distribution, yellow contours marking the positions of the dynamic pulses.

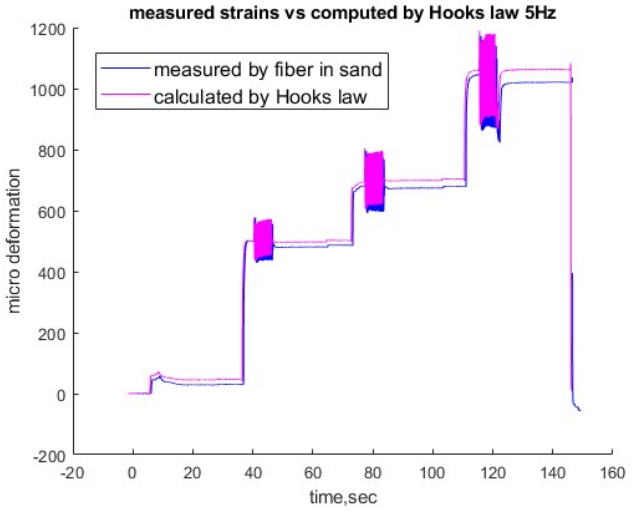

Figure 4. Strains measured by optic fiber vs strains comput ed by Hook's law, in test at 5HZ.

This is also consistent with the shown in Figure 5 representing the strains experienced along the nail, which has almost a uniform profile. A minimal friction is thus experienced between the soil and inclusion. The fact that the nail was inserted into the sand without being grouted, as well as the low density of confinement achieved (67.87%) is to be considered. Throughout previous studies (mentioned in the introduction), it has been shown that the roughness possessed by the interface has a major effect on the interaction mechanism occurring between the inclusion and the sand, which may be the reason to obtain these values.

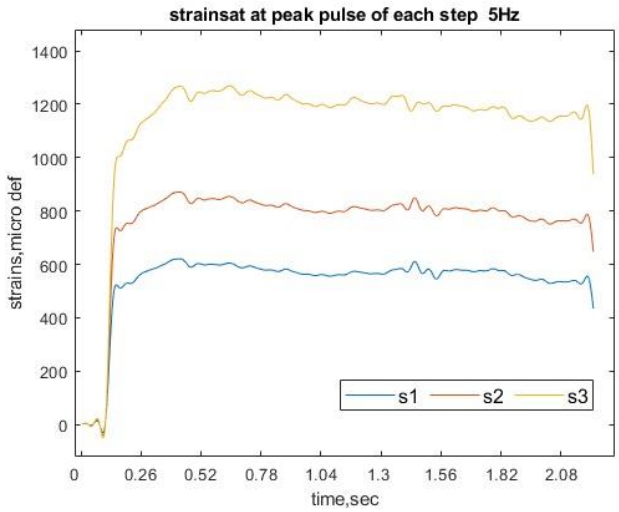

Figure 5. Strains during peak of the dynamic pulse at 5Hz at different steps.

5 CONCLUSIONS

A new impulsive device designed to study dynamic pull-out of nails has been developed and presented in this paper. The performance of this device has been examined through series of tests, with the aid of measurements obtained by optic fiber. The employment of the optic fiber allowed for accessing the strains all over the nail, which are essential to understand the interface behavior.

The tests allowed to assess the new dynamic device's capacity, and validity of the measurements of the optic fiber in case of dynamic pulses present. A consistency between the measurements of the sensors is achieved, as well as a uniform load transmission of the load through the nail. However, the measurements obtained by the optic fiber has shown no friction, eventually almost no interaction at the interface. This is due to the absence of grouting around the nail affecting the interface's roughness. This is to be tackled in the upcoming tests, where proper grouting of the nail will be done.

ACKNOWLEDGEMENTS

The authors address their sincere appreciation to the technical team responsible for the design and production of the device, in addition to their expertise during the performance of the tests.

REFERENCES

Poulos, H. (1989) 'Cyclic Axial Loading Analysis of Piles in Sand', *Journal of Geotechnical Engineering* [Preprint].https://www.academia.edu/7687163/Cyclic_Axial_Loading_Analysis_of_Piles_in_Sand (Accessed: 30 January 2023).

Schlosser, F. and Unterreiner, P. (1991) 'Soil Nailing in France: Research and Practice'.

Shahraki Ghadimi, A., Ghanbari A., Sabermahani M. and Yazdani M. (2017) 'Effect of soil type on nail pull-out resistance', *Proceedings of the Institution of Civil Engineers - Ground Improvement*, 170(2), pp. 81–88. https://doi.org/10.1680/jgrim.15.00038.

Su, L. (2006) 'Laboratory pull-out testing study on soil nails in compacted completely decomposed granite fill'. The Hong Kong Polytechnic University Available at [https://theses.lib.polyu.edu.hk/handle/200/2652](Accessed: 17 February 2023).

Tabucanon, J., Airey, D. and Poulos, H. (1995) 'Pile Skin Friction in Sands from Constant Normal Stiffness Tests', *Geotechnical Testing Journal - GEOTECH TESTING J*, 18. https://doi.org/10.1520/GTJ11004J.

Tan, S.A., P.H.Oo, T. S. Park, and W. L. Cheang. (2008) 'Rapid Pullout Test of Soil Nail'. *Journal of Geotechnical and Geoenvironmental Engineering,* Vol. 134, No. 9, September 1, 2008. https://doi.org/10.1061/(ASCE)1090-0241(2008)134:9(1327)

Tei, K. and Milligan, G.W.E. (1998) 'The Pull-Out Resistance of Model Soil Nails', 地盤工学会論文報告集,38(2),pp. 179–190. https://doi.org/10.3208/sandf.38.2_179.

Tufenkjian, M.R. and Vucetic, M. (2000) 'Dynamic Failure Mechanism of Soil-Nailed Excavation Models in Centrifuge', *Journal of Geotechnical and Geoenvironmental Engineering*, 126(3), pp. 227–235.https://doi.org/10.1061/(ASCE)1090-0241(2000)126:3(227).

Vucetic, M., Tufenkjian, M.R. and Felio, G.Y. (1998) *The Loma Prieta, California, earthquake of October 17, 1989--earth structures and engineering characterization of ground motion*. Edited by H. THOMAS L. Washington: U.S. G.P.O. (Earth structures and engineering characterization of ground motion). Available at: https://catalog.hathitrust.org/Record/011195881 (Accessed: 30 January 2023)

Xu, P., Hatami, K. and Jiang, G. (2020) 'Study on seismic stability and performance of reinforced soil walls using shaking table tests', *Geotextiles and Geomembranes*, 48(1), pp. 82–97.:https://doi.org/10.1016/j.geotexmem.2019.103507.

Yazdandoust, M. (2017) 'Experimental study on seismic response of soil-nailed walls with permanent facing', *Soil Dynamics and Earthquake Engineering*, 98, pp.101119.https://doi.org/10.1016/j.soildyn.2017.04.009.

Zeybek, A. (2017) 'Air Injection Technique to Mitigate Liquefaction beneath Shallow Foundations'. University of Cambridge. Available at [https://www.researchgate.net/publication/321048895_Air_Injection_Technique_to_Mitigate_Liquefaction_beneath_Shallow_Foundations].

Zhou, W., Zhen G., Lizhong W. and Jiahao L. (2020) 'Sand-steel interface behaviour under large-displacement and cyclic shear', *Soil Dynamics and Earthquake Engineering*, 138, p. 106352. https://doi.org/10.1016/j.soildyn.2020.106352.

Proceedings of the XVIII ECSMGE 2024
GEOTECHNICAL ENGINEERING CHALLENGES
TO MEET CURRENT AND EMERGING NEEDS OF SOCIETY
© 2024 the Authors
ISBN 978-1-032-54816-6
DOI 10.1201/9781003431749-79
Open Access: www.taylorfrancis.com, CC BY-NC-ND 4.0 license

ECSMGE 24
XVIII EUROPEAN CONFERENCE ON SOIL MECHANICS AND GEOTECHNICAL ENGINEERING

Use of BIM methodology in Geotechnical Projects – Construction of underground reservoirs

L'utilisation de la méthodologie BIM dans les projets géotechniques - Construction de réservoirs souterrains

A. Henriques*, N. Silva, M. Lopes
JET_{SJ} Geotecnia Lda, Lisbon, Portugal

**ahenriques@jetsj.com*

ABSTRACT: Building Information Modelling (BIM) is a digital technology-based methodology that is widely used in the Architecture, Engineering, and Construction (AEC) industry. The application of BIM to geotechnical projects can provide significant benefits. This paper aims to present the use of this methodology in the geotechnical and structural design of two reservoirs inserted in Belo Horizonte's Flood Control System. These reservoirs are comprised of three 40 m diameter secant circular shafts around 35 m deep, in an area of approximately 3500 m^2. The geotechnical and structural design was conducted in a PLAXIS 3D model generated by importing an IFC with geological surfaces defined in GEO5 with the interpolation of boreholes results. Also, a geometrical model was developed in REVIT which allowed a better visualization and interpretation of the construction stage planning, interaction and clashing between different structures before construction and accurate quantities estimation of all elements. All steel rebars were modelled and detailed using REVIT or TEKLA, which improved the accuracy of rebar placement and design, and reduced error and omissions during the construction. This case study allowed us to conclude that the integration of specialized software in a unique collaborative environment can have several advantages leading to a better project and construction outcome.

RÉSUMÉ: La Modélisation des Informations du Bâtiment (BIM) est une méthodologie basée sur la technologie numérique largement utilisée dans l'industrie de l'Architecture, de l'Ingénierie et de la Construction (AEC). L'application du BIM aux projets géotechniques peut offrir des avantages significatifs. Cet article vise à présenter l'utilisation de cette méthodologie dans la conception géotechnique et structurelle de deux réservoirs. Ces réservoirs sont composés de trois puits circulaires sécants d'un diamètre de 40 mètres, d'une profondeur d'environ 35 mètres, sur une superficie d'environ 3500 mètres carrés. La conception géotechnique et structurelle a été réalisée dans un modèle PLAXIS 3D généré en important un fichier IFC avec des surfaces géologiques définies dans GEO5 grâce à l'interpolation des résultats de sondages. De plus, un modèle géométrique a été développé dans REVIT, permettant une meilleure visualisation et interprétation de la planification des étapes de construction, des interactions et des conflits entre différentes structures avant la construction. Toutes les armatures en acier ont été modélisées et détaillées à l'aide de REVIT ou TEKLA, améliorant la précision du placement et réduisant les erreurs et les omissions pendant la construction. Cette étude de cas nous a permis de conclure que l'intégration de logiciels spécialisés dans un environnement collaboratif unique peut présenter plusieurs avantages pour le projet et la construction.

Keywords: BIM methodology, 3d analysis, deep excavations, diaphragm walls.

1 INTRODUCTION

In this article, the application of the BIM methodology for the execution and construction of the "Nado 1" and "Vilarinho 2" reservoirs is presented. This project is part of the restructuring of the drainage system of the city of Belo Horizonte, state of Minas Gerais, Brazil (Figure 1).

The city has approximately 90 risk areas, classified according to the number of points per municipality, with the Venda Nova region, where both reservoirs are located, being the region with the highest incidence of flood records, with approximately 20 classified points (Cistini, 2018).

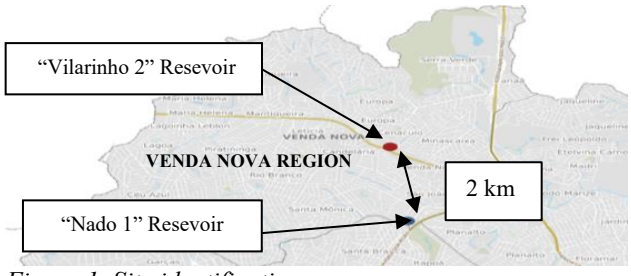

Figure 1. Site identification.

The construction of two large reservoirs with approximately 3500 m^2 and a considerable depth of about 35 m), situated in a densely populated region of the city of Belo Horizonte, results in a complex process marked by complex soil-structure interaction,

influenced by various factors such as structural symmetry, geological-geotechnical asymmetry, flow analysis, stability of the excavation bottom (hydraulic failure) through permeable formations, construction phasing, and demanding control of settlements in the surrounding space. In this context, three-dimensional analyses were conducted to obtain results with greater reliability, capturing the soil-structure interaction appropriately. These analyses were made through the use of the BIM methodology by the creation and integration of geotechnical, numerical, and geometrical models of the reservoir's elements and structures in the Vilarinho area (Figure 2) and Nado area (Figure 3).

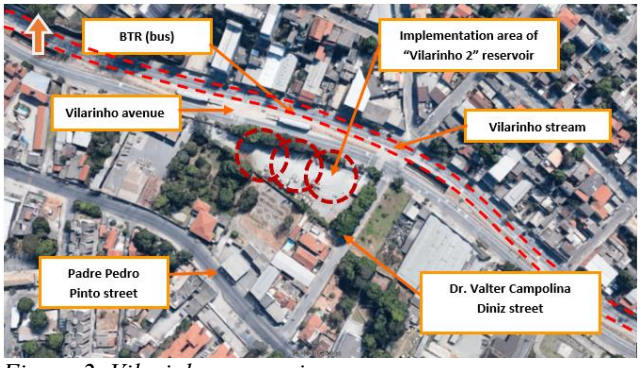

Figure 2. Vilarinho reservoir.

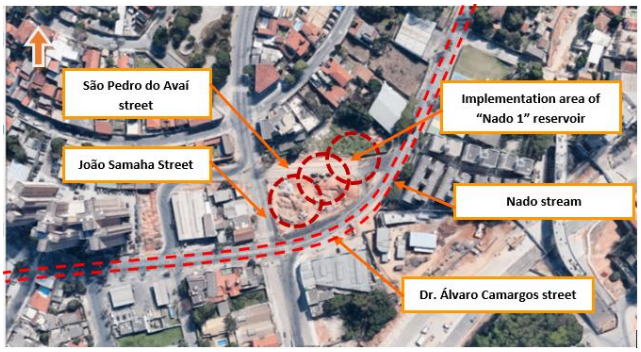

Figure 3. Nado reservoir.

2 STRUCTURAL SOLUTION

The main concept for the project aimed at controlling deformations in the influence area of the excavation, with the goal of minimizing its impact on existing infrastructures as well as neighboring buildings. Given the substantial depth of the planned excavation and the nature of the geological formations encountered, a solution in diaphragm walls was chosen, materialized by three intersecting circular shafts. At the intersection points, the execution of two reinforced concrete frames is designed, materialized by a set of columns and struts braced at various levels to reduce their respective bending lengths.

To ensure the proper functioning of the retaining structure when existing possible deviations from the verticality of the diaphragm wall panels, various bracing rings were designed along the perimeter of the wall. These rings are responsible for transmitting axial loads to the different levels of struts of the frames (Figure 4).

The regulatory soil pressures and overloads acting on the face of the diaphragm walls are, in turn, transmitted by bending/shear to the rings and, equally, by axial forces from the rings to the two reinforced concrete frames.

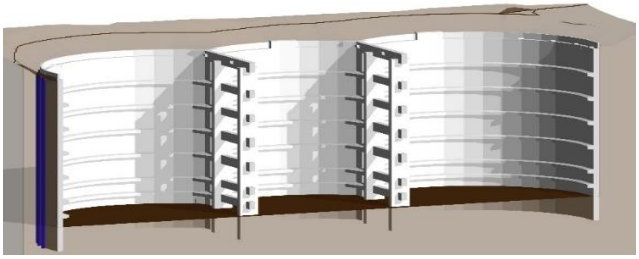

Figure 4. Excavation structure of the reservoirs.

The structure of the reservoir cover essentially consists of pre-slabs supported by prefabricated beams, which in turn are supported on reinforced concrete columns with a height equal to that of the reservoir (Figure 5).

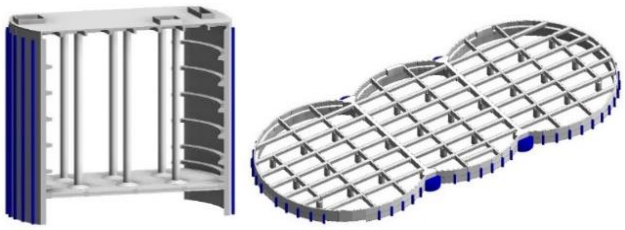

Figure 5. Cover structure of the reservoirs.

3 USE OF BIM TOOLS

3.1 Introduction

Considering the development and importance of using BIM tools in civil construction, especially in geotechnical projects (Vaníček et al, 2021), the decision was made to carry out this project in a collaborative environment, integrating and coordinating the geometry of the reservoir structure and associated structures with its reinforcement, and ensuring compatibility between the structure and the surrounding geological-geotechnical environment. The development of the project through this methodology also allowed for the identification of various incompatibilities among the different constituent structures of the reservoir, which were

timely corrected in the design phase, prior to construction phase.

3.2 Geotechnical modeling

In order to identify the geological formations to be intersected by the excavation, geologic-geotechnical campaigns were conducted at both locations. These campaigns included mechanical drilling, geophysical surveying and in-situ and laboratory tests.

It is observed that the local geological environment generally involves a superficial layer of modern anthropogenic, alluvial, and colluvial materials, referred to as "fill deposits" and "alluvial/colluvial deposits," respectively. Underlying these formations there is a substratum dating from the Archean, representing the lithostratigraphic unit designated as the "Belo Horizonte Complex", composed superficially of residual soils/saprolites covering a gneiss rock mass with a degree of weathering ranging from sound to highly weathered.

In order to make a more accurate assessment of the materials intersected by the diaphragm walls (Tawelian et al, 2016), as well as to determine the various excavation volumes of these materials and the position of the existing water table, a three-dimensional modeling of the geological structure was carried out based on the information provided by the extensive geologic-geotechnical plan.

This model was developed using the Stratigraphy tool in the GEO5 software, which allows, through the input of various point field test data (drillings, wells, CPT, DPT, SPT, DMT, and PMT) and topographic surveying, to interpret and generate a geological model consisting of a set of transition surfaces between the various formations that constitute the terrain in the reservoir areas (Figure 6). The creation of this model was done iteratively, through the interpretation and analysis of the model until it aligned with the geological-geotechnical study results.

All this information was input into the program through georeferencing points with X, Y, and Z coordinates, allowing for subsequent export to the numerical and geometrical modeling program in the universal IFC format.

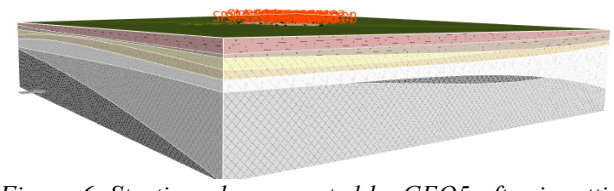

Figure 6. Stratigraphy generated by GEO5 after inputting geotechnical test data.

3.3 Numerical modeling

In an effort to assess the impact of geological-geotechnical asymmetry, structural asymmetry and the presence of neighboring structures and infrastructure, and thereby estimate the forces and deformations on the structure, three-dimensional finite element analyses were conducted using the PLAXIS 3D software, simulating the key construction phases (Figure 7).

The geometry of the numerical calculation models, particularly concerning the spatial definition of the geological structure, was based on the three-dimensional geological models presented in the previous chapter.

To achieve this, aiming to generate suitable finite element meshes, geotechnical boundary points (generated in the GEO 5 model) were first imported into AutoCAD 3D. Subsequently, Non-Uniform Rational Basis Spline (NURBS) surfaces were created at the transition between the various formations constituting the terrain in the reservoir areas. Finally, these surfaces were imported into the PLAXIS 3D numerical calculation program. This entire process was carried out iteratively until a finite element mesh with sufficient quality for the analysis of all structural elements and neighboring infrastructure was generated.

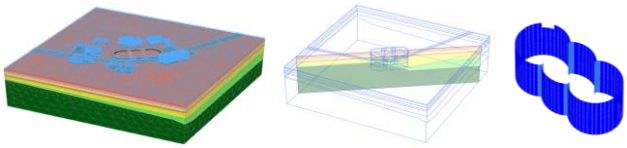

Figure 7. Geometry and finite element mesh of the three-dimensional calculation model of a reservoir and its structural elements (PLAXIS 3D).

3.4 Geometric modeling

Based on the structural preliminary design drawings created in AutoCAD, the decision was made to do the geometric modeling of the reservoir structure and adjacent structures in REVIT.

To make the project more comprehensive, enhance the understanding of all constituent elements of the models, and facilitate the extraction of material quantities from various components of the reservoir, including formwork, concrete, and reinforcements, various construction phases were created to simulate the reservoir's construction process (Figure 8)

It is also noteworthy that creating the model using these phases was crucial for all stakeholders involved in the construction of the reservoirs (designers, builders, inspectors, and the owner) to have a clear understanding of the planning and execution of the project.

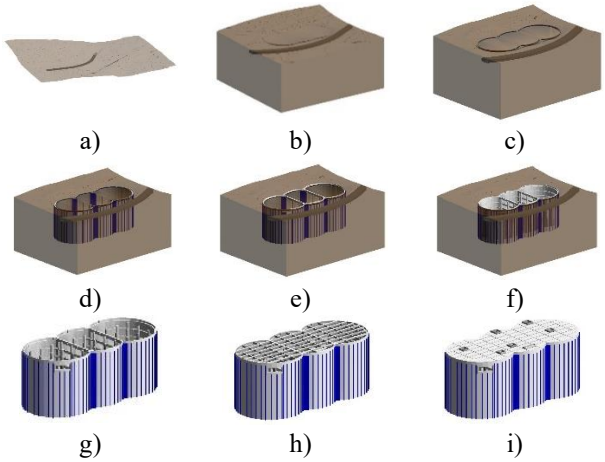

Figure 8. Phases for the execution of the structure: a) existing; b) excavation; c) guide wall; d) panels and jet grouting; e) first beam; f) rings and struts; g) structural columns; h) cover beams; i) roof slabs.

3.5 Rebar modeling

The reinforcement rebars of the elements of the reservoir were modeled in REVIT and TEKLA software to ensure that, during the construction phase, there were no doubts or errors in the assembly of the reinforcements.

Modeling of simpler and longer-developed elements such as the panels of the diaphragm wall, was carried out in REVIT (Figure 9), while modeling of more complex elements, such as beams and slabs of the cover, was performed in TEKLA (Figure 10).



Figure 9. Modeling the reinforcements' panels and assembling them on-site.

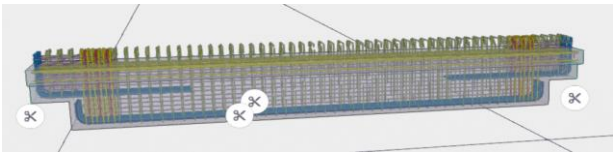

Figure 10. Modeling the reinforcements of the cover beams.

Despite being time-consuming, this modeling approach offers numerous advantages for geotechnical projects, particularly for designers and builders, including th reduction of steel wastage on the construction site, reduction of time spent on presenting and measuring reinforcements compared to traditional CAD methods, correction of errors and incompatibilities between reinforcements in a preliminary phase and evaluation of all necessary details for proper execution.

4 FINAL REMARKS

The present article addressed the use of the BIM methodology for the design and construction of two underground reservoirs with approximately 35 m of depth, integrated into the flood control system of the city of Belo Horizonte, Brazil.

The geological-geotechnical models, along with their iterative integration with numerical and geometrical models allowed for a better visualization and more comprehensive analysis of geotechnical data. This led to a correct simulation of the soil-structure interaction and, consequently, more realistic and optimized solutions.

The application of the BIM methodology in this geotechnical project facilitated coordination among different disciplines and structures involved. It has provided a better and more effective interpretation of different construction phases from the early design stage, avoiding coordination errors during the execution phase. Thus, this methodology represents a significant evolution in the approach to geotechnical projects and in their execution in a more efficient way.

ACKNOWLEDGEMENTS

The authors express gratitude for the authorization from SUDECAP and the CME consortium for the publication of this article and for their collaboration and willingness in providing the necessary data for the document's preparation.

REFERENCES

Cristini F. (2018) "*BH tem quase 90 áreas sujeitas a inundações; saiba onde ficam*" Available at https://g1.globo.com/mg/minas-gerais/noticia/2018/09/27/bh-tem-quase-90-areas-sujeitas-a-enchentes-saiba-onde-ficam.ghtml, acessed 26/02/2024.

Vaníček I., Jirásko D. and Vaníček M. (2021), "*Role of Geotechnical Engineering in BIM process modelling*" in 14th Baltic Sea Region Geotechnical Conference (2021), Helsinki, Finland. Doi: 10.1088/1755-1315/727/1/012007.

Tawelian L. and Mickovski S. (2016), "*The implementation of Geotechnical Data Into the BIM Process*", ProcediaEngineering Volume143, Pages734–741, Doi: https://doi.org/10.1016/j.proeng.2016.06.115.

Proceedings of the XVIII ECSMGE 2024
GEOTECHNICAL ENGINEERING CHALLENGES
TO MEET CURRENT AND EMERGING NEEDS OF SOCIETY
© 2024 the Authors
ISBN 978-1-032-54816-6
DOI 10.1201/9781003431749-80
Open Access: www.taylorfrancis.com, CC BY-NC-ND 4.0 license

ECSMGE 24
XVIII EUROPEAN CONFERENCE ON SOIL MECHANICS AND GEOTECHNICAL ENGINEERING

Evaluation of some "similar" dissipation tests

Évaluation de quelques tests de dissipation "similaires"

E. Imre*
Óbuda University, Bánki Donát Fac. of Mechanical and Safety Eng., Budapest Hungary

L. Bates
University of Newcastle, Newcastle, Australia

D. Marchetti
Studio Prof. Marchetti, Italy

**imre.emoke@uni-obuda.hu*

ABSTRACT: Various types of extremely short (<< 1 min) in situ, CPT related dissipation tests in 3 test sites were evaluated statistically using simple, closed form, parametric functions. The parameters identified from the measured data linked with soil plasticity information showed strong correlation for granular matter, more scatter for clays. A recently suggested horizontal consolidation model was used to explain the soil type dependence. The consolidation model - based on time dependent constitutive law and K_0 condition at the outer boundary – was verified by the evaluation of a few in situ total stress dissipation tests, where a similar, one-dimensional version of the model was used instead of the cylindrical version.

RÉSUMÉ: Des tests de dissipation totale courte de 3 sites ont été évalués par des fonctions paramétriques. Des diagrammes de profilage du sol ont été réalisés en reliant les parametres identifiés la plasticité du sol. Les diagrammes ont montré une forte corrélation pour la sols granulaire fins, une certaine dispersion pour les argiles. Les résultats ont été expliqués de models de consolidation couplés ont été élaborées. Dans l'évaluation précise d'essai de dissipation totale des contraintes longue in situ, la similarité du modele d'essai de relaxation et in situ a été utilisée.

Keywords: Oedometer relaxation test; sand; soil profiling; displacement pile; total stress dissipation test.

1 INTRODUCTION

The few-second-long, total stress related, f_s, q_c and DMTA dissipation tests are made in the technical breaks of the steady penetration of the CPT equipment (S832 or Geomil CPT, see eg., Imre et al, 1995, 2023).

The test records are reflecting the following phenomena. (i) The CPT equipment is a model pile, and a residual stress state builds up at the stop of the penetration, which is negligible in soft clay but entails huge negative shaft resistance in sand (Poulos, 1987), which may redistribute (Prodinger, 1983). (ii) The dynamic-static transition in the soil constitutive equation, (iii) then horizontal consolidation (depending on soil type and initial condition) takes place.

The total stress dissipation tests are not evaluated (Baligh et al., 1985), or are evaluated approximately (Marchetti at al., 1986) in present practice.

This review type paper discusses how a newly suggested model family may explain the short, total stress related dissipation tests and the soil profiling charts. The content of the paper is as follows. The various dissipation tests, test sites and the statistical evaluation with the soil profiling charts are shown in Sections 2 to 3, the model is presented in Section 4, the model validation and the parameter analyses are presented in Sections 5 to 6.

2 MEASURED DATA

2.1 Szeged, Debrecen and Szeged-ELI sites

In the frame of the research started in 1998, some 10 to 20 m deep borings and S832 CPT's short f_s and q_c dissipation tests were made in Szeged side of Tisza river and in Debrecen city.

The slightly OC (crust) and NC soil layers of Szeged and eolian sand layer of Debrecen city are listed in Figure 1 and Tables 1 to 3. Szeged city was divided into 3 parts, in parts A and B,the soil was non-saline, in part C (including the ELI site) the soil was spotlike saline (Imre et al., 2010).

In Szeged outskirts, 20 to 80 m deep borings and various dissipation tests were made in the expertise on ELI building (Figure 2).

Concerning the S832 short f_s and q_c dissipation tests made in Szeged side of Tisza river and in Debrecen,

mean dissipation test was determined for each group (Figure 3, within layers 1 to 5 and part A, B and C in Szeged, various plasticity). The. Some DMTA dissipation test records and some Geomil q_c dissipation test data were made in Szeged ELI site, the initial part of the tests are shown in Figure 4.

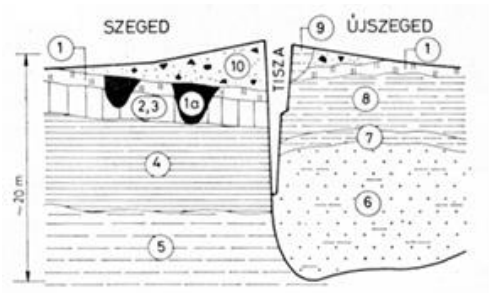

Figure 1. Layers in Szeged side of river (Rétháti, 1988).

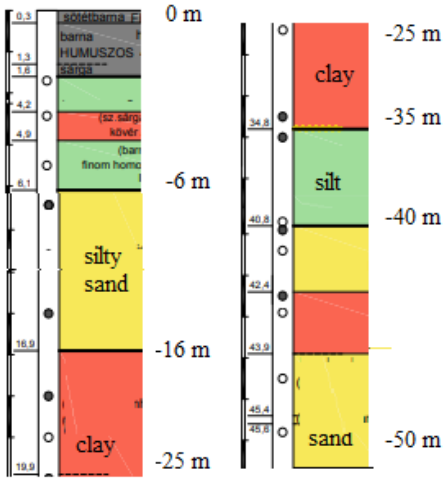

Figure 2. Szeged, ELI, a profile indicating location of the soil samples and dissipation tests (u2, qc, DMTA). 0-50m.

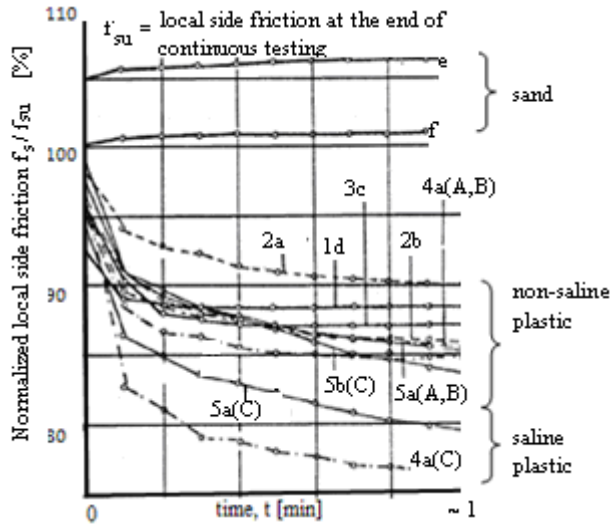

Figure 3. Szeged city and Debrecen sand data, mean short CPT f_s dissipation tests, see Tables 1-2, (Imre, 1995).

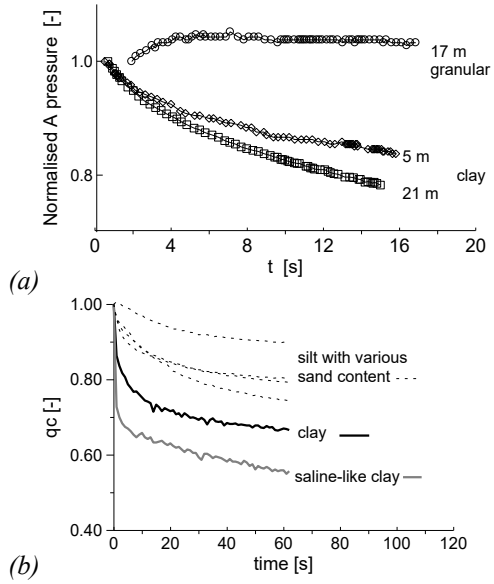

Figure 4. Szeged, ELI site. (a) Short DMTA dissipation test results in sand and in clay (b) Geomil, short q_c dissipation tests in sandy silt and in clay.

Table 1. Layers in the upper 20 m, Szeged Tisza bank.

Layer	Soil
1	Loess
2	Upper yellow lacustrine clay, OC
3	Silty inclusion
4	Lower yellow lacustrine clay, NC
5	Blueish fresh-water deposit, NC

Table 2. Soil classification, Szeged and Debrecen.

Notation	Category limits
a	> 25 I_p [%]
b	15-25 I_p [%]
c	10-15 I_p, [%]
d	5-10 I_p, [%]
e	d_{30}>0.1mm
f	d_{30}<0.1mm

Table 3. Some soil properties in Szeged, non-saline soils.

Layer	I_p [%]	C_U [kPa]	k[m/s]	e[-]
1	7.4	86.2	$6.1.10^{-8}$	0.68
2	28.9+	92.7	$3.9.10^{-8}$	0.76
3	19.	75.3	$3.8.10^{-8}$	0.76
4	36.3	95.0	$2.5.10^{-g}$	0.85
5	30.01	60.0	$6.3.10^{-8}$	0.80

2.2 The Araquari test site

The project was developed on a coastal plain in Araquari, Brazil (Figures 5, 6) where marine sandy terraces were formed in the Pleistocene. The testing program consisted of short DMTA dissipation tests in every 20 cm with data sampling in a frequency of 20 millisecond, in 3 days (Imre et al., 2023(a and b)).

3 SOIL PROFILING CHARTS

The following empirical parameters were defined for the various short dissipation test records (Imre, 1995; Imre et al, 2023(b)). A "stress delta" parameter:

$$\Delta\sigma = \sigma(t_i) - \sigma(t_i + \Delta t); \quad (1)$$

In case of the short DMTA test, the initi time t_i was the first recorded time and 15 s was the final time value.

In case of the short Sz832 CPT f_s and q_c dissipation tests, the t_i was the time when the immediate stress drop (due to dynamic-static transition) was ended, and about 30 s was the final time value depending on the personnel.

Between these times, the stress variation is described by the following parametric functions for DMTA and CPT dissipation tests, resp.:

$$\sigma(t) = at^b \quad (2)$$

$$\sigma(t) = \sigma_\infty + (\sigma_0 - \sigma_\infty)\ e^{-\frac{t}{\upsilon}} \quad (3)$$

Analysing the parameters, the stress delta parameter is negative/positive for stress increase/decrease, the reverse is true for the exponent *b*. Linking the parameters with plasticity index or soil type, soil profiling diagrams are shown in Figure 7 related to DMTA and fs dissipation tests.

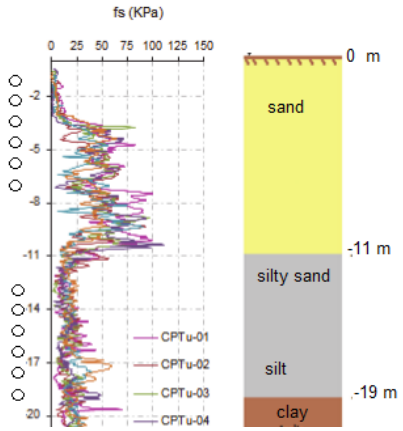

Figure 5. Araquari test site. Soil profile and CPTu fs data (Brocheroa and Schnaid, 2020). No test in the dense sand.

4 JOINED MODEL

A coupled 1 consolidation model family (oedometer, cylindrical, spherical model, space dimension 1, 2, 3), was derived by using displacement boundary condition at „outer" boundary (Imre et al., 2010).

In the cylindrical version of the model, the constant displacement boundary condition is the K_0 condition which is more realistic than the constant total stress boundary condition.

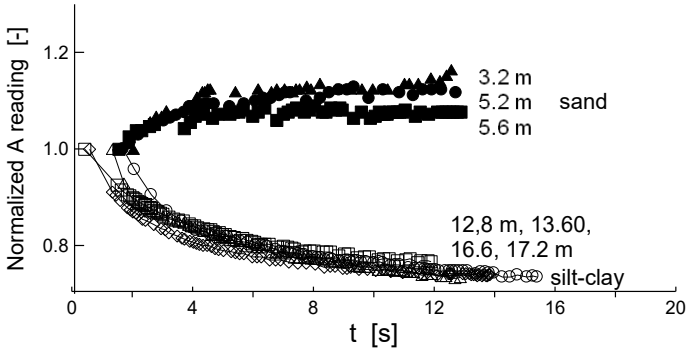

Figure 6. Araquari test site. Short DMTA dissipation test records, in sand and in silt - clay layer.

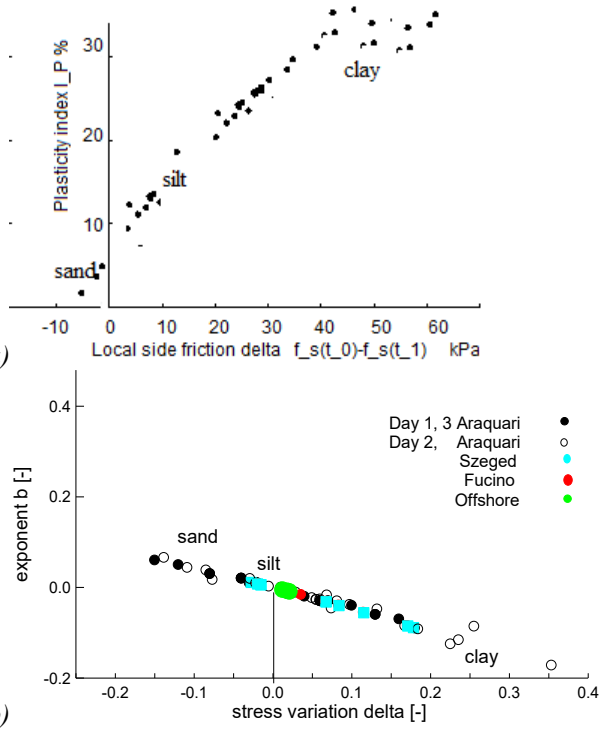

Figure 7. Soil profiling diagrams by linking identified parameters with soil plasticity. (a) Szeged, S832 CPT fs diagram. (b) All test sites, DMTA diagram. Strong correlation for granular matter, scatter for clays.

By adding a relaxation part-model, the joined 1 model family is resulted (Imre et al., 2010):

$$\sigma(t, r_0) = \sigma^c(t, r_0) + \Delta\sigma^r(t, r_0) = \sigma_\infty + \sigma^t(t, r_0) + \Delta\sigma^r(t, r_0) \quad (4)$$

where superscripts c and r indicate consolidation and, relaxation, resp. The relaxation model was follows:

$$\Delta\sigma^r(t,r_0) = -s\,\sigma(0,r_0)\frac{1}{1-s\,b}\log\left[\frac{t+t_1}{t_1+t_3}\right];\ t > t_1+t_3 \quad (5)$$

where s is coefficient of relaxation, t_1 and t_3 time constants, b model parameter.

It follows from Eq (5) that the total stress decreases at r_0 with time due to relaxation if the elapsed time is greater than $t_1 + t_3$. The t_3 and b are zero if no partial unloading takes place in the displacement load at the boundary r_0.

The qualitative behaviour of the consolidation model is determined by the initial condition as follows. Concerning the total stress variation, the transient part of the horizontal total stress at the boundary r_0 is equal to the mean excess pore water pressure (ment on the space domain):

$$\sigma_r^t(t,r_0) = u_{mean}(t) \quad (6)$$

Its final value is equal to zero. It follows that the total stress changes with time due to consolidation by the initial value. This is a decrease or stress drop if the initial mean pore water pressure is positive and an increase if it is negative (see Eq (6)).

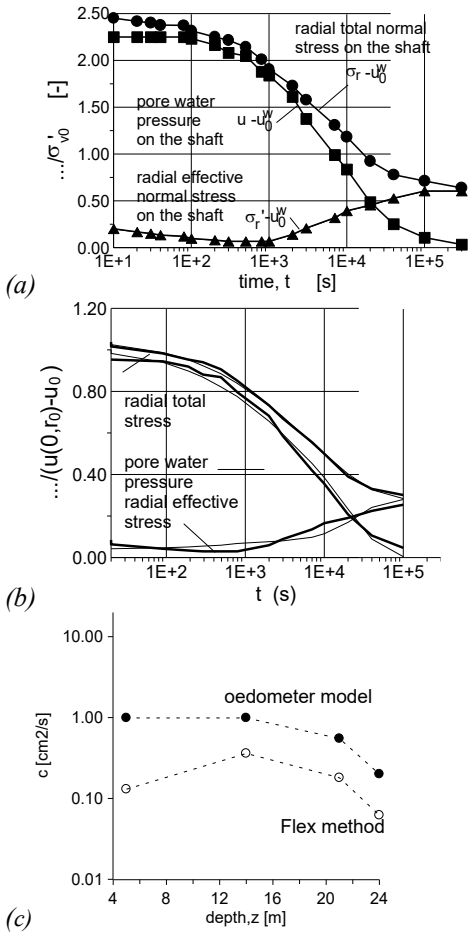

Figure 8. (a) and (b): The piezo-lateral stress cell test data and evaluation results. (d) Evaluation results of DMTA long dissipation tests, made in Szeged-ELI site.

Concerning the horizontal effective normal stress at boundary r_0, if positive initial excess pore water pressure dissipates, then it increases due to consolidation and decreases due to relaxation, according to Eq (5).

5 MODEL VALIDATION

In the case of the piezo-lateral stress cell test made in Boston Blue Clay (Figure 8(a), Baligh et al., 1985), the measured radial total stress decreases by 73%. The measured radial effective stress at the shaft decreases then increases with time. (No similar measured data set is available in case of granular matter.).

The evaluation was made by using the oedometer relaxation test model. The measured and fitted data are shown in Figure 8(b). The identified c and the identified initial pore water pressure distribution were slightly over-predicted in both cases due to the elastic deformation of the equipment (since during the time dependent stress release, the diameter of the equipment slightly decreases).

The same method was applied to evaluate the DMTA dissipation tests in Szeged-ELI site. Some pore water pressure data were derived beforehand using Eq (6), then the oedometer test model was fitted on the A readings and the generated pore water pressure data. Some results are shown in Figure 8(c).

6 SIMULATIONS

A parameter analyses was made assuming positive initial excess pore water pressure distribution, the radius $r_1 = 37r_0$ was used, the steady-state part of solution and initial condition was estimated from the PSL cell test record in Boston Blue Clay (Figure 8(a)).

In case of varying coefficient of consolidation c and relaxation s, the parameter analysis gave the following result. The radial total stress at r_0 decreased with time both due to consolidation and relaxation, with rate depending on the foregoing parameters (Figure 9), the total stress drop in short testing in soft clay can be explained by this (Figures 4, 6).

The time variation of the effective normal stress at boundary r_0 was an increase due to consolidation and a decrease due to relaxation, with rate depending on the coefficient of consolidation (c) and the coefficient of relaxation (s), see Figure 9. For large/small permeability soil, the increase/decrease with time was dominant in the first seconds, respectively.

The local side friction increase for large c and decrease for small c (shown in Figure 3) can be explained by the model simulations including the scatter due to effect of parameter s for soft clays.

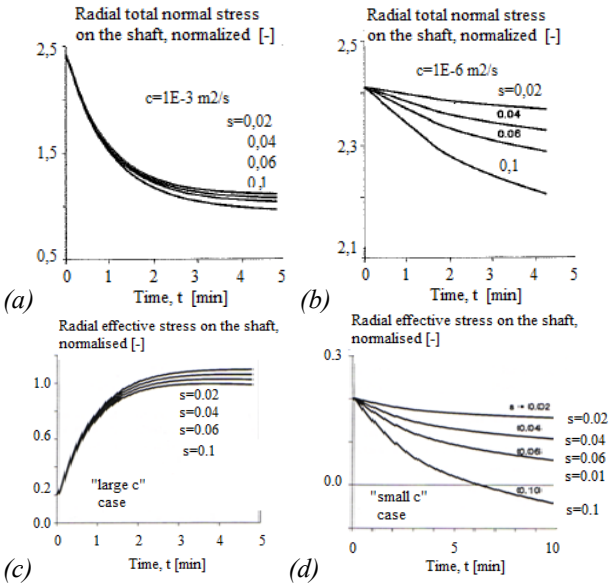

Figure 9. Parameter analysis, various c and s values (positive initial excess pore water pressure distribution). (a) and (b) The radial total normal stress on the shaft, large / small c (or permeability), resp. (c) and (d) The radial effective stress on the shaft, large and small c, resp.

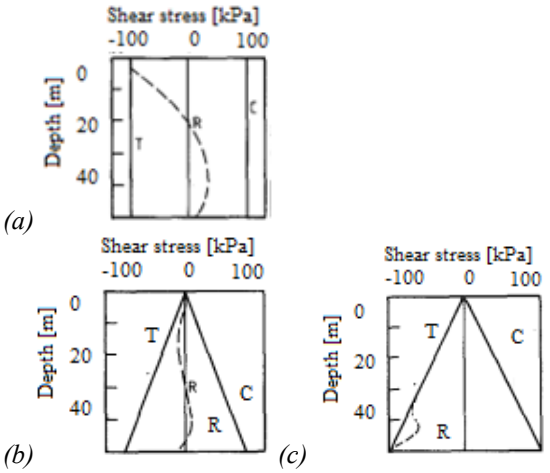

Figure 10. (a) to (c) to (d): Residual shear stresses, stiff clay, soft clay, sand, resp. Legend: R: Residual stress. T: Stress for tensile failure. C: Stress for compression failure. (after Poulos, 1987).

7 DISCUSSION

The excess pore water pressure in coarse sands is assumed as zero being the state fully drained by Campanella & and Robertson, 1991.

The theoretical works (Kouretzis et al., 2014) indicate high negative excess pore water pressures and phase change in coarse, dense sand after penetration. Negative excess pore water pressure is generally measured in most sands after penetration (see eg., Imre et al, 2021), which may increase the shaft resistance.

The theoretical work of (Poulos, 1987) indicate that the residual stress state is different in sand and in soft clay (see Figure 10). In sand, there are high negative, residual shaft stresses at the stop of the penetration. In accordance to this, Schnaid et al (2015) mention that in Araquari sand site „the equipment was unable to push the standard DMT through the upper dense sand due to a buildup of resistance during the pause to perform the standard DMT measurements“ (Figure 5). Similarly, huge re-driving resistance of displacement piles is mentioned by (Yang 1956) in sand.

Measurements during a time interval show that time dependent stress re-distribution takes place (Prodinger, 1983). The vertical equilibrium condition of the CPT equipment - soil system (Imre, 1988) and the frictional nature of the shaft force may result in a saw-tooth-like stress variation at the tip level.

8 CONCLUSION

The evaluation of the total stress dissipation tests is hindered by the fact that the CPT equipment is a displacement model pile with residual stress state, which is less important in soft clay and more important in sand.

The evaluation of simultaneous total stress and pore water pressure dissipation records were successful in soft clay verifying the suggested model. However, the result (identified positive excess pore water pressure initial condition, parameter *c*) reflected that the stress release in the equipment modified the rigid body boundary condition. Similar evaluation can theoretically be made in the case of medium amd coarse sand, however, very few pieces of information on the long-term behavior and on the initial condition are available.

The result of the statistical evaluation - showing soil type dependences – were explained here by a point-symmetric, coupled 1 consolidation model completed with a relaxation part-model (Imre et al., 2010) as follows. Concerning fine-graded soils, the parameter analysis made using a fixed, positive initial excess pore water pressure distribution and varying (the soil type dependent) coefficient of consolidation *c* and coefficient of relaxation *s* explained the short dissipation test results and the soil profiling diagrams constructed from short, DMTA, f_s and q_c dissipation test records, including the scatter for soft clays.

Concerning medium and coarse sands, the time dependent A pressure increase during the DMTA dissipation test was tentatively explained by the suggested consolidation model assuming negative initial excess pore water pressure distribution and partial unloading at the soil-blade interface.

Experiences and theoretical works support these assumptions since negative excess pore water pressure

is measured and theories predict dilating sand behaviour along the shaft after penetration, moreover, significant change in equipment forces with negative residual side friction forces occurs at the stop of penetration. However, very few pieces of information are available on long-term phenomena in medium and coarse sand.

REFERENCES

Baligh M. M.; Martin R. T.; Azzouz A. S. & Morrisson M. J. (1985). The piezo-lateral stress cell. *Proc. of the 11th ICSMFE* San Francisco. (2) pp. 841-844.

Imre, E. (1995). "Statistical evaluation of simple rheological CPT data". *XI. ECSMFE*, 1995. 1. 155-161.

Imre, E. (1988). Skin bearing capacity of piles. *Proc. 1st Int. Geotech. Seminar on Deep Foundations on Bored and Auger Piles* pp. 421-429. , 9 p.

Imre E., Rózsa P., Bates L., Fityus S. (2010). Evaluation of monotonic and non-monotonic dissipation tests. *Computers and Geotechnics*. (37): pp. 885-904. https://doi.org/10.1016/j.compgeo.2010.07.008.

Imre E.; Schanz T.; Hortobágyi Zs.; Singh V.P;. Fityus S. (2015). Oedometer relaxation test. *XVI ECSMGE* London, UK, ICE Pub. pp. 3347-3352.

Imre, E., Bates, L., Fityus, S.; Hegedűs, M., Singh P. (2021). Coupled models for dissipation tests *ISC6*. https://doi.org/10.53243/ISC2020-269.

Imre E., Marchetti D., Juhász M., Bates L., Fityus S. (2023a). Least Squares evaluation of DMT dissipation test data –preliminary results. *Proc. 8th IS-Porto*, isdcg2023-216-1-c.pdf. 8p.

Imre E., Marchetti D., Juhasz M., Bates L., Fityus S. (2023b). The short DMTA dissipation test. *Proc. 8th IS-Porto*, Sept. 3-6, 2023.isdcg2023-217-1-c.docx (issmge.org). 8p.

Kouretzis G. P., Sheng D. & Wang D. (2014). Numerical simulation of cone penetration testing using a new critical state constitutive model for sand. *Computers and Geotechnics* (56) pp. 50–60. 10.1016/j. compgeo. 2013.11.002.

Marchetti S., Totani G., Campanella R. G., Robertson P. K., Taddei B. (1986). The DMT_{hc} Method for Piles Driven In Clay, *Proceedings of In Situ '86.* GT. Div. ASCE, June 23-23, Blacksburg. 765-779.

Poulos H. G. (1987). Analysis of residual stress effects in piles. *J. Geotech. E. ASCE*. 113:216-22. doi. org/10.1061/(ASCE)0733-9410(1987)113:3(216).

Prodinger W. (1983). Measurement of the Redistribution of Stress Around Deep Foundations. *Proc. Int. Symposium*. Zurich, 09. 5-8, 1983 543-553.

Rétháti, L. (1988). *Probabilistic solutions in Geotechnics* Amsterdam. Elsevier.

Robertson P.K., Campanella R. G., Gillespie D.G., Greig J. (1986). Use of piezometer cone data. *ASCE Specialty conference IN-SITU'86.* SM 92.1263-1280.

Schnaid, F., Odebrecht, E., Sosnoski, J. and Robertson, P.K. (2016). Effects of test procedure on flat dilatometer test (DMT) results in intermediate soils. *Canadian Geot. Journal*, 53(8), pp.1270-1280. doi.org/10.1139/cgj-2015-0463.

Yang N.C. (1956). Re-driving characteristics of piles. *ASCE Jl. of Soil Mech. and Found. Div*. 1026-1.

APPENDIX

Two equations of coupled consolidation:

$$E_{oed}\frac{\partial \varepsilon}{\partial r} - \frac{\partial u}{\partial r} = 0 \tag{7}$$

$$-\frac{k}{\gamma_v}\Delta\, u + \frac{\partial \varepsilon}{\partial t} = 0 \tag{8}$$

where ε volumetric strain, v is the radial displacement, u is the excess pore water pressure, r and t are the space and the time co-ordinates respectively, E_{oed} is the oedometric modulus. The boundary conditions:

$$u(t,r)|_{r=r_1} = 0\,,\ \frac{\partial u(t,r)}{\partial r}|_{r=r_0} \equiv 0\,,\ v(t,r)|_{r=r_0} \equiv v_0 > 0\,,\quad v(t,r)|_{r=r_1} \equiv 0 \tag{9-12}$$

The solution of the excess pore water pressure and the transient part of the radial total stress in the cylindrical case is:

$$u = \sum_{k=0}^{\infty} \lambda_k C_k\, e^{-\gamma_k^2 \cdot c_h \cdot t} \left\{ \begin{matrix} [I_0(\lambda_k r) + \mu_k Y_0(\lambda_k r)] \\ -[I_0(\lambda_k r_1) + \mu_k Y_0(\lambda_k r_1)] \end{matrix} \right\} \tag{13}$$

$$\sigma = \sum_{k=0}^{\infty} \lambda_k C_k\, e^{-\gamma_k^2 \cdot c_h \cdot t} \left\{ -[I_0(\lambda_k r_1) + \mu_k Y_0(\lambda_k r_1)] \right\} + \sigma_\infty \tag{14}$$

where I_0 and Y_0 are Bessel functions, λ_k, μ_k are the roots of the boundary condition equations; C_k (k=1, 2, 3) are the l coefficients determinable from the initial condition, c_h is coefficient of consolidation.

The solution of the excess pore water pressure and the transient part of the radial total stress for the oedometric relaxation test model is:

$$u(t,y) = -\sum_{i=1}^{\infty} \varphi_i [\cos(y(i\pi/H) - 1]\ e^{-i^2 \pi^2 T} \tag{13}$$

$$\sigma(t) = -\sum_{i=1}^{\infty} \varphi_i\, e^{-i^2 \pi^2 T} + \sigma_\infty \tag{14}$$

where $T = ct/H^2$ the time factor, c coefficient of consolidation, ϕ_i are Fourier coefficients related to the initial condition, H length between model boundaries.

Proceedings of the XVIII ECSMGE 2024
GEOTECHNICAL ENGINEERING CHALLENGES
TO MEET CURRENT AND EMERGING NEEDS OF SOCIETY
© 2024 the Authors
ISBN 978-1-032-54816-6
DOI 10.1201/9781003431749-81
Open Access: www.taylorfrancis.com, CC BY-NC-ND 4.0 license

ECSMGE 24
XVIII EUROPEAN CONFERENCE ON SOIL MECHANICS AND GEOTECHNICAL ENGINEERING

A closed-form equation for the failure locus of pile groups subjected to generalized loading conditions

Une équation de forme fermée pour le lieu de rupture de groupes de pieux soumis à des conditions de chargement généralisées

M. Iovino*
University of Napoli 'Parthenope', Naples, Italy

C. Iodice, R. Di Laora
University of Campania 'Luigi Vanvitelli', Aversa, Italy

L. de Sanctis
University of Napoli 'Parthenope', Naples, Italy

A. Mandolini
University of Campania 'Luigi Vanvitelli', Aversa, Italy

**maria.iovino@assegnista.uniparthenope.it*

ABSTRACT: A closed-form solution for the failure locus of piled foundations in the force space is presented and discussed. Based on recent works published in the literature dealing with the problem of the bearing capacity of pile groups under inclined eccentric load, the expression of the failure locus is derived by combining a parabola in the vertical force – moment plane and a Granville egg in the vertical force – horizontal force plane. The complete three-dimensional failure surface requires only a few parameters that can be evaluated even by hand calculation through simplified methods existing in literature. The predictive ability of the proposed equation is validated against the data available from previous works on piled foundations subjected to inclined eccentric loads.

RÉSUMÉ: Une nouvelle solution de forme fermée pour le lieu de rupture des fondations sur pieux dans l'espace des forces est présentée et discutée. Basé sur des travaux récents publiés dans la littérature traitant du problème de la capacité portante des groupes de pieux sous charge excentrique inclinée, l'expression du lieu de rupture est dérivée en combinant une parabole dans le plan force vertical – moment et un œuf de Granville dans le plan force vertical – force horizontal. La surface de rupture tridimensionnelle complète ne nécessite que quelques paramètres qui peuvent être évalués même par calcul manuel grâce à des méthodes simplifiées existant dans la littérature. La capacité prédictive de l'équation proposée est validée par rapport aux données disponibles dans de travaux antérieurs sur des fondations sur pieux soumises à des charges excentriques inclinées.

Keywords: Pile group, bering capacity, failure locus, inclined eccentric loads.

1 INTRODUCTION

The evaluation of the pile group bearing capacity under vertical, Q, horizontal, H, and moment, M, loads can be conveniently carried out employing simple solutions as alternative tools to more complex and time-consuming numerical analyses. In this context, interaction domains can be used in engineering practice for a quick and reliable evaluation of the foundation resistance necessary to fulfil design Ultimate Limit State, ULS, checks.

An exact solution for vertical eccentric load has been proposed by Di Laora et al. (2019) using the theorems of limit analysis; this solution is based on the hypotheses of rigid-plastic behaviour of individual piles whose hinged heads are connected through a rigid cap of infinite strength. In the same fashion, to consider general loading conditions, Iovino et al. (2021) and Di Laora et al. (2022) furnished solutions for pile groups under inclined eccentric load postulating the formation of a double plastic hinge at failure to describe the response of the group to the horizontal component (Broms 1964 a, b).

Based on the above works, a closed-form solution for the failure locus of pile groups is derived. In particular, the three-dimentional domain is a combination of a parabola approximating the shape of the interaction diagram in the axial load – moment

plane (Di Laora et al., 2019) and a Granville egg to replicate the shape of the surfaces in planes parallel to the axial load – horizontal load plane (Iovino et al. 2021; Di Laora et al. 2022). The use of the proposed domain is straightforward since the constants needed are already required in routine design.

In the following sections the mathematical formulation of the failure locus is presented and a discussion about the selection of the ingredients needed for its construction is provided. Finally, the ability of the proposed expression to match the failure surface of pile groups is demonstrated by comparison with data borrowed from a recent numerical work on pile groups subjected to combined loads.

2 FORMULATION OF THE FAILURE LOCUS

For the sake of simplicity, the formulation of the failure locus is herein shown for the case of a row of four equally-spaced, identical piles. Dealing with the (Q, M) and (Q, H) planes separately, the final three-dimensional expression is presented as a combination of the two.

In Figure 1 a plot of the domain for vertical eccentric load is presented employing the closed-form solution by Di Laora et al. (2019), whose boundary can be reasonably approximated with a parabola passing through the points:

1. (Q_c, 0), where Q_c is the bearing capacity of the pile group in compression;
2. (Q_t, 0), where Q_t is the bearing capacity of the pile group in uplift;
3. ((Q_c+Q_t)/2, M_{max}), where M_{max} is the maximum moment capacity of the pile group.

By imposing such conditions, the following equation is obtained:

$$\left|\frac{M}{M_{max}}\right| = 4\frac{(Q_c-Q)(Q-Q_t)}{(Q_c-Q_t)^2} \tag{1}$$

Any section of the failure locus in planes parallel to (Q, H) can be obtained using a trapezium (Figure 2a) whose inclined side connects the points of coordinates (Q_c, H_c) and (Q_t, H_t), where H_c and H_t are the horizontal capacity of the pile group calculated at Q_c and Q_t, respectively (Di Laora et al., 2022). The equation of the inclined line is therefore:

$$H = H_t + \frac{(H_c-H_t)}{(Q_c-Q_t)}(Q-Q_t) = H_t + i_h(Q-Q_t) \tag{2}$$

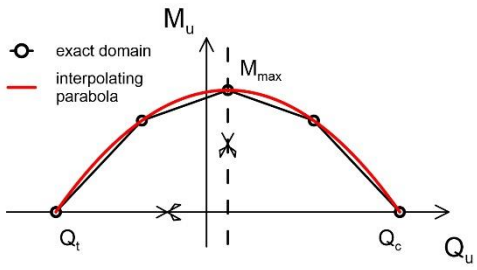

Figure 1. Failure locus for H = 0: exact domain and approximating parabola.

To obtain a smoother shape, the Granville egg was selected and its graphical construction is explained in the following. Consider a circle with centre C and radius r, a point A on the x-axis and a line t parallel to the y-axis (Figure 2b). For any point P with coordinates (x_P, y_P) lying on the circumference, the segment AP intersects line t in point T with coordinates (x_T, y_T). Point Q belonging to the Granville egg has coordinates (x_P, y_T). The whole function is found repeating the above construction for any point of the circumference and can be expressed as:

$$\begin{cases} x_Q = x_p = b + r\cos\omega \\ y_Q = y_T = a\tan\omega = \frac{a\,r\sin\omega}{d+a-r\cos\omega} \end{cases} \tag{3}$$

where b is the abscissa of point C, ω is the central angle defined by points P and A, a is the distance between point A and line t, d is the distance between point C and line t. The Cartesian form may be obtained by manipulating Equations (3) as:

$$y^2 = \frac{a^2[r^2-(x-b)^2]}{[(d+a)-(x-b)]^2} \tag{4}$$

To obtain a good approximation of the failure interaction diagram in the (Q, H) plane for M = 0, the passage through the following points is imposed:

1. (Q_c, 0);
2. (Q_t, 0);
3. point E on the inclined side of the trapezium whose position controls the shape of the egg, with coordinates (Q_E, H_E) = (Q_t + 2βR, H_t + 2$i_h\beta R$), where β is a dimensionless position, and r = R = (Q_c – Q_t)/2;

In addition to the above, the following condition is also considered:

4. horizontal tangent at $Q = Q_E$, i.e. $H_E = H_{max}$.

The parameters in Equation (4) can be therefore expressed as:

$$\begin{cases} b = \frac{Q_c+Q_t}{2} \\ r = R = \frac{Q_c-Q_t}{2} \\ a = 2\frac{H_t+2i_h\beta R}{2\beta-1}\sqrt{\beta(1-\beta)} \\ d = \frac{R}{2\beta-1} - a \end{cases} \quad (5)$$

For β it is suggested to take:

$$\begin{cases} \beta = \frac{1+2\psi}{2(1+\psi)} \\ \psi = 1 - \frac{H_t}{H_c} \end{cases} \quad (6)$$

The parameter β varies monotonically within the range [0.5, 0.75]. It is equal to 0.5 when the two lateral capacities are identical and to 0.75 when the failure domain degenerates in a triangle, that is for $H_t = 0$. Also, the Granville egg is defined only for H_c strictly larger than H_t; when H_c tends to H_c the egg approaches an ellipse.

Finally, the equation of the Granville egg for $M = 0$ is:

$$\left(\frac{H}{H_{max}}\right)^2 = \frac{4\beta(1-\beta)\left[\left(\frac{Q-b}{R}\right)^2-1\right]}{\left[(2\beta-1)\left(\frac{Q-b}{R}\right)-1\right]^2} \quad (7)$$

Note that the symmetric portion of the domain in the (Q, M) and (Q, H) planes can be obtained by changing the sign on the right-hand side of Equations (1) and (7), respectively.

To construct the three-dimensional surface starting from the above-defined sections for $H = 0$ and $M = 0$, the following procedure is established.

For any value of $M \neq 0$ it is possible to use Equation (1) to determine the corresponding Q_1 and Q_2 on the parabola as:

$$\begin{cases} Q_1 = \frac{Q_c+Q_t}{2} - R\sqrt{1-\frac{M}{M_{max}}} \\ Q_2 = \frac{Q_c+Q_t}{2} + R\sqrt{1-\frac{M}{M_{max}}} \end{cases} \quad (8)$$

The loads Q_1 and Q_2 can be used in Equation (2) to calculate the interaction domain in the (Q, H) plane for $M \neq 0$:

$$\begin{cases} H_1 = H_t + i_h(Q_1 - Q_t) \\ H_2 = H_t + i_h(Q_2 - Q_t) \end{cases} \quad (9)$$

This failure domain can be still interpolated by the Granville egg using as ultimate loads in Equations (5) and (6) the values calculated through Equations (8) and (9).

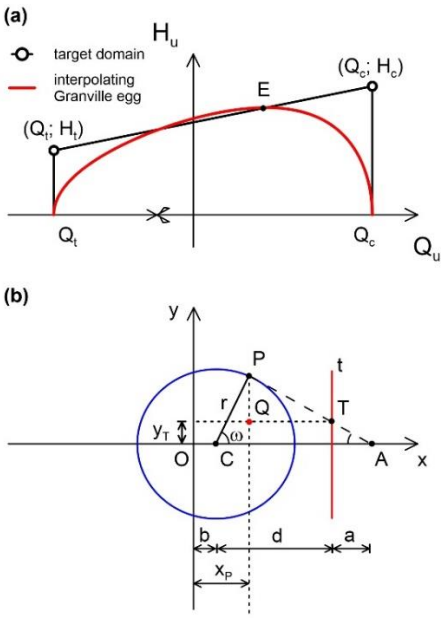

Figure 2. Fitting of Granville's egg to the target domain in the (Q, H) plane (a); graphical example of Granville's egg construction.

Substituting Equation (9) into Equation (7) yields to:

$$f = \left\{H^2\left[R\sqrt{1-\frac{M}{M_{max}}} - (2\beta-1)(Q-b)\right]^2 + 4\beta(\beta-1)\left[R^2\left(1-\frac{M}{M_{max}}\right) - (Q-b)^2\right]\left[H_{max} + i_h R(2\beta-1)\left(\sqrt{1-\frac{M}{M_{max}}} - 1\right)\right]^2\right\}/(2\beta-1)^2 = 0 \quad (10)$$

which is the explicit expression of the 3D failure locus (Figure 3).

Equation (10) is completely defined by only 5 parameters, (Q_c, Q_t, H_c, H_t, M_{max}) which can be determined even by hand calculation. In particular, Q_c and Q_t can be easily derived from the axial capacities in compression (N_u) and uplift ($-S_u$) of the isolated pile employing one of the possible approaches available in literature (e.g., Fleming et al, 2008; Letizia et al., 2018) and considering the efficiency at failure (e.g., Vesic, 1969; De Mello, 1969); M_{max} is evaluated form Q_c and Q_t using the approach proposed by Di Laora et al. (2019); H_c and H_t can be calculated from the horizontal capacities of the isolated pile subjected to an axial load equal to N_u and $-S_u$, respectively, as shown by Iovino et al. (2021) and Di Laora et al. (2022).

It is worth mentioning that Equation (10) can be conveniently used in routine engineering for ULS checks of pile foundations when subjected to the contemporary presence of three load components or incorporated in more complex mathematical frameworks, such as macroelements, serving as failure surface for the evaluation of the foundation response (Iodice et al., 2023, 2024).

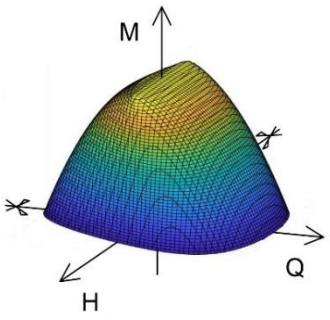

Figure 3. 3D failure surface.

3 VALIDATION AGAINST NUMERICAL ANALYSES

To show the predictive capabilities of the proposed failure surface, the latter is compared to the results of the Finite Element analyses available in literature on small pile groups subjected to an inclined eccentric load by Psychari & Anastasopoulos (2022). The Authors performed a series of analyses on (2 × 1), (3 × 1) and (4 × 1) pile groups. In the following only the comparison with the (2 × 1) group is presented since the results at failure are available for all the load components solely for this case.

The FE analysis involve a load path with an initial branch in which the group is only loaded vertically; after that, the horizontal load is applied under constant eccentricity represented by the pier height, h_{pier} = 6 m or 20 m. An idealized, homogeneous clay deposit with uniform undrained shear strength s_u = 100 kPa is considered. The soil behaviour is modelled with a kinematic hardening model with von Mises failure criterion and associated flow rule, while Reinforced Concrete (RC) piles are idealized by a combination of non-linear continuum elements for the concrete and surface elements for the longitudinal reinforcement so as to simulate the dependence of the plastic yielding moment of the pile cross-section, M_y, from the axial load, N. To investigate in detail the mechanism of interaction under combined loads, Psychari & Anastasopoulos (2022) distinguish between the moment component due to the axial resistance of the piles and that associated to the flexural strength of the concrete cross-section, referred to in the original work as M_{ax} and M_b, respectively. Since in the present formulation M_b is neglected, the focus is set only on the first contribution, M_{ax}.

The 5 parameters to employ in Equation (10) are derived as detailed in the ensuing and summarized in Table 1. The axial capacities in compression, Q_c, and tension, Q_t, of each pile group are evaluated from the axial capacities of the isolated pile, N_u and ($-S_u$), determined by employing analytical solutions. An efficiency factor of unity is adopted in this case. The moment capacity of the group, M_{max}, is calculated from N_u and ($-S_u$), using the solution by Di Laora et al. (2019). Considering the layout of the longitudinal reinforcement and the material properties of the RC piles, the horizontal capacities of the single pile are first estimated applying the Broms (1964a) theory for fixed head piles in clay with a yielding moment calculated by the closed-form expression proposed by Di Laora et al. (2020) under an axial force equal to N_u or ($-S_u$); then, the horizontal capacities of the group, H_c, and H_t, are obtained postulating an efficiency factor under horizontal load equal to unity.

Table 1. Parameters of the failure surface adopted to reproduce the analyses by Psychari & Anastasopoulos (2022) for (2 × 1) pile group.

Q_c (MN)	Q_t (MN)	M_{max} (MNm)	H_c (MN)	H_t (MN)
8.48	-7.07	11.66	4.15	0.15

The results of the comparison are shown in Figure 4 for the two cases of h_{pier} = 6 m and 20 m. The sections of the interaction domains in the (Q, M) plane are reported for H = 0 and $H = H_f$, H_f being the horizontal failure load at the end of the applied multicomponent load path as derived from the proposed failure locus; likewise, the sections in the (Q, H) plane are plotted for M = 0 and $M = M_f$, M_f being the moment at failure for the applied multicomponent load path as derived from the proposed failure locus. Note that since the vertical load is very small (10% of the group vertical bearing capacity) and $M_f \approx M_{max}$, the three-dimensional shape of the failure locus is such that the sections for $M = M_f$ in the (Q, H) plane are very narrow (a zoom is provided in the rightmost side of the figure). It can be stated that Equation (10) matches in a satisfactory way the data from FE analyses. The difference in the previsions (e.g., M_f = 0.85 and 0.9 M_{FE}, for h_{pier} = 6 m and 20 m, respectively, M_{FE} is the moment derived from FE analyses) can be explained inspecting the moment – rotation and horizontal load–horizontal displacement curves by Psychari & Anastasopoulos (2022), not reported here for space limitations. Note that the proposed failure locus is inherently not able to replicate the hardening response as predicted by the FE model at very large rotations.

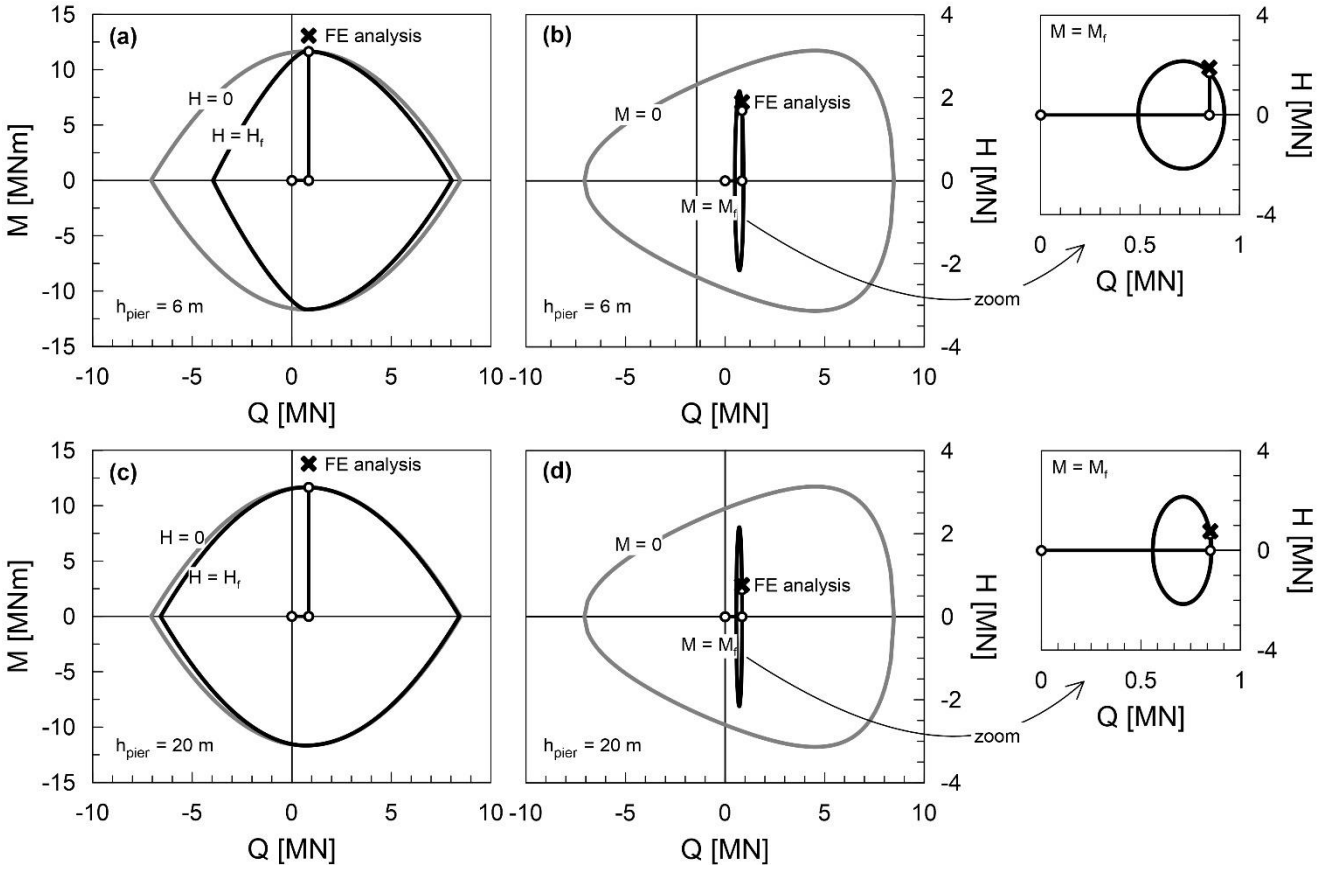

Figure 4. Comparison between Equation (10) and the FE analyses by Psycari and Anastasopoulos (2022).

4 CONCLUSIONS

The work describes a closed form equation for the evaluation of the failure locus of a pile group subjected to a multicomponent load including vertical, horizontal and moment components. The three-dimensional locus is obtained as a combination of a parabola and the Granville egg. In particular, the parabola is used to approximate the shape of the interaction diagram in the axial load–moment plane, while the Granville egg is employed to replicate the shape of the surfaces in planes parallel to the axial load–horizontal load plane. The use of the proposed failure domain is straightforward since the parameters needed for its construction are simple to determine even with hand calculations and anyhow are already required in routine design.

The ability of the failure locus in predicting the behaviour of pile groups subjected to vertical eccentric load has been checked against data from rigorous numerical analyses on small pile groups available in literature, providing generally good performance.

The proposed closed form equation can be conveniently employed for ULS analysis and design of a pile group when subjected to multicomponent loads; in addition, it may serve as an ingredient of more complex mathematical approaches (e.g., macroelements) to derive the load-displacement response of the group under generalized load paths.

ACKNOWLEDGEMENTS

The authors are grateful for the financial support provided by the Italian Ministry for Research and University. The project presented in this article is supported by MIUR PRIN 2017 ‘A new macro-element model for pile groups under monotonic, cyclic and dynamic loadings’.

REFERENCES

Broms, B.B. (1964a) Lateral resistance of piles in cohesive soils. *Journal of Soil Mechanics Foundation Division* 90(2):27–63. https://doi.org/10.1061/JSFEAQ.0000611.

Broms, B.B. (1964b) Lateral resistance of piles in cohesionless soils. *Journal of Soil Mechanics Foundation Division* 90(3):123–156. https:doi.org/10.1061/JSFEAQ.0000614.

De Mello, V. F. B. (1969). Foundations of Buildings on Clay. In State of the Art Report, *Proceedings of the 7th International Congress on Soil Mechanics and Foundation Engineering*, Vol. 1, pp. 49-136.

Di Laora, R., de Sanctis L., Aversa S. (2019). Bearing capacity of pile groups under vertical eccentric load. *Acta Geotechnica*. 14 (1), 193–205. https://doi.org/10.1007/s11440-018-0646-5.

Di Laora, R., Galasso, C., Mylonakis, G., Cosenza, E. (2020). A simple method for N-M interaction diagrams of circular reinforced concrete cross sections. *Structural Concrete*, 21(1), 48-55. https://doi.org/10.1002/suco.201900139.

Di Laora, R., Iodice, C., Mandolini, A. (2022). A closed-form solution for the failure interaction diagrams of pile groups subjected to inclined eccentric load. *Acta Geotechnica*, 17(8), 3633-3646. https://doi.org/10.1007/s11440-021-01439-8.

Fleming K.,Weltman, A., Randolph, M., Elson, K. (2008). *Piling engineering*. CRC Press. https://doi.org/10.1201/b22272.

Iodice, C., Iovino, M., Di Laora, R., de Sanctis, L., Mandolini, A. (2023). A Macro-element for Pile Groups Subjected to Vertical Eccentric Load. In *Proceedings of the National Conference of the Researchers of Geotechnical Engineering*, Cham: Springer Nature Switzerland, pp. 201-217. https://doi.org/10.1007/978-3-031-34761-0_26.

Iodice, C., Iovino, M., Di Laora, R., de Sanctis, L., Mandolini, A. (2024). A strain-hardening macro-element model for pile groups under vertical-horizontal-moment loading. *Acta Geotechnica*, 1-15. https://doi.org/10.1007/s11440-023-02174-y.

Iovino, M., de Sanctis, L., Maiorano, R.M.S., Aversa, S. (2021). Failure envelopes of pile groups under inclined eccentric load. *Géotechnique Letters*, 11(4), 247-253. https://doi.org/10.1680/jgele.21.00059.

Letizia, N., Iodice, C., Mandolini, A. (2018). A local design method for pile foundations. *Advances in Civil Engineering*. https://doi.org/10.1155/2018/9486945.

Psychari, A., Anastasopoulos, I. (2022). Combined loading of RC pile groups in clay accounting for N–M interaction. *Soil Dynamics and Earthquake Engineering*, 163, 107490. https://doi.org/10.1016/j.soildyn.2022.107490.

Vesić, A. (1969). Experiments with instrumented pile groups in sand. In *Performance of deep foundations*. ASTM International. https://doi.org/10.1520/STP47286S.

Proceedings of the XVIII ECSMGE 2024
GEOTECHNICAL ENGINEERING CHALLENGES
TO MEET CURRENT AND EMERGING NEEDS OF SOCIETY
© 2024 the Authors
ISBN 978-1-032-54816-6
DOI 10.1201/9781003431749-82
Open Access: www.taylorfrancis.com, CC BY-NC-ND 4.0 license

ECSMGE 24
XVIII EUROPEAN CONFERENCE ON SOIL MECHANICS AND GEOTECHNICAL ENGINEERING

Cyclic properties of sand-clay mixtures at low confining stresses

Propriétés cycliques des mélanges sable-argile à faibles contraintes de confinement

V. Jagodnik*
Center for Artificial Intelligence and Cybersecurity/University of Rijeka, Rijeka, Croatia; Faculty of Civil Engineering/University of Rijeka, Rijeka, Croatia

D. Marušić, J. Peranić, M. Vivoda Prodan, Ž. Arbanas
Faculty of Civil Engineering/University of Rijeka, Rijeka, Croatia

D. Katalinić
GP Krk, Krk, Croatia

**vedran.jagodnik@gradri.uniri.hr*

ABSTRACT: Small strains and shear stresses induced by railroad vibration, dynamic compaction, or earthquakes can cause strength degradation, pore pressure build-up, and accumulation of strains at large number of load cycles. In general, strength degradation and pore water pressure build-up are correlated with the plasticity index and thus the content of fine particles, meaning that a threshold for strength degradation will be lower for sands than for silty and clayey sands. Confining stresses play a significant role in soils shear behaviour. Fully saturated soil at low confining stresses is likely to have a significant strength reduction compared to the soil at higher confining stresses if loaded to the same number of cycles. This is very important for slopes that are prone to shallow sliding. This paper presents the test results of an artificial mixtures of sand and kaoline used for a small-scale physical model of slope subjected to cyclic loading. Mixtures are tested using cyclic triaxial apparatus under undrained condition at low confining stresses. The results show that the sand-clay mixture with 15% of kaoline powder exhibit larger pore water pressure than the mixtures with lower percentage of kaoline.

RÉSUMÉ: De petites déformations et contraintes de cisaillement induites par les vibrations ferroviaires, le compactage dynamique ou les tremblements de terre peuvent provoquer une dégradation de la résistance, une augmentation de la pression interstitielle et une accumulation de déformations sur un grand nombre de cycles. En général, la dégradation de la résistance et l'accumulation de pression interstitielle sont corrélées à l'indice de plasticité et donc à la teneur en particules fines, ce qui signifie qu'un seuil de dégradation de la résistance sera plus bas pour les sables que pour les sables limoneux et argileux. Les contraintes de confinement jouent un rôle important dans le comportement au cisaillement des sols. Un sol entièrement saturé à de faibles contraintes de confinement est susceptible de présenter une réduction significative de sa résistance par rapport au sol soumis à des contraintes de confinement plus élevées s'il est chargé selon le même nombre de cycles. Ceci est très important pour les pentes sujettes à des glissements peu profonds. Cet article présente les résultats d'un mélange artificiel de sable et de kaoline utilisé pour un modèle physique à petite échelle de pente soumise à un chargement cyclique. Les mélanges sont testés à l'aide d'un appareil triaxial cyclique dans des conditions non drainées et à faibles contraintes de confinement. Les résultats montrent que le mélange sable-argile contenant 15 % de poudre de kaoline présente une pression d'eau interstitielle plus élevée que les mélanges contenant un pourcentage plus faible de poudre de kaoline.

Keywords: Low confining stress; cyclic soil behavior; sand-clay mixtures, cyclic triaxial test, strain-controlled test.

1 INTRODUCTION

The study of sand-clay and sand-silt mixtures has a rich history in both monotonic and cyclic soil behaviour. Past investigations (e.g., (Thevanayagam, 1998), (Yamamuro et al., 1999), (Seed, 2010)) have extensively explored this area, and the area knowledgebase still continues to be expanded (e.g., (Othman et al., 2022), (Ranga Swamy et al., 2021), (Lü et al., 2022)). Understanding the mechanics of interparticle contacts in silty and clayey sandy soils is a challenging endeavour due to the presence of clay minerals. Benessalah et al. (2021) examined the intergranular void ratio and the undrained monotonic behaviour of sand containing low plasticity fine particles. Their findings revealed that the fines' content exerts a substantial influence on the instability stress,

as defined by the undrained instability state (Murthy et al., 2007). Another significant contribution was made by Nougar et al. (2021), who conducted a thorough investigation into the impact of fines content on the mechanical behaviour of mixtures. Their research highlights a clear trend: as the fines content increases, the strength of these mixtures decreases. The work of Dafalla et al. (2020) pointed out that higher fines content leads to reduced dilatation in mixtures. Furthermore, Akhila et al. (2019) observed that non-plastic silty sands and loamy sands with a low plasticity index (up to 15) exhibit greater susceptibility to liquefaction than fine sands. Wu et al. (2019) provided insightful documentation on the behaviour of artificial sand-clay mixtures, revealing a complex interplay of transitional and secondary compression behaviour. This response is significantly influenced by the creep of the fine fraction, emphasizing the material's complex nature. Balreaddy et al. (2021) unveiled that cyclic strength decreases with an increase in fines content by up to 20%. Surprisingly, with further increase in the proportion of fines, cyclic strength experiences an upswing, indicating that fines content becomes the predominant factor in controlling soil behaviour. Karim and Alam (2014) conducted a series of cyclic triaxial tests on specimens with a 20% silt content. Their study revealed that the rate of pore pressure generation initially rises with increased silt content, only to begin decreasing afterwards. Cyclic resistance experiences a decrease until a silt content limit of approximately 35% is reached, after which it stabilizes. These studies collectively contribute to the understanding of the complex behaviour of mixtures involving sand and clay material and their implications for geotechnical engineering. Another important role in the soil behaviour is govern by the confining pressure. According to White (2020) the secant shear modulus, denoted as Gs, was observed to decline as the number of cycles increased and as the effective stress decreased. Kumar et al. (2017) observed that the specimen exposed to lower levels of effective stresses (50 kPa) exhibited a higher damping ratio compared to the specimens exposed to higher levels of effective stresses (100 and 150 kPa). This difference can be attributed to the relatively high stiffness caused by the constraints on the specimen. In their investigation, Shaoli et al. (2003) highlighted that clean sand has a substantial dilating behavior at lower effective stresses. As a result, compared to behavior at high effective stresses, clean sand is more resilient under low effective stresses. The influence of clay content on the soil behaviour under low confining stress has to be examined further.

As part of two research projects, “Laboratory research of static and cyclic behavior at landslide activation (uniri-tehnic-18-113),” funded by the University of Rijeka, and “Physical modelling of landslide remediation constructions’ behavior under static and seismic actions (ModLandRemSS, IP-2018-01-1503),” funded by the Croatian Science Foundation, a series of physical model tests was conducted on small-scale slopes subjected to dynamic loading using a shaking table platform.

To gain a comprehensive understanding of the material’s response used in small-scale slope models, a series of cyclic triaxial tests were carried out on the artificial sand-clay mixtures used for the construction of the small-scale slope models. This paper focuses on presenting the preliminary findings derived from undrained, strain-controlled cyclic triaxial tests conducted on these mixtures. The results provide valuable insights into the material’s behaviour under cyclic loading conditions, which is essential for the assessment and understanding of slope stability subjected to cyclic loading.

2 METHODOLOGY

2.1 Material properties and specimen preparation

Industrial kaoline powder and homogeneous Drava River sand are combined to create artificial sand-clay mixtures. Artificial mixtures are named based on the mass ratio of sand (S) and kaoilne (K). The characteristics of Drava River sand (herein SK0) and kaoline powder (herein SK100) are well documented (Jagodnik & Arbanas, 2022; Marušić & Jagodnik, 2023; Pajalić et al., 2021). A mixture containing 10% kaoline powder per mass ratio (herein SK10) and a mixture containing 15% kaolinite powder per mass ratio (herein SK15) are prepared and tested in the dynamic triaxial apparatus. Physical properties of material are summarized in Table 1.

Using the undercompaction method for specimen preparation proposed by Ladd (Ladd, 1978), specimens were prepared with 5% undercompaction. The method's positive and negative aspects are documented by (Frost & Park, 2003; Jagodnik & Arbanas, 2022; Kodicherla et al., 2018; Raghunandan et al., 2012). Before the saturation stage, each specimen was percolated with CO_2, followed with water percolation as well. Upon finished saturation (B value above 0.95), specimens were isotropically consolidated at effective confining stress of 25 kPa or 50 kPa.

2.2 Testing procedure

Undrained strain-controlled cyclic triaxial tests were performed using dynamic triaxial apparatus manufactured by Controls Group Ltd. (Controls Group, 2023). Tests were performed on the previously defined soil mixtures to determine the cyclic behaviour, the strength degradation, and the change of pore water pressure ratio, at low confining stresses.

Table 1. Physical properties of the used specimens

Property	SK0	SK10	SK15	SK100
Specific gravity, Gs	2.70	2.69	2.67	2.60
D10 [mm]	0.183	0.054	0.0045	N/A
D60 [mm]	0.320	0.307	0.303	N/A
Uniformity coef-ficient, Cu [-]	1.749	5.685	67.333	N/A
Curvature coef-ficient, Cc [-]	0.959	2.893	31.123	N/A
Minimum void ratio, e_{min} [-]	0.547	0.596	0.640	0.849
Maximum void ratio, e_{max} [-]	0.856	1.022	1.128	1.636
Plastic limit [%]	N/A	5.8	9.6	21.6
Liquid limit [%]	N/A	17.9	17.9	48.3
Percent of clay particles ($\leq 0.002mm$) [%]	0	1	1.5	10

N/A – non applicable

Strain-controlled tests were performed in nine straining stages, each having a consolidation stage between (e.g. (Jagodnik & Arbanas, 2022; Vucetic et al., 2021)). Table 2 shows the corresponding cyclic axial deformation for each straining stage and equivalent shear strain. The specimens were tested in an undrained condition hence the shear strain can be calculated using :

$$\gamma = 1.5 \cdot \varepsilon_a \quad (1)$$

Table 2. Cyclic testing stages and equivalent cyclic axial and cyclic shear strain.

Testing stage	Cyclic Axial Strain $\varepsilon_{a,c}$ (%)	Cyclic Shear Strain $\gamma_{a,c}$ (%)
1	0.0033	0.005
2	0.005	0.0075
3	0.0067	0.01
4	0.013	0.02
5	0.033	0.05
6	0.05	0.075
7	0.067	0.1
8	0.133	0.2
9	0.333	0.5

3 RESULTS AND DISCUSSION

In the following section, the results of strain-controlled tests are summarized. The influence of low confining stresses on the artificial mixtures are presented with the strength degradation and normalized pore water pressure response build-up. In cyclic simple shear, the degradation index in strain-controlled tests can be calculated as a ratio of the shear stress in current loading cycle with respect to the shear stress at first cycle (Mortezaie & Vucetic, 2013). Contrary to simple shear, in cyclic triaxial test the cyclic loop is nonsymmetric so the average value of secant shear modulus have to be taken into consideration (e.g., (Jagodnik & Arbanas, 2022; Kumar et al., 2017)). In this case, degradation index is calculated using the as:

$$\delta_N = \frac{|q_{C,N}| + |q_{E,N}|}{|q_{C,1}| + |q_{E,1}|} \quad (2)$$

where $q_{C,N}$ and $q_{E,N}$ are the maximum and minimum deviatoric stress in compression and extension, respectively, at Nth cycle and $q_{C,1}$ and $q_{E,1}$ are the maximum and minimum deviatoric stress in compression and extension, respectively, in the first cycle.

Deviatoric stress is calculated as a difference in effective triaxial stresses:

$$q = \sigma_1' - \sigma_3' \quad (3)$$

where σ_1' is the vertical effective stress and σ_3' is radial effective stress.

Normalized pore water pressure ratio is calculated as a change of pore water pressure during loading cycle with respect to confining effective stress:

$$r_u = \frac{\Delta u}{\sigma_c'} \quad (4)$$

where Δu is the change of pore water pressure during the test and σ_c' is the effective confining stress which corresponds to cell pressure σ_3'.

Figure 1 present the degradation (δ_N) of artificial mixtures "SK10" and "SK15" at effective confining stresses 25 kPa and 50 kPa, respectively, with respect to the number of cycles (N).

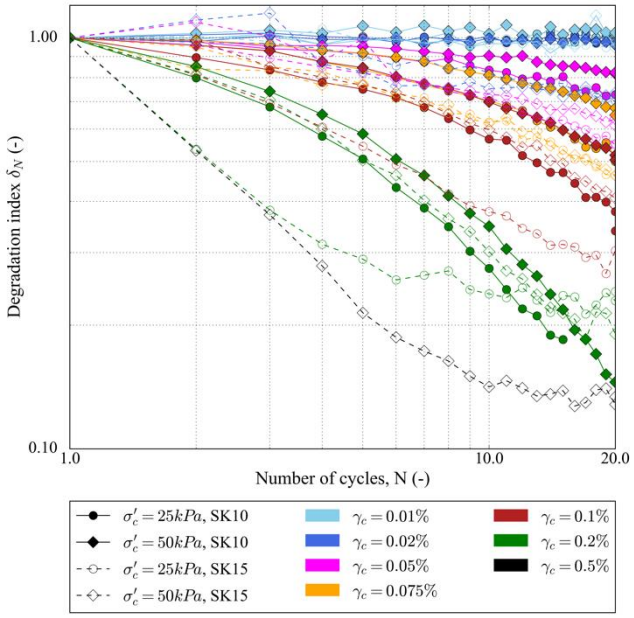

Figure 1. Degradation index change with number of cycles.

The maximum level of cyclic shear strain reached by the specimen labelled as "SK10" was 0.2% for both 25kPa and 50kPa confining stress. When subjected to a higher level of confining pressure, the specimen withstands 20 load cycles, while at 25 kPa confining stress, it only withstands 15 cycles. The decline in performance of the "SK10" specimen exhibits a somewhat non-linear nature, which can be attributed to the relatively low clay content present in the sand-clay matrix. Contrarily, the specimen labelled as "SK15" exhibits an almost linear decline in performance up to a relative cyclic shear strain of 0.2% under a confining stress of 25 kPa and 0.5% under a confining stress of 50 kPa. Degradation is initiated after reaching a cyclic shear strain of 0.02%, in contrast to the "SK10" specimen where degradation initiates upon reaching 0.05%.

Figure 2 presents the relation between the degradation index (δ_N), as defined by equation (2), and the normalized pore water pressure ratio (r_u), as defined by equation (4). Additionally, it illustrates the impact of effective confining stress on the degradation index.

A higher confining pressure allows the soil to withstand more shear cycles before reaching the same degradation index and pore water pressure ratio. The nonlinearity of the curves indicates the influence of the sand grain, which differs from the results of specimen "SK15" where the degradation is almost linear in relation to the pore pressure ratio.

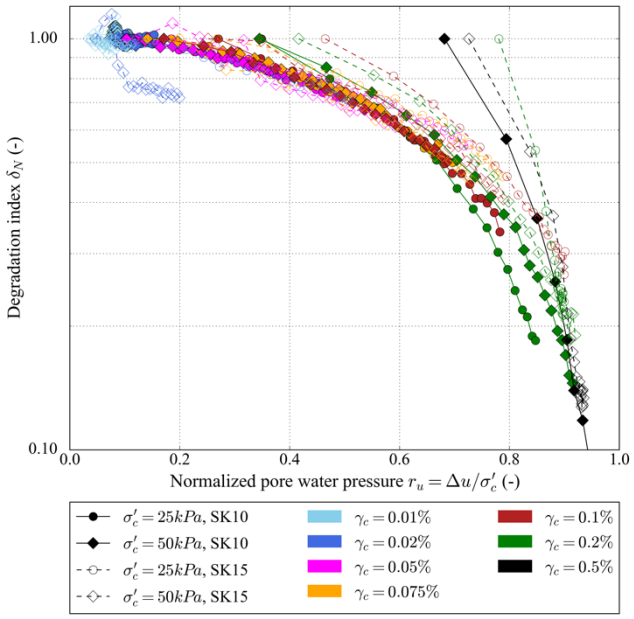

Figure 2. Degradation index change with normalized pore water pressure.

4 CONCLUDING REMARKS

A mixture of sand and kaoline clay in mass ratios of 10% and 15% were subjected to an undrained cyclic strain-control triaxial tests at low confining stresses.

At lower levels of confining stress, specimen containing 10% clay exhibit a smaller degradation index compared to those with a clay content of 15% for a range of cyclic shear strain up to 0.1%. The average degradation index at 10th cycle is 0.6. Specimen with 15% clay content at 25kPa showed smaller degradation index at 10th cycle (around 0.4), which means that almost 60% of strength was lost during previous loading cycles at cyclic shear strain of 0.1%.

The degradation of specimen containing 10% of the clay fraction exhibits a nonlinear behaviour once higher cyclic shear strain is applied. The specimens with 15% of clay display an almost linear behaviour until the interparticle connections are disrupted, resulting in a manifestation of high nonlinearity in the degradation index. The normalized pore water pressure ratio (r_u) experiences a rapid increase when the r_u gets the value of 0.6. Taking for example cyclic shear strain of 0.2%, the mixtures with 10% of kaoline can withstand from 3 to 5 cycles of loading, depending on the confining stress, until the r_u value of 0.6 is reached. For the mixtures containing 15% of kaoline, the role of confining stress is significant. At the confining stress of 25 kPa, r_u value is around 0.78 in the first cycle, while at the 50 kPa confining stress, it takes 2.5 cycles to reach the $r_u$value of 0.6. Higher cyclic shear strain was only possible under the

effective stress of 50 kPa, generating the normalized pore water pressure r_u in the first cycle of around 0.7, followed with the rapid degradation.

The executed experimental findings have revealed that the presence of 15% of clay particles within a specimen exerts a greater effect on the formation of pore pressure compared to a specimen composed of 10% of clay particles, under the same magnitude of relative cyclic shear deformation.

According to the presented test results, a slope under cyclic excitation such as earthquake, and in undrained condition, can exhibit large strength degradation if the clay content is lower than 20%.

The results of the conducted experiments will be important in the calibration of numerical models using the results of the experiments in the next phase of the research.

ACKNOWLEDGEMENTS

This research was funded and supported by the following projects: "Laboratory Research of Static and Cyclic Behavior at Landslide Activation" (uniri-tehnic-18-113) funded by the University of Rijeka, Croatia; and "Physical Modelling of Landslide Remediation Constructions Behavior under Static and Seismic actions" (ModLandRemSS, IP-2018-01-1503) funded by the Croatian Science Foundation. This support is gratefully acknowledged.

REFERENCES

Akhila, M., Rangaswamy, K., & Sankar, N. (2019). Liquefaction susceptibility of silty sands and low plastic clay soils. International Journal of Geotechnical Earthquake Engineering, 10(2), 1–17. https://doi.org/10.4018/IJGEE.2019070101.

Balreddy, M. S., Dinesh, S. V., & Sitharam, T. G. (2016). Influence of sand and low plasticity clay mixtures on the liquefaction and postliquefaction behavior. Japanese Geotechnical Society Special Publication, 2(21), 806–810. https://doi.org/10.3208/jgssp.IND-10.

Balreddy, M. S., Dinesh, S. V., & Sitharam, T. G. (2021). Liquefaction behavior of low to medium plasticity sand-fines mixtures (pp. 181–191). https://doi.org/10.1007/978-981-33-4001-5_17.

Benessalah, I., Arab, A., & Meziane, E.-H. (2021). Intergranular void ratio and undrained monotonic behavior of Chlef sand containing low plastic fines. Acta Mechanica, 232(4), 1621–1640. https://doi.org/10.1007/s00707-020-02923-0.

Controls Group. (2023). Dynamic triaxial tests system—DYNATRIAX, Soil mechanics testing equipment, Controls. https://controls-group.com/product/dynamic-triaxial-system-dynatriax-ems-controls/.

Dafalla, M., Shaker, A., Elkady, T., Almajed, A., & Al-Shamrani, M. (2020). Shear strength characteristics of a sand clay liner. Scientific Reports, 10(1), 18226. https://doi.org/10.1038/s41598-020-75188-1.

Frost, J., & Park, J.-Y. (2003). A Critical Assessment of the Moist Tamping Technique. Geotechnical Testing Journal, 26(1), 9850. https://doi.org/10.1520/GTJ11108J.

Jagodnik, V., & Arbanas, Ž. (2022). Cyclic Behaviour of Uniform Sand in Drained and Undrained Conditions at Low Confining Stress in Small-Scale Landslide Model. Sustainability, 14(19), 12797. https://doi.org/10.3390/su141912797.

Karim, M. E., & Alam, Md. J. (2014). Effect of non-plastic silt content on the liquefaction behavior of Sand–Silt mixture. Soil Dynamics and Earthquake Engineering, 65, 142–150. https://doi.org/10.1016/j.soildyn.2014.06.010.

Kodicherla, S. P. K., Gong, G., Fan, L., Moy, C. K. S., & He, J. (2018). Effects of preparation methods on inherent fabric anisotropy and packing density of reconstituted sand. Cogent Engineering, 5(1), 1533363. https://doi.org/10.1080/23311916.2018.1533363.

Kumar, S. S., Krishna, A. M., & Dey, A. (2017). Evaluation of dynamic properties of sandy soil at high cyclic strains. Soil Dynamics and Earthquake Engineering, 99, 157–167. https://doi.org/10.1016/j.soildyn.2017.05.016.

Ladd, R. S. (1978). Preparing test specimens using under compaction. Geotechnical Testing Journal, 1(1), 16–23. https://doi.org/10.1520/GTJ10364J.

Lü, X., Xue, D., Zhang, B., & Zhong, Q. (2022). Experimental Studies and Constitutive Modeling of Static Liquefaction Instability in Sand–Clay Mixtures. International Journal of Geomechanics, 22(9), 04022149. https://doi.org/10.1061/(ASCE)GM.1943-5622.0002472.

Marušić, D., & Jagodnik, V. (2023). Determination of the Atterberg Limits Using a Fall Cone Device On Low Plasticity Silty Sands. Rudarsko-Geološko-Naftni Zbornik, 38(3), 133–145. https://doi.org/10.17794/rgn.2023.3.11.

Mortezaie, A. R., & Vucetic, M. (2013). Effect of Frequency and Vertical Stress on Cyclic Degradation and Pore Water Pressure in Clay in the NGI Simple Shear Device. Journal of Geotechnical and Geoenvironmental Engineering, 139(10), 1727–1737. https://doi.org/10.1061/(ASCE)GT.1943-5606.0000922

Murthy, T. G., Loukidis, D., Carraro, J. A. H., Prezzi, M., & Salgado, R. (2007). Undrained monotonic response of clean and silty sands. Géotechnique, 57(3), 273–288. https://doi.org/10.1680/geot.2007.57.3.273.

Nougar, B., Brahimi, A., Bouri, D. E., Arab, A., & Benessalah, I. (2021). Laboratory investigation into the effect of fines plasticity on the mechanical behavior of Sand/Fines mixtures. Transportation Infrastructure Geotechnology, 8(3), 438–451. https://doi.org/10.1007/s40515-020-00144-5.

Othman, B. A., Marto, A., Uzuoka, R., Ueda, K., & Satar, M. H. M. (2022). Liquefaction Resistance of Sand-Kaolin Mixtures: Effect of Sand Sizes. IOP Conference

Series: Earth and Environmental Science, 1103(1), 012026. https://doi.org/10.1088/1755-1315/1103/1/012026.

Pajalić, S., Peranić, J., Maksimović, S., Čeh, N., Jagodnik, V., & Arbanas, Ž. (2021). Monitoring and data analysis in small-scale landslide physical model. Applied Sciences (Switzerland), 11(11). https://doi.org/10.3390/app11115040.

Raghunandan, M. E., Juneja, A., & Hsiung, B. C. B. (2012). Preparation of reconstituted sand samples in the laboratory. International Journal of Geotechnical Engineering, 6(1), 125–131. https://doi.org/10.3328/IJGE.2012.06.01.125-131.

Ranga Swamy, K., Akhila, M., & Sankar, N. (2021). Effects of fines content and plasticity on liquefaction resistance of sands. Proceedings of the Institution of Civil Engineers - Geotechnical Engineering, 174(6), 697–706. https://doi.org/10.1680/jgeen.19.00270.

Seed, R. B. (2010). Soil Liquefaction During Earthquakes (Issue UCB/GT-2010/01) [Technical review and comments]. University of California at Berkeley. https://vulcanhammernet.files.wordpress.com/2017/01/liquefactionreview.pdf.

Shaoli, Y., Sandven, R., & Grande, L. (2003). Liquefaction of sand under low confining pressure. Journal of Ocean University of Qingdao, 2(2), 207. https://doi.org/10.1007/s11802-003-0053-9.

Thevanayagam, S. (1998). Effect of Fines and Confining Stress on Undrained Shear Strength of Silty Sands. Journal of Geotechnical and Geoenvironmental Engineering, 124(6), 479–491. https://doi.org/10.1061/(ASCE)1090-0241(1998)124:6(479)..

Vucetic, M., Thangavel, H., & Ahmadreza Mortezaie. (2021). Cyclic secant shear modulus and pore water pressure change in sands at small cyclic strains. Journal of Geotechnical and Geoenvironmental Engineering, 147(5), 04021018. https://doi.org/10.1061/(ASCE)GT.1943-5606.0002490.

White, J. R. F. (2020). A Laboratory Investigation Into the Behaviour of Sand at Low Confining Stresses. University of Oxford. https://books.google.hr/books?id=fG9gzgEACAAJ.

Wu, Z., Deng, Y., Cui, Y., Chen, Y., Wang, Q., & Feng, Q. (2019). Investigations on secondary compression behaviours of artificial soft sand-clay mixtures. Soils and Foundations, 59(2), 326–336. https://doi.org/10.1016/j.sandf.2018.11.008.

Yamamuro, J. A., Covert, K. M., & Lade, P. V. (1999). Static and cyclic liquefaction of silty sands. In P. V. Lade & J. A. Yamamuro (Eds.), Physics and Mechanics of Soil Liquefaction (1st ed., pp. 55–65). Routledge. https://doi.org/10.1201/9780203743317-5.

Proceedings of the XVIII ECSMGE 2024
GEOTECHNICAL ENGINEERING CHALLENGES
TO MEET CURRENT AND EMERGING NEEDS OF SOCIETY
© 2024 the Authors
ISBN 978-1-032-54816-6
DOI 10.1201/9781003431749-83
Open Access: www.taylorfrancis.com, CC BY-NC-ND 4.0 license

ECSMGE 24
XVIII EUROPEAN CONFERENCE ON SOIL MECHANICS AND GEOTECHNICAL ENGINEERING

Measuring the undrained shear strength of very soft, clay-rich sediments

Mesure de la résistance au cisaillement non drainé des sédiments argileux très mous

L. Jaksic*, M. Konstadinou, A. Talmon, T. van Kessel
Deltares, Delft, The Netherlands

E. Meshkati
Boskalis, Papendrecht, The Netherlands

**luka.jaksic@deltares.nl*

ABSTRACT: This study examines what measuring devices can best be used to measure the undrained shear strength of very soft, clay-rich sediments that are in between solid and fluid states. Although in recent years interest in these sediments for construction purposes has been growing, little information is currently available on what laboratory testing devices can be used for this purpose. In this study, kaolinite-based clay samples are prepared at different liquidity index values (in the range of 0.4 to 1.9) and tested using a Fall Cone, Lab Vane, and Direct Simple Shear device. The results show that the measured shear strength (in the transitional range of 1-10 kPa) strongly depends on the applied test conditions. The Fall Cone and Lab Vane tests provide shear strength values in the same order of magnitude. The measured strength values from Direct Simple Shear testing depend on the applied consolidation stress level but are typically lower compared to the Fall Cone and Lab Vane tests. The findings of this research indicate that the results of different devices converge when the testing conditions are moved closer together. A full overlap of the results is not likely possible as it would require the test conditions to be pushed outside the validated range of operations or simply because some test conditions are inherent to the type of test.

RÉSUMÉ: Cette étude examine les dispositifs de mesure les plus adaptés pour mesurer la résistance au cisaillement non drainé des sédiments très mous, riches en argile, se situant entre les états solide et liquide. Bien que ces sédiments aient suscité un intérêt croissant ces dernières années dans le milieu de la construction, peu d'informations sont disponibles sur les dispositifs de test en laboratoire pouvant être utilisés à cette fin. Dans cette étude, des échantillons d'argile à base de kaolinite sont préparés à différentes valeurs d'indice de liquidité (variant entre 0.4 et 1.9) et testés à l'aide d'un pénétromètre à cône, d'un scissomètre de laboratoire, et d'un appareil de cisaillement simple direct. Les résultats des tests montrent que la résistance au cisaillement non drainé (variant entre 1 et 10 kPa) dépend fortement des conditions de test appliquées. Les tests avec le pénétromètre à cône et du scissomètre de laboratoire fournissent des résistances au cisaillement non drainé de même ordre de grandeur. La résistance au cisaillement non drainé obtenue à partir du test de cisaillement simple direct dépend du niveau de contrainte de consolidation appliqué, mais est généralement inférieure aux résultats obtenus avec les autres méthodes. Les conclusions de cette recherche indiquent que, plus les conditions de test sont proches, plus les résultats des différents dispositifs convergent. Une coïncidence complète des résultats est probablement impossible, car cela nécessiterait que les tests soient effectués dans des conditions hors de leur plage opérationnelle validée, ou tout simplement parce que certaines conditions de test sont inhérentes au type de test.

Keywords: Very soft clays; undrained shear strength; direct simple shear device; fall cone; lab vane test.

1 INTRODUCTION

The strength properties of very soft, clay-rich sediments are important as interest in these sediments is growing, e.g., for wetland (re)construction, to strengthen foreshores against sea level rise or as building material for dikes. An example hereof is the "Growing Dike" initiative in the Netherlands, where locally dredged material is placed on top of a dike, with the intention to strengthen the dike as it transforms from a sediment suspension to a soil. To guarantee that these very soft materials can withstand exposure, such as wave attack, knowledge of how to measure their undrained shear strength is needed.

Measuring the undrained shear strength of very soft, clay-rich sediments is challenging as these sediments display a specific deformation behaviour that differs from that of water or most soils (Meshkati et al., 2021). As these sediments are in a transition between a fluid and solid state, they are considered

(ultra-)soft from a soil mechanics perspective, but rather strong from a fluid mechanics perspective. Although the undrained shear strength (Su) is a geotechnical parameter used for soils ($Su > 10\ kPa$), similar parameters exist in the field of fluid dynamics – albeit measured with different devices and protocols and used for much softer materials ($Su < 1\ kPa$).

It remains uncertain what devices and protocols within soil and fluid mechanics are appropriate for measuring undrained shear strengths beyond the typical range of interest for both disciplines ($1 < Su < 10\ kPa$). Meshkati et al. (2021) anticipate that the suitability of devices may vary, considering that the differences in stress and strain levels studied in both disciplines span multiple orders of magnitude.

Building on Meshkati et al. (2021), a Direct Simple Shear device, Lab Vane, and Fall Cone are used to measure the undrained shear strength of artificial clay samples between fluid and solid states. The aim is to evaluate suitable measuring devices within this transitional strength range ($1 < Su < 10\ kPa$).

2 USED MATERIALS

To assess the performance of the measuring devices for the whole range of strengths that bridges the gap between fluids and solids, different clay samples were prepared with water contents between 23 and 120%.

The tested samples were predominantly kaolinite-based to minimize thixotropic behaviour. These inactive clay samples were prepared by mixing FT-S1 powder and tap water in a lab mixer. Once prepared, the samples were placed in cups, wrapped in plastic foil and given one hour to rest before testing. In addition, a stiffer prefabricated pottery clay, namely the Vingerling K147 clay by Sibelco, was used. Table 1 summarizes the tested clay sample characteristics.

Table 1. Clay characteristics.

WC (%)	LI (-)	VR (-)	Properties
Mixture FT-S1 and tap water			
118-120	1.87-1.91	3.01-3.69	KC = 64 %
94	1.44	2.44-2.88	LL = 70-80 %
58-59	0.78-0.80	1.54-1.77	PL = 15-20 %
47-51	0.59-0.66	1.26-1.54	PI = 60-75 %
43-43.3	0.51-0.52	1.14-1.30	
Vingerling K147			
22.6-24	0.41-0.50	0.60-0.64	KC = 70-90 % LL = 32.3 %* PL = 15.8 %* PI = 16.5 %*

*Note: KC is the Kaolinite Content, LL the Liquid Limit, PL the Plastic Limit, and PI the Plasticity index, PI=LL-PL. WC is the water content and LI the Liquidity Index, LI=(WC-PL)/(LL-PL). VR is the estimated void ratio. *Based on De Lange et al. (2018).*

3 TESTING APPARATUS & PROCEDURES

The strength of the clay samples is measured using the Lab Vane, Fall Cone and Direct Simple Shear device.

3.1 Lab Vane test

The Lab Vane test was performed following ASTM D4648, which entails the rotation of a vane at a constant shear strain rate within the clay specimen. The vane size is adjusted based on the material's stiffness to ensure that the device remains within its calibrated range.

The measured peak stress is known as the static peak shear stress, which is considered equivalent to Su in soil mechanics. Both parameters are shear strain rate dependent, exhibiting higher values at increased strain rates. To assess shear strain rate dependency, the blade's rotation speed is varied at 0.01, 0.1, 0.5 and 1 RPM. As the Lab Vane does not measure the corresponding shear strain rates $\dot{\gamma}$ [1/s], $\dot{\gamma}$ is estimated with the analytical approach by Maron & Krieger (1952) by performing a Controlled Shear Stress ramp-up protocol (Meshkati et al., 2021). The estimated strain rate at the clay's static yield point is in the order of $1 \times 10^{-3}\ 1/s$ for the Vingerling clay, and between 1 and $5 \times 10^{-3}\ 1/s$ for the FT-S1 specimens with water contents between 43 and 120%.

3.2 Fall Cone test

The Fall Cone test was performed in accordance with ISO 17892-6 and with 5 repetitions per clay specimen. Two different cones were used depending on the specimen's water content (WC). The stiffest Vingerling clay (WC=23%) was tested with a cone of 80g and 30° aperture, while the softest clays (WC > 90%) used a cone of 60g and 60° aperture. Intermediate water contents were assessed with both cones. The undrained shear strength (Su) [kPa] was derived from the cone penetration depth (d) [mm] using Hansbo's empirical equation:

$$Su = K\frac{m\,g}{d^2} \qquad (1)$$

where g is gravitational acceleration [m/s^2], m is the cone mass [g], and K is a dimensionless constant (0.27 and 0.8 for the 60 and 80-gram cone, respectively).

3.3 Direct Simple Shear device

The Direct Simple Shear (DSS) tests followed ASTM D6528–17 and used specimens with a diameter of 63mm and a height of 21mm.

Prior to shearing the specimen at a constant speed of 8% of the sample height per hour (hr), a vertical consolidation stress ($\sigma_{v,i}$) was applied. $\sigma_{v,i}$ values as

low as 3 kPa were used; lower consolidation stress values were unfeasible due to difficulties in maintaining grip during shearing. The sample height is kept constant during shearing to prohibit any volume changes and mimic undrained conditions. The shear strain rate dependency is tested by applying an increased, non-standard shear strain rate of 100%/hr.

The undrained shear strength (Su) is the measured peak stress level, or in the absence of a peak stress, the strength taken at 38% shear strain (γ). Note that strength measurements are corrected for ring friction and membrane effects, which amount to roughly 1 kPa. The DSS tests are conducted for water contents below 55% due to handling limitations with softer materials. Table 2 outlines the test specifications.

Table 2. Overview Direct Simple Shear (DSS) tests.

WC (%)	Shear rate (%/hr)	$\sigma_{v,i}$ (kPa)	γ (%)
Mixture FT-S1 and tap water			
49.9	8	3	38
47.2	100	3	38
	8	3	38
43.3	100	3	38
	8	5	38
Vingerling K147			
22.9	8	3	38
22.6	100	3	28*

*Note: WC is the Water Content (WC), $\sigma_{v,i}$ the initial consolidation stress, and ϵ the shear strain level at which the undrained shear strength is determined. *Corresponds to peak stress level.*

4 TEST RESULTS

Figure 1 shows the variation in undrained shear strength (Su) with the liquidity index (LI) for all tests performed in this study. The results are expressed in terms of LI to provide an indication of the clays' plasticity and to enable a direct comparison of the two mineralogically-distinct clays, Vingerling and FT-S1. For comparison purposes, an empirical relation between LI and Su is shown, as derived by Vardanega et al. (2014) based on extensive Fall Cone testing on fine-grained materials.

For the Fall Cone and Lab Vane tests, the results show comparable undrained shear strength values, Su. Both tests closely adhere to the theoretical relation proposed by Vardanega et al. (2014).

The alignment of the DSS results with the Fall Cone, Lab Vane, and Vardanega et al. (2014), strongly depends on the applied testing conditions.

For very soft clays ($Su < 10\,kPa$), the Su values obtained through DSS testing are typically lower than those measured with the Fall Cone and Lab Vane; with variations influenced by the applied consolidation stress level ($\sigma_{v,i}$) and strain rate ($LI \geq 0.5$ in Figure 1).

Increased consolidation stress levels ($\sigma_{v,i}$) result in higher Su values. Still, even at the highest stress level of $\sigma_{v,i} = 5kPa$, the measured undrained shear strength remains at the lower bound of the Su values measured in Lab Vane and Fall Cone tests. It should be noted that the Lab Vane and Fall Cone tests are performed in the absence of a consolidation stress ($\sigma_{v,i} = 0\,kPa$).

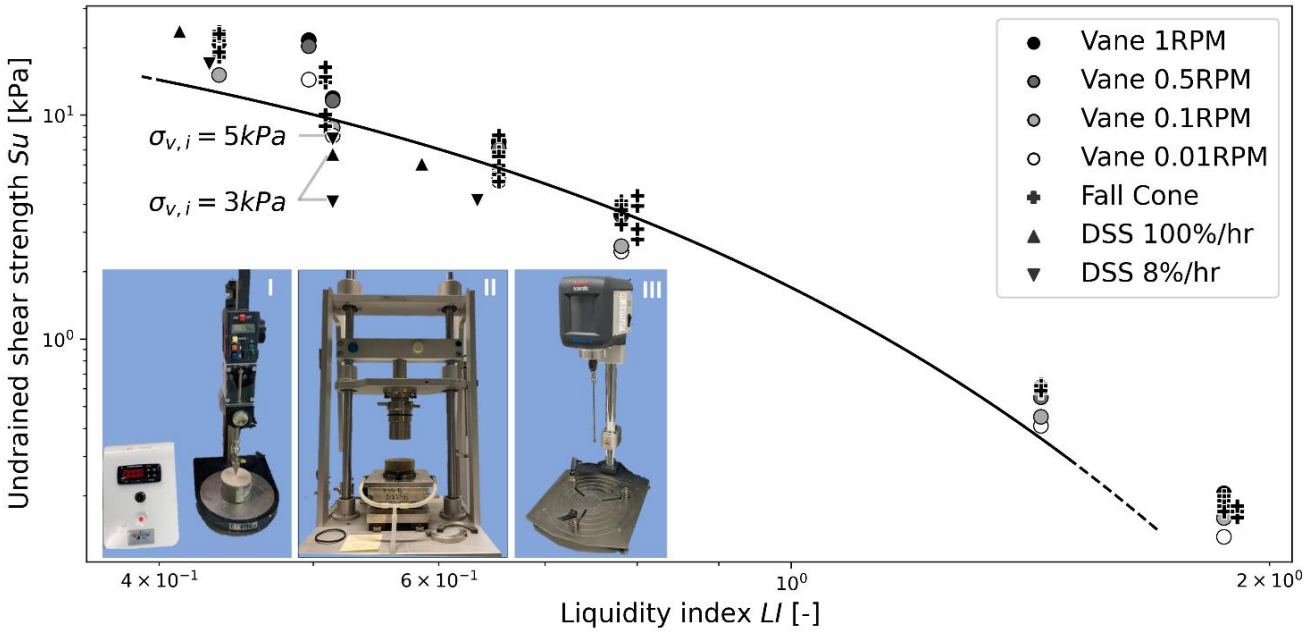

Figure 1. Undrained shear strength (Su) [kPa] at different liquidity index (LI) [-] values as calculated by the Fall Cone, Direct Simple Shear (DSS) and Lab Vane. ▼ and ▲ indicate DSS results with a shear strain rate of 8 and 100% of the sample's height per hour, respectively. The Lab Vane's rotation speed is indicated with shades of grey. The black line shows the empirical relation between Su and LI as derived by Vardanega & Haigh (2014); the dotted part is outside the validated range. The used Fall Cone (I), DSS (II) and Lab Vane (III) are shown in the lower left corner.

However, when the applied shear strain rate of the DSS approaches that of the Lab Vane, the measured undrained shear strengths are in better agreement. The Lab Vane exhibits relatively high strain rates, $\dot{\gamma}$, in the order of $10^{-3}\ 1/s$. In general, the undrained shear strength tends to increase for higher strain rates (Lefebvre and LeBoef, 1987). Accordingly, the DSS underestimates the undrained shear strength compared to the Lab Vane when operating at a lower strain rate of $\dot{\gamma} = 2.2 \times 10^{-5}\ 1/s$ (i.e. 8%/hr) (▼ in Figure 1, for $LI \geq 0.5$, $\sigma_{v,i}$=3 kPa). At the fastest applied shearing rate of $\dot{\gamma} = 2.8 \times 10^{-4}\ 1/s$ (i.e., 100%/hr), the DSS results approach the Lab Vane results (▲ in Figure 1).

For the stiffest Vingerling clay ($Su > 10\ kPa$, $LI < 0.5$ in Figure 1), the DSS results align well with the Su_p values obtained with the Fall Cone and Lab Vane for both applied shear strain rates (8 & 100%/hr). Please note that Sheahan et al. (1996) show that that the clay's sensitivity to shear strain rate decreases with an increasing over-consolidation ratio (OCR), and that the Vingerling clays are over-consolidated (OCR>1). During preparation, the Vingerling clay experienced higher consolidation stress levels than during the test. In contrast, the FT-S1 clay samples are tested under normally consolidated conditions, OCR=1.

5 DISCUSSION

Comparable undrained shear strength values, Su, are obtained between the Fall Cone and Lab Vane tests, aligning with Canelas et al. (2018) tests based on cohesive soil samples with water contents around their liquid limit. Interestingly, our results indicate that this conclusion holds even under significant variations in the Lab Vane's shear strain rate (0.01 – 1 RPM).

The results indicate that the observed discrepancy in the undrained shear strength response among the DSS and the Lab Vane device is to an extent attributed to differences in the applied shear strain rates.

Meshkati et al. (2021) argue that in geomechanics mostly small displacement are studied (small shear strains) to ensure geotechnical stability, whereas in fluid mechanics flowing materials and thus large shear strains are studied. Meshkati et al. (2021) anticipate a similar difference in the shear strain rates that are applied in both fields of discipline. This is in line with the findings in this study which shows a notable discrepancy in shear strain rates between the DSS device, commonly employed in soil mechanics, and the Lab Vane, extensively utilized in fluid mechanics.

6 CONCLUSION

This work has investigated the variation in the undrained shear strength (Su) of very soft, kaolinite-based clays for different devices and test conditions. The Fall Cone and Lab Vane tests yielded comparable Su values, whereas the Direct Simple Shear (DSS) results showed a dependency on the applied shear strain rate and consolidation stress level. The Su from DSS testing aligned well with Fall Cone and Lab Vane results for stiffer clays ($Su > 10kPa$). For very soft clays ($Su < 10kPa$), this is the case when the difference in the shear strain among the different devices is minimized. A full overlap of the undrained shear strength is not likely to be possible as this would require the shear strain rate to be pushed outside the validated range of operations or simply because some test conditions – such as a non-zero consolidation stress – are inherent to the type of test.

REFERENCES

Canelas, D., Fernandes, I., Lopes, M. (2018). Use of Fall Cone Test for the determination of undrained shear strength of cohesive soils, In: MATEC Web Conf. https://doi.org/10.1051/matecconf/201825104067.

De Lange, D.A., Terwindt, J., van der Linden, T.I. (2018). CPT in thinly inter-layered soils, In: *International Symposium on Cone Penetration Testing*, Delft, the Netherlands, pp. 383-388.

Krieger, I.M., Maron, S.H. (1952) Direct Determination of the Flow Curves of Non-Newtonian Fluids. III. Standardized Treatment of Viscometric Data, *J. of Applied Physics*, 25, pp. 72-75. https://doi.org/10.1063/1.1721523.

Lefebvre G., Leboeuf D. (1987). Rate effects and cyclic loading of sensitive clays, *J. Geotech. Eng.*. 113, pp. 476-489. https://doi.org/10.1016/0148-9062(87)92312-6.

Meshkati, E., Talmon, A., Luger, D., Bezuijen, A. (2021). Rheology of clay rich soft sediments: from fluid to geo-mechanics, In: *CEDA Dredging Days*. Central Dredging Association.

Sheahan, T.C., Ladd, C.C., Germaine, J.T. (1996). Rate-dependent undrained shear behavior of saturated clay, *J. of Geotech. Eng.*, 122, pp. 99-108. https://doi.org/10.1061/(ASCE)07339410(1996)122:2(99).

Vardanega, P.J., Haigh, S.K. (2014). The undrained strength - liquidity index relationship, *Canadian Geotech. J.*, 51(9), pp. 1073-1086, https://doi.org/10.1139/cgj-2013-0169.

Proceedings of the XVIII ECSMGE 2024
GEOTECHNICAL ENGINEERING CHALLENGES
TO MEET CURRENT AND EMERGING NEEDS OF SOCIETY
© 2024 the Authors
ISBN 978-1-032-54816-6
DOI 10.1201/9781003431749-84
Open Access: www.taylorfrancis.com, CC BY-NC-ND 4.0 license

ECSMGE 24
XVIII EUROPEAN CONFERENCE ON SOIL MECHANICS AND GEOTECHNICAL ENGINEERING

Settlement evaluation of reinforced embankment over a soft subgrade: Numerical modelling with different soil models based on a full-scale study

Évaluation des tassements d'un remblai renforcé sur une couche de fondation meuble: Modélisation numérique avec différents modèles de sol basés sur une étude à l'échelle réelle

B. Janevski*
Civil Engineering Institute "Macedonia", Skopje, RN Macedonia

J. Br. Papić
Faculty of Civil Engineering, Skopje, RN Macedonia

A. Skejić
Faculty of Civil Engineering, Sarajevo, Bosnia and Herzegovina

A. Turalić
Design & QC, Sarajevo, Bosnia and Herzegovina

**bojan.janevski@gim.mk*

ABSTRACT: This paper presents results from comparative numerical analyses for an experimental study performed to investigate the soil behaviour for airfield pavement design in Bihać, Bosnia and Herzegovina. A 300 m long and 45 m wide multilayer reinforced embankment is constructed and surcharged in three zones by static loads over thick soft deposits. The monitoring comprises the observation of the settlements with a geodetic survey, horizontal inclinometers, and magnetic extensometers. Different constitutive models are used to model the terrain and estimate the settlements, and the results are compared to the monitoring. Although the results of the analyses generally confirm the terrain response, regardless of how precisely the terrain is modelled, it is difficult to accurately model all loading phases with constant values of the input parameters. The findings obtained through the numerical modelling are presented in the paper.

RÉSUMÉ: Cet article présente les résultats d'analyses numériques comparatives pour une étude expérimentale réalisée pour étudier le comportement du sol pour la conception de la chaussée d'un aérodrome à Bihać, en Bosnie-Herzégovine. Un remblai renforcé multicouche de 300 m de long et 45 m de large est construit et surchargé en trois zones par des charges statiques sur d'épais dépôts d'argiles molles et de limons. La surveillance sur le terrain comprend l'observation des agglomérations avec un levé géodésique, des inclinomètres horizontaux et des extensomètres magnétiques. Différents modèles constitutifs sont utilisés pour caractériser le terrain et estimer les tassements, et les résultats sont comparés au suivi. Bien que les résultats des analyses confirment généralement la réponse du terrain, quelle que soit la précision avec laquelle le terrain est modélisé, il est difficile de modéliser avec précision toutes les phases de chargement avec des valeurs constantes des paramètres d'entrée. Les résultats obtenues grâce à la modélisation numérique sont présentés dans l'article.

Keywords: Embankment; monitoring; numerical modelling; settlements; soft soil.

1 INTRODUCTION

The evaluation of the consolidation settlements in soft soils represents an everyday challenge, and it is a subject of research by many authors, starting from the constitution of the theory of consolidation (Terzaghi, 1925) until today. The engineer should precisely assess the uncertainties about the geological and hydrogeological conditions, correctly interpret the field investigations and the laboratory test results, and evaluate the influence of the construction phases and the structure on the terrain, the variation of the stresses, the total stresses, etc. The construction activities on soft soils commonly include placing layers of geosynthetic reinforcement and controlled fill material beneath the loading area to enhance performance, especially in embankments, unpaved roads, and large stabilized areas like car parks or

platforms (Giroud et al., 1984; Rowe and Soderman, 1986; Love et al., 1987; Rowe and Li, 2005).

The benefits of geosynthetic as a reinforcing layer between the fill and the subsoil offers benefits such as a potential for reduction in fill thickness for specified compaction values and bearing capacities and a decrease in rut formation, thereby extending the serviceable life of the track (Hufenus et al., 2006). The large and small-scale experiments generally illustrate that the geogrid aids in spreading the applied load over a broader area on the subgrade layer, leading to reduced permanent deformation accumulation in the subgrade (Abu-Farsakh and Chen, 2011; Demir et al., 2013; Kapor et al., 2023a, 2023b). However, the case studies supported by back-numerical analyses using relatively complex soil models are somewhat limited.

This paper briefly presents an experimental study investigating soil behaviour for airfield pavement design in Bihać, Bosnia and Herzegovina. Unlike Skejić and Turalić (2022), the numerical analyses included a complex soil model with stress and time-dependent parameters. Good agreement was achieved between the model and in-situ records. Finally, some conclusions and recommendations are emphasized for future similar projects.

2 DEFINING THE PROBLEM

2.1 Geotechnical characteristics

Up to a depth of about 1,5 m, the terrain for the airfield is composed of sandy clays and silts (CL/ML) with low plasticity and soft to very soft consistency. There are silts and clays with organic content (OL) in a liquid-consistent state under it, with a thickness of around 17 m. Under these quaternary deposits, there are practically impermeable Miocene sediments with very low compressibility. The average groundwater level is 0.5 m below the terrain. Table 1 shows the parameters of the represented soil layers.

Table 1. Geotechnical parameters of the soil materials.

Parameter	CL/ML	OL
γ [kN/m^3]	16,5 – 19,0	16,5 – 18,5
φ [°]	18 – 22	16 – 18
c [kPa]	10 – 15	10 – 15
q_c [MPa]	0,5 – 4,0	0.2 – 1.0
N_{spt} [/]	2 – 4	1 – 2
E [MPa]	1,5 – 7,0	0,7 – 2,3
k_f [m/s]	5×10^{-6} – 5×10^{-8}	5×10^{-8} – 1×10^{-9}

2.2 Brief overview of the experimental study

An experimental study was conducted to investigate the soil behaviour for an airfield pavement design (Nuhić et al., 2021).

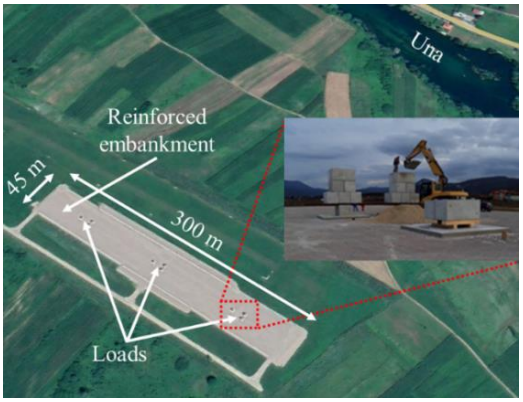

Figure 1. Aerial view of the subject location.

The embankment was constructed in three reinforced and compacted layers with a total height of 1,1 m over a very soft subgrade, where static loads are applied on top (Figure 1). All three layers are reinforced with geogrids 60/60 kN/m. The compressive modules of the embankment layers are 25/60/90 MPa, with construction time of 30/33/42 days, respectively. The static loads were applied in 1 day, in three zones, 40 days after the completion of the embankment. They simulate a load of 20 kN on an area of 16 m^2. The characteristic cross-section of the reinforced embankment is shown in Figure 2.

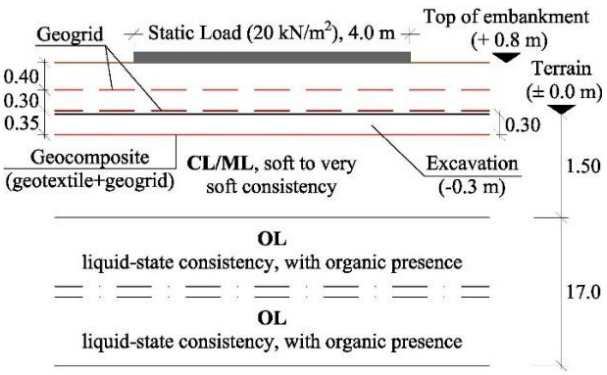

Figure 2. Characteristic cross-section of the study.

2.3 Results from the monitoring

The settlements were monitored continuously with geodetic measurements, horizontal inclinometers, and magnetic extensometers. The inclinometers were placed along the entire embankment width, 35 cm under the loads. The initial measurement was done immediately after loading. The average cumulative settlement 170 days after the loading was 8,4 cm and 8,2 cm as measured by geodetic monitoring and the horizontal inclinometer readings, respectively. The

settlement distribution presented in Figure 3 shows the impact of the loads on the embankment.

The magnetic extensometers were placed on the contact between the first two embankment layers when the initial measurement was performed.

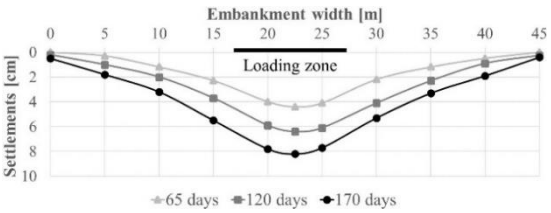

Figure 3. Embankment settlement distribution along its width (readings from horizontal inclinometers).

Figure 4 shows characteristic settlement curves for different depths. The primary consolidation has a significant part in the cumulative settlements since most of the deformations occur after the construction of the embankment. The secondary consolidation is not completed as there is no flattening of the settlement curve. A relatively short monitoring period represents a drawback of the experimental study, where the monitoring was unfortunately stopped due to unclear reasons.

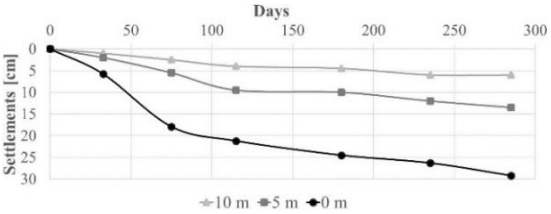

Figure 4. Magnetic extensometer measurements.

3 NUMERICAL CALCULATIONS

The three-dimensional numerical simulation was performed in Plaxis 3D software (Bringreve and Manoj, 2019). The half-space is discretized with 10-noded tetrahedral finite elements. The soil is characterized according to the Mohr-Coulomb (MC) criterion and Soft-Soil (SS) model. The simulation is conducted in several successive phases, according to the stages of the experimental study, that is:

- Phase 1: initial state (before construction);
- Phase 2: topsoil excavation (30 cm);
- Phase 3: construction of 1st layer, t=30 days;
- Phase 4: construction of 2nd layer, t=33 days;
- Phase 5: construction of 3rd layer, t=42 days;
- Phase 6: consolidation, t=40 days;
- Phase 7: static loading p=20 kN/m^2, t=1 day;
- Phase 8: consolidation, t=170 days.

The input parameters, depending on the model, are shown in Table 2, based on the in-situ and laboratory test results. For the Soft-Soil model, correlations from contemporary literature were used (see Van Baars, 2003, and Long et al., 2020).

Table 2. Input parameters in the software Plaxis 3D.

	CL/ML		OL		
	MC-p	MC-c	MC-p	MC-c	SS-c
γ [kN/m^3]	17,0	17,0	16,5	16,5	16,5
φ [°]	20,0	20,0	17,0	17,0	29,0
c [kPa]	10,0	10,0	10,0	10,0	0,0
E [MPa]	4,5	7,0	1,2	2,2	/
k_f[m/s]	/	5*10^{-6}	/	5*10^{-7}	2*10^{-8}
C_c [/]	/	/	/	/	1,0
C_s [/]	/	/	/	/	0,22
λ* [/]	/	/	/	/	0,145
k* [/]	/	/	/	/	0,064

* MC = Mohr-Coulomb; SS = Soft-Soil; p = plastic; c = consolidation

The geogrids are defined with elastoplastic behaviour and isotropic characteristics, with axial stiffness EA_1=EA_2=1200 kN/m and maximum tensile force $N_{p,1}$=$N_{p,2}$=60 kN. Due to small deviations in the results compared to the monitoring, a calibration of the permeability (k_f) and the deformation modulus (E) was conducted. These parameters are not constant in reality but are directly dependent on the degree of the stresses and the time, that is from the analysed phase. Namely, the deformation modulus tends to increase with the stresses while the permeability decreases and vice versa. Therefore, the analyses are repeated using a variable set of parameters: for the sandy clays and silts (CL/ML), E_{oed}=1,5-7,0 MPa, and for the silts with organic content (OL), E_{oed}=0,7-2,25 MPa and k_f=1*10^{-7}-1*10^{-8} m/s.

Figure 5 shows an overview of the settlement evaluation in Plaxis 3D, depending on the analyzed phase, the model used, and the calculation method, compared to the average values of the settlement obtained during the monitoring. The highest value of settlements (30,38 cm) is obtained using a variable set of parameters and the Soft-Soil model, where the settlement curve is the closest to the monitoring curve. The deformed mesh in the vertical direction for this analysis is shown in Figure 6.

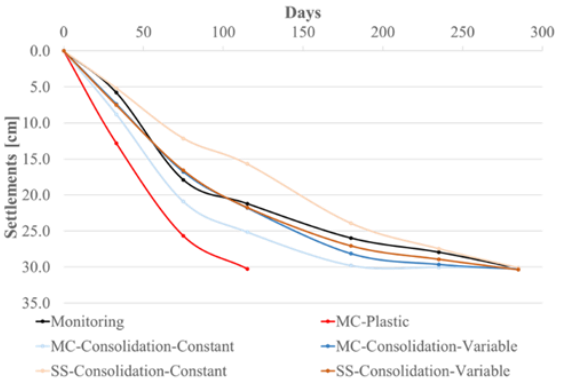

Figure 5. Settlement curves obtained in Plaxis 3D.

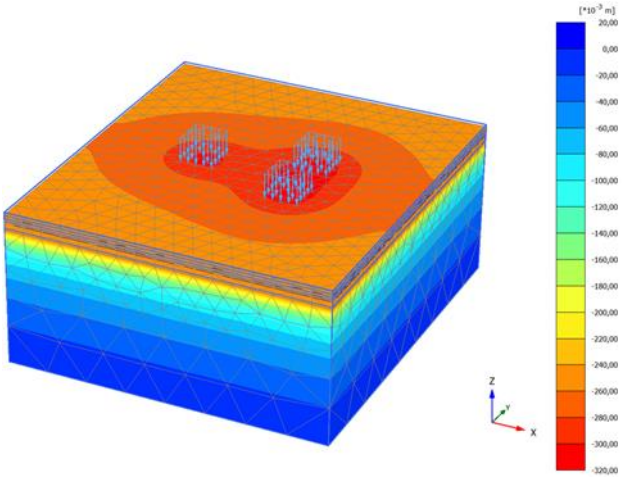

Figure 6. Deformed mesh in Plaxis 3D, using variable parameters in the Soft-Soil model.

4 CONCLUSIONS

3D numerical analyses with different constitutive models were performed to study the soil behaviour for airfield pavement design in Bihać, Bosnia and Herzegovina. The results are compared to findings from field monitoring at 300 m long and 45 m wide surcharged multilayered reinforced embankment over thick deposits of soft clays and silts.

According to the numerical analyses, it can be concluded that although there is a certain deviation between the settlement curves, the cumulative value of the settlements is very similar to the measured settlements. It should also be emphasized that when using variable parameters directly dependent on the degree of stresses and time, the settlement curves are much more realistic when compared to the analyses where only one set of parameters is applied.

The next step of this research will be to investigate the dependence between the degree of the stresses on one side and the values of the compressibility modulus and permeability on the other.

REFERENCES

Brinkgreve, R.B.J., Zampich, L. and Manoj, N.R. (2019). Plaxis 3D Connect edition manual. Delft University of Technology & PLAXIS bv, Netherlands.

Hufenus, R., Rueegger, R., Banjac, R., Mayor, P., Springman, S.M. and Brönnimann, R. (2006). Full-scale field tests on geosynthetic reinforced unpaved roads on soft subgrade. *Geotextiles and Geomembranes*, 24(1), 21-37. http://doi.org/10.1016/j.geotexmem.2005.06.002.

Demir, A., Laman, M., Yildiz, A. and Ornek, M. (2013). Large scale field tests on geogrid-reinforced granular fill underlain by clay soil. *Geotextiles and Geomembranes*, 38, 1-15. http://doi.org/10.1016/j.geotexmem.2012.05.007.

Kapor, M., Skejić, A., Medić, S. and Balić, A. (2023a). DIC assessment of foundation soil response for different reinforcement between base and soft subgrade layer – physical modeling. *Geotextiles and Geomembranes*, 51(3), 390-404. http://doi.org/10.1016/j.geotexmem.2023.01.003.

Kapor, M., Skejić, A., Medić, S. and Balić, A. (2023b). Experimental evaluation of relative soil-geotextile displacements Induced by strip footing pressure on a reinforced foundation bed over soft subgrade. *International Journal of Geosynthetics and Ground Engineering*, 9(6), 82. http://doi.org/10.1007/s40891-023-00503-5.

Long, M., Trafford, A. and Grimstad, G. (2020). Prediction of embankment settlement on Swedish peat using the soft soil creep model. *Proceedings of the Institution of Civil Engineers – Geotechnical Engineering*. http://doi.org/10.1680/jgeen.20.00141.

Love, J.P., Burd, H.J., Milligan, G.W.E. and Houlsby, G.T. (1987). Analytical and model studies of reinforcement of a layer of granular fill on a soft clay subgrade. *Canadian Geotechnical Journal,* 24(4), 611-622. https://doi.org/10.1139/t87-075.

Nuhić, S., Rekanović-Nuhić, F., Abdihodžić, M. and Muratović-Isović, E. (2021). Script with technical solutions and presentation of test and measurement results on the test section of the Airfield Bihać, Euroing doo, Bihać.

Rowe, R.K. and Li, A.L. (2005). Geosynthetic-reinforced embankments over soft foundations. *Geosynthetics International*, 12(1), 50-85. https://doi.org/10.1680/gein.2005.12.1.50.

Rowe, R.K. and Soderman, K.L. (1986). Reinforced embankments on very poor foundations. *Geotextile and Geomembranes*, 4(1), 65-81. https://doi.org/10.1016/0266-1144(86)90037-3.

Skejić, A. and Turalić, A. (2022). Analysis and numerical modelling of full-scale study related to settlements of multilayer reinforced earth platform over a soft subgrade. *19th International Symposium of Macedonian Association of Structural Engineers (MASE)*, Ohrid, Macedonia.

Van Baars, S. (2003). Soft soil creep modelling of large settlements. *2nd International Conference on Advances in Soft Soil Engineering and Technology*, Kuala Lumpur, Malaysia.

Proceedings of the XVIII ECSMGE 2024
GEOTECHNICAL ENGINEERING CHALLENGES
TO MEET CURRENT AND EMERGING NEEDS OF SOCIETY
© 2024 the Authors
ISBN 978-1-032-54816-6
DOI 10.1201/9781003431749-85
Open Access: www.taylorfrancis.com, CC BY-NC-ND 4.0 license

ECSMGE 24
XVIII EUROPEAN CONFERENCE ON SOIL MECHANICS AND GEOTECHNICAL ENGINEERING

A study on ultimate vertical bearing capacity of spread foundations of sand-clay two layers ground

Une étude sur la capacité portante verticale ultime des fondations étalées sur un sol à deux couches sablo-argileux

K. Kaneda*
Department of Civil Engineering, Chiba Institute of Technology, Narashino, Japan
S. Ohtsuka
Department of Civil and Environmental Engineering,Nagaoka University of Technology, Nagaoka, Japan
**kazuhiro.kaneda@p.chibakoudai.jp*

ABSTRACT: A rigid–plastic finite element analysis was used to study the bearing capacity of a two-layered ground consisting of sand and clay in the upper and lower layers, respectively. In general, a phenomenon in which a load propagating through a sand layer is distributed over a clay layer and applied to shear the clay layer is called distributed failure. Depending on the strength ratio of sand and clay, either the sand layer fails or distributed failure occurs in the clay layer. In addition, size effects occur when the foundation width increases in the sand layer. In this study, the ultimate bearing capacity of a spread foundation of two layers of sand and clay was examined using a higher-order function as a constitutive equation that considers the size effect. When the strength of the lower clay layer was relatively low, dispersion fractures were likely to occur.

RÉSUMÉ: L'analyse par éléments finis plastique rigide a été utilisée pour étudier la capacité portante d'un sol à deux couches constitué d'une couche de sable dans la couche supérieure et d'une couche inférieure dans la couche inférieure. En général, un phénomène dans lequel une charge se propage à travers une couche de sable, est répartie sur une couche d'argile et est appliquée pour cisailler la couche d'argile est appelé rupture distribuée. En fonction du rapport de résistance du sable et de l'argile, on considère que seule la couche de sable se brise ou qu'une rupture distribuée se produit dans la couche d'argile. De plus, des effets de taille sont connus lorsque la largeur des fondations augmente dans la couche de sable. Dans cette étude, la capacité portante ultime de la fondation étalée composée de deux couches de sable et d'argile a été examinée en utilisant une fonction d'ordre supérieur comme équation constitutive pouvant prendre en compte l'effet de taille. Il a été constaté que lorsque la résistance de la couche inférieure d'argile est relativement faible, une fracture par dispersion est susceptible de se produire.

Keywords: Ultimate vertical bearing capacity; RPFEM; size effect; two layered ground; distributed failure.

1 INTRODUCTION

Calculation of the ultimate bearing capacity of soil is important when designing a building (Terzaghi and Peck, 1967). The ultimate bearing capacity formulae for building foundations are specified in the guidelines published by the Architectural Institute of Japan (AIJ, 2019). These formulae are based on experimental and theoretical considerations of risk avoidance. However, the vertical bearing capacity of two-layered clayey soils has not been adequately investigated. Kaneda et al. (Kaneda et al., 2018) clarified the mechanism of bearing capacity considering squeeze breakdown of clayey soils. However, Kaneda et al. (Kaneda et al., 2018) investigated only clay grounds with two layers and did not consider cases in which the bottom layer was sand. In addition, when considering the vertical bearing capacity of spread foundations on sandy soil, the size effects must be considered. Nguyen Du et al. (Nguyen Du et al, 2016)explained the size effect by introducing a higher-order yield function using rigid plastic finite element method (RPFEM), which was developed separately by Tamura et al. (Tamura et al., 1984) and Asaoka and Ohtsuka (Asaoka and Ohtsuka, 1986). This method was employed to estimate the ultimate bearing capacity of the footings. The Drucker–Prager and high-order yield functions were adopted as the soil constitutive equations, and associated and non-associated flow rules were introduced to establish the configuration relationship of the ultimate state. Using this method, a structural safety assessment and calculation of the soil-bearing capacity were performed. In contrast to deformation

analysis, RPFEM is applicable to limited soil constants. It uses only strength parameters, such as cohesion and friction angle, since it addresses the limit state directly by disregarding the deformation of the building and ground. Since the RPFEM uses the upper-bound theorem of plastic theory, the end result is slightly larger than the true value. In this study, the vertical bearing capacities of two-layered clay and sandy soils were analyzed using numerical simulations.

2 BRIEF OUTLINE OF HIGH ORDER YIELD FUNCTION

The high-order yield function can be expressed as follows:

$$f(\boldsymbol{\sigma}) = aI_1 + (J_2)^n - b = 0 \tag{1}$$

where a, b, and n represent the material parameters. When n = 0.5, Eq. (1) corresponds to the Druker Prager model (DP model) function: assuming an associated flow rule, the strain rate and volumetric strain can be derived using Eqs. (2) and (3), respectively:

$$\dot{\boldsymbol{\varepsilon}} = \lambda \frac{\partial f(\boldsymbol{\sigma})}{\partial \boldsymbol{\sigma}} = \lambda \frac{\partial}{\partial \boldsymbol{\sigma}} \left(aI_1 + (J_2)^n - b \right) = \lambda \left(a\mathbf{I} + nJ_2^{n-1}\mathbf{s} \right) \tag{2}$$

$$\dot{\varepsilon}_v = tr\dot{\boldsymbol{\varepsilon}} = tr\left(\lambda \left(a\mathbf{I} + nJ_2^{n-1}\mathbf{s} \right) \right) = 3a\lambda = \frac{3a}{\sqrt{3a^2 + 2n^2 (b - aI_1)^{2-1/n}}} \dot{e} \tag{3}$$

where denotes the plastic multiplier. Based on Eqs. (1)–(3), the first stress invariant can be expressed as:

$$I_1 = \frac{b}{a} - \frac{1}{a} \left\{ \frac{1}{2n^2} \left[\left(3a \frac{\dot{e}}{\dot{\varepsilon}_v} \right)^2 - 3a^2 \right] \right\}^{\frac{n}{2n-1}} \tag{4}$$

Finally, the rigid plastic equation was calculated as follows:

$$\boldsymbol{\sigma} = \frac{1}{n} \left\{ \frac{9a^2}{2n^2} \left[\left(\frac{\dot{\mathbf{e}}}{\dot{\varepsilon}_v} \right)^2 - \frac{3a^2}{2n^2} \right] \right\}^{\frac{n}{2n-1}} \left[3a \frac{\dot{\boldsymbol{\varepsilon}}}{\dot{\varepsilon}_v} - a\mathbf{I} \right] + \frac{1}{3} \left[\frac{b}{a} - \frac{1}{a} \left\{ \frac{9a^2}{2n^2} \left(\frac{\dot{\mathbf{e}}}{\dot{\varepsilon}_v} \right)^2 - \frac{3a^2}{2n^2} \right\}^{\frac{n}{2n-1}} \right] \mathbf{I} \tag{5}$$

3 THEORETICAL DISTRIBUTED FAILURE

Regarding the vertical bearing capacity of the two-layered ground with a sand layer at the top and a clay layer at the bottom, the bearing capacity of the clay layer was evaluated by considering the load distribution by the sand layer. Figure 1 and Eq. (6) show the concept and evaluation formula for a distributed failure (Yamaguchi, 1963). If the foundation width (B) is larger than the sand layer thickness (H_s), the shear failure zone will reach the clay layer from the sand layer, and the shear resistance of the clay soil will affect the ultimate bearing capacity of the foundation considering the influence of ϕ. However, if $B<H_s$, shear failure occurs within the sand layer. Distributed failure is the phenomenon in which the load propagates through the sand layer and is distributed over the clay layer, causing shear failure of the clay layer.

$$q_{ac} = \frac{N_c B'}{F_b B} c + \gamma_t D + \frac{H_s p_o' K_0}{F_b B} \tan \phi' \tag{6}$$

where q_{ac} is bearing capacity of distributed failure (kPa), N_c is the bearing capacity coefficient, B is the foundation width (m), F_b is the safety factor, c is the cohesion (kPa), γ_t is the unit weight (kN/m^3), D is the penetration depth (m), and H_s is the upper sand layer thickness (m), p'_0 is the static coefficient, and K_0 is the earth pressure at rest, ϕ 'is the shear resistance angle of upper sand. $B'=B+2(H_s-D)\tan\alpha$. $p_0' = \gamma_t h_w + \gamma'(H_s - h_w)$ is the effective soil overburden pressure on the bottom surface of the sand. α is a dispersion angle.

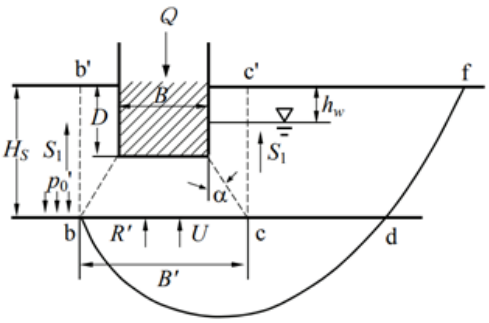

Figure 1. Distributed failure.

4 ANALYSIS CONDITIONS

Set B from 1m to 10 m; and set H_s to 0.5B, 1B, and 1.5B relative to foundation width B. Figure 2 shows the simulation mesh for a foundation width of 1 m and an upper sand layer of 1.5 m. The thickness and horizontal distance of the lower clay layer were set

such that a shear failure occurred within the simulation mesh, corresponding to the width of the foundation. The shear resistance angle ϕ was 30° and 40° for the upper sand layer, and the cohesion of lower clay layer was 20, 50, 100, and 150 kPa. The parameters of the higher order yield function were a=0.175, b=1.0, and n=0.526 for the ϕ 30° ground, and a=0.257, b=1.0, and n=0.526 for the ϕ 40° ground. The unit weight of the sand and clay layers was γ=18 kN/m^3, and the foundation rigidity was high. A vertical load was applied to the foundation to determine the ultimate vertical bearing capacity.

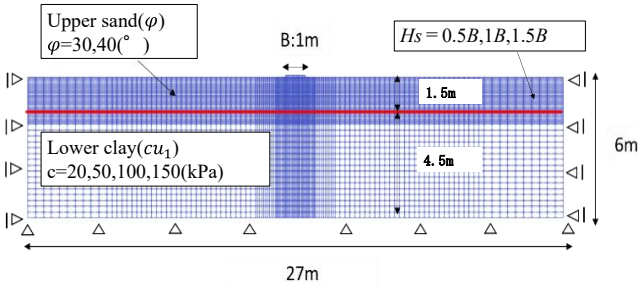

Figure 2. Simulation mesh (1m).

5 SIMULATION RESULTS

We investigated whether the simulation results were closer to a sand layer failure or distributed failure. The simulation results were organized by dividing them by the theoretical bearing capacity of sand layer failure and the theoretical bearing capacity of distributed failure (Eq. (6)). Note that the dispersion angle α in Figure 1 is 26.6° (1:2) and K_0 = 0.5. Figure 3 shows the relationship between the simulation results/sand layer failure (red), simulation results/distributed failure (blue), and the clay layer. The closer these values(the simulation results/sand layer failure or distributed failure) are to 1, the more it becomes clear whether the simulation result is a sand layer failure or a distributed failure. Also, ■ indicates the upper sand layer 0.5B, ▲ indicates 1B, and ● indicates 1.5B.

The focus was on the case where B=10 m. For ϕ =30°, if the strength of the lower clay layer is low, distributed failure is likely to occur, and if the strength of the lower clay layer is high, sand layer failure occurs. Figure 4 shows the shear strain distribution contours at failure at H_s = 1B (10 m) for the clay strength of (a) 50 kPa and (b) 150 kPa. Figure 4(a) shows a distributed failure including the lower clay layer, whereas form Figure 4(b), although there is some failure of the clay layer, most of the failure is of the sand layer. Next, considered ϕ =40°. Figure 5 shows the shear strain distribution contours at failure at H_s = 1B (10 m) with the clay strength of (a) 50 kPa and (b) 150 kPa. Figure 5(a) shows a distributed failure including the lower clay layer; however, a dispersion angle of 40° was more consistent with the analysis results than that of 26.6° from the appearance of shear failure. When calculating the theoretical value at the dispersion angle 40°, the simulated results/theoretical distributed failures were approximately 1.0. In contrast, in Case (b), a distributed fracture with a dispersion angle of 26.6° was observed.

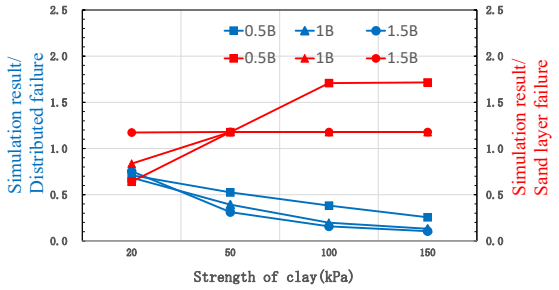

(a) B=1 m ϕ=30 ° (sand)

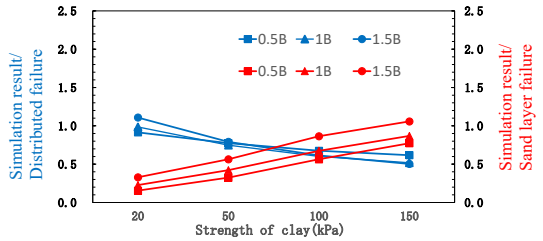

(b) B=1 m, ϕ=40 ° (sand)

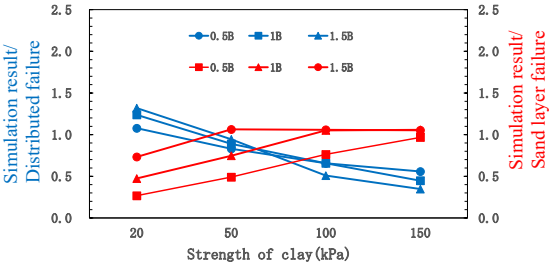

(c) B=10 m ϕ=30 ° (sand)

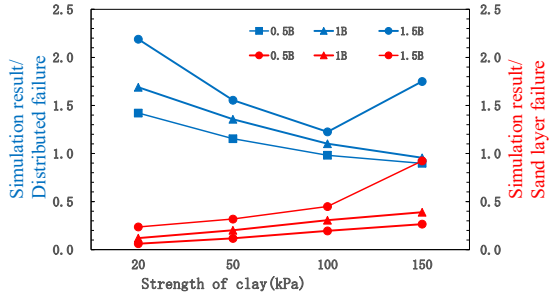

(d) B=10m, ϕ=40 ° (sand)

Figure 3. Relationship between the simulation result/sand layer failure (red), simulation result/ distributed failure (blue), and underlying clay layer.

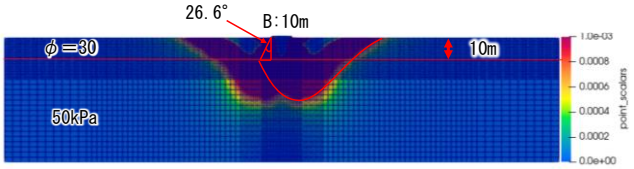

(a) Clay strength of 50 kPa

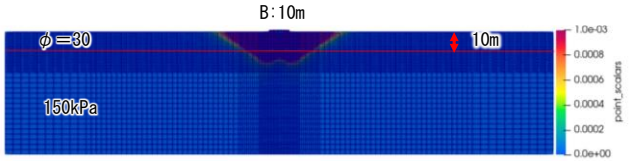

(b) Clay strength of 150 kPa

Figure 4. shear strain distribution contours at failure at H_s = 1B (10 m), ϕ=30 ° (sand).

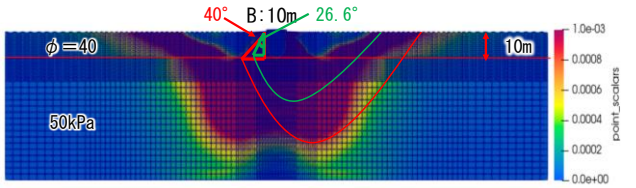

(a) Clay strength of 50 kPa

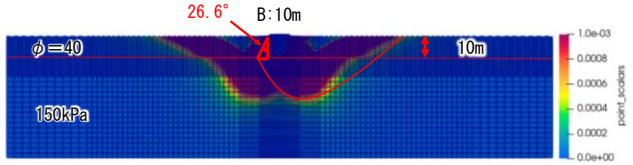

(b) Clay strength of 150 kPa

Figure 5. shear strain distribution contours at failure at H_s = 1B (10 m), ϕ=40 ° (sand).

6 CONCLUSIONS

The vertical bearing capacity of the two-layered soil was investigated using the RPFEM with higher-order yield functions.

For the strength of the upper sand layer of ϕ = 30° and a low strength of the lower clay layer, a distributed failure occurs, and conversely, for a high strength of the lower clay layer, a sand layer failure occurs. The dispersion angle is 26.6°.

For the strength of the upper sand layer of ϕ = 40°, a distributed failure occurs, and for the low strength of the lower clay layer, the dispersion angle is large, and conversely, for the high strength of the lower clay layer, the dispersion angle is 26.6°.

ACKNOWLEDGEMENTS

We would like to thank Takumi Araki, second year master's student at Chiba Institute of Technology for organizing these simulations.

REFERENCES

Architectural Institute of Japan (2019). AIJ. Recommendations for design of building foundation, pp. 112–136. (in Japanese).

Asaoka, A. and Ohtsuka, S. (1986). The analysis of failure of a normally consolidated clay foundation under embankment loading, Soils and Foundations, 26(2), pp. 47–59. https://doi.org/10.3208/sandf1972.26.2_47

Hakujyu Yamaguchi (1963). Practical formula of the bearing capacity for two layered ground, *Proceedings of 2nd ARCSM*, Vol. 1.

Kaneda, K., Aoki, M. and Ohtsuka, S. (2018). Ultimate bearing capacity of footing of two layered clayey soil system by rigid-plastic finite element method, *Proceedings of 8th International Conference on Geotechnique, Construction Materials and Environment, Kuala Lumpur, Malaysia*, Nov. 20-22, ISBN: 978-4-909106001 C3051.

Nguyen Du L., Ohtsuka S., Hoshina T. and Isobe K. (2016). Discussion on size effect of footing in ultimate bearing capacity of sandy soil using Rigid plastic finite element method, Soils and Foundations, Vol 56, No.1, pp. 93-103. https://doi.org/10.1016/j.sandf.2016.01.007

Tamura, T., Kobayashi, S., and Sumi, T. (1984). Limit analysis of soil structure by rigid plastic finite element method, Soils and Foundations, 24(1), pp. 34–42. https://doi.org/10.3208/sandf1972.24.34

Terzaghi, K. and Peck, R.B. (1967). Soil Mechanics in Engineering Practice, John Wiley & Sons, pp. 472–569.

Proceedings of the XVIII ECSMGE 2024
GEOTECHNICAL ENGINEERING CHALLENGES
TO MEET CURRENT AND EMERGING NEEDS OF SOCIETY
© 2024 the Authors
ISBN 978-1-032-54816-6
DOI 10.1201/9781003431749-86
Open Access: www.taylorfrancis.com, CC BY-NC-ND 4.0 license

ECSMGE 24
XVIII EUROPEAN CONFERENCE ON SOIL MECHANICS AND GEOTECHNICAL ENGINEERING

Numerical modelling of soil-pile interaction in a subsiding soil

Modélisation numérique de l'interaction sol-tas dans un sol affaissé

J.G. Kania*, L.L.C.G. de Sousa, O. Hededal
COWI A/S, Kongens Lyngby, Denmark

K.K. Sørensen
Aarhus University, Aarhus, Denmark

**jbka@cowi.com*

ABSTRACT: This paper presents a suitable constitutive and interface model of soil-pile interaction in a subsiding soil (gyttja) using PLAXIS 2D software. The model was calibrated by simulating the results of soil settlement, excess pore water pressure, drag force and unit shaft resistance along the uncoated steel test pile obtained in the field triggered by placing a 2 m high fill embankment around the piles. Such calibrated model could serve as a basis for further numerical simulations of the soil-pile interaction for both single-pile and pile groups.

RÉSUMÉ: Cet article présente un modèle constitutif et d'interface approprié de l'interaction sol-tas dans un sol affaissant (gyttja) à l'aide du logiciel PLAXIS 2D. Le modèle a été calibré en simulant les résultats du tassement du sol, de la pression excessive de l'eau interstitielle, de la force de traînée et de la résistance unitaire de l'arbre le long du pieu d'essai en acier non revêtu obtenu sur le terrain, déclenché en plaçant un remblai de 2 m de haut autour des pieux. Un tel modèle calibré pourrait servir de base à d'autres simulations numériques de l'interaction sol-pieu pour des groupes de pieux simples et de pieux.

Keywords: PLAXIS 2D; soft soils; interface; drag force; instrumentation.

1 INTRODUCTION

An expansion of the Randers Harbour, Denmark, is forthcoming. The first step of the site development plan was to employ vertical drains across a vast area to accelerate consolidation process. Later steps will involve piles installed through compressible gyttja surcharged by fill. Placing fill induces soil subsidence and develops negative skin friction along piles (Fellenius, 1984). Therefore, an experimental programme has started in the Randers Harbour to investigate force distribution along uncoated and bitumen coated, steel and precast concrete driven piles installed in gyttja (Kania et al., 2023). Vibrating wire piezometers, magnetic extensometers and strain gauges along piles were employed.

The aim of this paper is to validate a numerical soil and interface model of soil-pile interaction using PLAXIS 2D software (Bentley Systems, 2022). The soil model was calibrated by simulating field results obtained after placing a 2 m high fill embankment. The soil-pile interaction was examined focusing on the results from the uncoated steel pile.

2 MATERIALS AND METHODS

2.1 Soil and ground water conditions

The boreholes and results of two CPTU soundings carried out prior to the pile installation indicated a soil profile consisting of an 1.1 m old fill underlain by an 8 to 10 m thick gyttja (a post-glacial organic clayey sandy silt of marine origin) layer on top of a post-glacial, marine, medium dense sand. The ground water table was located 0.4 m below the ground surface.

The average unit density, ρ, of gyttja was 1,430 kg/m³ ranging from 1,390 to 1,510 kg/m³. The water content, w_n, ranged from 70% to 110% and was close to the liquid limit. The undrained shear strength, $c_{u;FVT}$, determined from the field vane shear tests (adjusted by plasticity index factor of $\mu = 0.77$) ranged from 13 to 35 kPa with an average of 21 kPa. Consolidated undrained triaxial tests indicated an angle of friction $\varphi'_{tr} = 34°$ and an effective cohesion $c' = 8$ kPa.

Two oedometer tests performed on specimens from 2.6 and 4.5 m depth showed an average compression index, C_c, of 1.14, swelling index, C_s, of 0.15 and creep index for secondary compression, C_α, of 0.014. An average initial void ratio, e_{init}, was 2.9. Both specimens were found to be overconsolidated with an average

preconsolidation stress of about 20 kPa, which corresponds to an *OCR* at 2.6 and 4.5 m depths of about 2.1 and 1.7, respectively. An average coefficient of permeability, *k*, between initial and final (after placing the fill) effective stress was $9.5 \cdot 10^{-10}$ m/s.

2.2 Test setup and programme

Two instrumented Ø 406 diameter (8 mm wall thickness) closed-end steel piles (with and without bitumen coating) and two instrumented 400 mm square precast concrete piles were installed at the test site. All piles were instrumented with vibrating wire strain gauges and distributed fibre optic sensors. The steel and precast concrete driven piles were installed to the approximate depth of 13.8 m and 12.8 m, respectively.

The ground monitoring system consisted of vibrating wire piezometers and magnetic extensometers was installed at different depths prior to the pile installation.

The test programme consisted of two phases. The first phase focused on the pile installation effects and the second phase on placing of the fill. The embankment footprint area was 10 x 19 m and a slope of 45°. All piles were sleeved using a plastic pipe prior to placing of the fill to avoid load transfer from the fill to the piles. This paper addresses only the effects of the second phase.

Details about the test setup and programme are reported in Kania et al. (2023).

2.3 Numerical model

PLAXIS 2D V22.02 (Bentley Systems, 2022) was used for the numerical analysis. The uncoated steel test pile (STP1) was considered as a single pile in an axisymmetric model. The model had a radius of 1.5 m corresponding to the half spacing between the piles. The lower boundary was located 10 times the pile diameter below the pile toe elevation. A 15-noded triangular mesh elements with medium distribution and enhanced mesh refinement were employed in the model. The obtained average mesh quality was 0.9.

The soil stratigraphy and parameters are shown in Table *1*. The old fill and sand layer were modelled using a drained Mohr-Coulomb soil model. Their parameters were adopted from Belinchon et al. (2016), who performed a numerical analysis of a previous test setup located next to the one described in this paper. The gyttja layer was modelled using an undrained (type A) Soft Soil Creep model following the observations from the oedometer tests regarding the secondary compression. The model is described by modified compression index, $\lambda^* = \frac{C_c}{(1+e_0)\ln 10}$, swelling index, $\kappa^* = \frac{C_s}{(1+e_0)\ln 10}$, and creep index, $\mu^* = \frac{C_\alpha}{(1+e_0)\ln 10}$. An average coefficient of permeability obtained within the change in effective stress was initially used in the model. The flow conditions along the vertical boundaries of the model within gyttja layer were set as "closed" to prevent water flow across it.

Table 1. Model soil stratigraphy and parameters.

Parameter	Old fill	Gyttja	Sand
y_{min} [m]	0.0	-1.1	-9.5/-10.9[1)]
y_{max} [m]	-1.1	-9.5/-10.9[1)]	-17.86
γ [kN/m³]	18.0	14.3	16.0
e_{init} [-]	0.5	2.898	0.5
E'_{ref} [kN/m²]	10000	-	30000
ν [-]	0.25	0.15[2)]	0.3
c'_{ref} [kN/m²]	6	8	1
φ' [°]	25	34	35
k_x [m/day]	0.6	$0.0821 \cdot 10^{-3}$	0.6
k_y [m/day]	0.6	$0.0821 \cdot 10^{-3}$	0.6
λ^* [-]	-	0.1269	-
κ^* [-]	-	0.0333	-
μ^* [-]	-	0.0016	-

[1)] Two different levels due to inclination of the layer
[2)] ν_{ur}

The steel pile was modelled as a solid cluster using a Linear Elastic material model with an equivalent saturated unit weight of 16.7 kN/m³ (to represent a tubular steel pile) and stiffness of 210 GPa.

Interface elements, to simulate the soil-pile interaction, were created by adopting the method used by Belinchon et al. (2016). They were placed along the vertical and horizontal pile cluster limit and extended by 0.5 m in both directions at the pile toe level in order to avoid non-physical stress oscillations. The soil-pile interaction was defined by a strength reduction factor R_{inter}.

The fill was represented by uniformly distributed load with a magnitude of 36 kPa (applied in two 18 kPa load steps simulating half- and full completion of the fill embankment) located along the top, horizontal boundary between the pile cluster and the vertical boundary of the model.

The first construction stage represented the initial conditions. The second stage simulated completion of a half of the fill embankment (i.e. 1 m high). The next stage was a short (1 day) consolidation stage before a full embankment fill was completed (i.e. 2 m high). The last stage was a consolidation stage until all excess pore pressures in the geometry have reduced to a predefined minimum value of 1 kPa.

3 ANALYSIS

To calibrate the soil model, the dissipation of excess pore water pressure and ground settlement obtained in the field and in the finite element model were compared. In order to assess the soil-pile interaction the strength reduction factor was modified. Due to inclination of the gyttja layer, the bottom of the layer for calibrating the soil and soil-pile interaction model was assumed at 9.5 m and 10.9 m depth, respectively.

3.1 Excess pore water pressure dissipation

The measured (at 5.8 m depth) and simulated dissipation of excess pore water pressure with time after starting construction of the fill embankment is presented in Figure 1 The field records show unexpectedly low maximum excess pore water pressure of 17 kPa at the end of constructing the fill embankment and indicate stable readings after about 80 days after placing the fill. In general, a faster dissipation of excess pore water pressure was expected based on the results from the previous test setup reported by Sørensen (2015). This can be explained in part by the existence of vertical drains about 10 m from the test site. However, erroneous readings of the piezometers cannot be ruled out since all three piezometers installed in gyttja showed similar trend. In order to simulate the accelerated consolidation time and match the ground settlement with time, the coefficient of permeability was increased 5 times, i.e. $k_x=k_y=0.41\cdot10^{-3}$ m/day. Another way of simulating the observed settlements, without changing the coefficient of permeability, was to create a 7 cm thick vertical sand drain along the boundary of the model. The sand drain had a coefficient of permeability equal to 0.01 m/day. Both simulations are shown in Figure 1.

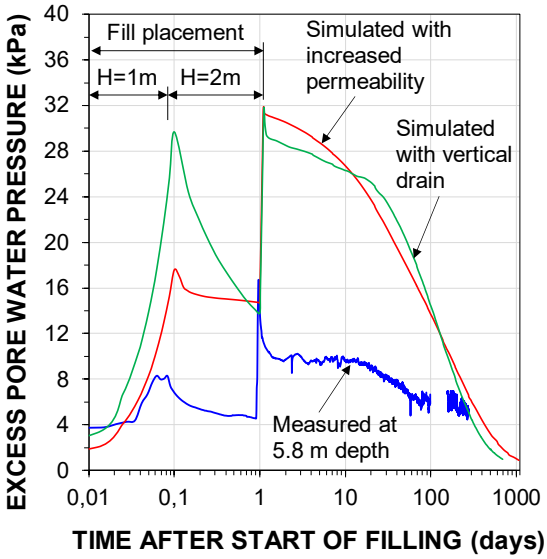

Figure 1. Excess pore pressure dissipation with time due to fill placement (measured data based on Kania et al. (2023)).

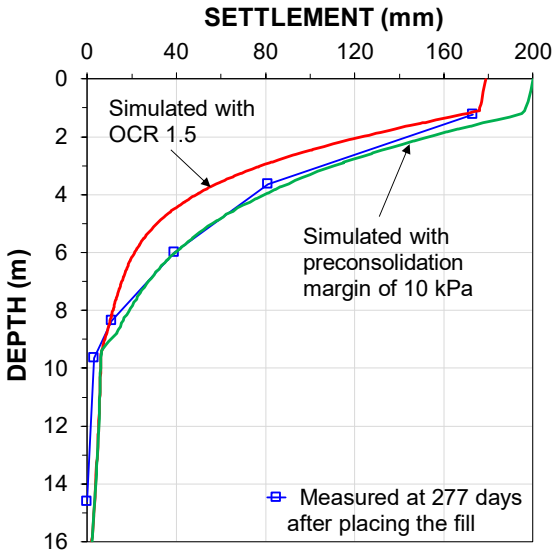

Figure 2. Measured and simulated settlement 277 days after placing the fill (measured data based on Kania et al. (2023).

3.2 Ground settlement

The apparent preconsolidation of the gyttja layer in the upper part was assumed to decrease with depth. Therefore, the OCR and the preconsolidation margin used in the PLAXIS models were reduced to 1.5 and 10 kPa, respectively. Figure 2 shows the measured and simulated soil settlement profile 277 days after placing the fill. The model with vertical sand drain served as a basis to compare two different ways of generating initial preconsolidation stress in PLAXIS. As shown in the figure, both methods provide good agreement with the measured data. By using the OCR method, the simulated soil settlement profile differs from the observed one within the gyttja layer, however, it has a perfect match at the top of the gyttja layer. In contrast, by using the preconsolidation margin method the soil settlement is slightly different only in the upper part of the curve. This difference can be explained in part by the fact that an OCR is a ratio function, while a preconsolidation margin is a stress difference.

3.3 Drag force distribution and negative skin friction along the uncoated steel pile

To calibrate the soil-pile interaction model, the strength reduction factor, R_{inter}, was adjusted using the PLAXIS model with the vertical sand drain and the preconsolidation margin of 10 kPa. The simulated and measured drag force distributions obtained 277 days after placing the fill are presented in Figure 3. As shown in the figure, the R_{inter} of 1.0 provided 2 times higher drag force than the measured value. However, a good agreement was obtained using the R_{inter} of 0.45. This finding is consistent with Potyondy (1961), who

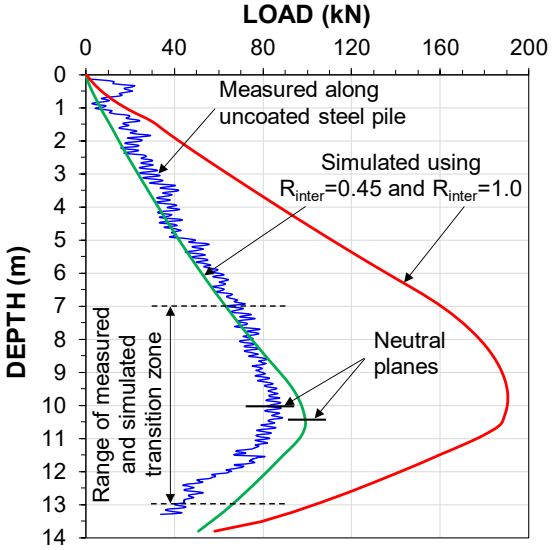

Figure 3. Measured and simulated drag force distributions (measured data based on Kania et al. (2023)).

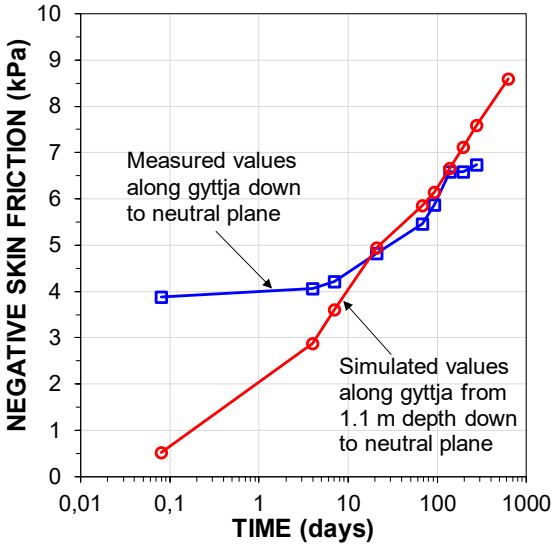

Figure 4. Measured and simulated development of negative skin friction with time after fill placement (measured data based on Kania et al. (2023)).

proposed a strength reduction factor of 0.5 (average value) between rough steel and cohesive granular material. A neutral plane, a point of force equilibrium, and a transition zone, at which negative skin friction gradually changes into positive shaft resistance, were located at similar depths in both, measured and simulated drag force distributions.

The development of negative skin friction with time after fill placement is presented in Figure 4. Both measured and simulated values are comparable. However, measured negative skin friction started to increase about 8 days after placing the fill, while the simulated curve shows a logarithmic relationship shortly after placing the fill. A possible explanation for this is that the shearing rate effect was not correctly simulated in the PLAXIS model.

4 CONCLUSIONS

The purpose of the current study was to determine a suitable constitutive and interface model of soil-pile interaction in gyttja using PLAXIS 2D software. This study has shown that it was possible to simulate the ground settlement and derive a more realistic dissipation of excess pore water pressure. The second major finding was that good agreement between measured and simulated drag force distribution was obtained using the strength reduction factor of 0.45. The current study has only examined the behaviour of a single uncoated steel driven pile in an axisymmetric model. Further work needs to be done to establish a response of different piles, e.g. concrete driven piles or bitumen coated piles. It would be also interesting to assess the group effect using PLAXIS 3D software.

ACKNOWLEDGEMENTS

The authors are grateful to Aarhus University for providing access to the electronic data from the field and laboratory tests. The funding provided by COWI is also highly appreciated.

REFERENCES

Belinchon, P., Sørensen, K. K. and Christensen, R. (2016). A case study of the interaction between a pile and soft soil focusing on negative skin friction using finite element analysis. In: *Proceedings of the 17th Nordic Geotechnical Meeting*, Reykjavik, Island, pp. 513-522.

Bentley Systems (2022). PLAXIS 2D, CONNECT Edition (V22.02).

Fellenius, B. H. (1984). Negative skin friction and settlement of piles. In: *Proceedings of the Second International Seminar, Pile Foundations, Nanyang Technological Institute*, Singapore, 12 p.

Kania, J. G., Sørensen, K. K. and Fellenius, B. H. (2023). The development of unit shaft resistance along driven piles in subsiding soil. *Canadian Geotechnical Journal*. https://doi.org/10.1139/cgj-2022-0694.

Potyondy, J. G. (1961). Skin friction between various soils and construction materials. *Géotechnique,* 11(4): 339-353, https://doi.org/10.1680/geot.1961.11.4.339.

Sørensen, K. K. (2015). Fuldskala pæleforsøg på Randers havn/Full-scale pile testing at Randers Harbour/, presentation at the Danish Geotechnical Society meeting (in English)

Proceedings of the XVIII ECSMGE 2024
GEOTECHNICAL ENGINEERING CHALLENGES
TO MEET CURRENT AND EMERGING NEEDS OF SOCIETY
© 2024 the Authors
ISBN 978-1-032-54816-6
DOI 10.1201/9781003431749-87
Open Access: www.taylorfrancis.com, CC BY-NC-ND 4.0 license

ECSMGE 24
XVIII EUROPEAN CONFERENCE ON SOIL MECHANICS AND GEOTECHNICAL ENGINEERING

Nonlinear numerical analysis of foundations on basis of plate load test results

Analyse numérique non linéaire des fondations sur la base du résultat du test de charge sur plaque

Y. Kirichek*, O. Tregub
Pridniprovska State Academy of Civil Engineering and Architecture, Dnipro, Ukraine
**kirichek.yurii@pdaba.edu.ua*

ABSTRACT: The nonlinear analysis method for shallow foundations is presented in the article. The study of more than 50 results of plate load tests on sandy and clayey soils allow the improvment of the settlement computation of the shallow foundation by the numerical method with the nonlinear dependence between stresses and deformations. Comparison of calculation data with the field test results showed that the proposed nonlinear numerical method provides the necessary accuracy of settlement computation in the nonlinear range of stresses up to $0.5q_{ult}$ in sand and up to $0.6q_{ult}$ in clay. The proposed method of nonlinear settlement calculation significantly reduces the impact of the difference between the behaviour of real soil and the ideal material assumed in the theory on the accuracy of computation.

RÉSUMÉ: La méthode d'analyse non linéaire par approximation successive pour les fondations superficielles est présentée dans l`article. L'étude de plus de 50 résultats d'essais de plaques de charge sur sols sableux et argileux nous permet d'améliorer le calcul du tassement des fondations superficielles par la méthode numérique avec la dépendance non linéaire entre contraintes et déformations. La comparaison des données de calcul avec les résultats des tests sur le terrain a montré que la méthode numérique non linéaire proposée fournit la précision nécessaire pour le calcul du tassement dans la gamme non linéaire de contraintes allant jusqu'à 0,5 q_{ult} dans le sable et jusqu'à 0,6 q_{ult} dans l'argile. La méthode proposée de calcul du tassement non linéaire réduit l'influence significative des différences entre le comportement du sol réel et le matériau idéal supposé dans la théorie.

Keywords: Shallow foundation; nonlinear numerical analysis; plate load test.

1 NONLINEAR COMPUTATION OF SHALLOW FOUNDATION

In theory, the key point in shallow foundation design is to determine the allowable bearing capacity based on the ultimate bearing capacity and settlements of the footing, and the calculated settlement is usually the determining factor. In fact, the task is to determine the required range of bearing capacity as the difference between the ultimate bearing capacity and the allowable bearing capacity. This is essentially the reserve bearing capacity of the foundation, which is the main determinant of the safety of the foundation design. However, foundation construction costs are significant, so the value of the reserve bearing capacity of the foundation directly affects the economic efficiency of construction, especially in difficult soils. The analyses carried out show that application of non-linear methods of settlement calculation and, as a consequence, justified increase of loads on spread footings from 1 m to 5 m in width and from 1 m to 5 m in depth on sand and clay contributes to cost savings ranging from 12 to 47%. Footings of medium dimensions (from 2 m to 3 m in width) rested on medium dense sand and stiff cohesive soils have greater cost savings than footings of larger and smaller dimensions (Kirichek and Tregub, 2015).

1.1 The purpose of the research

A reliable nonlinear method for computing the settlement of shallow foundation makes it possible to reasonably reduce the reserve bearing capacity of the foundation, which allows reducing the cost of construction with guaranteed reliability of the foundation. The purpose of this research is to improve the settlement computation process of the shallow foundation by the mixed numerical-experimental technique with the nonlinear dependence between loads and deformations.

1.2 Accuracy assessment of engineering nonlinear settlement methods

The nonlinear calculation methods of spread footings based on experimental studies of settlements had recently been developed by many authors, and this paper has used the results of some plate load tests: Cimbal and Sheikhnazari (2011), Kusner (2008), Klepikov (1996), Malyshev (1982, 1996), Shvets (2002) and Timchenko (2009). The size of the plates allows the plate load tests to be considered as full scale load tests, and field test results from real sites have also been used.

The computed settlements based on engineering methods were compared with the test results on sandy and clayey soils. Figure 1 shows a comparison of the results of the settlement calculation according to the nonlinear models and PLAXIS with the results of full scale load test on dense silty sand f`=36˚, c`=10kPa, E=34.7 MPa, γ=16.6 κN/m^3, R=0.53 MPa, P_u=4.65 MPa, (Kushner, 2008) and Figure 2 for full scale test on stiff loam, f`=23˚, c`=43 kPa, E=19MPa, γ=18.7kN/m^3, R=0.54 MPa, Pu=1.09 MPa, (Klepikov, 1996).

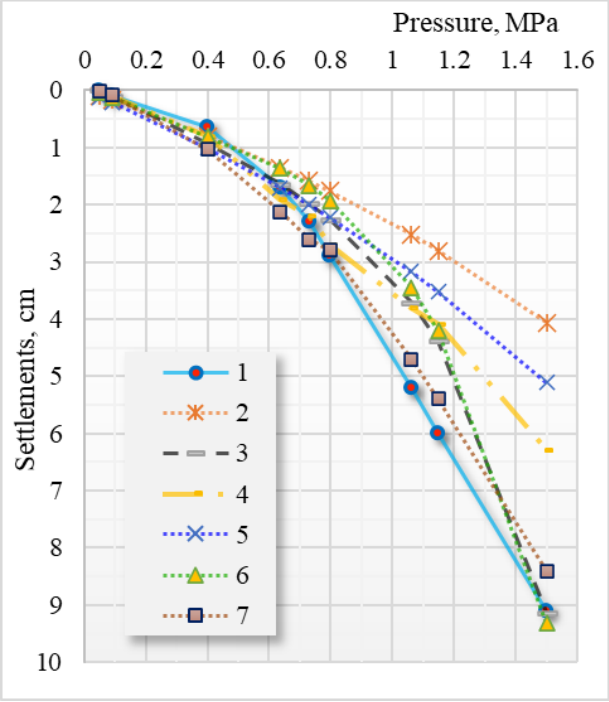

Figure 1. Comparison of computed settlements and test result for the plate of 1x1m, and 2.2 m depth on dense silty sand: 1 - the test; 2 - Klepikov's method; 3 - Malyshev's method (1982); 4 - Kushner's method; 5 - Popov's method; 6 - Malyshev's method (1996); 7 – PLAXIS 3D.

The results of numerical modelling of settlements in PLAXIS 3D of the considered experimental foundations at the applied pressure on the soil R<P<P_u corresponding to the nonlinear deformation stage are shown in Figures 3 and 4, where R (MPa) is the computed resistance of the foundation according to Ukrainian State Building Standard DBN V.2.1-2018, as linear limit in the applied pressure-settlement relationship and P_u is the ultimate bearing capacity (MPa).

The considered nonlinear models for calculating settlements were applied to homogeneous soil massifs within the depth of soil deformation zones, which, according to the results of calculations in Figures 3 and 4, ranged from 2.8B to 3.2B, where B is the width of the footings.

Engineering calculation methods showed a deviation of the calculated settlements from the test data of approximately 19% at the linear stage of settlement, and up to 45% beyond the linear stage of settlement as a function of load, with the error increasing as the load increases.

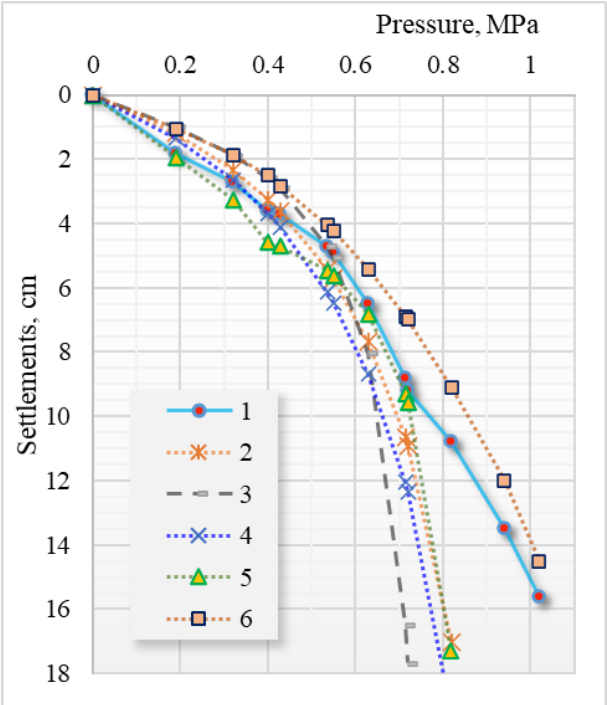

Figure 2. Comparison of computed settlements and test result for the plate of 1.4x1.6 m, and 0 m depth on stiff loam: 1 - the test; 2 - Klepikov's method; 3 - Malyshev's method (1982); 4 - Popov's metod; 5 - Malyshev's method (1996); 6 – PLAXIS 3D.

The calculation by the numerical finite element method in PLAXIS 3D using the the linear-elastic perfectly-plastic Mohr-Coulomb model showed the best convergence with the settlement curve of the full scale load test, compared to analytical methods. The deviation of PLAXIS 3D data from the full-scale settlement at pressures $R < P \leq 1.5R$ was 16-21%.

Insufficient accuracy of nonlinear methods for settlement calculations is obviously one of the

reasons for limiting the loads on foundations to 1.2R in the State building codes of Ukraine. The engineering method of Malyshev (1996), which is an improvement of the previous method (1982), can be further developed by the use of the empirical relationship between settlements, loads, soil properties and foundation dimensions on the basis of the comparison of test results and calculated settlements with different nonlinearity parameters.

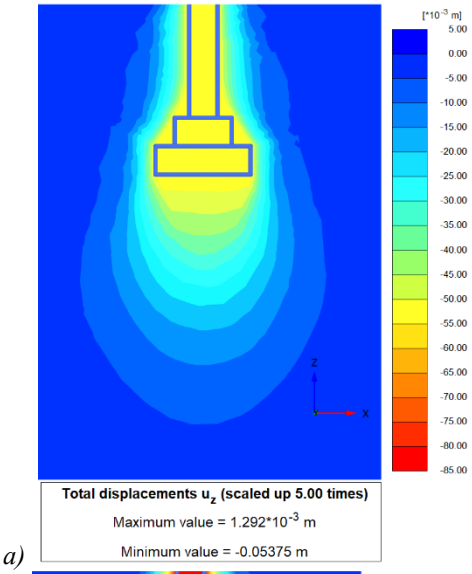

a)

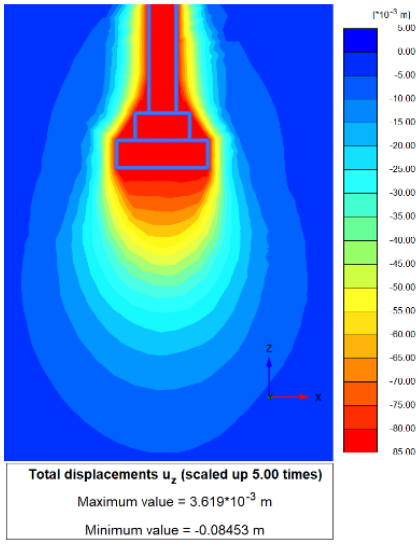

b)

Figure 3. Numerical modelling of the settlement of 1x1m plate at the depth of 2.2m on dense silty sand: a - pressure P=1.15 MPa, settlements S=5.4 cm; b - P=1.5 MPa, S=8.5 cm.

1.3 Improving the method of the nonlinear settlement computation

In this research, the use of the Malyshev (1996) method for calculating settlements with a non-linearity parameter has been substantiated. In order to make more rational use of the bearing capacity reserves of the shallow foundations in the design, it is necessary to obtain pressure-settlement dependencies from the full scale test data in the formula:

$$S = S_R \left\{ 1 + \left(\frac{P_u - R}{P_u - P} \right)^n \cdot \frac{P - R}{R - \sigma_{zg,0}} \right\} \qquad (1)$$

where S_R (cm) is the settlement of the footing under pressure corresponding to the computed resistance of the foundation R (MPa), as linear limit in the applied pressure-settlement relationship;

P is the applied pressure on the soil (MPa);

$\sigma_{zg,0}$ is overburden pressure (MPa);

n is a nonlinearity parameter which characterizes the nonlinear dependence of the settlement on the applied pressure, and which can be established empirically.

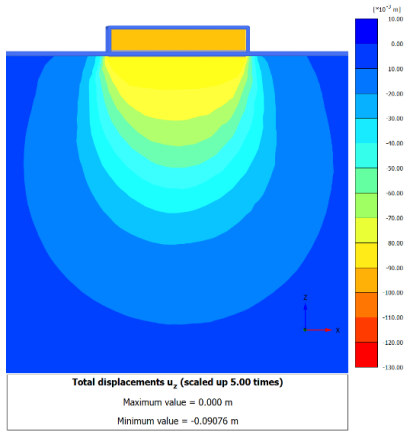

a)

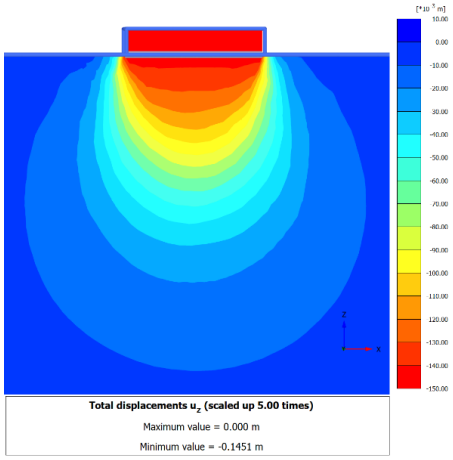

b)

Figure 4. Numerical modelling of the settlement of 1.4x1.6 m plate at the depth of 0 m on stiff loam: a - P=0.82 MPa, S=9.1 cm; b - P=1.02 MPa, S=14.5 cm.

1.4 Determination of empirical parameters of the nonlinear model

The study of pressure-settlement curves for full scale load tests on different types of soil was carried out to determine the dependence of the nonlinearity parameter n on the characteristics of the foundations. The nonlinearity parameter values were determined

by comparing the calculated settlements with the test results. In total, more than 50 data from field tests and full-scale load tests were examined. Some results presented in Figures 5-8 were used in the nonlinear model calculation.

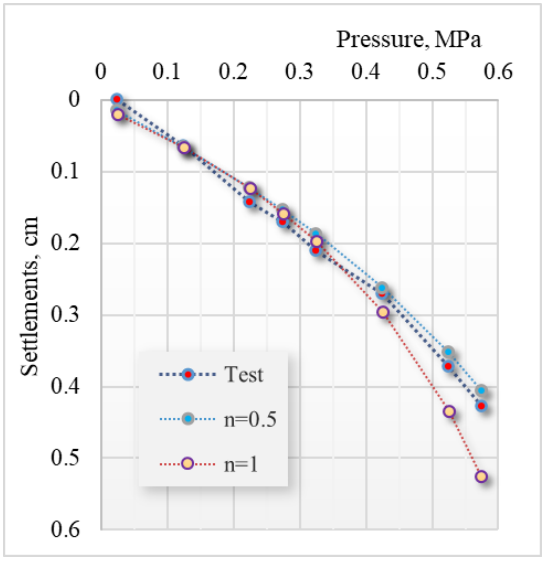

Figure 5. The nonlinearity parameter n for a round plate with diameter of 1 m, and 0.5 m depth on dense fine sand: f`=36$^0$, c`=4 kPa, E=86 MPa, γ=17.99kN/m^3, n=0.5 (Shvetz, 2002).

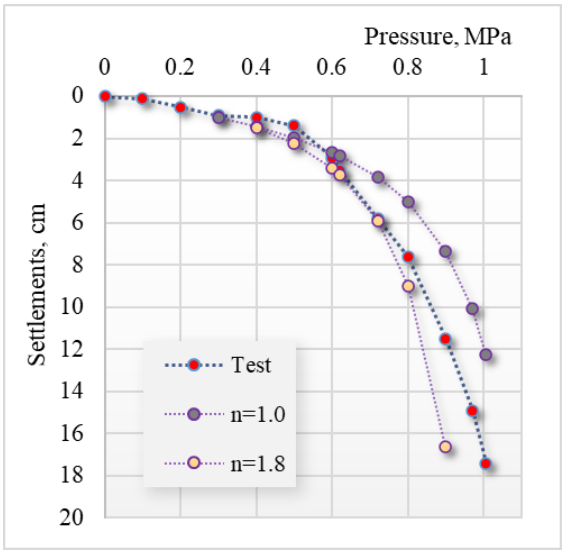

Figure 6. The nonlinearity parameter n for plate of 1.2 x 2.4 m and 0 m depth on semi-solid loam: f`=32.2, c`=20 kPa, γ=19.6 kN/m^3, n=1.8 (Timchenko, 2009).

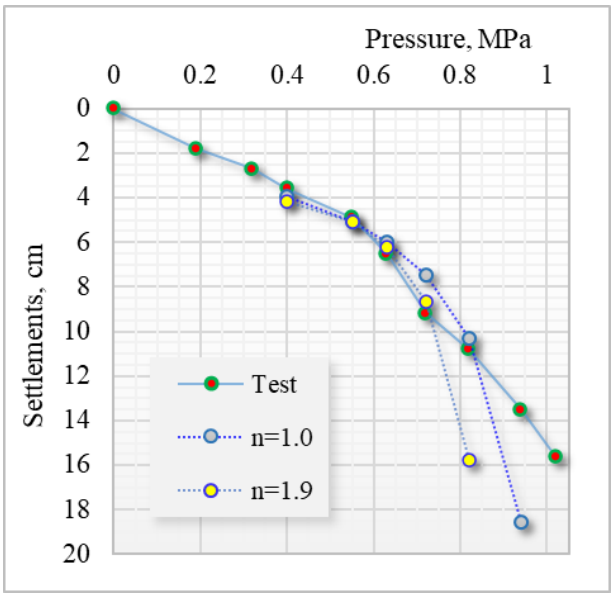

Figure 7. The nonlinear parameter n for the plate of 1.4 x 1.6m, and 0 m dept on semi-solid loam: f`=23$^0$, c`=43 kPa, E=13.1 MPa, γ=18.7 kN/m^3 n=1.9, (Klepikov, 1996).

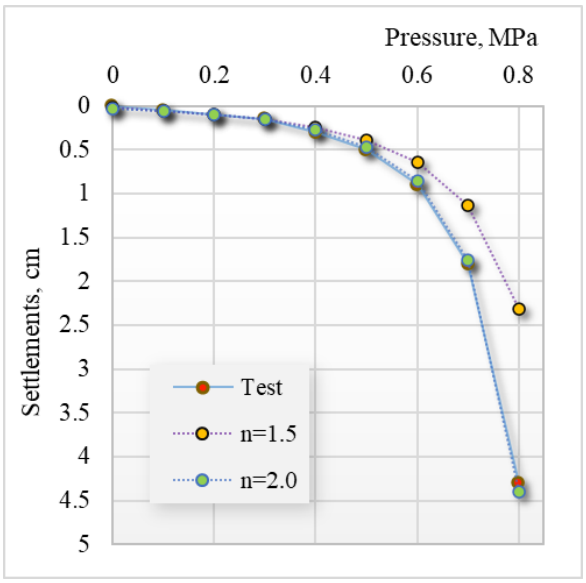

Figure 8. The nonlinearity parameter n for the plate of 1x1m, and 0.9 m depth on dense coarse sand: f=33^0, E=20.7 MPa, γ=20 kN/m^3, n=2.0 (Cymbal, 2011).

The factors influencing the adopted computational model were determined using the method of correlation analysis. On the basis of these data, regression equations were obtained that reflect the dependencies of the nonlinearity parameter n on the characteristics of the foundations and the relative foundation depth D/B. The non-linearity parameter equation was obtained:

$$n = -0{,}306 + 1{,}175\frac{P_u}{P_{u0}} + 0{,}177\frac{D}{B} - \\ -0{,}052\left(\frac{P_u}{P_{u0}}\right)^2 - 0{,}051\frac{P_u}{P_{u0}}\frac{D}{B} + 0{,}055\left(\frac{D}{B}\right)^2, \quad (2)$$

where: P_{u0}=1MPa;

D is footing depth;

B is footing width.

The determination coefficients of the equations were r^2 = 0.7 – 0.9, which indicates a sufficiently satisfactory agreement between the computed data and the field test results.

Figure 9 shows the dependences n=f(Pu, D/B), calculated using formulas (1, 2). It is noted that with an increase in the relative depth of foundation D/B and the value of the bearing capacity of the foundation, the nonlinearity parameter on the settlement-load diagrams increases.

Figures 10-13 show the results of comparing the calculated settlements according to the proposed nonlinear model for the calculation of settlements of spread foundations using the obtained empirical equation with the field data and full scale load test results on sandy and clayey soils.

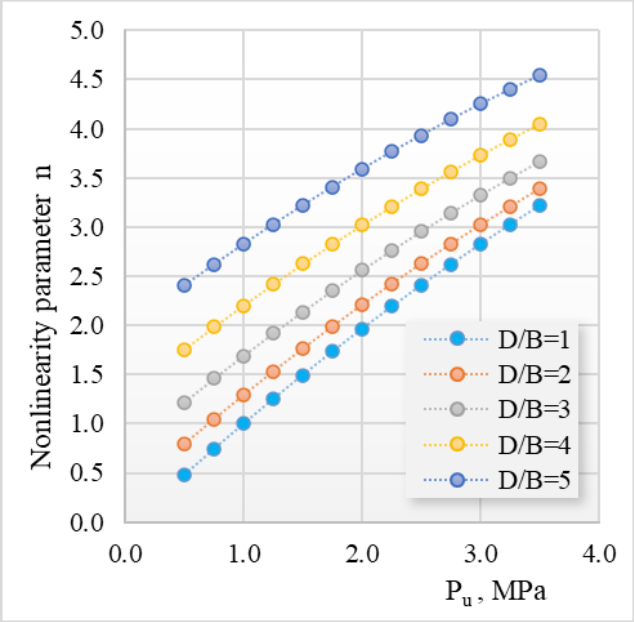

Figure 9. Dependences of the nonlinearity parameter n on the ratio of the depth of embedment to the width of the foundation D/B and the ultimate bearing capacity P_u.

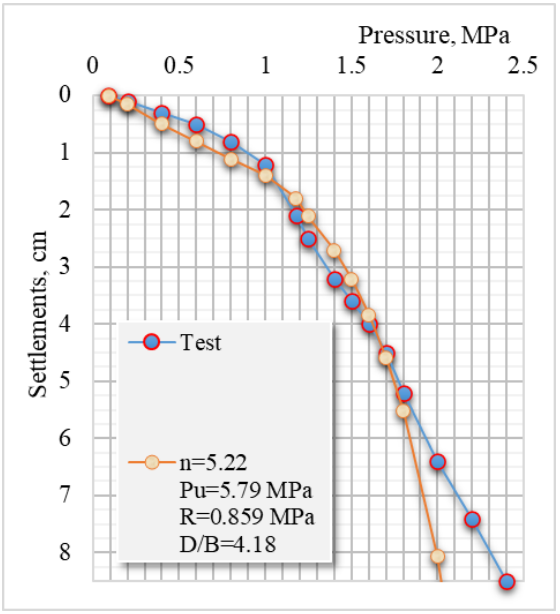

Figure 10. Comparison of computed settlements and full scale load test result for the plate of 1.0 x1.0 m, and 4.18 m depth on the medium dense silty sand: f`=37$^0$, c`=10kPa, E=53 MPa, γ=16.8 kN/m^3 (Kushner, 2008).

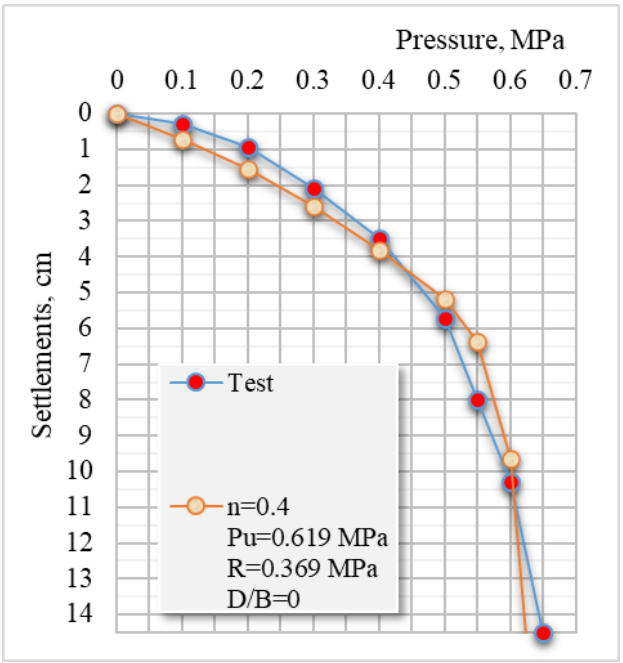

Figure 11.Comparison of computed settlements and field test result for the plate of 1.2 x 1.4 m, and 0 m depth on the firm clay: f`=24$^0$, c`=45 kPa, E=20 MPa, γ=19.6 kN/m^3, (Timchenko, 2009).

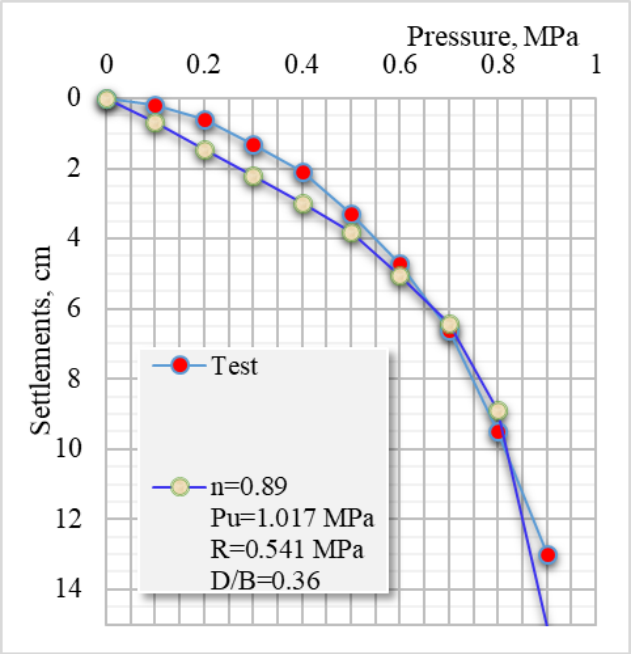

Figure 12. Comparison of computed settlements and field test result for the plate of 1.4 x 1.6 m, and 0.5 m depth on the stiff loam: f`=27$^0$, c`=57 kPa, E=24 MPa, γ=19.8 kN/m^3 (Timchenko, 2009).

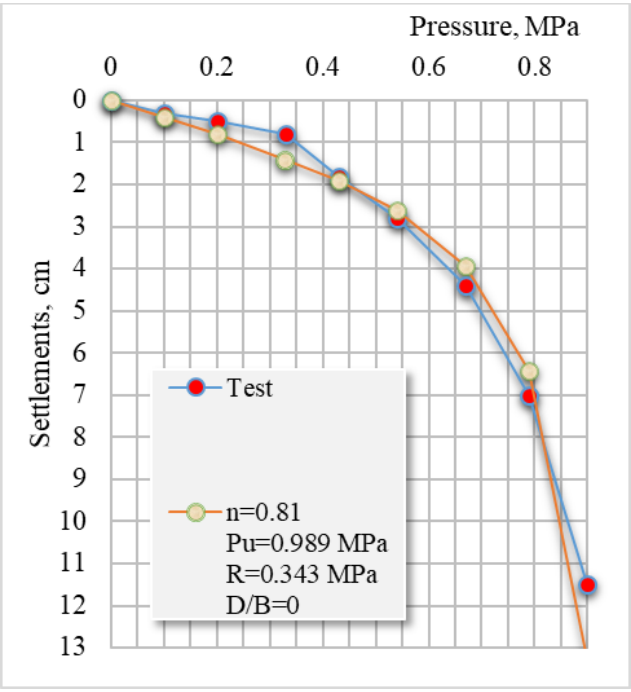

Figure 13. Comparison of computed settlements and field test result for the plate of 1.2 x 2.4 m, and 0 m depth on the stiff loam: f`=35$^0$, c`=28 kPa, E=34MPa, γ=19.2 kN/m^3 (Timchenko, 2000).

The comparative analysis indicated that the adopted nonlinear model allowed performing calculations of settlements of spread foundations with sufficient accuracy for practical use in the pressure range of up to $0.4P_u$ on sandy soils and up to $0.6P_u$ on clayey soils.

4. CONCLUSION

The conducted research makes it possible to propose mixed numerical-experimental technique for computing settlements of spread foundation on the basis of full scale test results characterizing the non-linear relationship between loads and settlements.

ACKNOWLEDGEMENTS

The authors are grateful to all researchers who have provided the results of the tests.

REFERENCES

Cimbal, S.Y., Sheikhnazari, H.R. (2011) Static testing of pad foundations on soil of Iran, In: *Foundation,* v.32, KNUBA, Kyiv, Ukraine, pp. 159-164.

Kirichek, Y., Tregub, A., (2015) Limit Sate Design of Shallow Foundation in *Fifth International Symposium on Geotechnical and Risk (ISSGR*), Rotterdam, The Netherlands, pp. 374 – 379.

Klepykov S.N., (1996), *Calculation of the constriction on deformable soil*, NIISK, Kyiv, Ukraine, 202 p.

Kushner, S.G., (2008), *The computation of the foundation deformation*, IPO Zaporozhye, Ukraine, 496 p.

Malyshev, M.V., Nikitina, N. S., (1982) Computation of foundation settlements with nonlinear dependence between stresses and deformations in soils, *Foundations and soil mechanics,* 2, pp. 21–25.

Malyshev, M.V., (1996) Prognosis of foundation settlements of shallow deposits with the use of both criteria of limit states, *Foundations and soil mechanics*, 1, pp. 2–4.

Shvetz, V.B. (2002) On the issue of assessing the stressed deformed state of layered soil foundations, In: *Construction, materials science, mechanical engineering,* PDABA, Dnipropetrovsk, Ukraine pp. 34-38.

Timchenko, R.A. (2009) Interaction of mat foundation with a non-uniformly deformable base under complex loading: In *Thesis of Doctor of Engineering Sciences,* Dnepropetrovsk, Ukraine, 387 p.

Proceedings of the XVIII ECSMGE 2024
GEOTECHNICAL ENGINEERING CHALLENGES
TO MEET CURRENT AND EMERGING NEEDS OF SOCIETY
© 2024 the Authors
ISBN 978-1-032-54816-6
DOI 10.1201/9781003431749-88
Open Access: www.taylorfrancis.com, CC BY-NC-ND 4.0 license

ECSMGE 24
XVIII EUROPEAN CONFERENCE ON SOIL MECHANICS AND GEOTECHNICAL ENGINEERING

Multidisciplinary design optimisation of vibro stone columns and dynamic replacement

Optimisation multidisciplinaire des colonnes ballastées et substitution dynamique

B. Knabe*, C. Tinat
Menard GmbH, Seevetal, Germany

M. Rosenberg
TU Braunschweig, Institut für Geomechanik und Geotechnik, Braunschweig, Germany

**bknabe@menard.gmbh*

ABSTRACT: The evaluation of construction processes regarding environmental aspects is becoming more important and is of particular interest for the construction business. An evaluation method for stone columns using vibro replacement technique (VRSC) and dynamic compaction with execution of large stone pillars, called dynamic replacement (DR), is presented. The analysis includes both technical and environmental criteria. Life cycle assessment (LCA) is used to evaluate the environmental criteria. The global warming potential (GWP) is considered as relevant indicator because of its informative value regarding climate change. The result of the two analysed ground improvement methods considered here are columns consisting of granular material. With DR an additional improvement can be obtained in the underlying layers through the transmission of the energy of the weight at depth. The results of a logistic centre case study show advantages of DR in terms of environmental impact. With the defined maximum settlement of 1.5 cm, the DR pillars can save approx. 60 % of the GWP compared to the VRSC technique. If larger settlements are allowed, the environmental impacts of both methods can be further reduced. In the future, this decision will have to be made by the investors. In the present example of a so-called "positive footprint building", the multiobjective optimisation for the ground improvement is carried out with the criteria of minimising the settlement as well as the GWP to reach both targets.

RÉSUMÉ: L'évaluation de l'impact environnemental dans les processus de construction devient de plus en plus important et présente un intérêt majeur pour le secteur de la construction. Cet article présente une méthodologie pour évaluer sur un plan environnemental et technique les colonnes ballastées avec une aiguille vibrante (VRSC), et du compactage dynamique avec installation de colonnes de gros diamètre de matériaux granulaires compactés, appelée substitution dynamique (DR). L'analyse du cycle de vie (LCA) s'avère être la méthode la plus appropriée pour l'évaluation des aspects environnementaux. Le potentiel de réchauffement planétaire (PRP) semble être une mesure pertinente pour ces aspects, ayant l'avantage d'englober plusieurs phénomènes impactant le climat. Les deux méthodes d'amélioration des sols examinées ici produisent des colonnes granulaires. La substitution dynamique génère une amélioration significative des propriétés du sol au-dela la base de la colonne du fait de l'énergie dissipée par la masse lors de l'impact. Avec l'étude de cas d'un centre logistique, les résultats de l'analyse montrent les avantages de la substitution dynamique en terme d'impact environnemental. Avec un tassement admissible de 1,5 cm maximal spécifié, la substitution dynamique permette d'économiser environ 60 % du PRP par rapport aux colonnes ballastées. Si des tassements plus importants sont acceptés, les impacts environnementaux des deux méthodes peuvent être encore réduits. À l'avenir, cette décision devra être prise par les investisseurs. Dans le présent exemple d'un bâtiment à empreinte positive, l'optimisation multiparamétrique est réalisée avec pour objectif de minimiser le tassement ainsi que le PRP pour être conforme aux spécifications.

Keywords: Ground imrovement; life cycle assessment; multiobjective optimisation; dynamic replacement.

1 INTRODUCTION

Climate change and the global warming is one of the biggest challenges of our time and of the future generations. Industrial societies in particular bear a significant responsibility to achieve global climate targets and the necessary mitigation of impacts.

In geotechnical designs of ground improvement works or typical piling, the emissions of the appropriate methods and the construction process itself have not yet been given high priority when selecting the method and awarding contracts. However, a variant investigation with a qualified analysis of the environmental impact based on a life

cycle assessment could already be carried out in the early planning stage and thus be included in the decision process of investors. For this purpose CO_2 balancing will play a decisive role in the evaluation of geotechnical concepts.

Ground improvement allows a wide range of technically equivalent methods with different materials and equipment. Technically equivalent solutions lead to different environmental impacts which have only been marginally evaluated so far.

Under uniformly loaded structures such as embankments and slabs-on-grade, stone columns are installed on a regular grid to improve the soil parameters on a defined area. There is not only one geotechnical solution to reach the settlement criteria, but rather a variety of possibilities by varying the grid, diameter or column length. Furthermore, there are different methods in terms of machinery and type of pushing the material into the ground to form the column.

A multidisciplinary evaluation method is presented for two methods of stone column installation. This includes the disciplines of geotechnical engineering and environmental management. Geotechnical engineering considers technical aspects such as bearing capacity and settlement behaviour after treatment. Environmental management identifies the reduction potential regarding environmental impacts by means of a life cycle assessment. The combined method enables the evaluation of individual solutions and optimisation.

2 METHODOLOGY

2.1 Life cycle assessment

The life cycle assessment is a method for the ecological balancing of a product system. The LCA considers the relative environmental impacts of a product system over its entire life cycle. The principles and framework conditions of a life cycle assessment are specified in EN ISO 14040. The EN ISO 14044 provides detailed instructions for drawing up a life cycle assessment. The environmental impacts are quantified using various impact indicators that describe the different environmental impacts.

LCA has become established in the construction industry for quantifying and evaluating environmental impacts (Röder and Finkbeiner, 2021) which can thus lead to optimisation respecting environmental impacts. The LCA includes in addition to the used materials, for example, the handling of construction vehicles during the construction stage (Ays and Geimer 2017). For processes without the use of concrete, the use of fuels and transport accounts for a significant part of the CO_2 consumption, see Figure 1 (Bunieski et al., 2023). Therefore, not only the material consumed can be compared.

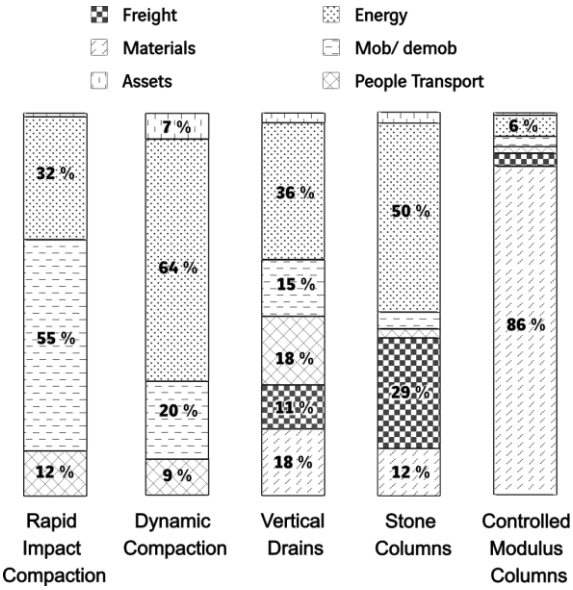

Figure 1. Embodied Carbon Breakdown per Ground Improvement Technique (Bunieski et al., 2023).

So far, no specific regulations exist for the preparation of life cycle assessments of construction processes. For this reason, the presented study is also based on EN ISO 14040 and EN ISO 14044 for the preparation of the LCA. These standards were designed for balancing product systems. From the authors' point of view the basic assumptions can be used and transferred for the preparation of a life cycle assessment for special civil engineering measures.

In general, several impact indicators could be considered in a life cycle assessment (LCA). In this study the CO_2 emissions were analysed. In an LCA, the CO_2 emissions are described by the global warming potential (GWP) indicator. The GWP is calculated by multiplying the quantity by the emission factor. The value is given in tonnes of CO_2 equivalent (tCO_2eq). For example, the calculation of the GWP of the gravel volume:

$$\mathrm{GWP}_{\mathrm{gravel}}[\mathrm{tCO_2eq}] = \mathrm{gravel}\,[\mathrm{m^3}] \cdot \mathrm{emissionfactor}\,[\frac{\mathrm{tCO_2eq}}{\mathrm{m^3}}]$$

The emission factor is taken from a database such as the German ÖKOBAUTDAT. It is also possible to use a product-specific emission factor like an environmental product declaration (EPD). The GWP in this study is calculated for the materials used, the fuel for transport, the site facilities and the fuel for the equipment.

2.2 Multiobjective optimisation

Multiobjective optimisation can be used in the planning of a structure by automatically checking a big amount of different parameter combinations and therefore supporting the decision process. Multiobjective optimisation is particularly suitable for complex systems that are influenced by several variables and that are strongly impacted by only one variable.

In geotechnical engineering only random variants with few selected parameter combinations are calculated and compared currently (Seitz and Grabe, 2018).

Multiobjective optimisation considers two or more objective functions to be optimised, which can also compete. Objective functions in civil engineering can refer to the minimisation of financial costs, materials, construction time, energy used and thus also to the minimisation of resources. Restrictive conditions can be stability verifications, settlement criteria or other limitations. (Seitz and Grabe, 2018)

The solution of a multiobjective optimisation usually has no absolute minimum or maximum. There is no solution that fulfils all objective functions, but a solution set. This solution set is called pareto set and consists of solutions that dominate other solutions but are not dominated. A dominating solution in this case means that a solution is better in at least one objective and yet not worse in any other objective. A solution is not dominated if one solution is better than another in one objective, but the other solution is better in another objective and the two solutions are therefore not comparable. Accordingly, the pareto set describes all optimal solutions that cannot be improved in one objective without simultaneously degrade another objective. The pareto set is represented graphically by the pareto front in Figure 2. The grey dots represent all solutions from the parameter combinations, the pareto-optimal solutions are highlighted with red circles. (Knowles, 2008)

The presented multidisciplinary optimisation approach can be understood as a special form of multiobjective optimisation. It includes the disciplines of geotechnical engineering and environmental management. The discipline of geotechnics can be considered, for example, through the criteria of stability or serviceability of the structure. Environmental management deals with the environmental impacts caused by the execution of ground improvement works within the framework of a life cycle assessment.

The considered geotechnical criterion is settlement, which must not exceed a limit value or should be minimised. The LCA sets its criteria through various impact indicators which should also be minimised.

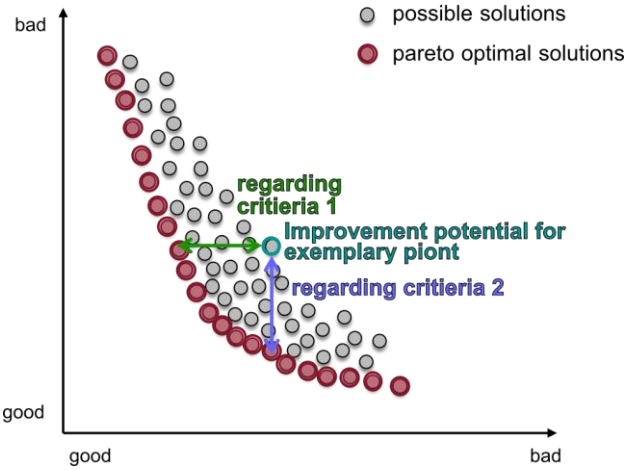

Figure 2. Example for possible pareto-front.

2.3 Technical and environmental aspects of the ground improvement methods

The ground improvement methods considered in this case study are stone columns using vibro replacement technique (VRSC) and dynamic replacement (DR). Both methods are briefly explained below as the basis for the following life cycle assessments.

Classical stone columns are formed by inserting a vibratory probe to incorporate granular material into the ground and create vertical inclusions with small diameters of approx. 0.5 - 0.8 m.

Stone columns are formed by inserting a hydraulic or electric vibroflot equipped with a pressure chamber equipment using air as a jetting fluid. The execution of stone columns requires a rig, as well as a feeding unit for filling the material. Various equipment combinations are available, depending on the diameter and depth of the columns.

Dynamic replacement (DR) is an extension of dynamic compaction to highly compressible and weak soils. In this application, the tamping energy drives granular material down into the compressible soils to form large diameter soil reinforcement columns (with diameter around 2 to 3.5 m). Additional improvement can be obtained in the underlying layers by transferring the energy of the weight at depth. This method combines advantages from both dynamic consolidation and stone pillars by creating large-sized dynamic replacement inclusions with high internal shear resistance. Dynamic replacement columns are formed by dropping a 10 to 35 tons pounder from heights ranging from 10 to 30 m. With this technique replacement ratios of up to 20 to 25 % can be achieved.

In the case of weakly permeable soils the columns are made in several phases so that excess pore water

pressure can dissipate. For this technique a crawler crane is used and the filling for the craters is done by a crawler, see Figure 3. Recycled crushed concrete material can be used as fill material which is an advantage over the deep vibrator of the VRSC technique.

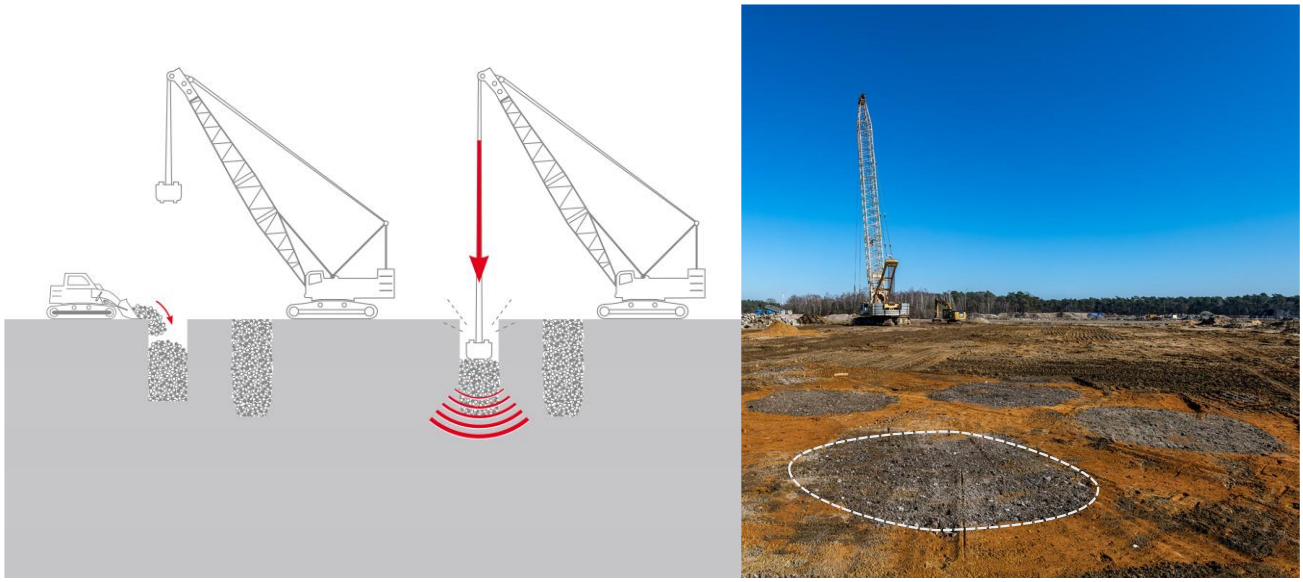

Figure 3. left: principle of DR with crane and compaction below; right: surface of DR pillars in the Dorsten project.

3 APPLICATION EXAMPLE LOGISTICS CENTRE

The developed method was used for the foundation of a logistics centre which requires piling or ground improvement. A high-bay warehouse for Levi Strauss & Co. is being built on a former coal mine area in Dorsten-Wulfen in Germany. The Positive Footprint Wearhouse® is a representative example of sustainable construction. Materials and processes that save resources as much as possible are used and the core of the building is realised according to the Cradle-to-Cradle (C2C) principle.



Figure 4. Levi Strauss & Co Positive Footprint Wearhouse®.

The existing soil was too soft to reach the settlement requirements of the structure. Therefore, piling and different ground improvement methods were considered for the stabilisation of the slab and the single foundations. Finally, the VRSC and DR technique were analysed to achieve the required stiffness of the ground in the high-bay part of the warehouse.

The design method according to (Priebe, 1995) is a frequently used method to estimate the behavior of the reinforced soil. The DR can also be designed as granular columns according to the basic assumptions of Priebe. However, plastic deformations and bulking of the pillars can be neglected because of the geometry (large diameter and shorter length).

4 MULTIDISCIPLINARY ASSESSMENT METHOD

The multiobjective optimisation considers the settlement and the environmentally impact. Accordingly, two objective functions are used: minimising the settlement and the GWP.

The variable design parameters are the column diameter, the column spacing and the column length. The optimisation problem is solved by a self-developed algorithm using the software package Matlab. This calculates every possible parameter combination of the three variable parameters. For each possible parameter combination, the settlement and the GWP are calculated. The settlements are calculated with an implemented function for an infinite spread load. In the calculation the improved stiffness of the soil after treatment are applied according to the Priebe approach (Priebe, 1995). The paretoQS function is used to determine the pareto-optimal solutions (Tom R, 2022).

The parameters are varied in different limits. In the script of the stone columns about 3,900 and of the DR about 5,300 parameter sets are calculated.

To decide on a solution, it has to be weighed up which settlements are acceptable in order to reduce the GWP (definition of settlement criterion). A larger grid spacing and a smaller column diameter can reduce the column volume and the construction time whereby the GWP is reduced. Varying the grid, the column diameter or the column length show the optimisation potential and the multitude of optimal solutions. Based on the selection of a priority, a solution can be chosen from a set of optimal solutions.

The result of this multiobjective optimisation for stone columns, with the objective functions of GWP and settlement, is shown in Figure 5. Each marker represents a parameter set for the VRSC design.

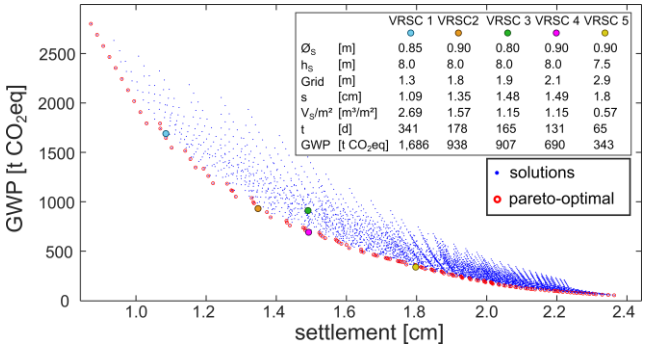

Figure 5. Multiobjective optimisation vibro replacement stone columns (GWP vs. settlement).

A reference design and an optimised design are selected to compare the results indicated by the green and pink circles respectively. The reference design (VRSC 3) has been chosen prior to optimisation as possible VRSC layout in order to demonstrate the optimisation possibilities of the algorithm. The reference solution is a non pareto-optimal solution. More than 200 t CO_2 equivalent can be saved with the VRSC 4 solution with almost the same settlement. The construction time of the VRSC is calculated based on the installation performance which depends on the column length. The diameter of the columns is not included in the calculation of the construction time. However, the diameter is considered by the volume of fill material.

Figure 6 shows the results of the multiobjective optimisation for the DR pillars with the objective functions of the GWP and the settlement.

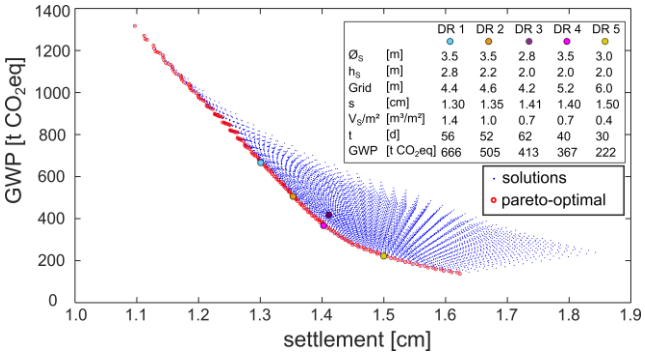

Figure 6. Multiobjective optimisation DR-pillars (GWP vs. settlement).

The reference solution DR 3 is a non pareto-optimal solution, there are solutions with the same settlement, but with a smaller GWP. By choosing the solution DR 4, about 50 t CO2 equivalent can be saved compared to DR 3.

The lengths of the pillars of the pareto-optimal solutions are shorter compared to the VRSC. The underlaying soil layers are compacted by the pounder and represent an additional improvement of the deeper ground. The construction time is calculated via the specified installation performance. The installation performance of the DR pillars is significantly dependent on the grid spacing and soil conditions. Consequently, a larger grid spacing, in addition to a low material requirement, contributes significantly to minimising the GWP.

The pareto-optimal solutions of both methods are shown in Figure 7. The DR pillars shows the best solutions possible to the optimisation problem for minimising settlement and GWP. With a settlement criterion of 1.5 cm applied for this study, the DR columns can save about 60 % of the GWP compared to the VRSC.

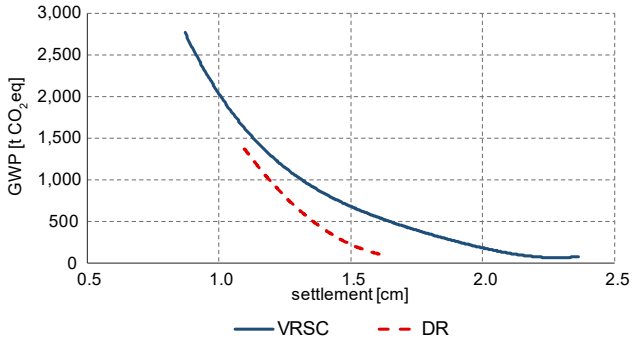

Figure 7. Comparison of the global warming potential of the pareto-optimal solutions (criteria: GWP – settlement).

Considering the entire building the ground improvement has only a small share of the GWP of the overall balance - with piling it would be much more. This kind of building has a GWP of around 15,000 to

20,000 t CO_2 equivalent only from the materials used in the shell, without including the construction process. The GWP of the ground improvement with DR pillars of 285 t CO_2 equivalent has a share of 1 to 2 % of the GWP of the material used in the building shell. The environmental impact and thus the savings potential in the structural engineering part is significantly higher. The optimisation of ground improvements in terms of environmental impact is nevertheless important. Due to the many variation possibilities savings in GWP are possible without increasing settlement or decreasing the bearing capacity. Further, saving GWP means also saving costs. Therefore, a contribution to saving resources and emissions can also be made in foundation engineering.

5 CONCLUSIONS

Overall, the developed evaluation method is a good way to find optimal solutions for the considered ground improvement methods. An increase of the maximum allowable settlements by a few millimetres can reduce the environmental impact to a minimum. The multiobjective optimisation can be performed with the criteria of settlement and global warming potential for VRSC and DR. The evaluation method can be applied to other projects, as only the input parameters of the optimisation code (like soil parameters and layers). The determination of the construction time is sufficiently accurate. A determination of the construction time by means of a construction process model would include all influencing aspects on the construction time and thus lead to an even more accurate result. The presented evaluation method represents an easy-to-use and practical application to optimise the design of ground improvement methods about settlement and environmental impacts. The extension to other techniques is given.

REFERENCES

Ays, I. and Geimer, M. (2017). CO2e Quantifizierung von mobilen Arbeitsmaschineneinsätzen im Erdbau, Steinbruch, Straßen- und Hochbau*,* CO2e quantification of mobile machine operations in earthworks, quarries, road construction and building construction (in: german)*,* In: *Hybride und energieeffiziente Antriebe für mobile Arbeitsmaschinen: 6. Fachtagung, 15. Februar 2017,* Wissenschaftlicher Verein für Mobile Arbeitsmaschinen, KIT Scientific Publishing, Karlsruhe, Germany, pp. 145–161.

Bunieski, S.; Boyd, G. and Isenegger, N. (2023). Methodology to calculate and compare Embodied Carbon associated with Ground Improvement techniques. *Geo Saskatoon 2023*, Saskatoon, Canada.

Röder, A. and Finkbeiner, M. (2021). Was jeder im Bauwesen über Ökobilanzen wissen sollte, What everyone in the construction sector should know about life cycle assessments (in: german), In: *Nachhaltigkeit, Ressourceneffizienz und Klimaschutz: Konstruktive Lösungen für das Planen und Bauen: aktueller Stand der Technik*, Wilhelm Ernst & Sohn, Berlin, Germany, pp. 137–145.

Knowles, J.; Corne, D. and Deb, K. (2008). Introduction: Problem Solving, EC and EMO, In: Knowles, J. et al. [Ed.] *Multiobjective Problem Solving from Nature*. Berlin, Heidelberg: Springer Berlin Heidelberg, Germany, pp. 1–28. https://doi.org/10.1007/978-3-540-72964-8_1.

Priebe, H. J. (1995) Die Bemessung von Rüttelstopfverdichtungen, The design of vibro compaction (in: german), *Bautechnik 72. 1995, Nr. 3*, pp. 183–191.

Seitz, K.-F. and Grabe, J. (2018). Einsatzmöglichkeiten der multikriteriellen Optimierung im digitalen Bauen, Possible applications of multiobjective optimisation in digital construction (in: german), In: *Digitale Infrastruktur und Geotechnik 2018, Jg. 42 von Veröffentlichungen des Instituts für Geotechnik und Baubetrieb der Technischen Universität Hamburg*, Hamburg, Germany, pp. 169-181.

Tom, R. (2022). *Find multi-objective Pareto front using modified quicksort.* [software]. https://www.mathworks.com/matlabcentral/fileexchange/73089-find-multi-objective-pareto-front-using-modified-quicksort, MATLAB Central File Exchange. [acess on: 09.07.2022].

Proceedings of the XVIII ECSMGE 2024
GEOTECHNICAL ENGINEERING CHALLENGES
TO MEET CURRENT AND EMERGING NEEDS OF SOCIETY
© 2024 the Authors
ISBN 978-1-032-54816-6
DOI 10.1201/9781003431749-89
Open Access: www.taylorfrancis.com, CC BY-NC-ND 4.0 license

ECSMGE 24
XVIII EUROPEAN CONFERENCE ON SOIL MECHANICS AND GEOTECHNICAL ENGINEERING

On the use of compliance correction for performing truly constant volume cyclic direct simple shear tests on sands

Sur l'utilisation de la correction de conformité pour la réalisation d'essais de cisaillement simple cyclique à volume vraiment constant sur les sables

M. Konstadinou*
Deltares, Delft, The Netherlands

A. Bezuijen
Ghent University, Ghent, Belgium

**maria.konstantinou@deltares.nl*

ABSTRACT: The cyclic undrained Direct Simple Shear (DSS) response of sand samples is predominantly influenced by the stiffness of the apparatus. Recent findings have shown that a stiffer apparatus results in a lower cyclic resistance response compared to a more flexible apparatus for which the number of cycles to liquefaction is higher. Consequently, the cyclic response of the sand samples is not only controlled by the soil behaviour itself but by the stiffness of the DSS device. High quality DSS test results on dense sand require a very stiff device that minimizes compliance to ensure truly constant volume (undrained) conditions. In this study, the device compliance is reduced to tolerated limits via actively correcting the vertical displacement response of the system during testing such that the height of the sample remains constant. Cyclic DSS tests on dense sand samples are performed and presented in this study for different compliance correction equations.

RÉSUMÉ: La réponse cyclique non drainée en cisaillement direct (DSS) d'échantillons de sable est principalement influencée par la rigidité de l'appareillage. Des découvertes récentes ont montré qu'un appareillage plus rigide entraîne une réponse de résistance cyclique inférieure par rapport à un appareillage plus flexible, pour lequel le nombre de cycles jusqu'à la liquéfaction est plus élevé. Par conséquent, la réponse cyclique des échantillons de sable n'est pas uniquement contrôlée par le comportement du sol lui-même, mais aussi par la rigidité du dispositif DSS. Pour obtenir des résultats de test DSS de haute qualité sur du sable dense, il est essentiel d'utiliser un dispositif très rigide qui minimise la conformité pour assurer des conditions vraiment constantes de volume (non drainées). Dans cette étude, la conformité de l'appareil est réduite à des limites tolérables en corrigeant activement la réponse de déplacement vertical du système pendant les essais, garantissant que la hauteur de l'échantillon reste constante. Des essais cycliques DSS sur des échantillons de sable dense sont réalisés et présentés dans cette étude en utilisant différentes équations de correction de conformité.

Keywords: Direct simple shear tests; apparatus stiffness; cyclic testing; dense sands.

1 INTRODUCTION

To mimic undrained behaviour, the DSS apparatus uses the conservation of volume by inhibiting any volume strain changes of the sample during shear. Following Dyvik et al. (1987), the change in vertical stress during shearing under constant height conditions, is assumed to be equal to the excess pore water pressure generation. However, the apparatus will have a finite stiffness. This means that a stress reduction, as will occur during cyclic loading, will lead to some volume change of the sample. Konstadinou et al. (2020), showed that the stiffness of the DSS apparatus is of major importance as it proved to control the cyclic behaviour of dense sand samples. ASTM D6528 states that for an undrained monotonic constant volume test the DSS device shall allow a sample change in height of less than 0.05%. To comply with this allowable limit, the DSS devices in use must be very stiff. To the authors' knowledge, however, most DSS devices in use today are unable to satisfy such high stiffness requirements. This paper presents a methodology for performing DSS tests that comply with the 0.05% criterion. Herein a series of cyclic DSS tests is performed for which the system compliance introduced during shearing is compensated by actively changing the vertical displacement response of the system to keep the height of the sample constant. Furthermore, to evaluate if truly constant volume conditions are achieved, the volume change of the samples during cyclic loading is measured.

2 MATERIAL & TESTING CONDITIONS

The tests were carried out in the geotechnical laboratory of Deltares in The Netherlands. For measuring volume changes of the samples during testing, the DSS apparatus is equipped with a water tank connected with a closed system to the inlet at the top of the sample. The water tank is placed on a precision weighing balance which continuously monitors the inflow/outflow of fluid in the water tank. Tests were performed on cylindrical samples having a diameter of 63 mm and a height at preparation of approximately 20 mm. A standard research sand, the Toyoura sand is used which has been extensively used in previous studies (e.g., Kiyota et al. 2008; Chiaro et al. 2012). All samples were prepared by the air pluviation method (Mulilis et al. 1977). The initial relative density of the samples is $D_{r,i} \approx 80\%$, and the samples were consolidated to 200 kPa starting from an initial stress state at preparation of 10 kPa. The samples were saturated by flushing carbon dioxide through the voids among the sand particles and by subsequently percolating de-aired water from the bottom to the top of the sample. The samples were saturated to allow measurement of volume change during consolidation and shearing. The volume change is determined from the amount of water that is expelled from or drawn into the sample. After saturation, the samples were consolidated to σ_{vi}' = 200 kPa. The samples were presheared (drained) at $\tau_{SA}/\sigma_{vi}' = 0.03$ for 400 cycles, where τ_{SA} is the single-amplitude cyclic shear stress, with a frequency of 1 Hz. Samples were presheared to mitigate sample inhomogeneity and to replicate the in-situ stress history of soils subjected to drained preshearing prior to the main design event. After a consolidation period of 1 hour, the samples were subjected to cyclic loading under undrained simple shear conditions at $\tau_{SA} = \pm$ 20 kPa. Cyclic loading was applied by way of a sinusoidal shear at a frequency of 0.02 Hz. The samples in this study were laterally confined by means of a rigid metal ring stacks enclosing an unreinforced rubber membrane. Table 1 summarizes the testing conditions of all the tests reported in this study.

Table 1. Sample characteristics.

Test	CC	D_r (%)	N_f (-)	K_m (kPa/mm)
NC_1	NC	88	86	
NC_2	NC	85	113	K_i =4,049
NC_3	NC	86	74	
WC_A_1	A	89	29	'infinite'
WC_B_1	B	88	51	12,727
WC_B_2	B	90	47	

Note: CC, Compliance Correction; NC, No Compliance correction; WC, With Compliance correction; D_r, relative density after consolidation; N_f, number of cycles required to develop single amplitude of shear strain, γ_{SA} = 5%; K_i, apparatus stiffness, K_m, modified apparatus stiffness.

3 SYSTEM COMPLIANCE

Compliance tests were conducted on a 20 mm thick dummy aluminium sample, which was subjected to three loading - unloading vertical load loops within the stress range of interest in this study, close to the sample's consolidation stress level of 200 kPa (compliance stress range: 10 – 300 kPa). In the years of operation of the DSS apparatus mobilized herein, several compliance tests were performed on aluminium samples. Figure 1(a) shows the upper and lower bound best fit lines to the compliance data from such tests which will be refer to in this paper as compliance "Correction A" and "Correction B" curves respectively and are described with a 4th degree polynomial equation. It should be noted that the compliance test on an aluminium sample performed prior to the start of the current test series agrees with the compliance "Correction A" data. The secant apparatus stiffness, K_i, as determined from the compliance "Correction A" curve at the consolidation stress level of 200 kPa is K_i = 4,049 kPa/mm.

To account for compliance, "Correction A" and "Correction B" equations have been implemented in the active height control loop of the apparatus. During shearing and for an applied vertical load, the LVDT vertical displacement response of the system is adjusted to compensate for the compliance displacement as derived via the employed correction equations. When no compliance correction is applied, the LVDT vertical displacement values are negligible as shown in Figure 1(b). Figures 1(c) & 1(d) plot the measured LVDT vertical displacement with the applied vertical displacement as calculated via the use of "Correction A" and "Correction B" compliance equations respectively. It should be noted that in Figure 1 a positive measured LVDT displacement corresponds to a movement in the opposite direction of displacement due to compliance. By employing compliance corrections, the stiffness of the apparatus is modified. The modified stiffness, K_m, is higher compared to the original apparatus stiffness (K_i = 4,049 kPa/mm, no compliance correction) and has a value of K_m = 12,727 kPa/mm for the compliance "Correction B" tests while in theory an 'infinite' apparatus stiffness is achieved for the compliance "Correction A" test.

4 TEST RESULTS

Figure 2 presents the development of volumetric strain, ε_v, with vertical stress ratio, $\Delta\sigma_v'/\sigma_{vi}'$, during shearing of the samples up to reaching failure. Note that in this figure, a positive volumetric strain corresponds to a volume reduction of the sample.

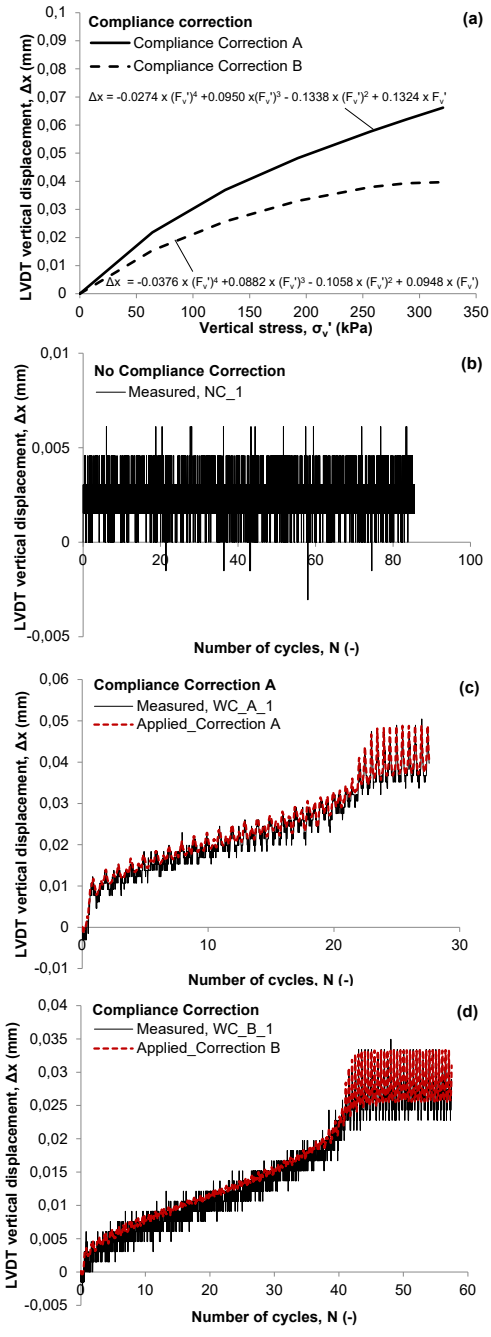

Figure 1. (a) Best fit compliance curves. Measured and applied LVDT vertical displacement as function of the number of loading cycles for tests with (b) no compliance correction, (c) compliance "Correction A" and (d) compliance "Correction B". The units in the compliance correction equations in Figure 1(a) are given in mm for the LVDT vertical displacement, Δx, and in kN for the vertical force, F_v'. The DSS sample diameter is 63 mm.

It is noteworthy that the sample for which no compliance correction is applied has a higher volumetric strain compared to the samples with compliance correction [Figure 2(a) cf., Figure 2(b) & 2(c)]. Using compliance "Correction A" and "Correction B" equations, the predicted volumetric strain distribution is also plotted against the experimental data in Figure 2. In overall, Figure 2 shows that only when compliance corrections are applied, the volumetric strain remains within the maximum tolerated change of ±0.05% as prescribed in ASTM D6528. In Figure 3 the number of cycles, N_f, required to develop a single-amplitude shear strain γ_{SA}=5% is plotted versus the modified apparatus stiffness, K_m, for the tests in this study performed with and without the use of compliance correction equations. As aforementioned, the influence of the apparatus stiffness on the cyclic response of dense Toyoura sand samples has been investigated by Konstadinou et al. (2020). To evaluate this influence, the stiffness of the apparatus has been altered via the use of spring rings attached to the apparatus. The test data reported in Konstadinou et al. (2020) are also shown in Figure 3. It is evident that the resistance to cyclic loading depends on the rigidity of the DSS apparatus. Particularly for the employed apparatus, the number of cycles required to reach γ_{SA} = 5% decreases by about 70% when the apparatus is tricked to operate at its stiffest mode ('infinite' stiffness). In practice, the data in Figure 3 indicate that past results of cyclic DSS tests, particularly those on dense sand samples, should be treated with caution if the apparatus stiffness has not been considered in the data interpretation.

5 CONCLUSIONS

The performance of truly constant volume cyclic direct simple shear tests can be achieved only when the compliance of the system within the height control measurement area is 'infinite'. This is practically impossible as the apparatus will have a finite stiffness. Two options are available to reduce the system's compliance to allowable limits. That is to use a DSS apparatus that: (i) meets the high stiffness requirements or (ii) controls the height of the sample alone and keeps it constant with high accuracy. Modifying the DSS devices in use today to allow for the above options can be costly or simply not feasible. An alternative option has been explored in this paper based on which the sample's volumetric strain is kept within tolerated limits by correcting the displacement during shearing to account for the system's compliance. This option is recommended to be applied to every cyclic DSS test, but it requires, however, an

active height control system that reacts swiftly to changes in the vertical load. For a slower system, compromises must be made on the value of the applied loading frequency.

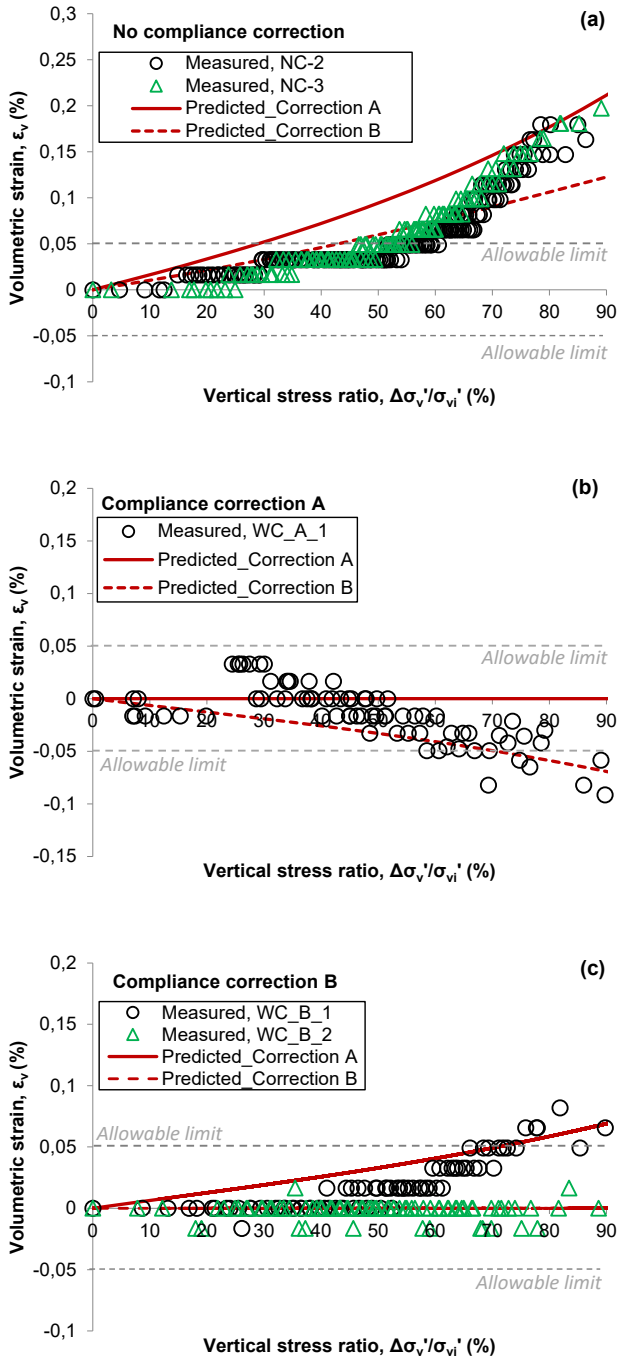

Figure 2. Measured and predicted volumetric strain, $\Delta\varepsilon_v$, against vertical stress ratio $\Delta\sigma_v'/\sigma_{vi}'$, for tests: (a) with no compliance correction (NS_1, NS_2 & NS_3), (b) with compliance correction A (WC_A_1) and (c) with compliance correction B (WC_B_1 & WC_B_2).

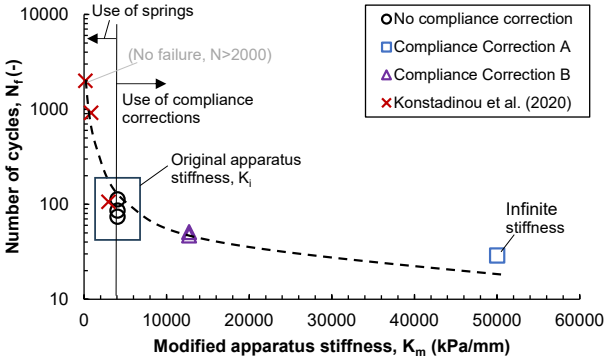

Figure 3. Relationship between number of cycles to develop a single amplitude of shear strain of γ_{SA} = 5 % and modified apparatus stiffness, K_m.

REFERENCES

ASTM D6528 (2017). Standard test method for consolidated undrained direct simple shear testing of fine grain soils. *ASTM International*, West Conshohocken, PA, www. astm.org.

Chiaro, G., Koseki, J., and Sato, T. (2012). Effects of initial static shear on liquefaction and large deformation properties of loose saturated Toyoura sand in undrained cyclic torsional shear tests. *Soils Found.*, Vol. 52(3), pp. 498 – 510. https://doi.org/10.1016/j.sandf.2012.05.008.

Dyvik, R., Berre, T., Lacasse, S., and Raadim, B. (1987). Comparison of truly undrained and constant volume direct simple shear tests. *Géotechnique*, Vol. 37(1), pp. 3-10. https://doi.org/10.1680/geot.1987.37.1.3.

Kiyota, T., Sato, T., Koseki, J., and Abadimasand, D. (2008). Behaviour of liquefied sands under extremely large strain levels in cyclic torsional shear tests. *Soils Found.,* Vol. 48(5), pp. 727 – 739. https://doi.org/10.3208/sandf.48.727.

Konstadinou, M., Bezuijen, A., Greeuw, G., Zwanenburg, C., Van Essen, H.M and Voogt, L. (2020). The influence of apparatus stiffness on the results of cyclic direct simple shear tests on dense sand. *Geotechnical Testing Journal*, Vol. 44(5), pp. 1501-1525. https://doi.org/10.1520/GTJ20190471.

Mulilis, J. P., Arulanandan, K., Mitchell, J. K., Chan, C. K., and Seed, H. B. (1977). Effects of sample preparation on sand liquefaction. *J. Geotechnical Eng. Division ASCE*, 103(GT2), pp. 91 – 108. https://doi.org/10.1061/ajgeb6.0000387.

Proceedings of the XVIII ECSMGE 2024
GEOTECHNICAL ENGINEERING CHALLENGES
TO MEET CURRENT AND EMERGING NEEDS OF SOCIETY
© 2024 the Authors
ISBN 978-1-032-54816-6
DOI 10.1201/9781003431749-90
Open Access: www.taylorfrancis.com, CC BY-NC-ND 4.0 license

ECSMGE 24
XVIII EUROPEAN CONFERENCE ON SOIL MECHANICS AND GEOTECHNICAL ENGINEERING

Effects of physical characteristics on the shear behaviour of Foulum glaciofluvial sand

Effets des caractéristiques physiques sur le comportement en cisaillement du sable fluvio-glaciaire du Foulum

J.Z. Krabbe*
Aarhus University/NIRAS, Aarhus, Denmark

K.K. Sørensen
Aarhus University, Aarhus, Denmark

M.R. Lodahl
COWI, Aalborg, Denmark

**jzkr@niras.dk*

ABSTRACT: The geotechnical properties of sand deposits are heavily influenced by their physical characteristics, making their characterization essential. By subjecting 15 specimens to isotropic triaxial tests and by using a simple table scanner to collect 2D-oriented projections of the sand grains, the study aims to present a comprehensive physical characterization of Foulum high quartz glaciofluvial sand, with an emphasis on its implications on the shear behaviour and drained peak friction angle φ'_p of the tested sand. The results revealed the multifaceted nature of granular material behaviour. In particular, the stress dependency and initial conditions emerged as extremely important, in line with previous research. The study also highlights the importance of the sample size when considering particle shape (sphericity in particular) on the geotechnical properties.

RÉSUMÉ: Les propriétés géotechniques des sediments sableux sont fortement influencées par leurs caractéristiques physiques, ce qui rend leur caractérisation essentielle. En soumettant 15 spécimens à des essais triaxiaux isotropes et en utilisant un scanner à plat pour collecter des projections orientées en 2D des grains de sable, cette étude vise à présenter une caractérisation physique complète des sédiments fluvio-glaciaire à haute teneur en quartz de Foulum, en mettant l'accent sur ses implications sur le comportement au cisaillement et l'angle de frottement maximal drainé φ'_p des échantillons testés. Les résultats ont révélé les comportements très diversifiés des matériaux granulaires. En particulier, la dépendance aux contraintes et conditions initiales ont émergé comme étant extrêmement importantes, conformément aux études précédentes. L'étude met également en évidence l'importance de la taille de l'échantillon lors de la prise en compte de la forme des particules (en particulier la sphéricité) sur les propriétés géotechniques.

Keywords: Shear behaviour; triaxial tests; particle shape; sphericity; drained peak friction angle.

1 INTRODUCTION

Knowledge of the peak drained friction angle of sands φ'_p is important for the construction and safety of most geotechnical designs such as foundations, excavations, tunnels, slopes, and many other important civil engineering works. In contrast to the critical state friction angle, φ'_{cs}, the peak friction angle φ'_p is not a fundamental soil property but depends on the sands' capacity to dilate. Thus, it changes with mineralogy, particle shape, particle irregularities and distribution of soil particles, the magnitude of the effective confining stress, the initial void ratio, the applied stress path, and much more. This has led to the peak friction angle in designs being largely dependent on the geotechnical engineers' experience. Nevertheless, extensive studies (i.e., Bolton 1986, among others) have sought to formulate mathematical expressions for triaxial compression loading based on the confining stress, relative density, and fitting parameters based on the mineralogy and particle shape.

This study aims to characterise and link the physical and mechanical shearing properties of a Danish high quartz glaciofluvial sand. Additionally, the study seeks to investigate the extent to which experimental studies conducted on sands accurately reflect the geological context and variability, and how this can be better incorporated into subsequent analyses, with an emphasis on its implications on the shear behaviour and drained peak friction angle φ'_p.

2 TEST MATERIAL AND METHODS

The investigated "Foulum sand" is a natural high quartz glaciofluvial sand collected at the Foulum test site near the Danish glacial front line in the middle of Jutland, Denmark, from a depth of 2 m to 14 m.

The grain size distribution obtained using dry sieving method classifies the sand as a clean sand (FC < 5%) and poorly graded (SP) group according to the United Soil Classification System with a coefficient of uniformity $U = 2 - 4$ and a coefficient of curvature $Z <$ 1.3. Visual and chemical composition analysis showed that the mineral composition of Foulum Sand is dominated by Quartz (> 80%) in addition to feldspar. The specific gravity (G_s) was found to range between 2.62 to 2.67 (mean 2.64), accurately representing a mineral composition of primarily quartz and feldspar with some fines content present. Standard Danish laboratory procedures were used to determine the void ratio limits. The minimum void ratio e_{min} ranged from 0.36 to 0.52 (mean 0.44) the maximum void ratio e_{max} ranged from 0.72 to 1.01 (mean 0.8).

2.1 Experimental program and procedures

In addition to the standard index properties a detailed analysis has been carried out to characterise the particle shapes. Three main scales which define particle shape irregularities exist (considering a 2D projection). While sphericity is related to the 'form' and thus sensitive to particle elongation, roundness reflects the variations and sharpness of particle corners (i.e., angularity) and roughness describes surface texture at the smallest scale, cf. Figure 1a.

In this study a 'CanoScan LiDE 300' table scanner with a 1200 DPI resolution was used to facilitate the collection of 2D-oriented projections of sand grains. A sample size of least 1000 particles have been considered to capture the grain variability as suggested by Rorato (2019). After the scan was performed the image was prepared (increasing the image size) using the commercial program ImageJ Fiji (Schindelin et al. 2012) and subsequently binarised, segmented, and labelled using the open-source python package SPAM (Stamati et al. 2020) as shown in Figure 1b. The Python script originally developed by Rorato (2019) was used to compute the mean value and standard deviation of the distribution of 2D perimeter sphericity, S_p, of the grains.

In addition, the freely available commercial program ImageJ Fiji and the Particle8_Plus plugin (Landini 2008) have been used as an alternative method to determine the sphericity (S) and roundness (R) from square pixels to extract the features:

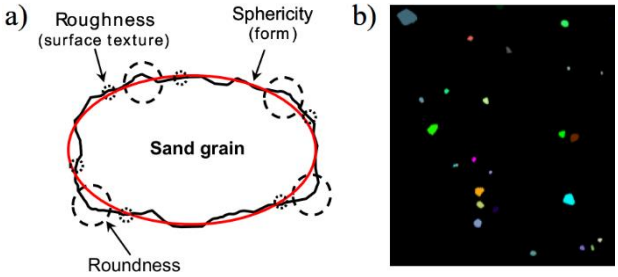

Figure 1. a) Particle shape characterisation at different scales, b) Obtained 2D-oriented projections of sand grains - Labelled image.

$$S = \frac{R_i}{R_c}, R = \frac{4A_c}{\pi L_{major}^2} \quad (1)$$

In Eq. (1) R_i is the radius of the inscribed circle, R_c is the radius of the circumscribed circle at the center of mass, A_c is the cross-sectional area, and L_{major} is the length of the major axis.

For examining the shear strength, 15 isotropically consolidated drained triaxial compression tests (CID) with pore water pressure measurements were performed on clean Foulum sand. The CID tests were dry reconstituted by the undercompaction method by Ladd (1978) and prepared using an equal height to diameter ratio (h/d = 1) while employing lubricated ends. The normally consolidated specimens were consolidated to an isotropic compression mean effective stress p'_c between 35 and 255 kPa.

3 LABORATORY TEST RESULTS

The index relationships and strength results for the tested Foulum sand specimens are presented in Table 1.

The computed mean values of S_p were found to range from 0.83 to 0.95 with a standard deviation between 0.03 to 0.06, indicating that the sand is highly spherical. Conversely, using the methodology presented in Eq. (1) the sphericities were found to vary between 0.61 to 0.68. This underscores the significance of the selected computational framework. The range of void ratio before shearing e_s varied from as low as 0.49 to as high as 0.82 (mean 0.62), corresponding to a relative density range of 38.2% < D_R < 66.6% with a mean of D_R = 49.8%.

The mean stress at failure, p'_f, was observed to be between 65 kPa to 577 kPa, resulting in normalised peak shear stresses q/p'_f in the range of 1.37 to 1.74, overall, with a tendency to increase in value for greater values of confining p'_c. Distinct dilative behaviour was obtained on specimens recompacted to D_R values higher than about 40%, generally attaining peak angle of dilation (ψ_p) values greater than 7° at observed peak

Table 1. Summary of index and strength properties for the tested specimens.

Nr.	Grain size distribution				Particle shape			Shearing state and properties						
	FC (%)[a]	D_{50} (mm)	U^b (−)	Z^c (−)	S_p (−)	S (−)	R (−)	D_R (%)	e_s (−)	p'_c (kPa)	p'_f (kPa)	ψ_p (°)	φ'_p (°)	φ'_{cs} (°)
1	2.30	0.37	2.92	1.18	0.91	0.66	0.58	39.0	0.82	35	65	0.9	34.0	33.4
2	2.41	0.34	2.87	1.18	0.93	0.66	0.58	41.5	0.76	53	101	3.8	35.1	32.9
3	0.85	0.57	2.56	0.87	0.92	0.67	0.60	53.5	0.57	71	169	14.9	42.3	35.3
4	2.71	0.46	3.32	1.12	0.89	0.68	0.59	56.1	0.55	81	191	14.2	41.5	34.9
5	2.03	0.51	2.93	1.00	0.88	0.65	0.58	54.2	0.56	90	204	11.9	41.0	34.8
6	5.78	0.49	4.57	1.30	0.85	0.63	0.55	40.4	0.58	99	215	11.1	39.5	34.7
7	2.23	0.47	3.25	1.09	0.95	0.67	0.60	52.2	0.57	125	276	12.4	40.1	34.6
8	2.47	0.46	2.93	1.06	0.86	0.68	0.61	65.5	0.52	146	349	14.0	42.5	35.0
9	4.03	0.36	3.13	1.21	0.84	0.67	0.60	38.2	0.73	43	82	3.6	34.0	32.2
10	2.53	0.35	2.72	1.27	0.87	0.65	0.57	43.2	0.67	88	182	9.2	37.5	33.1
11	2.89	0.34	2.88	1.22	0.85	0.64	0.57	48.8	0.63	107	230	9.6	38.6	33.4
12	3.36	0.39	3.26	1.21	0.83	0.66	0.58	51.8	0.59	126	258	8.2	37.2	33.4
13	3.69	0.38	3.29	1.22	0.87	0.64	0.56	48.6	0.61	144	289	6.7	36.7	33.5
14	4.72	0.33	3.12	1.05	0.93	0.64	0.58	46.8	0.66	225	422	2.4	34.3	33.2
15	4.67	0.19	2.51	1.03	0.83	0.64	0.58	66.6	0.49	255	577	13.6	40.7	34.3

[a]Fines content < 0.075mm; [b]Coefficient of uniformity $U = D_{60}/D_{10}$; [c]Coefficient of curvature $Z = D_{30}^2/(D_{60} \times D_{10})$

strength. In four cases, the reconstituted specimens showed contractive behaviour and much lower shear strength. The drained peak friction angles φ'_p were observed to lie between 34° to 42.5°, commonly reached at about an axial strain of ε_a = 6 − 8%. The critical state friction angles φ'_{cs} were observed to lie between 32.2° to 35.3°, although some tests were not run to sufficiently large strains for a complete critical state to be reached. The level of dilatancy during shearing is presented in Figure 2a and are seen to vary approximately linearly with ψ_p giving the relationship $\varphi'_p = \varphi'_c + 0.48\psi_{max}$.

4 CORRELATIONS BETWEEN DATA

A multivariable linear regression analysis has been performed to investigate the interdependencies between the physical attributes of Foulum glaciofluvial sand and its shear behaviour. The sensitivity analysis presented in Table 2 highlights and serves as a valuable reference for understanding the observed trends.

The three parameters exerting the most significant influence on the φ'_p are e_s, $\ln p'_c$ and D_R. This is evidenced by low p-values at 1.6%, 1.8% and 6.2%, respectively, indicating a strong significance in the model and strong linear relationship. This is consistent with the work of Bolton (1986) and others, who demonstrated that for a given granular material, the difference $\varphi'_p - \varphi'_{cs}$ generally varies approxi-mately linearly with the logarithm of vertical stress. Moreover, the slope of this linear variation changes systematically with the sample's relative density.

Interestingly, the analysis revealed that incorporating S_p (6.2%) plays a more crucial role than S (10.8%) likely due to its equivalency to the 3D true sphericity for the 2D particle (Rorato 2019). Similar p-values of those attained by S are obtained by other various sphericity descriptors, such as the area-, diameter-, and ks sphericity. This highlights the importance of considering different measures of sphericity in geotechnical analysis and underscores the complexity of granular material behaviour. The influence of roundness was found insignificant. Of the particle shape properties, the roundness indicates the lowest level of statistical significance at 27.6%.

The grain size distribution (GSD) further revealed the importance of several other parameters, albeit to a lesser extent. The Z and D_{50} emerged as the most significant properties.

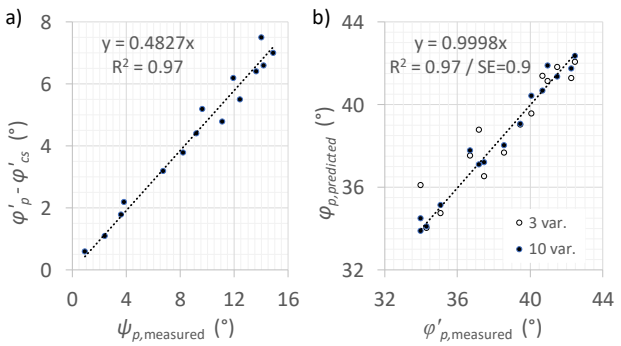

Figure 2. a) Level of dilatancy during shearing, b) measured vs. predicted peak drained friction angle φ'_p (trendline for 10 variables).

Table 2. Sensitivity analysis for φ'_p, φ'_{cs} and ψ_p. Percentages given for the properties indicate their respective p-values.

	Grain size distribution				Particle shape			Shearing state and properties			Combined statistics		
	FC (%)	D_{50} (%)	U (%)	Z (%)	S_p (%)	S (%)	R (%)	D_R (%)	e_s (%)	$\ln p'_c$ (%)	p (%)	SE (°)	R^2 (−)
φ'_p	21.4	13.2	16.2	8.9	6.2	10.8	27.6	6.2	1.6	1.8	1.00	0.92	0.97
φ'_{cs}	6.7	13.0	4.0	0.6	3.4	41.9	27.7	–	–	–	24.1	0.62	0.71
ψ_p	33.1	33.9	21.0	15.2	10.3	26.9	35.2	39.5	0.5	3.1	1.28	1.52	0.97

Figure 2b depicts the measured versus predicted peak drained friction angle φ'_p for 3 (shearing state properties) and 10 included variables. When considering the combined statistics of all the variables, the model was found to be statistically significant with a p-value of 0.95%. The R^2 value of 0.97 was found to provide a strong fit, ultimately resulting in a standard error (SE) of 0.92°. Thus, the variables included in the model appear to be good predictors, providing a robust and accurate model.

The variable φ'_{cs}, which is independent of shearing state and properties, reveals four index parameters (Z, S_p, U and FC) as particularly influential, with respective p-values of 0.6%, 3.4%, 4.0%, and 6.7%. This aligns with the critical state concept of dependence on factors such as mineralogy, particle shape and particle irregularities. It is noted that S_p emerges as vastly superior to S, while R also provides a low level of statistical significance. It is likely that the table scanner is not able to present a high enough quality scan for the algorithm to sufficiently capture the roundness. The combined variables yield a p-value of 24.1%, R^2 value of 0.71 and SE of 0.62°. These results are likely influenced by the fact that some tests were not performed at strains large enough to achieve a fully developed critical state.

In the sensitivity analysis conducted for the peak angle of dilation ψ_p, the variables exhibited varying degrees of statistical significance. As sands ability to exhibit dilating behaviour is directly related to shearing state and the applied confining pressure, it is unsurprisingly that e_s and $\ln p_c$ indicates a very strong significance with p-values of 0.5% and 3.1%, respectively. It is noteworthy that the inclusion of the last 8 variables only marginally increases the predictive abilities from an R^2 value of 0.92 to 0.97. This suggests that these variables, while contributing to the model, do not drastically improve its predictive power.

5 CONCLUSION

This study delves into the characterization of high quartz glaciofluvial sand through a meticulous examination of its physical and mechanical properties.

The findings provide insights into the role of particle shape, in particular different measures of sphericity. Furthermore, the findings underscore the multifaceted nature of granular material behaviour and highlight the need for a comprehensive approach in geotechnical analysis that considers a wide range of parameters.

ACKNOWLEDGEMENTS

The authors would like to acknowledge the support from COWI fonden. Further, thank you to Marcos Arroyo from Universitat Politècnica de Catalunya (UPC), Riccardo Rorato (formerly at UPC) and Marco Previtali from the University of Dundee for providing the necessary scripts for image analysis.

REFERENCES

Bolton, M. D. (1986), The strength and dilatancy of sands, *Géotechnique,* 36(1), pp. 65-70, https://doi.org/10.1680/geot.1986.36.1.65.

Ladd, R. S. (1978), Preparing test specimens using undercompaction, *Geotechnical testing journal,* 1(1), pp. 16-23, https://doi.org/10.1520/GTJ10364J.

Landini, G. (2008), Advanced shape analysis with ImageJ, *Proceedings of the Second ImageJ user and developer Conference*, Available at https://blog.bham.ac.uk-/intellimic/g-landini-software/, accessed: 08/10/2023.

Rorato, R. (2019), *Imaging and discrete modelling of sand shape,* Doctoral dissertation, Universitat Politècnica de Catalunya. Available at: https://upcommons.upc.edu, accessed: 08/10/2023.

Schindelin, J., Arganda-Carreras, I., Frise, E., Kaynig, V., Longair, M., Pietzsch, T., Preibisch, S., Rueden, C., Saalfeld, S., Schmid, B. and Tinevez, J.Y. (2012), Fiji: an open-source platform for biological-image analysis, *Nature methods*, 9(7), pp. 676-682. https://doi.org-/10.1038/nmeth.2019.

Stamati, O., Andò, E., Roubin, E., Cailletaud, R., Wiebicke, M., Pinzon, G., Couture, C., Hurley, R.C., Caulk, R., Caillerie, D. and Matsushima, T. (2020), Spam: software for practical analysis of materials, *Journal of Open Source Software*, 5(51), 2286, https://doi.org-/10.21105/joss.02286.

Proceedings of the XVIII ECSMGE 2024
GEOTECHNICAL ENGINEERING CHALLENGES
TO MEET CURRENT AND EMERGING NEEDS OF SOCIETY
© 2024 the Authors
ISBN 978-1-032-54816-6
DOI 10.1201/9781003431749-91
Open Access: www.taylorfrancis.com, CC BY-NC-ND 4.0 license

ECSMGE 24
XVIII EUROPEAN CONFERENCE ON SOIL MECHANICS AND GEOTECHNICAL ENGINEERING

An advanced method to predict umbrella arch behaviour in soft ground tunnelling

Une méthode avancée pour prédire le comportement de voûte parapluie dans la réalisation de tunnels en sol meuble

S. Kuder*, J. Klopčič, B. Pulko, J. Logar
Faculty of Civil and Geodetic Engineering, University of Ljubljana, Slovenia
**skuder@fgg.uni-lj.si*

ABSTRACT: When tunnelling in soft ground, umbrella arch is often being used to improve the conditions around tunnel face. The paper describes an advanced method to predict the umbrella arch behaviour based on the displacement measurements. An established empirical method initially proposed by Barlow is used as the foundation. The displacement functions for sections ahead of the face and for the supported part of the tunnel are retained while in the unsupported area and unexcavated area close to the face the functions are modified by introducing a set of analytical equations. For the arch element the elastic beam theory is adopted in combination with the theory of the beam on elastic foundation (Winkler soil model). The proposed method is kept relatively simple by adopting analytical solution for semi-infinite beam in front of the tunnel face. The analytical solution is compared to the results of 3D numerical analysis. Despite the simplification in the approach the analytical solution gives very similar results both in terms of beam displacement and bending moment.

RÉSUMÉ: Lors du creusement de tunnels dans un sol meuble, la voûte parapluie est souvent utilisée pour améliorer les conditions autour du front du tunnel. L'article décrit une méthode avancée basée sur des mesures de déplacement pour prédire le comportement de la voûte parapluie. Une méthode empirique établie, initialement proposée par Barlow, est utilisée comme base de cette méthode. Les fonctions de déplacement pour les sections en avant du front et pour la partie supportée du tunnel sont conservées tandis que dans la zone non supportée et la zone non excavée proche du front, les fonctions sont modifiées en introduisant un ensemble d'équations analytiques. Pour la voûte, la théorie des poutres élastiques est utilisée en combinaison avec la théorie des poutres sur fondation élastique (modèle de Winkler). La méthode proposée reste relativement simple en adoptant une solution analytique pour une poutre semi-infinie devant le front du tunnel. La solution analytique est comparée aux résultats de l'analyse numérique 3D. Bien que l'approche soit simplifiée, cette méthode donne des résultats similaires à ceux de l'analyse numérique, tant en termes de déplacement de la poutre que de moment fléchissant.

Keywords: Tunnel; umbrella arch; displacement function; 3D analysis.

1 INTRODUCTION

Umbrella arch also known as pipe roof is one of the pre-support methods in tunnelling used to improve stability and safety conditions around the unsupported section of the tunnel. For safe but also cost-efficient design of umbrella arch it is necessary to understand the behaviour of the pipe elements during the excavation. To design umbrella arch several analytical methods exist, but none has achieved widespread acceptance (Oke et al., 2016).

An empirical method proposed by Barlow (1986) and further modified by Sellner (2000) describes the tunnel displacements as a function of time and excavation advancement. The method has proven to give very good results describing the tunnel displacements, however it has some limitations with regard to describing the umbrella arch displacements. The paper proposes a modification of the method to overcome these shortcomings.

2 TUNNEL DISPLACEMENT METHOD

The displacement function defines vertical displacements of tunnel crown at a given chainage (monitoring section) as a function of time and the distance between tunnel face position and the observed chainage. Barlow proposed three separate functions to describe tunnel crown displacement along a tunnel section: displacement in front of the face (Eq. 1), displacement in unsupported section (Eq. 2) and displacement in supported section (Eq. 3):

$$C_{pf}(x,t) = \left[Q_1 \cdot C_{pf}(x) - Q_k \cdot P_k^+(x)\right] \cdot \left[C_{x\infty} + A \cdot C_2(t)\right] \quad (1)$$

$$C(x,t) = [Q_1 + Q_2 \cdot C_1(x) - Q_k \cdot P_k^+(x)] \cdot [C_{x\infty} + A \cdot C_2(t)] \quad (2)$$

$$C(x,t) = \frac{[Q_1 + Q_2 \cdot C_1(x) + K \cdot C_S - Q_k \cdot P_k^-(x)]}{[1 + K \cdot (C_{x\infty} + A \cdot C_2(t))]} \cdot [C_{x\infty} + A \cdot C_2(t)] \quad (3)$$

where Q_1 is a displacement proportion ahead of the face, C_{pf} is a displacement function ahead of the face, Q_k is a displacement proportion to account for the effect of support, P_k^+ is a support function ahead of support installation point, $C_{x\infty}$ is time independent displacement, A is a displacement proportion to account for the effect of time, C_2 is a displacement function to account for time effect, Q_2 is a displacement proportion behind the face, C_1 is a displacement function behind the face, P_k^- is a support function behind the support installation point, K is a support stiffness and C_S is the convergence at the point of support installation.

The advantage of the method is relatively small number of parameters. Four main parameters ($C_{x\infty}$, Q_1, A, K) govern the shape of three functions, which makes the process of fitting calculated to measured displacements relatively straightforward. Since the displacements of umbrella arch don't differ significantly from the ground displacement, the displacement function can be used to describe the umbrella arch behaviour. Once the deformed shape of umbrella arch is known, internal forces can be easily calculated.

However, as it can be seen from Figure 1, the analytical displacement functions describe continuous displacements, whereas their derivatives are not continuous at the connection points between individual displacement functions. Such displacement functions do not represent the actual behaviour of tunnel lining well enough to be used for the assessment of umbrella arch internal forces due to ground displacements. Although the arch elements aren't very stiff compared to the ground, they can still locally redistribute stresses from the unsupported section to the tunnel support on one side and to unexcavated ground ahead of the face. This results in a more gradual displacement curve around two crucial points (Figure 1, red line). In the next chapter, a modification of displacement functions is proposed.

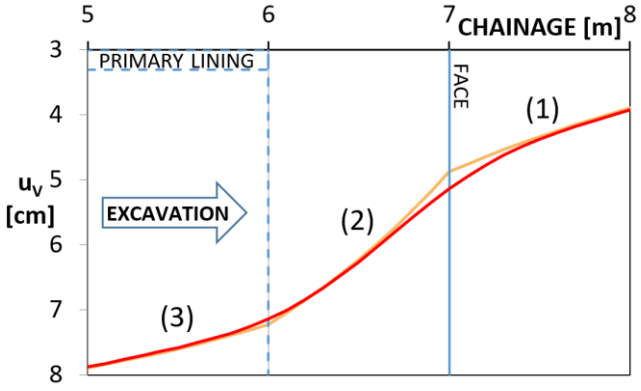

Figure 1. Three displacement functions (brown curve) and measured/numerically obtained displacement curve (red).

3 MODIFICATION OF EMPIRICAL METHOD

As shown in Figure 1, redefinition of the intermediate displacement function (Equation 2) is particularly required. Similarly, the function ahead of the face at close proximity to the face also deviates considerably from measured curve (Figure 1) and needs an adjustment having in mind that we are interested in obtaining good estimates of derivatives, which will yield bending moment and shear force distribution in arch elements. Therefore, two new intermediate functions are proposed.

Sequential excavation method is considered in the study and this results in an oscillating pattern of bending moment and shear force distribution along the arch element (Figure 2). The original displacement function formulation doesn't allow to simulate such behaviour. The proposed modification of displacement functions is therefore written in terms of displacement increments between two consecutive excavation stages instead of total displacements.

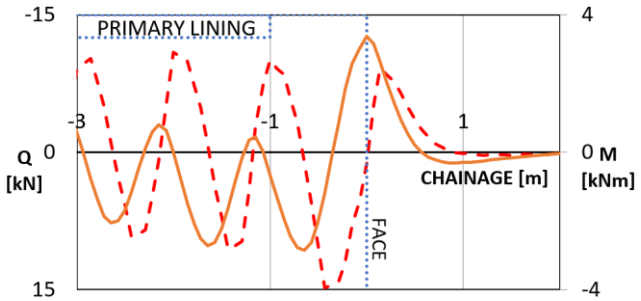

Figure 2. Bending moment curve (solid line/secondary axis) and shear force curve (dashed line) of the arch element.

3.1 The model assumptions

The modified model for the description of the arch element behaviour is based on the following assumptions:

- the arch element is modelled as linear elastic beam with known relations between displacements and internal forces,
- the model comprises four functions: two original displacement functions at both ends and two modified analytical intermediate functions. The first intermediate function starts at certain distance ahead of the face and ends approximately at the face of the tunnel. From this point onwards the second one describes displacements in the unsupported section and extends slightly into supported section,
- four boundary conditions (displacement, rotation, bending moment, shear force) are fulfilled at each joint between two adjacent functions,
- functions ahead of the face (Eq. 1) and in supported section (Eq. 3) are fitted to measured/calculated displacement increments,
- two intermediate functions are based on analytical solutions for elastic beam and derived at the incremental level (see 3.2 and 3.3). The values a_L, a_M, a_R, a_T and p_L, p_M, p_R, p_T defining load pattern (Figure 4) acting on elastic beam are again obtained by fitting procedure,
- the derivatives and resulting inner forces are obtained analytically.

3.2 Arch load in unsupported section

To model the load in the unsupported section the results of numerical analyses were thoroughly studied. Different distributions were considered (polynomial, trigonometric), but finally the load pattern was simplified to triangular load at the initial part of supported section and two rectangular loads in unsupported section (Figure 3), which significantly reduces the number of parameters but still provides very good agreement with numerical results.

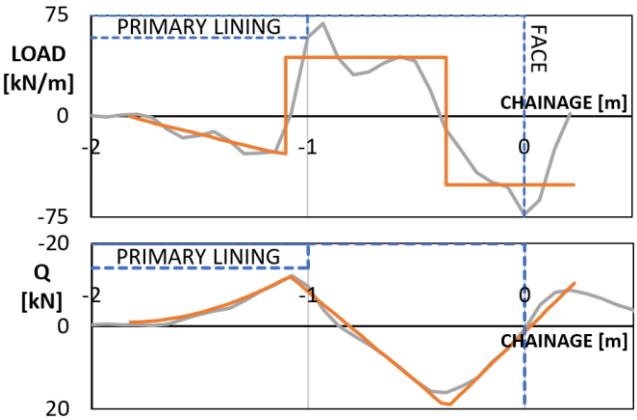

Figure 3. The load distribution in unsupported section (above) and shear force curve (below). Comparison of numerical results (gray) and analytical model (orange).

3.3 Intermediate function ahead of face

The second intermediate function ahead of the face is based on Winkler subgrade model. The analytical solutions for the semi-infinite elastic beam were adopted (Young and Budynas, 2002). This beam type was chosen to keep the solution relatively simple and with low number of parameters. Figure 2 shows that the resulting values of internal forces vanish quickly as one would expect.

The superposition approach was adopted to model the load in both intermediate sections. The ground load was modelled by triangular load p_T (Figure 4) and solutions for concentrated force and moment were included to meet the boundary conditions at the face.

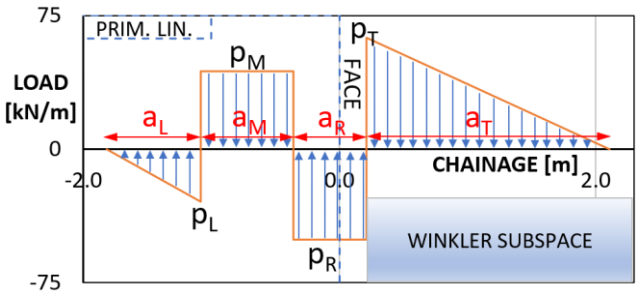

Figure 4. Load and ground model around the tunnel face.

4 RESULTS

The intended use of the proposed method is primarily during tunnelling by fitting displacement functions to measured displacements of a tunnel lining. In this paper, instead of using measurements, displacements were obtained by advanced 3D numerical models. A series of numerical analyses with different scenarios were performed (Kuder et al., 2022) by using Plaxis 3D finite element software (Figure 5). Results of one such case are presented in this paper using the properties shown in Table 1.

Hardening soil material model was used for the ground. Primary lining was modelled with special concrete constitutive model.

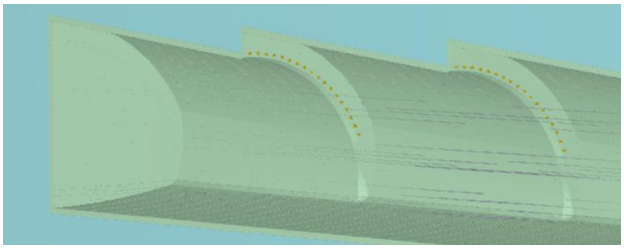

Figure 5. 3D model of top heading with temporary invert.

To acquire the parameters, four functions were fitted to numerically obtained displacement curves by using MS Excel solver. Table 2 shows the fitted

displacement function parameters for analysed case. Figure 6 shows very good agreement for both incremental displacement and bending moment.

Table 1. Main properties of numerical model.

Parameter	Value
Average top heading radius	approx. 6 m
Overburden height	55 m
Shotcrete thickness	25 cm
Ground angle of internal friction	28°
Ground cohesion	35 kPa
Ground modulus $E_{50} = E_{oed}$	100 MPa
Pipe diameter	114 mm
Pipe bending stiffness	655 kNm^2

Table 2. Displacement function properties.

Parameter	Value
$C_{x\infty}$	9.88 cm
Q_1	0.26
K	46.3 m^{-1}
Fitting parameter X	2.46 m
Subgrade modulus	260 MN/m^3
Load p_L	-29.5 kN/m
Load p_M	43.6 kN/m
Load p_R	-50.9 kN/m
Load p_T	62.6 kN/m
Load area a_L	0.73 m
Load area a_M	0.73 m
Load area a_R	0.57 m
Load area a_T	1.90 m

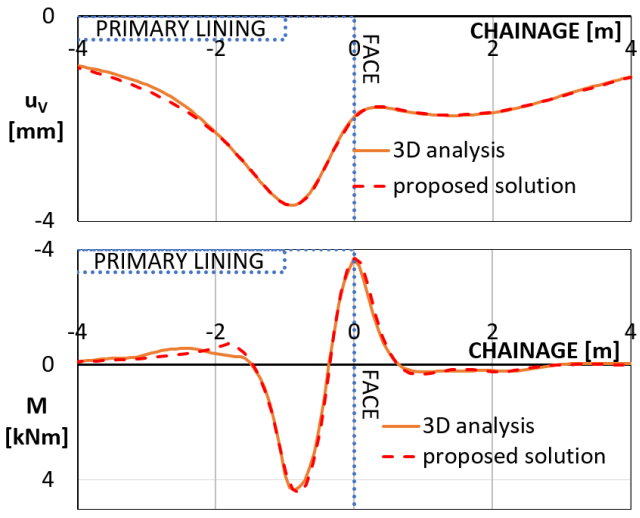

Figure 6. Incremental phase displacement (above) and resulting bending moment (below).

5 CONCLUSION

The paper presents an advanced method for predicting umbrella arch behaviour. For this purpose, the established displacement function has been modified. The proposed analytical solution for intermediate unsupported section behind the excavation face efficiently connects two original empirical displacement functions and provides such derivatives that perfectly fit the numerically obtained bending moments and shear forces within umbrella arch pipe.

Complex 3D numerical analyses are usually required to design an umbrella arch efficiently. The proposed solution is useful as complementary method during tunnel construction to make use of usually reliable displacement measurements and when calibration of sophisticated numerical models may not be a proper choice. The results of the analyses on a test case show that the proposed method can perform this task very well.

REFERENCES

Barlow, J. P. (1986). *Interpretation of Tunnel Convergence Measurements*. Master thesis. University of Alberta, Department of Civil & Environmental Engineering, Edmonton, Alberta, Canada.

Kuder, S., Logar, J., Klopcic, J. (2022). *The numerical study of umbrella arch behavior in soft ground tunneling.* Proceedings of the 20th International Conference on Soil Mechanics and Geotechnical Engineering– Rahman and Jaksa (Eds). Australian Geomechanics Society, Sydney, Australia.

Oke, J., Vlachopoulos N., Diederichs M. S. (2016). *Semi-analytical model for umbrella arch systems employed in squeezing ground conditions*, Tunnelling and Underground Space Technology, 56. https://doi.org/10.1016/j.tust.2016.03.006.

Sellner, P. J. (2000). *Prediction of Displacements in Tunneling*. Doctoral Thesis. Graz University of Technology, Institute for Rock Mechanics and Tunnelling.

Young, W. C. and Budynas, R. G. (2002). *Roark's formulas for Stress and Strain*, 7th Edition, McGraw Hill.

Proceedings of the XVIII ECSMGE 2024
GEOTECHNICAL ENGINEERING CHALLENGES
TO MEET CURRENT AND EMERGING NEEDS OF SOCIETY
© 2024 the Authors
ISBN 978-1-032-54816-6
DOI 10.1201/9781003431749-92
Open Access: www.taylorfrancis.com, CC BY-NC-ND 4.0 license

ECSMGE 24
XVIII EUROPEAN CONFERENCE ON SOIL MECHANICS AND GEOTECHNICAL ENGINEERING

Repeated LWD test to assess the stiffness properties of clayey soil

Essai répété de LWD pour évaluer les propriétés de rigidité d'un sol argileux

D. Kuttah*
Swedish National Road and Transport Research Institute,VTI, Road and Track Engineering Division, Linköping, Sweden
**dina.kuttah@vti.se*

ABSTRACT: Geotechnical failures are often the result of not recognizing or adequately evaluating conditions prior to construction of a pavement system. The dominant geotechnical factor(s) for many pavement distresses is/are the stiffness and/or strength of the subgrade materials (U.S. Department of Transportation, 2006). To investigate further the stiffness properties of geotechnical materials, the current study has been undertaken to evaluate the feasibility of using a new multifunctional light weight deflectometer (LWD) to determine the in-situ dynamic deformation moduli (Evd) of clayey soil under repeated loading. This method is considered simple and a time saving technique to measure the in- situ dynamic properties of geotechnical materials. A sandy silty clay soil has been chosen for testing. At the beginning, the soil was compacted in a test pit, and then, series of in-situ repeated LWD were conducted at different ranges of water contents (namely 16%, 19% and 24%) under various applied stress levels (namely, 24 kPa, 38 kPa and 50 kPa). The test results have showed that increasing the water content decreases the dynamic deformation moduli, similarly, increasing the applied stresses decreases the dynamic deformation moduli as well. The multiple regression analysis has been used to model the dynamic deformation moduli of the tested soil based on the measurements reported from repeated in-situ LWD tests. A strong correlation has been found between the Evd and the water content, degree of saturation and applied axial stresses for the tested soil with high correlation coefficient of 0.99.

RÉSUMÉ: Les défaillances géotechniques sont souvent le résultat d'un manque de reconnaissance ou d'évaluation adéquate des conditions avant la construction d'un système de chaussée. Le(s) facteur(s) géotechnique(s) dominant(s) pour de nombreuses dégradations des chaussées est/sont la rigidité et/ou la résistance des matériaux de fondation (U.S. Department of Transportation, 2006). Afin d'étudier plus avant les propriétés de rigidité des matériaux géotechniques, la présente étude a été entreprise pour évaluer la faisabilité de l'utilisation d'un nouveau déflectomètre léger multifonctionnel (LWD) pour déterminer les modules de déformation dynamique in situ (Evd) d'un sol argileux soumis à des charges répétées. Cette méthode est considérée comme une technique simple et peu coûteuse en temps pour mesurer les propriétés dynamiques in situ des matériaux géotechniques. Un sol argilo-sableux a été choisi pour les essais. Au début, le sol a été compacté dans une fosse d'essai, puis une série d'essais LWD répétés in situ ont été effectués à différentes gammes de teneurs en eau (à savoir 16%, 19% et 24%) sous différents niveaux de contraintes appliquées (à savoir 24 kPa, 38 kPa et 50 kPa). Les résultats des essais ont montré que l'augmentation de la teneur en eau diminue le module de déformation dynamique, de même que l'augmentation des contraintes appliquées diminue également le module de déformation dynamique. L'analyse de régression multiple a été utilisée pour modéliser les modules de déformation dynamique du sol testé sur la base des mesures rapportées par les tests LWD in situ répétés. Une forte corrélation a été trouvée entre l'Evd et la teneur en eau, le degré de saturation et les contraintes axiales appliquées pour le sol testé avec un coefficient de corrélation élevé de 0,99.

Keywords: Applied stress levels; multiple regression analysis; repeated LWD test; stiffness properties; water content.

1 INTRODUCTION

With the introduction of the concept of resilient modulus (*Mr*) as the material stiffness, considerable attention has been dedicated to evaluating the behaviour of subgrade soils using repeated load triaxial test (Gomes Correia & Gillett, 1996, Lekarp et al., 2000). However, the resilient modulus tests are relatively expensive and time consuming. As a result, many of the pavement design standards are based on material properties evaluated using simpler and faster tests such as the static plate loading test, static *CBR*, and others (Razouki and Kuttah, 2004, Araya, et al. 2012). Although these static tests are very common all over the world, they cannot always be correlated efficiently to the dynamic response of the pavement structure under the actual traffic loading of moving vehicles. Therefore, it has become necessary to estimate the material properties using simple dynamic

tests (preferably, field tests) to reduce the gap between the requirement on material stability and properties measured in the field and that used in Mechanistic-Empirical Pavement Design (*MEPD*) (Kuttah, 2020, 2021 and 2023). Therefore, this study was mainly dedicated to assessing the efficiency of using the light weight deflectometer devise (*LWD*) in computing the dynamic moduli of fine-grained subgrade soil directly in-situ. For this purpose, several in-situ *LWD* tests have been carried out to measure the dynamic deformation moduli of clayey subgrade soil. The *LWD* tests have been carried out for many successive falling weight's drops at each tested point to eliminate as much as possible the plastic deformations that usually take place at the beginning of the test and as a result, the measured deformation moduli have mainly been related to the elastic deformations as confirmed in previous similar projects. The new procedure has been found to be quite useful to estimate the dynamic behavior of the selected soil tested in this study.

2 THE MODULUS OF ELASTICITY

The modulus of elasticity given in the following equation is calculated for one-layer system based on Boussinesq theory (1885).

$$E=2k(1-v^2)/Ar_o \quad (1)$$

where,

k=Load (peak)/deformation (peak)

r_o = The plate radius.

A= Stress distribution factor

v= Poisson's ratio

Note that $A= \pi$ for uniform stress distribution shape (mixed soil)

$A= 3\ \pi/4$ for parabolic stress distribution (Granular material)

A=4 for inverse-parabolic stress distribution (Cohesive soil)

This equation assumes the test media to be a linearly elastic, isotropic, homogeneous semi-infinite continuum. Two of the parameters required for determining the modulus, the shape factor for distribution of the contact stress between the plate and the soil (A) and Poisson's ratio (v), are assumed. Some *LWD* manufacturers give users the option of selecting values for A and v while others assume fixed values.

For the current study, the *Evd* is calculated using Eq. 1, assuming, A=4 and v= 0.35.

Although the setup and test times for *LWD* are relatively short (Siekmeier et al. 2009), there are some concerns about the effectiveness of the *LWD* in testing layered systems. This concern is mainly attributed to the fact that the *LWD's* zone of influence may extend beyond the thickness of the tested layer. Elhakim et.al. (2014) investigated the zone of influence of the *LWD* by performing the *LWD* test on calcareous and siliceous sands placed in layers with varying thicknesses (10, 20, 40, 60, and 80 cm) resting on a rigid boundary (concrete floor). They found that the *LWD* reading reflects the stiffness of both the tested soil and the rigid boundary. The influence of the rigid base boundary on the *LWD* modulus diminishes with increasing the thickness of the sand layer. For soil layer thickness to plate diameter ratios of 1.5 to 2, the effect of the rigid layer is considered negligible. Furthermore, tests performed using siliceous sands show similar findings. Tompai (2008) and Nazzal (2003) found also that the zone of influence of the *LWD* to vary between 1 and 2 times the plate diameter something which is in good agreement with the findings reported by Elhakim et. al. (2014). These findings have been considered during *LWD* tests performed in this study.

3 TESTING METHODOLOGY

A commonly available sandy silty clay subgrade soil was selected to be used in the current project. Material classification tests have been carried out to define the main physical and mechanical properties of the materials to be used for testing (e.g. particle size distribution, liquid limit (*LL*) and plastic limit (*PL*), compaction characteristics and specific gravity).

The in-situ *LWD* tests were carried out on a compacted layer of the chosen soil in a test pit located at the backyard of *VTI* in Linköping using a multi-functional *LWD*. During the in-situ *LWD* tests, the deformation moduli have been measured under repeated loading at different stress levels and water content conditions. Laboratory moisture tests have been carried out using oven drying method in parallel with the *LWD* tests. The Nuclear Density Gauge (*NDG*) was also used in this study to determine the in-situ density and moisture content of the tested soil in the test pit. The in-situ repeated *LWD* tests have been carried out at stress levels of about 24 kPa, 38 kPa, and 50 kPa. These stress levels have been chosen to simulate the real ranges of applied stresses on such weak clayey subgrade soil by moving vehicles for subgrade used for paved and unpaved roads. Due to the expected low bearing capacity of the tested soil, a maximum stress level of 50 kPa has been adopted. Note that *LWD* testing at stress levels lower than 24 kPa cannot be achieved using in-situ *LWD* with 30 cm plate diameter (as the one used in this study). This is because generating lower loads requires to reduce the

drop height significantly and, if so, the dropping weight will bounce faster than one manages to grab it resulting in uncounted additional successive rebound blows of the *LWD* weight.

4 CHARACTERISTICS OF THE TESTED SOIL

The particle size distribution test has been performed for the selected soil according to SS-EN 933-1 (2004) and the result of the test is illustrated in Figure 1 below.

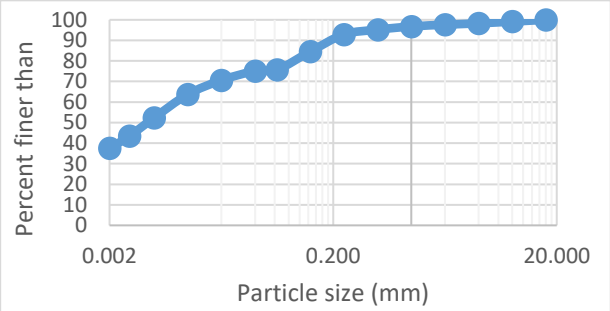

Figure 1. Particle size distribution of the tested soil.

The clay content in the soil was tested by sediment method at *SGI* (Swedish Geotechnical Institute) and the test results showed that the soil consisting of 37.5% clay particles (≤ 0.002 mm), fine content of 75.7% (clay and silt), the sand fraction was 21.9% and gravel fraction was 2.4%. The specific gravity of the selected soil was tested according to SS 027115 (1989), and it was found to be 2.65. The liquid and plastic limits were determined at *SGI* according to SS 027120 (1990) and SS 027121 (1990) respectively. The tests results revealed a liquid limit (*LL*) of 37% and a plastic limit of (*PL*) 17.8% resulting in a plasticity index of 19.2%.

The compaction properties of the soil under study were determined by modified Proctor test as per ASTM D1557 (2012). The soil samples were compacted at different molding water contents ranging between 7 to 27% to determine the water-density relationship, see Figure 2.

The results reveled that the compaction curve is irregularly (double peak) shaped as shown in Figure 2. The results of the compaction tests revealed that the tested soil has a maximum dry density of 1.825 g/cm^3 at two optimum moisture contents of 9.5% and 16.5%.

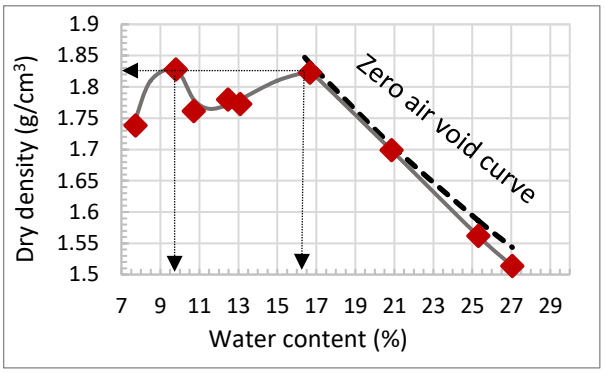

Figure 2. Compaction curve of the tested soil.

5 IN-SITU TESTING OF THE SELECTED SUBGRADE SOIL

In-situ tests were carried out on the selected soil, namely, field density and moisture content tests, and repeated in-situ *LWD* tests using *VTI's* multifunctional *LWD*, see Figure 3.

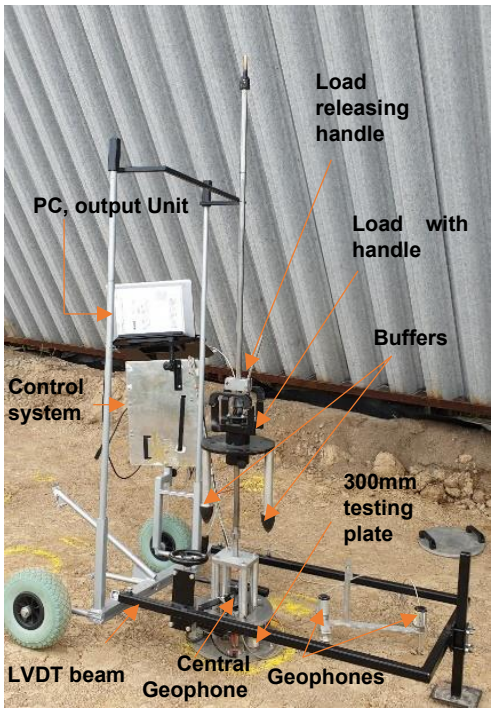

Figure 3. The VTI's light weight deflectometer used in this study.

These tests were carried out in a test pit compacted with the selected soil under controlled conditions. The test pit is located at the backyard of the Swedish Road and Transport Research Institute (*VTI*) and it is approximately 10 m long x 5 m width x 1.5 m depth. It has been equipped with a concrete well with a water discharging motor that can be used to control the ground water level during testing. The test pit is also instrumented with an electric drive motor roof panel that can be opened and closed with the help of an

electric motor to control as much as possible the testing conditions in the test pit.

6 RESULTS AND DISCUSSIONS

6.1 In-situ measurements of deformation moduli *Evd*

Figure 4 shows the effect of consecutive dropping of the falling weight on the average *Evd* of various points tested at three different moisture contents under 24 kPa, 38 kPa and 50 kPa applied stresses.

In Figure 4 with (16%) water content (i.e., the lowest tested water content), one can notice obvious fluctuation in readings of *Evd* with the number of falling weight drops while for higher water contents the fluctuation in readings almost diminished. This could be attributed to the high particle interlocking and shearing between the particles at the lowest water content of 16% which is near the optimum. This high particle interlocking, and high friction between the particles enables the energy transfer between the particles and hence rearrangement of particles within the soil matrix under the plate after each *LWD* drop something which causes fluctuation in readings with the successive falling weight drops. In the case of higher moisture content and hence high degree of saturation, as for the case of 19% and 24% water content, the friction between the particle has been decreased and less rearrangement of particles has been taken place with successive *LWD* drops something which resulted in more even *Evd* readings. Also, it can be noticed that for the case of tests carried out at 16% water content, the trendlines indicate that *Evd's*, in general, have been increasing slightly with increasing the number of *LWD* drops for the three applied stress levels conditions. This increase in *Evd* with increasing the number of repeated load cycles owing to the densification. With increasing the water contents, such increasing trend of *Evd* with the number of *LWD* drops has been diminished. This means that *Evd* attained a steady state due to the steadiness of the elastic deformation with the number of load cycles.

Furthermore, it can be seen from Figure 5 that increasing the water content decreases the dynamic moduli. The *Evd's* dropped from about 35kPa to about 20 kPa when the water contents increased from 16% to 24% for the case of 24 kPa applied pressure. Similarly, the *Evd's* dropped from about 23kPa to about 6 kPa for the same increase in water content for the case of 50 kPa applied pressure.

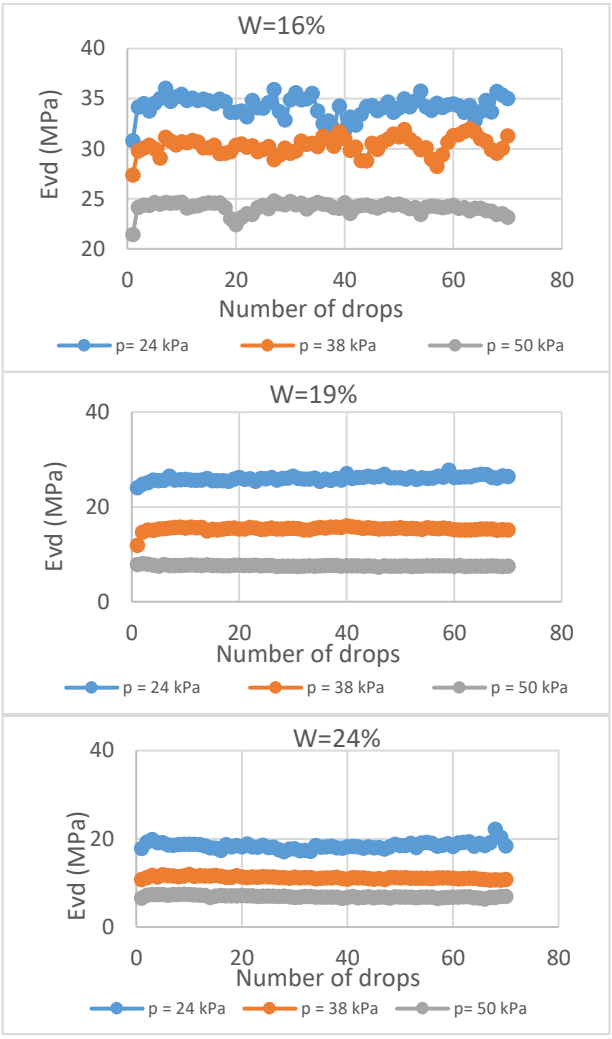

Figure 4. The average Evd measured by in-situ LWD tests on many points tested at various water contents under different applied pressures of 24, 38 and 50 kPa.

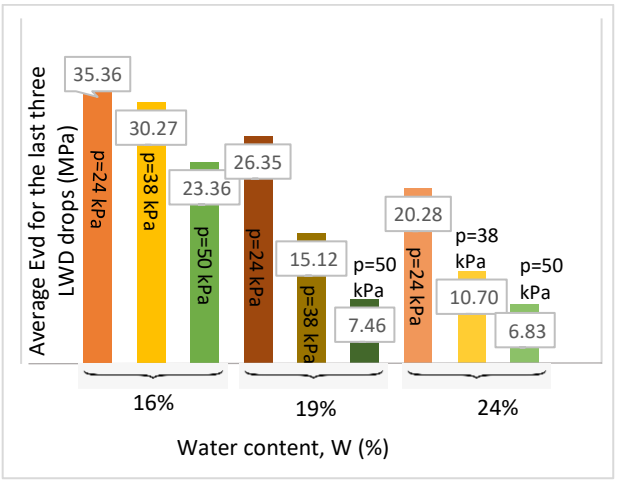

Figure 5. Effect of water contents and applied stresses on the LWD measurement for the tested clayey soil.

Thom and Brown (1987) attributed this behaviour to the effect of water since stiffness of the compacted material decreases due to the reduction of inter-particle bonds. Also, these tests are carried out at different

densities, so the changes in stiffness observed are due to different densities.

6.2 Modelling of the measured deformation moduli *Evd's*

Over the last decades, a lot of effort has been made to develop models that can describe and predict the non-linear resilient behavior of road materials.

In this study, multiple regression analysis has been used to correlate the measured deformation moduli *Evd's* to the water content, applied pressure and degree of saturation or density parameters, as given in the following equations, see Figure 6:

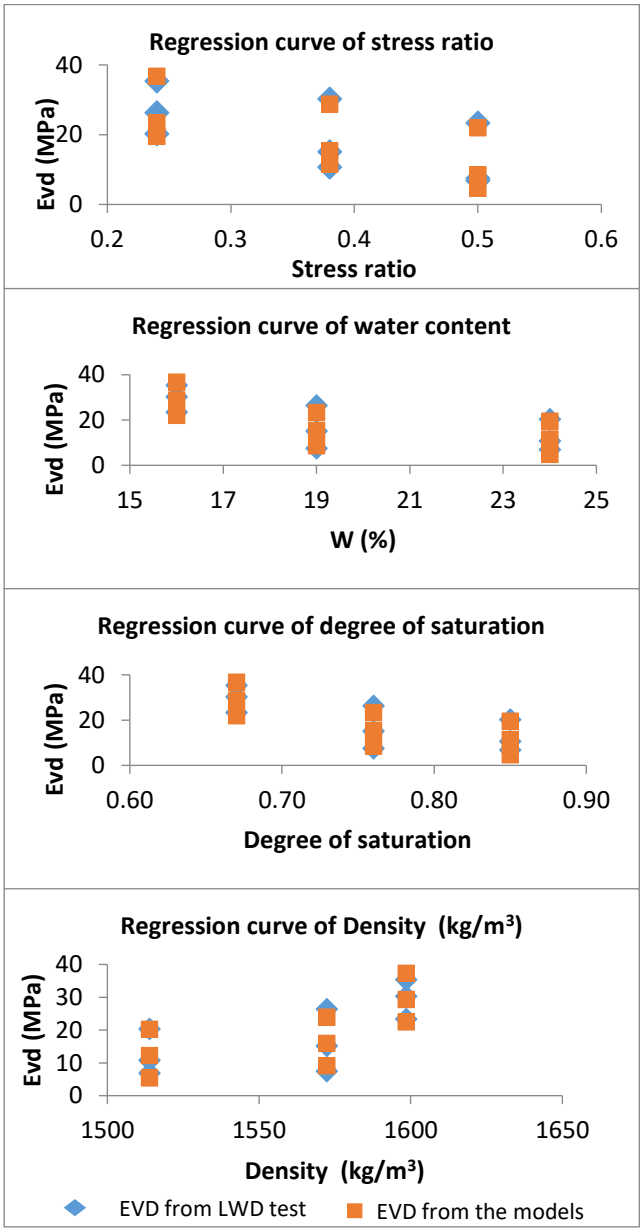

Figure 6. Regression curves describing the correlation between measured Evd and calculated Evd using Eq. 2.

$$Evd = 180.9 - 57(S) + 4.8(W) - 309.3(SR) \quad (2)$$

$$Evd = 2292.8 - 57(S) - 15{,}3(W) - 1{,}248(D) \quad (3)$$

where, *Evd* is the deformation moduli in MPa, *S* is the normalized applied stress level = *p/pa*, *p* is the axial applied stress during repeated *LWD* tests, *pa* is a reference stress of 100 kPa, *W* is the water content in %, *SR* is the degree of saturation and D is the field dry density in kg/m3.

A strong correlation has been found with multiple correlation coefficient of 0.988 representing very strong correlation after Ott and Longnecker (2010), see Figure 6.

7 CONCLUSIONS AND RECOMMENDATIONS

The overall tests results have been analyzed and the relations between the materials parameters collected from in-situ repeated *LWD* tests and those predicted by defined equations has been identified for the sandy silty clay tested in this project, as follows:

1. It has been observed that for the case of *LWD* tests carried out at 16% water content, the *Evds* curves reported slight increasing trend with increasing the number of LWD drops for the three applied stress levels conditions. With increasing the water contents, such increasing trend of Evd with the number of LWD drops has been diminished.
2. It has been noticed that for tests carried out at 16% water content, the lowest tested water content adopted in this study, the readings fluctuated with the number of falling weight drops while for higher water contents of 19% and 24%, the fluctuation in readings almost diminished. It has also been noticed that increasing the water content decreases the dynamic moduli, similarly, increasing the applied stresses decreases the dynamic deformation moduli as well.
3. Regarding the prediction of the dynamic deformation moduli *Evd*, a strong correlation has been found between the *Evd* and the water content, applied axial stresses, and degree of saturation or density for the tested soil with high correlation coefficient of 0.988.

The models adopted in this study to estimate the dynamic deformation moduli, namely Eq. 2 and Eq.3, are sophisticated enough and easy to use. These models are valid for the material used in this study and can be used to solve practical problems concerning the stiffness estimation under repeated traffic loading for engineering purposes.

ACKNOWLEDGEMENTS

The author is grateful for the financial support provided by the Swedish Transport Administration.

Thanks also to KUAB AB for developing further the VTI's lightweight deflectometer in cooperation with the author.

REFERENCES

Araya, A. A., Huurman, M., Molenaar A. A. and Houben L.J.M. (2012). Investigation of the resilient behavior of granular base materials with simple test apparatus, *Materials and Structures* 45:695-705. https://doi.org/10.1617/s11527-011-9790-1.

ASTM D1557 (2012). Standard test methods for laboratory compaction characteristics of soil using modified effort (56,000 ft-lbf/ft^3-2,700 kN-m/m^3, ASTM International, West Conshohocken, PA, United States.

Boussinesq, M. J. (1885). *Application des potentiels a l'étude de l'équilibre et du mouvement des solides élastiques, avec des notes étendues sur divers points de physique mathématique et d'analyse*, Paris: Gauthier-Villard imprimeur libraire.

Elhakim, A. F., Elbaz, K., and Amer, M. I. (2014). The use of light weight deflectometer for in situ evaluation of sand degree of compaction, Housing and Building National Research Center HBRC Journal, 10, 298-307. http://ees.elsevier.com/hbrcj.

Gomes Correia, A. and Gillett, S. (1996). *Resilient behaviour of Soils*, In Flexible pavements edited by Gomes Correis, A. , Balkema, Rotterdam, ISBN 90 5410 523 2, resilient.pdf (uminho.pt).

Kuttah, D. (2020). Simple and quick evaluation of unbound materials bearing capacities that could be used as input data in Mechanistic-Empirical Pavement Design, VTI report 1054, ISSN 0347-6030, in Swedish. VTI rapport 1054 (diva-portal.org).

Kuttah, D. (2021). Determining the resilient modulus of sandy subgrade using cyclic light weight deflectometer test, *Transportation Geotechnics* 27, 100482, ISSN 2214-3912, https://doi.org/10.1016/j.trgeo.2020.100482.

Kuttah, D. (2023). Assessing the interactions among factors affecting the light weight deflectometer measurements, *Bulletin of Engineering Geology and the Environment*, 82, 238. https://doi.org/10.1007/s10064-023-03231-2.

Lekarp F, Isacsson U, Dawson A (2000). State of the art. II: Permanent strain response of unbound aggregates.", *J. Transp. Eng.* 126(1):76–83. https://doi.org/10.1061/(ASCE)0733-947X(2000)126:1.

Nazzal, D. M. (2003). *Field evaluation of in-situ test technology for QC/QA during construction of pavement layers and embankments*, (Master's thesis), Louisiana State University, Baton Rouge.

Ott, L. and Longnecker M. (2010). *An Introduction to Statistical Methods and Data Analysis*, Sixth Edition, Brooks/Cole, Cengage Learning, USA. ISBN-13: 978-0-495-01758-5.

Razouki, S. S. and Kuttah, D. K., (2004). Effect of Soaking Period and Surcharge Load on Resilient Modulus and California Bearing Ratio of Gypsiferous soils, *Quarterly Journal of Engineering Geology and Hydrogeology,* London, Vol. 37, pp. 155-164. http://qjegh.geoscienceworld.org/content/37/2/155.

Siekmeier, J., Pinta, C., Merth, S., Jensen, J., Davich, P., Camargo, F. & Beyer, M. (2009). Using the dynamic cone penetrometer and light weight deflectometer for construction quality assurance, Minnesota Department of Transportation, Report No. MN/RC 2009-12. https://www.lrrb.org/pdf/200912.pdf.

SS-EN 933-1 (2004). Tests for geometrical properties of aggregates, Part 1 "Determination of particle size distribution – sieving method, SIS, Swedish Standards Institute, Stockholm, Sweden.

Swedish Standard SS 027115 (1989). Geotechnical tests – Grain density and specific gravity. Edition 3, Swedish Standards Institute, Stockholm.

Swedish Standard SS 027120 (1990). Geotechnical tests - Cone liquid limit. Edition 2, Swedish Standards Institute, Stockholm.

Swedish Standard SS 027121 (1990). Geotechnical tests – Plastic limit. Edition 2, Swedish Standards Institute, Stockholm.

Thom, N. H. and Brown,S. F. (1987). Effect of Moisture on the Structural Performance of a Crushed-limestone Road Base, *Transportation Research Board, Transportation Research Record* 1121. http://worldcat.org/isbn/0309045010.

Tompai, Z. (2008). Conversion between static and dynamic load bearing capacity moduli and introduction of dynamic target values, *Periodica Polytechnica, Civil Engineering*, Hungary, 52–2: pp. 97-102. https://doi.org/10.3311/pp.ci.2008-2.06.

U.S. Department of Transportation (2006). Geotechnical Aspects of Pavements Reference Manual, Federal Highway Administration, Publication No. FHWA NHI-05-037, NHI Course No.132040, https://www.fhwa.dot.gov/engineering/geotech/pubs/05037/.

Proceedings of the XVIII ECSMGE 2024
GEOTECHNICAL ENGINEERING CHALLENGES
TO MEET CURRENT AND EMERGING NEEDS OF SOCIETY
© 2024 the Authors
ISBN 978-1-032-54816-6
DOI 10.1201/9781003431749-93
Open Access: www.taylorfrancis.com, CC BY-NC-ND 4.0 license

ECSMGE 24
XVIII EUROPEAN CONFERENCE ON SOIL MECHANICS AND GEOTECHNICAL ENGINEERING

Some applications of interaction domains to pile foundations design

Quelques applications des domaines d'interaction à la conception de fondations sur pieux

A. Lambrughi*, A. Chiarelli, M. Orlandini
Webuild s.p.a, Rome, Italy

A. Mandolini
Università degli studi della Campania "Luigi Vanvitelli", Dipartimento di Ingegneria, Aversa (CE), Italy

a.lambrughi@webuildgroup.com

ABSTRACT: Pile foundations are generally checked against eccentric vertical loads by referring to the most loaded pile in the group, whose length is set to achieve a design bearing capacity at least equal to its design vertical load. All other piles in the group are then assigned the length obtained in this way. Intuitively, any pile group designed with this method is left with plenty of spare bearing capacity, well beyond the demand from minimum safety factors. In contrast, interaction domains allow to treat a pile group as a whole system and to include the contribution of each pile into the overall bearing capacity of the foundation, allowing the mobilisation of limit bearing capacity for most piles in the group. The lack of closed-form solutions made in the past the use of interaction domains impractical. However, some recent advances now provide analytical relationships for the full shape of the domain, without limitations to the pile group geometry.Some applications of interaction domains are presented in the paper for two Italian High Speed Railway projects, currently under construction.

RÉSUMÉ: Les fondations sur pieux sont généralement vérifiées contre les charges verticales excentriques en se référant au pieu le plus chargé du groupe, dont la longueur est définie pour atteindre une capacité portante de conception au moins égale à sa charge verticale de conception. Tous les autres pieux du groupe se voient ensuite attribuer la longueur ainsi obtenue. Intuitivement, tout groupe de pieux conçu avec cette méthode dispose d'une grande capacité portante disponible, bien au-delà de l'exigence des facteurs de sécurité minimaux. En revanche, les domaines d'interaction permettent de traiter un groupe de pieux comme un système global et d'inclure la contribution de chaque pieu dans la capacité portante globale de la fondation, permettant ainsi de mobiliser la capacité portante limite pour la plupart des pieux du groupe. Le manque de solutions de forme fermée a rendu par le passé l'utilisation de domaines d'interaction peu pratique. Cependant, certaines avancées récentes fournissent désormais des relations analytiques pour la forme complète du domaine, sans limitations à la géométrie du groupe de pieux. Certaines applications des domaines d'interaction sont présentées dans l'article pour deux projets de chemin de fer italien à grande vitesse, actuellement en construction.

Keywords: Pile groups; interaction domains; pile capacity.

1 INTRODUCTION

Axially loaded pile foundations shall be designed to provide adequate strength against a bearing capacity failure.

Routine design approach is typically based on three fundamental steps:

- Assessment of the compression (F_c) or tension (F_t) load acting on each pile belonging to the pile foundation,
- Evaluation of the individual axial capacity of the single pile under compressive (R_c) or tensile (R_t) loads,
- Estimate of the most probable failure mechanism (individual pile failure mechanisms or block failure mechanism).

With the only exception of groups with piles embedded in fine-grained soils at spacing s smaller than some critical value (say 2–4 times the pile diameter d; de Sanctis and Mandolini, 2006), individual pile failure mechanism occurs, and the axial pile resistance of the pile group R_g is evaluated as follows:

$$R_g = \sum_1^N R_i \qquad (1)$$

Checks against ULS (Ultimate Limit State) are then generally made with reference to the most loaded pile within the group, in practice selecting pile length L and diameter d for all the piles in order to satisfy the following inequality according to EC7:

$$R_{i,d} \geq F_{i,d,max} \qquad (2)$$

where: $R_{i,d}$ = single pile design resistance; $F_{i,d,max}$ = maximum design action on single pile.

However, it is all too evident that achievement of the axial capacity on the most loaded pile does not represent a failure condition for the whole group and can be viewed just as the onset of yielding. At this point, the pile group is still capable to carry a further increase in the external load taking advantage from the ductility of the system.

To consider this aspect, in the past attention has been placed on the assessment of interaction diagrams of pile groups under vertical eccentric loads, although limited to experimental observations on reduced scale pile groups resting on homogeneous soils (for instance, Meyerhof et al., 1983; Meyerhof and Yalcin, 1984). Recently, a closed-form exact solution for the interaction domains of pile groups under vertical eccentric loads has been proposed by Di Laora et al. (2019) to describe the failure of a group of piles considered as a whole, then also extended to the case of inclined eccentric load (Di Laora et al., 2022).

In the following, the advantages coming from the applications of the interaction domains approach will be shown with reference to examples taken from two Italian High Speed Railway Line (HSRL) projects, currently under construction. Both projects constitute an important part of the European TEN-T program for sustainable transport, which aims to transfer 50% of the currently road freight traffic to railway by 2050, triple the high-speed rail network and connect the main seaports to the railways and reduce emissions from transport by 60%.

2 VERONA-PADUA HSRL PROJECT

Figure 1 shows the pile group layout for Pier 3 of one of the viaducts crossing the HSRL. The group is composed by eight bored cast in situ piles with d=1.2m, installed at spacing s=3.6m=3·d. Piles are connected to a stiff rectangular raft having B_{max}=13.2m and B_{min}=6m.

Local ground conditions feature predominantly cohesive soils, as summarised in Table 1 (unit soil weight, γ; friction angle, ϕ).

Compression conditions were found to govern single pile sizing. In particular, the design maximum compression load on a single pile was found to be equal to $F_{c,d}$=4900kN, which from single pile bearing capacity check would have required a pile length of 44m ($R_{c,d}$=4910kN). This design bearing capacity value was calculated according to the ULS approach in the Italian Building Code (shaft for compression, $\gamma_{s,c}$=1.15; shaft for tension, $\gamma_{s,t}$=1.25; base, γ_b=1.35; number of soil profiles n=1 → ξ_3=ξ_4=1.70)

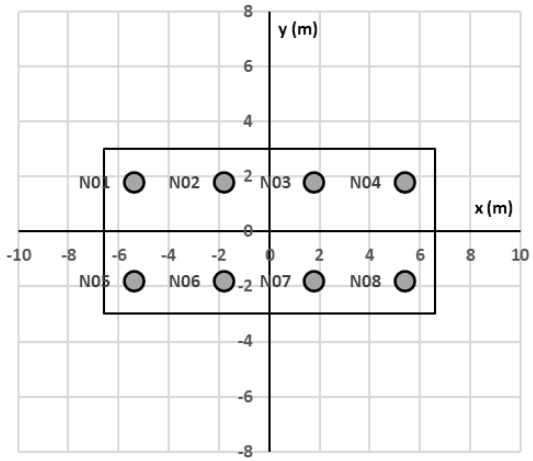

Figure 1. Pile group layout for Verona-Padua HSRL.

Table 1. Soil properties for Verona-Padua HSRL.

Soil	Thickness [m]	γ [kN/m³]	ϕ [°]
Gravels	3	19	40
Clayey silts	18	19	26
Silty sands	2	19	35
Clayey silts	>25	19	26

The design was then optimised iteratively by means of the interaction domains, by investigating pile group capacity for shorter pile lengths. Figure 2 shows the interaction domains with respect to the symmetry axes of the group and for piles length of 38m (i.e. based on $R_{c,d}$ and $R_{t,d}$ values of 4395kN and 3818kN, respectively). Also shown are the total external loads on the pile group, in terms of axial force and moment (N_d=25.2MN, $M_{x,d}$=4.6MNm, $M_{y,d}$=4.3MNm), which fall into the two domains and prove that the design bearing capacity of the group is sufficient to carry the design external loads.

Implementing the interaction domains led then to a net reduction of 6m length for each of the piles of the group.

3 NAPLES-BARI HSRL PROJECT

In Figure 3 is reported a typical solution adopted for one of the many piers of the project. Twelve bored cast in situ piles with L=30m and d=1.5m were installed at

spacing s=4.5m=3·d. Piles were connected to a stiff rectangular raft having B_{max}=16.5m and B_{min}=12m.

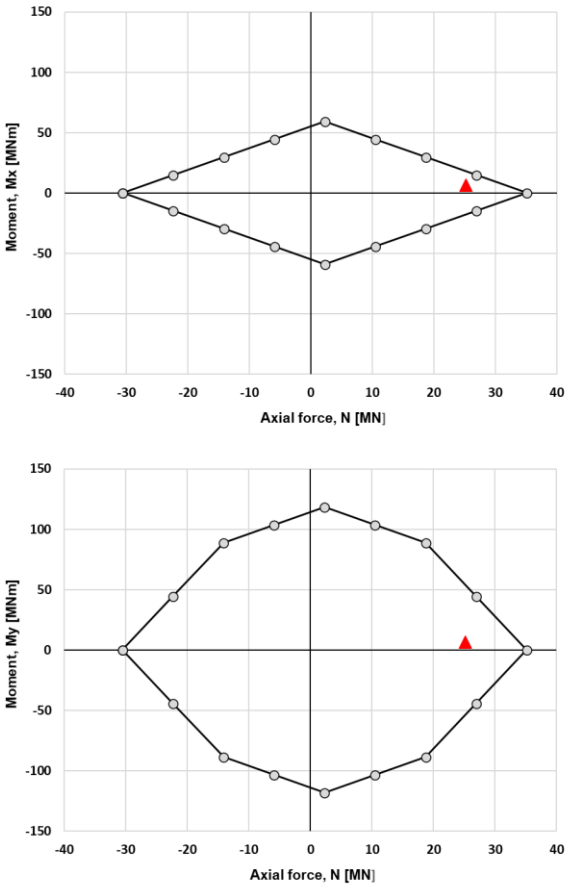

Figure 2. Interaction domains (L = 38m) for Verona-Padua HSRL.

Boreholes and in situ tests revealed the presence of a thick deposit of pyroclastic cohesionless soils up to 50m depth from ground surface, whose main properties for bearing capacity evaluation are listed in Table 2.

According to the evaluation made by designer, the calculated single pile bearing capacity under compressive load is $R_{c,cal}$ = 9.98MN. Adopting the partial factors according to Italian Code (shaft for compression, $\gamma_{s,c}$=1.15; shaft for tension, $\gamma_{s,t}$=1.25; base, γ_b=1.35; number of soil profiles n=1 → ξ_3=ξ_4=1.70), the design compressive resistance is $R_{c,d}$=5.08MN. Since the design action $F_{c,d}$ for the most loaded pile is 5.02 MN, ULS check (eq. 2) is satisfied with a ratio $R_{c,d}/F_d$=1.01.

In Figure 4 is reported the interaction domain evaluated on the basis of the design resistances. In the same figure is also reported the point representative of the worst loading design condition for the pile group (N_d=49MN, $M_{x,d}$=18.1MNm, $M_{y,d}$=19.5MNm), clearly falling within the domain.

During the installation of piles, some construction issues occurred. Non-destructive ND tests carried out on all piles revealed that problems occurred near the pile base with a maximum length of 4m, thus reducing in this case the effective length to 26m from the original 30m.

In such situations, typically the first practical solution aimed to re-establish the desired safety margin against failure is that of replacing defective piles with additional piles installed close to the original position of the defective ones.

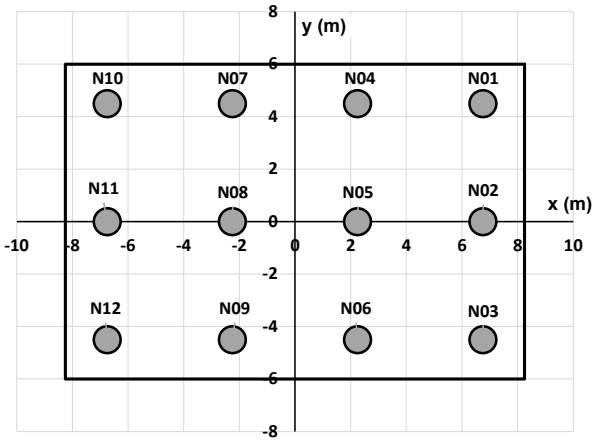

Figure 3. Pile group layout for Naples-Bari HSRL.

Table 2. Soil properties for Naples-Bari HSRL.

Soil	Thickness [m]	γ [kN/m³]	ϕ [°]
Remoulded pozzolana	4	16.0	30
Silty sand with interbedded pozzolana layers	7	16.0	34
Medium dense pozzolana	7	15.0	37
Dense pozzolana	32	16.0	39

The use of interaction domains, on the contrary, allows to accept the pile group with defects because, although reduced, it was found that the point representative of the worst loading condition kept inside the interaction domain (Figure 5).

Adopting this approach for all those piled foundations where ND tests revealed defects of different types, the number of cases where additional piles had to be installed reduced significantly.

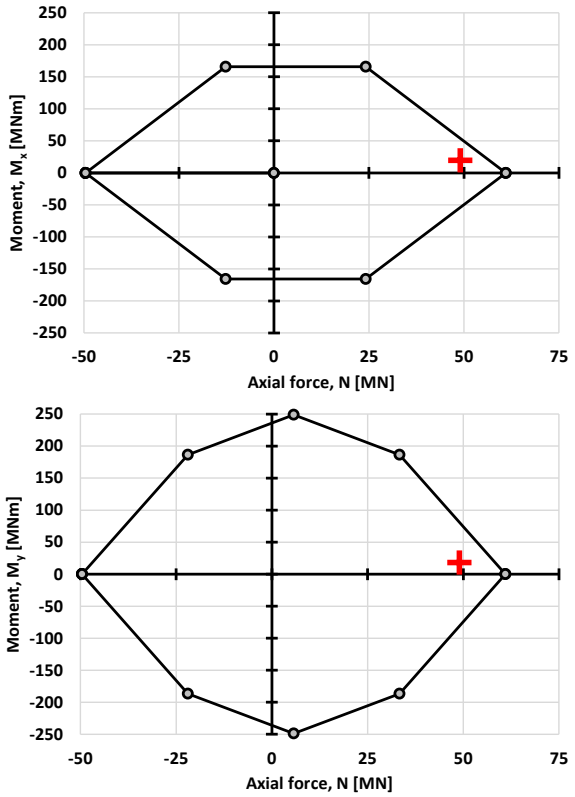

Figure 4. Interaction domains (L = 30 m) for Naples-Bari HSRL.

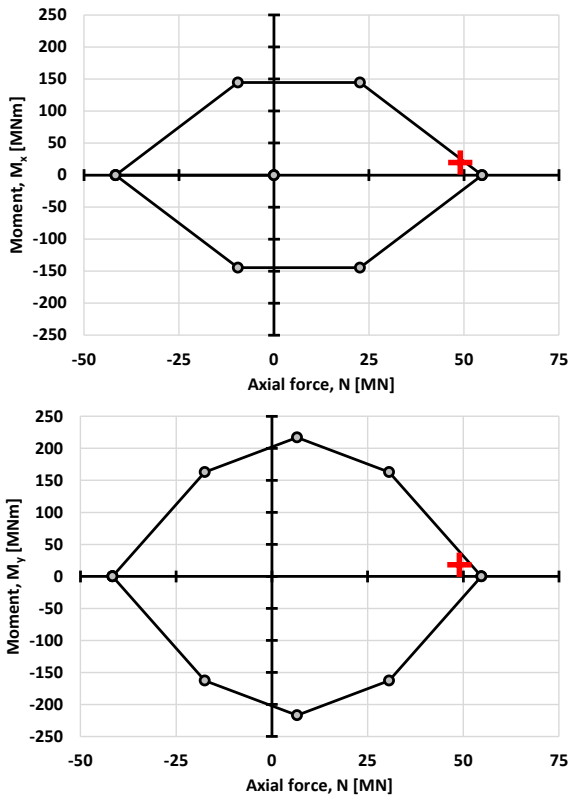

Figure 5. Interaction domains (L = 26 m) for Naples-Bari HSRL.

4 CONCLUSIONS

Pile sizing through single pile bearing capacity checks generally leads to overdesigned pile groups, which are left with some supplementary bearing capacity. On the contrary, interaction domains allow direct comparison between overall group capacity and total external loads on the group by taking into consideration the contribution from all piles.

Two example applications of interaction domains have been presented, one for the optimisation of design obtained from a traditional single pile bearing capacity check and one for the closure of non-conformities that resulted from construction issues.

The benefits from the method are evident. The routine adoption of interaction domains in pile foundation design would allow for more efficient design and avoid in some cases unnecessary re-work.

REFERENCES

Di Laora R., de Sanctis L. and Aversa S. (2019). Bearing capacity of pile groups under vertical eccentric load. *Acta Geotechnica*, 14: 193–205. https://doi.org/10.1007/s11440-018-0646-5.

Di Laora R., Iodice C. and Mandolini A. (2022). A closed-form solution for the failure interaction diagrams of pile groups subjected to inclined eccentric load. *Acta Geotechnica*, 17: 3633-3646. https://doi.org/10.1007/s11440-021-01439-8.

de Sanctis L. and Mandolini A. (2006). Bearing Capacity of Piled Rafts on Soft Clay Soils. *ASCE Journal of Geotechnical and Geoenvironmental Engineering*, 132: 1600-1610. https://doi.org/10.1061/(ASCE)1090-0241(2006)132:12(1600).

Meyerhof, G.G. and Yalcin A.S. (1984). Pile capacity for eccentric inclined load in clay. *Canadian Geotechnical Journal*, 21: 389–396. https://doi.org/10.1139/t84-043.

Meyerhof, G.G., Yalcin A.S. and Mathur S.K. (1983). Ultimate pile capacity for eccentric inclined load. *Journal Geotechnical Engineering ASCE*, 109: 408–423. https://doi.org/10.1061/(ASCE)0733-9410(1983)109:3(408).

Proceedings of the XVIII ECSMGE 2024
GEOTECHNICAL ENGINEERING CHALLENGES
TO MEET CURRENT AND EMERGING NEEDS OF SOCIETY
© 2024 the Authors
ISBN 978-1-032-54816-6
DOI 10.1201/9781003431749-94
Open Access: www.taylorfrancis.com, CC BY-NC-ND 4.0 license

ECSMGE 24
XVIII EUROPEAN CONFERENCE ON SOIL MECHANICS AND GEOTECHNICAL ENGINEERING

Discrete modelling of stress relaxation in crushable sands based on fracture theory

Modélisation discrète de la relaxation des contraintes dans les sables concassés basée sur la théorie de la fracture

J. Lei*, M. Arroyo
Department of Geotechnical Engineering and Geosciences, Polytechnic University of Catalonia (UPC), Barcelona, Spain

M.O. Ciantia
School of Science and Engineering, University of Dundee, Dundee, UK
Università Degli Studi di Milano Bicocca, Milan, Italy

N. Zhang
Institute of Geomechanics and Underground Technology, RWTH Aachen University, Aachen, Germany

**jiangtao.lei@upc.edu*

ABSTRACT: Stress relaxation of quartz sand is simulated using a recently proposed physically based time-to-fracture discrete element method (DEM) framework. The relaxation of stress on sands under high confining pressure is modelled using stress-corrosion induced grain fracture. This feature is embedded into a pre-existing particle-splitting based rough crushable model for Fontainebleau sand. A controlled on-off computational strategy is adopted to advance the simulation. The computed oedometer stress relaxation curve compares favourably with previous experimental results. Triaxial stress relaxation results indicate that stress relaxation increases linearly with time. Contact forces become more homogenous during stress relaxation; as a result, the sample becomes more stable. These microscopic behaviours agree with some observations in pile ageing, suggesting that the model may be adopted directly to investigate such engineering scale phenomena due to its conceptual simplicity, computational efficiency and ease of calibration.

RÉSUMÉ: La relaxation des contraintes du sable de quartz est simulée à l'aide d'un cadre de méthode des éléments discrets (DEM) récemment proposé, basé sur la physique. La relaxation des contraintes sur les sables soumis à une pression de confinement élevée est modélisée à l'aide de la fracture des grains induite par la corrosion sous contrainte. Cette fonctionnalité est intégrée dans un modèle broyable brut préexistant basé sur la division des particules pour le sable de Fontainebleau. Une stratégie de calcul marche-arrêt contrôlée est adoptée pour faire avancer la simulation. La courbe de relaxation des contraintes calculée par l'œdomètre se compare favorablement aux résultats expérimentaux précédents. Les résultats de la relaxation des contraintes triaxiales indiquent que la relaxation des contraintes augmente linéairement avec le temps. Les forces de contact deviennent plus homogènes lors de la relaxation des contraintes; en conséquence, l'échantillon devient plus stable. Ces comportements microscopiques sont en accord avec certaines observations sur le vieillissement des pieux, suggérant que le modèle peut être adopté directement pour étudier de tels phénomènes à l'échelle technique en raison de sa simplicité conceptuelle, de son efficacité de calcul et de sa facilité d'étalonnage.

Keywords: Stress relaxation; discrete-element-modelling; particle crushing; time dependence.

1 INTRODUCTION

Sand stress relaxation is observed when stress decreases under zero deformation. Circumferential stress relaxation, which may strengthen the radial stress along the pile shaft, has been long regarded as one of the most plausible reasons for pile aging (Axelsson, 2000). At high stress levels grain breakage is at root of sand stress relaxation (Lade and Karimpour, 2013).

Current laboratory observations include oedometric stress relaxation tests (Levin et al., 2021) and triaxial stress relaxation tests (Pham Van Bang et al., 2007; Lade and Karimpour, 2015). Different from oedometric stress relaxation where deformation is nil, triaxial stress relaxation is observed by just keeping the axial strain constant under constant cylindrical stress conditions. A linear relationship between the deviatoric stress relaxation and log scale time was observed in those tests.

The discrete element method (DEM) is a very useful tool to find grain-scale explanations of specimen-scale observations. However, as an explicitly advancing method, DEM computation timesteps are always below 1 μs, leading to an overwhelming computational cost for simulating stress relaxation experiments lasting hours to even years. To overcome this difficulty, Wang and Xia (2021), using a rate process theory (RPT) model to simulate stress relaxation in granular materials, scaled up the model viscous parameters by very large numbers to accelerate the simulation. The model is then hard to apply to engineering scale since those scaled parameters lack a clear physical basis and are directly calibrated on specimen-scale responses.

Another option for simulating stress relaxation in sand is based on grain fracture. Xu et al. (2018) adopt a fracture based DEM model to simulate stress relaxation of granular materials. Time advancing is achieved using an on-off computation strategy: a strength ageing model to advance time and DEM dynamic computation only switched on when model equilibrium is required. Xu et al. (2018) used bonded agglomerates, which strongly limits the number of particles in the model, and calibrated parameters on specimen-scale.

In this work we use a time-to-fracture rough crushable DEM sand model to simulate stress relaxation. The model is physically based, computationally efficient and easy to calibrate.

2 MODEL DESCRIPTION

A rough surface Hertzian contact model proposed by Otsubo et al. (2017) was incorporated into the Fontainebleau sand crushable model in Ciantia et al. (2019) by Zhang et al. (2021), to achieve the simulation of mechanical behaviour and accompanied grain sized evolution of real Fontainebleau NE34 sand. The particle strength dominated failure criterion of the model is described in Equation (1):

$$F_n \leq \sigma_{lim,0} \left(\frac{d}{d_0}\right)^{\frac{-3}{m}} f(var)\pi r'\delta \qquad (1)$$

where F_n is the contact normal force, the right hand side of equation is limit force F_{lim}, and it includes two parts: particle strength is $\sigma_{lim,0} \left(\frac{d}{d_0}\right)^{\frac{-3}{m}} f(var)$, both considering strength variance $f(var)$ and size effect $\left(\frac{d}{d_0}\right)^{\frac{-3}{m}}$ in real quartz sand. $\sigma_{lim,0}$ is particle strength at a reference diameter d_0. $\pi r'\delta$ is Hertz contact area. Detailed means of the parameters are shown in Zhang et al. (2021).

Independent of particle strength dominated failure, A crack propagation model proposed by Lei et al. (2024) is adopted here which is an adapted version of normalized Charles (1958) law to determine the crack velocity:

$$v = v_0 (\frac{\sigma}{\sigma_{lim}})^n \qquad (2)$$

where v is crack velocity, v_0 is the reference velocity (0.1 m/s according to Tapias et al., (2015)). σ is the maximum normal contact stress acting on a particle, σ_{lim} is particle strength, which is already defined in Equation (1). n is the stress corrosion index.

Crack half-length a is updated every time interval Δ_t as:

$$a = a_0 + v \times \Delta_t \qquad (3)$$

where a_0 is the initial crack length seeded into each particles following a random uniform distribution ranging from $0.001d$ to $0.5d$, and d is particle diameter.

When $F_n > F_{\text{lim}}$ or $a > 0.5d$, the particle splits into 14 particles, and of which the local axis rotates to direction of normal component of maximum contact force.

Details on the particle splitting mechanism and calibration procedure for the rough crushable time-to-fracture model are given in Zhang et al. (2021) and Lei et al. (2023). Calibrated parameters are presented in Table 1.

Table 1. Model parameters for Fontainebleau sand REV (Lei et al. 2023).

Category	Parameter/unit	Value
Particle failure criteria	G/GPa	32
	ν	0.19
	μ	0.275
	m	12
	$\sigma_{lim,0}$/GPa	3.75
	var	0.38
	d_c/d_{50}	0.55
	d_{max}/mm	0.27
	d_{min}/mm	0.01
Contact roughness	S_q/μm	0.6
	n_1	0.05
	n_2	5
Crack Propagation	v_0	0.1
	n	60

Note: G=shear modulus; ν = Poisson's ratios; μ = interparticle friction coefficient; dc= particle comminution limit; d_{50}=50% pass particle size; d_{max}, d_{min}=maximum, minimum particle diameter; S_q=particle surface roughness; n_1, n_2= roughness parameters.

2.1 Off-DEM ageing

Off-DEM ageing is a strategy to advance time during DEM simulation since the extreme small timestep (below 10^{-6} s) makes impossible continuous simulation of experiments lasting hours to days. The details of Off-DEM ageing are described in Lei et al. (2023, 2024). The simulation begins with a dynamic computation with all model features activated, lasting at least 150,000 cycles. Then it switches to Off-DEM ageing, where only particle crack growth is activated, at a constant velocity given by that at the end of the previous dynamic computation. Potential broken particles during off-DEM (N_{break}) are counted, and once this number reaches a target (in this work N_{break} = 30), dynamic computation is switched on again to break those particles. Those two steps are carried out alternately until the target relaxation time is reached.

3 STRESS RELAXATION SIMULATION

A Fontainebleau sand (quartz) representative element volume (REV) cube containing 11500 particles, of 4mm side with target void ration of 0.65 was formed in PFC3D 5.00.40. Stress relaxation servo-control was achieved by rigid wall motion, setting as boundaries of the REV cube.

3.1 Oedometric stress relaxation

Oedometric stress relaxation with initial vertical stress of 7.5 MPa was carried out to compare with the laboratory results of medium dense sand. Stress during relaxation is normalized by the value at 4s. An acceptable agreement can be observed even if the rough-crushing contact model was initially calibrated to represent a different sand. For the simulation curve, red dots correspond to the periods of dynamic computation, and the time between two red dots is the off-DEM ageing time.

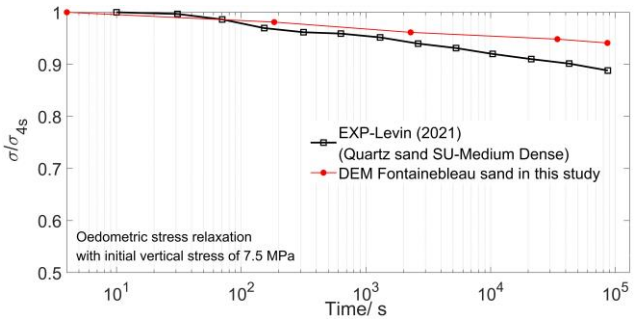

Figure 1. Comparison of DEM model stress relaxation and laboratory results for medium dense quartz sand.

3.2 Triaxial stress relaxation

Triaxial stress relaxation tests were carried out at a high confining pressure of 10 MPa to ensure the sample is in a particle breakage dominated state. Triaxial shearing to failure (30% deviatoric stain) of REV was carried out first to find out the maximum deviatoric stress q_{max} (22.6 MPa). Then stress relaxation tests were conducted maintaining mobilized strength (q/q_{max} = 0.7) for 1 day.

Taking the 4th dynamic computation of triaxial stress relaxation as an example (which denotes the 4th data point in Figure 3), the fluctuation of confining pressure and generated volumetric strain due to previous off-DEM ageing is shown in Figure 2. Figure 2(a) indicates that the confining pressure fluctuation remains a low value during stress relaxation, and Figure 2(b) indicates that although the triaxial stress relaxation accompanying with the generation volumetric strain, the strain remains moderate. These results indicate that dynamic disruption generated by off-DEM ageing remains moderate, and that the control value (N_{break} = 30) in switching to DEM is appropriate (see also Lei et al. (2023), for a parametric study on N_{break}).

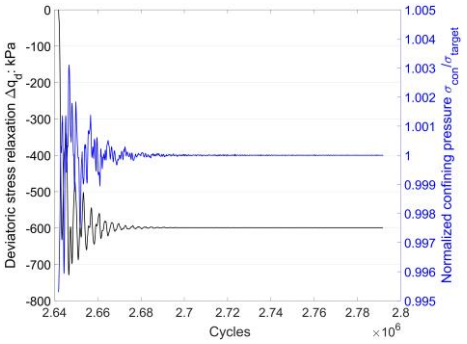

(a)

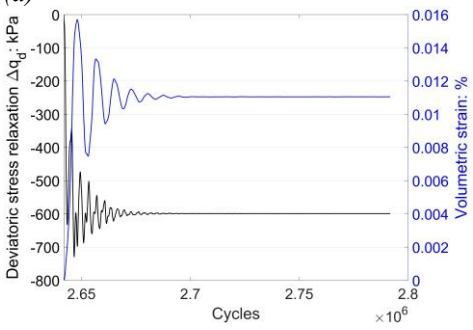

(b)

Figure 2. Confining pressure fluctuation(a) and generated volumetric strain (b) during 4th dynamic computation of triaxial stress relaxation.

Figure 3 shows the simulated triaxial stress relaxation with time. A linear relationship can be observed, and similar relaxation trends were also

observed in Lade and Karimpour (2015) and Pham Van Bang et al. (2007) for quartz sands.

Figure 4 shows the standard deviation evolution of normal contact forces F_n and tangential contact forces F_t during stress relaxation. A decreasing trend can be observed for all cases, indicating how stress relaxation homogenizes contact forces. The similar stress homogenization was also observed by Zhang and Wang (2015) for Toyoura sand around pile after pile set-up, in which they adopt tiny sensing elements to measure the normal contact stresses.

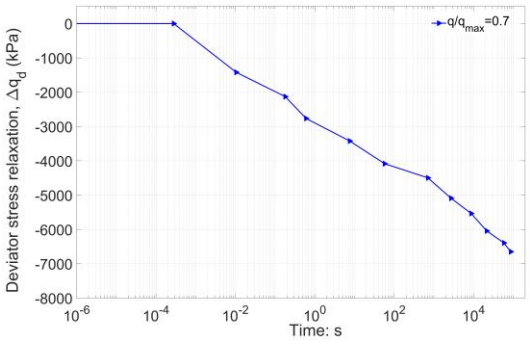

Figure 3. Triaxial stress relaxation with time in DEM simulation.

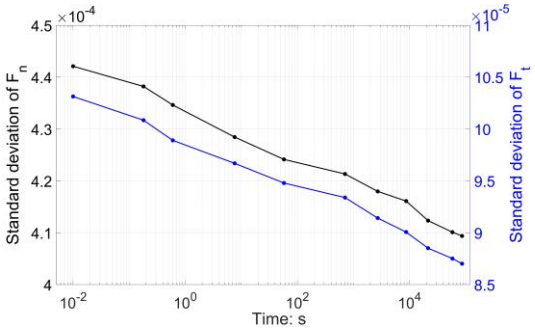

Figure 4. Standard deviation evolution of (a) normal contact forces (b)tangential contact forces.

4 CONCLUSIONS

A fracture based rough crushable Fontainebleau sand DEM model is applied here to simulate stress relaxation, and a good agreement with laboratory results of quartz sands can be found. Contact forces homogenization during relaxation indicates the possible association between stress relaxation and pile set-up.

ACKNOWLEDGEMENTS

The first author is supported by Chinese Government Scholarship CSC (No.202108390006). Spanish Research Agency support (AEI) through research project PID2020-119598RB-I00 is also acknowledged.

REFERENCES

Axelsson, G. (2000). "Long-term set-up of driven piles in sand." Ph.D. thesis, Royal Institute of Technology, Stockholm, Sweden.

Charles, R. J. (1958). Static fatigue of glass. *Journal of Applied Physics* 29(11): 1549–1560.

Ciantia, M. O., Arroyo, M., O'Sullivan, C., Gens, A., and Liu, T. (2019). Grading evolution and critical state in a discrete numerical model of Fontainebleau sand. *Geotechnique*, *69*(1): 1–15. https://doi.org/10.1680/jgeot.17.P.023.

Lade, P. v., and Karimpour, H. (2015). Stress relaxation behavior in Virginia Beach sand. *Canadian Geotechnical Journal*, *52*(7): 813–835. https://doi.org/10.1139/cgj-2013-0463.

Lei, J., Arroyo, M., Ciantia, M. and Zhang, N. (2023) A time-to-fracture DEM model for simulating creep in rough crushable sand.*10th European Conference on Numerical Methods in Geotechnical Engineering, London, UK.* https:// 10.53243/NUMGE2023-37.

Lei, J., Arroyo, M., Ciantia, M., & Zhang, N. (2024). A fracture-based discrete model for simulating creep in quartz sands. *Géotechnique*, 1–43. https://doi.org/10.1680/jgeot.23.00068.

Levin, F. (2021). Time-Dependent Compression Behavior of Sands under Oedometric Conditions. *J. Geotech. Geoenviron.*, *147*(12). https://doi.org/10.1061/(ASCE)GT.1943-5606.0002664.

Otsubo, M., O'Sullivan, C., Hanley, K. J., and Sim, W. W. (2017). The influence of particle surface roughness on elastic stiffness and dynamic response. *Geotechnique*, *67*(5): 452–459. https://doi.org/10.1680/jgeot.16.P.050.

Pham Van Bang, D., di Benedetto, H., Duttine, A., & Ezaoui, A. (2007). Viscous behaviour of dry sand. *Int. J Numer. Anal. Met*, *31*(15): 1631–1658. https://doi.org/10.1002/nag.606..

Tapias, M., Alonso, E. E., and Gili, J. (2015). A particle model for rockfill behaviour. *Geotechnique*, *65*(11): 975–994. https://doi.org/10.1680/jgeot.14.P.170.

Wang, J., and Xia, Z. (2021). DEM study of creep and stress relaxation behaviors of dense sand. *Computers and Geotechnics*, *134*. https://doi.org/10.1016/j.compgeo.2021.104142.

Xu, M., Hong, J., and Song, E. (2018). DEM study on the macro- and micro-responses of granular materials subjected to creep and stress relaxation. *Computers and Geotechnics*, *102*: 111–124. https://doi.org/10.1016/j.compgeo.2018.06.009.

Zhang, N., Ciantia, M. O., Arroyo, M., and Gens, A. (2021). A contact model for rough crushable sand. *Soils and Foundations* 61(3): 798–814. https://doi.org/10.1016/j.sandf.2021.03.002.

Zhang, Z., and Wang, Y. H. (2015). Examining Setup Mechanisms of Driven Piles in Sand Using Laboratory Model Pile Tests. *Journal of Geotechnical and Geoenvironmental Engineering*, *141*(3). https://doi.org/10.1061/(ASCE)GT.1943-5606.0001252.

Proceedings of the XVIII ECSMGE 2024
GEOTECHNICAL ENGINEERING CHALLENGES
TO MEET CURRENT AND EMERGING NEEDS OF SOCIETY
© 2024 the Authors
ISBN 978-1-032-54816-6
DOI 10.1201/9781003431749-95
Open Access: www.taylorfrancis.com, CC BY-NC-ND 4.0 license

ECSMGE 24
XVIII EUROPEAN CONFERENCE ON SOIL MECHANICS AND GEOTECHNICAL ENGINEERING

Assessing tunnel-structure interaction effects in London Clay

Évaluant les effets de l'interaction structure-tunnel dans l'argile de Londres

J. Liu*, A. Tsiampousi, A. Ruiz López, D.M.G. Taborda
Imperial College London, London, UK

j.liu22@imperial.ac.uk

ABSTRACT: In the context of tunnelling in urban areas, the serviceability of existing infrastructure must be guaranteed when these structures are subjected to tunnelling activities in their vicinity. Tunnel construction inevitably causes movements in the tunnel surroundings. It can also lead to potentially differential settlements of existing buildings with associated serviceability problems. To prevent such problems, the accurate prediction of tunnelling-induced building settlements becomes essential. In this paper, the case study of the construction of the Elizabeth line beneath a site in Whitechapel, London, is simulated using 2D finite element (FE) analysis. The investigation considers first the analysis of greenfield conditions, for which field measurements are available. The numerical results are shown to be in very good agreement with field measurements which validates the adopted soil models. The second part of the study involves the analysis of tunnelling beneath a building, where the influence of the building and the characteristics of its foundations on the shape of the settlement trough is evaluated.

RÉSUMÉ: Dans le contexte du creusement de tunnels en zones urbaines, la fonctionnalité des infrastructures existantes doit être garantie lorsque ces structures sont soumises à des activités de tunnelisation. La construction de tunnels provoque inévitablement des mouvements dans les environs du tunnel, comme des tassements différentiels des bâtiments existants avec des problèmes de fonctionnalité associés. Pour prévenir ces problèmes, la prédiction précise des tassements des bâtiments dus à la tunnelisation devient essentielle. Dans cet article, la construction de la ligne Elizabeth sous le site de Whitechapel, Londres, est simulée à l'aide d'une analyse par éléments finis en 2D. Cet article commence par l'analyse des conditions de terrain vierge. Les résultats numériques sont en très bon accord avec les mesures sur le terrain, ce qui valide les modèles de sol adoptés ainsi que leur calibration. La deuxième partie de l'étude concerne l'analyse de la tunnelisation sous le bâtiment, où l'influence du bâtiment et des fondations sur pieux sur la forme de la cuvette de tassement est évaluée.

Keywords: Tunnelling; finite element analysis; tunnel-structure interaction; piled raft foundations; London Clay.

1 INTRODUCTION

Space overuse has been a worrying issue in big cities. Therefore, due to space limitations, new developments have made greater use of underground space. One concern impeding underground construction is that this may cause potential effects on the surrounding superstructures. In London, tunnel excavation and its influence on neighbouring structures has been a widely researched topic.

Tunnelling can cause ground loss which leads to surface settlement, which affects the structures above. Many studies have been carried out to predict the influence of tunnel excavation on existing superstructures (Potts and Addenbrooke, 1997; Franzius et al., 2004). However, existing studies regarding tunnel-structure interaction mostly assume buildings or foundations sitting on ground surface, overlooking more complicated deep foundations, which could change the building response.

This paper is based on a case study, using greenfield data to validate the numerical model, then explores influence of tunnelling on the building with piled raft foundation using 2D Finite Element (FE) analysis.

2 FINITE ELEMENT ANALYSIS

2.1 Geometry

The chosen case study is the construction of the Elizabeth Line, west of Whitechapel underground station in East London. This site consists of Vallance Road Gardens and a building nearby supported by a piled raft foundation along Castlemain Street, which offers adequate field data for both greenfield and superstructure existing conditions to validate the analysis results and study tunnel-structure interaction.

The ground profile found at this site is recognized to be typical London geology, with Made Ground being the top layer of 4.2 m thickness, followed by River Terrace Gravel (3.3 m thick), London Clay (36.4 m thick), Lambeth Group Clay (5.9 m thick) and

Lambeth Group Sand (4 m thick). They are underlaid with the Thanet Sands Formation, which is 11.5 m thick, with the Chalk bedrock set as the bottom boundary of the FE model (Chong, 2015).

The building modelled in this analysis is a 3-storey structure found nearby Vallance Road Gardens which is 86 m long, 10 m wide and 10.5 m high. It is sitting on a piled raft foundation, which is assumed to consist of a 1.5 m thick foundation slab and 20m long piles, spaced 4 m apart and with a diameter of 0.5 m.

The two vertical boundries of the model are set to be normally fixed and impermeable. The bottom horizontal boundry is set to be fully fixed and the top horizontal boundry is free to deform in any directions. Both are set to be permeable.

2.2 Soil properties and initial stresses

Made Ground is modelled as a linear elastic-perfectly plastic material with a Mohr-Coulomb failure criterion, a Young's modulus of $E = 10$ MPa, a Poisson's ratio of 0.25 and a friction angle of 25°. The other strata are modelled using a perfectly plastic Mohr-Coulomb yield surface combined with an isotropic small-strain stiffness model to describe their elastic response (Taborda et al., 2023a, 2023b). The soil model parameters were adopted from Gawecka et al. (2017) and are listed below in Table 1 and Table 2.

The initial vertical total stress is prescribed by the saturated unit weight of the soil ($\gamma = 19$ kN/m^3 for Made Ground and $\gamma = 20$ kN/m^3 for the remaining materials). The coefficient of earth pressure K_0 is taken as 0.5 for the Made Ground and River Terrace Gravel. For London Clay, K_0 is equal to 1.5 for the top 10 m, 1.25 for the next 10 m and 1 for the remainder and all the other layers below London Clay, a variation which is based on the profile described in Schroeder (2003).

The initial effective stress is also affected by the pore water pressure distribution. This site has a perched aquifer above the London Clay, with the water table found to be 4.2 m below ground level, and a bottom aquifer in the Thanet Sands with the pressure head at 40 m below ground level, as indicated in Environmental Agency (2010). All clay layers are considered as undrained materials and the following nonlinear anisotropic variation of permeability with depth is adopted (Taborda et al., 2023c):

$$log_{10}k_y = a(y - y_{LC}) + b \quad (1)$$

$$k_y > k_{y,min} \quad (2)$$

$$k_x = 2 \cdot k_y \quad (3)$$

where y_{LC} is the value of the coordinate y at the top of London Clay; k_x and k_y are permeabilities along directions x and y, respectively; $k_{y,min}$ is the minimum permeability along direction y; a and b are model parameters, here assumed to take the values of 0.0215 and -4.5259, respectively. This variation of permeability matches that adopted in Avgerinos (2014) who calibrated it based on data reported for Heathrow Terminal 5 by Hight et al. (2007).

2.3 Modelling of tunnel

There are three major tunnels passing through this site, which are the Running Tunnel East (RTE), Crossover tunnel and the Tunnel Boring Machine tunnel. The first two are Sprayed Concrete Lining (SCL) tunnels. The axes of these three tunnels are all set to be 25.9 m below the ground surface around this area. For simplicity, only the RTE tunnel is considered, as it was excavated first. The construction sequence consists of a pilot tunnel (6.2 m diameter, 250 mm lining thickness), which is then enlarged to obtain the final diameter (9.12 m, 350 mm lining thickness). The RTE tunnel lining was simulated with the plate element, adopting a Young's modulus of 30 GPa and a Poisson's ratio of 0.15. The unit weight of shotcrete was taken as 24 kN/m^3.

3 GREENFIELD CASE

A 2D plane-strain FE model is set up in PLAXIS 2D based on the Vallance Road Gardens area to simulate the tunnelling effect without the influence of buildings above. The tunnelling process is simulated using the volume loss method, where the unloading level associated with tunnel excavation is varied until the desired volume loss is obtained. The ground surface settlements obtained in the analysis are presented in Figure 1 along with the field data (Chong, 2015).

The maximum settlement obtained for the pilot tunnel is 14.9 mm, which is slightly bigger than the field data (12.4 mm). An excellent match is obtained for the remainder of the settlement trough. For the enlargement tunnel, the numerical model yielded a maximum settlement of 29.7 mm, which is very close to the field measurements (30.4 mm). The very good agreement between field data and numerical results validates the adopted modelling approach.

Table 1. Mohr-Coulomb strength properties adopted (Gawecka et al., 2017).

Material	Angle of shearing resistance ϕ (°)	Cohesion c (kPa)	Dilatancy angle ψ (°)
River Terrace Gravel	35	0	17.5
London Clay	25	5	12.5
Lambeth Group Clay	27	25	13.5
Lambeth Group Sand	34	0	17
Thanet Sands	40	0	20

Table 2. Small-strain stiffness properties adopted assuming $p'_{ref} = 100\ kPa$ (Gawecka et al., 2017).

Material	G_{ref} (kPa)	m_G	a	b	$R_{G,min}$	G_{min} (kPa)
River Terrace Gravel	41939.61	1.0	0.000145	1.00	0.03511	3000
London Clay	51743.55	1.0	0.000056	0.90	0.06450	2667
Lambeth Group Clay	51924.52	1.0	0.000110	0.95	0.04662	2667
Lambeth Group Sand	81346.31	1.0	0.000015	1.00	0.14557	1000
Thanet Sands	65275.23	1.0	0.000046	0.85	0.02631	2000
Material	K_{ref} (kPa)	m_K	r	s	$R_{K,min}$	K_{min} (kPa)
River Terrace Gravel	49843.08	1.0	0.000247	1.25	0.15440	3000
London Clay	26692.73	1.0	0.000127	1.80	0.13275	5000
Lambeth Group Clay	61331.71	1.0	0.000065	1.40	0.07589	5000
Lambeth Group Sand	49843.08	1.0	0.000026	0.90	0.08377	5000
Thanet Sands	29813.53	1.0	0.000155	1.10	0.27947	5000

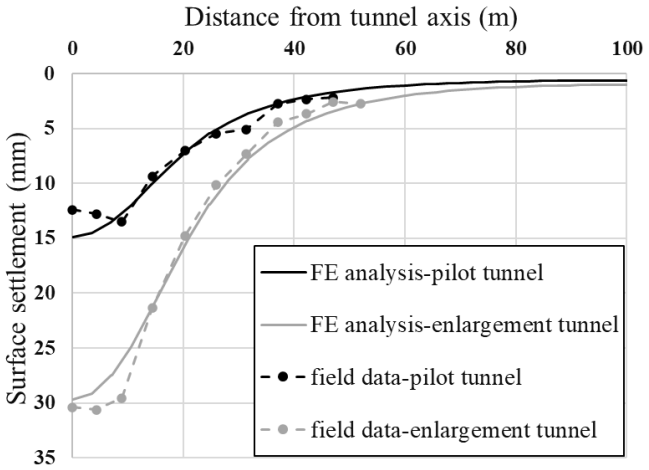

Figure 1. Comparison of 2D FE analysis results with field data (Chong, 2015).

4 TUNNEL-STRUCTURE INTERACTION

The tunnels at this site were excavated after the construction of the building along the Castlemain Street. In the numerical model, once building construction is complete, the ground is set to consolidate under the building load for 14 years before tunnel construction. The construction sequence of the RTE tunnel includes excavation of pilot tunnel, pilot tunnel lining construction, excavation of enlargement tunnel and enlargement tunnel lining construction.

Three different scenarios are considered herein to study the influence of piles and the building stiffness on the surface settlement. The first case analysed consists of a simplified model containing only the foundation slab and building load (i.e. the influence of piles is disregarded). Subsequently, two more analyses are carried out, introducing first the pile foundations and then the building stiffness.

In these analyses, the concrete foundation slab is modelled with solid elements, adopting a Young's modulus of 30 GPa for concrete. The building stiffness is added using additional plate elements in PLAXIS2D, with the stiffness corresponding to the 3-storey building: the Young's modulus E is taken as 30 GPa, while the second moment of area I is calculated using the parallel axis theorem assuming the neutral axis is located at mid-height of the building (Franzius et al., 2004). The equivalent cross section area A of the plate is the sum of the cross-sectional area of the three slabs. The piles are modelled with plate elements, correcting for pile spacing in the out of plane direction, adopting a Young's modulus of 30 GPa.

The results obtained for the three analyses are shown in Figure 2 in terms of surface settlement troughs, using the same unloading values as in the greenfield model, since the same tunnelling technology was employed. Piles are shown to have a rather significant influence on the ground surface settlement trough due to tunnelling. The maximum settlement of the piled raft foundation at tunnel axis after enlargement is approximately 1.3 times larger than that obtained when having only the raft foundation. However, it is also clear that a much narrower trough is obtained when the presence of piles is considered, leading to larger differential settlements and distortions. These differences are perhaps caused by the transmission of loads to greater depths when

including pile foundations, as well as effects associated with the bending sriffness of the piles.

After adding building stiffness, the shape of settlement trough is significantly shallower and wider than either of the two previous cases, suggesting that neglecting this important factor would be overly conservative when assessing the impact of tunnelling on the building.

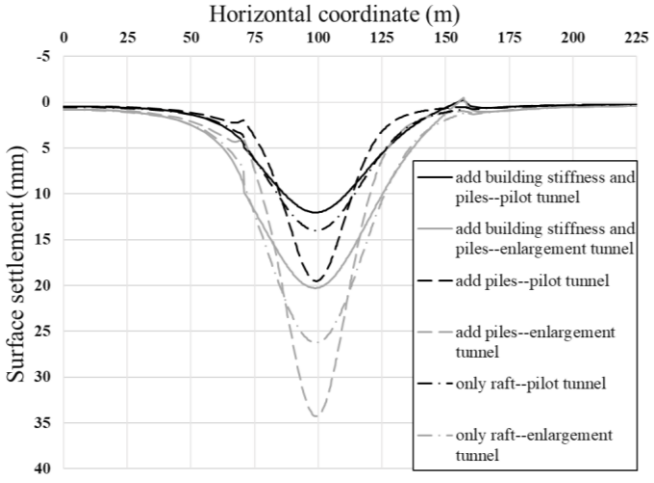

Figure 2. Influence of building stiffness on settlement trough.

5 CONCLUSIONS

The present paper investigates the effect of tunnelling works on surrounding buildings. To this end, plane-strain Finite Element analyses are carried out based on a typical London site. A greenfield analysis is performed first to validate the adopted soil models and a good agreement with field measurements is reached. Subsequently, a tunnel-building interaction study is conducted, characterising the influence of the presence of piles and that of the building stiffness on the settlement trough. The obtained results show that the piled raft foundation has a different response to tunnelling, leading to a deeper and narrower settlement trough when compared to the case where only a raft is considered. Furthermore, the inclusion of the building stiffness has a significant impact on the deformations associated with tunnelling, leading to shallower and wider settlement troughs.

REFERENCES

Avgerinos, V. (2014). *Numerical investigation of tunnelling beneath existing tunnels*, PhD thesis, Imperial College London.

Chong, H.Z. (2015). *Influence of tunnelling on a piled structure-Crossrail case study*, MEng thesis, Imperial College London.

Environmental Agency (2010). Management of the London Basin Chalk Aquifer. Status Report 2010.

Franzius, J.N., Potts, D.M., Addenbrooke, T.I. and Burland, J.B. (2004). The influence of building weight on tunnelling-induced ground and building deformation, *Soils and Foundations*, 44(1), pp. 25-38, https://doi.org/10.3208/sandf.44.25

Gawecka, K.A., Taborda, D.M.G., Potts, D.M., Cui, W., Zdravković, L. and Haji Kasri, M.S. (2017). Numerical modelling of thermo-active piles in London Clay, *Proceedings of the Institution of Civil Engineers - Geotechnical Engineering*, 170(3), pp. 201-219, https://doi.org/10.1680/jgeen.16.00096

Hight, D.W., Gasparre, A., Nishimura, S., Minh, N.A., Jardine, R.J. and Coop, M.R. (2007). Characteristics of the London Clay from the Terminal 5 site at Heathrow Airport, *Geotechnique*, 57 (1), pp. 3-18, https://doi.org/10.1680/geot.2007.57.1.3

Potts, D.M. and Addenbrooke, T.I. (1997). A structures influence on tunnelling induced ground movements, *Proceedings of the Institution of Civil Engineers-Geotechnical Engineering*, 125(2), pp. 109-125, https://doi.org/10.1680/igeng.1997.29233

Schroeder, F.C. (2003). *The influence of bored piles on existing tunnels*, PhD thesis, University of London, Imperial College of Science, Technology and Medicine.

Taborda, D.M.G., Kontoe, S. and Tsiampousi, A. (2023a). IC MAGE Model 01—strain-hardening/softening Mohr-Coulomb failure criterion with isotropic small strain stiffness (Version 2.0), *Zenodo*. https://doi.org/10.5281/zenodo.7565062

Taborda, D. M. G., Kontoe, S. and Tsiampousi, A. (2023b). IC MAGE UMIP – universal model interface for PLAXIS (Version 3.3), *Zenodo*. https://doi.org/10.5281/zenodo.7564989

Taborda, D.M.G., Kontoe, S. and Tsiampousi, A. (2023c). IC MAGE Flow Model 01 –Nonlinearly varying anisotropic permeability (Version 1.0), *Zenodo*. https://doi.org/10.5281/zenodo.7796383

Proceedings of the XVIII ECSMGE 2024
GEOTECHNICAL ENGINEERING CHALLENGES
TO MEET CURRENT AND EMERGING NEEDS OF SOCIETY
© 2024 the Authors
ISBN 978-1-032-54816-6
DOI 10.1201/9781003431749-96
Open Access: www.taylorfrancis.com, CC BY-NC-ND 4.0 license

ECSMGE 24
XVIII EUROPEAN CONFERENCE ON SOIL MECHANICS AND GEOTECHNICAL ENGINEERING

Centrifuge modelling of sand and sawdust embankments on peat for sustainable infrastructure development

Modélisation par centrifugation de remblais de sable et de sciure sur tourbe

M. Long*
University College Dublin (UCD), Dublin, Ireland

L. von der Tann
Norwegian Geotechnical Institute (NGI), Oslo, Norway

S. Ritter
Norwegian Geotechnical Institute & Oslo Metropolitan University, Oslo, Norway

P. Paniagua
Norwegian Geotechnical Institute & Norwegian University of Science and Technology, Trondheim, Norway

M. Dahl
Romerike Geoteknikk AS, Frogner, Norway (formerly Norwegian Public Roads Administration (NPRA), Oslo)

M. Konstantinou, C. Cengiz
Deltares, Delft, The Netherlands

**Mike.Long@ucd.ie*

ABSTRACT: Previously accepted methods to develop infrastructure across peatlands such as roads or railways typically excavated out the peat and substituted it with granular material. Such solutions, especially the alteration to drainage, can disturb peatlands and emit large amounts of greenhouses gases. The work on the GEOLAB / CLARIFIER (Centrifuge modeLling of peat embAnkments foR critical inFrastructure In EuRope) project explores the use of an innovative combination of sawdust and sand as embankments for rural roads, a technique which has previously been used in Norway. Although this previous work shed light on the deformation behaviour, very little is currently known about the performance during traffic loading and about the failure mechanisms of such embankments. A series of centrifuge tests were performed as plate loading tests and on sawdust and sand embankments at Deltares. The testing was carried out on intact peat using large block samples which were recovered from a site in Trondheim, Norway. In addition to extensive instrumentation, two colour cameras were used to capture images throughout the centrifuge tests to allow image-based deformation analysis. This paper provides an overview of the project as well as some preliminary results.

RÉSUMÉ: Les méthodes précédemment acceptées pour développer des infrastructures à travers les tourbières, telles que des routes ou des voies ferrées, consistaient généralement à extraire la tourbe et à la remplacer par des matériaux granulaires. De telles solutions, notamment la modification du drainage, peuvent perturber les tourbières et émettre de grandes quantités de gaz à effet de serre. Les travaux du projet GEOLAB / CLARIFIER (Centrifuge modelling of peat emAnkments for crucial inFrastructure In EuRope) explorent l'utilisation d'une combinaison innovante de sciure de bois et de sable comme remblais pour les routes rurales, une technique qui a déjà été utilisée en Norvège. Bien que ces travaux antérieurs aient mis en lumière le comportement en déformation, on sait actuellement très peu de choses sur les performances lors du chargement du trafic ucialet sur les mécanismes de rupture de tels remblais. Une série d'essais de centrifugation ont été réalisés sous forme d'essais de chargement de plaques et sur des remblais de sciure et de sable à Deltares. Les tests ont été effectués sur de la tourbe intacte à l'aide de gros blocs d'échantillons récupérés sur un site de Trondheim, en Norvège. En plus d'une instrumentation étendue, deux caméras couleur ont été utilisées pour capturer des images tout au long des tests de centrifugation afin de permettre une analyse de déformation basée sur l'image. Cet article fournit un aperçu du projet ainsi que quelques résultats préliminaires.

Keywords: Peat; embankments; centrifuge; soil characterisation; DIC: digital image correlation.

1 INTRODUCTION

There is an increasing need to develop roads and other critical infrastructure across peatlands, e.g. for low trafficked roads in rural areas, housing estates and for upland renewable energy projects. In the past the peat would have been dug out and replaced by imported

granular material. This type of solution is no longer acceptable for environmental and cost reasons. This project investigates the use of innovative, low cost and sustainable road construction in peatland using a combination of sawdust and sand to form the road embankments. The main knowledge gap is that the failure mechanism of such a construction on natural fibrous peat is unknown. There are no methods available to design such systems against bearing capacity failures or to assess whether the structure remains within serviceability limits. To address this some centrifuge testing of model embankments was carried out over 1 month at the facilities of Deltares in The Netherlands as part of the project CLARIFIER, funded by the EU GEOLAB scheme. This paper gives an overview of the project and some preliminary results.

2 ABOUT GEOLAB

GEOLAB is a European network of renowned institutes bringing together eleven unique installations in Europe aimed to study subsurface behaviour and the interaction with structural elements, and the environment. Critical Infrastructures (CI) and their service in the water, energy, urban and transport sectors are at risk due to climate change, extreme weather, geohazards, and aging. The overarching aim of GEOLAB is to integrate and advance these key national research infrastructures for performing ground-breaking research and innovation that enhances the resilience of Europe's CI. GEOLAB is led by Deltares and has received funding from the European Union's Horizon 2020 Research and Innovation program under grant agreement No. 101006512 (https://project-geolab.eu/).

3 THE DELTARES CENTRIFUGE

The GeoCentrifuge at Deltares is a beam centrifuge with a 260 g-tonne capacity and a platform radius of 5.0 m. The device is produced by Actidyn and the model designation is C72-31. The platform of the centrifuge can house test subjects with dimensions up to 1.2 m × 1.2 m × 1.2 m. The data-acquisition system is supplied by HBM and has 56 channels with a simultaneous sampling rate of 100 kHz. Beyond conventional sensors, the centrifuge is equipped with two 4K cameras and two high-speed cameras which are routinely used for digital image correlation (DIC) applications. While the 4K cameras can capture images with 31 MP (megapixel) resolution at 26 fps frame rate, the high-speed cameras can capture images with a resolution of 2 MP at 2500 fps frame rate for a period of 4 s. Figure 1 illustrates the CLARIFIER test setup onboard the platform of the Deltares GeoCentrifuge.

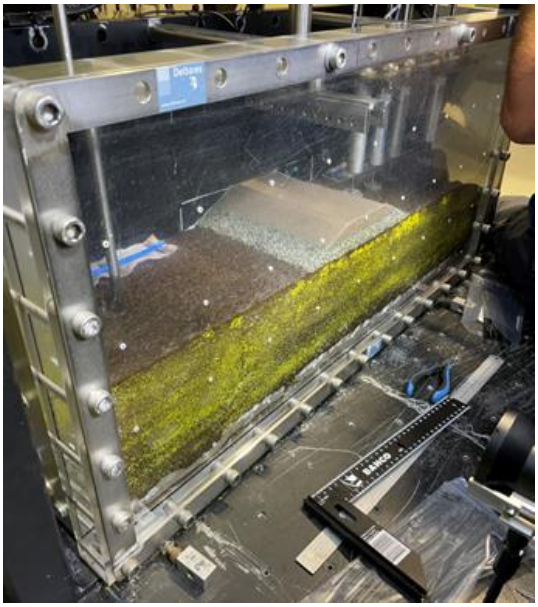

Figure 1. Deltares centrifuge with the test setup (notice the green tracers/speckles for DIC).

4 MOTIVATION AND AIMS OF PROJECT

The motivation for this project was the availability of construction records and long term settlement data from four trial embankments constructed of sawdust and sand which were placed directly on peat by NGI and NPRA in 1963 and 1964. These embankments are still accessible. Their purpose was to investigate the use of sawdust for low cost lightly trafficked roads and railway lines in rural areas. The embankments were constructed in Kongsvinger in south-eastern Norway and at Slåttemyra in Nordmark just north of Oslo. A summary of the experience gained from these embankments is given by Long et al. (2023).

5 SOIL SAMPLING

Large block samples of natural peat were extracted from a site at Tiller-Flotten some 11 km south of Trondheim city centre (Figure 2). The peat research area is located immediately adjacent to the Norwegian Geo-Test Site (NGTS) quick clay area (L'Heureux et al., 2019). Sampling was carried out to ISSMFE (1981). The block samples were cut using a serrated knife and subsequently sealed with cling film to avoid drying. Wooden boxes with dimensions of 930 (length) x 280 (width) x 215 (height) mm and 930 x 280 x 315 mm were used for transport. Eight of these samples were successfully transported to Delft from Trondheim via car and ferry.



Figure 2. Block sampling at Tiller-Flotten site.

6 PEAT CHARACTERISATION

The peat from Tiller-Flotten is characteristic of other peats in the Trondheim area and in Norway in general (Long et al., 2022). It is a very soft highly compressible fibrous peat. It has an average water content of 1150%, a density of 1.05 Mg/m^3 and its loss on ignition (LOI) is between 95% and 98%. Its von Post degree of decomposition (H) is equal to 3.

7 OVERVIEW OF CENTRIFUGE TESTS

An overview of the seven centrifuge tests carried out is given on Table 1. Three of the tests involved plate loading tests to investigate failure mechanisms during loading with different g levels being used. The remaining four tests involved a model embankment made of sand and sawdust. The test layout, for the tests where a model embankment was included, is shown in Figure 3. The intention was to test a prototype peat layer of 7.5 m in thickness. Therefore, for the plate loading tests the samples were trimmed to between 150 mm and 250 mm in height. For the embankment tests a uniform g level of 50 was assumed, giving a 150 mm peat height and a total embankment height of 40 mm in model scale. Water level was maintained at the top of the peat.

Data obtained during the testing included vertical displacement of the surface of the peat using displacement transducers (LVDT in Figure 3), pore water pressures, total pressures as well as the load versus displacement of the loading piston. A mini cone penetration test (CPT) with a diameter of 11 mm was conducted on each test specimen. In addition to the instruments in the strongbox, soil deformations on the front window of the strongbox were derived using the open-source DIC software GeoPIV (Stanier et al., 2015) from pictures taken with two cameras.

Table 1. Overview of centrifuge tests.

No.	g-level	Plate (P) or embankment (E)	Peat water content (%)	von Post H
1	50	P	1423	3
2	30	P	1314	4
3	75	P	788	3
4	50	E	1137	4
5	50	E	695	3
6	50	E	639	3 to 4
7	50	E	663	3

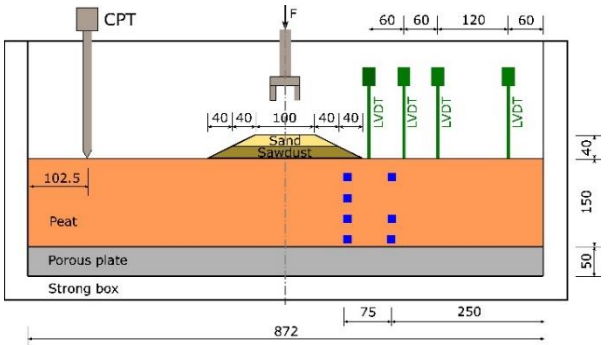

Figure 3. Test layout. CPT = mini cone penetrometer test, F = load cell, LVDT = linear variable differential transformers and P = pore pressure transducers. Dimensions in mm and model scale.

8 SOME PRELIMINARY TEST RESULTS

Figure 4 shows preliminary results from the plate loading tests. The load was measured by a load cell while keeping the displacement rate constant. The peat displacements were analysed using GeoPIV and are shown as vertical and horizontal contours.

Typical images obtained during the centrifuge test series to subsequently perform the image-based measurement technique are shown in Figure 5. Figure 1 shows the sand and sawdust embankment on the natural peat before starting the centrifuge test. Peat and embankment deformation due to increase of the gravitational acceleration can be seen in Figure 5a. Figure 5b shows the deformed embankment and peat due to traffic loading.

An interesting observation from Figures 4 and 5b is that the peat deformations during loading are different to typical bearing capacity failures. This implies that design concepts for mineral soils may not apply for peat. The design of such embankments on peat may be governed by the serviceability limit state. Some impressions from the tests can be found on the movie: Deltares Clarifier Project – YouTube and the CLARIFIER data is available on the ZENODO platform; DOI: 10.5281/zenodo.8099793.

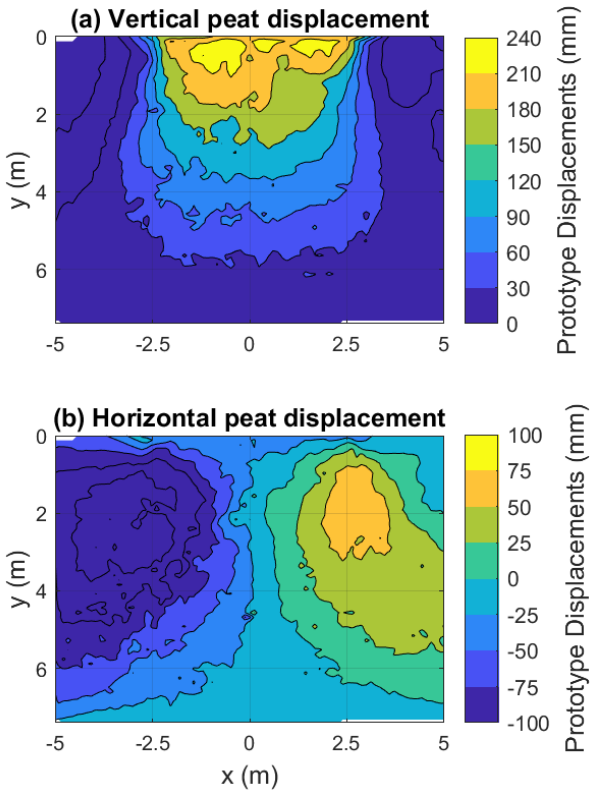

Figure 4. Example results from a plate loading test: (a) vertical displacement contours and (b) horizontal displacement contours.

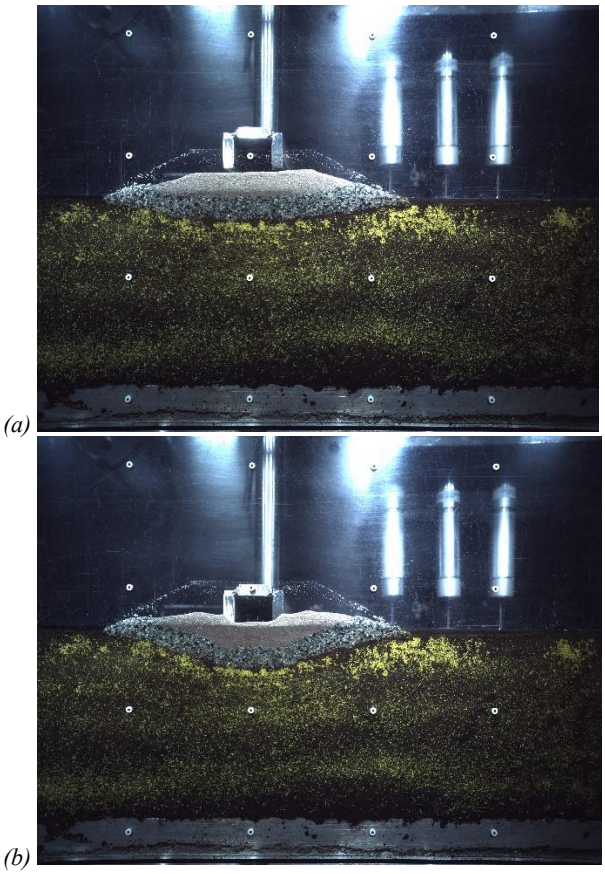

Figure 5. Observations during a sand and sawdust embankment test: (a) spin-up and (b) traffic loading.

9 CONCLUSIONS AND FUTURE WORK

This contribution introduces a centrifuge tests series which studies the performance of an intact peat during loading and its interaction with an embankment composed of sand and sawdust. Block samples of intact peat were obtained from Tiller-Flotten, Norway. The centrifuge tests of these samples were carried-out at Deltares and were part of the GEOLAB project. Preliminary results indicate that failure mechanism suggested for embankments on mineral soils may not apply for peat. Future work will focus on detailed analysis of the experimental data. In addition, the data will be explored to calibrate numerical models.

ACKNOWLEDGEMENTS

The authors are grateful for the financial support provided by the European Union's Horizon 2020 Research and Innovation program under grant agreement No. 101006512 and the Norwegian Research Council through the basic grants (GBV) 20220120 and 20230065. The authors thank the technicians at Deltares for their support while performing these experiments.

REFERENCES

ISSMFE (1981). *International manual for the sampling of soft cohesive materials*, Published by Tokai University Press, Tokyo on behalf of the International Society of Soil Mechanics and Foundation Engineering.

L'Heureux, J.-S., Lindgård, A. And Emdal, A. (2019). The Tiller-Flotten research site: Geotechnical characterisation of a sensitive clay deposit. *AIMS Geosciences*, 5(4), pp 831–867. https://doi.org/10.3934/geosci.2019.4.831.

Long, M., Paniagua, P., Grimstad, G., Trafford, A., Degago, S. and L'Heureux, J.-S. (2022). Engineering properties of Norwegian peat for calculation of settlements". *Engineering Geology*, Vol. 308. https://doi.org/10.1016/j.enggeo.2022.106799.

Long, M., Paniagua, P., Grimstad, G. Egil Berg Antoniazzi Sponås, E.G.A., Bjertness, E. and Ritter, S. (2023). Behaviour of 60-year-old trial embankments on peat. *Engineering Geology*, Vol. 323. https://doi.org/10.1016/j.enggeo.2023.107226.

Stanier, S.A., Blaber, J., Take, W.A. and White, D.J. (2015). Improved image-based deformation measurement for geotechnical applications. *Canadian Geotechnical Journal*, 53(5): 727 - 739. https://doi.org/10.1139/cgj-2015-0253.

Proceedings of the XVIII ECSMGE 2024
GEOTECHNICAL ENGINEERING CHALLENGES
TO MEET CURRENT AND EMERGING NEEDS OF SOCIETY
© 2024 the Authors
ISBN 978-1-032-54816-6
DOI 10.1201/9781003431749-97
Open Access: www.taylorfrancis.com, CC BY-NC-ND 4.0 license

ECSMGE 24
XVIII EUROPEAN CONFERENCE ON SOIL MECHANICS AND GEOTECHNICAL ENGINEERING

Interpretation of pressuremeter tests in clays with non-linear elastic behaviour

Interprétation des essais pressiométriques dans les argiles tenant compte du comportement élastique non-linéaire

A. Lopes dos Santos*, T. Nader, J. Habert
Terrasol (setec), Paris, France

**alexandre.lopes@setec.com*

ABSTRACT: Pressuremeter tests are an efficient tool to derive shear modulus of soils and its decay with shear strain. Non-linear behaviour of soils during cavity expansion, and its consequence on stress and shear modulus with the distance to the pressuremeter cavity have to be taken into account. This paper presents several methods based both on the monotonic loading and on subsequent unload-reload loops to derive shear modulus decay as a function of the shear strain for tests performed in saturated clays, where constant volume can be assumed, by means of several but distinct interpretation methods: i) retrofitting based on closed form solutions integrating the non-linear elastic behaviour, ii) comparisons to numerical modelling by finite difference analysis and iii) approaches integrating prior strains transformations. The different results are compared to each other and to other investigation tests providing the initial shear modulus G_0 associated with very small shear strain levels, in order to validate the different interpretation methods.

RÉSUMÉ: Les essais pressiométriques sont un outil efficace pour déterminer le module de cisaillement des sols et sa décroissance en fonction de la déformation de cisaillement (ou distorsion). Le comportement non linéaire des sols pendant l'expansion de la cavité, et ses conséquences sur la contrainte et le module de cisaillement en fonction de la distance à la cavité du pressiomètre, doivent être pris en compte. Pour les essais réalisés dans des argiles, pour lesquelles on peut supposer un volume constant pendant le test, cet article présente plusieurs méthodes pour déterminer la décroissance du module de cisaillement en fonction de la déformation de cisaillement, basées à la fois sur l'essai de chargement monotone et sur les boucles de déchargement-rechargement ultérieures, au moyen de plusieurs méthodes d'interprétation distinctes: i) adaptation basée sur des solutions analytiques intégrant le comportement élastique non linéaire, ii) comparaisons avec la modélisation numérique par analyse en différences finies et iii) approches intégrant les transformations de déformations préalables. Les différents résultats sont comparés les uns aux autres ainsi qu'à d'autres types d'essais fournissant le module de cisaillement initial G_0 associé à de très faibles niveaux de déformation de cisaillement, afin de valider les différentes méthodes d'interprétation.

Keywords: Pressuremeter tests; shear modulus; non-linear elasticity; clay.

1 INTRODUCTION

Pressuremeter tests (PMT) are cylindrical cavity expansion tests that can be performed either on a pre-bored cavity, in a cavity created by pushing the probe into the ground, or in a self-bored cavity. Several testing procedures exist, enabling the determination of both deformation and strength parameters of the ground. In France, the most known procedure is the Ménard one, which yields the Ménard pressuremeter modulus (E_M) and the pressuremeter creep and limit pressures (p_f, p_{lM}). In French practice, those parameters are used in semi-empirical and direct correlations, to determine the bearing capacity and stiffness of foundations and retaining walls. Since the beginning of the development of the pressuremeter, Ménard and other contemporary authors focussed on the semi-empirical approach due to its ease of use (Ménard and Rousseau, 1962): these approaches are still successful used in French practice (Frank, 2017), but is less frequently implemented in foreign practices.

Other approaches exist, based on an analytical background that confirms that it is possible to determine intrinsic ground properties from the pressuremeter. This theoretical background is remarkably strong and straightforward to use in saturated fine soils, where undrained conditions prevail and where one can assume that there are no volume variations during the test. In these cases, additional parameters can be determined: undrained shear strength, maximum shear modulus, or shear modulus decay. Whatever the aim is, it can be noted that the initial expansion curve is sensitive to

disturbances due to probe insertion, that led to prefer the use of unload-reload loops.

2 PRESENTATION OF THE INTERPRETATION METHODS

Several interpretation methods exist enabling the determination of ground moduli based on the measured cavity expansion curve. Historically, linear elasticity has been frequently used, supposing that ground response is linear, and that elasticity Young's modulus *E* (or shear modulus *G*) can be determined from the slope of the pressuremeter curve:

$$G = \frac{1}{2}\frac{dP}{d\epsilon_c} = \frac{E}{2(1+\nu)} \quad (1)$$

where dP is the variation in cavity pressure and $d\epsilon_c$ is the variation in cavity strain within a range of values assumed to be linear. Cavity strain is the ratio between the variation of cavity radius and the initial or current cavity radius, depending if analyses are in small strains or large strains, $\epsilon_c = \Delta r/r$.

Elasticity modulus determined in that manner, does not capture true ground behaviour that is not actually linear. If moduli determined in that manner are intended to be used for geotechnical modelling, correlations of many different types are required to adjust it for the appropriate level of shear strain associated with the soil-structure interaction problem being modelled.

In a pressuremeter test, the response measured at the cavity wall corresponds to an integration of the elementary ground behaviour around the cavity and is dependent on the non-homogeneous stress and strain variations with the distance to the cavity. If the hypothesis of linear elasticity could be verified, pressuremeter moduli would indeed correspond to ground moduli. However, this is not the case, because non-linear behaviour makes that the response at the cavity wall apparent to be stiffer than the elementary response and only "apparent" moduli may be derived from pressuremeter tests if no appropriate and further analysis is carried out.

Methods recognising and integrating the non-linear response of ground have been proposed by Briaud *et al.* (1983), Wood (1990), Jardine (1992), Ferreira et Robertson (1992), Bolton and Whittle (1999).

Briaud *et al*. (1983) observed that the ground response to a pressuremeter unload-reload loop can be considered to be hyperbolic, and that the inverse of the secant "apparent" modulus can be described by a linear relationship of the form:

$$\frac{1}{G_{s,app}} = a_0 + a_1\epsilon_c \quad (2)$$

where ϵ_c is the cavity strain and a_0 and a_1 can be determined from linear regression from the pressuremeter loop data.

From this assumption, the authors point to the possibility to derive the initial modulus of the ground from a pressuremeter unload-reload loop. Secant moduli calculated in that manner are, however, apparent, and do not integrate the ground behaviour around and with the distance to the cavity.

Wood (1990) presents the theoretical background linking secant "apparent" pressuremeter modulus with the elementary modulus (secant, or tangent) of the ground at different shear strain levels.

Based on a comparison of "apparent" pressuremeter modulus and modulus determined from laboratory tests for several types of soils, Jardine (1992) proposes the so-called strain transformation approach. It consists in a direct method enabling to transform the strains associated to an "apparent" pressuremeter modulus to the strains associated to the same modulus, obtained using elementary laboratory testing.

Ferreira and Robertson (1992) assume that the elementary behaviour of the ground is hyperbolic and that the modulus decay with shear strain can be described by a Hardin-Drnevich type function. The authors integrate this behaviour to the cavity expansion problem and obtain an analytical solution that enables to determine the maximum ground modulus from the pressuremeter curve. They state that it is preferable to use the method within an unload path, to avoid potential disturbance due to probe insertion.

Bolton and Whittle (1999) assume the elementary ground behaviour is associated with a secant shear modulus (G_s) decay following a power law function of the shear strain (γ), yielding an expression for the shear modulus that is parametrized by coefficients α and β that can be determined from pressuremeter unload-reload loops:

$$G_s = \alpha\gamma^{\beta-1} \quad (3)$$

According to the authors, this expression can be used to derive shear modulus decay from a strain range between 10^{-4} and 10^{-2}. As the method does not enable an assessment of G_0, it will not be further explored in this paper.

Habert and Burlon (2021) proposed an interpretation method for undrained cavity expansion that considers that ground behaviour is hyperbolic according to a Hardin-Drnevich function (4),

following Ferreira and Robertson (1992). The following relationship is proposed:

$$\frac{G_s}{G_0} = \frac{1}{1+\frac{s_u}{G_0}\gamma} \quad (4)$$

$$p_c = p_0 + s_u\, ln\left(1 + \gamma_c \frac{G_0}{s_u}\right) \quad (5)$$

where p_c is the pressure at the cavity wall, p_0 is the initial horizontal pressure, s_u is the ground undrained cohesion, G_0 is the initial shear modulus of the ground, and γ_c is the shear strain at the cavity wall.

The authors propose the following interpretation procedure to determine G_0 from a pressuremeter curve: use the cavity expansion curve to derive the undrained cohesion using the slope of $dp_c/dln(\Delta V_c/V_c)$ ratio for the last points of the virgin expansion curve, where V_c is the cavity volume. The authors argue that s_u is marginally sensible to variations in p_0 and thus, the method used for the determination of p_0 lead to minor impact on the value of S_u. The Ménard limit pressure can be assessed using conventional methods.

3 EXAMPLES OF APPLICATION

3.1 Tests without unload-reload loops

Ménard pressuremeter tests performed according to standard ISO 22476-4 (AFNOR, 2015), monotonic, can be interpreted taking the non-linear response of the ground into account using Eq. 5, provided ground response is undrained.

Figure 1 presents an example of interpretation of a pressuremeter test performed in the north of France in overconsolidated Flander's clays. The pressure and volume measurements are used. Values of radial strain at the cavity wall γ_c are calculated from the volumetric measurements as $\gamma_c = \Delta V_c/V_c$, where V_c is the current volume measured at the cavity wall and ΔV_c is the volume variation corresponding to the initial cavity volume, $\Delta V_c = V_c - V_c(p = p_0)$.

The interpretation procedure consists on:

(1) estimate the initial horizontal pressure at rest (p_0),
(2) calculate values of shear strain at the cavity wall,
(3) extrapolate the curve to determine the limit pressure and the undrained cohesion,
(4) use Eq. (5) to evaluate G_0.
(5) Hardin Drnevich relationship can be used to estimate the shear modulus decay curve.

The interpretation procedure presented above and illustrated in Figure 1 was applied to Ménard type tests in Flander's clays and further compared to the results of cross hole tests performed on the same site. Results and discussion are presented in paragraph 4.

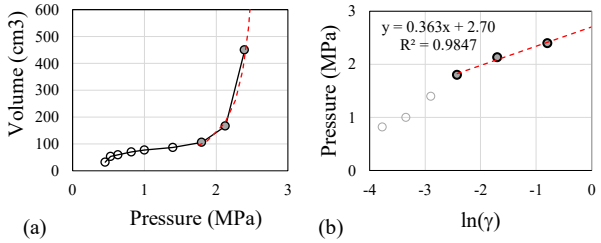

Figure 1. Example of interpretation of pressuremeter test to determine the initial shear modulus G_0 (undrained conditions). Overconsolidated Flander's clay at 37.5m depth.

Three cross hole profiles available on site enable a comparison between G_0 from the PMT. Figure 2 shows an example for the test at 37.5m and compares the initial shear modulus to the ones obtained from 3 cross hole tests between 35 to 39 m depth. From this figure, it is also possible to see that the method enables an evaluation of the reference shear strain, $\gamma_{0.5} = s_u/G_0$, for which $G_s = G_0/2$.

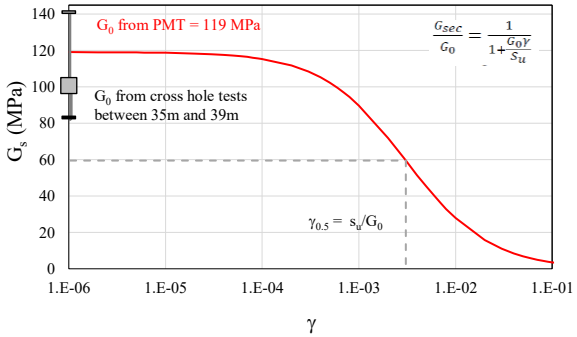

Figure 2. Shear stiffness decay curve derived from pressuremeter test showing the value of G0 compared to Cross Hole tests nearby.

3.2 Tests with unload-reload loops

Pressuremeter tests including unload-reload loops enable to enhance the reliability on the evaluation of the deformation modulus of the ground. Unload-reload loops are less susceptible to disturbance due to probe insertion; Furthermore, in undrained conditions, loops initiated at different cavity pressure levels should lead to similar results, which provides redundancy and easiness to verify and validate the test results. Yet, the interpretation procedure for monotonic tests can still be applied to these tests, providing another way to check its robustness.

Figure 3 presents an example of pressuremeter test performed at 4.8m depth in the Whitby Mudstone in

the UK. The test includes two unload-reload loops performed during the loading. An additional loop is performed while unloading the cavity and is not the scope of this paper. Initial horizontal stress at rest was evaluated using lift off method and p_0 = 76 kPa. Figure 4 presents a detail of the loop 1, showing the interpreted curves obtained using Eq. (2) fitted.

The interpretation procedure for Eq. (2) is:

(1) Define the origin of the unload loop
(2) Calculate secant shear modulus $G_{s,app}$ for all points measured in the unload loop
(3) Plot $1/G_{s,app} = f(\gamma_c)$, and determine a_0 and a_1 by linear regression
(4) G_0 is calculated as $1/a_0$
(5) Use strain transformation approach to determine shear modulus decay $G_s = f(\gamma)$

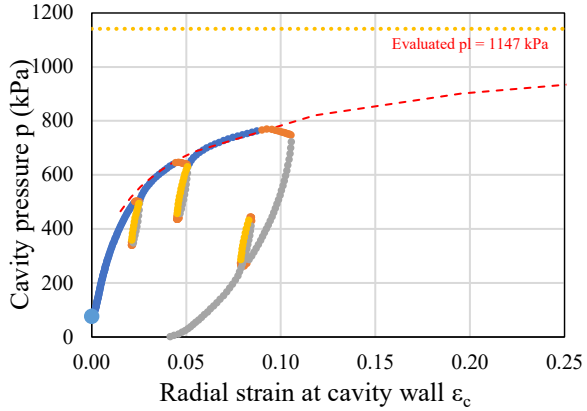

Figure 3. Pressuremeter test with unload-reload loops performed in the Whitby Mudstone at 4.8m depth.

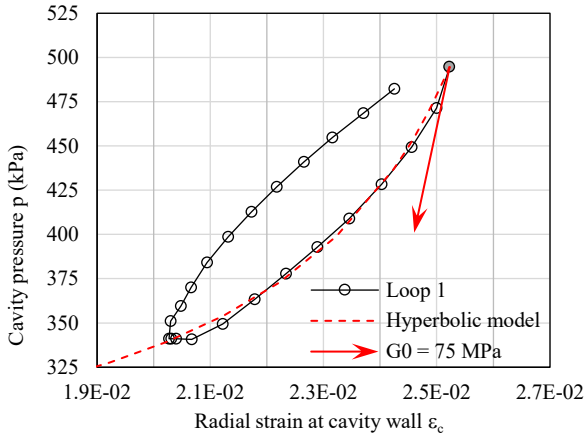

Figure 4. Detail of loop 1 showing the interpreted curves from Eq. (2) fitted.

3.3 Comparison of the methods

Figure 5 presents a comparison of the quoted interpretation methods: Eq. (2) applied to loop 1, and Eq. (5) applied to the plastic phase, both applied to the test shown on Figure 3. The following main differences can be underlined between the proposed interpretation methods:

- Both methods are based on a hyperbolic ground behaviour and enable the determination of the maximum shear modulus of the ground. The results obtained for G_0 should, in principle, be the same, which is not the case in this example. As will be explained in paragraph 4, this is due to the limited expansion of the probe, leading to an important amount of extrapolation (the evaluated limit pressure is about 40% higher than the maximum pressure measured during the test, which makes the method less reliable.
- This highlights the advantage of performing both analyses on a same test, providing redundancy and facilitating the verification of test results. As it can be seen here, the value obtained with the unload loop is close to what has been measure on site using seismic CPT.
- Regarding the shear modulus decay rate, there are two possibilities when hyperbolic ground behaviour is considered: (1) if strain transformation methods are adopted, the shear modulus decay rate will be a function of a_0 and a_1 and of the transformation function applied. There is some amount of empiricism on the determination of the transformation functions. (2) if Eq (5) is considered, the shear modulus decay rate is constrained and will be a function of the undrained cohesion, as per Hardin-Drnevich function.

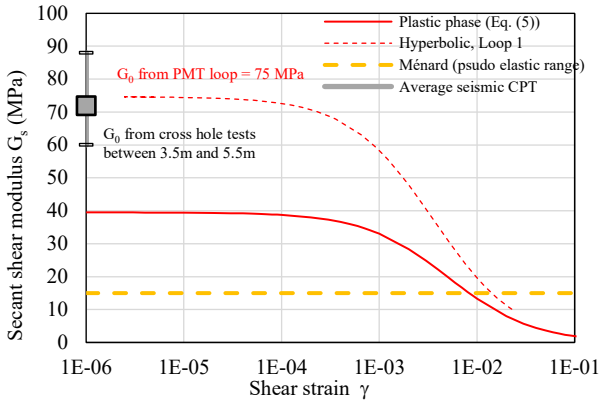

Figure 5. Comparison of the interpretation methods applied to the loop 1 and the plastic phase.

4 COMPARISON WITH OTHER MEASUREMENTS

Ménard pressuremeter tests were conducted as part of a quay project near Dunkirk, in the north of France. Other investigation campaigns, including cross-hole geophysical tests, were carried out on the same site and

nearby. The encountered stratigraphy consists of an approximately 25m thick layer of sands, followed by the overconsolidated Flanders clay. This clay exhibits a plasticity index ranging from 40% to 70%.

The interpretation of the pressuremeter tests in this paper was limited to tests conducted in the clays, whose behaviour is assumed to be undrained. Tests with expansion curves considered to be disturbed (poor probe-soil contact, incomplete expansion) were excluded. The obtained values of G_0 from the studied tests (as per Eq. (5) as the tests are associated to monotonic loading) were compared to the shear modulus results determined by cross hole tests. The results are presented in Figure 6.

The G_0 values evaluated from the pressuremeter tests interpreted according to the proposed method are close to those measured by cross-hole tests. In the figure, two groups of results have been distinguished: for the pressuremeter tests where the limit pressure was obtained by extrapolation up to 15% of the measured maximum pressure value (Group 1), and the tests for which the extrapolation is less than 10% of the measured maximum pressure (Group 2). It is observed that, for this second group, the results are closer to the geophysical measurements.

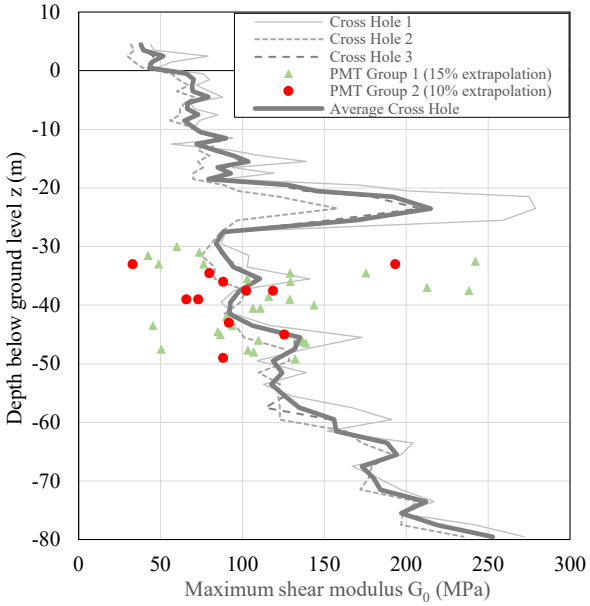

Figure 6. Comparison of the maximum shear modulus obtained through interpretation of the pressuremeter tests and measurements from cross hole tests in the Flanders clays.

The average ratio between the maximum shear modulus evaluated with the pressuremeter and the one measured from cross hole tests was calculated. For Group 1, this ratio is of ±25%. For Group 2, this ratio is of ±16%. This magnitude of error is considered to be sufficient for many types of projects. And this result points out to the interest of pushing the pressuremeter tests expansion level far enough to get the closest as possible to the conventional limit pressure, reducing the extrapolation levels and thus reducing errors.

Ten pressuremeter tests were carried out from 4.8m to 28m depth in the Whitby Mudstone, the UK. Tests at 4.8m and 10m depth were carried out using self-bored pressuremeter, with loops, and interpreted using both Eq. (2) and (5). Seismic CPT tests were performed from ground surface to approximately 10m depth, providing an estimate of the maximum shear modulus G_0. Plasticity index of the ground varies from an average of 33% to 28% as depth increases. The maximum shear modulus determined from the unload loops is compared to the values assessed from seismic CPT (Figure 7).

Three seismic tests performed on the formation lead to an average maximum shear modulus of 81 MPa and 56 MPa, respectively, at 4.8 and 10.0m depth.

Maximum shear modulus evaluated through unload loops using Eq. (2) is of 68 MPa and 49 MPa for these same depths, so an error of the magnitude of 15%.

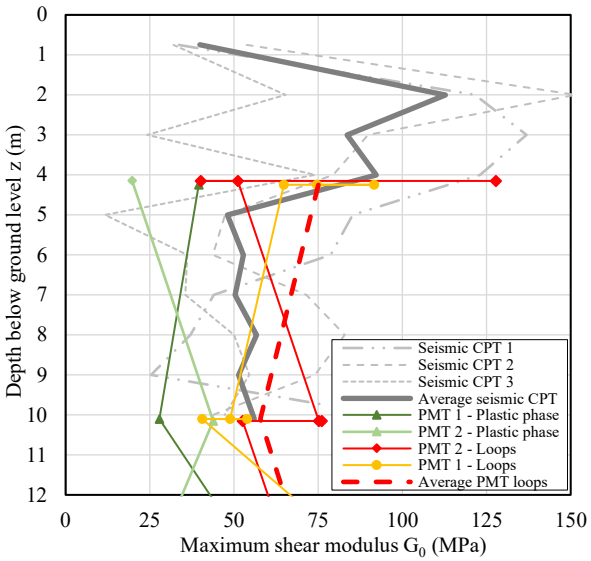

Figure 7. Comparison of the maximum shear modulus obtained through interpretation of the pressuremeter tests and seismic CPT tests in Whitby Mudstone.

Values of maximum shear modulus obtained using Eq. (5) for the plastic phase are of 40 MPa and 28 MPa, so 50% error in comparison to seismic CPT. As stated previously, this error can be explained by the excess of extrapolation required to evaluate the limit pressure: for the self-bored pressuremeter tests concerned, the cavity expansion has been limited to the magnitude of 10% radial strain. 42% radial strain is required to effectively measure the limit pressure. For these tests, the extrapolation ratio between the limit pressure extrapolated and the maximum pressure measured during the test is of approximately 40%.

While the unload loops yield a good estimate of the maximum shear modulus, an immediate recommendation that can be drawn from these results is to push the pressuremeter tests farther in expansion, to reduce the extrapolation ratio and enhance reliability.

5 SUMMARY AND CONCLUSION

Pressuremeter tests can be interpreted in considering the background of non-linear elasticity theory. In the case of undrained ground behaviour, the determination of the maximum shear modulus of the ground and the shear stiffness decay curve is straightforward.

Interpretation methods can be applied either in monotonic tests, such as tests performed using Ménard type procedures, or in tests including unload-reload loops, yielding two proposed methods. For high quality pressuremeter tests, both methods will lead to an evaluation of G_0 with an average error of the magnitude of 15%.

While both methods should be equivalent, methods based on unload reload loops enable to add redundancy and enhance reliability for the test interpretation. Loops are less susceptible to being disturbed due to probe insertion and its interpretation is less dependent on the assumption of the initial horizontal stress at rest.

Pressuremeter tests including several unload-reload loops and for which the cavity expansion is carried out sufficiently far (less than 10% extrapolation ratio) provide a reliable estimation of G_0. As different interpretation methods can be applied, all leading, in theory, to the same result, makes the test results to be easily verifiable and robust.

REFERENCES

AFNOR. 2015. Geotechnical investigation and testing − Field testing − Part 4: Ménard pressuremeter test. French standard NF EN ISO 22476-4.

Bolton, M.D., and Whittle, R.W. 1999. A non-linear elactic/perfectly plastic analysis for plane strain undrained expansion test. Géotechnique, 49(1): pages 133-141. https://doi.org/10.1680/geot.1999.49.1.133.

Briaud, J.L., Lytton, R.L., and Hung, J.T. 1983. Obtaining moduli from cyclic pressuremeter tests. Journal of Geotechnical Engineering, 109(5): 657–665. https://doi.org/10.1061/(ASCE)0733-9410(1983)109:5(657).

Ferreira, R. S., & Robertson, P. K. 1992. Interpretation of undrained self-boring pressuremeter test results incorporating unloading. Canadian Geotechnical Journal, 29(6), 918-928. https://doi.org/10.1139/t92-103.

Frank, R. 2017. Some aspects of research and practice for pile design in France. Innovative Infrastructure Solutions, 2(1): 32. Springer International Publishing. https://doi.org/10.1007/s41062-017-0085-4.

Habert, J., & Burlon, S. 2021. Taking into account inhomogeneous distortion around the pressuremeter probe to determine shear modulus. 6th International Symposium on Site Characterization. Budapest, Hungary.

Jardine, R.J. 1992. Nonlinear stiffness parameters from undrained pressuremeter tests. Canadian Geotechnical Journal, 29: 436–447. https://doi.org/10.1139/t92-048.

Ménard, L., and Rousseau, J. 1962. L'évaluation des tassements. Tendances Nouvelles. Sols Soils, 1(1): 13–29.

Wood, D.M. 1990. Strain-dependent moduli and pressuremeter. Géotechnique, 40(3): 509–512. https://doi.org/10.1680/geot.1990.40.3.509.

Proceedings of the XVIII ECSMGE 2024
GEOTECHNICAL ENGINEERING CHALLENGES
TO MEET CURRENT AND EMERGING NEEDS OF SOCIETY
© 2024 the Authors
ISBN 978-1-032-54816-6
DOI 10.1201/9781003431749-98
Open Access: www.taylorfrancis.com, CC BY-NC-ND 4.0 license

ECSMGE 24
XVIII EUROPEAN CONFERENCE ON SOIL MECHANICS AND GEOTECHNICAL ENGINEERING

Soil-pile interaction mechanisms under compressive service load

Mécanismes d'interaction sol-pieu sous charge de service en compression

J.C. Lourenço*
Universidade de Coimbra & TPF Consultores, Portugal

J.A. Santos
Instituto Superior Técnico – Universidade de Lisboa, Portugal

**jclourenco@uc.pt*

ABSTRACT: The evaluation of the response of piles subjected to compressive load is a common geotechnical problem. For non-displacement piles, the contribution of the lateral resistance for the global equilibrium is typically substantial under the service load level. For instance, the lateral resistance can be mobilised for small soil-shaft relative displacements, but the base resistance requires much larger displacements. Due to the pile's shortening and toe displacements, a narrow shear band is formed in the soil surrounding the pile's shaft, which is responsible for most lateral resistance development. In this shear band, shear and volumetric strains of complex evolution occur. However, the induced shear strain will be related to the thickness of the shear band, with the mobilised resistance and with the elastic shortening of the pile and toe displacements. In this work, a simplified model is presented to evaluate the order of magnitude of the shear band strain and its variation in depth, to understand the influence of the shear band thickness and the influence of the axial stiffness of the pile in the mobilisation of the shaft resistance even at very small toe displacements.

RÉSUMÉ: L'évaluation de la réponse des pieux soumis à une charge de compression est un problème géotechnique courant. Pour les pieux sans déplacement, sous le niveau de charge d'utilisation, la contribution de la résistance latérale à l'équilibre global est généralement substantielle. Par exemple, la résistance latérale peut être mobilisée pour de petits déplacements relatifs sol-puits, mais la résistance de base nécessite des déplacements beaucoup plus importants. En raison du raccourcissement du pieu et des déplacements de la pointe, une étroite bande de cisaillement se forme dans le sol entourant la tige du pieu, qui est responsable de la majeure partie du développement de la résistance latérale. Dans cette bande de cisaillement, des déformations de cisaillement et volumétriques d'évolution complexe se produisent. Cependant, la déformation de cisaillement induite sera liée à l'épaisseur de la bande de cisaillement, à la résistance mobilisée et au raccourcissement élastique du pieu et aux déplacements de pointe. Dans ce travail, un modèle simplifié est présenté pour évaluer l'ordre de grandeur de la déformation de la bande de cisaillement et sa variation en profondeur, pour comprendre l'influence de l'épaisseur de la bande de cisaillement et l'influence de la rigidité axiale du pieu dans la mobilisation de la résistance de l'arbre même en cas de très petits déplacements des orteils.

Keywords: Pile; service load; shaft resistance; shear band strain.

1 INTRODUCTION

The bearing capacity of the soil for compression piles is influenced by various factors, such as the nature and conditions of the soil, the presence of water, installation effects, the interface between the pile and the soil, the type of load, time effects, among others, and can be determined as the sum of the mobilised portions at the tip and along the shaft. In piles without the tip activated after installation (common situation in non-displacement piles), the load applied at the top is transferred to the soil through the shaft and progressively to the tip as the lateral resistance from top to bottom is depleted. On the other hand, for many practical situations, the contribution of lateral resistance is dominant for service load levels; that is, it is still far from reaching the ultimate bearing capacity.

This work focuses on the analysis of resistance mobilisation using a simplified model, which assesses the level of shear strain at the soil-pile lateral interface and its relationship with the mobilised resistance and the elastic shortening of the pile. Various scenarios are analysed, with piles of different lengths and diameters, where the tip contribution is 20% of the load applied at the top. Finally, a critical review of the values obtained for elastic shortening is discussed.

2 DESCRIPTION OF THE SIMPLIFIED MODEL

The total resistance (R_t) of a compression pile is given by the sum of two components: lateral resistance (R_s) and base resistance (R_b). The involved resistances are calculated as follows:

$$R_t = R_b + R_s - W \quad (1)$$

$$R_b = A_b\, q_b \quad (2)$$

$$R_s = A_s\, q_s \quad (3)$$

where W is the weight of the pile (often neglected due to its magnitude compared to other forces involved), A_b is the base area of the pile, q_b is the unit base resistance, A_s is the shaft area, and q_s is the unit lateral resistance.

Defining the parameter β as the ratio of q_s to σ'_{v0} (initial effective vertical stress of the soil), the accumulated lateral resistance (R_s) from the surface (z=0) to a depth of $z=L$ is calculated as:

$$R_s = \int_0^L P_s\, q_s\, dz = \int_0^L P_s\, \beta\, \sigma'_{v0} dz \quad (4)$$

where P_s corresponds to the perimeter of the pile at depth z. Usually, constant values for β are adopted with depth. Assuming a constant value neglects the effect of soil dilatancy. In practice, this is not observed since β has a maximum value at the surface, decreasing with depth. The superficial soil tends to be over-consolidated, dilating before reaching the critical state under shearing. Under confined conditions, the increase in soil volume results in increased average stresses and, consequently, increased normal stress around the pile. As granular soil is a material with frictional resistance, the increase in normal stress causes an increase in the lateral resistance of the pile. In more considerable depth, the soil is typically normally consolidated to slightly over-consolidated. Distortional deformations cause small soil contraction deformations, and the unit resistance tends towards a particular value, often represented by $sin\phi'_{cs}$, where ϕ'_{cs} is the angle of shear resistance at the critical state (Lourenço, 2020). Based on load test records on piles compiled by Fellenius (2019), this model adopts the following form for the function $\beta(z)$:

$$\beta(z) = a\, z^b + c \quad (5)$$

where a, b, and c are constants. Lourenço & Santos (2021), fitting equation (5) to the results of Fellenius (2019), yields values of a=2.8184, b=−0.6249, and c=0.25. Note that this type of function allows for a curve with a horizontal asymptote for z=0 and a vertical asymptote for z=+∞ with a value of 0.25. This value corresponds physically to $k_0 \times sin\phi'$ (i.e. 0.5×sin30°).

Since, as defined earlier, $\beta = q_s/\sigma'_{v0}$, adopting a constant value for the soil unit weight yields the evolution of the unit lateral resistance with depth:

$$q_s(z) = \left(a\, z^b + c\right) \gamma\, z \quad (6)$$

Figure 1 presents the evolution of the $\beta(z)$ and $q_s(z)$, determined by equations (5) and (6). For these curves, a unit weight value of 18 kN/m^3 was assumed.

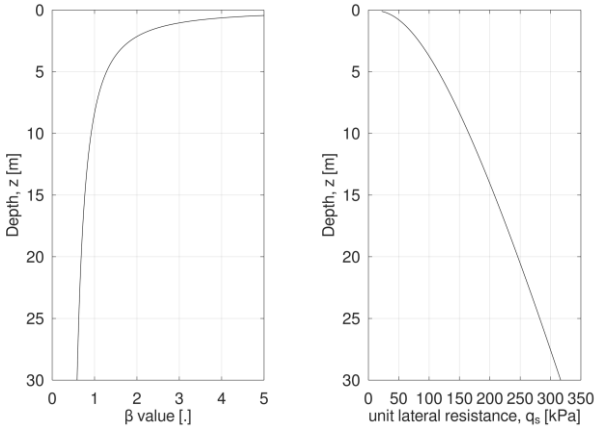

a) β value *b) unit lateral resistance (q_s)*

Figure 1. Evolution of the β and unit lateral resistance with depth

Knowing the load that the structure transfers to the top of the pile (Q_T), which is balanced by the lateral and tip resistance of the pile ($Q_T = R_s + R_b$), it is possible to know the axial force along the pile. For this, it is necessary to integrate equation (6) from the surface to the desired depth, resulting in the following equation:

$$N(z) = Q_T - \int_0^z \pi D\, q_s(z)\, dz = Q_T - \pi D \left(\frac{a\, \gamma\, z^{(b+2)}}{b+2} + \frac{c\, \gamma\, z^2}{2}\right) \quad (7)$$

where πD corresponds to the perimeter of the pile (assuming the pile has cylindrical geometry). Finally, the evolution of elastic shortening with depth ($\rho(z)$) is obtained through the depth integration of (7) divided by the axial stiffness modulus (EA):

$$\rho(z) = \int_0^z \frac{N(z)}{EA}\, dz = \frac{1}{EA}\left(Q_T\, z - \pi\, D \left(\frac{a\, \gamma\, z^{(b+3)}}{(b+2)(b+3)} + \frac{c\, \gamma\, z^3}{6}\right)\right) \quad (8)$$

The above equation allows determining the total elastic shortening (ρ_L), corresponding to the value of elastic shortening calculated at the base of the pile. This value will estimate the shear strain imposed on the shear band generated along the lateral interface. The thickness of this shear band is difficult to predict because: i) it is not an intrinsic characteristic of either the soil or the interface, also depending on the boundary conditions of the problem; ii) the thickness of the shear band tends to decrease with decreasing soil compactness; iii) the thickness of the shear band increases with the roughness of the pile-soil interface.

However, Fioravante (2002) sought to systematise the issue for pile cases, proposing that the interface thickness be about 2 to 5 times D_{50} for piles with a smooth interface and 10 to 15 times D_{50} for piles with a rough interface (where D_{50} corresponds to the average effective diameter of the soil particles).

To estimate the shear band's shear strain, it is assumed that the pile moves due to elastic shortening and the surrounding soil remains fixed, i.e., the relative displacement (d_{rel}) can be determined by the difference between the total elastic shortening of the pile and the elastic shortening at a depth determined through (8), as indicated in the following equation:

$$d_{rel}(z) = \rho_L - \rho(z) \tag{9}$$

Therefore, all soil deformation is concentrated in the shear band, and the shear strain (γ) in each point is given by the relative interface displacement determined through (9) divided by the shear band thickness (t_{intf}), as indicated by the following expression:

$$\gamma(z) = \frac{d_{rel}(z)}{t_{intf}} \tag{10}$$

Considering cast-in-place piles installed in sands, it is assumed that the effective diameter of the soil (D_{50}) will vary between 0.1 and 1 mm, generating shear bands with thicknesses of 1 to 15 mm. From the analysis of a series of interface test results compiled by Lourenço (2020), the mobilisation of maximum resistance is obtained from a shear strain level ranging from about 100% to 200%.

3 MODEL FOR PILES UNDER LOW-SERVICE LOAD

A model was developed for typical service conditions, where the applied load is resisted mostly by lateral resistance. For the development of the model, the following assumptions were adopted:

- the pile is cylindrical, with a diameter (D) ranging from 0.30 to 2.00 m;
- the ratio Length/Diameter (L/D) ranges from 5 to 50, which correspond from very short to very long piles;
- the pile is made of reinforced concrete (E = 30 GPa);
- the soil has a constant unit weight of 18 kN/m^3 without water-table;
- two types of soils are analysed: a fine sand, with a D_{50} of 0.1 mm, and a medium sand, with D_{50} of 1 mm; it is assumed that the shear band for these cases will have a thickness of 1 mm and 10 mm, for fine sand and medium sand respectively;
- the lateral resistance of the pile corresponds to 80% of the total resistance (i.e., the base resistance accounts for 20% of the total resistance);
- the tip of the pile lies on a very stiff soil, and it has no displacements.

The results of this parametric calculation are presented in Figure 2. From the analysis of the figure, it can be observed that:

i) in all cases, it is assumed that the lateral resistance is fully mobilized. From equation (6), it is possible to determine the relationship between the lateral resistance (R_s) and the length (L) of the pile, expressed through the following equation (Lourenço & Santos, 2021) presented in Figure 2a:

$$R_s[kN] = D\gamma(6.44L^{1.3751} + 0.393L^2) \tag{11}$$

ii) lateral resistance (R_s) is directly proportional to the diameter (D) and varies with the length of the pile (L) raised to the exponent of 1.38 to 2. Values between approximately 1 and 30 MN of lateral resistance were obtained (Figure 2a).

iii) the total elastic shortening is inversely proportional to the pile's diameter and modulus of elasticity. From equation (8), it is possible to determine the relationship:

$$\rho[mm] = \frac{L^{2.375}}{245.2D} + \frac{L^3}{3635.8D} \tag{12}$$

iv) It varies with the pile length raised to the exponent comprised between 2.38 and 3; in other words, the value of the shortening is mainly conditioned by the length of the pile (Figure 2b); for example, a pile with a length of 20 m and a diameter of 0.5 m has approximately the same lateral resistance as a pile with a length of 10 m and a diameter of 1.5 m; however, the elastic shortening of the former is about 15 mm, and the latter is 1 mm.

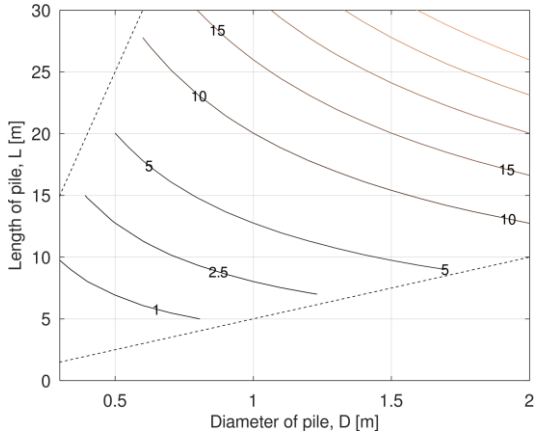

a) lateral resistance (MN)

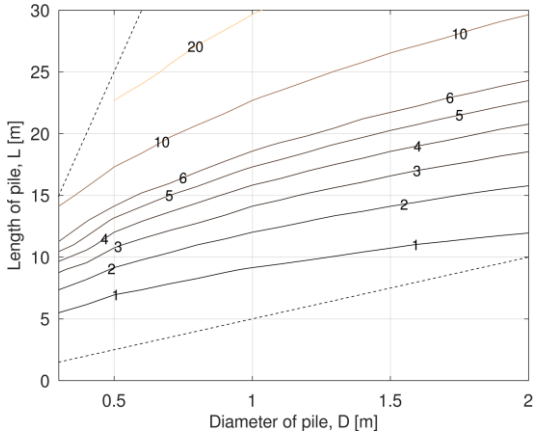

b) total elastic shortening, ρ_L (mm)

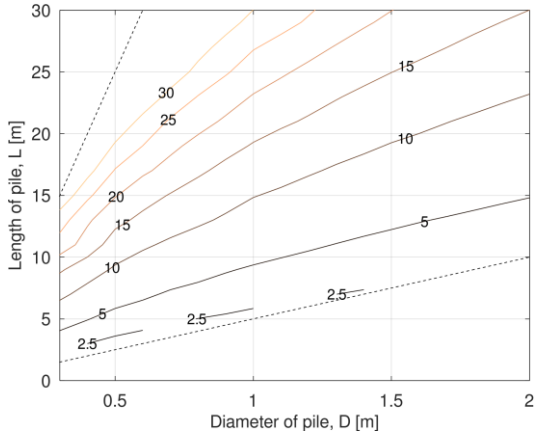

c) top pile axial stress (MPa)

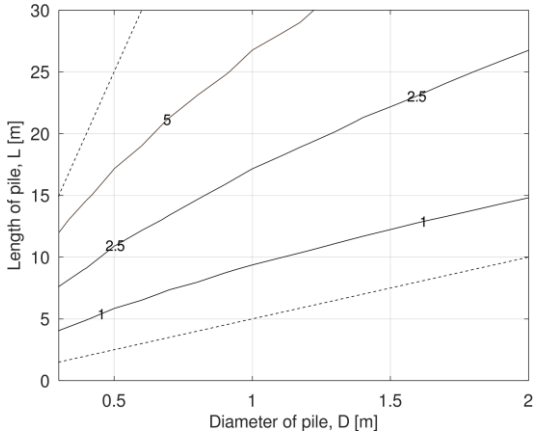

d) tip pile axial stress (MPa)

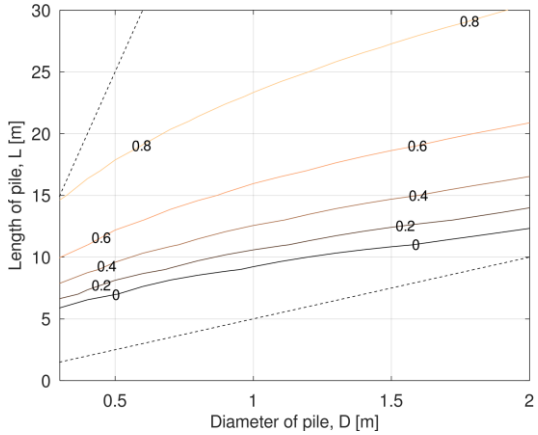

e) ratio of the shaft area where interface shear strain is greater than 1, for the pile installed in fine sand (t_{inf}=1 mm)

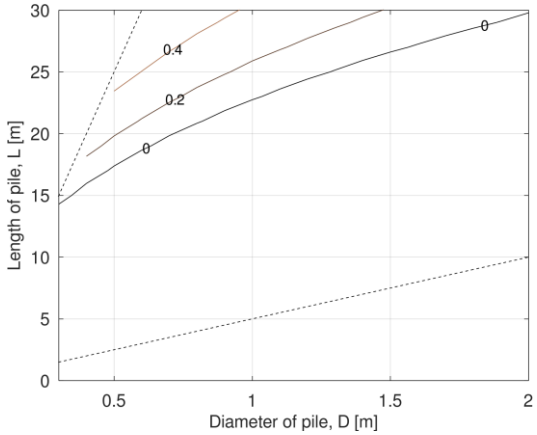

f) ratio of the shaft where interface shear strain is greater than to 1, for the pile installed in medium sand (t_{inf}=10 mm)

Figure 2. Parametric study results.

v) elastic shortening is very small, typically on the order of millimeters; in slender piles, shortening may reach 2 cm (Figure 2b);vi) the maximum base stress at the tip of the pile is usually smaller than 5 MPa (Figure 2d);

vii) for piles installed in fine sand, the ratio of the shaft where interface shear strain is greater than 1 is considerable; for example, if $L>5.9D+8.2$, more than top 60% of pile has the lateral resistance fully mobilized (Figure 2e); for short piles, the values presented in Figure 2e are merely indicative, as the influence of the tip should be greater than assumed;

viii) for piles installed in medium sand, the ratio of the shaft where interface shear strain due to elastic shortening allows some lateral resistance is

considerable; for exasmple, if $L<8.8D+12.4$, no lateral resistance occurs (Figure 2e);

ix) if tip settlement occurs in the pile installed in fine sand, all interface is fully mobilized for a tip settlement of 1 mm;

x) from Figure 2f, it can be inferred that for mobilizing the lateral resistance in medium sand, the tip settlement should be around 1 cm, which can be quite high, when considering the pile tip axial stress due to service loads. So, the full mobilization of the lateral resistance may not occur in all cases.

4 CONCLUSIONS

This article discussed the application of the beta method in assessing the strain level of the shear band mobilised for lateral resistance. It was observed that the mobilisation of lateral resistance corresponds to maximum relative displacements of a few millimetres. However, these displacements are sufficient to mobilise the entire resistance, as the strains resulting from the adopted model are typically over 100%.

As discussed in this article, the capacity for lateral resistance to be fully mobilised with elastic shortening will depend on the shear strain imposed on the shear band, which will have a thickness depending on the soil's particle size. The shear band will be a few millimetres thick for fine to medium sands. For coarser soils, where the shear band thickness is in order of centimetres, elastic shortening will not be sufficient to deplete the ultimate lateral resistance.

REFERENCES

Fellenius, B. (2019). Basics of foundation design. Pile Buck International, Inc.

Fioravante, V. (2002). On the shaft friction modeling of non-displacement piles in sand. *Soils and Foundations*, 42(2), pp. 23–33, https://doi.org/10.3208/sandf.42.2_23

Lourenço, J.C. and Santos, J. (2021) Assessment of the shortening of a pile based on the beta method. 17º Congresso Nacional de Geotecnia, Lisboa, Portugal.

Lourenço, J.C. and Santos, J. (2023) Assessment of the shaft interface shear strain for a pile under compressive loading (in Portuguese). 18º Congresso Nacional de Geotecnia, Lisboa, Portugal.

Lourenço, J.C. (2020). Numerical Modelling of Non-Displacement Piles in Sand. The importance of the dilatancy in the resistance mobilization. PhD Thesis. Instituto Superior Técnico and Centralesupélec.

Proceedings of the XVIII ECSMGE 2024
GEOTECHNICAL ENGINEERING CHALLENGES
TO MEET CURRENT AND EMERGING NEEDS OF SOCIETY
© 2024 the Authors
ISBN 978-1-032-54816-6
DOI 10.1201/9781003431749-99
Open Access: www.taylorfrancis.com, CC BY-NC-ND 4.0 license

ECSMGE 24
XVIII EUROPEAN CONFERENCE ON SOIL MECHANICS AND GEOTECHNICAL ENGINEERING

Seismic stability of gravity retaining walls: reliability assessment and web application

Stabilité sismique des murs de soutènement gravitaires: évaluation de la fiabilité et application web

Z. Luo*
Tolunay-Wong Engineers, Inc., Beaumont, USA

B.M. Das
California State University, Sacramento, USA

K. Sobhan
Florida Atlantic University, Boca Raton, USA

**zluo77@gmail.com*

ABSTRACT: This paper introduces a reliability-based seismic stability analysis of gravity retaining walls using a classical model and Monte Carlo simulation method. It empowers engineers to make informed design decisions based on acceptable probabilities of failure, thereby enhancing the reliability of their projects. The resulting web-based application provides an interactive platform for engineers and researchers to input seismic and soil parameters and perform the geotechnical design under seismic loads.

RÉSUMÉ: Ce document présente une analyse de stabilité sismique des murs de soutènement gravitaires basée sur la fiabilité, en utilisant un modèle classique et la méthode de simulation de Monte Carlo. Il donne aux ingénieurs la possibilité de prendre des décisions de conception éclairées en se basant sur des probabilités de défaillance acceptables, améliorant ainsi la fiabilité de leurs projets. L'application web résultante offre une plateforme interactive permettant aux ingénieurs et chercheurs de saisir des paramètres sismiques et géotechniques et d'effectuer la conception géotechnique sous des charges sismiques.

Keywords: Seismic stability; reliability-based design; retaining walls.

1 INTRODUCTION

Gravity retaining walls serve as critical components of geotechnical engineering, especially in ensuring the structural stability during seismic occurrences. This paper builds upon the extensive body of knowledge developed over the years in the domain of seismic design principles and the behaviour of gravity retaining walls. The primary aim of this paper is to introduce a reliability-based approach to analysing the seismic stability of such walls, offering both theoretical insights and practical solutions.

2 LITERATURE REVIEW

The seismic design of gravity retaining walls is a critical component of geotechnical engineering, addressing the stability of these structures during earthquake events. The study by Richards and Elms (1979) offers insights into early research on the seismic behavior of gravity retaining walls, providing a foundation for subsequent studies. Whitman et al. (1985) contributed to our understanding of seismic design principles for gravity retaining walls, providing historical context and insights into design methods. Notably, Das and Luo (2017) summarized the fundamental principles of soil behavior that underlie seismic analysis and design, providing essential groundwork for subsequent research.

In recent years, Srikar and Mittal (2020) proposed a modified pseudodynamic approach for seismic analysis and this approach is particularly relevant when assessing retaining walls subjected to surcharge loads, enhancing our methods for evaluating their seismic response. Srikar and Mittal (2021) presented a modified pseudo-dynamic analysis for rigid gravity retaining walls with specific soil and surcharge conditions and offered a more tailored approach to seismic analysis. Jadhav and Prashant (2023) developed charts for permanent displacement-based seismic design of cantilever retaining walls.

3 DESIGN MODEL

The design procedure documented in Das (2024) is used in this study for seismic stability analysis of gravity retaining walls. Figure 1 illustrates the design scheme. The wall has a height of H on the underlain soils with friction angle (ϕ_2) and unit weight (γ_2). The backfill materials have friction angle (ϕ_1) and unit weight (γ_1). The friction angle (δ) between the wall and the backfill is 2/3 of (ϕ_1). The active earth pressure coefficient under seismic condition is:

$$K_{ae} = \frac{sin^2(\phi_1+\beta-\theta')}{cos\theta' sin^2(\beta-\theta'-\delta)\left[1+\sqrt{\frac{sin(\phi_1+\delta)sin(\phi_1-\theta'-\alpha)}{sin(\beta-\delta-\theta')sin(\alpha+\beta)}}\right]} \quad (1)$$

Next, the required weight of wall for a tolerable wall displacement (Δ) is given:

$$W = \left[\frac{1}{2}\gamma_1 H^2(1-k_v)K_{ae}\right]C_{IE} \quad (2)$$

where

$$C_{IE} = \frac{sin(\beta-\delta)-cos(\beta-\delta)tan\phi_2}{(1-k_v)(tan\phi_2'-tan\theta')} \quad (3)$$

$$\theta' = tan^{-1}\left(\frac{k_h}{1-k_v}\right) \quad (4)$$

$$k_h = A_a\left(\frac{0.2A_v^2}{A_a\Delta}\right) \quad (5)$$

where, α is the slope angle of the backfill, and β is the angle of the wall heel. The coefficients k_h and k_v are the horizonal seismic acceleration and vertical seismic acceleration, over the acceleration due to gravity, respectively. The values of A_a and A_v are documented in Applied Technology Council (1978).

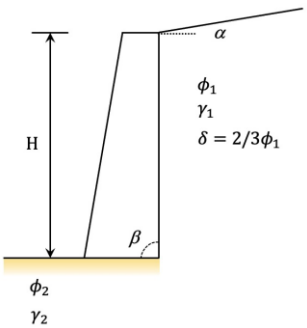

Figure 1. Scheme of a gravity retaining wall for earthquake conditions.

The parameter values in the design of a gravity retaining wall under seismic condition documented in Das (2024) are adopted and shown in Table 1. Additionally, α is zero and β equals 90°. Following Eq. (2), the required weight of wall that meets the displacement requirement is determined to be 54.1 kN/m. This result does not consider the factor of safety.

Table 1. Parameters and their values in the design of a gravity retaining wall under seismic condition.

Variable	Symbol	Value
Height of wall	H	5 m
Limiting wall horizontal displacement	Δ	38 mm
Friction angle of backfill	ϕ_1	36°
Unit weight of backfill	γ_1	16 kN/m^3
Friction angle of underlain soil	ϕ_2	36°
Normalized vertical seismic acceleration	k_v	0
Coefficient	A_a	0.2
Coefficient	A_v	0.2

4 PROBABILISTIC DESIGN

Next, the above procedure is repeated in a Monte Carlo simulation (MCS) framework. For simplicity, only the soil strength parameters (ϕ_1 and ϕ_2) are chosen as normally distributed variables, while all other parameters are assumed to be constant. It is assumed that the coefficient of variation (COV) of ϕ_1 is 0.10 and the COV of ϕ_2 is 0.15, respectively. Their mean values follow Table 1 and are 36°.

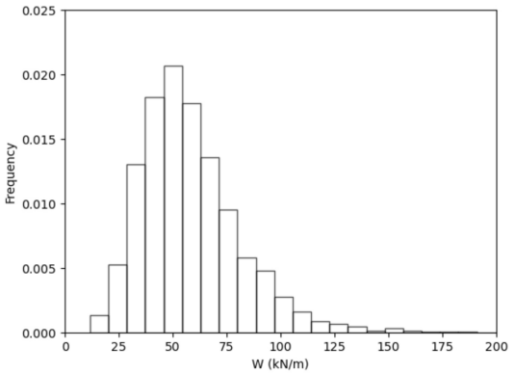

Figure 2. Resulting histogram of wall weight (W) from Monte Carlo simulation.

The number of MCS is 5000. Figure 2 shows the resulting histogram of the required wall weight. The Shapiro-Wilk test shows that this resulting distribution does not follow a lognormal distribution. Based on Figure 2, the 95th percentile of W is 100.7 kN/m. It indicates that if the design target is to ensure there is only 5% of chance to fail, the designed wall weight should be 100.7kN/m. Similarly, the 99.75th percentile of W is 161.5 kN/m. If the wall weight is designed to be 161.5 kN/m, the probability of failing to meet the

required wall displacement is reduced to 0.25%. The smaller the target probability of failure is, the larger designed wall weight will be, leading to more project cost. This demonstrates that the probabilistic approach can not only quantify the uncertain of soil parameters, but also ensure a rational design based on the acceptable probability of failure.

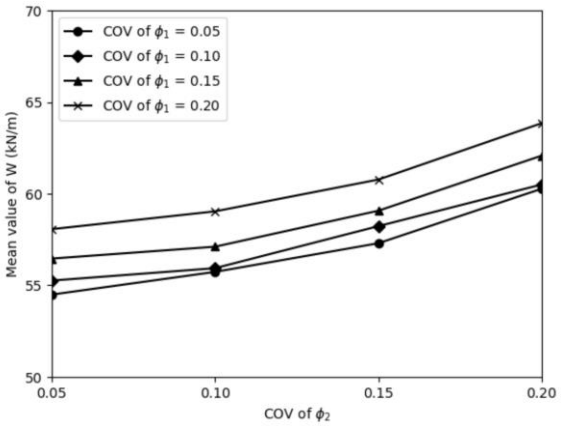

Figure 3. The mean values of wall weight (W) for various pairs of coefficient of variation (COV) for ϕ_1 and ϕ_2.

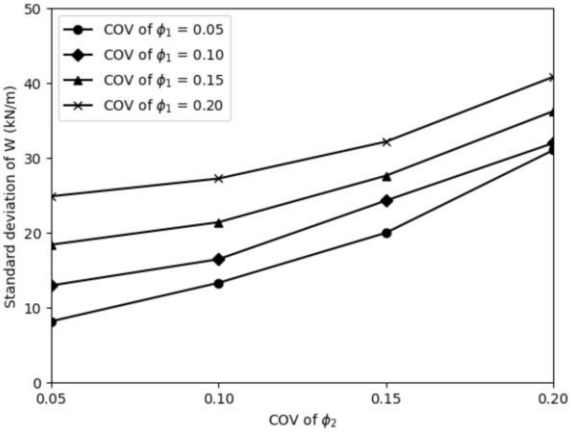

Figure 4. The standard deviations of wall weight (W) for various pairs of coefficient of variation (COV) for ϕ_1 and ϕ_2.

To better understand the uncertainty propagation in the geotechnical design of gravity retaining walls under seismic condition, a series of parametric study is performed. The following *COV* values for ϕ_1 and ϕ_2 are considered: 0.05, 0.10, 0.15 and 0.20. For each pair of *COV*, a number of 5000 MCS is performed. Based on the resulting distributions of the required all weight (*W*), the mean values and standard deviations are obtained and presented in Figure 3 and Figure 4, respectively. Figure 3 shows that when the *COV* of ϕ_1 is held constant, the mean *W* increases with the *COV* of ϕ_2. For the same level of *COV* of ϕ_2, the mean W increases with *COV* of ϕ_1. It indicates that the mean required wall weight to satisfy the required wall displacement in seismic condition increases in the variability in either ϕ_1 or ϕ_2.

Figure 4 shows that when the *COV* of ϕ_1 is held constant, the standard deviation (*SD*) of *W* increases with *COV* of ϕ_2. For the same level of *COV* of ϕ_2, the *STD* of *W* increases with the *COV* of ϕ_1. It indicates that the variation in the required wall weight to satisfy the required wall displacement in seismic condition increases in the variability in either ϕ_1 or ϕ_2.

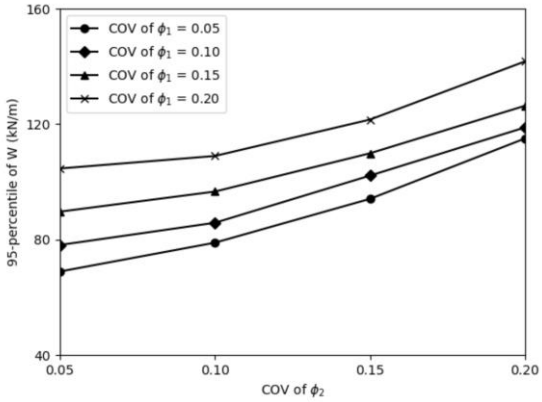

Figure 5. The 95th percentile of the required wall weight (W) for various pairs of coefficient of variation (COV) for ϕ_1 and ϕ_2.

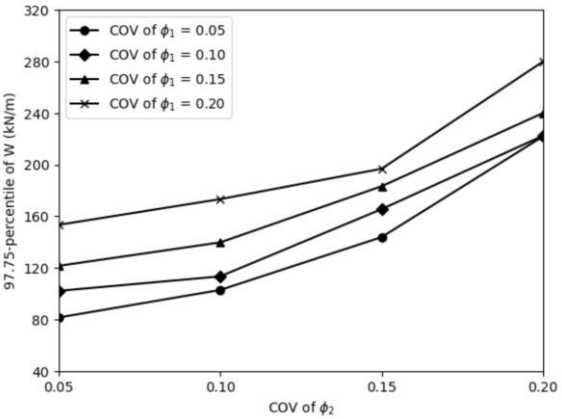

Figure 6. The 99.75th percentile of the required wall weight (W) for various pairs of coefficient of variation (COV) for ϕ_1 and ϕ_2.

Figure 3 and Figure 4 explicitly demonstrate that the uncertainty in soil strength parameters has inevitable impact on the geotechnical design of gravity retaining walls under seismic condition. The geotechnical design can then be realized based on the outcomes of MCS. The percentiles of the resulting probability distribution of *W* can be readily obtained for some target probability of failure. Figure 5 shows the 95th percentile of the required W that satisfies the required wall displacement for various pairs of coefficient of variation (*COV*) for ϕ_1 and ϕ_2. Figure 5 can serve as a design chart for the target probability of

failure of 5%. Given a known pair of COV for ϕ_1 and ϕ_2, the designed W can then be interpolated in this chart. Similarly, Figure 6 shows the 99.75th percentile of the required W that satisfies the required wall displacement for various pairs of coefficient of variation (COV) for ϕ_1 and ϕ_2. Figure 6 corresponds to the design chart for the target probability of failure of 0.25%. It is obvious that compared to 5% probability of failure, the designed W values in Figure 6 are much greater.

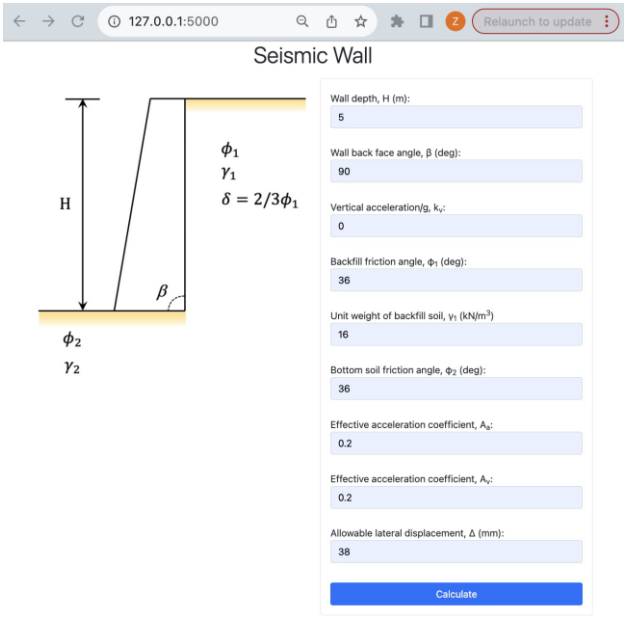

Figure 7. User interface of the developed application

5 WEB APPLICATION

A Flask application has been created to support the seismic design of gravity retaining walls, with a specific focus on implementing the mathematical model described in Eq (2) for deterministic analysis. The application addresses the time-consuming and error-prone nature of manual seismic design calculations for such structures. Engineers and designers often face challenges in performing these calculations, which involve intricate parameters like wall geometry, soil properties, and seismic coefficients. Our Flask app aims to simplify this process, reduce errors, and provide a user-friendly interface to efficiently obtain critical design information, such as the required unit weight of the wall (in kN/m). By streamlining seismic design calculations, this application contributes to the safety and reliability of gravity retaining walls during seismic events.

6 DISCUSSION AND CONCLUSION

This paper ventures into the realm of probabilistic design by conducting a Monte Carlo simulation, demonstrating the capacity to quantify uncertainties in soil strength parameters. It is commonly understood that reliability is represented by one minus the probability of failure. This approach empowers engineers to make informed design decisions based on acceptable probabilities of failure, thereby enhancing the reliability of their projects. The significance of uncertainty in geotechnical design is underscored through parametric studies, highlighting the influence of soil strength parameter variations on the required wall weight. This reinforces the importance of considering uncertainty as an integral part of the design process. Lastly, the research transcends theory to practicality with the introduction of a user-friendly Flask web application.

REFERENCES

Applied Technology Council. (1978). Tentative Provisions for the Development of Seismic Regulations for Buildings. Publication ATC-3-06.

Das, B.M. (2024). Principles of Foundation Engineering, 10th Edition. Cengage Learning. ISBN-10: 0357684656. ISBN-13: 9780357684658.

Das, B.M. and Luo, Z. (2017). Principles of Soil Dynamics, 3rd Edition. Cengage Learning. ISBN-10: 1305389433. ISBN-13: 9781305389434.

Jadhav, P.R. and Prashant, A. (2023). Charts for Permanent Displacement-Based Seismic Design of Cantilever Retaining Walls. Journal of Earthquake Engineering, 27:12, 3341-3361. https://doi.org/10.1080/13632469.2022.2134943

Richards Jr, R., and Elms, D. G. (1979). Seismic behavior of gravity retaining walls. Journal of the Geotechnical Engineering Division, 105(4), 449-464.

Srikar, G., and Mittal, S. (2020). Seismic analysis of retaining wall subjected to surcharge: A modified pseudodynamic approach. International Journal of Geomechanics, 20(9), 06020022. https://doi.org/10.1061/(ASCE)GM.1943-5622.0001780

Srikar, G., and Mittal, S. (2021). Modified pseudo-dynamic analysis of rigid gravity retaining wall with cohesion-less backfill and uniform surcharge. Geomechanics and Engineering, 26(5), 453-464. https://doi.org/10.12989/gae.2021.26.5.453

Whitman, R. V., Liao, S., and Massachusetts Institute of Technology. Department of Civil Engineering. (1985). Seismic design of gravity retaining walls (pp. 533-540). US Army Engineer Waterways Experiment Station.

Proceedings of the XVIII ECSMGE 2024
GEOTECHNICAL ENGINEERING CHALLENGES
TO MEET CURRENT AND EMERGING NEEDS OF SOCIETY
© 2024 the Authors
ISBN 978-1-032-54816-6
DOI 10.1201/9781003431749-100
Open Access: www.taylorfrancis.com, CC BY-NC-ND 4.0 license

ECSMGE 24
XVIII EUROPEAN CONFERENCE ON SOIL MECHANICS AND GEOTECHNICAL ENGINEERING

Direct design method of shallow foundation based on in situ tests results, application to dynamic cone penetrometer

Méthode de conception directe des fondations peu profondes basée sur les résultats des essais in situ, application au pénétromètre dynamique

T.A. Luong
Sol Solution, Riom/Université Gustave Eiffel, Champs-sur-Marne, France

P. Reiffsteck*, F. Szymkiewicz
Université Gustave Eiffel, Champs-sur-Marne, France

M. Benz-Navarrete
Sol Solution, Riom, France

**philippe.reiffsteck@univ-eiffel.fr*

ABSTRACT: The University G. Eiffel has built a light surface foundation test station to perform loading test campaign on experimental sites. This paper presents the test campaigns on shallow foundations carried out to failure with the contribution of optic fibre strain measurement in ground mass. Prediction of bearing capacity may be realized with direct design method based on limit resistance of in situ tests. Several methods based on limit pressure, static and dynamic penetration resistance and SPT blow count will be compared. The results are qualified with a database of 160 load tests with detailed ground investigation. This paper presents a simple, economic, and sound design method that could be easily implemented worldwide, based on a Dynamic Penetration Test (DPT) device.

RÉSUMÉ: L'Université G. Eiffel a construit une station d'essais de fondations superficielles légères pour réaliser des campagnes d'essais de chargement sur des sites expérimentaux. Cet article présente les campagnes d'essais sur les fondations superficielles menées jusqu'à la rupture avec l'apport de la mesure de déformation par fibre optique dans la masse du sol. La prédiction de la capacité portante peut être réalisée avec une méthode de conception directe basée sur la résistance limite des essais in situ. Plusieurs méthodes basées sur la pression limite, la résistance à la pénétration statique et dynamique et le nombre de coups SPT seront comparées. Les résultats sont qualifiés à l'aide d'une base de données de 160 essais de charge avec une étude détaillée du sol. Cet article présente une méthode de conception simple, économique et solide qui pourrait être facilement mise en œuvre dans le monde entier, basée sur une nouvelle génération d'appareils d'essai de pénétromètre dynamique (DPT).

Keywords: Shallow foundation; direct design method; ground investigation; penetration test.

1 INTRODUCTION

The design of shallow foundations is carried out within the framework of Eurocode 7 using two main methods. The first, based on laboratory tests, requires the angle of friction to be determined (Terzaghi and Peck, 1948). This is often determined indirectly from in situ tests by correlation which may be a source of uncertainties. The second one based on the assumption of a similarity of the failure mechanism observed under the shallow foundation and during in situ test, propose a direct calculation using the equivalent resistance of the soil estimated using this test under foundation and the bearing capacity.

This paper describes the shallow foundation tests carried out by the Univ. G. Eiffel/IFSTTAR and the direct design method developed on the basis of the results obtained during the study and those in the database collected in the bibliography. The method derived from the database is discussed.

2 SHALLOW FOUNDATION DATABASE

The development of methods for the design of shallow foundations has always been based on the analysis of test campaigns involving the loading of shallow foundations by dedicated structures. Numerous national research bodies and universities have undertaken parametric test campaigns on sites of various types (Table 1). A complete summary of these tests was produced by Canépa and Garnier

(2004) for the symposium on surface foundations organised by the LCPC in 2003. The tests listed in Table 1 may have varied in their protocol, but follow more or less the same test procedure.

Table 1. Some tests listed in database.

Country	Site	Soil class	Reference
Thaïland	Bangkok	Soft clay	Brand et al,(1972
Irland	Belfast, Kinnegar	Clayey silt	Lehane (2003)
UK	Bothkennar Cowden Shellhaven	Marine soft clay	Jardine et al, (1995) Lehane et Jardine (2003)
Brasil	Porto Alegre	residual soil	Consoli et al, (1998)
Germany	DEGEBO	Sand and coarse sand	Muhs and Weiß (1971)
Koweit	Koweit city	Silty sand	Ismael (1984)
Australia	Shenton Park, Perth	Sand	Lehane et al. (2008)
Portugal	Porto	Silty sand and saprolitic clay	Viana da Fonseca (2001)
Norway	Haga	Firm clay	Andersen and Stenhamar (1982)
Canada	Ottawa	sand	Shields and Bauer (1975)
USA	Texas A & M FHWA	Silty sand Sand clay	Briaud and Gibbens (1999) Lutenegger and de Groot (1995
Sweden	Kolbyttemon Tornhill Vagverket Vattahammar	clay till silt	Bergdahl, et al., (1985) Larsson (2001) Larsson (1997)

Some complementary tests are needed to add some configuration (eccentricity, cyclic solicitation), soil types.

2.1 Shallow foundation loading test

The foundation or plate loading test consists of measuring the settlement corresponding to a succession of load steps applied to the soil by the plate. The test is carried out using the device arrangement shown in Figure 1.

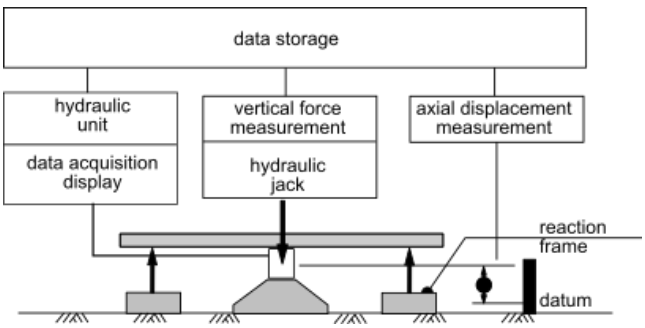

Figure 1. Loading test equipment.

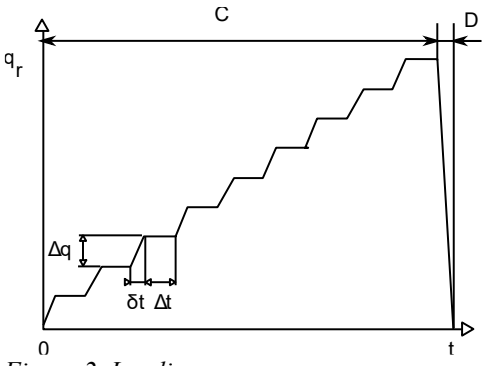

Figure 2. Loading program.

The test is continued:

- either until the ground is punched, conventionally defined as B/10,
- or to the limit of the reaction device.

Each loading stage is kept constant until the curve representing settlement as a function of the logarithm of the time of application is linear, or for 30'. The settlement is measured using comparators uniformly distributed around the plate, the attachment points of which are fixed to a non-deformable frame resting on the ground at points that must remain immobile during the test. Figure 2 and 3 gives example of test realised in this research to increase test results in database.



Figure 3. Test on sandy site.

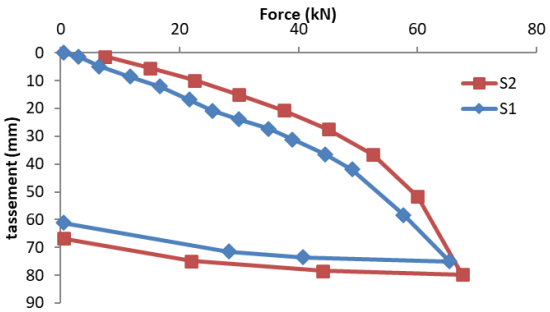

Figure 4. Test result on a soft clay site.

3 DIRECT DESIGN METHOD

This method, standardized in France since the seventies was developed by Menard mainly for the pressuremeter and adopted in French design rules for

CPT since 1988, and also proposed in other studies (Lehane, 2019). It has been extended in this research, to dynamic and standard penetration tests. Almost all the cases studied, listed in Table 1 and the one stored in French database have been described by a detailed ground investigation campaign including dynamic and standard penetration soundings.

3.1 Calculation of bearing capacity from the in situ test

The formula used to calculate the net failure stress (bearing capacity per unit area) of a foundation subjected to a centred vertical load from the results of considered test is:

$$q_{net} = k_{test} \cdot x_c \qquad (1)$$

with

q_{net} net stress,

k_{test} bearing capacity factor (i.e. k_d for DPT, k_c for CPT, etc.)

x_c equivalent resistance.

The equivalent resistance x_c is the average soil strength that can be defined by averaging resistance on a DPT or SPT or CPT, profile for a depth of 1.5 the width of the foundation.

In the case of dynamic penetration test, the average bearing factor k_d is observed to be equal to 0.225 (Amar et Morbois, 1985). The coefficients a, b and c of the curves defined by equation (2), to match the experimental data as closely as possible (Figure 5 and Table 2):

$$k_{test;\frac{B}{L}} = k_{test;0} + \left(a + b.\frac{D_e}{B}\right) \cdot \left(1 - e^{-c.\frac{D_e}{B}}\right) \qquad (2)$$

The dispersion of the dynamic penetrometer bearing factor k_d is similar to that observed for the bearing factor k_p defined for the pressuremeter test.

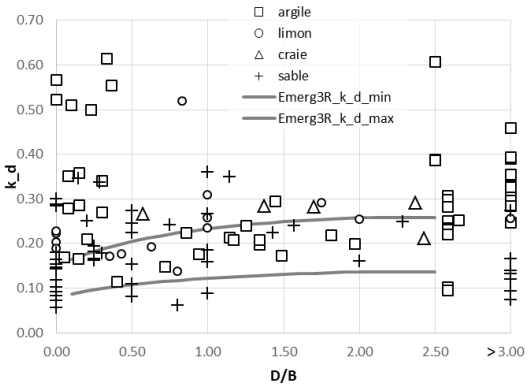

Figure 5. Effect of embedment for the different soils for the dynamic penetrometer method.

In the case of a water table at depth in sand, we consider that during a penetration test in moderately compact sand, a "liquefaction" phenomenon (thixotropy) may occur which affects the dynamic resistance of the soil (sensitivity coefficient, s_L=2). So for any test under the water table and in sand, we take:

$$q_d = q_{d\,test} \cdot s_L \qquad (3)$$

Table 2. Coefficients in the expression of the bearing capacity factor k_d.

Soil category	curve	Coefficient formula (2)			
		a	b	c	$k_{d;0}$
Clay and loam	L/B=∞ : Q1	0.04	0.007	1.3	0.15
	L/B=1: Q2	0.10	0.007	1.5	0.15
Sand and gravel	L/B=∞ : Q3	0.04	0.009	2	0.08
	L/B=1: Q4	0.03	0.04	5	0.08
Chalk	L/B=∞ : Q5	0,06	0,03	3	0,2
	L/B=1 : Q6	0,09	0,04	3	0,2

It is noted that these coefficients vary little from those adopted for the static penetrometer.

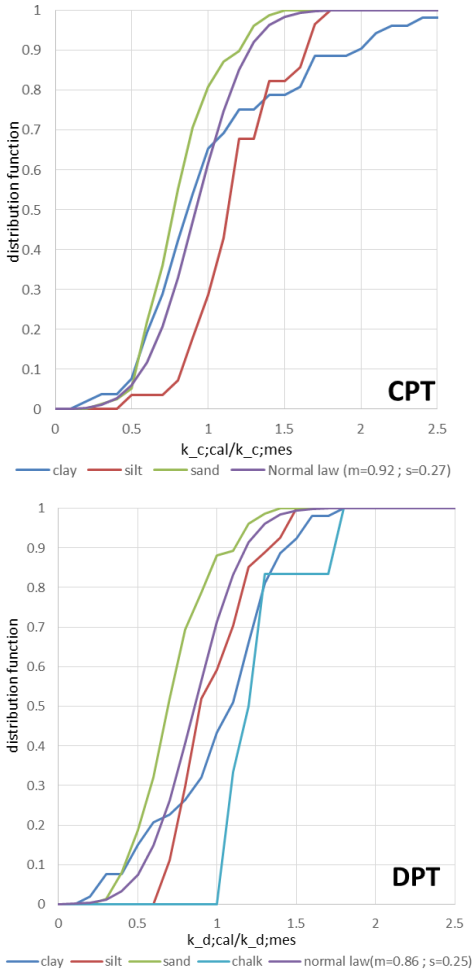

Figure 6. Distribution curves of direct design method for (a) CPT (b) DPT for different soils,

3.2 Evaluation of the method on the basis of existing data

Figure 6 compares the distribution curves of the ratios between the calculated and measured bearing capacity factors, with 147 cases collected for CPT and 98 tests for DPT. It should be noted that the calculation using the proposed relationship has a sigmoidal shape very close to that of a normal distribution for most soils. The level of safety represented by the deviation from a mean value of 1 is not observed to be totally identical in the various cases, but it remains very close to that observed on the same database for estimates based on the results of pressuremeter tests.

4 CONCLUSIONS

This paper presents the extension of the direct design method for assessing the bearing capacity of shallow foundations in situ to dynamic penetration tests. New tests have been performed to supplement the database of tests already collected in bibliography to validate the design method.

A method for estimating the bearing capacity using a dynamic penetrometer with constant and variable energy was presented and its results compared with the elements in the database, demonstrating a good quality of prediction, which should be taken into account in the French design standard NF P92-261 under revision.

ACKNOWLEDGEMENTS

The authors are grateful for the financial support provided by ANRT funding agency.

REFERENCES

Amar S., Morbois A., (1985), Contribution au dimensionnement des fondations superficielles à l'aide de l'essai au pénétromètre statique, *BLPC* 141:37-43 (in French).

Andersen, K.H. and Stenhamar, P. (1982). Static plate loading tests on overconsolidated clay. *JGED, ASCE*, 108(GT7):919-934. https://doi.org/10.1016/0148-9062(84)91235-x.

Bergdahl, U., Hult, G., & Ottosson, E. (1985). Calculation of settlements of footings in sands. In *Proc. 11th ICSMFE.* Rotterdam: Balkema. 3(8/C/5):2167-2170,

Brand, E.W., Muktabhant, C., and Taechathummarak, A. (1972). Load tests on small foundations in soft clay, *Performance of Earth and Earth-Supported Structures. ASCE*, 1(2):903-928 • https://doi.org/10.1016/0148-9062(74)92802-2.

Briaud J.L., Gibbens R. (1999) Behavior of Five Large Spread Footings in Sand. *JGGE*, 125(9): 787-796. https://doi.org/10.1061/(ASCE)1090-0241(1999)125:9(787).

Canépa Y., Garnier J. (2004) "Etudes expérimentales du comportement des fondations superficielles - Etat de l'art", *Proc. Int Symp. Fondsup 2003*, Paris, Presses de l'ENPC/LCPC, Magnan (éd), 2:155-260 (in French).

Consoli, N. C., Schnaid, F., and Milititsky, J. (1998). Interpretation of plate load tests on residual soil site. *JGGE*, 124(9):857–867. https://doi.org/10.1061/(ASCE)1090-0241(1998)124:9(857.

Ismael, N. F. (1985). Allowable pressure from loading tests on Kuwaiti soils. *CGJ*, 222:151–157.

Jardine, R.J., Lehane, B.M., Smith, P.R., Gildea, P.A. (1995). Vertical loading experiments on rigid pad foundations at Bothkennar *Géotechnique*, 45(4):573-597 https://doi.org/10.1680/geot.1995.45.4.573.

Larsson R. (1997) Investigations and Load Tests in Silty Soils. SGI, Report n° 54, 266 pages.

Larsson R. (2001) Investigations and Load Tests in Clay till, SGI, Report No 59, 169 pages.

Lehane, B., Jardine, R.J., (2003). Vertically loaded shallow foundation on soft clayey silt: A case history, *Proc. ICE, Geotech. Eng.*,.156(1):17–26.

Lehane, B.M., Doherty, J.P. & Schneider, J.A. (2008). Settlement prediction for footings on sand. *Deformation characteristics of geomaterials; Proc. 4th intern. symp.*, 1:133–150.

Lehane, B.M. (2019). CPT-based design of foundations. E.H. Davis Memorial Lecture (2017), *Australian Geomechanics*, 54(4):23-48.

Lutenegger A.-J., De Groot D.-J., (1995), Settlement of shallow foundations on granular soils. UMass, 233 pages.

Muhs, H. and Weiß, K. (1971). "Untersuchung von Grenztragfahigkeit und Setzungsverhalten flach gegründeter Einzelfundamente im ungleichförmigen nichtbindigen Boden." Berichte aus der Bauforschung, DEGEBO, Berlin, heft 69. (in German).

Shields D., Bauer G. (1975), Determination of the modulus of deformation of a sensitive clay using laboratory and in situ tests. *Proc. Spec. Conf. on In Situ Meas. Soil Prop.,* ASCE, (1):395-421.

Terzaghi K. , Peck R. (1948*) Soil Mechanics in Engineering Practice,* 1st edition, New York Wiley, 719 pages.

Viana da Fonseca A. (2001), Load tests on residual soil and settlement prediction on shallow foundation, *JGGE*, 127(10): 869-883 https://doi.org/10.1061/(ASCE)1090-0241(2001)127:10(869.

Proceedings of the XVIII ECSMGE 2024
GEOTECHNICAL ENGINEERING CHALLENGES
TO MEET CURRENT AND EMERGING NEEDS OF SOCIETY
© 2024 the Authors
ISBN 978-1-032-54816-6
DOI 10.1201/9781003431749-101
Open Access: www.taylorfrancis.com, CC BY-NC-ND 4.0 license

ECSMGE 24
XVIII EUROPEAN CONFERENCE ON SOIL MECHANICS AND GEOTECHNICAL ENGINEERING

Key concepts in soil mechanics: simple hands-on and team-based strategies to promote active learning

Concepts clés en mécanique des sols: stratégies pratiques simples pour promouvoir l'apprentissage actif

J. Macedo, M. Pinho-Lopes*
RISCO, University of Aveiro, Aveiro, Portugal
**mlopes@ua.pt*

ABSTRACT: Soils are particulate materials, which exhibit mechanical and hydraulic responses, very different from other civil engineering materials. This response poses additional challenges to students. A new pedagogical practice was implemented, combining hands-on and team-based learning to promote deep learning of fundamental concepts in Soil Mechanics: phase relationships and total and effective stresses in soils. The implementation occurred in the first semester of 2022/2023 in an introductory course on Soil Mechanics (Civil Engineering degree) at University of Aveiro, Portugal. To illustrate the topics covered simple experiments were used, setup with basic materials and accessories, thus simple to replicate in different contexts. Most activities took place in a room with modern equipment and furniture, designed to promote active learning. The model promotes deep learning and student engagement. Students appreciated the model, the sessions dynamic, the learning environment and the interaction between peers and with teachers. They recognised the importance of adopting different learning strategies. Not all students engaged with preparation activities, which compromises the benefit from the sessions. The model is sufficiently robust and versatile to be replicated in different contexts. The authors believe that using technology, while adopting hands-on strategies (with simple physical models and illustrations) and promoting critical thinking is an excellent way of promoting engagement and deep learning in Soil Mechanics.

RÉSUMÉ: Les sols sont des matériaux particulaires qui présentent des réactions mécaniques et hydrauliques très différentes des autres matériaux de génie civil. Cette réponse pose des défis supplémentaires aux étudiants. Une nouvelle pratique pédagogique a été mise en œuvre, combinant l'apprentissage pratique et l'apprentissage en équipe pour promouvoir l'apprentissage approfondi des concepts fondamentaux de la mécanique des sols: relations de phase et tensions totales et effectives dans les sols. L'implémentation a eu lieu au cours du premier semestre 2022/2023 dans le cadre d'un cours d'introduction à la mécanique des sols (diplôme de génie civil) à l'université d'Aveiro, Portugal. Pour illustrer les sujets abordés, des expériences simples ont été utilisées, préparées avec des matériaux et des accessoires de base, donc faciles à reproduire dans différents contextes. La plupart des activités se sont déroulées dans une salle dotée d'un équipement et d'un mobilier modernes, pour favoriser l'apprentissage actif. Le modèle favorise l'apprentissage en profondeur et l'engagement des étudiants. Les élèves ont apprécié le modèle, la dynamique des sessions, l'environnement d'apprentissage et l'interaction entre pairs et les enseignants. Ils ont reconnu l'importance d'adopter différentes stratégies d'apprentissage. Tous les étudiants n'ont pas participé aux activités de préparation, ce qui compromet le bénéfice des sessions. Le modèle est suffisamment solide et polyvalent pour être reproduit dans différents contextes. Les auteurs estiment que l'utilisation de la technologie, tout en adoptant des stratégies pratiques (avec des modèles physiques et des illustrations simples) et en encourageant la pensée critique, est un excellent moyen de promouvoir l'engagement et l'apprentissage approfondi de la mécanique des sols.

Keywords: Soil Mechanics; hands-on learning; phase relationships; effective stresses.

1 INTRODUCTION

Fostering deep understanding through active learning strategies is a critical priority in the education of engineering students. Engineering is a complex domain that demands more than just a superficial acquisition of knowledge. It requires a deep understanting of fundamental principles and the ability to relate and apply them to solve complex problems that very often require innovative solutions. Active learning strategies, which require students to engage with the content, solve problems, and collaborate with each other, are essential for achieving this depth of understanding.

In this paper, a pedagogical practice is presented and described, which was designed to promote deep learning of fundamental concepts in Soil Mechanics, and that combines two different active learning strategies: hands-on learning and team-based learning.

2 METHODOLOGY

2.1 Pedagogical context

The pedagogical strategies described herein were implemented on the course Soil Mechanics I (SMI) of the 1st cycle degree *Licenciatura* in Civil Engineering of the University of Aveiro (UA), Portugal. Within the European Credit Transfer and Accumulation System (ECTS), the *Licenciatura* programme consists of 180 ECTS credits, and SMI corresponds to 6 ECTS credits. At UA, 1 ECTS is assigned to a workload of 27 hours.

2.2 Course

This is an introductory course on Soil Mechanics. The aim is that the students understand the basic concepts and the fundamental quantities associated, so they can later apply those concepts to the design of civil engineering structures. At the end of SMI, successful students should be able to: enunciate and apply the fundamental concepts of Soil Mechanics; define a laboratory test program to characterize soil samples and interpret their results; determine the stresses in a soil profile under different conditions; compare the stress state of soils with their shear strength; identify the water flow phenomena in soils and associated risks; predict settlements due to consolidation of clay soils and design systems to accelerate them; use computer programs to solve problems of Soil Mechanics; demonstrate capacity to work in teams; and communicate effectively (orally and in writing).
In 2022/2023, the SMI course had 21 students: 18 from the Civil Engineering programme and 3 from Erasmus.

2.3 Teaching and learning models

2.3.1 Overview of the models

The teaching and learning models adopted are varied; some are implemented during contact hours, are theoretical-practical (TP) and practical (P).

TP lessons are often expositive, with presentation of relevant content, and solving illustrative exercises or presenting and discussing realistic/real cases. Some lessons are prepared using team-based learning (TBL).

Some P lessons include "Explore first" activities; students carry out experiments and then relevant concepts are presented and discussed. Other P lessons are dedicated to solving exercises (simple to complex and realistic/real-life cases).

Project-based learning (PjBL), outside contact hours, is used to tackle realistic problems and includes experimental, analytical and/or numerical work.

Herein, particular focus is given to hands-on and team-based learning activities.

2.3.2 Pedagogical goal

As particulate materials, soils exhibit mechanical and hydraulic responses that are very different from other materials studied in civil engineering. This creates additional challenges to students. The pedagogical practice described herein was designed to promote deep learning of fundamental concepts in Soil Mechanics. The fundamental concepts reported in this paper are phase relationships for soils (section 3.1) and total and effective stresses in soils (section 3.2).

2.3.3 Hands-on learning

The learning activities were divided in two periods. During the first period, students carried out a simple experiment in groups, to visualise and demonstrate the chosen essential principles and concepts. In the second period, to trigger discussion and promote further learning, a team-based learning session was held combining previous knowledge, observations from the experiment and application activities (section 2.3.4).

2.3.4 Team-based learning

TBL is centred around a readiness assurance process using Readiness Assurance Tests, RAT (Koh et al., 2019). The TBL activities included: 1) preparation for the TBL session; 2) individual quiz (iRAT); 2) then, the students tackled the same quiz in a team (tRAT); 3) lastly, a discussion period in the large group, to analyse the correct answers, systematise contents and to present a final summary of the theoretical basis.

To prepare for the TBL sessions, students were invited to view online lessons on relevant topics. The lessons were developed by the authors in 2020/2021, when they taught the course using flipped learning (Pinho-Lopes and Macedo, 2022). Each online lesson includes a short video-lecture; a small question, with immediate feedback; a brief summary of key messages from the online lesson. The online lessons are available to students via the learning management system (LMS) of University of Aveiro (Moodle).

To promote deep learning, the quizzes (iRAT and tRAT) were developed to include questions ranging in complexity and mobilising varying levels of knowledge. The quizzes were designed to mix different types of questions: conceptual, about the different concepts and principles involved in the experiments; application exercises, where those are applied to particular problems. These quizzes were implemented using Microsoft Forms (Office 365). Thus, after login using the institutional credentials, each student answered individually to the iRAT. After the group discussion, one representative per group submitted their answers to the tRAT.

2.3.5 Learning spaces

Adequate learning spaces, for each type of activity, are key. The spaces used in the activities reported herein were the laboratory (for the first hands-on session) and the Space for Active Learning and Teaching (SALT) of the University of Aveiro, for the TBL sessions. SALT was created for promoting pedagogical innovation at University of Aveiro, by offering the physical, digital, and training environments necessary for the adoption of active, student-centred teaching and learning approaches. SALT provides adaptable configurations through furniture suitable for individual and group work, and different technological resources to support the activities developed.

2.4 Assessment of the models

To assess the models, different approaches can be used. First, an analysis of the students' answers to the TBL quizzes was carried out. Comparing the answers to the identical quiz given to each student individually (iRAT) and after the small group discussion (tRAT), it was possible to understand how learning evolved throughout the TBL session. This approach was used and presented in Macedo and Pinho-Lopes (2023) where a quantitative analysis is included.

Second, a survey prepared and given out at the end of each TBL session was used to collect the students' perceptions about the hands-on activities and the TBL sessions: STOP, START & CARRY ON (SS&Co) survey. The three open-ended questions that students answered anonymously and digitally were: 1) STOP. State what you do not like about SMI and WHY; 2) START. State what you would like to see improved in SMI and WHY; 3) CARRY ON. State what you like best about SMI and WHY.

In this paper, the results and discussion refer to the teachers' (the authors) and the students' perceptions on the teaching and learning models implemented. The authors reflections are included, as well as suggestions to enable other teachers to implement similar models.

3 IMPLEMENTATION AND DISCUSSION

3.1 Key concepts A – phase relationships for soils

The hands-on and TBL learning activities used for promoting deep learning of the phase relationships for soils have been described in detail by Macedo and Pinho-Lopes (2023). These activities are organised at the start of the semester, namely the first P lesson and the second TP lesson.

3.1.1 Hands-on learning

The hands-on learning activity took place at the Civil Engineering laboratory. The activity is similar to the "Jar of Rocks" demonstration proposed by Elton (2015). During the experiment students measured the mass of specimens of known volume of a gravel placed on a small jar under different conditions: dry; partially saturated; and fully saturated.

The students organised themselves in small groups (up to 3 students). They were given a laboratory sheet (without theoretical explanation, written or verbal) that included information on the sequence of activities to carry out (details in Macedo and Pinho-Lopes, 2023) and a table, to record the observations. After the experiment was finished, students received a second hand-out which included: equations that define the phase relationships for soils; information on unit conversions; a table to fill-in with the values of the phase relationships for the three specimens (dry, partially saturated, and fully saturated).

3.1.2 Team-based learning

The TBL session included a new subtopic, relations between phase relationships. Students were asked to engage with an online lesson on the topic beforehand.

The quiz used in the TBL session included four sections: 1) asking students if they watched the online lesson; 2) simple calculation exercise, similar to the one carried out during the hands-on activity; 3) conceptual questions, to promote discussion and critical thinking; 4) application exercise, using relations between phase relationships for soils. The quiz is included in Macedo and Pinho-Lopes (2023).

3.2 Key concepts B – total and effective stresses in soils

The hands-on and TBL learning activities about total and effective stresses in soils took place on a single TP lesson, at the start of the second chapter of the syllabus. Students were asked to view two online lessons before the session: Lesson 1 (Chapter 2) about stresses in soils and the principle of effective stress, and Lesson 2 (Chapter 2) covered the at-rest stress state and the at-rest earth pressure coefficient.

3.2.1 Hands-on learning

The hands-on experience was adapted from Elton (2001) using the "The Bucket of Bolts Experiment", which consists of placing loose aggregate in a bucket, surrounding bolts with nuts at the top, tightened; up turning the bucket does not result in dumping the aggregate out of the bucket. The procedures were explained verbally to students. At the start of the session, they carried out the experiment in small

groups and observed the response of the aggregate, when the container was turned over.

3.2.2 Team-based learning

The TBL activities (mostly held at the second part of the session) included: 1) preparation for the TBL session (before the session); 2) individual quiz (iRAT); 2) group quiz (tRAT); 3) large group discussion.

The quiz (iRAT) developed for this TBL session is summarised in Table 1. The quiz tackled in group (tRAT) included an additional question (Table 2). The different activities had allocated times.

Table 1. Quiz (iRAT) used in the TBL session on Key concepts B – total and effective stresses in soils.

Section	Question	Type of answer
1 | Experience	Explain the phenomenon you observed in the experiment carried out at the start of the session.	Open question (text)
2 | Preparation for the session	Did you watch *Lesson No. 1 of Chapter 2 | Principle of effective stress* on e-learning?	Multiple choice (Yes | I forgot | No)
3 | Conceptual questions	3.1. Positive stresses in a soil are tensile stresses.	True / False
	3.2. The stress applied to a soil is that obtained through the forces between particles divided by the contact surface between the soil particles.	True / False
	3.3. The stress acting on the boundary of a soil element is called: a) Total stress | b) Effective stress | c) Pore water pressure	Multiple choice
	3.4. The effective stress corresponds to the portion of the pore water pressure that is actually installed in the solid skeleton of the soil.	True / False
	3.5. In a soil, the structure formed by the pores is connected to each other, forming a single continuous "body".	True / False
4 | Preparation for the session	Did you watch *Lesson No. 2 of Chapter 2 | At-rest stress state* on e-learning?	Multiple choice (Yes | I forgot | No)
5 | Conceptual questions	5.1. The stresses in the ground are due exclusively to the soil unit weight.	True / False
	5.2. In which case (A to E) is the water pressure at the base greater? Choose the correct option. 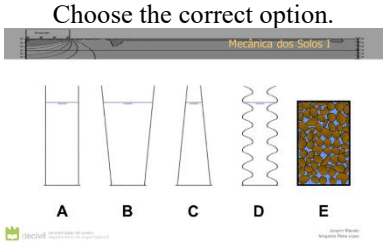	Multiple choice (multiple answers accepted)
	5.3. Consider a homogeneous soil mass with horizontal surface and a point P located at depth z. The effective stress at this point will always be greater when the soil is dry than when it is saturated (water table at ground surface).	True / False
	5.4. In a very old clay ground that has undergone several loading-unloading cycles, the probable value of the at-rest earth pressure coefficient will be: a) Smaller than 1 | b) Equal to 1 | c) Larger than 1	Multiple choice
6 | Application exercise	The aim is to determine the at-rest stress of a homogeneous soil mass with a horizontal surface and where the water table coincides with the surface. Data: Soil unit weight 18 kN/m^3; water unit weight 9.81 kN/m^3; at-rest earth pressure coefficient K_0=0.5 For a point P at 5 m depth, calculate: a) total vertical stress | b) pore water pressure | c) effective vertical stress d) effective horizontal stress | e) total horizontal stress	Numerical

Table 2. Additional question on the group quiz (tRAT) used in the TBL session on Key concepts B – total and effective stresses in soils.

Section	Question	Type of answer
7 | Application exercise	Graphically represent the variation in depth of the stress state of the soil profile, up to a depth of 10 metres. Include the total vertical and horizontal stresses, the effective horizontal and vertical stresses and the pore water pressure on the same graph. A minimum of 5 points must be included, between 0 m and 10 m depth. Submit an excel file with the calculations and the graph.	Numerical

3.3 Results and discussion

3.3.1 Students' engagement and perceptions

The number of students actively participating in the course varied (between 15 and 17). The Erasmus students did not participate in most activities, and 1 other student did not engage at all with the course. The attendance to the sessions is summarised in Table 3.

Table 3. Attendance and engagement in the sessions.

Key concepts | session	N. of students attending	N. answers to the iRAT	N. of students engaging with the online lessons
A | hands-on session	18	-	-
A | TBL session	15	12	11: Chapter 1 | Lesson 1
B | hands-on and TBL session	15	10	8: Chapter 2 | Lesson 1 6: Chapter 2 | Lesson 2

Of the 15 students attending sessions on key concepts A and B, only some answered the iRAT. A few students forgot to login in Office 365 before attempting to answer the quiz and, thus, their answers were not recorded. This led to only 12 and 10 answers for sessions A and B, respectively. Of the students answering the iRAT, 92% prepared in advance for session A, while 60% viewed the 2 online lessons for session B (80% viewed 1 only). These numbers showed a decrease in the engagement of students with the pre-session activities, which affected their performance on both the iRAT and tRAT and how much they could gain from the TBL session.

Table 4 summarises the results of SS&Co survey.

Table 4. Results of the SS&Co survey (in %).

	Comments	A	B
STOP	Nothing / Students liked everything	50	43
	Hand-out given after the session	0	7
	No answer / Do not know	50	50
START	Nothing / Students liked everything	50	7
	More classes at SALT	33	50
	Better theoretical introduction	0	7
	No answer / Do not know	17	36
Carry on	Class dynamics / interaction	44	40
	Diversity of learning strategies	19	10
	Existence of video contents	13	5
	Real / realistic case studies	13	0
	Quality of SALT	0	15
	Hands-on activity	0	15
	Group work	0	5
	No answer / Do not know	13	10

Overall, students were happy with the course and the hands-on and TBL activities. The SS&Co survey results (Table 4) showed that the teaching and learning models implemented were well accepted by the students.

Students enjoyed the teaching space (SALT) and asked for more sessions in that room. They also appreciated the use of different teaching and learning strategies and the class dynamics associated to the hands-on and TBL activities.

3.3.2 Teachers' perceptions

The teachers' (authors') perceptions are included in two different dimensions: 1) discussion on whether the teaching and learning model adopted worked well and allowed better and deeper construction of knowledge by students; 2) how the model can be adapted by other teachers to their contexts.

These two strategies combined, hands-on and TBL, were well accepted by students. However, the pre-session activities were often overlooked by students. That is particularly relevant as the semester advances. For the case described herein, the demands of different courses reduced student engagement with the online lessons from the first to the second session. As discussed before, the lack of preparation for the sessions reduces their effectiveness and how much students gain. Another important aspect is the discussion within the groups to answer the tRAT. In some groups, a few students convinced the others of wrong answers, propagating misconceptions, and errors. These were later deconstructed during the final, large group discussion. Thus, final discussion periods are key for the success of these strategies; allocating enough time for this is essential. Time management is an issue that requires some attention. For the whole TBL process to develop, time periods appropriate to all tasks are needed. To actively involve students in the process, it is important to ensure that the session is dynamic and engaging. Therefore, the space where the session takes place must be suitable for the various activities, such as carrying out simple experiences, problem solving and discussing in small groups, and large group discussion. Finally, this methodology promotes the development of some soft skills such as teamwork, communication, problem solving.

These reflections aim at encouraging other teachers to implement similar strategies, as they are simple to implement and rather effective. The hands-on experiments are straightforward, and do not require sophisticated equipment or materials. Although the iRAT and tRAT have been implemented digitally (using Microsoft Forms), they can be done using printed versions. The digital format allows checking

for changes in answers and the progress of students quickly, if that type of analysis is considered useful. The preparation activities adopted were the online lessons, previously available because of the teaching and learning strategies adopted during the COVID19 pandemics. If this type of resource is not available, alternatives need to be found, such as printed handouts. Such materials tend to be less appealing for many students. Dedicated and specially designed spaces for promoting active learning (such as SALT) are not essential for the success of the model. Ideally, the TBL session should be held in rooms where the furniture can be moved, alternating between individual, small group, and large group work.

4 CONCLUSIONS

Soils are particulate materials, which exhibit mechanical and hydraulic responses that are very different from other materials studied in civil engineering. This response poses additional challenges to students. A new pedagogical practice was implemented, combining hands-on and team-based learning (TBL) to promote deep learning of fundamental concepts in Soil Mechanics. The fundamental concepts reported in this paper are phase relationships for soils and total and effective stresses in soils. The main conclusions of this paper are:

- The model promotes active learning and student engagement during the sessions.
- Students appreciate the model, the dynamic of the sessions, the learning environment and interaction between peers and with the teachers. They recognised the importance of adopting different learning strategies.
- Not all students engaged with the preparation activities, which compromises the benefit they get from the sessions.
- Realistic allocated times for the different tasks is an essential feature for the success of this model. This is enhanced by a multifunctional space, designed for active teaching and learning.
- The model is sufficiently robust and versatile to be replicated in different contexts, regardless of the availability of technology.
- The TBL discussions, in the small and the large group, promote argumentation skills and critical thinking.
- From the teachers' perspective, the model worked well and promoted deep learning. The hands-on experiments become references that can be used when recalling concepts (often used as a reminder in later sessions).

The authors believe that using technology, while adopting hands-on strategies (with simple physical models and illustrations) and promoting critical thinking is an excellent way of promoting engagement and deep learning in Soil Mechanics.

ACKNOWLEDGEMENTS

This work was supported by: Pedagogical Innovation Projects, University of Aveiro; Foundation for Science and Technology (FCT) - Aveiro Research Centre for Risks and Sustainability in Construction (RISCO), Universidade de Aveiro, Portugal [FCT/UIDB/ECI/04450/2020]; Human Capital Operational Program (POCH) - Project Skills 4 Pós-COVID – Competências para o futuro no Ensino Superior, POCH-02-53I2-FSE-000022.

REFERENCES

Elton, D. J. (2001). *Soils magic*. American Society of Civil Engineers, Reston, Virginia, United States of America.

Elton, D. J. (2015). *Grounded!: amazing classroom demonstrations in soil mechanics*. American Society of Civil Engineers, Reston, Virginia, United States of America.

Koh, Y. Y. J., Rotgans, J. I., Rajalingam, P., Gagnon, P., Low-Beer, N. and Schmidt, H. G. (2019). Effects of graded versus ungraded individual readiness assurance scores in team-based learning: a quasi-experimental study. *Advances in Health Sciences Education*, 24, 477-488. https://doi.org/10.1007/s10459-019-09878-5.

Macedo, J. and Pinho-Lopes, M. (2023). Blending Hands-on Learning and Team-based Learning in Soil Mechanics: Phase Relationships for Soils. In: *2023 5th International Conference of the Portuguese Society for Engineering Education* (CISPEE). Guimarães, Portugal, pp. 1-7. https://doi.org/10.1109/CISPEE58593.2023.10227626.

Pinho-Lopes M. and Macedo J. (2022). Mecânica dos Solos – implementação de flipped learning em ensino híbrido. In: *CNaPPES21 - 7.º Congresso Nacional de Práticas Pedagógicas no Ensino Superior*, 12 a 16 julho 2021, Livro de Atas.

Proceedings of the XVIII ECSMGE 2024
GEOTECHNICAL ENGINEERING CHALLENGES
TO MEET CURRENT AND EMERGING NEEDS OF SOCIETY
© 2024 the Authors
ISBN 978-1-032-54816-6
DOI 10.1201/9781003431749-102
Open Access: www.taylorfrancis.com, CC BY-NC-ND 4.0 license

ECSMGE 24
XVIII EUROPEAN CONFERENCE ON SOIL MECHANICS AND GEOTECHNICAL ENGINEERING

Concrete arches and reinforced soil: a sustainable alternative structure for road bridges

Arches en béton et sol renforcé: une structure alternative durable aux ponts routiers

K. Malekmohammadi*, A. Moncada
Department of Civil and Environmental Engineering, Universitat Politècnica de Catalunya·BarcelonaTech (UPC) / International Centre for Numerical Methods in Engineering (CIMNE), Barcelona, Spain

I.P. Damians
International Centre for Numerical Methods in Engineering (CIMNE), Universitat Politècnica de Catalunya·BarcelonaTech (UPC) / VSL International, Barcelona, Spain

**khashayar.malekmohammadi@upc.edu*

ABSTRACT: Road bridges are necessary infrastructures for transportation. As such, they are subject to thorough scrutiny for their environmental, social, and economic impacts. An adequate substantiality assessment applied to bridge design must minimize the negative impacts of the structure on the surrounding environment. A concrete deck and piles, together with cantilever abutments, is a well-established and conventional bridge design option. An alternative solution is precast concrete arches, widely used in bridge and tunnel constructions, providing stable, long-lasting support even under heavy load conditions. Concrete arches can be constructed together with reinforced soil walls (RSW) solutions, for both embankment and abutment zones, which are considered cost-effective solutions with short construction periods, making them an attractive option for such structural and geotechnical engineering projects. The compound concrete arch and RSW structure results in a resilient, efficient, and cost-effective design. This study presents a simple approach for an environmental and economic assessment of two bridge designs: a classical solution with cantilever abutments and a concrete deck slab, and concrete arches with RSW on top. Based on the environmental impact, and associated costs, the precast arch bridges with RSW solution are judged to be the better alternative.

RÉSUMÉ: Les ponts routiers sont une infrastructure nécessaire au transport. À ce titre, ils font l'objet d'un examen minutieux quant à leurs impacts environnementaux, sociaux et économiques. Une évaluation adéquate du caractère substantiel appliquée à la conception du pont doit minimiser les impacts négatifs de la structure sur l'environnement environnant. Un tablier et des pieux en béton, ainsi que des culées en porte-à-faux, constituent une conception de pont bien établie. Une solution alternative consiste en des arches en béton préfabriqué, largement utilisées dans la construction de ponts et de tunnels, offrant un support stable et durable, même dans des conditions de charge lourde. Les arches en béton peuvent être construites avec des solutions de murs en sol renforcé (RSW), tant pour les zones de remblai que de culées, qui sont considérées comme des solutions rentables avec des périodes de construction courtes, ce qui en fait une option attrayante pour de tels projets d'ingénierie structurelle et géotechnique. L'arche en béton composée et la structure RSW donnent lieu à une conception résiliente, efficace et rentable. Cette étude présente une approche simple pour une évaluation environnementale et économique de deux modèles de pont: une solution classique avec des culées en porte-à-faux et une dalle de tablier en béton, et des arches en béton avec un RSW. Sur la base de l'impact environnemental et des coûts associés, les ponts en arc préfabriqués avec la solution RSW sont considérés comme la meilleure alternative.

Keywords: Geosynthetic reinforcement; precast arch bridges; reinforced soil walls; sustainability assessment.

1 INTRODUCTION

Civil engineering works encompass a wide range of structures, including, but not limited to, buildings, pavements, bridges, foundations, and reinforced soil structures. The inclusion of sustainability criteria in the decision-making process of civil engineering design, including geotechnical engineering projects, is becoming prevalent (Aguado et al., 2012; MacAskill and Guthrie, 2013, Basu et al., 2014). Sustainability encompasses the fulfillment of three distinct sets of criteria regarding environmental, economic, and societal/functional aspects (Afnor Group, 2012; ISO, 2006). Bridges made of concrete arches with reinforced soil walls (RSW) are used for pedestrians, road, and rail traffics. The complexity of concrete arch

and reinforced soil bridge systems resides in the proper assessment of soil-structure interaction, the impact of lateral soil pressure, and the boundary condition at the base of the bridge supports. This study presents a simplified and reduced approach and results to evaluate and compare the environmental and economic aspects of a sustainability assessment of two bridge designs composed of (i) cantilever abutments and concrete deck slab, and (ii) precast concrete arches and back-to-back reinforced soil wall embankment/abutment. The assessment of environmental factors is conducted utilizing a reduced Life Cycle Assessment (LCA) methodology (e.g., Damians et al., 2016). Ideally, a LCA should comprehensively evaluate all potential environmental implications associated with the construction process and materials employed in project activities.

2 CASE STUDY AND METHODOLOGY

Figure 1 shows a schematic representation of the two types of road bridges included in this study. Dimensions were determined through conventional design methods. To properly evaluate the environmental impact across both alternative solutions, a Functional Unit (FU) must be defined. In this particular scenario, the comparative FU is defined as a bridge with a width of 12 meters and a span of 10 meters, designed to accommodate a two-lane civilian roadway with a distributed traffic surcharge load of 10 kPa, over a design life of 100 years. In this study, it is assumed that both alternatives are installed on a competent/stiff foundation and does not take into account the environmental and economic implications of site preparation and final grading (i.e., foundation preparation), as these impacts are expected to be comparable between the two types of structures. In the same way, the scope of this study is restricted to the bridge span S (see Figure 1). The analysis of the Cantilever+deck bridge does not take into account the material/filling located behind the cantilever abutments. Likewise, the Arch+RSW solution does not consider the RSW beyond the length S (see the limit of the study detailed zone in Figure 1). For the Arch+RSW bridge design, the back-to-back reinforced soil structure uses polymeric strap reinforcement and precast reinforced concrete panels.

The life-cycle stages encompass the entire process from the extraction of raw materials from the natural environment. Intermediate stages include material processing to create the necessary components, transportation of materials/components, installation work, etc.

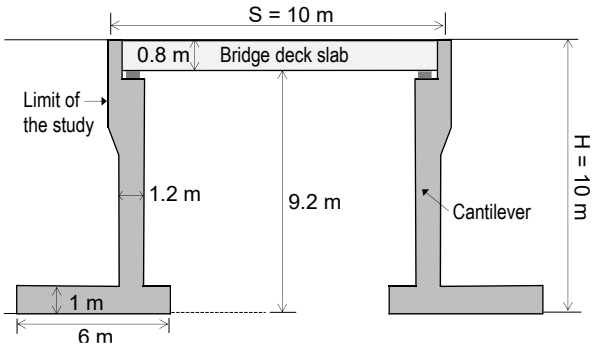

(a) Geometry of Cantilever+deck.

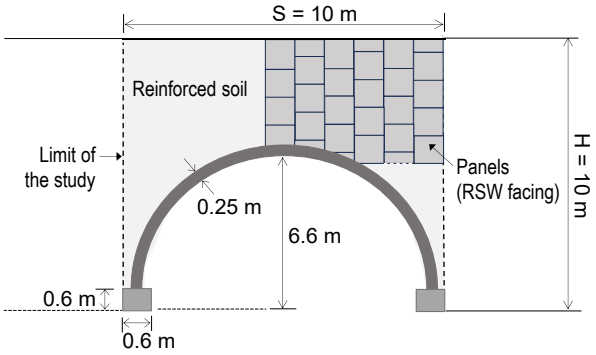

(b) Geometry of Arch+RSW.

Figure 1. Schematic geometry for (a) Cantilever+deck and (b) Arch+RSW.

Table 1 shows the environmental inventory pertaining to the materials and construction-related activities included in the present investigation. The deck bridge and cantilever abutment alternative requires considerably more concrete and reinforcing steel (i.e., rebar) compared to the arch bridge segments and back-to-back RSW solution. The main structural component of the conventional bridge is the reinforced concrete, while that of the arch bridge is the reinforced soil (i.e., backfill and polymeric strap reinforcements).

Backfill material is assumed to be brought from a distance of 10 km. The cantilever+deck bridge includes on-site concrete pouring. The expected distance for the transportation of precast concrete panels and precast concrete arches from the manufacturing site was 10 km. In addition, the transportation distances for concrete mix trucks, steel rebar, and polymeric reinforcement straps were assumed to be 10 km because of consideration of the same distance/condition of transportation for all solutions.

Life cycle assessments (LCA) were carried out using SimaPro v9.4.0.2 software (PRé Consultants B.V., 2010). Input values for material and energy usage were obtained using the Ecoinvent v3.8 database (Ecoinvent Centre, 2014) and ReCiPe 2016 method v1.1 (Huijbregts et al., 2017), all available within SimaPro. The economic analysis was conducted for

both solutions using the ITeC BEDEC cost database. The environmental impact is assessed using only two midpoint indicators: the Global Warming Potential (GWP), which measures the impact of carbon dioxide equivalent (amount of CO_2 eq.) emissions on the atmosphere, and the Cumulative Energy Demand (CED), employed for the assessment of energy consumption (in Joules). Both environmental indicators are analyzed across the whole life cycle of the main involved materials, products, processes, and/or construction-related activities in both proposed bridge construction alternatives.

3 ENVIRONMENTAL AND ECONOMIC ASSESSMENT

Figure 2 shows the total GWP (2a) emissions and CED (2b) of both alternatives. As anticipated, the traditional solution (Cantilever+deck) results in the highest emissions of CO_2 eq. and energy consumption. GWP and CED values of the Arch+RSW structure were found to be about 85% and 82% lower than those of the Cantilever+deck design, respectively. This is explained by the high energy requirements in the production of steel and concrete, which serve as the main structural components of the conventional bridge case. Combined contributions of concrete and steel components are the most significant factors in the overall environmental impact of both cases, accounting for 58% and 37% of total CO_2 eq. and 46.2% and 45% of CED values, for the conventional and arch solutions, respectively. Compared to concrete and steel, construction activities and material transportation contribute a small portion of total CO_2 eq. and GJ values. Furthermore, according to the outcomes of the economic analysis, Arch+RSW solution led to about 47% reduction in construction costs with respect to the conventional bridge structure (Figure 3). In this solution, the RSW structure contributes most of the construction costs, at 56.7%, because more components need to be used for construction.

Table 1. Environmental inventory including materials, construction activities and transportation details.

Case	Category	Items	Unit	Value
Cantilever+deck	Structural material	Concrete	m^3	501.6
		Reinforcing steel (rebar)	t	39.3
	Construction	Pouring concrete	h	16.72
		Reinforcing (rebar) fixing	h	263.3
		Formwork installation	h	796
	Transportation	Concrete, reinforcing steel, etc.	km	10
Arch+RSW	Structural material	Concrete (footing)	m^3	8.4
		Precast arches	m^3	55.32
		Precast panels	m^2	100.2
		Polymeric strap	kg	288
	Construction	Reinforced backfill	m^3	601.2
		Panel installation	h	44.5
		Earth work (backfilling and compacting)	h	22.5
	Transportation	Concrete, precast arches/panels, reinfs., etc.	km	10
		Backfill material	km	10

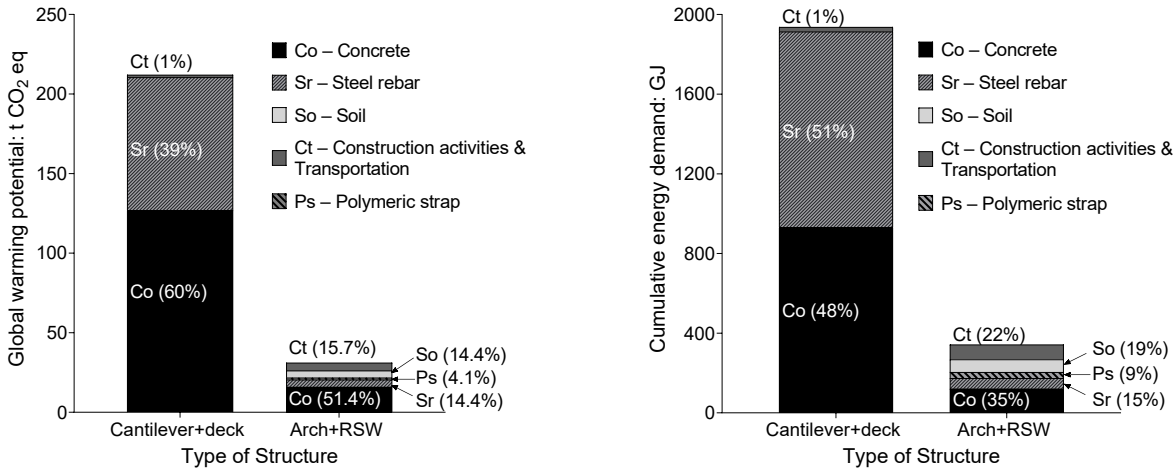

(a) Total GWP for both bridges. *(b) Total CED for both bridges.*

Figure 2. Total (a) GWP, (b) CED of construction for both bridge solutions.

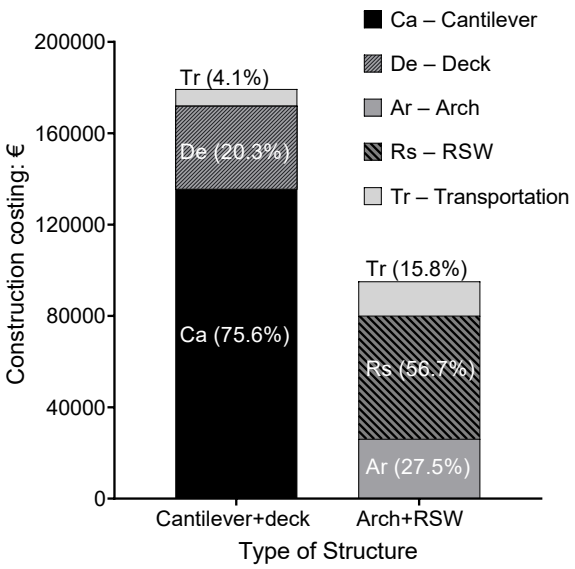

Figure 3. Construction costs for both bridge solutions.

4 CONCLUSIONS

A simplified life-cycle and economic assessment of Cantilever+deck and Arch+RSW bridge solutions that satisfy the same function were performed, and some results were presented. The primary findings of the comparison are as follows:

- Arch+RSW with reinforced soil structures showed reduced CO_2 eq. emissions and energy requirements compared to a conventional Cantilever+deck bridge design. Arch+RSW solutions resulted in reductions of about 85% and 82% for CO_2 eq. emissions and CED, respectively, with regards to the Cantilever+deck design approach.
- Reduced environmental indicators of the arch bridge alternative are attributed to the use of compacted soil and polymeric reinforcements as the primary structural elements, as opposed to concrete and steel in the conventional solution.
- Arch+RSW bridges can result in construction cost reductions of about 50%.

This study was limited to the environmental and economic impacts of two different bridge types: cantilever abutment with bridge deck slab and reinforced soil walls over precast arches. Forthcoming research requires a comprehensive study of full sustainability assessment including environmental, economic, and societal/functional/ technical aspects through multi-criteria analysis and different stakeholder scenarios. Furthermore, it is recommended to expand the scope of this study to encompass various types of bridges, including different dimensions and technologies.

ACKNOWLEDGEMENTS

The authors wish to acknowledge the support received from VSL Construction Systems (Spain) and Eng. Vitomir Nikolic for his valuable data on construction methods, GECO Industrial (Korea, Rep. of), the Department of Civil and Environmental Engineering (DECA) of Universitat Politècnica de Catalunya·BarcelonaTech (UPC), and the International Centre for Numerical Methods in Engineering (CIMNE).

REFERENCES

Afnor Group (2012) CEN/TC 350: Sustainability of Construction Works. Afnor Group, Paris, France. See http://portailgroupe.afnor.fr/public_espacenormalisation/CENTC350/index.html (accessed: 05/08/2016).

Aguado, A., Caño, A. D., de la Cruz, M. P., Gómez, D., and Josa, A. (2012). Sustainability assessment of concrete structures within the Spanish structural concrete code. *J. of Constr. Eng. and Manag.*, 138(2), 268-276. https://doi.org/10.1061/(ASCE)CO.1943-7862.0000419.

Basu, D., Misra, A., and Puppala, AJ. (2014). Sustainability and geotechnical engineering: perspectives and review. *Can. Geotech.* J., 52(1): 96–113. https://doi.org/10.1139/cgj-2013-0120.

Damians, IP., Bathurst, RJ., Adroguer, E., Josa, A., and Lloret, A. (2016).Environmental assessment of earth retaining wall structures. *Environ. Geotech.* http://dx.doi.org/10.1680/jenge.15.00040.

Ecoinvent Centre. (2014). Ecoinvent database v3.1. Ecoinvent Centre, Swiss Centre for Life Cycle Inventories, Zurich, Switzerland. See http://www.ecoinvent.ch/ (accessed 02/02/2016).

Huijbregts, M.A.J., Steinmann, Z.J.N., Elshout, P.M.F., et al. (2017). ReCiPe2016: a harmonised life cycle impact assessment method at midpoint and endpoint level. Int J Life Cycle Assess, 22, 138–147. https://doi.org/10.1007/s11367-016-1246-y.

MacAskill, K., and Guthrie, P. (2013). Risk-based approaches to sustainability in civil engineering. *In Proc. of the Inst. of Civ. Eng.-Eng. Sustain.* 166 (4) pp. 181-190. Thomas Telford Ltd. https://doi.org/10.1680/ensu.12.00001.

Institute of Construction Technology of Catalonia (ITeC BEDEC). Avaialble at: https://metabase.itec.cat/vide/es/bedec/itec accesed: 10/09/2023.

ISO (International Organization for Standardization) (2006a) ISO 14040: Environmental management – life cycle assessment – principles and framework. ISO, Geneva, Switzerland.

PRé Consultants B.V. (2010) SimaPro software, v.8.0.2. Amersfoort. Utrecht, Netherlands. See http://www.presustainability.com (accessed 02/02/2016).

Proceedings of the XVIII ECSMGE 2024
GEOTECHNICAL ENGINEERING CHALLENGES
TO MEET CURRENT AND EMERGING NEEDS OF SOCIETY
© 2024 the Authors
ISBN 978-1-032-54816-6
DOI 10.1201/9781003431749-103
Open Access: www.taylorfrancis.com, CC BY-NC-ND 4.0 license

ECSMGE 24
XVIII EUROPEAN CONFERENCE ON SOIL MECHANICS AND GEOTECHNICAL ENGINEERING

Analytical method to check the uplift of a jet-grouting plug

Méthode analytique pour vérifier le soulèvement d'un bouchon de jet-grouting

A.B. Martínez-Bacas*
Ferrovial Construction, Madrid, Spain
**abmartinez@ferrovial.com*

ABSTRACT: The construction of jet-grouting plugs is a common practice to carry out underground works, such as underground lines, underpasses, shafts, etc. Many times, these constructions are developed in clayey soils with low resistance capacity, where the open excavations are carried out below the water table. This situation makes necessary to carry out very deep walls to avoid uplift of the bottom slab. To shorten the length of the walls and guarantee the stability of the bottom slab, it is possible to execute jet-grouting column plugs, improving the stiffness of the wall embedment level and the waterproofing of the excavation, as well as ensuring that the bottom uplift does not occur due to water pressure. This article presents a new method to analyse the uplift of the jet-grouting plugs, based on an analytical calculation of the wall-plug system, assimilating the behaviour of the jet-grouting plug to a thick beam subjected to uniformly distributed pressure. Also, a study of the same problem has been carried out using numerical modelling through the finite element method, that confirms that both numerical and analytical models result in similar stress fields at the wall/ jet-grouting plug interface.

RÉSUMÉ: La construction de bouchons de jet-grouting est une pratique courante pour réaliser des travaux souterrains, tels que des lignes souterraines, des passages souterrains, des puits, etc. Souvent, ces constructions sont développées dans des sols argileux à faible capacité de résistance, où sont réalisées les excavations à ciel ouvert en dessous de la nappe phréatique. Cette situation nécessite de réaliser des murs très profonds pour éviter le soulèvement de la dalle inférieure. Afin de raccourcir la longueur des murs et de garantir la stabilité de la dalle de fond, il est possible d'exécuter des bouchons de colonne par jet-grouting, améliorant la rigidité du niveau d'encastrement du mur et l'étanchéité de l'excavation, en plus d'assurer que le soulèvement du fond ne se produit pas en raison de la pression de l'eau. Cet article présente une nouvelle méthode d'analyse du soulèvement des bouchons de jet-grouting, basée sur un calcul analytique du système mur-chevilles, assimilant le comportement du bouchon de jet-grouting à une poutre épaisse soumise à une pression uniformément répartie. En outre, une étude du même problème a été réalisée en utilisant une modélisation numérique par la méthode des éléments finis, qui confirme que les modèles numériques et analytiques aboutissent à des champs de contraintes similaires à l'interface mur/bouchon de jet-grouting.

Keywords: Jet-grouting plug; uplift; diaphragm wall/jet-grouting plug interface; analytical method; deep beam.

1 INTRODUCTION

The subject of this article is the checking of the design and the uplift of the bottom plug of the diaphragm wall (D-wall).

The chosen D-wall is located in the Llobregat Delta area, within soils with low resistance and a shallow water level. Thus, a bottom plug was executed, using jet-grouting columns, causing stiffening of the wall embedment, as well as waterproofing of the excavation.

The purpose of this article is, on one hand, to verify with an analytical calculation the thickness of the jet-grouting plug and the safety factor against the uplift due to water pressure. On the other hand, to compare and analyze the results, applying the finite element method using a 3D geotechnical model.

2 DESCRIPTION OF THE DIAPHRAGM WALL AND THE JET-GROUTING PLUG

The substructure of the extension of the Barcelona Airport was executed with diaphragm walls. These walls reach a depth of 33 m. The dimensions of the D-wall are 32.20 m length and 23.43 m span (see Figure 1). The thickness of the D-wall is 1.20 m and it is always below the water table. The bottom slab has a variable thickness between 2.00 m and 3.68 m.

The jet-grouting plug dimensions are 21 m wide with a variable thickness between 9.43 m and 7.43 m.

3 SOILS

3.1 Material

The D-wall construction area comprises the following geotechnical units:

- UG0: Made ground fill and organic soils. Thickness 1.5m.
- UG1: Continental clays and silts. Thickness 2 m
- UG2: Silty sands, fine to medium sands. Thickness 11 m.
- UG3: Clays, clayey silts of low plasticity with a high content of organic matter. Thickness 31m.
- UG4: Gravel and sand. Dense.

3.2 Geotechnical parameters

The geotechnical parameters of the soils are summarized in Table 1.

The jet-grouting plug is in the UG3 soil layer. The geotechnical parameters of the jet-grouting plug are presented in Table 2.

The jet-grouting plug/D-wall interface is considered only frictional, see parameters in Table 3.

Table 1. Soil parameters.

Parameter	UG0	UG1	UG2	UG3	UG4	Unit
Unit Weight, γ	17.50	20.00	20.00	19.00	28.00	kN/m^3
Young Mod.	2000	16000	9600	3940	39100	kN/m^2
Poisson coef.	0.30	0.35	0.35	0.40	0.33	
Fric. Angle, δ	22	24	32	26	38	(°)
Cohesion,c	0	10	5	15	0	kPa

Table 2. Jet-grouting plug parameters.

Parameter	Value	Unit
Unit Weight, γ_j	19	kN/m^3
Young Mod., E_j	$2{\cdot}10^6$	kN/m^2
Poisson coef., v_j	0.3	
Fric. angle, δ_j	34	(°)
Cohesion, c_j	930.5	kN/m^2
Simple comp. strength, σ_c	3500	kN/m^2

Table 3. Jet-grouting plug/D-wall interface parameters.

Parameter	Value	Unit
Unit Weight, γ_{jp}	19	kN/m^3
Young Mod., E_{jp}	$2{\cdot}10^6$	kN/m^2
Poisson coef., v_{jp}	0.3	
Fric. angle, δ_{jp}	34	(°)
Cohesion, c_{jp}	0	kN/m^2

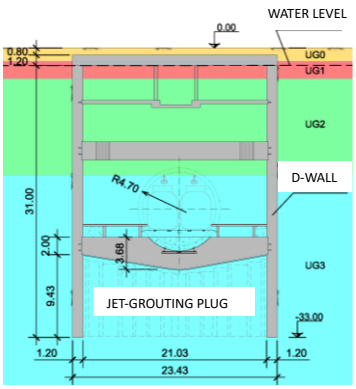

Figure 1. Cross-section of the D-Wall. Cross-section of the Barcelona subway structure executed with diapharfn walls and jet-grouting plug.

4 ANALYTICAL METHOD

4.1 Theoretical base

For the first analysis the plastic balance of the plug and its jet-grouting plug/D-wall interface is considered, meaning that the plug does not uplift due to water pressure. Thus, the plug must prop-up against the D-wall, creating an axial compression force that should be equal to the characteristic compression resistance of the jet-grouting material (Table 2, σ_c).

To calculate the axial compression force, the concept of a deep beam with a uniform distributed load is used (Leonhardt, 1985). The jet-grouting plug is like a deep beam and the uniform load is the water pressure minus the plug weight.

Since the Airport substructure is a linear structure, a slice is analysed in a two-dimensional model using plane strain model. Therefore, considering the deep beam theory, a parabolic unloading arch is formed into the jet-grouting plug, that will have a minimum thickness for its propping up happen (Figure 2).

Once, it checked that the weight of the jet-grouting plug did not balance the water uplift pressure, there must be a shear strength between the D-wall and the jet-grouting plug that adds resistance against the plug uplift. This tangential strength can be obtained using the analogy of the deep beam supporting a uniformly distributed load.

Finally, it must also be verified that the axial unloading arch does not exceed the compression strength of the jet-grouting material (σ_c).

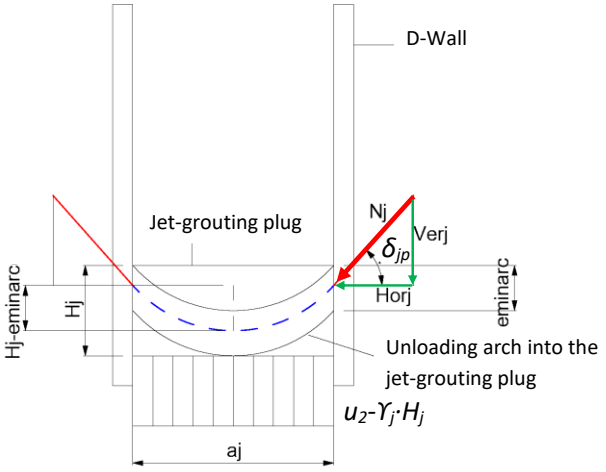

Figure 2. Deep beam analogy.
Sketch of the deep beam analogy for the jet-grouting plug

Where:

H_j:	jet-grouting plug thickness
a_j:	jet-grouting plug length
$emin_{arc}$:	minimum thickness of unloading arch
u_2:	uniform water pressure
δ_{jp}:	friction angle plug/wall interface
γ_j:	unit weight of the jet-grouting
N_j:	axial force on the unloading's arch developed into the jet-grouting plug
Hor_j:	Horizontal force on the jet-grouting plug
Ver_j:	Verical force on the jet-grouting plug

4.2 Practical application

The steps to use the analytical method to check or to pre-design the jet-grouting plug are as follows:

- Total water pressure on the bottom jet-grouting plug, U_2:

$$U_2 = u_2 \cdot a_j \quad (1)$$

- Jet-grouting plug weight, w_j:

$$w_j = H_j \cdot a_j \cdot \gamma_j \quad (2)$$

- Minimum thickness of the unloading parable (Leonhardt, 1985), so that the plug rests on the D-wall and it is in limit equilibrium, avoiding the uplifting of the bottom, $emin_{arc}$:

$$\tan \delta_{jp} = \frac{(H_j - emin_{arc})}{\left(\frac{a_j}{4}\right)} \quad (3)$$

- Vertical force (Ver_j) and horizontal force (Hor_j) on the plug for an uplift safety factor, SF:

$$Ver_j = \frac{(SF \cdot U_2 - w_j)}{2} \quad (4)$$

$$Hor_j = \frac{Ver_j}{\tan \delta_{jp}} \quad (5)$$

- Axial force on the jet-grouting plug, N_j:

$$N_j = \sqrt{\left(Ver_j^2 + Hor_j^2\right)} \quad (6)$$

- Compression stress on the jet-grouting plug, σ_{cj}:

$$\sigma_{cj} = \frac{N_j}{emin_{arc}} \quad (7)$$

where σ_{cj} should be lower than the compression carachteristic strength of the jet-grouting material (σ_c).

4.3 Analytical results

Table 4 and Table 5 summarize the results of the analytical calculation of the jet-grouting plug presented in Figure 1.

In this case, the minimum thickness of the unloading arch is 3.85 m, which requires a minimum thickness of the jet-grouting plug of 7.43 m for the development of the unloading arch, see Table 4.

Once the value of the $emin_{arc}$ has been obtained, the SF is calculated, being the multiplier of the total water pressures (U_2) that create the maximum compression stress of the plug (Table 5).

Thus, the geometric design of the jet-grouting plug that balances the water pressure depends exclusively on the plug dimensions and the angle of friction of the jet-grouting plug/D-wall interface.

Table 5 shows the safety margin of the simple compression resistance of the jet-grouting needed to prevent failure, presenting a maximum safety factor of 2.7, reaching the maximum simple compression strength of the jet-grouting material.

Table 4. Design of the plug. Analitical results.

H_j (m)	a_j (m)	w_j (kN/m)	u_2 (kN/m²)	$emin_{arco}$ (m)
7.43	21.03	2968.8	310	3.85

Table 5. Safety Factor. Analytical results.

FS	σ_{cj} (kN/m²)	σ_c (kN/m²)	$\sigma_{cj} < \sigma_c$
1	826.5	3500	Yes
1.3	1280		Yes
2.0	2339		Yes
2.7	3398		Yes

5 NUMERICAL METHOD

5.1 Model

The 3D model of the D-wall has the next dimensions: 124 m long x 25.10 m wide x 55 m depth (Figure 3). The number of zones is 55033.

For both the soil layers and the jet-grouting plug, the drained Mohr Coulomb elastoplastic model has been used, applying the parameters of Table 1 and Table 2 respectively.

The jet-grouting plug/D-wall interface has been simulated using a frictional Mohr Coulomb model, see parameters in Table 3.

The D-walls and middle struts have been simulated using zones and the linear elastic model of concrete, see Table 6.

The upper struts are pipes Φ355.6x14 mm separated 3.85 m. These structures have been modeled with beam elements, whose characteristics are presented in Table 7.

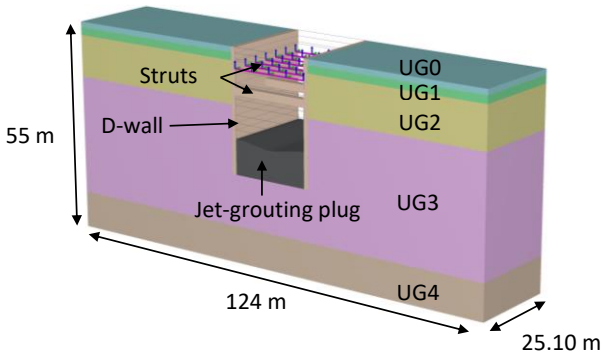

Figure 3. Geometry of the 3D model. Geotechnical 3D Model of the D-Wall and jet-grouting plug.

Table 6. Concrete parameters.

Parameter	Value	Unit
Unit Weight	21	kN/m^3
Young Mod.	$30 \cdot 10^6$	kN/m^2
Poisson coef.	0.2	

Table 7. Struts parameters.

Parameter	Value	Unit
Material model	Elastic	
Unit Weight	78.5	kN/m^3
Young Mod.	$200 \cdot 10^6$	kN/m^2
Area	0.015	m^2
Moment inertia	$0.278 \cdot 10^{-3}$	m^4
Elastic yield, σ_e	275	MN/m^2

5.2 Results of the critical phase

Figure 3 presents the critical construction phase of the construction process, the end of the excavation before execution of the bottom slab. In this case the total excavation depth is 24 m.

Figure 4 shows the principal stresses direction into the jet-grouting plug, where the unloading arch obtained with the analytical method has clearly been developed, as indicated in Figure 2. Figure 4 shows the unloading arch showed in Table 4.

Figure 5 shows a band of shear plastic points in the jet-grouting plug/D-wall interface, where the maximum friction is mobilized. This shear plastic band has a thickness of 4 m. In this way, the thickness of the interface plastic area equals the unloading arch minimum thickness, $emin_{arc}$, 3.85 m obtained with the analytical method (Table 4).

Figure 6 shows the variation of the angle of friction mobilized along the thickness of the interface during the critical phase. It is observed that in the upper 0.6 m thickness there is a tension plastic band, caused by the rotation and support of the D-wall in this band. Thus, this band should not be considered as shear resistance. Therefore, the plastic shear area develops from 0.6 m to 4.8 m, mobilizing the maximum friction angle 34° (Table 3).

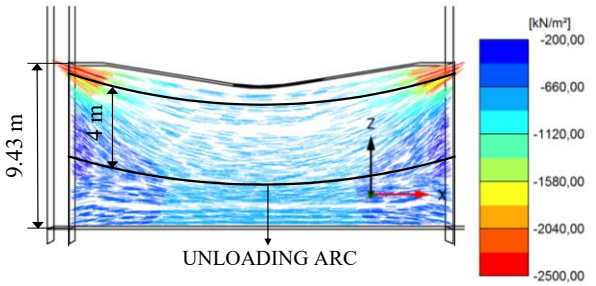

Figure 4. Principal stresses into the jet-grouting plug. Principal stresses direction into the jet-grouting plug, where the unloading arch has been developed.

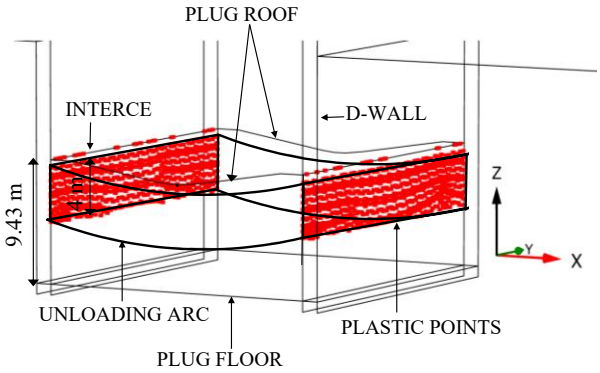

Figure 5. Shear plastic points in the plug/wall interface. Shear plastic points in the jet-grouting plug/D-wall interface, where the maximum friction is mobilized.

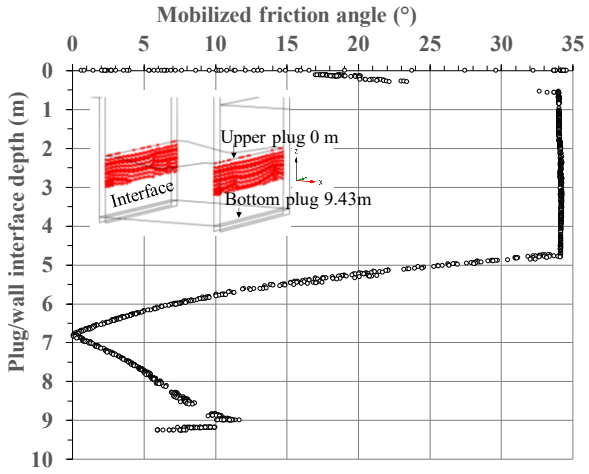

Figure 6. Shear plastic points along the jet-grouting plug/D-wall interface. Variation of the angle of friction mobilized along the thickness of the interface during the critical phase

6 CONCLUSIONS

This paper presents a structural analysis of jet-grouting plugs for the open excavations constructed with diaphragm walls. This model considers the behavior of the jet-grouting plug as a deep beam with uniform distributed water pressure. This pressure is resisted via the mobilization of the frictional strength when the jet-grouting plug props-up against the diaphragm wall. The following conclusions are obtained:

- Fitting the plug geometrically, the analogy of a deep beam bearing a uniform load can be used, assuming the equilibrium limit state against the upward forces.
- The uniform loading on the plug is resisted by the formation of a structural unloading arch in equilibrium with the reaction at the jet-grouting plug/D-wall interface.
- It is very important that the prop-up effect between the jet-grouting plug and the D-wall develops, in order to ensure that the shear resistance prevents the uplift of the jet-grouting plug. In many cases this resistance becomes more important than the value of the unit weight of the jet-grouting. Thus, during the construction process, it must be guaranteed that the jet-grouting and the D-wall contact is continuous, otherwise the system may fail due to lack of friction.
- It is important to consider the width/thickness ratio of the plug. The greater ratio, the more extended the unloading arch, and the greater horizontal stresses are developed, which can exceed the simple compression resistance of the jet-grouting.

Verification using a numerical model yields the following conclusions:

- The principal stresses develop within the jet-grouting plug in an arch-shaped form as considered in the analytical study.
- At the jet-grouting plug/D-wall interface, a plastic zone develops, that corresponds to the jet-grouting/diaphragm wall propping-up area, and it is similar to the minimum thickness of the parabolic unloading arch obtained in the analytical method.
- Therefore, the analytical method provides a preliminary design of a jet-grouting plug, verifying the minimum conditions of the plug and the uplift safety factor.

REFERENCES

Fritz Leonhardt. 1985. *Estructuras de hormigón armado. Casos especiales del dimensionado de structuras de hormigón armado*. Tomo II. Editorial El Ateneo.

Muttoni, A., Schwartz, J., Thürlimann, B. 1996. *Design of concrete structures with stress fields*. Editorial Birk Häuser.

Proceedings of the XVIII ECSMGE 2024
GEOTECHNICAL ENGINEERING CHALLENGES
TO MEET CURRENT AND EMERGING NEEDS OF SOCIETY
© 2024 the Authors
ISBN 978-1-032-54816-6
DOI 10.1201/9781003431749-104
Open Access: www.taylorfrancis.com, CC BY-NC-ND 4.0 license

ECSMGE 24
XVIII EUROPEAN CONFERENCE ON SOIL MECHANICS AND GEOTECHNICAL ENGINEERING

Parameter identification for constitutive models based on pressuremeter test

Identification des paramètres pour les modèles constitutifs basés sur test pressiométrique

I. Marzouk*, F. Tschuchnigg, H.F. Schweiger
Graz University of Technology, Graz, Austria

N. Hödlmoser
Bridge construction and foundation consulting, City of Vienna, Vienna, Austria

**islam.marzouk@tugraz.at*

ABSTRACT: The application of numerical methods for performing SLS and ULS design of complex geotechnical structures requires the usage of appropriate advanced constitutive models. Determination of input parameters for these models becomes a key aspect. The logical choice of parameter determination based on laboratory experiments may suffer from effects of sample disturbance and therefore the in-situ behaviour may not be captured with sufficient confidence. Alternatively, in-situ measurements such as CPT or pressuremeter test provide information of the in-situ behaviour but this approach has the disadvantage that parameters cannot be directly identified. Therefore, the in-situ test has to be modelled as a boundary value problem and parameter identification has to be based by applying appropriate parameter identification procedures or by simple curve fitting approaches. In this paper pressuremeter tests are numerical simulated and parameters for the well-known Plaxis Hardening Soil Small model are derived based on these analyses. The authors believe that this is a promising way forward for obtaining realistic input parameters for advanced constitutive models and thus improve the prediction capabilities of numerical methods in geotechnical engineering.

RÉSUMÉ: L'application de méthodes numériques pour la conception SLS et ULS de structures géotechniques complexes nécessite l'utilisation de modèles constitutifs avancés appropriés. La détermination des paramètres d'entrée de ces modèles devient un aspect essentiel. Le choix logique d'une détermination des paramètres basée sur des expériences en laboratoire peut souffrir des effets de la perturbation de l'échantillon et, par conséquent, le comportement in situ peut ne pas être capturé avec suffisamment de confiance. D'autre part, les mesures in situ telles que les essais CPT ou pressiométriques fournissent des informations sur le comportement in situ, mais cette approche présente l'inconvénient de ne pas permettre l'identification directe des paramètres. Par conséquent, l'essai in situ doit être modélisé comme un problème de valeur limite et l'identification des paramètres doit être basée sur l'application de procédures appropriées d'identification des paramètres ou sur des approches simples d'ajustement de courbes. Dans cet article, les essais pressiométriques sont simulés numériquement et les paramètres du célèbre modèle Plaxis Hardening Soil Small sont dérivés sur la base de ces analyses. Les auteurs pensent qu'il s'agit d'une voie prometteuse pour obtenir des paramètres d'entrée réalistes pour les modèles constitutifs avancés et améliorer ainsi les capacités de prédiction des méthodes numériques dans le domaine de l'ingénierie géotechnique.

Keywords: SBPMT; Parameter determination; numerical modelling; nonstitutive model calibration.

1 INTRODUCTION

Over the past years, there has been significant progress in the development of soil constitutive models. Advanced models are able to represent soil behaviour much better than simpler models. However, the more advanced the model, the more parameters are required. The proper determination of these parameters is one of the key factors for carrying out numerical analyses successfully. It is often the case that these parameters are determined based on laboratory tests (e.g., triaxial and oedometer tests), which are not always available on all projects (especially in the early design stages).

Alternatively, constitutive model parameters can be determined from in-situ tests. In-situ testing is faster, cheaper and causes (often) less soil disturbance than laboratory testing. However, it is not possible to determine the parameters directly from field results (measured data). Recommendations on how to interpret results from pressuremeter tests (PMT) are given e.g., in (Mair and Wood 1987; Yu 2010; Clarke 2023).

This paper presents an approach for deriving Plaxis HS Small model (Benz 2007) parameters by modelling the self-boring pressuremeter test (SBPMT) as a boundary value problem and comparing the results of the analysis with field measurements.

2 SELF-BORING PRESSUREMETER TESTS

2.1 Test site

SBP tests were conducted in Vienna, Austria for a construction project. The testing programme included 18 tests performed in three boreholes at depths ranging from 7 to 50 m. This paper focuses on three tests from the same borehole conducted at depths of 15.8, 30.95, and 36.5 m, respectively.

The stratification is deduced from the borehole log and is illustrated in Figure 1. Beneath the ground level lies a layer of backfill with a thickness of 0.6 m. Below the backfill, a 3.7 m layer of gravel is present. Silt was first encountered at a depth of 4.3 m below the surface.

The groundwater level is located at a depth of around 8.3 m below ground level in this borehole. According to the borehole log, the soil tested in all three tests was mainly silt. Within the silt, a small amount of clay was encountered at the depth of the first test (at 15.8 m), while some fine sand was present at the depth of the second test (at 30.95 m) and some dense to fine sand was found at the third test depth (at 36.5 m). The results of those tests are presented in Figure 2.

In addition to the SBP tests, laboratory tests were conducted. Those tests were used to assess the strength parameters and the unit weight of the silt layers.

2.2 Test interpretation

The tests were performed employing a 6-arm probe with an 88 mm diameter. The field measurements were used to determine the total in-situ horizontal stress (σ_{h0}) and yield stress (P_{yield}). Theoretically, the SBP is drilled into the soil with no disturbance. Consequently, the in-situ horizontal stress could be determined directly. Nevertheless, there is always some minor disturbance to the ground around the probe. Therefore, it is essential to assess this disturbance to ensure accurate determination of the total in-situ horizontal stress. There are several methods to interpret the in-situ horizontal stress from SBP results. In this analysis, the lift-off method has been used to assess the total in-situ horizontal stress.

According to Marsland and Randolph (1977), the behaviour of the soil is elastic in the vicinity of in-situ horizontal stress. For undrained conditions the onset of yield is represented by reaching the undrained shear strength (s_u) of the soil in the cavity wall. The yield stress is determined as follows:

$$P_{yield} = \sigma_{h0} + s_u \quad (1)$$

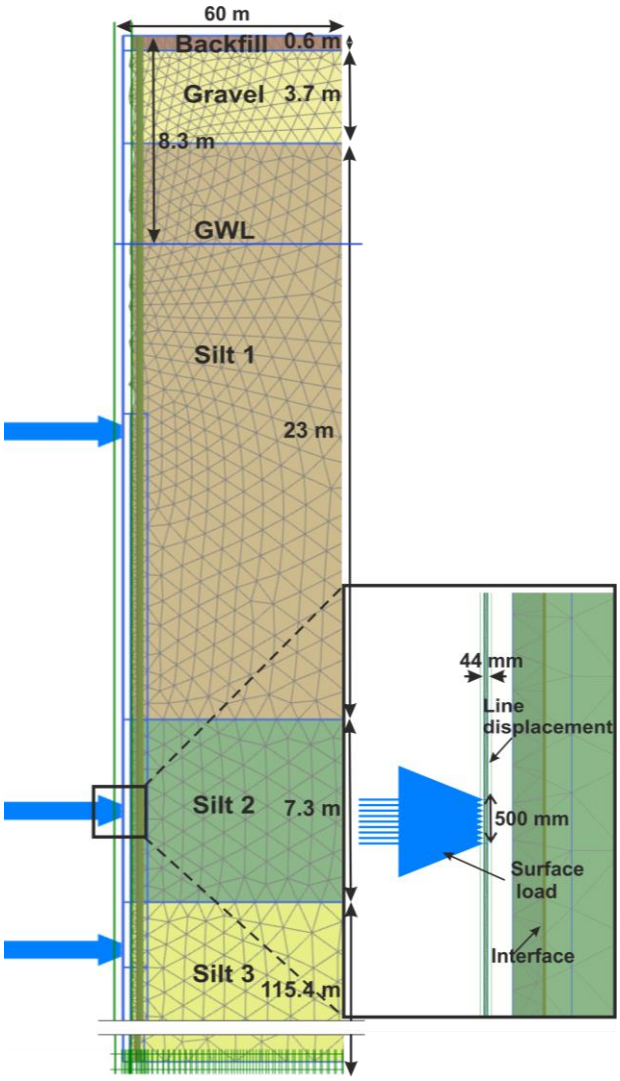

Figure 1. 2D FE model – SBPMT and soil stratification.

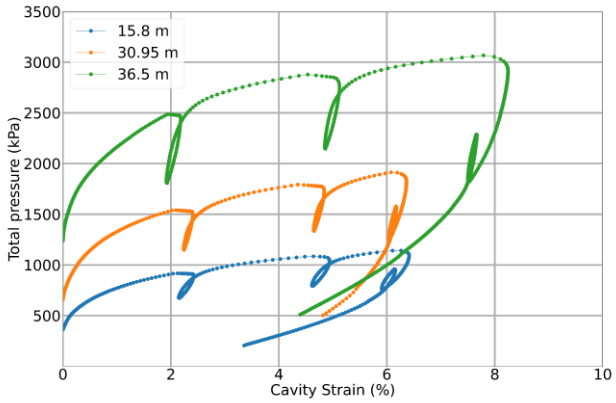

Figure 2. Pressure – strain response for the three selected tests.

The effective in-situ horizontal and yield stress were used to calculate the coefficient of earth pressure at rest (K_0) and the overconsolidation ratio (OCR), as elaborated in the following section.

3 NUMERICAL ANALYSIS

In literature, several attempts have been made to model the SBP tests as a boundary value problem, such as (Tschuchnigg and Schweiger 2016; Gaone at al. 2019). A 2D axisymmetric finite element model was created to model the field SBP tests and the obtained results were compared with field measurements. SBP tests were modelled in Plaxis 2D V21 (Plaxis 2021). The model is presented in Figure 1, it consists of 9630 15-noded elements.

3.1 Finite element model

The model has a width and a depth of 60 m and 150 m, respectively. A parametric study was performed to examine the effect of the boundaries on the simulations. The thickness of each layer is displayed in Figure 1; layer Silt 3 extends all the way to the bottom boundary of the model. The left boundary is positioned at a distance of 0.044 m (equal to the radius of the SBP membrane) from the vertical axis of symmetry. At the left boundary, a line displacement (which is fixed in horizontal direction and free in vertical direction) and an impermeable interface are created.

The total horizontal stresses were determine based on the lift-off method and were obtained from the SBPMT report. Afterwards, the vertical stresses were computed. From the vertical and horizontal effective stresses, K_0 values for the three tests were identified. Furthermore, the "effective" yield stresses were computed using the yield stresses provided in the SBPMT report through Eq. 1 for the three silt layers to calculate OCR. As different values for K_0 and OCR were obtained for the three tests, the silt layer was divided into three layers (Silt 1, Silt 2, and Silt 3). The values of K_0 and OCR for the respective layers are presented in Table 1.

3.2 Constitutive model and soil parameters

The silt layers were simulated using the Hardening Soil Small model (HSS) (Benz 2007). It is an elasto-plastic constitutive model characterized by the ability to account for both deviatoric and volumetric hardening while considering stress-dependent stiffness. The HSS model is an extension to the Hardening Soil model (HS) (Schanz et al. 1999), where it incorporates the high stiffness at very low strains. Compared to the HS model, the HSS model requires two additional parameters to describe the small-strain stiffness. These parameters are the initial shear modulus (G_0) and the shear strain level ($\gamma_{0.7}$), which denotes the amount of shear strains where the secant shear modulus is reduced to 70% of its initial value. The parameters of the HSS model are presented in Table 1.

The strength parameters ($c'$and φ') were determined from consolidated undrained triaxial tests. K_0 and OCR were calculated based on the total horizontal stress and yield stress values obtained from the SBPMT report. The stiffness parameters were calibrated through back analyses of the SBP tests. Additionally, the unit weight (γ_{unsat}) was determined from the laboratory tests.

Table 1. HSS model parameters used for the 3 silt layers.

Parameter	Silt 1	Silt 2	Silt 3
$\boldsymbol{\gamma_{unsat}(kN/m^3)}$	20	20	20
$\boldsymbol{E_{50}^{ref}(kPa)}$	13000	16500	18000
$\boldsymbol{E_{oed}^{ref}(kPa)}$	13000	16500	18000
$\boldsymbol{E_{ur}^{ref}(kPa)}$	39000	49500	54000
$\boldsymbol{m(-)}$	0.8	0.8	0.8
$\boldsymbol{c'(kPa)}$	8	8	8
$\boldsymbol{\varphi'(°)}$	28	28	28
$\boldsymbol{\gamma_{0.7}(-)}$	0.0001	0.0001	0.0001
$\boldsymbol{G_0^{ref}(kPa)}$	60000	70000	120000
$\boldsymbol{p^{ref}(kPa)}$	100	100	100
$\boldsymbol{K_0(-)}$	1.17	1.08	2.12
$\boldsymbol{OCR(-)}$	1.73	1.77	2.76

4 RESULTS

The three tests presented in Section 2 and Figure 2 were modelled and the simulation results were compared with field measurements. As the SBP tests were executed in silty soil, undrained material behaviour was considered.

The simulations were carried out in five calculation steps. Following the initial phase (K_0 procedure), the vertical line displacement (refer to Figure 1) is activated. In the subsequent step, the vertical line displacement corresponding to the membrane's height (500 mm, refer to Figure 1) is deactivated and a linear load (equivalent to the effective horizontal stress) is applied. Afterwards, the loading phase takes place by applying a uniform load that corresponds to the maximum horizontal pressure obtained from the field results. Finally, the unloading phase commences by applying a uniform load lower than the maximum horizontal pressure.

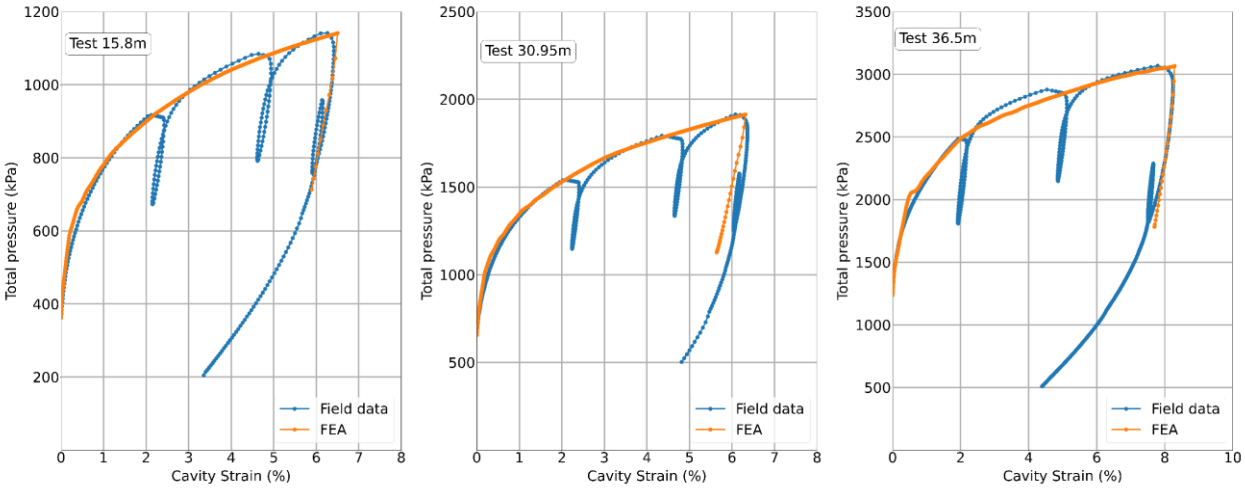

Figure 3. Comparison between field measurements and simulated tests.

The results of the simulations are presented in Figure 3. It can be seen that the HSS model produces a good agreement with the field measurements. It is worth noting that the third test (36.5 m) shows a slightly softer behaviour compared to the field data at cavity strains between 2.8% and 4.8%. Nevertheless, the calibrated stiffness parameters produced very good match with the field data.

5 CONCLUSIONS

There are various benefits to deriving soil parameters from in-situ tests. However, the primary constraint lies in the interpretation of the results as it is not possible to assess the parameters directly. Several attempts have been made to automate the process of parameter determination and to increase the confidence in the parameters derived from in-situ tests, such as (Marzouk et al. 2023a, 2023b).

In the present contribution, an efficient and practical approach to derive constitutive model parameters from SBP tests was illustrated. The numerical results show that it is possible to calibrate constitutive model parameters based on field measurements. The automated optimization of the parameters to accelerate the parameter determination process is part of ongoing research.

REFERENCES

Benz, T. (2007). *Small-strain stiffness of soils and its numerical consequences*. PhD thesis, University of Stuttgart, Germany.

Clarke, B. G. (2023). *Pressuremeters in geoetechnical design*, 2nd ed., Boca Raton: CRC Press.

Gaone, F. M., Doherty, J. P. and Gourvenec, S. (2019). An optimization strategy for evaluating modified Cam clay parameters using self-boring pressuremeter test data. *Can. Geotech. J.* 56 (11), pp. 1668–1679. DOI: 10.1139/cgj-2018-0385.

Mair, R. J. and Wood, D. M. (1987). *Pressuremeter Testing. Methods and Interpretation*. Kent: Elsevier Science.

Marsland, A. and Randolph, M.F. (1977). Comparison of the results from pressuremeter tests and large in situ plate tests in London Clay. *Géotechnique*, 27, (2), 217-243. DOI: 10.1680/geot.1977.27.2.217

Marzouk, I., Tschuchnigg, F. and Brinkgreve, R.B.J. (2023a). Expansion of an automated system for determining soil parameters using in-situ tests. *In: Proc 10th European Conference on Numerical Methods in Geotechnical Engineering 2023.*

Marzouk, I., Oberhollenzer, S. and Tschuchnigg, F. (2023b). An automated system for determining soil parameters: Case study. *In: Proc 8th International Symposium on Deformation Characteristics of Geomaterials 2023.*

Plaxis bv. (2021). *PLAXIS 2D Reference Manual*. Bentley Systems, Incorporated, Netherlands.

Schanz T., Vermeer P.A. and Bonnier P.G. (1999). The hardening-soil model: formulation and verification. *In: Beyond 2000 in computational geotechnics,* Rotterdam: Balkema, p. 281-90.

Tschuchnigg F. and Schweiger H.F. (2016). Embankment and footing prediction by means of 2D and 3D finite element analyses. *In: Proc embankment and footing prediction symposium 2016,* p. 366–90.

Yu, H-S (2010). *Cavity Expansion Methods in Geomechanics, 1st ed.* Dordrecht: Springer.

Proceedings of the XVIII ECSMGE 2024
GEOTECHNICAL ENGINEERING CHALLENGES
TO MEET CURRENT AND EMERGING NEEDS OF SOCIETY
© 2024 the Authors
ISBN 978-1-032-54816-6
DOI 10.1201/9781003431749-105
Open Access: www.taylorfrancis.com, CC BY-NC-ND 4.0 license

ECSMGE 24
XVIII EUROPEAN CONFERENCE ON SOIL MECHANICS AND GEOTECHNICAL ENGINEERING

Advanced numerical modelling using the Hardening Soil Small Strain material model for sensitive excavations adjacent to a metro station

Modélisation numérique avancée utilisant le Hardening Soil Small Strain pour des excavations sensibles adjacentes à une station de métro

C. Merino*, J. González
Ove Arup & Partners SAU, Madrid, Spain

A. Prados
Former Ove Arup & Partners SAU, Madrid, Spain

**carlos.merino@arup.com*

ABSTRACT: This study focuses on the advanced numerical modelling of retaining structures for deep excavations in urban areas using the Plaxis Hardening Soil model with small-strain stiffness (HSS). The main objective is to provide a safe and stable solution for deep excavations next to metro stations and tunnels. This model is utilized to simulate soil response and soil-structure interaction. The numerical results are validated and calibrated against field measurements to update models for additional accuracy and reliability. The advanced numerical modelling approach based on HSS material models can effectively predict the behaviour of the soil and retaining structures and provide valuable information for the design and construction of retaining structures for deep excavations in urban areas.

RÉSUMÉ: Cette étude se concentre sur la modélisation numérique avancée de structures de soutènement pour des excavations profondes dans les zones urbaines en utilisant le modèle HS Small Strain de Plaxis. L'objectif principal est de fournir une solution sûre et stable pour les excavations profondes à proximité des stations de métro et des tunnels. Le modèle HSS est utilisé pour simuler la réponse du sol et l'interaction sol-structure. Les résultats numériques sont ensuite validés et calibrés par rapport aux mesures sur le terrain pour mettre à jour les modèles pour plus de précision et de fiabilité. La modélisation numérique avancée basée sur le modèle HSS de Plaxis peut prédire efficacement le comportement du sol et des structures de soutènement et fournir des informations précieuses pour la conception et la construction de structures de soutènement pour des excavations profondes dans les zones urbaines.

Keywords: Metro; deep excavations; HSS (Hardening Soil model with small-strain stiffness); tunnel; sensitive infrastructure

1 INTRODUCTION

We present a deep basement excavated next to a metro station and tunnel, that had to remain operational and safe during all works. A detailed understanding of the soil behaviour was crucial for predicting ground movements, settlements, and potential impacts on nearby structures. This required the use of models that could accurately simulate the soil behaviour and predict ground movements and settlements. Finite element models were created to numerically simulate the expected soil response. The HS-Small Strain model (Benz, 2007) was used to simulate soil behaviour since these deep excavations typically involve small strains, especially in the early stages of the excavation process. This model was tailored to specific well known geological and soil conditions at the site in Madrid.

2 BACKGROUND

The proposed site is located in the vicinity of the centre of Madrid. It was occupied by an industrial building bounded by Dédalo Street to the south and Alcalá Street to the north. Adjacent to the plot (less than 1m in some areas) and along Alcalá Street, there is an existing metro station (Torre Arias Station –Line 5 Madrid Metro) was built in the 80s. The proposed building is 80m long and 74m wide, five storeys high above ground floor and has three basement levels below the street level.

Given the presence of Torre Arias metro station, contiguous bored pile retaining walls with diameters of 850mm, 650 mm and 450mm were required to support the ground and adjacent structures.

Temporary propping and ground anchors were required in some areas during construction to support

the retaining wall prior to construction of the permanent basement structure (Figure 1).

Wall thicknesses and construction details of Torre Arias station were undocumented. To avoid damage or distress to the underground station and to confirm the validity of the proposed design, it was necessary to undertake intrusive investigations inside the station to determine material and construction details of the metro structures. The investigations included core drilling to confirm wall thicknesses (and strength) at several different station facilities, core drilling in the crown and shoulders of the tunnel and CCTV survey of the drains and ventilation shafts to establish more detailed information adjacent to the piling works. As part of the characterization campaign, concrete cylinders for compression testing were taken to determine the compressive strength of the concrete used in construction in the 80s.

Given the proximity of adjacent structures it was necessary to assure a high overall stiffness for the pile retaining wall, in order to reduce the overall lateral deformation, through anchors, berms with struts inclined to the ground on strip foundations, and diagonal steel struts specifically in the northeast corner of the plot (Figure 2).



Figure 1. Front view of the retaining wall during the construction works (©Arup).

A strategy for monitoring both pile retaining wall and adjacent metro infrastructures before, during and after construction works, was implemented to assess the influence of the excavation on the nearby infrastructures. The monitoring system comprised inclinometers in the embedded wall, convergence monitoring and tape extensometers for the tunnel and different station facilities.

3 GROUND CONDITIONS AND PARAMETERS

Having analysed the project details, the two most representative sections are shown on Figure 3. The natural stratigraphy comprised anthropic fill (R) overlying 'Facies Madrid' sediments, as follows in depth: sands and clayey sands '*Arenas de Miga*' (AM), overconsolidated sandy/silty clays '*Toscos Arenosos*' (TAR) and '*Toscos Arcillosos*' (TARC). The stratigraphic columns adopted in the calculations are shown in Table 1 and Table 2.

Table 1. Stratigraphic column of section S3.

Soil unit	Top elevation (masl)	Bottom elevation (masl)	Thickness (m)
R	652.00	648.50	3.50
AM	648.50	640.40	8.10
TAR	640.40	634.80	5.60
TARC	634.80	To depth	-

Table 2. Stratigraphic column of section S6.

Soil unit	Top elevation (masl)	Bottom elevation (masl)	Thickness (m)
R	651.00	645.30	5.70
AM	645.30	639.60	5.70
TAR	639.60	634.20	5.40
TARC	634.20	To depth	-

A detailed ground investigation was carried out to derive representative geotechnical parameters for the soil units indicated above. They are shown in Table 3:

Table 3. Geotechnical parameters adopted.

Unit	R	AM	TAR	TARC
Model	MC	HSS	HSS	HSS
γ (kN/m^3)	19	20	20	20
c' (kPa)	0	10	20	50
Φ' (°)	28	34	32.5	29
E_{50}^{ref}/E' (MPa)	10	90	100	120
υ_{ur}/υ	0.35	0.20	0.20	0.20
G_o^{ref} (MPa)	-	661.3	976	976
$\gamma_{0.7}$	-	6E-05	6E-05	6E-05



Figure 2. Front view of the strutting system (©Arup).

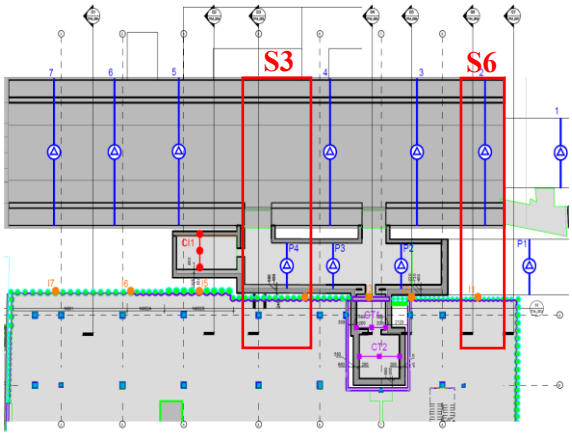

Figure 3. Plaxis 2D sections and inclinometer locations.

4 NUMERICAL ANALYSIS

The piled wall structure and its supporting elements (temporary strand anchors, strutting system at the northern east excavation corner), along with the nearby underground structures, were modelled with Plaxis 2D under plane-strain conditions.

Prior to starting the construction of the piled wall, it was essential to obtain the initial stresses acting on the ground. For that purpose, the construction sequence of the existing nearby tunnel and its galleries were simulated and, later, the displacements were set to zero. The construction sequence and overall geometric properties of the tunnel lining were provided by the asset owner.

The HSS model was calibrated using downhole geophysics for small strains and presuremeter tests for larger strains, alongside comparison to published literature on Madrid soils. The free-length of the cable anchors and its bond length (i.e. grout body) were modeled with node-to-node anchor and embedded beam row elements, respectively. For modelling the steel lattice beam elements of the strutting system and the concrete slab floors of the projected building were used fixed-end anchor elements. The geometry of the temporary anchors and prestress load are included in Table 4.

Table 4. Temporary anchors geometry.

Elev. (masl)	Free length (m)	Bond length (m)	$L_{spacing}$ (m)
648.50	17.0	8.5	1.60

A detailed staged analysis was defined considering up to 14 phases including intermediate excavation phases, installation of ground anchors/strutting system, berms, localised excavation for foundations and final support from basement concrete slabs. This allowed monitoring to be checked during all stages of the works.

Figure 4 compares the displacements predicted at sections 3 and 6 with the measurements taken in-situ by the nearest inclinometers (I1 and I4 respectively), once the final excavation level was reached and concrete slab floors built, along with the removal of supporting structures (earth berm, strutting system and temporary anchors). As shown above, there is a tight correspondence between predictions and measurements in section S6. However, differences of up to 10mm were observed in section S3, suggesting that the anchors did not behave as initially expected.

Constant monitoring of the wall displacements allowed for immediately warning of these unexpected displacements during one of the excavation phases. A more intensive anchor testing campaign was proposed to determine the causes. The tests revealed that some anchors had lost a significant portion of the applied prestressed load in spite of following standard BS EN 1537:2013 procedures. Further investigations revealed the existence of backfill material in this area that had not been identified during the geotechnical survey. To address this issue, the free anchor length was reduced from 17m to 9m, the spacing between anchors was reduced to 0.80m and the prestressed load was reduced.

Also, the frequency of the inclinometer readings was increased. Thereby, the displacements could be properly controlled to meet the requirements imposed by the metro station asset owner and the building construction was safely completed. Figure 5 and

Figure 6 show the sections in the final Plaxis model, before starting the building's construction.

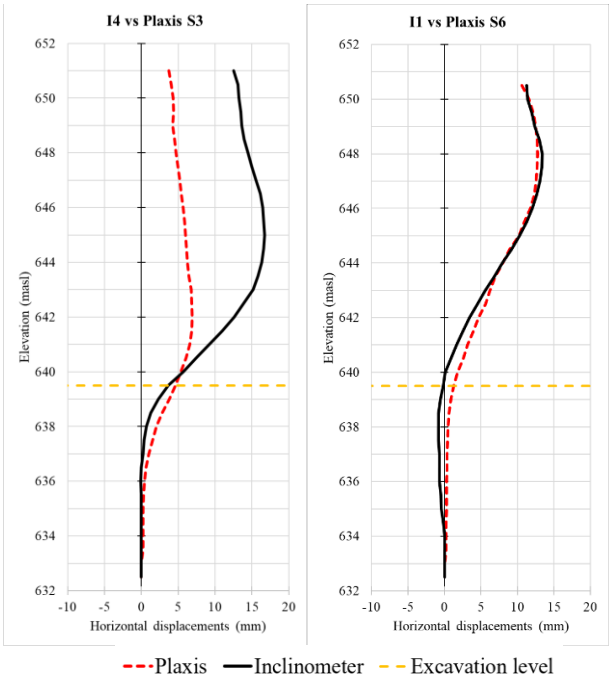

Figure 4. Horizontal displacements. Piled wall.

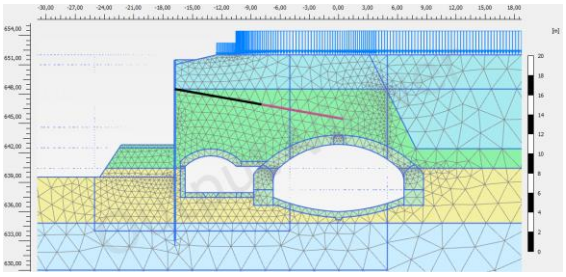

Figure 5. Plaxis Section 3 (anchor, earth berm).

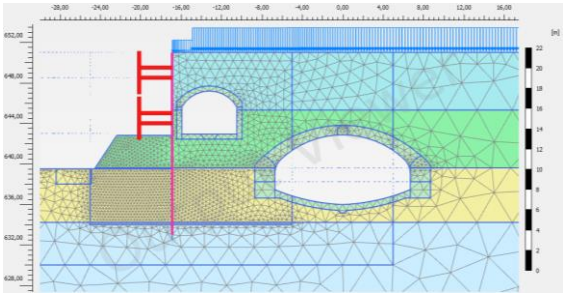

Figure 6. Plaxis Section 6 (strutting system, earth berm).

5 SUMMARY AND CONCLUSIONS

Using advanced constitutive models such as the Plaxis HS Small Strain model to simulate soil response and soil-structure interaction was essential to accurately assess potential impacts on a nearby sensitive metro station infrastructure. Overall, the numerical models allowed for a comprehensive understanding of soil behavior and its implications on adjacent structures. It facilitated effective design, risk mitigation, and optimized construction methods to ensure the safety and stability of both the excavation and nearby sensitive infrastructure. Another advantage was that the finite element models integrated both geotechnical and structural analysis, providing a holistic understanding of the interaction between the excavation, the soil, and nearby structures. This helped in making in-formed design decisions.

A detailed monitoring scheme alongside the use of numerical models was incorporated to enhance the safety and success of construction project. It enabled a proactive and responsive approach, allowing for timely adjustments and mitigations based on real-time data and observations such as:

- Real-Time performance evaluation
- Early detection of issues
- Validation of analytical models
- Calibration of design assumptions
- Confirmation of safety measures
- Record and benchmark for future projects
- Digital data-driven decision making
- Record of compliance verification

Finally, this case study showed it is crucial not only to accurately characterize the ground around the retaining structures but also at the anchor locations. In congested urban areas or near critical infrastructure these locations may vary considerably and end up being distant from the retaining structures. Unexpected displacements can compromise the excavation and safety of nearby structures unless a strict monitoring scheme is implemented, with suitable remedial measures that have been incorporated previously into the design as part of the decisionmaking process.

ACKNOWLEDGEMENTS

The authors are grateful to Metro de Madrid, S.A. for their active involvement during both design and construction phase. We would also like to give thanks to other collaborators involved in the project.

REFERENCES

Benz T. (2007). Small-strain stiffness of soils and its numerical consequences. *Ph.D. Thesis, University of Stuttgart.*

Oteo Mazo C. and Rodriguez Ortiz JM. (1997). Subsidence and monitoring in the Madrid Subway Network. *Revista de Obras Públicas Nº3.369. October 1997.*

Proceedings of the XVIII ECSMGE 2024
GEOTECHNICAL ENGINEERING CHALLENGES
TO MEET CURRENT AND EMERGING NEEDS OF SOCIETY
© 2024 the Authors
ISBN 978-1-032-54816-6
DOI 10.1201/9781003431749-106
Open Access: www.taylorfrancis.com, CC BY-NC-ND 4.0 license

ECSMGE 24
XVIII EUROPEAN CONFERENCE ON SOIL MECHANICS AND GEOTECHNICAL ENGINEERING

Axial behaviour of displacement pile groups in sand based on model tests in a calibration chamber

Comportement axial des groupes de pieux de déplacement dans le sable sur la base d'essais modèles dans une chambre d'étalonnage

F. Mitlmeier*, Ch. Moormann
University of Stuttgart, Institute of Geotechnical Engineering, Stuttgart, Germany
**felix.mitlmeier@igs.uni-stuttgart.de*

ABSTRACT: This paper presents results of physical model tests with a 3 x 3 displacement pile group in sand. The test results are evaluated to investigate mainly the influence of spacing on the axial group bearing behaviour. Accordingly, the instrumentation of the model piles allows one to identify the effect of pile-pile interaction on skin friction and tip resistance of the group piles depending on their position inside the group. First results of this experimental study show that for a spacing of three pile diameters the resistance of a driven group pile in medium-dense sand is higher than the resistance of a comparable unaffected single pile. This insight substantiates that there is a great potential in an optimized design assessment of the axial resistance of displacement pile groups which is intended to be considered for a sustainable pile design in future.

RÉSUMÉ: Cet article présente les résultats d'essais sur modèle physique avec un groupe de pieux à déplacement 3 x 3 dans le sable. Les résultats des essais sont évalués pour étudier principalement l'influence de l'espacement sur le comportement axial du groupe de pieux. En conséquence, l'instrumentation des pieux modèles permet d'identifier l'effet de l'interaction pieu-pieu sur le frottement cutané et la résistance de pointe des pieux du groupe en fonction de leur position à l'intérieur du groupe de pieux. Les premiers résultats de cette étude expérimentale montrent que pour un espacement de trois diamètres de pieux, la résistance d'un groupe de pieux enfoncés dans du sable moyennement dense est plus élevée que la résistance d'un pieu unique comparable non affecté. Cette constatation montre qu'il existe un grand potentiel dans l'évaluation optimisée de la résistance axiale des groupes de pieux de déplacement, ce qui devrait être pris en compte pour une conception durable des pieux à l'avenir.

Keywords: Displacement pile group; pile-pile-interaction; group efficiency; axial behaviour; calibration chamber test.

1 INTRODUCTION

The pile-pile interaction of displacement piles in sand both due to installation and due to loading and the resulting impact on the axial pile bearing behaviour has so far not been intensively investigated and clarified. While for bored pile groups a reduction of skin friction due to pile group effects is already often considered in pile design (DGGT, 2013), for displacement pile groups it is not clear, whether installation effects and the resulting modifications of status variables as soil density and stress status compensate group effects due to axial loading resulting in a reduction of shaft resistance or even lead to a higher axial pile resistance in comparison to an unaffected single pile.

To investigate the static axial load-bearing behaviour of displacement pile groups, a new calibration chamber was designed at the Institute of Geotechnical Engineering (IGS) at the University of Stuttgart. The chamber allows single displacement piles as well as 2 x 2 and 3 x 3 displacement pile groups up to a pile center distance of 6·D to be investigated under real stress scenarios. In the following, the pile-pile interaction is quantified and the findings from existing literature are provided. Thereafter the experimental setup, testing program, pile installation results, and the test outcomes of a 3 x 3 displacement pile group with a pile spacing of 3·D and the corresponding single piles in medium dense sand are described in detail.

2 GROUP EFFICIENCY AND MODEL TESTS OF OTHER AUTHORS

To compare the ultimate axial resistance of a pile group with that of an aggregate of unaffected single piles, Vesić (1969) as well as Valsangkar and Meyerhof (1983), among others, use group efficiency η defined as:

$$\eta = \frac{Q_g}{n\, Q_s} \qquad (1)$$

where Q_g is the ultimate load capacity of a pile group, n is the number of piles in a group and Q_s is defined as the ultimate resistance of a single pile.

Model tests on 3 x 3 jacked displacement pile groups in sand were performed e.g. by Hanna (1963), Vesić (1969), Tejchman (1973) and Le Kouby et al. (2006), see Figure 1. In loose non-cohesive soils, it is evident that the group efficiency η is always greater than 1.0, extending up to a 6·D pile spacing. Moreover, the highest group efficiency occurs within the range of 2·D to 3·D pile spacing. In medium-dense sands, conflicting results emerge regarding group effectiveness: Studies by Vesić (1969) and Tejchman (1973) demonstrated η-values greater than 1.0 up to 6·D, while Le Kouby et al. (2006) reported a significantly lower value with η = 0.64 in a pile group test with 2.8·D pile spacing. In dense sands, research by Hanna (1963) consistently indicated that the bearing capacity of the pile group is always less than that of an equivalent number of individual piles, irrespectively of the pile center distance.

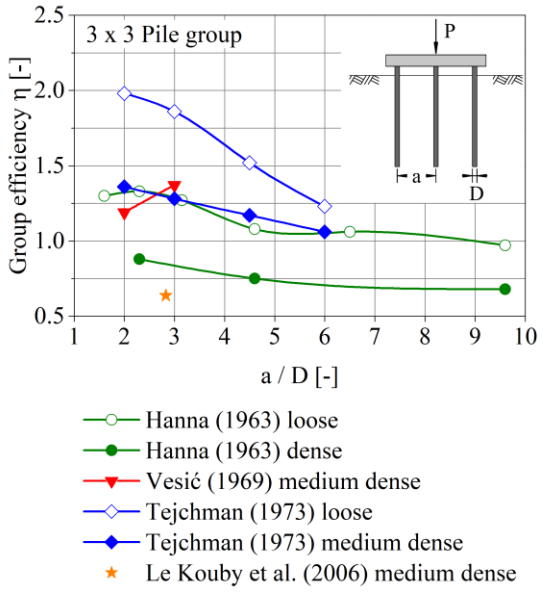

Figure 1. Group efficiency of 3 x 3 displacement pile groups in non-cohesive soils from model tests at a settlement s = 0.1·D.

3 EXPERIMENTAL SET-UP

Within the new calibration chamber developed at IGS (Figure 2), it is possible to regulate the vertical stress state. A categorization by Salgado et al. (1998) identifies this type of calibration chamber as 'BC3'. Application of the surface load is facilitated by a rigid 25 cm thick reinforced concrete slab, braced to the test tank with a system of preload beams, anchor rods and hydraulic presses. The new chamber accommodates a soil body measuring 1980 x 1980 x 1400 mm³. The results of the experiments shown herein correspond to using an air-dried, narrow-graded, medium-coarse sand known as *Berlin Sand* (Taşan, 2011, Le, 2015). The upright sand column method (Walz et al., 1975) is applied to create a homogenous medium-dense sand body of the specified dimensions.

The density of this sand body is determined directly by the volume of soil that has been poured. An indirect determination of the soil density is conducted through light dynamic probing (DPL-5) before and after pile installation. A distance of at least 9·D between the DPL-5 and installed piles is maintained to prevent any change in the soil density.

The model piles are driven vertically into the soil using a new designed model guide. The pile (group) test is controlled by force using a hydraulic control and regulation unit, transferring the force through a single press into a rigid pile head plate. Composed of aluminium, the model piles measure D = 40 mm in outer diameter and 1150 mm in length. After installation, they are embedded in the soil up to L = 750 mm (Figure 3), resulting in an L/D ratio of 18.75. These model piles are expected to represent a reinforced concrete displacement pile with a smooth pile surface and a flat pile tip, having an equivalent pile diameter (D_{eq}) of 0.5 m and an embedment depth of 10 m at a real scale. The ratio of chamber width B = 1980 mm to the diameter of a single pile, being 50, minimizes boundary effects. Additionally, a sufficient distance of 16·D from pile base to tank bottom is provided.

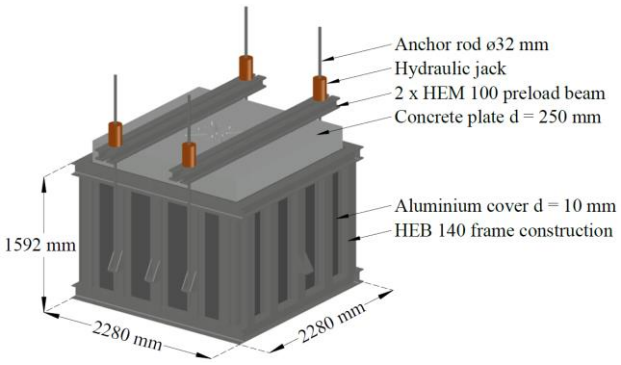

Figure 2. IGS calibration chamber – isometric view.

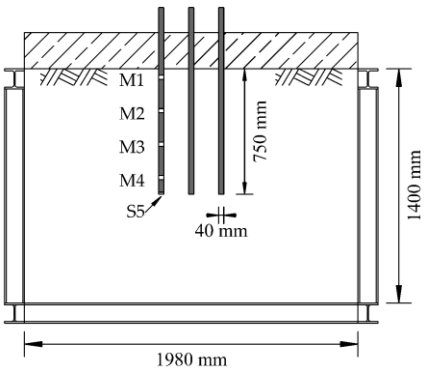

Figure 3. Cross section through IGS calibration chamber, model pile dimension and instrumentation.

In the 3 x 3 pile group test, one edge, one corner and one center pile (Figure 4 a) are instrumented with four measuring levels (M1 - M4) of strain gauges along the pile shaft and one at the pile base (S5), as shown in Figure 3, to determine the pile normal force as well as skin friction and tip resistance.

4 TEST PROGRAM

Following the preparation of the soil in a medium-dense packing with I_D = 37 %, it is consolidated under a vertical surface load of 200 kN/m². Afterwards either the group or individual piles are installed by hammering. The ratio of driving weight to pile weight is 2:1, providing a theoretical driving energy of 22.5 N·m per blow. In the pile group test, the piles (P1 - P9) are driven from left to right at a horizontal and vertical pile center distance of 3·D = 120 mm (Figure 4 b). During installation, the number of blows and the pile penetration are monitored to determine the theoretical driving energy per penetration depth. After completing the installation of all group piles, a load test of the pile group involving an initial loading, unloading and reloading phase is conducted, following the guidelines of DGGT (2013).

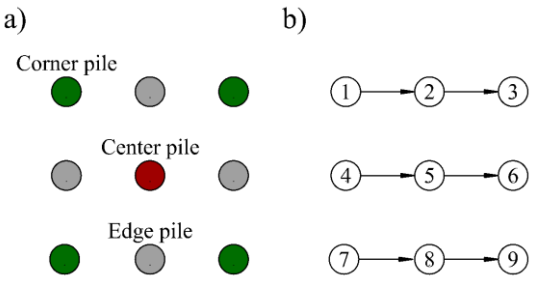

Figure 4. a) Group pile definition, b) installation order.

The corresponding individual pile tests (P10, P11 and P12) are conducted in a separate test for the same experimental conditions and soil density. The elapsed time of the single pile P10 after installation up to its test loading aligns with the elapsed time of the group piles (approx. 18 h to 24 h). Conversely, the single piles P11 and P12 were tested immediately after driving.

5 EXPERIMENTAL RESULTS

5.1 Pile installation data

Figure 5 displays the number of blows (N_5) and the theoretical driving energy per 5 cm of penetration, as well as the energy sum for both the group piles P1 to P9 (pile positions acc. to Figure 4 b) and the unaffected single piles P10 to P12. According to model tests conducted by Le Kouby et al. (2016) involving jacked displacement piles in sand, it was observed that the installation force increased with each additional group pile. Similarly, in a field test with medium-dense to dense gravel-sand mixtures (Garbers et al., 2022), there was a consistent rise in the pile energy sum for subsequently installed group piles within a 3 x 3 driven pile group. Briaud et al. (1989) also noted an increase in the number of blows for each sequentially installed pile in a driven 5-pile group in sand.

Regarding the current test, it can be stated initially that the energy sums of the group piles range from 2430 N·m (P3) to 3038 N·m (P1). It becomes apparent, starting from about half of the final penetration depth of 750 mm, that - except for the first pile installed (P1) - a greater driving energy per 5 cm of penetration is required compared to the group piles installed later.

The sum of energy of the single pile P10, with an elapsed time corresponding to that of the group piles, is 2745 N·m, falling within the range of the group piles.

5.2 Single pile and pile group tests

The results of the pile group test with a pile spacing of a = 3·D and a testing load of 50 kN are illustrated in Figure 6 (left). Following the guidelines from DGGT (2013), the resistance of the pile group, as well as that of the single or group piles in the ULS, corresponds to an average pile cap settlement or a pile head settlement of 0.1·D = 4 mm.

To assess the load-settlement behaviour under service load conditions, the resistances at a pile head settlement of 0.025·D = 1 mm were also evaluated. All measuring levels were reset to zero before the

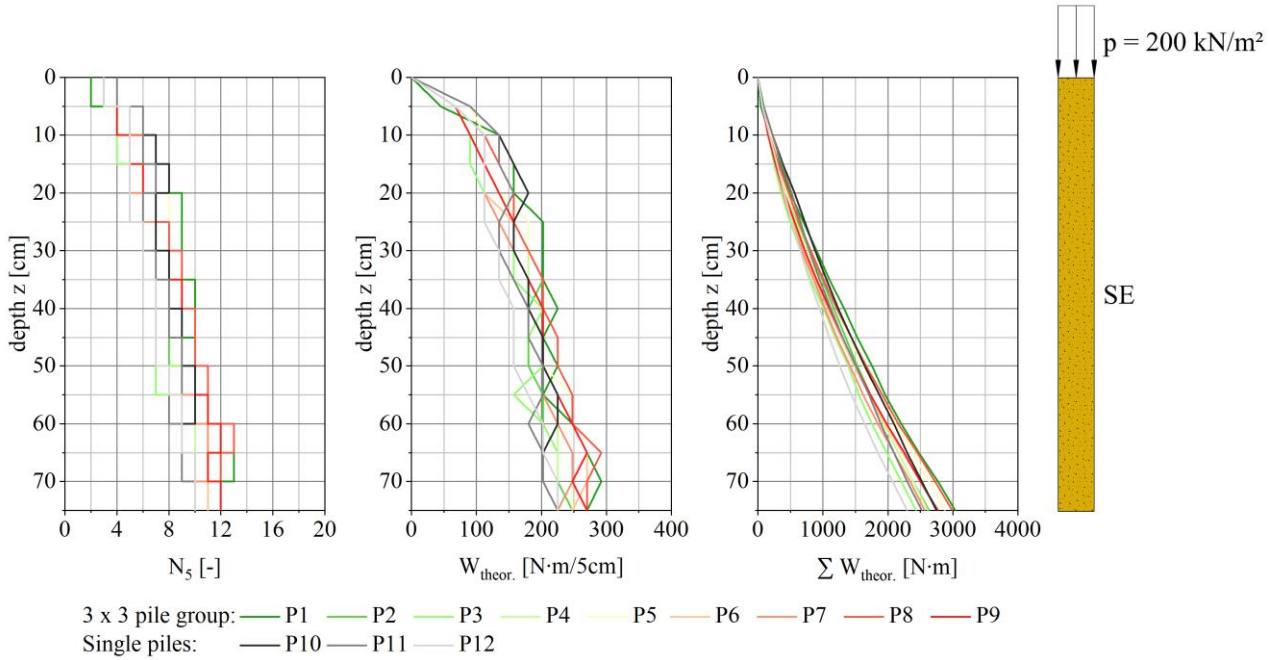

Figure 5. Number of blows N_5, theoretical driving energy per 5 cm of penetration $W_{theor.}$ and energy sum $\sum W_{theor.}$ for the group piles P1 - P9 (acc. to Figure 4 b) and the unaffected single piles P10 - P12.

tests, eliminating residual forces from pile driving. At a settlement of s = 0.1·D, the resistance of the 9-pile group measures 42.47 kN, significantly exceeding that of $9 \cdot Q_s$. Comparison with $9 \cdot$ P10 yields a group effectiveness $\eta_{s=0.1 \cdot D} = 1.26$, while with $9 \cdot$ P11 it reaches $\eta_{s=0.1 \cdot D} = 1.36$. These results align closely with those of previous studies: Tejchman (1973) and Vesić (1969) found a group efficiency of $\eta = 1.26$ and $\eta = 1.37$ when the piles were spaced at 3·D. Hanna (1963) determined a group efficiency in loose sand with a 3.15·D pile spacing at $\eta = 1.27$, as shown in Figure 1.

A positive group effect is also apparent under service load conditions at a settlement of 1 mm: Compared with $9 \cdot$ P10, it results in a group effectiveness of $\eta_{s=0.025 \cdot D} = 1.20$.

Figure 6 (right) shows the axial resistance of the representative group piles under the pile group test load and the axial resistances of the unaffected individual piles. The efficiency of the group piles in SLS and ULS and are summarised in Tables 1 and 2.

Table 1. Axial resistance of the group piles and group pile efficiency at s = 0.025·D (SLS).

	Q (s=0.025·D)	**η (s=0.025·D)**
Center pile	2.56 kN	1.28
Corner pile	2.56 kN	1.28
Edge pile	2.64 kN	1.32
Single pile P10	2.00 kN	-

Table 2. Axial resistance of the group piles and group pile efficiency at s = 0.1·D (ULS).

	Q (s=0.1·D)	**η (s=0.1·D)**
Center pile	5.48 kN	1.46
Corner pile	4.42 kN	1.18
Edge pile	4.88 kN	1.30
Single pile P10	3.75 kN	-

The results in Table 1 confirm that a positive group effect is evident even under service load conditions. At this settlement, the resistances are evenly distributed among the center, edge and corner pile. As the load increases and reaches the limit settlement of 4 mm, it can be seen that the center pile bears increasingly more load compared to the other group piles. This can be attributed to the increased stress status in the pile group area. This effect decreases at the edges and is least noticeable at the corners, a trend also reflected in the efficiencies of the group piles (Table 2).

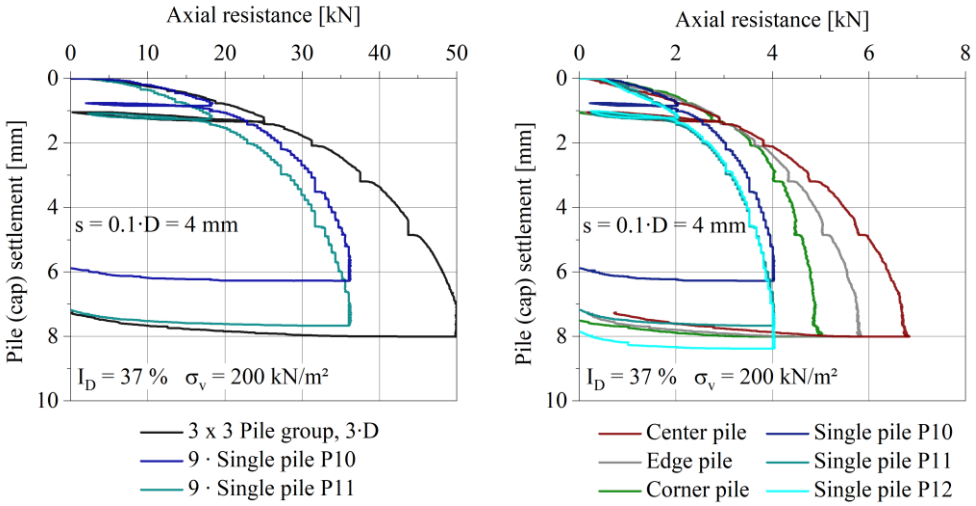

Figure 6. Pile group resistance and resistance of an equivalent amount of unaffected single piles (left) - group pile and single pile resistances (right) in medium dense Berlin Sand.

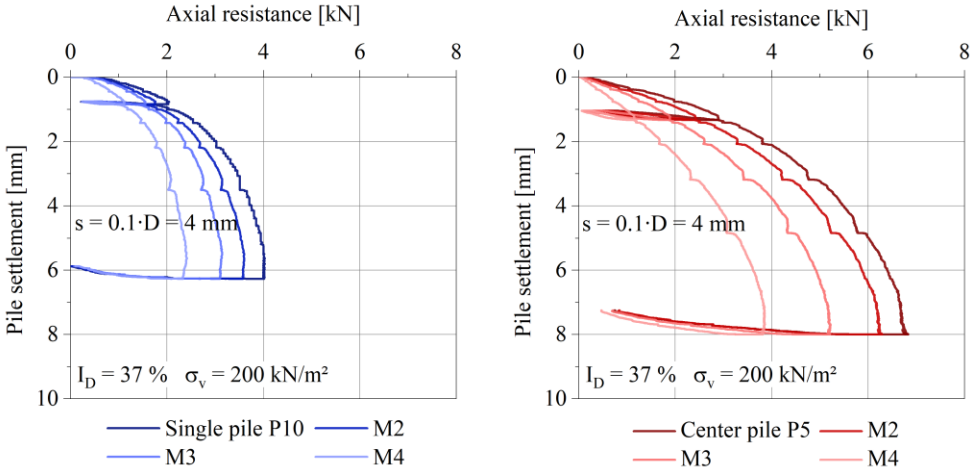

Figure 7. Single pile (P10) resistance, shaft distribution (left) and center pile resistance, shaft distribution (right) in medium dense Berlin Sand.

Unlike the individual piles, where no significant increase in load-bearing capacity is recognisable after the settlement s = 0.1·D, the elevated stress level in the pile group test leads to an increase in axial capacity, particularly noticeable for the center and edge piles, which clearly exceed the resistance determined at 4 mm.

Figure 7 illustrates the load-deformation curve of the single pile P10 (left) and that of the center pile (right), along with the distribution of the axial normal force over the measuring levels. The measuring level M4 at the lower pile shaft corresponds to level S5 at the pile base, enabling the determination of the proportion of the pile's normal force from base resistance Q_{base} and shaft resistance Q_{shaft}, see Table 3.

The results indicate that 41 % of the single pile's normal force is transferred through skin friction and 59 % via end bearing. For the center pile, on the other hand, 62 % of the axial resistance at a settlement of 1 mm is attributed to skin friction mobilisation. At a settlement of s = 0.1·D, the proportion of load transfer via skin friction is 0.47. These findings highlight that the increased axial resistance of the group piles, exemplified by the center pile, is due to an increased mobilisation of skin friction compared to the individual pile, as previously demonstrated by Vesić (1969).

Moreover, it is noticeable that the single pile exhibits no residual forces after the pile test when fully unloaded. However, for the center pile, a residual force of up to 0.74 kN is detected across the entire pile shaft after complete unloading of the pile cap. This residual force accounts for approximately 11 % of the maximum normal force of the center pile, which is 6.8 kN at a settlement of 8 mm.

Table 3. Ratio of pile normal force induced by skin friction to pile resistance of the respective piles at s = 0.025·D and s = 0.1·D.

	s=0.025·D: Q_{shaft} / Q	**s=0.1·D: Q_{shaft} / Q**
Single pile P 10	0.41	0.41
Center pile	0.62	0.47

6 CONCLUSIONS AND OUTLOOK

Model scale tests at the Institute of Geotechnical Engineering at the University of Stuttgart, assessing a displacement pile group in a calibration chamber in medium dense sand and a pile spacing of 3·D, illustrate a positive group efficiency of η = 1.26 aligning with findings by relevant researchers. It has also been demonstrated that the increase in axial resistance of the group piles is primarily attributed to increased skin friction.

Despite this potential, the current pile design does not consider these positive effects on the axial behaviour of displacement group piles. Therefore, an additional test series examines the influence of key aspects like the pile center distance, initial soil density, stress state within the calibration chamber, and the influence of the installation method.

REFERENCES

Briaud, J.L., Tucker, L.M., & Ng, E. (1989). Axially loaded 5 pile group and single pile in sand, In: *Proc. 12th Int. Conf. on Soil Mechanics and Foundation Engineering*, Rio de Janeiro, Brazil, pp. 1121-1124.

DGGT (2013). *Recommendations on Piling (EA-Pfähle)*. John Wiley & Sons.

Garbers, T., Mitlmeier, F., Moormann, Ch., Wardinghus, P. (2022). Zum Gruppentragverhalten von Verdrängungspfählen - Untersuchungen zu Interaktionseffekten bei Installation und axialer Beanspruchung, In: *Vorträge der 37. Baugrundtagung*, Wiesbaden, Germany, pp. 181-190.

Hanna, T.H. (1963). Model studies of foundation groups in sand. *Géotechnique*, 13(4), pp. 334-351. https://doi.org/10.1680/geot.1963.13.4.334

Le, V.H. (2015). *Zum Verhalten von Sand unter zyklischer Beanspruchung mit Polarisations-wechsel im Einfachscherversuch*, PhD thesis, Veröffentlichungen des Grundbauinstituts der Technischen Universität Berlin, Heft 66.

Le Kouby, A., Canou, J., Dupla, J.C. (2006). Group effect on model piles under axial monotonic load-ing, In: *Proc. 4th Int. Conf. on Soft Soil Engineering*, Vancouver, Canada, pp. 179-187.

Le Kouby, A., Dupla, J.C., Canou, J., Francis, R. (2016). The effects of installation order on the re-sponse of a pile group in silica sand. *Soils and Foundations*, 56(2), pp. 174-188. https://doi.org/10.1016/j.sandf.2016.02.002

Salgado, R., Mitchell, J. K., Jamiolkowski, M. (1998). Calibration chamber size effects on penetration resistance in sand. *Journal of Geotechnical and Geoenvironmental Engineering*, 124(9), pp. 878-888. https://doi.org/10.1061/(ASCE)1090-0241(1998)124:9(878)

Taşan, E. (2011). *Zur Dimensionierung der Monopile-gründungen von Offshore-Windenergieanlagen*, PhD thesis, Veröffentlichungen des Grundbauinstituts der Technischen Universität Berlin, Heft 52.

Tejchman, A.F. (1973). Model investigations of pile groups in sand. *Journal of the Soil Mechanics and Foundations Division*, 99(2), pp. 199-217. https://doi.org/10.1061/JSFEAQ.0001852

Valsangkar, A.J., Meyerhof, G.G. (1983). Model studies of the collapse behaviour of piles and pile groups, In: *Developments in Soil Mechanics and Foundation Engineering*, Vol. 1, pp. 65-109.

Vesić, A.S. (1969). Experiments with instrumented pile groups in sand. *Performance of Deep Founda-tions, ASTM STP 444*, pp. 177-222. https://doi.org/10.1520/STP444-EB

Walz, B., Schober, H.-D., Diekmann, N. (1975). Untersuchungen zum lagenweisen Einbau von Sandvolumina für bodenmechanische Modell-versuche, In: *Aus Theorie und Praxis des Grundbaus und der Bodenmechanik, Festschrift zum 70. Geburtstag von Herrn Prof. Dr.-Ing. Hans Lorenz,* Berlin, Germany, pp. 219-247.

Proceedings of the XVIII ECSMGE 2024
GEOTECHNICAL ENGINEERING CHALLENGES
TO MEET CURRENT AND EMERGING NEEDS OF SOCIETY
© 2024 the Authors
ISBN 978-1-032-54816-6
DOI 10.1201/9781003431749-107
Open Access: www.taylorfrancis.com, CC BY-NC-ND 4.0 license

ECSMGE 24
XVIII EUROPEAN CONFERENCE ON SOIL MECHANICS AND GEOTECHNICAL ENGINEERING

Terramesh: Solutions for great heights. Design and durability

Terramesh: Solutions pour de grandes hauteurs. Conception et durabilité

L. Molano*, D. García, D.C. Freitas, G.M. Torres, M. Jimenez
A.Bianchini Ingeniero, S.A, Barcelona, Spain

**l.molano@maccaferri.com*

ABSTRACT: A wide variety of construction systems to execute reinforced ground structures exist. Reinforced soil structures consist of improving the properties of the soil by installing reinforcement with metal strips or synthetic mesh, with the aim of providing tensile strength. The implementation of geogrids in the market is a competitive alternative with the added value of environmental sustainability. The geogrids work as a reinforcement element for each layer, distributing the efforts and generating friction due to the soil-reinforcement interaction, in such a way that the friction angle of the ground increases. Consequently, it is possible to use as structural material, tolerable soils with low mechanical properties, thus avoiding the transport of material and making its use viable. In 1979, the first officially executed structure with the combination of gabions and mechanically reinforced soil was built. At the time, a 14-meter structure was verticalized and as these results were extremely satisfactory, the solution was used again in other applications. From this work, the evaluation studies of the use of the double torsion hexagonal mesh as a reinforcement element in private and international laboratories resulted in the creation of the Terramesh System. This type of structure replaces the classic concrete structures which reduces the environmental impact. The mechanical and environmental characteristics are certified in accordance with international institutions and standards that include the CE mark. In this presentation, we want to demonstrate the main criteria, advantages, and durability of the Terramesh systems that have been studied in recent years.

RÉSUMÉ: Il existe une grande variété de systèmes de construction pour réaliser des structures de sol renforcé. Les structures de sol renforcé consistent à améliorer les propriétés du sol en installant un renforcement avec des bandes métalliques ou un treillis synthétique dans le but de fournir une résistance à la traction. L'introduction de géogrilles sur le marché constitue une alternative compétitive avec une valeur ajoutée en termes de durabilité environnementale. Les géogrilles agissent comme un élément de renforcement pour chaque couche, répartissant les efforts et générant des frottements dus à l'interaction entre le sol et le renforcement, de telle sorte que l'angle de frottement du sol augmente. Par conséquent, il est possible d'utiliser des sols tolérables ayant de faibles propriétés mécaniques en tant que matériau structural, ce qui évite le transport de matériau et rend son utilisation viable. En 1979, la première structure officiellement réalisée avec la combinaison de gabions et de sol mécaniquement renforcé a été construite. À l'époque, une structure de 14 mètres a été verticalisée, et comme ces résultats étaient extrêmement satisfaisants, la solution a été réutilisée dans d'autres applications. A partir de ce travail, les études d'évaluation de l'utilisation du treillis hexagonal double torsion comme élément de renforcement dans des laboratoires privés et internationaux ont abouti à la création du Système Terramesh. Ce type de structure remplace les structures classiques en béton ce qui réduit l'impact environnemental. Les caractéristiques mécaniques et environnementales sont certifiées conformément aux institutions internationales et aux normes qui incluent la marque CE. Dans cette présentation, nous souhaitons démontrer les principaux critères, avantages et durabilité des systèmes Terramesh qui ont été étudiés au cours des dernières années.

Keywords: Soil reinforced; durability; ecological; CE mark; software design.

1 INTRODUCTION

There are several established construction systems to execute reinforced soil slope (RSS) due to the economic advantages over conventional retaining walls (Hatami, et al., 2001). The range of products offered as reinforcing material has expanded over the years. There are materials for soil reinforcement: steel and geosynthetics as geogrids. The suitable design RSS involves understanding the different responses of the reinforcement under load. The geosynthetics are characterized by having a time-load sensitive response because of the creep effect, and instead, the steel has a constant rigid elastoplastic response.

The hybrid reinforcement consists of a combination of steel wire mesh and geogrids, where the steel component provides a function as secondary reinforcement (modular ready-to-use facing units) and the geogrids provide the primary reinforcement functions. After making a preliminary numerical approach applying mixed reinforcement configurations, the results indicate a response under

load resembling a theoretical uniform reinforcement pattern (Vicari, 2009). Additionally, significant progress has been achieved with the development of the numerical simulations which showed that a hybrid reinforcement scheme appears to be a more effective reinforcement arrangement (Vicari, 2009). These outcomes indicated that a smaller gap between the reinforcement layers is a suitable setting to minimize facing deformation (Vicari, 2009). Thus, the same results are not achieved using stiffer reinforcement layers at greater distances.

1.1 Background

The Terramesh System was designed based on the principle of reinforced soil system developed in the early 1960s, where steel ties were used as reinforcement. The first officially executed structure was built in Sabah (Malaysia) in 1979 which was a design ahead of its time (Egoavil, 2011). This consisted of building a gabion-facing anchored to the embankment by inserting stainless-steel strips. Over the years there has been an evolution in the structural design replacing the stainless-steel strips by double-twist woven steel wire mesh panels. In this way, continuous and longitudinal reinforcement is achieved with high interlocking forces involved.

The experience acquired since this first construction promoted broader studies in this area, encouraging the simplification of placement phases on site. The findings have led to the design of the hybrid RSS from the combination of steel wire mesh and geogrids.

1.2 Description of Terramesh Solutions

The hybrid RSS is composed of a front facing element of the Terramesh family, geogrids, the drainage system, and the material fill. The Terramesh family involves three options of front facings: Terramesh, Green, and Mineral Terramesh. The first type can provide a mechanically stabilized earth wall with a gabion lining finish. Another option for a stone finish is the Mineral Terramesh, which are factory-pre-assembled units with inclined surfaces filled with stone. In contrast, the Terramesh Green is an environmentally friendly modular system with a surface vegetation finish (green). Perspective views of each type of modular system is shown in Figure 1. However, this paper focuses only on structures with gabion facings, whose units are formed by creating the rectangular-shaped cells used to contain the stones.



Figure 1. Elements of Terramesh Solutions.

The Terramesh units are 3.0 (W) x 3.0m (L) x 1.0m (H) as indicated in Figure 2. The cladding section is formed by connecting a back panel and diaphragms to the main front panel, thus creating the rectangular-shaped cell used to contain the stones. It is worth highlighting that these units are filled with rock varying in size between 15cm and 20cm properly graded to provide a high packing density. The gabion front facing does not comply with a structural function within the RSS because its main function is cladding and erosion control of the facing. To stabilize the facing, a wire mesh tail with a length of 3m is required, and the geogrids spacing should not exceed 2m.

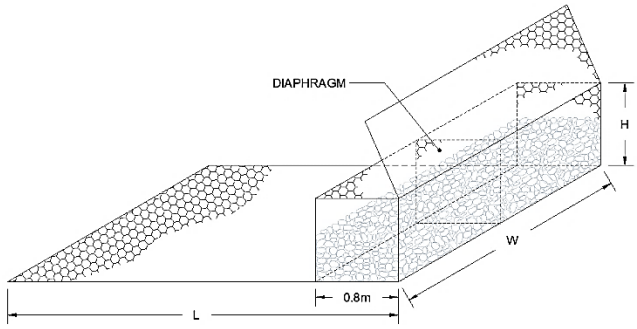

Figure 2. Typical Terramesh Dimensions.

In general terms, the main advantage of the RSS is the economic affordability compared to most of the classic concrete wall solutions. In addition, using gabion lining has the benefit of ensuring soil drainage on the front face. For this reason, the cladding is not subject to the actions of hydrostatic forces. Reducing emissions derived from the transportation of materials represents a distinctive characteristic of being environmentally friendly.

2 CERTIFIED QUALITY

The design process of the Terramesh solution is based on test campaigns and investment in performance evaluation. Different trials were carried out to define the strength and anchoring features of the double twisted hexagonal steel mesh and the structural behavior of the Terramesh System. Mesh testing took place at Universidad New South Wales (1990), STS Consultant Lab. (1989), and Bathurst Clarabut

Geotechnical Testing Inc. (2001) (Egoavil, 2011). The assessment of the mesh consists of its deformation modulus behavior that varies if the mesh is in the air or confined. According to the results, the mesh in air stretches to close transversally and elongates longitudinally resulting in high deformation (or low deformation modulus); while the mesh in contact with soil prevents the starching (Zannoni, et al., 2011).

Besides, trials developed in real structures were carried out in cooperation with laboratories and universities (Ghionna, et al., 2002), where two aspects were examined: the pull-out and the strength of the mesh. The structural analysis needs an overall evaluation of the reinforcement system. Considering that the double-twisted hexagonal wire mesh behaves elastically instead, the geogrid reinforcement is influenced by viscous deformation.

The efforts in the field of research have resulted in an assembly of quality certifications such as BBA, and the CE mark. Those certifications with international institutions and standards evidence the quality management checks and production inspections. It is also committed to following the International EPD System to communicate environmental characteristics transparently and comparably.

2.1 Durability

Durability depends not only on the manufacturing process but also on the technical characteristics of the materials used. The wire complies with the strictest international standards (EN 10218-2, ASTM A 641), moreover, the protection revetments selected to provide optimum durability for up to 120 years. The steel wire is coated with an alloy of Zn95-Al5 to protect against corrosion and it in addition to the galvanization, it is coated with an innovative polymer. It is therefore a highly abrasion and UV-resistant coating, which protects the steel wire mesh underneath against ever more severe environmental and mechanical effects.

The aggressiveness of the environment depends on the location construction site because the degree of corrosion is associated with the exposure time to humidity combined with other factors such as temperature, atmosphere chemical composition, and the nature of the material. The effect of atmospheric corrosion and abrasion are assessed as the major risks that affect the service life of metal structures. Currently, the standard establishes a relation between the type of galvanization, the coating, and the estimated service life, based on the accelerated artificial aging test of the official regulations.

3 DESIGN TOOLS

In the field of geotechnical engineering, the analysis of stability and safety is essential for the design of reinforced soil for different applications. For the design of slopes and retaining structures, computational tools are used to evaluate the behavior of different types of soil reinforcement and the evaluation of their performance in terms of stability.

The software for the RSS with Terramesh is based on the Limit Equilibrium Method with the possibility to introduce the mechanical characteristics of synthetic or metallic reinforcements and define the regulations. Stability checks are carried out with references to the geometry, soil typologies, and the hydraulic characteristics of the site. Therefore, the initial phase of the design aims to achieve the RSS sketch and then it could be analyzed with FEM to interpret deformations.

The accurate choice of reinforcement material from a deformation point of view is essential to not compromise the serviceability limit of the structure (Zannoni, et al., 2011). Therefore, the evaluation of performances in the short- and long-term including safety factors, can provide the difference between an effective design and an overdesign. The reinforced soil deformations can be vertical or horizontal, where the vertical movements are attributed to soil behavior and the horizontal ones occur due to the facing or the reinforcement (Zannoni, et al., 2011). The design parameters to characterize the reinforcement material are configured for the end of the service life of the structure. In the short term, deformations develop during the construction phase, where the soil deforms until the equilibrium between soil and reinforcement is achieved (Zannoni, et al., 2011). The steel reinforcement of the Terramesh is only evaluated in the short-term deformations because steel does not present creep phenomena as does geosynthetics. After the soil consolidation process, the deformations are associated with viscous behavior which is partially offset by the effective performance of geosynthetic.

Regarding the introduction of Building Information Modeling, all the objects and libraries were created. In the case of complex projects, the project management will improve by integrating all the construction processes, thus avoiding interferences and errors on site. Inside each object, there is a large amount of information available such as quality certifications and technical data sheets.

4 CONCLUSIONS

The Terramesh System is a technically and cost-effective solution for the construction of reinforced

soil structures. The design of the pre-assembled units with gabion facing was focused on test campaigns and investments in performance evaluation of the solution. Additionally, research suggests that the best reinforcement assembly is the hybrid combining the geogrids as the primary reinforcement and steel wire mesh as the second one.

In addition, the technical design of RSS is supported by software with good modeling capabilities using limit equilibrium. The analysis considers the quality and technical characteristics of the materials to provide optimum durability for up to 120 years. To ensure the stability of the structure the software incorporates the majority of international regulations. Finally, it is encouraged in further research focused on the monitoring of strength and deformation reinforcements in the long-term using remote sensors.

REFERENCES

Egoavil, H. (2011). Reinforced Earth Walls Terramesh Systems in Mining Projects, Lima: Maccaferri.

Ghionna, V. N., Fioravante, V., & Vicari, M. (2002). Full scale test on a retaining wall with non-uniform reinforcements. *Geosynthetics-7th ICG*, 279-282.

Hatami, K., Bathurst, R. J. & Di Pietro, P. (2001). Static response of reinforced soil retaining walls with nonuniform reinforcement. *International Journal of Geomechanics*, Vol. 4, pp. 477-506.

FHWA-NHI-10-024 (2009). Design and Construction of Mechanically Stabilized Earth Walls and Reinforced Soil Slopes.

Vicari, M. (2009). 10 years of experience with reinforced soil structures, Bologna, Italy: Maccaferri.

UNE-EN 10223-3 (2014). Steel wire and wire products for fencing and netting - Part 3: Hexagonal steel wire mesh products for civil engineering purposes.

UNE-EN ISO 22479 (2023). Corrosion of metals and alloys - Sulfur dioxide test in a humid atmosphere (fixed gas method) (ISO 22479:2019).

UNE-EN ISO 9227 (2023). Corrosion tests in artificial atmospheres - Salt spray tests (ISO 9227:2022).

Zannoni, E., Vicari, M. & Scotto, M. (2011). Deformations of Soil Reinforced Walls in Relationship with Reinforcement Used. *Proceedings of the 15th African Regional Conference on Soil Mechanics and Geotechnical Engineering*, Vol IOS Press, pp. 228-236.

Proceedings of the XVIII ECSMGE 2024
GEOTECHNICAL ENGINEERING CHALLENGES
TO MEET CURRENT AND EMERGING NEEDS OF SOCIETY
© 2024 the Authors
ISBN 978-1-032-54816-6
DOI 10.1201/9781003431749-108
Open Access: www.taylorfrancis.com, CC BY-NC-ND 4.0 license

ECSMGE 24
XVIII EUROPEAN CONFERENCE ON SOIL MECHANICS AND GEOTECHNICAL ENGINEERING

Assessment of the degree of saturation in sands by bender element testing

Évaluation du degré de saturation dans les sables par des tests d'élément Bender

F. Molina-Gómez*, A. Viana da Fonseca, C. Ferreira
CONSTRUCT-GEO, Universidade do Porto (FEUP), Porto, Portugal

G. Cascante
University of Waterloo, Waterloo, Canada

**fausto@fe.up.pt*

ABSTRACT: The propagation of the P-wave is affected by the compressibility of the porous fluid in the granular media. This effect provides alternatives to estimate the degree of saturation of sands by measuring the P-wave velocity. In the laboratory, such an estimate is usually made using Skempton's B-value (or B-value). However, the B-value is not suitable for use in the field because undrained conditions cannot be guaranteed during measurement. This study aims to assess the degree of saturation in partially to fully saturated sands using P-wave velocity measurements obtained by bender element tests. The measurements of P-wave velocity were compared with theoretical predictions based on Biot-Gassmann theory of wave propagation in fluid-saturated granular media. Therefore, the P-wave velocity proved a more reliable approach to assess the degree of saturation, as shown by the good agreement between the theoretical predictions and experimental results.

RÉSUMÉ: La propagation de l'onde P est influencée par la compressibilité du fluide poreux dans les milieux granulaires. Cet effet offre des alternatives pour estimer le degré de saturation des sables en mesurant la vitesse de l'onde P. En laboratoire, cette estimation est généralement réalisée en utilisant la valeur B de Skempton (ou valeur B). Cependant, la valeur B n'est pas adaptée à une utilisation sur le terrain car les conditions non drainées ne peuvent pas être garanties lors de la mesure. Cette étude vise à évaluer le degré de saturation dans les sables partiellement à entièrement saturés en utilisant les mesures de la vitesse de l'onde P obtenues par des tests à élément bender. Les mesures de la vitesse de l'onde P ont été comparées aux prédictions théoriques basées sur la théorie de Biot de la propagation des ondes dans les milieux granulaires saturés de fluide. Par conséquent, la vitesse de l'onde P s'est avérée être une approche plus fiable pour évaluer le degré de saturation, comme le montre la bonne concordance entre la prédiction théorique et les résultats expérimentaux.

Keywords: Laboratory tests; wave propagation; sands; soil dynamics.

1 INTRODUCTION

The degree of saturation (*Sr*) significantly impacts the mechanical behaviour of sands as it affects pore pressure build-up (Ishihara, 1993). In the laboratory, *Sr* is typically estimated by the pore pressure coefficient B (or *B*-value) originally introduced by Skempton (1954). However, measurements of *B*-value in the field due to the difficulty in controlling undrained conditions (Gu et al., 2021; Naesgaard et al., 2007). This limitation has prompted the development of alternative methods for field-based Sr assessment.

According to (Biot, 1956), changes in the degree of saturation affect the propagation of P-waves. Studies conducted by diverse authors (Astuto et al., 2023; Kumar & Madhusudhan, 2012; Leong & Cheng, 2016; Tsukamoto et al., 2002) have demonstrated that alterations in *Sr* effectively result in variations of the P-wave velocity (V_P). This response is because P-wave travels through the fluid (a mixture of water and air) rather than through grains contacts. Consequently, in fluid-saturated granular media, *Sr* can be estimated by measuring *Vp*.

This paper assesses *Sr* by a novel and reliable procedure Bender Element (BE) tests to generate P-wave. based on V_P measurements. Experimental results were compared against theoretical predictions based on the wave propagation theory or Biot-Gassmann theory (Biot, 1956). The wave-based approach of this study has proven to be a method more reliable for estimating *Sr* in sands.

2 MATERIALS AND METHODS

In this study, TP-Lisbon sand was used. This sand is an alluvial granular soil with origin in the late Quaternary, which has sedimented next to the Tagus River in the historical centre of Lisbon (Molina-Gómez & Viana da Fonseca, 2021). Figure 1 exhibits the grain size distribution of TP-Lisbon sand. Table 1 summarises the parameters derived from the grain size distribution, specifically the mean diameter (D_{50}), the coefficient of curvature (Cc), the coefficient of uniformity (Cu) and the fines content (FC). This table also presents the following physical properties: the specific gravity of solids (G_s), the minimum void ratio (e_{min}) and the maximum void ratio (e_{max}).

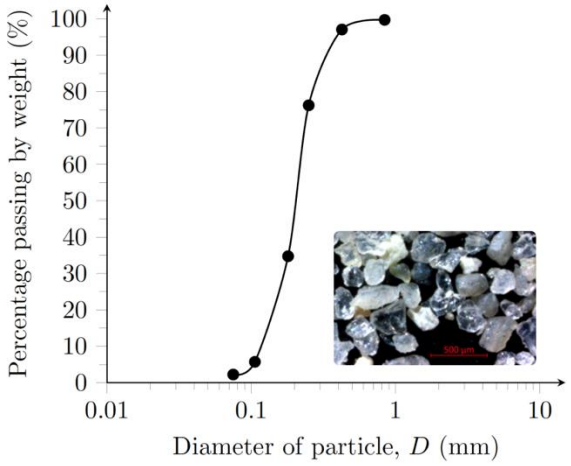

Figure 1. Grain size distribution of TP-Lisbon sand.

Table 1. Physical properties of TP-Lisbon sand.

Parameter	Value
D_{50} (mm)	0.21
Cu	1.69
Cc	1.13
FC (%)	2.21
Gs	2.66
e_{min}	0.64
e_{max}	1.01

A series of soil specimens were reconstituted to achieve a relative density (Dr) of 30% using the air pluviation method (Yamashita et al., 2009). This procedure allows replicating the initial fabric of alluvial soil deposits (Molina-Gómez et al., 2020). The tests were conducted in a triaxial cell equipped with a pair of BE to measure the seismic wave velocities, specifically P- and S-wave velocities (V_P and V_S).

These waves were generated by exciting the BE using sine-wave pulses with various frequencies (Ferreira et al., 2021). For P-wave, input frequencies (F) ranging from 30 to 75 kHz were employed; while S-wave F ranged from 1 to 10 kHz. BE testing involved the analysis of wave propagation using four different F (Viana da Fonseca et al., 2009). V_P and V_S were estimated by computing the ratio between the tip-to-tip distance (L_{tt}) and the travel time of wave propagation (t_t). L_{tt} was accurately monitored by local instrumentation, that is, a series of Hall-Effect transducers installed directly to the soil specimen (Molina-Gómez et al., 2023). The t_t was estimated by the identifying the first arrival time of the signals with different F.

As previously mentioned, the dry pluviation method was used, ensuring a Sr = 0% at the beginning of all tests. For soil saturation, the carbon dioxide method was implemented. After the carbon dioxide flushing, deaired water was flushed through the soil specimen under a constant hydraulic gradient, pushing out the carbon dioxide through the top drainage line. To guarantee the effective removal of the gas, the water volume should be twice the estimated volume of voids (Viana da Fonseca et al., 2021). An automatic volume change gauge was utilised to measure the volume of water that passed through the soil specimen. The water that did not remain in the specimen was estimated by collecting this water in a graduated cylinder.

Gas bubbles may remain in the soil skeleton even after flushing. To achieve the full saturation of the soil, the backpressure (BP) was gradually increased under a confinement pressure of 10 kPa. Measurements of Vp and Vs were conducted during BP increments of 50 kPa, corresponding to BP of 0, 50, 100, 150, 200, 250, and 300 kPa. Throughout the BP increments, the ingress of water into the soil specimen was monitored using a volume gauge, and changes in volume were measured by Hall-Effect transducers. This method ensures accurate estimation of Sr at each BP value by calculating the phase relationships (Molina-Gómez et al., 2023).

The soil was considered fully saturated when Vp exceeded 1482 m/s—the Vp of water (Astuto et al., 2023). All soil specimens reported the full saturation condition at the end of testing. The evolution of the Sr was confirmed by the final water content, ω_f, (Viana da Fonseca et al., 2021). To estimate ω_f, the specimens were carefully removed from the cell, avoiding possible loss of soil grains and water, as suggested by Verdugo & Ishihara (1996).

3 RESULTS AND DISCUSSION

Figure 2 displays the typical P- and S-wave signals obtained from BE tests. The analysis of the fist arrival time of seismic waves reveals that the P-wave propagation changes with the variation of Sr, while S-wave propagation remains constant. These results

confirmed that the increment in *Sr* causes a V_P increasing, demonstrating that P-wave is effectively transmitted through the fluid-saturated granular media.

Figure 3 shows the evolution of *Vp* as a function of *Sr* in TP-Lisbon sand. Besides, Figure 3 compares experimental data against theoretical predictions performed based on Biot-Gassmann theory:

$$Vp = \sqrt{\frac{K_{soil} + \frac{4}{3}G_{soil}}{\rho_{soil}}} \quad (1)$$

where K_{soil} is the bulk modulus of the soil (comprising the sum of the bulk moduli of soil grains, K_g, and suspension K_{sus}), G_{soil} is the shear modulus of the soil and ρ_{soil} is the density of the soil. *Vs* measurements were used for estimating the soil stiffness using the shear modulus of the soil ($G_{soil} = \rho_{soil} Vs^2$). ρ_{soil} was estimated by:

$$\rho_{soil} = (1-n)\rho_g + n[(1-Sr)\rho_a + Sr\rho_w] \quad (2)$$

where *n* is the porosity, ρ_{soil} is the density of grains, ρ_a is the density of the air/gas, and ρ_w is the density of the water. In this study, K_g equal to 3.5 GPa was adopted, as suggested by Santamarina *et al.* (2005); Kumar and Madhusudhan (2012). K_f computation involved the bulk modulus of liquid (i.e. water equal to 2.2 GPa) and gas (i.e. carbon dioxide equal to 0.1 GPa).

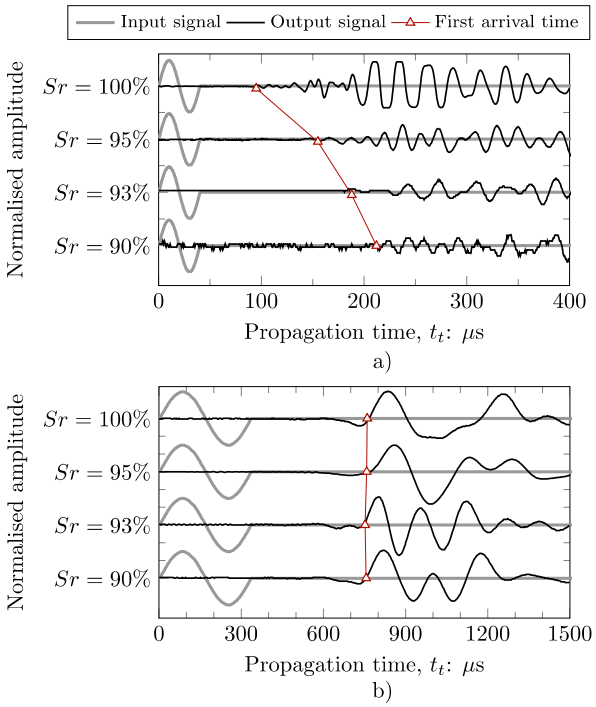

Figure 2. Typical BE signals: a) P-wave; b) S-wave.

Figure 3 demonstrates the effects of *Sr* in V_P due to a good agreement between experimental results and theoretical predictions based on Biot-Gassmann theory. This agreement establishes a solid framework to assess the *Sr* in partially saturated sands, i.e. *Sr* ranging from 80% to 100%. From Figure 3, it can be observed that *Vp* has a gradual change until *Sr* of about 85%. Afterwards, *Vp* sharply increased until converging to a *Vp* value exceeding 1500 m/s. This *Vp* increment was attributed to the partially saturated condition of the soil, where occluded air bubbles are present in the fluid without interacting with the soil grains. In this state, the P-wave propagation is controlled by the fluid instead of the contacts in the granular medium, clarifying the sharp increment in *Vp*, as also observed by Leong and Cheng (2016); Gu *et al.* (2021).

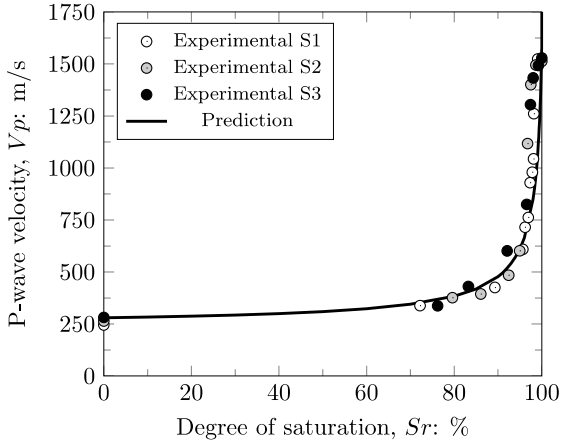

Figure 3. Relationship between V_P and Sr.

Figure 4 demonstrates the effectiveness of the P-wave-based approach by providing a direct comparison between the experimental V_P results and the theoretical V_P values for the same *Sr*. This comparison fits within a difference factor of ±10% for all soil specimens. These results validate that the approach proposed herein can estimate *Sr* with an accuracy well within the ±10% range.

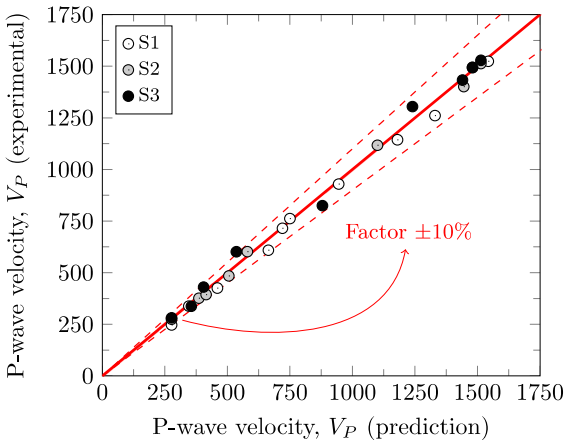

Figure 4. Experimental results vs. predicted values.

4 CONCLUSION

This study has evaluated the use of *Vp* for estimating the degree of saturation in sands, utilising BE testing. Tests involved reconstituted soil specimens of TP-Lisbon sand with a relative density of 30%. The P-wave propagation changes with the *Sr* variation due to the compressibility of the pore fluid type and occluded air/gas bubbles in the soil skeleton. A comparison between experimental results and theoretical predictions based on Biot-Gassmann theory validated this approach. The results offer a versatile method for degree of saturation estimation in sands, demonstrating the effectiveness of P-wave estimation in both laboratory and field testing.

ACKNOWLEDGEMENTS

This work was financially supported by: Base Funding - UIDB/04708/2020 with DOI 10.54499/UIDB/04708/2020 and Programmatic Funding - UIDP/04708/2020 with DOI 10.54499/UIDP/04708/2020 of the CONSTRUCT - Instituto de I&D em Estruturas e Construções - funded by national funds through the FCT/MCTES (PIDDAC). The first author acknowledges the support of FCT, through the grant SFRH/BD/146265/2019. The third author acknowledges the support of FCT in the EXPL/ECI-EGC/1420/2021 project. The fourth author acknowledges the support provided by Natural Sciences and Engineering Research Council of Canada (NSERC), the University of Waterloo.

REFERENCES

Astuto, G., Molina-Gómez, F., Bilotta, E., Viana da Fonseca, A., & Flora, A. (2023). Some remarks on the assessment of P-wave velocity in laboratory tests for evaluating the degree of saturation. *Acta Geotechnica*, 18(2), 777–790. https://doi.org/10.1007/s11440-022-01610-9.

Biot, M. A. (1956). Theory of Propagation of Elastic Waves in a Fluid-Saturated Porous Solid I. Low-Frequency Range. *Journal of the Acoustical Society of America*, 28, 168–178. https://doi.org/https://doi.org/10.1121/1.1908239.

Ferreira, C., Díaz-Durán, F., Viana da Fonseca, A., & Cascante, G. (2021). New approach to concurrent Vs and Vp measurements using bender elements. *Geotechnical Testing Journal*, 44(6), 1801. https://doi.org/10.1520/GTJ20200207.

Gu, X., Zuo, K., Tessari, A., & Gao, G. (2021). Effect of saturation on the characteristics of P-wave and S-wave propagation in nearly saturated soils using bender elements. *Soil Dynamics and Earthquake Engineering*, 145, 106742. https://doi.org/10.1016/J.SOILDYN.2021.106742.

Ishihara, K. (1993). Liquefaction and flow failure during earthquakes. *Géotechnique*, 43(3), 351–451. https://doi.org/10.1680/geot.1993.43.3.351.

Kumar, J., & Madhusudhan, B. N. (2012). Dynamic properties of sand from dry to fully saturated states. *Géotechnique*, 62(1), 45–54. https://doi.org/10.1680/geot.10.P.042.

Leong, E. C., & Cheng, Z. Y. (2016). Effects of Confining Pressure and Degree of Saturation on Wave Velocities of Soils. *International Journal of Geomechanics*, 16(6), D4016013. https://doi.org/10.1061/(ASCE)GM.1943-5622.0000727.

Molina-Gómez, F., & Viana da Fonseca, A. (2021). Key geomechanical properties of the historically liquefiable TP-Lisbon sand. *Soils and Foundations*, 61(3), 836–856. https://doi.org/10.1016/j.sandf.2021.03.004.

Molina-Gómez, F., Viana da Fonseca, A., Ferreira, C., & Caicedo, B. (2023). Experimental Wave-Based Assessment of Liquefaction Resistance for Different Degrees of Saturation. *Geotechnical Testing Journal*, 46(6), 968–985. https://doi.org/10.1520/GTJ20230299.

Molina-Gómez, F., Viana da Fonseca, A., Ferreira, C., & Camacho-Tauta, J. (2020). Dynamic properties of two historically liquefiable sands in the Lisbon area. *Soil Dynamics and Earthquake Engineering*, 132, 106101. https://doi.org/10.1016/j.soildyn.2020.106101.

Naesgaard, E., Byrne, P. M., & Wijewickreme, D. (2007). Is P-Wave Velocity an Indicator of Saturation in Sand with Viscous Pore Fluid? *International Journal of Geomechanics*, 7(6), 437–443. https://doi.org/10.1061/(asce)1532-3641(2007)7:6(437).

Santamarina, J. C., Rinaldi, V. A., Fratta, D., Klein, K. A., Wang, Y.-H., Cho, G. C., & Cascante, G. (2005). A Survey of Elastic and Electromagnetic Properties of Near-Surface Soils. In D. K. Butler (Ed.), *Near-Surface Geophysics* (pp. 71–87). Society of Exploration Geophysicists. https://doi.org/10.1190/1.9781560801719.ch4.

Skempton, A. W. (1954). The Pore-Pressure Coefficients A and B. *Géotechnique*, 4(4), 143–147.

https://doi.org/10.1680/geot.1954.4.4.143.
Tsukamoto, Y., Ishihara, K., Nakazawa, H., Kamada, K., & Huang, Y. (2002). Resistance of partly saturated sand to liquefaction with reference to longitudinal and shear wave velocities. *Soils and Foundations*, 42(6), 93–104. https://doi.org/10.3208/sandf.42.6_93.
Verdugo, R., & Ishihara, K. (1996). The Steady State of Sandy Soils. *Soils and Foundations*, 36(2), 81–91. https://doi.org/10.3208/sandf.36.2_81.
Viana da Fonseca, A., Cordeiro, D., & Molina-Gómez, F. (2021). Recommended Procedures to Assess Critical State Locus from Triaxial Tests in Cohesionless Remoulded Samples. *Geotechnics*, 1(1), 95–127. https://doi.org/10.3390/GEOTECHNICS1010006.
Viana da Fonseca, A., Ferreira, C., & Fahey, M. (2009). A Framework Interpreting Bender Element Tests, Combining Time-Domain and Frequency-Domain Methods. *Geotechnical Testing Journal*, 32(2), 100974. https://doi.org/10.1520/GTJ100974.
Yamashita, S., Kawaguchi, T., Nakata, Y., Mikamt, T., Fujiwara, T., & Shibuya, S. (2009). Interpretation of international parallel test on the measurement of Gmax using bender elements. *Soils and Foundations*, 49(4), 631–650. https://doi.org/10.3208/sandf.49.631.

Proceedings of the XVIII ECSMGE 2024
GEOTECHNICAL ENGINEERING CHALLENGES
TO MEET CURRENT AND EMERGING NEEDS OF SOCIETY
© 2024 the Authors
ISBN 978-1-032-54816-6
DOI 10.1201/9781003431749-109
Open Access: www.taylorfrancis.com, CC BY-NC-ND 4.0 license

ECSMGE 24
XVIII EUROPEAN CONFERENCE ON SOIL MECHANICS AND GEOTECHNICAL ENGINEERING

Characterization of intermediate soils by innovative in-situ testing procedures using Medusa DMT

Caractérisation des sols intermédiaires par des procédures innovantes d'essais in-situ à l'aide de la Medusa DMT

P. Monaco*
University of L'Aquila, L'Aquila, Italy

S. Amoroso
University of Chieti-Pescara, Pescara, Italy; Istituto Nazionale di Geofisica e Vulcanologia, L'Aquila, Italy

A. Chiaradonna
University of L'Aquila, L'Aquila, Italy

D. Marchetti
Studio Prof. Marchetti, Rome, Italy

T.M.H. Le, J.-S. L'Heureux
Norwegian Geotechnical Institute, Trondheim, Norway

**paola.monaco@univaq.it*

ABSTRACT: This paper illustrates early findings obtained using the Medusa DMT/SDMT – the newest fully automated version of the flat/seismic dilatometer – at the benchmark silt test site of Halden, Norway, part of the Geo-Test Sites (NGTS) research infrastructure managed by the Norwegian Geotechnical Institute. The comparison of results obtained by Medusa (S)DMT tests carried out adopting standard and variable penetration/pressurization rates permits to identify some trends in response to different test rates in the silt layers. These preliminary results support the potential of this approach for improving the in-situ characterization of intermediate soils.

RÉSUMÉ: Cet article illustre les premiers résultats obtenus à l'aide du Medusa DMT/SDMT – la version la plus récente entièrement automatisée du dilatomètre plat/sismique – sur le site d'essai de référence (limon) de Halden, Norvège, qui fait partie de l'infrastructure de recherche Geo-Test Sites (NGTS) gérée par Norwegian Geotechnical Institute. La comparaison des résultats obtenus par essais Medusa (S)DMT réalisés en adoptant des taux de pénétration/pressurisation standard et variables permet d'identifier certaines tendances en réponse à des taux d'essai différents dans les couches limoneuses. Ces résultats préliminaires attestent le potentiel de cette approche pour améliorer la caractérisation in-situ des sols intermédiaires.

Keywords: Intermediate soils; in-situ testing; Medusa DMT; benchmark test sites.

1 INTRODUCTION

The Critical Infrastructure (CI) of Europe in the water, energy, urban and transport sector is currently facing major challenges related to climate change, extreme weather, geo-hazards, aging and increased usage in combination with pivotal changes to meet long-term societal goals. Improvements in geotechnical approaches to enhance the resilience of the CI rely significantly on an in-depth understanding of soil behaviour. A major challenge, due to uncertainties in assessing partial drainage effects, is the characterization of intermediate soils (silty sands, silts, sandy silts, and other soil mixtures), frequently encountered in densely populated and risk-sensitive areas. The results presented in this paper were obtained as part of the Transnational Access project JELLYFISh (A Just-released innovativE in-situ soiL testing technoLogY (Medusa DMT/SDMT) For enhancing the resilience of the critical InfraStructure in Europe) funded by H2020-GEOLAB. The project is based on an extensive in-situ testing campaign with the Medusa DMT/SDMT – the newest fully automated version of the flat/seismic dilatometer – carried out in June 2022 in different soil types at four well-known benchmark test sites in Norway: Halden (silt), Onsøy (soft clay), Tiller-Flotten (quick clay), and Øysand (sand). These benchmark sites, largely documented in previous research, are part of the Geo-Test Sites

(NGTS) research infrastructure managed by the Norwegian Geotechnical Institute. In particular, this paper presents early findings obtained from Medusa (S)DMT tests carried out in silts at the Halden test site, adopting both standard and variable penetration/pressurization rate test procedures.

2 MEDUSA SDMT EQUIPMENT AND TEST PROCEDURE

The Medusa DMT (Figure 1) is a self-contained probe able to perform dilatometer tests using a standard blade without the pneumatic cable, the control unit and the gas tank required in the traditional pneumatic DMT. A motorized syringe hydraulically expands the membrane to obtain the DMT *A*, *B*, *C* pressure readings, which are acquired and stored automatically at each test depth. The probe can operate in cableless mode. An optional electric cable may be used to obtain real-time data during test execution. The Medusa SDMT incorporates additional sensors and components (Figure 1) for the measurement of the shear wave velocity, in addition to the DMT measurements. The standard Medusa DMT test procedure is the same as for the traditional pneumatic DMT (ASTM D6635-15; ISO 22476-11:2017(E)), using an internal automated pressurization system instead of an external manually operated pressure source and regulation system. The standard pressurization rate is regulated to obtain the *A*-pressure reading 15 s after start of pressurization and the *B*-pressure reading 15 s after the *A*-pressure reading. The automatic volume-controlled hydraulic pressurization of the membrane is highly repeatable and permits to impose a programmable timing to obtain the pressure readings, i.e., the standard timing or different time intervals corresponding to variable pressurization rates. This capability of the Medusa DMT has prompted its use for performing dilatometer tests adopting variable pressurization rates, in combination with variable penetration rates, to investigate the behaviour of intermediate soils.

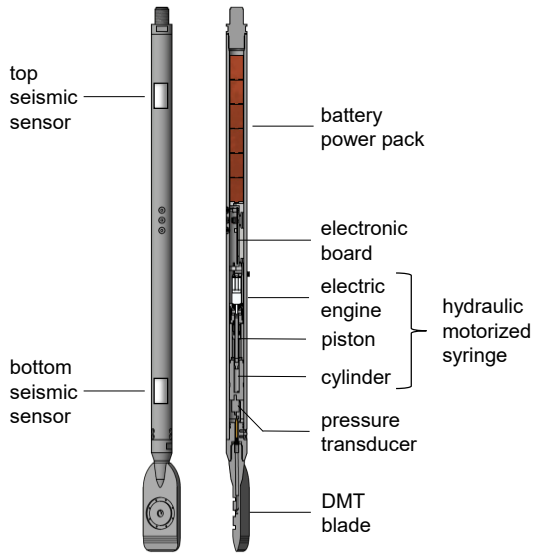

Figure 1. Medusa SDMT equipment.

3 MEDUSA SDMT TESTS AT HALDEN

3.1 Test site conditions

The Halden test site is located in south-eastern Norway, approximately 120 km south of Oslo. This site has been thoroughly characterized by geological, geophysical and geotechnical in-situ and laboratory tests. The stratigraphy of the Halden test site, reconstructed based on all available data (Blaker et al., 2019), includes four soil units down to 20 m:

- Unit I: silty-clayey loose to medium dense sand, extending to about 4.5-5 m depth;
- Units II and III: clayey silt, separated into two soil units based on in-situ and index test results but regarded as the same material with the same geologic origin; the silt extends to about 15-16 m depth and becomes sandier close to this depth;
- Unit IV: low to medium strength clay.

The soil unit weight is approximately 19 kN/m^3 down to 11-12 m depth, and increases to 20 kN/m^3 from there to 20 m depth. The fines content in silt (Units II and III) is generally higher than 80%, slightly decreasing towards the interface with Unit IV. The clay content (particle size < 0.002 mm) is fairly constant at around 8% in Units II and III. The natural water content generally decreases with depth from about 31% at 4 m to about 26% at 16 m depth. The overconsolidation ratio is estimated in the range 1 to 1.3. The undrained shear strength in silt increases from 20-40 kPa at 5 m to 60-90 kPa at 15 m depth. The remoulded undrained shear strength lies around 5-15 kPa, and the sensitivity is around 2-7. The effective friction angle from triaxial tests on block samples lies around 36°, with cohesion $c' = 0$.

3.2 Medusa (S)DMT testing program

The field testing program at Halden (Figure 2) included one Medusa SDMT sounding (HALD02) carried out by the standard procedure and four Medusa DMT soundings (HALD03 – HALD06) carried out adopting variable penetration rates (slower and faster than standard), combined with variable pressurization rates (slower and faster than standard) achieved by regulating different time intervals for the *A* and *B*

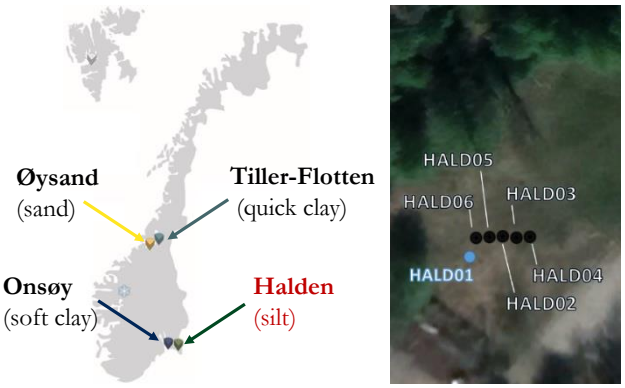

Figure 2. Location of Medusa (S)DMT (HALD02–HALD06) and traditional SDMT (HALD01) at Halden.

Table 1. Summary of Medusa (S)DMT tests at Halden.

Sounding ID	Test type	Penetration rate (mm/s)	Time to A-reading (s)	Time to B-reading (s)
HALD02	standard (baseline)	20	15	15
HALD03	slow rate	2	15	15
HALD04	slow rate/ slow press	2	30	30
HALD05	fast rate	86	15	15
HALD06	fast rate/ fast press	75	7.5	7.5

pressure readings (Table 1). Several Medusa DMTA dissipation tests were also carried out. All Medusa (S)DMT soundings reached a depth of about 19-20 m and were located close to one traditional pneumatic SDMT sounding (HALD01) performed by the NGI in 2018. More details can be found in Monaco et al. (2023).

3.3 Medusa (S)DMT test results

Figure 3 summarizes some significant results obtained from Medusa (S)DMT tests at Halden, in terms of depth profiles of the DMT pressure readings p_0, p_1, p_2 (A, B, C corrected for membrane stiffness), as well as of the material index I_D and the pore pressure index U_D (Marchetti, 1980; Marchetti et al., 2001). To assess the combined effects of both variable penetration and pressurization rate, only the results obtained from the standard "baseline" HALD02 compared with the "slowest" HALD04 (slow rate/slow press) and the "fastest" HALD06 (fast rate/fast press) are shown in Figure 3. The in-situ pore pressure u_0 profile, shown in the p_2 graph, was assumed as non-hydrostatic with a groundwater table at 1.30 m (u_0 = 155 kPa at 20 m depth), based on piezometer measurements. Figure 3 highlights that:

(a) The p_0 obtained using slow penetration/ pressurization rates in silt (Units II and III) are lower than the p_0 obtained using the standard rates. This can be explained considering that in fine-grained soils p_0 (total pressure) incorporates the excess pore pressure Δu induced by blade penetration: the slower the penetration rate, the lower will be Δu, hence p_0. An opposite trend was expected for the p_0 obtained using fast penetration/pressurization rates, as observed by Monaco et al. (2021) in a different silt deposit in Italy. However, at Halden the "fastest" p_0 are nearly coincident with the baseline values suggesting that the standard penetration/pressurization rates impose fully undrained conditions, which do not evolve to "more undrained" using faster rates. Similar considerations apply for p_1.

(b) In sand p_2 closely approximates the in-situ pore pressure u_0, while in clay $p_2 > u_0$ due to Δu induced by blade penetration. Consistently, the p_2 obtained in silt using slow penetration/pressurization rates are lower than the p_2 obtained using the standard rates, reflecting lower Δu induced by penetration. As for p_0, the p_2 from fast penetration/pressurization rates are substantially equal to the baseline p_2.

(c) In sand (Unit I) and clay (Unit IV) the p_0, p_1, p_2 obtained at different penetration/pressurization rates remain substantially unchanged, indicating fully drained or fully undrained response, respectively, under any test conditions.

(d) The material index I_D is an indicator of soil type (clay, silt, sand) which broadly reflects soil behaviour rather than real grain size distribution, while the pore pressure index U_D can help discern between drained, undrained or partially drained soil behaviour (Marchetti et al., 2001). In silt (Units II and III) the slower the penetration/pressurization rate, the more "drained" the test, with lower p_2 and U_D (moving to the left towards the "fully drained" $U_D = 0$ vertical line); accordingly, I_D moves to the right towards the "sand" region. On the other hand, no apparent evolution towards more "undrained" conditions is observed when using faster penetration/pressurization rates.

(e) For the standard test conditions I_D fails to correctly identify the silt Units II and III, which are wrongly classified as "very clayey" clays. Such misinterpretation, sometimes observed in the transition region of silt-mixture soils, is attributed to partial dissipation of the Δu induced by penetration in the time interval from p_0 to p_1. Consequently, p_1 will not be the "proper match" of p_0 and all the parameters proportional to $(p_1 - p_0)$, namely I_D , will be "too low". Partial drainage effects in silts, reflected by I_D values close to zero, are more pronounced in Unit III than in Unit II. Such persistent very low I_D are a "signature" feature, indicative of silts in the "niche" of partial drainage. In such silts, the parameters obtained by common DMT interpretation are misleading.

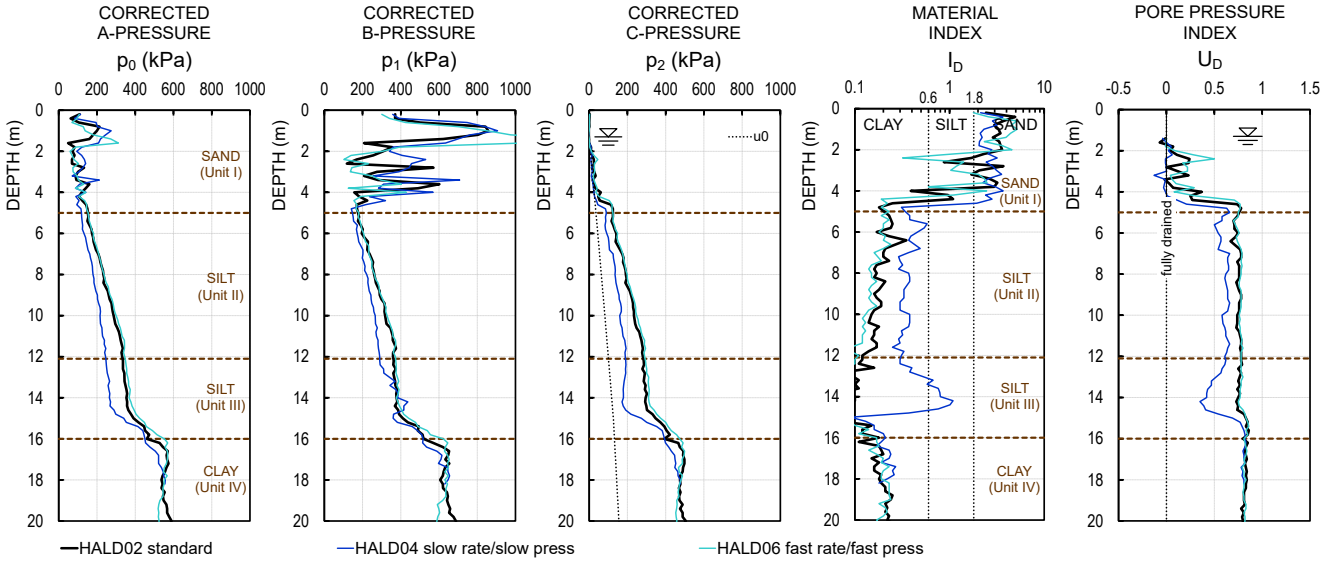

Figure 3. Combined effects of variable penetration and pressurization rates on Medusa (S)DMT results at the Halden test site (schematic soil stratigraphy after Blaker et al., 2019).

4 CONCLUSIONS

The preliminary results obtained at the Halden test site support the potential use of the Medusa (S)DMT for investigating the behaviour of intermediate soils by adopting variable penetration/pressurization rates. At Halden it was found that a slower (than standard) penetration/pressurization rate "shifts" the interpretation towards drained behaviour, while a faster (than standard) penetration/pressurization rate provides the same results obtained using the standard rates. This suggests that in the Halden silt the standard test rates impose fully undrained conditions, which do not evolve to "more undrained" using faster rates as observed in different silt deposits (Monaco et al., 2021). These results, combined with data available from previous investigations at the Halden site (e.g., variable-rate piezocone tests, Carroll and Paniagua, 2018) and from other well-documented silty sites, provide a basis for improving the in-situ characterization of intermediate soils.

ACKNOWLEDGEMENTS

This project has received funding from the European Union's Horizon 2020 research and innovation programme under Grant Agreement No. 101006512.

REFERENCES

ASTM D6635-15 (2015). Standard Test Method for Performing the Flat Plate Dilatometer. ASTM International, West Conshohocken, PA, USA.

Blaker, Ø., Carroll, R., Paniagua, P., DeGroot, D. and L'Heureux, J.-S. (2019). Halden research site: geotechnical characterization of a post glacial silt. *AIMS Geosciences*, 5(2): 184-234. https://doi.org/10.3934/geosci.2019.2.184.

Carroll, R. and Paniagua, P. (2018). Variable rate of penetration and dissipation test results in a natural silty soil. *Proc. 4th Int. Symp. on Cone Penetration Testing CPT'18*, pp. 205-212.

ISO 22476-11:2017(E) (2017). Geotechnical Investigation and Testing – Field Testing – Part 11: Flat Dilatometer Test. International Organization for Standardization, Geneva, Switzerland.

Marchetti, S. (1980). In Situ Tests by Flat Dilatometer. *Journal of Geotechnical Engineering Division*, 106(GT3): 299-321.

Marchetti, S., Monaco, P., Totani, G. and Calabrese, M. (2001). The Flat Dilatometer Test (DMT) in Soil Investigations – A Report by the ISSMGE Committee TC16. *Proc. Int. Conf. Insitu Measurement of Soil Properties and Case Histories*, pp. 95-131, reprinted in *Proc. 2nd Int. Conf. on Flat Dilatometer*, 2006, pp. 7-48.

Monaco, P., Chiaradonna, A., Marchetti, D., Amoroso, S. and Le, T.M.H. (2023). GEOLAB – Transnational Access project JELLYFISh – Field testing of Medusa DMT (Version 0) [Data set]. Zenodo. https://doi.org/10.5281/zenodo.7695740.

Monaco, P., Tonni, L., Amoroso, S., Garcia Martinez, M.F., Gottardi, G., Marchetti, D. and Minarelli, L. (2021). Use of Medusa DMT in alluvial silty sediments of the Po river valley. *Proc. 6th Int. Conf. Geotech. Geophys. Site Characterisation ISC'6*. https://doi.org/10.53243/ISC2020-424.

Proceedings of the XVIII ECSMGE 2024
GEOTECHNICAL ENGINEERING CHALLENGES
TO MEET CURRENT AND EMERGING NEEDS OF SOCIETY
© 2024 the Authors
ISBN 978-1-032-54816-6
DOI 10.1201/9781003431749-110
Open Access: www.taylorfrancis.com, CC BY-NC-ND 4.0 license

ECSMGE 24
XVIII EUROPEAN CONFERENCE ON SOIL MECHANICS AND GEOTECHNICAL ENGINEERING

Performance of cantilever sheet pile walls in sensitive clays: Case study Campus Ullevål

Performance des murs de palplanches en porte-à-faux dans les argiles sensibles: Étude de cas Campus Ullevål

E. Monsås*, S. Oberhollenzer, E.J. Lande, M. Løyland
Norwegian Geotechnical Institute, Oslo, Norway

*egil.monsas@ngi.no

ABSTRACT: The continuous development of urban areas often requires underground constructions close to existing structures and in challenging ground conditions. In Norway, deep excavations in soft marine clays are usually supported by sheet pile walls (SPW) and tieback anchors or internal struts to safeguard the excavation pit and its surroundings until sufficient support is provided by the permanent structure. Cantilever SPWs are rarely used, as deflections are often quite significant. Furthermore, the acting earth pressure distribution, and consequently also the deflection profile, is often difficult to predict. Particularly, the earth pressure distribution and its development over time warrants further investigation.
The research project CURIOUS (Campus Ullevål: Research and Instrumentation Of Underground Structures) was initiated at NGI to study and improve the design of cantilever SPW in sensitive clays. A six-meter-deep excavation pit in Oslo was equipped with an elaborate monitoring system, including strain sensors on the SPW, inclinometers, load cells on temporary struts and geodetic points, to gain a better understanding of the earth pressure development along the retaining structure during the different construction stages. In this paper, results of the instrumentation are presented for different construction phases. The earth pressure distribution acting along the SPW was back calculated based on monitoring data and further compared with predicted distributions.

RÉSUMÉ: Le développement continu des zones urbaines nécessite souvent des constructions souterraines à proximité des structures existantes et dans des conditions de sol difficiles. En Norvège, les excavations profondes dans les argiles marines molles sont généralement soutenues par des murs de palplanches (SPW) et des ancrages de liaison ou des étançons internes pour protéger la fosse d'excavation et ses environs jusqu'à ce que la structure permanente fournisse un soutien suffisant. Les parois de palplanches en porte-à-faux sont rarement utilisées, car les déformations sont souvent très importantes. En outre, la distribution de la pression du sol, et par conséquent le profil de déflexion, sont souvent difficiles à prévoir. En particulier, la distribution de la pression du sol et son évolution dans le temps méritent d'être étudiées plus en détail.
Le projet de recherche CURIOUS (Campus Ullevål: Research and Instrumentation Of Underground Structures) a été lancé au NGI afin d'étudier et d'améliorer la conception des SPW en porte-à-faux dans les argiles sensibles. Une fosse d'excavation de six mètres de profondeur à Oslo a été équipée d'un système de surveillance élaboré, comprenant des capteurs de déformation sur le SPW, des inclinomètres, des cellules de charge sur des étançons temporaires et des points géodésiques, afin de mieux comprendre l'évolution de la pression de la terre le long de la structure de soutènement au cours des différentes étapes de la construction. Dans cet article, les résultats de l'instrumentation sont présentés pour différentes phases de la construction. La distribution de la pression de terre agissant le long du SPW a été calculée sur la base des données de surveillance et comparée aux distributions prédites.

Keywords: Case study; cantilever sheet pile wall; monitoring; sensitive clay.

1 INTRODUCTION

Many parts of Norway are characterized by challenging ground conditions, including soft marine clays (e.g., quick clays). The continuous development of urban areas increases the demand for construction measures in such ground conditions, often close to existing structures. Deep excavations in soft marine clays are usually supported by sheet pile walls (SPW) in combination with tieback anchors or internal struts to safeguard the excavation pit and its surrounding until sufficient support is provided by the permanent structure. Cantilever sheet pile walls have not been widely used in Norway for deep excavations in soft clay, due to the large displacements that occur when not supported by struts or tie-backs anchors.

The design of retaining structures in Norway is performed according to standards such as the Eurocode. The distribution of the acting earth pressure is often assumed based on literature recommendations

(e.g., Terzaghi, 1943), as monitoring results are usually not available for similar boundary conditions. Today, design is most often supported with numerical analyses to predict the system behaviour. However, high-quality data of in-situ and laboratory tests are required to define the input parameter for constitutive soil models. The latter input parameters can further be updated during and after construction by back calculating monitoring results. However, different parameter sets can be used to reproduce the monitoring results.

The construction project Campus Ullevål (Oslo, Norway) offers the opportunity to investigate the performance of cantilever sheet pile walls for excavation support in soft marine clays. An extensive monitoring concept was installed to characterize the deformation behaviour and earth pressure distribution during construction. The results in combination with numerical analyses should further be used to (i) validate existing and (ii) elaborate new design procedures for cantilever sheet pile walls in soft clays.

In this paper, the monitoring setup is presented, and preliminary results of strain sensors on the SPW, inclinometers as well as load cells on temporary struts are shown. Furthermore, the monitoring data is used in the second step to estimate the acting total earth pressure along the SPW at different stages of excavation.

2 CANTILIVER SHEET PILE WALL

Cantilever sheet pile walls are used to support soils for low to moderate depth of excavation. The earth pressures generated at both sides of the retaining structure distribution fulfils the force and moment equilibrium (Gopal Madabhushi and Chandrasekaran, 2005) and were studied by various researchers (e.g., Terzaghi, 1934; Bransby and Milligan, 1975).

The earth pressure theories according to Rankine or Coulomb are usually applied in practical engineering to predict the acting earth pressure along the SPW. However, previous investigations showed that certain deformations are required to mobilize the active and passive earth pressure (Terzaghi, 1934).

For the stability of the excavation, the installation depth of the SPW represents a key design parameter. Various design principles for cantilever sheet pile walls were elaborated by researchers (e.g., Terzaghi, 1934; Padfield and Mair, 1984; Broms, 1995) and were summarized to design guidelines (e.g., Bolton, 1991a, 1991b).

3 CAMPUS ULLEVÅL

3.1 Project description

This case involves construction of a 10-storey building, with two basement storey in Oslo, Norway. For this, an excavation pit up to 7 m deep was required. Due to the location in urban environment close to existing structures, a retaining structure was designed and installed to support the excavation. The retaining structure was comprised by an internally supported 15 meter deep floating SPW. At a final stage, the SPW wall cantilevered up to 7 m from a concrete base slab. During excavation, the SPW was supported internally with ground reinforcement.

3.2 Ground conditions

The ground surface is nearly flat at the construction site, ranging between +97.1 and +98.3 m above the sea level. The top layer, composed of fill material and dry crust clay, shows a thickness of 1 to 2 m. A medium stiff to stiff, low-sensitive clay of 6 to 7 m thickness is situated below the top layer and overlays a soft to medium-stiff quick clay down to bedrock. The clay is interbedded by silt and sand layers (between +83 m down to bedrock) in the northern part of the site. These sand and silt layers can range in thickness from a few cm to 2 m. The ground water table was situated 1 to 1.5 m below the original terrain during the investigations.

The typical unit weight for the clay is 19.3 kN/m^3, and a water content around 30 %. Undrained shear strength c_u^A varies from 75 kPa in the dry crust, before falling to a bottom plateau around 40 kPa, before rising linearily 2.5 kPa/m from approx. 10 m depth.

3.3 Excavation work

The final excavation depth is situated at +91.4 m, approx. 7 m below the original terrain. The working steps for excavation is illustrated in Figure 1 and can be summarized as follows:

I. The sheet pile profiles (type AZ17-700) were driven 14.5 m into the soil and approx. 1 m top soil was excavated. Soil improvement with *lime-cement (*LC*)* was installed to support the excavation. The LC was installed in a ribbed pattern perpendicular to the SPW (lengths and depths of individual ribs amount to 20 m). The LC ribs are spaced approx. 3.5 m apart (see Figure 2) and are composed of overlapping columns (Ø600 mm).
II. The soil in the central part of the pit was excavated down to the final level (7 m below original ground surface). The SPW was supported

during excavation by a soil berm (4 m wide plateau, 1:1.5 inclination). Struts and walers were installed approx. 0.5 m below original terrain. The strut is disposed approx. 23° and further connected to a concrete slab at the excavation floor.

III. The berms supporting the SPW were excavated, and the slab was extended and cast into contact with the SPW. This work was carried out in small sections of 6 m width and symmetrically in both sides of the construction site, ensuring global stability of the concrete slab.

IV. Struts and walers were removed, leaving the SPW cantilevered from the concrete slab.

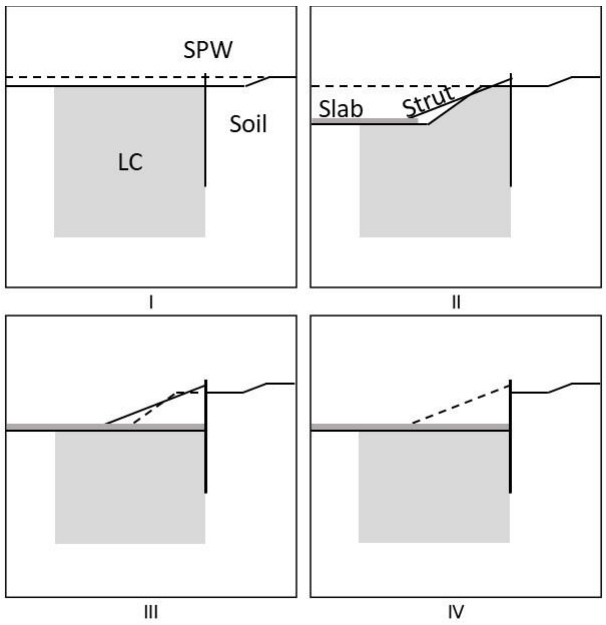

Figure 1. Working sequence of the excavation. Dashed lines indicate the excavation or removal of struts prior to a given stage.

3.4 Instrumentation

The monitoring concept is composed of *fiber optic strain gauges* (FOSG) attached to the SPW; three *inclinometers* (INC) installed on the soil side of the SPW; and tracking of three *geodetic points* (GEO) along the top of the SPW. For an overview of the installed instrumentation, reference is made to Figure 2. Further instrumentation was installed at the site but not further discussed in this paper.

The deformation behaviour of the SPW and the adjacent soil was measured by three inclinometers and geodetic points tracked by automatic surveying equipment. Two inclinometers, INC1 and INC2, were installed immediately behind the SPW. INC3 was installed 5 m behind the SPW (see Figure 2).

The deflection curve of the SPW was measured with fiber-optic sensors. Two sensors, one on each flange of a single Z-profile, measured the strains along the SPW at an interval of 0.5 m (see Figure 2).

The instrumentation shown in Figure 2 can be summarized as follows:

① Geodetic point, GEO1 GEO2 and GEO3 are placed at equivalent locations further along the SPW.
② Fiber optic strain gauges on the SPW.
③ Inclinometer, INC1 – 0.5 m resolution, biaxial
④ Inclinometer, INC2 – 2.0 m resolution, uniaxial
⑤ Inclinometer, INC3 – 2.0 m resolution, uniaxial

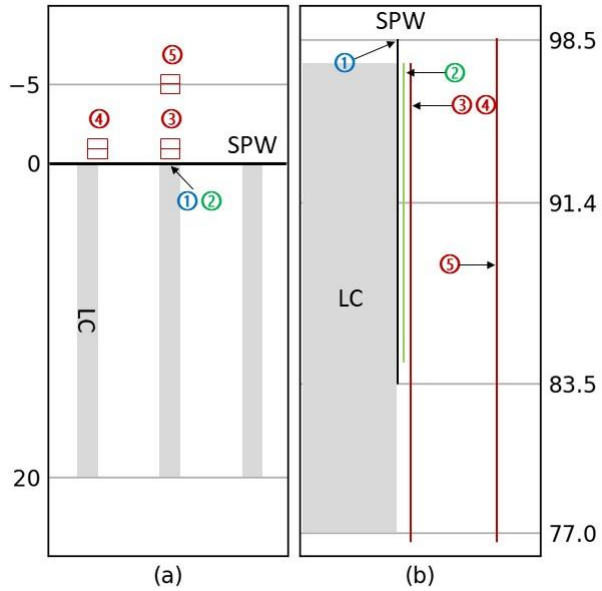

Figure 2. Overview of the instrumentation setup. (a): Plan view, (b): Section view. Annotative colors: blue = geodetic points, green = fiber optics strain gauges, red = inclinometers.

4 RESULTS

4.1 Deformations

Figure 3 shows the measured displacements of the inclinometers (INC1, INC2, INC3) and geodetic points (GEO1, GEO2, GEO3) for three construction stages, namely excavation in the central part of the building pit (see II in Figure 1), full excavation with struts installed (see III in Figure 1), and the cantilever stage (see IV in Figure 1). It should be mentioned for stage IV that the measurements were taken immediately after removing the struts and installing the foundaton slab. It can be seen that the deformations increase with the excavation process. While INC1 and INC2 (both situated behind the SPW) are in good agreement, INC3 shows smaller displacements in all three excavation stages (see Figure 3). While the maximum displacements of INC1 and INC2 amounts

to approx. 150 mm in stage IV, only 65 mm head displacements was measured at INC3. The results of the geodetic points show a wide scatter (stage II: 26 – 38 mm, stage III: 50 – 130mm and stage IV: 135 – 210 mm), leading to a poor agreement with INC1 and INC2, both installed directly behind the SPW. While GEO2 and GEO3 show similar trends in phases III and IV, the displacements of GEO1 are significantly larger in the latter phases.

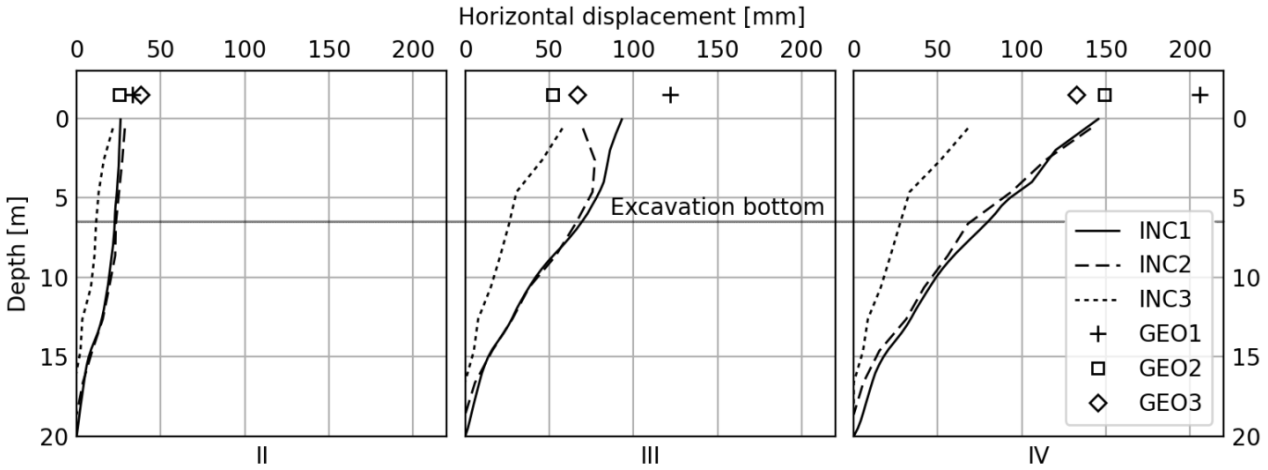

Figure 3. Measured deflection of the soil and SPW at different stages of excavation. (II) partial excavation, (III) full excavation with struts installed, (IV) cantilevered stage.

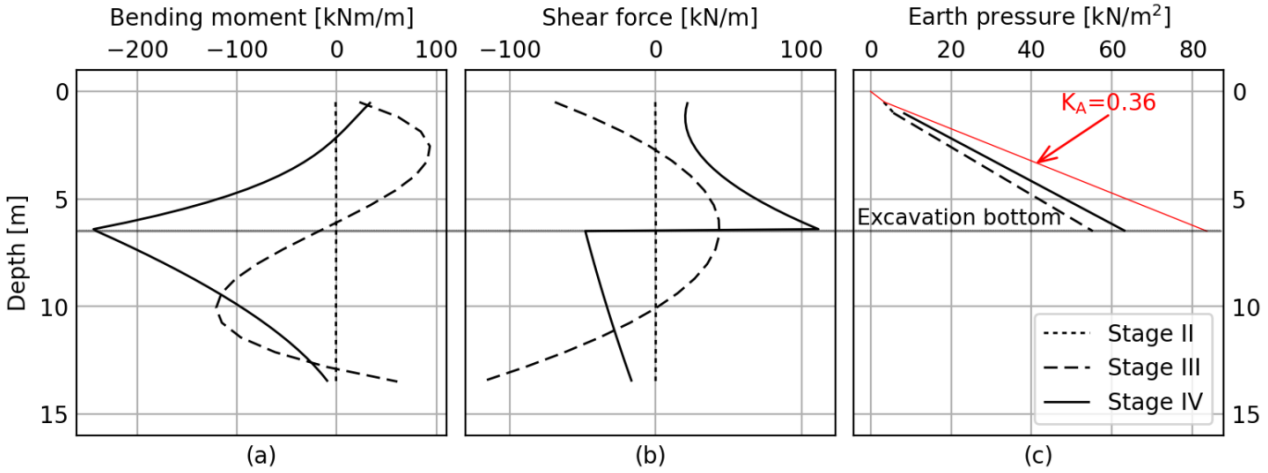

Figure 4. Structural forces along the SPW derived from FOSG monitoring data. (a): Bending moment (b): Shear force (c): Earth pressure

4.2 Structural forces and earth pressure

The bending moments M, the shear forces V and the acting earth pressure along the SPW, all derived from the measured deflection curve κ from FOSG data, are shown in Figure 4. The construction stages II, III and IV, defined in Figure 1, are indicated by different line strokes. The deflection curve κ was derived by fitting a 3rd degree polynomial to the strain measurements. For the cantilevered system in stage IV, the deflection curve was composed by two 3rd degree polynomials joined at the excavation bottom, to fit better with the expected profile. The bending moments *M* were estimated according to Equation (1) by assuming linear elastic beam theory:

$$M = -EI \cdot \kappa \quad (1)$$

where *EI* represents the bending stiffness (76.08 MNm²/m for AZ17-700). The shear forces *V* and the acting earth pressures *p* represent the first and second derivative of the moment curve, respectively. The earth pressure is only shown in Figure 4 (c) for full excavation stages (III and IV), and only down to the excavation floor. The active earth pressure, calculated according to Rankine (1856) assuming a friction angle φ = 28°, is additionally given in red.

M and *V* approximate zero for stage II, as no defection of the SPW was measured. An S-shaped bending moment distribution was observed after excavating the berms (stage III). The derived earth

pressure shows an increase over depth, albeit slightly smaller compared to the calculated active earth pressure according to Rankine theory (1856). The maximum moment is observed at the excavation bottom after removing the struts and extending the foundation slab (see solid, black line in Figure 4 (a). The kink in the moment curve leads to a corresponding discontinuous shear force profile. The earth pressure profile (by definition, a straight line with the approach used in this paper) increases slightly in stage IV compared to stage III but remains smaller than the estimated active earth pressure.

5 DISCUSSION

The displacements of the geodetic survey points (GEO1, GEO2, GEO3, installed at the SPW) and the head displacements of inclinometers (INC2, INC3, installed close to the SPW) show a certain scatter. Different observations are discussed in the following:

- The measured displacements at the upper part of INC1 and INC2 show a difference at stage III, as the SPW was only partly shimmed to the waler at this stage. While the single sheet pile was not supported by the waler and strut close to INC1, a support is given at INC2 (see Figure 3,III). The deflection curve for INC1 resembles a cantilevered system, as opposed to INC2, which clearly shows the effect of the strut and waler. At stage IV, where the gap between SPW and waler was closed, both inclinometer measurements are in good agreement.
- The bottom of the inclinometers is not fully fixed as they are situated on top of bedrock, enabling horizontal displacements without measuring deflections. As GEO2 and GEO3 show a good agreement with results of INC1 and INC2 it is assumed that movements at the inclinometer foot can be neglected.
- It is assumed that the large deviation of GEO1 from INC1 and INC2 cannot be related to measurement inaccuracy only (see Figure 3,III and IV). It must be further investigated whether human influence or other reasons cause this deviation.

Contrary to expectation, the bending moment M and shear force V do not converge to 0 at the top of the SWP for the cantilevered system (see stage IV in Figure 4). It is assumed that the fiber optic strain gauges were influenced by thermal or mechanical effects. Exposing the sensors to high heat while removing the walers with blowtorches could affect the measurements. Mechanical effects such as bending of the SPW can be caused during the construction work. It is feasible that other causes affecting the readings can also be present.

A spurious earth pressure profile is derived when including the topmost strain measurement datapoint. Therefore, the topmost datapoint were neglected when deriving the profiles shown in Figure 4 (c).

The derived acting earth pressure profile is increasing from stage III to stage IV. Typically, as deflections outwards increase, the earth pressure is expected to decrease. One possible explanation might be related to the consolidation process, as the clay behind the SPW progresses into a partially drained state. This explanation must be further investigated.

6 CONCLUSION

The performance of cantilever sheet pile walls in soft Norwegian clays is investigated within the research project CURIOS. An extensive monitoring concept, including inclinometers, geodetic points and fiber optic strain gauges, was installed to study the displacement behaviour and the acting earth pressure along the SPW.

This paper presents results of the instrumentation for different stages of excavation. Furthermore, results of fiber optic strain gauges are used to calculate structural forces acting on the sheet pile wall as well as the acting earth pressure. The results indicate that the derived earth pressure is smaller compared to the active earth pressure, derived according to Rankine (1856).

Further analyses of the measured data are required to characterize the deformation behaviour, the structural forces, and the acting earth pressure for different stages, considering consolidation processes. In a second step existing design procedures for cantilever sheet pile walls will be validated and/or revised for Norwegian, soft clays.

ACKNOWLEDGEMENTS

The authors are grateful for the funding provided by the Research Council of Norway (RCN), through the public basic funding programme for research institutes. Further, the authors thank contractors Skanska and E-Service as well as NGI's instrumentation division, for their cooperation and expertise making this project possible.

REFERENCES

Bransby, P.L. and Milligan, G.W.E. (1975). Soil deformations near cantilever sheet pile walls. *Geotechnique*, https://doi.org/10.1680/geot.1975.25.2.175

Bolton, M.D. (1991a). Geotechnical stress analysis: A possible approach for cantilever retaining walls on spreap foundations. TRRL Report No. 271, United Kingdom.

Bolton, M.D. (1991b). Geotechnical stress analysis for bridge abutment design. TRRL Report No. 270, United Kingdom.

Broms, B.B. (1995). Design of sheet pile walls. Foundation engineering, Geotexts & Publications.

Gopal Madabhushi, S.P. and Chandrasekaran, V.S. (2005). Rotation of Cantilever Sheet Pile Walls. *Journal of Geotechnical and Geoenvironmental Engineering*, https://doi.org/10.1061/(ASCE)1090-0241(2005)131:2(202)

NS-EN 1997-1:2004+A1+NA (2020). Eurocode 7 – Geotechnical design, Part 1: General rules. Standard Norge.

Padfield, C.J. and Mair, R.J. (1984). The design of propped cantilever walls embedded in stiff clays. Report No. 104. CIRIA (Construction Industry Research and Information Association), London.

Rankine, W.J.M. (1856). On the stability of loose earth. Philosophical Transactions of the Royal Society of London, 147:9-27.

Terzaghi, K. (1934). Large retaining wall tests. I. Pressure of dry sand. *Engineering News-Record*, 85(1):136-140.

Terzaghi, K. (1943). *Theoretical Soil Mechanics.* John Wiley & Sons.

Proceedings of the XVIII ECSMGE 2024
GEOTECHNICAL ENGINEERING CHALLENGES
TO MEET CURRENT AND EMERGING NEEDS OF SOCIETY
© 2024 the Authors
ISBN 978-1-032-54816-6
DOI 10.1201/9781003431749-111
Open Access: www.taylorfrancis.com, CC BY-NC-ND 4.0 license

ECSMGE 24
XVIII EUROPEAN CONFERENCE ON SOIL MECHANICS AND GEOTECHNICAL ENGINEERING

Morphological characterization of grain-scale sphericity using 2D x-ray microtomography images

Caractérisation morphologique de la sphéricité à l'échelle des grains à l'aide d'images de microtomographie à rayons x 2D

T.K. Moura*, L.C.S.M. Ozelim
University of Brasilia, Brasília, Brazil

G.M. Alelvan
Federal University of Minas Gerais, Belo Horizonte, Brazil

T.D. Rosa
National Department of Transport Infrastructure, Brasília, Brazil

M.D.T. Casagrande
University of Brasilia, Brasília, Brazil

**thais.moura@aluno.unb.br*

ABSTRACT: Geotechnical engineering has traditionally used laboratory or in situ testing to determine soil properties. With the advancement of computational techniques and data processing performances, new possibilities have been investigated. In the context of morphological and geometric characterization on a grain scale, X-ray computed tomography (μCT) has served as an input for determining these parameters. The challenge still lies in standardizing the analysis methodologies into an appropriate and applicable approach for larger groups of granular materials. In this context, this article aims to propose a new algorithm implemented in Python to determine the overall sphericity classification of soil samples through a computational tool that analyses high-resolution particle-scale images from microtomography tests. The focus of this research is on performing the morphological analysis of the sphericity of particles using 2D images. The code was implemented in an open-source programming language and its applicability has been shown for an uncontaminated sand sample, based on experimental results. This method allows for more accurate determination of soil parameters and has the potential to reduces operational costs related to some laboratory tests.

RÉSUMÉ: L'ingénierie géotechnique utilise traditionnellement des essais en laboratoire ou in situ pour déterminer les propriétés du sol. Avec les progrès des techniques informatiques et des performances de traitement des données, de nouvelles possibilités ont été étudiées. Dans le contexte de la caractérisation morphologique et géométrique à l'échelle du grain, la tomographie à rayons X (μCT) a servi d'intrant pour la détermination de ces paramètres. Le défi consiste toujours à normaliser les méthodologies d'analyse en une approche appropriée et applicable à des groupes plus importants de matériaux granulaires. Dans ce contexte, cet article vise à proposer un nouvel algorithme implémenté en Python pour déterminer la classification globale de la sphéricité des échantillons de sol par le biais d'un outil informatique qui analyse les images haute résolution à l'échelle des particules provenant des tests de microtomographie. Cette recherche se concentre sur l'analyse morphologique de la sphéricité des particules à l'aide d'images 2D. Le code a été mis en œuvre dans un langage de programmation libre et son applicabilité a été démontrée pour un échantillon de sable non contaminé, sur la base de résultats expérimentaux. Cette méthode permet une détermination plus précise des paramètres du sol et a le potentiel de réduire les coûts opérationnels liés à certains tests de laboratoire.

Keywords: Microtomography; sphericity; grain-scale; image processing; python.

1 INTRODUCTION

In pursuit of solving problems and improving results, engineering has evolved and benefited from technology to enhance and optimize processes and outcomes. In this context, geotechnical engineering may encounter situations of uncertainty and variability in laboratory investigations, which need to be addressed in order to minimize or eliminate errors in soil property measurements. These errors, as indicated by Vanmarcke (1977), constitute one of the three sources of uncertainties in soil structure characterization, in addition to knowledge gaps, as outlined by Lacasse and Nadim (1996), and parameter

uncertainty due to human errors or deficiencies in the equipment used to determine soil properties, as stated by Morgenstern (1995).

One of the alternatives for mitigating the impact of these sources of uncertainty is the use of equipments with pore-scale accuracy for geometric particle characterization, which can reveal the soil structure through computational procedures such as the processing and analysis of X-ray microtomography images. The interest of geotechnical engineering in obtaining these characterizations is particularly significant in the study and prediction of soil infiltration capacity, a crucial factor in engineering solutions such as stormwater management in urban centers, peak flow reduction, and contamination plume studies (Durand et al., 2012), as well as the study of micro-scale mechanical behavior, such as particle crushing and rearrangement (Cheng et al., 2019). Specifically regarding geometric sphericity characterization, it plays a significant role in influencing anisotropy levels (Oboudi et al., 2016), experimental effects on mechanical strength (Casagrande, 2005), and drag coefficient in particle-fluid systems (Mendes and Melo, 2011).

Therefore, this paper aims to propose an alternative approach involving the use of microtomography images combined with open-source image processing codes, aiming for reduced human interference and consequently minimizing errors and rework, saving time and effort in obtaining sphericity measurements.

2 MATERIALS AND METHODS

In this article, the study material consisted of microtomography images from Zubeldia (2013). These images were obtained from common construction sand in the Federal District, supplied by the Geotechnical Laboratory of the University of Brasília, and were described by the author as pure and poorly graded sand according to the Unified Soil Classification System (USCS). Specimens were molded in Polymerase Chain Reaction (PCR) tubes and microtomographed using the Sky Scan 1172, producing 610 2D images (slices) with a resolution of 5.94 μm per pixel.

From the 2D images generated on the Sky Scan 1172 microtomography machine, the code available at https://github.com/thaiskogui/ECSMGE24 was created and executed, which uses open-source computer vision Python libraries such as OpenCV, Pillow, Scikit-Image as well as other libraries such as NumPy, Matplotlib and Pandas, to identify the sphericity of particles. In short, the algorithm-covers the following steps: pre-processing of 2D images; particle segmentation; and calculation of the sphericity parameter in 2D images according to Rittenhouse (1943).

During the preprocessing of 2D images, GaussianBlur filter was applied to minimize noise and maintain the main structures of the images, yielding better results for global image thresholding using the Otsu method. The Otsu method determines an ideal automatic threshold value from histogram analysis, separating the foreground elements (particles identified as white) from the background (black).

Following the thresholded image obtained during preprocessing, particle segmentation was performed using the Watershed segmentation technique. This technique is particularly useful for cases of overlapping or closely adjacent objects, which are often observed in the 2D microtomography images in this study due to the proximity of sand particles. After segmentation, each particle was individually identified and assigned a unique identifier. All these previous steps are exemplified in one of the 2D images as shown in Figure 1.

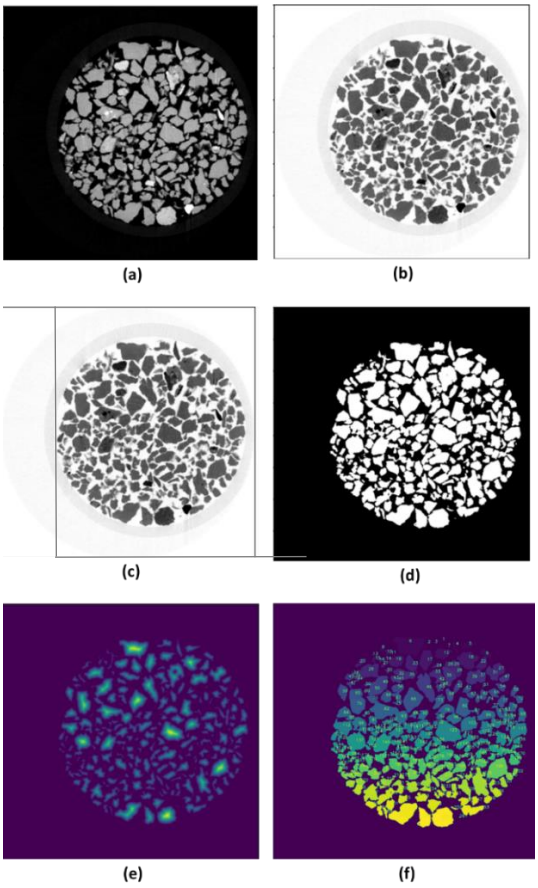

Figure 1. Image processing flowchart (a) original 2D image; (b) inverted image matrix; (c) GaussianBlur filter implementation; (d) binarization by Otsu method; (e) watershed implementation; and (f) numbered distinction of each grain.

The last step of calculating the sphericity parameter in 2D images was based on the definition presented by Rittenhouse (1943), who defined sphericity as the relationship between the diameter of the circle with an area equal to the projection of the particle and the diameter of the smallest circumscribed circle to the particle. This relationship can also be represented by the ratio between the area of the grain and the area of the smallest circle circumscribed by the grain, as demonstrated in:

$$S_i = \frac{d_{pp,i}}{d_{sc,i}}\ 100\% = \frac{\left(\frac{\pi d_{pp,i}^2}{4}\right)}{\left(\frac{\pi d_{sc,i}^2}{4}\right)} 100\% = \frac{A_{g,i}}{A_{sc,i}} \qquad (1)$$

where Si (dimensionless) is the sphericity of the grain; dpp,i (L) is the diameter of the circle with an area equal to the projection of a particle; dsc,i (L) is the diameter of the smallest circle circumscribed in a particle; Ag,i (L^2) is the area of grain i; and Asc,i (L^2) is the area of the smallest circle circumscribed by a grain i.

To minimize the computational cost, the relationship between areas in Equation 1 was used as an equivalent to the definition of Rittenhouse (1943), which indicated that the degree of sphericity varies from 0 to 1, taking values of 0.45 as a practical reference for more elongated particles and 0.97 for very spherical particles.

It is worth noticing that recent studies indicated that 2D measure can reasonably approximate the real 3D sphericity, using as projection direction called “plane of greatest stability” (Rorato et al., 2019). Other measures, such as perimeter sphericity, could be also considered, but are not considered in the present paper for simplicity and since the main goal is to provide a open-source implementation of the general procedure, not of a particular assessment method.

However, it was possible to find, in each of the 2D microtomographic sections, the sphericity of each identified grain, generating data for analysis of the sphericity frequency distribution of the specimen and its representative average sphericity.

3 RESULTS AND DISCUSSION

After completing the three steps (pre-processing, particle segmentation and calculation of the sphericity parameter), 152,028 sand grain particles were identified, each with their respective particle area data, smallest circle circumscribed to the particle and calculation of sphericity according to Equation 1.

From the data on the sphericities of each grain and a previous treatment of the data with the identification and removal of outliers, the following descriptive statistics in Table 1 were obtained.

Table 1. Descriptive statistics of sphericity.

Parameter	Value
Mean	0.535516
Standard deviation	0.102641
Minimum	0.299322
Quartile 1	0.461724
Quartile 2 (Median)	0.540525
Quartile 3	0.612649
Maximum	0.758905

Hence, it was possible to evaluate the frequency distribution of the sample's sphericities, as well as its cumulative distribution, respectively represented in Figure 2 and Figure 3.

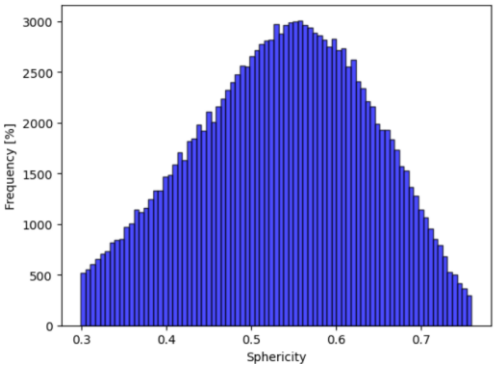

Figure 2. Distribution of sphericity frequency.

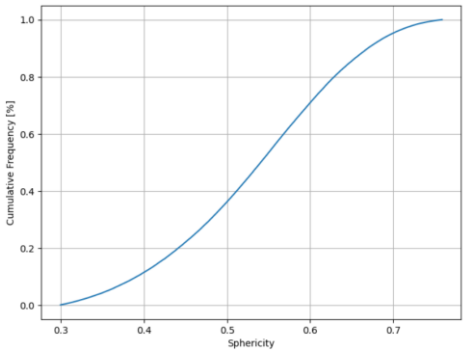

Figure 3. Cumulative distribution of sphericity.

To classify the sphericity of the sample, the sphericity index intervals mentioned by Nunes et al. (2021) as shown in Table 2.

Table 2. Classification by sphericity interval.

Classification	Sphericity interval
Lamellar/elongated	≤ 0.5
Low sphericity	0.5 – 0.6
Medium sphericity	0.6 – 0.8
High sphericity	> 0.8

Thus, considering Table 2 and the sample in general, the average sphericity obtained of approximately 53% indicates a low sphericity classification.

4 CONCLUSIONS

As shown in the present work, it is possible to infer the sphericity parameter based on 2D images, reducing procedural efforts in laboratory tests, simply by scanning the sample using x-ray microtomography and executing the suggested algorithm.

It is important to highlight that prior treatment of sphericity data is recommended, such as the identification and removal of outliers, to obtain less distortion in the results of descriptive statistics, since in image processing, the singular non-identification of a particle may occur due to joining it with another very close one, or also the creation of particles from noise in the image.

Furthermore, it is important to highlight that 2D analysis has inherent limitations and is a simplification of the real 3D nature of the soil, however, there are correlations between 2D and 3D analysis algorithms, achieving the objective of this article of presenting a simple procedure based one theoretical and computational approaches. Future works may address the generalization of the procedures hereby presented, incorporating other 2D sphericity assessment algorithms as well as 3D analyses.

REFERENCES

Casagrande, M.D.T. (2005). Comportamento de Solos Reforçados com Fibras Submetidos a Grandes Deformações. Behavior of Fiber Reinforced Soils Subjected to Large Deformations. In portuguese. Doctoral Thesis. Federal University of Rio Grande do Sul. Available at: https://lume.ufrgs.br/handle/10183/5345.

Cheng, Z., Wang, J., Coop, M.R. and Ye, G. (2019) A miniature triaxial apparatus for investigating the micromechanics of granular soils with in situ X-ray micro-tomography scanning. Frontiers of Structural and Civil Engineering, 14: 357-373. Doi: 10.1007/s11709-019-0599-2.

Durand, R., Farias, M.M. and Carvalho, J. C. (2012). Tópicos sobre infiltração: teoria e prática aplicada a solos tropicais. Topics on infiltration: theory and practice applied to tropical soils. In portuguese. Faculty of Technology, University of Brasília. Brasília, Brazil, 287-308.

Lacasse, S. and Nadim, F. (1996). Uncertainties in Characterizing Soil Properties – Plenary paper. In Proceedings of ASCE Special Technical Publication No. 58: Uncertainty in the Geologic Environment-From Theory to Practice. Madison, Wisconsin, USA, 1: 49–75.

Mendes, L.V.R. and Melo, T.M. (2011). Avaliação da Esfericidade como um Fator de Forma na Interação Partícula-Fluido. Assessment of Sphericity as a Shape Factor in Particle-Fluid Interaction. In portuguese. Federal University of Rio de Janeiro, Rio de janeiro, RJ. Available at: https://pantheon.ufrj.br/handle/11422/18706.

Morgenstern, N. R. (1995). Managing Risk in Geotechnical Engineering. Proceeding of the 10th Pan American Conference on Soil Mechanics and Foundation Engineering, Guadalajara, Mexico, 4: 102-126.

Nunes, J. J. B. C., Teixeira, A. M. A. J. and Saraiva, R. M. D. C. (2021) Caracterização morfológica do agregado leve de argila expandida brasileira com utilização do AIMS. Morphological characterization of lightweight Brazilian expanded clay aggregate using AIMS. In portuguese. Ambiente Construído, Porto Alegre, Brazil. 21 (3): 213-227. http://dx.doi.org/10.1590/s1678-86212021000300547.

Oboudi, M., Pietruszczak, S. and Razaqpur, A.G. (2016). Description of Inherent and Induced Anisotropy in Granular Media with Particles of High Sphericity. International Journal of Geomechanics, 16 (4). https://doi.org/10.1061/(ASCE)GM.1943-5622.0000635.

Rittenhouse, G. (1943). A visual method of estimating two-dimensional sphericity. Journal of Sedimentary Petrology, 13: 79-81. Available at: https://api.semanticscholar.org/CorpusID:127241668.

Rorato, R., Arroyo, M., Andò, E. and Gens, A. (2019) Sphericity measures of sand grains, Engineering Geology, 254: 43-53. https://doi.org/10.1016/j.enggeo.2019.04.006.

Vanmarcke, E. H. (1977). Probabilistic Modeling of Soil Profiles. Journal of the Geotechnical Engineering Division, ASCE, 103 (11): 1227-1246. https://doi.org/10.1061/AJGEB6.0000517.

Zubeldia, E. H. (2013). Uso dos autômatos celulares bidimensionais e imagens tomográficas na geração de meios porosos artificiais. Use of two-dimensional cellular automata and tomographic images in the generation of artificial porous media. In portuguese. Masters dissertation. University of Brasilia. Available at: http://repositorio.unb.br/handle/10482/15280.

Proceedings of the XVIII ECSMGE 2024
GEOTECHNICAL ENGINEERING CHALLENGES
TO MEET CURRENT AND EMERGING NEEDS OF SOCIETY
© 2024 the Authors
ISBN 978-1-032-54816-6
DOI 10.1201/9781003431749-112
Open Access: www.taylorfrancis.com, CC BY-NC-ND 4.0 license

ECSMGE 24
XVIII EUROPEAN CONFERENCE ON SOIL MECHANICS AND GEOTECHNICAL ENGINEERING

Accuracy of in-situ assessment of soil density and moisture content using the non-nuclear method

Précision de l'évaluation in situ de la densité et de la teneur en eau du sol à l'aide de la méthode non nucléaire

J. Neves*
CERIS, Instituto Superior Técnico, Universidade de Lisboa, Lisboa, Portugal

C. Lopes
Construções Gabriel A.S. Couto S.A., Vila Nova de Famalicão, Portugal

C. Silva
RELACRE, Lisboa, Portugal

**jose.manuel.neves@tecnico.ulisboa.pt*

ABSTRACT: The in-situ determination of the conditions of the materials in the pavement and subgrade layers (density and water content) is essential in quality control. In addition to the traditional tests of the sand replacement method (density) and the oven drying method (moisture content), the nuclear method based on the gamma-densimeter device has been one of the most used due to its ease and quick operation. Non-nuclear alternative methods can be used, such as the electromagnetic method contemplated in the ASTM D7830/D7830M. The paper presents a study on the potential application of this method to quality control of earthworks, road pavement layers (unbound granular layers of base and sub-base) and subgrade. The paper describes an application of this test method to the case of soil, including a comparative analysis with other test methods, such as sand replacement and nuclear methods. The study's main results confirmed the method's feasibility and identified aspects of its practical application.

RÉSUMÉ: La détermination in situ des conditions des matériaux dans les couches de chaussée et de fondation (densité et teneur en eau) est essentielle au contrôle qualité. Outre les tests traditionnels de la méthode de remplacement du sable (densité) et de la méthode de séchage au four (teneur en humidité), la méthode nucléaire basée sur le dispositif gamma-densimètre a été l'une des plus utilisées en raison de sa facilité et de sa rapidité d'opération. D'autres méthodes alternatives non nucléaires peuvent être utilisées, comme la méthode électromagnétique envisagée dans l'ASTM D7830/D7830M. L'article présente une étude sur l'application potentielle de cette méthode au contrôle de la qualité des travaux de terrassement, des couches de chaussée routière (couches granulaires non liées de base et de sous-couche) et du sol de fondation. L'article décrit une étude sur l'application de cette méthode d'essai au cas d'un sol, comprenant une analyse comparative avec d'autres méthodes d'essai, telles que la méthode de remplacement du sable et la méthode nucléaire. Les principaux résultats de l'étude ont confirmé la faisabilité de la méthode et identifié les aspects de son application pratique.

Keywords: Density; moisture content; non-nuclear method; quality control.

1 INTRODUCTION

Compaction is a process of great relevance in geotechnical structures, such as hydraulic works (embankment dams), retaining structures (earth retaining walls) and transport infrastructures (roads, railways, and airfields construction). Compaction is fundamental for the adequate behaviour of the structures (resistance, deformability, permeability). Therefore, compaction quality control is of relevant importance and the most common procedures are based on the direct assessment of the density and water content of the compacted layers. In general, current specifications establish compaction acceptance criteria based on the maximum limit of the variation range of water content in relation to the optimum value and the minimum limit of dry density, normally expressed in terms of the degree of compaction established for maximum dry density. Those limits should consider the nature of the material, the type of application and the compaction equipment.

There are several methods that can be used to evaluate in situ density and water content. Over time, the sand replacement method, in conjunction with the determination of water content, has been considered the reference method in determining dry unit weight of

soils in natural conditions or after compaction. However, other methods were developed with the aim of allowing the non-destructive in-place quality control more adjusted to the construction and continuous monitoring of the quality of roads or other infrastructure works (Wang et al., 2022), including intelligent compaction (Kumar et al., 2016, Chen et al., 2023), and artificial intelligence (Wang et al., 2022, Wang et al., 2023).

The nuclear method has been one of the most used in Portugal. This method uses a nuclear density gauge, which is a radioactive equipment composed of gamma ray and neutron sources that allows direct measurement of density and water content. However, the current licensing process for radioactive source equipment, such as the nuclear density gauge, has led to a preference for using alternative methods to control compaction. The preference for methods based on density and water content measurement has the advantage of being in accordance with the compaction control methodology contained in the specifications.

The paper describes an experimental study to validate the application of the electromagnetic soil density gauge (non-nuclear method) to the soil density and water content control, based on proficiency tests. The proficiency tests also included the sand bottle method and the nuclear method.

2 METHODOLOGY

2.1 Equipment

One of the non-nuclear methods for measuring wet density and water content is the electromagnetic method which is based on the use of electromagnetic impedance spectroscopy device. The electromagnetic properties of the soil are evaluated for certain frequencies through changes induced in the electromagnetic field and which can be correlated with density and water content. Figure 1 shows an electromagnetic gauge (SDG 200 from TransTech Systems). The equipment consists of the following main components: the circular sensor (1) located at the base of the equipment and where the induction and electromagnetic field measurement electrodes are located; the unit where the internal circuits, batteries and the infrared temperature measuring device are located (2); the interface display for reading, managing, and storing measurement results (3). The equipment also consists of a handle for transport and operation (4). As shown in Figure 1, during measurement the equipment is supported on the ground surface. Electromagnetic equipment has the advantage of controlling compaction based on the measurement of density and water content in a simple and quick way. Another advantage of electromagnetic equipment is related to the exemption from licensing, which has contributed to the greater interest in using this equipment to control compaction to the detriment of the nuclear method. The non-nuclear method is included in the ASTM D 7830/D 7830 M.

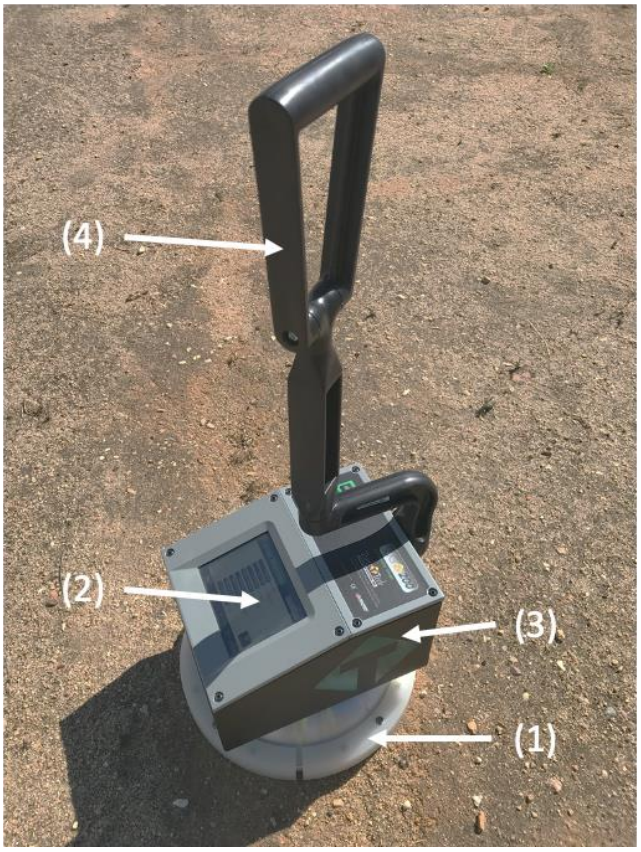

Figure 1. Electromagnetic gauge.

2.2 Proficiency tests

The Association of Accredited Laboratories of Portugal (RELACRE), representative of Portuguese laboratories at EUROLAB, has more than two decades of experience in organizing proficiency tests in the context of construction and building materials (tests of soils, aggregates, bitumen, bituminous mixtures, and concrete). Since 2010, RELACRE has also organized proficiency tests relating to in-place tests carried out on pavement and sub-grade layers (Neves et al., 2013). The proficiency tests follow the methodology of the ISO/IEC 7043 standard.

In 2022, a proficiency test was carried out including the following test methods related to quality compaction control based on dry density and water content:

- Determination of “in situ” density by the nuclear method considering measurements at the surface (backscatter mode) and at a depth of

200 mm (direct transmission mode) of wet density and water content, according to ASTM D 6938.

- Determination of "in situ" density by the sand replacement method, using a sand cone apparatus, according to LNEC E 204 (Portuguese specification based on ASTM D 1556 and ASTM D 1557).

The proficiency test was carried out in a compacted soil. The local was sectioned into three large zones and each zone was divided into nine test points. The zones and points were selected to guarantee homogeneity of state conditions (density and water content). The distance between test points was at least three meters. The soil was a clayey sand (SC) with the properties listed in Table 1 (grain size distribution and plasticity).

Table 1. Properties of the soil.

Properties		Values
Percent passing (Sieve size, mm)	19.0	100
	9.5	98
	4.75	96
	2.00	84
	0.850	53
	0.425	29
	0.250	21
	0.106	17
	0.075	16
Liquid Limit, LL (%)		27
Plasticity Index, PI (%)		11

Seven laboratories participated in the evaluation of wet density and water content using the nuclear method. Each laboratory carried out measurements in three randomly chosen locations: one test point in each zone. At each test point, measurements were taken first at the surface (backscatter) and then at depth (direct transmission). In both operating modes of the nuclear equipment, three measurements were taken at the test site, characterized by a reading time of sixty seconds, with an interval of three minutes between successive measurements. Each laboratory carried out a total of nine measurements of wet density and water content. In the case of the sand replacement method, five laboratories participated and followed a similar procedure to the nuclear method. They carried out a test in each of the three zones, for a total of three measurements of wet density.

In addition, the non-nuclear method was also used in the organization of the proficiency test. Three measurements of wet density and water content were carried out with the electromagnetic gauge. Measurements of the nuclear method were carried out at the surface (backscatter).

3 RESULTS AND DISCUSSION

Figure 2 presents the mean of the values measured by all laboratories for each parameter of the nuclear method and the sand replacement method. Neves et al. (2013) concluded that, in general, the wet density measured at depth (direct transmission) tends to be higher than the wet density value measured at the surface (backscatter). The same authors also found that measuring wet density at depth is the closest to the sand replacement method. The results presented in Figure 2 confirm those conclusions. It was also observed that the standard deviation was smaller in the direct transmission mode. These results reinforce the recommendation of using the direct transmission mode to measure wet density. In relation to water content: the measurements were similar in both modes of nuclear gauge operation: 2,7% (direct transmission) and 3,0% (backscatter).

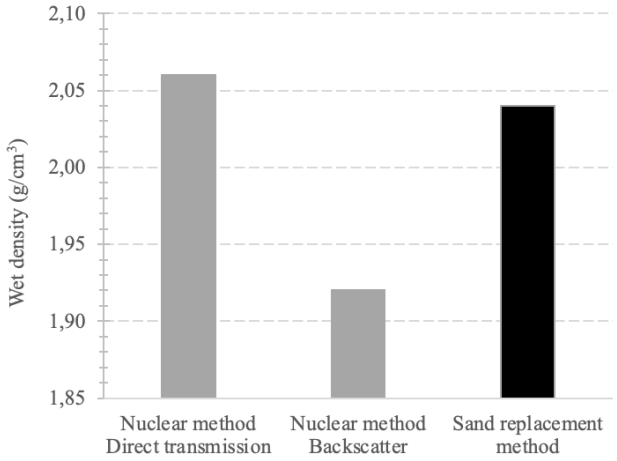

Figure 2. Comparison of wet density measurements.

Regarding the comparison between nuclear and non-nuclear methods, Table 3 presents the values of wet density and water content (mean and standard deviation, SD, of three measurements). The values measured by the non-nuclear method resulted from correction of the equipment in accordance with the manufacturer's methodology. The correction procedure is based on knowledge of the material's identification properties (granulometry and plasticity) and their comparison with values established by the manufacturer for standard samples. For each type of material, correction factors for wet density and water content (offset) are established, which are added to the measured values to obtain the corresponding final values. From the analysis of Table 2, it appears that the corrected values obtained in the non-nuclear method are practically coincident with the values from the nuclear method (backscatter).

Table 2. Comparison of nuclear and electromagnetic methods.

Test	Parameter	Mean	SD
Nuclear method (backscatter)	Wet Density (g/cm^3)	1.927	0.003091
	Water content (%)	2.57	0.0471
Non-nuclear method	Wet Density (g/cm^3)	1.927	0.002974
	Water content (%)	2.57	0.0471

4 CONCLUSION

The paper presented a study on the application of the electromagnetic method to control the compaction of clayey sand, in comparison with the nuclear method. The study was carried out as part of a proficiency test that included the nuclear method and the sand replacement method. The study allowed to conclude that the values of wet density and water content measured by nuclear and non-nuclear (after correction) methods were practically coincident. The study also highlighted the importance of correcting the values measured by the electromagnetic equipment, in accordance with the procedure established by the manufacturer and considering the main properties of the soil (granulometry and plasticity). In addition, the study also provided a comparison between the nuclear and the sand replacement methods. The wet density measurement at depth through the nuclear method was the closest to the sand replacement method.

These conclusions provide confidence in the use of the electromagnetic method to control soil compaction, as an alternative to the nuclear method. However, it will be desirable to validate this study by applying the non-nuclear method to other compacted soils for different conditions (density and humidity).

ACKNOWLEDGEMENTS

The first author is grateful for the support of the Foundation for Science and Technology (FCT) through funding FCT-IDB/04625/2020 from the research unit CERIS (Center of Civil Engineering Research and Innovation for Sustainability).

REFERENCES

ASTM D 1556 (2007). Standard test method for density and unit weight of soil in place by the sand-cone method. American Society for Testing Materials.

ASTM D 6938 (2010). Standard test method for in-place density and water content of soil and soil-aggregate by nuclear methods (shallow depth). American Society for Testing Materials.

ASTM D 7830/D 7830M (2014). Standard test method for in-place density (unit weight) and water content of soil using an electromagnetic soil density gauge. American Society for Testing Materials.

Chen, C., Hu., Y., Jia, F., Wang, X., La, X., Zhang, R. (2023). *Intelligent compaction quality evaluation using Morse wavelet transform and deep neural network*. Construction and Building Materials 400, 132697. https://doi.org/10.1016/j.conbuildmat.2023.132697.

ISO/IEC 17043 (2010). Conformity assessment – General requirements for proficiency testing. International Organization for Standardization.

Kumar, S. A., Aldouri, R., Nazarian, S., Si, J. (2016). *Accelerated assessment of quality of compacted geomaterials with intelligent compaction technology*. Construction and Building Materials 113, 824–834. http://dx.doi.org/10.1016/j.conbuildmat.2016.03.117.

LNEC E 204 (1967). Determination of in situ dry density using the sand replacement method. National Laboratory for Civil Engineering, Lisbon, Portugal (in portuguese).

Neves, J., Duarte, A. M., Silva, C., Candeias, R. (2013). *Contribution of PTS to the laboratory and in situ studies related to soils compaction tests*. Proceedings of the 4th International Proficiency Testing Conference, Brasov, Romania, pp.17–24.

Wang, S., Sui, X., Jiang, J., Lu, G. (2022). *Asphalt pavement density measurement using non-destructive testing methods: current practices, challenges, and future vision*. Construction and Building Materials 344, 128154. https://doi.org/10.1016/j.conbuildmat.2022.128154.

Wang, X., Dong, X., Zhang, Z., Zhang, J., Ma, G., Yang, X. (2022). *Compaction quality evaluation of subgrade based on soil characteristics assessment using machine learning*. Transportation Geotechnics 32, 100703. https://doi.org/10.1016/j.trgeo.2021.100703.

Wang, X., Cheng, C., Li, J., Zhang, J., Ma, G., Jin, J. (2023). *Automated monitoring and evaluation of highway subgrade compaction quality using artificial neural networks*. Automation and Construction 145, 104663. https://doi.org/10.1016/j.autcon.2022.1046.

Proceedings of the XVIII ECSMGE 2024
GEOTECHNICAL ENGINEERING CHALLENGES
TO MEET CURRENT AND EMERGING NEEDS OF SOCIETY
© 2024 the Authors
ISBN 978-1-032-54816-6
DOI 10.1201/9781003431749-113
Open Access: www.taylorfrancis.com, CC BY-NC-ND 4.0 license

ECSMGE 24
XVIII EUROPEAN CONFERENCE ON SOIL MECHANICS AND GEOTECHNICAL ENGINEERING

Analysis and modelling of Resonant Column test results on reconstituted specimens of a saturated pyroclastic soil

Analyse et modélisation des résultats d'essais en colonne résonante sur des échantillons de sol pyroclastique saturé reconstitué

G. Nicodemo*, N. Poursalimi, V. Foresta, S. Ferlisi
Department of Civil Engineering, University of Salerno, Fisciano (SA), Italy
**gnicodemo@unisa.it*

ABSTRACT: In the last decades, several efforts have been made by the Scientific Community to properly investigate the role played by the factors that affect the soil dynamic behaviour and define reliable interpretation models. With the general intent to provide a further contribution on the topic, this paper shows the results of laboratory tests carried out with a Resonant Column (RC) equipment on reconstituted specimens of a pyroclastic soil widely diffused in the Campania region (southern Italy) in saturated conditions. In particular, the laboratory tests are specifically aimed at investigating the effects of confining stresses on the soil shear stiffness modulus (G) at either very small or small shear strains (γ). The test results are also used to calibrate the values of parameters involved in modelling the G–γ relationships for the saturated pyroclastic soil under consideration.

RÉSUMÉ: Au cours des dernières décennies, plusieurs efforts ont été faits par la communauté scientifique pour étudier correctement le rôle joué par les facteurs qui affectent le comportement dynamique du sol et pour définir des modèles d'interprétation fiables. Avec l'intention générale de fournir une contribution supplémentaire sur le sujet, cet article montre les résultats d'essais de laboratoire effectués avec un équipement de colonne résonnante (RC) sur des spécimens reconstitués d'un sol pyroclastique largement diffusé dans la région de la Campanie (Italie du Sud) dans des conditions saturées. En particulier, les essais de laboratoire visent à étudier les effets des contraintes de confinement, de l'historique des contraintes et du fluage sur le module de rigidité de cisaillement du sol (G) à des déformations de cisaillement très faibles ou faibles (γ). Les résultats des essais sont également utilisés pour calibrer les valeurs des paramètres impliqués dans la modélisation des relations G–γ pour le sol pyroclastique saturé considéré.

Keywords: Pyroclastic soil; dynamic behaviour; resonant column; shear stiffness; small strains.

1 INTRODUCTION

Soil shear stiffness modulus (G) is one of the key parameters that must be considered to properly address issues concerning geotechnical dynamic analysis and design. For a given soil under certain confining stresses (p), its value is mainly related to the current shear strain (γ) level. In this regard, Hardin and Black (1968) separated the range of shear strains in which the shear stiffness modulus is almost constant (G_0) from that in which G decreases as shear strains increase.

To provide a further contribution to the topic, this paper shows the results of laboratory tests carried out with a Resonant Column (RC) equipment on reconstituted specimens of a pyroclastic soil widely diffused in the Campania region (southern Italy) in saturated conditions. In particular, the laboratory tests are specifically aimed at investigating the effects of confining stresses on the soil shear stiffness modulus (G) at either very small or small shear strains (γ).

The test results are also used to calibrate the values of parameters involved in modelling the G–γ relationships for the saturated pyroclastic soil under consideration.

2 TESTED SOIL AND RC DEVICE

In this work, reconstituted specimens of pyroclastic (ashy) soil originating from the strombolian activities of the Vesuvius volcano (Campania region, southern Italy) were tested.

The reconstituted specimens were prepared according to the following steps (Figure 1). The oven-dried soil was taken and mixed with a fixed water content equal to 15%. Then, the specimen was reconstituted in a cylinder mould (of 140 mm height and 70 mm large) by compacting three layers of soil, utilizing the moist tamping technique, up to attain a target porosity of 53% corresponding to the minimum

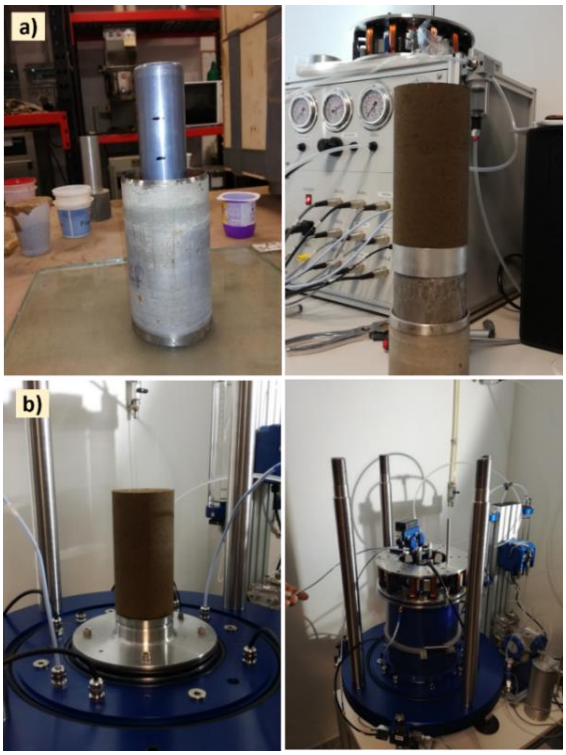

Figure 1. a) Soil specimen preparation; (b) its assemblage within the RCTS equipment.

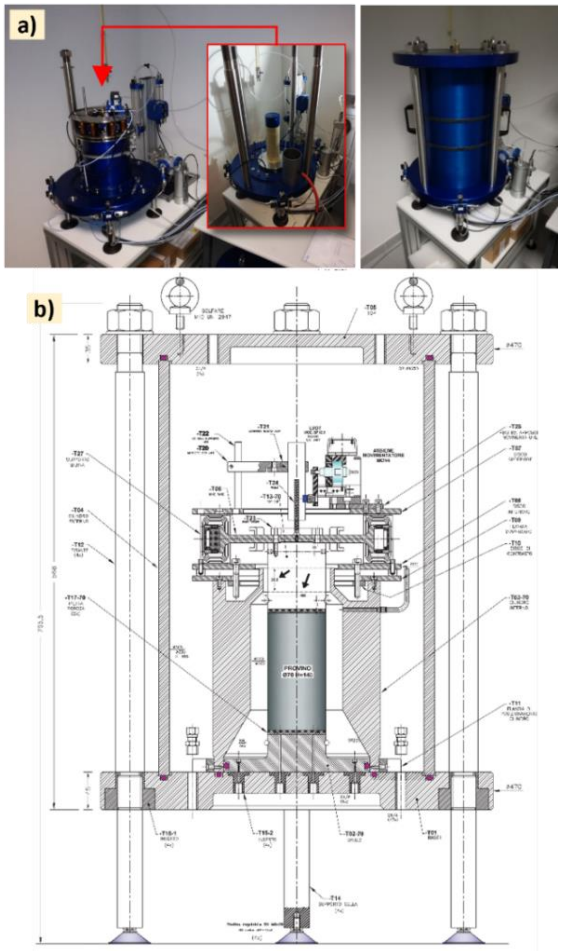

Figure 2. a) Photos and b) detailed scheme of the used RCTS equipment.

value measured in the field (Bilotta et al., 2005).

To reach a uniform distribution of both the water content and matric suction inside the specimen, a time lasting (at least) 24 hr was needed.

The soil testing system consists of a combined suction-controlled Resonant Column-Torsional Shear (RCTS) equipment generally aimed at retrieving the stress-strain behaviour of soil under cyclic loading in either saturated or unsaturated conditions. The RCTS apparatus is comprised of three main parts, namely: the excitation system, the electro-dynamic drive system, and the measurement system (Figure 2).

To pursue the main goal of this work, only the RC component was used. In particular, the reconstituted soil specimen is held fixed at the base. The electrodynamic drive system applies a torsional stress M_t (torque) to the top of the specimen by regulating a sinusoidal electrical signal V (voltage) with a torque/voltage ratio equal to 0.268 Nm/V. The drive consists of a plate with eight magnets, twelve drive coils and a power current amplifier. Each coil is shaped so that the magnets can move as the soil specimen volume changes during the consolidation phase.

3 EXPERIMENTAL TESTS

The experimental tests were carried out on saturated soil specimens to check the performance of the equipment and to gather information about the initial small-strain shear modulus (G_0) and the G–γ relationships.

Once the soil specimen is assembled in fixed-free conditions, the experimental procedure involves considering different steps. In the first step, the saturation is made by increasing the pore water pressure (u_w) at the base of the specimen, from a negative (initially measured) to a positive value, by contextually increasing the cell (p) and the pore air (u_a) pressures step by step (keeping constant their difference at 5 kPa as initial consolidation) until the measured u_w reach the minimum controlling value. The u_w can be measured/applied at the base drainage line while the u_a is applied at the top drainage line of the specimen. In this way, by first regulating u_w to the value reached by u_a and then opening the water drainage valve, the amount of water in the sample is forced to change until the difference between u_a and u_w is zero within the entire specimen. The saturation phase ends when water is visible in the upper drainage line. At this point, the two drainage lines are closed and a B-test is carried out.

As for the consolidation phase (second step) and the dynamic phase (third step), they are differentiated

according to the aim of the test. In particular, in the case with the aim of G_0 estimation, gradually increasing confining stresses – at a rate of 4 kPa per hr – from 5 kPa to 200 kPa (loading phase) and vice versa (unloading phase) are applied to the soil specimen. Two RC tests per hr (1 each 30 min) are performed during the ramp of confining stress, with constant voltage amplitude (0.001 V) and variable frequencies (range of 20 to 80 Hz), to find the resonance frequency of the soil specimen. Resonance frequency allows computing shear-wave propagation velocity and the corresponding shear modulus G, while the measured rotation of the specimen free head allows computing the corresponding shear strains.

On the other hand, if the goal is to retrieve the G–γ relationship, the soil specimen is subjected to multiple consolidation stages imposing confining stresses equalling 20 kPa, 40 kPa, 60 kPa, 80 kPa, 100 kPa, and 150 kPa. In such a case, the dynamic tests are performed with a range of different voltage amplitudes starting from 0.001 V until a maximum of 2.8 V according to the confining stress (to minimize the destructive effects on the specimen), which allows investigating a range of shear strains from 10^{-4} % to 5×10^{-1} %.

4 RESULTS

The analysis and modelling of test results were focused, separately, on the linear and non-linear soil behaviour based on the attained shear strain level. In the former case, information about the initial shear stiffness modulus (G_0) values was gathered; in the latter case, the soil response in terms of G–γ relationship was retrieved. The obtained test results are plotted in the graphs of Figure 3 and Figure 4. As expected, the experimental data highlight that the confining stress has a direct effect on the soil dynamic response – in both linear and non-linear parts – with a general increase of the shear stiffness (G) as the confining stress increases; while G gradually decreases when the applied shear strain (γ) increases.

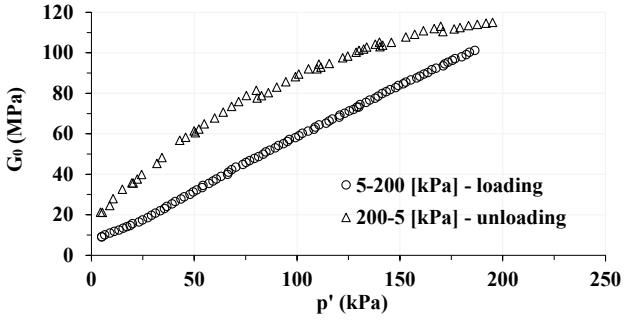

Figure 3. Initial shear stiffness modulus (G_0) vs. confining stress in loading and unloading phases.

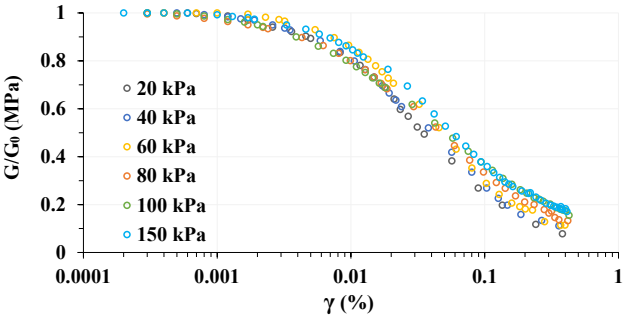

Figure 4. Normalized shear stiffness modulus (G/G_0) vs. shear strain (γ) for different confining stresses.

To model the non-linear soil behaviour, several mathematical formulations were proposed in the scientific literature. In particular, Darendeli (2001) suggested adopting a hyperbolic equation – like the one given by Hardin and Drnevich (1972) – which involves using a reference shear strain (γ_r) at $G/G_0 = 0.5$ and a curvature coefficient (α):

$$\frac{G}{G_0} = \frac{1}{1+\left(\frac{\gamma}{\gamma_r}\right)^{\alpha}} \quad (1)$$

Figure 5 highlights that the Equation (1) allows modelling with sufficient accuracy the test results shown in Figure 4 for the different confining stresses and over a wide range of shear strains.

Nevertheless, to have a best-fit model of the shear modulus reduction curve for the investigated pyroclastic soil, a modified equation was proposed by introducing a further curvature parameter (β):

$$\frac{G}{G_0} = \left(\frac{1}{1+\left(\frac{\gamma}{\gamma_r}\right)^{\alpha}}\right)^{\beta} \quad (2)$$

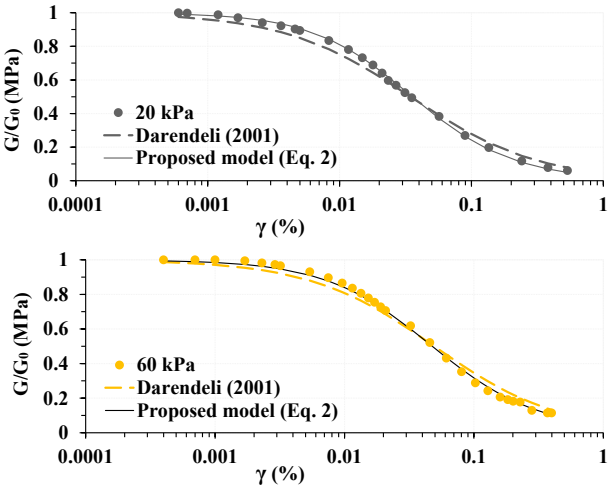

Figure 5. Application of the Darendeli (2001) model and proposed model on the test results in terms of normalized shear stiffness modulus vs. shear strain for different confining stresses values.

In Equation (2), each dimensionless parameter was estimated as a function of the confining stress (p) using Equations (3), (4) and (5) for α, β and, γ_r respectively:

$$\alpha = -7 \times 10^{-5} p^2 + 0.0057p + 1.0747 \quad (3)$$

$$\beta = -1 \times 10^{-5} p^2 + 5 \times 10^{-5} p + 0.8007 \quad (4)$$

$$\gamma_r = -3 \times 10^{-6} p^2 + 4 \times 10^{-4} p + 0.0188 \quad (5)$$

As for the initial shear modulus (G_0), the mathematical formulation given by Rampello et al. (1995) was first considered:

$$G_0 = A \cdot p_{atm}^{1-n} \cdot (p')^n \cdot (OCR)^m \cdot f(e) \quad (6)$$

In Equation (6) p_{atm} is the atmospheric pressure, A is a dimensionless stiffness index, n is a stiffness coefficient expressing the rate of sensitivity of G_0 on the current stress state, p' is the mean effective stress, OCR is the over-consolidation ratio and $f(e)$ is a suggested function of void ratio e ($f(e) = \frac{(2.97-e)^2}{1+e}$).

By plotting the curve relating $f(e)$ vs. e (-), it can be observed that the suggested function does not provide a good match with the test results (Figure 6). Thus, Equation (6) was adapted for the pyroclastic soil under consideration by introducing two new dimensionless parameters (B and C):

$$f(e) = \frac{(B-e)^C}{1+e} \quad (7)$$

On the other hand, the parameter A was calibrated according to the equation (Kokusho,1987):

$$G_0 = A \cdot f(e) \cdot (p')^n \quad (8)$$

Finally, the values of A = 0.18, B = 4.80, and C = 1.89 were obtained. The good match of data coming from Equation (7) to the test results is shown in Figure 6.

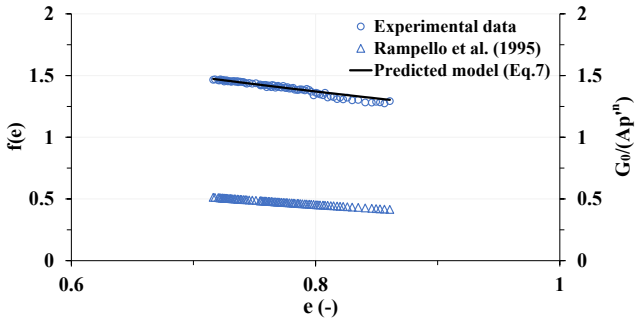

Figure 6. Comparison of the f(e) vs. e experimental data with the mathematical formulation given by Rampello et al. (1995) and the new predicted model proposed in this work.

On the other hand, to model the loading and unloading curves in the G_0–p'graph, the m parameter related to over-consolidation was calibrated too so obtaining a value equal to 0.37 (Figure 7).

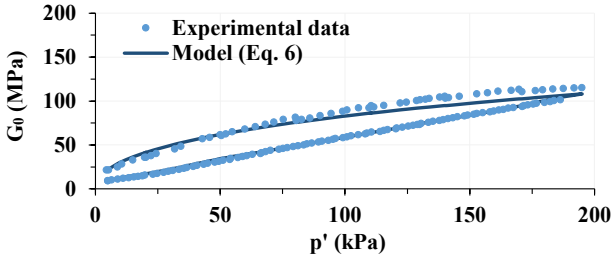

Figure 7. Experimental and modelled $G_0 - p'$ curves.

5 CONCLUSIONS

This paper showed the preliminary results of laboratory tests carried out with a Resonant Column (RC) equipment on reconstituted specimens of a pyroclastic soil widely diffused in the Campania region (southern Italy). The collected experimental data allowed providing new mathematical formulations useful to model either the linear or nonlinear behaviour of the investigated soil in saturated conditions under different confining stresses.

REFERENCES

Bilotta, E., Cascini, L., Foresta, V., and Sorbino, G. (2005). Geotechnical characterization of pyroclastic soils involved in huge flowslides. *Geotechnical and Geological Engineering*, 23:365-402. https://doi.org/10.1007/s10706-004-1607-3.

Darendeli, M.B. (2001). Development of a new family of normalized modulus reduction and material damping curves. *Ph.D. Thesis, University of Texas at Austin,* pp. 362.

Hardin, B.O., and Drnevich, V.P. (1972). Shear modulus and damping in soils: measurement and parameter effects (Terzaghi lecture). *Journal of the soil mechanics and foundations division,* 98(6): 603-624. https://doi.org/10.1061/jsfeaq.0001756.

Kokusho, T. (1987). In-situ dynamic soil properties and their evaluations. In *Proc. of 8th Asian Regional Conference on Soil Mechanics and Foundation Engineering,* Kyoto (Japan), Vol. 2, pp. 215-240.

Rampello, S., Silvestri, F., and Viggiani, G. (1995). The dependence of G_0 on stress state and history in cohesive soils. In: *Pre-failure e-failure deformation of geomaterials – Measurements and application*, IS-Hokkaido, Sapporo 1994, Balkema, Rotterdam, Vol. 2, pp. 1155-1160.

Proceedings of the XVIII ECSMGE 2024
GEOTECHNICAL ENGINEERING CHALLENGES
TO MEET CURRENT AND EMERGING NEEDS OF SOCIETY
© 2024 the Authors
ISBN 978-1-032-54816-6
DOI 10.1201/9781003431749-114
Open Access: www.taylorfrancis.com, CC BY-NC-ND 4.0 license

ECSMGE 24
XVIII EUROPEAN CONFERENCE
ON SOIL MECHANICS AND
GEOTECHNICAL ENGINEERING

Accumulated axial strains for bentonite sand mixture due to cyclic loading with low confining pressures

Déformations axiales accumulées pour le mélange de sable bentonite en raison d'un chargement cyclique avec de faibles pressions de confinement

T. Nishimura*
Ashikaga University, Tochigi, Japan
**nishimura.tomoyoshi@g.ashikaga.ac.jp*

ABSTRACT: A certainly design, construction, management and observation of geological repositories is crucial key to address the safety disposal of radioactive waster including LLWs and HLWs. This study focused on dynamic properties for unsaturated-saturated bentonite sand mixture used as one of engineered barrier system, which composed sodium bentonite and silica sand. Cyclic triaxial apparatus is used for determination of reduction amplitude stress, stress-strain behaviour and changing of cyclic stress ratio. Also, shear strength parameters are measured from monotonic loading tests for unsaturated-saturated bentonite sand mixture, which are angle of shear resistance and apparent cohesion, and failure envelopes are estimated, proceeding of faire conditions are observed in between principal means stress and principal deviator stress. Specimens used in this study are unsaturated condition and saturated condition, and unsaturated specimens are applied high suction controlling by vapor pressure technique in order to prepare variety of soil moisture and various of dry density. Owing suction control by vapor pressure technique, it proves that specimens have hydration effect associated to strength parameters and stress-strain properties in dynamic loading. Also, it is found out that accumulated axial strains for unsaturated bentonite sand mixture with various of high suctions verified the influence of initial cyclic stress ratio and suction value, and accumulated axial strains are slightly when suction is over 83 MPa. Other hands, specimens are decrement to the resistance in cyclic loading due to increment of soil moisture induced by relative humidity of 98%, and strains in compression side.

RÉSUMÉ: La conception, la construction, la gestion et l'observation de dépôts géologiques sont certainement essentielles pour assurer l'élimination en toute sécurité des déchets radioactifs, y compris les déchets de faible activité et les déchets de haute activité. Cette étude s'est concentrée sur les propriétés dynamiques d'un mélange de sable de bentonite insaturé-saturé utilisé comme système de barrière technique, composé de bentonite de sodium et de sable de silice. L'appareil triaxial cyclique est utilisé pour déterminer la contrainte d'amplitude de réduction, le comportement contrainte-déformation et la modification du rapport de contrainte cyclique. En outre, les paramètres de résistance au cisaillement sont mesurés à partir d'essais de chargement monotones pour un mélange de sable de bentonite insaturé-saturé, qui sont l'angle de résistance au cisaillement et la cohésion apparente, et les enveloppes de rupture sont estimées, les conditions de déroulement sont observées entre la contrainte moyenne principale et la contrainte déviatrice principale. Les spécimens utilisés dans cette étude sont en condition insaturée et saturée, et les spécimens insaturés sont soumis à une aspiration élevée contrôlée par une technique de pression de vapeur afin de préparer une variété d'humidité du sol et diverses densités sèches. Grâce au contrôle de l'aspiration par la technique de pression de vapeur, il prouve que les éprouvettes ont un effet d'hydratation associé aux paramètres de résistance et aux propriétés contrainte-déformation en chargement dynamique. En outre, il a été découvert que les déformations axiales accumulées pour un mélange de sable de bentonite insaturé avec diverses succions élevées ont vérifié l'influence du rapport de contrainte cyclique initial et de la valeur de succion, et que les déformations axiales accumulées sont légères lorsque la succion est supérieure à 83 MPa. D'autre part, les éprouvettes subissent une diminution de la résistance en chargement cyclique en raison de l'augmentation de l'humidité du sol induite par une humidité relative de 98% et des déformations axiales côté compression.

Keywords: Bentonite; unsaturated soil; suction; dynamic properties; vapor pressure technique.

1 INTRODUCTION

The aspect of high-level radioactive waste (HLW) repository commonly includes environmental engineering artificial barrier system. The system has compacted bentonite blocks with some sand mixture are established around the strong waste canister, which Sellin and Leupin, (2013) mentioned detail. It is generally accepted that after construction the high-level radioactive waste (HLW) repository, the compacted bentonite become gradually absorb or hydration with groundwater at deeply place to recognize essential buffer functions such as sealing

some gaps due to swelling, subsequently supporting the canister with steady. The mathematical models regard to artificial barrier have been suggested including thermal-hydration-mechanical-chemical couple phenomena (Villar et al. (2010), Yong-Gui Chen at al. (2015), Yong-Gui Chen et al. (2017), Yong-Gui Chen et al. (2019)) that contribute accuracy simulations in swelling processes. The cyclic strength and deformations are generally a problem in liquefaction for loose sand and few refreshes are report clay material and unsaturated soils. This study focused on dynamic properties for unsaturated-saturated bentonite sand mixture used as one of engineered barrier system. The controlling suctions have a range from 2.8 MPa to 148 MPa and three different suction are required that translated relative humidity are 98%, 75% and 33%. The maximum cyclic of number is 10 times, and loading-unloading frequency is 0.1 Hz, which is not so large cyclic application. Furthermore, this study has more consideration that both heating application and chemical effort to bentonite sand mixture specimen. 80 degree Celsius and 100 degrees Celsius are controlled to the specimen heating application accomplish.

2 TESTING PROCEDUE

2.1 Soil material and specimens

Considering, Kunigel V1, a sodium bentonite, is used in some series of testing programs to confirm cyclic loading properties in experimental laboratory studies. Owing to its high montmorillonite content, the bentonite has a fines content greater than 95%. In this testing program all of specimens mixed a silica sand, named Iitoyo No.4, into the sodium bentonite, which has a uniformity grain size distribution.

All specimens had a diameter of 38 mm and a height of 76 mm for all of series of testing programs that are statically compacted using a hydraulic oil jack. The bentonite sand mixture is put into the stiffness steel mold with an inner diameter of 38.0 mm, a thickness of 18.0 mm and a height of 76.0 mm. The initial specimens have the following physical properties: a dry density of 1.600 Mg/m^3, void ratio of 0.710, and degree of saturation of 65.6%.

2.2 Apparatus and programs

This study used cyclic triaxial test apparatus for investigation of axial deformations for unsaturated specimen and saturated specimens. This testing program has majority two parts that one is

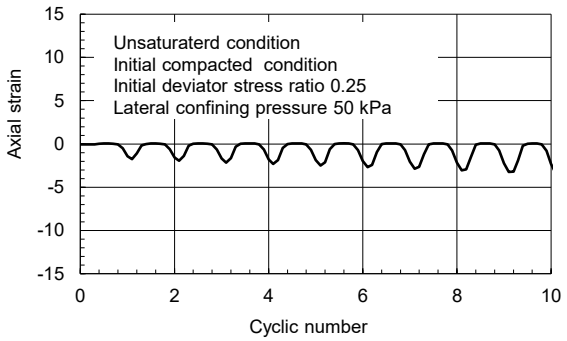

Figure 1. Initial condition at compaction.

unsaturated specimens cyclic loading test and other one is saturated specimen cyclic loading test. Furthermore, unsaturated specimens cyclic loading test divided as followings; the specimens are prepared with and without suction controlling. Suction controlling is performed using vapor pressure technique, which is used salt solutions and have a range from 2.8 MPa to 2986 MPa. This testing program attempt three suction (i.e., 98%, 75% and 33% in relative humidity), which are 2.8 MPa, 39 MPa and 148 MPa. Then, saturated specimens are prepared due to soaking. The salinity water has concentration of 0.85% or 1.2%. After the specimens approach to be fully saturation, and saturated specimens placed on the pedestal and the cyclin triaxial apparatus is set up. It is common between unsaturated specimen test and saturated specimen test that lateral confining pressure is 50 kPa and loading frequency is 0.1 Hz. End of cyclic loading test is determined till cyclic number is ten.

3 TEST RESULTS

3.1 Compacted bentonite sand mixture

Axial strains in both compression side and expansion side are described as shown in Figure 1. Compression side is positive value and expansion side is negative value. During cyclic loading, compression strain and expansion strain are further small, which are less than 0.2%. The specimen has steady small strain with cyclic number, the increment is not found. The difference between compression axial strain expansion strain remain the same.

3.2 Unsaturated bentonite sand mixture subjected to suction

Comparing the axial strain behaviour during cyclic loading through as shown in Figs. 2, 3 and 4 that the different phenomena is clear. When the specimen has equilibrium to RH 98%, the specimen has a suction of 2.8 MPa, and the axial strain through cyclic

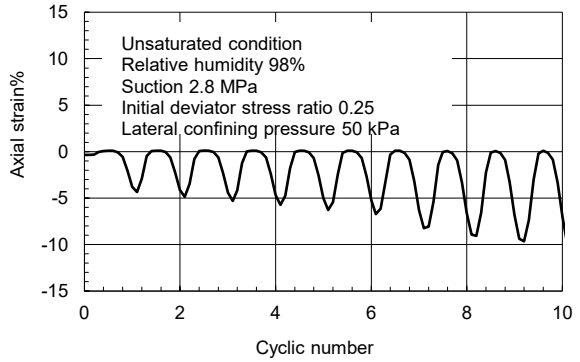

Figure 2. Unsaturated specimen for suction of 2.8 MPa.

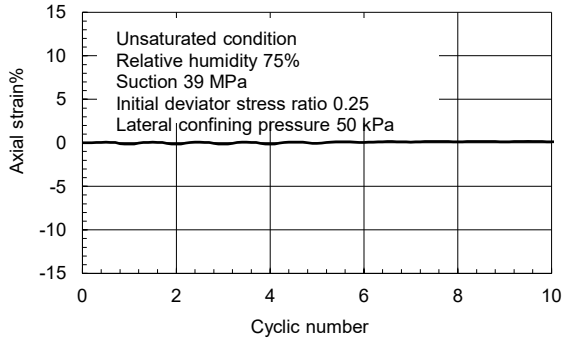

Figure 3. Suction of 39 MPa.

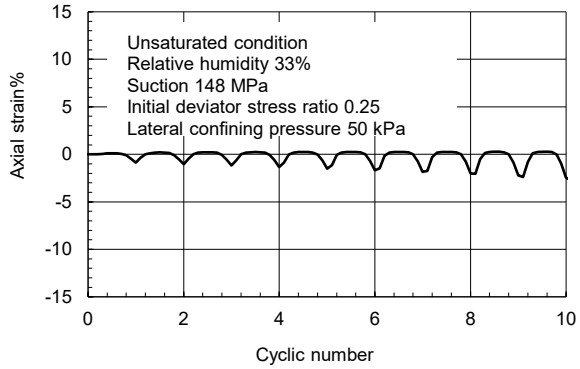

Figure 4. Suction of 148 MPa.

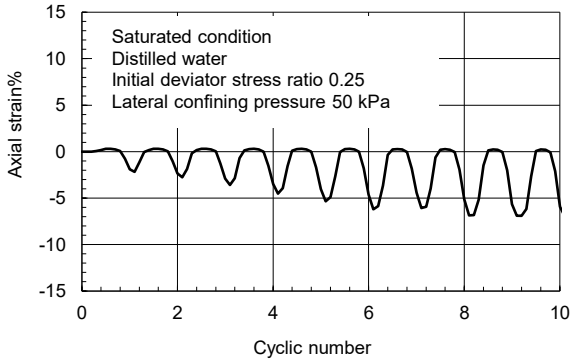

Figure 5. Saturated specimen (Distilled water).

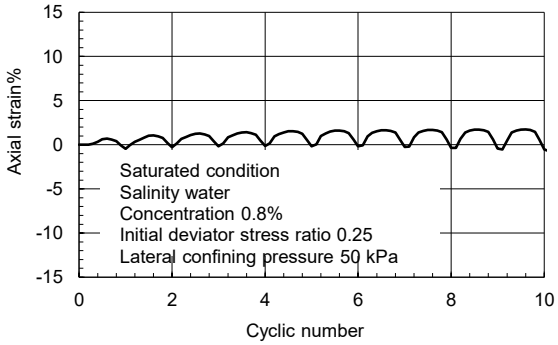

Figure 6. Saturated specimen (0.8%).

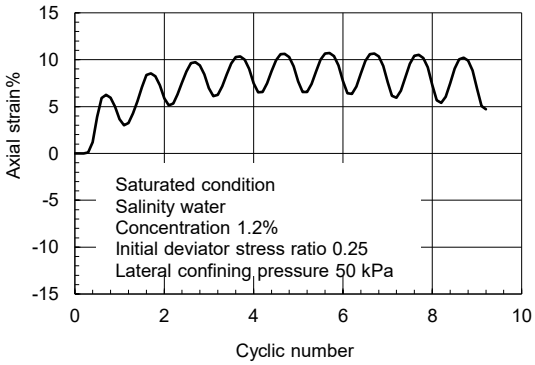

Figure 7. Saturated specimen (1.2%).

loading is measured as shown in Figure 2. Expansion axial strain is occurred at beginning of loading and unloading which is -4.3%. Processing compression loading and expansion loading, the deformations are employed toward to expansion side. The failure for specimen with suction of 98% is impossible to observed through the test. Other hands, the specimen is applied relative humidity of 75% corresponding to 39 MPa that two times difference between two relative humidity value for suction value. Similar cyclic loading is required, changing of axial strain is verified as shown in Figure 3. Providing that small axial strain is measured for both compression side and expansion side during cyclic loading, which each strain is 0.15%.

3.3 Saturated bentonite sand mixture

Saturated specimen due to distilled water indicate the axial strains with vibration as shown in Figure 5, and almost of deformation are occupied in expansion side that compression deformations are less than 0.2%. According to expansion deformations increase with cyclic number, and approach to 7.0% at end of test. In case of absorbed water change to salinity water, Figure 6 shows the compression side deformations are advantage compare to expansion deformation for salinity water with concentration of 0.8%. Maximum axial strain in compression side is 1.5%. Furthermore, significant different properties are measured as shown in Figure 7. The specimen occurred large compression deformation, and the compression deformation remine the increment of axial strain with number.

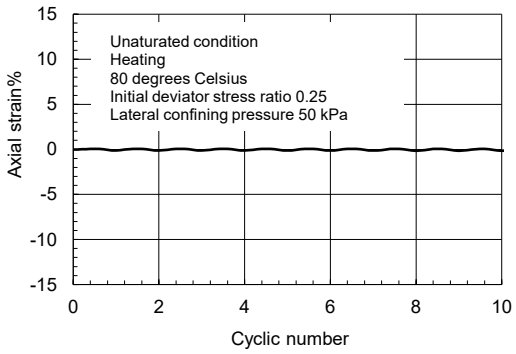

Figure 8. 80 degrees Celsius.

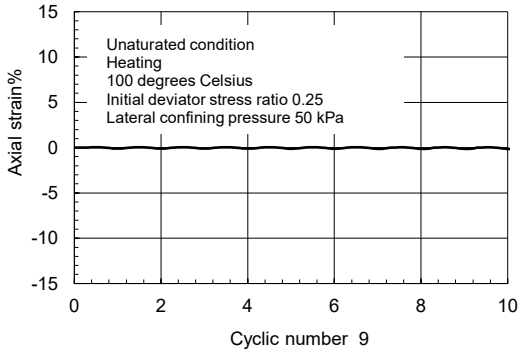

Figure 9. 100 degrees Celsius.

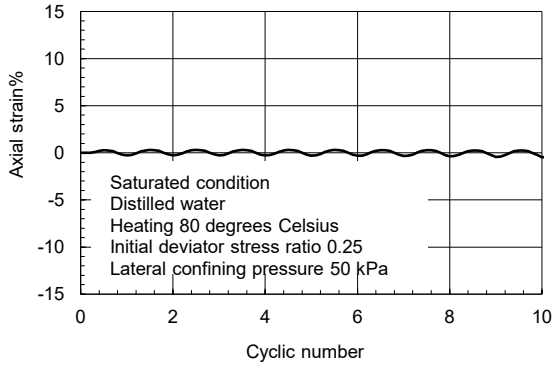

Figure 10. Saturated specimen at 100 degrees Celsius.

Expansion axial strains are not measured. Also, the deference between compression axial strain and expansion axial strain are almost 5% through the cyclic numbers.

3.4 Influence of heating action on deformations

Unsaturated bentonite sand mixture specimens have conductive under 80 and 100 degrees Celsius and subsequently cyclic loading test are conducted. The relationship between cyclic number and axial strain are shown in Figs. 8 and 9. The measured axial strains are less than 0.2% and expansion side that the occurrence of axial strains is resist through the test. Saturated bentonite sand mixture specimen subjected to heating application (i.e. 80 degrees Celsius) that the strains are similar to the result in Figures. 8 and 9. A few axial strains are measured as shown in Figure 10.

4 CONCLUSIONS

This study focused on dynamic properties for unsaturated-saturated bentonite sand mixture with variety functions. The obtained summaries are as followings: The unsaturated bentonite sand mixture specimen subjected to suction control that the further small axial strain is measured for both compression side and expansion side during cyclic loading. Its tendency related to increase the suction that is relative humidity decrease. Saturation specimen due to distilled water verify the large expansion axial strains, and it is obviously that saturated specimens in salinity water with concentration of 1.2%.

REFERENCES

Sellin, P., Leupin, O. X. (2013). The use of clay as an engineered barrier in radioactive-waste management–a review. Clays and Clay Minerals, 61(6):477-498. https://doi.org/10.1346/CCMN.2013.0610601.

Villar M.V., Gómez-Espina R., Lloret A. (2010). Experimental investigation into temperature effect on hydro-mechanical behaviours of bentonite, Journal of Rock Mechanics and Geotechnical Engineering, 2(1):71-78. https://doi.org/10.3724/SP.J.1235.2010.00071.

Yong-Gui Chen, Chun-Min Zhu, Wei-Min Ye, Yu-Jun Cui, Qiong Wang. (2015). Applied Clay Science, Swelling pressure and hydraulic conductivity of compacted GMZ01 bentonite under salinization–desalinization cycle conditions, 114:454-460. https://doi.org/10.1016/j.clay.2015.06.033.

Yong-Gui Chen , Ling-Yan Jia , Quan Li , Wei-Min Ye , Yu-Jun Cui , Bao Chen. (2017). Swelling deformation of compacted GMZ bentonite experiencing chemical cycles of sodium-calcium exchange and salinization-desalinization effect, Applied Clay Science, 141: 55-63. https://doi.org/10.1016/j.clay.2015.06.033.

Yong-Gui Chen , Xin-Xin Dong, Xu-Dong Zhang , Wei-Min Ye , Yu-Jun Cui. (2019). Cyclic thermal and saline effects on the swelling pressure of densely compacted Gaomiaozi bentonite, Engineering Geology, 255, 18: 37-47. https://doi.org/10.1016/j.enggeo.2019.04.016.

Proceedings of the XVIII ECSMGE 2024
GEOTECHNICAL ENGINEERING CHALLENGES
TO MEET CURRENT AND EMERGING NEEDS OF SOCIETY
© 2024 the Authors
ISBN 978-1-032-54816-6
DOI 10.1201/9781003431749-115
Open Access: www.taylorfrancis.com, CC BY-NC-ND 4.0 license

ECSMGE 24
XVIII EUROPEAN CONFERENCE ON SOIL MECHANICS AND GEOTECHNICAL ENGINEERING

PIV analysis of ground during horizontal pile loading by centrifuge tests

Analyse par PIV du sol pendant le chargement horizontal de pieux par essais en centrifugeuse

M. Odagiri*, T. Takatoshi, Y. Asaka
Shimizu Corporation, Tokyo, Japan

**odagiri.m@shimz.co.jp*

ABSTRACT: Examining the ground's deformation characteristics is valuable in assessing the impact of ground behavior around piles on horizontal resistance. In this study, horizontal pile loading experiments in a centrifugal 50G field and PIV image analysis were conducted. The ground deformed three-dimensionally when the pile was loaded horizontally. Therefore, two experiments were conducted: one to observe the ground surface and another to observe the ground section. The displacement distribution of the ground surface was nearly circular, while that of the ground section was triangular in the initial stage of loading and became quadrangular as the pile head displacement increased. The size of the three-dimensional deformation area of ground in front of a pile at each loading stage was analyzed, and the results indicated that the horizontal resistance of a pile is related to the size of the deformation area of the ground.

RÉSUMÉ: Examiner les caractéristiques de déformation du sol est important afin d'évaluer l'impact du comportement du sol autour de pieux à résistance horizontale. Dans cette étude, des expériences de chargement horizontal de pieux dans un champ centrifuge de 50G et une analyse d'images par PIV (vélocimétrie par image de particules) ont été réalisées. Le sol se déformait tridimensionnellement lorsque le pieu était chargé horizontalement. Par conséquent, deux expériences ont été menées : une première afin d'observer la surface du sol et une seconde afin d'observer la section du sol. La distribution du déplacement de la surface du sol était quasiment circulaire, tandis que celle de la section du sol était triangulaire lors de la phase initiale de chargement, puis devenait quadrangulaire au fur et à mesure que le déplacement au point d'application augmentait. La taille de la zone de déformation tridimensionnelle du sol devant un pieu à chaque phase du chargement a été analysée, et les résultats indiquent que la résistance horizontale d'un pieu est liée à la taille de la zone de déformation du sol.

Keywords: Particle image velocimetry; pile; lateral loading; lateral resistance; centrifugal test.

1 INTRODUCTION

The pile foundations of buildings are subjected to horizontal loads due to earthquakes and winds. The evaluation of the horizontal resistance of piles is one of the most important issues in the design of pile foundations. Although many studies have focused on pile stress, it is essential to understand the deformation characteristics of the ground during pile loading. The ground resistance area and the resistance mode affect the horizontal resistance of the pile and the pile group effect.

Reese et al. (1974) performed horizontal loading tests on a full-size pile on site and determined the ultimate resistance of a laterally loaded pile, assuming a three-dimensional (3D) wedge-shaped failure pattern on sand. In recent years, laboratory tests have been conducted in addition to field tests. Various techniques, including X-ray computed tomography (CT) and particle image velocimetry (PIV), have been used to visualize ground behavior. Using X-ray CT to observe the ground during horizontal pile loading, Otani et al. (2006) proposed a cone shaped 3D failure pattern for sand. Hajialilue-Bonab et al. (2011) and Yuan et al. (2017) studied the ground deformation patterns under the horizontal loading of piles based on small-scale models in the laboratory and PIV. The authors also conducted ground surface observation experiments during horizontal pile loading in a 1G field and reported the displacement distributions on the ground surface (Odagiri et al. (2023)).

Although some studies have focused on soil deformation characteristics, as shown above, most experiments used small-scale models in a laboratory, making it difficult to quantitatively evaluate ground

behavior. Since the strength of friction material is dependent on the confining pressure, it is difficult to quantitatively evaluate the behavior of the ground in a 1G field. Therefore, experiments in a centrifugal field are essential. In this study, horizontal pile loading tests in a centrifugal field and PIV image analysis were conducted. Soil deforms three- dimensionally when a pile is loaded horizontally. Therefore, two experiments were conducted under similar conditions: one to observe the ground surface and another to observe the ground section.

2 METHODOLOGY OF HORIZONTAL LOADING TEST AND PIV

2.1 Experimental model

The experiments were conducted using a beam-type centrifuge at a centrifugal acceleration of 50 G at the ground surface, and the experimental models are shown in Figure 1. The experiment conducted to observe the ground surface is called the "full-section experiment," and the experiment conducted to observe the ground section is called the "half-section experiment." In the half-section experiment, the pile and ground models were half of those in the full-section experiment. The rigid soil container was 690 mm long, 510 mm wide, and 450 mm high. The soil container was identical in both experiments. In the half-section experiment, one side of the wall was removed, and a glass window was installed at the center of the container.

The piles were designed assuming cast-in-place concrete piles. The specifications of the piles are listed in Table 1. The pile for the full-section experiment (full-section pile) was an aluminum pipe with a diameter (D) of 20 mm (prototype scale: 1m), a thickness of 1 mm, and a length of 350 mm. The plate thickness was set such that the flexural rigidity of the pile was equivalent to that of a cast-in-place concrete pile of the same pile diameter. The strain gauges were affixed to eight levels inside the pile. The pile used for the half-section experiment (half-section pile) was a half-section aluminum pipe of equal size to the full-section pile. The inside of the half-section pile was filled with a silicone sealant, and a Teflon sheet was

Table 1. Specifications of the pile.

	prototype pile	**model pile**
Diameter (D)	1m	20mm
Thickness	-	1mm
Length	17.5m	350mm
Embedded length	15m	300mm
Flexural rigidity	1.14GN·m^2	183N·m^2

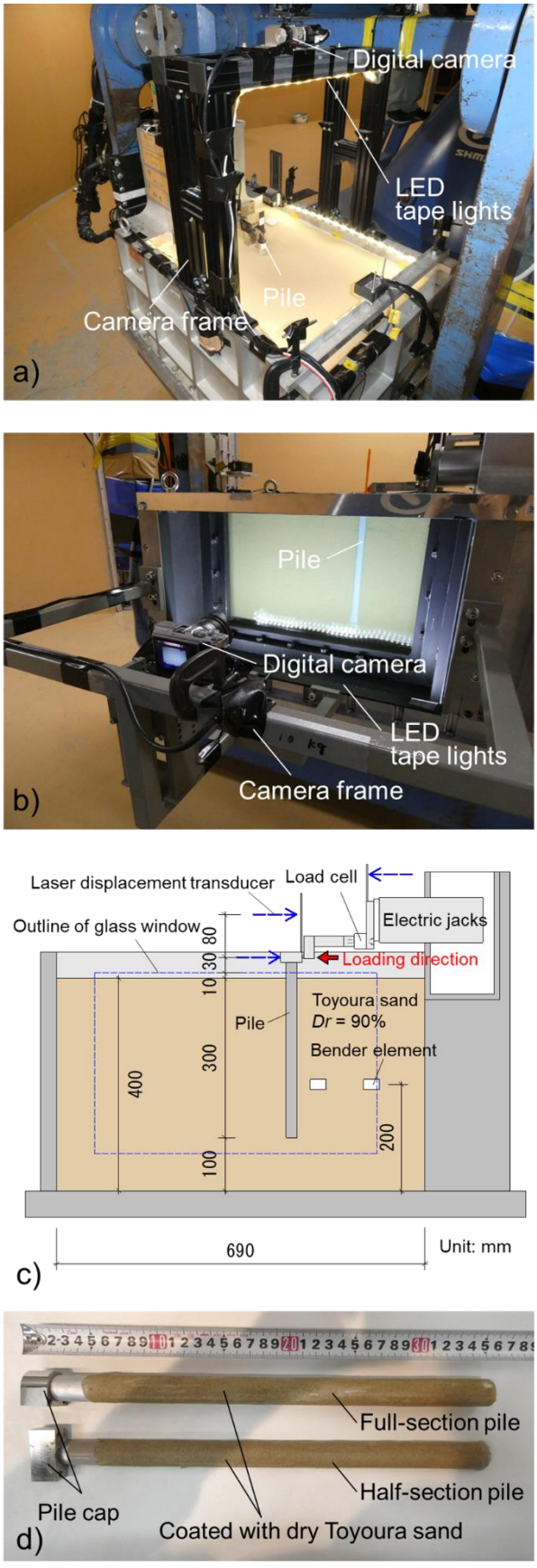

Figure 1. Experimental model: a) Full-section experiment, b) Half-section experiment, c) Detail plan, d) model piles.

bonded to the glass contact surface to reduce friction between the glass and pile. The pile surfaces were adhered to Toyoura sand to account for the friction between the pile and ground. The ground conditions, loading conditions and sensor arrangement were the same for both experiments.The ground models were 400 mm high (20 m). The embedment length of the piles in the ground was 300 mm (15 m). Dry Toyoura sand was used as ground material. Figure 2 shows the grain size distribution curve. The average grain size (D_{50}) of the Toyoura sand was 0.196 mm and the relative density (D_r) of the ground was set to 90% using the air pluviation method. A model pile was set up when the ground was piled up to 100 mm from the bottom of the soil container, and a surface layer was then formed. Bender elements were used to measure the shear wave velocity at the center depth of the ground. Horizontal loading was applied to the pile cap (40 mm above the ground surface) using an electric jack at a loading rate of 0.5 mm/min. The pile head was free. Load cells were used to measure the load on the pile head, and laser displacement transducers were used to measure the horizontal displacement of the jack, pile head at the loading level, and upper part of the pile 80mm above the loading point (Figure 1 (c)) .

2.2 Photographic method and post processing

A digital camera with a resolution of more than 20 million pixels (Fujifilm X-A5) was used. A single-focus lens was used in this study. A digital camera was placed on a frame fixed to the soil container. Photographs for image analysis were captured from the top of the soil container in the full-section experiment and from the side of the container in the half-section experiment. During the experiment, the room lights were turned off, and the ground surface was lit using LED tape lights placed in the soil container and camera frame. Instead of lighting from a single spot, lights were placed around the pile to prevent shadows from forming in the analysis area. The ground was captured every 5 s during the holizontal pile loading.

PIV is used for obtaining displacement by calculating the cross-correlation coefficient of the luminance distribution of two images. PIV is commonly used for the visualization of ground behavior (e.g., White et al. (2003)).The image analysis steps were as follows. 1) Photographs were selected for every 1 mm of pile head displacement. 2) The positions in the photographs were corrected. 3) The photographs were trimmed around the piles. 4) The relative displacements were obtained using PIV between the image at a 0-mm pile head displacement (initial pile head displacement) and each photo at

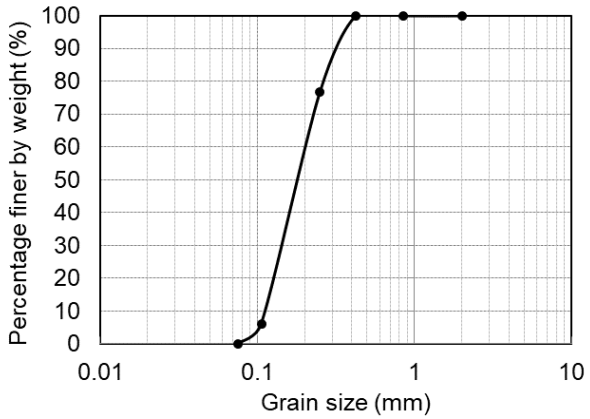

Figure 2. Grain size distribution curve of Toyoura sand.

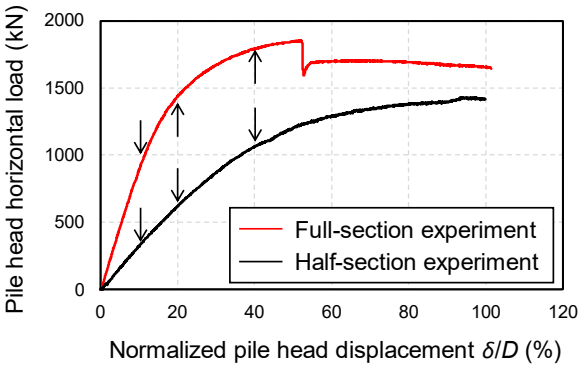

Figure 3. Relationships between horizontal load and displacement at the pile head.

every 1-mm pile head displacement. In this study, the open-source platform JPIV was used for PIV analysis. The size of one pixel in the ground plane was 0.15 mm square in the full-section experiment, and 0.14mm square in the half-section experiment, which are approximately equal in size. Therefore, the variance in the image analysis results owing to differences in the conditions of the two experiments is expected to be negligible.

3 EXPERIMENTAL AND IMAGE ANALYSIS RESULTS

3.1 Pile head load and displacement relationship

The experimental results are presented on a prototype scale. The shear velocity at the center depth of the ground was 247 m/s in the full-section experiment and 244 m/s in the half-section experiment at a centrifugal acceleration of 50G. The ground conditions for both experiments were approximately the same. Figure 3 shows the relationship between the horizontal load of the pile head and pile head displacement (loading point height). The pile head displacement δ was normalized

by the pile diameter D. In the full-section experiment, the pile-head load decreased rapidly when the pile-head displacement was 52% of the pile diameter. After the test, the pile exhibited significant residual deformation, and buckling was considered to have occurred when the pile head displacement was 52% of the pile diameter. Therefore, the image analysis results showed pile head displacement of up to 50% of the of the pile diameter.

In the full-section experiments, the pile head load increased almost linearly until the pile head displacement was about 15% of the pile diameter, and the increase in pile head load became smaller when the pile head displacement exceeded 20% of the pile diameter. In the half-section experiments, the pile head load increased almost linearly until the pile head displacement is about 30% of the pile diameter, and the increase in pile head load became smaller when the pile head displacement exceeded 40% of the pile diameter. The initial slope of the pile head load in the half-section experiment was approximately 40% of that in the full-section experiment.

3.2 Deformation of ground surface during horizontal pile loading

Figure 4 shows contour charts of the ground surface displacement. Ground surface displacement occurred during the loading stages of 10, 20, and 40% of the pile diameter, as indicated by the arrows in Figure 2. The black circles in Figure 4 represent the projections of the pile at the loading point height on the ground surface, and the loading equipment is indicated in gray. The contour lines of the displacement are shown every 10 mm (0.01D). As the pile head displacement increased, the deformed area of the ground widened almost circularly. When the pile head displacement was 40% of the pile diameter, the area of displacement beyond 10 mm expanded 5.7 m in the loading direction and 7.5 m orthogonal to the loading direction.

Figure 5 shows the displacement in the loading direction, the displacement in direction orthogonal to the loading and the displacement vector of the ground surface. The ground in the area close to the axis of the loading direction was displaced primarily in the

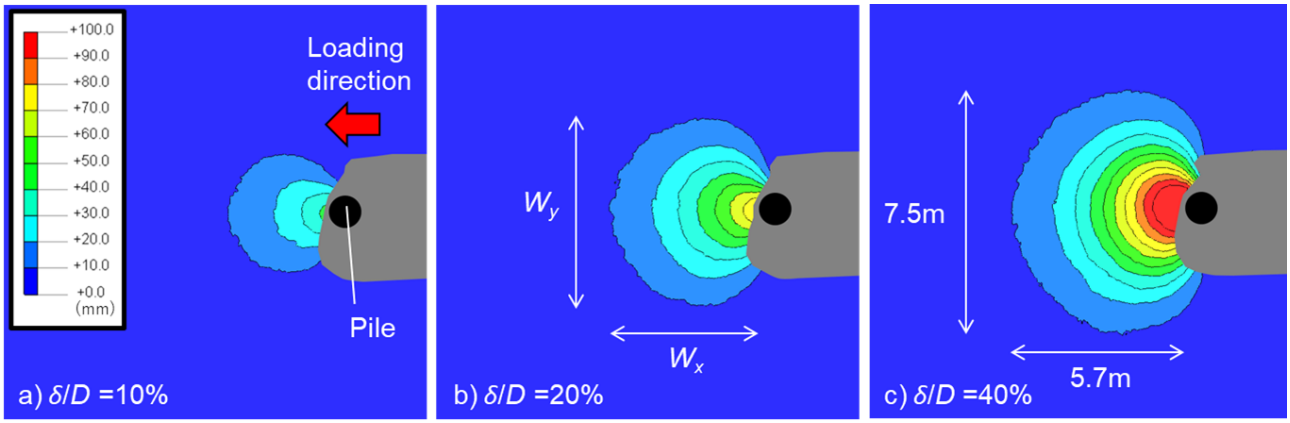

Figure 4. Displacement of the ground surface: pile head displacements of a) 100 mm (δ/D=10%), b) 200mm (δ/D=20%), and c) 400mm (δ/D=40%).

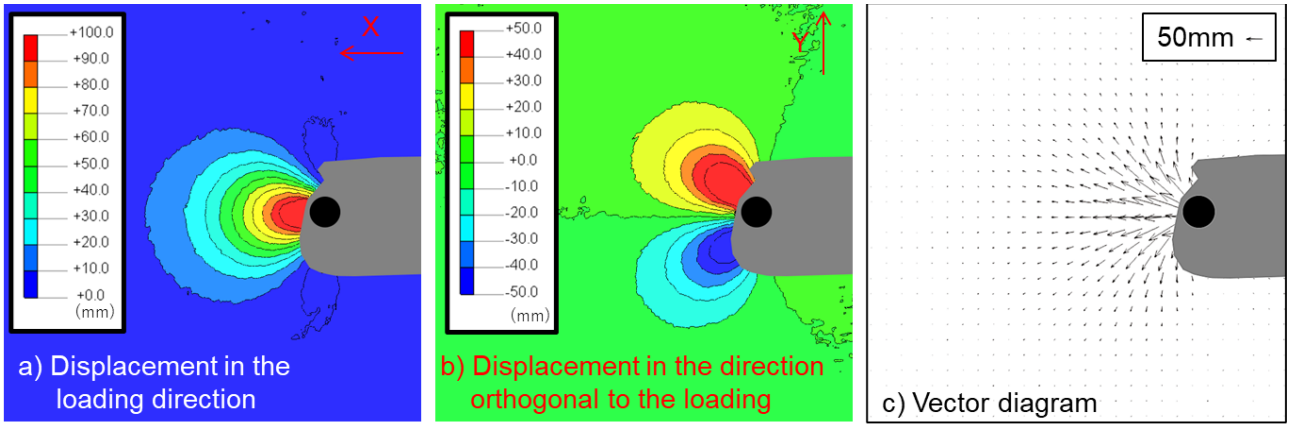

Figure 5. Displacement of the ground surface at pile head displacements of 400mm (δ/D=40%): a) loading direction, b) direction orthogonal to the loading, and c) vector diagram.

loading direction and not in the orthogonal direction of loading. As shown in Figure 5 (b), the ground in the area located at a distance from the loading axis was also displaced in a direction orthogonal to the loading.

3.3 Deformation of ground section during horizontal pile loading

Figure 6 shows the contour charts of the ground section displacement. This occurred during the loading stages at 10, 20, and 40% of the pile diameter. In the initial stage of loading, the displacement distribution in front of the pile was triangular (Figure 6 (a)), and as the pile head displacement increased, the displacement distribution became into a quadrant (Figure 6 (c)). When the pile head displacement was 40% of the pile diameter (Figure 6 (c)), the area of displacement beyond 10 mm expanded 6 m in the depth direction and 5.7 m in the loading direction, which is approximately the same as the results of the full-section experiment. On the rear side of the pile, the ground within 2.1 m of the pile was displaced.

Figure 7 shows the displacement in the loading direction, the vertical displacement, and the displacement vector of the ground section. Figure 7 (b) shows that ground shallower than 3.2 m in depth was displaced vertically upward, and Figure 7 (c) shows that the ground in that area was displaced in the surface direction. Deeper ground was displaced horizontally. The ground at the rear side of the pile settled significantly.

3.4 Size of the three-dimensional deformation area of ground

Since the ground deformed as the load was transmitted, and the deformation area of the ground was quantified. W_x is the extent of the ground deformation area in front of the pile in the loading direction with a displacement of 10 mm (0.01D) or more (from the results of the full-section experiment). The extent of the deformation area in the direction orthogonal to the loading is W_y, and the extent of the deformation area in the depth direction is W_z. Figure 8 shows the relationship between pile head displacement and the extent of deformation area. The pile head displacement and extent of the deformation area were normalized by pile diameter D. When the pile head displacement was 50%

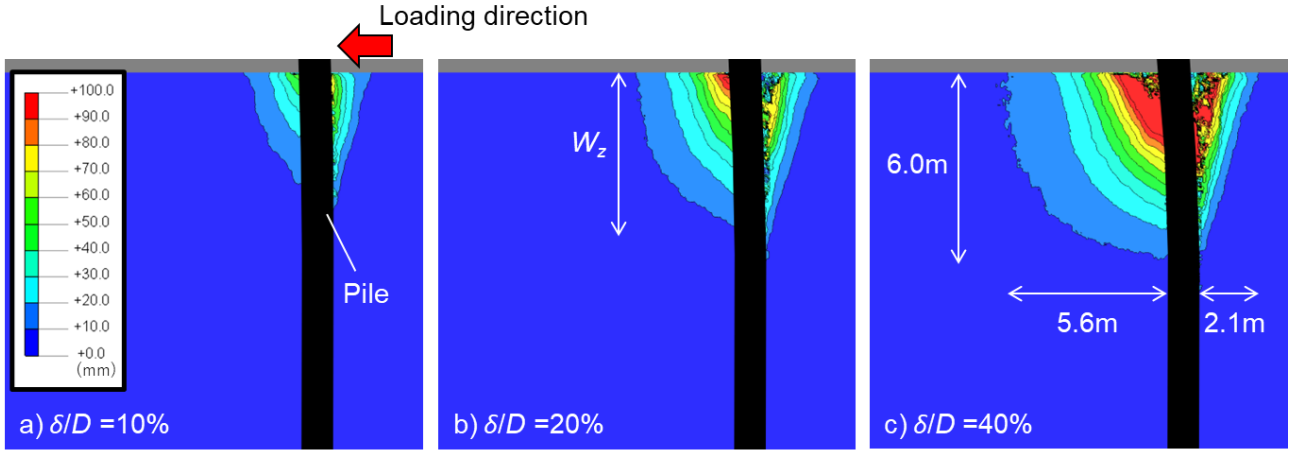

Figure 6. Displacement of the ground section: pile head displacements of a) 100 mm (δ/D=10%), b) 200mm (δ/D=20%), and c) 400mm (δ/D=40%).

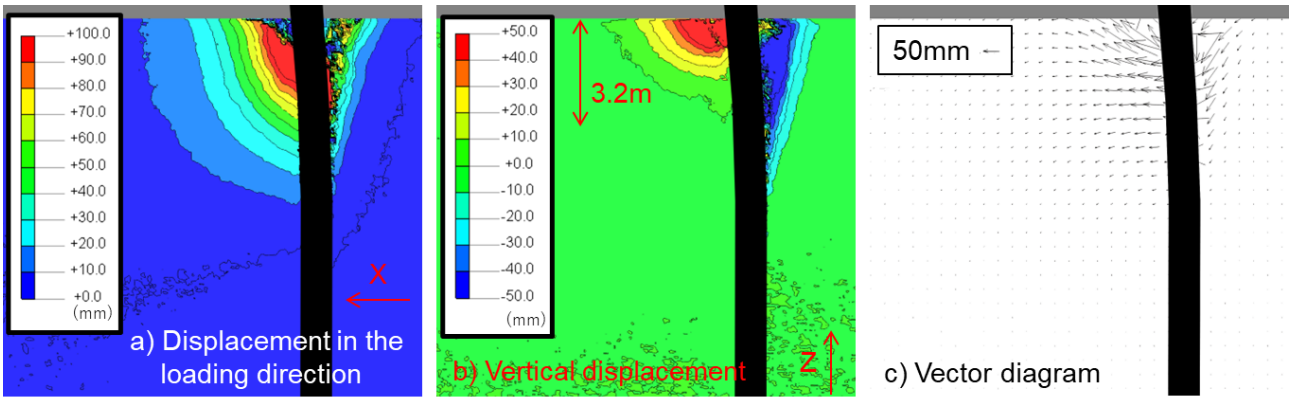

Figure 7. Displacement of the ground section at pile head displacements of 400mm (δ/D=40%): a) loading direction, b) vertical displacement, and c) vector diagram.

of the pile diameter, W_x and W_z were approximately six times the pile diameter, and W_y was approximately eight times the pile diameter. Odagiri et al. (2023) reported that a 0.01D displacement occurred at a distance 10 times the pile diameter (10D) in the loading direction from the pile when the pile head displacement was 20% of the pile diameter in a 1G field test. The results of this centrifugal field experiment demonstrated that the size of the deformed region was smaller than that in a 1G field. This is because the results of this centrifugal experiments were able to take into consideration the effect of ground confining pressure, which closely approximates actual ground conditions.

Figure 9 shows the relationship between the pile head horizontal load and the extent of the deformation area. The results are shown for pile head displacements up to 50% of the pile diameter, at which point the pile head load has almost reached its ultimate state. The pile head load on the horizontal axis was determined by the full-section experiment. As the pile head load increases, W_x, W_y, and W_z increase almost linearly. Thus, the size of the deformation area in the front of the pile is related to the resistance force of the pile.

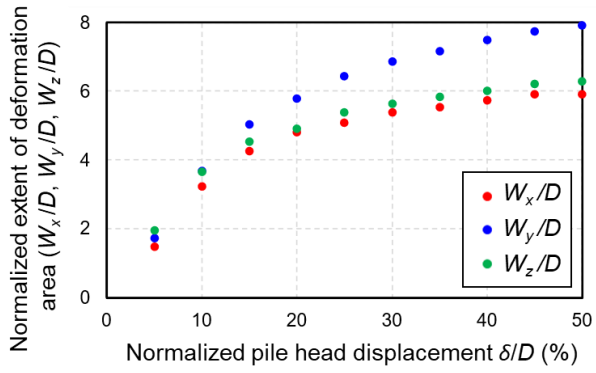

Figure 8. Relationships between the extent of deformation area and the displacement at the pile head.

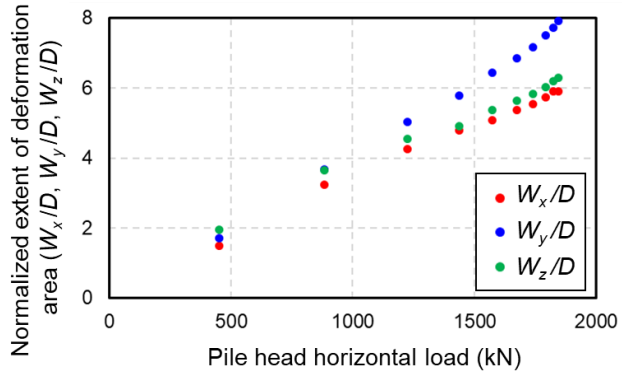

Figure 9. Relationships between the extent of deformation area and the pile head horizontal load.

4 CONCLUSIONS

The behaviors of the ground surface and section during horizontal pile loading in the centrifugal field were observed. The displacement distribution in front of the pile on the ground surface exhibited a nearly circular pattern, whereas that on the ground section exhibited a triangular pattern during the initial loading and became quadrangular as the pile head displacement increased. The shallow part of the ground in front of the pile was displaced in the direction of the ground surface owing to pile displacement. The size of the 3D deformation area of the ground in front of a pile at each loading stage was analyzed, and the results indicated that the horizontal resistance of a pile is related to the size of the deformation area of the ground.

REFERENCES

Hajialilue-Bonab, M., Azarnya-Shahgoli, H. & Sojoudi, y. (2011). Soil deformation pattern around laterally loaded piles, *International Journal of Physical Modelling in Geotechnics*, 11 (3), 116-125. https://doi.org/10.1680/ijpmg.2011.11.3.116.

JPIV. https://eguvep.github.io/jpiv/, accessed: 2023/10/17.

Odagiri, M., Kiriyama, T. & Asaka, Y. (2023). Behavior of soil surface due to a laterally loaded pile based on a 1G model test and PIV, *Proceedings of the 5th international conference on geotechnics for sustainable*, Hanoi, Vietnam.

Otani, J., Pham, K. D. & Sano, J. (2006). Investigation of failure patterns in sand due to laterally loaded pile using X-ray CT, *Soils and Foundations*, 46 (4), 529-535. https://doi.org/10.3208/sandf.46.529.

Reese, L. C., Cox, W. R. & Koop, F. D. (1974). Analysis of laterally loaded piles in sand, *Offshore Technology Conference*, Dallas, TX, OTC2080. https://doi.org/10.4043/2080-MS.

Yuan, B., Xu, K., Wang, Y., Chen, R., & Luo, Q. (2017). Investigation of deflection of a Laterally loaded pile and soil deformation using the PIV technique, *International Journal of Geomechanics,* 17 (6), 04016138. https://doi.org/10.1061/(ASCE)GM.1943-5622.0000842.

White, D.J., Take, W.A. & Bolton, M.D. (2003). Soil deformation measurement using particle image velocimetry (PIV) and photogrammetry, *Géotechnique*, 53 (7), 619-631. https://doi.org/10.1680/geot.2003.53.7.619.

Proceedings of the XVIII ECSMGE 2024
GEOTECHNICAL ENGINEERING CHALLENGES
TO MEET CURRENT AND EMERGING NEEDS OF SOCIETY
© 2024 the Authors
ISBN 978-1-032-54816-6
DOI 10.1201/9781003431749-116
Open Access: www.taylorfrancis.com, CC BY-NC-ND 4.0 license

ECSMGE 24
XVIII EUROPEAN CONFERENCE ON SOIL MECHANICS AND GEOTECHNICAL ENGINEERING

Correlating q_{net} to E_{ur} of Paleogene clays of high plasticity

Corréler q_{net} à E_{ur} des argiles Paléogènes de haute plasticité

N. Okkels*, L. Bødker, T. Thorsen
Geo, Aarhus, Denmark

**nio@geo.dk*

ABSTRACT: This paper provides a practical formulation for correlating net-corrected cone resistance q_{net} to the drained unloading and reloading stiffness E_{ur} in highly overconsolidated, fissured, marine Paleogene clays of very high plasticity as observed in Aarhus, Denmark. E_{ur} is used for analysis of soil deformations using Hardening Soil models, which is particularly advantageous to use rather than more traditional Mohr-Coulomb soil models when the soil model has to handle both loading and unloading. By correlating E_{ur} from 34 drained triaxial tests to q_{net} from CPTu's near the boreholes from which the triaxial-samples are extracted, a linear correlation between these two properties is found. This formulation makes it possible to derive E_{ur} directly from CPTu for use in preliminary analysis of deformations. More importantly, the correlation supports the final derivation of E_{ur} for 3D finite element models once the results of all field and laboratory tests for the construction project are available.

RÉSUMÉ: Cet article fournit une formulation pratique pour corréler la résistance du cône corrigée nette q_{net} à la rigidité drainée de déchargement et de rechargement E_{ur} dans des argiles marines paléogènes fortement surconsolidées et fissurées de très haute plasticité, comme observé à Aarhus, au Danemark. E_{ur} est utilisé pour l'analyse des déformations du sol à l'aide de modèles de sol durcis sables, ce qui est particulièrement avantageux à utiliser plutôt que des modèles de sol Mohr-Coulomb plus traditionnels lorsque le modèle de sol doit gérer à la fois le chargement et le déchargement. En corrélant l'E_{ur} de 34 tests triaxiaux drainés avec le q_{net} des CPTu proches des forages d'où les échantillons triaxiaux sont extraits, une corrélation linéaire entre ces deux propriétés est trouvée. Cette formulation permet de dériver E_{ur} directement à partir de CPTu pour une utilisation dans l'analyse préliminaire des déformations. Plus important encore, les corrélations soutiennent le calcul final de l'E_{ur} pour les modèles d'éléments finis 3D une fois que les résultats de tous les tests sur le terrain et en laboratoire pour le projet de construction seront disponibles.

Keywords: Clay; overconsolidated; very high plasticity; cone resistance; drained unloading-reloading stiffness.

1 INTRODUCTION

It has become common practice to perform triaxial tests to determine the drained triaxial unloading and reloading stiffness for use in Hardening Soil (HS) models and Hardening Soil small strain (HSs) models when analyzing the deformations of high-rise buildings in the city of Aarhus, Denmark.

At the same time, CPTu has become the preferred investigation method because it is the most effective way to illuminate how stratigraphy, strength and stiffness varies spatially. In order to exploit this commercially, Geo has derived an Aarhus correlation between the net-corrected cone resistance q_{net} from the CPT's and the drained triaxial unloading and reloading stiffness E_{ur}.

The CPTu's are performed in a single continuous stroke from the ground surface to target depth using Geo's enhanced CPT-system, which reduce the friction on the rod and makes it possible to push the cone through more than 80 meters of very firm clays.

Geo's CPT-crawler with a maximum push capacity of 15 ton is used together with a 10 or 15 cm^2 piezoelectric cone from the manufacturer A.P. van den Berg. The equipment and the execution are in agreement with ISO 22476-1 with continuous measurement of tip resistance, sleeve friction, pore pressure (measured behind the tip of the probe) and inclination of the probe.

The CPTu's are supplemented with geotechnical boreholes for use in interpreting the CPTu's and for extracting soil samples for classification and advanced laboratory tests.

2 THE PALEOGENE STRATIFICATION

In costal parts of Aarhus, the Paleogene stratification is found near the surface only covered by fill and/or a thin series of glacial and or postglacial layers. The following stratification is typically found, cf. figure 1:

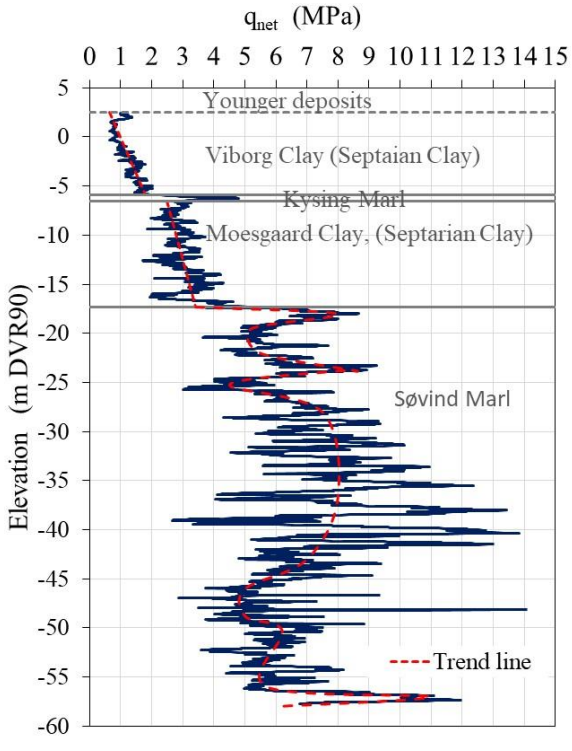

Figure 1. An example of a q_{net}-profile calculated from one of nine CPTu's included in this study.

- Topmost 5-9 meter Viborg Clay, which is an Oligocene clay of very high plasticity with mica.
- The Viborg clay is underlain by 0.5-2 meters Kysing Marl, which is a highly glauconitous, highly calcareous and high to very high plasticity clay from the top of the Eocene Søvind Marl formation. It is quite similar to the underlying Søvind Marl, but the geotechnical properties are better.
- Below the Kysing Marl typically 9 to 13 meters of Moesgaard Clay - which is an Eocene clay of very high plasticity with mica - is found. This clay is somewhat reminiscent of the overlying Viborg Clay in terms of appearance and geotechnical properties. The trivial name "Septarian Clay" is traditionally used for both clay types.
- Søvind Marl underlies Moesgaard Clay. Søvind Marl is a clay of very high plasticity that makes up the majority of the Søvind Marl formation. It is predominantly very calcareous. However, calcareous free or slightly calcareous zones frequently alternate with more calcareous ones.

All these clays are deposited in a deep ocean and with exception of the Kysing Marl, they are all fissured with slickensides. Due to removal of younger layers by erosion and the weight of numerous glaciers during the Quaternary period, they are also highly overconsolidated with a geological preconsolidation stress greater than two MPa.

Large variations in plasticity and calcium carbonate content indicate that also strength and deformation properties vary a lot down through the formations. Variability in CPTu cone resistance confirms this, cf. figure 1. If cone resistance is decomposed into a trend component and a fluctuating component, the CPTu's show, that the fluctuating component is characterized by frequent and violent fluctuations around a trend line. Through the Septarian clays, the trend line is directly proportional to depth, but in the Søvind Marl it varies in large irregular cycles.

3 TEST PROCEDURES

The primary target for the triaxial tests has been to determine the drained unloading and reloading stiffness E_{ur}.

The tests are performed on nominally undisturbed specimens extracted from Shelby-tube samples with a diameter of 70 mm and a height to diameter ratio of 1. Smooth and lubricated end plates are used.

All tests are carried out isotopically consolidated with a drained failure state (CID) according to the guidelines in ISO 17892-9. De-aired tap water is used. It also applies, that a plasticity index I_P and a calcium carbonate content are determined on the specimen material itself and/or the trimming material.

Due to the swelling potential of the clays, it is necessary to set the isotropic chamber pressure during the initial flushing and water saturation of the system so high that the samples are prevented from swelling. The chamber pressure is determined corresponding to the specimen's effective in situ mean stress, which is initially estimated from the vertical effective in situ stress and a coefficient of lateral earth pressure, K_0 (between 1.3 and 2.5). If the specimen swell, the chamber pressure is increased until swelling is prevented.

Next, the specimens are isotopically pre-consolidated to a conservatively estimated pre-consolidation stress (mean stress determined from a cautious estimated vertical pre-consolidation stress and K_0 = 0.4 to simulate a normal consolidated state prior to the geological unloading). The consolidation phase is carried out according to Danish tradition in order to reduce the influence from the inevitable sample disturbance (Jacobsen, 1970). Finally, the specimen is isotopically unloaded to a stress corresponding to the chamber pressure found during the initial phase, from which the shearing phase starts.

The applied rate of strain during shearing is chosen according to ISO 17892-9 to ensure slow enough rates

to achieve full equalization of pore water pressures in the specimen. For very high plasticity clay, this means that the applied strain rate is around 0.02-0.05%/hr. All tests are continued until failure.

$E_{ur;TX}$ is determined as the secant stiffness from the unloading and reloading loop. In the calculation, the strain is corrected for the compression of the lubricated latex sliding membranes, which are placed at both ends of the samples to ensure smooth endplates. Tests carried out with identical equipment show that the compression (strain) of the membranes can be evaluated from the following expression (for a 70 mm high specimen):

$$\epsilon_{membran} = 0.070\, ln\sigma'_V + 0.31 \qquad (1)$$

where σ'_V is the effective vertical stress acting on the specimen.

E_{ur} is stress-dependent, as it (regarding to the soil models HS or HSs) depends on the minimum principal stress σ'_3 - which initially is vertical in overconsolidated soil. For a given type of soil, the stiffness E_{ur} therefore varies with σ'_3 (typically corresponding to stiffness increasing with depth).

Only if the triaxial test is carried out at an effective chamber pressure $\sigma'_{3;TX}$, which is equal to the vertical effective in situ stress σ'_{v0} at the level where the soil sample is taken, the measured stiffness $E_{ur;TX}$ corresponds to the in situ stiffness. Due to the swelling pressure, however, the tests are typically performed at a higher chamber pressure. Therefore, it is necessary to correct the measured stiffness, if the stiffness is to be correlated with the q_{net} value measured at the same depth. This is necessary because the stiffnesses of the overconsolidated Paleogene clay types naturally fluctuate significantly with depth.

The in situ stiffness $E_{ur;insitu}$ for use in the correlation with q_{net} is calculated from equation 2 (Brinkgreve and Vermeer, 2015):

$$E_{ur;insitu} = E_{ur;TX}\left(\frac{c\,cos\varphi + \sigma'_{v0}\,sin\varphi}{c\,cos\varphi + p^{ref}\,sin\varphi}\right)^{m} \qquad (2)$$

where p^{ref} is replaced with $\sigma'_{3;TX}$. The tests indicate effective strength parameters $\varphi' = 22°$ and $c' = 40$kPa for Septarian clays and $\varphi' = 30°$ and $c' = 40$kPa for Søvind Marl. Simulations in Plaxis Soil Test indicate that the stress-dependency parameter $m \approx 0.7$. The $E_{ur;insitu}$ calculation is checked in Figure 2.

As part of commercial ground investigations, $E_{ur;TX}$ and $E_{ur;insitu}$ are derived from a total of 16 triaxial tests with Septarian Clay types and 21 triaxial tests with Søvind Marl and presented in Table 1 and 2. A total of 9 pairs of CPT's and borings are included in this study.

Table 1. Test results Septarian Clays (I_P = 56-100%).

Geo ID	σ'_{v0} [kPa]	$\sigma'_{3;TX}$ [kPa]	q_{net} [MPa]	$E_{ur;TX}$ [MPa]	$E_{ur;insitu}$ [MPa]
204608 1;34	173	341	2.60	30.0	21.5
204296 1;37	170	211	3.93	38.8	35.2
205173 2;17	80	200	1.40	29.1	20.4
205173 2;41	186	246	3.50	80.2	70.2
205231 1;20	102	207	2.33	30.7	22.9
205231 1;12	70	122	1.65	20.8	17.3
204607 1;11	60	80	1.13	13.8	12.7
204607 1;15	75	23	1.45	12.3	15.7
204607 1;19	90	50	1.75	16.4	19.3
204607 1;27	125	101	2.13	22.1	23.9
206449 15;39	185	287	3.32	44.7	36.1
206449 15;47	220	485	4.00	40.9	26.8
206449 15;55	250	407	4.50	39.9	30.8
206374 1;25	131	268	1.95	50.7	36.6
206374 1;33	167	239	3.10	84.5	71.5
206385 4;31	160	247	2.25	29.9	24.4

Table 2. Test results for Søvind Marl (I_P = 67-192%).

Geo ID	σ'_{v0} [kPa]	$\sigma'_{3;TX}$ [kPa]	q_{net} [MPa]	$E_{ur;TX}$ [MPa]	$E_{ur;insitu}$ [MPa]
204608 1;58	269	324	5.40	50.1	45.1
204608 1;66	301	348	6.50	67.5	62.1
204608 1;82	365	470	9.40	56.8	48.8
204296 1;77	330	331	11.0	157.7	157.4
204296 1;101	425	463	5,80	55.6	52.8
204296 6;53	240	340	6,00	41.2	33.9
204296 6;85	365	547	4.90	69.9	54.7
204296 6;125	520	621	6.10	92.5	82.8
205173 2;65	289	365	8.90	90.5	79.1
205173 2;81	457	454	8.70	86.5	86.8
205173 2;97	428	541	5.00	96.8	83.9
205231 1;44	198	265	5.75	58.0	49.6
205231 1;28	134	201	3.20	40.0	32.9
204607 1;35	157	122	3.55	37.4	42.1
204607 1;39	175	144	4.00	28.9	31.8
206374 1;41	131	281	5.00	43.9	29.7
206374 1;57	270	330	6.50	62.0	55.3
206374 1;81	372	581	6.50	52.8	40.2
206374 1;89	406	641	7.00	92.7	70.0
206385 4;51	250	294	4.70	34.5	31.5
206385 4;61	295	352	5.50	81.1	73.3

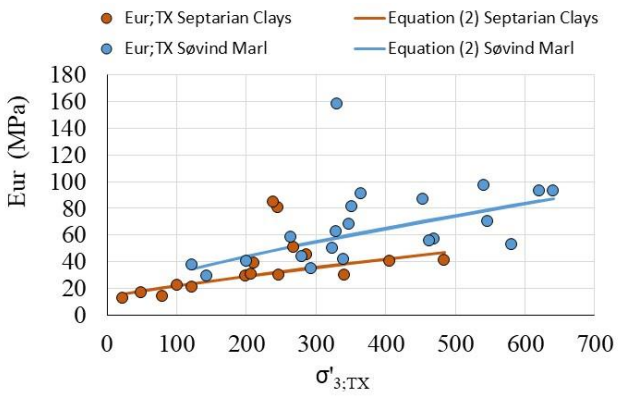

Figure 2. Check of equation (2) and the derived soil parameters.

4 CORRELATING QNET AND EUR

In commercial ground investigations about a handful or two of triaxial tests are usually carried out per site. Consequently, the soil volume with which tests are carried out is typically in the order of one billionth of the soil volume that is subsequently modelled when the settlements are to be calculated. It is therefore only possible to establish a statistically acceptable basis for deriving a valid input to a soil model if it is included the knowledge that CPTs and strength measurements in boreholes provide about the spatial variation of the stiffness. In practice, this is done by correlating the results of laboratory tests with field tests such as CPT and field vane tests.

However, the number of tests remains insufficient considering the large natural fluctuations that naturally occur in the stiffness of the overconsolidated clays cf. Figure 1. Therefore, it is necessary to improve the statistical basis by including a priori knowledge about the stiffness parameters. This is done by including corresponding correlations between measured stiffnesses and CPT-data collected in connection with previous ground investigations in the same clay types.

Only in this way is it possible to create an acceptable statistical basis for deriving a valid 3D stiffness model for use in settlement calculations.

Corresponding values of $E_{ur;insitu}$ and the net cone resistance q_{net} are plotted in Figure 3, where q_{net} is measured in a nearby CPTu at the same level as samples for the triaxial test were extracted from the boreholes (mean value of q_{net} over 0.2 m CPT).

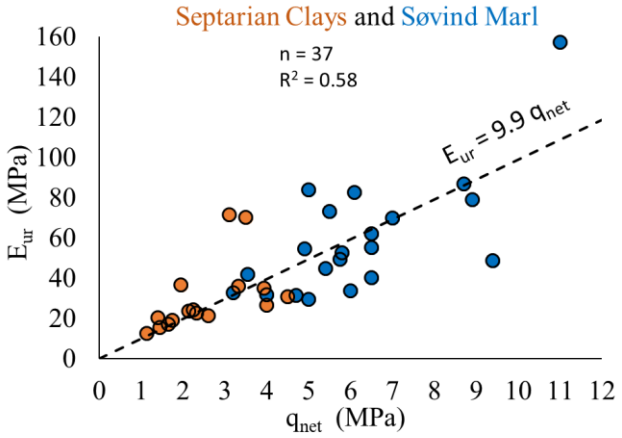

Figure 3. Correlation between q_{net} and the drained E_{ur}.

The CPTu's are typically performed approximately two meter from the borehole. However due to the inevitable deflection, the distance may be different at target depth. The distance introduces uncertainty and thus scatter when the highly fluctuating CPTu measurements are correlated with measured soil parameters from in situ testing and from laboratory testing on soil samples extracted from the boring. Therefore, a large number of tests is required to achieve a satisfactory strong correlation.

Based on available data, the following Aarhus correlation is derived for Septarian Clays and Søvind Marl:

$$E_{ur} \approx 9.9\, q_{net} \qquad (3)$$

A confidence interval for the proportionality factor was computed to be $CI(95) = 9.9 \pm 1.4$.

According to Figure 3, the deviation appears to increase as q_{net} increases. Since the overall trend is that q_{net} also increases with depth and q_{net} at the same time fluctuate violently around its overall trend cf. Figure 1, the inevitable inclination means that the distance between CPTu probe and extracted samples changes with depth and thereby deteriorates the correlation between q_{net} and E_{ur}.

5 SUMMARY AND CONCLUSION

During ground investigations for high-rise buildings in Aarhus, Geo has determined the drained unloading and reloading stiffness from 16 triaxial tests with Septarian Clays and 21 triaxial tests with Søvind Marl. On this basis, an Aarhus correlation between q_{net} the E_{ur} has been derived cf. eq. (3).

The proposed correlation makes it possible to transform CPTu-profiles into drained unloading and reloading stiffness E_{ur}-profiles for use in preliminary analysis of deformations. More importantly, the correlations support the final derivation of E_{ur} for 3D finite element models once the results of all field and laboratory tests for the construction project are available.

The derived local correlation between q_{net} and E_{ur} indicates that it is also possible to formulate similar correlations between q_{net} and other stiffness parameters such as the small strain shear modulus G_{max} and the oedometer stiffness E_{oed} for reloading in these highly overconsolidated, fissured, marine Paleogene clays of very high plasticity.

REFERENCES

Brinkgreve R.B.J, Vermeer, P.A. (2015). *PLAXIS-Finite element code for soil and rock analysis, Plaxis 3D*. Manuals, Delft University of Technology & Plaxis bv, The Netherlands.

Jacobsen, M. H. (1970). *New oedometer and new triaxial apparatus for firm soils*, The Danish Geotechnical Institute (Geo), bull. 27, Copenhagen.

Proceedings of the XVIII ECSMGE 2024
GEOTECHNICAL ENGINEERING CHALLENGES
TO MEET CURRENT AND EMERGING NEEDS OF SOCIETY
© 2024 the Authors
ISBN 978-1-032-54816-6
DOI 10.1201/9781003431749-117
Open Access: www.taylorfrancis.com, CC BY-NC-ND 4.0 license

ECSMGE 24
XVIII EUROPEAN CONFERENCE ON SOIL MECHANICS AND GEOTECHNICAL ENGINEERING

High embankments on soft soils – geotechnical design based on field monitoring and back analysis, Romania, Sebeş-Turda motorway

Emploi élevé sur sols mous – conception géotechnique basée sur la surveillance de terrain et la rétro-analyse, Roumanie, autoroute Sebeş Turda

A.C. Olteanu, T. Malancu*, C. Tomsa
Technical University of Civil Engineering, Bucharest, Romania
teodor.malancu@gmail.com

ABSTRACT: This paper presents an analysis of a high embankment on a compressible soil area on the newly designed highway route Sebes Turda, 2nd Lot, km26+000 (Romania, Transylvania, Alba County). Due to the difficult soil conditions and hydro geological issues of the analysed area, the configuration of the newly designed structure of the railway passage and especially the proposed consolidation solution required validation by geotechnical monitoring. Given the intensity of some geomorphological processes and the acceleration of soil degradation in certain sectors as a result of anthropic intervention, several consolidation works were proposed consisting in the use of earthworks (reinforced with geosynthetics) and / or stone columns (with radial drainage and reinforcement function), that were numerically modelled and studied in order to determine the values of the settlements and especially consolidation time. The validation of the designed solutions is decided based on results obtained from experimental trials instrumented by means of monitoring deformations, pressures, and water level variations (free and under pressure). The results based on monitoring represent criteria for choosing the consolidation solution and especially a validation / correction of the constitutive model for the foundation ground. Details regarding laboratory test results correlated with in situ testing and modelling of soil structure interaction will be approached, as well as presented by comparison with back analysis results.

RÉSUMÉ: Cet article présente une étude de cas détaillée d'une solution de remblai élevé adoptée pour une zone de sol compressible sur la nouvelle route routière Sebeş Turda, 2e lot, km26+000 (Roumanie, Transilvanie, comté d'Alba). En raison des conditions pédologiques difficiles et des enjeux hydrogéologiques de la zone analysée, la configuration de la structure nouvellement conçue du passage ferroviaire et surtout la solution de consolidation proposée ont nécessité une validation par suivi géotechnique. Compte tenu de l'intensité de certains processus géomorphologiques et de l'accélération de la dégradation des sols dans certains secteurs suite à l'intervention anthropique, plusieurs travaux de consolidation ont été proposés consistant en l'utilisation de terrassements (renforcés de géo synthétiques) et/ou de colonnes en pierre (avec drainage radial et renforcement fonction), qui ont été modélisés et étudiés numériquement afin de déterminer les valeurs des tassements et surtout le temps de consolidation. La validation des solutions conçues est décidée sur la base des résultats obtenus à partir d'essais expérimentaux instrumentés par le suivi des déformations, des pressions et des variations du niveau d'eau (libre et sous pression). Les résultats basés sur le suivi représentent des critères de choix de la solution de consolidation et surtout une validation/correction du modèle constitutif du sol de fondation. Les détails concernant les résultats des tests en laboratoire corrélés aux tests in situ et à la modélisation de l'interaction sol-structure seront abordés, ainsi que présentés par comparaison avec les résultats des analyses rétrospectives.

Keywords: Compressible soil; high embankments; monitoring.

1 INTRODUCTION

The site is located along the Sebes-Turda motorway, which connects the cities of Turda, Alba Iulia and Sebes, figure 1. The monitored sector is a high bridge ramp, figure 2 located on a very compressible alluvial soil, figure 3. The foundation solutions consisted of a combination of several consolidation works in order to achieve the desired results according to the beneficiary's requirements, i.e. settlements of less than 2 cm. Therefore, due to the lithology and hydrogeological conditions of the foundation ground, the nature of the passageway structure, and particularly the proposed consolidation solution required validation through geotechnical monitoring.

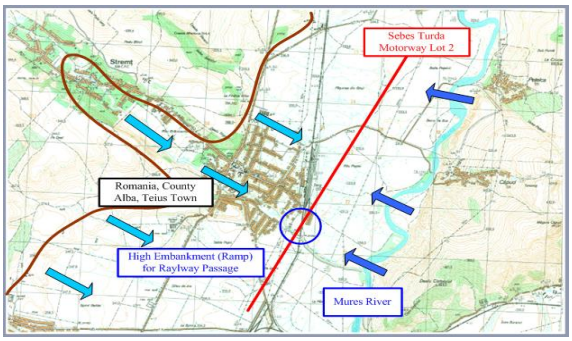

Figure 1. Plan.

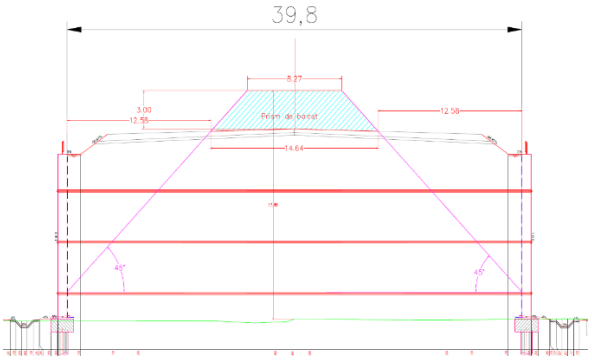

Figure 2. Analysed characteristic profile.

2 HYDRO, GEOLOGICAL AND MORPHOLOGYCAL CONDITIONS OF THE SITE

From a morphological point of view, the analysed site is located at the southern edge of the hilly area of the Transylvanian Depression, which presents various geomorphological processes. This perimeter is approximately 400÷600 m above sea level, surrounded on all sides, except for the north-western region, by the hilly area and mountains. The area has been divided by several rivers to form a rolling relief, with alluvial plains at the valley bottom.

For the site under analysis, it can be said that the relief is developed on clays and marls specific to the hilly regions of the Transylvanian Depression. The relief has regionally differentiated features, depending on the variety of clay rocks, on the stage of evolution and on the specificity of the action of the environmental modelling factors. The mineralogical composition, the physical-mechanical properties and the textural peculiarities show great differences from one relief unit to another.

A particular feature area is the montmorillonite clays present in marine and volcano-sedimentary formations, clays with high sensitivity to mass displacements. The analysed geographical area is mainly characterised by concave slopes with a broadly undulating or stepped profile, the lower third of which is covered by thick colluvial-deluvial deposits.

2.1 Selection the critical section

The profile was selected based on geometry, corresponding to an area with the highest embankment height and difficult foundation ground.

The calculation values for the geotechnical parameters resulted from the values determined from the corrected laboratory and field tests and following a statistical calculation of the values grouped by soil types, where these laboratory data were insufficient. The chosen section can be found in figure 2.

The parameters of the deformation process in time were determined (consolidation process) based on the in situ and laboratory geotechnical investigation. The lithological column used for the calculation and for the monitoring correlation is shown in the following figure. 3.

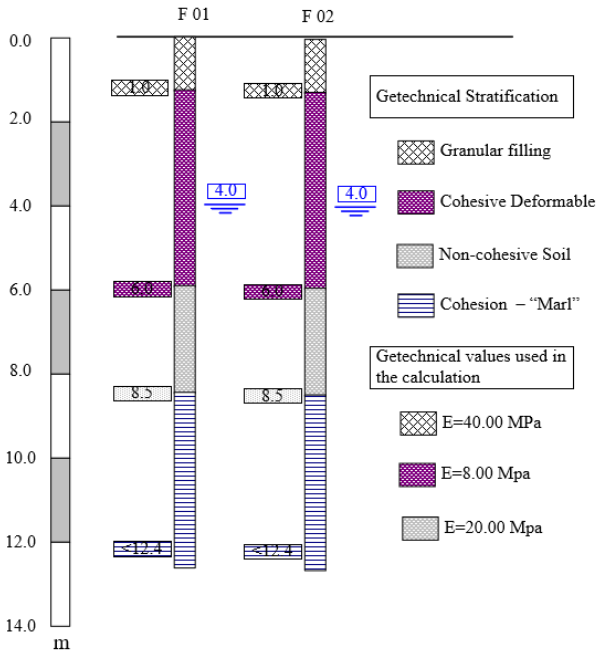

Figure 3. Lithology of the site.

2.2 Selection of the consolidation solution

The purpose of the calculation notes was to determine the maximum values of the settlement of the new embankment at the level of the foundation ground and in the upper part, in the axis.

If the results of the calculations show that the foundation ground does not have the capacity to bear the loads of the embankment or suffers from significant settlements that may endanger the safety of the construction, the possibility of improving the properties of the soil in the respective layer so that it meets the conditions of a proper foundation ground should be examined.

The proposed foundation solutions with the use of earthworks (reinforced with geosynthetics) and / or stone columns (with radial drainage and reinforcement function) have been numerically modelled in order to determine the values of the settlements and in particular the consolidation time.

The optimal solution chosen was the solution with stone columns (with radial drainage and reinforcement function), stone blocking and the application of an overload to speed up settlement. Following the analysis of this solution, figure 4, settlement values (S=31 cm) and the degree of consolidation, 80% that could be implemented in the project were obtained.

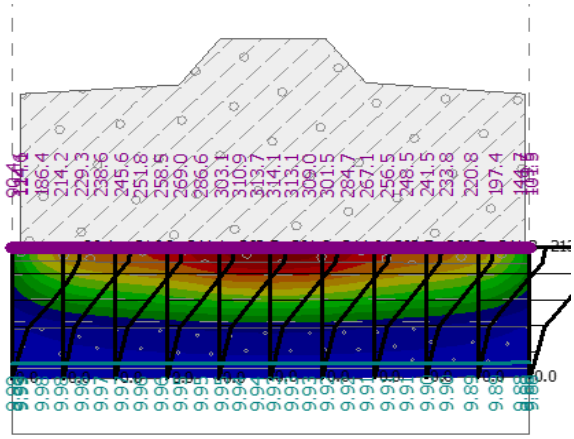

Figure 4. Settlement calculation result.

2.3 Geotechnical monitoring

Geotechnical monitoring consisted of the installation of a piezometer, outside the ramp, and a Tasometer, in the area with the highest ramp height, figure 5.

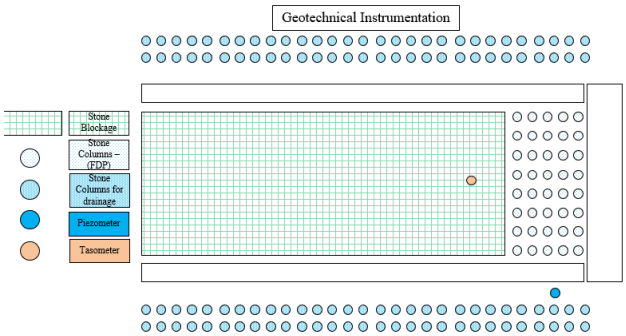

Figure 5. The location of the monitoring sistems.

For the Monitoring System - Piezometer with Free Level ""Right Wall" it was desired to identify the effects of the realization of the Embankment, the realization of the Overload and the Efficiency of the perimeter drainage conditions by correlating the Execution Stages versus Time with the measurements of the Water Levels (Compression and Drainage Process)

The monitoring was designed to cover all construction phases of the embankment and highlight the effects of each stage.

The following stages are presented as Preloading Structure Realization Stages and Monitoring Realization Stages respectively:

1.System Data Initialization Stage
2.Monitoring with reference to 1.0m Embankment figure 6.
3.Monitoring with reference to 5.0m Embankment
4.Monitoring with reference to 8.0m Embankment
5.Monitoring with reference to 12.0m Embankment
6.Monitoring with reference to 15.0m Embankment
7.Monitoring with reference to 15.0m Embankment 3m Overload– Ballast, figure 7

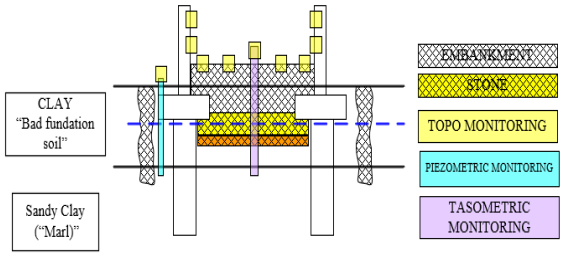

Figure 6. Etap 2 embankment 1.0 m.

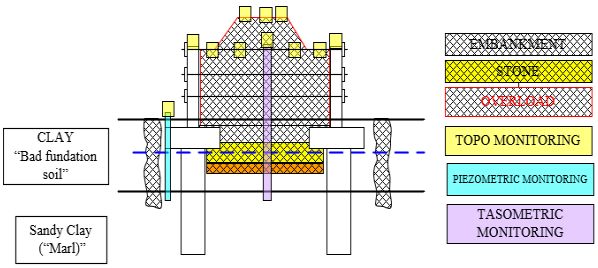

Figure 7. Etap 7 embankment 15.00 m plus overload.

The validation of the Design (solution) is decided based on results obtained from experimental sectors instrumented with equipment for monitoring deformations, pressures, variations of water level (free and under pressure). The results based on monitoring represent criteria for confirmed the consolidation solution and especially for validation / correction of the constitutive model for the foundation ground.

3 GRAPHICAL REPRESENTATION OF RESULTS

The recorded data allow the representation of the consolidation curve of the foundation ground (the high compressibility cohesive alluvial horizon being prioritized in the analysis).

The graphical representation indicates that the Primary Consolidation Process is 80% completed and that the applied overload (3.0 m ballast which

represents ~ 20% of the structure height and 10% of the structure overload value) brings an additional contribution of 2÷ 3 cm (10% of the 26 cm of the Primary Consolidation Process), figure 8.

The period of occurrence of the recorded deformations indicates a high speed of the Settlement Process (2÷3 cm <30 days of overload application).

From the point of view of the recorded deformation values, it is accepted to eliminate the overloads and to continue the project, provided that the monitoring conditions for the tasometer are ensured during the operation of the infrastructure.

Table 1. Position of the sensor relative to ground elevation.

Sensor nr.	Depth (m)
6	0.42
5	1.270
4	1.390
3	7.920
2	13.000
1	14.100

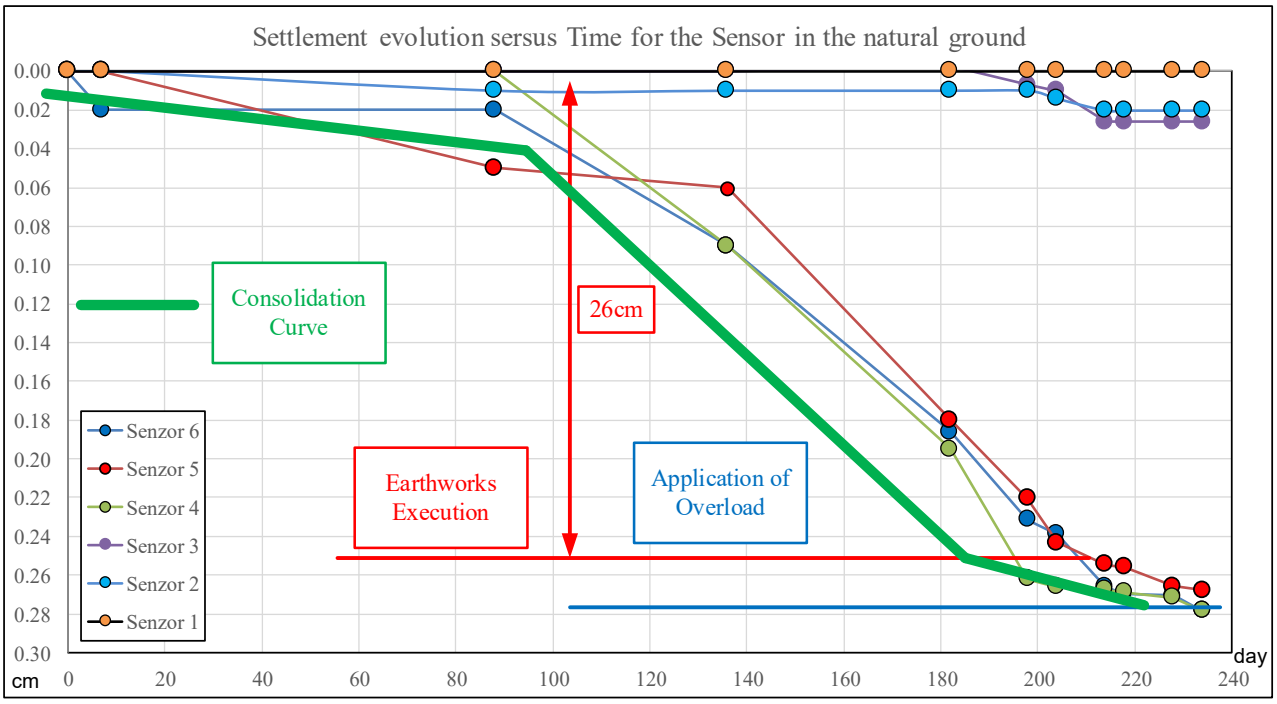

Figure 8. Graphical representation of the results.

4 CONCLUSIONS

The recorded deformations and their evolution over time confirm the effectiveness of the application of the Structure Preloading Solution in consuming settlements. For the foundation ground situation (CTN Reference) 2.0 m blockage, 4.0 m compressible ground E~8000kPa, the consolidation time related to a consolidation degree of 80% is considered. The high deformability of the foundation ground in the area adjacent to the support structures ("walls founded on fixed elements") is confirmed as a (possible) result of a reduced volume (geometry) of the blocking layer. It is confirmed that the blocking layer leads to the occurrence of a uniform deformation (it has the role of a "preliminary slab").

REFERENCES

Dunnicliff, J. (1994). *Geotechnical Instrumentation for Monitoring Field Performance*. John Wiley & Sons.

Terzaghi, K. (1943). *Theoretical Soil Mechanics.* John Wiley & Sons.

Win Bo, MyInt. Barrett, J (2023). *Geotechnical Instrumentation and Applications*. Springer, Berlin

Hanna, H,T (1973). *Foundation Instrumentation*. Trans Tech Publications.

Caicedo, B. (2019). *Geotechnics of Roads: Fundamentals*. Taylor & Francis Group, London UK.

Proceedings of the XVIII ECSMGE 2024
GEOTECHNICAL ENGINEERING CHALLENGES
TO MEET CURRENT AND EMERGING NEEDS OF SOCIETY
© 2024 the Authors
ISBN 978-1-032-54816-6
DOI 10.1201/9781003431749-118
Open Access: www.taylorfrancis.com, CC BY-NC-ND 4.0 license

ECSMGE 24
XVIII EUROPEAN CONFERENCE ON SOIL MECHANICS AND GEOTECHNICAL ENGINEERING

Assessing the impact of correlated geotechnical properties on the behaviour of retaining structures

Évaluation de l'impact des propriétés géotechniques corrélées sur le comportement des structures de retenue

E. Panagiotis*, I. Rocchi, V. Zania
Technical University of Denmark, Kongens Lyngby, Denmark
**eftpan@dtu.dk*

ABSTRACT: This study investigates the geotechnical intricacies of Copenhagen's Quaternary upper clay till deposits, characterized as highly over-consolidated and significantly heterogeneous, and their impact on the structural performance of secant pile walls. Through rigorous analysis, 5000 samples were generated using multivariate distribution functions. These functions were developed to probabilistically calibrate the HS-small constitutive model, taking cross correlations into account. Additionally, 5000 more samples were generated assuming independence. These samples serve as the basis for a finite element model, providing crucial data on lateral wall deflections and bending moments. The impact of cross correlations among geotechnical properties on secant pile wall response is evident. The study quantifies this impact, showing a substantial reduction in standard deviation for lateral deflections (about 20%) compared to interdependent samples. The maximum bending moment during the final excavation stage sees a more modest 50% decrease. This study not only sheds light on the importance of considering dependencies among geotechnical properties in deep excavation design but also provides a practical framework for optimizing performance and safety in similar projects.

RÉSUMÉ: Cette étude explore les subtilités géotechniques des dépôts argileux quaternaires à Copenhague, fortement surconsolidés et très hétérogènes, et leur impact sur les performances structurelles des parois moulées. En analysant rigoureusement 5000 échantillons générés par des fonctions de distribution multivariées, le modèle constitutif HS-small a été probabilistiquement calibré en tenant compte des corrélations croisées. Ces échantillons, à la base d'un modèle par éléments finis, fournissent des données clés sur les déformations latérales et les moments de flexion des parois. L'impact des corrélations croisées sur la réponse des parois moulées est mis en évidence, montrant une réduction significative de l'écart type des déformations latérales (environ 20%) par rapport aux échantillons interdépendants. La diminution du moment de flexion maximal lors de la phase finale d'excavation est plus modeste, à hauteur de 50%. Cette étude souligne l'importance de considérer les dépendances entre les propriétés géotechniques dans la conception des excavations profondes, offrant un cadre pratique pour optimiser les performances et la sécurité dans des projets similaires.

Keywords: Multivariate distribution functions; cross correlations; deep excavation design; secant pile walls.

1 INTRODUCTION

Deterministic approaches, which are most commonly employed for geotechnical design, can fail to accurately predict soil structure interaction in complex geotechnical conditions, because they rely on single-value properties. Representing geotechnical properties as probability distribution functions enables the incorporation of inherent uncertainties and variations in a more comprehensive manner. In particular, advanced probabilistic techniques, such as bivariate or multivariate distributions, account for the correlation among geotechnical properties and establish a platform to gauge the potential influence of correlated parameters on structural performance through reliability-based design (RBD) techniques.

In the field of geotechnical engineering, a multitude of multivariate distribution functions have been developed, drawing from both regional and global databases (Ching and Phoon 2012, Liu et al. 2016, Zang et al. 2020). These functions share a common aim: to effectively capture cross correlations among various geotechnical properties. Macroscopic geotechnical properties, such as shear strength, permeability, and stiffness are in fact governed by the same physical parameters and microscopic features, therefore they exhibit inherent interdependencies. Multivariate distribution functions describing these correlations lessen uncertainty, provide a complete overview of overall variations, and assist in developing precise transformation models for particular situations.

Despite the acknowledged correlation among geotechnical properties, a noticeable gap persists in the literature regarding the integration of these correlations into reliability-based design studies for deep excavations, as highlighted in various published studies (Gong et al., 2016; Wang et al., 2020). The majority of these studies have treated geotechnical properties as independent variables, neglecting the intricacies of real-world behaviour or focus solely on specific ones, such as the extensively studied relationship between effective cohesion (c´) and angle of shearing resistance (φ´). This gap is further underscored by the absence of established multivariate distribution functions aimed at calibrating soil constitutive models in a probabilistic manner.

This paper aims to investigate the impact of considering the cross-correlation between different geotechnical properties on the performance of single-anchored secant pile walls embedded in a uniform clay till layer. To achieve this, soil samples were generated based on established multivariate distribution functions developed by Panagiotis et al. (2023) for the Copenhagen upper clay till. These functions aimed to probabilistically calibrate the HS-small constitutive model and were used to explore two scenarios. In the first scenario, samples were generated while considering the observed cross-correlations among geotechnical properties. In the second scenario, the selected geotechnical properties were treated as independent probability density functions, resulting in a correlation matrix being an identity matrix. For each scenario, a total of 5000 generated samples were incorporated into a finite element model (FEM) created in PLAXIS 2D. This model was employed to calculate and compare wall deflections and maximum bending moments at both initial and final excavation stages between the two scenarios. The comparisons were conducted using various statistical measurements, including standard deviation and confidence intervals.

2 METHODOLOGY

2.1 Geology of Copenhagen (clay till dep)

The greater Copenhagen's geology dates to the Paleogene and Quaternary epochs. Thicker glaciers covered the area twice, causing Paleogene deposits (limestone) to be overlaid by glacial deposits. These glacial deposits are categorized into clay, sand, and gravel tills based on their natural moisture content, rather than their grading (Frederiksen et al., 2003). The Quaternary upper clay till in Copenhagen is the focus of this study, which is characterized as a highly over-consolidated (OCR ~ 1-20) low to medium plastic clay (I_p < 15%), with a clay fraction varying from 15% to 30%.

2.2 Multivariate distribution functions

Due to the limited and incomplete database for calibrating the Hardening small-strain stiffness (HS-small) constitutive model, Panagiotis et al. (2023) constructed two distinct multivariate distribution functions: one based on anisotropically consolidated drained/undrained tests and soil classification, and the other on oedometer and soil classification, sharing four common parameters. Geotechnical data from triaxial and oedometer functions were combined based on minimum differences for the common parameter, assuming similar samples with matching stress and index properties. This approach capitalizes on shared characteristics to effectively merge information from the two multivariate functions. The first multivariate distribution function comprised eight parameters (q/p´, OCR, E^{ref}_{50}, e_0, LL, depth, p'_i, p'_{peak}) and the second comprised seven parameters ($E^{ref}_{oed,u}$, OCR, C_k, e_0, LL, depth, $E^{ref}_{oed,l}$). The correlation matrix after the combination of the two multivariate distribution functions is presented in Table 1.

Table 1. Correlation matrix among the geotechnical properties adopted in this study.

C_{xx}	e_0	q/p´	E_{50}^{ref}	OCR	C_k	$E_{oed,l}^{ref}$
e_0	1.00	-0.22	-0.92	-0.13	0.54	-0.41
q/p´		1.00	0.42	0.52	-0.08	-0.22
E_{50}^{ref}			1.00	0.36	-0.43	0,34
OCR	Symmetric			1.00	0.16	0.03
C_k					1.00	-0.32
$E_{oed,l}^{ref}$						1.00

Initially, 5000 samples were generated using multivariate distribution functions that considered cross correlations, while an additional 5000 samples were generated assuming independence. These samples were imported into the FEM model developed on PLAXIS 2D and lateral wall deflections and bending moments were calculated. The generated samples used for the analyses on the two scenarios are illustrated in Figure 1.

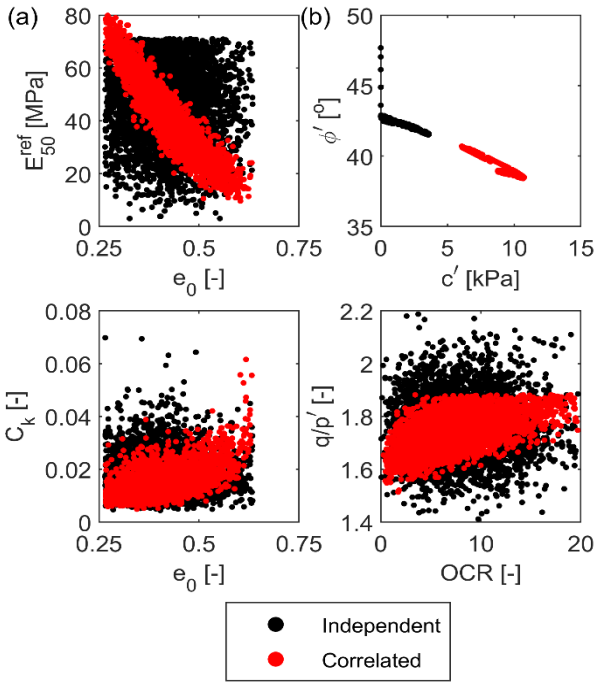

Figure 1. Scatter plots of generated samples implemented in PLAXIS 2D for the two scenarios.

2.3 Design of secant pile walls

The deep excavation analyzed in this study was embedded within Copenhagen's clay till unit, supported by 15m long secant pile walls and one row of anchors. Secant pile walls were designed according to free earth support method. A schematic view of the deep excavation with the excavation characteristics is illustrated in Figure 2.

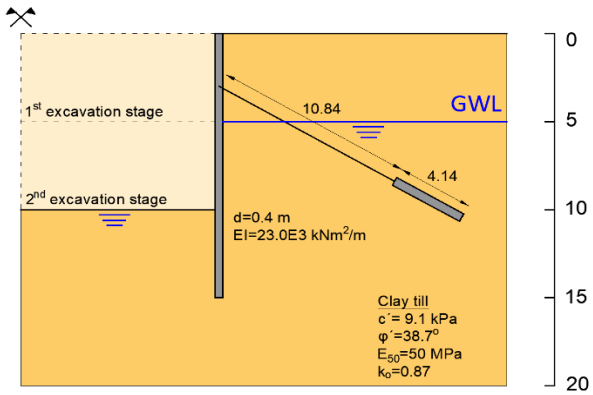

Figure 2. Cross section of the deep excavation analyzed in this study.

It is important to highlight that a c-φ′ reduction analysis was conducted on the developed finite element model in PLAXIS 2D. This was done to ensure that the design of the deep excavation was not overly conservative, resulting in a safety factor of approximately one. This decision was made because our objective was to assess the impact of cross correlations among geotechnical properties on an excavation designed to its limit. The construction sequence of the modelled deep excavation consisted of:

Stage 1: Wall installation
Stage 2: Excavation stage 1 (from +0 to -5.00m)
Stage 3: Anchor activation (-3.00 m)
Stage 4: Ground Water Lowering (from -5.00 to -10.00m)
Stage 5: Final excavation stage (from -5.00 to -10.00m)

3 RESULTS

The lateral wall deflections and bending moments during both the initial and final excavation stages are depicted in Figure 3 and Figure 4, respectively. It is evident that the variability in the response of the secant pile wall is consistently reduced when cross correlations among the geotechnical properties are taken into account. To quantitatively assess the impact of considering cross correlations, the standard deviations of the maximum lateral wall deflections and bending moments were estimated and are presented in Table 2.

Table 2. Standard deviations of the maximum lateral deflections and bending moments for two scenarios during the first and last excavation stage. Confidence intervals (95%) are displayed in parentheses (Lower-Upper bound).

Stage	1st Exc. stage	Final exc. stage
Maximum lateral deflections [mm]		
Independent	23.7 (45.75-47.43)	25.8 (48.55-50.38)
Correlated	5.1 (19.10-19.45)	5.5 (23.47-23.85)
Maximum bending moment [kNm/m]		
Independent	28.5 (70.61-72.63)	12.8 (86.51-87.93)
Correlated	7.3 (30.30-30.79)	6.8 (65.57-66.12)

The most significant reduction in standard deviation was observed in lateral wall deflections, where it decreased to approximately 20%, equivalent to a five-fold decrease compared to samples with correlated properties. In contrast, the reduction in standard deviation for maximum bending moments during the final excavation stage was 50%, indicating a two-fold decrease. When confidence intervals are utilized to determine the required reinforcement, it becomes evident that the required reinforcement area is reduced by 33% when considering correlations. This reduction, in turn, leads to significant reductions in CO2-eq emissions.

4 CONCLUSIONS

In this study, an investigation was conducted into the effect of cross correlations among geotechnical parameters on the structural performance of secant pile walls, with a specific focus on the Copenhagen Quaternary upper clay till. The construction sequence of a deep excavation was simulated considering wall installation, excavation stages, anchor activation, and groundwater lowering.

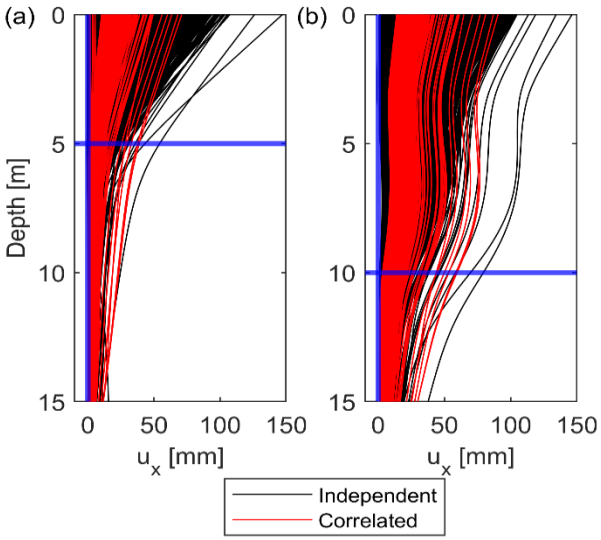

Figure 3. Lateral wall deflections with respect to depth for the two scenarios during the: (a) first excavation stage and (b) final excavation stage.

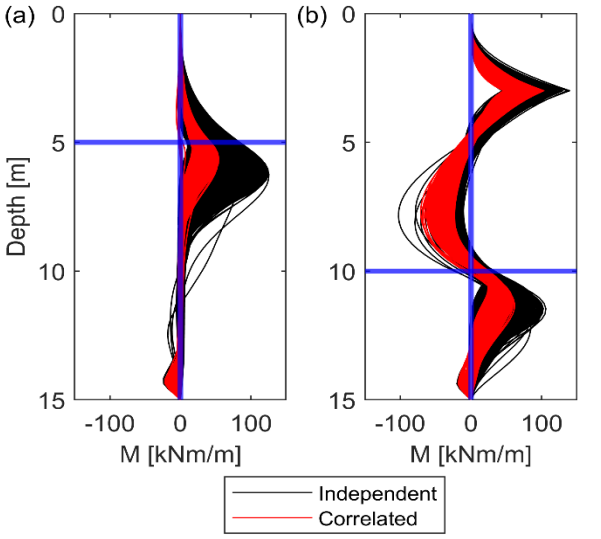

Figure 4. Bending moments with respect to depth for the two scenarios during the: (a) first excavation stage and (b) final excavation stage.

PLAXIS 2D numerical analyses were performed using 5000 samples generated under the consideration of cross correlations, and an additional 5000 samples assuming independent distributions. Lateral wall deflections and bending moments were derived showing a remarkable reduction in variability in the response of the secant pile wall, particularly in lateral wall deflections, when cross correlations were considered. This was quantified by estimating the standard deviations of maximum lateral wall deflections and bending moments, revealing a substantial reduction in standard deviation for lateral deflections of samples having cross correlated properties. Overall, this study highlights the significance of considering dependencies among geotechnical properties in the design and analysis of deep excavations supported by secant pile walls.

REFERENCES

Ching, J., and Phoon, K.-K. (2012). Modelling parameters of structured clays as a multivariate normal distribution. Can. Geotech. J. 49, 522-545.https://cdnsciencepub.com/doi/10.1139/t2012-015.

Gong, W., Juang, H., and Martin, J. R. (2016). Numerical integration method for computing reliability index of geotechnical system, Georisk: Assessment and Management of Risk for Engineered Systems and Geohazards, 10:2, 109-120.https://doi.org/10.1080/17499518.2015.1102292.

Hansbo, S. (1957). A new approach to the determination of the shear strength of clay by the fall-cone test. Royal Swedish Geotechnical Institute; 1957.

Kulhawy, F. H., and Mayne, P. W. (1990). Manual on Estimating Soil properties for Foundation Design, Electric Power Research Institute EL-6800, Project 1493-6, Electric Power Research Institute, Palo Alto, Calif.

Liu, S., Zou, H., Cai, G., Bheemasetti, T. V., and Puppala, A. J., Lin, J. (2016). Multivariate correlation among resilient modulus and cone penetration tests parameters of cohesive subgrade soils. Eng. Geol. 209, 128-142. http://dx.doi.org/10.1016/j.enggeo.2016.05.018.

Panagiotis, E., Rocchi, I., and Zania, V (2023). Multivariate probabilistic assessment of a regional database in Copenhagen. 8th International Symposium on Deformation Characteristics of Geomaterials (ISDCG2023).

Wang, M.-X., Tang, X.-S., Li, D.-Q., and Qi, X.-H. (2020). Subset simulation for efficient slope reliability analysis involving copula - based cross-correlated random fields. Comp. and Geotech. 118,103326.http://dx.doi.org/10.1016/j.compgeo.2015.08.002.

Zhang, D., Zhou, Y., Phoon, K. K., and Huang, H. (2020). Multivariate probability distribution of Shanghai clay properties. Eng. Geol. 273, 105675. https://doi.org/10.1016/j.enggeo.2020.105675.

Proceedings of the XVIII ECSMGE 2024
GEOTECHNICAL ENGINEERING CHALLENGES
TO MEET CURRENT AND EMERGING NEEDS OF SOCIETY
© 2024 the Authors
ISBN 978-1-032-54816-6
DOI 10.1201/9781003431749-119
Open Access: www.taylorfrancis.com, CC BY-NC-ND 4.0 license

ECSMGE 24
XVIII EUROPEAN CONFERENCE ON SOIL MECHANICS AND GEOTECHNICAL ENGINEERING

A new approach for evaluation of remoulded shear strength in clays using the cone penetration test

Une nouvelle approche pour évaluer la résistance au cisaillement remaniée dans les argiles à l'aide du piézocône

P. Paniagua*
Norwegian Geotechnical Institute and Norwegian University of Science & Technology, Trondheim, Norway

P.W. Mayne
Georgia Institute of Technology, Atlanta, USA

B. Di Buò
Tampere University and Ramboll Finland, Tampere, Finland

S.S. Agaiby
Cairo University, Giza, Egypt

priscilla.paniagua@ngi.no

ABSTRACT: Interpretation of remoulded shear strength in soft clays based on lab and/or in-situ traditional testing can be simple and challenging, depending on the adopted approach. A new approach that uses *CPTU* data in the calculation of the slope parameter $a_q = B_q - 1/Q$, together with laboratory fall cone and field vane shear tests data from 15 sites, demonstrates that when $a_q > 0.5$, the clay under study can be considered as sensitive clay. The proposed relation is intended to be used as a first-order approximation of the remoulded shear strength that can be used as an indication of clay sensitivity. Further data and extended verification of the proposed approach are encouraged in the future for further validation.

RÉSUMÉ: L'interprétation de la résistance au cisaillement à l'état remanié des argiles molles est traditionnellement basée sur des résultats de test au laboratoire ou en chantier. Ce genre d'interprétation peut souvent être difficile dépendamment de la méthode choisie. Une nouvelle approche qui utilise les données *CPTU* dans le calcul du paramètre de pente $a_q = B_q - 1/Q$, ainsi que les données de pénétration au cône et du scissomètre de chantier provenant de 15 sites, démontre que lorsque $a_q >$ 0,5, l'argile étudiée peut être considérée comme argile sensible. La relation proposée est destinée à être utilisée comme approximation du premier ordre de la résistance au cisaillement à l'état remanié pouvant être utilisée comme indication de la sensibilité de l'argile. Des données supplémentaires et une vérification approfondie de l'approche proposée sont encouragées à l'avenir pour une validation plus approfondie.

Keywords: Clay; *CPTU*; remoulded shear strength; vane shear tests; fall cone.

1 INTRODUCTION

General practice and previous studies have shown that the measured sleeve friction resistance (f_s) from cone penetration tests (*CPTU*) can be considered as a remoulded shear strength in non- or low-sensitive clays. However, this approach does not work well when dealing with sensitive and quick clay deposits. Moreover, the sleeve friction in soft (and sensitive) clays is not so reliable (Powell and Lunne, 2005; Lunne, 2010), and the correction of f_s to a total sleeve resistance (f_t) requires a sleeve net ratio from triaxial tests and both measurements of pore pressures at the shoulder (u_2) and behind the sleeve friction (u_3) (Lunne et al. 1997), where the latter one is not typically measured in practice.

Other approaches applying traditional soil behaviour type (*SBT*) charts often fail to identify the material as sensitive (Mayne and Benoit, 2020; Agaiby and Mayne, 2021). Some new approaches propose modified SBT charts using the pore pressure measurements at the tip (u_1) (Gylland et al., 2017) or the added measurement of resistivity, designated *RCPTU* (Sandven et al. 2016; Gylland et al. 2017); however, then require certain additional sensors that are not usually present in traditional *CPTU* testing.

A new approach for calculating the remoulded shear strength (s_{ur}), which can then be applied as an indicator for classifying a soil material as sensitive, is presented in this paper. The approach uses the total cone resistance (q_t) and the u_2 data collected from a

standard *CPTU* test for calculating the slope parameter $a_q = B_q - 1/Q$, where B_q = pore pressure ratio and Q = normalized cone tip resistance. Then, based on previous observations stating that when $a_q > 0.5$, the clay under study can be considered sensitive (see Section 2), and using empirical data, a relation for calculating s_{ur} is presented. This relation is a first-order correlation based on data from 15 sites and can be employed to evaluate remoulded shear strength based on *CPTU* data. The paper summarizes and verifies the approach using a global database of *CPTU*, field *VST* (field vane shear test), and laboratory *FC* (fall cone) results compiled from Norway, Finland, Canada, and USA sites.

2 THE SLOPE PARAMETER a_q

The slope parameter a_q can be determined as a single value for any clay layer or uniform clay deposit by taking the slope of a plot of the parameter (U-1) versus Q, or alternatively taken as the slope of ($u_2 - \sigma_{vo}$) versus ($q_t - \sigma_{vo}$). Mathematically speaking, it can be calculated as $a_q = (U - 1)/Q = (u_2 - \sigma_{vo})/(q_t - \sigma_{vo}) = B_q - 1/Q$, where $U = \Delta u_2/\sigma_{vo}'$ and $Q = q_{net}/\sigma_{vo}'$. Di Buo et al. (2019) presented the friction angle ratio ϕ'_{peak}/ϕ'_{MO} as a function of the slope parameter a_q for kaolin, natural clays, and sensitive clays. It was observed that sensitive clays are found mainly when $a_q > 0.5$, i.e., the sensitivity of the clays studied increased when the friction angle ratio decreased. This trend was already presented by Bjerrum and Simons (1960) when comparing the ratio of $tan\phi'_{peak}/\ tan\phi'_{MO}$ from triaxial tests with sensitivity: $S_t = s_{uc}/s_{ur}$. That is the ratio of $\tan\phi'_{peak}/\ \tan\phi'_{MO}$ decreases with an increase in sensitivity. The premise of the present study is that when $a_q > 0.5$, then the material is probably a sensitive clay, and that S_t increases with increasing a_q. However, evaluating S_t can be difficult since that value then depends on the testing method being used to define the reference or benchmark S_t. Specifically, the value of S_t could be assessed using field *VST*, laboratory *FC*, or other approaches like full flow penetrometers, including the T-bar and/or ball (Abuhajar et al. 2010). This paper focuses on the remoulded shear strength as an initial evaluation for clay sensitivity.

3 FIELD AND LAB DATABASE

A database of 15 clay sites has been used to study the relation between the remoulded shear strength from field *VST* and/or lab *FC* tests and the *CPTU* data. Table 1 presents the main characteristics of the sites included. The sites marked with red in the table are sensitive clay sites. The data have been collected from previous publications and technical reports, including *CPTU* and field *VST* data for all the sites except Onsøy, where just lab *FC* data were obtained. The following list presents the reference publications from where data were collected from:

- Bothkennar, UK (Hight et al. 2003)
- Burswood, A.U. (Low et al. 2011)
- Dover, NH (Mayne & Benoît 2020)
- Gloucester, ON (Mayne et al. 2019)
- Gulf of Guinea (Low et al. 2010)
- Kreuzlinger, SW (Springman et al. 1999)
- Louiseville, QC (Leroueil et al. 2003)
- Newbury, MA (DeGroot et al. 2019)
- Northwestern NGES (Finno et al. 2000)
- Perniö, Finland (Di Buo et al. 2019)
- Tiller-Flotten, Norway (L'Heureux, et al. 2019)
- Mink Creek, BC (Geertsema and Torrance 2005)
- Onsøy, Norway (Lunne, Long, & Forsberg 2003)

Table 1. Sites included in the present study.

Site	w_n [%]	*P.I.* [%]	*L.L.* [%]
Bothkennar, UK	56-67	35-44	64-76
Burswood, A.U.	62-88	35-65	64-95
Dover, NH	31-49	9-17	30-42
Gloucester, ON - A	52-56	21-30	36-60
Gloucester, ON - B	51-90	19-35	39-64
Gloucester, ON - C	60-73	20-31	40-57
Gulf of Guinea	104-130	79-122	120-164
Kreuzlinger, SW	29-36	20-25	35-41
Louiseville, QC	70-89	40-47	62-72
Newbury, MA	39-54	19-21	43-49
Northwestern NGES	24-27	15-16	33-34
Pernio, Finland	82-103	21-37	45-66
Tiller-Flotten, Norway	30-44	7-19	25-39
Mink Creek, BC	23-33	4-19	23-40
Onsøy, Norway	55-70	20-50	50-80

w_n: natural water content, *P.I.*: plasticity index, *L.L.*: liquid limit

Figure 1 and Figure 2 present the observed relationships between the parameter a_q and the ratio $s_{ur}/\Delta u_2$. Figure 1 includes the s_{ur} data measured by field *VST*, while Figure 2 includes the s_{ur} data measured by lab *FC*. All data in the database are presented in both figures, and a large scatter is observed; however, a clear distinction between sensitive and non-sensitive clays is distinguished at the threshold: $a_q = 0.5$, as expected. When taking the average values for each site (Figure 3 and Figure 4), a relationship between the ratio $s_{ur}/\Delta u_2$ and a_q is proposed.

4 VERIFICATION WITH KLETT CLAY

Long et al. (2019) summarized the characteristics of Klett clay, Norway. The Klett site comprises non-

sensitive clay to about 6 m to 8 m and quick clay with significant silt lenses below this down to at least 30 m depths. The materials encountered are typical of the marine clays found in Scandinavia and North America. The *CPTU* data at Klett showed that above 7.5 m, the values of f_s are close to 4 kPa, and these fit well with the s_{ur} data reported using the lab *FC* tests. The clay is a quick-clay below 7.5 m depth, and s_{ur} < 0.5 kPa based on lab *FC* were reported. Some limited field *VST*s were available but higher than those obtained from the lab *FC*. The authors mentioned that this finding is consistent with that observed for other Norwegian clays, especially quick clays, and is attributed to uncertainties in rod friction at depth and torque measurements taken from the surface.

Figure 5 presents the estimated s_{ur} when applying the approach presented in this paper (i.e. equation in Figure 4). A sufficient match is obtained with the data from lab *FC* tests. The observed differences might be attributed to the intrinsic variability in the data from the database (i.e., data coming from different sources where different approaches for interpretation may differ depending on the applicable standard for interpretation of the lab *FC* tests). Still, the estimated values are in the same range of the ones measured.

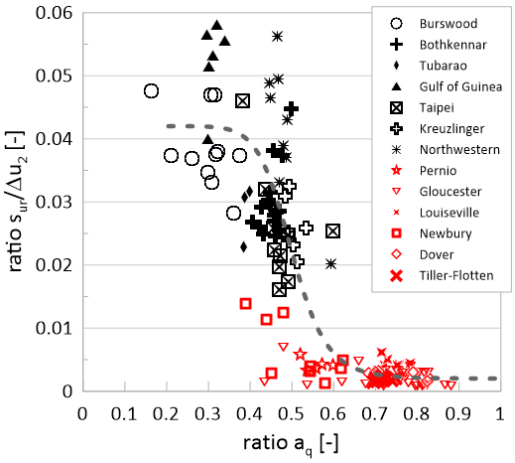

Figure 1. All data sets containing s_{ur} from field VST.

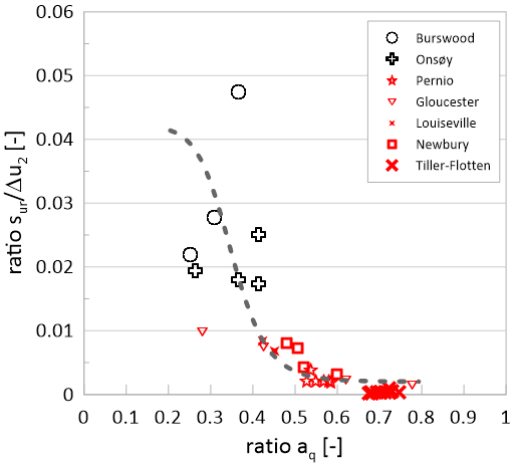

Figure 2. All data sets containing s_{ur} from lab FC.

The approach presented in this paper may be applied as a first-order approximation of the s_{ur} to indicate clay sensitivity.

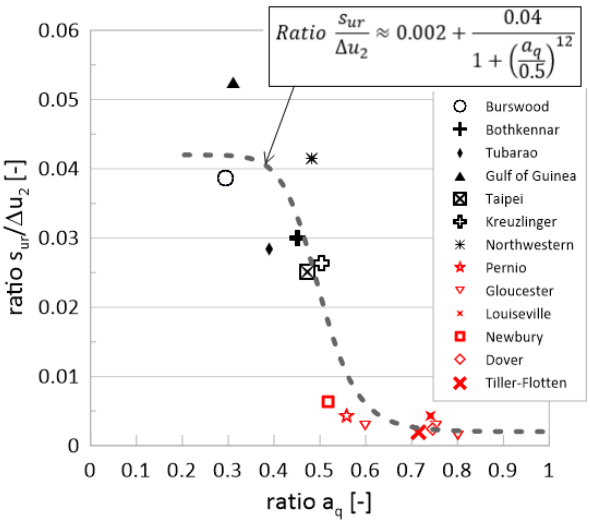

Figure 3. a_q vs. $s_{ur}/\Delta u_2$, average values & s_{ur} from field VST.

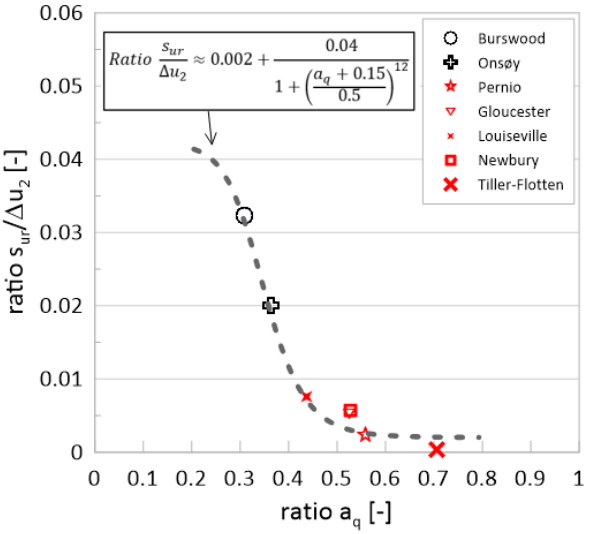

Figure 4. a_q vs. $s_{ur}/\Delta u_2$, average values & s_{ur} from lab FC.

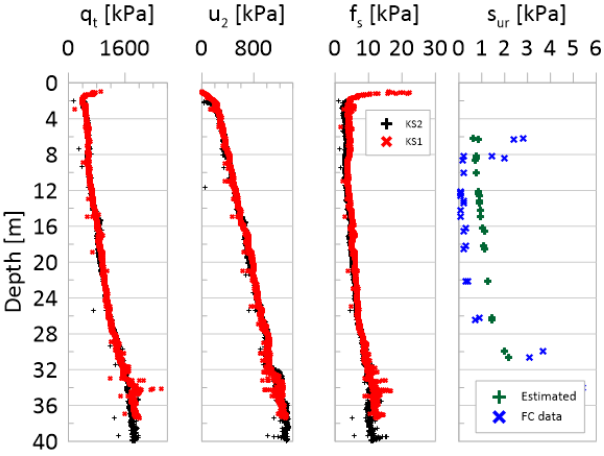

Figure 5. Verification of proposed approach at Klett site.

5 CONCLUSIONS

A discussion of remoulded shear strength of clays based on cone penetration test data has been presented. A novel approach relates the slope parameter a_q and the remoulded shear strength evaluated by either the field vane shear test or the laboratory fall cone test. The approach is verified at an independent testing site having layers of sensitive and non-sensitive clay. The proposed relation is intended to be used as a first-order approximation of the remoulded shear strength that can be used as an indication of clay sensitivity. Further data and extended verification of the proposed approach are encouraged in the future for further validation. Finally, the empirical data used in the present study confirms previous observations stating that when $a_q > 0.5$, the clay under study can be considered sensitive.

REFERENCES

Abuhajar, O., El Naggar, M.H., and Newson, T. (2010) Review of available methods for evaluat soil sensitivity seismic design. *Proc Int Conf Rec Adv Geotech Earthq Eng & Soil Dyn*. California, 1- 8.

Agaiby, S., and Mayne, P.W. (2021). CPTU identification of regular, sensitive, and organic clays towards evaluating preconsolidation stress profiles. *AIMS Geosciences* 7(4): 553-573.

Bjerrum, L., and N.E. Simons. (1960). Comparison of shear strength characteristics of normally consolidated clay. *Proc. Research Conf on Shear Strength of Cohesive Soils*, ASCE: 1771–1726.

DiBuo, B., D'Ignazio, M., Selãnpaã, J., Länsivaara, T. And Mayne, P.W. (2019). Yield stress evaluation of Finnish clays based on analytical CPTu models. *Canadian Geotech J* (11): 1623 – 1638.

DeGroot, D.J., Landon, M.M. and Poirer S.E. (2019). Geology and engineering properties of sensitive Boston Blue Clay at Newbury, Massachusetts. *AIMS Geosciences* 5(3): 412-447.

Finno, R.J., Gassman, S.L. and Calvello, M. (2000). NGES at Northwestern University. *National Geotechnical Experimentation Sites*, Geotechnical Special Pub 93. ASCE, Reston, VA: 130–159.

Geertsema, M. and Torrance, J.K. (2005). Quick clay from the Mink Creek landslide near Terrace, BC. *Canadian Geotech J* 42 (3): 907-918.

Gylland, A., Sandven, R., Montafia, A. et al. (2017). CPTU classification diagrams for ident of sensitive clays. *Landslides in Sensitive Clays* 46. Springer.

Hight, D.W., Paul, M.A., Barras, B.F., Powell, J.J.M., et al. (2003). The characterisation of the Bothkennar clay. *Charact and Eng Properties of Natural Soils* 1, Balkema, Lisse: 543–597.

L'Heureux, J-S., Lindgård, A. and Emdal, A. (2019). The Tiller-Flotten research site: Geotechnical characterization of a very sensitive clay deposit. *AIMS Geosciences* 5 (4): 831-867.

Leroueil, S., Hamouche, K., Tavenas, F., Boudali, M., Locat, J., Virely, D., Roy, M., La Rochelle, P., and Leblond, P. (2003). Geotechnical characterization and properties of a sensitive clay from Québec. *Characterization and Engineering Properties of Natural Soils* 1, Balkema, Lisse: 363-394.

Long, M., L Heureux, J.S., Bache, B.K.F., Lund, A. K., Hove, S., Sødal, K.G., Amundsen, H.A., Nordal, S., and Montafia, A. (2019). Site characterisation and some examples from large scale testing at the Klett quick clay research site. *AIMS Geosciences*, 5(3): 344-389.

Low, H.E., Lunne, T., Andersen, K.H., Sjursen, M.A., et al. (2010). Estimation of intact and remoulded undrained shear strengths from penetration tests in soft clays. *Geotechnique* 60 (11): 843-859.

Low, H.E., Maynard, M., Randolph, M.F., and DeGroot, D.J. (2011). Geotechnical characterization and engineering properties of Burswood clay. *Geotechnique* 61 (7): 575–591.

Lunne, T., Robertson, P.K. & Powell, J. (1997) *CPT and piezo-cone testing in geotechnical practice*. Textbook, Taylor and Francis Company, London.

Lunne, T., Long, M., and Forsberg, C.F. (2003). Characterization and engineering properties of Onsøy clay. *Charact and Eng Properties of Natural Soils* 1, Balkema, Lisse: 395-428.

Lunne, T. (2010). The CPT in Offshore Soil Investigation: a historic perspective. Proc. CPT'10, Los Angeles, May 2010: 71–113.

Mayne, P.W. and Benoît, J. (2020). Analytical CPTU models applied to sensitive clay at Dover, New Hampshire. ASCE *Journal of Geotechnical & Geoenvironmental Engineering* 146 (12*)*.

Mayne, P.W., Cargill, E. and Miller, B. (2019). Geotechnical characteristics of sensitive Leda clay at Canada test site in Gloucester, Ontario. *AIMS Geosciences* 5(3): 390-411.

Powell, J.J.M. & Lunne, T. 2005. Use of CPTU data in clays/fine grained soils. *Studia Geotechnica*. XXVII (3 – 4): 29–65.

Sandven, R., Gylland, A., Montafia, A., Kåsin, K., Pfaffhuber, A.A. and Long, M. (2016). In-situ detection of sensitive clays - Part I: selected test methods. *Proc. 17th Nordic Geotechnical Meeting.* No. 054, Reykjavik.

Springman, S., Trausch, J., Heil, H.M., and Heim, R. (1999). Strength of soft Swiss lacustrine clay: cone penetration and triaxial test data. *Transportation Research Record* 1675: 99-0981, National Academy Press, Washington, DC: 1-9.

Proceedings of the XVIII ECSMGE 2024
GEOTECHNICAL ENGINEERING CHALLENGES
TO MEET CURRENT AND EMERGING NEEDS OF SOCIETY
© 2024 the Authors
ISBN 978-1-032-54816-6
DOI 10.1201/9781003431749-120
Open Access: www.taylorfrancis.com, CC BY-NC-ND 4.0 license

ECSMGE 24
XVIII EUROPEAN CONFERENCE ON SOIL MECHANICS AND GEOTECHNICAL ENGINEERING

Alert soil mechanics instructors of the main unsaturated soil issues: What and how to teach when experts disagree

Alerter les formateurs en mécanique des sols sur les principales questions relatives aux sols non saturés: Quoi et comment enseigner lorsque les experts ne sont pas d'accord

M. Pantazidou*
National Technical University of Athens, Zografou, Greece

S. Houston
Arizona State University, Phoenix, USA

J. McCartney
University of California San Diego, La Jolla, USA

A. Tarantino
University of Strathclyde in Glasgow, Scotland, UK

M. Bardanis
Edafos Engineering Consultants, S.A., Athens, Greece

**mpanta@central.ntua.gr*

ABSTRACT: The team project described in this paper is a brainchild of technical committee TC106 on Unsaturated Soils, which has been advocating for years the teaching of unsaturated soil mechanics, and technical committee TC306 on Geo-engineering education, which learned in 2020 about a technical disagreement within the unsaturated soils community. The 8th International Conference on Unsaturated Soils (UNSAT 2023) was an opportunity for the two committees to collaborate on tackling together the specific issue of teaching unsaturated soil mechanics and the broader issue of expert disagreement. Understanding the nature of the disagreement was attempted mainly by having specialists answer a list of questions phrased by the non-specialist first author after having been tutored by the last author, also a specialist. The answers revealed a significant disagreement on the variables selected to describe the behavior of unsaturated soils. Until the disagreement is satisfactorily settled within the unsaturated soils community, interim solutions are proposed for instruction.

RÉSUMÉ: Le projet d'équipe décrit dans cet article est une idée du comité technique TC106 pour les sols non saturés, qui préconise depuis des années l'enseignement de la mécanique des sols non saturés, et du comité technique TC306 pour l'enseignement de la géo-ingénierie, qui a appris en 2020 l'existence d'un désaccord technique au sein de la communauté des sols non saturés. La 8e conférence internationale sur les sols non saturés (UNSAT 2023) a été l'occasion pour les deux comités de collaborer pour aborder ensemble la question spécifique de l'enseignement de la mécanique des sols non saturés et la question plus large du désaccord entre experts. La compréhension de la nature du désaccord a été tentée principalement en demandant à des spécialistes de répondre à une liste de questions formulées par le premier auteur, non spécialiste, après avoir été encadré par le dernier auteur, également spécialiste. Les réponses ont révélé un désaccord important sur les variables choisies pour décrire le comportement des sols non saturés. En attendant que ce désaccord soit résolu de manière satisfaisante au sein de la communauté des sols non saturés, des solutions provisoires sont proposées pour l'enseignement.

Keywords: Geotechnical engineering education; unsaturated soils instruction; effective stress.

1 INTRODUCTION

Unsaturated soil mechanics is moving from research to instruction primarily in courses taught by unsaturated soils specialists, including members of the technical committee TC106 on Unsaturated Soils of the International Society for Soil Mechanics and Geotechnical Engineering (ISSMGE) (Houston et al., 2014; McCartney, 2021). With the exception of a section on compacted soils, few introductory geotechnical engineering textbooks cover or even draw attention to unsaturated soils. The ISSMGE technical committee TC306 on Geo-engineering Education became aware of a technical disagreement

within the unsaturated soils community thanks to the 2nd Burland Lecture and accompanying paper by Jaksa (2020), who presented two different expressions for the shear strength of unsaturated soils.

This paper describes a collaborative project of TC106 and TC306 targeting non-specialist soil mechanics instructors who would be interested in presenting in their courses some elements of unsaturated soil mechanics, provided they are aware of the main issues. The opportunity for the collaboration was given by the organization of the UNSAT 2023 conference and a proposal of the last author (the conference chair) to the first author to organize a panel session on education. Together, they decided to help non-specialist instructors understand in broad strokes the disputed issues. Guidance to the non-specialists would be given mainly in a question-and-answer form. To this end, a set of 14 questions was prepared by the non-specialist first author after being tutored by the specialist last author. This collaboration was crucial: without the specialist's involvement, the non-specialist would not have the necessary stamina to translate bewilderment about outstanding issues in unsaturated soil mechanics into questions. The three other specialist authors of this paper accepted the invitation to participate in the panel and agreed to provide written answers. In addition, they agreed to evaluate educational material used by the non-specialist member of the author team in an introductory course in soil mechanics.

The goal of the paper is three-fold: (i) to advance the collective understanding (i.e. within the wider geotechnical engineering community) of the technical disagreement within the unsaturated soils community (Section 2), (ii) to explore approaches to handle technical disagreement (Section 3) and (iii) to offer interim suggestions for teaching (Section 4) until the disagreement is resolved or becomes irrelevant. The paper provides a record of the aforementioned novel inter-committee collaboration and its outcomes so far, including a link to all the background materials produced, which are available in an online supplement (Houston et al., 2023).

2 UNSATURATED SOILS QUESTIONS AND DISCUSSION OF ANSWERS

Table 1 includes somewhat shorter forms of the 14 questions posed to three of the specialist co-authors, arranged in six groups, A through F. The full questions and the complete answers provided by the three specialists are available in the Supplement (Houston et al., 2023). Instructors reading the complete answers will notice that some combine technical and pedagogical/didactical arguments. These instances do not come through in the discussion of this section, which attempts when possible, for each of the six groups of questions, a rough synthesis of only the technical arguments of the answers.

2.1 Soil profile above the water table

The specialists agree that, above the water table, the pore water pressure is negative and a wide variation is expected for pore water pressure and its associated variables saturation and water content. Some of the earliest measurements of field suction for geotechnical applications concerned slope stability (Sweeney, 1982). In general, there seems to be a dearth of pressure measurements to sizeable depths: one such record (9-meter long) was located in Herraman (2019: Figure 4). One approach would then be to consider an equilibrium hydrostatic distribution as an idealized reference case. In cases of net rain infiltration, higher pressures than in the hydrostatic case will exist (less negative), while net evaporation will result in water pressures lower than hydrostatic, see also Houston et al. (2023).

2.2 Effective stress & state variables

This is an area of considerable disagreement, which could be described with the question "may we find a single expression for a saturated soil-equivalent effective stress for unsaturated soils?", such as the expression proposed by Bishop (1959):

$$\sigma' = \sigma - u_a + \chi\,(u_a - u_w) \qquad (1)$$

where σ' and σ are effective and total stress, u_a and u_w are air and water pressures, and χ is a parameter that depends on the type of soil. The term "equivalent" is key here, since there is no full agreement even in soil mechanics textbooks about what effective stress is capable of describing (Houston et al., 2023) – but this bigger discussion is beyond the scope of this paper. Three answers, summarized from the experts' differing opinions, are delineated next.

2.2.1 Opinion 1 – two state variables: net stress and suction

When dealing with unsaturated soils, we cannot use a single equation, but we need to think, simultaneously, about two stress variables. The measurable and controllable stress variables which have been found to govern the behavior of unsaturated soils are: net total stress (or net stress) ($\sigma - u_a$) and soil suction $s = (u_a - u_w)$, which is a strong function of soil water content (Fredlund and Morgenstern, 1977).

Table 1. Puzzlement questions about unsaturated soils phrased by a non-specialist.

No	Group A of questions: Soil profile above the water table
1	What is the distribution of pore water pressure above the water table in the field? In a soil column?
2	May we talk of an "equilibrium" water pressure distribution in the field other than hydrostatic?
3	Is it reasonable to assume that equilibrium conditions are rare in the field for low permeability soils?
	Group B of questions: "Effective stress" or in general "variables we need to keep track of in order to describe and predict soil behavior"
4	From the perspective of an unsaturated soils specialist, can the existing alternative expressions for effective stress that include both air pressure and water pressure be excusable for explaining concepts in an introductory course? [Example: Bishop's Equation: $\sigma' = \sigma - u_a + \chi (u_a - u_w)$]
5	What is really the "claim to prediction" of effective stress? [Textbooks do not agree: see Houston et al., (2023).] If we have excused other description/prediction failures of the effective stress for saturated soils, then why are we so strict for the failure of effective stress to describe/predict states in unsaturated soils?
	Group C of questions: Sand castles & other demonstrations for effective stress (e.g. Elton, 2001)
6	Is it wrong to tell students that sand castles stand due to higher effective stress? Should we say instead that the castle stands due to higher shear strength?
7	Is it wrong to tell students that vacuum-packed coffee is strong due to higher effective stress?
	Group D of questions: Shear strength
8	Considering that there are several alternative expressions for Mohr-Coulomb-type failure criteria for shear strength, non-specialist instructors are likely to avoid mentioning unsaturated soils in the context of soil behavior under shear stress. Do they have a better simple alternative?
9	Is there any simple demonstration based on principles (not on examples, e.g. sand castles) of suction contributing to shear strength?
10	If the answer to the question "which shear strength equation to use" is contested within the unsaturated soils community (Question No 8), a follow up question is whether the choice of shear strength criterion is a main issue within the community. If not, perhaps other more important/applied issues should take precedence.
	Group E of advanced questions: Motivation for teaching unsaturated soil mechanics
11	Which geotechnical problems require knowledge of unsaturated soil behavior for the analysis that will produce their solution?
12	Are there any applications of unsaturated soil mechanics in the field? Has the unsaturated soils community recorded some case studies?
	Group F of advanced questions: Evidence for the practical need of an unsaturated soils approach
13	If instructors are to give up effective stress, they need to understand its main shortcoming(s) for unsaturated soils. Does it fail to predict volume change? Or deformation? Or both?
14	What would be a good set of experimental results, ideally from both the laboratory and the field, showing the inability of effective stress to predict … (whatever is the answer to Question 13) and the successful prediction of a suitable unsaturated soil mechanics approach.

2.2.2 Opinion 2 – Bishop effective stress and its variations

It is possible to use a single expression for the effective stress when interpreting the shear strength of unsaturated soils (e.g. Lu et al., 2010) or the elastic volume change of unsaturated soils (e.g. Khalili et al., 2004). A single expression of effective stress can also be used to represent inelastic deformations of unsaturated soils as long as an elasto-plastic model is used with a yield function that depends on suction (e.g. Mun and McCartney, 2017). Several different equations have been proposed for the effective stress in unsaturated soils, including one where χ in Equation (1) is replaced with the effective saturation, $S_e = (S - S_r)/(100 - S_r)$, where S is saturation and S_r is residual saturation (Lu et al., 2010).

2.2.3 Opinion 3 – Two effective stresses

Once it is clarified that the concept of effective stress is more complex for unsaturated soils to the point that the mechanical behavior of unsaturated soils needs to be represented by two effective stresses (or, equivalently, two stress state variables), it can be stated that:

- As far as the shear strength is concerned, the Bishop effective stress, i.e. Equation (1), (with $\chi=S_e$) is an appropriate effective stress for coarse-grained materials and can be considered acceptable from a qualitative standpoint for fine-grained materials.
- For deformation problems, the Bishop effective stress is not generally sufficient to interpret/model the mechanical response of unsaturated soils, even from a qualitative standpoint.

2.3 Sand castles and other demonstrations

This group of questions concerns only teaching and in particular the choice of comments that accompany the demonstrations used for explaining the implications of the particulate nature of soil. The answers of the specialists to this group of questions reflect their perspectives on effective stress. To avoid disagreeing with any specialist, instructors may choose to state that sand castles stand due to higher shear strength associated with the existence of suction in moist sand. Proponents of Equation (1) may say either one, i.e. due to higher effective stress or higher shear strength.

2.4 Shear strength

Although TC306 became aware of technical disagreements within the unsaturated soils community regarding the expression for shear stress at failure (Jaksa, 2020), the specialists agree (Question 10) that this is not a key issue in unsaturated soils, since any disagreements are due to the empirical nature of the equation. In fact, they all accept as useful (see also Table 2) the following expression for shear strength τ (for $u_a = 0$):

$$\tau = c' + \sigma \tan\varphi' + f(s, S) \tan\varphi' \qquad (2)$$

where c' is the saturated soil effective cohesion intercept (typically equal to zero unless the soil is cemented), φ' is the saturated soil effective angle of shearing resistance and $f(s, S)$ is a function of suction and degree of saturation that expresses their contribution to the shear strength of the soil.

2.5 Motivation for teaching unsaturated soils

Some answers to Question 11 seem not to address the question about performing design calculations for unsaturated soils cases but rather the related question about studying unsaturated soil problems. Examples given include problems involving water flow that lead to changes in stiffness or shear strength, which are relevant to pavements and retaining walls, rainfall-induced instability of man-made and natural slopes, and damages of buildings caused by drought-induced foundation subsidence. The case studies offered as examples to Question 12 concern either unusual critical structures or research projects (see also Section 2.6). An exception is the practical application reported by Rahardjo et al. (2019), which is described in some detail in the Supplement, together with two more case studies deemed appropriate for an introduction on unsaturated soils (Houston et al., 2023).

2.6 Evidence from unsaturated soil studies

This group of questions gave the specialists the opportunity to express some closing remarks on the perspectives presented in Section 2.2. From this group of answers, it is worth mentioning a nicely presented case study, of the research project type (Alonso et al., 1999): with inspiration from a partial slope failure due to heavy rainfall, the authors investigated with the use of a numerical code some "what if" scenarios for continuing rainfall (for additional details see Houston et al., 2023).

3 FRAMING DISAGREEMENT

An equal-distances attitude may help in studying disagreement. Such a stance has already been expressed within the unsaturated soils community. Recently, Ng et al. (2023) reproduced the following statement by Gens et al. (2006) "Bishop stresses and net stresses stand on an equal footing and the matter of adopting one or the other must be decided using criteria of convenience", who compared the two stresses from a work rate point of view. A more liberal interpretation of the quoted statement, but also more useful to the non-specialist, is as follows: the pair made of "Bishop stress and suction" and the pair made of "net stress and suction" stand on an equal footing when interpreting unsaturated soils phenomena.

Given the foundational nature of the disputed concepts for soil mechanics, it is useful to seek insights on how to approach disagreement in different geotechnical engineering problems, such as the case study presented by Alonso (2023): a heaving claystone was being described for years with a suction-based model, until mounting evidence and an equally good-fitting model showed that it was a crystal growth problem. The ability of two models based on markedly different mechanisms to reproduce well the actual laboratory and field behavior may serve as a potent reminder to abstain from taking sides. Stepping further aside from unsaturated soils to a different thematic field may also be useful. Biology can be a source of inspiration because, like soil mechanics, concepts play a greater role in theory formation than laws, according to the prominent biologist and philosopher of biology Mayr (1997). The similarity between the two fields can be understood by comparing the role of (i) Terzaghi's effective stress in the theory of consolidation and the birth of soil mechanics to (ii) Darwin's natural selection in the birth of evolutionary biology. Seeking inspiration in biology is useful because it has experienced quite a few controversies that were ultimately resolved. After the resolution of the disputes, it was clear that even the "wrong"

alternatives had valid portions to offer, which may be overlooked if we hasten to take sides.

Another source of disagreement that should not be neglected is the instructors' pedagogical beliefs regarding how much to expose undergraduate students to contested and complex topics, typically slated for graduate courses. Instructional decisions on controversial topics must take into account the centrality of these topics within a thematic field; for key foundational topics, it is recommended that the controversy is mentioned in an introductory course and explained later in an elective or graduate course. Whether a topic is contested or merely complex, the advice from the late professor Harry Seed (1986) is apropos herein: "I would not say in an undergraduate course anything that I would have to take back in a graduate course".

4 PROPOSALS FOR TEACHING

The Supplement includes a five-point list to introduce key issues in unsaturated soils, with variations to accommodate different perspectives (Houston et al., 2023). After having been made aware of the disputed issues, instructors will likely elect to adapt suggestions according to a gradation of different aims, such as:

- Instructor aims to remove something that is "plainly wrong" (unacceptable) from any unsaturated soils perspective. The respective aim for the students is that they would not have to "unlearn" something before expanding their own knowledge of unsaturated soils in a subsequent course (Harry Seed's advice).
- Instructor aims to clarify that a statement or an equation is –from an unsaturated soils perspective– a simplification, and state the range of validity of the statement/equation. The focus here is on alerting the students that they learn principles and calculations suitable for only subsets of reality (e.g. saturated soils).
- Instructor aims to create "receptors" for future knowledge about unsaturated soils, i.e. when students later see something in a more advanced geotechnical engineering course, they will recognize that it fits with what they have seen in the introductory course.

The specialists' evaluation of the educational materials created by the non-specialist first author for an introductory soil mechanics course provides an example of the necessity to modify existing material in light of the answers to the questions in Table 1, filtered through the pedagogical beliefs of an instructor. The Supplement (Houston et al. 2023) includes four items that make reference to unsaturated soils, both before and after the evaluation by the three specialists, who were asked to rate the "before" version as useful (3 points), acceptable (1 point), excusable (0 points) or unacceptable (-3 points). The four items are summarized in Table 2, which also includes the grades provided by the specialists. Disagreement among specialists is reflected in the spread of the grades, which creates decision space for the instructors.

From the four items, only item 2, Equation 3 for the effective stress in unsaturated soils, requires immediate attention to at least eliminate the unacceptable rating (-3 points) given by two of the three specialists. The low rating of this item came as a surprise to the non-specialist author, since the effective stress Equation 3 in Table 2 is an alternative way to write Equation 1, i.e. the Bishop effective stress, with $\alpha = \chi$ and $\beta = 1 - \chi$. However, the specialists did not approve of the fact that suction $(u_a - u_w)$ and net stress $(\sigma - u_a)$ are not recognizable in this alternative version. They also did not approve of calling α and β area ratios. Considering that all three specialists do not approve of Equation 3, and two of the three specialists are at least skeptical about the validity of its original version, i.e. Equation 1, the non-specialist will stop including in her course an equation for effective stress for unsaturated soils.

Table 2. Four references made to unsaturated soils by a non-specialist and respected ratings by three specialists.

No	Item referenced	Ratings[a]
1	Sand castles & video by Burland (2023) "The effect of water on soil strength" [link]	3, 3, 3
2	A version of Bishop's equation for effective stress that separates water pressure from air pressure (Briaud, 2013: Eq. 10.54): $\sigma' = \sigma - \alpha\, u_w - \beta\, u_a$ (3) where α and β are water and air area ratios ($\alpha + \beta = 1$)	-3, -3, 0
3	Distribution of quantities above the water table (see Figure S2 in Supplement)	1, 3, 1
4	Equation 2 for shear strength of unsaturated soils, $\tau = c' + \sigma \tan\varphi' + f(s, S) \tan\varphi'$	1, 1, 3

[a] *3 = useful, 1 = acceptable, 0 = excusable, -3 = unacceptable.*

5 CONCLUSIONS

The team project described herein set out to answer the question what and how can instructors teach when experts disagree. A complementary question that comes up is whether it is best to avoid in instruction topics associated with debates, especially since such situations are considered to be rare in engineering education and collective experience on how to approach them is missing. Understanding the nature of the disagreement was attempted in two complementary ways, by having specialists (i) answer a list of questions phrased by the non-specialist author after being tutored by the last author, also a specialist

and (ii) evaluate educational material created by the non-specialist author for an introductory soil mechanics course. This combined approach revealed, as expected, differences in the preferred variables to use in theory and constitutive modelling of unsaturated soils. There is agreement that unsaturated soil behavior is controlled by net total stress and suction, but there is also open debate concerning the use of the term effective stress for unsaturated soils. Given the centrality of the concept under dispute, it does not seem prudent to avoid it, even in introductory courses. For non-specialist instructors, a sensible approach would be to acknowledge the opposing approaches and focus on topics where viewpoints diverge the least. Such a topic is shear strength of unsaturated soils.

Judging by the relative dearth of design case studies, geotechnical engineering practice does not signal that there is current understanding for a need for professionals cognizant of unsaturated soils theory, in spite of the actual prevalence of applications involving soils in an unsaturated state. But, this may be a chicken-and-egg situation. Considering that geotechnical engineering researchers are branching out to a variety of research topics, better funded than and further removed from core topics of soil mechanics, it is possible that the unsaturated soils community will bring about the next breakthrough in understanding better the fundamental behavior of soils.

REFERENCES

Alonso, E. (2023). The positive history of an error. Modelling the heave of a nuclear power station, *Proc. 8th Int. Conf. on Unsaturated Soils (UNSAT 2023)*. https://doi.org/10.1051/e3sconf/202338200002.

Alonso, E., Lloret, A. and Romero E. (1999). Rainfall induced deformations of road embankments, *Rivista Italiana di Geotecnica* N.1/1999:(8-15).

Bishop, A.W. (1959). The Principle of Effective Stress, lecture delivered in Oslo, Norway, in 1955, published in *Teknisk Ukeblad*, 106(39):859-863.

Briaud, J.-L. (2013). *Geotechnical Engineering: Unsaturated and saturated soils*, John Wiley & Sons, Hoboken, NJ.

Burland, J.B. (2023). *Bare Essentials of Soil Mechanics*, Expedition Workshed Videos. https://expeditionworkshed.org/sub_categories/soil/

Elton, D. (2001). *Soils Magic*, Geotechnical Special Publication 114, ASCE, Reston, VA.

Fredlund, D. G. and Morgenstern, N. R. (1977). Stress state variables for unsaturated soils. *ASCE J. of Geotechnical and Geoenvironmental Engineering*, 103(5):447-466. https://doi.org/10.1061/ajgeb6.0000423.

Gens, A., Sánchez, M., and Sheng D. (2006). On constitutive modelling of unsaturated soils, *Acta Geotech*, 1(3):137-147. https://doi.org/10.1007/s11440-006-0013-9.

Herraman, R. (2019). A Lightweight Soil Nail Retaining Wall in Unsaturated Clay, *Int. J. of Geoengineering Case Histories*, 5(1):1-11, http://dx.doi.org/10.4417/IJGCH-05-01-01.

Houston, S., Savenye, W., Zapata, C. and Ornelas, A. (2014). *Introducing Unsaturated Soil Mechanics in the Undergraduate Curriculum*. https://www.nsf.gov/awardsearch/showAward?AWD_ID=1044012.

Houston, S., McCartney, J., Tarantino, A. and Pantazidou, M. (2023). Online Supplement. https://www.mygeoworld.com/file/139953/teaching-unsaturated-soils-paper-supplement.

Jaksa, M.B. (2020). Reflections on some contemporary aspects of Geotechnical Engineering Education – From critical state to virtual immersion, 2nd John Burland Lecture, *Proc. of the ISSMGE Int. Conf. Geotechnical Engineering Education (GEE 2020)*. https://www.issmge.org/uploads/publications/3/102/Jaksa.pdf.

Khalili, N., Geiser, F. and Blight, G.E. (2004). Effective Stress in Unsaturated Soils: Review with New Evidence, *ASCE Int. J. of Geomechanics*, 4(2):115-126. https://doi.org/10.1061/(ASCE)1532-3641(2004)4:2(115).

Lu, N., Godt, J.W. and Wu, D.T. (2010). A closed-form equation for effective stress in unsaturated soil, *Water Resources Research*, Vol. 46, W05515. https://doi.org/10.1029/2009WR008646.

Mayr, E. (1997). This is biology, Harvard University Press, Cambridge, MA.

McCartney, J. (2021). Building an understanding of the impacts of transient flow processes on the mechanical behavior of unsaturated soils. Part of the webinar "*Teaching unsaturated soil mechanics at the undergraduate level*" organized as pre-conference activity for the Pan-American UNSAT, July 17.

Mun, W. and McCartney, J.S. (2017). Constitutive model for the drained compression of unsaturated clay to high stresses. *ASCE J. of Geotechnical and Geoenvironmental Engineering*. 143(6), 04017014. https://doi.org/10.1061/(ASCE)GT.1943-5606.0001662

Ng, C.W.W., Zhou, C., Zhang, S. and Zhang, Q. (2023). Effects of thermal cycles on soil behaviour: theoretical and experimental studies, *Proc. 8th Int. Conf. on Unsaturated Soils (UNSAT 2023)*. https://doi.org/10.1051/e3sconf/202338200003.

Rahardjo, H., Satyanaga, A., Gofar, N., Leong, E. C., Kew, J. H., Wang, C. L. and Wong, J. L. (2019). Geobarrier System for Protection Against Rainfall-induced Slope Failure, *Int. J. of Geoengineering Case Histories*, 5(1):26-42. http://dx.doi.org/10.4417/IJGCH-05-01-03.

Seed, H.B. (1986). Oral remark during lecturing at UC Berkeley.

Sweeney, D. J. (1982). Some in situ soil suction measurements in Hong Kong's residual soil slopes. *Proc. of the 7th Southeast Asian Regional Conference*, Hong Kong, 91–106.

Proceedings of the XVIII ECSMGE 2024
GEOTECHNICAL ENGINEERING CHALLENGES
TO MEET CURRENT AND EMERGING NEEDS OF SOCIETY
© 2024 the Authors
ISBN 978-1-032-54816-6
DOI 10.1201/9781003431749-121
Open Access: www.taylorfrancis.com, CC BY-NC-ND 4.0 license

ECSMGE 24
XVIII EUROPEAN CONFERENCE ON SOIL MECHANICS AND GEOTECHNICAL ENGINEERING

From EN 1998-5:2004 to prEN 1998-5:2023: Has the calculation of earth pressures improved or deteriorated?

De la norme EN 1998-5:2004 à la prEN 1998-5:2023: Le calcul des pressions terrestres s'est-il amélioré ou détérioré?

L. Pantelidis*
Cyprus University of Technology, Limassol, Cyprus
**lysandros.pantelidis@cut.ac.cy*

ABSTRACT: This paper critically examines the transition from EN1998-5:2004 to prEN1998-5:2023 in the context of calculating lateral earth pressures. The Mononobe-Okabe method, a long-standing normative approach, is replaced by a new informative method in the latest draft standard. This study explores the implications of this change, assessing the conservatism of both methods, their treatment of cohesive soils, sloping backfill, the negative square root problem, and the impact of wall roughness. The paper highlights the potential challenges and considerations that engineers may face with the adoption of the new standard.

RÉSUMÉ: Ce document examine de manière critique la transition de la norme EN1998-5:2004 à la norme prEN1998-5:2023, en se concentrant sur le calcul des pressions latérales de la Terre. La méthode de Mononobe-Okabe, une approche normative de longue date, est remplacée par une nouvelle méthode informative dans le dernier projet de norme. Cette étude évalue les implications de ce changement, en analysant le conservatisme des deux méthodes, leur traitement des sols cohésifs, des remblais en pente, du problème de la racine carrée négative, et l'impact de la rugosité des murs. Le document met en évidence les défis et les considérations que les ingénieurs pourraient rencontrer avec l'adoption de la nouvelle norme.

Keywords: Active and passive earth pressures; EN 1998-5:2004; prEN 1998-5:2023; seismic situation.

1 INTRODUCTION

As known, EN1998-5:2004 (2004) incorporates the Mononobe-Okabe (M-O) method (Okabe 1926; Mononobe and Matsuo 1929) for calculating the active and passive earth pressures for the seismic situation. The coefficient of active or passive earth pressures is:

$$K_{(A/P)E} = \begin{cases} \dfrac{\sin^2(\psi+\varphi'-\theta)}{\cos\theta\cdot\sin^2\psi\cdot\sin(\psi\mp\theta-\delta)[1\pm\rho]^2} \\ \rho = \sqrt{\dfrac{\sin(\varphi'+\delta)\cdot\sin(\varphi'\mp\beta-\theta)}{\sin(\psi\mp\theta-\delta)\cdot\sin(\psi\pm\beta)}} \end{cases} \quad (1)$$

The symbol $K_{(A/P)E}$ denotes either the active or the passive coefficient (K_{AE} and K_{PE} respectively). Having no provision for the cohesion of soil, the total active or passive resultant earth pressure force exerted on the retaining structure as per the EN 1998-5:2004 standard is:

$$E_{(A/P)E} = \frac{1}{2}\gamma(1-a_v)K_{(A/P)E}H^2 + E_{ws} + E_{wd} \quad (2)$$

ψ and β are the inclination angles of the back of the wall and backfill surface from the horizontal line, φ' is the effective angle of shearing resistance of soil, θ is the apparent inclination of the gravity field in the seismic situation, i.e., $\tan\theta = a_h/(1 \pm a_v)$, and δ is the friction angle between the soil and the wall (δ is ignored in the passive state; $\delta = 0$), γ is the unit weight of soil, a_h and a_v are the horizontal and vertical seismic coefficient respectively, H is the height of the retaining structure and E_{ws} and E_{wd} are the static and hydrodynamic water force.

In the draft standard prEN1998-5:2023 (2023) the M-O earth pressure coefficients have been replaced by the following expression (presented in combined form):

$$K_{(A/P)E\gamma} = \frac{\cos\delta\left(\cos\delta\mp\sqrt{\sin^2\varphi'-\sin^2\delta}\right)}{\cos(\beta\pm\theta_{eq})\pm\sqrt{\sin^2\varphi'-\sin^2(\beta\pm\theta_{eq})}}\cdot \frac{\cos\beta}{\cos\theta_{eq}}e^{\mp 2\psi_{(A/P)}\tan\varphi'} \quad (3)$$

$$\psi_{(A/P)} = 0.5\left\{\arcsin\left(\frac{\sin\delta}{\sin\varphi'}\right)\right\}\mp \arcsin\left[\frac{\sin(\beta\pm\theta_{eq})}{\sin\varphi'}\right]\mp\delta+\beta\mp\theta_{eq} \quad (4)$$

The total earth pressure at depth z is:

$$\sigma_{(A/P)E} = K_{(A/P)E\gamma}(\sigma_v - u) + K_{(A/P)Eq} \mp \mp c' K_{(A/P)Ec} + u \quad (5)$$

where, $\tan\theta_{eq} = a_h$ or $\tan\theta_{eq} = a_h\sigma_v/(\sigma_v - u)$ in the absence or in the presence of pore water pressure respectively, c' is the effective cohesion of soil, σ_v is the total overburden pressure and u is the pore water pressure. The coefficients $K_{(A/P)Eq}$ and $K_{(A/P)Ec}$ have been defined as follows:

$$\begin{cases} K_{(A/P)Eq} = K_{(A/P)E\gamma}/\cos\beta \\ K_{(A/P)Ec} = \pm\left(1 - K_{(A/P)E\gamma}\right)/\tan\varphi' \end{cases} \quad (6)$$

Both methods are critically reviewd below.

2 CRITICAL REVIEW

2.1 "Normative" versus "informative"

It is noteworthy that a method which was "normative" for about 20 years (Equations 1 and 2) has been replaced by an "informative" one (Equations 3 to 6). This change seemingly undervalues the new method and can be interpreted in two ways. On one hand, if the new Eurocode exhibits less confidence in its new choice, practicing engineers are likely to do the same, sticking to the old method. On the other hand, the decision to not use a method included in the Eurocode, even if it is labeled as informative, might be viewed as risky. In the event of a failure or issue, not following a method outlined in the Eurocode could be seen as neglecting a recognized standard, even if compliance with that specific method is not legally mandated. This perspective might lead to the practical obligatory use of the new method, as engineers may prefer to align with the latest standards to safeguard against potential liability or to ensure they are using the most current practices.

A third option would be for engineers to use the most conservative method, namely, the one included in prEN1998-5:2023. The relative conservatism of the two methods is discussed in the following section.

2.2 Assessing the conservatism of the two methods

In recent decades, a significant number of experimental and numerical studies (Fragaszy et al. 1987; Gazetas et al. 2004; Sitar and Al Atik 2012; Lew et al. 2010; Al Atik and Sitar 2010; Agusti and Sitar 2013; Mikola and Sitar 2013; Mikola et al. 2016; Wagner et al. 2017) have indicated that the Mononobe-Okabe method yields conservative active earth pressure values, particularly for PGA (peak ground acceleration) values greater than 0.4g. Indeed, some authorities, recognizing the conservatism of the Mononobe-Okabe method, have adopted the standard design practice of using a reduction coefficient for the expected PGA. In this context, AASHTO (2010) considers a horizontal seismic coefficient equal to half the PGA. Conversely, the prEN1998-5:2023 method appears to be even more conservative, as shown in Table 1. A substantial number of finite element results supporting this can be found in Pantelidis and Christodoulou (2022) . The excessive conservatism of the two Eurocode 8-5 methods, as well as the validity of the AASHTO correction on PGA, can also be validated by contemporary centrifuge tests, the results of which are revealing. Referring to the "Loma Prieta SC" test conducted by Mikola and Sitar (Mikola and Sitar 2013), the resultant seismic force (excluding the static force) calculated by the M-O, AASHTO, and prEN1998-5:2023 methods was 54.7, 76.0, and 32.8 kN, respectively; Mikola and Sitar found a value approximately equal to 29 kN, which is very close to AASHTO's prediction. Referring now to the "Kobe TAK090" test by Mikola and Sitar, the resultant seismic force was 70.2, 111.0, and 36.1 kN, respectively; the experimental value was approximately 35 kN, again very close to AASHTO's prediction. The static force, in both cases, was equal to 20.2 kN. Mikola and Sitar used a dry medium-dense sand with a relative density of 75% to 80% as backfill. The friction angle and the unit weight of the sand were φ' =35° and γ =16.6 kN/m³, respectively. The "Loma Prieta SC" wall was tested for a_h=0.51, while the "Kobe TAK090" wall was tested for 0.61. Both walls had height equal to 3m.

Table 1. K_{AE} values for various α_h and φ values calculated according to EN1998-5:2004 (M-O), AASHTO (M-O with PGA/2) and prEN1998-5:2023.

a_h	φ (°)	M-O	AASHTO	prEN1998-5
0.2	20	0.672*	0.569	0.714
	30	0.473*	0.397	0.501
	40	0.328*	0.268	0.350
0.4	20	n/a	0.672*M-O	n/a
	30	0.697	0.473*M-O	0.861
	40	0.488	0.328*M-O	0.611

2.3 Dealing with cohesive soils

The earth pressure analysis method included in Annex F.3 of prEN1998-5:2023 is a lower-bound solution originally proposed by Lancellotta (2007) for purely frictional soils being in the passive failure state (hereinafter referred to as "RL method"). This method

was subsequently expanded from Eurocode 8-5 to deal with the active failure state and to apply to cohesive-frictional soils. For converting the passive state formula to the respective active state, Eurocode 8-5 follows the common practice of changing the proper signs into the formula from "+" to "-" or vice versa (see Equations 3 and 4). Regarding cohesion, in the initial drafts of prEN1998-5, soil cohesion was incorporated into the total earth pressure calculation as follows:

$$\sigma_{(A/P)E} = K_{(A/P)E}(\sigma_v - u) \mp 2c'\sqrt{K_{(A/P)E}} + u \quad (7)$$

The reasoning was that the term $2c'\sqrt{K_{XE}}$ ($X = A$ or P) is equivalent to the corresponding $2c'\sqrt{K_X}$ term of prEN1997-3 for static conditions (see §10.3.2 in the draft version of prEN1998-5, dated 2022-09). In a rational approach, the cohesion term emerges naturally during the derivation of the earth pressure coefficient (as in the case of Rankine's theory, extended by Bell; Rankine 1857; Bell 1915). The numerical examples given in Pantelidis and Christodoulou (2022) clearly demonstrate that this approach (Equation 7) is rather destructive and indeed, on the non-conservative side for the passive state.

In its final form, the total earth pressure is given by Equation 5. One would expect the value calculated by the term $\{c'K_{(A/P)Ec}\}_{v2023}$ to be equal to the value calculated by the earlier term $\{2c'\sqrt{K_{(A/P)E}}\}_{v2022}$. However, as shown in Figure 1, the two approaches yield completely different results. Indeed, the K_{AEc} coefficient becomes smaller as φ' decreases and turns negative for φ less than a certain value (e.g., around 26° for $a_h = 0.4$). According to current knowledge and common sense, the cohesion of soil reduces the earth pressures on the wall, and this effect becomes less significant as the soil's friction angle decreases. A third problem, also indicated in Figure 1, refers to the negative root problem, but this is discussed later.

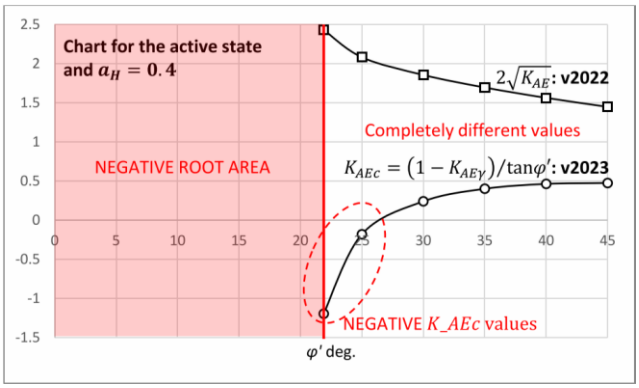

Figure 1. Comparison of the cohesion terms in the active state as per prEN1998-5, versions 09/2022 and 2023 (final version).

2.4 Dealing with sloping backfill

A brief overview of Rankine's theory at this point is deemed necessary. According to this theory, the passive earth pressure coefficient is given as follows:

$$K_P = \cos\beta \frac{\cos\beta + (\cos^2\beta - \cos^2\varphi\prime)^{1/2}}{\cos\beta - (\cos^2\beta - \cos^2\varphi\prime)^{1/2}} \quad (8)$$

Perhaps few have noticed that a positive (and therefore, favourable) angle β results in an unfavorable K_P coefficient (and vice versa). This is obviously not acceptable. Considering that Rankine's theory and the RL method share the same line in Mohr's chart with inclination β (as shown in Figure 2), this presents a strong indication of an erroneous practice in the RL method, despite the fact that this method yields favorable K_P values for favorable β values. The explanation is straightforward. Schematically, for sloping ground inclined at an angle of β to the horizontal, the active Rankine's earth pressure is defined by point B in Figure 2 ($\sigma_{A\prime}$). The fact that $\sigma_{A\prime} > \sigma_A$, as explained below, does not mean that $\sigma_{A\prime}$ is the correct answer to Rankine's problem. In this context, point E provides the answer. Point E defines the corresponding passive Rankine's earth pressure ($\sigma_{P"}$), which is smaller than σ_P; the latter obviously should not be the case. This discrepancy is a strong indication that the line OE in Figure 2 does not represent the ground inclination. Another indication is that the vertical stress of the sloping ground in the active state is less than that of the horizontal ground ($\sigma_{V\prime} < \sigma_V$), which is also incorrect. A third indication is that the same point in the ground has different vertical stress depending on whether the problem is examined from the "active" or "passive" perspective (i.e., $\sigma_{V\prime} \neq \sigma_{V"}$; point C ≠ point D). This is also not acceptable since the vertical stress in the ground should be independent of the state of the soil. In this respect, the RL method used point D to calculate the vertical stress $\sigma_{V"}$ (see Figure 2), through which the passive earth pressure coefficient was derived.

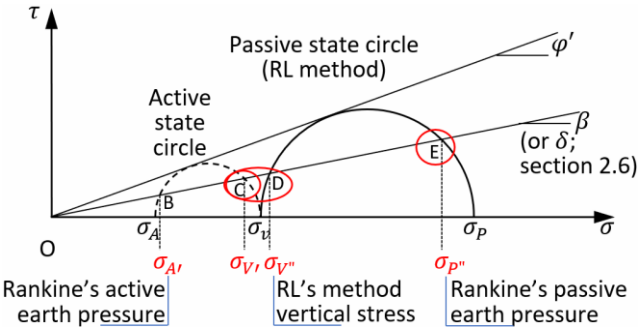

Figure 2. Rankine's theory for sloping ground for the active and passive state.

2.5 The negative square root problem

Although the RL method has been developed on a completely different basis than the Mononobe-Okabe method, it presents the same negative root problem, also for $\varphi' - \theta_{eq} \mp \beta < 0$ (the upper sign stands for the active state, while the lower one for the passive state). This similarity raises suspicions that the cause might be common to both methods. It is undoubtedly true that $K_{AE} > K_A$ (also, $K_{PE} < K_P$). In a seismic situation, the active (or passive) state of the soil is also a failure state, and we should be able to represent this failure with the corresponding Mohr circle. However, because the Mohr's circle for the seismic situation is smaller than that for the static condition, it does not seem to "touch" the failure criterion, as shown in Figure 3a. On the other hand, literature sources (e.g., Srbulov 2008) indicate that during seismic excitation, the shear strength of soils decreases ($c_m < c'$ and $\varphi_m < \varphi'$). Lower shear strength values, in turn, define their own failure criterion that starts at the same point on the normal stress axis but has a gentler slope, as depicted in Figure 3b. The slope decreases with the intensity of the seismic event.

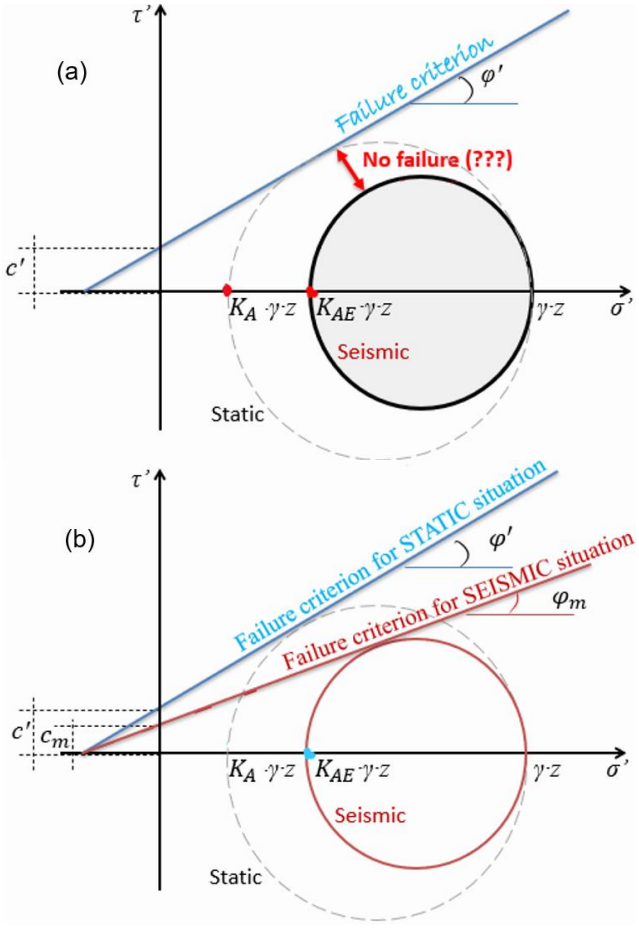

Figure 3. a) Static and seismic Mohr's circle, b) Mohr-Coulomb criterion for static and seismic situation ($a_v = 0$).

The official position of the CEN/TC 250/SC 8 committee is that "the negative square root problem corresponds to a physical situation when the rotated slope angle is larger than the friction angle" (CEN/TC 250/SC 8; document N 1267). However, this is not accurate. The negative root problem exists even for $\beta = 0°$ (for example, for $a_h = 0.5$ and $\varphi' = 26.5°$, which is a quite common case). Moreover, according to the $\varphi' - \theta_{eq} - \beta < 0$ restriction, a slope with c'= 0, φ' = 30°, θ_{eq}= 20° (a_h= 0.364), H =1.176 m and β = 10° is marginally stable (safety factor FS equal to 1), because $\varphi' - \theta_{eq} - \beta = 0$. However, this slope yields an FS of 1.17 with finite elements and FS=1.15 with the method of slices (using the Bishop, Janbu, or Spencer method). This slope stability problem has been analyzed using Rocscience's RS2 (a finite element program) and Rocscience's Slide2 (a limit equilibrium program). In addition, slopes with cohesion do not have this slope angle restriction. In fact, even if the backslope fill cannot remain stable during an earthquake event, we should be able to calculate the seismic earth pressure on the wall.

For the history, when $\varphi' - \theta_{eq} \mp \beta < 0$, EN1998-5:2004 replaces the entire square root in Equation 1 with zero, while prEN1998-5:2023 states "the coefficient $K_{AE\gamma}$ cannot be taken larger than the value corresponding to $\theta_{eq} = \varphi' - \beta$; the coefficient $K_{PE\gamma}$ cannot be taken smaller than the value corresponding to $\theta_{eq} = \varphi' + \beta$". When interpreting the prEN1998-5:2023 statement, it is unclear whether Eurocode 8-5 is simply highlighting the problem with the formula (since it is evident that $K_{AE\gamma}$ and $K_{PE\gamma}$ cannot take the mentioned values) or if it silently suggests bypassing the negative root problem, as in the case of EN1998-5:2004 (replacing the square root in the denominator of Equation 3 with zero and the second arcsin in Equation 4 with π/2). In any case, this replacement leads to the paradox where a soil with a greater friction angle appears more unfavorable than a soil with a smaller friction angle, as shown in Figure 4.

2.6 Dealing with wall roughness

The line inclined at an angle β is one of the two lines used for deriving the RL method. A similar line, also starting from point O, but with an inclination angle of δ, represents the friction angle between the ground and the retaining wall (see Figure 2). While one might mistakenly associate the inclination of the first line with that of dry, cohesionless soil due to their similar range of values, from zero to φ' (the latter being the angle of repose of the material in question), the second line with angle δ is not as intuitively interpretable. Therefore, its use in the RL method seems

unjustifiable. Consequently, this major and arbitrary assumption is unlikely to yield correct results.

The influence of wall roughness on earth pressure was initially introduced by Coulomb (1776). Coulomb analyzed the equilibrium of a soil wedge, treating it as a single block that either moves or rotates as a whole. This block was assumed not to undergo internal strain or deformation, such as compression or extension. In reality, however, soil can expand or compress as the wall moves away from or toward it (active and passive states, respectively). When dealing with an undeformable body, the friction at its boundaries plays a crucial role in its equilibrium. Nevertheless, this effect is likely to be weaker, or even negligible, for deformable bodies like soil, especially in the active state where the soil loosens and flows.

In this context, the author presents a finite element analysis example to indicate the impact of wall roughness. The finite element model, along with its parameters used, are shown in Figure 5. Unless specified otherwise, default parameter values were used. The analysis was carried out using Rocscience's RS2 (version 11.012), a 2D finite element program. The problem involves a (flexible) embedded wall, where all states coexist in the same example, and was solved twice: first by assuming the wall to be rough, and then by considering it as smooth. The findings, which are quite revealing, are illustrated in Figure 6. They indicate that the impact of wall roughness on earth pressure is, in fact, negligible. Additionally, Figure 7 demonstrates that wall roughness has only a minor influence on wall deflection.

A uniform horizontal displacement equal to 0.0001m was applied to the wall to achieve more stable results. These results were found to be independent of the direction of the displacement.

2.7 Validation

According to the CEN/TC 250/SC 8 committee (document N 1267), the validity of the prEN1998-5:2023 method has been checked by *direct comparison* with upper bound solutions and by *indirect comparison* with numerical analyses and results of centrifuge experiments. However, similar solutions, which share the same problems (such as those mentioned in the present paper) are expected to yield comparable results. Also, the term "*indirect comparison*" is somewhat ambiguous. As of 2023, *direct comparison* with results from numerical analyses and centrifuge experiments has become a standard procedure. In this respect, a direct comparison containing centrifuge tests results and tens of finite element results is detailed in Pantelidis and Christodoulou (2022).

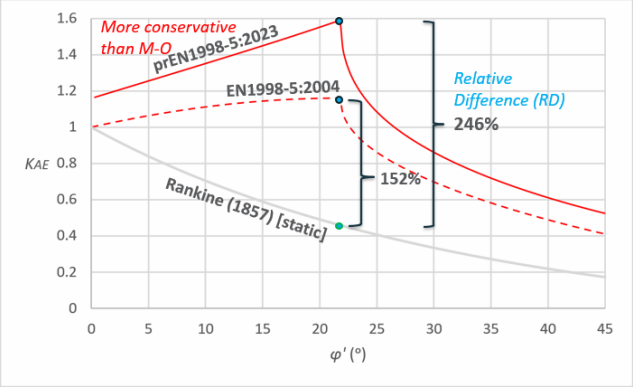

Figure 4. Active earth pressure coefficient versus φ' chart. The two Eurocode 8-5 methods have been used for $a_h = 0.4$ and $a_v = 0$. All methods refer to non-battered, frictionless wall with zero backfill inclination.

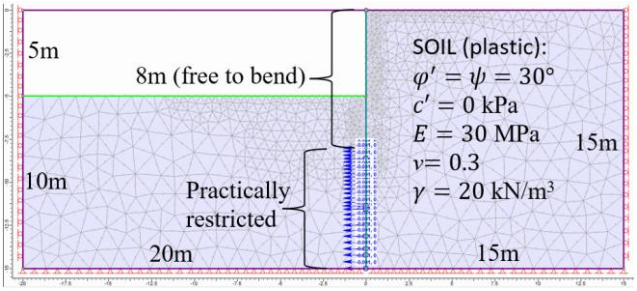

Figure 5. RS2 model of embedded wall. WALL (Timoshenko elastic beam): $E_w = 200$ GPa, $v_w = 0.3$, Thickness: 0.3m; INTERFACE: $\varphi_{int} = 0.1$ or 30°, Normal stiffness=300 MPa/m, Shear stiffness=30 MPa/m.

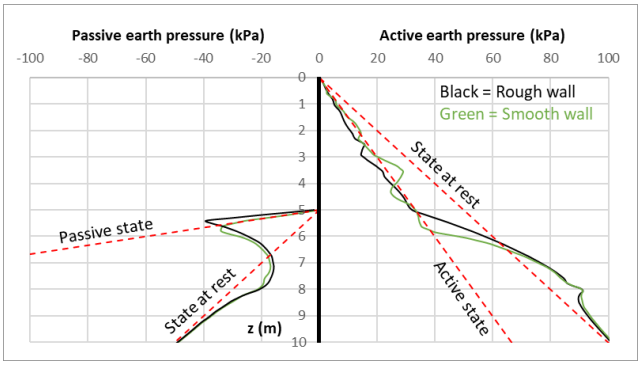

Figure 6. Earth pressure chart (example). Negative values simply indicate the passive state.

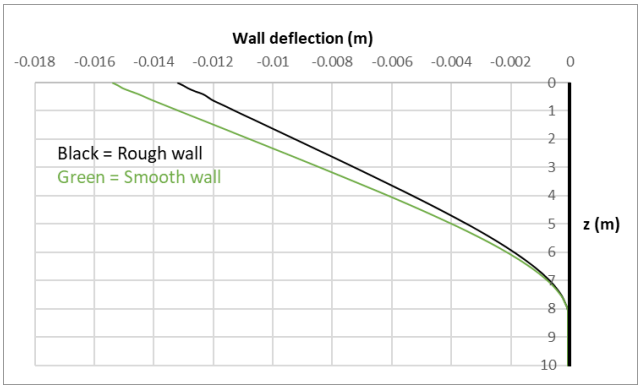

Figure 7. Wall deflection chart (example).

3 CONCLUSIONS

The transition from EN1998-5:2004 to prEN1998-5:2023 in calculating lateral earth pressures adopts a more conservative stance, while it introduces additional complexities and challenges. This study points out that although the Mononobe-Okabe method is already conservative, especially for higher Peak Ground Acceleration (PGA) values, prEN1998-5:2023 is even more so, as shown by finite element analysis and centrifuge testing. The updated standard complicates accurate soil cohesion accounting, causing discrepancies in earth pressure calculations, and incorrectly addresses sloping backfill. Both standards struggle with the negative square root issue, highlighting a fundamental problem in modelling seismic soil failure. Finite element analysis also shows that wall roughness has minimal impact on earth pressure, questioning its traditionally assumed importance. Ultimately, prEN1998-5:2023 introduces complexities and inaccuracies that necessitate careful consideration in engineering applications.

REFERENCES

AASHTO (2010). LRFD Bridge Design Specifications, 5th ed., American Association of State Highway and Transportation Officials, Washington, DC.

Agusti GC, Sitar N (2013) Seismic Earth Pressures on Retaining Structures in Cohesionless Soils, California Department of Transportation, Sacramento CA, USA, Rep. CA13-2170.

Al Atik, L., Sitar, N. (2010). Seismic Earth Pressures on Cantilever Retaining Structures, *Journal of Geotechnical and Geoenvironmental Engineering*, 136, pp. 1324–1333. https://doi.org/10.1061/(ASCE)GT.1943-5606.0000351.

Bell, A.L. (1915). The lateral pressure and resistance of clay and the supporting power of clay foundations. In: *Minutes of the Proceedings of the Institution of Civil Engineers*, Thomas Telford-ICE Virtual Library, pp. 233–272.

Coulomb, C.A. (1776*) An attempt to apply the rules of maxima and minima to several problems of stability related to architecture,* Mémoires l'Académie Royale des Sciences, 7: 343–382.

EN1998-5:2004 (2004). Eurocode 8 - Design of structures for earthquake resistance - Part 5: Geotechnical aspects, foundations, retaining walls and underground structures, CEN, Brussels, Belgium.

Fragaszy, R.J., Dendy, G., Higgins, J.D. (1987). Seismic response of tieback retaining walls, Phase I, Pullman, WA., USA, Rep. WA-RD 138.1.

Gazetas, G., Psarropoulos, P.N., Anastasopoulos, I., Gerolymos, N. (2004). Seismic behaviour of flexible retaining systems subjected to short-duration moderately strong excitation, *Soil Dynamics and Earthquake Engineering*, 24, pp. 537–550. https://doi.org/10.1016/j.soildyn.2004.02.005

Lancellotta, R. (2007). Lower-bound approach for seismic passive earth resistance, *Géotechnique*, 57, pp. 319–321. https://doi.org/10.1680/geot.2007.57.3.319

Lew, M., Sitar, N., Atik, L. Al (2010). Seismic earth pressures: Fact or fiction?, In: *Earth Retention Conference* 3, pp. 656–673.

Mikola, R.G., Candia, G., Sitar, N. (2016). Seismic earth pressures on retaining structures and basement walls in Cohesionless Soils, *Journal of Geotechnical and Geoenvironmental Engineering*, 142, 04016047. https://doi.org/10.1061/(ASCE)GT.1943-5606.0001507.

Mikola, R.G., Sitar, N. (2013). Seismic Earth Pressures on Retaining Structures in Cohesionless Soils, California Department of Transportation, Sacramento CA, USA, Rep. UCB GT 13-01.

Mononobe, N., Matsuo, H. (1929) On the determination of earth pressures during earthquakes. In: *World Engineering Congress*. Tokyo

Okabe, S. (1926). General theory of earth pressure. *Japan Society of Civil Engineers*, 12.

Pantelidis, L., Christodoulou, P. (2022). Comparing Eurocode 8-5 and AASHTO methods for earth pressure analysis against centrifuge tests, finite elements, and the Generalized Coefficients of Earth Pressure, ResearchSquare (preprint). [online] Available at: https://doi.org/10.21203/rs.3.rs-1808466/v3, accessed: 27/02/2024.

prEN1998-5:2023 (2023). Eurocode 8 - Earthquake resistance design of structures - Part 5: Geotechnical aspects, foundations, retaining walls and underground structures, CEN, Brussels, BE.

Rankine, W.J.M. (1857). On the stability of loose earth. *Philosophical Transactions of the Royal Society of London*, 9–27.

Sitar, N., Al Atik, L. (2012). Dynamic centrifuge study of seismically induced lateral earth pressures on retaining structures. In: *Geotechnical Earthquake Engineering and Soil Dynamics IV*. pp 1–11. https://doi.org/10.1061/40975(318)149.

Srbulov, M. (2008). *Geotechnical earthquake engineering: simplified analyses with case studies and examples*. Springer Science & Business Media.

Wagner, N., Candia, G., Mikola, R.G., Sitar, N. (2017). Seismic earth pressures – Experiments and Analyses. In*: Proceedings of the 3rd International Conference on Performance-Based Design in Earthquake Geotechnical Engineering*, Vancouver, BC, Canada, pp. 16-19.

Proceedings of the XVIII ECSMGE 2024
GEOTECHNICAL ENGINEERING CHALLENGES
TO MEET CURRENT AND EMERGING NEEDS OF SOCIETY
© 2024 the Authors
ISBN 978-1-032-54816-6
DOI 10.1201/9781003431749-122
Open Access: www.taylorfrancis.com, CC BY-NC-ND 4.0 license

ECSMGE 24
XVIII EUROPEAN CONFERENCE
ON SOIL MECHANICS AND
GEOTECHNICAL ENGINEERING

Influence of carbonate content on the shear strength of a beach sand from the northeastern coast of Brazil

Influence du teneur en carbonate sur la résistance au cisaillement d'un sable de plage de la côte nord-est du Brésil

K. Polemis Júnior*, A.S. Moura, C.U.V. Verissimo, F.C. Silva Filho, D.A. Nascimento, R.A. Cordeiro Silva
Universidade Federal do Ceará, Fortaleza/CE, Brasil

D.R. de Lima
Universidade de Brasília, Brasília/DF, Brasil

*konstantinos@alu.ufc.br

ABSTRACT: This study assesses how variations in carbonate content affect the shear strength of beach sand from Caucaia, Brazil, a region where specific data on coastal sands' behaviour are limited. Recognizing the relevance for maritime constructions and offshore wind tower foundations, this research focused on two Northeastern coastal sand samples. These were subjected to direct shear tests under stresses of 50, 100, and 200 kPa, with carbonate content variations introduced through Cariri stone waste at low (less than 1%), medium (around 50%), and high (over 80%) levels. Findings reveal a direct impact of carbonate content on sand shear strength, with medium levels enhancing strength uniformly across samples. However, at high carbonate levels, responses varied, indicating a complex relationship between carbonate content and soil mechanical properties. One sample showed increased strength, while the other did not, suggesting a threshold effect where additional carbonate may not consistently benefit soil strength. This nuanced understanding challenges simplistic models of soil behaviour, emphasizing the need for detailed geotechnical analysis in carbonate-rich coastal areas. The study emphasizes the critical need to incorporate carbonate content assessment into the geotechnical evaluation for coastal infrastructure design. It provides foundational data that advances the understanding of soil behaviour in carbonate-enriched environments, essential for optimizing the construction and stability of maritime and wind energy structures.

RÉSUMÉ: Cette étude évalue comment les variations de teneur en carbonate affectent la résistance au cisaillement du sable de plage de Caucaia, au Brésil, une région où les données spécifiques sur le comportement des sables côtiers sont limitées. Reconnaissant l'importance pour les constructions maritimes et les fondations de tours éoliennes offshore, cette recherche s'est concentrée sur deux échantillons de sable côtier du nord-est. Ces derniers ont été soumis à des essais de cisaillement direct sous des contraintes de 50, 100 et 200 kPa, avec des variations de teneur en carbonate introduites par le biais de déchets de pierre de Cariri à des niveaux bas (moins de 1%), moyen (environ 50%) et élevé (plus de 80%). Les résultats révèlent un impact direct de la teneur en carbonate sur la résistance au cisaillement du sable, les niveaux moyens améliorant uniformément la résistance à travers les échantillons. Cependant, à des niveaux élevés de carbonate, les réponses varient, indiquant une relation complexe entre la teneur en carbonate et les propriétés mécaniques du sol. Un échantillon a montré une augmentation de la résistance, tandis que l'autre non, suggérant un effet de seuil où l'ajout supplémentaire de carbonate ne bénéficie pas systématiquement à la résistance du sol. Cette compréhension nuancée remet en question les modèles simplistes du comportement du sol, soulignant le besoin d'une analyse géotechnique détaillée dans les zones côtières riches en carbonate. L'étude souligne le besoin crucial d'intégrer l'évaluation de la teneur en carbonate dans l'évaluation géotechnique pour la conception d'infrastructures côtières. Elle fournit des données fondamentales qui font avancer la compréhension du comportement du sol dans des environnements enrichis en carbonate, essentielle pour optimiser la construction et la stabilité des structures maritimes et éoliennes.

Keywords: Carbonate content; shear strength; geotechnical engineering; offshore wind energy.

1 INTRODUCTION

The exploration of renewable energy sources, particularly in coastal regions, is a topic of increasing relevance in the context of global energy transition efforts. Among these sources, offshore wind energy stands out due to its vast potential for sustainable power generation. This study is situated in the broader context of renewable energy development, focusing specifically on the Northeast coast of Brazil, a region identified for its significant wind energy potential.

Within the field of geotechnical engineering, the behaviour of coastal sands, especially those with high

carbonate content, has been a subject of ongoing research (Poulos, 1988; Watson et al., 2019; Salem et al., 2021). Studies have indicated that such soils can present challenges, notably changing of shear stiffness (Sterianos, 1988; Hassanlourad et al., 2014; Wang et al., 2016; Wei et al., 2021). However, there is a notable gap in specific information regarding the behaviour of Northeast Brazilian coastal sands, which are prevalent in areas earmarked for renewable energy projects, such as the state of Ceará.

Addressing this gap, the current study aims to investigate the impact of varying levels of carbonate content on the shear strength of coastal sands. Given the prevalence of carbonate-rich soils along the Brazilian Northeastern coastline, understanding their mechanical properties is essential for informed geotechnical decision-making in the context of offshore wind farm construction. By evaluating the effect of different carbonate contents on the shear strength of these sands, the study seeks to provide a clearer picture of the mechanical behaviour of coastal soils under varied geotechnical conditions.

Through this research, the aim is to advance the understanding of coastal sand behaviour, particularly in response to carbonate content variations. The findings are expected to be a valuable addition to the field of geotechnical engineering, providing insights that could improve the design and construction practices for renewable energy infrastructures in coastal environments.

2 MATERIALS AND METHODS

This study focused on the shear strength characteristics of quartz beach sands from Pacheco Beach in Caucaia, Brazil, with a particular emphasis on the impact of varying carbonate content. The soil samples, designated SM1 and SM2, were typical quartz sands characteristic of the Brazilian Northeastern coastline, exhibiting naturally low carbonate levels (LCC - Low Carbonate Content).

To establish a comparison, the physical properties of SM1 and SM2 were detailed, including their maximum and minimum specific weights, water content, and void ratios, as summarized in Table 1.

To simulate varying carbonate conditions, limestone residue from Cariri stone, characterized by its higher carbonate content and mechanically processed to a maximum grain diameter of 2.0 mm, was blended with the quartz sands from Pacheco Beach. This residue predominantly consists of silt-sized particles and coarse sand. The beneficiation process ensured homogenized particle sizes suitable for this study experimental investigation. A 50% limestone to quartz sand ratio was used to create a medium carbonate content mixture (MCC), and an 80% limestone to 20% quartz sand ratio was prepared to represent high carbonate content conditions (HCC). These artificial mixtures were then subjected to direct shear tests to examine the altered mechanical behaviours under simulated carbonate-enriched environments, performed under normal stresses of 50, 100, and 200 kPa.

Table 1. Physical properties of SM1 and SM2.

Header	unit	SM1	SM2
Max. specific weight	g/cm^3	1.69	1.80
Min. specific weight	g/cm^3	1.46	1.51
Water content	%	3.23	3.42
Max. void ratio	-	0.78	0.81
Min. void ratio	-	0.53	0.52
Specific gravity	-	2.51	2.64
Gravel (>2 mm)	%	12	2
Coarse Sand (0.60 - 2.00 mm)	%	33	9
Medium Sand (0.20 - 0.60 mm)	%	23	34
Fine Sand (0.075 - 0.20 mm)	%	22	35
Fines (<0.075 mm)	%	10	20

3 RESULTS AND DISCUSSION

The analysis of the shear stress versus horizontal displacement curves for samples SM1 and SM2 across different carbonate content levels reveals a nuanced influence of carbonate content on the shear strength properties of the soil samples. As seen in Figures 1, 2, and 3, the shear strength of both samples generally decreases with an increase in carbonate content under the same normal stress condition. This can be attributed to the alteration in the soil structure and interparticle forces due to the presence of carbonate, which seems to reduce the soil's resistance to shear under loading.

For low carbonate content (LCC), the shear strength curves of both SM1 and SM2 exhibit a relatively steep initial ascent, followed by a more gradual increase, with SM1 showing a consistently higher shear stress across all normal stresses compared to SM2. This suggests that SM1, potentially with a denser packing or better particle interlock, can sustain higher shear stresses before reaching a critical displacement. In contrast, the high carbonate content (HCC) curves demonstrate a marked reduction in shear strength for both samples, particularly noticeable at higher normal stresses, indicating that the presence of carbonate at this level may be leading to a weakening of the soil structure or a reduction in frictional resistance between particles.

The intermediate carbonate content (MCC) shows a transitional behaviour between LCC and HCC, where the reduction in shear strength is evident but not as pronounced as in HCC. Interestingly, the response under 50 kPa normal stress for both SM1 and SM2 in MCC does not follow the same decreasing trend as seen under higher stresses, which could suggest that at lower normal stresses, the carbonate content's effect on the soil's shear strength might be less significant or that other factors, such as particle size distribution or shape, could be influencing the behaviour.

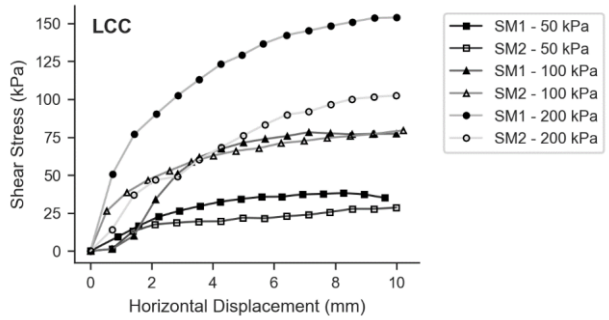

Figure 1. Shear stress vs. horizontal displacement curves of SM1 and SM2 with low carbonate content.

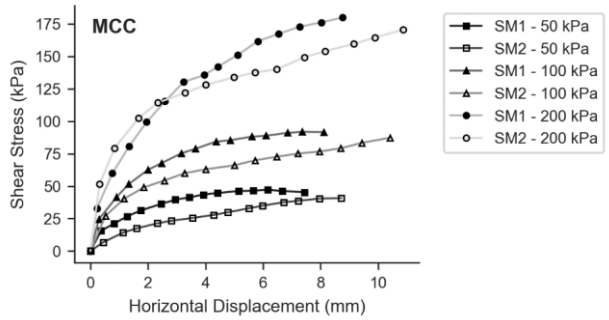

Figure 2. Shear stress vs. horizontal displacement curves of SM1 and SM2 with medium carbonate content.

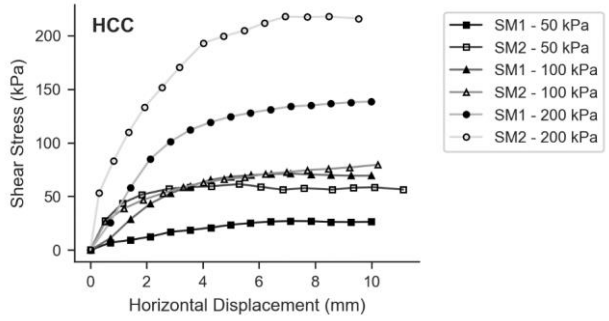

Figure 3. Shear stress vs. horizontal displacement curves of SM1 and SM2 with high carbonate content.

The vertical versus horizontal displacement outcomes for soil samples SM1 and SM2, depicted in Figure 4, exhibit distinctive deformation behaviours under various levels of normal stress, reflecting their respective compressibility and dilatancy during shear. The control of initial density was carefully managed by maintaining a consistent methodology for sample preparation across all tests.

Under the lesser normal stress of 50 kPa, SM1 shows notable compression, suggesting consolidation under modest confining pressures. As normal stress escalates to 100 kPa and subsequently 200 kPa, SM1 transitions to a dilatant response, as evidenced by the increase in vertical displacement. This behaviour suggests a particle rearrangement and shear band formation, which is typical in densely packed granular soils when subjected to elevated confining pressures.

In contrast, SM2 consistently displays dilatancy across all examined normal stresses. Even under lower stresses, SM2's dilatant behaviour suggests an initially looser packing or more angular particle shape, causing a volume increase upon shearing. Such dilatancy is significant when assessing the potential for soil liquefaction or in the design to prevent bearing capacity failure, as it influences the soil's ability to support loads.

At medium and high carbonate content levels, both samples show enhanced dilatancy, corresponding with the trends noted in the shear stress versus horizontal displacement data. The presence of carbonate appears to amplify the volume increase during shearing, possibly due to its effect on soil fabric and the ratio between particles.

The combined analysis of shear and volumetric behaviour reinforces the need to understand the influence of carbonate content on the mechanical behaviour of soils. It underlines the complex interplay between soil fabric, stress conditions, and carbonate content, which must be considered for accurate predictions of soil response under shear loading in geotechnical engineering practice.

In the evaluation of shear strength parameters, as delineated in Figures 5, 6, and 7, an analysis of the friction angles for SM1 and SM2 across varying carbonate contents reveals the significant role of carbonate content in influencing soil behaviour. Notably, for SM1, an unexpected decrease in friction angle was observed at high carbonate content (HCC), diverging from the anticipated trend of increased shear resistance with carbonate addition. This phenomenon suggests that, beyond a certain carbonate concentration threshold, there may be a diminution in frictional performance, likely due to alterations in particle interlock and soil fabric that require further investigation.

For low carbonate content (LCC), SM1 demonstrates a higher friction angle compared to SM2, potentially attributed to differences in particle shape or texture, which are known to influence shear strength. As carbonate content escalates to medium levels

(MCC), the friction angles of both samples converge, suggesting that the effects of carbonate content on shear strength behaviour become increasingly pronounced.

The behaviour of SM2, particularly its increased friction angle at high carbonate content, underscores the complex nature of soil-carbonate interactions and points to the potential for carbonate content to enhance soil mechanical properties under specific conditions. These observations indicate that the relationship between carbonate content and soil mechanical behaviour is intricate and multifaceted, highlighting the importance of a nuanced approach to geotechnical analysis in carbonate-rich soils.

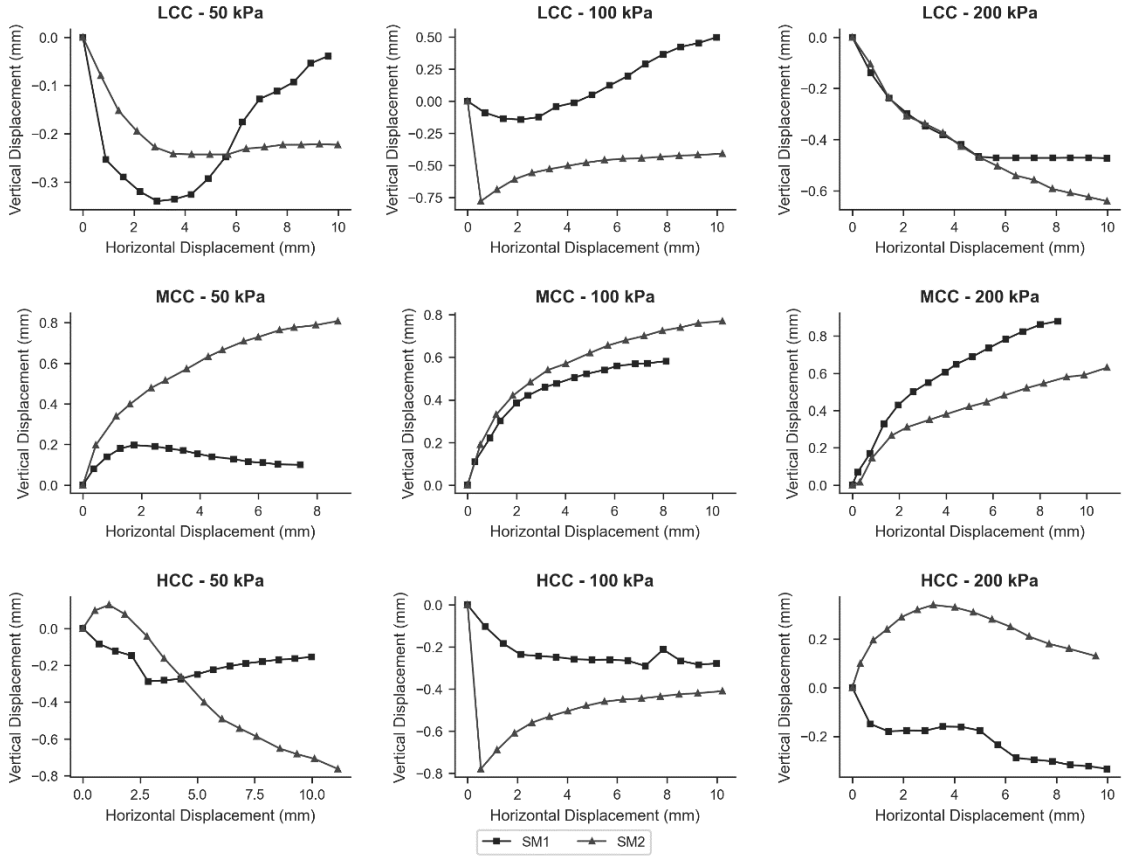

Figure 4. Vertical displacement vs. horizontal displacement for samples SM1 and SM2.

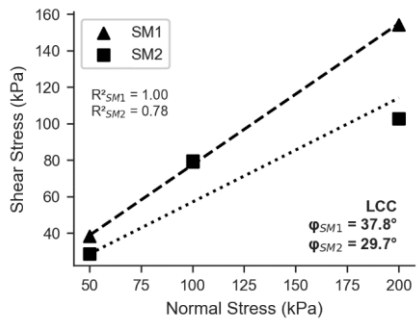

Figure 5. Failure envelope for the direct shear test of SM1 and SM2 with low carbonate content.

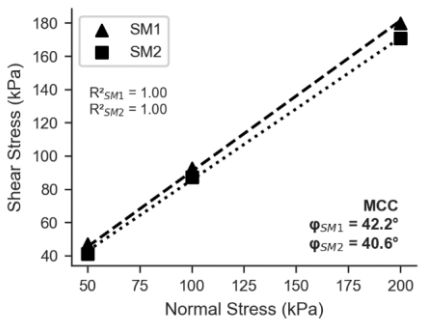

Figure 6. Failure envelope for the direct shear test of SM1 and SM2 with medium carbonate content.

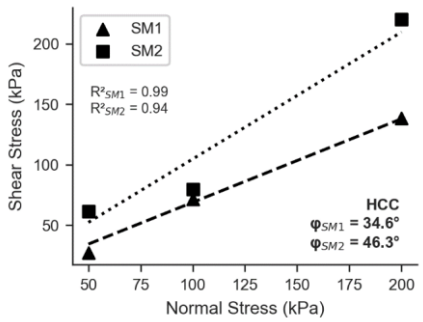

Figure 7. Failure envelope for the direct shear test of SM1 and SM2 with high carbonate content.

4 CONCLUSIONS

The research presented in this paper provides a critical assessment of the mechanical behaviour of Caucaia beach sands, with a specific examination of the effects of carbonate content variations. The study contributes to a nuanced understanding of coastal sands with high carbonate content, which are often categorized as problematic due to their propensity for rapid shear stiffness degradation. The findings are particularly relevant for geotechnical applications along the Northeast Brazilian coast, an area with significant potential for wind energy exploitation and corresponding maritime construction activities.

The study's findings indicate that the relationship between carbonate content and soil mechanical properties is more complex than previously understood. An increase in carbonate content, particularly up to a medium level, was observed to enhance the effective friction angle. This improvement in friction angle for mixtures incorporating up to 50% limestone residue from Cariri stone is consistent with other research findings, suggesting that the mechanical processing of the limestone grains contributes to a more angular grain shape, thereby enhancing soil resistance. Such changes are attributed to the distinct grain morphology introduced by the processed limestone, known for its inherent high resistance due to the Cariri stone origin.

However, upon increasing the carbonate content to high levels (i.e., an 80% limestone to 20% quartz sand ratio representing high carbonate content conditions), the behaviour diverges between samples. While one sample continued to exhibit an increase in friction angle, indicative of strengthened soil properties, the other did not follow this trend, suggesting that there is a threshold beyond which additional carbonate content may not uniformly contribute to soil strength enhancement. This deviation underscores the complexity of soil behaviour in response to carbonate content, challenging the assumption of a straightforward relationship between increased carbonate and soil strength.

The differences observed in friction angles at higher carbonate levels emphasize the importance of a detailed approach in understanding the role of carbonate content on soil mechanics. These results bring to light the necessity of considering grain shape and processing techniques in geotechnical analysis and design, particularly for projects involving carbonate-rich soils. The findings suggest that current models might not fully account for the nuanced effects of elevated carbonate levels on soil mechanical properties, signaling a need for more sophisticated models that accurately reflect these detailed interactions.

ACKNOWLEDGEMENTS

This study was financed in part by the Coordenação de Aperfeiçoamento de Pessoal de Nível Superior – Brasil (CAPES) – Finance Code 001 – and the Conselho Nacional de Desenvolvimento Científico e Tecnológico (CNPq). The authors appreciate the financial support from PETROBRAS. Gratitude is also extended to the DEHA department's postgraduate program at Universidade Federal do Ceará (UFC) for their support.

REFERENCES

Hassanlourad, M., Rasouli, M.R., and Salehzadeh, H. (2014) A comparison between the undrained shear behavior of carbonate and quartz sands, International Journal of Civil Engineering, 12(4), pp. 338-350. Available at: https://ijce.iust.ac.ir/article-1-923-en.pdf , accessed: 12/March/2024.

Poulos, H.G. (1988). The mechanics of calcareous sediments (John Jaeger Memorial Address). *Australian Geomechanics, pp. 8-41*. Available at: https://www.issmge.org/publications/publication/the-mechanics-of-calcareous-sediments , accessed: 12/March/2024.

Salem, T.N., Elkhawas, N.M., and Elnady, A.M. (2021) Behavior of Offshore Pile in Calcareous Sand—Case Study, *Journal of Marine Science and Engineering*, 9(8), p. 839. https://doi.org/10.3390/jmse9080839.

Sterianos, B. (1988). Geotechnical properties of carbonate soils with reference to an improved engineering classification. *Master's thesis*, University of Cape Town. [online] Available at: https://open.uct.ac.za/server/api/core/bitstreams/41e2cbb7-65a3-4d1e-9149-9301d8e65403/content , accessed: 12/March/2024.

Wang, X.Z., Wang, X., Jin, Z.C., et al. (2016) Shear characteristics of calcareous gravelly soil, *Bulletin of*

Engineering Geology and the Environment, 76(2), pp. 561-573. https://doi.org/10.1007/s10064-016-0978-z.

Watson, P.G., Bransby, M.F., Delimi, Z.L., Erbrich, C.T., Finnie, I., Krisdani, H., Meecham, C., O'Neill, M., Randolph, M.F., Rattley, M.J., and Silva, M. (2019). Foundation design in offshore carbonate sediments-building on knowledge to address future challenges. In XVI Pan-American Conference on Soil Mechanics and Geotechnical Engineering (XVI PCSMGE), *From Research to Applied Geotechnics*, pp. 240-274. [online] Available at: https://www.issmge.org/uploads/publications/84/85/9-keynote-lecture-s8-watson.pdf , accessed: 12/March/2024.

Wei, H., Yin, M., Zhao, T., et al. (2021) Effect of particle breakage on the shear strength of calcareous sands, *Marine Geophysical Research*, 42, 23. https://doi.org/10.1007/s11001-021-09440-2.

Proceedings of the XVIII ECSMGE 2024
GEOTECHNICAL ENGINEERING CHALLENGES
TO MEET CURRENT AND EMERGING NEEDS OF SOCIETY
© 2024 the Authors
ISBN 978-1-032-54816-6
DOI 10.1201/9781003431749-123
Open Access: www.taylorfrancis.com, CC BY-NC-ND 4.0 license

ECSMGE 24
XVIII EUROPEAN CONFERENCE ON SOIL MECHANICS AND GEOTECHNICAL ENGINEERING

Soil plugging in small diameter tube samplers in silty soils

Le bouchage du sol dans les échantillonneurs de tubes de petit diamètre dans les sols limoneux

E. Pöyry*, M.S. Farhadi, M. Haikola, T.T. Länsivaara
TERRA Research Center, Department of Civil Engineering, Faculty of Built Environment, Tampere University, Tampere, Finland

**eetu.poyry@tuni.fi*

ABSTRACT: One of the challenges in a geotechnical ground investigation is to obtain high quality samples, especially from coarser soils like sands and silts. Piston samplers are commonly used in the Nordic countries to take undisturbed soils samples. For coarser soils, one commonly reported issue is that the sample is disturbed particularly during withdrawal, causing even loss of sample. To avoid this, different types of catchers can be used. The paper presents some preliminary results of a study aimed to improve sampling quality for silty soils. ST1 and ST2 piston samplers with different setups are compared in a test site near Pori, Finland. One important observation of the study was that in some conditions the sampler was plugged, causing densification, disturbance and partly empty sample tubes. To avoid plugging, lubricant was used both inside the tube as well as on the outside surface. In this paper results from four different type of sampling setups will be presented, namely 1) ST1 with lubricant 2) ST2 with lubricant 3) ST1 with catcher, and 4) ST1 without lubricant. Type 4 presents the standard method used in Finland. The amount of soil plugging was measured after sampling. The sample quality is assessed by comparing unit weight and water content. The results show that plugging appears the most for ST1 sampler with the catcher, but to some extent plugging was an issue even without the catcher. The applied lubricant reduced the plugging effect quite effectively. Another important conclusion from the study is that plugging, due to its densification effect, may lead to results on the unsafe side. This has traditionally not necessarily been noted, as the lack of sample has been interpreted as loss of sample rather than plugging.

RÉSUMÉ: L'un des défis d'étude géotechnique est de prélever des échantillons de bonne qualité, en particulier aux sols plus grossiers, comme les sables et les limons. Les échantillonneurs à piston sont couramment utilisés dans les pays nordiques pour prélever des échantillons de sols non perturbés. Pour les sols plus grossiers, un problème fréquemment signalé est que l'échantillon est perturbé, en particulier lors du retrait. Pour éviter cela, différents types de récupérateurs peuvent être utilisés. Le présent document présente les résultats préliminaires d'améliorer la qualité de l'échantillonnage pour les sols limoneux. Les échantillonneurs ST1 et ST2 avec différentes configurations sont comparés sur un site d'essai près de Pori, en Finlande. Une observation importante de l'étude était que dans certaines conditions, l'échantillonneur était bouché, provoquant de densification, perturbation et des tubes d'échantillons partiellement vides. Pour éviter le bouchage, un lubrifiant a été utilisé à l'intérieur du tube et sur la surface extérieure. Dans ce document, les résultats de quatre types différents de configurations d'échantillonnage seront présentés, 1) ST1 avec lubrifiant 2) ST2 avec lubrifiant 3) ST1 avec récupérateur, et 4) ST1 sans lubrifiant. Le type 4 représente la méthode standard utilisée en Finlande. La quantité de bouchage du sol a été mesurée après l'échantillonnage. La qualité de l'échantillon est évaluée en comparant le poids unitaire et la teneur en eau. Les résultats montrent que le bouchage apparaît le plus pour l'échantillonneur ST1 avec le récupérateur. Le lubrifiant appliqué a réduit l'effet de bouchage. Une autre conclusion importante de l'étude est que le bouchage, en raison de son effet de densification, peut conduire à des résultats du côté dangereux. Cela n'a pas nécessairement été noté traditionnellement, car le manque d'échantillon a été interprété comme une perte d'échantillon plutôt que comme un bouchage.

Keywords: Soil sampling; sample quality; piston samplers; soil plug; silts.

1 INTRODUCTION

One of the main objectives of geotechnical investigation is to obtain representative samples of the subsurface soil. However, sampling is not a trivial task, especially for coarser soils like sands and silts, which are prone to disturbance and loss during the sampling process. Disturbed samples may not reflect the real in-situ conditions of the soil and may lead to erroneous or unreliable results in the laboratory tests. Disturbance can affect the soil structure, density, water content, and strength, leading to inaccurate or misleading results (Clayton, Matthews, & Simons, 1982). Therefore, it is important to minimize the disturbance and maximize the recovery of undisturbed samples.

As a popular sampler in Nordic countries, piston sampler can take high quality samples in soft clays, but it may encounter difficulties in silty and sandy soils, especially during the withdrawal stage, when the sample may drop. One of the problems is also the soil plugging effect, which occurs when the soil inside the tube is compressed, as a result of sampler diameter, wall friction, length of the sampler tube, soil cohesion, etc. (Baligh, Azzouz, & Chin, 1987; Carroll & Long, 2017). To prevent or reduce the soil dropping or plugging, different techniques can be used, such as applying lubricant to the inner surface, or using a catcher at the tip of the tube to retain the sample.

This study aims to compare the most common soil sampling methods used in Finland. The preliminary results are presented herein to improve the sampling quality for silty soils. The performance of two types of piston samplers, ST1 and ST2, are compared with different setups and modifications.

2 TESTING SITE

The testing site is located in the southwest of Finland, at Haistila, which is located in Pori (according to: https://www.google.com/maps/). The location of the testing site is shown in Figure 1.

The Haistila testing site is close to the Gulf of Bothnia, and it has been covered by sea in the past. The sulphide soil is verified there, approximately deeper than 2 m.

The information on the sampling boreholes IDs and the sampler types are presented in Table 1. The boreholes are located at least 2 m far from each other, and the farthest distance between them is about 6 m.

Table 1. The sampler types for each borehole at Haistila; mentioned by S2~S7, in the Borehole IDs.

Borehole ID	Sampler type
HAI22-S2-S050	ST2
HAI22-S5-S060	ST1-FIN with friction tapes
HAI22-S4-S070	ST1-FIN with catcher
HAI22-S3-S090	ST1-normal
HAI22-S7-S100	ST1-FIN without lubricant

2.1 Soil type

The CPTu-based soil stratification profiles, using the $RIGTOSS_{Fr\text{-}Qt}$ and $RIGTOSS_{Bq\text{-}Qt}$ models (Farhadi et al., 2022; Farhadi, Länsivaara, & Tonni, 2022; Farhadi & Länsivaara, 2022), are presented in Figure 2. The identified soil behavior type (SBT) in Figures 2-(a,b) show mainly three or four layers, with SBT values as 6, 5, 4 and 3, respectively at the depth ranges of 1-1.7, 1.7-2.8, 2.8-4.1, and 4.1-10 m; including some minor variations. Distribution of data points on the two related charts of F_r-Q_t and B_q-Q_t in Figures 2-(c,d) confirm the identified layers.



Figure 1. Location of the testing site at Haistila, located in Pori (https://asiointi.maanmittauslaitos.fi/karttapaikka/).

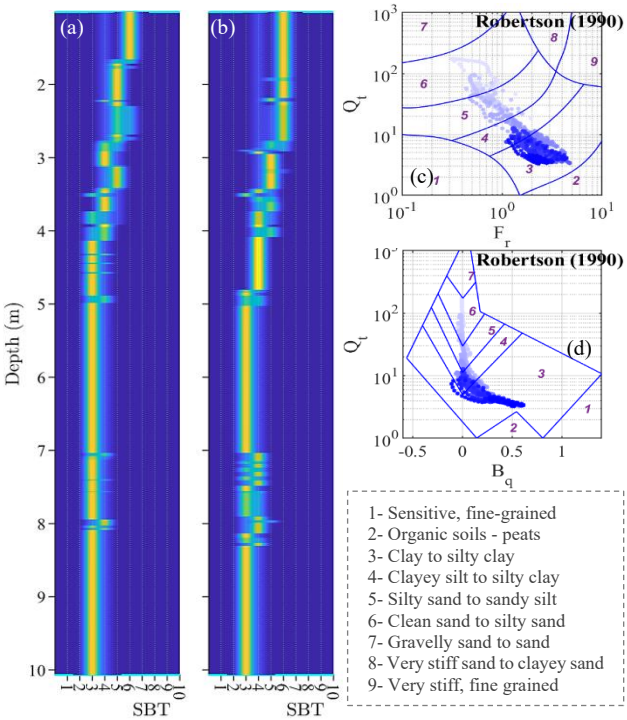

Figure 2. (a) $RIGTOSS_{Fr\text{-}Qt}$, and (b) $RIGTOSS_{Fr\text{-}Bq}$ stratification-characterization profiles of the Haistila testing site, and (c,d) distribution of data points on the characterization charts, by Robertson (1990). The legend introduces different soil behavior types (SBTs) numbers.

The grains size distributions at different depths, for the Haistila testing site are shown in Figure 3. The chart shows that the soil type at the site is silty, and the size of the particles reduces with depth; which is in agreement with the SBT profiles in Figure 2.

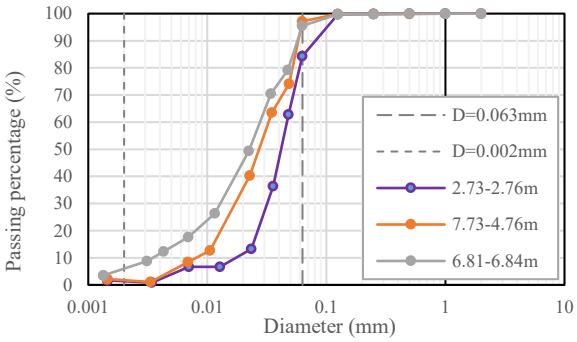

Figure 3. Grains size distribution of the soil at different depths, at the testing site, Haistila. The diameter of the silt particles range from 0.002 to 0.063 mm are marked on the chart by the dotted grey gridlines.

3 METHODOLOGY

The study focuses on identifying plugging and how it affects the soil properties, such as the bulk unit weight, γ, and natural water content, w_n. Herein, plugging is simply defined by the 'core recovery' parameter, defined as the height of the soil taken inside the sampling tubes, H_F, to the theoretical sample height, H_T; i.e. $H_P=H_F/H_T$. Additionally, we estimated plugging by measuring the weights of the three 170 mm inner tubes (higher, middle, and lower sampling tubes) at each sampling depth: 2.5, 4.5, and 6.5 m. The masses of the sample tubes were used to estimate the intensity of the potential plugging and its effect on the unit weight of the soil.

The sampler penetration rate into ground varied for different techniques and depths between 0.8 and 2.2 cm/s, and was kept as constant as possible because it was found that the penetration rate influences the soil plugging, i.e., the intrusion of the soil into the sampler tubes.

The two 50 mm piston samplers used here are ST1 and ST2. The details can be sought in the guidelines of Finnish Geotechnical Society (Suomen Geoteknillinen Yhdistys, 2023). As mentioned in Table 1, sampler with catcher is used at borehole HAI22-S4-S070. Its photo is shown in Figure 4-(a). As a novel method, the ST1 sampler is modified in this study, and used at HAI22-S5-S060. Several friction tapes are mounted at six slots, in a 4 cm high inner tube, added behind the cutting shoe of the sampler. It can be seen in Figure 4-(b). Lubricant was used at every borehole except HAI22-S7-S100.

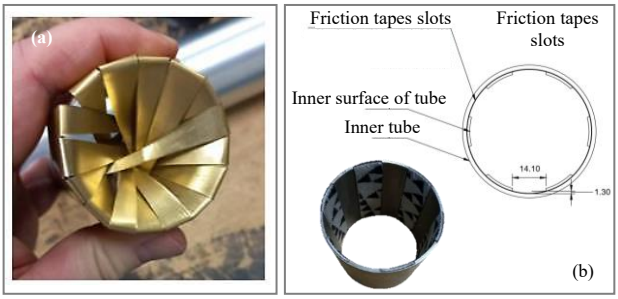

Figure 4. a) photo of the sampler catcher, and, b) the friction tape inner tube of the ST1 sampler.

4 RESULTS

The results indicate that there are correlations between plugging and the soil properties w_n and γ; which are explained in the following section.

4.1 Field observations

Plugging is compared for five different sampling techniques at the boreholes S050, S060, S070, S090 and S100 (the full ID of the boreholes are mentioned in Table 1). For each borehole, the weight of the inner tubes is measured, and the measurement results are shown in Figure 5.

Based on the results, it is found that at the boreholes S070 and S100, the sample tubes differ mostly from the average of the results, and the difference is the greatest at the reference depths of 2.5 and 4.5 m.

In addition, at the depth of 4.5 m, it is observed that the lowest sample tubes are partly empty at the boreholes S090 and S100, resulting in much lower sample tube masses. Most likely, part of the samples is dropped when the withdrawal of the sampler started. This phenomenon occurred with ST1 samplers with polymer and without polymer gel. Thus, it is concluded that the polymer gel could not significantly contribute to the retention of the samples within the sampling tube, during the sample lifting phase in the field.

In addition to the dropping of the samples, the other observed problem was the soil plugging into the sampler tubes. As presented in Table 2, plugging is observed especially at the sampling points S070 and S100. The lowest core recovery is found at the sampling depths 2.5 and 4.5 m, which equals 57 and 89%, respectively. The soil at these depths have been coarser; in contrast to the soil at 6.5 m. The higher masses of the lowest tubes at the depths 2.5 and 4.5 m confirm the densification of soil, at boreholes S070 and S100. Table 2 also indicates that the lubricant has a positive impact to reduce the soil plugging, comparing the sampling points S090 and S100 (ST1

sampler with and without the polymer gel at the inner sampling tubes). Using lubricant at S090 has led to 100% core recovery.

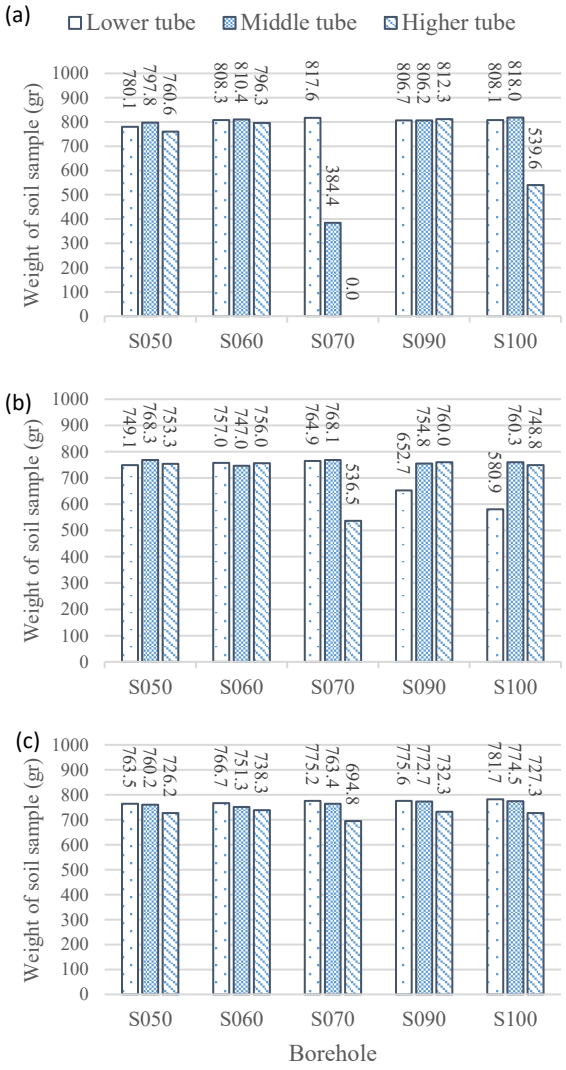

Figure 5. Weight of soil samples at approximate depths of: a) 2.5, b) 4.5, and c) 6.5 m. The boreholes full IDs are mentioned in Table 1, which are shortened herein as the x-axis labels; for example, S050 stands for HAI22-S2-S050.

Table 2. Core recovery for the three reference depths.

	Core recovery (%)		
Borehole ID	**2.5**	**4.5**	**6.5**
HAI22-S2-S050	100	100	100
HAI22-S5-S060	100	100	100
HAI22-S4-S070	57	89	98
HAI22-S3-S090	100	100	100
HAI22-S7-S100	86	100	99

4.2 Unit weight

The water content, w_n, and bulk unit weight, γ, results are shown in Figure 6. It shows significant variations in both w_n and γ, for different samplers, at the same depth. The variation is greatest at the reference depths of 4.5 and 6.5 m, while at the reference depths of 2.5 m, the results are closer together.

Figure 6-a shows that there is a natural variation in γ in depth, due to different soil types; which is approved by the CPTu results shown in Figure 5-b. The maximum γ is measured at the depth of 2.5 m, where the soil contains more sand, in contrast to 4.5 m and 6.5 m. However, it is also found that there are differences between different sampling methods, as there is considerable variation in the γ of samples taken from the same depth. Based on the results, it can be concluded that the γ of the sample is increased by the plugging, mainly due to the large friction of the sampler's wall. Plugging has occurred mostly at the boreholes S070 and S100, where γ has been also the highest, especially at the depth of 2.5 m. But some impacts on γ can also be seen in 4.5 and 6.5 m depth, in Figure 6-(a). At the depth of 4.5m, it seems that catcher has a negative impact on γ. At this depth, the γ values for the low and middle tubes are highest among all tested samplers, which means densification of soil; and at the top tube (which has been left partly empty) γ is the lowest. At the depth of 6.5 m, the highest γ is measured when the lubricant is not used. Definitely, the whole sampling process (transportation and lab test preparation) may affect the results which can magnify the variation.

4.3 Water content

Based on the results in Figure 6, it is found that the higher bulk unit weight, γ, is correlated with the lower water content, w_n, especially at 2.5 m, where the soil is coarser. However, for silts at 4.5 and 6.5 m, the measured parameters are more variable, for different samplers. At the depth of 2.5 m the lowest value of w_n has been measured when using catcher, at the borehole S070. At the depth of 4.5 m, the lowest values of w_n is measured at the boreholes S060 and S070, and at the depth of 6.5 m, the lowest values are measured at the borehole S100. At the same points, γ has been the highest value. It seems that soil densification resulting from the shear and vertical strains during penetration of the sampler causes higher pore pressure in the samples and the escape of water, which could also have led to lower w_n – discussed also by (Baligh, Azzouz, & Chin, 1987; Bjerrum, 1973).

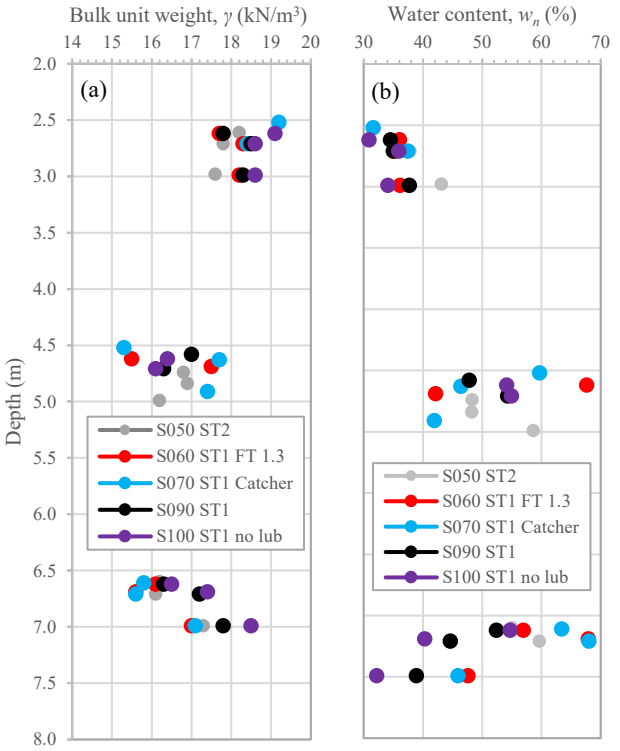

Figure 6. Bulk unit weight, γ, and water content, w_n, measurements for different samplers. (FT stands for friction tapes, used at S060; and 'no lub' shows not using lubricant.).

5 CONCLUSIONS

In this study, several small diameter samplers are employed in silty and sandy soils. They are used mainly in a testing site, Haistila, Ulvila, in Finland. The problem of soil plug in sampling is addressed by the assessment of some sampling and soil properties, such as core recovery, bulk unit weight, γ, and natural water content, w_n. The study led to several concluding marks, for instance:

- Using catcher led to the highest soil densification, and the smallest core recovery.
- Using lubricant lead to less plugging. Plugging was also observed when the lubricant was not applied to the samplers.
- Plugging affected the measurements of γ and w_n, more in silty soils rather than sandy soils. The higher the densification, the higher the γ, and the lower the w_n.
- The novel idea to modify the samplers with friction tapes prevented the soil drop during the withdrawal of the sampler, not leading to plugging and soil densification.

ACKNOWLEDGEMENTS

The authors are grateful for the financial support provided by Tampere University.

REFERENCES

Baligh, M. M., Azzouz, A. S., & Chin, C.-T. (1987). Disturbances due to "ideal" tube sampling. *Journal of geotechnical engineering*, *113*(7), 739-757. https://doi.org/10.1061/(ASCE)0733-9410(1987)113:7(739).

Bjerrum, L. (1973). Problems of soil mechanics and construction on soft clays and structurally unstable soils. *State-of-the-art report, Session IV, Proc. 8th Int. Conf. Soil. Mech. and Found. Eng., Moscow., Volume 3, pp. 111—159.*

Carroll, R., & Long, M. (2017). Sample disturbance effects in silt. *Journal of Geotechnical and Geoenvironmental Engineering*, *143*(9), 04017061. https://doi.org/10.1061/(ASCE)GT.1943-5606.0001749.

Clayton, C. R., Matthews, M. C., & Simons, N. E. (1982). *Site investigation*. Granada London.

Farhadi, M., Länsivaara, T., L'Heureux, J.-S., & Lunne, T. (2022). Application of two novel CPTu-based stratification models. In *Cone Penetration Testing 2022* (pp. 400-406). CRC Press. https://doi.org/10.1201/9781003308829-55.

Farhadi, M., Länsivaara, T., & Tonni, L. (2022). Application of integrated Game Theory-optimization subground stratification (-IGTOSS) model to Venetian Lagoon deposits. In *Cone Penetration Testing 2022* (pp. 394-399). CRC Press. https://doi.org/10.1201/9781003308829-54.

Farhadi, M. S., & Länsivaara, T. (2022). Development of an integrated game theory-optimization subground stratification model using cone penetration test (CPT) measurements. *Engineering with Computers*, *38*(Suppl 2), 1227-1242. https://doi.org/10.1007/s00366-020-01243-0

Suomen Geoteknillinen Yhdistys. (2023). *Kairausopas III: Näytteenotto geoteknisiä tutkimuksia varten*.

Proceedings of the XVIII ECSMGE 2024
GEOTECHNICAL ENGINEERING CHALLENGES
TO MEET CURRENT AND EMERGING NEEDS OF SOCIETY
© 2024 the Authors
ISBN 978-1-032-54816-6
DOI 10.1201/9781003431749-124
Open Access: www.taylorfrancis.com, CC BY-NC-ND 4.0 license

ECSMGE 24
XVIII EUROPEAN CONFERENCE ON SOIL MECHANICS AND GEOTECHNICAL ENGINEERING

A glimpse into the future of site supervision: Data collection during pile installation at the Amaliahaven construction site

Un aperçu du futur de la supervision de site: Collecte de données pendant l'installation des pieux sur le chantier de construction d'Amaliahaven

J. Putteman*, P.S.F. Le Lan, C.J.F. van Marrewijk, T. Jottier
SBE Engineering Consultants, Rotterdam, The Netherlands

J.N. Bruens
Port of Rotterdam, Rotterdam, The Netherlands

A.A. Roubos
Port of Rotterdam, Rotterdam, The Netherlands/Delft University of Technology, Delft, The Netherlands

M. van der Pol
Maarten van der Pol, Utrecht, The Netherlands

**jan.putteman@sbe-engineering.nl*

ABSTRACT: The Amaliahaven project in the Port of Rotterdam involves the construction of quay walls and a back crane track. Given the enormous quantities of foundation piles and anchors included in the design, it was decided to collect and store the installation data in a uniform and structured manner. The goal was to improve quality control and support site supervision through efficient data analysis and, in addition, to acquire new knowledge. This paper presents a framework for automated data collection and validation. Despite the high level of automation, manual verifications of the data through Site Acceptance Tests remain crucial. The data of driven foundation piles can be used quite easily by site supervisors and geotechnical engineers when assessing the load-bearing capacity of these piles. In fact, the initial knowledge from the coarse-meshed CPT grid is updated with additional insights obtained from the fine-meshed pile installation grid. For grouted anchors, there is significant improvement potential to create added value based on the recorded data. The findings of this paper can play a crucial role in the quality control procedure of foundation piles and can serve as direct input for reverse engineering of quay walls, and presumably also for other types of port infrastructure.

RÉSUMÉ: Le projet Amaliahaven dans le port de Rotterdam implique la construction de quais et d'une voie de grue arrière. Compte tenu des quantités énormes de pieux et d'ancrages, il a été décidé de collecter et de stocker les données d'installation de manière uniforme et structurée. L'objectif était de soutenir la supervision du site grâce à une analyse efficace des données et, en même temps, d'acquérir de nouvelles connaissances. Un cadre pour la collecte automatisée et la validation des données est présenté. Malgré le niveau élevé d'automatisation, les vérifications manuelles des données lors des tests d'acceptation sur site restent essentielles. Les données des pieux battus peuvent être relativement facilement utilisées par les superviseurs de site et les ingénieurs géotechniciens pour évaluer la capacité portante des pieux. Il s'avère que les connaissances initiales issues de la grille CPT à mailles larges sont mises à jour avec des informations supplémentaires obtenues à partir de la grille d'installation plus fine des pieux. Pour les tirants d'ancrage, il existe un potentiel d'amélioration significatif pour créer une valeur ajoutée basée sur les données enregistrées.

Keywords: Pile; anchor; data; database.

1 INTRODUCTION

Container volumes in Rotterdam (the Netherlands) are expected to continue to grow strongly in the coming years. For this reason the Port of Rotterdam Authority invests in the further expansion of the Prinses Amaliahaven quay walls located on Maasvlakte II. The project involves the construction of:

- 1,825 metres of deep sea quay wall, with a soil retaining height of 29 metres.
- 1,825 metres of back crane track with pile foundation
- 160 meters of inland shipping quay wall
- Construction works started in 2021. A large amount of foundation elements are installed, including:

- ca. 700 open-ended tubular piles (combined wall)
- ca. 700 intermediate sheet piles (combined wall)
- ca. 2100 vibro piles (driven cast-in-situ piles)
- ca. 1300 screw injection anchors

In recent quay wall construction projects, installation data from pile and anchor installation was collected (e.g. blow count, rotations per minute, flow, pressure, torque, grout volume, …). Due to unclear agreements, this data was provided by the contractor in various file formats (handwritten, Excel files, PDFs, etc.), and there was no consistent formatting of the files. This made it very impractical to process this large amount, and as a result, this source of data was underutilized.

Given the enormous quantities of foundation piles and anchors in the Amaliahaven project, it was decided to collect and store the data in a uniform and structured manner. The goal was to improve quality control and support site supervision through efficient data analysis and, in addition, to acquire new knowledge.

2 DATA STANDARD

The SBEGEO standard is an in-house developed general data standard to which the registrations must adhere. This data standard was included in the tender documents for the construction and consequently constituted a contractual obligation for the contractor. The corresponding SBEGEO transfer file (Figure 1) is a computer file formatted uniformly with the intention of enabling the transfer of data between different platforms in a standardized manner and allowing smooth database processing. The main characteristics of the transfer file are:

- The file is text-formatted (UTF-8)
- The extension is *.txt
- The transfer file consists of two parts. The top section includes the header data, the bottom section includes the data series.

3 COMPLIANCE CHECK AND STORAGE

The .txt transfer file is uploaded to the port's database by the contractor, according to the following process:
Step 1: Upload .txt transfer file to web application.
Step 2: Automated file compliance check.
Step 3a: If the file compliance check fails, the user receives an error message in the web application, with identification of the error (example in Figure 2 left).
Step 3b: If the file compliance check is successful, the user receives a message (example in Figure 2 right) and the .txt file is parsed to .JSON and saved to the PostgreSQL database.

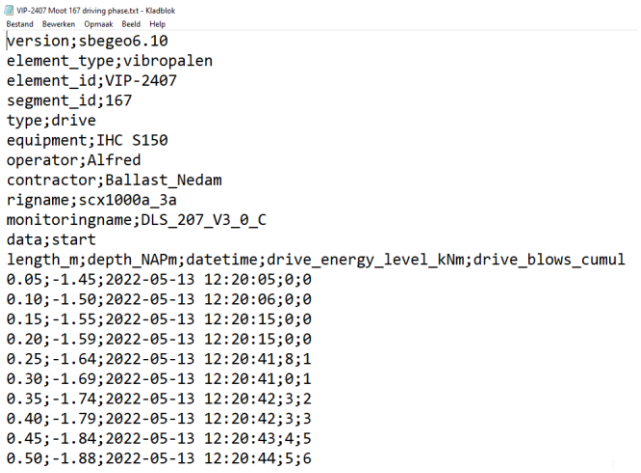

Figure 1. Example of SBEGEO transfer file (.txt).

Step 4: Data transformation and visualisation in the web application, ready to be viewed by e.g. port's site supervisors, technical back-office and contractor.

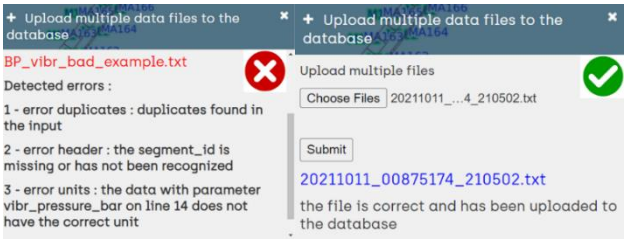

Figure 2. Automated file compliance checks: messages.

4 SITE ACCEPTANCE TESTS

In recent years, the capabilities for automated data capture during the installation of foundation piles and anchors have significantly expanded. However, it is crucial to verify the accuracy of the collected data through regular Site Acceptance Tests (SAT).

A fundamental understanding of the functioning of the monitoring equipment is of utmost importance. It is most important to know whether a parameter is measured directly or indirectly. In the latter case, the accuracy of the final parameter relies on the conversion formula provided by the manufacturer of the equipment, which is often taken for granted. An example is the indirect measurement of the energy level of a diesel hammer. Instead of measuring the actual drop height from the cylinder relative to the hammer, the energy is calculated from the drop height. The drop height is calculated from the measured number of blows per minute cfr. manufacturer's specifications. Interruptions in the driving process, e.g. due to stalling and restarting of the diesel hammer when penetrating through weak layers, result in a reduced number of blows per minute, and consequently an (incorrect) increase of energy. This is illustrated in Figure 3 and Figure 4. Drops in the blows

per minute because of stalling and restarting of the hammer, or by incorrect time registration, are falsely translated into an increase of the drive energy (peaks). On the other hand, for the hydro hammer, which is shown in the same figures, the energy is directly calculated from the measured acceleration of the hammer. Figure 4 clearly shows that the energy measurement of the hydro hammer is not being influenced by the peaks in the blows per minute registration. This example shows that a fundamental understanding of the data collection process is crucial to correctly interpret installation data.

During construction, frequent Site Acceptance Tests on the registration equipment are performed to verify the accuracy of the measurements. For each installation technique (driving with diesel or hydro hammer, vibratory driving, drilling) a SAT protocol was drafted. The SAT is performed at regular time intervals. In between limited testing was performed, related to changes in the piling or registration equipment. The SAT includes e.g.:

- Comparison of visual readings of pressure gauges with the automated registrations of hydraulic pressure.
- Verification of RPM (indirectly calculated from measured flow) with manual tachometer.
- Verification of pull-down with dynamometer.
- Filling a 10 m³ water container to verify the flow rate and volume registered by anchor drilling rig.

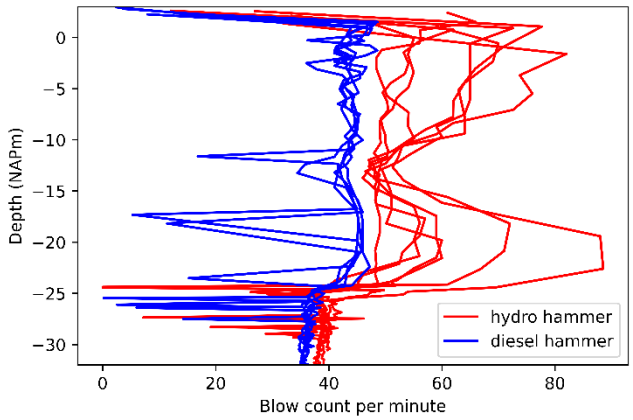

Figure 3. Comparison of blow count per minute for Delmag D-100 diesel hammer and IHC S-150 hydro hammer.

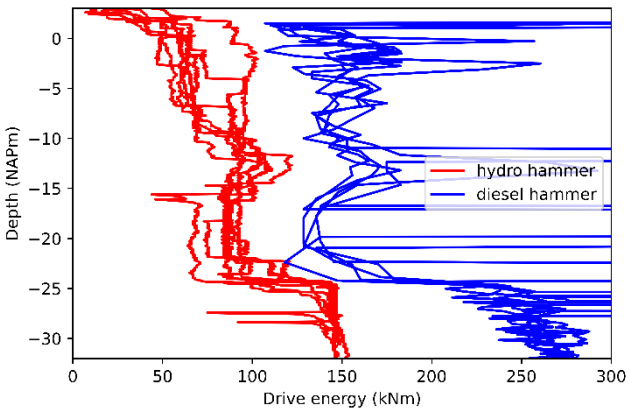

Figure 4. Comparison of drive energy for Delmag D-100 diesel hammer and IHC S-150 hydro hammer.

5 FUTURE OF SITE SUPERVISION: CASE STUDIES

5.1 Pile installation data enhance the understanding of the local geology

The pile design of the back crane track was based on CPT's available at 25m center-to-center (c.t.c.) grid distance. Figure 5 shows the plan view of a 80m stretch of the back crane track. Figure 6 shows the CPT's available for the pile design. The upper boundary of the dense Pleistocene sand layer, varies from NAP -28.50m in CPT1 to NAP -22.50m in CPT4.

Figure 7, Figure 8 and Figure 9 show the data of the driven cast-in-situ piles, installed with IHC S-150 hammer. The blow count per 25cm is influenced by the blow energy setting of the hammer. The blow energy setting is set by the operator of the piling rig, and varies with depth. The higher the blow energy, the lower the blow count per 25cm, and vice versa (for the same soil resistance). For this reason the total driving energy per 25cm is calculated. The total driving energy per 25cm is the blow count per 25cm multiplied by the blow energy setting. The total driving energy per 25cm is an unambiguous measure of the amount of energy inserted into the ground to achieve 25cm of pile settlement. The total driving energy per 25cm correlates with the local resistance of the soil. Figure 9 shows that the driving data of every single pile provides a clear indication of the exact location of the upper boundary of the dense sand layer.

For the geotechnical design of a single pile, all the surrounding CPT's are considered. One can imagine a (fictitious) situation for a pile in between CPT2 and CPT3: for the design of the pile length, CPT2 with dense sand layer at NAP -27.00m will be decisive. However, as the pile is located in between CPT2 and CPT3, at the pile's location the sand layer might be at NAP -25.00m. This results in heavier pile driving than

was anticipated based on CPT2 which is decisive for geotechnical design, or even refusal. As the c.t.c. distance of the piles is 3m, the knowledge resulting from the driving data is supplementary to the initial CPT's with c.t.c. distance of 25m. This helps the site supervisor and geotechnical engineer to better understand the variation in geology and reasons for heavy pile driving or pile refusal. Assuming the data is considered accurate enough and taking into account the level of flexibility permitted by local design codes, this could ultimately aid in evaluating whether the piles possess adequate bearing capacity.

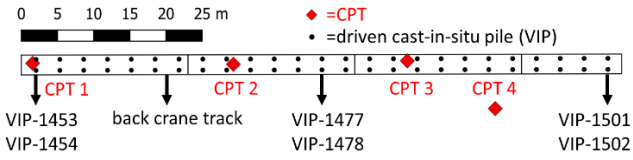

Figure 5. Plan view of 80m stretch of the back crane track.

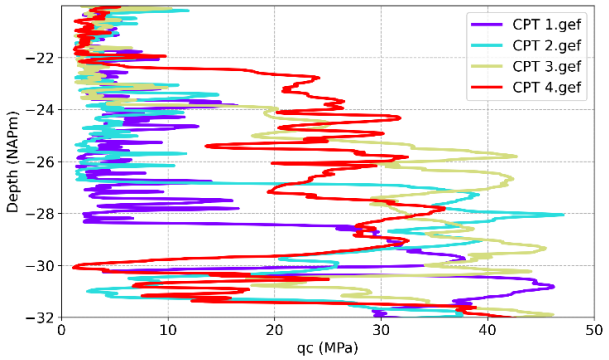

Figure 6. CPT's at back crane track location.

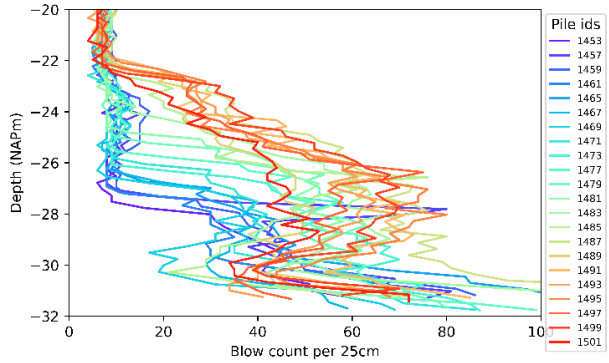

Figure 7. Blow count per 25cm.

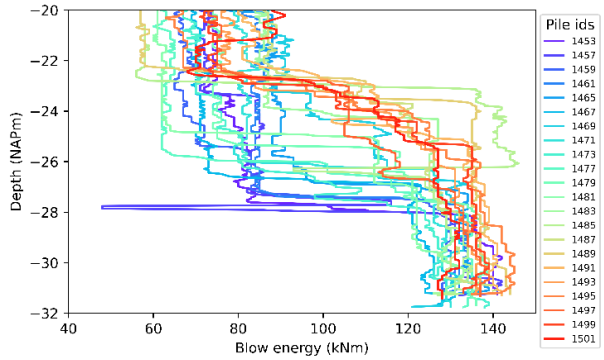

Figure 8. Drive energy.

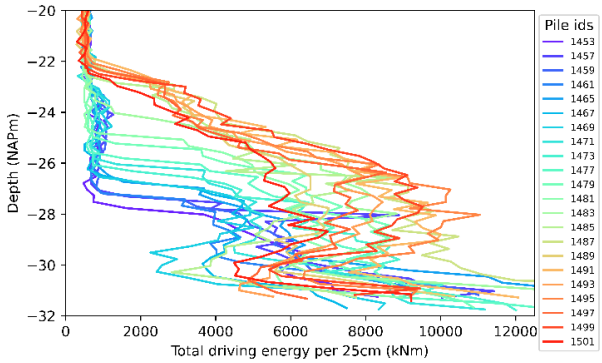

Figure 9. Total driving energy per 25cm.

5.2 Correlation between driving data and cone resistance: detecting (soft) intermediate layers

Westerbeke (2021) demonstrates the correlation between the total driving energy per 25cm and cone resistance for MV-piles. For all piles it was found that a fixed ratio of 2% between energy (kNm) and cone resistance (MPa) is valid along the entire depth of the CPT's (ca. 30m). An example from Westerbeke (2021) is shown in Figure 10. The MV-pile consists of a steel beam with a grouted cover. As the grout surrounds the pile, the shaft friction during pile driving is significantly reduced. Most of the driving energy is transferred to the pile tip to overcome the resistance of the soil. This explains the good correlation with cone resistance.

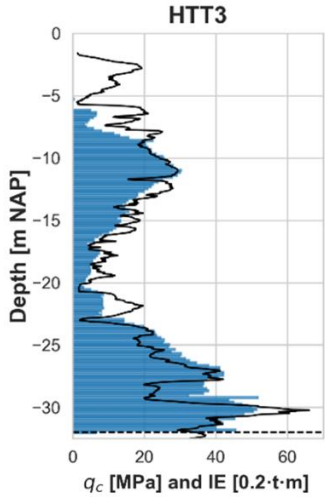

Figure 10. Cone resistance and installation energy for MV-piles (Westerbeke, 2021).

For a driven cast-in-situ pile, the shaft friction during pile driving is substantial, thus a weaker correlation is expected. However, from Figure 11 and Figure 12 it is concluded that the correlation (fixed ratio of 1%) is still fairly good. Moreover, the response of driving energy to the reduction in cone resistance at depth NAP -30.00m is observed. The drop in cone

resistance in Figure 12 is caused by a silty layer with thickness of ca. 20cm. This shows that the driving data can precisely detect soft intermediate layers. The observations of the driving data can be used for quality assurance and reverse engineering of the bearing capacity of the piles.

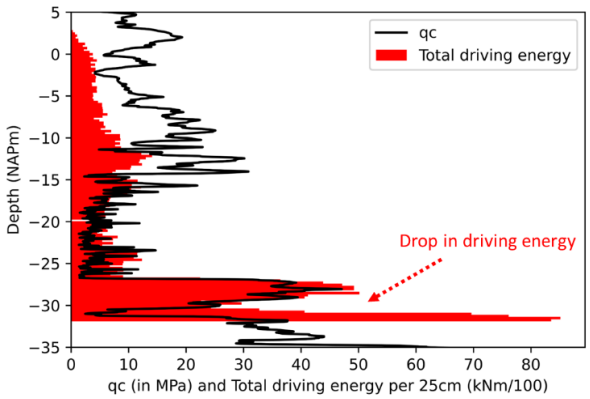

Figure 11. Cone resistance and total driving energy per 25cm with IHC S-150 hammer: example 1.

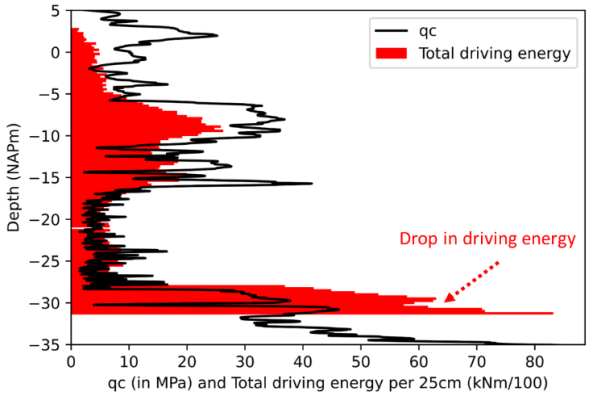

Figure 12. Cone resistance and total driving energy per 25cm with IHC S-150 hammer: example 2.

5.3 Anchor drilling parameters and measured apparent free length

Every ground anchor is subjected to a acceptance or suitability test to verify if the measured creep rate and apparent free length are within the tolerances cfr. EN-1537. The deepsea quay wall is equipped with Leeuwankers®, which are a type of self-drilling anchor with a helicoidal drill tip. The free length of this anchor is created through drilling with water. As soon as the drilling tip approaches the location of the grout body, the operator switches from water to grout.

As a tendency towards undershooting of the permissible free length has been identified, an investigation has been conducted to determine if a relationship can be found between the grout consumption and the measured apparent free length (Figure 13). To account for the variation in design length of the grout body along the length of the quay wall, both X and Y axis are normalised by dividing them by the design length of the grout body. The obtained linear trend line is included in the graph. Although the trendline suggests that an increase in grout consumption is associated with a decrease in free length, the scatter between the data points is very large. This could be partially explained by the registration method of the time at which the operator switches from water to grout. The registration of this moment in time is done manually. It is advisable to eliminate any human influence in the registration process by exploring options for complete automation. This indicates that there are still opportunities for improvement in both measuring and interpreting the installation data of this type of anchor.

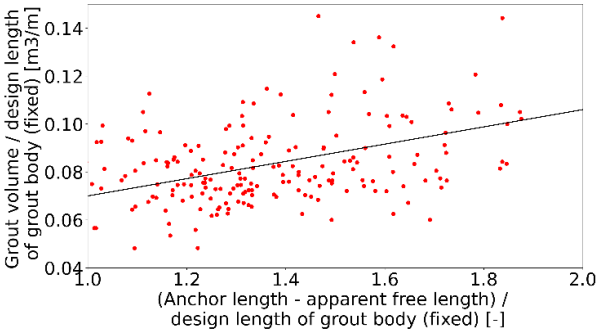

Figure 13. Normalised grout consumption vs. anchor length – apparent free length. Linear trendline in black.

6 CONCLUSIONS

A framework for automated data collection during foundation pile and anchor installation is presented. The main challenge in building a reliable database is the verification of the data through Site Acceptance Tests. The data of driven piles can be used quite easily by site supervisors and geotechnical engineers in assessing the load-bearing capacity of the piles. In fact, the initial knowledge from the coarse-meshed CPT grid is updated with additional insights obtained from the fine-meshed pile installation grid. For grouted anchors, there is significant improvement potential to create added value based on the recorded data. The findings of this paper can play a crucial role in the quality control procedure of foundation piles and can serve as direct input for reverse engineering of quay walls, and presumably also for other types of port infrastructure.

REFERENCES

Westerbeke, F.Y.H. (2021). *Geotechnical bearing capacity of MV-piles. Improving the design based on full scale load tests in the Port of Rotterdam.* Master thesis, Delft University of Technology, the Netherlands.

Proceedings of the XVIII ECSMGE 2024
GEOTECHNICAL ENGINEERING CHALLENGES
TO MEET CURRENT AND EMERGING NEEDS OF SOCIETY
© 2024 the Authors
ISBN 978-1-032-54816-6
DOI 10.1201/9781003431749-125
Open Access: www.taylorfrancis.com, CC BY-NC-ND 4.0 license

ECSMGE 24
XVIII EUROPEAN CONFERENCE ON SOIL MECHANICS AND GEOTECHNICAL ENGINEERING

Influence of the subgrade geomechanical classification on the short term and long-term performance of a railway track

Influence de la classification géomécanique de la plate-forme sur la performance à court et à long terme d'une voie ferrée

A. Ramos*
CONSTRUCT-LESE Faculty of Engineering of the University of Porto

A. Gomes Correia
ISISE and Department of Civil Engineering of University of Minho

R. Calçada
CONSTRUCT-LESE Faculty of Engineering of the University of Porto

**aramos@fe.up.pt*

ABSTRACT: The type of subgrade of a railroad foundation is an important aspect in the evaluation of a railway track. Indeed, with the environmental changes and tonnage and train speed increase, the influence and type of subgrade are vital in the railroad track structure performance. The subgrade geomechanical classification includes the combination of both short and long-term behaviour through the evaluation of the stiffness (resilient modulus) and permanent deformation, respectively. This work aims to evaluate the impact of this classification on the global performance of the track. Thus, a ballasted track is analysed which is associated with different values regarding the subgrade geomechanical classification (QS1 and QS2). Thus, the performance of the tracks is analysed in detail and compared. This work is supported by advanced numerical modelling tools and includes a hybrid methodology that combines both short and long-term performance. This is a first attempt to deeply estimate the influence of subgrade geomechanical classification, which can be a useful tool in the evaluation and modelling of the foundation of railway structures.

RÉSUMÉ: Le type de plate-forme d'une fondation ferroviaire est un aspect important de l'évaluation d'une voie ferrée. En effet, avec les changements environnementaux et l'augmentation du tonnage et de la vitesse des trains, l'influence et le type de plate-forme sont vitaux pour la performance de la structure de la voie ferrée. La classification géomécanique de la plate-forme comprend la combinaison du comportement à court et à long terme par l'évaluation de la rigidité (module réversible) et de la déformation permanente, respectivement. Ce travail vise à évaluer l'impact de cette classification sur la performance globale de la voie. Ainsi, une voie ballastée est analysée, associée à différentes valeurs concernant la classification géomécanique de la plate-forme (QS1 et QS2). Les performances des voies sont ainsi analysées en détail et comparées. Ce travail s'appuie sur des outils de modélisation numérique avancés et comprend une méthodologie hybride qui combine à la fois les performances à court et à long terme. Il s'agit d'une première tentative d'estimation approfondie de l'influence de la classification géomécanique du sol, qui peut être un outil utile dans l'évaluation et la modélisation de la fondation des structures ferroviaires.

Keywords: Railways; short and long-term performance; geomechanical classification; numerical modelling.

1 INTRODUCTION

The understanding of the deformation and failure mechanisms of geomaterials under cyclic loading is of utmost importance for designing and planning maintenance in railway structures (Luo et al., 2017, Mones Ruiz et al., 2019, Alabbasi and Hussein, 2021). Typically, the subgrade layer of a railway track consists of mainly coarse-grained soils, chosen for their superior performance compared to fine-grained soils.

The subgrade layer exhibits two types of deformation when subjected to cyclic loads: resilient and permanent deformations. These two types of deformation significantly impact the short and the long-term performance of the substructure (Ling et al., 2017, Lu et al., 2021).

Resilient deformation, which was first introduced by AASHTO (1994) in 1986, is a property frequently used to characterise materials in various railway layers (Liang et al., 2008, Nguyen and Mohajerani, 2016, Titi and Matar, 2018). On the other hand, accurately

estimating the cumulative settlement is crucial for railway structures to ensure optimal long-term performance and reduce annual maintenance costs (Puppala et al., 1999).

Indeed, both resilient and permanent deformations are essential parameters for designing railway structures (Burrow et al., 2007, Sun et al., 2016). However, laboratory tests to determine these deformations can be complex and time-consuming, especially when evaluating permanent deformation. Therefore, predictive models based on available data from laboratory and field results have been developed.

In this context, the primary objective of this study is to compare the performance of a ballasted track when considering different subgrade materials with different classifications. These materials were already classified based on their properties and are included in a ballasted track model in order to assess the short and long-term performance using a novel hybrid methodology that includes a 3D model of the track and the implementation of an empirical permanent deformation model.

2 GEOMECHANICAL CLASSIFICATION

The geomechanical classification is based on a previous work developed by Gomes Correia and Ramos (2022). In this study, a parametric study was conducted to classify different materials. Thus, two models were selected to characterise the resilient modulus and permanent deformation of geomaterials. Indeed, this choice represents an attempt to establish a relationship between the resilient modulus and permanent deformation under specific stress conditions.

In this analysis, only two materials were selected. The selected materials are described in Table 1. This choice is dependent on the type of material, resilient modulus value, and permanent deformation value.

Regarding the well-graded sand, the resilient modulus was obtained based on the RLT from the laboratory. The sample was first subjected to confining stress (6 kPa, 12 kPa, 24 kPa, 48 Kpa and 96 kPa), and then, in a force-controlled mode, a minor static vertical stress was applied. Posteriorly, the actuator applied a half since shaped cyclic stress. Since granular materials show a stress-dependent behaviour, the cyclic triaxial test was performed at various stress combinations. Based on the tests performed and coefficients obtained, and considering a cyclic deviator stress of 24 kPa and a constant confining stress of 60 kPa (representative of the stress state at the subgrade level (Ramos et al., 2020)), a resilient modulus of 509 kPa was determined.

Table 1. Properties of the materials.

UIC ASTM	Materials	Properties	Obs.
QS1 SM	Silty Sand (42.2% fines)	Cu≈28; Cc≈0.54; Gs=2.68; Fine content=42.2%; Maximum dry density =19.6 kN/m3; Wopt =10.1%. c=15.82 kPa ϕ=36.18°	Compacted at optimum compaction – standard Proctor
QS2 SP	Well-graded Sand	C_u=2.10; C_c=1.05; Maximum dry Density = 16.90 kN/m^3; W_{opt}=12.5%; c=5.60kPa; ϕ=48.2^0;	Compacted at optimum compaction – standard Proctor

The resilient modulus and permanent deformation of the selected materials are presented in Table 2. The resilient modulus of the silty sand was determined in the laboratory from the RLT (repeated loading testing). During the tests, Erlingsson et al. (2017) defined different approaches: 1) resilient modulus as a function of various w (S) where the cyclic deviator stress is constant and equal to 69 kPa (w=3% - S=30%, w=6.4% - S=50%, w=10.1% - S=79.3%, w=12% - S=94.3%); 2) resilient modulus as a function of S for various deviator stresses (28 kPa, 48 kPa, 69 kPa, 98 kPa, 165 kPa). Based on several tests, Huurman (1997) defined the model parameters that conduct a resilient modulus of 258 MPa in the geomechanical analysis (considering a cyclic deviator stress of 24 kPa and a constant confining stress of 60 kPa).

Table 2. Resilient modulus and permanent deformation of the selected materials.

Materials Classification	Resilient Modulus	Permanent Deformation
Silty Sand (42.2% fines) QS1-SM	M_r= 258 MPa	ε_p=0.01385 %
Well-graded sand QS2-SP	M_r= 509 MPa	ε_p=0.00003%

From the previous work (Gomes Correia and Ramos, 2022), it was possible to define guiding values associated with UIC classification: QS1, QS2, and QS3 (UIC, 2008). The preliminary geomechanical

classification should be viewed as a preliminary version.

The presented geomechanical classification serves as an innovative and practical guide intended to support the modelling and design of substructures. This novel classification system aims to rank soils in a manner closely aligned with the approach pioneered by Coronado et al. (2011), which drew inspiration from EN13286-7 (2004). The presented work provides valuable insights into acceptable values of permanent deformation and resilient modulus based on the material type and its classification. Specifically, the UIC (2008) classification was adopted, as illustrated in Figure 1, to facilitate the establishment of the mechanical classification.

Analysing Figure 1, it becomes evident that a significant range of values has been observed within each classification. This variability is expected, given the diverse mineralogical nature and physical properties inherent to each material. These factors can exert a notable influence on several parameters employed in determining both resilient modulus and permanent deformation.

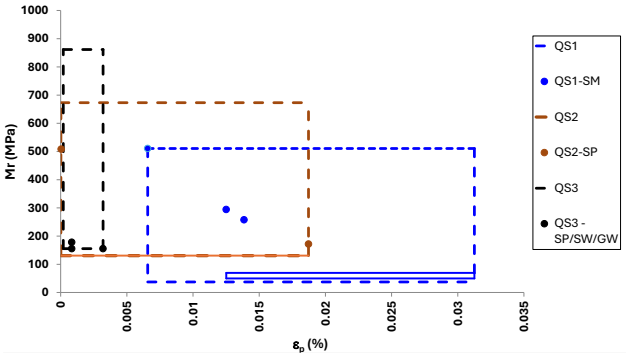

Figure 1. Mechanical classification based on the resilient modulus and permanent deformation (Gomes Correia and Ramos, 2022).

In the case of materials falling under the QS1 classification (comprising fine soils), the material type (CL, CH, ML, or MH), in conjunction with its plasticity's characteristics, consistency index, and the percentage of fines can exert a substantial impact on both permanent deformation and resilient behaviour. This relationship is evidently illustrated in Figure 1.

Similarly, for materials categorized as QS2 and QS3, factors such as material type (sand or gravel), granulometry (well-graded or poorly graded), and the presence of fines (particularly in well-graded materials) can significantly influence the material's response in terms of both resilient and permanent deformations.

In Figure 1, it is possible to perfectly identify the materials selected in this work: QS1-SM (blue point) and QS2-SP (brown point). More details can be found in Gomes Correia and Ramos (2022).

3 NUMERICAL MODELLING

The numerical model represents a ballasted track consisting of rails, railpads, ballast, sub-ballast, and a substructure that encompasses subgrade, as depicted in Figure 2. The ballast presents a thickness of 0.3, the sub-ballast has a thickness of 1 m and the subgrade has a thickness of 11.5 m The material characteristics can be found in Table 3.

In this analysis, damping coefficients were determined using the *Rayleigh* damping matrix. Assuming equal damping $\xi_1 = \xi_2$ and using $\xi = 0.01$ for concrete materials and $\xi = 0.03$ for geomaterials, the αi and βi values were derived from receptance curves and the chosen frequency range, identifying the resonant frequencies. A hysteretic damping of $\xi = 0.05$ was applied to rail pads, considering their solid element representation. Additional details on this methodology are available in Ramos et al. (2022). A frequency range of 5 Hz to 200 Hz was adopted, which is sufficient for an accurate track response.

The numerical model, as illustrated in Figure 2, spans a total length of 30 meters. To enhance computational efficiency, the symmetric boundary conditions were employed as well as an optimized mesh structure. The distance between the symmetry plane and the vertical boundary measures 6 meters.

The analysis is focused on the passage of the Portuguese *Alfa Pendular* train at 220 km/h. The train model properties can be found in Table 4. In this study, the train's components include the bogies, primary suspension, mass, and wheelset axles, while incorporating Hertzian stiffness to replicate the vehicle-track interaction. The properties of the track were adjusted by a factor of two since only half of the track's was considered. Concerning the applied load, a constant value of 67.5 kN (135/2) was adopted. Although load distribution varies slightly along the train, these variations are negligible. To simulate both short-term and long-term track responses, the passage of the initial first bogie was simulated.

To avoid spurious reflections and attenuate the waves that impinge the vertical boundaries, viscous dampers were adopted using the *Lysmer* formulation. Indeed, this approach has been used in the scope of 3D modelling with effective results.

The materials were modelled with solid elements with 8 nodes using linear elastic models. The rail was modelled using the beam theory (2D element) and the railpads were modelled with a spring-damper element.

Moreover, contact elements were implemented between the train and track to simulate the interaction between the two bodies and between the sleepers and the ballast. More details about the modelling of the contact elements can be found in Ramos et al. (2022), which includes information about the Normal penalty stiffness factor. The dynamic analysis was performed in the software *ANSYS* using the *Newmark-Raphson* method with a time step equal to 0.002 s.

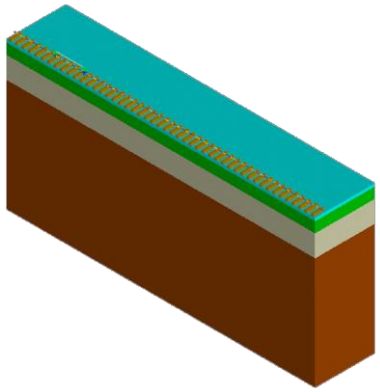

Figure 2. Numerical model.

Table 3. Material Properties.

Ballast	E=67.5 MPa; ν=0.20; ρ=1800 kg/m^3 α=1.84; β=4.66× 10^{-5}
Sub-ballast	E=161.7 MPa; ν=0.30; ρ=2100 kg/m^3 α=1.84; β=4.66× 10^{-5}
Subgrade 1: QS1	E=258.3 MPa; ν=0.3; ρ=1998 kg/m^3 α=1.84; β=4.66× 10^{-5}
Subgrade 2: QS2	E=508.62 MPa; ν=0.3; ρ=1723 kg/m^3 α=1.84; β=4.66× 10^{-5}

Table 4. Characteristics of the Alfa Pendular train adopted in this study.

Component		Values
Bogie: M_b/2		4932/(2*2.7) [kg]
Primary suspension	K_p/2	3420×10^3 (/2) [N/m]
	c_p/2	36×10^3 (/2) [N.s/m]
Wheelset Mass: M_e/2		1800 (/2) [kg]
K_h/2		2.4×10^9 (/2) [N/m]

3.1 Short-term performance

The objective of this study is to examine the impact of the subgrade type and classification on the dynamic response of a ballasted track Consequently, two different simulations considering two distinct subgrades were conducted. These materials were selected to assess the performance of a high-speed railway line.

The short-term performance assessment encompasses the analysis of displacements and stresses induced in different track components during the passage of the *Alfa Pendular* train. In this case, the focus is the subgrade material.

Thus, the maximum displacements in the top of the rail and subgrade were obtained in the alignment under the load (Figure 3 and Figure 4). The results indicate higher displacements in subgrade QS1 when compared to the subgrade QS2. However, the differences are higher at the subgrade level than at the rail. At the subgrade, there is an increment in the displacement's maximum magnitude of 92% between QS2 and QS1. At the rail level, this increment is only 11%. Moreover, at the subgrade level, it is not possible to identify the axles of the bogie in both subgrades.

3.2 Long-term performance

In this analysis, the prediction of the permanent deformation is only carried out on the subgrade. The permanent deformation is determined by applying the empirical model developed by Chen et al. (2014):

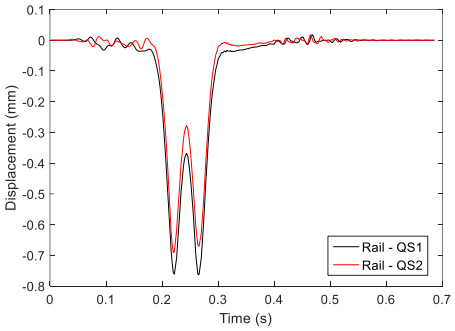

Figure 3. Rail displacement.

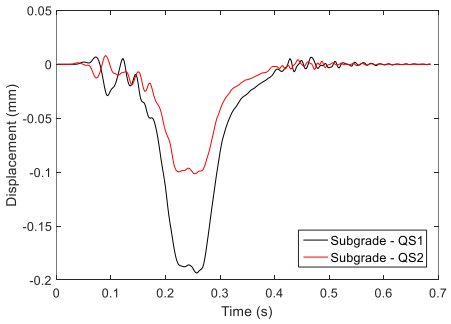

Figure 4. Subgrade displacement.

$$\varepsilon_1^p(N) = \varepsilon_1^{p0}[1 - e^{-BN}]\left(\frac{\sqrt{{p_{am}}^2+{q_{am}}^2}}{p_a}\right)^{a} \cdot \frac{1}{m\left(1+\frac{p_{ini}}{p_{am}}\right)+\frac{s}{p_{am}}-\frac{(q_{ini}+q_{am})}{p_{am}}} \quad (1)$$

where the parameters ε_1^{p0}, B and a are the material's constants of the model, m and s are defined by the yielding criterion q=s+m·p, N is the number of loading cycles, p_{ini} and q_{ini} are the initial stress state and p_{am}

and q_{am} are the stress levels induced in the subgrade during the passage of the train. The constants employed to characterize the empirical permanent deformation model are presented in Table 5.

Table 5. Materials constants of the permanent deformation model.

Material	ε_1^{p0}	B	a
Subgrade 1 - QS1	0.0067	0.2	0.65
Subgrade 2 – QS2	0.0505	0.0018	0.0104

The developed methodology relies on the number of load cycles, and it is intricately tied to the stress levels experienced by the substructure due to the passage of the train. In this context, each cycle (N) corresponds to the passage of one of the axles of the *Alfa Pendular* train. However, the material constants values and stress values are not enough to obtain the induced permanent deformation. It is necessary to characterize the materials considering their mechanical properties: Subgrade 1 (QS1): ϕ=36.18° and c=15.82 kPa; Subgrade 2 (QS2): ϕ=48.20° and c=5.60 kPa.

This methodology involves the development of a powerful 3D numerical model of the vehicle-track system within ANSYS software. Thus, a dynamic analysis is performed considering the vehicle-track interaction and including contact elements. From the numerical results, the stresses in the subgrade are obtained in all directions and all elements and nodes. These stress values are then exported to MATLAB to predict the permanent deformation based on the implementation of the empirical permanent deformation model.

In this analysis, each curve of the permanent deformation corresponds to 1 million load cycles. Thus, during the calculation of the permanent deformation.

Despite the importance of the permanent deformation, the results are analysed in terms of cumulative permanent settlements to have the magnitude of the track's settlement:

$$\delta = \sum_{i=1}^{n} \varepsilon_{p;i} H_{s;i} \qquad (2)$$

where i corresponds to the number of elements that constitute a certain material, $H_{s;i}$ corresponds to the thickness of each element (in m), $\varepsilon_{p;i}$ is the permanent deformation at the center of each element, and δ is the cumulative permanent deformation (in m).

Following the developed methodology, the maximum cumulative permanent settlements occurring in the subgrade were calculated under the load alignment, as illustrated in Figure 5. The results show the variation of the maximum cumulative permanent deformation along the track. The influence of the loading on the first meters (-30<x<-18) is not presented as well as the influence of the end of the model (x=0). The results show that there is a difference between the subgrade QS1 and QS2 in terms of permanent displacements. However, the difference is not significant, and it is close to 0.1 mm.

4 CONCLUSIONS

This work presents the performance of the ballasted track considering two different subgrades: subgrade QS1 and subgrade QS2, classified according to UIC. The results show, as expected, that the performance is better when considering a better material. In this case, regarding the short-term performance, the difference is significantly higher at the subgrade level when compared to the rail level. Concerning the long-term performance, the difference between the QS1 and QS2 subgrades is for the data used as input parameters not significant (below 0.1 mm).

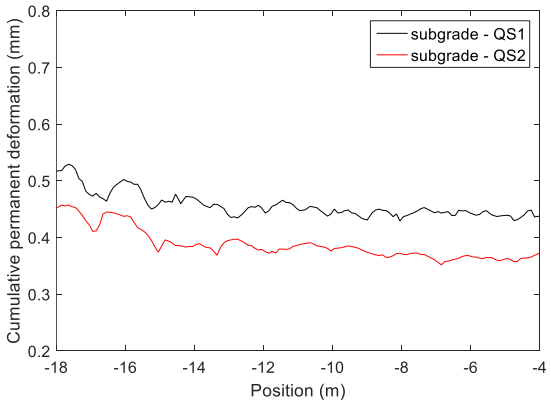

Figure 5. Maximum cumulative permanent deformation.

ACKNOWLEDGEMENTS

This work was partially carried out under the framework of In2Track3 (a project of Shift2Rail). This work was also partly financed by FCT / MCTES through national funds (PIDDAC) under the R&D Unit Institute for Sustainability and Innovation in Structural Engineering (ISISE), under reference UIDB / 04029/2020 and it was supported by: Base Funding – UIDB/04708/2020 of the CONSTRUCT – Institute of R&D in Structures and Construction – funded by national funds through the FCT/MCTES (PIDDAC).

REFERENCES

Ashto 1994. Standard test method for determining the resilient modulus of soils and aggregate materials.

Alabbasi, Y. & Hussein, M. 2021. Geomechanical Modelling of Railroad Ballast: A Review. *Archives of Computational Methods in Engineering,* 28(3)**:** 815-839. http://doi.org/10.1007/s11831-019-09390-4.

Burrow, M., Bowness, D. & Ghataora, G. 2007. A comparison of railway track foundation design methods. *Proceedings of The Institution of Mechanical Engineers Part F-journal of Rail and Rapid Transit - PROC INST MECH ENG F-J RAIL R,*221:1-12. http://doi.org/10.1243/09544097JRRT58.

Chen, R., Chen, J., Zhao, X., Bian, X. & Chen, Y. 2014. Cumulative settlement of track subgrade in high-speed railway under varying water levels. *International Journal of Rail Transportation,* 2(4)**:** 205–220. http://doi.org/10.1080/23248378.2014.959083.

Coronado, O., Caicedo, B., Taibi, S., Correia, A. G. & Fleureau, J.-M. 2011. A macro geomechanical approach to rank non-standard unbound granular materials for pavements. *Engineering Geology,* 119:64-73).

EN13286-7 2004. Unbound and hydraulically bound mixtures. *Part 7: Cyclic load triaxial test for unbound mixtures* Brussels.: CEN-European Committee for Standardization.

Erlingsson, S., Rahman, S. & Salour, F. 2017. Characteristic of unbound granular materials and subgrades based on multi stage RLT testing. *Transportation Geotechnics,* 13:28-42. http://doi.org/10.1016/j.trgeo.2017.08.009.

Gomes Correia, A. & Ramos, A. 2022. A geomechanics classification for the rating of railroad subgrade performance. *Railway Engineering Science,* 30(3)**:** 323-359. http://doi.org/10.1007/s40534-021-00260-z.

Huurman, M. 1997. *Permanent deformation in concrete block pavement.* PhD Thesis, Delft University of Technology, Netherlands.

Liang, R. Y., Rababah, S. & Khasawneh, M. 2008. Predicting moisture-dependent resilient modulus of cohesive soils using soil suction concept. *Journal of Transportation Engineering,* 134(1)**:** 34-40. http://doi.org/10.1061/(ASCE)0733-947X(2008)134:1(34).

Ling, X., Li, P., Zhang, F., Zhao, Y., Li, Y. & An, L. 2017. Permanent deformation characteristics of coarse grained subgrade soils under train-induced repeated load. *Advances in Materials Science and Engineering,* 2017 (15).

Lu, C., Chen, J., Gu, C., Wang, J., Cai, Y., Zhang, T. & Lin, G. 2021. Resilient and permanent deformation behaviors of construction and demolition wastes in unbound pavement base and subbase applications. *Transportation Geotechnics,* 28(100541). http://doi.org/https://doi.org/10.1016/j.trgeo.2021.100541.

Luo, X., Gu, F., Zhang, Y., Lytton, R. L. & Zollinger, D. 2017. Mechanistic-empirical models for better consideration of subgrade and unbound layers influence on pavement performance. *Transportation Geotechnics,* 13:52-68. http://doi.org/10.1016/j.trgeo.2017.06.002.

Mones Ruiz, H. A., Gräbe, P. J. & Maina, J. W. 2019. A mechanistic-empirical method for the characterisation of railway track formation. *Transportation Geotechnics,* 18:10-24. http://doi.org/https://doi.org/10.1016/j.trgeo.2018.10.003.

Nguyen, B. T. & Mohajerani, A. 2016. Resilient modulus of fine-grained soil and a simple testing and calculation method for determining an average resilient modulus value for pavement design. *Transportation Geotechnics,* 7:59-70. http://doi.org/https://doi.org/10.1016/j.trgeo.2016.05.001.

Puppala, A. J., Mohammad, L. N. & Allen, A. 1999. Permanent deformation characterization of subgrade soils from RLT test. *Journal of Materials in Civil Engineering,* 11(4)**:** 274-282. http://doi.org/10.1061/(ASCE)0899-1561(1999)11:4(274).

Ramos, A., Gomes Correia, A., Calçada, R. & Connolly, D. P. 2022. Ballastless railway track transition zones: An embankment to tunnel analysis. *Transportation Geotechnics,* 33:100728. http://doi.org/https://doi.org/10.1016/j.trgeo.2022.100728.

Ramos, A., Gomes Correia, A., Indraratna, B., Ngo, T., Calçada, R. & Costa, P. A. 2020. Mechanistic-empirical permanent deformation models: Laboratory testing, modelling and ranking. *Transportation Geotechnics,* 23:100326. http://doi.org/https://doi.org/10.1016/j.trgeo.2020.100326.

Sun, Q. D., Indraratna, B. & Nimbalkar, S. 2016. Deformation and Degradation Mechanisms of Railway Ballast under High Frequency Cyclic Loading. *Journal of Geotechnical and Geoenvironmental Engineering,* 142(1)**:** 04015056.http://doi.org/doi:10.1061/(ASCE)GT.1943-5606.0001375.

Titi, H. H. & Matar, M. G. 2018. Estimating resilient modulus of base aggregates for mechanistic-empirical pavement design and performance evaluation. *Transportation Geotechnics,* 17:141-153.http://doi.org/https://doi.org/10.1016/j.trgeo.2018.09.014.

UIC 2008. UIC Code 719 R. Earthworks and Track Bed for Railway Lines. International Union of Railways.

Proceedings of the XVIII ECSMGE 2024
GEOTECHNICAL ENGINEERING CHALLENGES
TO MEET CURRENT AND EMERGING NEEDS OF SOCIETY
© 2024 the Authors
ISBN 978-1-032-54816-6
DOI 10.1201/9781003431749-126
Open Access: www.taylorfrancis.com, CC BY-NC-ND 4.0 license

ECSMGE 24
XVIII EUROPEAN CONFERENCE ON SOIL MECHANICS AND GEOTECHNICAL ENGINEERING

Prediction of resilient modulus of unsaturated soils considering inter-particle suction bonding

Prédiction du module de résilience des sols non saturés en tenant compte de la liaison par succion entre les particules

A. Rana, A. Azizi*
University of Portsmouth, Portsmouth, UK

A. Kumar
Indian Institutes of Technology, Mandi, India

M. Lloret-Cabot, D.G. Toll
Durham University, Durham, UK

**arash.azizi@port.ac.uk*

ABSTRACT: Understanding the behaviour of compacted soils in road and railroad formations is crucial for ensuring the long-term performance of transportation infrastructure. These formations are often under unsaturated conditions and their response to repeated traffic-induced loads is significantly influenced by soil water content and suction (i.e., water retention), which vary due to environmental factors such as precipitation and evaporation. This paper proposes a predictive framework to establish a relationship between the mechanical cyclic response and water retention properties of unsaturated compacted soils. The proposed framework employs two constitutive variables, i.e. Bishop's stress and an inter-particle bonding parameter, and is intended to predict the resilient modulus of unsaturated compacted soils subjected to repeated traffic and environmental loading. Both constitutive variables allow consideration of the effects of the degree of saturation and suction on the compacted soil behaviour and facilitate a smooth transition between unsaturated and saturated states. The proposed model is used to predict the resilient modulus of various unsaturated soils subjected to cyclic loading. The results show a good agreement between the predictions of the model and experimental data.

RÉSUMÉ: La compréhension du comportement des sols compactés dans les formations routières et ferroviaires est cruciale pour garantir la performance à long terme des infrastructures de transport. Ces formations sont souvent sous des conditions non saturées et leur réponse aux charges répétées induites par le trafic est significativement influencée par la teneur en eau du sol et la succion (c'est-à-dire, la rétention d'eau), qui varient en raison de facteurs environnementaux tels que les précipitations et l'évaporation. Cet article propose un cadre prédictif pour établir une relation entre la réponse mécanique cyclique et les propriétés de rétention d'eau des sols compactés non saturés. Le cadre proposé utilise deux variables constitutives, c'est-à-dire, la contrainte de Bishop et un paramètre de liaison entre particules, et vise à prédire le module de résilience des sols compactés non saturés soumis à des charges répétées et environnementales. Les deux variables constitutives permettent de prendre en compte les effets du degré de saturation et de la succion sur le comportement du sol compacté et facilitent une transition fluide entre les états non saturés et saturés. Le modèle proposé est utilisé pour prédire le module de résilience de divers sols non saturés soumis à un chargement cyclique. Les résultats montrent un bon accord entre les prédictions du modèle et les données expérimentales.

Keywords: Unsaturated soils; suction; resilient modulus; bonding.

1 INTRODUCTION

The resilient modulus is a crucial parameter in the design of roads and railways, playing a fundamental role in assessing the integrity and durability of transportation infrastructure. It represents the stiffness and elastic response of their formation materials under repeated traffic induced loading, making it instrumental in ensuring long-term performance. Climatic conditions, such as precipitation and evaporation, influence the moisture levels experienced by the formation materials of roads and railways which are often unsaturated. The behaviour of these unsaturated materials is sensitive to changes in their water retention properties. This implies that their resilient modulus undergoes continuous changes in response to seasonal variations. Therefore, it is crucial to reflect the effect of water content and suction on the resilient modulus in the design phase to ensure the

development of sustainable and climate-resilient transportation infrastructure.

With the advancement in understanding of suction mechanisms and its measurement methods (Kumar et al. 2021), suction together with water content and have been considered to interpret the hydromechanical behaviour of unsaturated soils. Azizi et al. (2023) proposed a framework to establish a correlation between the mechanical cyclic response and the water retention properties of an unsaturated soil, using two constitutive variables, namely, Bishop′s stress and a bonding parameter, while both constitutive variables allow considering the effects of the water content (or degree of saturation) and suction on the behaviour of soils subjected to cyclic loading. This paper examines the capability of the proposed framework in predicting the resilient modulus of several soils with varying water content and suction levels.

2 RESILIENT MODULUS MODEL

The model proposed by Azizi et al. (2023) employs two constitutive variables: (i) Bishop′s stress p^* (Bishop, 1959) accounting for the effect of suction (s) on the average stress acting on the soil skeleton:

$$p^* = p_n + S_r s \quad (1)$$

where p_n is the net stress and S_r is the degree of saturation; (ii) A bonding parameter ξ accounting for the normal force acting at soil particle contacts due to the presence of water menisci (Gallipoli et al., 2003):

$$\xi = (1 - S_r) f_s \quad (2)$$

$(1 - S_r)$ accounts for the number of water menisci and f_s accounts for the increase in the inter-particle force exerted by a single meniscus with suction. $f_s = 0.838\, s^{0.06}$ was assumed to estimate the values of the inter-particle force within a soil consisting of identical sphere particles having radii of 1 μm (Fisher, 1926). The empirical equation used in this study to predict resilient modulus (M_R) takes the form as below:

$$M_R = (p^*/p_r)^{k_1} . \left(1 + q_{cyc}/p_r\right)^{-k_2} + M_0 exp\,(k_3 \xi) \quad (3)$$

where p_r = 1 (kPa) is the reference mean stress. k_1, k_2, k_3 and M_0 are model parameters. The first term accounts for the effect of mean Bishop′s stress p^* whereas the second term incorporates the effect of the cyclic deviatoric stress q_{cyc}. The last term is dependent on the bonding parameter and allows consideration of the effect of suction bonding on the resilient modulus.

3 EXPERIMENTAL DATA

Table 1 presents the properties of four subgrade materials including Residual Soil (Soil I), Pulverised Mudstone (Soil II), Decomposed Tuff (Soil III) and Guangdong Subgrade Soil (Soil IV). For Soils I, II, and III, samples were compacted at the optimum water content (w_{opt}) and maximum dry density (ρ_{dmax}) while in the case of Soil IV, samples were compacted at a relative compaction of 85%. These samples were subjected to varying cyclic deviatoric stresses at constant confining pressure and constant suction or water content using triaxial apparatus to measure resilient modulus, allowing for the determination of values for p_n, q_{cyc} and M_R. The suction and degree of saturation were also obtained to determine p^* and ξ.

Table 1. Properties of subgrade soils used in this study.

Soils	**Soil I** Yang et al. (2008)	**Soil II** Yang et al. (2008)	**Soil III** Ng et al. (2013)	**Soil IV** Zhang et al. (2021)
Sand (%)	3	1	24	46.5
Silt (%)	43	60	72	53.6
Clay (%)	54	39	4	
PI (%)	19	15	14	19.1
w_{opt} (%)	18.3	16.8	16.3	12.5
ρ_{dmax} (Mg/m^3)	1.76	1.77	1.76	1.89
Testing Procedure				
p_n (kPa)	21	21	30	30
Freq. (Hz)	1	1	1	1
q_{cyc} (kPa)	21, 34, 48, 69, 103	21, 34, 48, 69, 103	30, 40, 55, 70	10, 20, 30, 40
Initial s (kPa)	50, 150, 450	50, 150, 450	0, 30, 60, 100, 150, 250	1040, 438, 226, 94, 46
Loading condition	suction controlled	Suction controlled	Suction controlled	Constant w

4 DATA ANALYSIS

The experimental data shows that the resilient modulus of all four subgrade soils is significantly dependent on suction and deviatoric stress. Figure 1 shows example M_R values for Soils II and III measured at two suction levels and varying q_{cyc} while p_n is constant. M_R reduces with an increase in q_{cyc}, providing that the permanent strain of the soil samples increases with q_{cyc}. Consequently, the samples experiencing higher strains exhibit lower resilience and M_R. While M_R decreases with q_{cyc} across all four soils, different trends are noticeable. For example, the declining rates

of M_R at the two suction levels for Soils III is dissimilar, or the relationship between M_R and q_{cyc} for Soil II exhibits scattering.

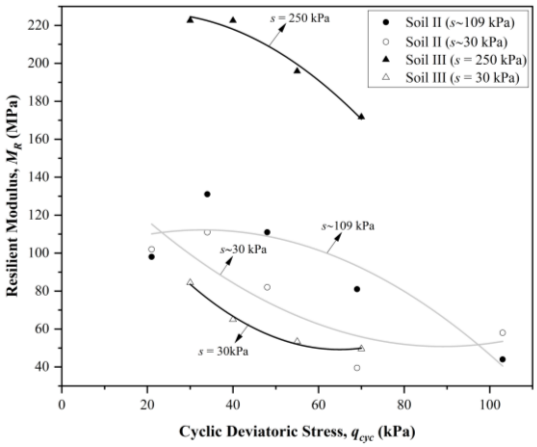

Figure 1. Variations of resilient modulus with cyclic deviatoric stress at constant suction levels.

Figure 2 shows the example data for the variation of M_R with respect to suction for the tests carried out at two constant cyclic deviatoric stresses. Since the increase in suction leads to increase in bonding between soil particles, the stiffness and in turn, the resilient modulus of all four soils increases with suction. However, the discrepancy in the pattern of the relationship between resilient modulus and suction for these soils can be detected. This is evident, for example, when comparing the inclining rates of M_R for Soils II and III at the two cyclic deviatric stress shown in Figure 2.

Although the experimental data show an apparent trend and agreement between the resilient modulus and the cyclic deviatoric stress along with the suction, it is evident that this relationship is not consistently robust. This suggests that other factors, particularly the degree of saturation, may be needed to account for an accurate determination of the resilient modulus.

5 PREDICTING RESILIENT MODULUS

The contribution of the degree of saturation and suction can be incorporated through Bishop′s stress and the bonding parameter using the proposed model. The least squares method is employed to calibrate the parameters of the model for the best fit. The parameters of the model for the soils used in this study are shown in Table 2. These values for k_1 and k_2 are determined based on the impact of p^* and q_{cyc} on the resilient modulus, respectively. M_0 represents the reference resilient modulus in the saturated state which is assumed to be constant. The parameter k_3 is calibrated by considering the effect of suction bonding and ξ on M_R.

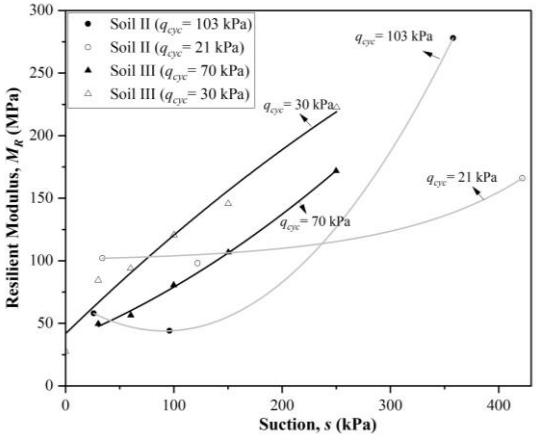

Figure 2. Variations of resilient modulus with suction at constant cyclic deviatoric stress.

Table 2. Model parameters for soils used in this study.

Soils	Soil I	Soil II	Soil III	Soil IV
k_1	0.51	0.94	1.45	0.93
k_2	1.48	0.12	0.52	0.68
k_3	0.47	1.52	1.41	0.50
M_0	119	38	10	72

M_R measured at two different q_{cyc} levels for Soil II and Soil III are shown in Figures 3 and 4, respectively, in terms of mean Bishop′s stress p^* and the bonding parameter ξ. M_R increases with p^* while the rate of this increase declines as the cyclic deviatoric stress level rises. The impact of suction bonding is also evident where the increase in ξ enhances the soil resilience, consequently elevating M_R. The example M_R values lie on two distinct surfaces, predicted by the proposed model accounting for p^* and ξ, due to their different cyclic deviatoric stress levels.

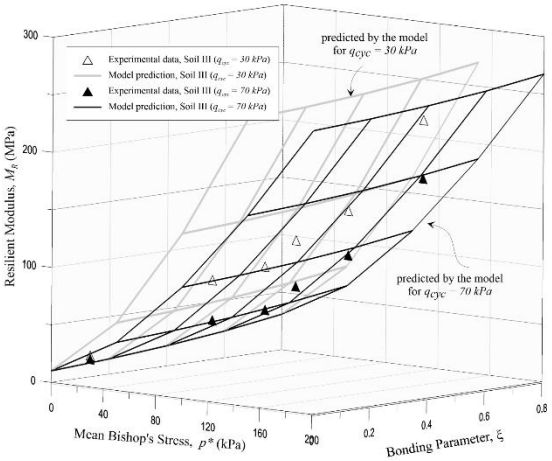

Figure 3. Variations of resilient modulus with Bishop′s stress and the bonding parameter for Soil II.

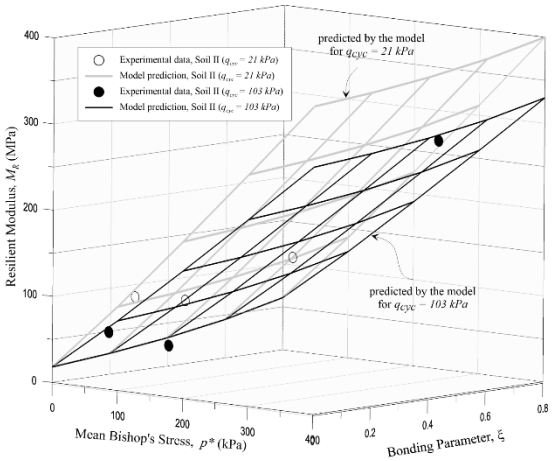

Figure 4. Variations of resilient modulus with Bishop's stress and the bonding parameter for Soil III.

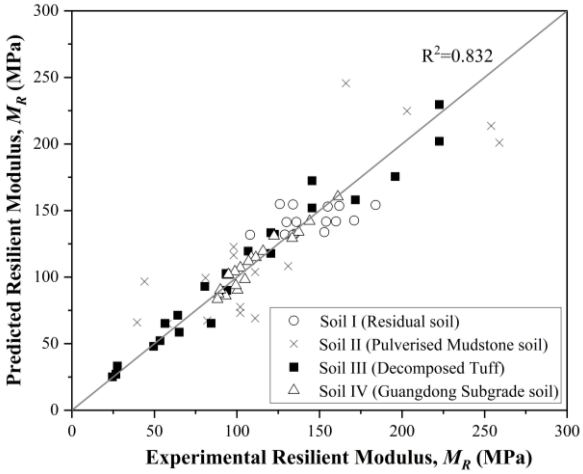

Figure 5. Predicted and measured resilient modulus values for all soils used in the present study.

The results show an increase in the suction stress modifies the average soil skeleton, reducing the possibility of slippage at the particle contacts and thereby enhancing M_R. The stiffness is further influenced by the bonding effect at soil inter-particle contacts, restraining the slippage of soil particles and contributing to an increase in M_R.

Figure 5 shows the predicted values of the resilient modulus plotted against the experimental data. The good agreement between the experimental values and the model predictions across all soil types is evident.

6 CONCLUSIONS

A predictive framework is employed that incorporates the effect of suction and degree of saturation through Bishop′s stress and the bonding parameter to predict the resilient modulus of four different soils. The comparison between the predicted and experimental resilient modulus for all soils used in the study indicates a good agreement, highlighting the efficacy of the proposed model in addressing the impact of soil water retention properties on the cyclic behaviour of unsaturated soils. The proposed framework allows for the consideration of the coupled effects of cyclic traffic-induced and environmental loads on the long-term performance of geotechnical infrastructure.

ACKNOWLEDGEMENTS

The authors acknowledge the funding received from UK Engineering and Physical Research Council for ‘Sustainability and resilience of transportation infrastructure in African countries’.

REFERENCES

Azizi, A., Kumar, A., & Toll, D. G. (2023). Coupling cyclic and water retention response of a clayey sand subjected to traffic and environmental cycles. *Géotechnique* 73 (5), 401-417. https://doi.org/10.1680/jgeot.21.00063.

Bishop, A. W. (1959). The principle of effective stress. *Tecknisk Ukeblad* 106 (39), 859–863. https://cir.nii.ac.jp/crid/1570009749802798848.

Fisher, R. A. (1926). On the capillary forces in an ideal soil; correction of formulae given by WB Haines. *The Journal of Agricultural Science* 16 (3), 492-505. https://doi:10.1017/S0021859600007838.

Gallipoli, D., Gens, A., Sharma, R. & Vaunat, J. (2003). An elasto-plastic model for unsaturated soil incorporating the effects of suction and degree of saturation on mechanical behaviour. *Géotechnique* 53 (1), 123–135. https://doi.org/10.1680/geot.2003.53.1.123.

Kumar A, Azizi A, Toll DG (2022) Application of suction monitoring for cyclic triaxial testing of compacted soils. *Journal of Geotechnical and Geoenvironmental Engineering* 148 (4). https://doi.org/10.1061/(ASCE)GT.1943-5606.0002766.

Ng, C.W.W., Zhou, C., Yuan, Q. & Xu, J. (2013). Resilient modulus of unsaturated subgrade soil: experimental and theoretical investigations. *Canadian Geotechnical Journal* 50 (2), 223–232. https://doi.org/10.1139/cgj-2012-0052.

Yang, S. R., Lin, H. D., Kung, H. S. & Huang, W. H. (2008). Suction-controlled laboratory test on resilient modulus of unsaturated compacted subgrade soils. Journal of Geotechnical and Geoenvironmental Engineering 134 (9), 1375–1384. https://doi.org/10.1061/(ASCE)1090-0241(2008)134.

Zhang, J., Peng, J., Liu, W., & Lu, W. (2021). Predicting resilient modulus of fine-grained subgrade soils considering relative compaction and matric suction. *Road Materials and Pavement Design* 22 (3), 703-715. https://doi.org/10.1080/14680629.2019.1651756.

Proceedings of the XVIII ECSMGE 2024
GEOTECHNICAL ENGINEERING CHALLENGES
TO MEET CURRENT AND EMERGING NEEDS OF SOCIETY
© 2024 the Authors
ISBN 978-1-032-54816-6
DOI 10.1201/9781003431749-127
Open Access: www.taylorfrancis.com, CC BY-NC-ND 4.0 license

ECSMGE 24
XVIII EUROPEAN CONFERENCE ON SOIL MECHANICS AND GEOTECHNICAL ENGINEERING

Evolution of shallow foundation load test from static to cyclic loading

Évolution de l'essai de chargement de fondations superficielles, de la charge statique à la charge cyclique

P. Reiffsteck*, F. Szymkiewicz, C. Minatchy
Université Gustave Eiffel, Champs-sur-Marne, France

T. Sanagawa, D. Yokoyama
Railway Technical Research Institute, Kokubunji, Japan

**philippe.reiffsteck@univ-eiffel.fr*

ABSTRACT: The conventional bearing capacity of a shallow foundation under vertical centered loading measured under static and cyclic loading differs. This observation is of crucial importance to anticipate behaviour of structure under cyclic loads with or without eccentricity. The most important factor appears to be the ratio of the cyclic load amplitude to the maximum static bearing capacity. This paper presents an experimental study during which a 0.1m square steel footing was statically and cyclically loaded. A parametric study was carried out by performing tests on a physical model based on a sand mass reconstituted at a fixed density index. Complementary tests were performed on an intact silty soil on an experimental test site. The loading frequency was kept below 1Hz, which is lower than the natural frequency of the foundation. Prior to testing, cone penetration test and laboratory tests were performed to determine engineering properties of the soil. An analysis of the results and a comparison with previous tests available in the literature are presented. Predictions of the footing settlement were made by traditional methods, which were then modified to take into account of the effect of cyclic loading.

RÉSUMÉ: Les capacités portantes conventionnelles d'une fondation superficielle sous une charge verticale centrée mesurées sous une charge statique et cyclique diffèrent. Cette observation est d'une importance cruciale pour anticiper le comportement de la structure sous des charges cycliques avec ou sans excentricité. Le facteur le plus important semble être le rapport entre l'amplitude de la charge cyclique et la capacité portante statique maximale. Cette communication présente une étude expérimentale au cours de laquelle une semelle carrée en acier de 0,1 m de coté a été soumise à des essais de chargement statiques et cycliques. Une étude paramétrique a été réalisée en effectuant des essais sur un modèle physique basé sur une masse de sable reconstituée à un indice de densité fixe. Des essais complémentaires ont été réalisés sur un sol limoneux intact sur un site d'essai expérimental. La fréquence de chargement a été maintenue en dessous de 1 Hz, ce qui est inférieur à la fréquence naturelle de la fondation. Avant les essais, des essais de pénétration au cône et des essais en laboratoire ont été réalisés pour déterminer les propriétés techniques du sol. Une analyse des résultats et une comparaison avec les essais précédents disponibles dans la littérature sont présentées. Les prévisions du tassement de la semelle ont été faites par des méthodes traditionnelles, qui ont ensuite été modifiées pour prendre en compte l'effet de la charge cyclique.

Keywords: Shallow foundation; load test; static; cyclic.

1 INTRODUCTION

The appearance of load eccentricity can have a major impact on the behaviour of the foundation systems of certain statically or cyclically loaded structures. In this paper we consider the case of shallow foundations on granular soil.

Current methods of calculating bearing capacity, either indirect methods based on soil mechanical parameters deduced from laboratory tests or correlation tests (Terzaghi and Peck, 1948) or direct methods based on correlation with the results of in-situ tests (Briaud, 1992; AFNOR, 2013; Lehane, 2019), only consider the static case. For low frequencies where inertial and kinematic effects are not predominant, fatigue induced by the action of cycles can lead to failure of the soil beneath the foundation (Andersen, 2009). With this in mind, we carried out cyclic loading tests on foundations with different eccentricity and loading amplitude conditions.

2 TESTS PRESENTATION

The tests were carried out at the RTRI facilities using a hydraulic loading frame enhanced by a speed-

controlled loading system developed by the University of Tokyo.

2.1 Sand

The sand N°6 used in this study is a clean sand with a narrow grain size similar to Toyoura sand. Figure 1 shows its particle size distribution.

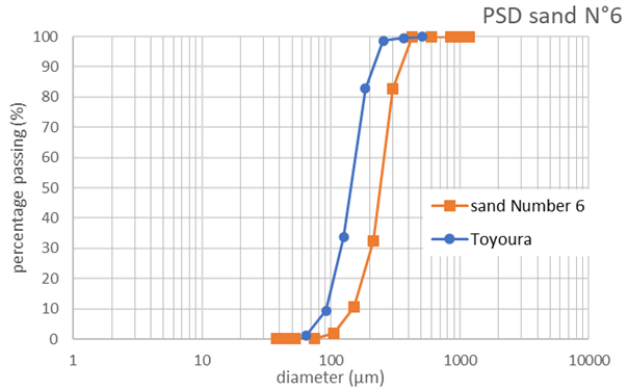

Figure 1. Particle size distribution.

The dry sand mass was reconstituted by tamping to a relative density of 80%. The peak friction angle at this relative density is 42°.

2.2 Foundation and equipment

The foundations are square stainless-steel plates, 100 mm wide and 25 mm thick. A simple spherical connection was used for the initial tests, but this was replaced as the tests began to introduce eccentricity to limit slippage. A spherical washer resting on a conical seat was used afterwards as the ball joint.

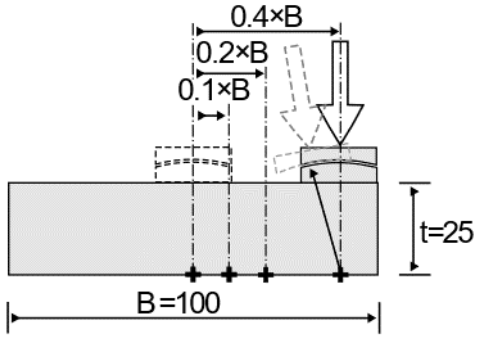

Figure 2. Foundation geometry.

The radius of the ball-joint was chosen to be very close to plate thickness t, in order to keep the point of load application at the base of the footing. A schematic drawing of the foundation is shown in Figure 2.

Foundations were placed diagonally in a soil container wide enough to avoid any interference from sides, regarding the failure zones

2.3 Testing program

As shown on Figure 3, two types of loading were studied. Loading by force step, as used during the on-site tests, was used to define the maximum vertical loads acceptable by the foundation. Each load step is maintained 5 minutes. Cyclic loading between two force values was applied , followed by a final loading to failure.

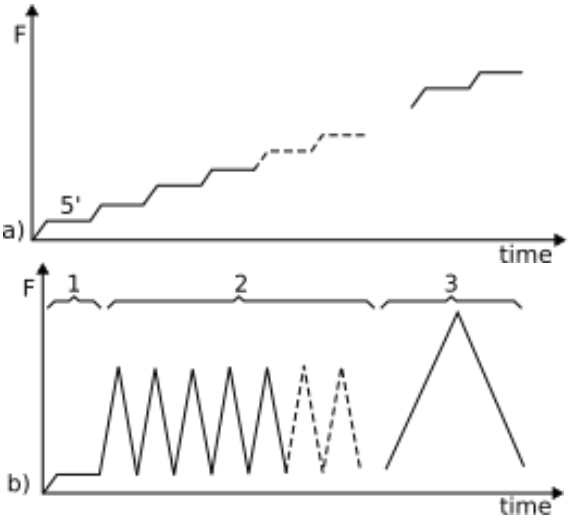

Figure 3. Loading program.

Ratios ranging from 40% to 80% of the maximal vertical load were considered and studied excentricity ranged from 0.1 to 0.4xB. All tests were performed at soil surface without embedment.

A load sensor and four displacement transducers placed at each corner were used to record force and settlement during the tests. At the end of the load test, i.e. when a settlement greater than B/10 was reached, the equipment was removed, the tank emptied and refilled for the next set of load tests.

3 TEST RESULTS

Table 1 summarize the main characteristics of the 21 tests performed in this test session. For the monotonic loading, the maximum vertical load V_0 is derived from the load-settlement curve using B/10 method (Briaud and Gibbens, 1999). Two types of loads may be defined for cyclic test, the load observed at end of phase 1 that may be obtained during monotonic test at the same settlement, and the maximal load reached during the final monotonic loading.

3.1 Monotonic loading - Influence of eccentricity

Figure 4 shows the load settlement curve of the monotonic loading of the shallow foundation according to the eccentricity.

Table 1. Main tests results.

Test	Tank	e/B	V/V_0	Load	V_{min}	V_{max}	V_0
01	1	0		S			1430
02	1	0		S			1150
03	1	0		S			1350
04	2	0.1		S			1100
05	2	0.2		S			788
06	2	0.2	0.4	C	50	370	1000
07	3	0.2	0.6	C	50	530	782
08	4	0.4		S			384
09	4	0.2	0.8	C	50	690	1221
10	4	0.1	0.4	C	50	490	2000
11	5	0.4	0.8	C	50	370	486
12	5	0.4	0.4	C	50	210	509
13	5	0.4	0.6	C	50	290	510
14	6	0.1	0.6	C	50	710	1913
15	6	0.1	0.8	C	50	930	2185
16	6	0	0.4	C	50	1170	2670
17	7	0.4		S			406
18	7	0	0.6	C	50	890	1765
19	7	0	0.4	C	50	610	1965
20	8	0		S			1084
21	8	0	0.4	C	420	980	1286

The mean settlement indicated in the following Figures has been computed at the rotation point for each test as illustrated on Figure 2.

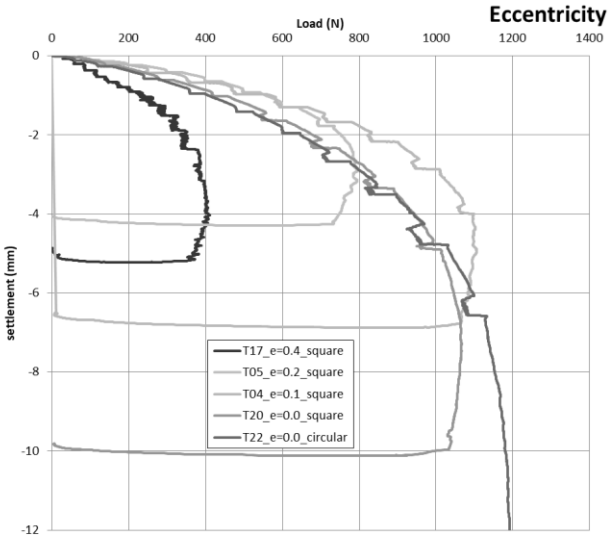

Figure 4. Load settlement curve of monotonic tests.

Figure 5 shows the evolution of the load reduction coefficient with respect to the relative eccentricity e/B. The relationships $i_e = 1 - 2 \cdot {}^{e}/_{B}$ and $i_e = \left(1 - 2 \cdot {}^{e}/_{B}\right)^2$ are also shown. This evolution had already been observed in the first studies on small foundation models by Meyerhof (1951), which enabled him to suggest the relationship mentioned above.

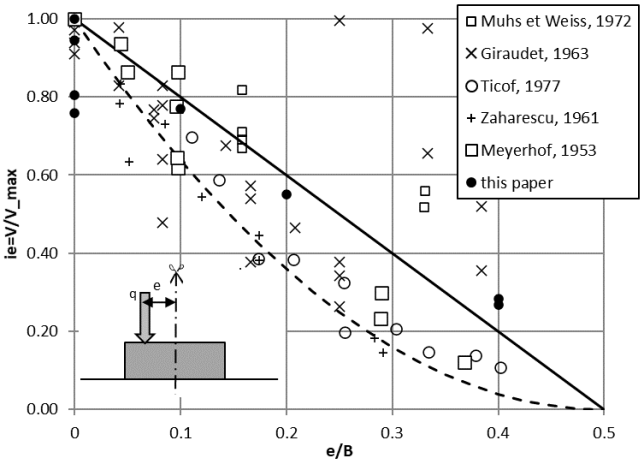

Figure 5. Evolution of normalized maximum load according to relative eccentricity.

Results of monotonic tests performed during this first phase of the research are in accordance with previous research.

3.2 Cyclic loading - Influence of eccentricity

Figure 5 shows test 18 performed in the second phase of the research program. The three loading phases may be identified clearly.

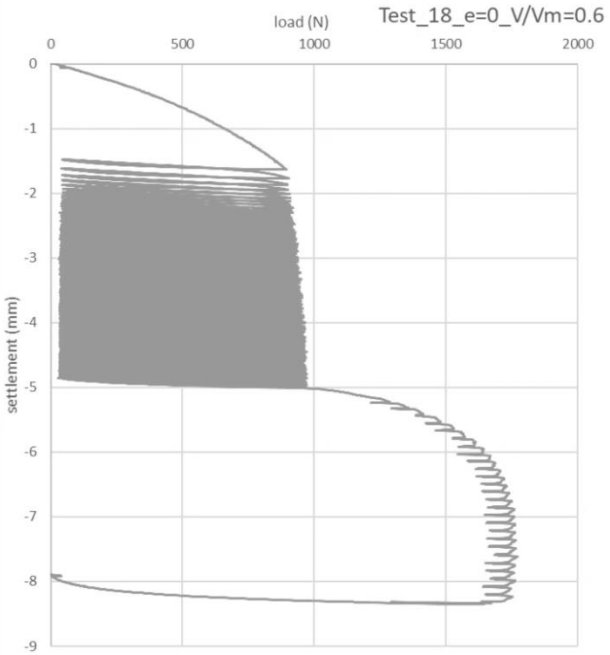

Figure 6. Load settlement curve of test 18.

Figure 7 illustrates the fact that cyclic loading has a positive influence on the maximum load achievable after a post-cyclic monotonic loading (phase 3). However for eccentricity higher thar 0.2 this effect disappears.

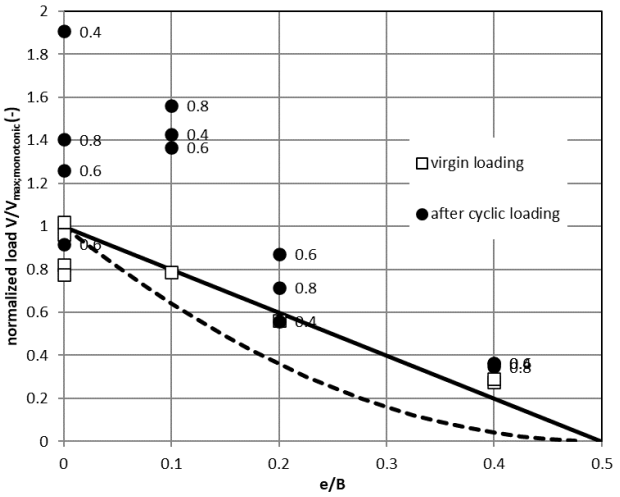

Figure 7. Influence of cyclic phase on final step loading.

Figure 8 shows that settlements here extrapolated at 10000 cycles increase at higher stress amplitude $\Delta V/V_0$.

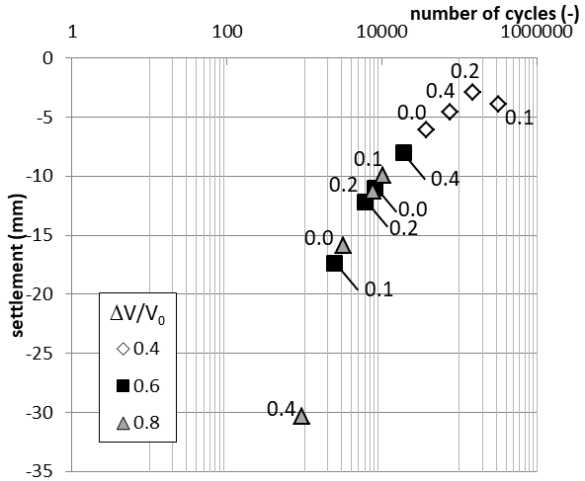

Figure 8. Influence of cyclic phase on settlement (eccentricity is attached to the symbols)

It may be noted that in these experiments, foundations were unloaded to a force of 40 N.

4 CONCLUSIONS

Experiments on shallow foundations submitted to cyclic loading under different eccentricity have been presented. Preliminary results have shown the effect of cycling on a further monotonic loading to failure, and the effect of eccentricity on the settlement reached after a given number of cycle for increasing amplitude.

ACKNOWLEDGEMENTS

The authors are grateful for the financial support provided by University G. Eiffel and RTRI.

REFERENCES

AFNOR (2013) Justification of geotechnical work - National application standards for the implementation of Eurocode 7 - Shallow foundations, NF P94-261, p. 160.

Amar, S., Baguelin, F., and Canepa, Y. (1998). Shallow foundations – experimental study under cyclic loading. *Proceedings of Geotechnical Hazards*, Rotterdam, pp. 477-483.

Andersen, K. H. (2009) *Bearing capacity under cyclic loading — offshore, along the coast, and on land*. Can. Geotech. J., 46: 513–535 https://doi.org/10.1139/T09-003.

Briaud, J.-L., (1992), The pressuremeter, CRC, 340 pages

Briaud, J.L., Gibbens R. (1999) *Behaviour of Five Large Spread Footings in Sand*, ASCE, JGGE, 125(9): 787-796. https://doi.org/10.1061/ (ASCE)1090-0241(1999)125:9(787).

Das, B., Yen, S., Singh, G. (1995) Settlement of Shallow Foundation on Sand Due to Cyclic Loading, *3rd Int. conf. on recent advances in Geotech. Earthquake Eng. And Soil Dynamics*, Vol. 1, pp 385-388.

Giraudet, P (1965) Recherches expérimentale sur les fondations soumis à des efforts inclinés ou excentrés. Ann Ponts Chaussées 3: pp. 167–193.

Lehane, B.M. (2019). *CPT-based design of foundations*. E.H. Davis Memorial Lecture (2017),Australian Geomechanics, 54(4), pp. 23-48.

Meyerhof, G.G. (1953). The Bearing Capacity of Foundations under Eccentric and Inclined Loads. *Proc. 3rd ICSMFE*., vol. I, Zurich.

Muhs, H. and Weiß, K. (1973). Inclined load tests on shallow strip footings, *Proc. 8th ICSMFE*, Vol 2, pp. 173–179.

Raymond, G.P., Komos, F. El (1978), Repeated load testing of a model plane strain footing, *Canadian Geotechnical Journal*, 15, pp.190-201 https://doi.org/10.1139/t78-019.

Sawicki, A., Swidzinski W., Zadroga B. (1998) *Settlement of Shallow Foundation Due to Cyclic Vertical Force*, Soil and Foundation, 38(1), pp 35-43, DOI: 10.3208/sandf.38.35.

Terzaghi, K., Peck R. (1948) Soil Mechanics in Engineering Practice, 1rst edition, New York Wiley , 719 pages

Ticof, J., (1977) Surface footings on sand under general planar loads University of Southampton PhD Thesis

Zaharescu, E., (1961) Sur la stabilité des fondations rigides, 4ème Conf Int. Méca. des Sols, Paris, 3A/52, pp.867-871.

Proceedings of the XVIII ECSMGE 2024
GEOTECHNICAL ENGINEERING CHALLENGES
TO MEET CURRENT AND EMERGING NEEDS OF SOCIETY
© 2024 the Authors
ISBN 978-1-032-54816-6
DOI 10.1201/9781003431749-128
Open Access: www.taylorfrancis.com, CC BY-NC-ND 4.0 license

ECSMGE 24
XVIII EUROPEAN CONFERENCE ON SOIL MECHANICS AND GEOTECHNICAL ENGINEERING

A novel undrained saturation method for triaxial testing of cohesive specimens

Une nouvelle méthode de saturation non drainée pour les essais triaxiaux d'échantillons cohésifs

A. Rismanchian*, A. Tavallali
Geotechnologies Intelligence (GeoIntel)
*aris@geointel.eu

ABSTRACT: In triaxial testing, achieving saturation of cohesive specimens obtained below the water table is paramount. ISO and ASTM standards advocate back pressure methods, yet these pose risks of sample damage and extended saturation periods, leading to reduced effective stresses and prolonged consolidations. To counter these drawbacks, an undrained saturation technique is proposed that aims to preserve specimen integrity and expedite saturation and consolidation times. Initial trials on over 90 overconsolidated triaxial specimens confirmed an average time reduction of 7 days for saturation compared to traditional methods. Reduced consolidation times, maintaining in situ stresses, further amplified time savings. Several labs, upon receiving instructions, consistently reproduced the method, reducing saturation times significantly.

RÉSUMÉ: Dans les tests triaxiaux, saturer les échantillons cohésifs sous la nappe phréatique est essentiel. Les normes ISO et ASTM préconisent la pression arrière, risquant dommages et saturation longue. Nous proposons une technique non drainée préservant l'intégrité des échantillons, accélérant la saturation et la consolidation. Essais sur 90 spécimens montrent une réduction moyenne de 7 jours pour la saturation. Plusieurs laboratoires, après avoir reçu des instructions, ont reproduit la méthode, réduisant significativement les temps de saturation et évitant les dommages aux échantillons.

Keywords: Saturation; triaxial; overconsolidated clay; intact; offshore; sample damage; time saving.

1 INTRODUCTION

Triaxial testing demands specimens to be adequately saturated, enabling the application of "saturated soil mechanics" equations for accurate analysis of soil behaviour. Therefore, a saturation phase is introduced to eliminate air from the void spaces, allowing subsequent testing stages to provide reliable data on pore water pressure (PWP) variations, essential for effective stress determination (Head, 1980). Standards such as ASTM D4767 and ISO 17892-9 emphasize the prevention of undesirable prestressing or swelling of specimens during this saturation stage.

Traditionally, saturation is achieved through back pressure, involving the addition of water to the specimen. ASTM guidelines specify a limit for the differential pressure (cell pressure minus back pressure) not exceeding 35 kPa or the specimen swelling pressure, while ISO standards lack a specific value for back pressure and mandate that effective stresses on the specimen should not surpass specified consolidation stresses. To mitigate risks, many UK laboratories adhere to the recommended 20 kPa back pressure limit outlined in BS 1377-8:1990.

However, applying back pressure to specimens with intricate structures, fissures, interbedding, or low plasticity can adversely impact soil shear strength properties. In cases where swelling could significantly influence sample behaviour or when re-imposing in-situ stress conditions, saturating specimens at a constant water content becomes imperative (Head, 1980). ISO 17892-9 clause 6.3.2.3 suggests saturating specimens incrementally with closed drainage, stipulating that observed increases in PWP during cell pressure increments should correspond to at least 90% of the cell pressure increase, which is not a realistic condition for highly OC clays based on our experience on numerous samples from different sites.

Challenges arise particularly with highly overconsolidated stiff clays retrieved from below the water table. ASTM D4767 acknowledges the dependency of the PWP parameter 'B' on soil stiffness. Consequently, higher mean effective stress values than routinely adopted in laboratories are often required, especially for stiff clays, to achieve the 90% B-value suggested by ISO 17892-9. Furthermore, achieving a PWP of at least 300 kPa, as specified by ISO for reliable saturation, proves challenging in meeting the

prescribed B-value requirement, necessitating the utilization of back pressure.

Thus, these clays are typically saturated using back pressure despite its detrimental impact on shear strength properties. For instance, in a site located in the North Sea, various tests, including Cone Penetration Test (CPT), Direct Simple Shear (DSS), Undrained Unconsolidated (UU), and Consolidated Undrained (CU) triaxial tests, were conducted on intact very high strength overconsolidated CLAY with pockets of silt, with a liquid limit of 75% and a Plasticity Index of 46%.

During the saturation stage of the CU triaxial test, back pressure with a differential pressure of 5 kPa was applied. Although the undrained shear strength (s_u) values obtained from UU and CPT tests demonstrated a close match, it was approximately 40% lower for CU test. Remarkably, the s_u of CU even fell below that of the DSS test.

This disparity between the undrained shear strengths obtained from different testing methods strongly suggests that back pressuring the CU specimen had a detrimental effect on its s_u.

Moreover, back pressuring proves time-consuming, resulting in specimens with low effective stress, requiring extended consolidation times to match in-situ conditions. These additional durations significantly impact project timelines and outcomes.

The limitations of the existing back pressure saturation method underscore the need for alternative techniques that preserve sample integrity, minimize damage, and reduce both saturation and consolidation durations for cohesive soil specimen.

2 SUGGESTED METHOD

This method is suitable for high-quality intact samples obtained below the water table, especially in offshore environments, where in-situ saturation has occurred. It is applicable when aiming for effective stress values equivalent to or higher than in situ conditions during consolidation.

1. *Initial Pressure Increase:* Increase cell pressure to 600 kPa in an undrained condition within 3 hours.

2. Stepwise Pressure Increase: If PWP < 300 kPa, incrementally raise cell pressure in undrained condition, checking the B-value at each step.

- Note 1: Perform B-value checks within one hour for stages where PWP remains < 300 kPa.
- Note 2: Measured B-values are nominal.
- Note 3: Limit this stage to a maximum of 2 days.

3. *B-value Check:* Once PWP > 300 kPa, continue raising cell pressure in undrained condition until target B-value is achieved. Perform longer-duration B-value checks to allow PWP stabilisation within the specimen (maximum 4 hours).

If B-value < 0.95 or mean effective stress reaches 80% of the target consolidation pressure, proceed to the next step.

- Note 4: Consideration of 80% consolidation pressure prevents excessive effective stress if back pressure becomes necessary.

4. *Reporting to the Engineer*: Communicate PWP, B-value, and mean effective stress related to recent cell pressure steps to the engineer ordering the tests.

5. *Engineer Assessment*: Evaluate likelihood of exceeding the target effective stress if undrained saturation continues. B-value exceeding 70% often indicates specimen can achieve saturation before reaching the target consolidation pressure.

6. *Continued Saturation*: Carry on with Engineer's instructions until the specimen is saturated. Consider going back to item 4 when B-value is less than 85%.

- Note 5: Maintain consistent waiting periods for B-value determination across different cell pressure steps.

7. *Completion Criteria:* Saturation is deemed complete when the final B-value is > 0.95 and recorded PWP is > 300 kPa.

3 METHOD VALIDATION

When intact soil samples are extracted from the ground, they tend to expand due to the removal of in situ stresses. This phenomenon generates negative PWP or suction equivalent to the in situ mean effective stress, particularly when the air entry of the soil matrix surpasses the in situ mean effective stress, and there's no dissolved gas in the pore water to be released after sampling.

Rismanchian et al. (2020) conducted a comprehensive study using Kaolin clay triaxial sample to validate the suggested saturation method. They created a cylindrical triaxial specimen from Kaolin clay consolidated to 200 kPa in a press, with dimensions of 70 mm in diameter and height. The specimen was placed on a saturated porous stone on a triaxial bottom platen, sealed in a membrane, and a top cap housing a tensiometer was positioned atop the specimen without employing top drainage.

Their study involved several steps:

- Initially achieving a B-value higher than 0.95.
- Isotropically consolidating to around 500 kPa.
- Incrementally consolidating to 1000 kPa followed by swelling steps to 250 kPa to analyse overconsolidated specimen behaviour.

- Further consolidation steps until reaching a maximum mean effective stress of around 1120 kPa.

Between each consolidation or swelling step, they reduced the cell pressure to zero while maintaining undrained conditions to simulate the stress loss experienced during sampling. Subsequently, they increased the cell pressure in undrained conditions to its previous value and measured the B-value.

When conducting the above tests, it was observed that while increasing the cell pressure in undrained conditions, satisfactory B-values were consistently achieved when measuring PWP using the tensiometer. However, in most cases, PWP measurements from the base filter stone were unresponsive until reaching nearly 300 kPa. This discrepancy led to contrasting mean effective stress calculations between the tensiometer and base measurements. Consequently, it was evident that base PWP readings were unreliable at lower pressure values.

This disparity between readings underscores the unreliable nature of base pore water pressure measurements at lower values. In situations where ISO 17892-9 recommendations are followed, back pressuring should have commenced when the B-value calculated from base pore pressure readings fell below 90%. Meanwhile, the tensiometer readings indicated acceptable B-values already. This observation justifies the significant increase in cell pressure in the initial step of the suggested procedures.

4 PRACTICAL IMPLEMENTATION OF THE INTRODUCED METHOD

In a comprehensive geotechnical investigation conducted in an offshore North Sea site, notably thick, highly overconsolidated clay deposits were encountered. The observed overconsolidated clay exhibited significant depth, measuring over 70 meters based on various boreholes surveyed in the area.

Results from both CPT and laboratory consolidation tests revealed an apparent overconsolidation ratio exceeding 7 at the upper section of the clay layer, gradually declining to 2 at a depth of 50 m. Considering the expanse and condition of the site, over 90 CU triaxial tests were assigned.

Initially, the back pressure method was utilized for the saturation of samples in four CU triaxial tests. However, this method proved time-consuming, taking approximately 8 to 12 days on average to achieve the targeted B-value of 0.95. Moreover, the mean effective stress of the triaxial specimens at the end of the saturation stage was significantly lower than the target consolidation pressure, further contributing to lengthened consolidation periods.

Table 1 provides insight into selected stages from the saturation phase of one of the abovementioned triaxial specimens, where cell pressure increments were restricted to 50 kPa to limit the increase in back pressure. Simultaneously, maintaining a high differential pressure was prioritized to prevent specimen swelling. Despite these concerted efforts, the saturation of this specimen took over 12 days to achieve the desired saturation level.

Table 1. Selected back pressure (BP)saturation stages.

Stage	Time (hr)	Cell (kPa)	BP. (kPa)	B-Value
1	0.1	50	14	0.31
2	0.1	100	22	0.23
12	8.2	500	125	-
13	9.6	550	150	0.49
18	24.2	600	250	-
19	11.5	650	288	0.75
21	18.1	650	325	-
22	6.5	700	368	0.88
27	16.4	900	559	0.99
28	0.6	950	607	0.98

To expedite the saturation phase, the novel undrained saturation method, as detailed in Section 2, was applied to three samples. Remarkably, using this method significantly reduced the required saturation time, bringing it down to an average of merely 2 days to achieve the B-value target. Moreover, the mean effective stress at the end of the saturation stage was close to the in situ mean effective stress, resulting in lower consolidation time.

Table 2 provides detailed insights into the stages of the undrained saturation phase of one of these triaxial specimens, showcasing the tangible benefits of adopting this method. Notably, saturation was successfully attained within a mere 19 hours, a substantial reduction compared to traditional methods. Additionally, the table highlights observations regarding ‘apparent’ mean effective stress levels during early saturation stages. For instance, the apparent mean effective stress measured 465 kPa at the end of the first stage, decreasing to 412 kPa by the conclusion of the saturation phase. These findings reinforce the assertions made in Section 3 regarding the unreliability of pore pressure readings below 300 kPa and indicate anomalous B-value results at certain stages (e.g. stage 2 in Table 2). Furthermore, the table elucidates a significant improvement in B-value as the PWP approaches the 300 kPa threshold, providing

empirical evidence supporting the effectiveness of this method in achieving the desired B-value targets.

Table 2. Undrained saturation stages.

Stage	Time (hr)	Cell (kPa)	PWP (kPa)	B-Value
1	3.2	600	135	0.23
2	4.0	650	248	1.34
3	4.0	700	294	0.93
4	4.0	750	340	0.92
5	3.9	800	388	0.97

Upon witnessing the promising and satisfactory outcomes of the newly proposed method, we decided to implement it across multiple laboratories spanning four different countries to saturate a collective total of more than 90 triaxial specimens. The method's reproducibility among these diverse laboratories was notable, resulting in a commendable reduction in saturation time. Across most samples, the saturation phase duration ranged from 2 to 5 days, with an average of around 3 days. This consistent performance and effectiveness across various laboratory settings underscored the method's reliability and contributed to the notable reduction in saturation duration.

This transition from the back pressure method, which averaged around 10 days, to the undrained saturation method, averaging approximately 3 days, effectively saved an average of 7 days for the saturation phase of the highly overconsolidated clay samples. Consequently, this transition resulted in a remarkable saving of more than 630 days solely on the saturation process. The overall time saved was considerably higher when factoring in the reduced consolidation duration, given that the mean effective stress at the end of saturation closely approached the in-situ value. Beyond the benefits derived from reduced project time, another crucial aspect was the prevention of specimen damage incurred by back pressuring.

It's noteworthy that in a few isolated instances, undrained saturation was halted to prevent excessive stress on specimens. In such cases, backpressure was judiciously applied to facilitate specimen saturation while trying to maintain their integrity and reliability.

5 CONCLUSION AND RECOMMENDATIONS

The study underscores the limitations of the traditional back pressure saturation method in triaxial testing, particularly in dealing with highly overconsolidated clay specimens. The proposed undrained saturation method not only addresses these limitations but also significantly reduces saturation and consolidation durations. This novel technique, validated across various laboratory settings, consistently achieved target B-values and effectively preserved specimen integrity, substantially reducing saturation times from an average of 10 days to approximately 3 days. The reduced duration and preservation of sample integrity signify substantial advantages over conventional back pressure methods. We recommend adopting this undrained saturation method for similar overconsolidated soil types, to expedite testing processes and prevent sample damage. Additionally, further studies on different soil types and conditions can enhance the method's applicability and efficacy.

Furthermore, it's imperative to note that ASTM currently doesn't allow undrained saturation. With upcoming large offshore windfarm constructions on sites with overconsolidated clays, updating ASTM standards becomes crucial to prevent sample damage during saturation stages.

ACKNOWLEDGEMENT

The authors extend their appreciation to Geotechnologies Intelligence (GeoIntel) for their financial support and permission to publish this work.

REFERENCES

ASTM (2020) D4767 Standard test method for consolidated undrained triaxial compression test for cohesive soils, DOI: 10.1520/D4767-11R20.

BS 1377-8 (1990) Methods of test for soils for civil engineering purposes - Shear strength tests (effective stress).

Head, K. H. (1980). *Manual of soil laboratory testing*, Pentech Press Limited, UK.

ISO (2018) 17892 Geotechnical investigation and testing — Laboratory testing of soil — Part 9: Consolidated triaxial compression tests on water saturated soils.

Rismanchian, A., Carrington, T., Snelling, K., and Sutton, J. (2020). Indirect determination of soils in-situ horizontal stress from matric suction measurements: developing a new tensiometer, In: *4th ISFOG*, Austin, USA.

Proceedings of the XVIII ECSMGE 2024
GEOTECHNICAL ENGINEERING CHALLENGES
TO MEET CURRENT AND EMERGING NEEDS OF SOCIETY
© 2024 the Authors
ISBN 978-1-032-54816-6
DOI 10.1201/9781003431749-129
Open Access: www.taylorfrancis.com, CC BY-NC-ND 4.0 license

ECSMGE 24
XVIII EUROPEAN CONFERENCE ON SOIL MECHANICS AND GEOTECHNICAL ENGINEERING

Large scale direct shear tests on rockfill 63/180mm

Essais de cisaillement direct de grandes dimensions dans enrochement 63/180mm

J. Rocha*, P. Mengé
DEME NV, Zwijndrecht, Belgium

M. Muñiz-Menéndez
Laboratorio de Geotecnia - CEDEX, Madrid, Spain

**rocha.jose@deme-group.com*

ABSTRACT: This paper presents the results of a large-scale direct shear test campaign (1.0 m x 1.0 m x 1.2 m) performed on rockfill material, grading 63/180 mm, that was used as a foundation base for an offshore jack-up vessel. The tests were performed for normal stresses ranging between 50 kPa and 800 kPa, with the main goal of estimating the peak friction angle of the material for a normal stress of 1000 kPa. A description of the material properties is presented together with the equipment characteristics and adopted test procedures. The test results were evaluated according to the non-linear failure method proposed by De Mello (1977).

RÉSUMÉ: Cet article présente les résultats d'une campagne d'essais de cisaillement direct de grandes dimensions (1,0 m x 1,0 m x 1,2 m) réalisée sur un matériau d'enrochement, de granulométrie 63/180 mm, utilisé comme base de fondation pour un navire autoélévateur offshore. Les essais ont été réalisés pour des contraintes normales comprises entre 50 kPa et 800 kPa, avec l'objectif principal d'estimer l'angle de frottement maximal du matériau pour une contrainte normale de 1000 kPa. Une description des propriétés des matériaux est présentée avec les caractéristiques de l'équipement et les procédures d'essai adoptées. Les résultats des essais ont été évalués selon la méthode de rupture non linéaire proposée par De Mello (1977).

Keywords: Rockfill; direct shear; large scale; peak friction angle.

1 INTRODUCTION

As part of an offshore wind-farm project, rockfill with grading 63/180 mm was selected as foundation material for offshore jack-up vessels, used to load turbines and other components near a quay-wall. A minimum peak friction angle of 40 degrees under a normal stress of 1000 kPa was defined in the contract specifications.

The simplest way to determine the friction angle of a granular material is testing a sample using a shear box apparatus (Tanghetti et al., 2019). The main difficulty to perform direct shear tests in rockfill material is the large size of the particles, which does not allow for the use of conventional equipment (Marachi et al, 1969).

In order to avoid some scale effects, some limits are proposed in ASTM D3080, where the maximum diameter of the particles must be ten times smaller in comparison with the smallest shear plane, while the height of the equipment must be at least six times larger in comparison with the largest particle of the sample. Fu *et al*. (2015) tested two samples in equipment with different dimensions and got to more stringent results than the limits proposed in ASTM D3080, i.e., fifteen times for the ratio between smaller shear plane dimension and maximum particle size and ten times for the ratio between height of equipment and maximum particle size.

In the current work it was not possible to follow the limits mentioned above because of the maximum particle size of the material, 180 mm, and the target dates for the conclusion of the tests. No equipment was found available that would be compatible with the required limits and planning for the test campaign, thus it was decided to conduct the tests at Laboratorio de Geotecnia (CEDEX), in Madrid, where a large direct shear box is available. Approximately 9500 kg of material were sent to Spain from a rock quarry located in Norway for the execution of the tests.

The test results were evaluated according to the non-linear failure method proposed by De Mello (1977).

2 TESTING PROGRAM

2.1 Equipment details

The tests were performed in a large direct shear apparatus available at Laboratorio de Geotecnia - CEDEX. The shear plane has an area of 1.0 m^2 and the height of the shear box is 1.2 m.

Horizontal and vertical stresses up to 1000 kPa can be applied based on the type of material being tested. The shear force is applied by a constant horizontal displacement rate, ranging between 0.5 and 45 mm/min, until a maximum horizontal displacement of 250 mm. The vertical displacements are recorded by four transducers LVDT located on corners of the top plate.

Due to the large particle size of the rockfill it was decided to limit the vertical stress to a maximum of 800 kPa in order to guarantee a constant load during the full shearing phase. This was required because of the vertical deformations (dilatant/contractive behaviour) and response of the hydraulic system responsible for the shear force.

The control and data collection are performed by means of a multichannel controlling system. The system records the vertical and horizontal forces, and the displacements at the four transducers with an acquisition rate of 0.1 Hz.

2.2 Material properties

The rockfill material used in the testing campaign was produced in a rock quarry located in *Sogn og Fjordane*, Norway. The bedrock at the quarry consists of hard, low weathering grade rock (Devonian rock), described as a metamorphosed quartzite with presence of laminations (Figure 1).

The intrinsic properties of the rockfill material produced at the quarry are classified as excellent according to The Rock Manual (CIRIA, 2007).

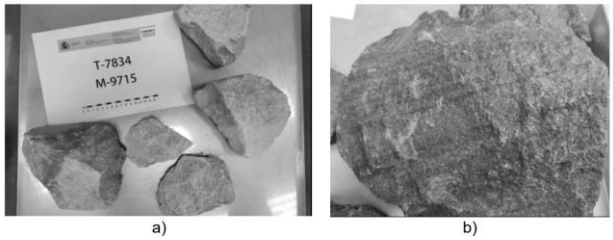

Figure 1. a) Individual particles; b) Detail of laminations.

Ten particle size distribution curves (PSDs) were performed to verify the compliance with the requirements defined in British Standard, BS EN 13383-1: 2002, for $CP_{63/180}$ materials (Figure 2).

Regarding the shape of the particles, determined by a length-to-thickness ratio larger than 3, also defined by the same standard, the material belongs to category LT_A. The broken surface was visually evaluated, and the material is defined as RO_5 according to the same standard.

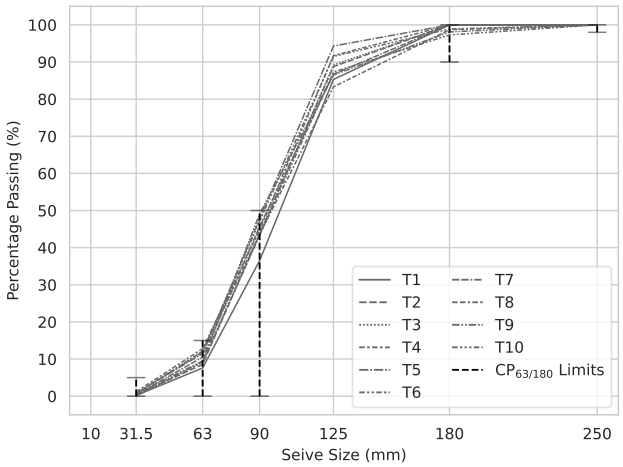

Figure 2. Particle size distribution curves.

Besides the tests and verifications described above, three specimens were cored from the biggest particles and unconfined compression tests (UCS) were performed. The dimension of the specimens and the results of the tests are summarised in Table 1.

Table 1. UCS test results.

Sample	A	B	C
Diameter (mm)	37.6	37.5	37.5
Height (mm)	92.7	93.9	92.7
Unit Weight (kN/m^3)	26.7	26.6	26.5
UCS (MPa)	125.0	128.0	92.2

2.3 Test procedures

The rockfill material will be used underwater, but this condition could not be reproduced because the shear box is not watertight. Following a request from the Client, it was decided to add water to the material during the sample preparation. For comparison purposes, one test (normal stress of 800 kPa) was executed without addition of water.

The material was placed inside the shear box in three layers, with a thickness of approximately 30 cm. The first two layers were manually installed while the last layer was installed by gravity, after cutting the sample box above the shear box.

A slight compaction was applied to the material, after the installation of each layer, by a vertical stress of 50 kPa. The main goal of this step was to guarantee the correct rearrangement between the particles. Once the installation of the third layer was completed, the required normal stress was applied, and the vertical deformations were registered.

The shear of the samples was executed with a constant rate of 0.8mm/minute and the tests were completed once a maximum horizontal displacement of 240mm was reached.

2.4 Sample conditions

Six samples were prepared following the procedures described above and tested for normal stresses between 50kPa and 800kPa.

Table 2 presents the initial conditions of the samples and Table 3 presents the sample conditions after the required normal stress was applied.

Table 2. Sample initial conditions.

Test	w (kg)	WC (%)	h_0 (mm)	γ_0 (kN/m^3)
T50	1229.5	1.30	905	13.50
T200	1405.0	1.40	996	14.03
T400	1253.0	1.50	890	14.01
T600	1236.5	1.30	890	13.80
T800	1250.0	1.50	890	13.98
T800d	1278.5	1.40	960	13.24

Table 3. Sample conditions after application of normal stress.

Test	σ (kPa)	δv (mm)	h_f (mm)	γ_f (kN/m^3)
T50	50	15.5	889.5	13.73
T200	200	24.6	971.4	14.38
T400	400	19.3	870.7	14.32
T600	600	33.7	856.3	14.34
T800	800	30.1	859.9	14.47
T800d	800	34.2	925.8	13.73

In those tables:

- w = weight of the sample in kg
- WC = water content in %
- h0 = initial height of the sample in mm
- γ0 = initial unit weight in kN/m^3
- σ = normal stress in kPa
- δv = vertical displacement in mm
- hf = final height of the sample in mm
- γf = final unit weight in kN/m^3.

3 TEST RESULTS

The results of the tests are presented in Figure 3.

As it can be seen, the difference in results between the dry test (T800d) and the equivalent wet test is negligible. The addition of water seems to produce no significant change in the behaviour of the material.

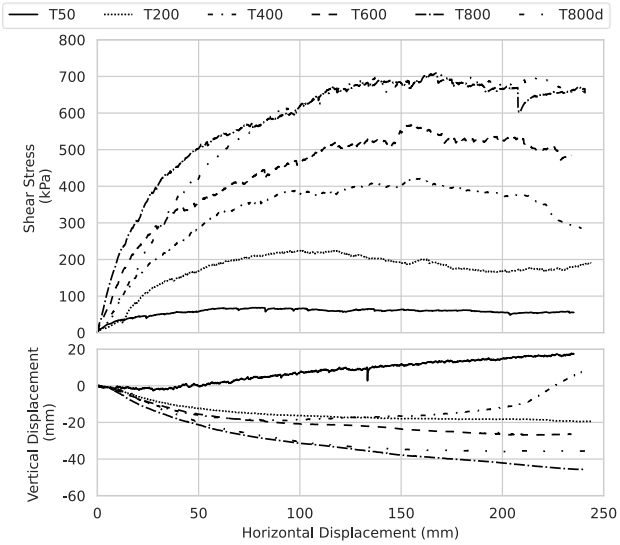

Figure 3. Shear stress and vertical displacement versus horizontal displacement.

The peak shear stresses in function of the normal stress (Figure 4) are well fitted with a non-linear regression curve, as proposed by De Melo (1977).

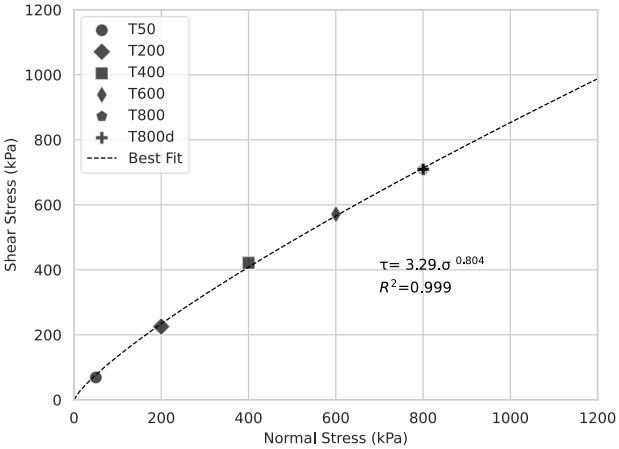

Figure 4. Peak shear stress versus normal stress.

Non-linear equation that resulted in the best fit to the test results is the following:

$$\tau = a' \times \sigma^b = 3.29 \times \sigma^{0.804} \qquad (1)$$

This result is in line with the work of several authors (Barton, 2013; Frossard *et al*. 2012; Indraratna, 1994) that have proposed non-linear failure modes for this type of material.

The constants *a'* and *b* were compared with a compilation made by Muñiz-Menéndez & Estaire (2022), including test performed at CEDEX and results published by other authors. As shown in Figure 5, the current results are in good agreement with values found in literature.

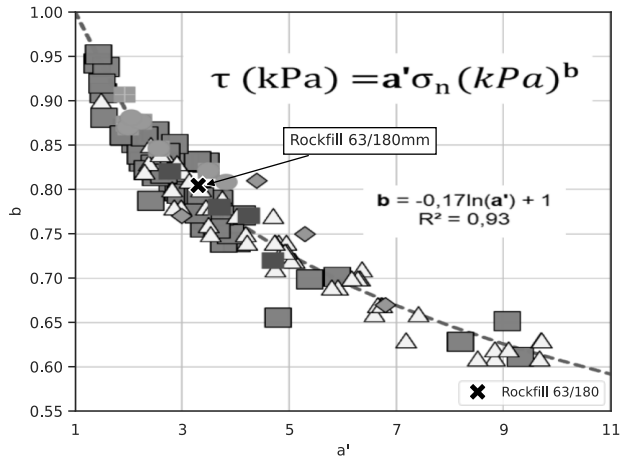

Figure 5. Relation between a' and b parameters compiled by Muñiz-Menéndez & Estaire (2022) including results of rockfill 63/180mm.

The estimated effective friction angle for a normal stress of 1000 kPa (Figure 6) was found equal to 40.5 degrees which was just above the minimum value defined in the project specifications.

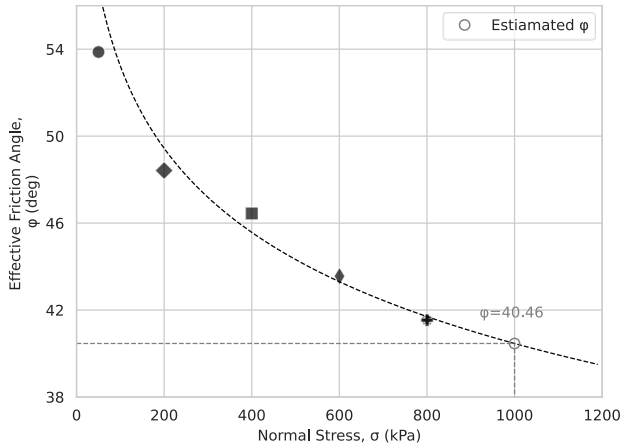

Figure 6. Estimated peak friction angle for a normal stress equal to 1000 kPa.

4 CONCLUSIONS

Six samples of rockfill, grading 63/180mm, were tested on a large-scale direct shear apparatus for normal stresses ranging between 50 kPa and 800 kPa. A non-linear regression resulted in a very good fit to the data, and a peak friction angle of 40.5 degrees was estimated for a normal stress of 1000 kPa.

REFERENCES

ASTM Standard (2023). ASTM D3080. Standard Test Method for Direct Shear Test of Soils Under Consolidated Drained Conditions. ASTM International, West Conshohocken, 10 p.

Barton, N.R. (2013), Shear strength criteria of rock, rock joints, rockfill and rock masses: Problems and some solutions. *Journal of Rock Mechanics and Geotechnical Engineering*, 5(4), pp. 249-261.

British Standard Institute (2002). BS EN 13383-1:2002. Armourstone-Specification. British Standards Institute, London, 38 p.

CIRIA, CUR, CETMEF (2007). The Rock Manual. The use of rock in hydraulic engineering (2nd edition). C683, CIRIA, London, pp.135.

De Mello, V. F. B (1977). Reflections on design decisions of practical significance to embankment dams. *Géotechnique*, 27(3), pp. 281-355.

Marachi, N. N., Chan, C. K., Seed, H. B., Duncan, J. M. (1969). Strength and deformation characteristics of rockfill materials. Report No. TE-69-5. Department of Civil Engineering, University of California, Berkeley.

Frossard, E., Hu, W., Dano, C., Hicher, P.Y. (2012). Rockfill shear strength evaluation: a rational method based on size effects. *Géotechnique*, 62(5), pp. 415-427.

Fu, X., Zheng, X., Lei, X. Deng, J. (2015). Using a modified direct shear apparatus to explore gap and size effects on shear resistance of coarse-grained soil. *Particuology*, 23, pp.82-89. https://doi.org/10.1016/j.partic.2014.11.013.

Indraratna, B. (1994). Implications of non-linear strength criteria in the stability assessment of rockfill dams. *Proceedings of the 13th International Conference on Soil Mechanics and Foundation Engineering*, New Delhi, India, pp. 935-938.

Tanghetti, G., Goodey, R.J., Divall, S., MacNamara, A. M., McKinley, B. (2019). Design and development of a large shear box for testing working platform material. In *Proceedings of the 17th European Conference on Soil Mechanics and Geotechnical Engineering*, pp. 267–274. Reykjavik,Iceland. http://doi.org/10.32075/17ECSMGE-2019-0267.

Muñiz-Menéndez, M. Estaire, J. (2022). Experimental study on the shear strength of medium-coarse rockfill, *Proceedings of the 20th International Conference on Soil Mechanics and Geotechnical Engineering*. Sydney, Australia, pp. 169-173. https://www.issmge.org/uploads/publications/1/120/ICSMGE_2022-30.pdf.

Proceedings of the XVIII ECSMGE 2024
GEOTECHNICAL ENGINEERING CHALLENGES
TO MEET CURRENT AND EMERGING NEEDS OF SOCIETY
© 2024 the Authors
ISBN 978-1-032-54816-6
DOI 10.1201/9781003431749-130
Open Access: www.taylorfrancis.com, CC BY-NC-ND 4.0 license

ECSMGE 24
XVIII EUROPEAN CONFERENCE ON SOIL MECHANICS AND GEOTECHNICAL ENGINEERING

Numerical modelling of unsaturated bentonite subjected to different hydro-mechanical stress paths

Modélisation numérique de bentonite insaturée soumise à différents chemins de contraintes hydromécaniques

C.E. Rodríguez*
UPC, Barcelona, Spain

A. Gens, R. Vasconcelos, J. Vaunat
UPC, CIMNE, Barcelona, Spain

**carlos.rodriguez.romero@upc.edu*

ABSTRACT: Bentonite-based materials such as MX-80 bentonite have been considered for their use as engineering barriers (EB) in deep radioactive waste geological repositories, mainly due to their low permeability, swelling pressure, and radionuclide retention properties. To ensure their integrity and to know their influence, different hydro-mechanical stress paths must be assessed. The European project BEACON (Bentonite Mechanical Evolution), addressed the behaviour of MX-80 bentonite subjected to different conditions including laboratory hydration tests carried out by EPFL (École Polytechnic Fédérale de Lausanne). For the fulfilment of the task, the constitutive response of the model is evaluated, decreasing the suction linearly to zero from its initial value simultaneously in the entire domain of analysis. A purely mechanical constitutive model calculation and no-flow conditions are enforced to probe the predictive power of the proposed numerical model. The paper presents a comparison between these numerical simulations and the laboratory test data showing satisfactory results.

RÉSUMÉ: Les matériaux à base de bentonite tels que la bentonite MX-80 ont été envisagés pour leur utilisation comme barrières techniques (EB) dans les dépôts géologiques profonds de déchets radioactifs, principalement en raison de leur faible perméabilité, de leur pression de gonflement et de leurs propriétés de rétention des radionucléides. Pour garantir leur intégrité et connaître leur influence, différents chemins de contraintes hydromécaniques doivent être évalués. Le projet européen BEACON (Bentonite Mechanical Evolution), a abordé le comportement de la bentonite MX-80 soumise à différentes conditions dont ces tests d'hydratation en laboratoire réalisés par l'EPFL (École Polytechnic Fédérale de Lausanne). Pour l'accomplissement de la tâche, la réponse constitutive du modèle est évaluée, en diminuant la succion linéairement jusqu'à zéro depuis sa valeur initiale simultanément dans tout le domaine d'analyse. Un calcul de modèle constitutif purement mécanique et des conditions d'absence de débit sont appliqués pour sonder le pouvoir prédictif du modèle numérique proposé. L'article présente une comparaison entre ces simulations numériques et les données d'essais en laboratoire montrant des résultats satisfaisants.

Keywords: MX-80 bentonite; hydro-mechanical; double porosity model; engineering barriers; stress path.

1 INTRODUCTION

The hydro-mechanical (HM) behaviour of bentonite-based materials has been extensively studied due to their potential use as sealing barriers in deep geological repositories for nuclear waste. These materials present appealing characteristics for their use, such as low hydraulic conductivity, swelling potential and sealing capacity. The bentonite is installed in an unsaturated state, but, due to environmental conditions, the barrier evolves to a saturated state. Because of its importance, it is necessary to verify their long-term behaviour to ensure their integrity under different hydro-mechanical stress paths. The Bentonite Mechanical Evolution project (BEACON), addressed the behaviour of samples of granular MX-80 bentonite subjected to different conditions such as those laboratory hydration tests carried out by EPFL (École Polytechnic Fédérale de Lausanne).

The occurrence of an active interaction between fabric and microfabric of active clays due to the physicochemical processes taking place at the particle level (Gens and Alonso, 1992) restricts the use of single-porosity formulations. In this respect, the development of mechanical constitutive models by Alonso et al., (1999) and Sánchez et al., (2005) considering the existence of two-pore structural levels

constituted a crucial enhancement of previous constitutive formulations for unsaturated clayey soils. In this work, the modelling is performed using this double-porosity model (DPM).

2 DESCRIPTION OF THE CONSTITUTIVE MODEL

The HM formulation requires a set of constitutive laws for dealing with the HM coupled processes that take place in geotechnical porous media.

An unsaturated soil is usually treated as a porous multi-phase medium composed of solid grains, water (as liquid water or vapour in the gas phase) and air (as dry air or dissolved in the liquid phase) (Olivella et al., 1996). Three-phase diagrams representing a soil element as a double porosity medium are shown in Figure 1. It can be easily noted that the volume of voids in the soil (V_p) is the sum of the volume occupied by macro-pores (V_{pM}) and micro-pores (V_{pm}). The volume of microstructure (V_m) includes the volume of the intra-aggregate pores (micro-pores) and the volume occupied by the solid phase (V_s).

Porosities (ϕ and ϕ_m) and void ratios (e and e_m) for the two porous media (the soil and the clay aggregate) are defined as:

$$\phi = \frac{V_p}{V} = \frac{V_{pm}}{V} + \frac{V_{pM}}{V} = \bar{\phi}_m + \bar{\phi}_M \quad (1)$$

$$\phi_m = \frac{V_{pm}}{V_m} \quad (2)$$

where $\bar{\phi}_m$ and $\bar{\phi}_M$ are the pore volume fractions associated with microstructure and macrostructure, respectively (Ruiz, 2020).

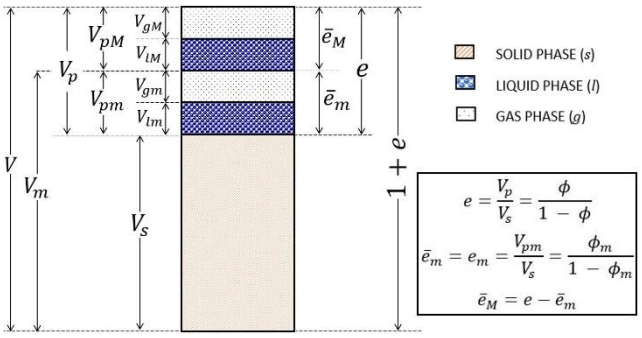

Figure 1. Phase diagram of a double structure unsaturated medium.

2.1 Mechanical model

In the current double porosity approach, the well-known BBM model (Alonso et al., 1990) is used for the macrostructural constitutive equation; the evolution of the yield surface in the stress space is dependent on the stress state, history variables and macro suction. The yield function for a general state, F_{LC}, in terms of the stress invariants (p, J, θ), is defined as:

$$F_{LC} = 3J^2 - M_F^2 \left(\frac{g_F(\theta)}{g_F\left(-\frac{\pi}{6}\right)} \right)^2 (p + p_s)(p_0 - p) = 0 \quad (3)$$

where M_F is the slope of the critical state line; g_F is a function of Lode's angle (θ); p_s expresses the dependence of the shear strength on macro suction and temperature; and p_0 is the apparent non-saturated pre-consolidation pressure that defines the Loading-Collapse (LC) locus in the $p{:}\, s_M$ plane according to

$$p_0 = p_c \left(\frac{p_0^*}{p_c} \right)^{\frac{\lambda(0) - \bar{\kappa}_M}{\lambda(s_M) - \bar{\kappa}_M}} \quad (4)$$

where p_0^* is the pre-consolidation pressure at saturation; p_c is a reference pressure; $\lambda(0)$, $\lambda(s_M)$ are the macro-structural compressibility at saturated and non-saturated conditions, respectively; and $\bar{\kappa}_M$ is the elastic stiffness parameter at macro for changes in the mean stress, p.

The microstructural mechanical behaviour is described by the following nonlinear elastic relationship:

$$K_m = \frac{1 + e_m}{\kappa_m} p_m \quad (5)$$

where K_m is the microstructural bulk modulus, p_m the effective mean stress acting on the microstructure and κ_m a model parameter.

It is assumed that microstructural volumetric deformation is fully reversible but can generate plastic deformation at macrostructural level ($\dot{\bar{\varepsilon}}^p_{M,\beta}$) and is defined by:

$$\dot{\bar{\varepsilon}}^p_{M,\beta} = f_\beta(\dot{\bar{\varepsilon}}^e_m) \quad (6)$$

where f_β defines a pair of coupling functions dependent on the degree of compactness of macro-structure (μ_β) and on the sign of the mean effective stress increment at the micro-structural domain $(\dot{p}_m)$

$$f_\beta = \begin{cases} f_{MC}^{(1)} + \left(f_{MC}^{(0)} - f_{MC}^{(1)}\right)(1 - \mu_\beta)^{n_{MC}} if\ \dot{p}_m > 0 \\ f_{MS}^{(1)} + \left(f_{MS}^{(0)} - f_{MS}^{(1)}\right)(1 - \mu_\beta)^{n_{MS}} if\ \dot{p}_m < 0 \end{cases} \quad (7)$$

$f_{MC}^{(0)}$, $f_{MC}^{(1)}, n_{MC}$ and $f_{MS}^{(0)}$, $f_{MS}^{(1)}, n_{MS}$ are model parameters that define the coupling function in micro-structural contraction (*MC*) and micro-structural swelling (*MS*) paths, respectively.

2.2 Hydraulic model

Volumetric advective fluxes are formulated for the macro-structural domain, since the liquid and gas advective fluxes through micro-pores have been neglected. Therefore, the generalized Darcy's law ($\boldsymbol{q}_{\alpha M}$) for the α phase (liquid, l; gas, g) in expansive clays can be expressed as:

$$\boldsymbol{q}_{\alpha M} = -\boldsymbol{k}_M \frac{k_{r\alpha M}}{\mu_{\alpha M}} (\nabla P_{\alpha M} - \rho_{\alpha M} \boldsymbol{g}) \quad (8)$$

The intrinsic permeability tensor for the macrostructure, $\boldsymbol{k}_M$, is only dependent on its pore structure, according to the modified Kozeny-Carman equation:

$$\boldsymbol{k}_M = \boldsymbol{k}_{0,M} \frac{\bar{\phi}_M^3}{(1-\bar{\phi}_M)^2} \frac{(1-\bar{\phi}_0)^2}{\bar{\phi}_0^3} \quad (9)$$

$\bar{\phi}_0$ is the pore fraction for which the reference intrinsic permeability tensor $\boldsymbol{k}_{0,M}$ is estimated. The phase relative permeability, $k_{r_\alpha M}$, expresses the dependence of hydraulic permeability on the degree of saturation of the macrostructure. The decrease in liquid permeability with the reduction of the liquid saturation in macro-pores is defined through the following exponential function:

$$k_{r_l M} = A_{rl} \left(S_{el,M}\right)^{\lambda_r} \quad (10)$$

where the effective degree of saturation of macrostructure, $S_{el,M}$, is defined by:

$$S_{el,M} = \frac{S_{lM} - S_{lr,M}}{S_{ls,M} - S_{lr,M}} \quad (11)$$

in which S_{lM}, $S_{lr,M}$, $S_{ls,M}$ are the current, the residual and the maximum degree of saturation of the macrostructure, respectively; A_{rl}, λ_r are model parameters.

The water retention curve (WRC) of a porous medium relates its water content (or degree of saturation) to the pore-water potential (suction). Due to the assumption that micro-pores may be unsaturated, it is also necessary to define hydraulic constitutive laws for the microstructure by the definition of a WRC for this pore domain as well. In CODE_BRIGHT the water retention capacity of a porous medium is described by a modified van Genuchten law, as follows:

$$S_{el,\beta} = \left(1 + \left(\frac{s_\beta}{P}\right)^{\frac{1}{1-\lambda_{r\beta}}}\right)^{-\lambda_{r\beta}} \cdot \left(1 - \frac{s_\beta}{P_{d,\beta}}\right)^{\lambda_{d\beta}} \quad (12)$$

where s_β is the matric suction; $\lambda_{r\beta}$, $\lambda_{d\beta}$ are model parameters; P is a parameter related to the pore-air entry value dependent on temperature; and $P_{d,\beta}$ is the suction value at fully dry conditions.

Hydraulic equilibrium between the two structural levels is not assumed, which leads to a local exchange of mass of water and air between micro- and macro-pores. Sánchez, (2004) and Gens et al., (2011) proposed that the pore-water transferred between microstructure and macrostructure (Γ^w) is proportional to the difference in micro (s_m) and macro (s_M) suctions, that is,

$$\Gamma^w = \gamma^w (s_m - s_M) \quad (13)$$

The leakage parameter, γ^w, is related to the geometric characteristics of the porous media (Sánchez, 2004; Alonso and Navarro, 2005).

3 DESCRIPTION OF THE TEST

Tests were performed using a high-pressure oedometric cell that allows keeping the volume constant while measuring the axial load. Water is supplied from the bottom and top bases of the oedometric cell with a constant pressure of 20 kPa. The cell is made of stainless steel and holds an oedometric ring with height of 12.5 mm and diameter of 35.0 mm. The tested material is granular MX-80 bentonite with an initial void ratio in the range of 0.83-0.85 and a total suction is 110 MPa.

Path 1 (A-B-C-D) consisted on a hydration phase under constant vertical stress of 21 kPa. Path 2 (A-B'-D) also consisted of a hydration phase but at constant-volume conditions. Vertical stresses in both tests were increased in steps up to 20 MPa once full saturation was reached (Figure 2). Additional details of the test are provided in Ferrari et al., (2022).

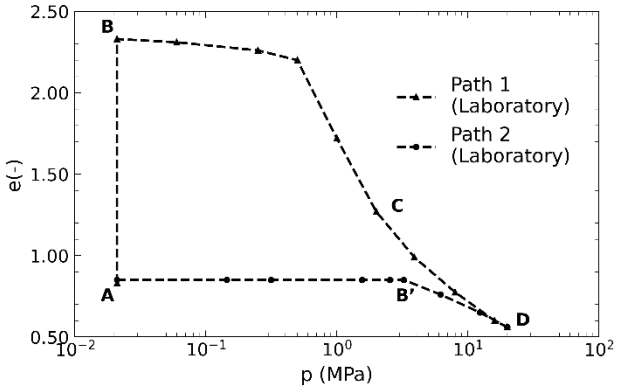

Figure 2. Hydro-mechanical stress paths under constant axial stress and constant volume conditions.

4 MODEL PARAMETERS

The HM parameters required in the numerical modelling were fitted using the experimental data in the literature (Seiphoori et al., 2014, 2015) and by back-calculating the results of the tests.

However, some other model parameters had to be calibrated during the modelling of this modelling task to fit the model predictions to the data from the laboratory tests. The main input parameters used to simulate the hydration tests are listed in Table 1.

Table 1. Main HM parameters for MX-80 bentonite.

Water Permeability Macro			
$k_{M,0}$	$[m^2]$	4e-21	Eq. (9)
$\bar{\phi}_{M,0}$	$[-]$	0.20	Eq. (9)
A_{rl}	$[-]$	1.0	Eq. (10)
λ_{rl}	$[-]$	6.0	Eq. (10)
Local Water Transfer			
γ^w	$\frac{kgs^{-1}m^{-3}}{MPa}$	5e-03	Eq. (13)
WRC (Macro)			
P_0	$[MPa]$	12.0	Eq. (12)
λ_{rM}	$[-]$	0.55	Eq. (12)
P_{dM}	$[-]$	1e27	Eq. (12)
λ_{dM}	$[-]$	3.90	Eq. (12)
WRC (micro)			
P_0	$[MPa]$	90.0	Eq. (12)
λ_{rm}	$[-]$	0.65	Eq. (12)
P_{dm}	$[-]$	1e27	Eq. (12)
λ_{dm}	$[-]$	0.8	Eq. (12)
Expansive Behaviour			
$\bar{\kappa}_M$	$[-]$	0.19e-4	Eq. (4)
$\bar{\kappa}_s$	$[-]$	0.28e-2	Eq. (4)
p_0^*	$[MPa]$	2.5	Eq. (4)
$\lambda(0)$	$[-]$	0.3	Eq. (4)
$f_{MS}^{(0)}$	$[-]$	4.0	Eq. (9)
$f_{MS}^{(1)}$	$[-]$	0.0	Eq. (9)
n_{MS}	$[-]$	2.0	Eq. (9)

5 NUMERICAL RESULTS AND DISCUSSION

A cubic sample of expansive soil, with a volume of 1.0 cm^3, was selected to represent the geometry. The tests were modelled by means of the finite element code CODE_BRIGHT. The generated mesh is composed of 125 identical hexahedral elements. The suction is decreased linearly to zero from its initial value simultaneously in the entire domain of analysis. It is a purely mechanical constitutive model calculation and no flow conditions are enforced.

In the wetting path at constant load conditions ("free swelling"), the confining pressure is applied on the upper surface and the four lateral surfaces. Under such conditions, vertical displacements (in the z-axis direction) are not allowed at the lower surface.

In contrast, in the isochoric condition path, the vertical displacements are restricted in all surfaces of the volume until the suction is reduced to a value of 0.

The FE mesh and three orthogonal views with the applied mechanical boundary conditions for the wetting path under unconfined (free swelling) and confined (isochoric) conditions are displayed in Figure 3.

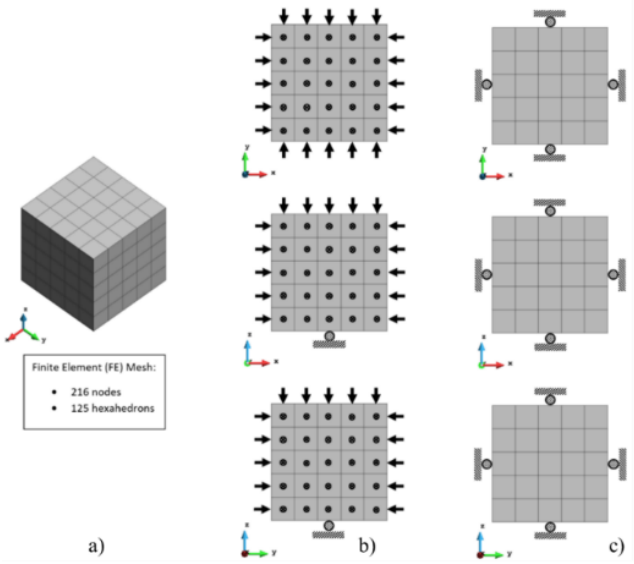

Figure 3. Schematic representation of the modelled geometry (FE mesh) of a cubic element of expansive soil together with the mechanical boundary conditions under (b) unconfined and (c) confined swelling/shrinkage evolution.

5.1 Analysis of stress path 1

In path 1 the swelling of the clay aggregates leads to an increase in macro-porosity, which produces a global expansion of the soil element (increase in total porosity). It can be seen that during the swelling stage (A-B) the LC curve moves to the left (Figure 4) in response to the plastic swelling strains taking place in

the macrostructure. This is due to the low isotropic stress ratio p/p_0. When this ratio is low, it implies a dense packing of the clay aggregates and, under this condition, the micro-structural swelling (MS path) affects strongly the global arrangements of clay aggregates, inducing large macro-structural plastic strains and a macro-structural softening.

After saturation, subsequent loading (B-D) takes the LC again to the right to the final load value of approximately 8.0 Mpa (Figure 5). During the subsequent loading (B-D), under saturated conditions, the deformation of the macrostructure is significant but it is not due to micro-structural strains that are now quite small.

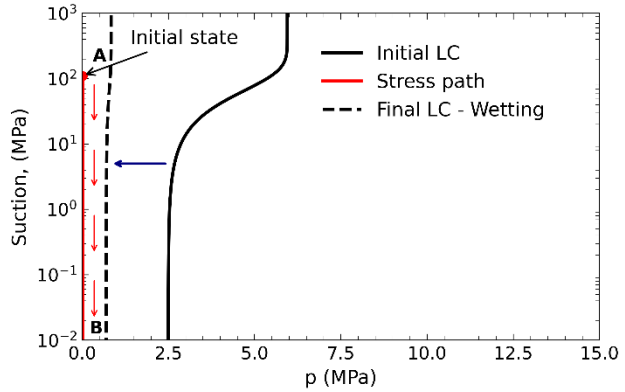

Figure 4. Schematic representation of Path 1. Wetting at constant confining pressure (in the p:s_M plane).

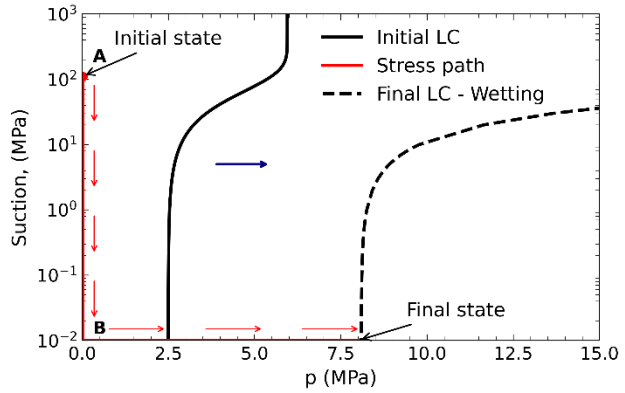

Figure 5. Schematic representation of Path 1. Subsequent load after wetting (in the p:s_M plane).

5.2 Analysis of stress path 2

For the isochoric test, since the modelling of these stress paths is merely constitutive, the value of the macro-structural liquid pressure is prescribed at all nodes of the FE mesh. Null displacements were prescribed at all nodes of the mesh to reproduce the test under costant volume conditions. The initial location of the LC curve is presented along with the different positions of the LC yield curve during the performance of the test (Figure 6). Initially, the stress increases due to the development of swelling pressure. Once the LC yield surface is reached, the vertical stress drops to compensate for the tendency of the macrostructure to collapse so that the sample length is maintained constant. It can be seen that during the wetting stage (A-B') the LC curve moves slightly to the right in response to macro-structural hardening. In the final stage (B'-D), the reduction of pores can be observed; it is related to the progressive increase of vertical stress (Figure 7). Comparing the numerical predictions with the experimental results in path 2, a good agreement is obtained.

Figure 8 shows the comparison between model and experimental results for paths 1 and 2. As can be seen, the agreement with experimental data is reasonably satisfactory although some departures from observations can be noted. Specifically, the following features have been correctly reproduced: large swelling strains upon wetting under low applied stresses, a clearly defined yield point when loading after wetting, stress path dependency comparing the swelling pressure test and the swell-load test (although the void ratio difference is overestimated by the model) and a realistic value of swelling pressure. In contrast, the convergence of the loading compression lines is not captured by the model.

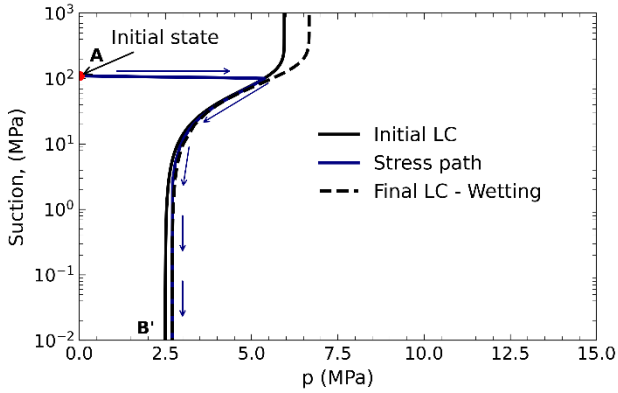

Figure 6. Schematic representation of Path 2. Wetting at constant volume conditions (in the p:s_M plane).

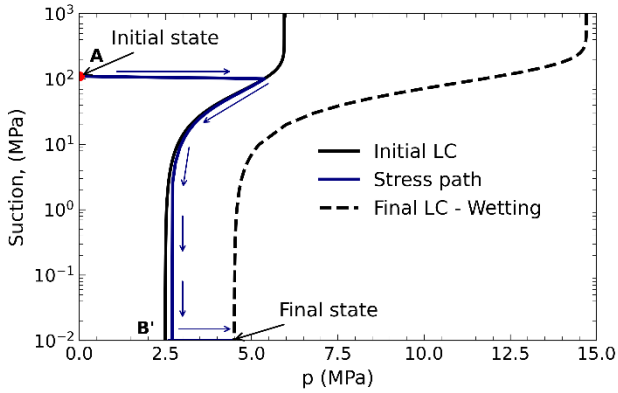

Figure 7. Schematic representation of Path 2. Subsequent load after wetting (in the p:s_M plane).

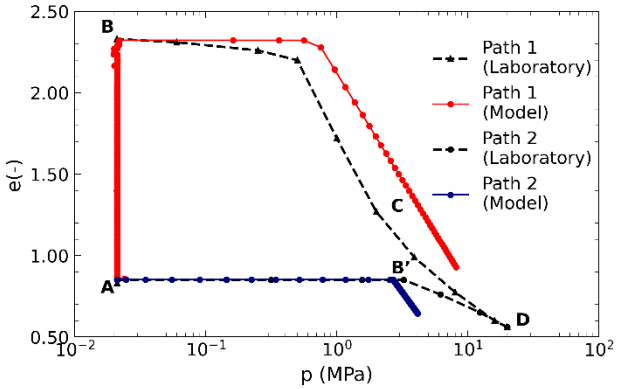

Figure 8. Laboratory and modelling path results.

6 CONCLUSIONS

The capabilities of the double-porosity model to reproduce the swelling response of expansive materials under hydration conditions have been evaluated through the performance of constitutive problem analyses. The overall variation of the void ratio along the two stress paths has been satisfactorily reproduced by the constitutive model, however, the convergence of the compression lines is not captured.

ACKNOWLEDGEMENTS

The work presented has been developed in the frame-work of the Bentonite Mechanical Evolution Project (BEACON). The project receives funding from the Euratom research and training programme 2014-2018 under grant agreement No 745942. The support of Conacyt (Id. no. 710153) to the first author is also gratefully acknowledged.

REFERENCES

Alonso, E.E., Gens, A., Josa, A., (1990). A constitutive model for partially saturated soils. *Géotechnique*, 40, pp. 405–430. https://doi.org/10.1680/geot.1990.40.3.405.

Alonso, E.E., Vaunat, J., Gens, A., (1999). Modelling the mechanical behaviour of expansive clays. *Engineering Geology,* 54, pp. 173-183. https://doi.org/10.1016/S0013-7952(99)00079-4.

Alonso, E.E. and Navarro, V., (2005). Microstructural model for delayed deformation of clay: loading history effects, *Canadian Geotechnical Journal*, 42, pp. 381-392. https://doi.org/10.1139/t04-097.

Ferrari, A., Bosch, J.A., Baryla, P., Rosone, M., (2022). Volume change response and fabric evolution of granular MX80 bentonite along different hydro-mechanical stress paths, *Acta Geotechnica*, 17, pp. 3719-3730. https://doi.org/10.1007/s11440-022-01481-0.

Gens, A., Alonso, E.E., (1992). A framework for the behaviour of unsaturated expansive clays. *Canadian Geotechnical Journal,* 29, pp. 1013-1032. https://doi.org/10.1139/t92-120.

Gens, A., Valleján, B., Sánchez, M., Imbert, C., Villar, M.V. and Van Geet, M., (2011). Hydromechanical behaviour of a heterogeneous compacted soil : experimental observations and modelling, *Géotechnique*, (5), pp. 367–386. https://doi.org/10.1680/geot.SIP11.P.015.

Olivella, S., Gens, A., Carrera, J. & Alonso, E.E., (1996). Numerical formulation for a simulator (CODE_BRIGHT) for the coupled analysis of saline media, *Engineering Computations*, 13 (7), pp. 87-112. https://doi.org/10.1108/02644409610151575.

Ruiz, D., (2020). *Hydro-mechanical analysis of expansive clays constitutive and numerical modelling*. PhD Thesis, Technical University of Catalonia (UPC). Available at: https://upcommons.upc.edu/handle/2117/192447.

Sánchez, M., (2004). *Thermo-hydro-mechanical coupled analysis in low permeability media*. PhD Thesis, Technical University of Catalonia (UPC). Available at: https://upcommons.upc.edu/handle/2117/107703.

Sánchez, M., Gens, A., Guimarães , L. do N., Olivella, S., (2005). A double structure generalized plasticity model for expansive materials. *International Journal for Numerical and Analytical Methods in Geomechanics*. 29, 751-787. https://doi.org/10.1002/nag.434.

Seiphoori, A., Ferrari, A. and Laloui, L., (2014). Water retention behaviour and microstructural evolution of MX-80 bentonite during wetting and drying cycles. *Géotechnique*, 64(9), pp.721-734. http://dx.doi.org/10.1680/geot.14.P.017.

Seiphoori, A., (2015). Thermo-hydro-mechanical characterisation and modelling of Wyoming granular bentonite. NAGRA, Switzerland, Technical Report 15-05.

Vasconcelos, R., (2021). *A double-porosity formulation for the THM behaviour of bentonite-based materials*, PhD Thesis, Technical University of Catalonia (UPC). Available at: https://upcommons.upc.edu/handle/2117/349570.

Proceedings of the XVIII ECSMGE 2024
GEOTECHNICAL ENGINEERING CHALLENGES
TO MEET CURRENT AND EMERGING NEEDS OF SOCIETY
© 2024 the Authors
ISBN 978-1-032-54816-6
DOI 10.1201/9781003431749-131
Open Access: www.taylorfrancis.com, CC BY-NC-ND 4.0 license

ECSMGE 24
XVIII EUROPEAN CONFERENCE ON SOIL MECHANICS AND GEOTECHNICAL ENGINEERING

Bi-directional testing of bored piles in chalk

Essais bidirectionnels de pieux forés dans la craie

M. Roed*, J.S. Steenfelt, O. Hededal
COWI A/S, Kongens Lyngby, Denmark

**mcro@cowi.com*

ABSTRACT: Large diameter bored piles (Ø1800 mm) will be used as foundation for a new railway bridge crossing Guldborgsund between the Danish islands of Falster and Lolland. The ground conditions at site are dominated by 10-15 m of glacial and late- postglacial deposits above relatively soft Cretaceous chalk. The experience with bored piles in chalk in Denmark is limited and a conservative design approach would have to be used due to lack of testing. Therefore, two full-scale, instrumented piles (26m and 31m long) were constructed and tested using bi-directional loading by means of O-cell technology. The piles were instrumented with tell-tales and strain gauges to allow for determination of the mobilized unit shaft resistance as function of depth and soil type. The piles were loaded to 22.5 MN and 30 MN, respectively, which significantly exceeded the capacity predicted by normal design methods. Based on calibration of an α-method for shaft resistance versus local CPT profiles, it was possible to establish a site-specific design model allowing for optimization of the production piles.

RÉSUMÉ: Les pieux forés de grand diamètre (Ø1800 mm) seront utilisés comme fondation pour un nouveau pont ferroviaire traversant le Guldborgsund entre les îles danoises de Falster et Lolland. Les conditions du sol sur le site sont dominées par 10 à 15 mètres de dépôts glaciaires et tardifs/post-glaciaires au-dessus de la craie crétacée relativement tendre. L'expérience avec les pieux forés dans la craie au Danemark est limitée, et une approche de conception conservatrice devra être utilisée en l'absence d'essais. Par conséquent, deux pieux à pleine échelle instrumentés (26 m et 31 m de long) ont été construits et testés en utilisant une charge bidirectionnelle grâce à la technologie O-cell. Les pieux étaient équipés de “tell-tales” et de jauges de contrainte pour permettre la détermination de la résistance à la traction unitaire mobilisée en fonction de la profondeur et du type de sol. Les pieux ont été chargés à 22,5 MN et 30 MN respectivement, dépassant significativement la capacité prédite par les méthodes de conception normales. En se basant sur l'étalonnage d'une méthode α pour la résistance à la traction du fût par rapport aux profils locaux CPT, il a donc été possible d'établir un modèle de conception spécifique au site permettant l'optimisation des pieux de production.

Keywords: Bored piles; Pile loading test; chalk, CPT based methods.

1 INTRODUCTION

In connection with the construction of the Fehmarnbelt tunnel connecting Denmark and Germany from 2029, the railway between Copenhagen and the tunnel are currently being upgraded to meet European interoperability standards. For parts of railway with only a single track, a second track is to be constructed. This also requires construction of a new bridge to carry the extra track across the strait of Guldborgsund between the islands of Falster and Lolland.

The bridge will be constructed next to the existing Kong Frederik IX's bridge (E3006 project) carrying a single railway track. The new bridge will be built as a bascule bridge similar to the existing bridge. The bridge will be founded on Ø1800 mm bored piles, two at each pier location. The bored piles will be installed into Cretaceous chalk formation and equipped with flat-jacks to ensure immediate activation of both toe and shaft resistance.

Danish experience with bored piles in un-indurated chalk is limited. The Danish Annex to Eurocode 7, Dansk Standard (2021), sets strict limits on the shaft and toe resistance without testing. This leads to significantly lower design resistance than found e.g. using the recommendations from CIRIA (1999). To optimize the pile design, it was therefore chosen to test two full scale piles by means of bi-directional loading tests to establish a site-specific design model that could be used to optimize the production piles.

2 TEST SETUP

2.1 Bi-directional loading test

The loading tests on bored piles at the E3006 project are carried out as bi-directional loading test using Osterberg cells (O-cells). The O-cell is a hydraulic jack that is installed inside the reinforcement case of

the bored pile. During a loading test, the pile is loaded by expanding the O-cell inside the pile. The O-cell is cast into the pile and the pile itself acts as a reaction system, see Figure 1.

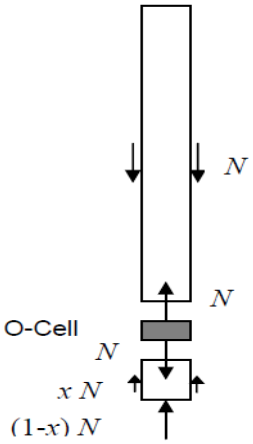

Figure 1. Principle of bi-directional test.

Using strain gauges and tell-tales at different levels of the pile, it is possible to derive the shaft resistance above the O-cell and the end-bearing and shaft resistance below the O-cell from the bi-directional loading test. Ideally, the O-cell should be placed at the location where the resistance above the O-cell is equal to the resistance below.

For this project two test piles were constructed; Test Pile 1 (TP1) and Test Pile 2 (TP2) with a length of 31 m and 26 m, respectively. The O-cells were placed 4 m above the toe of TP1 and 1 m above the toe of TP2. The position of the O-cell means that the piles are in principle loaded from the bottom and the chalk layers will therefore be activated before the glacial deposits. In this project focus was on evaluating the strength of the chalk.

2.2 Flat-jack preload system

The flat-jack system is installed at the bottom of the reinforcement case, as shown on Figure 2. The flat-jack system is used to preload the pile by introducing base grouting over a controlled area at the toe level of the pile after casting to establish full contact and prestressing at the pile toe.



Figure 2. Flat-jack system used for the E3006 project.

The installation of the flat-jack system allows for a degree of mobilization of the end-bearing resistance without any notable deformation and for prestressing of the shaft resistance. If the flat-jack is loaded to or above the SLS load, the settlement of the pile at SLS loads will be limited.

The activation of the flat-jack is in principle a primitive bi-directional loading test on a working pile giving a check of the pile installation and adding robustness to the design.

The flat-jacks are prestressed to 3 MN and 2 MN for TP1 and TP2, respectively. The diameter of the flat-jacks are 1650 mm with a maximum inflation height of 70 mm.

2.3 Site conditions

The soil strata at the test site (on land close to the bridge site) is evaluated based on one borehole and one CPT. Fill is found to 5 m below ground level, followed by glacial deposits down to 11 m below ground level. Below the glacial deposit, a glacially disturbed chalk layer (K2) is encountered to 21 m below ground level, after which competent chalk (K3) is found to large depth.

For both test piles, the piles were instrumented with six levels of strain gauges (SG) and 4 level of tell-tales. The instrumentation of TP1 is shown schematically in Figure 3.

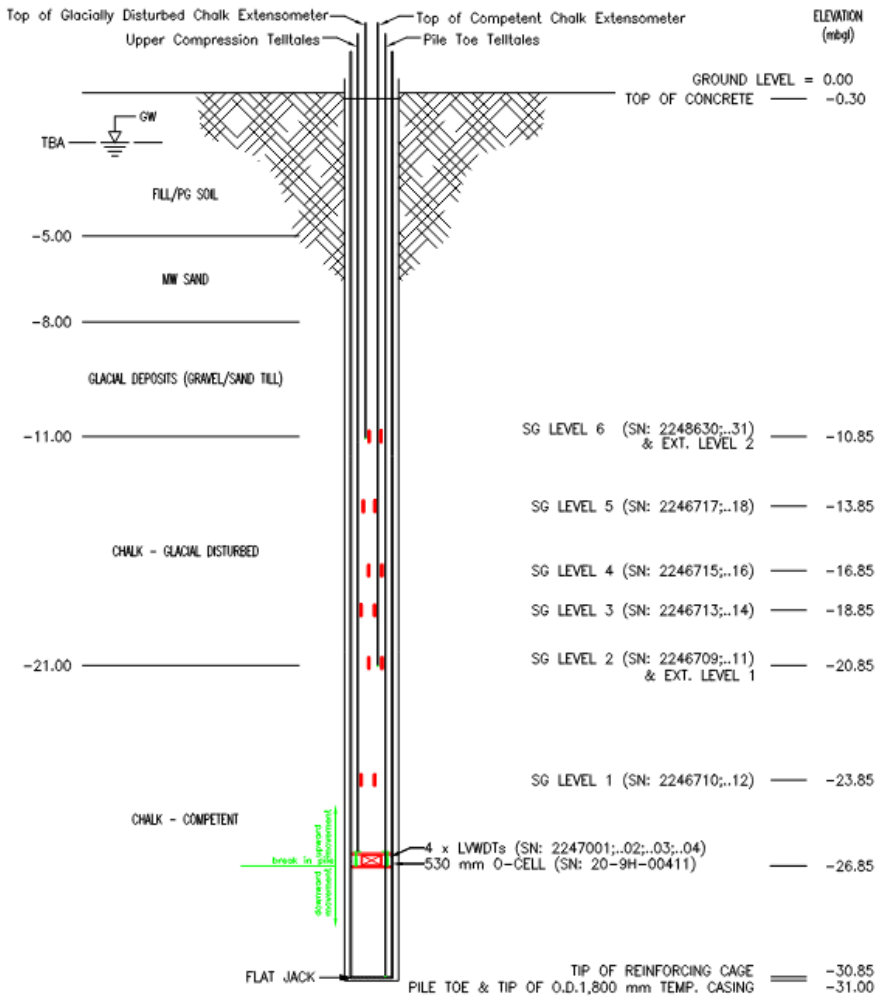

Figure 3. Instrumentation of TP1 together with approximate soil profile

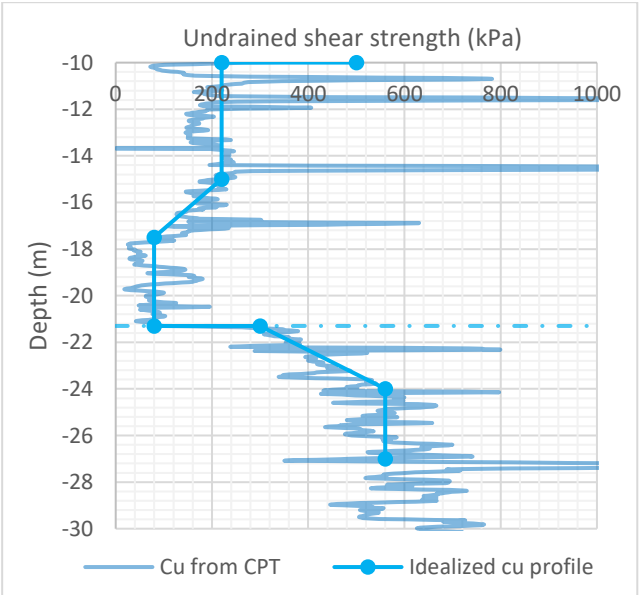

Figure 4. Undrained shear strength profile based on CPT for the test site (in the chalk layers).

From the CPT investigation a c_u – profile for the test site can be evaluated based on the corrected cone resistance (q_t) and the vertical stress (σ_{v0}). The c_u – profile is used for developing the design model for bored piles in chalk. The c_u parameter can be evaluated using the following method:

$$c_u = \frac{q_t - \sigma_{v0}}{N_{kt}} \quad (1)$$

A cone factor of $N_{kt} = 20$ has been derived for the chalk (both K2 and K3) based on laboratory tests. The derived c_u – profile is shown in Figure 4.

2.4 Loading schedule

The loading schedule consisted of two load cycles:

In the first load cycle, the O-cell was loaded to 6 MN in four (4) steps of 1.5 MN with a holding time in each step of 50 minutes or until the rate of creep (measured as expansion of the O-cell) was less than 2 mm/log cycle of time. The pile was then unloaded in three (3) steps to 4.5 MN, 3 MN and 0 MN.

The second load cycle aimed to load the pile to failure in maximum 12 steps (of 1.5 MN) with a holding time in each step of 60 minutes or until the rate of creep (measured as expansion of the O-cell) was less than 2 mm/log cycle of time. Finally, unloading was done in six (6) steps of 3MN.

In the tests, failure was assumed to be reached either if the measured pile head movement exceeds 20 mm (maximum shaft resistance reached) or if the rate of O-cell expansion exceeds 10 mm/lct after 50 min sustained loading.

3 TEST RESULTS

3.1 Load-displacement behaviour

The pile head and toe displacement for both test piles are shown in Figure 5.

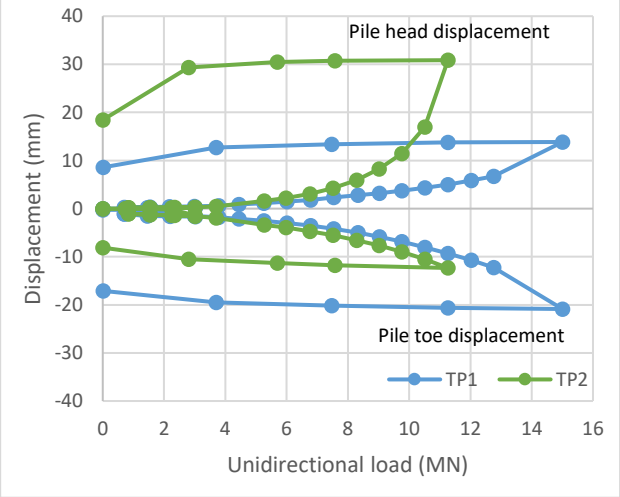

Figure 5. Pile head and toe displacement for all loading – unloading steps for both TP1 and TP2.

Figure 5 shows that the measured pile head displacement exceeded 20 mm for unidirectional load 11.3 MN for TP2, while the measured pile head movement is below 20 mm for unidirectional load of 15 MN for TP1. This means that TP2 is in failure. This is also confirmed by the creep rates of the O-cell expansion for the final loading step for both test piles, see Figure 6. For TP1, the creep rate at a unidirectional load of 15 MN was 2.8 mm/lct, which is below the failure criterion. For TP2, the creep rate at a unidirectional load of 11.3 MN was 15.2 mm/lct, which is above the defined failure criterion.

Note that even though the failure criterion is met for TP2, the pile is not in ultimate failure. While the shaft resistance is fully mobilized, the working curve for the tip resistance does not show any indication of imminent end bearing failure.

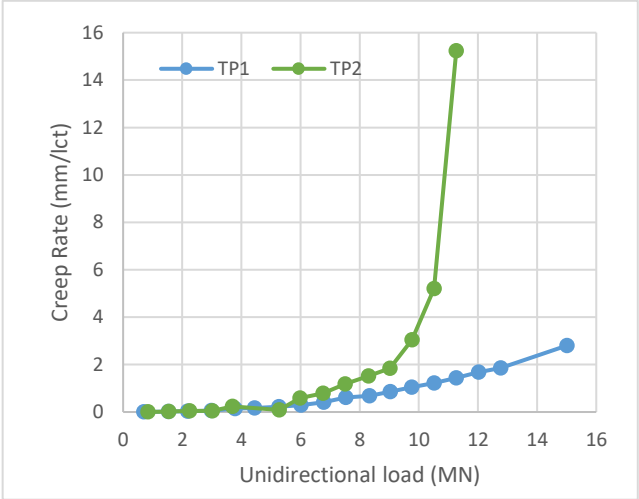

Figure 6. Development of creep rates for increasing unidirectional load

3.2 Flat-jacks

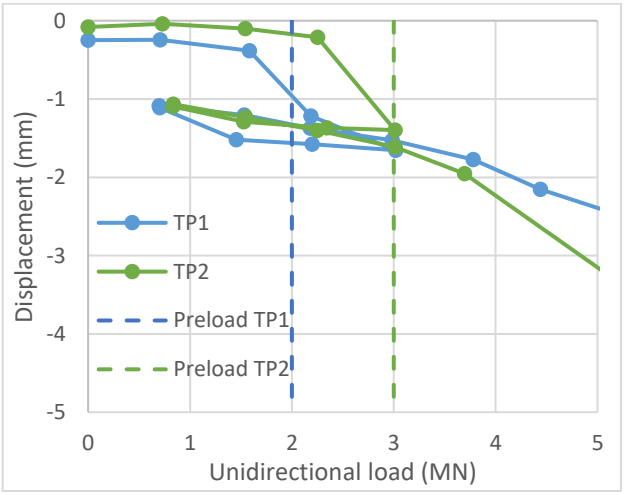

Figure 7. Pile toe displacement for prestress range of the flat-jack.

Flat-jacks are used to ensure that there is full contact between the toe of the bored pile and the chalk below. In the tests, the flat-jacks for TP1 and TP2 were preloaded to 2 MN and 3 MN, respectively. The preload not only secures a stiff initial response, but also preconsolidates the chalk – indicated by the shift of the pile toe displacement when the preload is exceeded as seen in Figure 7. Preloading flat-jacks to or above the maximum service load on the bored piles may therefore in practice eliminate future SLS pile movements.

4 INTERPRETATION

For both piles, six levels of strain gauges have been installed above the O-cell. From the strain gauges, the

mobilized shaft resistance of the part of the pile above the O-cell can be assessed.

The assessment of the mobilized shaft resistance and end-bearing (toe) resistance below the O-cell carries some uncertainty. The toe resistance can only be deduced by assuming a constant shaft resistance below the O-cell (as no strain gauge measurement are available). Here, the shaft resistance is assumed constant below the O-cell level and subtracted from the downward O-cell load to provide the toe resistance.

The load transfer along the piles from the O-cell to the top of chalk are shown in Figure 8. The load transfer is found based on interpretation of the strain gauge measurements.

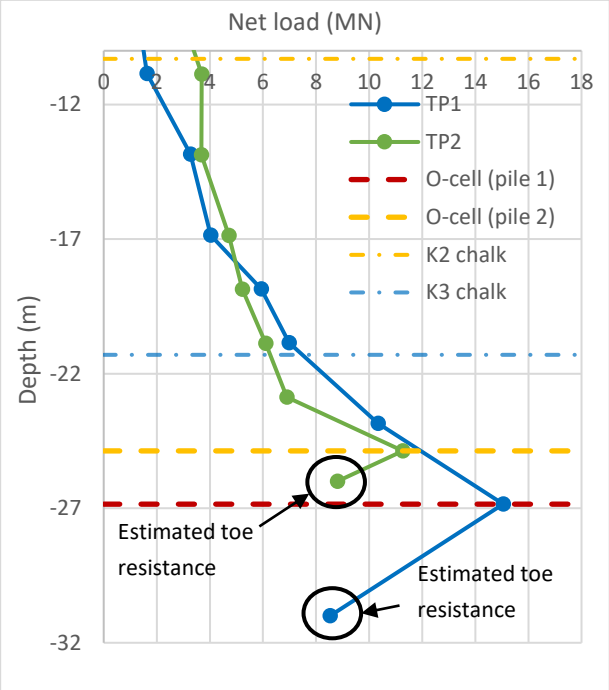

Figure 8. Load transfer head to toe based on strain gauge measurements and O-cell load for the last loading step.

The unit skin friction can then be derived along the pile from the load transfer results, see Figure 9. From the analysis of the strain gauge on TP2, it was found that the results of strain gauge level 6 were unreliable and therefore disregarded in the analysis of shaft resistance.

4.1 Shaft resistance

The shaft resistance of the piles was evaluated using the α-method. The α-values in the chalk were evaluated based on the load transfer along the pile shown on Figure 8. The α-values for both test piles are derived based on the average shaft resistance in K2 and K3 versus the average c_u value for each layer. The average c_u values are found from the idealized c_u-profile shown in Figure 4.

The derived α-values for TP1 and TP1 are given in Table 1 and Table 2, respectively.

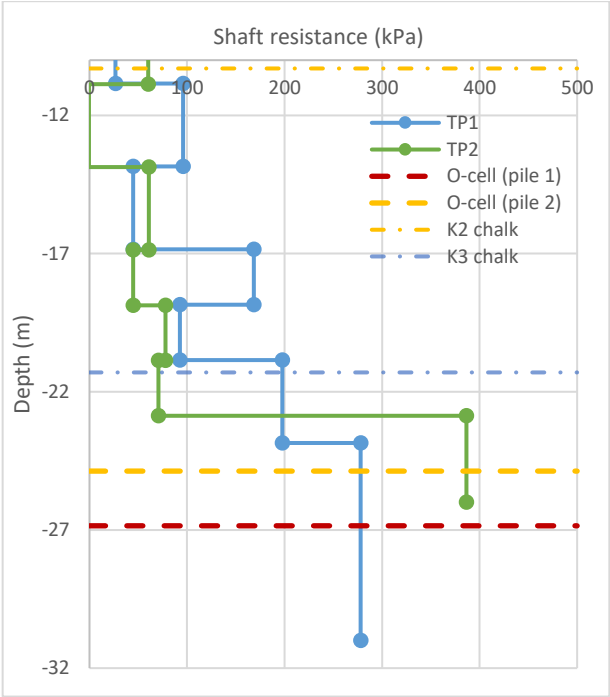

Figure 9. Unit shaft resistance along the shaft.

Table 1. α-values for test pile 1.

Soil unit	Average shaft resistance (kPa)	Average c_u (kPa)	a-value (-)
K2	99.01	151.36	0.65
K3	241.11	508.47	0.47

Table 2. α-values for test pile 2.

Soil unit	Average shaft resistance (kPa)	Average c_u (kPa)	a-value (-)
K2*	61.59	124.85	0.49
K3	247.64	461.68	0.54

*Strain gauge level 6 gives unreliable results and not included in the analysis

Figure 10 shows the load distribution along both TP1 and TP2 together with the estimated load distribution based on calculated shaft resistance using the α-values for K2 and K3 chalk given in Table 1 and Table 2. In Figure 10, an estimated load distribution using a constant α-value of 0.55 for both K2 and K3 chalk is also shown. The calculated load distributions are found using the load at O-cell level, distributing the load upwards along the pile.

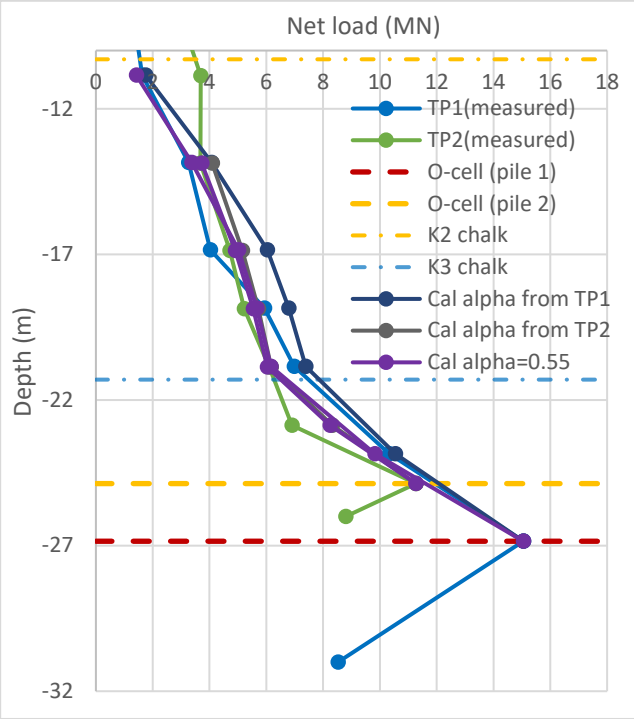

Figure 10. Model prediction against measured net load distribution from pile loading test on both test piles.

The back-calculated load distribution using an α-value of 0.55 for both K2 and K3 chalk gives a conservative solution compared to the measured load distribution. An α-value of 0.55 is adopted for the design of the bored piles in chalk.

4.2 Toe resistance

The toe resistance of 8.5 – 8.8 MN corresponds to a mobilized contact pressure of approximately 3340 – 3458 kPa. Based on the CPT profile, it is assessed that $c_u \approx 560$ kPa around the toe of the piles. Back-calculating from the estimated toe resistance, the end-bearing factor (N_{cu}) is found to vary between 6.7 and 6.9 for the two test piles. This end-bearing factor is below the commonly used value of 9 for fine-grained materials, indicating – as also observed from the load-displacement curves for the pile toe – that the toe resistance is not fully mobilized. In the design model, it is chosen to use a maximum bearing pressure of $q_{bk} = N_{cu} c_{uk} = 6\, c_{uk} \leq 2670$ kPa (model factor $\xi = 1.25$), where the cap is cautiously chosen as the maximum applied bearing pressure in the tests.

5 CONCLUSIONS

The load test performed on two bored piles at the E3006 project showed that the overall shaft resistance in the chalk is considerably higher than estimated based on common Danish Practice (as low as 25 kPa).

For the design of bored piles in chalk on the E3006 project an α-value of 0.55 is found to provide a reasonable fit for both K2 and K3 soil compared to the test piles.

Based on the two available pile loading test, the design methodology for the E3006 project was to take the full shaft resistance and a characteristic toe resistance of 2670 kPa into account, in contrast to 30% shaft resistance of an equivalent driven pile and maximum toe resistance of 1000 kPa specified in the Danish Annex to Eurocode 7, Dansk Standard (2021).

ACKNOWLEDGEMENTS

The authors are grateful to MT Højgaard for performing the bi-directional loading test and for granting permission to use the data from the pile loading tests.

REFERENCES

CIRIA (1999). *Piled foundation in weak rock.* CIRIA 181, Ed. Gannon, Masteron, Muir Wood & Wallace, London.

Danish Standard (2021) DS/EN 1997-1 DK NA:2021. *National annex to Eurocode 7: Geotechnical design – Part 1: General rules.*

Proceedings of the XVIII ECSMGE 2024
GEOTECHNICAL ENGINEERING CHALLENGES
TO MEET CURRENT AND EMERGING NEEDS OF SOCIETY
© 2024 the Authors
ISBN 978-1-032-54816-6
DOI 10.1201/9781003431749-132
Open Access: www.taylorfrancis.com, CC BY-NC-ND 4.0 license

ECSMGE 24
XVIII EUROPEAN CONFERENCE ON SOIL MECHANICS AND GEOTECHNICAL ENGINEERING

Monitoring pile construction impact near sheet pile quay walls: Some remarks

Auscultation de l'impact de la construction de pieux près des murs de quai en palplanches: Quelques remarques

P. Ruggeri*, M. Senigagliesi, P. Alesiani, V.M.E. Fruzzetti
Università Politecnica delle Marche, Ancona, Italy

p.ruggeri@staff.univpm.it

ABSTRACT: During structural renovation of sheet pile quay walls, monitoring is an essential tool to anticipate possible failure events. When monitoring displacements, the objective is to compare measured with expected values to detect possible reduction of the safety margin. This study presents findings from monitoring activities during execution of piles near an old sheet pile quay wall in the Port of Ravenna. Collected data include geodetic measurements of displacements of the top beam, an inclinometer profile and elongations from strain gages fixed on a horizontal anchor. The study highlights the influence of constructing a pile near the monitored quay wall; the possibility of predicting such effect by referring to analytical solutions and 3D finite element analysis is explored to provide a tool to anticipate anomalous behaviour of the structure and to minimize risk of brittle failures.

RÉSUMÉ: Cette étude présente les données d'auscultation pendant l'exécution de pieux à proximité d'un ancien quai portuaire en palplanches dans le port de Ravenna. L'objectif est de comparer les valeurs mesurées aux valeurs attendues afin de détecter une éventuelle réduction du facteur de sécurité. Les données d'auscultation comprennent des mesures topographiques des déplacements de la poutre supérieure, des mesures inclinométriques des déplacements horizontaux en profondeur ainsi que des déformations le long d'un tirant d'ancrage équipé de jauges de contrainte. L'influence de la réalisation des pieux a été mise en évidence et une rétro-analyse détaillée a permis d'explorer la possibilité de prédire les impacts des travaux sur la base de solutions analytiques ainsi qu'en exploitant les résultats de modèles 3D aux éléments finis.

Keywords: Sheet pile quay walls; monitoring; displacement; failure risk.

1 INTRODUCTION

Carrying out renovation works on old port quay walls is never an easy task, which is why careful monitoring during the execution of the site activity is essential to detect signs of structural distress and anticipate failure events. This is especially true when considering that normal site operations are often able to impact on existing structures, particularly when the structure is old and the soil soft. In addition, when the monitoring system is accurate, some effects are always detected. Consequently, the site engineers are charged to assess if the observed effects are a tolerable consequence of the ongoing operations or a warning sign of an impending failure.

In the outlined context this paper examines the monitoring data collected during the execution of medium diameter displacement piles behind an existing anchored quay wall, that are part of retrofitting works in an Italian major port. The installation of the piles caused a small displacement of the top wall beam which was clearly detected by the accurate monitoring systems even without any sign upon visual observation. This situation called the attention of the site engineer because it was not easy to assess with certainty the relevance of the observations. Also, as often, the project only provided the indication of a tolerable displacement based on general assessment of the entire work without offering any prediction of expected effects related to a single site activity.

Pile installation effect is a well-documented issue, even though not many experiences are available in the literature for piles near retaining walls. From a theoretical perspective, the theme is classically analysed referring to the cavity expansion theory, in which soil displacement is assumed to be caused by an expanding cylindrical cavity without considering soil movements at and below the pile toe. Randolph et al. (1979), by using radiographic techniques, investigated the deformation pattern around a pile driven into clay obtaining fundamental results in understanding the

disturbance effect caused by pile penetration. Massarsch and Wersall (2013), based on model test and numerical analysis, proposed a method to estimate the cumulative lateral soil displacements caused by the installation of a pile group in soft clay. Regarding case studies, Vytiniotis et al. (2018) showed the relevant lateral movements of a pile-supported retaining wall caused by nearby pile driving in a clay soil, with not negligible effects produced from pile driven even at distances greater than 50 times the pile diameter.

After a brief description of the considered case study, the paper compares the observed effects with the expected ones on the bases of the analytical solutions of the problem provided in the literature for ideal scenarios. Also, a 3D finite element model was implemented to evaluate the potential of a numerical analysis on the estimation of the pile installation effect near the quay wall of interest.

2 THE CASE STUDY

The operative quay of interest is located in the port channel of Ravenna, a major Italian harbour on the Adriatic Sea, northern Italy, along the coast of the river Po Plain. The quay is a combined HZ/AZ steel sheet pile wall, constrained at the top by horizontal strands to an anchor plate, 40 m away from the wall. The work, completed in the 2000, was designed for a seabed of 11.5 m below m.s.l., by considering an operative surcharge of 60 kPa and a bitt force of 500 kN every 25 m. Each anchor is made up of 16 strands (0.6S″) every 4 m. The quay, that has a length of about 250 m, is divided in 5 segments by expansion joints on the top beam.

In the context of a general upgrading works of the port infrastructure of Ravenna (see also Ruggeri et al., 2021), the seabed had to be deepened to -14.50 m above sea level. To fulfil this target, a strengthening intervention was designed by considering the structural deficiencies of the current quay as well as its relatively robustness and young age.

2.1 Intervention of upgrading

The adopted solution for strengthening the work has focused on reducing the horizontal soil pressure by creating a series of piles in the active wedge capable of transferring large part of the operational surcharge to the deep soil layers. This type of intervention is part of the strategies outlined in Ruggeri et al (2019) for quay walls.

In the considered case, the treatment involved the construction of 4 lines of piles, spaced 4.00 m × 3.20 m, 600 mm diameter, 29 m long. To limit the cost of disposing excavated soil, screw displacement piles (SDP) were chosen (Krasiński, 2014). To improve the efficiency of the load transfer, a pile cap is built on each pile and a geogrid is adopted to complete the system. The plain view and the cross-section of the central segment of the quay is represented in Figure 1a-c. Here, both the existing structure and the new piles are represented. Note that only the new piles are represented in the cross section, because subsequent activities are of no interest in this context.

2.2 Geotechnical situation

The geotechnical situation of the area is characterised by the presence of a thick deposit of recently sedimented soils characterized by poor geotechnical properties. As shown in the cross section of Figure 1c, under an anthropic landfill, we find a layer of Soft Clay belonging to the old coastal marsh, followed by the Silty Sand of the ancient beach. Then, we find a thick layer of normally consolidated Clayey Silt, sedimented in a marine environment, of very poor geotechnical properties. Under this deposit we have a little stratum of Silty Sand that identifies the passage to the older deposit of continental origin. Here, at 26 m below m.s.l., the mechanical properties of the soil increase, both due to the different geologic history and the greater lithostatic level of stress.

2.3 Monitoring data and site observations

To limit the relevance of some confounding effects, we focused on the central sector of the quay wall. The response of the existing structure was monitored by specific instruments installed before the start of the activities. As shown in Figure 1, in the middle of the segment, just behind the top beam, a 38 m deep inclinometer tube was installed. Two topographic targets were placed on two bitts of the top beam, at 1/3 and 2/3 of the segment length. Also, a couple of strain gages were joined to two strands of a horizontal anchor, near the inclinometer tube. These sensors made it possible to estimate the initial load acting on the anchor by carrying out a specific test as well as to measure the evolution of the tensile load with time.

The installation of the displacement piles in the segment of interest took place between 12th and 27th of July 2022.

The zero reading of the inclinometer was made on 1-07-2022. Then, two readings are available, on 8-08-2022 and 14-10-2022. It means that all the piles were in place at the time of the second readings. Looking at the cumulative displacement of the inclinometer (Figure 1e), it is possible to recognize a maximum displacement of 10 mm at 10 m b.m.s.l., that reduces to 7 mm at the top and extends up to 25 m b.m.s.l.,

where the effects become negligible. The reading on 14-10-2022 exhibits the same shape of the first one but with an increase of the max displacement up to 15 mm and 12 mm at the top. Now, some effect appeared up to 30 m b.m.s.l. The lack of relevant site activity between the two readings may be interpretated as a short- vs long-term effect of the pile installation, respectively.

Topographic survey of the bitts begun on 27-06-2022. Next readings happened on 4thJuly, 11th July, 8th August 2022, then on 8th February and on 8th June 2023. Measurements give displacements between 14 and 17 mm which do not longer evolve after the 8th August 2023.

Strain gages measurements started on 4th July 2022, with two sensors placed on two different strands of the same anchor. Data was recorded daily from 18th to 29th July, then some sporadic reading is available until June 2023. The raw readings give the local deformation of the tendon and can be transformed in the displacement of the top beam by assuming a constant strain for the entire tendon. Doing that, we obtain an elongation of the anchor equal to 12 mm. However, this estimation represents the lower bound of the real displacement because any tensile force increment requires a further mobilization of the soil resistance in front of the plate which adds an amount of displacement that is not quantifiable by sensor readings alone. In this sense, the appearance of two millimetric cracks on the pavement near the plate confirms that the real displacement of the top beam exceeds what is evaluated from the strain gages measurements. The cracks could also explain the displacement recorded by inclinometer and targets that was not detected by the strain gages on the strands.

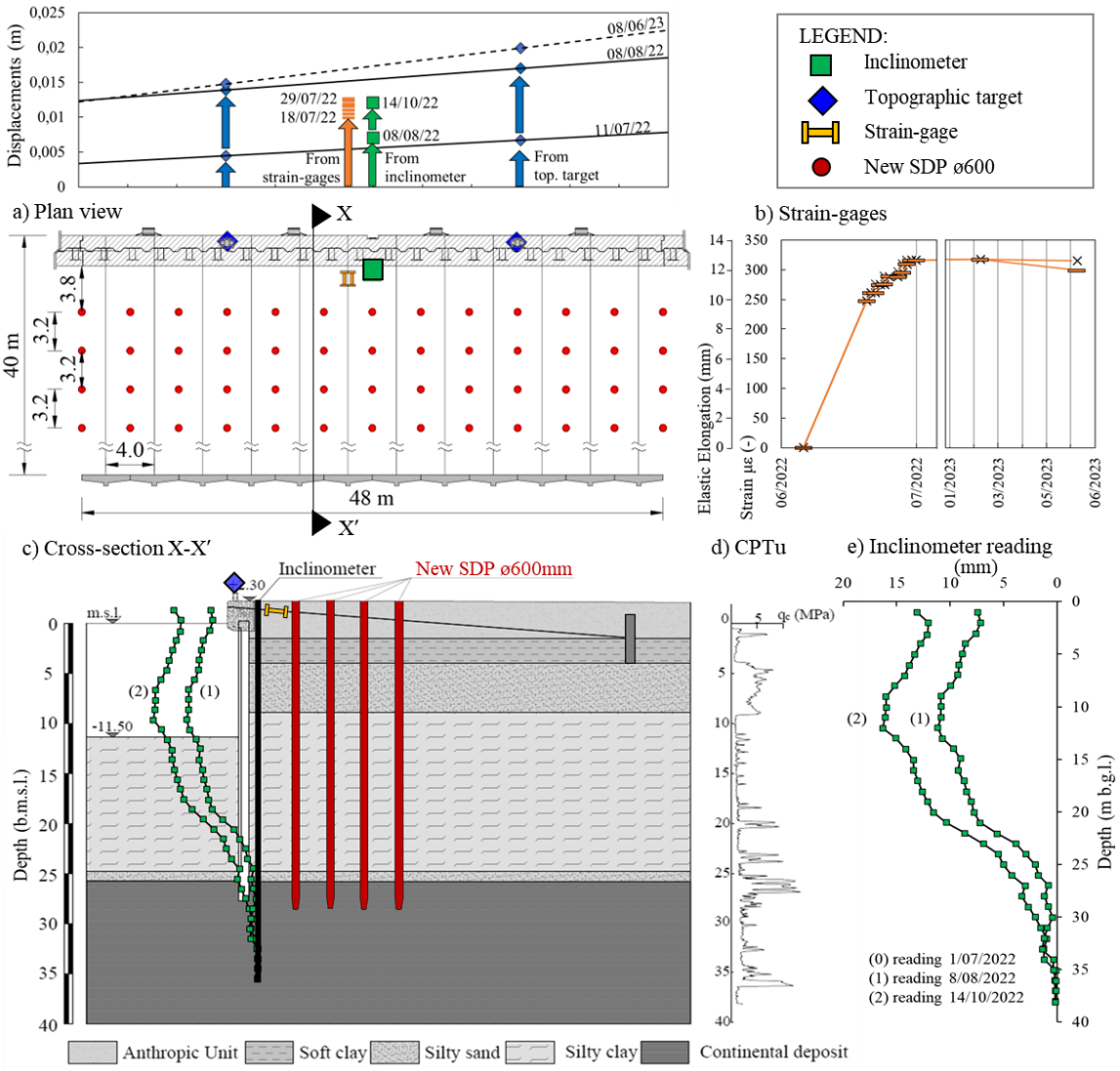

Figure 1. Plan view and cross section of the quay segment of interest with indication of SDP grid and monitoring data.

3 PILE INSTALLATION EFFECT ON THE QUAY WALL

While ground movement caused by the installation of driven pile on horizontal ground was investigated by several Authors, the effect of the pile installation close to a retaining wall does not seem extensively addressed in the literature. Therefore, the first idea is to adopt the superposition of the effects referring to some classical solutions developed for the installation of a single pile on horizontal ground, neglecting the presence of the excavation. Then, the possibility of obtaining a prediction using a 3D numerical analysis will be considered.

3.1 Analytical methods

Closed form solutions for displacement induced by pile installation have been developed under the hypothesis of linear elastic soil behaviour. In 1979, Randolph et al (1979) proposed an equation based on the cavity expansion theory in which only the pile radius (r_0) and the distance (r) affect the lateral displacement (u), as indicated in:

$$\frac{u}{r_0} = \left[\left(\frac{r}{r_0}\right)^2 + 1\right]^{0.5} - \frac{r}{r_0} \qquad (1)$$

More recently, Sagaseta and Whittle (2001) proposed an equation, based on the stress strain path method (SSPM), in which the lateral displacement (u) is function both of pile radius (r_0), distance (r) and pile length (L), in the form reported in:

$$u = \frac{r_0^2}{2}\frac{L}{r\sqrt{r^2+L^2}} \qquad (2)$$

It is worth noting that these two formulations were calibrated for clayey soil under undrained conditions and axial symmetric deformation field.

Equation (1) gives an estimation of the displacement at each depth while Equation (2) provides the displacement at the ground level only. As a first approximation, such value was considered constant with the depth.

The case study under examination does not match exactly all the hypotheses of the presented formulations, especially the undrained behaviour of the soil and the infinite half-space. However, they provide some reference values that can be compared with those observed on site or predicted by using numerical analysis. Also, the presence of multiple piles to be installed in the volume of interest has to be considered. Generally speaking, multiple piles generate an amplification of the effect, as well as the sequence and time interval of installation. In this study, we assumed that: (1) no shield effect due to construction sequence happens and (2) superposition principle can be applied to estimate the total displacement. Note that, according to Massarsch and Wersall (2013), the sequence of construction seems to play a secondary role on the final displacement produced by the pile group installation, so the first assumption appears acceptable.

Furthermore, limiting the distance of influence (i.e. the distance beyond which the installation of a pile has negligible effect on the point of interest) appears necessary. Here, we have considered the following situations (see Figure 2): a) only 1 pile produces effects on the wall; b) only the 4 piles included within 30 radii produce effects on the wall; c) all the piles in the circular sector enclosed between lines inclined ±45° from the orthogonal to the retaining wall and within 50 radii produce effects on the wall. By adopting these hypotheses, the displacement expected on the wall is indicated in Figure 2. It can be noted that the expected displacements are generally greater than those observed. Values similar to the observed ones are obtained if only the closest pile (situation "a") or the 4 closer piles (situation "b") to the quay wall are considered.

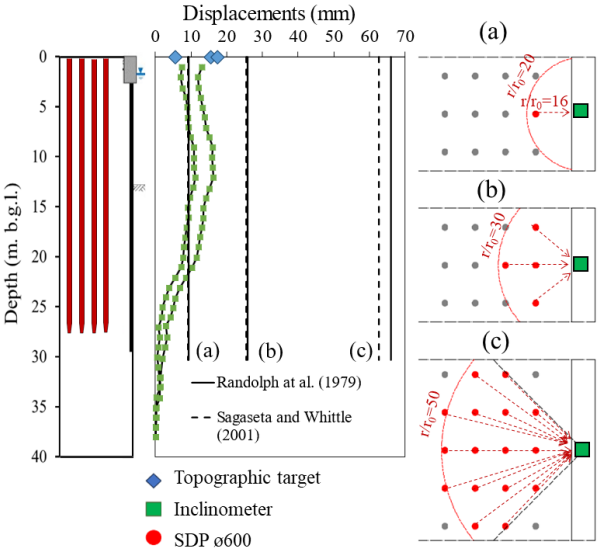

Figure 2. Prediction of displacement due to SDP installation according to analytical methods.

3.2 Preliminary numerical analysis

A 3D numerical model was implemented on the FE code Plaxis 3D to evaluate the pile installation effect on the quay wall. This method has already been applied to serviceability analysis of quay walls at the same site of interest, showing encouraging results (Alesiani et al., 2023).

The symmetry of the problem made it possible to limit the extension of a representative numerical model to a single row of 4 piles (see Figure 3).

Soil was modelled using 10-node tetrahedral elements with a linear elastic (LE) and Linear Elastic Perfectly Plastic Mohr-Coulomb (MC) constitutive relationship; the adopted soil parameters are shown in Table 1.

Table 1. Input parameters for soils.

Soil Unit	**γ** (kN/m³)	**E** (MPa)	**υ** (-)	**φ′** (°)	**c′** (kPa)
Anthropic	18.0	13	0.32	30	-
Soft Clay	18.0	3	0.35	28	-
Silty Sand	19.0	12	0.29	36	-
Clayey Silty	19.0	6	0.32	31	-
Silty Sand	19.0	12	0.30	35	-
Cont. Dep.	19.0	25	0.32	31	20

To model the piles installation in FE code, it is usual to activate a volume and then expand it simulating a cylindrical cavity expansion. Carter et al. (1979) suggest to activate an initial pile whose diameter is $a_0 = 0.577\ r_0$. This means that an expansion from a_0 to $2a_0$ (i.e. 100% expansion) reproduces the real volume displaced by the pile limiting at the 15% the extra-diameter of the modelled pile in its final configuration.

Two soil responses were considered:

1. drained (i.e. drained behaviour for all soils);
2. undrained (i.e. undrained behaviour only for fine-grained soils).

The undrained behaviour of soils were simulated by referring to effective stress parameters with invariability of the soil volume (i.e. so-called undrained A-Type behaviour).

Two models were considered to explore the reliability of the numerical analysis: the first one (Model A) with horizontal ground surface, without excavation or structures (see Figure 3a); the second one (Model B) in which the real situation is included (see Figure 3b). In particular, the measured value of the tensile stress on the anchors before the installation of the piles was reproduced by acting on the prestressing value.

In Figure 3 the results of the numerical modelling, in terms of induced displacements on a vertical section behind the wall, are shown. FE analysis for 100% pile expansion indicates that:

- the magnitude of displacements is in line with that expected from situation "c" of analytical method (i.e. all piles relevant for displacement are considered);
- undrained response produces larger displacements than drained response;
- LE and MC models predict similar displacements, despite the development of the plastic annulus around the piles for MC model;
- the magnitude of displacements ranges from 40 mm (for LE Model A in drained conditions) to 100 mm (for MC Model A in undrained conditions);
- MC-Model A (without structures and excavation) exhibits slightly larger displacements than MC-Model B (with structures and excavation);
- the overall shape of predicted displacements agrees with the observed one;
- all the considered models predict displacements 5-10 times greater than observed; even the predicted strand elongations are much larger than measured.

In Figure 4 the comparison of horizontal displacement field in the mid-section of the FEM model due to pile installation, in drained condition, is shown for the two model.

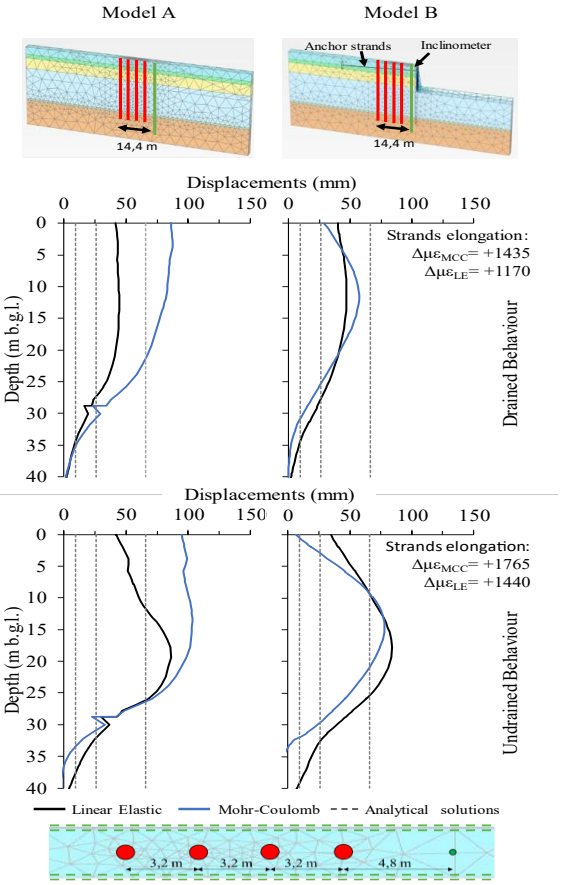

Figure 3. Prediction of displacement due to SDP installations from FEM analysis in drained and undrained condition: Model A) 4 rows of piles on horizontal ground; Model B) 4 rows of piles behind anchored sheet pile wall.

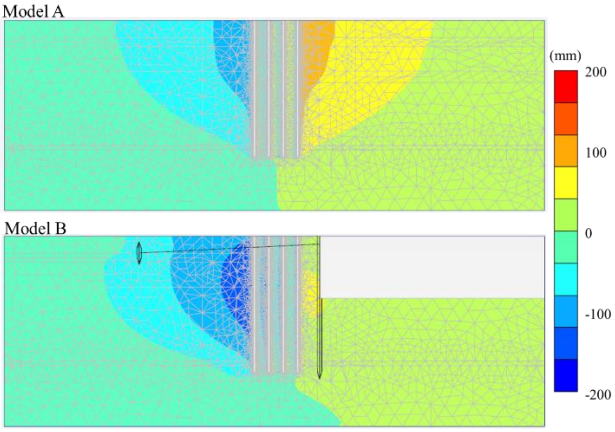

Figure 4. Comparison of horizontal displacement field due to pile installation for Model A and B, drained condition.

4 CONCLUSIONS

In the paper we have presented a case study in which the installation of several Screw Displacement Piles (SDP), medium diameter, near an existing anchored retaining quay wall induced not negligible displacement on the structure.

Being the issue relevant for the evaluation of the safety during the execution of the work, a number of analyses have been carried out to investigate whether the impact of the pile installation can be predicted at the design stage.

The adoption of analytical methods, even though not developed for similar situations, can provide some useful indications. However, the complex evaluation of the distance beyond which the pile installation impact is negligible makes it difficult to adopt such approach in practice.

On the other hands, the adoption of 3D finite element analysis is promising but difficult to implement. First results from 3D FEM analysis, developed by adopting linear elastic and elasto-plastic constitutive models for soils, indicate a general overestimation of the impact of the pile installation on the quay wall. Therefore, further investigations and analyses are underway to explain the mismatching and to reduce the current gap between displacements predicted by FEM analysis and monitoring data.

It is worth noting that the presented case study confirms the relevance of adopting a detailed and targeted monitoring when carrying out infrastructure works, especially considering the difficulties of obtaining accurate predictions in geotechnical situations involving existing structures.

ACKNOWLEDGEMENTS

The authors are grateful to the Autorità di Sistema Portuale del Mare Adriatico centro settentrionale, to the site Supervisor and to the General Contractor for making available the data used in the paper.

REFERENCES

Alesiani, P., Ruggeri, P., Fruzzetti, V. M. E., & Scarpelli, G. (2023). The potential of 3D numerical modelling for the interpretation of load tests on a sheet pile quay wall. Proc. 10th NUMGE. https://doi.org/10.53243/NUMGE2023-5

Carter, J. P., Randolph, M. F., & Wroth, C. P. (1979). Stress and pore pressure changes in clay during and after the expansion of a cylindrical cavity. International Journal for Numerical and Analytical Methods in Geomechanics, 3(4), 305-322. https://doi.org/10.1002/nag.1610030402

Krasiński, A. (2014). Numerical simulation of screw displacement pile interaction with non-cohesive soil. Archives of Civil and Mech. Eng. 14(1): 122-133. https://doi.org/10.1016/j.acme.2013.05.010

Massarsch, K. R., & Wersäll, C. (2013). Cumulative lateral soil displacement due to pile driving in soft clay. In: Sound Geotechnical Research to Practice: Honoring Robert D. Holtz II (pp.462-479).https://doi.org/10.1061/9780784412770.031

Randolph, M.F., Steenfelt, J.S. and Wroth, C.P. (1979). The effect of pile type on design parameters for driven piles. Proceedings VII ECSMFE 1979, Brighton, Design Parameters in Geotechnical Engineering, Vol. 2, pp.107 – 114.

Ruggeri, P., Fruzzetti, V. M. E., & Scarpelli, G. (2019). Renovation of quay walls to meet more demanding requirements: Italian experiences. Coastal Engineering, 147, 25-33. https://doi.org/10.1016/j.coastaleng.2019.01.003

Ruggeri, P., Fruzzetti, V. M. E., & Scarpelli, G. (2021). Upgrading of quay walls at the Ravenna port, Italy: evaluation of the steel piles degradation after a long working life. Structure and Infrastructure Engineering, 17(2), 249-259. https://doi.org/10.1080/15732479.2020.1736101

Sagaseta, C., & Whittle, A. J. (2001). Prediction of ground movements due to pile driving in clay. J. of Geot. Geoenv. Eng., 127(1), 55-66. https://doi.org/10.1061/(ASCE)1090-0241(2001)127:1(55)

Vytiniotis, A., Casey, B., & Sykora, D. W. (2018). Lateral soil movements due to pile driving: a case study in soft clays. In IFCEE 2018 (pp. 113-128).

Proceedings of the XVIII ECSMGE 2024
GEOTECHNICAL ENGINEERING CHALLENGES
TO MEET CURRENT AND EMERGING NEEDS OF SOCIETY
© 2024 the Authors
ISBN 978-1-032-54816-6
DOI 10.1201/9781003431749-133
Open Access: www.taylorfrancis.com, CC BY-NC-ND 4.0 license

ECSMGE 24
XVIII EUROPEAN CONFERENCE ON SOIL MECHANICS AND GEOTECHNICAL ENGINEERING

Applying machine learning to the development of surrogate models for shafts in clay

Application de l'apprentissage automatique au développement de modèles de substitution pour les puits dans l'argile

A. Ruiz López*, D.M.G. Taborda, A. Tsiampousi
Imperial College London, London, UK

A.M.G. Pedro
Universidade de Coimbra, ISISE, ARISE, Coimbra, Portugal

S. Hardy
Ove Arup & Partners, London, UK

**a.ruiz-lopez17@imperial.ac.uk*

ABSTRACT: Surrogate models are machine learning-based models that approximate aspects of interest of a reference numerical model while being considerably faster to run. This feature makes them very attractive for engineering purposes, such as design optimisation and back-analysis. A surrogate model capable of predicting the short-term vertical movements around a shaft excavated in clay is developed in this paper. The surrogate model consists of an artificial neural network (ANN) which is trained with an extensive database generated from a finite element (FE) model considering variations in shaft geometry (diameter and depth). Correspondingly, the ANN is established to predicting the surface and subsurface vertical displacements around the structure for a given shaft geometry. The procedure followed for handling the data inputs as well as optimising the training of the ANN is described. Furthermore, the predictive capabilities of the ANN are thoroughly assessed against the numerically-generated data demonstrating an overall excellent performance. This suggests that the FE model of the shaft can be confidently replaced by the ANN in preliminary design stages.

RÉSUMÉ: Les modèles de substitution sont des modèles basés sur l'apprentissage automatique qui se rapprochent des aspects intéressants d'un modèle numérique de référence tout en étant considérablement plus rapides à exécuter. Cette caractéristique les rend très attrayants à des fins d'ingénierie, telles que l'optimisation de la conception et la rétro-analyse. Un modèle de substitution capable de prédire les mouvements verticaux à court terme autour d'un puits creusé dans l'argile est développé dans cet article. Le modèle de substitution consiste en un réseau neuronal artificiel (RNA) qui est entraîné à l'aide d'une vaste base de données générée à partir d'un modèle d'éléments finis (EF) prenant en compte les variations de la géométrie du puits (diamètre et profondeur). En conséquence, le RNA est réglé pour prédire les déplacements verticaux de surface et de subsurface autour de la structure pour une géométrie du puits donnée. La procédure suivie pour traiter les données d'entrée et optimiser l'entraînement de le RNA est décrite. Les capacités prédictives de le RNA sont minutieusement évaluées par rapport aux données générées numériquement, ce qui démontre une excellente performance globale. Cela suggère que le modèle EF du puits peut être remplacé en toute confiance par le RNA dans les étapes préliminaires de la conception.

Keywords: Shafts; excavations; machine learning; surrogate modelling; artificial intelligence.

1 INTRODUCTION

Surrogate models, or meta-models, present several potential advantages in engineering design due to their fast evaluation, rendering them particularly suitable for back-analysis (Ferrero et al., 2023) or design optimisation. In this paper, a surrogate model is proposed as a pre-design tool for estimating ground movements due to shaft excavation in London Clay. Typically, these are evaluated based on empirical expressions established from limited field data (New and Bowers, 1994) and their performance is often limited to geometries similar to those employed in case histories. This severely limits their applicability to new infrastructure where a range of possible geometries may be considered throughout the various design stages. Alternatively, detailed finite element analyses can be performed, although their accuracy is highly dependent on the material models used and the available information for their effective calibration.

Surrogate models, established based on datasets obtained from detailed finite element modelling offer a third approach, combining the ease of use and fast evaluation of empirical expressions with the physics-based accuracy typical of numerical models. This is of relevance to early design stages where ground characterisation and a detailed construction sequence are generally unavailable and thus simplifications introduced by the use of surrogate models are comparatively less important. This paper presents the procedure followed to establish a surrogate model capable of predicting ground vertical displacements due to shaft excavation in London Clay for a wide range of shaft geometries with an accuracy comparable to that of detailed finite element simulations of this problem.

2 REFERENCE NUMERICAL MODEL

The generation of a surrogate model requires detailed numerical analysis of several variants of a given structure. This can, for example, consist of different soil parameters in the case of using surrogates in the context of back analysis of a well-defined structure (Ferrero et al., 2023). In the present case, the stratigraphy and the material parameters were assumed to be known, while the geometry of the shaft was allowed to vary within pre-defined limits (see Section 3.1). Therefore, PLAXIS 2D's Python API had to be employed in order to generate, calculate and post-process axisymmetric finite element models where the geometry of a typical shaft was defined parametrically in terms of its diameter, D, and depth, H.

An idealisation of the stratigraphy typically encountered in London was assumed, with $2\,m$ of Made Ground ($\gamma = 18\ kN/m^3$, $K_0 = 0.5$, linear elastic stiffness with $E = 10\ MPa, \nu = 0.2$, strength defined by the Mohr-Coulomb failure criterion with $\phi = 30°, c = 0\ kPa$ and non-associated plasticity with $\psi = 0°$), overlying a deep layer of London Clay ($\gamma_{sat} = 20\ kN/m^3$, K_0 varying with depth identical to that used in Sailer et al. (2019)). A hydrostatic initial pore water pressure profile with the groundwater table positioned at the top of London Clay was adopted. The behaviour of the latter was modelled using the IC MAGE M01 model (Taborda et al., 2023b), which combines a non-associated Mohr-Coulomb failure criterion ($\phi = 25°, c = 5\ kPa, \psi = 12.5°$) with cyclic non-linear elasticity to describe the highly non-linear variation of stiffness with stress and strain levels. The parameters adopted for this component of the constitutive model are identical to those proposed in Sailer et al. (2019), and are briefly outlined in Table 1. A value of $p'_{ref} = 100\ kPa$ is assumed throughout. Lastly, the anisotropic permeability of London Clay ($k_h = 2 \cdot k_v$) was described using the following expression, implemented as a User-Defined Flow Model in PLAXIS (Taborda et al., 2023a) and calibrated based on data by Hight et al. (2007):

$$log_{10}\, k_v = 0.0215 \cdot (y + 2) - 9.427 \qquad (1)$$

where y is the vertical coordinate ($y = 0\ m$ denotes the ground surface), and k_v and k_h are the vertical and horizontal permeabilities in m/s, respectively.

Table 1. Stiffness properties for London Clay.

Shear stiffness		**Bulk stiffness**	
G_{ref}	$51.7\ MPa$	K_{ref}	$26.7\ MPa$
a	5.6×10^{-5}	r	1.27×10^{-4}
b	0.9	s	1.8
$R_{G,min}$	0.0645	$R_{K,min}$	0.13275
G_{min}	$2.67\ MPa$	K_{min}	$5\ MPa$

The excavation of the shaft (with diameter D and depth H) was simulated in $1\ m$ steps, with each ring being built concurrently with the next excavation (i.e. the support trailed the excavation by one step). The duration for each excavation stage was, for simplicity, set to $D/10$ days. For the top half of the shaft, pre-cast concrete segments ($E = 37\ GPa,\ \nu = 0.2$) were adopted for support, while sprayed concrete was used in the lower half. For both cases, a thickness of $0.35\ m$ was assumed based on typical geometries of shafts built in London. The mechanical behaviour of the shotcrete support was simulated using the IC MAGE M07 model (Taborda et al., 2023c), which introduces a time-dependent Young's modulus following the expression proposed by the CEB-FIP Model Code 90 (CEB-FIP, 1993) with $E_{28} = 30\ GPa, s = 0.25$ and $\nu = 0.2$. The interaction between the support and the soil was modelled using interface elements with their strength reduced to two thirds of that of the soil ($c_{int}/c_{soil} = \tan\phi_{int} / \tan\phi_{soil} = 2/3$), and normal and tangential stiffness values of $10^6\ kN/m^3$.

3 SURROGATE MODEL

In this study, the numerical model described in Section 2 was surrogated with an artificial neural network (ANN) from the deep learning framework *Keras* (Chollet et al., 2015). The ANN was trained, using synthetically generated data, to predict the surface and subsurface settlement from an input shaft geometry. The procedures followed in the creation of the surrogate model including data generation, training of the ANN and its evaluation are described subsequently.

3.1 Synthetic database

A synthetic database of numerical analyses, for different shaft geometries, was generated using the numerical model described above; the database comprised a total of 100 analyses.

The Latin Hypercube Sampling (LHS) method (McKay et al., 1979) was employed to define the combined shaft depth and diameter for each of the *samples* (analyses) in the database. In simple terms, the LHS generalises the concept of a latin square, i.e. a square grid of equally-spaced intervals where only one sample point is located in each row and column of the grid, to arbitrary input dimensions. Bounds for the input parameters are required by the LHS and these were taken as 2.5 m and 20 m for the shaft diameter and 20 m and 70 m for the shaft depth. These bounds were aimed to cover a large portion of the shaft geometries to be potentially constructed in London.

Displacement troughs from the end of the excavation were extracted from the analysis results at interval depths corresponding to $0.1H$ (where H is the shaft depth), from the surface to the base of the shaft. Correspondingly, 11 curves were produced per analysis. Each of these curves extended radially from 0.1 m to $2H$ and included 201 equally-spaced points. Note that the movement of the points located at the shaft boundary can be largely affected by the presence of the interface element, hence it was decided to shift the starting point of the troughs 0.1 m away from the boundary.

3.2 Training procedure

The synthetic dataset was divided into the training (70%), validation (10%) and testing (20%) datasets. The validation dataset was employed to assess the generalisation ability of the ANN model at the model tuning stage; the performance of the ANN, adopting its final configuration, was evaluated against the testing dataset. The ANN was trained to predict the ground displacement given the following input variables: shaft depth (H) and diameter (D), the ratio z/H (where z is the depth of the point to be evaluated) and the ratio x/H (where x is the radial distance from the point to the shaft boundary). To ensure that all the input variables were in the same scale prior to training of the model, they were normalised by the maximum absolute value of each variable found in the training dataset.

The ANN adopted a feedforward architecture, the *adam* optimiser (Chollet et al., 2015) and the rectified linear unit activation function for all hidden layers. The number of hidden layers, the number of neurons for each hidden layer and the learning rate were fine-tuned through exploration of a large number of combinations of the abovementioned hyperparameters. A summary of the hyperparameters adopted by the ANN is presented in Table 2.

Table 2. Summary of hyperparameters adopted by the ANN.

Hyperparameter	Value
Hidden layers	{640,704,832,320,576,864,288}
Activation function	Relu
Optimiser	Adam
Learning rate	$3.747 \cdot 10^{-5}$

3.3 Performance evaluation

Figure 1 and Figure 2 depict regression plots where the displacement predicted by the surrogate model is plotted in the vertical axis against the actual displacement (i.e. that obtained numerically) for the training and testing datasets, respectively. Note that negative displacements indicate settlement of the ground. The solid black line signifies a perfect agreement between predictions and target values. It can be seen that data points generally plot in a narrow band around the black line which illustrates the overall excellent performance of the surrogate. In quantitative terms, the coefficient of determination (R^2), which yields a value of 1 when the residual between observations and predictions is zero, was obtained as 0.998 and 0.996 for the training and testing datasets, respectively. Similarly, the Mean Absolute Error (MAE) was determined as $6.7 \cdot 10^{-5}$ m and $9.5 \cdot 10^{-5}$ m for the two datasets.

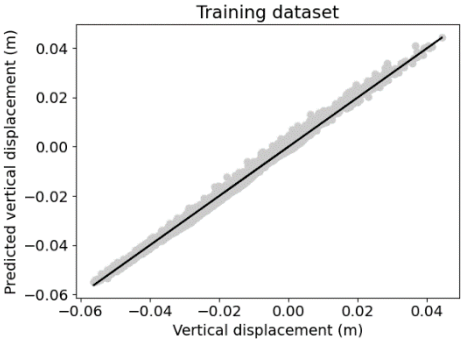

Figure 1. Regression plot of the training dataset.

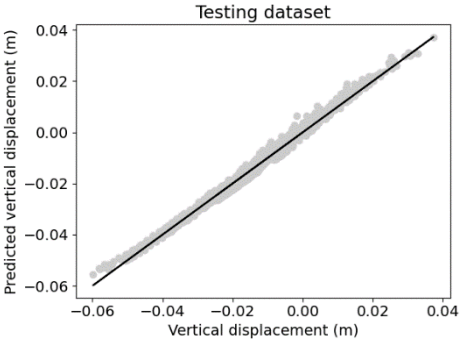

Figure 2. Regression plot of the testing dataset.

Figure 3 shows the displacement troughs at depths ranging from 0 m to depth H for a shaft of 10.1 m diameter and 36 m depth, part of the database described in Section 3.1. The troughs from the numerical data are shown according to the data split (training, testing and validation) they belonged to. According to the numerical analyses, the settlement magnitudes reduce gradually with depth such that for z/H larger than about 0.6 there is heave next to the shaft. It can be observed that the surrogate model is capable of reproducing that trend as well as the shape of the displacement troughs at different depths. Overall, the results demonstrate that the surrogate model can be used with confidence for the prediction of ground movements around a newly constructed shaft. It is useful to note that while each of the numerical analyses described in this paper took several hours to complete, the surrogate model can make predictions almost instantaneously, allowing for quick estimates in the early design stages.

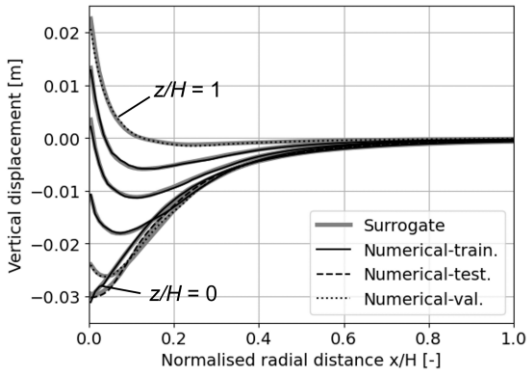

Figure 3. Settlement troughs at different depths for a shaft of 10.1 m diameter and 36 m depth.

4 CONCLUSIONS

A dataset consisting of vertical movements due to shaft excavation in London Clay was created for a wide range of geometries by performing detailed coupled consolidation axi-symmetric finite element analyses. The obtained data were subsequently used to create a surrogate model using an ANN, which was shown to reproduce with a high level of accuracy the numerical data. This work paves the way for greater adoption of this type of data-centric models in the pre-design of geotechnical structures.

ACKNOWLEDGEMENTS

The work presented in this paper was carried out within the scope of project *SIDeTools*, funded by the Engineering and Physical Sciences Research Council (EPSRC) (grant number: EP/X52556X/1).

REFERENCES

CEB-FIP (1993). CEB-FIP Model Code 90. Thomas Telford, London.

Chollet, F., & others. (2015). Keras. GitHub. Retrieved from https://github.com/fchollet/keras.

Ferrero, J. A., Ruiz Lopez, A., Taborda, D. M. G., Brasile, S. (2023) Applying the observational method to a deep braced excavation using an artificial neural network. *Proceedings of the 10th European Conference on Numerical Methods in Geotechnical Engineering*, London, UK. http://doi.org/10.53243/NUMGE2023-303.

Hight, D. W., Gasparre, A., Nishimura, S., Minh, N. A., Jardine, R. J., Coop, M. R. (2007) Characteristics of the London Clay from the Terminal 5 site at Heathrow Airport, *Géotechnique*, 57(1), pp. 3-18. http://doi.org/10.1680/geot.2007.57.1.3.

McKay, M. D. Beckman, R. J. Conover, W. J. (1979) A Comparison of Three Methods for Selecting Values of Input Variables in the Analysis of Output from a Computer Code, *Technometrics*, 21 (2), pp. 239-245. http://doi.org/10.1080/00401706.2000.10485979.

New, B. M., Bowers, K. H. (1994) Ground movement validation at the Heathrow Express trial tunnel. *Proceedings of the 7th international symposium Tunnelling '94*, Boston, MA, pp. 301-329.

Sailer, E., Taborda, D. M. G., Zdravkovic, L., Potts, D. M. (2019) Fundamentals of the coupled thermo-hydro-mechanical behaviour of thermo-active retaining walls. *Computers and Geotechnics*, 109, pp. 189-203. http://doi.org/10.1016/j.compgeo.2019.01.017.

Taborda, D. M. G., Kontoe, S. & Tsiampousi, A. (2023a) IC MAGE Flow Model 01 – Nonlinearly varying anisotropic permeability (Version 1.0). *Zenodo*. http://doi.org/10.5281/zenodo.7796383.

Taborda, D. M. G., Kontoe, S. & Tsiampousi, A. (2023b) IC MAGE Model 01 – Strain hardening /softening Mohr-Coulomb failure criterion with isotropic small strain stiffness (Version 2.1). *Zenodo*. http://doi.org/10.5281/zenodo.8239422.

Taborda, D. M. G., Kontoe, S. & Tsiampousi, A. (2023c) IC MAGE Model 07 – Simple non-linear time-dependent stiffness model for concrete (Version 1.4). *Zenodo*. http://doi.org/10.5281/zenodo.8234140.

Proceedings of the XVIII ECSMGE 2024
GEOTECHNICAL ENGINEERING CHALLENGES
TO MEET CURRENT AND EMERGING NEEDS OF SOCIETY
© 2024 the Authors
ISBN 978-1-032-54816-6
DOI 10.1201/9781003431749-134
Open Access: www.taylorfrancis.com, CC BY-NC-ND 4.0 license

ECSMGE 24
XVIII EUROPEAN CONFERENCE ON SOIL MECHANICS AND GEOTECHNICAL ENGINEERING

Field investigations of combined raft-pile foundation with adjustable interaction between the raft and the piles

Test sur le terrain d'une fondation combinée radeau-pieux avec interaction réglable entre le radier et les pieux

O. Samorodov*, S. Tabachnikov, O. Dytiuk, O. Krotov
O.M. Beketov National University of Urban Economy in Kharkiv, Kharkiv, Ukraine

Y. Vynnykov
National University "Yuri Kondratyuk Poltava Polytechnic", Poltava, Ukraine

Y. Kirichek
State Higher Educational Establishment "Prydniprovska State Academy of Civil Engineering and Architecture", Dnipro, Ukraine

V. Shapoval
National Technical University "Dnipro Polytechnic", Dnipro, Ukraine

**osamorodov@ukr.net*

ABSTRACT: A new design of a combined raft pile foundation, which is devoid of the shortcomings of similar existing design solutions and installation methods, and an engineering method for determining its main parameters, are proposed. This technical solution has been implemented at one of the construction sites in Kharkiv (Ukraine). The proposed design makes it possible to efficiently use the load-bearing capacity of the soil base by involving the raft part in response to the loading in a controlled manner with the transfer of up to 50% of the total load to this without going beyond the allowable strains of the soil base. The remaining 50% of the load is taken up by piles. After determining the multiplicity of the pile spacing and their parameters costs can be reduced by up to 35% in comparison with other design solutions for combined raft pile foundations. The results of field surveys of the initial settlements of the piles as part of a combined raft pile foundation (CRPF) are presented, which is not in contact with the raft that settles during the construction of a multi-story building. Based on the field investigations, a qualitatively new dependency of the pile deformation on the effect of additional loading forces of soil friction was found, which shows the upward sliding effect of the pile because forces of friction are higher than the resistance forces on the lateral surface of the pile with the manifestation of reverse (elastic) deformations of the soil base of the pile, which indicates the need to consider this phenomenon when setting the size of the gap between the raft and the piles in the designs of similar CRPF.

RÉSUMÉ: Une nouvelle conception d'une fondation combinée sur pieux sur radier, dépourvue des inconvénients des solutions de conception et des méthodes d'installation existantes similaires, ainsi qu'une méthode d'ingénierie pour déterminer ses principaux paramètres, sont proposées. Cette solution technique a été mise en œuvre sur l'un des chantiers de construction à Kharkiv (Ukraine). La conception proposée permet d'utiliser efficacement la capacité portante de la base du sol en impliquant la partie radier dans la réponse à la charge de manière contrôlée avec transfert jusqu'à 50 % de la charge totale vers celle-ci sans dépasser la déformations admissibles de la base du sol. Les 50 % restants de la charge sont repris par des pieux. Après avoir déterminé la multiplicité de l'espacement des pieux et leurs paramètres, les coûts peuvent être réduits jusqu'à 35 % par rapport à d'autres solutions de conception pour les fondations sur pieux combinés. Les résultats d'enquêtes sur le terrain des tassements initiaux des pieux dans le cadre d'une fondation sur pieux à radeau combiné (CRPF) sont présentés, qui n'est pas en contact avec le radier qui se tasse lors de la construction d'un bâtiment à plusieurs étages. Sur la base des enquêtes sur le terrain, une dépendance qualitativement nouvelle de la déformation du pieu à l'effet des forces de chargement supplémentaires dues au frottement du sol a été trouvée, ce qui montre l'effet de glissement vers le haut du pieu dû au fait que les forces de frottement sont supérieures aux forces de résistance. Sur la surface latérale du pieu avec manifestation de déformations inverses (élastiques) de la base du sol du pieu, ce qui indique la nécessité de prendre en compte ce phénomène lors de la définition de la taille de l'espace entre le radier et les pieux dans les conceptions similaires CRPF.

Keywords: Combined raft pile foundation; soil base; negative friction forces; settlement; slipping; reverse.

1 INTRODUCTION

In the construction of multi-storey and high-rise buildings in the last twenty years in the world practice, one of the advanced developments has been a combined raft pile foundation (CRPF), where the loads from the building are distributed between the piles and the raft, allowing up to 50% of the structural load being taken by the raft. (Katzenbach et al. 2016).

The choice of effective solutions for such foundations depends on many factors, such as the features of soil conditions, the parameters and spacing of piles, the rigidity of the raft, the model of the base and the nature of the interaction between the piles, raft and soil, and others. Therefore, the design of the "base – foundation – structure" system is possible only with the help of numerical methods implemented in powerful computer systems such as WinTUBE (SOFISTIK), Plaxis etc. taking various individual approaches to modeling such systems with a significant number of assumptions which, as a rule, do not have a full-scale experimental base in terms of the actual resistance of the soil base under the raft.

Thus, the development of a new design of a combined raft pile foundation and a method for determining its main parameters is a relevant objective.

2 NEW DESIGN OF A COMBINED RAFT PILE FOUNDATION

A new design of a combined raft pile foundation (Utility model patent, 2020) is proposed, which is devoid of the shortcomings of similar existing design solutions and methods of arrangement, and engineering methods for determining its rational parameters are proposed (Samorodov, 2017 and Samorodov et al., 2022). A combined raft pile foundation (as shown in Figures. 1, 2) consists of the raft **1** and the piles **2** with the diameter *d*, with the gap **3** of the height *Δ* provided between the raft and the piles. Moreover, for technological convenience to ensure the absence of contact between the raft and the pile heads within the concrete bed **4** installation under the raft, the gap can be filled with a low-modulus material such as foamed plastic. Soil base shown **5**.

Further, it is proposed to consider the development of an engineering method for designing a raft pile foundation proceeding from the maximum allowable settlement of a structure s_u (DBN V.2.1-10:2018, 2018), considering the design model for the interaction between a nominally solid foundation and a linearly deformed soil mass (see Figure 2).

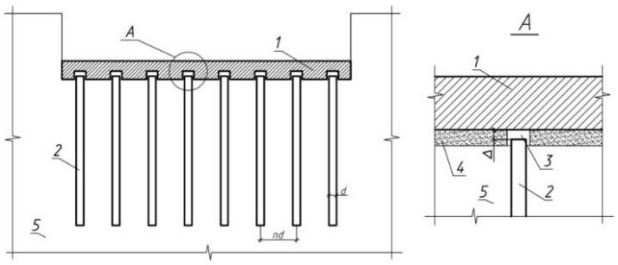

Figure 1. A combined raft pile foundation (CRPF).

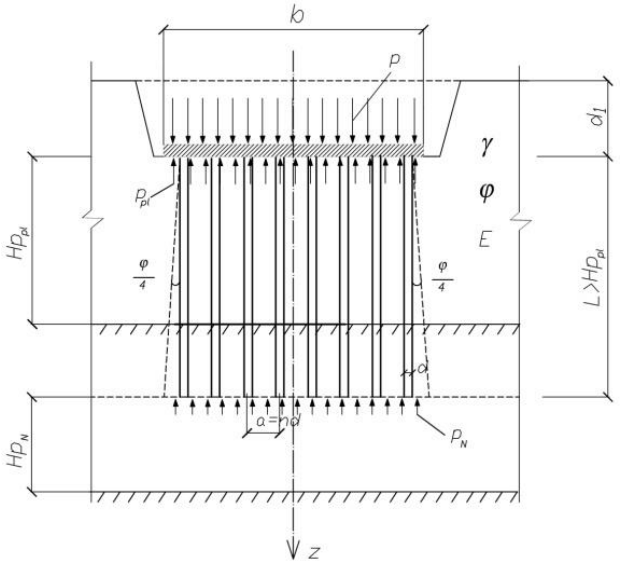

Figure 2. Design model for the interaction between a combined raft pile foundation and the soil mass.

A special feature of the methodology for determining the main parameters of the CRPF is the determination of the raft settlement s_{pl} and the initial settlement of the piles $S_{pile}^{P_n}$ to adjust the gap height *Δ:*

$$\Delta = s_{pl} - S_{pile}^{P_n} \quad (1)$$

3 FIELD INVESTIGATIONS

The object of observation is a 9-storey residential building with a technical floor and a basement located at 5, Myra Street in Kharkiv, Ukraine (see Figure 3). The project organization and general contractor is PrJSC TRUST ZHYTLOBUD-1 (Kharkiv). The height of the building is *35 m* (measured from the top of the foundation). The structural scheme of the building is frameless with longitudinal and transverse walls and precast floor slabs. The load-bearing walls of the building are made of silicate brick with a thickness of *510 mm* and *380 mm*. The floor slabs are hollow-core reinforced concrete slabs with a thickness of *220 mm*. The basement walls are precast of concrete blocks of various thicknesses from *400 mm* to *800 mm*.



Figure 3. View of the building.

The cast in-situ combined raft pile foundation is composed of a raft measuring in plan *26.2 m* by *27.0 m*, with a thickness of *800 mm*, with a linear arrangement under the load-bearing walls of bored piles with a diameter of *d=500 mm* and a length of $L=10.0\ m \approx H_{p_{pl}}$, which are not connected to the raft (see Figures 4, 5, 6).

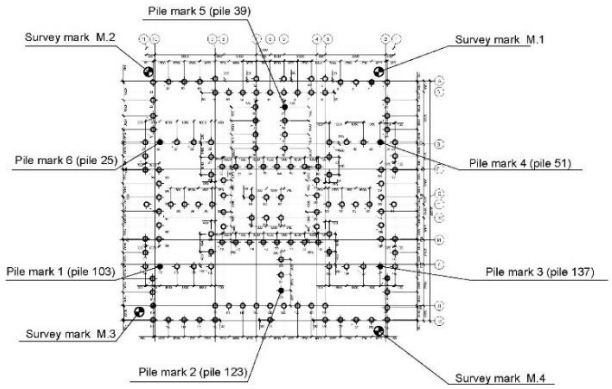

Figure 4. A schematic plan showing the arrangement of test piles and survey marks.

For the combined foundation (see Figs. 2, 5, 6) the distribution of resistance between the raft and the piles was taken to be 70/30, i.e. 70% is taken up by the raft ($p_{pl}=119$kPa) and 30% by the piles ($p_N=48$kPa); therefore, the design gap between the raft and the piles is taken to be $\Delta=5cm$ according to the method (Samorodov, 2017 and Samorodov et al., 2022). The accepted gap value $\Delta=5cm$ also guaranteed that the over-standard tilt of the building would be prevented in the event of a possible emergency local soaking of the Layer-2 subsiding soils under the raft during the construction process; however, this did not occur.

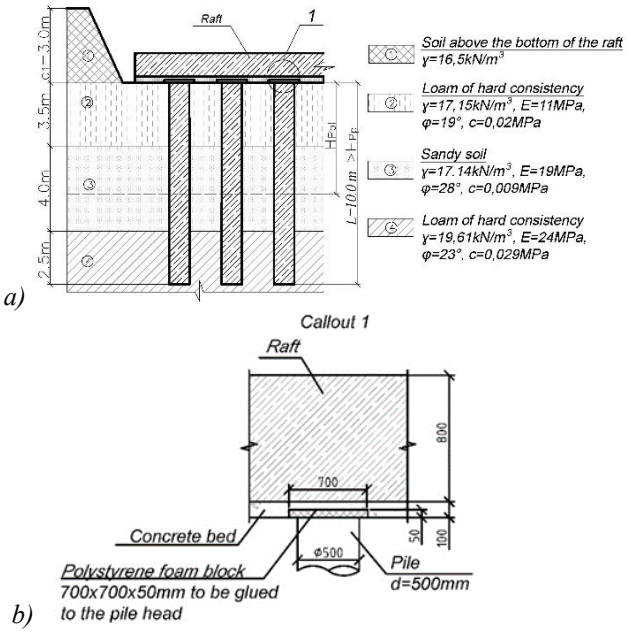

Figure 5. A schematic drawing of a CRPF: (a) in the engineering geological section; (b) raft-pile junction.

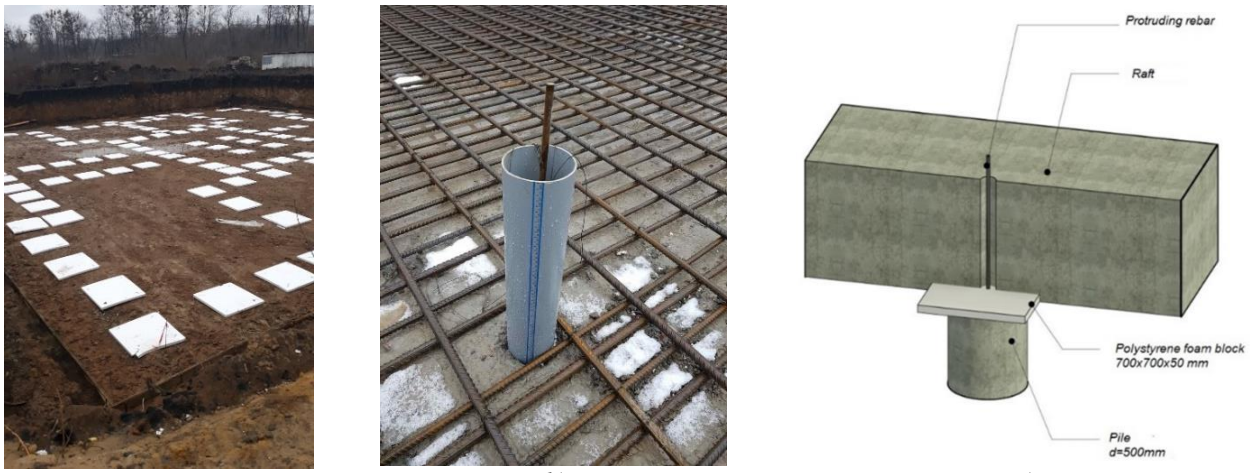

a) *b)* *c)*

Figure 6. Installing a CRPF and devices for surveying the initial settlements of piles: (a) Laying a low-modulus material (polystyrene foam) above the pile heads; (b) A rebar protruding from the pile in a protective sleeve (tube); (c) Axonometric diagram.

The vertical settlements $S_{pile}^{P_n}$ of six piles and the settlement of the building s_{pl} (equal to the settlement of the raft) have been investigated in parallel since July 2020 as part of the scientific and technical support to the construction object (geodetic work performed by Ass. Prof., PhD T.A. Nalyvayko).

The settlements s_{pl} of the building were surveyed during construction and operation using high-precision Class 2 leveling methods. Survey marks M.1, M.2, M.3, and M.4, which were laid at the level of the basement floor of the building (see Figure 4).

The settlements of the piles (see Figure 7) at each stage of the investigation were determined by the formula:

$$S_{pile}^{P_n} = s_{pl} - u_{pile} \quad (2)$$

where s_{pl} is the settlement of the raft (building), mm; u_{pile} is the deformation of the pile relative to the raft, mm, determined by a caliper according to the diagram in Figure 7a.

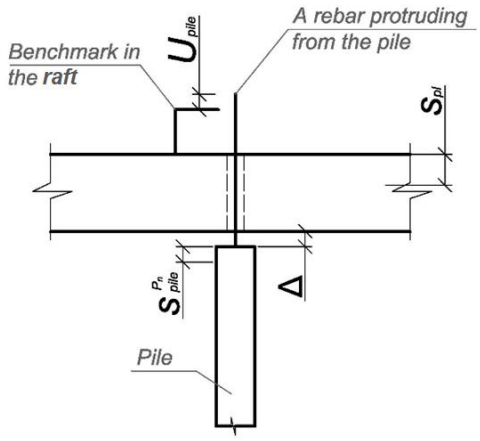

a)



b)

Figure 7. Determining the pile deformation u_{pile}: (a) schematic of deformations; (b) determining u_{pile} using a caliper.

3.1 Research results

Figure 8 schematically shows the values of the settlements of the survey marks (M.1, M.2, M.3, and M.4) and the deformations of six separate piles in plan for each stage as visual diagrams according to the schematic plan in Figure 4.

Table 1 gives the values of the average settlements of the raft s_{pl} and the initial settlements of the piles $S_{pile}^{P_n}$ (based on the statistical processing of data for six piles) owing to the actual controlled pressure under the raft p_{pl} (only the deadweight of the erected structures without the use of increasing factors was taken into account) for each stage of the investigation, and Figure 9 shows the corresponding dependency graphs.

Table 1. The average settlements for the CRPF insert.

Date of measurement	**Number of stories**	**Average pressure under the bottom of the raft**	**Average settlement of the raft (building)**	**Average initial settlement for the piles based on data statistical processing**	**Compressible mass of the base of the raft (theoretical value)**
Month.Year	n	p_{pl}, kPa	s_{pl}, mm	$S_{pile}^{P_n}$, mm	$H_{p_{pl}}$, m
07.2020	Basement	0.00 (conditionally)	0.00	0.00	0
09.2020	3	60.6	-3.33	-2.28	6.7
11.2020	6	85.1	-4.58	-1.91	8.5
03.2021	9	109.6	-13.18	-8.54	10.1
07.2021	10	≈119	-13.53	-6.86	10.7

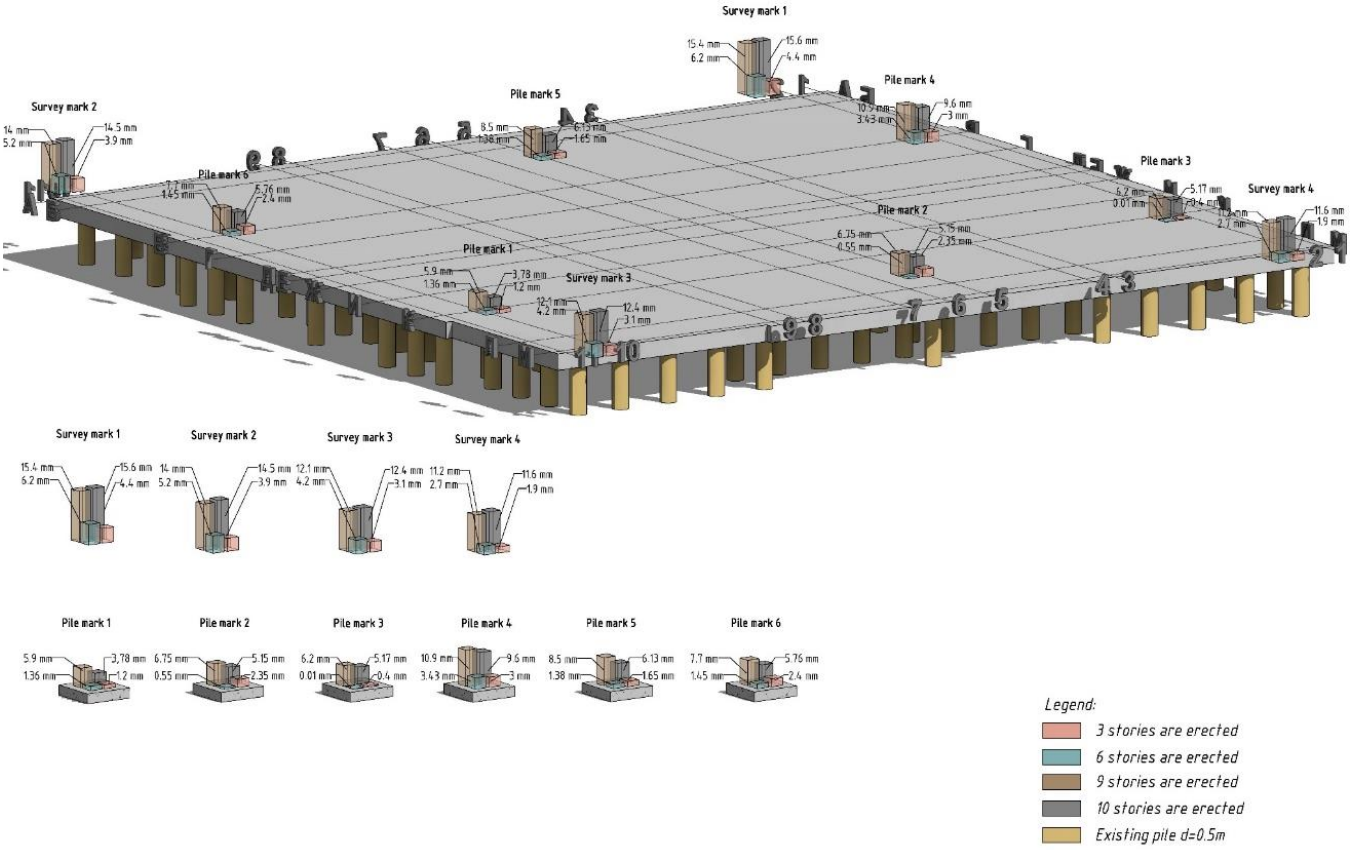

Figure 8. The settlement of the raft s_{pl} and the relative deformations of the piles u_{pile} at each stage of the investigation.

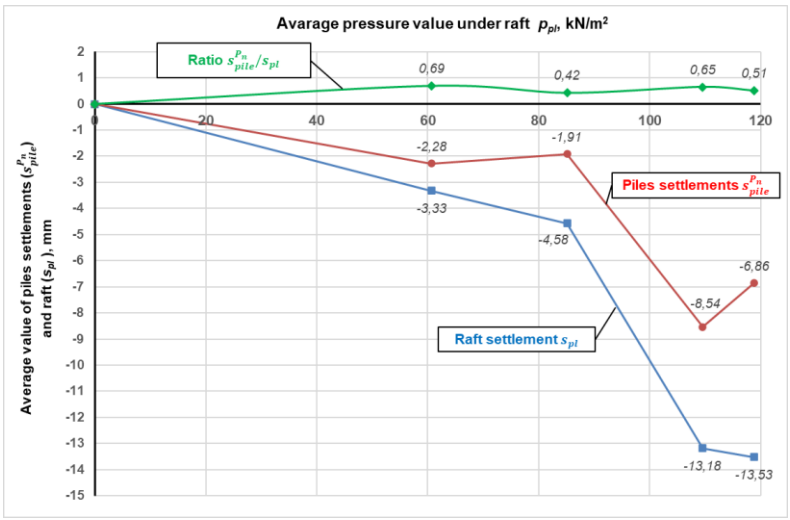

Figure 9. The dependency graphs of the average settlements of the raft s_{pl} and the initial settlements of the piles S_{pile}^{Pn} on the average pressure under the raft p_{pl} and their ratio.

As can be seen from the graph of the absolute settlements of the piles in Figure 9, there is an upward sliding effect of the piles at different pressures under the bottom of the raft, which is explained by the fact that the loading forces of friction are higher than the resistance forces on the lateral surface of the piles with the manifestation of reverse (elastic) deformations of their soil base. It should be noted that this behavior is observed for all six piles in different places in plan (see Figure 4) and is not related to the statistical processing of the experimental results.

4 CONCLUSIONS

(1) A new design of a combined raft pile foundation has been developed, which is able to distribute in a real and controlled manner the resistance between the raft and the piles by arranging a gap between them, where the raft and then the piles are fully involved in the response to the loading from the building.

(2) The impact of loading forces of friction along the lateral surface of the piles on their settlement was confirmed, which was also observed by other researchers. In this case, it can be stated that when the pressure under the bottom of the raft is up to p_{pl}≈119kPa, the ratio of the stabilized settlement of the piles to the settlement of the raft in the large-size foundation is: $S_{pile}^{P_n}/s_{pl} \geq 1/2$.

(3) For the first time, a qualitatively new dependency of the deformation of piles on the action of loading forces of soil friction was found, which shows the upward sliding effect of piles because the forces of friction are higher than the resistance forces on the lateral surface of the piles with the manifestation of reverse (elastic) deformations of the soil base of the piles.

REFERENCES

DBN V.2.1-10:2018 Osnovy Ta Fundamenty Budynkiv I Sporud. Osnovni Polozhennia. Bases and foundations of buildings and structures. Main provisions. Kyiv: Ministry of Regions of Ukraine, State Enterprise Ukrarchbudinform, 2018. 36 p.

Katzenbach R., Leppla S. and Choudhury D. 2016; Foundation Systems for High-Rise Structures, published by CRC Press, Taylor & Francis Group, USA and UK.

Samorodov, O.V. *Proyektirovaniye effektivnykh kombinirovannykh svaynykh i plitnykh fundamentov mnogoetazhnykh zdaniy* [Designing high-performance combined pile and raft foundations for multi- storey buildings]. Monograph. O.V. Samorodov. Kharkiv: Tipografiya Madrid, 2017, 204 p.

Samorodov, O. New design of a combined pile raft foundation for a multi-storey building with determination of its main parameters: [text] / O. Samorodov, D. Muliar, S. Tabachnikov, O. Krotov, Y. Vynnykov, M. Zotsenko, V. Shapoval // Proceedings of the 20th International Conference on Soil Mechanics and Geotechnical Engineering. Sydney, Australia: 2022. – P. 3493-3497.

Utility model patent No. 148444, Ukraine IPC E02D 27/12 (2006/1). COMBINED RAFT PILE FOUNDATION (O.V. Samorodov, O.Ye. Dytyuk, D.L. Mulyar, and S.V. Tabachnikov). KhNUCEA. Appl. November 09, 2020. Publ. August 11, 2021. Bull. No. 32, 4 p.

Proceedings of the XVIII ECSMGE 2024
GEOTECHNICAL ENGINEERING CHALLENGES
TO MEET CURRENT AND EMERGING NEEDS OF SOCIETY
© 2024 the Authors
ISBN 978-1-032-54816-6
DOI 10.1201/9781003431749-135
Open Access: www.taylorfrancis.com, CC BY-NC-ND 4.0 license

ECSMGE 24
XVIII EUROPEAN CONFERENCE ON SOIL MECHANICS AND GEOTECHNICAL ENGINEERING

Seismic and load inclination factors for estimating the bearing capacity of strip footings

Facteurs sismiques et d'inclinaison de charge pour estimer la capacité portante des semelles filantes

T. Santana*, N. Guerra, A. Antão, M. Vicente da Silva
UNIC, NOVA School of Science and Technology, Almada, Portugal

**mtgs@fct.unl.pt*

ABSTRACT: Bearing capacity of shallow foundations is commonly determined using formulations initially considering centered vertical loading on a strip horizontal footing and then corrected for taking into account deviations from this ideal situation, such as eccentricity and inclination of the loads and of the shape of the foundation. Most bearing capacity formulations don't include correction factors considering seismic actions. In this work, pseudostatic limit analysis calculations simulating the seismic action with horizontal and vertical seismic coefficients, were performed with *mechpy*, a program developed within the authors' team which implements a finite element formulation of the limit analysis theorems. Based on the results of both lower and upper bound calculations, seismic and load inclination bearing capacity factors are proposed.

RÉSUMÉ: La capacité portante des fondations superficielles est généralement déterminée à l'aide de formulations considérant initialement les charges verticales centrées sur une semelle horizontale filante, puis corrigée pour tenir compte des écarts par rapport à cette situation idéale, tels que l'excentricité et l'inclinaison des charges et de la forme de la fondation. La plupart des formulations de capacité portante n'incluent pas de facteurs de correction prenant en compte les actions sismiques. Dans ce travail, des calculs d'analyse limite pseudostatique simulant l'action sismique avec des coefficients sismiques horizontaux et verticaux ont été réalisés avec *mechpy*, un programme développé au sein de l'équipe des auteurs qui implémente une formulation par éléments finis des théorèmes d'analyse limite. Sur la base des résultats des calculs des limites inférieure et supérieure, des facteurs de capacité portante sismique et d'inclinaison de charge sont proposés.

Keywords: Bearing capacity; seismic actions; seismic factors; load inclination factors; limit analysis.

1 INTRODUCTION

Terzaghi's bearing capacity equation for strip footing continues to be used in practice. In its simple form, it is applicable to strip footings, with vertical and centered loading, and it is then modified, mainly through correction factors to take into account the deviations from the original simple case. Inclination of the loads applied to the footing and seismic effects can be taken into account in this way.

In this paper, soil is assumed to be purely frictional. A rigid strip footing is considered, with rough base and the load is centered and can be inclined. Seismic effects are considered by a pseudo-static approach: on the footing the effects are considered included in this load, and on the soil they are applied through seismic coefficients k_h and k_v on the horizontal and vertical directions, respectively. Numerical bearing capacity calculations are performed using *mechpy*, a finite element code developed within the authors' team, implementing the upper and lower bound theorems of limit analysis (Vicente da Silva and Antão, 2013).

The numerical calculations are performed to determine correction factors for the inclination of the load and for the seismic effects on the soil. These are initially determined separately and compared with results from Cascone and Casablanca (2016) and Conti (2018). Then, the superposition of both effects is considered, this being the main contribution of the paper. Equations for the above mentioned factors are proposed for application to design.

2 THE PROBLEM

The following equation for the bearing capacity will be considered:

$$q_r = \frac{1}{2}\gamma(1+k_v)BN_\gamma i_\gamma e_\gamma + q(1+k_v)N_q i_q e_q \quad (1)$$

where γ is the unit weight if the soil, B is the width of the footing, q is the loading caused by the soil above the footing base, N_γ and N_q are the bearing capacity factors, i_γ and i_q are the load inclination factors, e_γ and e_q are the seismic factors and k_v is the vertical seismic coefficient. Both k_h and k_v will affect the seismic factors. The two summands of eq. (1) are determined independently, as was the initial proposal for Terzaghi's equation, following what is presented in Figure 1. Coefficient k_v can be positive or negative.

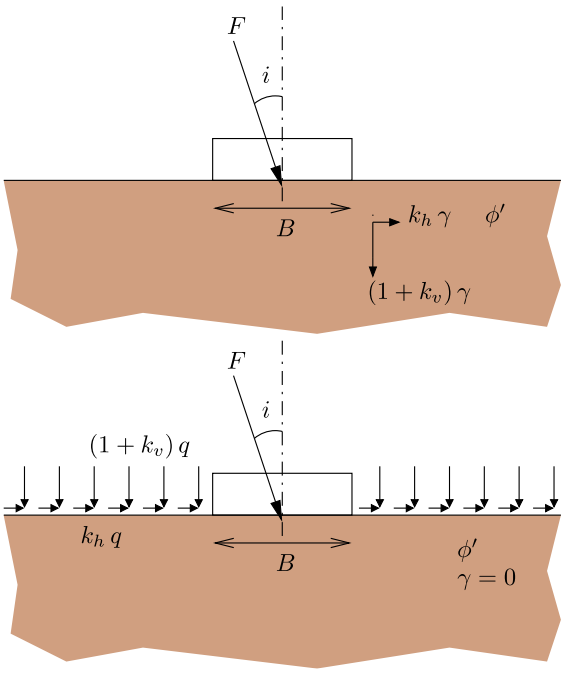

Figure 1. Problem considered for determining i_γ and e_γ (top) and i_q and e_q (bottom). Note: k_v can be positive or negative.

3 NUMERICAL CALCULATIONS

3.1 Bearing capacity factors

Numerical upper and lower bound limit analysis calculations were performed using program *mechpy*, which has been successfully used for determining collapse loads, namely in three-dimensional conditions, of a variety of geotechnical problems: earth pressures (Antão et al., 2011; Santana et al., 2023), bearing capacity of shallow foundations (Antão et al., 2012), tunnels stability (Antão et al., 2021) and slope stability (Deusdado et al. 2016). Initial calculations were performed to obtain N_γ and N_q for different friction angles, and therefore determining the collapse loads for angle $i=0$ and $k_h=k_v=0$ (see Figure 1), where i is the inclination of the loading. The results obtained are presented in Figure 2, where they are compared with Martin's solution (Martin, 2005) for N_γ and with the known exact solution for N_q. A good agreement can be observed.

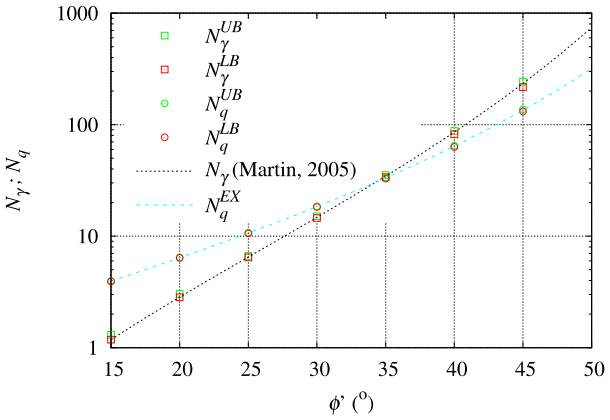

Figure 2. Bearing capacity factors obtained from upper (UB) and lower bound (LB) numerical calculations; comparison with known solutions.

3.2 Load inclination and seismic factors

Two sets of calculations were then performed: for determining the load inclination factors, no seismic action was considered; for the seismic factors, no load inclination was applied.

For the first set, three values of tan(i) were considered: 0.1, 0.2 and 0.3. The results are presented in Figures 3 and 4. In these figures, the factors identified as *UB* or *LB* were obtained from the *UB* or *LB* calculations: for example, i_γ *(UB)* was obtained through $q_{r,\gamma\neq0,\ q=0,\ i\neq0}/q_{r,\gamma\neq0,\ q=0,\ i=0}$; this means that i_γ *(UB)* is the ratio between two UB values and not necessarily an upper bound anymore. It can be seen in Figures 3 and 4 that there is some dependency of the friction angle and not only on the load inclination, as in some simplified proposals for these coefficients. It was found that the numerical results could be fitted by the following equations:

$$i_\gamma = \left(1 - \frac{\tan i}{\tan \phi\prime}\right)^{(1.3\tan i + 3)(\tan \phi\prime)^a} \quad (2)$$

$$i_q = \left(1 - \frac{\tan i}{\tan \phi\prime}\right)^{2.3(\tan \phi\prime)^b} \quad (3)$$

where:

$$a = 0.88\tan i + 1.19 \quad (4)$$

$$b = 1.06\tan i + 1.37 \quad (5)$$

These equations are also represented in Figures 3 and 4.

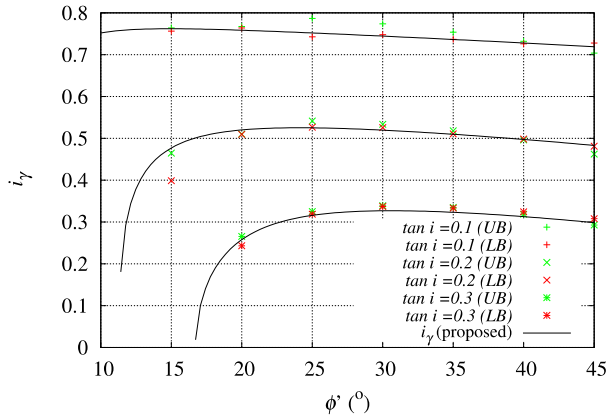

Figure 3. Load inclination factor i_γ obtained from upper (UB) and lower bound (LB) numerical calculation; comparison with proposed equation (2).

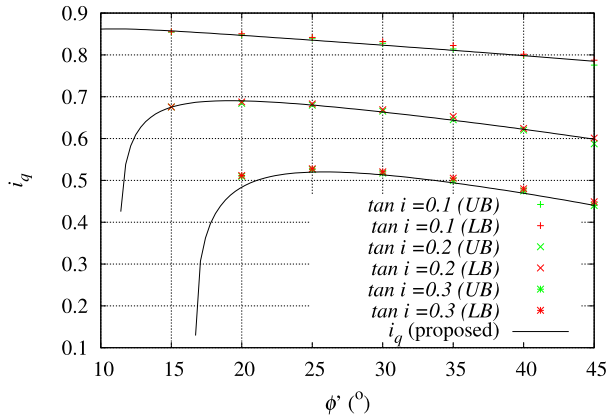

Figure 4. Load inclination factor i_q obtained from upper (UB) and lower bound (LB) numerical calculations; comparison with proposed equation (3).

For the second set of calculations, the load was considered vertical and the seismic coefficients were applied as represented in Figure 1. The following values of k_h were considered: 0.1, 0.2, 0.3, 0.4 and 0.5; the coefficient k_v was assumed 0, $+k_h/2$ and $-k_h/2$. For some lower friction angles, results could not be obtained, as this seismic loading was not stable. It was found that using equation (1) results for the seismic factors would depend only on angle θ, equal to:

$$\theta = atan\frac{k_h}{1+k_v} \qquad (6)$$

The obtained values are represented in Figures 5 and 6. In the same figures, other results obtained within this work are also represented and will be addressed in the next section.

It was found that the obtained results could be fitted with the following equations:

$$e_\gamma = \left(1 - 0.9\frac{tan\,\theta}{tan\,\phi\prime}\right)^{0.57} \qquad (7)$$

$$e_q = \left(1 - 0.9\frac{tan\,\theta}{tan\,\phi\prime}\right)^{tan\,\phi' exp(-0.76 tan\,\phi\prime)} \qquad (8)$$

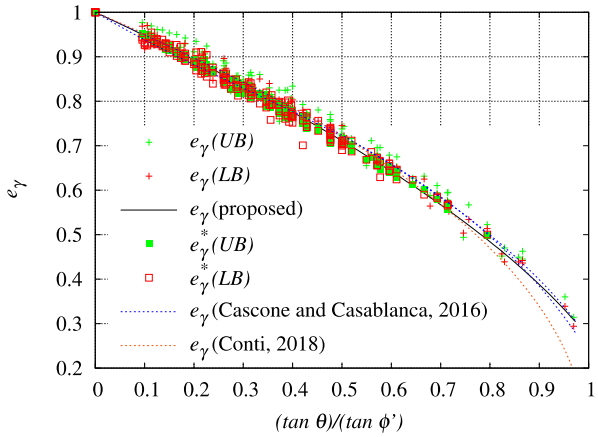

Figure 5. Seismic factor e_γ obtained from upper (UB) and lower bound (LB) numerical calculations; comparison with proposed equation (7) and with other proposals.

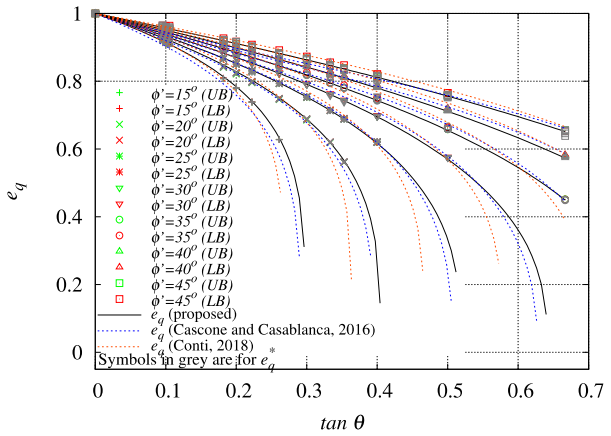

Figure 6. Seismic factor eq obtained from upper (UB) and lower bound (LB) numerical calculations; comparison with proposed equation (8) and with other proposals.

These equations are also represented in Figure 5 and 6, where good agreement can be observed. In the same figures, the proposals for the same coefficients from Cascone and Casablanca (2016) and Conti (2018) are also represented, also showing a good general agreement.

3.3 Seismic factors with load inclination

Numerical calculations for obtaining seismic factors when inclined loading is applied were also performed. They are referenced in the present paper as e^*_γ and e^*_q and are also represented in Figures 5 and 6. It is observed that they can be described by the same equations (7) and (8).This occurs for all cases.

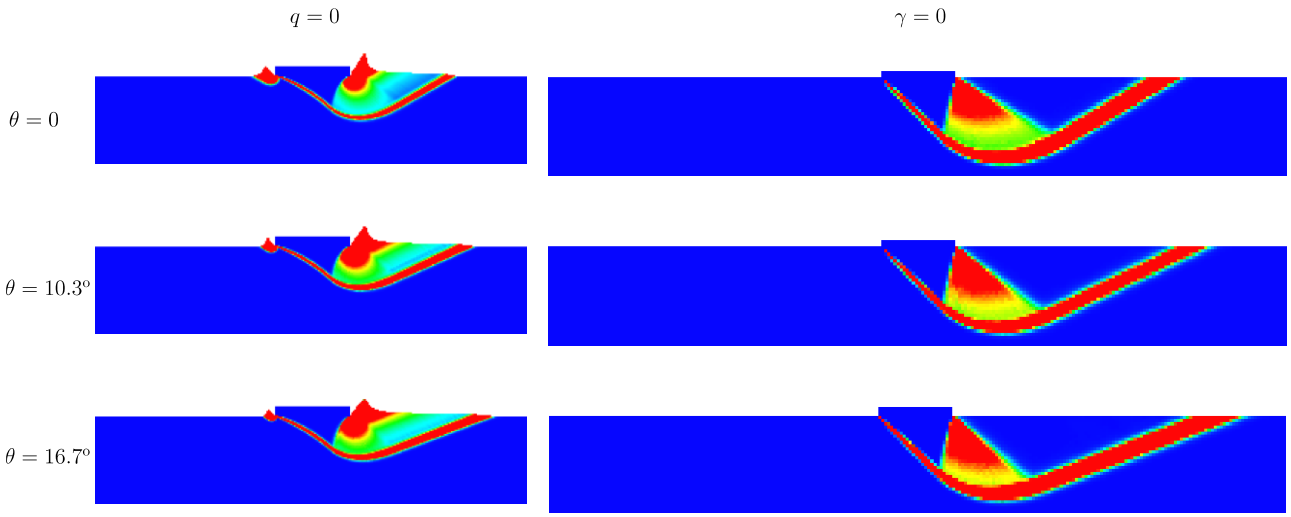

Figure 7. Maximum plastic distortion zones obtained from UB calculations for φ'=30° and tan i=0.2.

analysed, for e_q, and for the cases where $i+\theta<\phi'$, for e_γ.

Figure 7 shows the maximum plastic distortion zones obtained from upper-bound calculations for $\phi'=30^{o}$, tan $i=0.2$, three values of θ and for $q=0$ and $\gamma=0$. From the images on this figure, the mechanisms involved in each case can be inferred.

4 CONCLUSIONS

Correction factors for the bearing capacity of strip shallow foundations for cohesionless soils under drained conditions for load inclination and seismic actions were determined using limit analysis calculations with program *mechpy*. It was found that the results from upper- and lower-bound calculations are quite close. Equations to approximate those factors were proposed and compared with other solutions from the literature.

It was shown that these factors can be combined as long as $i+\theta<\phi'$.

REFERENCES

Antão, A., Santana, T., Vicente da Silva, M., Guerra, N.M.C. (2011). Passive earth-pressure coefficients by upper-bound numerical limit analysis. *Can. Geotech. J.* 48 (5), 767–780. https://doi.org/10.1139/t10-103

Antão, A., Vicente da Silva, M., Guerra, N., Delgado, R. (2012). An upper bound-based solution for the shape factors of bearing capacity of footings under drained conditions using a parallelized mixed f.e. formulation with quadratic velocity fields. *Comput. Geotech.* 41, 23–35. https://doi.org/10.1016/j.compgeo.2011.11.003

Antão, A., Vicente da Silva, M., Monteiro, N., Deusdado, N. (2021). Upper and lower bounds for three-dimensional undrained stability of shallow tunnels. *Transp. Geotech.* 27, 100491. https://doi.org/10.1016/j.trgeo.2020.100491

Cascone, E. and Casablanca, O. (2016). Static and seismic bearing capacity of shallow strip footings. *Soil Dyn. Earthq.* Eng. 84, 204–223. https://doi.org/10.1016/j.soildyn.2016.02.010

Conti, R. (2018). Simplified formulas for the seismic bearing capacity of shallow strip foundations. *Soil Dyn. Earthq. Eng.* 104, 64–74. https://doi.org/10.1016/j.soildyn.2017.09.027

Deusdado, N., Antão, A.N., Vicente da Silva, M., Guerra, N.C. (2016). Application of the upper and lower-bound theorems to three-dimensional stability of soil slopes. In: *Advances in Transportation Geotechnics 3. The 3rd International Conference on Transportation Geotechnics (ICTG 2016).* 143, SPG, pp. 674–681. http://dx.doi.org/10.1016/j.proeng.2016.06.097.

Martin, C.M. (2005). Exact bearing capacity calculations using the method of characteristics. *Proc. 11th Int. Conf. IACMAG*, Vol. 4, pp. 441-450, Turin.

Santana, T., Antão, A., Vicente da Silva, M., Guerra (2023). Upper bounds for the three-dimensional seismic active earth pressure coefficients. *Géotechnique Letters*. 13, 65-74. https://doi.org/10.1680/jgele.22.00096

Vicente da Silva, M. and Antão, A.N. (2013). Program mechpy. http://geocluster.dec.fct.unl.pt/mechpy/.

Proceedings of the XVIII ECSMGE 2024
GEOTECHNICAL ENGINEERING CHALLENGES
TO MEET CURRENT AND EMERGING NEEDS OF SOCIETY
© 2024 the Authors
ISBN 978-1-032-54816-6
DOI 10.1201/9781003431749-136
Open Access: www.taylorfrancis.com, CC BY-NC-ND 4.0 license

ECSMGE 24
XVIII EUROPEAN CONFERENCE ON SOIL MECHANICS AND GEOTECHNICAL ENGINEERING

Conception d'un remblai avec prise en compte de la succion d'un sol non saturé pour justifier la stabilité

Design of an embankment using cohesion due to suction of an unsaturated soil for stability calculation

V. Savatier*, C. Nogue Sanchez
EGIS, Toulouse, France

D. Mahmutovic, O. Denk
EGIS, Seyssins (Grenoble), France

**vincent.savatier@egis-group.com*

RÉSUMÉ: Ce papier présente la conception d'un remblai ferroviaire constitué de « Limons des plateaux » à talus raidis à 3H/2V protégés contre l'imbibition par des barrières capillaires au-dessus des plus hautes eaux et sous la couche de forme de façon à pouvoir prendre la succion en compte dans le dimensionnement. Cette configuration de remblai a été conçue dans le cadre d'un concours pour le lot G de la ligne ferroviaire du Grand Paris Express. Les types de rupture possibles ont été étudiées: rupture de peau par imbibition et rupture d'ensemble (corps de remblai et fondation). Ce papier montre que les barrières capillaires permettent de garantir que, pour la rupture d'ensemble, le cas de calcul le plus défavorable est la fin de construction. Les essais à inclure dans une étude de compactage conduite pour prendre en compte la succion sont présentés: Etude Proctor avec indice de portance immédiat à 2 ou 3 énergies (au moins Proctor Normal et Modifié) et mesure de la succion sur tous les points; pour des densités et teneurs en eau encadrant l'objectif de compactage choisi à partir du Proctor: essais double œdomètre avec mesure de succion initiale et finale; essais triaxiaux CD sur éprouvettes saturées. La saturation de l'air ambiant qui créé une succion moyenne en surface du sol est pris en compte dans cette approche. Une analyse de stabilité paramétrique montre que pour le compactage étudié on peut justifier des remblais jusqu'à 20 m de haut avec un berme tous les 10m et des talus à 3H/2V.

ABSTRACT: This paper presents the design of a railway embankment composed of silts with steep slopes at 3H/2V, protected against imbibition by capillary barriers above the highest water level and beneath the subgrade layer, in order to consider suction in the design. This embankment configuration was developed as part of a competition for Lot G of the Grand Paris Express railway line. Possible failure modes were studied: skin failure due to imbibition and overall failure (embankment body and foundation). The paper demonstrates that capillary barriers ensure that, for overall failure, the most unfavorable calculation scenario is the end of construction. The tests to be included in a compaction study conducted to account for suction are presented: Proctor test with immediate bearing capacity index at 2 or 3 energies (at least Normal and Modified Proctor) and measurement of suction at all points; for densities and water contents encompassing the chosen compaction target from the Proctor test: double oedometer tests with measurement of initial and final suction; CD triaxial tests on saturated specimens. The saturation of ambient air, which creates an average suction at the soil surface, is taken into account in this approach. A stability analysis shows that for the retain compaction target stability is reached for 20 meters high fill with slope at 3H/2V and a berm each 10 meters.

Keywords: Windblow silt and clay suction; unsaturated soil; embankment stability; soil compaction.

1 CONSTITUTION DU REMBLAI

La Figure 1 décrit la géométrie et la constitution du remblai proposé. Ce dernier présente des pentes de talus raidies à 3H/2V. Le cœur de remblai est protégé contre les infiltrations capillaires par deux barrières étanches. La barrière b_1 supérieure a pour but de protéger le corps de remblai contre les infiltrations d'eau venant de la plateforme. Elle est constituée de 2 couches de 0.35m de sol fin l_2 stabilisées à la chaux enrobant une couche drainante de sable s_1. La barrière b_2 est placée 0.3m au-dessus des plus hautes eaux.

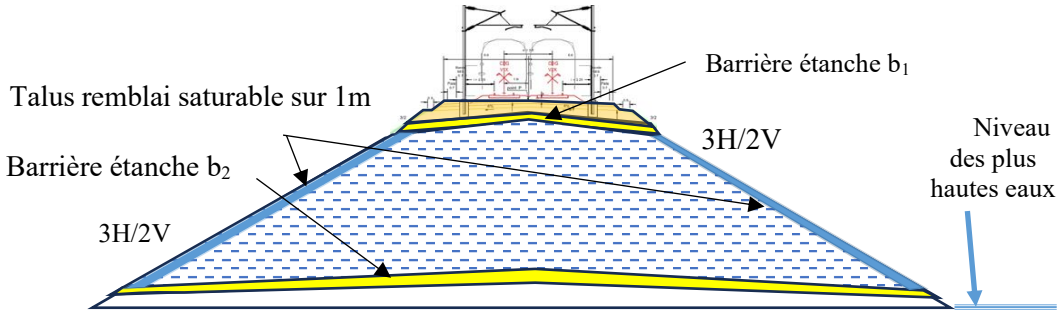

Figure 1. Coupe type du remblai.

Elle repose sur une arase des terrassements peu déformable pour permettre un compactage efficace en pied de remblai (typiquement on cherchera un module à la plaque EV2>50 MPa et EV2/EV1<2.2). Elle est constituée de 0.3m de sable s_1 surmontée d'une assise de 0.35m de sol l_2. Les barrières étanches b_1 et b_2 sont pentées à 4% vers l'extérieur du remblai et ont un exutoire sur le talus. Les sols l_2 sont des limons ou des argiles F2 ou F3 du GTR_{2023} traités à 2% de CAO et compactées à 95% de l'Optimum Proctor Normal (OPN).

Les sables s_1 sont roulés avec un passant à 10% d_{10} supérieur à 0.2mm. Ils ont une hauteur capillaire inférieure à 20 cm.

Le cœur de remblai est constitué par des limons F2 ou F3 du GTR_{2023} (limite d'Atterberg Wl= 44%) compactés à 95% de l'OPN coté humide (teneur en eau de mise en œuvre W= 16.5 %; teneur en eau et densité sèche à l'optimum WOPN= 16% γ_{OPN}=17 kN/m^3). En phase Avant-Projet, la succion de mise en œuvre a été estimée selon la formule de Fleurot (2002).

$$u_w(\Delta w_{OPT}, Wl) = -0.118 Wl^{1.98}.10^{\left(\frac{-\Delta W_{OPN}}{0.54+0.03.Wl-[3.3.10^6]Wl^2}\right)} \quad (1)$$

u_w: succion; Δw_{OPT} écart de la teneur en eau par rapport à l'optimum Proctor; Wl limite de liquidité d'Atterberg.

2 PRINCIPES DE FONCTIONNEMENT DE L'OUVRAGE

2.1 Variation de la succion due à la montée du remblai

La succion au sein d'une couche compactée va diminuer au cours de la montée du remblai.
Cette diminution peut être estimée par diverses approches:

- Première approximation par la méthode de Hilf (1948) pour un remblai de grande hauteur avec des succions modérées.
- Méthode déduite des travaux de L. Boutonnier (2007) et D.Mahmutovic (2016) utilisable sur la ligne optimale de compactage ou coté humide de l'optimum Proctor. Elle consiste à calculer la variation de pression interstitielle sous l'effet d'une surcharge en passant par le coefficient B de Skempton dépendant lui-même du coefficient de compressibilité du fluide interstitiel.

$$\Delta u_w = B\,\Delta\sigma_v \quad (2)$$

- Méthode résultant des travaux de Lloret et Alonzo dans Couzy et all (2002) qui définit 8 paramètres fixant les variations de l'indice des vides e et de la teneur en eau w en fonction de la variation de la contrainte moyenne:

$$e = d - a\log(\sigma'_m) - b\log(s') + c\log(s')\log(\sigma'_m)$$
$$w = e - f\log(\sigma'_m) - g\log(s') + h\log(s')\log(\sigma'_m) \quad (3)$$

σ'$_m$: contrainte nette moyenne; s': succion nette égale à la succion augmentée de la pression atmosphérique. Cette méthode est utilisée par Savatier (2014) pour l'amélioration des essais double oedomètre.

2.2 Variation de la succion à long terme

Au niveau des talus du remblai et sur une épaisseur variant de 0.5 à 1.2m (1m en général) la succion sera variable et s'annulera en période pluvieuse. La stabilité devra donc être assurée avec les caractéristiques saturées.

Au cœur de remblai, le massif étant protégé contre les infiltrations et contre les remontées capillaires par les barrières b_1 et b_2, sa teneur en eau ne va varier qu'en fonction des échanges au niveau des talus. La succion et la teneur en eau vont converger vers la succion moyenne de l'air atmosphérique au niveau des talus.

La succion atmosphérique peut être estimée par la formule:

$$s = 10^{-3}\left[\frac{RT\rho}{ma}\right] ln\left(\frac{Pvs}{Pv}\right) \quad (4)$$

Pv: pression partielle en vapeur d'eau dans l'air; Pvs: pression saturée de vapeur d'eau; ma: masse vol. de l'air, ma = 1,204 kg/m^3 à 20°C; R: constante des gaz parfaits, R = 8,314 J mol^{-1}K^{-1}; T: température à 20°C, T = 293 K; s: succion en kilopascal; ρ: masse volumique du sol, ρ = 1 800 kg/m^3.

Le Tableau 1 donne les succions calculées pour différents degrés de saturation de l'air.

Les degrés de saturation donnant ces succions peuvent être comparés aux degrés de saturation moyens annuels de l'air en France Hexagonale donnés Tableau 2.

Tableau 1. Succion fonction de la saturation de l'air.

Saturation %	PVS/PV	ln(P_{VS}/P_V)	s (kPa)
50%	2,000	0,693	2524
85%	1,176	0,163	592
90%	1,111	0,105	384
95%	1,053	0,051	187
99%	1,010	0,010	37

Les succions à long terme en cœur de remblai restent donc supérieures à la succion à la mise en œuvre. Celle-ci sera donc dimensionnante pour le calcul de l'ouvrage.

Tableau 2. Humidités relatives moyennes en divers points de France Hexagonale.

Humidité relative moyenne annuelle par an (%)		
Pointe du Raz:86%	Poitiers: 79 %	Clermont-Ferrand: 73 %
Brest: 84 %	Biarritz: 78 %	Salon de Provence: 70 %
Lille: 83 %	Toulouse: 78 %	Saint Auban: 67 %
Reims: 82 %	Paris: 76 %	Nîmes: 66 %
Luxeuil: 82 %	Lyon: 76 %	Embrun: 64 %
Bordeaux: 81 %	Antibes: 76 %	Toulon: 56 %
Strasbourg: 79 %	Carcassonne: 75 %	Le Luc: 43 %

3 ETUDE DE COMPACTAGE POUR LA DETERMINATION DES PARAMETRES INITIAUX DU REMBLAI

3.1 Les essais réalisés et leurs objectifs

Les essais de laboratoire réalisés avaient pour objectif de reproduire l'état de compactage du sol avant montée du remblai. Cela dans l'optique d'estimer son état initial, son évolution en fonction de la teneur eau et sous l'effet d'un chargement. L'objectif final étant d'alimenter les paramètres utilisés dans les calculs de stabilité.

A cet effet un programme de laboratoire alliant essais de terrassement classiques et essais de mécanique des sols a été mis en œuvre. Ce dernier s'est basé sur:

- des essais d'identifications afin de vérifier l'homogénéité des matériaux testés et leur concordance avec ceux du projet;
- des essais Proctor avec mesure de succion au papier filtre entre-calées entre les couches compactées afin de déterminer les références de compactage et la valeur de la succion initiale en fonction de la teneur en eau de compactage;
- des essais œdométriques au double œdomètre afin d'observer l'effet de la perte de succion sous imbibition;
- des essais triaxiaux afin de déterminer les paramètres de cisaillement en condition drainée;
- des essais IPI et CBRi afin d'étudier la traficabilité en fonction de la teneur en eau initiale et donc de la succion initiale.

3.2 Les résultats obtenus

La figure ci-dessous est un exemple de résultats obtenus, à savoir la densité sèche, la succion et la cohésion non drainée (à l'essai triaxial) en fonction de la teneur en eau de compactage, et ceci pour deux énergies de compactage: l'OPN et l'OPM.

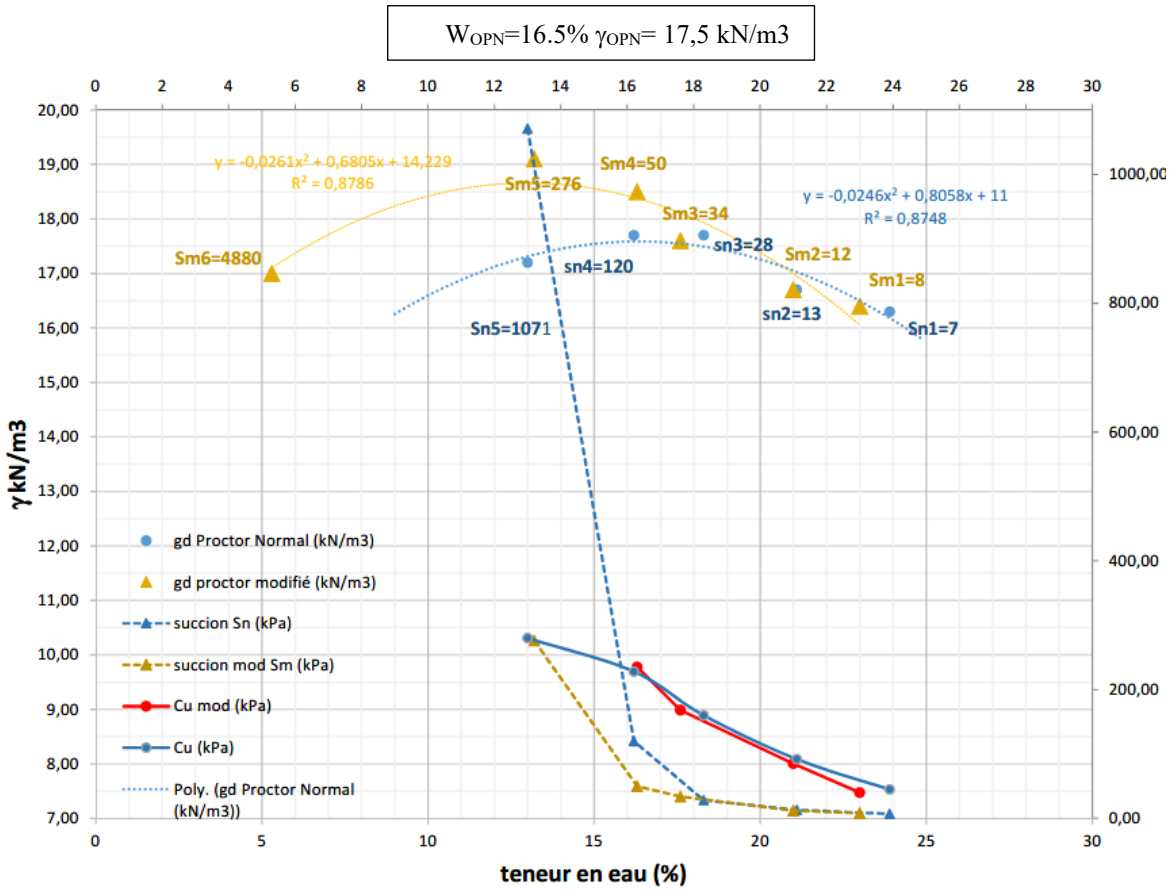

Figure 2. Essai Protor Normal et Modifié avec mesure de la succion.

Ces essais ont permis de déterminer les paramètres suivants:

- Identification: sol F2 ou F3 du GTR_{2023} dans un sol « m » ou « h »; teneur en eau 17.6<W<27.6 %; teneur en eau moyenne W_{moy}=23% limite d'Atterberg moyenne Wl=32 à 36 IP=11 à 15.
- Proctor Normal teneur en eau W_{OPN}= 16.5% masse volumique sèche γ=17.7kN/m; succion 50 kPa;
- Proctor Modifié teneur en eau à l'Optimun $W_{OPM=}$ 12.4% masse volumique sèche γ_{OPM}= 18.8 kN/m^3 succion 270 kPa
- Essai triaxial saturé angle de frottement ϕ'= 28° cohésion c'=7 kPa.

Si l'on choisit une consigne de mise en œuvre des limon avec un compactage à 98% de l'OPN pour des teneurs en eau variant de 98% de l'OPN+0.5% à 95% de l'OPM+0.5% côté humide, on obtient les paramètres donnés dans le Tableau 3:

Tableau 3: succion et saturation pour les optimum Proctor et les objectifs de compactage.

	W(%)	gd (kN/m^3)	w_{sat} (%)	Sr (%)	Succion (kPa)
OPN	16,5	17,7	19,5	85%	50
95% OPN W_{OPN}+0,5	17	16,8	22,4	76%	50
OPM	12,4	19,1	15,3	81%	276
95% OPM W_{OPM}+0,5	13	18,1	18,1	72%	276

4 ETUDE DE STABILITE DU REMBLAI

4.1 Stabilité générale

Un calcul de stabilité de remblai a été mené en considérant les caractéristiques de compactage présentées précédemment.

Le calcul a été mené pour un remblai de hauteur variant entre 7 m et 20 m avec une risberme à 10 m et avec une cohésion homogène dans le remblai comprise entre 7 à 35 kPa. L'augmentation de la cohésion par rapport aux mesures triaxiales est due à la prise en compte de la succion par application de la formule suivante:

$$C_{cor}=c'+F(u_a-u_w; s_{air}, S_{rair}) \tan(\phi') \quad (5)$$

Avec:

- Domaine quasi saturé (Boutonnier 2007):

$$F(u_a-u_w;\ s_{air},\ S_{rair}) = -u_w \qquad (6)$$

A noter que l'augmentation de la cohésion due à la succion n'est pas considérée sur une bande de 1 m au droit des talus (voir Figure 1 et Figure 4).

L'évolution de la succion initiale sous l'effet d'un chargement a été vérifiée par une méthode calculatoire via l'approche quasi saturée dépendant de la compressibilité du fluide interstitiel (Boutonnier 2007 et Mahmutovic 2016). Les résultats sont présentés sur la figure ci-dessous.

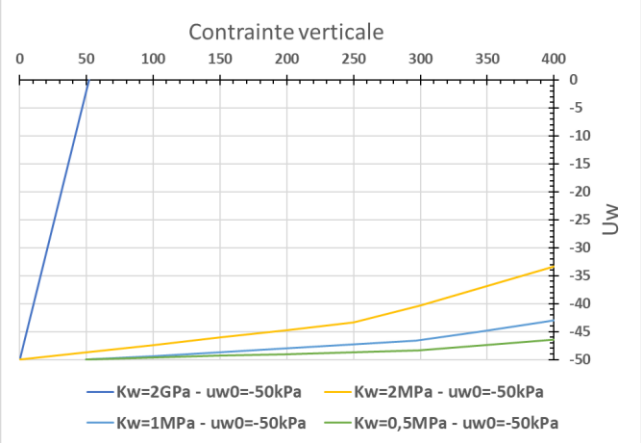

Figure 3. Evolution de la succion en fonction du chargement vertical.

La courbe bleue correspond à un sol complétement saturé en considérant un fluide interstitiel ayant la compressibilité d'une eau pure. Les autres courbes correspondent à un sol quasi saturé compacté dans les conditions mentionnés ci-avant. La succion varie entre 47 kPa et 33 kPa sous l'effet d'une montée de remblai de 20m, ce qui équivaut à une cohésion équivalente du sol non saturé c_{cor} compris entre 24 kPa et 32 kPa.

Le Tableau 5 donne les coefficients de sécurité pour des calculs de stabilité réalisés avec le logitiel Talren. La coupe de calcul type utilisée avec Talren est donnée Figure 4:

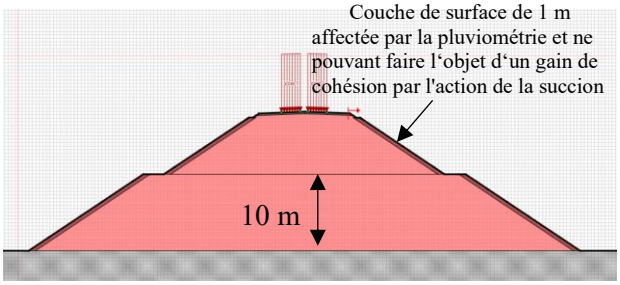

Figure 4. Coupe de calcul Talren pour un remblai de plus de 10m.

Ces calculs sont fait pour des cohésions équivalentes c_{cor} allant de 7 à 35 kPa et pour des hauteurs de remblai: de 7 à 35m. (résultats sont donnés Tableau 5).

Chaque calcul est fait avec les coefficients partiels de l'Eurocode 7 donnés Tableau 4.

Tableau 4.Eurocode coefficients de sécurité retenus.

Nom du coefficient partiel Eurocode	**EC7 Situation Fondamentale pour un Ouvrage Courant**
Γ_φ	1.25
Γ_c	1.25
Γ_{cu}	1.40
Γ_{Q}(1)	1.0 défavorable/1.3 variable défavorable (1)
Γ_{s3}	1.2 (ouvrage sensible aux déformations)

Tableau 5. Coefficients de sécurité – calculs Talren.

F	H_R (m)	9	11	13	15	18	20
C cor (kPa)	7	0,92	0,92	0,92	0,90	0,86	0,83
	15	1,12	1,12	1,11	1,06	0,99	0,97
	20	1,24	1,29	1,20	1,15	1,07	1,03
	25	1,35	1,4	1,30	1,24	1,15	1,11
	30	1,46	1,50	1,39	1,32	1,24	1,17
	35	1,60	1,60	1,51	1,42	1,32	1,24

Le Tableau 5 montre que la stabilité du remblai n'est pas garantie pour une cohésion de 7 kPa. La prise en compte d'une cohésion corrigée de l'ordre de 15 kPa due à la succion dans les sols non saturés se trouvant au sein du remblai permet de garantir la stabilité pour toutes les hauteurs testée sauf 20m (F=0.97).

4.2 Recommandations pour l'utilisation de cette approche

La prise en compte d'une succion dans les calculs de stabilité doit être accompagnée:

- D'un programme de laboratoire initial pour identifier les variations de succion en fonction de la teneur en eau et de l'énergie de compactage;
- D'une estimation de la variation de la succion en fonction du chargement vertical;
- La réalisation d'une planche d'essai de compactage pour confirmer les paramètres de compactage;
- D'un contrôle strict des matériaux durant le chantier, notamment les teneurs en eau de compactage se rapprochant de ce qui est fait dans le domaine des barrages;
- Le suivi via une auscultation des succions présentes dans le corps de remblai pendant 1

ans. Ceci peut être fait par la méthode du papier filtre placé dans une chambre ménagée par forage dans le corps du remblai. On peut également utiliser des tensiomètres placés dans le corps de remblai. Des questions de qualité de la mise en place, de temps de réponse et de fiabilité dans le temps vont alors se poser. D'une manière plus prospective on pourrait envisager d'utiliser des pénétromètres statiques ou des pressiomètres à mesure de succion conçus en utilisant les développements théoriques présentés dans Savatier (2016) et Savatier et all (2020).

5 CONCLUSIONS

Ce papier a montré qu'il était possible, sous certaines conditions, de prendre en compte la succion initiale après compactage dans les calculs de stabilité d'ouvrages en terre. Cette approche permet de raidir les talus et donc de faire des économies au niveau des emprises au sol et en quantité de matériaux. Il convient pour cela de parfaitement identifier les paramètres après compactage et l'évolution de ces derniers durant la montée du remblai. Par ailleurs, des dispositions constructives afin de limiter les transferts d'eau au sein du remblai doivent être prises en compte, tout comme une auscultation spécifique.

REFERENCES

Boutonnier L. (2007). Comportement hydromécanique des sols fins proches de la saturation. Cas des ouvrages en terre: coefficient B, déformations instantanées et différées, retrait / gonflement. Thèse INPG Grenoble soutenue le 23 octobre 2007.

Fleureau J-M., Verbrugge J-C., Huergo P-J., Gomes Correia A., Kheirbek-Saoud S. (2002). Aspects of the behavior of compacted clayey soils on drying and wetting paths. *Canadian Geotechnical Journal*, 39, p.1341-1357. DOI 10.1139/T02-100.

Hilf J-W. (1948). Estimating construction pore pressure in rolled earth dams. *Proceedings of 2nd International Conference on Soil Mechanics and Foundation Engineering. Rotterdam, vol. 3, p.234-240.*

Lloret et Alonzo (2002) dans Coussy O. et Fleureau J.M. *Mécanique des sols non Saturés, Traité Mim (2002), Ed Lavoisier, p 89.*

Mahmutovic D. (2016). Etude du comportement des sols proches de la saturation – validation numérique sur essais de laboratoire et ouvrages en terre. Thèse Université Grenoble Alpes soutenue le 8.Décembre.2016.https://jngg2016.sciencesconf.org/browse/speaker4866.html?authorid=378381,330788.

Savatier V. (2014)-Sol effondrable-essai double oedomètre-Interprétation et proposition d'amélioration.,JNGG2014. https://vdocuments.mx/sol-effondrable-cfmr-journees-nationales-de-geotechnique-et-de-geologie.html?page=1.

Savatier V. (2016) Stress path during pressuremeter test and link between shear modulus and Menard pressuremeter modulus in unsaturated fine soils. UNSAT 2016.

Savatier V, Silvestre-brac V , Cazaux-Ginestet G., (2020) essai de pénétration statique chemin de contrainte en sol non saturé JNGG 2020. https://www.geotechnique.org/jngg2020/index.html.

Collectif (2023) Guide des terrassements des remblais et des couches de forme édition 2023 *Editions CEREMA* Fascicule 2 Annexe1 p12.

Proceedings of the XVIII ECSMGE 2024
GEOTECHNICAL ENGINEERING CHALLENGES
TO MEET CURRENT AND EMERGING NEEDS OF SOCIETY
© 2024 the Authors
ISBN 978-1-032-54816-6
DOI 10.1201/9781003431749-137
Open Access: www.taylorfrancis.com, CC BY-NC-ND 4.0 license

ECSMGE 24
XVIII EUROPEAN CONFERENCE ON SOIL MECHANICS AND GEOTECHNICAL ENGINEERING

Shear and creep behaviour of frozen granular soils under compressive and tensile loading

Comportement en cisaillement et en fluage des sols granulaires gelés sous charge de compression et de traction

U. Schindler*, S. Chrisopoulos, S. Vogt, R. Cudmani
Technical University of Munich, Chair and Testing Institute of Soil Mechanics and Foundation Engineering, Rock Mechanics and Tunneling, Munich, Germany

u.schindler@tum.de

ABSTRACT: The mechanical behaviour of frozen soils currently gets progressively into the focus of fundamental research and is an ongoing challenge in the increasing use of artificial ground freezing as well as in the context of the thawing and refreezing of permafrost due to global warming. In both cases, frozen soils exhibit shear and creep deformation resulting from both compressive and tensile loading. However, relatively few experimental studies deal with the tensile shear and creep behaviour of frozen soils compared to investigations under compressive loading. Therefore, this study presents a comprehensive investigation of the tensile behaviour of frozen granular soils, including uniaxial shear and creep tests at various temperatures under compressive and tensile loading. Evaluation of the test data and comparison with data from the literature reveal the fundamental characteristics of two different frozen granular soils under tensile loading and highlight their essential differences from behaviour under compression. Overall, this comprehensive study aims to contribute to a more fundamental understanding of frozen soils' complex mechanical behaviour under both compressive and tensile loading.

RÉSUMÉ: Le comportement mécanique des sols gelés fait actuellement l'objet d'une recherche fondamentale progressive et constitue un défi permanent dans le cadre de l'utilisation croissante de la congélation artificielle des sols ainsi que dans le contexte du dégel et du regel du pergélisol en raison du réchauffement climatique. Dans les deux cas, les sols gelés présentent des déformations de cisaillement et de fluage résultant de charges de compression et de traction. Cependant, relativement peu d'études expérimentales traitent du comportement des sols gelés en matière de cisaillement et de fluage par rapport aux études sur les charges de compression. C'est pourquoi cette étude présente une étude complète du comportement en traction des sols granulaires gelés, y compris des essais de cisaillement uniaxial et de fluage à différentes températures sous charge de compression et de traction. L'évaluation des données d'essai et la comparaison avec les données de la littérature révèlent les caractéristiques fondamentales de deux sols granulaires congelés différents sous charge de traction et mettent en évidence leurs différences essentielles par rapport au comportement sous compression. Dans l'ensemble, cette étude complète vise à contribuer à une compréhension plus fondamentale du comportement mécanique complexe des sols gelés sous charge de compression et de traction.

Keywords: Frozen soil; shear; creep; tensile loading.

1 INTRODUCTION

In general, frozen soil is a complex multiphase material consisting of four components: mineral grains, unfrozen pore water, frozen pore water, and air voids. Particularly in saturated frozen granular soils with low fine content (i.e. < 0.06 mm), only two components are relevant as the grain skeleton is embedded in the ice matrix. As Cudmani et al. (2023) described, the frozen soil's shear resistance results from a complex interaction between the grain skeleton and the ice matrix. On the one hand, the ice hinders the dilatancy of the grain skeleton, leading to an increase in grain-to-grain contact forces and shear resistance. On the other hand, the grains retard the development and spreading of cracks in the ice matrix and enhance the shear resistance of the ice. Probably, the most interesting and distinctive feature of frozen soils is their rate- and temperature-dependence resulting from the viscous behaviour of the ice. For example, in uniaxial creep tests under compressive loading, the strain rate first decreases (primary creep), then reaches a minimum value (secondary creep) and afterwards increases with time (tertiary creep), resulting in unstable frozen soil behaviour at this point. Despite the well-studied shear and creep behaviour of frozen soils under compressive loading, comparatively fewer studies under tensile loading are available in the literature. However, from a practical point of view, taking into account the tensile strength of frozen soils has significant potential to improve the current

mechanical designs of frozen soil bodies. Moreover, in permafrost engineering scenarios such as slope and ground stability, frozen soils exhibit not only compressive loading, but also tensile loading. Here, understanding the complex frozen soil shear and creep failure processes under tension becomes even more relevant due to climate change and the temperature rises in permafrost regions. Therefore, in this study, we focus on the tensile behaviour of frozen granular soils in both shear and creep tests and compare it to that under compression, providing important insights into frozen soil engineering under compressive and tensile loading.

2 METHODS

2.1 Testing materials

This study introduces a lab testing programme, including standard uniaxial compression tests and special, indirect uniaxial tensile tests at a temperature of -5 °C. Both types of experiments were performed with frozen sandy gravel, which is obtained from drilling campaigns in southern Germany. Moreover, we use comprehensive experimental data of frozen medium sand by Eckardt (1979, 1982) to compare its uniaxial creep behaviour under compressive and tensile loading. Figure 1 shows the grain size distributions of both granular soils.

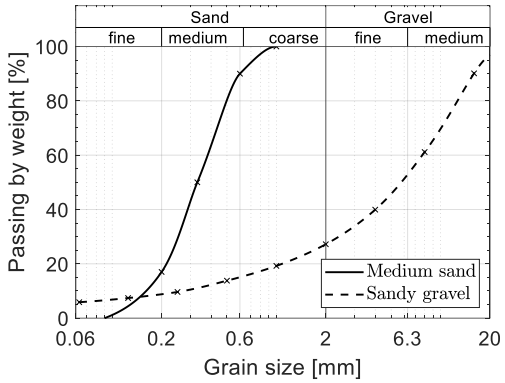

Figure 1. Grain size distributions of our own tested sandy gravel and medium sand after Eckardt (1982).

2.2 Sample preparation

Our experimental study includes two different sample types of frozen sandy gravel. We prepared full cylinder samples for uniaxial compression tests, while hollow cylinder samples were used for uniaxial tensile tests. Figure 2 illustrates examples of the prepared full and hollow cylinder samples with the frozen sandy gravel tested in this study. Firstly, we briefly summarise the sample preparation method for both specimen types. In both cases, dry material was filled into a cylindrical mould with a diameter of 100 mm and a height of 250 mm. Subsequently, the mould was closed and flushed with CO2 to displace the air within the sample. Next, the sample was slowly saturated from the bottom to the top with de-aired water. Afterwards, the mould was sealed airtight and placed into a cooling chamber to freeze the sample isotopically to the testing temperature of -5 °C. Finally, the frozen samples were pushed out of the mould, and their end plates were trimmed and smoothed out using cutting tools. At the end of the preparation procedure, the full cylinder samples had a diameter of about 100 mm and a height of about 200 mm.



Full cylinder *Hollow cylinder*

Figure 2. Examples of the two tested types of frozen sandy gravel samples.

In contrast to the above procedure, the preparation of the hollow cylinder samples began by placing a 40 mm diameter steel rod in the centre of the mould. The actual preparation process was then essentially the same as for the full cylinder samples, including pushing out the steel rod of the frozen sample. The hollow cylinder samples had an outer diameter of about 100 mm, an inner (hole) diameter of 40 mm and a height of about 200 mm.

The full and hollow cylinder sample characteristics were very similar, with an average gravimetric water content of 14.5 %, dry unit weight of 1.87 g/cm^3 and an average degree of saturation of 89 %.

2.3 Testing equipment for indirect tensile tests using the hydraulic fracturing method

In order to investigate the frozen soil tensile shear behaviour, either so-called direct or indirect tensile tests are reported in the literature. Although direct tensile tests are desirable, they are more challenging to perform and more time-consuming than indirect tensile tests. In fact, from a practical point of view, indirect tensile tests seem sufficiently accurate to approximate the tensile behaviour of frozen soils, with the advantage of reduced test effort and less complex measurement equipment (Wang et al., 2023). In this study, we performed indirect tensile tests on frozen gravel using a hollow-cylinder device based on the hydraulic fracturing method (HFM) proposed by Al-

Khateeb and Buttlar (2000) and Perras and Diederichs (2014) in the field of testing asphalt and rock mechanics. This practical and comparably simple testing method has recently been demonstrated by Wang et al. (2023) for frozen silt. In this study, we applied HFM to frozen coarse-grained soils for the first time. In the following, we briefly summarise HFM; for further details, see Al-Khateeb and Buttlar (2000) and Wang et al. (2023). HFM is similar to the dilatometer test conducted in boreholes in situ. The core aspect of HFM is the use of a hollow cylindrical specimen in which the internal pressure p is gradually increased. This pressure is applied until the specimen reaches its peak strength, indicating shear failure under tension (radial splitting of the sample). Since the internal pressure p can be well controlled, HFM allows different types of loading, such as monotonically increasing p or keeping p constant (creep). As such, HFM is comparatively cost-effective and provides a technically simple yet fundamental insight into the mechanical response of the specimen under stress. Figure 3 shows our used testing set-up and supplementary equipment to perform HFM on frozen gravel.

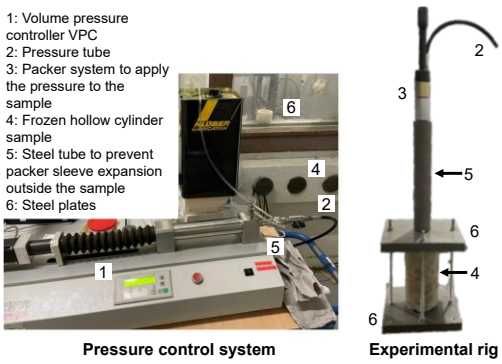

Figure 3. Experimental set-up to perform hollow-cylinder tensile tests (HFM) at the Center for Geotechnics of the Technical University of Munich.

As can be seen in Figure 3, the internal pressure p was applied to the sample via a conventional packer system commonly used for grouting works. The applied pressure was controlled by a volume pressure controller (VPC). In addition, a steel tube at the top and bottom of the packer prevented the packer membrane from expanding outside the sample. Consequently, only the packer membrane inside the hollow cylinder expanded and applied pressure to the sample. Steel plates at the top and bottom of the sample hindered vertical displacements of the sample. Hence, the sample only deforms radially during the tests. The packer membrane and the contact areas of the steel plates with the sample were lubricated to reduce friction. In order to convert the measured internal pressure p into the stress state of the sample, based on theoretical and mechanical considerations, Perras and Diederichs (2014) and Wang et al. (2023) proposed the following equation for the tangential stress σ_θ:

$$\sigma_\theta = \sigma_t = p\left(\frac{R^2+r^2}{R^2-r^2}\right) \quad (1)$$

In Equation 1, σ_θ corresponds to tensile stress σ_t in HFM, while p is the applied internal pressure. Moreover, r is the radius (location in the sample) at which σ_t is evaluated, and R is the outer radius of the hollow cylinder. Based on our tested sample dimensions for frozen gravel described in Section 2.2, Equation 1 results in $\sigma_t \approx 1.38 \cdot p$ at the outer surface with $r = 20$ mm and $R = 50$ mm.

2.4 Testing program

In order to investigate the difference in the shear behaviour between compressive and tensile loading, five uniaxial compression and five tensile tests on frozen gravel were performed at −5.0 °C. The results of these freezing tests are discussed in the next section.

3 EXPERIMENTAL RESULTS OF UNIAXIAL SHEAR TESTS

3.1 Uniaxial compression tests

Figure 4 depicts the experimental results of uniaxial compression tests with frozen gravel at -5 °C for different constant axial strain rates $\dot{\varepsilon}_1$ from 0.01 %/min to 1.0 %/min.

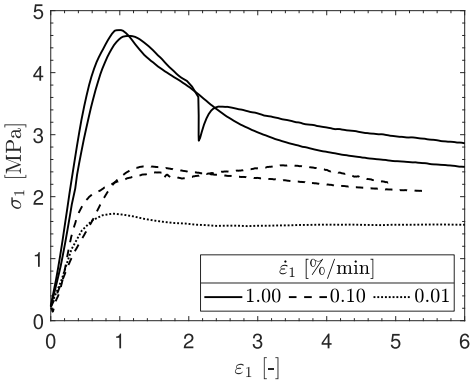

Figure 4. Evolution of axial stress σ_1 over axial strain ε_1 in uniaxial compression tests at -5 °C with different constant axial strain rates $\dot{\varepsilon}_1$ for frozen sandy gravel.

The test results in Figure 4 are in accordance with the well-known rate-dependent behaviour of frozen soils, as the uniaxial compression (peak) strength σ_c increases with increasing axial strain rate. In fact, σ_c ranges between 1.5 MPa up to about 4.5 MPa. This is consistent with studies like Zhao et al. (2020), who

reported a similar rate-dependent order of magnitude for frozen gravel at -5 °C.

3.2 Indirect uniaxial tensile tests (HFM)

After analysing the shear strength of frozen gravel in uniaxial compression tests, the uniaxial tensile behaviour is discussed and compared with that under compression. Figure 5 shows the experimental results of HFM on frozen sandy gravel at -5°C. In particular, Figure 5(a) describes the measured and evaluated volume increase of the packer membrane ΔV during the tests. The radial expansion of the packer membrane leads to radial deformation of the frozen soil sample and, after a particular stage, to tensile/shear failure. In this context, Figure 5(b) compares the tensile stress σ_t with ΔV, where σ_t is calculated from the measured inner pressure p according to Equation 1. At the beginning, σ_t slowly increases with increasing ΔV. Afterwards, there is complete contact between the packer membrane and the frozen soil sample. Hence, σ_t increases faster with ΔV until the peak tensile strength $\sigma_{t,u}$ is reached. The sample shows brittle failure by abruptly enlarging cracks (see Figure 6) and consequently, the stress instantaneously drops to zero.

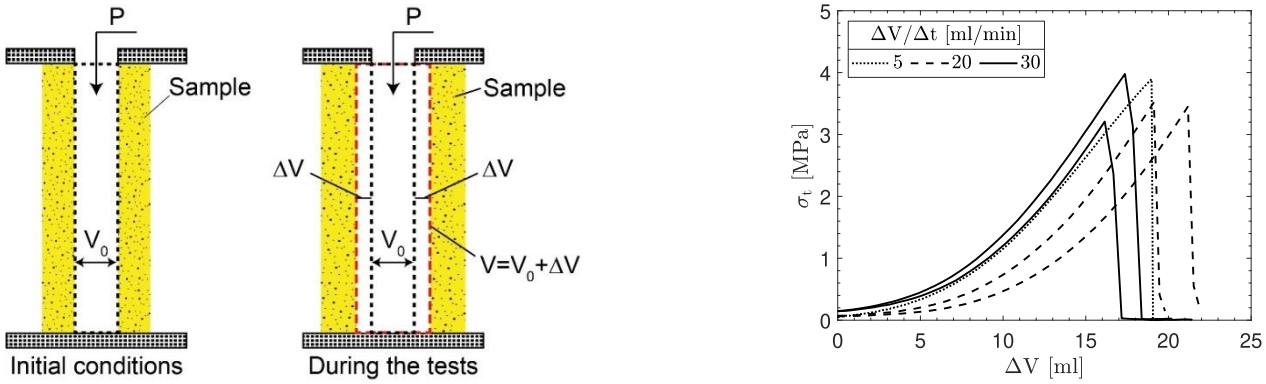

(a) Schematic view of HFM evaluation procedure for ΔV, which represents the change of the volume within the packer membrane.

(b) HFM test results on frozen gravel

Figure 5. Experimental results of HFM tests on frozen sandy gravel at -5°C. σ_t represents the uniaxial tensile strength of the sample.



Figure 6. Example of a sandy gravel sample tested and its corresponding crack pattern after tensile testing.

The peak strength $\sigma_{t,u}$ in Figure 5(b) ranges from 3.2 MPa to 4.0 MPa with an average value of 3.6 MPa. In addition, the experimental results do not indicate a pronounced rate-dependence of the frozen soil tensile behaviour, as $\sigma_{t,u}$ is mostly independent of the investigated incremental volume increase $\Delta V/\Delta t$. In fact, this is consistent with experimental observations by Schulson and Duval (2009), which revealed no significant rate-dependence of the tensile strength of polycrystalline ice. Therefore, the tensile shear behaviour of the frozen soil should also be less affected by the rate of shear loading, as the polycrystalline ice contained in the frozen soil controls the viscous behaviour. For validation purposes of the measured tensile strengths of $\sigma_{t,u}$, Figure 7 compares our own experimental results with literature data. As can be seen in Figure 7, the peak tensile strengths of frozen gravel generally align in terms of magnitude with data from the literature for other frozen soils. Note that the results from tensile testing generally show larger scatter compared to data from compressive tests. Therefore, we recommend conducting a sufficient number of tests to ensure reliability and accuracy for the evaluation of the data for tensile loading. A key observation from the comparison in Figure 7 is the tensile strength of pure ice (blue symbols), which is approximately 1 MPa and appears to be largely temperature-independent. The tensile strength of the frozen soils tested in Figure 7 is, with some exceptions, higher than that of the pure ice. This suggests a positive influence of the granular skeleton on the tensile strength as compared to pure ice. The granular skeleton hinders the weakening crack initiation and propagation in the ice matrix. Therefore, the tensile strength of frozen soils can be significantly higher than that of pure ice. Indeed, the shear resistance of the granular skeleton could also

contribute to the overall tensile strength. However, the measurement technology used in the reported tensile tests as well as in our tests by HFM is not sophisticated enough to confirm this assumption. Further investigations using the latest instrumentation and measurement techniques, focusing on micro-scale resolution, are required in the future. From a practical point of view, comparing the tensile strength $\sigma_{t,u}$ (Figure 5(b) and Figure 7) and the compression strength σ_c (Figure 4) of frozen gravel, we conclude that the ratio of $f_{t/c} = \sigma_{t,u}/\sigma_c$ is not constant for a given temperature. It rather depends on the considered compression strength σ_c and its corresponding axial strain rate $\dot{\varepsilon}_1$. For instance, assuming a mostly rate-independent tensile strength $\sigma_{t,u}$ even for very low shear rates, $f_{t/c}$ is only less than one for $\sigma_c(\dot{\varepsilon}_1 = 1.0\ \%/\mathrm{min})$, when comparing the results in Figure 4 with Figure 5(b).

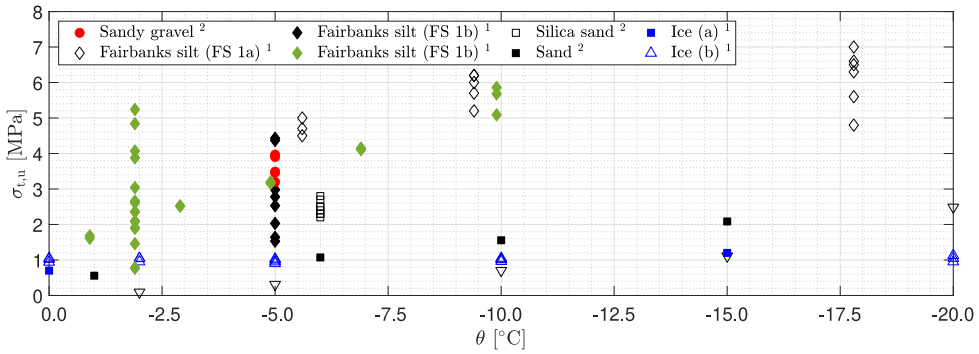

Figure 7. Comparison of the peak uniaxial tensile strength $\sigma_{t,u}$ obtained from our own tests with frozen sandy gravel (red symbols) and literature data at different temperatures. [1] direct tensile test; [2] indirect tensile test. FS 1a: Haynes and Karalius (1977). FS 1b/1c: Zhu and Carbee (1987). Silica sand: Bragg and Andersland (1981). Sand: Shen et al. (2022). Ice (a): Akagawa and Nishisato (2009). Ice (b): Schulson and Duval (2009).

For $\sigma_c(\dot{\varepsilon}_1 < 1.0\ \%/\mathrm{min})$, $f_{t/c}$ is greater one and thus, the tensile strength is greater than the compared compression strength.

In conclusion, our indirect tensile tests on frozen sandy gravel and their comparison with literature data demonstrate frozen soils' significant and considerably high tensile strengths. Taking into account physical considerations and experimental investigations on polycrystalline ice, the frozen soil tensile strength shall be mostly rate-independent. Consequently, the essential mechanical behaviour and the peak strength of frozen soils under tensile loading can differ significantly from the one under compressive loading.

4 COMPARISON OF UNIAXIAL CREEP TESTS UNDER COMPRESSIVE AND TENSILE LOADING

4.1 Creep tests on frozen medium sand after Eckardt (1979, 1982)

Although the experimental results and discussions in Section 3 indicate that in some cases, the uniaxial tensile strength is higher than the compressive strength for frozen soils, from a practical point of view in relation to the mechanical design of frozen soil bodies, the creep behaviour and therefore the service limit state is more important than the ultimate limit state. Based on the comprehensive experimental data by Eckardt (1979, 1982), we compare the creep behaviour of frozen medium sand under tensile and compressive loading and highlight their essential differences. In this context, Figure 8 depicts uniaxial creep tests for different axial compression (solid lines) and tensile (dashed lines) stresses at -5 °C and -10 °C. The results in Figure 8 show the typical creep behaviour, characterized by a continuous increase in axial strain over time under both tension and compression. However, a crucial observation is the time-dependent evolution of creep deformation under tensile loading, which in two cases ($\sigma_{1,c/t} = 1.0$ MPa and $\sigma_{1,c/t} = 2.0$ MPa) is notably faster than under equivalent compression stress state. This is illustrated by the sudden occurrence of creep failure in two tensile tests within a short period at -5°C and -10°C, whereas no such failure is observed in the equivalent compressive creep tests. Furthermore, the initial axial deformations during the load application ($t < 10$h) are higher under compression than under tension. This indicates a higher initial frozen soil stiffness under tension than under compression. Nevertheless, as can be seen in Figure 8, the subsequent creep phase under compression is significantly more ductile than that under tension, where it is predominantly brittle, with the potential for sudden failure.

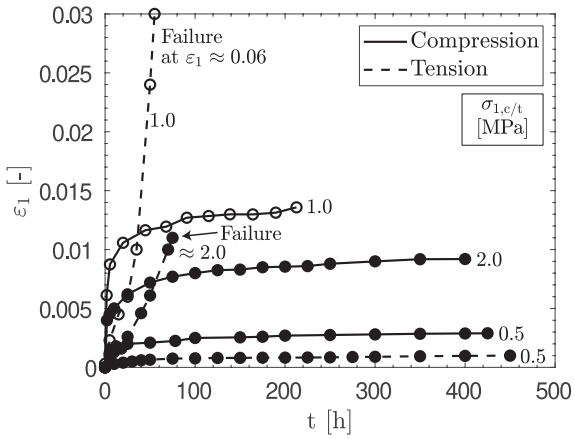

Figure 8. Experimental results of uniaxial creep tests with frozen medium sand under compressive and tensile loading. Open symbols at -5°C and filled symbols at-10°C. Data after Eckardt (1979, 1982).

In summary, the creep strength under tensile stress is significantly lower than the creep strength at the equivalent compressive stress state. Furthermore, the deformation behaviour under tension appears to be brittle, whereas the frozen soil exhibits largely ductile characteristics under compression. Note that further experimental investigation of the frozen soil creep behaviour under tensile loading is required to better understand and quantify these complex mechanical processes and differences from the known creep behaviour under compression.

5 CONCLUSIONS

This study presents a comprehensive analysis and comparison of the shear and creep behaviour of frozen sand and gravel under compressive and tensile loading. The experimental results show the following significant differences in mechanical behaviour between uniaxial compressive and tensile loading:

- The frozen soil tensile strength amounts to comparably high values and may even be higher than the corresponding compression strength.
- The uniaxial creep strength is lower in tension than in compression at the same stress levels and temperatures. Consequently, under the same stress and temperature conditions, creep failure will occur much earlier under tension than under compression.
- In both tensile shear and creep tests, frozen granular soil exhibits a pronounced brittle behaviour when compared to its ductile characteristics under compressive loading.

Taking into account the scatter and sudden failure observed in the tensile tests, we recommend extensive testing to obtain reliable data on the tensile behaviour of frozen soils before their tensile shear and creep strength are considered in practical applications.

REFERENCES

Akagawa, S., & Nishisato, K. (2009). Tensile strength of frozen soil in the temperature range of the frozen fringe. *Cold regions science and technology*, *57*(1), 13-22.DOI: https://doi.org/10.1016/j.coldregions.2009.01.002

Al-Khateeb, G. G., & Buttlar, W. G. (2000). Hollow-Cylinder Tensile Tester for asphaltic paving mixtures. In *Proceedings of the Mid-Continent Transportation Symposium* (pp. 14-19).

Bragg, R. A., & Andersland, O. B. (1981). Strain rate, temperature, and sample size effects on compression and tensile properties of frozen sand. *Engineering Geology,* 18(1-4), 35-46. DOI: https://doi.org/10.1016/0013-7952(81)90044-2

Christ, M., & Kim, Y. C. (2009). Experimental study on the physical-mechanical properties of frozen silt. *KSCE Journal of Civil Engineering*, *13*, 317-324. DOI: http://doi.org/10.1007/s12205-009-0317-z

Cudmani, R., Yan, W., & Schindler, U. (2023). A constitutive model for the simulation of temperature-, stress-and rate-dependent behaviour of frozen granular soils. *Géotechnique*, 73:12, 1043-1055. DOI: https://doi.org/10.1680/jgeot.21.00012

Eckardt, H. (1979). Tragverhalten gefrorener Erdkörper (Bearing capacity of frozen soil bodies). *PhD thesis*, University of Karlsruhe. Vol. 81. (in German).

Eckardt, H. (1982). Creep tests with frozen soils under uniaxial tension and uniaxial compression. In *Proceedings of the 4th Canadian Permafrost Conference*, pages 365–373, Calgary, Canada.

Haynes, F. D., & Karalius, J. A. (1977). Effect of temperature on the strength of frozen silt. *Report No. 77-3*. Department of Defense, Department of the Army, Corps of Engineers, Cold Regions Research and Engineering Laboratory.

Perras, M. A., & Diederichs, M. S. (2014). A review of the tensile strength of rock: concepts and testing. *Geotechnical and geological engineering*, *32*, 525-546. DOI: http://doi.org/10.1007/s10706-014-9732-0

Schulson, E. M., & Duval, P. (2009). *Creep and fracture of ice*. Cambridge University press.

Shen, M., Zhou, Z., & Ma, W. (2022). Tensile behaviors of frozen subgrade soil. *Bulletin of Engineering Geology and the Environment*, *81*(3), 122. DOI: http://doi.org/10.1007/s10064-022-02616-z

Wang, H., Zhou, Y., Zhao, X., Ji, Y., & Zhou, G. (2023). Experimental study on tensile strength of warm frozen soil based on hydraulic fracturing method. *Cold Regions Science and Technology*, *212*, 103883. DOI: https://doi.org/10.1016/j.coldregions.2023.103883

Zhao, J., Zhang, P., Yang, X., & Qi, J. (2020). On the uniaxial compression strength of frozen gravelly soils. *Cold Regions Science and Technology*, *171*, 102965.DOI: https://doi.org/10.1016/j.coldregions.2019.102965

Zhu, Y., Carbee, D.L., 1987. Tensile strength of frozen silt. *CRREL. Report 87–15*. US Army Cold Regions Research and Engineering Laboratory.

Proceedings of the XVIII ECSMGE 2024
GEOTECHNICAL ENGINEERING CHALLENGES
TO MEET CURRENT AND EMERGING NEEDS OF SOCIETY
© 2024 the Authors
ISBN 978-1-032-54816-6
DOI 10.1201/9781003431749-138
Open Access: www.taylorfrancis.com, CC BY-NC-ND 4.0 license

ECSMGE 24
XVIII EUROPEAN CONFERENCE ON SOIL MECHANICS AND GEOTECHNICAL ENGINEERING

Influence of installation effects on the performance of laterally loaded pile groups

Influence des effets de l'installation sur les performances des groupes de pieux chargés latéralement

T. Schlager*, C. Moormann, H. Schiewe
University of Stuttgart, Institute of Geotechnical Engineering, Germany
**tobias.schlager@igs.uni-stuttgart.de*

ABSTRACT: A profound knowledge of the performance of laterally loaded piled foundations is important for the assessment of critical infrastructure which is mostly founded on deep foundations and which to an increasing extend has to resist lateral loads resulting from structures, variable loads and geohazards. An in-depth understanding of the performance of piled foundations due to lateral loading is relevant for the reliable design of new structures and for the assessment of the stability and serviceability of existing infrastructure. Available investigations on laterally loaded pile groups and current empirical or analytical methods mainly focus on bored piles. Opposite to that, there is very limited knowledge about the performance of full displacement pile groups although it can be expected that their behaviour is significantly influenced by the installation effects, like the change of stress-state and soil density. For realisation, tests on groups of 9 piles, installed as bored-piles and as full-displacement piles, are performed at Deltares Centrifuge, to quantify the impact of installation effects on the lateral load-displacement behaviour of the pile groups. Therefore, the horizontal soil pressure was measured directly on the pile surface by small earth pressure cells. The pile installation and the loading were executed during spinning, enabled by an innovative experimental system. In the paper based on a state-of-art assessment of the design of laterally loaded pile groups, the concept and the results of the centrifuge tests are analysed demonstrating the characteristic differences between bored and displacement piles.

RÉSUMÉ: Une connaissance approfondie des performances des fondations sur pieux chargés latéralement est importante pour l'évaluation des infrastructures critiques qui reposent principalement sur des fondations profondes et qui doivent de plus en plus résister aux charges latérales résultant de géorisques. Une compréhension approfondie des performances des fondations sur pieux dues aux charges latérales est pertinente pour la conception fiable de nouvelles structures et pour l'évaluation de la stabilité et de l'aptitude au service des infrastructures existantes. Les recherches disponibles sur les groupes de pieux chargés latéralement et les méthodes empiriques ou analytiques actuelles se concentrent principalement sur les pieux forés. À l'opposé, les connaissances sur les performances des groupes de pieux à déplacement complet sont très limitées, bien que l'on puisse s'attendre à ce que leur comportement soit influencé de manière significative par les effets de l'installation, tels que le changement d'état de contrainte et la densité du sol. Pour la réalisation, des tests sur des groupes de pieux de 9 pieux, installés comme pieux forés et comme pieux à déplacement complet, sont effectués à la Centrifugeuse Deltares, pour quantifier l'impact des effets d'installation sur les performances des groupes de pieux. Par conséquent, la pression horizontale des terres a été mesurée directement sur la surface du pieu par de petites cellules de pression des terres. L'installation des pieux et le chargement ont été exécutés pendant le filage, grâce à un système innovant. Dans l'article, le concept et les résultats des essais de centrifugation sont analysés.

Keywords: Pile groups; centrifuge testing; earth pressure cells; bored piles; displacement piles.

1 INTRODUCTION

Regarding the basic concept of laterally loaded pile groups, Figure 1 illustrates schematically for a laterally loaded 3x3 pile group the pile-pile interaction by shadowing effects caused by adjacent piles when the pile-spacing (S/D) is close. There are various findings about the exact distance needed, to avoid interaction overlapping effects; In EA-Pfähle (2013) six times the diameter (6D) is suggested as minimum distance.

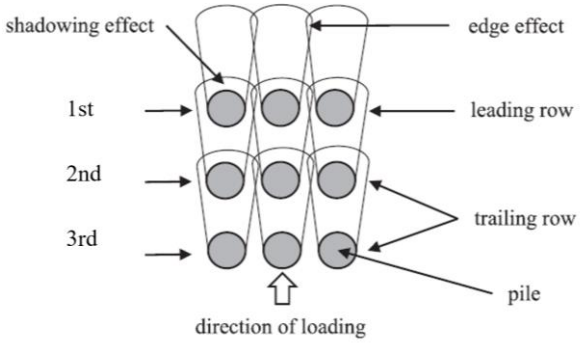

Figure 1. Scheme of a laterally loaded 3x3 pile group.

In Table 1 a selection of often cited research is documented. For driven piles, no tests were done at 1g gravity and for driven piles in the centrifuge, no pile-installation effects were considered. The values for the p-multipliers, an empirical reduction factor for p-y curves (Brown et al. (1988)), mentioned by Huang et al. (2001) for driven piles does not consider the impact of the installation method. Therefore, the performance of the piles in a group has to be reduced by a p-multiplier <1.0, in comparison to a single pile.

Table 1. List of p-multipliers from frequently cited research sorted by installation method.

Author	Testing	p-Multiplier			
Bored piles		1st	2nd	3rd	4th
Klüber*	1g	1.0	0.625	0.625	-
Kotthaus 1992	1g	1.0	0.72	0.64	-
Kotthaus 1992	ng	1.0	0.685	0.685	-
Huang 2001	In situ	0.93	0.7	0.74	-
Brown 1988	In situ	0.8	0.4	0.3	-
Driven piles		1st	2nd	3rd	4th
McVay 1994	ng	0.8	0.4	0.3	-
McVay 1995	ng	0.8	0.4	0.3	-
McVay 1998	ng	0.8	0.4	0.3	-
Rollins 2005	In situ	0.8	0.4	0.4	-
Huang 2001	In situ	0.89	0.61	0.61	0.66

Table 2 shows the p-multipliers from Huang et al. (2001) again, mentioned here as f_m-values for bored piles and for driven piles. The columns on the right-hand side show the installation-factors, called p_m-values, for both types of piles. The p_m-values can be regarded as extended p-multipliers, where the installation effects are already considered.

Table 2. P-multiplier by Huang et al. (2001) - with and without considering installation effects.

Row	Bored group piles		Driven group piles	
	f_m	p_m	f_m	p_m
1st (Leading)	0,93	0,88	0,89	1,57
2nd	0,7	0,66	0,61	1,08
3rd	0,74	0,7	0,61	1,08
4th	-	-	0,66	1,16

Objective of the proposed tests is to quantify the impact of pile group installation effects on the performance of laterally loaded pile groups covering replacement piles (bored piles) and full displacement piles (driven prefabricated piles) As shown before in Table 2, Huang et al. (2001) observed a potential of 76% higher load-factors (p-multiplier) for full displacement piles and in addition higher lateral pile resistances for piles in a group, compared to a single pile. Opposite to those findings, the load capacity of driven piles in a group must be currently reduced, recommended by official guidelines, e.g. EA-Pfähle (2013). By transferring Huang's findings from in-situ tests to centrifuge tests, the aim is to confirm the positive effects of a displacement pile installation for laboratory conditions, where boundary conditions can be controlled to generate reproduceable tests and to isolate the impact of the installation method.

2 EXPERIMENTAL METHODOLOGY

To realize the above-mentioned goals, six tests were performed in the Deltares Centrifuge.

Centrifuge modeling is indeed a technique used in geotechnical engineering to replicate the stress state experienced by full-scale prototypes in a scaled-down model. This technique allows to simulate the stresses and behaviors experienced by full-scale structures more accurately than traditional physical modeling methods.

Besides the already mentioned aspects of improving the understanding of the performance of laterally loaded pile groups, the way of performing this kind of pile group tests in a centrifuge is highly challenging. To model driven, fixed-headed piles in a centrifuge without stopping means that the piles have to be driven, rigidly fixed and loaded laterally in flight, without stopping the centrifuge in between. If the centrifuge would have to be stopped for further installations, this could cause significant changes of the stress state in the soil as well as for the soil-structure interaction. Due to the relaxation, the behaviour of the soil-structure interaction will fundamentally change. The results of the created output would be hardly definable. Outcomes could range from resembling driven piles to, in worst case, behaving like a bored pile group due to relaxation. Therefore, no installation effects would be figured out in the end. That's why maybe former research couldn't picture significant differences, affected by the method of pile installation.

2.1 Experimental layout

To enable in-flight installation and loading of the pile group construction, a special coupling system with a plug-in method was developed. The method allows to keep the piles in place, install them separately, fix the piles and the head plate together and load the system in horizontal direction at the pile-head level.



Figure 2. Plug-in method: open system before pile installation (left), coupled system after pile installation (right).

The intended gravity for the tests is 50g. Therefore, the planned scaling of the model is 1:50. The prototype of the piles is 18,75 m in length and 0.75 m in diameter. So, the model piles are scaled down to 37,5 cm in embedded-length and 1.5 cm in diameter.

As pictured in Figure 3, three levels of earth pressure cells (EPC) were mounted in the pile surface of the leading pile (LP) in the middle of the 1st row and the centre pile (CP) of the 3x3 pile group. The embedded depth of the EPC‘s is 1,5 m, 4,5 m and 7,5 m.

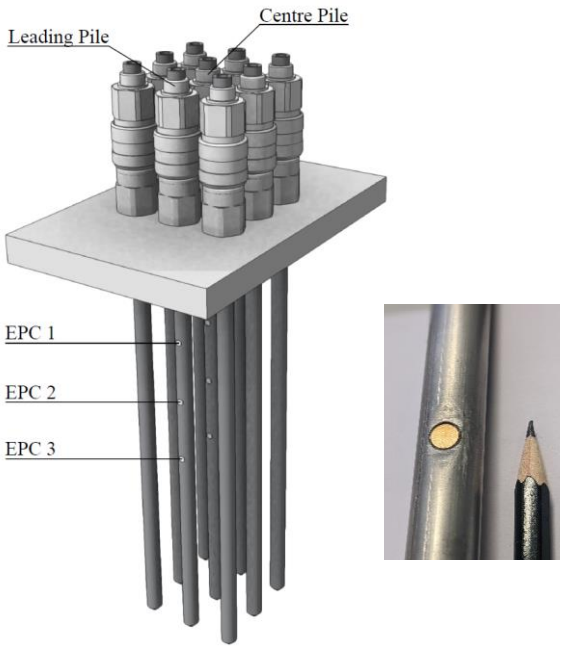

Figure 3. Model of fixed-headed pile group with applicated Earth pressure cells (EPC) in 3 levels at the centre pile (CP) and the leading pile (LP).

2.2 Test soil and sample preparation

The centrifuge tests take place in dry, Bascarp Sand No. 15 (Figure 4 & Table 3). The relative density of the sand was about $I_D = 55\%$ and $I_D = 30\%$. For sample preparation, the sand raining method was used.

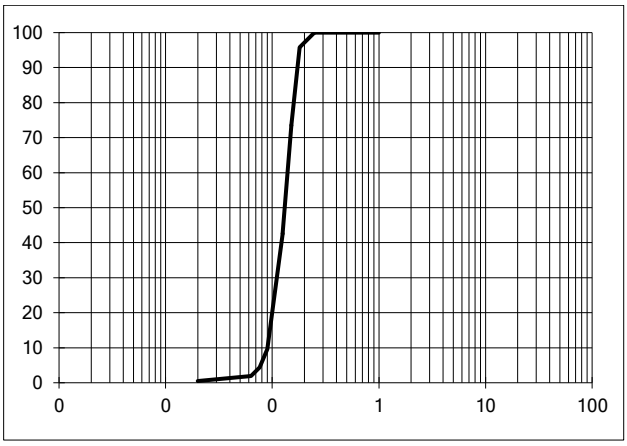

Figure 4. Grain size distribution Bascarp Sand No. 15.

Table 3. Properties of model sands for centrifuge tests (Nielsen & Nielsen (2018)).

Parameter		
Mean grain size (mm)	d_{50}	0,132
Maximum void ratio (-)	e_{max}	0,84
Minimum void ration (-)	e_{min}	0,56
Angle of repose (°)	φ	30,1
Critical state friction angle (°)	φ_c	34
Specific gravity (-)	G_s	2,63
Coefficient of uniformity (-)	U	1,53

2.3 Loading of pile group

The lateral load was applied path controlled with 0,1 mm/s. Kotthaus (1992) captured, that the load distribution is constant at a pile-head deflection of 10% of the pile diameter. Up to 10% deflection, the piles are acting as single piles in the beginning with no interaction, by increasing the deflection, the interaction of the piles develop and a reduction of the load-bearing capacity for following piles takes place. With a diameter of 15 mm, this would mean 1.5 mm horizontal deflection at the pile-head. For these tests, the horizontal deflection was chosen with 0,1·D, 0,2·D and 0,3·D. The deflection was applied successively starting with the lowest deflection and was kept for 40 to 70 seconds until the measured earth pressure showed almost a constant value (Figure 7, Figure 8). After every load step the piles were unloaded to the starting position.

2.4 Test program

Six tests were performed at Deltares Centrifuge. Therefore, a cylindrical container was filled in two steps, once with medium-dense and once with loose sand. For each density, three tests were performed. One single pile test and two tests with a pile group of 9 piles in a 3x3 arrangement.

Table 4. Test program centrifuge tests.

Test	Pile installation	Type of pile	I_D [%]
1	re- & displacement	single pile	0,58
2	re- & displacement	single pile	0,29
3	replacement	pile group 3x3	0,32
4	replacement	pile group 3x3	0,56
5	displacement	pile group 3x3	0,32
6	displacement	pile group 3x3	0,54

Figure 5 shows the 3x3 arrangement of the pile-head-plate. The spacing of the pile axes is three times the diameter (3D) in load direction and particular to that. Following the recommendations of ´EA Pfähle´ (2013), there should be no interaction effects out of the axis of load direction where no influences are expected with at least 3D spacing. In axes of the load direction the spacing is as well 3D. Here the crucial distance is assumed to be about 6D, therefore interaction effects can be expected. The two additional slots on the left and on the right side were made for the single pile tests, to enable four single piles to be tested simultaneously, see Figure 5 red marked dots. With a spacing of the pile axes of 8D in load direction, all overlapping effects can be ruled out.

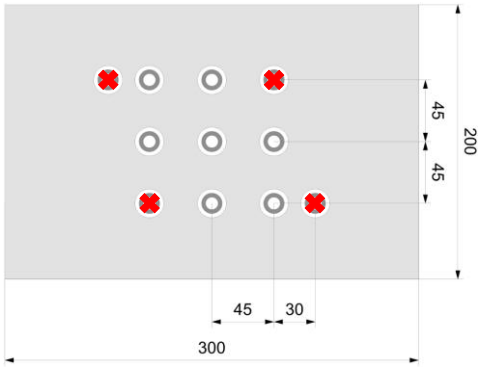

Figure 5. Top view of pile-head plate - values in [mm].

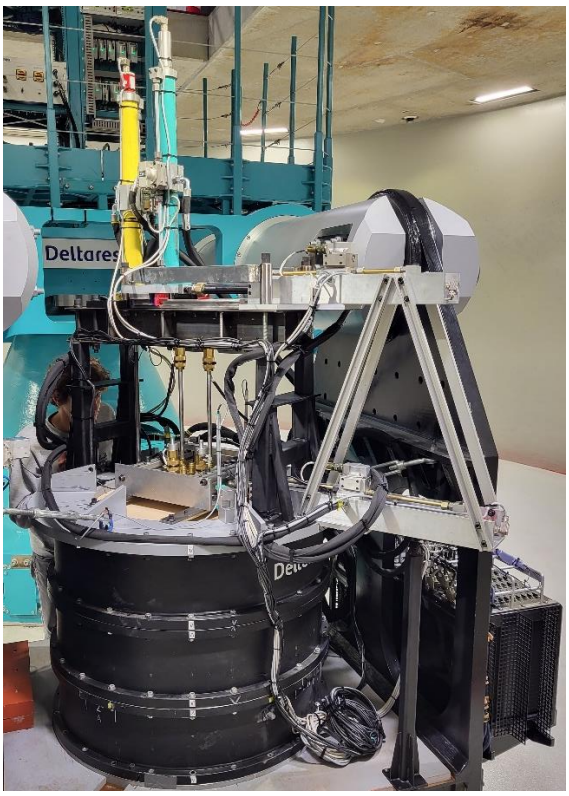

Figure 6. Full test set-up - Deltares Centrifuge.

3 TEST RESULTS

Five out of six tests were conducted successfully. A pile remained stuck in the precisely fitting holes of the pile-head-plate during installation and was thereby destroyed. Subsequently, the entrances of the holes were modified and round shaped to prevent any further complications during installation under high g-forces. The invented coupling system with a plug-in method to enable in-flight installation and loading of the pile group construction allowed to keep the piles in place, install them separately, fix the piles and the head plate together and load the system in horizontal direction at the pile-head level.

Figure 7 and Figure 8 is an idealized plot of the earth pressure of the interaction of the soil and the pile. The three peaks show the successively applied deflection of 0,1·D, 0,2·D and 0,3·D with an unloading to the starting postition inbetween.

In Figure 7 for Test 3, where a group of replacement piles in loose sand was investigated, the measured horizontal pressures at pile surface are evaluated. It is evident, that the measured earth pressure values for the leading pile (LP) are significantly higher for each depth than the values for the centre pile (CP).

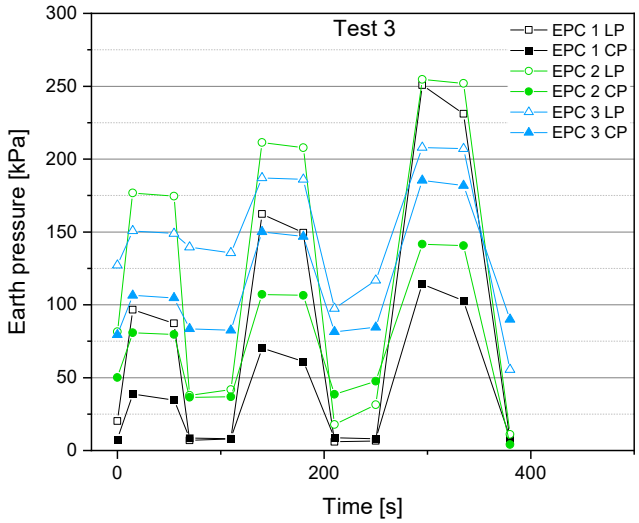

Figure 7. Data Test 3 - Earth pressure acting on Leading pile (LP) and on Centre pile (CP).

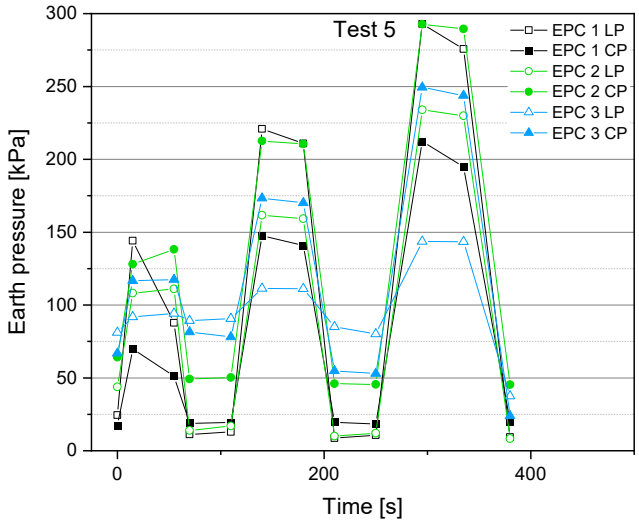

Figure 8. Data Test 5 - Earth pressure acting on Leading pile (LP) and on Centre pile (CP).

Figure 8 documents results of Test 5, where displacement piles in loose sand were modelled. With exception of the upper level EPC1, the distribution of the acting earth pressure on the piles is different for displacement piles. The measured values for EPC 2 and EPC 3 are significantly higher for the centre pile compared to the leading pile, if the installation effects are considered.

The ratio of the acting earth pressure between the leading pile and the centre pile is plotted in Figure 9 (Test 3 - replacement piles) and Figure 10 (Test 5 - displacement piles). For Test 3, higher values for the leading pile were detected at each applied deflection, especially in the two upper layers of EPC1 and EPC2. For Test 5, EPC1 shows still higher values for the leading pile, even if the ratio of acting earth pressure is significantly diminished. For EPC2 and EPC3 a ratio lower than 1.0 is observed, that indicate a higher acting earth pressure on the centre pile, than on the leading pile.

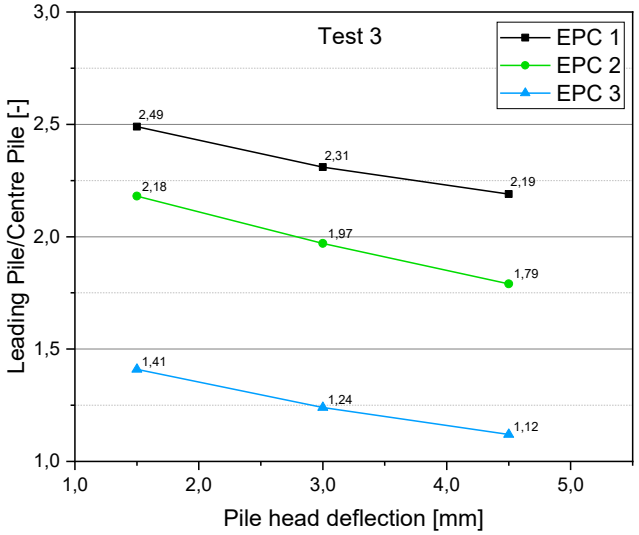

Figure 9. Test 3 - Replacement piles - Ratio of effective pressure for Leading Pile/Centre Pile.

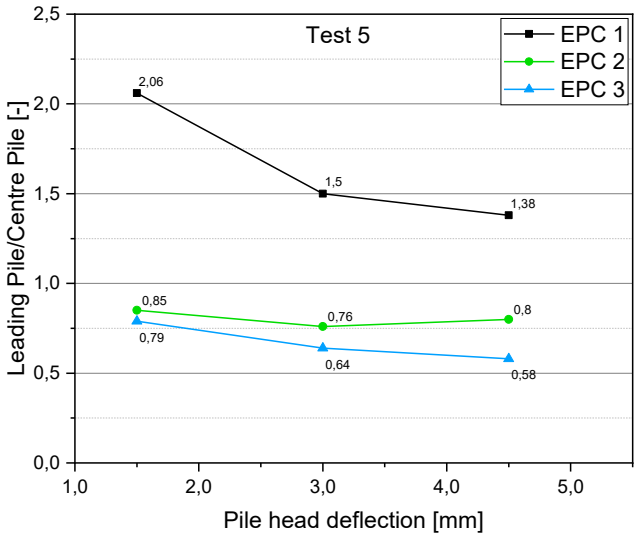

Figure 10. Test 5 - Displacement piles - Ratio of effective pressure for Leading Pile/Centre Pile.

The results indicate that installation effects exert a significant influence, with interaction effects being significantly attenuated. Soil compaction occurs in the mobilizable soil around the trailing piles, leading to increased soil-structure interaction and particularly affecting the central pile.

4 CONCLUSIONS

Through centrifuge testing conducted on a laterally loaded 3x3 pile group, this study examines the influence of installation effects on the load-displacement behavior of pile groups within dry sand.

Initial analysis of the data obtained from earth pressure cells reveals that these installation effects markedly affect both the load-bearing behavior and load distribution within the pile group. Specifically, displacement piles situated at the center of the 3x3 pile group exhibit notably higher earth pressure values on their embedded surfaces compared to bored piles.

These findings underscore the significant impact of pile installation methods on the load-bearing characteristics of pile groups. Consequently, it is evident that such installation techniques must be carefully considered in the design process. Further research is warranted to comprehensively investigate these effects and their implications for design methodologies.

ACKNOWLEDGEMENTS

The GeoLab project was a co-operation between Deltares and the University of Stuttgart.

The overall project is funded by the European Union's Horizon 2020 Research and Innovation programme.

REFERENCES

Brown, D. A., Morrison, C., & Reese, L. C. (1988). Lateral load behavior of pile group in sand. *Journal of Geotechnical Engineering, 114(11),* 1261-1276. https://doi.org/10.1061/(ASCE)0733-9410(1988)114:11(1261).

Deutsche Gesellschaft für Geotechnik Arbeitskreis Pfähle. (2013). *Recommendations on Piling (EA Pfähle)*. John Wiley & Sons.

Huang, A.B., Hsueh, C.K., O'Neill, M. W., Chern, S., & Chen, C. (2001). Effects of construction on laterally loaded pile groups. *Journal of Geotechnical and Geoenvironmental engineering*, 127(5), 385-397. https://doi.org/10.1061/(ASCE)1090-0241(2001)127:5(385).

Klüber E. (1988) Tragverhalten von Pfahlgruppen unter Horizontalbelastung. *PhD Dissertation,* Mitteilungen des Instituts für Grundbau, Boden- und Felsmechanik der TH Darmstadt; Heft 25.

Kotthaus M. (1992). Zum Tragverhalten von horizontal belasteten Pfahlreihen aus langen Pfählen in Sand. *PhD Dissertation*, Schriftreihe des Instituts für Grundbau, Ruhr-Universität Bochum, Heft 18 (in German).

McVay, M., Bloomquist, D., Vanderlinde, D., & Clausen, J. (1994). Centrifuge modeling of laterally loaded pile groups in sands. *Geotechnical Testing Journal, 17(2*), 129-137. https://doi.org/10.1520/GTJ10085J.

McVay, M., Casper, R., & Shang, T. I. (1995). Lateral response of three-row groups in loose to dense sands at 3D and 5D pile spacing. *Journal of Geotechnical Engineering, 121(5)*, 436-441. https://doi.org/10.1061/(ASCE)0733-9410(1995)121:5(436).

McVay, M., Zhang, L., Molnit, T., & Lai, P. (1998). Centrifuge testing of large laterally loaded pile groups in sands. *Journal of Geotechnical and Geoenvironmental Engineering, 124(10),* 1016-1026. https://doi.org/10.1061/(ASCE)1090-0241(1998)124:10(1016).

Nielsen, S.D., & Nielsen, B.N. Data report on Baskarp Sand No. 15 2018 Delivery.

Rollins, K. M., Lane, J. D., & Gerber, T. M. (2005). Measured and computed lateral response of a pile group in sand. *Journal of Geotechnical and Geoenvironmental Engineering, 131(1)*, 103-114. https://doi.org/10.1061/(ASCE)1090-0241(2005)131:1(103).

Proceedings of the XVIII ECSMGE 2024
GEOTECHNICAL ENGINEERING CHALLENGES
TO MEET CURRENT AND EMERGING NEEDS OF SOCIETY
© 2024 the Authors
ISBN 978-1-032-54816-6
DOI 10.1201/9781003431749-139
Open Access: www.taylorfrancis.com, CC BY-NC-ND 4.0 license

ECSMGE 24
XVIII EUROPEAN CONFERENCE ON SOIL MECHANICS AND GEOTECHNICAL ENGINEERING

Correlating CPTu to G_0 in high plasticity Paleogene clays

Corrélation des CPTu à G_0 dans des argiles Paléogènes de haute plasticité

E. Skouboe*, K.H. Lundvig, N. Okkels
Geo, Denmark
**esk@geo.dk*

ABSTRACT: This paper presents formulations for correlating the cone resistance q_c and net corrected cone resistance q_{net} to the maximum small-strain shear modulus G_0 in highly over-consolidated, fissured, marine Paleogene clays of very high plasticity, as observed in the Aarhus area of Denmark. CPTu tests performed in these Paleogene clays reveal fluctuating geotechnical properties both vertically and horizontally. Seismic CPTu tests (SCPTu) are often used to determine stiffness parameters for advanced soil models. However, they are more time-consuming, expensive, and may not always be performed to the required depth. To address this issue, two second-order relationships can be constructed by correlating G_0 values derived from SCPTu with corresponding q_c and q_{net} values. Both formulations provide more accurate G_0 values than conventional global CPTu correlations and demonstrate that local correlation is always preferable. These formulations make it possible to derive G_0 directly from ordinary CPT for use in preliminary analysis of deformations. More importantly, they support the final derivation of G_0 for 3D finite element analysis beyond seismic field and laboratory measuring points.

RÉSUMÉ: Cet article fournit des formulations pour corréler la résistance du cône q_c et la résistance nette corrigée du cône q_{net} au module de cisaillement maximal à petite déformation G_0 dans les argiles marines paléogènes fortement surconsolidées, fissurées et d'une plasticité très élevée, telles qu'observées dans la région d'Aarhus, au Danemark. En corrélant les valeurs G_0 dérivées de SCPTu avec les valeurs q_c et q_{net} correspondantes, deux relations de second ordre sont construites. Toutes deux fournissent des G_0 plus précis que les corrélations CPTu globales conventionnelles et démontrent que la corrélation locale est toujours préférable. Ces formulations permettent de dériver G_0 directement de la CPT ordinaire pour l'utiliser dans l'analyse préliminaire des déformations. Plus important encore, elles soutiennent la dérivation finale de G_0 pour l'analyse par éléments finis en 3D au-delà du champ sismique et des points de mesure en laboratoire.

Keywords: CPT; small-strain shear modulus; high plasticity clay; correlation.

1 INTRODUCTION

As part of the geotechnical investigations for high-rise buildings in Aarhus, Denmark, Geo has carried out 9 seismic cone penetration tests (SCPTu) at 6 different construction sites. For all high-rises in common, they are to be pile-founded in fissured, heavily over-consolidated, highly plastic Paleogene clay sediments, which pose complex and poor behaviour in terms of strength and deformation properties. To optimize the pile foundations, a hardening-soil small strain (HSS) model was chosen for the calculations of soil deformations. This model requires measurements of the small-strain stiffness G_0 and with this purpose in mind; Geo has carried out the seismic measurements.

This paper researches the correlation between G_0 and regular cone penetration tests (CPTu) data from two Paleogene clay types, Septarian Clays, and Søvind Marl.

1.1 Tests, equipment, and measurements

The SCPTu's are performed until a target depth of 60 – 86 meters below terrain with the recording of seismic traces for every one or two meters of penetration. However, individual seismic traces are rejected when the signal-to-noise ratio is less than 2 and seismic data is therefore typically not collected reliably all the way to the target depth. A total of 66 acceptable shear wave velocity v_s determinations were recorded in Septarian Clay, and 284 in Søvind Marl.

The CPTs are carried out with Geo's CPT crawler, which has a maximum pushing capacity of 20 tons, and a 10 or 15cm^2 piezoelectric probe from the manufacturer A.P. van den Berg (Icone) is used.

A threshold criterion of 25° inclination is set to discard unreliable measurements where the inclination exceeds this threshold.

For seismic SCPT testing, two A. P. van den Berg 3C accelerometers are attached behind the CPT cone with a fixed distance of 0.5 m between the two modules. During the recording of CPT data, the CPT operator stops the CPT cone at multiple depth positions. At each position, a shear wave generator runs through a series of multiple 'left blows' and 'right blows' generating seismic waves from the surface that

propagate through the subsurface. The accelerometers record the seismic waves as they pass by.

The estimation of the shear wave velocity v_s is based on the cross-correlation method from the recorded seismic traces. On the assumption that the generated waves propagate linearly from the source to the accelerometers, thereby ignoring the effect of refraction, the interval shear wave velocity between the two stacked signals is calculated using eq. (1):

$$v_s = \frac{D_2 - D_1}{\Delta t} \quad (1)$$

D_1 and D_2 are the straight slant distances from the source to the upper and lower accelerometer, respectively. Δt is the transit time between the two.

1.2 The Paleogene stratification

In costal parts of Aarhus, the following Paleogene stratification is typically found near the surface, cf. Figure 1:

- Topmost 15-20 m Septarian Clays of very high plasticity with a 0.5 – 2.0 meter thick layer of Kysing Marl which separate the upper Oligocene part (Viborg Clay) from the lower Eocene part (Moesgaard Clay).
- Søvind Marl is a clay of very high plasticity. It is predominantly very calcareous. However, calcareous-free or slightly calcareous zones frequently alternate with more calcareous ones.

The Paleogene clays are deposited in a deep ocean. Due to the removal of younger layers by erosion and the weight of numerous glaciers during the Quaternary period, they are also highly overconsolidated and fissured with slickensides. Index properties are given in Table 1.

Table 1. Natural water content w_{nat}, plasticity limit w_P, plasticity index I_P, and calcium content C_a. Values in %.

Soil type	w_{nat}	w_P	I_P	C_a
Septarian Clay	25-47	29-34	55-84	3-17
Søvind Marl	28-60	31-41	79-199	4-60

Large variations in plasticity and calcium carbonate content indicate that also strength and deformation properties vary. Variability in CPTu cone resistance confirms this. If the tip resistance is decomposed into a trend component and a fluctuating component, the CPTu's shows that the fluctuating component is characterized by frequent and violent fluctuations around a trend line as marked in Figure 1. Through the Septarian Clays, the trend line is directly proportional to depth, but in the Søvind Marl, it varies in large irregular cycles.

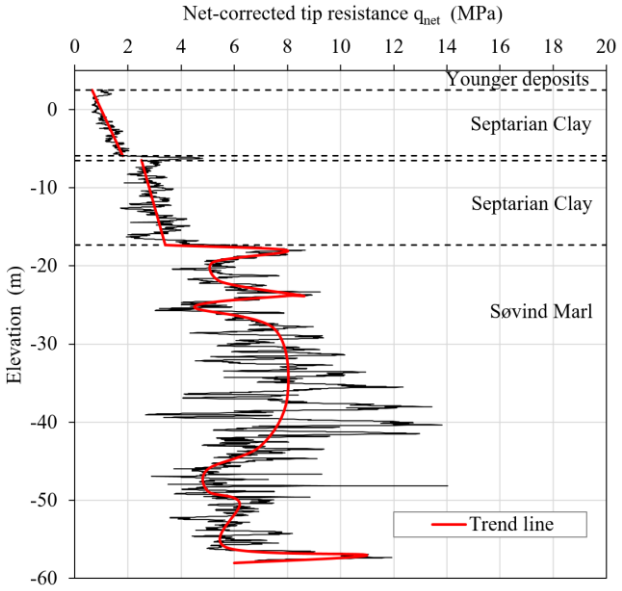

Figure 1. The net cone resistance q_{net} calculated from a CPTu in the Paleogene stratification in Aarhus.

2 DATA PROCESSING

The SCPT data is processed to determine the soil unit weight γ by (Mayne, 2001) and G_0 using eq. (1-3):

$$\gamma = 8.32\, log_{10}(v_s) - 1.61\, log_{10}(d) \quad (2)$$

$$G_0 = v_s^2 \rho \quad (3)$$

where d is the depth of seismic recording, and ρ is the soil density (kg/m^3).

As CPT data is measured on a cm-scale and v_s is measured over a depth interval of 0.5 m, CPT data was downscaled to a corresponding resolution. In practice, q_c was averaged over the same depth interval as v_s or ± 0.25 m around the depth midpoint.

The non-linear behaviour of the SCPT data with q_c does not increase directly proportional with q_c. The non-linear behaviour is captured by constructing a second order polynomial on the form of eq. (4) ($G_{0;CPT}$):

$$G_{0;CPT} = (a\, q_c + b)\, q_c = a\, q_c^2 + b\, q_c \quad (4)$$

where a and b are constants of the linear regression. The interval of validity in Septarian Clay is documented for $1 < q_c < 4$ MPa and in Søvind Marl for $3 < q_c < 9$ MPa.

In some cases, it may be appropriate to use the net-corrected tip resistance q_{net}, and a similar relation is therefore determined with eq. (4). For the derivation of q_{net}, eq. (5-6) by (Robertson and Cabal, 2022) is used:

$$q_t = q_c + (1 - a)\, u_2 \quad (5)$$

$$q_{net} = q_t - \sigma_{v0} \quad (6)$$

where u_2 is the pore pressure measured behind the cone, a is the net area ratio of the cone, q_t is the corrected cone resistance, and σ_{v0} is the total overburden pressure.

Other relations are used for the prediction of G_0 based on CPT input ($G_{0;CPT}$). (Mayne, 2007) proposed eq. (7) to determine v_s for Quaternary soils singularly based on the sleeve friction f_s. $G_{0;CPT}$ is then described following eq. (1-3). More directly, (Robertson, 2009) proposed eq. (8) to directly determine G_0 by employing the soil behaviour type index I_c and q_{net}:

$$v_s = 118.8\, log_{10}(f_s + 18.5) \quad (7)$$

$$G_{0;CPT} = 0.0188 \cdot 10^{0.55\, I_c + 1.68}\, q_{net} \quad (8)$$

3 RESULTS

The constants of the soil-specific models for Septarian Clay and Søvind Marl, q_c and q_{net}, are provided in Table 2 and used with eq. (4) in Figure 2.

Table 2. Constants derived from linear regressions.

	Constants for eq. (4)			
	Septarian Clay		Søvind Marl	
	q_c	q_{net}	q_c	q_{net}
a	0.33	0.32	2.11	1.79
b	23.74	25.74	10.25	14.02

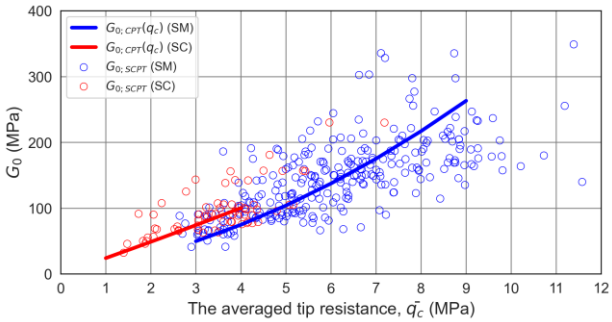

Figure 2. The performance of the models based on q_c for both soils.

The models are evaluated for both soil type data sets. The mean (μ), standard deviation (σ), and median (M) of their residuals are listed for each combination in Table 3. The centres of the sample distributions are relatively close to unity for both soils. Meanwhile, σ is largest for Søvind Marl which may be due to the wider range of tip resistances encountered in that soil. The magnitude of σ itself may is caused by the unpredictability in the mechanical behaviour of the soils, uncertainty involved in the data acquisition, and the fact that a static parameter (q_c) is sought related to a dynamic (G_0).

Table 3. Statistics of the residuals for all the models, including the models in comparison. SC is Septarian Clay and SM is Søvind Marl.

		Residuals $G_{0;SCPT} - G_{0;CPT}$ (MPa)			
x		$G(q_c)$	$G(q_{net})$	$G_{Robertson}$	G_{Mayne}
SC	μ	-8.83	-8.78	10.22	42.34
	M	-5.92	-5.97	14.49	55.38
	σ	26.54	27.62	31.12	37.54
SM	μ	4.35	5.53	25.88	-9.39
	M	-0.04	-0.71	27.78	-3.36
	σ	57.14	60.41	54.36	55.18

4 MODEL COMPARISON

The performances of the soil-specific models are compared to global models proposed by (Robertson, 2009) and indirectly by (Mayne, 2007). The statistics of the residuals for the global models are also presented in Table 3, and the derived Gaussian distributions are displayed in Figure 3. Figure 4 provides a regression plot comparison of the three models in both soils.

The model based on (Mayne, 2007) has the largest μ, M, and σ of all the models in Septarian Clay. It appears unrelated to $G_{0;SCPT}$ in both soils as the model was based on tests in Quaternary soils. Consequently, the regression lines in Figure 4 (green) show a low robustness for extrapolation to Paleogene soils.

The model by (Robertson, 2009) is based on I_c which is also used to classify the soil type. The model has the largest μ and M in Søvind Marl. The regression lines in Figure 4 (blue) show over-prediction for the majority of the inspected range.

Figure 4 shows that the soil-specific models for Septarian Clay and Søvind Marl predict very good estimations of G_0. The lower σ in Septarian Clay compared to Søvind Marl can be attributed to the generally lower q_c recorded in that soil type.

In general, the model based on q_{net} performs slightly worse than the model with q_c based on Table 3. This may be related to the u_2 measurements in eq. (5) used for the derivation of q_{net}. Upon penetrating these soil types, u_2 fluctuates similarly to q_c up to the nominal limit of the pore pressure sensor of 5 MPa which directly influences the corrected cone resistance.

Figure 5 is a proof-of-concept of the Søvind Marl model. On the left side, the soil-specific model based on q_c is shown with a lower and upper limit of $\pm\sigma$ to visualize the most likely prediction of $G_{0;SCPT}$. On the

right side, the model is compared to the other empirical models.

The derived second order polynomials for both soil types appear to provide a narrower fit around the observation values of $G_{0;SCPT}$ as expected from a soil-specific formulation. Neither of the empirical models captured the low $G_{0;SCPT}$ zone around 20 to 30 m depth in the first comparison. The proportionality of $G_{0;SCPT}$ with depth is clear, however, heavily influenced by fluctuations.

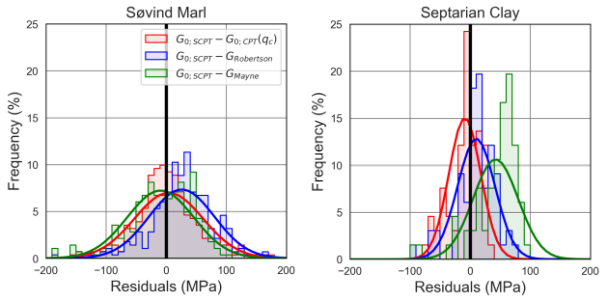

Figure 3. Comparing the histogram distributions of Søvind Marl with a bin size of 10 with $G_{0;CPT}$ based on q_c.

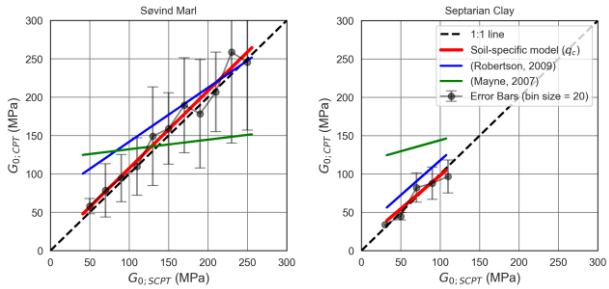

Figure 4. The second order models are based on q_c and error bars with a bin size of 20.

5 CONCLUSIONS

This paper has shown that second order polynomials as functions of only the cone tip resistance q_c, or the net-corrected q_{net}, can predict the in situ small-strain shear modulus G_0 in highly over-consolidated, fissured, marine Paleogene clays and marls of very high plasticity. The prediction accuracy is satisfactory given the unpredictability of the soils. As expected, the local relationships is shown to provide a more accurate match in comparison to existing global relationships by (Mayne, 2007) and (Robertson, 2009). In Mayne's case not least because his model does not include Paleogene soils. The results clearly demonstrate that local correlations always should be preferred for commercial purposes.

The relationships for Septarian Clay and Søvind Marl with q_c and q_{net}, respectively is:

$$SC: \quad G_0 = 0.33\,(q_c)^2 + 23.74\,q_c \qquad (9)$$

$$SC: \quad G_0 = 0.32\,(q_{net})^2 + 25.74\,q_{net} \qquad (10)$$

$$SM: \quad G_0 = 2.11\,(q_c)^2 + 10.25\,q_c \qquad (11)$$

$$SM: \quad G_0 = 1.79\,(q_{net})^2 + 14.02\,q_{net} \qquad (12)$$

The interval of validity is $1 < q_c < 4$ MPa in Septarian Clay and $3 < q_c < 9$ MPa for Søvind Marl.

These formulations makes it possible to derive G_0 directly from ordinary CPT for use in preliminary analysis of deformations. More importantly, they supports the final derivation of G_0 for 3D finite element analysis beyond the seismic field and laboratory measure points.

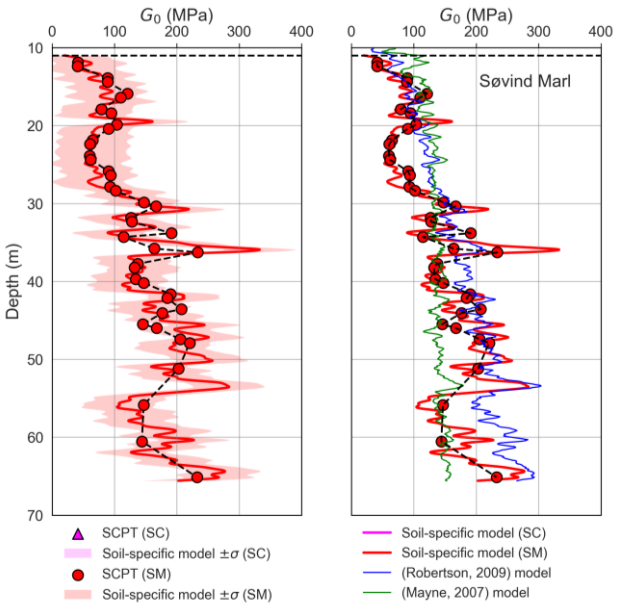

Figure 5. Comparison of $G_{0;SCPT}$ to the models. The soil-specific $G_{0;CPT}$ models are plotted with ± σ.

REFERENCES

Mayne, P.W. (2001). Stress-strain-strength-flow parameters from enhanced in-situ tests. *Proc. Int. Conf. on In Situ Measurement of Soil Properties and Case Histories*, Bali, pp. 27–47.

Mayne, P.W. (2007). In-situ test calibrations for evaluating soil parameters. *Characterisation and Engineering Properties of Natural Soils*, 3–4, pp. 1601–1652. https://doi.org/10.1201/NOE0415426916.CH2.

Robertson, P.K. (2009). Interpretation of cone penetration tests - a unified approach. *Canadian geotechnical journal*, 46(11), pp. 1337–1355. https://doi.org/10.1139/t09-065.

Robertson, P.K. and Cabal, K. (2022). Guide to Cone Penetration Testing.

Proceedings of the XVIII ECSMGE 2024
GEOTECHNICAL ENGINEERING CHALLENGES
TO MEET CURRENT AND EMERGING NEEDS OF SOCIETY
© 2024 the Authors
ISBN 978-1-032-54816-6
DOI 10.1201/9781003431749-140
Open Access: www.taylorfrancis.com, CC BY-NC-ND 4.0 license

ECSMGE 24
XVIII EUROPEAN CONFERENCE ON SOIL MECHANICS AND GEOTECHNICAL ENGINEERING

Numerical investigation on attenuation response of machine foundation under horizontal excitation

Étude numérique sur la réponse d'atténuation des fondations de machines sous excitation horizontale

A. Singh, P. Ghosh*
Indian Institute of Technology, Kanpur, India

S. Surapreddi
COEP Technological University, Pune, India

priyog@iitk.ac.in

ABSTRACT: The vibration transmitted through the ground from various sources like machine operation, railways, highways, and industrial activities poses several threats to nearby structures. Understanding the attenuation response of such vibrations is crucial. The current study examines the attenuation response of machine foundations under horizontal excitation using a 3D finite element (FE) analysis. The dynamic response is recorded at different monitoring points from the source of vibration at distinct frequencies. Furthermore, the influence of different parameters such as soil density, shear wave velocity, damping ratio, frequency of excitation, and Poisson's ratio is thoroughly investigated. The results indicate that the attenuation response of vertical and horizontal vibrations is found to vary significantly. In addition, the wave interference effect can be observed for horizontal vibration.

RÉSUMÉ: Les vibrations transmises par le sol à partir de diverses sources telles que le fonctionnement des machines, les chemins de fer, les autoroutes et les activités industrielles constituent plusieurs menaces pour les structures voisines. Comprendre la réponse d'atténuation de telles vibrations est crucial. La présente étude examine la réponse d'atténuation des fondations de machines sous excitation horizontale à l'aide d'une analyse par éléments finis (EF) 3D. La réponse dynamique est enregistrée à différents points de captage de la source de vibration à des fréquences distinctes. En outre, l'influence de différents paramètres tels que la densité du sol, la vitesse des ondes de cisaillement, le taux d'amortissement, la fréquence d'excitation et le coefficient de Poisson est étudiée de manière approfondie. Les résultats indiquent que la réponse d'atténuation des vibrations verticales et horizontales varie considérablement. De plus, l'effet d'interférence des ondes peut être observé pour les vibrations horizontales.

Keywords: Attenuation characteristics; dynamic response; finite element analysis; horizontal excitation; machine foundation.

1 INTRODUCTION

Ground-borne vibrations are typically produced by activities such as machine operations, traffic, blasting, and construction activities. Such vibrations may lead to structural damages, operational inefficiencies, and even safety hazards. Vibrations produced by different sources propagate through the soil media in the form of body and surface waves. Miller *et al.* (1955) examined the energy distribution between body waves and surface waves and reported that surface waves accounted for 67% of the total transmitted energy, whereas body waves accounted for 33% of the total transmitted energy. Generally, body waves attenuate more rapidly compared to surface waves (Richart *et al*. 1970). Furthermore, vibrations attenuate rapidly at higher frequencies compared to lower frequencies (Seed and Idriss, 1970). Han *et al.* (2016) performed a comprehensive investigation of compressional wave propagation in saturated soil by employing hydro-mechanically coupled analytical and numerical methods and found the existence of two types of compressional waves (the fast and slow waves) and their characteristics highly depend on critical geotechnical and seismic properties such as permeability, soil stiffness, and loading frequency. Park and Kaynia (2018) analyzed enhancements and characteristics of the widely utilized stiffness matrix approach employed for simulating the propagation of waves in layered soil media.

Several researchers studied the attenuation response (AR) of vibrations by performing large-scale field experiments. Auersch and Said (2010) evaluated the vibration characteristics generated by different

sources experimentally and analytically and reported that the attenuation response primarily depends on soil damping and excitation frequency. Surapreddi and Ghosh (2022a) used experimental and numerical studies to investigate the AR of machine foundations subjected to vertical harmonic excitation and reported that the attenuation characteristics of vertical and horizontal vibrations differ significantly. Earlier studies utilized different numerical approaches such as the boundary element method (BEM) (Ahmad and Al-Hussaini, 1991), limit analysis (Ghosh, 2010), and finite element method (FEM) (Saikia and Das, 2014; Surapreddi and Ghosh, 2022b). However, existing studies specifically focused on the behavior of machine foundations subjected to vertical harmonic excitation. A few studies focused on the attenuation characteristics under horizontal excitation. Dasgupta (1987) performed a numerical investigation using the BEM and evaluated the efficacy of open trenches in reducing horizontal vibration. Al-Hussaini and Ahmad (1991) investigated the efficiency of rectangular wave barriers to mitigate vibrations generated by surface waves, employing the BEM. However, the influence of different types of soil on the AR of machine foundations under horizontal excitation has not been thoroughly studied.

Accordingly, the current study focuses on investigating the AR of machine foundations subjected to horizontal excitation. This is accomplished by developing a 3D finite element (FE) model in ABAQUS and validating it against the outcomes reported in the existing literature. In addition, a comprehensive parametric analysis is performed to evaluate the impact of different parameters on the AR.

2 PROBLEM STATEMENT

A concrete footing of dimension 0.75 m × 0.75 m × 0.45 m is considered in the current study. A horizontal sinusoidal dynamic force ($P = P_0 \sin\omega t$) having a magnitude of 2 kN is applied on the top of the footing. The attenuation characteristics are evaluated by recording the vertical and horizontal vibration response at different monitoring points, as shown in Figure 1. The displacement amplitude at the monitoring points is normalized with respect to the width of the footing (b). The schematic representation of the problem definition and typical layout of monitoring points are shown in Figure 1.

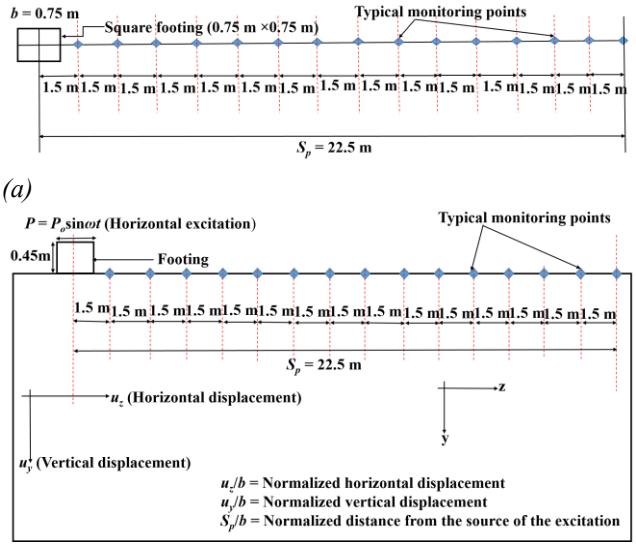

Figure 1. Schematic depiction of the problem (a) top view, and (b) cross-sectional view.

3 NUMERICAL MODELING

The current study investigates the AR of machine foundations subjected to horizontal excitation using the FE software ABAQUS. For analysis purposes, a full-domain 3D FE analysis is utilized. The soil and footing are discretized using 8-noded hexahedra (C3D8R) elements. To avoid wave scattering from the boundaries, first-order 8-noded semi-infinite boundaries are used (Lysmer and Kuhlemeyer, 1969). A graded meshing scheme is employed for discretizing the soil domain. The soil is modeled as homogenous, isotropic, and semi-infinite, while the constitutive behavior of the soil is taken as linear elastic (Surapreddi and Ghosh, 2023). The dimensions of the soil domain are adopted as L_x = 15 m, L_y = 15 m, and L_z = 25 m (Surapreddi and Ghosh, 2023), as shown in Figure 2.

4 FE MODEL VALIDATION

As mentioned earlier, limited studies are available on the AR of machine foundations under horizontal excitation. Therefore, the results reported in the literature on the AR of machine foundations exhibiting vertical excitation are used to validate the current FE model. The following properties are used for validation purposes: soil density, ρ = 1800 kg/m^3, shear wave velocity, V_s = 221.5 m/s, and Poisson's ratio, v = 0.3 (Surapreddi and Ghosh, 2022a). In the current study, a damping ratio (D) of 5% is used to estimate the Rayleigh damping coefficients (Al-Hussaini and Ahmad, 1991). A dynamic horizontal force of amplitude 2 kN is applied at a frequency (f)

of 50 Hz (Surapreddi and Ghosh, 2022a). For validation purposes, the vertical displacement amplitude at each monitoring point is normalized by the displacement obtained at the first monitoring point. Thus, the obtained normalized vertical displacements are compared with the results reported by Saikia and Das (2014), Mahdavisefat *et al.* (2018), and Surapreddi and Ghosh (2022a), as shown in Figure 3. Figure 3 depicts that the results obtained from the present FE analysis compare reasonably well with those reported in the earlier studies. As a result, the present FE model can be confidently used to evaluate the AR of machine foundations under horizontal excitation.

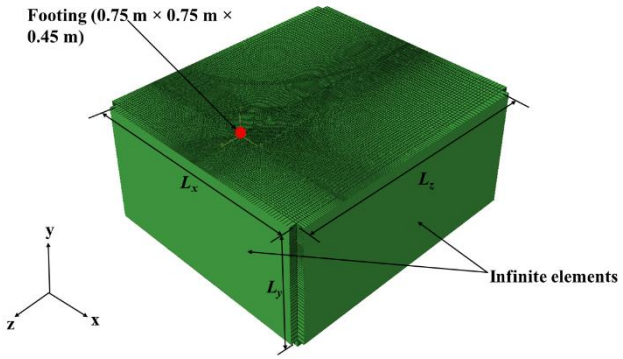

(a)

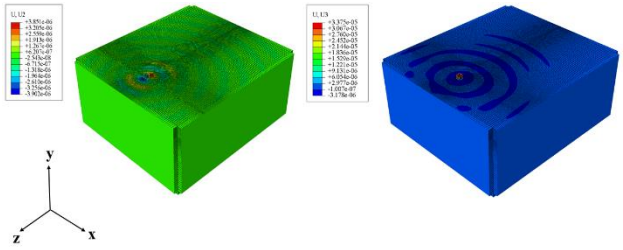

(b)

Figure 2. (a) FE mesh discretization featuring infinite elements along boundaries, and (b) contour depicting u_z, and u_y at the frequency of 50 Hz with ρ = 1800 kg/m^3, ν = 0.3, D = 5%, and V_s = 221.5 m/s.

5 RESULTS AND DISCUSSION

5.1 Attenuation response

The AR of both vertical and horizontal vibrations under horizontal excitation are presented in Figure 4. It can be observed from Figure 4 that the normalized horizontal displacement values (u_z/b) are lower than the normalized vertical displacement values (u_y/b), indicating that horizontal vibrations attenuate faster compared to vertical vibrations. Further, it can be observed that u_y/b decreases with an increase in S_p/b. In contrast, the same trend is not observed for u_z/b. Such a trend may be due to the wave interaction and superposition between horizontally propagating compressional waves (P-wave) and Rayleigh waves. Similar findings were also reported by Haupt (1985).

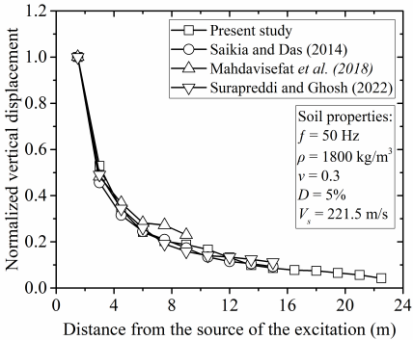

Figure 3. Comparison of present FEM results with available investigations.

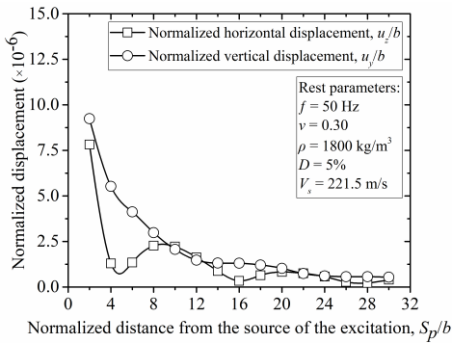

Figure 4. Variation of normalized displacement (u_z/b and u_y/b) with S_p/b under horizontal excitation at f = 50 Hz, ν = 0.3, ρ = 1800 kg/m^3, D = 5%, and V_s = 221.5 m/s.

5.2 Parametric study

A comprehensive parametric analysis is conducted in the current study to assess the influence of key parameters on the AR of both horizontal and vertical vibrations under horizontal excitation. This is accomplished by varying the key parameters such as ρ, V_s, ν, D, and f.

5.2.1 Effect of soil density and Poisson's ratio

The effect of ρ and ν on the AR of machine foundations under horizontal excitation is presented in Figures 5 and 6, respectively. It can be noted from Figure 5 that ρ does not influence the AR significantly. In contrast, it is seen that ν influences the AR (Figure 6) but not up to a large extent. It can be also noted that with an increase in ν from 0.20 to 0.40, u_y/b decreases as S_p/b increases (Figure 6(b)). However, such a well-defined trend is not observed in the case of u_z/b (Figure 6(a)). This may be attributed to the fact that the P-wave and Rayleigh wave interference effect is observed for horizontal vibrations. Similar findings were also reported by Surapreddi and Ghosh (2022a). As soil is

considered completely dry in this study and due to computational constraints in ABAQUS, the attenuation characteristics of incompressible soil (v = 0.495) have not been shown, but results for a value v = 0.45 very close to incompressibility are shown in Figure 6.

5.2.2 Effect of excitation frequency

The impact of f on the AR is presented in Figure 7. It can be noticed from Figure 7(a) that as f increases from 25 Hz to 45 Hz, u_z/b increases. With a further increase in f, u_z/b decreases. Similarly, u_y/b increases as f increases from 25 Hz to 40 Hz (Figure 7(b)). However, beyond f = 40 Hz, u_y/b decreases. Similar observations were reported by Surapreddi and Ghosh (2023).

5.2.3 Effect of shear wave velocity

Figure 8 presents the variation of u_z/b and u_y/b with S_p/b for V_s values ranging from 100 m/s to 400 m/s while keeping other parameters constant. It can be noted from Figure 8(a) that as V_s increases from 100 m/s to 400 m/s, u_z/b values decrease by 76.87% and 92.18% at S_p/b = 2 and S_p/b = 10, respectively. Similarly, at the same monitoring points for the same increase in V_s, u_y/b decreases by 82.94% and 80%, as shown in Figure 8(b). This may be attributed to the fact that stiff soils have higher V_s values compared to soft soils. Consequently, the displacement values decrease with an increase in V_s. Thus, it can be noted that the attenuation rate for both vibrations increases with an increase in V_s (Figure 8). It is worth noting that the interference effect of P-wave and Rayleigh wave on horizontal vibration decreases with an increase in V_s (Figure 8(a)).

5.2.4 Effect of damping

The influence of D on the AR is examined by varying D from 5% to 15% while keeping other parameters constant. The variations of u_z/b and u_y/b with S_p/b are depicted in Figure 9. As D increases from 5% to 15%, u_z/b decreases by 41.10% and 70.27% at S_p/b = 2 and S_p/b = 10, respectively, as shown in Figure 9(a). In contrast, u_y/b decreases by 39.83% and 72.47% at the same monitoring points, with an increase in D from 5% to 15%, as presented in Figure 9(b).

6 CONCLUSIONS

In this study, the AR of machine foundations subjected to horizontal excitation is investigated numerically using the FE software ABAQUS. The AR of machine foundations subjected to horizontal excitation and the influence of various parameters on the attenuation characteristics are thoroughly investigated. The important conclusions from the present study can be listed as

- u_y/b decreases as S_p/b increases, but u_z/b shows a different trend due to wave interaction and superposition.
- Horizontal vibration attenuates more rapidly compared to vertical vibration.
- ρ does not significantly influence the AR, whereas v affects the AR significantly.
- u_y/b decreases as v increases from 0.20 to 0.40 but this increment is very small, while u_z/b does not follow the same trend because of the interference effect of P-wave and Rayleigh wave on horizontal vibration.
- As f increases from 25 Hz to 45 Hz, u_z/b increases. However, beyond f = 45 Hz, u_z/b decreases with an increase in f. Similarly, u_y/b increases with an increase in f from 25 Hz to 40 Hz. beyond f = 40 Hz, any further increase in f results in a decrease in u_y/b.
- As D increases from 5% to 15%, u_z/b, and u_y/b both decrease.
- Horizontal and vertical vibrations attenuate faster with an increase in V_s.

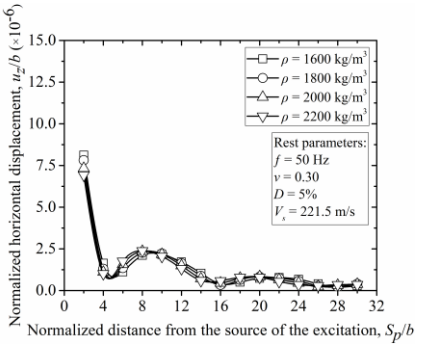

(a)

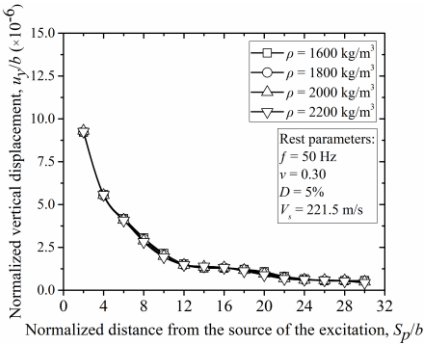

(b)

Figure 5. Variation of (a) u_z/b, and (b) u_y/b with S_p/b for different ρ at f = 50 Hz, v = 0.3, D = 5% and V_s = 221.5 m/s.

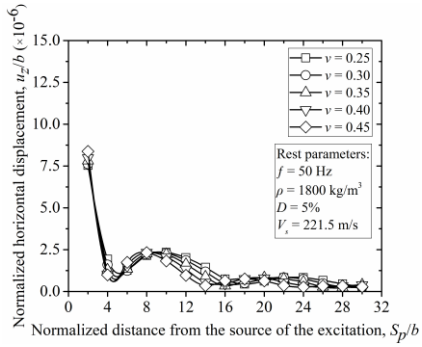

(a)

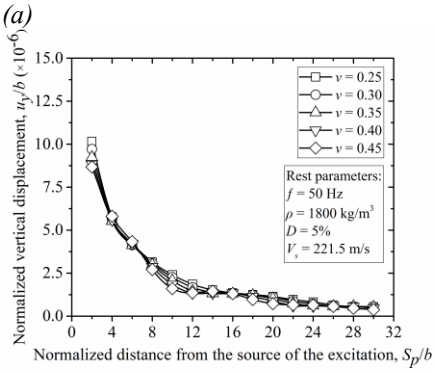

(b)

Figure 6. Variation of (a) u_z/b, and (b) u_y/b with S_p/b for different v at f = 50 Hz, ρ = 1800 kg/m^3, D = 5% and V_s = 221.5 m/s.

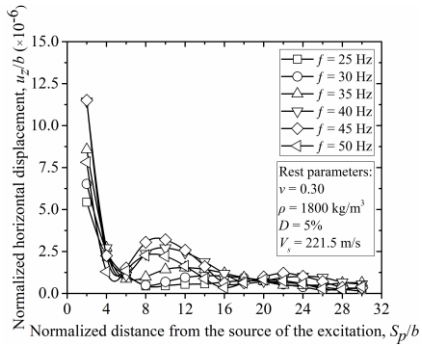

(a)

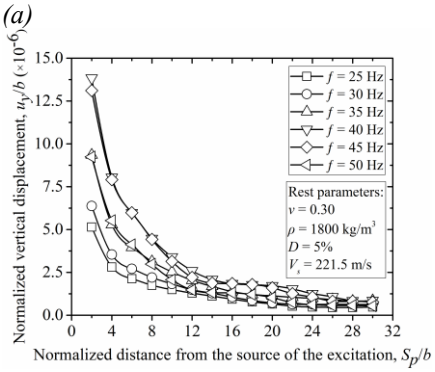

(b)

Figure 7. Variation of (a) u_z/b, and (b) u_y/b with S_p/b for different f at ρ = 1800 kg/m^3, v = 0.3, D = 5% and V_s = 221.5 m/s.

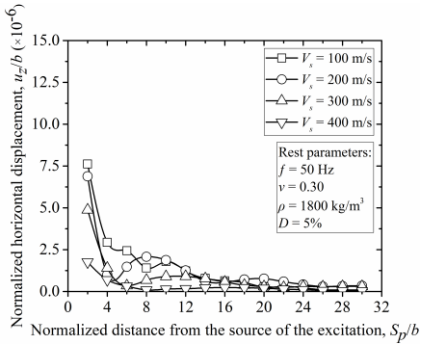

(a)

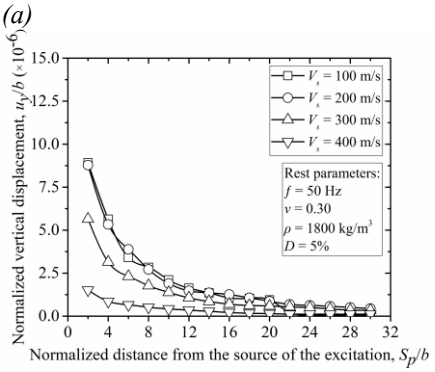

(b)

Figure 8. Variation of (a) u_z/b, and (b) u_y/b with S_p/b for different V_s at f = 50 Hz, v = 0.3, D = 5% and ρ = 1800 kg/m^3.

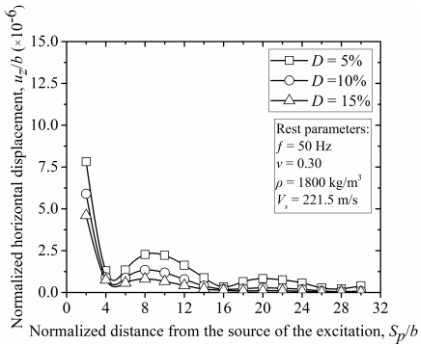

(a)

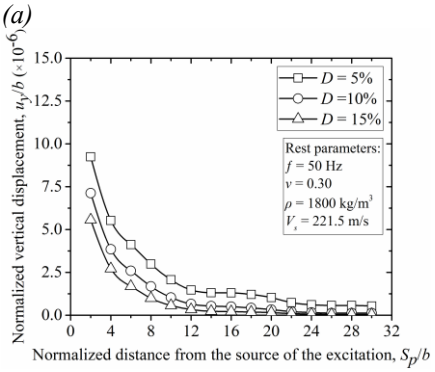

(b)

Figure 9. Variation of (a) u_z/b, and (b) u_y/b with S_p/b for different D at f = 50 Hz, v = 0.3, ρ = 1800 kg/m^3 and V_s = 221.5 m/s.

REFERENCES

Auersch, L. and Said, S. (2010). Attenuation of ground vibrations due to different technical sources. *Earthquake Engineering and Engineering Vibration,* 9(3): 337–344. https://doi.org/10.1007/s11803-010-0018-0.

Al-Hussaini, T. M. and Ahmad, S. (1991). Design of wave barriers for reduction of horizontal ground vibration. *Journal of Geotechnical Engineering*, 117(4): 616-636. https://doi.org/10.1061/(ASCE)0733-9410(1991)117:4(616).

Dasgupta, G. (1987). *Vibration isolation of structures in a homogeneous elastic soil medium.* Ph.D. thesis, University of Minnesota, Minneapolis, Minn.

Ghosh, P. (2010). Seismic uplift capacity of inclined strip anchors in sand using upper bound limit analysis. *Geomechanics and Geoengineering,* 5(4): 267-275. https://doi.org/10.1080/17486025.2010.492242.

Han, B., Zdravkovic, L. and Kontoe, S., (2016). Numerical and analytical investigation of compressional wave propagation in saturated soils. *Computers and Geotechnics*, 75: pp. 93-102. https://doi.org/10.1016/j.compgeo.2016.01.019.

Haupt, W. A. (1995). Wave propagation in the ground and isolation measures. *Proceedings of the International Conferences on Recent Advances in Geotechnical Earthquake Engineering and Soil Dynamics*, S. Prakash (ed.), Missouri, Louis, USA, Vol. 3, pp. 990-991.

Lysmer, J. and Kuhlemeyer, R. L. (1969). Finite dynamic model for infinite media. *Journal of the Engineering Mechanics Division*, 95(4): 859-877. https://doi.org/10.1061/JMCEA3.0001144.

Mahdavisefat, E., Salehzadeh, H. and Heshmati, A. A. (2018). Full-scale experimental study on screening effectiveness of SRM-filled trench barriers. *Géotechnique*, 68(10): 869-882. https://doi.org/10.1680/jgeot.17.P.007.

Miller, G. F., Pursey, H. and Bullard, E. C. (1955). On the partition of energy between elastic waves in a semi-infinite solid. *Proceedings of the Royal Society of London. Series A. Mathematical and Physical Sciences*, Vol. 233(1192), pp. 55-69. https://doi.org/10.1098/rspa.1955.0245.

Park, J., & Kaynia, A. M. (2018). Stiffness matrices for fluid and anisotropic soil layers with applications in soil dynamics. *Soil Dynamics and Earthquake Engineering*, 115: pp. 169-182. https://doi.org/10.1016/j.soildyn.2018.06.030.

Richart, F. E., Woods, R. D. and Hall, J. R. (1970). *Vibrations of Soils and Foundations*. Prentice-Hall, Saint Louis University, USA.

Saikia, A. and Das, U. K. (2014). Analysis and design of open trench barriers in screening steady-state surface vibrations. *Earthquake Engineering and Engineering Vibration*, 13(3): 545-554. https://doi.org/10.1007/s11803-014-0261-x.

Seed, H. B. and Idriss, I. M. (1970). Analyses of ground motions at Union Bay, Seattle during earthquakes and distant nuclear blasts. *Bulletin of the Seismological Society of America*, 60(1): 125-136. https://doi.org/10.1785/BSSA0600010125.

Surapreddi, S. and Ghosh P. (2022a). Experimental and numerical investigations on attenuation response of machine foundations under vertical excitation. *Geomechanics and Geoengineering*, 17(6): 1865-1886. https://doi.org/10.1080/17486025.2021.1980231.

Surapreddi, S. and Ghosh, P. (2022b). Impact of footing shape on dynamic properties and vibration transmission characteristics of machine foundations. *International Journal of Geosynthetics and Ground Engineering*, 8(2). https://doi.org/10.1007/s40891-021-00347-x.

Surapreddi, S. and Ghosh, P. (2023). Active vibration screening characteristics of bamboo in-filled wave barriers. *Soil Dynamics and Earthquake Engineering*, 171: 107945. https://doi.org/10.1016/j.soildyn.2023.107945.

Proceedings of the XVIII ECSMGE 2024
GEOTECHNICAL ENGINEERING CHALLENGES
TO MEET CURRENT AND EMERGING NEEDS OF SOCIETY
© 2024 the Authors
ISBN 978-1-032-54816-6
DOI 10.1201/9781003431749-141
Open Access: www.taylorfrancis.com, CC BY-NC-ND 4.0 license

ECSMGE 24
XVIII EUROPEAN CONFERENCE ON SOIL MECHANICS AND GEOTECHNICAL ENGINEERING

Evaluation full-scale mooring pile load test Rotterdam

Évaluation de l'essai de chargement de pieux d'amarrage grandeur nature Rotterdam

J.J.M. Sluis*, H.J. Lengkeek
Witteveen+Bos, Utrecht, The Netherlands

A.A. Roubos
Port of Rotterdam, Rotterdam, The Netherlands

**jasper.sluis@witteveenbos.com*

ABSTRACT: In the summer of 2022, a full-scale pile test was carried out in the Caland Canal on behalf of the Port of Rotterdam Authority. In this test, two large diameter mooring piles were pulled towards each other under lateral loading. The forces, displacements and strains were continuously monitored during 9 load-unload steps. The aim of the test was to gain a better insight into the load-displacement behaviour of a mooring pile during (repeated) loading, and more specifically into the fixation of the pile tip. The current design method proposed in the CROW publication Flexible Dolphins may result in mooring piles that are too long, due to the required fixation criterion in the publication. Witteveen+Bos performed the prediction and back analysis of the pile response with the use of the finite element method (FEM), the results of which are presented in this article. The results of the pile test highlight that the mooring pile may in fact be shorter with an alternative fixation criterion.

RÉSUMÉ: Au cours de l'été 2022, un essai de chargement chargement répétéde pieux grandeur nature a été réalisé dans le Canal Caland pour le compte de l'Autorité portuaire de Rotterdam. Lors de cet essai, deux pieux d'amarrage de grand diamètre ont été tirés l'un vers l'autre sous charges latérales. Les forces, déplacements et déformations ont été monitorés en permanence pendant 9 séries d'essais de chargements cycliques. L'objectif de cet essai grandeur nature est de mieux comprendre le comportement d'un pieu d'amarrage en déplacements lors d'un chargement (répété), et plus particulièrement la fixation de la pointe du pieu. La méthode de conception actuellement proposée dans la publication CROW Flexible Dolphins s'emble aboutir à des pieux trop longs, en raison du critère de fixation exigé dans la publication. Witteveen+Bos a réalisé la prédiction et la analyse réctrospective de la réaction du pieu avec la méthode des éléments finis (MEF), dont les résultats sont présentés dans cet article. Les résultats de l'essai de chargement chargement répétéde pieux démontrent que le pieu d'amarrage pourrait être plus court avec un critère de fixation alternatif.

Keywords: Mooring pile; full-scale-test; soil-structure interaction; pile design.

1 INTRODUCTION

In recent projects it has been noted that a number of design aspects included in the CROW publication Flexible Dolphins (CROW, 2018) could be improved. In particular, the degree of fixation of the mooring piles in the subsurface is a subject about which there is still a lot of uncertainty. The effect on the design outcomes can be significant.

The design method for determining the required pile length in CROW's Flexible Dolphins manual appears to be a conservative method, resulting in inefficient use of materials (piles that are too long).

The behaviour of a mooring pile under repeated loading is also uncertain. Soil reacts stiffer when reloaded, which means that in the event of a second and later mooring thrust, the displacement is smaller, and therefore also the capacity to absorb the energy of a mooring ship through pile deflection.

2 PILE DESIGN AND TEST SETUP

2.1 Pile design

The mooring piles have a diameter of 2.4 meters and are made up of sections with different optimized wall thicknesses, see Table 1.

The piles were dimensioned for energy absorption and resulting fender load (at NAP +1.7 m). In addition, the piles must be able to withstand a representative bollard load of 1500 kN, at approximately 0.5 m above the top of the pile, at NAP +6.5 m. The design value of the bollard load is 2025 kN.

The average water level is around NAP and the ground level in the channel near the mooring piles is approximately NAP -24 m. The pile tip level is NAP -42 m.

Table 1. Sections of mooring piles 81-D01 and 81-D04.

Part	Steel quality	Wall thickness [mm]	From [m NAP]	To [m NAP]
1	S355	25	+6.00	-0.75
2	X70	25	-0.75	-10.00
3	X70	30	-10.00	-12.75
4	X70	35	-12.75	-15.25
5	X70	40	-15.25	-18.25
6	X70	50	-18.25	-22.50
7	X70	55	-22.50	-34.00
8	X70	40	-34.00	-37.00
9	X70	30	-37.00	-42.00

2.2 Test setup and measurement equipment

The starting point for testing the piles was that no additional piles had to be placed for the test. For the test, a tensile connection was made at NAP +6.5 m between two planned mooring piles, 81-D01 and 81-D04, see Figure 1.

A jack was placed on top of pile 81-D04 (left), and a holding connection was attached to pile 81-D01 (right). In between, two GEWI bars Ø 57.5 mm were placed. To prevent the GEWI bars from sagging, a suspension bridge construction was created. The cylinders of the jack had a length of 2 meters, which means that both piles could be pulled towards each other up to approximately 1 meter.

During the test, the oil pressure and cylinder stroke of the jack were continuously measured. On and around both mooring piles the following measurement equipment was installed (Figure 2):

- glass fibers were placed on the inside of the piles to measure the elongation of the steel. The glass fibers were placed on the tension side, the compression side and the two neutral sides of the tubular pile. The glass fibers measured the strains between NAP -1.5 m and NAP -41.5 m;
- a SAAF (Shape Accel Array Field) inclinometer was placed on the outside of both piles, see Figure 2, which measured the deflection of the piles. The top of the SAAF was at NAP +4 m and extended to the pile tip at NAP -42 m.
- two reflectors were placed on the tube of the SAAF to measure the displacements with a total station, which was located onshore. Additionally, at the top of the pile two reflectors were placed, see Figure 2;
- the pore pressures were monitored in the subsurface sand layers at a distance of 5 m from both piles (in the pulling direction). The pore pressure meters were placed at -27.0, -28.5 and -30.0 m NAP.



Figure 1. Test setup, pile 81-D04 (left) and 81-D01 (right).

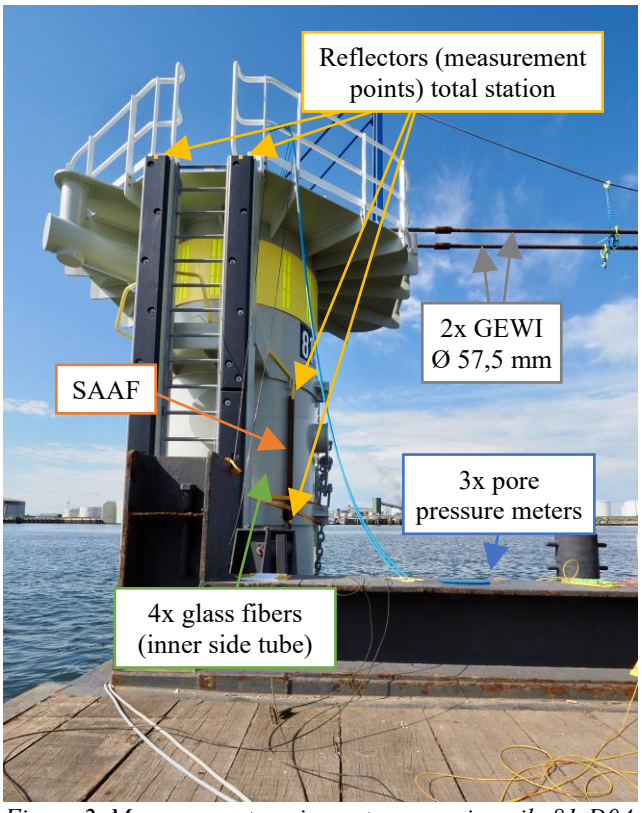

Figure 2. Measurement equipment on mooring pile 81-D04.

2.3 Loading scheme and displacement predictions

Prior to the test, finite element calculations were made using Plaxis 3D to predict the deformation of the mooring piles and to determine an acceptable loading schedule: it was necessary to prevent the piles from becoming too permanently tilted after testing.

The calculated pile head displacement was just over one meter, the residual displacement of the pile head after unloading was just over 0.3 m. In consultation with the Port of Rotterdam Authority this was seen as acceptable.

3 SUBSOIL CONDITIONS

The subsoil consists mainly of sand, see Table 2:

- up to approximately NAP -30 m: loose to moderately packed sand;
- up to approximately NAP -36 m (very) dense packed sand;
- up to approximately NAP -45 m: moderately packed sand (silty);
- below NAP -45 m: loose to moderately packed sand.

The soil layers were modelled with the Hardening Soil model with small-strain stiffness (HSs) (Bentley, 2022). Lab testing on sand samples was performed (triaxial tests with unloading-reloading step for varying relative density and oedometer tests). The procedure for obtaining the final parameter set consisted of the following steps:

1 determine the initial HSs parameter set based on empirical relationships between the cone resistance of CPT's, the relative density and the HSs parameters as described in Lengkeek (2022) and Brinkgreve et.al. (2010);
2 model the pile test in Plaxis 3D with the parameter set obtained from step 1;
3 determine the average strain and mobilized shear stress during the last loading step of the pile test. This is done for each soil layer;
4 use the Soil Test module (Bentley, 2022) to simulate a triaxial test on a soil type with the parameter set obtained in step 1 and compare with the results of the laboratory research;
5 iteratively adjust the HSs parameter set from step 1 to achieve the best fit with the results of the triaxial tests. This fit is performed in the range of strain as determined in step 3.

The final parameter set is presented in Table 3. An example of the fit of the Plaxis Soil Test with the triaxial test is shown in Figure 3.

Table 2. Stratification at mooring piles (top of layer in [m NAP]) and Re being the relative density of the sand [%]

Id	Layer	81-D01	81-D04	Re [%]
1	Sand 1	-24.25	-24.7	65
2	Sand 2	-30.0	-32.0	95
3	Sand 3	-37.5	-36.0	80
4	Sand 4	-45.0	-44.0	60

Table 3. Geotechnical parameters for HSs material model (expected values), see Bentley (2022) for parameter explanation.

Id	γ / γ_{sat} [kN/m^3]	c' [kN/m^2]	φ' [°]	ψ [°]	E_{50}^{ref} / E_{oed}^{ref} / E_{ur}^{ref} [MN/m^2]	$\gamma_{0.7}$ ·10^{-4}[-]	G_0^{ref} [MN/m^2]	m [-]	K_0^{nc} [-]	POP [kN/m^2]
1	18.7 / 20.1	0	39.8	9.6	65 / 78 / 130	5.0	80	0.4875	0.4510	65
2	19.9 / 21.1	0	44.0	24.0	80 / 65 / 160	5.0	80	0.4031	0.4499	100
3	19.2 / 20.8	0	39.5	15.5	54.8 / 58.5 / 164	1.3	137	0.4688	0.4423	39
4	18.2 / 20.0	0	37.2	4.44	33.6 / 33.9 / 101	1.6	97	0.5500	0.4379	30

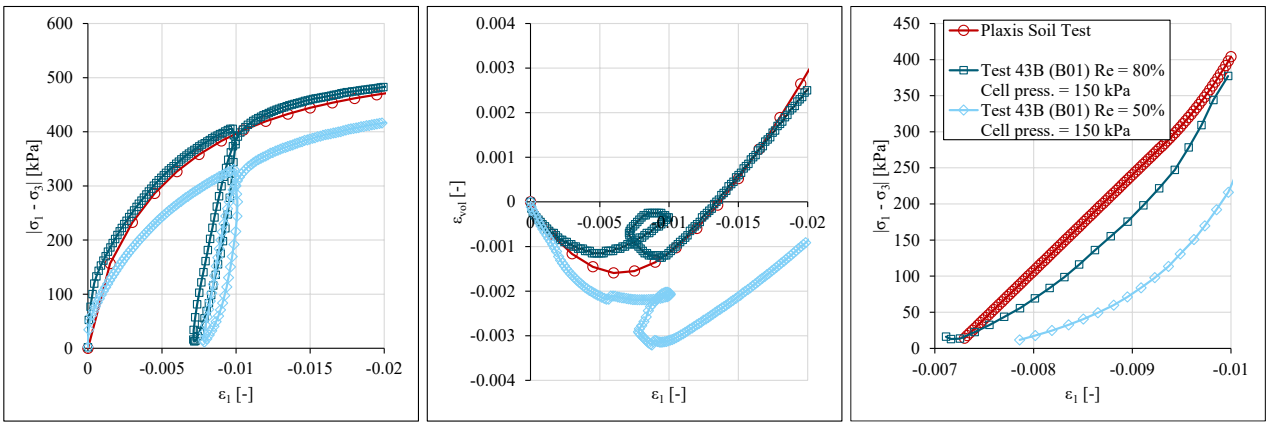

Figure 3. Comparison Plaxis soil test results and laboratory test data for sand 3.

4 BACK ANALYSIS RESULTS

4.1 Plaxis 3D modelling

The pile test was modelled in Plaxis 3D. To limit the calculation time, half of the pile was modelled with half the load on the pile. Afterwards a more extensive model was made in which, among other things, the adjacent (underwater) slope of the Caland Canal was modelled, but this turned out to have a negligible effect on the results.

The model was calculated with drained behaviour, without water over- or under-pressures. This was concluded from the pore pressure meters. These showed a consistent behaviour with the tide without deviations during the loading and unloading steps.

The calculation results of the FEM model in Plaxis 3D corresponded well with the measurement results, see Figure 4 - Figure 7. The difference in pile head displacement between the numerical analysis and the pile test was approximately 10%. The shape of the displacements matched good along the pile. The moment distribution, both under loading and unloading conditions, also corresponded well with the bending moment calculated from the strain measurements.

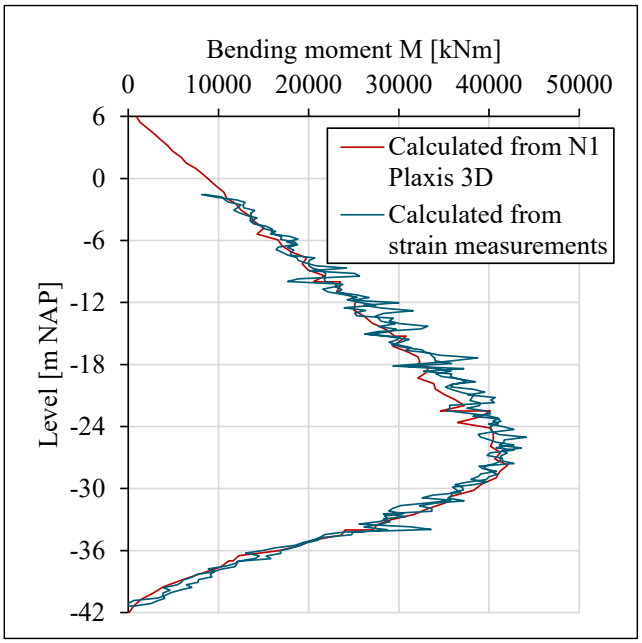

Figure 4. Bending moment mooring pile 81-D04 in loading step 8 at 1380 kN.

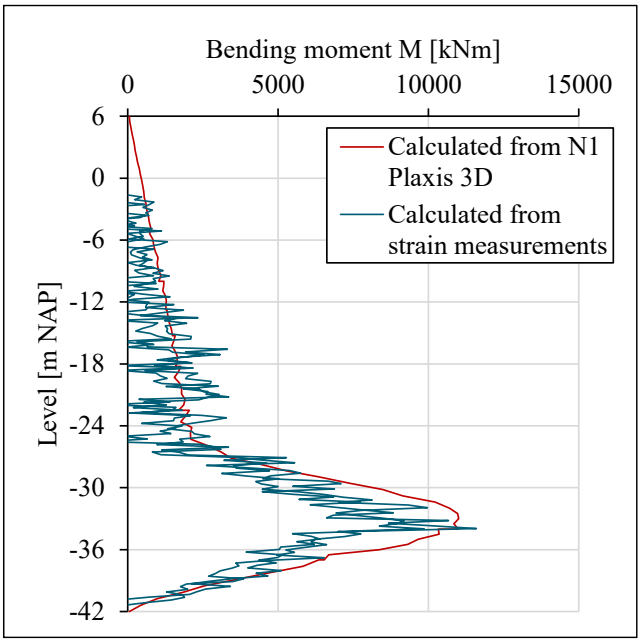

Figure 6. Bending moment mooring pile 81-D04 unloaded after loading step 8 (approximately 70 kN).

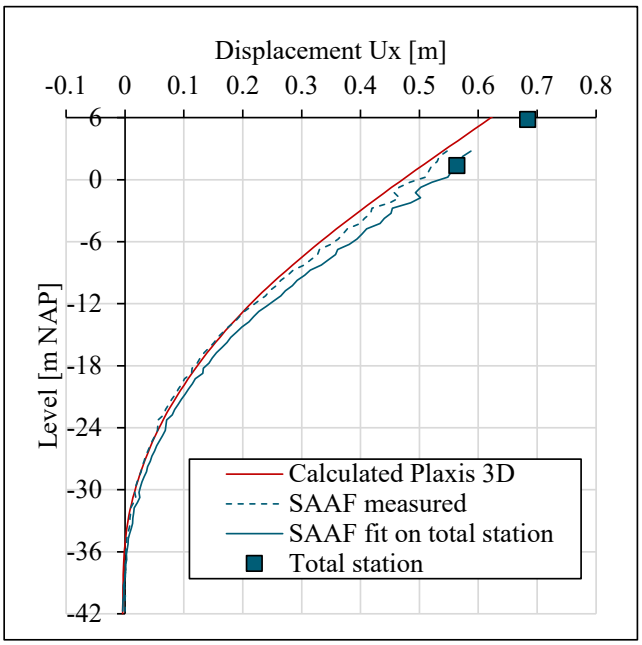

Figure 5. Displacement mooring pile 81-D04 in loading step 8 at 1380 kN.

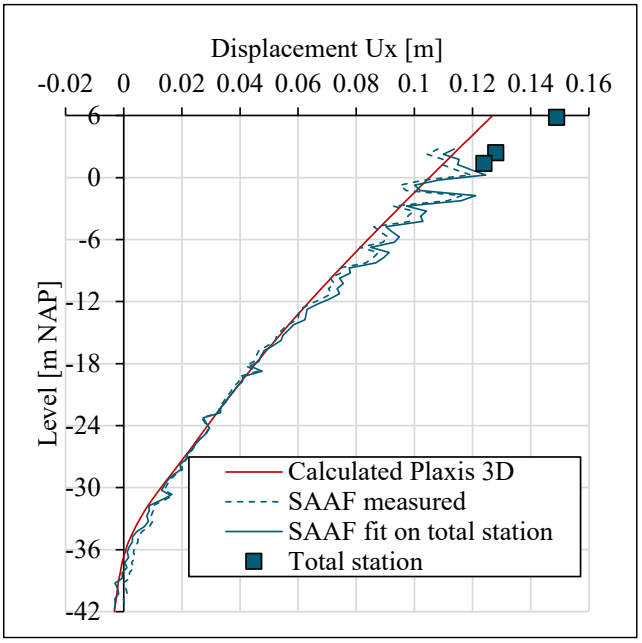

Figure 7. Displacement mooring pile 81-D04 unloaded after loading step 8 (approximately 70 kN).

The differences at the pile head of approximately 10% can be explained by uncertainties in the back analysis, including:

- the actual force on the pile. The forces from the jack pressure proved to be insufficiently reliable, the modelled force was derived from the strain measurements on the pile;
- strength and stiffness of the subsoil. Despite the extensive in-situ and lab testing, there was uncertainty in the fact that the sand samples were built in the lab at a certain relative density. Although the relative density was determined as best as possible based on lab testing and empirical correlations from CPT's, there is always a certain bandwidth. In addition to the relative density, other aspects such as stress history and structure were not represented by the remoulded sand samples.

Despite the uncertainties mentioned, the current FEM model in Plaxis 3D appeared to be sufficiently reliable to substantiate further conclusions with regard to unloading-reloading behaviour and the pile tip displacement (fixity check).

4.2 Unloading-reloading behaviour

One of the research questions of the test was how the mooring pile reacts as a result of repeated loading. The force-displacement diagrams as measured and calculated in Plaxis 3D are shown in Figure 8.

This figure shows that during initial (virgin) loading (or first impact), both in the test and in the modelling, the pile reacted less stiff than during unloading-reloading, which is also the expected behaviour of the subsoil. The absorbable mooring energy is therefore higher during the first mooring thrust (virgin loading). The displacement behaviour was comparable during the second and subsequent mooring thrusts (step 6 - 9 in Figure 8).

The pile test had sufficiently demonstrated that with repeated loading, the second impact already showed sufficiently representative reloading behaviour for any subsequent impacts. The resulting forces and displacements from the second mooring thrust with a serviceability limit state (SLS) mooring energy seemed sufficient to check the fixation of the mooring pile during the design of a mooring pile.

4.3 Pile tip displacement

The pile tip displacement during the pile test could not be directly derived from the SAAF measurements. To do this, the SAAF would have had to extend below the pile tip (fixed in the subsoil), but this turned out to be impracticable.

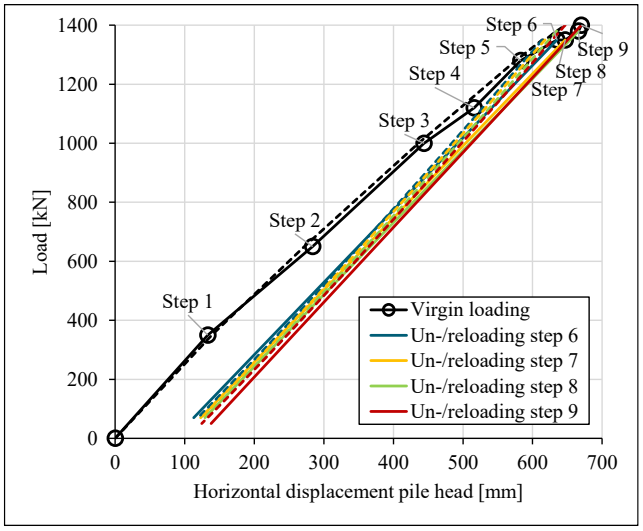

Figure 8. Load-displacement diagram with repeated unloading-reloading measured (continuous) and calculated in Plaxis 3D (dashed)

However, when the SAAF measurements were combined with the displacements from the FEM model in Plaxis 3D, see for example Figure 5, it became clear that a limited displacement of the pile tip (order of millimeters) was the most likely scenario.

5 FIXITY CHECK

5.1 Current fixity check

The purpose of the fixity check in the CROW publication 'Flexible Dolphins' is to make sure that plastic soil deformation at the pile tip does not contribute to energy absorption and/or result in permanent pile inclination (CROW, 2018).

According to the publication, it needs to be shown that the chosen embedment length has a limited effect on the displacement of the pile at the impact level. The recommended limit is 2% of extra deflection at impact level compared with an infinitely long pile. In practice, this can be done by comparison with the deflection of a longer pile by 5*D (CROW, 2018).

In practice, the current fixity check turns out to be governing for the design of the mooring pile in many cases. Especially for piles with long freestanding length, differences in deflection at impact level occurs quickly, while at the pile tip no significant deformations occur. Because calculated deformations of the pile tip are limited, also shown in the Caland Canal pile test, the current fixity check results in piles that are probably too long.

5.2 Adjusted fixity check

In the new edition of CROW Flexible Dolphins (to be published), an adjusted fixity check will be presented.

As explained above, the purpose of the fixity check is to avoid excessive plastic soil deformation. This is established by limiting the plastic deformation at the pile tip. For e.g. a spring model with PY-curves, mobilisation of the passive soil resistance σ_p should be limited to a maximum of 50% in SLS conditions.

In FEM models it is not straightforward how to derive the mobilised soil resistance, since this is not explicitly reported. Instead, a different approach is used, based on the amount of pile displacement needed to mobilise the soil resistance. This approximation is easier to use since displacement can be derived directly from the FEM calculation results.

The proposed method is based on appendix C.3 of EN 1997-1. For different modes of wall movement, required displacement in relation to soil mobilisation is given for 100% and 50% mobilisation. For mooring piles, Figure 9 is applicable, in which v_p is the displacement to mobilise passive soil resistance σ_p and h is the height difference between point of rotation and pile tip.

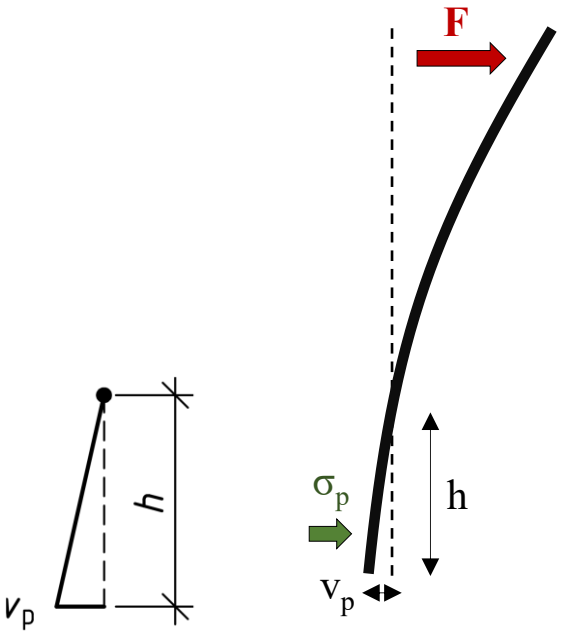

Figure 9. Mode of wall movement (left, EN 1997-1, 2005) and translation to mooring pile behaviour (right).

For ratio v_p/h, displacement criteria will be given in the updated version of CROW Flexible Dolphins, depending on the soil type the pile tip is in. The criteria are given for $0.5 \cdot \sigma_p$, i.e. 50% passive soil resistance mobilisation, which should be evaluated in SLS conditions.

For the determination of this new fixity check, multiple benchmark calculations were evaluated. The Caland Canal pile test represented the finalisation of this study, in which the FEM model of one of the benchmark calculation was validated.

6 CONCLUSIONS

During the Caland Canal pile test, two mooring piles were repeatedly loaded to approximately 1400 kN, which is approximately 70% of the ultimate load for which the pile was dimensioned. Back analysis was performed with a FEM model in Plaxis 3D, using HSs soil parameters. A good fit was found with the measured data, leading to the following conclusions:

- the surface of the mooring post reacts less stiff during the first load compared to the second and subsequent loads, which means that the energy absorption during repeated mooring thrust is lower than during the first mooring thrust. The forces and displacement resulting from the second mooring with a SLS mooring energy seem representative and can be used to check the fixation of the mooring pile;
- the pile tip displacement of the mooring piles in the Caland Canal was limited. The validated FEM model in Plaxis 3D was used to determine which optimization of the pile was possible with the adjusted fixity check. The piles could have been 2 m shorter and the wall thickness could have been reduced in several segments. In total, a reduction of 12.7% in the required amount of steel appeared to be possible for the mooring piles in the Caland Canal.

ACKNOWLEDGEMENTS

The authors would like to thank Port of Rotterdam Authority for the opportunity and financial support of the Caland Canal pile load test.

REFERENCES

Bentley (2022). PLAXIS 3D Reference Manual, PLAXIS CONNECT Edition V22.01.

Brinkgreve, R.B.J., Engin, E., Engin, H.K. (2010). Validation of empirical formulas to derive model parameters for sands. In: *Numerical methods in geotechnical engineering NUMGE 2010*, T. Benz, & S. Nordal (eds.), CRC Press, London, pp. 137-142. http://doi.org/10.1201/b10551-27.

CROW (2018). Flexible Dolphins

EN 1997-1:2005: Eurocode 7: Geotechnical design - part 1: General rules

Lengkeek, H.J (2022). Testing and modeling of sheet pile reinforced dikes on organic soils: Insights from the Eemdijk full-scale failure test (PhD thesis). https://doi.org/10.4233/uuid:78df5e2b-740e-4268-a821-ed0ccaae93e5. TU Delft.

Proceedings of the XVIII ECSMGE 2024
GEOTECHNICAL ENGINEERING CHALLENGES
TO MEET CURRENT AND EMERGING NEEDS OF SOCIETY
© 2024 the Authors
ISBN 978-1-032-54816-6
DOI 10.1201/9781003431749-142
Open Access: www.taylorfrancis.com, CC BY-NC-ND 4.0 license

ECSMGE 24
XVIII EUROPEAN CONFERENCE ON SOIL MECHANICS AND GEOTECHNICAL ENGINEERING

Compressibility characteristics and hydraulic conductivity of slurry clays using large diameter Rowe cell

Caractéristiques de compressibilité et conductivité hydraulique des argiles en suspension utilisant une cellule Rowe de grand diamètre

K. Soe, M. Swamynaidu, A. Tyagi*
Indian Institute of Technology Roorkee, Uttarakhand, India

**akanksha.tyagi@ce.iitr.ac.in*

ABSTRACT: Slurry clays are often encountered in mining and reclamation projects. Soil-bentonite slurries are also extensively used for vertical barriers, especially for contaminant containment. This study describes the experimental investigation of the compressibility and hydraulic conductivity of four different types of clay slurries using a large-diameter Rowe cell testing system. The slurries are made from two types of locally available high plastic clays, and two commercially available sodium bentonites from the state of Gujarat, India. The slurries are prepared at an initial water content of 1.5 times their corresponding liquid limits by mixing distilled water thoroughly in a Hobart mixer. After applying an initial effective stress of 2.5 to 3 kPa, the consolidation tests are performed at effective stresses of 25, 50, 100 and 200 kPa. The coefficient of volume compressibility (m_v), coefficient of consolidation (c_v), and saturated hydraulic conductivity (k) determined from the consolidation tests are compared for the locally available clays and bentonite slurries. The mineralogy and microstructure of the samples are also studied by using X-ray Diffraction (XRD) analysis and Scanning Electron Microscopy (SEM) analysis. The results show that the difference in hydraulic conductivities in natural clay slurries and bentonite slurries are more profound at low effective stresses i.e., 25 kPa. At the highest applied effective stress of 200 kPa, the hydraulic conductivity of all four slurries is found to be within the range of 1.3×10^{-9} m/sec to 8.6×10^{-11} m/sec. Hence, the potential of using natural and locally available clays in slurry wall backfills is assessed by comparing the compressibility, hydraulic conductivity, and microstructural characteristics.

RÉSUMÉ: Les argiles en suspension sont souvent rencontrées dans les projets d'exploitation minière et de remise en état. Les boues de sol-bentonite sont également largement utilisées pour les barrières verticales, notamment pour le confinement des contaminants. Cette étude décrit l'étude expérimentale de la compressibilité et de la conductivité hydraulique de quatre types différents de boues d'argile à l'aide d'un système d'essai à cellules Rowe de grand diamètre. Les boues sont fabriquées à partir de deux types d'argiles à haute teneur en plastique disponibles localement et de deux bentonites de sodium disponibles dans le commerce dans l'État du Gujarat, en Inde. Les bouillies sont préparées avec une teneur initiale en eau de 1,5 fois leurs limites de liquide correspondantes en mélangeant soigneusement de l'eau distillée dans un mélangeur Hobart. Après application d'une contrainte effective initiale de 2,5 à 3 kPa, les essais de consolidation sont réalisés à des contraintes effectives de 25, 50, 100 et 200 kPa. Le coefficient de compressibilité volumique (m_v), le coefficient de consolidation (c_v) et la conductivité hydraulique saturée (k) déterminés à partir des essais de consolidation sont comparés pour les argiles et les boues de bentonite disponibles localement. La minéralogie et la microstructure des échantillons sont également étudiées à l'aide d'une analyse par diffraction des rayons X (DRX) et d'une analyse par microscopie électronique à balayage (MEB). Les résultats montrent que la différence de conductivité hydraulique dans les boues d'argile naturelle et les boues de bentonite est plus profonde à de faibles contraintes effectives, c'est-à-dire 25 kPa. À la contrainte effective appliquée la plus élevée de 200 kPa, la conductivité hydraulique des quatre boues se situe dans la plage de $1,3 \times 10^{-9}$ m/s à $8,6 \times 10^{-11}$ m/s. Par conséquent, le potentiel d'utilisation d'argiles naturelles et disponibles localement dans les remblais de murs en coulis est évalué en comparant la compressibilité, la conductivité hydraulique et les caractéristiques microstructurales.

Keywords: Rowe cell; slurry clays; bentonite; saturated hydraulic conductivity; coefficient of consolidation.

1 INTRODUCTION

Low permeable slurry clays are often used as hydraulic barriers for the containment of contaminants, to control the groundwater flow during deep excavations, and to control seepage in dams and levees. Slurry trench cutoff walls are effectively used as vertical barriers against contaminated soils in a number of landmark remediation projects (Cao et.al., 2021). The compressibility characteristics and hydraulic conductivity of slurry clays are significant for the design of such cutoff walls (Evans et al., 2002; Opdyke and Evans, 2005).

Numerous researchers have performed studies on the modification of bentonites and sand-bentonite mixtures in order to improve the efficiency of slurry walls, e.g., Sreedharan and Puvvadi (2013), Yang et al., (2017, 2018). The commercial bentonite powders are costly and often difficult to obtain. The locally available high-plastic clays are cheap alternatives and might be a potential replacement for bentonite powders. For example, Fan et al., (2014) investigated the compressibility and hydraulic conductivity characteristics of clayey soil/Ca-bentonite backfills. Di Emidio et al., (2017) also discussed the reuse of dredged clay sediments into various barrier applications as the modified clays.

Hence, in this paper, the consolidation characteristics and saturated hydraulic conductivity of four different types of clay slurries including two locally available clays are obtained using a large-diameter Rowe cell testing system. The mineralogy and microstructure of the samples are also studied and compared by using X-ray Diffraction (XRD) analysis and Scanning Electron Microscopy (SEM) analysis.

2 EXPERIMENTAL METHODS

2.1 Materials

Four types of materials are used for preparing slurry clays in this paper: the two different types of locally available clays and the two different sodium bentonites. The first one is fat clay, collected from a site near the Indian Institute of Technology (IIT) Roorkee, India and it shall be referred to as Roorkee clay in this paper. The second clay is black cotton soil, collected from the state of Madhya Pradesh, India and it shall be referred to as Madhya Pradesh (MP) clay. The rest two are the commercially available sodium bentonites, referred to as Ben I and Ben II, respectively, and are obtained from the state of Gujarat, India. Their physical properties are summarized in Table 1.

The grain size distribution curves for the four materials are illustrated in Figure 1.

2.2 Characterization of XRD and SEM

The powder clay samples smaller than 75µm are characterized by X-ray Diffraction (XRD) Analysis. A Bruker D8 X-ray Diffractometer is used with a LINXEYE XE detector. The analysis is performed in the Bragg angle (2θ) measuring range of 5° to 65° at a scanning rate of 2°/min. The morphology of the dried samples before and after consolidation is studied by using the Apreo S Low Vacuum model at the Institute Instrumentation Centre, IIT Roorkee. Before taking SEM images, a gold coating is applied to the samples for better resolution. The different characteristics between the raw powder samples and dried consolidated solid samples of the four materials are discussed later by SEM images.

Table 1. Physical properties of clays.

Properties	Roorkee clay	MP clay	Ben I	Ben II
G_s	2.65	2.65	2.64	2.42
LL (%)	65	52	118	450
PL (%)	28	26	30	59
PI (%)	37	26	88	391
Sand (%)	1	6	0	0
Classification (IS)	CH	CH	CH	CH
Free swell index	48	36	131	429
Activity	0.41	0.33	0.89	3.95

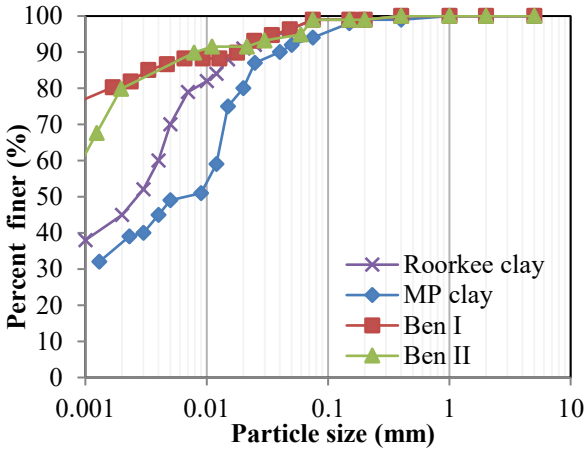

Figure 1. Grain size distribution curves.

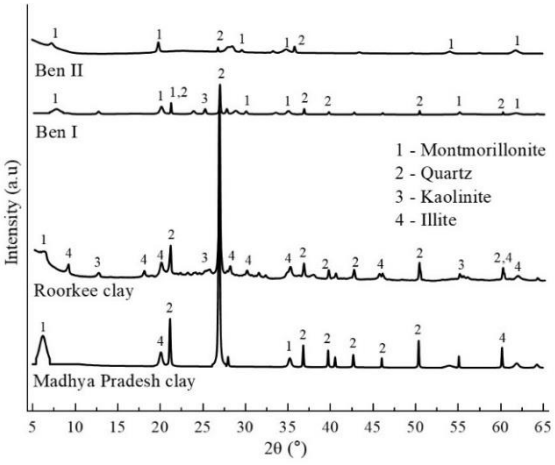

Figure 2. X-ray Diffraction patterns of the four clay samples.

The diffraction patterns of Roorkee clay, MP clay, Ben I and Ben II samples are illustrated in Figure 2. The XRD patterns of the four samples indicate the

presence of clay minerals such as montmorillonite, kaolinite, and illite with the common peaks of crystallized quartz. Roorkee clay is primarily composed of illite with small amounts of kaolinite. MP clay i.e., the black cotton soil has dominant montmorillonite and a low illite content. Montmorillonite is mainly observed in the Ben I and Ben II samples.

As shown in Table 1, the MP clay exhibits less swelling than Roorkee clay, despite having montmorillonite as the dominant clay mineral. This may be because of the presence of sand fraction in the MP clay. This may have also resulted in a lower liquid limit and plasticity index for MP clay as compared to Roorkee clay.

2.3 Sample preparation

The two natural clay samples (Roorkee clay and MP clay) are first soaked in potable water for approximately 48 to 72 hours before preparation and sieved through a 2 mm sieve. Bentonite slurries are prepared by mixing bentonite powder with the distilled water. In this paper, the water contents of all slurries are kept at 1.5 times their respective liquid limits i.e., 1.5LL. Slurries are then poured inside the large-diameter Rowe cell of 250 mm diameter up to 90 mm specimen height. The samples are carefully poured to avoid any entrapped air voids within. The prepared sample for Ben II slurry in the Rowe cell is shown in Figure 3.



Figure 3. Sample preparation for Ben II slurry.

2.4 Testing equipment and procedure

Due to the high compressibility of slurry clays, conventional small-diameter laboratory oedometers are inefficient in performing consolidation tests (Bo et al., 2003). There are several drawbacks to using conventional oedometers, such as the smaller sample size i.e., 60 or 75 mm, test arrangement using mechanical loading, and lack of drainage for pore pressure measurement.

A Rowe cell is a consolidation cell in which the total stress is applied using hydraulic pressure acting across a convoluted rubber jack (Rowe and Barden, 1966). In this paper, the slurry clays are tested using a VJ Tech large-diameter Rowe cell testing system at the geotechnical engineering laboratory, IIT Roorkee. The system consists of three major components: (i) a dual pro automatic pressure controller to apply the vertical load, (ii) a Rowe-type consolidation cell (250 mm diameter and 90 mm specimen height), and (iii) a linear variable displacement transducer and pore water pressure transducer. Figure 4 illustrates the setup of the system. The cell is capable of withstanding confining pressures up to 1000 kPa. It has the advantage of precisely controllable drainage and hydraulic loading.

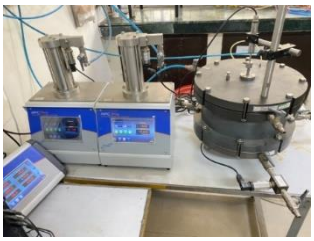

Figure 4. VJ Tech large-diameter Rowe cell testing system in the geotechnical engineering laboratory of IIT Roorkee.

In this paper, one-dimensional consolidation tests are performed for one-way vertical drainage by free strain loading in a large-diameter Rowe cell. The initial effective pressure of 2.5 to 3 kPa is first applied as the seating load. Then, the effective pressures of 25, 50, 100, and 200 kPa are consecutively applied to all four samples. The coefficient of volume compressibility (m_v), coefficient of consolidation (c_v), and hydraulic conductivity (k) of the slurries for each applied pressure is obtained.

For each given load increment, coefficient of consolidation (c_v) value is obtained using logarithm-of-time method (Casagrande and Fadum, 1940).

3 RESULTS AND DISCUSSION

Figure 5 shows the c_v values of four slurries at different effective stresses. For each effective stress, the c_v value of Roorkee clay slurry is found to be higher than that of MP clay, Ben I and Ben II slurries. The c_v value for Roorkee clay seems to decrease drastically with the increase in effective stress. On the other hand, the effect of vertical effective stress on the c_v values of the other three slurries is mostly insignificant. Regardless of the high variation in the plasticity index of bentonite powders, the difference in c_v values of Ben I and Ben II slurries is also found to be insignificant.

Figure 6 shows the variation of the coefficient of compressibility (m_v) and the reciprocal of the constrained modulus ($1/E'_{oed}$) obtained for different effective stresses. There is a sharp decrease in the m_v value of MP clay with the increase in the effective stress. In general, it is observed that the m_v values decrease with increasing effective stresses. For

effective stress of 200 kPa, Ben II slurry is found to have the highest susceptibility to volume compression with the largest m_v value. Nearly the same m_v values are obtained in Ben I and Roorkee clay slurries, while the Ben I slurry is slightly more compressible. Among the four slurries, Madhya Pradesh clay has the lowest volume compressibility value after consolidation. The completely reverse trends are observed for the constrained modulus E'_{oed}, which is the reciprocal of m_v. For the 200 kPa effective stress, the range of E'_{oed} is obtained as approximately 900-1600 kN/m^2.

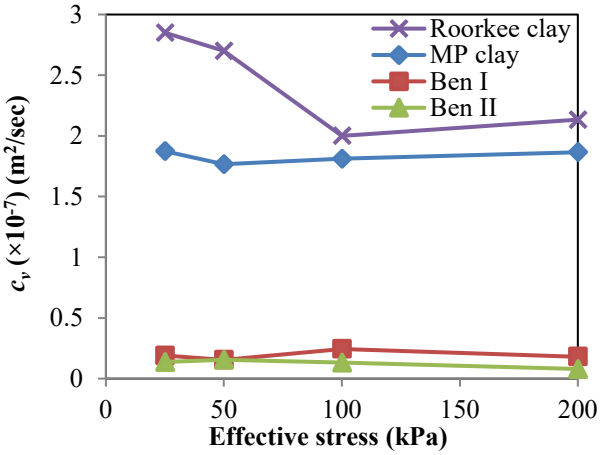

Figure 5. Coefficient of consolidation (c_v) versus effective stress.

Figure 7 shows the values of hydraulic conductivity obtained at different effective stresses for the four slurries. At low effective stress, the difference in hydraulic conductivities is quite significant. For example, at 25 kPa effective stress, the values of hydraulic conductivity of Roorkee clay, MP clay, Ben I and Ben II are 4.4 x 10^{-9} m/sec, 2.2 x 10^{-8} m/sec, 9.5 x 10^{-10} m/sec and 7.9 x 10^{-10} m/sec, respectively. The hydraulic conductivity decreases strikingly with the increase in effective stress from 25 to 100 kPa, while the decrease is gradual from 100 to 200 kPa for both Roorkee clay and MP clay. At 200 kPa effective stress, the hydraulic conductivity of Ben II is the lowest being 8.6 x 10^{-11} m/sec. Except for the MP clay at 25 kPa effective stress, the obtained values are lower than the typically specified value of 1 x 10^{-8} m/sec in the design of seepage control projects (Ryan and Day, 2002). However, hydraulic conductivity of less than 10^{-9} m/s is often required for soil-bentonite slurry walls (Opdyke and Evans, 2005).

The c_v, m_v and k values for the maximum effective stress of 200 kPa are summarized in Table 2. As distilled water is typically recommended due to its high purity and absence of dissolved ions, the use of potable water may introduce some variations in the consolidation properties of clayey soil slurries.

Figures 8(a) to (h) show the SEM images of the four clay samples before and after consolidation. In the SEM images of powder samples before consolidation, book-like stacks of kaolinite in small amounts and the dominant particles of irregular platy illite sheets can be seen in Roorkee clay. In Madhya Pradesh clay, stacks of transparent layers of montmorillonite are present. Montmorillonite is mostly observed in Ben I and Ben II powders. These SEM observations are consistent with the XRD results.

After consolidation of the 200 kPa effective stress, the inter-particle pores are closely packed with each other, and thus the proportion of void spaces is obviously reduced. The soil particles are also densely compressed into a group of particles acting as a unit. The formation of these compacted units mainly controls the compressibility characteristics of clay slurries. Within the clusters, nearly parallel stacks of dispersed structures are mostly observed. As can be observed from Figures 8 (e) to (h), less porous microstructures are observed for Ben I and Ben II.

4 CONCLUSIONS

The paper discusses the compressibility and hydraulic characteristics of four different slurries made of two locally available clays and two commercially obtained sodium bentonites. While Roorkee clay has illite as the dominant mineral, MP clay has montmorillonite as the dominant mineral. It is observed that the c_v values are lowest for Ben II, while similar values were obtained for Roorkee clay and MP clay.

Table 2. Compressibility and hydraulic conductivity values for 200kPa effective stress.

Properties	Coefficient of consolidation, c_v (m^2/sec)	Coefficient of volume compressibility, m_v (m^2/kN)	Constrained modulus, E'_{oed} (kN/m^2)	Hydraulic conductivity, k (m/sec)
Roorkee clay	2.13×10^{-7}	0.00061	1616.7	1.32×10^{-9}
MP clay	1.87×10^{-7}	0.00041	2426.0	7.69×10^{-10}
Ben I	1.80×10^{-8}	0.00062	1608.2	1.12×10^{-10}
Ben II	7.96×10^{-9}	0.00107	927.1	8.58×10^{-11}

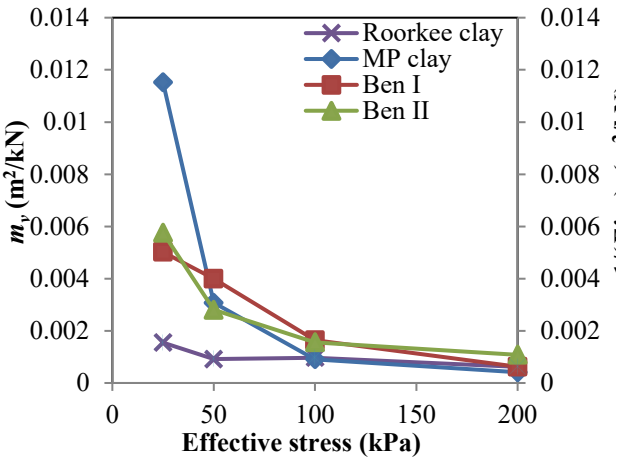

Figure 6. Coefficient of volume compressibility (m_v) and reciprocal of constrained modulus ($1/E'_{oed}$).

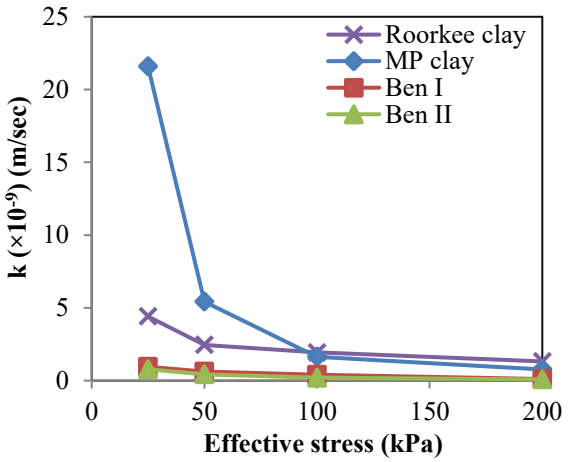

Figure 7. Hydraulic conductivity (k) versus effective stress.

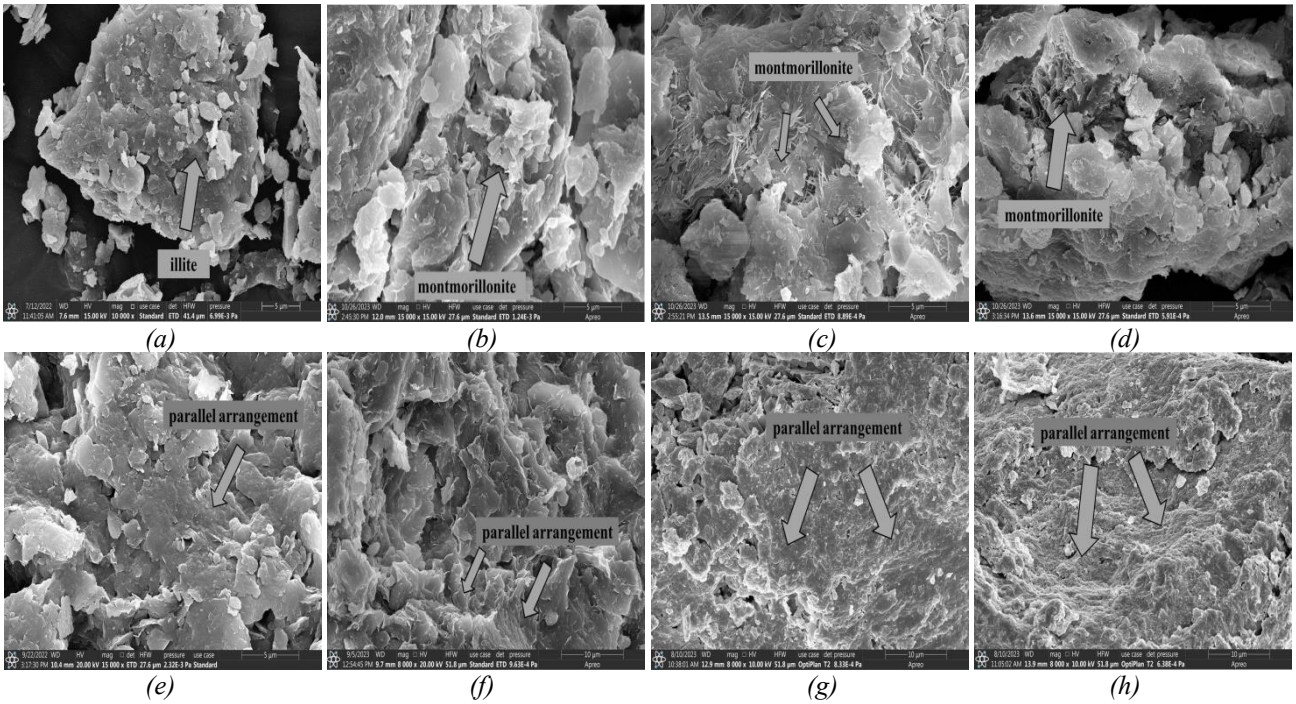

Figure 8. SEM images of the four clay samples, (a)-(d) before consolidation for Roorkee clay, Madhya Pradesh clay, Ben I and Ben II, (e)-(h) after consolidation for Roorkee clay, Madhya Pradesh clay, Ben I and Ben II.

The difference in hydraulic conductivities is more profound at low effective stresses i.e. 25 kPa, for which the values of hydraulic conductivity of Roorkee clay, MP clay, Ben I and Ben II are 4.4 x 10^{-9} m/sec, 2.2 x 10^{-8} m/sec, 9.5 x 10^{-10} m/sec and 7.9 x 10^{-10} m/sec, respectively. The hydraulic conductivity was found to decrease sharply with the increase in effective stress from 25 to 100 kPa, while gradually from 100 to 200 kPa for both Roorkee clay and MP clay. At 200 kPa effective stress, the hydraulic conductivity of Roorkee clay, MP clay, Ben I and Ben II are 1.3 x 10^{-9} m/sec, 7.7 x 10^{-10}, 1.1 x 10^{-10} m/sec and 8.6 x 10^{-11} m/sec, respectively. Although most of the obtained values are lower than the typically specified value of 1 x 10^{-8} m/sec in the design of seepage control projects, the hydraulic conductivity of less than 10^{-9} m/s is typically required for soil-bentonite slurry walls (Ryan and Day, 2002; Opdyke and Evans, 2005). Moreover, the contamination and exposure to salts often lead to a decrease in the efficiency of soil-bentonite walls. This necessitates the use of organic molecules or polymers, chemicals, etc. (Sreedharan and Puvvadi, 2013; Yang et al. 2017, 2018).

Nonetheless, given ease of availability, economy, and zero environmental impact, natural clay slurries may be used as a constituent for low permeable barriers.

ACKNOWLEDGEMENTS

The authors are grateful for the financial support provided to the first author by the Indian Council for Cultural Relations (ICCR) under the General Scholarship Scheme. The authors are also thankful to the Ministry of Education, Government of India, for providing the financial assistantship to the second author.

REFERENCES

Bo, M. W., Sin, W. K., Choa, V., & Ing, T. C. (2003). Compression tests of ultra-soft soil using an hydraulic consolidation cell. *Geotechnical Testing Journal*, *26*(3), 310–319. https://doi.org/10.1520/gtj11310j.

Cao, B., Xu, J., Wang, F., Zhang, Y., & O'connor, D. (2021). Vertical barriers for land contamination containment: A review. In *International Journal of Environmental Research and Public Health* (Vol. 18, Issue23).MDPI.https://doi.org/10.3390/ijerph182312643.

Casagrande, A., & Fadum, R. E. (1940). Notes on soil testing for engineering purposes. *Harvard University Graduate School of Engineering Publication No. 8*.

Di Emidio, G., Verastegui-Flores, R. D., Mazzieri, F., & Dominijanni, A. (2017). Modified clays for barriers: a review. In *Innovative Infrastructure Solutions* (Vol. 2, Issue 1). Springer. https://doi.org/10.1007/s41062-017-0073-8.

Evans, J. C., Dawson, A. R., & Opdyke, S. M. (2002). Slurry walls for control of contaminant migration a comparison of UK and US practices. *ASCE/PENNDOT Central PA Geotechnical Conference*, 105–120.

Fan, R.-D., Du, Y.J., Reddy, K.R., Liu, S.Y., Yang, Y.L. (2014). Compressibility and hydraulic conductivity of clayey soil mixed with calcium bentonite for slurry wall backfill: Initial assessment. Applied Clay Science, 101, 119-127. https://doi.org/10.1016/j.clay.2014.07.026.

Opdyke, S. M., & Evans, J. C. (2005). Slag-Cement-Bentonite Slurry Walls. *Journal of Geotechnical and Geoenvironmental Engineering*, *131*(6), 673–681. https://doi.org/10.1061/(asce)1090-0241(2005)131:6(673).

Rowe, P. W., & Barden, L. (1966). A new consolidation cell. *Geotechnique*, *16*(2), 162–170. https://doi.org/10.1680/geot.1966.16.2.162.

Ryan, C. R., & Day, S. R. (2002). *Soil-Cement-Bentonite Slurry Walls*. *Ryan 1985*, 713–727. https://doi.org/10.1061/40601(256)51.

Sreedharan, V., & Puvvadi, S. (2013). Compressibility behaviour of bentonite and organically modified bentonite slurry. *Geotechnique*, *63*(10), 876–879. https://doi.org/10.1680/geot.SIP13.P.008.

Yang, Y.L., Du, Y.J., Reddy, K.R., Fan, R.D. (2017). Phosphate-amended sand/Ca-bentonite mixtures as slurry trench wall backfills: Assessment of workability, compressibility and hydraulic conductivity. *Applied Clay Science*, 142, 120–127. https://doi.org/10.1016/j.clay.2016.10.040.

Yang, Y.L., Reddy, K.R., Du, Y.J., Fan, R.D. (2018). SHMP amended calcium bentonite for slurry trench cutoff walls: Workability and microstructure characteristics. Canadian Geotechnical Journal. 55, 528–537. https://doi.org/10.1139/cgj-2017-0291.

Proceedings of the XVIII ECSMGE 2024
GEOTECHNICAL ENGINEERING CHALLENGES
TO MEET CURRENT AND EMERGING NEEDS OF SOCIETY
© 2024 the Authors
ISBN 978-1-032-54816-6
DOI 10.1201/9781003431749-143
Open Access: www.taylorfrancis.com, CC BY-NC-ND 4.0 license

ECSMGE 24
XVIII EUROPEAN CONFERENCE ON SOIL MECHANICS AND GEOTECHNICAL ENGINEERING

Application of the new Brazilian pavement design method (MeDiNa) in the design of flexible pavement structures using fine-grained tropical soils

Application de la nouvelle méthode Brésilienne de conception des revêtements routiers (MeDiNa) dans le dimensionnement des structures de revêtements flexibles utilisant des sols tropicaux à grains fin

M.A.S. Sousa
State University of Maranhão, São Luís, Brazil

R.Q. Coutinho
Federal University of Pernambuco, Recife, Brazil

L.M.G. Motta
Federal University of Rio de Janeiro, Rio de Janeiro, Brazil

C.D. Castro*
Pontifical Catholic University of Rio de Janeiro, Rio de Janeiro, Brazil

**carmendc@puc-rio.br*

ABSTRACT: This article discusses the utilization of MeDiNa, a novel Brazilian pavement design method, in the construction of flexible pavements using fine-grained tropical soils. In Brazil, the conventional pavement design relies on empirical equations that consider load applications, material attributes, and CBR assessments. MeDiNa, introduced in 2021 and named after Professor Jacques de Medina, incorporates principles of pavement mechanics and deformation interactions, employing the Elastic Analysis of Multiple Layers (AEMC) technique. The study concentrates on the analysis of fine-grained tropical soils from Pernambuco, Brazil, examining their properties. Various pavement configurations, traffic levels, and materials are assessed. The study demonstrates MeDiNa's capability to suggest cost-effective pavement structures with thinner layers, even when local materials possess low CBR values and fine granulometry. Results from 26 design simulations, encompassing variations in fatigue class, traffic levels, material types, and layer thicknesses, confirm MeDiNa's proficiency in recommending economical solutions. Both the percentage of cracked area and Wheel Tracking Rutting values consistently adhere to acceptable limits (30% and 10 mm, respectively), showcasing MeDiNa's ability to design enduring pavements. In conclusion, this research underscores MeDiNa as a significant advancement in pavement analysis, providing a more economical and efficient approach to pavement design by utilizing local resources and enhancing construction efficiency, thereby contributing to cost reduction in infrastructure projects and fostering sustainable development in the Brazilian context.

RÉSUMÉ: Cet article examine l'utilisation de MeDiNa, une nouvelle méthode brésilienne pour concevoir des chaussées flexibles avec des sols tropicaux fins. Au Brésil, les chaussées sont généralement conçues en se basant sur des équations empiriques prenant en compte divers facteurs tels que la charge, les matériaux et l'évaluation CBR. En 2021, MeDiNa a été introduit comme une approche novatrice nommée d'après le professeur Jacques de Medina. Elle intègre des principes de mécanique des chaussées et d'interactions de déformation en utilisant l'Analyse Élastique de Couches Multiples (AEMC). L'étude se concentre sur les sols tropicaux fins de Pernambuco, au Brésil, en examinant leurs propriétés. Elle évalue diverses configurations de chaussées, niveaux de trafic et matériaux. Les résultats de 26 simulations confirment la capacité de MeDiNa à proposer des structures de chaussées économiques avec des couches plus minces, même lorsque les matériaux locaux ont des valeurs CBR faibles et une granulométrie fine. Les critères de fissuration de surface et d'affaissement des roues restent constamment dans les limites acceptables (30 % et 10 mm, respectivement). En conclusion, cette recherche souligne que MeDiNa représente une avancée significative dans la conception de chaussées au Brésil, offrant une approche plus économique et durable en utilisant les ressources locales et en améliorant l'efficacité de la construction, contribuant ainsi à la réduction des coûts dans les projets d'infrastructure et favorisant le développement durable.

Keywords: Pavement design; fine-grained soils; tropical soils; cracked area; wheel track sinking.

1 INTRODUCTION

In Brazil, the design of asphalt pavements has historically relied on empirical formulas based on load applications, material coefficients, and CBR tests, resulting in fixed asphalt thicknesses determined by load applications and subgrade quality (Balbo, 2007; Bernucci et al., 2022). However, authors like Sousa (2021), Sousa et al. (2021), Guimarães (2009), and Motta (1991) have emphasized the need for pavement designs that account for the specific conditions of tropical environments, considering the elastic and plastic properties of materials and material selection criteria, including repeated load tests.

Although standards for measuring the resilient modulus of soils and asphalt mixtures were available in Brazil since the 1980s, they gained broader academic use only recently. The SISPAV program, developed as a result of Franco's doctoral thesis (2007), aimed to address these issues, incorporating design criteria (Medina and Motta, 2015). Building upon SISPAV, the Brazilian National Department of Transport Infrastructure (DNIT) launched the MeDiNa program in 2021, honoring Professor Jacques de Medina, who pioneered the introduction of Pavement Mechanics and repeated load tests in the country. MeDiNa utilizes the AEMC (Elastic Analysis of Multiple Layers) technique to calculate stresses and deformations in pavement structures, accounting for road standard axles with an 8.2 ton-force load. It requires data related to pavement composition, material types, thicknesses, Poisson ratio, modulus, as well as parameters describing material resilience and permanent deformation, which are determined through experimental tests.

In contrast, conventional geotechnical material classifications, designed for non-tropical and temperate environments, impose strict criteria primarily favoring granular materials for fundamental pavement layers, like base and sub-base (Sousa, Motta, Coutinho, 2021). These criteria often exclude or underutilize fine-grained tropical soils. Nevertheless, numerous studies by scholars such as Nogami and Villibor (1991), Guimarães (2009), Sousa (2016, 2021), Lima et al. (2019), and Sousa, Motta, and Coutinho (2021) suggest that fine-grained soils, not neatly categorized under existing systems like the Unified Soil Classification System (USCS) and Transportation Research Board (TRB), can perform adequately in tropical regions.

This article applies the MeDiNa Method to design various pavement structures under different traffic levels, incorporating fine-grained tropical soils from Pernambuco, Brazil, in different layers. The results are assessed for geotechnical properties, including resilience, permanent deformation (PD), and the MCT (Miniature, Compact, Tropical) Classification of materials.

2 MATERIALS AND METHODS

2.1 Fine-grained tropical soils

The research used two soils from a humid tropical climate (01 - clayey soil and a 02 - sandy soil). These fine-textured soils (following the MCT Methodology, with up to 10% retained on a 2 mm sieve) were collected in Pernambuco, Brazil. They are from the Barreiras Geological Formation, known for sediment variations, diverse grain sizes (fine to coarse), yellowish to reddish colors, and occasional presence of pebble-sized grains and ferruginous concretions (Coutinho et al., 2019).

The laboratory tests followed DNIT standards. Traditional characterization, classification, CBR and repeated load tests necessary for the application of MeDiNa were carried out. The mechanical tests were carried out at optimum humidity and Intermediate Proctor energy (26 strokes per layer, DNIT Standard 164/2013-ME).

The equations for the resilient behavior are based on the composite model, while the DP equations follow the Guimarães (2009) model. For details on the types and test standards used to carry out the RM and PD tests, see Sousa (2021).

2.2 Data included in simulations in the MeDiNa program

In the simulations, fine soils from Pernambuco were used with various pavement and traffic configurations. Light traffic employed Double Surface Treatment (DST), while other levels used asphalt concrete (across various fatigue classes, with a preference for CAP 50/70, common in the region according to Moreira, 2021). Figure 1 displays models of the structures simulated in MeDiNa.

Table 1 presents materials from MeDiNa data base, which were used in the simulations, and their respective resilient modulus (RM). Further data can be consulted directly in: https://www.gov.br/dnit/pt-br/assuntos/planejamento-e-pesquisa/ipr/medina .

The soils used as subgrade in most cases included the soils in the research. However, in some structures, for comparison purposes, a Non-Lateritic Silty Soil (NS') from the MeDiNa database was also used.

Two approaches were considered in thickness design in MeDiNa (1. Evaluates with predefined thicknesses and 2. Sizes specific layer thickness.), resulting in numerous simulations. In the results, only

the most economical and essential thicknesses are shown, reducing construction expenses.

For traffic and design, a standard axle of 8.2 tons for 10 years was adopted. Primary Arterial Road type, criteria: 30% Cracked Area (AT) and 13 mm Wheel Tracking Rutting (ATR) at the end, with 85% reliability according to MeDiNa.

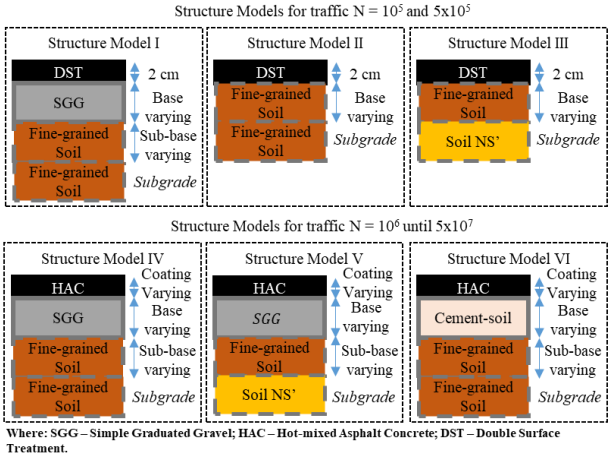

Figure 1. Pavement design models by simulation using MeDiNa software with soils from Pernambuco (Brazil).

Table 1. Resilient modulus data of materials from MeDiNa software database that were used in this research.

Material	RM (MPa)	Model
DST (Double Surface Treatment)	1,000	Linear
Asphalt concrete - Class 1	5,764	Linear
Asphalt concrete - Class 2	6,743	Linear
Asphalt concrete - Class 3	8,000	Linear
Asphalt concrete - Class 4	10,492	Linear
Simple graded crushed stone (BGS)	381	Linear
Soil NS' (Non-Lateritic Silty Soil)	189	Linear
Soil - Cement	9,230	Sigmoidal (max RM)

3 RESULTS AND DISCUSSIONS

3.1 Physical and mechanical characterization and soil classification

Table 2 presents basic characterization results (Real Density, Granulometry, Atterberg limits, MCT and TRB Classification and USCS (Unified Soil Classification System), as well as data from the Mechanical tests (Compaction, RM and PD).

TRB and USCS classify soils as fine sandy loam with poor sub-base performance. MCT Classification for tropical soils categorizes them as clay and sandy clay with laterite behaviour, promising for sub-base and base use. Nevertheless, the CBR and expansion test results indicate that both soils do not comply with the conventional specifications for the base layer (CBR > 60% for light traffic volume, DNIT (2006)). Concerning the sub-base (CBR > 20%, DNIT (2006)), soil 02 exhibits acceptable load-bearing capacity (30%) and zero expansion (0.00%).

Table 2. Physical-mechanical test results and soil classification.

Test		Soil 01	Soil 02
Real Density	δ (g/cm³)	2.634	2.679
Granulometry	Clay % (ø < 0.002mm)	48.71	42.00
	Silt % (0.002mm < ø < 0.074mm)	15.66	5.70
	Sand % (0.075mm < ø < 4.75mm)	35.57	52.30
	Gravel % (4.75mm < ø < 75mm)	0.06	0.00
Atterberg Limits	Liquid Limit (LL)	35.60	34.70
	Plasticity Index (PI)	10.60	9.80
MCT	c'	2	0.92
	e'	0.94	0.91
	Class	LG'	LA'
TRB	Class	A-6	A-4
USCS	Class	ML	SM
Compaction	MEAS	1.79	1.9
	$W_{ót}$	17.4	12.7
CBR	%	12.8	30.0
Expansion	%	30.0	0.00
Resilient Modulus	Average value (MPa)	438	488
Composite Model (CM)	K_1	354.12	601.39
	K_2	*0.33*	*0.362*
	K_3	-0.515	-0.358
	R^2	0.81	0.87
Permanent Deformation (PD)	In mm, under Confined Strength = 120 kPa / Deviant Stress = 360 kPa	6,5	0,7
Model from Guimarães, 2009 (PD)	Ψ_1	0.209	0.076
	Ψ_2	-0.447	0.043
	Ψ_3	1.727	0.912
	Ψ_4	0.056	0.047
	R^2	0.89	0.93

RM and PD align with literature, with lateritic soils commonly showing high resilient modulus and low permanent deformation, supported by Costa and Motta (2007), Guimarães (2009), Dalla Rosa and Motta (2018), Lima (2020) and other researchers.

3.2 Application of the new Brazilian pavement design method (MeDiNa)

Table 3 summarizes MeDiNa simulation results for pavements meeting established requirements: ATR (wheel track sinking) < 13 mm, % Cracked Area < 30%, service life of 10 years). Table details minimum layer thicknesses for various traffic levels (ranging from 10^5 to $5x10^7$), along with sizing results (cracked area and ATR). A total of twelve structures with soil 01 and fourteen with soil 02.

Figure 2 (a) and (b) present, respectively for the structures in which soils 01 and 02 were used, the Rutting results in millimeters and the percentage of Cracked Area of all simulations realized.

The first two structures tested with soil 01 considered a light traffic scenario ($1x10^5$), with application of double surface treatment (DST) and lower layers with different materials. Structure I was composed of 15 cm of simple graded gravel (SGG) as base and 30 cm of fine soil (soil 01) as sub-base.

In Structure Model II, the SGG base layer was replaced with a 30 cm layer of soil 01, eliminating the subbase layer. Pavement performance was similar in the two structures, highlighting the viability of land use, in addition to a clear advantage in terms of construction costs. In DST pavements, the design criterion is solely ATR.

In Structure III, the thicknesses remained identical to those in Structure II, however, there was an increase in traffic to $5x10^5$ (still classified as light intensity). The subgrade was changed to an NS' soil with a lower RM. There was a reduction in the structure's contribution to permanent deformation in the subgrade. The ATR value remained significantly below the 13 mm road category limit (Figure 2a).

With the increase in traffic level to 10^6, the use of DST was no longer possible, so the coating was replaced by a layer of asphalt concrete. Structure IV was composed with Class 1 of asphalt mixtures (5 cm), 15 cm of base with SGG, 30 cm of sub-base with soil 01 and the subgrade of the same soil. In Model V, the structure remained the same, but the subgrade was changed to NS' soil. Both sections showed similar performance in terms of fatigue and permanent deformation (Figure 2a).

In Structure Model V* was composed of a base with SGG (20 cm), sub-base with fine soil (20 cm) and subgrade with NS' soil and traffic was increased to $5x10^6$. Despite thicker base and coating, a significant increase in AT percentage was observed.

The Structure Models tested for a traffic of 10^7 (medium-heavy), were composed of a SGG base (20 cm), sub-base (30 cm) and subgrade with soil 01. The fatigue classes (according to the bench data from MeDiNa) of the asphalt mixtures were varied (Structure Models: IVa - Class 1, IVb - Class 2, IVc - Class 3 and IVd - Class 4), revealing that the simple change in the fatigue class of the mixture caused a considerable change in the thickness required for the coating. Using a Class 4 asphalt mixture it was possible to reduce the required thickness by practically 50%, in relation to section IVa, and still meet the requirements established.

In Model V (traffic 10^7), the configuration matched Section IVd, with the subgrade changed to NS' soil. Thickness increased by 0.5 cm, highlighting the economic benefits of lateritic soil over non-lateritic soil according to MCT Classification.

Finally, for soil 01, in structure VI, the possibility of using soil for heavy traffic ($5x10^7$) was explored through the adoption of a 15 cm soil-cement base. The result was satisfactory, indicating a lower total permanent deformation than all other structures tested under light traffic. The percentage of cracked area was also lower than those observed for traffic levels of $5x10^6$ and 10^7 (Figure 2a).

In the case of soil 02, at light traffic levels for the simulated structures (II and IV), only a base layer was required, with a considerably thin thickness of 15 cm, composed of a fine soil reffered in this research. The first simulations indicated a better performance of the sandy soil with lateritic behavior (LA') compared to soil 01 (clayey soil with lateritic behavior). In these first simulations with surface treatment on the coating, it was noted that, in both cases, the Wheel Tracking Rutting (ATR) was low and equivalent (Figure 2b).

For medium traffic (10^6), two structures (IVa and V) were simulated with a Class 1 asphalt mixture coating of 5 cm, a SGG base of 15 cm and a sub-base of fine soil 02. Varying the subgrade material between the research soil and NS' soil, both sections presented similar percentages of cracked area and Wheel Tracking Rutting(Figure 2b). However, for traffic of $5x10^6$ and using an asphalt mixture with CAP 50/70, it was only possible to obtain a satisfactory service life by increasing the sub-base thickness to 30 cm and program the software to design the asphalt layer. This resulted in a lower coating thickness in the section with the subgrade composed of the research soil (IVa) compared to the subgrade with the NS' soil (V).

For traffic 10^7, the simulations were realized by varying only the fatigue class of the asphalt mixture. It was observed that as the class of the asphalt mixture increased (and its resilient modulus, according to Table 2), the thickness required for the coating decreased, as for the simulations with soil 01. Simulation with structure V, changing the subgrade to NS' soil, led to a thicker coating than needed with soil 02 subgrade in this study.

Last test with soil 02 and heavy traffic suggests a thinner cemented base (5 cm) and smaller sub-base layer (15 cm) than required for soil 01 (30 cm). The percentage of cracked area in structure VI (for both soils) is considerably lower due to the cemented base layer. It should be noted that the method used in the work considers fatigue cracking only in layers composed of asphalt mixtures.

Table 3. Results of the MeDiNa in the dimensioning of flexible pavement structures using fine-grained tropical soils.

Traffic		**Light**			**Medium**			**Mid-heavy**					**Heavy**
N		**10^5**		**$5x10^5$**	**10^6**		**$5x10^6$**	**10^7**					**$5x10^7$**
Results of simulations on MeDiNa for Soil 01													
Structure Model		**I**	**II**	**III**	**IVa**	**V**	**V***	**IVa**	**IVb**	**IVc**	**IVd**	**V**	**VI**
Thickness (cm)	Coating	2	2	2	5	5	9	14,5	12	10	7,5	8	5
	Base	15	30	30	15	15	20	20	20	20	20	20	15
	Sub-base	30	-	-	30	30	20	30	30	30	30	30	30
Crack Area (%)		**-**	**-**	**-**	**6,3**	**6,6**	**28,4**	**28,5**	**29,2**	**29**	**28,1**	**29,2**	**17,3**
Rutting (mm)		**10,5**	**10,3**	**7,9**	**11,4**	**8,8**	**5,4**	**5,9**	**6,9**	**7,6**	**9,1**	**6,6**	**4,9**
Results of simulations on MeDiNa for Soil 02													
Structure Model		**II**	**III**	**II**	**III**	**IVa**	**V**	**IV***	**V***	**IVa**	**IVb**	**IVc**	**IVd**	**V**	**VI**
Thickness (cm)	Coating	2	2	2	2	5	5	7,7	8,5	14	12	10	8	9	5
	Base	15	15	15	15	15	15	15	15	15	15	15	15	15	15
	Sub-base	-	-			15	15	30	30	30	30	30	30	30	15
Crack Area (%)		-	-	-	-	**6,3**	**6,9**	**29,1**	**29,2**	**29**	**28,4**	**28,7**	**28,6**	**28,3**	**17,7**
Rutting (mm)		**1,4**	**3,0**	**1,5**	**3,3**	**3,2**	**4,5**	**3,1**	**3,4**	**2,5**	**2,7**	**2,8**	**3,3**	**3,5**	**1,0**

Where: IVa, IVb, IVc and IVd are structures with differents classes of Hot-mixed asphalt concrete (HAC), according to the MeDiNa database, Classes 1, 2, 3, and 4, respectively. The * in sctructures models subjected to 5x106 traffic load, it indicates that the binder used in the pavement was changed to the most commonly used in the research region (northeast), the 50/70 type (classified by penetration).

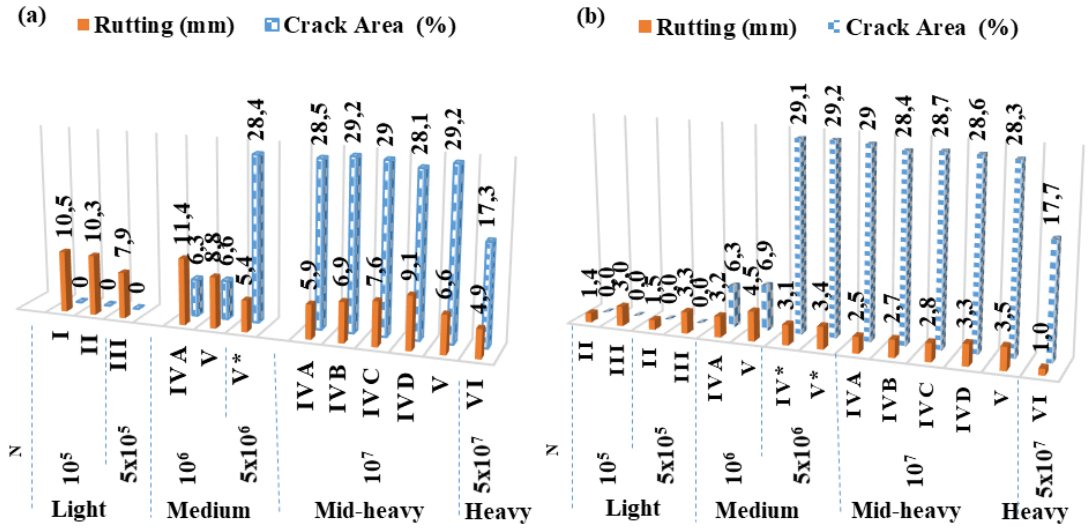

Figure 2. Results of Cracked Area and Rutting obtained in simulations with soils 01 e 02 in different structure models.

Based on the results presented and discussed in this article, it is demonstrated that the MeDiNa program has the capacity to recognize the potential of fine soils, typical of the Brazilian tropical environment. In this work alone, 26 different pavement structures were proposed, using these materials (which in Brazil are still, in many cases, summarily discarded for use in pavement, due to their granulometry and low CBR), in different layers of the flexible pavement and being subjected at varying traffic levels.

Several proposed structures had thin 15 cm layers, showing modern pavement mechanics can provide economical and durable solutions with up to 10 years of service life.

4 CONCLUSIONS

This study applied the Brazilian MeDiNa pavement design method to create structures using fine-grained tropical soils. Two soils from Pernambuco were characterized, and tests were conducted with a Primary Arterial System Road type, meeting criteria for Wheel Tracking Ruttingand cracked area percentage.

The results of 26 design simulations were presented in total, with six different structural models, in which varied the fatigue class of the asphalt mixture, the traffic levels (light to heavy), the types of materials and the thicknesses of the coating layers, base, sub-base and sub-grade. The percentage of cracked area varied between 6.3 and 29.2% and the Wheel Tracking Ruttingvalues obtained for all structures reached a maximum of 11.4 millimeters at the end of the service life of the pavement.

The results attest the ability of the new design method (MeDiNa) to propose economic structures using fine-grained soils used, regardless of their CBR values and granulometry, taking as a reference the behavior of the materials in terms of their deformability (resilience and permanent deformation). This discovery allows flexible pavement designers to propose the use of local resources in infrastructure projects, contributing to the reduction of costs related to transportation and the acquisition of crushed materials, in addition to improving construction efficiency. The importance of MeDiNa stands out as a significant advance in pavement analysis, based on mechanistic principles, allowing the proposition of more economical and long-lasting solutions.

REFERENCES

Balbo, J. T. (2007) *Pavimentação Asfáltica: materiais, projetos e restauração*. São Paulo: Oficina de Textos. *(in portuguese)*

Bernucci, L. B.; L. M. G. Motta.; J. A. P. Ceratti e J. B. Soares (2022) *Pavimentação Asfáltica: formação básica para engenheiros*. Rio de Janeiro: Petrobras - Abeda. *(in portuguese)*

Costa, J. H. e L. M. G. Motta. (2007) Caracterização Geotécnica dos solos finos, do litoral do Estado de Sergipe, visando aplicação em pavimentos de rodovias de baixo volume de tráfego. *Revista Pavimentação*, p. 45- 57, ano II. *(in portuguese)*

Coutinho, R. Q., Silva, M. M., Santos, A. N. D., & Lacerda, W. A. (2019). Geotechnical characterization and failure mechanism of landslide in granite residual soil. Journal of *Geotechnical and Geoenvironmental Engineering*, 145(8), 05019004.

Dalla Roza, A. E. e L. M. G. Motta (2018) Classificação MCT com relação ao comportamento resiliente e deformação permanente em solos do Mato Grosso. Anais do *XIX Congresso Brasileiro de Mecânica dos Solos e Engenharia Geotécnica* – COBRAMSEG, Bahia. *(in portuguese)*

DNIT, Departamento Nacional de Infraestrutura de Transportes (2006) Manual de pavimentação (n. 719). 3ª ed. 274p. Rio de Janeiro. *(in portuguese)*

DNIT, Departamento Nacional de Infraestrutura de Transportes (2021) IS-247: Estudos para Elaboração de Projetos de Implantação usando o Método de Dimensionamento Nacional – MeDiNa.

DNIT, Departamento Nacional de Infraestrutura de Transportes (2013) DNIT 164/2013-ME – Solos – Compactação utilizando amostras não trabalhadas – Método de Ensaio. *(in portuguese)*

Franco, F. A. C. P (2007) *Método de dimensionamento mecanístico-empírico de pavimentos asfálticos - SISPAV*. PhD thesis, COPPE/UFRJ, Rio de Janeiro.

Guimarães, A. C. R. (2009) *Um Método Mecanístico Empírico para Previsão da Deformação Permanente em Solos Tropicais Constituintes de Pavimentos*. PhD thesis, COPPE/UFRJ, Rio de Janeiro. *(in portuguese)*

Lima, C. D. A.; L. M. G. Motta.; F. T. S. Aragão e A. C. R. Guimarães (2019) Mechanical Characterization of Fine-Grained Lateritic Soils for Mechanistic-Empirical Flexible Pavement *Design. Journal of Testing and Evaluation*. ASTM International. DOI: 10.1520/JTE20180890.

Lima, C. D. A. (2020) *Avaliação da deformação permanente de materiais de Pavimentação a partir de ensaios triaxiais de cargas repetidas*. PhD thesis, COPPE/UFRJ, Rio de Janeiro.

Medina, J. e L.M.G. Motta (2015) *Mecânica dos Pavimentos*. 2a. ed. Rio de Janeiro: Editora Interciência. *(in portuguese)*

Moreira, M. R. P. (2021) *Uma abordagem da gestão da infraestrutura urbana versus a operação do sistema de transporte coletivo: a necessidade de uma visão holística do processo*. PhD thesis. Federal University of Pernambuco (UFPE).

Motta, L. M. G. (1991) *Método de dimensionamento de pavimentos flexíveis: critério de confiabilidade e ensaios de cargas repetidas*. PhD thesis, COPPE/UFRJ, Rio de Janeiro. *(in portuguese)*

Nogami, J. S. e D. F. Villibor, (1991) Use of lateritic fine-grained soils in road pavement base courses. *Geotechnical and Geological Engineering*, n. 9, p. 167-182.

Sousa, M. A. S. (2021). *Contribuição ao estudo de solos tropicais finos para uso na pavimentação rodoviária*. PhD thesis. Federal University of Pernambuco. Pernambuco. *(in portuguese)*

Sousa, M. A. S., Motta, L. M. G., & Coutinho, R. Q. (2021). Análise da aplicabilidade de solos tropicais finos em estruturas de pavimento flexível utilizando o novo Método de Dimensionamento Nacional (MeDiNa). In 35º *Congresso de Pesquisa e Ensino em Transportes* (ANPET). *(in portuguese)*

Proceedings of the XVIII ECSMGE 2024
GEOTECHNICAL ENGINEERING CHALLENGES
TO MEET CURRENT AND EMERGING NEEDS OF SOCIETY
© 2024 the Authors
ISBN 978-1-032-54816-6
DOI 10.1201/9781003431749-144
Open Access: www.taylorfrancis.com, CC BY-NC-ND 4.0 license

ECSMGE 24
XVIII EUROPEAN CONFERENCE ON SOIL MECHANICS AND GEOTECHNICAL ENGINEERING

Combined pile-raft and raft foundation modelling and design for three distinct office buildings in Lisbon, Portugal

Modélisation et conception combinées de fondations sur pieux et sur radiers pour trois différents immeubles de bureaux à Lisbonne, au Portugal

A. Sousa*, A. Pinto, N. Silva
JETsj Geotecnia, Lisbon, Portugal

**asousa@jetsj.com*

ABSTRACT: In recent years many projects were designed using the Combined Pile-Raft Foundation (CPRF) concept. Combined Pile-Raft Foundations have a complex soil-structure interaction scheme including the pile-soil interaction, pile-pile interaction, raft-soil interaction, and finally the pile-raft interaction. Consequently, there is a need for 3D numerical models that can study this complex interaction. In this paper, several 3D models are presented and discussed for the foundation design of three office buildings, that were built using the Combined Pile-Raft and Raft Foundations solutions, near the right bank of the Tagus River in Lisbon, Portugal. The study was based on geotechnical information provided by the site investigation and by Static and Dynamic Load Tests on Driven Piles, both performed in several spots evenly distributed at the site. The developed 3D model was able to simulate the behaviour of the piled raft foundation system.

RÉSUMÉ: Ces dernières années, de nombreux projets ont été conçus en utilisant le concept de fondation combinée sur pieux et radeau. Les fondations combinées pieux-radeau ont un schéma d'interaction sol-structure complexe comprenant l'interaction pieu-sol, l'interaction pieu-pieu, l'interaction radeau-sol et enfin l'interaction pieu-radeau. Par conséquent, il existe un besoin de modèles numériques 3D capables d'étudier cette interaction complexe. Dans cet article, plusieurs modèles 3D sont présentés et discutés pour la conception des fondations de trois immeubles de bureaux, qui ont été construits à l'aide des solutions de fondations combinées Pile-Raft et Raft, près de la rive droite du Tage à Lisbonne, au Portugal. L'étude s'est basée sur les informations géotechniques fournies par l'investigation du site et par des essais de charge statique et dynamique sur pieux battus, tous deux effectués à plusieurs endroits uniformément répartis sur le site. Le modèle 3D développé a pu simuler le comportement du système de fondation sur radiers sur pieux.

Keywords: 3D modelling; raft foundation; combined pile-raft foundation; finite element method.

1 INTRODUCTION

The use of piles, strategically located, within a raft foundation has been a commonly accepted practice, which has been used in many projects, to improve both the ultimate load capacity and the settlement and differential settlement performance of the raft.

This paper presents the modelling and geotechnical design of pile-raft and raft foundation solutions for three office buildings built close to the Tagus River, in Lisbon, Portugal (Figure 1). The proximity to the river brought geological and geotechnical restraints that will be further discussed and analysed in the next sections.

The three lots had different constraints regarding the number of basements, and the total number of stories as shown in Table 1:

Table 1. Geometry information table on the 3 lots.

Designation	Area (m2)	Stories	Basements	Excavation Depth (m)
Lot 1	2000	12	3	11
Lot 2	6350	9	2	6
Lot 3	5000	8	2	7



Figure 1. (Google Earth) Satellite location of the 3 lots.

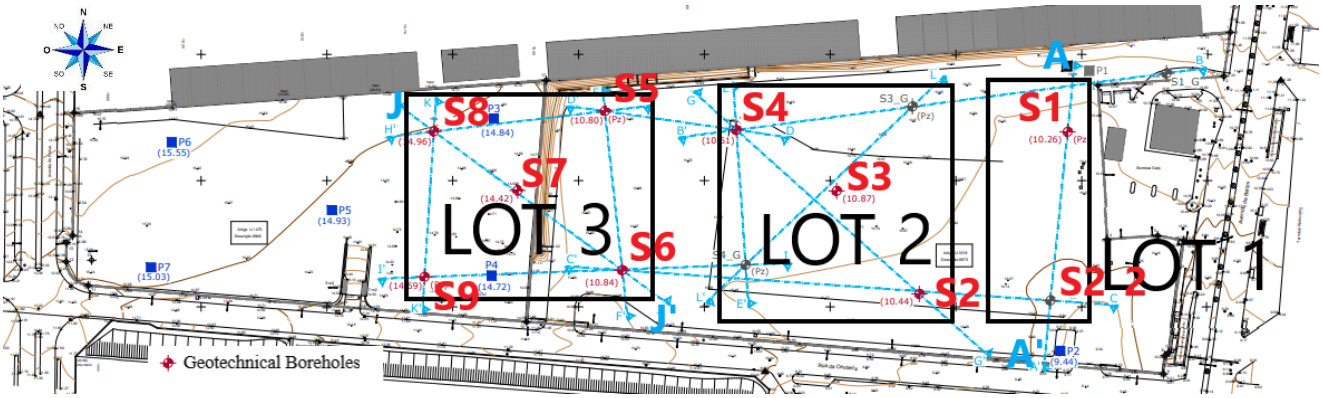

Figure 2. Building lots and boreholes for geotechnical investigation.

2 GEOTECHNICAL CONSTRAINTS

This section presents the main geotechnical constraints that affected the solutions studied.

2.1 Geotechnical investigation

A site investigation campaign consisting of eleven boreholes was conducted with SPT tests. The location of the boreholes is shown in Figure 2.

In general, the area where the lots are located is at a low topography level in an alluvial zone, corresponding to old water courses that formerly flowed into the Tagus River, with a general orientation WNW-ESE (main water course) and SW-NE (secondary water course). Under these alluvial deposits layer is the Miocene layer, characterized by the "Areolas de Braço de Prata" which is formed by dense sands and clays (as illustrated in Figure 3 Figure 4).

Throughout the area landfill deposits were identified, resulting from various anthropic actions developed over time and of diverse nature.

Table 2 shows the several layers detected in the investigation campaign, along with the SPT test results.

Table 2. Prospected layers by the investigation campaign.

Geotechnical Zone	Lithology	NSPT
ZG1	Landfill and other materials that may have been displaced	1-17
	Alluvial Deposits	0-8
ZG2A	Fine silty-clayey sands and sandy silts	10-41
ZG2B	Silty clays, clayey silts and sandy silts	24-60
ZG2C	Fossiliferous lumachelic/calcarenite levels	>60

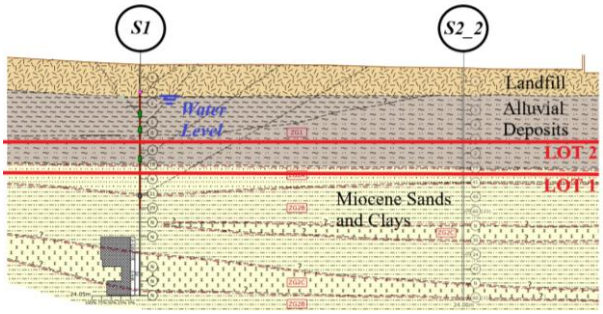

Figure 3. Site investigation geotechnical profile (Section Cut AA' from S1 to S2_2 at lot 1).

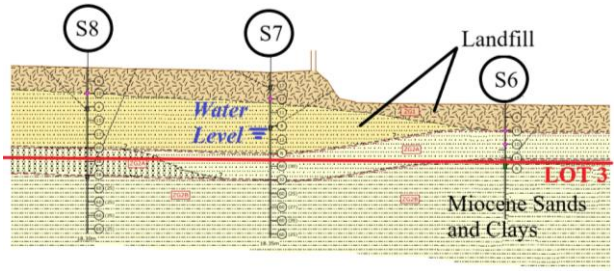

Figure 4. Site investigation geotechnical profile (Section Cut JJ' from S8 to S6 at lot 3).

2.2 Hydrology and permeability

The study of the ground permeability, as well as of the water lines crossing the site area, proved to be particularly important for the design and execution of the foundation solutions.

These permeabilities were evaluated based on laboratory analyses of samples taken during the boreholes drilling.

The Miocene layers in the investigated area are composed of fine silty-clayey sands, sandy silts, and silty clays, sometimes with the intercalation of very fossiliferous levels. In general, this Miocene complex has porosity permeability (primary), but locally it may present fissure permeability in the more carbonate/fossiliferous layers (secondary permeability).

This Miocene complex, due to its fine sandy, silty-sandy, and clayey-sandy composition, has overall moderate to low permeability, providing unfavourable

conditions for water percolation, with moderate to not significant flows. The retaining walls for the excavation of all lots reached this layer with lower permeabilities, which drastically reduced the water inflow into the excavation pits. In general, the foundations for the three lots were several meters below the investigated ground water level.

3 FOUNDATION SOLUTIONS

Two types of foundation solutions were adopted for the three lots.

The main criteria for choosing the solution was the control of differential settlements. In cases where the foundation level was directly over the more dense Miocene layer, a raft solution was recommended. When the foundation level intersected alluvial deposits, a combined pile-raft foundation solution (CPRF) was studied to control deformations.

3.1 Raft foundation

The raft foundation solution consists of a continuous slab, connected to the retaining walls by bolts. In the areas where there are higher loads, as for example under the lifts and stairs boxes, greater thicknesses were considered in order to better control differential settlements.

This type of solution allows the hydrostatic vertical uplift pressures, which can be mobilized in the long term, to be accommodated, without having to provide an extensive drainage solution.

3.2 Combined pile-raft foundation

The combined pile-raft foundation (CPRF) consists of a raft foundation (as described before) with soil inclusions in areas with greater concentration of loads. In this case, rectangular barrettes were considered, using the same diaphragm wall technology used for the execution of the retaining walls. At areas under structural columns, thicker areas of the slab were adopted, with driven precast piles resting over the more dense Miocene layer (Miocene sands and clays), in order to reduce settlement in these areas and to homogenise displacements throughout the foundation (Figure 5).

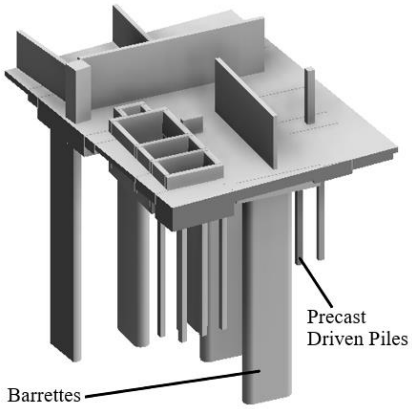

Figure 5. Pile-raft foundation solution at lot 2.

4 STRUCUTRAL DESIGN

4.1 Raft foundation design

The design of a raft foundation consists of the distribution of the loads that come from the structure to the slab, which in turn will transmit them to the ground.

The key issue to this type of design is to minimise the differential settlements derived from the heterogeneous spatial distribution of structural loads.

In this particular case, there is also the action of uplift hydrostatic pressures, which were taken into account in the long-term design of this slab.

To reduce the differential settlements, thicker areas of the foundation slab were adopted under the structural columns and walls.

The design of raft foundation solutions considered the following main design states:

- Maximum total settlements;
- Differential settlements;
- Bending moments and shear forces at the raft.

4.2 Combined pile-raft foundation design

There are several design methods for combined piled-raft foundations, with guidelines from Poulos (2000, 2001), Poulos et al. (2011), Fellenius (2015), among others. The main goal is that the load is transferred to the ground by both the raft and piles. The loads are resisted by the bearing capacity between the raft and soil and by the lateral friction and end bearing capacity of the piles. The design method should comprise 4 phases:

- Preliminary study where the viability of the solution is analysed;
- Mapping of the piles and definition of their general characteristics;
- Detailed study of the optimal number of piles;

- Estimation of settlements, bending moments, and shear forces at the raft, as well as axial loads and bending moments at the piles.

The design of CPRF solutions considers, according to Poulos (2001):

- Ultimate bearing load for axial, shear stresses, and bending moments;
- Maximum total settlement;
- Differential settlement;
- Bending moments and shear forces at the raft;
- Bending moment and axial loads at the piles.

5 IN SITU TESTS – PDA

To estimate the real bearing capacity of the precast driven piles, 9 load dynamic load tests were performed using the "Pile Driving Analyser (PDA)" method. The tests were performed on a square prefabricated reinforced concrete piles of section 300x300mm2 (Figure 6).

The results obtained from the dynamic load test indicate several layers of low to medium strength up to a depth of approximately 2.9 to 13.1 m, where the shaft resistance is lower than 90 kPa. Under this layer, a zone of higher resistance was found, with a shaft resistance ranging from 128 to 524 kPa. The tip resistance for these piles was between 14.6 and 18.2 MPa.

These values (both for the shaft and tip resistance) are an underestimation since low energy was being transferred during these tests to guarantee pile integrity.



Figure 6. Pile Driving Analyser preliminary tests being executed at lot 2.

6 MODELLING

The modelling was performed using software PLAXIS 3D. For the pile-raft foundation of lot 2, PLAXIS 2D axisymmetric analysis were also used for the calibration of the modelled inclusions with empirical methods widely used in the past.

6.1 FE models for structural elements

Different finite element (FE) models were chosen for each of the structural elements to simulate their behaviour in both the short and long term.

6.1.1 Foundations *slabs*

The foundation slabs were modelled with plate elements (PLAXIS, 2023).

6.1.2 Precast driven piles and barrettes

Both the precast driven piles and the barrettes were simulated using the embedded beam element in PLAXIS 3D. These elements describe the interaction between the piles and the surrounding soil. The interaction at the shaft and at the tip is described by means of embedded interface elements. The pile is considered as a beam which can cross a volume element at any place with any arbitrary orientation. Due to the existence of the beam element three extra nodes are introduced inside the volume element.

6.1.3 Connection between the foundation slab and the retaining wall

The retaining wall and the foundation slab are connected by a linear element which allows shear forces to be transmitted, however rotations are free. This behaviour allows the simulation of the bolted connection between the two elements.

6.1.4 Structural columns and walls

The structural loads for all relevant combinations, are simulated in the model by means of point loads applied at the gravity centre of the structural columns and walls.

The structural wall behaviour was simulated by implementing a rigid beam along the wall centreline, which will redistribute the point load along the walls path, and therefore avoiding any numerical problems that may appear due to the high concentrated loads (applied at the walls gravity centres).

6.1.5 Soil elements

The soil was modelled using the hardening soil model, with volume elements in the 3D models. The Miocene sand layers were set to respond with a drained behaviour and the Alluvial deposits, and the Miocene clay layers were set to respond with an undrained behaviour (effective stress analysis) (Table 3, Table 4 and Table 5).

Both short term and long-term situations were accounted for in the analysis.

Table 3. Material models adopted in the 3D Model.

	Properties	
	Material model	**Drainage type**
ZG1	HS	Undrained (A*)
ZG2A	HS	Drained
ZG2B	HS	Undrained (A*)
ZG2C	HS	Undrained (A*)

**Undrained calculations were performed using effective stress properties. Long-term behaviour was also considered in the model.*

Table 4. Material stiffness in the 3D Model.

	Stiffness		
	E_{50}^{ref} (kPa)	**E_{oed}^{ref} (kPa)**	**E_{ur}^{ref}(kPa)**
ZG1	10000	10000	30000
ZG2A	50000	50000	150000
ZG2B	100000	100000	300000
ZG2C	150000	150000	450000

Table 5. Material strength parameters in the 3D Model.

	Resistance	
	c'^{ref} (kPa)	**φ' (º)**
ZG1	1	28
ZG2A	1	38
ZG2B	40	36
ZG2C	20	39

6.1.6 PLAXIS 2D axisymmetric modelling for embedded beam behaviour calibration

The three-dimensional model for lot 2 was calibrated using the axisymmetric mode of PLAXIS 2D, where the response of the embedded beams was compared with the real pile behaviour.

The results (illustrated on Figure 7) show that the loads, for the failure criterion, estimated using the 2D axisymmetric model match the maximum service load calculated using empirical methods (Bustamante and Gianeselli, 1993, 1998).

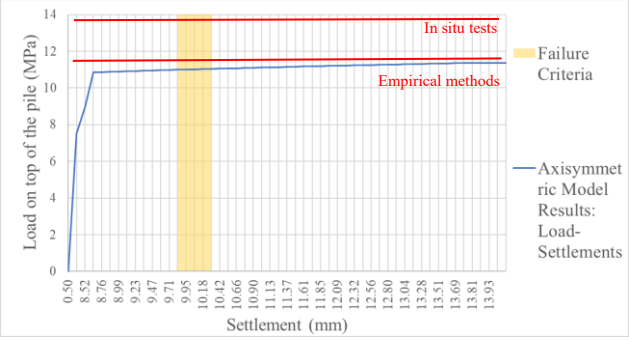

Figure 7. Load-Settlement obtained in the 2D model.

An ultimate load of 990kN was obtained for the failure criteria, for the precast driven piles.

These results were lower than the values obtained in the PDA tests. This shows that the empirical methods used, that are based on a collection of data from numerous field trials, take on assumptions so that the calculated values (using the methods) for the bearing capacity are, in most cases, conservative in relation to their actual capacity.

7 FINAL DESIGN

For the safety verification against relevant limit states, partial safety factors relative to both the actions and the materials, were adopted according to the European standard regulations.

7.1 Ultimate limit states

The final design of the foundation slab and the deep foundation elements was made using the results of the three-dimensional models, duly calibrated.

A load envelope was considered for each structural element, based on the most relevant combinations.

It should be noted that the lots in question are located in a seismic zone, and therefore there are, in all the buildings, sets of stairs and lift boxes and walls that have severe loads that need to be transmitted to the foundations.

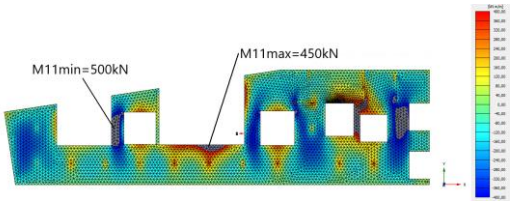

Figure 8. Bending moments M11 at the raft plate for a single combination in the lot 1 model.

Figure 8 shows the distribution of the bending moments in the lowest thickness slab. The distribution of loads on the slab leads to cylindrical bending between the spans without deep foundation elements. The areas over deep foundations will be stiffer, and therefore behave as supports for the hydrostatic uplift pressures.

Both solutions were designed against punching. It's crucial to thoroughly assess the hydrostatic uplift pressures exerted on the bottom of the foundations in these types of solutions, especially considering that the column loading acts in a different direction.

All the precast driven piles and the barrettes were checked for combined axial force and biaxial bending, adopting the results from the model (Figure 9).

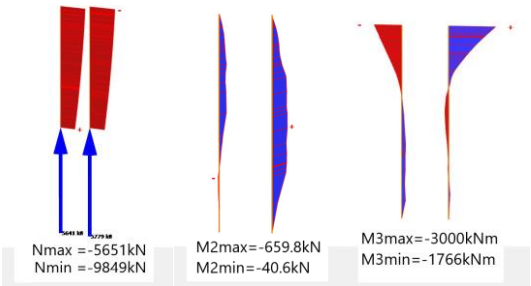

Figure 9. Forces in a pair of barrettes, modelled as embedded beams, for a single combination at lot 2.

7.2 Service limit states

7.2.1 Verification of the maximum settlements

The maximum settlement for each model was accessed and checked, for the relevant combinations. The maximum values of 6.7 mm, 20.3 mm and 16.3 mm were obtained, respectively, for lots 1, 2 and 3.

7.2.2 Verification of differential settlements

To check the differential settlements, the maximum rotations over two points in the foundations system were estimated for each model.

Equation (1) shows the formula used to check the rotations at lot 1.

$$\tan(\theta_{rel,max}) = \tan\left(\frac{(\delta_{max}-\delta_{min})\times 10^{-3}}{distance}\right) = \tan\left(\frac{(6.7-2)\times 10^{-3}}{15}\right) = 5.5\times 10^{-5} \leq \frac{1}{2000} = 5\times 10^{-4} \quad (1)$$

where $\theta_{rel,max}$ is the rotation (angle) between two points with the settlements δ_{max} and δ_{min}

7.2.3 Verification of the global settlements near the façade, due to architectural limitations

Due to architectural constraints, it was necessary to verify the differential settlements at the lots peripherical zones. The models provided the ability to quickly access this information, as shown in Figure 10, for lot 2.

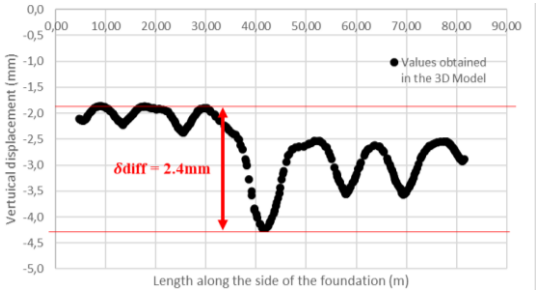

Figure 10. Long-term total settlements from two corners at the lot 2 model.

8 CONCLUSIONS

Higher processing power and access to smaller and greater data storage units are allowing more complex models to be quickly assembled. The described type of model can now be built, calibrated, and ran within most foundation projects time frame and enables the study of crucial issues in this type of project, such as soil-structure interaction, soil permeability, different settlements caused by different foundation stiffness zones, geological and geotechnical changes throughout the area site and much more, to be simulated effectively, henceforth allowing for optimized foundation solutions.

ACKNOWLEDGEMENTS

The authors would like to thank the Contractor "HCI construções" and the owner "EXPO ATLÂNTICO, EPII INVESTIMENTOS IMOBILIARIOS S.A. "for authorising the writing and presentation of this article.

REFERENCES

Bustamante, M. and Gianeselli, L. (1993). Design of auger displacement piles from in situ tests. *Deep Foundations on Bored Auger Piles, BAP II*, Balkema, Rotterdam, 21-34. https://doi.org/10.1201/9781003078517-12.

Bustamante, M. and Gianeselli, L. (1998). Installation parameters and capacity of screwed piles. *Deep Foundations on Bored Auger Piles, BAP III*, Balkema, Rotterdam, 95-108.

Fellenius, B. H. (2015). *Basics of foundation design (Revised IE)*. Retrieved from www.Fellenius.net.

PLAXIS bv. (2023). PLAXIS 3D Version 2023.1, *Reference Manual*. Delft, The Netherlands. https://doi.org/10.1155/2023/6693876.

Poulos, H. G. (2000). Practical Design Procedures for Piled Raft Foundations. In J. Hemsley, *Design Applications of Raft Foundations,* 425-467. London: ICE Publishing. https://doi.org/10.1680/daorf.27657.0016.

Poulos, H. G. (2001). *Piled Raft Foundations: Design and Applications. Geotechnique*, 51(2), 95-113.

Poulos, H. G., Small, J. C., Chow, H. (2011). Piled Raft Foundations for Tall Buildings. *Geotechnical Engineering Journal of the SEAGS and AGSSEA*, 42(2), 78-84.

Proceedings of the XVIII ECSMGE 2024
GEOTECHNICAL ENGINEERING CHALLENGES
TO MEET CURRENT AND EMERGING NEEDS OF SOCIETY
© 2024 the Authors
ISBN 978-1-032-54816-6
DOI 10.1201/9781003431749-145
Open Access: www.taylorfrancis.com, CC BY-NC-ND 4.0 license

ECSMGE 24
XVIII EUROPEAN CONFERENCE ON SOIL MECHANICS AND GEOTECHNICAL ENGINEERING

Advanced constitutive model parameter determination, optimisation and selection using a database of triaxial tests and machine learning tools

Détermination, optimisation et sélection des paramètres d'un modèle constitutif avancé à l'aide d'une base de données d'essais triaxiaux et d'outils d'apprentissage automatique

M.T. Stals*
Delft university of technology/Fugro, Delft/Leidschendam, The Netherlands

K. Siderius
Fugro, Groningen, The Netherlands

R.B.J. Brinkgreve
Delft university of technology, Delft, The Netherlands

**Michael.Stals@gmail.com*

ABSTRACT: Numerical modelling in Geo-Engineering is used to solve complex problems by simulating, analysing, or predicting soil behaviour under certain loading and boundary conditions. The soil behaviour is simulated by constitutive models that describe the relationship between stresses and strains through a mathematical formulation. Model parameters are used to calibrate model behaviour to physical soil behaviour measured during in-situ testing (e.g. CPT) or laboratory testing (e.g. triaxial testing). The selection of model parameters is challenging as it needs to cope with aspects as, constitutive model limitations, laboratory test limitations, sample disturbance, soil heterogeneity and many other. In this paper a database with over 3000 stress-strain paths measured during triaxial tests is used to derive model parameters for the Hardening Soil Small Strain Stiffness model (HS small). A procedure/algorithm has been developed to calibrate model parameters by comparing measured stress-strain paths to a simulated response from a single stress point constitutive driver. Several data analysis techniques, including machine learning tools, have been used to investigate the relationship between soil properties, soil parameters and HS small model parameters. In this paper the developed methodology and the results of the data analysis are presented.

RÉSUMÉ: La modélisation numérique en géo-ingénierie est utilisée pour résoudre des problèmes complexes en simulant, analysant ou prédisant le comportement du sol sous certaines charges et conditions limites. Le comportement du sol est simulé par des modèles constitutifs qui décrivent la relation entre les contraintes et les déformations par le biais d'une formulation mathématique. Les paramètres du modèle sont utilisés pour calibrer le comportement du modèle par rapport au comportement physique du sol mesuré lors d'essais in situ (par exemple CPT) ou d'essais en laboratoire (par exemple essais triaxiaux). La sélection des paramètres du modèle est un défi car elle doit prendre en compte des aspects tels que les limites du modèle constitutif, les limites des essais en laboratoire, la perturbation de l'échantillon, l'hétérogénéité du sol et bien d'autres. Dans cet article, une base de données contenant plus de 3000 trajectoires de contrainte-déformation mesurées lors d'essais triaxiaux est utilisée pour dériver les paramètres du modèle de rigidité des sols durcissants à faible déformation (HS small). Une procédure/algorithme a été développée pour calibrer les paramètres du modèle en comparant les trajectoires de contrainte-déformation mesurées à une réponse simulée à partir d'un pilote constitutif à point de contrainte unique. Plusieurs techniques d'analyse de données, y compris des outils d'apprentissage automatique, ont été utilisées pour étudier la relation entre les propriétés du sol, les paramètres du sol et les paramètres du modèle HS small. Cet article présente la méthodologie développée et les résultats de l'analyse des données.

Keywords: Triaxial test; parameter determination; constitutive models; machine learning.

1 INTRODUCTION

Numerical methods, like the finite element method (FEM), have gained popularity and an increasing importance in Geo-engineering. They are widely accepted and are now considered a standard design tool. This is firstly because the (commercial) software

has been developed to the point where it is easy to operate and secondly because of the availability of appropriate constitutive models that describe the mechanical behaviour of soils in a continuum framework (Schweiger et al. 2019). Model parameters are required to quantify certain features of the soil behaviour. In general, simple constitutive models require less input parameters than more advanced models, but they may therefore lack some essential features of soil behaviour (Brinkgreve et al. 2010). Parameter determination is a heavily debated and researched topic in the field of Geo-Engineering, due to the complexity of these heterogeneous, natural building materials and the amount of engineering judgement required. This paper aims to elaborate on the methodology (Chapter 2), results and discussion (Chapter 3), and conclusion (Chapter 4) of the parameter determination, optimisation and selection for the HS small model parameters.

2 METHODOLOGY

Over the past decades a large number of triaxial tests on soil samples from across the Netherlands have been conducted by Fugro Netherlands according to the NEN-EN-ISO 2018 standard, or one of its predecessors. This data offers the opportunity to perform an analysis on, and research (new) statistics and correlations based on the full measured stress paths. This paper focuses on the Consolidated Isotropic Drained and Undrained Multi Stage triaxial tests.

2.1 Soil properties

Each text file, in which the triaxial test measurements are stored contains information regarding the soil sample like the initial weight, dry weight, volumes etc. With this information soil properties can be determined (γ, w, γ_d, e_0 and n), which provide information about the soil sample. These results can be used to formulate correlations with other parameters.

2.2 Soil parameters

The triaxial measurements were used to derive the classic soil parameters, the internal friction angle (φ') and the cohesion (c') were determined at 2% strain using the p-q stress space, also known as the Cambridge stress space (Roscoe et al. 1958). The stress-strain path was used to determine the secant stiffness (E_{50}) at 50% peak deviatoric stress. Determining the stiffness as such for different confining stress levels also enables determining the power of stress level dependency of stiffness (m).

2.3 Model parameters

The Hardening Soil with small-strain stiffness (HS small) was selected as constitutive model to describe the stress-strain relationship of all tested soils, since it is an advanced model for soil in general (Brinkgreve 2005). It requires 13 model parameters. An initial parameter set was derived by expanding upon the soil parameters, using common correlations and default values from the literature (the traditional method). A simulation of the triaxial test is performed using the SoilTest facility in the PLAXIS software package using this initial parameter set and the stress-strain path is compared to the laboratory measurement (Figure 1). It can be seen that the simulation with the initial parameter set is not optimal in approximating the measurement, since this is only the starting point of the optimisation algorithm.

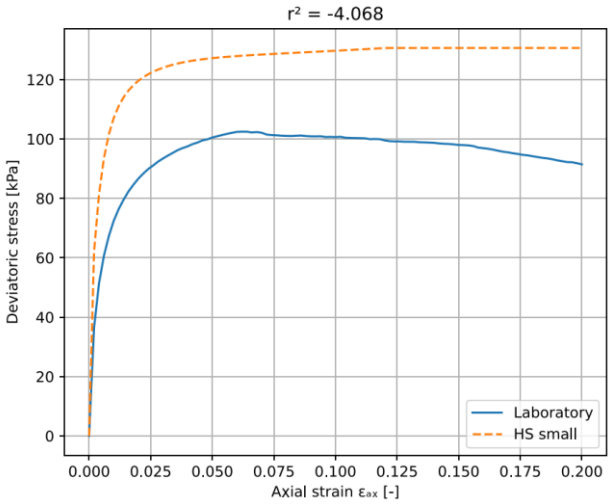

Figure 1. Example of comparison of triaxial test simulation with the initial parameter set (HS small with measurement (Laboratory)).

The procedure is to fit the stress-strain path of the simulation to the measured stress-strain path in the laboratory by calibrating the HS small parameters. The goodness of the fit will be quantified using the coefficient of determination (r^2) and the aim is to reach a value close to 1, where $r^2 = 1$ is a perfect fit. The schematic overview of the algorithm is presented in Figure 2. The sequence in which the parameters were optimised was based on the sensitivity of the individual parameter with regard to the test results.

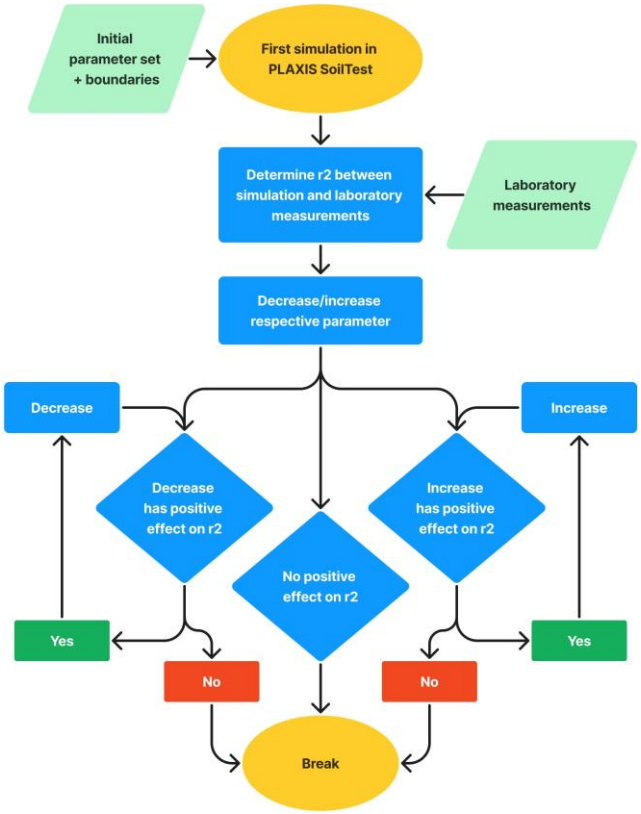

Figure 2. Schematic overview of the algorithm.

Individually matching the stress-strain curve resulted in a singularity, meaning that the parameter set after optimisation could be very different depending on the initial parameter set or optimisation order, which is why an additional feature needed to be fitted simultaneously. The selected additional feature was the ε_{vol}-ε_{ax} for the drained tests and the u_{excess}-ε_{ax} for the undrained tests. After the optimisation the stress-strain curves matched significantly better, an example of an optimised curve is shown in Figure 3.

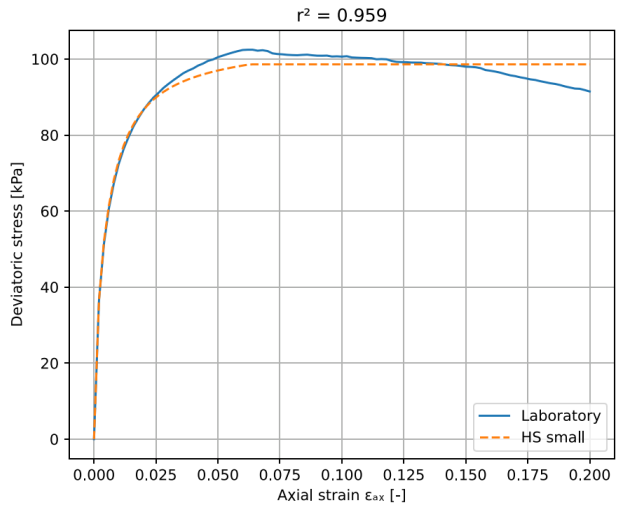

Figure 3. Example of comparison of triaxial test simulation with the optimised parameter set (HS small with measurement (Laboratory)).

3 RESULTS AND DISCUSSION

The optimisation algorithm has been deployed for 3073 tests in total. The tests are subdivided in categories based on the main soil type classification available in the text file. It is important to note that the soil type given does not mean that it only consists of this specific soil. Descriptions in the text file are often quite long (and subjective), E.g. ”CLAY= slightly silty = slightly organic grey”. In this example, the sample is labelled as clay since this is the main component. The optimisation results for all 3073 tests are presented in Table 1 and Figure 4, the left graph shows the r^2 of the initial parameter set an the right graph shows the r^2 of the optimised parameter set. The median r^2 of the comparison between the simulated triaxial test and the measurement improved significantly when the optimised parameter set was used. Softer soils like clay and peat showed a better performance in terms of r^2 than sand and silt. The poorer performance for sand and silt can be explained due to limitations of the HS small model. Sand and silt sometimes show a high peak strength and low residual strength, this softening behaviour cannot be captured by the HS small model.

Table 1. Optimisation results (median r^2).

Soil [-]	Quantity [-]	Initial r^2 [-]	Optimised r^2 [-]
Clay	1707	-0.51	0.92
Sand	718	0.36	0.71
Peat	374	0.55	0.99
Silt	274	-5.39	0.09

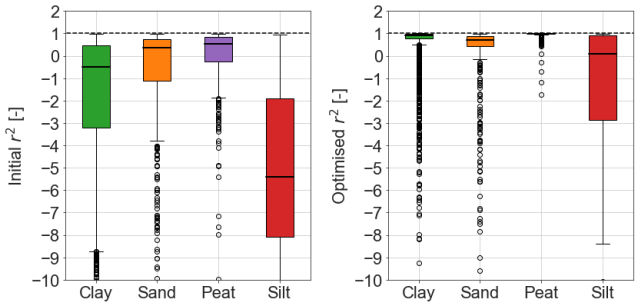

Figure 4. Results in terms of r^2 of comparison between simulated and measured stress-strain path for initial parameters set (left) and optimised parameter set (right).

The results of the optimisation are stored in a database which consist of soil properties, soil parameters and optimised model parameters. The soil properties are relatively easy to obtain. For this reason data analysis techniques have been used to predict soil parameters and optimised model parameters based on soil properties.

The soil properties (γ, w, γ_d, e_0 *and* n) showed a strong correlation with 5 parameters, the soil parameter φ’ and the optimised model parameters

E_{50}^{ref}, E_{oed}^{ref}, E_{ur}^{ref} and G_0^{ref}. The single linear/-exponential regression managed to find a fit with an $r^2 > 0.4$ for these parameters. Still, a lot of scatter in the graphs was noticed which is why more advanced machine learning methods were explored. The machine learning models: Multiple Linear Regression (MLR) Artificial Neural Network (ANN), Gradient Boosting (GBR) and Kernel Ridge Regression (KRR) were selected based on an initial analysis on the data set, and a literature study in which similar models were used. Different input sets were presented to the machine learning model, input set 1 only consisted of the soil type (s) as classified in the laboratory, every successive input set added a soil property in the same order as mentioned above. The soil parameters and optimised model parameters are the output. After training, the machine learning models were able to make significant better predictions for the same 5 parameters, with an increase of r^2 in the range of 0.05-0.27 (average of 0.2), compared to the single linear/exponential regression methods. Providing the machine learning models with more soil properties generally resulted in an increase in performance. An example for the prediction of the E_{ur}^{ref} is presented in Figure 5, where the x-axis shows the different Machine learning models, the y-axis the input sets and the z-axis the r^2 score. All the results were evaluated using (group)k-fold.

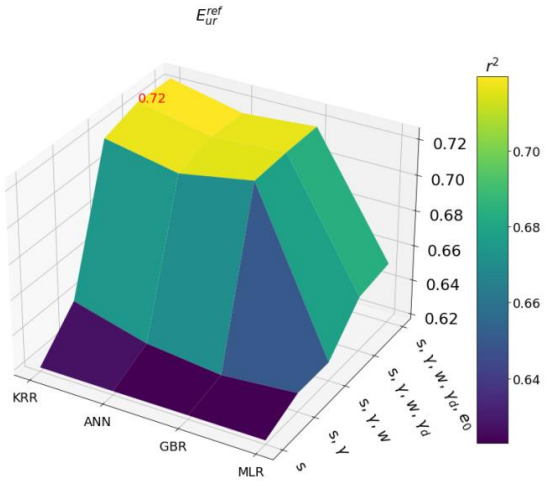

Figure 5. Machine learning prediction result.

4 CONCLUSIONS

This paper presents methods to provide guidance in the parameter determination, optimisation and selection for the HS small model parameters.

An initial parameter set was derived by expanding upon the soil parameters (traditional method). This resulted in relatively poor results when comparing the stress-strain curve of the simulation to that of the measured one in the laboratory. It is therefore concluded that the traditional method could only be used as a first estimate to determine the model parameters.

The developed optimisation algorithm was deployed for all triaxial tests and a significant improvement in r^2 was observed, the median r^2 increased from -0.61 to 0.81. The developed algorithm can optimise the initial HS small parameter sets, by matching the simulated/calculated stress-strain curve.

The trained machine learning models, could be used to select the soil parameter φ' and the optimised HS small model parameters E_{50}^{ref}, E_{oed}^{ref}, E_{ur}^{ref} and G_0^{ref} with an r^2 in the range of 0.6-0.74 by using 1 to 5 soil properties as input parameters in the ML algorithm. The linear/exponential regression results come in the form of equations that can also be used, and they may even be easier to apply, but these have a significantly lower r^2 score in the range of 0.41-0.56.

It is important to note that these methods, results and conclusions are based on triaxial test and have not been validated for other tests and engineering practices.

ACKNOWLEDGEMENTS

Authors would like to thank Dr. Ir. M.A. Cabrera and Dr. Ir. G. Rongier of TU Delft for their input.

REFERENCES

Brinkgreve, R. (2005). Selection of soil models and parameters for geotechnical engineering application, In: *Congress Austin*, Texas, American Society of Civil Engineers (ASCE), pp. 69–98., https://doi.org/10.1061/40771(169)4.

Brinkgreve, R., Engin, E. and Engin, H. K. (2010), Validation of empirical formulas to derive model parameters for sands, in 'Numerical methods in geotechnical engineering', Vol. 137, CRC Press/Balkema, Rotterdam, the Netherlands, p. 142., http://doi.org/10.1201/b10551-25.

'NEN-EN-ISO17892-9: (2018): Geotechnical investigation and testing – laboratory testing of soil - part 9: Consolidated triaxial compression tests on water saturated soils'.

Roscoe, K. H., Schofield, A. and Wroth, a. P. (1958), 'On the yielding of soils', Geotechnique 8(1), 22–53., https://doi.org/10.1680/geot.1958.8.1.22.

Schweiger, H., Fabris, C., Ausweger, G. and Hauser, L. (2019), 'Examples of successful numerical modelling of complex geotechnical problems', Innovative Infrastructure Solutions 4(1), 1–10., https://doi.org/10.1007/s41062-018-0189-5.

Proceedings of the XVIII ECSMGE 2024
GEOTECHNICAL ENGINEERING CHALLENGES
TO MEET CURRENT AND EMERGING NEEDS OF SOCIETY
© 2024 the Authors
ISBN 978-1-032-54816-6
DOI 10.1201/9781003431749-146
Open Access: www.taylorfrancis.com, CC BY-NC-ND 4.0 license

ECSMGE 24
XVIII EUROPEAN CONFERENCE ON SOIL MECHANICS AND GEOTECHNICAL ENGINEERING

Effective strength parameters of Danish clay tills - revisited

Résistance effective paramètres des sols argileux Danois - revisité

J.O. Steensen-Bach*, J.S. Steenfelt, O. Hededal
COWI A/S, Kongens Lyngby, Denmark

*jess@cowi.com

ABSTRACT: Effective strength parameters φ' and c' cannot be measured in tests. They are derived from the linear equation defining the tangent to a point on the failure envelope and cannot be addressed individually. For years Danish Practice has been to assess the effective stress failure envelope from the linear stress path in undrained triaxial compression tests (CAU_c), or alternatively assuming that the effective friction angle is a function of Plasticity Index (using $\varphi'=A-B\cdot logI_P$) in combination with effective cohesion as function of the undrained shear strength ($c'=C\cdot c_u$). The paper discusses the shortcomings of these practices for Danish clay tills and presents a model that ensures that paired values of φ' and c' can be consistently addressed from curved failure envelopes that are uniquely defined by void ratio and Plasticity Index.

RÉSUMÉ: Les paramètres de résistance effective φ' et c' ne peuvent pas être mesurés lors d'essais. Ils sont dérivés de l'équation linéaire définissant la tangente à un point sur l'enveloppe de rupture et ne peuvent pas être traités individuellement. Pendant des années, la pratique danoise a consisté à évaluer l'enveloppe de rupture sous contrainte effective à partir du chemin de contrainte linéaire dans les essais de compression triaxiale non drainée (CAU_c), ou en supposant que l'angle de frottement effectif est une fonction de l'indice de plasticité (en utilisant $\varphi'=A-B\cdot logI_P$) en combinaison avec la cohésion effective en fonction de la résistance au cisaillement non drainé ($c'=C\cdot c_u$). L'article discute des lacunes de ces pratiques pour les sols argileux danois et présente un modèle qui garantit que les valeurs appariées de φ' et c' peuvent être traitées de manière cohérente à partir d'enveloppes de rupture courbes qui sont définies de manière unique par le taux de vide et l'indice de plasticité.

Keywords: Clay till; effective strength parameters; curved failure envelope; triaxial tests; plate load tests.

1 INTRODUCTION

Effective strength parameters, φ' and c' cannot be measured in tests. These parameters are substitutes for the effective shear strength as modelled by Mohr-Coulomb. Their derivation comes from an evaluation of tests using the slope and interception point of the tangent to each point on the effective strength failure envelope.

Since the pioneering works by Jacobsen (1970), the most common test in Denmark for adressing the effective strength parameters for cohesive soils (including overconsolidated clay tills) is the anisotropically consolidated triaxial compression test CAU_c with reconsolidation to preconsolidation stress and unloading typically to the in situ stress, see Figure 1.

The effective friction angle φ'_{tr} (Eq.1) and the effective cohesion c'_{tr} (Eq.2) in a single CAU_c test is derived from the tangent fitting the linear part of the stress path using the slope $tan\beta$ and interception point a, i.e., assuming a linear failure envelope for the stress interval covered by the tangent.

$$\varphi'_{tr} = arcsin\left(\frac{1}{1+2tan\beta}\right) \quad (1)$$

$$c'_{tr} = a \cdot tan\beta \cdot tan\varphi'_{tr} \quad (2)$$

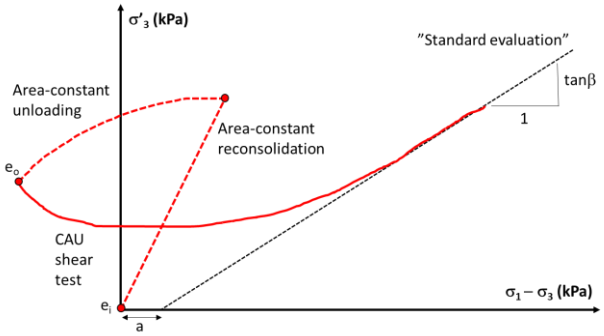

Figure 1. Danish "standard evaluation" of CAU_c triaxial tests. Reconsolidation and unloading changes specimen void ratio from its initial value e_i to e_o

It was suggested by Jacobsen (1970) that the effective strength parameters in triaxial compression tests could be described solely as a function of the initial void ratio, e_i:

$$\varphi' = 35.3^0 - 9e_i \qquad (3)$$

$$c' = 422kPa \cdot exp(-7.3e_i) \qquad (4)$$

Jacobsen (1970) found that the use of φ'_{tr} and c'_{tr} from directly derived from triaxial tests (CAU_c and CAD_c) in many cases overestimated the bearing capacity observed in drained plate load tests in clay tills. The same was observed using Eqs.(3)-(4) and Jacobsen (1970) suggested Eq.(5) as an alternative to Eq.(4) to be used in combination with φ'_{tr}.

$$c' = \frac{N_{co}c_u}{N_c} = \frac{5.14c_u}{(N_q - 1)cot\varphi'_{tr}} \qquad (5)$$

However, the use of Eqs. (3)-(4) or φ'_{tr} and Eq.(5) does not remove the mismatch between predicted and recorded bearing capacity in drained plate load tests. This questions the use of φ'_{tr} and c'_{tr} based on a linear failure envelope for a selected stress range (say σ'_3 = 100-150 kPa).

If no site specific tests are available, the obsolete Danish Codes (DS415:1977, 1984) suggest the use of $c' = 0.1c_u \leq 20\,kPa$ in combination with $\varphi' = 30^o$ for preliminary analyses. Unfortunately a common misuse of $c' = 0.1c_u$ (without the cap on c') in combination with $\varphi' > 30^o$ has sneaked into practice, although it clearly disregards that $\varphi'$and c' cannot be assessed separately.

The ratio $c'/c_u = 0.1$ has its origin in triaxial tests by Jacobsen (1970) showing $c'/c_v \geq 0.1$ (see Table 3) in which c_v is the vane shear strength. The 20 kPa cap on the effective cohesion c' is likely to have its origin from Jacobsen's (1970) observation that by using φ'_{tr} in back calculation of c' from the plate load tests resulted in values $c' < c'_{tr}$ and $c' \leq 20$ kPa.

The relationships Eqs.(3)-(4) by Jacobsen (1970) are still in use, but has been surpassed in Danish practice by the approach where φ' taken as a function of Plasticty Index I_p, (Eq.6), and c' assessed using Eq.(5) in combination with φ':

$$\varphi' = 45^o - (14^o\ a\ 15^o) \cdot log\left(\frac{I_p}{1\%}\right) \qquad (6)$$

Equation (5) indicates a coupling between c' and φ' as $N_c = f\{\varphi'\}$, However, most often this coupling is neglected by simply applying $c' = 0.1c_u$.

The arbitrariness of Eqs.(3)-(6) is exposed by comparing their assessment to the values of φ'_{tr} and c'_{tr} from triaxial tests. Figures 2 and 3 show that classification parameters like void ratio and Plasticity Index individually cannot properly describe the effective strength parameters φ'_{tr} and c'_{tr}.

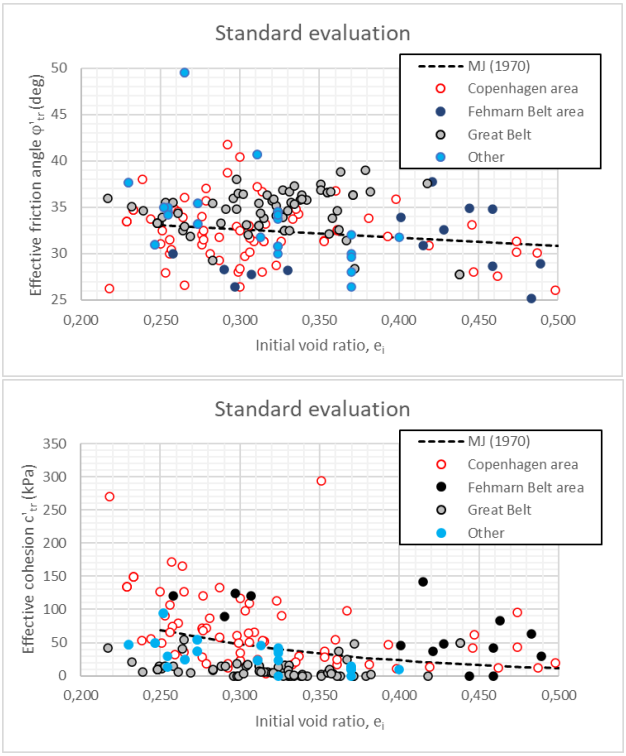

Figure 2. Effective strength parameters φ' and c' assessed using Eqs.(3)-(4) compared to φ'_{tr} and c'_{tr} from CAUc tests (H/D=1) using standard interpretation (Figure 1).

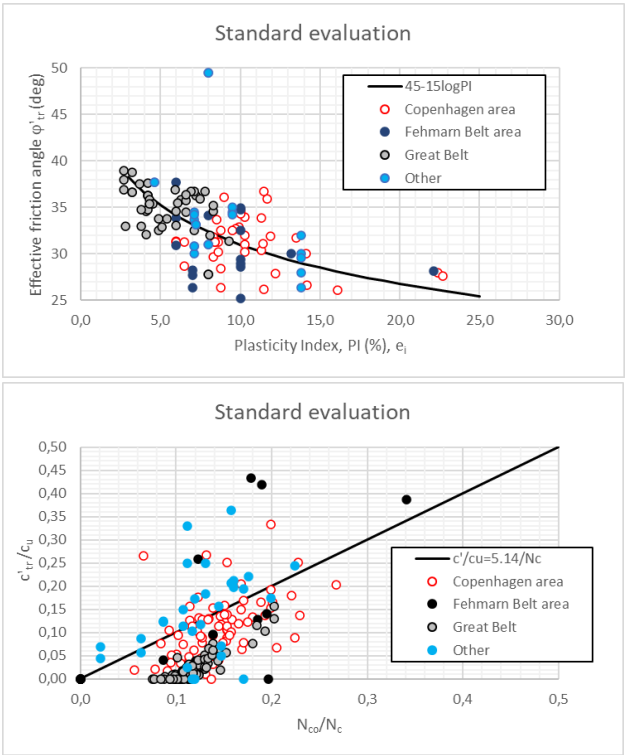

Figure 3. Effective strength parameters φ' and c' assessed using Eqs.(4)-(6) compared to φ'_{tr} and c'_{tr} from standard evaluation of CAUc tests(H/D=1).

2 FAILURE ENVELOPE FOR CLAY TILL

In relation to the København Tunnelbane project in the mid 1970ies, a series of drained triaxial compression tests (MCIDc) was performed with fixed axial stress (σ'_1) and decreasing confining stress (σ'_3) until failure. These showed very high friction angle and low effective cohesion at low effective stress levels at failure, $(\sigma'_3)_f$, indicating a curved failure envelope.

Therefore, a curved failure envelope is adopted in the proposed "*CAU-PI-e_o model*" (Steensen-Bach, 2023) being a function of void ratio and Plasticity Index. The failure envelope is assumed to follow a power law of $(\sigma'_3)_f$ (Eqs. (7)-(13) with coefficients as functions of the void ratio e_o, and Plasticity Index I_p).

$$(\sigma_1 - \sigma_3)_f = k_1 \cdot \left(\frac{\sigma'_3}{1kPa}\right)^{k_2} \quad (7)$$

$$k_1 = a_1 \cdot (e_o)^{-b_1} \quad (8)$$

$$k_2 = a_2 \cdot (e_o)^{b_2} \quad (9)$$

$$a_1 = 2.76675 + 0.053924 \cdot \frac{I_p}{1\%} \quad (10)$$

$$b_1 = 0.907 + 0.001620 \cdot \frac{I_p}{1\%} \quad (11)$$

$$a_2 = 0.8327 - 0.004004 \cdot \frac{I_p}{1\%} \quad (12)$$

$$b_2 = 0.02515 + 0.000816 \cdot \frac{I_p}{1\%} \quad (13)$$

The effective strength parameters φ' and c' are assessed from the tangent to each point on the curved failure envelope using Eqs.(14)-(15) as input in Eqs. (1)-(2).

$$tan\beta = \frac{1}{k_1 k_2} \cdot \left(\frac{\sigma'_3}{1kPa}\right)^{1-k_2} \quad (14)$$

$$a = k_1 \cdot \left(\frac{\sigma'_3}{1kPa}\right)^{k_2} - \frac{\sigma'_3}{tan\beta} \quad (15)$$

An example of the curved failure envelopes is shown in Figure 4 for the case of I_p = 10% and various void ratios in the range e_o = 0.25-0.40.

Figure 5 shows the curved failure envelope for the case e_o = 0.3 and I_p = 5-20%, and the related effective strength parameters φ' and c' as function of σ'_3. Similar curves can be obtained for other e_o and I_p with the validity ranges e_o = 0.25-0.45 and I_p = 3-20%.

Figure 6 compares measured triaxial test values of $(\sigma_1\text{-}\sigma_3)_{max}$ to modelled values $(\sigma_1\text{-}\sigma_3)_f$ using the *CAU-PI-e_o model*.

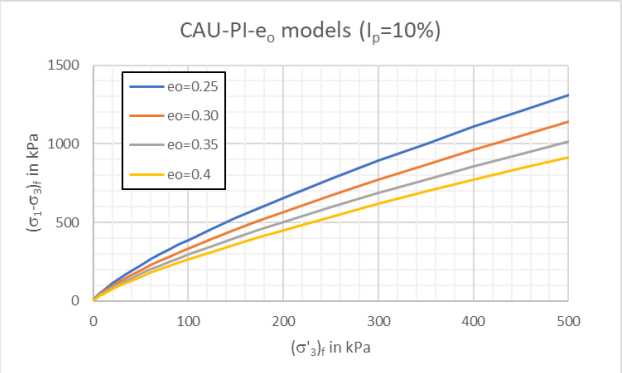

Figure 4. Curved failure envelope for CAU$_c$ tests using Plasticity Index I_p=10% and some selected void ratios.

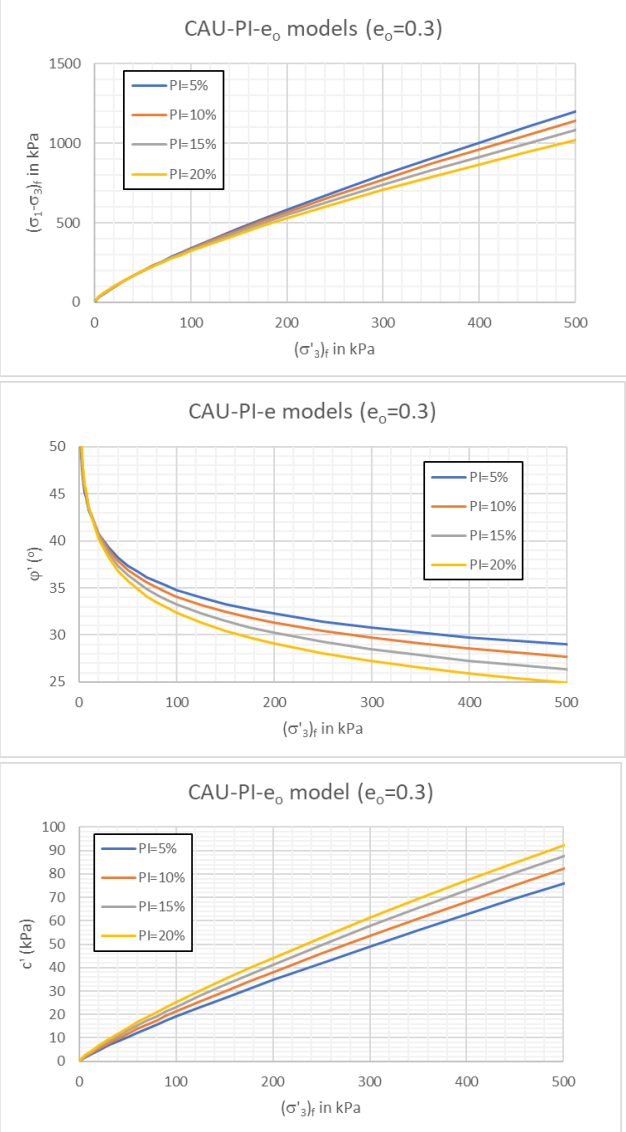

Figure 5. Curved failure envelope and effective strength parameters for CAU-PI-e_o model at selected e_o and I_p.

Table 1 summarizes the ranges of initial void ratio (e_i) and at start of shear phase (e_o), and Plasticity Index (I_p) for CAU$_c$ and CAD$_c$ tests on Danish clay tills shown in Figure 6, and CID$_c$ tests in Figure 7.

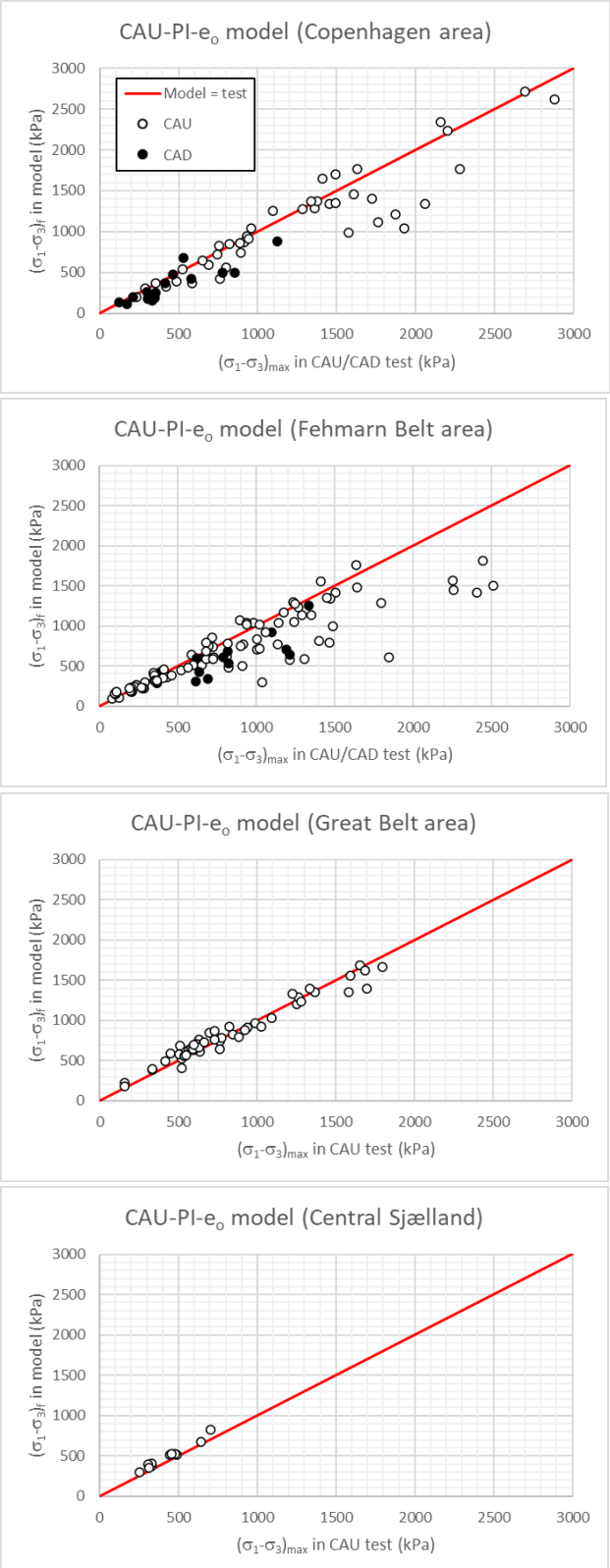

Figure 6. Prediction of $(\sigma_1-\sigma_3)_{max}$ in 186 CAU$_c$ tests and 33 CAD$_c$ tests on Danish clay tills (Clay content L= 10-25%) using the CAU-PI-e$_o$ model, Eqs.(7)-(13).

The use of the *CAU-PI-e$_o$ model* appears also to be applicable for some clay tills outside Denmark, as illustrated in Figure 7 for a Canadian clay till.

Table 1. Test type and basic classification parameters for clay tills tests analysed in this document.

Test	H/D	I_p (%)	e_i (-)	e_o (-)
CAU$_c$	1	2.7-22.7	0.23-0.55	0.16-0.49
CAD$_c$	1	3.0-27.1	0.17-0.47	0.15-0.41
CID$_c$	2	5.0-16.0	0.22-0.72	0.20-0.65

H/D = height to diameter ratio of specimen.

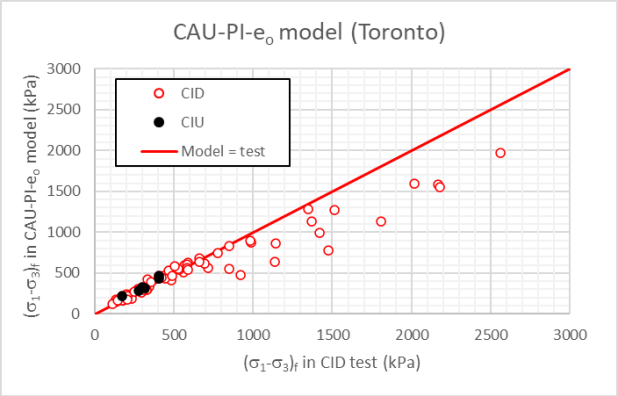

Figure 7. Prediction of $(\sigma_1-\sigma_3)_{max}$ in 71 CID$_c$ and 6 CIU$_c$ tests on clay till from Toronto (OCR$_{test}$=1-2, Clay content L= 9-42%) using the CAU-PI-e$_o$ model, Eqs.(7)-(13).

The *CAU-PI-e$_o$ model* underestimates $(\sigma_1-\sigma_3)_{max}$ in CAD$_c$ tests (see Figure 8) and thus provides a conservative estimate of the effective strength parameters in drained tests.

It is believed that the main reason for some CAD$_c$ tests being stronger than predicted by the *CAU-PI-e$_o$ model* is related to the strain-hardening due to dilation taking place in drained tests, but not in undrained tests. The difference in strain hardening between CAD$_c$ and CAU$_c$ tests increases with increasing OCR and could explain why the Toronto tests (OCR=1-2) are better predicted by *CAU-PI-e$_o$ model* than CAD$_c$ tests on the more heavily preconsolidated Danish clay tills.

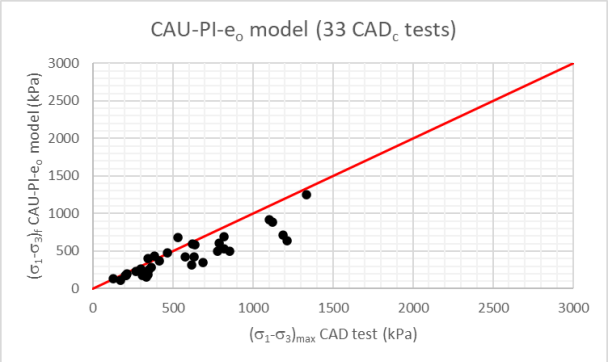

Figure 8. Prediction of $(\sigma_1-\sigma_3)_{max}$ in 33 CAD$_c$ tests on Danish clay tills using the CAU-PI-e$_o$ model, Eqs.(7)-(13).

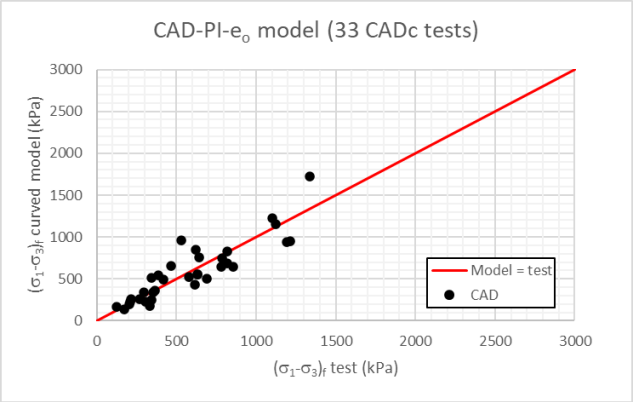

Figure 9. Prediction of $(\sigma_1-\sigma_3)_{max}$ in 33 CAD$_c$ tests on Danish clay tills using the CAD-PI-e$_o$ model, Eqs.(16)-(22).

To account for the strain-hardening in CAD$_c$ tests and obtaining a better prediction of the drained tests (see Figure 9) the coefficients a_1, b_1, a_2 and b_2 used in the *CAU-PI-e$_o$ model* are modified in the curved failure envelope for CAD$_c$ tests (*CAD-PI-e$_o$ model*). The coefficients a_3, b_3, a_4 and b_4 in the *CAD-PI-e$_o$ model,* Eqs.(16)-(18), are given by Eqs.(19)-(22).

$$(\sigma_1-\sigma_3)_f = k_3 \cdot \left(\frac{\sigma'_3}{1kPa}\right)^{k_4} \quad (16)$$

$$k_3 = a_3 \cdot (e_o)^{-b_3} \quad (17)$$

$$k_4 = a_4 \cdot (e_o)^{b_4} \quad (18)$$

$$a_3 = 0.8 \cdot a_1 \quad (19)$$

$$b_3 = 1.3 \cdot b_1 \quad (20)$$

$$a_4 = 1.05 \cdot a_2 \quad (21)$$

$$b_4 = 1.4 \cdot b_2 \quad (22)$$

The coefficients a_1,b_1,a_2 and b_2 are given by Eqs. (10)-(13). The effective strength parameters φ' and c' for each point on the curved failure envelope (*CAD-PI-e$_o$*) are derived using Eqs.(23)-(24).

$$tan\beta = \frac{1}{k_3 k_4} \cdot \left(\frac{\sigma'_3}{1kPa}\right)^{1-k_4} \quad (23)$$

$$a = k_3 \cdot \left(\frac{\sigma'_3}{1kPa}\right)^{k_4} - \frac{\sigma'_3}{tan\beta} \quad (24)$$

There is no significant effect of Plasticity Index I_P or void ratio e_o on the ratio between $(\sigma_1-\sigma_3)_{max}$ in the CAD$_c$ tests and $(\sigma_1-\sigma_3)_f$ modelled using the *CAD-PI-e$_o$ model.* This is valid within the ranges of void ratio (e_o=0.15-0.40, e_{mean} = 0.27) and Plasticity Index (I_P=3-27%, $I_{p,mean}$ =11%) covered by the CAD$_c$ tests.

3 DRAINED PLATE LOAD TESTS

For curved failure envelopes the question is how to assess the relevant stress level $(\sigma'_3)_f$. Meyerhof (1950) suggested that stress level (drained bearing capacity of footings, p_f) is obtained through an iterative process solving Eqs.(25)-(26):

$$(\sigma'_3)_f = f(p_f) \quad (25)$$

$$p_f = \frac{1}{2}\gamma' B s_\gamma N_\gamma + q' s_q N_q + c' s_c N_c \quad (26)$$

The function $f(p_f)$ for clay till that relates to the *CAU-PI-e$_o$ model*, is established using the 28 drained plate load tests on four clay tills (Table 2), using circular plates of diameter D tested at effective overburden pressure q', as reported by Jacobsen, (1970).

The width B in Eq.(26) has been taken for the circular plates as for an equivalent square footing $B \approx 0.866D$. Bearing capacity factors N_γ, N_c, N_q and shape factors for square footing (s_γ=0.6, s_q=s_c=1.2) as given in DS415:1984. For clays, it is Danish practice to use the triaxial friction angle in N_γ, N_c and N_q.

For each plate load test the bearing capacity is modelled using the *CAU-PI-e$_o$ model*. Figure 10 shows that on the relevant failure envelope (e,I_p) there is a unique σ'_3 and thus (φ',c') for each plate test, where modelled capacity $p_{f,model}$ equals $p_{f,test}$.

Table 2. Drained plate load tests on clay tills (L=15-25%).

	Carls. I	**Carls. II**	**Kratbj.**	**Sabro**
Nos.	1	6	17	4
D (cm)	7.5	7.5-25	5-15	15-30
q' (kPa)	23	0-30.5	0-20.5	1-7.8
e	0.24	0.30	0.32	0.52
I_p (%)	10.3	8.8	7.1	13.8
c_v (kPa)	700	250	200	58
φ'_{tr} (°)	33.0	30.6	32.6	30.6
c'_{tr} (kPa)	70.6	27.9	39.2	10.8

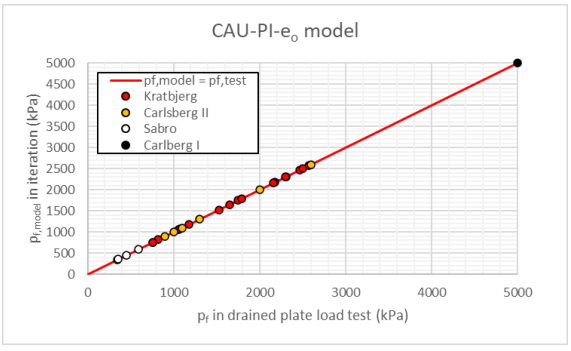

Figure 10. Bearing capacity in test (Jacobsen, 1970) and for selected σ'_3 in CAU-PI-e$_o$ model giving $p_{f,model}$=$p_{f,test}$.

Figure 11 shows that for three of the clay tills investigated there is a distinct relationship between bearing capacity p_f in test and σ'_3. The coefficients a and b (Eq.19) are modelled as functions of in situ void ratio e and I_p (Steensen-Bach, 2023):

$$f\{p_f\} = b \cdot \left(\frac{p_f}{1kPa}\right)^a \qquad (27)$$

$$a = 1.5724 + 0.05974\left(\frac{I_p}{1\%}\right) - 0.004098\left(\frac{I_p}{1\%}\right)^2$$

$$b = 0.002731 - 0.0232(e) + 0.004968(e)^2 \geq 0.000242 \qquad (28)$$

The coefficient a (ranging 1.62-1.79) decreases with increasing I_p and coefficient b (ranging 0.000242-0.0041) increases with increasing in situ void ratio e. The lower bound of b = 0.000242 (e = 0.3) is applied to Carlsberg I clay till.

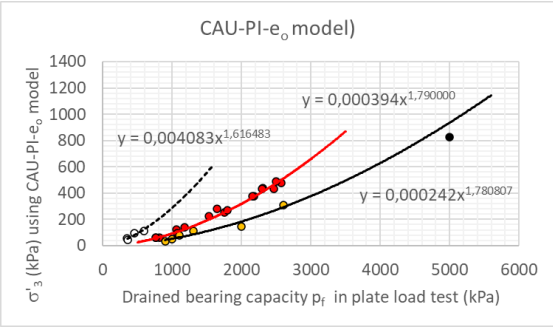

Figure 11. Required stress level σ'_3 in CAU-PI-e_o model to model drained bearing capacity in plate load tests.

Figure 12 shows a comparison of the vertical bearing capacity in Jacobsen's drained plate load tests to the bearing capacity predicted using the *CAU-PI-e_o model* with $(\sigma'_3)_f$ assessed using Eqs.(25)-(28).

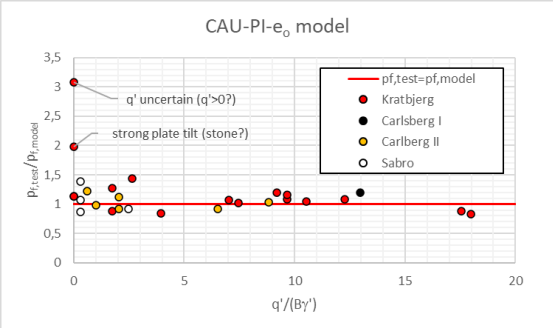

Figure 12. Comparison of measured and predicted values of drained vertical bearing capacity in plate load tests on clay tills using CAU-PI-e_o model and assessing stress level from the iteration model, (Eqs.25-28).

Figure 13 shows the comparison of drained bearing capacity in plate load tests using the commonly used approaches i.e., Eqs.(5)-(6) using I_p and field vane shear strength c_v, or the effective strength parameters from the linear failure envelope parameters (Table 2).

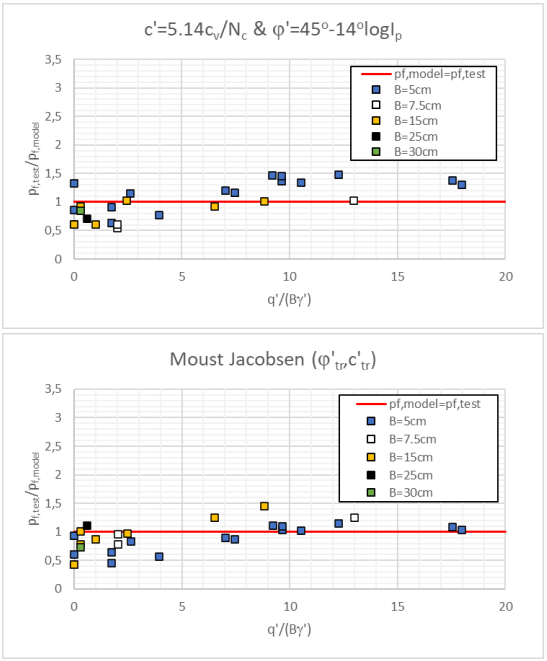

Figure 13. Comparison of measured values and predicted drained vertical bearing capacity in plate load tests.

4 CONCLUSIONS

No amount of modelling can beat parameters established through site specific testing. However, analyses demonstrate the inadequacy in predicting the drained bearing capacity using constant values of φ' and c' from CAU_c or CAD_c tests.

The *CAU-PI-e_o model* offers a rational alternative to the models currently used in practice and can be used to support sites where low number of tests prevents establishing local (curved) failure envelope models.

Instead of the arbitrary selection of constant values of φ' *and* c', the models support the Danish Practice using undrained triaxial tests to derive effective strength parameters, provided the undrained tests are analysed with due respect to the impact of I_p, in situ e (replaces e_o in models) and $(\sigma'_3)_f$.

REFERENCES

Jacobsen, M. (1970): *Strength and deformation properties of preconsolidated moraine clay.* Danish Geotechnical Institute, Bulletin No.27.

Steensen-Bach, J.O. (2023): *Effective strength parameters for clay till*. Unpubl. COWI memo.

Proceedings of the XVIII ECSMGE 2024
GEOTECHNICAL ENGINEERING CHALLENGES
TO MEET CURRENT AND EMERGING NEEDS OF SOCIETY
© 2024 the Authors
ISBN 978-1-032-54816-6
DOI 10.1201/9781003431749-147
Open Access: www.taylorfrancis.com, CC BY-NC-ND 4.0 license

ECSMGE 24
XVIII EUROPEAN CONFERENCE ON SOIL MECHANICS AND GEOTECHNICAL ENGINEERING

Digital geotechnical information management in a life cycle perspective

Gestion numérique des informations géotechniques dans une perspective de cycle de vie

M. Svensson*
Tyréns AB, Helsingborg, Sweden

O. Friberg
Tyréns AB, Malmö, Sweden

**mats.svensson@tyrens.se*

ABSTRACT: Heading towards sustainability a lifetime perspective is required for geotechnical information management. The GeoBIM concept has been developed, always enabling 1) Easy access to all geotechnical data for all stakeholders, 2) Design managed by geotechnical uncertainty control, 3) Flexible workflow and quick adaption to the user needs. This allows a smooth, quality assured and efficient workflow for any geotechnical design applications, and a significantly updated geotechnical process. Gathering different data sets in the same digital environment enables joint interpretation of any data sets, allowing use of the whole available data set in the most optimal way. Common issues in geotechnical engineering are uncertainties concerning the geological model and the design values. Tools have been developed for handling uncertainties of the layering, i.e., the bedrock model, and the design values. By adding as built geotechnical information to the database (surveyed bedrock model, geotechnical structures) a digital geotechnical asset management model (digital twin) could be handed over to the client for maintenance. A new geotechnical workflow is suggested, governed by a constant update of the uncertainties. Following this process activities like investigation program could be optimized and risk sharing between client and contractor could be clearer.

RÉSUMÉ: Pour parvenir à la durabilité, une perspective de vie est nécessaire pour la gestion des informations géotechniques. Le concept GeoBIM a été développé, permettant toujours 1) un accès facile à toutes les données géotechniques pour toutes les parties prenantes, 2) une conception gérée par contrôle de l'incertitude géotechnique, 3) un flux de travail flexible et une adaptation rapide aux besoins de l'utilisateur. Cela permet un flux de travail fluide, de qualité assurée et efficace pour toutes les applications de conception géotechnique, ainsi qu'un processus géotechnique considérablement mis à jour. La collecte de différents ensembles de données dans le même environnement numérique permet une interprétation conjointe de tous les ensembles de données, permettant ainsi d'utiliser l'ensemble des données disponibles de la manière la plus optimale. Les problèmes courants en ingénierie géotechnique sont les incertitudes concernant le modèle géologique et les valeurs de conception. Des outils ont été développés pour gérer les incertitudes de la stratification, c'est-à-dire le modèle du substrat rocheux et les valeurs de conception. En ajoutant des informations géotechniques telles que construites à la base de données (modèle de substrat rocheux étudié, structures géotechniques), un modèle numérique de gestion des actifs géotechniques (jumeau numérique) pourrait être remis au client pour maintenance. Un nouveau workflow géotechnique est proposé, régi par une mise à jour constante des incertitudes. En suivant ce processus, les activités telles que le programme d'enquête pourraient être optimisées et le partage des risques entre le client et l'entrepreneur pourrait être plus clair.

Keywords: GeoBIM; uncertainties; geomodels; MVA; digital twin.

1 INTRODUCTION

When a road, bridge or railway is to be built it is crucial to know the geotechnical conditions, including hydrogeology and the environmental situation. All information about the subsurface conditions is most often collected using geotechnical drill rigs and is done to a different extent depending on current project type and project phase. At an early stage only archive material is used, whereas at a later stage more detailed investigations are carried out. Every investigation gains valuable information which nowadays most often is digitally collected. Heading towards sustainability and hence a lifetime perspective, today we also need to take the geotechnical asset management phase into account.

Although different initiatives on handling smooth transferring and standardization of geotechnical data formats have been ongoing since many years (AGS, LAS, SGF, buildingSmart, OGC, IFC, CoClass) there is still a long way to go until full compatibility between all data and all software in the geotechnically related subsurface disciplines will come true. Therefore, still planning of geotechnical investigations are often non-optimized and the full potential of the whole geotechnical data set is seldom used. Sometimes data sets are even lost between different phases and different stakeholders.

With the vision of full transparency between all project phases and all stakeholders from idea to demolition of a structure the GeoBIM concept has been developed, enabling:

- Easy access to all data (geotechnical, environmental, geology/rock, groundwater) for all stakeholders always
- Design managed by known geotechnical uncertainties
- Flexible workflow and quick adaption to the user needs and specific software

This not only allows a smooth, quality assured and efficient workflow for any geotechnical design applications, it also enables a significantly updated geotechnical process.

2 DIGITAL GEOTECHNICAL PLATFORM

With the initial driver of developing a digital platform where all geotechnically related data in a large infrastructure project carried out could be gathered and easily accessible the GeoBIM database was developed, see Figure 1.

Considering all the subsurface disciplines – geotechnics, hydrogeology, geology, rock mechanics, environmental, geophysics – and both field and laboratory data, the number of data types in a large infrastructure project could be >100.

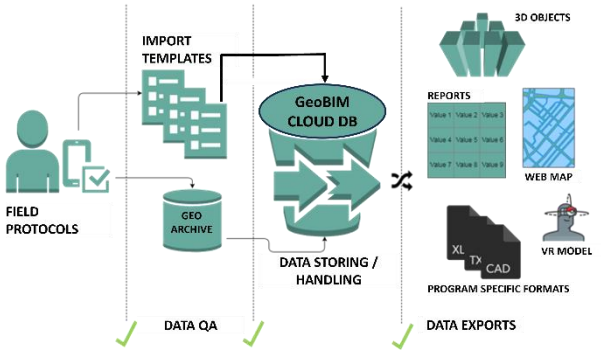

Figure 1. The GeoBIM concept process, enabling a completely closed digital chain from field data collection to 3D geo-model. (Svensson and Friberg, 2019).

In Sweden only the geotechnical data collected with the drill rigs are standardized, SGF (2012). Also internationally only a few of the data types are standardized. While waiting for the international geotechnical community to agree on common standards for all data types used, experts were asked for best practise concerning which parameters that should be logged. This was followed by developing standardized import scripts and a database accessible via a web interface, see Figure 1.

3 GEOTECHNICAL BIM COMPATIBILITY

To allow full BIM compatibility for geotechnical data and geotechnical objects three key elements must be fulfilled: All objects must: 1) be digital, 2) carry information of itself, 3) carry information of its relation to all other objects in the total digital model, see Figure 2. The CoClass code system has recently developed codes for classifying geotechnically related data, (Svensson and Friberg, 2019). Data and models stored in the GeoBIM database could also be assigned CoClass codes to allow full BIM compatibility.

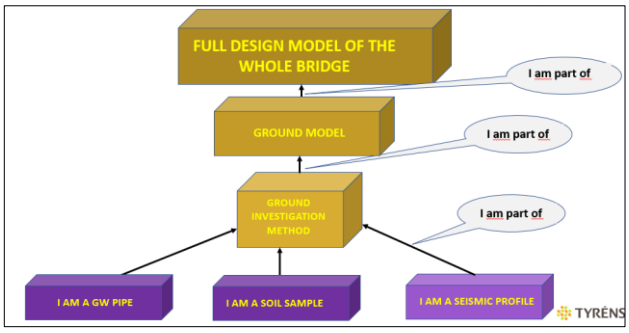

Figure 2. Principle of the BIM hierarchy. Each digital object carries information about itself and its relation to all other digital objects in the total (bridge) model. (Svensson, 2021).

4 GEOTECHNICAL DESIGN MANAGED BY UNCERTAINTY CONTROL

Having good order of all data in a digital format and easy access to it opens for validation, quality assurance and a wide flexibility of using the data - fundamental analyses in spread sheets, VR models, export for further 3D geological modelling etc. Maybe most important, enabling joint interpretation of any data sets, using the whole available data set in the most optimal way. One of the applications that has been developed is handling of uncertainties.

A big issue in geotechnical engineering is the large proportion of uncertainties concerning both the geological model and the design values. There are a

few reasons for this – the natural geological variation, transformation errors when converting from sounding results to engineering properties etc. The results are presented in factual reports and design reports (GBR, GDR). However, there is no standardized procedure for specifying the uncertainties, neither concerning the stratigraphy or the design values, i.e., undrained shear strength.

Tools have been developed for handling both the uncertainties of the layering, i.e., the bedrock model, (Svensson and Friberg, 2022), and the design values, (Prästings, 2019). For determining the uncertainties of the bedrock an algorithm based on individual uncertainties assigned to each sounding has been developed. Also, the distance to the nearest sounding point is used in the algorithm. After a Monte Carlo simulation (1 000 models) the outcome are three bedrock models and an uncertainty map, see Figure 3.

The algorithm that has been developed is validated to five uncovered and surveyed bedrocks in infrastructure projects in Sweden, (Svensson and Friberg, 2022). The prediction accuracy was shown to be 0.4-0.9 m.

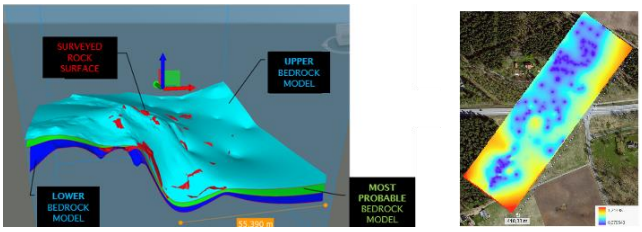

Figure 3. Results from modelling the top of the bedrock, (Svensson et al, 2022). Left: most probable bedrock model, upper and lower bedrock models within 95% probability. Right: Uncertainty map, plan view of most probable bedrock model.

To get an objective prediction of the undrained shear strength a tool using Multivariat analysis (MVA) has been developed. The methodology for geotechnical applications is well validated in (Prästings, 2019). The GeoBIM platform has implemented a module grabbing data of the user's choice in the database and performing an analysis using the MVA methodology. The result is presented with an objectively determined undrained shear strength accompanied by a known uncertainty (COV), see Figure 4.

All GeoBIM functionality has been implemented in the general Microsoft 365 Teams platform, including both the geometry uncertainty tool and the MVA tool. Each tool is run upon request and the geometry uncertainty models and the MVA results are stored in the digital platform, see Figure 6, and could be added to the final BIM design model if decided.

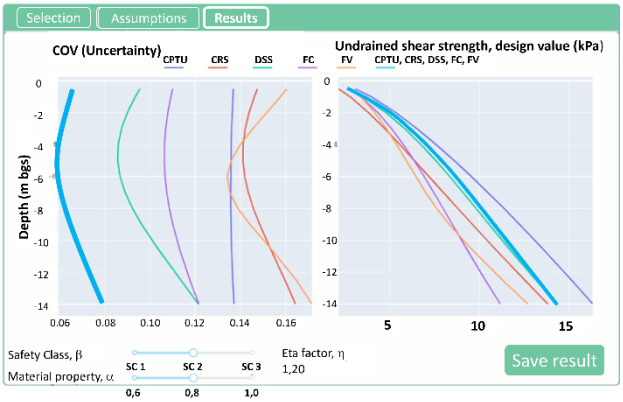

Figure 4. The undrained shear strength determined using MVA methodology. The combined uncertainty is significantly lower than the individual uncertainties from each method. (Svensson et al., 2022).

5 INCLUDING GEOTECHNICAL STRUCTURES

Saving information on all the geotechnical structures installed during a project´s lifetime contributes to sustainability. By adding as built geotechnical information to the database, a digital geotechnical asset management model could be handed over to the client for maintenance use during the operation phase, see Figure 5.

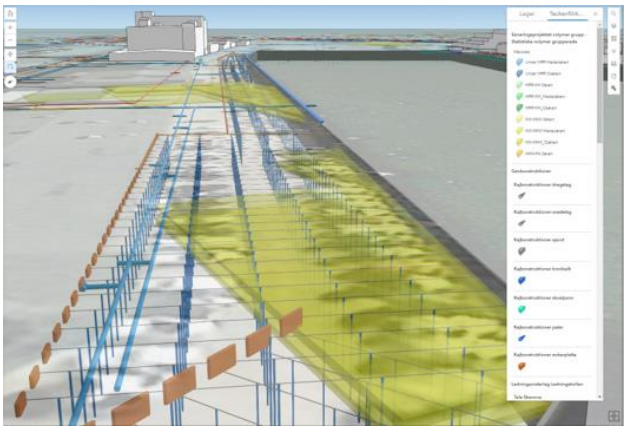

Figure 5. Digital geotechnical asset management model visualizing both geotechnical borehole information, contamination levels (yellow) and geotechnical sheet pile walls with anchors in the Nyhamnen area, Malmö, Sweden. All information is kept in the database. (Svensson, Friberg and Hagerberg, 2023).

6 NEW GEOTECHNICAL DESIGN PROCESS

In this article it has been shown that keeping all geotechnical data well-structured and in good order in a professional database advanced and novel applications, such as uncertainty models of geometries

and MVA methodology for objective determination of design values, could be implemented.

Irrespective of phase in a project this opens for defining a new geotechnical process and workflow, based on known uncertainties, see Figure 6. A new geotechnical workflow is suggested, governed by a constant update of the uncertainties both concerning the geologic model and the design values. As soon as any new information is added to the database the uncertainties are recalculated and compared to the allowed uncertainty criteria decided at the beginning of the project or current phase. Following this process activities like investigation program could be optimized, risk sharing between client and contractor could be clearer and the GBR/GDR will also become more defined.

With the vision of this suggested workflow, not taking legal aspects into account, all stakeholders constantly have access to the same updated information via the same digital platform/database where both data and models could be visualized.

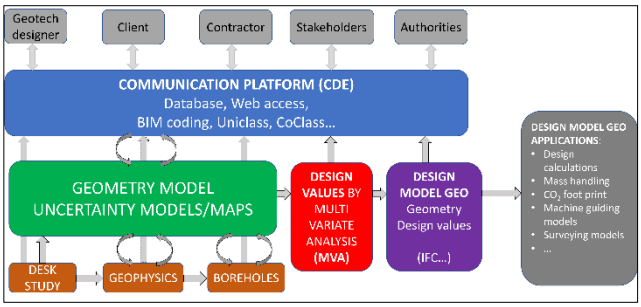

Figure 6. A new geotechnical process is suggested, based on uncertainties that is now possible to define. (Svensson and Friberg, 2022).

7 CONCLUSIONS

A digital geotechnical information management platform for a LCC perspective has been developed, based on the GeoBIM concept. The database and the accompanying methodology enables qulaity assurance, easy access to data, models and geotechnical structures for all stakeholders through all phases. This would decrease geotechncially related risks, miscommunication and the number of claims. It also allows flexible and advanced analyses using the whole data set. This opens for a new updated geotechnical process governed by uncertainty control of geotechnical parameters. At the end of a project a complete geotechnical model could be handed over to the client for maintanence use.

Implementing a new geotechnical design process as suggested requires overcoming legal issues and since long well established workflows. Good use cases, eduaction of the geotechnical community, including the environmental, geophysics, rock and groundwater disciplines, and openminded early adoptors among all strakeholders are key elements for succeeding.

ACKNOWLEDGEMENTS

The authors are grateful for the financial support provided by Sven Tyréns Foundation, Smart Built Environment, Swedish Rock Engineering Research Foundation (BeFo), The Development Fund of the Swedish Construction Industry (SBUF), Swedish Road Administration (TRV) and the City of Malmö.

REFERENCES

Prästings, A. (2019). *Managing uncertainties in geotechnical parameters: From the perspective of Eurocode 7*, PhD thesis, KTH School of Architecture and the Built Environment (ABE), Civil and Architectural Engineering, Soil and Rock Mechanics, ORCID iD: 0000-0001-5243-4650.

SGF (2012), SGF Rapport 3:2012 (in Swedish), Swedish Geotechnical Society, Linköping.

Svensson, M. (2021). Optimized joint interpretation using BIM methodology combining CoClass and GeoBIM, In: *Proceedings EAGE Near Surface Geoscience Conference 29 Aug-2 Sept,* Bordeaux, France.

Svensson, M., Hansson, P., Johansson, S., Duvaldt, M. and Friberg, O. (2022). Uncertainty models – for optimal use of geo related resources in infrastructure planning, BeFo Report 232, Sweden (*in Swedish*).

Svensson, M. and Friberg, O. (2022). GeoBIM for handling geological and geotechnical uncertainties in tunnelling, In: *Proceedings World Tunnelling Congress, 2-8 September,* Copenhagen, Denmark.

Svensson, M. and Friberg, O. (2019). Full underground BIM via development of CoClass for geotechnical data, models, and objects, In: *Proceedings ECSMGE, 1-6 September*, Reykjavik, Iceland.

Svensson, M., Friberg, O. and Hagerberg, D., (2023). GeoBIM for increased efficiency of the remediation process of contaminated sites, Smart Built Environment Report nr U8-2020-06, (*in Swedish*).

Proceedings of the XVIII ECSMGE 2024
GEOTECHNICAL ENGINEERING CHALLENGES
TO MEET CURRENT AND EMERGING NEEDS OF SOCIETY
© 2024 the Authors
ISBN 978-1-032-54816-6
DOI 10.1201/9781003431749-148
Open Access: www.taylorfrancis.com, CC BY-NC-ND 4.0 license

ECSMGE 24
XVIII EUROPEAN CONFERENCE ON SOIL MECHANICS AND GEOTECHNICAL ENGINEERING

Behaviour of continuous flight auger piles in homometric and carbonated sands

Comportement des pieux à la tarière creuse dans les sables homométriques et coquilliers

F. Szymkiewicz*, L. Makki, S. Fanelli, C. Minatchy, F. Guirado
Université Gustave Eiffel – SRO Laboratory, Champs sur Marne, France

J. Habert
Terrasol, Paris, France

**fabien.szymkiewicz@univ-eiffel.fr*

ABSTRACT: Continuous flight auger piles allow for a quick on-site installation, short execution time and a bearing capacity usually much higher than that of other bored piles. For these reasons, they are the most common piles in France, whether the encountered soils be fine or granular. However, homometric and carbonated sands are identified as 'problematic' for these kinds of piles, either in terms of execution or with regard to the bearing capacity, without the reasons being clearly stated in the scientific literature and technical documents. This communication presents the results of static loading tests carried out on three sites and on seven CFA piles in order to better understand the behaviour of these piles in this type of sands and to optimize their design. The geological and geotechnical context is first described in details. The implemented instrumentation and the obtained results are then presented. An analysis is then carried out, in the light of mechanical tests and further identification of the sandy soil, making it possible to understand the atypical behaviour of these piles in such soils, as well as to propose amended procedures for the design of continuous flight auger piles in these sands.

RÉSUMÉ: Les pieux réalisés à la tarière continue permettent une installation rapide sur site, un temps d'exécution court et offrent une capacité portante généralement bien supérieure à celle des autres pieux forés. Pour ces raisons, ce sont les pieux les plus couramment réalisés en France, que les sols rencontrés soient fins ou granulaires. Cependant, les sables homométriques et carbonatés sont identifiés comme 'problématiques' pour ce type de pieux, que ce soit en termes d'exécution ou de portance, sans que les raisons soient clairement énoncées dans la littérature scientifique et les documents techniques. Cette communication présente les essais de chargement réalisés sur trois sites et sur sept pieux CFA afin de mieux comprendre le comportement de ces pieux dans ce type de sables et d'optimiser leur conception. Le contexte géologique et géotechnique est d'abord décrit en détail. L'instrumentation mise en place et les résultats obtenus sont ensuite présentés. Une analyse est ensuite menée, à la lumière d'essais mécaniques et d'une identification plus poussée du sol sableux, permettant de comprendre le comportement atypique de ces pieux dans de tels sols, ainsi que de proposer de nouvelles valeurs à retenir pour le dimensionnement des pieux à tarière creuse dans ces sables.

Keywords: Deep foundations; carbonated sands; static load tests; design.

1 STUDY BACKGROUND

Continuous flight auger (CFA) and displacement piles are the most common types of piles used in Northern France. They offer a number of advantages: high production rates and expected axial resistance, and the equipment required for their realisation is limited compared with other techniques.

For research purposes, seven static loading tests were carried out on these types of piles at three sites between the cities of Calais and Dunkirk, on the French North See Coast. The piles are all founded in the quaternary sands of the Middle Flandrian, which are fine, homometric and shell-bearing.

The piles were all tested in compression, with the exception of one in tension. Loading tests were carried out until the piles reached geotechnical failure.

The strain instrumentation used on the piles varied from sites to sites, ranging from LCPC removable extensometers to fiber optics, vibrating string extensometers and strain gauges.

For all seven piles, the results obtained showed a systematically lower bearing capacity than that calculated according to current French rules.

This communication presents in detail these tests, the geotechnical context of the sites and the results obtained, and proposes an attempt to explain the low bearing capacities observed. New values of parameters k_p and $\alpha_{pieu\text{-}sol}$, defined as the pressuremeter bearing capacity and used to calculate the base resistance, and as a parameter depending on both the soil types and the pile technique and used to determine unit shaft friction, respectively, are proposed for CFA piles in these sands, which are known to be a potential source of problems both during the execution phase and with regard to bearing capacity.

2 TEST SITES AND TEST PILES SPECIFICATIONS

2.1 Location and geological/geotechnical context

The loading tests were carried out in three test plots carried out between 2011 and 2020.

Geotechnical investigations were carried out at the test sites, using core sampling and pressuremeter drilling.

The geotechnical cross-sections obtained from the various boreholes are presented in Table 1.

Table 1. Geotechnical models at Calais (a), Coudekerque (b) and Loon (c).

Depth of the layer (m)	Nature
0	Fills
1,4	Clays / Sands alternations
2,7	Coarse sand
3,7	Flandrian sand

(a)

Depth of the layer (m)	Nature
0	Silts
3	Flandrian fine sand

(b)

Depth of the layer (m)	Nature
0	Fills
0,6	Clays
2,2	Flandrian fine sand

(c)

The particle size analyses carried out on the samples recovered from the sands show them to be fine and very uniform with a coefficient of uniformity (D_{60}/D_{10}) less than 1.5.

The pressuremeter tests carried out at the three sites are shown in Figure 1. The p_{lM}* Ménard pressuremeter net limit pressure values are very comparable from one site to the next, with values increasing with depth in the homometric sand layers.

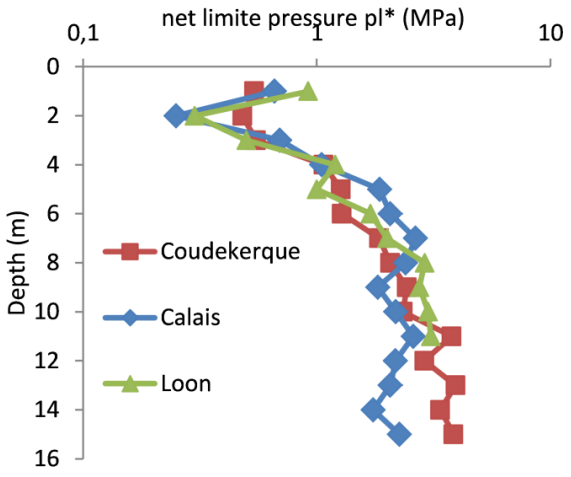

Figure 1. Evolution of net limit pressure as a function of depth at the three sites.

Moreover, the sands encountered are carbonated sands, being largely made up of pieces of shellfish shells, the presence of which was confirmed by the observation of a clear effervescence when drops of hydrochloric acid were applied, reflecting the presence of calcium carbonate. A more precise analysis allowed to quantify the carbonate content of these sands, with values up to 10%.

Uniform sands have been identified abroad as problematic during the execution phase of hollow auger or cast screw piles, but also with regard to bearing capacity (Brown et al., 2007 and Van Weele, 1988).

With regard to carbonated (shell) sands, Spagnoli et al. (2015) and Agemeer et al. (1973) pointed out that the constituent grains of these soils are fragile and often hollow, and can easily break during shearing, resulting in a reduction in volume and therefore limited friction (which can sometimes be as little as 10% of that expected for conventional sand). Noorany (1985) found that this limited friction is not due to a low pile-soil friction angle, but rather to the low horizontal stresses prevailing at the soil-pile interface.

However, current European and French rules for the execution and justification of deep foundations devote only one line to these soils, saying only that they "require special analysis due to their specific behaviour, which can result in very low resistances" (AFNOR, 2012 and AFNOR, 2015).

2.2 Test Piles

The seven piles tested on the three sites are hollow auger bored piles corresponding, according to standard NF P94-262, to category 6 piles (FTC).

Table 2 gives the details of the various piles at the Calais, Coudekerque and Loon sites. All the piles were instrumented, with the exception of the pile tested in tension at Loon. This instrumentation, irrespective of the measurement technology used, enables the shaft resistance R_s of the compression-tested piles to be dissociated from the base resistance R_b, and to estimate the axial unit shaft friction that can be mobilized in the various horizons crossed (Szymkiewicz et al., 2021).

Analysis of the drilling parameters for the seven piles also confirmed that the work was carried out without any particular problems.

Table 2. Geometric characteristics, types and strengths of piles tested in accordance with French design method.

	Coudekerque			Calais		Loon	
	P1	**P2**	**P3**	**P1**	**P2**	**P1**	**P2**
Length (m)	12	12	12	10	10	8	10,5
Diameter (m)	0.52	0.52	0.52	0.52	0.52	0.42	0.42
Type	FTC	FTC	FTC	FTC	FTC	FTC	FTC
Instrumented	yes	yes	yes	yes	yes	yes	no
Test	compression						traction
Rc (kN)	3297	3297	3297	2438	2438	1588	
Rs (kN)	2088	2088	2088	1685	1685	959	1685
Rb (kN)	1209	1209	1209	753	753	629	

3 LOADING TEST RESULTS AND ANALYSIS

The loading tests were carried out in compliance with the requirements of the test standards in force at the time.

3.1 Resistance of the piles

It is important to note first of all that the P2 and P3 piles at the Coudekerque site were subjected to heating-cooling cycles for 4 months and it has been shown that these cycles had an impact on the shaft resistance of these piles (Szymkiewicz et al., 2015). Therefore, for this study, only the base resistance was compared to the theoretical resistance.

The tests were all carried out at near failure, taking as the failure criterion a displacement of the pile head equal to B/10. At these displacement levels, the base and shaft resistances were almost completely mobilized (Figure 2). It should be noted that, for piles tested in compression, the normalized load-displacement curves are quite similar.

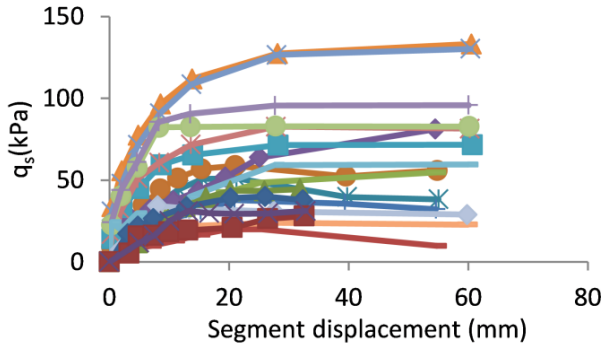

Figure 2. t-z curves in sands, for all piles.

In general, the measured tensile and compressive strengths ($R_{t/c\ ;\ m}$) are well below the expected theoretical strengths ($R_{t/c\ ;\ cal}$, estimated in accordance with NF P94-262). Measured ultimate strengths are at best 74% of theoretical ultimate strengths (Table 3), for the P1 pile tested at the Coudekerque site, while for the other three the difference is even greater, with an average ratio of 64%.

The shaft resistances of the instrumented piles tested in compression and of the one tested in tension are also well below the expected resistances. In the case of the Coudekerque P1 pile, measured resistances represent at best 84% of the theoretical resistance, and only 61% on average, with a minimum of 54% (Table 3).

The base resistances of the instrumented piles tested in compression are below the expected strengths, too. Measured resistances represent at

best 92% of the theoretical resistance (extrapolating the peak resistance for a limit resistance of 1100 kN and considering the shaft friction fully saturated during the last maintained bearing) for the P1 pile in Loon, and only 70% on average, with a minimum of 58% (Table 3).

It is interesting to note that at all three sites, shaft resistance is on average the most overestimated, but at the Coudekerque site, the opposite is observed.

Table 3. Theoretical (cal) and measured (m) limit (c/t), shaft (s) and base (b) resistances, and ratios.

	$R_{s;\,cal}$	$R_{s;\,m}$	$R_{s;\,m}$ / $R_{s;\,cal}$	$R_{b;\,cal}$	$R_{b;\,m}$	$R_{b;\,m}$ / $R_{b;\,cal}$	$R_{c\,cal}$	$R_{c\,m}$	$R_{c;\,m}$ / $R_{c;\,cal}$
Calais P1	1685	898	0,53	753	577	0,77	2438	1475	0,61
Calais P2	1685	925	0,55	753	550	0,73	2438	1475	0,61
CDK P1	2088	1751	0,84	1209	699	0,58	3297	2450	0,74
CDK P2	-	-	-	1209	726	0,6	-	-	-
CDK P3	-	-	-	1209	752	0,62	-	-	-
Loon P1	959	521	0,54	629	579	0,92	1588	1100*	0,69
Loon P2	1334	820	0,61	-	-	-	-	-	-

* CDK = Coudekerque

3.2 Axial unit shaft friction mobilization friction mobilization and values

Analysis of the t-z transfer curves achieved via the instrumentation reveals that the curves all have virtually the same shape, with no softening (Figure 2). This shape is characteristic of a rather loose sand, by analogy with a shear test on sand.

Generally speaking, we note that the unit shaft friction q_s measured are well below that expected according to standard NF P 94-262 (Figure 3).

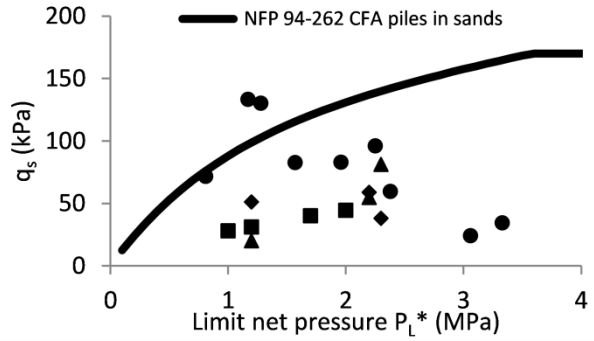

Figure 3. Measured q_s against net limit pressure, and comparison with the French theoretical values.

It is also interesting to note that the friction measured in the top layers is on average higher than expected and therefore 'compensates' in part for the low friction in the sands.

4 RESULTS EXPLANATIONS

The results achieved in these seven tests assess the fact that the bearing capacity of CFA piles in this type of soil is much lower than expected.

As stated previously, there is already some tentative explanations for these low values. However, another alternative explanation could be related to the homometric properties of the sands.

Indeed, homometric granular soils are known to exhibit a dilatant behavior during the shearing process. This shearing process occurs naturally during the pile loading, at the interface soil-pile, but also already during the pile execution process, when the auger penetrates the soil. Therefore, it may be interesting to look at the residual effective friction angle and to compare it to the peak friction angle.

To evaluate the possible decrease of the friction angle, it was decided to perform shearbox tests as well as alternate shearbox tests.

Peak friction angle was determined to be equal to 41°, while the residual friction angle was derived as 34°. This induces a decrease of the friction of about 22 %, which could explain the low values of resistance achieved during these tests.

However, it is difficult to conclude, as the shape of the t-z curves, with no softening, is more clearly linked to a contractant behavior.

Furthermore, the sands of this study show a fairly high voids ratio, consistently above 0.6. Using the e_{max} and e_{min} values available in the literature, it is possible to estimate the soil relative density, in order to better classify these sands. They are fairly loose to very loose, except at the Loon site, where the sand is moderately dense.

This contradicts our proposed explanation, and implies that the study of this topic should be continued.

5 NEW DESIGN PARAMETERS FOR CFA PILES IN HOMOMETRIC CARBONATED FINE SANDS

Even if the reasons for the low values are still not clear, it is possible to propose new values for design parameters, in order to increase the safety when planning for CFA in these sands.

First, regarding the determination base resistance, determined following the French method according to Eq. (1), the pressuremeter bearing capacity k_p factor shall be decreased from 1.65 as stated in the French standard to 1.1:

$$R_b = A \times k_p \times p^*_{le} \quad (1)$$

where A is the base area, and p_{le}^* is the equivalent net limit pressure around the base of the pile.

Regarding the shaft resistance, in order to limit the design values of q_s, determined following the French method according to Eq. (2), it is recommended to decrease the value of the parameter $\alpha_{pieu\text{-}sol}$, that depends on both the soil types and on the pile categories, and to leave unaffected the f_{sol} function that is defined by parameters a, b and c dependant only on the soil types (Eq. (3)). The proposed value is 0.7, compared to the 1.8 given by the French standard:

$$q_s = a_{pieu-sol} \times f_{sol} \quad (2)$$

with

$$f_{sol} = (a \times p_{lM} + b) \times (1 - e^{-c \times p^*_{lM}}) \quad (3)$$

It also necessary to limit the maximum value of the unit shaft friction q_{smax} to a much lower value of 70 kPa, compared to the 170 kPa allowed at the moment. The new curve of mobilizable limit unit shaft friction in these sands is shown in Figure 4.

It is now possible to compare the measured data of these tests with the new theoritical values: this is what is done in Table 6.

It can be seen that, on average, the measured friction resistance is now 25% higher than the friction resistance with this new $\alpha_{pile\text{-}soil}$ value. The case of P1 de Coudekerque remains problematic, as the friction resistance is largely underestimated.

The base resistance measured remains on average 5% higher than that measured with this k_p value. However, this value is biased by the results obtained on the P1 pile in Loon. If this pile is discarded, the ratio $R_{b;\,m}$ / $R_{b;\,cal}$ drops to 0.99.

Table 6. Ratios between measured and calculated resistances, with the new proposed values of $\alpha_{pile\text{-}soil}$ and k_p.

	$R_{s;\,m}$ / $R_{s;\,cal}$	$R_{b;\,m}$ / $R_{b;\,cal}$	$R_{c/t;\,m}$ / $R_{c/t;\,cal}$	$R_{c/t;\,cr;\,m}$ / $R_{c/t;\,cr;\,cal}$
Calais P1	1,10	1,15	1,12	1,20
Calais P2	1,14	1,10	1,12	1,12
Coudekerque P1	1,79	0,87	1,37	1,88
Coudekerque P2	-	0,90		-
Coudekerque P3	-	0,93		-
Loon P1	1,02	1,38	1,18	1,27
Loon P2	1,22	-	1,22	1,51

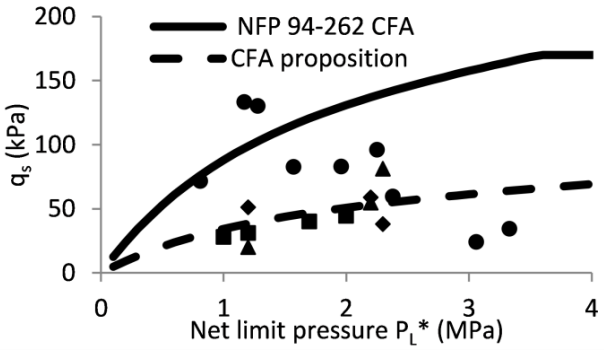

Figure 4. New proposition for a q_s – P_l curve for CFA piles in homometric carbonated sands.*

On the other hand, if we look at the limit resistances, we see that the ratio $R_{c/t;\,m}$ / $R_{c/t;\,cal}$ averages 1.20. It is therefore possible to adjust the proposed values while maintaining a certain degree of safety.

6 CONCLUSIONS

Various Tests carried out on CFA piles have shown that the limit resistance of these piles are systematically overestimated in homometric carbonated sands.

A possible explanation for the low value of shaft friction and base resistance could be the dilatant behaviour of the soil associated to the pile realisation process. However, further tests are needed to assess the validity of this hypothesis.

Nevertheless, the results achieved allowed for the proposition of new design values for the $\alpha_{pile\text{-}soil}$ and k_p parameters, ensuring a safer design of CFA in these very special sands.

It is also necessary to propose lower values for the $\alpha_{pile\text{-}soil}$ and k_c parameters, as well as the q_{smax}, allowed for the CPT method, insofar as testing is possible in these soils.

Further loading tests in these soils are still necessary, not only to gain a better understanding of the behaviour of these piles, but also to analyze these data according to the principles used to draw up standard NF P94-262, so as to confirm the proposals presented in this report. A similar study on other types of piles should also be carried out, as all categories of piles are impacted by these very particular soils: two cast screw piles tested on the Calais site gave similarly poor results.

Finally, a further laboratory study focusing solely on the impact of sand particle friability could be carried out, with additional tests on homometric quartz sands.

REFERENCES

AFNOR (2012). NF P 94-262 Justification des ouvrages géotechniques - Normes d'application nationale de l'Eurocode 7 - Fondations profondes, France.

AFNOR (2015), NF EN 1536+A1 Execution of special geotechnical work - Bored piles, France.

Angemeer J., Carlson E. and Klick J. H. (1973). Techniques and results of offshore pile load testing in calcareous soil. *Proceedings of the 5th Offshore Technology Conference*, Houston, USA, Paper 1894.

Brown D., Dapp S.,, Robert Thompson W., and Lazarte C. (2007). Geotechnical engineering circular no. 8: Design and Construction of Continuous Flight Auger (CFA) Piles, USA, Report FHWA-HIF-07-03.

Noorany I. (1985) Side friction of piles in calcareous sands. *Proceedings of 11th International Conference on Soil Mechanics and Foundation Engineering*, San Francisco, USA, pp. 1611-1614.

Spagnoli G., Doherty P., Wu D. and Doherty M. (2015), Some mineralogical and geotechnical properties of carbonate and silica sands in relation to a novel mixed-inplace pile, *12th Offshore Mediterranean Conference and Exhibition*, Ravenna, Italy.

Szymkiewicz, F., S. Burlon, F. Guirado, C. Minatchy and Vinceslas G. (2015). Experimental study of heating-cooling cycles on the bearing capacity of CFA piles in sandy soils, *Proceedings of the XVI ECSMFE: Geotechnical Engineering for Infrastructure and Development*, Edinburgh, UK, pp. 2647-2652.

Szymkiewicz F., Minatchy C. and Reiffsteck P. (2021). *Static pile load tests: contribution of the measurement of strains by optical fiber*, International Journal of GEOMATE, Vol. 20, Issue 81, pp. 44-51, DOI: https://doi.org/10.21660/2021.81.6330.

Van Weele, A.F., (1988). Cast-in-situ piles — Installation methods, soil disturbance and resulting pile behaviour, *Proceedings of Deep Foundations on Bored and Auger Piles*, Ghent, Belgium, pp. 219–226. https://doi.org/10.1016/0148-9062(90)90854-U.

Proceedings of the XVIII ECSMGE 2024
GEOTECHNICAL ENGINEERING CHALLENGES
TO MEET CURRENT AND EMERGING NEEDS OF SOCIETY
© 2024 the Authors
ISBN 978-1-032-54816-6
DOI 10.1201/9781003431749-149
Open Access: www.taylorfrancis.com, CC BY-NC-ND 4.0 license

ECSMGE 24
XVIII EUROPEAN CONFERENCE ON SOIL MECHANICS AND GEOTECHNICAL ENGINEERING

Static load tests on raft on rigid inclusions

Essais de chargement statiques sur fondations superficielles posées sur des inclusions rigides

F. Szymkiewicz*
Université Gustave Eiffel – SRO Laboratory, Champs sur Marne, France

C. Bohn
KELLER Holding, Offenbach am Main, Allemagne

L. Briançon
INSA LYON, Lyon, France

S. Lambert
KELLER Fondations Spéciales, Duttlenheim, France

P. Garnier
COLAS, Merignac, France

L. Carpinteiro
GINGER CEBTP, Elancourt, France

**fabien.szymkiewicz@univ-eiffel.fr*

ABSTRACT: A full-scale experimentation of static loading tests on square footings on rigid inclusions has been performed in the framework of the research project ASIRI+. This experiment aimed to assess the effect of a load transfer platform between the shallow foundation and the rigid inclusions on the behaviour of the footing and the reinforced soil. To do so, three configurations of load distribution platforms were tested, under different loading conditions (vertical catered, vertical with eccentricity, horizontal-vertical combined loading…). Preliminary load tests on instrumented isolated rigid inclusions were carried out to study their behaviour under compression. A complete instrumentation solution was designed and implemented (including strain gauges, inclinometers, and total stress sensors…), to assess in detail the distribution of the load between the soil and the inclusions, This publication presents the geotechnical context of the study, the instrumentation implemented, and the different load cases. Results as then presented, and conclusions are drawn, allowing a better understanding of the behaviour of the reinforced soil under the footings.

RÉSUMÉ: Une expérimentation en grandeur réelle d'essais de chargement statique sur des semelles carrées sur inclusions rigides a été réalisée dans le cadre du projet de recherche ASIRI+. Le but de cette expérience était d'évaluer l'effet de la présence d'une plate-forme de transfert de charge entre la fondation superficielle et les inclusions rigides sur le comportement de la semelle et du sol renforcé. Pour ce faire, trois configurations de plates-formes de répartition des charges ont été testées, dans différentes conditions de chargement (vertical avec trappe, vertical avec excentricité, chargement combiné horizontal-vertical...). Des essais de charge préliminaires sur des inclusions rigides isolées et instrumentées ont été réalisés pour étudier leur comportement en compression. Une solution d'instrumentation complète a été conçue et mise en œuvre (comprenant des jauges de déformation, des inclinomètres, des capteurs de contrainte totale...), afin d'évaluer en détail la répartition de la charge entre le sol et l'inclusion. Cette publication présente le contexte géotechnique de l'étude, l'instrumentation mise en œuvre, et les différents cas de charge. Les résultats sont ensuite présentés et des conclusions sont tirées, permettant une meilleure compréhension du comportement du sol renforcé sous les semelles.

Keywords: Soil improvement; rigid inclusions; foundations; static load tests.

1 STUDY BACKGROUND

This study aimed to compare the behaviour of the footing with or without the presence of a granular load-transfer platform. Indeed, current French recommendations (ASIRI, 2012) recommend only a solution with a granular platform interposed between the inclusions and the footing. However, more and more companies want to be able to dispense with this platform constraint.

The ASIRI+ project therefore aims to offer a more open solution for dimensioning footings on rigid inclusions.

Centered vertical, eccentric vertical and horizontal loading tests was thus performed footings on rigid inclusions, with instrumentation used to monitor load transfer to the inclusions, footing displacement, soil and inclusion settlement. Two isolated inclusions were also tested to determine their behavior under static and cyclic loading.

2 TEST SITES AND TEST SPECIFICATIONS

The loading tests were carried out in Dourges, in the northern part of France. The geological/geotechnical context was quite simple, with a single layer of silts encountered.

All the tests were performed on the same precast reinforced concrete 1.8 m x 1.8 m x 0.5 m footing.

The implemented instrumentation included vibrating wire strain gauges, displacement sensors, soil settlement sensors, total earth pressure cells, and an inclinometer.

The rigid inclusions executed on this site were continuous flight auger inclusions, 4.5 m long and with a 0.27 m diameter.

The different test configurations are shown schematically in Figure 1, along with the results of the penetrometer tests, and summarized as follows:

- Configuration 0: two isolated inclusions.
- Configuration 1: a footing on four rigid inclusions without a load transfer platform.
- Configuration 2: a footing on four rigid inclusions with a load transfer platform of 30 cm of granular material.
- Configuration 3: a footing on four rigid inclusions with a 10 cm leveling sand layer.

The testing program is shown in Table 1.

Table 1. Testing program for each configuration

Test	Eccentricity	Loadings
E1	e = 0	V : 0 → 650 kN
E2	e = 0.3 m	V : 0 → 650 kN
E3	e = 0.45 m	V : 0 → 450 kN
E4	e = 0	V = 650 kN,
E5	e = 0	V = 650 kN, H : 0 → 250 kN
E6	e = 0	V : 0 → failure

The vertical loads were applied through the solicitation of a reaction frame identical to a typical one used for piles testing. For the horizontal solicitations, the reaction was achieved via the use of a concrete block founded on four large piles.

A 5 MN hydraulic jack was used for the vertical loadings and a 1 MN hydraulic jack for the horizontal loadings. Each of the two jacks was actuated independently, with its own hydraulic pump.

The testing program was very dense and rich, with many loading configurations tested (Table 1), and this communication will only present some of them.

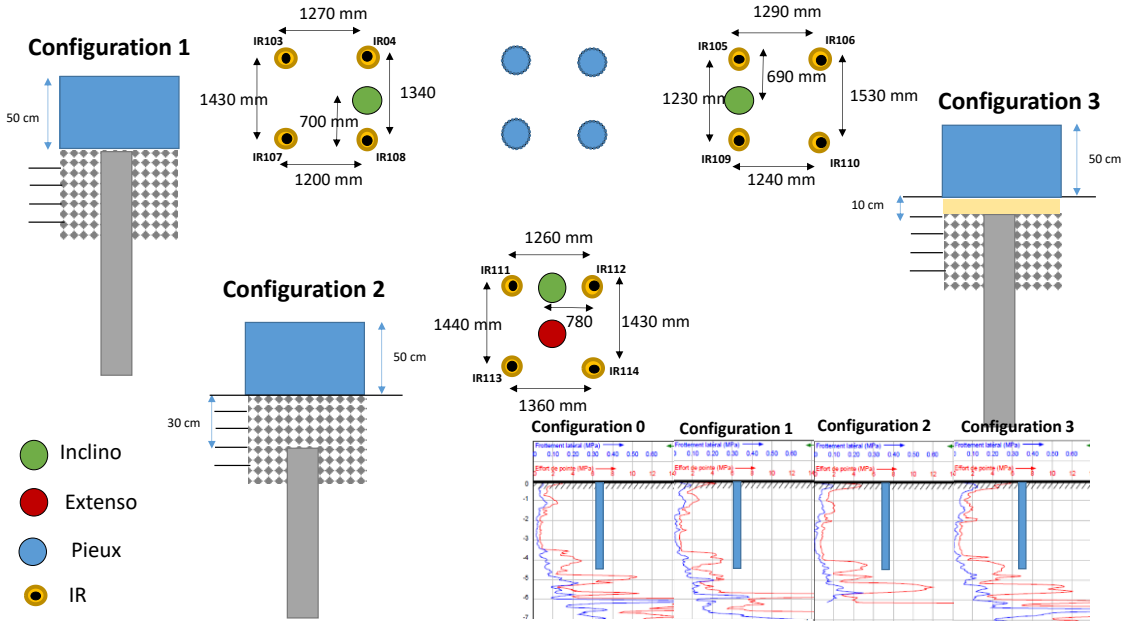

Figure 1. Tests configurations, implemented instrumentation, and CPT results.

3 LOADING TEST RESULTS

3.1 Stress distribution over the four inclusions

Figure 2 shows the stress increases measured on the rigid inclusions of configurations 1, 2 and 3 at the end of the test for the centered vertical loading E1 and E4.

It can be seen that for all three configurations, the footing never rests on the four inclusions. The same observation was made on a similar experimental test (Pham et al., 2019). Nevertheless, configuration 3, with the leveling sand layer, seems to allow a better distribution on the inclusions.

Configuration 2, with the granular platform, generates lower stress on the inclusions.

Furthermore, there is a difference in stress distribution between tests E1 and E4, which can be attributed to the installation of the soil reinforcement device during the first loading. This effect of the first loading has been observed in the footing displacement recorded at the end of tests E1 and E4.

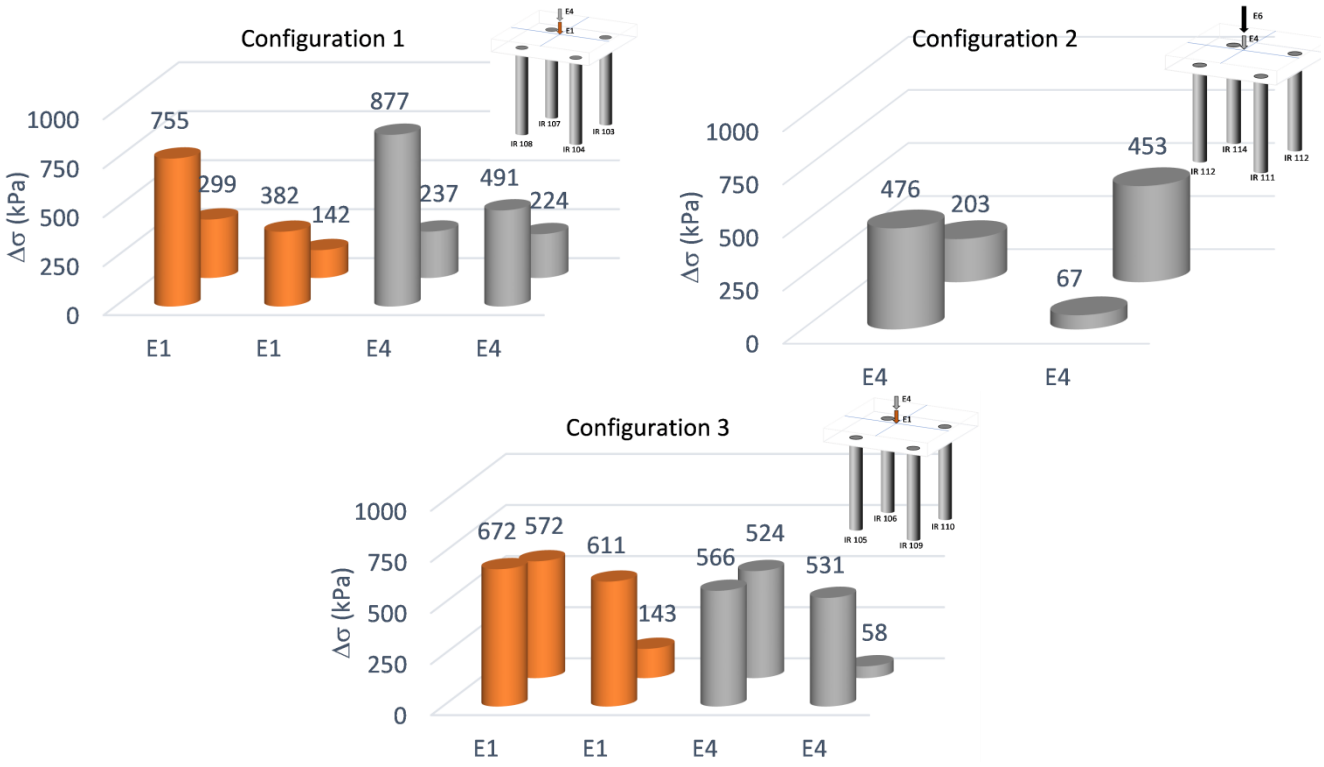

Figure 2. Stress measures at inclusions head, for configuration 1 to 3, during tests E1 and E4.

3.2 Influence of the eccentricity

Figure 3 shows the stress increases measured on the rigid inclusions of configurations 1 and 3 at the end of the test for centered vertical loading (E4), eccentric vertical loading at 30 cm (E2) and eccentric vertical loading at 45 cm (E3).

To avoid errors linked to the first loading, the E4 centered vertical test was preferred to the first E1 test for this comparison. Furthermore, to verify the influence of eccentricity, average values are presented for the two inclusions perpendicular to the direction of eccentricity.

An imbalance (60%-40%) is observed for the centered vertical test, even when a leveling layer of sand is disposed between the footing and the inclusions. At the 30 cm eccentricity, there is a slight tilting towards the two inclusions located on the eccentricity side. This tilting is much more pronounced at an eccentricity of 45 cm, where two inclusions take up 77% and 95% respectively of the load applied to configurations 1 and 3, respectively. This difference can be explained by the fact that, in configuration 1, the eccentricity was applied in the opposite direction to the two most heavily loaded inclusions, whereas for configuration 3, the eccentricity was applied in the same direction.

3.3 Failure tests

Test E6 brought each configuration to failure. The creep load was estimated at 900 kN, 950 kN, and 850 kN respectively for configurations 1, 2, and 3.

Results also showed that the settlement of the soil was greater than that of the inclusions. Plotting the differential settlement of soil and inclusions (Figure 4), we can see a change in behaviour from creep load onwards: for configuration 1, the soil-inclusion assembly settles homogeneously; for configuration 3, this homogeneous settlement occurs later. It should be noted that the differential measurements recorded are millimetric, and we can conclude that the reinforced soil settles homogeneously after the creep load for both configurations.

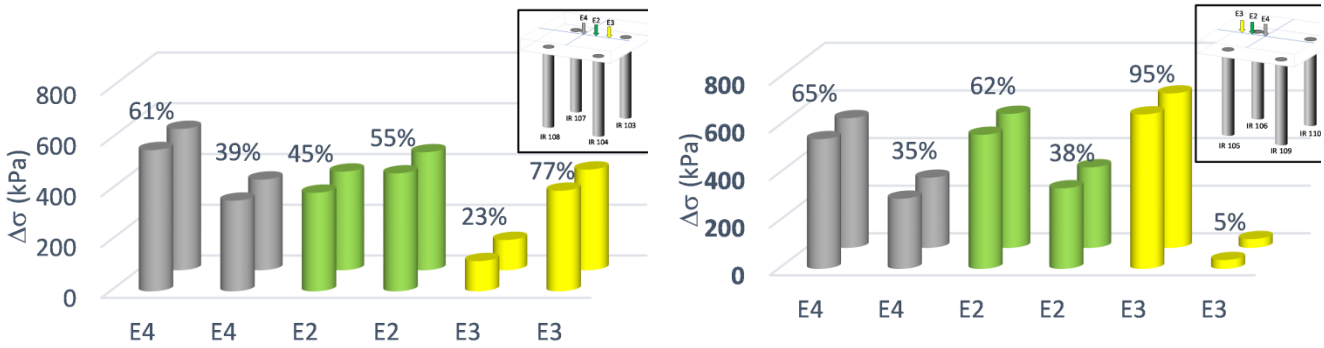

a *b*

Figure 3. Stress evolution at inclusions head, for configuration 1 (a) and 3 (b), during tests E4, E2 and E3.

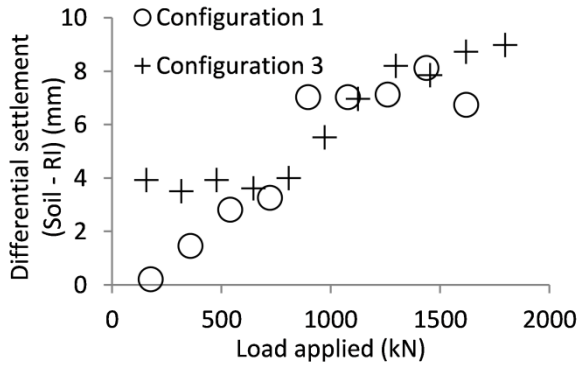

Figure 4. Differential settlement between soil and inclusions for configurations 1 and 3.

4 CONCLUSIONS

This full-scale experiment with footings on rigid inclusions is rich in lessons learned, despite the difficulty of accurately comparing the results of the three plots, particularly due to the different initial conditions. In fact, for each block, the first test highlighted conditions of preferential load transfer to two or three inclusions, making it difficult to exploit the results.

Tests with vertical load eccentricity revealed a strong load transfer to two inclusions. The presence of a granular platform reduces the load transferred directly to the inclusion heads (part of which must be transmitted by friction), but does not modify the overall behavior for vertical loading to failure. Load tests carried out to the failure demonstrated the behaviour of the reinforced soil after the creep load. These tests will enable the ASIRI+ project partners to calibrate their numerical models. This experimental study will be completed by another on-site tests campaign as well as a centrifuge test campaign, for which the initial conditions will be better controlled and which will enable an easier analysis of the behaviour of the various configurations tested, as the setup conditions and the reliability and reproductibility of all measures are difficult to assess with only one campaign.

ACKNOWLEDGEMENTS

The authors are grateful for the participation of all the 42 partners of the ASIRI+ National Project to this collaborative work.

REFERENCES

ASIRi (2012). Recommandations pour la conception, le calcul, l'exécution et le contrôle des ouvrages sur sols améliorés par inclusions rigides verticales (Recommandations Projet National ASIRi), Presse des Ponts - IREX Paris.

Pham V.H., Briançon L., Dias D., Racinais J. (2019). *Footings over rigid inclusion-reinforced soft soil. Experimental and numerical approaches*. Canadian Geotechnical Journal, 56(12), pp. 1940-1952. https://doi.org/10.1139/cgj-2018-0495

Proceedings of the XVIII ECSMGE 2024
GEOTECHNICAL ENGINEERING CHALLENGES
TO MEET CURRENT AND EMERGING NEEDS OF SOCIETY
© 2024 the Authors
ISBN 978-1-032-54816-6
DOI 10.1201/9781003431749-150
Open Access: www.taylorfrancis.com, CC BY-NC-ND 4.0 license

ECSMGE 24
XVIII EUROPEAN CONFERENCE ON SOIL MECHANICS AND GEOTECHNICAL ENGINEERING

Simplified methodology to evaluate the stability of a group of isolated caisson-type maritime infrastructures

Méthodologie simplifiée pour évaluer la stabilité d'un groupe d'infrastructures maritimes de type caisson isolé

D. Tarragó*, A. Gens
Centre Internacional de Mètodes Numèrics en Enginyeria (CIMNE), Barcelona, Spain
Universitat Politècnica de Catalunya (UPC), Barcelona, Spain
dani.tarrago@upc.edu

ABSTRACT: With the recent development of finite element programs for 3D geotechnical analysis, and the concurrent reduction in computational costs, the number of 3D simulations has significantly increased. Despite the benefits of 3D simulations, they are often complex and require a greater amount of work than their 2D counterparts. The methodology presented simplifies the stability analysis of isolated maritime caissons (3D) into a 2D problem. Specifically, the problem considers a group of caissons separated by tens of meters and founded on soft soil. The methodology is based on adjusting the load applied on the caisson and the weight of the caissons. The stability results indicate a satisfactory agreement when compared to the same case simulated in 3D, as well as a significant reduction in computational costs. This methodology does not propose abandoning 3D evaluation of the problem; rather, it aims to provide a reliable preliminary result that can help in reducing the updates to the geometry (remeshing) of 3D simulations and the overall computational costs in the project.

RÉSUMÉ: Avec le développement récent de programmes d'éléments finis pour l'analyse géotechnique 3D, et la réduction concomitante des coûts de calcul, le nombre de simulations en 3D a considérablement augmenté. Malgré les avantages des simulations en 3D, elles sont souvent complexes et nécessitent un travail plus important que leurs homologues en 2D. La méthodologie présentée simplifie l'analyse de stabilité des caissons maritimes isolés (3D) en un problème 2D. Plus précisément, le problème considère un groupe de caissons séparés par des dizaines de mètres et fondés sur un sol meuble. La méthodologie se base sur l'ajustement de la charge appliquée sur le caisson et du poids des caissons. Les résultats de stabilité indiquent un accord satisfaisant par rapport au même cas simulé en 3D, ainsi qu'une réduction significative des coûts de calcul. Cette méthodologie ne propose pas d'abandonner l'évaluation en 3D du problème ; elle vise plutôt à fournir un résultat préliminaire fiable qui peut contribuer à réduire les mises à jour de la géométrie (remaillage) des simulations en 3D et les coûts de calcul globaux du projet.

Keywords: Stability; 2D-analysis; 3D-analysis; caissons.

1 DESCRIPTION

The construction of a new mooring dolphin using caissons in a section of the Energy quay at the Port of Barcelona has required the numerical simulation of a proposed project solution. During the analysis, a methodology was developed to optimize the analysis, with the primary objective of avoiding excessive computation time in the 3D design simulations.

The use of mooring dolphin structures is often implemented in ports with limited draughts for the installation of isolated elements such as bollards, pipelines, and more. The project solution is depicted in Figure 1, along with a cross-sectional view (Figure 2).

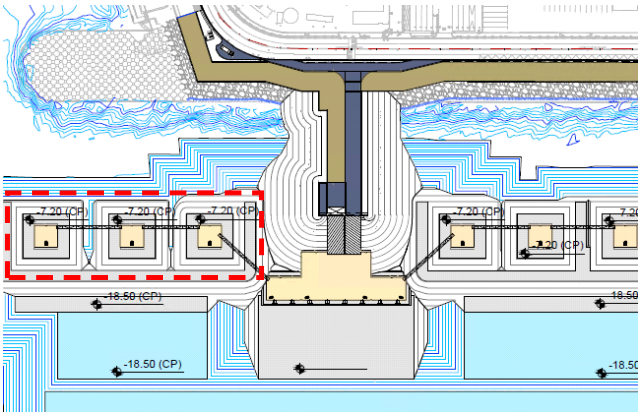

Figure 1. Plan view of the new mooring dolphin using caissons at the Energy quay of Barcelona port.

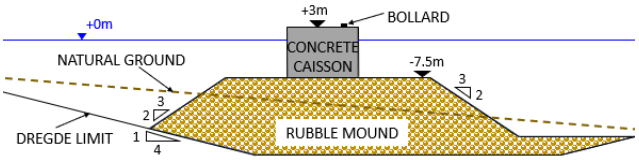

Figure 2. Cross section of the mooring dolphin with caisson (landside is on the left).

The construction process consists of three main phases: (i) dredging of the natural ground, (ii) placement of the rubble mound, generally to an elevation higher than the initial one, and (iii) placing of the individual concrete caissons on the rubble mound and subsequent filling.

To simulate this solution and optimize the dredging depth and rubble mound thickness and area, it was necessary to carry out a 3D simulation considering all the present structures, as there is considerable interaction between them. The solution could be simulated and optimized in a simplified and somewhat conservative manner by a 3D simulation considering three isolated caissons of identical dimensions -red squared zone of Figure 1-, together with common dredging and rubble mound. Nevertheless, a 3D simulation is highly complex and comes with a significant computational cost in terms of time and computing resources. To reduce time and complexity, it should be simulated in 2D. However, a plain strain 2D simulation would not be suitable for this problem. To use a 2D simulation for this problem, a methodology is implemented that allows obtaining a simulation that closely approximates a 3D model.

For this purpose, it must be considered that the stability of the solution will essentially depend on the strength of the soft soil foundation, composed of clayey silts (Alonso et al., 2008; Tarragó, 2021; and Madrid, 2021). The undrained shear strength of the soil behaviour follows the law of Equation (1).

$$c_u = 0.25 \cdot [\sigma'_v]^{OCR^{\Lambda}} \qquad (1)$$

where σ'_v is the effective vertical stress, OCR is the overconsolidation ratio and Λ is $\lambda/(\lambda-\kappa)$. λ is the compresion ratio and κ is the unloading reloading ratio.

Therefore, the behaviour of the problem regarding failure will be influenced by: (i) the undrained shear strength of the soil, (ii) the effective weight of the caisson, and (iii) the strength of the material constituting the rubble mound.

2 METHODOLOGY

The proposed methodology incorporates approximately the 3D effects on strength in a 2D plain strain model by incorporating the equivalent effective weight based on the spacing between isolated caissons and the equivalent loads on the caisson. To achieve this, the effective weights of the caisson and the loads on the caissons are weighted according to the spacing as shown in Figure 3.

The percentage of the length of 3 caissons (41.1 m) against the total length (95 m) in the direction of the caisson alignment is 43%.

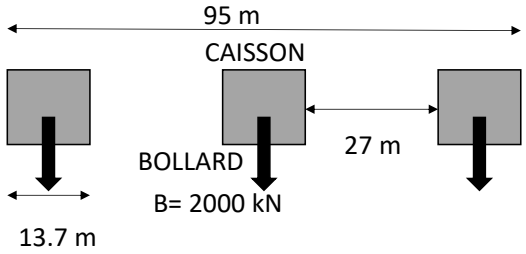

Figure 3. Diagram of the location of the caissons and the horizontal loads.

The effective weight ($\gamma_{effective} = \gamma - \gamma_w$) of the caisson is calculated by adding the weights of the submerged caisson, 10.94 kN/m^3 × 7.5 m (between the anchoring elevation of -7.5 m and +0 m), and the emerged caisson, 20.94 kN/m^3 × 3m (between +0m and +3m), resulting in 144 kN/m^2. When this weight is weighted by the percentage of caisson length, it yields an equivalent $\gamma_{effective}$ of 62.3 kN/m^2. The total equivalent weight will be 137.3 kN/m^2. Using this total weight, the equivalent specific weight of the caisson (13.08 kN/m^3) is determined, which will be utilized in the 2D analysis to account for the strength.

Finally, the point loads from the existing bollards on each caisson (2000 kN) are also accounted for in a weighted manner, resulting in a load of 63 kN/m

3 ANALYSES

The analyses were conducted using 2D plane strain and 3D simulations. The material parameters in both of them were the same, as well as the meshes in 2D and 3D.

3.1 Materials

The simulated materials are the concrete caisson, the rubble mound, and the natural soft soil. The caisson is simulated with a linear elastic model having a Young's modulus (E) of 20,000 MPa and a variable specific weight according to the proposed methodology. The

rubble mound consists of coarse granular quarry material and is simulated using a Mohr-Coulomb model with a friction angle of 38° and E = 30 MPa. Finally, to account for the effect of the effective weight on the undrained shear strength of the soft soil, its behaviour is simulated using a modified Cam Clay constitutive model (Brinkgreve, 1994).

3.2 Simulation conditions

The simulations replicate the various stages of the construction process, up to the final stage of applying the bollard loads. Drained stages are considered during construction until the final stage of applying the bollard load, which is done in an undrained manner. Finally, it should be noted that safety factors are evaluated using the phi-c reduction method.

4 RESULTS

4.1 Methodology for 2D analysis

Initially, the stability is assessed for two cases using the 2D geometry of the section:

A. Applying the spread out bollard load ($Q_{B\ eq}$ = 63 kN/m) and not applying any modification to the caisson weight ($\gamma_{caisson}$ = 20.94 kN/m^3).
B. Using the proposed methodology: $Q_{B\ eq}$ = 63 kN/m and $\gamma_{caisson}$ = 13.08 kN/m^3.

The results of the obtained safety factor (FoS) indicate that for case A, FoS = 1.40 whereas for case B, FoS = 1.69. The geometry of the two failures is similar; they both extend from the top to the bottom of the rubble mound, reaching the natural soil where they deepen a few meters before re-emerging on the seabed on the other side of the caisson, as shown in Figure 4.

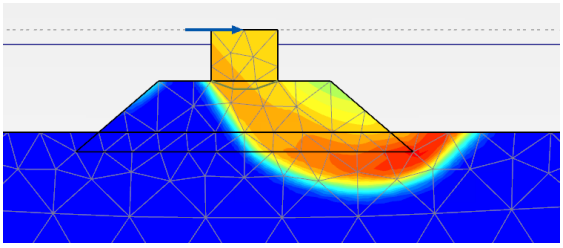

Figure 4. Incremental displacements of 2D simulation, case B, FoS=1.69, bollard loading phase.

4.2 3D and methodology verification

The results obtained in the 2D model are now validated using a 3D model of the problem. In order to accomplish this, an equivalent 3D model of the extruded 2D section has been created. For case A, the 3D model yields a FoS of 1.43 similar to those of case A in the 2D model. Figure 5 shows the failure mechanism. The agreement in FoS indicates that the number of elements in the 3D model is sufficient to ensure similar results to the 2D model.

Using the same mesh, a 3D simulation with three isolated caissons of identical dimensions has been performed, including a point load of 2000 kN applied to each caisson.

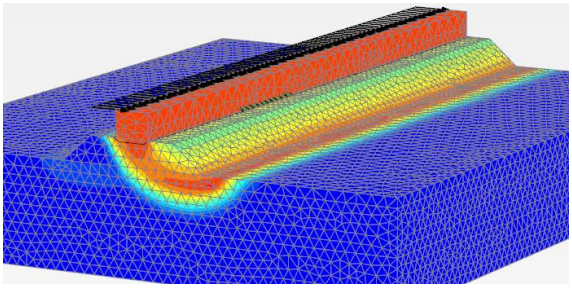

Figure 5. Incremental displacements of 3D (extruded 2D simulation) case A, FoS=1.43, bollard loading phase.

The FoS obtained in the 3D analysis, FoS=1.73 (Figure 6), a value similar to that of case B using the 2D methodology, FoS=1.69. The results are consistent as the FoS obtained from the 3D simulation and the 2D simulation are similar for this case.

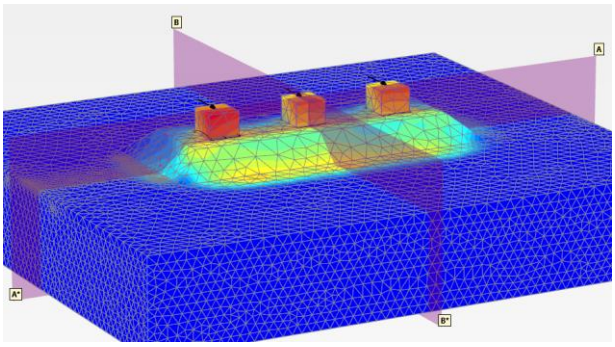

Figure 6. Incremental displacements of 3D model, FoS=1.73, bollard loading phase.

5 DISCUSSION

The results obtained demonstrate the effectiveness of the proposed methodology because the safety factors obtained are similar for the 3 caissons. While the failure shapes are similar in the central area (Figure 7: section B-B' from Figure 6), at the edges of the 3D model (Figure 8: section A-A' from Figure 6), the failure naturally takes on a somewhat different shape. For this reason, the FoS in the 3D model is possibly slightly higher than that of the 2D model.

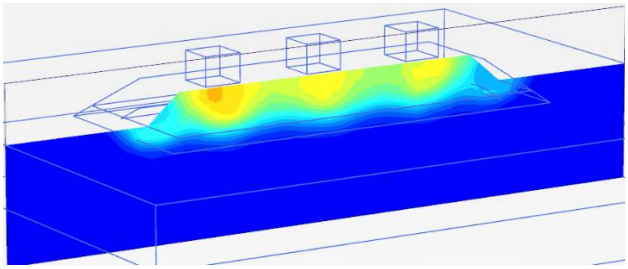

Figure 7. Cross-section A-A' of incremental displacements from 3D model, FoS=1.73, bollard loading phase.

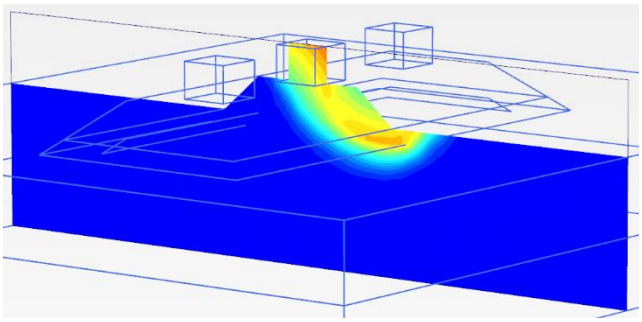

Figure 8. Cross-section B-B' of incremental displacements from 3D model, FoS=1.73, bollard loading phase.

A slight difference in the failure mode is also observed: in the 2D simulation, the failure primarily occurs at the foundation base, whereas in the 3D simulation, there is a combination of the previous mode and overturning. This overturning component is directly related to the point load applied by the bollard in the 3D case.

Additionally, stability has been evaluated with the same mesh using 1 and 2 caissons to assess the edge effects on the failure. The FoS is 1.73 for the simulation with 2 caissons and 1.77 for the simulation with 1 caisson, Figure 9. These results reinforce the idea that the edge effects increase modesty the FoS.

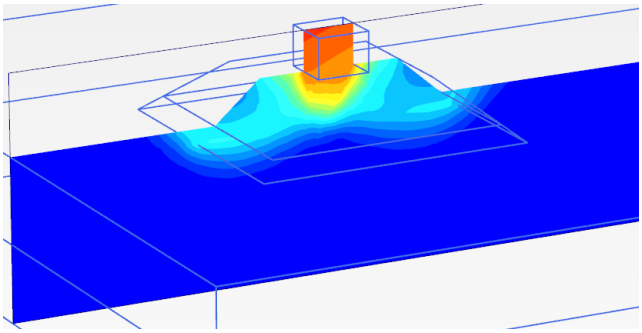

Figure 9. Cross-section A-A' of incremental displacements from 3D model with 1 caisson, FoS=1.77, bollard loading phase.

The computation time for the proposed 2D analysis is at least 20 times less than the time for the 3D simulation to achieve a similar result, provided that no changes to the mesh are required.

6 CONCLUSIONS

A proposed methodology for the analysis of a group of mooring dolphin caissons founded on soft soils -soils ruled by undrained shear strenght-, has proved highly beneficial for the optimization of the dredging depth and rubble mound thickness and area during the design and project phase. Since these types of structures are common in numerous port works, as are the prevalence of soft soils, the importance of simplification and time reduction in analysis using the presented methodology is evident.

It has been demonstrated that by using an effective weight of the caissons and bollard loads, it is possible to accurately assess the problem of isolated group of caissons in a 2D simulation. However, it may be necessary to resort to a 3D simulation to incorporating features that cannot be implemented in a 2D model, such as asymmetric loads, adjacent structures influencing behavior, lateral variation in soil properties, and more. In any case, a 3D analyses for checking the performace of the methodology in each particular case is recommended.

ACKNOWLEDGEMENTS

The authors are grateful for the technical and financial support provided by the Barcelona Port Authority.

REFERENCES

Alonso, E., Gens, A., Madrid R., Uzcanga, J. (2007). The soft foundation soils of new breakwaters at the port of Barcelona. European *Proceedings of the 14th European Conference on Soil Mechanics and Geotechnical Engineering*. IOS Press (eds.), Madrid, pp. 1765-1770. ISBN: 978-90-5966-055-7.

Brinkgreve, R. B. J. (1994). Geomaterial models and numerical analysis of softening. *Ph. D. Thesis, TU Delft. Available at: https://repository.tudelft.nl/islandora/object/uuid%3A6738de62-4dde-45b0-b3bd-3635504767c2*.

Madrid, R. (2021). Construction and post-construction performance of vertical breakwaters on soft soils: the Port of Barcelona case. *Ph. D. Thesis. UPC, Departament d'Enginyeria Civil i Ambiental*.

Tarragó, D. (2021). Hydraulic fills liquefaction: effect on quay stability. *Ph. D. Thesis. UPC, Departament d'Enginyeria Civil i Ambiental.*

Proceedings of the XVIII ECSMGE 2024
GEOTECHNICAL ENGINEERING CHALLENGES
TO MEET CURRENT AND EMERGING NEEDS OF SOCIETY
© 2024 the Authors
ISBN 978-1-032-54816-6
DOI 10.1201/9781003431749-151
Open Access: www.taylorfrancis.com, CC BY-NC-ND 4.0 license

ECSMGE 24
XVIII EUROPEAN CONFERENCE ON SOIL MECHANICS AND GEOTECHNICAL ENGINEERING

Viscous resistance of clay soil under kinematic shear

Résistance visqueuse des sols argileux sous cisaillement cinématique

A.Z. Ter-Martirosyan, L.Yu. Ermoshina*
National Research Moscow State University of Civil Engineering, Research and Educational Center "Geotechnics" named after Z.G. Ter-Martirosyan, Moscow, Russia
**lyubov.ermoshina1801@mail.ru*

ABSTRACT: Based on the concept proposed by N.N. Maslov, the ultimate shear resistance of clay soil can be represented as the sum of Coulomb friction, structural cohesion and cohesion of water-colloidal bonds. However, this concept doesn't take into account the influence of shear rate. Note that during kinematic shear in a soil medium that has viscosity, viscous resistance may appear. In this regard, within the framework of this work, it was proposed to present the general cohesion in clay soil as a sum of three components: structural cohesion, cohesion of water-colloidal bonds and viscous soil resistance. To take into account the influence of shear rate on the shear resistance of clay soil, experimental studies were carried out on samples of clay soil in a simple shear device in a kinematic loading mode. The tests were carried out at four different shear rates and at three different values of constant vertical load. The design of the simple shear device used during testing allows for the realization of a homogeneous stress-strain state inside the soil sample during testing, since each individual elementary layer of the sample moves by the same amount during shear. Based on the results of experimental and theoretical studies, a new rheological equation was obtained, which simultaneously takes into account the influence of Coulomb friction, structural cohesion, cohesion of water-colloidal bonds and viscous resistance of the soil. The resulting equation can be used for further improvement of methods for quantitative assessment of the stress-strain state of foundations composed of weak clay soils.

RÉSUMÉ: Basé sur le concept proposé par N.N. Maslov, la résistance ultime au cisaillement d'un sol argileux peut être représentée comme la somme du frottement coulombien, de la cohésion structurelle et de la cohésion des liaisons eau-colloïdales. Cependant, ce concept ne prend pas en compte l'influence du taux de cisaillement. Notez que lors d'un cisaillement cinématique dans un milieu de sol ayant une viscosité, une résistance visqueuse peut apparaître. A cet égard, dans le cadre de ce travail, il a été proposé de représenter la cohésion générale dans les sols argileux comme la somme de trois composantes : la cohésion structurelle, la cohésion des liaisons eau-colloïdales et la résistance visqueuse du sol. Pour prendre en compte l'influence du taux de cisaillement sur la résistance au cisaillement des sols argileux, des études expérimentales ont été réalisées sur des échantillons de sol argileux dans un dispositif de cisaillement simple en mode de chargement cinématique. Les tests ont été effectués à quatre taux de cisaillement différents et à trois charges verticales constantes différentes. La conception du dispositif de cisaillement simple utilisé lors des essais permet de réaliser un état de contrainte-déformation homogène à l'intérieur de l'échantillon de sol pendant les essais, puisque chaque couche élémentaire individuelle de l'échantillon se déplace de la même quantité pendant le cisaillement. Sur la base des résultats d'études expérimentales et théoriques, une nouvelle équation rhéologique a été obtenue, qui prend simultanément en compte l'influence du frottement coulombien, de l'adhésion structurelle, de l'adhésion des liaisons eau-colloïdale et de la résistance visqueuse du sol. L'équation résultante peut être utilisée pour améliorer encore les méthodes d'évaluation quantitative de l'état de contrainte-déformation des fondations composées de sols argileux faibles.

Keywords: Viscous resistance; kinematic shear; simple shear device; creep.

1 INTRODUCTION

Due to the high pace of development of housing, transport and hydraulic engineering over the past hundred years, the study of the phenomenon of creep in clay soils has become the subject of scientific research.

The process of creep of clay soils in nature manifests itself in the form of long-term settlements, displacements, tilts, horizontal movements of structures, as well as in the form of slow sliding of clay masses along the natural slopes and slopes of structures made from soil materials.

In order to describe the rheological properties (creep) of clayey soils, various techniques are currently widely used (Meschyan, 2005; Shirinkulov and Zareckij, 1986; Ter-Martirosyan, 1990; Ter-Martirosyan and Ter-Martirosyan, 2020), which are based on the use of mechanical models, the theory of plastic flow and hereditary creep, etc., on the basis of

which various equations of state are derived (Bodas Freitas, Potts and Zdravkovic, 2011; Chen, Weiqiang, Chen and Yin, 2023; Gu, Zou, Fang, and Hu 2018; Li and Yue 2014; Santa Maria and Santa Maria, 2018), containing several parameters that can be determined during experimental studies of soil in various instruments (Roman and Kotov, 2016; Yuan, Wang, Chen and Huang , 2023).

2 MATERIALS AND METHODS

Based on the concept proposed by N.N. Maslov, the ultimate shear resistance of clay soil can be represented as the sum of Coulomb friction ($\sigma tg\varphi$), structural cohesion (c_c) and cohesion of water-colloidal bonds (c_w):

$$\tau^* = \sigma tg\varphi + c_c + c_w \qquad (1)$$

However, the presented concept (1) doesn't take into account the influence of shear rate ($\dot{\gamma}$).

Note that during kinematic shear ($\dot{\gamma} = const$) in a soil medium that has viscosity, viscous resistance may appear ($c_{\dot{\gamma}}$).

If we assume that viscous resistance is due to the viscosity of the soil as a whole, then during kinematic shear viscous resistance will arise ($c_{\dot{\gamma}} = \dot{\gamma}\eta$). Therefore, we represent the general cohesion in clay soil as a sum of three components:

$$c = c_c + c_w + c_{\dot{\gamma}} \qquad (2)$$

In order to take into account the effect of the shear rate ($\dot{\gamma}$) on the shear resistance of clay soil in the laboratory of the REC "Geotechnics" named after Z.G. Ter-Martirosyan (National Research University MGSU), experimental studies were carried out in a simple shear device in a kinematic loading mode ($\dot{\gamma} = const$) at four different shear rates ($\dot{\gamma}_1 > \dot{\gamma}_2 > \dot{\gamma}_3 > \dot{\gamma}_4$) and at three different values of constant compaction load ($\sigma_1 < \sigma_2 < \sigma_3$) acting on the soil sample during testing.

Pre-compacted samples of fluid-plastic loam (I_P = 10,60, I_L = 0,80) with a diameter d = 71,4 mm and a height h = 22 mm were tested in a simple shear device in the kinematic loading mode ($\dot{\gamma} = const$) (at a constant shear displacement rate equal to $\dot{u} = \dot{\gamma}h$), under the action of a constant vertical compaction load ($\sigma = const$), as well as with constant measurement of the shear force.

3 RESULTS

Figures 1-4 show the results of testing fluid-plastic loam in a simple shear device in a kinematic loading mode ($\dot{\gamma} = const$).

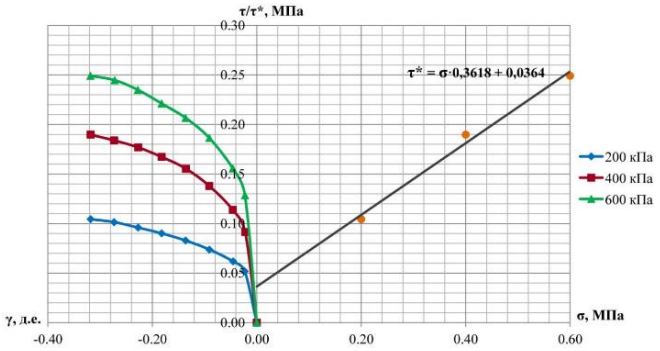

Figure 1. A graph of the dependence of the acting shear stresses on shear strains ($\tau - \gamma$) and a graph of the dependence of the ultimate shear stresses on normal stresses ($\tau^* - \sigma$) at a constant shear displacement rate equal to $\dot{u}$ = 5 mm/min.

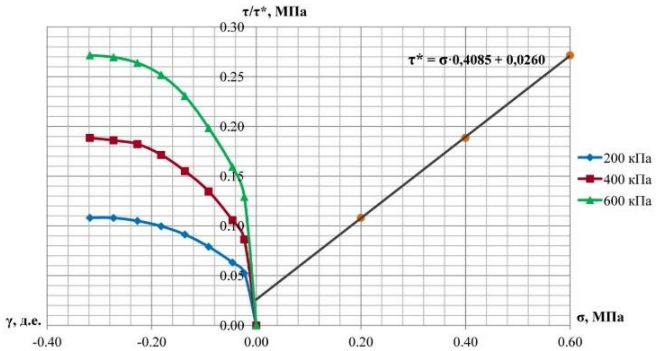

Figure 2. A graph of the dependence of the acting shear stresses on shear strains ($\tau - \gamma$) and a graph of the dependence of the ultimate shear stresses on normal stresses ($\tau^* - \sigma$) at a constant shear displacement rate equal to $\dot{u}$ = 0,5 mm/min.

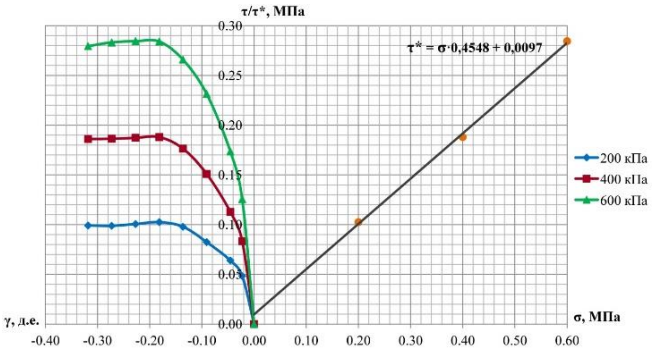

Figure 3. A graph of the dependence of the acting shear stresses on shear strains ($\tau - \gamma$) and a graph of the dependence of the ultimate shear stresses on normal stresses ($\tau^* - \sigma$) at a constant shear displacement rate equal to $\dot{u}$ = 0,05 mm/min.

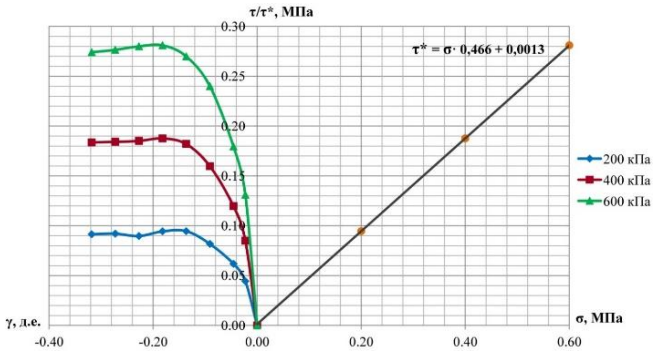

Figure 4. A graph of the dependence of the acting shear stresses on shear strains $(\tau - \gamma)$ and a graph of the dependence of the ultimate shear stresses on normal stresses $(\tau^* - \sigma)$ at a constant shear displacement rate equal to $\dot{u}$ = 0,005 mm/min.

Numerous experimental tests of quaternary clay samples of disturbed and undisturbed structure, carried out in the kinematic loading mode $(\dot{\gamma} = const)$ and at different values of vertical stress σ (100, 200, 300 and 500 kPa), described in the work of M.B. Kornouhov, showed (Figure 5) that the limit lines at different shear rates $(\dot{\gamma}_1 > \dot{\gamma}_2 > \dot{\gamma}_3 > \dot{\gamma}_4)$ have the same slope equal to $\varphi = const$, and this angle doesn't depend on the shear rate $(\dot{\gamma})$.

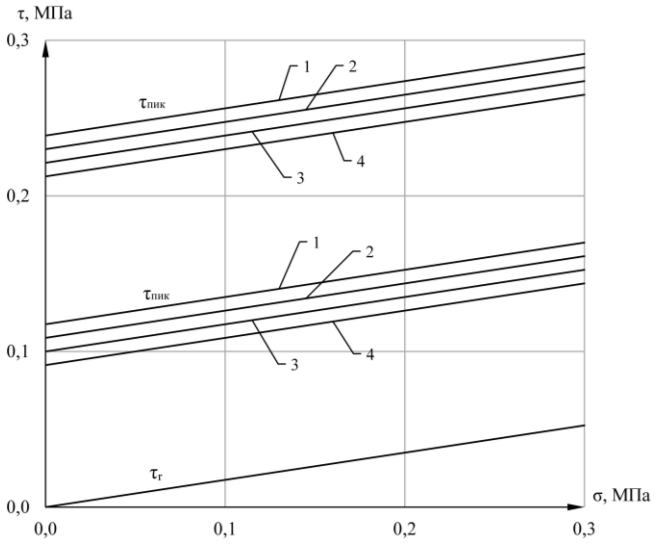

Figure 5. Graph of the dependence of the peak and residual strength of quaternary clay of an undisturbed structure (a) and a disturbed structure (b) on vertical stress (σ_{n_1} = 0,1 MPa; σ_{n_2} = 0,2 MPa and σ_{n_3} = 0,3 MPa), acting on the sample at different shear rates: 1 - $\dot{\gamma}_1$ = 0,066 min^{-1}; 2 - $\dot{\gamma}_2$ = 0,0041 min^{-1}; 3 - $\dot{\gamma}_3$ = 0,00026 min^{-1}; 4 - $\dot{\gamma}_4$ = 0,00002 min^{-1}.

The ultimate value of shear resistance (τ^*) largely depends on the angle of internal friction (φ) and the general cohesion (c). And the general cohesion (c) significantly depends on the shear rate $(\dot{\gamma})$, and as the shear rate increases, the ultimate shear resistance also increases in direct proportion $ln\,\dot{\gamma}$ (Figure 6).

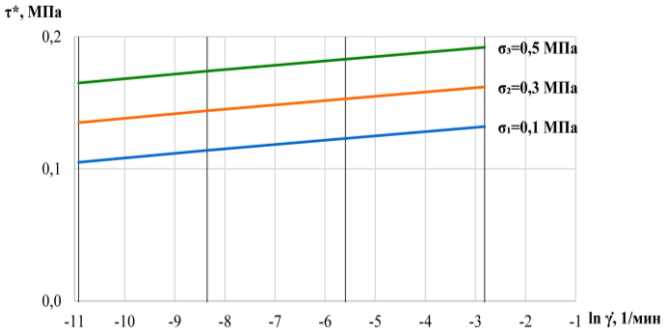

Figure 6. Graph of the dependence of the peak strength of quaternary clay of a disturbed structure on the deformation rate.

Since, according to the results of experimental studies, it was found that the structural cohesion (c_c) and the angle of internal friction (φ) don't depend on the shear rate $(\dot{\gamma})$, the viscous resistance was presented in the following form:

$$c_{\dot{\gamma}} = c_{\dot{\gamma}_0} + \alpha\, ln(\dot{\gamma}/\dot{\gamma}_1) \qquad (3)$$

where α is a parameter determined on the basis of experimental data.

Based on the Maxwell elastic-viscous body model, we present the rheological equation for kinematic shear in the following form:

$$\dot{\gamma} = \frac{\tau - \tau^*}{\eta} + \frac{\dot{\tau}}{G} \qquad (4)$$

where $\tau^* = \sigma tg\varphi + c_0$ (and $c_0 = c_c + c_w$); η is the viscosity of the soil as a whole; $\dot{\tau}$ - rate of change of shear stress; G - soil shear modulus.

Having performed a certain grouping in equation (4), we obtain a differential equation of the following form:

$$\dot{\tau} + \tau \cdot \frac{G}{\eta} = \frac{G}{\eta} \cdot \left(c_{\dot{\gamma}} + \tau^*\right) \qquad (5)$$

The solution to equation (5) at a constant shear rate $(\dot{\gamma} = const)$ has the form:

$$\tau(t) = (\sigma tg\varphi + c_c + c_w + c_{\dot{\gamma}}) \cdot (1 - e^{-\frac{G \cdot t}{\eta}}) \qquad (6)$$

At $t \to \infty\ \tau(\infty) = \sigma tg\varphi + c_c + c_w + c_{\dot{\gamma}}$, and $c_{\dot{\gamma}} = \dot{\gamma}\eta$.

The obtained result corresponds to our ideas about the ultimate shear resistance (2). However, it should be noted that in this case, the viscous resistance $c_{\dot{\gamma}}$

increases in direct proportion to the shear rate ($\dot{\gamma}$), and this doesn't correspond to the results obtained during experimental studies (3). However, if we take dependence of the form (7) as a rheological model, we obtain a result corresponding to the experimental data:

$$(\dot{\gamma}/\dot{\gamma}_1)^{\alpha/\eta} = e^{\left(\frac{\tau-\tau^*}{\eta}+\frac{\dot{\tau}}{G}\right)} \quad (7)$$

where $\tau^* = \sigma tg\varphi + c_c + c_w$.

Equation (4) can also be represented as follows:

$$\frac{\alpha}{\eta} ln(\dot{\gamma}/\dot{\gamma}_1) = \frac{\tau-\tau^*}{\eta} + \frac{\dot{\tau}}{G} \quad (8)$$

The solution to equation (8) has the following form:

$$\tau(t) = (\sigma tg\varphi + c_c + c_w + \alpha\, ln(\dot{\gamma}/\dot{\gamma}_1)) \cdot (1 - e^{-\frac{G\cdot t}{\eta}}) \quad (9)$$

For $t \to \infty$ $\tau(\infty) = \sigma tg\varphi + c_c + c_w + \alpha\, ln(\dot{\gamma}/\dot{\gamma}_1)$.

From equation (9) it follows that $c_{\dot{\gamma}} = \alpha\, ln(\dot{\gamma}/\dot{\gamma}_1)$.

The obtained result concurs with the result of experiment (3), and using equation (9) it is possible to construct a diagram $(\tau^* - ln\dot{\gamma})$ (Figure 6).

By replacing time t with the value $\gamma/\dot{\gamma}$ in equation (9), we obtain the dependence $(\tau - \gamma)$:

$$\tau(\gamma/\dot{\gamma}) = (\sigma tg\varphi + c_c + c_w + \alpha\, ln(\dot{\gamma}/\dot{\gamma}_1)) \cdot (1 - e^{-\frac{G}{\eta}\cdot(\gamma/\dot{\gamma})}) \quad (10)$$

4 CONCLUSION

The results of experimental studies carried out in a simple shear device in a kinematic loading mode showed that the shear rate has a significant effect on the cohesion of clay soil.

However, due to the limited scope of tests performed, additional research is required on clay soil samples with different plasticity numbers I_P and fluidity index I_L in order to identify and determine correlation dependencies.

Earlier in the works of many authors, it has been noted that total adhesion can be decomposed into two components: structural cohesion (c_c) and cohesion of water-colloidal bonds (c_w). Based on the results of experimental studies presented in Figures 5 and 6, and their analysis, it is explicitly shown that general cohesion also depends on the shear rate $\dot{\gamma}$.

REFERENCES

Bodas Freitas, T.M., Potts, D. and Zdravkovic, L. (2011). A time dependent constitutive model for soils with isotach viscosity. *Computers and Geotechnics*, 38(6), pp. 809-820. http://dx.doi.org/10.1016/j.compgeo.2011.05.008.

Chen, Z-J., Weiqiang, F., Chen, W-B. and Yin, J-H. (2023). A thermal elastic visco-plastic model for soft clayey soils. *Canadian Geotechnical Journal*, pp. 1-68.http://dx.doi.org/10.1139/cgj-2022-0279

Gu, R., Zou, Y., Fang, Y.-G. and Hu, Y.-G. (2018). Rheological model of soft soils using nonlinear instantaneous elastic modulus. *Yantu Lixue/Rock and Soil Mechanics*, 39(1), pp. 237-241. http://dx.doi.org/10.16285/j.rsm.2016.0237

Li, R. and Yue, J. (2014). Nonlinear rheological constitute of soft soil based on fractional order derivative theory. *Journal of Basic Science and Engineering*, 22(5), pp. 856-864. http://dx.doi.org/10.3969/j.issn.1005-0930.2014.05.002

Meschyan S. R. (2005). *Experimental rheology of clayey soils. 3rd edition [Eksperimental'naya reologiya glinistyh gruntov. Izdanie 3-e]*. Gitutyun, Yerevan (in Russian)

Roman, L. T. and Kotov, P. I. (2016). Viscosity of frozen and thawed soil. *Soil Mechanics and Foundation Engineering*, 53(1), pp. 1-23. http://dx.doi.org/10.1007/s11204-016-9358-8

Santa Maria, P. and Santa Maria, F. C. M. (2018). One-Dimensional Consolidation Considering Viscous Soil Behaviour and Water Compressibility - Viscoconsolidation. *Soils and Rocks*, 41(1), pp. 033-048. http://dx.doi.org/10.28927/SR.411033

Shirinkulov, T. SH. and Zareckij, YU.K. (1986). *Creep and soil consolidation [Polzuchest' i konsolidaciya gruntov]*. Fan, Tashkent (in Russian)

Ter-Martirosyan, Z. G. (1990). *Rheological parameters of soils and calculations of foundations of structures [Reologicheskie parametry gruntov i raschety osnovanij sooruzhenij]*. Strojizdat, Moscow, Russia (in Russian)

Ter-Martirosyan, Z. G. and Ter-Martirosyan A. Z. (2020). *Soil mechanics in high-rise construction with a developed underground part: a textbook [Mekhanika gruntov v vysotnom stroitel'stve s razvitoj podzemnoj chast'yu: uchebnoe posobie]*. ACB, Moscow, Russia (in Russian)

Yuan, J., Wang, T. J., Chen, J. and Huang, J. A. (2023). Microscopic mechanism study of the creep properties of soil based on the energy scale method. *Frontiers in Materials*, 10, pp. 1-8. http://dx.doi.org/10.3389/fmats.2023.1137728

Proceedings of the XVIII ECSMGE 2024
GEOTECHNICAL ENGINEERING CHALLENGES
TO MEET CURRENT AND EMERGING NEEDS OF SOCIETY
© 2024 the Authors
ISBN 978-1-032-54816-6
DOI 10.1201/9781003431749-152
Open Access: www.taylorfrancis.com, CC BY-NC-ND 4.0 license

ECSMGE 24
XVIII EUROPEAN CONFERENCE ON SOIL MECHANICS AND GEOTECHNICAL ENGINEERING

Applications of PS suspension logging test in port infrastructures

Applications de l'essai de diagraphie de la suspension PS dans les infrastructures portuaires

A. Tijera*, E. Asanza, R. Ruiz
Centro de Estudios y Experimentación de Obras Públicas, Madrid, Spain
Universidad Politécnica de Madrid, Madrid, Spain

**angel.tijera@cedex.es; a.tijera@alumnos.upm.es*

ABSTRACT: This work has its origin in a research project focused on the characterisation by geophysical methods of different materials present in port infrastructures and the seafloor on which they are founded. The study centered on obtaining the mechanical properties of the materials, so mainly seismic methods were applied. One of the most important conclusions of the study was the verification of the excellent results provided by the PS suspension logging test, which is the reason why this technique has subsequently been used in different technical assistance and research works applied in several Spanish ports. It is a very versatile technique as it only requires one borehole which can be cased or uncased and, in addition, the values of V_P and V_S can be obtained very accurately at any depth. This paper presents the results obtained with the PS suspension logging probe in different applications: temporal evolution of the stiffness of landfills and ground improvement treatments, localisation of the rocky substrate, checking the state of the concrete of old quays, characterisation of the natural seafloor for the construction of a new quay, etc. With these results, on the one hand, the main advantages of the PS logging probe are highlighted: versatility and accuracy; on the other hand, its most important limitations are also indicated: length of the probe and sensitivity to high seismic noise.

RÉSUMÉ: Ce travail trouve son origine dans un projet de recherche axé sur la caractérisation par des méthodes géophysiques de différents matériaux présents dans les infrastructures portuaires et le fond marin sur lequel elles sont fondées. L'étude s'est concentrée sur l'étude des propriétés mécaniques des matériaux, c'est pourquoi des méthodes sismiques ont été appliquées. L'une des conclusions les plus importantes de l'étude a été la vérification des excellents résultats fournis par le test de diagraphie de la suspension PS, raison pour laquelle cette technique a ensuite été utilisée dans différents travaux d'assistance technique et de recherche appliqués dans plusieurs ports espagnols. Il s'agit d'une technique très polyvalente car elle ne nécessite qu'un seul trou de forage qui peut être tubé ou non tubé et, en outre, les valeurs de V_P et V_S peuvent être obtenues avec une grande précision à n'importe quelle profondeur. Cet article présente les résultats obtenus avec la sonde PS dans différentes applications: évolution temporelle de la rigidité des décharges et des traitements d'amélioration du sol, localisation du substrat rocheux, vérification de l'état du béton des anciens quais, caractérisation du fond marin naturel pour la construction d'un nouveau quai, etc. Ces résultats mettent en évidence, d'une part, les principaux avantages de la sonde de diagraphie PS: polyvalence et précision ; d'autre part, leurs principales limites: longueur de la sonde et sensibilité aux bruits sismiques élevés.

Keywords: PS logging, port infrastructures, stiffness, S-wave.

1 INTRODUCTION

Between 2016 and 2019, a research project was conducted to characterize port fill materials and the underlying natural ground using various geophysical methods. The study aimed to find the most suitable combination of methods and compare results with other geotechnical tests for validation. In this study, it was of particular interest to understand the mechanical properties of the materials, so seismic methods were primarily applied.

The work was addressed in two phases: in the first, the effectiveness of different geophysical techniques applied was verified at a site where the geotechnical profile was known; The second phase consisted of the application of some of these methods to study the foundation of a maritime station to be built on a port reclamation land that has been in service for several years. One of the most important conclusions of the study was the verification of the excellent results provided by the PS suspension logging test (Tijera et al., 2019), which is the reason why this technique has

subsequently been used in different technical assistance and research works applied in several Spanish ports. It is a very versatile technique as it only requires one borehole which can be cased or uncased and, in addition, the values of V_P and V_S can be obtained very accurately at any depth.

In this paper, different applications of this technique in port infrastructures have been selected to illustrate its versatility.

2 PS SUSPENSION LOGGING

The PS suspension logging is employed to accurately determine the mechanical properties of the ground surrounding a borehole at various depths.

This technique involves measuring the propagation velocities of elastic waves (V_P and V_S) within a 1-meter radius around the borehole walls. The waves are induced by an impulsive source inside the equipment, necessitating the borehole to be filled with water or mud to ensure the transfer of disturbance from the source to the borehole walls and subsequently to the ground. The resulting waves, traveling parallel to the borehole axis, are detected by sensors positioned 1 meter apart in depth within the probe and recorded in a central unit (Kitsunezaki, 1980). The primary goal is to achieve precise measurements of ground properties through this logging technique.

Its main advantage is its precision at any depth. Its main weaknesses are high sensitivity to ambient noise, spurious vibrations (Tijera et al., 2023); and its length, the probe is about 6 m long.

3 APPLICATIONS

3.1 Characterisation of hydraulic fills and natural ground

In this initial example, a summary of the results obtained using PS suspension logging is presented in the context of a geotechnical study aimed at determining the design of the foundation for a maritime station in the Port of Ibiza. This work constituted the second phase of the research project mentioned in the introduction. The geophysical investigation was carried out in the esplanade of a dock that, at that time, was used for material storage. The esplanade was composed of a fill of clayey sands, and the main objective of the geophysical campaign was to identify the presence of the rock bed.

The measurement campaign, conducted in 2018, was divided into two trial groups: those performed from the surface and those carried out inside two previously drilled mechanical boreholes. From the surface, the Surface Wave Seismics (SASW) and Multichannel Analysis of Surface Waves (MASW) techniques were applied (Foti et al., 2017), while inside the boreholes, measurements were conducted using the PS logging probe, as well as electromagnetic and natural gamma probes (Ellis et al, 2007).

The combination of seismic methods both on the surface and inside the boreholes enhances the results, leveraging the accuracy of internal measurements and the extrapolation capability to large areas, such as port areas.

The PS logging probe played a crucial role in calibrating continuous measurements taken from the surface, allowing for a precise determination of the depth of the rock beneath the port area. In Figure 1, the results of V_S obtained through various techniques, namely PS logging, MASW, and SASW, are presented. The survey extensions for SASW and MASW, as depicted, were centered on the borehole where PS logging was introduced. The rock at that point was accurately located at a depth of 19 m, as indicated by the red dotted line in the figure. Measurements with the PS logging were made every 0.5 m depth. The spacing of the sensors in the SASW test varied between 0.5 m and 20 m. In the MASW tests, an array of 24 geophones spaced 2 m was used and moved along the entire length of the esplanade. The results are presented from the first-metre depth to avoid the high-velocity layer of the surface pavement.

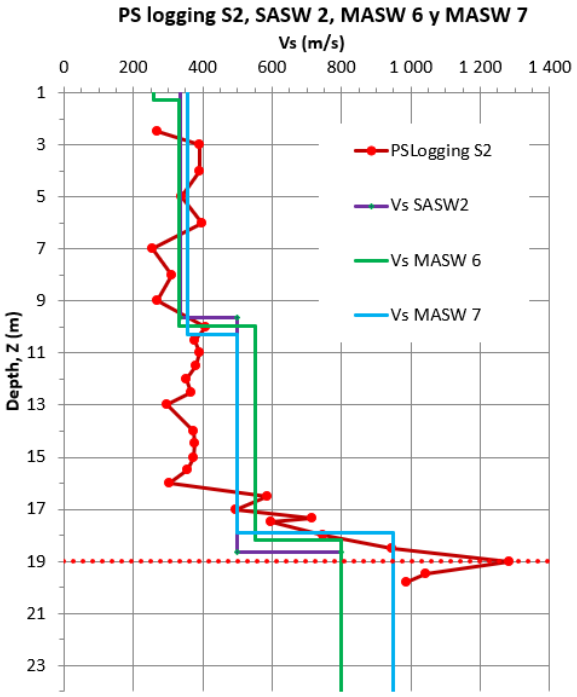

Figure 1. Vs values obtained with the different seismic tests in the vertical of one of the drilled boreholes. The rock is located 19 m at that point.

3.2 Assessment of the integrity and quality of port quays

The second example chosen to illustrate the good results of the PS probe is its application to study possible structural damage in a port quay. The work aimed at assessing the integrity and quality of a reinforced concrete diaphragm wall in the Port of Huelva, Spain, using a combination of field and laboratory tests. The diaphragm wall consists of 250 T-shaped elements which are strongly reinforced. Each element is 3 m wide and long and 0.6 m thick, and all of them are anchored to a rear passive wall. The depth of the diaphragm wall is 34 m, counting the capping beam (3 m). The contact with the seabed is 12 m from the surface. In 2018 a series of sinkholes appeared in the quay near the cantilever beam, prompting this research work.

The study employs seismic methods, including PS suspension logging tests and seismic tomography combining surface and borehole tests, to assess anomalies in wave propagation velocities (V_P and V_S) associated with material continuity loss. These tests help identify defects in the structure, particularly at joints. Additionally, laboratory tests, such as unconfined compression and ultrasonic pulse velocity tests on borehole specimens, are conducted to quantify concrete quality.

In 2019, a 3D ground-penetrating radar (GPR) campaign revealed anomalies near the capping beam, and a visual inspection exposed defects in joints. Subsequently, in May 2020, 5 vertical boreholes were drilled at different points of the quay to assess the condition of the concrete. The boreholes served multiple purposes: visual inspection, laboratory testing, seismic testing, and installation of inclinometer pipes for monitoring potential movements.

The field tests, including PS suspension logging and seismic tomography, consistently show high values of V_P and V_S below the capping beam, indicating good concrete quality. Laboratory tests on extracted cores further confirm the high quality of the concrete, with unconfined compression and ultrasonic pulse velocity values within ranges associated with excellent quality.

The study emphasizes the good correlation between field and laboratory results, reinforcing the conclusion that the concrete within the diaphragm wall is of good quality. PS logging played a key role in this study as it provided a link between the large-scale surface tests (tomography) and small-scale laboratory tests. The results obtained with PS logging helped to determine that the defects were in the joints, ruling out large losses of material inside each element. Figure 2 shows the values of V_P and V_S obtained in the different boreholes studied with PS suspension logging. The high velocity values indicate the good quality of the concrete in the section of the screen above the seabed (12 m), which is the area susceptible to material leakage. These results agree with those of the other tests:

- Seismic tomography: 4300 m/s<V_P<5000 m/s
- Laboratory tests: 4200m/s<V_P< 5000 m/s.

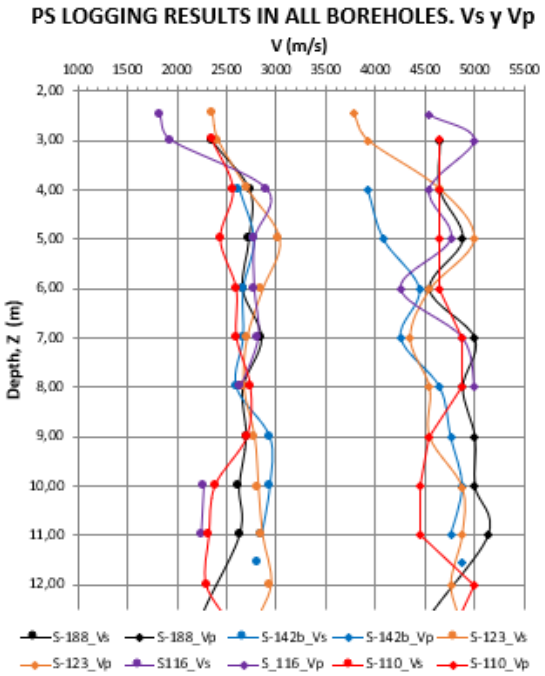

Figure 2. V_S and V_P values obtained in the different boreholes in the section of the screen above the seabed.

3.3 Time evolution of mechanical properties

Finally, to highlight the precision and versatility of this technique, two examples are presented next, in which it was used to study the temporal evolution of different materials that constitute part of port infrastructures. In the first, the short-term stiffening of soil subjected to an improvement treatment is verified. In the second, the long-term evolution of the natural ground under the fill in the platform of a maritime terminal is studied.

3.3.1 Short term

The Port Authority of Valencia conducted groundwork to increase the draft in the South Basin of the Port of Valencia. The project involved reinforcing dock foundations using jet grouting treatment in two phases at different locations. However, during the first phase, the leaning of caissons and differential movements occurred at the surface, prompting further monitoring. The main cause appeared to be differences in soil stiffness due to local strength loss during injection. Based on this problem, in the second phase of

execution, it was considered to search for a method to investigate the evolution of the stiffness of the columns, especially at early ages, between hours and days. To fulfill this main objective, PS suspension logging was used innovatively (Tijera et al., 2023).

Figure 3 shows the results obtained for V_S in the tests carried out during the first hours after the injection of the jet.

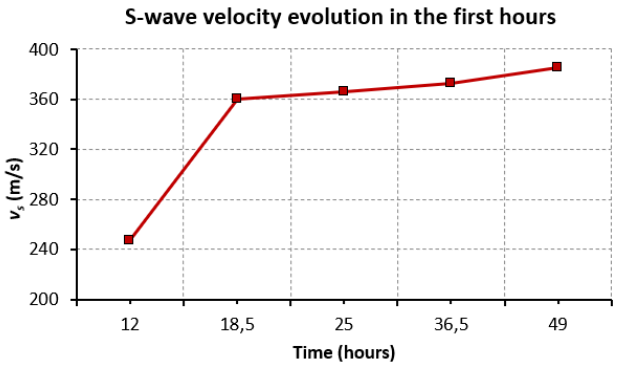

Figure 3. Obtained V_S values during the first hours after injection.

3.3.2 Long term

The study took place at the new container terminal of the Port of Cádiz, constructed using floating caissons and a closing dike. Hydraulic fills, mainly sands, were deposited on soft natural clays. Construction began in 2014, and in 2016, two boreholes were drilled for pressuremeter tests after an accelerated consolidation process. The boreholes were then protected with PVC pipes for the insertion of different geophysical probes. Since then, some PS logging measurements have been carried out at different times. The results are shown in Figure 4.

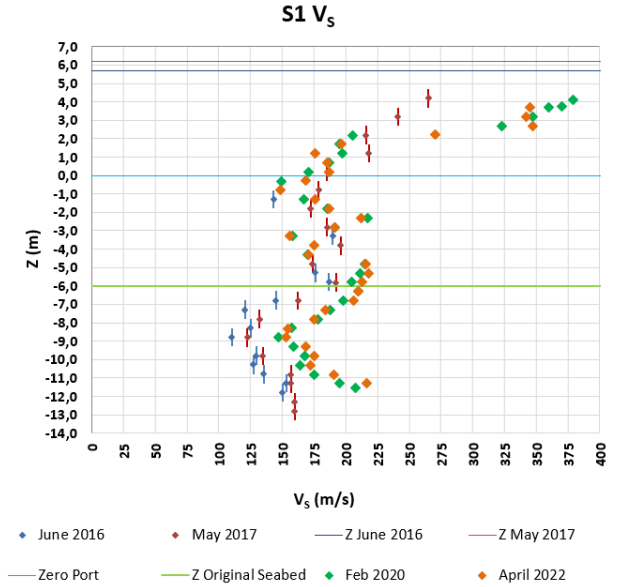

Figure 4. V_S values obtained at different times in one of the studied boreholes.

Even though the natural soil materials under the fill were undergoing a process of secondary consolidation from the beginning of the measurements, a slight increase in the V_S values could be observed. In Figure 4, the horizontal lines represent the height of the esplanade at different moments (red and dark blue), the zero level of the port (light blue), and the position of the original seabed (green).

4 CONCLUSIONS

The presented application cases have been chosen to demonstrate that the PS logging technique can be applied in studies with diverse objectives and showcase the main advantages of this technique: its versatility and precision.

Despite its great usefulness, its main drawbacks should not be forgotten: its high sensitivity to noise and the length of the probe.

ACKNOWLEDGEMENTS

All the works presented in this paper were carried out by the Geotechnical Laboratory of Centro de Estudios y Experimentación de Obras Públicas, CEDEX (R+D+i Centre of the Spanish Ministries of Transport and Environment). This study is part of the agreement that CEDEX and Puertos del Estado (the Spanish state-owned Port Agency) have subscribed for technical assistance and applied research in matters of interest for the Spanish state-owned port system.

REFERENCES

Ellis, D.V. (2007). *Well logging for earth scientist*. Springer, Dordrecht.

Foti, S., Lai, C., Rix, G. and Strobbia, C. (2017). *Surface Wave Methods for Near-Surface Site Characterization*. CRC Press, Taylor and Francis Group, Boca Raton, Florida.

Kitsunezaki C. (1980). A new method of shear wave logging. *Geophysics*, 45: 1489-1506.

Tijera A., Asanza E., Ruiz R., and Ruiz J.M. (2019). Geophysical and geotechnical characterization of soft marine soils in port infrastructures. *XVII European Conference on Soil Mechanics and Geotechnical Engineering, ISSMGE*, September 1-6. Reykjavik.

Tijera, A., Asanza, E., Galindo, R. and Burgos, M. (2023) Stiffness evolution of jet grouting columns performed under port caissons using PS suspension logging. *Near Surface Geophysics*, 21, 444–457. https://doi.org/10.1002/nsg.12258.

Proceedings of the XVIII ECSMGE 2024
GEOTECHNICAL ENGINEERING CHALLENGES
TO MEET CURRENT AND EMERGING NEEDS OF SOCIETY
© 2024 the Authors
ISBN 978-1-032-54816-6
DOI 10.1201/9781003431749-153
Open Access: www.taylorfrancis.com, CC BY-NC-ND 4.0 license

ECSMGE 24
XVIII EUROPEAN CONFERENCE ON SOIL MECHANICS AND GEOTECHNICAL ENGINEERING

On the modelling of state and history dependency of small strain stiffness of soils with application to 1D settlement analysis

Sur la rigidité des sols en petite déformations et son application pour analyse de tassement unidimensionnelle

A.B. Tsegaye*, J.-S. L'Heureux
Norwegian Geotechnical Institute, Trondheim, Norway

**anteneh.biru.tsegaye@ngi.no*

ABSTRACT: Soil mechanics is increasingly focusing on understanding the deformation characteristics of soils under small strains. At small strains, soil stiffness is notably high, but its decay with increasing shear strains or stresses is rather fast and nonlinear. Accounting for small strain stiffness is crucial for accurately calculating deformations and minimizing the influence of distant fields in numerical simulations of boundary value problems. This paper offers a comprehensive overview of factors, including state and loading history dependencies, that impact the shear modulus of soils. It introduces an explicit 1D small-strain model, expanding upon Janbu's stress-dependent stiffness, to incorporate small strain considerations into 1D settlement analysis.

RÉSUMÉ: L'un des domaines qui attirent l'attention en mécanique des sols est le comportement des sols à petite déformations. À ce niveau, la rigidité des sols est relativement élevée et décroit non-linéairement avec l'augmentation des contraintes. Le module de cisaillement à petite déformation est un paramètre crucial pour calculer précisément les déformations et pour minimiser l'influence des conditions limite en analyse numérique. Cet article présente une synthèse des facteurs qui influencent le module de cisaillement des sols. Un modèle 1D à petites déformations est proposé en utilisant le modèle à contrainte dépendante de Janbu lors d'analyse de tassement.

Keywords: Small strain stiffness; stress dependency of stiffness; soil deformation.

1 INTRODUCTION

Researches on soil stiffness indicate that the tangent shear modulus is a function of several state variables and history of loading (Länsivaara, 1999; Benz, 2007; Tsegaye, 2014)

$$G = f(\sigma, e, \gamma, S_r, c_i, F, T, S_s, H_l), \quad (1)$$

where σ is effective stress, e is void ratio, γ is shear strain amplitude, S_r is saturation level, c_i are soil properties linked to grain shape, size and grading, F is loading frequency, T is temperature, S_s is soil structure, H_l is loading history. The relevant variables may be combined in several ways. Several authors in the literatures put the various factors in a multiplicative form. Accordingly, Tsegaye (Tsegaye, 2014) wrote the shear modulus, G, as

$$G = \alpha_G f_e f_\sigma f_H f_\varepsilon p_a, \quad (2)$$

where α_G is a dimensionless parameter, sometimes also called shear modulus number and p_a is atmospheric pressure. The soil constant α_G is may depend on grain characteristics such as grain shape, size and grading, (Wichtmann et al., 2011). The functions f_e, f_σ, f_H, and f_ε take into account the dependence of the shear modulus on void ratio, effective stress, loading history and strain amplitude respectively. The stress dependency and the void ratio dependency may be collectively called *state dependency* whereas the strain and loading history dependency may be called *memory dependency*.

This paper presents a synthesis of factors that influence the shear modulus of soils at small strain. Following the review, application of small strain stiffness is demonstrated by enhancing Janbu's stress dependent stiffness using novel small strain overlay formulations.

2 STATE DEPENDENCY

State dependency includes stress dependency and void ratio dependency of stiffness. Each is briefly discussed in the sub-sections below.

2.1 Stress dependency

According to (Tsegaye, 2014), the stress dependency factor may be multiplicatively split into effective confining pressure dependency factor, f_p, and stress-ratio dependency factor, f_η, say $f_\sigma = f_p f_\eta$.

The effective confining pressure dependency of stiffness of soils was proposed as early as the late 1930's by (Ohde, 1939). On the basis of numerous oedometer and triaxial compression tests, (Janbu, 1963) proposed a formulation of soil stiffness as power function of stress. The usual form of the stress-dependency function is of the form

$$f_\sigma = f_p = \left(\frac{p}{p_a}\right)^n, \tag{3}$$

where p is the effective confining stress, n is the Ohde-Janbu stress dependency parameter that ranges between 0.5 and 1 for several types of soils. A similar power law has been proposed to describe stress dependency of stiffness in the small strain regime as well, *e.g.*, (Hardin and Drnevich, 1969). Some researchers use the minor effective principal stress instead of the effective confining pressure, *e.g.*, (Duncan and Chang, 1970; Schanz et al., 1999), Janbu's formulation is in terms of the axial (vertical) stress. In the literature, the geometric mean stress $(\sigma_i\sigma_j)^{\frac{1}{2}}$ has also been used for sands instead of the arithmetic mean, p (Ni, 1987; Hardin and Blandford, 1989) where σ_i and σ_j are the principal stresses in the plane G is measured.

When the stress dependency function is a function of the effective confining pressure alone, the resulting stiffness is none-conservative and may result in physically incorrect solution during repeated actions of loading-unloading (Zytynski et al., 1978; Lade and Nelson, 1987; Houlsby et al., 2005). To this end, several conservative stress-dependent elastic stiffness formulations have been proposed, *e.g.*, (Vermeer, 1980; Lade and Nelson, 1987; Molenkamp, 1988; Einav and Puzrin, 2004; Houlsby et al., 2005). For example, (Lade and Nelson, 1987) derived a conservative stress-dependent elastic shear modulus with the stress-dependency function specified as

$$f_\sigma = \left(\frac{p}{p_a}\right)^{2\lambda_1} f_\eta^{L-N}, \tag{4}$$

wherein f_η^{L-N} is the Lade-Nelson stress ratio dependency function and is given by

$$f_\eta^{L-N} = (9 + R\eta^2)^{\lambda_1}, R = 2\frac{1+\upsilon}{1-2\upsilon}, \tag{5}$$

R and λ_1 are material parameters. R is given in terms of Poisson's ratio, υ, (which is assumed constant.) According to (Lade and Nelson, 1987), all these parameters can be determined from conventional triaxial compression tests with unloading-reloading cycles. The Lade-Nelson exponent may be estimated with $\lambda_1 = \frac{n}{2}$, leading to a range of λ_1 roughly between 0.25 and 0.5. (Lade and Nelson, 1987) reported values of λ_1 between 0.2 and 0.3 for different types of sands.

2.2 Void ratio dependency

Interlocking and intergranular contacts decrease with increasing void ratio, e. It is generally known that the denser the soil, the higher is its shear stiffness. (Hardin and Richart, 1963) proposed $f_e = \frac{(a_e - e)^2}{1+e}$, where a_e depends on the nature and grading of soils (Hicher, 1996). In general, a_e in the range 1.4 - 7.3 has been reported, *e.g.*, (Hardin and Richart, 1963; Hardin and Black, 1968; Kokusho et al., 1982; Wichtmann and Triantafyllidis, 2004). The higher values are reported for clayey soils. The other redundantly appearing equation in the literature is an exponential function of the form, $f_e = e^{-x_e}$. Values of x_e between 1 and 2 have been reported, *e.g.*, (Lo Presti et al., 1993; Lo Presti and Jamiolkowski, 1998; Fioravante, 2000).

3 MEMORY DEPENDENCY

Soil stiffness is known to depend on both strain magnitude, stress and loading direction. This dependency may in general be referred to as memory dependency. This is briefly discussed in this section.

3.1 Strain dependency

The stiffness of soils is strain dependent in general. But the decay is highly nonlinear and faster in the small strain region. It is often postulated that the small strain region can be defined with a certain limit, say $f_\varepsilon \geq f_{\varepsilon-lim}$ although there is no agreement in the literature on the question "how small is small strain?" For example, (Atkinson, 2000) states that the strain range can be sub-divided into very small ($\gamma \leq 10^{-6}$), small ($10^{-6} \leq \gamma \leq 10^{-3}$) and large strain ($\gamma \geq 10^{-3}$). Moreover, (Bui, 2009) proposed sub-divisions and different ranges, namely: small strain ($\gamma \leq 10^{-5}$), medium strain ($10^{-5} \leq \gamma \leq 10^{-3}$), large strain

($10^{-3} \leq \gamma \leq 10^{-2}$) and failure strain ($\gamma > 10^{-2}$). The complexity of the stiffness-strain relationship even in this range is difficult to account for using proper elastic formulations.

There are various proposed formulations that aim at capturing the nonlinear decay of secant shear modulus with shear strain in the small strain regime. Several of those are in the form

$$f_\varepsilon = \frac{1}{1+a_\gamma\left(\frac{\gamma}{\gamma_{ref}}\right)^{\alpha_\gamma}}, \quad (6)$$

where γ is the shear strain, γ_{ref} is a reference shear strain, and a_γ, α_γ and γ_{ref} are model parameters (Tsegaye, 2014). Early proposition by (Hardin and Drnevich, 1969), for example, was $a = 1$, $\alpha_\gamma = 1$ and $\gamma_{ref} = \tau_{max}/G_{max}$, where τ_{max} is the maximum shear stress. (Stokoe et al., 2004) considered $a = 1$, $\alpha_\gamma = 1$ and $\gamma_{ref} = \gamma_{0.5}$. (Santos and Correia, 2001) modified the same equation considering $a_\gamma = 0.385$, $\alpha_\gamma = 1$ and $\gamma_{ref} = \gamma_{0.7}$. The reference shear strains $\gamma_{0.5}$ and $\gamma_{0.7}$ are shear strains at which the stiffness has decayed by 50% and 30% respectively. In (Benz, 2007), $\gamma_{0.7}$ is determined at a slightly different point, where the stiffness has degraded 27.8%. When a_γ and α_γ are fixed, only one parameter, namely γ_{ref} is required to define the strain dependency curve. A cut-off is required for using Eq. (6) as an overlay for enhancement of elastoplastic models. The cut-off criterion can be either in terms of stiffness or in terms of strain. Where there is lack of data, defining $\frac{\gamma_{cut-off}}{\gamma_{ref}} = 10$, the cut-off stiffness for the small strain overlay may be set $f_\varepsilon \geq (f_{\varepsilon-cut-off} \approx 0.2)$.

3.2 Loading history dependency

According to (Atkinson et al., 1990), the stiffness of overconsolidated soils depends not only on the current state but also on the stress history. They distinguish the stress history into the overall history "which may be best described by overconsolidation ratio" and the recent history "which may be related to a sudden change of direction or a period of time at constant stress." (Tsegaye, 2014) formulated this as

$$f_H = f_{OCR} f_\theta, \quad (7)$$

where f_{OCR} accounts for overconsolidation history dependency and f_θ considers recent loading history (in terms of magnitude and direction). (Hardin and Black, 1968) proposed $f_{OCR} = OCR^{n_o}$, where n_o is a material parameter. For granular materials such as sands, (Tsegaye, 2014) suggested that the ratio $\frac{e_c}{(e_c-\langle\Psi\rangle)}$ may be considered instead, where e_c is the critical state void ratio and Ψ is the state parameter according to (Been and Jefferies, 1985).

(Atkinson et al., 1990) performed laboratory tests on reconstituted overconsolidated samples of London Clay aiming at influence of rotation of stress on subsequent stiffness. Their test results demonstrated clearly that change of loading direction has a significant effect on stiffness of soils, *Figure 1b*.

At small stress ratio, it is seen that the stiffness increases linearly with the magnitude of the rotation angle of the stress path, the highest being for the 180 degrees, i.e., load reversal. However, this difference vanishes at higher mobilizations.

On the theoretical end, (Simpson, 1992) proposed a physical analogue to describe the effect of arbitrary changes of loading direction on stiffness of soils. He considered a man dragging a series of bricks that are tied on separate strings, *Figure 1a*. According to Simpson, if the man "walks continuously in one direction the brick will line up behind him and follow…if he turns back the bricks initially do not move then the ones on a shorter string start to move, gradually followed by the longer strings…if he turns 90^0, the bricks initially keep moving in their previous direction but gradually swing round behind him". Simpson formulated his ideas in strain space such that the man is taken a point in strain space, each brick represents the proportion of a soil element while the movement of a brick represents plastic strains and the difference between the movement of the man and the sum of the movements of the bricks represents elastic strains. (Länsivaara, 1999) proposed two hypotheses which are in line with Simpson's brick analogue. Namely, soil remembers stress history and that its stiffness depends thus on how the direction of the stress increment relates to the previous states; and that the recent stress history has the greatest influence on stiffness, while the effect of older stress states slowly diminishes to zero, *i.e.*, more weight should be placed on recent history. Few models have been developed based on the very recent stress (strain) history, *e.g.*, (Niemunis and Herle, 1997; Länsivaara and Nordal, 2001; Benz, 2007).

The higher stiffness observed at the beginning of loading and during the change of loading direction may also be alternatively reasoned as follows (Tsegaye, 2014). At the rest state of the soil mass that is in equilibrium, the soil grains are arranged in a stable configuration state. The degree of stability generally depends on the arrangement, the time it stayed in the given configuration state and the loading history it has been subjected to. Initialization of deformation

requires destabilizing this stable configuration and the initial resistance can be significantly high. Upon continuous loading, the order and interaction of particles changes (Klausner, 1991), the established resistance gives way to a new order in an attempt to form a new stable state that accommodates the external action if the action is sustained. Changing the loading direction would be once again met with a higher resistance until such a state change is accommodated. This concept is called *resistance of an established state to change* in (Tsegaye, 2014).

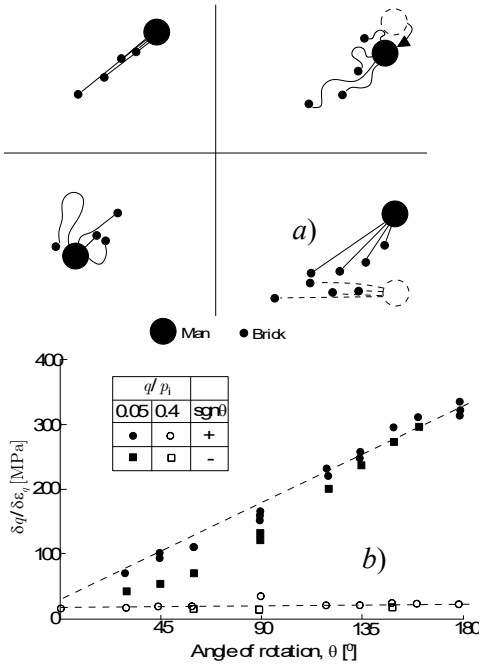

Figure 1. a) Simpson's brick illustration (Simpson, 1992)), b) Variation of stress path shear stiffness with change of direction in constant effective confining pressure laboratory tests on reconstituted London Clay after (Atkinson et al., 1990).

Let $G^{\theta} = m_{\theta} G_r$, where G^{θ} is the shear stiffness immediately after a change in the loading direction and G_r be a certain reference shear modulus. The reference shear modulus may be selected at the strain level where the influence of stress rotation has vanished by more than 90%, *i.e.*, swept out of memory, as (Gudehus, 1977) calls it. Let the factor m_{θ} at $\theta = 0^0$, 90^0 and 180^0 be given respectively by 1, m_{90} and m_{180} with $1 \geq m_{90} \geq m_{180}$. Assuming linear interpolation between these boundary conditions (Tsegaye, 2014) found:

$$m_{\theta} = m_{90} + (1 - 2m_{90} + m_{180})\theta^{+} \cos\theta + (m_{90} - m_{180}) \cos\theta, \quad \theta^{+} = \langle \mathrm{sgn}(\cos\theta) \rangle \tag{8}$$

where θ is the angle between the memorized previous loading direction and the current loading direction. Considering a linear increase of stiffness with $\cos\theta$ one may set $m_{90} = 1 + 0.5(m_{180} - 1)$.

The stiffness interpolation function can then be completely specified by specifying m_{180}. Where data is lacking $m_{180} = 5$ may be set. In addition, for virgin loading, $m_i G_r$, where $m_i = m_{180}$ may be considered.

We may further consider (Niemunis and Herle, 1997) intergranular strain formulation for the modelling the stiffness decay with strain. See (Tsegaye, 2014) for application of the intergranular strain concept to elastoplastic models. For the same, Eq. **(5)** may be extended as

$$m_{\theta} = m_{90\rho} + (m_{i\rho} - 2m_{90\rho} + m_{180})\theta^{+} \cos\theta + (m_{90\rho} - m_{180}) \cos\theta, \quad \theta^{+} = \langle \mathrm{sgn}(\cos\theta) \rangle \tag{9}$$

where $m_{90\rho} = m_{180} - \rho_I^{\chi}(m_{180} - m_{90})$, $m_{i\rho} = m_{180} + \rho_I^{\chi}(1 - m_{180})$, ρ_I is the normalized magnitude of the intergranular strain accroding to (Niemunis and Herle, 1997).

If the most recent memorized direction is say $\hat{\mathbf{h}}$ and the current loading direction is, say $\mathbf{d}$, the $\cos\theta$ in Eqs. (8) and (9) can be replaced by the scalar product $\hat{\mathbf{h}}:\mathbf{d}$, Figure 2.

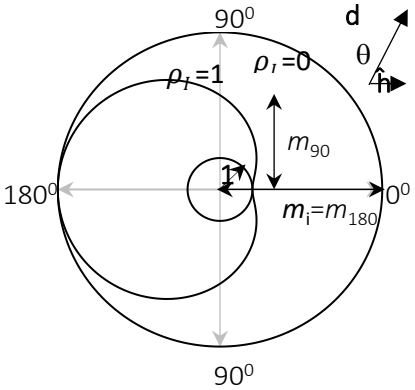

Figure 2. m_{θ} according to Eq. (9), $m_{90} = 1 + 0.5(m_{180} - 1)$, $m_i = m_{180} = 5$ considered.

4 APPLICATION OF SMALL STRAIN OVERLAY TO JANBU'S 1D SOIL STIFFNESS FORMULATION

In this section, we would like to demonstrate the small strain overlay approach in a 1D. For simplifying the treatment, let us set f_e and f_H to unity. An enhanced form of Janbu's stress dependent stiffness is considered such that the vertical stress increment, $\mathrm{d}\sigma_z$, is given by:

$$\mathrm{d}\sigma_z = \alpha_G r_v f_{\varepsilon} f_{\sigma} p_a \mathrm{d}\varepsilon_z, \; r_v = \frac{1-\nu}{1-2\nu}. \tag{10}$$

where $d\varepsilon_z$ is the vertical strain increment, v is Poisson's ratio, α_G is considered a soil constant, and f_ε and f_σ are defined respectively by

$$f_\varepsilon = \begin{cases} \dfrac{1}{\left(1 + a_\gamma a\left(\gamma/\gamma_{0.7}^{ref}\right)\right)^2}, G \geq G_r \\ 1, G < G_r \end{cases} \quad (11)$$

$$f_\sigma = (\sigma_z/p_a)^n, 0 \leq n \leq 1 \quad (12)$$

where G is the shear modulus at a given shear strain within the small strain limit. From experience, n may be set 0.5 for sandy and coarser materials and 1 for clay soils. The stress dependency equation can lead to a numerical issue when $\sigma_z = 0$. This may be resolved by adding attraction to both the numerator and the denominator in Eq (12).

Upon integration, for $0 \leq n < 1$, we have:

$$\left(\frac{\sigma_z}{p_a}\right)^{1-n} - \left(\frac{\sigma_{z,0}}{p_a}\right)^{1-n} = \frac{\alpha_G r_v (1-n) {\gamma_{0.7}^{ref}}^2 \left(\varepsilon_z - \varepsilon_{z,0}\right)}{\left(a_\gamma \varepsilon_{z,0} + \gamma_{0.7}^{ref}\right)\left(a_\gamma \varepsilon_z + \gamma_{0.7}^{ref}\right)} \quad (13)$$

and for $n = 1$,

$$\frac{\sigma_z}{\sigma_{z,0}} = \exp\left\{\frac{\alpha_G r_v \gamma_{0.7}^{ref}\left(\varepsilon_z - \varepsilon_{z,0}\right)}{\left(a_\gamma \varepsilon_{z,0} + \gamma_{0.7}^{ref}\right)\left(a_\gamma \varepsilon_z + \gamma_{0.7}^{ref}\right)}\right\} \quad (14)$$

It is natural to assume that the initial state is unstrained and hence $\varepsilon_{z,0} = 0$ which simplifies the equations further. Note that Eqs. (13) and (14) can be easily inverted.

During 1D settlement calculation, it is customary to limit the stress increment that causes settlement in an arbitrary depth where $\Delta\sigma_z \geq 0.2\sigma_{z0}$. This can now be more objectively set using a strain limit.

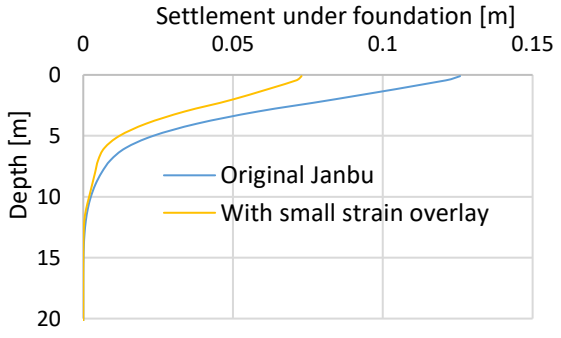

Figure 3. Comparison of original Janbu and small strain enhanced Janbu formulations in a 1D settlement analysis ($\alpha_G = 286$, $n = 1$, $\gamma_{0.7}^{ref} = 10^{-4}$, $a_\gamma = 0.385$. Janbu's original formulation is used beyond the small strain limit).

5 SUMMARY

This paper undertakes a comprehensive examination of soil stiffness at small strains, categorizing the factors influencing it into state and memory dependency. State dependency pertains to variables independent of a reference system, such as stress and void ratio, while memory dependency does not generally align with this criterion. Various formulations are explored to encompass the dependency of soil stiffness on both state and memory dependency, considering monotonic loading as well as changes in loading directions. Additionally, a straightforward 1D small strain overlay model is introduced to augment Janbu's stiffness formulation, illustrating the integration of small strain models with those designed for analysis of soil deformation at larger strains.

REFERENCES

Atkinson, J. H. (2000). Non-linear soil stiffness in routine design. *Géotechnique* 50(5): 487-508.DOI: https://doi.org/10.1680/geot.2000.50.5.487.

Atkinson, J. H., Richardson, D. and Stallebrass, S. E. (1990). Effect of recent stress history on the stiffness of overconsolidated soil. *Géotechnique* 40(4): 531-540.DOI: https://doi.org/10.1680/geot.1990.40.4.531.

Been, K. and Jefferies, M. G. (1985). A State Parameter for Sands. *Géotechnique* 35(2): 99-112.DOI: https://doi.org/10.1680/geot.1985.35.2.99.

Benz, T. (2007). Small strain stiffness of soils and its numerical consequences. PhD, Stuttgart University.

Bui, T. M. (2009). Influence of some particle characteristics on the small strain response of granular materials. PhD, University of Southampton: School of Civil Engineering and the Environment

Duncan, J. M. and Chang, C. Y. (1970). Nonlinear analysis of stress and strain in soils. *Soils and Found. Eng., ASCE*: 1629-1653.DOI: https://doi.org/10.1061/JSFEAQ.0001458.

Einav, I. and Puzrin, A. M. (2004). Pressure dependent elasticity and energy conservation in elastoplastic models for soils. *J. Geotech. Geoenviron. Eng.* 130(1): 81-92.DOI: 10.1061/(ASCE)1090-0241(2004)130:1(81).

Fioravante, V. (2000). Anisotropy of small strain stiffness of Ticino and Kenya sands from seismic wave propagation measured in triaxial testing. *Soils and Foundations* 40(4): 129-142.DOI: https://doi.org/10.3208/sandf.40.4_129.

Gudehus, G., Ed. (1977). Stability of saturated granular bodies under cyclic loads. Plastic and Long-term Effects in Soils. Karlsruhe, Balkema.

Hardin, B. O. and Black, W. L. (1968). Vibration modulus of normally consolidated clay. *Proc. ASCE* 94(SM2): 353-369.DOI: https://doi.org/10.1061/JSFEAQ.0001100.

Hardin, B. O. and Blandford, G. E. (1989). Elasticity of Particulate Materials. *J. Geotech. Eng. ASCE* 115(6): 788-805.DOI: https://doi.org/10.1061/(ASCE)0733-9410(1989)115:6(788.

Hardin, B. O. and Drnevich, V. P. (1969). Shear modulus and damping in soils: Design equations and curves. *Journal of Soil Mechanics and Foundations Division, ASCE* 95(SM6): 1531-1537.DOI: https://doi.org/10.1061/JSFEAQ.0001760.

Hardin, B. O. and Richart, F. E. (1963). Elastic wave velocities in granular soils. *Journal of Soil Mechanics and Foundations Division, ASCE* 89(SM1): 33-65.DOI: doi/10.1061/JSFEAQ.0000493.

Hicher, P. Y. (1996). Elastic properties of soils. *J. Geotech. Eng. ASCE* 122(8): 641-648.DOI: Doi 10.1061/(Asce)0733-9410(1996)122:8(641).

Houlsby, G. T., Amorosi, A. and Rojas, E. (2005). Elastic moduli of soils dependent on pressure: a hyperelastic formulation. *Géotechnique* 55(5): 383-392.DOI: DOI 10.1680/geot.55.5.383.66021.

Janbu, N. (1963). Soil compressibility as determined by oedometer and triaxial tests. *Proc. 3rd Eur. Conf. Soil Mech.*, Weisbaden.

Klausner, Y. (1991). *Fundamentals of Continuum Mechanics of Soils*. London, Springer-Verlag.

Kokusho, T., Yoshida, Y. and Esashi, Y. (1982). Dynamic properties of soft clay for wide strain range. *Soils and Foundations* 22(4): 1-18.DOI:
10.3208/sandf1972.22.4_1.

Lade, P. V. and Nelson, R. B. (1987). Modelling the elastic behavior of granular materials. *Int. J. Numer. Anal. Meth.Geomech.* 11: 521-542.

Lo Presti, D. C. F. and Jamiolkowski, M. (1998). Discussion: Estimate of elastic shear modulus in holocene soil deposits. *Soils and Foundations* 38: 263-265.

Lo Presti, D. C. F., Pallara, O., Lancellotta, R., Armandi, M. and Maniscalco, R. (1993). Monotonic and cyclic loading behaviour of two sands at small strains. *Geotechnical Testing Journal* 16(4): 409-424.DOI: https://doi.org/10.1520/GTJ10281J.

Länsivaara, T. (1999). A study on mechanical behaviour of soft clay. PhD, Norwegian University of Science and Technology.

Länsivaara, T. and Nordal, S. (2001). Loading history model for small strain behaviour of soils. *Proceedings of the 15th International Conference on Soil Mechanics and Geotechnical Engineering*, Istanbul, Turkey.

Molenkamp, F. (1988). A simple model for isotropic non-linear elasticity of frictional materials. *Int. J. Numer. Anal. Meth. Geomech.* 12: 467-475.DOI: https://doi.org/10.1002/nag.1610120502.

Ni, S.-H. (1987). Dynamic properties of sand under true triaxial stress state from resonant column / torsional shear tests PhD thesis, University of Texas.

Niemunis, A. and Herle, I. (1997). Hypoplastic model for cohesionless soils with elastic strain range. *Mechanics of Cohesive-Frictional Materials* 2(4): 279-299.DOI: 10.1002/(Sici)1099-1484(199710)2:4<279::Aid-Cfm29>3.0.Co;2-8.

Ohde, J. (1939). Zur theorie der Druckverteilung im Baugrund. *Der Bauingenieur* 20: 451-459.

Santos, J. A. and Correia, A. G. (2001). Reference threshold shear strain of soil. Its application to obtain a unique strain-dependent shear modulus curve for soil. . *15th Int. Conf. SMGE*, Istanbul.

Schanz, T., Vermeer, P. A. and Bonnier, P. G. (1999). Formulation and verification of the Hardening-Soil model. Beyond 2000 in Computational Geotechnics. Rotterdam, Balkema**:** 281-290.

Simpson, B. (1992). Retaining structures: displacement and design. *Géotechnique* 42(4): 541-576.DOI: https://doi.org/10.1680/geot.1992.42.4.541.

Stokoe, K. H., Darendeli, M. B., Gilbert, R. B., Menq, F.-Y. and Choi, W. K. (2004). Development of a new family of normalized modulus reduction and material damping curves. *International Workshop on Uncertainties in Nonlinear Soil Properties and Their Impact on Modeling Dynamic Soil Response*, UC, Berkley, Canada.

Tsegaye, A. B. (2014). On the Modelling of State Dilatancy and Mechanical Behaviour of Frictional Materials. PhD, Norwegian University of Science and Technology.

Tsegaye, A. B. (2014). On the Modelling of State Dilatancy and Mechanical Behaviour of Fritional Materials. PhD, Norwegian University of Science and Technology.

Vermeer, P. A. (1980). Formulation and analysis of sand deformation problems Dissertation, Delft University of Technology.

Wichtmann, T., Hernandez, M. N., Martinez, R., Graeff, D. and Triantafyllidis, T. (2011). Estimation of the small-strain stiffness of granular soils taking into account the grain size distribution curve. 5th International Conference on Earthquake Geotechnical Engineering. Santiago, Chile.

Wichtmann, T. and Triantafyllidis, T. (2004). Influence of a cyclic and dynamic loading history on dynamic properties of dry sand, Part I: cyclic and dynamic tensorial prestraining. *Soil dynamics and Earthquake Engineering* 24(2): 127-147.

Zytynski, M., Randolph, M. F., Nova, R. and Wroth, C. (1978). On modelling the unloading-reloading behaviour of soils. *Int. J. Numer. Anal. Meth.Geomech.* 2: 87-94.DOI: https://doi.org/10.1002/nag.1610020107.

Proceedings of the XVIII ECSMGE 2024
GEOTECHNICAL ENGINEERING CHALLENGES
TO MEET CURRENT AND EMERGING NEEDS OF SOCIETY
© 2024 the Authors
ISBN 978-1-032-54816-6
DOI 10.1201/9781003431749-154
Open Access: www.taylorfrancis.com, CC BY-NC-ND 4.0 license

ECSMGE 24
XVIII EUROPEAN CONFERENCE ON SOIL MECHANICS AND GEOTECHNICAL ENGINEERING

The influence of clay and silt content on reducing stiffness of soil in a small range of strains

L'influence de la teneur en argile et en limon sur la réduction de la rigidité de sol dans une petite gamme de souches

W. Tymiński*, T. Kiełczewski, P. Stajszczak
GEOTEKO Geotechnical Consultants, Warsaw, Poland

**wojciech.tyminski@geoteko.com.pl*

ABSTRACT: Stiffness parameters are defined as the ratio of stress to strain and depend on many factors, e.g. on soil type, stress conditions, stress history. The stress–strain behaviour of soil is highly non-linear. Therefore, the moduli - i.e. parameters characterizing soil stiffness - are not constant and, in addition to the previously mentioned factors, also depend on the deformation level. The initial soil stiffness is assumed as moduli values for strains smaller than approximate $1x10^{-4}$%. It can be determined on the basis of shear wave velocity measurement or tests in a resonant column. It is assumed that these are non-destructive tests, carried out in the range of very small soil strains. Resonant column test allows to determine the shear modulus in the range of shear strains 10^{-4}÷10^{-1}%. As the deformation increases, the soil stiffness decreases. The change in stiffness occurs faster for less cohesive soils than for very cohesive soils. The paper presents the analysis of resonant column test results in terms of soil stiffness reduction along with deformation for different soils. The authors of the paper proposed a relationship between shear modulus and values of shear strains based on the initial stiffness and basic soil index properties.

RÉSUMÉ: Les paramètres de rigidité sont définis comme le rapport entre la contrainte et la déformation et dépendent de nombreux facteurs, par exemple du type de sol, des conditions de contrainte, de l'histoire de la contrainte. Le comportement contrainte-déformation du sol est fortement non linéaire. Par conséquent, les modules - c'est-à-dire les paramètres caractérisant la rigidité du sol - ne sont pas constants et, en plus des facteurs mentionnés précédemment, dépendent également du niveau de déformation. La rigidité initiale du sol est supposée correspondre aux valeurs du module pour des déformations inférieures à 1x10-4%. Elle peut être déterminée sur la base d'une mesure de la vitesse des ondes de cisaillement ou d'essais dans une colonne résonante. On suppose qu'il s'agit d'essais non destructifs, réalisés dans le domaine des très petites déformations du sol. L'essai sur colonne résonante permet de déterminer le module de cisaillement dans la plage de déformations de cisaillement 10-4÷10-1 %. À mesure que la déformation augmente, la rigidité du sol diminue. Le changement de rigidité se produit plus rapidement pour les sols moins cohérents que pour les sols très cohérents. L'article présente l'analyse des résultats des tests de la colonne résonante. Les résultats des tests ont été analysés en termes de réduction de la rigidité du sol ainsi que de déformation pour différents sols. Les auteurs de l'article ont proposé une relation entre le module de cisaillement et les valeurs des déformations de cisaillement, basée sur les propriétés de rigidité initiale et d'indice de base du sol.

Keywords: Soil stiffness; resonant column tests; small strains.

1 INTRODUCTION

In the resonant column device, it is possible to determine soil stiffness expressed by shear modulus (G) also called Kirchoff's modulus, in the range of small strains; γ: 10^{-4}÷10^{-1}% (Atkinson and Sallfors 1991, Mair 1993). According to ASTM D4015, ASTM D8295 the value of modulus obtained in the range of strains γ: 10^{-4} is taken as the maximum value (G_0 or G_{max}). This value is called the initial soil stiffness and can also be determined from the shear wave velocity propagation in soil. The studies on the soil stiffness concept in the range of small strains, based on laboratory results, have led to the development of empirical formulae to estimate the maximum values of shear modulus G_{max} in an indirect manner (e.g. Hardin and Black, 1968; Kim and Novak, 1981). The empirical equations describing the reduction of shear modulus (G) with shear strains (γ) were proposed by among others, Ishibashi and Zhang (1993); Darendeli (2001); Zhang et al. (2005); Kallioglou et al. (2008); Vardanega and Bolton (2013). The computational formulae proposed in the literature allow the approximation of small strain behaviour of soil considering: selected soil index properties, expressed

by plasticity index (PI) and void ratio (e), stress history, expressed by overconsolidation ratio (OCR), effective stress, applied to the soil sample tested, correction factors, adopted in the individual calculation formulas.

The scope of application of the formulae developed so far may be limited to specific soil types. The formulae described in the work of Vardanega and Bolton (2013) allow reliable distributions of G/G_{max} values as a function of shear strain γ for cohesive soils of plasticity index (10-150%); and void ratio, (0.480-6.150). The equations proposed by them predicted over 90% of the G/G_{max} ratios within a margin of +/-30% across the full range of values from 0 to 1.0 for all soils, with the exception of certain London Clay data. Ishibashi and Zhang (1993) analysed available in literature experimental data and attempted to establish unified formulas for shear moduli to cover wide variety of soils ranging from sands to highly plastic clays such as Mexico City clay. Empirical relationships to evaluate reduction of the normalized stiffness (G/G_{max}) together with the shear strains (γ) are also formulated for non-cohesive soils (e.g. Oztoprak & Bolton (2013)). The parameters such as effective stress, plasticity index PI, void ratio (e) and overconsolidation ratio OCR are the components of most of the proposed equations describing G/G_{max} vs. γ relations. However, it should be noted that these parameters are determined indirectly and in extreme cases their values may be subject to considerable error or, in case of plasticity index, may be completely impossible to determine (soils bordering on fine- and coarse-grained soils - ISO 17892-12). In this study, a formula is proposed to predict the reduction of the normalised stiffness (G/G_{max}) together with the shear strains (γ) taking into account the changes in clay and silt fractions content. (fines content FC<0.063mm). The proposed relationship applies to cohesive, pre-consolidated soils.

2 CHARACTERISTIC OF TESTED SOILS

The tested soil samples came from the area of Poland, also from the areas located in the Baltic Sea. The basic index properties of the tested soils are presented below (Table 1). Index properties tests were performed in accordance with ISO 17892 group of standards. The analysed soils are mainly clay with sand and silt. (see Table 1).

Table 1. Index properties of tested soils

Sample	Depth	Gravel	Sand	Silt	Clay	Silt+Clay	Type of soil according to PN-EN ISO 14688-2:2006	Natural water content	Plastic limit	Liquid limit	Plasticity index	Liquidity index	Consistency index
								w	**w_p**	**w_L**	**PI**	**LI**	**I_C**
	m	**[%]**	**[%]**	**[%]**	**[%]**	**[%]**		**[%]**	**[%]**	**[%]**	**[%]**	**[-]**	**[-]**
1	5.4	1	25	46	28	74	sasiCl	31.4	15	38	23	0.71	0.29
2	28.8	4	41	32	23	55	saCl	12.9	15	25	10	-0.26	1.26
3	30.4	0	28	47	25	72	sasiCl	25.1	32	48	16	-0.43	1.43
4	33.8	0	33	44	23	67	sasiCl	20.4	20	42	22	0.02	0.98
5	35.1	4	50	28	18	46	sasiCl	8.8	12	24	12	-0.27	1.27
6	35.2	4	20	43	33	76	Cl	21.9	15	31	16	0.43	0.57
7	40.6	0	46	33	21	54	sasiCl	20.2	27	35	8	-0.85	1.85
8	41.1	1	24	45	30	75	saCl	19.2	15	30	15	0.29	0.71
9	44.0	0	41	39	20	59	sasiCl	19.2	23	40	17	-0.22	1.22
10	58.1	0	3	41	56	97	Cl	21.3	29	54	25	-0.31	1.31

3 RESONANT COLUMN TESTS

The tests were performed in a resonant column manufactured by GDS Instruments (Stokoe Type – Figure 1). According to ASTM D4015, this is a Fixed-Base - Type 1 (DT1) column where the passive end platen is connected to the fixed base (no torque transducer). The test comprised three stages: back pressure saturation, isotropic consolidation (overload), isotropic consolidation (unload) and a resonant test for several different vibration amplitudes. Based on the resonant frequencies, the moduli of elastic strain (G) were calculated for elastic strains in the variation range of approx. $5x10^{-5}$ to 10^{-1}%. The stress conditions under which the tests were carried out are shown below in Table 2. The results of the resonant column tests are shown in Figure 2 as a plot of the reduction of normalised shear modulus against shear strain.



Figure 1. Fixed-Base - Type 1 Resonant Column made by GDS Instruments

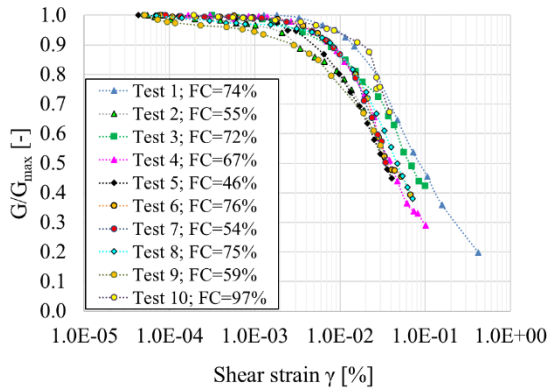

Figure 2. G/G_{max} reduction curves from resonant column tests.

Table 2. Values of consolidation stress applied during resonant column tests.

Sample	Test name	Consolidation stress	
		I Stage overloading	II Stage unloading
		[kPa]	[kPa]
1	Test 1	40	30
2	Test 2	900	360
3	Test 3	900	340
4	Test 4	900	330
5	Test 5	900	490
6	Test 6	900	380
7	Test 7	900	500
8	Test 8	900	480
9	Test 9	900	480
10	Test 10	900	540

4 ANALYSIS OF TEST RESULTS

The test results confirm that reduction of soil stiffness with deformation is more pronounced for low-cohesive soils than for very cohesive soils (e.g. Vutecic and Dobry 1991). In Figure 3, the relationship between G/G_{max} and fines content is presented on the basis of the obtained test results. The relationship is described by the linear equation:

$$\frac{G}{G_{max}} = a \cdot FC + b \quad (1)$$

where: a – slope, b – intercept, FC – fines content (<0.063 mm)

As it can be seen in Figure 3 for some tests no G/G_{max} value was obtained for a strain of 0.04%. The results for this strain value were not considered for further analyses. Both parameter 'a' and 'b' vary with the shear strains. The following equations describing the relationship are proposed (Figure 4).

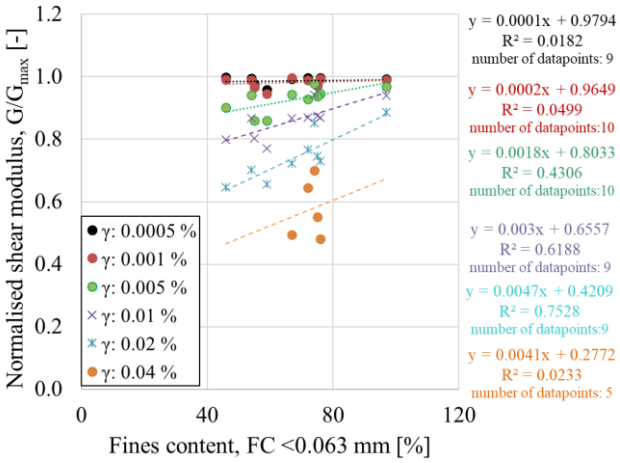

Figure 3. Relationship between G/G_{max} and fines content.

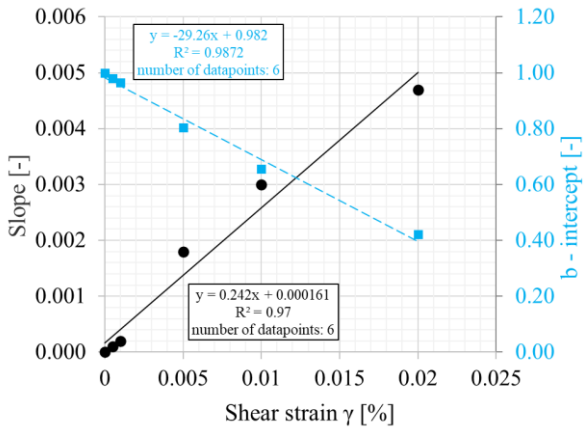

Figure 4. Relationship between parameters a,b and shear strain.

Using the above relationships, the following equation was proposed from which the value of G/G_{max} can be estimated.

$$\frac{G}{G_{max}} = (0{,}242\gamma + 0{,}000161) \cdot FC - 29{,}26\gamma + 0{,}982 \quad (2)$$

The comparison of the G/G_{max} values obtained directly from the tests and based on the proposed equation for the three selected tests is shown below

in Figure 5. Soils with different fine fraction contents were selected for comparison. The next figure (Figure 6) presents the compatibility of obtained values depending on the shear strains. The largest scatter of results was obtained for shear strains of 0.04%. This can be concluded to represent the limit of applicability of the proposed formula.

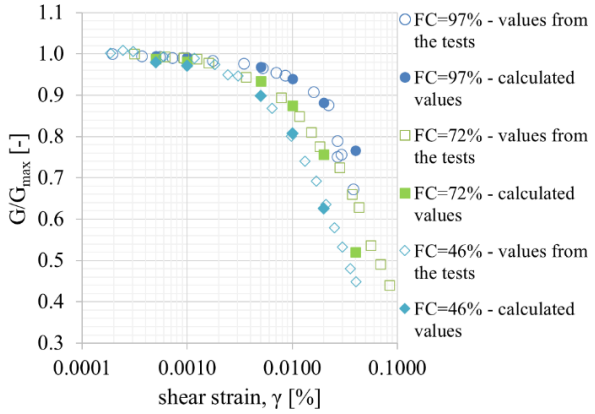

Figure 5. $G/G_{max} - \gamma$ curves obtained directly from the tests and from the proposed equation.

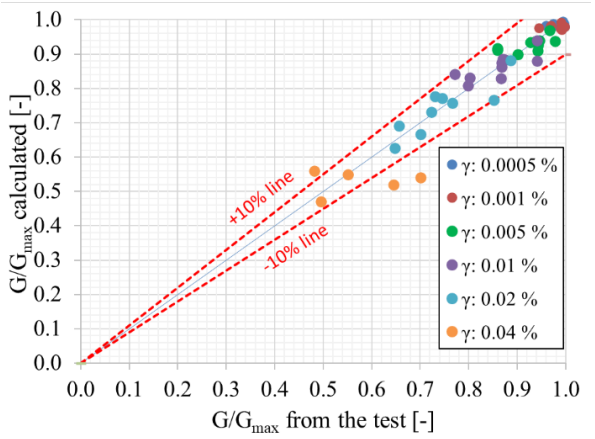

Figure 6. Comparison of G/G_{max} values obtained from the tests and from the proposed equation.

5 CONCLUSIONS

The following conclusions can be drawn from the tests carried out:

- The results of the normalised shear modulus (G/G_{max}) obtained directly from laboratory tests and from the proposed empirical formula are comparable. According to the authors, the proposed formula can be used to estimate (G/G_{max}) values for different cohesive preconsolidated soils.
- Calculated values of normalised shear modulus for shear strains above 0.04% differ significantly from the results obtained from the tests. Therefore, the value of shear strains 0.04% is a limitation of the applicability of the proposed formula.
- The G/G_{max} values calculated from equation (2) do not differ from the measured values by more than +/- 10% of the measured value (Figure 6).
- The proposed formula is based only on fines contnent. The soil stiffness depends on many other factors (effective stress, stress history, void ratio, soil cementation), and the given solution can be used for preliminary estimation of G/G_{max} values.

REFERENCES

Atkinson, J. H.; Sallfors, G. (1991) Experimental determination of soil properties. General Report to Session 1, *Proceedings of 10th ECSMFE*, Florence, Vol. 3, pp. 915–956.

Darendeli, M.B. (2001) Development of a new family of normalized modulus reduction and material damping curves. Ph.D. Thesis, The University of Texas at Austin, Austin, TX, USA.

Hardin, B.O.; Black, W.L. (1969) Vibration modulus of normally consolidated clay–closure. *Journal of the Soil Mechanics and Foundations Division*, 95, 1531–1537. https://doi.org/10.1061/JSFEAQ.0001364[DOI].

Ishibashi, I.; Zhang, X. (1993) Unified dynamic shear moduli and damping ratios of sand and clay. *Soils and Foundations*, 33, 182–191. https://doi.org/10.3208/sandf1972.33.182[DOI].

Kallioglou, P.; Tika, T.H.; Pitilakis, K. (2008) Shear Modulus and Damping Ratio of Cohesive Soils. *Journal of Earthquake Engineering*, 2, 879–913. https://doi.org/10.1080/13632460801888525[DOI].

Kim, T.; Novak, M. (1981) Dynamic properties of some cohesive soils of Ontario. *Canadian Geotechnical Journal*, 18, 371–389. https://doi.org/10.1139/t81-044[DOI].

Mair, R.J. (1993). Developments in geotechnical engineering research: application to tunnels and deep excavations. *Proc. Inst. Civil Engineers*, Civil Engineering. 93, 27-41.

Oztoprak, S. and Bolton, M. D. (2013). *Stiffness of sands through a laboratory test database*. Geotechnique 63, No. 1, 54–70. https://doi.org/10.1680/geot.10.P.078[DOI].

Vardanega, P.J.; Bolton, M.D. (2013) Stiffness of clays and silts: Normalizing shear modulus and shear strain. *Journal of Geotechnical and Geoenvironmental Engineering*, 139, 1575–1589. https://doi.org/10.1061/(ASCE)GT.1943-5606.0000887[DOI].

Vucetic, M. and Dobry, R. (1991) Effect of Soil Plasticity on Cyclic Response. *Journal of Geotechnical Engineering*, 117, 89-107.

Zhang, J.; Andrus, R.D.; Juang, C.H. (2005) Normalized shear modulus and material damping ratio relationships. *Journal of Geotechnical and Geoenvironmental Engineering*, 131, 453–464. https://doi.org/10.1061/(ASCE)1090-0241(2005)131:4(453)[DOI].

Proceedings of the XVIII ECSMGE 2024
GEOTECHNICAL ENGINEERING CHALLENGES
TO MEET CURRENT AND EMERGING NEEDS OF SOCIETY
© 2024 the Authors
ISBN 978-1-032-54816-6
DOI 10.1201/9781003431749-155
Open Access: www.taylorfrancis.com, CC BY-NC-ND 4.0 license

ECSMGE 24
XVIII EUROPEAN CONFERENCE ON SOIL MECHANICS AND GEOTECHNICAL ENGINEERING

Geotechnical and structural design of primary support for shaft and tunnelling construction works at Santos station-Lisbon subway - a 3D FE modelling approach

Conception Géotechnique et Structurelle du Support Primaire pour les Travaux de Construction de Puits et de Tunnels à la Gare de Santos - Métro de Lisbonne. Une Approche de Modélisation aux EF 3D

M. Unas*, S. Ferreira, F. Bernardo, R. Pistone
COBA, Consultores de Engenharia e Ambiente, S.A., Lisboa, Portugal

R. Pina
Metropolitano de Lisboa, Lisboa, Portugal

A. Tavares
Metro Santos Sodré ACE, Linda-a-Velha, Portugal

m.unas@cobagroup.com

ABSTRACT: As part of the extension of the Yellow and Green lines of the Lisbon Subway, the underground alignment of lot 2 starts at Santos Station and runs southwards ending at the terminal of the Cais do Sodré Station. The design of a new underground station – Santos Station has been considerably demanding. The highly complex geological and geotechnical challenges and the constraints related to surface occupation in a densely populated part of the city, where ground movement assessment is paramount, played a significant role in the selection of available design options for enabling the shaft and tunnelling works of the station. The geological and geotechnical challenging conditions are expressed by highly complex multi-layered terrain with formations of diverse nature such as Made Ground, Miocene formation, the upper cretaceous Lisbon Volcanic Complex, and the underlying Cretaceous formation. The scope of the article is to provide an insight of the achievements made by means of the design tool that has been adopted for the assessment of the stress and strain conditions of the surrounding ground due to the shaft and tunnelling construction works, as well as the assessment of forces and displacements on the primary support, enabling the carrying-out of stability checks and design optimization. As such, for this purpose, 3D FE models (Plaxis 3D 2022.01) have been developed. The ground and groundwater conditions, the constitutive modelling of ground behaviour, the structure-ground-structure interaction and the construction sequence of the shaft and tunnelling works have been comprehensively considered in these analyses.

RÉSUMÉ: Dans le cadre du prolongement des lignes Jaunes et Vertes du Métro de Lisbonne, le tracé souterrain du lot 2 commence à la gare de Santos et se dirige vers le sud pour se terminer au terminal de la gare de Cais do Sodré. La conception d'une nouvelle station de métro – la gare Santos – a été très exigeante. Les défis géologiques et géotechniques très complexes et les contraintes liées à l'occupation de la surface dans une partie densément peuplée de la ville, où l'évaluation des mouvements de terrain est primordiale, ont joué un rôle important dans la sélection des options de conception disponibles pour permettre les travaux de puits et de tunnels de la station. Les conditions géologiques et géotechniques difficiles s'expriment par un terrain multicouche très complexe avec des formations de nature diverse telles que terrain remblayé, la formation du Miocène, le Complexe Volcanique de Lisbonne du Crétacé supérieur et la formation sous-jacente du Crétacé. Le but de l'article est de donner un aperçu des réalisations réalisées grâce à l'outil de conception qui a été adopté pour l'évaluation des conditions de contrainte et de déformation du sol environnant dues aux travaux de construction de puits et de tunnels, ainsi que les évaluation des efforts et des déplacements sur le revêtement primaire, permettant de réaliser des contrôles de stabilité et d'optimiser la conception. À cet effet, des modèles Plaxis 3D 2022.01 ont été développés. Les conditions du sol et des eaux souterraines, la modélisation constitutive du comportement du sol, l'interaction structure-sol-structure et la séquence de construction des travaux de puits et de tunnel ont été largement prises en compte dans ces analyses.

Keywords: Constitutive modelling of ground behaviour; structure-ground-structure interaction; staged construction; 3D FE modelling; tunnelling design.

1 INTRODUCTION

The primary support works at Santos Station may be categorised into 4 parts: Central shaft, access shaft, underground works - north side, and underground works - south side.

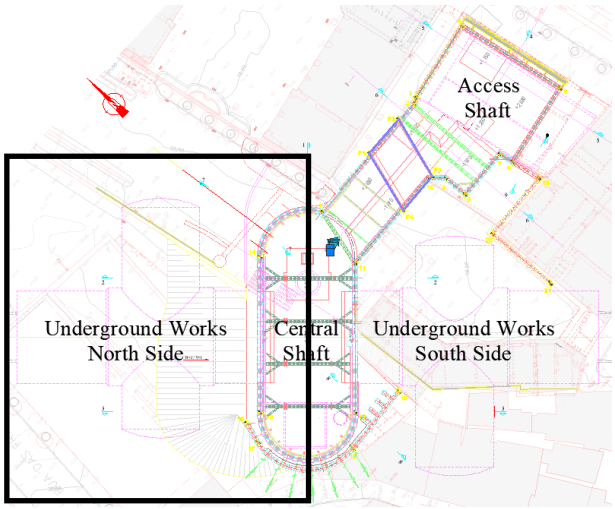

Figure 1. Plan view of primary support works at Santos Station.

The present article will be focused on the modelling procedures that have been developed for enabling tunnelling design check on the northern side of the underground works.

2 MODEL OVERVIEW

The 3D FE model considers the northern half of the central shaft, the central gallery, and the transversal gallery of the underground works on the northern side of Santos Station.

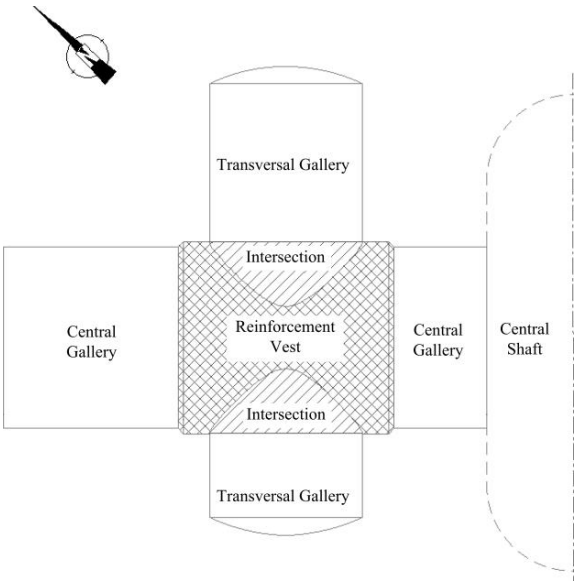

Figure 2. Plan view of the northern side of Santos Station.

The works started with the construction of a local pile wall, consisting in the installation of 0.8m diameter and 1m spaced contiguous piles, for enabling the creation of the working site at level 21.6mAOD from where the shaft construction will take place.

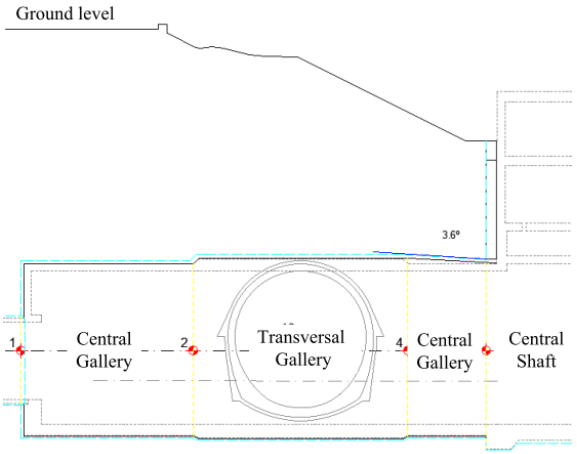

Figure 3. Longitudinal profile of the northern side of Santos Station.

The 45m long, 16m wide (total) and 30m deep central shaft comprises the installation of 1m diameter reinforced concrete piles spaced by 1.5m, a sequence of excavation down to design levels (20.3mAOD, 14.2mAOD, 9.23mAOD, 4.03mAOD, -1.07mAOD and -8.84mAOD) followed respectively by the installation of propping and/or anchoring sub-structures (21.1mAOD, 15.0mAOD, 9.9mAOD, 4.8mAOD, -0.5mAOD and -0.3mAOD).

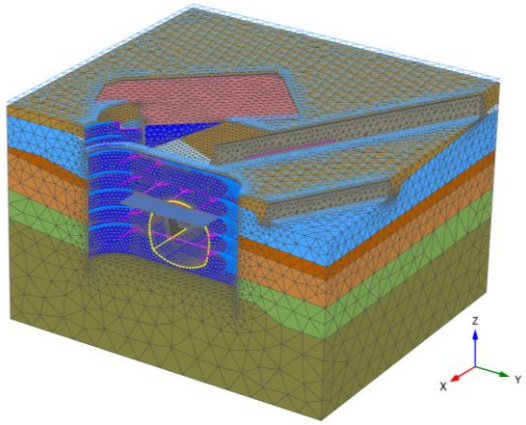

Figure 4. Plaxis 3D FE model of the primary support works of the northern side of Santos Station (Plaxis 3D).

The size of the 3D FE model has been established for ensuring that forces and displacements on the primary support are not impacted by the effects of the boundary fixity conditions. As such, the dimensions of the model are approximately 100m by 100m in plan view and 65m in height ($Z_{máx}$=28.7mAOD and Z_{min}=-35mAOD).

3 DESIGN STRATEGY

The tunnelling design strategy consisted in the development of a 3D FE model that is implicitly and explicitly capable of providing reliable output results for performing safety check calculations, according with the NP EN 1992 (EC2), NP EN 1993 (EC3) and NP EN 1997 (EC7), for all the failure mode mechanisms that have been identified. In order to accomplish such goal, the 3D FE model considered the following features:

- the heterogeneity of geological and geotechnical ground conditions;
- groundwater conditions and respective dewatering effects in the primary support;
- spatial distribution of loading conditions at the ground surface;
- ground-structure interaction and boundary conditions;
- explicit modelling of reinforcement elements of the primary support;
- ageing of shotcrete along the staged construction;
- comprehensive modelling of construction sequence of shaft and tunnelling works.

3.1 Modelling of ground conditions

The geological conditions at the Santos Station site, shown below in Figure 5, are characterized by a top Made Ground layer overlying a sequence of Miocene formation (blue layers) and the upper cretaceous Lisbon Volcanic Complex (CVL) which is composed by weathered and fractured Basalt (dark brown layer) overlying Tuffs (light brown layer). Underlying the CVL formation it has also been identified the presence of the Bica Limestone formation (green layers).

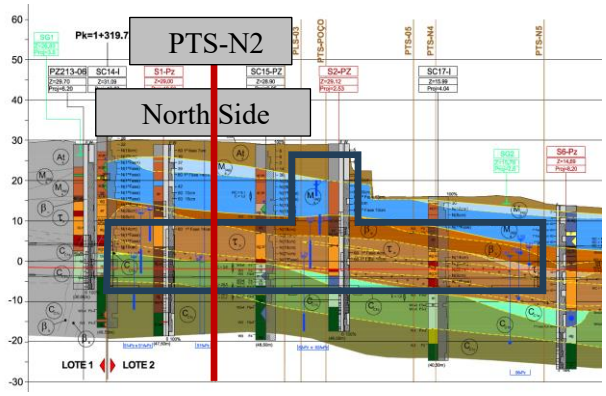

Figure 5. Geological and geotechnical longitudinal profile at Santos Station.

As it can be seen above in Figure 5, the tunnelling works are mainly developed through CVL materials i.e., generally highly fractured, and weathered Basalts and Tuffs. With greater expression on the northern side of the tunnelling works, the underlying cretaceous Limestone is also foreseen to be intersected throughout the excavation of the lower bench.

The idealised ground model on the northern side of the tunnel considers a critical geological cross-section (PTS-N2) while maintaining constant the thickness of strata along the longitudinal axis of the tunnel.

While the behaviour of the cretaceous Limestone (Bica Formation) has been modelled by means of the Hoek-Brown constitutive model for the remaining strata (Soils and Weathered Rock) a Hardening Soil like behaviour has been adopted, given that these materials are deemed to exhibit stress dependent stiffness.

Provided the temporary nature of the works under assessment, undrained behaviour has been assigned to the cohesive Miocene Formation.

3.2 Groundwater conditions

The piezometric readings and the observed waterflow concentrated in the region of Santos Station suggests that the underground works are likely to occur partially below the groundwater table. As such, for design purposes an initial groundwater table (GWT) at 14.8mAOD has been assumed.

During the tunnelling works a system of systematic drainage holes have been installed along the contour of excavation, especially in formations like the Cretacic where the presence of groundwater is likely. This has been thus implicitly considered by means of imposing localised dewatering conditions at the tunnel location down to the desired levels (Z=-0.5mAOD for top heading excavation and Z=-9.5mAOD for bench excavation).

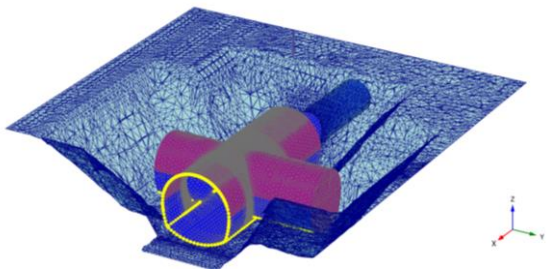

Figure 6. Groundwater surface condition for dewatering at level Z=-9.5mAOD (Plaxis 3D).

3.3 Loading conditions

Permanent and variable loading conditions have been considered such as the self-weight of the ground, groundwater, primary support, and existing structures. In places where ground surface circulation is possible a nominal live load of 10kPa has been assigned, with its magnitude conveniently adjusted for Ultimate Limit State (ULS) calculations.

3.4 Ground-structure interaction

The volume elements that are modelling existing structures at the ground surface level and the plate elements modelling the shaft have been provided with interface elements for mobilising an interface strength reduction of 0.7 (R_{inter}~2/3φ′). The plate elements modelling the primary support of the tunnel have been provided with interface elements with R_{inter}=1.0 for simulating a rigid condition between the shotcrete and the surrounding ground.

3.5 Boundary conditions

In terms of the boundary conditions of the model, the bottom boundary is fully fixed, the lateral boundaries are all normally fixed and the upper boundary is free for deformation.

The connectivity conditions between structural elements with limited capacity for loading transfer has been considered between the central shaft and the tunnel, the top heading and the temporary invert, the bench, and the invert. In such connections the degree of freedom for rotation has been assigned (sections with no capacity for bending moment transfer).

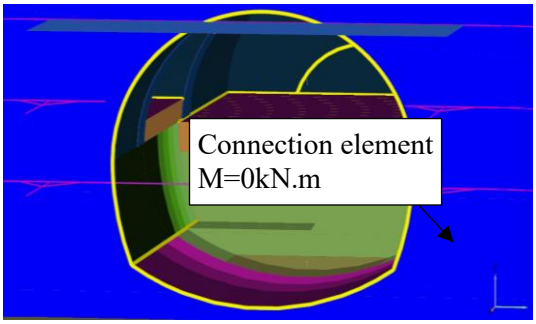

Figure 7. Connection elements for modelling limited capacity for load transfer (Plaxis 3D).

3.6 Primary support and reinforcement

The primary support is composed by a 300mm thickness shotcrete layer reinforced with steel fibres and 1000mm spaced TH-29 profile girders. The primary support has been modelled by means of isotropic plate elements with combined effects of shotcrete and steel girders.

At the intersection between the central and transversal galleries an additional 100mm thickness reinforcement vest has been introduced by means of a linear elastic volume element with a dummy plate element placed at the middle fibres of the volume element.

The 12m long forepole umbrellas to be installed both at the portal and tunnel intersections have been installed with 0.4m spaced 76mm diameter, 14.6mm thickness steel tubes. These rigid bodies have been modelled with embedded beam elements only capable of mobilizing lateral resistance, the value of which has been conveniently assessed by means of the Bustamante and Doix empirical formulation.

The 1.5m by 1.5m layout of 76mm diameter grouted holes reinforced with 28mm diameter fibre-glass nails, to be installed at the top heading of the tunnel face, have been modelled with beam elements. At their installation stage their length is 12m. After 4 advancements with step of 2m, their length is reduced from 12m to 4m, the moment of which another set of 12m long ground nails is installed. This trimming and installation sequence is repeated along the whole excavation of the top heading both for central and transversal galleries.

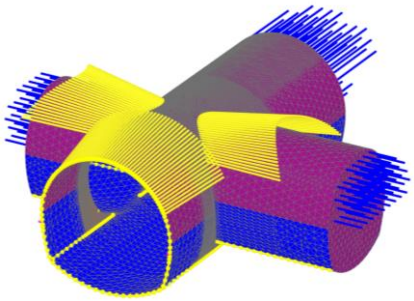

Figure 8. Primary support and reinforcement elements of north side tunnel (Plaxis 3D).

3.7 Ageing of shotcrete

The ageing of shotcrete has been modelled by means of stiffness increments which have been based on the curve extracted from the CEB-FIP Model Code 1990 shown below in Figure 9. For each sequence of excavation followed by lining installation a time increment of 1 day has been assumed.

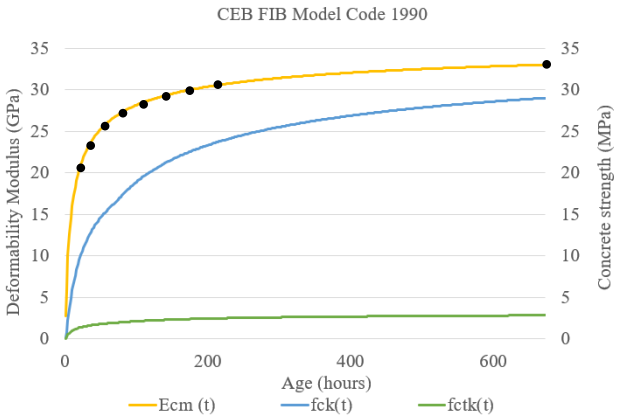

Figure 9. CEB-FIP Model Code 1990 Curves.

For reducing the modelling working time without compromising the validity of safety checks, the ageing of shotcrete has been modelled in steps of 1 day (24 hours) until 8 days (192 hours) from which the age of

shotcrete is set to 28 days. As shown in Figure 9, the stiffness variation of shotcrete between 8 and 28 days is just about 3GPa, as such, refinement along these ages was deemed to bring negligible gains.

3.8 Staged construction

The modelling of the staged construction may be subdivided in 7 main parts, which are briefly described below:

- Initial conditions (phase 0 to phase 2) – Initial stress calculations with KO-procedure, plastic-nil phase, and application of loading pre-conditions at the ground level.
- Shaft construction (phase 3 to phase 18) – Shaft lining installation, staged excavation followed by activation of propping structures.
- Top heading of the central gallery (phase 19 to phase 109) – Installation of the starting forepole umbrella and tunnel face nails, excavation in advancement steps of 2m and installation of the primary support.
- Top heading of the transversal galleries (phase 110 to phase 141) – Installation of the reinforcement vest, activation of the intersection forepole umbrellas and tunnel face nails, excavation in advancement steps of 2m, installation of the primary support.
- Shaft Construction (phase 142 to phase 143) Excavation down to the minimum shaft design level followed by the installation of the propping substructure.
- Bench of central gallery (phase 144 to phase 233) – Excavation in advancement steps of 2m followed by primary support installation.
- Bench of transversal galleries (phase 233 to phase 265) – Installation of the reinforcement vest, excavation in advancement steps of 2m followed by primary support installation.

The central and transversal galleries of the north tunnel have been partialized has shown below in Figure 10.

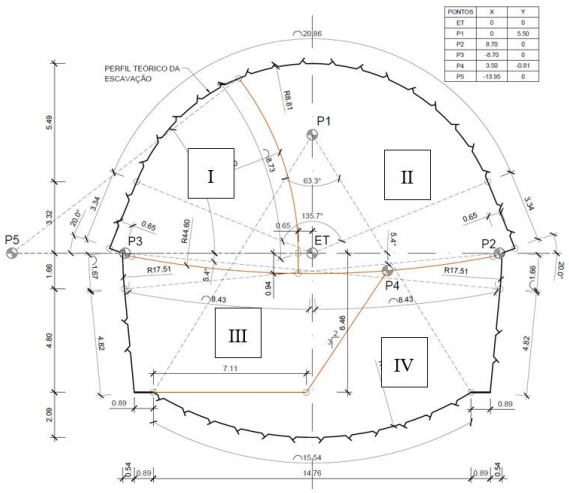

Figure 10. Partialization of the tunnel excavation.

The top heading works consists of excavation and support of sectors I and II with a maximum out-of-phase excavation of 8m. The sept that separates sectors I from II is uninstalled in each 4m of advancement of sector II, the moment of which temporary shotcrete invert is applied. Once the tunnel faces of sectors I and II are in-phase, works in sector II stops and in sector I restarts, with the sequence above described being repeated until tunnelling completion.

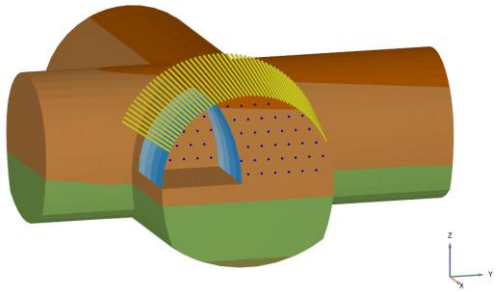

Figure 11. Excavation and support of sector I (Plaxis 3D).

Likewise, the bench excavation is done in two stages (sectors III and IV) with an out-of-phase excavation of 8m. Shotcrete invert is applied in each 4m of advancement.

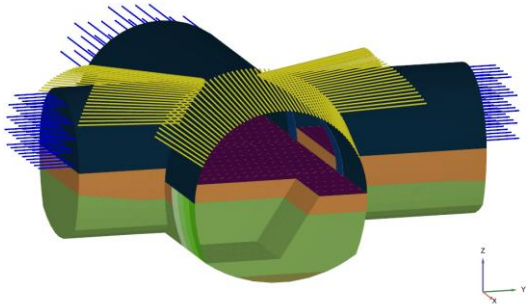

Figure 12. Excavation and support of sector III (Plaxis 3D).

4 SAFETY CHECKING

The output results of the 3D FE model enabled performing the required ULS and SLS safety checks which have been carried out according to the EC2, EC3, and EC7 (Design Approach 1 Combinations 1 and 2 – C1 and C2).

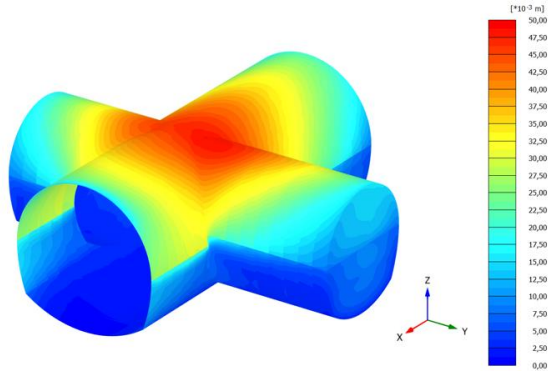

Figure 13. Total displacements (Plaxis 3D).

ULS safety checks:

- Shotcrete lining (*):
  - Bending resistance (C1)
  - Shearing resistance (C1)
  - Compression/tension resistance (C1)
- TH-29 steel girders:
  - Bending resistance (C1)
  - Shearing resistance (C1)
  - Bearing resistance of foundation ground (C2) (**)
- Forepole umbrellas:
  - Bending resistance (C1)
  - Shearing resistance (C1)
- Tunnel face:
  - Global stability analysis (C2) (***)

SLS safety checks:

- Displacements and convergences of tunnel section.
- Settlements of existing structures located in the region of influence of the tunnelling excavation.

(*) The safety check of both the shotcrete lining and shotcrete lining reinforced with steel fibres, has been performed at the early age of 1 day and for 28 days of age.

(**) The bearing resistance of foundation ground has been performed by means of a P2D model conveniently calibrated with the results obtained from the P3D model.

(***) The global stability analysis has been performed by means of the strength reduction method with ground parameters and loading conditions set according to C2.

5 CONCLUSIONS

The 3D FE model provided the necessary output results (forces and displacements) for performing the required safety checks against all identified failure mechanisms of the tunnelling works. Given the comprehensive modelling of the staged construction and mesh refinement that has been duly implemented, the present limit state analysis with FEM solution likely approximates the exact solution, as such, optimised design is plausible. On the other hand, a 3D FE modelling design approach for complex problems, as was the case, is recognized to be time consuming, machine demanding and requires expertise FE modellers with sound geotechnical engineering background.

Finally, the author hopes that the present article may have contributed to improve the awareness and acknowledgement of 3D FE modelling as a compelling tool for the future of geotechnical design.

REFERENCES

Bauduin, C., Bakker, K.J., Frank, R. (2005). *Use of finite element methods in geotechnical ultimate limit state design*. Proceedings of the 16th International Conference on Soil Mechanics and Geotechnical Engineering.

Bentley, Plaxis 3D - Reference Manual, Material Models Manual, (2022).

Brinkgreve, R.B.J., Post, M. (2013). *On the use of finite element models for geotechnical design*. Bernessen mit numerishen methoden Workshop. (Veroffentlichungen des Institutes, 27) 111-222.

Bustamante, M., Doix, B. (1985). *Une méthode pour le calcul des tirants et des micropieux injectés* – Bulletin de Liaison des Laboratoirs des Pont et Chaussés, Paris.

CEB-FIP model code (1990) Fédération internationale du béton.

Hoek, E., Carranza-Torres, C., Corkum, B. (2002). *Hoek-brown failure criterion*. In Proc. 5th North American Symposium. NARMS-TAC, Toronto, Canada.

NP EN 1992-1-1 (2010) Eurocode 2 - Design of concrete structures. Part 1-1: General rules and rules for buildings. European Committee for Standardization, Brussels.

NP EN 1993-1-1 (2010) Eurocode 3 – Design of steel structures. Part 1-1: General Rules and rules for buildings. European Committee for Standardization, Brussels.

NP EN 1997-1 (2009) Eurocode 7 – Geotechnical Design. Part 1: General Rules. European Committee for Standardization, Brussels.

Proceedings of the XVIII ECSMGE 2024
GEOTECHNICAL ENGINEERING CHALLENGES
TO MEET CURRENT AND EMERGING NEEDS OF SOCIETY
© 2024 the Authors
ISBN 978-1-032-54816-6
DOI 10.1201/9781003431749-156
Open Access: www.taylorfrancis.com, CC BY-NC-ND 4.0 license

ECSMGE 24
XVIII EUROPEAN CONFERENCE ON SOIL MECHANICS AND GEOTECHNICAL ENGINEERING

Static load tests on energy piles: Effects of thermal cycles

Essais de chargement statiques sur des pieux énergétiques: Effets des cycles thermiques

R. Vasilescu
Pinto, France

F. Szymkiewicz*, C. Minatchy, F. Guirado
Université Gustave Eiffel – SRO Laboratory, Champs sur Marne, France

V.T. Nguyen, A.M. Tang, J.M. Pereira
Navier, Ecole des Ponts, Univ Gustave Eiffel, CNRS, Marne-la-Vallée, France

**fabien.szymkiewicz@univ-eiffel.fr*

ABSTRACT: Although energy geostructures, and among them thermoactive piles, have been in use for almost 50 years, design offices and decision makers are still reluctant to routinely integrate this technique in the final design solutions, as some unresolved technical issues appear to remain, as well as comprehensive guidelines based on in situ tests and projects feedback. Indeed, one of the remaining issues is the potential effect of temperature and more importantly of the accumulation of heating-cooling cycles on the soil-pile interface and therefore on the long-term behaviour of a pile, as well as on its bearing capacity. With the ever increasing cost of fossil energy, and the need to propose green solutions limiting global warming and its consequences, it is of the upmost importance to address these issues. To do so, five thermoactive continuous flight auger piles were thus constructed on two different sites (one mostly sandy and the other mostly made of clay and marls). They were mechanically loaded at different levels ranging from the quasi-permanent Serviceability Limit State (SLS) to the characteristic SLS, and submitted to multiple thermal cycles. They were then loaded to the failure, to assess the impact of these cycles on the bearing capacity. The embedded instrumentation (fiber optic, strain gauges, etc.) allowed estimating the distribution of the load along the shafts, and the possible effect of the repeated thermal loadings on the shaft and base resistances. This paper shows that the bearing capacity of piles executed in fine soils does not seem to be affected by temperature cycles, while that of piles executed in sandy soils shows a noticeable increase.

RÉSUMÉ: Bien que les géostructures énergétiques, et notamment les pieux géothermiques, soient utilisés depuis près de 50 ans, les bureaux d'études et les décideurs hésitent encore à intégrer systématiquement cette technique dans les solutions de conception finales, car certaines questions techniques non résolues semblent subsister ; de même, les recommandations basées sur des essais in situ et le retour d'expérience des projets sont encore assez peu nombreux. Notamment, l'une des questions en suspens est l'impact potentiel de la température et, plus important encore, de l'accumulation des cycles de chauffage et de refroidissement sur l'interface sol-pieu et, par conséquent, sur le comportement à long terme d'un pieu, ainsi que sur sa capacité portante. Avec l'augmentation constante du coût des énergies fossiles et la nécessité de proposer des solutions vertes pour limiter le réchauffement climatique et ses conséquences, il est de la plus haute importance d'aborder ces questions. Pour ce faire, cinq pieux réalisés à la tarière creuse et géothermiques ont été réalisés sur deux sites différents (l'un principalement sableux et l'autre principalement constitué d'argile et de marnes). Ils ont été chargés mécaniquement à différents niveaux allant de l'état limite de service quasi-permanent à l'état limite de service caractéristique, et soumis à de multiples cycles thermiques. Ils ont ensuite été chargés jusqu'à la rupture, afin d'évaluer l'impact de ces cycles sur la capacité portante. L'instrumentation embarquée (fibre optique, jauges de contrainte, etc.) a permis d'estimer la distribution de la charge le long des futs, et l'impact possible des chargements thermiques répétés sur les résistances par frottement et de pointe. Cette communication montre que la portance des pieux réalisés dans des sols fins ne semblent pas impactés par les cycles de température, au contraire de celle de pieux réalisé dans des sols sableux, qui a montré une augmentation notable.

Keywords: Deep foundations; energy geostructures; static load tests.

1 INTRODUCTION

The thermo-active pile technique involves integrating heat exchanger elements into deep foundations. This offers the advantage of reducing the drilling cost when compared to vertical geothermal probes. In addition, this technology is considered eco-friendly

since it minimizes the consumption of fossil energy sources and the energy bill.

The technique has been used successfully for over 50 years in various countries with more and more reported cases in the past several years (Abdelaziz et al., 2016, Bourne-Webb et al., 2009, Di Donna et al., 2017, to name a few). However, with the exception of a few guidline documents (Rotta-Loria et al. 2020) there is no established design method yet for justifying the geotechnical resistance of the thermo-active piles. Therefore, contractors have been constructing buildings with these piles based on empirical knowledge or conservative designs (Boënnec, 2009 and Knellwolf et al., 2011).

A few tests have been carried out to investigate the thermomechanical behaviour of the soil and of the soil-pile interface, but experimental data remains scarcely available and not generally applicable.

In France, due to insufficient information available regarding the effect of temperature and heating-cooling cycles on the mechanical characteristics of the soil, this technology is still viewed with some skepticism.

Nevertheless, this technology must now be considered as a viable option, with the new regulations and the ever increasing price of energy. Therefore, five continuous flight auger (CFA) piles, fully instrumented, were built and then subjected to combined mechanical and thermal loadings. This communication presents the tests carried out and the obtained initial results.

2 TEST SITES AND TEST PILES SPECIFICATIONS

2.1 Location and geological/geotechnical context

The loading tests were carried out on two sites: the first one Coudekerque-Branche (CDK), and the second one in Champs-sur-Marne (CSM), in France. Geotechnical investigations were carried out at the test sites, using core sampling and pressuremeter tests.. The pressuremeter tests carried out at the two sites are shown in Figure 1.

At Coudekerque-Branche, the piles were anchored in the quaternary sands of the Middle Flandrian, which are fine, homometric and shelly (carbonated). These sands were encountered at 3m deep, with the overtopping layer being silts.

At Champs sur Marne, fills were encountered throughout the first 0.7m, then came silty clay until 2m deep, then Green clay from Romainville (Early Oligocene, late Eocene), and then the Marls of Pantin, from the late Eocene, in which the bases of the piles were embedded.

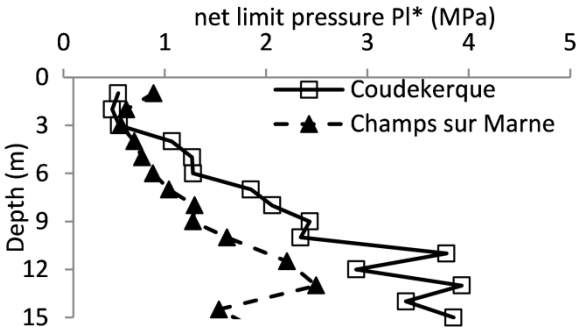

Figure 1. Evolution of net limit pressure as a function of depth at the two sites.

2.2 Test Piles

The five piles tested on the two sites are continuous flight auger piles corresponding, according to standard NF P 94-262 (AFNOR, 2012), to category 6 piles (CFA). This technique was chosen as it is the most common type of piles used in Northern France. It offers a number of advantages: high production rates and expected axial strengths, and the means required for their execution are limited compared with other techniques.

Table 1 details the characteristics of the piles at both the Coudekerque and Champs-sur-Marne sites.

Table 1. Geometric characteristics, types and strengths of piles tested in accordance with French design method.

	Coudekerque	**Champs-sur-Marne**
	P1/P2/P3	**P1/P2**
Length (m)	12	12
Diameter (m)	0.52	0.42
Type	CFA	CFA
Instrumented	yes	yes
Test	compression	
R_c (kN)	3297	1856
R_s (kN)	2088	1357
R_b (kN)	1209	499

All the piles were instrumented with various sensors, ranging from LCPC removable extensometers to fiber optics and strain gauges, from which efforts at different depths were derived. As demonstrated by (Szymkiewicz et al., 2021), the instrumentation technology used does not impact the results.

The piles were all tested in compression, and loading tests were carried out until the piles reached geotechnical failure.

3 THERMAL LOADING

Piles CDK P2 and P3 and piles CSM P1 and P2 were subjected to a thermal loading for several months.

More specifically, CDK P2 underwent both thermal and mechanical loading for a duration of five months. During this period, the mechanical load applied at the top of the pile was equivalent to 30% of the bearing capacity determined during the static load test carried out on CDK P1. As for CDK P3, it was loaded only thermally, for a period of five months. No mechanical load was applied on its head during this period.

The thermal cycles applied during these five months were the same for both piles CDK P2 and P3. The duration of normal heating-cooling cycles was around 14 days, with 7 days allotted to heating and an additional 7 days to cooling. However, during the tests, the duration of these cycles had to be adjusted as necessary. The heat pump was programmed to provide fluid at a temperature of 30 C during the heating phase of the cycle and 2 C during the cooling phase.

At Champ-sur-Marne, the pile CSM P1 was first mechanically loaded to 30% of its estimated bearing capacity. Three series of heating-cooling cycles (called H and C on Figure 2, respectively) were then applied over the duration of seven weeks. For each cycle, the temperature of the refrigerated and heated circulating fluid was increased to 30 C and kept constant for one week and then decreased to 0°C and kept constant for another week. The thermal loading test was stopped during the fourth cycle due to a thermal loading system malfunction. After three weeks of thermal recovery, during which the ground cooled back to its initial temperature, the pile was unloaded. Figure 2 shows the evolution of its head settlement as temperature varies during the thermal cycles.

The pile CSM P2 was in turn mechanically loaded to 50% of its estimated bearing capacity. Five series of heating-cooling cycles were then applied over the duration of ten weeks. For each cycle, the temperature of the refrigerated and heated circulating fluid was increased to 30°C and kept constant for one week and then decreased to 5°C and kept constant for another week.

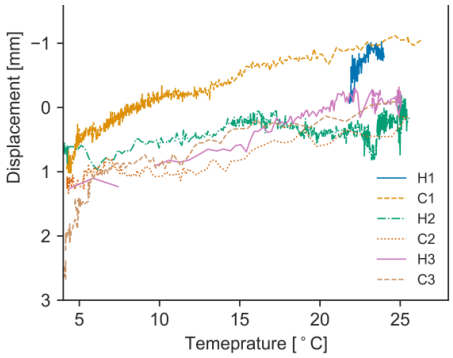

Figure 2. Displacement –Temperature relationship for CSM P1.

4 RESISTANCE OF THE PILES

After the thermal cycles were finished, CDK P2 and P3 and CSM P1 and P2 were loaded to the failure. CDK P1 was loaded without having been previously subjected to any thermal loading.

The loading tests were carried out in compliance with the requirements of the test standards in force at the time and the base resistances (R_b) and shaft resistances (R_s) were derived from the strain measurements along the shaft of the piles, using the estimated deformation modulus of the pile. It is to note that strain recordings encountered some problems for CSM P2, and therefore base and shaft resistances for this pile are not presented.

Table 2 summarizes the results achieved during these tests. From these results, it is clear that multiple thermal cycles performed on CSM P1 and P2 did not affect the resistance, as it is very close to the expected theoretical value (Figure3). However, the distribution of the load at failure between the base and the shaft is not as expected. It is something somewhat usual, as the French design method is calibrated on global resistance and not on local values, which can vary greatly for a number of reasons (heterogeneity of the soil, slight variation of stiffness of the shaft, etc.).

For CDK P2 and P3, it can be seen that they exhibit a higher resistance than the one achieved on CDK P1. Furthermore, these values are quite similar to the theoretical one, while the resistance of CDK P1 is much lower. This was explained by the nature of the sand encountered and by the installation methods (Szymkiewicz et al., 2024), for which the French standard seems over-optimistic.

For the tests at Coudekerque, it is clear that the base resistance is not impacted by the thermal cycles, but that the shaft resistance is strongly impacted, on the other end. However, this impact is on the positive side, as the shaft resistance increases by 40%, thus increasing naturally the bearing capacity by 30%, in this configuration.

Table 2. Measured (m) limit (R_c), shaft (R_s) and base (R_b) resistances, and ratios to calculated (cal) values.

Pile	$R_{s;\,m}$ (kN)	$R_{s;\,m}$ / $R_{s;\,cal}$	$R_{b;\,m}$ (kN)	$R_{b;\,m}$ / $R_{b;\,cal}$	$R_{c\,m}$ (kN)	$R_{c;\,m}$ / $R_{c;\,cal}$
CDK P1	1751	0.84	699	0.58	2450	0.74
CDK P2	2450	1.17	726	0.60	3176	0.96
CDK P3	2450	1.17	752	0.62	3202	0.96
CSM P1	1100	0.81	700	1.40	1800	0.97
CSM P2					1800	0.97

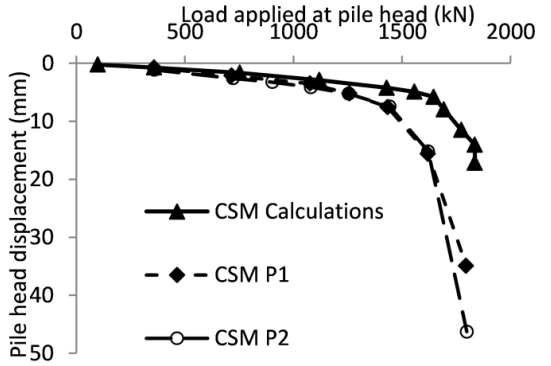

Figure 3. Calculated and experimental load-displacement curves for piles CSM1 and CSM 2.

5 CONCLUSIONS

Five CFA geothermal piles, two installed in fine-grained soils and two in sands, were loaded to the failure, after having been subjected to several thermal cycles.

The results show that the bearing capacity of the piles installed in fine-grained soils was not affected by the thermal loading, while that of the piles installed in sands was clearly affected by the thermal cycles. In particular, it was exclusively the shaft resistance that was impacted. However, this impact appeared to be positive, as the bearing capacity increased by 30% after the thermal cycles.

More tests should be carried out in the near future to validate these results: in particular, other tests should be carried out in another type of sand.

Furthermore, a test on a pile without any thermal history should be carried out on the Champs-sur-Marne site, so as to assess the experimental bearing capacity. This will be done, among other tests, during the research project “COOP”, funded by a grant from the French National Research Agency (ANR-22-CE22-0007) and involving Université de Lille, Université Gustave Eiffel, Ecole des Ponts ParisTech and Pinto.

REFERENCES

Abdelaziz, S. and Ozudogru, T.Y. (2016). Non-uniform thermal strains and stresses in energy piles. *Environ. Geotech.* 3 (4), pp. 237-252, DOI: https://doi.org/10.1680/jenge.15.00032.

AFNOR (2012). NF P 94-262 Justification des ouvrages géotechniques - Normes d'application nationale de l'Eurocode 7 - Fondations profondes, France.

Boënnec, O. (2009). *Piling on the Energy*, GeoDrilling International, 150, pp. 25 - 28.

Bourne-Webb, P.J., Amatya, B.L., Soga, K., Amis, T., Davidson, C. and Payne, P. (2009). Energy pile test at Lambeth College, London: geotechnical and thermodynamic aspects of pile response to heat cycles. *Geotechnique* 59 (3), pp. 237-248, DOI : https://doi.org/10.1680/geot.2009.59.3.237.

Di Donna, A., Barla, M. and Amis, T. (2017). Energy geostructures: analysis from research and systems installed around the world. In: Proceedings of 42nd DFI Conference.

Knellwolf, C., Peron H. and Laloui L. (2011). Geotechnical Analysis of Heat Exchanger Piles, *Journal of Geotechnical and Geoenvironmental Engineering* 137(10), pp. 890-902, DOI : https://doi.org/10.1061/(ASCE)GT.1943-5606.0000513

Rotta Loria, A. F., Bocco, M., Garbellini, C., Muttoni, A., and Laloui, L. (2020). The role of thermal loads in the performance-based design of energy piles. Geomechanics for Energy and the Environment, 21, 100153, DOI : https://doi.org/10.1016/j.gete.2019.100153.

Szymkiewicz F., Minatchy C. & Reiffsteck P. (2021). Static pile load tests: contribution of the measurement of strains by optical fiber, *International Journal of GEOMATE*, Vol. 20, Issue 81, pp. 44-51, DOI: https://doi.org/10.21660/2021.81.6330.

Proceedings of the XVIII ECSMGE 2024
GEOTECHNICAL ENGINEERING CHALLENGES
TO MEET CURRENT AND EMERGING NEEDS OF SOCIETY
© 2024 the Authors
ISBN 978-1-032-54816-6
DOI 10.1201/9781003431749-157
Open Access: www.taylorfrancis.com, CC BY-NC-ND 4.0 license

ECSMGE 24
XVIII EUROPEAN CONFERENCE ON SOIL MECHANICS AND GEOTECHNICAL ENGINEERING

Uncovering soft soils with 3D Empirical Bayesian Kriging: A case study on cone penetration test data

Révélation des sols meubles avec la Krigeage Bayésien Empirique en 3D: Une étude de cas sur les données des essais de pénétration au cône

J. Viegas*, A. Gallardo
TPF Consultores de Engenharia e Arquitetura S.A, Lisbon, Portugal

A.C. Costa
NOVA Information Management School (NOVA IMS). Universidade Nova de Lisboa, Lisboa, Portugal

R. Marinaro
Vale S.A, Nova Lima, MG, Brazil

**jeniffer.viegas@tpf.pt*

ABSTRACT: The present work investigates the coexistence of soft and very soft soils in the foundation of a dam and aims to create a 3D map of excess pore pressure using the 3D Empirical Bayesian Kriging geostatistical method. A previous study had revealed that the only distinctive property in these residual soils is the generation of excess pore pressure during shear, which varies significantly depending on the weathering process of the parent rock, and so the pore-pressure parameter is the main feature here. The purpose of the study is not only to demonstrate that zoning the foundation of the dam is possible, but also to clarify that this zoning is more than a simply geometric delimitation of geotechnical units with previously defined deterministic properties. The values of the geotechnical properties of the equivalent soil grouped in a unit, regardless of the zoning method adopted, must represent the partial contributions of each of the soils gathered there, in variable and uncertain proportions, but estimable with some level of confidence. The study concludes that geostatistical methods are useful tools for creating balanced and reliable geotechnical models, particularly when the values of the target properties vary drastically. Overall, the study highlights the importance of accurately representing the properties of soils in geotechnical models to ensure safe and reliable engineering structures.

RÉSUMÉ: Le travail présent étudie la coexistence de sols mous et très mous dans les fondations d'un barrage et vise à créer une carte 3D de la pression de pore excessive à l'aide de la méthode géostatistique de Krigeage Bayésien Empirique en 3D. Une étude précédente avait révélé que la seule propriété distinctive de ces sols résiduels est la génération de pression de pore excessive lors du cisaillement, qui varie significativement en fonction du processus d'altération de la roche mère, entre autres, le paramètre de pression de pore étant ici la caractéristique principale. L'objectif de l'étude n'est pas seulement de démontrer que la zonification des fondations du barrage est possible, mais aussi de préciser que cette zonification va au-delà de la simple délimitation géométrique des unités géotechniques avec des propriétés déterministes préalablement définies. Les valeurs des propriétés géotechniques du sol équivalent regroupées dans une unité, quel que soit la méthode de zonage adoptée, doivent représenter les contributions partielles de chacun des sols regroupés là-bas, dans des proportions variables et incertaines, mais estimables avec un certain niveau de confiance. L'étude conclut que les méthodes géostatistiques sont des outils utiles pour créer des modèles géotechniques équilibrés et fiables, en particulier lorsque les valeurs des propriétés cibles varient considérablement. Globalement, l'étude met en évidence l'importance de représenter avec précision les propriétés des sols dans les modèles géotechniques pour garantir des structures d'ingénierie sûres et fiables.

Keywords: 3D empirical bayesian kriging; cone penetration test; pore pressure parameter; tropical residual soils.

1 INTRODUCTION

The characterization of a material in terms of its strength and deformability is fundamental for any geotechnical project, and equally important is the accurate spatial definition of each material. Incorrectly placing a more resistant material in a potential failure zone could create a false sense of security.

Defining boundaries between materials, such as soil, which exhibit significant spatial variability, is a challenging task fraught with uncertainties. Determining what cannot be seen based on pointwise data requires the interpreter's discernment and some level of confidence (or skepticism) in the models being produced. All models, be they geological or otherwise, are inherently imperfect due to simplifications or

assumptions. It is the responsibility of the technician to determine the degree of error that can be tolerated.

When creating a model, it is of utmost importance to evaluate its implications for the real-world problem. For example, what would happen if a material extended a few meters more than initially assumed or if it turned out to be deeper than anticipated? Could it create a plane of weakness or affect the percolation regime? Whenever a model is presented, it should ideally be accompanied by a map of uncertainties, allowing engineers to account for less favourable scenarios.

This study focuses on a tailings dam located in the Quadrilátero Ferrífero, an iron ore-rich region in Minas Gerais, southwestern Brazil. The dam's foundation comprises two residual soils of dolomitic phyllite, with one significantly softer than the other. This very soft soil exhibits low tip resistance and a high pore pressure ratio, as determined through Cone Penetration Tests (CPTu) detailed in (Viegas et al., 2023). The extent and location of this very soft soil critically affect the dam's factor of safety (FS) since the critical failure surface may intersect this material.

The primary objective of this study is to map this very soft residual soil by interpolating the pore-pressure ratio (B_q) data obtained from CPTu surveys. The aim is to demonstrate how the material's strength, situated on a potential failure surface, can be quantified. For a better understanding, imagine a failure surface passing through a specific area of the foundation and encompassing a certain mass of soil. The goal would be to define, with some confidence and a few parameters, the strength that would be available on average along this surface. Considering a slope stability model discretized into slices, one would be looking for the available resistance at the base of each slice, considering the possibility of stress redistribution between elements (meaning that the material exhibits some ductility).

2 METHODOLOGY

In this section, we describe the methodology employed in this study to map the very soft residual soil within the context of the tailings dam in the Quadrilátero Ferrífero. We utilized the pore-pressure ratio parameter, B_q, which follows a skewed normal distribution and exhibits non-stationarity.

To address the challenges posed by limited data and the absence of stationarity, we applied the geostatistical method known as Empirical Bayesian Kriging (EBK). EBK combines the principles of kriging and Bayesian statistics, and it assumes that the study variable follows a Gaussian distribution. Hence, since the distribution of the data was skewed, a Gaussian transformation was applied. It generates priors and posteriors distributions, providing more accurate estimates than classical kriging methods and quantifying uncertainty in predictions. EBK represents the stochastic spatial process as a random field, allowing parameters to vary across space, crucial for materials with significant spatial variability, as is often the case with geological materials. For readers interested in a more detailed exploration of the EBK method, we recommend referring to the works of Gribov and Krivoruchko (2020) and Krivoruchko and Gribov (2019).

The model presented here was created using the implementation of EBK 3D in ArcGIS Pro 3.0, and several sensitivity tests were performed to determine the most suitable semivariogram and calibrate model parameters such as the subset size, the number of simulations, the overlap factor and the semivariograma type.

3 RESULTS

The final model is presented in Figure 1, in which the pore-pressure parameter, B_q is displayed with a colour scale, where yellow represents high values of B_q, correlated to the very soft residual soil of dolomitic phyllite and confirmed by the boreholes in that area. The blue colour represents low values of B_q. To evaluate the model, a cross-validation was performed, where the observed data were compared against the calculated data. The Average Continous Ranked Probability Score (CRPS) is low, with a value of 0.006, the Root-Mean-Square (RMS) and an average standard error are 0.023, reflecting good data reproduction. The Root-Mean-Square Standardized (RMSE) is 0.94, suggesting slight overfitting. The results presented here could be as diverse as possible, depending on the choice of modelling parameters; however, this study serves to illustrate an approach to model soil properties rather than specifically create a terrain model.

Isolating the material with $0.15 \leq B_q \leq 0.29$ (Figure 2) shows the material generating these pore-pressure intervals is concentrated on the right side but not exclusively there, with minor presence in the rest of the model. How do we create the geotechnical model to be used for stability analysis? If we were to create discrete zones, or 'balls' of materials, there would be a risk of misplacing these zones or overlooking their true dimensions. So, the question arises: How can we construct a geotechnical model that accounts for the geological uncertainty? It is not feasible to assert that

where there is residual soil, there is no presence of very soft residual soil; these materials could coexist.

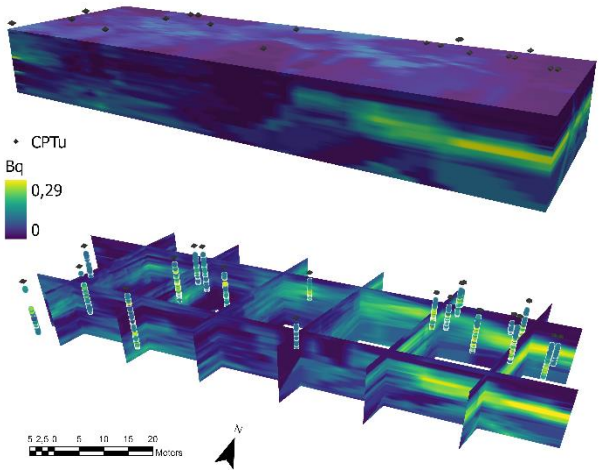

Figure 1. Recovered Model: 3D model of the subsurface colored by the pore-pressure parameter, B_q, where yellow represents high values of B_q, and blue low values.

Creating a model with distinct delineations for these materials poses a significant challenge. Our approach revolves around defining a criterion that permits the coexistence of both materials in varying proportions simultaneously. This can be achieved using a mean parameter and its associated standard deviation.

Another possible approach would be to calculate a confidence interval for the pore-pressure parameter and its uncertainty, but would be necessary to perform several simulations, applying for example Direct Sequential Simulation (DSS) as described in Soares, A. (2001), which falls outside the scope of this study.

In practice, it is more useful to have an average parameter associated with a standard deviation. Therefore, the mean value and standard deviation of each pixel along the cross-section were calculated, resulting in a mean section and a standard deviation section. The same procedure was repeated in the longitudinal direction. Figure 3 shows the mean cross-section and longitudinal section at a depth of 12.07 m, which was chosen due to its intersection with the high pore-pressure zone (yellow in the figure). Figures 3a) and 3b) depict the mean (the mean of the values of each pixel in the interpolated cube) longitudinal and cross-section, respectively. A black dashed line used for comparison at a depth of 12.07 m is also shown. Figures 3c) and 3d) illustrate the variation in the mean value of the parameter B_q along this line in each of the directions. Notice a higher variability of the mean in the cross-section.

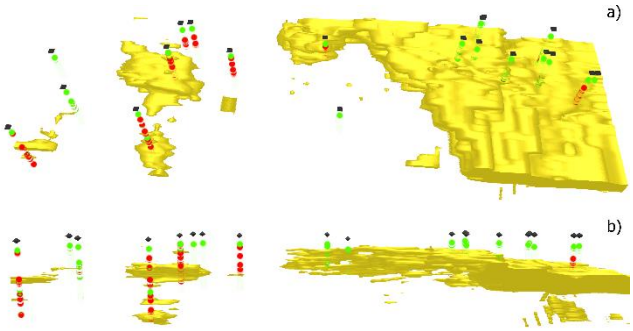

Figure 2. Mass of soil with $0.15 \leq B_q \leq 0.29$. The black dots represent the available CPTu. The CPTu data are plotted in terms of pore-pressure ratio, B_q, where the green points have $B_q < 0.15$, and the red points have $B_q \geq 0.15$.

Similarly, Figure 4 presents the associated standard deviation. In the cross-section, the area with high pore-pressure is sharp and clear, while in the longitudinal section, it appears blurry, reflecting the higher standard deviation in this direction. Figure 5 shows the mean value of the B_q parameter in black and a cautious value in red, calculated by adding half of the standard deviation to the mean, for a depth of 12.07 meters in both sections.

Since, as illustrated in Figure 1, we cannot isolate a specific area where the very soft soil exists, nor can we disregard its coexistence with other materials, one possible approach to addressing this weaker soil in the geotechnical model for obtaining the dam's safety factor may involve considering that this material represents a certain percentage of the total soil mass.

Considering that B_q is the parameter describing the excess of pore-pressure during CPTu, and A_f is the parameter describing excess of pore-pressure at failure in a triaxial test, even though a theoretical relationship between them has not been established, we can say that, albeit distinct, both parameters measure the response of the same soil when subjected to rapid loading.

Assuming it was possible to carefully separate the results of the triaxial tests into two groups: one corresponding to residual soil and the other to very soft residual soil, and that both soils appear in space without explanation (randomly). Also, assuming that in any failure surface that cuts through the soil mass, the available resistance there, on average, results from the spatial weighting of the occurrence of one or the other soil simultaneously along that surface. For illustrative purposes, if $B_{q,maximum} = 0.29$ corresponds to the group of samples (CIUC tests) of the very soft residual soil and $B_{q,minimum} = -0.11$ is equivalent to the group of samples (also from CIUC tests) of residual

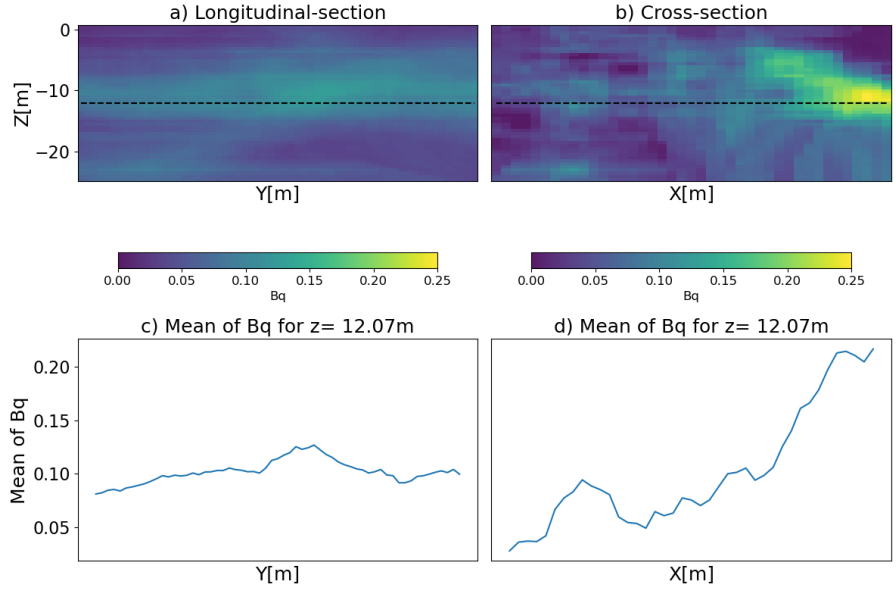

Figure 3. Mean value of B_q for the longitudinal and cross-section at the depth of z=12.07m.

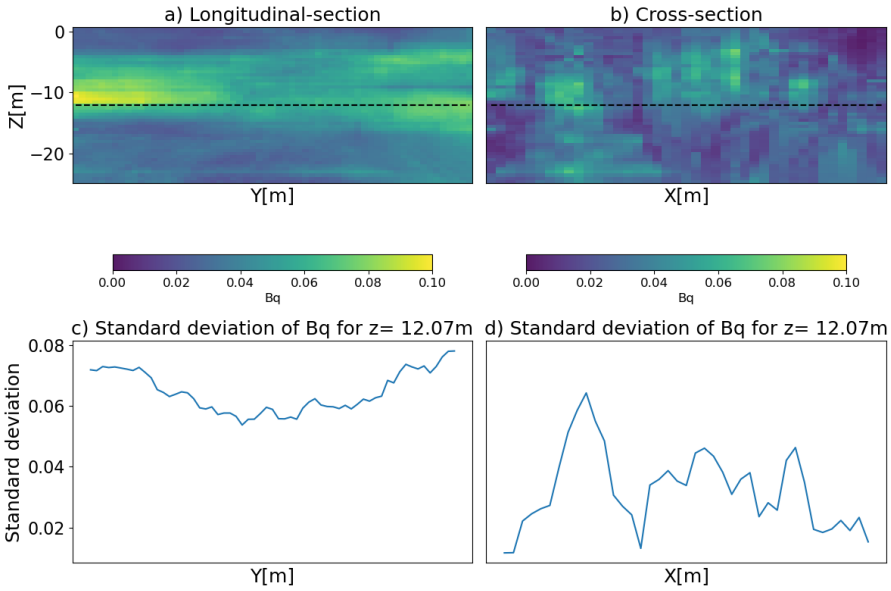

Figure 4. Standard deviation of B_q for the longitudinal and cross-section at the depth of z=12.07m.

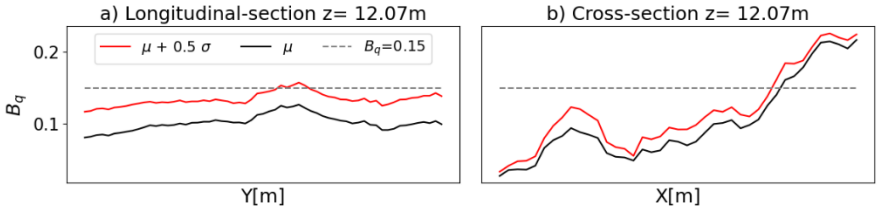

Figure 5. Mean and cautious value of B_q. In black, the mean value of the parameter B_q is presented, as shown in Figure 3, and in red, the mean value plus half of the standard deviation, with a reference to a depth of 12.07 meters.

soil, we can use random fields (Baecher and Christian, 2005; Griffiths and Fenton, 2007) to infer that any property X (such as undrained shear strength) related to the generation of excess pore pressure will be:

$$\bar{X}(\bar{B}_q) = \alpha \cdot X(B_{q,minimum}) + (1-\alpha) \cdot X(B_{q,maximum}) \approx \bar{X}(\alpha \cdot B_{q,minimum} + (1-\alpha) \cdot B_{q,maximum}) \quad (1)$$

that is:

$$\alpha = \frac{B_{q,maximum} - \overline{B_q}}{B_{q,maximum} - B_{q,minimum}} \quad (2)$$

In the equations above, $\overline{B_q}$ represents a cautious estimation of the mean value of B_q. Returning to the example, with $\overline{B_q}$ = 0.15, we would have $\alpha \approx 0.35$. This would mean that in a simplified model where the entire foundation of residual soil is treated as a homogeneous and isotropic unit of an equivalent soil, the value of the variable $\bar{X}$ would correspond to a combination of 35% of residual soil with $X(B_{q,min})$ and 65% of very soft residual soil with $X(B_{q,max})$. Regardless of the theoretical ambiguity, this example serves to illustrate that:

- In summary, any attempt at zoning the foundation, including its absence, is valid, depending solely on the representativeness of the values of the parameters assigned to each zone.
- Zoning the foundation is entirely legitimate when, as in this example, one can conclude that there is a region in space with markedly distinct properties and dimensions capable of influencing the results of stability analyses. Otherwise, we would fall into excessive pessimism in the general case and dangerous optimism in the specific case.
- Selective and biased sampling, if not subsequently subjected to any form of weighting, will likely result in a biased perception of the values of soil properties available on average in each zone of the terrain. This weighting should and can be done in field tests, considering the volumes of soil involved in the failure mechanism we are interested in analysing.
- Unless there is an explanation for the occurrence of very soft soils within residual soils, and it is demonstrated that very soft soils occur, without a known pattern, with greater or lesser frequency in the upper alteration horizon of the massif, it is not simply credible and immediately prudent to reduce zoning to the distinction between two extreme soils, one very good and the other very bad (the case of $\alpha = 0$ or $\alpha = 1$).

4 CONCLUSIONS

By applying EBK in this context, we aim to provide a robust and data-driven method for mapping and characterizing the very soft residual soil, thereby enhancing our understanding of its influence on the safety and stability of the tailings dam. This methodology allows us to not only estimate material properties but also assess the associated uncertainties, which is essential for informed decision-making in geotechnical projects.

The pore-pressure parameter proved effective in distinguishing residual soil and the very soft residual soil. Based on known values, a geostatistical method was adopted to predict the parameter across the entire study area. This type of interpolation is widely used and is applied in geological modelling commercial software. Despite being an extremely powerful tool, it has limitations, highlighting the need for model weighting by the interpreter and its association with the uncertainty. This method allows us to have an idea of the areas where we could find soils that generate high pore-pressure values. It is not prudent to deny the coexistence of the residual soil within the very soft residual soil, as it has been observed that, even in a smaller proportion, the very soft residual soil may appear across the entire analysed extent.

However, the interpolation result suggests the existence of a zone where the very soft soil concentrates (zone on the right in Figure 1), which could be explicitly considered in the geotechnical model, thus allowing the formation of mechanisms that pass through this zone. In this case, the definition of the B_q parameter representative of the mass of the very soft soil (where, in addition to the very soft soil, soils with different B_q values and consequently different strengths are involved) could be determined as a value lower than the lowest one found in this mass. On the other hand, if the decision is made not to explicitly specify this zone and to model it as a single equivalent soil, the ability of the geotechnical model to influence the formation of failure mechanisms would be lost. However, for the same mechanism, if the resistance weighting in this zone is cautious, it is possible to arrive at the same safety factor, since on average, the available resistance would be similar.

It is not possible to assert that there are no small contributions of the very soft residual soil within any region where the more consistent residual soil may be predominant (zone on the left in Figure 1). In the

absence of an explanation for the spatial occurrence of the very soft soil and given the spatial variability of the chosen variable (B_q), it is possible to make some judgment about the spatial contribution of each of the materials at different stages of alteration. In this study, it is assumed that softer soils may randomly appear within other soils and coexist with them. The study allows for rationalizing the choice of resistance parameters in most of the foundation, where it is not possible to discern a geometric shape that encompasses soils with specific properties, evaluating in what proportion each soil appears. This weighting is purely statistical and does not allow determining how zones with different incidences of softer soils respond physically.

Despite all the limitations of statistical methods, without their application, it would not be possible to understand how to spatially weigh the properties of each soil and choose parameters based on this weighting. In the specific case under study, one could choose to specify the mass of very soft soil evident in the zone on the right of Figure 1 and homogenize the soil on the left, characterizing it with an equivalent resistance parameter, calculated cautiously based on the proportion of each material.

REFERENCES

Baecher, G.B., and Christian, J.T. (2005). *Reliability and statistics in geotechnical engineering*. John Wiley & Sons.

Gribov, A., & Krivoruchko, K. (2020). Empirical Bayesian kriging implementation and usage. *Science of the Total Environment*, 722, 137290. https://doi.org/10.1016/j.scitotenv.2020.137290.

Griffiths, D. V., & Fenton, G. A. (Eds.). (2007). *Probabilistic methods in geotechnical engineering*. Springer Science & Business Media.

Krivoruchko, K., & Gribov, A. (2019). Evaluation of empirical Bayesian kriging. *Spatial Statistics*, 32, 100368. https://doi.org/10.1016/j.spasta.2019.100368.

Soares, A. (2001). Direct sequential simulation and cosimulation. *Mathematical Geology*, 33, 911-926. https://doi.org/10.1023/A:1012246006212.

Viegas, J., Gallardo, A., Bottaro, L., Marinaro, R. (2023). Identifying Soft Soils using Pore-Pressure Parameters: A Machine Learning Approach. *International Journal of Civil Infrastructure*. DOI: 10.11159/ijci.2023.002.

Proceedings of the XVIII ECSMGE 2024
GEOTECHNICAL ENGINEERING CHALLENGES
TO MEET CURRENT AND EMERGING NEEDS OF SOCIETY
© 2024 the Authors
ISBN 978-1-032-54816-6
DOI 10.1201/9781003431749-158
Open Access: www.taylorfrancis.com, CC BY-NC-ND 4.0 license

ECSMGE 24
XVIII EUROPEAN CONFERENCE ON SOIL MECHANICS AND GEOTECHNICAL ENGINEERING

Mechanical behaviour of geosynthetic sheets used to reinforce load transfer mattresses in the case of embankments on soft soils reinforced by rigid inclusions

Comportement mécanique des nappes géosynthétiques utilisées pour renforcer les matelas de transfert de charge dans le cas des remblais sur sols mous renforcés par inclusions rigides

P. Villard*
3SR/CNRS UMR 552/University Grenoble Alpes, Grenoble, France
**pascal.villard@univ-grenoble-alpes.fr*

ABSTRACT: Geosynthetic sheets are commonly used to improve the mechanical performances of soft soils reinforced by rigid inclusions and a granular load transfer embankment. In order to establish a design method for such reinforcement a DEM numerical analysis was performed. It was clearly demonstrated that the load due to the granular embankment is transferred on the one hand to the piles by load transfer within the granular embankment and by membrane effect induced by the deformation of the geosynthetic sheet, and on the other hand by the soft soil, which undergoes settlement. From the numerical results, it was shown that the main part of the load transmitted to the piles by membrane effect is due to the deformation of the geosynthetic strips located between the piles. It was also demonstrated that the geometry of the distribution of load supported by membrane effect takes a polynomial shape with concentration of loads at the vicinity of the piles.

RÉSUMÉ: Les nappes géosynthétiques sont couramment utilisées pour améliorer les performances mécaniques des sols mous renforcés par inclusions rigides et par un matelas granulaire de transfert de charge. Afin d'établir une méthode de dimensionnement pour ce type de renforcement, une analyse numérique DEM a été réalisée. Il a été clairement démontré que la charge transmise au remblai granulaire est transférée, d'une part aux pieux par transfert de charge au sein du matelas granulaire et par effet membrane suite à l'incurvation de la nappe géosynthétique, et d'autre part, par le sol compressible qui subit un tassement. A partir des résultats numériques, il a été montré que l'essentiel de la charge transmise aux pieux par effet membrane est due à la déformation des bandes de géosynthétiques situées entre les pieux. Il a également été démontré que la géométrie de la répartition des charges supportées par effet membrane prend une forme polynomiale avec une concentration des charges au voisinage des pieux.

Keywords: Geosynthetic; reinforcement; rigid inclusions; DEM.

1 INTRODUCTION

Soil reinforcement using Rigid Inclusions is a now common technique which, compared to other reinforcement methods, presents certain technical and economic advantages. Geosynthetic sheets are sometimes used to increase the effectiveness of the reinforcement and limit surface settlements to allowable values. The vertical forces acting on the granular mattress are partly transferred to the piles either by membrane effect (contribution of the geosynthetic to the reinforcement) or directly by the arch effect which develops within the granular material (LTP-Load Transfer Platform). The forces not redirected towards the piles are transmitted to the supporting soil that deforms more or less strongly depending on the intensity of the transmitted load.

The membrane effect is the mechanism of deformation of the sheet that allows it, by curving, to balance by its tensioning the forces initially applied perpendicular to its plane (weight of the overlying embankment and the applied overloads). The membrane effect is not proportional to the intensity of the applied load, i.e. significant initial displacements are necessary to generate noticeable tensile forces in the sheet. When the sheet has deformed into a membrane, it is able to support immediately additional vertical forces without deforming too much.

The arching or load transfer mechanisms in the LTP initiate within the granular layer following a

modification of the boundary conditions in displacement of the compressible horizon. They consist of a reorientation of forces towards fixed zones (shear forces in the load transfer platform or rotation of the principal stresses when the formation of an arch is possible). The intensity of the load transfer depends on the characteristics of the granular soil, the height of the LTP, the spacing between inclusions and their diameter.

The numerical tool chosen for this study is a numerical software (Villard, 2009) based on the discrete element method (DEM) that makes it possible to take into consideration the discrete nature of the soils, the texture of the reinforcement and the interaction on a local scale between the granular particles and the reinforcement. The simulations were carried out with the aim of describing the in-service behavior of a structure subjected to settlements of reasonable amplitude. Figure 1 presents the basic geometry used for the modeling. To limit calculation times, a quarter of the mesh of the pile network was subsequently modeled.

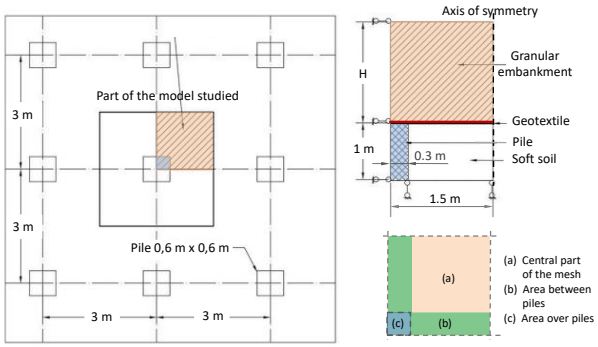

Figure 1. Geometry of the numerical application.

2 PRINCIPLE OF THE DISCRETE ELEMENT MODELLING

The discrete element method (Cundall and Strack, 1979) consists of discretizing any medium by a set of elementary particles of different sizes which interact with each other at their contact points. Interaction laws are introduced locally at the contact level (microscopic laws) which give the whole a specific macroscopic behavior. This behavior depends on the shape, the granular distribution of the particles, the apparent density of the granular medium and the microscopic contact parameters (Salot et al., 2009; Szarf et al., 2011). Considering that there is no direct relationship between the microscopic parameters (normal and tangential stiffness, contact friction coefficient, particle size, particle shape and density of the numerical sample) and the macroscopic parameters (modulus of Young, Poisson's ratio and internal friction angle), a specific calibration process is necessary. A classic way to obtain micro-mechanical parameters is to simulate laboratory tests (triaxial tests in general) carried out under well-controlled conditions and to compare the numerical and experimental results. DEM makes it possible to take into account large displacements between particles (particles can be separated from each other or brought into contact at any time). By its nature, DEM is well suited to granular materials modelling. It allows, among other things, to simulate load transfers, arching, fracturing, compaction, expansion and the evolving behavior of the material following the variation in its density (due to the expansion or shear mechanisms, for example). Specific elements (thin triangular elements) are used to model the geosynthetic reinforcement and to account for its tensile and membrane behavior (Villard, 2009).

The numerical model (Tran, 2019) consists of a granular mattress (apparent density of 1550 kg/m^3) made up of clumps arranged in such a way that the macroscopic behavior of the numerical sample corresponds to a granular material with an internal friction angle at the peak of 40° and a Young modulus of 20 MPa (Figure 2). Each clump is made up of two spheres of diameter D, overlapped and inseparable, whose centers are spaced a distance of 0.8 D. Several heights of the granular embankment were tested: H1=0.75 m (16000 clumps), H2=1.5 m (32000 clumps), H3=2.25 m (48000 clumps) and H4=3m (64000 clumps).

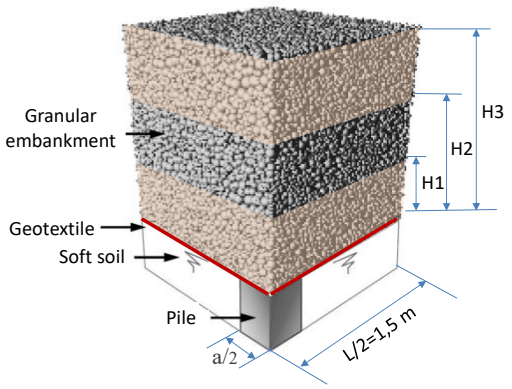

Figure 2. Description of the numerical model (H3).

The geosynthetic layer (2738 thin three nodes triangular elements), positioned at the base of the granular embankment, is reinforced in two directions (longitudinal and transverse directions). The tensile stiffnesses of the geosynthetic in the longitudinal and transverse directions are respectively: J_x=3000 kN/m and J_y=3000 kN/m. A set of spheres regularly distributed under the geosynthetic reinforcement is used to materialize the soft soil and the action of the

piles on the reinforcement sheet. The behaviors of the compressible soil and the piles are governed by springs that act vertically on the particles located under the geosynthetic. The compressibility modulus of the soil K_s is defined as the ratio between the oedometric modulus of the soil and the thickness of the soft soil (by default a value of 0.2 MN/m^3 is used for the soft soil and a value of 2000 MN/m^3 for piles). In the following, the interface friction angle between the granular layer, the soft soil and the geosynthetic is 31.5°. Frictionless vertical walls are applied around the perimeter of the model to ensure symmetry conditions.

3 NUMERICAL RESULTS

3.1 Analysis of load transfer mechanisms

The discrete modelling makes it possible to determine the displacements and contact forces between all the particles and elements of the model. It is therefore easy to distinguish the forces that act on the soft soil from those which act on the pile heads or on different areas of the geosynthetic sheet. We thus define the total efficiency of the load transfer mechanism as the ratio between the load supported by the piles and the loads inherent to the weight of the backfill.

In Figure 3 we compare, for different thicknesses of the granular mattress, the total efficiencies of the load transfer mechanisms for embankments on rigid inclusions reinforced by geosynthetics (solid lines) or not reinforced (dotted lines) and this for different values of the stiffness Ks of the soft soil.

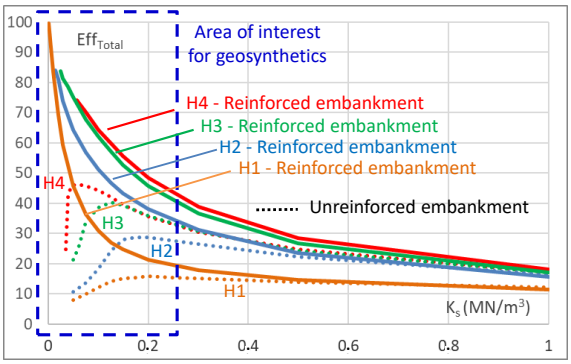

Figure 3. Load transfer efficiency versus the soft soil stiffness.

The results in Figure 3 show that the presence of geosynthetic reinforcement increases the overall efficiency of load transfer to the rigid inclusions, which has the effect of reducing settlement. The interest in using a geosynthetic sheet appears for soft soil stiffnesses that are sufficiently low. Beyond a certain compressibility of the soft soil, reinforcement is of only limited interest. This is explained by the need to produce significant displacements to mobilize membrane effects. In Figure 3, we see, as expected, that the greater the thickness of the LTP, the greater is the efficiency of the load transfers.

The contribution of the geosynthetic sheet to the load transfers mechanism towards the piles is obtained by comparing the sum of the vertical forces acting on the upper face of the geosynthetic sheet to those acting under the sheet. Knowing the total load transfered to the pile it is then possible to determine the load transfer fraction that only develops within the granular mattress. The contributions of the geosynthetic sheet (green dotted line) and the granular mattress (blue dotted line) to the load transfers are presented in Figure 4. It can be seen that the geosynthetic brings a significant contribution to the load transfers. We also note that the load transfers within the granular mattress are quite similar in the reinforced (blue dotted line) and non-reinforced (black dotted line) cases.

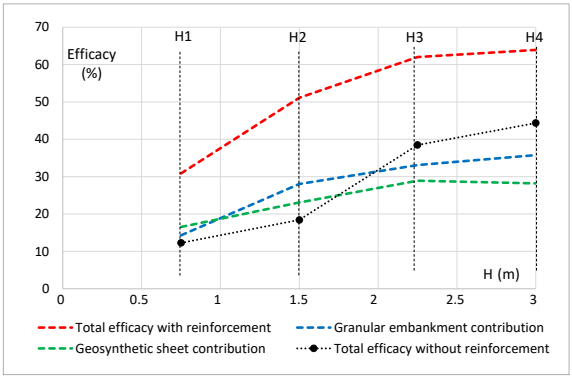

Figure 4. Load transfer mechanisms as a function of the height of the granular platform (K_s = 0.1 MN/m^3).

3.2 Contribution of the geosynthetic sheet to reinforcement

The analysis of the tensile forces in the geosynthetic sheet (Figure 5) shows that it is the geosynthetic strips located between the piles that are mainly stressed in tension.

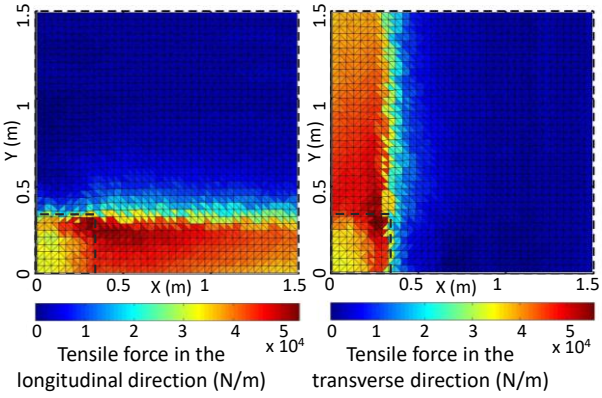

Figure 5. Tensile forces in the longitudinal and transverse directions (K_s=0.2 MN/m^3 - H2).

Between the piles, the distribution of tensions in the geosynthetic sheet (Figure 6) is not uniform due to the frictional forces between it, the soil of the granular mattress and the soft soil. The maximum tensile forces are, as might be expected, concentrated in the vicinity of the piles.

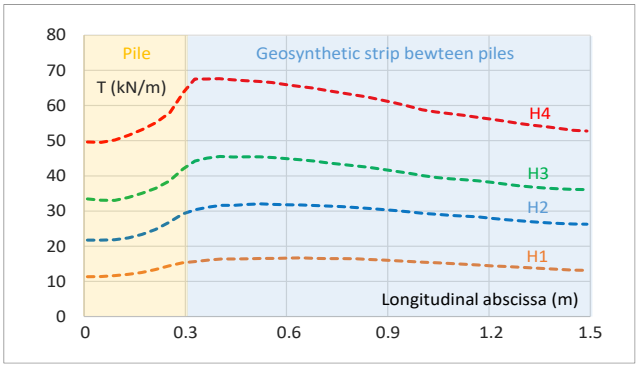

Figure 6. Tensile forces within the geotextile strip located between the piles (Ks=0.2 MN/m³).

When the geosynthetic sheet curves, it can mobilize part of the vertical forces applied to it through the membrane effect. By comparing the vertical stresses acting on and below the sheet, it is possible to determine the contribution of the geosynthetic to the load transfer mechanism. A zero stress difference means that the vertical forces acting on the sheet are fully transmitted to the soft soil while a non-zero stress difference means that the part of the sheet concerned is stressed by the membrane effect.

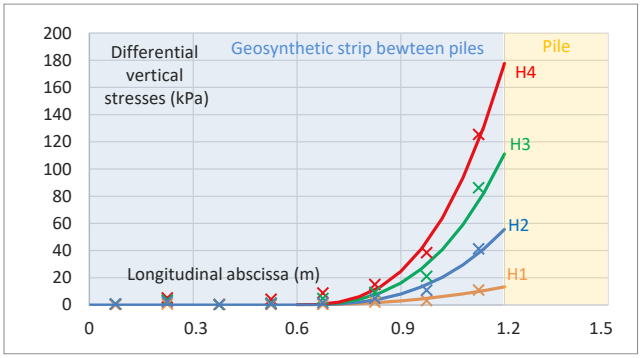

Figure 7. Differential vertical stresses acting on the geosynthetic strip located between piles (Ks=0.2 MN/m³).

On the strip of geosynthetic located between the piles (Figure 7) we see that the distribution of the differential stresses (difference between the upper and lower stresses) is non-uniform. This distribution is similar to a third-degree polynomial distribution, whatever the height of the granular mattress modeled. This distribution reflects the fact that the geosynthetic sheet is strongly curved in the vicinity of the piles and remains flattened in the center part of the network of piles. The analyze of the distribution of differential stresses on one mesh of the pile network shows that the geosynthetic strips located between the piles mobilize 85% of the whole differential stresses supported by the geosynthetic sheet. So, these geosynthetic strips mainly contribute to the reinforcement.

4 CONCLUSIONS

The numerical results showed that the vertical loads due to the granular emankment are transferred, on the one hand to the piles by load transfer within the granular mattress, by membrane effect following the curvature of the geosynthetic sheet, and to the soft soil which undergoes a vertical settlement. The geosynthetic strips located between the piles are the most stressed and contribute mainly to the reinforcement. The distribution of stresses on these geosynthetic strips takes a third degree polynomial form from which it con be deduced that 85% of the total loads are mobilized by the geosynthetic sheet. It has also been shown that the load transfer mechanisms within the granular fill are little affected by the presence of the geosynthetic sheet. All these conclusions will lead, by studying the vertical equilibrium of a portion of the geosynthetic sheet, to the development of a design method for the geosynthetic.

REFERENCES

Cundall, P.A., Strack, O.D.L. (1979). A discrete numerical modelling method for granular assemblies. *Geotechnique.* 29 (1), 47-65.

Salot, C., Gotteland, Ph., Villard, P. (2009). Influence of relative density on granular materials behavior: DEM simulations of triaxial tests. *Granular Matter*. 11 (4), 221-236. https://doi:10.1007/s10035-009-0138-2

Szarf, K., Combe, G., Villard, P. (2011). Polygons vs. clumps of discs: A numerical study of the influence of grains shape on the mechanical behaviour of granular materials. *Powder Technology.* 208(2), 279-288. https://doi:10.1016/j.powtec.2010.08.017

Tran, Q.A., Villard, P., Dias, D. (2019). Discrete and continuum numerical modeling of soil arching between piles. *International Journal of Geo-mechanics*.19(2). https://doi:10.1061/(ASCE)GM. 1943-5622.0001341

Villard, P., Chevalier, B., Le Hello, B., Combe, G. (2009). Coupling between finite and discrete element methods for the modelling of earth structures reinforced by geosynthetics. *Computer and Geotechnics*. 36, 709-717. https://doi: 10.1016/j.compgeo.2008.11.005

Proceedings of the XVIII ECSMGE 2024
GEOTECHNICAL ENGINEERING CHALLENGES
TO MEET CURRENT AND EMERGING NEEDS OF SOCIETY
© 2024 the Authors
ISBN 978-1-032-54816-6
DOI 10.1201/9781003431749-159
Open Access: www.taylorfrancis.com, CC BY-NC-ND 4.0 license

ECSMGE 24
XVIII EUROPEAN CONFERENCE ON SOIL MECHANICS AND GEOTECHNICAL ENGINEERING

Assessment of shear wave velocity variation in compacted soil using pulse transmission techniques

Évaluation de la variation de la vitesse des ondes de cisaillement dans un sol compacté à l'aide de techniques de transmission d'impulsions

C. Walker*, A. Heitor
University of Leeds, Leeds, UK
**cn19cbw@leeds.ac.uk*

ABSTRACT: In this paper, two techniques for benchmarking shear wave velocity in compacted soil during drying are compared. The two techniques considered are both pulse transmission techniques, i.e. bender elements and ultrasonic pulse testing. In past studies, bender elements have been used to monitor the shear wave velocities in soil media whereas ultrasonic pulse tests have been mainly used for determining pulse velocities of rocks because the soil media have higher damping characteristics. While the ultrasonic pulse test system is less established in geotechnical engineering applications compared to bender elements, it is less intrusive as the specimens do not need to be protruded. The results suggest that both pulse transmission systems provide comparable wave responses and thus appropriate for more wide use in geotechnical applications.

RÉSUMÉ: Dans cet article, deux techniques d'évaluation de la vitesse des ondes de cisaillement dans un sol compacté pendant le séchage sont comparées. Les deux techniques considérées sont des éléments de flexion-extension et des tests d'impulsions ultrasonores. Dans des études antérieures, des éléments de flexion-extension ont été utilisés dans le sol, tandis que les tests d'impulsions ultrasoniques ont été utilisés dans le roches. Bien que le système de test par impulsions ultrasoniques soit moins établi que les éléments de flexion -extension, il est moins intrusif car les échantillons n'ont pas besoin de faire saillie. Les résultats suggèrent également que les deux systèmes de transmission d'impulsions fournissent des réponses comparables et donc appropriés pour une utilisation plus large dans les applications géotechniques en sols.

Keywords: Pulse transmission test; unsaturated soils; compacted soils; ultrasonic testing; bender elements.

1 INTRODUCTION

Two configurations of the piezoelectric elements are used for soils testing, namely bender elements and ultrasonic transducers (Figure 1). The former is characterised by two piezoelectric ceramic elements joined to each side of an intermediate conduction shim, mounted vertically and embedded in a specimen (Santamarina et al., 2001). When a DC voltage, usually in the form of a sine wave, is applied to the bender element it deforms converting the electrical input into mechanical energy in the form of a shear wave. Comparatively, ultrasonic transducers consist of a polarised piezoelectric element with two electrodes on either face, bonded to a low impedance platen (wear plate). Excitation to produce shear waves is achieved when a voltage is applied to the element, aligning the polarized molecules causing it to change shape (Suwal and Kuwano, 2013). The piezoelectric element in the transducer is generally one half the thickness of its selected frequency. Unlike bender elements the frequency of the ultrasonic tests can not be altered during testing. The platen is also one quarter the thickness of the selected frequency of the transducer to ensure it is in phase with the piezoelectic element. The backing material generally has low impedance to attenuate waves travelling into the transducer. A couplant is also required between the platen and the specimen to ensure good contact to efficiently transmit the shear wave. Due to this configuration ultrasonic transducers do not require penetration of the specimen to transmit a wave, thus negating disturbance due to the insertion of the bender element tip, waterprofing and element robustness problems. This is especially important when considering changes in water content, as penetration may be difficult in dry clays or initial penetration may become too large or small due to volume changes. Despite this ultrasonic transducers are less common. Table 1 summarises the testing conditions of ultrasonic and acoustic testing in a variety of soils. Its clear that ultrasonic tests have only been conducted on a limited range of soils and few comparisons have been made between ultrasonic and

bender element testing techniques. This is important to consider due to the differences in wave propagation and configuration.

This paper therefore presents a comparison between the shear modulus results for bender elements and ultrasonic shear wave transducers upon drying for compacted kaolin clay at different water content levels.

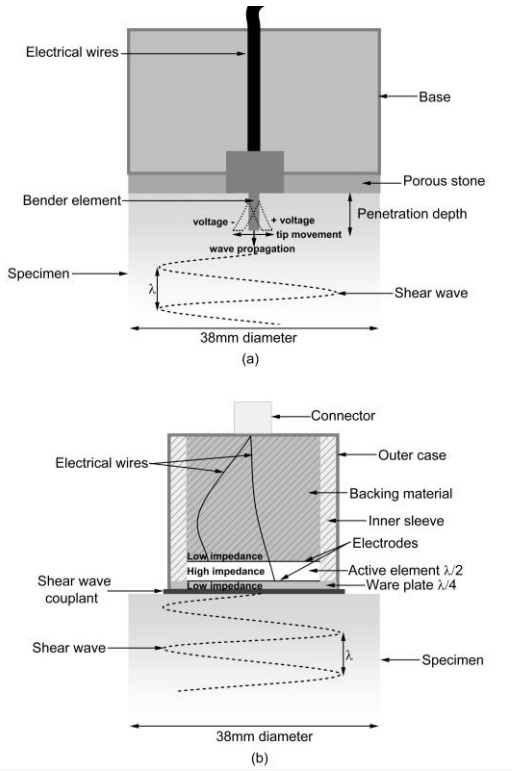

Figure 1. Pulse transmission tests: (a) bender elements and (b) typical ultrasonic transducer.

2 EXPERIMENTAL WORK

2.1 Compaction characteristics and drying

The kaolin clay specimens used in this study comprise of 62% medium and fine silt and 38% clay, with a liquid limit of 56% (fall cone), plasticity index of 23% and specific gravity of 2.61 (BS EN ISO 17892-12:2018+A2:2022). The specimens were statically compacted using a static stress of 1400 kPa (76mm x ⌀38mm). Compaction was completed in two layers to ensure consistent density througout the specimes (Walker et al., 2023). Figure 2 shows a comparison between standard Proctor (BS 1377-2:2022), and static compaction at 1400 kPa. Results show that at the optimum moisture content after static compaction specimens achieve >90% of the maximum Proctor dry unit weight. Statically compacted specimens were prepared at the OMC to mimick field conditions. Air drying was conducted at constant 40°C from the compacted water content (28.0%) to target water contents levels including 21.5% and 15.0%. Water content was controlled during drying by monitoring the weight of specimens to target weights. To ensure an even distribution of water content prior to the measurement of small strain stiffness, specimens were allowed to equilibrate for a minimum of 24 hours. This was determined by prior testing presented in Walker et al. (2023).

Table 1. Summary of literature testing conditions used in ultrasonic and acoustic pulse transmission techniques.

	Materials	Dimensions (diameter × length; mm)	Confining stress (kPa)	Testing frequency
Leong et al., 2004	kaolin	70 × 60	800	P wave: 90 kHz S wave: 76 kHz
	Compacted residual mudstone (S_r 1.0 and S_r 0.6)	70 × 105-118	800	
Brignoli et al., 1996	Saturated Ticino sand	50 × 100	30-500	P wave: 100 kHz S wave: 3 – 10 kHz
	Reconstituted saturated Pontida silty clay	50 × 100	50-500	
	Undisturbed offshore clay	50 × 100	30-100	
Cheng and Leong, 2014	Saturated kaolin	60 × 100-140	-	P wave: 100 kHz S wave: 49 kHz
	Changi sand (S_r 0.5)	60 × 100-140	-	
Mulmi et al., 2008	Dry Toyoura sand	50 × 100	50, 100, 200, 400	P wave: 4 – 16 kHz S wave: 4 – 16 kHz
Miturski et al., 2021	Compacted stabilized clay	80 × 80	Unconfined	P wave: 54 kHz
Slavova et al., 2010	Low plasticity silt	70 × 50	Unconfined	P wave: 46 kHz S wave: 39 kHz
Nakagawa et al., 1996	Saturated kaolin Saturated fine sand	- × 101	98 -490	P wave:200 kHz S wave: 3-5 kHz
George, 2009	Bonny silt	100 × 125	Unconfined	P wave: 20 kHz S wave: 20 kHz
	Heterogeneous mixture of sand, silt and clay			

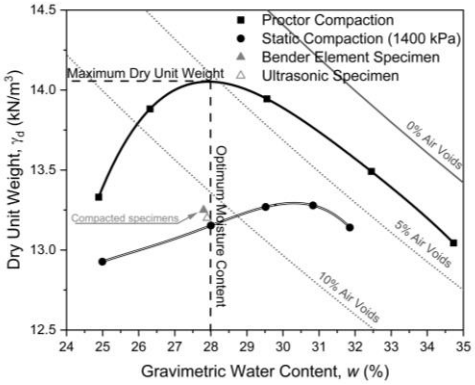

Figure 2. Compaction for kaolin clay (modified after Walker et al., 2023).

2.2 Pulse transmission tests

The bender elements (BE) system (VJ Tech) comprises of two elements (11.25mm long, 1.8mm wide, protruding thickness of 3.2mm) cantilevered in a pedestal and top cap. The signal was generated by a sine wave (VJ Tech Clisp software) and data was acquired using a sampling rate of 1000 kHz and 16-bit resolution for frequencies between 0.5 to 15 kHz. The shear wave for the ultrasonic system (USS) was generated by a 2 volt square wave (Pundit Lab system). A digital oscilloscope with a 12 bit resolution and 6250 kHz sampling rate was used to capture the data. Olympus normal incidence shear wave transducers (V150-RB), were used to transmit and capture the shear wave response and couplant was used to ensure good contact. Staking of approximelty 20 signals was used to mitigate background noise. The travel time (Δt_s) of the shear wave was detemined from the intial drop in the square wave (USS) and first rise in the sinusoidal wave (BE), to the first deflection of the received wave for both systems to allow suitable comparison. The shear modulus (G_0) was subsquently calculated as follows:

$$V_s = \frac{L_{pp/tt}}{\Delta t_s} \quad (1)$$

$$G_0 = \frac{\gamma_b}{g} V_s^2 \quad (2)$$

where the V_s is the shear wave velocity, L_{tt} and L_{pp} is the tip to tip or platen to platen distance, γ_b is bulk unit weight and g is the gravity acceleration. The 2.4 μs delay derived from the travel of the shear wave through the ultrasonic transducer's platen was also considered in the V_s calculation (Walker et al., 2023).

3 RESULTS

Identical compacted kaolin specimens (Table 2) were dried to selected gravimetric water contents and both bender elements and ultrasonic systems captured the variation in shear wave velocity. The shear wave response for both systems is presented in Figure 3, in addition to the wave travel path and wave length ratio ($L_{tt/pp}/\lambda$) of the chosen waveforms required to mitigate the influence of the near field effects (Arulnathan et al., 1998). Notably due to the increased frequency of ultrasoinc testing, the impact of the near field effect is mitigated. Tests were conducted at different water content levels show a reduction in travel time attributed to the increase in matric suction and thus stiffness of the soil. The arrival time of the BE is less than the USS as a result of the shorter distance between piezoelectric crystals due to the required BE specimen penetration. A comparison between the shear modulus for each technique is presented in Figure 4. The results show good agreement between both techniques at the selected water contents. The small discrepancy between techniques likely originates from interpretation of the waveforms in the time domain.

4 CONCLUSIONS

The benchmarking results established for both configurations of piezoelectric elements (BE and USS pulse transmission testing) show comparable shear waves response for both techniques. The results demonstrate the feasibility to conduct shear wave measurements without penetration using ultrasonic equipment. The implementation of ultrasonic testing in geotechnical applications not only can help reduce specimen disturbance but also problems due to penetration in dry soils. The results also demonstrate the feasibility of higher frequencies associated with ultrasonic testing for compacted soils. However, it must be noted that frequency during ultrasonic testing cannot be altered.

Table 2. Initial compacted conditions used in the bender element and ultrasonic testing.

Pulse Transmission	Material	Gravimetric Water Content, w: %	Dry Unit Weight, γ_d:KN/m^3	Void Ratio, e
Bender elements	kaolin clay	27.9	13.2	0.931
Ultrasonic	kaolin clay	27.5	13.3	0.927

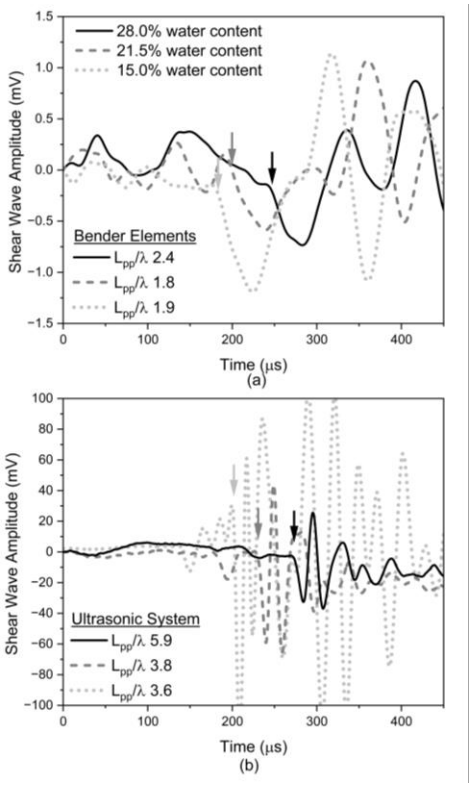

Figure 3. Received waveforms for compacted kaolin clay for (a) BE and (b) USS; arrows indicate Vs arrival.

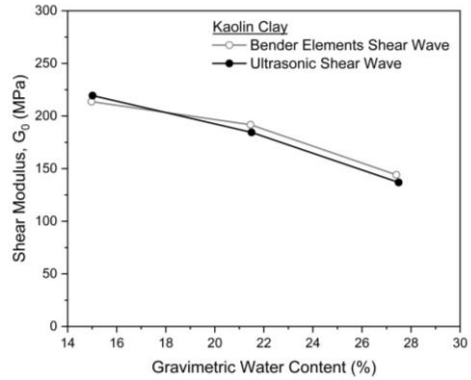

Figure 4. G_0 comparison between BE and the USS during drying at selected water contents.

ACKNOWLEDGEMENTS

The authors gratefully acknowledge the support provided by the School of Civil Eng. and financial support provided by EPSRC (EP/T517860/1). The assistance provided by Andrew Birch and Prof. Barry Clarke is gratefully appreciated.

REFERENCES

Arulnathan, R., Boulanger, R. W. and Riemer, M. F. (1998). Analysis of bender element tests. *Geotech. Testing Journal*, 21(2), pp.120-131. https://doi.org/10.1520/gtj10750j.

Brignoli, E. G., Gotti, M. and Stokoe, K. H. (1996). Measurement of shear waves in laboratory specimens by means of piezoelectric transducers. *Geotech. testing journal*, 19(4), pp.384-397. https://doi.org/10.1520/gtj10716j.

British Standards Institution. (2022). BS 1377-2:2022: Methods of test for soils for civil engineering purposes. BSI: London.

British Standards Institution. (2022). BS EN ISO 17892-12:2018+A2:2022. Geotechnical investigation and testing. BSI: London.

Cheng, Z. and Leong, E. C. (2014). A hybrid bender element-ultrasonic system for measurement of wave velocity in soils. ASTM International. https://doi.org/10.1520/gtj20120158.

George, L. (2009). *Characterization of unsaturated soils using acoustic techniques*. PhD, University of Vermont.

Leong, E.C., Yeo, S. H. and Rahardjo, H. (2004). Measurement of wave velocities and attenuation using an ultrasonic test system. *Canadian Geotechnical Journal*, 41(5), pp.844-860. https://doi.org/10.1139/t04-041.

Miturski, M., Sas, W., Radzevičius, A., Šadzevičius, R., Skominas, R., Stelmaszczyk, M. and Głuchowski, A. (2021). Effect of dispersed reinforcement on ultrasonic pulse velocity in stabilized soil. *Materials*, 14(22), p.6951. https://doi.org/10.3390/ma14226951.

Mulmi, S., Sato, T. and Kuwano, R. (2008). Performance of plate type piezo-ceramic transducers for elastic wave measurements in laboratory soil specimens. *Seisan Kenkyu*, 60(6), pp.565-569. https://doi.org/10.11188/seisankenkyu.60.565.

Nakagawa, K., Soga, K. and Mitchell, J.K. (1996). Pulse transmission system for measuring wave propagation in soils. *Journal of Geotechnical Engineering*, 122(4), pp.302-308. https://doi.org/10.1061/(ASCE)0733-9410(1996)122:4(302).

Santamarina, J. C., Klein, A. and Fam, M. A. (2001). Soils and waves: Particulate materials behavior, characterization and process monitoring. *Journal of Soils and Sediments*, 1(2), pp.130-130. https://doi.org/10.1007/bf02987719.

Slavova, D. Z., Weidinger, D. M., Sevi, A. F. and Ge, L. (2010). Evaluation of compacted silt characteristics by ultrasonic pulse velocity testing. *Proceedings of GeoFlorida 2010: Advances in Analysis, Modeling & Design*, West Palm Beach, USA, (pp. 1284-1293). https://doi.org/10.1061/41095(365)128.

Suwal, L. P. and Kuwano, R. (2013). Disk shaped piezo-ceramic transducer for P and S wave measurement in a laboratory soil specimen. *Soils and foundations*, 53(4), pp.510-524. https://doi.org/10.1016/j.sandf.2013.06.004.

Walker, C., Heitor, A. and Clarke, B. G. (2023). Impact of drying-wetting cycles on the small strain behaviour of compacted clay. *Transportation Geotechnics*, 42, p.101063. https://doi.org/10.1016/j.trgeo.2023.101063.

Proceedings of the XVIII ECSMGE 2024
GEOTECHNICAL ENGINEERING CHALLENGES
TO MEET CURRENT AND EMERGING NEEDS OF SOCIETY
© 2024 the Authors
ISBN 978-1-032-54816-6
DOI 10.1201/9781003431749-160
Open Access: www.taylorfrancis.com, CC BY-NC-ND 4.0 license

ECSMGE 24
XVIII EUROPEAN CONFERENCE ON SOIL MECHANICS AND GEOTECHNICAL ENGINEERING

Mechanical and physicochemical study of a cemented sand exposed to wetting and drying cycles

Etudes mécanique et physico-chimique d'un sable cimenté soumis à des cycles hydriques

A. Wassermann, A. Abdallah, O. Cuisinier*
LEMTA – Université de Lorraine – CNRS – Nancy, France

C. Diliberto, J.-M. Mechling
IJL - Université de Lorraine – CNRS – Nancy, France

**Olivier.Cuisinier@univ-lorraine.fr*

ABSTRACT: The core objective of this study was to analyze the impact of wetting/drying cycles on the mechanical behavior of a cement-treated sand. A comprehensive microstructural and physicochemical analysis were also performed to determine the physicochemical processes occurring in the samples along the cycles. Two types of wetting and drying cycles were applied to a 4%-cement treated sand. The results showed that although the cycles only slightly altered mechanical performance, they induced major mineralogical transformations in the cementitious phases. The results underline the importance of a protocol of imposing wetting/drying cycles for a more accurate assessment of the long-term performance of treated soils.

RÉSUMÉ: L'objectif principal de cette étude était d'analyser l'impact des cycles d'humidification/séchage sur le comportement mécanique d'un sable traité au ciment. Une analyse microstructurale et physicochimique complète a également été réalisée pour déterminer les processus physicochimiques se produisant au cours des cycles. Deux types de cycles hydriques ont été appliqués à un sable traité au ciment à 4 %. Les résultats ont montré que bien que les cycles n'altèrent que faiblement la performance mécanique, ils induisent des transformations minéralogiques majeures des phases cimentaires. Les résultats soulignent l'importance du protocole de cycles d'humidification/séchage imposé pour une évaluation plus précise de la performance à long terme des sols traités.

Keywords: Soil stabilisation; shear strength; dilatancy; microstructure; durability.

1 INTRODUCTION

Soil stabilization with hydraulic binders is employed to improve soil properties for the construction of earth structures such as road bases and subbases, dikes, and backfills. Several authors have shown that wetting/drying cycles can alter the mechanical behaviour of treated soils. The extent of the degradation is a function of several parameters, such as the initial dry density of the stabilized soil, the moisture content, mineralogy, and the amount of binder. An important additional factor is the method employed to apply wetting and drying cycles in laboratory studies. Numerous approaches for imposing drying/wetting cycles have been employed with varying durations for the wetting and drying phases, wetting techniques (such as capillary rise or immersion), and drying phase temperatures (air-drying or oven-drying). Most earlier studies applied cycling conditions derived from the ASTM D559 (ASTM 2015) standard, which suggests immersing for 5 hours in water at room temperature, followed by 42 hours of oven-drying at 71°C. However, this method can be considered to be aggressive compared to solicitations endured on-site by geotechnical structures since it includes full immersion of the samples and complete drying under temperature. Some authors evaluated the impact of the amplitude of the wetting and drying cycle; for instance, by applying suction control techniques. They reported that mechanical performance degradation increased with the magnitude of the wetting/drying cycles (e.g. Menaceur et al., 2021). The impact of the wetting protocol should also be carefully considered. The immersion of samples in water can also induce progressive leaching of the treatment product over time, which may result in lowering the soil performance in the long term. Thermal conditions are also of primary importance since the setting reactions of cement are impacted by temperature.

Varying experimental conditions may also trigger different alteration mechanisms associated with the cycles leading to significant behaviour change compared with what could occur in situ. Some authors also highlighted the role of carbonation on the long-term behaviour of stabilized soils. The extent of the degradation caused by carbonation is a function of temperature and relative humidity (Vitale et al. 2021).

In this context, the main purpose of this study was to analyse the impact of the drying protocol on the ageing of cement-treated sand exposed to wetting and drying cycles at different scales. The analysis of the mechanical behaviour of the samples was associated with an investigation of the microstructure after the cycles, and completed by a physico-chemical analysis of the cement-treated sand.

2 MATERIALS AND METHODS

2.1 Sample preparation

The selected soil is a sand sampled in the eastern part of France. According to the French classification system (GTR, 2023), it is classified as an S1-type soil, and in accordance with the Unified Soil Classification System, it is categorized as an SW soil. The D_{50} is 0.8 mm. The Portland cement chosen for this study is CEM I 52.5 N. This cement has a specific gravity of 3.15. The sand and cement were hand-mixed, and then water was added to reach a water content of 7%. Once the mixture was homogeneous, the blend was compacted in three layers with a piston and a manual press in a two-part mould (100 mm high and 50 mm wide). The targeted dry unit weight was 17 $kN.m^{-3}$.

2.2 Wetting and drying cycle protocol

To assess the impact of the intensity of the cycles on the mechanical behaviour, two different methods of wetting/drying cycles were used. The ASTM standard D559 (ASTM, 2015) served as the basis for the type-I cycle. The samples were wetted by being submerged in water at room temperature for 8 hours and dried in an oven for 16 hours at 65 °C. The type-II cycle protocol was inspired by the literature (Mehenni, 2015). Water immersion for 48 hours was used to achieve the wetting process. The drying phase was conducted in a climatic chamber at a temperature of 20 °C and a relative humidity of 50% for 120 hours.

The main difference between the two cycles is the drying protocol. Compared to the type-I cycle, the type-II cycle was thought to be less aggressive. Its purpose was to impose weathering in accordance with the environmental conditions that an engineered structure is anticipated to be exposed to over the course of its lifespan.

2.3 Triaxial tests

Triaxial testing campaign was carried out with consolidated drained (CD) tests that were run on a conventional triaxial system apparatus. In this paper, only the results obtained with one confining effective pressure of 100 kPa are introduced. The shearing velocity was fixed at 0.1 mm/min. More details about the experimental protocol are available in Wassermann et al. (2022).

2.4 Physico-chemical test protocols

Microlevel observations were performed on fresh breaks on the sample using a scanning electronic microscope (SEM). Secondary electron (SE) images were processed at an accelerating voltage of 15 kV and a working distance of 15mm. The SEM used in this study was a TESCAN® Vega3. The samples were stored in a desiccator after the cycles or after curing time before being oven-dried at 65°C. Then, they were cut into 1 to 2cm cubic pieces, and the surface was metallized. The X-ray diffraction technique (XRD) and thermogravimetric analysis/differential thermal analysis (TGA/DTA) were used to track any alteration of the cementitious phases during the cycles.

2.5 Experimental program

Specimens prepared with 4% cement were submitted to wetting/drying cycles. Each specimen was duplicated with a control specimen that was made at the same time and kept in sealed containers at a controlled room temperature. While the test sample was put through wetting-drying cycles, the control specimen was not subjected to any solicitation. The triaxial tests were then performed on the same day on the two samples after 1, 3, 6, 9, 12, 18 and 24 cycles. For the type-I cycles, the whole procedure required almost one month of experiments, while it required 6 months for the type-II cycles. The physico-chemical analyses and the microstructural investigations were performed on samples exposed to 24 cycles as well as on a sample cured in a sealed container.

3 MECHANICAL BEHAVIOUR

For a 4%-cement-treated sand after a 14-day cure at a constant water content, the maximum deviatoric stress q_{max} has been determined to be close to 1550 kPa by performing 4 triaxial tests. This value will be taken as a reference to quantify the impact of the cycles.

After one cycle, q_{max} was equal to 1146 kPa and 1268 kPa for the type-I and type-II cycles (Figure 1 & 2). The first cycle decreased the maximum deviatoric stress by 26% for the type-I cycle and by 18% for the type-II cycle compared to the reference specimen cured at a constant water content. Subsequent cycles led to a slight increase in q_{max}. For both cycle types, there was an increase in q_{max} after the first three cycles, up to 1376 kPa for the type-I cycles and to 1323 kPa for the type-II cycles. For the type-I cycles, the maximum deviatoric stress then decreased until the 12th cycle, reaching a value of 1022 kPa. Then, until the 24th cycle, the maximum deviatoric stress tended to stabilize. One can notice a decrease in the secant modulus at 50% strength, E_{50}, with cycles.

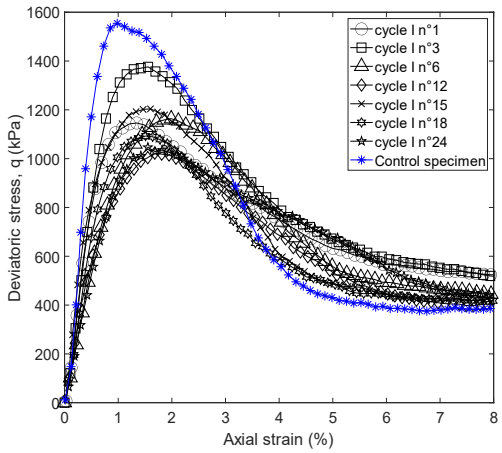

Figure 1. Influence of the wetting–drying cycles on the stress–strain behaviour after type-I cycles.

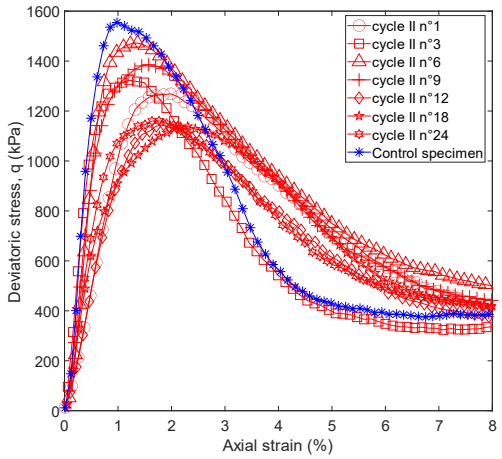

Figure 2. Influence of the wetting–drying cycles on the stress–strain behaviour after type-II cycles.

Concerning the type II cycles, q_{max} continued to increase until the 6th cycle to reach a value of 1472 kPa. Then, it decreased until the 12th cycle down to 1145 kPa (-26% compared to the control specimen). Similarly to the type-I cycles, the values of the maximum deviatoric stress remained constant until the 24th cycle (1138 kPa after 18 cycles and 1160 kPa after 24). A comparison of the maximum deviatoric stresses after each cycle is shown in Figure 3. A decrease in the E_{50} stiffness with cycles can also be noticed.

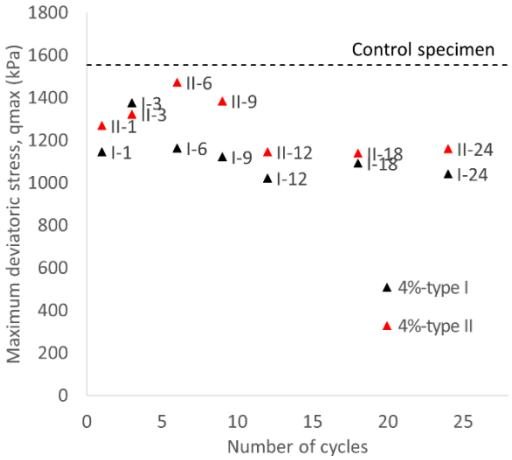

Figure 3. Influence of the type and the numbers of wetting–drying cycles on the maximum deviatoric stress.

4 SEM OBSERVATIONS

The cementitious gel seems to homogeneously encapsulate the surface of the sand grains and create a coating on the grains (Figure 4a and b). After 24 type-I cycles, the porosity remains open with pores of approximately a few tens of micrometers (Figure 4c and d). At 350X magnification, the cementitious paste still seems to coat the sand grains. Some cracks are noticeable all over the surface and are observed in what appeared to be secondary compounds. These cracks are more visible at a magnification of 1000X. Additionally, at this magnification, some needle-shaped compounds of approximately 20 µm in length were detected inside the pores. After 24 type-II cycles the porosity seems more closed than in the other samples (Figure 4e and f). At a higher magnification factor, needle-shaped components are found; they seem to be more frequent than after type-I cycles and cover almost the entire surface of the observed quartz grains. Additionally, the needles appear longer than 20 µm, indicating that they are likely to still be developing in the pores.

5 THERMOGRAVIMETRIC ANALYSIS

For the sample cured at a constant water content, there is a peak at approximately 110 °C to 180 °C, which corresponds to the decomposition of hydrated cementitious compounds such as ettringite or CSH and also residual water (Figure 5). There is a peak at approximately 450 °C, which is the identification peak for portlandite decomposition. The TGA for the

samples after cycles (types I and II) showed that there is an important mass loss between 600 °C and 800 °C, which corresponds to the loss of carbonates ($CaCO_3$) such as calcite. In the case of the sample after 24 type-II cycles, there is a large peak in the range of 110 to 180 °C, indicating the presence of cementitious compounds such as ettringite. This peak is less visible after the type-I cycles. For the two samples after the cycles, there is no peak at approximately 450°. The amount of calcite is higher after type-II cycles than after type-I cycles, which is in good agreement with the XRD observations.

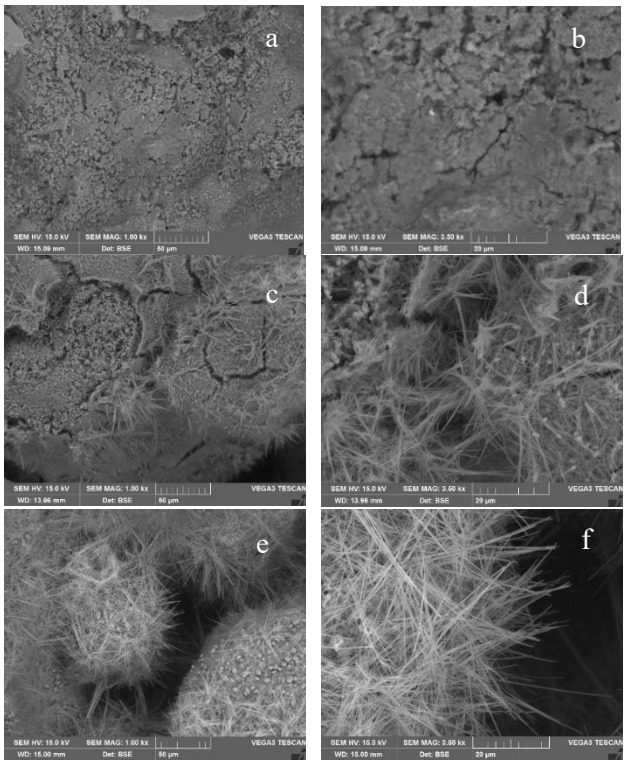

Figure 4. Microstructure of the samples before (a & b) and after 24 cycles I (c & d) and 24 cycles II (e & f).

6 CONCLUSION

The aim of this study was to better understand the processes induced by a large number of wetting/drying cycles, both mechanical and physicochemical. The results showed that the cycles induced a limited degradation of the mechanical macroscopic behaviour of the sand samples after the 24th cycle. Despite this limited impact of the cycles at the macroscale, the physico-chemical analysis and the microscopy showed that the cycles had a strong impact on the binding phases with two major processes associated: carbonation and the formation of ettringite.

Modifying the wetting and drying processes not only slightly impacted the macromechanical behaviour but also the microstructure by influencing the physico-chemical processes involved. Indeed, hydraulic binders are sensitive to several external conditions, such as temperature or humidity variations, that could promote processes such as carbonation. This phenomenon was evidenced in the samples after the wetting and drying cycles.

This study demonstrated that the intense mineralogical transformations that affected the bonding only had a limited effect on the macroscopic mechanical behaviour of the cement-treated soil. It also highlighted the importance of the cycling conditions. Indeed, it has been shown that the type of cycles has an impact on both the mechanical behaviour and its degradation as well as on the extent of ettringite formation and carbonation.

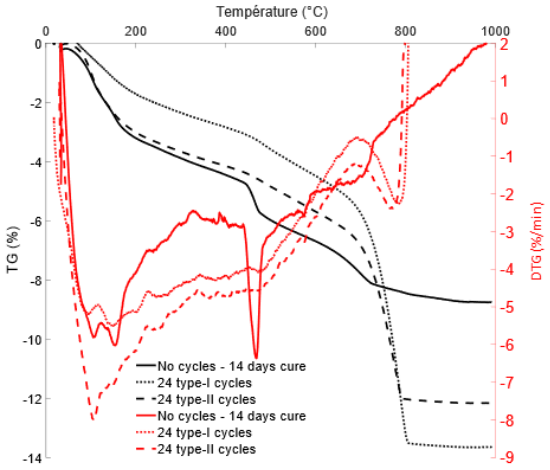

Figure 5. Thermogravimetric analysis curves after curing at constant water content and after the cycles.

REFERENCES

ASTM (2015) D559/D559M − 15 : Standard Test Methods for Wetting and Drying Compacted Soil-Cement Mixtures.

Cerema (2023) IDRRIM. Guide des terrassements des remblais et des couches de forme. Fascicule 1 - Principes Généraux

Mehenni A (2015) Comportement hydromécanique et érosion des sols fins traités. Thèse de doctorat, Université de Lorraine, France.

Menaceur H, Cuisinier O, Masrouri F and Eslami H (2021) Impact of monotonic and cyclic suction variations on the thermal properties of a stabilized compacted silty soil. Transportation Geotechnics 28:100515.

Vitale E, Deneele D and Russo G (2021) Effects of carbonation on chemo-mechanical behaviour of lime-treated soils. Bull Eng Geol Environ 80:2687–2700.

Wassermann A, Abdallah A and Cuisinier O (2022) Impact of wetting and drying cycles on the mechanical behaviour of a cement-treated soil. Transportation Geotechnics 36.

Proceedings of the XVIII ECSMGE 2024
GEOTECHNICAL ENGINEERING CHALLENGES
TO MEET CURRENT AND EMERGING NEEDS OF SOCIETY
© 2024 the Authors
ISBN 978-1-032-54816-6
DOI 10.1201/9781003431749-161
Open Access: www.taylorfrancis.com, CC BY-NC-ND 4.0 license

ECSMGE 24
XVIII EUROPEAN CONFERENCE ON SOIL MECHANICS AND GEOTECHNICAL ENGINEERING

Application of the isotache law and the power creep law on prediction of long-term consolidation behaviour

Application de la loi isotache et de la loi de fluage à la prédiction du comportement de consolidation à long terme

Y. Watabe*
Hokkaido University, Sapporo, Japan

Y. Miyata
National Defence Academy, Yokosuka, Japan

**watabe@eng.hokudai.ac.jp*

ABSTRACT: In this study, it was shown that the isotache law is essentially the same as the power creep law, but the formulations of these two are different. The model equations are applied to the results of the multi-stepwise constant rate of strain (CRS) consolidation test. It was clarified that the isotache law (or power creep law) is applicable for the test result. Strain rate dependency of two Osaka Bay clays (marine clays collected from the Kansai International Airport and the Yumeshima Island) was discussed through comparison of isotache parameters.

RÉSUMÉ: Dans cette étude, il a été démontré que la loi d'isotache est essentiellement la même que la loi de fluage, mais que les formulations de ces deux lois sont différentes. Les équations du modèle sont appliquées aux résultats de l'essai de consolidation à vitesse de déformation constante (CRS) en plusieurs étapes. Il a été précisé que la loi d'isotache (ou loi de fluage) peut s'appliquer aux résultats de l'essai. La dépendance de la vitesse de déformation de deux argiles de la baie d'Osaka (argiles marines prélevées à l'aéroport international du Kansai et sur l'île de Yumeshima) a été examinée en comparant les paramètres d'isotache.

Keywords: Long-term consolidation; strain rate dependency; isotache; creep.

1 INTRODUCTION

Over the past 70 years, many researchers have attempted to apply the isotache law, which expresses a unique relationship among stress-strain-strain rate, i.e., the strain rate dependency of compression curve, focusing on the effect of viscosity in long-term consolidation of clay.

In this study, first, it was shown that the isotache law is essentially the same as the power creep law, which is one of the classical mechanical models, but the formulations of these two are different. Based on the isotache law and the power creep law, model equations were derived, respectively. And then, the model equations are applied to the results of the multi-stepwise constant rate of strain (CRS) consolidation test. Finally, strain rate dependency of two Osaka Bay clays (marine clays collected from the Kansai International Airport and the Yumeshima Island) was discussed through comparison of isotache parameters used in the models, and calculated long-term consolidation settlement behaviour as well.

2 MODEL DESCRIPTION

The first author and his colleagues (Watabe et al. 2008; 2012; Watabe and Leroueil 2015) have conducted long-term consolidation tests and multi-stepwise CRS consolidation tests for various worldwide clays, including the marine clays at the Kansai International Airport, and have modelled the strain rate dependency in long-term consolidation behaviours. The strain rate dependency has been rheologically modelled as "isotache law", which is essentially the same approach as "power creep law in conjunction with overstress concept" in the classical mechanics, even though these are expressed by different equations. An outline of these models is described as follows.

The isotache law of compression curve in consolidation behaviour was first found by Šuklje (1957). In previous studies by the first author and his colleagues, the "isostache law" is rheologically modelled by finding the strain rate dependency of the consolidation yield stress by fitting the "shape" of the compression curve which is normalized by the

consolidation yield stress σ'_p based on the method proposed by Leroueil et al. (1985)

The equations can be written in the form of visco-plastic strain ε_{vp} and described by Equations (1) – (3):

$$\varepsilon_{vp} = \varepsilon - \varepsilon_e \quad (1)$$

$$\sigma'/\sigma'_p = f(\varepsilon_{vp}) \quad (2)$$

$$\sigma'_p = g(\dot{\varepsilon}_{vp}) \quad (3)$$

Watabe et al. (2008) showed that the consolidation yield stress converges to the lower limit σ'_{pL} as the visco-plastic strain rate $\dot{\varepsilon}_{vp}$ decreases, and proposed Equation (4) for the strain rate dependency of the consolidation yield stress σ'_p:

$$\ln\frac{\sigma'_p-\sigma'_{pL}}{\sigma'_{pL}} = c_1 + c_2\ln\dot{\varepsilon}_{vp} \quad (4)$$

where c_1 and c_2 are constants, and together with the lower limit of consolidation yield stress, σ'_{pL}, are referred to as isotache parameters. Watabe et al. (2012) conducted experiments for a variety of clays and found that the values of the isotache parameter are almost common regardless of the clay type or condition. The parameters commonly applicable to many clays are $\sigma'_{pL}/\sigma'_{p0}$ = 0.70 and c_1 = 0.935, where σ'_{p0} is the consolidation yield stress corresponding to $\dot{\varepsilon}_{vp} = 1.0 \times 10^{-7}$ s^{-1} that is almost equivalent to the strain rate at elapsed time of 24 hours in incremental loading oedometer test. Using these values, the parameter c_2 is automatically determined as in Equation (5):

$$c_2 = \frac{\ln\frac{\sigma'_p-\sigma'_{pL}}{\sigma'_{pL}} - c_1}{\ln\dot{\varepsilon}_{vp}} = \frac{\ln\frac{1-0.7}{0.7} - 0.935}{\ln(1.0\times10^{-7})} \quad (5)$$

Equation (4) models the fact that the consolidation yield stress σ'_p converges to the lower limit σ'_{pL} when the strain rate becomes infinitesimal, but it can be easily transformed into an equation similar to the power creep law in conjunction with overstress concept expressed as Equation (6) (Watabe and Leroueil, 2015):

$$\dot{\varepsilon}_{vp} = c_3\left(\frac{\sigma'_p-\sigma'_{pL}}{\sigma'_{pL}}\right)^{c_4} \quad (6)$$

where $c_3 = \exp(-c_1/c_2)$ and $c_4 = 1/c_2$. Hereafter, calculations using this method will be referred to as "calculation with isotache law" evaluated by rheological approach.

On the other hand, the description of the power creep law in conjunction with overstress concept in classical mechanics is expressed as follows: Visco-plastic strain occurs when the present effective stress σ' is larger than the present yield stress σ'_y (which, as described later, corresponds to the lower limit of consolidation yield stress σ'_{pL} in the isotache law in the initial state). The model is based on the concept that creep deformation in consolidation will eventually terminate as the structure gradually becomes denser (harder), and the strain rate is expressed as Equation (7):

$$\dot{\varepsilon}_{vp} = a\left(\frac{\sigma'-\sigma'_y}{\sigma'_y}\right)^b \quad (7)$$

where a and b are constants.

Hereafter, calculations using this method will be referred to as "power creep law" based on the classical mechanical model. The isotache law and the power creep law, although formulations of these methods are different as described above, these two laws are essentially the same.

In the model equations above, the compression curves obtained from the tests can be used directly. However, as with constitutive models of soil in general, a compression curve expressed in strain is assumed as a bi-linear relationship expressed by the compression index λ_ε and the swelling index κ_ε. The parameters for the Pleistocene clay Ma9 collected at the construction site of the Kansai International Airport in Osaka Bay are shown in Table 1 as the representative values obtained in the previous studies, and used in the following calculations.

Table 1. Input parameters for calculation (c_3 and c_4 are calculated from c_1 and c_2, respectively).

	Kansai Airport	**Yumeshima Island**
$\sigma'_{pL}/\sigma'_{p0}$	0.70	0.70
σ'_{p0} (kPa)	1408	242
σ'_y (kPa)	980	169
c_3, a	2.127×10^{-4}	7.889×10^{-4}
c_4, b	9.043	7.873
σ'_{v0} (kPa)	1016	550
e_0	1.420	2.067
C_c (λ_ε)	1.000 (0.1790)	1.204 (0.1705)
C_s (κ_ε)	0.100 (0.0179)	0.126 (0.0179)

The simulation results of the multi-stepwise CRS consolidation test, in which the strain rate was varied stepwise by one order of magnitude sequentially for each 1% increment of strain in the range of 3.3×10^{-12} s^{-1} to 3.3×10^{-5} s^{-1} after the strain reached 5%, are shown in Figure 1. The results calculated based on the isotache law and the power creep law are superimposed on the same figure, but the results are coincident with each other and cannot be distinguished

between them. Here, for the calculation with the power creep law, it was assumed that $\sigma'_y = \sigma'_{pL}$ in the initial state. That means that σ'_y corresponds to the consolidation yield stress of the compression curve with infinitesimal strain rate, considering the relation of $\sigma'_{pL}/\sigma'_{p0}$ (= 0.7). Even in the case of multi-stepwise CRS consolidation test, in which the strain rate is stepwise varied sequentially, isotache properties in strain rate dependency are consistent with the isotache compression curves.

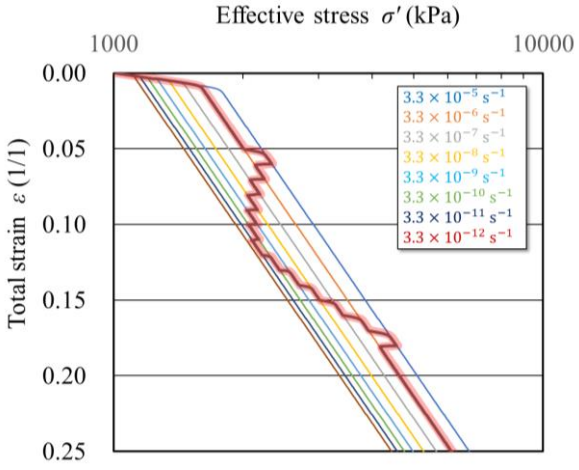

Figure 1. Calculation results for the strain rate dependency (isotache properties) of the compression curve for Ma9 collected from the Kansai International Airport.

3 MULTI-STEPWISE CRS CONSOLIDATION TEST

Constant rate of strain (CRS) consolidation test was conducted in the manner proposed by Watabe et al. (2019) for Pleistocene clay Ma9 collected from the Kansai International Airport in Osaka Bay under back pressure of 200 kPa. Consolidation pressure was increased to the effective overburden stress σ'_{v0} by applying a constant strain rate of 3.3×10^{-6} s^{-1}, then switched to constant stress control and preliminary consolidation under the effective overburden stress was conducted for 7 days, and then, a constant strain rate (3.3×10^{-6} s^{-1}) loading was applied. After the specimens were sufficiently yielded, the strain rate was stepwise varied sequentially from 3.3×10^{-5} s^{-1} to 3.3×10^{-8} s^{-1}, and the loading pattern was set so that the specimens would experience twice at each strain rate. Figure 2 shows the compression curve obtained by multi-stepwise CRS consolidation test after preliminary consolidation at the effective overburden stress. The vertical axis of the figure is the total strain, however, the value shown in the figure were obtained by offsetting at the completion of 7 days of preliminary consolidation at the effective overburden stress.

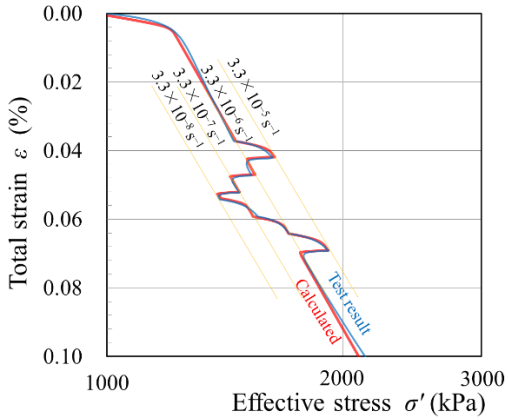

Figure 2. Comparison of test result and calculation result of the muti-stepwise strain-rate loading consolidation test for Ma9 collected from the Kansai International Airport.

To obtain a better fitting to the test results, the compression index C_c (or λ_ε) and the swelling index C_s (or κ_ε) were modified by a factor of 0.97 from the value shown in Table 1 and the value of parameter c_1 by a factor of 0.877. The strain rate dependency of the compression curves obtained as a test result can be well expressed by the isotache model.

Similar tests were conducted for Pleistocene clay Ma12 collected from the Yumeshima Island in Osaka Bay, and an example of the results is shown in Figure 3. The strain on the vertical axis is calculated from the initial specimen height, but is shown offset by the amount of strain at the elapsed time of 7 days in the preliminary consolidation under the effective overburden stress σ'_{v0}.

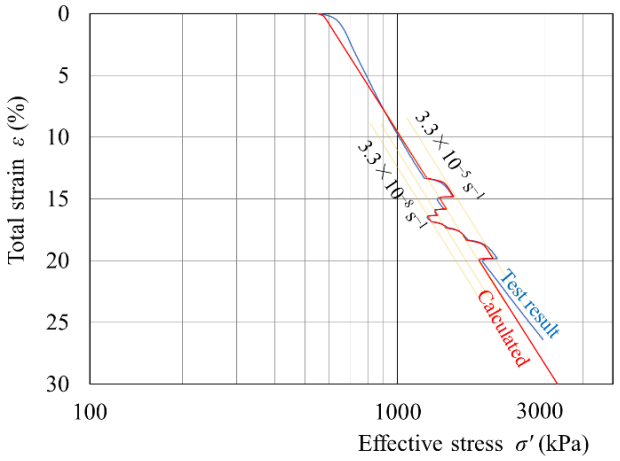

Figure 3. Comparison of test result and calculation result of the muti-stepwise strain-rate loading consolidation test for Ma12 collected from the Yumeshima Island.

The strain rate dependency of the compression curve is modelled and expressed by the isotache law using Equation (4) or Equation (5) (note here that it is the same as the power creep law using Equation (6)). The parameters used in the calculation are listed in Table 1. The isotache parameters were set to $\sigma'_{pL}/\sigma'_{p0}$ =

0.7 (from previous studies) and c_1 = 1.20 (by fitting) and c_2 = 0.127 (automatically calculated from both $\sigma'_{pL}/\sigma'_{p0}$ and c_1). Calculated curve corresponding to multi-stepwise CRS loading is well expressed the test results.

4 DISCUSSION

Because naturally deposited intact clay sample was examined in this study, the compression curve in the normal consolidation domain is slightly convex downward. In the calculation, the compression curve was represented by a bi-linear relationship with compression index λ_ε and swelling index κ_ε expressed in terms of strain, therefore, there are some deviations in the low and high consolidation pressure domains. However, the fitting was successful, especially for the portion of the multi-stepwise CRS loading (Figures 2 and 3).

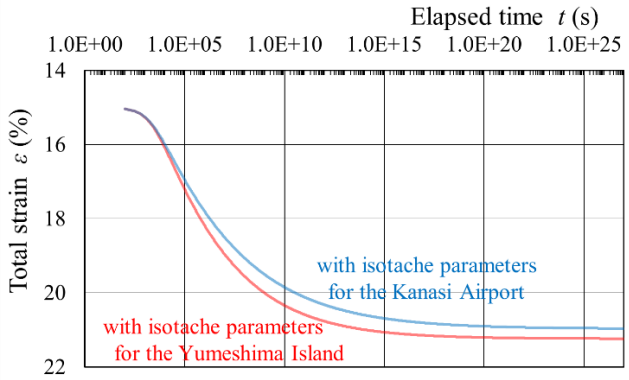

Figure 4. Calculated results of long-term consolidation settlement for the clay collected from the Yumeshma Island as a relationship between total strain and elapsed creep time.

Aiming to express all test results at each site using the same isotache parameters, $\sigma'_{pL}/\sigma'_{p0}$ = 0.7 (obtained from previous studies) was fixed, and c_1 = 1.20 (by fitting) and c_2 = 0.127 (automatically calculated) were obtained. According to a previous studies, the isotache parameters for marine clays at the Kansai International Airport are commonly determined with $\sigma'_{pL}/\sigma'_{p0}$ = 0.7, c_1 = 0.935, and c_2 = 0.111. The value of c_1 for marine clays at the Yumeshima Island is 28% larger than that of marine clays at the Kansai International Airport.

Figure 4 shows an example of calculated results showing how this difference affects the long-term consolidation behaviour. In these calculations, soil parameters obtained for the clay at the Yumeshima Island were used, but only isotache parameters were set respectively for each clay. In the figure, the data is plotted only in creep stage starting at a total strain of 15% against the elapsed creep time. It can be seen that secondary consolidation proceeds slightly faster in the Yumeshima clay than in the Kansai Airport clay, and that the final settlement is slightly larger.

5 SUMMARY

In this study, isotache properties in consolidation behaviour were evaluated based on isotache law, and power creep law as well. Even though the two laws are based on different approaches to express strain rate dependency in consolidation behaviour, these laws are essentially the same, which expresses strain rate dependency using a power law with overstress concept.

The strain rate dependency of consolidation behaviour was experimentally investigated by multi-stepwise CRS test for seabed clays in Osaka Bay. The strain rate dependency of the clay collected from the Yumeshima island showed isotache parameter c_1 of 1.20, which is slightly larger than c_1 of 0.935 for the clays collected from the Kansai International Airport.

REFERENCES

Leroueil, S., Kabbaj, M., Tavenas, F. and Bouchard, R. (1985). Stress-strain-strain rate relation for the compressibility of sensitive natural clays. *Géotechnique*, 35(2), 159–180. https://doi.org/10.1680/geot.1985.35.2.159.

Šuklje, L. (1957). The analysis of the consolidation process by the isotache method. *Proceedings of the 4th International Conference on Soil Mechanics and Foundation Engineering*, Vol. 1, Butterworths, London, pp. 200–206.

Watabe, Y. and Leroueil, S. (2015). Modelling and implementation of isotache concept for long-term consolidation behavior. *International Journal of Geomechanics*, ASCE, 15(5), A4014006. http://dx.doi.org/10.1061/(ASCE)GM.1943-5622.0000270.

Watabe, Y., Udaka, K. and Morikawa, Y. (2008). Strain rate effect on long-term consolidation of Osaka bay clay, *Soils and Foundations*, 48(4), 495–509. http://dx.doi.org/10.3208/sandf.48.495.

Watabe, Y., Udaka, K., Nakatani, Y. and Leroueil, S. (2012). Long-term consolidation behavior interpreted with isotache concept for worldwide clays. *Soils and Foundations*, 52(3), 449–464. http://dx.doi.org/10.1016/j.sandf.2012.05.005.

Watabe, Y., Yoneda, A., Hashizume, H. and Ono, Y. (2019): Multi-stepwise strain-rate loading consolidation test to evaluate strain rate dependency, *Proceedings of Geotec Hanoi 2019*, *Geotechnics for Sustainable Infrastructure Development*, Springer Singapore, pp.1253–1258.

Proceedings of the XVIII ECSMGE 2024
GEOTECHNICAL ENGINEERING CHALLENGES
TO MEET CURRENT AND EMERGING NEEDS OF SOCIETY
© 2024 the Authors
ISBN 978-1-032-54816-6
DOI 10.1201/9781003431749-162
Open Access: www.taylorfrancis.com, CC BY-NC-ND 4.0 license

ECSMGE 24
XVIII EUROPEAN CONFERENCE ON SOIL MECHANICS AND GEOTECHNICAL ENGINEERING

The impact of small strain stiffness parameters on geotechnical numerical modelling: a case study in Budapest, Hungary

L'impact des paramètres de rigidité des petites déformations sur la modélisation numérique géotechnique: une étude de cas à Budapest, Hongrie

Á. Wolf*, K. Ficzek
Széchenyi István University, Győr, Hungary

Zs. Szilvágyi
Geoplan Ltd., Budapest, Hungary

**wolf@sze.hu*

ABSTRACT: Geotechnical numerical modelling has become a standard tool for analyzing complex geotechnical structures. However, determining small strain stiffness parameters presents challenges for engineers. The widely used HSSmall model requires estimation of the initial shear modulus (G_0) and shear strain parameter ($\gamma_{0.7}$), which significantly influence the behaviour. In this study, their impact was investigated on numerical modelling results using soil data from a site in Hungary. We compare the results of seismic CPT and MASW, which yielded slightly different results for shear wave velocity with depth. Plaxis 2D software is used to analyze the effects of parameters on different geotechnical structures. Additionally, we conduct a comprehensive parameter analysis to assess the influence of G_0 and $\gamma_{0.7}$. Our findings provide valuable insights into the significance of small strain stiffness parameters in geotechnical numerical modelling and highlight the need for accurate determination of these parameters for reliable predictions of structural behaviour. This research contributes to improving the understanding of the challenges associated with small strain stiffness parameters and their impact on numerical modelling and can aid geotechnical engineers in selecting appropriate parameter values for their projects.

RÉSUMÉ: La modélisation numérique géotechnique est devenue un outil standard pour l'analyse des structures géotechniques complexes. Cependant, la détermination des paramètres de rigidité pour les petites déformations représente un défi pour les ingénieurs. Le modèle HSSmall, largement utilisé, nécessite l'estimation du module de cisaillement initial (G_0) et du paramètre de déformation de cisaillement ($\gamma_{0.7}$), qui influencent considérablement le comportement. Dans cette étude, nous étudions leur impact sur les résultats de la modélisation numérique en utilisant les données du sol d'un site en Hongrie. Nous comparons les résultats de la CPT sismique et de la MASW, qui ont donné des résultats légèrement différents pour la vitesse des ondes de cisaillement en fonction de la profondeur. Le logiciel Plaxis 2D est utilisé pour analyser les effets des paramètres sur différentes structures géotechniques. En outre, nous effectuons une analyse complète des paramètres pour évaluer l'influence de G_0 et de $\gamma_{0.7}$ sur les résultats de la modélisation. Nos résultats fournissent des indications précieuses sur l'importance des paramètres de rigidité des petites déformations dans la modélisation numérique géotechnique et soulignent la nécessité d'une détermination précise de ces paramètres pour des prévisions fiables du comportement structurel. Cette recherche contribue à améliorer la compréhension des défis associés aux paramètres de rigidité des petites déformations et leur impact sur la modélisation numérique et peut aider les ingénieurs géotechniques à sélectionner les valeurs de paramètres appropriées pour leurs projets.

Keywords: HSS soil model; FEM; parametric study; small strain stiffness.

1 INTRODUCTION

Nowadays, more and more projects require a more accurate description of the complex behaviour of structures. To this end, in addition to the superstructure, two- or three-dimensional finite element modelling is also used to understand the expected behaviour of the soil environment to analyse the construction, renovation and restoration phases. Numerical modelling is becoming increasingly widespread and is now part of the design practice to deal with complex tasks and to find optimal technical and economic solutions.

Advanced material models of geotechnical finite element software are used to describe the soil behaviour, but the determination of parameters is a critical point in the process. Using advanced material

models requires the study of parameters describing the complex – nonlinear, time-dependent – behaviour of soils. These can usually be determined by specific, targeted tests, but in their absence their value can only be estimated from other measurement data based on recommendations in the literature. Furthermore, the extrapolation of small sample test results and the scatter of measurement results, introduces uncertainty in the determination of parameters, and parameter analysis is therefore carried out in design practice to understand the impact of them.

The most widely used material model in Hungarian practice (both for design and research, Hübner and Mahler, 2020) today is the HSSmall (Benz, 2007, Plaxis, 2022), a double hardening material model that considers the higher stiffness of soils in the small strain range as well. The influence of two parameters describing the stiffness variation with strain level on the calculation results is analysed in this paper based on the results of investigations carried out at a specific site in Hungary for typical geotechnical structures.

2 EXAMINATION PROGRAM

In the framework of this study, we aimed to assess how much the calculation results differ in the case of parameters obtained by different measurement and estimation models, what effect the inherent uncertainty in the parameters has. For this purpose, we used measurement data from a site in Budapest, where, in addition to 10 large diameter boreholes and 4 CPT tests, 1 seismic CPT (SCPT) and a surface wave measurement (MASW) for research purposes (Szilvágyi et al, 2017) were also performed to record the shear wave propagation velocity profile.

The typical stratification of the area and the parameters that have been obtained based on the soil tests are summarised in Table 1.

Table 1. Soil parameters.

Soil layer	fill	sand	Danube sedim.	Mioc clay
depth, z [m]	0-2	2-7.5	7.5-14	14-
friction angle, φ [°]	28	31	38	26
cohesion, c [kPa]	0	0	0	80
unit weight, γ [kN/m^3]	18	19	21	21
oedemetric mod., E_{oed} [MPa]	8	12	50	15

To analyze the effect of the small strain parameters under investigation, three shear wave propagation profiles were investigated. In addition to the results of the two targeted tests, seismic CPT and MASW measurements, the evolution of the shear wave propagation velocity (CPT-R) was estimated from the CPT data according to Robertson (2009) (Szilvágyi et al, 2017).

The three resulting profiles are shown in Figure 1. The notation given here is later used for comparison. In the figure, it can be observed that in the upper 6 m thick soil zone the MASW measurement values are larger than the SCPT and CPT-R data series.

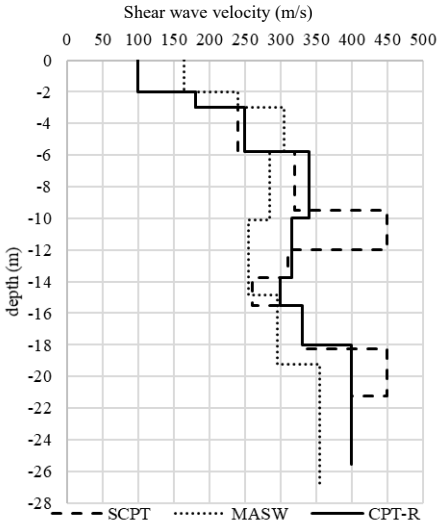

Figure 1. Shear wave velocity profiles.

The shear modulus at in situ stress state was estimated from the shear wave velocity (v_s) profiles and the soil density (ρ) based on the equation.

$$G_0 = \rho \cdot v_s^2 \qquad (1)$$

Important to note, that the difference between the three shear-wave propagation velocity values based on each test appears squared in terms of shear modulus value.

The shear strain, where the shear modulus is 70% of its maximum value is estimated according to the recommendation of Plaxis (2022)

$$\gamma_{0.7} = \frac{1}{9G_0}[2c'(1 + cos2\varphi') - \sigma_1'(1 + K_0)sin2\varphi'] \qquad (2)$$

All the input stiffness parameters were calculated for a reference stress of p^{ref} = 100 kPa using the Plaxis material model (Plaxis, 2022).

First, the impact of the three soil profiles on the calculation results was investigated. Second, a parameter analysis was performed to study the variation of the two input parameters over a larger range, for which the parameter values were modified – separately – based on the CPT-R profile as shown in the table below.

Table 2. Parameter study.

parameters	modification multipliers			
shear modulus, G_0	0.50	0.75	1.25	1.50
shear strain, $\gamma_{0.7}$		0.75	1.25	1.50

In the framework of the research, we investigated the use of Plaxis 2D software for strip footing, excavation support, slab foundation, combined pile-raft foundation and rigid inclusion. In the present paper, the results of these calculations are summarized for a back-anchored diaphragm-wall excavation support, a 40 cm thick slab foundation placed near the surface and a rigid inclusion foundation system with D = 60 cm diameter concrete piles distributed in a 2 m by 2 m grid. The structures investigated are illustrated in the following figures.

For the modelling of the excavation support, the calculation was carried out following the real construction phases, i.e. after the completion of the diaphragm wall, the soil was removed to the anchorage level in the first phase, the anchors were activated in a separate phase with the pre-stressing force, and the complete 10 m excavation was carried out in the last calculation step.

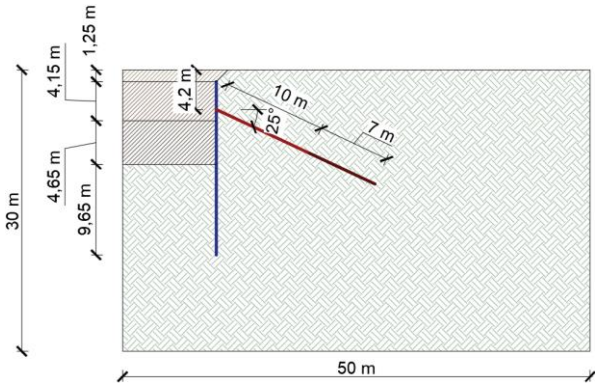

Figure 2. Cross section of diaphragm wall.

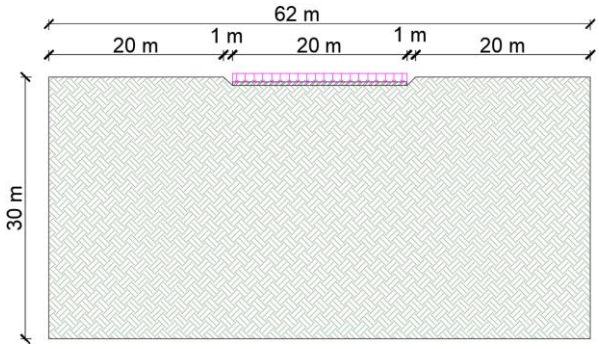

Figure 3. Cross section of slab foundation.

For the slab foundation and the rigid inclusion, a uniformly distributed load of 80-200-250 kPa was activated on the upper plane of the plate, and the resulting deformations and stresses were analysed.

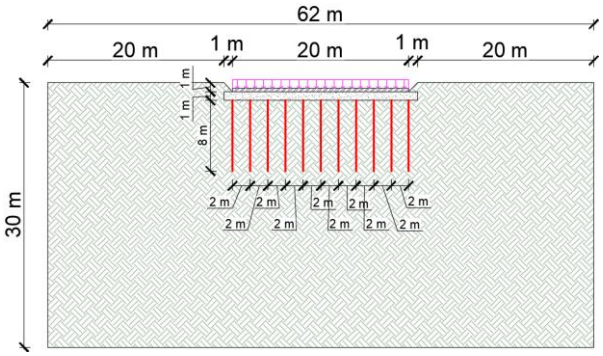

Figure 4. Cross section of rigid inclusion foundation system.

3 RESULTS

3.1 Excavation support

Of the results obtained with the soil models from the field measurements, the SCPT and CPT-R models gave almost identical results, and the MASW soil model showed a significant difference. This is illustrated in Figure 5, which shows the evolution of the bending moments at the end of the first excavation (red-FK2), anchoring (green-H) and full excavation (blue-FK3+V) phases.

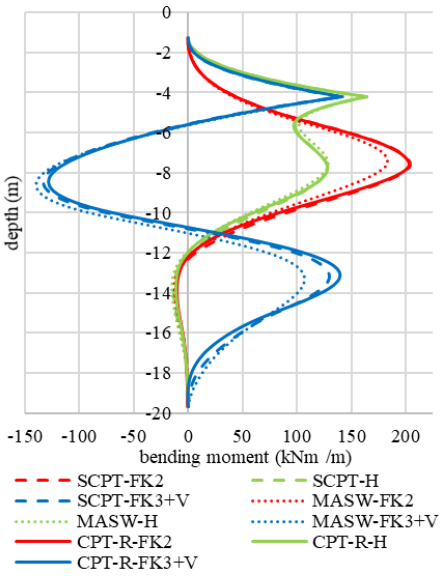

Figure 5. Bending moment of diaphragm wall.

This shows that in the final state, the difference between the maximum moments above the excavation plane is only 10%, which has no significant effect on the design of the structure. Below the excavation level, however, the MASW bending moment value is only 75% of the result obtained with the other two soil models. The differences start to develop from 5 m below the surface, where the MASW measurement shows that the stiffness is higher at small strain level. However, below the working pit level, in the

confinement zone, the MASW recorded a lower shear wave velocity value, therefore there is less support stiffness, and thus the wall "moves out of the ground", and thus the stresses are slightly lower. There is little variation in displacement between the models.

The parameter analysis by varying the initial shear modulus showed significant differences in both structural stress and deformation. The effect of the initial shear modulus is largest in the final state (blue curves) (see Figure 6). At a depth of 8.5 m from the surface, the moment was 140% of the original value with the modulus halved and 67% with the modulus one and a half times the original value, with a difference of more than two times between the two extreme values.

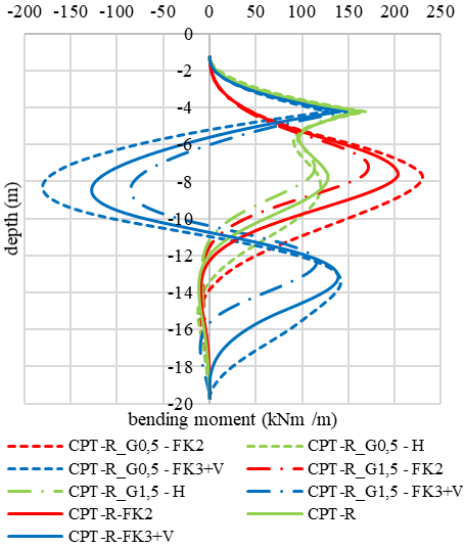

Figure 6. Bending moment of diaphragm wall, G_0 varied.

As shown in Figure 6, at the highest initial stiffness, the bending moment decreases rapidly below the excavation level, i.e. within a small distance, support of the structure is assured. As the modulus decreases, the stiffness of the supporting structure transmits the earth pressure of the background area to a deeper and deeper range, therefore the maximum stress in this range becomes larger and its decay reaches a greater and greater depth. With higher soil stiffness, no substantial stress is experienced in the lower support zone of the diaphragm, but with decreasing stiffness, significant stress is experienced. This is consistent with the calculated shear force distribution, which shows that at higher soil stiffness, the shear stress in the lower part of the diaphragm is small but increases with decreasing stiffness.

The change in the small strain shear modulus has no significant effect on the anchor force: the difference is only 3-4% compared to the baseline value, varying between 564-594 kN. Compared to the soil model estimated from the soil test, changing the small strain modulus without changing the moduli in the large strain range results in a difference in the peak displacement of almost the same proportion (see Figure 7). This is essentially due to the different support stiffness in the confinement range, with the higher part of the structure essentially rotating rigidly as a result of the different support.

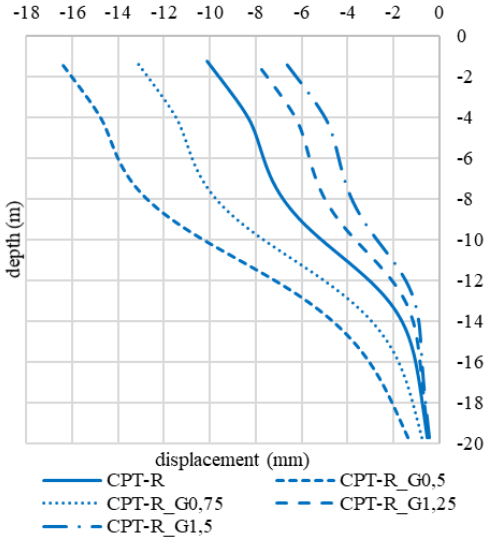

Figure 7. Displacement of the diaphragm wall, G_0 varied.

The sensitivity analysis of $\gamma_{0.7}$, which defines the shape of the modulus degradation curve, shows that its effect on the computed results is smaller than that of G_0, but the mechanisms show good agreement. In the intermediate construction phase, both the moments and shear forces vary nearly identically within a narrow range as a function of $\gamma_{0.7}$. Again, the largest deviations are in the final phase. As the reference shear strain decreases, the soil stiffness decreases more rapidly as the deformation level increases, with a consequent decrease in the support stiffness. Accordingly, as the value $\gamma_{0.7}$ decreases, a larger soil zone provides passive lateral support, whereas as it increases, a soil layer of smaller thickness is able to exert resistance. At the same time, the difference between the two extreme values is only about 15% in the maximum bending moment below the excavation level, and its position changes by only ~1 m.

3.2 Slab foundation

Figure 8 shows the variation of the bending moment in the slab as a function of the load and the soil profile recorded from the field measurements. In the figure, the line type indicates the soil model, and the colour indicates the load level. In general, it can be observed that the curvature of the plate is slightly reduced in the axis of symmetry, with the maximum curvature and hence the maximum moment occurring at ¼ length of

the plate. This is related to the fact that the uniformly distributed load results in a shifted soil pressure towards the edges due to the stiffness of the plate, where it is higher. For all three load cases, the moment developed in the plate was almost identical for the SCPT and CPT-R models, but the MASW calculation showed a significant difference. Examining the ratio of moments at the maximum load location, at one quarter of the length of the plate, the value from the SCPT model was 1.5 times the MASW model's value for 80 kPa, 2.7 times for 200 kPa and four times for 250 kPa, so the difference increased with increasing load.

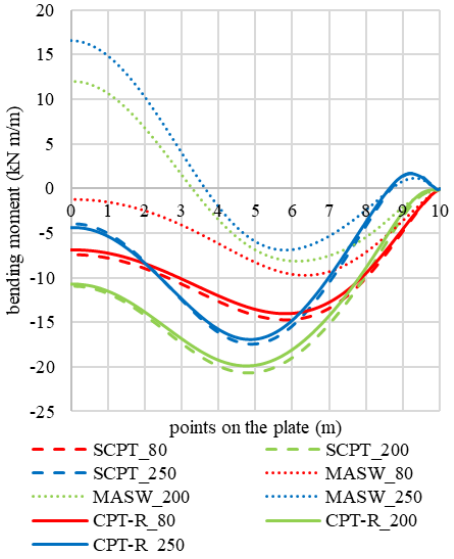

Figure 8. Bending moment along slab foundation.

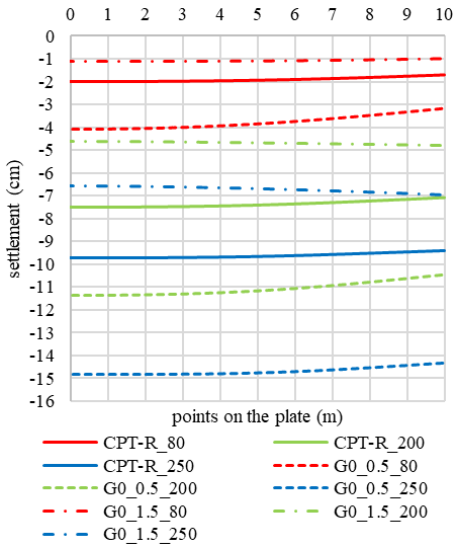

Figure 9. Settlement of plate foundation, G_0 varied.

The results of the parameter analysis regarding the small strain shear modulus and the value of $\gamma_{0.7}$ confirmed the previous findings. A larger change in the small strain modulus also had a significant effect on the range of deformation, and the change was almost directly reflected in the calculated settlement range (see Figure 9).

The deformation of the slab clearly shows that at high soil stiffness the central area of the slab curved in the opposite direction, i.e. tension appeared in the top of the slab. The change in the shear strain value has no such significant effect.

By reducing the reference value, the calculated settlement increased slightly, but the plate shape did not change. However, increasing the reference shear strain reduced the deformations, and in some cases the curvature of slab also switched.

3.3 Rigid inclusion

In the case of the 2D modelling of rigid inclusion soil improvement, the uncertainty inherent in the field measurements did not make a significant difference. Although the variation between the soil models is observed with increasing load, it is moderate. A similar trend to the slab was observed in the bending moment plot. The peak of the bending moment developed at about 2 m from the edge of the plate and tension appeared in the top of the section in the middle of the plate due to the high load (see Figure 10).

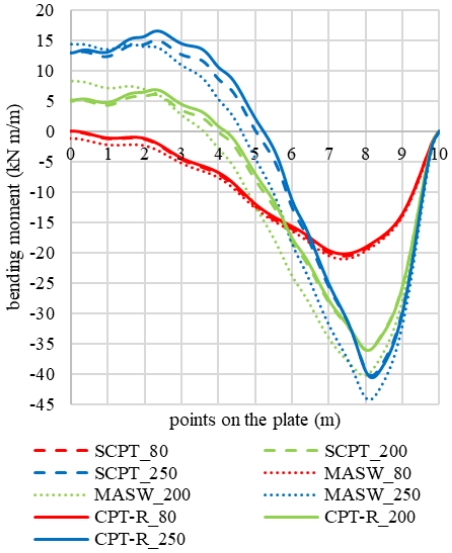

Figure 10. Bending moments in the plate on rigid inclusion.

Increasing the initial shear modulus by one and a half times along the entire length caused little change at all three load levels. At lower loads, the decrease in modulus increased the shear stress along the entire length. Under loads of 200 and 250 kPa, the moment at the plate edges was less sensitive to the change in shear modulus, but there was a significant difference at mid-plate, with tension appearing in the bottom section of the plate.

The effect of the change in the reference shear strain value was smaller for rigid inclusion than for pure slab foundation. For the smallest value, the displacements were 110% of the original value, and for the larger reference shear strain, the displacements were 80% of the original value.

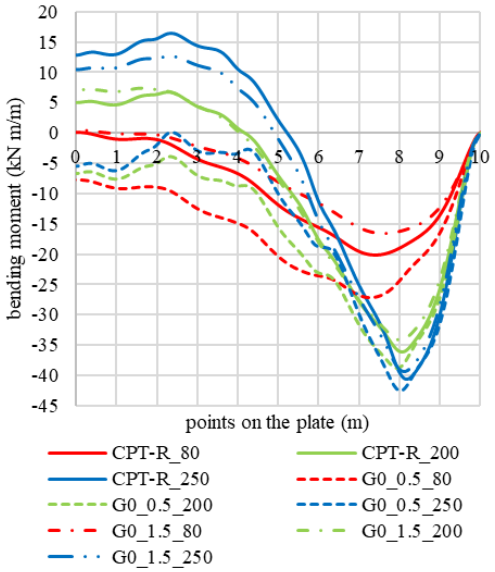

Figure 11. Effect of G_0 on bending moment in plate on rigid inclusion.

4 CONCLUSION

For numerical modelling, the determination of the material model parameters is of paramount importance, and the uncertainties inherent in them will appear in the computational results. In this paper, we investigate how small strain stiffness parameters affect behaviour of typical geotechnical structures.

We have shown, how different shear wave velocity measurements have a significant effect on calculation results for the slab, and a more moderate effect in the case of a diaphragm wall and a rigid inclusion foundation system. A significant effect of the small strain parameters has been identified in the case of the slab bending moments.

Next a parameter study showed, that changing the small strain shear modulus and the value of $\gamma_{0.7}$ over a larger range resulted in significant differences for all three structures. In the case of the excavation support, the change in the stiffness conditions of the embedment area also affected the deformations and bending moment distribution, with the structure being more sensitive to changes in the small strain shear modulus. The behaviour of the slab foundation was fundamentally influenced by the shear modulus, and the results varied substantially in proportion to it. Shear strain parameter had a minor effect also here. For the rigid inclusion, the effect of G_0 decreased with increasing load, as the near-surface layers, which determine the behaviour, were subjected to larger deformation.

Overall, the determination of the G_0 value has a greater impact on the structural behaviour, hence it should be determined by targeted field measurements as precise as possible. The estimation of the shear deformation parameter, which defines the shape of the degradation curve, has shown to have a moderate impact in the modelling of these structures.

REFERENCES

Benz, T (2007) Small-Strain Stiffness of Soils and its Numerical Consequences. *PhD thesis*, University of Stuttgart, 2007.

Ficzek, K. (2023) A talajok kis alakváltozási paramétereinek hatása, Effect of small strain parameters of soil – numerical parametric study, final work (in Hungarian), SZE, Győr.

Hübner, B., Mahler, A. (2020) Analysis of Seismic Fragility Functions of Highway Embankments, *Periodica Polytechnica Civil Engineering*, 64(4), pp. 1162–1169 https://doi.org/10.3311/PPci.16483.

Mahler, A. (2018) A talajkörnyezet modellezése. Modelling of soil enviroment In: Wolf Á. (eds): *Geotechnikai végeselemes modellezés Geotechnical numerical modelling* (in Hungarian). MMKGT, Kontraszt Plus Kft., Budapest, pp. 32-46.

PLAXIS (2022) Plaxis 2D - Material Models, Delft.

Robertson, P. (2009) Interpretation of cone penetration tests - a unified approach. Canadian Geotechnical Journ., Vol 46., pp. 1337-1355, DOI: 10.1139/T09-065.

Szepesházi, R. (2008) Geotechnika, Geotechnics (in Hungarian) Széchenyi István University, Department of Structural Engineering, Győr.

Szilvágyi, Zs. (2018) Dynamic soil properties of Danube Sands, *PhD Dissertation*, Széchenyi István University Győr, MMTDI, Hungary, DOI: 10.15477/SZE.MMTDI.2018.002.

Szilvágyi Zs. (2012) Dinamikus talajparaméterek meghatározása, Determination of dynamic soil parameters (in Hungarian), *Tavaszi Szél 2012 Konferencia*, DOSZ, pp 458-465.

Szilvágyi, Zs., Panuska, J., Kegyes-Brassai, O., Wolf, Á., Tildy, P., Ray, R. P. (2017). Ground Response Analyses in Budapest Based on Site Investigations and Laboratory Measurements, *Int. Jour. of Env., Chem., Eco., Geol. and Geoph. Eng.* 11 (4), DOI doi.org/10.5281/zenodo.1130023.

Vucetic, M., Dobry, R. (1991). Effect of soil plasticity on cyclic response, *Jour. of Geotech. Eng.*, ASCE, 117 (1), pp. 89-107, DOI https://doi.org/10.1061/(ASCE)0733-9410(1991)117:1(89).

Proceedings of the XVIII ECSMGE 2024
GEOTECHNICAL ENGINEERING CHALLENGES
TO MEET CURRENT AND EMERGING NEEDS OF SOCIETY
© 2024 the Authors
ISBN 978-1-032-54816-6
DOI 10.1201/9781003431749-163
Open Access: www.taylorfrancis.com, CC BY-NC-ND 4.0 license

ECSMGE 24
XVIII EUROPEAN CONFERENCE ON SOIL MECHANICS AND GEOTECHNICAL ENGINEERING

Numerical study of ground movements induced by traditional foundation underpinning

Etude numérique des mouvements de terrain induits par les fondations traditionnelles en sous-œuvre

J. Woodcock*, A. Fasano, A. Nikolic
A-Squared Studio Engineers Ltd, London, UK

**james.woodcock@a2-studio.com*

ABSTRACT: Traditional concrete underpinning is a commonly adopted technique for the construction of basements beneath or beside existing buildings, in congested urban settings. The successful implementation of underpinning schemes places a significant reliance on suitable construction means and methods to limit impacts on neighbouring assets. Case study data regarding the ground movements induced by construction of underpins are very limited. This presents a challenge when assessing the potential impact of underpinning works on nearby existing structures and assets, with practitioners frequently adopting inappropriate empirical relationships based on other construction activities. This paper presents the results of a series of finite element soil-structure interaction analyses, assessing ground movements arising from underpinning of an idealised strip footing foundation. The impact of underpin depth on induced ground movements has been investigated, simulating an idealised construction sequence and considering two typical ground models. Proposed charts of normalised ground movements are presented for use in practice.

RÉSUMÉ: La sous-construction traditionnelle en béton est une technique couramment adoptée pour la construction de sous-sols sous ou à côté de bâtiments existants, dans des contextes urbains encombrés. La mise en œuvre réussie des projets de sous-construction repose dans une large mesure sur des moyens et des méthodes de construction appropriés pour limiter les impacts sur les actifs voisins. Les données des études de cas concernant les mouvements de terrain induits par la construction des fondations sont très limitées. Cela présente un défi lors de l'évaluation de l'impact potentiel des travaux de soutien sur les structures et les actifs existants à proximité, les practiciens adoptant fréquemment des relations empiriques inappropriées basées sur d'autres activités de construction. Cet article présente les résultats d'une série d'analyses d'interaction sol-structure par éléments finis, évaluant les mouvements du sol résultant de la reprise en sous-œuvre d'une fondation à semelle filante idéalisée. L'impact de la profondeur du sous-sol sur les mouvements de sol induits a été étudié, en simulant une séquence de construction idéalisée et en considérant deux modèles de sol typiques. Des graphiques proposés de mouvements du sol normalisés sont présentés pour une utilisation pratique.

Keywords: Underpinning; ground movement; numerical modelling.

1 INTRODUCTION

As part of many projects, especially those in congested urban areas, designers are required to demonstrate that ground movements induced by a new development will not have an unacceptable impact on existing adjacent assets.

Where structures are founded on shallow footings and located close to proposed excavations, traditional mass concrete underpinning is frequently used to reduce the impact of construction activities on these structures or to avoid loss of usable basement space which would result from using embedded retaining walls.

Traditional underpin construction involves local excavations beneath the live foundations of the structure, carried out following a hit-and-miss sequence. Construction of these underpins is frequently undertaken with relatively limited/low stiffness excavation support and therefore has the potential to induce ground movements in the nearby area.

The availability of case study data for ground movements induced by underpin construction is extremely limited. Geotechnical engineers therefore typically make use of other existing empirical relationships to determine likely ground movements. Ground movement relationships put forward in CIRIA C760 (Gaba et al., 2017) for installation of piled or diaphragm walls are commonly used in UK practice. The construction methodologies are clearly very different and ground movement predictions made

using this type of methods should be viewed with appropriate caution.

This paper presents the findings of a series of parametric numerical simulations, to provide practitioners with normalised ground movement charts, in the style of CIRIA C760. These may be used in the early stages of design to provide an indication of the impact of underpinning activities.

2 METHODOLOGY

2.1 Structure and underpinning procedure

A parametric study has been carried out using the commercially available software program Plaxis 3D (Bentley Systems, 2023).

This study examined the development of ground movements during underpinning of a 10m long strip footing, 1m wide, founded 1m below ground surface level, as indicatively shown in Figure 1. This footing is sufficiently long in relation to the underpin depth, so that relatively uniform ground movements, broadly representative of plane strain conditions, are expected to occur along most of its length.

A 5-stage underpinning sequence has been simulated, based on proposals made in Underpinning: Good practice guidance (2023), as schematically reproduced in Figure 2. These underpins are 1m wide. Underpins of depth (H) varying between 1.5m and 2.5m have been examined, to allow the resulting ground movements to be normalised, in a similar fashion to the CIRIA C760 ground movement curves.

A load of 100kN/m has been applied to the footing throughout the underpinning sequence, to represent the building load. The footing itself has been placed at the edge of the finite element mesh (thereby restraining the footing from moving horizontally) in order to model the restraint provided by the superstructure and any form of temporary propping which may be installed along the footing, and prevent rigid body rotation of the footing.

2.2 Ground model

Two idealised ground profiles have been examined as part of this study.

Firstly, a ground profile consisting entirely of stiff clay has been considered.

Secondly, a ground profile consisting entirely of dense gravel has been considered. Since the underpins are cut vertically in each case, a nominal cohesion has been assumed in the gravel to prevent excavation collapse in the temporary condition.

The standard Hardening Soil Model available in Plaxis 3D has been used for the gravel, while the version including the small strain stiffness feature has been used for the clay. The input parameters for both materials are summarised in Table 1. The adopted clay parameters are based on the work by Pillai et al. (2023) to simulate the behaviour of London Clay. The gravel parameters are based on the authors' previous experience with dense River Terrace Gravels in the London area.

For the purpose of the outline assessment undertaken, a groundwater level lower than the underpin depth has been assumed, therefore ignoring the impact of any potential dewatering works.

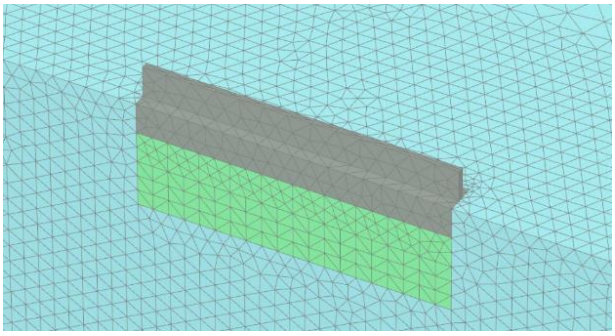

Figure 1. View of finite element mesh (Initial Phase).

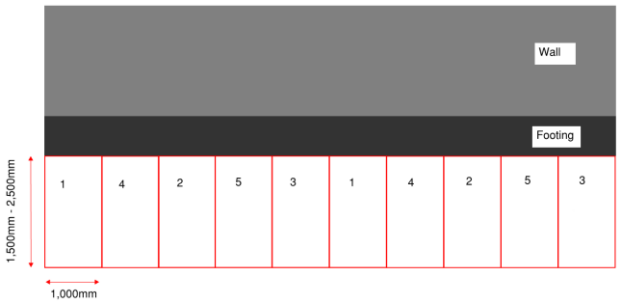

Figure 2. Underpinning sequence – vertical cross-section along wall (numbers refer to installation order/sequence).

Table 1. Material parameters.

Parameter	Stiff Clay	Dense Gravel
c' (kPa)	5	5
ϕ' (deg)	24	34
E_{50}^{ref} (MPa)	11.75	100
E_{oed}^{ref} (MPa)	9.4	100
E_{ur}^{ref} (MPa)	23.5	300
m (-)	0.8	0.5
p_{ref} (kPa)	100	100
G_0^{ref} (MPa)	57.13	-
$\gamma_{0.7}$ (-)	0.096×10^{-3}	-
K_0	1.0	0.44

3 RESULTS

The zone of influence of the underpinning operations and the maximum ground movement immediately adjacent to the footing are observed to be generally

uniform along the footing. Results have been extracted at a representative cross-section perpendicular to the footing.

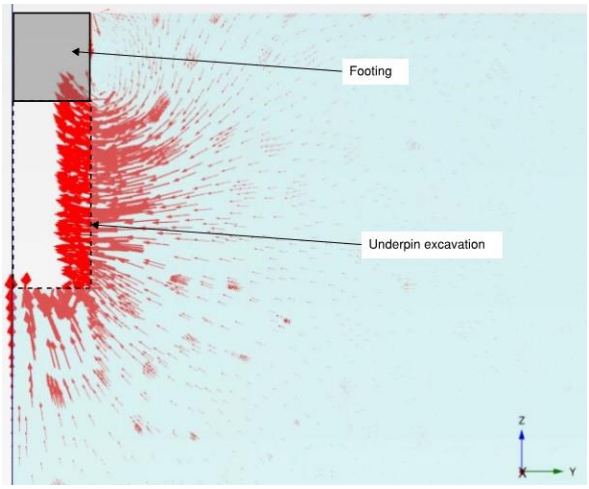

Figure 3 Exaggerated vectors of ground movement during excavation of 2.5m deep underpin in stiff clay.

The predicted soil displacement field is relatively localised (refer to Figure 3), with horizontal movements of the excavation face leading to vertical movements at ground level in the soil above, immediately adjacent to the footing.

Horizontal movements at ground surface are restrained by the presence of the footing, and initiall increase slightly moving away from it, before decreasing.

Ground movements were observed to be proportional to the depth of the underpin (H).

In the case of the underpins in stiff clay, a maximum ground surface settlement (u_z) of 7mm and maximum horizontal movement at ground level (u_y) of 1mm were observed for a 2.5m deep underpin.

In the case of the underpins in dense gravel, a maximum ground surface settlement (u_z) of 5mm and maximum horizontal movement at ground level (u_y) of 1mm were observed for a 2.5m deep underpin.

Ground movement results at ground surface for the two ground models have been normalised by distance from the footing (d) and are presented in Figure 4 to Figure 7.

4 CONCLUSIONS

This paper presents the results of a series of three-dimensional finite element analyses of traditional underpin construction.

Two idealised ground models have been considered, comprising stiff clay and dense gravel, respectively. The analyses have been carried out in a parametric fashion, varying the underpin depth from 1.5m to 2.5m.

The predicted ground movements have been normalised by the depth of the underpins to allow practitioners to apply the results to their own projects. The normalised ground movement profiles are relatively consistent for the various underpin excavation depths adopted in the study.

Results indicate a relatively localised ground movement field in proximity of the footing, rapidly dissipating when moving away from the it. The designer should consider the impact of this on any nearby assets being assessed.

The results presented represent a greenfield condition and practitioners should exercise their own judgement in applying these curves to the assessment of neighbouring structures.

Further research is required, considering a wider range of ground conditions, potentially considering the effect of dewatering and including deeper underpinning schemes, e.g. multi-level underpinning.

REFERENCES

Gaba, A., Hardy, S., Doughty, L., Powrie, W. & Selemetas, D. (2017) Guidance on embedded retaining wall design, Construction Industry Research and Information Association (CIRIA), London, Rep. C760

Pillai, A., Patel, B., Hardy, S., (2023) Validation of advanced soil constitutive models for use in numerical modelling to represent London Clay. Emap Ground Engineering Magazine (Apr 2023).

Underpinning: Good practice guidance (2023). Temporary Works Forum & Association of Specialist Underpinning Contractors, Rep. TWf2023:02

Bentley Systems (2023) Plaxis 3D (Version 2023.2) [Computer Program].

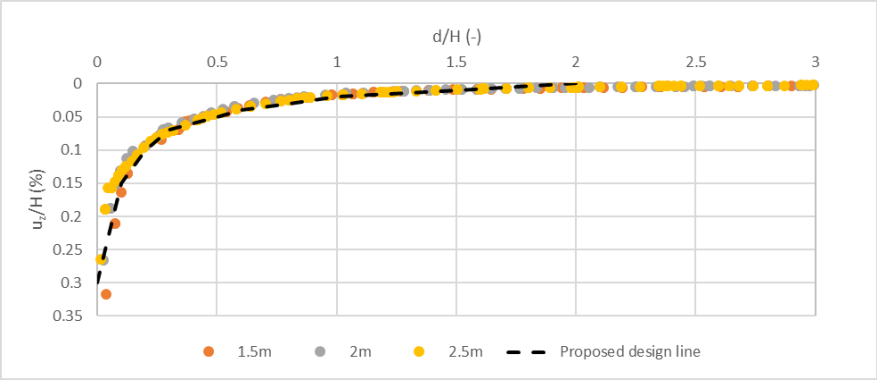

Figure 4. Normalised settlements at ground level in stiff clay for various depths of underpin, with suggested design curve.

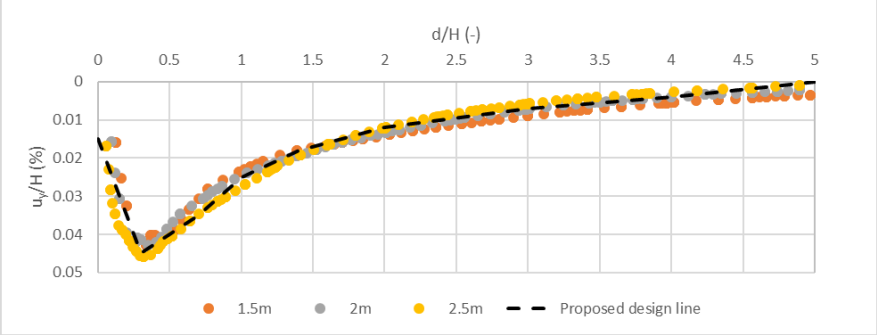

Figure 5. Normalised horizontal movements at ground level in stiff clay for various depths of underpin, with suggested design curve.

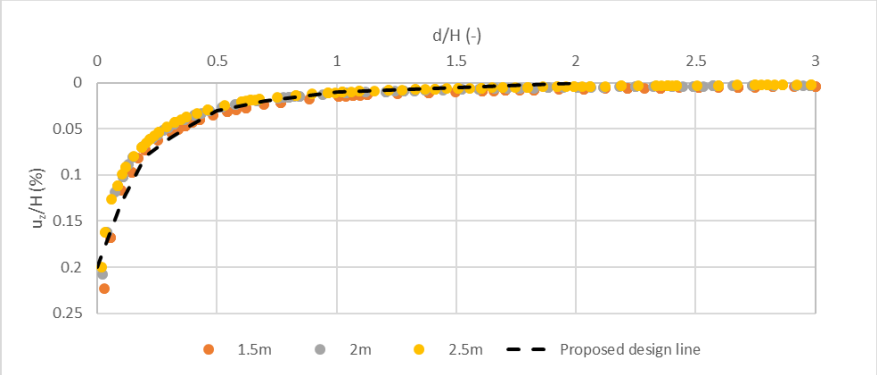

Figure 6. Normalised settlements at ground level in dense gravel for various depths of underpin, with suggested design curve.

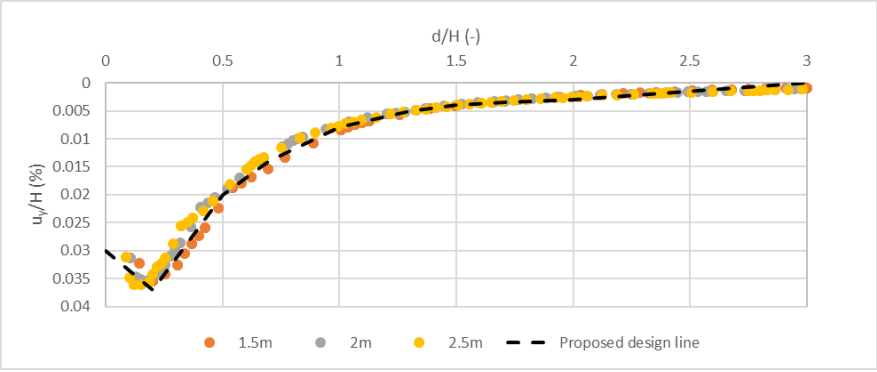

Figure 7. Normalised horizontal movements at ground level in dense gravel for various depths of underpin, with suggested design curve.

Proceedings of the XVIII ECSMGE 2024
GEOTECHNICAL ENGINEERING CHALLENGES
TO MEET CURRENT AND EMERGING NEEDS OF SOCIETY
© 2024 the Authors
ISBN 978-1-032-54816-6
DOI 10.1201/9781003431749-164
Open Access: www.taylorfrancis.com, CC BY-NC-ND 4.0 license

ECSMGE 24
XVIII EUROPEAN CONFERENCE ON SOIL MECHANICS AND GEOTECHNICAL ENGINEERING

Comparison of Markov Chain Monte Carlo and Sequential Monte Carlo inference techniques for calibrating soil parameters in a braced excavation

Comparaison des techniques d'inférence de chaîne de Markov Monte Carlo et de Monte Carlo séquentielle pour étalonner les paramètres du sol dans une excavation avec soutènement

N. Yang, T. Le*
Civil and Environmental Engineering, Imperial College London, United Kingdom
L.T. Nguyen
Boley Geotechnik GmbH, Munich, Germany
**truong.le@imperial.ac.uk*

ABSTRACT: Data assimilation has gained significant attention for the sequential updating of soil parameters, particularly in the context of automatic back-analysis. Compared to traditional manual calibration methods, continuous Bayesian calibration provides a formal approach to merge measured data with model predictions. The performance of two prevalent inference algorithms, namely the Markov chain Monte Carlo (MCMC) and Sequential Monte Carlo (SMC), are compared in back-analyzing the parameters of a synthetic braced excavation problem. Model parameters are sequentially inferred using inclinometer data calculated during a typical excavation project based in London. The accuracy of the MCMC and SMC samplers in inferring the synthetic ground truth is compared systematically. Results reveal that back-analysis using MCMC is better for problems which involve high-dimensionality in the output space, while SMC yields faster inference results, especially in cases which involve a lower dimensional output space. This study demonstrates the effectiveness of the two methods in sequential Bayesian updating and outlines their benefits and limitations in identifying soil parameters for a synthetic problem.

RÉSUMÉ:. L'assimilation de données a suscité beaucoup d'attention pour la mise à jour séquentielle des paramètres du sol, notamment dans le contexte de la rétro-analyse automatique. Comparée aux méthodes traditionnelles de calibrage manuel, la calibration bayésienne continue offre une approche formelle pour fusionner les données mesurées avec les prédictions du modèle. La performance de deux algorithmes d'inférence prévalents, à savoir la chaîne de Markov Monte Carlo (MCMC) et le Monte Carlo séquentiel (SMC), est comparée dans la rétro-analyse des paramètres d'un problème synthétique d'excavation avec soutènement. Les paramètres du modèle sont inférés séquentiellement en utilisant des données d'inclinomètre calculées lors d'un projet d'excavation typique basé à Londres. L'exactitude des échantillonneurs MCMC et SMC dans l'inférence de la vérité synthétique du sol est comparée de manière systématique. Les résultats révèlent que la rétro-analyse utilisant MCMC est meilleure pour les problèmes impliquant une grande dimensionalité dans l'espace de sortie, tandis que SMC donne des résultats d'inférence plus rapides, notamment dans les cas impliquant un espace de sortie de dimension inférieure. Cette étude démontre l'efficacité des deux méthodes dans la mise à jour bayésienne séquentielle et décrit leurs avantages et limites dans l'identification des paramètres du sol pour un problème synthétique.

Keywords: Data assimilation; Bayesian calibration; excavation; MCMC; particle filter.

1 INTRODUCTION

The use of a probabilistic back-analysis or inverse analysis based on field observations in a braced excavation process has been widely reported (e.g. Hsein et al., 2013; Lo and Leung 2019; Jin et al., 2021). Among the different probabilistic inverse methods, such as maximum likelihood, maximum a posteriori and Monte Carlo, Bayesian updating using the entire probability distribution stands out as the most attractive option as it provides a quantitative framework for updating the probability distributions of input parameters. This is achieved by assimilating prior probability distributions with observed data via the likelihood function. However, as many geotechnical projects are carried out in stages, a recursive updating scheme is often formulated to align

with the construction stages. Through a sequential Bayesian calibration approach, the updated soil parameters facilitate the predicted wall deflections with improved confidence with each subsequent excavation stage. This process can be repeated at each stage until the construction is complete.

For any problem which employs a Bayesian framework, the posterior distribution cannot typically be calculated analytically and must, therefore, be approximated numerically. In geotechnical engineering, the prevailing approaches used to estimate the posterior distribution are the family of Markov Chain Monte Carlo (MCMC) methods (see Andrieu et al., 2003 and Murakami et al., 2023 for an overview) and the sequential Monte Carlo approach (SMC) (e.g., particle filter). Despite the numerous studies employing either MCMC and SMC for back-analysis, there have been limited attempts to identify the merits of these two popular approaches at solving typical geotechnical problems.

The aims of this study are two-fold: (1) provide an overview on the principles of MCMC and SMC inference approach, (2) based on an artificial multi-stage excavation with known soil parameters as our ground truth values, assess the feasibility and effectiveness of the two sampling approaches in inferring the model parameters.

2 SAMPLING METHODS

The aim of a sampling algorithm is to approximate the posterior $p(z|y)$ for the soil parameters z given observed data y. Efficient sampling methods are a topic of active research, with numerous techniques proposed in the past few years. (see Murphy, 2022). This study will primarily focus on the two prevailing sampling methods, namely, MCMC and SMC. Both methods follow a straightforward Monte Carlo style approach to estimating the posterior: generate s samples from the *t-th* step posterior, $z_t^s \sim p(z_t|y_t)$, and then use these to aggregate any quantity of interest $\mathbb{E}[f|y_t] \approx \frac{1}{S}\sum_{s=1}^{S} f(z_t^s)$ given suitable function *f*. Any desired level of accuracy of the posterior distribution can be achieved by generating a sufficiently large set of samples.

Both MCMC and SMC can be employed in sequential Bayesian inference for soil parameters in excavation. The overall structure of sequential Bayesian inference is illustrated in Figure 1. Throughout the excavation steps, the posterior of the unknown parameters z_t at the current stage t is fed into the inference as prior at the next stage $t+1$. As new observation y_{t+1} become available, new stage parameters z_{t+1} can be updated. Though MCMC and SMC share the common ingredients during the Bayesian inference, there are some fundamental differences in how samples are proposed and weighted.

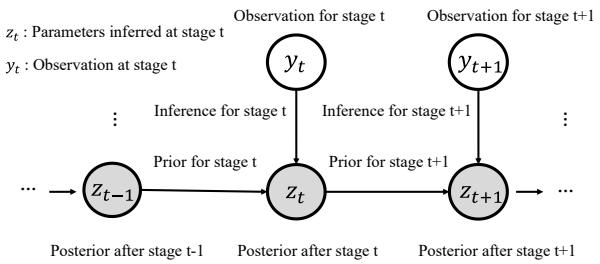

Figure 1. Sequential Bayesian inference for soil parameter.

2.1 Markov Chain Monte Carlo (MCMC)

Markov Chain Monte Carlo (MCMC) algorithms are methods for randomly sampling from an arbitrary distribution based on Markov chains. Different from non-iterative Monte Carlo methods (e.g., rejection sampling or importance sampling), MCMC can build a series of dependent and sequential samples. Instead of drawing samples independently, the samples in the Markov chain depend on the last adjacent sample. Many different MCMC sampling techniques share similar ingredients. For simplicity and clarity, here we take Metropolis–Hastings (MH) algorithm as example, but alternative more effective sampling methods can be also easily implemented.

The basic idea in MH is to define a proposal distribution $q(z_t^{s+1}|z_t^s), s = 1, \dots, n$, between two adjacent samples from the current sample point z_t^s to the new point z_t^{s+1}. For any given distribution $p(z_t^s)$, we define the acceptance function, which is used to decide whether to accept this move, as follows:

$$f(z_t^{s+1}|z_t^s) = \min(1, \alpha) \quad (1)$$

$$\alpha = \min\left(1, \frac{q(z_t^s|z_t^{s+1})p(z_t^{s+1}|y_t)}{q\left(z_t^{s+1}\middle|z_t^s\right)p(z_t^s|y_t)}\right) \quad (2)$$

$$f(z_t^{s+1}|z_t^s) = \min(1, \alpha) = \min\left(1, \frac{p(z_t^{s+1})}{p(z_t^s)}\right) \quad (3)$$

If $\alpha > 1$, which implies $q(z_t^s|z_t^{s+1})p(z_t^{s+1}|y_t) > q(z_t^{s+1}|z_t^s)p(z_t^s|y_t)$, we accept the candidate sampled point from $q(z_t^s|z_t^{s+1})$. If $\alpha < 1$, we accept the candidate point with probability α. A commonly used proposal distribution is Gaussian distribution centered on the current point z_t^s. The acceptance function can be modified as Equation (3). The process of MH sampling is shown in *Algorithm 1*. Typically, convergence improves with the number of paralleled chains and iterative steps used .

In a multi-stage excavation problem, the t-step posterior of the calibrated soil parameters z_t can be readily explored and extracted with paralleled MCMC. Based on these distributions, we can then draw samples for predictive purpose. Additionally, upon acquiring new observations y_{t+1} in the subsequent stage, the $t+1$ -step soil parameters z_{t+1} can be updated using obtained samples z_t^s as priors for the next stage, ensuring a continuous calibration for z_{t+1}^s.

2.2 Sequential Monte Carlo (SMC)

SMC, also known as particle filter, is initialized by generating a population of independent particles (each particle corresponding to a possible soil parameter set). It will filter these particles in a way that the final distribution of particles approximates the posterior distribution. This filtering typically consists of three steps: initial samples, weighting, and resampling, which are sequentially applied while a new observation is added.

The recursive filtering process can be treated as a predict-correct step shown in *Algorithm 2*. Each particle generated is assigned a weight, usually proportional to its likelihood $\mathcal{L}(z_t|y_t)$. In the next step, the weights of these particles are reassigned with replacement, with their sampling probabilities given by their normalized weights ω_t^s. This means that particles with low weights (bad fit) tend to be less likely, whereas particles with high weights (good fit) are more likely to be saved. This study adopts a particle filter with sequential importance sampling as described in Nguyen et al. (2014).

Unlike MCMC samplers, where new soil parameter sampling point z_t^{s+1} is generated based on the current z_t^s, SMC sampling points $z_t^{1:s}$ can be processed simultaneously.

Algorithm 1 Metropolis Hastings algorithm at t-th step

1 Initialize z_t^0;
2 **for** $s = 0,1,2,\dots n$ **do**
3 Candidate sample $z_t^{s+1} \sim q(z_t^{s+1}|z_t^s)$;
4 Compute acceptance probability α;
Compute $f(z_t^{s+1}|z_t^s) = \min(1,\alpha)$;
5 Sample $u \sim U(0,1)$;
6 Set new sample to

$$z_t^{s+1} = \begin{cases} z_t^{s+1} & if\ u < f(z_t^{s+1}|z_t^s) \\ z_t^s & if\ u \geq f(z_t^{s+1}|z_t^s) \end{cases}$$

Algorithm 2 Particle filtering

1 **for** $s = 1,2,\dots n$ **do**
2 Draw $z_t^s \sim q\left(z_t^s \middle| z_{t-1}^s, y_t\right)$;
3 Compute weight $\omega_t^s \propto \omega_{t-1}^s \frac{p(y_t|z_t^s)p(z_t^s|z_{t-1}^s)}{q(z_t^s|z_{t-1}^s,y_t)}$;
4 Normalized weights: $\omega_t^s = \frac{\omega_t^s}{\sum_{s=1}^S(\omega_t^s)}$;

3 MODEL SETUP

The ground stratigraphy and construction sequence is modelled based on an excavation project described by Chen (2020). An artificial and symmetric 2D FE excavation model has been set up using Imperial College Finite Element Program (ICFEP). The excavation was modelled using bottom-up construction method in nine stages (with a final excavation depth of 28.9m) with the support of concrete diaphragm walls and steel props. The wall is modelled as a beam element, and the props are modelled as bar elements only accounted for axial force. The soil elements adopt modified Cam Clay model with small strain stiffness model. The soil profile and the excavation depth in each stage are shown in Figure 2. In order of increasing depth below ground level, the soil profile has six layers: made ground, Terrace Deposits, London clay A-3, London clay A2, Lambeth Group Upper Mottled Clay and Lambeth Group Lower Mottled Clay. The excavation width is 27.0m and the extension length for the mesh is 100m to avoid boundary effect. In these analyses, Bayesian updating was employed to determine the best-estimate small-strain stiffness soil parameters, G_0, to replicate measured wall deflection. Details for the model setup and construction stages can be found in Chen (2020) and Fu (2023).

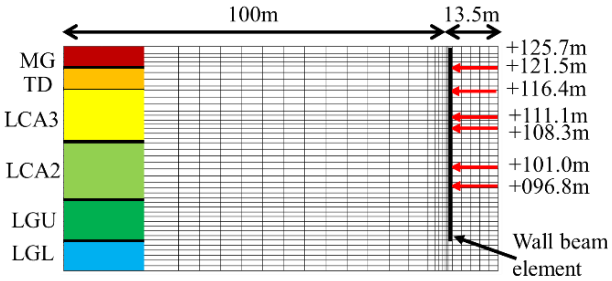

Figure 2. Detailed configurations of the excavation.

As the Bayesian updating process becomes significantly more difficult with increasing number of soil layers and complexity. The number of parameters to be calibrated should be carefully balanced with the amount computational resources available. As this study focuses on the differences of MCMC and SMC samplers in excavations problems, only a smaller number of parameters are treated as random variables in order to preserve the effect of individual soil layers while exploring the influence of the sampling methodology. In order to focus on the ability of the methods to capture the non-linear shear stiffness profile of the soil response, only the maximum shear modulus of each layer, namely G_1 to G_6, is consider. The remaining parameters, such as shear stiffness

degradation parameters, limiting stiffness and plastic parameters, are kept constant. Table 1 summarize the soil parameters varied in the analysis. The ranges for the input parameters are deliberately assumed to be very large as to be difficult to back-analyze without prior knowledge of the solution. To establish comparability between MCMC and SMC, the same run outputs were used as the training dataset for both methods. An artificial solution (ground truth) was obtained by adding 3% Gaussian noise to a synthetic run of the simulation with known input values within the prior range. The artificial run is excluded from the training data set, thereby excluding the exact solution from both MCMC and SMC. Differences in the ground truth values between Case A and Case B are a result of the different seeds upon initializing.

Typically, the total number of runs is controlled by the computational time of the FE model, and as such, there are no fixed rules in place. In this study, Latin hypercube sampling is used for a balance approach to draw from the prior distribution. To ensure comparability is achieved between the two methods, emulated outputs are generated using a surrogate model at each stage over the prior range of parameters (experimental design space). The performance of each of the surrogates have been validated with mean square error percentage and are found to have an error of less than 0.1%. It is noted that although a surrogate is not mandatory for SMC updating, it is employed to ensure that the number of particles in SMC are comparable to the number of samples evaluated using MCMC. The use of surrogate model also allows the MCMC resampling scheme to interpolate particles on the fly, without the need for the expensive FE model. For the SMC scheme used in this study, a unique set of emulated particles are evaluated using the surrogate models every stage to replicate the behaviour of a traditional PF scheme.

4 RESULTS AND DISCUSSION

4.1 Case A

To demonstrate the working principles between SMC and MCMC in greater detail, Case A only considers two stiffness input variables. To determine the most appropriate pair of input parameters, sensitivity analysis was performed using Sobol's indices. Results showed that the first-order index for G_3 and G_4 were the greatest among the 6 possible parameters at 66% and 34%, respectively. A simple analysis consisting of only 30 runs was therefore performed with only these two parameters as random variables. Figures 3 and 4 shows the evolving distributions of these two parameters using either MCMC and SMC for the sequence of excavation.

Figures 3(a) and 3(b) illustrate the evolution of the mean value (μ) and the standard deviation (σ) of G_3 and G_4 with respect to the excavation stages. Both SMC and MCMC are shown to reliably converge towards the artificial ground truth. By the final excavation stage, parameters determined by SMC and MCMC result in a root mean square errors of 0.6% and 1.0% respectively.

In SMC method as shown in Figure 4(a)-(c), the underlying principle is to iteratively filter a population of particles with respect to their fit to new observations. The color change in the figure reflects the resampling weight assigned to the particles, which gradually narrows down the confidence range until only a few particles with the highest weight remain. The samples with the red ellipse show the one standard deviation confidence interval ($\mu \pm \sigma$). Practically, the reweighting procedure of SMC is achieved using all the data at once. This non-iterative nature leads to particles being independent of each other. Consequently, it is necessary to generate all potential particles before the updating process. Particle positions therefore remain unchanged during the calibration process, as the updates primarily affect the weights assigned to the particles, rather than the particles themselves.

Unlike SMC, MCMC treats samples from posterior equally and specifies a random walk-in parameter space. Further, the samples in MCMC are not predefined and are constructed in a correlated manner. A uniform distribution is chosen as the non-informative prior, as shown Figure 4(d). As new observation is incorporated, as shown in Figure 4(e), newly generated samples tend to be clustered near the vicinity of the *maximum a posteriori* estimation, while samples in less likely regions will be disregarded during the burn-in process. After multiple stages of random walk and burn-in, corresponding to the construction sequences, a region where the parameters are most likely expected is established.

In terms of computational efficiency, the models were executed on a PC equipped with a 32-core Intel(R) Xeon(R) Silver 4216 CPU @ 2.10GHz and 256GB of memory. SMC, employing 5000 particles, completes the analysis in mere 10 minutes. In contrast, MCMC, with 800 steps and 30 chains, takes over 30 minutes to achieve the same results.

From the comparison, we can see that in a low dimensional problem, the main differences between the two methods is in the speed at which stable confident estimate is achieved. It is shown that, the SMC approach is substantially quicker than the MCMC approach at a achieving a unique solution.

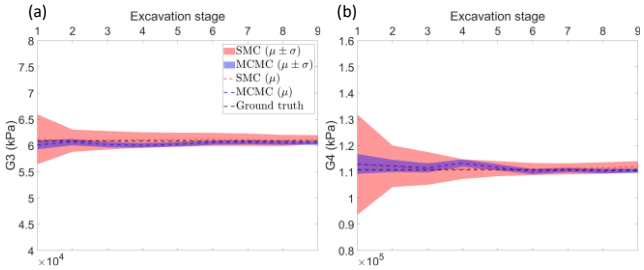

Figure 3. Summary for SMC and MCMC with excavation stages (a) G_3 parameter (b) G_4 parameter.

4.2 Case B

In Case B, the performance of MCMC and SMC is compared for a problem with a higher-dimensional input space; this problem now involves six soil parameters as outlined in Table 1. Sensitivity analysis reveals that G_2 (17.3%), G_3 (76.3%), and G_4 (2.6%) are the most influential variables among the 6 parameters. In this study, despite the importance of a few, all parameters from G_1 to G_6 are recognised to increase the complexity of the inference process. Figure 5 summarizes the mean (μ) and one standard deviation (σ) confidence range for both MCMC and SMC as excavation progresses through various stages. Notably, G_1, G_5, and G_6 struggle to approximate the ground truth due to their low Sobol's indices.

As shown in Figures 5(b)-5(d), both MCMC and SMC initially exhibit wider result spreads at the beginning of the analysis, which gradually narrow as excavation progresses. While SMC yields a smaller variance, MCMC proves more adept at exploring samples in high-dimensional spaces. As shown in Figures 5(b)-5(d), as we acquire new observational data, the posterior distribution obtained through MCMC effectively encompasses the true underlying information. In contrast, SMC does not converge to the same ground truth and demonstrates a more pronounced bias.

5 CONCLUSIONS

This study conducted a comparative analysis of the performance of Markov Chain Monte Carlo (MCMC) and Sequential Monte Carlo (SMC) methods for calibrating soil parameters in the context of an artificial braced excavation. Both methods demonstrated their effectiveness in updating soil parameters, particularly in low-dimensional settings.

MCMC, with its random walk approach, showcased its proficiency in exploring high-dimensional parameter spaces, making it a suitable choice for complex and multifaceted problems. On the other hand, SMC, with its non-iterative nature, offered the advantage of parallel processing, significantly enhancing computational efficiency. This attribute makes SMC a favourable option when quick results are imperative. However, it is crucial to consider that SMC, while delivering rapid outcomes, might exhibit a narrower variance in results and may not guarantee the same level of accuracy as MCMC in high-dimensional scenarios. Therefore, the choice between these methods should be guided by the specific needs and priorities of the analysis, whether precision or computational efficiency takes precedence.

CODE AVAILABILITY

Sampling methods for Markov Chain Monte Carlo and Sequential Monte Carlo are both based on MATLAB software. MCMC is performed using an open-source toolbox UQLAB available at https://www.uqlab.com/. SMC is available at https://github.com/luan-th-nguyen/ParticleFilter.

REFERENCES

Andrieu, C., N. De Freitas, A. Doucet, and M. I. Jordan. 2003. "An introduction to MCMC for machine learning." *Mach Learn*, 50: 5–43. Springer. https://doi.org/10.1023/A:1020281327116.

Chen, Y. 2020. *Application of new observational method on deep excavation retaining wall design in London Clay*, PhD dissertation, Cambridge University, UK.

Fu, F. H. 2023. *Back-analysis and simple demonstration of surrogate model on wall deflection, with case study of Crossrail Tottenham Court Road Station,* MSc dissertation, Imperial College London, UK.

Hsein Juang, C., Z. Luo, S. Atamturktur, and H. Huang. 2013. "Bayesian updating of soil parameters for braced excavations using field observations." *Journal of Geotechnical and Geoenvironmental Engineering*, 139 (3): 395–406. American Society of Civil Engineers. https://doi.org/10.1061/(ASCE)GT.1943-5606.0000782.

Jin, Y., G. Biscontin, and P. Gardoni. 2021. "Adaptive prediction of wall movement during excavation using Bayesian inference." *Comput Geotech*, 137: 104249. Elsevier https://doi.org/10.1016/j.compgeo.2021.104249.

Lo, M. K., and Y. F. Leung. 2019. "Bayesian updating of subsurface spatial variability for improved prediction of braced excavation response." *Canadian Geotechnical Journal*, 56 (8): 1169–1183. NRC Research Press. https://doi.org/10.1139/cgj-2018-0409.

Murakami, A., Fujisawa, K. and Shuku, T., 2023. Developments of inverse analysis by Kalman filters and Bayesian methods applied to geotechnical engineering. *Proceedings of the Japan Academy, Series B*, *99*(9), pp.352-388. https://doi.org/10.2183/pjab.99.023.

Murphy, K. P. 2022. *Probabilistic machine learning: an introduction*. MIT press.

Nguyen, L. T., T. Nestorović, K. Fujisawa, and A. Murakami. 2014. "Particle filter-based data assimilation for ide

ntification of soil parameters with application in tunneli ng." *Proceedings of the 14th International Conference of International Association for Computer Methods and Recent Advances in Geomechanics*, 1241–1246. https://doi.org/10.1201/b17435-218.

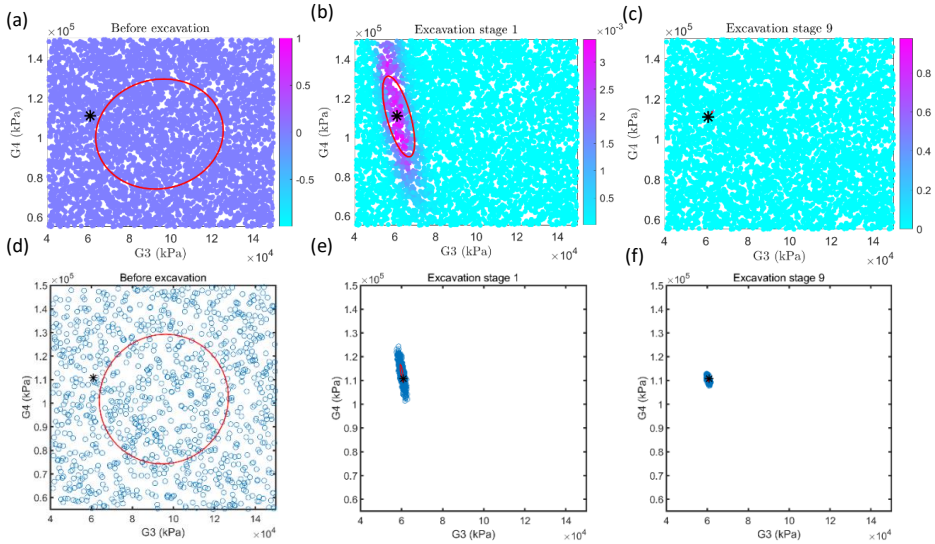

Figure 4. Bayesian Calibration of SMC and MCMC: (a)-(c) for SMC, (d)-(f) for MCMC.

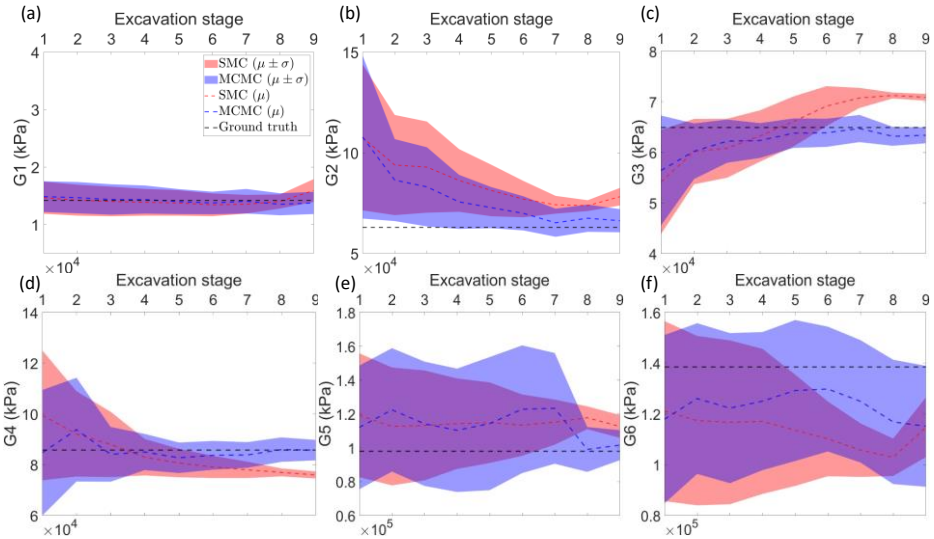

Figure 5. Summary for SMC and MCMC on parameters: (a) G_1, (b) G_2, (c) G_3, (d) G_4, (e) G_5, (f) G_6,.

Table 1. Summary of analysis and soil parameters for calibration.

Case	Input parameter range (MPa)		Ground truth (MPa)	Sampler method	FE Simulation runs
A	G_3	38.9-150	60.8	MCMC/SMC	30
	G_4	53.5-150	110.8	MCMC/SMC	
B	G_1	10-20.2	14.213	MCMC/SMC	120
	G_2	53-227.4	62.915	MCMC/SMC	
	G_3	38.9-150	64.906	MCMC/SMC	
	G_4	53.5-150	85.774	MCMC/SMC	
	G_5	55-183	97.856	MCMC/SMC	
	G_6	55-183	138.519	MCMC/SMC	

Proceedings of the XVIII ECSMGE 2024
GEOTECHNICAL ENGINEERING CHALLENGES
TO MEET CURRENT AND EMERGING NEEDS OF SOCIETY
© 2024 the Authors
ISBN 978-1-032-54816-6
DOI 10.1201/9781003431749-165
Open Access: www.taylorfrancis.com, CC BY-NC-ND 4.0 license

ECSMGE 24
XVIII EUROPEAN CONFERENCE ON SOIL MECHANICS AND GEOTECHNICAL ENGINEERING

Simulation of sand-fines mixtures behaviour based on bounding surface plasticity and equivalent void ratio

Simulation du comportement des mélanges sable-fines basée sur la plasticité de la surface de confinement et de l'indice de vide équivalent

F.H. Yeh*
National Taiwan University of Science and Technology, Taipei, Taiwan

L.F. Prada-Sarmiento
Aarhus University, Aarhus, Denmark

M. Tafili, D. Sarkar, T. Wichtmann
Ruhr-University Bochum, Germany

L. Ge
National Taiwan University, Taipei, Taiwan

**fhyeh@mail.ntust.edu.tw*

ABSTRACT: Binary materials are sand-fines mixtures where the mechanical behaviour transitions from a configuration where the entire forces are transmitted between the grain contacts (no fines) to an array where all voids are filled with fines and contribute to the force transmission. The fines content controls this complex transition, and as such, it has been incorporated into the definition of the equivalent void ratio concept. The macromechanic modelling of sand-fines mixture soils is challenging. Conventional constitutive models are formulated and calibrated either to work for granular or fine-grained soils. This article presents an application of the boundary surface plasticity model proposed by Dafalias and Manzari in 2004, incorporating the equivalent void ratio concept. The model is tested with a series of monotonic triaxial results on Vietnam silica sand and non-plastic fine sand mixtures. Investigations about the inclusion of the equivalent void ratio as a promising option to model binary mixtures before undertaking substantial changes in the structure of well-established constitutive models are explored. Recommendations on the critical void ratio line based on the experimental observations are also provided.

RÉSUMÉ: Les matériaux binaires sont des mélanges de sable et de fines dont le comportement mécanique passe d'une configuration où toutes les forces sont transmises entre les contacts des grains (pas de fines) à une configuration où tous les vides sont remplis de fines et contribuent à la transmission des forces. Cette transition complexe est contrôlée par la teneur en fines et, en tant que telle, elle a été incorporée dans la définition du concept de taux de vide équivalent. La modélisation macromécanique des sols à mélange de sable et de fines est un défi. Les modèles constitutifs conventionnels sont formulés et calibrés soit pour les sols granulaires, soit pour les sols à grains fins. Cet article présente une application du modèle de plasticité de surface limite proposé par Dafalias et Manzari (2004), incorporant le concept de rapport de vide équivalent. Le modèle est testé avec une série de résultats triaxiaux monotones sur des mélanges de sable siliceux du Vietnam et de limon non plastique. Les recherches sur l'inclusion du rapport de vide équivalent en tant qu'option prometteuse pour modéliser les mélanges binaires, avant d'entreprendre des changements substantiels dans la structure de modèles constitutifs bien établis, sont explorées. Des recommandations sur la ligne de rapport de vide critique, basées sur les observations expérimentales, sont fournies.

Keywords: Equivalent void ratio; bounding surface plasticity; binary mixtures; sand-fines mixtures; triaxial simulation.

1 INTRODUCTION

Sand behaviour is influenced by sundry aspects such as grain size distribution, grain shape, sample preparation methods, preloading history, drainage conditions, partial saturation among others. Many research works published in the last decades have studied those effects using extensive experimental campaigns based mostly on triaxial tests for monotonic and cyclic loading conditions (e.g., Wichtmann and Triantafyllidis (2016). Based on those observations on clean sands, different constitutive models have been developed, calibrated, validated and tested in boundary value problems. However, granular soils are

mixed with finer non-plastic fractions in many depositional environments. Those silty sands are idealised as a binary combination of coarse particles (sand) and fine particles (fine sands, silts), and new definitions of fundamental state variables like the equivalent void ratio have been proposed to consider the effect of the fine fraction on the mechanical transfer of forces between the coarse grains. Experimental observations have demonstrated that for binary mixtures, the critical state line (CSL) becomes a function of fines content (Thevanayagam, 1998; Yang et al, 2006; Rahman and Lo, 2008; Rahman et al., 2011; Goudarzy et al. 2022). Applying the critical state soil mechanics framework to sand with fines is challenging because a specific critical state line (CSL) is required for each fine content (f_c). At a specific f_c value, the rotation of the CSL with respect to change in f_c reverses. This specific fines content value is known as the threshold fines content (f_{thre}). It indicates a change in soil fabric from "fines-in-sand" to "sand-in-fines" (Rahman et al., 2011). An alternative way to consider the changes in the CSL induced by the fines content in binary mixtures is to use the concept of equivalent granular void ratio e^* (Rahman et al., 2011; Thevanayagam, 1998; Nguyen et al. 2017; Chang and Deng, 2019; Tamang et al., 2023; Tafili et al., 2022) instead of the conventional void ratio e:

$$e^* = \frac{e+(1-b)f_c}{1-(1-b)f_c}; 0 < b < 1 \qquad (1)$$

where b denotes the portion of the fine grains that contribute to the active intergranular contacts. Parameter b depends on grain size disparity and grain characteristics and there are different approaches to estimate its value (Rahman et al., 2011; Thevanayagam 1998; Nguyen, Benahmed and Hicher, 2017; Chang and Deng, 2019; Tamang et al., 2023).

This article explores the convenience of incorporating different definitions of equivalent void ratio in the description of the CSL in the SaniSand bounding surface plasticity model proposed by Dafalias and Manzari (2004) to reproduce the experimental behaviour of binary mixtures observed on a series of monotonic triaxial tests conducted on the Vietnam silica sand.

2 MATERIALS AND METHODS

2.1 Materials

The behaviour of binary mixtures can be controlled by coarse-grained, fine-grained (non-plastic or a small amount of plastic), or a combination of both fractions. Two different grain size distributions of silica sands from Vietnam were selected to apply alternative definitions for the equivalent void ratio e^*. Figure 1 presents coarse and fine sand grain size distribution curves for the sand-fines mixture. The main properties of both materials are summarized in Table 1. Vietnam silica sand is characterized by a specific gravity (G_s) of 2.66, the plasticity index (PI) is zero, and the mean grain sizes (D_{50}) of the coarse sand and fine sand are 0.904 mm and 0.081 mm, respectively. The coarse sand has a uniformity coefficient of C_u = 1.49 and a coefficient of gradation of C_c = 0.98, while the fine sand has a uniformity coefficient of C_u = 1.89 and a coefficient of gradation of C_c = 1.13.

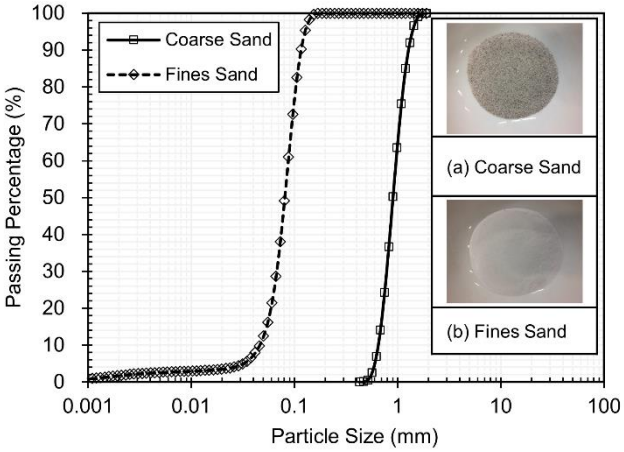

Figure 1. Particle size distribution curves of Vietnam Silica Sand: (a) coarse sand; (b) fine sand.

Nine strain-controlled monotonic triaxial tests were conducted on reconstituted specimens of Vietnam silica sand. Four drained and one undrained tests were performed on Vietnam sand with no fines, whereas three drained and one undrained tests were undertaken on mixtures with 15% fines content. A summary of initial conditions and critical values for each triaxial test is presented in Table 2, where the monotonic triaxial test under drained conditions is named TMD, and the triaxial test under undrained conditions is named TMU.

Table 1. Physical properties of Vietnam silica sand.

Mixtures	**Coarse-dominated**			χ
	D_{50} [mm]	e_{max} [-]	e_{min} [-]	D_{50}/d_{50} [-]
Vietnam silica sand	0.904	0.976	0.621	11.2
	Fines-dominated			
	D_{50} [mm]	e_{max} [-]	e_{min} [-]	
	0.081	1.323	0.671	

2.2 Model calibration

Five different models (shown in Table 3) based on the concept of the equivalent granular void ratio e^* and the parameter b were calibrated to describe the critical state line obtained experimentally for specimens with fines content f_c = 0% and f_c = 15%. Figure 2 shows in the e or e^*-log(p') plane the critical state points obtained from the interpretation of drained and undrained triaxial tests, and the equivalent void ratios for the specimens with f_c = 15%. From the comparison of different approaches to calibrate e^*, it is clear that the model after Thenvanagan et al. (2002) produces the best fitting. The blue curve in Figure 2 represents the CSL used in the SaniSand model (Dafalias and Manzari, 2004), and was fitted considering the critical void ratios obtained for Vietnam silica sand specimens with f_c = 0% and for the e^* calculated after Thevanayagam et al. (2002) for the f_c = 15% results.

Table 2. Test program and critical state results for the Vietnam Silica sand.

Test	f_c [%]	p'_0 [kPa]	e_0 [-]	e_{cri} [-]	p'_{cri} [kPa]	e^*_{cri} [-]
TMD	0	100.0	0.716	0.921	218.8	-
TMD	0	200.0	0.695	0.879	386.3	-
TMD	0	300.4	0.684	0.829	679.9	-
TMD	0	400.0	0.685	0.810	694.0	-
TMD	15	100.6	0.638	0.704	254.0	0.904
TMD	15	200.2	0.633	0.670	475.3	0.865
TMD	15	399.6	0.629	0.649	860.7	0.842
TMU	0	149.0	0.672	0.672	1134.3	-
TMU	15	150.3	0.639	0.639	912.8	0.831

Table 3. Prediction of b-value for the f_c = 15% binary mixture of Vietnam silica sand.

References	Function b()	Calibrated b
Thevanayagam et al. (2002)	constant	0.3
Rahman and Lo (2008), Rahman (2009), and Rahman, Lo, and Baki (2011)	$b(f_c, r)$	0.219
Nguyen, Benahmed, and Hicher (2017)	$b(f_c, e, \chi)$	Not a constant (0.702 ~ 0.711)
Chang and Deng (2019)	$b\left(\frac{d_{50}}{D_{50}}\right)$	0.23
Tamang et al. (2023)	$b(\chi)$	0.7

The SaniSand version proposed by Dafalias and Manzari (2004) was implemented as a user material Fortran routine (UMAT) in IncrementalDriver (Niemunis, 2014). Table 4 presents the set of calibrated parameters for the Vietnam silica sand. Calibration was based on the simulation of drained triaxial test on the sand fraction (f_c = 0%), following the recommendations presented in Wichtmann et al. (2019).

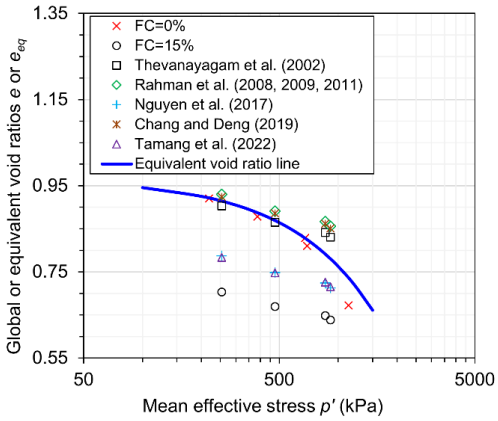

Figure 2. Critical state line and equivalent void ratios for f_c = 15% using different approaches to estimate b.

Figure 3 shows the comparison between experimental results and the simulation of drained triaxial tests with different initial mean pressures for the sand specimens with no fines (f_c = 0%). The description of initial stiffness, peak shear strength and volumetric strain is adequate between triaxial results and SaniSand simulations.

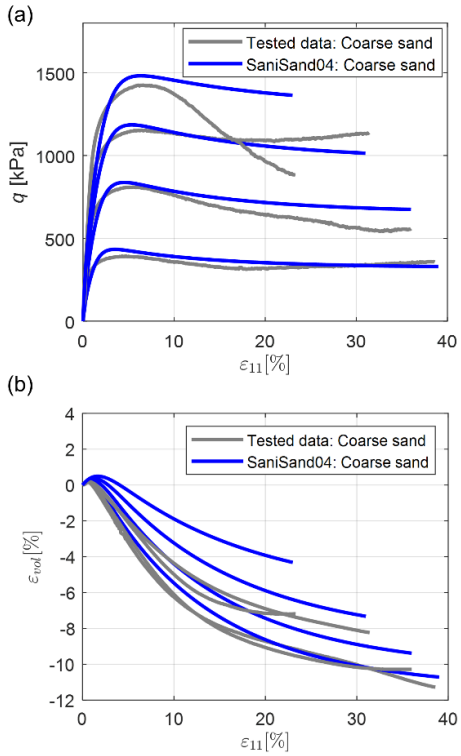

Figure 3. Comparison of experimental and simulated triaxial curves for the Vietnam silica coarse sand (f_c = 0%) under drained conditions: a) Deviatoric stress q vs axial strain ε_{11} curves. b) Volumetric strain ε_{vol} vs axial strain ε_{11} curves.

Table 4. Calibrated parameters of the Sanisand model (Dafalias and Manzari, 2004) for the Vietnam silica sand.

e_0	λ	ξ	M_c	M_e	m
0.966	0.0206	1	1.567	1.029	0.1
G_0	ν	H_0	c_h	n_b	A_0
100	0.25	8	0.95	0.75	1.1
n_d	Z_{max}	c_z	b		
1.3	20	5000	0.3		

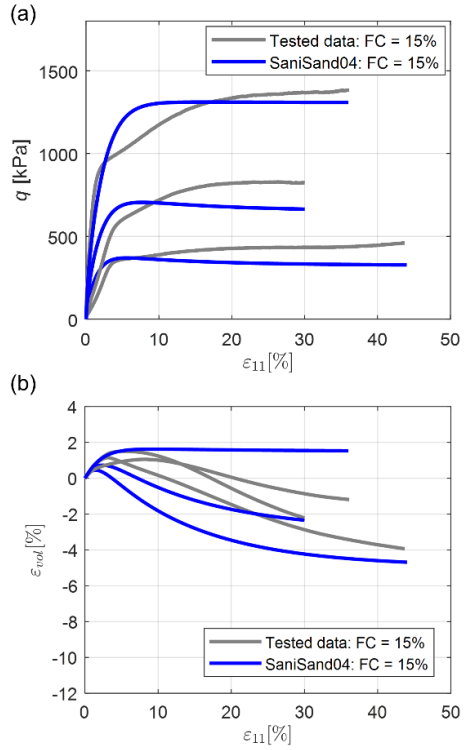

Figure 4. Comparison of experimental and simulated triaxial curves for the Vietnam silica coarse sand (f_c = 15%) under drained conditions: a) Deviatoric stress q vs axial strain ε_{11} curves. b) Volumetric strain ε_{vol} vs axial strain ε_{11} curves.

3 RESULTS AND DISCUSSION

The series of drained triaxial tests for the binary mixture with f_c = 15% was simulated, using the equivalent void ratio e^* calculated with the Thevanayagam et al. (2002) formula for fine contents of 15% as the initial void ratio e_0 in IncrementalDriver. Figure 4 summarizes the comparison between experimental results and simulations with SaniSand for three different mean initial stresses (p'_0 = 100, 200, 400 kPa), considering e^*. The increase in the fines content in the binary mixture of Vietnam silica sand is reflected in the change from strain softening behaviour observed for samples with f_c = 0% (Figure 3-a) to strain hardening for specimens with f_c = 15% (Figure 4-a). This trend is well reproduced by the numerical simulations with SaniSand and the equivalent void ratio e^*. The effect of fines content is also clearly observed on the volumetric behaviour. For the specimens with f_c = 15% a reduction of approximately 50% in the dilatancy was observed. Once again, simulations using SaniSand and the equivalent void ratio managed to reproduce the reduction in dilatancy, as shown in Figure 4-b.

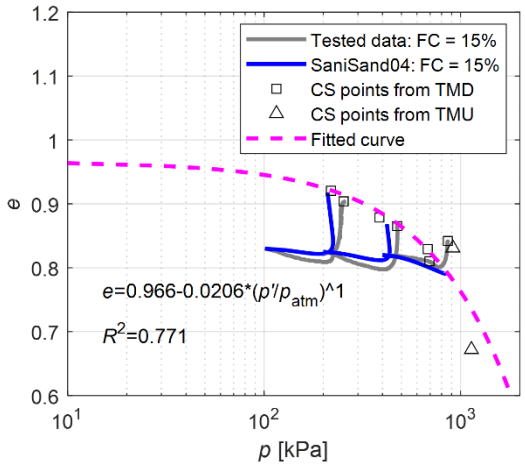

Figure 5. Comparison between experimental and simulated mean effective stress versus void ratio paths for Vietnam silica sand with f_c=15%.

Figure 5 presents the evolution of void ratio e vs mean effective stress p' for the three drained triaxial tests with f_c = 15%. Simulations for p'_0 = 100, 200 kPa match the experimental observations, describing the transition between contractancy and dilatancy behaviour. For p'_0 = 400 kPa, the model describes well the contracting phase but then it reaches the critical state, whereas the experiments exhibit first contractancy followed by a dilatant stage that exceeds the fitted critical state line.

Additionally, simulations of two undrained triaxial tests for specimens with fine contents f_c = 0, 15% and mean confining pressure p'_0 = 150 kPa were conducted (Figure 6). Simulations for the coarse Vietnam silica sand with no fine content agree well with the description of the stiffness, but overestimate the shear strength measured in the laboratory. Similarly, the curves describing the evolution of the excess pore water pressure Δu_w vs the axial strain ε_{11} coincide well in the transition between positive and negative Δu_w up to $\varepsilon_{11} \approx 3\%$ between experimental and simulation results. SaniSand results for the binary mixture with f_c = 15% exhibit in average a similar trend, but the model underestimates the shear strength and the steady state excess pore water pressure.

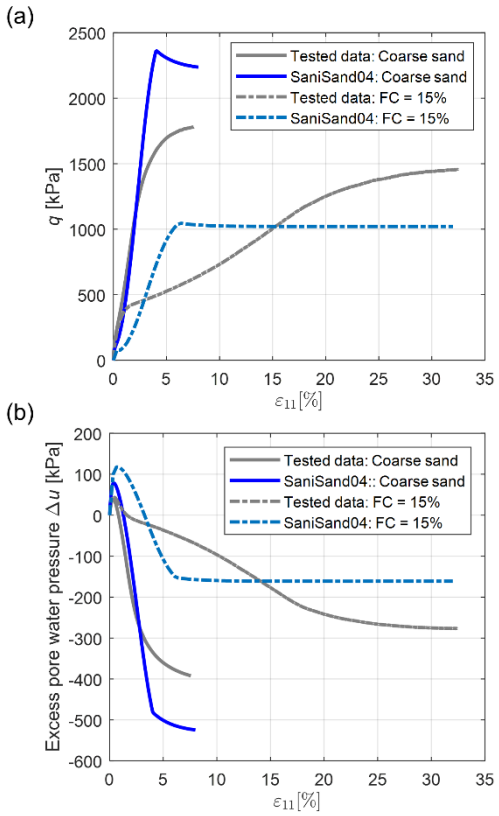

Figure 6. Simulations for the coarse sand and mixture under undrained conditions: (a) Deviatoric stress v.s. Axial strain and (b) Excess pore water pressure v.s. Axial strain.

4 FINAL REMARKS AND FUTURE WORK

This work presented experimental results of drained and undrained monotonic triaxial tests performed on coarse Vietnam silica sand and binary mixtures thereof with fines content f_c = 15%. Five different equations to estimate the equivalent granular void ratio e^* were calibrated for the available experimental set of results. The Thevanayagam et al. (2002) model delivered the best description of critical void ratios for mixtures with fine contents. Experimental points in the space $e^* - \log p'$ considering the coarse specimens and the mixtures with f_c = 15% were used to fit the critical state line, following the definition used in the SaniSand model (Dafalias and Manzari, 2004). Simulations of experiments with the popular SaniSand model incorporating the concept of e^* both for the CSL and as the initial void ratio were presented. Results showed that the concept of e^* can account for the effects of fines content on granular binary mixtures, especially well for drained triaxial tests. However, additional modifications to the constitutive model might be needed to improve the prediction of undrained tests. Further validation with other materials like the Karlsruhe fine sand is planned, considering drained and undrained triaxial tests.

ACKNOWLEDGEMENTS

The authors are grateful for the financial support provided by the National Science and Technology Council (NSTC), Taiwan, R.O.C., and the German Academic Exchange Service (DAAD), Germany.

REFERENCES

Chang, C. S., Deng., Y. (2019) Revisiting the concept of inter-granular void ratio in view of particle packing theory, *Géotechnique Letters*, Vol. 9 (2), pp. 121-129. https://doi.org/10.1680/jgele.18.00175.

Dafalias, Y., Manzari, M. (2004) Simple plasticity sand model accounting for fabric change effects, *Journal of Engineering Mechanics*, Vol. 130 (6), pp. 622-634. https://doi.org/10.1061/(ASCE)0733-9399(2004)130:6(622).

Goudarzy, M., Sarkar, D., Lieske, W., Wichtmann, T. (2022) Influence of plastic fines content on the liquefaction susceptibility of sands: monotonic loading, *Acta Geotechnica*, Vol. 17, pp. 1719-1737. https://doi.org/10.1007/s11440-021-01283-w.

Nguyen, T. K., Benahmed, N., Hicher, P.Y. (2017) Determination of the equivalent intergranular void ratio - Application to the instability and the critical state of silty sand, In *EPJ Web of Conferences*, Vol. 140, Montpellier, France, EDP Sciences, pp. 02019. https://doi.org/10.1051/epjconf/201714002019.

Niemunis, A. (2014). Incremental Driver User's manual. Available at: https://www.soilmodels.com/idriver/, accessed: 13/01/2018.

Rahman, M. M., Lo., S. R. (2008) The prediction of equivalent granular steady state line of loose sand with fines, *Geomechanics and Geoengineering: An International Journal*, Vol. 3 (3), pp. 179-190. https://doi.org/10.1080/17486020802206867.

Rahman, M. M., Lo, S. R., Baki, M. A. L. (2011) Equivalent granular state parameter and undrained behaviour of sand–fines mixtures, *Acta Geotechnica*, Vol. 6, pp. 183-194. https://doi.org/10.1007/s11440-011-0145-4.

Rahman, M. M. (2009) Modelling the influence of fines on liquefaction behaviour. PhD diss., UNSW Sydney. https://doi.org/10.26190/unsworks/22259.

Tafili, M., Knittel, L., Gauger, V. (2022) Experimentelle und numerische Untersuchungen zum Kompressionsverhalten von Sand-Schluff-Gemischen, Experimental and numerical studies on the compression behavior of sand-silt mixtures, *Geotechnik*, Vol. 45 (1), pp. 3-15. (in [German]). https://doi.org/10.1002/gete.202100006.

Tamang, B., Kim, U., Jin, J., Lee, S., Kim, Y. (2023) Undrained monotonic shear behavior of sand mixed with a small amount of fines content, *Acta Geotechnica*, Vol. 18 (6), pp. 2915-2927. https://doi.org/10.1007/s11440-022-01776-2.

Thevanayagam, S. (1998) Effect of fines and confining stress on undrained shear strength of silty sands, *Journal*

of geotechnical and geoenvironmental engineering, Vol. 124 (6), pp. 479-491. https://doi.org/10.1061/(ASCE)1090-0241(1998)124:6(479).

Thevanayagam, S., Shenthan, T., Mohan, S., Liang, J. (2002) Undrained Fragility of Clean Sands, Silty Sands, and Sandy Silts, *Journal of Geotechnical and Geoenvironmental Engineering*, Vol. 128 (10), pp. 849-859. https://doi.org/10.1061/(ASCE)1090-0241(2002)128:10(849).

Wichtmann, T., Fuentes, W., Triantafyllidis, T. (2019) Inspection of three sophisticated constitutive models based on monotonic and cyclic tests on fine sand: Hypoplasticity vs. Sanisand vs. ISA, *Soil Dynamics and Earthquake Engineering*, Vol. 124, pp. 172-183. https://doi.org/10.1016/j.soildyn.2019.05.001.

Wichtmann, T., Triantafyllidis, T. (2016) An experimental data base for the development, calibration and verification of constitutive models for sand with focus to cyclic loading: part I—Tests with monotonic loading and stress cycles, *Acta Geotechnica*, Vol. 11 (4), pp. 739-761. https://doi.org/10.1007/s11440-015-0402-z.

Yang, S. L., Sandven, R., Grande, L. (2006) Steady-state lines of sand–silt mixtures, *Canadian Geotechnical Journal*, Vol, 43 (11), pp. 1213-1219. https://doi.org/10.1139/t06-069.

Proceedings of the XVIII ECSMGE 2024
GEOTECHNICAL ENGINEERING CHALLENGES
TO MEET CURRENT AND EMERGING NEEDS OF SOCIETY
© 2024 the Authors
ISBN 978-1-032-54816-6
DOI 10.1201/9781003431749-166
Open Access: www.taylorfrancis.com, CC BY-NC-ND 4.0 license

ECSMGE 24
XVIII EUROPEAN CONFERENCE ON SOIL MECHANICS AND GEOTECHNICAL ENGINEERING

Load bearing mechanism of screw piles under compressive loading in clayey soil

Mécanisme porteur des pieux vissés sous chargement de compression dans un sol argileux

P. Zahedi*, D. Igoe
Trinity College Dublin, Ireland
**zahedip@tcd.ie*

ABSTRACT: In this study the load transfer mechanism of screw piles under compressive loading in clayey soils is studied. 3D Finite Element analysis was used to estimate the load bearing mechanism of screw piles. The results revealed that the pile head load-displacement response of the screw pile with inter-helix spacing ratio smaller than 3 can be captured in a piecewise curve in three stages: (i) an initial linear stage; (ii) a non-linear stage and (iii) a final linear stage. For an inter-helix spacing ratio greater than 3, the load-displacement curve can be described by the first two stages without the final linear stage. During the initial linear stage of the pile response, the performance of the screw pile is linear elastic. At the second stage, most of the soil strains are concentrated in the vicinity of the helix plates where behave as individual plates with little interaction between them. At the third stage, the bearing mechanism forms a cylindrical shear band leading to a linear response. The load associated with the intersection point of the 2nd and 3rd stages of the pile response was recognized as the phase transition load, which the load bearing mechanism of the screw pile changes. The phase transition load of the screw piles depends on the pile geometry.

RÉSUMÉ: Dans cette étude, le mécanisme de transfert de charge des pieux vissés sous chargement de compression dans des sols argileux est étudié. Initialement, un nouveau principe a été établi pour estimer le mécanisme porteur des pieux vissés à l'aide de courbes charge-déplacement. En outre, les résultats ont révélé que la réponse des pieux vissés avec un rapport d'espacement inter-hélices inférieur à 3 peut être capturée dans une courbe par morceaux en trois étapes: (i) et étape linéaire initiale; (ii) une étape non linéaire et (iii) une étape linéaire finale. Pour un rapport d'espacement inter-hélices supérieur à 3, la courbe charge-déplacement peut être décrite par les deux premières parties sans la partie linéaire finale. Pendant la partie linéaire initiale de la réponse du pieu, la performance du pieu vissé est élastique linéaire. Dans la deuxième partie, la plupart des déformations du sol sont concentrées au voisinage des plaques hélicoïdales qui se comportent comme des plaques individuelles avec peu d'interaction entre elles. Au troisième étage, le mécanisme de roulement forme une bande de cisaillement cylindrique conduisant à une réponse linéaire. La charge associée au point d'intersection des 2ème et 3ème étapes de la réponse du pieu a été reconnue comme la charge de transition de phase, dont le mécanisme porteur de charge du pieu vissé est modifié. La charge de transition de phase des pieux vissés dépend de la géométrie du pieu.

Keywords: Screw pile; inter-helix spacing; finite element analysis; plaxis; clay.

1 INTRODUCTION

The main geometrical features which affect the axial capacity of screw piles are the pile length (L), space of helix plates (S), helix number (n) and helix diameter (D_h). The behavior of screw piles under compressive loads depends on the spacing of the helix plates, which is generally described by the ratio of plates spacing to helix diameter (S/D_h).

Several studies have been conducted to identify the axial performance of the screw piles. Cerfontaine et al. (2019) carried out two-dimensional finite element analysis with various soil properties to recognize the failure mechanism of screw piles and stress distribution at failure. The results showed that soil deformation modifies the stress field around the anchor and enhances the uplift capacity. Stuedlein and Uzielli (2013) and Merifield (2010) studied the uplift performance of helical anchors in clay. A practical design framework for multi-plate circular anchor foundations was established by Merifield. Three-dimensional finite-element (3DFE) analysis was conducted by Al-Baghdadi et al. (2017) to investigate the behavior of screw piles under combined vertical and lateral loading in sandy soil. The results of the analysis revealed that vertical compressive loads enhance the lateral capacity of the screw piles. On the other hand, vertical uplift loads marginally reduce the lateral capacity. Li et al. (2017) performed field tests

including axial compression and tension tests to study the axial - load transfer mechanism of helical piles within sandy and clayey soils. They estimated the area along the shaft where the shear resistance was negligible to be 2.5 – 5 times the helix diameter. Meng et al. (2017) performed field study to investigate the influences of drilled displacement (*DD*) piles with a screw-shaped shaft in soft clay of Shanghai. The results revealed that the horizontal soil displacements induced by the installation of a *DD* pile are focused within a circular region with a radius smaller than six times the pile external diameter.

The so-called phase transition load, where the interaction of the plates forms a cylindrical failure mechanism in the soil, has not been widely investigated. The aim of this study is to investigate the axial load-displacement curves of the screw piles under compressive loading in clay soils and to estimate the phase transition load using 3DFE modelling.

2 NUMERICAL MODELLING

2.1 Pile characteristics

3DFE analyses was undertaken using Plaxis 3D software. A 3-helix screw pile with pile length (L), shaft diameter, helix diameter (D_h) and helix thickness of 10, 0.1, 0.4 and 0.02 m, respectively, was considered as a base model. The helix plates were simplified by circular disks and linear elastic model was used to model the pile materials with properties listed in Table 1.

2.2 Soil properties

Since the main objective of this study was to investigate the long-term drained performance of screw piles in clay, a clay with specifications listed in Table 2 was assumed (taken from Azarbaijan Shahid Madani University tech.lab dataset). A linear elastic-perfect plastic Mohr-Coulomb model was used to model the behaviour of the clay.

Table 1. Pile material properties (Tokhi, 2016).

Parameters	Values
Poisson ratio, υ	0.33
Pile unit weight, γ (kN/m^3)	78
Modulus of elasticity of pile, E (GPa)	210

Table 2. Soil properties.

Parameters	Values
Internal friction angel, ϕ_i (deg)	20
Cohesion, c_i (kN/m^2)	50
Poisson ratio, υ_i	0.33
Unit weight, γ_i (kN/m^3)	18
Elastic modulus, E_i (MPa)	20

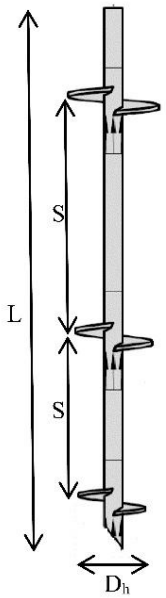

Figure 1. Schematic representation of screw pile geometry.

2.3 Model dimension and meshing

The width and depth of the model were considered twice and three times the pile length, respectively (Salhi et al., 2013). Vertical boundaries of the model were fixed in *x*-direction and y-direction and the bottom boundary of the model was fixed in all directions, and ground surface is free in all directions. Mesh generation performed with fine 10-node tetrahedral elements and a very fine meshing was applied for the soil zone around the pile because of the considerable changes of stress and strain of soil (Figure 2). The pile shaft and helix plates were modeled by 6-node plate element with virtual thickness. To simulate the pile and soil interaction, interface elements were utilized and Mohr-Coulomb criteria was used to describe the interface material behavior. A shear strength reduction factor (R_{int}) of 0.5 was adopted, based on recommendations of Brinkgreve et al. (2002), to model interface materials.

2.4 Parametric analysis

In this study, the load-displacement response of the pile head was analyzed and the relationship between the pile head response and the load bearing mechanism of the screw piles (i.e. soil strains) were presented. The impact of the pile geometry such as pile length and helix number on the load-bearing mechanism of the screw piles were also investigated.

The (S/D_h) values of 1, 2, 3 and 5 were selected to study the load transfer mechanism of the screw pile under compressive loading. For evaluating the impacts of the pile geometry such as pile length (L) and helix number (n) on the pile response, the values of L changed from 8 m to 15 m and n increased from 1 to

4. In all of these analyses, the base soil properties were used.

3 RESULTS AND ANALYSIS

In this section, the results of the numerical analyses, including the load transfer mechanism of screw piles in clay and the effect of pile geometry on the load-bearing mechanism and bearing capacity of the screw piles are presented and discussed.

3.1 Pile response

The pile head response as well as the development of shear strain within the soil around screw piles with different inter-helix spacing are presented in this section. The axial force-displacement of screw piles for S/D_h values smaller than 3 consists of three stages, including an initial linear stage (I), non-linear stage (II) and final linear stage (III). For S/D_h ratios greater than 3, the pile response can be reduced to the first two stages. The intersection point between stage I and II is referred to as the initial transition point (T_f) and the intersection point of the stage II and stage III is referred to as the second transition point (T_s) (Figure 3). The non-linear stage (II) of the pile response extends when the S/D_h value increases. While the first linear stage (I) of the pile response appears independent of the inter-helix spacing.

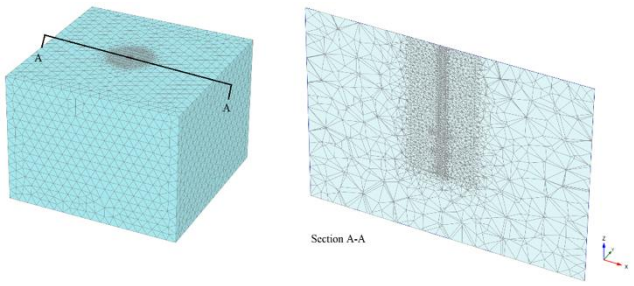

Figure 2. A typical view of the model meshing.

3.2 Development of shear strains during loading

For piles with small S/D_h = 2, the screw pile behaves linear elastic (I) for loading values smaller than Q_f, and shear strains initially form at the vicinity of helix plates, when the loading value passes Q_i and pile response transfers from stage (I) to stage (II) (see point B in Figure 4(b)). As the loading increases, the shear strains around each helix plate begin to interact and create cylinder zone around the edge of the helixes where the soil is shearing. Once this occurs the pile head load-displacement response enters the 3rd stage (III) (see points E – F in Figure 4(b)).

For piles with large S/D_h (S/D_h = 5), screw pile acts linear elastic for loading values smaller than Q_{Tf}. The shear strains form within the soil around the helix plates when the loading value passes Q_{Tf} and pile response enters the nonlinear stage II. In this case, because of large spacing between the helix plates, they act individually and therefore do not enter stage III for the levels of displacement investigated (see Figure 5).

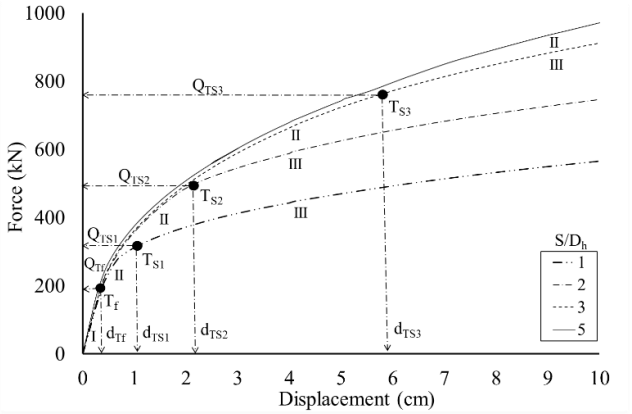

Figure 3. Force-displacement of screw pile with S/D_h values of 1, 2, 3 and 5.

3.3 Impact of pile geometry

The axial load-displacement of the screw pile with S/D_h = 2 and different values of the pile length illustrates that with an increase in pile length, L, and number of helixes, n, the displacement at which the transition occurs, d_{TS}, remains fixed and the Q_{TS} value increases (note: the pile is assumed rigid in this analysis). It means that by increasing the pile length and helix number, the rate of proceeding of the shear strains within the soil between helix plates reduces and transformation of the load-bearing mechanism of the screw pile occurs at greater loads. However, the d_{Tf} and Q_{Tf} values are independent of the pile length and helix number (Figure 6).

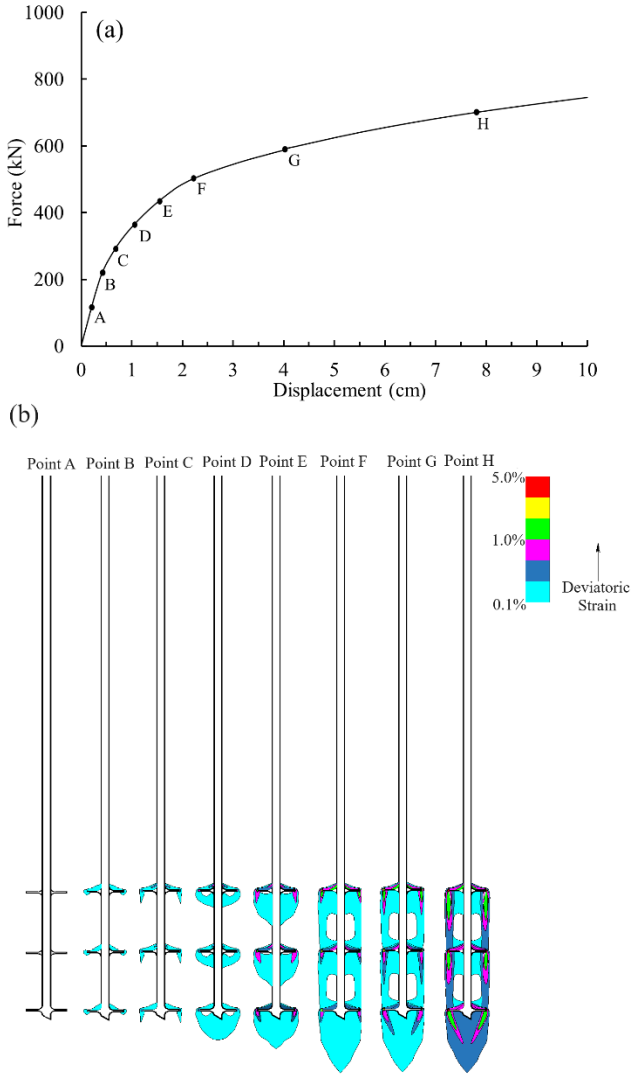

Figure 4. (a) Pile response curve of screw pile with S/D_h of 2, (b) shear strain development patterns of the soil around helix plates at given points of the pile response curve during loading process.

3.4 Axial capacity

The axial capacity of the screw pile (Q_u) is considered to be the load that produces a settlement value of 10 percent of the largest helix diameter (Mohajerani et al., 2016). For the piles with inter-helix spacing ratio (S/D_h) lower than 3, the axial compression capacity of the screw pile increases with the S/D_h value. While for S/D_h values greater than 3, the effect of S/D_h on compression capacity is negligible (Figure 7). For S/D_h values greater than 3 there is no interaction between the helix plates (see, Fig 5(b)) and the compression capacity is a combination of the summation of the bearing load of each helix plate along with the shaft friction along the side of the pile. While for S/D_h values smaller than 3, the cylindrical shear zone forms around the pile and the compression capacity is a result of the soil shear strength mobilized in this cylindrical shear zone along with the end bearing load of the lower most helix. In this case, by increasing the S/D_h value, the length of the soil cylinder rises, therefore the bearing capacity of the screw pile increases. It can be concluded that at screw piles embedded within the clay studies in this paper, the optimum spacing of the helix plates is 3 times of the helix plate's diameter.

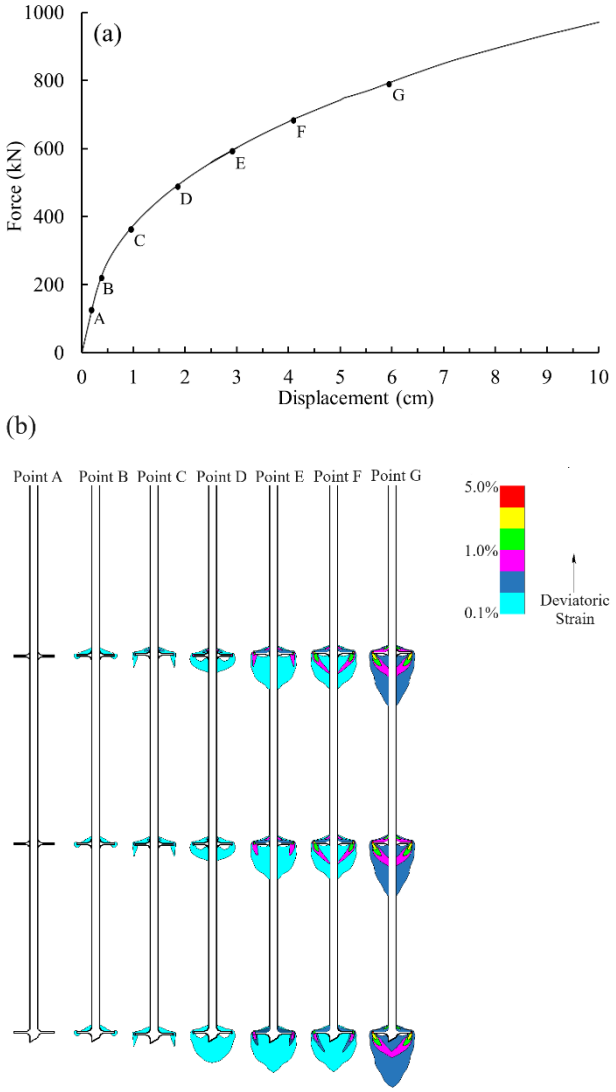

Figure 5. (a) Pile response curve of screw pile with S/D_h of 5, (b) shear strain development patterns of the soil around helix plates at given points of the pile response curve during loading process.

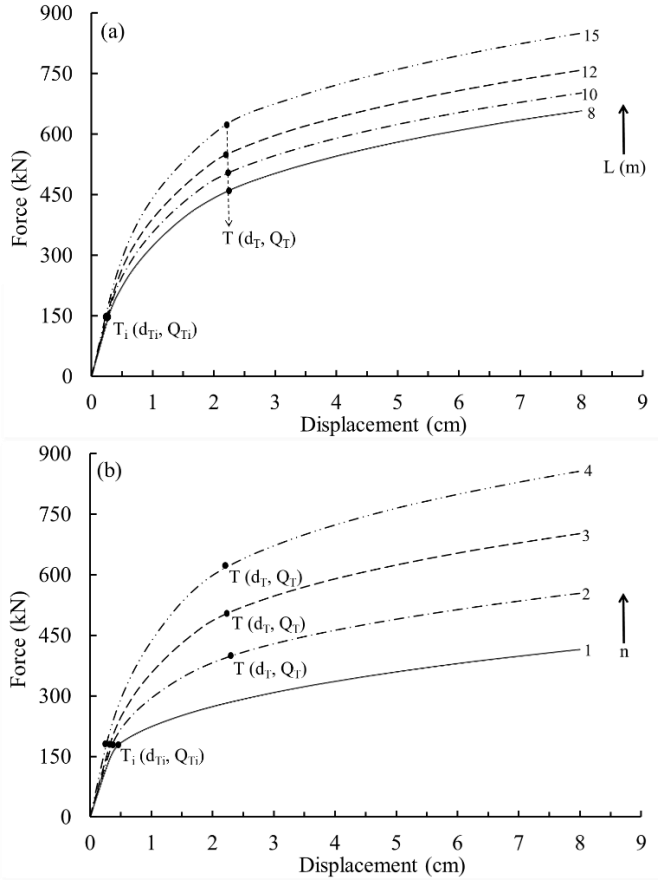

Figure 6. Force-displacement of screw pile with various values of: (a) Pile length, (b) helix number.

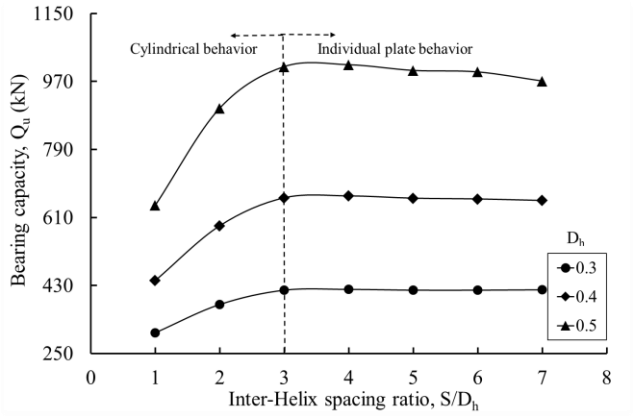

Figure 7. Bearing capacity of screw pile with different inter-helix spacing ratio (S/D_h).

4 CONCLUSIONS

The present study examines the effect of screw pile geometry on the load bearing mechanism and bearing capacity of screw piles in clay soils under drained loading. Based on the results obtained from analysis undertaken in Plaxis 3D, the following conclusions can be made:

1) The pile axial load-displacement response of a screw pile with inter-helix spacing ratio less than 3 was seen to consist of three stages, (I) an initial linear stage, (II) a non-linear stage and (III) a final linear stage. For inter-helix spacing ratio great than 3, only the first and second stages were evident.
2) During the initial stage of the pile response, the screw pile behaves linearly. In the second stage the plastic strains within the soil are concentrated at the vicinity of the helix plates which pile behaves individually without interacting.
3) During the third stage a linear response is observed as a result of the helix plates interacting and the formation of a cylindrical shear failure zone surrounding the plates.
4) The load associated with the beginning of interaction between the helix plates (i.e. the intersection point of the 2nd and 3rd stages of the pile response) is referred to as the phase transition load.
5) The value of the phase transition load depends on the geometry of the screw pile.

Further work is underway to examine the effect of using more advanced soil models and soil properties to identify if the response can be generalized to a range of soil types.

ACKNOWLEDGEMENTS

The authors are grateful for the financial support provided by the Science Foundation Ireland Centre for Applied Geosciences (ICRAG), grant number 13/RC/2092_2 who provided support for this work.

REFERENCES

Al-Baghdadi, T.A., Brown, M.J., Knappett, J.A., and Al-Defae, A.H. (2017), Effects of vertical loading on lateral screw pile performance, Proceeding of Institution of Civil Engineers - Geotechnical Engineering,https://doi.org/10.1680/jgeen.16.00114.

Brinkgrevee, R.B.J., Broere, W., Waterman, D. (2002). Plaxis V8, Reference manual. Delft University of Technology and PLAXIS, Netherlands.

Cerfontaine, B., Knappett, J.A., Brown, M.J., and Bradshaw, A.S. (2019). Effect of soil deformability on the failure mechanism of shallow plate or screw anchors in sand, Computers and Geotechnics, https://doi.org/10.1016/j.compgeo.2019.01.007.

Li, W., Zhang, D.J.Y., Sego, D.C., and Deng, L. (2017). Field testing of axial performance of large-diameter helical piles at two soil sites, International

Journal of Geotechnical and Geoenvironmental Engineering, 144 (3), 06017021.

Mohajerani, A., Bosnjak, D., Bromwich, D. (2016). Analysis and design methods of screw piles: a review,

Soils and Foundations, https://doi.org/10.1016/j.sandf.2016.01.009.

Meng, Z., Chen, J.J., Zhang, L., Wang, J.H., and Yao, J.M. (2015). Field tests to investigate the installation effects of drilled displacement piles with screw-shaped shaft in clay, International Journal of Geotechnical and Geoenvironmental Engineering, 141 (12), 06015010.

Merifield, R.S. (2010). Ultimate uplift capacity of multiplate helical type anchors in clay, International Journal of Geotechnical and Geoenvironmental Engineering, https://doi.org/10.1061/(ASCE)GT.19435606.0000478.

Salhi, L., Nait-Rabah, O., Deyrat, C., and Roos, C. (2013). Numerical modeling of single helical pile behavior under compressive loading in sand, Electronic Journal of Geotechnical Engineering, 4319-4338.

Stuedlein, A.W., and Uzielli, M. (2014). Serviceability limit state design for uplift of helical anchors in clay, Geomechanics and Geoengineering, https://doi.org/10.1080/17486025.2013.857049.

Tokhi, H.A. (2016). A study of new screw soil nail. MSc. thesis, RMIT University, Civil Environmental and Chemical Engineering, Melbourne, Australia.

Proceedings of the XVIII ECSMGE 2024
GEOTECHNICAL ENGINEERING CHALLENGES
TO MEET CURRENT AND EMERGING NEEDS OF SOCIETY
© 2024 the Authors
ISBN 978-1-032-54816-6
DOI 10.1201/9781003431749-167
Open Access: www.taylorfrancis.com, CC BY-NC-ND 4.0 license

ECSMGE 24
XVIII EUROPEAN CONFERENCE ON SOIL MECHANICS AND GEOTECHNICAL ENGINEERING

Simplified finite element modeling of TBM tunneling

Modélisation numérique simplifiée du creusement au tunnelier

H. Zaiter*, H. Mroueh
Université de Lille, Lille, France

E. Bourgeois
Université Gustave Eiffel, Marne-la-Vallée, France

**hadia.zaiter@univ-lille.fr*

ABSTRACT: Numerical modelling of TBM tunneling remains a difficult problem due to the complexity of the phenomena involved and the large number of parameters that need to be taken into account. Conventional numerical models generally associate stress relaxation forces on the tunnel contour and compressive forces representing the action of both the TBM and the grout on the ground. These models have certain drawbacks, the main one being the difficulty of calibrating the parameters used. In this paper, we propose a model that takes as input data the control parameters of the TBM and models the injection of the grout by applying compressive forces to the contour of a zone of the mesh. This model combines stress relaxation forces and compressive forces in a single step by applying the final stress directly to the tunnel contour. In particular, it allows the grouting pressure to be taken into account only where it is greater than the initial mean stress in the soil. The approach is implemented in the finite element code CESAR and compared with experimental data from the TULIP project (Tunneling and Limitation of Impacts on Piles); in particular, the influence of the model parameters on the width of the surface settlement trough and the lateral displacements of the soil at different depths are discussed.

RÉSUMÉ: La modélisation numérique du creusement des tunnels au tunnelier reste un problème difficile en raison de la complexité des phénomènes mis en jeu et du grand nombre de paramètres à prendre en compte. Les modèles classiques associent le plus souvent des forces de déconfinement sur le contour du tunnel et des forces de confinement représentant l'action du tunnelier et du mortier de bourrage sur le terrain. Ces modèles présentent un certain nombre de limites, la principale étant la difficulté de caler les paramètres utilisés. Dans ce papier, on propose un modèle qui prend comme données d'entrée les paramètres de pilotage du tunnelier et modélise les injections de bourrage en imposant une contrainte sur le contour d'une zone du maillage. Ce modèle combine en une seule étape des forces de déconfinement et des forces de pression en appliquant directement la contrainte finale sur le contour du tunnel. Il permet notamment de prendre en compte la pression d'injection uniquement aux endroits où elle est supérieure à la contrainte moyenne initiale dans le sol. L'approche est implémentée dans le code de calcul par éléments finis CESAR, et mise en œuvre sur les données expérimentales du projet TULIP (Tunneliers et Limitation des Impacts sur des Pieux) ; on discute en particulier l'influence des paramètres du modèle sur la largeur de la cuvette de tassement en surface et les déplacements latéraux du sol en profondeur.

Keywords: Tunnels; numerical modelling; expansion model; settlement.

1 INTRODUCTION

In recent years, TBM excavation has been increasingly used, particularly in projects like the Grand Paris Express in France, which involves over 20 TBMs excavating more than 200 kilometers of tunnels. Understanding the TBM's impact on foundations is a complex challenge. In 2021, the TULIP project prediction exercise (Berthoz et al., 2022) was enlightening. It showed a lack of consensus in simulating excavation and its effects on deep foundations: a wide variety of numerical approaches were adopted by the participants. Results exhibited a large discrepancy and diverged significantly from measurements. To provide a simple methodology, Mohamad (2022) proposed to model the TBM advance by means of "prescribed strains" applied to groups of elements in the mesh, which proved efficient to discuss the response of existing piles to the TBM passage. The calculations are straightforward to implement, but the technique takes as input data the volume loss: a modelling technique taking as input data the TBM parameters would be of greater practical interest.

2 A SIMPLE MODELLING APPROACH FOR TBM TUNNELING

2.1 Basic principle of the approach

In the context of modelling the excavation process, a new approach is proposed, taking into account the

control and injection parameters as input data. This approach, called the "swelling model", accurately incorporates these parameters to provide a simplified method with the same accuracy as conventional methods. It consists in defining a "reference stress" type loading. The definition of such a reference stress at each integration point makes it possible to calculate a vector of nodal forces, resulting in the application of a surface force on the boundary of the swelling zone, as shown in Figure 1.

2.2 Implementation

The calculation principle entails correcting stresses in a designated mesh zone at integration points, transforming these corrections into nodal forces. This indirect method imposes swelling stress on element groups within the corrected zone. In the application under discussion, the zone subjected to the “swelling stress” corresponds to the space in which grout is injected between the lining and the ground. It must be underlined that this zone must be given an extremely low Young's modulus (with respect to the properties of the adjacent materials), so that the surfaces forces applied to the ground and the lining are actually equal to the prescribed value (otherwise part of the applied nodal forces is required to deform the grout zone).

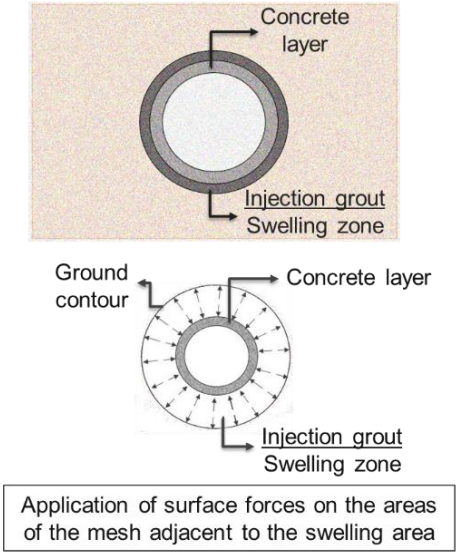

Figure 1. Principle of the swelling model.

In CESAR, the data for the swelling stress model are provided among the properties of the groups of elements (or zones) in the mesh, using a keyword "GONF" and a sequence of integer or reals parameters. The approach makes it possible to account for various types of reference stress (isotropic or not, homogeneous or not, etc.). In general, the reference stress is associated with a pressure varying linearly with depth, defined by the value of a reference pressure p_{ref} at a given depth z_{ref} and the pressure gradient, i.e. the group volume weight.

Tests have been carried out to check that the procedure gives the same results as the classical procedure, which combines stress relaxation forces and weighing fluid pressure forces. However, the preparation of the data is very simple with the new procedure.

The approach offers the possibility to calculate the difference between the final applied stress (derived from the grout pressure) and the stress in the ground before grouting operations, specifically at the end of the TBM shield. This is illustrated by the red curve in Figure 2, where correction of the stress state is taken into account only at the points where the grout pressure is larger than the initial stress: the model attempts to represent the fact that no grout can be injected if the pressure is not large enough.

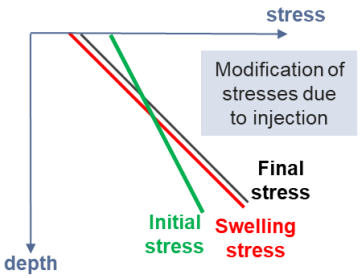

Figure 2. "GONF" model with loads defined by difference with the initial stress.

2.3 Application

During the TULIP (Tunnelling and Limitation of Impacts on Piles) research project, led by the Society of Grand Paris in collaboration with the French Centre for Tunnel Studies (CETU), ENTPE, and Université Gustave Eiffel, a full scale experiment has been carried out to study the influence of a TBM on existing deep foundations, in the area of the future Line 16 of the Grand Paris Express.

2.3.1 Presentation of the problem

A plane strain model of the TULIP experiment was used (Figure 3). The layers found in the site are a layer of made ground (MG), Saint Ouen limestone layer, divided into two parts, one above the water table (SOLdry), and a second below the water table (SOLsat), and three layers of Beauchamp (BS), Marly Limestone (ML) and Coarse limestone layer (CL). Furthermore, pile P3 from the TULIP project is included in the modelling. Calculations are performed in greenfield condition, or in the presence of the pile, either loaded with a 2100 kN applied load at the head or unloaded. Moreover, the behavior of the grout is

assumed to be elastic, and the shield conicity is neglected.

The soil mechanical properties are modelled with the Hardening Soil Model (HSM) in all layers, except the CL layer, considered as a very stiff elastic layer.

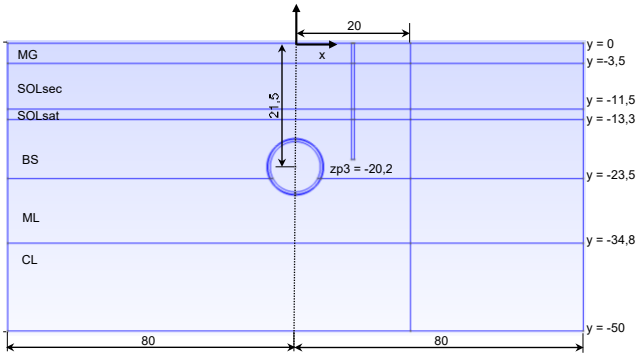

Figure 3. Geometry of the model..

The values of the mechanical parameters, presented in Table 1, are taken from (Mohamad, 2022). Both vertical and horizontal displacements at set to zero at the base of the mesh, as well as horizontal movements at the left and right edges of the mesh. The initial (effective) stresses are assumed to be geostatic, defined by the unit weight and the earth pressure coefficient (K_0) for each layer.

Table 1. Reference model parameters

	MG	SOLdry	SOLsat	BS	ML
z top of layer (m)	0	-3.5	-11.5	-13.3	-23.5
Unit weight (kN/m³)	19	18	18	21	20
E_{50ref} (MPa)	102	180	327	504	790
E_{urref} (MPa)	307	541	982	1510	2370
p_{ref}(kPa)	17	71	111	142	198
ν	0.3	0.3	0.3	0.3	0.3
c' (kPa)	0	10	10	5	15
φ' (°)	28	33	33	35	38
ψ (°)	0	3	3	5	8
R_f	0.95	0.95	0.95	0.95	0.95
m	0.5	0.5	0.5	0.5	0.5
Coefficient of earth pressure K_0	0.53	0.45	0.45	0.43	0.38

We have used the CESAR solver and the CESAR pilot which can be used to script the calculations in Python (CESAR, 2023), i.e. to specify properties of different mesh zones, boundary conditions and loadings. Additionally, the external open source software GMSH was used to generate the mesh. The surface mesh was composed of approximately 3400 quadratic triangular elements, and 7200 nodes.

2.4 Calculation Results

We present three simple parametric studies to illustrate the results of the proposed approach.

2.4.1 Influence of the swelling zone stiffness

As mentioned in the introduction, the results obtained with the "swelling stress" approach depends on the stiffness of the concerned zones. Figure 4 shows the variation of the settlement trough width *i* (according to the familiar Gaussian distribution proposed by (Peck, 1969), *i* is the distance from the axis for which the settlement is equal to 60% of the maximum settlement) for different values of the Young's modulus of the swelling layer E_m. The injection pressure is equal to 100 kPa (no gradient). The results stabilize for values of E_m values below 20 kPa. It should be noted that this module allows the parametrization of the grout layer behaviour for computational purposes, ie. is not a physical parameter, and does not need to be calibrated to a realistic value.

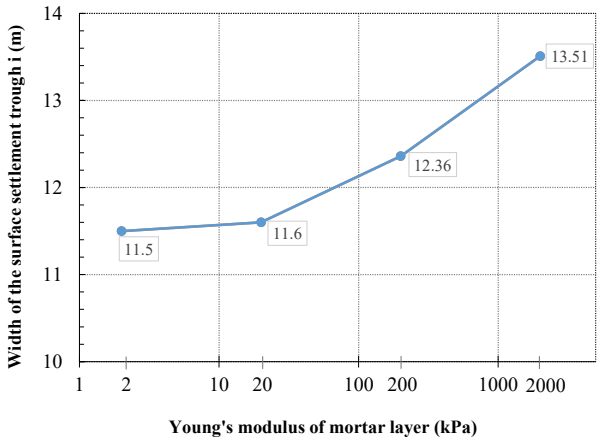

Figure 4. Influence of Young's modulus E_m on the width of the surface settlement trough.

2.4.2 Influence of the reference pressure p_{ref}

In this section, the injection pressure at the depth of the tunnel axis (equal to 21.5 m) is set to pref, with a vertical gradient of 22 kN/m3. Figure 5 shows the surface settlement distribution (in the case of a loaded pile), for different injection values of the reference pressure p_{ref}: 70, 100 and 180 kPa.

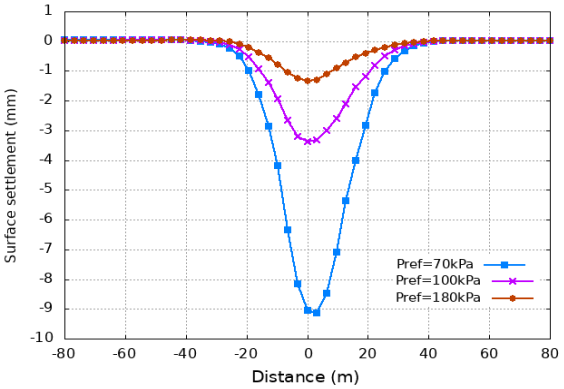

Figure 5. Influence of the reference pressure on the surface settlement.

The variations in the settlement trough width *i* is shown in Figure 6, in greenfield conditions, with the pile loaded or unloaded. The width of the settlement trough width depends on the reference pressure, which is noteworthy, since many models propose correlations between the settlement trough width and the nature of the ground alone, disregarding the influence of the construction method.

The results also show that the width of the settlement trough is reduced in presence of an unloaded pile, and slightly increased for a loaded pile.

As calculation is performed into plane strain condition, confining pressure at the front face is not modelled. Moreover, in this condition, structural element behave as plate element rather than one-dimensional one.

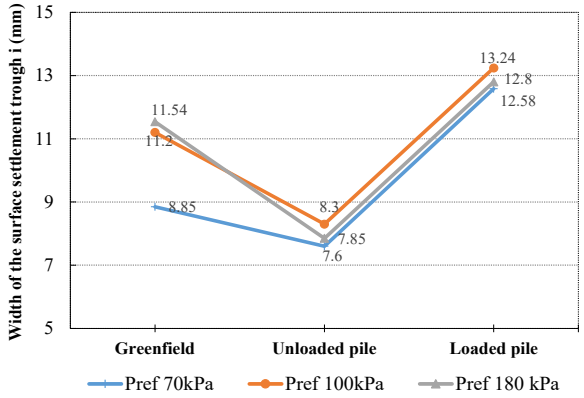

Figure 6. Width of surface settlement in greenfield condition, in the presence of unloaded and loaded pile.

2.4.3 Influence of the mortar density

In the last place, we have discussed the influence of the injection pressure gradient. It does not notably affect the results for p_{ref} equal to 100 and 180 kPa in terms of maximum settlement and settlement trough width (see Figure *7*). However, for p_{ref}=70 kPa, a 7% reduction is observed between the values of 8 kN/m^3 and 22 kN/m^3 of the injection pressure gradient.

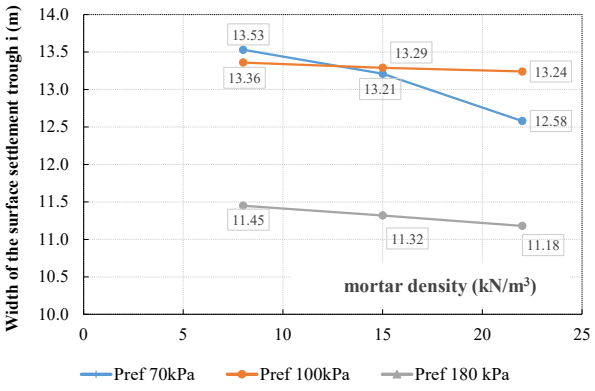

Figure 7. Width of surface settlement for different values of mortar density.

3 CONCLUSIONS

We have so far only validated the principle of the approach, but tunnel applications clearly require 3D calculations; this work is currently in progress. The new approach makes it possible to take into account the difference between injection pressure and in-situ stress, which would be rather complex with a more conventional modeling approach. It is recalled that it is essential to adopt a very low stiffness in the area where the injection occurs, which can be perceived as a limitation of the method. We will seek to explore ways to improve this aspect.

In the last place, it is worth noting that the procedure makes it possible to discuss the influence of injection pressure on the settlement trough width: it is generally assumed that the width parameter depends mainly on the characteristics of the soil being traversed, but results presented here show here that it also depends on the parameters of the tunnel-boring machine.

ACKNOWLEDGEMENTS

The results presented in this paper have been obtained within the framework of the French research Project E-PILOT (Evaluation of the impact on PILes response during Tunneling) E-PILOT ANR-21-CE22-0011.

E-PILOT is a joint industry project dedicated to the behaviour of piles during Tunneling. The project, driven by University Gustave Eiffel involves 4 contracting or consulting companies of the civil engineering sector, 2 contracting authorities and 4 universities and research laboratories. The project is funded by the partners, ANR and MTE.

REFERENCES

Berthoz, N., Bourgeois, E., Branque, D., Michalski, A., Mohamad, W., Le Kouby, A., Szymkiewicz, F., & Kreziak, C. (2022). Impact du creusement au tunnelier sur un pieu : synthèse de l'exercice de prévision TULIP. *Revue Française de Géotechnique*, 173, 2. https://doi.org/10.1051/geotech/2022015.

CESAR (2023). Available at: https://cesar.univ-gustave-eiffel.fr/, accessed: 20/12/2023.

Mohamad, W. (2022). *Effet de la construction des tunnels sur les fondations profondes : Cas du Grand Paris Express.* Thèse de Doctorat, Université Gustave Eiffel, France.

Peck, R. B. (1969). Deep Excavation and Tunneling in Soft Ground. *Proceedings of the 7th International Conference on Soil Mechanics and Foundation Engineering*, Mexico, pp. 225-290.

Proceedings of the XVIII ECSMGE 2024
GEOTECHNICAL ENGINEERING CHALLENGES
TO MEET CURRENT AND EMERGING NEEDS OF SOCIETY
© 2024 the Authors
ISBN 978-1-032-54816-6
DOI 10.1201/9781003431749-168
Open Access: www.taylorfrancis.com, CC BY-NC-ND 4.0 license

ECSMGE 24
XVIII EUROPEAN CONFERENCE ON SOIL MECHANICS AND GEOTECHNICAL ENGINEERING

Determining the modulus of subgrade reaction for piled raft foundations by numerical modelling

Détermination du modulus de réaction du sous-sol pour les systèmes de radier sur pieux par modélisation numérique

B. Zarazvand*, J. Frankovska
Slovak University of Technology, Bratislava, Slovakia
**bahman.zarazvand@stuba.sk*

ABSTRACT: The modulus of subgrade reaction, commonly recognised as the stiffness of the foundation, plays an essential role in predicting the behaviour of foundations. This research explores the characterisation and estimation of this coefficient for piled raft foundations. This hybrid foundation system finds frequent application in high-rise structures, especially in challenging soil conditions. Following a validation phase, the research identifies the system's ultimate bearing capacity and then uses a computational approach to derive the modulus of the subgrade reaction. Utilising advanced numerical tools, this research simulated the interaction between piled raft foundations and the underlying soil to estimate the modulus of subgrade reaction in the form of a 2D contour map, illustrating the coefficient distribution throughout all points of the piled raft components. This research underscores the importance and efficiency of numerical modelling in determining the modulus of subgrade reaction for piled raft foundations. It offers insights to enhance foundation design, ultimately contributing to safer and more economical infrastructural developments.

RÉSUMÉ: Le module de réaction du sous-sol, couramment reconnu comme la rigidité de la fondation, joue un rôle essentiel dans la prévision du comportement des fondations. Cette recherche explore la caractérisation et l'estimation de ce coefficient pour les fondations sur radier renforcé, un type hybride de système de fondation fréquemment utilisé dans les structures de grande hauteur, en particulier dans des conditions de sol difficiles. Suite à une phase de validation, la recherche détermine la capacité portante ultime du système puis utilise une approche computationnelle pour déduire le module de réaction du sous-sol. En utilisant des outils numériques avancés, cette recherche simule l'interaction entre les fondations sur radier renforcé et le sol sous-jacent pour estimer le module de réaction du sous-sol sous forme de carte de contour 2D, illustrant la distribution du coefficient en tous points des composants du radier renforcé. Cette recherche souligne l'importance et l'efficacité de la modélisation numérique pour déterminer le module de réaction du sol pour les fondations sur pieux et radier. Elle offre des perspectives pouvant conduire à une conception de fondation améliorée, contribuant finalement à des développements infrastructurels plus sûrs et plus économiques.

Keywords: Modulus of subgrade reaction; piled raft foundation; numerical modelling.

1 INTRODUCTION

Piled raft foundations represent a hybrid foundation system that combines the advantages of pile groups and raft foundations, offering enhanced stability for structures built on challenging soil conditions. These foundations are particularly crucial in regions with soft or heterogeneous soil profiles where traditional foundation systems might not provide adequate support. The modulus of subgrade reaction, often termed Ks, plays an essential role in geotechnical design. It is a measure that quantifies the soil's response to applied loads and is instrumental in understanding the intricate dynamics of soil-structure interaction. Historically, various methodologies have been employed to determine this modulus, ranging from plate load tests to more advanced numerical simulations. However, as construction practices evolve and the demand for taller and more complex structures increases, there is a pressing need to revisit and refine our understanding of the modulus of subgrade reaction, especially in the context of piled raft foundations (Kim et al., 2001; Randolph, 2003; Chan et al., 2009). Historically, the modulus of subgrade reaction for piled raft foundations has been determined through various empirical and analytical methods. A conventional approach entails evaluating the stiffness and capacity of pile foundations when subjected to seismic forces. Although this method can be applied to various forms of dynamic excitation, it might not fully consider the complex interactions between soil and structure (Pender, 1993). Another

approach focuses on the optimal pile arrangement to minimise differential settlements in piled raft foundations, where the foundation is modelled as a plate based on Mindlin theory, and the soil and piles are represented as Winkler coupled springs (Kim et al., 2001). However, while insightful, these methods can sometimes lead to overdesign or unexpected foundation behaviour, emphasising the need for optimisation techniques, such as hybrid genetic algorithms, to improve the design process (Chan et al., 2009).

With the recognised limitations of traditional methods in determining the modulus of subgrade reaction for piled raft foundations, the geotechnical community has turned to numerical modelling as a promising alternative. Numerical modelling offers a comprehensive approach to simulate intricate soil-structure interactions, capturing the behaviour of foundations under various conditions (Batini et al., 2015). Furthermore, the optimisation of pile groups and piled rafts, especially in terms of pile length distribution, has been explored through numerical methods, demonstrating the potential for increased stiffness and reduced differential settlements (Leung et al., 2010). These advancements underscore the potential of numerical modelling in providing more accurate, efficient, and versatile solutions for piled raft foundation design and analysis.

The main goal of this study is to assess the effectiveness of numerical modelling in determining the modulus of subgrade reaction for piled raft foundations. Given the increasing complexity of geotechnical projects and the need for accurate modelling tools, it is crucial to assess the capabilities of advanced software like Plaxis 3D in simulating real-world conditions and providing reliable results. Specifically, this study aims to investigate the accuracy of Plaxis 3D in modelling the behaviour of piled raft foundations under vertical loading conditions, as understanding the behaviour of such foundations is essential for safe and efficient design. The load-settlement relationship derived from the model was cross-referenced with findings from detailed research by Raut et al. (2014), which utilised the Poulos-Davis-Randolph (PDR) analytical approach. Following this, the contact pressure of the piled raft was ascertained, leading to the calculation of the modulus of the subgrade reaction.

2 MATERIALS

The geotechnical properties of the soil and the mechanical properties of the pile and raft used in the analysis are following the soil parameters of Raut et al. (2014). The geological profile consists of homogenous sandy clay soil, with the groundwater level at the ground surface to ensure full saturation of the soil layer. The Mohr-Coulomb (MC) model was employed to reflect the mechanical behaviour of the soil in terms of the material model, as indicated in Table 1. As for the raft and piles, it is assumed that they were constructed using C30-grade concrete, as shown in Table 2.

Table 1. The properties of the sandy clay soil.

Characteristic	Unit (SI)	Value
Natural unit weight	kN/m^3	18.5
Saturated unit weight	kN/m^3	19.5
Cohesive Strength	kPa	50
Angle of Internal Friction	(°)	20
Elastic Modulus	MPa	7
Poisson's Ratio	-	0.3

Table 2. The properties of concrete (grade C30).

Characteristic	Unit (SI)	Value
Unit weight	kN/m^3	25
f_{ck}	MPa	30
f_{ctm}	MPa	2.9
Elastic Modulus	GPa	32.8
Poisson's Ratio	-	0.2

3 METHODOLOGY AND MODELS

The piled raft foundations consist of a rectangular raft foundation measuring 18 meters in length and 8 meters in width, with a thickness of 0.5 meters. It is accompanied by 16 uniformly arranged piles, each having a length of 12 meters and a diameter of 0.6 meters.

The numerical analysis in this study was conducted utilising PLAXIS 3D software, employing mesh discretisation through the utilisation of 15-node elements. To accurately represent the geological layer, a single borehole was defined, with the groundwater level set at ground surface level.

To comprehensively model the soil-structure interaction, including the interaction between pile skin and soil, pile base and soil and raft subsurface interaction with the soil, both piles and raft elements were designated as volume clusters. It is worth highlighting that the interaction between the soil and concrete structure was defined by specifying interface surface elements with a strength reduction factor of 0.67, adhering to the reference guidelines provided by PLAXIS (Bentley, 2023).

To validate the process, settlement magnitudes were compared with the analytical model of PDR. Subsequently, the modulus of subgrade reaction for each element within the piled raft system was

computed using Equation 1 at various points throughout the system (Winkler, 1867).

$$K_s = \frac{\sigma'_N}{s} \quad (1)$$

where K_s (MN/m^3) is the modulus of subgrade reaction, σ'_N is the effective contact stress, and s is the settlement.

4 RESULTS AND DISCUSSIONS

The load-settlement curve of the piled raft system, depicted in Figure 1, exhibits a close match between the results from the numerical model and those obtained using the PDR method, as calculated by Raut et al. (2014). PDR and FEM methods predict a total deformation of 61.79 mm and 60 mm, respectively, for an ultimate load of 22 000 kN.

Figure 2 illustrates the horizontal cross-section surfaces on the deformed shape of the model, which is utilised to extract the distribution of contact stress and the corresponding settlement. Figure 3 depicts the contact stress distribution at the base of the raft with a total resultant force of 5 560 kN, while Figure 4 shows the contact stress distribution at the top of the piles with a resultant force of 16 440 kN. These results reveal that the pile groups bear 75% of the total force, with the load shared by the raft accounting for the remaining 25%.

Furthermore, in the cross-section marked as B-B, it is evident that 9 150 kN is supported by the bearing mechanism, which implies that the skin friction mechanism must equal 7 290 kN.

The numerical values of the modulus of subgrade reaction for all points along the horizontal cross sections of A-A* and B-B* are graphically presented using contour plots, as depicted in Figures 6 and 7. Figure 6 illustrates the distribution of the modulus of subgrade reaction for the raft foundation, which can be categorised into three regions: the centre, the perimeter, and the transitional zone between them. The center region registers the minimum value, equaling 1.25 MN/m³, whereas the perimeter records the highest value at 5 MN/m³. Furthermore, a significantly higher Ks value of 60 MN/m³ is observed at the pile tips.

5 CONCLUSIONS

The validation of the FEM model for a piled raft system was conducted using the analytical PDR method, focusing on a comparative analysis of the load-settlement graph. The study progressed by extracting contact stress and settlement data from the nodes along various key cross sections, including those at the raft base, pile tops, and pile base surfaces. This data was used to calculate the modulus of subgrade reaction at the mentioned points, with the results then visualised through a contour map. The outcome of the study not only delivers a detailed visual representation of the modulus of subgrade reaction distribution in piled raft systems but also establishes a specific method for incorporating these findings into superstructure design. The modulus of subgrade reaction, which signifies the interaction between soil and structure, can be effectively modelled and integrated into any structural model as the stiffness of area and point springs.

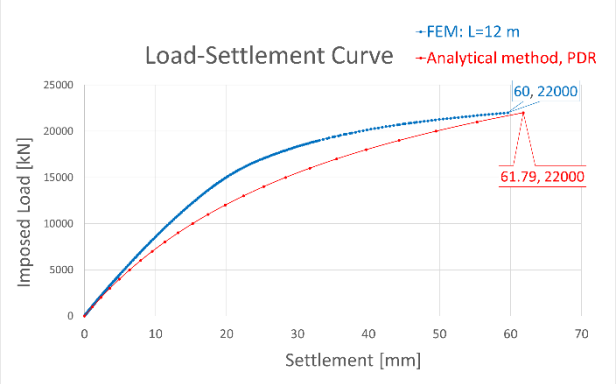

Figure 1. Comparison of the pile raft foundation load-settlement curve derived from analytical (PDR) and numerical methods.

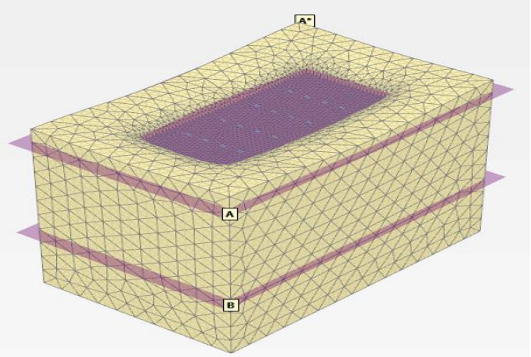

Figure 2. Horizontal cross-sections marked as A-A and B-B*, respectively, at the base of the raft and the piles.*

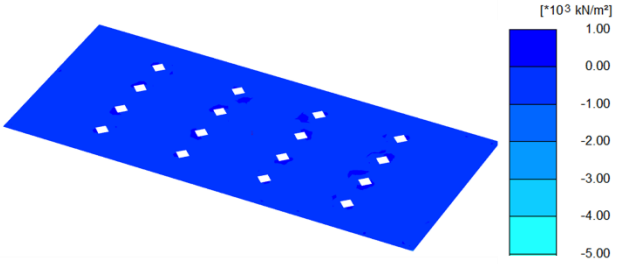

Figure 3. Distribution of contact stress at the base of the Raft.

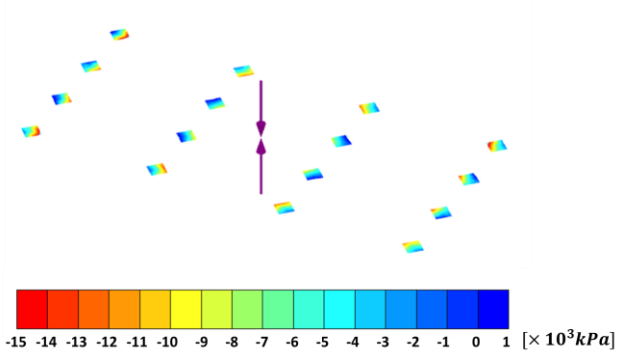

Figure 4. Distribution of contact stress at the top of the piles.

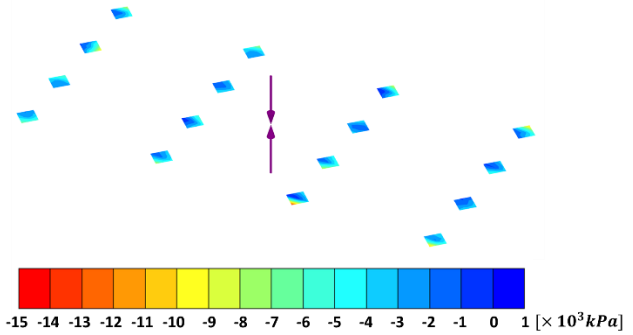

Figure 5. Distribution of contact stress at the base of the piles.

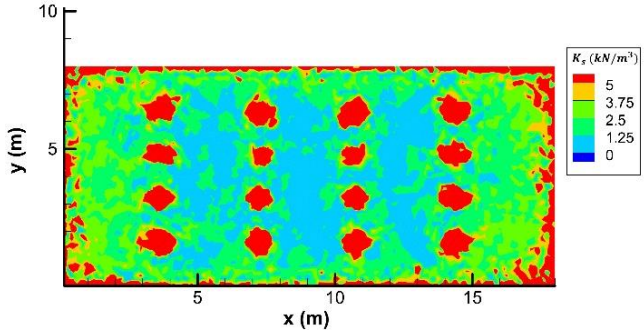

Figure 6. Modulus of subgrade reaction at the base of the Raft.

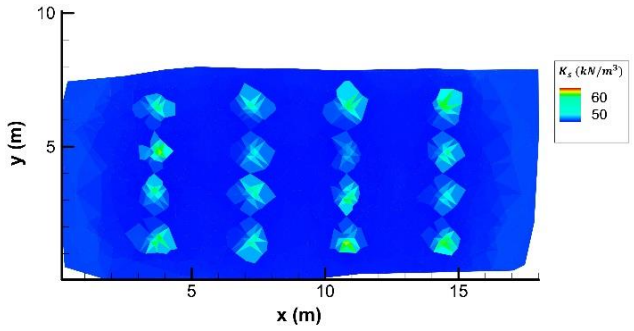

Figure 7. Modulus of subgrade reaction at the base of the piles.

ACKNOWLEDGEMENTS

The authors are grateful for the financial support provided by the Grant Agency of the Ministry of Education, Science, Research and Sport of the Slovak Republic. The project presented in this article is supported by grant project VEGA 1/0745/21.

REFERENCES

Batini, N., Rotta Loria, A. F., Conti, P., Testi, D., & Grassi, W. (2015). Energy and geotechnical behaviour of energy piles for different design solutions. *Applied Thermal Engineering*, 85, 250-262. DOI: 10.1016/j.applthermaleng.2015.04.050.

Chan, C. M., Zhang, L. M., & Ng, J. T. M. (2009). Optimisation of Pile Groups Using Hybrid Genetic Algorithms. *Journal of Geotechnical and Geoenvironmental Engineering*, 135(4), 497-505. DOI: 10.1061/(asce)1090-0241(2009)135:4(497).

Kim, K. N., Lee, S. H., Kim, K. S., Chung, C. K., Kim, M. M., & Lee, H. S. (2001). Optimal pile arrangement for minimising differential settlements in piled raft foundations. *Computers and Geotechnics*, 28(6), 411-431. DOI: 10.1016/s0266-352x (01)00002-7.

Leung, Y. F., Klar, A., & Soga, K. (2010). Theoretical Study on Pile Length Optimization of Pile Groups and Piled Rafts. *Journal of Geotechnical and Geoenvironmental Engineering*, 136(11), 1554-1564. DOI: 10.1061/(asce)gt.1943-5606.0000206.

Pender, M. J. (1993). Aseismic pile foundation design analysis. *Bulletin of the New Zealand Society for Earthquake Engineering*, 26(1), 49-160. DOI: 10.5459/bnzsee.26.1.49-160.

Randolph, M. F. (2003). Science and empiricism in pile foundation design. *Géotechnique*, 53(10), 847-875. DOI: 10.1680/geot.2003.53.10.847.

Winkler, E. (1867) Die Lehre von Elastizitat und Festigkeit (on Elasticity and Fixity). Dominicus, Prague.

Raut JM, Khadeshwar SR, Bajad SP, & Kadu MS (2014) "Simplified design method for piled raft foundations. " Advances in Soil Dynamics and Foundation Engineering, GSP 240 ASCE 2014. DOI: 10.1061/9780784413425.047.

Bentley Systems, Plaxis 3D-Reference Manual 2023.

Proceedings of the XVIII ECSMGE 2024
GEOTECHNICAL ENGINEERING CHALLENGES
TO MEET CURRENT AND EMERGING NEEDS OF SOCIETY
© 2024 the Authors
ISBN 978-1-032-54816-6
DOI 10.1201/9781003431749-169
Open Access: www.taylorfrancis.com, CC BY-NC-ND 4.0 license

ECSMGE 24
XVIII EUROPEAN CONFERENCE ON SOIL MECHANICS AND GEOTECHNICAL ENGINEERING

Examining the behavior of laterally loaded large-diameter monopiles using coupled FDM-DEM simulations

Examen du comportement des monopieux de grand diamètre chargés latéralement à l'aide de simulations FDM-DEM couplées

Z. Zhang*, Z.-T. Zhang, X.-D. Zhang
China Institute of Water Resources and Hydropower Research, Beijing, China.

W. Wang, G.-M. Yu, Z.-Q. Zhang
China Three Gorges Corporation, Beijing, China

**zhangzt@iwhr.com*

ABSTRACT: In order to examine the load-transfer mechanisms of large-diameter monopiles from a microscopic perspective, three-dimensional FDM-DEM simulations on a centrifuge model pile test were carried out. The simulation results show great resemblance to the measurements from the centrifuge test, suggesting capability of the proposed FDM-DEM simulation framework, which considers rolling-resistance in the contact model and involves a careful calibration based on triaxial tests. The simulation results shed light on the complex interactions between monopile and the surrounding soils in terms of deformation patterns of the monopile, the displacement field and the force chain evolution of surrounding soils. This do not support the basic assumption of p-y curve method that the soil-pile interaction at a particular depth is independent of the soil behavior at all other depths. The research findings help to deepen our understanding on the behavior of monopiles from a microscopic perspective, and to provide a theoretical basis for the optimization of associated design approaches.

RÉSUMÉ: Afin d'examiner les mécanismes de transfert de charge des monopieux de grand diamètre d'un point de vue microscopique, des simulations tridimensionnelles FDM-DEM ont été réalisées sur un modèle de pieu en centrifugeuse. Les résultats de la simulation présentent une grande similitude avec les mesures du test en centrifugeuse, suggérant la capacité du cadre de simulation FDM-DEM proposé, qui prend en compte la résistance au roulement dans le modèle de contact et implique un étalonnage minutieux basé sur des essais triaxiaux. Les résultats de la simulation mettent en lumière les interactions complexes entre le monopieu et les sols environnants en termes de motifs de déformation du monopieu, de champ de déplacement et d'évolution de la chaîne de forces des sols environnants. Cela ne soutient pas l'hypothèse de base de la méthode de la courbe p-y selon laquelle l'interaction sol-pieu à une profondeur particulière est indépendante du comportement du sol à toutes les autres profondeurs. Les résultats de la recherche contribuent à approfondir notre compréhension du comportement des monopieux d'un point de vue microscopique et à fournir une base théorique pour l'optimisation des approches de conception associées.

Keywords: Large-diameter monopile; discrete element method; lateral loading; displacement field; force chain evolution.

1 INTRODUCTION

More than 70% of offshore wind turbines are founded on monopiles, which become increasingly large in terms of diameter to support wind turbines with extremely large capacities in recent years. The maximum diameter of monopiles used in offshore wind power farms reaches 10.5m in China. Although many efforts have been made to explore the behaviour of large-diameter monopiles, the pile-soil interaction still remains unclear (Choo and Kim, 2016).

Field tests were usually carried out on piles with diameters not exceeding 2.5 meters, while the prototype diameters were usually smaller than 6.5 meters in centrifuge tests (Choo and Kim, 2016; Truong, 2019). The authors designed and manufactured an innovative device for centrifuge modelling of the super-large monopiles with diamteres of 9 meters. A series of tests were carried out using the device and an advanced 400 g-ton beam centrifuge with maximum centrifugal acceleration of 1000g at China Institute of Water Resources and Hydropower Research (IWHR). Details of the device and the experimental tests can be found in (Zhang et al. 2023, Wang et al. 2023). The experimental results shed light on the distribution of bending moment for monopiles under static loading. However, the displacement field and force chains of surrounding soils remain unknown.

In order to examine the micro-mechanical behaviour of surrounding soils of super-large monopiles subjected to static loading, this paper carried out simulations using a coupled Finite Difference-Discrete Element (FDM-DEM) method. The research findings help to deepen our understanding on the behavior of monopiles from a microscopic perspective, and to provide a theoretical basis for the optimization of associated design approaches.

2 DETAILS OF THE SIMULATION

One simulation was carried out to model a centrifuge test on a large-diameter monopile in sandy soils. As shown in Figure 1, the level-ground with a thickness of 490 mm was prepared using silty sands with a mean diameter d_{50} close to 0.125mm. The dry density was 1.55g/cm³, and the relative density was 62%, indicating a medium dense state. The model pile made by aluminium alloy had an outer diameter of 90 mm, a wall thickness of 3 mm, an elastic modulus of 69 GPa, an anchoring depth of 470 mm. The monopile was subjected to a monotonic unidirectional loading at 100g, where g is the gravitational acceleration. The loading point was located 510 mm above the mudline.

The simulation utilized discrete spherical particles with a diameter of 0.125 mm, mirroring the experimental conditions closely, particularly the d_{50} of the silty sands employed. The inter-locking effects among real soil particles were accounted for using the built-in rolling resistance linear model. As illustrated in Table 1 and Figure 2, the parameters were carefully calibrated based on triaxial compressioin tests on the same material. The monopile was modelled in a continuum way, and a linear elastic model was ultilized. The parameters were the same as that used in the centrifuge test. The wall-zone coupling scheme was employed, and PFC walls were created coinciding with zone faces of monopile to ensure the interaction between DEM and FDM components. In order to reduce the computational cost, the gravity acceleration was set as 10, 000g, equivalent to 100 times the gravity used in the centrifuge test. Although the sizes of ground and monopile were 1/100 of those used in the centrifuge test, the size of the particles remained consistent between the simulation and the centrifuge test, adhering to the scale law conventionally employed in centrifuge testing. Hence, the simulation and the centrifuge test referred to the same prototype. Horizontal loading was simulated by imposing a constant horizontal velocity 1×10^{-10} m/s at pile head.

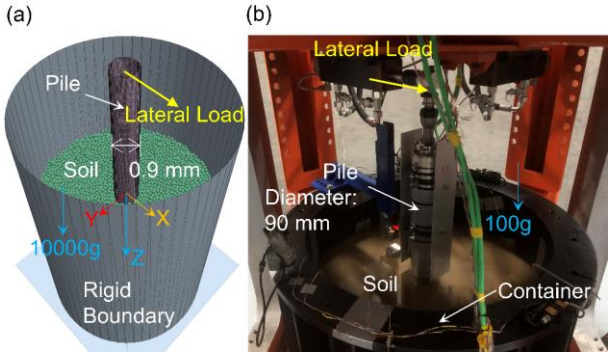

Figure 1. Setups of (a) simulation and (b) cenrifuge test.

Table 1. Contact model parameters.

Parameters	Value
Normal stiffness k_n (N/m)	2×10^4
Shear stiffness k_s (N/m)	2×10^4
Friction coefficient μ	0.35
Rolling friction coefficient μ_r	0.55

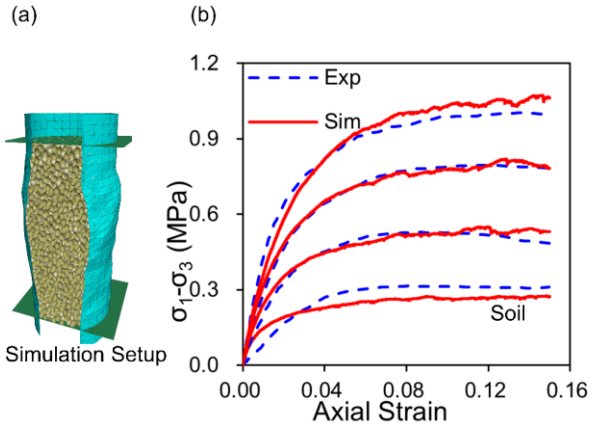

Figure 2. Comparison between numerical and experimental results: stress-strain relation during triaxial compression.

3 RESULTS AND DISCUSSIONS

Since the rotation angle at mud line θ_0 could hardly be monitored in the experiment, two laser displacement sensors were used to monitor the average rotation θ' of a monopile segment with a length of 300mm and located 140 mm above the seabed at model scale (see Figure 1). Figure 3 compares the experimental and numerical results in terms of the relationship between horizontal loading force H and θ'. The simulation results show great resemblance to the measurements from the centrifuge test. This suggests the capability of the proposed FDM-DEM simulation framework. The rotation angle at mud line θ_0 is also added in Figure 3. The horizontal resistance is 17.48 MN when the rotation angel reaches 0.25° at mud line.

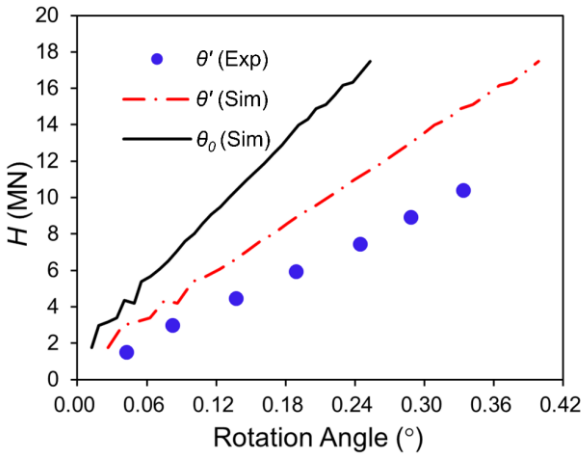

Figure 3. Relationships between horizontal loading force and rotation angles.

3.1.1 Deformation Patterns of Monopile

Figure 4 presents the distributions of lateral displacement y and rotation angle θ along depth for monopiles under various horizontal forces. There is a rotation center where y equals zero, and this center moves towards pile tip when the horizontal forces increase. When the force increases from 6.51MN to 17.48MN, the total increment of ration center depth is only 3.8m, which accounts for 8% of embedment depth.

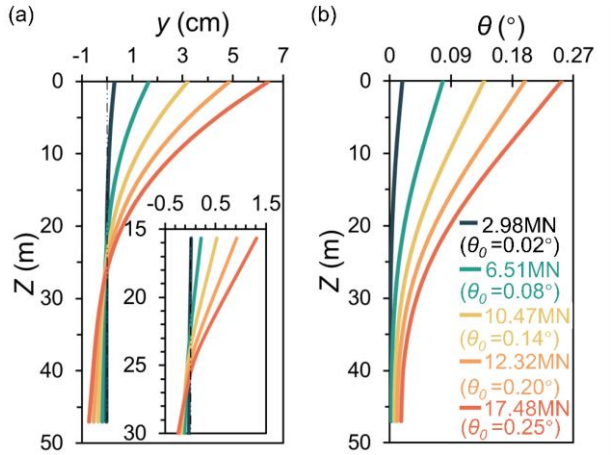

Figure 4. Distributions of (a) lateral displacement and (b) rotation angle along depth.

3.1.2 Displacement Field of Soil Particles

Figure 5 presents the section views of displacement field at $Y = 0$. Figures 6 and 7 shows section views at $Z = 15$ m above rotation center and $Z = 30$ m below it, d_p equals the displacement of soil particles in the prototype. The surrounding particles seem rotate around the rotation center of monopile. The displacement pattern is far more complex than that of small-diameter long piles where the soil particles move horizontally. This observation may elucidate the substantial discrepancy observed when employing the *p-y* curve method for analyzing the force-deformation relationship of large-diameter monopiles, which has been discussed by numerous studies (Choo and Kim, 2016; Li, 2017; Zhu, 2011). The point will be further discussed in clause 3.1.3.

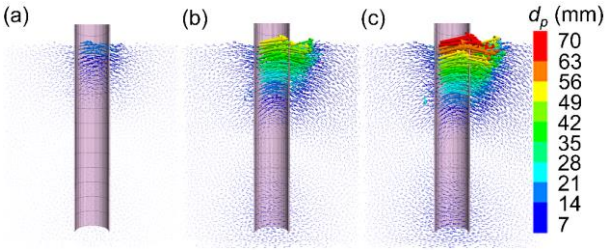

Figure 5. Section views of displacement fields at Y = 0: (a) H = 6.51 MN, θ0 = 0.08°; (b) H = 12.32 MN, θ0 = 0.14°; (c) H = 17.48 MN, θ0 = 0.25°.

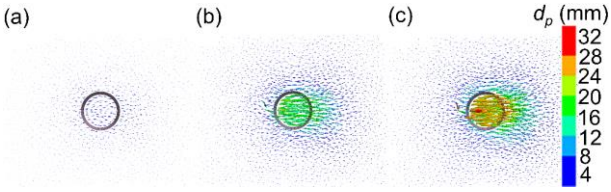

Figure 6. Section views of displacement fields at Z= 10m: (a) θ0 = 0.08°; (b) θ0 = 0.14°; (c) θ0 = 0.25°.

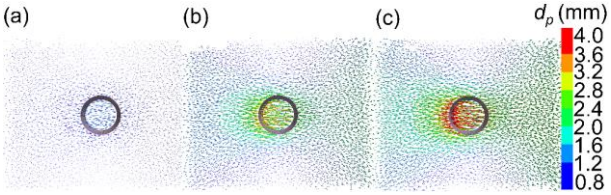

Figure 7. Section views of displacement fields at Z = 30m: (a) θ0 = 0.08°; (b) θ0 = 0.14°; (c) θ0 = 0.25°.

3.1.3 Force Chains Evolution

Figure 8 illustrates the force chains before loading and at a rotation angle θ_0 of 0.25°. The value α equals $F_m/F_{m,mean}$, where F_m is the total contact force at a specific contact and $F_{m,mean}$ represents the mean value of total contact forces of all particles. Due to gravitational forces, the strong force chains are mainly aligned along the vertical direction before loading. When lateral loading is applied on the monopile, the force chains gradually evolve. For the soils in the superficial zone in front of the pile, more strong force chains become inclined from the vertical direction at $\theta_0 = 0.25°$. The pile-soil interaction force at shallow depths is transferred to much deeper soils.

The force chain evolution and the aforementioned displacement field of surrounding soils might indicate that the assumption of the *p-y* curve method may overlook certain evident issues. The *p-y* curve method is based on the assumption that the soil-pile interaction at a particuar depth is independent of the soil behavior at all other depths (Reese et al., 1974). This

assumption seems not true for large-diameter monopiles. The surrounding particles in the superficial zone in front of the pile rotate along a center and move in an inclined direction. The strong force chains become inclined from the vertical direction and then transfer force to much deeper soils. Therefore, the soil-pile interaction at a particuar depth is also influenced by the soils at deeper depths. This does not support the basic assumption of *p-y* curve method.

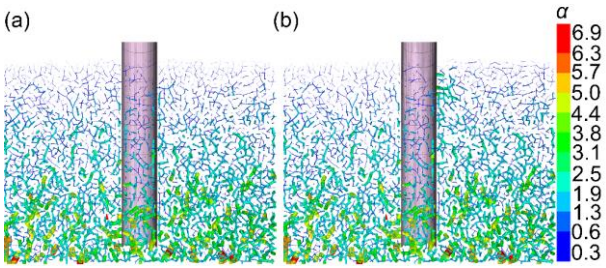

Figure 8. Force chains (a) before loading and (b) at θ0 = 0.25°

4 CONCLUDING REMARKS

In this study, FDM-DEM simulations were conducted to analyze the load-transfer mechanisms of large-diameter monopiles. The simulation results show great resemblance to the measurements from the centrifuge test. This suggests the capability of the proposed FDM-DEM simulation framework, which considers rolling-resistance in the contact model and involves a careful calibration based on triaxial tests.

The simulation results shed light on the the complex interactions between monopile and the surrounding soils in terms of deformation patterns of the monopile, the displacement field and the force chain evolution of surrounding soils. The surrounding particles in the superficial zone in front of the pile rotate along a center and move in an inclined direction. The strong force chains become inclined from the vertical direction and then transfer force to much deeper soils. Therefore, the soil-pile interaction at a particuar depth is also influenced by the soils at deeper depths. This does not support the basic assumption of *p-y* curve method that the soil-pile interaction at a particuar depth is independent of the soil behavior at all other depths.

ACKNOWLEDGEMENTS

This research was supported by Research Fund Program of China Three Gorges Corporation (202103016) and National Natural Science Foundation of China (51809290).

REFERENCES

Choo, Y. W., & Kim, D. (2016). Experimental development of the p-y relationship for large-diameter offshore monopiles in sands: Centrifuge tests. *Journal of Geotechnical and Geoenvironmental Engineering*, 142(1): 04015058. https://doi.org/10.1061/(ASCE)GT.1943-5606.000137.

Li, W., Zhu, B., & Yang, M. (2017). Static response of monopile to lateral load in overconsolidated dense sand. *Journal of Geotechnical and Geoenvironmental Engineering*, 143(7), 04017026. https://doi.org/10.1061/(ASCE)GT.1943-5606.0001698.

Reese, L. C., Cox, W. R., & Koop, F. D. (1974, May). Analysis of laterally loaded piles in sand. In *Offshore Technology Conference*(pp. OTC-2080). OTC. https://doi.org/10.4043/2080-MS.

Truong, P., Lehane, B. M., Zania, V., & Klinkvort, R. T. (2019). Empirical approach based on centrifuge testing for cyclic deformations of laterally loaded piles in sand. *Géotechnique*, 69(2), 133-145. https://doi.org/10.1680/jgeot.17.P.203.

Wang, W., Zhang, Z. T., Yu, G. M., Zhang, X. D., Zhang Z. C., Song J. Z., Zhang, Z. (2023). Small-displacement behavior of offshore wind power monopiles subjected to static lateral loading. submitted to *Chinese Journal of Geotechnical Engineering* (under review, in [Chinese]).

Zhang, Z. T., Wang, Z., Zhang, X. D., Guangming Yu, G. M., Hu, J. (2023). An innovative experimental device for characterizing the responses of monopiles subjected to complex lateral loading. In *Proceedings of the 8th International Symposium on Deformation Characteristics of Geomaterial*. Porto, Portugal.

Zhu, B., Zhu, R. Y., Luo, J., Chen, R. P., Kong, L. G. (2011). Model tests on characteristics of ocean and offshore elevated piles with large lateral deflection. *Chinese Journal of Geotechnical Engineering*, 32(4), 521-530. (in Chinese).

Proceedings of the XVIII ECSMGE 2024
GEOTECHNICAL ENGINEERING CHALLENGES
TO MEET CURRENT AND EMERGING NEEDS OF SOCIETY
© 2024 the Authors
ISBN 978-1-032-54816-6
DOI 10.1201/9781003431749-170
Open Access: www.taylorfrancis.com, CC BY-NC-ND 4.0 license

ECSMGE 24
XVIII EUROPEAN CONFERENCE ON SOIL MECHANICS AND GEOTECHNICAL ENGINEERING

Research on macro-meso relationship of geological materials based on Discrete Element Method: Review and prospect

Recherche sur la relation macro-méso des matériaux géologiques basée sur la Méthode des Éléments Discrets: Revue et perspective

M. Zhou*
Arup Group Limited, Beijing, China
Q. Zhang
China Institute of Water Resources and Hydropower Research, Beijing, China
R. Ding
Tsinghua University, Beijing, China

*monica.zhou@arup.com

ABSTRACT: The discrete element method has been widely adopted in the geotechnical engineering. In this paper, the discrete element study on the soil-rock mixtures, and the crushing as well as creep properties of rockfill materials, are reviewed. The development trend of discrete element method in geotechnical engineering is introduced, and the main issue is the determination of meso-parameters in the model. In addition, by combining the large amount of discrete element data and machine learning technology, it seems that the intelligent constitutive models can be reasonably established.

RÉSUMÉ: La méthode des éléments discrets a été largement adoptée dans l'ingénierie géotechnique. Dans cet article, l'étude des éléments discrets sur les mélanges sol-roche, ainsi que les propriétés de concassage et de fluage des matériaux d'enrochement, sont passées en revue. La tendance de développement de la méthode des éléments discrets dans l'ingénierie géotechnique est introduite, et le problème principal est la détermination des méso-paramètres dans le modèle. De plus, en combinant la grande quantité de données sur les éléments discrets et la technologie d'apprentissage automatique, il semble que les modèles constitutifs intelligents puissent être raisonnablement établis.

Keywords: Macro-micro analysis; discrete element method; constitutive relationship; data-driven predictions

1 INTRODUCTION

Although soil is often treated as a continuous medium in theoretical or numerical methods (Luo and Yao, 2010; Liu et al., 2015), it is actually a bulk material with complex structures in the mesoscopic scale, especially for soil-rock materials and rockfill materials. As a numerical method suitable for bulk materials, DEM has been widely applied in geotechnical engineering (Xu et al., 2003). DEM can reproduce the soil characteristics in laboratory tests with multi-stress path and are capable of preparing soil materials with different meso-structures, thus it is very suitable for macro-meso mechanism study. In addition, DEM is a suitable method to study the failure process of geotechnical engineering for its capability of large deformation problems and macro-meso mechanisim. This article will review the current state of discrete element simulations of soil-rock mixtures and crushing creep properties of rockfill, as well as its application prospects of engineering simulation and consititutive construction.

2 MESO BEHAVIOR SIMULATION OF SOIL-ROCK MIXTURES

The soil-rock mixture is a special engineering geological material, which is mainly adopted in the geotechnical slope and subgrade engineering. The soil-rock mixture is formed by the accumulation of rock blocks with a certain size and high elastic modulus, as well as the soil with low elastic modulus, thus its physical and mechanical properties are between the soil mass and the fractured rock mass. Numerical methods such as DEM, particle flow (PFC) and finite element-based discrete element method (CDEM) are playing an increasingly important role.

It is a potential method to analyze and predict the deformation and failure behavior of soil-rock mixture based on its structural model. Most of the structural models of soil-rock mixtures are based on macroscopic statistical laws, which mostly use regular geometric shapes, such as rectangles, circles, triangles and ellipses, to represent rock blocks. There is a large gap from the actual structure (Huang et al., 2013). Recently,

the structural model generated based on digital images can accurately reflect the actual distribution of blocks and soil in the mixed body (Figure 1) (Xu and Wang, 2016; Jia et al., 2022). However, it is still not suitable for large-scale engineering problems due to the limitation of the ability of acquisition and recognition equipment.

The deformation and failure of soil-rock mixture is not only related to the geometric characteristics, strength and deformation properties of the soil or Rock, but also closely related to the motion state, the contact property, friction characteristics and other factors. At present, there is a lack of quantitative experimental research and analysis methods for this internal meso-mechanism.

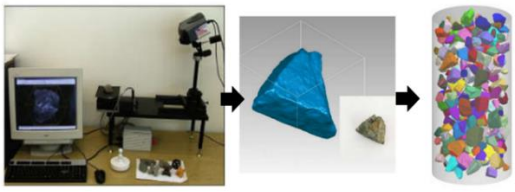

(a) Blocks based on computer 3D scanning



(b) Soil-rock mixture model

Figure 1. Reconstruction of a real soil-rock mixture (Zhang et al., 2019).

3 CRUSHING & CREEP SIMULATION OF ROCKFILL

Particle breakage and its size effect are the typical properties of rockfill material due to its irregular shapes and large particle size. In the engineering of dams and high filled foundations, the quantitative law of size effects is one of the main technical difficulty to predict the in-situ settlement due to the limitation of test scale. Numerical simulation of the test considering particle breakage is regarded as one of the solutions (Alonso et al., 2012).

Among many DEM models reported in literature, the bonded-particle model (BPM), which is formed by bonding small balls together, is one of the most popular models for particle breakage simulation. Recently, Wu & Wang (2020) demonstrated the capability of reproducing the realistic particle breakage behaviors of BPM by generating initial flaws based on the realistic fracture surfaces obtained from the experiment. Cil et al. (2020) & Zhou (2021) adopted random and size-dependent bond strength in BPM and showed at both particle and assembly scale that the proposed modelling strategy can be a viable approach to capture the mechanics of size-dependent granular matter.

To establish the bridge between grain-scale phenomena and continuum-scale processes, the more accurate DEM model as well as the summary of the law of test results are the future study plan, in which photo elastic test, X-ray technology and DIC technology provide the possibility. In addition, compared to the modelling of particle breakage, the simulation of creep gained relatively less attention. Soil creep may be caused by delayed grain breakage and reorientation or time-delayed sliding of particles (Figure 2) (Zhou and Song, 2016).

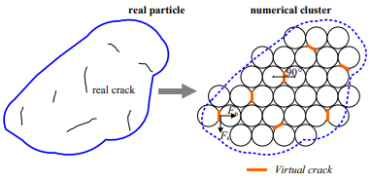

(a) Random Virtual Crack Model

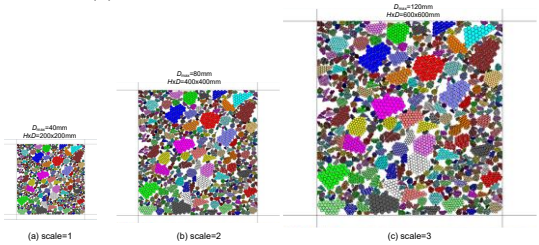

(b) Models of different test sizes

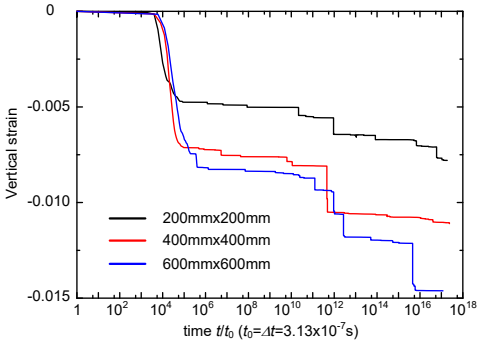

(c) Size effects of creep properties

Figure 2. Discrete element study of the size effect of creep behaviour for rockfill material (Zhou and Song, 2016).

4 THE FAILURE PROCESS SIMULATION OF GEOTECHNICAL ENGINEERING

Discrete elements not only have good applicability in the mechanism study at material mesoscale, but also are suitable to the study of large deformation problems

with obvious block properties at the engineering scale. For geotechnical and hydraulic engineering, the DEM shows strong superiority in numerical simulation problems such as landslide, rockfall motion, seepage field analysis and so on. Zhang et al. (2010) and Hu (2010) established the discrete element theory for three-dimensional modal deformation body and simulated the dam failure process of the Meihua arch dam. Pekau et al. (2004) and Hou (2005) combined the finite element method, discrete element method and fracture mechanics to analyze the failure process of Koyna concrete gravity dam. Su et al. (2019) simulated the embankment engineering by DEM, analyzed the influence of particle scale parameters on the macro-mechanical parameters of the embankment, and simulated the process from local failure to overall instability. It is found that, in recent years, the application of DEM to solve practical problems of engineering scale structures is in a rapid development stage, and good progress has been made in phenomenon reproduction and structural simulation, but the above research also has problems such as difficulties in the calibration of discrete element mesoscopic parameters.

There are relatively few studies on the correlation between cross-scale parameters of rockfill materials and meso-parameter calibration methods. Ma (2020) proposed a new parameter calibration method for rockfill meso-contact model based on the dam structure monitoring data and machine learning technology. The multiple data samples related to the meso-contact model parameters in DEM and the engineering scale dam deformation are first established based on the DEM simulation of stress-strain curves of rockfill material, parameter determination of macroscopic constitutive models and finite element analysis of dam structures. Then the machine learning is adopted to train and propose a fast-prediction model for the cross-scale relationship between meso-contact model parameters in DEM and the engineering scale dam deformation. Finally, the quantum genetic algorithm is used to find the minimum error between predicted and measured dam deformation, and the DEM meso parameters are determined.

5 DATA-DRIVEN INTELLIGENT CONSTITUTIVE PREDICTION

Meso-scale DEM simulation has been shown to be effective in simulating the constitutive behavior of granular materials. Compared with laboratory triaxial tests of granular materials, DEM virtual triaxial tests are less expensive, more efficient, and more convenient to consider various loading conditions. The constitutive model based on deep learning uses neural networks to establish the mapping relationship between stress and strain. Usually the input parameter is the strain tensor, and the output parameter is the stress tensor. The stress response of granular materials has obvious characteristics of strain history and strain path dependence, and a material constitutive response model that can reflect complex stress-strain path conditions must have the ability to "remember" the stress or strain history, so the constitutive model is essentially a time series model or process model (Figure 3).

Yu (2021) used the DEM to establish a particle material model sample, and carried out a total of 96 sets of triaxial compression simulations with different groups of confining pressure, strain rate, and loading/unloading conditions. The stress-strain relationship curve obtained by numerical simulation and the internal variable data such as porosity, coordination number, and composition tensor were used as the training and verification datasets, and the constitutive relationship was proposed and verified by deep autonomous reinforcement learning algorithm. Qu et al. (2021) proposed a deep learning strategy guided by mechanical knowledge by adopting the small strain theory of granular materials based on the homogenization assumption of Vogit. DEM simulation of triaxial experiments were used to generate stress-strain data. The results show that the trained deep learning model can effectively capture the stress-strain response relationship under complex multiaxial loading conditions, with good interpolation and extrapolation prediction capabilities.

Based on experimental data and deep learning model, the key constitutive parameters or complete stress-strain relationship of rockfill material can be predicted, and the strength parameters or stress-strain relationship are directly obtained from the basic physical parameters of rockfill. At present, the research on rockfill constitutive model based on machine learning/deep learning method is still in its infancy. The DEM, as a powerful means to expand datasets and provide key information such as internal variables, has initially demonstrated its advantages in considering different loading paths. There is still a lot of work to be done to consider the different gradings, initial state and particle crushing.

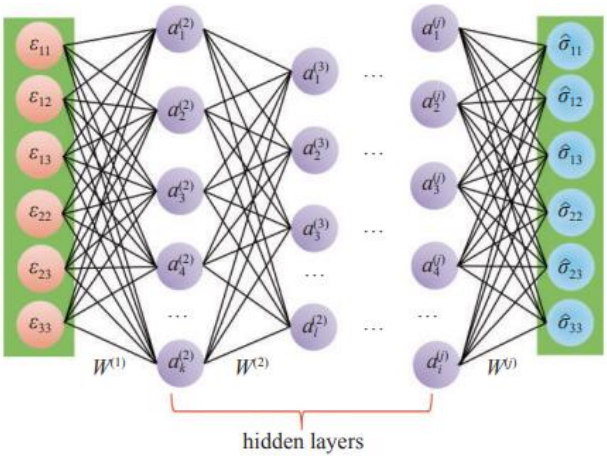

Figure3. Schematic diagram of a constitutive model based on deep learning (Qu et al., 2021).

REFERENCES

Alonso, E.E., Tapias, M., and Gini, J. (2012). Scale effects in rockfill behaviour. *Géotechnique Letters*, 2(3):155-160. DOI:10.1680/geolett.12.00025.

Cil, M.B., Sohn, C., and Buscarnera, G. (2020). DEM modeling of grain size effect in brittle granular soils. *J. Engng Mech.*, 146(3): 04019138. DOI: 10.1061/(ASCE)EM.1943-7889.0001713.

Hou, Y.L. (2005). *A coupling rupture model of distinct element and fracture mechanics for concrete dam-foundation*. PhD thesis, Tsinghua University, Beijing, China.

Hu, W. (2010). *Simulation of damage-collapse process and safety evaluation for arch dams*. PhD thesis, Tsinghua University, Beijing, China.

Huang, J., Xu, S., and Hu, S. (2013). Effects of grain size and gradation on the dynamic responses of quartz sands. *Int J Impact Eng*, 59: 1-10. DOI: 10.1016/j.ijimpeng.2013.03.007.

Jia, M.K., Wang, W., Zhang, B., et al. (2022). Numerical study on fabric properties of random dense packing structures of complex convex polyhedrons: Effects of shape parameters. *Chinese Journal of Computational Mechanics*, 39(3): 273-282.

Liu, Y., Zhao, C.G., and Cai, G.Q. (2015). *Rational soil mechanics and thermodynamics*. Science Press.

Luo, T., and Yao, Y.P. (2010). *Constitutive relation of soil*. China Communication Press.

Ma, C.H. (2020). *Intelligent inversion analysis of macro- and microparameters of rockfill based on discrete element method and it's engineering application*. Master's thesis, Xi'an University of Technology, Xi'an, China.

Pekau, O.A., and Cui, Y.Z. (2004). Failure analysis of fractured dams during earthquakes by DEM. *Engineering Structures*, 26(10): 1483-1502. DOI: 10.1016/j.engstruct.2004.05.019.

Qu, T.M., Feng, Y.T., Wang, M.Q., et al. (2021). Constitutive relations of granular materials by integrating micromechanical knowledge with deep learning. *Chinese Journal of Theoretical and Applied Mechanics*, 53(9): 2404-2415.

Su, H., Fu, Z., Gao, A., et al. (2019). Numerical simulation of soil levee slope instability using particle-flow code method. *Natural Hazards Review*, 20(2): 04019001. DOI:10.1061/ (ASCE)NH.1527-6996.0000327.

Wang, Y., Li, X., Zhang, B., et al. (2014). Meso-damage cracking characteristics analysis for rock and soil aggregate with CT test. *Sci. China Technol. Sci.*, 57, 1361-1371. DOI: 10.1007/s11431-014-5578-1.

Wu, M., Wang J. (2020). A DEM investigation on crushing of sand particles containing intrinsic flaws. *Soils Found.*, 60(2): 562-572. DOI: 10.1016/j.sandf.2020.03.007.

Xu, W.J., and Wang, S. (2016). Meso-mechanics of soil-rock mixture with real shape of rock blocks based on 3D numerical direct shear test. *Chinese Journal of Rock Mechanics and Engineering*, 35(10): 2152-2160.

Xu, Y., Sun, Q.C., Zhang, L., et al. (2003). Research progress of particle discrete element method. *Advances in Mechanics*, 33(2): 251-260.

Yu, H.L. (2021). *Research on establishing method of granular material constitutive laws based on data-driven strategy*. Master's thesis, Harbin Engineering University, Harbin, China.

Zhang, C., and Jin, F. (2010). Three-dimensional modal deformable discrete element method and its application study. *Design of Hydroelectric Power Station*, 26(3): 1-9.

Zhang, Q., Wang, X.G., Zhao, Y.F., et al. (2019). 3D random reconstruction of meso-structure for soil-rock mixture and numerical simulation of its mechanical characteristics by particle flow code. *Chinese Journal of Geotechnical Engineering*, 41(1): 60-69.

Zhou, M.J. (2021). A crack theory-based bonded-particle model for rock particles considering size effects. *Géotechnique letters*, 11(4): 340-349. DOI: 10.1680/jgele.21.00022.

Zhou, M.J., and Song, E.X. (2016). A random virtual crack DEM model for creep behavior of rockfill based on the subcritical crack propagation theory. *Acta Geotechnica*, 11(4): 827-847. DOI: 10.1007/s11440-016-0446-8.

Proceedings of the XVIII ECSMGE 2024
GEOTECHNICAL ENGINEERING CHALLENGES
TO MEET CURRENT AND EMERGING NEEDS OF SOCIETY
© 2024 the Authors
ISBN 978-1-032-54816-6
DOI 10.1201/9781003431749-171
Open Access: www.taylorfrancis.com, CC BY-NC-ND 4.0 license

ECSMGE 24
XVIII EUROPEAN CONFERENCE ON SOIL MECHANICS AND GEOTECHNICAL ENGINEERING

Numerical simulations of soil tests emulating ground behaviour beneath super-tall building foundations

Simulations numériques d'essais de sol reproduisant le comportement du sol sous les fondations d'immeubles de grande hauteur

Y. Zhou*, T. Kiriyama
Shimizu Institute of Technology, Tokyo, Japan
**y.zhou@shimz.co.jp*

ABSTRACT: Recently, the number of super-tall buildings has been increasing in Japan. The soil beneath such buildings undergoes significant unloading in the excavation phase followed by significant loading during construction, with the latter exceeding 1000 kN/m^2 in some cases. Therefore, it has become increasingly important to consider the confining pressure dependency of the soil when predicting rebound and settlement of the bearing ground during construction. In a previous study, the authors presented a new constitutive model for soil where both the confining pressure dependency and strain dependency are considered. The stress–strain relation was defined using hyperbolic function in the deviatoric stress–strain plane, and its applicability was shown through numerical analysis of soil tests of Toyoura sand. In this work, an improved constitutive model based on modified Ramberg-Osgood (RO) model is proposed. Using the improved model, a series of soil tests on three different undisturbed samples taken from the construction site of a super-tall building is numerically simulated. The improved model is able to replicate the stress–strain relationship with a reasonable degree of accuracy.

RÉSUMÉ: Récemment, le nombre de bâtiments très hauts a augmenté au Japon. Le sol sous ces bâtiments subit une décharge importante lors de la phase d'excavation, suivie d'une charge importante pendant la construction, cette dernière dépassant 1000 kN/m^2 dans certains cas. Par conséquent, il est devenu de plus en plus important de prendre en compte la dépendance de la pression de confinement du sol lors de la prédiction du rebond et du tassement du sol porteur pendant la construction. Dans une étude précédente, les auteurs ont présenté un nouveau modèle constitutif pour le sol dans lequel la dépendance de la pression de confinement et la dépendance de la déformation sont prises en compte. La relation contrainte-déformation a été définie à l'aide d'une fonction hyperbolique dans le plan déviatorique contrainte-déformation, et son applicabilité a été démontrée par l'analyse numérique d'essais de sol de sable de Toyoura. Dans ce travail, un modèle constitutif amélioré basé sur le modèle Ramberg-Osgood (RO) modifié est proposé. En utilisant le modèle amélioré, une série d'essais de sol sur trois différents échantillons non perturbés prélevés sur le site de construction d'un immeuble de grande hauteur est simulée numériquement. Le modèle amélioré est capable de reproduire la relation contrainte-déformation avec un degré raisonnable de précision.

Keywords: Super-tall building; ground settlement; triaxial test; numerical modelling; numerical simulation.

1 INTRODUCTION

In recent years, the number of super-tall buildings (i.e., structures over 300 m high) in Japan has been increasing. The soil beneath such buildings undergoes significant unloading during excavation and then significant loading when the structure is built, with the latter exceeding 1000 kN/m^2 in some cases. Maximum local contact pressure can be as high as 1500 kN/m^2. During the construction process, the stiffness of the bearing ground decreases during the excavation phase before increasing again as the structure is built, due to the confining pressure dependency of soil stiffness. Since the unloading and subsequent loading values are so large, it has become increasingly important to consider the confining pressure dependency of the soil when predicting the rebound and settlement of the bearing ground for super-tall buildings. This contrasts with the need to consider only the strain dependency of the soil in the case of smaller buildings.

Around the world, settlement analysis for super-tall buildings with this level of self-weight, such as Burj Khalifa in Dubai (Poulos et al., 2008), Shanghai Tower in China (Xiao et al., 2011), and Lotte World Tower in Korea (Sze et al., 2019), has been performed using conventional constitutive models of soil. However, owing to the differing geotechnical conditions, it is unclear whether the same methods can be used for super-tall buildings in Japan. Tamaoki et al. (1993) proposed a method for predicting soil stiffness based on case studies of buildings with weight per unit area

up to 500 kN/m^2 in Japan. Because the weight of upcoming new super-tall buildings is significantly larger than this, the applicability of this method is questionable.

In a previous study (Zhou et al., 2022a), the authors presented a new constitutive model for geomaterials where both the confining pressure and strain dependency are considered. The stress–strain relation was defined using hyperbolic function in the deviatoric stress–strain plane, and its applicability was demonstrated through numerical analysis of soil tests on Toyoura sand. In this study, an improved constitutive model based on modified Ramberg-Osgood (RO) model (Tstsuoka et al, 1978), which is more versatile in compared to hyperbolic model, is presented. The applicability of the improved model is verified by performing a series of numerical analyses of soil tests previously carried out (Zhou et al., 2022a) on three different undisturbed samples taken from the construction site of a super-tall building, including both sandy and silty samples.

2 CONSTITUTIVE MODEL OF SOIL WITH BOTH CONFINING PRESSURE AND STRAIN DEPENDENDCY

A constitutive model is proposed for three-dimensional numerical analysis in which both the confining pressure and strain dependency are considered. To accommodate loading in an arbitrary direction (i.e., regardless of element coordination), the stress–strain relation is defined in the principal stress–strain space. The stress increment is defined separately for its deviatoric and volumetric components, as shown in Figure 1 and Equation 1:

$$d\boldsymbol{\sigma}' = d\boldsymbol{s} + d\boldsymbol{p}' \quad (1)$$

where $d\boldsymbol{\sigma}'$ is the effective stress increment vector, while $d\boldsymbol{s}$ and $d\boldsymbol{p}'$ are its deviatoric and volumetric components, respectively.

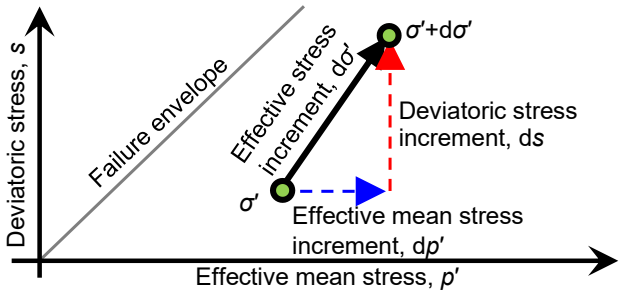

Figure 1. Separation of deviatoric and volumetric components of stress increment.

The skeleton curve of the deviatoric stress–strain (s~ϵ_{dev}) relationship, with consideration of both the confining pressure and strain dependency, is given in incremental form by Equation 2:

$$ds = \partial f/\partial p' \cdot dp' + \partial f/\partial \epsilon_{dev} \cdot d\epsilon_{dev} \quad (2)$$

where s (kPa) is deviatoric stress (=[σ'_1-σ'_3]/2), p' (kPa) is effective mean stress (=[σ'_1+σ'_2+σ'_3]/3), ϵ_{dev} is deviatoric strain (=ε_1-ε_3), and f is an arbitrary function. In the previous study (Zhou et al., 2022a), hyperbolic function was chosen as a first step. In this study, modified RO model is used because it provides more versatile in replicating the nonlinearity of the soil obtained from laboratory tests. This stress–strain relationship is given by Equations 3–6:

$$\epsilon_{dev} = \frac{h_1 s}{G_0}(1 + \alpha|s|^\beta) \quad (3)$$

$$\alpha = \left(\frac{2}{\epsilon_r \cdot G_0}\right)^\beta \quad (4)$$

$$G_0 = G_{0i} \cdot (p'/p'_i)^{n_1} \quad (5)$$

$$\epsilon_r = \epsilon_{ri} \cdot (p'/p'_i)^{n_2} \quad (6)$$

where h_1 is a fitting parameter for the initial stiffness on the skeleton curve, α and β are parameters for the modified RO model, G_0 (kN/m^2) is initial shear modulus, G_{0i} and ϵ_{ri} are normalized shear modulus and reference shear strain at unit effective mean stress (p'_i=1 kPa), and n_1 and n_2 are parameters for the confining pressure dependency of stiffness and reference shear strain, respectively. By substituting Equations 3–6 into Equation 2, the skeleton curve of the modified RO model is obtained in incremental form as shown in Equation 7:

$$ds = \left[\frac{n_1 s}{p'} + \frac{\alpha\beta n_2 |s|^\beta}{\{1+\alpha(1+\beta)|s|^\beta\}p'} s\right] \cdot dp' + \frac{G_0}{h_1 \cdot \{1+\alpha(1+\beta)|s|^\beta\}} \cdot d\epsilon_{dev} \quad (7)$$

The first line in the equation represents confining pressure dependency and the second line represents strain dependency. The skeleton curve of the effective mean stress versus volumetric strain (p'~ε_v) relationship was not explicitly defined in the previous study. In this study, it is defined as shown in Equations 8 and 9 in incremental form:

$$dp' = K_{0i} \cdot (p'/p'_i)^{n_1} \cdot d\varepsilon_v/h_1 \quad (8)$$

$$K_{0i} = 2G_{0i}(1+\nu)/[3(1-2\nu)] \quad (9)$$

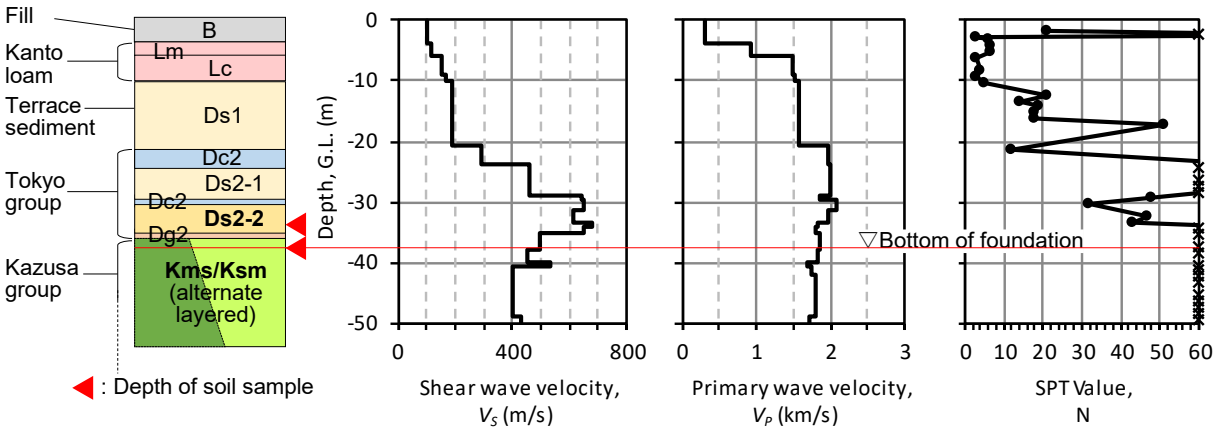

Figure 2. Soil profile of the site where the undisturbed soil samples are taken from.

Table 1. Characteristics of soil samples.

Specimen	**Ds2-2**	**Ksm**	**Kms**
Material	Very dense sand	Consolidated sandy silt	Very dense silty sand
Depth (m)	-33	-37	-37
SPT value, N	32~64	57~100	57~100
Shear wave velocity, V_S (m/s)	600	500	500
Wet density, ρ_t (g/cm^3)	1.68	1.82	1.92
Dry density, ρ_d (g/cm^3)	1.50	1.32	1.51
Cohesion, c_u (kN/m^2)	83	608	85
Internal friction angle, φ (deg)	35	20	34

where ε_v is volumetric strain ($=\varepsilon_1+\varepsilon_2+\varepsilon_3$), K_{0i} is normalized bulk modulus at unit effective mean stress (p'_i=1 kPa), and ν is Poisson's ratio. As a first step, only the confining pressure dependency is considered in this study.

In the previous study (Zhou et al., 2022a), only the skeleton curve was modelled as a first step. In this study, to accommodate cyclic loading, hysteresis curve is modelled by applying Masing's rule. For simplicity, however, only the strain dependency is considered for the deviatoric component, as shown in Equation 10, while the volumetric component is entirely elastic as shown in Equation 11:

$$ds = \frac{G_0}{h_2 \cdot \left\{1+\alpha(1+\beta)\left|\frac{s}{2}\right|^{\beta}\right\}} \cdot d\epsilon_{dev} \qquad (10)$$

$$dp' = K_0 \cdot d\varepsilon_v / h_2 \qquad (11)$$

$$G_0 = G_{0i} \cdot (p'_{rev}/p'_i)^{n_1} \qquad (12)$$

$$K_0 = K_{0i} \cdot (p'_{rev}/p'_i)^{n_1} \qquad (13)$$

In these equations, h_2 is the fitting parameter for the initial stiffness on the hysteresis curve and p'_{rev} (kPa) is the effective mean stress at the last unloading point.

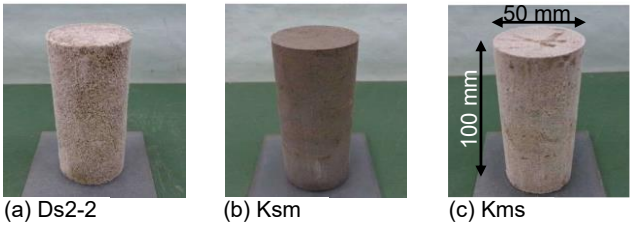

Figure 3. Soil specimens for K0 triaxial tests.

Note that, for Equations 10 and 11, all stresses and strains are given relative to the last unloading point.

3 K0 TRIAXIAL COMPRESSION TESTS OF UNDISTURBED SOIL BENEATH SUPER-TALL BUILDING FOUNDATION

In a previous work, undisturbed soil samples of three different strata were obtained for the purpose of performing K0 triaxial compression tests (Zhou et al., 2022b). The samples were taken using the block sampling method from the construction site of a super-tall building in Tokyo during the excavation phase. Figure 2 shows the soil profile and Table 1 summarizes the characteristics of the sampled soils. The samples consist of two sandy soils (Ds2-2 and Kms) and a silty soil (Ksm) and are all highly dense. The sample soil blocks measured 150 mm in diameter and 150 mm in

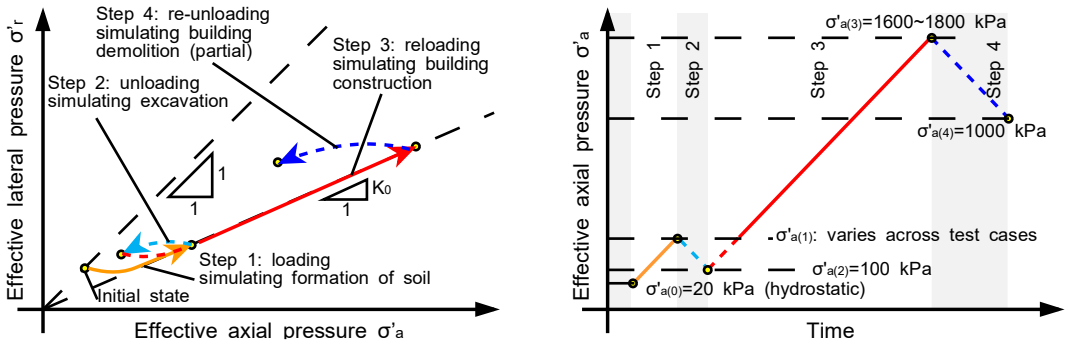

Figure 4. Schematics of stress path and timeline of K0 triaxial compression tests.

Table 2. List of cases and loading sequence for K0 triaxial compression tests.

Case ID	Effective axial pressure σ'_a (kPa)			
	(1)	(2)	(3)	(4)
500	500	100	1600 (Ds2-2) 1800 (Ksm, Kms)	1000
1000	1000			
1500	1500			

Table 3. Parameters for numerical simulation of K0 triaxial compression test.

Parameters		Ds2-2	Ksm	Kms
Normalized shear modulus, G_{0i} (kN/m^2)		23931	88348	15622
Poisson's ratio, v		0.3	0.3	0.25
Normalized reference shear strain, ϵ_{ri}		7.26×10^{-5}	3.00×10^{-5}	6.11×10^{-5}
Parameter for modified RO model, β		1.506	1.506	1.506
Parameter for confining pressure dependency	Stiffness, n_1	0.483	0.227	0.515
	Reference shear strain, n_2	0.517	0.773	0.485
Fitting parameter for initial stiffness	Skeleton curve, h_1	20	10	10
	Hysteresis curve, h_2	10	5	5

height, from which cylindrical specimens 50 mm in diameter and 100 mm in height were cut out, as shown in Figure 3.

In the series of K0 triaxial compression tests performed on these specimens, the stress path of soil under a super-tall building foundation during the excavation and construction phases was simulated (Zhou et al., 2022b). Figure 4 shows schematics of the stress path and timeline of the tests. That is, the specimens were subjected to an axial loading and unloading sequence that emulates the stress path the soil undergoes during the construction process. To simulate the boundary condition of the bearing ground, the lateral strain ε_r was constrained to zero ($\varepsilon_r \equiv 0$) by controlling the effective lateral pressure σ'_r, to maintain the specimen in the K0 condition. The tests were performed by applying incremental axial loading.

Table 2 lists the loading cases and corresponding step-by-step loading sequences. A different axial pressure $\sigma'_{a(1)}$ was chosen for each case at step 1 to simulate the effective overburden pressure of soil at different depths. Loading case IDs correspond to the value of $\sigma'_{a(1)}$. Each test case is referred to as [name of specimen]-[loading case ID] (e.g., Ds2-2-500). Full test results are presented and discussed in the previous paper (Zhou et al., 2022b).

4 NUMERICAL SIMULATIONS OF K0 TRIAXIAL COMPRESSION TESTS

Numerical simulations of the K0 triaxial compression tests described above are performed using the proposed constitutive model to verify its applicability.

Table 3 shows the parameters for the simulations. G_{0i} and n_1 are obtained by measuring the shear wave velocity of the specimens using bender elements during isotropic consolidation tests that were conducted separately, and n_2 is given by n_2=1-n_1. v is

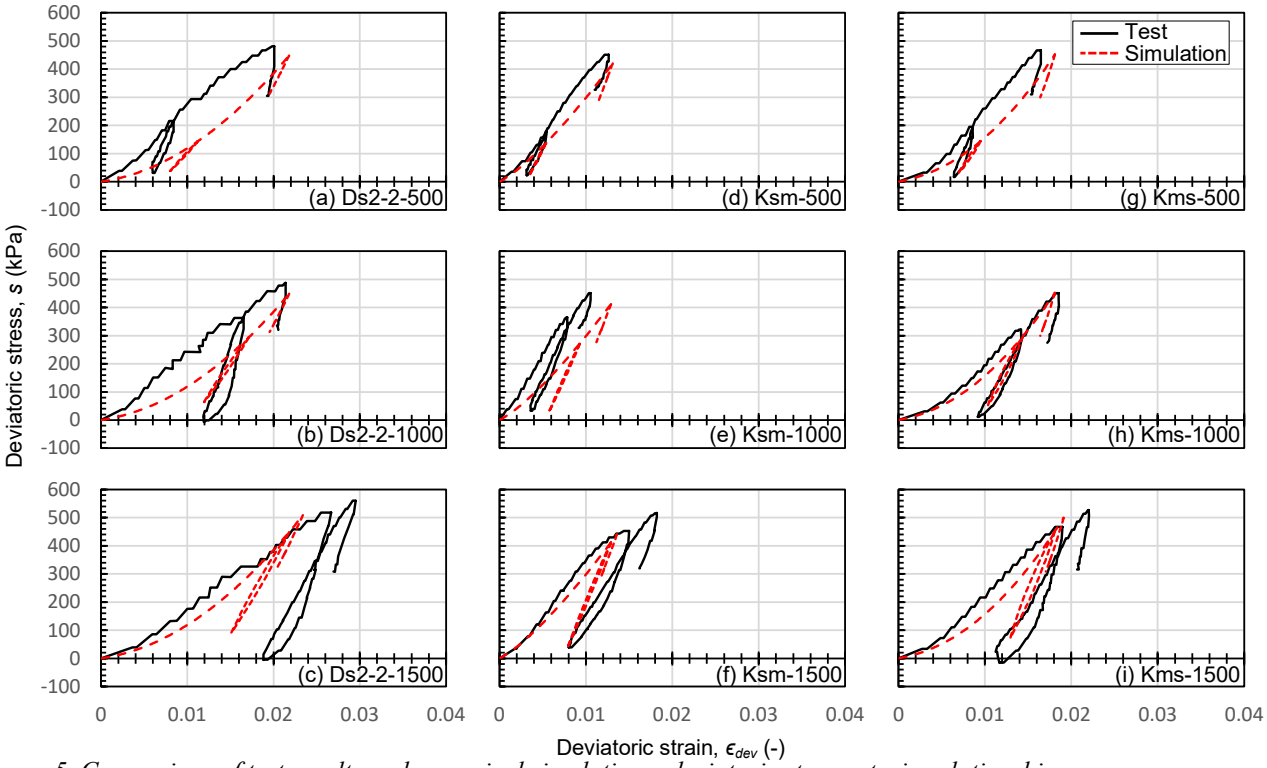

Figure 5. Comparison of test results and numerical simulations: deviatoric stress–strain relationship.

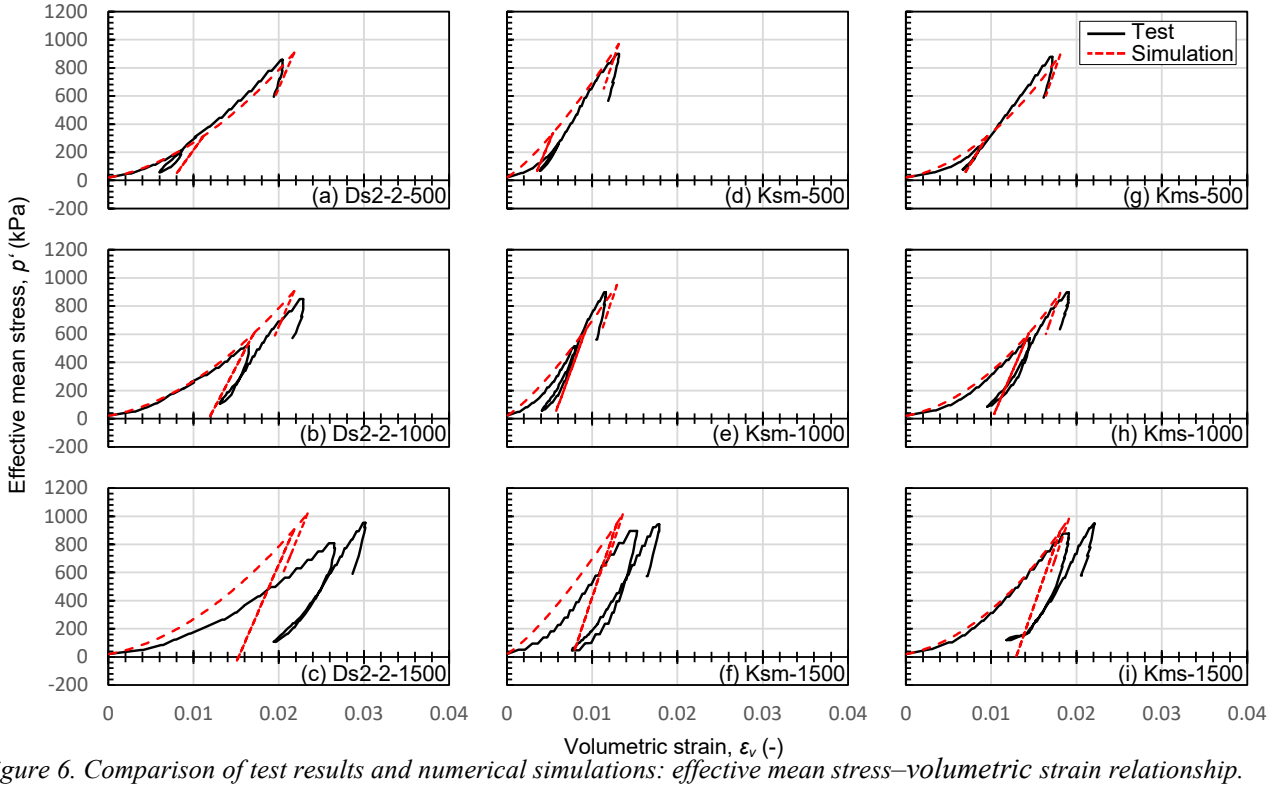

Figure 6. Comparison of test results and numerical simulations: effective mean stress–volumetric strain relationship.

determined from the ratio between the effective lateral and axial stresses (σ'_r/σ'_a) during the K0 triaxial tests (Zhou et al., 2022b). ϵ_{ri} and β are obtained from cyclic shear tests that were conducted separately. h_1 and h_2 are determined by fitting the initial stiffness to the test results. The lateral boundary is fixed for the simulation, and the same loading sequences as the tests are applied.

Figure 5 shows the deviatoric stress–strain (s~ϵ_{dev}) relationships and Figure 6 shows the effective mean stress–volumetric strain (p'~ε_v) relationships,

comparing the results of the tests and numerical simulations for all cases respectively. (Test results are plotted with black lines and simulation results with red dashed lines.)

In the test results, the skeleton curves of both s~ϵ_{dev} and p'~ε_v relationships exhibit notably downward convex curves in all cases, suggesting that the gradually increasing stiffness due to confining pressure dependency has a dominant effect on the stress–strain relationships for all the three samples. As for the s~ϵ_{dev} relationships, the skeleton curves tend to transition to upward convex shapes as the strain increases, forming slightly S-shaped curves overall. The simulations are able to reproduce the downward convex shape of the p'~ε_v skeleton curves (Figure 6). Although the simulated s~ϵ_{dev} skeleton curves do not exhibit the S-shape seen in the tests, the stress–strain relationships are in overall good agreement with the test results.

Looking at hysteresis curves, the limitations of the simplistic approach taken in this study mean that the simulated p'~ε_v hysteresis is notably linear, as opposed to the overall upward convex shape seen in the test results (Figure 6). Overall, however, the simulations are able to reproduce the cyclic stress–strain relationships as affected by both confinement pressure and strain dependency to a reasonable degree.

The results demonstrate that the proposed constitutive model has a certain degree of applicability in predicting the rebound and settlement of bearing ground during the construction of super-tall buildings.

5 CONCLUSIONS

A constitutive model is proposed for geomaterials that takes into consideration both confining pressure and strain dependency. This proposed constitutive model, which is based on modified Ramberg-Osgood model, is used to numerically simulate previously reported K0 triaxial compression tests on undisturbed soil samples from the bearing ground of a super-tall building. Overall, the simulations are able to reproduce the cyclic stress–strain relationships as influenced by both confinement pressure and strain dependency to a reasonable degree. This suggests that the proposed model has applicability in predicting the rebound and settlement of bearing ground during the construction of super-tall buildings.

Future work for the authors is to modify the modelling of hysteresis curve to improve the reproducibility of unloading and reloading behaviour. The authors also plan to use the proposed constitutive model to analyse the settlement of existing super-tall buildings.

REFERENCES

Poulos, H. G. and Bunce, G. (2008). Foundation design for the Burj Dubai–the world's tallest building. In: *Proceedings of 6th Conference of the International Conference on Case Histories in Geotechnical Engineering*, Arlington, VA, 14. Available at: https://scholarsmine.mst.edu/icchge/6icchge/session_01/14, accessed 19/10/2023.

Sze, J. and Lam, A. K. (2019). A Combo Foundation Does the Job: Piled-Raft Foundation Design for a Supertall Skyscraper. *Geo-Strata—Geo Institute of ASCE*, 23(4), pp. 42-49. https://doi.org/10.1061/geosek.0000152.

Tamaoki, K., Katsura, Y., Nishio, S. and Kishida, S. (1993). Estimation of Young's Moduli of Bearing Soil Strata. In: *Excavation in urban areas: Proceedings of 2nd Kansai international geotechnical forum on comparative geotechnical engineering (KIGForum'93)*, pp. 23-33.

Tatsuoka, F. and Fukushima, S. (1978). 砂のランダム繰返し入力に対する応力～歪関係のモデル化について(1) (Stress-Strain Relation of Sand for Irregalar Cyclic Excitation (1)). *Journal of Institute of Industrial Science*, The University of Tokyo. 30(9), pp. 356-359. (In Japanese) Available at: https://ndlsearch.ndl.go.jp/books/R000000004-I1962092, accessed 27/02/2024.

Xiao, J. H., Chao, S. and Zhao, X. H. (2011). Foundation design for the Shanghai Center Tower. *Advanced Materials Research*, Vol. 243, pp. 2802-2810. https://doi.org/10.4028/www.scientific.net/AMR.243-249.2802.

Zhou, Y. and Kiriyama, T. (2022a). Numerical Implementation of Ground Behaviors Beneath Super-Tall Building Foundations During Construction. In: *Proceedings of 4th International Conference on Performance Based Design in Earthquake Geotechnical Engineering (PBD-IV 2022)*, Beijing, China, pp. 1277-1285. https://doi.org/10.1007/978-3-031-11898-2_108.

Zhou, Y., Kiriyama, T. and Saito, A. (2022b). 超々高層建物基礎下地盤の施工時挙動を再現した要素試験 (Element Tests Simulating the Behavior of Soil under Supertall Building during Construction). In: *Proceedings of 57th Japan National Conference on Geotechnical Engineering*, Niigata, Japan, 20-8-3-2~3 (In Japanese).

Proceedings of the XVIII ECSMGE 2024
GEOTECHNICAL ENGINEERING CHALLENGES
TO MEET CURRENT AND EMERGING NEEDS OF SOCIETY
© 2024 the Authors
ISBN 978-1-032-54816-6
DOI 10.1201/9781003431749-172
Open Access: www.taylorfrancis.com, CC BY-NC-ND 4.0 license

ECSMGE 24
XVIII EUROPEAN CONFERENCE ON SOIL MECHANICS AND GEOTECHNICAL ENGINEERING

Challenges in characterisation of natural sands with fines

Défis liés à la caractérisation des sables naturels contenant des fines

H. Zhou*, S. Sharma
Norwegian Geotechnical Institute, Perth, Australia
**hzh@ngi.no*

ABSTRACT: Characterisation of sands with fines has been historically challenging due to the difficulty in recovering intact samples. For this reason, very often advanced laboratory tests are performed on reconstituted specimens, which are typically prepared to the *in situ* density estimated based on the concept of relative density (D_r) derived from *in situ* testing results, typically cone penetration tests. However, the reliability of most of reconstitution techniques in replicating the *in situ* conditions can be questionable, especially for sands with fines. This is because it is not only difficult to accurately estimate the *in situ* density, but also difficult to reproduce *in situ* conditions, such as fabric and ageing, in the laboratory. In this paper, the commonly used procedure for specimen reconstitution is reviewed first and the limitations associated with the D_r-based and state parameter (ψ)-based correlations for inferring *in situ* conditions is discussed, especially towards characterisation of sands with fines. Subsequently, some preliminary results are reported from an experimental study on a natural sand with plastic fines. The performance of the D_r- and ψ- based approaches are compared and recommendations are provided towards developing a practical and more reliable procedure for characterising natural sands with fines.

RÉSUMÉ: La caractérisation des sables contenant des fines a toujours été un défi en raison de la difficulté de récupérer des échantillons intacts. Pour cette raison, des tests de laboratoire avancés sont très souvent effectués sur des échantillons reconstitués, qui sont généralement préparés à la densité in situ estimée sur la base du concept de densité relative (D_r) dérivé des résultats des tests in situ, généralement des tests de pénétration au cône. Cependant, la fiabilité de la plupart des techniques de reconstitution pour reproduire les conditions in situ peut être discutable, en particulier pour les sables contenant des fines. En effet, il est non seulement difficile d'estimer avec précision la densité in situ, mais également de reproduire en laboratoire les conditions in situ, telles que le tissu et le vieillissement. Dans cet article, la procédure couramment utilisée pour la reconstitution des échantillons est d'abord passée en revue et les limites associées aux corrélations basées sur D_r et sur les paramètres d'état (ψ) pour déduire les conditions in situ sont discutées, en particulier en ce qui concerne la caractérisation des sables contenant des fines. Par la suite, quelques résultats préliminaires sont rapportés à partir d'une étude expérimentale sur un sable naturel contenant des fines plastiques. Les performances des approches basées sur D_r et ψ sont comparées et des recommandations sont fournies pour développer une procédure pratique et plus fiable pour caractériser les sables naturels avec des fines.

Keywords: State parameter; fabric; sand; reconstitution; relative density.

1 CHARACTERISATION OF SANDS

Characterisation of natural sands and silts has been historically challenging due to the difficulties in recovering intact samples. To date, the main technique for recovering undisturbed samples is *in situ* ground freezing. This technique, however, is very costly and cannot be easily adopted for most commercial projects offshore. Therefore, laboratory testing on reconstituted specimens is the most commonly used method for characterisation purposes.

A general procedure for reconstitution-based sand characterisation is depicted on Figure 1, which also compares the reconstituted specimens with undisturbed samples, in terms of void ratio, e (i.e., *in situ* void ratio, $e_{\text{on-situ}}$, vs. e of reconstituted specimens, e_{rect}), fabric and ageing, in order to highlight the key differences. Note that in this paper the terminology of 'fabric' follows the same definition proposed by Mitchell & Soga (2015), i.e., the particle sizes, shapes, and their distribution along with the arrangement of grains and their contacts in a given soil.

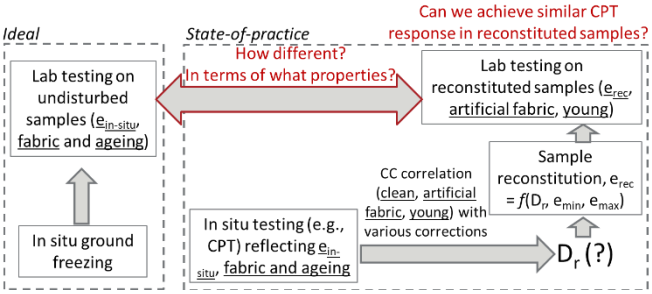

Figure 1. Sand characterisation: undisturbed vs. reconstituted.

In the reconstitution-based approach, the concept of relative density (D_r) is typically adopted (when dealing with 'conventional' silica sands) to link *in situ* soil conditions to the reconstituted conditions in a lab, as illustrated on Figure 1. It should be appreciated that D_r-based approach assumes that:

- If $e_{rec} = e_{in\text{-}situ}$, then the reconstituted specimens will exhibit comparable behaviour to the corresponding natural sand *in situ*.
- D_r can reliably link the densities between the *in-situ* soil and the reconstituted specimens.

Unfortunately, these two assumptions are not always valid. Firstly, the vast majority, if not all, of the empirical correlations, which relates the CPT data to D_r, were developed from the fresh (non-aged), clean silica sands reconstituted in the Calibration Chambers (CC) by dry pluviation, where cones were penetrated under fully drained conditions, e.g., Baldi et al. (1986); Jamiolkowski et al. (2003). As such the empirical correlationships may not be representative of the *in situ* soils, especially the *in situ* 'aged' sands with (plastic) fines. Secondly, the value of D_r measured for the reconstituted specimens in the lab is teemed with uncertainties, as detailed in Lunne et al. (2019). For sands with fines, the uncertainty becomes even larger.

An alternative approach is to use the state parameter, ψ, (Been & Jefferies, 1985) to determine the target e for specimen reconstitution. One of the main advanctages of the concept of ψ over D_r is that it not only accounts for the stress dependency of the soil behaviour, but also the effects of fines on the soil response. This study assesses the feasility of this alternative approach for characterising the sands containing plastic fines, which this is found to be the most difficult and least researched material.

As part of the research, a literature review was performed firstly, concentrating on the effects of non-plastic and plastic fines, fabric and ageing on soil behaviour. These factors are believed to be largely responsible for the limitations associated with the D_r- and ψ-based approaches on specimen reconstitution used for characterising natural sands with fines. Due to space limit, the findings cannot be elaborated here. In a nutshell, not only the fabric and ageing may have significant impact, but also soil plasticity (or clayey particles), is found to influence the sand behaviour significantly, though in a more complicated manner (Carraro et al.,2009; Georgiannou et al., 1990). It becomes even more complicated when coupled with the ageing effect (Kokusho et al., 2012). In view of the different trends shown in field and on reconstituted specimens, it is reasonable to believe that the effects of the fines may be overly exaggerated by tests on reconstituted specimen for some fines-containing sands (e.g., Huang and Huang, 2007).

2 CASE STUDY

Considering the differences between D_r- and ψ-based approach in estimating *in situ* density, an internal research project has been carried out at NGI to comparing these two approaches. This paper presents some preliminary results and findings.

For the current stage of the research project, the testing is focusing on investigating the behaviour of the specimen reconstituted using Moist Tamping (MT) method. However, the fabric effect due to use of different reconstitution methods, such as dry pluviation and slurry deposition, may have significant impact (Hoeg et al., 2000), which is outside the scope of this study.

2.1 Basic soil information

The soil used for testing was recovered as part of offshore site investigation within the Norwegian sector of the central North Sea, in water depths of around 70 m. Geologically, the samples belong to the Forth Formation according to the British Geological Survey classification scheme. The soil is primarily composed of fine sand/ silty sand with widely spaced beds of firm to stiff clay. The materials were deposited in a shallow marine environment after the last glacial stage (from late Weichselian to Holocene) and has therefore not been subjected to ice loading. However, it is likely to have undergone extensive post-depositional wave loading as sea level rose during the end of the Weichselian glacial stage.

For this study, two batches of samples (i.e., Batch A and Batch B) were created using the material recovered from depth ranges as indicated by the coloured boxes shown on Figure 2a. The material used for batching was selected considering the corresponding cone resistance (q_c) and excess pore-water pressure ratio (B_q) obtained from adjacent locations. The q_c and B_q profiles are shown on Figure 2(a) and Figure 2(b), respectively, along with measured fines content (C_{fines}) and clay-sized particle content (C_{clay}). Note that two horizontal axes have been used for both sub-plots: one axis for C_{fines} and C_{clay}, and the other for q_c and B_q, respectively, in Figure 2(a) and Figure 2(b). These two axes are differentiated by colours. The Particle Size Distributions (PSDs) of the created batches are plotted on Figure 3, with both C_{fines} and C_{clay} being annotated. Note that the definition of C_{fines} is the soil fraction with particle size < 63 μm.

As can be seen on Figure 2(a), the approximate q_c range for Batch A is about 6MPa to 14MPa, which is much lower than Batch B of about 25MPa to 40MPa. Seemingly, the soil with less fines (and clay-sized particles) has higher q_c and near-zero B_q (Figure 2).

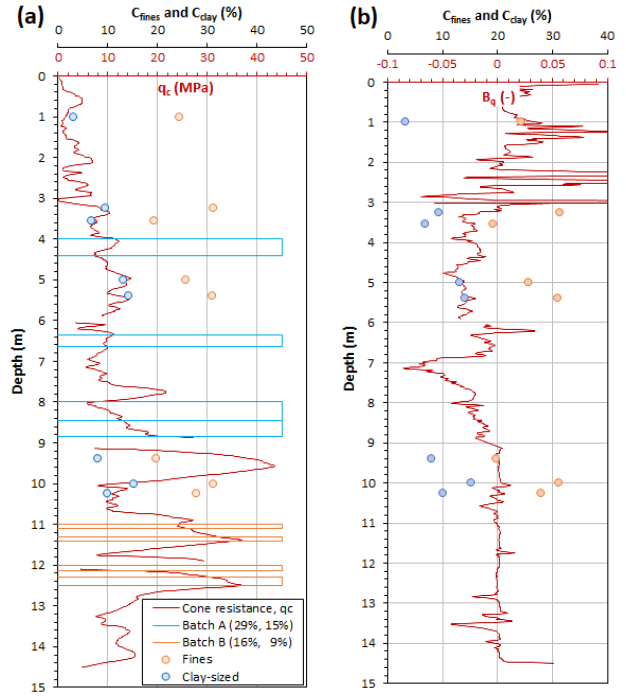

Figure 2. Fines content (C_{fines}), clay-sized particle content (C_{clay}) and (a) q_c profile and sample locations for creating Batch A and B; and (b) B_q profile.

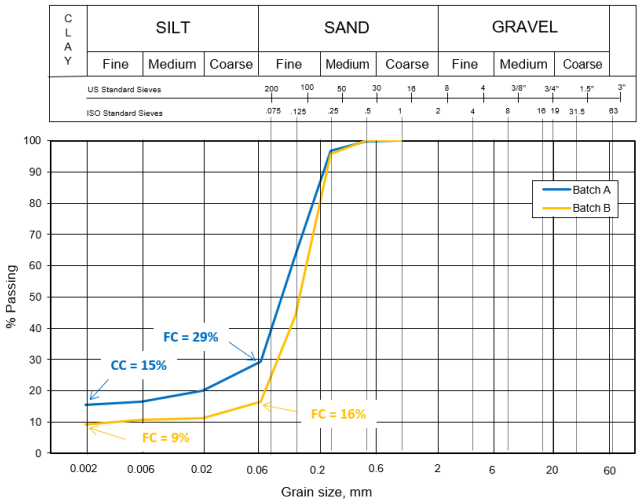

Figure 3. Grain size distribution of Batch A and Batch B.

2.2 Soil reconstitution and triaxial tests

2.2.1 Mounting reconstituted sand

Reconstituted sand specimens were prepared using MT method, which is a slightly modified version of under-compaction method described by Ladd (1978). First the dry soil is mixed with water to attain a typical water content around 5%. For triaxial test specimens the soil is tamped into the mould in six layers. The initial bottom layer is compacted to a lower density than upper layers so that the final density of each specimen layer is approximately uniform.

2.2.2 Monotonic shearing

Shearing starts at a constant rate of axial strain after the specimen is saturated and consolidated under the specified stresses. The rate of strain is 1.4%/hour for undrained tests, and sufficiently low to avoid development of pore water pressure for drained tests. The total radial stress is kept constant while the total axial stress is increased in compression tests for isotropically consolidated samples (CIUc for undrained tests and CIDc for drained tests) or anisotropically consolidated samples (CAUc).

2.2.3 Measuring end-of-test *e*

For sand characterisation, *e* is typically the targeted parameter, regardless of whether D_r- or ψ-based approach is used. Hence it is important to measure its value of the tested specimens accurately.

Without reliable internal instrumentation, the potential error in the conventional approach (with an assumption on the sample geometry before shearing) used for estimating *e* can be substantial and has been demonstrated by many, such as Sladen & Handford (1987). Therefore, the end-of-test sample freezing method introduced by Sladen & Handford (1987) was used in this study for measuring *e*. This study also confirms the deficiency of the conventional approach in estimating *e* - most of the measurements have an error of less than 20%, and the worst one reaches about 40%.

2.3 Preliminary results

2.3.1 Critical State Line (CSL) in the *e-p'* space

For clarification, the results obtained from triaxial tests are plotted on Figure 4(a) for Batch A and on Figure 4(b) for Batch B in the void ratio – mean effective stress (*e-p'*) space, along with the tentatively selected CSLs represented by the dashed line. Both CSLs and the CSL for a North Sea clean sand (Zhou et al., 2024) are compared on Figure 5.

As shown on Figure 5, the CSL of Batch A is lower than that of Batch B, due to higher FC for Batch A. This is consistent to the findings for Ticino sand mixture with various amount of non-plastic fines in Porcino et al. (2021). It is generally observed that the CSL moves downward initially with increasing fines until reaching the transition value of fines content, then moves back upward (e.g., Porcino et al., 2021).

It should be noted that the CSLs currently selected for Batch A and Batch B are preliminary only and some confirmatory tests are still required, especially associated with the level-off at the end. In comparisons with the CSL for the clean sand on Figure 5, and also with those reported in the literature, such as in Jefferies

& Been (2015) and in Porcino et al. (2021), these two CSLs appear to be somewhat unusual in terms of the location in the *e-p'* space (at lower *e* for similar *p'*) and also the trend (level-off) at the relatively high stress level. This may be something to do with the relatively high content of clay-sized particles in these two batches, which have significant impact on the overall behaviour, as discussed in Section 2. Note that almost all of the CSLs reported in the public domain are for clean sands or sands with non-/ low-plasticity fines.

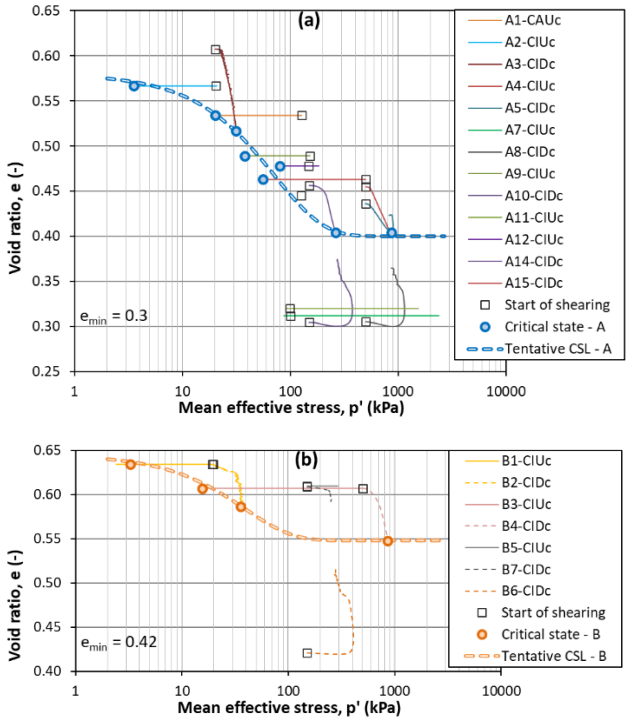

Figure 4. Determination of tentative CSLs for Batch A (a) and Batch B (b).

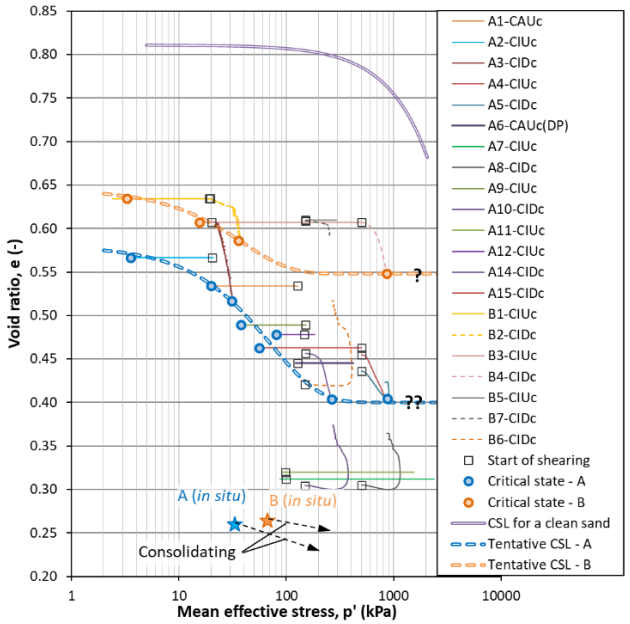

Figure 5. Comparison of CSLs.

2.3.2 Transitional D_r

As discussed in Cubrinovski & Ishihara (2000), the CSL in the *e-p'* space could be used approximately to identify whether the sand behaviour upon monotonic undrained shearing is likely to be strain-softening (contractive) or strain-hardening (dilative). Therefore, the corresponding D_r, termed as 'transitional D_r', where behaviour changes from contractive to dilative or vice versa, has been calculated based on the tentative CSLs for Batch A and Batch B and also using the CSL for a North Sea clean sand (Zhou et al., 2023), as all shown on Figure 5. The results are plotted on Figure 6, as a function of *p'*. Consistent to the observations by Cubrinovski & Ishihara (2000), the results show transitional D_r is higher for the sands with higher FC and increases with stress level.

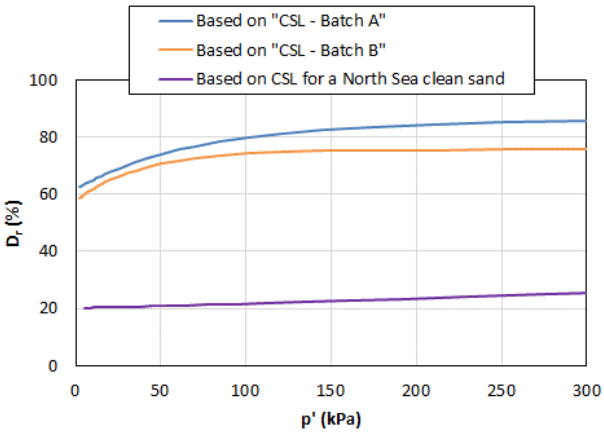

Figure 6. Variation of Transitional D_r with p'.

Traditionally, D_r is used as an index paramater to classify sand into several groups ranging from "very loose" to "very dense". This range is then used as a guide to infer other parameters for design purpose. Although this approach may be convenient for design purpose, it does not take into acccount of the effect of FC and stress level, hence is not a reliable measure of soil behaviour, as suggested by the results on Figure 6 and others, e.g., Cubrinovski & Ishihara (2000). The value of D_r alone does not provide any information regarding potential soil behaviour – contractive or dilative. This is especially the case for sands with fines. As can be seen from Figure 6, the transition from contractive to dilative behaviour can vary from D_r of ~20% for the North Sea clean sand to >70% for Batch A and Batch B under a relatively high stress level. Also it can be seen that soil behaviour depends on stress level which is not captured by D_r. In conclusion, use of D_r to infer soil behaviour/ parameter is rather limited, especially for sands with fines.

Alternatively, the concept of ψ as proposed by Been & Jefferies (1985) captures not only the effect of density (void ratio) and stress level but also indirectly

captures the effect of FC on the soil behaviour (note the FC changes the CSL and hence the value of ψ). In that sense, the ψ-based approach is better suited to assess the effect of FC on sand behaviour. This is further discussed in the following sections.

2.3.3 $e_{in\text{-}situ}$ estimated based on D_r or ψ correlations

This section compares $e_{in\text{-}situ}$ derived with the D_r-based and ψ-based approaches. The *in situ* D_r profile is plotted on Figure 7(a), derived based on the empirical equation plus correction for saturation (Jamiolkowski et al., 2003) and assuming a coefficient of lateral earth pressure at rest of $K_0 = 0.6$.

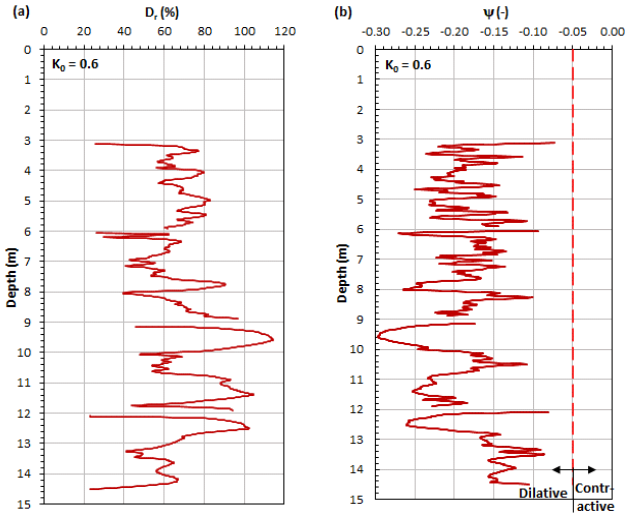

Figure 7. Derived profiles of in situ (a) D_r and (b) ψ.

The *in situ* ψ profile is plotted on Figure 7 (b) along with the boundary between contractive to dilatative response (as shown by dashed line), is derived based on the semi-empirical approach proposed in Plewes et al. (1992), with a soil specific critical state friction angle of 32° and K_0 = 0.6. Comparing between Figure 7 (a) and Figure 7 (b), one obvious difference is that the value of ψ indicate soil behaviour directly, while D_r is not as straightforward, as there is no fixed D_r limit between contractive to dilative response for sands with fines, as discussed earlier on.

Estimated values of $e_{in\text{-}situ}$ following the D_r-based and ψ-based approaches are summarised in Table 1. A representative value of D_r = 70% has been assumed for Batch A and D_r = 90% for Batch B (see Figure 2(a)). Alternatively, using the ψ-based approach, a representative value of ψ can be estimated as -0.25 and -0.3 for Batch A and B, respectively. $e_{in\text{-}situ}$ can then be estimated assuming Batch A is at 6m below seafloor (p' = 35kPa) and Batch B at 12m below seafloor (p' = 70kPa). Their states are also annotated on Figure 5 represented by a star symbol. The equivalent D_r values are also calculated in Table 1, which are significantly higher than the D_r profile shown on Figure 7 (a).

Table 1. Estimated $e_{in\text{-}situ}$.

Batch No.	D_r-based		ψ-based		
	D_r (%)	$e_{in\text{-}situ}$ (-)	ψ (-)	$e_{in\text{-}situ}$ (-)	Equi. D_r (%)
A	70	0.52	-0.25	0.26	105
B	90	0.42	-0.3	0.265	130

It may be worth noting that the measured lowest $e_{in\text{-}situ}$ for the recovered samples is about 0.53 for the depth range from 3m to 14.5m. This is higher than that estimated using either D_r- or ψ-based approach (Table 1); may be partly due to (1) sample disturbance; and (2) effect of fabric and ageing on CPT response.

This also raises a question regarding whether the reconstituted specimens prepared in the laboratory for testing purpose should be created at $e_{rec} = e_{in\text{-}situ}$ or $e_{rec} > e_{in\text{-}situ}$ in order to match *in situ* soil behaviour (due to the effects of *in situ* fabric and ageing) via a higher e_{rec}. Here again, the ψ-based approach may be more relevant for specimen reconstitution purpose as it allows comparison of expected soil response (contractive versus dilative) of the specimens reconstituted in a lab and of the *in situ* soil, which is inferred from the *in situ* testing results.

Finally, for the foundation design where the underlying soil is expected to experience consolidation under sustained loads before being subjected to design loads, the soil state will change from the *in situ* state. This is illustrated on Figure 5 by dashed arrows starting from the *in situ* condition represented by a star symbol. This may affect subsequent soil behaviour, hence should be incorporated properly into the laboratory tests. This can be inferred using the ψ-based approach but is not possible with the D_r-based one.

3 CONCLUSIONS

In this paper, reliability of the D_r-based specimen reconstitution practice is critically reviewed for sands with fines, and the usefulness of alternative ψ-based approach is explored. The following conclusions and recommendations may be drawn:

- It is emphasised that specimen reconstitution should be taken as a last resort, instead of a default option for characterising *in situ* sand behaviour. This is mainly because, irrespective of reconstitution methods used, it is difficult to recreate the '*in situ*' conditions in the lab. This is especially the case for sands with fines where the beneficial effects of soil fabric and ageing

on behaviour (e.g., higher strength and stiffness parameters) are expected to be significant.

- Where reconstituted specimens are required, it is important to bear in mind the potential issues associated with the methods. It is recommended to investigate different specimen reconstitution techniques and try to identify the practical method that best replicate the *in situ* conditions.
- As a potential alternative to the D_r-based approach, the ψ-based reconstitution has a stronger theoretical basis and some useful advantages, hence worth considering in case reconstitution is the only option.
- Where reconstituted specimens are used, it is important to check whether the reconstituted specimens have actually achieved similar behaviour to its *in situ* counterpart, by inspecting its behaviour against that suggested by the *in situ* tests, as highlighted on Figure 1.

ACKNOWLEDGEMENTS

The authors acknowledge soil samples donated by Aker BP and permission of publishing some project data. The authors are grateful of the financial support provided by NGI and the Research Council of Norway through GBV fund. All the laboratory tests were performed at NGI lab in Oslo by the laboratory team led by Dr. Camelia Dominguez Quintans. Their expertise and reliable supports are very much appreciated.

REFERENCES

Baldi G., Bellotti R., Ghionna V., Jamiolkowski M. and Pasqualini E. (1986). Interpretations of CPT's and CPTU's, 2nd Part: Drained Penetration of Sands. In *4th Int. Conf. on Field Instrumentation and in-Situ Measurements*, Singapore, 143-156.

Been K. and Jefferies M.G. (1985). A state parameter for sands. *Géotechnique*, 35(2), 99-112. DOI: 10.1680/geot.1985.35.2.99.

Carraro J.A.H., Prezzi M. and Salgado R. (2009). Shear Strength and Stiffness of Sands Containing Plastic or Nonplastic Fines. *J. Geotech. Geoenviron. Eng.*, 2009, 135(9): 1167-1178. DOI: 10.1061/(ASCE)1090-0241(2009)135:9(1167).

Cubrinovski M. and Ishihara K. (2000). Flow potential of sandy soils with different grain compositions, *Soils and Foundations*, 40(4), 103-119. DOI: 10.3208/sandf.40.4_103.

Georgiannou V.N., Burland J.B., and Hight D.W. (1990). The undrained behaviour of clayey sands in triaxial compression and extension. *Géotechnique*, 40(3), 431–449. DOI: 10.1680/geot.1990.40.3.431.

Hoeg K., Dyvik R. and Sandbækken G. (2000). Strength of un-disturbed versus reconstituted silt and silty sand specimens. *J. Geotech. Geoenviron. Eng.*, 126(7), 606-617. DOI: 10.1061/(ASCE)1090-0241(2000)126:7(606).

Huang A.B. & Huang Y.T. (2007). Undisturbed sampling and laboratory shearing tests on a sand with various fines con-tents. *Soils and Foundations*, 47(4). DOI: 10.3208/sandf.47.771.

Jamiolkowski M., Lo Presti D., & Manassero M. (2003). Evaluation of Relative Density and Shear Strength of Sands from CPT and DMT. *Geotechnical Special Publication*. 201-238. DOI: 10.1061/40659(2003)7.

Jefferies M. and Been K. (2015). *Soil liquefaction, a critical state approach (2nd edition)*. CRC Press.

Kokusho T., Ito F., Nagao Y. and Green R. (2012). Influence of non/low-plastic fines and associated aging effects on liquefaction resistance. *J. Geotech. Geoenviron. Eng.*, ASCE, 138(6):747–56. DOI: 10.1061/(ASCE)GT.1943-5606.0000632.

Ladd R.S. (1978). Preparing Test Specimen using Undercompaction. *Geotechnical Testing Journal*, 1(1), pp. 16-23. DOI: 10.1520/GTJ10364J.

Lunne T., Knudsen S., Blaker Ø., Vestgården T., Powell J.J.M., Wallace C.F., Krogh L., Thomsen N.V., Yetginer G., and Ghanekar R.K. (2019). Methods used to determine maximum and minimum dry unit weights of sand: Is there a need for a new standard? *Can. Geotech. J.* 56(4): 536-553. DOI: 10.1139/cgj-2017-0738.

Mitchell J. & Soga K. (2005). *Fundamentals of Soil Behaviour, 3rd Edition*.

Plewes H.D., Davies M.P., and Jefferies M.G. (1992). CPT based screening procedure for evaluating liquefaction susceptibility. In *Proceedings of the 45th Canadian Geotechnical Conference*, Toronto, Ont., 26–28 October 1992. pp. 41–49.

Porcino D., Triantafyllidis T., Wichtmann T., and Tomasello G. (2021). Application of Critical State Approach to Liquefaction Resistance of Sand–Silt Mixtures under Cyclic Simple Shear Loading. *J. Geotech. Geoenviron. Eng.*, 147. DOI: 10.1061/(ASCE)GT.1943-5606.0002470.

Sladen, J. A. & Handford, G. (1987). A potential systematic error in laboratory testing of very loose sands. *Can. Geotech. J.*, 24(3), 462–466. DOI: 10.1139/t87-058.

Zhou H., Sharma S., Joer H., Petter H. and Boylan N. (2024). Trial of Nor-Sand Model for Practical Characterisation of a North Sea Clean Sand. *Proceedings of the Institution of Civil Engineers – Geotechnical Engineering*. In preparation.

Proceedings of the XVIII ECSMGE 2024
GEOTECHNICAL ENGINEERING CHALLENGES
TO MEET CURRENT AND EMERGING NEEDS OF SOCIETY
© 2024 the Authors
ISBN 978-1-032-54816-6
DOI 10.1201/9781003431749-173
Open Access: www.taylorfrancis.com, CC BY-NC-ND 4.0 license

ECSMGE 24
XVIII EUROPEAN CONFERENCE ON SOIL MECHANICS AND GEOTECHNICAL ENGINEERING

Smart foundations for undermined and seismically affected territories

Des fondations intelligentes pour des territoires minés et touchés par les séismes

A. Zhussupbekov
L.N. Gumilyov Eurasian National University, Astana, Kazakhastan
Saint-Petersburg State Architecture and Civil Engineering University, Saint-Petersburg, Russia

B. Bazarov
Karaganda Industrial University, Temirtau, Kazakhastan

A. Sarsembayeva*, A. Omarov, S. Mussakhanova, D. Mukhanov
L.N. Gumilyov Eurasian National University, Astana, Kazakhastan

**assel_enu@mail.ru*

ABSTRACT: Significant territories of Kazakhstan are located in the zones of influence of underground mining and also seismically hazardous areas, leading to the displacement of rocks and uneven deformations (precipitations) of the earth's surface. Seismically dangerous are the territories of the south and south-east of Kazakhstan, where up to 40 percent of the country's population lives. A new design of the conical foundation developed by the Geotechnical Institute at the L.N. Gumilyov Eurasian National University in Astana and Karaganda Industrial University in Temirtau was presented. The design of the conical foundation proposed by the authors is 2/3 of its height immersed with a tip into the soil base, which increases its bearing capacity under the influence of technogenic impact, since the area of the tapered foundation structure raises with immersion into the soil base, i.e. the settlement of the tapered foundation has a positive effect on its bearing capacity. The round shape of the base of the inverted cone eliminates the concentration of stresses near the corners and the formation of cracks at the corner points. Model tests of conical foundations were carried out on a specially developed stand for modelling the deformability of the undermined foundation. A volumetric stand allowed individual sections to move in a horizontal plane and drop individually, thereby simulating the subsidence and displacement of the base soil.

RÉSUMÉ: Des territoires importants du Kazakhstan sont situés dans les zones d'influence de l'exploitation minière souterraine et également dans des zones à risque sismique, entraînant le déplacement de roches et des déformations inégales (précipitations) de la surface de la Terre. Les territoires du sud et du sud-est du Kazakhstan, où vit jusqu'à 40 pour cent de la population du pays, sont à risque sismique. Une nouvelle conception de la fondation conique développée par l'Institut Géotechnique du L'Université nationale eurasienne L.N. Goumilyov d'Astana et l'Université industrielle Karaganda de Temirtau ont été présentées. La conception de la fondation conique proposée par les auteurs est immergée aux 2/3 de sa hauteur avec une pointe dans la base du sol, ce qui augmente sa capacité portante sous l'influence d'un impact technogénique, puisque la surface de la structure de fondation conique augmentée avec immersion dans la base du sol, c'est-à-dire le tassement de la fondation conique a un effet positif sur sa capacité portante. La forme ronde de la base du cône inversé élimine la concentration de contraintes près des pièces et la formation de fissures aux points des pièces. Des essais sur modèle de fondations coniques ont été réalisés sur un support spécialement développé pour modéliser la déformabilité de la fondation minée. Un support volumétrique permettait aux sections individuelles de se déplacer dans un plan horizontal et de tomber individuellement, simulant ainsi l'affaissement et le déplacement du sol de base.

Keywords: Undermined soils; smart foundations; cone shape foundation; bearing capacity of soils.

1 INTRODUCTION

Extensive regions of Kazakhstan are in areas affected by both underground mining and seismic hazards. This dual influence leads to the displacement of rocks and uneven deformations known as subsidence of the earth's surface and horizontal displacements of strata (Bakhurin, 1946; S.G. Avershin, 1947). The southern and southeastern territories of Kazakhstan, where almost 40 percent of the country's population lives, are particularly susceptible to seismic risk (Belleri and Marini, 2016). The aforementioned issues have become the catalyst for the development of smart

foundations and methods for securing soil foundations in exploited areas and seismic risk zones, taking into account the soil conditions specific to Kazakhstan (R. Sadyrov and U. Beiskhanova, 2020; Zhussupbekov, 1996; Zhusupbekov and Bazarov, 1996).

Studies carried out by (Usanov, et. al., 1986) and other researchers highlight that, in the context of underground mining, the configuration of the displacement trough is influenced by the depth of development and the dimensions of the excavations. The findings derived from their research on the displacement of the Earth's surface under different conditions of coal seam occurrence (Marschalko et al., 2012; Baek et al., 2008).

The primary objective of the research was to develop stable foundations capable of effectively responding to substantial soil displacement, with the overarching aim of preventing emergencies and lowering construction costs. In this study, foundation block models with a right circular cone shape were employed. Comparative loading experiments were conducted on both conical and columnar foundation models, having the same diameter. The goal was to assess soil settlement and bearing capacity under horizontal soil displacement induced by horizontal tensile strains in areas affected by underground mining and seismic activities.

2 METHOD

2.1 Laboratory testing

Models of conical foundations with an apex angle of 90 and 80 degrees and conical models with a stand pile were made out from aluminium alloy (Figure 1) to be tested in the 3-dimentional volumetric stand which fulfilled the horizontal tensile strains replicating the undermined basement (Figure 2).

The setup involved an expanding box made of steel channels and sealed with thick rubber, fastened together with bolts. The unscrewing of these bolts causes the rubber spacer between the channels to expand, resulting in an increase in dimensions.

The compaction process involves manually compacting soil in 5 cm layers using a 10 kg roller into the volumetric expandable box. Physical and mechanical characteristics of tested soils are presented in Table 1. According to Askar Zhussupbekov (1996) for given values of cohesion corresponding to their bulk unit weight for natural soil and equivalent material the modelling scale was:

m_l = 0.9/40 x 20.5/17.0 = 1/40



Figure 1. Cone foundation models for laboratory test.

Table 1. Physical and mechanical characteristics of soil.

Soil characteristics	Units	Natural soils	Equiv. material
Bulk unit weight (γ)	N/cm^3	20.5	17.0
Cohesion, c	kPa	40.0	0.9
Angle of internal friction, φ	degree	29	37
Modulus of deformation, E	MPa	-	0.24
Poisson ratio, ν	-	-	0.25

The foundation models were placed on the compacted soil immersed 0.75 R into the base and underwent a static loading by steps of 0.001 MP, sustained until settlement conditionally stabilized, defined as settlement less than 0.01 mm within 15 minutes. The settlement of foundation models was measured by vertical dial gauges with a reading accuracy of up to 0.01 mm. The maximum load was identified as the point at which the model lost load-bearing capacity, accompanied by continuous settlement/movement.



Figure 2. Laboratory testing.

Horizontal deformations were induced by unscrewing joints between channel sections, extending the box length by 3, 6, and 9 mm/m. This induced horizontal soil movement and displacement of foundation models, monitored both vertically and horizontally.

To compare the bearing capacity of a conical foundation with the traditional type, under the same loading conditions, a model of a columnar foundation with a diameter corresponding to the conical one at the intersection with the ground surface was tested. More details for laboratory test parameters are presented in Zhussupbekov et al. (2024).

2.2 Numerical modelling

The numerical modeling of the conical foundation was conducted through computational methods using the Plaxis 2D program. Due to the axisymmetric nature of the problem, a two–dimensional (2D) axisymmetric finite element (FE) formulation is used to model the soil domain and conical footing.

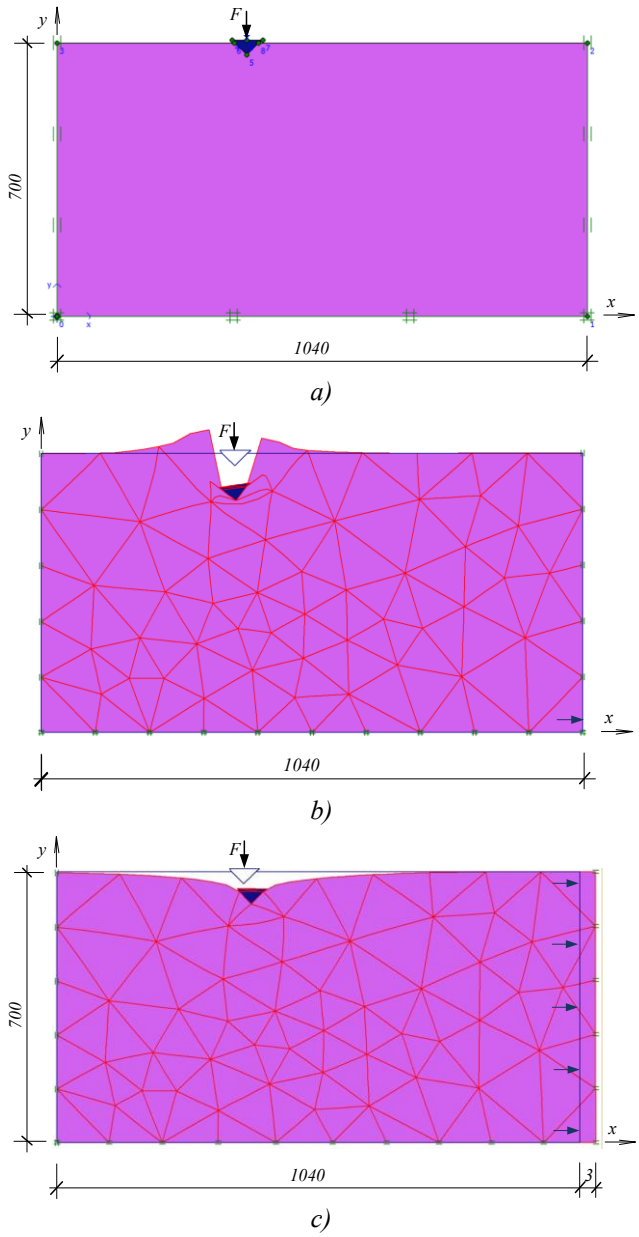

Figure 3. Numetical modelling of cone foundation models.

Initial parameters for the model were derived from soil characteristics obtained during laboratory tests. Loading for conical foundations modelling was set without soil displacement (Figure 3a, 3b) and with horizontal displacement of 3, 6, 9 mm/m (Figure 3c). For columnar foundations modeling under the same testing conditions, it's presented in Figure 4.

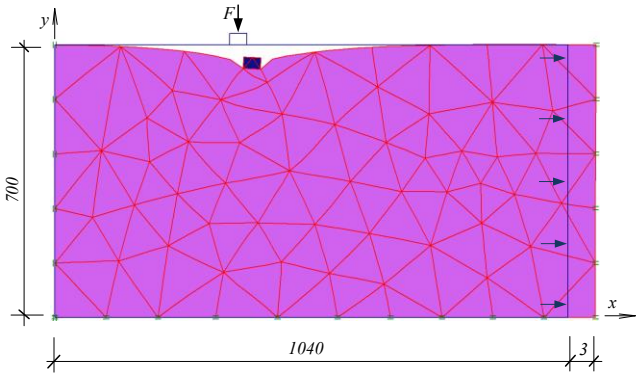

Figure 4. Numetical modelling of columnar (isolated) foundation model.

3 RESULTS AND DISCUSSION

The results of the loading demonstrated clear advantage of conical models over columnar (Figure 5 and 6), among which the bearing capacity conical foundations with a pile stand (Figure 7) among which the latter is 10 percent higher than conical foundations with an apex angle of 90°and 15 percent higher than conical foundations with an opening angle of 80 °, but 25 percent higher than traditional columnar foundation models. The results of numerical simulation are presented by dashed lines in Figures 5-7.

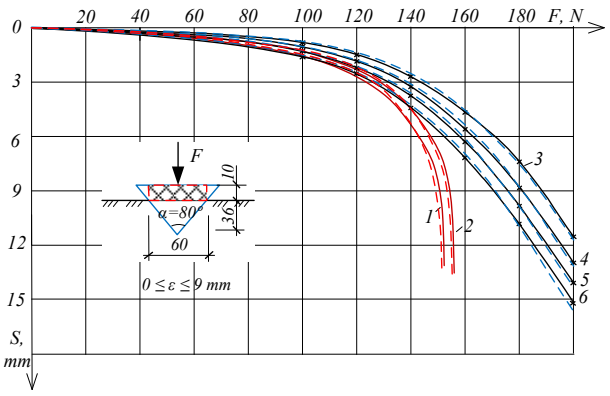

Figure 5. Results of the loading test of conical foundation models with aperture angle 80° and columnar isolated foundations, where: 1,2 – curves obtained for isolated shallow foundation for horizontal tensile strains ε=0, 3 mm/m; 3, 4, 5, 6 - curves obtained for conical foundation for horizontal tensile strains ε=0, 3, 6 and 9 mm/m.

For cone foundation with an apex of 80° the settlement under a load of 200 N without horizontal tensile strains reached 11 mm, while for models with an apex of 90° it was 9 mm. The highest load-bearing capacity was observed for conical foundations with a pile stand, the settlement of which at 200 N was 6.5 mm (Figure 5). In contrast, columnar foundation models lost their bearing capacity upon reaching a load of 140 N.

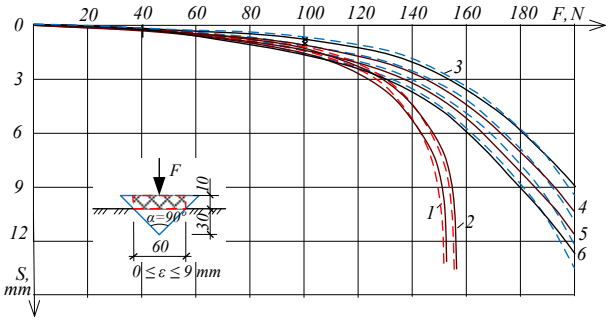

Figure 6. Results of the loading test of conical foundation models with aperture angle 90° and columnar isolated foundations, where: 1,2 – curves obtained for isolated shallow foundation for horizontal tensile strains ε=0, 3 mm/m; 3, 4, 5, 6 - curves obtained for conical foundation for horizontal tensile strains ε=0, 3, 6 and 9 mm/m.

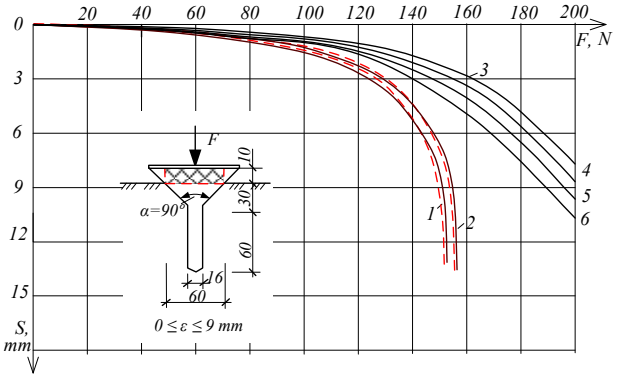

Figure 7. Results of the loading test of conical foundation models with stand pile and columnar isolated foundations, where: 1,2 – curves obtained for isolated shallow foundation for horizontal tensile strains ε=0, 3 mm/m; 3, 4, 5, 6 - curves obtained for conical foundation for horizontal tensile strains ε=0, 3, 6 and 9 mm/m.

Numerical modelling results marked on the graphs in Figures 5-7 by dashed curves confirmed the results of loading test obtained in laboratory testing with a small difference of 7%. At the beginning of the loading, the simulation curve lagged the laboratory testing settlement in Figures 5 and 6, and after 170 N the simulation settlement results became greater than the laboratory loading test values. This is explained by the heterogeneity of the soil composition and possible differences in the composition of particles.

Figure 8 shows a graphical expression of numerical modeling for cone foundation models in the form of displacement from an applied load without horizontal tensile strains in soils (a,b) and at 3 mm/m displacement (c,d).

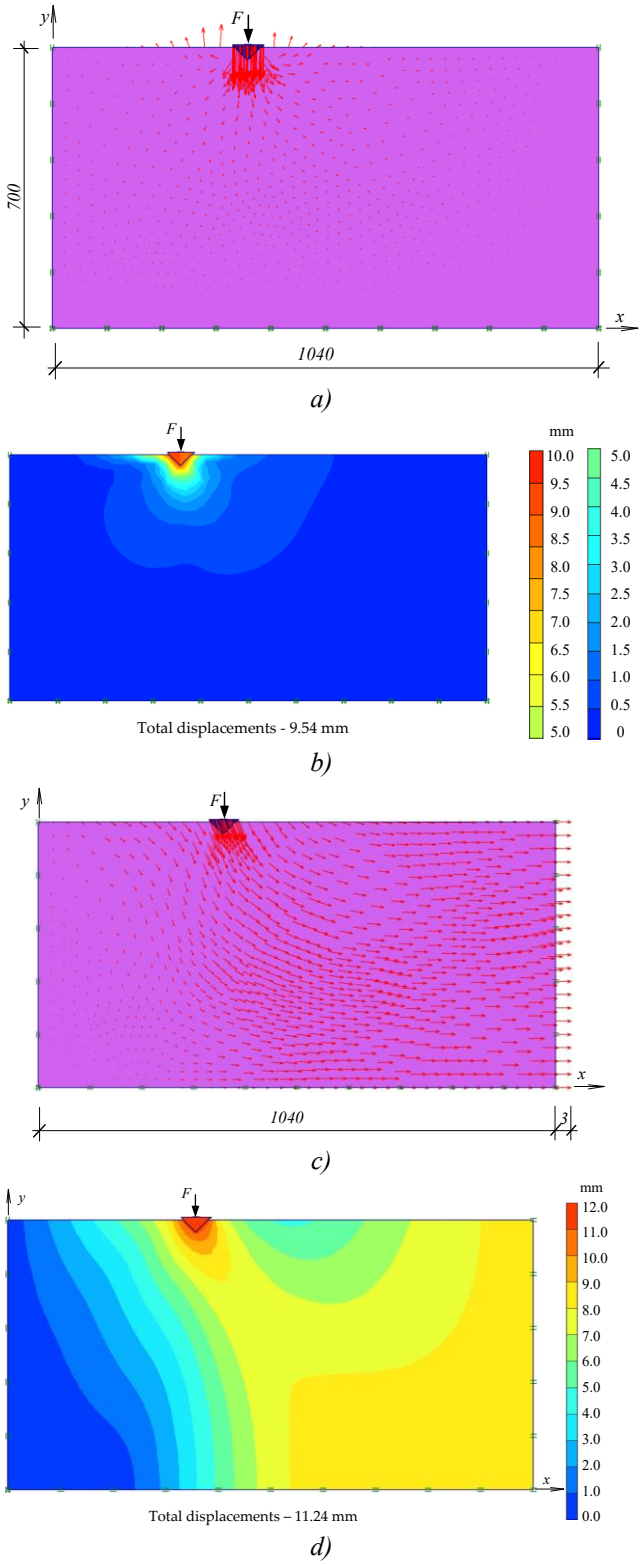

Figure 8. Results of numerical modelling for cone foundation models without horizontal tensile strains (a,b) and at 3 mm/m displacement (c,d).

Collapse was recorded for columnar (isolated) foundation under a load of 150 N. Therefore, the maximum load for these soils was taken to be 140 N (Figure 9).

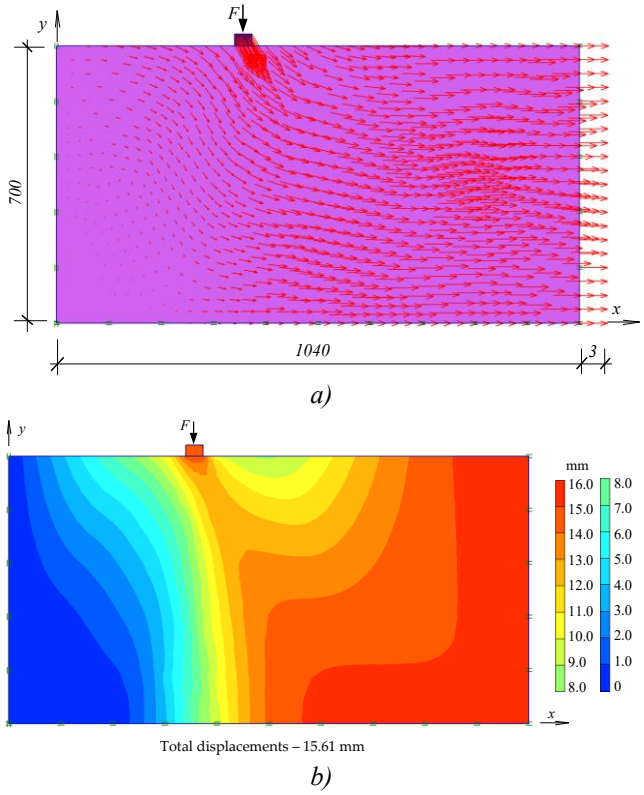

Figure 9. Numerical modelling for columnar foundation models with horizontal tensile strains (a,b) of 3 mm/m.

Horizontal tensile strain of 3 mm/m cased loose of bearing capacity by 3-4% in all type of foundations (Figure 8, 9). Soil settlement of 6 mm was reached at 147 N load in columnar foundations, 182 N and 170 N loading of cone shape foundations 90° and 80° accordingly, and 188 N loading of cone models with stand pile.

4 CONCLUSIONS

The research aimed to create stable foundations that respond effectively to significant soil displacement, with the overarching goal of preventing emergencies and reducing construction costs. To achieve this, the study proposed models of conical foundations designed for high load-bearing capacity, particularly in areas prone to horizontal tensile strains due to underground mining and seismic activities. According to the results the following points were highlighted:

1. Experimental studies revealed that in the elastic stage of deformation the load-settlement curve is identical for conical and columnar models.
2. With increasing load, cone foundations demonstrated a 20 percent raise in load-bearing capacity compared to columnar foundations at the same load settlement. While cone models with pile stand by 28 percent increased the load-bearing capacity at the same loading settlement.
3. Numerical modelling results confirmed the behaviour of the load-settlement curve of laboratory studies with a small difference of 7%.
4. Horizontal tensile strain of 3 mm/m cased loose of bearing capacity by 3-4% in all type of foundations.
5. The ultimate limiting state of cone foundations has not been reached due to the increase in bearing area as it sinks into the ground under load.
6. Cone models with pile stand are recommended for use in highly loaded foundations in the undermined and seismic areas with horizontal tensile strains.

ACKNOWLEDGEMENTS

This work was funded by the Science Committee of the Ministry of Science and Higher Education of the Republic of Kazakhstan, grant number AP13268861 «Development of structures of smart foundations in undermined and seismically hazardous territories».

REFERENCES

Jin, B., Kim, S.W., Park, H.J., Jung, H.S., Kim, K.D. and Kim, J.W. (2008). Analysis of Ground Subsidence in Coal Mining Area Using SAR Interferometry. *Geosciences Journal* 12 (3): 277–84. https://doi.org/10.1007/s12303-008-0028-3.

Bakhurin, I.M. (1946). *Movement of Rocks under the Influence of Mining*. State scientific-technical publishing house of petroleum and mining fuel literature. https://books.google.ru/books?id=XalBAAAAIAAJ.

Belleri, A., and Marini, A. (2016). Does Seismic Risk Affect the Environmental Impact of Existing Buildings. *Energy and Buildings* 110 (January): 149–58. https://doi.org/10.1016/j.enbuild.2015.10.048.

Fadeev, A. B., Kleshchev, P. E. and Zhusupbekov, A. Zh. (1986). 'Variation in the Bearing Capacity and Pliability of Undermined Beds'. *Soil Mechanics and Foundation Engineering* 23 (2): 63–68. https://doi.org/10.1007/BF01880312.

Marschalko, M., Bednárik, M., Yilmaz, I., Bouchal, T. and Kubečka, K. (2012). Evaluation of Subsidence Due to Underground Coal Mining: An Example from the Czech Republic. *Bulletin of Engineering Geology and the Environment* 71 (1): 105–11. https://doi.org/10.1007/s10064-011-0401-8.

Sadyrov, R. and Beiskhanova, U. (2020). Methods of Seismic Protection of Buildings and Structures. *Bulletin of Kazakh Leading Academy of Architecture and Construction* 78 (4): 240–49. https://doi.org/10.51488/1680-080X/2020.4-36.

Avershin, S.G. (1947). *Movement of Rocks during Underground Development*. Moscow: Ugletekhizdat. https://www.dissercat.com.

Usanov, S. V., Konovalova, Yu. P. and Usanova, A. V. (2023). Investigation of the Causes of Damage to Residential Low-Rise Buildings in the Zone of Influence of Underground Mining. *Proceedings of the Tula States University-Sciences of Earth* 2: 334–46.

Zhussupbekov, A. Zh. (1996). *Scientific basis for predicting the bearing capacity and rigidity of undermined soil foundations. Dissertation for the degree of Doctor of Technical Sciences.* Karaganda: Karaganda Industrial Institute.

Zhusupbekov, A. Zh., and B. A. Bazarov. (1996). Performance of Conical Foundations at Underworked Sites. *Soil Mechanics and Foundation Engineering* 33 (5): 169–73. https://doi.org/10.1007/BF02354242.

Zhussupbekov, A., Sarsembayeva, A., Bazarov, B., Omarov, A. (2024). Design of Conical Foundations with Increased Bearing Capacity in Areas of Undermined Soils. *Applied Sciences* 14(5):1816. https://doi.org/10.3390/app14051816.

Proceedings of the XVIII ECSMGE 2024
GEOTECHNICAL ENGINEERING CHALLENGES
TO MEET CURRENT AND EMERGING NEEDS OF SOCIETY
© 2024 the Authors
ISBN 978-1-032-54816-6
DOI 10.1201/9781003431749-174
Open Access: www.taylorfrancis.com, CC BY-NC-ND 4.0 license

ECSMGE 24
XVIII EUROPEAN CONFERENCE ON SOIL MECHANICS AND GEOTECHNICAL ENGINEERING

Method for triaxial experiments for unconventional strain paths and back-calculation using Neohypoplasticity

Méthode d'essais triaxiaux pour des trajectoires de déformation non conventionnelles et calcul rétrospectif avec Neohypoplasticity

J. Zürn*, L. Mugele, H.H. Stutz
Institute for Soil Mechanics and Rock Mechanics / Karlsruhe Institute of Technology, Karlsruhe, Germany
jochen.zuern@kit.edu

ABSTRACT: Triaxial tests are commonly used in soil mechanics to determine the shear strength of soils. In standard tests, either the development of volumetric strain is restricted (undrained), or the development of pore water pressure is inhibited (drained). In this work, a new approach to triaxial testing is proposed that couples the evolution of pore water pressure with the development of volumetric strain. The resulting unconventional strain and stress path is referred as a partially drained path. The experiments can be interpreted as true partially drained since time dependence due to pore water flow does not occur. This new approach offers a third possibility for conducting triaxial tests as element tests, besides fully drained or undrained tests. A series of monotonic tests were conducted on Karlsruhe fine sand. The obtained unconventional strain paths were simulated using Neohypoplasticity, a novel constitutive model for sand. The simulation results were evaluated concerning the experimental data. A good agreement between the experimental results and numerical calculations can be shown.

RÉSUMÉ: Les essais triaxiaux sont couramment utilisés en mécanique des sols pour déterminer la résistance au cisaillement des sols. Dans les essais standard, soit le développement de la déformation volumétrique est restreint (non drainé), soit le développement de la pression de l'eau interstitielle est inhibé (drainé). Ce travail propose une nouvelle approche des essais triaxiaux qui associe l'évolution de la pression de l'eau interstitielle au développement de la déformation volumétrique. La trajectoire de déformation et de contrainte non conventionnelle qui en résulte est appelée trajectoire partiellement drainée. Les expériences peuvent être interprétées comme de véritables essais partiellement drainés puisque la dépendance temporelle due à l'écoulement de l'eau interstitielle ne se produit pas. Cette nouvelle approche offre une troisième possibilité de réaliser des essais triaxiaux en tant qu'essais d'éléments, en plus des essais entièrement drainés ou non drainés. Une série d'essais monotones a été réalisée sur du sable fin de Karlsruhe. Les trajectoires de déformation non conventionnelles obtenues ont été simulées à l'aide de la Neohypoplasticity, un nouveau modèle constitutif pour le sable. Les résultats de la simulation ont été évalués par rapport aux données expérimentales. Une bonne concordance entre les résultats expérimentaux et les calculs numériques peut être démontrée.

Keywords: Partial drainage; triaxial; experiments; Neohypoplasticity.

1 MOTIVATION

In the realm of classical triaxial experiments performed mostly on fully saturated soils, a popular distinction emerges between two testing paradigms: (1) drained and (2) undrained conditions. In drained testing, the primary objective is to have a constant pore fluid pressure and to measure the volumetric deformations, while undrained testing seeks to have a constant volume of the sample. Due to some insufficiencies, it is important to note that undrained tests should not be considered isochoric because of membrane penetration and the compressibility of the substance consisting of grains, water, and gas (Niemunis and Knittel, 2020). Nevertheless, the in situ conditions in saturated soils often pose a challenge, where both pore water pressure changes and volumetric deformations occur simultaneously.

This phenomenon is commonly known as partially drained conditions, and frequently arises in geotechnics such as the foundation of offshore piles or structures in saturated soils.

This paper presents a novel experimental approach that couples the volumetric strain rate and pore water pressure rate within a specimen during a globally undrained triaxial test. This coupling is achieved by using the compressibility of a precisely defined gas bubble enclosed within the experimental setup. In such an experiment, strains, pore water pressure, and stresses within the specimen can be considered as uniform fields. Methods presented in the literature for

partially drained tests typically manipulate drainage resistance (Suzuki et al., 2020, Umehara et al., 1985) and are therefore not time-independent. In contrast, the presented novel approach can be assumed as a triaxial element test (Zürn et al., 2023). Consequently, this approach allows for unconventional stress and strain paths that bridge the gap between well-established drained and undrained conditions.

In this paper, the novel approach is introduced. Experimental data were obtained from a series of 8 monotonic triaxial tests. The novel constitutive model of Neohypoplasticity was used to recalculate the experimental results.

2 EXPERIMENTAL METHOD

To achieve the partial drainage conditions, a modification of a common triaxial set-up is sufficient. The experimental setup is shown in Figure 1. An enclosed gas bubble with adjustable initial volume $V_{a,0}$ and gas bubble pressure $p_{a,0}$ is connected to the pore water of the sample via the burette and drainage system.

A change in the sample volume ΔV leads to an outflow or inflow of water from the sample and a change of V_a. According to the law of Boyle-Mariotte $p_a \cdot V_a = \text{const.}$, such a change of V_a leads to a change of p_a. With the known initial variables $p_{a,0}$ and $V_{a,0}$ and the measurement of p_a using the pore pressure transducer, the actual gas bubble volume V_a can be calculated. Assuming that the change in volume of the sample is equal to the change in gas bubble volume $\Delta V \approx \Delta V_a$, we can calculate the volumetric deformation of the sample ε_{vol}.

3 EXPERIMENTAL RESULTS AND BACK-CALCULATION

3.1 Experiments

A series of monotonic tests was carried out with Karlsruhe fine sand (KFS), a uniformly graded fine sand. The grading curve and characteristic values of KFS can be found in the literature (Wichtmann , 2016). The tests which were conducted are given in Table 1. All medium-dense tests were prepared by moist tamping, the dense tests were prepared by air pluviation. For comparison, two additional tests (TMU6 and TMD23) from the literature were used (Wichtmann and Triantafyllidis, 2016).

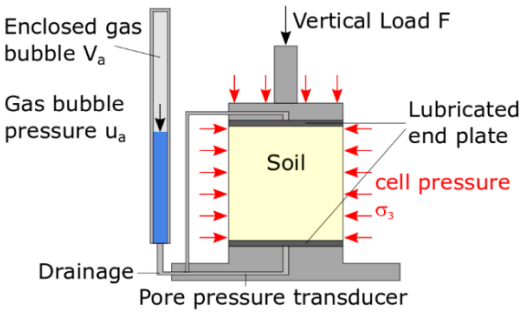

Figure 1. Experimental setup for the testing of partially drained conditions.

First, Figure 2 shows the evolution of the bulk moduli in the experiments calculated using

$$K_m = \dot{p}_f / \dot{\varepsilon}_{vol} \quad (1)$$

whereby, the pore fluid pressure p_f and the volumetric strain ε_{vol} are measured directly. First of all, it should be mentioned that the initial values of K_m can be reproduced well. However, the bulk modulus changes significantly during the test.

The well-known initial contractancy of the sample leads to a compression of the gas bubble. The bubble becomes smaller and stiffer, which increases the bulk modulus. In a subsequent dilatancy, the gas bubble becomes larger and softer, resulting in a decreased bulk modulus. The observed differences in the maximum strains are the result of test termination due to large stresses.

The stress path in the p - q diagram and the strain path in the ε_1 - ε_{vol} diagram are shown together with the corresponding simulations in Figure 3-6. It can be seen that all the test results are between the limits of the drained and undrained test and both volumetric deformations and pore water pressure changes occur simultaneously.

As the size of the gas bubble increases, the behavior of the tests changes from more undrained to drained conditions.

Table 1. Overview of the experiments on KFS.

Test	e_0 [-]	I_{D0} [-]	p_0 [kPa]	Gas bubble size
V1	0.896	0.42	200	large
V2	0.910	0.38	200	medium
V3	0.901	0.39	200	small
V4	0.698	0.95	200	large
V5	0.702	0.93	200	medium
V6	0.694	0.96	200	small
U1	0.901	0.41	200	zero (undrained)
D1	0.898	0.41	200	infinite (drained)
TMU6	0.728	0.87	200	zero (undrained)
TMD23	0.706	0.92	200	infinite (drained)

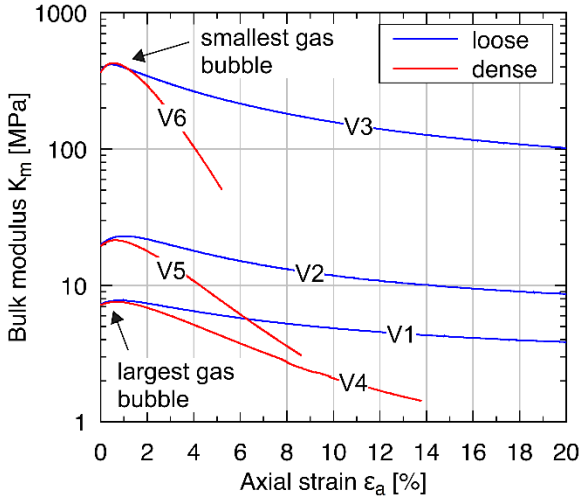

Figure 2. Evolution of the bulk modulus K_m for the different tests.

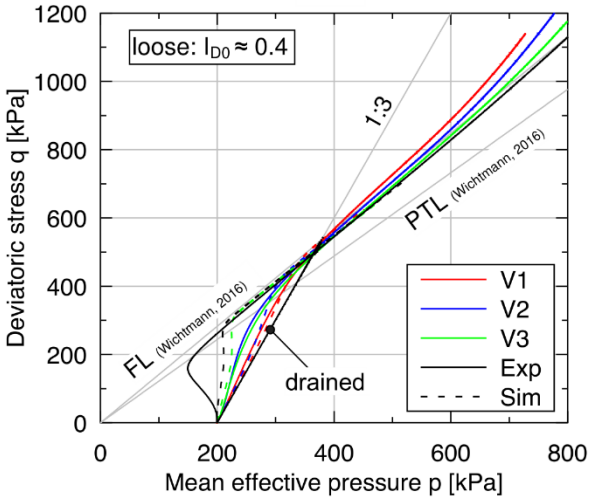

Figure 3. Stress paths for triaxial tests under different drainage conditions of loose KFS: experiments (solid lines) versus simulations with NHP (dashed lines).

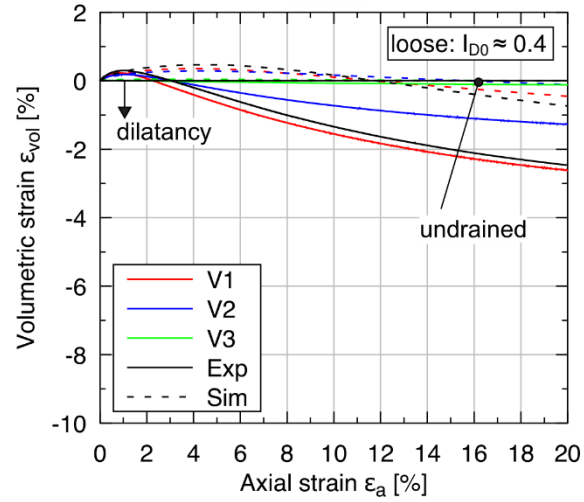

Figure 4. Strain paths for triaxial tests under different drainage conditions of loose KFS: experiments (solid lines) versus simulations with NHP (dashed lines).

The volumetric deformations increase, while the change in pore water pressure decreases. The tests can therefore be considered as partially drained.

The low initial contractancy of the medium-dense samples compared to the dense ones is due to the different preparation methods of the tests, as shown in the literature for KFS (Wichtmann, 2016).

3.2 Simulations using Neohypoplasticity

The Neohypoplasticity (NHP), which is a novel hypoplastic constitutive model for sand was used to recalculate the experimental results for partially drained conditions. For the main rate equation applies

$$\mathring{\boldsymbol{\sigma}} = k\,\overline{\mathrm{E}}\colon(\dot{\boldsymbol{\varepsilon}} - \boldsymbol{m}Y \parallel \dot{\boldsymbol{\varepsilon}} \parallel - \omega \boldsymbol{m}^z\langle -\boldsymbol{z}\colon\dot{\boldsymbol{\varepsilon}}\rangle - \boldsymbol{m}^d Y_d \parallel \dot{\boldsymbol{\varepsilon}} \parallel) \qquad (2)$$

were $\mathring{\boldsymbol{\sigma}}$ is the objective Jaumann-Zerema stress rate and $\dot{\boldsymbol{\varepsilon}}$ is the strain rate. More details about NHP can be found in the literature (Mugele et al. 2023).

In NHP, the mechanical behavior of non-cohesive soil is described using four state variables: (1) stress $\boldsymbol{\sigma}$, (2) void ratio e, (3) structure variable $\boldsymbol{z}$ and (4) last strain reversal $\boldsymbol{h}^r$. However, for the presented simulations the structure variable is initialized in such a way that their influence on the mechanical response vanishes. The small strain stiffness (increase due to $\boldsymbol{h}^r$) at the beginning of the monotonic deformation is fully considered. The constitutive parameters for KFS were taken from the literature (Mugele et al., 2023) and the test results presented in this work were not considered in the parameter calibration.

The element test simulations were conducted using the program code IncrementalDriver. A challenge for the recalculation of the partially drained tests of the experimental method presented is the bulk moduli, which varies significantly over the test (Figure 2). This corresponds to a non-linear restriction between the effective stress rates and the strain rates.

However, using the incremental driver, only linear restrictions between stress and strain rates can be specified. For simplicity, we have chosen the bulk modulus as a constant. The used value of K_m was calculated as the average value over the total strain of the test. For example, a value of $K_m = 4.99$ MPa was obtained for test V1. A

restriction between the effective stress and strain rates can be calculated. This restriction depends on the chosen bulk modulus and is therefore different for the different tests.

The comparison of the simulations with the experiments indicates that the soil behavior can be qualitatively reproduced with the coarse estimation of the bulk modulus.

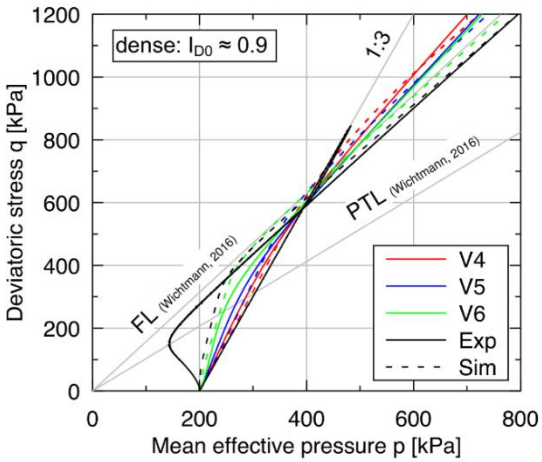

Figure 5. Stress paths for triaxial tests under different drainage conditions on dense KFS: experiments (solid lines) versus simulations with NHP (dashed lines).

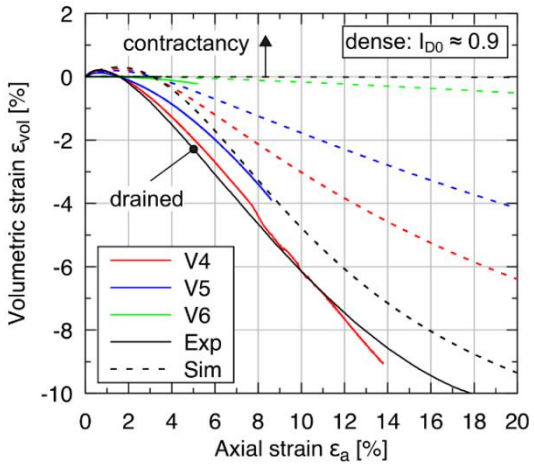

Figure 6. Strain paths for triaxial tests under different drainage conditions on dense KFS: experiments (solid lines) versus simulations with NHP (dashed lines).

The more drained the test is, i.e. the larger the gas bubble and the smaller the bulk modulus, the smaller the deviations of the stress path in the p - q diagram from the 1:3 line (corresponds to the drained test). Simultaneously, these tests and the simulations showed a larger volumetric deformation.

The opposite can be observed for a smaller gas bubble that results in a larger bulk modulus. Smaller volumetric deformations occur but deviations from the 1:3 line become larger.

4 CONCLUSION

The present study presents a method for conducting triaxial tests under partially drained conditions. It was found that:

- The experimental method presented was verified using a series of monotonic tests.
- Partially drained experimental element tests result in stress and strain paths lying between the two well-known extreme cases of undrained and drained tests.
- Simulations of the unconventional test results demonstrate that Neohypoplasticity can qualitatively reproduce the results.
- The quantitative discrepancies between the simulations and the experimental results could probably be improved by considering the nonlinear bulk modulus more accurately, calibrating the parameters, and initializing the structure variable.

REFERENCES

Niemunis, A. and Knittel, L. (2020): Removal of the membrane penetration error from triaxial data, *Open Geomechanics*, 2, https://doi.org/10.5802/ogeo.7

Mugele, L., Niemunis, A. and Stutz, H.H. (2023) Neohypoplasticity Revisitied, *International Journal for Numerical and Analytical Methods in Geomechanics*, https://doi.org/10.1002/nag.3640

Suzuki, Y.; Carotenuto, P.; Dyvik, R. and Jostad, H.P. (2020): Experimental Study of Modeling Partially Drained Dense Sand Behavior in Monotonic Triaxial Compression Loading Tests. *Geotechnical Testing Journal*, 43(5), pp. 1174-1190, https://doi.org/10.1520/GTJ20190097

Umehara, Y.; Zen, K. and Hamada, K. (1985): Evaluation of soils liquefaction potentials in partially drained conditions, *Soils and Foundations*, 25(2), pp. 57-72, https://doi.org/10.3208/sandf1972.25.2_57

Wichtmann, T. (2016): Soil behaviour under cyclic loading – experimental observations, constitutive description and applications. Habilitation, Karlsruher Institut für Technologie, 181.

Wichtmann, T. and Triantafyllidis, T. (2016) An experimental database for the development, calibration and verification of constitutive models for sand with focus to cyclic loading: part I—tests with monotonic loading and stress cycles, *Acta Geotechnica*, 11(1), pp. 739-761, https://doi.org/10.1007/s11440-015-0402-z.

Zürn, J., Mugele, L. and Stutz, H.H. (2023) Novel experimental method for rate-independent triaxial tests with partial drainage conditions, submitted 21.12.2023.

Proceedings of the XVIII ECSMGE 2024
GEOTECHNICAL ENGINEERING CHALLENGES
TO MEET CURRENT AND EMERGING NEEDS OF SOCIETY
© 2024 the Authors
ISBN 978-1-032-54816-6
DOI 10.1201/9781003431749-175
Open Access: www.taylorfrancis.com, CC BY-NC-ND 4.0 license

ECSMGE 24
XVIII EUROPEAN CONFERENCE ON SOIL MECHANICS AND GEOTECHNICAL ENGINEERING

Creep of organic soils due to small load increments

Fluage des sols organiques dû à de faibles augmentations de charge

C. Zwanenburg*
Deltares – Delft University of Technology, Delft, The Netherlands

B. Wittekoek, M. Konstadinou
Deltares, Delft, The Netherlands

**cor.zwanenburg@deltares.nl*

ABSTRACT: Organic soils are susceptible to creep. When predicting settlement of organic deposits due to small load increments, the initial conditions, particularly the initial strain rate should be assessed carefully. Recent developments in predicting creep behaviour of clays are tested in an ongoing study on organic soil behaviour. A series of incremental loading tests on peat and organic clay shows that a framework of undisturbed isotachs cannot be used to predict strain rates in over-consolidated conditions. This complicates the applicability of conventional incremental loading test results for assessing field conditions. Additionally, the tests show the relevance of a large strain approach when dealing with soft organic soils.

RÉSUMÉ: Les sols organiques sont susceptibles de fluer. Lors de la prévision du tassement des dépôts organiques dû à de faibles incréments de charge, les conditions initiales, en particulier la vitesse de déformation initiale, doivent être évaluées avec soin. Les développements récents dans la prévision du comportement au fluage des argiles sont testés dans une étude en cours sur le comportement des sols organiques. Une série d'essais de chargement incrémentiel sur tourbe et argile organique montre qu'un cadre d'isotaches non perturbés ne peut pas être utilisé pour prédire les taux de déformation dans des conditions sur-consolidées. Cela complique l'applicabilité des résultats des tests de chargement incrémentiels conventionnels pour évaluer les conditions sur le terrain. De plus, les tests montrent la pertinence d'une approche à grandes déformations lorsqu'il s'agit de sols organiques mous.

Keywords: Settlement; creep; organic soils.

1 INTRODUCTION

Organic soils are known for their tendency to creep. Yet, most 1D creep theories are typically derived for clays. This paper discusses some results of a study that examines the applicability of the 1D creep theories for organic soils.

This study focusses on small load increments. These are increments for which the soil stress remains below the yield stress. For predicting creep due to small load increments, the initial conditions, such as strain rate prior to loading, play an important role.

2 TESTED MATERIAL

Two material types are selected for testing: peat sampled at Zegveld and an organic clay sampled near Bleskensgraaf, The Netherlands. Table 1 and Table 2 present the characteristics of the tested materials.

The material was sampled by the DLDS sampler. This sampler takes block samples, 400 mm in diameter and 500 mm in height. Details of the sampler are given by Zwanenburg (2017).

Table 1. Characteristics of the tested peat samples.

sample	Depth [m]	W [%]	γ [kN/m^3]
25	-3.90	673	9.41
26	-3.90	675	9.34
42	-7.48	830	9.13
55	-3.13	578	9.80
65	-7.71	843	9.60
67	-3.42	420	9.40
97	-3.42	585	9.58
99	-3.31	656	9.02
9	-2.93	587	9.57

Table 2. Characteristics of the tested organic clay samples.

sample	Depth [m]	W [%]	γ [kN/m^3]
1	-3.04	62	15.2
2	-3.04	118	13.0

The volumetric weights indicate that the samples might be unsaturated, which is explained by the presence of gas in the peat deposits. As indicated by Persekian (2011), the gas content might run up to 30%. The organic content of the tested peat samples is in the order of 79%.

The organic clay samples show natural heterogeneity, as shown by the water content, W and

volume weight, γ. The organic content of the clay is in the order of 3.6% for test 1 and 6.5% for test 2.

3 THEORY

This study follows the isotach frame as discussed by Leroueil (2006), Yin & Graham (1989), Den Haan (1992, 1999), Den Haan & Edil (1994), Leroueil et al. (1985).

The 1D creep compression and creep rate follows from:

$$\varepsilon_c = C_\alpha \log\left(\frac{\tau}{\tau_0}\right), \dot{\varepsilon}_c = \frac{C_\alpha}{2.3\tau} \quad (1)$$

in which, ε_c represents linear strain due to creep, $\dot{\varepsilon}_c$ creep strain rate, C_α creep parameter, τ intrinsic time and τ_0 reference intrinsic time, τ_0 = 1 day. With intrinsic time, τ as the time scale for soil deformation related to the isotach field, Den Haan (1992, 1999).

The relation between changes in intrinsic time and load steps follows from:

$$\tau_i = \tau_{i-1}\left(\frac{\sigma'_{i-1}}{\sigma'_i}\right)^{\frac{CR-RR}{C_\alpha}} \quad (2)$$

in which τ_i and τ_{i-1} represent the different intrinsic time values in the different load steps, σ'_i, σ'_{i-1} the effective stresses during these steps, CR the compression ratio and RR the recompression ratio.

For specific stress conditions, the intrinsic time can be found by Equation (2). When referring to the 1-day compression line, τ_{i-1} = 1 day, σ'_{i-1} is the yield stress, σ'_{vy} and OCR = over-consolidation ratio, Equation (2) turns into:

$$\tau = OCR^{\frac{CR-RR}{C_\alpha}} \quad (3)$$

Recent developments (Yuan & Whittle, 2018) allow for a constant or non-constant spacing between the isotachs by introducing a parameter β. For $\beta = C_\alpha/(CR\text{-}RR)$, the Yuan & Whittle model aligns with Eq. (2). Smaller values for β mimic the conditions of reducing distance between the isotachs. The Yuan & Whittle model also introduces an activation of creep on changes in loading.

Vergote (2020) describes non-linear isotachs caused by structural changes due to unloading. Disturbed isotachs will lead to larger strain rates on unloading compared to the undisturbed isotachs.

4 TEST SET UP

In total 9 incremental loading tests, IL, have been conducted on peat and 2 IL tests on the organic clay. The applied loading scheme is given in Figure 1. Additional testing, including constant rate of strain, CRS testing is still ongoing.

The tests use a WILLE oedometer test set-up. A 1 kN load cell provides the load measurement. An LVDT is placed directly on the top cap to measure vertical displacements. The initial sample height, h_0, was 20 mm for the peat samples and 30 mm for the organic clay samples.

To validate Equations (1) and (2), the tests include multiple loading and unloading steps. The duration of the different load steps is 24 hours except for the steps 2 and 10 which were extended to 168 hours (1 week). This loading scheme allows to determine the relevant parameters from the conventional 24 h loading steps to examine the creep strain and strain rate for the 168-hours steps. In this way parameters are derived and applied in the analysis of the same test, eliminating the possible effect of heterogeneity between the samples. For the organic clay tests only 24 hours load steps were applied. After the unloading step, multiple loading steps with reducing OCR have been applied. This allows for examining the influence of OCR on the calculated and observed strain rates.

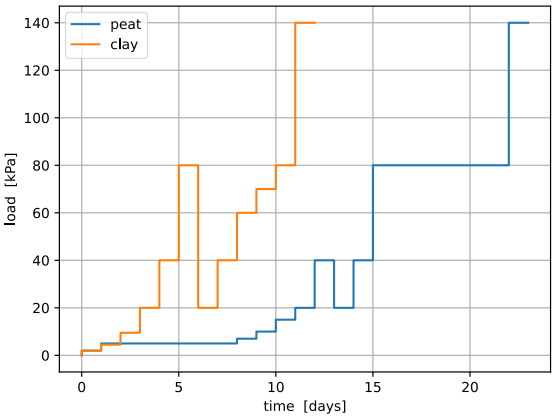

Figure 1. Applied loading schemes.

5 RESULTS TESTED PEAT SAMPLES

Figure 2 shows some results for test 25, which are considered typical for the tests on peat.

Table 3 shows that the ratio (CR-RR)/C_α ranges from 8.3 to 19.7 for the tested peat and 11 to 23 for the tested organic clay, see Table 5. Consequently, the relation between load increments and intrinsic time increments is highly non-linear and small deviations in for example OCR in Eq. (3) has a strong influence on the calculated intrinsic time.

The 1-day compression line, Figure 2a, starts to bend at $\varepsilon_a > 0.4$. This is explained by the finite layer thickness and can be addressed by using a large strain approach (Den Haan, 1999). The strain rate in step 2, with a vertical load of 5 kPa and representing OC conditions is clearly lower than found in step 10, with a vertical load of 80 kPa, representing NC conditions.

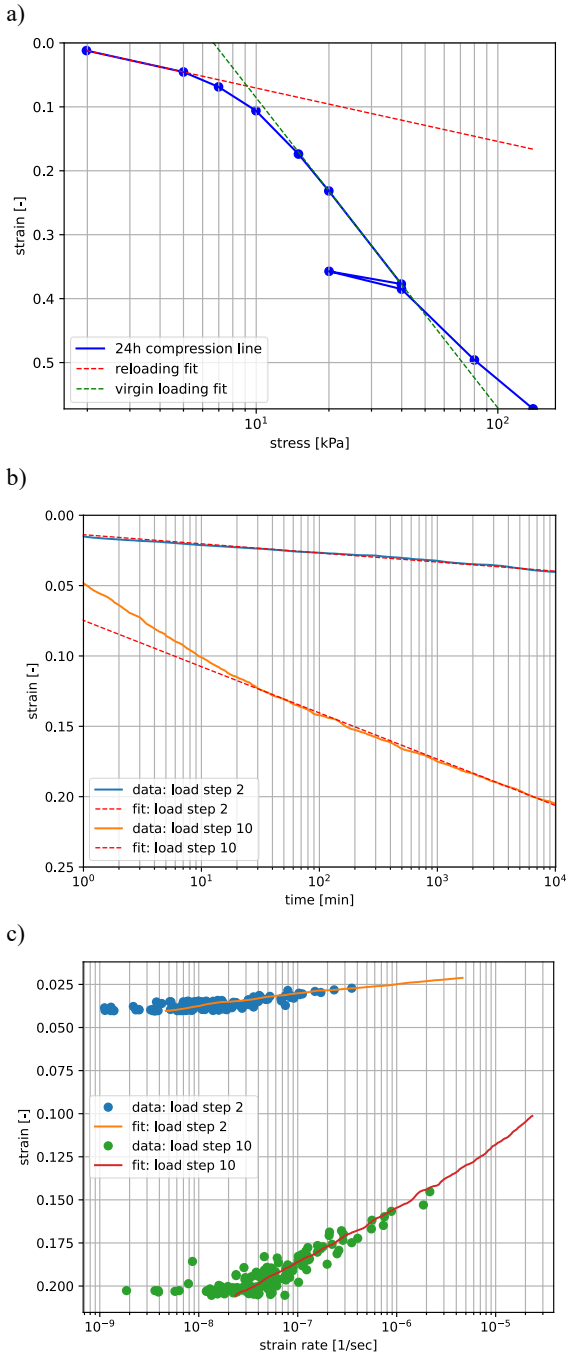

Figure 2. Results of test 25, a) 24h compression curve, b) time – strain development for load steps 2 and 10, c) strain rate – strain development for load steps 2 and 10.

Table 3. Comparison between calculated and measured creep strain rate at the end of step 2, OCR_2 = OCR in step 2, $C_{\alpha,10} = C_\alpha$ derived from step 10.

nr	(CR-RR) /C_α	$C_{\alpha,10}$	OCR_2	$\dot{\varepsilon}_{cal}\times10^{-9}$ [1/s]*	$\dot{\varepsilon}_m\times10^{-9}$ [1/s]
25	12.7	0.0329	1.8	0.073	4.6
26	13.4	0.0315	2.1	0.0084	3.2
42	15.9	0.0303	2.7	0.00003	2.1
55	19.7	0.0309	3.1	4.0×10^{-8}	1.0
65	10.7	0.0344	2.3	0.03	4.6
67	8.8	0.0374	2.2	0.21	8.8
97	8.7	0.0372	2.2	0.2	7.4
99	8.3	0.0429	1.8	1.5	13
9	11.2	0.0391	2.5	0.0074	3.2

**Calculated using Equation (1).*

Table 3 summarizes the results. The creep parameter is evaluated from step 10, $C_{\alpha,10}$, by curve fitting, as indicated by the red dotted line in Figure 2b. The curve fitting yields $\mu_{C\alpha} = 0.035$ with coefficient of variation, COV = 0.12. The OCR in step 2 fluctuates around 2.3.

Figure 2a shows the curve fitting of the compression line providing the RR and CR values, which are combined with $C_{\alpha,10}$ to obtain (CR-RR) /C_α values as presented by Table 3.

The last column in Table 3 presents the measured creep strain rates found at the end of loading phase 2. The obtained values are in the order of 10^{-9} to 10^{-8} 1/s. Using Eq. (1), the strain rates are assessed for the same test phase. The calculated values, column 5 of Table 3, show a large variety and clearly underpredict the measured values. Small changes in (CR-RR)/C_α cannot explain the differences.

Using $\dot{\varepsilon}_m$, Eq. (1) and (3) yield an effective OCR, OCR_{eff}, which corresponds to the observed strain rates. Table 4 compares OCR_{eff} and OCR. On average, OCR_{eff} is 62% of OCR.

Table 4. Comparison of OCR_{eff} and applied OCR

nr	OCR_{eff}	OCR_2	OCR_{eff}/OCR_2
25	1.33	1.8	0.74
26	1.34	2.1	0.64
42	1.31	2.7	0.48
55	1.29	3.1	0.42
65	1.40	2.3	0.61
67	1.42	2.2	0.64
97	1.45	2.2	0.66
99	1.40	1.8	0.78
9	1.44	2.5	0.58

It should be noted that for normally consolidated conditions, step 10, the calculated and measured strain rates are in good agreement. This is visualised by test 25. For $C_\alpha = 0.0329$, see Table 3, and $\tau = 10^4$ min (6×10^5 sec), Eq. (1) gives $\dot{\varepsilon}_{cal} = 2.4\times10^{-8}$1/s, which

corresponds nicely to the measured creep strain rate at the end of loading stage 10 in Figure 2c.

6 RESULTS ORGANIC CLAY

Figure 3 shows the compression curve as a function of void ratio for the two oedometer tests on organic clay. Table 6 shows a good agreement between the measured and calculated strain rates for normally consolidated conditions. For over-consolidated conditions, however, the measured strain rate decreases mildly whereas the calculated strain rate is orders in magnitude smaller. It should be noted that when including a reducing C_α, the calculated strain rates would reduce even stronger for increasing OCR.

Table 5. re-compression ratio, RR, compression ratio, CR, creep parameter C_α and yield stress σ'_{vy} for oedometer test 1 and 2.

Test	RR	CR	C_α	$(CR-RR)/C_\alpha$	σ'_{vy} [kPa]
1	0.011	0.16	0.0065	22.9	14
2	0.025	0.29	0.025	10.6	22

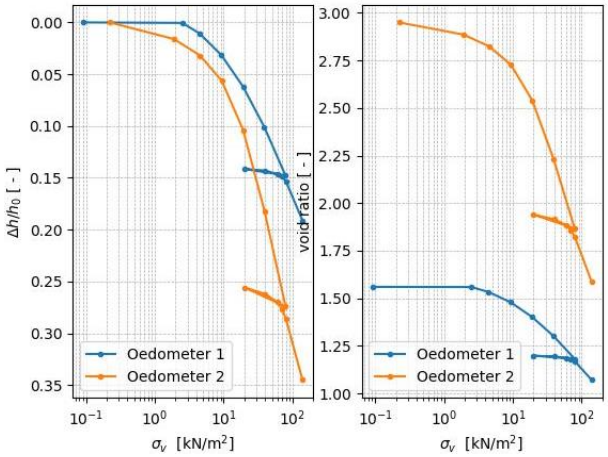

Figure 3. 24h compression curves, left) stress vs strain right) stress vs void ratio, e.

Table 6. Results for Test 1 and 2 on organic clay

Step nr	OCR		$\dot{\varepsilon}_m$ [1/s] $\times 10^{-8}$		$\dot{\varepsilon}_c$ [1/s]*	
	1	2	1	2	1	2
2	4.5	4.4	0.15	1.5	3.4×10^{-23}	1.8×10^{-14}
3	2.2	2.1	0.7	2.5	6.6×10^{-16}	4.2×10^{-11}
4	1.0	1.0	2.8	5.7	0.8×10^{-8}	4.8×10^{-8}
5	1.0	1.0	2.27	11.8	1.5×10^{-8}	6.1×10^{-8}
6	1.0	1.0	3.3	19.3	1.5×10^{-8}	6.1×10^{-8}
8	2.0	2.0	0.07	0.37	5.2×10^{-15}	8.9×10^{-11}
9	1.3	1.3	0.32	0.31	5.6×10^{-11}	6.2×10^{-9}
10	1.1	1.1	0.26	1.9	0.2×10^{-8}	2.6×10^{-8}
11	1.0	1.0	0.57	4.6	1.5×10^{-8}	6.2×10^{-8}
12	1.0	1.0	3.60	11.7	1.5×10^{-8}	6.1×10^{-8}

**Calculated using Equation (1).*

7 CONCLUSIONS

The tests on peat and organic clay show the same tendency. Calculated creep strain rates for normally consolidated conditions correspond to the measured creep strain rates. For over-consolidated conditions, however, calculations following Den Haan (1992, 1999) underpredict the creep strain rates. The difference between the measured and calculated creep strain rates increases for increasing OCR.

A reducing C_α with OCR does not improve the calculations. Instead, disturbed isotachs (Vergote 2020), might provide a framework within which an explanation for this behaviour could be found. This will be part of a follow-up study.

The tests on organic clay show that the difference between the measured and predicted strain rate is found for both, the initial re-loading steps below the natural yield stress as well as for the re-loading steps in the second part of the test. In the field, initial strain rates are induced typically by long term creep or aging and unloading might not be relevant field conditions. This difference in stress conditions between field and incremental loading tests results in a difficulty for the assessment of the initial creep strain rate in the field.

The last loading steps, in the tests on peat, show an increase in stiffness, which is explained by the finite layer thickness. This shows the relevance for a large strain approach when dealing with organic soils.

REFERENCES

Den Haan E.J. (1992) The formulation of virgin compression of soils Géotechnique, vol 42, p 465-483 DOI: 10.1680/geot.1992.42.3.465

Den Haan E.J., Edil T.B. (1994) Secondary and tertiary compression of peat *in: Advances in understanding and modelling the mechanical behaviour of peat, den Haan, Termaat & Edil (eds),* Balkema Rotterdam

Den Haan E.J. (1999) Stress independent parameters for primary and secondary compression *in: Proceedings XIIIth International Conference on Soil Mechanics and Foundation Engineering,* New Delhi, Vol I, p 65 – 70

Leroueil S., Kabbaj M., Tavenas F., Bouchard R. (1985). Stress-strain-strain rate relation for the compressibility of sensitive natural soils *Géotechnique* **35**(2) 159-180 doi:/10.1007/978-3-642-32814-5_15

Leroueil S. (2006) The isotach approach. Where are we 50years after its development by Professor Šuklje? *in: Proceedings of the 13th Danube-European Conference on Geotechnical Engineering, Prof. Suklje's memorial lecture*, Ljubljana 2006 pp 55-88

Persekian A.D. (2011). *Geophysical estimation of free-phase gas content and distribution in peatlands PhD Thesis* State University of New Jersey

Vergote T.A. (2020). *Deformation of soils: time and strain effects after unloading* PhD thesis National University

Singapore. Downloadable: https://scholarbank.nus.edu.sg/handle/10635/185992

Yin J.-H., Graham J. (1989). Viscous-elastic-plastic modelling of one-dimensional time-dependant behaviour of clays *Canadian Geotechnical Journal* **26** 199-209, doi.org/10.1139/t89-029

Yuan, Y., & Whittle, A.J. (2018). A novel elasto-viscoplastic formulation for compression behaviour of clays. *Géotechnique* **68**(12), 1044, doi: 10.1680jgeot.16.P276

Zwanenburg C. (2017). The development of a large diameter sampler *in: proc. 19th international conference on soil mechanics and geotechnical engineering,* Seoul

B - Geohazards
B - Géorisques

Proceedings of the XVIII ECSMGE 2024
GEOTECHNICAL ENGINEERING CHALLENGES
TO MEET CURRENT AND EMERGING NEEDS OF SOCIETY
© 2024 the Authors
ISBN 978-1-032-54816-6
DOI 10.1201/9781003431749-176
Open Access: www.taylorfrancis.com, CC BY-NC-ND 4.0 license

ECSMGE 24
XVIII EUROPEAN CONFERENCE ON SOIL MECHANICS AND GEOTECHNICAL ENGINEERING

Discharge flow rate under sheet piles, a prediction model

Débit de décharge sous palplanches, un modèle de prédiction

A. Ahangar Asr*
School of Science, Engineering and Environment (SEE), University of Salford, Manchester, UK
A. Johari
Department of Civil and Environmental Engineering, Shiraz University of Technology, Shiraz, Iran
A.A. Javadi
College of Engineering, Mathematics and Physical Sciences, University of Exeter, Devon, UK EX4
**a.ahangarasr@salford.ac.uk*

ABSTRACT: The discharge flow rate beneath water-retaining structures is an important parameter in designing water retaining structures. This paper presents a framework to model and predict discharge flow rate using an evolutionary-based technique. The proposed method is data-driven and searches mathematical structures to representing a complicated system. A comprehensive data set including around a thousand data lines is used to create and test the prediction model. Data divided into training and testing data sets (testing data set not introduced to the model in the training stage) using special statistical approach to ensure relevance, validity and compatibility of the training and testing data sets. The main advantage of the proposed models is to provides an optimum explicit structure for the model directly from the data unlike black box models and the capability of the model is tested by introducing an unseen data set to ensure the model is capable of generalisation. Results revealed the high accuracy of the developed model in predicting flow rates both for seen and unseen data cases. A parametric study on the presented models confirmed consistency of the parameter relationships with the database and expected behaviour of the system based on traditional empirical methods.

RÉSUMÉ: Le débit de rejet sous les ouvrages de rétention d'eau est un paramètre important dans la conception des ouvrages de rétention d'eau. Cet article présente un cadre pour modéliser et prédire le débit de rejet à l'aide d'une technique basée sur l'évolution. La méthode proposée est basée sur les données et recherche des structures mathématiques pour représenter un système complexe. Un ensemble de données complet comprenant environ un millier de lignes de données est utilisé pour créer et tester le modèle de prédiction. Données divisées en ensembles de données de formation et de test (ensemble de données de test non introduits dans le modèle lors de la phase de formation) en utilisant une approche statistique spéciale pour garantir la pertinence, la validité et la compatibilité des ensembles de données de formation et de test. Le principal avantage des modèles proposés est de fournir une structure explicite optimale pour le modèle directement à partir des données, contrairement aux modèles de boîte noire, et la capacité du modèle est testée en introduisant un ensemble de données invisible pour garantir que le modèle est capable de généralisation. Les résultats ont révélé la grande précision du modèle développé dans la prévision des débits pour les cas de données visibles et invisibles. Une étude paramétrique sur les modèles présentés a confirmé la cohérence des relations entre les paramètres avec la base de données et le comportement attendu du système sur la base des méthodes empiriques traditionnelles.

Keywords: Sheet piles; seepage; flow rate; evolutionary computing.

1 INTRODUCTION

One of the most important interests of geotechnical researchers is to look into the safety of structures like dams that are used to retain water bodies. The rate at which the water outflows from the body of such structures is the core of this research attention, because it could potentially be a starting point for any failure due to seepage-related issues which could be catastrophic i.e. the piping phenomenon to name an example. The amount of water seeping out and the rate at which the discharge happens therefore is the main focus point for design safety of these. Large exit quantity of water from the structure on the downstream side can be dangerous as it could threaten stability of the structure as a whole due to increases possibility of piping phenomenon. Therefore, mechanisms must be in place to ensure the exit quantity of water is kept under watch and indeed limited to ensure structural safety and stability. The high values of the discharge flow rate can endanger the water retaining structure stability. One of the very commonly used tools to contribute to this aim is sheet pile. Sheet piles can in fact be considered an effective shield and are used to

cut the discharge rate and volume of water passing through the porous medium (geotechnical materials) under the water retaining structure. There is a mathematical constitutive differential equation that governs the seepage flow rate and various methods have been used to solve the equation (Zhang et al. 2017).

While analytical methods offer much more desirable exact solutions to the problems, they cannot be used in analysing large scale problems due to calculations getting too complicated. Numerical approaches however offer approximate but with high enough accuracy levels solutions to complicated large scale problems. Numerical methods can hit problems numerically when singularity occurs (i.e. sharp shaped corners etc.) in discretisation process which makes solving the problem numerically further problematic (Lei et al., 2020).

Scaled Boundary Finite Element Method (SBFEM) introduced by Song and Wolf (1997) aimed at removing some limitations with existing finite element based numerical techniques and been used so far by many researchers (Johari and Heydari, 2018). As per any other method SBFEM has a downside too and it is the fact that each calculation of discharge flow must be analysed by an expert. Data mining and machine learing approches have been used by researchers therefore to overcome this issue as the analysis could be done by models that learn from data eliminating the lenghty manual case-by-case analysis (Yalchin et al 2019).

In this research an evolutionary data mining -based method called Evolutionary Polynomial Regression (EPR) is implemented to learn the behavioural pattern and make predictions for the rates of discharge flow that happens through (passing under) sheet piles. The database used to train and develop the model was built of one thousand lines that were created synthetically using SBFEM.

2 EVOLUTIONARY POLYNOMIAL REGRESSION

To be able to learn and make predictions of the behaviour of the system being modelled, EPR uses data and in the data it looks to find trends and relations presents them in the form of a set of explicit polynomial expression which is accessible by the user and could be judged for suitability considering the known effect of any parameter used as input and how it is expected to affect the output. Therefore, if a model deemed not representative then the user could pick another more suitable one. The maximum number of terms in the mathematical expression can be adjuted to avoid over complexity or under-representavieness of the models by the user to strike the right balance. This is the very important advantage of EPR compared to blackbox systems like ANN.

$$y = \sum_{j=1}^{n} F(X, f(X), a_j) + a_0 \tag{1}$$

Where **y** = outputs (vector)**;** $\mathbf{a_j}$ = parameters of the model; **F** = EPR-developed function; **X** = inputs (variable); **f** = user-defined fuction; **n** = terms number (how many) in polynomial that user wants to see as the maximum. The general functional structure is constructed from elementary functions by EPR using a Genetic Algorithm (GA) strategy.

EPR is very interactive in communicating with the users as the output is an explicit expression mathematical terms relating the variables to the output; therefore, use has full access to the model and is able to check that the contribution by various inputs are in line with the understanding of the phenomena by the engineers (Ahangar Asr et al., 2023).

3 PREPARING DATA

A thousand line of data used to train the EPR model in this work. These data lines were developed using an SBFEM model (figure 1) and many possible scenarios were considered to ensure that the data set contains almost all aspect of the behaviours of water passing through these water retaining structures (Ahangar Asr et al., 2023).

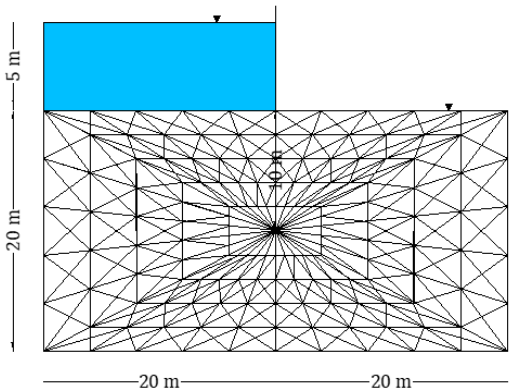

Figure 1. SBFEM model.

4 MODEL DEVELOPMENT

The source of data containing the thousand data line were divided into two subsets. The larger data set containing about eighty percent of data was the used to develop the model by training EPR and the

remaining was not introduced to EPR at all therefore suitable to test the outcome models. This approach is very robust as it not only tests the capability of the model in making accurate predictions but also because the test data are not seen by EPR when the model was being developed, the testing process also shows the generalisation capabilities of the developed model to the cases that are not experienced by EPR when training. This does not mean that the model extrapolates. The data was statistically analysed to ensure an even distribution is made and the training and testing sets are close statistically to avoid extrapolation (Ahangar Asr et al., 2023). Table 1 shows the input parameters and training and testing subsets of data used to develop and verify the model are presented in figures 2 and 3.

Table 1. Input parameters.

Parameters	**Range**
Input parameters	
Sheet pile's height (D)	0.25-10 m
Upstream water level (H)	1-5 m
Anisotropy ratio of deposit materials (K)	0.2-1
Output parameter	
Normalized flow rate Q_{Nor}	1.42×10^{-6} – 8.54×10^{-5}

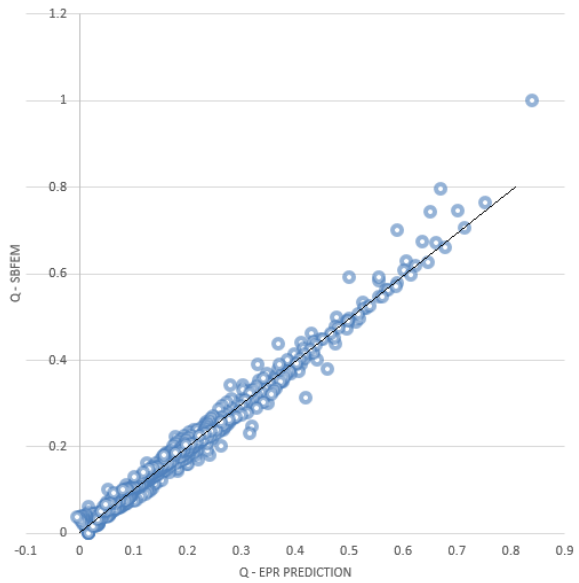

Figure 2. Training data against predictions.

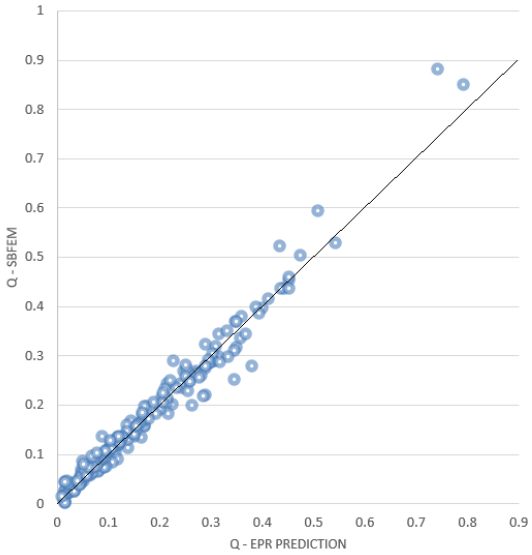

Figure 3. Test data against predictions.

The parameter defined as coefficient of determination or COD (Eqn. 2) was used by EPR to judge the accuracy levels of the models developed:

$$\mathbf{COD} = 1 - \frac{\sum_{N}(\mathbf{Y}_a - \mathbf{Y}_p)^2}{\sum_{N}\left(\mathbf{Y}_a - \frac{1}{N}\sum_{N}\mathbf{Y}_a\right)^2} \qquad (2)$$

Where $\mathbf{Y}_a$ = value of the output (actual); $\mathbf{Y}_p$ = value of the output (EPR prediction); N = count of the data point used to calculate the coefficient of determination (COD) value.

Coefficient of determination values calculated for training data was 98.11%. This showed exceptional capability of the EPR model to learn from the data patterns presented and make predictions for the data which was used to train the model. The coefficient of determination calculated for the testing data which has not been previously introduced to EPR in training stage was 97.24%. This clearly shows that not only the suggested evolutionary polynomial regression technique was able to, to a very high degree of accuracy, capture the seepage phenomena behaviour under the sheet piles, but also can very rigorously generalise the predictions to cases that were not previously familiar to (not seen by EPR). EPR learns form data no matter where it comes from. Actual data from field measurements and synthetic data could therefore be used in one set. Synthetic data could be the main data source or could be simply used to fill any gaps in data where no measured data is available.

5 UNDERSTANDING THE EFFECTS OF CONTRIBUTING PARAMETERS

To understand whether the developed model is a true representation of any contributing parameter effect on the phenomenon, meaning that changes in every individual parameter or any combination of them - where applicable - are having the effect on the model output that is also expected in the real world, an analysis on the parameters is conducted. All parameters were allocated with their average values in the range used apart from the parameter effect of its change on the model was being scrutinised. The change in the model output values then was recorded as the parameter in question varied from its minimum to maximum values. The effects on the predictions of the EPR model was then shown in the form of a series of graphs, each produced for an input parameter. Figure 4 shows an example analysis outcome of this type. It can be seen for instance that the model shows that as the cut off wall length increases (generally meaning that the wall penetrates deeper in the soil), the flow rate drops. Which is consistent with the behaviour expected from the interaction between a cut of wall and the seepage phenomenon.

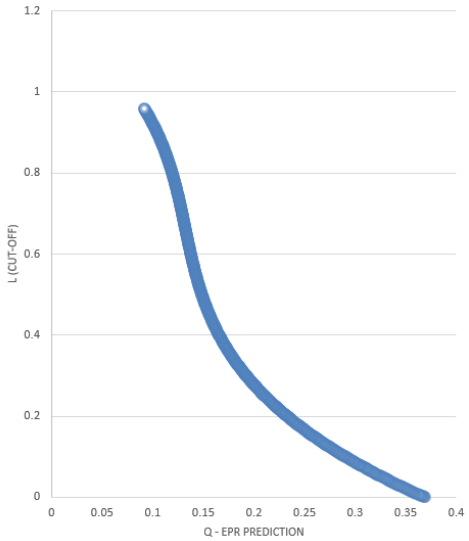

Figure 4. EPR prediction variations as the cut-off wall length changes.

6 DISCUSSION AND CONCLUSIONS

A model was produced by an artificial intelligence-based machine learning technique to simulate and represent the seepage flow rate under sheet piles. The data was divided into training and testing subsets. Relevant pre-analysis was conducted on the data to ensure that the two subsets were statistically consistent. Testing data ensured not to be shown to the EPR during the training stage and once the models developed, they then used to measure the generalizations (but not extrapolation) capabilities of the developed models. Effect of individual contributing parameters on the developed model predictions was assessed. It was shown that the proposed method developed a model that could predict discharge flow rate under sheet piles to a very high accuracy level. This was particularly important because the model could make predictions for the cases where the data were not seen by EPR during the model development processes, to a similar level of accuracy. It can be concluded that the model has successfully captured and learned the underlying relations between the contributing input parameters and was able to replicate their true (expected) effects on the model outcome. An advantage of the proposed modelling data is that as new and more comprehensive data becomes available, the EPR could be retained, and the model amended to ensure more realistic and up to date predictions are made in light of the new data becoming available.

REFERENCES

Ahangar Asr A., Johari, A. and Javadi, A. A. (2023). An evolutionary-based polynomial regression modeling approach to predicting discharge flow rate under sheet piles. *Engineering with Computers* 39, 4093–4101. https://doi.org/10.1007/s00366-023-01872-1.

Johari A., and Heydari A. (2018). Reliability analysis of seepage using an applicable procedure based on stochastic scaled boundary finite element method. *Engineering Analysis with Boundary Elements*, 94, 44-59. https://doi.org/10.1016/j.enganabound.2018.05.015.

Lei X., He S., Chen X., Wong H., Wu L. and Liu E. (2020). A generalized interpolation material point method for modelling coupled seepage-erosion-deformation process within unsaturated soils. *Advances in Water Resources*, 141, 103578. https://doi.org/10.1016/j.advwatres.2020.103578.

Song C. and Wolf J. P. (1997). The scaled boundary finite-element method—alias consistent infinitesimal finite-element cell method—for elastodynamics. *Computer Methods in applied mechanics and engineering*, 147(3-4), 329-355. https://doi.org/10.1016/S0045-7825(97)00021-2.

Yalcin Y., Orhon M. and Pekcan O. (2019). An automated approach for the design of Mechanically Stabilized Earth Walls incorporating metaheuristic optimization algorithms. *Applied Soft Computing*, 74, 547-566. https://doi.org/10.1016/j.asoc.2018.09.039.

Zhang W., Dai B., Liu Z. and Zhou C. (2017). Unconfined seepage analysis using moving kriging mesh-free method with Monte Carlo integration. *Transport in Porous Media*, 116(1), 163-180. https://doi.org/10.1007/s11242-016-0769-9.

Proceedings of the XVIII ECSMGE 2024
GEOTECHNICAL ENGINEERING CHALLENGES
TO MEET CURRENT AND EMERGING NEEDS OF SOCIETY
© 2024 the Authors
ISBN 978-1-032-54816-6
DOI 10.1201/9781003431749-177
Open Access: www.taylorfrancis.com, CC BY-NC-ND 4.0 license

ECSMGE 24
XVIII EUROPEAN CONFERENCE ON SOIL MECHANICS AND GEOTECHNICAL ENGINEERING

Contract for the stabilization of the north cliff in Azenhas do Mar

Travaux de stabilisation de la falaise nord d'Azenhas do Mar

S. Almeida*, M. Pereira
Mota-Engil Engenharia S.A, Portugal

**sergioa@mota-engil.pt*

ABSTRACT: The Mota-Engil Engenharia S.A. Special Foundations Department executed the stabilization contract of the North Cliff of Azenhas do Mar located in Sintra for the Portuguese Environment Agency (APA). The intervened area extended along the northern Cliff section under the urban core of Azenhas do Mar with about 125 m of development and a maximum height of 45 m. This project was developed with two key objectives. The first was the need to seek to preserve the core of traditional housing that were built on top of the Cliff, considered of great patrimonial interest; the second with the requirement to increase the level of security of the area overlooking the restaurant and the ocean pool, built at the base of the Cliff whose attendance increases significantly during the Summer. The great exposure of this Cliff, either to the direct action of sea wave, or to atmospheric phenomena, more specifically to the formation of fog and fog with some persistence, contributes to a process of continuous erosion that was causing its progressive retreat, thus endangering the stability of buildings and other structures that are built at their top, especially those that are closer to the edge.It is intended to address in the first place the challenge of accessing the work area since it was delimited to the west by the sea and east by the buildings of Azenhas do Mar housing core. At the same time will also be addressed the means involved in the execution of work, deforestation, reperfilation of the Cliff, nailing, sprayed concrete and recovery and execution of new walls of mortar stone, procedures adopted, as well as the complexity related to the execution of works of this nature in a protected and national interest landscape.

RÉSUMÉ: Le Département des Fondations Spéciales de Mota-Engil a exécuté les travaux de stabilisation de la falaise nord d'Azenhas do Mar, située dans la municipalité de Sintra, pour le compte de l'Agence portugaise de l'environnement (*Agência Portuguesa do Ambiente - APA*). La zone d'intervention s'étend le long du tronçon de la falaise nord, en contrebas du centre urbain d'Azenhas do Mar, qui s'étend sur près de 125 mètres pour une hauteur maximale de 45 mètres. Ce projet a été développé avec deux objectifs fondamentaux en tête: Le premier concernait la nécessité de préserver le cœur de la ville construite au sommet de la falaise, considérée comme présentant un grand intérêt patrimonial, le second était lié au besoin d'augmenter le niveau de sécurité dans la zone surplombant le restaurant et la piscine océanique, construits au pied de la falaise, dont l'occupation augmente considérablement pendant la saison balnéaire. La grande exposition de cette falaise, tant à l'action directe des vagues qu'aux phénomènes atmosphériques, plus précisément à la formation de brumes et de brouillards qui persistent dans la région, contribuent à un processus continu d'érosion qui a conduit à son recul progressif, mettant ainsi en péril la stabilité des bâtiments et autres structures qui sont construits sur son sommet, en particulier ceux qui sont les plus proches de son bord. L'objectif est de répondre dans un premier temps à la problématique d'accès à la zone de travaux telle qu'elle était délimitée à l'Ouest par la mer et à l'Est par les bâtiments de cette zone résidentielle. En parallèle, les moyens mis en œuvre pour réaliser les travaux de déboisement, de reprofilage de la falaise, de clouage, de béton projeté, de récupération et de construction de nouveaux murs en pierre avec application de mortier, les procédures adoptées, la phase de construction et la complexité liée à la réalisation de travaux de cette nature dans une zone de paysage protégé et d'intérêt national élevé seront également abordés.

Keywords: Cliff; stabilization; erosion.

1 INTRODUCTION

In 2014, the Portuguese Environment Agency (*Agência Portuguesa do Ambiente - APA*) has promoted a competition for the development of a project covering: The stabilization of the northern cliff section under the urban area of Azenhas do Mar, near Sintra (Portugal), with about 125 m in length and a maximum height of 50 m, as we can see on figure 1. The rehabilitation of the ocean pool and surrounding areas, located at the base of that cliff.



Figure 1. Before the intervention.

This project was developed with two key objectives: The first was the need to preserve the core of traditional housing built on top of the Cliff, considered of great heritage interest.

The second should meet the requirement to increase the level of security of the area overlooking the restaurant and the ocean pool, built at the base of the Cliff, whose attendance increases significantly during the Summer.

The great exposure of this cliff, either to the direct action of sea waves or to atmospheric phenomena, more specifically to the formation of haze and fog with some persistence in the area, contributes to a process of continuous erosion causing its progressive retreat, thus endangering the stability of buildings and other structures built on top of it, especially those closer to the edge.

This situation of imminent danger was evidenced by the fact that a large part of the walls delimiting the properties at the top of the cliff were over areas that were already cantilevered, sometimes by two or more meters. To deal with this situation, it was necessary to intervene along a large part of the height of the cliff, in order to stabilize it. Regarding the restaurant and pool area, the existing stone cladding built in the 1950s and 1960s had to be rehabilitated to protect the cliff surface from erosion.

Some more specific work was carried out in some areas that were not yet covered and whose evolution has contributed to an increase in the risk of material falling from the cliff.

On figure 2 we can see the cliff after the intervention.



Figure 2. After the intervention.

2 CONSTRUCTION STAGES

One of APA's requirements was that, on the one hand, the project should contribute to attenuating erosion processes and consequently to minimizing the geomorphological evolution of the cliff surface and, on the other hand, that it should have as little impact on the landscape as possible, so as not to deprive the site of its characteristics, given that it is considered to be of high landscape interest. To this end, all the concrete solutions that were planned in the area visible from both the pool and the cliff on the south side of the river were clad in stone, so that they would have similar visual characteristics to the cladding already in place in the area overlooking the ocean pool.

Another requirement from the Portuguese Environment Agency (APA) was to start working on this project outside the bathing season so as to lessen the impact on the many bathers that often attend the beach of Azenhas do Mar. Prior to the actual work of stabilizing the cliff, Mota-Engil, together with the client APA, held several meetings to reach an agreement with some landowners so that they would provide access to their land to enable the work to be carried out, in particular through the possibility of setting up two tower cranes to access the work fronts.

It would not have been possible to carry out such work without the cooperation of the owners, as we would not have had the access to carry it out. One of the owners, Mr. Theber, made the entrance to his property available in order to provide the main access for equipment and materials and, consequently, for the assembly of the first tower crane with a 30-metre reach. Another owner, Sandra Ramos, provided access to her condominium terrace to allow a second tower crane with a reach of 64m to be erected, located in the center of the project, with capacity to reach the entire radius of the project (125m long).

Due to the need to carry out a large part of the work using a basket suspended on the tower crane, all

activities were conditioned by weather conditions, especially the wind speed, which is often high in the fall and spring in that part of the country.

For safety reasons, a system was implemented on the tower cranes that allowed us to check the wind speed. One of the major constraints of this project, in addition to what has already been said, was the fact that the number of workers was limited to the basket capacity (2 to 3 people), which largely affected the performance of these tasks.

After consignment on May 20, 2019, and following approval from the DPSS, we began the contract activities in accordance with the approved work plan: setting up the construction site, providing access to the work front, signs, fencing, demolition of two existing ruined buildings, laying foundations for the implementation of tower cranes. The project was drawn up by Mota-Engil's project team. These foundations were made using 22m long TM-80 ø139.7mm micropiles, 10 units for each foundation rock mass.

The equipment used was a Klem 803 extendable tower and the drilling method was rotopercussion.

2.1 Tower cranes assembly

Assembly was carried out using an auto car crane, duly dimensioned and stabilized on the work platform for the assembly of crane No. 2. Subsequently, crane No.1 was assembled with support of crane no. 2. Two safety cameras were installed on each of the cranes, so that crane operators had a field of vision in perfect safety conditions.

The equipment was rented from Ibergru. Once assembly was complete, the company EQS was asked to certify the set: crane, basket and drilling equipment.

A redundant system was manufactured and applied to both cranes.

2.2 Clearing of vegetation and all loose material Sanitation and partial demolition of blocks and partial reprofiling of cantilevered rock layers

Figure 3 shows one moment of the cleaning process.



Figure 3. Clearing and cleaning using ropes.

As it was not possible to carry out the dismantling through the use of explosives, other methods had to be used. One of the techniques used was the application of expansive cement.

The designated supplier was Geotek, which was supplying the material and was also available to monitor the work.

2.3 Shotcrete and systematic soil nailing

In order to protect and reinforce the entire upper area of the cliff, from the top to around +30.00 m above sea level, due to the need to prevent decompression of the area underlying the existing buildings, a systematic cladding was carried out using shotcrete with a minimum thickness of 0.10 m, combined with nailing with A500 NR ø32 mm steel rods, quincunx-patterned in a 2.0Vx2.0H mesh, 12.0 m to 10.0 m long.

Nailing was carried out at an inclination of 15º to the horizontal, in holes measuring 4" (approximately 101 mm) in diameter and sealed with cement grout. All soil nailing metal elements were hot-dip galvanized. The shotcrete used was c40/50 with metal fibers.

The areas where treatment was not planned were properly protected with a geotextile blanket. In figure 4 we can see the drilling and nailing process.



Figure 4. Drilling – Nailing.

2.4 Mortared stone cladding and recovery of the existing stone

In order to allow for a new work front, a properly dimensioned scaffolding was erected, thus allowing the existing stone to be recovered in that specific area, as we see on figure 5.

Catari was the supplier appointed to assemble the scaffolding. Scaffolding dimensions: 20 m long x 25 m high, the shoring was done to the slab of the existing restaurant building.



Figure 5. Recovery of the existing stone.

It was decided on site and recorded in a memo that the view from the viewpoint would determine which area would be covered in mortared stone. Thus, in the northernmost area with no view from the viewpoint, the final cladding would be with pigmented shotcrete and no mortared stone. In order to make it as homogeneous as possible, it was decided on site that pigmented concrete would be sprayed over the entire targeted area of the cliff before the stone was laid. This work allowed the areas where it was not possible to apply the mortared stone to be as homogeneous as possible. In our opinion, this measure added value to the aesthetics of the project. The work on the cliff crest was largely carried out using lifelines and ropes.

All the material to be used in the stone cladding was collected from the base of the cliff.

This material was treated and transported by buckets and placed in the baskets for application. One of the important works to stabilize the cliff was the retreat of the houses' walls. A glass railing was applied to the top of the wall, a solution chosen by the owner, and the existing ditch along the south façade of the "Cabana Mar" house was improved along the cliff. In some specific areas, caves/cavities in the cliff were also filled with cyclopean concrete.

After the work was completed, it was necessary to ensure the renaturation of the occupied areas, namely the construction site and the area in front of the site, where tower crane no. 2 was erected. The project was drawn up by Vibeiras and approved by the Institute for the Conservation of Nature and Forests (ICNF). Vibeiras, a company belonging to the Mota-Engil group, drew up the project and carried out the work.

2.5 Quality plan

Figure 6 shows the nailing test. The following tests were carried out prior to the work, in order to check and control the materials used on site: Preliminary tests on shotcrete designed with fibers (compression / bending and energy absorption); Compressive strength test on the cement grout used to seal nailing; Preliminary test on nailing Execution of three molds to choose the final coating and its grain size, as well as the tone and spacing of the joints between the limestone; Fiber-reinforced cement and setting accelerator; Compression test; Bending test; Punching-bending test (energy absorption); Compression test: The compressive strength of fiber-reinforced shotcrete was determined by a simple cylinder compression test.

The concrete was poured into a projection box with dimensions of 60x60[cm] at the base, 80x80[cm] at the top and 20 cm high, and 6 cylindrical test specimens with a diameter of 6 cm and a height of 12 cm (ground) were removed. The compression tests were carried out every 50m3. Bending test: The bending test carried out by recording the Load-Deformation curve allows the behavior of fiber-reinforced shotcrete to be assessed. Concrete is shot on a panel that would allow 3 beams of 50(L)x12.5(W)x7.5(H)[cm] to be taken from it. Punching-bending test: The punching-bending test carried out on a shotcrete slab, recording the Load-Deformation curve, makes it possible to appreciate the multidirectional action of the fiber network. In these tests, the energy absorption is measured in a test on a 60x60x10 cm slab, supported on all 4 edges, leaving a free span of 50 cm.

The load is applied to the center of the slab with a contact surface of 10 cm x 10 cm (EFNARC). In the diagram, by recording the load and the deformation in the center of the slab, the energy absorbed up to a deformation of 25 mm at 28 days is then calculated. This energy will be 700 J as a minimum.

Nailing Control Tests: Compression/viscosity and decantation testing: The compressive strength of the cement grout was determined by a simple compression test on a cylinder. The cylindrical specimens were identified, 3 specimens at 3 days. 3 at 7 days and 3 at 28 days, requiring at least the following compressive strengths: During the course of the work, three control tests made per type of geological formation. The control tests were carried out up to a force at least equal to 1.1 TL, where TL is the service tensile strength (defined by the designer).

The tests were carried out at the same speed and with the same force and displacement readings as the previous tests.

The test was carried out by applying loading and unloading cycles, with a successive increase in the test load in each cycle, up to a given maximum cycle load value. The maximum load proposed in this case was 0.80 fy, steel yield load = 442kN and 80% fy = 354kN. The load is then increased smoothly up to the maximum value of the cycle or test or until failure by pull-out occurs, Rt. The maximum number of load increments should be sufficient to define the shape of the load-displacement curve and should not normally exceed 20% of the maximum.After applying each load increment, the load is kept constant until the nailing displacement stabilizes, that is, the displacement measured between two consecutive readings (s1 - s2) must be less than 0.5 mm with readings taken at times: T= 0 min, 1 min, 2 min, 5 min, 10 min, 15 min, 20 min. Once the maximum load of the Rt or Pp cycle has been reached and the necessary waiting time has elapsed, the test nailing must be unloaded to the reference load P0 and the residual displacement shall be recorded. Additional load cycles can be carried out if necessary.

Bearing in mind the landscape and heritage value of the northern cliff of Azenhas do Mar, it was necessary to assess the characteristics of the final coating. To this end, three experimental panels were carried out to choose the final finish of the mortared stone cladding.

Study proposals were presented to define the thickness of the joints between stones, the color of the mortar, the type and color of the stone, the regularity of the face, among other characteristics. The study proposals for defining the thickness of the joints between stones, the color of the mortar, the type and color of the stone, the regularity of the face, among other characteristics, were submitted for approval by the land management bodies with jurisdiction over the site, namely the Portuguese Environment Agency (APA), Sintra Municipal Council (CMS) and the Institute for Nature Conservation and Forests (ICNF).



Figure 6. Nailing test.

3 RELEVANT QUANTITIES

- Systematic nailing with 10 and 12 meters - 3300m
- Nailing where required with 4.6 and 8 meters 909.40m
- Geodrains ø50mm - 132.00m
- Shallow drains - 220 units
- Shotcrete C-30/37 with metallic fibers - 654m3
- Fracture sealing - 42.83m3
- Clearing - 870m2
- Sanitation - 780m2
- Reprofiling - 372.50 m3
- Recovery of the existing stone - 380 m2
- Mortared stone cladding - 1889 m

4 FINAL CONSIDERATIONS

As a final note, we'd like to highlight that the European Commission (EC) selected the Azenhas project as an excellent example of a climate change adaptation project.

The inauguration of the project was attended by Mr. Eng. Matos Fernandes, Minister of the Environment, and his delegation. We would like to thank the entire Mota-Engil technical team, project manager Eng. Sérgio Almeida, technical director Dr. Miguel Pereira, safety technician Mr. Carlos Lalim, foreman Mr. Fernando Mesquita and his work team, who showed total dedication to the work in question, the Inspection team, Afaplan employees, Mr. Paulo Rangel, Eng. Igor Mateus, the owner of APA, in the person of Dr.

Catarina Patriarca, also Dr. Cátia Valente and the architect Paulo Figueiredo, for their total and constant availability. In figure 7 we can see the final work at the moment of the inauguration of the contract in the presence of the minister for the Enviromment, Mr. Matos Fernandes.



Figure 7. Inauguration of the contract in the presence of the Minister for the Environment, Mr. Matos Fernandes.

Proceedings of the XVIII ECSMGE 2024
GEOTECHNICAL ENGINEERING CHALLENGES
TO MEET CURRENT AND EMERGING NEEDS OF SOCIETY
© 2024 the Authors
ISBN 978-1-032-54816-6
DOI 10.1201/9781003431749-178
Open Access: www.taylorfrancis.com, CC BY-NC-ND 4.0 license

ECSMGE 24
XVIII EUROPEAN CONFERENCE ON SOIL MECHANICS AND GEOTECHNICAL ENGINEERING

Overcoming geotechnical challenges to maximise re-use of an existing brownfield site for use as a rail test track

Surmonter les défis géotechniques pour optimiser la réutilisation d'un ancien site industriel comme voie d'essai ferroviaire

P. Anning*, J.K. Thillainadarajah, A. Kushwaha
AtkinsRéalis, London, UK

**peter.anning@atkinsrealis.com*

ABSTRACT: The Global Centre for Rail Excellence (GCRE) is a purpose-built rail facility for train testing and rail industry research. The project will comprise a looped track supported on significant cuttings and embankments. The project will be constructed on a site containing backfilled opencasts (pits) from previous coal mining, with the remaining site consisting of spoil tips, forestry and undisturbed common land. The site has a varied topography with the level difference of around 125m below the highest and lowest point. Various geotechnical challenges were encountered during the design development. With an aim to become UK's first net zero railway, the earthworks design aspired to utilise all site won material - mainly opencast mining waste / backfill. This material would not typically conform with the fill classes of the National Highways Specification for Highway works (SHW 2017). Trial embankments were constructed to test the suitability of site-won materials and compaction required to achieve specified stiffness at rail formation level. Prediction of settlement of the earthworks within the footprint of the historical open cast back fill is a major challenge. Historical underground mine workings are present beneath the site, shallow mine entries and workings are within influencing distance of the scheme. Remediation design has been undertaken to reduce the instability risk to the scheme utilising a risk based approach in partnership with the client.

RÉSUMÉ: Le Centre Global d'Excellence Ferroviaire (GCRE) est une installation spécialement conçue pour des essais de véhicules et la recherche dans l'industrie ferroviaire. Le projet comprendra une piste en boucle nécessitant des terrassements importants. Le projet sera construit sur un site contenant d'anciennes mines de charbon à ciel ouvert remblayées, des terrils, des forêts et de terres communales non développées. Le topographie du site est variable avec un dénivelé maximal d'environ 125 m.Divers défis géotechniques ont été rencontrés au cours de l'étude de conception. Avec pour objectif d'en faire le premier chemin de fer à zéro émission nette du Royaume-Uni, la conception des travaux de terrassement visait à utiliser tous les matériaux issus du site, principalement les anciens remblais. Cependant, ce matériau n'est généralement pas conforme aux classes de remblai définies dans les codes pour les Travaux Autoroutiers des Autoroutes Nationales (National Highways SHW 2017). Des remblais d'essai ont donc été construits pour vérifier la compatibilité des matériaux revalorisés avec le compactage requis pour une rigidité adéquate de la nouvelle plateforme. L'estimation des tassements des zones remblayées est un défi majeur, car des mines abandonnées sont présentes dans l'emprise du site, avec des structures d'accès peu profondes et des réseaux de mines présentes à proximité du site. Pour réduire le risque d'instabilité, la conception de cette réutilisation adaptative a utilisé une approche de gestion des risques en partenariat avec le maître d'ouvrage.

Keywords: Geohazards; risk; sustainability; instability; settlement.

1 INTRODUCTION

The Global Centre for Rail Excellence will form a purpose built site for train testing and rail industry research for the UK and European markets. An electrified high speed loop, approximately 7km in length to test trains at speeds up to 177km/h is proposed, the scheme will also include a platform test environment, rolling stock storage and maintenance facilities, operations and control offices, staff accommodation and a connection to the rail network via the Swansea to Onllwyn branch line (Figure 1). Once completed, this will be the world's first integrated testing facility for rail infrastructure and rolling stock.

The site covers 440ha in an area and is located at the head of the Dulais and Swansea valleys on the former Nant Helen opencast coal site and Onllwyn washery in Neath Port Talbot/Powys, Wales, UK. Planning permission for the scheme was granted in

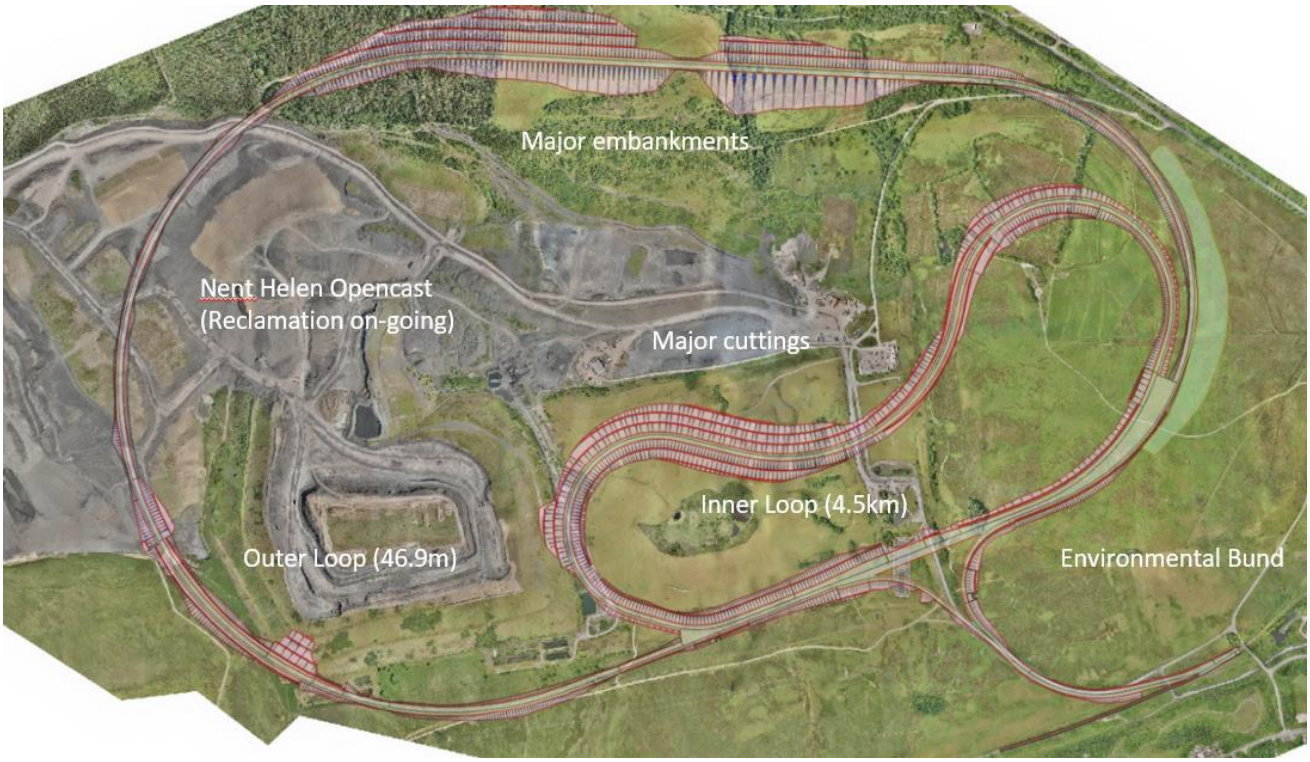

Figure 1. Earthworks layout in March 2023, the earthworks design is subject to change as the project progresses.

summer 2021. In June 2022 the contract for the detailed design and construction of the scheme's significant earthworks was awarded to Hirwaun-based Walters Group, with AtkinsRéalis as its design partner.

The contract covers approximately 3.5Mm3 of earthworks. The AtkinsRéalis scope also includes design of temporary and permanent drainage for the construction stage, landscape design and providing environmental services to support discharging planning conditions.

The design and construction schedule is currently undergoing optioneering with the earthwork layout and alignment subject to change however the challenges and geohazards discussed in this paper are relevant for all layouts.

2 GROUND CONDITIONS

Ground conditions at the site are dominated by the recent history of extensive opencast mining for coal. The depth of opencast workings varied from 40m to 150m, the opencasts have been subsequently backfilled with overburden and other waste material (Figure 2). Large tips of mining waste are also present above the original ground surface.

Outside the footprint of the opencast workings and tips, mining waste / Made Ground of variable thickness is present across the site at surface. Natural deposits of glacial till and peat are occasionally present in some, less disturbed parts of the site overlying weathered South Wales Coal Measures (SWCM) which become less weathered with depth.



Figure 2. Opencast mining backfill material.

3 GEOTECHNICAL DESIGN CHALLENGES

Historical open cast mining activities and the resulting variable ground conditions are the source of the main geotechnical challenges at the GCRE project. The thickness and extent of opencast backfill / tipped waste / Made Ground varies significantly across the site, superficial Glacial Till deposits are also present or absent variably across the site. The SWCM bedrock was encountered at variable depth, typically shallowly.

The variability in ground conditions is most pronounced at the transition between backfilled opencast workings and the wider site area where great thicknesses of opencast backfill gives way to shallower horizons of Made Ground and superficial deposits. The rate and amount of settlement varies such that differential settlement is a significant issue.

To better understand the variability in ground stiffness and susceptibility to settlement, the whole site was modelled in Leapfrog using data from current and historic boreholes combined with mine restoration plans. This information was used to identify locations of transition where ground stiffness was expected to change dramatically, and a remedial transition zone design was prepared.

One of the key goals of the GCRE project was to reduce the need to import fill and maximise the use of site won material (backfill / mining waste) which is mainly constituted of processed SWCM and does not conform to the fill classes of the Standards for Highways, Specification for Highway Works (2017). Although this could be achieved by processing through crushers and screen, it would significantly add to the cost and programme and increase the carbon footprint of the project.

As the material is significantly over size, the proportion of material of less than 37.5mm is likely to be less than 25% from particle size distribution. The determination of optimum moisture content and maximum dry density, therefore, becomes unrepresentative of the placed material as a whole. It was proposed that the quality of the earthworks construction is controlled by the use of plate load testing, where an acceptable subgrade stiffness isderived from the Ev2 load cycle. The Ev2 is the formation static modulus measured in accordance with Network Rail Standard NR/L2/TRK/4239 (Network Rail, 2020) and German Standard DIN 18134 (Normenausschuss Bausen, 2012). This method of quality control is commonly used on earthworks in France. It has also been used to evaluate compaction trials on High Speed 2 projects.

As part of detailed design, trial embankments were constructed on site to evaluate the performance of backfill / mining waste under compaction and understand the resultant stiffness. Four trial embankments ranging from 1m to 4m in height, and with different compaction layer thicknesses of 0.5m, 1.0m and 2.0m, were constructed and tested. Based on the assessment of the results, it was concluded that 1m thickness for fill layers would provide a balanced approach between earthworks stiffness/required compaction efforts and speed of construction to meet the programme.

Another key geotechnical challenge was creep settlement. The opencasts have historically been backfilled by tipping mining waste in an uncontrolled manner without systematic compaction, as a result the backfill material is experiencing continuous creep settlement. An ongoing surface monitoring regime suggests that the current rate of settlement is varying from 10mm to about 90mm per year, depending on depth of opencast mine fill and the associated backfill dates.

The predictions of the magnitude of creep settlement have been undertaken in accordance with the Building Research Establishment publication "Building on fill: geotechnical aspects" (Watts & Charles, 2015). An interpretation and extrapolation of the monitoring data from surface arrays installed at each opencast site, as well as historical satellite monitoring InSAR (Interferometric synthetic aperture radar) information, have been used to validate the creep settlement predictions, see Figure 3.

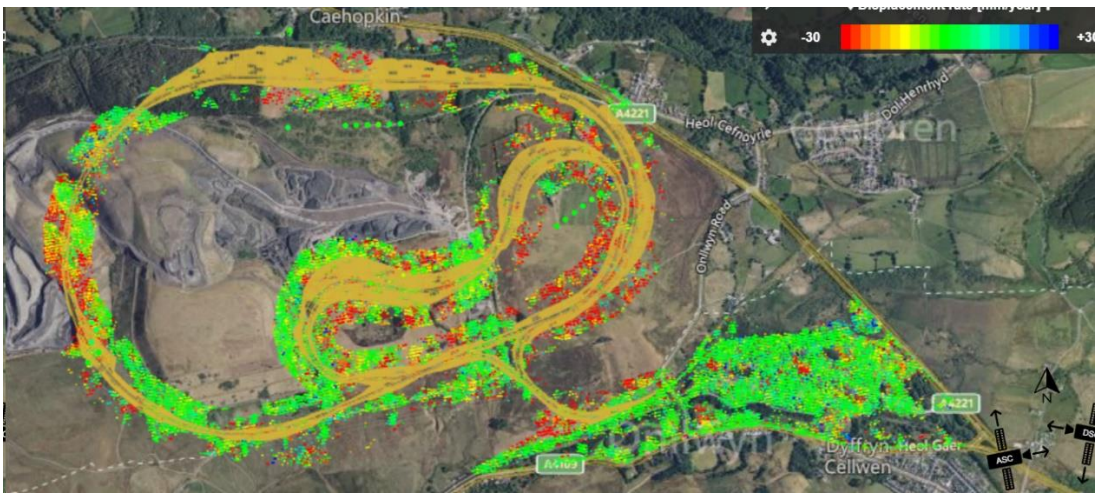

Figure 3. Extract from InSAR for GCRE.

The ongoing ground movement across the site is likely to result in settlements exceeding the widely accepted industry tolerances. GCRE aims to adopt an innovative approach to risk management and will

continuously monitor, inspect, survey and tamp tracks to ensure compliance. A possible redesign of the vertical alignment has been accepted as a likely mitigation measure in operation to accommodate excessive earthworks settlements.

4 UNDERGROUND MINING CHALLENGES

As well as open cast mining, the site has a long history of underground coal working. A desk based review was undertaken following the principles of the CIRIA Abandoned Mine Workings Manual C758D (Parry and Chiverrell, 2019) including, but not limited to, review of Coal Authority reports, mine abandonment plans, client records and ground investigation data.

The assessment concluded that underground workings and mine entries are very likely present across the site. Workings pose a risk to the proposed scheme given the shallow depth and lateral extent, and considering the mining method likely to have been employed which is liable to leave mining voids. The potential for collapse and void migration to surface from workings was identified particularly in the south and east (Figure 3). Untreated mine entries also posing a collapse risk are present at discrete locations across the site.

A risk-based remediation strategy was developed including phased ground investigation works, targeting the high-risk mining areas and sensitive operational locations. “Drill and grout” and “excavate and replace” treatment methods are proposed for shallow workings with additional capping and grouting of mine entries.

The remediation strategy was developed with the client, partners and stakeholders to reduce the mining risk to the scheme and enabling construction, as well as being economical, sustainable and able to meet programme and operational requirements.

5 CONCLUSION

Earthworks design has had to overcome a number of challenges in order to redevelop an existing brownfield site with a long history of opencast coal mining. The key geotechnical challenges are differential settlement, creep settlement and potential for site won material not conforming to standards.

Mine working and entry remediation design has been undertaken to protect the proposed earthworks, this has been done collaboratively with the client adopting a risk based approach to ensure an economic approach and programme needs are met.

The design work undertaken will allow the GCRE project to ‘reuse’ a landscape already significantly impacted by industrial activity and make use of the waste products of this industry.

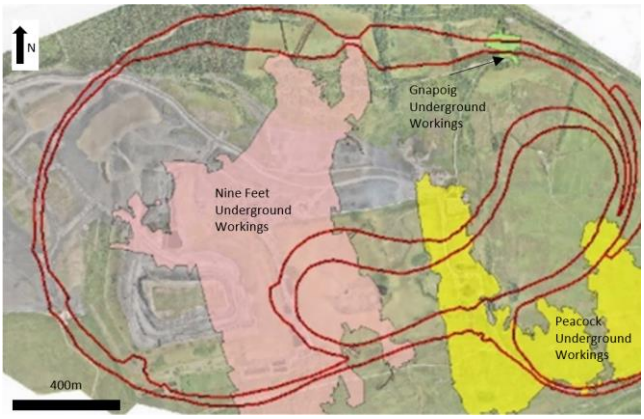

Figure 4. Shallow underground workings in three seams were assessed to be shallow enough to pose an instability risk to the project.

REFERENCES

National Highways, Transport Scotland, Welsh Government, Department for Infrastructure, (2017). Standards for Highways, Specification for Highway Works [online]. Available at: https://www.standardsforhighways.co.uk/mchw, accessed 01/07/2022.

Network Rail (2020). NR/L2/TRK/4239, Track Bed Investigation, Design and Installation, Network Rail, London, UK.

Normenausschuss Bausen (2012). DIN 18134, Soil – Testing Procedures and Testing Equipment, DIN Deutsches Institut fur Normung, Berlin.

Parry, D. and Chiverrell, C. (eds) (2019). *Abandoned Mine Workings Manual*, C758D, CIRIA, London, UK.

Watts, K. and Charles, A. (2015). *Building on Fill: Geotechnical Aspects,* 3rd ed., BRE Press, Bracknell, UK.

Proceedings of the XVIII ECSMGE 2024
GEOTECHNICAL ENGINEERING CHALLENGES
TO MEET CURRENT AND EMERGING NEEDS OF SOCIETY
© 2024 the Authors
ISBN 978-1-032-54816-6
DOI 10.1201/9781003431749-179
Open Access: www.taylorfrancis.com, CC BY-NC-ND 4.0 license

ECSMGE 24
XVIII EUROPEAN CONFERENCE ON SOIL MECHANICS AND GEOTECHNICAL ENGINEERING

Ravines in collapsible soils of Luanda, Angola: forms of erosion – state of the art

Ravines dans les sols effondrés de Luanda, Angola: formes d'érosion – état des conaissances

F.M. António*
University of Aveiro, RISCO - Research Centre for Risks and Sustainability in Construction, Aveiro, Portugal

F.A.B. Bonito
Angola Engineering Laboratory, Luanda, Angola

A.A.R.C.A. Benta
University of Aveiro, RISCO - Research Centre for Risks and Sustainability in Construction, Aveiro, Portugal

**francisco.m.antonio@ua.pt*

ABSTRACT: The upper part of Luanda is mainly made up of red sands, known locally as "muceque" soil. Luanda's red sands have collapsible characteristics and a metastable structure, prone to erosion phenomena that have caused much damage to the foundations of buildings, roads, airfields, and agricultural areas, with significant socio-economic consequences for the population. Despite the danger posed by the erosion of these soils, few studies on soil erosion by water have been conducted locally to date. To contribute towards filling this gap, this paper aims to review the literature on water erosion processes in these soils, highlighting the controversies in the literature regarding the designations and sequences of the forms of soil erosion that generally predominate. It stresses the need for a more significant effort to standardise criteria for classifying forms of soil erosion despite the complexity of the problem under study. Although the local bibliography is scarce, this work could be valuable in encouraging further research since erosion processes have created many problems in these soils.

RÉSUMÉ: La partie supérieure de Luanda est principalement constituée de sables rouges, connus localement sous le nom de "muceque". Les sables rouges de Luanda présentent des caractéristiques d'effondrement et une structure métastable, propices aux phénomènes d'érosion qui ont causé de nombreux dommages aux fondations des bâtiments, des routes, des aérodromes et des zones agricoles, avec des conséquences socio-économiques importantes pour la population. Malgré le danger que représente l'érosion de ces sols, peu d'études sur l'érosion des sols par l'eau ont été menées localement à ce jour. Pour contribuer à combler cette lacune, cet article vise à passer en revue la littérature sur les processus d'érosion hydrique dans ces sols, en soulignant les controverses dans la littérature concernant les désignations et les séquences des formes d'érosion du sol qui prédominent généralement. Il souligne la nécessité d'un effort plus important pour standardiser les critères de classification des formes d'érosion des sols malgré la complexité du problème étudié. Bien que la bibliographie locale soit peu abondante, ce travail pourrait être utile pour encourager des recherches plus approfondies car les processus d'érosion ont créé de nombreux problèmes dans ces sols.

Keywords: Red sands; rill; gully; ravine erosion; barroca.

1 INTRODUCTION

The occurrence of erosion phenomena on Luanda's "muceque" soils or red sands for several decades is a serious problem that needs urgent solutions (Nascimento, 1952). The red sands of Luanda are soils with collapsible characteristics and a metastable structure, prone to the appearance of erosion processes that have caused much damage to the foundations of buildings, roads, airfields, and agricultural areas, with significant socio-economic consequences for the population (Ferreira & Silva, 1957). There are various definitions of soil erosion in the literature. El-Swaify et al. (1982), for example, defined erosion as the "wearing away of the soil surface by erosive agents such as running water and wind", while Foth (1990) and Goudie (2004) defined erosion as "a three-stage process: detachment followed by transport and deposition", considering a third stage, called deposition, which occurs when there is no longer enough energy to transport the particles.

On the other hand, Nascimento (1952), Morgan (2005) and Lal (2006) define soil erosion as a two-stage process consisting of the detachment of particles

from the soil mass and their transportation by erosive agents, such as running water and wind, to another location.

The first research on soil erosion in Luanda documented in the literature dates back to 1949 when the Overseas Urbanization Office invited Portugal's National Civil Engineering Laboratory (LNEC) to carry out a "Study of the Regularization and Protection of Luanda's Gullies (Barrocas)" (Nascimento, 1952). At the time, the problem that most concerned the engineers was the appearance of gullies in lateritic sands, which were highly erodible compared to clay soils (Nascimento, 1952).

Lateritic sands are another name for Luanda's red sands or "muceque" soils, which are collapsible, metastable, and highly erodible. Despite the danger posed by their erosion, few studies on soil erosion by water have been conducted locally.

To contribute towards filling this gap, this paper aims to review the literature on water erosion processes in these soils, highlighting the controversies in the literature regarding the designations and sequences of the forms of soil erosion by water that generally predominate. It stresses the need for a more significant effort to standardise criteria for classifying forms of soil erosion despite the complexity of the problem under study.

2 LITERATURE REVIEW

2.1 Red sands of Luanda, Angola

In Angola, the first research work on collapsible soils documented in the literature dates back to the 1950s, when engineers from the Engineering Laboratory of the Directorate of Public Works and Transport Services of Angola encountered problems of cracking and settlement in buildings, road pavements, and the Luanda aerodrome, which were founded on this soil (Ferreira & Silva, 1957).

The upper part of Luanda consists mainly of red sands, locally known as "muceque" soil (Silva, 1965). The main geological and geotechnical characteristics of the red sands of Luanda were studied by Silva (1970), Silva and Teixeira (1973) and are summarised below. The geological formations of the Luanda region are divided into two groups, corresponding to the Quaternary and Tertiary periods, respectively. The Quaternary consists of islands, beaches and alluvial fans; coastal cordons; Cazenga Formation and Muceque or Quelo Formation, while the Tertiary consists of the Luanda Formation, Cacuaco Formation and Quifangondo Formation. The red sands belong to the Muceque or Quelo Formation (Pleistocene) and constitute most of the foundation soil on the "plateau" of Luanda, and its layer has thicknesses ranging from a few centimetres to 17 metres in the foral area and can reach 50 metres (Nascimento, 1952; Silva & Teixeira, 1973).

The granulometric distribution of the red sands / "muceque" soil is composed of sand particles (≥ 75%), silt particles (1% - 5%) and clay particles (8% - 20%). While the sand and silt particles have a similar mineralogical composition, based on quartz and feldspar, the clay fraction consists of kaolinite, illite and iron oxides (geotite and hematite) (Silva, 1970; Silva & Teixeira, 1973).

From a geotechnical point of view, the red sand or "muceque" soil has been classified, according to the Unified Soil Classification System, as sandy-clay soil (SC), sandy-silt soil (SM) or a combination of both sandy-clay-silt soil (SC-SM) (Silva & Teixeira, 1973). The collapsible behaviour of Luanda red sands was demonstrated by Novais-Ferreira and Silva (1961) using plate load tests and pile tests, while Silva (1970) demonstrated the collapsibility of this soil by performing oedometer tests. The results of these tests show that, with low moisture content, the soil can withstand high loads (up to 800 kPa) with little settlement. However, as soon as it becomes saturated, even with small loads, it settles drastically due to the failure of the bonds between the particles.

2.2 Red sands erodibility

The Erodibility is defined as the soil's resistance to detachment by splashing during precipitation, surface runoff or both (Renard et al., 1997; Morgan, 2005; Bastos, 2004). The erodibility of a given soil is closely related to its properties, for example, granulometric distribution, permeability, organic matter content and structure (Zhang et al., 2004; Morgan, 2005).

Bastos (2004) mentions that since the 1960s, studies on soil erodibility have been carried out by the National Civil Engineering Laboratory (LNEC) in Portugal and the Engineering Laboratory of Angola (LEA) to obtain erodibility criteria for tropical soils involved mainly in road cuts. The author cited Meireles (1967), who studied the soils of Angola, classifying them as *strongly*, *moderately* and *weakly erodible* according to criteria based on granulometry and plasticity. For the author, strongly erodible soils have low plasticity, represented by a liquidity limit (wl) < 21% and a plasticity index (PI) < 8%.

As for particle size, a criterion was established based on the percentage passing the #200 sieve: % passing #200 ≤ 20% - *strongly erodible soils*; 20% < % passing #200 < 40% - *moderately erodible soils*; % passing #200 ≥ 40% - *weakly erodible soils*.

Bastos (2004) analysed the geomechanical properties of unsaturated soils in relation to erodibility. The author found that the collapse coefficient was not related to erodibility (K). Nevertheless, it was assumed that the disintegration of the soil in water is related to the collapse and erosion phenomena; the differences in the efforts involved explain the results.

2.3 Forms of soil erosion by water

The primary forms of soil erosion are mentioned in the early days of the study of erosion in 1939 when Bennet (1939) considered that the way water flows over the surface of the soil essentially takes three forms (see Figure 1): sheet/interrill erosion, rill erosion, and gully erosion (Bennet, 1939; Hurni, 1975; El-Swaify et al., 1982; Brady, 1984; Goudie, 2004; FAO, 2019).

In the literature, the forms of soil erosion by water are identified by groups related to their origin; the most important are listed below: Rainfall causes *splash erosion*; Surface runoff causes *sheet/interrill*, *rills*, *gullies* and *ravines erosion*; and Subsurface runoff which gives rise to *pipe/tunnel erosion* (Adhikary, 2020) (see Table 1). Below, we analyse the various forms of soil erosion by water resulting from Precipitation, Surface runoff, and Subsurface runoff.

2.3.1 Splash erosion

Splash erosion is the process of removing particles from the soil mass due to the impact of raindrops (Telkar et al., 2015). As a result, aggregates can be broken and soil particles thrown several centimetres away (Brady, 1984; Morgan, 2005). El-Swaify et al. (1982) cited Ellison (1947), stating that raindrops initiate the erosion process.

2.3.2 Sheet erosion or interrill erosion

Sheet erosion is caused by the action of raindrops (splashing) and the transport of detached soil particles by flowing water in a thin sheet of surface runoff that contributes to the removal of a relatively uniform thickness of soil (Brady, 1984; Lal, 2006; Goudie, 2004; Telkar et al., 2015; Balasubramanian, 2017; Saroha & Ambedkar, 2017; FAO, 2019; Adnan et al., 2021).

2.3.3 Rill erosion

Rill erosion is a form of linear soil erosion with depths (H) < 0.5 m that creates small, shallow incisions/channels resulting from the concentration of water flow in depressions, tillage marks or previously eroded grooves on the soil surface (Gobin et al., 1999; Goudie, 2004; FAO, 2019). Soil detachment in rills is largely because of flow shear stress forces acting on the wetted perimeter of the rill channel (Flanagan, 2006).

2.3.4 Gully erosion

Gully erosion is an obvious and prominent form of linear soil erosion consisting of deeper incisions with depths (H) ranging from $0.5 \leq H \leq 5$ m that usually result in open and unstable channels, as well as a long evolution that can be characterised by several stages of development (Gobin et al., 1999; Dagar, 2018).

The "barranco" - a term used in Portugal - is the form of soil erosion that assumes other designation terms worldwide. For example, in English, it is called "gully erosion", which is known as "ravine" in France, "cárcava" in Spain, "lavaka" in Madagascar, "wadi" in Arabic, "donga" in South Africa, "barranco" in Argentina, while in Brazil it is known as "voçoroca/boçoroca" (Castillo & Gómez, 2016) and "barroca" in Angola (Nascimento, 1952; Bastos, 2004).

2.3.5 Ravine erosion

According to Dagar (2018), the advanced stage of gully erosion is the formation of ravines, which is considered the extreme and most dangerous form of soil erosion with depths (H) > 5 m (Gobin et al., 1999; Dagar, 2018).

2.3.6 Tunnel / pipe erosion

Tunnel erosion (piping erosion) is a specific form of underground erosion. It occurs mainly on soils characterised by specific properties (e.g. loess soils). Subsurface water flows can be concentrated in natural drains, which, like the surface, depending on their speed, tend to remove particles from the soil mass and transport them elsewhere (Valentin & Rajot, 2018).

Due to the widening and deepening of these piping or tunnels as erosion continues and the consequent weakening of the ceiling, the stability of the overlying layers is impaired, resulting in gully erosion (after the collapse of the ceiling) (El-Swaify et al., 1982; Goudie, 2004; Valentin et al., 2005).

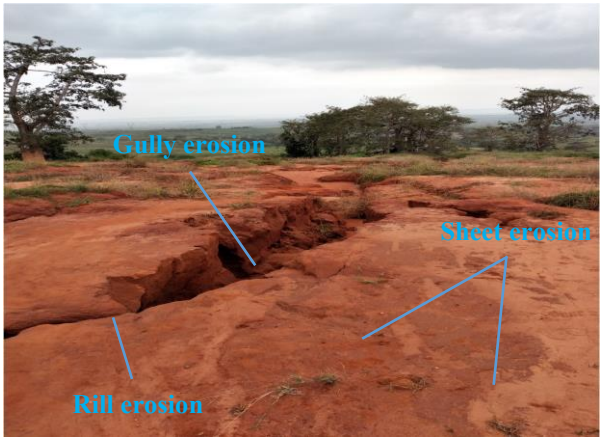

Figure 1. Examples of forms of soil erosion by water on a slope, Zango 5 – Luanda, Angola.

3 RESULT AND DISCUSSION

Based on consultation of the specialised literature, it was possible to compile Table 1, in which the stages of soil erosion were organised into three groups: 1. Precipitation (stage 1); 2. Surface runoff (stage 2, stage 3, stage 4, stage 5); and 3. Subsurface runoff (single stage).

The major controversies in the literature on soil erosion by water lie in the naming and sequencing of the forms of soil erosion, from the boundaries between interrill and rill to the confusion between the concepts of rill and gully as well as gully and ravine (Goudie, 2004). The discussion follows to understand better.

Table 1 shows that most of the discrepancies lie in soil erosion resulting from surface runoff, since precipitation and subsurface runoff both have a single, well-known erosion stage/form. Therefore, Hurni (1975), El-Swaify et al. (1982), Brady (1984), Foth (1990), Goudie (2004), Morgan (2005), Flanagan (2006), Valentin & Rajot (2018) and FAO (2019) considered three stages of erosion with the same designations and the following sequence: sheet, rill and gully, with gully being the advanced stage of surface erosion. On the other hand, Zachar (1982) considered four stages with two similar names but different meanings and sequences: sheet, gully, multi-form erosion, and rock erosion. In this case, sheet erosion includes splash and the related sheet erosion mentioned above, while gully corresponds to rill erosion.

The third group of researchers also consider four stages with different name meanings and the following sequence: sheet, rill, ravine, and gully (Guerra, 1997; Bastos, 2004; Vieira et al., 2019). Here, unlike the first group, these scholars consider interrill, rill, and ravine as the first three stages of surface erosion. The same authors consider the gully as the fourth and most advanced stage of surface erosion.

In addition, Gobin et al. (1999), Telkar et al. (2015), Saroha & Ambedkar (2017), Dagar (2018), and Bhat et al. (2019) also considered four stages of erosion with similar names but different sequences: sheet, rill, gully, and ravine being ravine the most advanced stage of surface erosion.

The last group of researchers also considers four stages with the same names and sequence as the previous first three stages, but the last name differs. They are in the following sequence: sheet, rill, gully, and stream bank erosion (Balasubramanian, 2017; Adhikary, 2020; Adnan et al., 2021). Here, unlike the previous group, these scholars consider stream bank erosion the fourth and most advanced stage of surface erosion.

The latter two groups of researchers consider ravine erosion and stream bank erosion to be their fourth stages, respectively. This is also contradictory because, according to Valentin & Rajot (2018), stream bank erosion is one form of soil mass movement.

With regard to the boundaries between interrill and rill, Goudie (2004) considers that the boundaries between them in hillside areas are often ill-defined and constantly changing. Regarding the difference between rill and gully, Goudie (2004) defines rill as incisions in the topsoil (A horizon), while gully are incisions in the subsoil (B or C horizons).

Other authors have established the difference between rill erosion and gully erosion as a function of depth (H) or size (depth (H) and drainage area (Ad)): Gobin et al. (1999) considered rill when $H < 0.5$ m, while Castillo and Gomez (2016) when depths (H) < 0.30 m. The Gully erosion has the following definitions: Gobin et al. (1999) when depth (H) ranges from $0.5 \leq H \leq 5$ m, while Castillo and Gomez (2016) when depths (H) > 0.30 m.

The difference between a gully and a ravine can be established by depth (H) or size. For this case, the information on gully erosion is described below to be compared with following paragraph about ravine.

Dagar (2018), citing Frevert et al. (1955), classified gully erosion based on their size into small gullies ($H < 1$ m and $Ad < 2$ ha), medium gullies ($1 \leq H \leq 5$ m and $2 \leq Ad \leq 20$ ha) and large gullies ($H > 5$ m and $Ad > 20$ ha).

On the other hand, Dagar (2018) citing Tejwani et al. (1975) mentions that in India ravines are classified based on Bed width (L), Depth (H) and Side slope (D) into Small ravine: L >18 m; H < 3 m; D (%) - variable; Medium ravine: L >18 m; H = 3-9 m; D (%) = 8-15 (uniform); Narrow ravine: L = variable; H > 9 m; D (%) - vertical (mostly steep).

Table 1. Summary of the forms of erosion proposed by some authors (Zachar, 1982; Valentin & Rajot, 2018; Adhikary, 2020).

	Designation of Forms / Stages of Soil Erosion by water					
	Rainfall	**Surface runoff**				**Subsurface runoff**
		no channel	channel			
Autores	stage 1	stage 2	stage 3**	stage 4**	stage 5	single-stage
Hurni (1975); El-Swaify et al. (1982); Brady (1984); Foth (1990); Goudie (2004); Morgan (2005); Flanagan (2006); Valentin & Rajot (2018); FAO (2019)	splash erosion	sheet / interrill	rill	gully	-	piping erosion
Zachar (1982)	sheet erosion		gully erosion	multi-form erosion	rock erosion	tunnel erosion
Guerra (1997); Bastos (2004); Vieira (2019)	-	sheet / interrill	rill	ravine	gully	piping erosion
Gobin et al. (1999); Telkar et al. (2015); Saroha & Ambedkar (2017); Dagar (2018); (Bhat et al., 2019)	splash erosion	sheet / interrill	rill	gully	ravine	-
Balasubramanian (2017); Adhikary (2020); Adnan et al (2021)	splash erosion	sheet / interrill	rill	gully	stream bank	pipe erosion

**These two forms of soil erosion (rill and gully) can result from subsurface erosion after the collapse of the pipe's erosion cover (Valentin et al., 2005).

While, Gobin et al. (1999) defined ravine erosion when the depth (H) > 5 m.

4 CONCLUSIONS

The review confirms that the soil analysed is very prone to erosion phenomena, as previous studies have shown. It also confirms the controversies in the literature regarding the designations and sequences of soil erosion forms.

There are cases of similar terms having different meanings and different sequences (for example, a ravine in the fourth and a ravine in the fifth stage). With regard to the depths of the forms, we found different values for the same erosion form. All this makes it difficult to understand the subject and communicate with people working in the sector, so we suggest a more significant effort is needed to standardise the criteria for classifying soil erosion forms.

ACKNOWLEDGEMENTS

Thank you to the Portuguese Foundation for Science and Technology (FCT) for funding the SFRH/BD/151471/2021 PhD scholarship.

REFERENCES

Adhikary, R. (2020). Causes and Effect of Soil Erosion and its Preventive Measures. *Advanced Agriculture*, *August*. https://doi.org/10.30954/ndp-advagr.2020.19

Adnan, S., Aldefae, A. H., & Humaish, W. H. (2021). Soil erosion and the influenced factors: A review article. *IOP Conference Series: Materials Science and Engineering*, *1058*(1), 12. https://doi.org/10.1088/1757-899x/1058/1/012041.

Balasubramanian, A. (2017). Soil Erosion- Causes and Effects. In *Research Gate* (Issue February). https://doi.org/10.13140/RG.2.2.26247.39841

Bastos, C. A. B. (2004). *Estudo Geotécnico Sobre a Erodibilidade de Solos Residuais Não Saturados*. Universidade Federal do Rio Grande do Sul.

Bennet, H. H.. (1939). *Soil Conservation*. McGraw Hill Book Co, New York.

Bhat, S. A., Dar, M. U. D., & Meena, R. S. (2019). Soil Erosion and Management Strategies. *Research Gate*, *October*, 1–41. https://doi.org/10.1007/978-981-13-8832-3.

Brady, N. C. (1984). *The Nature and Properties of Soils* (Macmillan Publishing Company & Collier Macmillan Publishers (eds.); Ninth). Cornell University and United States Agency for International Development.

Castillo, C., & Gómez, J. A. (2016). A century of gully erosion research: Urgency, complexity and study approaches. *Earth-Science Reviews*, *160*, 300–319. https://doi.org/10.1016/j.earscirev.2016.07.009.

Dagar, J. C. (2018). Ravines: Formation, extent, classification, evolution and measures of prevention and

control. In S. N. S. P. Ltd. (Ed.), *Ravine Lands: Greening for Livelihood and Environmental Security* (pp. 19–67). Springer Nature Singapore Pte Ltd. 2018. https://doi.org/10.1007/978-981-10-8043-2_2.

El-Swaify, S. A., Dangler, E. W., & Armstrong, C. L. (1982). *Soil Erosion by Water in the Tropics* (Issue December, pp. 1–184). University of Hawaii.

Ellison, W. D. (1947). *Soil erosion studies. Soil detachment hazard by raindrop splash. Agric. Eng. 28:197-201.* (Vol. 2).

FAO. (2019). Soil erosion: the greatest challenge to sustainable soil management. In FAO (Ed.), *FAO Soil Bulletin* (pp. 1–104). FAO. https://creativecommons.org/ licenses/by-nc-sa/3.0/igo/legalcode/legalcode

Ferreira, H. N., & Silva, L. J. (1957). O Muceque como Fundação de Edificios e Base de Pavimentos. In *Jornada de Estradas* (p. 24). Laboratório de Engenharia da D.S.O.P. e T. de Angola.

Flanagan, D. C. (2006). Erosion. In *Soil Science* (Rattan Lal, pp. 523–526). United States Department of Agriculture-Agricultural Research Service (USDA-ARS), West Lafayette, Indiana, U.S.A.

Foth, H. D. (1990). *Fundamentals of Soil Science: Vol. New* (J. & S. Wiley (ed.); 8th ed.). John Wiley & Sons.

Frevert, R., Schwab, G., Edminister, T., & Barnes, K. (1955). *Soil and water conservation engineering*. Wiley, New York.

Gobin, A. M., Campling, P., Deckers, J. A., Poesen, J., & Feyen, J. (1999). Soil erosion assessment at the Udi-Nsukka Cuesta (southeastern Nigeria). *Land Degradation and Development*, *10*(2), 141–160. https://doi.org/10.1002/(SICI)1099-145X(199903/04)10:2<141::AID-LDR325>3.0.CO;2-N.

Goudie, A. S. (2004). *Encyclopedia of Geomorphology* (A. S. Goudie (ed.)). Routledge Taylor & Francis Group.

Guerra, A. J. T. (1997). Ravinas: processo de formação e desenvolvimento. *Anuário Do Instituto de Geociências*, *20*(1945), 9–26. https://doi.org/10.11137/1997_0_9-26

Hurni, H. (1975). *Forms in theSimen*. 93–100.

Lal, R. (2006). *Encyclopedia of Soil Science* (R. Lal (ed.); Second Edi, pp. 1–1941). Taylor & Francis.

Meireles, J. M. F. (1967). Erosão de Taludes de Estradas. *Jornadas Luso-Brasileiras de Engenharia Civil, 2. Anais...Rio de Janeiro/RJ - São Paulo/SP*, 204–211.

Morgan, R. P. C. (2005). Soil Erosion & conservation. In B. S. Ltd (Ed.), *National Soil Resources Institute - Cranfield University* (Third Edit). Blackwell Publishing company.

Nascimento, U. (1952). *Estudo da Regularização e Protecção das Barrocas de Luanda* (No. 30; pp. 1–39). Laboratório Nacional de Engenharia Civil (LNEC), Lisboa.

Novais-Ferreira, H., & Silva, C. A. F. (1961). Soil Failure in the Luanda Region. Geotechnique Study of these Soils. *Proc. 5th Int. Conf. Soil Mech. Found. Eng. Paris*.

Renard, K. G., Foster, G. R., Weesies, G. A., Mccool, D. K., & Yoder, D. C. (1997). *Predicting Soil Erosion by Water: A Guide to Conservation Planing with the Revised Universal Soil Loss Equation (RUSLE)*. U.S. Dept. of Agriculture, Agricultural Research Service.

Saroha, J., & Ambedkar, B. R. (2017). Soil Erosion: Causes, Extent and Management in India. *International Journal of Creative Research Thoughts*, *5*(4), 1321–1330. www.ijcrt.org.

Silva, J. A. H. da. (1965). *Contributo para o Conhecimento das Areias Vermelhas da Região de Luanda "Muceque": Estudo da Fracção Argilosa* (Memória nº127-Boletim Nº 12; p. 8). Serviços de Geologia e Minas de Luanda. https://doi.org/C.D.U. 549.9:553.623 (673.2).

Silva, J. A. H. da. (1970). *Nota sobre as Características Geológico-Geotécnicos dos Terrenos do Muceque Lixeira, Bungo e Boavista* (p. 20). Laboratório de Engenharia de Angola - LEA. https://doi.org/Nº 11.797.

Silva, J. A. H., & Teixeira, J. A. P. G. (1973). *Carta Geotécnica da Região de Luanda - 1ª Aproximação* (Publicação Nº 183; p. 11). Laboratório de Engenharia de Angola - LEA. https://doi.org/550.8:526.8(673).

Tejwani, K. G., Gupta, S. K., & Mathur, H. N. (1975). Classification, control and reclamation of ravine lands. Soil and Water Conservation Research (1956–1971). *Indian Council of Agricultural Research Publication, New Delhi*, 254–310.

Telkar, S. G., Solanki Singh, P. S., Dey, J. K., & Kant, K. (2015). Soil Erosion : Types and Their Mechanism. *International Journal of Economic Plants*, *2*(4), 178–180.

Valentin, C., Poesen, J., & Li, Y. (2005). Gully erosion: Impacts, factors and control. *Catena*, *63*(2–3), 132–153. https://doi.org/10.1016/j.catena.2005.06.001.

Valentin, C., & Rajot, J. L. (2018). Erosion and principles of soil conservation. *Soils as a Key Component of the Critical Zone 5: Degradation and Rehabilitation*, *5*, 39–82. https://doi.org/10.1002/9781119438298.ch3.

Vieira, L. H., Rodriguez, T. T., & Barra, M. F. W. (2019). Erodibilidade de Solos Residuais de Feição Erosiva e Mecanismo de Propagação. *Brazilian Journal of Development*, *5*(12), 30585–30599. https://doi.org/10.34117/bjdv5n12-175.

Zachar, D. (1982). *Soil Erosion* (10th ed., p. 548). Elsevier Scientific Publishing company.

Zhang, K., Li, S., Peng, W., & Yu, B. (2004). Erodibility of agricultural soils on the Loess Plateau of China. *Soil and Tillage Research*, *76*(2), 157–165. https://doi.org/10.1016/j.still.2003.09.007.

Proceedings of the XVIII ECSMGE 2024
GEOTECHNICAL ENGINEERING CHALLENGES
TO MEET CURRENT AND EMERGING NEEDS OF SOCIETY
© 2024 the Authors
ISBN 978-1-032-54816-6
DOI 10.1201/9781003431749-180
Open Access: www.taylorfrancis.com, CC BY-NC-ND 4.0 license

ECSMGE 24
XVIII EUROPEAN CONFERENCE ON SOIL MECHANICS AND GEOTECHNICAL ENGINEERING

Reliability analysis of a Po River embankment affected by underseepage

Analyse de fiabilité d'une digue du Fleuve Pô affectée par sous-infiltration

I. Bertolini, M. Marchi*, L. Tonni, G. Gottardi
DICAM Department, University of Bologna, Italy

**michela.marchi@unibo.it*

ABSTRACT: Backward erosion piping (BEP) is an internal erosion process that may develop as a consequence of seepage processes through the aquifers underneath river embankment structures. This phenomenon can be identified in the field by observing the formation of sand boils on the ground surface at or near the embankment toe. Along the Po River, more than 130 sections are affected by periodical sand boils, especially located in its middle-lower stretch. The paper presents the results of reliability analyses referred to BEP phenomena in a riverbank section located in Mazzorno Sinistro, in the province of Rovigo (Italy), whose stability has been threatened by periodical reactivations of this phenomenon. Fragility curves, describing the probability of BEP initiation with hydrometric level, are elaborated based on a two-dimensional model of the groundwater flow through the river section and on the application of the First-Order-Second-Moment (FOSM) method, assuming the main parameters as probabilistic variables. The soil profile and the probability distribution of the geotechnical parameters were obtained from the interpretation of several recent in situ and laboratory tests. Model results are compared to those obtained by applying the USACE theory and to the evidence of past reactivations.

RÉSUMÉ: Les canalisations d'érosion vers l'arrière (BEP) sont un processus d'érosion interne qui peut se développer à la suite de processus d'infiltration dans les aquifères situés sous les structures de digues fluviales. Ce phénomène peut être identifié sur le terrain en observant la formation de bouillons de sable à la surface du sol près du pied de la digue. Le long du Pô, plus de 130 sections sont affectées par des ébullitions de sable périodiques, en particulier dans sa partie moyenne-inférieure. L'article présente les résultats d'analyses de fiabilité relatives au phénomène BEP dans une section riveraine située à Mazzorno Sinistro, dans la province de Rovigo (Italie), dont la stabilité a été menacée par les réactivations périodiques de ce phénomène. Les courbes de fragilité, décrivant la probabilité d'initiation du BEP avec le niveau hydrométrique, sont elaborées sur la base d'un modèle bidimensionnel de l'écoulement des eaux souterraines à travers la section de la rivière et de la méthode du premier ordre-second-moment (FOSM), en supposant les principaux paramètres comme variables probabilistes. Le profil du sol et la distribution de probabilité des paramètres géotechniques ont été obtenus à partir de l'interprétation de plusieurs récentes essais in situ et en laboratoire. Les résultats du modèle sont comparés à ceux obtenus en appliquant la théorie bien connue de l'USACE et aux preuves de réactivations passées.

Keywords: Backward erosion piping; river embankment; fragility curve; USACE method; probabilistic analysis.

1 INTRODUCTION

Backward erosion piping (BEP) is an internal erosion process that excavates pipes in sandy foundations beneath river embankments, typically during high-water events. Its initiation and progression require a peculiar soil stratigraphy: a sandy foundation (aquifer), in hydraulic communication with the river, confined above by a fine-grained layer (blanket), characterized by a lower hydraulic load. The differential water head between the blanket and the aquifer can result in the concentration of hydraulic gradients in pre-existing holes or local discontinuities in the top layer, where flow velocities and gradients may become higher enough to drag sand particles to the surface forming sand volcanoes around the exit hole (sand boils). The ongoing process produces a progression upstream of erosion channels that weaken the foundation, potentially leading to embankment failure or breach, particularly during prolonged high-water periods or repeated reactivations. The Po River (Italy) counts more than one hundred sand boils of remarkable size (Gottardi et al., 2015). This generates the need to develop reliable strategies to quantify the potential risks for these critical structures connected to BEP. The analyses presented in this paper have been developed on a Po River embankment section located in Mazzorno Sinistro (RO), affected by three historic sand boils (Bertolini, 2024). The current study focuses on the most active one, located landside, within a ditch (Figure 1).

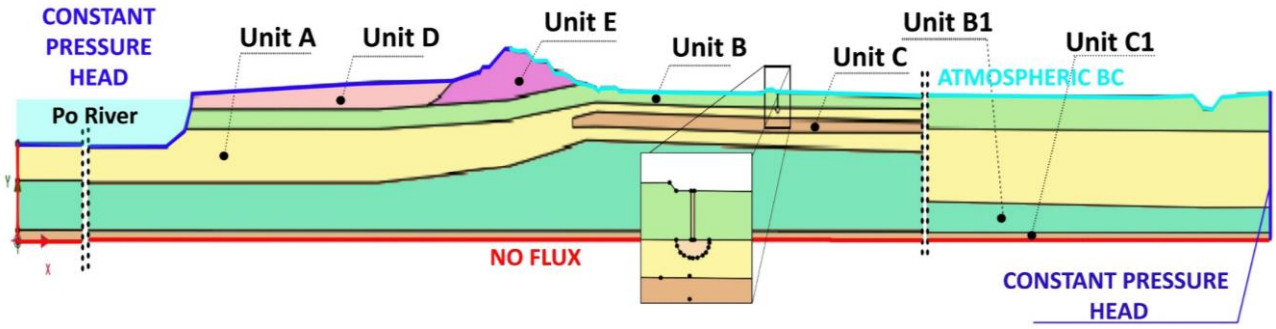

Figure 2. Soil stratigraphy of the investigated river section as adopted in the numerical modelling. The vertical dimension is magnified by double to ease its reading.

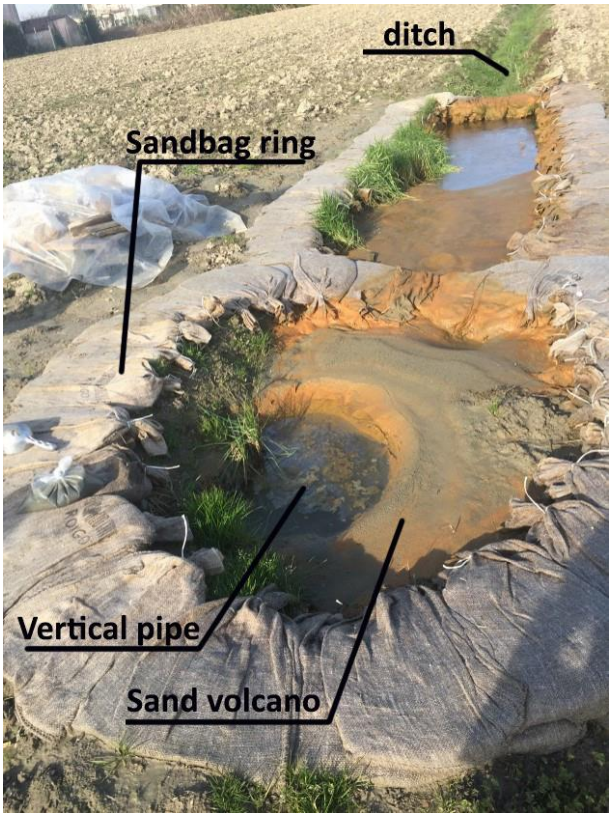

Figure 1. Photo of the sand boil reactivated in Mazzorno Sinistro in November 2019. The sandbag ring was positioned as an emergency measure to stop the progression of the erosion.

Fragility curves were calculated to assess the likelihood of BEP initiation, considering the probability distribution of the hydraulic soil properties obtained by laboratory and in-situ tests and multiple possible exit-hole configurations, and correlating it with river water levels. This involved employing two different strategies: the numerical results of a 2D finite element model simulating seepage beneath the river embankment and the analytical results obtained by applying the well-established Blanket Theory (USACE, 2000). The results of both strategies have been elaborated using a probabilistic approach, applying the First-Order-Second-Moment (FOSM) method (USACE, 1999).

2 THE 2D NUMERICAL MODEL

A 2D finite element (FE) model has been developed to simulate the saturated groundwater flow beneath the examined embankment section. Its primary objective was to compute the distribution of pore water pressure in proximity and within the exit hole of the historic sand boil, correlating it with incremental variations in river water head (H). The soil stratigraphy adopted in the model was deduced from in situ tests while the external profile of the section is from a topographic survey (Figure 2). The soil units involved in the process are the aquifer (unit A) and the overlying blanket (unit B). A peculiarity of the investigated site is the presence of an interbedded cohesive layer (named unit C) within unit A, which greatly reduces the thickness of the filtration section (from 9.4m to 6.9m) around the exit hole. The spatial domain, 36m x 1556m (length x height), has been discretized in 22524 triangular elements and 183541 nodes, with an average element size of 1.9m, refined up to 2cm in the proximity of the sand boil pipe and of the model boundaries subjected to imposed pressure heads.

The boundary conditions (BC) applied to the model are summarized in Figure 2. A no-flux boundary is applied to the base of the model since located within a low permeable clayey layer (Unit C1) not affected by the BEP phenomenon. The left-side of the model corresponding to the centerline of the river, for symmetry reason is associated to a no flux condition. On the berm and the riverside slope, it is imposed a Dirichelet condition in the form of a series of constant prescribed pressure heads simulating hydrometric levels of the river. In particular, the hydraulic loads are imposed to this boundary in 15 steady-state increments. To compare the 2D model's results with USACE ones, the loads have been referred to the landward phreatic level. Thus, hydraulic loads (H) equal to 0m and 8.85m correspond to the level of the phreatic water table and the crest, respectively. The landward water table in proximity of the sand boil is located ~0.65m below ground level, as revealed by the installed piezometric monitoring system. The

boundary conditions applied to the right side of the model are meant to reflect the groundwater condition of far-field which have been set as a series of constant hydraulic heads according to field monitoring data provided by a piezometer installed in unit A, 1123m distance from the embankment toe, landside. Atmospheric boundary conditions are applied to the outer slope and the landside field.

The described 2D numerical model has been adopted to generate fragility curves. Six random variables have been adopted to this scope: the permeability coefficients of units A, B and C (k_A, k_B, k_C), the diameter of the vertical exit hole (d_{exit}), the diameter of the hemisphere located at the base of the pipe and simulating the soil volume eroded by previous reactivations (d_{sphere}) and the permeability coefficient of both the exit hole and of the hemisphere (k_{exit}). Table 1 reports the mean value and the standard deviation of these random variables. CPT tests have been used to estimate the distribution of the hydraulic conductivities, which turned out to be well interpolated by a Gaussian distribution. A previous calibration of the 2D model over past sand boil reactivations suggested an optimal configuration of the existing exit pipe with a permeability coefficient equal to double the one of Unit A (k_A), then it varies in the range [k_A; 3 x k_A]. The average diameter of the exit hole is assumed equal to 0.2m, in accordance with field evidences (Marchi et al., 2021; Garcia Martinez et al., 2020a; 2020b) observed in another river embankment section located along the Po River (Bertolini et al., 2022a; 2022b). A value of 0.1m is assumed as the diameter of first activation and thus as lower boundary for the variation range of this random variable. As a result, the gaussian variation interval explored in the probability analysis results within the limits: average value +/- the standard deviation, that is [0.1;0.3]. Since the hemisphere is a stratagem of modelling whose geometry is not directly measurable but function of the erosive process occurred in the past reactivations, a diameter range of attempt between 0m and 4m has been adopted. The assessment of reactivation of the sand boil was carried out by comparing the critical hydraulic gradient of Terzaghi's (1960) formulation (i_{crit} ~0.969) with the average gradient within the vertical pipe, deduced from the numerical model. In particular, the average hydraulic gradient (i_{avg}) is estimated as the ratio between the pressure head loss between the top and bottom of the pipe and the length of the pipe itself (~2.68m in the selected location) while the critical hydraulic gradient of reactivation (~0.969) is defined as the gradient causing sand particles flotation within the open vertical pipe which occurs when the drag forces on the particles equal their submerged weight. A critical hydraulic gradient of first activation (~0.87) required to cause heaving of the landside top stratum prior to the piping have been also adopted.

A series of 13 simulations were conducted, which have been used to generate the fragility curves shown in Figure 3.

Table 1. Mean values of input parameters for the 2D numerical model of piping reactivation. In square brackets the SD.

Probabilistic variables	
Mean values [SD]	
k_A=3.19E-05 m/s [3.66E-07]	d_{pipe}=0.2m[0.1]
k_B=4.69E-09 m/s [3.21E-09]	d_{sphere}=2m [2]
k_C=7.86E-10 m/s [8.11E-10]	
k_{exit}=6.38E-05 m/s [3.19E-05]	

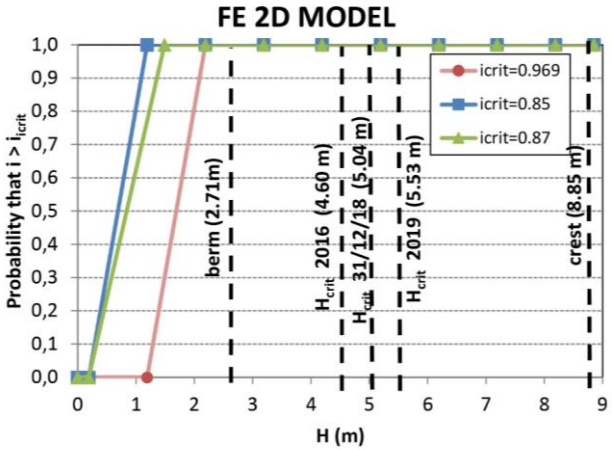

Figure 3. Cumulative probability of BEP initiation elaborated adopting the FE 2D numerical model.

A probability of 1 (i.e., certain BEP occurrence) is registered for hydraulic loads greater than 2m. It is also interesting to notice that an increase of 1m (from ~1m to ~2m) in the hydraulic load turns a likelihood of occurrence from 0 to 100%. The most significant random variables (for H=8.85m) are the permeability of the exit pipe (~55%) and the pipe diameter (~42%), while the remaining have low or null significance. In 2018, a reactivation of the sand boil was registered for a minimum hydraulic load of 5.04m. Another two reactivations of the same sand boil occurred a few years earlier, but the exact day of the BEP trigger and the (minimum) critical operating hydraulic load at the time are unknown. The peaks of these high-water events, under which surely the sand boil was active, were registered for hydraulic loads equal to 4.60m and 5.53m in the 2016 and 2019 events, respectively. The cumulative probability curve of BEP initiation forecasts correctly the three past activations but overestimates the minimum critical hydraulic load

being equal to H=2.5m the flood peak registered in May 2023 (25/5/23) which did not induce sand boil reactivation.

3 THE USACE APPROACH

The Blanket Theory was introduced within the technical manual USACE (1956) and is also described in the 2000 edition (USACE, 2000). The solution for semi-pervious top stratum of uniform thickness that extends infinitely landward of the levee, sketched in Figure 4 (case 7a of the methodology), was adopted for this study.

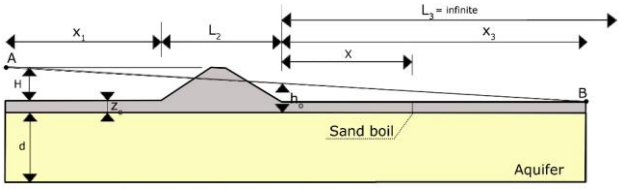

Figure 4. Scheme 7a of a section affected by BEP phenomenon characterized by a semi-pervious top stratum of uniform thickness riverside and landside (modified from USACE, 2000).

Table 2. Mean values of input parameters for the probabilistic safety assessment of the investigated section using USACE approach. In square brackets the standard deviation.

USACE APPROACH	
Deterministic variables	**Probabilistic variables**
x_1= 131.8 m	d= 6.13 m [2.47]
L_2= 66.4 m	z_b= 2.68 m [0.06]
L_3= infinite	k_A/k_B = 6818 [78]
x= 96.2 m	

The safety factor against (first) boiling or heaving computed according to the USACE approach is defined as the ratio of the exit gradient (i_{exit}) at the sand boil location to the critical gradient (i_{crit}). The exit gradient is a function of several variables, including the thickness of the aquifer and the blanket ("d" and "z_b," respectively), the ratio of permeability between the aquifer and the top stratum (k_A/k_C), the embankment base length (L_2), and the residual water pressure head at the embankment toe (h_o). Table 2 reports the "exact" values of the deterministic variables and the probabilistic distributions (in terms of mean value and standard deviation) of the stochastic variables assumed for the analysis. Among the latter, the thickness ranges of variation for the aquifer (d) and the blanket (z_b) have been retrieved from CPT test data. In particular, the range of variation of "d" is obtained from the interpretation of all the CPT tests performed in the section, while z_b from a selected number of tests performed in proximity of the sand boil, in order to be more representative of the blanket condition at the outflow point. Moreover, the depth of the ditch (~0.45m) in which the sand boil occurred has been subtracted from the estimated z_b value, to have an exit hole configuration more representative of site conditions and similar to the one adopted in the 2D FE model. Starting from the presumed expected values and standard deviation of the random variables, the moments of the performance functions were derived using Taylor's series method (specifically, the first-order second-moment - FOSM). The obtained fragility curves are presented in Figure 5.

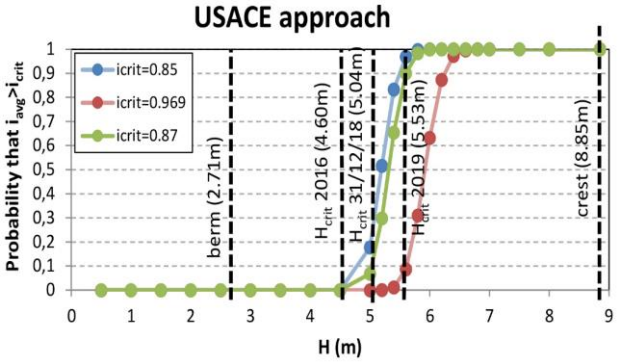

Figure 5. Cumulative probability of BEP initiation as deduced from the Blanket Theory.

The cumulative probability of BEP initiation remains null up to hydraulic loads of 4.5m and 5.5m, obtained for critical hydraulic gradients of 0.85/0.87 and 0.969, respectively. What emerges clearly is that for critical (first activation) gradients of 0.85 and 0.87, two of the three reactivations (i.e., 2016 and 2018) are not caught properly by the USACE approach, which underestimates the minimum critical hydraulic load causing sand boil activation. Similarly, the adoption of a critical (reactivation) gradient of 0.969 does not correctly predict all the three reactivations. Regarding this last observation, note that the analytical equations at the base of the Blanket Theory to estimate the seepage flow and the substratum pressure underneath the section are relative to an embankment configuration prior the possible formation of a landside open exit being these analyses usually performed in a design phase. It is also relevant to observe that the USACE solution is particularly sensitive to the thickness of the aquifer and of the blanket, with percentage of total variance equal to ~76% and ~24%, respectively (for H=8.85m).

4 CONCLUSIONS

The study describes the results of an analytical approach (Blanket Theory) and of a numerical FE

analysis, which can be adopted to predict the probability of BEP initiation in a river embankment along the Po River, prone to periodic sand boil reactivations during high-water events.

The soil profile, as well as the physical, mechanical and hydraulic properties of the site, have been deduced from field investigations and laboratory tests. The outcomes of the two different strategies were represented as fragility curves, denoting the probability of BEP initiation with increasing hydraulic loads. Results have been discussed considering observed reactivation in several real high-water events. The Blanket Theory tends to underestimate the probability of BEP reactivation. On the contrary, the FE analysis slightly overestimates the observed behaviour. Although these analyses are not directly comparable to each other, their application to this well-documented section suggests that the FE model can produce better results. In the near future, possible new reactivations should provide additional piezometric data that would enable the improvement of the calibration of FEM parameters.

ACKNOWLEDGEMENTS

This study was carried out within the RETURN Extended Partnership and received funding from the EuropeanUnion Next-GenerationEU (National Recovery and Resilience Plan – NRRP, Mission 4, Component 2, Investment 1.3 – D.D. 1243 2/8/2022, PE0000005 - Spoke TS 2).

REFERENCES

Bertolini, I., Gottardi, G., Marchi, M. and Tonni, L. (2022a). Probability of reactivation of a sand boil near a river embankment of the Po River (Italy). Proceedings of the 8th International Symposium on Geotechnical Safety and Risk (ISGSR 2022) 14–16 December, Newcastle, Australia, pp. 835-840. ISBN: 978-981-18-5182-7.

Bertolini, I., Gottardi, G., Marchi, M., Tonni, L., Bassi, A. and Rosso, A. (2022b). Application of CPT to the evaluation of permeability in a Po river embankment prone to backward erosion piping. *Proc. 5th International Symposium on Cone Penetration Testing (CPT'22)*, G. Gottardi and L. Tonni (eds), CRC Press, The Netherlands, pp. 300-305. https://doi.org/10.1201/9781003308829.

Bertolini, I. (2024). Field data based numerical analysis of sand boil reactivation along river embankments. *Proceedings 28th European Young Geotechnical Engineers Conference, EYGEC 2024*, 25-29 June 2024.

García Martínez, M.F., Tonni, L., Marchi, M., Tozzi, S. and Gottardi, G. (2020a). A numerical tool for the prediction of sand boil reactivations near river embankments. *Journal of Geotechnical and Geoenvironmental Engineering*, 146 (12) 06020023.https://doi.org/10.1061/(ASCE)GT.1943-5606.0002380.

García Martínez, M.F., Gottardi, G., Marchi, M., Tonni, L. (2020b). On the Reactivation of Sand Boils Near the Po River Major Embankments. *Lecture Notes in Civil Engineering*, 40: 328- 337. https://doi.org/10.1007/978-3-030-21359-6_35.

Gottardi, G., Marchi, M., Tonni, L. (2015). Static stability of Po river banks on a wide area. *Geotechnical Engineering for Infrastructure and Development - Proceedings of the XVI European Conference on Soil Mechanics and Geotechnical Engineering*, ECSMGE 2015, 4, pp. 1675 – 1680.

Marchi, M., García Martínez, M.F., Gottardi, G. and Tonni, L. (2021). Field measurements on a large natural sand boil along the river Po (Italy). *Quarterly Journal of Engineering Geology and Hydrogeology*, 54(4). https://doi.org/10.1144/qjegh2020-097.

Terzaghi, K. (1960). *From theory to practice in soil mechanics*, Wiley, New York, pp. 114-118. https://doi.org/10.2136/sssaj1961.03615995002500010002x.

USACE (1956*). Investigation of Underseepage and its Control, Lower Mississippi River Levees*. Technical memorandum No. 3-424, Vol. 1, Waterways Experiment Station, Vicksburg, Mississippi.

USACE (1999). *Evaluating the reliability of existing levees*. ETL 1110-2-556, App. B, U.S. Army Core of Engineers, Washington, DC.

USACE (2000). *Design and Construction of Levees*. U.S. Army Corps of Eng., Manual No. 1110-2-1913, Washington DC.

Proceedings of the XVIII ECSMGE 2024
GEOTECHNICAL ENGINEERING CHALLENGES
TO MEET CURRENT AND EMERGING NEEDS OF SOCIETY
© 2024 the Authors
ISBN 978-1-032-54816-6
DOI 10.1201/9781003431749-181
Open Access: www.taylorfrancis.com, CC BY-NC-ND 4.0 license

ECSMGE 24
XVIII EUROPEAN CONFERENCE ON SOIL MECHANICS AND GEOTECHNICAL ENGINEERING

Concept for sustainable lab and in-situ research on earthquake induced geohazards

Concept de recherche durable en laboratoire et in situ sur les géorisques induits par les tremblements de terre

J. Bojadjieva*, V. Sheshov, K. Edip, T. Kitanovski, D. Ivanovski, I. Gjorgjeska, A. Bogdanovic

Ss. Cyril and Methodius University in Skopje, Institute of earthquake engineering and engineering seismology-IZIIS, Skopje, Macedonia

**jule@iziis.ukim.edu.mk*

ABSTRACT: Geohazards related to earthquakes, such as amplification effects, liquefaction, soil-structure interaction etc. are complex phenomena which need to be investigated with diverse set of approaches, both experimental and in-situ. In this paper two state of the art facilities for earthquake geotechnical research are presented, established in the Laboratory for soil dynamics and foundation engineering in IZIIS, Skopje, Macedonia. At first, in laboratory conditions, experimental setup consisted of original laminar container and detailed soil material characterization – Skopje sand is presented along with obtained results from series of element and shaking table tests. Second, an in situ geotechnical laboratory was established in urban part of Ohrid, N. Macedonia at the site of a nine-story building with two accelerometers installed on the building, 4 instruments installed at the foundation level as well as one surface and three downhole accelerometers 125 meters down the bedrock. With recent activities, real time recording, and health monitoring processes are enabled at the location. The large set of in-situ investigation, characterization of the geotechnical profile and enabled real–time earthquake recordings are valid data for detailed studies of amplification of site effects, liquefaction and SSI at the site. In the paper overall comments on obtained results from both facilities is obtained, with aspects for future application, correlation, and obstacles. Both resources, experimental and in-situ represent a well-proven example of a facility for continuous and sustainable research in earthquake geotechnical engineering.

RÉSUMÉ: Les géorisques liés aux tremblements de terre, tels que les effets d'amplification, la liquéfaction, l'interaction sol-structure, etc. sont des phénomènes complexes qui doivent être étudiés à l'aide de diverses approches, à la fois expérimentales et in situ. Dans cet article, deux installations de pointe pour la recherche géotechnique sismique sont présentées, établies dans le Laboratoire de dynamique des sols et d'ingénierie des fondations à IZIIS, Skopje, Macédoine. Au début, dans des conditions de laboratoire, le dispositif expérimental consistait en un conteneur laminaire d'origine et une caractérisation détaillée des matériaux du sol – le sable de Skopje est présenté ainsi que les résultats obtenus à partir d'une série de tests d'éléments et de tables vibrantes. Deuxièmement, un laboratoire géotechnique in situ a été créé dans la partie urbaine d'Ohrid, en Macédoine du Nord, sur le site d'un bâtiment de neuf étages avec deux accéléromètres installés sur le bâtiment, 4 instruments installés au niveau des fondations ainsi qu'un en surface et trois en fond de trou. Accéléromètres à 125 mètres sous le substrat rocheux. Avec les activités récentes, les processus d'enregistrement en temps réel et de surveillance de la santé sont activés sur place. Le vaste ensemble d'investigations in situ, de caractérisation du profil géotechnique et d'enregistrements sismiques en temps réel permis sont des données valables pour des études détaillées de l'amplification des effets de site, de la liquéfaction et des SSI sur le site. Dans le document, des commentaires globaux sur les résultats obtenus dans les deux installations sont obtenus, avec des aspects d'application future, de corrélation et d'obstacles. Les deux ressources, expérimentales et in situ, représentent un exemple éprouvé d'installation de recherche continue et durable en ingénierie géotechnique sismique.

Keywords: Skopje sand, laminar container, in-situ lab, geotechnical monitoring.

1 INTRODUCTION

Earthquakes, a significant natural hazard, affects built and human environment in seismic-prone regions globally, leading to social and economic losses. Recent notable earthquakes worldwide, including the most recent series in Turkey in 2023, highlight that geotechnical hazards play a substantial role in causing damages and economic losses. Instances of geohazards have been documented after earthquakes in Southern Europe, such as the 1979 event in Montenegro, the Emilia earthquake sequence in Italy in 2012, the Kraljevo earthquake in Serbia in 2013, the Durres

earthquake in Albania and the most recent Petrinje Earthquake in Croatia in 2020.

2 SUSTAINABLE LAB RESEARCH

2.1 Justification

While there were no well documented cases of liquefaction during the 1963 Skopje earthquake with a magnitude of 6.1, significant structural damage was attributed to pronounced site amplification effects in the Vardar valley.

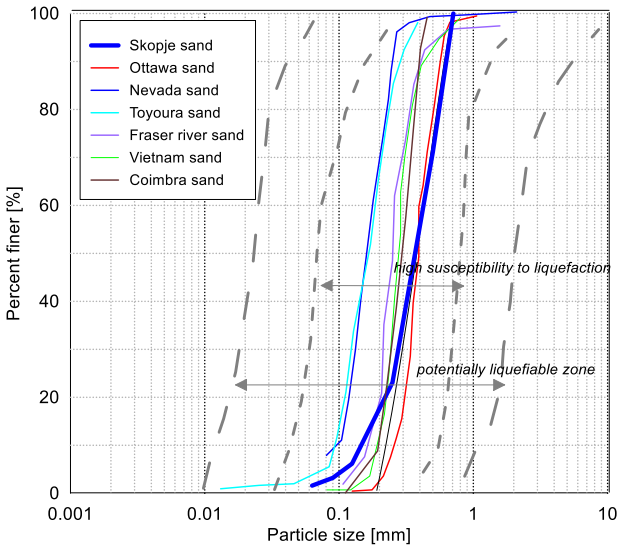

Figure 1. Grain size distribution compared with other sands from the literature (Bojadjieva et al., 2015).

Given the absence of seismic geotechnical codes in the region at that time, the lack of a seismic monitoring network, and limited knowledge about the city's geotechnical properties, there is assumption that liquefaction might have occurred but went undocumented and unassessed due to the overwhelming structural damage and other post-earthquake disaster management activities. Recent incidents in the Balkan region have underscored the importance of re-evaluating and enhancing understanding of soil behavior under cyclic loading.

To address these requirements, comprehensive experimental investigation to examine the monotonic and cyclic behavior of Skopje sand, has been proposed starting from 2013 and still ongoing.

2.2 Material

The material used for sustainable research in the lab, denoted as Skopje Sand, is chosen for testing not only based on the assumption that it is likely associated with liquefaction and significant deformations during earthquakes but is also justified by its potential for sustained, long-term use in experimental laboratory research. This continuous usage maintains consistent characteristics and facilitates ongoing improvements in results (Bojadjieva et al., 2022).

The grain size distribution curve of the sand (ISO/TS 17892-4:2004) is depicted in Figure 1, alongside other standard sands used in literature for investigating liquefaction phenomena. It is evident that the Skopje sand aligns well with the boundaries specified by Terzaghi (1996) for sands highly susceptible to liquefaction. Detailed analysis indicates that the sand is predominantly composed of silica oxides, allowing it to be classified as a siliceous sand material or soil class SP based on the USCS soil classification.

2.3 Research objectives – current states

Table 1 summarizes the so far performed research on the testing material. Figure 2 represents typical cyclic test for D_r = 55%, CSR = 0.20.

Table 1. Comprehensive research program -Skopje sand

Type of study	Topic	Reference
Simple shear tests	Cyclic behaviour	Bojadjieva (2015)
Triaxial tests	Monotonic, cyclic behaviour	Bojadjieva et al. (2015)
Shaking table tests	Cyclic behaviour, Liquefaction	Bojadjieva et al. (2022)
Simple shear tests	Liquefaction	Kitanovski (2018)
Triaxial tests	Monotonic, cyclic with fly ash	Angelova (2023)
Comparison triaxial vs simple shear tests	Liquefaction	Bojadjieva et al, (2019)
Numerical simulation	Monotonic, cyclic with hypoplastic model	Bojadjieva et al., (2020)

The produced experimental data provide researchers and practicing engineers a baseline data set for validation of numerical simulations (such as previous study in Edip et al., 2018), focused on liquefaction phenomena as well as future-induced settlement of buildings and evaluation of effective mitigation strategies. Figure 2 presents selected results from cyclic test on Skopje sand Dr = 55%, CSR = 0.20. Skopje sand is representative for the alluvial deposits around the Vardar River and the performed investigations can be a good basis for further definition and raising awareness about the liquefaction hazard in N. Macedonia.

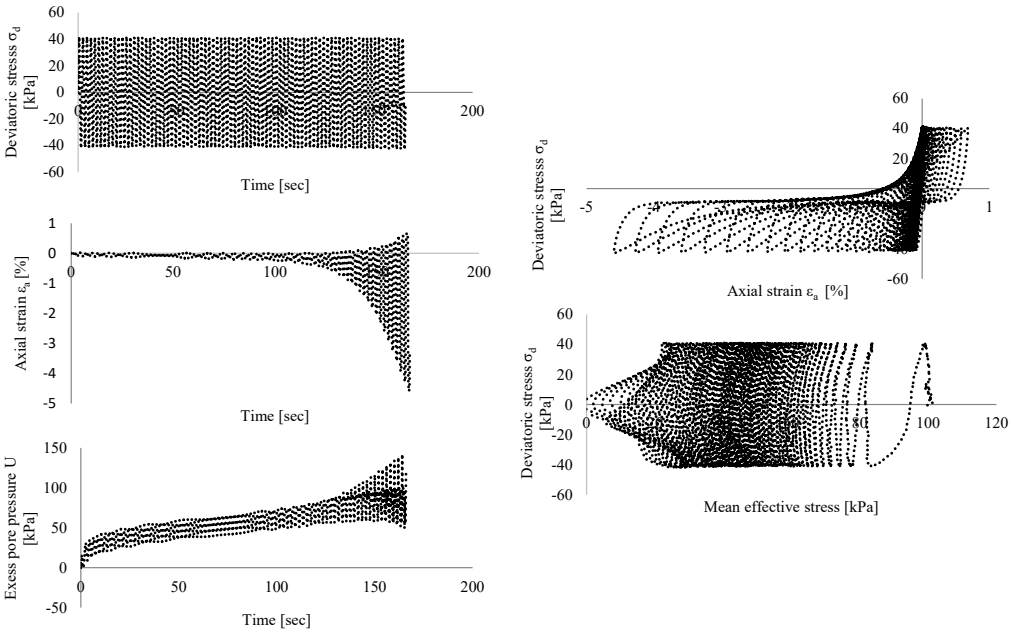

Figure 2. Results from cyclic test on Skopje sand for D_r = 55%, CSR = 0.20.

3 SUSTAINABLE IN-SITU RESEARCH

3.1 Ohrid 3d seismic network-Location Tower

Typically, monitoring is limited to either structures or testing sites, resulting in partial instrumentation either on the structures or in the soil.

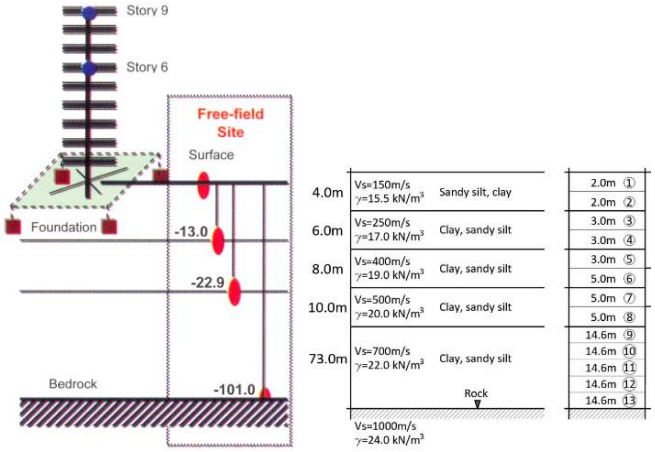

Figure 3. Instruments setup and soil model at the Location Tower.

The extent of damage to buildings, structures, and lifelines from earthquakes depends on the nature of the seismic energy and the characteristics of the soil and structures. To investigate the effects of local site conditions on strong ground motions and dynamic response of structural systems, a three-dimensional seismic network was established in the Ohrid Lake, N. Macedonia basin in the 1980s with support from the United States Geological Survey (USGS),(Petrovski et al., 1995). This array included three free field locations in the urban area of Ohrid, each with one surface and three downhole instruments, as well as a nine-story building site with instruments installed on the building and at the foundation level, and an outcropping rock site with one instrument. Since 2021, extensive efforts have been made to re-establish the network and provide continuous, real-time monitoring of the Location Tower (Bojadjieva et al., 2023), shown in Figure 3. Figure 4 represents recorded acceleration at bedrock and surface from the M. 4.8 earthquake - Kastoria, Greece, 24 km southeast of Korce, Albania, on 12 May 12:31 am (GMT +3).

Following the re-establishment, comprehensive research activities were conducted at the Location Tower, including geotechnical and geophysical in situ investigations using direct and indirect methods, direct simple shear and triaxial tests on soil specimens from various depths, and ambient vibration measurements of the structure.

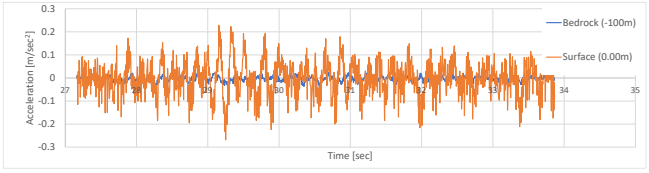

Figure 4. Recorded acceleration at bedrock (-101m and surface 0.0m).

The resulting dataset was used to achieve multiple research objectives, such as site response analysis, estimation of the small strain dynamic shear modulus G_{max} through comparison of different approaches, and analysis of soil-structure interaction validation with

records from the Location Tower, Figure 5. The Location is characterized with significant site effects as noted in Bojadjieva, 2019.

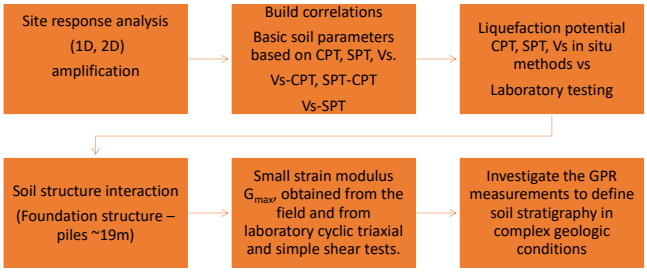

Figure 5. Concept of learning objectives at the in-situ laboratory.

4 FUTURE APPLICATIONS & CHALLENGES

The study on Skopje sand serves as a well-established source of laboratory-available sand, supporting ongoing research in earthquake geotechnical engineering. The achieved study reviewed in this paper is going towards significant contribution to the global database on the behavior of soil materials under cyclic conditions.

On othe other hand the Ohrid 3d seismic network, and particularly the Location Tower, with its unique instrumentation data, is important in-situ facility by providing high-quality earthquake records for both soil and structures in the urban area of the Balkan region. The revitalization of the network provides an opportunity to study the real-time interaction effects of earthquakes on structures and soil, thereby creating a solid foundation for enhancing earthquake resilience. Both presented concepts are sustainable and are expected to help towards reducing risk from earthquake induced geo-hazards.

ACKNOWLEDGEMENTS

The authors are grateful for the continuous support provided by the Institute of earthquake engineering and engineering seismology -IZIIS.

REFERENCES

Angelova, E., V. Angelov, V. Sheshov, J. Bojadjieva, K. Edip, T. Kitanovski, D. Ivanovski, and S. Dimitrijević. (2023). "Effects of fly ash on sand behaviour in monotonic triaxial tests." In *Smart Geotechnics for Smart Societies*, pp. 691-695. CRC Press, 2023. https://doi.org/10.1201/9781003299127

Bojadjieva, V. E. K., Sesov, J., & Edip, K. (2015). Experimental setup for sand liquefaction studies on shaking table. In *Proceeding of 6th international conference on earthquake geotechnical engineering (6ICEGE)*. https://www.issmge.org/news/proceedings-from-6th-international-conference-on-earthquake-geotechnical-christchurch-2015-available-in-open-access

Bojadjieva, Julijana, Vlatko Sheshov, Kemal Edip, and Toni Kitanovski. (2022). "Verification of a System for Sustainable Research on Earthquake-Induced Soil Liquefaction in 1-g Environments." Geosciences 12, no. 10 (2022): 363. https://doi.org/10.3390/geosciences12100363

Bojadjieva, J., V. Sheshov, K. Edip, T. Kitanovski, J. Chaneva, and D. Ivanovski. "Comparison of cyclic simple shear and triaxial tests on natural sand." (2019). Ecsmge, Reykjavík, Iceland. 10.32075/17ECSMGE-2019-0988

Bojadjieva, J., Sheshov, V., Edip, K., Chaneva, J., Kitanovski, T., & Ivanovski, D. (2019). GIS-based assessment of liquefaction potential for selected earthquake scenarios. In Earthquake Geotechnical Engineering for Protection and Development of Environment and Constructions (pp. 1453-1460). CRC Press. https://doi.org/10.1201/9780429031274

Bojadjieva, J., Bogdanovic, A. et al. (2023). 1 Seismic site investigation and structural amplification based on geotechnical and structural health monitoring. *Data-Centric Structural Health Monitoring: Mechanical, Aerospace and Complex Infrastructure Systems*. https://doi.org/10.1515/9783110791426

Edip, K., Sesov, V., Butenweg, C., & Bojadjieva, J. (2018). Development of coupled numerical model for simulation of multiphase soil. *Computers and Geotechnics*, *96*, 118-131. https://doi.org/10.1016/j.compgeo.2017.08.016

Kitanovski, Toni, Vlatko Sheshov, Julijana Bojadjieva, Kemal Edip, and Dejan Ivanovski (2023). "Effect of prior cyclic loading on triaxial monotonic experiments." 2nd Crocee, Zagreb, Croatia. https://crocee.grad.hr/event/2/attachments/197/300/2CroCEE%20Proceedings.pdf

Petrovski J. et al. (1995). Characteristics of Earthquake Ground Motions Obtained on the Ohrid Lake Three Dimensional Strong Motion Array in the R. N. Macedonia.10th ECEE, Duma (ed.) © 1995 Balkema, Rotterdam, ISBN 90 5410 528 3. https://www.tib.eu/en/search/id/BLCP:CN010534800/Characteristics-of-earthquake-ground-motions-obtained?cHash=b9fa72fb5b7f8d5765db57e693c7f0e4

Sesov V.(2003). Dynamic behavior of potentially nonstable layers and application of a model for decreasing the seismic risk of liquefaction occurrence. PhD Thesis. University Ss. Cyril and Methodius-Skopje, N. Macedonia.

Proceedings of the XVIII ECSMGE 2024
GEOTECHNICAL ENGINEERING CHALLENGES
TO MEET CURRENT AND EMERGING NEEDS OF SOCIETY
© 2024 the Authors
ISBN 978-1-032-54816-6
DOI 10.1201/9781003431749-182
Open Access: www.taylorfrancis.com, CC BY-NC-ND 4.0 license

ECSMGE 24
XVIII EUROPEAN CONFERENCE ON SOIL MECHANICS AND GEOTECHNICAL ENGINEERING

Seabed and sub-seabed boulders as an engineering hazard in the marine environment; a risk mitigation strategy for subsea cables

Les risques techniques liés aux blocs rocheux de surface et enfouis dans l'environnement marin; une stratégie d'atténuation des risques pour les câbles sous-marins

L.J. Burley, E. Tataki, H.M. Taylor*, V. Terente, N. Dyer
Cathie, Newcastle upon Tyne, UK

**Helen.Taylor@cathiegroup.com*

ABSTRACT: Every subsea cable development presents a unique set of conditions and constraints. The exact approach to seabed and sub-seabed boulder mitigation work is defined not only by the nature of the environment, but also the options open to the developer in terms of financial budgets and available construction timescales. Boulders represent a significant geohazard for trenching and installation operations of subsea cables. This paper proposes a comprehensive risk mitigation strategy for seabed and sub-seabed boulders in the marine environment. Once the magnitude of boulder risk is known through appropriate surveys and risk assessments, the following steps can be considered: avoidance, removal, reduction and/or relocation or remediation of residual risks. Working through these steps ensures a suitable mitigation strategy is followed, reducing the risk through adequate design, installation and remediation planning.

RÉSUMÉ: Chaque projet en mer présente un ensemble unique de conditions et de contraintes. L'approche exacte du travail d'atténuation des risques liés aux blocs rocheux pour tout type de développement est définie non seulement par la nature de l'environnement, mais aussi par les options ouvertes au développeur en termes de budgets financiers et de délais disponibles pour achever les travaux d'ingénierie. Les blocs rocheux présents sur le fond marin et enfouis représentent un risque géologique important pour les opérations de creusement de tranchées en mer et d'installation de câbles sous-marins. Cet article propose une stratégie globale d'atténuation des risques liés aux blocs rocheux de surface et souterrains dans l'environnement marin. Une fois l'ampleur de ces risques connue, grâce à des études et des évaluations appropriées, les options suivantes peuvent être envisagées: éviter, enlever, réduire et/ou déplacer ou remédier aux risques résiduels. Ces étapes permettent de définir une stratégie d'atténuation appropriée, grâce à une conception adéquate, au choix de l'installation adaptée et à la planification de la solution de mitigation.

Keywords: Boulder mitigation; mitigation strategy; surface boulders; sub-seabed boulders; subsea cables.

1 INTRODUCTION

Seabed and sub-seabed boulders pose a significant geohazard to a wide range of offshore wind activities, including trenching and installation of export and inter-array cables. In the marine environment, boulders are often found in areas previously influenced by glaciation, such as the North Sea, Baltic Sea, and East Coast of USA etc. The sediment formations containing boulders are often related to glacial features, such as moraines and outwash plains (Johnson et al., 1993). Glacial soils may consist of a mixture of sediments with a variety of degrees of sorting, including boulders (Clarke, 2018). These boulders can vary in shape and size, can be found at and/or below the seabed and can be isolated or in high density clusters (known as boulder fields). As per ISO 14688-1 (2017), boulders are defined as soil particles with diameter >0.20 m. However, for the purpose of this paper, and as it will be discussed in subsequent sections, mainly boulders with diameter >0.30 m are considered a risk to cable installation operations.

Where boulders are present, and as with any other hazard, the first step is identification and quantification of the risk across the site (Wetton et al., 2024). This information, together with knowledge on proposed operations and equipment limitations, will determine the impact, relative to size and density of boulders, and whether any mitigation is required.

If mitigation is required, measures such as, avoidance, removal/ relocation of boulders, reduction of the risk or/and remediation should be considered (Figure 1). Unanticipated requirements in overcoming boulder constraints may result in significant additional costs to developers and contractors, should the risk of boulders and a sufficient mitigation strategy not be identified from the early stages of the development.

The size and number of boulders, as well as whether they have been identified as isolated or in clusters, can significantly influence the methods used for mitigating the risk. Recommended best practises for subsea cables, such as the (DNV GL, 2021), highlight boulders as a geohazard that can affect cable routing, installation and protection, recommending the performance of boulder clearance campaigns, however, without presenting a recommended methodology to plan for remediation.

In this paper, the above-mentioned steps will be elaborated outlining a methodology for mitigating the risk of boulders to subsea cables.

It should be noted that a similar mitigation strategy can be suitable for boulder risk to offshore structure foundations, however this paper focuses only on subsea cables.



Figure 1. Boulder mitigation strategy.

2 MITIGATION STRATEGY

The selection of a suitable boulder mitigation strategy is governed by several factors which could include: boulder quantity, distribution, project location, commercial factors, project schedules, etc. Figure 1 outlines a proposed strategy method. Each step will be described in more detail in the subsequent sections.

2.1 Identify and quantify

The first step in the proposed mitigation strategy is to identify and quantify the boulders across the area of interest. This is achieved by planning a survey strategy ensuring the most suitable data is acquired by specifying appropriate survey techniques and correct resolutions (Carbon Trust, 2020). To ensure a suitable survey is being performed, the timing needs to be carefully considered. Prior to a survey, a cable corridor needs to have been defined with indicative cable burial and boulder clearance tools already in consideration (Wetton et al., 2024).

Once the data has been acquired, boulders are quantified by undertaking a 'boulder picking' exercise, an interpretive exercise where boulders are identified, located, and the dimensions measured to produce a boulder listing. This interpretive exercise should be tailored to a specific mitigation strategy it is targeting. For cable routing, a more efficient approach for quantifying the number of boulders, at an early stage, could be to focus on the areas posing the highest risk, e.g., large boulders >1.5 m and boulder fields. By only focusing on quantifying the critical areas, the picking exercise is less time demanding, and data could be available at an earlier stage without compromising understanding. At a later stage, data can be reinterpreted to a stricter specification, within a smaller study corridor once the preferred installation tool is selected. This approach could potentially save time and resource during the interpretation phase. As a development progresses the survey corridor may decrease from ~150 m to <20 m, rendering detailed interpretation outside of the reduced corridor obsolete.

Once the boulder listing is available, this can be used to estimate the likelihood of boulder encounter and impact of encountering areas with different boulder density (high to low), for each section of the proposed cable route.

2.2 Avoid

As with any hazard assessment, avoidance should be the first mitigation option, which in the case of subsea cables, is undertaken, where feasible, through route engineering (Figure 2). Route engineering is a process of designing the shortest and most practical cable route possible, whilst avoiding known physical risks. An outline of considerations is highlighted in (DNV GL, 2021).

Each identified risk is evaluated and assigned a design constraint. Constraints may be seen as "hard", must be avoided or as "soft", avoid if practical, as shown in Table 1.

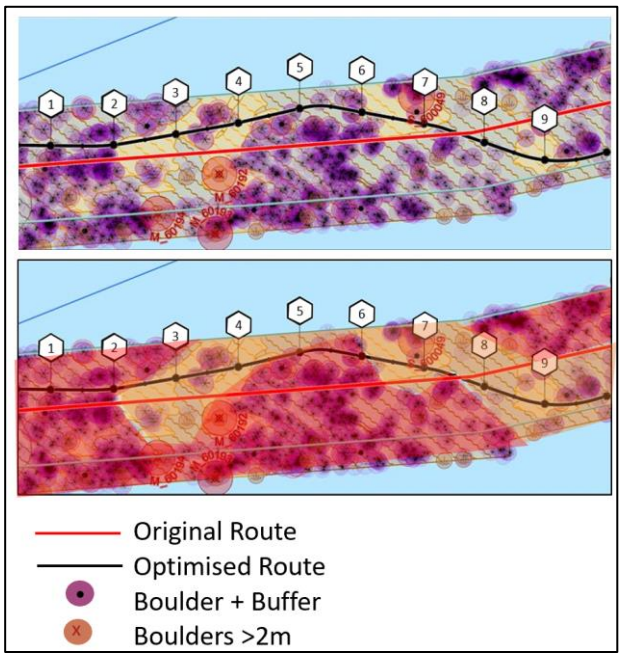

Figure 2. Route engineering example.

Table 1. Boulders as cable route constraints.

Individual Boulders Size (m)	Boulder Fields Density	Constraint Level	
< 0.5	Low		Low
0.5 - 1.5	Medium	Soft Constraint	Medium
1.5 - 2	High		Severe
> 2	-	Hard Constraint	

In most cases, it is impractical to avoid every boulder, especially where there is the presence of boulder fields, hence why boulder fields are not a hard constraint in Table 1. Together with boulders, there are other constraints to consider, which may take precedence over boulders, such as unexploded ordnance (UXO) and cable installation limitations (e.g. maximum bend radius and turning radius of tool). The aim of route engineering is to identify the most favourable route by avoiding any hard constraints and as many soft constraints as possible. Where soft constraints are intersected, the shortest route through, should be selected. Alongside reducing the risk of surface boulders, route engineering may assist with the mitigation of sub-seabed boulders. Where areas of concentrated sub-seabed boulders have been identified route engineering can also work to avoid these.

In practice, it is often the case, possibly due to limitations in identifying sub-seabed boulders, that only surface boulder information is available for a project. Actions can be taken, such as avoiding formations known to contain boulders, which can be identified through developing a geological Ground Model early in the project. Predicting or avoiding sub-seabed boulders may not always be possible and thus the risk remains as a residual risk within a project.

2.3 Remove/Relocate

Following route engineering and especially if there were areas of boulders where avoidance was not possible, a boulder clearance campaign may be required. Clearance campaigns mainly target surface boulders with mitigation methods including Boulder Grab (BG) and Clearance Plough (CP). For sub-seabed boulders, clearance is generally more challenging with tools such as pre-lay/pipeline ploughs existing in the industry. The following sections summarise some of the possible clearance methodologies.

2.3.1 Boulder Grab (BG)

BGs are used to remove and relocate boulders along a cable installation corridor. They resemble a mechanical claw and are typically fitted with thrusters, ultra-short baseline (USBL) and video feed to aid positioning over the boulder. The boulder is captured within the claws and relocated, to a pre-agreed location, off the main installation corridor.

BGs are suitable for areas with lower density of boulders or individual boulders rather than large boulders fields, due to time taken for vessel positioning and the operations undertaken to remove and relocate the boulder. Typically, the maximum boulder size a generic BG can relocate ranges from ~2 to 3 m. This will significantly depend on the percentage of the boulder that is buried, as a suction force can be created, increasing the working loads for the equipment.

Minimum survey requirements for this operation would include exact location and dimension of the boulder to be removed. An understanding of shallow geology of the soil matrix and boulder rock type would be beneficial.

Typical time duration for the relocation of one boulder, using this method, is 30-60 mins, depending on the relocation area and other seabed constraints. Note this does not include transiting times between individual boulders.

2.3.2 Clearance Plough (CP)

For sites with higher densities of boulders, a CP may be more suitable. CPs are towed along the seabed pushing/relocating surface, or near surface, boulders to either side, leaving a 'cleared' corridor of ~15 m width with a maximum penetration into the seabed of ~0.2 m (depending on soil type). CPs are generally limited to boulders up to ~1.5 – 2.0 m in size and therefore if larger boulders are present at the site, this method

would have to be used in conjunction with another, such as route engineering or a BG.

Minimum survey requirements for this operation would include location, including dimensions, of larger boulders (>1.5 m), location of boulder fields with density, high resolution bathymetric data and shallow geology information.

The operation speed of these ploughs is typically between 150-500 m/hr depending on the geotechnical conditions of the seabed and the density of boulders.

For boulder clearance within a Lease Area (i.e., for the inter-array cables), scheduling of the operations at the right development phase for the project should be considered. Preferably, seabed clearance operations should be carried out prior to installation. Should this operation be undertaken after the wind turbines generators (WTG) foundations have been installed, the vessel (and CP) would have to veer off a significant distance to avoid the structure and areas of seabed may be left uncleared which could later impact burial operations along the inter-array cable or require an alternative mitigation method.

2.3.3 Pre-Lay Plough (PLP)

PLP is a combined clearance and trenching plough, where the plough's share creates the "Y-shape" trench, with the mouldboards pushing the spoil away. PLPs are generally able to create a trench up to ~1.8 m deep, in a single pass. In certain conditions, the trenching capability may allow for mitigation of sub-seabed boulders, depending on the size and depth of the boulder. Advanced PLP systems also have the capabilities to include integrated backfill operations.

Similarly to the CP, the PLP requires the identification of boulders greater then ~1.5 – 2 m in diameter, as these will likely require a different mitigation measure. The scheduling should be considered, operations to be undertaken prior to construction of WTGs, as per the CP.

Similar survey requirements to the CP are required for a PLP, with the addition of more detailed understanding of the shallow geology to predict tow forces and speed. Available information on sub-surface boulders, i.e. density and expected dimensions, are also useful.

PLPs require much higher tow forces than CPs, especially in sandy soils, with some of the larger ploughs requiring up to 300 tonnes of towing force. This results in the need for more specialised vessels with higher bollard pull or the addition of tug vessels. These larger ploughs may also require an "A Frame" launch and recovery system with sufficient deck space for the large plough.

Due to the specialised nature of this tool, there is limited availability on the market and can often be in high demand, emphasising the need for early planning.

2.3.4 Summary of removal methodologies

When selecting the most suitable solution for boulder removal, boulder density and location of the boulders should be considered, and it is likely to significantly influence the decision. Figure 3 shows a schematic of how the number of boulders affects the clearance operations duration for a BG (green line) and CP (red line). As can be seen with ploughing, dependent on density, operation speed is relatively consistent. Although, there will likely be some variation depending on soil type. Whereas with the BG, clearance would be more effective in low density areas. Operation time would also be heavily dependent on the spacing of the boulders.

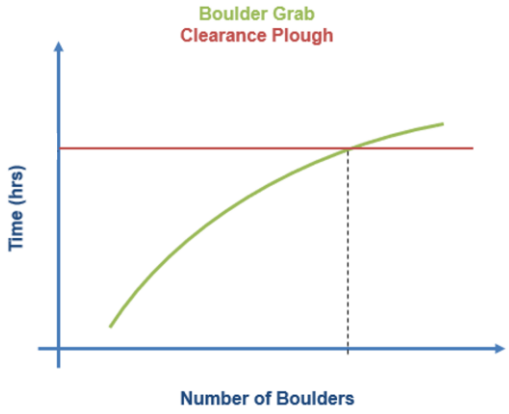

Figure 3. Effect of number of boulders to clearance operation timescales.

A brief suitability assessment for each of the methodologies is shown in Table 2. The table uses a traffic light ranking system for general suitability based on some of the main consideration factors; where green is high, orange is medium and red highlights low suitability for each solution. As can be seen, not one methodology is suitable for all factors. The final mitigation plan will likely include a combination of methodologies with the cable route zoned in accordance with the most suitable tool.

Table 2. Boulder clearance tools suitability assessment.

Consideration Factors	BG	CP	PLP
Time			
Cost			
Availability			
Sub-seabed boulder – clearance			
Efficiency – Higher density			
Efficiency – Lower Density			

2.4 Reduce

Detailed data on sub-seabed boulders are not always available. Consequently, even with the above mitigation measures of avoid and remove, the risk of sub-seabed boulders generally remains. The presence of sub-seabed boulders can result in reduced/no burial of a cable with contractors generally insisting on a *'Reasonable Endeavours'* clause within their contract.

Where sub-seabed boulders are expected, in order to reduce the risk, the selected cable installation tool should be considered based on the ground conditions and identified trenching risks (DNV GL, 2021). Some installation tools can be fitted with a structure, similar to a small scale 'clearance plough', to protect the installation tool from boulders.

Most installation contractors will highlight all boulders >0.3 m as potential risk to cable installation for all tools. However, some cable installation tools may be more suitable than others, e.g., a cable plough would likely be able to withstand larger boulders compared to other trenching tools. Table 3 below summarises the advantages and disadvantages, with regards to boulders, of the three most commonly used installation tools.

2.5 Remediate

Following the above mitigation steps, the risk to boulders should be considerably reduced. However, if boulders still pose a risk to a site and cannot be further mitigated against, additional costs should be factored into a project to allow for external protection for the cables if required. Areas with significant number of unmitigated boulders could lead to shallow/no burial of the cable leaving it exposed to external hazards such as fishing, shipping and on-bottom stability. Some remedial measures for protecting exposed/reduced burial areas of cable are listed below.

Rock fill protection: a rock berm could be specifically designed with sufficient height to cover and protect the cable. Rock berms are installed using specific vessels fitted with a fall pipe, used to place the rocks on the seabed over a cable.

Rock Bags: bags are placed on top of a cable to create a layer of protection. The bags are made from a durable material, often high strength geotextile or heavy-duty mesh, and filled with rocks of a specific size and weight to make them suitable to the local environment.

Concrete Mattressing: concrete or steel mats are placed over an exposed cable. The mats are generally made of heavy-duty panels that are interconnected to form a solid layer over a cable. These panels are designed to withstand the weight of the seabed and any external forces that may be encountered.

Cable Protection Systems (CPS): such as tubular protective sleeves that can be fitted around a cable to provide additional protection/armouring. These sleeves can be made from various materials, can be either flexible or rigid and are normally fitted during cable lay operations. Tubular sleeves are more susceptible to external hazards, such as anchoring, and are often used in combination with mattresses or rock placement.

Table 3. Advantages and disadvantages of commonly used trenching tools, with regards to boulders.

Tool	Advantages	Disadvantages
Jet Trencher	Fitted with retractable swords which can lift and/or widen the separation distance during trenching, potentially allowing for the swords to bypass any encountered boulders. Potential for remedial passes, should burial not be achieved on the first pass.	Contractors generally state that boulders >0.3 m will potentially impact burial. However high densities of boulders of smaller dimensions would also be problematic. Dependent on Contractor. If larger boulders are encountered, the jet swords could be damaged and a reduction in depth of lowering is observed.
Mechanical Trencher	Trencher may be able to manoeuvre boulders, depending on the soil type/matrix and size of the cutting chain. Should a boulder be encountered the mechanical cutting boom can be retracted, continuing burial albeit at a reduced burial depth.	Contractors generally state that boulders >0.3 m will potentially impact burial. However high densities of boulders of smaller dimensions would also be problematic. Dependent on Contractor. Boulders may generally lead to reduced lowering. Encountering boulders may result in cutting chain wear and cause damage to the cutting chain picks. If an area cannot be trenched due to significant density of boulders, the trencher would have to unload cable, recover and reposition, resulting in exposed cable and increased duration in operations.
Cable Plough	Cable ploughs generally have the capability to push the boulders to one side out of the cable lay path, depending on size and position.	Ploughs are generally not suitable for inter-array cables, as the vessel is forced to veer off on approach to WTG, leaving a section of un-buried/surface laid cable. Large boulders can misalign ploughs/plough ride out.

3 EXAMPLE THEORETICAL STUDY

When choosing the most appropriate mitigation method, it is likely that a combination of all of the above steps will be required in order to sufficiently mitigate the risk. The following describes a potential theoretical mitigation strategy following a survey, designed to identify the required range of boulders within a corridor wide enough to have a high likelihood of successful cable route engineering.

An export cable is to be installed through an area with identified (Identify - Step 1) surface and sub-seabed boulders, using the example from Figure 2. The original route is shown as a red line. Route engineering (Avoid - Step 2), has been carried out by avoiding any hard constraints (large boulders >~2 m) and choosing the shortest path through boulder fields, where possible. The optimised route is shown as black line Figure 4.

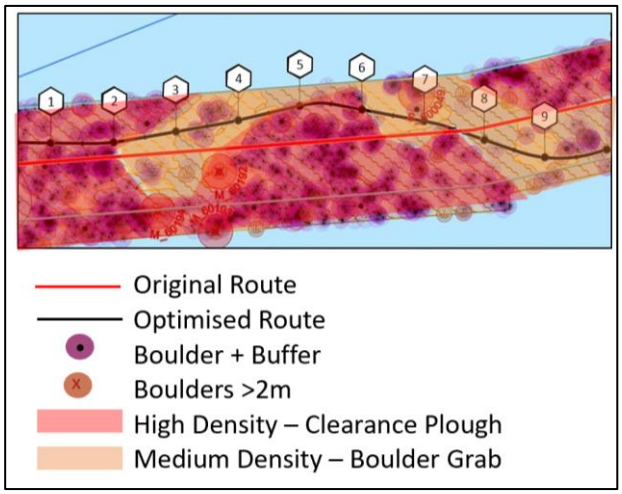

Figure 4. Example strategy.

Once the most optimum route is designed, and if boulders still pose a risk to the cable, removal/ clearance should be considered (Relocate - Step 3). As seen in Figure 4, a BG might be more suitable for the medium dense areas (e.g., between KP6 and KP8), whereas a CP would be more suited in denser areas (e.g., between KP1 and KP2). However, this will depend on distance between areas. In practice, a CP might be used for the full extent.

For Step 4 and 5 (Reduce and Remediate), the most suitable installation tool should be selected taking into consideration the ground conditions along the route, including any areas of boulders that could not be avoided or cleared by the above steps. For these 'un-cleared' areas, an allowance for remedial protection such as rock placement should be considered.

4 CONCLUSIONS

Whilst it is not always possible to remove the risk boulders pose to submarine cables entirely, the positive implications of investing project time and costs early on by following a mitigation strategy has proven to reduce unforeseen additional time and costs later on in a project.

Ensuring the most suitable detection method is chosen at the identification stage, as part of a survey campaign, is critical in detecting and measuring the presence of boulders. As part of the proposed Boulder Mitigation Strategy, the dimensions and distribution of boulders along a cable route is also key for selecting the most appropriate boulder clearance tool(s), if required. Poor selection of clearance tools can lead to downtime for several reasons i.e., tool damage etc.

If boulders remain a risk to the site and cannot be mitigated against employing the suggested strategy, it is important additional costs and time are factored into a project to accommodate the continually monitored risk of an unknown but expected boulder encounter.

REFERENCES

Carbon Trust (2020). Offshore Wind Accelerator. Guidance for geophysical surveying for unexploded ordnance and boulders supporting cable installation.

Clarke, B. G. (2018). The engineering properties of glacial tills. *Geotechnical Research, 5(4), 262-277.* DOI: 10.1680/jgere.18.00020

DNV GL (2021). DNVGL-RP-0360 Subsea Power Cables in Shallow Water. DNV GL AS.

ISO 14688-1 (2017), Geotechnical investigation and testing — Identification and classification of soil — Part 1: Identification and description.

Johnson, H, Richards, P C, Long, D, and Graham, C C. (1993). United Kingdom offshore regional report: the geology of the northern North Sea. *(London: HMSO for the British Geological Survey.)*

Wetton M.J., Vaughan D.P., Dyer N. (2024). Surface and sub-surface boulders as an engineering hazard in the marine environment; methods of detection and quantification. *Proceedings of the XVIII ECSMGE 2024.*

Proceedings of the XVIII ECSMGE 2024
GEOTECHNICAL ENGINEERING CHALLENGES
TO MEET CURRENT AND EMERGING NEEDS OF SOCIETY
© 2024 the Authors
ISBN 978-1-032-54816-6
DOI 10.1201/9781003431749-183
Open Access: www.taylorfrancis.com, CC BY-NC-ND 4.0 license

ECSMGE 24
XVIII EUROPEAN CONFERENCE ON SOIL MECHANICS AND GEOTECHNICAL ENGINEERING

The Tonbridge to Hastings undrained earthwork and modernisation programme and engineering research (THUMPER)

Programme de terrassement non drainé et de modernisation de Tonbridge à Hastings et de recherche en ingénierie (THUMPER)

D. Butcher*
Network Rail, UK

S. Fielder, S Holt, T. Hunt
AtkinsRéalis, UK

**Derek.Butcher@networkrail.co.uk*

ABSTRACT: Landslips continue to impart significant safety risk, disruption, and financial impact in the Southern Region of Network Rail (NR). Between 2019 and 2022 there were over 50 landslips (earthwork failures) per annum, causing between 7 and 9 line closures a year. The impact also has a significant financial burden, with annual repair and delay costs increasing by over £120m. An improvement / game changer was required to reverse the trend. The scope of the project was to consider a more radical identification and assessment methodology beyond the earthwork examination approach currently being undertaken.

RÉSUMÉ: Les glissements de terrain continuent d'entraîner des risques importants pour la sécurité, des perturbations et un impact financier dans la région sud de Network Rail (NR). Entre 2019 et 2022, il y a eu plus de 50 glissements de terrain (défaillances de terrassements) par an, provoquant entre 7 et 9 fermetures de lignes par an. L'impact a également un fardeau financier important, avec des coûts annuels du au réparations et au retards augmentant de plus de 120 millions de livres sterling. Une amélioration / un changement de jeu était nécessaire pour inverser la tendance. L'objectif du projet était d'envisager une méthodologie d'identification et d'évaluation plus radicale au-delà de l'approche d'examen du terrassement actuellement en cours.

Keywords: Earthwork; railway; landslip; hazard.

1 CONTEXT

Earthworks failures (landslips) continue to impart significant safety risk, disruption and financial impact in the Southern Region of the UK rail network, managed by Network Rail (NR). In the last 3 years there have been almost 50 earthwork failures per annum, causing between 7 and 9 line closures each year. Peaks in 2018/19 (69), 2019/20 (104) and 2020/21 (58) have pushed resources, budgets, and staff to breaking point.

This impact also has a significant financial burden, with individual failures costing on average c£3.5m (repair), c£1m (delay) and pushed annual repair costs to increase by over £100m. An improvement was required to undertake larger scale proactive remedial works in areas at risk of failure, rather than reactive works post-failure development. To achieve this requires a new way of thinking, to understand failure locations and triggers, and the development of optimal management strategies.

2 PROJECT

The THUMPER project commenced in October 2021. The initial focus was a detailed review of the Tonbridge to Hastings (TTH) railway line to better determine sections that at a higher risk of future failure. The line was selected as historically there have been a greater number of earthworks failures along its length than anywhere else in the Southern Region; in the last 20 years there have been 437 recorded failures in the Southern Region, 57 were located on the TTH line which equates to 13% of earthwork failures, 6 times the average number of failures for Southern Region. The present inspection driven intervention works are not preventing continuing earthwork failure

on the line. Currently there is a repetitive cycle of small reactive (often emergency) remedial fixes taking place on the TTH line, with works often being undertaken adjacent to or within the same earthwork length as previous failures. To better predict where earthwork failures are most likely in the future, a better understanding of the failure mechanisms and past earthwork performance on the line was required.

2.1 Basis of research

The research undertaken for the THUMPER project focussed on the natural geohazards, historical construction practices, subsequent earthwork performance and key trends relating to earthwork failures along the TTH line. All available geotechnical data has also been utilised to derive site specific geotechnical parameters and automated slope stability analysis unedertaken to support earthwork failure risk designation.

The initial consideration is the age of the assets present; the youngest earthwork on the TTH line is now 171 years old. These earthworks were constructed around 75 years prior to the conception of modern geotechnical design and were constructed to the basic empirical methods of the day, resulting in earthwork slopes that are over-steep by modern standards. Even if the earthworks had been constructed to modern standards, they are now over 50 years older than would be the standard 'design life' of such structures under Eurocode.

Given the age of earthworks on the line, general deterioration of the slope will have occurred by now and thus, if particular areas of the line are experiencing repeated failures, then other localised ground model changes in these locations must be driving the higher frequency of failures. However, the hisotric failure data available is very limited and the initial task was therefore to increase the amount of historic data through desk based geomoprhological mapping. The data was used to identify patterns within the past failures to determine conditions resulting in higher frequency of failures, consequently posing greatest risk of future failure. However, causality of the failures is ultimately more important and further detailed work will be required to take the findings of this work further.

2.2 Site setting

The TTH line is 32 miles 59 chains in length (approx. 52.7km) and is located in the south-east of England, running between the towns of Tonbridge in Kent and Hastings on the East Sussex coast. The railway crosses the central area of the Weald (an eroded anticline) along a generally northwest to southeast alignment and geology along the line is formed of alternating outcrops of the Tunbridge Wells Sand Formation, Wadhurst Clay Formation and Ashdown Formation which are heavily faulted (Gallois, 1965). The terrain is comprised of successive steep valleys and ridge lines reflective of the alternating ground conditions with numerous spring lines.



Figure 1. Location Plan.

3 FINDINGS

3.1 Construction History

The TTH line was built between 1844 and 1852, making earthworks on the route between and 171 and 179 years old. The relative age of the line in comparison with the rest of the UK network is highlighted on Figure 2.

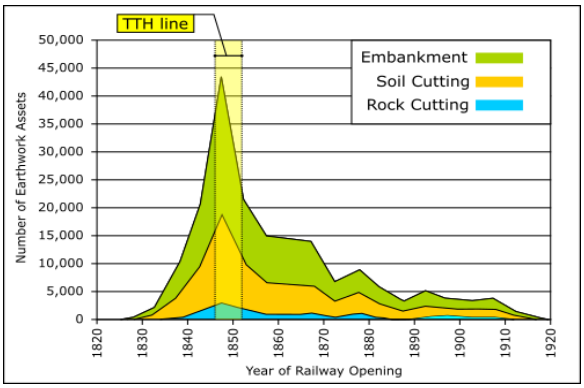

Figure 2. UK earthwork assets by date with the Tonbridge to Hastings Line highlighted (derived from Cobb, 2015).

Construction methods comprised large teams of manual labourers undertaking excavations using pick and shovel and utilising horse drawn wagons to end tip fill to form adjacent embankments, without any sorting or compaction (Skempton, 1996). Deliberate cost cutting by the contractors is documented on the TTH line tunnels and it was important to determine if any similar practices were employed on earthwork

construction that may have resulted in the particularly high number of failures on the TTH. It was thought likely that if present this would take the form of finished earthworks being steeper than than proposed, or omission of planned drainage. Both of these would result in huge reductions in volume of cut and fill over each construction section.

The available historical data indicated that the earthworks on the line were proposed at a gradient of 1V:1.5H (33°), although local variations where rock outcrops are present would be anticipated. The LiDAR data suggests that both cutting and embankment slopes along the line are typically at a slightly steeper angle of 34° to 36°.

No construction period drainage plans have been found; the earliest available data of any detail is from the British Railways drainage plans produced in the 1950s / 60s. Generally, the drainage along the route is less extensive than commonly seen on other lines of similar age. Furthermore, the drainage was found to vary considerably depending on area, with little or no drainage being provided in the northernmost section versus relatively comprehensive drainage in the lower section.

Although earthworks appear to have been finished to slightly steeper angles than proposed, no obvious trend was identified attributing a greater density of failures to a particular construction section. Some sections of the line did show a greater concentration of failures, however the rapidly changing geological conditions make it difficult to attribute poor earthwork performance to one factor. Given the distribution of failures along the line, it is believed that the key issues are primarily as a result of the geological conditions rather than faulty construction.

3.2 Earthwork & failure mapping

The 2020 NR LiDAR-derived bare-earth digital elevation models (DEMs) have been used to locate and map whole earthworks, earthwork failures and past remedial works along the line. A geodatabase was established to record key data for each failure including ground model, adjacent slope aspect, drainage, slope angle and other attributes to characterise each earthwork and failure.

Whole earthwork extents were mapped using the LiDAR data so that attributes and ground models could be assigned holistically, rather than continuing to look at the line in terms of the 5 chain asset lengths, as this artificially divides up the earthworks. This allowed the earthworks to be split up into sections reflecting the ground conditions and geomorphological features. In total 126 embankments, 147 cuttings were mapped along the TTH line.

A total of 458 individual failure locations have been identified based on the historical data, CIV185 data, and geomorphological mapping, comprising 176 within embankments and 282 within cuttings. Out of the 273 whole earthworks, 144 (53%) have failures mapped within their extent. The use of high-quality LiDAR data has resulted in the identification of 441 previously un-recorded earthwork failures or past remedial works. This has been of primary importance to both improve the overall failure data for the route, allowing greater analysis of failure trends, and to improve the accuracy of the spatial extent and attributes which are thought to act as precursors for failure.

3.3 Geographical & geological failure trends

Failure on the Up and Down sides of the line were found to be fairly evenly distributed, with no obvious trend suggesting that one side of the line was more susceptible to failure. Cutting failures were found to be more common (76% of total) where the adjacent land slopes towards the earthwork. This appears to indicate that failures within cuttings are more likely where these conditions prevail, although it is probable that the local dip of strata is a more important factor than aspect of the adjacent land in most locations, particularly cut slopes in the Wadhurst Clay Formation.

Cutting failures are more frequent within sections of the route with a composite slope where a geological boundary is present. At these locations spring lines are common and it is known that a large number of the cuttings on the line have notable seepage points within them. The presence of spring lines in cutting slopes is a key driving factor to future failure as evidenced by the highest risk cuttings being present where composite slopes are present.

Embankment failures appeared to show no obvious trend with regard to adjacent land aspect, but unsurprisingly were found to be most common in areas where the embankment was underlain (or likely to be underlain) by superficial deposits (46%) or where directly underlain by the cohesive Wadhurst Clay Formation (35%). It is important to note that due to the construction methodology employed on early railways, topsoil was not generally removed prior to the end tipping of unsorted fill, resulting in a relict low strength layer beneath the fill. This led to singificant settlement issues after tipping resulting in many large scale failures during or shortly after construction, as well as a legacy of instability issues.

3.4 Failure type and triggers

Historic earthwork failure data is limited, with nothing available outside of newspaper snippets prior to 1950;

good records of failures are available from 2000 onwards. Data on failure mechanism and triggering factors are only available for later failures recorded within NR's CIV185 failure database and selected historic failure records from the archives. Associated trends and are limited as a result.

Between 1950 (earliest available recorded failure data) and 2000 most recorded earthwork failures or remedial works are within embankments. Post 2000 most recorded failures are located within cuttings and are linked to heavy rainfall events and saturated ground conditions. There is an apparent trend of general increase in the reporting of cutting failures in recent years, although earlier failure datasets are potentially skewed due to the lack of reporting of small failures not affecting the track and more recent records by planned remedial work on embankments.

Cutting failures typically comprise relatively small scale shallow translational or rotational failures that occur repeatedly within the same whole earthwork, spreading laterally along the slope or re-occurring close to a previous failure / repair. In comparison, embankment failures are generally larger scale and many of them are thought to have occurred relatively soon after construction. As a result, cuttings are considered on a whole to pose the greatest risk of future ongoing failure, particularly considering that the youngest slopes on the line are now over 170 years old.

4 CONCLUSIONS

The TTH line review has allowed a greater understanding of the earthwork performance on the line as well as providing a historical baseline from which to judge this performance. It has allowed NR to identify a total 17 embankment and 47 cutting sites that are considered to be at risk of first-time failure or continuation of existing failures that were not previously considered a high priority based on earthwork exams alone. This has been based on the historical performance of the earthworks, as well as the specific geology and geometry of those assets.

This would not have been possible utilising inspection data; one of the key issues with using inspection data to identify areas of earthwork risk is that an earthwork close to its critical state may show no visible signs of movement, yet fail in the next few days. Furthermore, many of the initial indicators may be hidden by vegetation, infrastructure etc. or occur in a timescale that is less than the return frequency of inspections. Therefore, basing works off condition ratings is unlikely to fix the highest risk areas or prevent a continuation of the current issues on the TTH and elsewhere on the UK rail network.

The work on the TTH line has been wholly desk-based utilising existing available data. Whilst further work is required to refine the areas at risk, it has proved the value of undertaking such a review across a relatively wide area. Further targeted investigation into each of the sites will allow further refinement of the high priority sites and where applicable design appropriate poactive remedial works to improve the earthwork condition and reduce the likelihood of failure. This approach is far more sustainable than undertaking heavy engineering of failed sections and can often utilise lighter touch engineering such as targeted slope strengthening and drainage. Whilst undertaking large scale preventative works will be costly to implement, the longer-term savings vs emergency remedial works, delay compensation and safety of the operational railway in a location of known earthwork instability would be considerable and will work towards providing a more resilient network for the next 100 years.

ACKNOWLEDGEMENTS

The project presented in this article has also been supported by a number of AtkinsRéalis colleagues: Tim McAulay, Sam Rogers, Anurag Kushwaha, and Martin Kemp.

REFERENCES

Cobb, M. (2015). The Railways of Great Britain: A Historical Atlas. Riley Dunn & Wilson Ltd.

Skempton, A. W. (1996). Embankments and cuttings on the early railways. Construction History.

Gallois, R. (1965). The Wealden district British regional geology. British regional geology. 4th edition. London: HMSO.

Radley, J. D. (2006). A Wealden guide I: the Weald Sub-basin.. Geology Today, 22(3), 109-118., 2006.

Mellor, R. (2017) Development of a Global Stability and Resilience Appraisal for Network Rail earthwork assets. Ground Related Risk to Transportation Infrastructure. London, 26 – 27.

Network Rail. (2018). Earthworks Technical Strategy - Safety, Technical and Engineering.

Weeks, A. (1969). The stability of natural slopes in south-east England as affected by periglacial activity. Engineering Geol. Vol. 2, pp. 49-61.

Bromhead, E., Huggins M. (2000) Shallow Landslides in Wadhurst Clay at Robertsbridge Sussex UK. Proc 8th International Symposium on Landslides, Cardiff. Vol 1 pp287-292.

Pugh, R., Weeks, A., Hutchinson, D. (1991). Landslide and remedial works in Wadhurst Clay. Slope Stability Engineering, Thomas Telford, London.

Proceedings of the XVIII ECSMGE 2024
GEOTECHNICAL ENGINEERING CHALLENGES
TO MEET CURRENT AND EMERGING NEEDS OF SOCIETY
© 2024 the Authors
ISBN 978-1-032-54816-6
DOI 10.1201/9781003431749-184
Open Access: www.taylorfrancis.com, CC BY-NC-ND 4.0 license

ECSMGE 24
XVIII EUROPEAN CONFERENCE ON SOIL MECHANICS AND GEOTECHNICAL ENGINEERING

Centrifuge tests on the uplift and deformation patterns of clay cover layers in deltas

Essais en centrifugeuse sur les modèles de soulèvement et de déformation des couches d'argile dans les deltas

C. Cengiz*
Deltares, Delft, The Netherlands

M.A. Cabrera
TU Delft, Delft, The Netherlands

B. Wittekoek, M. Fransen, L. Wopereis, C. Zwanenburg
Deltares, Delft, The Netherlands

**cihan.cengiz@deltares.nl*

ABSTRACT: As the population in cities all over the world is increasing, the effects of climatic action on the resilience of communities is becoming more and more important. Cities situated in deltas are also under strong urbanization demands and these demands have to be met with due consideration of the challenges presented by climate change, land subsidence and sea-level rise. Within this context, the local geological conditions in the Netherlands present a particularly pressing challenge where water pressure under a clay cover may increase. The static equilibrium of the cover layer might be adversely affected, and uplift failure can be imminent. A recent research program into this failure path has been initiated. Besides the field tests and advanced numerical modelling approaches, the research program also made use of centrifuge tests to quantify the extent of uplift, cracking, and deformation phenomena. This contribution intends to exhibit the aspects of the centrifuge tests conducted as part of this study. The experimental setup design and design considerations will be explained as well as the instrumentation methodology and the reasoning behind the instrumentation choices. This contribution aims to improve the stability assessment of dikes under uplift conditions.

RÉSUMÉ: À mesure que la population des villes du monde entier augmente, les effets de l'action climatique sur la résilience des communautés deviennent de plus en plus importants. Les villes situées dans les deltas sont également soumises à de fortes demandes d'urbanisation et ces demandes doivent être satisfaites en tenant dûment compte des défis présentés par le changement climatique, l'affaissement des terres et l'élévation du niveau de la mer. Dans ce contexte, les conditions géologiques locales aux Pays-Bas présentent un défi particulièrement pressant, car la pression de l'eau sous une couverture argileuse peut augmenter. L'équilibre statique de la couche de couverture pourrait être affecté négativement et une rupture par soulèvement pourrait être imminente. Un programme de recherche récent sur cette voie d'échec a été lancé. Outre les essais sur le terrain et les approches avancées de modélisation numérique, le programme de recherche a également eu recours à des essais par centrifugation pour quantifier l'ampleur des phénomènes de soulèvement, de fissuration et de déformation. Cette contribution vise à exposer les aspects des essais de centrifugation menés dans le cadre de cette étude. La conception de l'installation expérimentale et les considérations de conception seront expliquées ainsi que la méthodologie d'instrumentation et le raisonnement derrière les choix d'instrumentation. Cette contribution vise à améliorer l'évaluation de la stabilité des digues en conditions de soulèvement.

Keywords: Dike stability, macro-stability, uplift failure, flood defences, centrifuge testing.

1 INTRODUCTION

In densely populated Dutch delta regions, an unfavorable geological condition is encountered where a thin clay cover is found over permeable layers. While this stratification does not pose significant challenges for most engineering applications, it creates a unique set of issues for dike engineering purposes. The problem is accentuated by large riverbeds and increasing severity and frequency of weather and precipitation extremes. The Dutch dike engineering approach focuses on macro-stability calculations, considering a scenario where the dike stability is lost due to buckling or uplifting of the clay cover. This concern arises when the water pressure within the sand beneath the top layer increases due to rising external water levels. When the water pressure matches the

weight of the top layer, it begins to rise or "float". Subsequently, under the influence of horizontal compressive forces, the top layer may experience deformation, potentially leading to buckling or bursting – this is a geometrically non-linear 'second-order' effect –. The expected formation of bending cracks, along with the resulting reduction in the bending capacity, can exacerbate the risk.

To address the risk of bursting, the current assessment and design approach involves a simple rule: for top layers with a thickness of 4 meters or less, no shear strength is assigned when the safety factor is 1 or lower. This particular rule is based on expert judgement without extensive support from calculations, experiments, or empirical data. However, it is widely believed that this approach errs on the side of caution and tends to lead to designs that are overly conservative. The above-mentioned risk is especially pressing in the Eastern part of the Netherlands, where the Holocene top layer is commonly situated on top of a relatively rigid and permeable Pleistocene sand layer. It is plausible that high-water levels in adjacent rivers and estuaries may generate locally high pore pressures directly under or beside a dike. Consequently, the effective normal stresses at the layer interface decrease, eventually to zero, giving rise to uplift and sliding failures (Van et al., 2005). A pictorial description of the problem is illustrated in Figure 1.

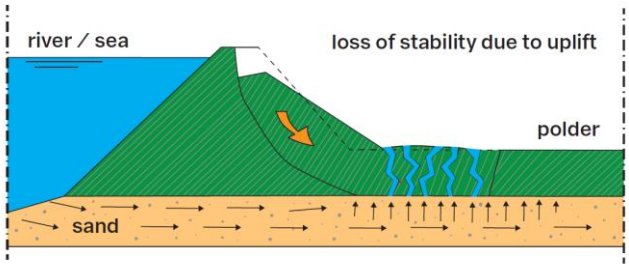

Figure 1. A sketch of buckling or uplifting mechanims over a dike clay cover.

In order to study the dike deformation mechanisms, a series of centrifuge experiments are carried out at the 5 m radius Deltares Geo-Centrifuge. The goal of the experimental program is to better understand the mechanisms that affect the behaviour of the dike and cover layer under extreme water levels. The forthcoming proceeding paper will introduce the experimental methodology and early findings of the experimental program by elaborating on an exemplar test carried out at the Deltares Geo-Centrifuge. It should be noted that centrifuge testing is part of the activities carried out under an overarching project, for a broader description, interested readers are referred to Zwanenburg et al. (2024). This project combines physical and numerical models as well as field experiments.

2 MATERIALS AND EXPERIMENTAL SETUP

Figure 2 illustrates a sketch of the experimental setup together with the soil layers, instrumentation details, and the model-scale dimensions.

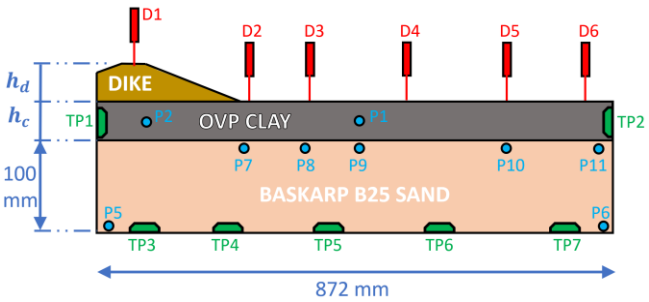

Figure 2. A sketch of the experimental setup.

2.1 Materials

The geo-materials used in the centrifuge model included Baskarp B15 and B25 sands and Oostvaardersplassen (OVP) clay. The model construction commenced with the addition of a precalculated amount of Baskarp B25 in the strongbox to serve as a permeable layer which underlies the cover layer (OVP Clay). The sand is placed by wet pluviation and tamping, achieving a relative density of 90%. Once the placement of the basal sand layer was finalized, remoulded OVP clay slurry was placed on top of the sand, being consolidated with an overburden pressure of 20 kPa within the strongbox and forming the cover layer. Please note that block samples consolidated to 40 kPa were also used in the wider experimental program. Upon completion of consolidation, the sand dike consisted of Baskarp B15 sand, constructed above the cover layer. Further details on the engineering properties of the OVP clay and Baskarp sands can be found in Fern et al. (2017) and Rosenbrand et al. (2022), respectively.

2.2 Experimental Setup

The models are prepared in a strongbox which can withstand the centrifugal accelerations and with a transparent window allowing in-flight image capture for digital image analysis. The width and length of the strongbox is 200 and 872 mm, respectively. The depth of the strongbox is 450 mm. The base plate of the strongbox is instrumented with total pressure sensors, abbreviated as ‘TP’ in Figure 2. Similarly, additional total pressure sensors are affixed to the side walls, capturing the lateral pressure changes in the cover

layer. An array of eleven pore water pressure sensors is distributed over the model, abbreviated as P in Figure 2. Notably, P5 and P6 indicate the pressure head of the influent and effluent flow. P7 to P11 measure the porewater pressure at the sand-clay interface. Finally, P1 and P2 give important insight into the pore water pressure within the OVP clay cover layer. Surface vertical deformations are monitored by six hard sensor points instrumented with DCDTs. These sensors are essentially similar to Linear Variable Differential Transformers (LVDT), but they do not incorporate any spring-loaded system, preventing jamming under the action of a centrifugal acceleration field. Beyond the conventional instrumentation, the deformations are monitored with a camera system, enabling post-testing digital image correlation analyses. Due to the large aspect ratio of the transparent window, a total of two cameras are used for monitoring the entirety of the model. A photograph of the intact dike is shown in Figure 3.

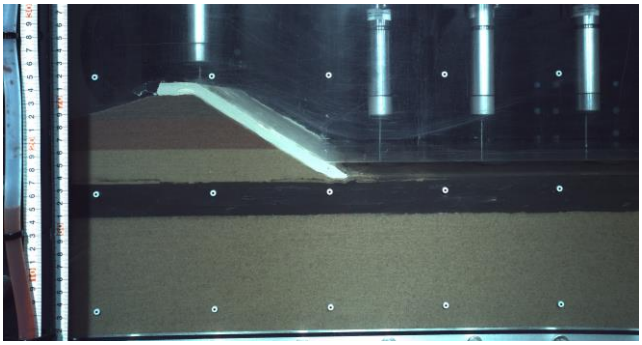

Figure 3. A photograph of the dike before failure occurs (note that a thin layer of Vingerling K147 clay (white) is used as an armor layer to retain water within the dike body).

3 EXPERIMENTAL METHOD

One of the primary objectives of the tests are to see if increments of hydraulic pressure on the riverside would cause uplift failure on the landside. With this in mind, during the centrifuge flight, the experimental assembly allows for adjustment of the hydraulic head on the river side while keeping the landside head constant. The influent flow is supplied from the left-hand-side, see Figure 2, using a series of diffusers. Water is allowed to leave the permeable sand from the right-hand side of the assembly.

The centrifugal acceleration regime applied to the model is illustrated in Figure 4. The hydraulic loading regime necessary to induce uplift is estimated on equivalent finite element calculations, assuming a stress field equivalent to an effective centrifugal acceleration of 80g. The hydraulic loading regime is illustrated in Figure 5, where the difference in influent (P5) and effluent (P6) pressure heads can be seen.

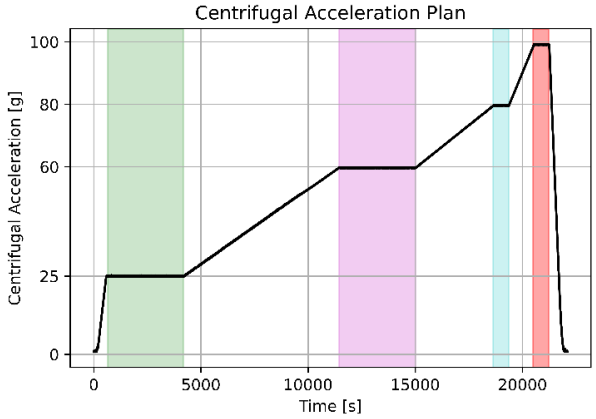

Figure 4. Centrifugal acceleration during the experiment.

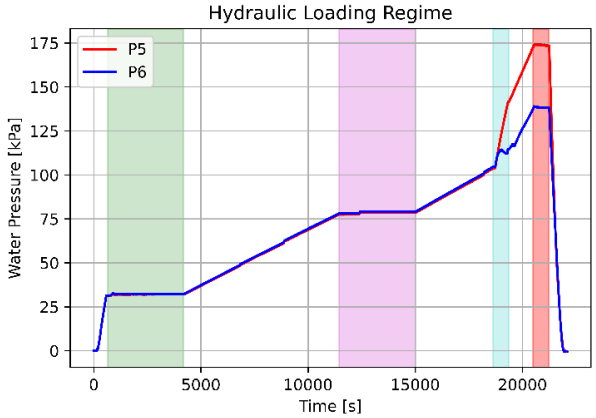

Figure 5. Hydraulic loading regime during the test.

As a result of increasing the hydraulic head difference across the model, uplift of the cover layer is triggered. Vertical displacements measured by the DCDTs are illustrated in Figure 6 (notice that the background coloring in the graph coincides with different phases of the experiment as illustrated in Figure 4 and Figure 5). A photograph capturing the moment of uplift is also shown in Figure 7.

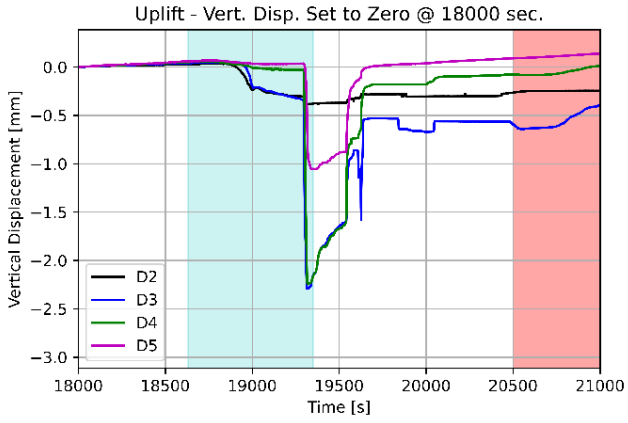

Figure 6. Vertical displacements measured by the DCDTs at the initiation of uplift.



Figure 7. Uplift and separation of the cover layer.

Figure 8 illustrates the overall deformation observed at the end of the test where multiple failure planes within the dike body are visible which also bring about settlements (reduced free-board). In addition to the dike body failure, the cover layer exhibits severe cracks, most notably at the toe. The cracks extend diagonally, and its slope is steeper than that of the dike slope. Multiple wells have also formed as a result of the increased hydraulic heads which reduce the integrity of the cover layer.

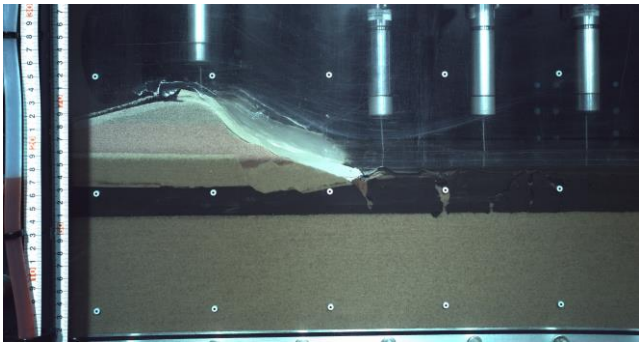

Figure 8. Overall deformation pattern of the model.

4 OBSERVATIONS AND CONCLUSIONS

This proceeding paper aimed at demonstrating the general aspects of the centrifuge scope undertaken at Deltares Geo-Centrifuge. Main observations and conclusions from the testing program can be summarized with the following items:

- Although the presently described test only constitutes a singular test within the experimental program, uplift of the cover layer was observed in all tests.
- Uplift phenomena occurs when the limit equilibrium state is satisfied, i.e., the ratio of the vertical pressure exerted by the cover layer is equal to the water pressure below the cover layer, or when $\sigma_v / \sigma_w = 1$.
- The cover layer cracks due to uplift. This crack is seen as a diagonal crack occurring at the toe of the dike, see Figure 7 (to the right of the first white dot in the figure).
- Uplift at a centrifugal acceleration of 80 g causes the cover layer to rise approximately 2.5 mm, see D4 measurements in Figure 6. There have been observations of much severe uplift deformations within the experimental program.
- When g-level increases the vertical displacement of the cover layer reduces. It should be noted that the cover layer remains in an uplifted condition and the ratio σ_v / σ_w remains unaltered when increasing the g-level. The exact cause of this is still under investigation.
- Figure 7 shows that in the uplifted zone the hydraulic head in the sand layer is maximised by the weight of the cover layer. A further increase in hydraulic head at the left boundary will further increase the head at the uplifted zone.
- Failure was found by a combination of a steep sliding plane at the active side that connects the opening at the cover layer with the sand layer.
- In the test series, no passive failure plane is visible, instead the cover layer seems to be horizontally compressed in combination with a further increase in curvature of the uplifted zone. The later could mean that the lateral stiffness of the cover layer might play a role in the observed deformation patterns.

ACKNOWLEDGEMENTS

The authors are grateful for the financial support provided by funding agency National Flood Protection Programme (HWBP) and Water Authority Drents Overijsselse Delta, WDOD.

REFERENCES

Fern, E.J., de Lange, D.A., Zwanenburg, C., Teunissen, J.A.M., Rohe, A., Soga, K., 2017. Experimental and numerical investigations of dyke failures involving soft materials. Engineering Geology 219, 130-139. 10.1016/j.enggeo.2016.07.006.

Rosenbrand, E., Beek, V.v., Bezuijen, A., Akrami, S., Terwindt, J., Koelewijn, A., Förster, U., 2022. Multi-scale experiments for a coarse sand barrier against backward erosion piping. Géotechnique 72, 216-226. 10.1680/jgeot.19.P.358.

Van, M., Koelewijn, A.R., Barends, F., 2005. Uplift phenomenon: Model, validation, and design. International Journal of Geomechanics 5, 98-106. 10.1061/(ASCE)1532-3641(2005)5:2(98).

Zwanenburg C., Koelewijn A., van der Kolk B., Förster U., Post, M. de Bruijn H. (2024). Small- and full-scale test programme on uplift induced slope failure *in: proceedings Proceedings of the XVIII ECSMGE,* Lisbon.

Proceedings of the XVIII ECSMGE 2024
GEOTECHNICAL ENGINEERING CHALLENGES
TO MEET CURRENT AND EMERGING NEEDS OF SOCIETY
© 2024 the Authors
ISBN 978-1-032-54816-6
DOI 10.1201/9781003431749-185
Open Access: www.taylorfrancis.com, CC BY-NC-ND 4.0 license

ECSMGE 24
XVIII EUROPEAN CONFERENCE ON SOIL MECHANICS AND GEOTECHNICAL ENGINEERING

UAS thermal imagers for monitoring and analysing landslide in a mudstone area

Imageurs thermiques UAS pour la surveillance et l'analyse des glissements de terrain dans une zone de mudstone

H.-W. Chen
Department of Environmental Science and Engineering, Tunghai University, Taichung City, Taiwan

C.Y. Chen*, Y.Y. Liu
Department of Civil and Water Resources Engineering, National Chiayi University, Chiayi City, Taiwan

**chienyuc@mail.ncyu.edu.tw*

ABSTRACT: Typhoon activities lead to numerous rainfall-induced erosions, debris flows, and landslides. Monitoring and analysing potential natural disasters are needed worldwide. Thermal imagers are characterized by noncontact and long-distance detection capabilities, rendering them suitable for landslide monitoring. The purpose of the study was to monitor the unstable slope in a mudstone area by analyzing surface infrared temperature changes. A landslide case in a mudstone area in southern Taiwan was monitored for this pilot study. Thermographs obtained by a handheld thermal imager from various times were analyzed for monitoring the surface temperature changes on slope faces. In addition, an unmanned aerial system (UAS) mounted thermal imager was used to capture digital orthophoto thermal images for setting up a three-dimensional monitoring net. Infrared temperature changes per unit time served as monitoring variables and were compared with isotherms for detecting infrared temperature changes. These images indicated that wet soil had higher water content and exhibited a lower surficial infrared temperature change. A thermal imager can reveal changes in surface radiation temperatures and can be used for monitoring landslide-induced surface temperature changes. Accordingly, the use of thermal imagers for potential unstable slope monitoring may be optional.

RÉSUMÉ: Les activités des typhons entraînent de nombreuses érosions, coulées de débris et glissements de terrain induits par les précipitations. La surveillance et l'analyse des catastrophes naturelles potentielles sont nécessaires dans le monde entier. Les imageurs thermiques se caractérisent par des capacités de détection sans contact et à longue distance, ce qui les rend adaptés à la surveillance des glissements de terrain. Le but de l'étude était de surveiller la pente instable dans une zone de mudstone en analysant les changements de température infrarouge en surface. Un cas de glissement de terrain dans une zone de mudstone du sud de Taiwan a été surveillé pour cette étude pilote. Des thermographes obtenus par une caméra thermique portative à différents moments ont été analysés pour surveiller les changements de température de surface sur les faces des pentes. En outre, un imageur thermique monté sur un système aérien sans pilote (UAS) a été utilisé pour capturer des images thermiques orthophoto numériques afin de mettre en place un réseau de surveillance tridimensionnel. Les changements de température infrarouge par unité de temps ont servi de variables de surveillance et ont été comparés aux isothermes pour détecter les changements de température infrarouge. Ces images ont indiqué que le sol humide avait une teneur en eau plus élevée et présentait un changement de température infrarouge superficiel plus faible. Une caméra thermique peut révéler les changements dans les températures de rayonnement de surface et peut être utilisée pour surveiller les changements de température de surface induits par les glissements de terrain. Par conséquent, l'utilisation de caméras thermiques pour la surveillance des pentes potentiellement instables peut être facultative.

Keywords: Landslide; monitoring; mudstone; unmanned aerial system.

1 INTRODUCTION

Taiwan has a monsoon climate. The west-south monsoon currently takes place in May to September affects the monsoon climate in Taiwan. Moreover, Taiwan is located in the path of typhoons in the Pacific Ocean area, which is prone to typhoons. High-intensity rainfall and prolonged high cumulative rainfall tend to initiate landslide and debris flow in Taiwan (Chen, 2016).

Mudrock is a class of fine-grained siliciclastic sedimentary rocks. Mudstone is a common type of mudrock in Taiwan. Mudstone strata are exposed in west-southern hillslopes along the south and east coasts of Taiwan. Mudstone is the most unstable type of sedimentary rock in the area and is prone to

weathering and water disintegration. Rainfall erosion of mudstone can be attributed to the formation of an erosion gully. The saline matter in mudstone is prone to dissolution by rainfall, which renders soil masses quite barren. Growth of plants is inhibited in such barren soil masses.

Mudstone has a complex structure and does not possess a bedding plane. The particle size of mudstone ranges between silt and clay, and its color varies from gray to black. Black mudstone consists of organic material. Mudstone is young in geologic age with poor cementation and is prone to disintegration because of softening by water. Mudstone is competent as stone under dry conditions but cracks easily on the surface under wet conditions. Cyclic dry and wet conditions cause surficial plate peeling in mudstone.

The evolution of a mudstone slope involves four stages (Lin, 1995): At the beginning, rainfall seeps into the surficial cracks of mudstone and then evaporates; finally, dry shrink occurs, and the base rock is separated. This separation enables further seepage of the rainfall into the cracks.

The separated mudrocks are eroded by rainfall, or they move down the slope due to gravity and continue to be deposited at the toe of the slope at a nearly 20° to 30° talus gradient. Rainfall continues to seep through the surficial cracks to deeper layers. Weathered slope surficial soil falls to the slope toe and retreats as the surficial layer of the mudstone collapses, thus engendering a repeated cycle.

The compression strength of the mudstone is 0.2–2.8 MPa (Lee et al., 1994). The average thickness of weathered surficial soil on the mudstone is from 2 to 10 m. In the bold area, the thickness of weathered surficial soil is less than 1 m, and the soil has low permeability to soluble salts, which reduces the survivability of plants and increases the ease of erosion (Wang, 1988). The index properties of the mudstone in southwestern Taiwan are outlined as follows: specific gravity, 2.67 to 2.77; water content, 1.73% to 17.91%; liquid limit, 24% to 42.2%; void ratio, 0.21 to 0.51; plastic limit, 7.4% to 25.4%; and plastic index, 10.5 to 18. The sand, clay, and silt particle contents are 2% to 23%, 16% to 42%, and 55% to 79 %, respectively; thus, the mudstone can be classified as CL-ML or CL (Chen, 2006).

In the mudstone area in the Kaohsiung City in southern Taiwan, various sunlight incident angles cause large infrared temperature changes in the east and west sides of the slopes (Figure 1). The maximum difference in temperature is 15–18 °C in winter and 2–5 °C in summer (Hsu et al., 2005).

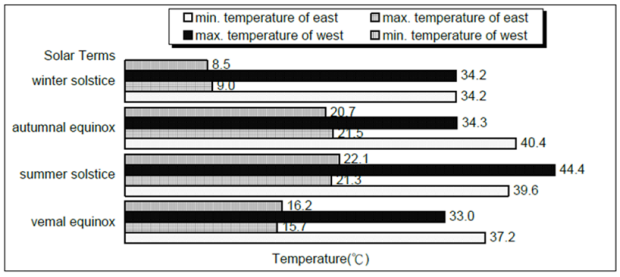

Figure 1. Infrared temperature changes at the east and west sides of the slopes (Hsu et al., 2005).

2 INFRARED TEMPERATURE CHANGES OF MUDROCK

A thermal imager is a noncontact, nondestructive, and rapid testing instrument for examining inner structural conditions through surficial infrared temperature. The imager's applications extend from military use to medicine, science, industry, agriculture, mining, and engineering.

The advantages of using a thermal imager for monitoring surficial infrared temperature changes of objects include remote monitoring, large-area monitoring, clear visibility, wide infrared temperature monitoring range, rapid response, and lightweight (Clark et al., 2003).

A previous study applied a thermal imager to monitor tension cracks on rock slopes (Baroň et al., 2014) and revealed that the thermal imager could provide information for rapidly evaluating the risk of rockfall and the distribution of tension cracks. In nondestructive inspections, a thermal imager has been used to inspect a shotcrete-protected slope (Wu et al., 2005; Chen and Jiang, 2018). The existence of caves behind the shotcrete surface results in higher infrared temperature changes than those observed under shotcrete surfaces without caves.

Applying thermal imagers for monitoring surficial infrared temperature changes necessitates environmental temperatures lower than the average temperature of rock surfaces, good visibility, low direct sun exposure, absence of heavy snow cover, and bare rock surfaces (Baroň et al., 2014).

The purpose of the study was to monitor the landslide in a mudstone area for testing the feasibility of thermal imagers for nondestructive inspections of surficial changes in a large area.

3 STUDY AREA AND METHOD

3.1 Study Area

The mudrock areas in the Kaohsiung City in southern Taiwan served as the study area. The annual rainfall in

the study area is up to 1800 mm, and the average temperature is between 23 and 25 °C. The area is bare with sparse vegetation.

A landslide disaster occurred in the study area at 11:00 on September 28, 2016 because of torrential rains engendered by Typhoon Megi. The landslide site was determined to be located at a latitude of 22°47'20.0"N and longitude of 120°22'45.7"E. The landslide buried one building and left three residents dead. The landslide area was measured to be 3000 m^2. A field investigation was conducted on October 6, 2016, a week after Typhoon Megi (Figure 2). The results of the field investigation revealed mudstone and sandstone with water-softened mud. Moreover, the results indicated high water content in the field mudstone and ground cracks. The landslide exhibited high soil mobility and mass movement and blocked the trail. The movement could have been induced by the softening of the mudstones because of the long-term high water content.

3.2 Geologic and Hydrologic Conditions

The landslide occurred at the Gutingkeng Formation between late Miocene and Pleistocene. The formation is a combination of gray mudstone and sandstone with interbedded limestone and exhibits a bare land after weathering.

The annual rainfall in the study area was 1747 mm in 2014, 1497 mm in 2015, and 3023 mm in 2016. The rainfall was 1255 mm on September, 2016 and up to 3023 mm in December, exceeding the average annual rainfall (i.e., 1800 mm) in the area. The landslide was induced by a cumulative rainfall of 482 mm engendered by Typhoon Megi on September 28, 2016; it occurred immediately after the rainfall (Figure 3). The area received 19 days of rainfall in September, which resulted in high water content and softened the mudstone.



Figure 2. The scar of the monitored landslide (October 6, 2016).

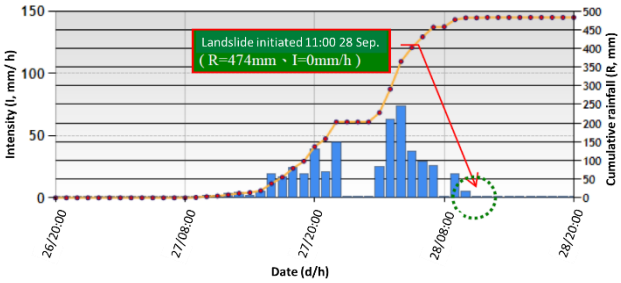

Figure 3. Rainfall time history at the nearest rain gauge station during Typhoon Megi (source NCDR, 2016).

3.3 Method

Two types of thermal imagers were used for monitoring the landslide area, namely a handheld infrared thermal imager (NEC G100D) and an unmanned aerial system (UAS). The handheld type was used for monitoring the facade of the landslide. The handheld imager has a sensitivity of 0.08 °C, image resolution of 200 megapixels, and focus length ranging from 10 cm to infinity. The UAS of the NEC F30W thermal imager is small in size and lightweight.

A post-processing package was used for thermal image analysis. The functions of the software include regional temperature distribution curves, infrared temperature profiles, isotherms, dynamic infrared temperature changes, and three-dimensional temperature change trends. Infrared temperature changes in multiple regions were analyzed to show the highest, average, and lowest temperatures in a regional area; the results were indicated on a thermal image (Figure 4).

This study monitored the landslide area to derive results that can be used for postdisaster prevention and mitigation. Changes in infrared temperature (△T) in a period (t) served as a monitoring index for the surficial temperature changes in the landslide area (Chen and Jiang, 2018). The landslide monitoring process in this study involved three stages. The first stage involved a preliminary field investigation and handheld thermal-imager-based monitoring at the landslide site for selecting the potential movement area for further monitoring. The second stage involved monitoring using the handheld thermal imager in the morning and afternoon. The third stage involved monitoring using the UAS thermal imager, and the derived results were compared with those obtained in the second stage.

4 RESULTS

4.1 Handheld Thermal Imager Monitoring

The landslide movement was monitored on March 24, 2017, using the handheld thermal imager.

Thermographs were divided into 36 grids (Figure 5) for the monitoring window from 09:00 to 13:30. The frequency of monitoring was 30 min. Figure 6 displays the thermographs obtained from the field investigation. The infrared temperature on the monitored slope increased from morning to noon. The main erosion gully as indicated in the middle of the thermograph, shows that the study area had a lower temperature than did other areas as well as the vegetation areas. The left side of the slope exhibiting a sandstone base and a small erosion gully had a lower temperature than did the right side of the slope exhibiting a mudstone area. The thermograph reveals different temperatures under different vegetation conditions and types of base materials.

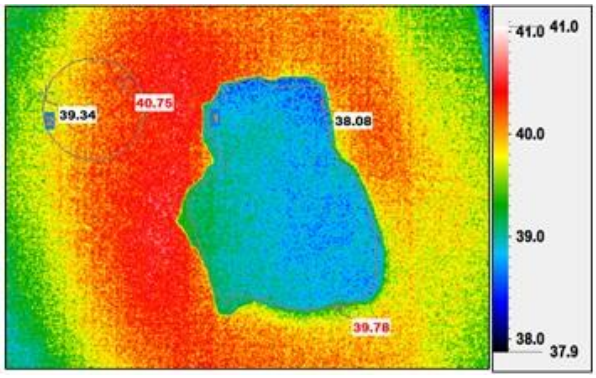

Figure 4. Example of multiregional thermal image analysis (temperature unit: degree).

The monitoring index △T/t can be calculated from the infrared temperature change △T for the current time minus the former time in the period t. The index changed as the environmental temperature increased. The index showed no obvious fluctuations between 09:57 and 10:24. The index exhibited high fluctuations in grids 7, 13, and 19, corresponding to the erosion gully on the left side of the monitored area, at 11:27. The main erosion gully in the middle of the area—represented by grids 11, 15, 21, and 28—revealed a high change in temperature at 11:58.

Figure 7 illustrates a histogram constructed for the changes in infrared temperature between 09:27 and 13:01, revealing that grids 7, 13, and 19 had the highest changes, followed by grids 14, 15, 20, and 21. The day of monitoring was sunny, and the sunshine streaked from the right to left of the imager in the afternoon. Shadow areas corresponding to grids 4, 5, 6, 10, 11, 12, 16, 17, 18, 22, 23, 24, 28, 29, and 30 demonstrated a low decrease in temperature. Grids 6, 12, 16, 17, 18, 20, 21, 22, and 23 exhibited a decrease in temperature engendered by the changes in solar orientation.

The erosion gully corresponding to grids 7, 13, and 19 showed a considerable change in ΔT/t. However, the main erosion gully of the landslide corresponding to grids 10, 16, and 22 was affected by the shadow and exhibited negligible changes. To identify potential high-change areas, an isothermal graph was overlapped with the visible image. The resultant image confirmed that the two gullies in the monitored landslide area had lower infrared temperature than did other naked areas (Figure 8).



Figure 5. Grid numbers for the monitoring of the landslide.

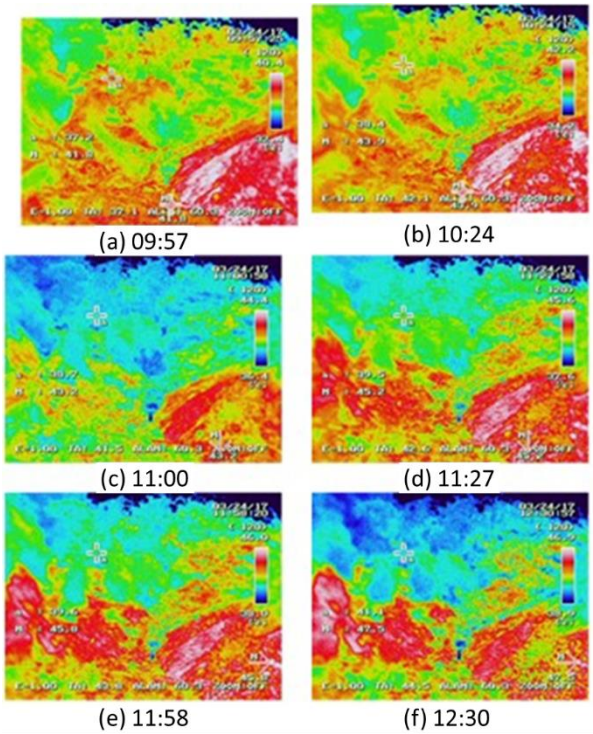

Figure 6. Thermographs of the monitored landslide (captured on March 24, 2017).

4.2 UAS Thermal Imager Monitoring

The thermal images obtained by the UAS thermal imager on April 28, 2017 were compared with those obtained by the handheld thermal imager. The UAS aerial thermograph revealed a lower temperature in the two erosion gullies and shadow areas than in other

areas (Figure 9). The highest temperature was 43.1 °C on the left side of the sandstone slope, and the lowest was 22.73 °C on the right side of the shadow gully. Compared with the thermograph obtained using the handheld thermal imager, the aerial thermograph obtained using the UAS thermal imager showed more considerable temperature changes in the gully areas. In terms of monitoring distance, the UAS thermal imager was closer to the landslide compared with the handheld thermal imager. However, the UAS image was limited because the imager was airborne for 15 min without finding a fixed position for monitoring.

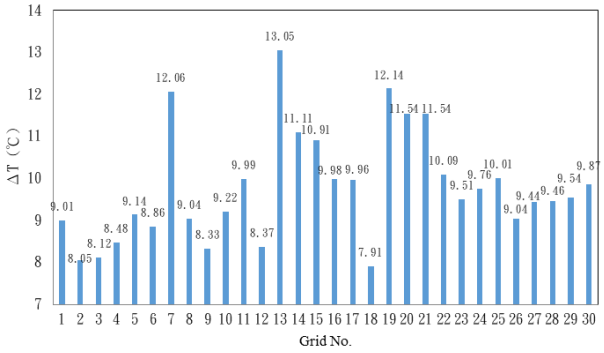

Figure 7. Statistics of the infrared temperature changes (⊿T) between 09:27 and 13:01 (recorded on March 24, 2017).

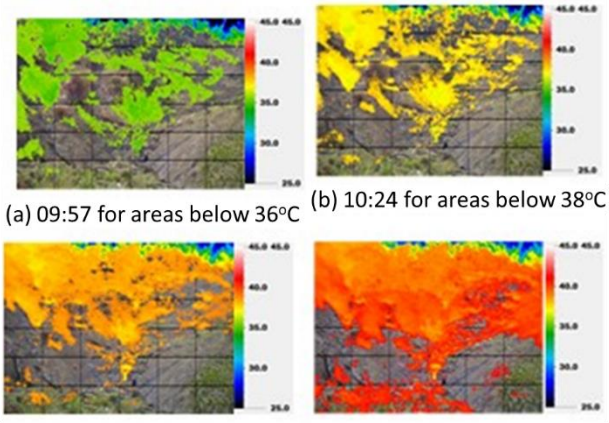

Figure 8. Handheld thermograph (captured on March 24, 2017).

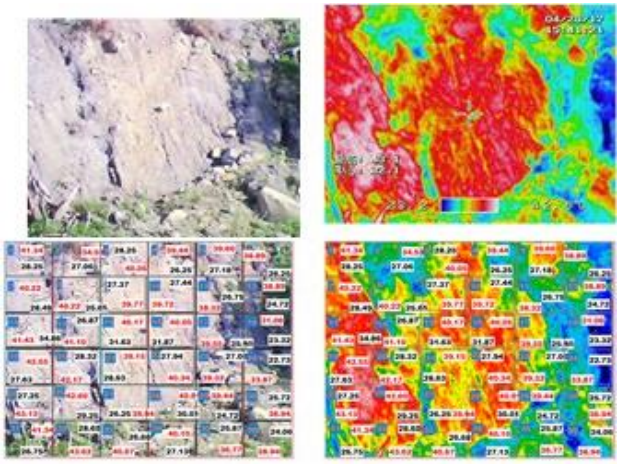

Figure 9. Aerial thermograph (captured by UAS thermal imager on April 28, 2017).

5 CONCLUSION

The study applied handheld and UAS thermal imagers for monitoring topography changes engendered by a landslide in a mudstone area. Field investigations showed that the landslide could be attributed to the torrential-rainfall-induced high water content in the mudstone and the surficial-rainfall-eroded gully. The derived thermal images demonstrated that the eroded gully exhibited a lower infrared temperature and was associated with higher temperature sensitivity when compared with the surrounding areas. Sandstone demonstrated a higher change in infrared temperature than did mudstone, in addition to being associated with higher temperature sensitivity. The erosion gully was associated with high sensitivity to infrared temperature changes and was affected by the shade. The infrared temperature image was overlapped with the visible image to find the high-water-content areas, bare land areas, and surficial cracks. Future research needs to prolong the monitoring period for better reflecting the changes in infrared temperature in slope areas.

ACKNOWLEDGEMENTS

Financial support provided by the National Science and Technology Council in Taiwan under contract NSTC 113-2914-I-415-001-A1.

REFERENCES

Chen, C.Y. (2016). Landslide and debris flow initiated characteristics after typhoon Morakot in Taiwan. *Landslides*, 13: 153-164. https://doi.org/10.1007/s10346-015-0654-6.

Lin, J.C. (1995). The evolutionary model of mudrock slope. *Journal of Geographical Science*, 18: 45-58.

Lee, D.H., Jhin, Y.Y. and Tien, K.G. (1994) Characteristics of mudstone and the methods for slope protection. *Sino-Geotechnics*, 48: 35-47.

Wang, S. (1988). *Research on the landscape conservation area of mudstone badland*. Council of Agriculture, Executive Yuan R.O.C., Report of Ecosystem Research No. 004.

Chen, H.L. (2006). *The study of the application of soil-tire-vegetation method in the mudstone slope with middle-high gradient*. Master thesis of Dept. of Civil Engineering in National Cheng Kung University in Taiwan.

Hsu, S.H., Huang, K.H. and Liao, S.Y. (2005). Application of thermo-tracer on studying surface temperature changes on mudstone slopes. *Crop, Environment & Bioinformatics*, 2: 148-156. https://doi.org/10.30061/CEB.200506.0007.

Hsu, S.H., Huang, K.H. and Liao, S.Y. (2005). Estimation of solar radiation on the mudstone slopes. *Crop, Environment & Bioinformatics*, 2: 211-220. https://doi.org/10.30061/CEB.200509.0004.

Clark, M.R., McCann, D.M. and Forde, M.C. (2003). Application of infrared thermography to the non-destructive testing of concrete and masonry bridges. *NDT & E International*, 36: 265-275. https://doi.org/10.1016/S0963-8695(02)00060-9.

Baroň, I., Bečkovský, D. and Míča, L. (2014). Application of infrared thermography for mapping open fractures in deep-seated rockslides and unstable cliffs. *Landslides*, 11: 15-27. https://doi.org/10.1007/s10346-012-0367-z.

Wu, J.H., Lin, H.M., Lee, D.H. and Fang, S.C. (2005). Integrity assessment of rock mass behind the shotcreted slope using thermography. *Engineering Geology*, 80: 164-173. https://doi.org/10.1016/j.enggeo.2005.04.005.

Chen, C.Y. and Jiang, Z.S. (2018). Application of thermal images for determining the vegetation coverage ratio at free-frame shotcrete grid beam protected slope. *MATEC Web of Conferences*, Vol. 206, 04003. https://doi.org/10.1051/matecconf/201820604003.

NCDR (2016). *Typhoon Megi Disaster Investigaton Report.* National Science and Technology Center for Disaster Reduction Center, Research Rep.

Proceedings of the XVIII ECSMGE 2024
GEOTECHNICAL ENGINEERING CHALLENGES
TO MEET CURRENT AND EMERGING NEEDS OF SOCIETY
© 2024 the Authors
ISBN 978-1-032-54816-6
DOI 10.1201/9781003431749-186
Open Access: www.taylorfrancis.com, CC BY-NC-ND 4.0 license

ECSMGE 24
XVIII EUROPEAN CONFERENCE ON SOIL MECHANICS AND GEOTECHNICAL ENGINEERING

Evaluating the interface shear strength of geocomposite drain and HDPE geomembrane layers in landfill cover systems

Évaluation de la résistance au cisaillement de l'interface entre le drain géocomposite et la géomembrane en PEHD dans les systèmes de clôture de décharge

F. Chihi*, G. Varga
Department of Engineering Geology and Geotechnics, Faculty of Civil Engineering, Budapest University of Technology and Economics. Budapest, Hungary

**chihi.feten@emk.bme.hu*

ABSTRACT: This study evaluates the shear strength of geosynthetic drain-HDPE geomembrane interfaces under dry and submerged conditions at normal stresses of 10, 20, and 30 kPa using a comprehensive large-scale direct shear testing program. Results revieled higher shear stress in dry conditions, with a significant reduction upon submersion due to water's lubricating effect. Despite a lower friction angle, the geocomposite drain maintains a consistent friction angle in residual shear strength tests, crucial for landfill cover stability. The geocomposite's lighter weight and reduced height are advantageous, potentially compensating for lower friction angles and contributing to slope stability. The outcomes of this study provide significant insights, which are essential in refining the engineering design of landfill cover systems incorporating geosynthetics. Further research is needed to fully understand the impact of the geocomposite physical properties on the overall slope stability.

RÉSUMÉ: Cette étude évalue la résistance au cisaillement des interfaces entre les drains géosynthétiques et les géomembranes HDPE sous conditions sèches et submergées à des contraintes normales de 10, 20 et 30 kPa, en utilisant un programme de tests de cisaillement direct à grande échelle. Les résultats révèlent un stress de cisaillement plus élevé en conditions sèches, avec une réduction significative lors de la submersion due à l'effet lubrifiant de l'eau. Malgré un angle de friction inférieur, le drain géosynthétique maintient un angle de friction constant dans les tests de résistance au cisaillement résiduel, crucial pour la stabilité des couvertures de décharge. Le poids plus léger et la hauteur réduite du géocomposite sont avantageux, compensant potentiellement les angles de friction inférieurs et contribuant à la stabilité des pentes. Les résultats de cette étude fournissent des aperçus significatifs, essentiels pour affiner la conception technique des systèmes de couverture de décharge incorporant des géosynthétiques. Des recherches supplémentaires sont nécessaires pour comprendre pleinement l'impact des propriétés physiques du géocomposite sur la stabilité globale des pentes.

Keywords: Landfill; geosynthetic drain; HDPE; hydraulic barrier; interface shear strength.

1 INTRODUCTION

The efficacy and sustainability of landfill sites critically depend on the performance of their cover systems, which serve as hydraulic barriers. These cover systems are designed to prevent environmental contamination by inhibiting water ingress into waste material. The integrity of these hydraulic barriers is essential in ensuring the long-term stability and environmental safety of landfill sites. Therefore, the engineering and material composition of landfill cover systems are areas of ongoing research and development, seeking to enhance their performance and durability under various environmental conditions.

However, the operational success of these landfill cover systems is frequently compromised by structural failures, predominantly manifested as sliding and slope instability (Cortellazzo et al., 2022; Shi et al., 2020). Such failures are largely attributed to a confluence of factors including low shear strength parameters, the excessive weight of conventional soil cover systems including granular drainage layers, and steep slope angles inherent in landfill designs (Zornberg et al., 2011). These failures not only pose significant risks to the structural integrity of the landfill but also have far-reaching implications for environmental safety. The low shear strength at the interfaces of different layers within the cover system is a critical factor contributing to these failures. The heavy weight of granular drains exerts substantial

pressure on the underlying structures, intensifying the risk of sliding, particularly on steeper slopes. Addressing these challenges is essential for the development of more robust and reliable landfill cover systems.

In response to these challenges, geosynthetics have emerged as a viable alternative to traditional materials in landfill cover systems (Müller & Saathoff, 2015). The use of geosynthetic drains offers a promising solution to reduce the overall weight of the cover system and optimize its design. Geosynthetics, known for their durability and versatility, can effectively enhance the stability of landfill covers. However, despite these advantages, the potential for sliding failures remains a concern. The interface shear strength between the geosynthetic layers and adjacent materials, especially under various hydraulic conditions, is a critical aspect that necessitates thorough investigation (Kavazanjian Jr. et al., 2006; Touze-Foltz et al., 2021). This understanding is essential to leverage the benefits of geosynthetics fully while mitigating the risks associated with their integration into landfill cover systems.

Therefore, this paper aims to experimentally evaluate the interface shear strength between geosynthetic drain and HDPE geomembrane (GM) layers in landfill cover systems. By conducting a series of tests under different hydraulic conditions, the study seeks to quantify the shear strength at these critical interfaces. These findings are compared with existing literature on traditional granular drains, offering a comprehensive understanding of the performance of geosynthetics in comparison to conventional materials. This research attempts to provide valuable insights into optimizing landfill cover designs, enhancing their stability, and ensuring environmental safety, thereby contributing significantly to the field of landfill engineering.

2 MATERIAL AND METHOD

2.1 Geocomposite drain

The triple layered geocomposite drain (GTD) is characterized by a tripartite structure, each layer contributing distinct functional properties to the overall system.

The upper and lower layers of the geocomposite drain consists of a needle-punched geotextile made from polypropylene (PP). Thes layers serve primarily as a filter, preventing the ingress of fine particles into the drainage core while allowing water to pass through. The needle-punching technique enhances the mechanical interlocking of the fibres, thus imparting both strength and durability to the geotextile.

At the heart of the triple-layered system lies an internal drainage core, made from PP. The core is designed in a "V" shape, which optimizes the flow of water through the drainage system. This configuration facilitates efficient drainage while maintaining structural integrity under varying stresses (Figure 1).



Figure 1. Geocomposite drain used in the testing program.

The entire structure is sewn together, creating a cohesive and robust drainage system. The triple drain exhibits a thickness of 5 mm, characterised by an opening size of 90 nm. The permeability on a plain surface is 100 mm/s. It weights 520 g/m^2, which is considered very light compared to the conventional granular drains, hence it contributes to its stability. It boasts a tensile strength of 16 kN/m, indicative of its ability to withstand significant mechanical stress without compromising its structural integrity or performance.

2.2 HDPE

The HDPE GM employed in this research is characterized by a smooth surface texture. With a thickness of 2 mm, it strikes a balance between flexibility and robustness.

2.3 Testing program

For the direct shear tests, geocomposite drain samples and HDPE GM were cut into 200x200 mm. A rigid, flat wooden board served as the substrate for the geosynthetic samples during the tests. To ensure the integrity of the samples during testing, each geocomposite drain specimen was carefully glued to the board to prevent any folds, wrinkles, or unwanted movements that could influence the test results (Figure 2).

The direct shear tests were carried out using a 200x200 mm test area. Each test was conducted under three different normal stresses: 10 kPa, 20 kPa, and 30 kPa representative of the stress exerted by a 1.5 m

thick cover system (Othman, 2016). To ensure the consistency each test was replicated three times. The shear parameters were then determined based on the average of these three results. Following the ASTM D5321/D5321M – 14 Standard, a constant shearing speed of 0.3 mm/min was maintained throughout all tests. The shear displacement was set to 10% of the shearing area, aligning with the standard testing protocols for such materials.

The lower HDPE specimen was first placed in the lower container of the direct shear apparatus, followed by the upper geosynthetic layer, along with its superstratum. Special attention was paid to ensuring that only the specimens were in direct contact within the test area.

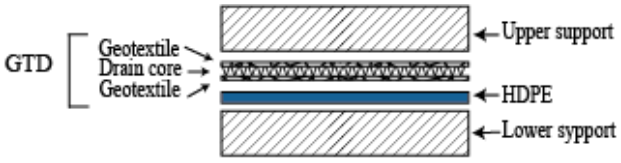

Figure 2. Test configuration.

To comprehensively evaluate the frictional characteristics under various service conditions, tests were performed under both dry and submerged scenarios. For the submerged tests, geosynthetic specimens were fully immersed in water before the beginning of the shearing process. This approach was integral in simulating the limit conditions that the HDPE-geocomposite drain interface might encounter in actual landfill cover systems.

3 RESULTS AND DISCUSSION

The direct shear tests conducted on the geosynthetic drain and HDPE geomembrane interfaces reveal their interaction under varying normal stresses and hydraulic conditions. The experimental outcomes, represented in Figure 3, demonstrate the shear stress response to shear displacement for both dry and submerged states at normal stresses of 10 kPa, 20 kPa, and 30 kPa.

The graphical representation outlines a clear escalation in shear stress levels corresponding to an increase in normal stress across both environmental conditions. This increment is consistent with the theoretical understanding that higher normal stresses engender an elevated frictional force at the interface.

The post-initial increments shear stress behaviour with respect to the shear displacement revealed a linear trend with no notable peak. Such steady-state friction behaviour is indicative of an absence of pronounced strain hardening or softening, which implies a stable interface shear strength within the displacement range and condition tested. The lack of peak shear stress values within the range of displacement tested suggests that the interface does not exhibit a failure indicating good interfacial compatibility and stability.

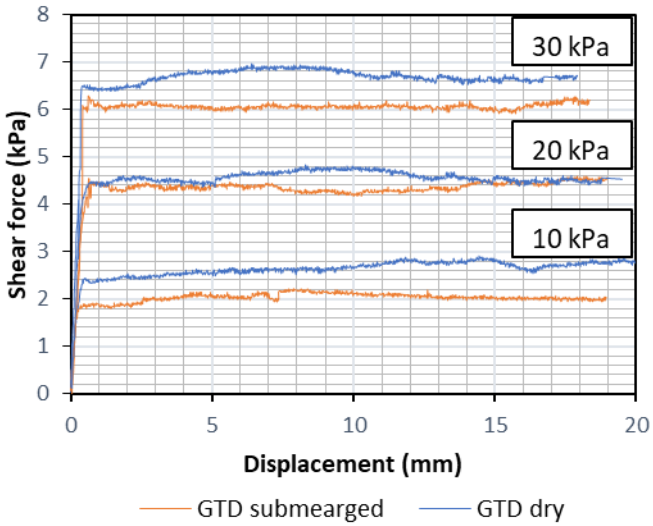

Figure 3. Shear stress and stress ratio vs. horizontal displacement of HDPE-GTD (average values).

The analysis of test results shows a clear difference in shear stress values between dry and wet conditions. When dry, the interface always showed higher levels of shear stress for all the different normal stresses compared to when it was wet. This phenomenon underlines the reduction in shear strength due to the lubricating effect of water at the interface. The reduction was reflected in the friction angle results (Table *1*) In the context of residual shear strength, both dry and submerged HDPE-GTD interfaces demonstrate a consistent friction angle, suggesting a stable residual strength. This is particularly significant for landfill cover system designs, where the post-peak strength is critical to long-term stability and safety.

The shear envelope representation of the test results presented in Figure 4, was compared to the trend line of smooth HDPE-coarse soil proposed by Dixon, et al. (2006). It shows that the shear strength obtained in the test is slightly lower.

Although the interface friction angle of the geocomposite drain-HDPE is lower than that of traditional granular soil drains, it is important to consider the overall stability factors in landfill cover system design. The geocomposite drain offers a considerable advantage due to its lighter weight and reduced height. These characteristics can significantly offset the lower interface friction angle by reducing the driving force on the slopes, thus enhancing stability.

Table 1. Geomembrane–Drain interface peak and residual shear strength parameters.

	Residual shear strength, τr	
Interface	Friction angle (°)	Friction angle (°)
HDPE-GTD (dry)	13.5	11
HDPE-GTD (submerged)	10	9.5

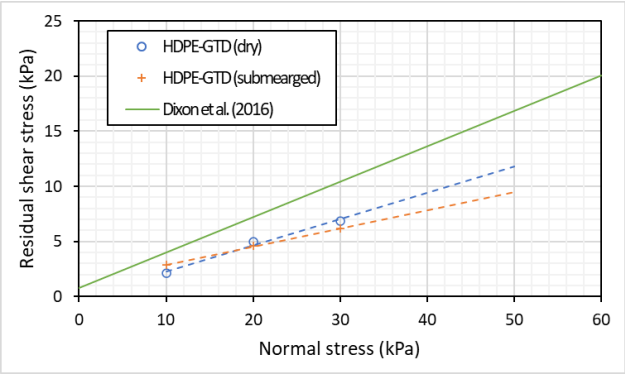

Figure 4. Residual strength envelopes (Dixon, et al. (2006)).

4 CONCLUSIONS

The direct shear tests on the geosynthetic drain-HDPE geomembrane interfaces have provided valuable insights into their interfacial behaviour under different conditions.

- The interface exhibits higher shear stress when dry compared to submerged, highlighting the reduction in shear strength due to the lubricating effect of water.
- Residual shear strength analysis reveals consistent friction angles for both dry and submerged conditions, important for the long-term stability of landfill covers.
- Although shear strength is slightly lower than that of traditional granular soil-HDPE interfaces, the geocomposite drain's lighter weight and reduced height enhance slope stability.

The characteristics of geocomposite drains effectively compensate for lower interface friction angles, advocating their use in landfill cover system design for balanced stability and safety. Future studies should investigate the drain's lighter weight and reduced height contributing to the overall slope stability of the cover system to further validate their suitability for landfill applications.

REFERENCES

ASTM. (2014). *D5321 / D5321M - 14. Standard Test Method for Determining the Shear Strength of Soil-Geosynthetic and Geosynthetic-Geosynthetic Interfaces by Direct Shear*. https://doi.org/10.1520/D5321_D5321M-14.

Cortellazzo, G., Russo, L. E., Busana, S., Carbone, L., Favaretti, M., & Hangen, H. (2022). Field trial of a reinforced landfill cover system: performance and failure. *Geotextiles and Geomembranes*, *50*(4), 655–667. https://doi.org/10.1016/j.geotexmem.2022.03.007.

Dixon, N., Jones, D. R. V., & Fowmes, G. J. (2006). Interface shear strength variability and its use in reliability-based landfill stability analysis. *Geosynthetics International*, *13*(1), 1–14. https://doi.org/10.1680/gein.2006.13.1.1.

Kavazanjian Jr., E., Dixon, N., Katsumi, T., Kortegast, A., Legg, P., & Zanzinger, H. (2006). Geosynthetic barriers for environmental protection at landfills. *Geosynthetics-8th International Conference on Geosynthetics*, *January 2006*, 152.

Müller, W. W., & Saathoff, F. (2015). Geosynthetics in geoenvironmental engineering. *Science and Technology of Advanced Materials*, *16*(3). https://doi.org/10.1088/1468-6996/16/3/034605.

Othman, M. (2016). *Interface Behaviour and Stability of Geocomposite drain/soil systems* (Issue March) [Loughborough University]. https://doi.org/10.13140/RG.2.2.22646.91204.

Quispe-Astete, E. R., Huallanca, W. J., & Parra, D. A. (2023). Shear Strength Evaluation of Soil–Geosynthetic and Geosynthetic–Geosynthetic Interfaces of Closure Cover Systems. *International Journal of Geosynthetics and Ground Engineering*, *9*(6). https://doi.org/10.1007/s40891-023-00504-4.

Shi, J., Shu, S., Qian, X., & Wang, Y. (2020). Shear strength of landfill liner interface in the case of varying normal stress. *Geotextiles and Geomembranes*, *48*(5), 713–723. https://doi.org/10.1016/j.geotexmem.2020.05.004.

Touze-Foltz, N., Xie, H., & Stoltz, G. (2021). Performance issues of barrier systems for landfills: A review. *Geotextiles and Geomembranes*, *49*(2), 475–488. https://doi.org/10.1016/j.geotexmem.2020.10.016.

Zornberg, J. G., Ph, D., Geosynthetics, I., & Igs, S. (2011). Advances in the Use of Geosynthetics for Waste Containment. *Fifteenth African Regional Conference on Soil Mechanics and Geotechnical Engineering*, *21*, 1–21. https://www.semanticscholar.org/paper/Advances-in-the-Use-of-Geosynthetics-for-Waste-Zornberg/3630d19d38ff87c57ba6e319dd620559b0c2c591.

Proceedings of the XVIII ECSMGE 2024
GEOTECHNICAL ENGINEERING CHALLENGES
TO MEET CURRENT AND EMERGING NEEDS OF SOCIETY
© 2024 the Authors
ISBN 978-1-032-54816-6
DOI 10.1201/9781003431749-187
Open Access: www.taylorfrancis.com, CC BY-NC-ND 4.0 license

ECSMGE 24
XVIII EUROPEAN CONFERENCE ON SOIL MECHANICS AND GEOTECHNICAL ENGINEERING

A simplified procedure for FE analysis of an earth dam under seismic loading

Une procédure simplifiée pour l'analyse EF d'un barrage en terre sous chargement sismique

A. Choudhury, P. Ghosh*, S.K. Mishra
Indian Institute of Technology Kanpur, Kanpur, India

**priyog@iitk.ac.in*

ABSTRACT: The behaviour of an earth dam under seismic conditions can be predicted by geotechnical engineers using a variety of numerical tools. This study performs the finite element (FE) analysis of an earth dam subjected to seismic ground motion. The choice of material constitutive model is critical in any numerical analysis as it should correctly simulate the soil behaviour under earthquake loadings. The current study proposes a simplified technique to avoid complicated user-defined material models. The shear modulus reduction of geomaterials under seismic loadings is introduced into the elastoplastic Mohr-Coulomb model available in the FE software ABAQUS using the user-defined field variable interface. By calibrating the damping of the model with the help of Rayleigh damping, the current numerical results are found to be in good agreement with those recorded using instruments and reported by other researchers using an advanced geotechnical engineering software. To reinforce the applicability of the proposed technique, the analysis is done with varying solver types and flow rules. Good and comparable results are obtained in all cases.

RÉSUMÉ: Le comportement d'un barrage en terre dans des conditions sismiques peut être prédit par les ingénieurs géotechniques à l'aide de divers outils numériques. Cette étude effectue l'analyse par éléments finis (EF) d'un barrage en terre soumis à un mouvement sismique du sol. Le choix du modèle constitutif du matériau est critique dans toute analyse numérique car il doit simuler correctement le comportement du sol sous les charges sismiques. La présente étude propose une technique simplifiée pour éviter les modèles de matériaux compliqués définis par l'utilisateur. La réduction du module de cisaillement des géomatériaux sous charges sismiques est introduite dans le modèle élastoplastique de Mohr-Coulomb disponible dans le logiciel FE ABAQUS à l'aide de l'interface de variables de champ définie par l'utilisateur. En calibrant l'amortissement du modèle à l'aide de l'amortissement de Rayleigh, les résultats numériques actuels s'avèrent être en bon accord avec ceux enregistrés à l'aide d'instruments et rapportés par d'autres chercheurs utilisant un logiciel d'ingénierie géotechnique avancé. Pour renforcer l'applicabilité de la technique proposée, l'analyse est effectuée avec différents types de solveurs et règles de flux. Des résultats bons et comparables sont obtenus dans tous les cas.

Keywords: Earth dam; finite element analysis; earthquake; seismic loading; ABAQUS.

1 INTRODUCTION

Earth dams are used worldwide to retain water or semi-fluid waste. The safety and stability assessment of such geotechnical structures under seismic loadings is an engrossing task. Several researchers (Prevost et al., 1985; Cascone and Rampello, 2003; Hwang et al., 2007; Rampello et al., 2009; Wu et al., 2021) used various numerical techniques to analyse the behaviour of earth dams under seismic conditions. The behaviour of earth dams was predicted using multiple techniques, including the finite element (FE) method, the finite difference method, and other numerical methods. Some of the researchers employed the equivalent linear technique to model geomaterials, while the hardening soil model (Schanz et al., 1999) or some other yielding constitutive model was utilised by others. The researchers conducted these numerical analyses using various commercially available software packages meant explicitly for geotechnical engineering applications. Sometimes, to study the behaviour of geotechnical structures in different physical settings, it becomes necessary to use some generalised multiphysics simulation tool. In that case, it is essential to implement soil models that can correctly simulate the behaviour of the soil under seismic conditions. Thus, coding complicated soil models as user-defined material models becomes necessary. To avoid this, the present study proposes a simplified procedure where, using the user-defined field variable interface of the FE software ABAQUS (Dassault Systèmes Simulia Corp., 2020), the shear modulus reduction of soil with respect to increasing

shear strain is introduced into the elastoplastic soil model following the Mohr-Coulomb failure criteria.

The proposed simplified procedure is used to analyse the behaviour of the Liyutan earth dam (situated in Taiwan) subjected to the Chi-Chi earthquake ground motion of 1999. Feng et al. (2010) investigated the response of this earth dam subjected to the same ground motion using the FLAC 6.0 code (Itasca, 2008). The results obtained using the proposed technique agree with the recorded values (by Central Water Resources Office, 1999) and those obtained by Feng et al. (2010).

2 MODEL DETAILS AND ANALYSIS METHODOLOGY

The simplified cross-section of the Liyutan dam employed by Feng et al. (2010) is used for the present analysis. The dam is divided into three sections – upstream shell (U/S), core and downstream shell (D/S), as shown in Figure 1. It is an earth dam with semi-permeable shells and an impervious core of clayey material. The FE mesh of the dam is also shown in Figure 1. The FE mesh contains 5523 four-noded plain strain elements (CPE4R). The size of the elements is chosen such that the length is less than one-tenth of the wavelength associated with the frequency of the input ground motion, which contains considerable energy (Kuhlemeyer and Lysmer, 1973).

The analysis consists of two broad steps – first is the static step, where the initial static state of the dam is established, and the second is the dynamic step (either explicit or implicit), which involves the time history analysis. The earthquake time histories in both horizontal and vertical directions are applied at the base of the dam, and the results are obtained in terms of the permanent horizontal and vertical displacement at the crest, mid-height of upstream (U/S) face and downstream (D/S) face. The accelerations at the crest are also noted. Similar to the research by Feng et al. (2010), the dynamic analysis is uncoupled; that is, the effect of transient seepage and excess pore water pressures is not considered. Feng et al. (2010) conducted a steady-state seepage analysis (with a 60 m water level) to get the initial stress state and then used that stress state to set the initial small strain shear modulus of the geomaterials. However, in the present analysis, the initial shear modulus is assumed to be constant and independent of the effective mean stress. Additionally, as the types of elements are different, ABAQUS by default does not let the seepage phase come before the dynamic step. Hence, the steady state seepage step is avoided in the current analysis, and the static stresses are directly established. Although user-defined elements can solve this problem, they are not considered to avoid complications.

The properties of the geomaterials that form the earth dam and the proposed simplified procedure are detailed in the subsequent sections.

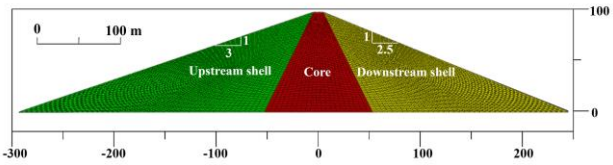

Figure 1. Simplified cross-section and FE mesh for the numerical analysis of the dam.

2.1 Material properties

The elastic and shear strength parameters of the three components of the earth dam are given in Table 1. The maximum shear modulus, i.e., the small strain shear modulus, is represented as G_{max}. The shear modulus (G) reduction curves of the geomaterials are shown in Figure 2.

The dam is modelled using the elastoplastic Mohr-Coulomb model. Initially, a non-associated flow rule (where the dilation angle is zero) is used. Results are later obtained using the associated flow rule and contrasted with the preliminary results. In this case, the dilation angle equals the friction angle of the soil. The shear modulus reduction of the soil is implemented in this model by the simplified procedure outlined in section 2.2. Rayleigh damping given by equation (1) is used to impose damping in the system:

$$[C] = \alpha[M] + \beta[K] \quad (1)$$

where $[C]$, $[M]$, and $[K]$ are the damping, mass and stiffness matrices, respectively. The terms α and β are the mass and stiffness proportional damping coefficients, respectively, which can be expressed as

$$\alpha = \xi \cdot \omega_i \quad (2)$$

$$\beta = \xi \cdot (\omega_i)^{-1} \quad (3)$$

where ξ is the damping ratio, and ω_i is the angular frequency. Typically, ω_i can be equal to the frequency that is in the middle of the dominant frequencies of the input wave (Itasca, 2008); alternatively, it can be equal to the fundamental frequency of the structure as that is the major mode of vibration (Idriss et al., 1973). In the present analysis, these two methods of calculating the damping coefficients are employed and the results are compared. Hereafter, the first method is referred to as R1, and the second as R2. The analysis is performed at three different values of damping ratio (ξ) – 5%, 10%,

and 15%, and the optimum value is found, which gives results close to the recorded (by Central Water Resources Office, 1999) and previously calculated values (by Feng et al., 2010).

The fundamental period of the dam is calculated using the default Lancozs solver in ABAQUS and is found to be 0.62 s.

Table 1. Elastic and shear strength properties of geomaterials (from Hnang, 1996 and Central Water Resources Office, 1995).

Zone	Density (t/m^3)	Shear modulus (G_{max}) (Pa)	Poisson's ratio (ν)	Cohesion c' (kPa)	Friction angle (ϕ) (°)
Upstream shell	2.18	5.0×10^8	0.34	94	41
Core	2.08	3.5×10^8	0.45	34	27
Downstream shell	2.18	6.0×10^8	0.3	82	35

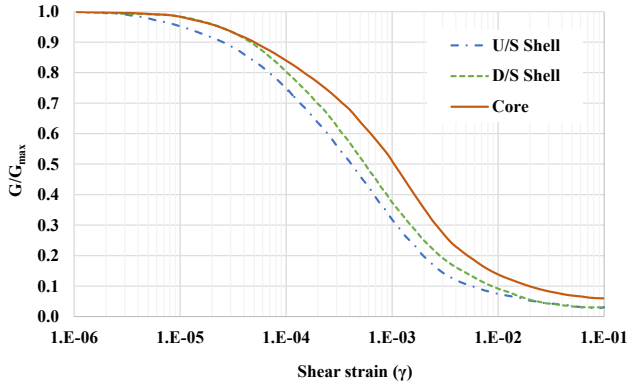

Figure 2. Shear modulus reduction curves of geomaterials (from Central Water Resources Office, 1995).

2.2 The simplified procedure

When the soil is subjected to a cyclic load, it loses its strength gradually. This reduction is represented as the shear modulus reduction curve, where the shear modulus reduces with increased shear strain. Parallel to this, due to the stress reversals and reduction in shear modulus, the damping of the soil increases as the shear strain increases. Using the user-defined field variable interface of the ABAQUS software the reduction in shear modulus with an increase in shear strain is implemented with the help of a simple algorithm, as shown in Figure 3.

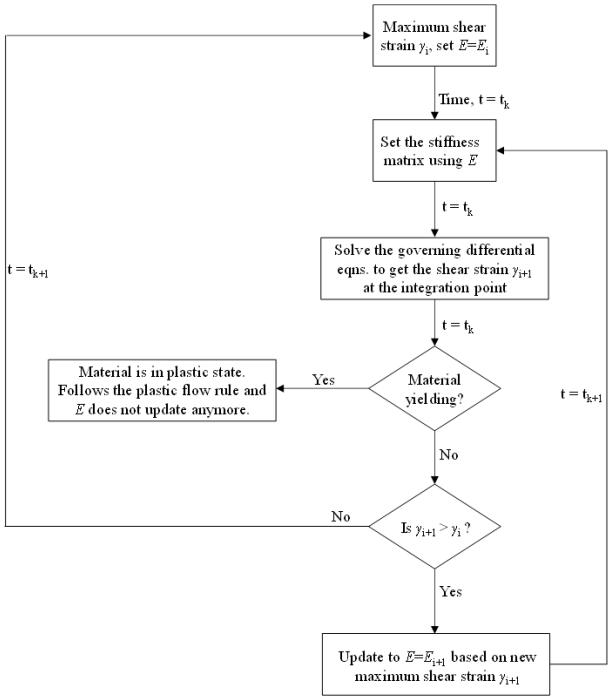

Figure 3. Flow chart for the algorithm used to implement the proposed simplified approach.

The soil is considered homogenous and isotropic; hence, the shear modulus (G) and elastic modulus (E) can be related by the following equation:

$$E = 2G(1 + \nu) \qquad (4)$$

where ν is the Poisson's ratio. Using Figure 2 and equation (4), the calculated elastic modulus (E) is assigned a field variable equal to shear strain in the ABAQUS material manager. The elastic modulus is updated at each integration point based on the maximum value of shear strain (i.e., the field variable) up to that time instant. The current new maximum shear strain is saved using the solution-dependent state variable. Feng et al. (2010) used the equivalent linear sigmoidal model with the Mohr-Coulomb failure model (Itasca, 2008), where the modulus reduction turns off when the material has plastic flow. Similarly, in this simplified approach, the elastic modulus stops reducing as soon as the material yields and enters a plastic flow state.

The proposed technique cannot reflect the hysteretic damping of the soil. Hence, considerably higher damping is enforced with the help of Rayleigh damping to substitute this in an average sense. Thus, this method ultimately gives an outcome that averages the effect of stress reversals and the number of cycles by giving weightage to the maximum strain generated from the peak seismic load during the time history.

2.3 Input ground motions

The horizontal and vertical ground motions recorded at the recording station at the base of the dam during the Chi-Chi earthquake of 1999 are used as input ground motions. These ground motions are shown in Figure 4 and Figure 5. The peak accelerations of horizontal and vertical ground motions are 0.149g and 0.108g, respectively. The horizontal ground motion has the following dominant frequencies – 0.244 Hz, 0.69 Hz, and 0.87 Hz, whereas the vertical ground motion has a dominant frequency of 0.255 Hz (Feng et al., 2010). The acceleration time histories are 45 s long, but the analysis is carried out for 60 s so that the transient response of the earth dam gets sufficiently attenuated.

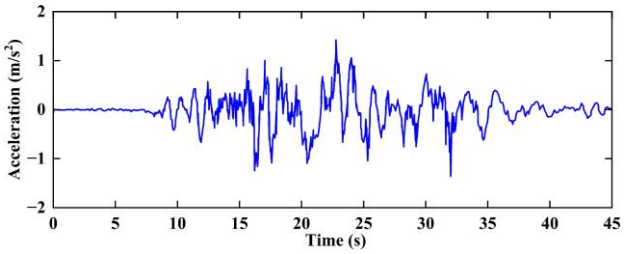

Figure 4. Horizontal acceleration recorded at the base of the Liyutan dam after the Chi-Chi earthquake of 1999 (from Feng et al.,2010).

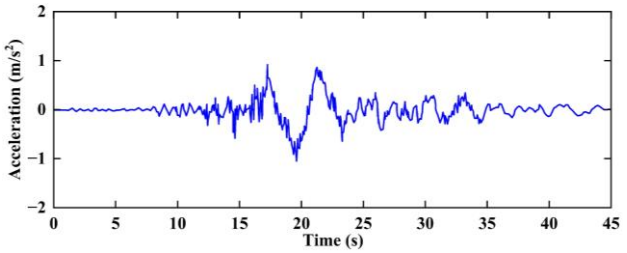

Figure 5. Vertical acceleration recorded at the base of the Liyutan dam after the Chi-Chi earthquake of 1999 (from Feng et al.,2010).

3 RESULTS

Four different time history analyses are carried out using ABAQUS varying the solver type – explicit (E) or implicit (I), method of selection of Rayleigh damping parameters – R1 or R2, and the flow rule – non-associated (N) or associated (A). These four analyses are named as – ER1N, ER2N, IR2N and ER2A, respectively.

The permanent horizontal (↔) and vertical (↕) displacements recorded by the Central Water Resources Office (1999) and those calculated by Feng et al. (2010) at the crest, mid-height (M/H) of upstream (U/S) face and downstream (D/S) face of the dam are given in Table 2. In comparison, the results obtained from the present analyses are tabulated in Table 3.

Table 2. Permanent horizontal and vertical displacements of the dam (in cm) from literature.

	Analysis type	
Location (direction)	**Recorded[a]**	**Calculated[b]**
U/S – M/H (↔)	-2.70 to -3.90	-2
U/S – M/H (↕)	-5.40 to -6.80	1.3
Crest (↔)	-0.70 to -4.30	-5.5
Crest (↕)	-5.00 to -7.90	-5.8
D/S – M/H (↔)	1.80 to 2.90	-0.4
D/S – M/H (↕)	-2.60 to -3.40	0.2

[a]Central Water Resources Office, 1999; [b]Feng et al., 2010

Note: Negative sign '-' means leftward horizontal (↔) or downward vertical (↕) displacement.

On comparing the results tabulated in Table 3 with those in Table 2, it can be seen that 10% Rayleigh damping gives permanent displacements that are a good fit with the recorded and calculated data in the literature. Method R2 gives mostly lower permanent displacements than R1 (except on the D/S side). Such observation agrees with the fact that the fundamental period of vibration of the dam is dominant during the vibration, and hence its damping affects the dynamic behaviour more. The implicit analysis gives results that are not much different from its explicit counterpart. But overall, it predicts slightly higher values. The associated flow rule predicts lower displacement in most of the cases. This is because the increase in dilation angle causes the yield acceleration to increase (Eskandarinejad and Shafiee, 2011; Sharifi et al., 2020).

The peak horizontal and vertical accelerations noted at the crest of the dam for 10% damping are close to the value obtained in the literature, which can be seen in Figure 6 and Figure 7. The comparison of horizontal and vertical acceleration time histories noted at the crest from the ER2N analysis for 10% Rayleigh damping with those from the literature are shown in Figure 8 and Figure 9, respectively. Time histories for the other three analyses are similar and not shown for brevity.

Table 3. Calculated permanent horizontal and vertical displacements (in cm) in the present study.

Location (direction)	Damping (%)	Analysis type ER1N	ER2N	IR2N	ER2A
U/S – M/H (↔)	5	-8.45	-5.82	-5.91	-5.87
	10	-4.09	-2.07	-2.49	-2.18
	15	-2.12	0.20	-0.02	0.18
U/S – M/H (↕)	5	-11.63	-10.04	-11.90	-9.88
	10	-8.12	-7.27	-8.72	-7.26
	15	-5.63	-4.95	-5.86	-4.86
Crest (↔)	5	-13.95	-9.42	-8.43	-10.83
	10	-6.43	-3.16	-2.64	-4.03
	15	-2.84	1.60	2.03	1.44
Crest (↕)	5	-28.90	-27.00	-35.40	-16.53
	10	-17.03	-16.95	-22.12	-10.23
	15	-11.57	-12.37	-16.41	-7.66
D/S – M/H (↔)	5	4.54	5.47	8.42	4.33
	10	1.97	3.49	4.83	3.40
	15	1.61	4.19	5.38	4.09
D/S – M/H (↕)	5	-3.77	-4.34	-6.20	-3.37
	10	-2.71	-3.00	-4.50	-2.75
	15	-2.20	-3.65	-4.91	-3.31

Note: Negative sign '-' means leftward horizontal (↔) or downward vertical (↕) displacement.

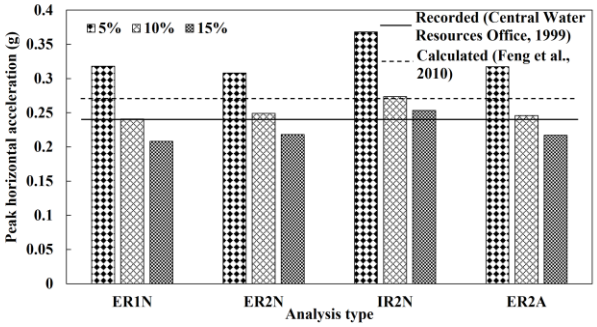

Figure 6. Variation of peak horizontal acceleration at the crest with damping ratio and type of analysis and its comparison with results obtained in the literature.

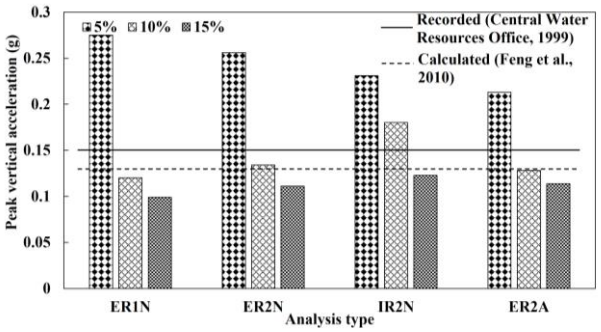

Figure 7. Variation of peak vertical acceleration at the crest with damping ratio and type of analysis and its comparison with results obtained in the literature.

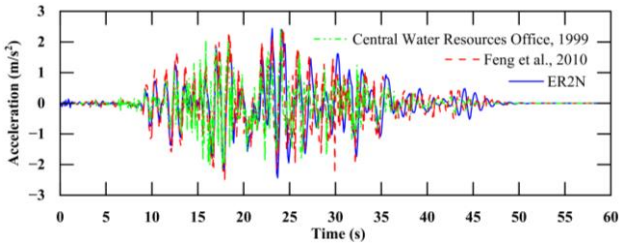

Figure 8. Horizontal acceleration time history at the crest of the dam.

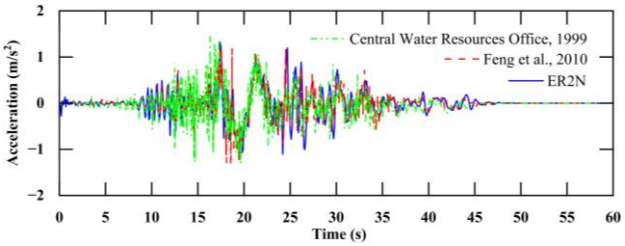

Figure 9. Vertical acceleration time history at the crest of the dam.

All the displacement and acceleration values at the crest are obtained by averaging the output of all the nodes at that level.

4 CONCLUSION

The FE analysis of an earth dam subjected to the Chi-Chi earthquake ground motion of 1999 is performed in the present study using the commercially available software ABAQUS. A simplified procedure to implement the shear modulus reduction of the soil subjected to cyclic loading is proposed and employed. Four different analyses are carried out by varying the solver type, method of calculating the Rayleigh damping parameters and the flow rule of the soil model. For a damping ratio of 10% enforced using Rayleigh damping, the permanent displacements and peak accelerations are found to be within an acceptable range compared to the recorded and calculated results in the literature. The implicit solver gives marginally higher values than the explicit solver, whereas the

associated flow rule predicts lower displacements and peak accelerations. Rayleigh damping parameter calculated using the fundamental frequency of the dam dampens the overall response more. Overall, the permanent displacements and accelerations are well predicted in the present study, except for the permanent vertical displacement of the crest (where a higher value is obtained). It is also to be noted that the results obtained here are the most critical values this scheme can give. Hence, the proposed simplified procedure can be judiciously used for the dynamic analysis, provided it is properly calibrated (using data recorded from instrumentation or analysis using comprehensive soil models) to get the correct damping ratio.

ACKNOWLEDGEMENTS

The authors are grateful for the financial support the Ministry of Education, Government of India, provided through the Prime Minister's Research Fellows (P.M.R.F) scheme.

REFERENCES

Cascone, E. and Rampello, S. (2003) Decoupled seismic analysis of an earth dam, *Soil Dyn. Earthq. Eng*., 23(5), 349-365, https://doi.org/10.1016/s0267-7261(03)00035-6.

Central Water Resources Office (1995). Regular monitoring and analysis report of Liyutan dam, Central Water Resources Office, Taichung, Taiwan (in Chinese).

Central Water Resources Office (1999). Chi-Chi earthquake analysis report of Liyutan dam, Central Water Resources Office, Taichung, Taiwan (in Chinese).

Dassault Systèmes Simulia Corp. (2020). ABAQUS (2020). Available at: https://www.3ds.com/products-services/simulia/products/abaqus/abaquscae/.

Eskandarinejad, A., & Shafiee, A. H. (2011) Pseudo-dynamic analysis of seismic stability of reinforced slopes considering non-associated flow rule, *Journal of Central South University of Technology*, 18, 2091-2099. https://doi.org/10.1007/s11771-011-0948-3.

Feng, Z., Tsai, P. H., & Li, J. N. (2010) Numerical earthquake response analysis of the Liyutan earth dam in Taiwan, *Natural Hazards and Earth System Sciences*, 10(6), 1269-1280. https://doi.org/10.5194/nhess-10-1269-2010.

Hnang, T. K. (1996) Stability analysis of an earth dam under steady state seepage, *Computers & structures*, 58(6), 1075-1082. https://doi.org/10.1016/0045-7949(95)00230-8.

Hwang, J. H., Wu, C. P., and Wang, S. C. (2007) Seismic record analysis of the Liyutan earth dam, *Can. Geotech. J.*, 44(11), 1351-1377. https://doi.org/10.1139/t07-062.

Itasca Consulting Group, Inc. (2008). *FLAC – Fast Lagrangian Analysis of Continua, Ver. 6.0 User's Manual*, Itasca, Minneapolis, USA.

Kuhlemeyer, R. L., & Lysmer, J. (1973) Finite element method accuracy for wave propagation problems, *Journal of the Soil Mechanics and Foundations Division*, 99(5), 421-427. https://doi.org/10.1061/jsfeaq.0001885.

ldriss, I. M., Lysmer, J., Hwang, R. and Seed, H. B (1973). *QUAD-4: a computer program for evaluating the seismic response of soil structure interaction by variable damping finite element procedures*, Report No. EERC 73-16, University of California, Berkeley, CA, USA.

Parish, Y., Sadek, M., and Shahrour, I. (2009) Review Article: Numerical analysis of the seismic behaviour of earth dam, *Nat. Hazards Earth Syst. Sci*., 9, 451-458, https://doi.org/10.5194/nhess-9-451-2009.

Prevost, J.H., Abdel-Ghaffar, A.M. and Lacy, S.J. (1985) Nonlinear dynamic analyses of an earth dam, *Journal of Geotechnical Engineering*, 111(7), 882-897, https://doi.org/10.1061/(asce)0733-9410(1985)111:7(882) .

Rampello, S., Cascone, E., and Grosso, N. (2009) Evaluation of the seismic response of a homogeneous earth dam, *Soil Dyn. Earthq. Eng*., 29(5), 782-798, https://doi.org/10.1016/j.soildyn.2008.08.006.

Schanz, T., Vermeer, P. A., & Bonnier, P. G. (1999) The hardening soil model: formulation and verification, *Beyond 2000 in computational geotechnics*, 1, 281-296, https://doi.org/10.1201/9781315138206-27.

Sharifi, P., Farzaneh, O., & Askari, F. (2020) Influence of Dilation Angle of Soil on Seismic Displacements of Gravity Retaining Walls using Upper Bound Limit Analysis Method, *Numerical Methods in Civil Engineering*, 4(4), 30-36, https://doi.org/10.52547/nmce.4.4.30.

Wu, Q., Li, D.Q., Liu, Y. and Du, W. (2021) Seismic performance of earth dams founded on liquefiable soil layer subjected to near-fault pulse-like ground motions, *Soil Dyn. Earthq. Eng*, 143, 106623, https://doi.org/10.1016/j.soildyn.2021.106623.

Proceedings of the XVIII ECSMGE 2024
GEOTECHNICAL ENGINEERING CHALLENGES
TO MEET CURRENT AND EMERGING NEEDS OF SOCIETY
© 2024 the Authors
ISBN 978-1-032-54816-6
DOI 10.1201/9781003431749-188
Open Access: www.taylorfrancis.com, CC BY-NC-ND 4.0 license

ECSMGE 24
XVIII EUROPEAN CONFERENCE ON SOIL MECHANICS AND GEOTECHNICAL ENGINEERING

Change of soil permeability during and after soil liquefaction

Changement de perméabilité du sol pendant et après la liquéfaction du sol

M.-C. Chu, C.-C. Tsai*, Y.-C. Kao, Y.-X. Liu, C.-Y. Jou
National Chung Hsing University, Taichung, Taiwan

**tsaicc@nchu.edu.tw*

ABSTRACT: In addition to the direct casualties caused by earthquakes, soil liquefaction induced by earthquakes can also lead to subsequent damage. Therefore, it is necessary to have a better understanding of soil liquefaction. Although previous studies have reported an increase in soil permeability during soil liquefaction, the rates of increase suggested by different scholars vary. As a result, this study conducts a series of shaking table liquefaction tests on loose to medium sand to further investigate this issue. The porewater pressure and settlement history are monitored, and the permeability history before, during, and after liquefaction is back-calculated based on the consolidation theory. The results show that the permeability during and after liquefaction is approximately 1.2 and 0.9 times the original value, respectively.

RÉSUMÉ: Outre les victimes directes causées par les tremblements de terre, la liquéfaction des sols induite par les tremblements de terre peut également entraîner des dommages ultérieurs. Il est donc nécessaire de mieux comprendre la liquéfaction des sols. Bien que des études antérieures aient signalé une augmentation de la perméabilité du sol lors de la liquéfaction du sol, les taux d'augmentation suggérés par différents chercheurs varient. En conséquence, cette étude mène une série d'essais de liquéfaction sur table vibrante sur du sable meuble à moyen pour approfondir cette question. La pression interstitielle et l'historique de tassement sont surveillés, et l'historique de perméabilité avant, pendant et après la liquéfaction est rétrocalculé sur la base de la théorie de la consolidation. Les résultats montrent que la perméabilité pendant et après la liquéfaction est respectivement d'environ 1,2 et 0,9 fois la valeur d'origine.

Keywords: Permeability, liquefaction, 1-D consolidation, shaking table.

1 INTRODUCTION

Most researches on soil liquefaction focus on the damages during shakings. However, damages may happen after shakings. Ambraseys and Sarma (1969) found sand boils occur at nearly 20 minutes after the Niigata earthquake during the dissipation of excess pore water pressure (EPWP). The EPWP dissipation rate is considered to be crucial for sand boil formation (Housner, 1958; Seed, 1979). Haigh et al. (2012) proved that the permeability (k) of sands increase with the generation of EPWP by experiments (Ueng et al., 2017). Adamidis and Madabhushi (2016) conducted one-dimensional tests to explain one-dimensional stiffness (E_0) changes with effective stress, in which stiffness during post-liquefaction EPWP dissipation is not constant. Brennan and Madabhushi (2011) proposed an EPWP function of time that could be used in back-calculating coefficient of consolidation (C_v), and the found C_v is not constant during dissipation, which indicates the permeability also varies. Zeybek and Madabhushi (2023) successfully simulate the post-liquefaction EPWP dissipation observed in the centrifuge tests, and found E_0 is more dominant than k in the consolidation process after liquefaction. In this study, the variation in permeability will be assessed using the test results obtained from torsional shaking table experiments, employing 1-D consolidation theory.

2 MATERIALS AND TEST SETUP

This study adopted the torsional shaking table to conduct model tests for observing the change of permeability during and after shakings. The configurations of test are shown in Figure1 (a). Four pore pressure transducers, an accelerometer, and a displacement (settlement) transducer are installed. The detailed configuration can be referred to Tsai et al. (2022). Moreover, seepage test can be also performed using the designed tube.

The testing material is C306 sand, categorized as SP, and its basic properties is provided in table 1. Water pluviation method is adopted in this study, and the schematic diagram is provided in Figure1 (b). The relative densities of specimens were set 68% (void ratio= 0.69). After finishing depositing specimens, torsional shakings were applied with a frequency range of 10 Hz to 25 Hz for 20 seconds to induce

liquefaction. In addition to the shaking test, constant-head seepage tests were performed for the same specimen prior and after vibration to obtain the permeability prior and after liquefaction, respectively.

Table 1. Basic Properties of C306 sand.

Materials	C306 Sand
Specific gravity of solids	2.65
Median size D_{50}(mm)	0.193
Coefficient of uniformity C_u	1.36
Coefficient of curvature C_d	1.1
e_{max}	0.922
e_{min}	0.598

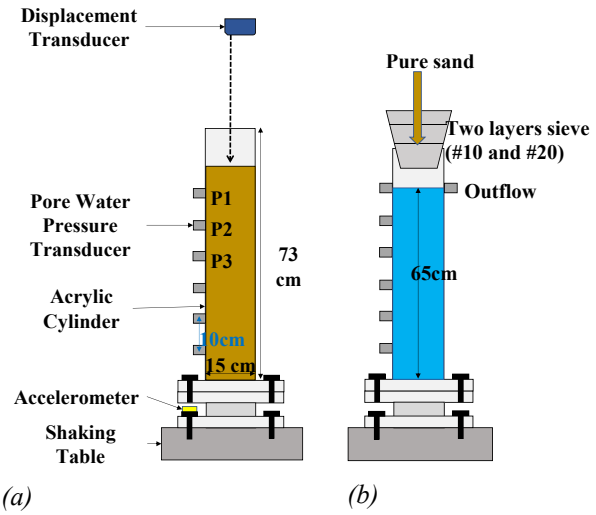

Figure 1. (a) Testing model (b) Specimen preparation method.

3 TEST RESULTS

Figure 2 shows the measured time history of PWP, settlement, and acceleration. Specimen liquefied within top 50-cm as indicated from the EPWP result (Figure 2(a)). The EPWP stayed at the high level (i.e. liquefaction condition) for a period of time (~ 20 sec) after shakings The high EPWP lasts differently at different elevations. Long durations were observed at the shallow depth, indicating the EPWP dissipates from the bottom to the top. On the other hand, it could be observed that settlement started right after shakings, and ended after fully dissipation of EPWP. The significant settlement rate was found during the shakings and the settlement continues after the shakings. These model tests with a relatively small size were conducted to observe the change of permeability during liquefaction under 1-g environment, and it may fail to offer an appropriate range in estimating the liquefaction permeability of soils in field due to the scale of tests.

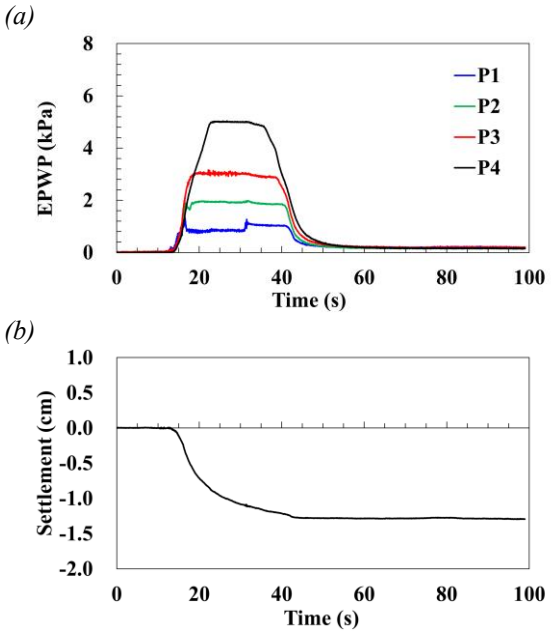

Figure 2. Test results (a) EPWP (b) settlement time history.

4 PERMEABILITY FROM 1-D CONSOLIDATION

From the additional 1-D consolidation tests of C306 sand, the relationships of E_0 and effective stress could be obtained, and could be explicated by the function (of effective stress) shown in Figure 3 with the suggestions from Zeybek and Madabhushi (2023). During the shaking table test, the effective stress in the specimen also varies due to EPWP. Hence, the changing r_u versus time (Figure 4) is considered in calculating changing E_0 due to varying effective stress. The consolidation degree (U) is estimated Equation (1) based on the measured settlement as shown in Figure 5.

$$U\ (\%) = \frac{S_n}{S_{final}} \tag{1}$$

where S_n is the settlement of each time step, and S_{final} is the final settlement of tests. Settlement initiates immediately after shakings and reaches its ultimate magnitude once the complete dissipation of EPWP has taken place. Hence, the settlement covers the time span from the initiation of shakings to the end of testing period. Afterward, C_v could be calculated during the test through Equation (2) to (4) as shown in Figure 6.

$$T_v = \frac{\pi}{4}\left(\frac{U}{100}\right)^2 \tag{2}$$

$$T_v = 1.781 - 0.933log(100 - U) \tag{3}$$

$$C_v = \frac{T_v H_{dr}^2}{t} \quad (4)$$

Where T_v Time factor calculated through Equation (2) or Equation (3) depending on U (60 or >60). After obtaining Tv, C_v (Figure 6) could be evaluated through Equation (4). H_{dr} is the longest drainage path for water in the specimen, and t is the consolidation time. Finally, k could be estimated from the obtained C_v and E0 (Haigh et al., 2012) per Equation (5).

$$k = \frac{C_v \gamma_f}{E_0} \quad (5)$$

As shown in Figure 7, k reach maximum of 0.035 cm/s during soil liquefaction and continue decreasing as the consolidation proceeds. According to the seepage test, k is 0.029 cm/s and 0.025 cm/s before and after liquefaction. The results indicate that liquefaction induces a higher permeability (about 15% higher) due to loosen contacts between particles. The loosen contacts make water flow through specimens more readily without bypassing grain contacts as explained by Ueng et al. (2017). However, after the liquefaction, k is lower caused by a denser condition due to consolidation. In Figure 7, k in the end of settlement is close to the value obtained from seepage test after liquefaction. Hence, k during the EPWP build-up process (beginning of settlement) lower than 0.029 that would be wrong was eliminated herein. This paper presented the view from 1-D consolidation to evaluate the changing permeability of sands during liquefaction, and it is worth noted that the evaluation of true E_0 of liquefied sands is critical.

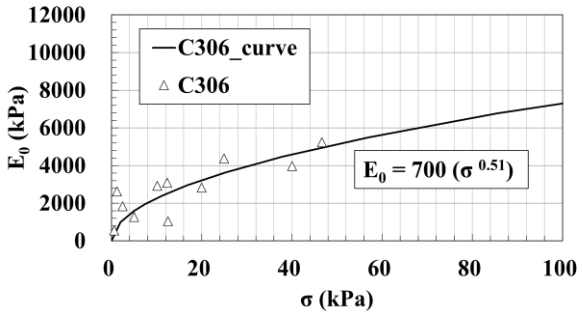

Figure 3. E0 versus 1-D stress based on 1D consolidation test.

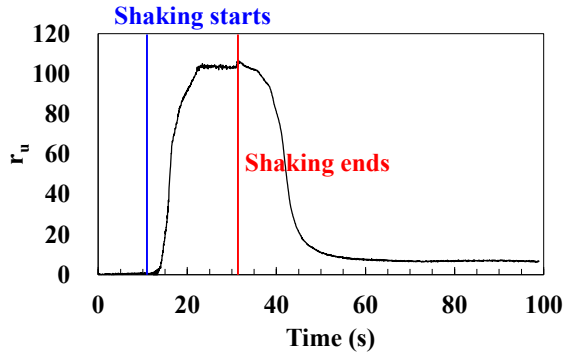

Figure 4. Measured ru time history.

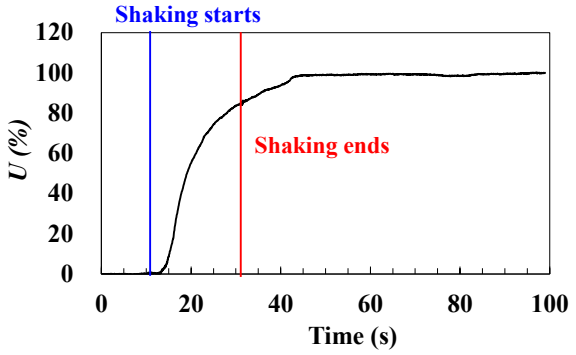

Figure 5. Consolidation degree (U) versus time.

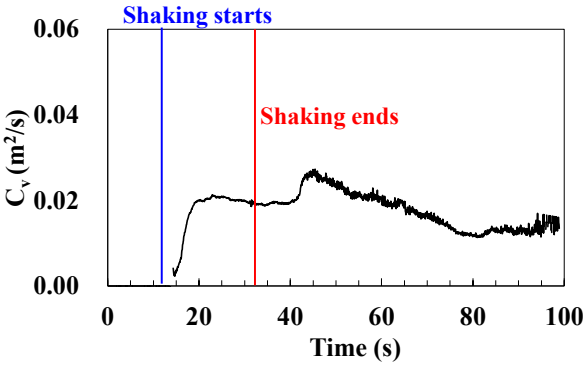

Figure 6. Derived Cv time history.

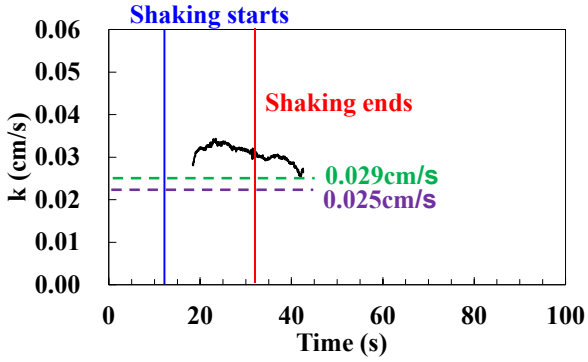

Figure 7. Derived k time history.

5 CONCLUSIONS

This study conducted torsional shaking table tests to evaluate permeability variations in liquefied soil. The settlement was measured, and in conjunction with 1-D consolidation theory, the permeability during soil liquefaction was calculated.

Notably, the onset of settlement was immediately observed following the shaking events. Furthermore, the test results demonstrated a notable increase in permeability (denoted as k) of up to 15% upon soil liquefaction. Interestingly, post-liquefaction, the permeability decreased due to a denser condition resulting from consolidation processes.

The current design practice did not consider the effect of changing permeability due to liquefaction. However, the changing permeability may be related to liquefaction settlement, which may influence the serviceability of structures with enough bearing capacity. These findings provide valuable insights into the dynamic behavior of liquefied soil, highlighting the temporal evolution of permeability and its correlation with settlement patterns.

REFERENCES

Adamidis, O., & Madabhushi, G. (2016). Post-liquefaction reconsolidation of sand. *Proceedings of the Royal Society A: Mathematical, Physical and Engineering Sciences*, 472(2186), 20150745.

Ambraseys, N., & Sarma, S. (1969). Liquefaction of soils induced by earthquakes. *Bulletin of the Seismological Society of America*, 59(2), 651-664. doi:10.1785/bssa0590020651.

Brennan, A., & Madabhushi, S. (2011). Measurement of coefficient of consolidation during reconsolidation of liquefied sand. *Geotechnical Testing Journal*, 34(2), 139-146. https://doi.org/10.1520/GTJ102914.

Haigh, S., Eadington, J., & Madabhushi, S. (2012). Permeability and stiffness of sands at very low effective stresses. Géotechnique, 62(1), 69-75. https://doi.org/10.1680/geot.10.P.035.

Housner, G. W. (1958). The mechanism of sandblows. *Bulletin of the Seismological Society of America*, 48(2), 155-161. https://doi.org/10.1785/BSSA0480020155.

Seed, H. B. (1979). Soil liquefaction and cyclic mobility evaluation for level ground during earthquakes. *Journal of the geotechnical engineering division*, 105(2), 201-255. https://doi.org/10.1061/AJGEB6.0000768.

Tsai, C.-C., Lin, W.-C., Chu, M.-C., & Chi, C.-C. (2022). Experimental study on the mechanism of sand boils and associated settlements due to soil liquefaction in loose sand. *Engineering Geology*, 306, 106708. https://doi.org/10.1016/j.enggeo.2022.106708.

Ueng, T.-S., Wang, Z.-F., Chu, M.-C., & Ge, L. (2017). Laboratory tests for permeability of sand during liquefaction. *Soil Dynamics and Earthquake Engineering*, 100, 249-256. https://doi.org/10.1016/j.soildyn.2017.05.037.

Zeybek, A., & Madabhushi, G. S. P. (2023). Assessment of soil parameters during post-liquefaction reconsolidation of loose sand. *Soil Dynamics and Earthquake Engineering*, 164, 107611. https://doi.org/10.1016/j.soildyn.2022.107611.

Proceedings of the XVIII ECSMGE 2024
GEOTECHNICAL ENGINEERING CHALLENGES
TO MEET CURRENT AND EMERGING NEEDS OF SOCIETY
© 2024 the Authors
ISBN 978-1-032-54816-6
DOI 10.1201/9781003431749-189
Open Access: www.taylorfrancis.com, CC BY-NC-ND 4.0 license

ECSMGE 24
XVIII EUROPEAN CONFERENCE ON SOIL MECHANICS AND GEOTECHNICAL ENGINEERING

Strength and rainfall-induced erosion resistance of bio-cemented soil slopes

Résistance et résistance à l'érosion induite par les précipitations des pentes en sol bio-cimenté

R. Devrani*, P. Vangla
Department of Civil Engineering, Indian Institute of Technology Delhi, India

S. Sharma
Department of Biochemical Engineering and Biotechnology, Indian Institute of Technology Delhi, India

cez198245@civil.iitd.ac.in

ABSTRACT: Rainfall-induced soil erosion in hilly regions is considered a significant geohazard due to its potential to cause substantial damage to infrastructure and human settlement. Soil improvement through microbial-induced calcite precipitation (MICP) using native bacterial strain is a novel approach that can alleviate concerns regarding this issue. The current study presents the soil improvement potential of a native urease-producing bacterial strain isolated from the slope failure region of Uttarakhand, India. The strength improvement and erosion resistance of treated soil were investigated through unconfined compressive strength (UCS) and rainfall-induced erosion tests, respectively. Further, the durability of the treatment was confirmed through the wet-dry cycle of the treated soils. The test results exhibited an enhancement in soil strength due to the binding of soil grains with precipitated calcite crystals. The rainfall simulation test revealed a significant reduction in soil mass loss after the MICP treatment, which was confirmed through microscopic investigations. Interestingly, the treated soil samples showed negligible soil erosion even after subjecting the samples to seven wet-dry cycles.

RÉSUMÉ: L'érosion des sols induite par les précipitations dans les régions montagneuses est considérée comme un géorisque important en raison de son potentiel de causer des dommages importants aux infrastructures et aux établissements humains. L'amélioration des sols grâce à la précipitation de calcite induite par des microbes (MICP) à l'aide d'une souche bactérienne native est une nouvelle approche qui peut atténuer les inquiétudes concernant ce problème. La présente étude présente le potentiel d'amélioration des sols d'une souche bactérienne produisant de l'uréase native isolée de la région de rupture de pente de l'Uttarakhand, en Inde. L'amélioration de la résistance et la résistance à l'érosion du sol traité ont été étudiées respectivement par des tests de résistance à la compression non confinée (UCS) et d'érosion induite par les précipitations. De plus, la durabilité du traitement a été confirmée par le cycle sec-humide des sols traités. Les résultats des tests ont montré une amélioration de la résistance du sol en raison de la liaison des grains du sol avec des cristaux de calcite précipités. Le test de simulation de pluie a révélé une réduction significative de la perte de masse du sol après le traitement MICP, ce qui a été confirmé par des analyses microscopiques. Il est intéressant de noter que les échantillons de sol traités ont montré une érosion négligeable même après avoir soumis les échantillons à sept cycles humides-secs.

Keywords: Rainfall-induced soil erosion; urease-producing bacteria; MICP; unconfined compressive strength.

1 INTRODUCTION

The hilly regions are prone to geohazards such as soil erosion, landslides, and debris flow (Froude and Petley, 2018), significantly impacting socio-economic facilities. These events occur over weathered soil slopes that possess soil mass of low strength characteristics and are susceptible to loss of strength due to natural agents such as rainfall. Traditional chemical soil stabilization methods, such as cement (Daraei et al., 2018), have been used to provide interparticle bonding, improving the soil slope characteristics. However, using these methods brings environmental concerns such as carbon emissions, due to which researchers are exploring different environmentally friendly soil stabilization methods that can reduce the dependency on these chemical stabilizers. Microbial-induced calcite precipitation (MICP) is a bio-engineering technique that uses the metabolic activity of the urease-producing bacteria to catalyze the urea hydrolysis process in the presence of urea and calcium chloride (Dejong et al., 2010). The $CaCO_3$ crystals formed due to the process bind the soil particles together and enhance the soil properties. This technique has been explored for applications such as soil erosion mitigation (Devrani et al., 2021; Dubey et

al., 2021), slope stabilization (Gowthaman et al., 2022) etc. However, few studies have been carried out on its application for rainfall-induced soil erosion such as Xiao et al. (2022). The surfaces of soil slopes are in close proximity to the atmosphere and experience periodic Wet-Dry (W-D) cycles as a result of diurnal shifts in cloudy and sunny weather, as well as the accompanying rainfall-evapotranspiration process (Tang et al., 2016). These cycles act as a slope weathering agent and is a severe concern for geotechnical and geological engineers, that results in irreversible deformations in the geomaterials and deteriorates its strength properties to a significant extent. The deterioration in the mechanical characteristics of the calcarenite rocks due to the W-D process was confirmed by Ciantia et al. (2013). Since the MICP-treated soils are often compared with the carbonate sediments, they may likely undergo deterioration due to the prolonged W-D process. Research studies such as Gowthaman et al. (2022) have investigated the effect of W-D cycles on the strength of MICP-treated soil. However, the result of the W-D cycle on the erosion resistance of MICP-treated soil under direct rainfall impact has not been studied before. Thus, the resilience of the MICP-treated soils against this process must be investigated.

Therefore, the current study investigates the potential of the MICP technique through a native bacterium from the hilly region for soil strength improvement and resistance against rainfall-induced soil erosion. Further, the durability of the treated soil sample was investigated by subjecting the soil samples to seven W-D cycles.

2 MATERIALS AND METHODS

2.1 Soil properties

A soil mixture of silty sand (85 % sand +15 % silt) was prepared and used to study the soil improvement through MICP. Table 1. presents the values of different soil properties and the testing method adopted.

Table 1. Soil properties.

Soil properties	Values	Testing method
Specific gravity	2.7	ASTM D854
Min. dry unit weight, kN/m^3 (γ_{dmax})	13.3	ASTM D4253
Max. dry unit weight, kN/m^3 (γ_{dmin})	16.2	ASTM D4254
Coefficient of uniformity (C_u)	5.2	ASTM D6913
Coefficient of curvature (C_c)	1.8	ASTM D6913

2.2 Ureolytic bacterium and bacterial suspension

A urease-positive bacterial isolate R1_5 was used to trigger the bio-cementation process. The bacterium was cultivated in nutrient broth (NB) medium (13 g/l) in a shaking incubator at 200 rpm for 18-24 h at 30ºC. The bacterial suspension with OD_{600} = 0.8-1.0 was used for soil treatment.

2.3 Soil sample preparation

A split mold set of 0.038 m diameter and 0.076 m height with an open top and closed bottom was used to prepare soil columns for the strength test. A circular splash cup of 0.1 m diameter and 0.025 m height was used to prepare soil samples for rainfall-induced erosion testing. Both soil mould and splash cups have a small opening at the bottom to facilitate drainage. A piece of filter paper was placed at the bottom of the mould and cup to prevent the migration of particles. The soil samples in both tests were prepared at 30% relative density, representing the loose soil condition using the air pluviation method followed by the tamping technique.

2.4 MICP-treatment

The soil treatment was carried out in stages. At each stage, one pore volume of solution was added through surface percolation in a split set mould and splash cup. The most feasible MICP-treatment sequence from Devrani et al. (2023) was adopted for soil treatment. For treatment, the soil was initially flushed with water to remove air voids. Then, a pretreatment solution with $NaHCO_3$ and NH_4Cl was added to advance the formation of bicarbonate radicals and the rate of hydrolysis, respectively, and left undisturbed for 6 h. The bacterial suspension of OD_{600}= 0.8-1.0 was added to allow uniform attachment of bacteria. Later, cementation solution (CS), which consisted of Urea, $CaCl_2.2H_2O$, $NaHCO_3$, and NH_4Cl, was prepared and added. Then, autoclaved nutrient broth (NB) and CS were added consecutively for 14 days. After that, the soil samples were rinsed with water and then oven-dried and tested.

2.5 Unconfined compressive strength testing

The treated soil column samples were dried, and unconfined compressive strength testing was carried out as per IS:2720 (Part 10). 1991. The sample was tested at a strain rate of 1 mm/min. The load values and vertical displacement were continuously recorded, and the axial stress corresponding to sample failure was reported as the unconfined compressive strength

(UCS) of the sample. The testing was performed on triplicate samples, and the average values is reported.

2.6 Rainfall-induced erosion testing

The untreated and treated splash cups were dried, and their initial weights were measured. Then, splash cups were placed under a simulated rainfall of 120 mm/h at a slope angle of 30º in a rainfall erosion simulator for 1 h and then allowed for oven-drying for a minimum of 42 h at 70 ± 1ºC to remove the moisture following the method suggested by ASTM (2003) and Gowthaman et al. (2022) and then final weight was measured. The weight difference between the initial weight, i.e., before the test, and the final weight, i.e., oven-dried weight, was used to calculate the percentage soil mass loss due to rainfall. The soil samples were subjected to 7 wet-dry cycles to investigate the potential of MICP-treated soil and were compared with untreated soil samples. Triplicates were investigated for untreated and treated soil samples, and their average and standard deviation are reported. Later, the erosion resistance of soil due to bacteria-induced bio-cementation was confirmed through scanning electron microscopy (SEM).

3 RESULTS AND DISCUSSION

3.1 Unconfined compressive strength of MICP-treated soil

The untreated soil was cohesionless with no strength. However, a solidified soil column was obtained upon treatment, and unconfined compression testing was performed. The test results demonstrate an unconfined compressive strength of about 495 kPa upon soil treatment. A typical stress-strain behavior of the MICP-treated soil is shown in Figure 1. The strength improvement in the soil is attributed to the precipitation of calcite crystals and the binding of soil particles together. It was also established that soil strengthening is possible in the presence of silt content; however, the strength values are reduced compared to strength values in soil with low silt content, as observed by Karimian and Hassanlourad (2022).

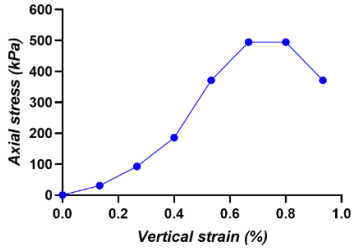

Figure 1. Typical stress-strain curve of MICP-treated soil.

3.2 Erosion of untreated and MICP-treated soil

The soil samples subjected to rainfall testing showcased soil loss in both untreated and treated samples. However, the soil loss rate in untreated samples was much higher and ranged from 22.11 % to 68.64 % after 1st and 7th wet-dry cycles, respectively. Whereas the soil samples upon MICP treatment reduced the soil loss to about 2.1 % after 1st cycle, which loss to only about 4.43 % after 7th cycle. Figure 2 represents the soil loss in untreated soil samples, ranging. However, the soil loss after MICP treatment was significantly lower. The reduction in soil loss values indicates improvement in shear strength characteristics of the soil due to the binding of soil particles together that does not allow the soil particles to disintegrate due to the impact of raindrops and runoff over the soil surface under high intense rainfall.

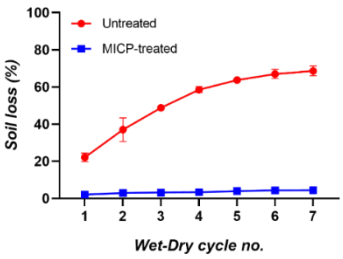

Figure 2. Soil loss in untreated and MICP-treated soil after different wet-dry cycles.

3.3 Scanning electron microscopy (SEM)

The soil specimens after the erosion testing were studied under scanning electron microscopy (SEM). Figure 3 and Figure 4 present the untreated and bio-cemented soil specimens after rainfall-induced erosion testing. The formation of calcite crystals due to bacteria-induced bio-cementation can be observed in Figure 4, and the resistance of the cemented soil particles against the rainfall can be speculated from the bound soil particles, which can be clearly visible even after being subjected to 7 wet and dry cycles, unlike untreated specimens in which only sub-angular shape soil grains with no binding can be observed. The strength improvement and erosion resistance of the bio-cemented soil particles is due to the calcite crystal formation that bonded the soil particles together.

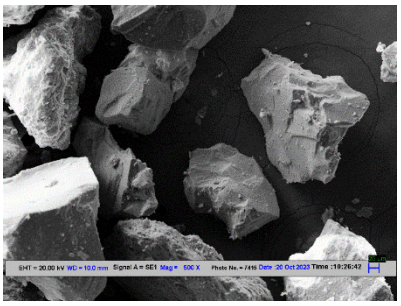

Figure 3. Untreated soil specimen after wet-dry cycle.

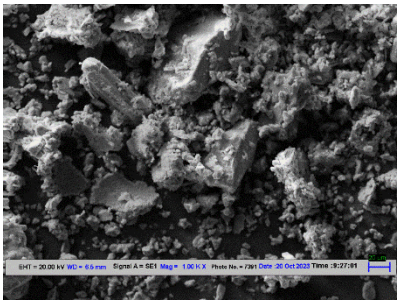

Figure 4. Bio-cemented soil specimen after wet-dry cycle.

4 CONCLUSIONS

The study investigates the potential of a ureolytic bacterial isolate for soil strength improvement and erosion resistance against rainfall-induced soil erosion. A solidified soil column with a UCS of 495 kPa was formed after MICP treatment with the bacterial isolate. The soil erosion test results revealed an 11-fold resistance of the treated samples against rainfall-induced erosion compared to untreated samples after 1st wet-dry cycle. Further, the erosion resistance in treated samples increased to 16-fold, when compared to untreated samples after 7 wet-dry cycles. The low values of soil loss in MICP-treated samples showcase the potential of the treated soil samples for resilience against a more significant number of wet-dry cycles, which can be investigated further.

ACKNOWLEDGEMENTS

The authors want to acknowledge the Central Research Facility (CRF) at IIT Delhi for the scanning electron microscopy (SEM) instrumentation facility.

REFERENCES

ASTM, M. (2003). Standard test methods for wetting and drying compacted soil-cement mixtures. West Conshohocken, PA: ASTM.

Ciantia, M. O., & Hueckel, T. (2013). Weathering of submerged stressed calcarenites: chemo-mechanical coupling mechanisms. *Géotechnique*, *63*(9), 768-785. https://doi.org/10.1680/geot.SIP13.P.024.

Daraei, A., Herki, B. M., Sherwani, A. F. H., & Zare, S. (2018). Slope stability in swelling soils using cement grout: a case study. *International Journal of Geosynthetics and Ground Engineering*, *4*, 1-10. https://doi.org/10.1007/s40891-018-0127-9.

DeJong, J. T., Mortensen, B. M., Martinez, B. C., & Nelson, D. C. (2010). Bio-mediated soil improvement. *Ecological Engineering*, *36*(2), 197-210. https://doi.org/10.1016/j.ecoleng.2008.12.029.

Devrani, R., Dubey, A. A., Ravi, K., & Sahoo, L. (2021). Applications of bio-cementation and bio-polymerization for aeolian erosion control. *Journal of Arid Environments*, *187*, 104433. https://doi.org/10.1016/j.jaridenv.2020.104433.

Devrani, R., Vangla, P., & Sharma, S. (2023). Effect of Treatment Strategies for MICP-Based Soil Improvement Using Urease-Producing Bacteria. In: *Geo-Congress 2023,* Reston VA, pp. 381-390. https://doi.org/10.1061/9780784484661.040.

Dubey, A. A., Ravi, K., Mukherjee, A., Sahoo, L., Abiala, M. A., & Dhami, N. K. (2021). Biocementation mediated by native microbes from Brahmaputra riverbank for mitigation of soil erodibility. *Scientific reports*, *11*(1), 15250. https://doi.org/10.1038/s41598-021-94614-6.

Froude, M. J., & Petley, D. N. (2018). Global fatal landslide occurrence from 2004 to 2016. *Natural Hazards and Earth System Sciences*, *18*(8), 2161-2181. https://doi.org/10.5194/nhess-18-2161-2018, 2018.

Gowthaman, S., Nakashima, K., & Kawasaki, S. (2022). Effect of wetting and drying cycles on the durability of bio-cemented soil of expressway slope. *International Journal of Environmental Science and Technology*, *19*(4), 2309-2322. https://doi.org/10.1007/s13762-021-03306-1.

IS: 2720 (Part 10), 1991. Indian Standard: Methods of test for soils, Part 10: Determination of unconfined compressive strength. Bur. Indian Stand. New Delhi 1–6.

Karimian, A., & Hassanlourad, M. (2022). Mechanical behaviour of MICP-treated silty sand. *Bulletin of Engineering Geology and the Environment*, *81*(7), 285. https://doi.org/10.1007/s10064-022-02780-2.

Tang, C. S., Wang, D. Y., Shi, B., & Li, J. (2016). Effect of wetting–drying cycles on profile mechanical behavior of soils with different initial conditions. *Catena*, *139*, 105-116. https://doi.org/10.1016/j.catena.2015.12.015.

Xiao, Y., Ma, G., Wu, H., Lu, H., & Zaman, M. (2022). Rainfall-induced erosion of biocemented graded slopes. *International Journal of Geomechanics*, *22*(1), 04021256. https://doi.org/10.1061/(ASCE)GM.1943-5622.0002239.

Proceedings of the XVIII ECSMGE 2024
GEOTECHNICAL ENGINEERING CHALLENGES
TO MEET CURRENT AND EMERGING NEEDS OF SOCIETY
© 2024 the Authors
ISBN 978-1-032-54816-6
DOI 10.1201/9781003431749-190
Open Access: www.taylorfrancis.com, CC BY-NC-ND 4.0 license

ECSMGE 24
XVIII EUROPEAN CONFERENCE ON SOIL MECHANICS AND GEOTECHNICAL ENGINEERING

Evaluating undrained shear strength and sensitivity in soft sensitive clay using piezocone and field vane tests

Évaluation de la résistance au cisaillement non drainé et de la sensibilité dans l'argile molle sensible en utilisant des essais au cône piézométrique et des essais au scissomètre sur le terrain

B. Di Buò*
Tampere University and Ramboll Finland, Tampere, Finland

P.W. Mayne
Georgia Institute of Technology, Atlanta, USA

P. Paniagua
Norwegian Geotechnical Institute and Norwegian University of Science & Technology, Trondheim, Norway

S.S. Agaiby
Cairo University, Giza, Egypt

**bruno.dibuo@tuni.fi*

ABSTRACT: Evaluating undrained shear strength in clayey soils, especially soft sensitive clays in Finland, is crucial for several geotechnical engineering applications. In-situ investigation methods, including field vane and piezocone testing, offer versatile methodologies to assess the soil parameters, overcoming issues related to undisturbed soil sampling. Challenges in using the field vane in soft sensitive clays are discussed, as well as the improvements offered by piezocone testing. However, evaluating cone factors to assess the undrained shear strength is not straightforward, owing to soil strength anisotropy and overconsolidation effects. The paper focuses on assessing the undrained and remoulded shear strength in Finnish soft sensitive clays based on an extensive experimental program conducted at four different test sites, comparing the results obtained from piezocone, field vane, and fall cone tests. Discrepancies among these methods are highlighted, as well as possible improvements in devices and test interpretation to assess the soil parameters correctly.

RÉSUMÉ: L'évaluation de la résistance au cisaillement non drainé dans les sols argileux, en particulier dans les argiles sensibles et molles de Finlande, revêt une importance cruciale pour plusieurs applications en génie géotechnique. Les méthodes d'investigation in situ, telles que le test de la gaine et le test de la piezocone, offrent des approches polyvalentes pour évaluer les paramètres du sol, surmontant ainsi les problèmes liés à l'échantillonnage non perturbé du sol. Les défis liés à l'utilisation du test de la gaine dans les argiles sensibles sont discutés, ainsi que les améliorations offertes par le test de la piezocone. Cependant, l'évaluation des facteurs de cône pour évaluer la résistance au cisaillement non drainé n'est pas aisée, en raison de l'anisotropie du sol et de la surconsolidation. L'article se concentre sur l'évaluation de la résistance au cisaillement non drainé et remaniée dans les argiles sensibles de Finlande, sur la base d'un vaste programme expérimental mené sur quatre sites d'essais différents, comparant les résultats obtenus à l'aide du piezocone, du test du scissomètre et du test du pénétromètre à cone tombant. Les divergences entre ces méthodes sont mises en évidence, de même que les améliorations possibles des dispositifs et de l'interprétation des essais pour évaluer correctement les paramètres du sol.

Keywords: Clays, cone penetration, fall cone, piezocone, sensitivity, shear strength, vane.

1 INTRODUCTION

The accurate determination of undrained shear strength (s_u) in clayey soils is a crucial aspect upon which critical decisions regarding foundation design, embankment stability, and overall geotechnical infrastructure depend. In the context of Finnish clays, undrained shear strength assessment has been a subject of particular interest, notably through the utilization of the Field Vane Shear Test (FVT) and the Cone Penetration Test with pore pressure measurements (CPTU) (Di Buò 2020; Selänpää 2021; Länsivaara et al. 2022). Furthermore, it is common practice to collect undisturbed samples for conducting the fall cone tests (FCT) to assess the intact and remoulded strength properties of soft sensitive clays in Finland.

FVT is established as a common practice for determining undrained shear strength. Recent research

studies conducted at Tampere University of Technology (Selänpää et al. 2017) have revealed the potential underestimation of undrained shear strength in soft sensitive clays when using FVT due in part to soil disturbance caused during predrilling and vane insertion, strain rate effects, non-uniform shear stress distribution around the vane, uncertainties in soil-rod friction evaluations, waiting time between vane insertion and rotation, apparatus maintenance, and calibration, as well as measurement system accuracy and errors.

Moving beyond the traditional FVT, the CPTU offers a rapid and continuous in-situ approach to evaluate s_u, providing readings of cone tip resistance (q_c), sleeve friction (f_s), and porewater pressure measured behind the shoulder (u_2) (Lunne et al. 1997).

Nevertheless, the cone factors N_{kt} and $N_{\Delta u}$ are needed to evaluate s_u from CPTU data based on the correlations $s_u=(q_t-\sigma_{v0})/N_{kt}$ and $s_u=(q_t-\sigma_{v0})/N_{\Delta u}$, where q_t is the corrected cone tip resistance for unequal end area effects (Jamiolkowski et al. 1985; Robertson and Campanella 1988; Lunne et al. 1997), σ_{v0} is the total vertical stress, and u_0 is the in-situ water pressure.

In overconsolidated clays, characterized by dilative stress-strain behaviour, the cone-bearing factor N_{kt} determination is rather challenging due to the strain level at which laboratory undrained strength is defined and the noted decrease of overconsolidation ratio (OCR) with depth (D'Ignazio & Lehtonen 2021).

Moreover, further challenges arise when taking into account the s_u anisotropy in clay in stability analysis, specifically active ($s_{u,A}$), passive ($s_{u,P}$), and direct simple shear ($s_{u,DSS}$) modes. These differences in undrained shear strength behavior occur due to the unique stress paths, direction of loading, and strain levels associated with each loading mode (Bjerrum 1973).

In this scenario, the CPTU data can be employed to assess the s_u in compression, whereas the FVT is more directly associated with determining simple shear, $s_{u,DSS}$. Consequently, making a direct comparison between these two tests may yield different results.

In the study of soft sensitive clays, a critical focus lies in assessing remoulded shear strength ($s_{u,rem}$) and soil sensitivity (S_t). These clays exhibit a relatively stiff response in their undisturbed state but transform into a viscous liquid upon remoulding, as initially noted by Rosenqvist (1953). The S_t is a parameter defined as the ratio of peak s_u to the corresponding $s_{u,rem}$ at the same water content (w). The term 'quick clay' characterizes highly sensitive clays with S_t values exceeding 50 and $s_{u,rem}$ values below 0.4 kPa (Rankka et al., 2004). However, establishing an unambiguous definition of quick clays remains challenging, as various classification systems have been put forth, including those by Rosenqvist (1953), Bjerrum (1954), Holtz et al. (2011), and Rankka et al. (2004).

Traditionally, $s_{u,rem}$ and S_t are determined through fall cone tests on soil samples. However, this method can be costly and time-consuming, especially when faced with the challenges of obtaining high-quality undisturbed samples (Ladd and DeGroot, 2003; Di Buò et al., 2019). Consequently, the prospect of assessing soil sensitivity through field testing becomes increasingly attractive.

CPTU provides a promising solution for estimating remoulded strength, utilizing f_s that reflects the frictional resistance encountered as the sleeve penetrates the soil. It is important to note that several authors have addressed concerns about the accuracy and resolution of sleeve friction measurements in soft, sensitive clays, where measured friction values can dip below 1 kPa (Lunne et al. 1997). These challenges can be mitigated by employing piezocones with higher resolution and precision (Di Buò et al., 2022).

Additionally, $s_{u,rem}$ can be measured using FVT. In this approach, the vane's rotational speed is increased to 6°/s, and measurements are taken after a 3600° vane rotation. Selänpää et al. (2017) discussed issues related to inaccuracies in remoulded strength evaluation based on FVT, which may stem from device-related factors, such as loose connections between the vane axle and the rotating system, vane tilt movements causing a 'wave' effect, and potential variations in pore pressure distribution around the remoulded area.

One aim of this paper is to exploit data obtained from an extensive experimental program conducted on Finnish soft sensitive clays (Di Buò 2020, Selänpää 2021, Länsivaara et al. 2022) and evaluate profiles of s_u from CPTU, FVT, and FCT test with particular emphasis on the values of the factors N_{kt} and $N_{\Delta u}$. Moreover, a comparative analysis is conducted among CPTU, FVT, and FCT methods to assess the remoulded shear strength, aiming to explore disparities arising from the diverse approaches.

In the following sections, the raw, direct measurements of FVT and FCT are utilized. They have not been empirically corrected based on plasticity.

2 EXPERIMENTAL DATA FROM SITES

The data included in this paper are a part of an extensive research project conducted by the Research Centre Terra at Tampere University in collaboration with the Finnish Transport Agency. The primary objective of this study was to establish robust correlations for estimating s_u and the preconsolidation stress (σ'_p) in Finnish soft clays. Furthermore, this research aimed to promote the utilization of CPTU as a solution to address challenges associated with the

traditional FVT method. For a more comprehensive understanding of this research and its findings, details are given by Di Buò (2020), Selänpää (2021), and Länsivaara et al. (2022).

The experimental program encompassed various test sites across Finland. However, the focus of this paper is on four specific sites within the country, namely Perniö, Masku, Paimio, and Sipoo. The main geotechnical properties of the investigated sites, including water content (w), plasticity index (PI), and soil sensitivity (S_t), are detailed in Table 1. The investigated clays are characterized by low OCR (1.2 – 1.50), high natural water content (40 – 120), and plasticity index, ranging between 20 and 70. The Masku and Sipoo clays are characterized by lower sensitivity compared to the Perniö and Paimio clays.

These sites have been investigated by using a low-capacity cone (7.5 MPa), which is suitable in sensitive clay deposits, and an innovative electric downhole FVT device equipped with a casing. Moreover, samples have been retrieved with a tube sampler to overcome the difficulties related to sample disturbance in soft sensitive clays. Details of the devices and testing procedure are discussed by Selänpää et al. (2017), Di Buò (2020), and Länsivaara et al. (2022).

Table 1. Geotechnical properties of the investigated clays.

Site	Depth	w (%)	PI (%)	S_t
Perniö	2.0 – 3.0	100 – 110	40	40 – 60
	3.0 – 4.0	70 – 100	30	50 – 70
	4.0 – 6.0	70 – 90	30	50 – 70
	6.0 – 8.0	90 – 110	40	70 – 90
Masku	3.0	80	40	20
	5.0	120	70	20
	7.0	60 – 80	50	20
Paimio	3.0 – 5.0	40 – 80	20	60 – 100
	6.0 – 7.0	90 – 110	40	80 – 90
	7.0 – 9.0	70 – 90	40	60 – 80
Sipoo	2.0 – 3.0	80 – 100	50	20 – 40
	5.0 – 7.0	90 – 110	60	20 – 30
	8.0 – 9.0	80 – 100	50	15

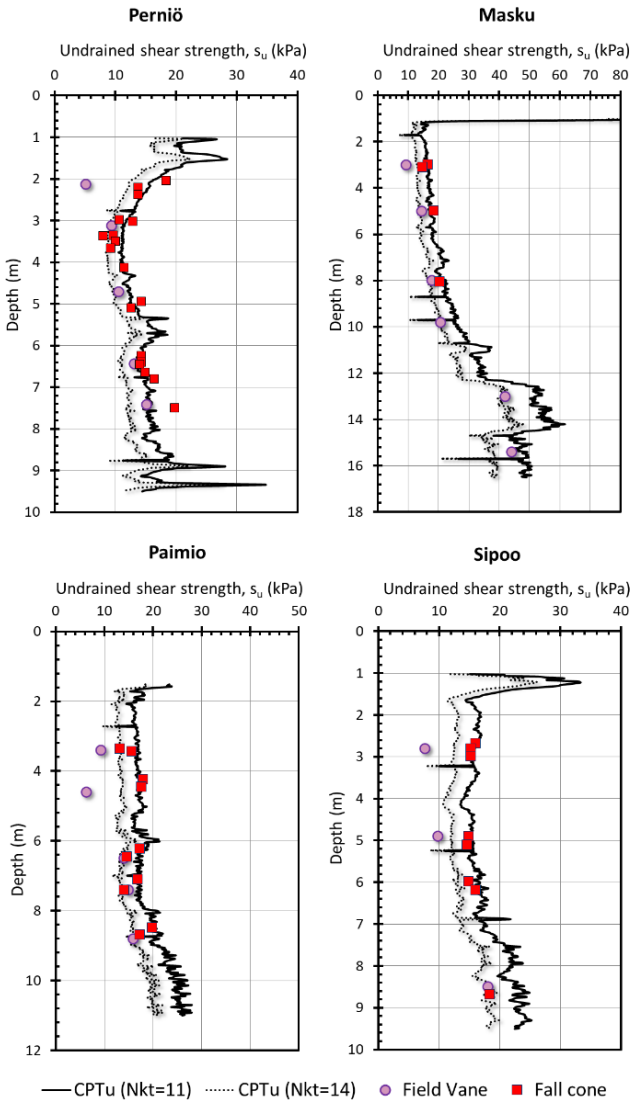

Figure 1. S_u profiles based on CPTU, FVT, and FCT with indications of the best-fit N_{kt} factor.

3 EXPERIMENTAL PROGRAM RESULTS

3.1 Undrained shear strength evaluation

The undrained shear strength profiles, derived from CPTU, and the intact strength determined using the FVT and FCT are illustrated in Figures 1 and 2 using q_{net} and Δu_2, respectively, for each of the 4 sites. Notably, a single representative CPTU profile was selected for each site, specifically those characterized by the highest data quality.

The N_{kt} and $N_{\Delta u}$ factors were assumed to optimize the fit of the FVT and FCT data. It is evident that, across all the sites examined, the s_u values determined by the FCT consistently exceed those obtained from the FVT. In some instances, such as Paimio and Sipoo, it is possible that the FVT data may have been affected by inaccuracies related to device or testing issues, resulting in unrealistically low s_u values.

The calculated N_{kt} values range from 11 to 14, while $N_{\Delta u}$ values range from 8 to 11, with the lower values providing a better fit to the FCT data. The variability in the evaluation of s_u results from many variables: soil heterogeneity, device precision and accuracy, interpretation methods, and operator skills, to name a few.

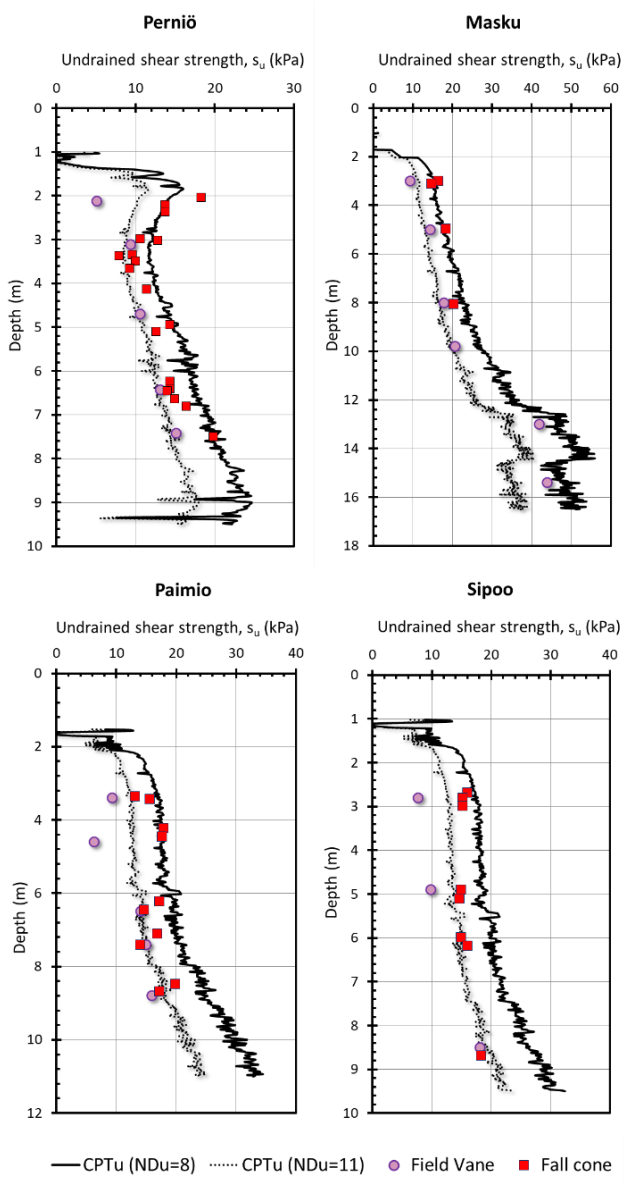

Figure 2. S_u profiles based on CPTU, FVT, and FCT with indications of the best-fit $N_{\Delta u}$ factor.

3.2 Evaluation of $s_{u,rem}$ and S_t

The assessment of $s_{u,rem}$, and S_t in soft sensitive clays presents notable challenges stemming from the inaccuracies associated with field test devices, including CPTU and FVT, as well as considerations related to sample quality and laboratory test procedures in the case of FCT. In the case of the FVT, the value of $s_{u,rem}$ is obtained from the residual torque reading after 10 full revolutions of the rotated vane. For the FCT, after a peak s_u is obtained, the sample is remoulded and tested again using a free-fall drop cone weight to obtain $s_{u,rem}$. For the CPTU, the normal assumption is that the remoulded strength is equal to the measured sleeve friction, i.e., $s_{u,rem} = f_s$ (e.g., Lunne et al. 1997). However, a recent database study (Mayne et al. 2023) has shown that while f_s provides a reasonable value of $s_{u,rem}$ in a variety of clays having low-medium sensitivity, in fact, f_s in highly-sensitive to quick clays overpredicts the $s_{u,rem}$ by a factor of 2 to 10.

Figure 3 presents a comparison of field data on 16 clays in terms of remoulded vane strength (s_{ur}) versus measures of sleeve friction (f_s). The database included 11 clays of low-medium sensitivity ($S_t < 15$) and 5 clays that are of high sensitivity ($S_t > 15$).

Notwithstanding these challenges, it is evident that FCT stands out as the most reliable method for evaluating $s_{u,rem}$, provided that the natural water content (w) is maintained. The data collected from the surveyed sites in Finland are presented in Figure 4, illustrating that CPTU is incapable of accurately directly estimating $s_{u,rem}$ due to limitations in sleeve sensor resolution. In contrast, FVT yields closer agreement with the values measured via FCT, although the results consistently exhibit higher values. These observations have been previously discussed by Selänpää et al. (2017) and Di Buò et al. (2022).

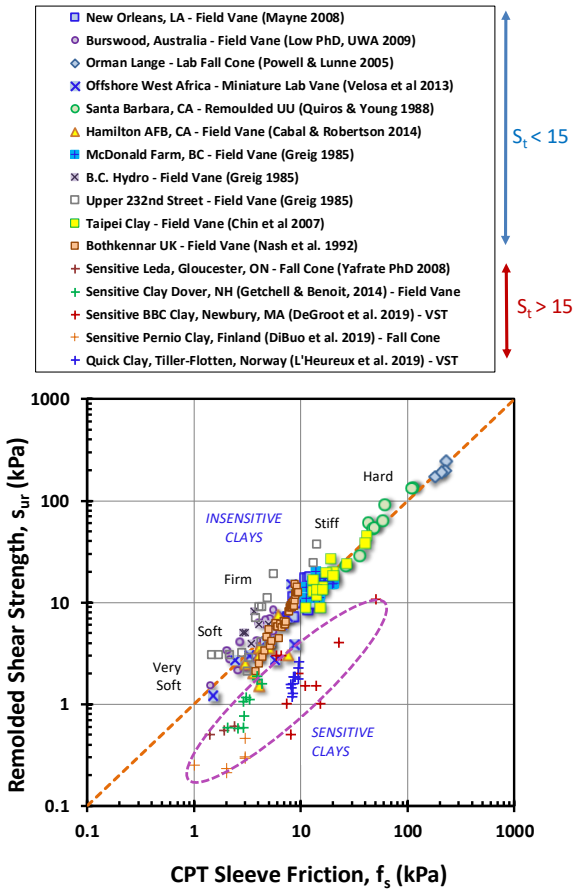

Figure 3. Measured values of remoulded undrained shear strength from FVT (s_{ur}) versus CPTU sleeve friction (f_s) for 16 clays (after Mayne et al. 2023).

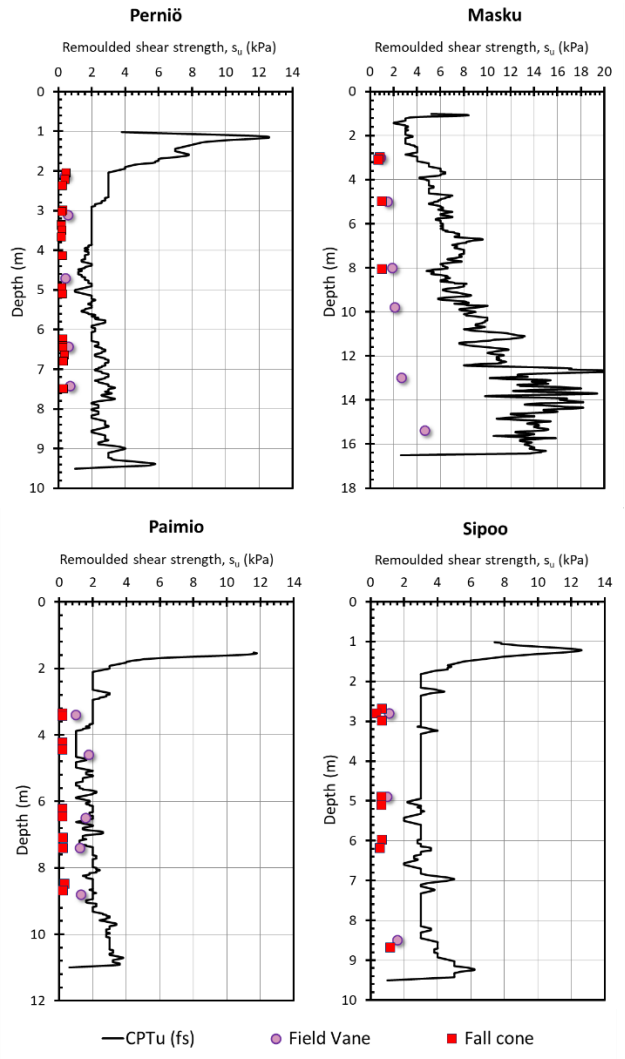

Figure 4. $S_{u,rem}$ profiles based on CPTU, FVT, and FCT.

4 CONCLUSIONS

Assessing the strength parameters s_u, $s_{u,rem}$, and S_t in soft sensitive clays is rather challenging, owing to several factors, including different devices, testing methodologies, interpretation methods, and soil properties variability. This paper reports findings obtained from 4 test sites located in soft sensitive clay deposits in Finland. The primary outcomes of this research study can be summarized as follows:

- The intact strength, as determined by the FCT, generally exceeds the s_u measured by the FVT.
- The best fit N_{kt} values fall within the range of 11 and 14, while $N_{\Delta u}$ values span from 8 to 11, with the lower value fits better the FCT data;
- The CPTU sleeve friction is not a suitable method to correctly estimate $s_{u,rem}$ due to the limited resolution of the load cell sensor, whereas the FVT provides comparable values to those measured through the FCT.

REFERENCES

Bjerrum, L. (1954). Geotechnical properties of Norwegian marine clays. Géotechnique, 4(2): 49- 69. https://doi.org/10.1680/geot.1954.4.2.49

Bjerrum, L. (1973). Problems of soil mechanics and construction on soft clays. State-of-the-art report. In *Proceedings, 8th ICSMFE*, Moscow. Vol. 3, pp. 111–159.

D'Ignazio, M. and Lehtonen, V. (2021). Using SHANSEP for verification of unreliable piezocone data in clays *IOP Conf. Ser.: Earth Environ. Sci.* 710 012011.

Di Buò, B., Selänpää, J., Länsivaara, T. and D'Ignazio, M. (2019). Evaluation of sample quality from different sampling methods in Finnish soft sensitive clays. *Canadian Geotechnical Journal*, 56(8): 1154-1168. https://doi.org/10.1139/cgj-2018-0066

Di Buò, B. (2020). *Evaluation of the Preconsolidation Stress and Deformation Characteristics of Finnish Clays based on Piezocone Testing*. PhD Thesis, Tampere University, Tampere, Finland. ISBN 978-952-03-1468-2.

Di Buò, B., D'Ignazio, M., Länsivaara, T. and Haikola, M. (2022). *Cone Penetration Testing 2022 - Proceedings of the 5th International Symposium on Cone Penetration Testing*, (CPT'22, Bologna), CRC-Taylor & Francis Group, London: 133–138.

Holtz, R.D., Kovacs, W.D. and Sheahan, T.C. (2011). *An Introduction to Geotechnical Engineering, Second Edition*, Pearson / Prentice-Hall, Upper Saddle River, NJ: 853 pages.

Jamiolkowski, M., Ladd, C.C., Germaine, J.T. and Lancellotta, R. (1985). New developments in field and laboratory testing of soils. *Proceedings of the 11th Intl. Conf. on Soil Mechanics and Foundation Engineering*, San Francisco, Vol. 1, pp. 57–153.

Ladd, C.C. and DeGroot, D.J. (2003). Recommended practice for soft ground site characterization: Arthur Casagrande Lecture. In *12th Panamerican Conference on Soil Mechanics and Geotechnical Engineering*, Vol. 1, pp. 1-57. Essen, Germany: Verlag GmbH.

Länsivaara, T., Di Buò, B., Selänpää, J., Knuuti, M. and Haikola, M.. (2022). Fincone: A study on the use of CPT in soft sensitive clays. *Cone Penetration Testing 2022 - Proceedings of the 5th International Symposium on Cone Penetration Testing,* (CPT'22, Bologna), CRC Press - Taylor & Francis Group, London: 497–502.

Lunne, T., Robertson, P.K. and Powell, J.J.M. (1997). *Cone Penetration Testing in Geotechnical Practice.* EF Spon Press/Blackie Academic, London: 312p.

Mayne, P.W., Cargill, E. and Greig, J. (2023). *The Cone Penetration Test: Better Information, Better Decisions.* A CPT Design Manual, published by ConeTec Group, Burnaby, B.C. www.conetec.com.

Rankka, K., Andersson-Sköld, Y., Hultén, C., Larsson, R., Leroux, V. and Dahlin, T. (2004). *Quick-clay in Sweden*, Technical Report No. 65, Swedish Geotechnical Institute, Linköping: 137 pages.

Robertson, P.K. and Campanella, R.G. (1988). *Guidelines for Geotechnical Design using CPT and CPTU.*

University of British Columbia, Vancouver, Department of Civil Engineering, Soil Mechanics Series, 120 pages.

Rosenqvist, I.T. (1953). Considerations on the sensitivity of Norwegian quick clays. *Géotechnique*, 3(5), 195-200. https://doi.org/10.1680/geot.1953.3.5.195.

Selänpää, J. (2021). *Derivation of CPTU Cone Factors for Undrained Shear Strength and OCR in Finnish Clays*. PhD Thesis, Tampere University, Tampere, Finland. ISBN:978-952-03-2156-7.

Selänpää, J., Di Buò, B., Länsivaara, T. and D'Ignazio, M. (2017). Problems related to field vane testing in soft soil conditions and improved reliability of measurements using an innovative field vane device. In *Landslides in Sensitive Clays: From Research to Implementation,* Springer, Cham, Switzerland: 109-119.

Proceedings of the XVIII ECSMGE 2024
GEOTECHNICAL ENGINEERING CHALLENGES
TO MEET CURRENT AND EMERGING NEEDS OF SOCIETY
© 2024 the Authors
ISBN 978-1-032-54816-6
DOI 10.1201/9781003431749-191
Open Access: www.taylorfrancis.com, CC BY-NC-ND 4.0 license

ECSMGE 24
XVIII EUROPEAN CONFERENCE ON SOIL MECHANICS AND GEOTECHNICAL ENGINEERING

Numerical analysis of an unstable slope

Analyse numérique d'une pente instable

A. Di Mariano*
Centre Internacional de Mètodes Numèrics a l'Enginyeria (CIMNE)/Universitat Politècnica de Catalunya · BarcelonaTech (UPC), Barcelona, Spain

J. Serna-Garcia, Y.F. Vargas-Alzate, A. Gens
Universitat Politècnica de Catalunya, BarcelonaTech (UPC)/ Centre Internacional de Mètodes Numèrics a l'Enginyeria (CIMNE), Barcelona, Spain

**adimariano@cimne.upc.edu*

ABSTRACT: A slope adjacent to a northbound regional motorway, outside the city of Barcelona, has shown signs of instability, which have affected the functionality of the road. An extensive instrumentation system has allowed to observe the movement of the slope and locate the slip surface in various sections. The paper presents the study of the instability phenomenon and its origin by means of 2D numerical analyses. Monitoring data has been used to validate the numerical model and to reproduce the observed slope behaviour. In the present work, the features of the numerical study are described and the results are then compared with the in-situ observations.

RÉSUMÉ: Une pente adjacente à une autoroute régionale en direction nord, à l'extérieur de la ville de Barcelone, a montré des signes d'instabilité qui ont affecté la fonctionnalité de la route. Un vaste système d'instrumentation a permis d'observer le mouvement de la pente et de localiser la surface de glissement dans différentes sections. L'article présente l'étude du phénomène d'instabilité et de son origine au moyen d'analyses numériques 2D. Les données de surveillance ont été utilisées pour valider le modèle numérique et reproduire le comportement de pente observé. Dans le présent travail, les caractéristiques de l'étude numérique sont décrites et les résultats sont ensuite comparés aux observations in situ.

Keywords: Slope analysis; numerical modelling; monitoring; stabilizing measures.

1 INTRODUCTION

Instability phenomena on natural and cut slopes are, in general, highly complex phenomena that must be properly identified to select appropriate stabilising measures (Alonso, 2021, Argyroudis et al., 2019). An incorrect estimation of these phenomena can lead to the adoption of ineffective or even counterproductive solutions for their stabilisation (Corominas, 2006).

Road networks are often exposed to the instability phenomena of nearby slopes, with the consequent impact on their users, as well as on the same transport infrastructures. Identifying problematic areas and managing the associated risks represent a priority to guarantee both the functionality and safety of road networks (Mavrouli et al. 2019).

The present work summarises the results of a 2D numerical finite element (FE) analysis carried out to study the stability of a slope adjacent to a road north of the city of Barcelona. Slope monitoring has provided detailed information on the instability mechanism and the location of the slip surface. The numerical results are compared with in-situ observations.

2 DESCRIPTION OF THE CASE STUDY

The slope object of this study borders a motorway whose construction dates back to the late 1980's. On the upper part of the slope an old quarry is present, the exploitation of which lasted a little over 40 years, from around 1960 to 2004 (Fig. 1). The materials extracted from the quarry were dolomites and limestones used mostly in the construction industry.

To reduce the environmental impact of the quarry and prevent the degradation of the slope, restoration measures were implemented once the activity of the quarry ended. The open-pit mine was hence converted into a construction and demolition waste (CDW) disposal deposit. A few years after the slope restoration began, a number of anomalies and defects signs repeatedly appeared on the pavement of the motorway, at the toe of the slope (Di Mariano and Gens, 2023).

The first study to determine the origin of the pavement's faults was carried out in 2008 and some corrective measures were implemented along the toe of the slope. At that time, the road deficiencies were

attributed to the possible presence of expansive materials below the pavement of the road. The implemented corrective measures, which included the construction of a gabion wall (Fig. 1), were nevertheless inadequate to definitely recover the road safety and functionality. Later on, in 2017, when significant repair works were being executed, the Contractor was able to relate the road deformation signs exclusively to the movement of its adjacent slope. An extensive monitoring plan was hence deployed to keep track of the slope instability phenomenon and properly define its limits.

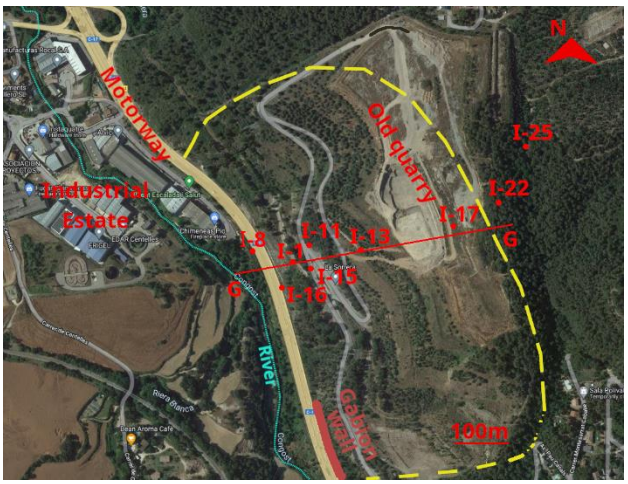

Figure 1. Layout of the motorway and the old quarry on the upper part of the slope (right-hand side). The picture also shows the industrial estate on the opposite side of the road with respect to the unstable slope (discontinuous line) and the location of Section G object of this study (Google maps image).

2.1 Geological Conditions

The lithological sequence of the slope in the area under study includes the materials listed in Table 1, from the most recent (RC) to the oldest (BC).

According to the latest available data, the failure surface of the slope is located at a depth of about 40 m, mainly placed within the shales layer (unit BC in Fig. 2), the upper part of which appears strongly weathered. During the exploitation of the old quarry, the excavation of the upper quaternary materials left the underlying shales layer exposed to atmospheric agents in many parts of the slope, probably favouring its weathering. When the restoration process began and the quarry was converted into a CDW disposal deposit, the hydraulic conditions of the slope changed mainly due to the fact that the base of the deposit was waterproofed.

The unstable slope directly affects the regional motorway, as well as nearly the entire old quarry location (Figs 1-2). It also indirectly affects the bed of a river located downhill from the motorway, an industrial estate located between the motorway and the river, as well as some telecommunications and electrical supply lines (Di Mariano et al., 2022).

Table 1. Lithological sequence of the slope under study.

Material	USCS	Description
RC	-	Construction waste materials
R	-	Anthropic fills
E	Not available	Eocene siltstones and sands
Q	GC	Sandy clays with gravel from the Quaternary Era
M*	CL	Alternation of dolomitic and calcareous rocks from the Middle Triassic
BC	SC, CL	Shale, claystone and sandstone deposits from the Lower Triassic

*(materials exploited in the old quarry)

2.2 Field Instrumentation

The motorway, its adjacent slope and the waste deposit, including their surroundings, are extensively instrumented. The monitoring system comprises topographic and geotechnical devices to control the evolution of both surface and subsurface ground movement, as well as to locate the slope slip surface (Figs 1-2 show all biaxial inclinometers, I, in section G). Topographic surveys include both geometric and GPS (Global Positioning System) levelling. Field monitoring also consists of open standpipes and vibrating wire piezometers (indicated as PZ in Fig. 2) to observe variations in the water table and pore water pressure evolution at the slip surface, respectively.

The main purpose of this extensive monitoring plan was to identify the origin of the slope instability. The observed movements indicated that the slope was indeed moving and that the depth of the slip surface was about 40 m (Fig. 2).

2.3 Origin of the instability and corrective measures

The removal of dolomitic and calcareous rocks from the head of the slope caused a gradual increase in the slope Safety Factor (SF), which decreased during the construction of the motorway, almost 30 years later, due to the cut made at the slope's toe. Later, when the old quarry was converted into a waste deposit, the head of the slope was loaded with time, producing a further and progressive decrease in its SF that eventually led to the instability of the slope when the restoration process was almost completed.

Once the origin of the problem in the motorway was identified, the Contractor performed some

numerical analyses to study the effect of possible corrective measures on the stabilisation of the slope. Different measures such as the construction of diaphragm walls as a reinforcement at the road level or the application of a ground load at the toe of the slope, with the consequent diversion of the river on the other side of the slope or the removal of the waste material at the head of the slope were considered. Among all of them, the latter was selected as the most appropriate in terms of environmental impact, flexibility, cost and time of execution. The unloading of the head of the slope began in 2018 and continued until February of 2022.

The slope movement rate varied over time with both the hydraulic conditions and the excavated volume of waste material. As soon as the unloading process started, the rate of the slope movement decreased, even though at the beginning it was yet quite sensitive to changes in pore water pressures. As the removal of waste material continuously reduced the driving forces on the slide, the movement became progressively slower. Currently, with the unloading process yet to be completed, the movement rate is approximately 0.3 mm/month.

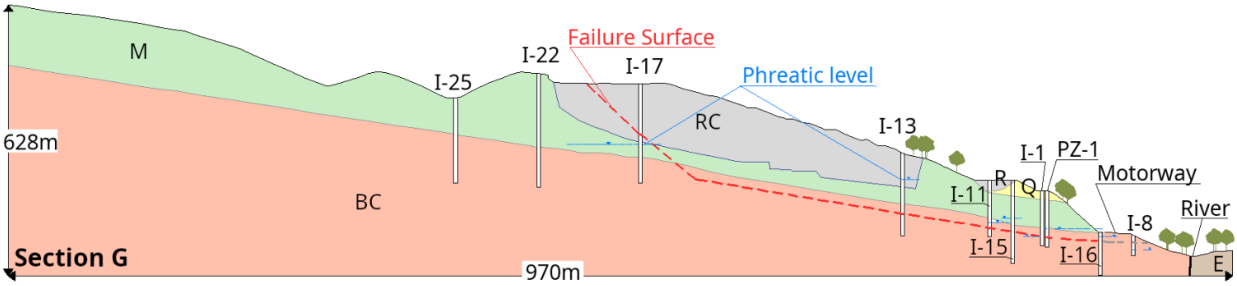

Figure 2. Geological profile along Section G of the slope. The failure surface observed through the inclinometer readings is indicated in red.

3 NUMERICAL MODEL

With all available data and information, the authors of the paper carried out new FE numerical analyses, with the commercial code PLAXIS 2D, to analyse the instability phenomenon in detail and reproduce the observed slope movement as well as the shape and dimensions of the observed slip surface.

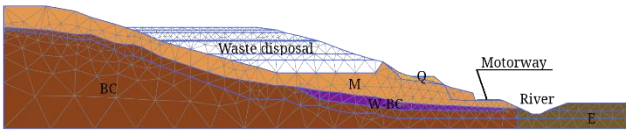

Figure 3. Detail of the FE mesh of the 2D numerical model.

Three different constitutive models were used to represent the ground materials behaviour, with the objective to analyse their influence on the movements distribution along the slope; the generalised Hoek-Brown criterion to account for the different weathering degrees of the rock masses (Hoek-Brown), a simple linear elastic perfectly plastic constitutive model (Mohr-Coulomb) and, finally, an advanced non-linear elastoplastic model with hardening plasticity (HS). The last two models are based on the Mohr-Coulomb failure criterion. In all numerical analyses, the hydraulic conditions approximately reproduce the evolution of the water table with time. Boundary conditions were standards, with a fixed lower boundary and the lateral ones allowing only vertical displacements. No restrictions were imposed on the top boundary.

At first, all numerical analyses were run with the numerical model shown in Figure 3, using the three previously mentioned constitutive models with equal, or equivalent, strength and stiffness parameters. The observed slope movement at inclinometer I-13 (Figs 1-2) and the numerical results associated to different constitutive laws are shown in Figure 4.

Table 2. Strength and stiffness parameters of the M, BC and W-BC deposits for the HS constitutive model.

Layer	c′ (kPa)	φ′ (°)	E_{50} (MPa)	E_{oed} (MPa)	E_{ur} (MPa)
M	20	30	1426	1069	2994
BC	33	38	8750	6560	18375
W-BC	0	18	10	7.5	21

The geomechanical parameters that characterize each ground layer were evaluated based on several laboratory and in situ tests. In Figure 3, the thin layer indicated with the symbol W-BC represents the upper weathered part of the BC deposit, identified from the boreholes, and along which part of the failure surface is located. This layer in the model is characterised by residual strength parameters and much lower stiffness values than those of the unweathered BC materials (Table 2). Such stiffness values were estimated from back-analysis. Table 2 contains the ground effective strength and stiffness parameters corresponding to the

HS constitutive model. As Figure 4 indicates, the HS model proved to be the one that best reproduces the slope horizontal movement with depth, confirming thus that it is indeed important to consider the strong non-linearity of ground materials. Also, in this case study, the unloading-reloading stiffness modulus (E_{UR}) plays a key role in characterising the ground behaviour; more relevant than the oedometric (E_{oed}) or secant modulus in drained triaxial tests (E_{50}).

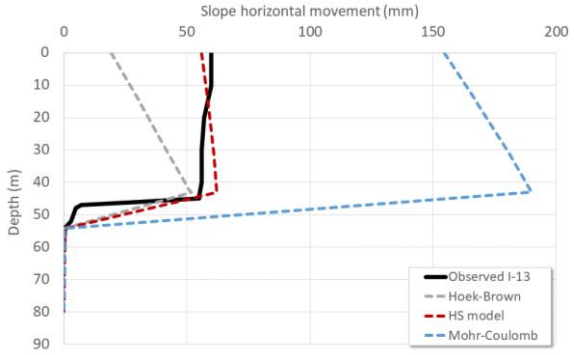

Figure 4. Observed horizontal movement with depth, at inclinometer I-13 and numerical results obtained with different constitutive models.

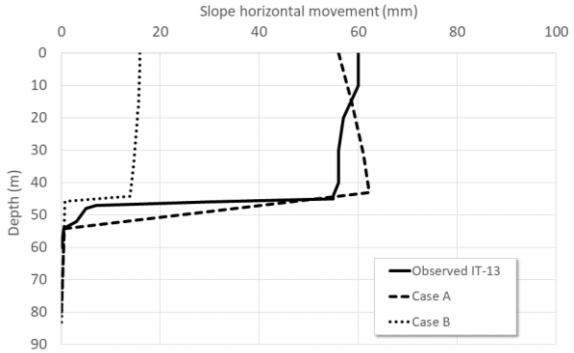

Figure 5. Observed horizontal movement, at inclinometer I-13 and numerical results, considering different slip surface thicknesses and the same HS constitutive model.

According to the different inclinometer readings, the thickness of the slip surface is not uniform throughout the slope, in general being thicker (up to about 10 m) further away from the motorway, as it is approximately represented by the varying thickness of the W-BC layer in Figure 3. In a second phase of this study, two different numerical models (both calculated with the HS model) were considered, each with a different thickness of the W-BC layer, in order to analyse how this feature affects the numerical results. Figure 5 shows the comparison between the observed slope horizontal movement, at inclinometer I-13, and the numerical results in two different scenarios: case (A), in which the thickness of the W-BC layer varies along the slope (Fig. 3) and case (B), in which the same layer has a uniform 2 m thickness. The results show that the thickness of this layer greatly affects the results and, in general, the movement of the slope.

4 SUMMARY AND CONCLUSIONS

The paper presents a case study about the instability phenomenon affecting a slope adjacent to a motorway connecting the city of Barcelona to the northern part of the Catalan region. To analyse the phenomenon and reproduce the slope movement as well as the observed failure surface, 2D finite element numerical analyses were carried out using different constitutive laws.

Considering the non-linearity of ground behaviour in elastoplastic models is crucial to reproduce the observed slope movement. The shape of the slip surface, as it is recorded by inclinometer readings, could only be adequately replicated considering the weathering of the shale deposits from the Lower Triassic. Ground movement distribution is strongly affected by the thickness of the failure surface.

ACKNOWLEDGEMENTS

The authors are grateful for the data and financial support provided by Infraestructures.cat.

REFERENCES

Alonso, E.E. (2021). Triggering and motion of landslides, *Géotechnique* 71, No. 1, 3–59 https://doi.org/10.1680/jgeot.20.RL.001.

Argyroudis, S.A., Mitoulis, S.A., Winter, M.G. and Kaynia, A.M., 2019. Fragility of transport assets exposed to multiple hazards: state-of-the-art review toward infrastructural resilience. *Reliab. Eng. Syst. Saf.* https://doi.org/10.1016/j.ress.2019.106567.

Corominas, J., 2006. El clima y sus consecuencias sobre la actividad de los movimientos de ladera en España. *Rev. C & G.*, 20 (3-4), 89-113.

Di Mariano & Gens (2023). Observation and Analysis of a Moving Slope. A. Ferrari et al. (Eds.): *CNRIG 2023, SSGG*, pp. 503–510, 2023. https://doi.org/10.1007/978-3-031-34761-0_61.

Di Mariano, A., Gost, X., Gens, A. & Álvarez E. (2022). Control and monitoring of an unstable slope. In: *Int. Symp. on Field Monitoring in Geomechanics. Conf. proceedings* ISFMG 2022, pp. 1–7. London: BGA.

Mavrouili, O., Corominas, J., Ibarbia, I., Alonso, N., Jugo, I., Ruiz, J., Luzuriaga, S., and Vavarro, J.A., 2019. Integrated risk assessment due to slope instabilities in the roadway network of Gipuzkoa, Basque Country. *Nat. Hazards Earth Syst. Sci.*, 19, 399–419, 2019 https://doi.org/10.5194/nhess-19-399-2019.

Proceedings of the XVIII ECSMGE 2024
GEOTECHNICAL ENGINEERING CHALLENGES
TO MEET CURRENT AND EMERGING NEEDS OF SOCIETY
© 2024 the Authors
ISBN 978-1-032-54816-6
DOI 10.1201/9781003431749-192
Open Access: www.taylorfrancis.com, CC BY-NC-ND 4.0 license

ECSMGE 24
XVIII EUROPEAN CONFERENCE ON SOIL MECHANICS AND GEOTECHNICAL ENGINEERING

Monitoring the hydro-mechanical effects of vegetation cover on shallow landslide triggering: Preliminary results from a case study in western Norway

Surveillance des effets hydromécaniques de la couverture végétale sur le déclenchement de glissements de terrain superficiels: Résultats préliminaires d'une étude de cas dans l'ouest de la Norvège

A. DiBiagio*
The Norwegian Geotechnical Institute, University of Oslo, Oslo, Norway

V. Capobianco, A. Oen
The Norwegian Geotechnical Institute, Oslo, Norway

L.M. Tallaksen
University of Oslo, Oslo, Norway

**amanda.johansen.dibiagio@ngi.no*

ABSTRACT: Rainfall-induced shallow landslides are amongst the most common gravitational mass movements on slopes in steep terrain. The use of vegetation as a nature-based solution for shallow landslide risk reduction is receiving increased attention in the scientific community. Until now, no studies on the effects of vegetation on slope stability have been conducted for Nordic conditions. Additionally, direct comparison between the hydrological conditions in a forest and a neighbouring open field has never previously been carried out in this region. To contribute to filling this knowledge gap, a monitoring program is installed, and field investigations are conducted in a natural slope in the Flåm valley, located in western Norway. The case study site is situated on a slope partially used as hayfield, and partially covered by deciduous forest. Both the hayfield and the forest are assessed to compare the effects of the presence of vegetation on slope stability. Herein, preliminary results are presented. A detailed analysis of the monitored variables and the laboratory test results must be carried out before to conclude on the effectiveness of the existing forest as a shallow landslide mitigation measure at the case study site.

RÉSUMÉ: Les glissements de terrain peu profonds induits par les précipitations sont parmi les mouvements gravitationnels les plus courants sur les pentes en terrain escarpé. L'utilisation de la végétation comme solution fondée sur la nature pour la réduction du risque de glissements de terrain peu profonds suscite un intérêt croissant au sein de la communauté scientifique. Jusqu'à présent, aucune étude des effets de la végétation sur la stabilité des pentes n'a été menée dans des conditions nordiques. De plus, aucune comparaison directe entre les conditions hydrologiques dans une forêt et un champ ouvert voisin n'a jamais été réalisée dans ces conditions. Pour contribuer à combler cette lacune de connaissances, un programme de surveillance est mis en place et des investigations de terrain sont menées sur une pente naturelle dans la vallée de Flåm, située dans l'ouest de la Norvège. Le site d'étude est situé sur une pente partiellement utilisée comme champ de foin et partiellement recouverte par une forêt caduque. Le champ de foin et la forêt sont tous deux évalués pour comparer les effets de la présence de végétation sur la stabilité de la pente. Dans ce document, des résultats préliminaires sont présentés. Une analyse détaillée des variables surveillées et des résultats des tests en laboratoire doit être effectuée avant de conclure sur l'efficacité de la forêt existante en tant que mesure d'atténuation des glissements de terrain peu profonds sur le site d'étude de cas.

Keywords: Monitoring; nature-based solutions; hydromechanical root-reinforcement; shallow landslides.

1 INTRODUCTION

Rainfall-induced shallow landslides are amongst the most common gravitational mass movements on slopes in steep terrain (Masi et al., 2021). These types of landslides usually interest the uppermost layer of soil or weathered rock (Phillips et al., 2021), posing a serious threat to people, infrastructure as well as agroforestry production in mountain areas. Lately, the

use of vegetation as a Nature-based Solution (NbS) as a mitigation measure for shallow landslides is receiving increased attention in the scientific community (Capobianco et al., 2022). Vegetation can contribute to slope stability through both hydrological and mechanical processes. Plants can provide mechanical reinforcement through the tensile strength of the root network and the interaction between the roots and the soil and/or bedrock (Bischetti et al., 2005). The hydrological reinforcement effects of plants consist of reducing the amount of water in the soil, i.e., reducing the driving forces in the slope caused by pore water pressures. The water content is reduced through plants' ability to intercept water on their canopies and by root water uptake through transpiration (Chirico et al., 2013). Furthermore, vegetation can affect the stability of a slope by surcharge due to self-weight (Gray & Megahan, 1981) and by being subjected to wind (Kim et al., 2020). Soil permeability is also affected by the presence of roots in the vadose zone, resulting in a change in the infiltration and drainage capabilities of the slope (Vergani & Graf, 2016).

Site specificities, such as climate seasonality, environmental conditions and soil conditions can play a role in how vegetation affects the soil hydro-mechanical properties (Boldrin et al., 2021). Until now, no studies on the effects of vegetation on slope stability has been conducted for Nordic conditions. Additionally, direct comparison between the hydrological conditions in a forest and a neighbouring open field has never previously been carried out in this region. To contribute to filling this knowledge gap, a monitoring program is installed and field investigations are conducted in a natural slope in the Flåm valley, located in western Norway. The case study site is situated on a slope partially used as hayfield, and partially covered by deciduous forest. Both the hayfield and the forest site are assessed to compare the effects of the presence of vegetation on slope stability. This paper provides an overview of the case study site, a description of the monitoring program, field and laboratory campaign and some preliminary results. Finally, the plans for further data analysis and research are presented.

2 MATERIALS AND METHODS

2.1 Case study site

The case study site, the farm Ryo, is situated on the hillslopes of the Flåm valley in western Norway (Figure 1). The area is composed of fjords and mountains with small, populated areas concentrated in the lower river valleys. This unique setting is recognized by UNESCO as a world heritage site, and the cultural landscape is maintained by the local inhabitants through traditional farming methods. The mountainsides are steep causing frequent shallow landslides, rock falls and avalanches. Ryo is located about 600 m.a.s.l., and the land is partially used as hayfield, and partially covered by a naturally growing deciduous forest composed by alder (*Alnus incana*), birch (*Betula pubescens*), aspen (*Populus tremula*), and willow (*Salix caprea*) trees (Figure 2, Figure 3). The slope angle of the hillslope is approx. 30° around the farm. The soil in the area consists generally of landslide debris of phyllite rock, which over the years has decomposed into well-graded material.

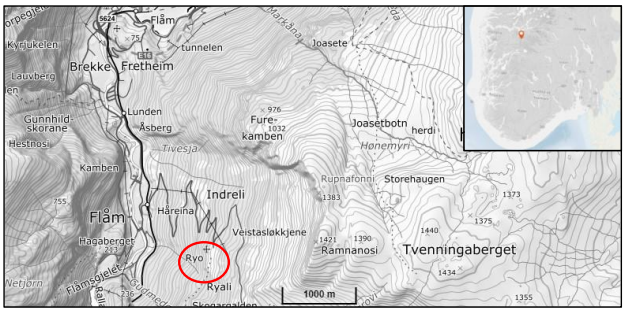

Figure 1. Location of the study site, Ryo. Source: www.norgeskart.no.

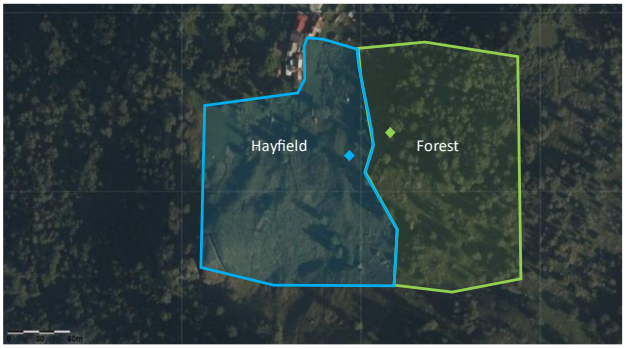

Figure 2. Satellite image of the case study site with approximate locations of the monitoring stations. Source: www.norgeibilder.no.



Figure 3. Photos from Ryo. Left: hayfield. Right: forested area before the growing season.

2.2 Monitoring setup

The locations of the two monitoring stations, one in the forest and one in the hayfield, are shown in Figure 2. In each location, a monitoring program was installed in May 2023, including two precision field tensiometers (Teros32), and four volumetric water content (VWC) sensors (Teros10, Teros 11) (Table 1). In addition to the measurement of VWC and soil suction, temperature is measured at all depths. The sensors are connected to data loggers, which log the measured variables every 15 minutes, and the data is wirelessly uploaded to the cloud through the cellular network. All the sensors and the data loggers were provided by the METER Company.

Table 1. Overview of monitoring equipment. T=Temp., c_ψ=matric potential and VWC=volumetric water content.

Depth [cm]	Variable	Sensor
10	VWC, T	Teros11
40	VWC, T, c_ψ	Teros10, Teros32
80	VWC, T, c_ψ	Teros10, Teros32
110	VWC, T	Teros11

In 2015, a weather station including, a Geonor T-200B series all weather precipitation gauge and a Lufft WS500 weather sensor measuring wind speed, direction, air temperature, relative humidity and air pressure, was installed at Ryo. Data from this weather station was intended to supplement the data collected by the monitoring equipment at the site. However, a site visit to the area showed that a component of the precipitation gauge had broken. Local, climatological data is therefore lacking from the start of our monitoring period (May 2023). To ensure a robust system for data collection of climate variables, a new weather station, of the model ATMOS 41W provided by the Meter Group, was installed in November 2023.

2.3 Field and laboratory investigations

Field investigations were conducted in September 2023. Soil profiles were excavated to a depth of approx. 60 cm respectively at 1.0 m and 2.5 m distance from the trunks of one young birch and one young alder, and at 1.0 m distance from an older birch in the forested area (Figure 4, left). The root distributions in the soil profiles were mapped in a grid of width 50 cm and depth 50 cm, with cell size of 10 cm x 10 cm (Figure 4, right). In each grid cell the root diameters were measured and the number of roots of different diameter classes (1-2 mm, 2-3 mm, …) was recorded. Roots with a diameter smaller than 1 mm were not counted.

Roots of different sizes were collected from each soil profile and brought to laboratory to test their tensional strength using a Quasar 250 Material Testing machine, developed by Galdabini SPA. To ensure proper preservation of the roots from collection to tensile testing, the roots were sprayed with a 20% alcohol solution and stored in the fridge before the tensile tests were performed (10 days from collection date). A total of 46 roots were tested. Thicker roots were debarked at their extremities and clamped directly, whilst the thinner roots were coiled around a rounded metal structure to distribute the stress and prevent breakage at the extremities. The results of the tensile tests have not yet been analysed and is therefore not presented herein.

Disturbed soil samples were collected from each sensor depth at the two monitoring locations (10, 40, 80 and 110 cm), and a total of eight undisturbed soil samples from depth 10-60 cm were collected from the soil profiles close to the three selected trees for soil characterisation in the laboratory. The undisturbed samples were collected using cylinders of Ø72 mm and length 20 cm.

The laboratory analysis of the collected soil samples is yet to be conducted. The laboratory campaign will include measurement of grain size distribution for all the samples, and soil density, organic content and field, residual, and saturated VWC for the undisturbed samples.



Figure 4. Left: Soil pits at dist. 1.0 and 2.5 m from a young birch. Right: Root distribution mapping grid. Cell size 10 x 10 cm.

3 PRELIMINARY RESULTS

3.1 Hydrological conditions

VWC and suction measured between May and October 2023 at 40 cm and 80 cm depth are presented in Figure 5. Air entry in the hayfield tensiometers around the beginning of June caused the sensors to malfunction until they were refilled the 12th of September. Suction data in this period are therefore not reliable. The forested area shows both higher suction and VWC values than measured for the hayfield. For both areas,

the deepest sensors shows both lower suction and VWC values than the shallowest sensors.

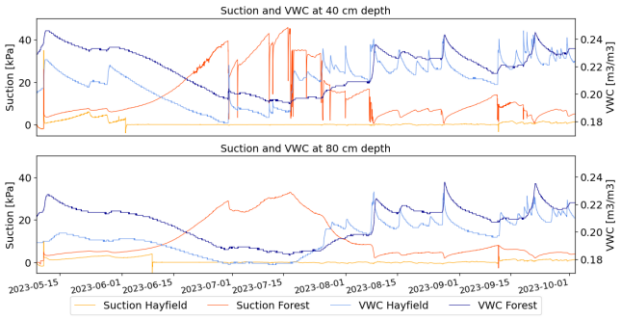

Figure 5. VWC and suction May-October 2023 at Ryo.

3.2 Root distribution

All trees have the highest number of roots in the smallest considered diameter class (1-2 mm). The younger trees do not have roots that are thicker than 15 mm, whilst it was recorded roots with diameters up to 27 mm for the older birch. The Root Area Ratio (RAR), i.e., the ratio between the rooted area and the total area of the soil profile, is calculated for each of the investigated trees (Figure 6). For the alnus, there is no clear difference in RAR from the soil profile at 1.0 m and 2.5 m distance from the stem. On the contrary, for the young birch, there seems to be a decrease in RAR with distance from the stem. The older birch has a peak in RAR at 20-30 cm depth, corresponding to the depth of its largest root (27 mm), whilst showing similar values as the younger trees otherwise. The obtained RAR values are of the same magnitude as found by Bischetti et al. (2005).

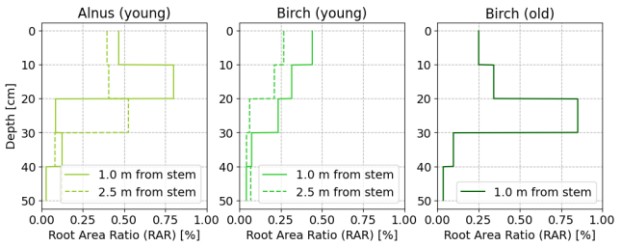

Figure 6. Root Area Ratio (RAR) with depth for the three investigated trees at Ryo.

4 FUTURE RESEARCH

The data gathered in this study will be analysed and used as input data for slope stability modelling, with the aim to assess the effectiveness of the existing forest at Ryo as a shallow landslide mitigation measure. Moreover, the effect of different forest management strategies for the area will be explored.

ACKNOWLEDGEMENTS

The authors would like to thank the Research Council of Norway for financial support, and the OsloMet Uni. for conducting the tensile tests on the roots.

REFERENCES

Bischetti, G. B., Chiaradia, E. A., Simonato, T., Speziali, B., Vitali, B., Vullo, P., & Zocco, A. (2005) Root strength and root area ratio of forest species in Lombardy (Northern Italy), *Plant and Soil*, 278(1), pp. 11-22, https://doi.org/10.1007/s11104-005-0605-4.

Boldrin, D., Leung, A. K., & Bengough, A. G. (2021) Hydro-mechanical reinforcement of contrasting woody species: a full-scale investigation of a field slope, *Geotechnique*, 71(11), pp. 970-984, https://doi.org/10.1680/jgeot.19.SiP.018.

Capobianco, V., Uzielli, M., Kalsnes, B., Choi, J. C., Strout, J. M., von der Tann, L., Steinholt, I. H., Solheim, A., Nadim, F., & Lacasse, S. (2022) Recent innovations in the LaRiMiT risk mitigation tool: implementing a novel methodology for expert scoring and extending the database to include nature-based solutions, *Landslides*, 19(7), pp. 1563-1583, https://doi.org/10.1007/s10346-022-01855-1.

Chirico, G. B., Borga, M., Tarolli, P., Rigon, R., & Preti, F. (2013) Role of vegetation on slope stability under transient unsaturated conditions, *Procedia Environmental Sciences*, 19, pp. 932-941, https://doi.org/10.1016/j.proenv.2013.06.103.

Gray, D. H., & Megahan, W. F. (1981) Forest vegetation removal and slope stability in the Idaho Batholith, *US Department of Agriculture, Forest Service*, 271.

Kim, Y., Rahardjo, H., & Tsen-Tieng, D. L. (2020) Stability analysis of laterally loaded trees based on tree-root-soil interaction, *Urban Forestry & Urban Greening*, 49, pp. 126639, https://doi.org/10.1016/j.ufug.2020.126639.

Masi, E. B., Segoni, S., & Tofani, V. (2021) Root Reinforcement in Slope Stability Models: A Review, *Geosciences*, 11(5), pp. 212, https://doi.org/10.3390/geosciences11050212.

Phillips, C., Hales, T., Smith, H., & Basher, L. (2021) Shallow landslides and vegetation at the catchment scale: A perspective, *Ecological Engineering*, 173, pp. 106436, https://doi.org/10.1016/j.ecoleng.2021.106436.

Vergani, C., & Graf, F. (2016). Soil permeability, aggregate stability and root growth: a pot experiment from a soil bioengineering perspective, *Ecohydrology*, 9(5), pp. 830-842, https://doi.org/10.1139/cjfr-2014-0095.

Proceedings of the XVIII ECSMGE 2024
GEOTECHNICAL ENGINEERING CHALLENGES
TO MEET CURRENT AND EMERGING NEEDS OF SOCIETY
© 2024 the Authors
ISBN 978-1-032-54816-6
DOI 10.1201/9781003431749-193
Open Access: www.taylorfrancis.com, CC BY-NC-ND 4.0 license

ECSMGE 24
XVIII EUROPEAN CONFERENCE ON SOIL MECHANICS AND GEOTECHNICAL ENGINEERING

Slope stabilization at Régua-Ferrão section of the Douro railway line

Stabilisation de talus sur le tronçon Régua-Ferrão de la ligne de chemin de fer du Douro

C.M. Dinis*, A.M. Pereira
Mota Engil Engenharia e Construção S.A., Lisbon, Portugal
**Carlos.Dinis@mota-engil.pt*

ABSTRACT: Mota-Engil Engenharia Deep Foundations Department has executed the slope stabilization works at the Régua - Ferrão section of the Douro railway line - Plot 3, for Infraestruturas de Portugal S.A. The works were consigned by 7th of January 2021, and completed by 10th of October 2022. The intervention area extended over 14 km on the right bank of the Douro River, divided by (10+1) slopes, between Peso da Régua and Ferrão railway stations at the district of Vila Real. The need for intervention on those slopes resulted from geological investigation, a survey of the slopes stability conditions, as well as of the slope areas with the greatest instability potential, combined with the risk factors identified, mainly the distance to the railway line and the boulders fall height, among others, resulted in an effective risk to people and goods including to railway line traffic. This contract covered the following tasks: nailing, nets, cable nets, slope crest drainage, railway line and slopes drainage, ballast guard walls and railway line ballast. Most of the intervened slopes did not have land access, so all the work had to be carried out using railway and river resources at night and under short railway line interdiction periods, resulting in very complex and demanding execution conditions.

RÉSUMÉ: Le Département des Fondations Spéciales de Mota-Engil Engenharia S.A. a exécuté les travaux de stabilisation des talus du tronçon Régua - Ferrão de la ligne du Douro - Plot 3, pour le compte de Infraestruturas de Portugal S.A. Les travaux ont démarré le 7 janvier 2021 et ont terminé le 10 octobre 2022. La zone d'intervention s'étend sur 14 kilomètres sur la rive droite du Douro, divisée par (10+1) talus, entre les gares ferroviaires de Peso da Régua et Ferrão, dans le district de Vila Real, au Portugal. La nécessité d'intervenir sur ces talus provient d'une reconnaissance géologique et d'une étude des conditions de stabilité du site, ainsi que des zones présentant le plus grand potentiel d'instabilité et de leurs modes de défaillance respectifs qui, combinés aux facteurs de risque identifiés, à savoir la distance par rapport à la voie ferrée et la chute de matériaux meubles ou instables en hauteur, entre autres, ont permis d'identifier un risque effectif pour les personnes et les marchandises et bien aussi pour le trafic ferroviaire. Des travaux de clouage, de pose de filets de guidage et de filets renforcés, de drainage des crêtes de talus, de drainage de la voie, de murs de protection du ballast et de ballastage de la voie ont été réalisés. La plupart des talus concernés n'ayant pas d'accès terrestre, tous les travaux ont dû être réalisés avec des moyens ferroviaires et fluviales, de nuit et sous accès fermé à la circulation, ce qui a ajouté des difficultés à la mise en œuvre déjà complexe des solutions de stabilisation.

Keywords: Slope stabilization; nails; reinforced concrete wall.

1 INTRODUCTION

The tender process launched by Infraestruturas Portugal began in May 2020, with an invitation letter to 13 Portuguese construction companies, of which only 3 responded to qualify. The most technically and economically advantageous proposal was presented by Mota Engil Eng. Construção SA, with the work being consigned in January 2021.

It is important to note that this project had initially been started by another contractor, in 2015, however, due to technical and economic difficulties on his part, he terminated the contract with the Construction Owner.

The project to stabilize the 10+1 slopes was carried out 90% under a nighttime railway ban, with the remaining 10% during daylight, with the respective railway safety measures.

During the almost 2 years of the project, there was a perfect harmonization of the project solutions and the construction conditions, which were always monitored by the inspection / Construction Owner, in the periodic fortnightly meetings, with the designer being involved in decisions whenever necessary. During the same period of work, the maximum labor load was around 30 workers, divided between 3 to 4 simultaneous work fronts.

During the same period of work, there was a need to apply or maintain speed restrictions on railway trains, for safety reasons, and some limitations were anticipated before the end of the project. Overall, the extremely difficult undertaking due to non-existent access and railway constraints was carried out regularly and in compliance with the partial deadlines that bound this contract.

2 CONSTRUCTION AND SLOPE STABILIZATION

The Douro railway line (Porto-Pocinho) from Km 103+900 to 117+930, intersects eleven unstable slopes between rail stations of Régua - Covelinhas and Ferrão (see Table 1). The work took place between the municipalities of Vila Real, Peso da Régua and Sabrosa.

The main players in this project were the following:

- Railway line owner: Infraestruturas de Portugal;
- Consultancy / designer: TPF;
- Contractor: consortium Mota Engil (MEEC) and Afavias;
- Supervision: consortium Gibb, Prospectiva and Quadrante.

2.1 Slope stabilization conceptual approach

Considering both the topographic, construction restraints and geological and geotechnical scenarios, the following main stabilization solutions were adopted at the eleven stabilized slopes (see Table 1):

- ϕ32mm steel nails combined with double torsion nets;
- ϕ32mm steel nails combined with double torsion steel nets and steel reinforcing cables;
- Underpinning with reinforced concrete walls lined by shale blocks;
- Cleaning, excavation, blocks removal, and slope reprofiling;
- Drainage systems improvement, mainly: deep drains, railway platform drains, slope crest and berms drains.

At the region where this section of the Douro railway line is located, between Peso da Régua and Ferrão, there are metamorphic formations of the Cambrian Schist-Grauvacic Complex. They are part of the Central Iberian Zone (ZCI) of the Hesperia Massif.

Table 1. Slopes identification and length.

Slope	Length	Note
Slope 1	200	Initial Contract
Slope 2	170	Initial Contract
Slope 3	180	Initial Contract
Slope 4	300	Initial Contract
Slope 5	350	Initial Contract
Slope 6	270	Initial Contract
Slope 7	200	Initial Contract
Slope 8	220	Initial Contract
Slope 9	250	Initial Contract
Slope 10	180	Initial Contract
Slope 11	50	New Contract

The structure of the rocky mass is dominated by the NW-SE orientation of the geological units and by the main fracture systems, with alignments between:

- NNE-SSW and ENE-WSW;
- NNW-SSE and NW-SE.

According to the Geological Chart of Portugal at scale of 1:50 000, Sheet 10-C of Peso da Régua and Sheet 10-D of Alijó, the metamorphic formations belong to the geological units of Allochthonous.

The geotechnical slope stabilization solutions were based on the studies carried out at the project first stage, supported by a parametric back-analysis.

Prior to all activities, land/rail access was created to the fronts of the slopes. To this end, MEEC transported the lighting towers to each specific location on the slopes, using a 2.4x18 (m) wagon; it prepared the temporary stockpiling areas for the materials; it made the necessary protections for the track and installed collective protections for these works and workers safety, lifeline systems for machines and climbing operators.

In this sense, as collective protection measures, steps were manually carved into the approximate contour of the slope to be intervened upon, to later allow the hammerers to enter for the construction of lifelines, topographical checks and markings, slope inspections and decision making/supervision of the work. The construction financial report is presented at the Table 2.

Table 2. Construction financial report.

Identification	Contract initial value	Final value
Contract	€3,558,056.89	€3,244,539.62
New 01	€99,699.44	€99,669.44
New 02	€281,133.51	€249,175.06
New 03	€21,449.32	€21,449.32
New 04	€251,092.90	€213,371.77
Price revision	-	€782,799.55
Total		€4,611,004.76

2.2 Slope stabilization solutions

The use of nailed nets was recommended in situations where the slope face was typically more decompressed, with small blocks (associated with fractures between F4-5 and F4-3), although the thickness of the decompression zone was expected to be relatively shallow (no more than 1m). The use of this system of nailed nets was also associated with slopes that typically showed inclinations of less than 3V:1H.

A system consisting of a triple-torsion hexagonal netting with an 8cm x 10cm mesh of Ø2.7mm wires galvanized in accordance with EN10264-2 was adopted. The net is associated with a 3m x 3m nailing mesh, measured on the slope face, and Ø12mm horizontal steel cables connected to the nailing heads.

The triple-torsion nets were hexagonal, with a mesh size of 8cm x 10cm, made of Ø2.7mm wires galvanized in accordance with NP EN 10244-2. The tensile strength of the Ø2.7 wire and the breaking load of the staples connecting the mesh panels was 1770 MPa. The system incorporated Ø8mm edge steel cables and exhibited a longitudinal tensile strength equal to or greater than 51kN/m, as well as a punching strength equal to or greater than 26kN.

The reinforcement cable panels consist of a mesh of Ø10mm steel cables, 40 x 40cm mesh, with double connections at the nodes. The cable netting panels are 6m high and 3m wide. The connections between adjacent panels were made with Ø12mm steel cables interwoven into the meshes.

The system was reinforced by a mesh of Ø16mm horizontal, vertical and perimeter steel cables. At the top of the panels (upper edges), a Ø20mm steel core cable was installed.



Figure 1. Multifunction drilling column under operation.

In the nailed net system (see Figure 1), nailing was made up of Ø32mm A500NRSD steel rods, sealed in Ø76 mm holes with cement grout, with lengths varying between 4.0 m, 6m and 8m. The nailing heads were made up of 200x200x10mm metal plates. Both the rod and all the metal elements of the nailing heads were galvanized to a thickness of 90 μm or more.



Figure 2. Multifunction drilling column MERLO 7028 with CPA 295 Montabert, working at railway line platform.

Several examples of the positioning and stabilization of drilling equipment (see Figure 2 and Figure 3), at height, on the railway platform, supported by a railway wagon, or suspended with drilling carts, connected to lifelines / suspension.

For the construction of the lifelines, we opted for standardized A500NRSD steel rods, Ø32mm, with a length of 2m and spaced 3m apart (double line).

The connection to the drilling equipment suspended/connected to the line was established using a mechanical TIRFOR, with a nominal load capacity of 16kN, properly connected with steel shackles of equal or greater load capacity.

For slope heights above 25m, it was decided to use suspended drilling carts, anchored to lifelines/built with nailed steel cables, as it was not possible to use conventional means of lifting the drilling columns (mobile crane or multifunction crane).

All the accessory and preparatory works related with the safety procedures and verification were set in accordance with Decree-Law 50/2005, which demands that the legal provisions defining that certifications of equipment anchored to lifelines / cart suspensions are currently necessary / required.

In most situations on the slopes of plot 3, with average heights of up to about 20m (see Figure 4), it was decided to use the lifting means, mobile crane or multifunction crane / equipped with a drilling column, stabilized at the track, at the railway platform level.

The set "mobile crane + wagon" was towed every night between Covelinhas Station, at PK 112+300, and the work site, varying between 113+400 and 117+940.



Figure 3. Multifunction drilling column working at the railway line platform.

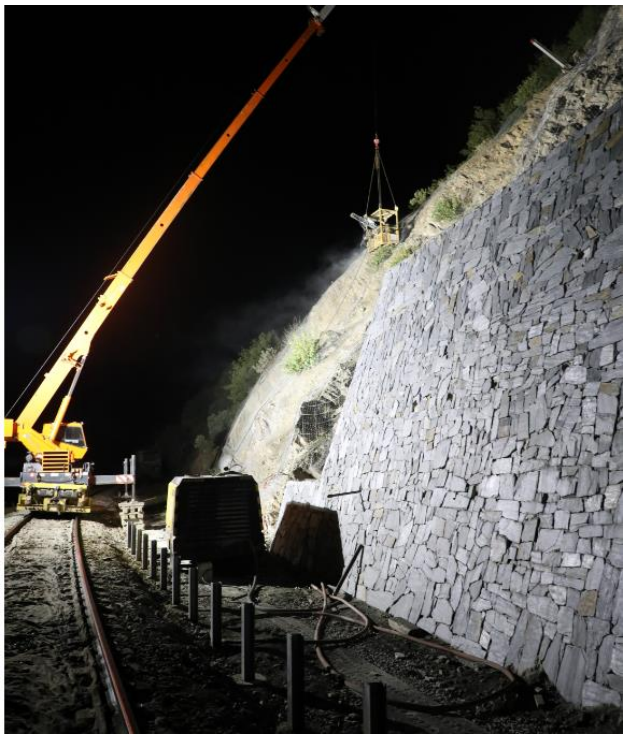

Figure 4. Crane position at railway line platform.

2.3 Underpinning reinforced concrete walls

For the underpinning reinforced concrete walls solutions, the concrete provided was part of resistance class C25/30, exposure class XC2(P), Dmax = 25 mm, chloride content equal to or less than 0.40 and slump class S3.

The concrete was stabilized and prepared for workability time of 3 hours, according to composition studies, since the shortest possible time between the end of manufacture and the start of unloading on site was around 2 to 2.5 hours.

The adoption of underpinning, rather than excavation work or stabilization with nets, was mainly associated with the existence of areas strongly conditioned by planar breakage and/or tilting phenomena involving large unstable volumes, in which, using excavation work, significant excavations would have to be carried out to properly stabilize the slope.

At those situations, nailed nets alone would not work as well as they could, especially for significant areas of cantilever or even with a negative slope inclination over the railway line.

There were two types of underpinning walls, with selection depending mainly on the slope geometry (height and inclination). For both types of underpinning walls, L-shaped nails were executed, and drains were installed, after the walls concreting, through Ø76mm holes. To facilitate drilling, it was recommended that empty holes should be placed at the walls before concrete pouring, using Ø90mm PVC pipes.

Still at the design stage, an attempt was made to avoid the use of reinforcement bars at the underpinning walls, as much as possible. There were many reasons for this, but the main advantage was that, by using simple concrete solutions, it was possible to define concretes with lower resistance and exposure classes, which was clearly suited to this type of work, since, due to access difficulties, the concrete was manufactured using rudimentary means, instead of concretes with the usual resistance classes chosen for regular reinforced structures.

The concreting activity was perfectly identified at the study and design stage. In order to better overcame the restraints, for the transport of ready-mixed concrete, two MEEC partner companies were involved:

- IED boats and river platforms;
- EDILAGES, which with one of its concrete mixer pump trucks, with a 28m boom, completed 90% of reinforced concrete underpinning walls.

Thus, using a river platform (SAPO) with a transport capacity of about 50ton, pulled by a tug (Pomba), some 800m^3 of concrete were transported between the banks of the Douro River, during approximately two months.

It should be pointed out some examples of complex works, as for instance: the positioning of scaffolding, the placement of formwork and the general civil works, alongside the railway line. Those works were carried out only with railway line traffic severe restrains or interdiction, as well as with constraints related to tight railway gauge in opposition to the geometry of the walls.

The construction works of the underpinning walls took place between March and July 2022, with concrete pouring works being done exclusively at night, with the support of railway and river resources that were adapted and provided specifically for this task (see Figure 5).



Figure 5. Railway loading gauge / scaffolding position close from railway line platform.

Concreting activities were always performed with the railway line closed between 9 p.m. and 6 a.m., where under optimal conditions 50m3 of concrete were transported and poured, in one night of work.

Coming from the Vila Real Hydraulic Plant, the ready-mixed concrete was transported to the left bank of the Douro River, where it was transferred to the concrete mixer on board at the Folgosa boat, provided by the IED company (Douro extractive industry). From there, it would continue for 10 to 25 minutes, depending on the distance from the slope (slope 10 to slope 6, respectively), where the river platform would be positioned, moored to the right bank. From this bank, it was then pumped up to the maximum height / elevation of the concrete underpinning wall (see Figure 6 and Figure 7).

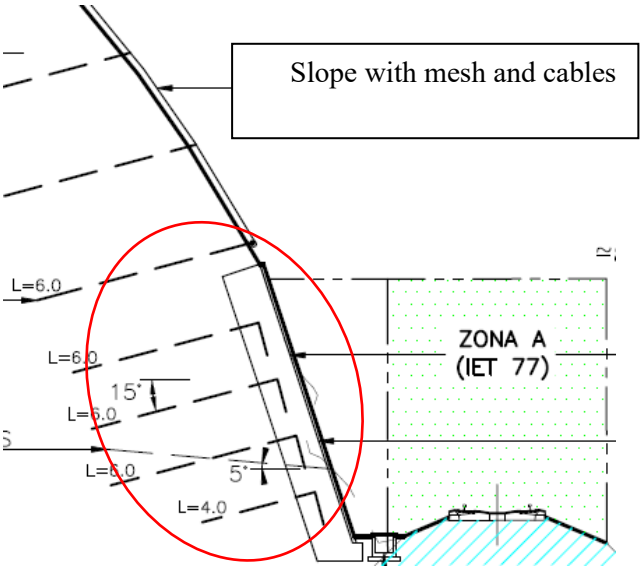

Figure 6. Underpinning wall with L shaped nails.



Figure 7. Underpinning wall concrete pouring operation.

Railway concrete transport equipment was also performed with the assistance of one concrete mixer wagon with a capacity of 6m^3 and a speeder for towing the set, which occasionally carried out transport between Ferrão Rail Station and Slopes 6 and 7 during the first phase of the works, while the river equipment was being prepared.

In the case of the concrete mixer wagon, transport times between the end of mixing and the start of pouring were still more than 2.5 hours, so it was quickly decided to use only the boat on-board mixer.

At Table 3 the main river/transport equipment's are presented.

Table 3. Main equipment at concrete wall transport.

Resource	Quant.	Note
Tug boat	1	4.92 TAB
Barge platform	1	42.4 TAB
generator	1	150Kva
lighting tower	1	Atlas Light V5+
Hydraulic crane	2	Gruman 19000
Concrete pump	1	Cifa
Auto concrete pump	1	Merceder + Cifa
Rail route machine	1	Liebherr 922

3 FINAL REMARKS

The railway slope stabilization complex works had to be linked with all the demanding restraints, as for instance from the delay in the departure time of the railway trains to the simple coordination of the concrete pouring time. The simultaneous execution of 10+1 slopes, when the main site access was just the railway line under daily operation, required a very demanding logistics and site activities management.

Carrying out construction work and stabilizing slopes exclusively at night was also extremely demanding physically and psychologically for those directly involved in the construction. Habituation, routines, and complex works, some of them performed with suspended ropes, in a night environment with assistance of artificial light creates accelerated tiredness on employees, increasing the risk for construction site accidents, including material goods and physical damage.

ACKNOWLEDGEMENTS

The authors are grateful to Infraestruturas de Portugal, Douro railway line owner, for the permission to present this paper. The authors also emphasize the important role of the following main suppliers for the works success:

- Newinfra Unipessoal, Lda., sub-contractor for civil construction and drainage works;
- A. Bianchini, steel nets and cables supplier;
- I.E.D – Indústria Extrativa do Douro, sub-contractor for river transport and platforms;
- Betão Liz, concrete ready-mix and hydraulic mixtures supplier;
- Eurogalva, galvanizing and anti-corrosion protection systems supplier.

Proceedings of the XVIII ECSMGE 2024
GEOTECHNICAL ENGINEERING CHALLENGES
TO MEET CURRENT AND EMERGING NEEDS OF SOCIETY
© 2024 the Authors
ISBN 978-1-032-54816-6
DOI 10.1201/9781003431749-194
Open Access: www.taylorfrancis.com, CC BY-NC-ND 4.0 license

ECSMGE 24
XVIII EUROPEAN CONFERENCE ON SOIL MECHANICS AND GEOTECHNICAL ENGINEERING

Resonant column round-robin testing

Essais de résonance en torsion: comparaisons inter et intra-laboratoires

N. Dufour*, H. Calissano, L. Batilliot
GéoCoD/Cerema/Aix-en-Provence, France

I. Rogoff, C. Simon, A. Disantantonio
EDF-TEGG, Aix-en-Provence, France

T. Lando, E. Bourguignon
ANTEA Group, Orleans, France

**nathalie.dufour@cerema.fr*

ABSTRACT: Faced with seismic risk, to better understand and characterize the behaviour of soils, advanced geotechnical laboratory tests are necessary. These include, for example, torsional resonance tests. The American standard (ASTM D4015 – 15), which describes the process for carrying out these tests, points out the lack of interlaboratory tests to determine their accuracy. As part of the ASIRI+ project, a cross-test campaign was launched in France from the beginning of 2023 on two types of sandy materials (HN31 and a mixture of HN38, HN34, HN31, HN04). Three independent laboratories participated. The results of resonant column tests obtained are presented. The following evolutions are discussed: shear modulus vs distortion, damping vs distortion. Results are compared to empirical models.

RÉSUMÉ: Face au risque sismique, pour mieux comprendre et caractériser le comportement des sols, des essais géotechniques avancés en laboratoire sont nécessaires. Ceux-ci comprennent, par exemple, des essais de résonance en torsion. La norme américaine (ASTM D4015-15), décrivant le processus de réalisation de ces tests pointe le manque de tests interlaboratoires pour déterminer leur précision. Dans le cadre du projet ASIRI+, une campagne de tests croisés a été lancée en France à partir de début 2023 sur deux types de matériaux sableux (HN31 et un mélange de HN38, HN34, HN31, HN04). Trois laboratoires indépendants ont participé. Les résultats des essais de colonne résonante obtenus sont présentés. Les évolutions suivantes sont discutées : module de cisaillement vs distorsion, amortissement vs distorsion. Les résultats sont comparés à ceux issus de modèles empiriques.

Keywords: Resonant column apparatus; round-robin test; shear modulus; damping.

1 INTRODUCTION

Dynamic soil response is of considerable importance for loadings produced by earthquakes, machine foundations, wind, waves, and impacts. Two of the most important parameters in any dynamic analysis involving soils are the shear modulus and the damping ratio. Both the shear modulus, G, and damping, D, are dependent on the shear strain, γ. For earthquake problems, the variation of G and D with shear strain must be considered. In laboratory, the resonant column apparatus (RCA) constitutes a means of determining these parameters. Precision of these results depends of the nature of tested soils, specimen variation, operator or laboratory testing variation (ASTM, 2021).

In the 1970's, USA organized resonant column round robin testing program for determining the dynamic shear modulus and the damping ratio of Monterey sands (Chung, 1982). At the beginning of 2023, in France, three independent laboratories decided to organize intercomparison testing on sandy reconstituted specimens.

For this study, the methodology was quite free: reconstitution method, apparatus, drainage conditions, method of determining depreciation are chosen by each operator according to their constraints and practices.

2 MATERIALS AND METHODS

2.1 Materials

The material used in this research work were two sands:

- Hostun HN31 sand whose properties have been extensively studied by many research laboratories (Baudouin, 2010).
- A mixture of Hostun sands composed of 25% in dry weight of the fraction HN38 HN34 HN32

and HN 04 (fraction HN 04 cut at 0.63 mm).

Particle size distributions of each material is shown in Figure 1. Their physical characteristics are given in Table 1. Different properties are presented: the effective Grain Size D_{10}, the median Grain Size D_{50}, the coefficient of uniformity $C_u = D_{60}/D_{10}$, the coefficient of curvature $C_c = {D_{30}}^2/D_{10}D_{60}$.

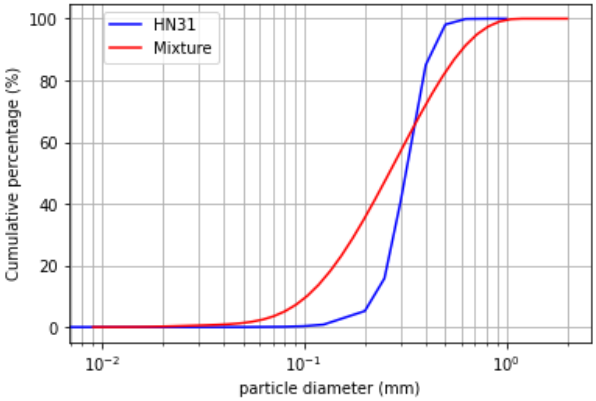

Figure 1. Particle-size size distribution (HN31 and mixture).

Table 1. Properties of HN31 and mixtures sands.

	HN31	**Mixture**
D_{10} (µm)	220	104
D_{50} (µm)	320	250
C_u	1.57	3.13
C_c	1.03	0.96

2.2 Specimen preparation

Three procedures of reconstitution of the samples were used: compaction, raining and compaction followed by freezing. Only the density was fixed. Grain bulk density was measured: 26.00 kN/m^3.

8 HN31 specimens and 7 mixture specimens were reconstitued in laboratories (with a density objective of respectively, 19.22 and 20.21 kN/m^3) . The height of the samples was about 100mm and the diameter about 50mm.

Void ratio of specimens before testing are presented in Figure 3 and Figure 4. HN31 and mixture specimens presented respectively density between 18.96 and 19.30, and between 19.63 and 20.11 kN/m^3).

2.3 Testing conditions

All specimens were saturated (Skempton coefficient 0,95<B<1,00). They were consolidated at an isotropic pressure σ'_0 = 100 kPa (HN31) or 300 kPa (Mixture). Some specimens were drained at their top and their base, others only at their base. Intermediate reconsolidation phases were carried out when the overpressures were too high (threshold determined by each laboratory).

2.4 Resonant column apparatus tests

The evolution of the shear modulus and the damping of a soil as a function of the distortion can be obtained by torsional tests on the RCA (Figure 2).



Figure 2. RCA in the Cerema laboratory.

The RCA is well suited for accurate measurements of soil stiffness and damping at low to medium shear strain amplitudes, typically between 0.0001% and 0.1% (ASTM, 2021). An axially and radially confined cylindrical sample is sheared by applying a sinusoidal torsional moment of predefined amplitude and increasing frequency to its top end, while the base end is fixed. Once the resonant frequency has been identified, it is used to calculate the soil shear modulus using a theoretical elastic model, which correspond to the applied shear strain amplitude. Two different approaches are generally applied to determine the damping rate using a RC test: steady-state and free vibration decay methods (Semblat et al., 2011). Both were used in this study.

The reduction in shear modulus and evolution of damping is obtained by repeating the test with increasing amplitudes.

The G modulus measured at the smallest amplitudes and distortions is called G_{max}.

3 RESULTS

3.1 Shear modulus as a function of distortion

Torsional RCA tests provide shear modulus decrease curves as a function of shear strain γ. The test results are presented for each type of specimens: HN31 (Figure 3) and mixture (Figure 4). Colors correspond to the initial void ratio of each specimen (from red to blue presented in the histogram).

Symbols correspond to different specimen preparation: ● is linked with compaction followed by freezing, + to raining and ★ to compaction.

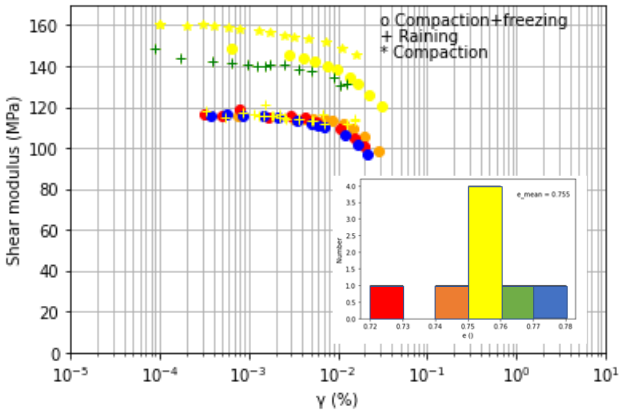

Figure 3. Shear modulus as function of distortion (HN31).

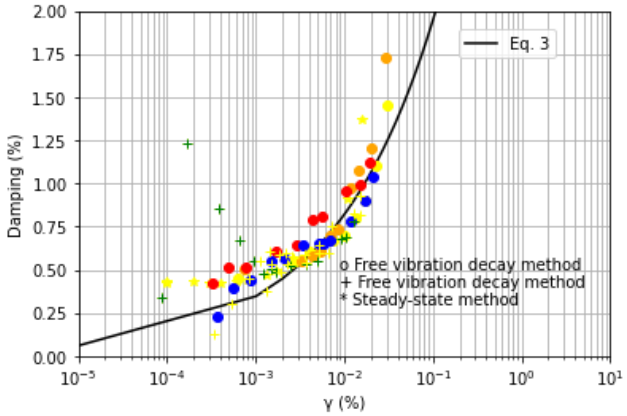

Figure 4. Soil damping as function of distortion (HN31).

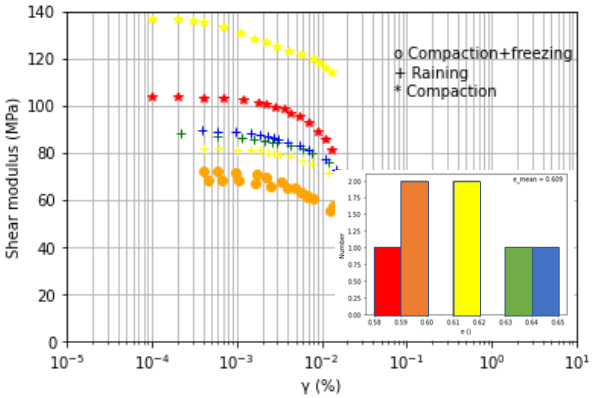

Figure 5. Shear modulus as function of distortion (Mixture).

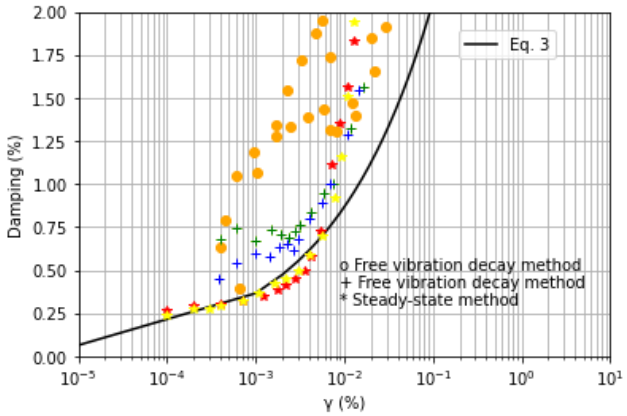

Figure 6. Soil damping as function of distortion (Mixture).

Two different apparatus were used (machine M1 ★ and machine M2 ● and +). Two different drainage conditions were used (drainage at the bottom of the specimen ★ and drainage at the top and the bottom of the specimen ● and +). The laboratories carried out several different tests on different specimens under the same drainage conditions and consolidation pressures.

The HN31 specimens present maximum shear modulus values varying between 120 and 160 MPa; those of the mixture, values between 65 and 140 MPa. The results of HN31 are less dispersed than those of the mixture. Results obtained with M1 (drainage only at the base of the specimen) are always higher than others. In Figure 3, yellow circle (●) and green plus (+) curves correspond to tests with technical problems (leak or inclination of the electro-magnets into the coils). Other curves are very closed but correspond to different initial void ratio. Void ratio after saturation and consolidation phases has to be considered, instead of initial one. In Figure 4, the yellow plus (+) curve corresponds to a laboratory test with a leak.

More generally, repeatability of tests for the same laboratory is observed.

3.2 Damping as a function of distortion

Torsional RCA tests also provide damping as a function of shear strain γ. The test results are presented for each type of specimens: HN31 (Figure 5) and mixture (Figure 6). Like for the previous figures, symbols are linked with specimen preparation and colors to the void ratio.

For both materials, the damping varies between 0 and 2%. The results of HN31 are less dispersed than those of the mixture. Steady-state and free vibration decay methods were used to determine the soil damping. The first one corresponds to ● and + symbols and the second one to ★ symbols. Figure 6 seems to show that steady-state method is more precise to determine the damping for very small distortions.

3.3 Discussion

Experimental results are compared to empirical relationships (solid and dotted black lines) that have been proposed in the literature for sandy soils in Figures 7, 8, 5 and 6. (Rollins et al., 2020) presented simplified equations for shear modulus degradation and damping of sandy soils in relation with confining

pressure and coefficient of uniformity (Equations. 1, 2 and 3):

$$\frac{G}{G_{max}} = \frac{1}{1+\left(\frac{\gamma}{0.0063{\sigma_0'}^{0.38}}\right)^{0.87}} \quad (1)$$

$$\frac{G}{G_{max}} = \frac{1}{1+\left(\frac{\gamma}{0.0046{C_u}^{-0.197}{\sigma_0'}^{0.52}}\right)^{0.84}} \quad (2)$$

$$D = 26{,}05\left(\frac{\gamma}{1+\gamma}\right)^{0.375} {C_u}^{0.08}{\sigma_0'}^{-0.07} \quad (3)$$

Normalized shear modulus is the current shear modulus G divided by G_{max}. In the Figure 7, measured values of G are above the empirical curves for HN31 specimens, whereas the empirical curves frame the measurements in the Figure 8 (mixture).

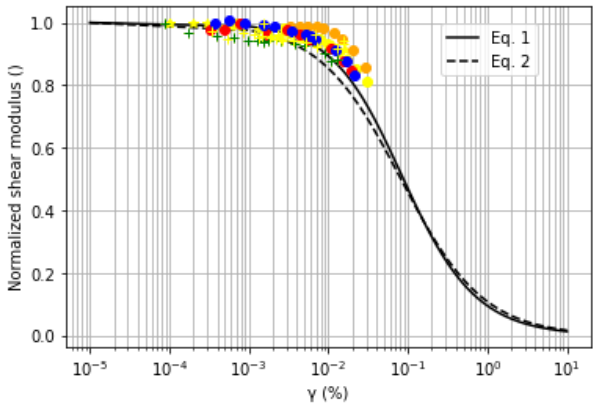

Figure 7. Normalized shear modulus as function of distortion (HN31).

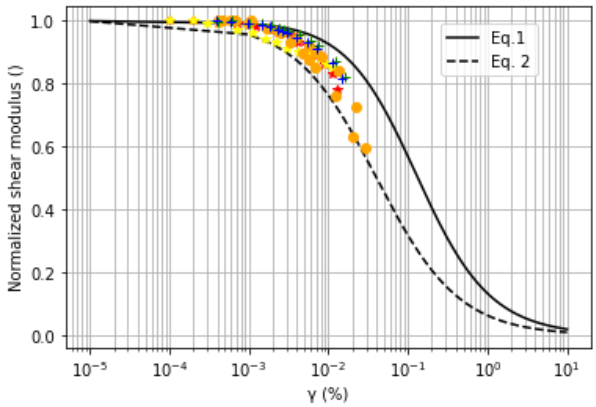

Figure 8. Normalized shear modulus as function of distortion (Mixture).

Regarding damping, the measured values coincide with the empirical curve proposed for the evolution of the damping of HN31 sand as a function of distortion (Figure 5). For the mixture, the empirical curve corresponds to the minimum of the measured values (Figure 6).

4 CONCLUSIONS

Finally, fifteen tests were carried out by three independent laboratories using a resonant column apparatus. Shear modulus and damping were determined on sandy specimens. In terms of shear modulus, the values are relatively dispersed explained by different sample preparation, different void ratio and hydromechanical problems during tests. However, the dimensionless modulus reduction curves are relatively close to each other and to the empirical curves in the literature. The HN31 sand damping values are also close to each other and are well reproduced by the empirical curves even though two different methods were used to determine them. An analysis of the test procedures and operating methods will be carried out to try to explain the dispersion of the curves. Other tests still need to be carried out.

ACKNOWLEDGEMENTS

The authors are grateful for the financial support provided by funding ANR (ANR-19-CE22-0015).

REFERENCES

ASTM. (2021). *ASTM D4015—21 Test Methods for Modulus and Damping of Soils by Fixed-Base Resonant Column Devices* (ASTM D4015-21). https://doi.org/10.1520/D4015-21.

Baudouin, G. (2010). *Sols renforcés par inclusions rigides : Modélisation physique en centrifugeuse de remblais et de dallage*. Université de Nantes.

Chung, R. M. (1982). *Contribution to the ASTM resonant column round robin testing program* (p. 78). U.S. DEPARTMENT OF COMMERCE.

Rollins, K. M., Singh, M., & Roy, J. (2020). Simplified Equations for Shear-Modulus Degradation and Damping of Gravels. *Journal of Geotechnical and Geoenvironmental Engineering*, *146*(9), 04020076. https://doi.org/10.1061/(ASCE)GT.
1943-5606.0002300.

Semblat, J.-F., Lenti, L., Jacqueline, D., Leblond, J.-J., & Grasso, E. (2011). Railway vibrations induced into the soil : Experiments, modelling and isolation. *Revue Française de Géotechnique*, *134-135*, 23-26. https://doi.org/10.1051/geotech/2011134023.

Proceedings of the XVIII ECSMGE 2024
GEOTECHNICAL ENGINEERING CHALLENGES
TO MEET CURRENT AND EMERGING NEEDS OF SOCIETY
© 2024 the Authors
ISBN 978-1-032-54816-6
DOI 10.1201/9781003431749-195
Open Access: www.taylorfrancis.com, CC BY-NC-ND 4.0 license

ECSMGE 24
XVIII EUROPEAN CONFERENCE ON SOIL MECHANICS AND GEOTECHNICAL ENGINEERING

Experimental investigation of influence of soil plasticity on compression characteristics and creep behaviour of clayey soils

Étude expérimentale de l'influence de la plasticité du sol sur les caractéristiques de compression et le comportement au fluage des sols argileux

M.N. Duy*, J. Jerman
Charles University, Prague, Czechia

**nguyendma@natur.cuni.cz*

ABSTRACT: Comprehending the creep mechanisms and determining the factors influencing compression and creep characteristics is indispensable for accurate long-term settlement predictions, a critical determinant of structural stability and safety of structures. Also, both natural and artificial slopes, as well as embankments, manifest varying rates of creep movements. Recent experimental investigations have highlighted the significant role played by the influence of soil composition, fabric structure, over-consolidation ratio (OCR), and plasticity in the time-dependent behaviour and compression characteristics of clays. However, a comprehensive description and correlation of these factors have yet to be proposed. To address this gap, an extensive experimental study was conducted under well-defined conditions. Reconstituted samples, including low-plasticity clay (kaolinite), high-plasticity clay (bentonite), and their mixtures, underwent standard and creep oedometric tests. We show that samples with lower plasticity exhibit reduced volume changes during compression and swelling and lower values of the creep coefficient (C_α). The stress dependency of C_α is more pronounced in mixtures containing bentonite compared to pure kaolinite. Also, strong OCR-dependency of C_α has been observed.

RÉSUMÉ: Comprendre les mécanismes de fluage et déterminer les facteurs influençant les caractéristiques de compression et de fluage est indispensable pour des prévisions précises de tassement à long terme, un déterminant essentiel de la stabilité structurelle et de la sécurité des structures. En outre, les pentes naturelles et artificielles, ainsi que les remblais, présentent des taux de fluage variables. Des recherches expérimentales récentes ont mis en évidence le rôle important joué par l'influence de la composition du sol, de la structure du tissu, du taux de surconsolidation (OCR) et de la plasticité dans le comportement dépendant du temps et les caractéristiques de compression des argiles. Cependant, une description complète et une corrélation de ces facteurs doivent encore être proposées. Pour combler cette lacune, une étude expérimentale approfondie a été menée dans des conditions bien définies. Les échantillons reconstitués, comprenant des argiles à faible plasticité (kaolinite), des argiles à haute plasticité (bentonite) et leurs mélanges, ont été soumis à des tests œdométriques standards et de fluage. Nous montrons que les échantillons ayant une plasticité plus faible présentent des changements de volume réduits lors de la compression et du gonflement et des valeurs plus faibles du coefficient de fluage (C_α). La dépendance du C_α à la contrainte est plus prononcée dans les mélanges contenant de la bentonite que dans la kaolinite pure. En outre, une forte dépendance de Cα à l'OCR a été observée.

Keywords: Soil plasticity; compression characteristics; creep behaviour; over-consolidation ratio; coefficient of secondary compression.

1 INTRODUCTION

Soil plasticity and composition have been shown to affect the mechanical response of clays, as has been presented by Olek (2022) in the context of creep behaviour. Soil creep characteristics are commonly described using a parameter known as the "coefficient of secondary compression - C_α" (Mesri, 1973). This parameter holds significance in engineering applications and constitutive modelling, particularly when estimating creep settlements. The time-dependent behaviour is traditionally characterised by linearly determining C_α through the relationship between the void ratio and the logarithmic function of time. Yin (1999) illustrated that the creep coefficient exhibits variation with the void ratio and the limitations associated with the logarithmic function used for linear performance. Nevertheless, for this paper, the linear formulation, as employed by Olek

(2022), is adopted to ascertain the parameter C_α. As for the stress dependency of C_α, there exist two conflicting perspectives. Barden and Laing (1969) assert that C_α is nearly independent of stress level, contrary to the findings of other researchers such as Lei et al. (2016).

Soil plasticity is the property governing deformation in soil without the occurrence of cracking or fracturing, making it a crucial aspect for analyzing long-term deformation, commonly known as creep deformation. The observed impact of clay plasticity on clay creep has been shown by Anagnostopoulos and Grammatikopoulos (2011), who conducted oedometer creep tests on thirteen types of natural clays in the broader Thessaloniki area, Greece. The findings suggest that the creep coefficient relies on both plasticity and water content. Additionally, Karstunnen and Yin (2010) established that the creep coefficient exhibits dependence on the process of destructuration specifically within intact natural clays. Despite these insights, there has been limited exploration into the influence of clay structure, including plasticity and its OCR on creep properties and soil responses, particularly when studying reconstituted samples of clays.

Varatharajan and Sivarajan (2011) observed that bentonite, a highly plastic clay, demonstrates more significant creep deformation compared to kaolin, a clay with lower plasticity. Nevertheless, the effect of long-term creep behaviour was not explored, leaving a gap in our understanding of this aspect. A comprehensive exploration of clay plasticity's influence on clay compression behaviour is lacking, highlighting a notable gap in our foundational understanding of time-dependent clay behaviour. To enhance our understanding of how soil plasticity influences the creep behaviour of clay soils, we have initiated a comprehensive experimental program involving the preparation of artificial mixtures of kaolin (K) and bentonite (B) and their mixtures.

2 METHODOLOGY AND MATERIAL

2.1 Methodology

The main goal of this contribution is to gather comprehensive experimental data on how plasticity influences compression (via standard oedometric tests) and creep behaviour (creep oedometric tests) of clays. Soil samples were prepared as mixtures with different proportion rates of kaolinite (K – low plasticity clay) and bentonite (B – high plasticity clay). Individual samples (further denoted as „mixtures“) are denoted such as 100K, 75K-25B, 50K-50B, 25K-75B, and 100B, showing the proportion of individual clays (such as 100K – 100% of kaolinite and 0% of bentonite clay). Plastic and liquid limits were determined for each mixture. Specifically, the plastic limit for each mixture was determined through interpolation using referenced values from (Sivapullaiah et al., 1985) and (Duque et al., 2022). For the determination of liquid limit (LL), the cone penetration method was employed. This method relies on the soil's shear strength, offering improved accuracy and preventing potential overestimation of the liquid limit, particularly in soils with LL exceeding 100% (e.g., bentonite) (Orhan et al., 2006).

Table 1 presents PL, LL, and plasticity index (PI) values. As anticipated, mixtures with a higher bentonite proportion demonstrate elevated PI values.

Table 1. PL, LL and PI of all mixtures.

Mixtures	PL(%)	LL(%)	PI
K	40	64.55	24.55
75K-25B	42.42	124.80	82.37
50K-50B	44.85	229.07	184.22
25K-75B	47.27	287.70	240.42
B	49.7	315.37	265.67

For oedometer tests, an analysis of soil compression, characterized by the critical state line slope (λ^*) in the e-ln(p) space, and swelling, represented by the unloading-reloading line slope (κ^*) in the same space, was performed. Parameters λ^* and κ^* are based on the definitions from the hypoplastic model for clays proposed by Masin (2005) and are equivalent to C_c and C_r. The creep oedometer tests undergo a minimum 7-day creep period after T_{eop}. This timeframe is deemed adequate, as indicated by prior research on reconstituted samples, where T_{eop} is typically achieved within 24 hours (Olek, 2022), (Lei et al., 2016). T_{eop} was determined for each creep stage by Casagrande‘s method (Taylor, 1948). The impact of soil plasticity on long-term settlement was explored by assessing the secondary compression coefficient (C_α):

$$C_\alpha = \frac{\Delta e}{\Delta \log t} \quad (1)$$

The current OCR was determined for every stress increment to address the influence of the OCR on determined soil characteristics. The OCR is defined as $\sigma'_p/\ \sigma'_z$, where σ'_p is the pre-consolidation stress and σ'_z is the applied experimental stress. In standard oedometer tests (refer to Table 2 for the applied stress levels), the kaolinite sample was subjected to a maximum of 1600 kPa, while the remaining samples were loaded to a maximum of 800 kPa due to the excessive deformation. In the case of creep oedometer

tests, bentonite is exposed to a maximum 200 kPa creep stage, while the other samples undergo a maximum of 400 kPa.

Table 2. Experimental plan, note the steps in brackets were performed only for mixtures and kaolinite.

Test	Creep Stress (kPa)/ Stress Increments (kPa)
Creep test	25-50-100-200(-400)
Standard oed. test	0-25-50-100-200-400-800(-1600-800)-400-200-100-50-25-0

2.2 Material

In preparing the investigated materials, specimens comprised dry kaolin and bentonite powder blended with distilled water. Prescribed guidelines dictate initial water content: W_i = 1.4-2.2LL for pure kaolinite tests, W_i = 1.2-1.6LL for pure bentonite tests, and equivalent water contents of 1.4-2.0LL for mixtures. Varied initial water content aims to assess its impact on compression characteristics and determine the content required for normal consolidation across diverse stress levels (e.g., 25, 50, 100 kPa), especially at low stresses. This procedure has been implemented to avoid comparing the mechanical behaviour of normally consolidated samples with over-consolidated ones.

3 RESULTS

3.1 Influence of initial water content on kaolinite compression characteristics

For kaolinite, we analysed compression curves and as expected, we found out that their shape is dependent on the initial water content, even after joining NCL as shown in Figure 1. The NCL is notably influenced by W_i, with a downward shift at lower W_i levels, converging after 200 kPa. This indicates over-consolidation at low stresses (~<200 kPa) for lower W_i. Utilizing the data, we establish a relationship between OCR and W_i, defining the highest NCL (W_i = 148.2%) as the benchmark for OCR = 1.0.

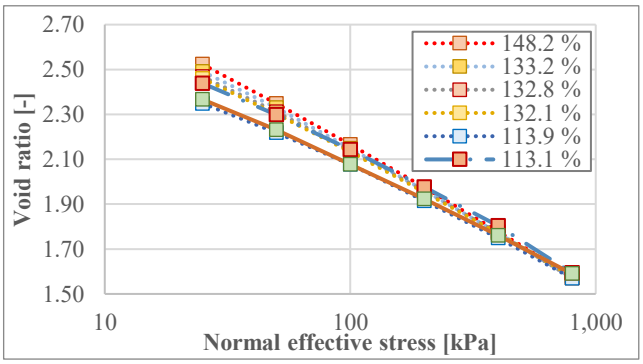

Figure 1. Influence of initial water content (W_i, in per cent) of reconstituted samples of kaolinite on NCL.

The OCR is referenced to the test with the highest initial water content, W_i = 148.2% (and thus the highest positioned NCL). Figure 2 depicts the relationship between OCR and W_i, revealing an inverse proportionality at low-stress levels. Around W_i = 130%, the OCR decreases to ~1.0 establishing this value as a limit. Beyond this limit, OCR remains stable. Thus, precise regulation of W_i is crucial to establishing an accurate NCL for the entire experimental scope. Figure 2 validates using W_i approximately twice the liquid limit for kaolinite, ensuring a normal consolidation state across all stress levels (25, 50, 100, 200, etc.)

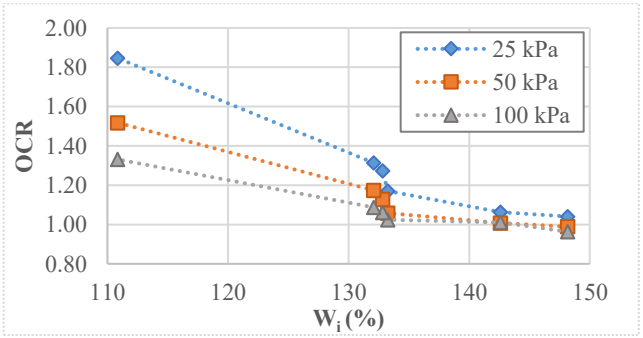

Figure 2. Correlation between initial water content and OCR of kaolinite at low-stress levels.

3.2 Influence of plasticity on soil compression characteristics

To examine the impact of plasticity on compression characteristics, Figure 3 illustrates the variation in λ^* and κ^* across all tested mixtures (represented by PI). The sample with lower plasticity (and lower proportion of bentonite) demonstrates reduced values of λ^* and κ^*, corresponding to lesser volume change during compression and swelling.

The primary consolidation duration (T_{eop}) is influenced by soil composition, as shown in Figure 4. Samples with higher bentonite percentages exhibit prolonged primary consolidation. Notably, for mixtures with bentonite (from 25K-75B to B), T_{eop}

reaches its maximum at 50 kPa, gradually decreasing until 200 kPa. In contrast, for kaolinite, T_{eop} is around 12 minutes at 25 kPa and remains relatively around 18 minutes during subsequent compression.

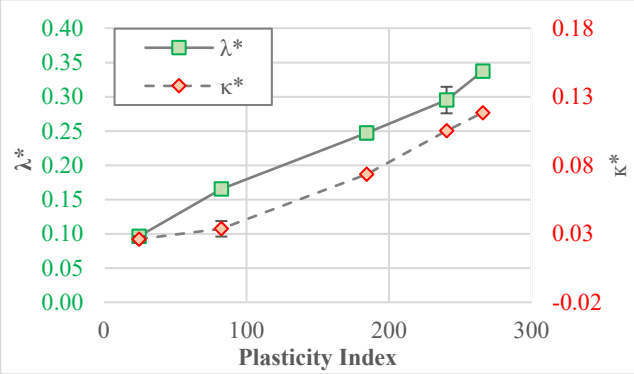

Figure 3. Evolution of compression indices (λ, κ*) with plasticity for different mixtures.*

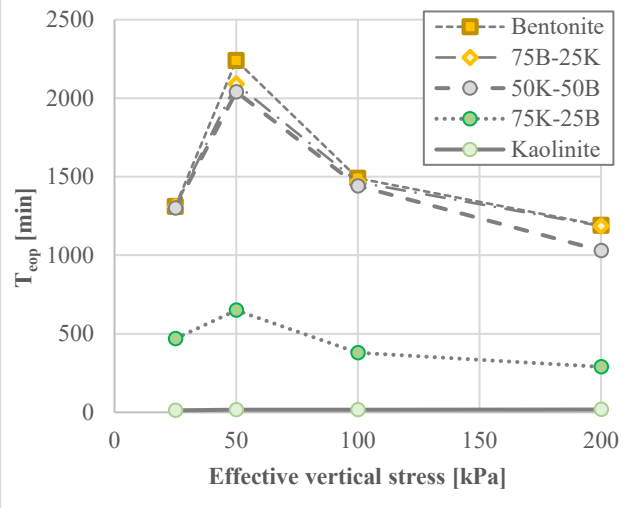

Figure 4. Influence of stress levels and soil plasticity on T_{eop}.

3.3 Influence of plasticity on creep behaviour

C_α is plotted against various soil compositions, represented by different Plasticity Index (PI) values at three stress levels (50, 100, 200 kPa), as depicted in Figure 5. Mixtures with higher plasticity manifest elevated C_α values, exhibiting significant changes among different stress levels. Conversely, the lower plasticity sample exhibits a contrasting trend; for instance, the C_α values for kaolinite remain nearly constant across all applied stress levels.

Figure 6 reveals another intriguing aspect: a trendline resembling the correlation between C_α and the stress level. Notably, the C_α values peak at 50 kPa across all mixtures containing bentonite. In the case of kaolinite, C_α for kaolinite shows only a statistically insignificant increase with applied stress across all applied stress levels. In the figures, we also present the values of OCR at all stress levels.

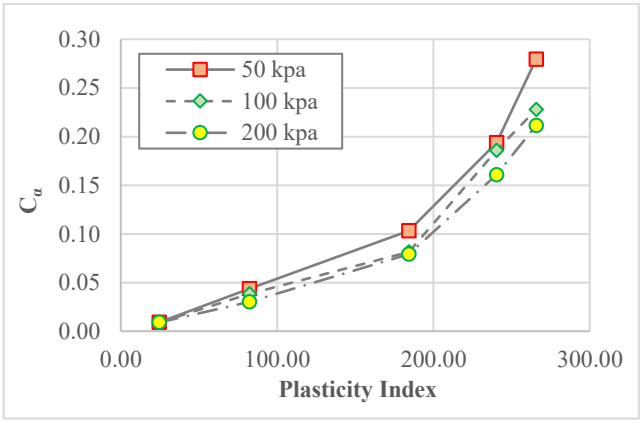

Figure 5. Correlation between C_α and soil plasticity.

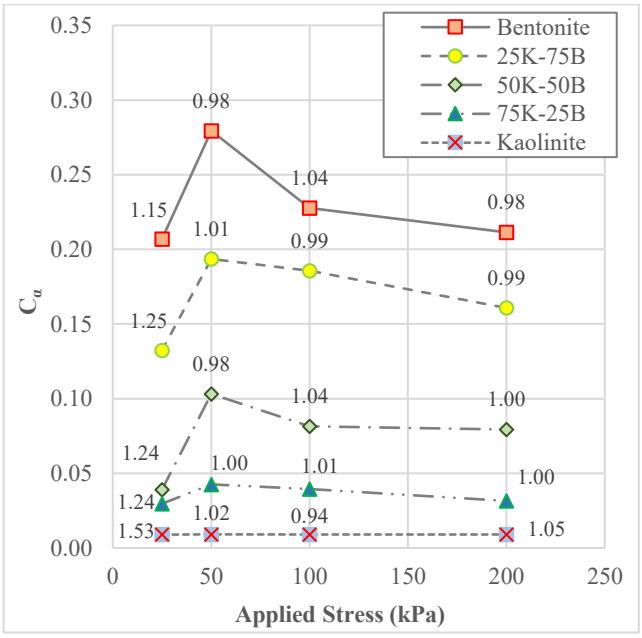

Figure 6. Influence of soil compositions on C_α at different stress levels. OCR at the current stress level is shown for all experiments.

All soil samples display over-consolidation in the 25 kPa stress range, with OCR values ranging from 1.1 to 1.53, and sample over-consolidation being the most likely factor in the low C_α at 25 kPa. Starting from 50 kPa, OCR values stabilize around 1. Capturing a definitive trend even for lower stresses requires additional experiments with high initial water content (W_i).

4 CONCLUSIONS

In this contribution, we presented an extensive experimental study consisting of 18 standard and 20 creep oedometric tests performed on low-plasticity clay (kaolinite), high-plasticity clay (bentonite), and their mixtures.

- Initial water content (W_i) plays a pivotal role in governing the OCR, especially at low stress

levels. Elevated W_i corresponds to a lower OCR value. Relatively low W_i (<130% for kaolinite) translates to samples being tested in overconsolidated state, which makes comparison of soil characteristics at low and high stresses impossible. It also induces a downward shift in the shape of NCL, evident at lower W_i levels and converging after reaching 200 kPa.

- Samples with lower plasticity exhibit reduced volume changes during compression and swelling, as evidenced by smaller values of λ* and κ*.
- Soils with higher plasticity display increased creep deformation, as indicated by higher values of the creep coefficient (C_α). The stress dependency of C_α is more pronounced in mixtures containing bentonite, as evidenced by a significant change in C_α, in contrast to the marginal change observed in kaolinite. Nevertheless, C_α attains its peak value at 50 kPa in all mixtures. A similar trend is also observed in T_{eop}. To accurately delineate the trend of C_α and T_{eop} with increasing stress levels, additional tests at higher W_i are essential. This precaution is necessary to prevent the manifestation of sample over-consolidation at 25 kPa, a probable cause for the lower C_α and T_{eop} at this stress level.
- Limitation of creep analysis arises from the limited amount of data, especially in case of bentonite and mixtures. That causes the shortcoming in investigating the influence of W_i on OCR at individual stress levels, correlation between OCR and C_α and statistical analysis of data.
- Primary objective is to correlate compression characteristics, creep coefficient, OCR, and soil plasticity. This requires thorough verification and determination of plasticity index values through an alternative experimental method for liquid limit, such as Cassagrande percussion cup method. Hence, more tests are essential to acquire a comprehensive dataset for subsequent statistical analysis.

ACKNOWLEDGEMENTS

This research was supported by the Johannes Amos Comenius Programme (P JAC), project No. CZ.02.01.01/00/22_008/0004605, Natural and anthropogenic georisks.

REFERENCES

Olek, B.S., 2022. An experimental investigation of the influence of plasticity on creep degradation rate. Acta Geotechnica, 17(3), pp.803-817. https://doi.org/10.1007/s11440-021-01272-z.

Mesri, G., 1973. Coefficient of secondary compression. Journal of the soil mechanics and foundations division, 99(1), pp.123-137. https://doi.org/10.1061/JSFEAQ.0001840.

Yin, J.H., 1999. Non-linear creep of soils in oedometer tests. Geotechnique, 49(5), pp.699- 707. https://doi.org/10.1680/geot.1999.49.5.699.

Barden, L., 1969. Time dependent deformation of normally consolidated clays and peats. Journal of the Soil Mechanics and Foundations Division, 95(1), pp.1-31. https://doi.org/10.1061/JSFEAQ.0001214.

Lei, H., Wang, X., Chen, L., Huang, M. and Han, J., 2016. Compression characteristics of ultra-soft clays subjected to simulated staged preloading. KSCE Journal of Civil Engineering, 20, pp.718- 728. https://doi.org/10.1007/s12205-015-0343-y.

Anagnostopoulos, C.A. and Grammatikopoulos, I.N., 2011. A new model for the prediction of secondary compression index of soft compressible soils. Bulletin of Engineering Geology and the Environment, 70, pp.423-427. https://doi.org/10.1007/s10064-010-0323-x.

Karstunen, M. and Yin, Z.Y., 2010. Modelling time-dependent behaviour of Murro test embankment. Géotechnique, 60(10), pp.735-749. https://doi.org/10.1680/geot.8.P.027.

Varatharajan S. 1D comperssion creep behavior of kaolinite and bentonite clay. department of civil engineering Calgary, Phd Thesis, Alberta. 2011 Jul.

Sivapullaiah, P.V. and Sridharan, A., 1985. Liquid limit of soil mixtures. ASTM International. https://doi.org/10.1520/GTJ10521J.

J. Duque, J. Roháč, D. Mašín &, Experimental investigation on Malaysian kaolin under monotonic and cyclic loading: inspection of undrained Miner's rule and drained cyclic preloading – 2022. https://doi.org/10.1007/s11440-022-01643-0.

Taylor, D.W., 1948. Fundamentals of soil mechanics (Vol. 66, No. 2,9. 161). LWW.

Orhan, M., Özer, M. and Işik, N., 2006. Comparison of Casagrande and cone penetration tests for the determination of the liquid limit of natural soils. Journal of the Faculty of Engineering and Architecture of Gazi University, 21(4).

Mašín, D., 2005. A hypoplastic constitutive model for clays. International Journal for numerical and analytical methods in Geomechanics, 29(4), pp.311-336. https://doi.org/10.1002/nag.416.

Proceedings of the XVIII ECSMGE 2024
GEOTECHNICAL ENGINEERING CHALLENGES
TO MEET CURRENT AND EMERGING NEEDS OF SOCIETY
© 2024 the Authors
ISBN 978-1-032-54816-6
DOI 10.1201/9781003431749-196
Open Access: www.taylorfrancis.com, CC BY-NC-ND 4.0 license

ECSMGE 24
XVIII EUROPEAN CONFERENCE ON SOIL MECHANICS AND GEOTECHNICAL ENGINEERING

Nonlinear finite element analyses of earthquake effects in slopes

Analyses non-linéaires par éléments finis des effets sismiques sur les pentes

A. Eikebrokk*, A.M. Kaynia
Norconsult, Sandvika, Norway

**anna.eikebrokk@norconsult.com*

ABSTRACT: Assessment of seismic slope stability traditionally rely on pseudo-static approaches whereby the seismic loads are simplified as static loads and applied to the model. These analyses tend to be conservative and may result in unnecessary and costly countermeasures. In many such cases, the slope will experience some permanent deformation, but it will not fail. Therefore, a more realistic approach is to assess the slope stability using finite element analyses and defining the seismic load in terms of acceleration time histories. The limit state is then defined by acceptable levels of displacements and strains, and satisfactory functionality of the construction possibly affected by the slope movement. In this study, the dynamics module of the finite element software *Plaxis 2D* has been utilized for the analyses. The conventional *Mohr-Coulomb model* is employed to characterize the soil's undrained behavior during the earthquake situation. This model is a linear elastic perfectly plastic material model in which the undrained shear strength is related to the soil's effective vertical stress. The cyclic shear strength in the model was determined through calculations and specialized cyclic laboratory tests conducted on soil samples from the site. The estimation of shear strength includes the effect of the static shear stress due to gravity, which was confirmed by the lab test results. Nonlinear finite element analyses using this approach have yielded promising results, suggesting that the approach is a more realistic method for assessing seismic slope stability.

RÉSUMÉ: Evaluation de la stabilité des pentes sismiques repose traditionnellement sur des approches pseudo-statiques où les charges sismiques sont simplifiées comme des charges statiques et appliquées au modèle. Ces analyses ont tendance à être conservatrices et peuvent entraîner des contre-mesures inutiles et coûteuses. Dans de nombreux cas, la pente subira une déformation permanente, mais elle ne faillira pas. Par conséquent, une approche plus réaliste consiste à évaluer la stabilité de la pente en utilisant des analyses par éléments finis et en définissant la charge sismique en termes d'historiques de temps d'accélération. L'état limite est alors défini par des niveaux acceptables de déplacements et de contraintes, et une fonctionnalité satisfaisante de la construction éventuellement affectée par le mouvement de la pente. Dans cette étude, le module de dynamique du logiciel d'éléments finis Plaxis 2D a été utilisé pour les analyses. Le modèle conventionnel de Mohr-Coulomb est employé pour caractériser le comportement non drainé du sol pendant la situation de séisme. Ce modèle est un modèle de matériau élastique parfaitement plastique linéaire dans lequel la résistance au cisaillement non drainé est liée à la contrainte verticale effective du sol. La résistance au cisaillement cyclique dans le modèle a été déterminée par des calculs et des tests de laboratoire cycliques spécialisés effectués sur des échantillons de sol du site. La résistance au cisaillement comprend l'effet de la contrainte de cisaillement statique due à la gravité, ce qui a été confirmé par les résultats des tests de laboratoire. Des analyses non linéaires par éléments finis utilisant cette approche ont donné des résultats prometteurs, suggérant que l'approche est une méthode plus réaliste pour évaluer la stabilité sismiques des pentes.

Keywords: Slope stability; earthquake; lab testing; cyclic loading.

1 INTRODUCTION

Most seismic codes, including Eurocode 8 (2014), require verification of ground stability for structures to be erected on or near natural or artificial slopes. The assessment of the seismic slope stability can be performed by a pseudo-static approach or by a dynamic analysis. However, a significant drawback of the pseudo-static analyses is that they tend to be too conservative. In cases where a pseudo-static analysis does not provide the required safety factor, it is advisable to base the assessment on a performance-based design whereby one can use a nonlinear dynamic analysis, for example in finite elements (FE) or finite difference (FD) and estimate the permanent displacements and shear strains in the slope. The assessment can then be based on the computed response against the required performance criteria. This method has been used extensively in soil and rock slopes in seismic areas with different computational solutions such as 2D/3D FE or FD, complex loading and geometry, and advanced constitutive modelling accounting for strain softening due to cyclic loading

and liquefaction among others. See, for example (Kaynia, 2018) for a review of these solutions.

In this study, the more realistic, dynamic analyses of the seismic slope stability are investigated together with a new procedure for determining the cyclic undrained shear strength in slopes.

The work showcased in this article was conducted in conjunction with the design of the Tangenvika railway bridge in Norway, to be constructed by the construction company Implenia for the Norwegian Rail Infrastructure, Bane NOR.

2 ANALYSIS METHOD

To assess the impact of earthquake on slope stability, the dynamics module of Plaxis 2D has been utilized. Three acceleration time histories scaled to the peak acceleration at site were used. Figure 1 shows the time history of Imperial Valley earthquake, 1979. The other two earthquakes were Nahanni (Canada, 1985) and Friuli (Italy, 1976).

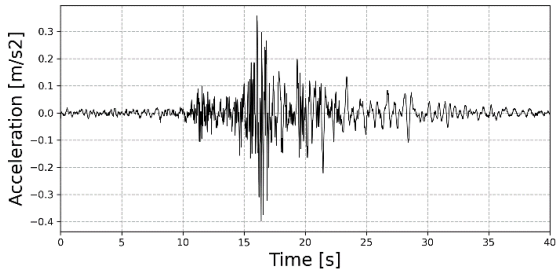

Figure 1. Acceleration time history for Imperial Valley earthquake scaled to peak acceleration at site.

To identify areas with potential stability issues, a seabed mapping was conducted using a multibeam echosounder (MBES). Based on the terrain analysis of this data along the bridge profile and geotechnical considerations, axis 10 was identified as the most vulnerable to earthquake shaking. The analyses related to this location are presented in this article. Figure 2 shows the Plaxis model used for the earthquake analyses of this slope.

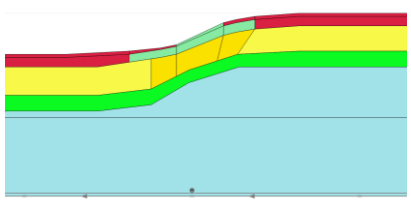

Figure 2. PLAXIS model of slope in axis 10.

To account for both the initial drained stresses in the silt and sand layers due to gravity and the cyclic undrained stresses during the earthquake, a new procedure based on the work of (Andersen, 2015) was used to estimate the shear strength of the soil. The procedure is outlined in the next section. The so-called *Shansep (Stress History and Normalized Soil Engineering properties) MC* model built in Plaxis allows an effective implementation of this procedure in the earthquake analyses.

2.1 Cyclic Shear Strength

Lab tests have shown that undrained cyclic shear strength can be increased in areas where consolidated static shear stresses are acting such as in slopes. The static shear stress will reduce the concurrent cyclic component of additional load. However, the total cyclic shear strength, $\tau_{f,cy}$, which is the sum of the static, τ_a, and cyclic shear component leading to failure, $\tau_{cy,f}$, will increase in most cases. The cyclic shear strength is the peak shear stress that can be mobilized during cyclic loading and is accordingly expressed as (Andersen and Lauritzen, 1988):

$$\tau_{f,cy} = \left(\tau_a + \tau_{cy}\right)_f \qquad (1)$$

Using published data (Andersen, 2015) one can estimate $\tau_{cy,f}$ in Eq. (1) using an interaction diagram as visualized in Figure 3. The intersection of the interaction line and the horizontal and vertical axes are correspondingly drained static shear strength and undrained cyclic shear strength under one-way loading. Using the average shear stress along the slope, the corresponding cyclic shear strength can be estimated from the interaction diagram. See example of the method applied further below.

The *Shansep MC model* introduces a cyclic factor, α, which normalizes the cyclic shear strength, $\tau_{f,cy}$, to the effective vertical stress, σ_v':

$$\alpha = \frac{\tau_{f,cy}}{\sigma_v'} \qquad (2)$$

For non-liquefiable soils, conservative values for the cyclic shear strength, $\tau_{cy,f}$, normalized with σ_v' as a function of Dr have been suggested (Andersen, 2015) which give normalized cyclic shear strength for the interpreted Dr = 40% for the silt and sand layers equal to 0.16.

Further, the estimated friction angle of the sand layer is 34 °, which gives static shear strength of the sand:

$$\tau_f = \sigma_n' \tan(34°) = \sigma_v' \sin(34°) \qquad (3)$$

where σ_n' is the effective normal stress on the failure plane and σ_v' is the corresponding vertical stress. Thus, the normalized static shear strength $\frac{\tau_f}{\sigma_v'} = 0{,}56$.

The average shear stress along the slope is correspondingly:

$$\tau_a = \sigma_v' \sin(\beta) \qquad (4)$$

where β is the angle of the slope.

Using the interaction diagram in Figure 3 and the average normalized shear stress along the slope, $\frac{\tau_a}{\sigma_v'} = 0.18$, one can estimate the normalized cyclic shear strength $\frac{\tau_{cy,f}}{\sigma_{v'}} = 0.11$. Therefore, the total normalized cyclic shear strength along the slope is 0.29 which is considerably larger than the cyclic shear strength without the effect of average shear stress.

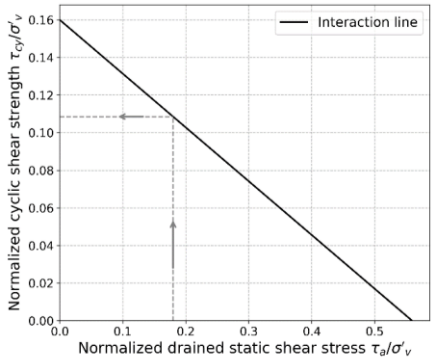

Figure 3. Interaction diagram for cyclic shear strength.

3 CYCLIC SIMPLE SHEAR TESTS

3.1 Laboratory Procedure

To investigate the actual in situ shear strength of the soil at the site and to confirm the selected strength parameters, cyclic direct shear tests (DSS) were carried out at NGI laboratory. The samples were taken from 3.4 m – 3.6 m below seafloor, where the sample quality was deemed best. Based on visual inspection, the material was described as clayey silt interspersed with thin sand layers and sporadic pockets of clay (Figure 4).



Figure 4. Tested specimen.

The DSS-tests were conducted one-way (unsymmetrical) and two-way (symmetrical, i.e., with no application of average shear stress). The unsymmetrical shear tests were intended to investigate the shear strength of the soil in sloping terrain. The equivalent number of stress cycles, *N*, for the design earthquake in the project site is about 5. However, the tests were conducted with additional cycles and increasing packets of higher shear stress to capture its ultimate strength. The experimental program is summarized in Table 1, while details for test ID 4 is given in Table 2.

Table 1. Laboratory programme, DSS cyclic tests.

Test ID	Test type	Depth below seafloor [m]	Consolidation stress [kPa]
1	Two way	3.43	24.0
4	One way	3.53	24.7
5	One way	3.56	24.9

Table 2. Stages of cyclic DSS test 4.

Stages	τ_a [kPa]	τ_{cy} [kPa]	N	$\frac{\tau_a}{\sigma_v'}$	$\frac{\tau_{cy}}{\sigma_v'}$
Cyclic 1	8.6	1.2	5	0.35	0.05
Cyclic 2	8.6	2.5	5	0.35	0.10
Cyclic 3	8.6	3.7	5	0.35	0.15
Cyclic 4	8.6	6.2	5	0.35	0.25
Cyclic 5	8.6	7.4	40	0.35	0.30

3.2 Experimental results

The test ID 4 results are shown in Figure 5. Calculated values for the cyclic factor, α, for all tests are summarized in Table 3.

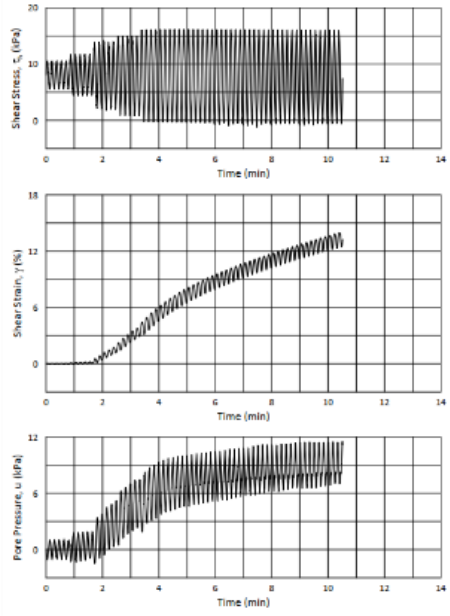

Figure 5. Laboratory results plotted vs time.

Table 3. Calculated cyclic shear stress factors from cyclic laboratory tests.

Test ID	1	4	5
Cyclic factor	0.33	0.65	1.16

4 RESULTS FINITE ELEMENT ANALYSES

Table 4 provides typical values for deformations and strains along the slope for the Imperial Valley acceleration time history which was found to give the largest response among the three selected earthquakes. Figure 6 and Figure 7 display the contours of the computed deformations and shear strains in the model. The permanent strain in the clay layer is approximately 0.6%, which is below the acceptable limits (Earthquake design at Norwegian Public Roads Administration, 2017). Consequently, the post-earthquake stability can be considered satisfactory.

Table 4. Typical responses in the slope for Imperial Valley time history.

Vertical deformation, u_y [mm]	Horizontal deformation, u_x [mm]	Strain, γ_{xy} [%]
42	50	2.0

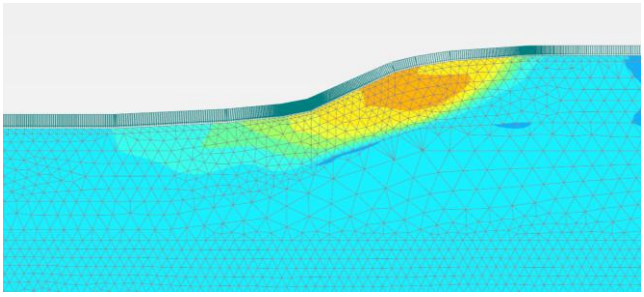

Figure 6. Contours of horizontal deformation, u_x.

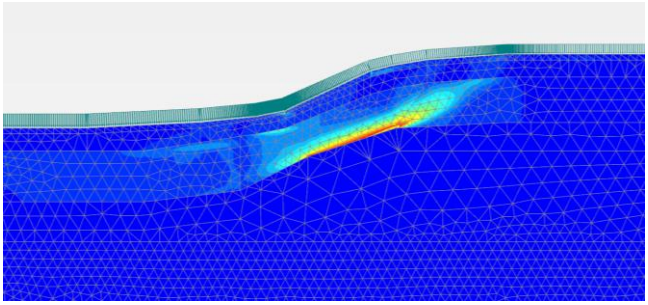

Figure 7. Contours of total shear strain, γ_{xy}.

5 CONCLUSIONS

This research has implemented a more realistic approach using nonlinear finite element analyses to investigate slope stability during the design earthquake. An integral aspect of this research was the determination of the cyclic shear strength. Recognizing that the presence of consolidated static shear stress enhances the cyclic strength has proved to be central to the analyses. The conducted laboratory investigations confirmed and further established a notably higher cyclic factor in slopes compared to flat terrains. Overall, these findings reinforce the potential of nonlinear finite element analyses in providing more accurate and realistic assessments of slope stability in earthquake-prone regions.

ACKNOWLEDGEMENTS

This work was made possible through the design contract for the construction company Implenia and the Norwegian Rail Infrastructure, Bane NOR. Their support during this study is gratefully acknowledged. Also, appreciation is extended to the Norconsult colleagues Magnar Myhre, project manager, and Kjetil Kildal, geotechnical discipline leader, for discussions and their collaboration throughout the study.

REFERENCES

Andersen, K.H. and Lauritzen R. (1988). Bearing capacity for foundations with cyclic loads. *Journal of Geotechnical Engineering,* Vol. 114, Issue 5. https://doi.org/10.1061/(ASCE)0733-9410(1988)114:5(540) .

Andersen, K.H. (2015). Cyclic soil parameters for offshore foundation design. The 3rd ISSMGE McClelland Lecture. In *Frontiers in Offshore Geotechnics III,* ISFOG, *Oslo, Norway, pp. 5-82.*

Kaynia, A.M. (2018). Earthquake geotechnics in offshore Engineering. *Recent Advances in Earthquake Engineering in Europe.* Vol. 46, pp. 263-288. http://doi.org/10.1007/978-3-319-75741-4_11.

SVV (2017). Earthquake design at Norwegian Public Roads Administration, Norwegian Public Roads Administration, Oslo, Norway, Rep. 604.

NS-EN 1998-1 (2014). Eurocode 8: Design of structures for earthquake resistance. Standard Norge.

Proceedings of the XVIII ECSMGE 2024
GEOTECHNICAL ENGINEERING CHALLENGES
TO MEET CURRENT AND EMERGING NEEDS OF SOCIETY
© 2024 the Authors
ISBN 978-1-032-54816-6
DOI 10.1201/9781003431749-197
Open Access: www.taylorfrancis.com, CC BY-NC-ND 4.0 license

ECSMGE 24
XVIII EUROPEAN CONFERENCE ON SOIL MECHANICS AND GEOTECHNICAL ENGINEERING

Appraisal of various measures for liquefaction flowslide mitigation in a mild sloping ground

Évaluation de diverses mesures d'atténuation des glissements de liquéfaction dans un terrain en pente douce

M.H. Fansuri*
Universitas Pertahanan Republik Indonesia (Unhan RI), Bogor, Indonesia

M. Chang, R.R. Rayhansyah, H.J. Lin
National Yunlin Univ. Sci. & Tech. (YunTech), Douliu, Taiwan, ROC

T.C. Upomo, R. Kusumawardani
Universitas Negeri Semarang (Unnes), Semarang, Indonesia

**hamzah.fansuri@idu.ac.id*

ABSTRACT: Liquefaction-induced flowslides would cause significant damages and casualties as the case of 2018.9.28 incidences of Palu, Sulawesi, Indonesia, where the flowslides occurred immediately after a severe earthquake and led to an extremely-long distance of sliding on mild sloping ground. The conditions that would favour soil liquefaction and the associated flowsliding hence become the focus of the incident. Another issue deserved further attention, however, would be strategy for preventing or mitigating the problem. In accordance, the aim of this study is to apprise the performance and effectiveness of various measures on the mitigation of soil liquefaction and flowsliding. The mitigation measures considered herein include: stone-column (SC), micro-pile (MP), densification (DS), encased stone column (ESC) soil grouting (GT), and groundwater lowering (GL), which are commonly adopted in engineering practice. The performance and effectiveness of the mitigation measures are assessed numerically in terms of their responses in the excess pore pressure generation in soil as well as the lateral deformation of soil deposit due to the excitation of seismic motion. Results generally indicate the SC, ESC, and DS options are more effective in prohibiting the generation of excess pore pressure, and hence in reducing soil liquefaction, than the other options. We also notice the MP, SC, and ESC options would be more effective in preventing the lateral deformation, and therefore in avoiding the flowslide or lateral spread in soil deposit.

RÉSUMÉ: Les glissements de terrain induits par la liquéfaction causeraient des dommages et des pertes importants, comme dans le cas des incidents du 28 septembre 2018 à Palu, Sulawesi, en Indonésie, où les glissements de terrain se sont produits immédiatement après un grave tremblement de terre et ont conduit à une distance de glissement extrêmement longue sur un terrain en pente douce. Les conditions qui favoriseraient la liquéfaction des sols et les glissements d'écoulement associés deviennent alors au centre de l'incident. Une autre question qui mériterait davantage d'attention serait celle de la stratégie visant à prévenir ou à atténuer le problème. Conformément, le but de cette étude est d'évaluer la performance et l'efficacité de diverses mesures d'atténuation de la liquéfaction des sols et des glissements de terrain. Les mesures d'atténuation envisagées ici comprennent: les colonnes de pierres (SC), les micro-pieux (MP), la densification (DS), les colonnes de pierres enrobées (ESC), l'injection de sol (GT) et l'abaissement des eaux souterraines (GL), qui sont couramment adoptées dans pratique de l'ingénierie. La performance et l'efficacité des mesures d'atténuation sont évaluées numériquement en termes de leurs réponses à la génération de pression interstitielle excessive dans le sol ainsi qu'à la déformation latérale des dépôts de sol due à l'excitation du mouvement sismique. Les résultats indiquent généralement que les options SC, ESC et DS sont plus efficaces pour empêcher la génération d'une pression interstitielle excessive, et donc pour réduire la liquéfaction du sol, que les autres options. Nous remarquons également que les options MP, SC et ESC seraient plus efficaces pour prévenir la déformation latérale, et donc pour éviter le glissement ou la propagation latérale dans les dépôts de sol.

Keywords: Mitigation measures; liquefaction flowslide; sloping ground; numerical assessment.

1 INTRODUCTION

Soil liquefaction is the phenomenon associated with strong earthquake which would be of the most catastrophic consequences of earthquake and thus has caused severe damage to the structures. Mainly, liquefaction induced earthquake might cause a significant loss of strength of soil masses with a progressive generation of pore pressure, and thus resulting in large permanent deformation, including

lateral spreading and settlement), and even flowslide failure of soils. Case histories were observed as the Petobo flow failure causing significant movement in a mildly sloping ground due to 2018 Palu-Donggala Indonesia earthquake (Kusumawardani, et al., 2021). Consequently, one of the most important strategy of earthquake-resistant design is to avoid or decrease liquefaction-induced deformations of foundation soils. Ground improvement and soil reinforcement are the most useful methods for improving the strength properties of soils and have been performed in order to avoid or decrease the liquefaction-induced soil deformations and associated damage. For example, the geosynthetics are main materials used for increasing the strength and stability of geotechnical structures (Hosseinpour et al., 2010). Several liquefaction mitigation techniques have been proposed over the years, including densification, grouting, and groundwater lowering. Although, the majority of these methods proves inapplicable or difficult to implement for various reasons and has been based on conceptual understanding or simplified analysis. Accordingly, the mitigation of liquefaction disasters would be a primary concern in engineering practice. Through rigorous finite element analyses, this paper addresses assessment of several liquefaction mitigation measures, including stone-column (SC), micro-pile (MP), densification (DS), encased stone column (ESC), soil grouting (GT), and groundwater lowering (GL), with an aim to provide a clearer understanding on effectiveness of ground improvement methods and to assess the liquefaction-induced soil deformations to acceptable levels for construction.

2 ANALYSIS METHOD

The assessment adopts a numerical tool for all simulations by using OpenSeesPL, which is a graphical user interface for conducting 3D ground-structure finite element analysis (http://opensees.berkeley.edu). A 20-8-node element is assumed, where 20 nodes are for solid translation degree for freedom and 8 corner nodes for fluid pressure. Multi-yield conical surfaces with considering phase transformation are applied for soils. The couple solid-fluid option of the software enables the performance of liquefaction studies. We describe the results of 3D seismic response with considering the behavior of soil in the center and the edge of soil column. In total, 88 simulations were performed to explore different combinations of influence factors, including the original cases (i.e., without any improvement).

Figure 1 indicates a typical soil column of the improved ground with a depth of 30 m, where a periodic boundary condition is assumed for the vertical faces and fix end at the base of column. Due to symmetric, only one half of the soil column is assumed in the numerical analysis. As indicated, the seismic shaking is assigned at the base of the soil column and acting in x-direction.

A liquefaction-prone area at Chuoshui river alluvial fan-delta (CRAFD; Chang et al., 2012) is selected as the target site with a groundwater level of 3.84 m below ground surface, where the log of Borehole W5-3, as shown in Figure 2, is adopted as the soil deposit with improvements by several mitigation measures in current study. It is noticed that the numerical analyses composed of clay and silt layers beneath a deposit of very loose sand to medium which are prone to liquefaction due to seismic shaking. Tables 1 and 2 indicate the assumed material parameters of soil deposit and mitigation as well as geosynthetic measures in numerical simulations.

The input motion of this study adopts the recorded motion at CHY002 station during 1999 Chi-Chi earthquake (M_W = 7.6) of Taiwan. The recorded motion, however, should be scaled to the design earthquake of the site (M_W = 7.1 and a_{max} = 0.308g) based on local building code (MOI, 2011), and then deconvoluted from ground surface to a depth of 30m of the site for OpenSeesPL analysis. Figure 3 shows the deconvoluted input motion for this study (a_{max} = 0.250g).

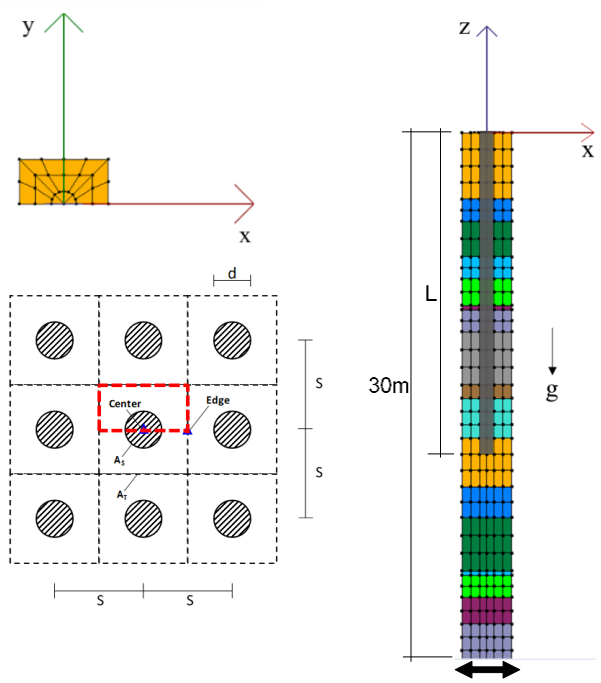

Figure 1. Finite element meshes of representative soil column for numerical simulations.

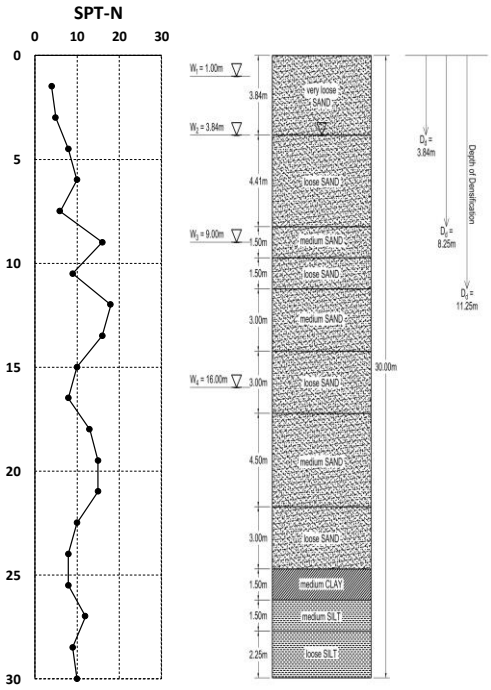

Figure 2. Typical soil/SPT-N profile, based on Borehole W5-3 in CRAFD, for current analysis.

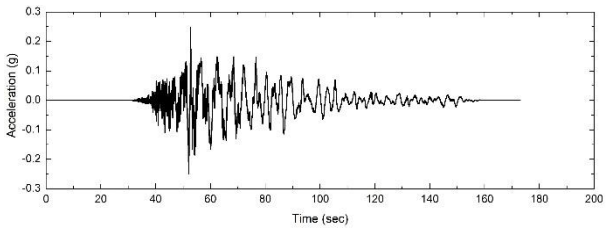

Figure 3. Deconvoluted input motion originally recorded at Station CHY002 (ground surface), in proximity of Borehole W5-3 with a distance < 2 km, during the 1999 Chi-Chi earthquake of Taiwan.

3 ASSESSMENT RESULTS

A comparative study of the seismic performance evaluation of stone-column (SC), micro-pile (MP), densification (DS), encased stone column (ESC), soil grouting (GT), groundwater lowering (GL) is compared with the original deposit (i.e., original ground, OG; without improvement). Typical range of design specifications for each of the options are selected, as indicated in the relevant figures, with varied spacing (s) for SC options, embedment depths (L) for MP options, depth of densification (D_d), thickness of geosynthetic (t) for ESC option, ground improvement ratio (Ir) for GT option, depth of groundwater (W) for GW option.

Table 2. Geosynthetic parameters.

Parameter	Geosynthetic	References
γ_{geosyn}(t/m^3)	0.13	IndoFelt Specification
v_{geosyn}	0.30	Murugesan and Rajagopal, 2006
E (kN/m^2)	1.00×10^6	Tang et al., 2015
k_{geosyn} (m/s)	1.00×10^{-3}	Tang et al., 2015
J (kN/m)	1.00×10^3	Tang et al., 2015
GJ (kN/m^2)	3.85×10^8	For t= 1mm, E= 10^6 kPa
k_{SC} (m/s)	1.00×10^{-2}	
G (kN/m^2)	3.85×10^5	
B (kN/m^2)	8.33×10^5	

Note: γ_{geosyn} = unit weight; v_{geosyn} = Poisson's ratio; E = Young's modulus; k_{geosyn} = permeability of geosynthetic; J = stiffness of geosynthetic; GJ = torsional rigidity; k_{SC} = permeability of stone-column; G = shear modulus of geosynthetic; B = bulk modulus of geosynthetic; Rayleigh damping for geosynthetic is 2%.

3.1 Excess pore pressure generation

For level ground, the computed excess pore pressure at a depth of 7m of deposit are shown in Figure 4. As seen, the SC, ESC, and DS options are more effective in dissipating the excess pore pressure than the other

Table 1. Adopted material parameters for original soil deposit (original ground; OG) and for liquefaction mitigation options of stone-column (SC) and micro-pile (MP).

Parameters	Original Ground (OG)						Stone Column (SC)	Micro Pile (MP)
	Very Loose SAND	Loose SAND	Medium SAND	Loose SILT	Medium SILT	Medium CLAY		
γ (kN/m^3)	16.7	16.7	18.6	16.7	18.6	14.7	18.5	24.5
ϕ (deg.)	29	29	33	29	33	0	33	-
c (kPa)	-	-	-	-	-	37	-	-
ϕ_{PT} (deg.)	29	29	27	29	27	-	27	-
G_r (kPa)	5.5E4	5.5E4	7.5E4	5.5E4	7.5E4	6.0E4	7.5E4	1.4E7
B_r (kPa)	1.5E5	1.5E5	2.0E5	1.5E5	2.0E5	3.0E5	2.0E5	-
K_{soil} (m/s)	6.6E-5	6.6E-5	6.6E-5	1.0E-7	1.0E-7	1.0E-9	-	-
K_{SC} (m/s)	-	-	-	-	-	-	1E-4, 1E-2, 1E0	-
E_r (kPa)	-	-	-	-	-	-	-	3.5E7
ν	-	-	-	-	-	-	-	0.2
σ_{py} (kPa)	-	-	-	-	-	-	-	5.2E4

Note: γ = unit weight; ϕ = friction angle; c = cohesion; ϕ_{PT} = phase transformation friction angle; G_r = shear modulus at a reference effective confining pressure of 80kPa; B_r = bulk modulus at a reference effective confining pressure of 80kPa; K_{soil} = hydraulic conductivity of soil; K_{SC} = hydraulic conductivity of stone-column; E_r = Young's modulus at a reference effective confining pressure of 80kPa; ν = Poisson's ratio; σ_{py} = yield stress.

options. The GT option shows decreasing in excess pore pressure and indicates no soil liquefaction at this depth. The results of excess pore pressure for GL option would be zero. Due to the soil-structure interaction, the excess pore pressure response in soil is oscillating severely by shaking for the MP option.

3.2 Lateral deformation time history

Figure 5 shows lateral deformation time histories computed at the depth of 7m of a mildly sloping ground (i=3deg.). As seen, the MP, SC, and ESC options would be more effective in preventing the lateral deformation than the other options, it is due to the increasing of the stiffness of soil mass. The GT and DS options would increase their inertia and lateral deformations are close or even more than the case of the original ground (OG).

3.3 Lateral deformation profile

Figure 6 shows the lateral deformation profiles of soil deposit with a slightly inclined ground (i=3deg.). Obviously, the MP, SC, and ESC options are most effective in preventing the lateral movement of soil deposits than the other options. The GL option would reduce the lateral movement by lowering the groundwater level down to 9m, however, not as effective as the MP, SC, and ESC options. The DS and GT options would densify or solidify the ground and reduce to some degree the generation of excess pore pressure, however, they tend to amplify the lateral movement as a result of the increase of soil density and inertia force by the shaking.

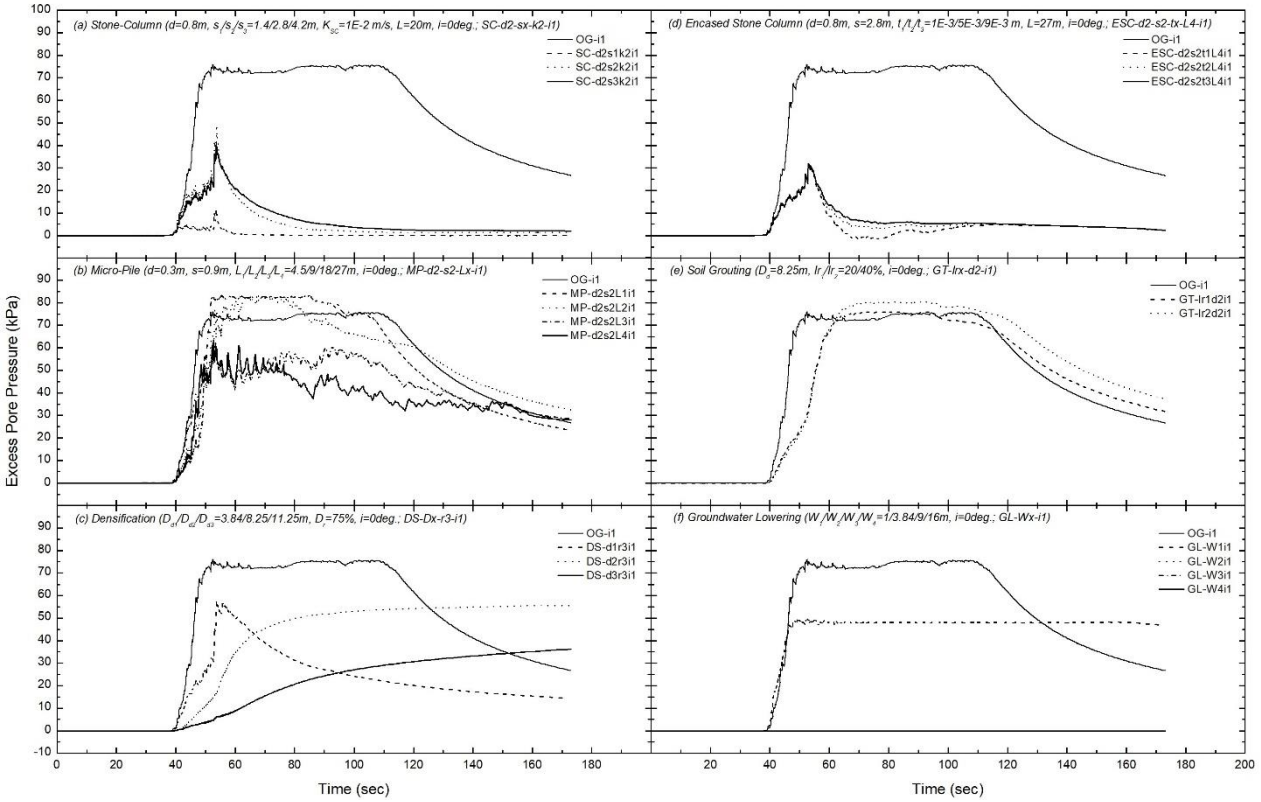

Figure 4. Computed excess pore pressure time histories at a depth of 7m (loose SAND) of the level ground (i=i_1=0deg.) for various liquefaction mitigation options. *(Note: OG – original ground; SC – stone-column; MP – micro-pile; DS – densification; ESC – encased stone column; GT – soil grouting; GL – groundwater lowering).*

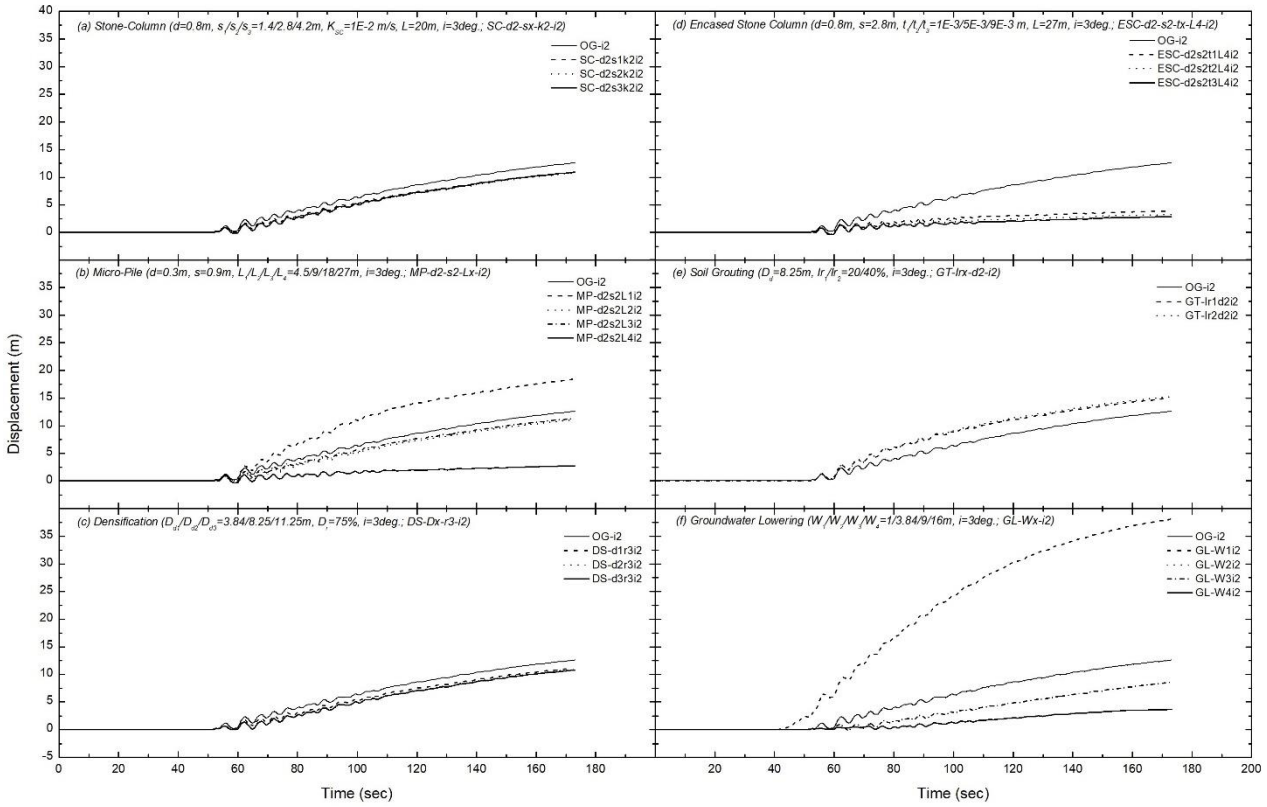

Figure 5. Computed lateral deformation time histories at a depth of 7m (loose SAND) of the inclined ground ($i=i_2$=deg.) for various liquefaction mitigation options. (Note: OG – original ground; SC – stone-column; MP – micro-pile; DS – densification; ESC – encased stone column; GT – soil grouting; GL – groundwater lowering).

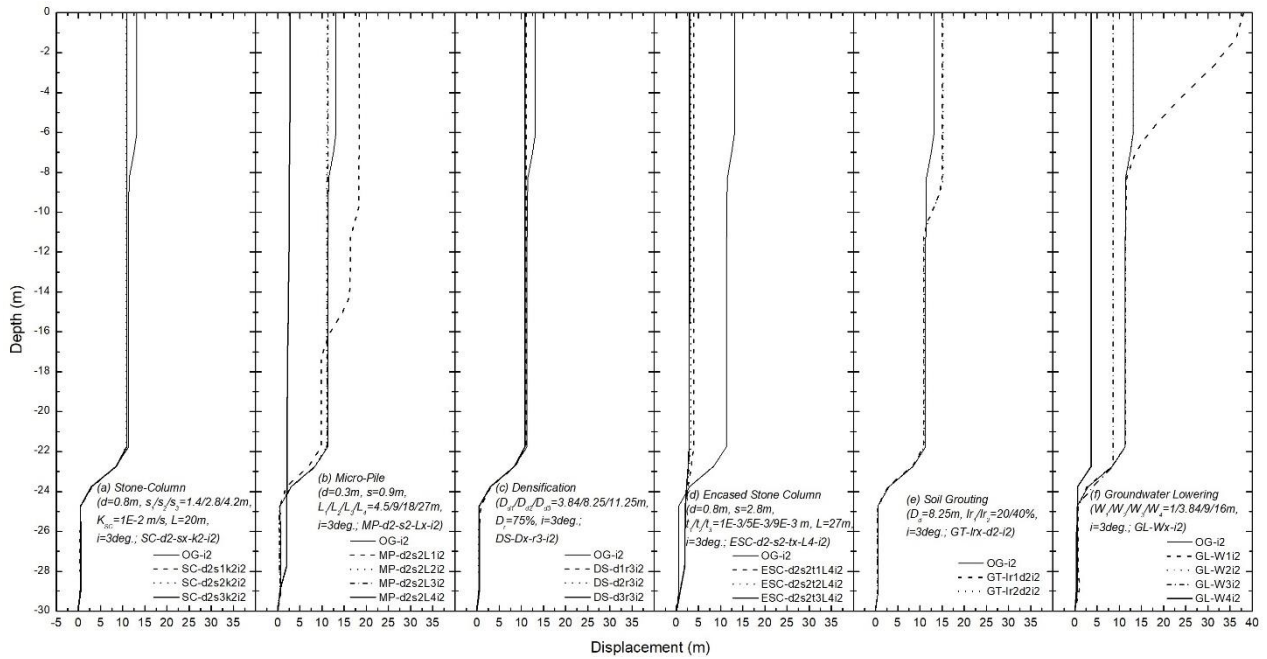

Figure 6. Computed lateral deformation profiles of an inclined ground ($i=i_2$=3deg.) for various liquefaction mitigation options. (Note: OG – original ground; SC – stone-column; MP – micro-pile; DS – densification; ESC – encased stone column; GT – soil grouting; GL – groundwater lowering).

4 CONCLUSIONS

Through a comprehensive numerical assessment of various liquefaction mitigation options, including stone-column (SC), micro-pile (MP), densification (DS), encased stone column (ESC) soil grouting (GT), and groundwater lowering (GL). Some key points and findings of the study are summarized as follows:

- The SC, ESC, and DS options are more effective in dissipating the excess pore pressure than the other options through drainage pathways and increased soil density. The ESC option would be improved soil stability by reinforcing the soil. The encasement provides additional lateral confinement to the stone column, facilitating efficient dissipation of excess pore pressure and enhancing soil stability.
- The GT and GL options would slightly reduce pore water pressure within the soil through soil densification and water table control, respectively. These options contribute to increased soil stability and decreased susceptibility to ground failure during seismic shaking.
- The MP, ESC, DS, and GT options are most effective in preventing the lateral deformation of soil deposits than the other options. They tend to increase the soil density, stiffness, and inertia force by shaking, thereby enhancing stability. The MP option would tend to amplify the lateral movement if the embedment depth is less than the liquefiable layers. The GT and GL options would tend to indirectly influence lateral deformation by stabilizing soil properties, though their direct impact on lateral displacement may vary.

REFERENCES

Chang, M., Kuo, C. P., Hsu, R. E., Shau, S. H. and Lin, T. M. (2012). Liquefaction potential and post-liquefaction settlement evaluations of Chuoshui River Allluvial Fan in Taiwan. *Bulletin of Engineering Geology and the Environment*, 7: 325-336. http://doi.org.10.1007/s10064-011-0390-7.

Hosseinpour, I., Mirmoradi, S. H., Barari, A. and Omidvar, M. (2010). Numerical evaluation of sample size effect on the stress–strain behavior of geotextile-reinforced sand. *Journal of Zhejiang University-Science A*, 11(8): 555–562. http://doi.org.10.1631/jzus.A0900535.

Kusumawardani, R., Chang, M., Upomo, T. C., Huang, R. C., Fansuri, M. H. and Prayitno, G. A. (2021). Understanding of Petobo liquefaction flowslide by 2018.09.28 Palu-Donggala Indonesia earthquake based on site reconnaissance. *Landslides*, 18: 3163-3182. http://doi.org.10.1007/s10346-021-01700-x.

Ministry of the Interior (MOI). (2011). *Construction and Planning Agency, Taiwan. Seismic Resistance Design of Buildings - Code and Explanations* (in Chinese).

Murugesan, S. and Rajagopal, K. (2006). Geosynthetic-encased stone column: Numerical evaluation. *Geotextiles and Geomembranes*, 24(6): 349-358. http://doi.org.10.1016/j.geotexmem.2006.05.001.

Tang, L., Cong, S., Ling. X., Lu, J. and Elgamal, A. (2015). Numerical study on ground improvement for liquefaction mitigation using stone columns encased with geosynthetics. *Geotextile and Geomembrane*, 43(2): 190-195. http://dx.doi.org/10.1016/j.geotexmem.2014.11.011.

Proceedings of the XVIII ECSMGE 2024
GEOTECHNICAL ENGINEERING CHALLENGES
TO MEET CURRENT AND EMERGING NEEDS OF SOCIETY
© 2024 the Authors
ISBN 978-1-032-54816-6
DOI 10.1201/9781003431749-198
Open Access: www.taylorfrancis.com, CC BY-NC-ND 4.0 license

ECSMGE 24
XVIII EUROPEAN CONFERENCE ON SOIL MECHANICS AND GEOTECHNICAL ENGINEERING

Coastal cliff stabilization and access stair reconstruction at Peneco beach, Algarve, Portugal

Stabilisation de la falaise côtière et reconstruction de l'escalier d'accès à la plage de Peneco, Algarve, Portugal

C. Fartaria*, A. Pinto
JETsj, Geotecnia, Lisbon, Portugal

J. Dinis, P. Nunes
Teixeira Duarte, Lisbon, Portugal

M. Silva
Câmara Municipal de Albufeira, Albufeira, Portugal

**cfartaria@jetsj.com*

ABSTRACT: The coastal cliffs erosion is a natural process that can lead to unstable occurrences and consequently high risk to the beach users. This paper describes the main solutions adopted at Peneco Beach, Algarve, Portugal aimed to mitigate the risk associated with space usage and access to the beach. Simultaneously, severe structural pathologies were also observed at the beach access stairs determining risk to users and therefore stabilization works were needed. The main goal was to develop solutions that could mitigate the users' risk while being conscious about environmental and aesthetics constrains as well as equipment accessibility restrains. The cliff stabilization solution used pigmented reinforced shotcrete combined with steel rockbolts, while the access stair was rebuilt using reinforced concrete and vertical rockbolts as foundation elements.

RÉSUMÉ: Les falaises côtières se détériorent en raison de l'érosion, qui est un processus naturel, mais qui peut conduire à des occurrences instables et, par conséquent, à un risque élevé pour les utilisateurs de la plage. Cet article décrit les principales solutions adoptées à Peneco plage, en Algarve, Portugal, visant à atténuer les risques associés à l'utilisation de l'espace et à l'accès à la plage. Dans le même temps, ont également été observées de graves pathologies structurelles au niveau des escaliers d'accès à la plage, déterminant le risque pour les usagers et donc des travaux de stabilisation ont été nécessaires. L'objectif principal était de développer des solutions capables d'atténuer les risques pour l'utilisateur tout en tenant compte des contraintes environnementales et esthétiques ainsi que des contraintes d'accessibilité des équipements. La solution de stabilisation de la falaise a utilisé du béton projeté renforcé pigmenté combiné à des clous de sol en acier, tandis que l'escalier d'accès a été reconstruit en utilisant du béton armé et des clous de sol verticaux comme de même de fondation.

Keywords: Coastal cliffs; risk mitigation; rockbolts; shotcrete.

1 INTRODUCTION

Coastal cliffs are areas of natural geological risk of instability due to their sedimentary genesis and exposure to atmospheric and marine agents with consequences for people and property. The risk associated with the instability of cliffs in beaches has been mitigated by several interventions along Portugal's coastline. At Peneco beach, Algarve, the reconstruction of the beach access staircase was implemented, restoring the safety conditions, and mitigating the erosion phenomena of the adjacent cliffs that determine an increased risk for people.

2 REFERENCE SCENARIO

At Praia do Peneco the morphology of the cliffs is a clear expression of the lithologies, as well as the processes and mechanisms of evolution present, mainly due to differential marine erosion. At the cliff face, erosion is accelerated by the intense vegetation that occurs in the place, since the growth of roots helps the opening of discontinuities and the consequent detachment of blocks (see Figure 1).



Figure 1. Cliff before intervention.

The top of the cliff is occupied by hotel and restaurant buildings and viewpoints, where small settlements, displacements and fractures were visible. The scarce presence of drainage and waterproofing devices in the area means that on days of high rainfall, water infiltrates into the existing cracks, dragging finer soil particles, promoting internal erosion phenomena.

The anomalies observed were representative of movements that have been progressively occurring over the years. The area of greatest concern corresponded to the top of the cliff, specifically to the viewpoint where tension cracks were observed in orientation parallel to the slope clearly showing signs of the occurrence of movements in this place.

The beach access staircase presented several structural pathologies caused by differential settlements (see Figure 2). The origin of such pathologies can be related to the lack of drainage devices, and a possible deficient foundation condition. Rainwater made its way to the foot of the cliff, infiltrating under the staircase by dragging particles, causing the observable differential settlements.



Figure 2. Staircase structural pathologies.

In this context, an intervention on cliffs stabilization and staircase reconstruction was considered critical for safety reasons.

3 MAIN CONSTRAINS

3.1 Geological and geotechnical constrains

Based on the Explanatory Report and the Geological Map of Portugal at a scale of 1:50000, sheet 52-B, it is possible to confirm the presence a Miocene unit (M^1) presented as carbonate rocks materializing the cliff (see Figure 3).

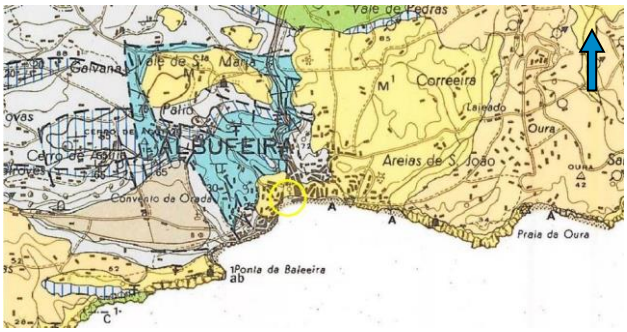

Figure 3. Portugal's Geological Map [sheet 52-B].

Field observation detected the presence of fine sandstones and siltstones, hard and compact, with yellowish tones, materializing metric benches, sometimes combined with centimetric horizons of silts and clays of grey tones (see Figure 4).



Figure 4. Cliff's surface before intervention.

The rock mass along the cliff is stiff and presents fractures that are moderately distant (F3-4). The transversal profiles of cliff can be described as slightly convex, steep slope and with sub-vertical sections, in the most competent rock formations. The cliff profiles are very rough, due to intense fracturing and high density secondary cementation of discontinuities (Marques, 1997).

The geological unit has, in general, a fissure-type permeability, where the circulation of water is essentially through the network of fractures and fissures. Thus, the circulation of groundwater is dependent on the degree of fracturing and weathering of the rock mass.

3.2 Other constrains

Given the location of the cliff, there were no significant constraints for access to the base of the cliff. However, given its height of about 20 m, the proposed solutions determined the need to use light weight equipment that could be operated hanging from a mobile crane.

The stabilisation solutions to be implemented had to use adequate materials considering the particularly aggressive environment due to the proximity to the sea. The interventions were also conditioned by the need to include the execution of a new rainwater drainage system, under the structure of the staircase.

Finally, it is also important to highlight the need to limit the impact of the intervention, especially in terms of the landscape and architectural framework of the proposed solutions always ensuring the indispensable safety conditions and their technical and economic suitability.

4 STABILIZATION SOLUTIONS

To mitigate the risk an intervention on cliffs stabilization and staircase reconstruction was implemented. For the cliffs surface a stabilization solution using rockbolts, geodrains and reinforced shotcrete was considered aiming the mitigation of the phenomena of superficial instability and erosion. Regarding the staircase pathologies a full reconstruction was proposed.

4.1 Cliff intervention

The intervention consisted of application of shotcrete, partially reinforced with metal fibres, and applied in layers with a total thickness of 12 cm. The application of shotcrete with C30/37 class resistance, took place by wet application and with the application of metal fibres, with a minimum dosage of 30 kg/m3, only in the first two layers. In the case of cavity areas, they were pre-filled, also with the application of layers of shotcrete. In the last layer of sprayed concrete, 4cm thick, applied without metallic fibres, a yellow pigment was incorporated for a better landscape integration of the solution (see Figure 5).

Rockbolts were materialized by 36 mm diameter bars, in A500/A550 continuous thread steel, in hot-dip galvanized rod with 85 µm minimum thickness by ISO 1461, placed in holes with a minimum diameter of 116 mm and sealed with cement grout of suitable characteristics. With this process, it was intended to disturb to a minimum the mechanical characteristics of the natural rock during the execution of the works. The diameter of the nails was defined considering a proper sacrificial thickness despite the galvanization.

With a length of 6 m and an inclination of 20º, in addition to fixing the layer of shotcrete, the nails crossed some existing sub-horizontal discontinuity planes near the cliff face. The nails were arranged in an approximate mesh of 3.0m (V) x 3.0m (H), and their position was adjusted during the works according to local needs.

To ensure the internal drainage, preventing the possible generation of hydrostatic pressure in the shotcrete coat, caused by water infiltration, sub-horizontal 4.0 m long geodrains were installed with 50 mm diameter perforated piped and wrapped in TecGeo 300 type geotextile. The gravitational flow of the captured waters is guaranteed because these elements were installed with an upward inclination of 5º with the horizontal.



Figure 5. Cliff's surface after intervention.

4.2 Staircase intervention

Given the severe structural pathologies of the staircase the intervention included its reconstruction executed on top of the existing one. Expanded clay aggregates were used for lightweight filling bellow the staircase concrete structure and rockbolts were used as foundation (see Figure 6).

For a conjoint behaviour of the entire structure, reinforced concrete cross beams were built to ensure a better connection between the various walls, and at the end of these a deep foundation was ensured, materialized by vertical rockbolts sealed in the rock mass.

Given the height of some retaining walls that materialize the staircase, geodrains were installed preventing the build-up of hydrostatic horizontal pressures behind those walls and using the drainage system, constructed bellow the new staircase, to drive those natural waters to the cliff base.

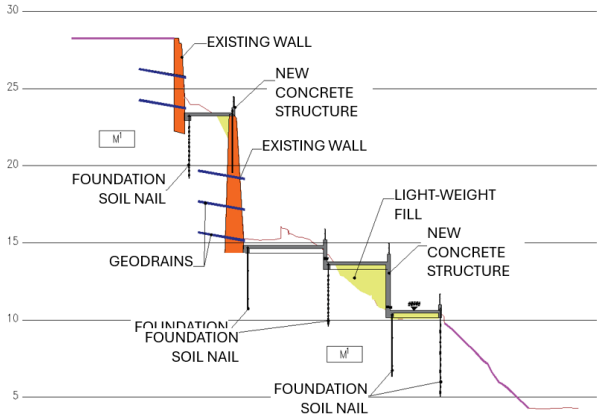

Figure 6. Staircase reconstruction – Cross section (not to scale).

5 MONITORING AND SURVEY PLAN

To monitor any relatively slow sliding movements, inclinometers were installed at the top of the cliff to measure the horizontal deformation of the rock mass. The intervention also provided for an observation plan, which should focus on the conservation and maintenance of the installed systems, to confirm the proper functioning of these structures. To this end, the observation of the intervened cliff will be made through the implementation of the following measures:

- Photographic coverage of the cliff after the intervention has been carried out, with the aim of defining an initial reference situation;
- Periodic photographic coverage in a manner similar to that recorded for the initial reference situation, in order to facilitate its comparison and the detection of any pathologies;
- Periodic reading of the inclinometers installed at the top of the cliff;
- Periodic inspection of the installed drainage systems and verification of their condition.

The information collected within the scope of the measures above described should be evaluated by a technical specialist to continuously validate the suitability of the solutions implemented and the need to carry out maintenance and conservation interventions or confirm the need for future stabilization interventions.

6 MAIN CONCLUSIONS

This article described the main solutions implemented and completed in the summer of 2022, with aim to mitigate the risk associated with the use of space and access to the bathing area at Praia do Peneco, in Algarve, Portugal (see Figure 7). The maintenance of the reinforcement elements and drainage elements installed, namely through the application of the defined monitoring plan, is fundamental to confirm the suitable behaviour of this type of structures and solutions during their lifetime. Special awareness should be considered within the monitoring plan implementation before and after periods of greater rainfall and greater sea agitation.

Coastal cliff erosion phenomenon can cause significant issues for public safety and serious damage to infrastructures. Thus, coastal cliffs stabilization solutions are crucial preventing the evolutive erosion that can lead to a natural disaster.



Figure 7. View after intervention.

ACKNOWLEDGEMENTS

The authors would like to thank the Albufeira City Council, the Owner, for the authorization for the writing and publication of this article. They also consider important to underline that the solutions implemented are the result of teamwork, in which the important role of the companies should be highlighted: GeoAlgar, the entity responsible for the preparation of the Geological and Geotechnical Study and Teixeira Duarte, Engenharia e Construções S.A., the contractor.

REFERENCES

Marques, Fernando (1997). *As arribas do Litoral do Algarve: Dinâmicas, processos e mecanismos*. Lisboa, Tese de Doutoramento (in Portuguese).

Proceedings of the XVIII ECSMGE 2024
GEOTECHNICAL ENGINEERING CHALLENGES
TO MEET CURRENT AND EMERGING NEEDS OF SOCIETY
© 2024 the Authors
ISBN 978-1-032-54816-6
DOI 10.1201/9781003431749-199
Open Access: www.taylorfrancis.com, CC BY-NC-ND 4.0 license

ECSMGE 24
XVIII EUROPEAN CONFERENCE ON SOIL MECHANICS AND GEOTECHNICAL ENGINEERING

A design procedure for high energy rockfall barriers

Conception des écrans pare-blocs à haute énergie

D. García*, L.Molano, G. Torres, D. Freitas
A. Bianchini Ingeniero, Barcelona, Spain

**dg.gordo@maccaferri.com*

ABSTRACT: The design of high energy rockfall barriers is traditionally carried out through trajectory simulations along the slope. The simplest way of designing these structures is comparing the energy level derived from these simulations with the results of the real scale tests according to the European Guideline Document 340059-00-0106 (which substitutes the previous ETAG 27-2008). This EAD is the harmonized document that defines how to test dynamic rockfall barriers and obtain their features (energy, residual height, deformation) in Maximum Energy Level (MEL) and Service Energy Level (SEL). Even though this guideline allows to compare in a reliable way the different barriers, this design procedure has limitations and doesn't consider how the real impact and installation conditions affect the barrier performance. In this paper, we give an overview of the contents of the EAD, and we show a design approach based on the Italian norm UNI 11211:2012, the mentioned EAD and the extensive experience of Maccaferri. Lastly, we will highlight the state of the art related to the foundation design.

RÉSUMÉ: La conception des écrans pare-blocs à haute énergie est traditionnellement réalisée par des simulations de trajectoire le long du talus. La manière la plus simple de dimensionner ces structures consiste à comparer le niveau d'énergie dérivé de ces simulations avec les résultats des essais en vraie grandeur conformément au Document d'Évaluation Européen 340059-00-0106 (qui remplace l'ancien ETAG 27-2008). Ce DDE est le document harmonisé qui définit comment tester les écrans pare-blocs dynamiques et obtenir leurs caractéristiques (capacité d'absorption d'énergie, hauteur résiduelle, déformation) au niveau d'énergie maximal (MEL) et au niveau d'énergie de service (SEL). Bien que ce guide permette de comparer de manière fiable les différentes barrières, cette procédure de conception présente des limitations et ne tient pas compte de la manière dont les conditions réelles d'impact et d'installation affectent la performance de la barrière. Dans cet article, nous donnons un aperçu du contenu du DDE, et nous présentons une approche de conception basée sur la norme italienne UNI 11211 :2012, le DDE mentionné et l'expérience approfondie de Maccaferri. Enfin, nous mettrons en lumière l'état de l'art lié à la conception des fondations.

Keywords: Rockfall protection systems; rockfall barrier; EAD 340059; new design approach.

1 INTRODUCTION

Rockfall dynamic barriers are kits designed to catch rock blocks that can fall from a slope. They are installed far from the detachment area; thus, they are classified as passive protection systems.

These systems can cover large surfaces that could not otherwise be protected with an active system (pinned drapery), they can absorb large impact energies, and they have been tested and certified by a recognised Technical Assessment Body.

1.1 EAD 340059-00-0106

The EAD 340059-00-0106 (hereinafter referred to as EAD) defines a dynamic rockfall barrier as a kit able to stop moving rock blocks on a slope with an energy level greater or equal to 100 kJ.

The kit is made up of:

- Interception structure: made of a principal net, and an optional additional layer usually with a finer mesh.
- A support structure: composed of metallic posts (minimum 4), with a separation distance between 8 and 12 meters.
- Connection components: consisting of metallic ropes, wire rope grips, and/or energy dissipating devices.

The foundation is not considered part of the kit.

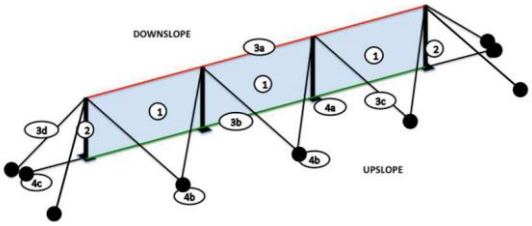

Figure 1. View of rockfall barrier components.

2 ROCKFALL SIMULATIONS

2.1 Input data

The first step to carry out the rockfall simulations in a reliable manner is to obtain the following:

- Geomechanical data: Type and dimensions of the rock blocks.
- Geological data: Type of ground in the hillside to obtain the restitution coefficients.
- Topographic data: To define the most unfavourable section, locate the rockfall detachment area, and choose the optimal location for the bar.

These parameters can be obtained with different degrees of accuracy, which will influence the Safety Factors for the calculations later.

2.2 Rockfall simulations

The rockfall simulations are done through several commercial softwares that rely upon different algorithms. These tools allow the designer to identify the block route and the parameters (velocity, energy, bounce height) at each point. For the numerical analysis, designers should take into account the following (Giachetti & Zotti, 2012):

- It is not advisable to directly use the kinetic energy given by the software, but to calculate it through the mass and translational velocity of the block ($E=1/2\ m \cdot v^2$), to avoid using abnormal data and to apply the corresponding safety factors.
- The rotational kinetic energy accounts for 10-15% of the total energy. Therefore, it can normally be disregarded.
- The statistical analysis allows for a 5% risk. Thus, the trajectories to consider should include the 95% confidence interval.

To validate the simulation, it is recommended to do back testing to check the results and the in-situ evidence, adjusting the restitution coefficients.

3 ROCKFALL BARRIER DESIGN

3.1 Design and safety factors

The EAD 340059 introduces the concepts of Maximum Energy Level (MEL) and Service Energy Level (SEL).

Generally, the MEL design is adopted if the frequency of the rockfalls is low, if individual blocks are expected, if the allowed risk is relatively high or if the maintenance tasks can be done with ease.

SEL design is adopted to reduce maintenance costs, when the allowed risk is low, or when multiple blocks are expected to impact. This criterion is more costly, as it implies the barrier must have a capacity three times higher (SEL = 1/3 MEL), but it enhances the safety of the site, and can be adequate in some cases (i.e. at the entrance of tunnel portals).

3.2 Energy of the barrier

The most important design parameter to determine is the energy level of the barrier, obtained with the following formula:

$$E_{sd} = \frac{E_b}{\gamma_E} \quad (1)$$

where E_{sd} = Block energy.
E_b = Nominal energy of the barrier, according to the EAD 340059.
γ_E = safety factor depending on the design criteria. 1.20 for MEL; 1.00 for SEL; 2.00 if the barrier is shorter than 30 m.

E_{sd} is defined with the classical formula of kinetic energy increased by a safety coefficient ($\gamma_R \geq 1.0$) which considers the human risk.

$$E_{sd} = \left(\frac{1}{2} M_d * {v_d}^2\right) \gamma_R \quad (2)$$

where M_d = Design mass of the block.
v_d = Design velocity of the block.
γ_R = 1.00 for a location of low economic value and easy repair; 1.20 for a location of high economic value and without possibility of repairing.

As per equation number (2); designers must define the design mass and velocity, which are obtained as following:

$$M_d = (Vol_B * \gamma)\gamma_{VOL} * \gamma_\gamma \quad (3)$$

$$v_d = (v_t * \gamma)\gamma_{Tr} * \gamma_{Dp} \quad (4)$$

where Vol_b = volume of the design block.
γ = Unit weight of the block.
γ_{vol} = safety coefficient related to the precision of the design block survey.
γ_γ = safety coefficient related to the evaluation of the unit weight of the rock of the block.
v_t = velocity calculated with the rockfall simulation and considering the 95th percentile of the velocities.

γ_{tr} = safety coefficient related to the reliability of the rockfall simulation.
γ_{Dp} = safety coefficient related to the quality of the topographic survey.

3.3 Height of the barrier

The minimum height of the barrier has to be defined considering the design height, a free zone, and the size of the block:

$$H_b > H_t * \gamma_{Tr} * \gamma_{Dp} + R * \gamma_R + f_{min} \quad (5)$$

where H_b = minimum height of the barrier.
H_t = Impact height of the block simulations, including the 95% confidence interval.
γ_{tr} = safety coefficient related to the reliability of the rockfall simulation.
γ_{Dp} = safety coefficient related to the quality of the topographic survey.
R = radius of the block.
γ_R = safety coefficient on the radius of the block (γ_R> 1.0)
f_{min} = safety zone that cannot be impacted (usually $f_{min} \geq 1.0$)

3.4 Separation distance of the barrier

The minimum distance between the barrier and the structure to be protected is determined as follows:

$$D_A \geq D_b * \gamma_d \quad (6)$$

where D_A = minimum distance between the barrier and the protected zone.
D_b = maximum dynamic deformation of the barrier, measured in accordance with the EAD.
γ_d = safety coefficient related to the energy level adopted during the design (γ_d>1.0 for MEL approach; γ_d=1.0 for SEL approach), the length of the barrier (γ_d>1.0 if the barrier is shorter than 30m) and to barrier-span impacted by the boulder (γ_d>1.0 if the lateral span of the barrier may be impacted)

4 FOUNDATION DESIGN

Even if the EAD does not define the foundations of the barrier as a component of the rockfall kit, these must be appropriately designed, regarding the type of barrier and the type of ground observed at the job site.

This implies that every barrier should have its proper anchoring system.

4.1 Load analysis

During the real scale tests, the suppliers must measure the forces transmitted to the anchors during the impact. Usually, the systems to measure the forces are a data logger connected to different load cells placed on the main foundations of the barrier.

The foundations are divided in 3 categories taking into consideration the worst load for each anchor:

- Post foundations: compression and shear stresses
- Upslope foundations: tensile stress (pull-out)
- Lateral foundations: tensile stress (pull-out)

Table 1 describes an example of the maximum loads in the anchors of the barrier RB 1500, obtained during the MEL crash test. These are the reference values for the design of the anchors, taking into account that this is the worst case scenario and the loads for the SEL test are lower.

Table 1. Forces in barrier RB 1500 during MEL.

Foundation	Type of force	Value
Posts	Compression	226,26 kN
	Shear	157,36 kN
Upslope foundations	Tensile	163,10 kN
Lateral foundations	Tensile	252,60 kN

4.2 Types of anchors

Foundations have to be able to transmit the load to the ground. Deep foundations are normally used in order to guarantee the best performance with a minimum cost. Generally, the anchoring systems are designed as follows:

- Post foundations: steel bars (for rock) or micropiles (usually for loose soil).
- Upslope and lateral foundations: flexible cable anchors (steel bars are not recommended due to the dynamic loads, which can pull the bar in different directions)

All the anchoring systems are considered passive because they start to work only if they are stressed by the impact. They are installed in drilled holes, and they are fully grouted along their entire length in order to develop the maximum anchor-grout and grout-ground friction.

The length and the diameter of the anchors as well as the drilling diameter depends on the design requirements. If the barrier is installed in an uneven terrain, a little concrete plinth can be foreseen to give a flat base for the posts of the fence.

5 CONCLUSIONS

The EOTA published in 2018 the EAD 340059, that replaces ETAG 27-2008 and defines standard procedures to evaluate the rockfall barriers in real scale tests, which allows to obtain the behaviour of the barriers and obtain the ETA and CE marking. Unfortunately, it describes the performance of the barrier in ideal conditions that differ from reality.

We have seen several cases where the consequences of the real installation conditions influence the behaviour of the rockfall barrier when impacted.

To design a rockfall barrier taking into account these factors, a new design approach based on the Italian norm UNI 11211:4-2012 has been defined to design the barriers in Ultimate Limit State and Service Limit State.

Even if the foundations are not considered part of the kit as per the EAD, these elements are crucial in the behaviour of the rockfall barrier. These foundations can dissipate the energy of the impact to prevent problems in other parts of the barrier and to reduce the maintenance costs.

The efforts of the main rockfall barrier suppliers are focused on delivering barriers with the following characteristics:

- Easy to install, through lesser anchors in the plate posts.
- Quick assembly, thanks to premounted elements such as the ring net.
- Effective, through their capability to absorb further impacts in Service Energy Level (SEL).

6 REFERENCES

EOTA (2018). European Assessment Document – EAD 340059-00-0106, Falling Rock Protection Kits. Brussels.

UNI (2012). UNI 11211-4:2012. Rockfall protective measures- Part 4: Definitive and executive design. Milan.

Grimod, A. and Giacchetti, G. (2013). New design approach for rockfall barrier.

Grimod, A. and Giacchetti, G. (2013). High energy rockfall barriers: a design procedure for different applications.

Giacchetti, G. and Zotti, I.M. (2012). Design approach for rockfall barriers. *Proceeding of the XI National Congress of Geothecnic*, San José, Costa Rica.

Proceedings of the XVIII ECSMGE 2024
GEOTECHNICAL ENGINEERING CHALLENGES
TO MEET CURRENT AND EMERGING NEEDS OF SOCIETY
© 2024 the Authors
ISBN 978-1-032-54816-6
DOI 10.1201/9781003431749-200
Open Access: www.taylorfrancis.com, CC BY-NC-ND 4.0 license

ECSMGE 24
XVIII EUROPEAN CONFERENCE ON SOIL MECHANICS AND GEOTECHNICAL ENGINEERING

Calibration of soil water retention parameters based on field measurements

Calibration des paramètres de rétention d'eau du sol basée sur des mesures sur le terrain

T.A.V. Gaspar*
University of Sheffield, Department of Civil and Structural Engineering, United Kingdom

S. Pradhan
Mott MacDonald, United Kingdom

A.S. Osman, D.G. Toll
Durham University, Department of Engineering, Durham, United Kingdom

**t.a.gaspar@sheffield.ac.uk*

ABSTRACT: It is well established that the relationship between soil water content and matric suction (referred to as the soil water retention curve (SWRC)), governs the behaviour of unsaturated soils. While SWRCs are typically measured in the laboratory, it is appreciated that the effects of soil structure can affect the shape of these curves. This paper presents calibration of the soil water retention parameters for an existing instrumented slope in Malaysia using field measurements of matric suction and volumetric water content and fully coupled flow-deformation analysis in PLAXIS. By systematically varying the SWRC parameters based on field measurements, this study attempts to improve the predictions of soil suction using a simplified rectangular soil section. Results from the analyses predicted slightly higher values of matric suction when compared with measured field data. However, the models were able to capture general trends and variations in matric suction in response to rainfall events.

RÉSUMÉ: Il est bien établi que la relation entre la teneur en eau du sol et la succion capillaire (appelée courbe de rétention d'eau du sol (SWRC)) régit le comportement des sols non saturés. Bien que les SWRC soient généralement mesurées en laboratoire, il est reconnu que les effets de la structure du sol peuvent affecter la forme de ces courbes. Cet article présente l'étalonnage des paramètres de rétention d'eau du sol pour une pente instrumentée existante en Malaisie en utilisant des mesures sur le terrain de la succion capillaire et de la teneur en eau volumétrique, ainsi qu'une analyse de déformation-débit entièrement couplée dans PLAXIS. En variant systématiquement les paramètres SWRC en fonction des mesures sur le terrain, cette étude tente d'améliorer les prédictions de succion du sol en utilisant une section de sol rectangulaire simplifiée. Les résultats des analyses ont prédit des valeurs légèrement plus élevées de succion capillaire par rapport aux données sur le terrain mesurées. Cependant, les modèles ont été capables de capturer les tendances générales et les variations de la succion capillaire en réponse aux événements de pluie.

Keywords: Unsaturated soils; slope stability; field monitoring; numerical modelling.

1 INTRODUCTION

Across the world, the effect of climate change and rapid development have increased the risks associated with landslides (Ozturk et al., 2022). In a review of fatal landslide occurrences, Froude & Petley (2018) found that a total of 55 997 fatalities occurred between 2004-2016, with a majority of landslides occurring within the tropics. A country which is particularly susceptible to fatal landslides is Malaysia (Lee et al., 2009). Several studies have attributed rainfall events as the triggering mechanism for landslides in Malaysia (Lee et al., 2009). It is therefore vital to understand the mechanisms for rainfall-induced slope instability.

Tropical humid regions are typically underlain by residual soils (Huat and Toll., 2012) with deep water tables, which result in large portions of the soil profile being unsaturated. Unsaturated soils are characterised by the presence of negative pore-water pressure (referred to as suction) which is related to soil water content through the soil water retention curve (SWRC). Simply put, a reduction in water content increases soil suction which results in an increase in shear strength. Conversely, if water content is increased (as would occur after a rainfall event), suction is reduced which

produces a lower shear strength and factor of safety (FoS).

To understand the behaviour of unsaturated soil subject to transient atmospheric processes, an unsaturated soil slope in Selangor Malaysia, approximately 20 km southeast of Kuala Lumpur was instrumented with suction and volumetric water content sensors. However, the absence of unsaturated soil test results limited the ability to predict the slope behaviour under present and future rainfall scenarios. This paper presents an initial numerical calibration that was undertaken to determine the SWRC parameters based on field-monitored data.

2 SITE DETAILS

The instrumented slope is located in Taman Bukit Mewah, Kajang, Selangor on the west coast of Peninsular Malaysia (2°59'11.7"N 101°47'56.6"E), approximately 20 km southeast of Kuala Lumpur. The location of the site is illustrated in Figure 1 with a cross section of the studied slope in Figure 2. The region chosen for this study has historically seen a vast number of landslides which have resulted in loss of life and severe economic consequences. For context, the location of the 1993 Highland Tower landslide which resulted in 48 fatalities (Jamaludin and Hussein, 2006) has also been highlighted in the figure.

Based on the existing geological maps, the site is underlain by residual granite soil, which occurs widely in Peninsular Malaysia as granites form a major part of the landmass (Singh et al., 2013). Ground investigation was undertaken at the site which indicated that the slope is underlain predominantly by medium brown to greyish brown silty CLAY from 0 to 9m bgl (below ground level), which transitions from being soft to medium stiff to stiff to very stiff below 7.5m.

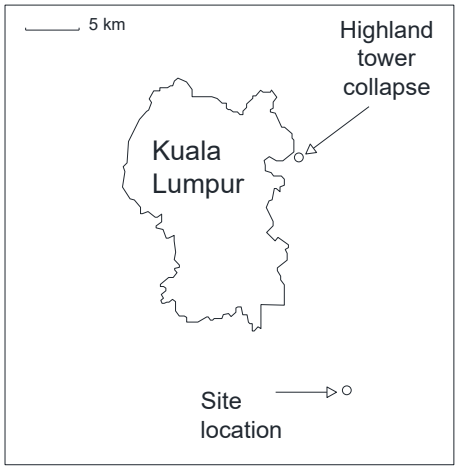

Figure 1. Site location.

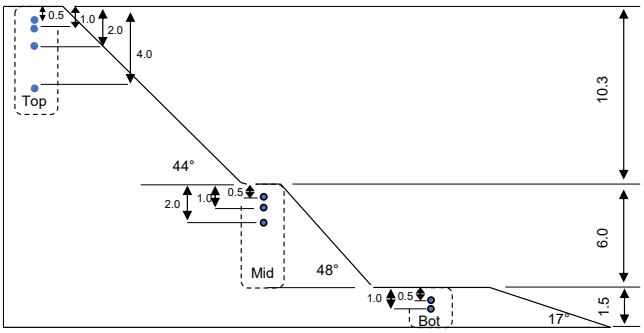

Figure 2. Cross-section of studied slope.

3 FIELD MONITORING

To enable long-term observation of rainfall patterns and hydraulic soil behaviour, a combination of instruments was installed at the selected site. A tipping-bucket rain-gauge, Terros 11 volumetric water content sensors, and Terros 21 soil water potential sensors were meticulously positioned at key locations: the crest, midsection, and toe of the slope. The installation depths are illustrated in Figure 2. By placing sensors at increasing depths within the soil profile, both volumetric water content of the soil and soil suction were measured over time.

4 NUMERICAL MODELLING FOR SWRC CALIBRATION

The soil water retention curve (SWRC) characterises the relationship between soil water content and suction. This relationship is crucial for modelling changes in soil suction, brought about by precipitation which can ultimately lead to the failure of a slope. Laboratory techniques are often used to establish the SWRCs. However, the soil type, initial water content, stress history and method of compaction can influence the shape of this curve which may not be accurately reproduced in the laboratory (Vanapalli et al., 1999).

Hence, this study attempts to derive the van Genuchten (1980) SWRC parameters by comparing the observed soil suction with those predicted through a fully coupled flow-deformation analysis conducted in the finite element program PLAXIS.

For this analysis, a simplified two-layered plane strain rectangular soil model (5 m×10 m) was created to simulate one dimensional infiltration and evaluate consequent changes in soil suction in response to rainfall (Figure 3). The finite element mesh constituted 434 triangular soil elements and 3605 nodes. Hydraulic parameters adopted for numerical modelling are given in Table 1.

The uppermost layer, extending 1.5 m below the top model boundary, represented desiccated surface

near the ground. This layer is known to possess a higher hydraulic conductivity than the underlying layers due to the presence of surficial cracks and plant roots (Toll et al., 2019). Hence, the hydraulic conductivity of Layer 1 representing the desiccated upper surface was adopted from the in-situ infiltration test results reported by Huat et al. (2012) and the hydraulic conductivity of the underlying Layer 2 was considered three orders of magnitude lower than the upper layer as suggested by Md. Rahim (2016) (Table 1).

The conventional Mohr-Coulomb model was used to represent the constitutive relationship of the soil layers. Due to limited testing, the strength properties were considered to be uniform with cohesion, $c' = 1$ kPa and effective angle of shearing resistance, $\phi' = 29^{o}$ based on a single set of consolidated undrained triaxial tests.

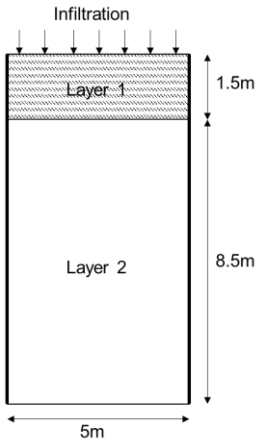

Figure 3. 2D soil model for numerical modelling.

Table 1. Hydraulic model parameters.

Saturated hydraulic conductivity, k_x, k_y (m/s)		1×10^{-5} m/s (Layer 1) 1×10^{-8} m/s (Layer 2)
Van Genuchten (1980) parameters	θ_r	0
	θ_s	0.45
	α (1/kPa)	0.18 (SWRC 1) 0.09 (SWRC 2) 0.154 (SWRC 3)
	n	2.8 (SWRC 1 and 3) 1.9 (SWRC 2)

To establish a representative SWRC for the desiccated surface at 0.5 m depth, upper and lower bound SWRCs were fitted using the van Genuchten (1980) hydraulic model (SWRC 1 and SWRC 2), as shown in Figure 4. The SWRCs for typical residual soils in Malaysia as outlined by Lee et al. (2009) are presented within the figure for context. Between the upper and lower bounds, the van Genuchten model parameters were systematically varied until the model prediction aligned closely with the fluctuations recorded in the field. In the flow-deformation analyses, hourly rainfall recorded between 28 October to 6 December 2021 was imposed as a top infiltration boundary (Figure 3). To simulate 1-D infiltration, the bottom model boundary was set to allow seepage and the left and right boundaries were closed. Initial porewater pressures were generated by assigning an initial degree of saturation, corresponding to the suction observed in the field.

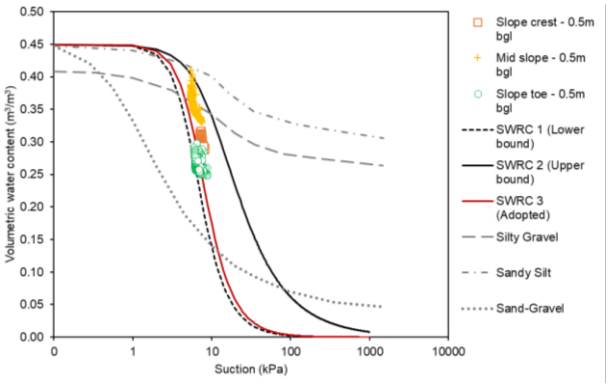

Figure 4. SWRCs plotted from the field measurements at 0.5m depth at the slope crest, mid and toe, and the typical SWRCs for soils found in the Malaysian Peninsula (modified from Lee et al. (2009)).

Figure 5 illustrates the predicted soil suction at 0.5 m depth, compared to the suction values measured at the same depths on the slope crest, mid and toe using 'SWRC 3' parameters. The model using 'SWRC 3' parameters slightly overestimated the suction compared to the onsite measurements. However, it effectively captured the overall trend, timing and magnitude of changes. Over a 922 hour-simulation, the model predicted suction changes between 6 and 11 kPa, while the monitored data showed fluctuations between 5 to 9 kPa. Therefore, with the adopted 'SWRC 3' parameters, the model closely predicted the hydraulic response during infiltration and intermittent dry periods and hence, this hydraulic model can be considered to be representative for this stratum.

It should be emphasised that the results presented in Figure 5, are for a single depth using a simplified rectangular soil model. In reality, the true geometry of the instrumented slope would have influenced infiltration. Additionally, modelling a single rectangular section does not incorporate changes in water content/suction induced by seepage to or from other locations of the slope. Nevertheless, the results provided in Figure 5 provide a useful first estimate of the SWRC which can be incorporated into subsequent slope stability analyses. A similar approach can be adopted in the future studies to calibrate the SWRCs for the underlying strata.

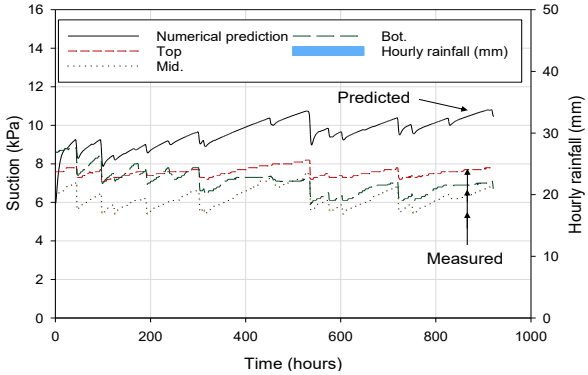

Figure 5. Observed and predicted changes in soil suction between 28 October 2021 to 06 December 2021.

5 CONCLUSIONS

Field monitoring offers an opportunity to calibrate water retention properties of existing unsaturated slopes, with limited disturbance to soil structure which is known to affect the SWRC. In this paper, water content and soil suction measured in-situ were integrated into fully coupled flow-deformation analyses of a rectangular soil section to identify optimal SWRC parameters, unique to the in-situ soil. While numerical simulations predicted slightly higher magnitudes of soil suction when compared to in-situ measurements, the models were able to capture general trends and suction fluctuations in response to rainfall events.

The calibration presented in this study aims only to provide an initial estimate of in-situ SWRC parameters. Using this calibration as a starting point, further analyses are required to accurately model the behaviour of the entire slope.

ACKNOWLEDGEMENTS

This work was funded by the Natural Environment Research Council for a project titled “Integrated Modelling of Landslides due to Hydrometeorological Impacts in Langat Basin, Peninsular Malaysia (iModelLandslides)”, Grant Ref: NE/S003347/1.

REFERENCES

Froude, M. J., and Petley, D. N. (2018). Global fatal landslide occurrence from 2004 to 2016. *Natural Hazards and Earth System Sciences*, 18(8), 2161–2181. https://doi.org/10.5194/nhess-18-2161-2018.

Huat, B. B. K. and Toll, D. G., and Prasad A. (2012). Chapter 11: Residual soils of Southeast Asia. *Handbook of tropical residual soils engineering*. https://doi.org/10.1201/b12302.

Huat, L.T., Ali, F. and Ibrahim, A.S. (2012). An investigation on one of the rainfall-induced landslides in Malaysia. *Electron. J. Geotech. Eng*. 17 D, 435–449.

Jamaludin, S., and Hussein, A. N. (2006). Landslide hazard and risk assessment: The Malaysian experience. *10th Congress of the Int. Ass. for Eng. Geol. and the Env.,* 455, 1–10.

Lee, L. M., Gofar, N., and Rahardjo, H. (2009). A simple model for preliminary evaluation of rainfall-induced slope instability. *Engineering Geology*, 108(3–4), 272–285. https://doi.org/10.1016/j.enggeo.2009.06.011.

Md. Rahim, M.S. (2016). Hydro-mechanical behaviour of a residual soil slope in Malaysia. *PhD Thesis*. Durham University.

Ozturk, U., Bozzolan, E., Holcombe, E. A., Shukla, R., Pianosi, F. and Wagener, T. (2022). How climate change and unplanned urban sprawl bring more landslides. *Nature*. Aug;608(7922):262-265. doi: 10.1038/d41586-022-02141-9. PMID: 35941295.

Singh, H., Jotisankasa, A. and Huat, B.B.K. (2013). Residual soils of Southeast Asia, in: Huat, B.B.K., David G. Toll, Arun Prasad (Eds.), *Handbook of Tropical Residual Soils Engineering.* CRC Press Taylor & Francis Group.

Toll, D.G., Md. Rahim, M.S., Karthikeyan, M., Tsaparas, I. (2019). Soil–atmosphere interactions for analysing slopes in tropical soils in Singapore. *Environ. Geotech.* 6, 361–372. https://doi.org/10.1680/jenge.15.00071.

van Genuchten, M.T. (1980). A Closed-form equation for predicting the hydraulic conductivity of unsaturated Soils. *Soil Sci. Soc. Am. J.* 44, 892–898.https://doi.org/10.2136/sssaj1980.03615995004400050002x.

Vanapalli, S.K., Fredlund, D.G. and Pufahl, D.E. (1999). The influence of soil structure and stress history on the soil-water characteristics of a compacted till. *Géotechnique* 49, 143–159. https://doi.org/10.1680/geot.1999.49.2.143.

Proceedings of the XVIII ECSMGE 2024
GEOTECHNICAL ENGINEERING CHALLENGES
TO MEET CURRENT AND EMERGING NEEDS OF SOCIETY
© 2024 the Authors
ISBN 978-1-032-54816-6
DOI 10.1201/9781003431749-201
Open Access: www.taylorfrancis.com, CC BY-NC-ND 4.0 license

ECSMGE 24
XVIII EUROPEAN CONFERENCE ON SOIL MECHANICS AND GEOTECHNICAL ENGINEERING

Use of Bayesian Kriging to develop new soil property maps for Quito, Ecuador

Utilisation du Krigeage Bayésien pour développer de nouvelles cartographies pédologiques pour Quito, Équateur

C.E.L. Gilder
Arcadis, Bristol, UK

M.M. Othman*, C. Zapata, E.A. Holcombe, R. De Risi, F. De Luca, P.J. Vardanega
University of Bristol, Bristol, UK

**li20946@bristol.ac.uk*

ABSTRACT: Seismic hazard assessment requires knowledge of regional geological and geotechnical parameters. Shear wave velocity averaged across the upper 30 m of soil (Vs_{30}) is a key parameter for site response studies in earthquake engineering. In the city of Quito, the capital of Ecuador, seismic data are scarce. This paper combines a recently compiled geotechnical database with a Bayesian Kriging technique to generate new soil geotechnical property maps for the city of Quito. The new QUITO/GEO-299 soil geotechnical database contains 299 records of soil geotechnical test results from across the Quito region. These datapoints were analysed using a Bayesian Kriging approach recently developed for generating seismic hazard data for the Kathmandu Valley in Nepal. The resulting Quito Vs_{30} map is compared to the corresponding map created using slope-based proxies implemented in the global Vs_{30} model presented by the U.S. Geological Survey. These new resources are useful for geotechnical engineers working in the Quito region, especially during project planning and preliminary design phases.

RÉSUMÉ: L'évaluation des risques sismiques nécessite la connaissance des paramètres géologiques et géotechniques d'une région. La vitesse moyenne des ondes de cisaillement dans les 30 m supérieurs du sol (Vs_{30}) est un paramètre clé pour les études de réponse des sites dans le domaine de l'ingénierie parasismique. Dans la ville de Quito, la capitale de l'Équateur, les données parasismiques sont rares. Cet article combine une base de données géotechniques récemment compilée avec des techniques de Krigeage Bayésien pour générer de nouvelles cartographies de propriétés géotechniques des sols pour la ville de Quito. La nouvelle base de données géotechniques QUITO-GEO-299 contient 299 enregistrements de résultats d'essais géotechniques du sol dans la région de Quito. Ces points de données ont été analysés à l'aide d'approches bayésiennes de krigeage récemment développées pour générer des données sur les risques sismiques dans la vallée de Katmandou au Népal. La carte Vs_{30} de Quito qui en résulte est comparée à la carte correspondante développée à l'aide d'approximations conventionnelles basées sur les pentes et mises en œuvre dans le modèle global Vs_{30} présenté par l'U.S. Geological Survey. Ces nouvelles ressources sont utiles pour les ingénieurs géotechniciens travaillant dans la région de Quito, en particulier pendant les phases de planification de projet et de conception préliminaire.

Keywords: Shear wave velocity; geodatabases; Bayesian Kriging, Quito.

1 INTRODUCTION

Average shear wave velocity over the upper 30 m of soil at a site (Vs_{30}) is commonly used for seismic microzonation studies. An assessment of the seismic hazard in a region is often carried out using Vs_{30} as a proxy for soil stiffness. (Foti *et al.,* 2018; De Risi *et al.,* 2019). However, due to the high costs associated with Vs_{30} testing, data availability for this parameter is limited especially in low income multi-hazard prone regions. Geospatial analysis of the geotechnical parameters in a region can provide maps of the estimated values such as Vs_{30} without extensive testing. To develop geotechnical parameter maps, an appropriate geospatial model is needed (see Gilder, 2022 and Gilder *et al.,* 2022). Kriging interpolation can be used to develop geospatial maps of various geotechnical parameters, including Vs_{30}, for data-scarce regions (Webster and Oliver, 2007).

A commonly used model for estimating soil Vs_{30} values relies on the topographic information obtained from Digital Elevation Models (DEM) and is currently implemented by the U.S. Geological Survey (USGS). The USGS model uses a slope-based estimation of Vs_{30} to produce estimates without testing (Wald and Allen, 2007; Allen and Wald, 2009). In the case of scarce

measurements (i.e. at few local points within a region), Bayesian Kriging approaches (Omre, 1987; De Risi *et al.,* 2021) can be used to produce a more robust estimation of Vs_{30} compared to the USGS model and may prove to have lower uncertainty compared to Simple or Ordinary Kriging approaches.

In this context, this study developed a Vs_{30} map of Quito, Ecuador, using the data available from a recently developed database (Othman *et al.,* 2023b) and the Bayesian Kriging framework developed by Gilder *et al.* (2022). Quito is in a multi-hazard region highly susceptible to seismic activities due to its location on a 60 km-long fault system (e.g. Vaca *et al.,* 2019). The region is also highly susceptible to rainfall-triggered landslides, debris flows and flooding (e.g. Zapata *et al.,* 2023). The city of Quito can be considered a 'data-scarce' region with respect to geotechnical data (Othman *et al.,* 2023a), and has limited Vs_{30} data available for use in construction design.

2 DATA SOURCES

The required data for the application of the Gilder *et al.* (2022) Bayesian framework for Quito is: (1) the Vs_{30} raster map obtained from the USGS repository (USGS, 2007) used as prior data; and (2) site-specific Vs_{30} data obtained from the open-access geotechnical database 'QUITO/GEO-299' (Othman *et al.,* 2023b) which includes Vs_{30} values and the geographical coordinates of these datapoints.

2.1 The USGS Vs_{30} map

The USGS (2007) open-access map repository contains rasterised global Vs_{30} mosaic maps based on the slope estimation of Vs_{30} using satellite DEM images. Using the data from the USGS raster, a Vs_{30} mosaic map for Quito is constructed, as shown in Figure 1. Using the generated map in Figure 1, the estimated Vs_{30} values for the different sections of the city of Quito can be used within the prediction.

2.2 The Quito geotechnical database

QUITO/GEO-299 database (Othman *et al.,* 2023b) presents comprehensive geological and geotechnical information on the soils of Quito. One of the parameters included in the database is the $Vs_{30,}$ along with the site location coordinates. The total number of available Vs_{30} data is 82 points.

The Vs_{30} data available in the database were reported as found in the source (45 points) or calculated from Vs measurements using CEN (2004) definition (21 points) or extrapolated for data points shallower than 30 m using Boore (2004) method (16 points). Figure 2 shows the location of each Vs_{30} measurement and the value of these measurements compared to the USGS model.

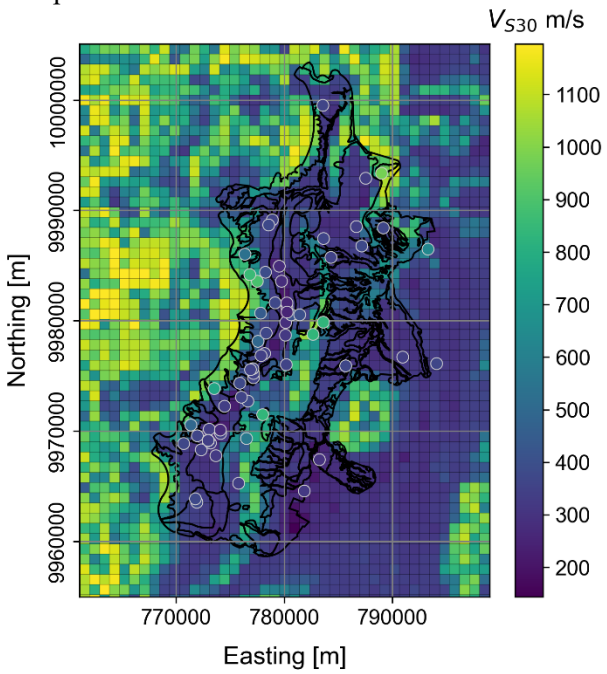

Figure 1. USGS Vs_{30} mosaic map for the Quito area; geology map polygons for the Metropolitan District of Quito (DMQ) from Municipio de Quito (2015).

The slope-based approach used as prior information in this study is known to provide an average overestimation of Vs_{30} with respect to data point measurements (e.g. Stewart *et al.,* 2014). This trend is also found in the area of study comparing the data points from 'QUITO/GEO-299' and the USGS estimates, see Figure 2.

3 ANALYSIS AND RESULTS

The steps described in Gilder *et al.* (2022) were followed: (1) selection of primary and secondary parameters; (2) removal of any bias or cluster from the data (i.e. debiasing or declustering); (3) variable transformation into a normally distributed variable; (4) use the primary variable, estimation of Vs_{30} using Simple Kriging (SK) method; (5) use the secondary variable, identifying the likelihood of the distribution; (6) map updating using the Bayesian method to present the final Kriging map. Based on the methodology described in Gilder *et al.* (2022), the data requires debiasing or declustering depending on the data availability. Histograms of the measured and estimated Vs_{30} are investigated (Figure 3) to determine which option to use. The measured data does not cover the higher values of Vs_{30}. Based on Gilder *et al.* (2022), the data was debiased following 'Option A' of the Gilder *et al.* framework.

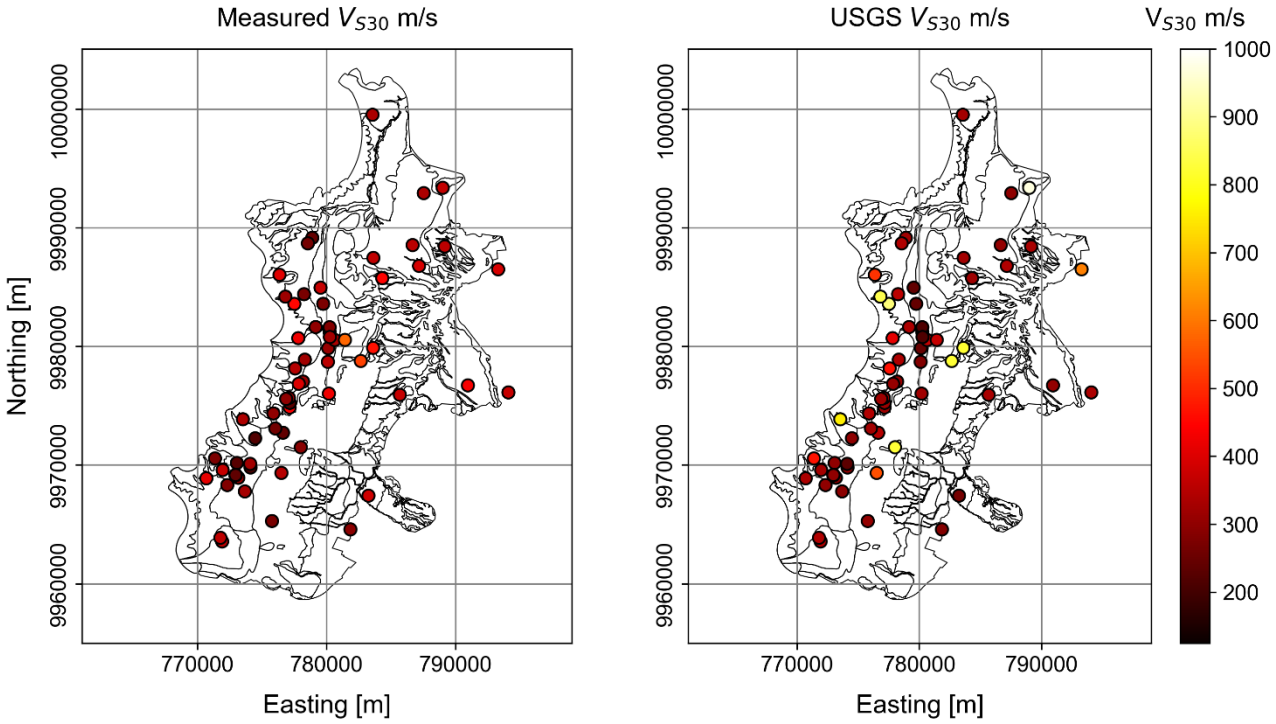

Figure 2. (left) The location and magnitude of each Vs_{30} measurement from QUITO/GEO-299 database compared with (right) values from USGS for the same location; geology map polygons in the DMQ from Municipio de Quito (2015).

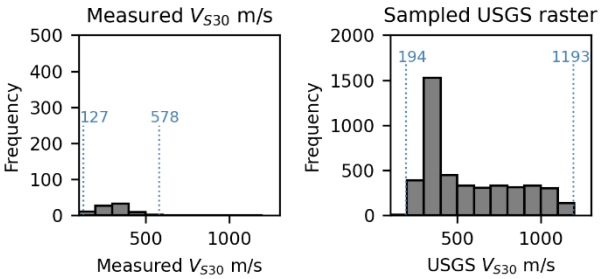

Figure 3. Comparison of the data histogram of the measured versus the sampled USGS raster in the same modelling area.

The updated Vs_{30} map using the Bayesian-Kriging model (Figure 4) shows higher accuracy in the Vs_{30} estimation compared to the map obtained from USGS in Figure 1. This increase in Vs_{30} accuracy is related to the additional information at Vs_{30} points obtained from the QUITO/GEO-299 database. Lower Vs_{30} estimations are observed compared to the USGS map. This outcome aligns with previous studies that suggest the USGS model tends to overestimate Vs_{30}. The updated Vs_{30} map captures differences in the properties of the different surface geology layers (including unconsolidated materials and soils) as described by Othman *et al.* (2023a) and shown in Figure 4.

The red region (*Qal*) in the geological map corresponds to lacustrine, fluvial and marsh deposits which are usually characterised by lower Vs_{30} values than the adjacent geological layer (*Qvi*, in purple) comprising material from pyroclastic flows, silts, lahars and volcanic sands. The Vs_{30} map in Figure 4 shows lower Vs_{30} with respect to the soil categories in the seismic code (ERN 2012).

4 SUMMARY AND CONCLUSIONS

The Bayesian-Kriging framework developed by Gilder *et al.* (2022) was employed to create a new map of Vs_{30} for Quito, Ecuador. Field measurements of Vs_{30} were obtained from QUITO/GEO-299 database (Othman *et al.,* 2023b). The resulting new Vs_{30} map aligns more closely with variations in the geology of the city – distinguishing between more deformable lacustrine soils and stiffer volcanic soils, which are not captured by the slope-based map of USGS or the soil classification of the latest seismic code (ERN, 2012). The new Vs_{30} map captures the difference between the geological formations and variability of this parameter within each formation, providing useful additional information for advanced soil modelling and for guiding future geotechnical investigations in the Quito Metropolitan Area.

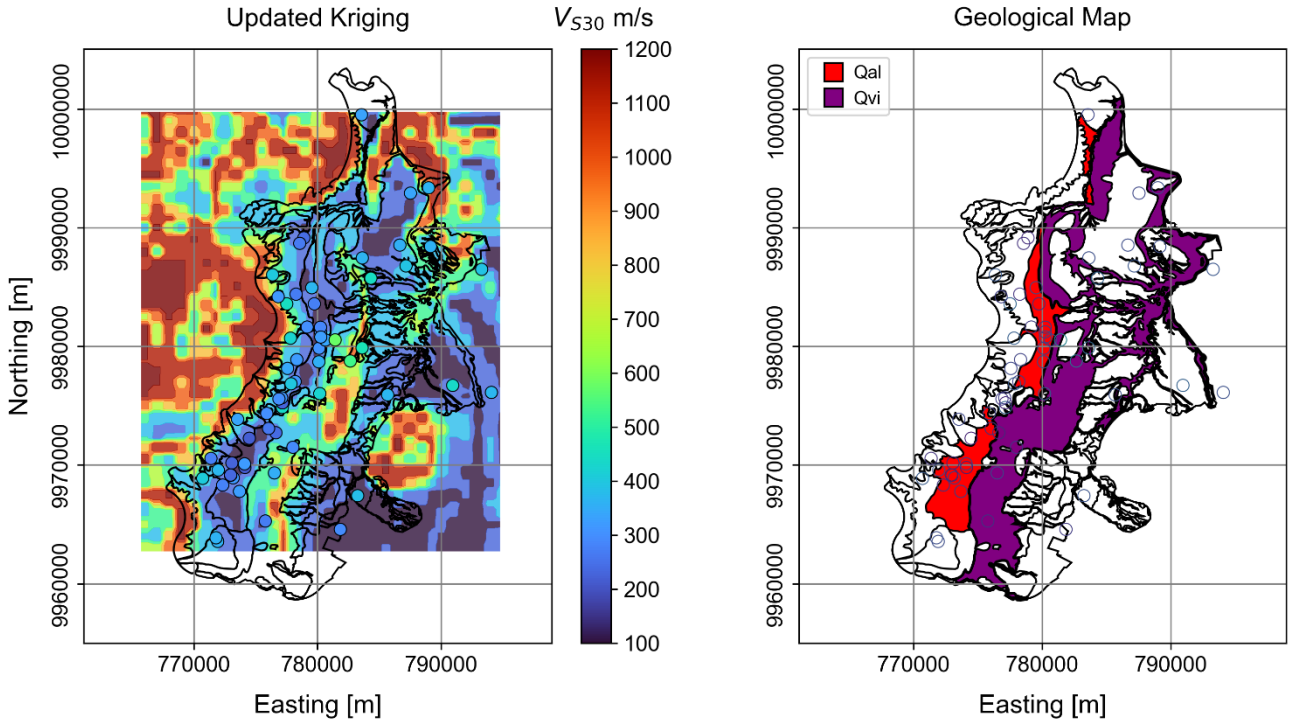

Figure 4. (left) Updated Vs_{30} map using the Bayesian Kriging model compared with (right) the geology of Quito; highlighted geological layers from Othman et al (2023a): Qal – in red – 'Lacustrine, fluvial and marsh deposits with silts and clays, in some sectors interspersed with levels of sand and lapillis from the volcanic centres that surround Quito', Qvi – in purple – 'Pyroclastic flows, silts, lahars; at the base of river-lake sequences sometimes very negligible and streams of volcanic sands (Cangahua formation)' (geological descriptions from Table 2 in Othman et al. 2023a). Geology map polygons in both maps are from Municipio de Quito (2015).

ACKNOWLEDGEMENTS

The authors acknowledge funding and support from UKRI Collective Fund under grant NE/S009000/1, Tomorrow's Cities UKRI GCRF: Urban Disaster Risk Hub. The second author acknowledges the support of AL-Zaytoonah University of Jordan. The authors thank Dr Ahmad EL Hajjar for the assistance with the French translation.

DATA AVAILABILITY STATEMENT

The underlying data used to generate the maps is available from the following sources: USGS (2007), Municipio de Quito (2015), Othman *et al.* (2023b). The raster file for Figure 4 (left) is available from the corresponding author upon request.

REFERENCES

Allen, T.I. and Wald, D.J. (2009). On the use of high-resolution topographic data as a proxy for seismic site conditions (VS30). *Bulletin of the Seismological Society of America*, 99(2A), pp. 935–943. https://doi.org/10.1785/0120080255.

Boore, D.M. (2004). Estimating V_S (30) (or NEHRP Site Classes) from Shallow Velocity Models (Depths < 30 m). *Bulletin of the Seismological Society of America*, 94(2), pp. 591–597. https://doi.org/10.1785/0120030105.

CEN (European Committee for Standardization) (2004). Eurocode 8: Design of Structures for Earthquake Resistance-Part 1: General Rules, Seismic Actions and Rules for Buildings, Brussels: CEN.

De Risi, R., Penna, A. and Simonelli, A.L. (2019). Seismic risk at urban scale: the role of site response analysis. *Soil Dynamics and Earthquake Engineering*, 123, pp. 320-336. https://doi.org/10.1016/j.soildyn.2019.04.011.

De Risi, R., De Luca, F., Gilder, C.E.L., Pokhrel, R.M. and Vardanega, P.J. (2021). The SAFER geodata-base for the Kathmandu valley: Bayesian kriging for data-scarce regions, *Earthquake Spectra*, 37(2), pp. 1108–1126. https://doi.org/10.1177/8755293020970977.

Evaluación de Riesgos Naturales (ERN) (2012). Microzonificación sísmica del Distrito Metropolitano de Quito. Estudio de la amenaza sísmica a nivel local. Programa de reducción de riesgos urbanos del Distrito Metropolitano de Quito.

Foti, S., Hollender, F., Garofalo, F., Albarello, D., Asten, M., Bard, P.Y., Comina, C., Cornou, C., Cox, B., Di Giulio, G., Forbriger, T., Hayashi, K., Lunedei, E., Martin, A., Mercerat, D., Ohrnberger, M., Poggi, V., Renalier, F., Sicilia, D. and Socco, V. (2018). Guidelines for the good practice of surface wave

analysis: A product of the InterPACIFIC project, *Bulletin of Earthquake Engineering*, 16(6), pp. 2367–2420. https://doi.org/10.1007/s10518-017-0206-7.

Gilder, C.E.L. (2022). Geotechnical data curation and a geostatistical multivariate framework for VS prediction in data scarce contexts, *Ph.D. thesis*, University of Bristol, Bristol, UK.

Gilder, C.E.L., De Risi, R., De Luca, F., Pokhrel, R.M. and Vardanega, P.J. (2022). Geostatistical framework for estimation of VS30 in data-scarce regions. *Bulletin of the Seismological Society of America*, 112(6), pp. 2981–3000. https://doi.org/10.1785/0120210266.

Municipio de Quito (2015). Actualización de la zonificación por amenaza de deslizamientos en el Distrito Metropolitano de Quito. Technical report.

Omre, H. (1987). Bayesian kriging—Merging observations and qualified guesses in kriging. *Mathematical Geology*, 19(1), pp. 25–39. https://doi.org/10.1007/BF01275432.

Othman, M.M., Hen-Jones, R., Zapata, C., Jiménez, E., De Luca, F., Holcombe, E.A. and Vardanega, P.J. (2023a). Geotechnical variability of the soils of Quito, Ecuador: a geodatabase study. *Bulletin of Engineering Geology and the Environment*, 82(11): [433] https://doi.org/10.1007/s10064-023-03438-3.

Othman, M., Hen-Jones, R., Zapata, C., Jiménez, E., De Luca, F., Holcombe, E.A. and Vardanega, P.J. (2023b). Quito Geotechnical Database (QUITO/GEO-299 v.1.1), University of Bristol, Bristol, UK. https://doi.org/10.5523/bris.ys9nfsd66knb21h3twx2rfin6.

Stewart, J.P., Klimis N., Savvaidis A., Theodoulidis N., Zargli E., Athanasopoulos G., Pelekis P., Mylonakis G. and Margaris B. (2014). Compilation of a local Vs profile database and its application for inference of VS30 from geologic- and terrain-based proxies. *Bulletin of the Seismological Society of America*, 104(6), pp. 2827–2841. https://doi.org/10.1785/0120130331.

USGS (2007). United States Geological Survey (USGS) V_{S30} map viewer. Data available at < https://usgs.maps.arcgis.com/apps/webappviewer/index.html?id=8ac19bc334f747e486550f32837578e1 > [12/04/2024].

Vaca, S., Vallée, M., Nocquet, J.M. and Alvarado, A. (2019). Active deformation in Ecuador enlightened by a new waveform-based catalog of earthquake focal mechanisms. *Journal of South American Earth Sciences*, 93, pp. 449-461. https://doi.org/10.1016/j.jsames.2019.05.017.

Wald, D.J. and Allen, T.I. (2007). Topographic slope as a proxy for seismic site conditions and amplification. *Bulletin of the Seismological Society of America*, 97(5), pp. 1379–1395. https://doi.org/10.1785/0120060267.

Webster, R. and Oliver, M.A. (2007). *Geostatistics for Environmental Scientists*, 2nd Edition, John Wiley and Sons Ltd., UK.

Zapata, C., Holcombe, E.A., Vardanega, P.J. and Jimenez, E. (2023). Modelling the effect of hydraulic conductivity variability on slope stability calculations for a site in South-East Quito, Ecuador. In: *European Geotechnical Engineering - Unity and Diversity*, Bucharest, Romania (Lungu, I., Teodoru, I-B. and Batali, L. (eds.)). Politehnium Publishing House, Işai, România, vol. 2, pp. 773-780.

Proceedings of the XVIII ECSMGE 2024
GEOTECHNICAL ENGINEERING CHALLENGES
TO MEET CURRENT AND EMERGING NEEDS OF SOCIETY
© 2024 the Authors
ISBN 978-1-032-54816-6
DOI 10.1201/9781003431749-202
Open Access: www.taylorfrancis.com, CC BY-NC-ND 4.0 license

ECSMGE 24
XVIII EUROPEAN CONFERENCE ON SOIL MECHANICS AND GEOTECHNICAL ENGINEERING

Liquefaction resistance of carbonate sands from cone penetration tests

Résistance à la liquéfaction des sables carbonatés issue d'essais de pénétration au cône

D. Giretti*
Department of Engineering and Applied Science, University of Bergamo, Italy
V. Fioravante
Engineering Department, University of Ferrara, Italy
**daniela.giretti@unibg.it*

ABSTRACT: Liquefaction assessment is normally carried out using semi-empirical approaches based on the pioneering study of Seed and Idriss (1982). The methods relate a penetration resistance measured in situ (preferably from cone penetration tests, CPTs) to observed instances of liquefaction and non-liquefaction of sandy deposits. However, the applicability of a simplified approach is questionable for materials which fall outside the range of silica sands and slightly silty sands for which it has been developed and extensively verified against field data. For such cases a more rigorous method is needed. Carbonate sands are well known and documented to behave differently from silica sands: at the same relative density, penetration resistance is generally lower than in siliceous sands, while cyclic laboratory testing indicates higher cyclic resistance. These observations cannot rationally be combined into the commonly used simplified liquefaction procedures. An experimental approach, based on the measured mechanical properties of the carbonate sands, is essential. This paper provides an example of calibration of liquefaction resistance from CPTU for a fill made of dredged carbonate sand, based on centrifuge CPTUs and cyclic laboratory tests.

RÉSUMÉ: L'évaluation de la liquéfaction est normalement effectuée en utilisant des approches semi-empiriques basées sur l'étude pionnière de Seed et Idriss (1982). Les méthodes relient une résistance à la pénétration mesurée in situ (de préférence à partir de tests de pénétration au cône, CPTs) à des instances observées de liquéfaction et de non-liquéfaction de dépôts sablonneux. Cependant, l'applicabilité de l'approche simplifiée est discutable pour les matériaux qui sortent du cadre des sables de silice et des sables légèrement silteux pour lesquels elle a été développée et largement vérifiée contre des données de terrain. Pour de tels cas, une méthode plus rigoureuse est nécessaire. Les sables carbonatés sont bien connus et documentés pour se comporter différemment des sables de silice: à la même densité relative, la résistance à la pénétration est généralement plus basse que dans les sables siliceux, tandis que les tests de laboratoire cycliques indiquent une résistance cyclique plus élevée. Ces observations ne peuvent pas rationnellement être combinées dans les procédures simplifiées de liquéfaction couramment utilisées. Une approche expérimentale, basée sur les propriétés mécaniques mesurées des sables carbonatés, est essentielle. Cet article fournit un exemple de calibration de la résistance à la liquéfaction à partir de CPTU pour un remblai fait de sable carbonaté dragué, basé sur des CPTUs de centrifugeuse et des tests de laboratoire cycliques.

Keywords: Liquefaction; carbonate sand; CPT; centrifuge.

1 INTRODUCTION

There is very little guidance in the literature on seismic liquefaction assessment of carbonate sands. Available information suggests that these materials have crushable grains and can be significantly more compressible than silica sands at the same relative density, resulting in a penetration resistance generally lower, Marioka and Nicholson (2000). However, laboratory testing such as cyclic simple shear or triaxial testing, indicates that, at the same relative density, carbonate sands have a higher cyclic resistance (Hyodo et al. 1998, Marioka and Nicholson 2000, Brandes 2011, Sandoval et al. 2011). These observations cannot rationally be combined into the commonly used simplified liquefaction procedures. This paper provides an example of a liquefaction assessment for a carbonate sand through an uncoupled total stress approach. The assessment compares the resistance to seismic loading to the seismic demand in terms of a factor of safety, FS_{liq}. The pore water pressure generated by seismic loading is computed from the value of FS_{liq}. Referring to a case study of a

hydraulic fill made of dredged carbonate sands, the steps of the assessment are the following:

- Determine seismic loading (cyclic stress ratio) based on site-specific ground response analysis;
- Determine in situ state parameter ψ ($\psi = e - e_{cs}$ where e = current void ratio; e_{cs} = void ratio on the critical state line at the same p', Been and Jefferies, 1985) based on the CPTU data;
- Determine cyclic strength of the sand, at the in situ state, based on laboratory cyclic shear strength tests; and,
- Compare cyclic resistance to the seismic loading to indicate the fill performance. Performance is measured in terms of whether liquefaction is likely or not, quantified by the factor of safety against liquefaction.

This engineering approach should be valid for any material that lies outside of the database of liquefaction case histories for which the NCEER (Youd and Idriss, 2001) approach is appropriate. This includes carbonate sands, as well as silts and tailings. It is also applicable for projects which are considered too complex for the simplified methods to apply.

2 SEISMIC LOADING

The reference case study is a 20 m thick hydraulic fill, made of a carbonate sand, dredged offshore, hydraulically placed and densified by vibrocompaction. The fill is located in the Persian Gulf.

The results of a regional seismic hazard analysis PSHA, indicating reverse and strike-slip earthquakes with moment magnitude of approximately $M_w = 6$, have been used as the basis for selecting and applying bedrock ground motions in the site response models. The number of cycles of loading, wich is mainly influenced by the magnitude, is N = 6, as defined by the PSHA.

The maximum cyclic stress ratio CSR through the depth of the fill has been determined through a series of site-specific dynamic soil response analyses using an uncopled total stress approach and a 1D nonlinear soil response model. Geotechnical and geophysical parameters measured for the calcareous sand fill and underlying geological materials have been used. It's worth noting that the 50 percentile value of the small strain shear modulus in the fill, derived from shear wave velocity measurements, was adopted in the analyses. This is considered appropriate since displacement compatibility is required and it is therefore the average stiffness that determines the cyclic strains. The non linear soil behaviour has been accounted for considering the experimental strain dependent stiffness and damping of the fill's sand.

The analyses output was a profile of maximum cyclic stress ratio, which was then multiplied by 0.65 to convert computed time histories of CSR containing transient peak amplitudes to an equivalent, uniform CSR profile, consistent with laboratory testing.

3 MECHANICAL PROPERTIES OF THE DREDGED CARBONATE SAND

3.1 ZS sand cyclic resistance

ZS sand, described in detail in Giretti et al. (2018a), is a biogenic carbonate sand with a carbonate content higher than 97%. The sand is composed of a major component referred to organigenic and bioclastic origin, clasts of micritic limestones, and minor component of sparry calcite. The prevalent mineral phases are calcite, aragonite and Mg-calcite. The grains are characterised by micro-porosity and fine borings due to action of endolithic algae are present in some cases.

Table 1 reports ZS grain size distribution parameters. Specific gravity, maximum and minimum density (as per ASTM D4254, ASTM D4253) and void ratio are summarised in Table 2. The ASTM procedure for maximum dry density was considered the more suitable to crushable carbonate sands, however the series of determinations carried out highlighted a significant range of variation, confirming the limited reliability of density as reference parameter to characterise carbonate sands.

The critical state line approximation of ZS in the e-$\log_{10}$(p') plane is shown in Figure 1.

To evaluate the cyclic resistance of ZS, many cyclic tests (both triaxial and simple shear) have been performed. The results have been interpreted to define relationships between the cyclic stress ratio CSR ($\Delta\sigma_a/2s'$, where $s' = (\sigma'_v+\sigma'_h)/2$, or τ/σ'_v) and the number of cycles N to cause liquefaction (defined as the condition when the double amplitude axial strain ε_{DA} equals 2.5% or the double amplitude shear strain γ_{DA} equals 5%), for different values of the state parameter ψ.

The cyclic resistance evaluated in triaxial condition has been converted to resistance in a simple shear condition using a multiplier factor (Ishihara et al., 1977, 1985) of 0.7. Data from triaxial tests corrected by this factor, for given values of the state parameter ψ, are compared in Figure 2 to data from cyclic simple shear tests.

Table 1. Grain size distribution parameters of ZS sand.

	D_{10} (mm)	D_{50} (mm)	D_{60} (mm)	U_C (-)	FC (%)	Gravel like (%)
ZS	0.085	0.339	0.474	5.57	7.9	0

Table 2. Index properties of ZS sand.

	γ_{min} (kN/m^3)	γ_{max} (kN/m^3)	e_{max} (-)	e_{min} (-)	G_S (-)
ZS	14.14	17.88	0.95	0.54	2.812

The relationships between the cyclic resistance CSR in simple shear conditions (τ/σ'_v) and N have been used to define relationships between CSR and the state parameter ψ at a given N, as shown in Figure 3. Equation 1, referred to the case of "failure" occurring on the 6th cycle of loading, is also reported in Figure 2.

$$CRR = 0.129 - 0.308 \cdot \psi \qquad (1)$$

This equation has been used to evaluate the *in situ* cyclic resistance as a function of the values of ψ estimated from CPTUs (using a properly calibrated correlation with the cone resistance, see next section).

The results of the cyclic tests have been also used to define a relationship between FS_{liq} and the excess pore pressure build up. For a given applied stress ratio τ/σ'_v, the number of cycles necessary to induce an excess pore pressure $Ru = \Delta u/\sigma'_v$ ranging from 0.1 to 0.95 has been evaluated. The relationship between τ/σ'_v and N for a given Ru value has then been determined. Example of the τ/σ'_v – N – Ru relationships are given in Figures 4a and b.

The FS_{liq} values at N=6 can be computed as the ratio between τ/σ'_v at Ru = 0.95 and τ/σ'_v at lower Ru values. The Ru – FS_{liq} relationships are shown in Figure 5. A unique relationship Ru – FS_{liq} has been found as shown in Figure 5, which can be interpreted with an inverse power law function:

$$Ru = \left(\frac{1}{FS_{liq}}\right)^{6.6} \qquad (2)$$

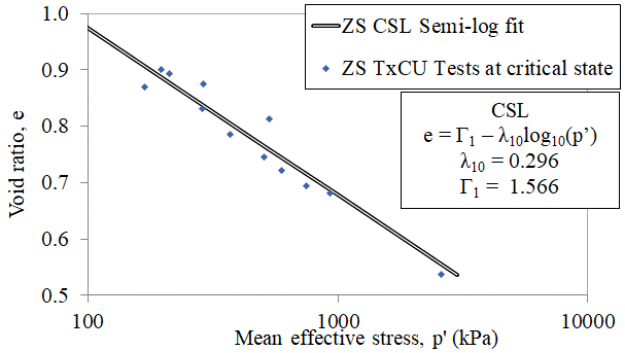

Figure 1. Critical state line of ZS Sand in the e - log$_{10}$(p') plane.

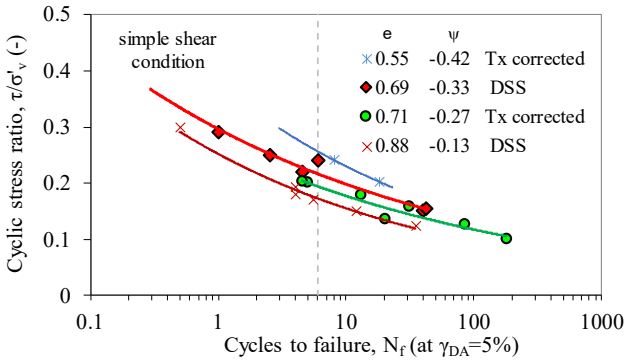

Figure 2. Cyclic Simple Shear Behaviour of ZS Sand.

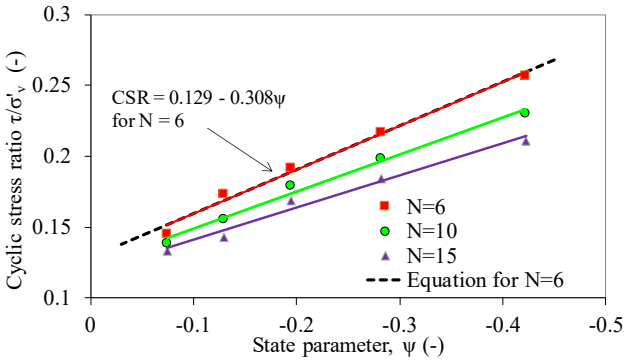

Figure 3. Cyclic stress ratio τ/σ' - number of cycles N relationships of ZS Sand.

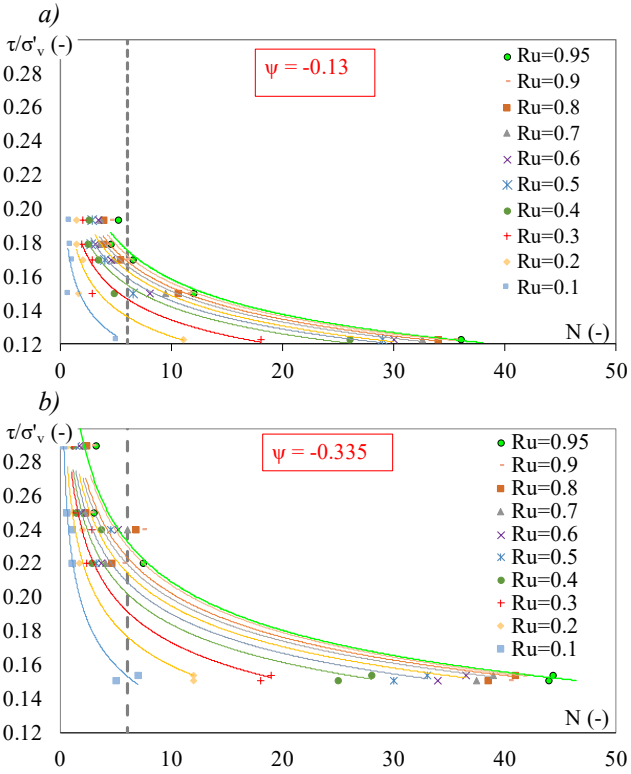

Figure 4. Cyclic stress ratio as a function of the number of cycles for Ru ranging from 0.3 to 0.95: a) ψ = -0.13; b) ψ = -0.335.

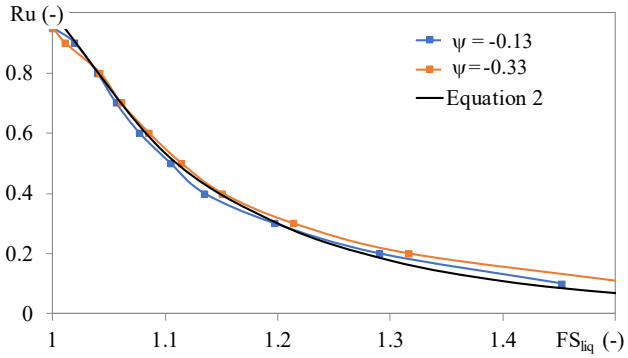

Figure 5. Ru - FS$_{liq}$ relationships.

3.2 Cone penetration resistance in ZS

As described in detail in Giretti et al. (2018b), a significant number of calibration CPTU tests in a centrifuge and in a large calibration chamber have been performed to calibrate correlations between the cone resistance q_t and the state parameter ψ for ZS.

Figures 6 and 7 show typical centrifuge calibration test results of dry and saturated ZS sand over a range of average void ratios (mean value at the end of inflight consolidation). The tip resistance is plotted against the vertical effective stress σ'$_v$, computed accounting for the acceleration field distortion in the centrifuge. Saturated as opposed to dry conditions have a significant effect on the measured tip resistance for ZS sand. Figure 8 shows the same centrifuge data from Figs. 6 and 7 but processed as a normalised tip resistance Q_p vs. to the state parameter, ψ, in which Q_p is:

$$Q_p = \frac{q_t - p}{p'} \quad (3)$$

where p and p' are the total and affective mean stress.

The state parameter is calculated for each Q_p point based on the vertical effective stress, horizontal effective stress from $K_0 = 0.5$, void ratio estimated at that point and a linear critical state line approximation characterised by $\lambda_{10} = 0.296$ and $\Gamma_1 = 1.566$ (see Fig. 1). It's worth noting that in a small scale accelerated model, the vertical effective stress increases significantly from top to bottom of the sample, thus the void ratio also varies through the model. The void ratio profile in the sample can be estimated using the compression coefficients measured in oedometer tests, but maintaining the measured average void ratio (average at the end of the inflight consolidation induced by the augmented gravity fill). The lines of data for dry and saturated conditions in Figure 8 describe two similar relationships, highlighting the significant influence of ψ on tip resistance in sands. Following Jefferies and Been (2006) the relationships have the following Equation:

$$Q_p = k \cdot e^{-m\psi} \quad (4)$$

in which the parameters *k*, *m* are 42 and 5.1 for dry models and 35 and 5.1 for the saturated models.

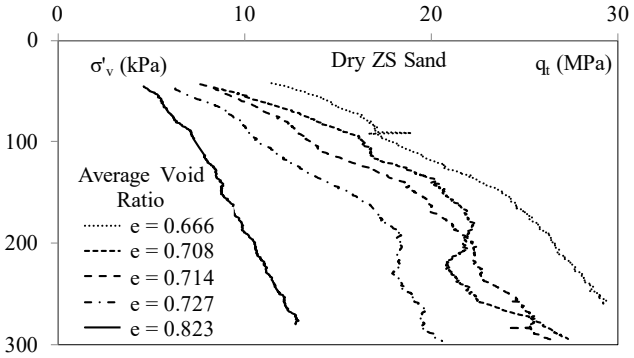

Figure 6. CPTUs in dry ZS.

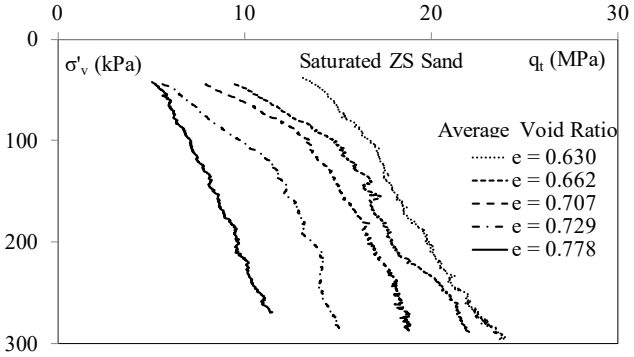

Figure 7. CPTUs in saturated ZS.

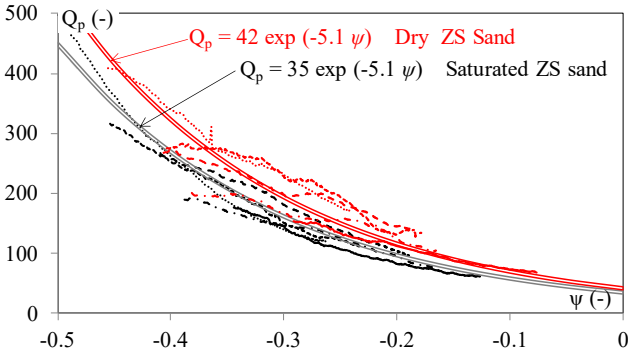

Figure 8. State parameter interpretation of centrifuge tests.

4 LIQUEFACTION ASSESSMENT

The first step of the liquefaction assessment consists in the determination of the in situ state of a sand fill through in situ CPTUs. The CPTU calibration summarised above provides the link between the measured tip resistance and the in situ state parameter. For a large volume of fill in which the in situ state is variable, the definition of a characteristic value for the liquefaction analysis is needed. For liquefaction to be a problem, a certain thickness of fill needs to be loose, and for this reason, 1 m thick layers or depth

increments can be considered. However, only a relatively small portion of a fill needs to liquefy for the overall performance of the fill to be unsatisfactory. The analysis therefore may consider the 20 percentile value of the in situ state in each metre interval. A one metre depth interval provides a good vertical definition of a fill profile in relation to the likely size of foundations and depth of fill. From a liquefaction perspective, a greater depth interval is not desirable as that relatively thin liquefied layers can be problematic.

Figure 9a shows, as an example, a groups of 4 CPTUs carried out in a 25 m x 25 m box of a compacted hydraulic fill made of ZS, and the 20 percentile values in 1 m depth intervals derived from the group. The 20 percentile profile is used to compute the characteristic in situ state parameter by means of the inverse form of Eq. 4, as shown on Figure 9b. For the inversion, an average depth of the groundwater table of 6 m was assumed. Figure 9c presents the comparison between the cyclic strength CRR, derived from the 20 percentile state parameter profiles by means of Eq. 1, with the seismic loading obtained from the site-specific dynamic soil response analysis.

Equation 1 (see also Fig. 2) has been employed to calculate cyclic strength from state parameter for N = 6 cycles. The seismic loading on Figure 9c is 0.65 times the maximum CSR from ground response analysis. The cyclic strength of the compacted fill is clearly well above the cyclic loading, representing a very low risk of liquefaction (or high factor of safety).

The CRR profile in Figure 9c derives from the combination of Eqs. 1 and 4 and can be written as:

$$\mathrm{CRR} = 0.129 - 0.308 \cdot \left(-\frac{1}{m} \cdot ln\frac{Q_P}{k}\right) \quad (5)$$

The ratio between the CSR and CRR profiles in Figure 9c is the factor of safety against liquefaction FS_{liq}, from whose values the pore pressure ratio Ru can be calculated using Eq. 2. The calculated pore pressure profiles for 7 groups of 4 CPTUs are shown on Figure 10. In general, the pore pressure ratio is less than about 0.1, with two locations showing values up to 0.37 in some layers.

These values are low in terms of liquefaction - a range of 0.3 to 0.5 is normally considered to signify the onset of strain softening during seismic loading, while 0.9 is considered liquefaction.

5 CONCLUSIONS

This paper presented an example of a liquefaction assessment for a carbonate sand with reference to a case study of a hydraulic fill made of dredged calcareous, biogenic sands. The two principal ingredients of the assessment are the determination of:

- the in situ state based on CPTU data and a properly calibrated correlation for the fill sand between the cone resistance and the soil state;
- the cyclic strength of the sand, at the in situ state, based on laboratory cyclic shear strength tests.

This assessment procedure has been developed given that carbonate sands lies outside of the range of materials for which the NCEER approach is appropriately applicable.

Core of the procedure is the adoption of the state parameter ψ (Been and Jefferies, 1985) as proper indicator of the state of the fill‘s sand, given that density alone (void ratio or relative density), without stress level, is not sufficient for defining the state of the soil and quantifying its stress-strain-strength behavior. The procedure described allows to assess the satisfaction of performance requirement (such as minimum safety factor against liquefaction) for compacted hydraulic fill on the basis of a directly relevant physical parameter, not affected by i) testing method, ii) the applicability of empirical correlations between cone resistance and liquefaction resistance, iii) potential errors associated with the nature of carbonate sand (e.g. high and variable compressibility and susceptibility to particle crushing).

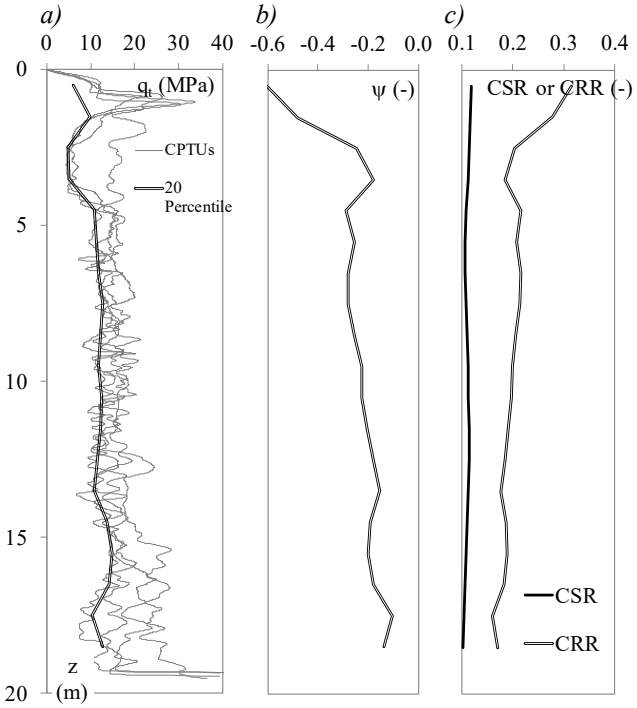

Figure 9. Liquefaction analysis for a group of 4 CPTUs: a) measured q_t profiles and corresponding 20 percentile value; b) characteristic in situ state parameter; c) cyclic resistance and cyclic stress ratio.

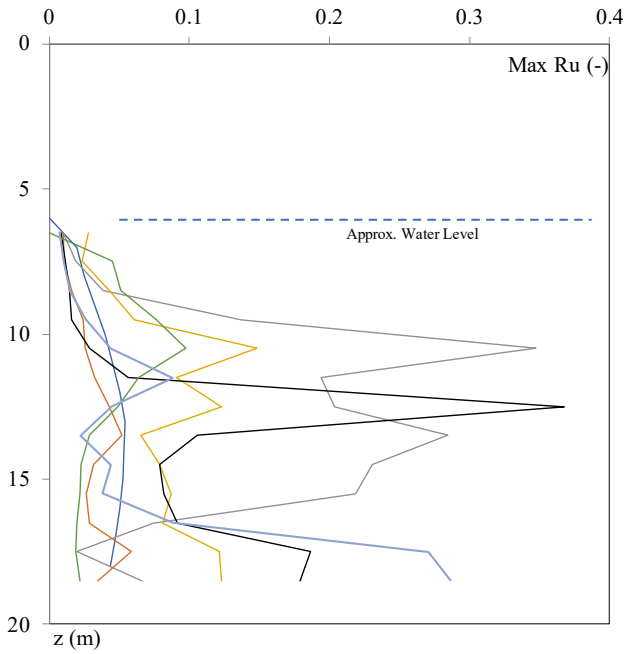

Figure 10. Ru from Uncoupled Liquefaction Analyses for 7 groups of 4 CPTUs.

ACKNOWLEDGEMENTS

The authors would like to express their deep gratitude to Ken Been for having been a fundamental partner of the research team which carried out the studies to which this note refers and having shared all his knowledge and professional experience on soil liquefaction.

REFERENCES

ASTM D4254 – 16. Standard Test Methods for Minimum Index Density and Unit Weight of Soils and Calculation of Relative Density.

ASTM D4253 – 16. Standard Test Methods for Maximum Index Density and Unit Weight of Soils Using a Vibratory Table.

Been, K. and Jefferies, M.G. (1985). A state parameter for sands. Géotechnique, 35(2), 99-112. https://doi.org/10.1680/geot.1985.35.2.99.

Brandes, H.G. (2011). Simple Shear Behavior of Calcareous and Quartz Sands. *Geotechincal and Geological Engineering*, 29(1), 113–126. https://doi.org/10.1007/s10706-010-9357-x.

Giretti, D., Fioravante, V., Been, K., Dickenson, S. (2018a). Mechanical properties of a carbonate sand from a dredged hydraulic fill. *Géotechnique*, 68(5), 410-420. https://doi.org/10.1680/jgeot.16.P.304.

Giretti, D., Been, K., Fioravante, V., Dickenson, S. (2018b). CPT Calibration and Analysis for a Carbonate Sand. *Géotechnique*, 68(4), 345-357. https://doi.org/10.1680/jgeot.16.P.312.

Hyodo, M., Hyde, A. F. L. & Aramaki, N. (1998). Liquefaction of crushable soils. *Geotechnique* 48(4), 527-543. https://doi.org/10.1680/geot.1998.48.4.527.

Ishihara, K., Iwamoto, S., Yasuda, S., and Takatsu, H. (1977). Liquefaction of anisotropically consolidated sand. *Proceedings 9th International Conference on Soil Mechanics and Foundation Engineering*, Japanese Society of Soil Mechanics and Foundation Engineering, Tokyo, Japan, Vol. 2, 261-64.

Ishihara, K, Yamazaki, A. and Haga, K. (1985). Liquefaction of K_0 consolidated sand under cyclic rotation of principal stress direction with lateral constraint, *Soils and Foundations*, Japanese, 5(4), 63-74.

Jefferies, M and Been, K. (2006). Soil liquefaction. A critical state approach. Taylor and Francis, London.

Marioka, B.T. and Nicholson, P.G. (2000). Evaluation of the liquefaction potential of calcareous sand. *Proceedings of the 10th International Offshore And Polar Engineering Conference*, Seattle, USA, 494-500.

Sandoval, E.A., Pando, M.A. and Olgun, G.C. (2011). Liquefaction susceptibility of a calcareous sand from Southwest Puerto Rico. *Proceedings of the 5th International Conference on Earthquake Geotechnical Engineering*, Santiago, Cile, paper No. LSOSA.

Seed, H. B. and Idriss, I. M. (1982). Ground motions and soil liquefaction during earthquakes. Earthquake Engineering Research Institute Monograph, Oakland, California.

Youd, T.L. and Idriss, I.M. (2001).Liquefaction Resistance of Soils: Summary Report from the 1996 NCEER and 1998 NCEER/NSF Workshops on Evaluation of Liquefaction Resistance of Soils. *Journal of Geotechnical and Geoenvironmental Engineering*, 127(4), 817-833. https://doi.org/10.1061/(ASCE)1090-0241(2001)127:4(297).

Proceedings of the XVIII ECSMGE 2024
GEOTECHNICAL ENGINEERING CHALLENGES
TO MEET CURRENT AND EMERGING NEEDS OF SOCIETY
© 2024 the Authors
ISBN 978-1-032-54816-6
DOI 10.1201/9781003431749-203
Open Access: www.taylorfrancis.com, CC BY-NC-ND 4.0 license

ECSMGE 24
XVIII EUROPEAN CONFERENCE ON SOIL MECHANICS AND GEOTECHNICAL ENGINEERING

2D Seismic response analyses from 3rd Level Seismic Microzonation in the Southern Italy: Approaches and applications

Analyses de réponse sismique 2D à partir de la microzonation sismique de 3e niveau dans le sud de l'Italie: Approches et applications

S. Grasso, M.R. Massimino
University of Catania, Catania, Italy

M.S.V. Sammito*
University "Kore" of Enna, Enna, Italy

**mariastellavanessa.sammito@unikore.it*

ABSTRACT: Seismic Microzonation studies of 3rd Level (SM3) have been performed for the emergency management and the reconstruction of several Municipalities in the eastern flank of Mt. Etna (Southern Italy) hit by the 2018 seismic sequence. The most energetic event (Mw=4.9) occurred on 26th December 2018, causing phenomena of superficial faulting along the Fiandaca Fault (FF), where the most damaged areas are located. In order to define the subsoil model for each seismic homogeneous microzone (SHM) and to perform extensive numerical analyses, intense investigations have been carried out including in situ and laboratory tests. For the estimation of the spatial variability in seismic response, the finite element code PLAXIS 2D has been employed. Moreover, the Hardening Soil model with small-strain stiffness (HS small model), which includes an increased soil stiffness for small strains, has been adopted in order to consider the soil non-linearity. For each SHM, results are presented in terms of acceleration response spectra and amplification factors (AFj). The latter are calculated for three different period intervals linked to the heights of buildings according to the Italian Guidelines and Standards. The results of this work provide important information for the development of urban planning aimed at reducing seismic risk.

RÉSUMÉ: Des études de microzonage sismique de 3e niveau (SM3) ont été réalisées pour la gestion des urgences et la reconstruction de plusieurs municipalités du flanc oriental de l'Etna (sud de l'Italie) touchées par la séquence sismique de 2018. L'événement le plus énergétique (Mw = 4,9) s'est produit le 26 décembre 2018, provoquant des phénomènes de failles superficielles le long de la faille de Fiandaca (FF), où se trouvent les zones les plus endommagées. Afin de définir le modèle de sous-sol pour chaque microzone sismique homogène (SHM) et d'effectuer des analyses numériques approfondies, des investigations intenses ont été menées, y compris des tests in situ et en laboratoire. Pour l'estimation de la variabilité spatiale de la réponse sismique, le code d'éléments finis PLAXIS 2D a été utilisé. De plus, le modèle Hardening Soil with small-strain stiffness (HS small model), qui inclut une rigidité accrue du sol pour les petites déformations, a été adopté afin de prendre en compte la non-linéarité du sol. Pour chaque SHM, les résultats sont présentés en termes de spectres de réponse d'accélération et de facteurs d'amplification (AFj). Ces derniers sont calculés pour trois intervalles de périodes différents liés aux hauteurs des bâtiments selon les directives et normes italiennes. Les résultats de ces travaux fournissent des informations importantes pour le développement d'une planification urbaine visant à réduire le risque sismique.

Keywords: Seismic microzonation studies; amplification factors; FEM analysis.

1 INTRODUCTION

Due to the seismic sequence that began on 23rd December 2018 and hit the eastern flank of Mt. Etna (Southern Italy), 3rd Level Seismic Microzonation studies were performed for several municipalities located in Eastern Sicily (Cavallaro et al. 2022; Grasso and Sammito, 2022). The sequence peaked in the Mw=4.9 seismic event occured on 26th December 2018 after many Mw>2.5 events causing serious damage to unreinforced masonry buildings.

Through intense field activities, the geological and geomorphological setting of the municipalities affected by the sequence was investigated. The physical phenomena govering the site response were studied by the finite element code PLAXIS 2D using

the Hardening Soil model with small-strain stiffness (HS small model).

2 DESCRIPTION OF THE CASE STUDY

Laboratory and in situ tests were performed for the 3rd Level Seismic Microzonation of several municipalities damaged by the 2018 seismic sequence. In this paper, the data collected for the municipality of Trecastagni are taken into consideration (Figure 1).

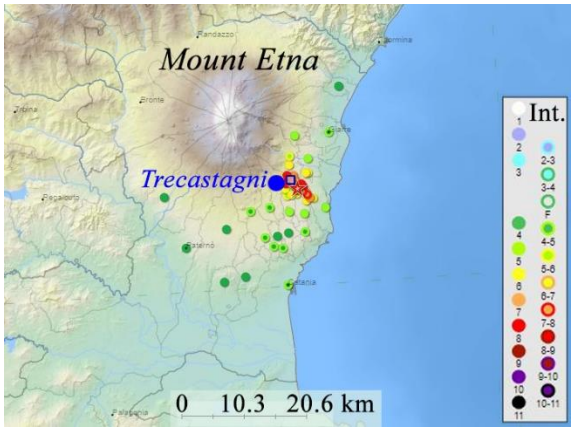

Figure 1. Intensity map. Earthquake of 26th December 2018 (from Rovida et al. 2020; 2022, modified).

To evaluate the local seismic response, laboratory and in situ tests were carried out including n. 8 Boreholes, n. 1 Down-Hole (DH) test, n. 9 Multichannel Analysis of Surface Waves tests (MASW), n. 24 Horizontal Vertical Spectral Ratio Test (HVSR) and n. 1 Direct Shear tests (DST). The shear wave velocities, V_S, obtained from the DH test, are shown against depth in Figure 2. In order to describe the dependence of the shear modulus and damping as a function of the shear strain, it was necessary to refer to dynamic curves from literature (Castelli et al., 2018). The definition of the Seismically Homogeneous Microzones (SHMs) is essential for the construction of the subsoil models (Castelli et al. 2023). Six SHMs were identified in the studied area. The SHMs Map includes also an "Attention zone for active and capable fault" (ACF) (Figure 3).

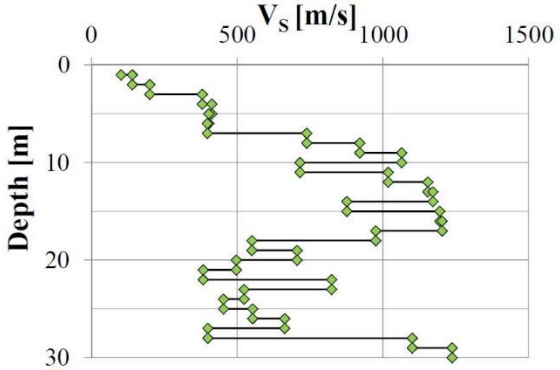

Figure 2. V_S from DH test in the municipality of Trecastagni.

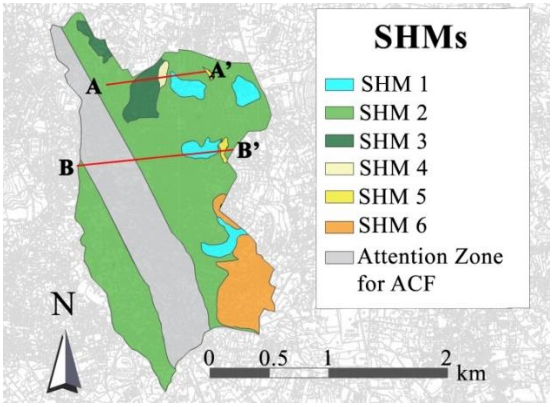

Figure 3. SHMs map with the indication of the studied geological cross-sections.

The main engineering-geological units (*gt-units*), identified by 2 to 4 letter acronyms, are the following: Backfill soil (RI), Silty gravels, gravel-sand-clay mixtures (GM), Coarse scoriaceous products in a predominantly sandy matrix (GW), Well-graded sands and gravelly sands, little or no fines (SW), Cover lithoid (LC), Fractured / altered geological bedrock alternation of lithotypes (SFAL). The 2D subsoil models are based on geological cross-sections that reproduce the geometry of the *gt-units* and the measured V_S from the geophysical tests. As example, the geological cross-sections B-B' is displayed in Figure 4.

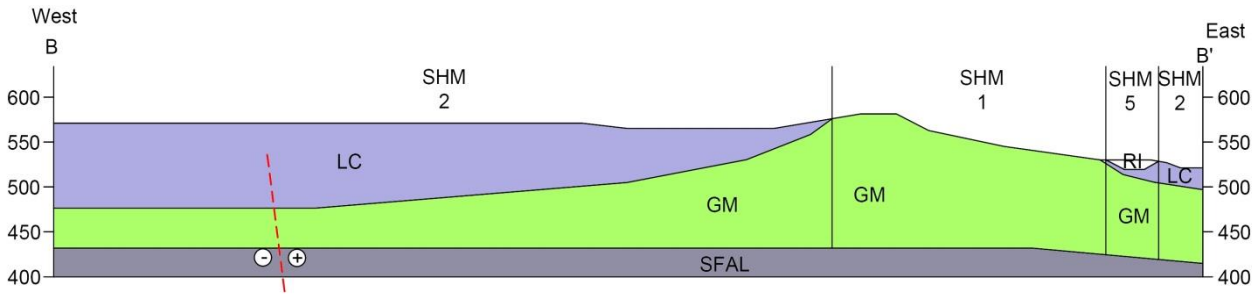

Figure 4. Geological cross-sections B-B'.

3 NUMERICAL MODELLING

For each municipality, the input motions consisted of a set of seven unscaled natural records selected from the European Strong-motion Database (ESM) (https://esm.mi.ingv.it/) to be compatible on average in the 0.1-1.1 s interval of period with the reference response spectrum for Soil Class A and for a return period of 475 year according to the Italian Building Code (NTC, 2018).

Natural records were selected using REXELite, a simplified online version of the computer program REXEL (Iervolino et al., 2009), through the Magnitude-Distance criterion based on disaggregation of seismic hazards (available at http://esse1-gis.mi.ingv.it).

The accelerograms used as input motion for Trecastagni area are listed in Table 1.

Table 1. Natural accelerograms selected as input motion for Trecastagni area.

ID	Mw	R[km]
A.MZ14.HNN.D	6.5	30.6
3A.MZ19.HNE.D	6.5	22.6
IT.CLO.HGN.D	5.9	10.8
IT.MMO.HGN.D	6.5	19.2
IT.SVN.HGE.D	4.9	4.5
IT.SVN.HGN.D	4.9	4.5
IV.T1212.HNN.D	6.5	10.5

The 2D analyses were performed through the finite element code PLAXIS2D using the HS small model.

The mesh was defined by 15-node triangular elements with a size that respects the Kuhlemeyer and Lysmer (1973) condition. With regard to the boundary conditions, the free field and compliant base boundary conditions were considered. The finite element mesh, reproducing the B-B' geological cross section for Trecastagni area, is reported in Figure 5.

The HS small describes the soil stiffness by using three different input parameters at the reference pressure p^{ref}: the secant stiffness in standard drained triaxial test, E_{50}^{ref}, the unloading/reloading stiffness, E_{ur}^{ref}, and the tangent stiffness for primary oedometer loading, E_{oed}^{ref}. To describe the variation of stiffness with strain, two additional parameters have to be considered: the reference shear modulus at very small strain, G_0^{ref}, and the shear strain level, $\gamma_{0.7}$, at which the secant shear modulus, G_S, is reduced to 72.2 % of G_0.

Table 2 reports the input parameters of the HS small model, i.e. for a GM layer, where: γ is the unit weight of soil, m is the power for stress-level dependency of stiffness, c' is the cohesion and φ' is the friction angle.

Table 2. Input parameters for the HS small model.

Symbol	Value	Unit
γ	20	kN/m^3
E_{50}^{ref}	36000	kN/m^2
E_{oed}^{ref}	36000	kN/m^2
E_{ur}^{ref}	108000	kN/m^2
G_0^{ref}	351324	kN/m^2
$\gamma_{0.7}$	0.00018	-
p^{ref}	100	kN/m^2
m	0.51	-
c'	10	kN/m^2
φ'	36	°

4 RESULTS

Once numerical ground response analyses is performed, another key aspect in a SM3 study is the evaluation of the Amplification Factors (AF) (Working Group ICMS 2008, 2011).

They are calculated as the ratio between the integral of the pseudo-acceleration elastic response spectrum of the output motion ($S_{,out}$) and the pseudo-acceleration elastic response spectrum of the input motion ($S_{,inp}$) in a defined interval of period (Pergalani et al., 2019):

$$AF_{T_n} = \frac{\int_{T_a}^{T_b} S_{,out} dT}{\int_{T_a}^{T_b} S_{,inp} dT} \; with \; n = 1,2,3 \qquad (1)$$

where Ta and Tb are the extremes of the defined interval of periods, Tn. The three different range of periods are: T_1= 0.1–0.5 s; T_2= 0.4–0.8 s and T_3= 0.7–1.1 s, in order to cover the fundamental periods of buildings in studied municipalities.

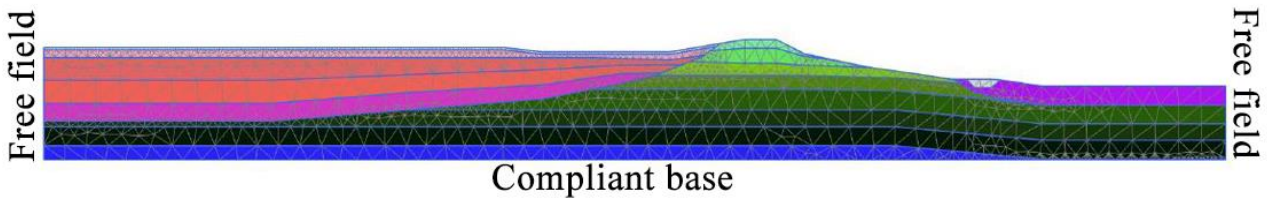

Figure 5. Finite element mesh reproducing the B-B' geological cross section used in numerical analyses for Trecastagni area.

In Figure 6, results are presented in term of response spectrum at the surface, i.e. for a SHM 2, obtained by setting a structural damping of 5%.

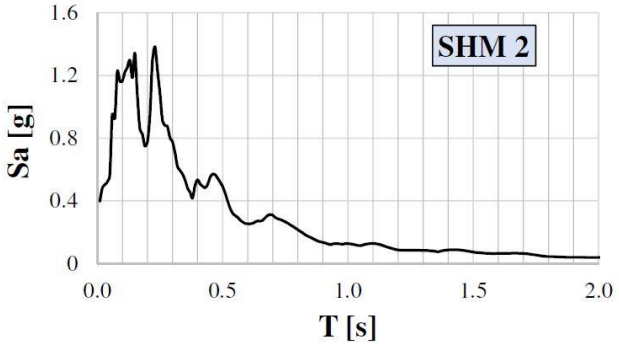

Figure 6. Elastic response spectrum obtained by numerical analyses.

According to the guidelines for Seismic Microzonation studies (Working Group ICMS 2008, 2011), AF factors were determined for each SHM encountered along the cross-sections, as summarize in Table 3. The amplification factors are named according to the related interval of periods: AF0105, AF0408 and AF0711.

Table 3. AF factors for each SHM.

SHM	AF0105	AF0408	AF0711
1	2.43	2.77	2.37
2	1.76	1.61	1.65
3	2.19	1.80	2.48
4	1.62	2.08	2.95
5	2.08	1.83	1.32

5 CONCLUSIONS

In this work, seismic microzonation studies were carried out for several municipalities in Eastern Sicily, after the effects of the 2018 seismic sequence. 2D site response analyses are presented to highlight approaches that could be applied for seismic microzonation studies in similar conditions. Relevant key aspects are reported focusing on a specific case study. Results are presented in terms of amplification factors of spectral acceleration defined according to national guidelines and standards for microzonation studies. The outcome of this paper provides a valuable base in developing urban planning oriented to seismic risk management.

REFERENCES

Castelli, F., Cavallaro, A., Ferraro, A., Grasso, S., Lentini, V. and Massimino, M.R. (2018). Static and dynamic properties of soils in Catania (Italy). Annals of Geophysics, 61(2), SE221. doi: 10.4401/ag-7706.

Castelli, F., D'Amico, S., Grasso, S., Lentini, V., Massimino, M.R. and Sammito, M.S.V. (2023). Seismic Hazard Assessment by the Application of a Synthetic Damage-Constrained Parameter. In: Ferrari, A., Rosone, M., Ziccarelli, M., Gottardi, G. (eds) Geotechnical Engineering in the Digital and Technological Innovation Era. CNRIG 2023. Springer Series in Geomechanics and Geoengineering. Springer, Cham. https://doi.org/10.1007/978-3-031-34761-0_72.

Cavallaro, A., Grasso, S. and Sammito, M.S.V. (2022). A Seismic Microzonation Study for Some Areas Around the Mt. Etna Volcano on the East Coast of Sicily, Italy. In book: Proceedings of the 4th International Conference on Performance Based Design in Earthquake Geotechnical Engineering, Beijing, China, 15-17 July. DOI: 10.1007/978-3-031-11898-2_61.

Grasso, S. and Sammito, M.S.V. (2022). Uncertainties in Performance Based Design Methodologies for Seismic Microzonation of Ground Motion and Site Effects: State of Development and Applications for Italy. In book: Proceedings of the 4th International Conference on Performance Based Design in Earthquake Geotechnical Engineering, Beijing, China, 15-17 July. DOI: 10.1007/978-3-031-11898-2_23.

Iervolino, I., Galasso, C. and Cosenza, E. (2009). REXEL: computer aided record selection for code-based seismic structural analysis. Bulletin of Earthquake Engineering. DOI: 10.1007/s10518-009-9146-1.

Kuhlemeyer, R.L. and Lysmer, J. (1971) Finite element method accurancy for wave propagation problems. Journal of Soil Mechanics and Foundation Devision. 99 (5): 421-427. https://doi.org/10.1061/JSFEAQ.0001885

NTC New Technical Standards for Buildings (2018). Available online: https://www.gazzettaufficiale.it/eli/gu/2018/02/20/42/so/8/sg/pdf.

Pergalani F, Pagliaroli A, et al. (2020). Seismic microzoning map: approaches, results and applications after the 2016–2017 Central Italy seismic sequence. Bulletin of Earthquake Engineering 18:5595–5629. https://doi.org/10.1007/s10518-019-00640-1.

Rovida, A., Locati, M., et al. (2020). The Italian earthquake catalogue CPTI15. Bulletin of Earthquake Engineering, 18(7): 2953-2984. https://doi.org/10.1007/s10518-020-00818-y.

Rovida, A., Locati, M., Camassi, R., Lolli, B., Gasperini, P. and Antonucci, A. (eds) (2022). Italian Parametric Earthquake Catalogue (CPTI15), version 4.0. Istituto Nazionale di Geofisica e Vulcanologia (INGV). https://doi.org/10.13127/CPTI/CPTI15.44.

Working Group ICMS (2008) Indirizzi e criteri per la microzonazione sismica – Guidelines for seismic microzonation. Conferenza delle Regioni e delle Province Autonome-Dipartimento della Protezione Civile.

Working Group ICMS (2011) Contributi per l'aggiornamento degli Indirizzi e criteri per la microzonazione sismica. Ing Sism anno XXVIII, 2.

Proceedings of the XVIII ECSMGE 2024
GEOTECHNICAL ENGINEERING CHALLENGES
TO MEET CURRENT AND EMERGING NEEDS OF SOCIETY
© 2024 the Authors
ISBN 978-1-032-54816-6
DOI 10.1201/9781003431749-204
Open Access: www.taylorfrancis.com, CC BY-NC-ND 4.0 license

ECSMGE 24
XVIII EUROPEAN CONFERENCE ON SOIL MECHANICS AND GEOTECHNICAL ENGINEERING

Slope stability modelling of urbanisation scenarios for communities in north Quito, Ecuador

Modélisation de la stabilité des pentes selon divers scénarios d'urbanisation: les communautés du nord de Quito, Équateur

R. Hen-Jones
Robertson Geo, Deganwy, North Wales, United Kingdom

C. Zapata, E. Jiménez
Escuela Politécnica Nacional, Quito, Ecuador

E.A. Holcombe, P.J. Vardanega*
University of Bristol, Bristol, United Kingdom

**p.j.vardanega@bristol.ac.uk*

ABSTRACT: Quito, Ecuador, is a rapidly expanding multi-hazard environment at increased risk of rainfall-triggered landslides. In such cities, information on the impact of urbanisation on slopes and rainfall intensity-duration thresholds for triggering landslides can be valuable for resilient urban planning. However, rainfall thresholds are usually generated from empirical landslide data, which is often unavailable. This paper presents an overview of recent stochastic landslide modelling work, enabling regional sensitivity analysis and the development of rainfall thresholds based on tens-of-thousands of physics-based slope stability simulations. Typical landslide-prone communities in north Quito are characterised in terms of degree of urbanisation, slope geometry, soil properties and rainfall scenarios. Soil data came from the new Quito soil geotechnical database and drone mapping successfully resolved slope geometries and more detailed information such as construction materials and slope features. An overview of the modelling methodology is presented. The key findings of the simulation study are that slope cutting, followed by removal of vegetation are the key drivers of slope instability. These findings are discussed in the context of recommendations for land use policy in the studied areas.

RÉSUMÉ: Quito, en Équateur, est un environnement multi-risques en expansion rapide, exposé à un risque accru de glissements de terrain provoqués par les précipitations. Les informations sur l'impact de l'urbanisation sur les pentes et les seuils d'intensité et de durée des précipitations déclencheurs de glissements de terrain peuvent être précieuses pour la planification urbaine. Cependant, les seuils de précipitations sont généralement générés à partir de données empiriques, souvenousat indisponibles. Cet article présente un aperçu des récents travaux de modélisation stochastique des glissements de thterrain, permettant une analyse de sensibilité régionale et le développement de seuils de précipitations basés sur des dizaines de milliers de simulations. Les communautés typiques sujettes aux glissements de terrain du nord de Quito sont caractérisées en termes de degré d'urbanisation, de géométrie des pentes, de propriétés du sol et de scénarios de précipitations. Les données pédologiques proviennent de la nouvelle base de données géotechniques des sols de Quito; la cartographie par drone a réussi à résoudre les géométries des pentes et des informations plus détaillées telles que les matériaux de construction et les caractéristiques des pentes. Un aperçu de la méthodologie de modélisation est présenté. Les principales conclusions de l'étude de simulation sont que la réduction des pentes, suivie de l'élimination de la végétation, sont les principaux facteurs d'instabilité des pentes. Ces résultats sont discutés dans le contexte de recommandations pour la politique d'aménagement du territoire dans les zones étudiées.

Keywords: Slope stability; CHASM; stochastic modelling; urbanisation.

1 INTRODUCTION

Quito, Ecuador is a multi-hazard environment and is subject to the effects of volcanic eruptions, seismic events and rainfall-triggered landslides (cf. O'Rourke and Crespo 1988). Municipal engineers and planners require hazard assessments to support effective disaster risk management practices and policies for today and the future, as urban development continues. Although there is a strong culture of geotechnical testing in the area, a dataset suitable for wide-area landslide hazard assessment was not readily accessible until the recent compilation, publication and statistical analysis of a new database

QUITO/GEO-299 (Hen-Jones et al. 2022; Othman et al. 2023a, b).

The development of this database followed the six-step methodology for data collection and curation in data-scarce regions presented by Vardanega et al. (2023, p.1268-9) summarised as follows: (1) assess the geotechnical-data landscape; (2) make use of local knowledge; (3) understand local practice; (4) undertake data harmonization and cleaning activities; (5) carry-out benchmarking analysis; (6) release the data. The new QUITO/GEO-299 database (Othman et al. 2023a) has enabled physics-based modelling and investigation of landslides in south Quito using the Combined Hydrology And Stability Model, CHASM (Zapata et al. 2023).

In this paper, geotechnical parameter distributions from the database are combined with data on slope geometries, rainfall, and slope features of three hillside communities in north Quito to enable stochastic CHASM modelling of landslide scenarios. The simulation outputs are analysed to find dominant slope instability drivers and rainfall intensity-duration thresholds likely to trigger urban landslides in north Quito. Triggering threshold estimation is usually only possible where landslide inventories are available (e.g., Larsen and Simon, 1993; Guzzetti et al., 2008). Identification of landslide drivers and thresholds can support landslide early warning and resilient land use practice and policy.

2 QUITO LANDSLIDE MODELLING

As part of the Tomorrow's Cities project (see Galasso et al. 2021) Hen-Jones et al. (2024), studied three communities in the northern parts of Quito. A stochastic modelling approach was adopted to allow a wide range of combinations of potential landslide preparatory and triggering factors to be investigated. The following simulation input data was prepared:

1) strata geotechnical properties: soil parameter ranges and distributions were determined from the new Quito geotechnical database, including effective strength parameters, hydraulic conductivity, and unit weight – more information on these geotechnical properties and their fitting parameters can be found in Hen-Jones et al. (2022) and Othman et al. (2023b).

2) natural and urban slope geometry: slope geometry data was derived from drone surveys carried out as part of community participatory activities that had been adapted due to the constraints on field work due to the Covid-19 pandemic. This was successful in capturing detailed information on the heights and angles of cut slopes associated with houses and roads (Hen-Jones et al. 2022). These data were statistically analysed to give distribution parameters for stochastic modelling.

3) urban slope features: drone surveys provided detailed information on house construction materials, urban drainage features and vegetation. Figure 1 indicates how urban slope features are represented in the CHASM urban slope analysis functions developed by Bozzolan et al. (2020). All simulations were run with and without the presence of vegetation.

4) design storms: rainfall intensity and duration ranges were sampled to generate the rainfall inputs that provide the dynamic driver for the hydrological response and stability of each slope in CHASM.

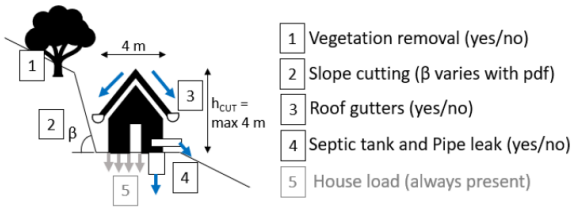

Figure 1. Urban properties of informal housing included in the slope stability analysis (from Bozzolan et al. 2020, used under the terms of the cc-by 4.0 licence).

The parameter ranges in the above four categories were stochastically sampled to generate tens-of-thousands of slope and rainfall scenarios representing the case-study communities. In each case CHASM was used to estimate the minimum slope factor of safety (FoS), where FoS < 1 defined slope failure (i.e. a landslide). CHASM uses Bishop's (1955) method of slices (a limit equilibrium method, LEM) and accompanying hydrological models (Darcy, 1856; Richards, 1931). More details on CHASM can be found in Wilkinson et al. (2002).

Global Sensitivity Analysis (GSA) and Regional Sensitivity Analysis (RSA) of the CHASM input factors and output FoS values were undertaken, allowing the effect of different input parameters on slope stability to be investigated. This analysis was carried out in Matlab using the SAFE Toolbox (Sarrazin et al. 2017; Noacco et al. 2019).

3 URBANISATION SCENARIOS

In this study, the effect of the urbanisation process on slope stability was assessed (Fig. 2) by representing the following stages: (Urb0) the initial plain slope; (Urb1) addition of a road; (Urb2) addition of sparse housing – this situation describes the first North Quito case study community. The other two communities are examples of subsequent urbanisation stages, either: (Urb3) unplanned/informal, high density urbanisation, or (Urb4) planned, low density

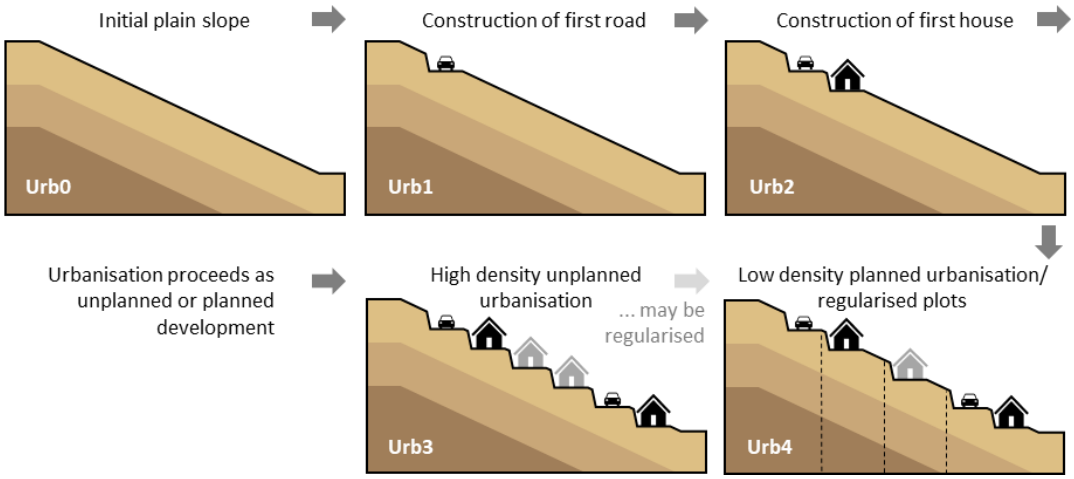

Figure 2. Modelled urbanisation scenarios on the N-S ridges of the Quito Fault System (from Hen-Jones et al. 2024). Urbanisation in east Quito often proceeds downslope from fault ridges or plateaus to lower elevations as the city expands.

urbanisation. Informal settlements often have makeshift drainage, adding to other destabilising factors including deforestation, blockage of natural drainage with solid waste, poor quality construction materials and poor engineering practices (Hen-Jones et al. 2024). Surface drainage features were modelled accordingly, as described in Hen-Jones et al. (2024).

4 RESULTS AND DISCUSSION

Hen-Jones et al. (2024) presents the full discussion of the results of this study. The sensitivity analysis revealed five key input factors dominating slope stability response: natural slope angle, effective cohesion, saturated hydraulic conductivity, height of the water table and rainfall duration. The influence of effective friction angle on slope stability did not feature strongly in the analysis. Given the importance of rainfall duration, rainfall-intensity duration thresholds were developed for north Quito, using the simulation results for all urbanisation stages (Urb0 to Urb4). Often intensity-duration thresholds are developed from smaller empirical datasets (see Table 2) rather than synthetic datasets, and usually presented in the form of Eq. (1):

$$I = a(D)^{-b} \quad (1)$$

where I = rainfall intensity (mm/hr); D = effective rainfall duration (hrs); a and b are fitting parameters. Thresholds were drawn at various percentiles of data capture as presented in Table 1. These can be compared to those from previous studies summarised in Table 2. The ranges of a and b values shown in these tables are broadly comparable but reflect significantly smaller datasets where empirical landslide and rainfall data are concerned (Table 2).

Table 1. Fitting parameters for Eq. 1 rainfall intensity duration thresholds (data from Hen-Jones et al. 2024).

Percentile	*a*	*b*
95	44.52	0.17
99	25.79	0.21
99.5	46.81	0.48
99.9	20.08	0.45
100	20.57	0.77

Table 2. Fitting parameters for I-D thresholds from previous studies.

Reference	Location	*a*	*b*
Larsen and Simon (1993)	Puerto Rico	91.46	0.82
Ahmad (2003)	Jamaica	11.5	0.26
Guzzetti et al. (2008)	Worldwide	6.68	0.52

A comparison of slope failure rates between the different modelled scenarios reveals that the most significant factor driving instability is the act of cutting into the slope (increase in failure rate from 2% to 6% for a plain, vegetated slope, Urb0), also observed in Bozzolan et al. (2020) which investigated the stability of informal housing in the humid tropics. The next most important parameter is the removal of slope vegetation (increase in failure rate from 6% to 13% for a slope with a road cut present, Urb1). Further urbanisation to include an additional road and minimal housing (Urb2) has a negligible effect on the failure rate, the slope stability already having been critically influenced by the initial road cut. When considering vegetated slopes, the unplanned, high density housing scenario (Urb3) gives a significant increase in failure rate compared to the minimal housing scenario (Urb2) of 4%, however, considering bare slopes, the absolute increase is only 1%.

5 CONCLUSIONS

Stochastic simulations have been used to develop I-D thresholds for north Quito, comparing reasonably with past studies. The most important factor affecting stability in the modelled communities is slope cutting, followed by vegetation removal. Analysis supports the importance of revegetation as a landslide management policy and highlights the merit of urban planning for new settlements.

ACKNOWLEDGEMENTS

Funding from UKRI GCRF under grant NE/S009000/1, Tomorrow's Cities Hub is acknowledged. *Data Availability:* The simulation data is available from the first author upon reasonable request.

REFERENCES

Ahmad, R. (2003). Developing early warning systems in Jamaica: rainfall thresholds for hydrogeological hazards. *National Disaster Management Conference*, Ocho Rios, St Ann, Jamaica, 9-10 September 2003. Office of Disaster Preparedness and Emergency Management. Available online at: < https://www.mona.uwi.edu/uds/rainhazards_files/frame.htm > [last accessed 17/03/2024].

Bishop, A.W. (1955). The Use of the Slip Circle in the Stability Analysis of Slopes. *Géotechnique*, 5(1): 7-17. https://doi.org/10.1680/geot.1955.5.1.7.

Bozzolan, E., Holcombe, E., Pianosi, F. and Wagener, T. (2020). Including informal housing in slope stability analysis – an application to a data-scarce location in the humid tropics. *Natural Hazards and Earth System Sciences*, 20(11): 3161-3177. https://doi.org/10.5194/nhess-20-3161-2020.

Darcy, H. (1856). *Les Fontaines Publiques da la Ville de Dijon*. Dalmont, Paris.

Galasso, C., McCloskey, J., Pelling, M. *et al.* (2021). Editorial. Risk-based, Pro-poor Urban Design and Planning for Tomorrow's Cities. *International Journal of Disaster Risk Reduction*, 58: [102158]. https://doi.org/10.1016/j.ijdrr.2021.102158.

Guzzetti, F., Peruccacci, S., Rossi, M. and Stark, C.P. (2008). The rainfall intensity-duration control of shallow landslides and debris flows: an update. *Landslides*, 5(1): 3-17. https://doi.org/10.1007/s10346-007-0112-1.

Hen-Jones, R., Vardanega, P.J., Zapata, C., Jiménez, E. and Holcombe, E.A. (2022). Developing a geotechnical database to improve slope stability assessments in Quito, Ecuador. *Proceedings of the 20th International Conference on Soil Mechanics and Geotechnical Engineering*, M.M. Rahman and M. Jaksa (eds.), Australian Geomechanics Society, vol. 2, pp. 2569-2574.

Hen-Jones, R., Zapata, C., Jiménez, E., Holcombe, E.A. and Vardanega, P.J. (2024). Community-scale slope stability assessment of urbanisation scenarios in North Quito, Ecuador. *under review*.

Larsen, M.C. and Simon, A. (1993). A Rainfall Intensity-Duration Threshold for Landslides in a Humid-Tropical Environment, Puerto Rico. *Geografiska Annaler. Series A, Physical Geography*, 75(1/2): 13-23. https://doi.org/10.2307/521049.

Noacco, V., Sarrazin, F., Pianosi, F. and Wagener, T. (2019). Matlab/R workflows to assess critical choices in Global Sensitivity Analysis using the SAFE toolbox. *MethodsX*, 6: 2258-2280. https://doi.org/10.1016/j.mex.2019.09.033.

O'Rourke, T.D. and Crespo, E. (1988). Geotechnical properties of cemented volcanic soil. *Journal of Geotechnical Engineering (ASCE)*, 114(10): 1126-1147. https://doi.org/10.1061/(ASCE)0733-9410(1988)114:10(1126) .

Othman. M., Hen-Jones, R., Zapata, C., Jiménez, E., De Luca, F., Holcombe, E.A. and Vardanega, P.J. (2023a). Quito Geotechnical Database (Quito/GEO-299 v.1.1). University of Bristol, Bristol, UK. https://doi.org/10.5523/bris.ys9nfsd66knb21h3twx2rfin6

Othman, M.M., Hen-Jones, R., Zapata, C., Jiménez, E., De Luca, F., Holcombe E.A. and Vardanega, P.J. (2023b). Geotechnical variability of the soils of Quito, Ecuador: a geodatabase study. *Bulletin of Engineering Geology and the Environment*, 82(11): [433]. https://doi.org/10.1007/s10064-023-03438-3.

Richards, L.A. (1931). Capillary Conduction of Liquids Through Porous Mediums. *Physics*, 1(5): 318-333. https://doi.org/10.1063/1.1745010.

Sarrazin, F., Pianosi, F. and Wagener, T. (2017). An Introduction to the SAFE Matlab Toolbox With Practical Examples and Guidelines. *Sensitivity Analysis in Earth Observation Modelling* 1st Edition, G. Petropoulos and P.K. Srivastava (eds.), Elsevier, Amsterdam, the Netherlands, pp. 363-378.

Vardanega, P.J., Gilder, C.E.L., De Risi, R., De Luca, F., Werner, M.J. and Pokhrel, R.M. (2023). Developing geodatabases in data-scarce regions: A case study of the Kathmandu Valley, Nepal. *Smart Geotechnics for Smart Societies*, A. Zhussupekov, A. Sarsembayeva and V.N. Kaliakin (eds)., CRC Press/Balkema, Abingdon, UK, pp. 1265-1270. https://doi.org/10.1201/9781003299127-182.

Wilkinson, P.L., Anderson, M.G. and Lloyd, D.M. (2002). An Integrated Hydrological Model For Rain-Induced Landslide Prediction. *Earth Surface Processes and Landforms*, 27(12): 1285–1297. https://doi.org/10.1002/esp.409.

Zapata, C., Holcombe, E.A., Vardanega, P.J. and Jiménez, E. (2023). Modelling the effect of hydraulic conductivity variability on slope stability calculations for a site in South-East Quito, Ecuador. *European Geotechnical Engineering - Unity and Diversity*, I. Lungu, I-B. Teodoru and L. Batali (eds.), Politehnium Publishing House, Işai, România, vol. 2, pp. 773-780.

Proceedings of the XVIII ECSMGE 2024
GEOTECHNICAL ENGINEERING CHALLENGES
TO MEET CURRENT AND EMERGING NEEDS OF SOCIETY
© 2024 the Authors
ISBN 978-1-032-54816-6
DOI 10.1201/9781003431749-205
Open Access: www.taylorfrancis.com, CC BY-NC-ND 4.0 license

ECSMGE 24
XVIII EUROPEAN CONFERENCE ON SOIL MECHANICS AND GEOTECHNICAL ENGINEERING

Forensic investigation of quick clay landslide released by construction work at Asak, Norway

Enquête sur un glissement de terrain d'argile sensible provoqué par des travaux de construction à Asak, Norvège

H. Heyerdahl*, Å.M.W. Amdal, R. Frauenfelder, K. Sverdrup-Thygeson, A.O.K. Lysdahl
Norwegian geotechnical Institute, Oslo, Norway

hakon.heyerdahl@ngi.no

ABSTRACT: In November 2016, a quick clay landslide was triggered at Asak in Eastern Norway. The landslide occurred in an area where a landfill was under construction. Six persons worked in the forest downslope of the area at the time of the landslide. Three of these were able to escape from the landslide runout, while three were killed. After the event, NGI investigated the cause of the landslide using available and new information. An important part of the documentation was reconstruction of the landfill work prior to the landslide release, using satellite images and other evidence. The slope geometry previous to the failure was reconstructed, and stability calculations were done based on ground investigations performed outside the landslide area. The performed analyses confirmed that the landfill, although reducing the slope inclination, had resulted in a drastic reduction in the undrained stability. Stability calculations performed with LEM and FEM methods to investigate the probable geometry of the failure plane matched well with field observations.

RÉSUMÉ: En novembre 2016, un glissement de terrain d'argile sensible a été déclenché à Asak, dans l'est de la Norvège. Le glissement de terrain s'est produit dans une zone où une décharge était en construction. Six personnes travaillaient dans la forêt en aval de la zone au moment du glissement de terrain. Trois d'entre elles ont pu s'échapper de l'éboulement, tandis que les trois autres ont été tuées. Après l'événement, NGI a enquêté sur la cause du glissement de terrain en utilisant les informations disponibles et les nouvelles informations. Une partie importante de la documentation a consisté à reconstruire les travaux de la décharge avant le déclenchement du glissement de terrain, à l'aide d'images satellites et d'autres preuves. La géométrie de la pente, avant la rupture, a été reconstituée et des calculs de stabilité ont été effectués sur la base d'études de sol réalisées en dehors de la zone du glissement de terrain. Les analyses effectuées ont confirmé que la décharge, bien que réduisant l'inclinaison de la pente, avait entraîné une réduction drastique de la stabilité non drainée. Des calculs ont été effectués avec les méthodes LEM et FEM pour étudier la géométrie probable du plan de rupture.

Keywords: Landslide; quick clay; investigation.

1 INTRODUCTION

The quick clay landslide at Asak in Eastern Norway occurred on 10 November 2016, around 3:15 pm. There was still daylight at the time of the landslide detachment, and a few eyewitnesses observed the landslide development. Around 5 pm NGI was summoned for assistance by the police and arrived at the landslide site ca. 5:30 pm. Due to wintertime, sunset was around 4 pm and there was no daylight when NGI arrived at the site. Nevertheless, after a short inspection with a rescue helicopter, it could be concluded that the event indeed was a large quick clay landslide, with a high, almost vertical back scarp, and runout covering a large area with remoulded quick clay.

The SAR operation established that six persons working with logging in the forest area downslope of the release area had been trapped by the landslide in the runout area. Three of the workers managed to escape from the landslide. Three others were missing at the time rescue personal and NGI arrived on site and were later declared dead. Two of these persons have yet not been recovered.

The landslide volume was estimated to approximately 350.000 m^3. The runout covered a large area with debris, including liquid remoulded quick clay that collected in the ravines. The debris blocked the downslope creek, floated upstream as well as downstream, crossed and blocked a road, and subsequently followed the creek downslope about 1 km. In this paper, the landslide cause will be discussed.

2 DATA COLLECTION

NGI was appointed by the court to investigate the landslide cause. The work was based on available evidence and on data collected after the landslide.

2.1 Initial evaluation of triggering causes

Many potential triggering causes were evaluated, such as natural triggering by rainfall, pore-water pressure or erosion, as well as human-induced triggering by construction of new buildings at the farm Asak, road construction downslope of the landslide, establishment of an activity park east of the landslide, logging of timber downslope of the landslide, earth works being performed to increase the agricultural area of the farm, and a large mass deposit by a large recycling company just north of the landslide release area. All natural triggering causes, as well as most of the potentially human-induced causes, could after an initial evaluation be eliminated. Erosion in nearby creeks could, e.g., be disregarded due to distance of the creek to the landslide toe, while antecedent rainfall and hydrogeological conditions not in any way were critical. Also, neither the recent construction of a road, new buildings on the farm, the activity park, or activities in a mass deposit next to the landslide release area could have had any direct physical influence of the slope stability. The only remaining activity in the area that could have influenced the slope stability in a negative way was the ongoing landfill performed to increase the area of agricultural land on the farm. Further investigations were therefore concentrated around this activity.

2.2 Satellite images

Images from the Copernicus Sentinel-2 satellite between April 1st and November 17th, 2016, were analysed to map surface changes in the later landslide area prior to the landslide, with the November image being the first image after the landslide event with sufficiently low degree of clouds. These images reveal whether the surface has been changed between the different image acquisitions; that is, whether vegetation has been removed, or soil excavated or filled. Actual topographical changes in the affected area, i.e., whether soil has been excavated or filled, can however not be concluded from these images. The resolution of the imagery is 10 m x 10 m, and only imagery acquired during clear-weather conditions and without snow cover were used. The used images were spread over several months, which means that no exact dates for observed areal changes can be attributed. It is however possible to conclude where on the terrain specific surface changes occurred in the time span between two consecutive images. Figure 1 presents the outline of the landslide release and runout areas, and the interpretation of surface changes based on four satellite images acquired prior to the landslide event.

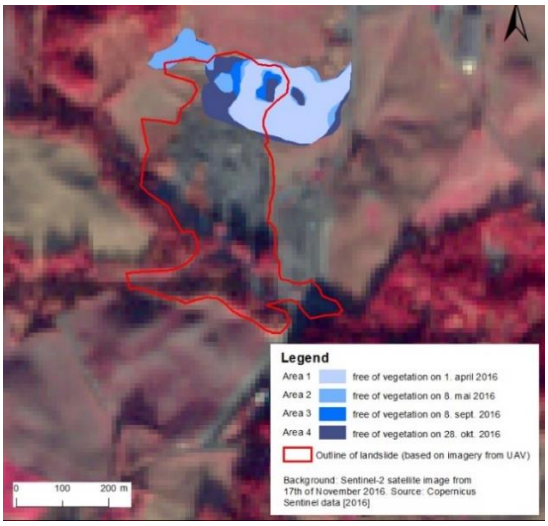

Figure 1. Surface changes interpreted from satellite images.

Zones where the surface had changed between image acquisitions are shown in shades of blue, with the oldest image (in light blue) on top, illustrating the progressive expansion of unvegetated areas into the landslide release area. The large development, indicated by a dark blue shading, shows that practically all the landslide release area was altered during the period ending with the imagery from 28 October, less than two weeks before the landslide.

2.3 Topographic changes

The landslide resulted in large topographic changes in release/runout areas that partly overlap, (Figure 2).

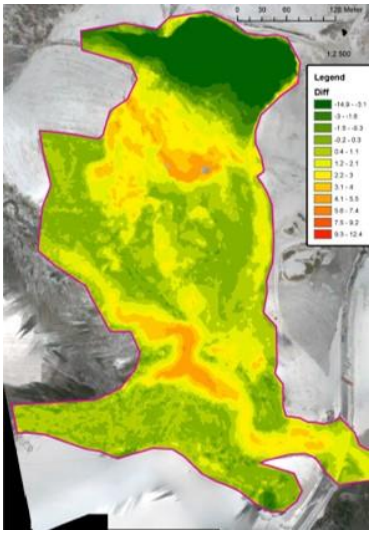

Figure 2. Topographic changes from landslide at Asak. Data before landslide does not include landfill. Map data from www.hoydedata.no.

Data before the landslide does not include landfill under construction. At the steep backscarp of the landslide, the soil surface was lowered by ca. 15 m.

2.4 Field observations

The mapped extent of the landslide (Figure 2) includes both release and runout area, which may be hard to distuingish. Based on field inspections the release area was defined to a limited area in the North. Downslope of this area, it was observed that the landslide had moved on top of the original soil surface. Large slabs of dry crust and landfill had moved down and rotated backwards from their original position, indicating retrogressive behaviour in several steps (Figure 3, Figure 5).



Figure 3. Runout area. Intact slabs have moved downslope and rotated backwards in several retrogressive steps.

The terrain model after the slide showed 5 m thick deposits adjacent to the release area. However, the landfill was not completed in the release area, and caution was taken when defining a the terrain model for subsequent stability analyses.

Landfill thickness was measured on intact slabs in the runout area to > 4 m (Figure 4).



Figure 4. Landfill thickness > 4 m found in runout area.

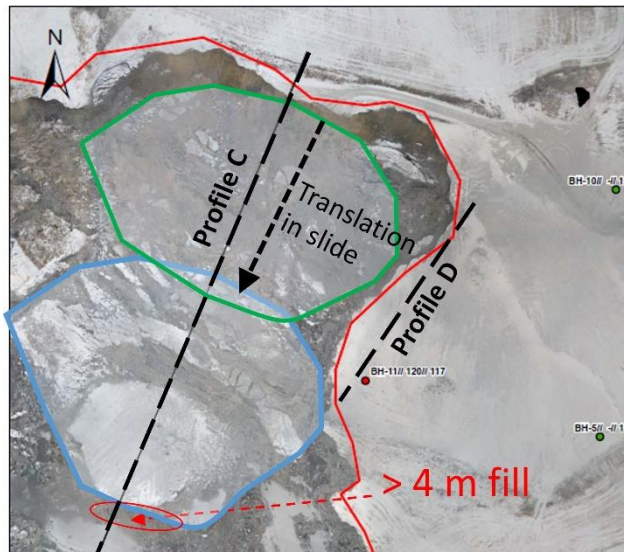

Figure 5. Translation of slabs of soil/fill. Position of soil thickness measurement in Figure 4 is indicated.

2.5 Ground investigations

In parallel with the forensic studies, NGI assisted the authorities with ground investigations and slope stability evaluations around (outside) the landslide area. Soil sampling confirmed quick clay in several bore points (Figure 6), and large amounts of remoulded quick clay were also confirmed in the runout area (Figure 3). Borings within the landslide extent line where performed before the landslide (in the South).

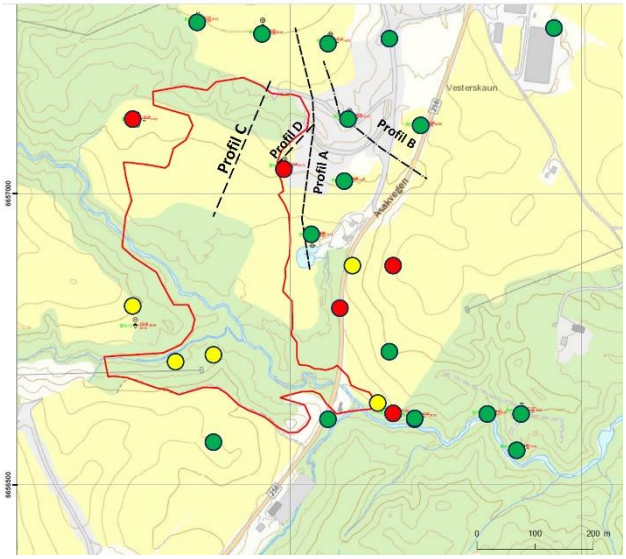

Figure 6. Ground investigations and stability profiles. Red points: QC (quick clay) confirmed by samples. Yellow: QC assumed based on soundings. Green: Not QC, based on soundings and/or samples.

3 EVALUATION OF SLOPE STABILITY

3.1 Slope stability outside the landslide area

East of the landslide scarp, the landfill was finished except from addition of topsoil. Stability profiles were constructed from Lidar data before and after the landslide. Soil parameters and layering were based on samples, total/CPTU soundings, and piezometers. Undrained shear strength of clay from CPTU was interpreted based on Karlsrud et al. (2005). No quick clay was encountered in this part of the slope but found close to the release area (Figure 5). Stability calculations for profile A just east of the landslide scarp and profile B further East showed that the undrained safety factor was reduced by the landfill, but that the safety margin with landfill was sufficient to avoid slope failure, both for drained and undrained conditions.

3.2 Slope stability in the release area

The landfill was built by dumping soil from trucks at a plateau at the top of the slope and pushing the material downslope with a bulldozer. Detailed slope geometry before the landslide release was not known, but reconstructed from topography along the landslide scarp, photos, and field observations. Soil parameters and layering were deduced from ground investigations after the landslide (Figure 6).

For profile C through the centre of the release area, slope stability analyses were performed using LEM and FEM (Figure 7). Results are summarized in Table 1. Undrained safety factor of critical sliding planes drops to values close to critical because of the landfill. Calculations were performed for different assumptions for soil parameters and topography, with similar main conclusions. Drained stability for the long-term situation is however satisfactory.

The failure geometry was validated by FEM analyses in Plaxis (Plaxis bv 2016). Resulting failure geometry (Figure 8) were similar to LEM results (Figure 7). Deep failure planes are critical for the undrained situation, and calculations match with field observation (large backward leaning slabs).

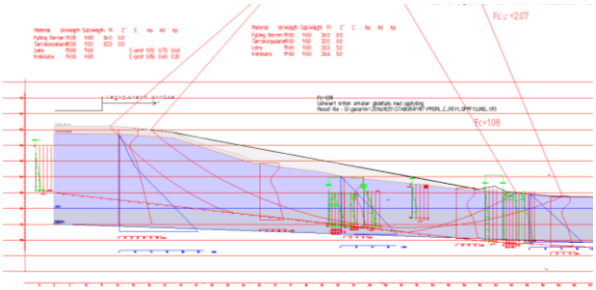

Figure 7. Slope stability C through landslide release area. Drained Fcφ and undrained Fc safety factors shown.

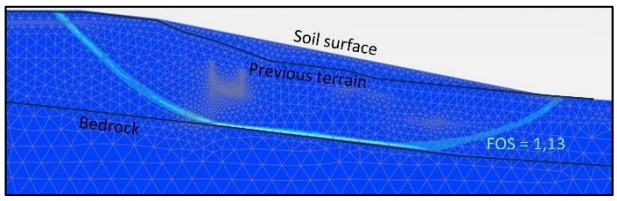

Figure 8. Results from FEM analysis (showing incremental shear strain) for profile C through landslide release area.

Table 1. Undrained safety factor with/without landfill.

Profile	Analysis	Before landfill	With landfill
C	Drained	1.57	2.02-2.07
C	Undrained	1.15-1.23	1.04-1.08 (1.13*)
D	Undrained	1.66-2.51	1.37-1.53

* Results from FEM

4 CONCLUSIONS

The investigation showed that lack of geotechnical design was the root cause of the failure, resulting in a disastrous quick-clay landslide and three fatalities as the consequence. If geotechnical design had been performed, undrained analyses would have shown that stabilising measures were necessary.

ACKNOWLEDGEMENTS

NGI wants to express our gratitude to Police Superintendent Mr. Svenn Roger Gundersen from East Police District, Economic and Environmental Crime Unit, for the opportunity to publish results from the forensic studies of the landslide.

REFERENCES

Karlsrud, K., Lunne, T. Kort, D.A. Strandvik, S. (2005). CPTU correlations for clays. *Proceedings of the 16th International Conference on Soil Mechanics and Geotechnical Engineering © 2005–2006 Millpress Science Publishers/IOS Press. doi:10.3233/978-1-61499-656-9-693*.

NGI (2017a): Sørum quick-clay landslide. Data report – ground investigations. *Report 20160826-01-R, rev. 1 (in Norwegian)*.

NGI (2017b): Sørum quick-clay landslide. Evaluation of landslide area. *Report 20160826-02-R, rev. 0 (in Norwegian).*

NGI (2018): Sørum quick-clay landslide – assistance to investigation. Cause of the landslide at Asak 10. November 2016. *Report 20160825-01-R, rev. 0 (in Norwegian)*.

Plaxis bv (2016). Plaxis 2D, version 2016.01.

Trimble (2017). GS Stability, version 15.3.0.0.

Proceedings of the XVIII ECSMGE 2024
GEOTECHNICAL ENGINEERING CHALLENGES
TO MEET CURRENT AND EMERGING NEEDS OF SOCIETY
© 2024 the Authors
ISBN 978-1-032-54816-6
DOI 10.1201/9781003431749-206
Open Access: www.taylorfrancis.com, CC BY-NC-ND 4.0 license

ECSMGE 24
XVIII EUROPEAN CONFERENCE ON SOIL MECHANICS AND GEOTECHNICAL ENGINEERING

Vulnerability assessment of buildings to landslides: application to Swiss case studies

Évaluation de la vulnérabilité des bâtiments aux glissements de terrain: application à quelques études de cas suisses

E.P. Howald
HEIG-VD, Yverdon-les-Bains, Switzerland

L. Francone, D. Martinelli*
Politecnico di Torino, Torino, Italy

**daniele.martinelli@polito.it*

ABSTRACT: Natural hazards such as floods, landslides, debris flows, earthquakes, and fires cause many disasters. In Switzerland, from 1972 to 2021, damage from floods, landslides, debris flows, and rockfalls amounted to approximately CHF 300 million annually. Climate change, settlement development, and increasing land use are some of the primary triggers of natural hazards. Permanent landslides generally have a lower probability of producing catastrophic events, but they can lead to structural damage to buildings and infrastructures. The aim of this work is the vulnerability analysis of selected building typologies exposed to the action of permanent landslides. Different building locations on the landslide body were chosen, after making simplifications, and then a vulnerability analysis was carried out on each one to define intensity and resistance parameters. The methodology makes it possible to obtain vulnerability curves depending on the type of building and its position in the landslide body. The method was applied to four case studies in southwest Switzerland: Hohberg Landslide, Converney-Taillepied Landslide, Pont Bourquin Landslide, and La Frasse Landslide. The methodology can be seen as validated since the results of the four case studies are within the range of values used to construct the vulnerability curves.

RÉSUMÉ: Les risques naturels tels que les inondations, les glissements de terrain, les laves torrentielles, les tremblements de terre et les incendies sont à l'origine de nombreuses catastrophes. En Suisse, de 1972 à 2021, les dommages causés par les inondations, les glissements de terrain, les laves torrentielles et les chutes de pierres se sont élevés à environ 300 millions de francs suisses par an. Le changement climatique, le développement de l'habitat et l'augmentation de l'utilisation des sols sont quelques-uns des principaux déclencheurs de risques naturels. Les glissements de terrain permanents ont généralement une probabilité plus faible de produire des événements catastrophiques, mais ils peuvent entraîner des dommages structurels aux bâtiments et aux infrastructures. L'objectif de ce travail est l'analyse de la vulnérabilité d'une sélection de typologies de bâtiments exposés à l'action de glissements de terrain permanents. Différents emplacements de bâtiments sur le glissement de terrain ont été choisis, en utilisant les simplifications nécessaires, puis une analyse de vulnérabilité a été réalisée pour chacun d'entre eux afin de définir les paramètres d'intensité et de résistance. La méthodologie développée permet d'obtenir des courbes de vulnérabilité en fonction du type de bâtiment considéré et de sa position dans le corps du glissement de terrain. La méthode a été appliquée à quatre études de cas dans le sud-ouest de la Suisse : Glissement de terrain du Hohberg, Glissement de terrain de Converney-Taillepied, Glissement de terrain de Pont Bourquin et Glissement de terrain de La Frasse. La méthodologie peut être considérée comme validée puisque les résultats des quatre études de cas se situent dans la fourchette des valeurs utilisées pour construire les courbes de vulnérabilité.

Keywords: Switzerland; landslides; structural harm; infrastructure; vulnerability analyses.

1 INTRODUCTION

Regarding natural hazards, landslides have one of the highest impacts worldwide in terms of loss of life and damage to public or private buildings, infrastructures, agricultural lands and economic activities. Population growth, hence more buildings in at-risk areas, climate change and intensification of land use have only increased the risk in recent years. Consequently, a rise in the frequency and intensity of natural disasters can be expected in the future: melting of glaciers and thawing of permafrost due to climate change threatens to displace vast amounts of soil, rock and stone, seriously endangering settlements and communication routes downstream (Swiss Federal Institute for Forest, Snow and Landscape Research, WLS). This paper focused on developing vulnerability curves in function

of the location and the typology of buildings on the landslide and their application to La Frasse landslide example.

2 METHODOLOGY

2.1 Building parameters

First, it is essential to consider the building locations in the landslide body. Four different building positions on the landslide body were analysed, and are:

A. The crown
B. The lateral edge
C. The middle
D. The foot

Then, buildings were classified according to material and number of floors. Buildings and human lives are the most critical elements in landslide risk assessment. The literature review shows that the main buildings damaged by landslides can be grouped into chalets, residential buildings and villas. Chalets are typical mountain buildings used for both residential and rural purposes. Some of them are entirely made of timber. Others have the first floor built in concrete and the second or third (if there is one) in timber. In this study, the foundations are always considered to be concrete. On the other hand, residential buildings and villas are mainly located at the valley bottom, at the base of the slopes, or in towns, which, in the present work, are small mountain towns composed of several hamlets also located at high altitudes. They are mainly constructed of concrete, stone and masonry. Some of them are built in both masonry and concrete because, as case the study of Lungro (Calabria, Italy) points out, reinforced concrete structures do not always guarantee less landslide damage if they are not accompanied by slope stabilisation measures (Antronico, et al., 2014). On the contrary, if located in a landslide area with specific features, masonry buildings can suffer irrelevant and widespread damage. Table 1 shows the structures analysed in this study and classified by building material and number of floors.

Table 1. Summary of structures vulnerable to landslides.

Building	Material	Number of floors
Chalet	Timber	1
	Timber and concrete	≥ 2
Residential building	Masonry	4
	Reinforced concrete	> 4
Residential villa	Masonry	2
	Concrete and masonry	3

Another critical parameter is the depth of the building foundations. As mentioned by the study of Chen & al 2020, related to the physical vulnerability of buildings affected by slow-moving landslides, the length, width and foundation depth are the three most critical factors that affect the vulnerability. It is highlighted that the higher the ratio of length to width of the building, the more serious the damage to it. Likewise, the shallower the foundation, the more severe the damage will be. Referring to the buildings considered in this work, the foundation's depth can be assumed to be approximately equal to:

- Greater than 1 m for concrete-built mountain chalets
- 1 m or greater than 1 m for residential villas
- Ranging from 2 m to 10 m, to more than 10 m for foundations of residential buildings

2.2 Intensity

"Intensity is the measure of geometrical and/or mechanical parameters, as maximum movement velocity, total displacement, differential displacement depth or volume of the moving mass, kinetic energy per unit area, relate to the destructive potential of a landslide" (Bonnard, et al., 2003). Intensity was quantitatively estimated with equations adapted to the slow-moving landslide. Two equations were used in function of the location of buildings on the landslide. For buildings in A, B or C areas, the impact of the moving mass is not considered because the effect of a slow-moving mass is visible only at the foundation level with subsidence, fractures, ground uplift and building inclinations. In these cases, the simplified intensity equation proposed in this paper refers to the general expression defined by (Li, et al., 2010):

$$I = I_{dyn} \cdot I_{dpt} \quad (1)$$

where I_{dyn} is the dynamic intensity factor and I_{dpt} is the debris-depth factor used to evaluate structures on the body of a slow-moving landslide:

$$I_{dyn} = \frac{1}{16} \cdot (log_{10} C + 0.3)^2 \quad (2)$$

with $C > 5 \cdot 10^{-1}$
where C is the average velocity of the sliding mass in mm/s

$$I_{dpt} = 0.1 \cdot D_{dpt} \quad (3)$$

where D_{dpt} is the debris depth expressed in meters, at the location of the building; considering a slow-moving landslide, the debris-depth also represents the

depth of the failure surface.

For buildings in D areas, the evaluation of landslide intensity refers to the general expression defined by (Kang & Kim, 2015); intensity is expressed as the impact pressure that the slowly moving landslide applies when it strikes structural elements.

$$P_t = \frac{1}{2} \cdot \rho_{df} \cdot g \cdot h + \rho_d \cdot v^2 \quad (4)$$

where ρ_{df} is the mean density of the material, g is the gravity acceleration, h is the height and v is the velocity of the moving mass.

2.3 Vulnerability

In the current and available literature, there are several studies that relate vulnerability and intensity to different parameters concerning landslides and buildings. These are to be considered preliminary to the quantitative study of landslide vulnerability as they must be adapted and calibrated based on actual landslide events or data collections from in-situ investigations. Research in this field is proceeding in this direction in order to refine the methodologies and make them more realistic. The present work mainly refers to four papers which analyse intensity and vulnerability (Li, et al., 2010), (Uzielli, et al., 2014)), (Chen, et al., 2020) (Miteva & Prina Howald, 2022). The vulnerability was analysed on average and is a function of intensity and resistance. Li's model gives the analytical structure, but the resistance formulation is adapted to the case of slow-moving landslides. The model used in this study is shown below, defining vulnerability in the range [0,1]:

$$V = \begin{cases} \frac{2 \cdot I^2}{R_B^2} & \frac{I}{R_B} < 0.5 \\ 1 - \frac{2 \cdot (R_B - I)^2}{R_B^2} & 0.5 \leq \frac{I}{R_B} \leq 1 \\ 1 & \frac{I}{R_B} > 1 \end{cases} \quad (5)$$

Based on Li's model, the proposed resistance formulation considers only structural elements. It is meant as follows: resistance to slow landslide movement for cases A, B and C and impact resistance for case D. Resistance (R) has been replaced by building resistance (R_B) in this work.

In the following formulas, ξfd is the parameter concerning foundation depth, ξcm is the construction material parameter, ξbi is the parameter concerning building inclination, ξnf is the parameter concerning the number of floors, and ξ_{ms} is the parameter concerning the maintenance state.

The resistance index R_B for cases A and C, where buildings are located in the crown and central part of the landslide, respectively, is calculated as follows:

$$R_B = \sqrt[2]{2 \cdot \zeta_{fd} + \zeta_{cm}} \quad (6)$$

The depth of the building foundation has a more significant influence on the building's vulnerability to slow-moving landslides than the construction material of the section above the ground level. This last section is supposed to be an integral part of the building's resistance as it interacts with the foundations by undergoing deformations in relation to its construction material. As the score does not change from one building to another, this factor is worth it. Therefore, the weights assigned to these two factors are 2 for the depth of building foundation (ξ_{fd}) and 1 for the construction material (ξ_{cm}). Table 2 shows the failure surface depth ranges considered in this study.

Table 2. Failure surface depth ranges.

Depth of the failure surface[m]
1.5 to 2
2 to 5
5 to 30
>30

For each failure surface depth range, a score is assigned to the factor concerning the depth of the building foundation. This depends on the foundation depth compared to that of the sliding plane. It will be the greater the shallower the foundation depth compared to that of the failure surface. This procedure is performed for all building materials considered, whose score is shown in Table 3. These scores were given on the basis of the tensile strength of the material.

Table 3. Scores relating to the type of building construction material (tensile strength).

Building	Material	Score
Chalet	Timber	0.6
	Timber and concrete	0.4
Residential building	Masonry	0.2
	Reinforced concrete	0.6
Residential villa	Masonry	0.2
	Concrete and masonry	0.3

The resistance index R_B for case B where buildings are located on the lateral edge of the landslide body, is calculated with:

$$R_B = \sqrt[3]{3 \cdot \zeta_{cm} + 2 \cdot \zeta_{bi} + \zeta_{nf}} \quad (7)$$

The parameters will be weighted according to their influence on the building's resistance capacity. The construction material has a greater influence on the building's vulnerability to slow-moving landslides than the building inclination and number of floors. Therefore, the weights assigned to these three factors are 3 for the construction material (ξ_{fd}), 2 for the building inclination (ξ_{bi}) and 1 for the number of floors (ξ_{nf}). Concerning the construction material parameter, scores assigned according to the type of buildings are the same used in cases A and C previously analyzed. ξ_{bi} is a parameter identifying the building inclination due to the structure's rotation at the boundary between the landslide body and the stable slope. According to the 'Code of Deformation Measurement of Building and Structure' it is possible to calculate the inclination of a building as follows:

$$i = tan\,\alpha = \frac{Y_m}{H} \qquad (8)$$

where i is the inclination of a building, α is the incline angle of the building, ym is the horizontal difference between the top and the bottom, and H is the vertical height of the tilted building calculated from the ground level.

Scores about building inclination are assigned based on threshold values provided by 'The Ministry of Housing and Urban-Rural Development of PRC, 2016'. Buildings with an inclination that exceeds the threshold values are considered dangerous and uninhabitable (Chen, et al., 2020). The present work proposes three inclination classes from very low to very high, shown in Table 4

Table 4. Scores relating to the building inclination.

Height [m]	Threshold value [i_m]	Classes	Score
H≤24	0.01	very low	1.2
24≤H≤60	0.007	medium	0.7
60≤H≤100	0.005	very high	0.1

Where : i<50%(i_m) →very low
50%(i_m)<i<100%(i_m) →medium
i>100%(i_m) →very high

Table 5 shows the scores provided by Li concerning the indicator of the number of floors/height. Four different ranges were distinguished.

Table 5. Scores relating to the number of floors/heights.

Number of floors	Score
1	0.1
2	0.3
3 to 4	0.9
More than 4	1.1

The resistance index R_B for case D where buildings are located at the toe of the slope, is calculated with:

$$R_B = \sqrt[3]{3 \cdot \zeta_{cm} + 2 \cdot \zeta_{nf} + \zeta_{ms}} \qquad (9)$$

The construction material significantly influences the building's vulnerability to slow-moving landslides more than the number of floors and the maintenance state, respectively. Therefore, the weights assigned to these three factors are 3 for the construction material (ξ_{fd}), 2 for the number of floors (ξ_{nf}) and 1 for the maintenance state (ξ_{ms}). The score assigned to the construction material, according to the building considered, can be seen in Table 6. Li's model is adopted for the attribution of this score by adapting it to the case of a moving mass hitting a structure with a certain pressure. These scores were given on the basis of the compressive strength of the material.

Table 6. Scores relating to the type of building construction material (compressive strength).

Building	Material	Score
Chalet	Timber	0.2
	Timber and concrete	0.6
Residential building	Masonry	0.8
	Reinforced concrete	1.5
Residential villa	Masonry	0.8
	Concrete and masonry	1.2

Concerning the indicator 'number of floors/height', the subdivision into four classes is the same as in case B.

The maintenance state describes the change in the building's performance; it is expressed in 5 classes from very poor to very good (Table 7), following the classification proposed by Li, et al.

Table 7. Scores relating to the maintenance state.

Maintenance state	Score
Very poor	0.1
Poor	0.4
Medium	0.8
Good	1.2
Very good	1.5

2.4 Results

Vulnerability curves were developed for each type of vulnerable structure in the four positions chosen in the landslide with the formulas presented above. Figure 1 shows an example of a vulnerability curve. The legend of each curve follows this scheme: Building Type _ Foundation Depth _ Material.

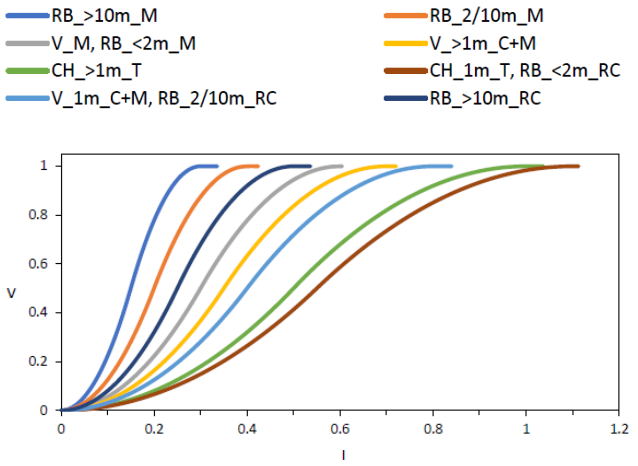

Figure 1. Vulnerability curves for case C when the depth of the sliding surface is between 5 and 30 meters.

3 APPLICATION

The methodology was applied to La Frasse's landslide, located in the Prealps (Vallée des Ormonts) of the Canton Vaud, Switzerland. La Frasse landslide is a huge slide with the toe continuously eroded by the Grande-Eau River. The most active part is the foot of the landslide crossed by the national road RC 705. The total landslide area exceeds 1 km2 with a length of approximately 2000 m oriented NW to SE and a width varying between 500 m in the landslide crown and 1000 m at the toe of the landslide body. Although the total volume of the landslide is approximately 73 million m^3, the volume of the active mass is 42 million m^3 because some portions have been stabilised. The depth of the unstable mass varies between 40 and 80 m, although the depth of the entire landslide reaches 110 m in the central part. The slope has an inclination of 11° in the upper part, reaching 20° in the lower part of the landslide. Concerning velocity, the landslide body could be divided into five main portions shown in Figure 2: Grand Glissement Supérieur, Lobe Sépey, Lobe Aigle, zone+ and zone ++ (Matti, Tacher et Commend 2012).

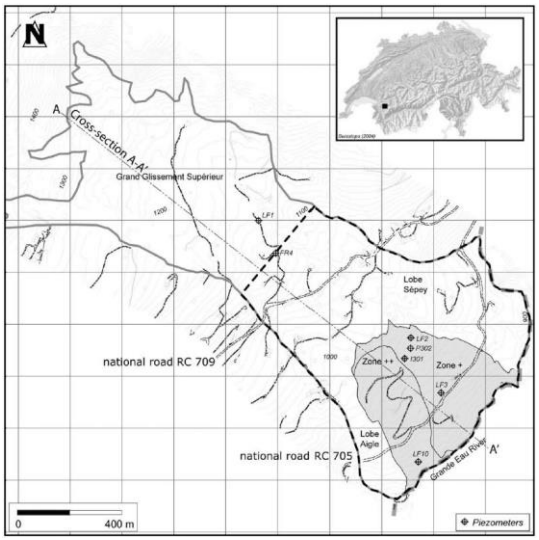

Figure 2. Location of La Frasse Landslide with subdivision in 5 main portions (Matti, Tacher et Commend 2012).

The activity of the La Frasse landslide dates back to 1863 with several reactivation phenomena, especially in the lower part, which occurred in 1910, 1914, 1966, 1981-1982 and 1993-1994. The long-term velocity in the upper and central part of the landslide is not affected by these reactivation events, constantly varying between 10 to 15 cm/year. In the lower part, however, it varies between 20 and 60 cm/year, with the maximum velocity reaching 1 m/week. Monitoring measures such as anchored piles or local pumping platforms, including drainage boreholes, decreased the movement velocity from 60 to 2.4 cm/year. The landslide's global behaviour is not yet wholly secure as near the Cergnat hamlet, and the landslide has been sliding at an average rate of about 13 cm/year for the past 200 years.

The methodology was applied to case C (central part of the landslide). Table 8 shows the data used for the application.

Table 8. Data used in the methodology application for case C, landslide central part.

Building	Height [m]	Velocity [cm/year]
Timber chalet	40	10
Timber & concrete chalet	50	13
Masonry & concrete villa	80	20
Masonry villa		60

The graph concerning case C, with indicators implemented based on the obtained data from the analysis of this case study, is shown in Figure 3.

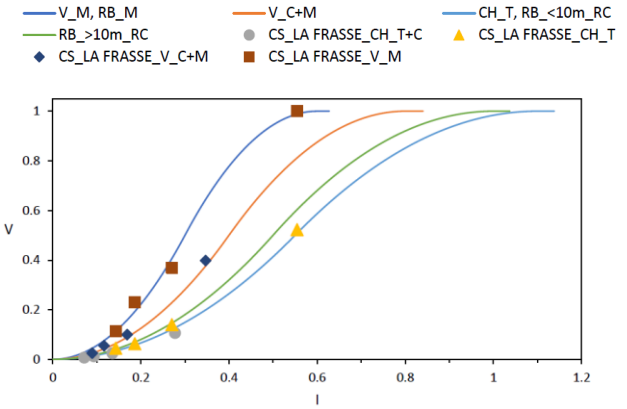

Figure 3. Vulnerability curves and indicators obtained for case C when the depth of the sliding surface is higher than 30 meters.

Since the central part of the landslide body is located in a mountainous area, the buildings considered are timber and concrete-timber chalets, masonry and concrete-masonry villas. In this case, the velocities used to calculate the indicators' vulnerability are relatively low, with a maximum of 60 cm/year. At the same time, the thickness of the landslide body is very high, reaching 80 m concerning the deepest sliding plane. The red square has a vulnerability value equal to 1 because, despite the failure surface being very deep, masonry is the least resistant material to tensile stress compared to concrete and wood. Compared to the red squares, the grey indicators have a considerably lower vulnerability calculated by referring to the higher strength parameters of timber and concrete. In addition, the high depth of the landslide body, relative to the deepest failure surface, and a velocity of more than 1 metre per year give a vulnerability of 1 for masonry buildings (material with the lowest tensile strength of those considered).

4 CONCLUSIONS

Construction in areas affected by more or less stabilised and ancient landslides, or in geologically sensitive sites where stability is a key issue, can lead to situations whose severity is difficult to predict. A minor environmental impact, such as overburdening or rainfall, can cause greater damage due to density, value of buildings and structures exposed, and extent that a small landslide can reach beyond its initial limits. The development of practical methods that consider slope instabilities and their evolution factors in the local planning of risk zones has to be considered. This work may open new perspectives to help spatial planning authorities select the most suitable areas for urbanisation. Furthermore, slope instability specialists should be required in the procedures for obtaining and granting building permits; this would be useful for both builders and local authorities to avoid building in geologically critical areas.

REFERENCES

Antronico, L. L., Borrelli, R., Coscarelli, e. G. & Gullà, (2014). Time evolution of landslide damages to buildings: the case study of Lungro (Calabria, southern Italy). *Springer-Verlag,* Volume 74, pp. 47-59. http://doi.org/10.1007/s10064-014-0591-y

Bonnard, Forlati & Scavia, (2003). Identification and Mitigation of large landslide risks in Europe. *Belkema Publisher.* http://doi.org/10.1201/9781482283877

Chen, et al., (2020). Assessment of the physical vulnerability of buildings affected by slow-moving landslides. *Natural Hzards and Earth System Sciences,* Volume 20, Issue 9, pp. 2547-2565. https://doi.org/10.5194/nhess-20-2547-2020

Kang & Kim, (2015). The physical vulnerability of different types of building structure to debris flow events. *Springer Science,* Volume 80, pp. 1475-1493. http://doi.org/10.1007/s11069-015-2032-z

Li, et al., (2010). Quantitative vulnerability estimation for scenario-based landslide hazards. *Springer-Verlag,* Volume 7, pp. 125-134. http://doi.org/ 10.1007/s10346-009-0190-3

Miteva & Prina Howald, (2022). Vulnerability assessment of different types of building structures to debris flow events. *GEAM,* Volume 1, pp. 14-21. http://doi.org/10.19199/2022.165.1121-9041.014

Uzielli, Catani, Tofani & Casagli, (2014). Risk analysis for the Ancona landslide- estimation of risk to buildings. *Springer Landslide,* Volume 12, pp. 83-100. http://doi.org/ 10.1007/s10346-014-0474-0

Proceedings of the XVIII ECSMGE 2024
GEOTECHNICAL ENGINEERING CHALLENGES
TO MEET CURRENT AND EMERGING NEEDS OF SOCIETY
© 2024 the Authors
ISBN 978-1-032-54816-6
DOI 10.1201/9781003431749-207
Open Access: www.taylorfrancis.com, CC BY-NC-ND 4.0 license

ECSMGE 24
XVIII EUROPEAN CONFERENCE ON SOIL MECHANICS AND GEOTECHNICAL ENGINEERING

Fire-induced changes in the geotechnical properties of a volcanic soil

Modifications des propriétés géotechniques d'un sol volcanique causées par le feu

L. Iervolino*, D. Peduto, V. Foresta
Department of Civil Engineering, University of Salerno, Fisciano, Italy
**liervolino@unisa.it*

ABSTRACT: Wildfires have been observed to significantly impact hillslope stability through the combustion of vegetation and changes in soil properties, mainly resulting in an increased proneness to post-fire rainfall-induced erosion and debris flows. In this regard, the existing literature on the fire-induced effects on soil properties has yielded divergent results mainly due to the inherent site-specificity that characterizes both wildfire and post-fire soil mobilization phenomena. To shed a light into the post-fire changes in both physical and hydromechanical properties of volcanic soils, an experimental laboratory study was conducted on soil samples collected from the Mt. Saro area in the Sarno municipality (Pizzo d'Alvano massif, Campania region, Italy). Here, a wildfire occurred on March 23, 2022. The experimental campaign pursued the geotechnical characterization of three classes of soil samples i) unburned, ii) wildfire-burned, and iii) laboratory thermally treated. The results unveiled pronounced changes in soil properties under both wildfire- and laboratory-burned conditions. In general, the fire-affected soil showed decreasing values of soil organic matter content, root content by weight, and soil shear strength when compared to the unburned control samples. Conversely, as the severity of the fire increased, we observed increases in soil hydraulic conductivity and cumulative infiltration. These findings can provide novel insights to enhance the comprehension of those processes presiding over post-fire slope instability and erosion in similar geo-environmental contexts.

RÉSUMÉ: Les feux de forêt ont été observés pour avoir un impact significatif sur la stabilité des versants par le biais de la combustion de la végétation et des modifications des propriétés du sol, principalement résultant en une plus grande propension à l'érosion induite par les pluies post-incendie et aux coulées de débris. Cependant, la littérature existante sur les modifications induites par le feu des propriétés du sol a produit des résultats divergents principalement en raison de la spécificité intrinsèque du site qui caractérise à la fois les phénomènes de feu de forêt et de mobilisation du sol après l'incendie. Afin d'éclairer les modifications post-incendie des propriétés physiques et hydromécaniques des sols volcaniques, une étude expérimentale en laboratoire a été menée sur des échantillons de sol prélevés dans la région du Mont Saro, dans la commune de Sarno (massif de Pizzo d'Alvano, région de Campanie, Italie). Dans cette région, un incendie s'est produit le 23 mars 2022. La campagne expérimentale visait à la caractérisation géotechnique des sols distingués en trois classes d'échantillons: i) non brûlés, ii) brûlés par le feu de forêt, et iii) soumis à un traitement thermique en laboratoire. Les résultats ont révélé des modifications marquées des propriétés du sol dans les conditions de feu de forêt et de traitement thermique en laboratoire. En général, le sol affecté par le feu a montré des valeurs décroissantes de la teneur en matière organique du sol, de la teneur en racines en poids, et de la résistance au cisaillement du sol par rapport aux échantillons témoins non brûlés. En revanche, à mesure que la gravité de l'incendie augmentait, nous avons observé des augmentations de la conductivité hydraulique du sol et de l'infiltration cumulative. Ces découvertes apportent de nouvelles perspectives qui renforcent la compréhension de la stabilité des pentes après un incendie et de l'érosion dans des contextes géoenvironnementaux similaires.

Keywords: Wildfires; laboratory testing; slope instability.

1 INTRODUCTION

Wildfires can affect hydrologic slopes response by burning vegetation and inducing changes in soil properties (Certini, 2005). Indeed, several literature studies recognize wildfire-burned watersheds as having an increased susceptibility to rainfall-induced surficial soil failures (e.g., Rengers et al., 2020). In the context of climate change scenarios, in which both frequency and intensity of wildfires are expected to increase, coupled with predicted shifts in precipitation patterns towards more frequent short-duration/high-intensity rainfall events, it is anticipated that the Mediterranean region, and particularly the southern Italy, will experience increasing post-fire surficial failures (Sousa, 2015). Thus, it is important to address

the possible threats that such events can pose to people, property, and infrastructure located downstream of the fire-affected area. In this regard, the geotechnical characterization of burned soil is key in providing quantitative information on post-fire soil behavior, as well as in trying to understand the triggering mechanisms of surficial failures on fire-affected slopes. The literature reveals that the possible fire-induced changes in soil properties are to be considered site-specific since both soil and wildfire characteristics can vary site by site according to local conditions such as geology, topography, and climate (Ulery and Graham, 1993; Certini ,2005).

Fire can impact soil organic matter (SOM) content. SOM may increase, decrease, or not change (Ulery and Graham, 1993). Key role is played by the temperature/duration conditions reached during wildfire, as well as by the types and characteristics of the affected SOM. Moderate to severe fires can permanently alter the grain size distribution (GSD) of the affected topsoil layer (Ulery and Graham, 1993). Similar to SOM, grain size may increase, decrease, or not change, mainly depending on soil type and its mineralogy. Generally, increases in GSD have been attributed with aggregation of fine particles into coarser composite stable particles (Ulery and Graham, 1993; Ketterings et al., 2000).

Although still limited, the existing literature on the effects of fire on soil mechanical properties highlights that the soil-root systems can lose their initial strength post-fire, by lowering the cohesion contribution to soil shear strength (Peduto et al., 2022a, 2022b).

For specific soil types and under certain thermal exposure conditions, soil-water repellency (SWR) may occur at a certain depth along the soil profile, which likely results in a decrease of rainwater infiltration, subsequently increasing the slope susceptibility to flooding and runoff-initiated soil mobilization phenomena (De Bano, 2000). The appearance of SWR in surficial topsoil layers can be related to i) the pore clogging by post-fire residues (e.g., ash, charcoal, burned leaves) (Woods and Balfour, 2006); ii) the temperature gradients experienced along the soil profile (De Bano, 2000). Literature studies suggest that an exposure temperature of 220-250 °C for a duration of 5-7 minutes is ideal conditions for the SWR formation. In contrast, more severe heating conditions (i.e., either longer duration or higher temperature) are reported to destroy either the intrinsic or the fire-induced SWR layer. Indeed, some studies also showed increases in soil infiltration and hydraulic conductivity because of the occurrence of severe wildfires, mainly due to the fire-induced loss of soil structure, attributable to roots and SOM burning (Peduto et al., 2022a, 2022b).

Given the site-specific nature of the possible fire effects on soil properties, this study focuses on the fire-induced changes in the physical and hydromechanical properties of the coarse-grained pyroclastic topsoil covering the Mt. Saro area (Pizzo d'Alvano massif, Campania region, Italy). Here, a wildfire occurred on 23 March 2022 (Figure 1). The slopes of the Pizzo d'Alvano massif are highly susceptible to fast-moving landslides and are also frequently affected by wildfires. Relatively thin pyroclastic soil layers, which derive from the past explosive activity of the nearby Somma-Vesuvius volcanic complex, cover the underlying bedrock (Rolandi et al., 1998).

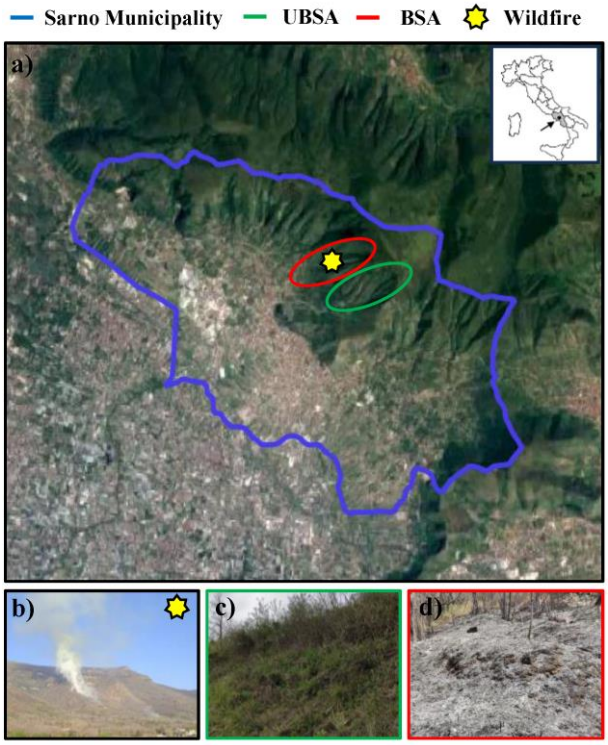

Figure 1. a) Overview of the study area with the indication of the sampling locations (i.e., UBSA: Unburned Sampling Area, BSA: Burned Sampling Area). b) Photo of the active wildfire taken on 23/3/2022. c) Photo of the UBSA. d) Photo of the BSA.

Soil sampling in undisturbed condition was conducted at 0-5 cm depth to limit the analyses to the shallow fire-affected topsoil layer. Both wildfire-burned and unburned soil samples were collected. In addition, laboratory burning treatments were carried out on unburned soil samples. For the purpose of data analysis, three different sample classes were distinguished i) "unburned", ii) "wildfire-burned", and iii) "laboratory thermally treated". Studies such as the one presented here can be useful to investigate mechanisms controlling post-fire erosion/instability slope responses in similar areas and to provide input

data for implementing prediction models and planning *in situ* monitoring systems.

2 EXPERIMENTAL PROGRAMME AND TESTING PROCEDURES

The sampling activity involved both burned (B-j) samples collected within the area affected by the 23 March 2022 fire (i.e., BSA: Burned Sampling Area) and unburned (UB-j) samples collected in the nearby control area (UBSA: Unburned Sampling Area), characterized by similar soil and vegetation conditions (Figure 1). Some of the samples from the UB-j class were also subjected to two different thermal treatments in the laboratory by using a propane burner placed 5 cm above the soil surface for 15- and 30-minutes duration, namely P15-j and P30-j sample classes, respectively.

For each sample class, we investigated the following soil characteristics i) soil grain size distribution (GSD) via particle-size by dry-sieving tests (ASTM D422-63, 2007); ii) root content by weight (RCW) through the procedure proposed by Schuurman and Goedewaagen (1965), iii) soil organic matter (SOM), via loss-on-ignition (LOI) tests (ASTM D7348-08, 2011) and specific gravity (G_s) tests (ASTM D 854, 2014), iv) soil shear strength through direct shear tests in saturated condition (ASTM D3080, 2011), v) soil saturated hydraulic conductivity following the standard method (ISO, 2004), and vi) soil infiltration via mini disk infiltrometer (MDI) tests (Robichaud et al., 2008).

Table 1. Performed laboratory tests and investigated soil properties.

Laboratory Tests	Soil Property
Particle-size by dry sieving	GSD
Schuurman and Goedewaagen (1965)	RCW
G_s and LOI	SOM
Direct Shearing	Shear strength
Constant head permeability	K_{sat}
Mini Disk Infiltrometer	K_{unsat} and infiltration

LOI and G_s tests were carried out to investigate indirectly any fire-related changes in SOM content. Basically, LOI tests involve the destruction by heat (i.e., exposure time of two hours at 550 °C) of SOM. The impact of increasing exposure temperatures on SOM and GSD was assessed. Specifically, LOI, G_s, and sieving tests were carried out on fixed soil material of the UB-j class. The tests were also performed on soil samples from the UB-j class after they were subjected to specific muffle furnace treatments. The latter involved heating soil samples for a duration of 30 minutes at progressively increasing temperatures, ranging from 100 to 600 °C. Direct shear tests were performed on saturated specimens at relatively low vertical pressures (i.e., 2, 10, 20, 30 kPa), given that fire can only affect the very surficial portion of the topsoil layer. To investigate any possible changes in soil infiltration characteristics for different post-burn conditions, we performed MDI tests by using the *Decagon Mini Disk Infiltrometer*.

3 RESULTS

Decreasing LOI and increasing G_s values were found as temperature increased (Figure 2a, 2b). Moreover, a decreasing trend in LOI was observed as G_s increased (Figure 2c). Relatively low LOI values (i.e., relatively high G_s values) are generally associated with low SOM contents (Schulte and Hopkins, 2015).

The obtained results reveal that the SOM decay increased at increasing temperatures, thus burned soil is expected to contain less organic matter than unburned soil.

The structure of the topsoil layer is generally dependent upon SOM content and GSD. By consuming SOM and altering soil GSD, fire can weaken soil structure (Gonzaléz Pérez et al., 2004). This may result in increased bulk density, reduced porosity, and decreased water storage capacity of the soil (Peduto et al., 2022a). Accordingly, along with the removal of ground cover, surface litter, and/or duff, a loss of SOM can significantly accelerate runoff resulting in increased susceptibility to erosion. Moreover, the percentage of soil material passing the 0.15 mm diameter sieve increased as the temperature of exposure increased. This finding could be linked to the thermal-induced weakening and subsequent disaggregation of the pumice particles that are typically found in pyroclastic soils. This statement agrees with past research findings on the topic (e.g., Stoof et al., 2011; Peduto et al., 2022a). Overall, the average RCW was found lower in the fire-affected samples (see table in Figure 3).

Accordingly, we can argue that both the wildfire and the laboratory thermal treatments caused the combustion of the existing soil-root systems and changed their initial characteristics. These findings can be related to the negative impacts of fire on soil shear strength arising from the obtained direct shear tests results (Figure 3). Indeed, a general reduction in the shear strength of B-j and P15/P30-j vs. UB-j samples was found. Notably, the shear strength envelopes exhibited up to almost 50% fire-induced decreases in soil cohesion values with respect to the control unburned samples. In contrast, the effective friction

angle value did not significantly change among the tested sample classes.

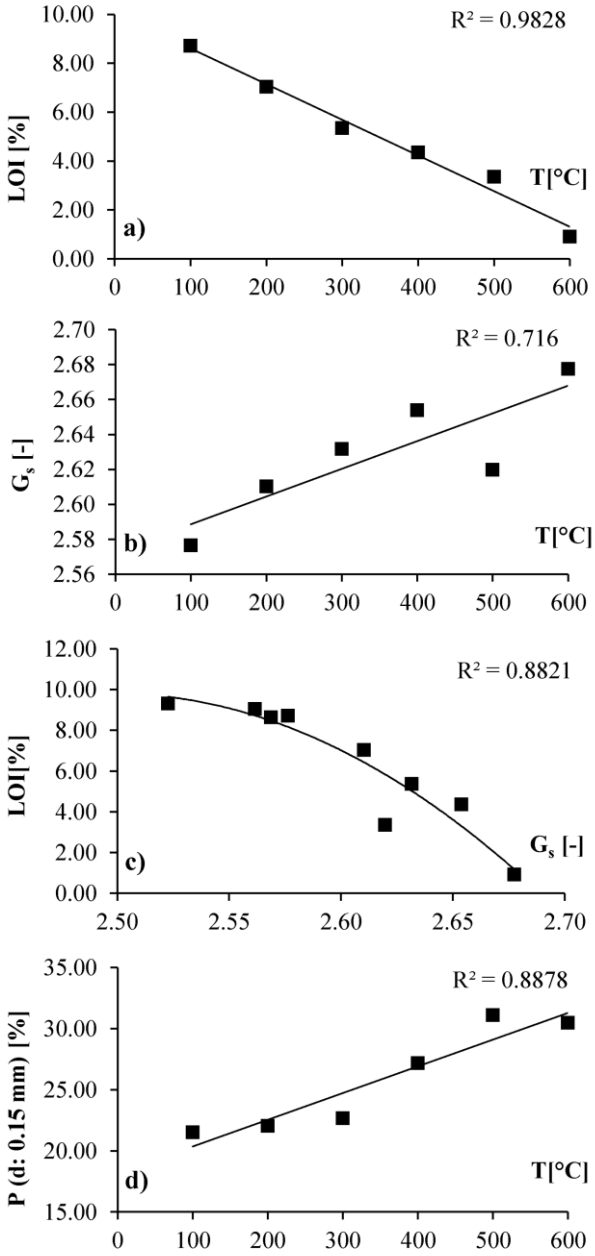

Figure 2. a) LOI, and b) G_s vs. T [°C]. c) LOI vs. G_s. d) percentage of soil passing 0.15 mm diameter sieve vs. T [°C]. The initial soil weight is fixed to 100 g for each heating treatment.

The investigated soils are loose and of pyroclastic origin, in a way that only their root systems and SOM aggregates may provide a cohesive contribution under saturated conditions (Peduto et al., 2022a, 2022b). The results reveal that fire can weaken surficial roots, reducing the associated contribution to the soil shear strength.

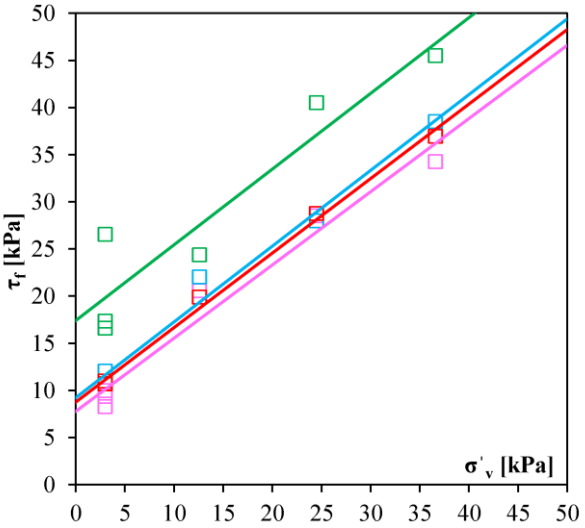

SAMPLE	SYMBOL	RCW [g]	c [kPa]	Φ' [kPa]
UB		1.25	17.4	46.0
B		0.09	8.7	45.3
P15		0.15	9.2	44.5
P30		0.12	7.8	46.0

Figure 3. Results from the direct shear tests in terms of shear strength failure envelopes for all the tested soil sample classes. "c" and "Φ'" are the soil cohesion, and the soil effective friction angle, respectively.

From the hydraulic point of view, the tested soil exhibited progressive fire-induced increases in soil cumulative infiltration, in contrast to most literature studies that report the occurrence of SWR (e.g., De Bano, 2000). However, it is worth noting that intensity and persistence of SWR usually differs with fire temperature and duration, vegetation type, soil moisture and texture, as well as time since burning (Huffman et al., 2001).

Overall, since wildfire impacts, vegetation cover, soil texture, and antecedent soil moisture all differ across a burned area, the occurrence and the spatial distribution, depth, and thickness of SWR may also differ considerably (Doerr and Moody, 2004; Woods et al., 2007). Indeed, the spatial distribution of water-repellent soils can range from isolated patches to discrete layers with discontinuities (Jackson and Roering, 2009), to continuous layers (Woods et al., 2007).

Moreover, increases in soil hydraulic conductivity, under both unsaturated and saturated conditions, were observed for fire-affected soil with respect to unburned soil (Figures 4a, 4b). We attributed the increases in both infiltration and hydraulic conductivity to the fire-related development of macropore flow pathways, mainly caused by the combustion of SOM and roots, as well as to alteration of soil GSD. This ends up creating post-fire interface priority flows.

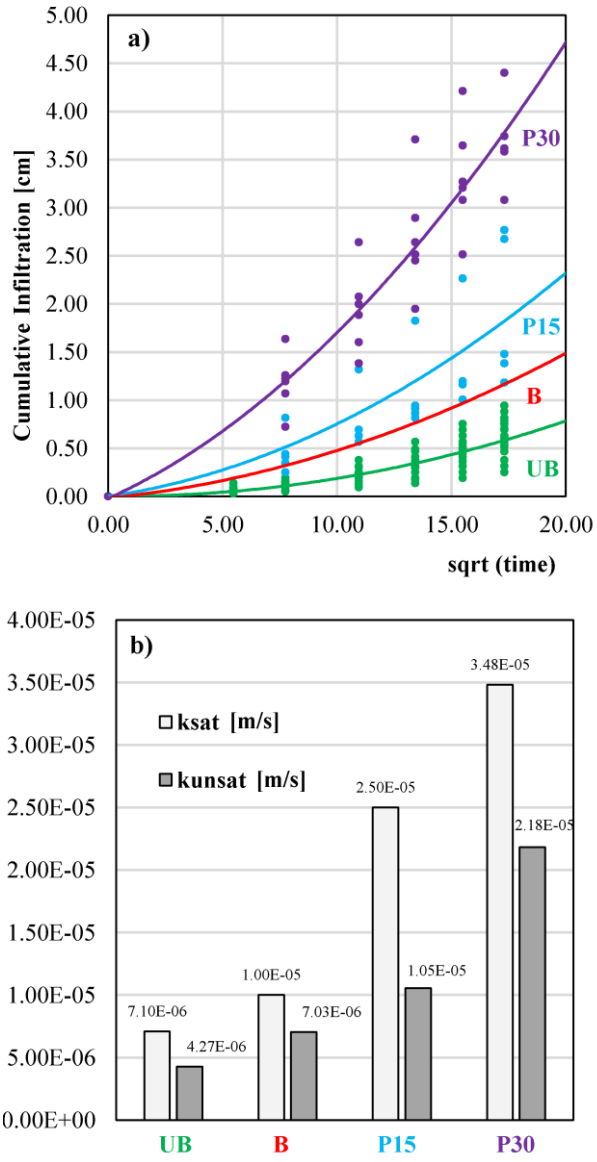

Figure 4. a) Cumulative infiltration vs. sqrt(time), derived from MDI tests. b) Average results in terms of hydraulic conductivity, in both saturated and unsaturated condition (i.e., k_{sat}, k_{unsat}), obtained through soil permeability and MDI tests, respectively.

4 CONCLUSIONS

The experimental results showed changes in the properties of soil sampled in the Mt. Saro wildfire-affected area or treated with laboratory burnings.

In general, the burned soil exhibits decrease in SOM content, RCW, and, consequently, soil shear strength. On the other hand, the increases in soil hydraulic conductivity and infiltration may be linked to the possible formation of macropore flow pathways induced by the burning of roots and SOM. In summary, we found that key role is played by SOM and RCW. By exposing the soil to increasing temperature, a reduction of SOM occurs, along with a possible weakening of the soil root systems, with consequences on both the soil mechanical and hydraulic properties. In turn, this may lead to an increase of the proneness to post-fire surficial soil failures. However, the tests carried out did not consider changes in mineralogy of the burned soil that could have affected GSD, LOI, and G_s.

Although deserving further deepening, the presented results could provide useful information for understanding the initiation mechanisms and assessing the susceptibility to post-fire soil mobilization phenomena.

REFERENCES

ASTM D3080 (2011). Direct Shear Test of Soils under Consolidated Drained Conditions, ASTM International, West Conshohocken, PA.

ASTM D422-63 (2007). Standard Test Method for Particle-Size Analysis of Soils, ASTM International, West Conshohocken, PA.

ASTM D7348-08 (2011). Standard Test Methods for Loss on Ignition (LOI) of Solid Combustion Residues, ASTM International, West Conshohocken, PA.

ASTM D854 (2014). Standard Test Methods for Specific Gravity of Soil Solids by Water Pycnometer, ASTM International, West Conshohocken, PA.

Certini G. (2005). Effects of fire on properties of forest soils: A review. Oecologia, 143:1-10. https://doi.org/10.1007/s00442-004-1788-8.

De Bano, L.F. (2000). The role of fire and soil heating on water repellency in wildland environments: a review. J Hydrol 231-232:195-206.

González-Pérez, J.A., González-Vila, F.J., Almendros, G. and Knicker, H. (2004). The effect of fire on soil organic matter - A review. Environ Int 30: 855-870. https://doi.org/10.1016/j.envint.2004.02.003.

ISO (2004). Geotechnical investigation and testing– Laboratory testing of soil - Part 11: Determination of permeability by constant and falling head, International Organization for Standardization, Geneva, Switzerland (accessed on 15/11/2023).

Ketterings, Q.M., and Bigham, J.M. (2000). Soil Color as an Indicator of Slash-and-Burn Fire Severity and Soil Fertility in Sumatra, Indonesia. Soil Sci. Soc. Am. J. 64: 1826-1833.

Peduto, D., Iervolino, L. and Foresta, V. (2022a). Experimental analysis of the fire-induced effects on the physical, mechanical, and hydraulic properties of sloping pyroclastic soils. Geosciences 12:198. https://doi.org/10.3390/geosciences12050198.

Peduto, D., Iervolino, L., Esposito, G., Matano, F. and Masi, R. (2022b). Clues of wildfire-induced geotechnical changes in volcanic soils affected by post-fire slope instabilities. Bull Eng Geol Environ 81. https://doi.org/10.1007/s10064-022-02947-x.

Rengers, F.K., McGuire, L.A., Oakley, N.S., Kean, J.W., Staley, D.M. and Tang, H. (2020). Landslides after

wildfire: initiation, magnitude, and mobility. Landslides, 17: 2631-2641. https://doi.org/10.1007/s10346-020-01506-3.

Robichaud, P.R., Lewis, S.A. and Ashmun, L.E. (2008). New procedure for sampling infiltration to assess post-fire soil water repellency. USDA For Serv - Res Note RMRS-RN 1–14.

Rolandi, G., Petrosino, P. and Mc Geehin, J. (1998). The interplinian activity at Somma-Vesuvius in the last 3500 years. J Volcanol Geoth Res 82: 19-52.

Schulte E.E. and Hopkins B.G. (2015). Estimation of soil organic matter by weight loss-on-ignition. Soil Org Matter Anal Interpret 49: 21-31. https://doi.org/10.2136/sssaspecpub46.c3.

Schuurman J.J. and Goedewaagen MA (1965). Methods for the examination of root systems and roots. Centre for agricultural publications and documentation, Wageningen.

Sousa, P.M., Trigo, R.M., Pereira, M.G., Bedia, J. And Gutiérrez, J.M. (2015). Different approaches to model future burnt area in the Iberian Peninsula. Agric. For. Meteorol. 202: 11-25. https://doi.org/10.1016/j.agrformet.2014.11.018.

Stoof, C.R., Moore, D., Ritsema, C.J. and Dekker, L.W. (2011). Natural and Fire-Induced Soil Water Repellency in a Portuguese Shrubland. Soil Sci Soc Am J 75: 2283-2295. https://doi.org/10.2136/sssaj2011.0046.

Ulery, A.L., and Graham, R.C. (1993). Forest Fire Effects on Soil Color and Texture. Soil Sci Soc Am J 57: 135-140. https://doi.org/10.2136/sssaj1993.03615995005700010026x.

Woods, S.W. and Balfour, V. (2006). Effect of vegetative ash on infiltration rates after forest wildfire in the Northern Rocky Mountain region, U.S.A. Biohydrology Conference, Prague, Czech Republic, 20-22 September 2006.

Proceedings of the XVIII ECSMGE 2024
GEOTECHNICAL ENGINEERING CHALLENGES
TO MEET CURRENT AND EMERGING NEEDS OF SOCIETY
© 2024 the Authors
ISBN 978-1-032-54816-6
DOI 10.1201/9781003431749-208
Open Access: www.taylorfrancis.com, CC BY-NC-ND 4.0 license

ECSMGE 24
XVIII EUROPEAN CONFERENCE ON SOIL MECHANICS AND GEOTECHNICAL ENGINEERING

Remote sensing techniques for soil-structure interaction health monitoring

Surveillance de la santé de l'interaction sol-structure grâce à des techniques de télédétection

D. Infante
Università Telematica Pegaso, Napoli, Italy

S. Moretti
SOCOTEC S.r.l., Roma, Italy

M. Zimbardo, A. Scotto di Santolo*
Università Telematica Pegaso, Napoli, Italy

**anna.scottodisantolo@unipegaso.it*

ABSTRACT: The paper aims to highlight the role of satellite data integrated with conventional monitoring results to support the soil-structure interaction analysis in Structural Health Monitoring (SHM) activities. DInSAR technology is a powerful tool to measure and monitor surface displacements both of ground and structures, without installing sensors or even accessing the structure, with millimetre precision. Using DInSAR data to integrate conventional SHM techniques allows to obtain, from a unique source of data, significant information on many structures, infrastructures, and landslides, detecting potential anomalies and triggering in-situ inspections, with clear benefits in terms of both time and resource management. In this work, results of some remote and contact monitoring techniques, applied in the small medieval village in Southern Italy, considering its complex morphology including underground cavities, have been discussed.

RÉSUMÉ: L'article vise à mettre en évidence le rôle des données satellitaires intégrées aux résultats de surveillance conventionnelle pour soutenir l'analyse des interactions sol-structure dans les activités de surveillance de la santé des structures (SHM). La technologie DINSAR est un outil puissant pour mesurer et surveiller les déplacements de surface du sol et des structures, sans installer de capteurs ni même accéder à la structure, avec une précision millimétrique. L'utilisation des données DInSAR pour intégrer les techniques SHM conventionnelles permet d'obtenir, à partir d'une source unique de données, des informations significatives sur un grand nombre de structures, d'infrastructures et de glissements de terrain, en détectant d'éventuelles anomalies et en déclenchant des inspections in situ, avec des avantages évidents en termes de temps et la gestion des ressources. Dans ce travail, les résultats de certaines techniques de surveillance à distance et par contact appliquées dans le petit village médiéval du sud de l'Italie, en tenant compte de sa morphologie complexe incluant des cavités souterraines, ont été discutés.

Keywords: DInSar; monitoring; resilience of cultural heritage; structural health monitoring.

1 INTRODUCTION

Analyses aimed at forecasting and preventing consequences induced by natural or manmade hazards on existing structures and infrastructures play a fundamental role in risk management activities. Among these, the phenomena of soil instability such as landslides and subsidence phenomena, widespread in geological contexts around the world, can generate considerable damage to existing heritage. Furthermore, historical urban centers are often characterized by cavity systems beneath the foundations or underground stories of masonry buildings, which can also modify the local seismic response (Scotto di Santolo et al., 2015; Piro et al., 2019). The presence in urban area of sectors affected by particular geological conditions has made it necessary to develop innovative monitoring techniques, in addition to conventional methods, in order to develop systems which can be supplied at different scales of analysis, information on the spatial and temporal evolution of current phenomena and their interaction with existing structures and infrastructures.

The integration of data obtained by different sources can be very helpful in understanding the mechanism, the geometry and the kinematic of complex instabilities affecting urban areas. In the past, many researchers demonstrated that the combination of different techniques allows a better understanding

of the instabilities process under investigation (e.g. Pastor et al., 2019). Amongst the complementary techniques that can be employed, satellite monitoring, and more specifically Differential Interferometry Synthetic Aperture Radar (DInSAR), have been widely investigated in recent yearsas a valid response to support structural health assessments, depending by a wide area coverage, millimetric accuracy, non invasiveness and cost-effectiveness of data (e.g. Infante et al., 2019). In addition, PhotoMonitoring techniques, based on Image Processing principles, allows to measure small displacements and deformations of the soil and structure aggregate at the same time, by comparing multi-temporal images of the continuously observed object using high-resolution cameras (e.g. Caporossi et al., 2018).

In this work, the feasibility and effectiveness of the combined use of satellite remote sensing technology and conventional in situ monitoring techniques in the structural health monitoring process for historical structures in Sant'Agata de' Goti village (Campania region, Italy) were evaluated.

2 THE CASE STUDY

The case study is a historic centre of Sant'Agata de' Goti, located in Campania Region, south Italy, resting on a rocky relief between two creeks, where many anthropic cavities, due to tuff quarrying activities, are present. The rock formation constituting the ridge is the Campanian Ignimbrite in its yellow and grey lithofacies, lying on a thin loose layer of pyroclastic soil and a Miocene flysch, Figure 1.

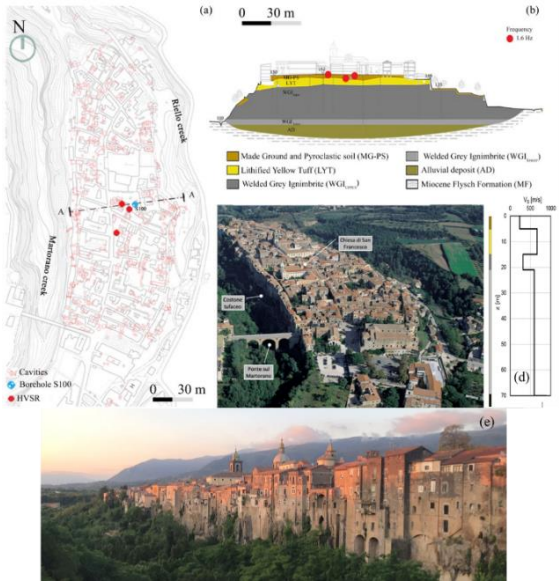

Figure 1. Sant'Agata de' Goti: (a) plan with location of the cavities and in situ tests, (b) A-A geological section, (c) aerial view with attention points; (d) shear wave velocity profile from DH; (e) view from the bridge (modified from Piro et al., 2019).

The western portion of the historic center of Sant'Agata de' Goti was built with rock quarried on site and is perched on tufaceous cliffs, with an often indistinguishable border, as can be observed from the bridge over the Martorano, Figure 2d. The upper portion of the cliffs houses cavities of anthropic origin which due to their position also amplify seismic effects (e.g. Scotto di Santolo et al., 2015; Piro et al., 2019).

The stress relief of the natural slope with the potential genesis of new fissure patterns, the river dynamics associated with the Martorano stream, the progressive alteration of the cortical portion of the promontory subjected to atmospheric agents, and the widespread presence of cavities can be considered overall factors of natural and anthropic risk that may have effects on the overlying inhabited center.

3 SOIL-STRUCTURAL INTERACTION HEALTH MONITORING RESULTS

Aimed to investigate the resilience of historic and cultural heritage, the Soil-Structural Interaction Health Monitoring require, as first step, a preliminary characterization of subsoil geological and geotechnical settings (§ 2). Subsequently, the integrated analysis of conventional and innovative monitoring data, performed also with remote sensing techniques, allows to achieve a validation of the results and to investigate preliminary cause-effect relationship between soil-structure interaction and related building structural behavior.

In the present work the attention is focused to:

- the tufaceous cliff overlooking the Martorano stream, and the corresponding structure including cavities;
- the Church of San Francesco that hosts an archaeological exhibition;
- the bridge over the Martorano stream, the main access to the historic center.

3.1 DInSAR and PhotoMonitoring analysis

Operating X-band Synthetic Aperture Radar sensors of the new generation COSMO-SkyMed satellite have provided long historical archives of motion rates and displacement time-series of whole Sant'Agata de' Goti urban centre, with a spatial resolution of 3x3 m and reduced revisiting time (16 days). In detail, 108 COSMO-SkyMed ascending images in the time-span October 2012–July 2019 and 128 descending images in the time-span February 2012–August 2019 have been processed by means of "Permanent Scatterers Interferometry" (Ferretti et al., 2001) to detect surface deformations of the considered area.

As a results, 'Line Of Sight-LoS' displacement rate maps and historical time series of scatterers identified within the whole urban center have been obtained (Figure 2a). Interferometric products show the occurrence of very slow-moving phenomena, with velocities of about some mm per year. Moreover, looking at the DInSAR scatterers identified above the bridge on Martorano river, a displacement means velocities of few mm/yr have been recorded in the considered period, thus confirming the absence of significant kinematics. As regards the San Francesco Church and palace, in order to analyze structural behavior, DInSAR data at ground level and on top of buildings were preliminarily differentiated, Figure 2b. The first are representative of ground kinematics condition while the second refer to structure deformation (e.g. Infante et al., 2019). Targets discriminated at ground and on top of structure show "LoS" displacement rates lower than 2 mm/year both on the Church and on the surrounding area, thus confirming that area is stable and structures do not show structural problems and deformations.

To evaluate the structure conditions of existing aggregate buildings and cliffs, an innovative remote monitoring system based on the Photomonitoring methodology has been set up (Figure 3). Digital Image Correlation (DIC) is an optical-numerical remote sensing technique that offers excellent opportunities to measure 'full-field' displacements and/or deformations on the surface of the monitored object, both in 2D and 3D.

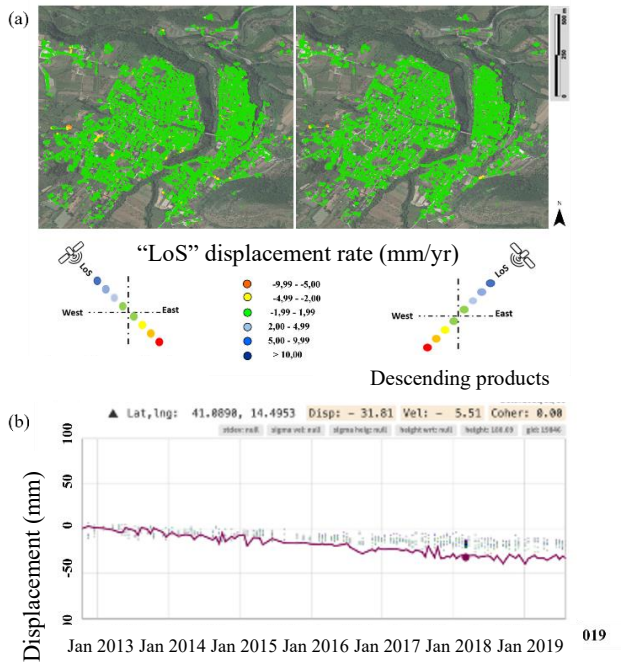

Figure 2. D-InSAR - LoS displacement velocity maps of Sant'Agata dei Goti urban area derived by COSMO-SkyMed SAR images in ascending and descending orbit (a); Displacement time series of significative scatterer identified (b).

This is made possible by comparing, tracing, and consequently, algorithmically correlating frames captured with a high-resolution optical camera at different time intervals. Through techniques based on Image Processing principles, it is possible to measure small displacements and deformations of the tufaceous promontory and building aggregate by comparing multi-temporal images of the continuously observed object using high-resolution cameras.

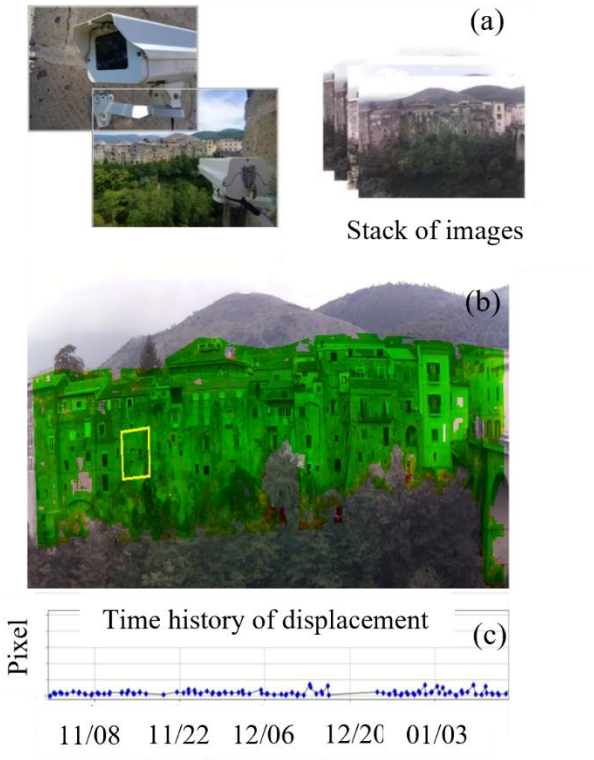

Figure 3. Monitoring of cliff-aggregate buildings movements through Photomonitoring technique: a) set-up and stack of captured images; b) interpretation of sectors; c) displacement time series for yellow area.

3.2 Conventional *in-situ* monitoring

The control and validation of the remote measurements will take place thanks to the installation of instruments on the ground. The wireless monitoring system of the bridge over the Martorano allows the survey, continuously and with high frequency, of the rotations of the bridge piers and cracks as well as the level of the Martorano stream. The system was completed with a total weather station, which allows the main environmental parameters to be recorded to correlate with the deformation behaviour of the structure during the monitoring phase of the work (Scotto di Santolo et al., 2022). In detail, the in-contact tools are:

1. 4 wireless biaxial electric clinometers with built-in temperature sensor, with high acquisition

frequency, located in the piers and abutments of the bridge (Figure 4).

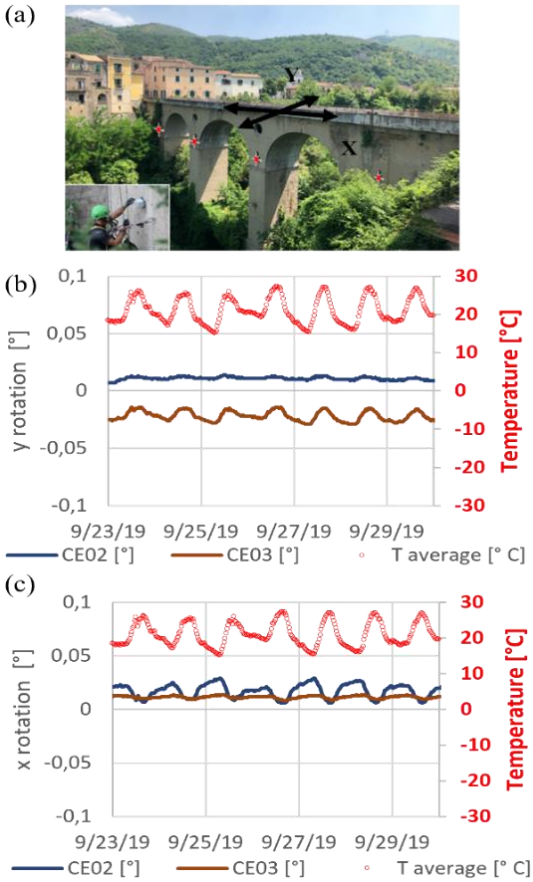

Figure 4 Bridge monitoring set-up (a); time series of air temperature and clinometers rotation in y (b) and x direction (c).

4 DISCUSSION AND CONCLUSION

This work shows the potentiality of remote sensing technique as a complementary tool for the analysis of Soil-Structural Interaction Health Monitoring of a emblematic historical village and its cultural heritage, proving the usefulness of the combination of different techniques. DInSar and Photomonitoring techniques can provide important information about structure conditions and help increase safety and optimize maintenance activities also in sterms of sustainability.

The interpretation process, preliminary includes geological, geotechnical and geomorphological data in determining the type of soil/rock directly interacting with building heritage.

Subsequently, the combined use of multi-source information has enabled performing a comprehensive investigation of structural performance as indicator of a preliminary cause-effect relationship with ground conditions.

The analysis of DInSAR and Photomonitoring displacement time series (Trend Change Detection Analysis) highlighted that no significant deformational trend was recorded, and no differential displacements have occurred, generating angular distortions (drift) consequently on the structures.

These results are confirmed by the stability of static and dynamic terrestrial data acquired in the first half of observation (July 2019 - January 2020): the clinometers integral with the structural elements of the bridge show negligible rotations in x and y direction, with dispersion of values between ± 0,05°, Fig. 4.

As it has been stated above, each of the techniques employed has been useful to understand the health of cultural heritage, considering the interaction with soil starting from the knowledge of geological and geotechnical site conditions.

REFERENCES

Ferretti, A., Prati, C., and Rocca, F. (2001). Permanent scatterers in SAR interferometry". In: *IEEE Transactions on Geoscience and Remote Sensing*, 39(1): 8-20. https://doi/10.1109/36.898661.

Infante, D., Tessitore, S., Confuorto, P., Sepe, C., Calcaterra, D., Di Martire D., Ramondini, M. (2019). Monitoring of strategic buildings in civil protection activities via remote sensing data. In: *IEEE Aerospace &Elect. Sys. Mag.*, 34(10): 6-16. https://doi.org/10.1109/MAES.2019.2915038.

Caporossi P., Bozzano F., Mazzanti P. (2018) Digital Image Correlation (DIC) Analysis of the 3 December 2013 Montescaglioso Landslide (Basilicata, Southern Italy): Results from a Multi-Dataset Investigation. *Int. J. Geo-Information,* 7(9): 372; https://doi.org/10.3390/ijgi7090372

Piro A., de Silva F., G. Martinelli, M. Meccariello Parisi F., Silvestri F., Scotto di Santolo A., 2019. Effects of the underground urban development on the seismic response of a historical centre in Italy. *Proc. 7th Int. Conf. on Earthquake Geotechnical Engineering ICEGE Roma, 17-20 June 2019.*

Scotto di Santolo A., de Silva F., Silvestri F., (2015). Site effects due to the presence of cavity near the cliffs. *Proc. of the 6th Int. Conf. on Earthquake Geotechnical Engineering, Christchurch, New Zealand, 1-4, November 2015.*

Scotto di Santolo A., Infante D., De Donato R., Moretti S., Petraglia G., Mammone A., Petraglia M., Spagnuolo A., Vetromile C., Bianchi A. (2022). Tecnologie e metodologie innovative e smart per un monitoraggio di borghi storici minacciati da rischi ambientali ed antropici. *Atti XVII Convegno Nazionale di Geotecnica, Reggio Calabria, 13-15 luglio 2022 (in italian).*

Proceedings of the XVIII ECSMGE 2024
GEOTECHNICAL ENGINEERING CHALLENGES
TO MEET CURRENT AND EMERGING NEEDS OF SOCIETY
© 2024 the Authors
ISBN 978-1-032-54816-6
DOI 10.1201/9781003431749-209
Open Access: www.taylorfrancis.com, CC BY-NC-ND 4.0 license

ECSMGE 24
XVIII EUROPEAN CONFERENCE ON SOIL MECHANICS AND GEOTECHNICAL ENGINEERING

Slope failures risk acceptance in the construction of roads on the clayey mine spoil dump, Czech Republic

Prise en compte des risques de rupture des pentes dans la construction de routes sur une décharge minière argileuse en République Tchèque

J. Jurko*
Colas Central Europe, Budapest, Hungary

N. Droniuc
Colas SA, Paris, France

**jozef.jurko@colas.com*

ABSTRACT: In this paper, we present a study of a large slope failure, which endangered the construction of a bridge, occurred in 24 m deep cutting with a main scarp upper edge extending over 70 m in length. The stability analysis is discussed, with a critical analysis of safety factors, according to the Eurocode. The important place takes the analysis of slope stability during construction, but also the analysis of long-term conditions, back-analysis, in anthropogenic site, conditions that are not completely covered by geotechnical codes. Lessons learned showed, that a design basis in such an anthropogenic environment should ensure an advanced geotechnical characterizations and parametric engineering assessments. Even in such a case, it will be necessary to acknowledge the risk of slope instability by all stakeholders, mainly due to uncertainties associated with a construction of clayey mine spoil heaps and a subsequent mechanical properties heterogeneity of stockpiled soils. The role of geotechnics is inevitable in such "natural" conditions of mine spoil dumps to provide necessary support throughout entire project life cycle.

RÉSUMÉ: On présente l'analyse des conditions de rupture d'une pente, lors de la construction d'un pont. La rupture s'est produite avec une extension de 70m en amont de la pente, avec un dénivelé de 24m. Les études suivent les règles définies par les Eurocodes, et une analyse critique des facteurs de sécurité est faite. L'analyse est faite en prenant en compte le phasage de construction. Ensuite, des études à long terme, en retro-analyse, avec les particularités d'un site anthropique, montrent que ces conditions ne sont pas prises en compte par les règles de calcul : le site est constitué de dépôts des matériaux argileux stériles provenant des mines de charbon. Les conclusions montrent que, dans des sites anthropiques, une importance considérable devra être portée à la caractérisation avancée des sols en place et qu'il est nécessaire que toutes les parties prenantes du projet prennent connaissance des risques encourus. La complexité du site, provenant de l'origine géologique des argiles à fortes hétérogénéité et remaniées lors de dépôts disparates, implique un comportement difficilement prévisible sur le long terme : le rôle et l'implication du géotechnicien, reste fondamentales tout au long de la vie de l'ouvrage .

Keywords: Slope stability; safety factor; anthropogenic site; clayey mine spoil; long term behaviour.

1 INTRODUCTION

As society develops, human activity has an increasing influence on the change of an environment. Mining activities and a subsequent processing of raw materials represent one of the world's biggest waste management challenges with a definite impact on the surrounding environment.

The north-west part of Czech Republic is characterized by the extensive open cast mining of brown coal for several decades. With the progress of open cast mining, overburden spoil material (clays primarily), covering brown coal reserves, is stockpiled in non-engineered manner into large spoil heaps/dumps, several tens of meters in height. These locations represent potential sites for infrastructure projects thanks to an interesting economical aspect. Even if the economic aspects are favourable, technical, and mainly geotechnical issues regarding possible developments represent significant challenge. One such particularity is the acceptance of the risk arising from the "natural" geotechnical conditions of the mine spoil heaps.

2 SPOIL HEAPS SPECIFICS

Vanicek and Vanicek (2008) and Najser (2010) summarized the uniqueness associated with the construction of clayey spoil dumps. During mining,

overburden clays in the form of irregular lumps typically 500 mm in size are stockpiled in large dumps. The total thickness of the layers is generally 20-50 m. The spoil material has a double porosity: the porosity of the clay lumps (primary intragranular) and the pores between the clay lumps (secondary intergranular). The total porosity can reach up to 70%. The clays are stockpiled top-down by free fall from a height of 15-30 m. Although the free fall allows some compaction, the resulting secondary porosity is considerably high, up to 35%. Generally, the loose material has the character of crushed stone material in an embankment with steep slopes of 1:1 (V:H) - 45-degree angle. The properties of the stockpiled material change with time due to increasing height and interaction with water. When the lumpy clays adversely change their mechanical properties due to interaction with water, the original hard clays/claystones change to clays of soft to very soft consistency. Such weakened soils present significant challenges to geotechnical engineering primarily due to significant settlement up to collapse and uneven settlements. Discovering of such altered layers in both vertical and horizontal directions is practically impossible, which greatly inhibits available options for subsoil improvement. Moreover, the progressive transformation from loose to fine-grained matrix with time makes the mechanical modelling of lumpy clays considerably uncertain.

3 CASE STUDY

This construction project including roads construction on the body of an external mine spoil dump was greatly influenced by certain technical challenges that had to be considered in such an anthropogenic environment.

The construction was realized on considerable thicknesses of spoil material, consisting of clayey soils and claystones with the thickness up to 70 m. These are Tertiary lacustrine clays and claystones (Cypress Formation) - kaolin-illite clays with variable minor content of montmorillonite.

During the construction of a bridge structure, a slope failure (landslide) occurred in the cutting with a total depth of approximately 24 m, and length of the main scarp upper edge approximately 70 m (Figure 1). The sliding surface was clearly characterized by a smoothed plane-slip surface with soil displacement of up to 5 m downward at a slope of approximately 45° (Figure 2). The landslide body covered an area of approximately 5000 m2 with a potential soil volume in the landslide of 50000 m3. Observations of the main sliding surface showed an interface of brown and distinctly coloured grey clays, which differentiated largely in consistency. The landslide body negatively affected the construction of the bridge structure and raised many questions about the next steps of the construction due to the geometric constraints of the planned construction. Removal of the landslide body at the bottom was not an option, however works, under increased safety precautions, had to be planned.

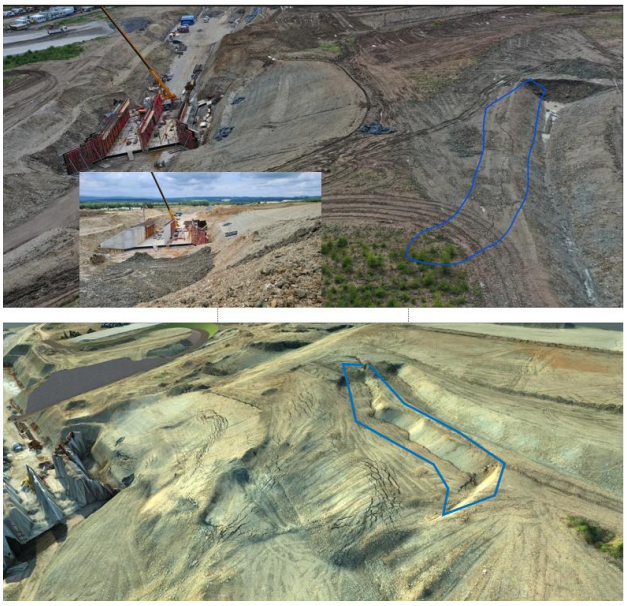

Figure 1. Landslide within 24m deep cutting (upper picture shows a situation before the failure).



Figure 2. Main scarp upper edge of the landslide.

4 BACK-CALCULATION

After the initial measures were taken to minimize the safety risk and based on the results of the daily monitoring, geotechnical assessments of the actual situation as well as back-calculated stability assessments were carried out. It should be paradoxically noted that the slope failure occurred after the construction of the stabilization berm at the toe, following the occurrence of a crack at the crown of the slope cut. Simultaneously, excavation works of soil in the upper part of the cut body were conducted to relief the associated stress just before the slope failure.

The numerical stability analyses results showed that the required theoretical safety factor was achieved in the phase of conducting stabilization measures, after the crack had occurred (Figure 3). Still, the question had arisen as to why the landslide occurred?

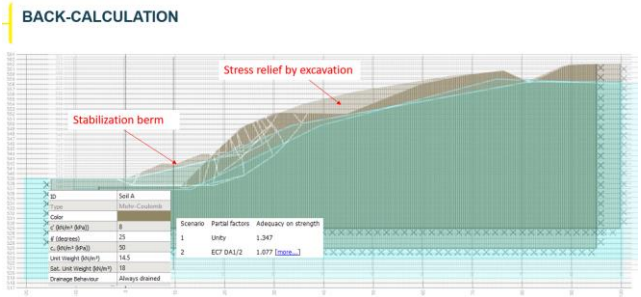

Figure 3. Back-analysis of the failure occurred after the construction of stabilization berm and excavation of upper part material.

The geotechnical back-analysis included parametric studies with different elements of instability. It turned out that a geometric instability element had to be present in the system (model), which was a prerequisite for the occurrence of the slope failure (Figure 4). By including such an instability element in the form of a completely thin layer of soft clay in the body of the landslide, the calculated degree of safety was insufficient, which also confirmed the theoretical possibility of a slope failure. Such calculated representation corresponded well with the site observations.

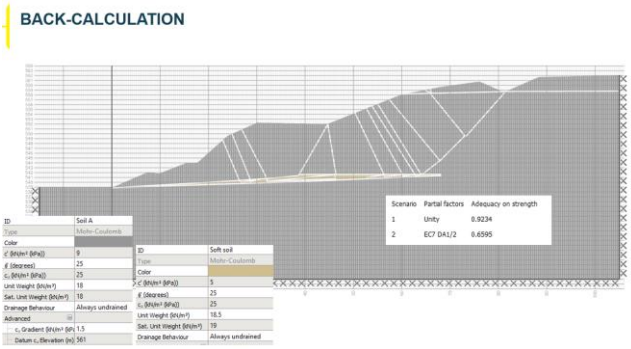

Figure 4. Back-analysis of the failure including an element of instability – 0.5m thick seam of soft soil in the cutting.

5 STATIC PENETRATION TESTS

As part of the investigation of the occurred slope failure, an additional geotechnical investigation by means of static penetration tests was carried out. The results provided detailed information regarding the subsoil profile, showing multiple low-peak locations, at different depths, with very low to low shear strength in the body of the landslide as well as in the wider area outside of the landslide body (Figure 5). These locations were local, very thin clay layers of very soft to soft consistency often only a few cm to a few dm thick. Thus, there was a practical confirmation of the hypothesis arising from the back-calculation, and that is a need for the presence of an element of instability in the system in order to model the theoretical failure. With the help of the interpretation of the static penetration results, the potential basal sliding surface was determined, which was necessary for the planning of remediation measures. The static penetration test results also indicated a random occurrence of very soft to soft clay deposits in locations outside the landslide itself. This confirmed the presence of the geotechnical risk arising from the nature of the spoil heap construction, the unpredictable interaction with water and the consequent change in the mechanical properties of the stockpiled clays.

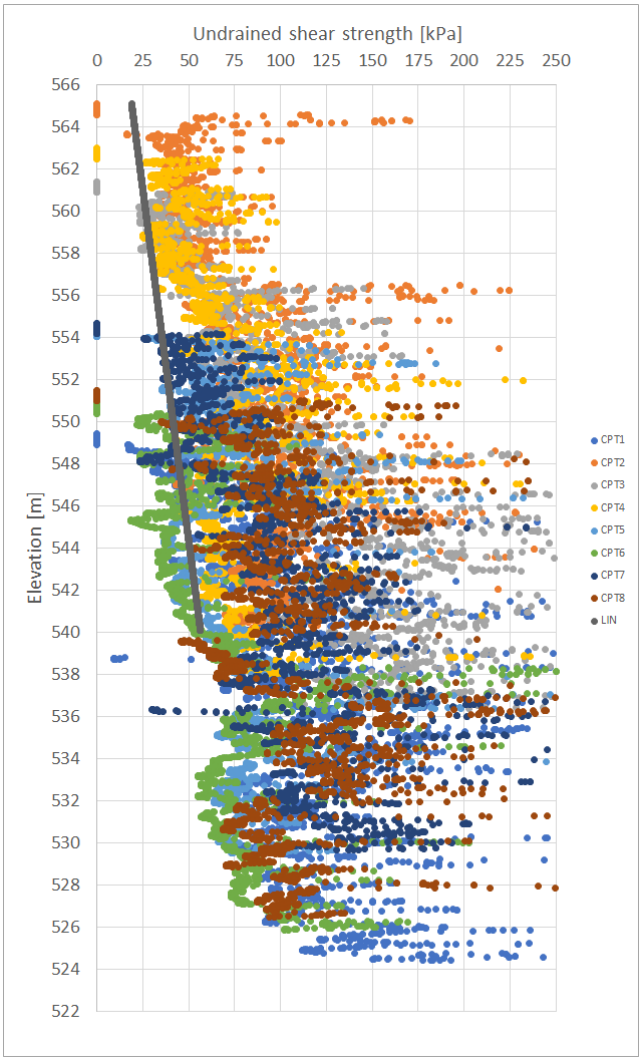

Figure 5. Static penetration test results showing potential basal sliding surface.

6 DISCUSSION

The entire construction site as formed of mine spoil heaps represented geotechnically challenging conditions. The main facts that underlined the geotechnical difficulty were the following:

- Obviously, the geotechnical properties were strongly dependent on the method of the spoil heap construction and in particular, on the interaction of the clay lumps with water long-term
- The construction of the spoil heap was carried out by free-fall of clay-claystone lumps under unknown and time-varying physical and weather conditions, without the classical engineered compaction known from road construction
- Although free-fall during construction allows some compaction, the resulting intergranular - lump porosity reached 35%, which in combination with water interaction varied over the time and created uncertainty to the geotechnical behaviour
- The relocated clay-claystone lumps (excavated and stockpiled) underwent a significant change in stress and depending on the water contact conditions (unknown, highly variable) the expected geotechnical behaviour is between rock type to soft clay type - this represented highly variable geotechnical conditions
- The whole process of stockpiling of clay mine spoil heaps led to an unpredictable alternation/intermixing of softer and stiffer layers/zones that randomly spread across the site
- Despite the site investigation carried out, there had always been uncertainty in the strength parameters and hydrodynamics due to the above facts

7 CONCLUSIONS

The construction site – clayey mine spoil dump represented a critical location predetermined to various forms of instability including slope failures, settlements, irregular groundwater seepage and erosion. Illogically, when the stabilizing measures were conducted, after a tension crack was observed at the crown of the cutting, and with a theoretically increasing factor of safety proved by calculations, a slope failure occurred. Geotechnical design of the 24 m deep cutting in such "natural" environment must ensure an advanced geotechnical characterisation as well as parametric stability assessments including different variables. Nevertheless, in such environments, all stakeholders must acknowledge the acceptance of the geotechnical risk, which would most likely require increased repair and maintenance costs.

REFERENCES

Najser, J. (2010). *Modelling of lumpy clay fills*. PhD thesis, Charles University in Prague, CZ.

Vanicek, I. and Vanicek, M. (2008). Earth structures in transport, water, and environmental engineering. Springer.

Proceedings of the XVIII ECSMGE 2024
GEOTECHNICAL ENGINEERING CHALLENGES
TO MEET CURRENT AND EMERGING NEEDS OF SOCIETY
© 2024 the Authors
ISBN 978-1-032-54816-6
DOI 10.1201/9781003431749-210
Open Access: www.taylorfrancis.com, CC BY-NC-ND 4.0 license

ECSMGE 24
XVIII EUROPEAN CONFERENCE ON SOIL MECHANICS AND GEOTECHNICAL ENGINEERING

Local site response analyses based on field measurements compared to v_{s30} site-condition and geologic and topographic constraints

Analyses de réponse du site local basées sur des mesures sur le terrain par rapport à l'état du site v_{s30} et aux contraintes géologiques et topographiques

O. Kegyes-Brassai*
Szechenyi István University, Gyor, Hungary

G. Kovacs, T. Toth
Geomega Ltd. / Eotvos Lorand University, Budapest, Hungary

B. Labar, A. Wolf
Szechenyi István University, Gyor, Hungary

**kegyesbo@sze.hu*

ABSTRACT: Earthquake forces can quickly cause vibrations that damage structures, leading to cracks and possible collapse. Buildings designed in accordance with EC8 (Eurocode 8) take into account soil properties based on ground motion amplification data. The use of average shear-wave velocity for the uppermost 30 m soil layers provides the core for soil type classification to determine the appropriate design acceleration response spectrum. On one hand, determining v_{s30} requires detailed investigations, however, lately intensive research has attempted to correlate v_{s30} data with slope and geology. On the other hand, previous results have demonstrated that the amplification of acceleration might differ even for the same soil category determined based on v_{s30}. In this paper v_{s30} is determined from field measurements, also taking into consideration the correlation between slope values and the measured V_{s30} profile. In addition to this result, 1-dimensional response analysis is also performed using STRATA software, obtaining the site-specific acceleration spectrum. The study highlights the importance of seismic site characterization and the usefulness of determining the local site effect.

RÉSUMÉ: Les forces sismiques peuvent rapidement provoquer des vibrations qui endommagent les structures, entraînant des fissures et un éventuel effondrement. Les bâtiments conçus conformément à la norme EC8 (Eurocode 8) prennent en compte les propriétés du sol sur la base des données d'amplification du mouvement du sol. L'utilisation de la vitesse moyenne des ondes de cisaillement pour les couches supérieures de 30 m du sol constitue la base de la classification des types de sol afin de déterminer le spectre de réponse d'accélération de conception approprié. D'une part, la détermination de v_{s30} nécessite des investigations détaillées, mais récemment, des recherches intensives ont tenté de corréler les données de v_{s30} avec la pente et la géologie. D'autre part, des résultats antérieurs ont démontré que l'amplification de l'accélération pouvait différer même pour la même catégorie de sol déterminée sur la base de v_{s30}. Dans cet article, v_{s30} est déterminé à partir de mesures sur le terrain, en tenant également compte de la corrélation entre les valeurs de pente et le profil v_{s30} mesuré. En plus de ce résultat, une analyse de réponse unidimensionnelle est également réalisée à l'aide du logiciel STRATA, obtenant ainsi le spectre d'accélération spécifique au site. L'étude souligne l'importance de la caractérisation sismique du site et l'utilité de déterminer l'effet site local.

Keywords: Site response; local site amplification, slope correlation; ground motion data; response spectrum analysis.

1 INTRODUCTION

The use of average shear-wave velocity for the uppermost 30 m soil layers provides the core for soil type classification, which is crucial for determining the appropriate design acceleration response spectrum. To assess the accuracy of the properties and behaviour of the soil, shear-wave velocity within this specific depth range (uppermost 30 m) is considered to enable the development of a response spectrum that aligns with the expected ground motion during seismic events. This information plays a vital role in designing structures and infrastructure that can withstand and effectively respond to the forces exerted by earthquakes or other ground vibrations (Weatherill et al., 2020, Mori et al., 2020, Thompson et al., 2012, 2014).

In a previous study conducted by Wang and Wang (2015), the focus was on examining the reliability of correlations between measured v_{s30} and estimated v_{s30} through the utilization of a statistical Pearson correlation coefficient (PCC). Furthermore, the accuracy of site classification was assessed by comparing estimated v_{s30} with measured v_{s30}. However, a significant limitation of the proposed correction method by Wang and Wang (2015) became apparent. This limitation manifested in larger relative errors for the depths in the model and an unacceptably large disparity between the curves of estimated v_{s30} and measured v_{s30}, which could potentially be attributed to the presence of interbedded layers with high shear-wave velocities.

Thompson and Wald (2012) conducted additional research that centred around the kriging-with-a-trend approach for mapping v_{s30}. They explored various methods of defining the trend by incorporating abundant v_{s30} measurements in Taiwan, considering geology, topographic slope, or both as potential factors. The aim was to evaluate the accuracy of v_{s30} maps by comparing them statistically to the standard deviation of the residuals. However, it was observed that the geology-based approach was unable to adequately fit the model and thus introduced the highest level of uncertainty in the results.

In a related study, Weatherill et al. (2020) constructed a comprehensive model comprising topographic/bathymetric elevation and a database of 30 m averaged shear wave velocity measurements (v_{s30}). The model incorporated both topography and geology as influential factors. The authors incorporated site amplification functions into the European Ground Motion Model (GMM), which was calibrated based on observed or inferred v_{s30} values derived from European geology and topography models. However, a notable limitation of this research emerged concerning the use of inferred v_{s30} properties such as topographic slope or seismic design code, as well as site class. These factors introduced increased uncertainty in the resulting site amplification estimates.

2 METHOD FOR LOCAL SITE SPECTRA

In this study, the shear modulus was determined through in-situ seismic methods to ascertain the shear wave velocity from two sites. The measurement was carried out by special seismic tool composed by Geomega Ltd. for local (few hundreds of meters long, few tens of meters deep) engineering geological purposes. S waves were triggered by Lightning electromechanical seismic source in every 3 meters along the 459 m (PCS) and 1065 m (KSZ) long sections. The generated seismic signal was 20 s long composed by frequencies 5-200 Hz. Three component geophones were set in an array in 3 m distance, which were used to record S waves' arrivals. Tomographic processing of the results was used to determine the shear wave velocities of the pre-defined 1.5 m size cells along the section. Considering the wave routes initiated from the surface, cells' velocities were modified in order to approximately get the measured arrival times. This inversion method was run in 4 iteration steps in order to decrease the differences between observed and modelled arrival times below the pre-defined threshold. Along the section vertical v_s trends were extracted where additional stratigraphy data were existing.

To enable the selection of appropriate seismic input for nonlinear dynamic analysis, REXEL was utilized for scaling and accurately estimating seismic performance based on the seismic hazard at the location site. This facilitates the proper selection of seismic input and earthquake records using fundamental probabilistic seismic hazard parameters. REXEL, a computer software, allows the construction of design spectra in accordance with Eurocode 8 (EC8). REXEL searches for sets of records for various structural applications, considering soil types, location, peak ground acceleration at the targeted location, and distance (Sgobba, 2019). This process aids in defining the elastic acceleration response spectrum based on the direction of earthquake motion, which can be easily utilized by STRATA, which may include horizontal or vertical components of motion.

Equally, STRATA which is an equivalent linear site response analysis software, was applied in the frequency domain using input motions scaled from REXEL within the time domain to perform random vibration theory (RVT), which enables the randomization of site properties. The 1-dimensional equivalent wave propagation software allows user to input soil layering parameters such as nonlinear properties (soil characteristics), layering thickness, shear-wave velocity, and depth to bedrock. It uses the time series method as a single motion to propagate motions through the site to compute the strain-compatible ground motion at the surface of the site at any depth in the soil column (Kottke, 2012).

Peak ground acceleration (PGA) was used as the primary parameter in the selection of input acceleration records from REXEL, using 0.09 g and soil type C as the intensity parameters to examine the frequency content and intensity relation, which has a significant association with seismic damage.

3 V_S TREND DATA 1-D ASSESSMENT

PCS measurements were carried out in a hilly area located in a tectonically and geomorphologically active area situated between the uplifting Hungarian Mountain Range and the relatively subsiding Danube valley (Ruszkiczay-Rüdiger et al., 2005). Highest point of the measured section is 300 m (asl) and the local relief (maximal height difference) is about 160 m. The area is covered by few meters thick Quaternary and/or late Miocene loess and lacustrine sediment in advance. The main mass of the measured strata consists of loose Oligocene silt, clay to depths down to at least 100 m below surface. Using refraction evaluation method several layer boundaries have been identified. S wave refractions appear at the depths of 3-5 m, 18 m and 45 m depths. Note that in the upper 3 layers (separated by the mentioned boundaries) the S wave velocity is lower than 400 m/s [PCS_1 and [PCS_2]. The P wave refraction based uppermost boundary is at the depth of 8-10 m. This correlates well with the depth where the increase of S wave velocity slows down or even starts decreasing. Based on the slope and geomorphology based v_{s30} map (Kovacs et al. 2023), the measurement site's soil class is B which contradicts the middle of soil class C measured v_s values (275 and 284 m/s). This contradiction can be explained by the active topography of the area: in steady-state the loose sediment would be flattened by preceding erosional processes resulting lower slope and lower predicted v_{s30} (thus may be soil class C), but the intense incision of the Danube river is resulting actively eroding surface with higher slope values and higher predicted v_{s30}.

KSZ measurements were carried out in the western foothills of relatively uplifting Mecsek Mountain (Sebe et al., 2008) which is a structurally and geologically complex shear zone. Surface elevation of the measurement area is 140-148 m (asl), whereas the lowest point in the surroundings is around 110 m (asl). In this measurement site, the two analysed v_s trends reflect significantly different geology. In the vicinity of [KSZ-2] at the depth of 30 m Permian-Triassic sandstone was drilled, however near [KSZ-1] below late Miocene lacustrine sediments (3-12 m) early Miocene strata were present down to the depth of 100 m. The section most likely runs along the edge of the fractured Permian-Triassic strata. S wave refraction method detected a boundary at 13 and 10 m depth (at 580 m and 220 m line distance respectively) which is probably the base of the late Miocene sediments. A deeper boundary reflects the top of a tuffic layer and the basement depth at 32 and 28 m depths. In this case v_{s30} map based on the surface slope provides soil type B that is consistent with the measured average v_s values (364 and 429 m/s). Note that soil type C appears 80 m from the KSZ-1 measurement point.

4 EVALUATION OF STRATA RESULTS

The upper soil layering at site PCS and KSZ in Figure 1 varied to determine the potential causes of the loop before 20 meters and at 40 meters, resulting from the intersection loop in the shear wave velocity profile. To assess the influence of the lower and upper layers of the site, we conducted STRATA analyses at 30, 40, 50, and 80 meters, respectively. For each case, we assumed and varied the bedrock shear wave velocity at 400, 600, and 800 m/s to ascertain the impact on the site results. This was done to rule out the effect on the response spectrum of the sudden jump in applied shear wave velocity (v_s) at bedrock.

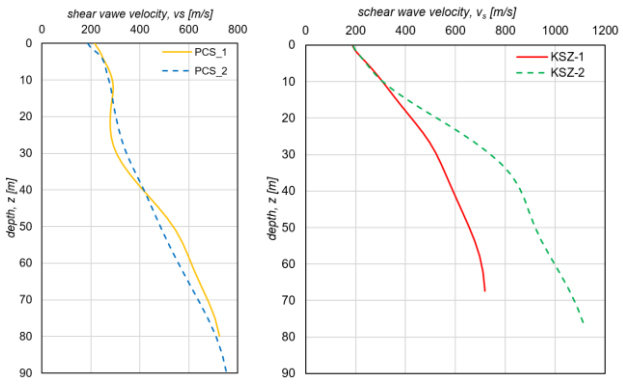

Figure 1. Two v_s trend for both PCS and KSZ location.

Changing the model depth at the two locations had different effects and results, which is in line with the v_s profiles. At PCS locations for all examined model depths, the v_s trends yielded almost identical results, the shape of the response spectra is very similar, their values show a difference mainly on the plateau.

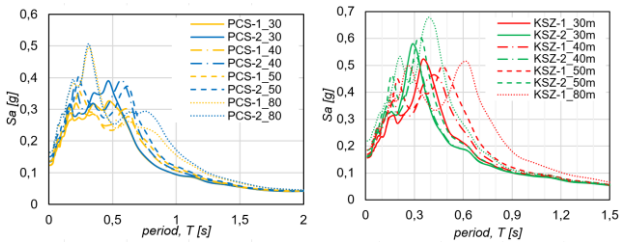

Figure 2. Response spectra for PCS and KSZ site considering two v_s trends and different bedrock depth.

In the case of KSZ sites different model depths, the difference in soil profiles is always apparent, with increasing depth, which is consistent with the fact that in one section the value of v_s increases faster with depth, and thus the average value of v_s, about the

difference between soil profiles as a function of model depth.

5 DISCUSSION

In case of PCS site the PCS-2 curve always gives a higher value at plateau. This fundamentally contradicts the fact that the average shear wave propagation speed determined for that profile is higher ($v_{s.30}$, $v_{s.40}$, $v_{s.50}$), on the basis of which we would expect an inverse ratio. The reason for this can be found in the fact that there is a dip in the PCS-1 v_s profile, which can affect the propagation of the wave towards the surface, in this zone the wave slows down, its amplitude increases, and then the wave accelerates again as it approaches the surface. This pulsation may cause the acceleration values on the plateau to be lower for this profile. The descending branches of the plateaus usually run along the same line, the connection point of the curve belonging to the two profiles is slightly shifted at the depth of 80 m. By increasing the depth of the model, the results given by the two soil profiles change according to almost the same trend. The effect of the depth can be summarized as follows: the average value of the plateau at the first three depths (30-40-50 m) does not change, it is shifting from the two-humped shape more and more towards one hump, within the plateau there is an increase parallel to the period in the case of a smaller depth, a constant for the two intermediate models, a decrease for the 80 m model, and even a marked difference for the latter. The beginning of the descending branch shifts to the right as the depth increases, but there is no significant difference between 40-50 m, and in the 80 m model, the plateau widens and only starts to decrease at a period time of 0.9 s, and it blends into the other curves at almost 2 s, in the case of the 30-40-50 m models it is already 1.2 s after that there is no significant difference.

In case of KSZ sites the shape of the plateau is almost the same for the 2 v_s trends, but in the case of KSZ-1 it is distributed over a larger period-time range than in the case of the KSZ-2 section, and this difference becomes more and more pronounced as the depth increases, the width of the plateau increases to a lesser extent in the KSZ-2 section by increasing the model depth as in the other section. The maximum acceleration value is usually in the very low period time range typical of the KSZ-2 section (depending on the depth T=0.2-0.4s), at the same time the average level of the plateau is almost the same, and in the range of T > 0.5 s, the value is usually smaller than that of KSZ-2, and in some places the difference is very marked, the two curves merge into each other at T = 1-1.6 s.

The effect of bedrock shear wave velocity is examined in case of PCS site, considering bedrock at 40 m, and bedrock v_s varied between 400-600 m/s. According to the calculation results the initial shear wave velocity does not modify the shape of the response spectrum, the run-off conditions, only the acceleration values on the plateau and its surroundings, it scales the ground response in this range. With a lower shear wave velocity, we get a less favorable response, which is in line with the fact that as the value of v_s decreases, the maximum acceleration increases, we get a less favorable effect. According to this result, it is important to really start the response spectrum analysis from the bedrock, and not to consider the range between the soil layers close to the surface and the bedrock with a "degraded" v_s value. Because we saw previously that increasing the depth of the model and taking into account the "real" v_s profile in that range also modifies the shape of the response spectrum, not just scales it. The deeper model is also justified by the fact that the effect is not clear as the model depth increases: it increases in a small period time range, then it decreases a little, but the plateau widens. This effect certainly depends on the soil profile and the accelerograms used.

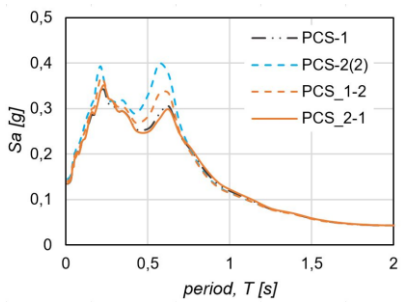

Figure 3. Response spectra for PCS and KSZ site considering two v_s trends and different bedrock depth.

To support the understanding of the results experienced at the different model depths at the PCS site, we made calculations where the layers above and below 14 m were mixed from the two sections (Fig. 3). Accordingly, a calculation was made where the v_s values of the upper 14 m were derived from section PCS-1, in the deeper range from PCS-2 (PCS_1-2) and the reverse of this (PCS_2-1). Both calculations were performed on the 40 m model with v_s 600 m/s at bedrock. The results are somewhat contradictory in terms of which layer is the defining one. As we can see, both versions are close to the PCS-1 profile, PCS_2-1 essentially coincides with it, i.e. according to this, the upper soil zone has no substantial influence here. At the same time, in the case of the other section,

it is closer to this, which would mean that the deeper layers do not have a marked effect either. A deviation is visible in the region of the response spectrum, where the two soil profiles produced a significant difference anyway, but the extent of this does not approach the distance of the two original profiles.

6 CONCLUSIONS

Determining local site spectra plays an important role in seismic design when designing earthquake-resistant structures. Determining $v_{s,30}$ provides insights into the stiffness and amplification properties of the near-surface geology. Based on the slope and geomorphology based v_{s30} map the category of the investigated area can be determined, and a EC8 code spectra can be used. However research conducted in this field applying 1-D STRATA analysis revealed that local site spectra might have higher values than the code spectra (Kegyes-Brassai et al, 2017). This underlines the necessity to evaluate more exactly the amplification potential.

This paper presented two soil profiles at two different sites and the v_s measured trend for each profile. 1-dimensional response analysis was performed using STRATA software, obtaining the site-specific acceleration spectrum. Varying the properties of the soil layering to take into account variability of soil, the mean value obtained for each site response were presented for each profile, PCS-1 and PCS-2, KSZ-1 and KSZ-2. Assuming different measured data local soil spectra were determined for different depth, with different shear wave velocity at bedrock, showing a similar trend in the response, however highlighting clear differences also, such as with increasing depth the plateau widens and the values decrease. Next the effect of the upper and lower layers on the response were also analysed. All the result highlighted that with more in-depth data more precise result can be obtained, and that there is a need for further investigations to be able determine the parameters that have a critical influence on seismic response analysis and the minimum requirement for on-site measurements like the depth, number of v_s-trends, etc. to be able to determine reliable response spectra for further seismic design.

REFERENCES

Sgobba, S. et al. (2019). REXELweb: A tool for selection of ground-motion records from the Engineering Strong Motion database (ESM). Conference proceedings of Eq. Geotechnical Eng. for Protection and Development of Environment and Constructions, Associazione Geotecnica Italiana, Rome, Italy, ISBN 978-0-367-14328-2.

Kegyes-Brassai. O.; Wolf A.; Szilvagyi, Zs.; Ray, P. R. (2017). Effects of local ground conditions on site response analysis results in Hungary. In: Proceedings of 19th Int. Conference on Soil Mechanics and Geotechnical Eng.: September 17-22, 2017, Seoul, South Corea, pp. 2003-2006. https://www.issmge.org/uploads/publications/1/45/06-technical-committee-13-tc207-17.pdf.

Phillips, C.; Kottke, A. R.; Hashash, Y. M.A.; Rathje, E. M. (2012) Significance of ground motion time step in one dimensional site response analysis, Soil Dynamics and Earthquake Engineering, Volume 43, pp. 202-217. ISSN 0267-7261, https://doi.org/10.1016/j.soildyn.2012.07.005.

Kovacs, G., Koroknai, B., Gyori, E., Németh, V., Balazs, L., Czecze, B., Bondar, I., Worum, G., Szabo, G., Kegyes-Brassai, O. & Toth, T. (2023) Seismotectonic hazard map of Hungary. Geomega Ltd. 1:500 000. https://doi.org/10.23928/foldt.kozl. 2023.153.4.mapE.

Mori, F. et al. (2020) A new Vs30 map for Italy based on the seismic microzonation dataset, Journal of Eng. Geology, Vol. 275, 105745, ISSN 0013-7952, https://doi.org/10.1016/j.enggeo.2020.105745.

Ruszkiczay-Rudiger, Zs., Fodor, L., Bada, G., Leel-Ossy, Sz., Horvath, E. & Dunai, T. J. (2005) Quantification of Quaternary vertical movements in the central Pannonian Basin: A review of chronologic data along the Danube River, Hungary. Tectonophysics, 410, pp. 157-172. https://doi.org/10.1016/j.tecto.2005.05.048.

Sebe, K., Csillag, G., & Konrad, Gy. (2008) The role of neotectonics in fluvial landscape development in the Western Mecsek Mountains and related foreland basins (SE Transdanubia, Hungary). Geomorphology, 102(1), pp. 55-67. https://doi.org/10.1016/j.geomorph.2007.05.018.

Thompson, E. M., & Wald, D. J. (2012). Developing Vs30 site-condition maps by combining observations with geologic and topographic constraints. In: The 15th World Conf. on Eq. Eng.: September 24-28, 2012, Lisbon, Portugal, pp. 24-28. https://doi.org/10.13140/RG.2.1.2248.5203.

Thompson, E. M., Wald, D. J., Worden, C. B. (2014) A VS30 Map for California with Geologic and Topographic Constraints, Bulletin of the Seismological Society of America, 104(5), pp. 2313–2321, http://doi.org/10.1785/0120130312.

Wang, H., & Suyang, W. (2015) A New Method for Estimating Vs (30) from a Shallow Shear-Wave Velocity Profile (Depth <30 m), Bulletin of the Seismological Society of America, 105(3), pp. 925–966, http://doi.org/10.1785/0120140103.

Weatherill, G., Crowley, H., Roullé, A., Tourlière, B., Lemoine, A., Gracianne, C., Kotha, S. R., Cotton, F. (2023). Modelling site response at regional scale for the 2020 European Seismic Risk Model (ESRM20). Bulletin of Eq. Engineering, 21, 665–714. https://doi.org/10.1007/s10518-022-01526-5.

Proceedings of the XVIII ECSMGE 2024
GEOTECHNICAL ENGINEERING CHALLENGES
TO MEET CURRENT AND EMERGING NEEDS OF SOCIETY
© 2024 the Authors
ISBN 978-1-032-54816-6
DOI 10.1201/9781003431749-211
Open Access: www.taylorfrancis.com, CC BY-NC-ND 4.0 license

ECSMGE 24
XVIII EUROPEAN CONFERENCE ON SOIL MECHANICS AND GEOTECHNICAL ENGINEERING

A geotechnical and geophysical characterization of the influence of seasonal variation on railway embankments

Une caractérisation géotechnique et géophysique de l'influence des variations saisonnières sur les remblais ferroviaires

Q. Khan, S. Donohue*
Department of Civil Engineering, University College Dublin, Dublin, Ireland

A. Trafford
Science Foundation Ireland Research Centre in Applied Geosciences (iCRAG), Dublin, Ireland

B. Dashwood, J.E. Chambers
British Geological Survey, United Kingdom

**shane.donohue@ucd.ie*

ABSTRACT: Seasonal variation causes the railway embankments in Ireland and the United Kingdom (UK) to experience significant changes in their pore water pressure throughout the year. Most of these embankments were constructed more than a 100 years ago with methods that did not comply with standard compaction methods used in modern embankments. As these embankments form a large portion of the railway infrastructure in the UK, their stability presents a geohazard. With the imminent effects of climate change on unstable seasonal variation in the weather patterns, understanding the behaviour of these embankments becomes even more critical. To understand the influence of such seasonal variation or hydraulic hysteresis, laboratory testing was conducted on clay-based embankment material sourced from an active railway embankment. Firstly, results of field measurements from sensors at the railway embankment are presented. Furthermore, results from shear wave velocity measurements of the material together with suction and moisture measurements are also presented.

RÉSUMÉ: Les variations saisonnières entraînent des changements importants dans la pression de l'eau interstitielle des remblais ferroviaires en Irlande et au Royaume-Uni tout au long de l'année. La plupart de ces remblais ont été construits il y a plus de 100 ans avec des méthodes non conformes aux méthodes de compactage standard utilisées dans les remblais modernes. Étant donné que ces remblais constituent une grande partie de l'infrastructure ferroviaire du Royaume-Uni, leur stabilité présente un géorisque. Avec les effets imminents du changement climatique sur les variations saisonnières instables des régimes météorologiques, il devient encore plus crucial de comprendre le comportement de ces remblais. Pour comprendre l'influence d'une telle variation saisonnière ou hystérésis hydraulique, des tests en laboratoire ont été réalisés sur un matériau de remblai à base d'argile provenant d'un remblai ferroviaire actif. Tout d'abord, les résultats des mesures de terrain effectuées à partir de capteurs situés sur le remblai ferroviaire sont présentés. En outre, les résultats des mesures de vitesse des ondes de cisaillement du matériau ainsi que les mesures de succion et d'humidité sont également présentés.

Keywords: Climate change; embankment stability; shear wave velocity; unsaturated soil; hydraulic hysteresis.

1 INTRODUCTION

Climate change is expected to lead to more frequent and severe weather events, resulting in wetter winters and hotter summers in the UK. For example, over 100 slope failures (significantly higher than usual) were recorded in southern UK in 2000/01 that was recorded as wettest winter on record (Dixon et al., 2008). The failure of these earthworks was attributed to excessive precipitation and a notable increase in saturation, highlighting the vulnerability of these structures to the impacts of extreme weather events. Railway infrastructure development in the UK surged during the industrialization period of the mid to late 19th century. Most of the railway embankments constructed during this pre-regulation era lacked a comprehensive understanding of the geophysical and geotechnical properties necessary for stable embankment design (Skempton, 2017). During construction, the foundations of these embankments were often left unprepared, with topsoil and soft surface deposits left in situ. O'Brien (2007) identified that this practice resulted in dumped clay fills exhibiting a clod-matrix structure, varying from compacted engineered fill to natural clay. The intact

clods could impact the compressibility and shear modulus of the dumped clay, while the remoulded clay matrix influenced permeability and shear strength (Briggs et al., 2017).

The seasonal variation in soil moisture content further influences the volumetric behaviour of embankment material (Briaud, 2013). In the presence of plastic clayey material, seasonal moisture fluctuations pose stability problems for pre-regulation embankments. High-plasticity soils, like soft clays, are more susceptible to excessive shrink-swell behaviour. Soil cracks resulting from clay shrinkage facilitate rainfall infiltration, leading to shallow slides and surface creep (Smethurst and Powrie, 2007). The inadequate compaction of early railway embankments would also have resulted in higher permeability levels and significant permeability fluctuations within the soil. This, in turn, amplifies pore water pressure variability, potentially increasing shrink-swell behavior and accelerating the aging rate (Glendinning et al., 2014). Due to poor compaction, dense vegetation and abundant presence of high-plasticity clays as embankment material, the hazard risk associated with failures of old railway embankments increases significantly with changing precipitation patterns as a result of climate change. Recent studies have employed seismic measurements, for assessing and monitoring the condition of embankments over extended periods (Bergamo et al. 2016). A crucial geophysical parameter derived from such investigations is the shear wave velocity (V_s) of the soil. Laboratory investigations into the impact of varying moisture levels on the mechanical behavior of soil can be conducted through the measurement of V_s using bender elements (Wheelar et. al., 2003). V_s measurements have demonstrated that clayey material exhibits greater sensitivity to changing moisture content (Dong and Lu, 2016). Additionally, higher plasticity in clayey soil has been associated with increased hysteresis (variations in suction within the soil between wetting and drying cycles) during wetting and drying cycles (Gapak and Tadikonda, 2018). Therefore, lab-based V_s measurements provide improved insights into the volumetric behavior of embankment material.

This study presents results from an investigation of the influence of hysteresis on the stiffness response of a clay-based embankment material sourced from an active railway embankment. By using V_s measurements obtained from bender elements, the specimen's stiffness variation with moisture levels is monitored. The moisture levels in the specimen are varied to reflect the suction levels during summer and winter seasons from an instrumented railway embankment.

2 METHODOLOGY

2.1 Materials

All the soil used for testing was collected from boreholes drilled on the Withy Beds embankment in the southeast England, between Effingham Junction Station and Cobham & Stoke d'Abernon (CSD) station. This embankment is part of the New Guildford Railway line. The soil is termed as London Clay. Its material properties are given in Table 1. The maximum dry unit weight and optimum moisture was found using standard proctor compaction method (BS 1377-4:1990). However, the in-situ dry density of the soil was found to be lower at 15 kN/m^3. For a better comparison of the volumetric behaviour of the soil with the in-situ conditions, the test specimen was prepared at the in-situ density with a moisture level of 30%.

2.2 Field instrumentation

Since December 2020, the Withy Beds site has employed different ground sensors, such as 5TE and T21, to capture data on volumetric water content (VWC), temperature, and soil suction. These sensors are located at 5 different locations spaced 66m apart.

2.3 Laboratory experimental setup

A cylindrical specimen was prepared (Dia=102mm and Height = 114mm) with a density of 1800 kg/m^3 at in-situ moisture content. Figure 1 shows the specimen setup for bender element and soil suction measurements. The specimen was fit into an acrylic casing that was fitted with inserts for the benders. MPS-6 tensiometer was embedded into specimen to measure suction. The V_s measurements were obtained using a system having a *Siglent* function generator and *Picoscope* 5000 series oscilloscope. A 10V sinewave was used as the input signal. As the stiffness of the specimen varies throughout the drying and wetting process, the input frequencies were adjusted to ensure that the wavepath-wavelength ratio (L_{tt}/λ) was above 3 at each moisture level (Leong. et al 2005).

Table 1. Geotechnical properties of embankment material.

Parameter	Value
Liquid Limit	60
Plasticity Index	29
Activity (%)	76
Maximum Dry Unit Weight (kN/m^3)	17
Optimum Moisture Content (%)	24
In-situ Moisture Content	30

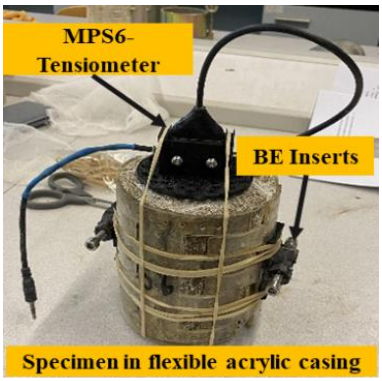

Figure 1. Assembly of specimen with Bender Element (BE) and Tensiometer.

3 RESULTS

3.1 Field measurements

The sensor measurements for soil moisture (VWC) and suction are provided in Figure 2. Averaged results from all five locations are depicted for both sensors. Furthermore, measurements from sensors located at the middle of the instrumentation layout are also provided in Figure 2. This is because the driest conditions were observed at this location with suction measurements exceeding 1000 kPa during the summer of 2022. During this year, high suction and low moisture levels were observed between early March and late October. Another feature of the measurements during the summers is the short-term variation in moisture levels. Due to rainfall events, short term reductions in suction measurements are observed that quickly return to higher values after the soil dries up. Therefore, the soil would likely experience several hysteresis cycles during summer.

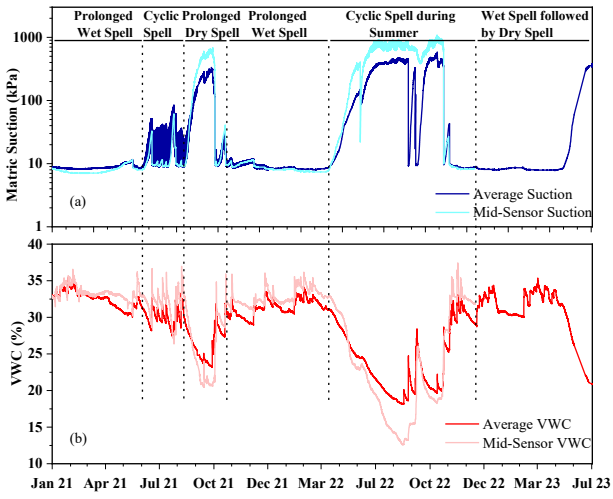

Figure 2. Field measurements, a) Suction Measurements, b) VWC Measurements.
Note: Mid-sensor data was recorded till Dec-2022.

Given the clayey nature of this material, the risk of rainfall induced failure due to crack formation from volumetric instability becomes greater. Consequently, laboratory testing is required to link the influence of hysteresis with the stiffness of the embankment material.

3.2 Laboratory testing

Testing was conducted on a specimen subjected to dry-wet cycles after being prepared at 30% gravimetric moisture content. The soil-water characteristic curve (SWCC) of the embankment clay is given in Figure 3. This curve was plotted using measurements from MPS-6 (up to 1200 kPa) and WP4C Potentiometer (beyond 1200 kPa and up to 75000 kPa). The MPS-6 measurements were obtained from the drying curve of the instrumented cylindrical specimen. The SWCC curve was modelled using the equation proposed by Fredlund and Xing (1994):

$$\theta = \left(1 - \frac{\ln\left(1+\frac{\psi}{\psi_r}\right)}{\ln\left(1+\frac{10^6}{\psi_r}\right)}\right)\left(\frac{\theta_s}{\left[\ln\left(e+\left(\frac{\psi}{a}\right)^n\right)\right]^m}\right) \quad (1)$$

where θ is the moisture content, θ_s is the saturated moisture content, ψ is the suction, ψ_r is residual suction and a, m and n are fitting parameters. Although the curve provides a good fit at suction levels beyond 200 kPa, the MPS-6 tensiometer does not have sufficient resolution for accurate suction measurements at suction levels closer to saturated state. Nevertheless, hysteresis is observed in the MPS-6 measurements on cylindrical specimen as shown by the wetting curve in Figure 3.

Figure 4 illustrates the variation of V_s with moisture content. The selection of a moisture variation range between 20% and 30% for the drying-wetting cycle was based on measurements from the mid-sensor in Figure 2.

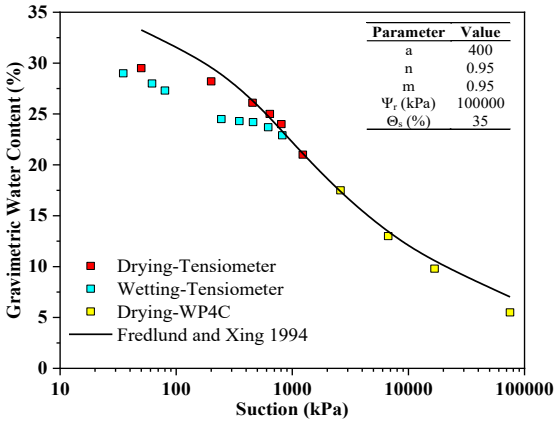

Figure 3. SWCC of embankment material.
Note: Parameters for equation 1 are given in the figure.

This is because the suction measured using MPS-6 tensiometer was approximately 1200 kPa at 20% moisture content, which is slightly higher than the maximum suction measured in the field based mid-sensor. In each drying cycle, the rate of increase in V_s of the specimen becomes higher. This rate of increase becomes evident in driest state where a 5% and 12% increase is observed in V_s at end of each drying cycle after the first cycle.

4 CONCLUSIONS

The influence of moisture variation on poorly compacted embankment material increases the hazard risks associated with embankment failure. These failures are common in old railways due to their clayey nature and insufficient compaction. The current study investigated the influence of moisture variation on stiffness of one such clayey material from an active railway embankment site. Using field-based sensors, soil suction and moisture data were obtained for nearly 30 months from the site. The data illustrated dry periods with episodes of extensive moisture variation during summers. Using laboratory-based testing, hysteresis was observed in the SWCC of the clay. Furthermore, V_s testing exhibited a stiffening influence of the repeated hysteresis. Consequently, the likelihood of rainfall-induced failure increases, primarily attributed to crack formations in the matrix of poorly compacted embankments. This risk is particularly heightened by the potential for seasonal extremes resulting from climate change. To investigate this risk, further studies are required to assess the impact of additional dry-wet cycles on the behaviour of clayey embankment material.

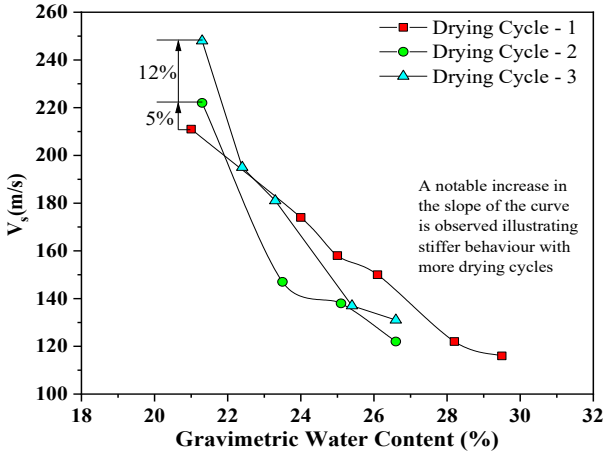

Figure 4. V_s variation with moisture content.

REFERENCES

Bergamo, P., Dashwood, B., Uhlemann, S., Swift, R., Chambers, J.E., Gunn, D.A. and Donohue, S. (2016) Time-lapse monitoring of climate effects on earthworks using surface waves, *Geophysics*, 81(2), pp.EN1-EN15, https://doi.org/[10.1190/geo2015-0275.1].

Briaud, Jean-Louis. (2013). *Geotechnical engineering: unsaturated and saturated soils*, 2nd ed., John Wiley & Sons.

Briggs, K.M., Loveridge, F.A. and Glendinning, S. (2017) Failures in transport infrastructure embankments, *Engineering Geology*, 219, pp.107-117, https://doi.org/[10.1016/j.enggeo.2016.07.016].

Dixon, N., Dijkstra, T.A., Glendinning, S., Hughes, P.N., Hughes, D.A.B., Clarke, D., Smethurst, J., Powrie, W., Toll, D.G. and Mendes, J. (2008). Climate change and slope stability–improving our forecasting capabilities. In: *Proceedings GeoEdmonton08-61st Canadian Geotechnical Conference.*

Dong, Y. and Lu, N. (2016) Dependencies of shear wave velocity and shear modulus of soil on saturation, *Journal of Engineering Mechanics*, 142(11), pp.04016083, https://doi.org/[10.1061/(ASCE)EM.1943-7889.0001147].

Fredlund, D.G. and Xing, A. (1994) Equations for the soil-water characteristic curve, *Canadian geotechnical journal*, 31(4), pp.521-532, https://doi.org/[10.1139/t94-061].

Gapak, Y. and Tadikonda, V.B. (2018) Hysteretic water-retention behavior of bentonites, *Journal of Hazardous, Toxic, and Radioactive Waste*, 22(3), pp.04018008, https://doi.org/[10.1061/(ASCE)HZ.2153-5515.0000398].

Glendinning, S., Hughes, P., Helm, P., Chambers, J., Mendes, J., Gunn, D., Wilkinson, P. and Uhlemann, S. (2014) Construction, management and maintenance of embankments used for road and rail infrastructure: implications of weather induced pore water pressures, *Acta Geotechnica*, 9, pp.799-816, https://doi.org/[10.1007/s11440-014-0324-1].

Leong, E.C., Cahyadi, J. and Rahardjo, H. (2009) Measuring shear and compression wave velocities of soil using bender–extender elements, *Canadian Geotechnical Journal*, 46(7), pp.792-812, https://doi.org/[10.1139/T09-026].

O'Brien, A. (2007). Rehabilitation of urban railway embankments: Investigation, analysis and stabilisation. In: *Proceedings of the 14th International Conference (SMGE)*, Madrid, Spain.

Skempton, A.W. (2017) Embankments and cuttings on the early railways, In: *The Civil Engineering of Canals and Railways before 1850*, 1st ed., Routledge, pp. 291-307.

Smethurst, J.A. and Powrie, W. (2007) Monitoring and analysis of the bending behaviour of discrete piles used to stabilise a railway embankment, *Géotechnique*, 57(8), pp.663-677, https://doi.org/[10.1680/geot.2007.57.8.663].

Wheeler, S., Sharma, R.S. and Buisson, M.S.R. (2003) Coupling of hydraulic hysteresis and stress–strain behaviour in unsaturated soils, *Géotechnique*, 53(1), pp.41-54, https://doi.org/[10.1680/geot.2003.53.1.41].

Proceedings of the XVIII ECSMGE 2024
GEOTECHNICAL ENGINEERING CHALLENGES
TO MEET CURRENT AND EMERGING NEEDS OF SOCIETY
© 2024 the Authors
ISBN 978-1-032-54816-6
DOI 10.1201/9781003431749-212
Open Access: www.taylorfrancis.com, CC BY-NC-ND 4.0 license

ECSMGE 24
XVIII EUROPEAN CONFERENCE ON SOIL MECHANICS AND GEOTECHNICAL ENGINEERING

Laboratory assessment of shear strength parameters in sandy soil by lime permeation method and sensitivity analysis from Doi Chang case study

Évaluation en laboratoire des paramètres de résistance au cisaillement dans un sol sablonneux par la méthode de perméation à la chaux et analyse de sensibilité à partir de l'étude de cas de Doi Chang

A. Koirala
Geotechnical Engineering Research and Development Center, Kasetsart University, Bangkok, Thailand

S. Soralump*
Geotechnical Engineering Division, Department of Civil Engineering, Faculty of Engineering, Kasetsart University, Bangkok, Thailand

*soralump_s@yahoo.com

ABSTRACT: In nature, slopy terrain or loosely compacted soil can have high permeability which can cause rise in groundwater table and may create stability problems. To minimize this phenomenon, hydrated lime slurry permeation can be used. Hydrated lime has been in use for many years. But using lime slurry to treat low shear strength soil can be a solution for slope stability. The purpose of this research is to increase the sand's shear strength by hydrated lime permeation under the influence of constant head. The test samples were obtained by passing through sieve #40 and retained on #200. After 66 days of lime permeation, permeability decreased by 94% and cohesion increased up to 77%. Also, to identify the mineral compounds and analyze the structure of crystalline materials, X-ray Diffraction Method (XRD) was used which showed formation of calcium cations along with the sand silica. The Sensitivity Analysis from Doi Chang mass movement case study (a village in Thailand having active mass movement currently) showed that the increase in cohesion help in the increase in factor of safety by 11.2% even though groundwater level was higher.

RÉSUMÉ: Dans la nature, un terrain en pente ou un sol peu compact peut avoir une perméabilité élevée, ce qui peut entraîner une montée de la nappe phréatique et créer des problèmes de stabilité. Pour minimiser ce phénomène, on peut utiliser la perméation à la boue de chaux hydratée. La chaux hydratée est utilisée depuis de nombreuses années, mais l'utilisation de boue de chaux pour traiter un sol de faible résistance au cisaillement peut être une solution pour la stabilité des pentes. Le but de cette recherche est d'augmenter la résistance au cisaillement du sable par perméation à la chaux hydratée sous l'influence d'une tête constante. Les échantillons de test ont été obtenus en passant à travers un tamis #40 et retenus sur le tamis #200. Après 66 jours de perméation à la chaux, la perméabilité a diminué de 94 % et la cohésion a augmenté jusqu'à 77 %. De plus, pour identifier les composés minéraux et analyser la structure des matériaux cristallins, la méthode de diffraction des rayons X (XRD) a été utilisée, montrant la formation de cations de calcium avec la silice du sable. L'analyse de sensibilité de l'étude de cas du glissement de terrain de Doi Chang (un village en Thaïlande connaissant actuellement des mouvements de masse actifs) a montré que l'augmentation de la cohésion contribue à augmenter le coefficient de sécurité de 11,2 %, même si le niveau de la nappe phréatique était plus élevé.

Keywords: Permeability; lime permeation; cohesion; XRD; sensitivity analysis.

1 INTRODUCTION

Lime treatment by permeation in porous soil is a challenge to let lime particles or soluble cations into the soil. However, pore size of the soil must be larger than the inherent lime particles. When lime is added to a fine-grained soil and intimately mixed, several reactions initiate. Cation exchange and agglomeration-flocculation reactions take place rapidly and produce immediate changes in soil plasticity, workability, and swell properties. A soil-lime pozzolanic reaction may commence depending on the characteristics of the soil being stabilized. The pozzolanic reaction results in the formation of various types of hydrated calcium silicate and calcium

aluminate cementing agents or both. The cementing agents increase strength and durability. Pozzolanic reactions are time dependent, and strength development is gradual but continuous for a long period of time (several years in some instances) (Thompson & Robnett, 1976).

Residual soil or colluvium is the heterogeneous mixture of boulder or granular soil and mixtures of both. The colluvium loses the valuable minerals under leaching such as iron, calcium, aluminum under high rainfall and form lateritic soils and andosols downslope. Many past studies have suggested that permeability in case of In situ residual soil is higher than compacted soil in laboratory and use of lime for high plasticity soils is effective except for organic soil (Townsend, 1985). Grouting by lime slurry with fly ash increased the alkalinity in time, having maximum concentration at 59 days. Also, grouting about 59-64%, hydraulic conductivity was found to decrease (Gabr et al., 1995). The hardening and strengthening of the lime mixture with soil depend on carbonation of the lime. This is likely because of the attachment of the calcite crystals to the surface of aggregate particles. The pore size of the soil is directly involved in the carbonation process (Lawrence et al., 2007).

Dissolving lime in water and intruding saturated lime solution (SLS) containing calcium cations into soil by means of gravity gradient resulted in an increase of 294% in cohesion and 222% in internal friction angle and a decrease of 58% in settlement of specimens (Davoudi et al., 2009).

The sequential permeation of $CaCl_2$ and NaOH solutions into compacted expansive soil resulted in the precipitation of lime in the expansive soil and increased pH level which is important for pozzolanic reactions to effectively reduce plasticity index and swell potential. This is an effective method for lime precipitation for stabilizing expansive soils (Thyagaraj et al., 2012; Thyagaraj & Zodinsanga, 2015).

Another study about the remediation of reactivated landslide used a method to introduce lime slurry into the sheared zone. Just after remediation of 10% of the slip surface by 7% lime, it caused increase in factor of safety from 1.1 to 2.89 after 5 weeks of curing (Moridzadeh, 2019).

X-Ray Diffraction (XRD) test is successful in identifying crystalline minerals such as calcite, illite, quartz, kaolinite and chlorite-serpentine mixed layers. It provides a powerful nondestructive technique for characterizing crystalline materials. It provides information on structures, phases preferred crystal orientation (texture), and other structural parameters, such as average grain size, crystallinity, strain and crystal defects (Moretti et al.,2020).

2 SPECIFIC OBJECTIVES OF THE RESEARCH

- To use lime stabilization to monitor the changes in cohesion and frictional properties of soil.
- To observe the relative changes in soil permeability before and after improvement using lime stabilization.
- To study the changes in soil structure using XRD.
- To perform sensitivity analysis in real case scenario with increase in cohesion.

3 METHODOLOGY

A laboratory set up was arranged using custom made constant head apparatus as in Figure 1. The top two containers contain two separate mixtures of 500 g and 4000 g solutions. The two small constant head containers take solutions to the samples separately. T1, T2 and T3 were passed through 500 g solution whereas T4, T5 and T6 were passed through 4000 g solution. An acrylic waterproof tube was made for testing samples. Altogether 6 sample tubes were prepared to test lime permeation. Samples were obtained from construction site and taken only samples passing #40 and retained on #200. A uniform density was maintained by mild compaction using Proctor for 25 blows at 5 cm each interval. Two solutions were prepared having 500 g and 4000 g for the same volume of water in separate containers. 500 g solution was passed through T1, T2 and T3 whereas 4000 g solution was passed through T4, T5 and T6. Continuous monitoring of the outlet permeability was done to measure and analyse the effectiveness of lime permeation. Samples were taken out at different time intervals to observe strength behaviour. Cohesion and friction angle were measured at different time intervals as in Figure 5 and Figure 6. A direct shear test method was used under drained conditions Also, X-Ray diffraction (XRD) test was done for T5 to see calcium ions within the samples. Finally, a sensitivity analysis was done using the laboratory data to evaluate possible changes in factor of safety in slope stability.

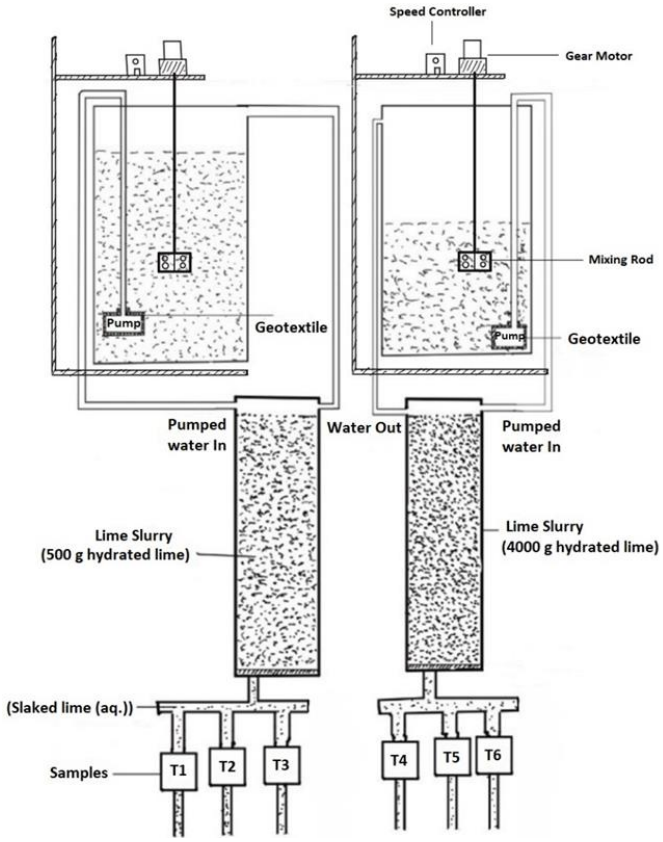

Figure 1. Schematic diagram of laboratory experiment.

4 FLOWCHART

The flowchart shows workflow and varieties of laboratory tests as shown in Figure 2.

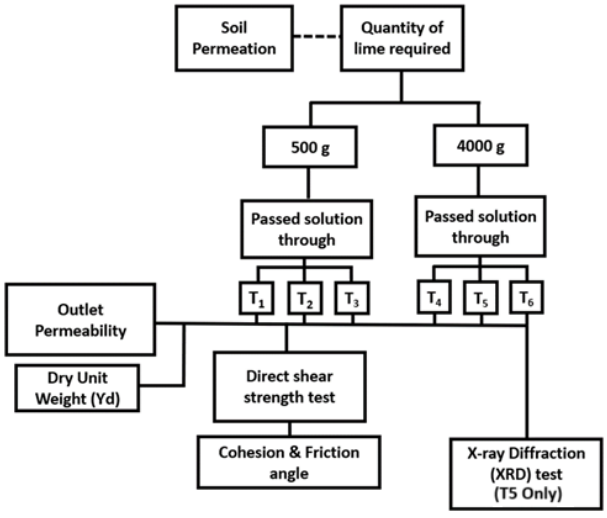

Figure 2. Flowchart of laboratory tests.

5 RESULT AND DISCUSSION

5.1 Unit Weight Variation

Lime water permeation method showed slight gain in the density of the sample i.e. increase in the unit weight of the soil by small percentage from original value. The value from 0.991% to 1.001% was the increased unit weight percentage range from T1 to T6. The result showed increase in unit weight percentage, which was higher in lime solution of 500 g than solution with 4000 g, as in Figure 3 below. 12 days and 66 days had similar results; however, 46 days results were reversed due to uneven flow and irregular permeability during treating.

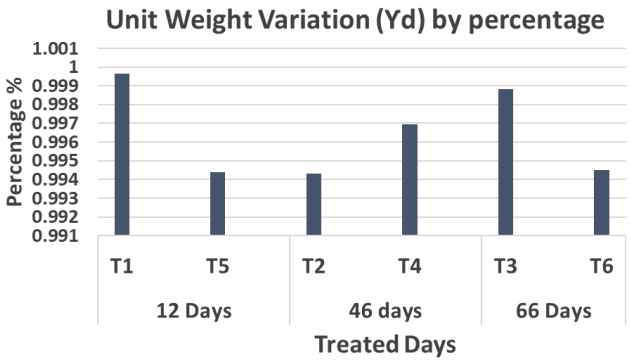

Figure 3. Percentage change in unit weight of the treated soil and its comparison.

5.2 Permeability

The permeability over the period of 2 months (66 days) showed a significant decrease in both 500 g and 4000 g solutions. In the Figure 4, the coefficient of permeability was seen to be slightly higher in 500 g mixture solution than that of 4000 g of solution because of the concentration of the lime particles. Also, as we could see T4 had minimum permeability from beginning due to apparatus misposition of perforated filter or apparatus failure, because of the insufficient permeation, it did not gain enough strength in strength test results. The ups and downs of values in the graph was due to clogging of lime particles. Frequent cleaning of inlet valves and pipes were done. However, this method could not show how much portion of the soil was impermeable and it requires another level of instrumentation or monitoring. The general graph of permeability for all soil samples in different time is in Figure 4 below.

5.3 Strength Test and Analysis

The samples were tested, and friction angle was found to fluctuate slightly lower than beginning as shown in Figure 5. The reduction in friction angle was uniform, which was not much affected by time whereas cohesion was increased exponentially. The friction angle reduction value ranges between 1-5.5% whereas cohesion was increased 0.4% in 12 days, 30% in 46 days and 77% in 66 days of treatment as in Figure 6.

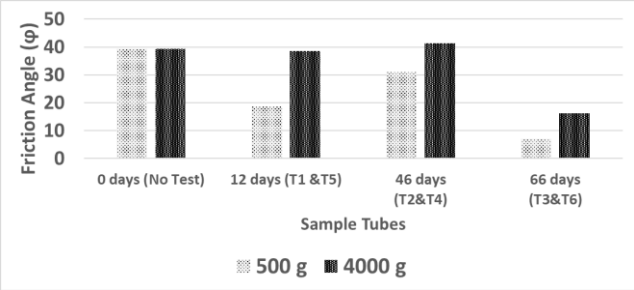

Figure 4. Coefficient of permeability for all samples at two different hydrated lime concentration.

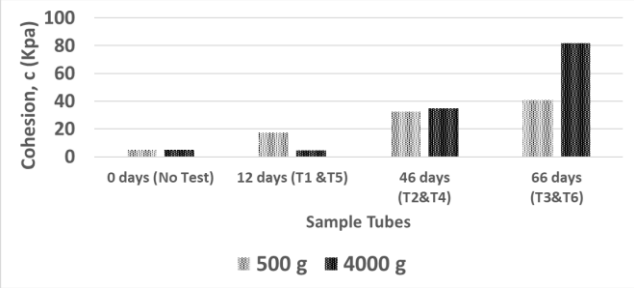

Figure 5. Comparison of friction angle of samples.

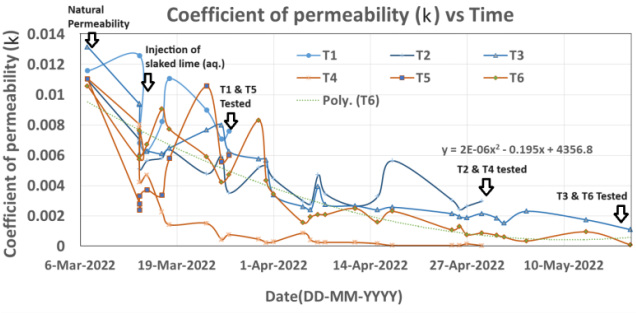

Figure 6. Comparison of Cohesion of samples.

5.4 XRD Test and Analysis

X-Ray Diffraction test was conducted to check the content of lime in compound form or formation of calcium carbonate. A sample tube T5 containing 4000 g solution was tested after 12 days of lime permeation. In a 2D section of the sample tube T5 as in Figure 7, altogether 6 samples were taken out for X-Ray Diffraction test from which Calcite and Quartz crystalline compounds were found. Quartz (SiO_2) is the silica found in sand itself, which had no change unless being mixed by lime particles. Calcite ($CaCO_3$) is the calcium carbonate compound being developed due to lime concentration. The X-ray diffraction was recorded based on reflected light and it is generally called 2θ (2 theta) which gives an angle made between incident and diffracted X-Rays. The result shows higher $CaCO_3$ in the beginning (i.e S51=1.30% and S52=3.46%). However in the middle (i.e S53=0.91%) and last part of the sample got lesser $CaCO_3$ after 12 days of treatment as in Figure 7.

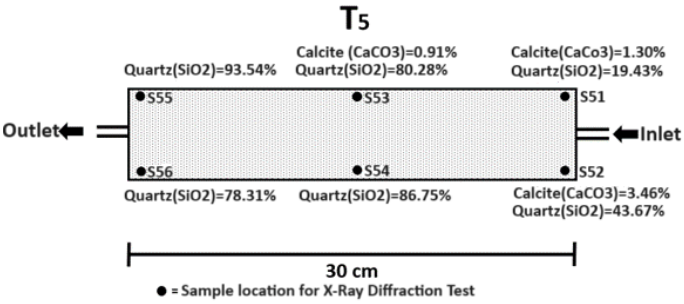

Figure 7. XRD result of T5 sample.

5.5 Sensitivity Analysis

A sensitivity analysis was used to determine the effect of various input parameters on slope stability. The effect of uncertainty or variability in the values of soil parameters could be explored. In this study, cohesion was more dominant parameter than friction angle. From the experiment, it was found that there was no significant change in friction angle values with respect to time; however cohesion was increased over time.

The residual cohesion of soil was found to be 7.84 kPa from a previous study. To check the effect of cohesion parameter in final factor of safety in the Doi Chang case, varying groundwater table and an infinite slope equation was used (Soralump et.al., 2021). In the performed experiment, the cohesion value had increased by 77% over 66 days of lime treatment. Using this cohesion value to simulate safety factor, an 11.2% increment in safety factor was of the unstable slope obtained. This showed that lime treatment would be an effective treatment for unstable slopes with high GWL.

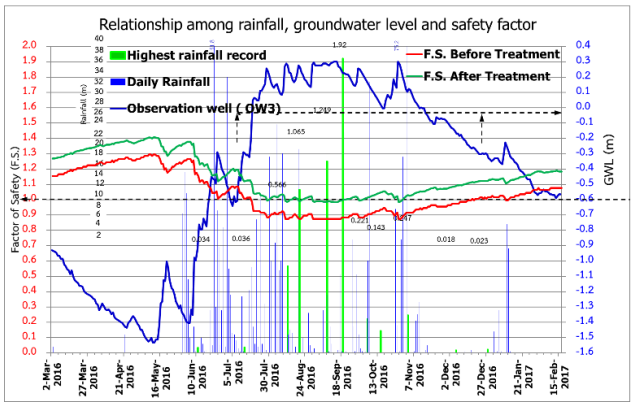

Figure 8. Relationship among rainfall, groundwater, and factor of safety before and after treatment of 66 days of lime permeation.

6 CONCLUSIONS

The lime permeation method is found to be effective for reduction in permeability in fine sand. However, uniform permeation is also a key to strengthen soil within its specimen. It can be greatly expected to have risen in strength where there is higher lime water permeation.

This method also increases cohesion in the cohesionless soil such as sand. However, permeability must be regular and not sudden drop in flow, which might result in the low treatment as in case of T4. Moreover, friction values are not affected much by this method. In case of fiction angle, reduction value ranges between 1-5.5% whereas cohesion was increased 0.4% in 12 days, 30% in 46 days and 77% in 66 days of treatment.

Moreover, presence of Calcium crystals detected by X-Ray Diffraction (XRD) shows successful treatment by lime permeation.

Also, sensitivity analysis for Doi Chang case study shows the cohesion increases by 77% resulting in increase in factor of safety by 11.2% even though high groundwater table is present.

ACKNOWLEDGEMENTS

The authors are grateful for the financial support provided by funding agency Department of Civil Engineering. The project presented in this article is supported by Geotechnical Engineering Research & Development (GERD), Bangkok, Thailand.

REFERENCES

Davoudi, M., Astaneh, F., & Alvandkoohi, H. (2009). Soft soil strengthening by calcium cation permeation. In: *17th International Conference on Soil Mechanics and Geotechnical Engineering*, Alexandria, Egypt, pp. 2354-2357, http://doi.org/10.3233/978-1-60750-031-5-2354

Gabr, M., Boury, E. M., & Bowders, J. J. (1995). Leachate characteristics of fly ash stabilized with lime sludge. *Transportation research record, 1486*, pp. 13-20, Available at: [http://onlinepubs.trb.org/Onlinepubs/trr/1995/1486/1486-002.pdf], accessed: 15/01/2022.

Lawrence, R. M., Mays, T. J., Rigby, S. P., Walker, P., & D'Ayala, D. (2007). Effects of carbonation on the pore structure of non-hydraulic lime mortars. *Cement and concrete research,* 37, pp. 1059-1069, https://doi.org/10.1016/j.cemconres.2007.04.011

Moretti, L., Natali, S., Tiberi, A., & D'Andrea, A. (2020). Proposal for a Methodology Based on XRD and SEM-EDS to Monitor Effects of Lime-Treatment on Clayey Soils, *Applied Sciences,* 10, pp. 14-17, https://doi.org/10.3390/app10072569

Moridzadeh, M. (2019). *Lime treatment to improve frictional resistance and stability of stiff clay slopes, Ph.D,* University of Illinois at Urbana-Champaign. [online] Available at: [https://www.ideals.illinois.edu/items/112318], accessed: 20/01/2022

Soralump, S., Shrestha, A., Thowiwat, W., Sukjaroen, R., Chaithong, T., Yangsanphu, S., . . . Jotisankasa, A. (2021). Assessment of landslide behaviour in colluvium deposit at Doi Chang, Thailand. *Scientific Reports, 11*, 22960, pp. 5-10, https://doi.org/10.1038/s41598-021-02363-3

Thompson, M. R., & Robnett, Q. L. (1976). Pressure injected lime for treatment of swelling soils, In: *54th Annual meeting of the TRB, TRR-568*, pp. 24-34, Washington DC, USA, Available at : [https://onlinepubs.trb.org/Onlinepubs/trr/1976/568/568.pdf#page=27], accessed: 15/01/2022

Thyagaraj, T., Rao, S. M., Sai Suresh, P., & Salini, U. (2012). Laboratory studies on stabilization of an expansive soil by lime precipitation technique. *Journal of Materials in Civil Engineering,* 24, pp. 1067-1075, https://doi.org/10.1061/(ASCE)MT.1943-5533.0000483

Thyagaraj, T., & Zodinsanga, S. (2015). Laboratory investigations of in situ stabilization of an expansive soil by lime precipitation technique. *Journal of Materials in Civil Engineering, 27*, pp. 1-7 , https://doi.org/10.1061/(ASCE)MT.1943-5533.0001184

Townsend, F. C. (1985). Geotechnical characteristics of residual soils. *Journal of Geotechnical Engineering,* 111, pp. 77-94, https://doi.org/10.1061/(ASCE)0733-9410(1985)111:1(77)

Proceedings of the XVIII ECSMGE 2024
GEOTECHNICAL ENGINEERING CHALLENGES
TO MEET CURRENT AND EMERGING NEEDS OF SOCIETY
© 2024 the Authors
ISBN 978-1-032-54816-6
DOI 10.1201/9781003431749-213
Open Access: www.taylorfrancis.com, CC BY-NC-ND 4.0 license

ECSMGE 24
XVIII EUROPEAN CONFERENCE ON SOIL MECHANICS AND GEOTECHNICAL ENGINEERING

Numerical and experimental evidence of the impact of soil nonlinearity on the response of an SSI system

Preuve numérique et expérimentale de l'impact de la non-linéarité du sol sur la réponse d'un système ISS

M. Koronides*
Cyprus university of technology, Limassol, Cyprus, Formerly: Imperial College London, London, UK

S. Kontoe
University of Patras, Patras, Greece. Imperial College London, London, UK

L. Zdravković, D.M. Potts
Imperial College London, London, UK

A. Vratsikidis, D. Pitilakis, A. Anastasiadis
Aristotle University of Thessaloniki, Thessaloniki, Greece

**marios.koronides@cut.ac.cy*

ABSTRACT: The influence of dynamic Soil-Structure-Interaction (SSI) phenomena on the response of structures under dynamic loading is widely recognised. These phenomena are more impactful on structures that are founded on soft soil sites, where soil nonlinearity can prevail. The present study examines this aspect by the means of three-dimensional nonlinear finite element analyses of real-scale free-vibration experiments on a steel frame structure. The structure has outer dimensions of 3×3×5m and is rested on a shallow foundation over a soft soil deposit. The numerical analyses focus on modelling experiments of different magnitude excitation forces, to allow the investigation of the SSI system for a wide strain range. Cyclic nonlinear models, which are typically used in numerical analysis to predict the hysteretic behaviour of soils, can simulate well either the stiffness degradation (G-γ) or the damping evolution (D-γ) with cyclic shear strain. Experimental strong motion data are compared against numerical results of analyses that adopt different G-γ-D curves for the shallow foundation soil. This investigation reveals that the choice of G-γ-D curves affects significantly the SSI free-vibration response, highlighting the importance of modelling the nonlinear behaviour of shallow soil appropriately. It also suggests that prioritising the calibration of the D-γ curve over G-γ is more applicable for most of the modelled experiments.

RÉSUMÉ: L'influence des phénomènes dynamiques d'interaction sol-structure (ISS) sur la réponse des structures soumises à des charges dynamiques est largement reconnue. Ces phénomènes ont un impact plus important sur les structures fondées sur des sols meubles, où la non-linéarité du sol peut prévaloir. La présente étude examine cet aspect au moyen d'analyses par éléments finis non linéaires tridimensionnels d'expériences de vibration libre à l'échelle réelle sur une structure en colonnes d'acier. La structure a des dimensions extérieures de 3×3×5 m et repose sur une fondation peu profonde au-dessus d'un dépôt de sol meuble. Les analyses numériques se concentrent sur les expériences de modélisation des forces d'excitation de différentes magnitudes, afin de permettre l'étude du système ISS pour une large gamme de déformations. Les modèles non linéaires cycliques, qui sont généralement utilisés dans l'analyse numérique pour prédire le comportement hystérétique des sols, peuvent bien simuler la dégradation de la rigidité (G-γ) ou l'évolution de l'amortissement (D-γ) avec la déformation cyclique de cisaillement. Les données expérimentales sur les mouvements forts sont comparées aux résultats numériques d'analyses qui adoptent différentes courbes G-γ-D pour le sol de fondation peu profond. Cette étude révèle que le choix des courbes G-γ-D affecte de manière significative la réponse en vibration libre du ISS, soulignant l'importance de modéliser de manière appropriée le comportement non linéaire du sol peu profond. Elle suggère également que la priorité donnée à l'étalonnage de la courbe D-γ par rapport à la courbe G-γ est plus applicable pour la plupart des expériences modélisées.

Keywords: Dynamic soil-structure interaction; finite element modelling; real-scale experiments; soil nonlinearity; constitutive model calibration.

1 INTRODUCTION

The significant role of soil nonlinearity on the dynamic response of soil-structure-interaction (SSI) systems with shallow foundations has been demonstrated in various studies in the past (e.g. Anastasopoulos et al., 2011; 2014; Gazetas et al., 2013). Most of these

studies focused on large strain problems, where soil plasticity is significantly engaged, however, soil nonlinearity associated with the small strain response has attracted less attention.

In problems dominated by the nonlinearity of soil behaviour at small strains, it is important to consider an appropriate set of stiffness degradation and damping ratio (G-γ-D) curves, due to the very limited linear elastic strains in such soils (e.g. Darendeli, 2001; Vucetic, 1993). Cyclic nonlinear models that are typically used in such analyses can simulate well either the stiffness or the damping curve (Taborda and Zdravkovic, 2012). It has been shown that the accurate prediction of the damping curve should be prioritised in free-field site response problems (e.g. Han et al., 2016; Papaspiliou et al., 2012), however there are no similar studies for SSI problems.

The present study discusses 3D nonlinear finite element (FE) simulations of real-scale free vibration tests on the prototype structure of EUROPROTEAS. Particular emphasis is placed on modelling the soil behaviour, investigating the impact of adopting different calibrations for the G-γ-D curves.

2 EXPERIMENTAL CAMPAIGN

2.1 Structure and experimental set-up

The examined structure is the prototype EUROPROTEAS structure that is 5m tall and 3 x 3m in plan. This frame structure comprises four steel columns (SHS 150 x 150 x 10mm), adjustable steel cross bracing system (L-shape 100 x 100 x 10mm), a reinforced concrete mat foundation (9Mg) and adjustable superstructural mass. Although different structural configurations were examined, the present study refers to one configuration only: a structure braced at all four sides and a superstructural mass of 18Mg (Figure 1).

The wider experimental campaign consisted of free and forced vibration tests (Koronides et al., 2023a), with the present study focusing on the former tests. The free vibration tests involved the application of a pull-out force at 9˚ angle to the horizontal plane on the top slab (Figure 1), via a wire rope tensioned by a pulling hoist. The force was measured in-situ by a load cell and upon reaching the desired magnitude, the wire was instantly cut, enabling the structure to oscillate until it came to rest. In both test types, the force was applied along the NS plane of symmetry of the structure, with reference to the coordinate system shown in Figure 1. The response of the SSI system was monitored by a comprehensive instrumentation that was placed on both the structure and the soil.

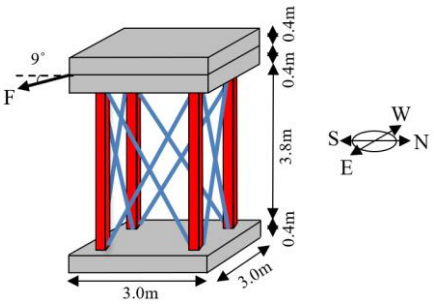

Figure 1. EUROPROTEAS' structural configuration.

2.2 Soil conditions

EUROPROTEAS is located at the TST site, the centre of Euroseistest site, within a valley in Northern Greece. The geotechnical and geological properties of the site are well documented by previous surveys (e.g. D. Pitilakis et al., 2018; K. Pitilakis et al., 1999), with Figure 2(a) and (b) presenting the resulting soil stratigraphy and shear velocity profiles, respectively. The shallow soil layers mainly consist of silty sand and low plasticity clay of very low stiffness, a condition that is anticipated to amplify SSI effects. The geotechnical site characterisation encompassed also resonant column and cyclic triaxial tests for soil samples retrieved from various depths, some of which are indicated in Figure 2(a). These tests produced stiffness degradation and damping ratio curves (G-γ-D) for the corresponding soil layers. The process of projecting the G-γ-D curves from lab conditions to site conditions is described in Koronides et al. (2023a).

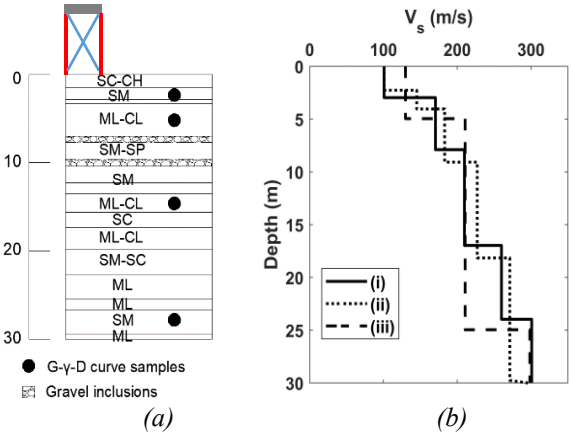

(a) *(b)*

Figure 2. (a) Soil stratigraphy, (b) shear wave profiles proposed by (i) K. Pitilakis et al. (1999), (ii) Raptakis et al. (2000) and (iii) Raptakis and Makra (2015).

3 NUMERICAL MODEL

Free vibration simulations were carried out using the Imperial College Finite Element Program (ICFEP) (Potts & Zdravković, 1999). Each simulation consists of three phases: a static phase where the deadloads are applied, a static phase where the pull-out force is

applied, and a dynamic phase where the free oscillation of the structure is computed.

3.1 Problem geometry and boundary conditions

The numerical model simulates only the half of the domain, exploiting the symmetry of the problem. Figure 3 presents the 3D mesh, dimensions and some of the boundary conditions.

The simulated soil domain has dimensions 15 x 7.5 x 6m, which were found to produce neglible boundary effects on the structural response and tolerable effects on the soil response. The 6m deep soil domain is divided into two soil layers (Figure 3a), as identified from the experimental studies, the results of which are shown in Figure 2(a). The domain consists of 20-noded brick elements, the size of which was based on the guidelines of Kuhlemeyer and Lysmer (1973). The corner nodes of the bottom boundary of the soil domain are fully fixed, while all nodes at the plane of symmetry (including the soil, base and top slab and braces) are fixed in the out-of plane (y) direction only. Dashpots and springs (Kontoe, 2006) are applied along the normal and tangential directions on the remaining soil boundary nodes, except those at the ground surface.

The numerical model explicitly simulates the dimensions of the actual structure (Figure 3(b)). The foundation and top slabs are modelled with 20-noded brick elements, while the steel columns and braces with 3-noded beam elements. To establish a moment connection between the columns and slabs, the beam elements of the columns extend into the brick elements of the slabs. The stiffness of the extended beam elements and the damping (ξ) of concrete and steel were calibrated in Koronides et al. (2023a). The remaining structural properties are chosen in accordance with modern regulations (i.e. British Standards Institution, 2004, 2005). All structural elements are assumed to be linear elastic, with their properties, including Young's modulus (E), Poisson's ratio (ν), density (ρ), cross sectional area (A), moment of inertia (I), torsional constant (J) and target Rayleigh damping (ξ), given in Table 1.

The excitation pull-out force (F) is applied at a node of top slab that lies in the plane of symmetry, as shown in Figure 3(a). Two free vibration experiments of 2.9kN and 15.7kN pull-out force are simulated. However, considering that only half of the problem geometry is modelled, half of the above magnitudes was applied in each analysis.

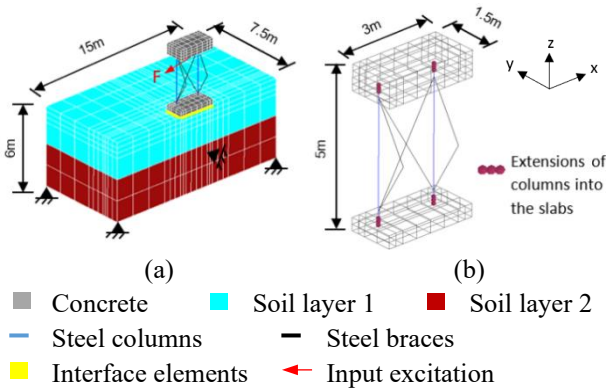

Figure 3. FE mesh, dimensions and some boundary conditions of the simulated experiments: (a) SSI system, (b) Structure.

3.2 Soil-foundation interface model

As discussed by Koronides (2023), field observations as well as strong motion data interpretation indicated permanent gap areas at the interface between the foundation and the soil. These played a crucial role in the response of the SSI system. The gap distribution and the interface model were calibrated by Koronides et al. (2022a, 2023a) against forced vibration measurements. The resulting distribution of permanent gaps is illustrated in Figure 4. Koronides et al. (2023b) demonstrated that during the various experiments carried out in the experimental campaign, temporary detachment and re-attachment of some foundation areas took place. However, they illustrated that for the present experiments, the above foundation behaviour could be reasonably neglected to reduce the computational cost. Therefore, the present analyses assume permanent interface gaps at the positions shown in Figure 4. only. For the interface model, elastic zero thickness interface elements (Day and Potts, 1994) are employed. These are characterised by shear and normal elastic stiffnesses, K_s and K_n, which control the relative elastic displacements between the foundation and the soil. A stiffness value of $K_s=K_n=1E8kN/m^3$ was adopted for the contact area, whereas $K_s=K_n=1E2kN/m^3$ was used for the non-contact area. The reduced interface stiffness of the latter area was shown equivalent to simulating permanent gaps, but at lower computational cost (Koronides et al., 2022b; 2023a; 2023b).

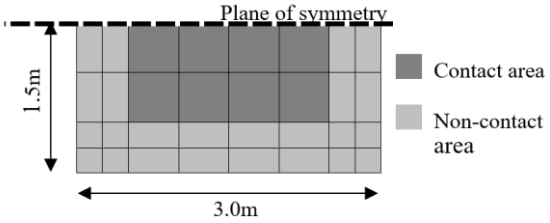

Figure 4. Permanent contact conditions at the soil-foundation interface.

Table 1. Elastic properties of the structural elements.

	E (GPa)	ν	ρ (Mg/m^3)	A (cm^2)	I (cm^4)	J (cm^4)	ξ (%)
Concrete	31	0.2	2.5	-	-	-	1
Braces	200	0.25	7.85	19.2	177	6.97	2
Columns	200	0.25	7.85	54.9	1770	2830	2
Beam elements extended into the foundation	200E4	0.25	0.05	54.9	1770	2830	-
Beam elements extended into the top slab	3	0.25	0.05	54.9	1770	2830	-

3.3 Nonlinear soil constitutive model

Koronides (2023) showed that for the examined SSI problem, soil nonlinearity extends within a very shallow soil zone. Herein, the first 0.8m of the soil domain is assumed to behave as nonlinear elastic material, while the remaining soil domain is prescribed as linear elastic. Table 2 presents the soil properties of the two layers at very small strains, that were inferred from previous site characterisation studies (Figure 2(b)). A target Rayleigh damping (ξ) of 5% was selected for the linear soil.

Table 2. Small strain soil properties.

	E (MPa)	ν	ρ (Mg/m^3)
Layer 1	100	0.25	2.0
Layer 2	186	0.20	2.1

For the nonlinear soil, the Imperial College Generalised Small Strain Stiffness (IC.G3S) model (Taborda et al., 2016) is used. The model prescribes the G-γ-D curves based on a predefined set of parameters. Figure 5 presents the three different G-γ-D curves, whose effect on the SSI response is investigated herein. These are compared with the reference curves, which were interpreted from resonant column and cyclic triaxial tests.

This type of cyclic models can describe well either the damping or shear stiffness curve, which is deemed the most important consideration on the calibration of the model's parameters. As Figure 5 shows and as highlighted by Taborda and Zdravkovic (2012), if the calibration prioritises the shear stiffness degradation curve (CalibrG), the soil damping is highly underestimated and highly overestimated at the very low and medium strain range, respectively. When, though, the calibration prioritises the damping ratio curve (CalibrD), the model underestimates the soil shear stiffness over the very small to small strain range. To further examine the impact of damping on the SSI response, an additional set of G-γ-D curves that predict a stiffness curve similar to CalibrD, but overestimates damping over a wide range of strains (CalibrDO) is also examined.

The adopted nonlinear constitutive model assumes soil shear stiffness as a function of mean effective stress. This is of paramount importance in SSI problems, where the presence of a structure contributes to a stiffer foundation soil in relation to the free-field conditions, affecting the response of the system.

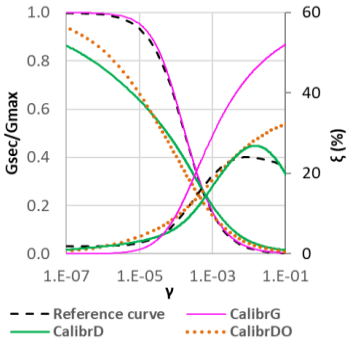

Figure 5. Examined calibrations of stiffness degradation and damping ratio curves.

4 RESULTS AND DISCUSSION

Figure 6 presents acceleration time histories and the corresponding Fourier spectra recorded at the top slab during the free vibration experiments of pull-out forces 2.9 and 15.7kN, as well as the linear elastic prediction. The accelerations were normalised by the magnitude of the pull-out force to allow comparison between different experiments, with any differences being attributed to nonlinear phenomena. The figure demonstrates that when larger pull-out force was applied, the response was more flexible and lower in amplitude. Possible nonlinearities are soil nonlinearity, interface nonlinearity and structural elements' nonlinearity. The latter is assumed negligible due to the weak bending of the structural elements (Koronides, 2023). Also, as shown by Koronides et al. (2022a; 2023a; 2023b), if interface nonlinearity was predominant, it would have led to a smaller interface contact area and, consequently, weaker radiation damping, resulting in motion amplification. This expectation contradicts the observed de-amplification, suggesting that the observed nonlinear phenomena can be predominantly assigned to soil nonlinearity. Figure 6 also demonstrates that a linear elastic analysis overpredicts both the natural frequency and the magnitude of the

SSI response, highlighting the necessity of incorporating soil nonlinearity.

*Figure 7*Figure 7 presents acceleration time histories and the corresponding Fourier spectra inferred from nonlinear analyses that assume different calibrations for the G-γ-D curves. CalibrG analysis predicts a larger natural frequency for both the small and larger strain response (i.e. F=2.9kN and F=15.7kN, respectively) and, most importantly, it strongly overdamps the motion of the system subjected to a larger force (i.e. F=15.7kN, shown in Figure 7b). Conversely, when the calibration prioritises the damping curve, e.g. CalibrD, the analysis accurately predicts the magnitude and frequency of both experimental responses. This observation demonstrates that, in SSI problems, the calibration of the G-γ-D curves should prioritise capturing the experimental damping curve well, accepting the limited consequences of underestimating the shear stiffness curve.The importance of damping in the examined SSI problem is further corroborated by the comparison of CalibrD and CalibrDO results. The two analyses predict similar response frequency, as a consequence of their similar soil stiffness simulation. However, CalibrDO, which overestimates damping, results in response overdamping for both small strain (i.e. F=2.9kN) and larger strain response (i.e. F=15.7kN). Hence, it can be concluded that a seemingly small damping overestimation can lead to significant errors, emphasizing the critical need for accurately simulating soil damping.

5 CONCLUSIONS

Three-dimensional FE simulations of real scale free vibration experiments have been presented. Although the field experiments induced small strains in the soil, soil nonlinearity was important, as indicated by both numerical and experimental data evidence.

Numerical results from analyses that adopt different calibrations for the G-γ-D curves were compared, demonstrating the necessity to simulate the damping behaviour of the soil appropriately. In fact, it is suggested that the calibration of cyclic nonlinear models should prioritise capturing the damping curve, even at the cost of underestimating the stiffness curve.

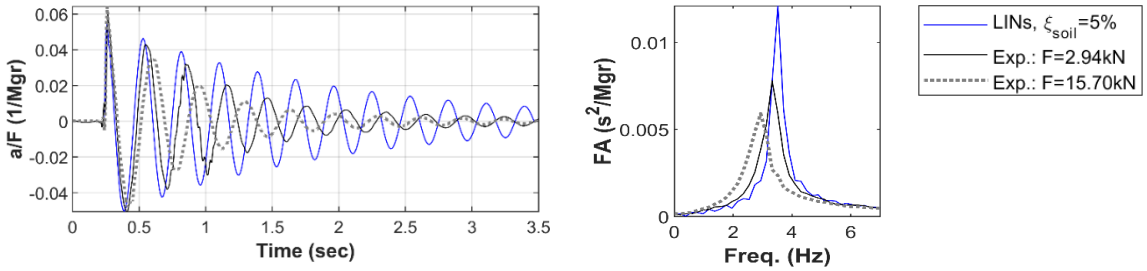

Figure 6. Normalised top slab acceleration time histories and the corresponding Fourier spectra inferred from linear analysis and experimental data.

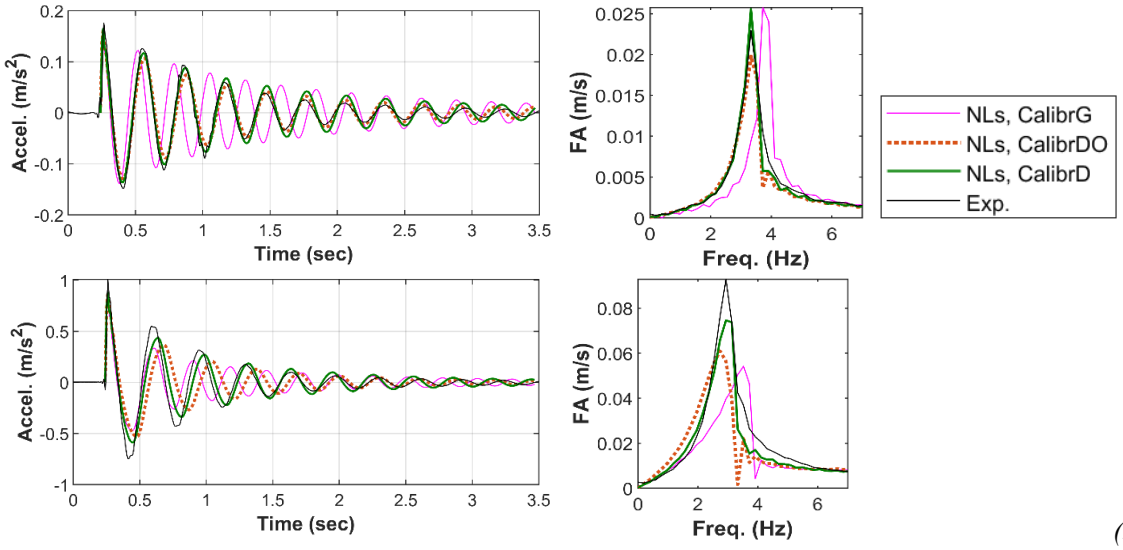

(a) F=2.9kN

(b) F=15.7kN

Figure 7. Top slab acceleration time histories and the corresponding Fourier spectra inferred from experimental data and nonlinear analyses with different calibrations.

The latter conclusion aligns with similar conclusions drawn from free-field site response analyses (e.g. Han et al., 2016; Papaspiliou et al., 2012).

ACKNOWLEDGEMENTS

The experiments were funded by SERA (Seismology and Earthquake Engineering Research Infrastructure Alliance for Europe). The first author wishes to thank Skempton Scholarship, A.G. Leventis and Cyprus State Scholarship Foundations for their support.

REFERENCES

Anastasopoulos, I., Gelagoti, F., Kourkoulis, R., Gazetas, G. (2011). Simplified Constitutive Model for Simulation of Cyclic Response of Shallow Foundations: Validation against Laboratory Tests. *Journal of Geotechnical and Geoenvironmental Engineering*, *137*(12), 1154–1168.

British Standards Institution. (2004). *BS EN 1992-1-1:2004. Eurocode 2. Design of concrete structures. General rules and rules for buildings*.

British Standards Institution. (2005). *BS EN 1993-1-1:2005, Eurocode 3. Design of steel structures. General rules and rules for buildings*.

Darendeli, M. B. (2001). *Development of a new family of normalized modulus reduction and material damping curves*. The University of Texas at Austin.

Day, R. A., Potts, D. M. (1994). Zero thickness interface elements—numerical stability and application. *International Journal for Numerical and Analytical Methods in Geomechanics*, *18*(10), 689–708. https://doi.org/10.1002/nag.1610181003.

Gazetas, G., Anastasopoulos, I., Adamidis, O., Kontoroupi, T. (2013). Nonlinear rocking stiffness of foundations. *Soil Dyn. Earth. Eng.*, *47*, 83–91.

Han, B., Zdravkovic, L., Kontoe, S., Taborda, D. M. G. (2016). Numerical investigation of the response of the Yele rockfill dam during the 2008 Wenchuan earthquake. *Soil Dynamics and Earthquake Engineering*, *88*, 124–142.

Kontoe, S. (2006). *Developement of time integration schemes and advanced boundary conditions for dynamic geotechnical analysis* (Issue May) [ICL].

Koronides, M. (2023). *Numerical and field investigation of dynamic soil structure interaction at full-scale*. Imperial College London.

Koronides, M., Kontoe, S., Zdravković, L., Vratsikidis, A., Pitilakis, D. (2023). Numerical simulation of SSI free and forced vibration experiments on real scale structures of different stiffness. *Soil Dyn Earth Eng*, *175*. https://doi.org/10.1016/j.soildyn.2023.108232.

Koronides, M., Kontoe, S., Zdravković, L., Vratsikidis, A., Pitilakis, D., Anastasiadis, A., Potts, D. M. (2022a). Numerical simulation of real-scale vibration experiments of a steel frame structure on a shallow foundation. In L. Wang, J.-M. Zhang, & R. Wang (Eds.), *Proc. 4th Int. Conf. on Performance-based Design in Earthquake Engineering* (pp. 1119–1127).

Koronides, M., Kontoe, S., Zdravković, L., Vratsikidis, A., Pitilakis, D., Anastasiadis, A., Potts, D. M. (2022b). Numerical simulations of field soil-structure interaction experiments on a shallow founded steel frame structure. *Proc. 3rd Int. Conf. on Natural Hazards & Infrastructure*.

Koronides, M., Kontoe, S., Zdravković, L., Vratsikidis, A., Pitilakis, D., Anastasiadis, A., Potts, D. M. (2023). Numerical simulation of soil-structure interaction experiments on shallow founded structures for different mass configurations. In L. Zdravkovic, S. Kontoe, D. M. G. Taborda, & A. Tsiampousi (Eds.), *Proc. 10th Eur. Conf. on Numerical Methods in Geotechnical Engineering*.

Kuhlemeyer, R. L., Lysmer, J. (1973). FINITE ELEMENT METHOD ACCURACY FOR WAVE PROPAGATION PROBLEMS. *Soil Mechanics & Foundations Div*, *99*(sm5), 421–427.

Papaspiliou, M., Kontoe, S., Bommer, J. J. (2012). An exploration of incorporating site response into PSHA-Part I: Issues related to site response analysis methods. *Soil Dynamics and Earthquake Engineering*, *42*, 302–315. https://doi.org/10.1016/j.soildyn.2012.06.011.

Pitilakis, D., Rovithis, E., Anastasiadis, A., Vratsikidis, A., Manakou, M. (2018). Field evidence of SSI from full-scale structure testing. *Soil Dyn. Earth. Eng.*, *112* (March), 89–106. https://doi.org/10.1016/j.soildyn.2018.04.024.

Pitilakis, K., Raptakis, D., Lontzetidis, K., Tika-Vassilikou, T., Jongmans, D. (1999). Geotechnical and geophysical description of euro-seistest, using field, laboratory tests and moderate strong motion recordings. *Journal of Earthquake Engineering*, *3*(3), 381–409.

Potts, D. M., & Zdravković, L. (1999). *Finite element analysis in geotechnical engineering: theory*. Thomas Telford, London.

Raptakis, D., Chávez-García, F. J., Makra, K., Pitilakis, K. (2000). Site effects at Euroseistest-I. Determination of the valley structure and confrontation of observations with 1D analysis. *Soil Dyn Earth Eng*, *19*(1), 1–22.

Raptakis, D., Makra, K. (2015). Multiple estimates of soil structure at a vertical strong motion array: Understanding uncertainties from different shear wave velocity profiles. *Eng. Geology*, *192*, 1–18.

Taborda, D. M. G., Potts, D. M., Zdravković, L. (2016). On the assessment of energy dissipated through hysteresis in finite element analysis. *Computers and Geotechnics*, *71*, 180–194.

Taborda, D. M. G., Zdravkovic, L. (2012). Application of a Hill-Climbing technique to the formulation of a new cyclic nonlinear elastic constitutive model. *Computers and Geotechnics*, *43*, 80–91.

Vucetic, M. (1993). Cyclic threshold shear strains in soils. *Journal of Geotechnical Engineering*, *120*(12), 2208–2228.

Proceedings of the XVIII ECSMGE 2024
GEOTECHNICAL ENGINEERING CHALLENGES
TO MEET CURRENT AND EMERGING NEEDS OF SOCIETY
© 2024 the Authors
ISBN 978-1-032-54816-6
DOI 10.1201/9781003431749-214
Open Access: www.taylorfrancis.com, CC BY-NC-ND 4.0 license

ECSMGE 24
XVIII EUROPEAN CONFERENCE ON SOIL MECHANICS AND GEOTECHNICAL ENGINEERING

Particle size distribution induced fabric effects on the onset and post liquefaction behaviours of soils

La distribution granulométrique induit des effets de tissu sur le comportement initial et post-liquéfaction des sols

J. Leak*, D. Barreto
Edinburgh Napier University, School of Computing Engineering and the Built Environment, Edinburgh

**J.leak@napier.ac.uk*

ABSTRACT: Liquefaction in soils is a detrimental phenomenon. Microscale behaviours and their influence on the macroscale response during and after the onset of liquefaction are not well understood. In particular, how contact behaviours effect macroscale properties such as gains in shear strength following the onset of liquefaction. Soil characteristics such as particle size distribution (PSD) are known to have important roles in determining a soils susceptibility to liquefaction. In this study, Discrete Element Simulations (DEM) are undertaken on soils with different PSDs to investigate how contacts at the microscale are influenced by PSD and how this influences the macroscale response. Consideration is given to these behaviours before and after the onset of liquefaction to gain insight into post-liquefaction strength behaviour. Using grading entropy coordinates, it is suggested that the PSD plays a key role in a soils ability to resist liquefaction. Larger grains appear to provide greater stability and an ability gain interparticle contacts post-liquefaction. This greater stability is suggested to come from the grain structure resisting being broken and remade during liquefaction, manifesting in greater isotropy throughout loading. Whereas soils with smaller PSDs are more prone to having their grain structure broken and remade, enabling them to become significantly more anisotropic, this appears to inhibit the ability to regain interparticle contacts.

RÉSUMÉ: La liquéfaction des sols est un phénomène néfaste. Les comportements à l'échelle microscopique et leur influence sur la réponse à l'échelle macro pendant et après le début de la liquéfaction ne sont pas bien compris. En particulier, comment les comportements de contact affectent les propriétés à l'échelle macro, telles que les gains de résistance au cisaillement après le début de la liquéfaction. Les caractéristiques du sol telles que la distribution granulométrique (PSD) sont connues pour jouer un rôle important dans la détermination de la susceptibilité des sols à la liquéfaction. Dans cette étude, des simulations d'éléments discrets (DEM) sont entreprises sur des sols présentant différentes PSD pour étudier comment les contacts à l'échelle microscopique sont influencés par la PSD et comment cela influence la réponse à l'échelle macro. Ces comportements sont pris en compte avant et après le début de la liquéfaction afin de mieux comprendre le comportement en matière de résistance après liquéfaction. En utilisant les coordonnées entropiques de gradation, il est suggéré que la PSD joue un rôle clé dans la capacité des sols à résister à la liquéfaction. Les grains plus gros semblent offrir une plus grande stabilité et une capacité à gagner des contacts interparticulaires après liquéfaction. Il est suggéré que cette plus grande stabilité provienne du fait que la structure des grains résiste à la rupture et à la reconstruction lors de la liquéfaction, se manifestant par une plus grande isotropie tout au long du chargement. Alors que les sols avec des PSD plus petits sont plus susceptibles de voir leur structure granulaire brisée et refaite, ce qui leur permet de devenir significativement plus anisotropes, cela semble inhiber la capacité à retrouver les contacts interparticulaires.

Keywords: Liquefaction; particle size distribution; grading entropy; soil fabric.

1 INTRODUCTION

Susceptibility to liquefaction can be determined with reference to a soils particle size distribution (PSD). Regarding this approach several methods have been proposed (e.g. Tsushida & Hayashi, 1971). The abundance of PSD based susceptibility criteria clearly indicate that a relationship exists between the initiation of liquefaction and grain size. Barreto et. al. (2019) assessed different susceptibly criteria using the grading entropy method proposed by Lőrincz (1986). This study affirmed a clear relationship between the entire PSD (i.e. including fines and gravel content) and liquefaction susceptibility, with reference to the grading entropy stability criteria. Moreover, the study highlighted the benefits of the grading entropy coordinates as a PSD based susceptibility criteria.

There is evidence to suggest that a relationship between PSD and increases in post-liquefaction shear

strength exist also. Whilst aspects such as confining stress, void ratio or relative density, fines content etc, are highly influential, PSD appears to be an important factor in the initiation of liquefaction and its ability to regain its strength following failure, via rebuilding interparticle contacts. It was discussed by Manmatharajan et al. (2023), that amongst varying PSDs, coarser well-graded PSDs showed greater post-liquefaction shear strength, particularly when compared to PSDs with the presence of fines, and poorly graded soils.

It has also been suggested that post-liquefaction shear strength may in part also be related to the orientation in particle fabric. For example, Wang et al (2020) investigated the post liquefaction shearing resistance of gravelly soils and found that the more anisotropic a soil is, the greater the difficulty it exhibits rebuilding shear strength and stable inter-particle particle contacts – leaving the soil vulnerable to secondary liquefaction. This was something also suggested by Otsubo et al. (2022), who stated that soils with a greater inherent isotropic fabric may have the potential to exhibit greater liquefaction resistance.

This study investigates the effect of PSD on the initiation and post-liquefaction contact behaviours of soils. Emphasis is placed on the influence of PSD and fabric behaviours, and exploring the role this plays in the development of liquefaction and a soils ability to regain interparticle contacts following failure. In this work, the entire PSD is assessed using grading entropy coordinates, enabling for the entire PSD to be represented.

2 GRADING ENTORPY

Proposed by Lőrincz (1986), grading entropy condenses the entirety of a PSD to a single point on a Cartesian plane. This is achieved by accumulating the information entropy within each soil fraction to ascertain the total grading curve entropy. The total grading entropy can then be split into two components which form a coordinate pair:

$$S = \Delta S + S_0 \tag{1}$$

where S is the total grading entropy, ΔS is the entropy increment, typically on the y-axis, and S_0 is the base entropy typically on the x-axis. The base entropy (S_0) is a logarithmic mean of the average grain diameter relating to the skewness of the PSD. ΔS is a measure of how much a PSD is influenced by all its fractions and relates to the kurtosis of the PSD.

ΔS and S_0 have normalised counterparts, where $0<A<1$ and $0<B<B_{max}$ 1.41. A is the normalised base entropy and B is the normalised entropy increment, given by:

$$A = \frac{S_0 - S_{0min}}{S_{0max} - S_{0min}} \tag{2}$$

$$B = \frac{\Delta S}{\ln(N)} \tag{3}$$

where N is the number of sieve fractions in the PSD. Whilst grading entropy coordinates may be related to commonly used descriptors, it should be noted that in contrast to these, ΔS, S_0 and A, B involve information about the entire PSD, not just specific particles diameters (e.g., d_{10}, d_{30}, d_{50}, d_{60}) and enables for the direct consideration of both fines and gravel content with no need for additional descriptors. In this study, only the normalised coordinates are used.

3 DEM SIMULATIONS & PSDs

Undrained monotonic DEM simulations were performed using the open-source software YADE. Specimens were randomly generated within cubical periodic boundaries and isotropically compressed prior to triaxial loading under constant volume conditions. A summary of the DEM input parameters is shown in Table 1.

Table 1. DEM Input parameters.

Description	Value
Confining Stress	200 kPa
Poisson's ratio (ν)	0.22
Particle density (ρ)	2650 kg/m^3
Inter-particle friction (μ)	26.6°
Young's Modulus (E)	70 GPa
Unbalanced force ratio	0.0001

These parameters where chosen to represent realistic values that have been measured experimentally by other researchers. Simulations were undertaken on uniform PSDs containing a single fraction, which are shown in Table 2:

Table 2. PSD ranges and entropy coordinates.

ID	Range	A	B
A1	1-2	1	0
A2	0.5-1	0.75	0
A3	0.25-0.5	0.5	0
A4	0.125-0.25	0.25	0
A5	0.0625-0.125	0	0

4 RESULTS

Figure 1 shows the deviatoric stress (q) during the first 5% axial strain (ε_a):

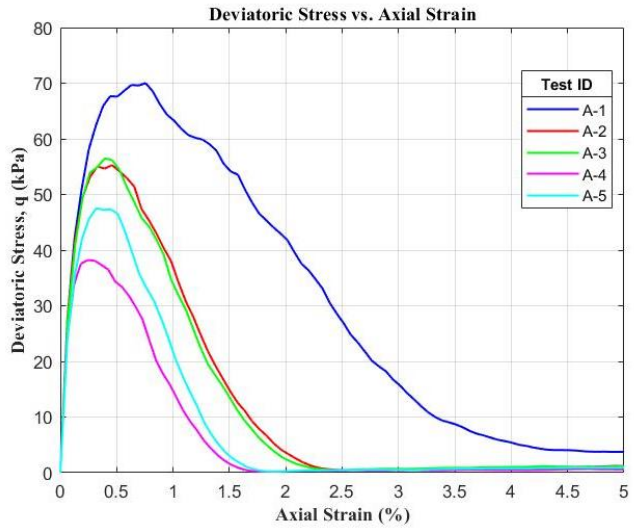

Figure 1. Deviatoric stress during the first 5% axial strain.

In all specimens but A-1, the deviatoric stress increases after the initiation of loading, but immediately reduce to near zero around 1.5% - 2.5% axial strain. Specimen A-1 shows the highest peak stress, followed by A-3, A-2, A-5 and A-4. Generally, as the A-coordinate increases, q_{peak} also increases, highlighting a relationship between stability and grain size. A-1, with the largest grain size, does not drop to a state $q=0$, indicating that it underwent more stable behaviours. Specimens A-2 and A-3 share similar stress relationships, with A-3 experiencing a slightly higher peak stress.

Figure 2 shows the initial mechanical coordination number (Zm_0) plotted with each specimen A-coordinate.

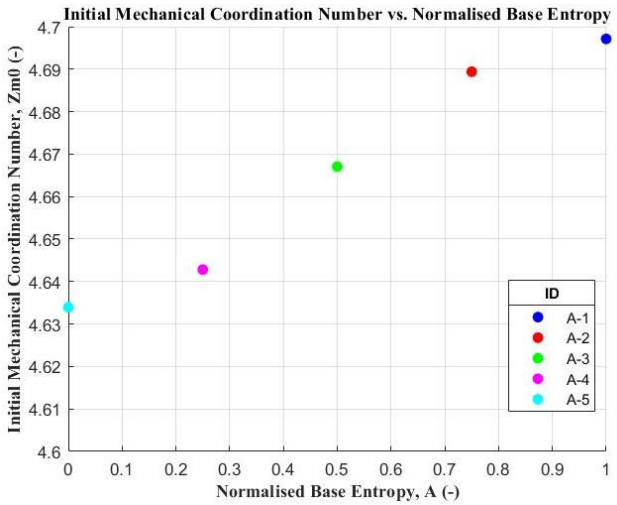

Figure 2. Initial mechanical coordination, Zm_0, number with normalised base entropy, A.

There is a relationship between the Zm_0 and decreasing A-coordinates. In other words, as the PSD decreases the specimens exhibit fewer stable tendencies. Note that these decreases in the Zm_0 align with the decreases in q_{peak} seen in Figure 1. It is suggested that as a result of changing the PSD, the ability for stress transmitting contacts to form is reduced; thus reducing the overall stability of the soil.

In Figure 3, to understand the contact behaviour at the initiation of liquefaction, Zm values corresponding to the minimum mean effective stress (p') in each specimen are plotted against their A-coordinates, i.e. the initiation of liquefaction. The decrease in Zm at the onset of liquefaction follows the same relationship seen in Figure 2, with Zm_0, indicating that the PSD influences stability (by means of particle contacts) during the initiation of liquefaction and this may be an inherent property of different PSDs. Whilst further research is needed, the results presented here may indicate that the threshold coordination discussed by Wen and Zhang (2022), amongst others, may be PSD dependant, at least under monotonic conditions.

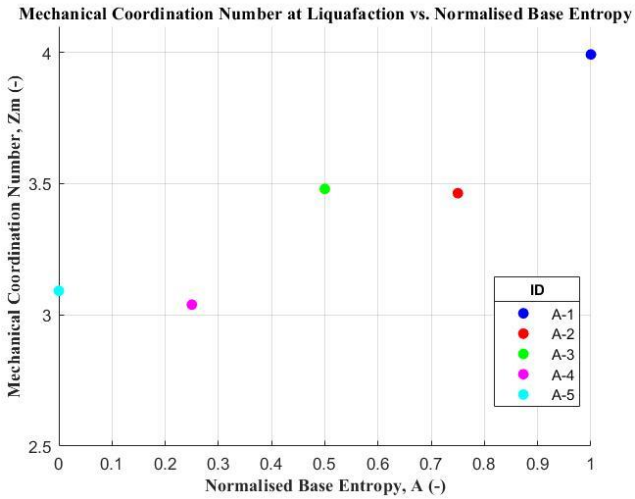

Figure 3. Mechanical coordination number, Zm at the initiation of liquefaction with normalised base entropy, A.

The figures thus far indicate that a correlation exists between the PSD and the stability of a soil during the initiation of liquefaction. This correlation may further be understood with reference to the deviatoric fabric component of the 2nd order fabric tensor (Φ_d), discussed by Satake (1982).

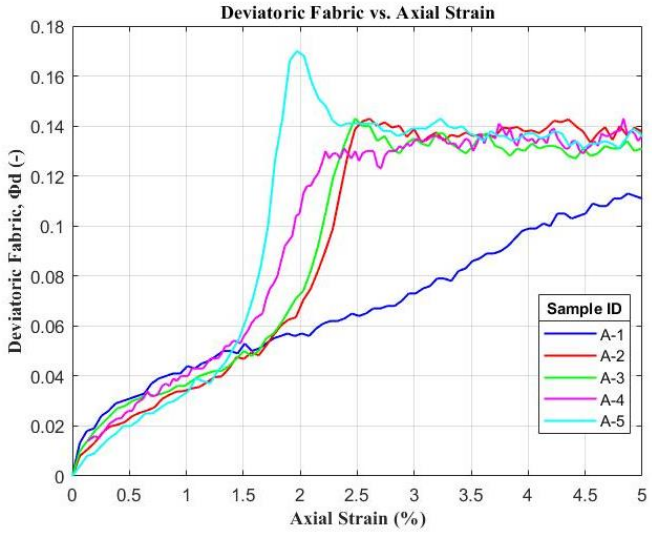

Figure 4. Deviatoric fabric during the first 5% axial strain.

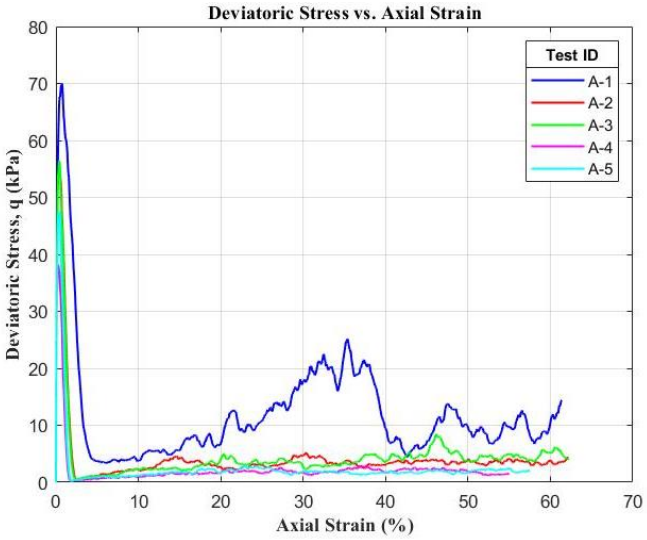

Figure 5. Deviatoric stress vs axial strain to simulation termination (55% - 60% strain).

Specimen A-1 shows a steady increase in Φ_d throughout the first 5% strain. Before q_{peak} at around 0.5% strain, A-1 has the largest Φ_d. In other words, it is the most anisotropic specimen at this point. It is important to note that changes in anisotropy in this work are not due to changes in stress path but are instead a result of changing PSD. A-1 is the most anisotropic specimen up to 1.5% strain. Following failure (2% - 2.5% strain), A-1 shows the lowest values of Φ_d, despite initially showing the largest values of Φ_d prior to failure. Despite this shift, A-1 presents a steadily growing fabric network as strain increases. Other specimens in Figure 4 show the opposite behaviour. They are generally more isotropic prior to failure but following the onset of liquefaction a notable shift in the fabric structure takes place and all specimens (except A-1) rapidly become significantly more anisotropic as their initial fabric was broken.

Figure 5 shows the q-ε_a relationship until a termination strain of 60%. The figure indicates that the initial fabric behaviours are evidently important throughout entirety of loading. Following failure, specimen A-1 exhibits large fluctuations in deviatoric stress indicating that within this specimen, new interparticle contacts were able to be created following failure. Specimen A-1 has been shown to be the most stable PSD throughout this work, which is also indicated by its drop to only around 5 kPa as opposed to near 0 kPa. The fluctuations in stress between 25% - 40% strain highlight the specimens inherent stability, which appears to be related to its ability to retain its grain structure. Whilst other specimens show some slight increases in stress post failure, it is evident that the change in the fabric structure at 2% - 2.5% strain has inhibited these specimens ability to regain interparticle contacts.

5 DISCUSSION AND CONCUSIONS

This work has presented undrained monotonic DEM simulations of 5 PSDs. A relationship has been seen between grain size and stability/resistance to liquefaction. By examining the contact behaviours, it is suggested that larger average grain sizes can greatly increase a soils stability by enabling the soil fabric structure to resist breaking and thus rearrangement, likely as a result of creating strong fabric networks. It was seen in A-1, with the largest grain size, that this specimen steadily increased its contact network following failure. Whereas specimens with smaller grains had their contact network broken, which inhibited their ability to regain contacts following liquefaction.

This also appears to be related to the anisotropy of the grains. Breaking the fabric network made it so that soils which initially showed greater degrees of isotropy become significantly more anisotropic during liquefaction. Whereas A-1, which initially showed the greatest anisotropy, became the most isotropic specimen following failure and was the most stable specimen. These results indicate that anisotropy in soils, resulting from PSD alone, may render soils more susceptible to liquefaction.

REFERENCES

Barreto, D., Leak, J., Dimitriadi, V., McDougall, J. (2019). 'Grading Entropy Coordinates and Criteria for Evaluation of Liquefaction Potential', In *Earthquake Geotechnical Engineering and Protection and Development of Environment and Constructions*, (1346-1353).

J. Lőrincz, (1986). Grading entropy of soils. Doctoral thesis, Technical Univ. of Budapest, Hungary.

Manmatharajan, M. V, Edouardine-Pascale. I., Alex, S. Ghafghazi, M (2023). 'Effect of particle size and particle size distribution on the post-liquefaction strength of granular soils', *Soils and Foundations*, 63(4), p. 101336. Available at: https://doi.org/10.1016/j.sandf.2023.101336.

Otsubo, M. Chitrave, S. Kuwano, R. Hanley, K. H, Kyokawa. J Koseki (2022) 'Linking inherent anisotropy with liquefaction phenomena of granular materials by means of DEM analysis', *Soils and Foundations*, 62(5), p. 101202. Available at: https://doi.org/10.1016/j.sandf.2022.101202.

Satake, M. (1982). 'Fabric tensor in granular materials', In: Vermeer PA, Luger HJ (eds) IUTAM symposium on deformations and failure of granular materials. Balkema, Rotterdam, pp 63–68.

Tsuchida, H. & Hayasi, S. (1971). 'Estimation of liquefaction potential of sandy soils', In *Proceedings of the Third Joint Meeting*, US-Japan Panel on Wind and Seismic Effects, UJNR, Tokyo, May 1971, pp. 91-109.

Wang, R. *et al.* (2020), 'Post-liquefaction Cyclic Shear Strain: Phenomenon and Mechanism', in *Model Tests and Numerical Simulations of Liquefaction and Lateral Spreading*. Cham: Springer International Publishing, pp. 653–656. Available at: https://doi.org/10.1007/978-3-030-22818-7_38.

Wen, Y., Zhang, Y (2022). 'Relation between void ratio and contact fabric of granular soils'. *Acta Geotech.* **17**, 4297–4312 https://doi.org/10.1007/s11440-022-01507-7.

Proceedings of the XVIII ECSMGE 2024
GEOTECHNICAL ENGINEERING CHALLENGES
TO MEET CURRENT AND EMERGING NEEDS OF SOCIETY
© 2024 the Authors
ISBN 978-1-032-54816-6
DOI 10.1201/9781003431749-215
Open Access: www.taylorfrancis.com, CC BY-NC-ND 4.0 license

ECSMGE 24
XVIII EUROPEAN CONFERENCE ON SOIL MECHANICS AND GEOTECHNICAL ENGINEERING

On the liquefaction induced pore water pressure ratio underneath existing buildings

Excès de pression d'eau interstitielle induit par liquéfaction sous les bâtiments

S. Lirer*
Department of Engineering Science/University Guglielmo Marconi, Roma, Italy

F. Valtucci, P. Bonassisa, L. Mele, A. Flora
Department of Civil, Environmental and Architectural Engineering/University of Napoli Federico II, Napoli, Italy

**lirer@unimarconi.it*

ABSTRACT: The catastrophic effects of seismically induced liquefaction recently observed during the Kahramanmaraş sequence (Turkey, 2023) confirmed the need of effective tools for predicting the effects of soil liquefaction on the built environment, to be used at the design stage. The main factors governing the seismic response of buildings founded on liquefiable sandy deposits are nowadays recognised. It is clear that the prediction of the damages depends on the correct estimation of earthquake induced excess pore water pressures Δu within the soil deposit, which cause the loss of soil shear strength and stiffness during the seismic shaking. While in free field conditions there are many models developed in literature able to predict the pore pressure ratio build-up ($r_{u,ff}$) induced by cyclic loading, the correct prediction underneath the footing ($r_{u,st}$) is a rather complex topic, still deserving research insight. By processing published centrifuge tests data, the paper proposes a simple expression of β (= $r_{u,st}/r_{u,ff}$) as a function of some relevant factors affecting the stress state within the liquefiable soil during the seismic shaking, grouped in a single, dimensionless parameter (Ψ).

RÉSUMÉ: Les effets catastrophiques de la liquéfaction induite par un tremblement de terre, récemment observés dans la séquence de Kahramanmaraş (Turquie, 2023), ont confirmé le manque d'outils efficaces pour prédire les effets de la liquéfaction du sol sur l'environnement bâti. La recherche expérimentale des dernières décennies a permis d'identifier les principaux aspects régissant la réponse des bâtiments et la manière dont leur comportement diffère des simples conditions de terrain libre. Il est clair que la prévention des dommages dépend de l'estimation correcte de la surpression de l'eau interstitielle induite par le tremblement de terre Δu dans le dépôt de sol, qui entraîne la perte de résistance et de rigidité du sol pendant la secousse sismique. Alors qu'en condition FF, il existe de nombreux modèles de génération de pression d'eau interstitielle capables de prédire l'accumulation de pression interstitielle induite par une charge cyclique ($r_{u,ff}$), la prédiction correcte sous la fondation ($r_{u,st}$) est un sujet plutôt complexe qui mérite encore d'être approfondi par la recherche. En traitant certaines données d'essais de centrifugation de la littérature, l'article propose une expression simple of β (= $r_{u,st}/r_{u,ff}$) en fonction de certains facteurs pertinents affectant l'état de contrainte dans le sol liquéfiable lors de la secousse sismique.

Keywords: Liquefaction, buildings, pore water pressure.

1 INTRODUCTION

Severe damages induced by soil liquefaction have occurred over time during some important earthquakes around the world (Anchorage, 1964; Niigata, 1964; Kobe, 1995; Kocaeli, 1999; Christchurch, 2010-2011; Emilia Romagna, 2012; Palu, 2018, Turkey, 2023). The effects of liquefaction on structures in these areas were catastrophic, with large settlements and rotations of entire structural complexes, leading to a loss of functionality and operative state. Liquefaction ground failure mechanisms (sand boils and cracks, sand ejecta, ground oscillation, settlements, lateral spreads) are due to the temporary transition of the granular soil from a solid to a fluid state because of the earthquake induced excess pore water pressure (Δu). Despite the experimental research efforts conducted in the last decades by many researchers to explain and understand the factors governing the liquefaction phenomena (cyclic liquefaction, cyclic mobility, and flow liquefaction), major gaps still exist regarding the ability to accurately assess liquefaction effects on the built environment (absolute and differential settlements, tilting, horizontal crack). The catastrophic effects of earthquake induced liquefaction recently observed during the Kahramanmaraş sequence (Turkey, 2023) have highlighted once more that all ground failure mechanisms induced by soil liquefaction are of minor interest in free field (FF), while the attention should be devoted to the built environment (i.e. Dashti et al., 2010a; Baris et al., 2021). As stated by Bray and Macedo (2017), liquefaction induced settlements of shallow founded

buildings are caused by shear (partial bearing failure, SSI induced building ratcheting) and volumetric strains (localized sand ejecta, sedimentation, and consolidation phenomena), that combine differently in time.



Figure 1. Example of liquefaction effects on a structure, with large settlements and tilt (Turkey 2023).

The relative relevance of these mechanisms depends on the characteristics of the earthquake motion, depth and thickness of liquefiable layer and building features (Dashti et al., 2010a, b).

This is the reason why the well-known semi-empirical procedure set out to compute the free field post liquefaction re-consolidation settlements (Zhang et al., 2002), usually gives only a rough prediction of the true building settlement. If we consider only the (minor) component linked to the post liquefaction volumetric strains, buildings settle more than the soil in free field conditions, even though is observed in many experiments (Dashti et al., 2010a-b; Bray and Macedo, 2017, Mehrzad et al., 2018) that the pore pressure ratio r_u ($r_u=\Delta u/\sigma'_v$) under them ($r_{u,st}$) is lower than in free field conditions ($r_{u,ff}$). This is due to the difference in the stress state underneath the foundation, linked to the higher vertical stresses ($=\sigma'_{v0}(z)+\Delta\sigma'_v(z)$) and the pre-existing static shear stresses. While in FF condition many excess pore water pressure generation models are nowadays available (Chiaradonna and Flora, 2020, Mele et al., 2022), the correct prediction of the pore pressure ratio underneath the foundation ($r_{u,str}$) is a rather complex topic still deserving research insight. Generally, the pore pressure ratio underneath the structure $r_{u,st}$ is expressed as a portion of the ones in free field $r_{u,ff}$:

$$r_{u,st}(z) = \beta \cdot r_{u,ff}(z) \qquad (1)$$

with $\beta \leq 1$. The knowledge of β is the key point for the estimation of the stress field underneath shallow founded structures and of the linked effects (i.e, vertical settlements, loss of bearing capacity). Experimental evidence (Dashti 2010 a,b, Bray and Dashti 2014, Bilotta et al, 2019, Ntritsos and Cubrinovsky, 2022) highlighted that β is a function of the foundation geometry, the applied load, the depth and thickness of the liquefiable layer, the presence of a non-liquefiable crust, and the seismic demand. Furthermore, $r_{u,st}$ is also affected by the partial drainage phenomenon within the soil volume under and near the building foundation caused by the fact $\Delta u_{,st} \neq \Delta u_{,ff}$.

Based on the results of a wide numerical study, Karamitros et al (2013) confirmed that the ratio between $\Delta u_{,st}/\Delta u_{ff}$ (named A in Figure 2), computed at a representative depth z under the footing, is lower than one, and it is coupled with the normalized seismic settlements (ρ_{dyn}/B). For large settlements ratio, Karamitros et al. (2013) suggest using the conservative value A=0.8 (Figure 2).

Since these indications are mostly based on numerical results, it is extremely relevant to verify them experimentally. To this aim, the paper collects several published centrifuge tests results, checking the effects of all the relevant factors, eventually proposing a simple expression of β as a function of them.

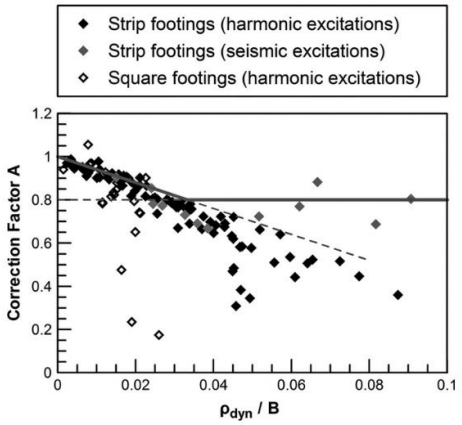

Figure 2. Dependence of the parameter A on the normalized dynamic building settlements (Karamitros et al. 2013) computed at a depth z=D+B, where D and B are respectively the depth and the width of the foundation.

2 EXPERIMENTAL MEASUREMENTS OF THE LIQUEFACTION INDUCED EXCESS PORE WATER PRESSURE

The performance of buildings founded on liquefiable soils has been investigated via centrifuge tests by many authors. In this paper, the well documented centrifuge tests carried out by Dashti (2009, 2010a, 2010b) and Bertalot and Brennan (2015) have been considered and processed.

Dashti (2009, 2010a, 2010b) tested three different (single degree freedom) elastic flexible structures (BLDG A,B and C, Figure 3) placed on a rigid mat

foundation of dimensions B×L loaded with realistic earthquake motions (see Table 1). The water table is at the depth D=1m below the ground level. The names of the tests reported in Table 1 report the thickness of the liquefiable Nevada Sand layer (H_L) and its relative density (i.e., T3-30 has H_L= 3m and Dr=30%). In test T3-50silt, a silty layer has been placed above the liquefiable layer.

The input motions are a scaled version of the ground motions recorded during the Kobe earthquake (1995) and the Chi-Chi event (1999). The objective was to analyse the dynamic response of structures with different degrees of liquefaction, using 'moderate' and 'large' events with different peak base accelerations. (Table 1).

The centrifuge tests carried out by Bertalot and Brennan (2015) involved four rigid square footings with different applied loads (30, 60, 90, and 130 kPa) placed on loose liquefiable sand deposits (Figure 4). The models had 15 m deep deposits of clean sand with a top loose liquefiable layer (Dr=40%) and a bottom dense layer (Dr=80%). The liquefiable layer thickness varied in each model. The input motion chosen was the 2010 Maule earthquake (Table 1).

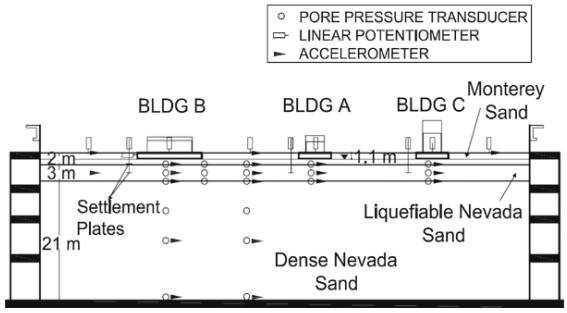

Figure 3. Section of the model used in the centrifuge tests (Dashti et al. 2010a).

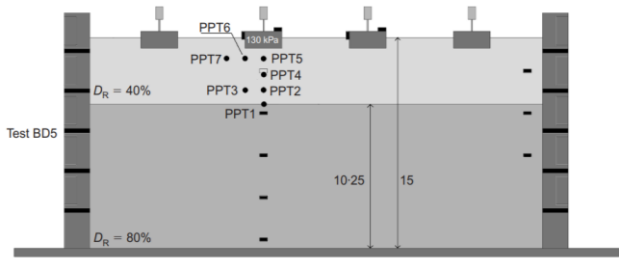

Figure 4. Section of the model used in centrifuge test BD5.

Table 1. Literature centrifuge tests.

Test	a_g (g)	H_L (m)	N_{eq}	q (kPa)	B (m)	L (m)
*T3-30	0.19 - 0.55	3	12-25	80-130	6-12	9-18
*T3-50	0.13 - 0.55	3	12-25	80	6	9
*T3-50silt	0.19 - 0.55	3	12-25	80-130	6-13	9-19
^BD5	0.6	4.75	20	120	2.75	2.75
^BD7	0.6	6.75	20	90	2.75	2.75

(*) Dashti et al. (2009-2010a, b) and Karimi and Dashti (2016)
(^) Bertalot and Brennan (2015)

In all centrifuge tests (Table 1), the excess pore water pressures induced by the imposed seismic demand at different depths under the structures have been measured and compared with the values at the same depth in FF conditions. The following considerations can be drawn to comment the overall results:

- at a given time and depth, $\Delta u_{st} \neq \Delta u_{ff}$;
- if liquefaction is attained, its triggering under the building generally happens at the bottom of the liquefiable layer with a certain time-delay compared to FF conditions (Figure 5);
- the shaking duration has an effect on the proportionality between $r_{u,st}$ and $r_{u,ff}$ (i.e. on β). In particular, when the soil liquefies in FF and $r_{u,st}$<1, the longer the shaking duration the higher the value of β;
- for the given constant stratigraphy, the values of $r_{u,st}$ are mainly affected by the foundation geometry and applied load (as sketched in Figure 6).

3 PROCESSING OF EXPERIMENTAL DATA

For all the selected centrifuge tests (Table 1), the ratio β (eq. 1) has been computed. As previously mentioned, it depends on all the parameters previously reported (i.e., foundation geometry and loads, characteristics of the dynamic action). Therefore, an attempt has been herein done to group them in a single, dimensionless parameter (Ψ) in such a way to correlate it directly to β. A possible form for Ψ is:

$$\Psi = \frac{5 \cdot \left(\frac{\Delta\sigma'_v}{\sigma'_{v0}}\right)^{0.8} \cdot D_r}{\left(a_g \cdot N_{eq}\right)^{0.5}} \qquad (2)$$

where $\Delta\sigma'_v$ is the effective vertical stress increment induced along the foundation axis at each depth z by the building load, $\sigma'_{v,0}$ is the lithostatic effective vertical stress at the same depth, N_{eq} is the equivalent number of cycles, a_g [g] is the non-dimensional peak ground acceleration.

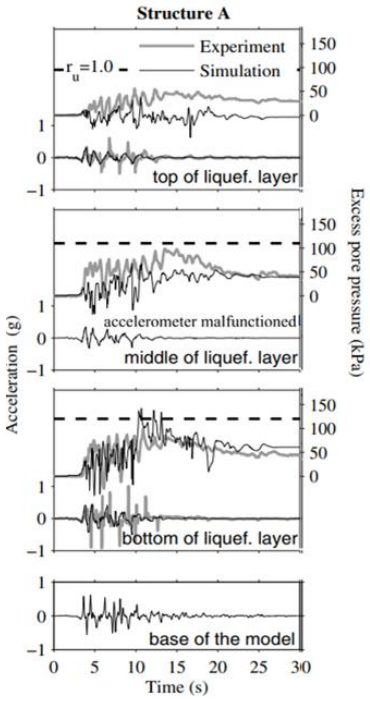

Figure 5. Centrifuge test T3-30, large event (Dashti et al. 2010a): comparison between excess pore water pressures measured under the structure A (at the top, bottom, and middle height of the liquefiable layer).

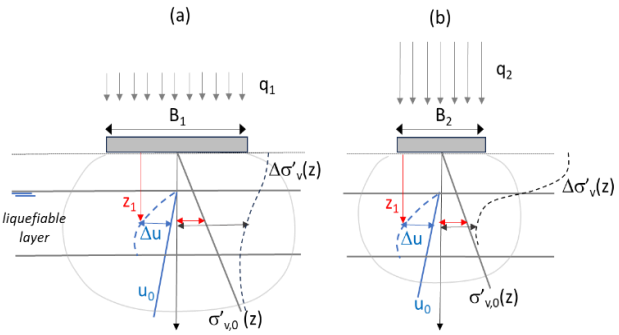

$$r_{u,st\,(z1,a)} < r_{u,st\,(z1,b)}$$

Figure 6. Sketch of the combined effect of the applied loads q and of the foundation width B on the excess pore water pressure ratio underneath the structure ($r_{u,st}$).

Figure 7 reports the experimental values of β as functions of Ψ.

Even though the data show some scatter, likely because of the simple expression adopted for Ψ (eq. 2), they confirm that the pore pressure ratio, underneath shallow founded buildings, differs from the one measured in free field conditions (i.e., β≤1). A clear trend can be also observed: as the parameter Ψ gets larger, the value of β (= $r_{ust}/r_{u,ff}$) clearly decreases. In other words, higher applied loads and/or larger foundations (both increasing the ratio $\Delta\sigma'_v/\sigma'_{v,0}$), and/or seismic actions with lower energy (i.e., with smaller values of N_{eq} and/or a_g) reduce the values of β and therefore of the pore pressure increment ratios underneath the foundation, in comparison to the free field values.

The experimental results also show that the simple indication of β=0.8 by Karamitros et al. (2013), regardless of the seismic actions and of the foundation properties and loads, is a bit oversimplified and can be unnecessarily conservative for Ψ≥1.5.

As a preliminary proposal to overcome this possible excessive overconservativeness, in this paper a simple yet conservative enveloping of the experimental data is proposed:

$$\beta = e^{-0.25\Psi} \qquad (3)$$

Valid for 0≤Ψ≤7, which covers a large part of the possible cases of engineering interest. For values of Ψ>7 it is reasonable to consider β=0.

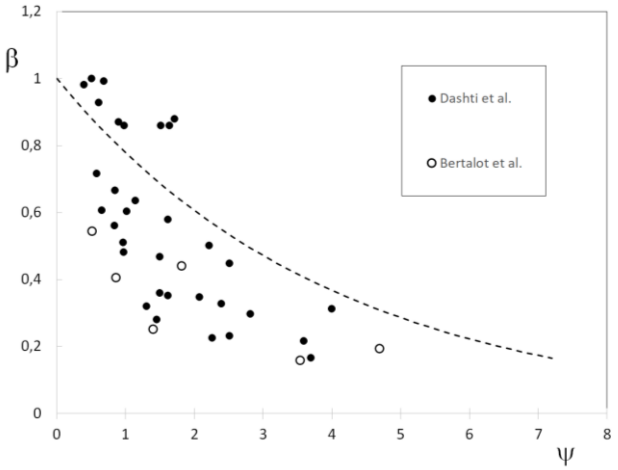

Figure 7. Experimental values of β (β=$r_{u,st}/r_{u,ff}$) measured in centrifuge tests (Table 1) as functions of the dimensionless parameter Ψ (eq.2).

4 NUMERICAL STUDY

A 2D numerical study has been carried out to check the validity of the proposed approach, starting from a simulation of T3-30 (Large P.I. event), and increasing the liquefiable thickness (H_L) to test the goodness of the relationship even deeper. The numerical study has been carried out with the code PLAXIS adopting the PM4Sand soil constitutive model for the liquefiable soil layer. The PM4Sand constitutive parameters (Table 2) have been calibrated on the results of

experimental data (VELACS project, Arulmoli K. 1992). The comparison between the pore pressure ratio time histories recorded (at z=3.5m) during the centrifuge test T3-30 test (Port Island PI large event, characterized by a PGA of 0.55g) and the ones computed by the numerical model (FF condition in Figure 8a, and underneath the structure in Figure 8b), confirm the effectiveness of the numerical model to capture the complex stress state induced by the seismic shaking within the soil volume.

After the calibration of PM4SAND, the numerical study has been extended considering the PI large event and the structure A founded on larger liquefiable soil (i.e., $3<H_L<6$ m). The numerical results in Figure 9, in terms of pore pressure ratio, highlighting how $r_{u,st}$ values. The volume affected is not only that located directly underneath the structure but also that beyond the edges of the structure due to the presence of the shear stresses; as it would be expected, the peak values of r_u in the two adjacent layers at high densities do not exceed values of 0.2-0.3.

Table 2. Calibrated PM4Sand model parameters.

PM4Sand Parameters	Nevada sand			Monterey sand
	Dr 40%	Dr 60%	Dr 90%	Dr 86%
G_0	524	710	1053	1092
hp_0	0.028	0.11	0.008	0.56
pA	101.3	101.3	101.3	101.3
e_{max}, e_{min}	0.78-0.51			0.81-0.51
n_b	0.5	0.5	0.5	0.5
n_d	0.1	0.1	0.1	0.1
ϕ_{cv}	33	33	33	33
ν	0.3	0.3	0.3	0.3
Q	9.5	9.5	9.5	10
R	1.4	1.4	1.4	1.5

The values of β (= $r_{u,st}/r_{u,ff}$) numerically computed at different depths have been reported in Table 3 and compared with the ones given by eq. 3. The numerical results are physically consistent (β_{Num} decreases for increasing values of the parameter Ψ), and β_{Num} is always lower than β_{Comp}, confirming the reasonable conservativeness of eq. (3).

Table 3. Comparison of β derived from eq. (3) and from the numerical analyses.

Ψ	β_{Num}	β_{Comp} (eq. 3)
0.17	1.00	0.96
0.34	0.60	0.92
0.41	0.70	0.90
0.60	0.50	0.86
0.80	0.60	0.81
0.98	0.55	0.78
1.20	0.52	0.74
1.60	0.40	0.67

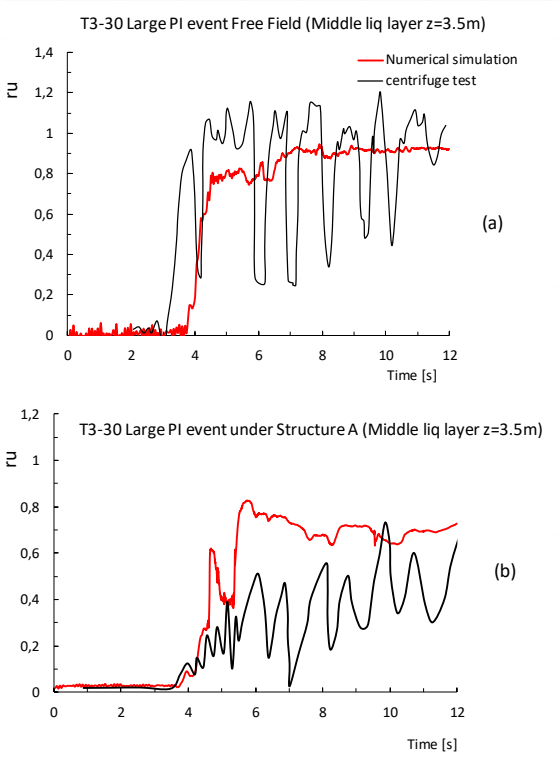

Figure 8. Comparison between the pore pressure ratio time histories recorded during T3-30 test (PI large event) and the numerical results (a: FF condition, b: underneath the structure A) at a depth z=3.5.

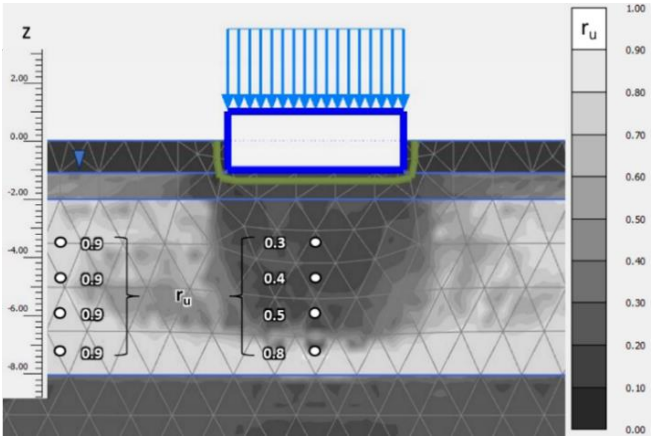

Figure 9. Peak values of the pore pressure ratio computed in the 2D numerical analysis of this work.

5 ACKNOWLEDGEMENTS

This study was carried out within the RETURN Extended Partnership and received funding from the European Union Next-GenerationEU (National Recovery and Resilience Plan – NRRP, Mission 4, Component 2, Investment 1.3 – D.D. 1243 2/8/2022, PE0000005).

6 CONCLUSIONS

Published centrifuge tests have been processed to provide an insight into the prediction of the pore pressure ratio $r_{u,st}$ caused by the seismic excitation of soil layers under shallow founded structures, expressing it as a function of the free field value $r_{u,ff}$ (relatively simply to compute) as $r_{u,st}=\beta \cdot r_{u,ff}$. Even though the considered data set does not cover the whole possible range of values of the involved variables, it is wide enough to conclude that for loose to medium dense soils the parameter β mainly depends on the foundation geometry and loads, as well as on the characteristics of the dynamic action. In this work, these factors were successfully grouped in the non-dimensional parameter Ψ (eq. 2). Figure 7 confirms that β depends on Ψ, allowing to derive a simple relationship between β and Ψ (eq. 3) which can be easily adopted to get a conservative estimate of the excess pore water pressure underneath shallow founded buildings ($r_{u,ff}$).

REFERENCES

Arulmoli K. et al. (1992) VELACS soil data report,National Science Foundation.

Baris, A., Spacagna, R. L., Paolella, L., Koseki, J., and Modoni, G. (2021). Liquefaction fragility of sewer pipes derived from the case study of Urayasu (Japan). *Bulletin of Earthquake Engineering*, *19*(10).

Bertalot, D., and Brennan, A. J. (2015). Influence of initial stress distribution on liquefaction-induced settlement of shallow foundations. *Geotechnical Earthquake Engineering - Geotechnique Symposium in Print 2015*, 89–99. https://doi.org/10.1680/geot.SIP.15.P.002

Bilotta, E., Chiaradonna, A., Fasano, G., Flora, A., Mele, L., Nappa, V., Lirer, S., Fioravante, V. (2019). Experimental evidences of the effective-ness of some liquefaction mitigation measures.

Bray, J. D., and Dashti, S. (2014). Liquefaction-induced building movements. *Bulletin of Earthquake Engineering*, *12*(3), 1129–1156. https://doi.org/10.1007/s10518-014-9619-8

Bray, J. D., and Macedo, J. (2017). 6th Ishihara lecture: Simplified procedure for estimating liquefaction-induced building settlement. *Soil Dynamics and Earthquake Engineering*, *102*, 215–231. https://doi.org/10.1016/j.soildyn.2017.08.026

Chiaradonna, A.,and Flora, A. (2020). On the estimate of seismically induced pore-water pressure increments before liquefaction. *Geotechnique Letters*, *10*(2), 128–134. https://doi.org/10.1680/jgele.19.00032

Dashti, S. (2009). *Toward Developing an Engineering Procedure for Evaluating Building Performance on Softened Ground*. Ph.D. Dissertation. University of California, Berkeley.

Dashti, S., Asce, M., Bray, J. D., Asce, F., Pestana, J. M., Riemer, M., and Wilson, D. (2010-a). *Centrifuge Testing to Evaluate and Mitigate Liquefaction-Induced Building Settlement Mechanisms*. https://doi.org/10.1061/ASCEGT.1943-5606.0000306

Dashti, S., Asce, M., Bray, J. D., Asce, F., Pestana, J. M., Riemer, M., and Wilson, D. (2010-b). *Mechanisms of Seismically Induced Settlement of Buildings with Shallow Foundations on Liquefiable Soil*. https://doi.org/10.1061/ASCEGT.1943-5606.0000179

Karamitros, D. K., Bouckovalas, G. D., Chaloulos, Y. K., and Andrianopoulos, K. I. (2013). Numerical analysis of liquefaction-induced bearing capacity degradation of shallow foundations on a two-layered soil profile. *Soil Dynamics and Earthquake Engineering*, *44*, 90–101. https://doi.org/10.1016/j.soildyn.2012.07.028

Karimi, Z., and Dashti, S. (2016). Seismic Performance of Shallow Founded Structures on Liquefiable Ground: Validation of Numerical Simulations Using Centrifuge Experiments. *Journal of Geotechnical and Geoenvironmental Engineering*, *142*(6). https://doi.org/10.1061/(asce)gt.1943-5606.0001479

Mehrzad, B., Jafarian, Y., Lee, C. J., and Haddad, A. H. (2018). Centrifuge study into the effect of liquefaction extent on permanent settlement and seismic response of shallow foundations. *Soils and Foundations*, *58*(1), 228–240. https://doi.org/10.1016/j.sandf.2017.12.006

Mele, L. (2022). An experimental study on the apparent viscosity of sandy soils: from liquefac-tion triggering to pseudo-plastic behaviour of liquefied sands. Acta Geotechnica, 17(2), 463–481. https://doi.org/10.1007/s11440-021-01261-2

Ntritsos, N., Cubrinovski, M. (2022). Some Important Limitations of Simplified Liquefaction Assessment Procedures. In Geotechnical, Geo-logical and Earthquake Engineering (Vol. 52, pp. 1638–1646). Springer Science and Business Me-dia B.V. https://doi.org/10.1007/978-3-031-11898-2_145

Zhang, G., Robertson, P. K., and Brachman, R. W. I. (2002). Estimating liquefaction-induced ground settlements from CPT for level ground. *Canadian Geotechnical Journal*, *39*(5), 1168–1180. https://doi.org/10.1139/t02-047

Proceedings of the XVIII ECSMGE 2024
GEOTECHNICAL ENGINEERING CHALLENGES
TO MEET CURRENT AND EMERGING NEEDS OF SOCIETY
© 2024 the Authors
ISBN 978-1-032-54816-6
DOI 10.1201/9781003431749-216
Open Access: www.taylorfrancis.com, CC BY-NC-ND 4.0 license

ECSMGE 24
XVIII EUROPEAN CONFERENCE ON SOIL MECHANICS AND GEOTECHNICAL ENGINEERING

Disintegration of natural granite residual soil and the geohazard implication

Désintégration du sol résiduel de granit naturel et implication des géorisques

X.Y. Liu*, Y. Miao
School of Civil and Hydraulic Engineering, Huazhong University of Science and Technology, Wuhan, China
X.W. Zhang, G. Wang, H.D. Gao
State Key Laboratory of Geomechanics and Geotechnical Engineering, Institute of Rock and Soil Mechanics, Chinese Academy of Sciences, Wuhan, China
**liuxinyu17@mails.ucas.ac.cn*

ABSTRACT: Collapsing gully as an erosional landform with a high sediment transfer rate is causing various hazards. Although it is widely acknowledged that the granite residual soil (GRS), especially its disintegration, plays a critical role, the quantitative characterizations of its disintegration behavior and the underlying mechanism remain to be revealed. In this study, laboratory disintegration tests were performed using a self-developed apparatus on natural GRS collected at various depths. The disintegration process was quantitatively traced through two types of parameters, namely disintegration ratio and disintegration rates. The disintegration behavior of natural GRS is classified accordingly. It is revealed that soil disintegration was triggered by cementation damage upon soaking which broke up the soil aggregates and reduced soil stability. In addition, previous studies overestimated the effect of particle composition on the disintegration of soil. This study provides quantitative characterizations of the disintegration behavior of GRS.

RÉSUMÉ: L'effondrement d'un ravin en tant que relief érosif avec un taux de transfert de sédiments élevé entraîne divers dangers. Bien qu'il soit largement reconnu que les sols granitiques résiduels (GRS), en particulier dans leur désintégration, jouent un rôle critique, les caractérisations quantitatives de leur comportement de désintégration et le mécanisme sous-jacent restent à révéler. Dans cette étude, des tests de désintégration en laboratoire ont été effectués à l'aide d'un appareil développé par nous-mêmes sur du GRS naturel collecté à différentes profondeurs. Le processus de désintégration a été suivi quantitativement à travers deux types de paramètres, à savoir le taux de désintégration et les taux de désintégration. Le comportement de désintégration du GRS naturel est classé en conséquence. Il est révélé que la désintégration du sol a été déclenchée par des dommages de cimentation lors du trempage, qui ont brisé les agrégats du sol et réduit la stabilité du sol. De plus, des études antérieures ont surestimé l'effet de la composition des particules sur la désintégration du sol. Cette étude fournit des caractérisations quantitatives du comportement de désintégration du GRS.

Keywords: Granite residual soil; disintegration; collapsing gully; microstructure; classification.

1 INTRODUCTION

A collapsing gully (CG) is an erosional landform (Xu, 1996) situated above the granite crust with a high sediment transfer rate. In 2005, a national-scale field investigation was performed by the Ministry of Water Resources of China and it is shown that more than 239,100 CGs exist in the south of China (Liang et al., 2009). As one of the most devastating types of soil erosion, CG is believed to be associated with different types of hazards, including soil and water loss, farmland degradation, infrastructure damage, and even loss of life. Specifically, Liang et al. (2009) indicated that the CGs in the south of China have resulted in the loss of more than 60 Mt of soil and 380,000 hectares of farmland, as well as a financial loss of more than 200 million Renminbi. The potential threat of CG has been long realized and researchers have characterized CG including its distribution (Xu, 1996), formation (Luk et al., 1997; Lin et al., 2015), classification (Zhong et al., 2013), development process (Lin et al., 2015), and controlling factors (Deng et al., 2018). However, in recent years, the number and the affected area of CGs still increased remarkably. This phenomenon is likely to be caused by a lack of firm understanding of its formation mechanism. Given that most of the CGs are found to occur in thick granite regolith, granite residual soil (GRS) therefore plays an important role in the formation mechanism serving as material for the CG. GRS is the in-situ product of parent rock weathering and has been studied extensively. The consensus is that this type of soil has fundamentally different geotechnical properties from

common sand and clay because of their difference in forming history (Liu et al., 2022). Despite the extensive studies performed on residual soil, little attention has been paid to the relationship between the geotechnical behavior of GRS and the development of CG. Among all aspects of geotechnical properties, disintegration referring to the crumbling of soil into small fragments and particles when a soil sample is immersed in water is believed to be tightly related to the formation of CGs because it involves soil–water interactions (Shit and Adhikary, 2020). Currently, the systematic information regarding the disintegration of GRS is still to be obtained, perhaps hindered by the limited apparatus available for soil disintegration tests. The test method for rock disintegration has been standardized by the American Society of Testing Methods (ASTM) but this is not the case for soil and only several researchers have performed disintegration tests either qualitatively or semi-quantitatively. For example, Shit and Adhikary (2020) performed disintegration tests on soil collected from a gully erosion area in India. The soil blocks were placed on a metal mesh underwater and the ultimate number of entirely disintegrated soil fragments was chosen to calculate the resistance to disintegration of soil. This method provides qualitative information on soil disintegration but cannot trace the disintegration process of soil quantitatively.

In response, this study investigates the disintegration of GRS collected at different depths quantitatively using a self-made apparatus. The disintegration process was quantitatively traced and three parameters are proposed to reflect soil disintegration rate. In addition, the disintegration rate is correlated to particle composition and shear strength parameters. This study improves the understanding of the soil-water interaction of GRS and the formation of CG.

2 MATERIALS AND METHODS

A typical CG area is selected at Jiangmen in Guangdong Province, China. In Jiangmen city, the total soil erosion area is estimated as 1225.82 km^2 which accounts for ~13% of this city's total area. This study focused on a CG near the Longmen (LM) reservoir (Figure 1), which is one of the largest CGs in this area. The studied CG was found to influence more than 10^5 hectares of farmland, 233 hectares of fishpond, and the safety of a minimum of 4000 local people. Unfortunately, the scale of this CG is still progressing.

A typical weathering profile has been established in this area and the sampling has occurred within the range of residual soil. This study uses a Mazier triple-tube core barrel to collect soil samples continuously from 0.3 to 12 m deep. This method can retrieve undisturbed residual soil which is sensitive to external disturbance. Table 1 lists the variations of clay content and shear strength parameters with depth and more details of soil properties of the studied soil are provided by Liu et al. (2022).



Figure 1. Photograph of CG.

Table 1. Soil index properties.*

Sampling depth (m)	w (%)	Clay content (%)	c' (kPa)	φ' (°)
0.3	40.90	48.7	23.4	26.6
1.3	39.40	42.4	26.3	27.2
2	40.87	39.3	27.4	31.5
3	38.07	38.4	26.8	33.6
4	34.77	29.4	28.5	33.3
6	36.10	26.6	28.0	33.6
8	36.20	23.2	31.1	34.1
10	35.07	13.4	29.2	36.6
12	35.83	10.2	27.1	36.4

*Note: w is the water content; c' and φ' are the effective cohesion and internal frictional angle, respectively.

The disintegration of residual soil is investigated using a purpose-built disintegration test apparatus (Figure 2). The soil specimen (cutting-ring sample, 61.8 mm in diameter and 40 mm in height) placed on a metal frame was immersed in distilled water. Upon the onset of soil disintegration, the produced fragments fall downward through the mesh of the plate. Concurrently, the mass variation of the sample was recorded by a digital dynamometer whose readings were output in real-time to a computer. A digital single-lens reflex camera was used to photograph the morphology of the specimen in the course of disintegration. The disintegration tests were terminated at either complete sample disintegration or a duration of 24 h. This study uses the disintegration ratio R_d and equivalent disintegration rates (v_I, v_{II}, and v_{III}) to quantitatively trace the disintegration process of GRS and the calculation is:

$$R_d = \frac{G' - G}{G' - G_0} \times 100\% \quad (1)$$

$$v_{\mathrm{I}} = \frac{R_{d10}}{t_{R_d=10\%}} \quad (2)$$

$$v_{\mathrm{II}} = \frac{R_{d30} - R_{d10}}{t_{R_d=30\%} - t_{R_d=10\%}} \quad (3)$$

$$v_{\mathrm{III}} = \frac{R_{d50} - R_{d30}}{t_{R_d=50\%} - t_{R_d=30\%}} \quad (4)$$

In Eq. (1), G_0 is the total weight of the float and metal plate. G is the nominal weight of the specimen as a function of time t, which is directly given by the reading of the dynamometer. G' is the initial value of G at $t = 0$. R_{d10}, R_{d30}, and R_{d50} are disintegration ratios of 10%, 30%, and 50%, respectively, and $t_{Rd=10\%}$, $t_{Rd=30\%}$, and $t_{Rd=50}$ is time needed to reach the above R_d values.

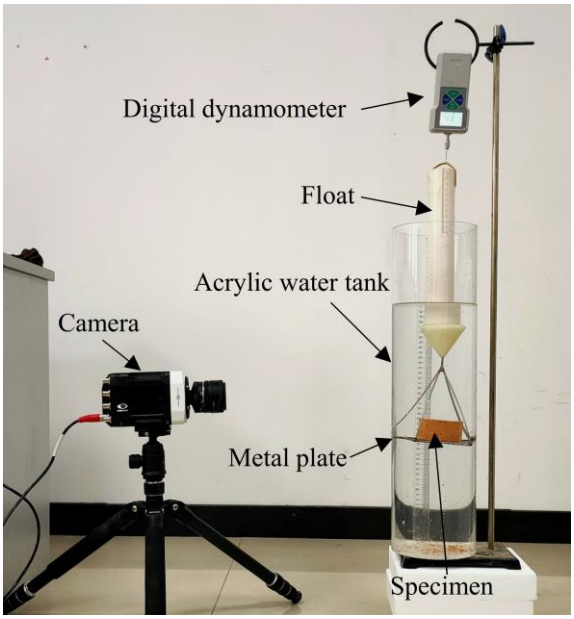

Figure 2. Adopted apparatus for disintegration test.

3 TEST RESULTS AND DISCUSSIONS

The disintegration behavior of natural GRS samples at different depths is given in Figure 3. Figure 4 gives typical photographs of the soil samples during the disintegration process. In addition, the relationships between the soil disintegration rates with the clay content and shear strength parameters are given in Figure 5.

It was found that the soils from a depth of 0.3 m and 1.3 m showed similar disintegration behaviors characterized by rapid climb of R_d to 100% within 5 min. The deeper soils (2 m and 3 m deep) also displayed complete disintegration (R_d = 100%), and the disintegration rate was generally high. Notably, these two samples show a temporary stop of disintegration, with the value of R_d being approximately constant. The GRS soil from the depth of 4.0–8.0 m disintegrated consistently over time but the disintegration rates gradually declined at the end of disintegration with the value of v_{III} being lower than 1%/min. The GRS at a depth of more than 10 m showed incomplete disintegration and the ultimate R_d was ~60%; a disintegration ratio of 100% has not been obtained even after 24 h.

The disintegration of GRS explains the occurrence of the CG. Upon heavy rainfall, the soil becomes rapidly saturated which degrades the cementation of surface soil. Therefore, the soil disintegrated into smaller fragments and particles, which were the major sources of colluvial deposits. These colluvial deposits were then transported to the LM reservoir.

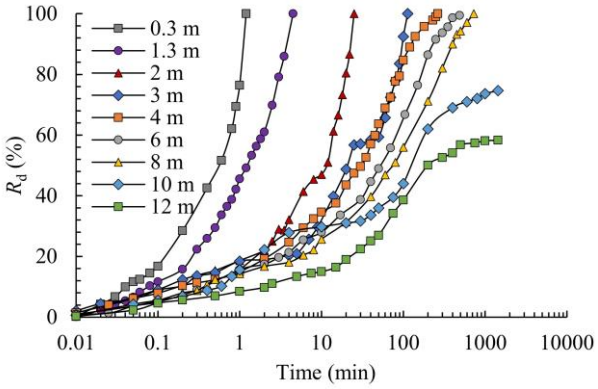

Figure 3. R_d–t curves for GRS from various depths.

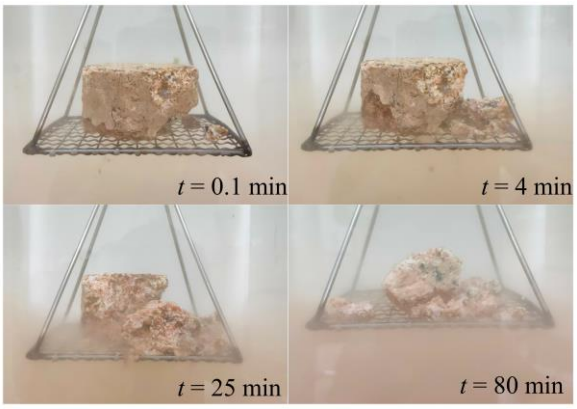

Figure 4. Photograph of the disintegration process.

In this study, a two-level classification system is adopted for soil disintegration. The soil was first classified according to the ultimate R_d value as completely disintegrative (R_d = 100%, type I) or incompletely disintegrative (R_d < 100%, type II).

Subsequently, the soil was further termed as stable (subtype A), incremental (subtype B), or rapid (subtype C) according to R_d–t curve shape. For type A, R_d increases stably to 100% and the disintegration rate reduces gradually. For type B, R_d increased incrementally to 100% and the ultimate time is approximately 100 min. For type C, R_d increased sharply to 100%. The combination of these two-level features produces a more reasonable classification. For example, GRS at 0.3 m deep was classified as I-C indicating the complete and rapid disintegration.

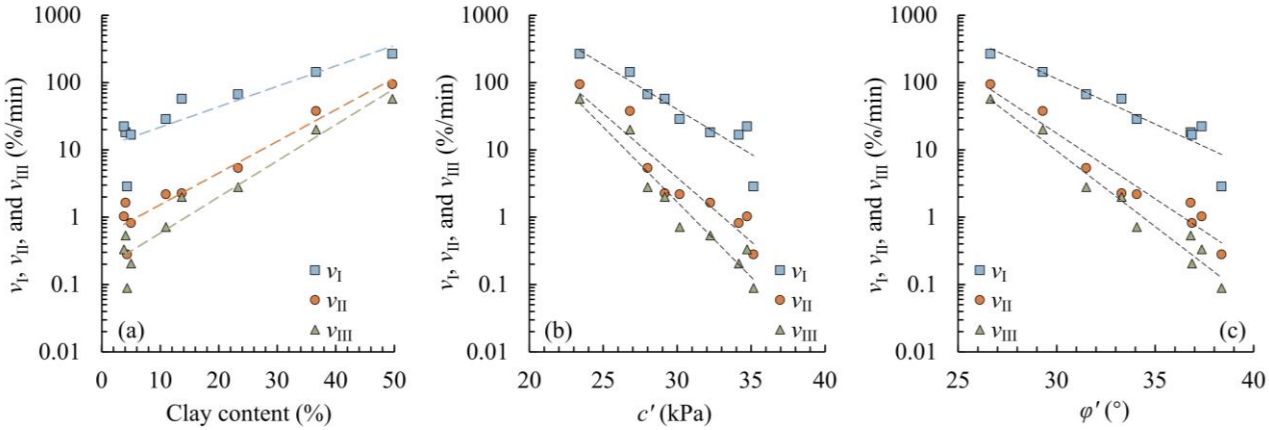

Figure 5. Correlations between disintegration rates and (a) clay content, (b) c', and (c) φ'.

Interestingly, the present results indicate that a higher clay content of GRS corresponds to less stable disintegration behavior. This is counterintuitive because of the higher interparticle forces within clays compared to the case of sand. This phenomenon shows that the particle composition may not be the dominant controlling factor of soil disintegration. It is also revealed that soils having higher c' and φ' are less disintegrative. It should be clarified that the shear strength of natural GRS is predominantly controlled by the interparticle cementation which binds the soil particles and forms larger aggregates. However, immersion of soil in water may damage the cementation and trigger disintegration.

4 CONCLUSIONS

This study presents the disintegration behavior of natural GRS collected from various depths. The GRS displays obvious disintegration when immersed. In addition, the disintegration of soil is affected by the soil depth, with the shallow soil showing less stable behavior. Different from the previous understanding, the particle composition was not a critical controlling factor at least for natural GRS; instead, the cementation among soil particles play critical roles.

ACKNOWLEDGMENTS

The authors thank the financial support from National Natural Science Foundation of China (Nos. 41972285, 41672293), and the opening fund of the State Key Laboratory of Geohazard Prevention and Geoenvironment Protection (No. SKLGP2023K011).

REFERENCES

Deng, Y., Duan, X., Ding, S. Cai, C., and Chen, J. (2018). Suction stress characteristics in granite red soils and their relationship with the collapsing gully in south China. *Catena*, 171: 505–522. https://doi.org/10.1016/j.catena.2018.07.043.

Liang, Y., Ning, D., Pan, X., Li, D., and Zhang, B. (2009). The characteristics of Benggeng erosion and its control in red soil region of southern China. *J. Soil Water Conserv.* 15: 31–34 (in Chinese). https://doi.org/10.14123/j.cnki.swcc.2009.01.009.

Lin, J., Huang, Y., Wang, M., Jiang, F., Zhang, X., and Ge, H. (2015). Assessing the sources of sediment transported in gully systems using a fingerprinting approach: an example from South-east China. *Catena*, 129: 9–17. https://doi.org/10.1016/j.catena.2015.02.012.

Liu, X., Zhang, X., Kong, L., Wang, G., and Liu, H., 2022. Formation mechanism of collapsing gully in southern China and the relationship with granite residual soil: A geotechnical perspective. *Catena*, 210, 105890. https://doi.org/10.1016/j. catena.2021.105890.

Luk, S., DiCenzo, P., and Liu, X. (1997). Water and sediment yield from a small catchment in the hilly granitic region, south China. *Catena,* 29: 177–189. https://doi.org/10.1016/S0341-8162(96)00054-9.

Shit, P.K., Adhikary, P.P. (2020). Gully Erosion Studies from India and Surrounding Regions, 1st ed., Springer, Cham. https://doi.org/10.1007/978-3-030-23243-6_2.

Xu, J.X. (1996). Benggang erosion: the influencing factors. *Catena.* 27: 249–263. https://doi.org/10.1016/0341-8162(96)00014-8.

Proceedings of the XVIII ECSMGE 2024
GEOTECHNICAL ENGINEERING CHALLENGES
TO MEET CURRENT AND EMERGING NEEDS OF SOCIETY
© 2024 the Authors
ISBN 978-1-032-54816-6
DOI 10.1201/9781003431749-217
Open Access: www.taylorfrancis.com, CC BY-NC-ND 4.0 license

ECSMGE 24
XVIII EUROPEAN CONFERENCE ON SOIL MECHANICS AND GEOTECHNICAL ENGINEERING

Endangered historic sites: The case study of Santa Croce in Ravenna (Italy)

Sites historiques en danger: L'étude de cas de Santa Croce à Ravenna (Italie)

M. Marchi*, I. Bertolini, G. Gottardi
DICAM Department, University of Bologna, Italy

**michela.marchi@unibo.it*

ABSTRACT: The city of Ravenna (Italy) is worldwide famous for the well-preserved late Roman and Byzantine architecture with eight buildings protected by UNESCO as part of the World Heritage Site "Early Christian Monuments of Ravenna". Climate change effects have increased the site vulnerability to natural hazards, in particular flooding and subsidence, two phenomena often strictly interrelated. The topic has been addressed with reference to the complex of Santa Croce in Ravenna (Italy), an emblematic case of the main hydrogeological and water-related threats affecting the city monuments. A recent geotechnical campaign and a new piezometric monitoring system helped to gain information on the local subsoil and on the drainage system, permanently operating in the area in order to maintain it dry; the 3D geometry of the complex was obtained by integrated geomatic techniques (mainly laser scanning and photogrammetry). The paper aims at presenting the main geotechnical issues affecting the site stability and its long-term preservation.

RÉSUMÉ: La ville de Ravenne (Italie) est mondialement connue pour son architecture de la fin de l'ère romaine et byzantine remarquablement préservée, avec huit bâtiments protégés par l'UNESCO dans le cadre du site du patrimoine mondial "Monuments du christianisme primitif de Ravenne". Les effets du changement climatique ont accru la vulnérabilité du site face aux risques naturels, notamment les inondations et l'affaissement, deux phénomènes souvent étroitement liés. Le sujet a été abordé en référence au complexe de Santa Croce à Ravenne (Italie), un cas emblématique des principales menaces hydrogéologiques et liées à l'eau affectant les monuments de la ville. Une récente campagne géotechnique et un nouveau système de surveillance piézométrique ont permis d'obtenir des informations sur le sous-sol local et sur le système de drainage fonctionnant en permanence dans la région afin de le maintenir sec; la géométrie en 3D du complexe a été obtenue grâce à des techniques géomatiques intégrées (principalement scanner laser couplé à un relevé photogrammétrique). L'article vise à présenter les principaux problèmes géotechniques affectant la stabilité du site et sa préservation à long terme.

Keywords: Historic site; Ravenna; Santa Croce church; land subsidence; drainage system.

1 INTRODUCTION

Ravenna (northern Italy) is renowned for its rich history, cultural heritage and stunning Byzantine mosaics that adorn its churches and monuments. As a UNESCO World Heritage Site, Ravenna boasts eight early Christian monuments that testify its significance during late Roman and Byzantine periods. However, these ancient historic sites face severe natural hazards that threaten their conservation. Being situated in a low-lying area, only few kilometres from the Adriatic Sea shoreline, the city is constantly prone to flooding. High tides, storm surges and heavy rainfalls - whose frequency is rapidly increasing as effect of climate change - can produce potentially significant damages to ancient sites and monuments, which have been historically subjected to relevant phenomena of land subsidence and are therefore located well below the current mean sea level. In order to mitigate such geohazards and preserve Ravenna's cultural treasures, numerous efforts have been made through many conservation and restoration projects, starting from an in-depth study of their current situation and thus devising possible solutions (Santangelo et al., 2022; Bertolini et al., 2023; Marchi et al., 2023a; Franzoni et al., 2023). Any conservation program aiming at safeguarding monuments and mosaics from environmental degradation and the impact of natural hazards should start from a diagnostical analysis trying to connect "root" causes to the effects on the structure (Gottardi et al., 2015; Bertolini et al., 2022; Marchi et al., 2019; Marchi et al., 2022a, Marchi et al. 2022b; Marchi et al., 2023b).

The paper addresses the steps taken to analyse, from a geotechnical point of view, the "state of health" of the archaeological site of the Santa Croce Church in Ravenna, encompassing the visual analysis of its decay due to the effects of natural and anthropic land subsidence with the preliminary results of a recent

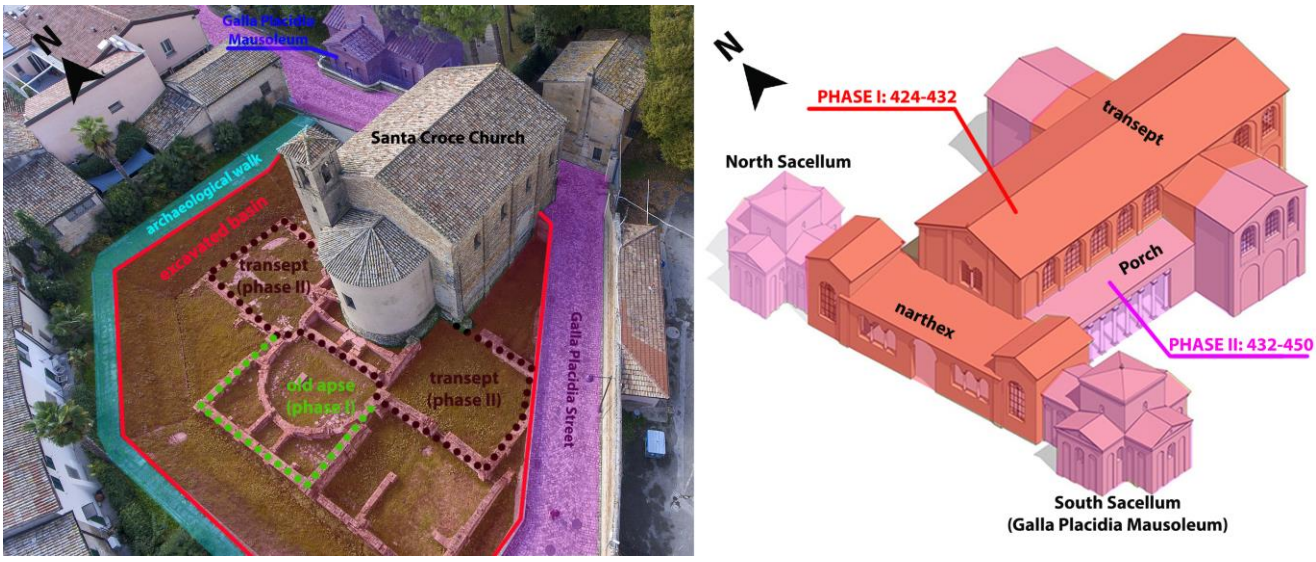

Figure 1. On the left, a bird's eye view of the area under study, with the excavated basin containing the archaeological remains and the Church. On the right, reconstruction of the geometry of the church at the end of the placidian era (modified from Cassanelli et al. (2013)).

geotechnical campaign investigating the local stratigraphy and the piezometric regime acting in the shallow aquifers as induced by a previously installed drainage system.

2 THE ARCHAEOLOGICAL SITE OF THE SANTA CROCE CHURCH

The archaeological site of Santa Croce is located in a buffer zone of the UNESCO early Christian monuments of Ravenna, adjacent to the world-famous San Vitale Basilica and Galla Placidia Mausoleum. While the two latter monuments are in good conservation conditions and are open to the public, the Santa Croce site appears in a partially abandoned state and is currently not accessible to visitors. The Church of Santa Croce, in ancient times, was a three-nave building preceded by a long portico (narthex) at the ends of which probably opened two symmetrical chapels (*sacellum*). The only surviving chapel is the south one, the so-called Mausoleum of Galla Placidia. The church was likely built in two phases on the structures of a roman *domus,* of which beautiful floor mosaics are preserved on site. The first church configuration dates back to the period between 424 and 432 A.D., constructed by the will of the roman empress Galla Placidia, and was followed by an enlargement between 432 and 450, precisely with the addition of two chapels and small adjacent porches next to the aisles, configured for funerary purposes (Figure 1, right). The early Christian church had a rich mosaic and stucco decorations, almost entirely lost today, similar in splendor to that still observable in the south *sacellum*. The old placidian church has been almost entirely reconstructed in time. In particular, at the beginning of the 17th century, the church front was set back and separated from the south chapel to make space for the Galla Placidia road today bordering two sides of the site. Concurrently, the apse has been demolished and reconstructed, in smaller dimensions, in correspondence of the old transept, considerably reducing the length of the church nave (Figure 1, left). In the 18th century, a bell tower, still observable today, has been added at the side of the apse.

2.1 Past and present hazards affecting the site

After the World War II, the economic recovery increased the need for fluid withdrawal from the subsurface. The exploitation of the Quaternary multiaquifer system underneath the Ravenna city centre and of new on-shore and off-shore gas reservoirs, increased the subsidence rate of the area from few millimetres/year (natural land subsidence rate before 1950) up to a peak value of ~80 mm/year recorded in the period 1972-73 (Carbognin et al., 1984). The cumulated subsidence in proximity of the Santa Croce site has been estimated ~1.3 m between 1897-2002, as a result of the superposition of natural and anthropic subsidence effects (Teatini et al., 2005), leaving evident signs of a marked decline in the urban and natural environment.

In the period between 1970 and 1980 the Santa Croce site was subjected to an important archaeological campaign aiming at bringing to light the archaeological stratification in the area. A basin was therefore excavated on three of the four sides of



Figure 2. On the left, scheme of the drainage system operating in the area. On the right, a picture taken during the drying procedures required following the basin's flooding caused by the malfunction of the two submersible pumps in 2021.



Figure 3. Pictures highlighting the different types of deterioration to the masonry structures and to the earthen slope of the basin, caused in time by the operating drainage system.

the church up to a depth of ~3.7m from the current street level (at ~1.5 m a.m.s.l) (Figure 1, left). The phreatic water level in the area is consistently located at ~1.5 m below the actual ground level; thus, to perform the excavation and maintain the archaeological remains in dry conditions a drainage system had to be set in place. A scheme of the drainage system, still in operation, is shown in Figure 2 (left). A perforated horizontal PVC tube (red line in Figure) bordering two sides of the excavated basin channels the water from well P1 through P2 and C1 to a buried concrete tank (indicated with a blue dot in Figure 2, left) containing two submersible pumps. The pumps lift the drained water to the street level and release them in the public sewer (light blue line in Figure 2). The subsequent piezometric lowering in the shallow aquifer initially produced new settlements in the overall site containing the church structure, the archaeological remains in the excavated basin and the private buildings standing at the site borders. Moreover, the lack of maintenance to the drainage system caused over the past years the progressive obstruction of the drainage pipes by soil particles. From a recent site inspection, the water still drained by the pumps flows along the soil surface, on a shallow trench self-created above the pipes (blue arrows in Figure 3, left), producing continuous shallow erosion and local instabilities. Despite the underpinning works operated in 1985 to the masonry remains in proximity of the tank, the negative effects of the continuous water withdrawal appears to have never stopped. In fact, the area in proximity of the concrete tank is clearly the most affected by settlements, as visible in all the close by masonry archaeological structures in

the south side of the church and in the deformation of the slope (Figure 3, right and left, respectively). Furthermore, occasional malfunctioning of the pumps in the past caused multiple flooding of the area with subsequent damages to the archaeological remains and to the roman mosaics (Figure 2, right).

2.2 The 2022 geotechnical investigation campaign and site monitoring

Funded under the European research program Horizon 2020, SHELTER (Sustainable Historic Environments holistic reconstruction through Technological Enhancement and community-based Resilience) project aims to increase the resilience of cultural heritage and reduce its vulnerability to natural and anthropic hazards through the elaboration of disaster risk management plans and protocols of intervention. The archaeological area of Santa Croce was selected as emblematic case study because it incorporates all the preservation issues characteristic of coastal, low-land, historic cities.

In 2022, among many other investigations, a geotechnical campaign was carried out, aiming at investigating the local soil stratigraphy and characteristics, together with the piezometric conditions in the area, as induced by the drainage system. Two piezocone penetration tests (CPTu), one seismic cone penetration test (SCPTu), one dilatometer test and three corings (two continuous and one destructive drillings) were executed in the area. Under a 5.5 m thick anthropic fill (unit R), rich in archaeological remains, the deposit turned out to be a succession of highly permeable aquifers (units U1 and U3) and low-permeable aquitards (units U2 and U4), up to the maximum investigated depth (~ 45 m) (Figure 4).

A piezometric monitoring system was thus installed in the site with the aim of recording in situ pore water pressure (pwp) data in the shallowest aquifers at different distances from the buried tank. As expected, the greatest dropdown in piezometric head is registered in PZ3, installed in the first aquifer and located in proximity of the pumps (Figure 5). The effects of the drainage system seem to reduce with distance in fact, PZ1, 50 m far from PZ3, has a higher piezometric head (with a difference of ~ 0.2 m). The deeper aquifer (monitored by PZ2) is only marginally influenced by the drainage conditions and tends to the undisturbed water level, located ~1.4 m below the street level (as measured locally at pumps shut down).

Various geomatics techniques were also integrated to create a highly detailed 3D model of the Santa Croce site (Bitelli et al., 2021). These geometrical data will support the creation of a seepage Finite Element (FE) model able to accurately reproduce the pwp distribution in the 3D system of aquifers as a consequence of the drainage currently in operation and to reproduce the effect of possible, more effective, solutions. Piezometric observed data will be used for a suitable calibration of the FE model parameters.

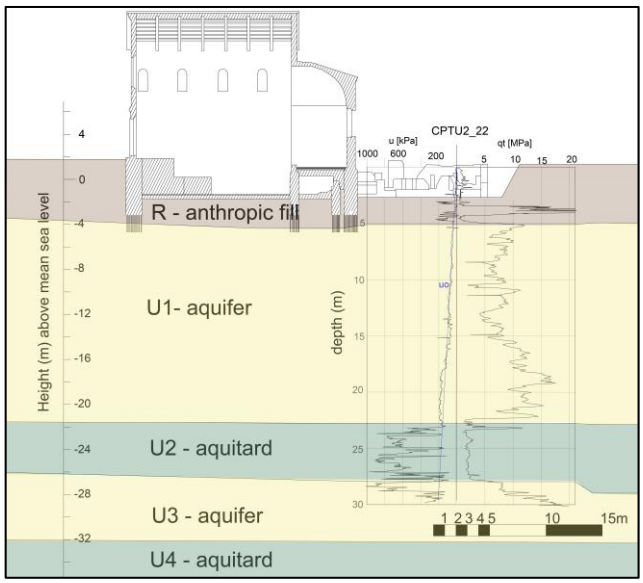

Figure 4. Soil stratigraphy in the investigated area with superimposition of the q_t and u profiles from a CPTU.

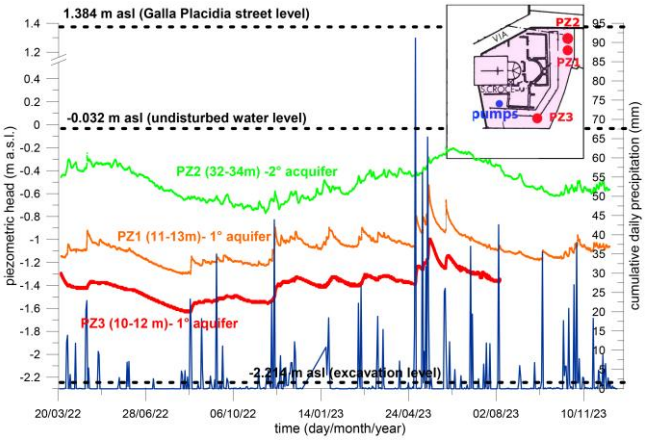

Figure 5. Piezometric head trends with time measured in PZ1 (1st aquifer), PZ2 (2nd aquifer) and PZ3 (1st aquifer).

3 CONCLUSIONS

The paper focuses on the precarious conditions and the number of hazards affecting the archaeological area of Santa Croce. This scrutiny has brought to light their significant implications to the preservation of such invaluable historic site. Diligent care and increased vigilance are required in order to effectively mitigate the associated risks, thereby enabling the safeguarding and future accessibility of the entire complex. The extensive field campaign conducted, coupled with the initial findings from on-site monitoring, represents a

valuable analysis of the current geotechnical situation. These findings not only shed light on the existing context but also pave the way for the formulation of well-informed management strategies essential for the preservation and sustainable use of the site. In this perspective, multiple solutions can be proposed to ensure an optimal control of the groundwater conditions in the area. Among them, a re-efficiency of the old drainage system in use or the design and implementation of a new dewatering system (e.g., well-points), able to guarantee spatial uniformity of pore pressure distribution and lower hydraulic gradients in the area.

ACKNOWLEDGEMENTS

This research, part of the H2020 SHELTER project, has received funding from the European Union's Horizon 2020 Research and Innovation Programme, under grant agreement no. 821282.

REFERENCES

Bertolini, I., Marchi, M., Gottardi, G. (2022). Learning from a well-documented geotechnical cold case: the Two Towers of Bologna, Italy. *International Journal of Architectural Heritage*, 17(5): 1607-1629. https://doi.org/10.1080/15583058.2022.2057828.

Bertolini, I., Gottardi, G., Marchi, M., Ugolini, A. (2023). Cultural heritage and subsidence: the emblematic case study of Santa Croce in Ravenna (Italy). *Proc.of the Tenth International Symposium on Land Subsidence, TISOLS 2023*, 17-21 April, Delft, Netherlands.

Bitelli, G., Barbieri, E., Girelli, V.A., Lambertini, A., et al. (2021). The complex of Santa Croce in Ravenna as a case study: integration of 3D techniques for surveying and monitoring of a historical site. *Proc. of the 9th ARQUEOLÓGICA 2.0 & 3rd GEORES*, Valencia, Spain, 26–28 April. https://dx.doi.org/10.4995/arqueologica9.2021.12164.

Carbognin, L., Gatto, P., Mozzi, G. (1978). Case history No. 9.15 Ravenna, Italy. In: Poland J.F. ed. Guidebook to studies of land subsidence due to ground-water withdrawal. UNESCO, pp. 291–305.

Cassanelli, R, Cirelli, E., Crociati, E., Civiletti, J.P. et al. (2013). *La Basilica di Santa Croce: nuovi contributi per Ravenna tardo-antica [The Santa Croce Basilica: new contributions for Late Antique Ravenna]*. Edited by David M., Edizioni del Girasole (in Italian).

Franzoni, E., Berk, B., Bassi, M., Marrone, C. (2023). An integrated approach to the monitoring of rising damp in historic brick masonry, *Construction and building materials*, 370: 1 – 11. https:/doi.org/10.1016/j.conbuildmat.2023.130631.

Gottardi, G., Lionello, A., Marchi, M., Rossi, P.P. (2015). Monitoring-driven design of a multiphase intervention for the preservation of the Frari bell tower in Venice. *Rivista Italiana di Geotecnica*, 49 (1): 45 – 64.

Marchi, M., Bertolini, I., Gottardi, G., Amorosi A., Bruno, L. (2019). From geological and historical data to the geotechnical model of the Two Towers in Bologna (Italy). Proceedings of the XVII ECSMGE-2019, 1-6 September, Reykjavik, Iceland. https://dx.doi.org/10.32075/17ECSMGE-2019-0269.

Marchi, M., Bertolini, I., Gottardi, G. (2022a). A geotechnical insight into the soil-foundation system of the Two Towers of Bologna, Italy. In *Geotechnical Engineering for the Preservation of Monuments and Historic Sites* III, Lancellotta et al. (eds), pp. 631-642, CRC Press, London. http://dx.doi.org/10.1201/9781003308867-46.

Marchi, G., Cremonini, C., Mastrangelo, A., Marchi, M., Bertolini, I., Lancellotta, R. (2022b). Assessing the causes of damages to the Osservanza Church in Bologna (Italy). In *Geotechnical Engineering for the Preservation of Monuments and Historic Sites* III, Lancellotta et al. (eds), pp. 619-630, CRC Press, London, http://dx.doi.org/10.1201/9781003308867-45.

Marchi, M., Bertolini, I., Gottardi, G. (2023a). Geotechnical investigations and monitoring of the archaeological site of Santa Croce in Ravenna (Italy). In: *Geotechnical Engineering in the Digital and Technological Innovation Era*. Ferrari, A. et al. (eds), CNRIG 2023, Springer Series in Geomechanics and Geoengineering, pp. 536-543. https://doi.org/10.1007/978-3-031-34761-0_65.

Marchi, M., Bertolini I., Marchi G., Lancellotta R. (2023b). Intrinsic and induced vulnerability of the Osservanza Church in Bologna (Italy). *Rivista Italiana di Geotecnica*, Vol. 4: 34 – 54. https://doi.org/10.19199/2023.4.0557-1405.034.

Santangelo A., Melandri, E., Marzani, G., Tondelli, S., Ugolini, A. (2022). Enhancing Resilience of Cultural Heritage in Historical Areas: A Collection of Good Practices, *Sustainability*, 14, 5171: 1 – 29. https://dx.doi.org/10.3390/su14095171.

Teatini, P., Ferronato, M., Gambolati, G., Bertoni, W., Gonella, M. (2005). A century of land subsidence in Ravenna. Italy. *Environ. Geol.*, 47: 831–846. https://doi.org/10.1007/s00254-004-1215-9.

Proceedings of the XVIII ECSMGE 2024
GEOTECHNICAL ENGINEERING CHALLENGES
TO MEET CURRENT AND EMERGING NEEDS OF SOCIETY
© 2024 the Authors
ISBN 978-1-032-54816-6
DOI 10.1201/9781003431749-218
Open Access: www.taylorfrancis.com, CC BY-NC-ND 4.0 license

ECSMGE 24
XVIII EUROPEAN CONFERENCE ON SOIL MECHANICS AND GEOTECHNICAL ENGINEERING

Coastal erosion process at Calhetas parish, São Miguel island, Azores

Processus d'érosion côtière dans la paroisse de Calhetas, île de São Miguel, Açores

F. Marques*, A.M. Malheiro, P. Amaral, A. Santos, L. Cunha
Laboratório Regional de Engenharia Civil (LREC), Ponta Delgada, Açores - Portugal

**Filipe.MP.Marques@azores.gov.pt*

ABSTRACT: The coastal cliffs on the north coast of the São Miguel Island, between Capelas and Rabo de Peixe parishes, due to its geology, composed by alternated fractured basaltic lava flows with breccia and/or unconsolidated pyroclastic deposits, are naturally predisposed to rock falls. Sea waves, meteorological agents and the anthropogenic activity that takes place near the cliffs are the main factors responsible for the erosive dynamics, with estimated retreat rates of up to 0.40 m/year. In this context, the urban settlements closest to the coastline are cyclically affected by landslides and rock falls. These geomorphological processes are responsible for the retreat of the cliffs, with the consequent loss of land, buildings and roads. Calhetas parish, in the municipality of Ribeira Grande, is one of those places that has recently been most affected by geomorphological instability. Since February 2023, a reactive phase of the cliff has been underway, with a consequent retreat of its crest. This paper describes the process that has affected this sector of São Miguel Island coast in recent years, with a particular focus on the phase that is currently underway. Displacements data are presented, obtained by fixed marks, as well as the measures that have been taken to mitigate the risk to the population. Finally, a discussion is presented on the solutions that are considered most appropriate for the problem.

RÉSUMÉ: Les falaises côtières de la côte nord de l'île de São Miguel, entre les paroisses de Capelas et Rabo de Peixe, en raison de leur géologie, composée d'alternances de coulées de lave basaltique fracturées avec des brèches et/ou des dépôts pyroclastiques non consolidés, sont naturellement prédisposées aux chutes de pierres. Les vagues de la mer, les agents météorologiques et l'activité anthropique qui se déroule à proximité des falaises sont les principaux facteurs responsables de la dynamique érosive, avec des taux de retrait estimés jusqu'à 0,40 m/an. Dans ce contexte, les agglomérations urbaines les plus proches du littoral sont cycliquement touchées par des glissements de terrain et des éboulements. Ces processus géomorphologiques sont responsables pour le retrait des falaises, avec pour conséquence la perte de terrains, de bâtiments et de routes. La paroisse de Calhetas, dans la municipalité de Ribeira Grande, est l'un des endroits les plus touchés récemment par l'instabilité géomorphologique. Depuis février 2023, une phase réactive de la falaise est en cours, avec pour conséquence un retrait de sa crête. Cet article décrit le processus qui a affecté ce secteur de la côte de l'île de São Miguel au cours des dernières années, avec un accent particulier sur la phase en cours. Les données de déplacements sont présentées, obtenues par notes fixes, ainsi que les mesures qui ont été prises pour atténuer le risque pour la population. Enfin, une discussion est présentée sur les solutions considérées comme les plus appropriées au problème.

Keywords: Geological risks; geomorphological instabilities; volcanic coast; cliff instability; coastal protection.

1 INTRODUCTION

The coastline of São Miguel Island, between the parishes of Capelas and Rabo de Peixe, has a morphology characterized by steep cliffs with heights between 10 and 20 m. From a geological point of view, these cliffs are made up of alternations of volcanic materials with different mechanical characteristics.

Maritime agitation, meteorological agents, and human activity that develop in the vicinity of these cliffs are mainly responsible for erosion dynamics, with estimates of the average retreat rate reaching 0.40 m/year (Borges, 2003).

Since the urban centres are located close to the crest of these cliffs, cyclically these villages are affected by retreat processes leading to the loss of land, buildings, and streets. The parish of Calhetas is one of these locations that periodically is affected by crises of geomorphological instability.

In February 2023, another geomorphological crisis began, and until December 2023, there have been several episodes of instability, three of greater dimensions and others of lesser importance.

During this crisis, some measures were implemented to mitigate the risk for the local

population. As part of this initiative, six pairs of marks were placed along two alignments of tension cracks that developed parallel to the crest of the cliff. These marks aimed to assess the rock mass kinematics and try to understand the dynamics of the process. The objective is, proactively, to anticipate potential cliff retreats and, consequently, promptly alert the population to ensure their safety.

2 CASE STUDY

2.1 Location and geological settings

The Azores archipelago is located at the triple junction between the Eurasian, African, and North American tectonic plates. Being recent volcanic islands, their rock formations are generally unaltered, and the soils are little altered. The cliffs present in São Miguel Island coastline between Capelas and Rabo de Peixe are characterized by being steep and made up of sub-horizontal layers of pomitic pyroclastic deposits without effective cohesion and/or by alternations of basaltic lava flows fractured with clinker.

The cliff under analysis in this study delimits the parish of Calhetas to the north and is around 20 m high, with a sub-vertical slope, with some of the strata partially suspended. The lower half of the cliff, geologically, is made up of soft formations, namely a level of pumice of trachytic nature, with interspersed ash of the same nature with variable thickness. The upper half is formed by lava flows of a basaltic nature (s.l.) with clinker intercalations. Finally, a small layer of surface soil (vegetable soil and/or landfill) can be seen. All these formations have varying thicknesses along the length of the cliff (Figure 1).

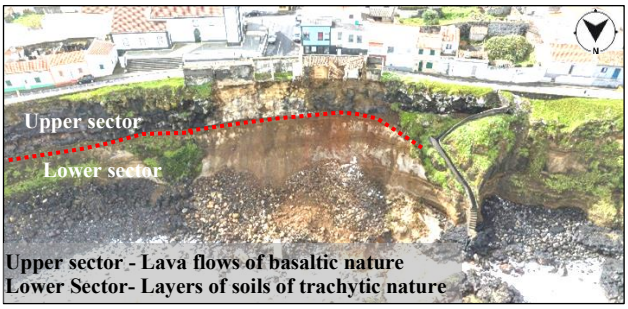

Figure 1. Geological constitution of the cliff at Calhetas.

In this sector of the coastline, close to the crest of the cliff and parallel to it, there are two streets with houses on the south side and some more scattered buildings on the north side over the crest of the cliff. With the inevitable progression of the cliff retreat process, the number of houses on the north side of the streets is increasingly reduced. Recently, the streets themselves have started to be threatened, restricting their use.

The erosion process in question consists of an intermittent phenomenon in time and space due to the intrinsic characteristics of the materials that constitute the cliffs and the action of triggering agents such as wave action, windstorms, intense precipitation, earthquakes, and anthropogenic actions (Di Crescenzo et al., 2021).

At the time of the beginning of this crisis, as the site was not being monitored, it was not possible to attribute any more intense meteorological phenomenon or any major anthropogenic action to trigger it, attributing its beginning to the progressive process of deformation of the massif and consequent increase in stress.

According to Borges (2003), who carried out quantitative studies of coastal retreat rates for the island of S. Miguel in the period between 1955 and 1999, the sector under analysis in this document points to values of average coastal retreat very heterogeneous cliff, varying between 0.1 m/year and 0.4 m/year.

Geologically, this cliff has a high propensity for the occurrence of these instability processes, considering that the base of the cliff is made up of material that is easily erodible by the action of the sea. So, periodically, the overlying basalt flows stay in cantilever. Furthermore, the alternation of basaltic flows with clinker levels, which are also quite erodible, leads to situations where the overlying strata also stay unsupported.

2.2 Description of occurrences

The current crisis began on February 2, 2023, at 8:00 pm, having destabilized an extension of the cliff measuring around 30 m and causing a retreat, which, in some places, reached 5 m (Figure 2).

In this episode, one of the affected buildings lost its back façade. It is important to note that the affected buildings were already vacant since the 2016-2017 crisis, except the structure located further west, which remained in use once it was a small warehouse.

After the first episode, the cliff became unstable again on March 1st, this time in a sector immediately to the west of the previous one, reaching a length of around 16 m and causing a retreat of around 2 m.

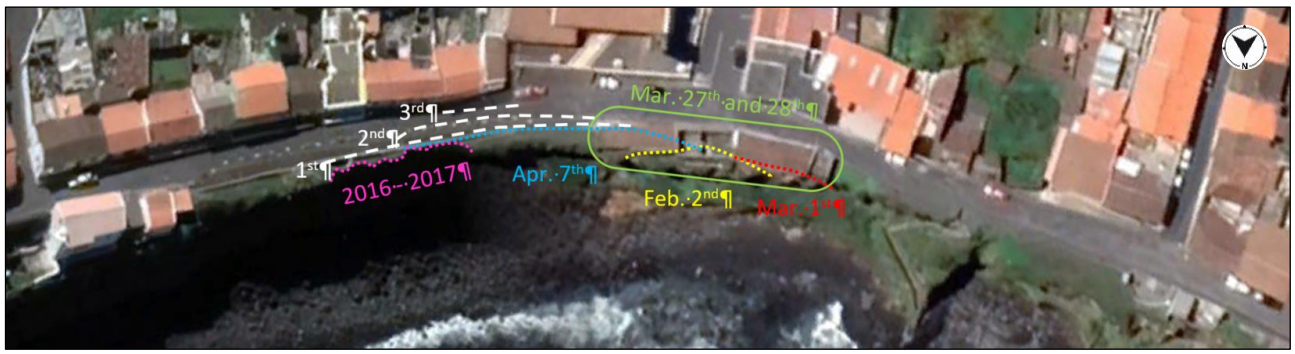

Figure 2. Affected areas on the Calhetas cliff: the alignment of existing cracks (dashed), the unstabilised areas (dotted) and the demarcation of demolished buildings / those affected by this crisis (continuous). Google Earth image (June 2022).

After this reactive phase, following a recommendation previously made by the Regional Laboratory for Civil Engineering, the four buildings located in the affected sector were demolished on the 24th, 27th, and 28th of March. This operation was done to relieve the load over the cliff and reduce the mass expected to become unstable once the cracks between the buildings and the adjacent sidewalk continued to evolve.

A few days before the demolitions began, it was found that the first and second alignment of cracks parallel to the coastline, already identified in 2016-2017, reactivated on the sidewalk and in the street pavement, resulting in an increase in the opening and the extension to the west of cracks. Furthermore, a new alignment of cracks further back was detected, the third (3rd) (Figure 2).

In March, the 2nd alignment (Figure 2) was located between 4.2 m and 6.2 m from the cliff crest, and the 3rd alignment was 1.6 m further back, thus compromising around 2/3 of the traffic lane.

On the night of April 7th, a few days after the demolitions had concluded, the cliff became unstable again. The sector now unstable was located immediately east of the initial one. With a length of around 50 m, it reached a retreat of 5 m in the sector of the demolished buildings (Figure 3).



Figure 3. The cliff after the instability of April 7.

After the instability of April 7th, the crest of the cliff retreated to the 1st alignment, becoming the 2nd alignment 2 to 3 m from the crest.

3 RISK MITIGATION MEASURES

3.1 Protection measures adopted

After the 2016-2017 crisis, when the retreat of the cliff reached the outer face of the road's guard wall, and the 1st and 2nd alignment of cracks appeared (Figure 2) parallel to the crest of the cliff, it was recommended that automobile circulation should be restricted on the affected extension of the road (70 m). It was also recommended to avoid activities or the presence of people and goods in the affected area until the 2nd crack alignment. For this purpose, it was suggested the placement of physical barriers like metal fences or blocks on the pavement. In addition, it was recommended the visual monitoring of the cliff quarterly, or after an abnormal worsening of weather conditions, to check for any retrogressive evolution of the site. In the case of activity, it was suggested the implementation of a monitoring system based on instrumental techniques to allow the detection of ground movements before the occurrence of instabilities. Although no movement was visually detected in the rock mass, marks were installed in the affected area, and the site was monitored for two years. Due to the movement being in its early stages or the limited accuracy of the total station used, no activity was detected, leading to monitoring discontinuation.

During the current crisis, and after the reactivation of the 2nd alignment and the emergence of the 3rd, it was recommended to increase the extension of the prohibited area for car traffic. This closure was extended to the west around 100 m, and in width, besides the entire sidewalk, 2/3 of the traffic lane was closed in the most critical area.

In May, after the crisis calmed down, six pairs of markers were placed along the two remaining crack alignments (2nd and 3rd) to evaluate its evolution weekly (Figure 4).

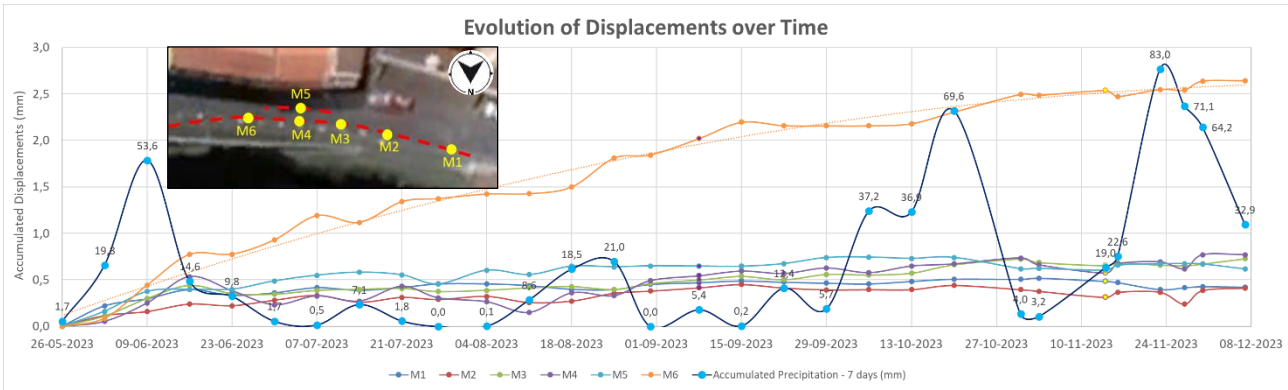

Figure 4. Evolution of the marks installed in the monitored cracks and precipitation.

3.2 Proposed solutions

To avoid the continued retreat of the cliff, it will be necessary to protect its base, which is made up of soft strata, as well as the stabilization of the overlying basalt flows that are fractured. For the lower sector, a rockfill prism adhering to the cliff can be done, which could serve as a base or foundation for the stabilization solution in the upper sector. Therefore, two possible solutions are proposed for the upper sector: one involves constructing an embankment along with small containment structures, while the other entails the installation of a reinforced concrete curtain anchored and nailed to the cliff.

At present, the authorities have granted a contract for the construction of a berm breakwater (a reshaping structure) for the base of the coastal cliff, without taking into account the solution to be implemented for the upper part. Even though the solution adopted isn't the one suggested, it has the advantage of needing smaller stones in the armour layer, making the construction process easier. Furthermore, although the project defines a reshapable berm, this intervention allows the execution of the solutions thought for the stabilization of the upper part of the cliff. Indeed, the breakwater has a wide stable crest, with a 15 to 23 m width.

In any case, until the entire cliff is protected and stabilized, new construction or rehabilitation should not be permitted on both sides of the street. Furthermore, it is essential to consider the necessity for new rehousing and relocation of structures, especially on the north side of the street.

4 CONCLUSIONS

The cliff that delimits the urban core of the parish of Calhetas to the north is cyclically plagued by crises of geomorphological instability.

The retreat of the cliff crest is the outcome of a natural process known as 'differentiated coastal erosion, occurring within various strata along the coastline.

In general, the occurrence of this type of phenomenon arises from the actions of different agents (e.g., high precipitation, intense maritime agitation, earthquakes, and vibrations resulting from human activity). Typically, there is a time interval of the order of hours or days between the request and the cliff's response to the action of the triggering agents in the rock mass.

During the current phase of the process, monitoring tension cracks near the crest of the cliff suggests that the mass rock does not react responsively to precipitation episodes, although, in the beginning, it seemed otherwise. Currently, this part of the cliff seems to have entered an inactive dormant state.

As this is a natural and irreversible process, there are two options: stabilization of the cliff or vacating the area near the ridge as the process progresses. In the latter case, proactive measures are necessary to minimize the exposed value. For this purpose, territorial planning tools are essential. Because both options have very high associated costs, each situation has to be viewed on a case-by-case basis. Regardless of the option adopted, it is essential to define clear policies to minimize losses and not create false expectations for the population.

REFERENCES

Borges, P. (2003) – Ambientes litorais nos Grupos Central e Oriental do Arquipélago dos Açores.

Di Crescenzo, G., Santangelo, N., Santo, A., & Valente, E. (2021). Geomorphological Approach to Cliff Instability in Volcanic Slopes: A Case Study from the Gulf of Naples (Southern Italy). Geosciences, 11(7), 289. https://doi.org/10.3390/geosciences11070289.

Proceedings of the XVIII ECSMGE 2024
GEOTECHNICAL ENGINEERING CHALLENGES
TO MEET CURRENT AND EMERGING NEEDS OF SOCIETY
© 2024 the Authors
ISBN 978-1-032-54816-6
DOI 10.1201/9781003431749-219
Open Access: www.taylorfrancis.com, CC BY-NC-ND 4.0 license

ECSMGE 24
XVIII EUROPEAN CONFERENCE ON SOIL MECHANICS AND GEOTECHNICAL ENGINEERING

Prediction program for slow moving landslides

Programme de prédiction des glissements de terrain à déplacement lent

R. Marte*, H. Ramoser
Institute of Soil Mechanics, Foundation Engineering and Computational Geotechnics, Technical University of Graz, Austria

**roman.marte@tugraz.at*

ABSTRACT: The deformation behaviour of large, slow moving landslides is often governed by rainfall characteristics. Whereas the average deformation rate per year of such landslides is often in the range of some mm to several cm, permanent deformation measurements for instance by means of permanently installed chain inclinometers show a far wider range of deformation rates especially after dry or very wet periods. If in addition to chain inclinometers, a weather station and permanent measured pore water gauges in the slip zone are installed one can identify in many cases a strong correlation between strong rain fall events, a time-delayed increase of the pore water pressure in the slip zone and simultaneously to this, an increase of the deformation rate of the landslide. So, based on these data, a good understanding of the above-mentioned correlation can be obtained. In this paper a newly developed analytical model which couples the relation between rainfall characteristics and the development of pore water pressures in the slip zone on one hand and the deformation behaviour of the slope on the other will be presented. The code allows a partition of the landslide in different sections to consider the often-observed time delayed deformation behaviour over the length of large landslides. The interrelation of shear resistance in the slip surface and deformation rate is defined by a logarithmic constitutive law. The calibration of the model is done by means of the above-mentioned permanent measurement data of precipitation, pore water pressures and deformation measurements.

RÉSUMÉ: Le comportement de déformation des grands glissements de terrain à déplacement lent est souvent régi par les caractéristiques des précipitations. Alors que le taux de déformation moyen par an de ces glissements de terrain est souvent compris entre quelques mm et plusieurs cm, les mesures permanentes de la déformation, par exemple au moyen d'inclinomètres à chaîne installés en permanence, montrent une gamme beaucoup plus large de taux de déformation, en particulier après des périodes sèches ou très humides. Si, en plus des inclinomètres à chaîne, une station météorologique et des jauges permanentes de l'eau interstitielle sont installées dans la zone de glissement, on peut identifier dans de nombreux cas une forte corrélation entre de fortes chutes de pluie, une augmentation différée de la pression de l'eau interstitielle dans la zone de glissement et, simultanément, une augmentation du taux de déformation du glissement de terrain. Ainsi, sur la base de ces données, une bonne compréhension de la corrélation susmentionnée peut être obtenue. Cet article présente un nouveau modèle analytique qui associe la relation entre les caractéristiques des précipitations et le développement des pressions d'eau interstitielle dans la zone de glissement, d'une part, et le comportement de déformation de la pente, d'autre part. Le code permet de diviser le glissement de terrain en différentes sections afin de prendre en compte le comportement de déformation souvent observé avec un décalage dans le temps sur la longueur des grands glissements de terrain. L'interrelation entre la résistance au cisaillement dans la surface de glissement et le taux de déformation est définie par une loi constitutive logarithmique. L'étalonnage du modèle est effectué à l'aide des données de mesure permanentes susmentionnées concernant les précipitations, les pressions de l'eau interstitielle et les mesures de déformation.

Keywords: Landslide; creep; inclinometer; pore water pressure; deformation rate.

1 INTRODUCTION

The deformation behaviour of large, slow moving landslides are often governed by rainfall and/or snow melting but sometimes also by man-induced processes. Such slow moving landslides (SMLS) are a common phenomenon in Alpine regions and their origin is often connected with erosion processes by glaciers during the last Ice Age, when steep mountain slopes have been left after the melting of the glaciers about 10.000 to 15.000 years ago. As a consequence, some of these steep mountain slopes developed to instable and large landslides, with low deformation rates in mm to cm per year and low factors of safety (FOS) (Marte & Hofmann 2020).

When infrastructure such as motorways, tunnels, railway tracks, water power plants, snow water storages on mountain slopes or constructions with a severe damage potential in general are endangered by such SMLS, an extensive assessment of the deformation behaviour, safety aspects as well as the

future behaviour of the slope is required (Leroueil, 2001; Hungr, 2016). Typical questions are (Marte, 2019):

- What is the expected deformation behaviour of the SMLS which needs to be considered for the life cycle of the objects?
- What is the "FOS" of the SMLS and how does it influence endangered objects?
- What are circumstances which could lead to a sudden failure of the SMLS?
- Is a sudden failure of the SMLS predictable and what is a proper observational instrumentation?
- What kind of remediation measures are applicable – what are their effects and their costs?

To work out proper answers for such questions geological survey (field work and subsoil exploration) and extensive measurement campaigns (e.g. inclinometer, geodetical, ground water resp. pore water measurements, installation of a weather station) are generally implemented (Ausweger, 2018, Marte & Hofmann, 2020). Based on results and data from this investigation geological, geotechnical and calculation models are developed. SMLS show in many cases complex geometrical and geological boundary conditions, a long history and often large movements in past as well as sometimes different triggers which govern the deformation behaviour. For such complex landslides – in many cases only simplified calculation models which prove to be valid only for some of the questions and aspects above, are available. Therefore a critical interpretation of calculation results is essential.

Improved calculation models allow a direct comparison of calculation results with measured data, which also allow a calibration of the most important input data. When for instance a calculation model delivers deformation (rate) and/or pore water pressures in the slip surface as results, this data can directly be compared to measurement data (Ausweger, 2018). On the other hand, a calculated FOS is a number which cannot be measured or controlled directly in the field, at most a change in FOS can be quantified indirectly by a change of deformation rate of the SMLS.

In the next chapter a new developed analytical model which couples the relation between rainfall characteristics, the development of pore water pressures in the slip zone and the deformation behaviour of the slope is presented. The model is calibrated on the bases of measured deformation and pore water pressure data over a longer period of time.

2 MODEL FOR SLOW MOVING LANDSLIDES

The presented model has been developed for SMLS, which are mainly triggered by rainfall (and snow melting) events. The primary input data therefore are precipitation data from a weather station (or artificial rainfall data for future events). The model is a combination of a hydrogeological model and a simple mechanical creep model (Leinenkugel, 1976). The hydrogeological model allows the calculation of pore water pressures along the slip zone over time as a function of the rainfall data. The mechanical creep model is used to calculate the deformation rate of the slope as a function of time and of pore water pressures in the slip zone.

2.1 Model description

The analytical model is based on the infinite slope model with an expansion that the SMLS is subdivided into several blocks, with the active earth pressure *Ea* at the upper end and a mobilisation function for the earth resistance *Er* at the lower end of the SMLS as shown in Figure.1 and Figure 2. The whole slope is split up into multiple finite blocks. Each block is a trapezoid with a vertical height at the lower end t_1, a vertical height at the higher end t_2 and a horizontal length l (Figure 1).

Additionally the inclination α of the slip plane is given. With that the geometry of each block is determined.

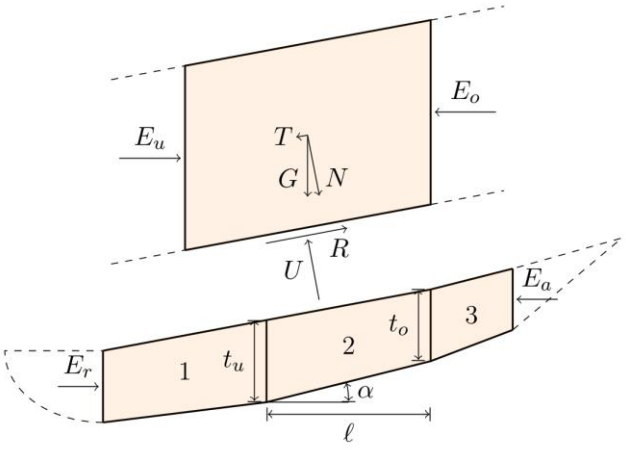

Figure 1. Model basics.

The model in the longitudinal section is shown in the lower part of Figure 1. A material is assigned to each block. The most important properties of the material are the weight γ to calculate the dead load *G* and with the geometrical data *N*, and *T* the normal and tangential component of *G*. Further input data are the friction angle Φ, the stiffness *E* and the creep index *Iv*.

The creep index *Iv* is a value that stems from the model after (Leinenkugel, 1976). The forces acting in the blocs are shown in the upper part of Figure 1:(*R* … shear resistance in the slip surface; *Eu* and *Eo* … Earth pressure at the lower and upper end of the bloc; *u* pore water pressure in the slip surface and *v* average deformation rate in a bloc). The number of blocs as well as the inclination of the surface and slip surface of each single bloc in the model is chosen individually for each SMLS. In the actual version the bloc stiffness is modelled by a Young's Modulus *E*, and the Poisson ratio is chosen ν=0, so the mechanical model can be seen as 1D model.

In this model the main mechanism that controls the deformations and velocity of the slope are the pore water pressures in the slip plane as well as the characteristics of the earth resistance and the mobilization function at the lower end respectively. A change in the pore water pressure results in a change of shear resistance and further on the velocity.

Each block has 5 degrees of freedom in the model. The general velocity of the block, the earth pressure force and the displacements on the the lower and upper side . The system of equation is split into 5 equations for the 5 degrees of freedom. The central equation (1) is the relationship between the changing forces at one block and the change of velocity:

$$(\Delta E_o - \Delta E_u) * \cos\alpha + \Delta u * \frac{l}{\cos\alpha} * \tan\phi - \tau_0 * I_v * \ln\left(\frac{v_i}{v_{i-1}}\right) * \frac{l}{\cos\alpha} = 0 \quad (1)$$

The first term describes the change of the earth pressure forces on the end of the blocks in direction of the slip plane. The second term describes the change of the resisting force in the slip plane due to a change of the pore water pressure. The last term describes the change of the resisting force due to the change of velocity whereas I_v is the creep index according to Leinenkugel (1976).

The second leading equation formulates the change of the length of each block by ($\Delta S_o - \Delta S_u$) the difference in displacements at the upper and lower end of a bloc) due of the changes of stress in the blocks ($\Delta E_{o,i}$, $\Delta E_{u,i}$) This is approximated with Hook's law:

$$(\Delta S_o - \Delta S_u) * \frac{\cos\alpha}{l} * E - \frac{1}{2}\left(\frac{\Delta E_u}{t_1} + \frac{\Delta E_o}{t_2}\right) = 0 \quad (2)$$

The third major equation describes the relationship between the change of displacements of the blocks in direction of the slip plane and the velocity of each bloc:

$$v_i * \Delta t - \frac{\Delta S_o + \Delta S_u}{2\cos\alpha} = 0 \quad (3)$$

And the last two field equations connects the change of earth pressure and change of displacements between two consecutive blocks:

$$\Delta E_{o,b} = \Delta E_{u,b+1} \quad (4)$$

$$\Delta S_{o,b} = \Delta S_{u,b+1} \quad (5)$$

To finish the system of equations two boundary equations are necessary. For the bottom boundary a mobilization function that combines the displacements of the lowest joint with an according earth pressure.

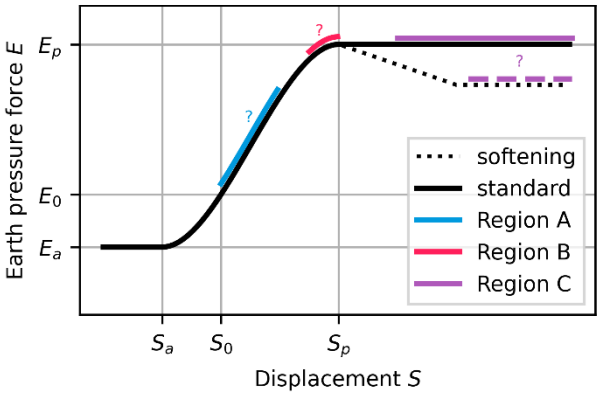

Figure 2. Mobilization Function for Er.

The mobilization function (Figure 2) is approximated as a polynom of third order that ranges from the active earth pressure E_a at the lower bound to the passive earth pressure E_p at the higher bound with a horizontal tangent at each point. The respective displacements s_a, s_0 and s_p in Figure 2 are calibration parameters of the model. The starting point on this function is another important initial parameter of the model and is understood as a representation of the history of the landslide. Region A (blue) in Figure 2 as starting point for the simulation shows a young SMLS with only small deformation in the past whereas Regions B and C show a SMLS with significant deformation in the past. Region C indicates two scenarios, one without softening and one with softening behaviour at large deformation.

In Figure 3 the principles of the hydrogeological model are presented for one single bloc which can be understood as a tank-like element. There are two types of such tank-like elements. The standard type that is modeled after the blocks in the Geomechanical Model and a source area element. The standard element takes the geometric properties of the block like the length, height and inclination. Other material properties like porosity *n*, saturation *Sr* and hydraulic conductivity *kf*

are added in the model to model the discharges through the block. Other properties are tuning factors for the amount of infiltration and influx that flows into the block from the sides. These elements are thought as 1m wide. The source area element, which describes the catchment area above the landslide, on the other hand has the same material and infiltration properties but has only an area and an inclination as geometric properties. In difference to the standard elements the source area element has two different flows out. One is the flow above the slip surface into the next bloc-element. To calculate the outflow into a 1 m wide bloc element the width of the bottom of the source area is given. The other outflow is below the slip surface that flows out of the system and does not inflence the behaviour of the SMLS anymore.

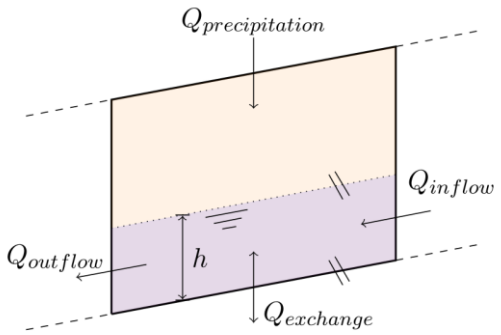

Figure 3. Hydrogeological Model.

Qprecipitation, Qinflow, Qoutflow respectively Qexchange in Figure 3. show water input and output in one bloc element.

So the model simulates a cascade of bloc elements in the direction of the slope. With the input of precipitation data the volume of water as well as a fictive water level in the elements, the flow between the elements and the pore water pressure in the slip surface is simulated. The cascade starts with the source area element from which the first flow to the top most block element is simulated. Further on an inflitration into each bloc element occur over the surface. At the bottom of the slope the discharges just flows out of the system.

For the simulation an initial water level is assigned for each element. This water level is then calculated into a volume with the length of the block, the porosity and the degree of saturation of the material.

Now every time step this volume is updated with the given flows between the elements and the infiltration over the surface and the new water level is calculated. As the system is a linear system of equations the whole calculation can be written in matrix form and solved with common linear system of equation solvers. The pore water pressures for each elemement are then saved as input for the Geomechanical Model.

2.2 Initial values and calibration parameters

To calculate the system a number of initial values have to be chosen. The initial velocity of all the blocks needs to be given together with the past displacement of the bottom block in order to initialize the mobilization function. With the initial earth resistance at the bottom block and the active earth pressure at the top most block an initial distribution of earth pressures along the slope is calculated. By multiplying the calculated earth pressures with the respective joint heights the initial forces Eo and Eu can be calculated in each joint. These earth pressures are then used to calculate an initial total resisting force in the slip plane that results from the earth pressure forces and the weight of the block. With these information the system can be calculated.

The calibration of the model, i.e. the determination of the major input data is done by comparing the calculation results for a certain time period respectively the rain fall data for this period with available measurement data from permanent pore water pressure measurements (PW-gauges) as well as data from chain inclinometer(s). Main input data are adjusted until a proper curve fitting of calculated and measured data are achieved. In Figure 4 measurement data from a case history, which are used to calibrate the model for this SMLS are shown exemplarily. The programming code for the model is written in Python 3.

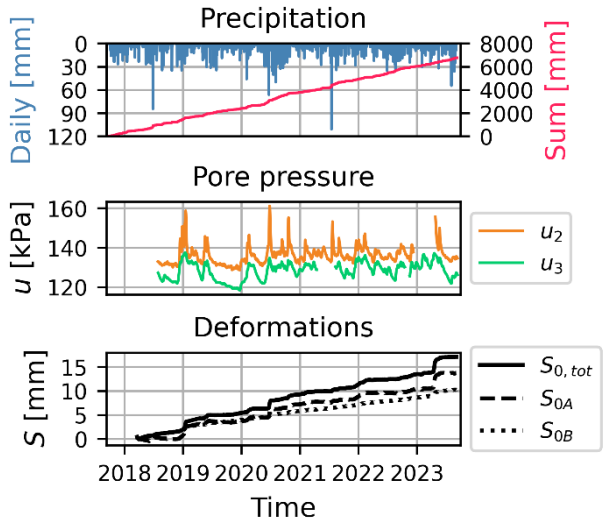

Figure 4. Measurement data for calibration of the model for a case history. Upper figure: Daily and cumulated precipitation data; Central figure: Measured pore water pressures in two points along the slip surface; Lower figure: Results (displacements) from an inclinometer measurement in different depths of the landslide.

3 CASE STUDY WITH ARTIFICIAL DATA

To present the general capacity of the model, Figure 5 shows the results of an artificial data set. A slope model with three blocks and a sinus shaped rainfall distribution over a time period of three years is modelled. The earth pressure Er at the lower end is assumed to start with earth pressure at rest E_0 at time zero. The infiltration of water in the slope is assumed in this simplified example only from the catchment area above the highest bloc of the landslide.

The results of pore water pressures in the slip surface show in accordance to the modelled sinus shaped rainfall distribution also a sinus shaped distribution over the year, with highest and temporary first peaks in the topmost bloc where the water inflow occurs first. The deformation curves for the different blocs show the highest deformation (rates) in the uppermost bloc and the lowest deformation (rates) in the lowest bloc where earth resistance is the highest and increases with further deformation.

This can also be seen in the lowest chart of Figure 5, where the earth pressure development over the three years is presented. On the upper end of the model the earth pressure remain on the level of the active earth pressure (red line). On the lower end the earth resistence increase with ongoing deformation according to the mobilization function as shown qualitively in Figure 2.

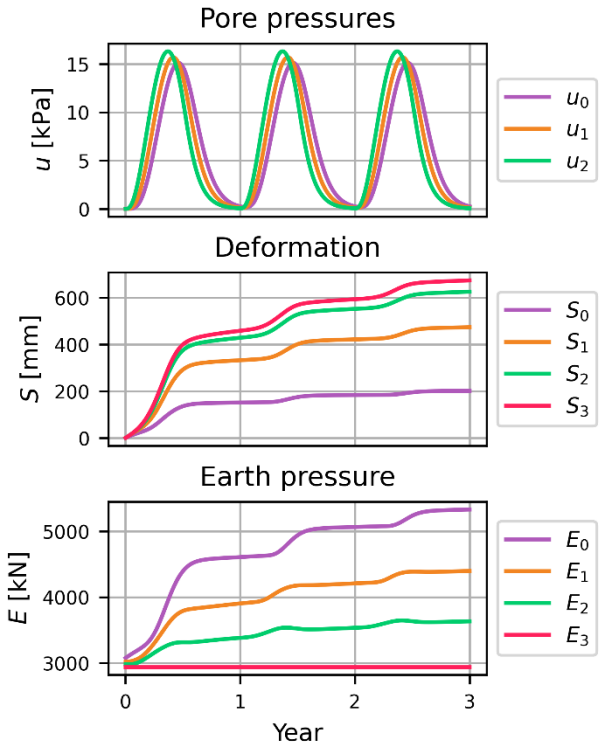

Figure 5. Calculation results for an artificial example.

It also can be seen that the same amount of pore water pressure peaks over the years lead to a decrease in ΔE over the time because of an increasing earth resistence with time. ΔE means the change of earth pressure in the bloc joints. E_3 in figure 5 is the constant active earth pressure at the upper end of the landslide, E_0 is the earth resistance (accorting to the moblization function) at the lower end of the landslide. E_1 and E_2 ar the earth pressures in the bloc joints of the model. This demonstrates the influence of the landslide history.

The application of the model for real case histories show on the one hand the applicablity and sgnificant improvements by the model compared to classical models with only discussing FOS. On the other hand the effort to get measurement data from chain inclinometers and permanent pore water pressure measurements in the slip surface as well as the challenge of a reliable calibration of the model specially for complex boundary conditions needs to be mentioned.

4 CONCLUSIONS

In this paper a combined hydrogeological-geomechanical model for slow moving large landslides is presented. For this type of landslides, the analytical model allows the simulation of the dependency of precipitation characteristics, time delayed pore water pressure developments in the slip surface and as consequence changes in the deformation rates. For slow moving landslides the model can be understood as supplement to classical analytical models which allow the calculation of FOS only. Assumed a successful calibration of the model is done, the prediction of further deformation behaviour as function of possible future rainfall events can be simulated. The model also is a good supplement for warning and alert plans, based on pore water pressure and deformation measurements, because a much deeper understanding of the deformation behaviour of the landslide is possible. Further developments of the model are necessary to simulate the influence of stabilization measures – such as anchors, dewatering measures but also the effect of pumping storages with changing water tables at the toe of such a SMLS.

REFERENCES

Ausweger, G.M. (2018) Influences of Water Level Changes on the Behaviour of a Slow Moving Landslide – In-situ Measurements, Model Tests and Numerical Analyses. Dissertation. Arbeitsgruppe Numerische Geotechnnik,

Institut für Bodenmechanik und Grundbau, Technische Universität Graz, Österreich.

Hungr, O. (2016) Landslides and Engineering Slopes. Experience, Theory and Practice. Proceedings of the 12th International Symposium on Landslides; Napoli, Italy.

Leinenkugel, H.J. (1976) Deformations- und Festigkeitsverhalten Bindiger Erdstoffe. Experimentelle Ergebnisse und ihre Physikalische Deutung. Veröffentlichungen des Institutes für Bodenmechanik und Felsmechanik der Universität Fridericiana in Karlsruhe; Herausgeber: A. Blinde, G. Gudehus, O. Natau; Heft 66.

Leroueil, S. (2001) Natural slopes and cuts: movement and failure mechanisms. Geotechnique 51, No. 3, 197-243.

Marte, R. (2019) Risikobeurteilung kriechförmig verlaufender Großmassenbewegungen. 68. Geomechanik Kolloquium, Spezialseminar: Umgang mit Risiken in der Geotechnik. Goricki & Kluckner (Herausgeber).

Marte, R.; Hofmann, R. (2020) Creeping large-scale landslides - Characterisation and assessment of safety. Geomechanics and Tunnelling, 13 (1) 1, S. 32-51. Doi.org/10.1002/geot.201900070.

Proceedings of the XVIII ECSMGE 2024
GEOTECHNICAL ENGINEERING CHALLENGES
TO MEET CURRENT AND EMERGING NEEDS OF SOCIETY
© 2024 the Authors
ISBN 978-1-032-54816-6
DOI 10.1201/9781003431749-220
Open Access: www.taylorfrancis.com, CC BY-NC-ND 4.0 license

ECSMGE 24
XVIII EUROPEAN CONFERENCE ON SOIL MECHANICS AND GEOTECHNICAL ENGINEERING

Mapping and monitoring tailings storage facilities with muography

Cartographie et surveillance des installations de stockage de résidus avec muographie

M.A. McLean
University of Melbourne, Parkville, Australia

F. Scutti, R. Seikel, S. Krishnan, C. Webster, S. Collins, S. Palanisamy, P.H. Panchal, J. Donovan, A.R. Duffy
Swinburne University of Technology, Hawthorn, Australia

C. Goss
BHP, Adelaide, Australia

A.N. Christensen*
mDetect, South Yarra, Australia

**achristensen@mdetect.com.au*

ABSTRACT: Tailings storage facilities present a global and growing challenge for mining companies. The management of tailings, which are the by-products of the mine processing plant, requires careful attention due to the potential risks they pose if the storage facility were to collapse. Such incidents can result in severe and lasting damage to the environment in downstream areas. Therefore, it is crucial to continuously monitor the structural stability of these facilities to ensure the safety and sustainability of active mining sites and legacy mines. This paper introduces a novel approach where muon tomography is employed to analyse the internal density structures of tailings dams. This work was conducted at the Prominent Hill Mine site in South Australia. We introduce an innovative method and technology for examining the internal density distribution of tailings storage facilities using muons, a natural source of radiation that can create X-ray-like scans of large structures. Muon technology provides a unique opportunity to provide insights into the inner structure of tailings storage facilities and potentially serves as a foundation for future research on developing early warning systems for detecting structural changes.

RÉSUMÉ: Les installations de stockage de résidus représentent un défi mondial et croissant pour les sociétés minières. La gestion des résidus, qui sont les sous-produits de l'usine de traitement minier, nécessite une attention particulière en raison des risques potentiels qu'ils posent en cas d'effondrement de l'installation de stockage. De tels incidents peuvent entraîner des dommages graves et durables à l'environnement dans les zones en aval. Il est donc crucial de surveiller en permanence la stabilité structurelle de ces installations afin de garantir la sécurité et la durabilité des sites miniers actifs et des mines existantes. Cet article présente une nouvelle approche où la tomographie muonique est utilisée pour analyser les structures de densité internes des barrages à résidus. Ce travail a été réalisé sur le site de la mine Prominent Hill en Australie méridionale. Nous introduisons une méthode et une technologie innovantes pour examiner la distribution de densité interne des installations de stockage de résidus à l'aide de muons, une source naturelle de rayonnement capable de créer des balayages de grandes structures semblables aux rayons X. La technologie des muons offre une opportunité unique de mieux comprendre la structure interne des installations de stockage de résidus et sert potentiellement de base à de futures recherches sur le développement de systèmes d'alerte précoce pour détecter les changements structurels.

Keywords: Tailings storage facilities; tailings wall monitoring; muon tomography; muography.

1 INTRODUCTION

Tailings Storage Facilities (TSF) are subject of long-term monitoring for stability and liquefaction assessments. Some remote monitoring capability for TSF is currently available with detection systems such as extensometers, LIDAR, total station, taseometers, and seismic sensors. However, their range and coverage of detection area are limited. Furthermore, background noise that inhibits detection ability, radiation licences that create barriers to deployment, and significant energy consumption of the systems either increase cost or restrict the longevity and flexibility of deployment.

The use of muons, naturally occurring particles from space, that impact a site and penetrate through hundreds of metres of rock with well-characterised frequency and direction, has long been considered a potential means to scan large volumes of matter.

Muons are continually being created by high-energy cosmic rays arriving from interstellar space and colliding with Earth's atmosphere at altitudes of about 15 kilometres. The average muon flux at sea level is about 1 muon per square centimetre per minute. The rate at which a muon loses energy as it interacts with matter is proportional to the density of the material it travels through.

Initially explored in 1955 to estimate tunnel overburden in the Snowy Mountains in Australia (George, 1955); detector capabilities have since greatly improved permitting mineral exploration (Bryman et al. , 2015), volcano monitoring (Nagamine et al., 1995), tide/tidal wave detection (Tanaka et al., 2022) and even mapping of corridors inside pyramids (Procureur et al., 2023).

In this paper we demonstrate a world-first use case of muon tomography in the context of TSF.

2 METHODOLOGY

The core detection unit is a 'telescopic' muon detector with several plastic scintillators that emit light when struck by a muon. This light is then received by mounted single-pixel silicon photomultipliers (SiPMs) (Krishnan et al., 2020). By utilising optically isolated sub-detectors within a panel plane, the arrival direction of intersecting muons can be estimated geometrically. The telescopic detectors provide angular coordinate uncertainty of less than five degrees within a field-of-view of order 17 × 17 degrees per pointing.

Two or more telescopic detectors are arranged along the embankment of a TSF to provide a limited 3D stereoscopic resolution of the muon flux detected across the extent of the embankment. Each detector observes multiple pointings over the course of several weeks to determine the muon flux as a function of angle across a TSF embankment (shown in Figure xxx). The observed muon flux depends on the elevation angle of observation and the opacity (or projected surface density), which is directly proportional to the muon path length inside the TSF embankment material and to the density of the material itself. Using at least two observation points separated by a known distance provides a stereoscopic 3D constraint on the material within overlapping fields of view.

The stand-alone telescopic muon detector system is solar powered with data transferred over 4G and can work independently of the mine power and communications infrastructure, easing many overheads and permissions from the host site.

Numerical simulations using the PUMAS library (Niess, 2022) and the Pyrate software package (Scutti, 2022) have been used to establish a relation between measured muon flux and observed opacity. This relation, which includes the correction for the elevation of observation, is used to convert the measured muon flux into observed opacity.

Assuming a geometry where the TSF can be subdivided into N 3D sub-blocks with uniform density ρ_j, the opacity Λ_i relative to a given muon path i inside the TSF is the sum of the products of individual path lengths Δl_{ij} and densities ρ_j for each sub-block j.

Simplifying assumptions about the interactions of muons with the medium of the TSF embankment are as follows. (1) Muons travel in straight lines for the energy ranges that predominate the ambient muon flux. (2) Muons are attenuated at a rate (Λ_i) proportional only to the density of the medium traversed (ρ_j) and distance traversed (Δl_{ij}) given as:

$$\sum_{j=1}^{N} \Delta l_{ij} \rho_j = \Lambda_i \qquad (1)$$

The basis of our adopted algorithm for 3D Muon Tomography is that of the Lines-Of-Sight (LOS) of different detectors intersecting common cells in the 3D block model space and by comparing observed LOS opacities against those computed by equation 1. The computed LOS opacity uses a 3D regular grid traversal algorithm (Figure 1) through an a priori discretised geological model of densities.

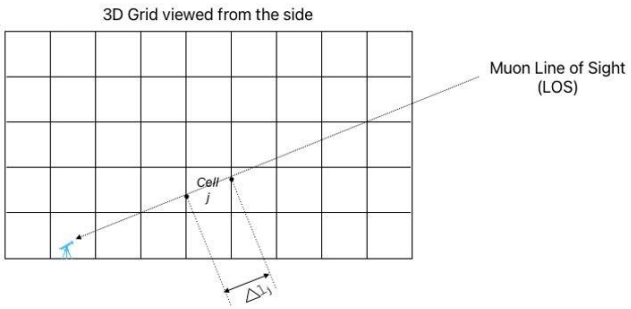

Figure 1. 3D Regular Grid Traversal Algorithm; with the opacity along a muon's line of sight (LOS) computed using equation 1.

The algorithm aims to find the density distribution of the medium traversed (ρ_j) such that equation 2 is minimised:

$$\left\| \Lambda_i - \left(\sum_{j=1}^{N} \Delta l_{ij} \rho_j \right) \right\| \qquad (2)$$

The algorithm developed to solve equation 1 is based on a Monte Carlo Markov Chain (MCMC) approach. Starting with an a-priori discretised geological model of densities to populate the initial guess for values of the image precomputed segment lengths of muon trajectories for the action, and reconstructed opacities derived from the observed muon events, an iterative method stochastically perturbs the image - one randomly selected cell at a time - looking to minimise equation 2.

This approach allows for geological constraints to be applied to the evolution of the model during its convergence (Guillen et al., 2004). The ability to use geological constraints is an advantage the MCMC approach offers over approximate imaging methods such as SIRT (Ren and Kalscheuer, 2020).

3 SURVEY

The Prominent Hill copper-gold mine is located approximately 640 km northwest of Adelaide in northern South Australia. Prominent Hill has one TSF impounded within the Integrated Waste Landform (IWL), shown in Figure 2. The TSF is a singular, circular facility containing tailings generated from processing ore from the open pit and underground mines. It has a diameter of 1750 m covering an area of about 2.4 km^2.

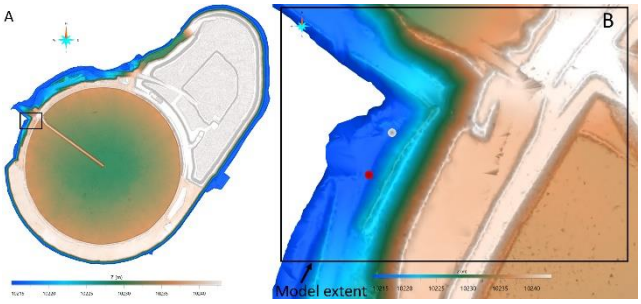

Figure 2. Topography surfaces generated from LiDAR data (blue colours are low elevations, white colours are high elevations) for: (A) the entire Prominent Hill tailings storage facility (black box shows the location of the scanned region), and (B) the scanned region zoom in, with the two telescopic detector deployments as the white and red dots.

Construction of the TSF has been ongoing, with five embankment lifts occurring since commissioning in 2009. The TSF embankment is a minimum 60 m wide waste rock dump rising 25 m high. On the tailings side of the embankment, a filter zone made up of finer waste rock, typically 3 m wide, was built concurrently with a 6m clay liner adjacent to the tailings.

Three detectors (seen in Figure 3) were used to monitor the region of interest identified in Figure 2. The primary and secondary detectors were telescopes used to scan the region dynamically. These detectors are placed approximately 10 m from the beginning of the rise, spaced 50 m from each other. The third reference detector was a simple muon counter recording the background rate.

The primary and secondary detectors were powered by an independent solar array with a single communication link used for data transfer and power distribution. Data acquisition and 4G gateway then arbitrated the data from all three detectors and forwarded data to the cloud.



Figure 3. Two muon detector telescopes mid-installation (note not their final placements), with the background muon counter as the small black box at its base.

Each detector observed multiple pointings over the course of nearly ten days to determine the muon flux as a function of angle across the TSF embankment.

The muon flux, detected across the extent of the embankment was converted to an opacity using an open-source muon physics transport engine, PUMAS (Niess, 2022). Regions in which opacities, or equivalently projected surface densities, had intersecting sightlines were then inverted to produce a 3D apparent density using the MCMC algorithm. These discrete points were then kriged to create a 3D volumetric apparent density, as shown in Figure 4.

The results of the muon-derived apparent densities, post-kriging, are found to be a distribution heavily skewed to the expected wall material density, with the 10th and 90th percentile found at 1.64 g/cm^3 and1.82 g/cm^3, respectively. While there are some outliers with unrealistically high apparent densities (over 10.0 g/cm^3), these make up a very small proportion of the scanned volume (0.3 per cent of the scanned volume falls between 3.0 g/cm^3 and 10.2 g/cm^3) and are numerical artefacts.

As shown in Figure 4, relatively high apparent densities (between 1.8 g/cm^3 and 2.2 g/cm^3) are robustly detected although their cause remains unclear. We suspect these values correspond to cemented backfill and basement waste which has been confirmed to have been used to build the TSF in the observed

direction of the telescope. Apparent densities estimated from muon tomography have tended to be slightly higher (median of 1.68 g/cm^3) compared with the measured value (1.495 g/cm^3).

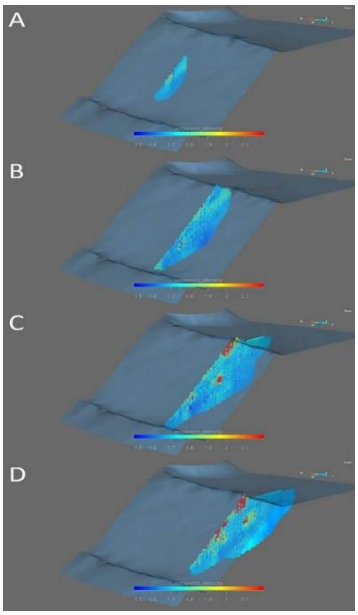

Figure 4. Apparent densities kriged throughout the scanned volume, shown as a progressive slice from North (A) to South (D). Cooler blue colours indicate low apparent densities, warmer red colours indicate high apparent densities. The transparent blue surface is the topography of the TSF. Note that only the rock fill embankment has been scanned.

4 CONCLUSIONS

Although only a limited area of the Tailings Storage Facility was scanned in this short deployment the utilisation and efficacy of muons for cheaply scanning large volumes, with no site disruption or installation requirements is clear. Muon technology provides a unique opportunity to provide insights into the inner structure of tailings storage facilities and potentially serves as a foundation for future research on developing early warning systems for detecting structural changes.

ACKNOWLEDGEMENTS

The authors gratefully acknowledge the support of the Prominent Hill mine in facilitating the trials, particularly Antoinette Stryk. mDetect recognises the valuable ongoing support of the Swinburne University of Technology, with special thanks to David Smoors for technical efforts. This work was made possible by the Australian Commonwealth Government's Advanced Manufacturing Growth Centre, AMGC, grant number C259.

REFERENCES

Bryman, D., Bueno, J., and Jansen, J., (2015). Blind Test of Muon Geotomography for Mineral Exploration, *ASEG Extended Abstracts*, pp 1–3. https://doi.org/10.1071/ASEG2015ab054.

George, E. P., (1955). Cosmic rays measure overburden of tunnel, *Commonwealth Engineer*, pp 455–457 (Tait Publishing Co.: Melbourne).

Guillen, A., Courrioux, G., Calcagno, P., Lane, R., Lees, T., and McInerney, P., (2004). Constrained gravity 3D litho-inversion applied to Broken Hill, *ASEG Extended Abstracts*. https://doi.org/10.1071/ASEG2004ab057.

Krishnan, S., Webster, C., Duffy, A. R., Brooks, G., Clay, R. and Mould, J., (2020). Improving the energy resolution while mitigating the effects of dark-noise, for a microcontroller based SiPM sensor, *JINST*, 15(9):P09028. https://doi.org/10.1088/1748-0221/15/09/P09028.

Nagamine, K., Iwasaki, M., Shimomura, K. and Ishida, K., (1995). Method of probing inner-structure of geophysical substance with the horizontal cosmic-ray muons and possible application to volcanic eruption prediction, *Nucl Instrum Methods Phys Res Section A*, 356:585–595. https://doi.org/10.1016/0168-9002(94)01169-9.

Niess, V., (2022). The PUMAS Library, *Comp Phys Comms*, 279:108438. https://doi.org/10.1016/j.cpc.2022.108438.

Procureur, S., Morishima, K., Kuno, M., et al. (2023). Precise characterization of a corridor-shaped structure in Khufu's Pyramid by observation of cosmic-ray muons, *Nature Communications*, 14:1144. https://doi.org/10.1038/s41467-023-36351-0.

Ren, Z. and Kalscheuer, T., (2020). Uncertainty and Resolution Analysis of 2D and 3D Inversion Models Computed from Geophysical Electromagnetic Data, *Surv Geophys*, 41:47–112. https://doi.org/10.1007/s10712-019-09567-3.

Scutti, F., (2022). Pyrate: a novel system for data transformations, reconstruction and analysis, *Journal of Physics*: Conference Series, 2438:012061. https://doi.org/10.1088/1742-6596/2438/1/012061.

Tanaka, H.K.M., Aichi, M., Balogh, S.J. et al. (2022). Periodic sea-level oscillation in Tokyo Bay detected with the Tokyo-Bay seafloor hyper-kilometric submarine deep detector (TS-HKMSDD). *Sci Rep* 12, 6097. https://doi.org/10.1038/s41598-022-10078-2.

Proceedings of the XVIII ECSMGE 2024
GEOTECHNICAL ENGINEERING CHALLENGES
TO MEET CURRENT AND EMERGING NEEDS OF SOCIETY
© 2024 the Authors
ISBN 978-1-032-54816-6
DOI 10.1201/9781003431749-221
Open Access: www.taylorfrancis.com, CC BY-NC-ND 4.0 license

ECSMGE 24
XVIII EUROPEAN CONFERENCE ON SOIL MECHANICS AND GEOTECHNICAL ENGINEERING

Liquefaction resistance of TP-Lisbon sand: A comparison between cyclic triaxial and cyclic direct simple shear tests

Résistance à la liquéfaction du sable TP-Lisbon: Une comparaison entre les essais triaxiaux cycliques et cisaillement simple direct cycliques.

F. Molina-Gómez*, A. Viana da Fonseca, C. Ferreira
CONSTRUCT-GEO, Universidade do Porto (FEUP), Porto, Portugal

B. Caicedo
Universidad de los Andes, Bogotá, Colombia

**fausto@fe.up.pt*

ABSTRACT: Soil liquefaction is one of the most complex phenomena characterised by the rapid loss of the strength and stiffness of soil. In the laboratory, the liquefaction resistance can be assessed by different testing procedures, involving axisymmetric and plain strain conditions. This paper addresses an experimental comparison between the results of cyclic triaxial and cyclic direct simple shear testing. The tests were conducted using a historically liquefiable sand from the city centre of Lisbon, denominated as TP-Lisbon sand. Findings showed a higher liquefaction resistance for axisymmetric conditions (cyclic triaxial tests) than plane strain conditions (direct simple shear tests). Therefore, a method to transform the results derived from either cyclic triaxial or direct simple shear is proposed. This method provides a reliable prediction of liquefaction resistance derived inversion and rotation of principal stresses in a single approach.

RÉSUMÉ: La liquéfaction des sols est l'un des phénomènes les plus complexes et instables, se caractérisant par une perte rapide de la résistance et de la rigidité du sol. En laboratoire, la résistance à la liquéfaction peut être évaluée par différentes procédures d'essai, impliquant des conditions axiales symétriques et de déformation simple. Cet article aborde une comparaison expérimentale entre les résultats des essais triaxiaux cycliques et des essais de cisaillement simple direct cycliques. Les essais ont été réalisés avec un sable historiquement liquéfiable du centre-ville de Lisbonne, sable TP-Lisbon. Les résultats ont montré une plus grande résistance à la liquéfaction dans des conditions axysy axisymétriques métriques (essais triaxiaux cycliques) par rapport aux conditions de contrainte pure (essais de cisaillement simple). Par conséquent, une méthode de transformation des résultats obtenus par des essais triaxiaux cycliques ou de cisaillement simple est proposée. Cette méthode permet de prédire la résistance à la liquéfaction en prenant en compte l'inversion et la rotation des contraintes principales au sein d'une seule approche.

Keywords: Liquefaction; laboratory testing; cyclic characterisation; sands.

1 INTRODUCTION

Liquefaction phenomena is characterised by the rapid loss of the strength and stiffness of soil due to the pore pressure build-up during cyclic or monotonic loading. Effective stress tends to zero during liquefaction due to the generation of pore pressure build-up (Ishihara, 1993). Around the world, liquefaction has seriously damaged a number of infrastructures. In Portugal, local liquefaction-induced damage dates from 1344, 1531, 1755 and 1909 when distant and local intraplate earthquakes (with a magnitude between 6.0 and 8.5) struck the Portuguese onshore mainland, mainly affecting the greater Lisbon area (Jorge, 1993). Therefore, the characterisation of the cyclic behaviour of liquefiable soils of Lisbon centre is essential to prevent damage and possible collapse of buildings and infrastructure in this region due to earthquake-induced liquefaction.

This paper presents the results of the liquefaction resistance characterisation of TP-Lisbon sand using cyclic triaxial tests (CTx) and cyclic direct simple shear tests (CDSS). TP-Lisbon sand was collected in a site locally denominated as 'Terreiro do Paço', located in the historical centre of Lisbon (Molina-Gómez & Viana da Fonseca, 2021). The experimental program focuses on the assessment of the effects of the inversion and rotation of principal stresses. A method to assess and compare these effects is proposed herein, proposing an estimation from a single approach. This method provides a reliable unification of both CTx and CDSS results to characterise the liquefaction resistance of TP-Lisbon sand.

2 MATERIALS AND METHODS

2.1 Description of TP-Lisbon sand

TP-Lisbon sand is an alluvial granular soil with origin in the late Quaternary, which has sedimented next to the Tagus River in the historical centre of Lisbon. This site is named by locals as 'Terreiro do Paço', (that in English means courtyard palace). The buildings surrounding this relevant historical spot correspond to old heritage Pombalino masonry buildings (Couto et al., 2020). The samples of TP-Lisbon sand were collected within the scope of geotechnical exploration for the construction of the Lisbon blue line tunnel of 'Metropolitano de Lisboa'. These samples were collected in a site investigation located into the 'Praça do Comércio', specifically at the coordinates 38º42'26.6"N–9º8'13.4"W (Molina-Gómez & Viana da Fonseca, 2021).

The specific gravity of solid particles (G_s), the minimum void ratio (e_{min}) and the maximum void ratio (e_{max}) are shown in Table 1. The parameters of the particle size distribution are also exposed in Table 2, including the mean diameter (D_{50}), the coefficient of curvature (Cc), the coefficient of uniformity (Cu) and the fines content (FC). The particle size distribution of TP-Lisbon sand is depicted in Figure 1. The unified soil classification system (USCS) classifies the TP-Lisbon sand as poorly graded (SP), with low values for Cu and Cc.

Table 1. Physical properties of TP-Lisbon sand.

Parameter	Value
Gs	2.66
e_{min}	0.64
e_{max}	1.01
D_{50} (mm)	0.21
Cu	1.69
Cc	1.13
FC (%)	2.21

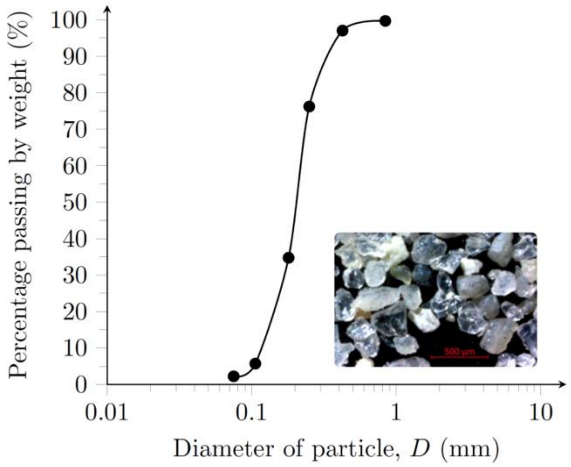

Figure 1. Particle size distribution of TP-Lisbon sand.

2.2 Testing devices and experimentation

The experimental programme for assessing the liquefaction resistance of TP-Lisbon sand involved an advanced testing programme in the laboratory involving cyclic triaxial (CTx) and cyclic direct simple shear (CDSS) tests. CTx and CDSS apparatuses allowed for the inversion and rotation of principal stresses, respectively. Therefore, the comparison between the results of both types of tests provided a comprehensive characterisation of cyclic behaviour and liquefaction resistance of TP-Lisbon sand.

The CTx apparatus featured a traditional triaxial cell equipped with a submersible load cell with a capacity of 1 kN. Cyclic loading was applied using a servo-actuator, consisting of a hydraulic piston for displacement or load control, with a frequency ranging between 0.001 and 2 Hz. A precise regulation of cell pressure and back-pressure was achieved using a pair of Pressure/Volume Controllers manufactured by Global Digital Systems (GDS). These controllers allowed for the automated increment of both pressures during the saturation and consolidation phases. To ensure reliable contact between the top cap and the hydraulic piston during cyclic loading, a rubber V-ring was employed to guarantee the inversion of principal stresses during the cyclic testing (Cordeiro et al., 2022; Molina-Gómez et al., 2023).

An advanced and fully automatic simple shear apparatus manufactured by Willie Geotechnik was employed. The equipment features two high-quality servomotors for vertical and horizontal loading, two local LVDT transducers to measure vertical and horizontal displacements and a multi-axis load cell. It enables static and cyclic tests under both strain and stress control by a SGI configuration. The SGI configuration comprises a series of stacked copper rings to maintain a constant cross-sectional area while allowing for shear distortion of the specimen. The cyclic loading was applied under constant volume conditions, ensuring an invariant height of the specimen through active control based on the vertical displacement reported by local LVDT. Constant volume tests are equivalent to undrained shear tests (Dyvik et al., 1987).

In this study, the following testing procedures were implemented for both CTx and CDSS tests. All samples were reconstituted to achieve a Dr of 50% using the dry pluviation method. This method was adopted due to its capability to replicate the initial fabric of alluvial soil deposits (Quinteros & Carraro, 2023). The samples were saturated by flushing carbon monoxide and de-aired water (Viana da Fonseca et al., 2021). The full saturation condition was confirmed through bender element tests by reporting P-wave

velocity values higher than 1482 m/s are needed to ensure the full saturation of the soil (Astuto et al., 2023). After saturation confirmation, the samples were consolidated for a mean effective stress (p'_0) of 50 kPa and effective vertical stress (σ'_0) of 80 kPa for CTx and CDSS tests, respectively. The soil samples were sheared using different cyclic stress ratio (CSR) combinations at a frequency of 0.1 Hz.

3 RESULTS AND DISCUSSION

3.1 Description of TP-Lisbon sand

Figure 2 shows the liquefaction resistance curves for TP-Lisbon sand derived from the results obtained from 5 CTx and 5 CDSS tests. These curves were derived by a power law that correlates the number of cycles liquefaction onset (N_L) for each CSR. N_L was identified when double axial strain exceeding 5.0% for CTx tests and double shear strain exceeding 7.5%.

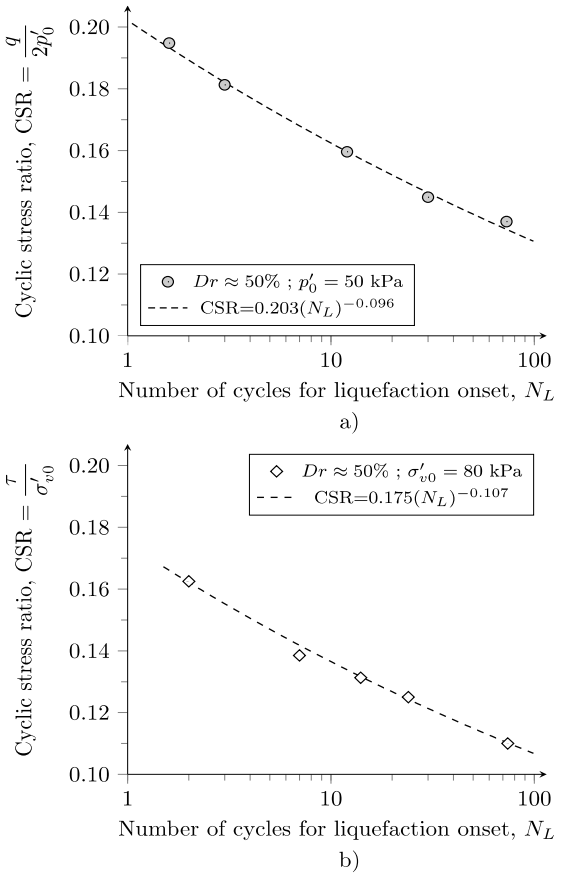

Figure 2. Liquefaction resistance curves: a) CTx results; b) CDSS results.

Experimental results in Figure 2 revealed that inversion of principal stresses (i.e. CTx tests) leads to a higher liquefaction resistance than rotation of principal stresses (i.e. CDSS tests). However, Figure 2 shows that the liquefaction resistance curves for TP-Lisbon sand are parallel, independently of the testing condition. The CTx and CDSS results have been contrasted (Giretti et al., 2018; Nong et al., 2021). Although the loading differences, these results can be correlated using a correction coefficient (*Cr*), which transforms liquefaction resistance from isotropic triaxial testing into liquefaction resistance in simple shear conditions:

$$CSR_{SS} = Cr \cdot CSR_{CTx} \quad (1)$$

Diverse authors (Castro & Poulos, 1977; Finn et al., 1971; Ishihara et al., 1985) demonstrated that *Cr* is a function of the lateral earth pressure coefficient at rest (K_0). Equation 2 presents a *Cr* correlation for TP-Lisbon sand.

$$Cr = \frac{2 + 3K_0}{4} \quad (2)$$

This correlation was obtained by adjusting the experimental results by the least-square method, obtaining a correlation coefficient $R^2 = 0.92$. For normally consolidated sands, K_0 is reasonably estimated by the approximation $K_0 = 1\text{-}\sin\phi_{cv}$ (Jaky, 1944). Molina-Gómez & Viana da Fonseca (2021) found that the friction angle at constant volume (ϕ_{cv}) of TP-Lisbon sand is 34º. Hence, *Cr* is equal to 0.83. Figure 3 demonstrates that the results obtained from both test types are associated since they fall into a single liquefaction resistance curve after applying the *Cr* transformation.

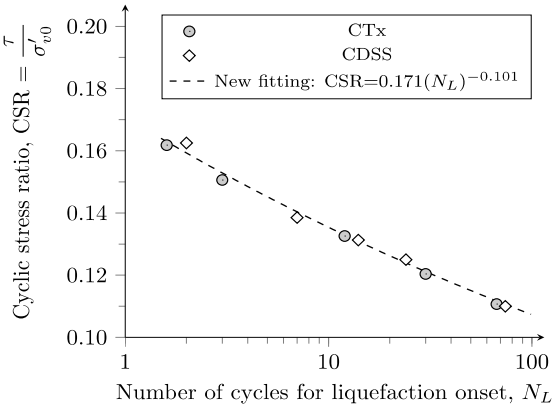

Figure 3. Transformed liquefaction resistance curve.

Figure 3 shows a good agreement between CTx and CDSS after results transformation. Hence, by using the *Cr* transformation, it is possible to compare the liquefaction resistance estimated by both testing procedures, providing a robust basis for cross-referencing their results and facilitating a more

comprehensive understanding of cyclic behaviour of TP-Lisbon sand.

4 CONCLUSION

This paper has presented a comprehensive characterisation of the liquefaction resistance of the TP-Lisbon sand using CTx and CDSS testing. Experimental results showed that the inversion of principal stresses leads to higher resistance than the rotation of principal stresses. This disparity between the two testing conditions can be overcome by introducing the correction coefficient, *Cr*. The transformation provided by *Cr* allows for a reliable approach, which provides a valuable approach to compare and understand the liquefaction resistance of TP-Lisbon sand under different stress paths.

ACKNOWLEDGEMENTS

This work was supported by Base Funding - UIDB/04708/2020 with DOI 10.54499/UIDB/04708/2020 and Programmatic Funding - UIDP/04708/2020 with DOI 10.54499/UIDP/04708/2020 of the CONSTRUCT – Instituto de I&D em Estruturas e Construções– funded by national funds through the FCT/MCTES (PIDDAC). Fausto Molina-Gómez acknowledges the support of FCT through the grant SFRH/BD/146265/2019.

REFERENCES

Astuto, G., Molina-Gómez, F., Bilotta, E., Viana da Fonseca, A., & Flora, A. (2023). Some remarks on the assessment of P-wave velocity in laboratory tests for evaluating the degree of saturation. *Acta Geotechnica*, 18(2), 777–790. https://doi.org/10.1007/s11440-022-01610-9.

Castro, G., & Poulos, S. J. (1977). Factors Affecting Liquefaction and Cyclic Mobility. *Journal of the Geotechnical Engineering Division*, 103(6), 501–506.

Cordeiro, D., Molina-Gómez, F., Ferreira, C., Rios, S., & Viana da Fonseca, A. (2022). Cyclic Liquefaction Resistance of an Alluvial Natural Sand: A Comparison between Fully and Partially Saturated Conditions. *Geotechnics*, 2(1), 1–13. https://doi.org/10.3390/geotechnics2010001.

Couto, R., Bento, R., & Gomes, R. C. (2020). Seismic performance and fragility curves of historical residential buildings in Lisbon downtown affected by settlements. *Bulletin of Earthquake Engineering*, 18(11), 5281–5307. https://doi.org/10.1007/s10518-020-00906-z.

Dyvik, R., Berre, T., Lacasse, S., & Raadim, B. (1987). Comparison of truly undrained and constant volume direct simple shear tests. *Géotechnique*, 37(1), 3–10. https://doi.org/10.1680/geot.1987.37.1.3.

Finn, W. D. L., Pickering, D. J., & Bransby, P. L. (1971). Sand Liquefaction in Triaxial and Simple Shear Tests. *Journal of the Soil Mechanics and Foundations Division*, 97(4), 639–659. https://doi.org/10.1061/JSFEAQ.0001579.

Giretti, D., Fioravante, V., Been, K., & Dickenson, S. (2018). Mechanical properties of a carbonate sand from a dredged hydraulic fill. *Géotechnique*, 68(5), 410–420. https://doi.org/10.1680/jgeot.16.P.304.

Ishihara, K. (1993). Liquefaction and flow failure during earthquakes. *Géotechnique*, 43(3), 351–451. https://doi.org/10.1680/geot.1993.43.3.351.

Ishihara, K., Yamazaki, A., & Haga, K. (1985). Liquefaction of K0-Consolidated Sand Under Cyclic Rotation of Principal Stress Direction With Lateral Constraint. *Soils and Foundations*, 25(4), 63–74. https://doi.org/10.3208/sandf1972.25.4_63.

Jaky, J. (1944). The coefficient of earth pressure at rest. In Hungarian "A nyugalmi nyomas tenyezoje." *Journal Society Hungarian Engineering and Architecture*, 355–358.

Jorge, C. (1993). *Zonation of Liquefaction Potential. Application Attempt to the Portuguese Territory*. New University of Lisbon.

Molina-Gómez, F., & Viana da Fonseca, A. (2021). Key geomechanical properties of the historically liquefiable TP-Lisbon sand. *Soils and Foundations*, 61(3), 836–856. https://doi.org/10.1016/j.sandf.2021.03.004.

Molina-Gómez, F., Viana da Fonseca, A., Ferreira, C., & Caicedo, B. (2023). Experimental Wave-Based Assessment of Liquefaction Resistance for Different Degrees of Saturation. *Geotechnical Testing Journal*, 46(6), 968–985. https://doi.org/10.1520/GTJ20230299.

Nong, Z. Z., Park, S. S., & Lee, D. E. (2021). Comparison of sand liquefaction in cyclic triaxial and simple shear tests. *Soils and Foundations*, 61(4), 1071–1085. https://doi.org/10.1016/J.SANDF.2021.05.002.

Quinteros, V. S., & Carraro, J. A. H. (2023). The initial fabric of undisturbed and reconstituted fluvial sand. *Géotechnique*, 73(1), 1–15. https://doi.org/10.1680/jgeot.20.P.121.

Viana da Fonseca, A., Cordeiro, D., & Molina-Gómez, F. (2021). Recommended Procedures to Assess Critical State Locus from Triaxial Tests in Cohesionless Remoulded Samples. *Geotechnics*, 1(1), 95–127. https://doi.org/10.3390/GEOTECHNICS1010006.

Proceedings of the XVIII ECSMGE 2024
GEOTECHNICAL ENGINEERING CHALLENGES
TO MEET CURRENT AND EMERGING NEEDS OF SOCIETY
© 2024 the Authors
ISBN 978-1-032-54816-6
DOI 10.1201/9781003431749-222
Open Access: www.taylorfrancis.com, CC BY-NC-ND 4.0 license

ECSMGE 24
XVIII EUROPEAN CONFERENCE ON SOIL MECHANICS AND GEOTECHNICAL ENGINEERING

Geotechnical interventions to mitigate the geomorphological risk of the access road to Ribeira Quente parish - Azores archipelago

Interventions géotechniques pour réduire le risque géomorphologique de la route d'accès a la paroisse de Ribeira Quente - archipel des Azores

L. Moniz*, P. Amaral, A.M. Malheiro, F. Marques, A. Santos
Laboratório Regional de Engenharia Civil, Ponta Delgada, Portugal

**Leticia.cm.moniz@azores.gov.pt*

ABSTRACT: The regional road no. 2-2ª is the only access to Ribeira Quente parish on the island of São Miguel (Azores). This road is approximately 5.5 km long and runs along the Ribeira Quente valley, with slopes that, in some cases, reach 450 m in height and with very steep gradients. The geology is very complex, with basaltic (*s.l.*) and trachytic (*s.l.*) lava flows, welded and non-welded ignimbrites, fall and flow pumice deposits, and slope deposits. Due to their geological, morphological, and hydrological characteristics, normally associated with episodes of intense and/or prolonged rainfall, the slopes often become unstable, isolating the population of Ribeira Quente parish from any kind of assistance by land. An example of this was the disaster that occurred on October 31, 1997, which left 29 people dead. Given the above, various consolidation works were carried out on the road's slope, of different types, namely: alteration of geometry, installation of external and internal drainage systems, ditches, application of shotcrete with nailing, and a semi-tunnel. This work presents the different interventions carried out along this regional road, as well as those that are planned to minimize and mitigate geomorphological risks. The aim is also to illustrate and emphasise the fact that any stabilisation solution needs to be properly dimensioned and have a maintenance plan after its implementation to guarantee its full functionality.

RÉSUMÉ: La route régionale n.° 2-2ª est le seul accès à la paroisse de Ribeira Quente sur l'île de São Miguel (Açores). Cette route, d'une longueur d'environ 5,5 km, longe la vallée de Ribeira Quente avec des pentes qui, dans certains cas, atteignent 450 m d'altitude et des dénivelés très importants. La géologie du site est très complexe, avec des coulées de lave basaltique (*s.l.*) et trachytique (*s.l.*), des ignimbrites soudées et non soudées, des dépôts de ponce de chute et de coulée et des dépôts de pente. En raison de leurs caractéristiques géologiques, morphologiques et hydrologiques, normalement associées à des épisodes de précipitations intenses et/ou prolongées, les pentes deviennent souvent instables, isolant la population de la paroisse de Ribeira Quente de toute forme d'assistance par terre. La catastrophe du 31 octobre 1997, qui a causé la mort de 29 personnes, en est un exemple. Compte tenu de ce qui précède, divers travaux de consolidation ont été réalisés sur le talus de la route, de différents types, à savoir: modification de la géométrie, installation de systèmes de drainage externes et internes, fossés, application de béton projeté avec clouage et un semi-tunnel. Ce travail présente les différentes interventions réalisées le long de cette route régionale, ainsi que celles qui sont prévues pour minimiser et atténuer les risques géomorphologiques. L'objectif est également d'illustrer et de souligner que toute solution de stabilisation doit être correctement dimensionnée, et disposer d'un plan d'entretien après sa mise en œuvre, afin de garantir sa pleine fonctionnalité.

Keywords: Geomorphological risks; slope instabilities; road protection; Azores.

1 INTRODUCTION

As a result of its volcanic-tectonic setting, the Azores archipelago has a wide variety of soils with different mechanical characteristics. The existence of slopes made up of volcanic deposits with different physical, mechanical, and hydrogeological characteristics are themselves predisposing factors to the occurrence of geomorphological instability processes, namely landslides, with consequences for people and property. Rainfall is one of the main factors triggering landslides in the Azores, as the increase in water in the materials leads to a decrease in shear strength, which can occur through the decrease in apparent cohesion (in unsaturated soils) or an increase in neutral pressures in the potential slip surface due the rise of the water table (Amaral, 2010 and Amaral *et al.*, 2010).

The regional road no. 2-2ª (E.R. 2-2ª), in the Ribeira Quente parish, on São Miguel Island (Azores), is flanked by slopes ranging in height from a few metres to approximately 450 meters, some with steep inclines. These slopes have a complex geological

constitution, ranging from basaltic (*l.s.*) and trachytic (*l.s.*) lava flows, welded and non-welded ignimbrites, pomitic pyroclastic deposits of fall and flow and gravitational deposits. Given the above, these slopes are highly prone to slope movements, particularly landslides and debris flows, which are usually associated with heavy and/or prolonged rainfall.

Over time, numerous episodes of heavy precipitation have triggered slope movements, resulting in the blockade of the road, often at multiple locations. This, in turn, isolates the local population, cutting off access to assistance by land. The most notable event took place in 1997, when 29 people died in the Ribeira Quente parish, and the most recent was in June 2023. Therefore, it has become imperative to intervene geotechnically along this road. The carried-out interventions aimed the improvement of safety conditions; however, if they are not supported by geological and geotechnical studies and maintenance actions, they risk not being functional in the long term. This article presents some slope consolidation works carried out at Ribeira Quente Road. In addition, the aim is to illustrate why any stabilisation solution must be the subject of a study, which supports the project, and must also include a long-term maintenance plan, which must be adhered to guarantee the functionality of the solutions.

2 STUDY AREA

The E.R. 2-2ª access road to the Ribeira Quente parish, in the Ribeira Quente valley, is one of the areas most affected by slope movements in the Azores archipelago. This road is the only access route to the parish.

The existing water lines in the Ribeira Quente valley, as well as the presence of concave morphologies expressed in the slopes, with continuity upstream, represent flow channels favourable to the mobilisation of debris flows.

Considering the susceptibility of this location to the occurrence of slope movements, Marques (2013), based on the work carried out by Marques et al (2009), produced a map of susceptibility and propagation of slope movements for the municipality of Povoação, including the Ribeira Quente parish (Figure 1).

From this map, it can be seen that this road is very vulnerable to geomorphological instability processes. Based on this information, which justifies the phenomena that have occurred in this location, it became imperative to implement actions to minimise some of the most serious situations, intending to improve safety conditions for passers-by. It is important to emphasise that these measures do not completely eliminate geomorphological risk (as we can see in the most recent situation), but only contribute substantially to reducing it.

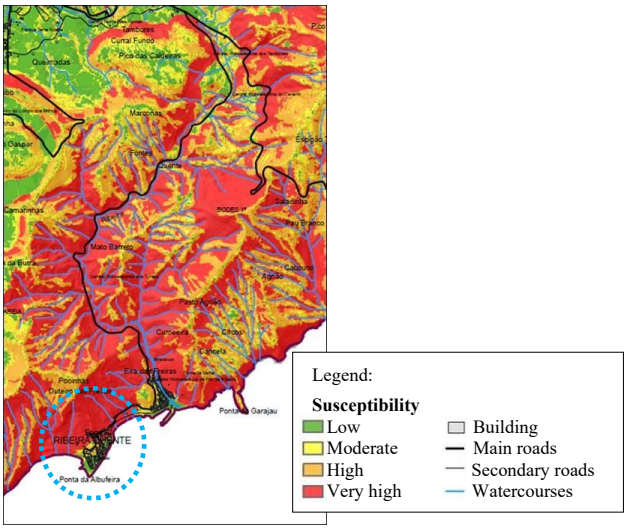

Figure 1. Map of susceptibility and propagation of occurrence of slope movements for the Ribeira Quente valley, outlined in blue (adapted from Marques, 2013).

3 RISK MITIGATION MEASURES

In recent years, 15 sites along the E.R. 2-2ª (Figure 2), which had been identified as critical, have been intervened. The risk mitigation measures to be implemented are: (1) re-profiling the slope, (2) a retaining wall with a ditch at the end, (3) construction of a semi-tunnel, (4) removal of rock blocks and (5) metal nets with nails and sometimes with shotcrete. This paper will present only 4 of the 15 sites intervened, corresponding to sites 4, 5, 12 and 14 (Figure 2), taking into account their representativeness in the overall context of the interventions.

Site no. 4 corresponds to a slope about 20 metres high and is made up of intercalations of trachytic pyroclastic deposits of different grain sizes. The intervention carried out at this site involves altering the geometry of the slope, softening its slope, and creating a bench at approximately half height (Figure 3).

The slopes adjacent to the E.R. 2-2ª usually have water levels. Evidence of this can be seen in the numerous springs and waterfalls that can be seen along the road. Despite this, no deep drainage system, such as sub-horizontal drains, has been installed at site no. 4. Thus, on the face of the slope, it is possible to observe signs of internal erosion caused by the outflow and accumulation of water, as well as gullies due to surface run-off (Figure 4 on the left). Apparently, no geological and geotechnical study or global stability analyses have been carried out on the slopes to be re-profiled to ascertain which tilt gives them stability.

Indeed, there have already been several surface geomorphological instabilities on the face of the re-profiled slopes. At site no. 6 (Figure 4 on the right), there was a superficial geomorphological instability on the face of the re-profiled slope.

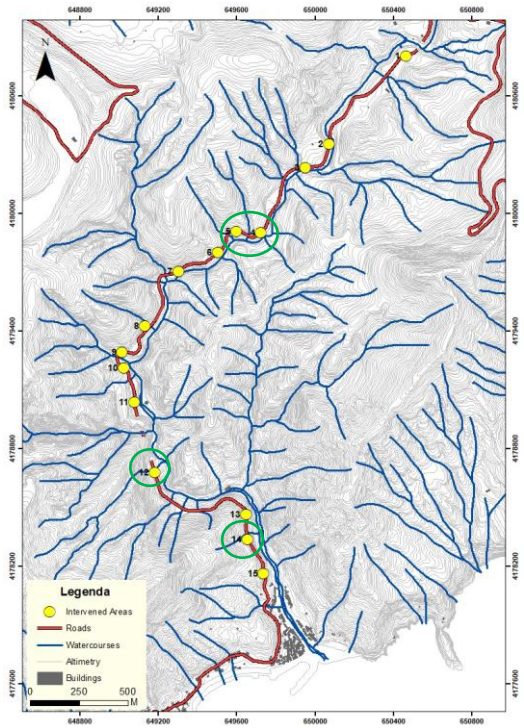

Figure 2. Location of the sections of the intervened areas. In green circles, the indication of the four sites presented in this work.



Figure 3. Site no. 4 - Slope re-profiling.



Figure 4. Site nº. 4 - Erosion on the slope face (on the left). Geomorphological instability at site no. 6 (on the right).

At site no. 5, a retaining wall was built with a ditch at its back, aiming to collect a large part of the material mobilised from upstream, preventing it from reaching the regional road platform (Figure 5). Over time, this measure has proved to be effective, as there have been several reports of these structures intercepting material that was heading towards vehicles travelling on the E.R. 2-2ª. However, these are measures that need to be maintained, in this specific case by removing the material that is trapped inside the ditch, so that it remains operational, a situation that does not always occur, as is the case at site no. 7 (Figure 5 on the right).



Figure 5. Site no. 5 – Waiting wall with ditch (on the left). Site no. 7 – No maintenance (on the right).

The slope adjacent to site no. 12 is 400 metres high. Taking into account the difficulty of implementing stabilisation measures there, a semi-tunnel was built, approximately 200 m long (Figure 6).



Figure 6. Site no. 12 – Semi-tunnel.

The length initially planned for the semi-tunnel was greater than that actually built. The initial extension was justified by the geological and morphological characteristics of the adjacent slopes. A heavy rainfall event in June 2023, which led to several landslides, debris flows, and debris avalanches, demonstrated

this. In fact, in this event, the most serious situation occurred on the slope adjacent to the section of the semi-tunnel that was chosen not to be intervened on (Figure 7). The unstable material was deposited at the entrance of the semi-tunnel, causing its interruption and, once again, leaving the population of the Ribeira Quente parish isolated for a few hours.

Finally, the last site presented (site no. 14) corresponds to the application of nailing, metal mesh and shotcrete (Figure 8).



Figure 7. Geomorphological instability, of debris avalanche type, on the slope adjacent to the semi-tunnel.



Figure 8. Site no. 14 - Application of nailing, metal mesh and shotcrete.

4 CONCLUSIONS

The Ribeira Quente valley, where the E.R. 2-2ª is located, is one of the places that has been most affected by slope movements. The wide variety of volcanic materials, combined with adverse weather conditions, promotes the occurrence of different types of slope failures, with different modes of mobilisation and destructive potential, which is why risk mitigation measures have been taken.

The stabilisation solutions implemented in the sectors identified as most critical were conditioned by the geology and morphology of the slopes adjacent to the E.R. 2-2ª. These measures aim to minimise the geomorphological risk of this road and its passers-by, although they will not eliminate it completely. The solutions involved re-profiling the slopes, building retaining walls with a ditch at the end, constructing a semi-tunnel, removing rock blocks, and the application of metal nets with nails, sometimes with shotcrete.

Throughout the document, it was possible to see the importance of a prior study of the site to be intervened, with geological and geotechnical studies, as well as global stability analyses. In addition, all the works carried out require periodic maintenance, with cleaning and removal of debris, in order to guarantee their effectiveness. It should be noted that the main problems were observed in the places where the stabilisation solution involved slope re-profiling, with the occurrence of surface ruptures. Furthermore, places where retaining walls were built with a ditch at the end found a lack of cleaning of the ditches where the unstable deposits were trapped in that structure.

REFERENCES

Amaral, P. (2010). Geotechnical and hydrological characterisation of volcanic deposits: modelling slope stability in the municipality of Povoação (S. Miguel Island - Azores). PhD dissertation in Geology, specialising in Volcanology. Department of Geosciences, University of the Azores, pp 277. in Portuguese.

Amaral, P., Marques, R., Zêzere, L.L., Queiroz, G., and Marques, F. (2010). Contribution of matrix suction to the dynamic assessment of the stability of natural slopes: the case study of the Regional Road Slope in the municipality of Povoação (S. Miguel Island, Azores). Publications of the Portuguese Association of Geomorphologists, Vol. VII, pp 41-49. in Portuguese.

Marques, R. (2013). Study of slope movements in the municipality of Povoação (São Miguel Island, Azores): Inventory, characterisation and analysis of susceptibility. PhD thesis in Geology, specialising in Geological Risks. University of the Azores, pp 456. in Portuguese.

Marques, R., Amaral, P., Zêzere, J.L., Queiroz, G. and Goulart, C. (2009). Comparative study of different probabilistic methods for assessing susceptibility to slope movements: a case study in the Ribeira Quente Valley (S. Miguel, Azores). Publications of the Portuguese Association of Geomorphologists, Vol. VI, p. 183-190. in Portuguese.

Proceedings of the XVIII ECSMGE 2024
GEOTECHNICAL ENGINEERING CHALLENGES
TO MEET CURRENT AND EMERGING NEEDS OF SOCIETY
© 2024 the Authors
ISBN 978-1-032-54816-6
DOI 10.1201/9781003431749-223
Open Access: www.taylorfrancis.com, CC BY-NC-ND 4.0 license

ECSMGE 24
XVIII EUROPEAN CONFERENCE ON SOIL MECHANICS AND GEOTECHNICAL ENGINEERING

Effect of bentonite permeation on the fabric and strength of Ottawa Sand

Effet de la perméation de la bentonite sur la structure et la résistance du Sable d'Ottawa

D. Mourtada, G.A. Jaoude*
Lebanese American University, Byblos, Lebanon
**grace.aboujaoude@lau.edu.lb*

ABSTRACT: This work aims to assess how the application of bentonite for soil liquefaction mitigation influences the soil fabric. Soil fabric controls the mechanical response of the soil through the interlocking forces between its particles. This is quantified using small-strain stiffness modulus G_{max}. Maintaining or increasing G_{max} is as important as increasing the cyclic resistance in any proposed mitigation measure against soil liquefaction. Previous studies have shown the effective use of bentonite in loose Ottawa sand samples for liquefaction mitigation using dry-mixing and permeation sample preparation techniques. However, resonant column tests on bentonite-treated dry mixed Ottawa Sand samples showed a decrease of the small strain stiffness modulus (G_{max}) and thus a decrease in the shear strength of the treated soil compared to that of clean Ottawa Sand samples. This work investigated the effect of permeation on the small-strain stiffness of bentonite-treated loose Ottawa sand samples. Static triaxial tests and bender element tests on these samples showed that bentonite-treated sand samples at least maintained the same shear strength and small-strain stiffness moduli as those of clean sand samples. This work proves the effectiveness of the use of the permeation method using bentonite as a non-disruptive liquefaction mitigation technique.

RÉSUMÉ: Ce travail vise à évaluer comment l'utilisation de la bentonite pour atténuer la liquéfaction des sols influence la structure du sol. La structure du sol contrôle la réponse mécanique du sol grâce aux forces d'imbrication entre ses particules. Ceci est mesuré par le module de module de cisaillement à petite déformation G_{max}. Le maintien ou l'augmentation de G_{max} est aussi important que l'augmentation de la résistance cyclique dans toute mesure d'atténuation proposée contre la liquéfaction du sol. Des études antérieures ont montré l'utilisation efficace de la bentonite dans des échantillons de sable meuble d'Ottawa pour atténuer la liquéfaction en utilisant des techniques de préparation d'échantillons par mélange à sec et par perméation. Cependant, les essais sur colonne résonante sur des échantillons de sable d'Ottawa mélangés à sec et traités à la bentonite ont montré une diminution du module de cisaillement à petite déformation (G_{max}) et donc une diminution de la résistance au cisaillement du sol traité par rapport à celle des échantillons de sable d'Ottawa propres. Ce travail a étudié l'effet de la perméation sur la rigidité à faible déformation d'échantillons de sable d'Ottawa meuble traité à la bentonite. Des essais triaxiaux statiques et des essais d'éléments de flexion sur ces échantillons ont montré que les échantillons de sable traité à la bentonite conservaient au moins les mêmes modules de résistance au cisaillement et de rigidité à faible déformation que ceux des échantillons de sable propre. Ce travail a prouvé l'efficacité de l'utilisation de la méthode de perméation utilisant la bentonite comme technique d'atténuation non perturbatrice de la liquéfaction.

Keywords: Bentonite; bender element; static triaxial testing; small strain stiffness modulus; soil fabric.

1 INTRODUCTION

Laboratory experiments have proven that the addition of 3% and 5% of plastic fines (bentonite) to sand increases the cyclic resistance by an order of magnitude in comparison to clean sand (El Mohtar et al., 2013; Haldavnekar et al., 2003). While extensive research has been conducted to study the effect of bentonite on the cyclic resistance of clean Ottawa Sand, the literature still lacks comprehensive information regarding the influence of bentonite on the fabric and strength of Ottawa Sand. El Mohtar et al. (2008) used the dry mix method to prepare sand mixtures with 3 and 5% bentonite (by mass of bentonite) and conducted static triaxial and resonant column tests to study the behaviour of the small strain stiffness modulus (G_{max}) during flushing and hydration, back saturation, and consolidation stages. Results showed that the G_{max} sharply drops after flushing the dry mixed samples with water. This was explained by the formation of a weak soft lubricant layer around the sand particles that is prevented from swelling due to contact stresses. As a consequence, the interlocking forces between the sand particles are

disturbed, hence, decreasing the G_{max}. During the consolidation stages at effective stress of 50 kPa, the G_{max} increased with time to values below those observed for clean sand samples. Moreover, El Mohtar et al. (2013) found that the yield stress friction angle of 3% and 5% dry mixed sand with bentonite samples decreased from 23° for a clean sand to 18° and 17°, respectively. The implications drawn from these findings suggested that the dry mix method altered the fabric of the sand and reduced the interlocking forces between the sand particles.

In this study, bentonite was introduced into a sand sample by permeation in an attempt to best represent the method that would be used on site. Bender element tests were performed on two types of samples: clean Ottawa Sand and permeated Ottawa Sand with 2% bentonite (by dry mass of sand). Samples were prepared at low relative densities (<35 or 40%). G_{max} values were obtained during the flushing and hydration (for clean sands), aging (for permeated samples), and over a range of consolidation stresses (50-300 kPa). Finally, strength properties were obtained following the shearing stage.

The results of the bender element tests were used to investigate the impact of the permeation method on the G_{max} and its correlation with the stress level. The preliminary findings provide insights on the effect of the selected laboratory sample preparation method on the fabric and strength of treated sand.

2 EXPERIMENTAL PROGRAM

2.1 Materials

The sand used for this study is Ottawa Sand C 778; a uniform clean fine to medium sand (D_{50}=0.4mm and C_u=1.7), having a specific gravity G_s=2.65, and minimum and maximum void ratios e_{min}=0.48 and e_{max}=0.78. The bentonite used is a commercial bentonite from Fisher Scientific finer than 0.075 mm. SPP (sodium pyrophosphate decahydrate) is used to decrease the yield stress and viscosity of the bentonite grout during permeation.

2.2 Sample preparation

Clean sand and permeated clean sand with 2% bentonite (by dry mass of sand) samples were prepared and tested. The clean sand samples were used as the reference samples to examine the effect of bentonite permeation on the fabric and the shear strength of the sand.

The clean sand samples were prepared directly on the triaxial machine. Ottawa Sand was air pluviated at zero drop height using a funnel to produce a loose sample with relative density below 35%. After assembling the samples and confining them at 25 kPa, CO_2 was flushed through the sample at a small rate for 15 mins to replace the air voids. Then, three pore volumes of distilled deaired water were flushed at a low gradient of 8 mL/min from the bottom to the top of the sample to achieve initial partial saturation while preventing the disturbance of the sand particles.

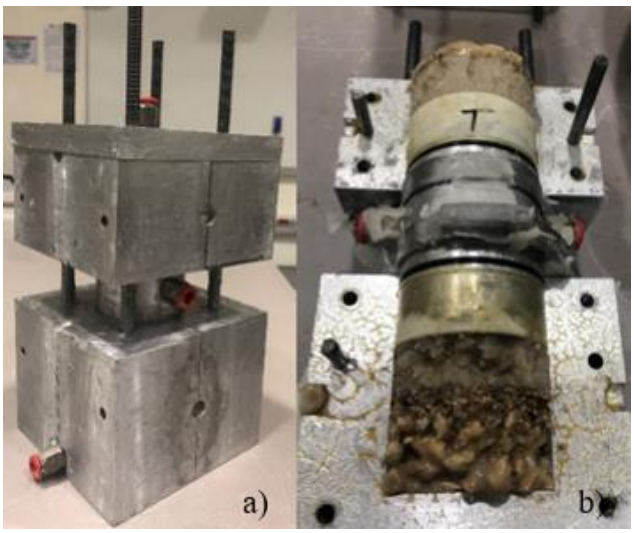

Figure 1. a) 3-way split mold b) Permeated sample after disassembly.

The permeated samples were prepared in a 3-way split mold, shown in Figure 1(a), that was first proposed by El Mohtar & Rugg, (2011). Due to impracticalities in performing the permeation process on the triaxial setup since cohesionless samples grouted with uncemented materials would collapse under their own weight, the mold provides adequate confinement to the sample during permeation. First, filter materials were first placed at the bottom of the mold consisting of a 20 mm layer of fine aggregates (diameter >4.75 mm) and a 20 mm layer of course sand (1.2>diameter>1.75 mm) to ensure a uniform permeation. A 10 mm layer of Ottawa Sand was placed above the filter material to allow for trimming any caking that would occur during the permeation process. Then, Ottawa Sand was air pluviated into the central section of the mold at zero drop height to achieve a relative density with a range of 33-42%. The properties of the clean sand and permeated samples are presented in Table 1. After air pluviation, another 10 mm layer of Ottawa Sand was placed on top of the central mold again for trimming purposes. Finally, a 20 mm layer of filter material was placed on top to prevent the sand from piping out of the mold during flushing and permeation. The CO_2 and distilled deaired water flushing procedures were done similar to the clean sand specimens. Bentonite suspensions with water to bentonite ratio of 8.55, equivalent to 2

Table 1. CS and PM sample properties.

Sample	Height (cm)	Diameter (cm)	Skeleton Relative Density (%)	Skeleton Void Ratio e_{sk}	Average % Bentonite
CS_20230831	9.7	4.9	33	0.68	-
CS_20230928	9.8	4.9	42	0.65	-
PM_20230710	10	5.0	37	0.67	1.95%
PM_20230724	10	5.0	35	0.67	2.00%
PM_20230911	10.1	5.0	41	0.66	1.74%

bentonite by dry mass of sand, and 0.5% SPP by mass of bentonite were prepared using a high shear mixer. The permeation process was done at 8 mL/min and pressures below 100 kPa after 3 pore volumes of distilled deaired water were flushed into the sample. All the flushing and permeation procedures were done using a peristaltic pump (see setup in Figure 2). Permeation stopped when the pressure build-up reached a steady state or when sufficient amount of bentonite escaped from the top outlet of the mold. After that, the mold was kept still for 72 hours to allow the bentonite to swell and hydrate before disassembling the mold and placing the sample on the triaxial machine for testing.

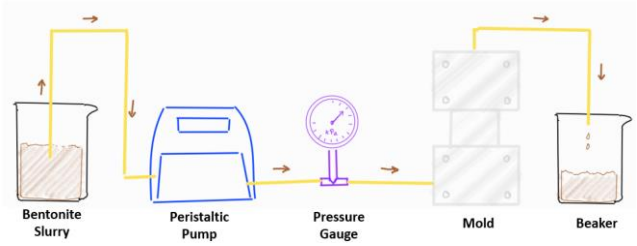

Figure 2. Permeation setup.

2.3 Static triaxial and bender element testing

A VJTech static triaxial machine was used to conduct consolidated undrained triaxial tests on both the clean sand and permeated specimens. First, a flushing and hydration stage for the clean sand samples and an aging stage for the permeated samples at a confinement of 25 kPa were done to ensure that the bentonite fully swells and hydrates for additional 72 hours. Second, back saturation begins to fully saturate the samples and reach a Skempton's B>0.95 (Black & Lee, 1973). The back pressures during this stage ranged between 500 and 600 kPa. Third, isotropic consolidation stages were done at effective pressures of 50, 75, 100, 200, and 300 kPa. Finally, undrained shearing was conducted to find the shear properties of the samples.

A VJTech bender element system embedded in the triaxial machine was used to fire S-wave signals from the top piezoelectric element placed in the top cap of the sample to the bottom piezoelectric element placed in the bottom cap of the sample. The travel time required for the S-wave to reach the bottom of the sample was used to calculate the shear wave velocity, knowing the height of the sample beforehand. The travel time was found using the peak-to-peak method. The small strain stiffness modulus (G_{max}) was calculated using equation (1):

$$G_{max} = \rho {v_s}^2 \quad (1)$$

where, ρ is the bulk density (Mg/m^3) of the sample and v_s is the shear wave velocity (m/s). Since bender element testing is non-destructive, it was conducted throughout the aging and consolidation stages of the triaxial testing at pulse frequencies 15 kHz, 10 kHz, and 5 kHz and amplitude 12 mV to study the behaviour of G_{max} and compare the values between the clean sand and permeated specimens.

3 RESULTS

3.1 Effect of flushing and hydration/aging on G_{max}

Figure 3 shows the behavior of G_{max} during the flushing and hydration period of clean sand (CS) samples and during the aging period of permeated (PM) samples. The data corresponding to these samples is representative of other tested samples. The clean sand sample shows a sudden rise in G_{max} after flushing the sample with water due to the increase of bulk density (ρ) and G_{max} remains constant after flushing because there is no change in the soil fabric with time. The permeated samples were prepared in the 3-way split mold and kept undisturbed for 72 hours for the bentonite to hydrate and to be able to disassemble the samples without it collapsing. After disassembling the samples (see Figure 1(b)), they were placed on the triaxial machine and confined at 25 kPa. Bender element signals were fired throughout the 72 hours of confinement. The permeated specimens showed almost a constant behavior of G_{max} with time. This is because the time needed for the bentonite to fully hydrate in the pore space is between 36 and 72 hours as discussed in El Mohtar (2008) and after that amount of time, no significant change in the soil fabric is observed.

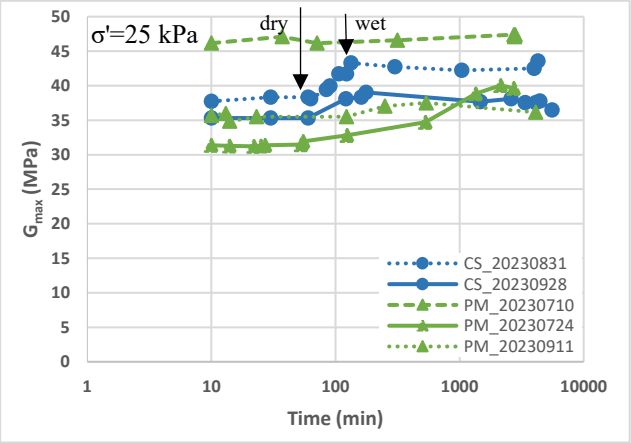

Figure 3. Gmax monitoring throughout the flushing and hydration/aging stages of CS and PM samples.

3.2 Effect of consolidation on G_{max}

Figure 4 shows the G_{max} results during the staged consolidation phases performed at 50, 75, and 100 kPa effective stresses. One clean sand sample (CS_20230928) was only consolidated at 50 kPa effective stress to obtain shearing results at this effective stress for at least one clean sand sample. The initial data point of each data set indicates the G_{max} value at the end of the flushing and hydration/aging stages. The curves indicate that the G_{max} values increase after dissipating the excess pore pressure and remain almost constant throughout the primary consolidation stage. The data also shows that the G_{max} exhibit greater values under higher effective stresses as can also be seen in Figure 5, where G_{max} increases linearly with effective stress during consolidation. This can be attributed to the increase of interlocking forces between the sand particles at higher confining stresses.

It can also be seen in Figure 4 that the G_{max} values of the permeated samples increase to values equal or slightly higher than those observed for the clean sand samples prepared at a loose state. These results suggest that unlike the dry mix method, the permeation method does not form a weak lubricating layer of bentonite coating around the surface of sand particles but instead, the grouted bentonite slurry fills the void space between the sand particles without affecting the frictional forces between the sand particles. Although the permeated samples were prepared using the same procedure, there was a slight difference in the G_{max} values between them. This can be attributed to the slight variation of properties of the samples (relative density and bentonite content).

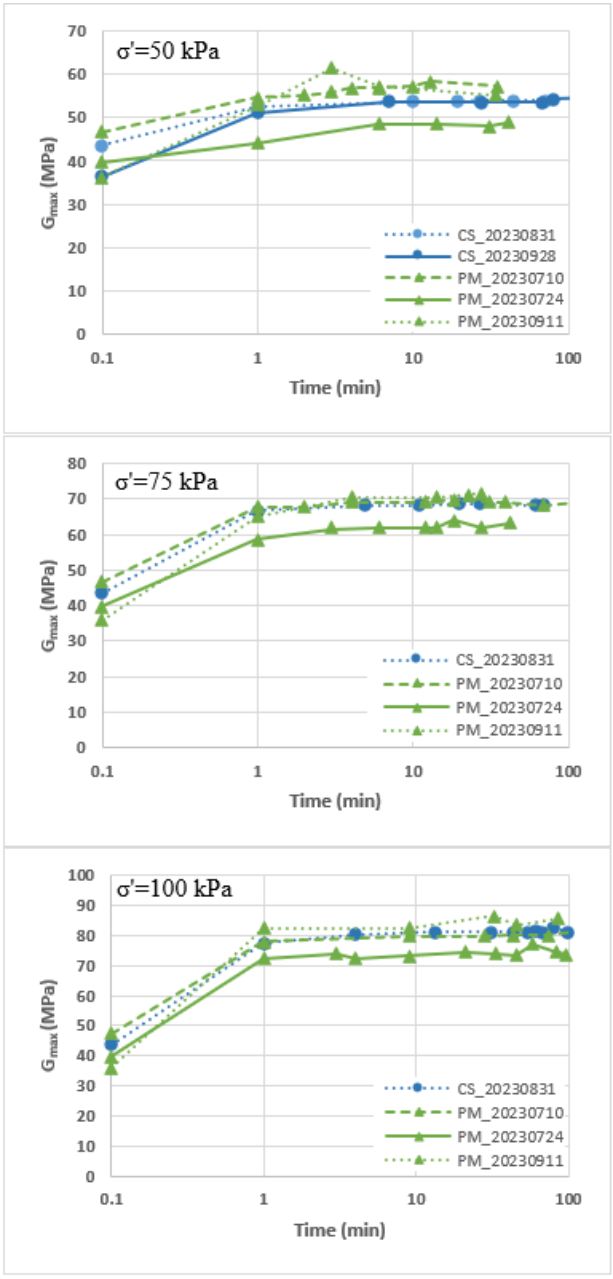

Figure 4. G_{max} monitoring throughout staged consolidation stages at 50, 75, and 100 kPa effective stresses.

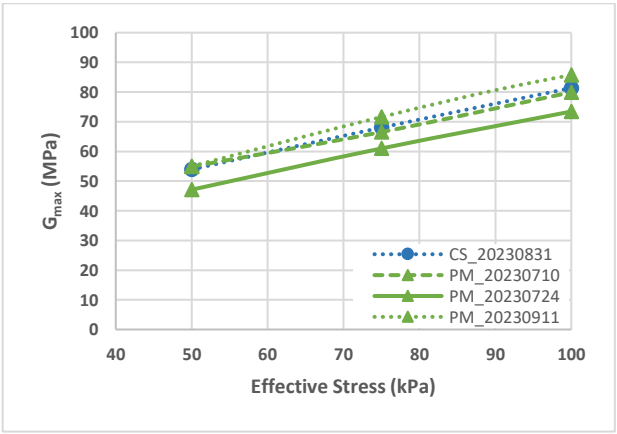

Figure 5. G_{max} versus effective confining stress.

3.3 Effect of bentonite permeation on shear strength

The shearing results of the 2% permeated specimens were consistent with those in the literature stating that the permeated specimens do not show a true undrained instability state (UIS) point, which is the point at which a loose or a medium loose sand start showing a tendency to liquefy and flow (Rugg et al., 2011). The yield stress friction angles were found at the corresponding UIS at the location of the initial change of slope in the stress-strain curves as shown in Figure 6. The yield friction angles were found using the Mohr's circle method. As reported in Table 2, for the permeated sand, the UIS friction angle is equal to that of the clean sand (19°). At the critical state, the permeated sand has a critical friction angle of 33°, which is almost equal to that of the clean sand (32°). Consistent with the literature, the results indicate that the shear strength of the sand samples is not affected by the permeation grouting of bentonite.

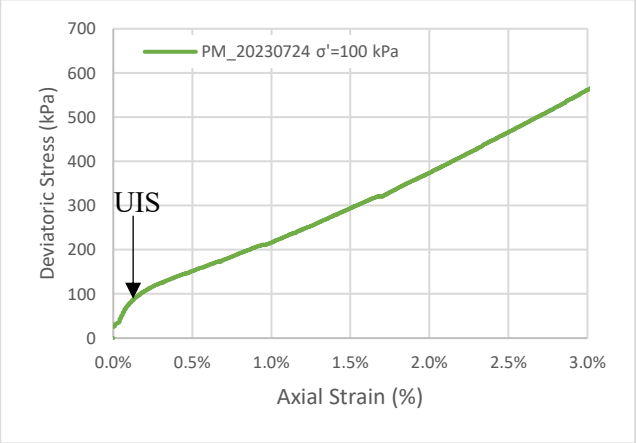

Figure 6. Consolidated Undrained Deviatoric Stress versus Axial Strain showing UIS.

Table 2. Yield and Critical Friction Angles of 0 and 2% bentonite-sand samples.

Shear Strength Parameter	**%Bentonite**	
	0%	**2%**
Yield Stress ϕ'	19	19
Critical State ϕ'	32	33

4 CONCLUSION

These results offer interesting insights on the different effects of laboratory sample preparation methods to introduce bentonite into a sand medium. In this study, preliminary results show that the fabric and the strength of Ottawa Sand, represented by G_{max} and friction angles, are not detrimentally affected by the bentonite in the pore space introduced through the permeation method. More samples need to be tested to reach a wide comparison between the fabric of the clean sand and the permeated samples in order to pave the way for onsite bentonite permeation applications.

ACKNOWLEDGEMENTS

This work was supported by the Lebanese American University President's Intramural Research Fund.

REFERENCES

Black, D. K., & Lee, K. L. (1973). Saturating Laboratory Samples by Back Pressure. *Journal of the Soil Mechanics and Foundations Division*, *99*(1), 75–93. https://doi.org/10.1061/JSFEAQ.0001847.

El Mohtar, C. S. (2008). *Pore fluid engineering: An autoadaptive design for liquefaction mitigation* [PhD Thesis, Purdue University]. https://search.proquest.com/openview/f1bbf27bd3b604d367dae4753b98a783/1?pq-origsite=gscholar&cbl=18750.

El Mohtar, C. S., & Rugg, D. A. (2011). New Three-Way Split Mold Design and Experimental Procedure for Testing Soft, Grouted Soils. Geotechnical Testing Journal, 34(6), 708–720. https://doi.org/10.1520/gtj103645.

El Mohtar, C. S., Bobet, A., Santagata, M. C., Drnevich, V. P., & Johnston, C. T. (2013). Liquefaction Mitigation Using Bentonite Suspensions. *Journal of Geotechnical and Geoenvironmental Engineering*, *139*(8), 1369–1380. https://doi.org/10.1061/(ASCE)GT.1943-5606.0000865.

El Mohtar, C. S., Santagata, M., Bobet, A., Drnevich, V., & Johnston, C. (2008). Effect of plastic fines on the small strain stiffness of sand. *Proc., 4th Int. Symp. on Deformation Characteristics of Geomaterials (IS-Atlanta)*, *1*, 245–251.

Haldavnekar, V., Bobet, A., Santagata, M., & Drnevich, V. (2003). Soil treatment with a thixotropic fluid: An autoadaptive design for liquefaction prevention. *Proceedings of the 11th International Conference on Soil Dynamics & Earthquake Engineering and 3rd International Conference on Earthquake Geotechnical Engineering*, *2*, 553–560.

Rugg, D. A., Yoon, J., Hwang, H., & El Mohtar, C. S. (2011). Undrained Shearing Properties of Sand Permeated with a Bentonite Suspension for Static Liquefaction Mitigation. *Geo-Frontiers 2011*, 677–686. https://doi.org/10.1061/41165(397)70.

Proceedings of the XVIII ECSMGE 2024
GEOTECHNICAL ENGINEERING CHALLENGES
TO MEET CURRENT AND EMERGING NEEDS OF SOCIETY
© 2024 the Authors
ISBN 978-1-032-54816-6
DOI 10.1201/9781003431749-224
Open Access: www.taylorfrancis.com, CC BY-NC-ND 4.0 license

ECSMGE 24
XVIII EUROPEAN CONFERENCE ON SOIL MECHANICS AND GEOTECHNICAL ENGINEERING

Mapping the 3D effect for slope stability analyses of quick clay slopes

Cartographie de l'effet 3D pour les analyses de stabilité des pentes en argile rapide

S.S. Nagula*, L. Rødvand, H.P. Jostad
Norwegian Geotechnical Institute, Oslo, Norway

S. Degago
The Norwegian Public Roads Administration, Oslo, Norway

**sparsha.nagula@ngi.no*

ABSTRACT: Industry quite often utilizes 2D limit equilibrium analyses to check the stability of sensitive and quick clay slopes. However, such analyses fail to capture the post peak reduction in undrained shear strength of these clays. In this work, finite element modelling with an appropriate constitutive model, capable of capturing strain softening, was used to compare 2D analyses against 3D analyses. Different slope widths were analysed, and results demonstrated that the width of the 3D model controls the width of the failure surface and thus also the factor of safety. The effect of strain softening was studied by means of simulations with and without strain softening. To emphasise the importance of considering spatially varying undrained shear strengths for strain softening clays, results from simulations with constant undrained shear strength were compared to ones with spatially varying undrained shear strengths. The analyses were used to develop a map for 3D effect factors for various kinds of idealized slopes with varying width, slope angle/height and undrained strength profiles.

RÉSUMÉ: L'industrie utilise assez souvent des analyses d'équilibre limite en 2D pour vérifier la stabilité des pentes en argile sensible et argile rapide. Cependant, de telles analyses ne parviennent pas à capturer la réduction post-pic de la résistance au cisaillement non drainé de ces argiles. Dans ce travail, la modélisation par éléments finis avec un modèle constitutif approprié, capable de capturer l'adoucissement sous contrainte, a été utilisée pour comparer les analyses en 2D aux analyses en 3D. Différentes largeurs de pentes ont été analysées, et les résultats ont démontré que la largeur du modèle 3D contrôle la largeur de la surface de rupture et donc aussi le coefficient de sécurité. L'effet de l'adoucissement sous contrainte a été étudié au moyen de simulations avec et sans adoucissement sous contrainte. Pour souligner l'importance de la prise en compte des résistances au cisaillement non drainé variant spatialement pour les argiles subissant un adoucissement sous contrainte, les résultats des simulations avec une résistance au cisaillement non drainé constante ont été comparés à ceux avec des résistances au cisaillement non drainé variant spatialement. Les analyses ont été utilisées pour élaborer une carte des facteurs d'effet en 3D pour divers types de pentes idéalisées avec une largeur variable, un angle/une hauteur de pente et des profils de résistance au cisaillement non drainé variables.

Keywords Quick clay; landslide; softening; 3D FEM.

1 INTRODUCTION

Soft sensitive clays like Norwegian quick clays undergo strain-softening under undrained loading, posing risks of catastrophic failure in slopes. Accurate modelling of slope stability (safety factor) is crucial. The progressive failure mechanism in strain-softening clays may reduce stability compared to non-softening materials with the same peak undrained shear strength. While two-dimensional studies explored the reduction (Fornes & Jostad, 2017 suggested 20%, Rødvand et al., 2022 found no significant reduction), the impact in three dimensions remains unclear. Current two-dimensional analyses don't fully represent the true three-dimensional nature of slope stability, and the effect of strain softening in three dimensions is not well-understood. This work aims to quantify strain-softening effects on three-dimensional stability using PLAXIS 3D V21 and the NGI-ADPSoft model for quick clay softening behaviour.

2 NUMERICAL & CONSTITUTIVE MODEL

This section describes the methodology employed in creation of the 3D quick clay slope model in PLAXIS

3D. The choice of constitutive model to capture the behaviour of the quick clay is explained.

2.1 Numerical model of slope

PLAXIS 3D V21 (2021) facilitated the creation and analysis of the 3D boundary value problem (BVP), referred to as the model. The model utilized 10-noded tetrahedral elements with second-order interpolation for displacements. Figure 1 outlines the dimensions of the 3D quick clay slope model, meshed with fully fixed bottom and laterally fixed boundaries against horizontal movement. The slope width (W) varied (H, 2H, 3H, 6H) to evaluate 3D effects, while the slope height (H) remained constant at 50 m. Note that Figure 1 models only half the slope width, exploiting symmetry. Although slope and clay layer depth influence 3D effects, this work concentrates on softening behaviour, maintaining constant depth and slope inclination for consistency. Once a trend is established for the selected slope geometry, previous work (Jostad & Lacasse, 2015) suggests that the same trend would extrapolate to other slope angles and depths.

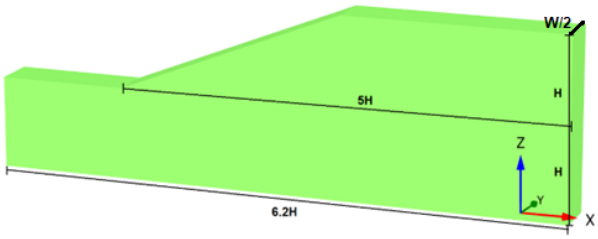

Figure 1. PLAXIS 3D model of the idealised quick clay slope.

2.2 Constitutive model: NGI-ADP Soft

NGI-ADP, an elastoplastic anisotropic shear strength-based model (Grimstad et al., 2012; PLAXIS V21, 2021), is used for capacity, deformation, and soil-structure interaction analyses under undrained loading of clay. It incorporates anisotropy based on the ADP framework (Bjerrum, 1973), where "A" is active, "D" is direct shear, and "P" is passive. Formulated for 3D stress states, NGI-ADP aligns undrained failure shear strengths and strains with experimental results, employing a translated Tresca criterion (Grimstad et al., 2012) and elliptical interpolation. With nine parameters directly obtainable from lab and in-situ testing, NGI ADP-Soft, an extension of NGI ADP, is capable of modelling undrained strain-softening behaviour, making it ideal for sensitive quick clays with distinct strain-softening beyond peak shear strength.

The focus of the work as discussed earlier was to study 3D effects in an ideal model with and without softening. Hence, material parameter values for the NGI ADP-Soft model were picked for a typical quick clay after Karlsrud's Bjerrum lecture (2010). Table 1 tabulates the material parameters; these parameters replicate the strains softening of the quick clay. Analyses conducted without softening used the same material parameters as in Table 1, barring the fact that residual strength was equal to 100 % of the peak strength. For constant undrained strength acrosss slope a value of 35 kPa was used. To study the effect of spatial variation of undrained strength on quick clay slope stability, an undrained shear strength of 20 kPa was assumed at the surface and assumed to linearly increase at a rate of 3 kPa/ unit depth.

Table 1. Material parameters used for quick clay.

Parameter		Value
Gur/su^A	Initial stiffness	300
$S_u^A ref\ (kPa)$	Reference active shear strength	35 kPa or varying with depth
$s_u{}^{DSS} / s_u{}^A$	Normalised DSS strength	0.59
$s_u{}^P / s_u{}^A$	Normalised passive strength	0.27
$s_{ur}{}^A / s_u{}^A$	Normalised residual active strength	0.1
$s_{ur}{}^{DSS} / s_u{}^A$	Normalised residual DSS strength	0.059
$s_{ur}{}^P / s_u{}^A$	Normalised residual passive strength	0.027
$\gamma_p{}^C\ (\%)$	Shear strain at peak in triaxial compression	0.6
$\gamma_p{}^{DSS}\ (\%)$	Shear strain at peak in DSS	0.7
$\gamma_p{}^E\ (\%)$	Shear strain at peak in triaxial extension	0.8
$\gamma_r{}^C\ (\%)$	Shear strain at residual state in triaxial compression	20
$\gamma_r{}^{DSS}\ (\%)$	Shear strain at residual state in DSS	20
$\gamma_r{}^E\ (\%)$	Shear strain at residual state in triaxial extension	20
$c1$	Shape parameter	1
$c2$	Shape parameter	1
v_u	Poisson's ratio, undrained conditions	0.495
$\gamma_{tot}\ (kN/m^3)$	Total unit weight	19.5

2.3 Simulation Methodology

Failure was achieved by load increments combined with indirect displacement control using the arc length

method. The standard phi/c strength reduction method cannot be used for a strain-softening material. The gravity increase method after Swan & Seo, (1999) was employed where gradually gravity loading was applied keeping other material properties constant until the slope became unstable. FoS was defined as the ratio of gravity at failure to actual gravity on earth. It was observed that shear force peaked at failure and eventually reduced as PLAXIS reduced gravity to maintain equilibrium. The analyses were continued 10 steps beyond failure, thus assuring that global failure had occurred rather than a local instability.

3 RESULTS OF NUMERICAL ANALYSIS

This section discusses in detail numerical simulation results for the ideal 3D quick clay slope. Strain softening constitutive model was used to describe the behaviour of the quick clay layer. However, no regularisation technique was used so the results would be mesh dependent. The FoS normalised by ratio of undrained shear strength to total stress at base of the slope ($\gamma H = 19.5 \times 50 = 975$), reduced as element sizes reduced as tabulated in Figure 2 and did not reach steady state indicating that results are discretisation sensitive and mesh regularisation techniques have to be employed while using a softening-based model, but this is out of scope of this work. A particular mesh discretisation was chosen and used in all the analysis to ensure consistency.

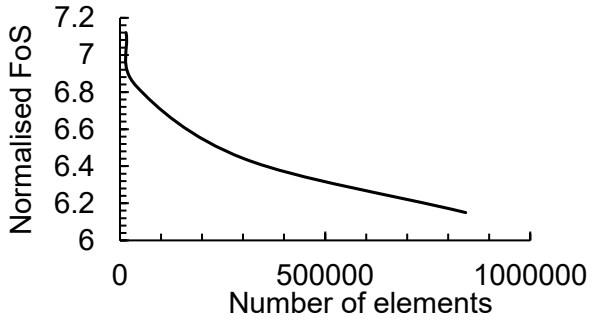

Figure 2. Effect on element size on factor of safety.

3.1 Effect of softening

The 3D model in Figure 1 simulated slope stability with and without softening effects for various widths: H (equal to slope height), 2H, 3H, and 6H, maintaining a 30 cm element size. Figure 3 displays normalized FoS for different widths, with the x-axis representing the inverse width ratio. To ensure accurate 3D effects, 2D cases were simulated in PLAXIS 3D with the same discretization error (Figure 3). The FoS decreases with wider slopes, and softening causes an 82 % drop with respect to analysis without softening. Conclusively, softening effects are comparable in 2D and 3D, consistent across varying slope widths.

3.2 3D effects with constant undrained shear strength

The model in Figure 1, featuring varied widths, maintained a constant undrained shear strength of 35 kPa across sensitive clay. Figure 4 depicts the 3D effect factor on the y-axis, representing the ratio of the factor of safety for a specific slope width to the factor of safety for a 2D plane strain model. Please note that the factor of safety at H/W=0 is 2D plane strain model factor of safety. The 3D effect factor peaked at around 90 % for narrow slopes and drops below 10 % for H/W < 0.17 (widths greater than 6H). Softening increased 3D effect factors compared to scenarios without softening. Results from PLAXIS 3D, with and without softening, are compared with Jostad and Lacasse (2015) results (b/w color scale), showing a similar trend. However, PLAXIS calculations exhibit lower 3D factors even without softening for steeper slopes (b represents the slope ratio of horizontal/vertical and d is ratio of depth to rock to height of slope, H/H here). This difference could stem from discretization variances, including the element types used in Bifurc3D and PLAXIS 3D (Zhang et al., 2013). Jostad and Lacasse (2015) used Bifurc3D, an in-house NGI development, employing isoparametric 20-noded brick elements, while PLAXIS 3D uses 10-noded tetrahedral elements.

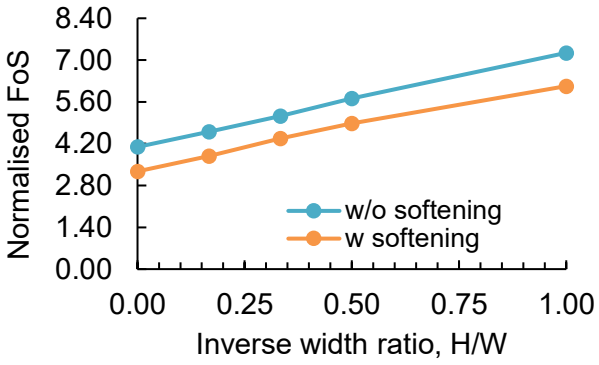

Figure 3. Variation of 3D FoS with width of slope with and without softening.

3.3 3D effects with varying undrained shear strength

To analyse the impact of varying undrained shear strength on the 3D effect factor, simulations were conducted with and without softening, where the undrained shear strength across the sensitive clay increased linearly with effective stress at a rate of 3

kPa/unit depth in m, starting at 20 kPa. Figure 5 illustrates the variation of the 3D effect factor with the inverse width ratio, showing an immediate reduction in the 3D effect as soon as a variation in undrained shear strength is considered. The case with softening exhibits higher 3D effect factors than the case without softening. A maximum 3D effect factor of 1.27 is observed for a narrow slope (H/W = 1). The 3D effect factor for a narrow slope (H/W = 1) with varying undrained shear strength with depth is 1.47 times lower than the 3D effect factor for the same slope with constant undrained shear strength. For slopes with widths larger than 6H (H/W = 0.166), the 3D effect factor with softening ranges between 1.05 and 1.07.

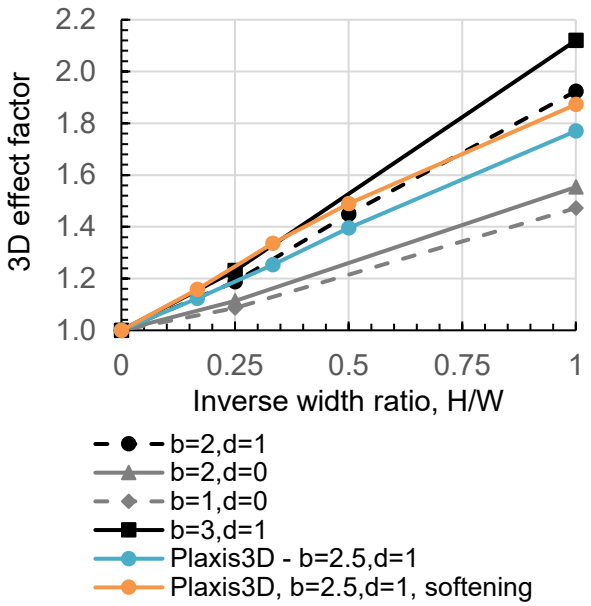

Figure 4. Variation of 3D effect factor with width of slope with and without softening for constant undrained shear strength (Jostad & Lacasse, 2015).

4 CONCLUSIONS

Wider slopes (width > 6 times height) can rely on 2D plane strain analysis due to reduced 3D effect with increasing undrained shear strength. For narrow slopes (width < 6 times height), significant 3D effects may occur, necessitating accurate 3D modeling. In cases where 3D modeling is impractical, scaling the 2D factor of safety using 3D effect factors is feasible, but attention to slope geometry is crucial. The impact of boundary conditions on softening along model edges is under study. The extent of influence is being studied by ensuring that softening to be predominant in the middle of the slope by having higher undrained strengths along slope edges.

ACKNOWLEDGEMENTS

The authors are grateful for the financial support provided by Norwegian Research Council.

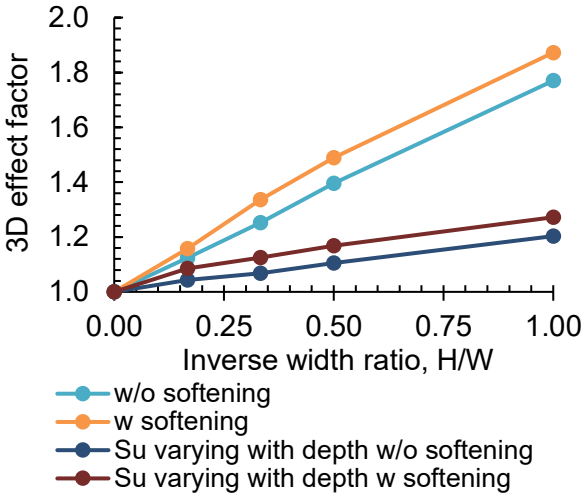

Figure 5. Variation of 3D effect factor with width of slope with and without softening for varying undrained shear strength (Jostad & Lacasse, 2015).

REFERENCES

Bjerrum L. (1973). Problems of Soil Mechanics and Construction on Soft Clays. State of the Art Report to Session IV. 8th International Conference on Soil Mechanics and Foundation Engineering, 111–159.

Fornes P. and Jostad H. (2017). Correction Factors for Undrained LE Analyses of Sensitive Clays. https://doi.org/10.1007/978-3-319-56487-6_20.

Grimstad G. Andresen L. and Jostad H.P. (2012). NGI-ADP: Anisotropic shear strength model for clay. International Journal for Numerical and Analytical Methods in Geomechanics, 36(4), 483–497.

Jostad H.P. and Lacasse S. (2015). 3D effects in undrained slope stability analysis of clays. Geotechnical Engineering for Infrastructure and Development, 1573–1578.

Rødvand L.A. Jostad H.P. Grimstad G. and Andresen L. (2022). Strain localisation in sensitive clays: can rate dependency provide mesh independent results? Computers and Geotechnics, 145, 104678.

Swan C.C. and Seo Y.K. (1999). Limit state analysis of earthen slopes using dual continuum/FEM approaches. International Journal for Numerical and Analytical Methods in Geomechanics, 23(12), 1359–1371.

Zhang et al. (2013). Effects of geometries on three-dimensional slope stability. *Canadian Geotechnical Journal*, 50, 233–249.

Proceedings of the XVIII ECSMGE 2024
GEOTECHNICAL ENGINEERING CHALLENGES
TO MEET CURRENT AND EMERGING NEEDS OF SOCIETY
© 2024 the Authors
ISBN 978-1-032-54816-6
DOI 10.1201/9781003431749-225
Open Access: www.taylorfrancis.com, CC BY-NC-ND 4.0 license

ECSMGE 24
XVIII EUROPEAN CONFERENCE ON SOIL MECHANICS AND GEOTECHNICAL ENGINEERING

Analysis of rock slope failures. Case studies on Romanian mountain roads

Analyse des ruptures de talus rocheux. Études de cas sur les routes de montagne roumaines

A.-Cs Nagy*
Technical University of Cluj-Napoca, Cluj-Napoca, Romania

C. Bruchental, D.M. Paşca, V.-S. Fărcaş, D.-V. Moldovan, L.-E. Moldovan
University of Agricultural Sciences and Veterinary Medicine of Cluj-Napoca

**andor.nagy@yahoo.com*

ABSTRACT: The evaluation of failure planes on rock slopes is always a great challenge, because of limited accessibility and natural hazards a failing cliff face could pose. Designing of retaining or protecting structure requires very specific data: maximal size and mass of rock that can dislocate from the slope, the highest point on the rock face of failure occurrence, depth of alteration, and a yearly estimate of volume and weight of fallen rocks. Often the devices and methods used for determining the aforementioned information may seem simplistic or disproportionately small in order to extrapolate to a large surface of rock slope, but many of them have proven to be efficient over time. One such method is the stereographic projection of discontinuities. This allows predicting the failure type based on determined pole density of the orientation of the discontinuity sets, that will be extensively explained in the paper. This study is based on results collected from two of the most spectacular mountain roads of Romania: the Transfagarasan highway, once described as the "best driving road in the world" by a famous british TV show, and the Transalpina, which may be less conspicuous, but is officially the highest road of the country. The paper highlights similarities and differences between resulting input data for consolidation and maintenance works.

RÉSUMÉ: L'évaluation des plans de rupture sur les pentes rocheuses est toujours un grand défi, en raison de l'accessibilité limitée et des risques naturels qu'une falaise défaillante pourrait poser. La conception d'une structure de soutènement ou de protection nécessite des données très spécifiques: taille et masse maximales de roches pouvant se disloquer de la pente, point le plus élevé de la paroi rocheuse où se produit une rupture, profondeur d'altération et estimation annuelle du volume et du poids des éboulis. Souvent, les dispositifs et les méthodes utilisés pour déterminer les informations susmentionnées peuvent sembler simplistes ou disproportionnellement petits pour pouvoir être extrapolés à une grande surface de pente rocheuse, mais plusieurs d'entre eux se sont révélés efficaces au fil du temps. Une de ces méthodes est la projection stéréographique de discontinuités. Cela permet de prédire le type de défaillance en fonction de la densité de pôles déterminée par l'orientation des ensembles de discontinuités, qui sera expliquée en détail dans l'article. Cette étude est basée sur les résultats recueillis sur deux des routes de montagne les plus spectaculaires de Roumanie: l'autoroute Transfagarasan, autrefois décrite comme la « meilleure route du monde » par une célèbre émission de télévision britannique, et la Transalpina, qui est peut-être moins visible , mais c'est officiellement la route la plus haute du pays. Le document met en évidence les similitudes et les différences entre les données d'entrée résultantes pour les travaux de consolidation et de maintenance.

Keywords: Rock slope failure; stereographic projection; compressive strength of rocks; Carpathian mountains geology.

1 INTRODUCTION

There are several recently published studies that investigate rock failures. Lagarde et al. (2023) applied a hidden Markov machine learning model to seismic data, revealing the temporal evolution of cracks prior to a major rockslide event in the Swiss Alps. After prolonged linear increase of the crack cumulative number, an S-shaped crack rate pattern occurred in the day before the rockslide. Total crack boundary length was described as the key factor controlling failure plane evolution immediately before mass movement. The study conclusions indicated that cracks should be treated as 2-D, rather than 1-D objects, and that slope failure can be driven predominantly by internal rather than external processes. Sečanj et al. (2019) presented preliminary rockfall susceptibility assessment based on remote

sensing and automated kinematic analysis for the steep slopes above the Town of Omiš. Their results of the spatial kinematic analysis and with the calculation of Kinematic Hazard Index, show that the most critical parts on the slopes for the occurrence of possible instability mechanisms can be identified. Resulting rockfall susceptible areas, unstable blocks and probable instability mechanisms on the investigated slopes provide the input data that can be used to determine critical areas for further deterministic slope stability analysis, as well as for rockfall hazard and risk assessment.

2 INVESTIGATION METHOD

Stereographic projection is the classical approach for the analysis of rock discontinuities. The concept and the graphical methods are widely used in rock engineering education to illustrate the orientation of planes of discontinuity and occurrence of failures. Described in Rock Slope Engineering by Hoek and Bray (1974), stereographic projection is a technique used to represent and analyze 3-D orientation data in a 2-D format. In this projection, a reference sphere is employed, with its equatorial plane positioned horizontally and its orientation fixed relative to the north. Among various projection methods, the equatorial projection is the preferred choice for plotting and analyzing discontinuity data in most cases. Equal area stereonets find particular utility in structural geology because they eliminate statistical bias when dealing with large datasets. They ensure that area preservation is maintained, meaning that, for instance, each 2-degree polygon on the stereonet possesses the same area. In structural geology, it is customary to consider the stereonet as a lower-hemisphere projection because all structural elements are assumed to be inclined below the horizontal plane.

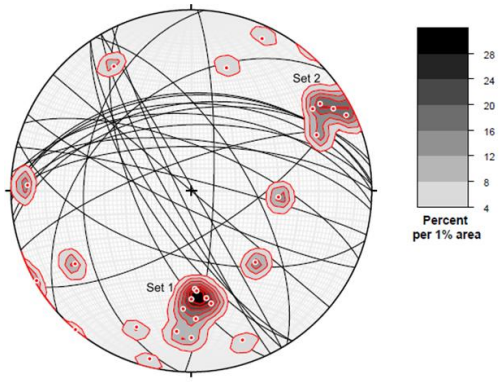

Figure 1. Plot of poles and great circles on stereonet (Schmidt) (km 132+760-132+860).

When representing a plane, such as a discontinuity surface, its intersection with the lower half of the reference sphere delineates a distinctive line on the stereonet (Wylie & Mah, 2004). This line typically takes the form of a circular arc known as a "great circle." Accurately plotting this great circle requires knowledge of both the dip direction and dip angle. The software Steronet v. 11 was used to plot the structural geology data (Allmendinger et all.2012, Cardozo & Allmendiger, 2013). Data collection in the field was done taking into account the ISRM 1981a guidelines.

2.1 Overview and geological conditions

Both studied areas are situated in the South Carpathians. The Transfagarasan was built in in the 1970s as a strategic military route, connecting Transylvania and Wallachia. The investigated areas are high above a steep valley. Excavation of rock slopes involved heavy blasting. Since 2009, the Transalpina has held the title of Romania's highest paved road, reaching an elevation of 7,037 feet (2,145 meters) above sea level at the Urdele Pass. Stretching for 92 miles (148 kilometers), the road meanders from Novaci in the southern region to Sebeș in the northern part, as it navigates its path through the magnificent Parâng Mountains within the Southern Carpathians. Throughout the ages, it has played pivotal roles in facilitating trade, communication, and transportation.

The geological structure of the South Carpathians is very complex, with an intricate pile of tectonic nappes, overthrusted from west eastward. The lithology consists of metamorphic rocks, mainly gneisses and mica schist (Mutihac,1990).

2.2 Transfagarasan

On the Transfagarasan three road segments were investigated. In the highest one (km 124+754-124+855), two sets of discontinuities were separated with mean dip direction and inclination of 052.6°/45.6°, respectively 063°/71°. The lithology is formed by mica schist, with irregular blocks and maximum block size of 5 m^3. The discontinuity spacing is moderate to wide, with medium persistence. In the middle segment (km 125+000-125+215), three sets of discontinuities were identified. The first discontinuity set is given by schistosity, with mean dip direction of 346.6° and inclination of 71°. The second and the third set of discontinuities have mean dip direction and inclination of 274.4°/61.4°, respectively 244.6°/64.8°.



Figure 2. An overview of the first segment on Transfagarasan (km 124+754-124+855). Notice the steep mountain slope, protected by a rock shed in the most dangerous area.

The lithology is formed by gneisses and mica schist, with the maximum block size of 7 m^3. At the lower end of this segment, there is a fault, with the fault zone, affected by parallel, close to moderate spaced discontinuities, with medium persistence. The fault zone is dump, but with no free water observed (rating IV). The filing material consists of saturated sand and clay. The fault does not seem to play an important role in overall slope stability; however it provides some small to medium blocks.

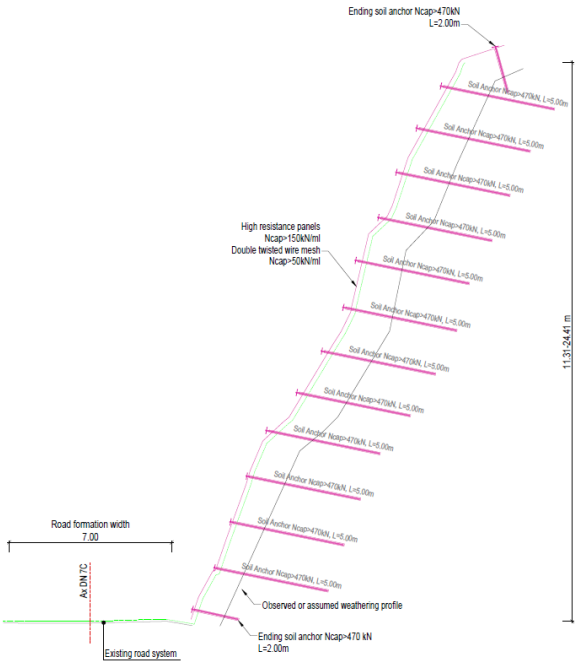

Figure 3. Observed or assumed weathering profile for the highest segment between km 124+754-124+855 on Transfagarasan Highway.

In the lowest segment (132+590-132+860), two set of discontinuities were identified, with mean dip direction and inclination of 358.3°/55° and 240.4°/75°. The lithology is formed by gneisses and sericite chlorite schist, mica schist, with the maximum block size of 3.36 m^3. The lower part of the segment is more affected by blasting, providing in general, small to medium blocks. This area is particularly unstable. A contour of the observed or assumed weathering profile for the highest segment between km 124+754-124+855 can be seen in Figure 3, together with the chosen retaining and protection systems.

2.3 Transalpina

On Transalpina six road segments were investigated. On the first segment (km 80+500-81+000) the lithology consists of gneisses with subordinate pegmatites, migmatites and amphibolite. The outcrop was a quarry not long ago. The slope face is at an angle between 45-60°. On the southern side of the quarry, there is an old magmatic intrusion. The schistosity plane dips towards NE, at 30-50°. Apart from the plane of schistosity, there are two sets of discontinuities dipping towards S and SW at 70-80°. Many discontinuities have at least 3 m persistence. The outcropping rocks are in general from fresh to slightly weathered, apart from the rocks at the top, that are moderately weathered. The maximum block size observed in the quarry is 20 m^3, but this is very likely the result of blasting. Most of the blocks are below 2 m^3 in volume. The maximum falling height is about 40 m.

The second segment (km 88+500-89+000) consists of fragmented and moderately altered gneisses. The rocks are highly affected by tectonics, and possibly blasting, with discontinuities dipping at high angles either towards E or W. The schistosity plane dips at 30-40° towards W. Because of the numerous discontinuities the maximum block size is below 1 m^3. The maximum falling height is 15 m.

The third segment (km 91+000-91+800) consists of mica schist followed by gneisses. Most rocks are moderately weathered, with the depth of weathering extending beyond 5 m. The are large blocks slipped over each other and precarious stabilized by vegetative cover. The lack of outcrops made it impossible to take compass reading. The maximum block size that reached the road is 2 m^3. In this area, there is a real risk of triggering a landslide, involving large blocks if any intervention is made without a careful planning.

The fourth road segment (km102+750-103+000) consists of slightly weathered gneisses and subordinate pegmatites. The weathered zone is below 2 m. The maximum block size is quite small 0.5 m^3. The schistosity plane dips towards SW, at 30-50°.

Apart from that, there is a set of discontinuities dipping almost at 90°, either towards NNE or SSW. Between km 102+950-102+980, the schistosity plane daylights on the slope face.

The fifth road segment (112+000-114+000) consists of slightly weathered gneisses and scree. At km 112+210, the slope face is almost vertical, with large unstable block. We were able to make only a small number of compass readings. The slope face with unstable scree, could fail in favourable conditions, but the size of blocks is small.

The sixth road segment (km 126+000-128+000) comprises areas with scree, with rock fragments caught in an argillaceous matrix (km 126+260-126+355; 127+330-127+240; 127+505-127+640) and areas with steeper slopes with mica schist and gneisses (km 126+490-127+020). The area with scree is in places protected with old gabions. This area is prone shallow circular failure. The area with steep slope is protected by an old wire mesh, which is broken in places, because of falling rocks, and inadequate wire mesh.



Figure 4. Closed spaced discontinuities on Transalpina favouring wedge failure. The slope is protected by a wire mesh that is teared-off in places.

2.4 Compressive strength

Estimation of the compressive strength of the rocks was done by uniaxial compressive strength (UCS) and point load test. The UCS of gneisses and amphibolite was between 68-165 MPa, and for mica schist 50-130 MPa. For some moderately weathered mica schist from Transalpina, the UCS was as low as 20 MPa. The moderately weathered rocks had UCS value well below the slightly weathered or fresh rocks.

3 CONCLUSIONS

The lithology of both area is very similar consisting of metamorphic rock, dominated by mica schist and gneisses. The Transfagarasan section belongs to a different tectonic unit, Supragetic Nappe, whereas Transalpina section belongs to Getic Nappe (Mutihac,1990). Transalpina section seems more affected by tectonics, with old igneous intrusions, folding and faulting. As a result, Transalpina section appear to be more affected by weathering. The discontinuity spacing is smaller on Transalpina, resulting in smaller falling block size. Wedge failure type predominate in both areas, but on Transalpina section, circular failure is likely on slopes covered by scree.

Although not part of the projects budget, the investition in these protection systems would have benefitted from using monitoring equipment that may have been installed in the slopes to measure displacements, strains, stresses or water pressure over time.

REFERENCES

Allmendinger, R. W., Cardozo, N., and Fisher, D., - Structural geology algorithms: Vectors and tensors in structural geology: Cambridge University Press, 2012

Cardozo, N., and Allmendinger, R.W., 2013, Spherical projections with OSXStereonet: Computers & Geosciences, v. 51, p. 193 – 205, doi:10.1016/j.cageo.2012.07.021.

International Society for Rock Mechanics (ISRM) (1981a) Suggested Methods for the Quantitative Description of Discontinuities in Rock Masses (ed. E. T. Brown). Pergamon Press, Oxford, UK, 211 pp.

Lagarde, S., Dietze, M., Hammer, C. et al. (2023). *Rock slope failure preparation paced by total crack boundary length.* Commun Earth Environ 4, 201 https://doi.org/10.1038/s43247-023-00851-0.

Mutihac, V. (1990) Structura Geologica a Teritoriului Romaniei. Ed. Tehnica, Bucuresti.

Sečanj, M. & Mihalić A., Snježana & Krkac, Martin & Bernat G., Sanja & Arbanas, Zeljko. (2019). Preliminary rockfall susceptibility assessment of the rock slopes above the Town of Omiš (Croatia).

Wylie D.C, Mah C. W., (2004). Rock slope engineering, Civil and Mining, 4th edition, „Based on Rock Slope Engineering (third edition, 1981) by Dr. Evert Hoek and Dr. Jhon Bray.” Spon Press, London and New York.

Proceedings of the XVIII ECSMGE 2024
GEOTECHNICAL ENGINEERING CHALLENGES
TO MEET CURRENT AND EMERGING NEEDS OF SOCIETY
© 2024 the Authors
ISBN 978-1-032-54816-6
DOI 10.1201/9781003431749-226
Open Access: www.taylorfrancis.com, CC BY-NC-ND 4.0 license

ECSMGE 24
XVIII EUROPEAN CONFERENCE ON SOIL MECHANICS AND GEOTECHNICAL ENGINEERING

Geotechnical seismic site characterization of deep alluvial sand sites in the South Iceland Lowland

Caractérisation géotechnique sismique des sites de sables alluviaux profonds dans les basses terres du sud de l'Islande

E.A. Olafsdottir*, S. Erlingsson, B. Bessason
Faculty of Civil and Environmental Engineering, University of Iceland, Reykjavik, Iceland
**elinasta@hi.is*

ABSTRACT: Thick deposits of post-glacial sediments are widely found along the coastline and close to main riverbeds in South Iceland. This work studies the feasibility of using a joint inversion of dispersion and ellipticity curves to characterize deep alluvial sand sites in the South Iceland Lowland. For this purpose, MASW (Multichannel Analysis of Surface Waves), small-aperture MAM (Microtremor Array Measurements) and MHVSR (Microtremor Horizontal-to-Vertical Spectral Ratio) field tests were conducted at selected locations along the Markarfljót River. The results provide the V_S profiles of the tested sites down to bedrock level at 120–190 m depth, along with the fundamental frequency (f_0) of the soil strata. Furthermore, simple correlations between f_0 and bedrock depth are evaluated against the measurement results, in order to identify suitable relationships for preliminary assessment of bedrock depths based on MHVSR measurements in South Iceland.

RÉSUMÉ: D'épais dépôts de sédiments post-glaciaires sont largement répandus le long du littoral et à proximité des principaux lits des rivières du sud de l'Islande. Ce travail étudie la faisabilité de l'utilisation d'une inversion conjointe des courbes de dispersion et d'ellipticité pour caractériser les sites de sable alluvionnaire profond dans les basses terres du sud de l'Islande. À cette fin, des tests sur le terrain MASW, MAM à petite ouverture et MHVSR ont été menés à des endroits sélectionnés le long de la rivière Markarfljót. Les résultats fournissent les profils V_S des sites testés jusqu'au niveau du substrat rocheux à 120–190 m de profondeur, ainsi que la fréquence fondamentale (f_0) des strates du sol. De plus, des corrélations simples entre f_0 et la profondeur du substrat rocheux sont évaluées par rapport aux résultats de mesure afin d'identifier les relations appropriées pour une évaluation préliminaire des profondeurs du substrat rocheux sur la base des mesures MHVSR dans le sud de l'Islande.

Keywords: Non-invasive site characterization; shear wave velocity; bedrock depth; South Iceland Lowland.

1 INTRODUCTION

The South Iceland Lowland is characterized by strike-slip earthquake activity and a geological environment shaped by volcanism and glacial impacts. Thick deposits of post-glacial sediments, resulting from repeated glacial outburst floods and accumulation of volcanic-originated materials, are widely found along the South Iceland coast and close to main riverbeds. The local soils are mostly normally consolidated coarse-grained basaltic materials and are often loosely compacted due to a rapid sediment build-up in catastrophic events.

This work focuses on an area along the Markarfljót River in South Iceland, between the Markarfljót Bridge and the Landeyjar Harbor (Figure 1a). The area is close to the eastern boundary of the South Iceland Seismic Zone (SISZ). The soil deposits along the glacier fed river primarily consist of sand and sandy gravel and were mainly created in outburst events. The river is highly dynamic with the river mouth moving in a cyclical pattern along a few-kilometre wide part of the coastline. It carries an estimated 100,000–200,000 m^3 of sand to the coastal zone annually (Pétursson et al., 2020).

Borehole logs for a site around 4.5 km east of the current study area indicate layers of sand and gravel down to a depth of 80 m and unspecified sedimentary layers down to 168 m. The borings were terminated before reaching competent bedrock. Seismic refraction surveys conducted in the 1970s (Mott MacDonald and Línuhönnun, 2004) further showed thick sediment formations in the area. The minimum sediment thickness was estimated as 40–50 m near the farm Kross, ca. 12 km west of the current study area. The depth to bedrock was then found to increase towards east, reaching up to 250 m near the farm Bakki, 2-3 km west of the Markarfljót River. No data exists for the sites considered in this work.

Non-invasive methods, specifically Multichannel Analysis of Surface Waves (MASW), Microtremor Array Measurements (MAM) and single-station microtremor measurements, are used to evaluate the shear wave velocity (V_S), depth to bedrock (H) and fundamental frequency (f_0) for selected sites within the area. Subsequently, simple equations relating f_0 and H are evaluated against the results to identify suitable correlations for preliminary assessment of bedrock depths for deep soil sites in South Iceland.

2 SITE CHARACTERIZATION

The surface wave tests in the Markarfljót area (Figure 1a) consisted of four MASW arrays (at S1–S4), two small-aperture MAM arrays (at S1 and S4) and single-station measurements at several locations, including S2 and in the vicinity of S3. This section provides an overview of the data acquisition (DAQ) and analysis. A more comprehensive description is given in Olafsdottir et al. (2023).

2.1 In-situ data acquisition

The MASW data was acquired using an array of twenty-four 4.5 Hz vertical geophones (receiver spacing of 0.5–2 m) and a 6.3 kg sledgehammer to generate the impact load. Repeated shots were collected along the same survey line whilst changing the receiver spacing, source offset and shot position. The MAM measurements were conducted using four Lennartz 5 s seismometers, each coupled with a Reftek digitizer. The seismometers were arranged in triangular-shaped arrays (circumradius of 12 m and 24 m) whose centroid was located at the midpoint of the respective MASW array. The single-station measurements at locations S2, S2b and S3a–d by the bridge and along the river (Figure 1a) were conducted using ETNA 2 accelerographs. As prior studies have recommended against the use of accelerometers for HVSR analysis (e.g., Guillier et al., 2008), the data acquisition was repeated at stations S1 and S1a using the ETNA 2 accelerographs and the resulting MHVSR compared (Figure 1b). The results show that comparable H/V ratios were obtained with both instruments, which is considered to support the use of the ETNA 2 accelerographs in this work.

2.2 Evaluation of f_0, V_S and H

The MHVSR (Microtremor Horizontal-to-Vertical Spectral Ratio) technique was used for evaluation of f_0. For each site, the three-component record (duration 50–100 min) was split into 50 s windows. The Fourier spectra of each component was smoothed using the Konno-Ohmachi function (with b = 40) and the H/V-ratio subsequently obtained by dividing the geometric mean of the horizontal spectra by the vertical spectrum. The resulting MHVSR curves are given in Figures 1b–e.

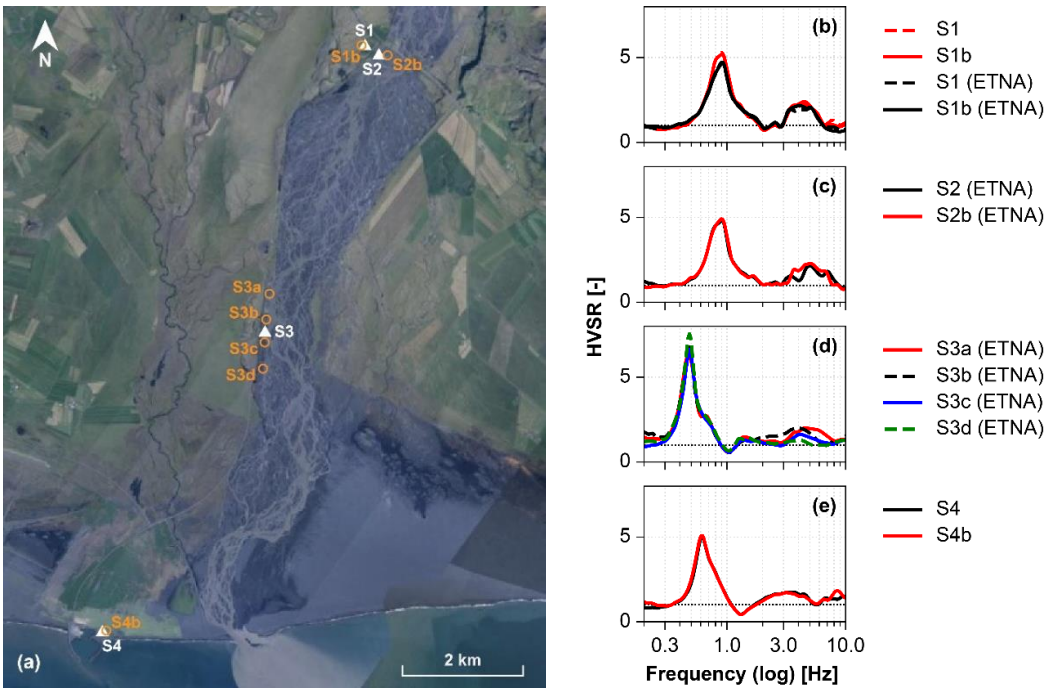

Figure 1. (a) Aerial image of the survey area along the Markarfljót River showing the test site locations. S1-S4: Evaluation of S-wave velocity profile, fundamental site frequency and depth to bedrock. S1b, S2b, S3a-d, S4b: Evaluation of fundamental site frequency. (b-e) Lognormal-median MHVSR curves for individual measurement stations.

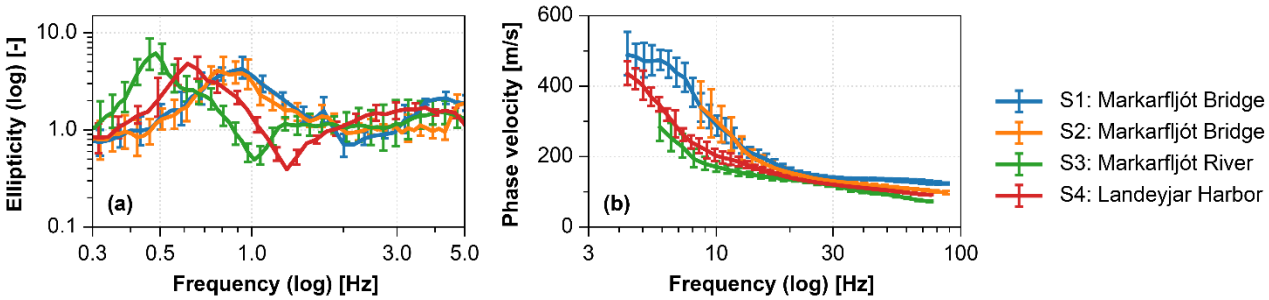

Figure 2. Experimental R-wave (a) ellipticity and (b) dispersion curves for sites S1-S4.

A joint R-wave dispersion-ellipticity inversion was used to evaluate V_S and H for sites S1–S4. The dispersion curve (DC) for each site was obtained from the active-source (MASW) and, where available, the passive-source (MAM) data. Each MASW shot gather was processed using the dispersion tool in MASWaves (Olafsdottir et al., 2018). The MAM data was processed using the MSPAC toolbox in Geopsy (Wathelet et al., 2020), with the 50–60 min recordings split into 12.5–15 min windows and each sub-record processed separately. An average DC (Figure 2b) was finally obtained by binning the dispersion data within log-spaced frequency bands.

The RayDec technique (Hobiger et al., 2009) was used to evaluate the R-wave ellipticity (Figure 2a), with the recorded microtremors split into 8–10 min windows. For S1 and S4, the ellipticity curves specified as inversion targets were obtained using the recordings of the central stations of the MAM arrays. For S2, a single-station measurement was conducted at the location of the MASW survey. The HVSR curves for stations S3a–d show limited variability (Figure 1d), thus indicating small variations in soil stratigraphy for the 1.2 km segment between S3a and S3d. Hence, the ellipticity for site S3 was estimated as the average ellipticity of S3b and S3c.

The inversion was conducted as described in Olafsdottir et al. (2023) using the Dinver module in Geopsy (Wathelet et al., 2020). The layer thicknesses and V_S in each layer were treated as unknowns to be established by the inversion, whilst the mass density was fixed as 2000 kg/m^3 and the Poisson's ratio confined to the range of 0.2–0.5 in lack of site-specific data. The inversion scheme was initiated five times with 75,000–90,000 models sampled in each initiation.

Following each inversion initiation, 100 models were randomly selected from the subset of sampled models whose dispersion-ellipticity misfit (m) fulfils $m \leq 1.25m_{min}$, with m_{min} being the minimum misfit value. The resulting collections of inverted velocity profiles, along with the associated ellipticity and dispersion curves, are shown in Figure 3 (sites S1, S2) and Figure 4 (sites S3, S4). Figure 5 illustrates the variation of the sediment V_S down to bedrock level and within the upper-most 30 m. Also shown is the lowest misfit model for each site.

The analysis points to a broadly similar velocity structure at all four sites along the river. Specifically, for the sandy and gravelly sediments, the developed velocity profiles indicate an increase in V_S from 70–130 m/s at surface to around 350–600 m/s.

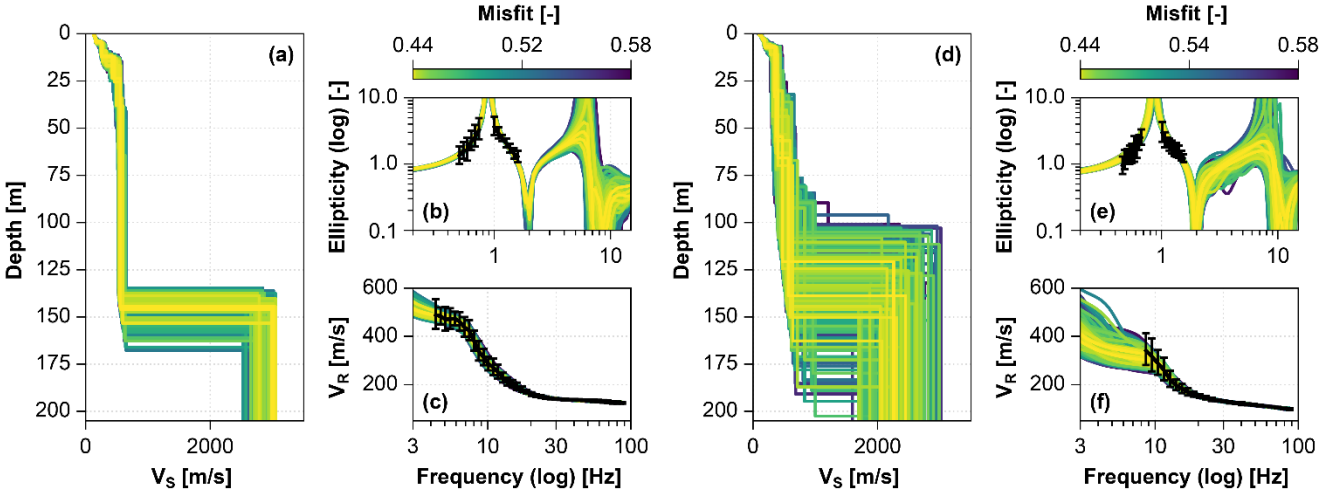

Figure 3. Joint dispersion-ellipticity curve inversion for Markarfljót Bridge sites (a-c) S1 and (d-f) S2. (a,d) Set of V_S profiles whose misfit values fulfil $m \leq 1.25m_{min}$. The associated theoretically computed ellipticity (b,e) and dispersion (c,f) curves are compared to the experimental data points specified as inversion targets.

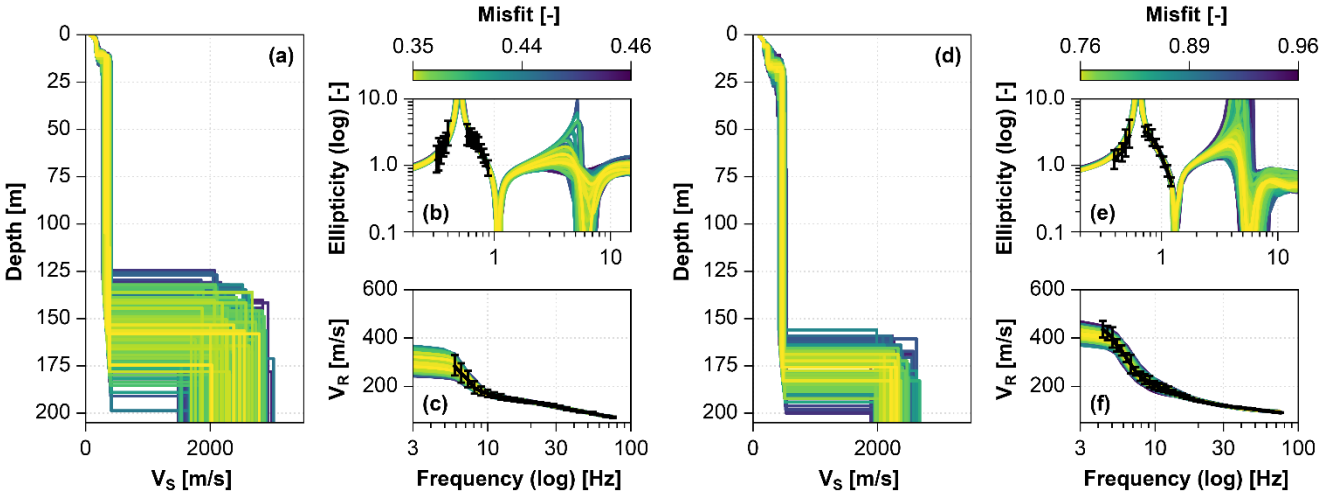

Figure 4. Joint dispersion-ellipticity curve inversion for (a-c) Markarfljót River site S3 and (d-f) Landeyjar Harbor site S4.

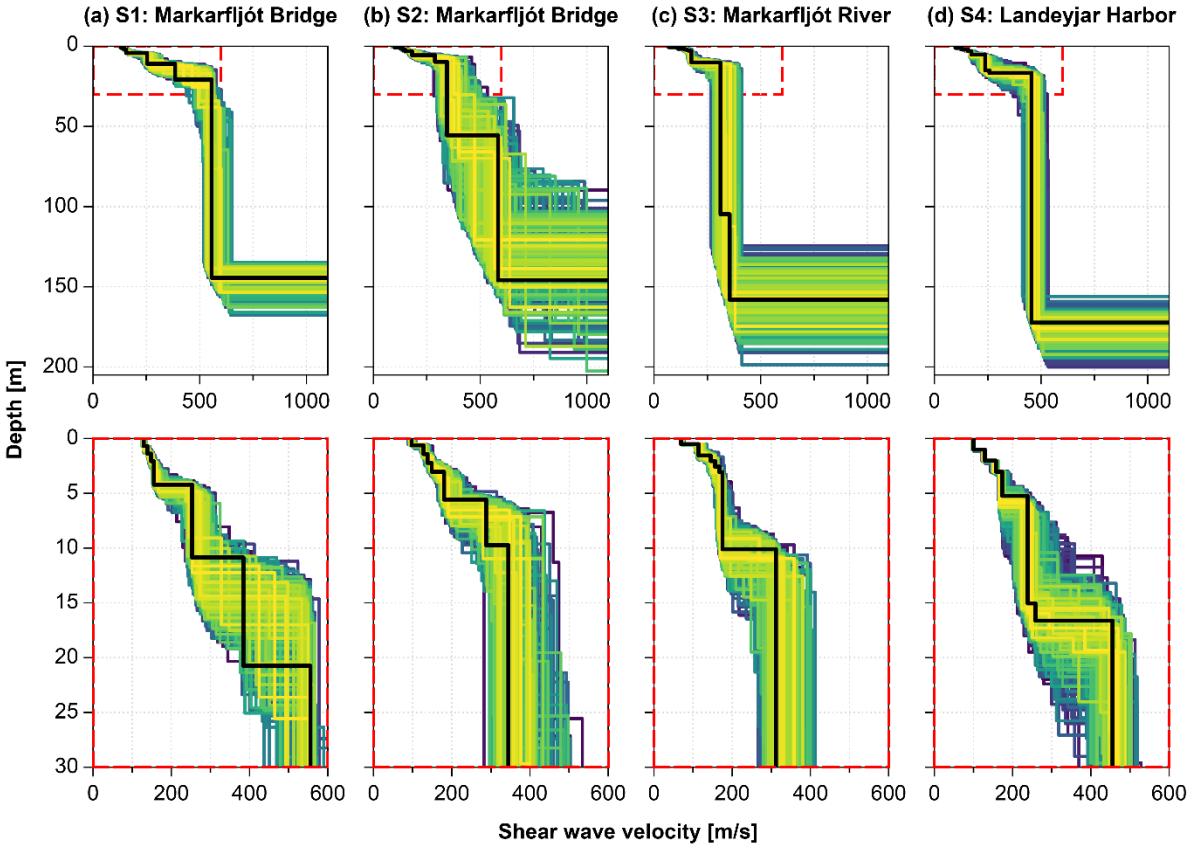

Figure 5. Variation of the sediment shear wave velocity predicted for sites (a) S1, (b) S2, (c) S3, and (d) S4 down to bedrock level (upper row) and down to a depth of 30 m (lower row). The colour scale used for each site refers to the misfit values in Figures 3 and 4. The lowest misfit shear wave velocity profile for each site is shown as a black line.

The strong impedance contrast at a depth of around 120–190 m is interpreted as depth to bedrock. However, the predicted bedrock velocity (>2000 m/s) may be affected by the uncertainty of the obtained data at depth. The time-averaged V_S for the top-most 30 m ($V_{S,30}$) is found to be in the range of 230–320 m/s. Down to bedrock level, the time-averaged V_S ($V_{S,H}$) is estimated as 290–480 m/s. Sediment thickness well exceeding 100 m is in line with available information on the Markarfljót area. It is noted that depth to bedrock was only retrieved at four locations. However, based on the results in Figure 5, a picture of increasing sediment thickness from north towards the sea emerges. Measurements at additional locations along the river are, however, required to conclude on this point.

The inversion results for the two sites by the Markarfljót Bridge (S1 and S2, Figures 3 and 5ab)

reveal a significantly more variation within the set of S2 V_S models as compared to those for S1. This is both observed in the predicted location of the sediment-bedrock interface, which is much better constrained for S1 than S2, as well as in the velocity estimates, particularly at depth. The observed difference is attributed to the narrower frequency range of the S2 dispersion curve, which results in a wider frequency gap between the right flank of the ellipticity peak and the experimental DC, as compared to that of S1. The lower surficial V_S for S2 (Figures 5ab) is consistent with prior expectations, as the surficial soil at S1 consisted of slightly compacted gravel whilst it was loose basalt sand at S2.

The results in Figures 4 and 5cd present a comparable trend for sites S3 and S4, as previously described for S1 and S2. Particularly, the lack of low-frequency components in the S3 DC (which results in a gap in the experimental data at 0.9–5.9 Hz) leads to increased difficulties in constraining the depth to bedrock. The effects of the lack of low-frequency DC components are also observed in the velocity estimates at depth, which are slightly less constrained at S3 than at S4. As shown in Figure 2b, the S3 DC presents the lowest phase velocity values out of the four experimental DCs, thus suggesting a somewhat softer surficial soil profile than at the other sites. However, the lack of data to constrain the theoretically computed DCs below 6 Hz is considered to affect the reliability of the velocity estimates for S3 at depth, possibly biasing the inverted V_S estimates to lower values and thereby also affecting the predicted bedrock depth. It would, therefore, be of value to gather MAM data at S3 in order to extend the experimental DC to lower frequencies. Consequently, the current estimate of the depth to bedrock and the corresponding value of $V_{S,H}$ for site S3 are considered more uncertain than those for S4.

3 SIMPLIFIED ESTIMATE OF H

In lack of site-specific measurements of velocity profiles or deep borehole logs, simple relationships providing a link between f_0 and H may be used to estimate depth to bedrock (or engineering bedrock) based on MHVSR measurements without inversion. Power-law regression models, i.e., $H = a \cdot f_0^b$, have been proposed by many authors, with the regression parameters a and b reflecting regional and geological characteristics. Thus, local calibration using data from multiple sites is required.

Assuming a one-dimensional soil model consisting of a soft sedimentary layer above bedrock, Eq. (1) relates f_0 and the average V_S of the sedimentary layer ($\overline{V}_S$) with H following a quarter-wavelength approach (Lachetl and Bard, 2011). A value of $\overline{V}_S$ = 300 m/s has previously been suggested to estimate sediment thickness based on measurements of f_0 (Nelson and McBride, 2019):

$$H = \frac{\overline{V}_S}{4 f_0} \quad (1)$$

Figure 6 compares the measurement results (i.e., MHVSR estimates of f_0 and the depth to bedrock level established based on the joint inversion) with values computed using Eq. (1) with $\overline{V}_S$ in the range of 200–600 m/s. For the softest site (S3), $\overline{V}_S$ = 300 m/s is found to provide an estimate of H that is consistent with the measured values. However, for S1, S2 and S4 a value of 300 m/s would lead to a significant underestimation of the depth to bedrock, with a $\overline{V}_S$ value in the range of 400–500 m/s seeming more appropriate. These results are consistent with the estimated $V_{S,H}$ for the four sites, i.e., around 300 m/s for S3, 410–420 m/s for S2 and S4, and up to 480 m/s for S1. This further correlates with the $V_{S,30}$ for the respective sites, which was estimated at around 230 m/s for S3 but showed values in the range of 260–280 m/s for S2 and S4 and exceeding 300 m/s for S1.

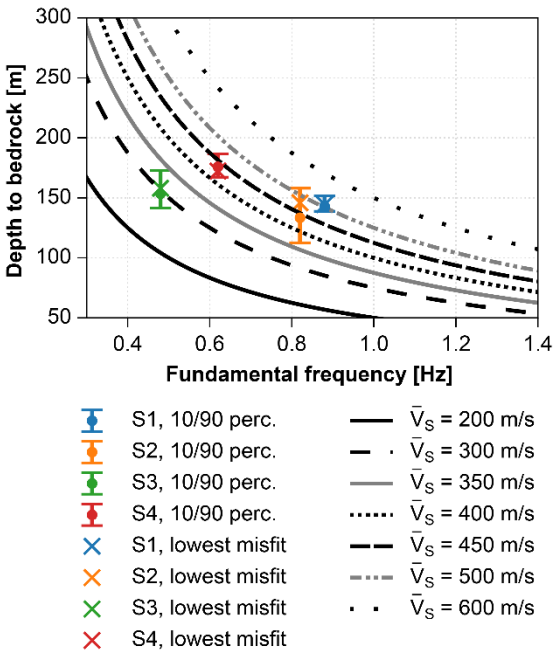

Figure 6. Comparison of measured values of depth to bedrock and values computed using Eq. (1) with $\overline{V}_s$ in the range of 200–600 m/s. For each site, the measured values are given as the 10th to 90th percentiles of the inverted bedrock depths (error bars) and the depth indicated by the lowest misfit velocity profile (crosses).

4 CONCLUSIONS

This study points at a joint dispersion-ellipticity inversion as a feasible method to retrieve the V_S distribution and depth to bedrock at deep soil sites in the South Iceland Lowland. For the conditions described here, a composite use of MASW and small-aperture MAM is further found highly beneficial to reduce the frequency gap between the experimental dispersion and ellipticity data, thus providing a more refined estimate of the sediment V_S and depth to bedrock. The bedrock depths estimated in this work are in line with available information on the wider Markarfljót area. However, existing data is limited to a few surveys, thus, comparison with direct measurements, e.g., deep boreholes, is considered beneficial for further verification of the results.

The results suggest that the quarter-wavelength approach (Eq. (1)) with $\overline{V}_S$ in the range of 300–500 m/s could be used for initial assessment of bedrock depths in the area based on MHVSR measurements of f_0. However, this study only includes data from four sites along the Markarfljót River. Further verification based on data from a larger number of sites is therefore required before general conclusions can be drawn. Future steps may also include calibration of power-law regression models relating f_0 and H to describe the local characteristics.

ACKNOWLEDGEMENTS

This work was supported by the Icelandic Research Fund (grants no. 206793-053, 218149-053), the Icelandic Road and Coastal Administration, and the Energy Research Fund of the National Power Company of Iceland.

REFERENCES

Guillier, B., Atakan, K., Chatelain, J.-L., Havskov, J., Ohrnberger, M., Cara, F., Duval, A.-M., Zacharopoulos, S., Teves-Costa, P., the SESAME team. (2008). Influence of instruments on the H/V spectral ratios of ambient vibrations. *Bulletin of Earthquake Engineering*, 6, pp. 3-31. https://doi.org/10.1007/s10518-007-9039-0.

Hobiger, M., Bard, P. Y., Cornou, C., Le Bihan, N. (2009). Single station determination of Rayleigh wave ellipticity by using the random decrement technique (RayDec), *Geophysical Research Letters*, 36, L14303. https://doi.org/10.1029/2009GL038863.

Lachetl, C., Bard, P.-Y. (2011) Numerical and theoretical investigations on the possibilities and limitations of Nakamura's technique. *Journal of Physics of the Earth*, 42(5), pp. 377–397. https://doi.org/10.4294/jpe1952.42.377.

Mott MacDonald, Línuhönnun. (2004). Independent Review of a Tunnel Connection to Vestmannaeyjar. Technical Report.

Nelson, S., McBride, J. (2019). Application of HVSR to estimating thickness of laterite weathering profiles in basalt. *Earth Surface Processes and Landforms*, 44(7), pp. 1365–1376. https://doi.org/10.1002/esp.4580.

Olafsdottir, E. A., Erlingsson, S., Bessason, B. (2018). Tool for analysis of multichannel analysis of surface waves (MASW) field data and evaluation of shear wave velocity profiles of soils, *Canadian Geotechnical Journal*, 55(2), pp. 217–233. https://doi.org/10.1139/cgj-2016-0302.

Olafsdottir, E. A., Erlingsson S., Bessason, B. (2023). Hybrid non-invasive characterization of soil strata at sites with and without embedded lava rock layers in the South Iceland Seismic Zone, *Bulletin of Engineering Geology and the Environment*, 82, 146. https://doi.org/10.1007/s10064-023-03136-0.

Pétursson, G. S., van Rijn, L., Pálmarsson, S. Ó., Myer, E. M., Ragnarsson, E. (2020). Landeyjahöfn harbour preliminary independent evaluation. Data review and assessment of harbour utilization, Ministry of Transport and Local Government, Reykjavik, Iceland, Rep. 20.07 / 2020-L-I.

Wathelet, M., Chatelain, J. L., Cornou, C., Di Giulio, G., Guillier, B., Ohrnberger, M., Savvaidis, A. (2020). Geopsy: A User-Friendly Open-Source Tool Set for Ambient Vibration Processing, *Seismological Research Letters*, 91(3), pp. 1878-1889. https://doi.org/10.1785/0220190360.

Proceedings of the XVIII ECSMGE 2024
GEOTECHNICAL ENGINEERING CHALLENGES
TO MEET CURRENT AND EMERGING NEEDS OF SOCIETY
© 2024 the Authors
ISBN 978-1-032-54816-6
DOI 10.1201/9781003431749-227
Open Access: www.taylorfrancis.com, CC BY-NC-ND 4.0 license

ECSMGE 24
XVIII EUROPEAN CONFERENCE ON SOIL MECHANICS AND GEOTECHNICAL ENGINEERING

Numerical modelling of the seismic site effects in Lisbon: role of buried and surficial morphology

Modélisation numérique des effets de site sismiques à Lisbonne: le rôle de la morphologie enfouie et superficielle

L. Oliveira*
Universidade de Lisboa, Faculdade de Ciências, Instituto Dom Luiz, Lisboa, Portugal

R.C. Gomes
CERIS, Instituto Superior Técnico, Universidade de Lisboa, Lisboa, Portugal

S. Amoroso
University of Chieti-Pescara, Department of Engineering and Geology, Pescara, Italy
Istituto Nazionale di Geofisica e Vulcanologia, L'Aquila, Italy

A. Pagliaroli
University of Chieti-Pescara, Department of Engineering and Geology, Pescara, Italy
Istituto di Geologia Ambientale e Geoingegneria, Consiglio Nazionale delle Ricerche, Montelibretti, Italy

P. Teves-Costa
CERU – European Centre on Urban Risks, Lisboa, Portugal

**lcaoliveira@ciencias.ulisboa.pt*

ABSTRACT: It is recognised that site effects have a great impact on seismic ground motion characteristics and this can lead to higher structural damage. Lisbon has a moderate to high seismic risk due to its historical seismicity, socio-economic importance and dense urbanisation. Furthermore, its geological setting is characterised by a complex lithostratigraphic structure, complex buried and surficial morphologies, shear wave velocity inversion and weathered rock layers. To assess the seismic site effects in Lisbon, a site response numerical analysis was performed along a profile characterised by the presence of a topographic relief and slightly inclined layers, considering the available geotechnical and geophysical data and the two types of seismic action defined in the Portuguese Annex of Eurocode 8. The results are shown in terms of amplification factors and acceleration response spectra at selected points. The physical phenomena governing the site response were also investigated by comparing 1D and 2D numerical analyses. At the top of the crest, an amplification factor equal to 3 was estimated within the period range of 0.05-2.50 s, which is related to bidimensional topographic effects.

RÉSUMÉ: Il est reconnu que les effets de site ont un grand impact sur les caractéristiques du mouvement sismique du sol ce qui peut accroître les dommages structurels. Lisbonne présente un risque sismique modéré à élever en raison de sa sismicité historique, de son importance socio-économique et de son urbanisation dense. De plus, son contexte géologique se caractérisé par une structure lithostratigraphique complexe, morphologies complexes enterrées et superficielles, l'inversion de la vitesse des ondes de cisaillement et des couches rocheuses altérées. Pour évaluer les effets sismiques du site à Lisbonne, des analyses numériques de la réponse des sites est réalisée le long d'un profil caractérisé par la présence d'un relief topographique et de couches légèrement inclinées, en tenant compte des données géotechniques et géophysiques disponibles et des deux types d'action sismique définis dans l'Annexe Portugais de l'Eurocode 8. Les résultats sont présentés en termes de facteurs d'amplification et de spectres de réponse d'accélération à certains points. Les phénomènes physiques qui sont responsables de la réponse du site sont également étudiés en comparant les analyses numériques 1D et 2D. Au sommet de la crête, un facteur d'amplification de 3 a été estimé entre 0.05 et 2.50 s, liés aux effets topographiques bidimensionnels.

Keywords: Site response analysis; site effects; amplification factors; complex morphological conditions; Lisbon.

1 INTRODUCTION

Since the combination of the many geological features of Lisbon's geological setting (Figure 1) increases the potential of site effects related to an earthquake, it is essential to identify and quantify them to delimit the areas of highest local hazard and contribute to long-term urban planning and seismic risk mitigation.

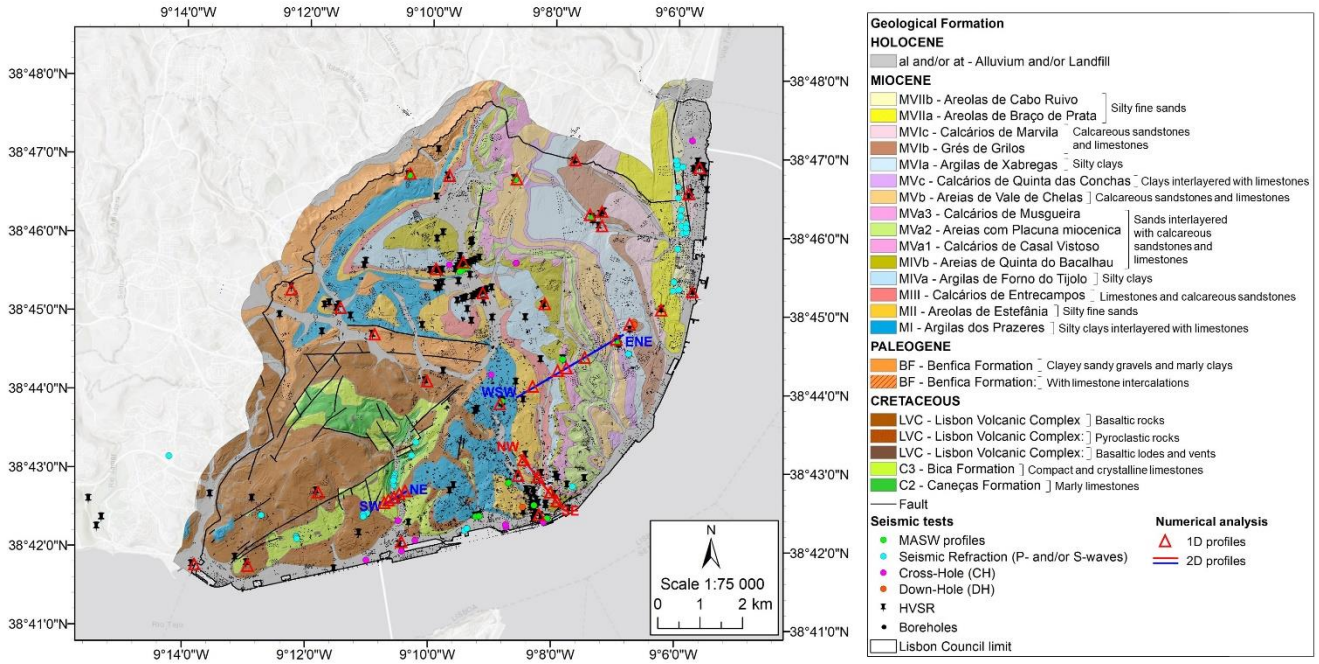

Figure 1. Geological map of Lisbon County (adapted from Almeida, 1986), displaying the spatial distribution of available geotechnical and geophysical data. The NW-SE profile is also identified with a red line.

This paper presents the results of numerical analyses carried out along a NW-SE profile characterised by topographic relief, slightly inclined layers and S-wave inversion. The profile was drawn based on the geological cross-section provided by Almeida (1986). The subsoil model was defined considering all the available geotechnical and geophysical data (see Figure 1), while the two types of reference spectra corresponding to seismic action type 1 (*AS1*) and seismic action type 2 (*AS2*) (return period of 475 years) defined in the Portuguese Annex of Eurocode 8 (IPQ, 2010) were considered to select two sets of seven accelerograms compatible with the reference spectral shapes. Figure 1 shows all of the 2D profiles that were modelled as well as the 1D analyses that were performed. However, due to limited space, the study focuses on the NW-SE profile.

The 1D numerical analyses were performed using STRATA (Kottke and Rathje, 2008), while the 2D analyses were carried out using LSR2D (www.stacec.com), with both employing an equivalent-linear viscoelastic approach. The 1D simulations were performed considering the same soil properties and input motions as the 2D response analysis. The compliant (elastic) base boundary condition was applied in both the 1D and 2D analyses. In 2D analysis, the free-field condition is applied to the lateral boundaries, leading them to operate as a system capable of absorbing reflected waves that would otherwise be artificially reintroduced into the model.

2 GEOTECHNICAL PROFILE

The NW-SE profile is characterised by a significant topographic variation, with the presence of a crest at 90 m a.s.l. and an adjacent shallow valley with a width of 95 m and filled by sediment of thickness around 15 m (Figure 2). Below the Miocene layers, the geological bedrock is composed of Cretaceous formations, including basalt rocks from the *LVC* and limestones from the *C3* and *C2* formations (Figure 1).

The shear wave velocity (V_S) of each geological unit was estimated through the site-specific V_S-depth equations developed for the Lisbon area (Oliveira et al., 2023), considering the average depth of each layer. The bedrock depth was calibrated to numerically reproduce the resonant frequencies measured through the noise (*HVSR*) measurements. Poisson's ratio (υ) was not directly measured in any geological formations. The Poisson's ratio was set at $\upsilon = 0.49$ for saturated soil, $\upsilon = 0.35$ for unsaturated soil and $\upsilon = 0.30$ for rocks (Oliveira et al., 2023).

The non-linear decay and damping curves computed for gravel soils by Rollins et al. (1998) were considered to describe landfill deposits and *MVa* complex (MVa3, MVa2 and MVa1 formations) behaviour due to their heterogeneous composition that can be comparable with gravel soil. The Darendeli (2001) curves were assigned to the alluvial deposit, *MIVb*, *MIVa*, *MII* and *MI* formations. The *LVC* behaviour is described by the Schnabel et al. (1972) curves and a linear viscoelastic behaviour was set for the *MIII*, *C3* and *C2* formations with damping D = 1%.

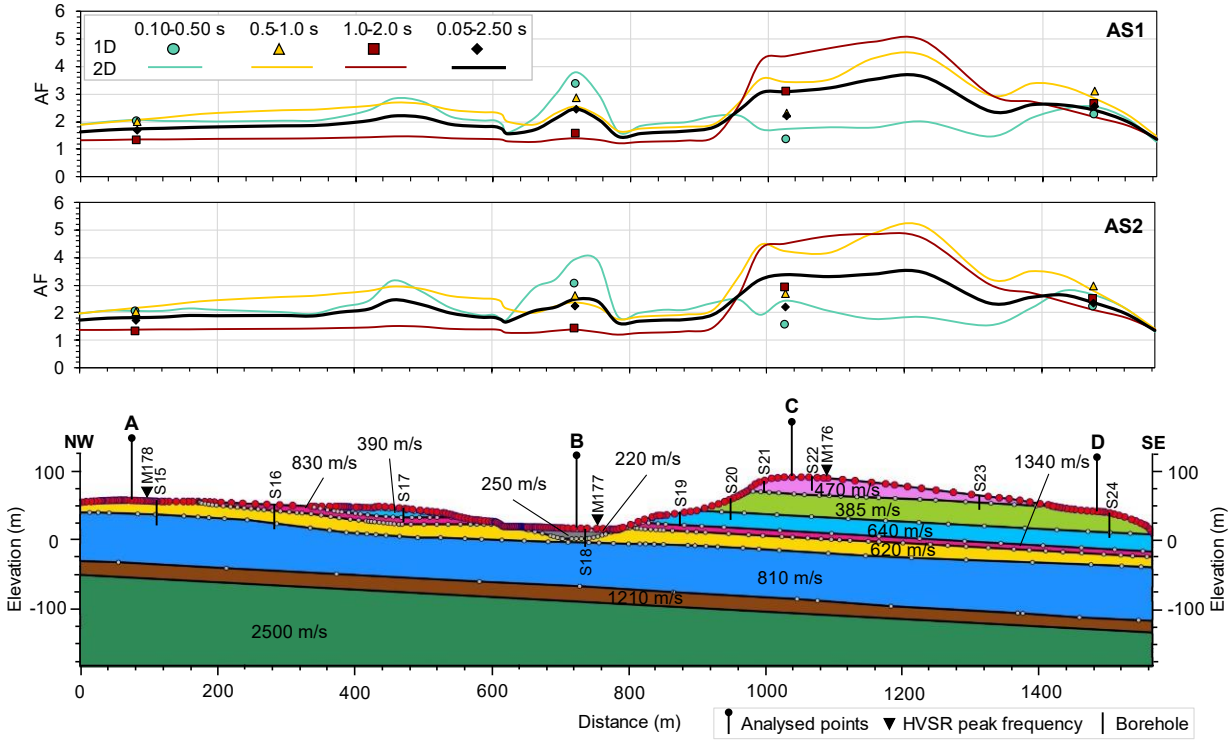

Figure 2. NW-SE profile: median total amplification factors (AF_{2D}) computed in the four period ranges T = 0.1–0.5 s; 0.5–1.0 s; 1.0–2.0 s; 0.05–2.50 s for AS1 (top) and AS2 (bottom) compared to the values computed through 1D seismic response analyses (AF_{1D}) along the verticals A, B, C and D. The geological formations are coloured according to Figure 1.

3 RESULTS AND DISCUSSION

Figure 2 shows the median AF_{2D} total amplification factor variation computed for periods 0.1–0.5 s, 0.5–1.0 s, 1.0–2.0 s and 0.05–2.50 s along the NW-SE profile, with the 2D response normalised by the input.

In the range 0.1–0.5 s the maximum amplification factors (*AFs*) occur in the middle of the valley (B). Conversely, at the top of the crest (C), the peak amplification factor (*AF*) occurs in the range 1.0–2.0 s. When the *AF* for the 0.1–0.5 s and 0.5–1.0 s period ranges are compared to the 1.0–2.0 s range in correspondence with the alluvial deposit (B), the expected dependence of *AFs* on the frequency and magnitude of the input motions is confirmed. On the other hand, a lower dispersion is associated with the outcropping stiff layers (e.g., A). Higher *AFs* occur in the intermediate to lower period ranges in correspondence of A and D for both *AS1* and *AS2*. At the top of the crest (C) and the centre of the valley (B), an *AF* of ~3-3.4 and ~2.5 are computed in the 0.05–2.50 s range, respectively. The comparison between the 2D median response spectra and median input spectra substantially confirms that the amplification takes place essentially for the periods lower than 0.5 s in the valley (B), more significant in *AS1*, and for the periods higher than 0.5 s at the top of the crest (C), observed in both *AS1* and *AS2* (Figure 3). The amplification takes place essentially for the periods higher than 0.3 s for *AS1* and for the periods lower than 0.3 s for *AS2* in A. The amplification is essentially observed for the periods higher than 0.1 s in D. Spectral accelerations as high as 13–20 $m.s^{-2}$ appear at B in the 0.3–0.5 s period range for *AS1* and *AS2*; on the contrary, the spectral acceleration is lower than 10–12 $m.s^{-2}$ at A, C and D in the whole period range.

To investigate the 2D physical phenomena that govern the local response, Figure 3 compares the 1D and 2D median response spectra for A, B, C and D, reporting the 2D/1D spectral ratios. 2D effects are noticed in B between 0.2 s and 0.4 s for *AS1* and *AS2* (peaks of the 2D/1D ratio), related to the valley effect and basin configuration; here the 2D analyses are ~1.2 (*AS1*) and ~1.3 (*AS2*) the amplitudes of ground motion predicted by 1D simulations (Figure 3). These effects are responsible for ground motion amplification in the 0.1–0.5 s period range mentioned above.

In C, clear 2D effects are observed in 0.5–1.0 s and 1.0–2.0 s ranges for *AS1* and *AS2*, evidencing the topographic effects related to the crest. In this case, the 2D analyses return ~1.5 (*AS1*) and ~1.6 (*AS2*) the amplitudes of ground motion predicted by 1D simulations (Figure 3). With reference to A and D, 1D and 2D computations are much closer for both *AS1* and *AS2*. The slight 2D effects are related to the buried morphology (i.e., inclined layers), leading to a residual

amplification factor. In this case, the amplification is mainly due to stratigraphic effects, which are well-predicted by 1D seismic response analysis (Figure 3).

According to the EC8 recommendations, the topographic amplification factor for ridges with crest width significantly narrower than base is 1.4 for slope angles $i > 30^{o}$ and 1.2 for gentler slope angles ($15^{o} < i < 30^{o}$) (CEN, 2004). In this study, the slope angle of the crest is roughly 20º and the maximum topographic amplification factor varies between 1.4 and 1.5, slightly higher than the EC8 recommended values.

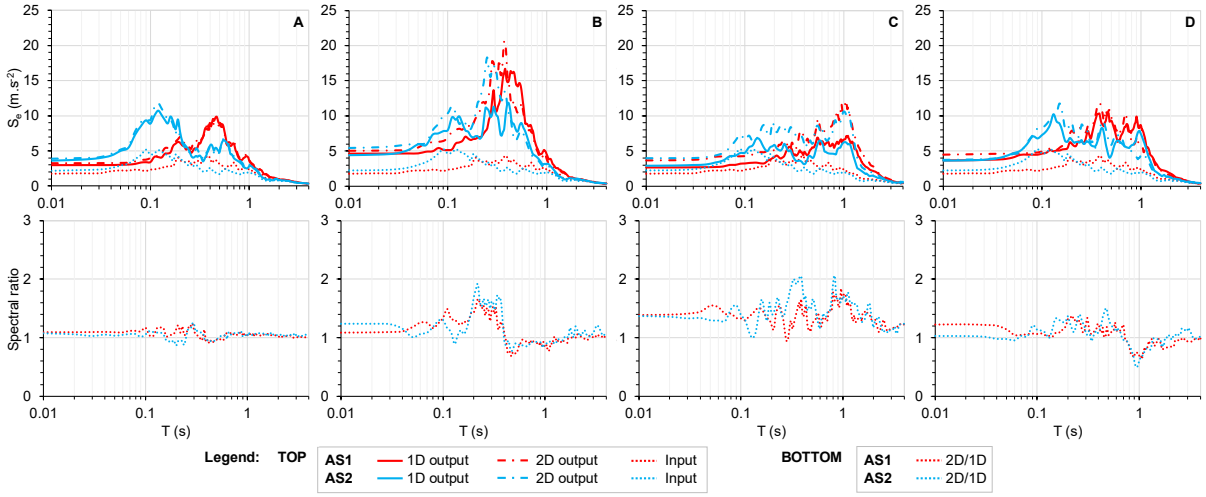

Figure 3. Response spectra (ξ = 5%) (top) and spectral ratios (bottom) from the 2D and 1D numerical analyses computed at points A, B, C and D for AS1 (red) and AS2 (blue).

4 CONCLUSIONS

This analysis shows that in an urban area like Lisbon, assessing seismic site effects is essential to mitigate the impact of a seismic event.

The presence of large topography differences, such as a crest and a valley filled with alluvial deposits, causes the observed valley and topographic effects. There are also slight 2D effects related to the buried morphology (i.e., inclined layers). Ground motion is aggravated by 2D site effects by a factor of 1.2-1.6 when compared to 1D prediction. The topographic amplification factors obtained at the top of the crest are 15% to 25% higher than the EC8 suggested values.

This methodology can be applied to quantify the impact of 2D effects in other parts of the city.

ACKNOWLEDGEMENTS

The authors are grateful for the financial support provided by the Portuguese Fundação para a Ciência e a Tecnologia (FCT) I.P./MCTES through national funds (PIDDAC)–UIDB/50019/2020 and (PIDDAC)–UIDB/04625/2020 and Liliana Oliveira acknowledges FCT for her Ph.D. Grant Ref. SFRH/BD/146030/2019.

REFERENCES

Almeida, F.M. (1986). *Geological map of Lisbon county 1:10 000.* Serviços Geológicos de Portugal, Lisbon, Portugal (in Portuguese).

Darendeli, M.B. (2001). *Development of a new family of normalized modulus reduction and material damping curves.* PhD thesis, University of Texas at Austin, p 394.

CEN (2004). *Design provisions for earthquake resistance of structures — Part 5: foundations, retaining structures and geotechnical aspects.* ENV 1998–5, CEN European Committee for Standardisation, Brussels.

IPQ (2010). *Eurocode 8: Design of structures to resist earthquakes – Part 1: General rules, seismic actions and rules for buildings, NP EN 1998-1.* Instituto Português da Qualidade, 230 p. (in Portuguese).

Kottke, A.R., Rathje, E.M. (2009). *Technical manual for strata.* PEER report 2008/10.

Oliveira, L., Gomes, R.C., Teves-Costa, P. (2023). Contribution to the seismic microzonation of Lisbon based on the integration of geological, geophysical, and geotechnical data. *Soil Dynamics and Earthquake Engineering*, Volume 171, 107965, ISSN 0267-7261. https://doi.org/10.1016/j.soildyn.2023.107965

Rollins, K.M., Evans, M.D., Diehl, N.B., Daily, W.D.I.I.I. (1998). Shear modulus and damping relationships for gravels. *J. Geotech Geoenvironmental Eng* 124(5):396–405. https://doi.org/10.1061/(ASCE)1090-0241(1998)124:5(396)

Schnabel, P.B., Lysmer, J., Seed, B. H. (1972). *SHAKE – A computer program for earthquake response analysis of horizontally layered sites.* Report No. EERC 72/12, Univ. of California, Berkeley, California.

Proceedings of the XVIII ECSMGE 2024
GEOTECHNICAL ENGINEERING CHALLENGES
TO MEET CURRENT AND EMERGING NEEDS OF SOCIETY
© 2024 the Authors
ISBN 978-1-032-54816-6
DOI 10.1201/9781003431749-228
Open Access: www.taylorfrancis.com, CC BY-NC-ND 4.0 license

ECSMGE 24
XVIII EUROPEAN CONFERENCE ON SOIL MECHANICS AND GEOTECHNICAL ENGINEERING

Expansive and collapsible soil behaviour under the Revised Soil Classification System

Compportement des sols gonflant ou affaissants selon le Système Révisé de Classification des Sols

R. Ortiz-Hernández*, E. Rojas-González
Universidad Autónoma de Querétaro, Santiago de Querétaro, México
**raforther@gmail.com*

ABSTRACT: Identifying expansive and collapsible soils is crucial for geotechnical engineering. Grain size distribution and Atterberg limits help identify such soils, and the Revised Soil Classification System enhances this identification. It primarily introduces a new testing protocol for the liquid limit of soils using various fluids. When assessing the plasticity behaviour of these soils under different levels of chemical stabilization, it is evident that the concentration of the stabilizing agent linearly reduces expansion or collapse potential. However, the liquid limit's behaviour under varying pore fluid chemistry and stabilizing agent concentration follows a non-linear trend.

RÉSUMÉ: L'identification des sols expansifs et pliables est cruciale pour l'ingénierie géotechnique. La distribution granulométrique et les limites d'Atterberg aident à identifier ces sols, et le système révisé de classification des sols améliore cette identification. Il introduit principalement un nouveau protocole de test de la limite de liquidité des sols utilisant divers fluides. Lors de l'évaluation du comportement plasticité de ces sols sous différents niveaux de stabilisation chimique, il est évident que la concentration de l'agent stabilisant réduit linéairement le potentiel d'expansion ou d'effondrement. Cependant, le comportement de la limite liquide selon la chimie du fluide interstitiel et la concentration de l'agent stabilisant varie suit une tendance non linéaire.

Keywords: Expansive soils; collapsible soils; geotechnical characterization; soil classification.

1 INTRODUCTION

In geotechnical engineering, certain soils pose risks during infrastructure construction. These include expansive and collapsible soils. Qualitatively identifying these soils based on their index properties is crucial in engineering practice to prevent costly foundation repairs resulting from misidentification.

Expansive soils alter their volume with changing saturation levels, expanding when saturated and contracting during desiccation (Zepeda, 2004). They are primarily characterized by their mineral composition, with clay minerals like smectite and illite being significant (Mitchell & Soga, 2005). The relationship between clay mineralogy and their position on the Casagrande Plasticity Chart has been established (Okkels, 2019).

Figure 1 illustrates that montmorillonite clay and illite fall above the A-Line (distinguishing clays from silts) and below the U-Line (indicating empirical clay behavior), classifying them both as "high plasticity clay," CH, under the Unified Soil Classification System (USCS). The primary difference between them is the value of the plasticity index (PI).

Collapsible soils remain stable under dry conditions but experience significant volume changes (shrinkage) when saturated under the same load (Ali, 2011). Indications of a collapsible soil include low volumetric weight and a high void ratio. The relationship between its dry volumetric weight and liquid limit (LL) (Rezaei et al., 2012) or the void ratios under natural conditions and at the LL (Denosov, 1951) has been established.

In soil classification advancements, the "Revised Soil Classification System (RSCS)" has been developed. It involves a review of the test protocol regularly used in the USCS to describe the fractions controlling the soil's mechanical and hydraulic behavior (Park & Santamarina, 2017). The RSCS is summarized graphically in the flow diagram presented in Figure 2.

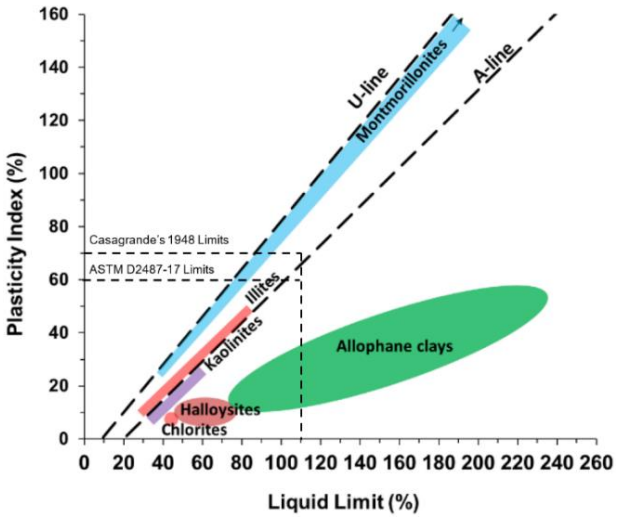

Figure 1. Fine-grained soils plasticity chart with mineralogy zones (adapted from Okkels, 2019).

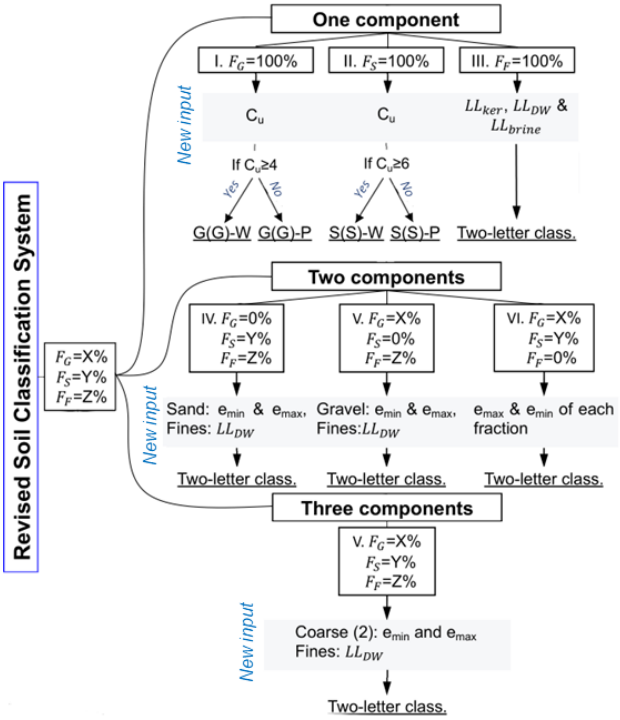

Figure 2. RSCS workflow (adapted from Castro et al, 2023).

For soils where the fine fraction influences the soil's mechanical and/or hydraulic behavior, the RSCS advises analyzing this fraction using the LL with various fluids. The LL is preferred due to its consistency, repeatability, and absence of segregation or edge effects (Jang & Santamarina, 2017).

The RSCS recommends using specific testing fluids: deionized water, enhancing double layer effects; kerosene, affecting van der Waals forces; and 2 M NaCl brine, causing the collapse of the diffuse double layer (Jang & Santamarina, 2017; Castro et al., 2022).

These fluid-based limits help establish relationships that express specific soil properties. The deionized water to brine water ratio denotes pore fluid permittivity, while the kerosene to brine ratio defines fluid electrical conductivity. These relationships lead to the determination of a new parameter called "Electrical Sensitivity" (Jang & Santamarina, 2017):

$$S_E = \sqrt{\left(\frac{LL_{dw}}{LL_{brine}} - 1\right)^2 + \left(\frac{LL_{ker}}{LL_{brine}} - 1\right)^2} \quad (1)$$

where S_E is the electrical sensitivity, LL_{dw} (%) is the deionized water LL, LL_{brine} (%) is the 2 M NaCl brine LL and LL_{ker} (%) is the kerosene LL.

When LL ratios are less than 1, their reciprocals are used to maintain a positive value in equation (1). To address density variations between kerosene (2) and deionized water and salt concentration in brine (3), these corrections are applied as outlined in Jang and Santamarina (2017):

$$\left.\frac{LL_{ker}}{LL_{brine}}\right|_{corr} = \frac{LL_{ker}}{LL_{brine}} \frac{1 - c_{brine}\frac{LL_{brine}}{100}}{G_{ker}} \quad (2)$$

$$\left.\frac{LL_{dw}}{LL_{brine}}\right|_{corr} = \frac{LL_{dw}}{LL_{brine}} \left(\frac{1 - c_{brine}\frac{LL_{brine}}{100}}{G_{ker}}\right) \quad (3)$$

where c_{brine} is the concentration of NaCl brine (mol/L) and G_{ker} is the specific gravity of kerosene.

The electrical sensitivity is a function of particle size, shape, mineralogy, surface, and edge charges, these in turn have an effect in the hydraulic conductivity, compressibility, and shear strength of the soil (Jang and Santamarina, 2016).

The electrical sensitivity and corrected brine LL are used in the RSCS Plasticity chart (Figure 3a), while the corrected LL ratios are depicted on a new electrical sensitivity chart (Figure 3b).

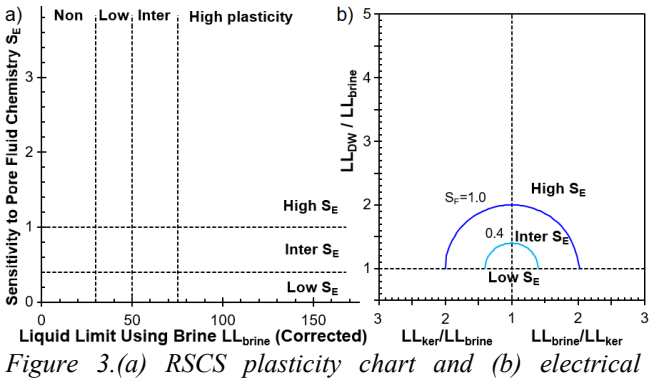

Figure 3.(a) RSCS plasticity chart and (b) electrical sensibility chart.

Tests using this new protocol reveal that soils with expansive minerals like montmorillonite exhibit high

plasticity with brine and an elevated electrical sensitivity. These findings group them into distinct sectors on the Plasticity Chart and Electrical Sensitivity Chart (Figure 4).

As of now, collapsible soils have not undergone this testing protocol, and thus, their position on the Plasticity and Electrical Sensitivity Charts remains uncertain.

This research aims to correlate a soil's expansive or collapsible behavior with its electrical sensitivity parameter due to the lack of knowledge regarding how special soils behave in various pore fluid conditions, both natural and when stabilized.

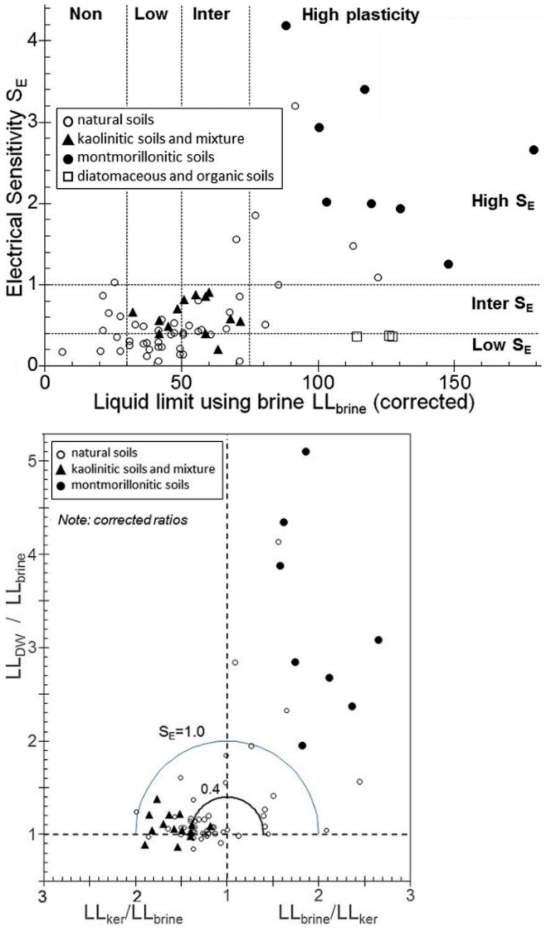

Figure 4. Soil mineralogy clusters in the RSCS plasticity and electrical sensitivity charts (adapted from Jang and Santamarina, 2017).

2 EXPERIMENTAL PROGRAM

The experimental program involved assessing a soil's expansion or collapse potential under natural conditions and applying a stabilizing agent at 3% and 5% concentrations while measuring electrical sensitivity. Additional tests for specific surface and specific gravity of soil solids were conducted to monitor material property changes.

The soil was dry sieved with a #200 sieve and dried at 60°C to prevent soil chemistry alteration (ASTM, 2010) before conducting expansion/collapse and LL tests.

The expansion potential was assessed using ASTM D4546-14 A-Method, while the collapse potential was determined following the ASTM D5333-12 standard. In both tests, the material was remolded to match the natural unit weight and water content reported by Verdín (2022) for expansive soil and Fonseca et al. (2014) for collapsible soil.

The electrical sensitivity parameter was calculated using the corrected LL ratios of the material with deionized water, reagent-grade kerosene, and 2 M NaCl brine using equations (2) and (3). The LL was determined using the fall cone method (BSI, 1990) and adjusted based on the fluid's concentration or specific gravity. To prevent material contamination, a fresh sample was used for each LL test and not reused between tests.

The 2 M NaCl brine is prepared by dissolving 117 grams of NaCl reagent in one liter of deionized water. Electrical sensitivity was calculated using the EGEL KAUST's spreadsheet for RSCS soil classification. Specific surface assessments for soils in their natural state and two stabilization levels were conducted with the "methylene blue" test (Santamarina et al., 2002), and the specific gravity of soil solids was determined following ASTM D854-10 standard.

3 RESULTS AND DISCUSSION

Chemical stabilization agents at 3% and 5% were employed, aligning with established practical geotechnical engineering ranges (Barma & Dash, 2022; Basma & Tuncer, 1992). Chemical stabilization was chosen due to its effectiveness in altering soil index properties, as other stabilization methods yielded less significant changes.

The soils used in these tests were previously identified as having expansion potential (Verdin, 2022) or collapsible behavior (Fonseca et al., 2014). Both soils primarily consist of fine particles. Key properties of the natural condition materials are detailed in Table 1.

Based on this data, both soils fall into the RSCS classification as F(F) soils, where the fine fraction governs the soil's mechanical and hydraulic characteristics. As a result, it's necessary to establish the LL of the materials using deionized water, kerosene, and brine as stated in the RSCS flowchart of Figure 2. The outcomes of the corrected LL tests are presented in Table 2, and their placement on the RSCS

Plasticity and Sensitivity Charts is depicted in Figure 5.

Expansion test results and electrical sensitivity data are displayed in the top section of Table 3, while potential collapse results and electrical sensitivity are presented in the lower section of the same table.

Table 1. Soil properties under natural conditions.

Material	Fractions			Atterberg Limits	
	G (%)	S (%)	F (%)	LL (%)	PL (%)
Expansive soil	0	16	84	76	39
Collapsible soil	0	3	97	63	39

Material	SUCS	Gs	Se (m²/g)
Expansive soil	CH	2.48	300
Collapsible soil	MH	3.15	27

Data obtained from Verdin (2022), Fonseca et al (2014) and the authors. G is Gravel, S is Sand, F is Fines, LL is Liquid limit, LP is Plastic limit, Gs is specific weight of soil solids, Se is specific surface.

Table 2. Liquid limits of soils under natural conditions and two stabilization levels in different pore fluid chemistry, electrical sensitivity and RSCS classification.

Material	LL_{dw} (%)	LL_{ker} (%)	LL_{brine} (%)	S_E	RSCS
Exp + 0%	67	41	46	0.47	F(F)-LL
Exp + 3%	66	46	46	0.32	F(F)-LI
Exp + 5%	63	49	50	0.29	F(F)-IL
Col + 0%	87	66	52	0.37	F(F)-II
Col + 3%	121	67	55	0.84	F(F)-IH
Col + 5%	109	61	60	0.54	F(F)-II

LLdw is LL with deionized water, LLker is LL with kerosene, LLbrine is LL with brine and S_E is Electrical Sensibility.

Table 3. Behaviour of expansive and collapsible soils under different stabilization levels.

Material	SP (kPa)	FSI (%)	S_E	Gs	Se (m²/g)
Exp + 0%	4.9	9.36	0.47	2.37	300
Exp + 3%	2.5	1.30	0.32	2.71	214
Exp + 5%	2.5	0.54	0.29	2.62	153

Material	CP (%)	S_E	Gs	Se (m²/g)
Col + 0%	4.61	0.37	2.76	27.07
Col + 3%	2.43	0.81	2.92	19.57
Col + 5%	1.50	0.54	2.92	17.13

SP is Swelling pressure, FSI is Free Swell Index, Gs is specific density of solids, SE is specific surface and CP is Collapse Potential Index.

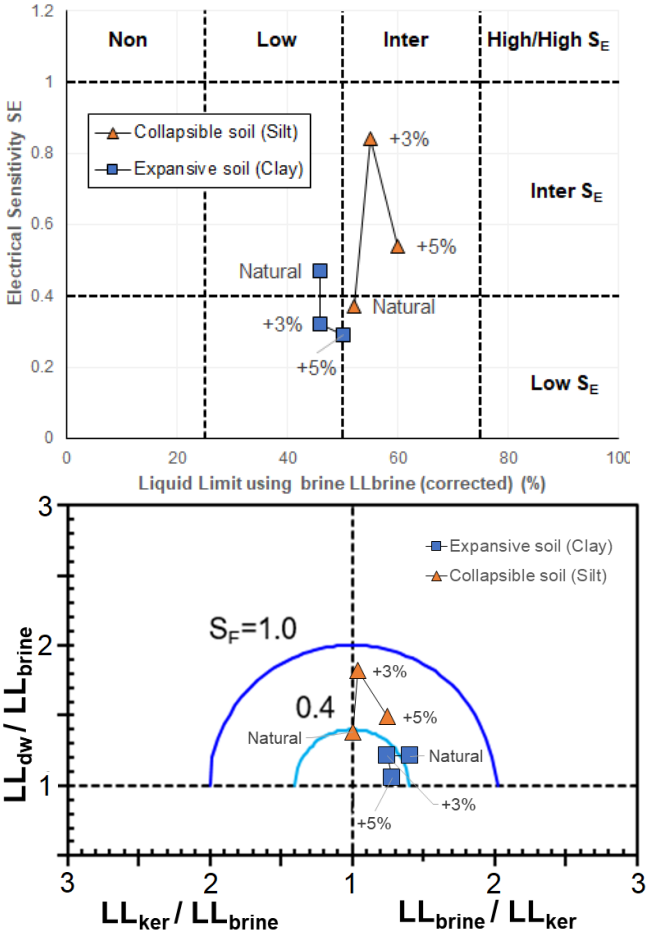

Figure 5. Evolution of the behaviour of expansive and collapsible soils in the RSCS plasticity and electrical sensitivity charts.

In the RSCS Plasticity Chart, expansive soils show that it has a natural low brine plasticity and low electrical sensibility, at a 3% stabilization agent concentration the soil presents a reduced electrical sensibility but no change in its brine plasticity, at a 5% stabilization the electrical sensitivity keeps decreasing but it presents an increase in brine plasticity. This effect could be attributed to the change lime produces on the ionic concentration of the soil and its effects on the double layers (Barman & Dash, 2022).

In collapsible soils, plasticity increases with greater stabilizing agent concentrations, however, in terms of electrical sensitivity there is a significant peak at a 3% concentration and a sharp decrease at 5%. The increase in deionized water and brine plasticity can be attributed to the microstructural mechanisms of hydration, surface deposition and shallow infilling of cementitious materials in the silt clusters (Basma and Tuncer, 1992).

In the Electrical Sensitivity Chart, expansive soils exhibit increased permittivity at 3%, followed by a reduction at 5%, with increased conductivity. Collapsible soils show reduced permittivity at 3% but increased permittivity at 5%.

No linear behavior was observed for both treated expansive or collapsible materials in both Plasticity and Electrical Sensitivity charts, so more experiments on higher concentrations are needed to establish a possible trendline, however these concentrations are purely for research purposes as these might be economically unfeasible for real-life applications.

In the complementary soil solid density measurements, the addition of the stabilizing agent increased the soil specific density, affirming a physical-chemical change in the soil's particles. As for specific surface, both lime and cement reduced the soil surface area with increasing concentration. Notably, the decrease in the collapsible silt surface area while the LL in both deionized and brine fluid increases during chemical stabilization suggests the presence of a distinct mechanism in the LL test, depending on the material's particle size and mineralogy, as noted by Sridharan and Prakash (2000).

During experimentation with the collapsible silt, an intriguing phenomenon occurred. It underwent a cementation reaction with both deionized water and brine, leading to an exothermic reaction with a temperature rise of 20°C, ultimately solidifying into a hard mass. To conduct the LL test, continuous stirring and fluid addition were essential to cool the mixture and prevent the formation of a non-workable paste.

Although the stabilization of these soils is a physical-chemical reaction that tends to continue to evolve over time, no significant change in LL results was recorded during the testing period of 14 days.

4 CONCLUSIONS

In the expansive soil, lime concentration inversely impacts expansion, with electrical sensitivity following a linear trend. However, brine plasticity exhibits a decreasing-then-increasing pattern.

For the collapsible soil, increased cement concentration reduces collapse potential. Electrical sensitivity displays a non-linear trend, while plasticity in brine rises with cement concentration.

In both cases, complementary tests reveal that chemical stabilization increases solids density and diminishes their specific surface area.

For establishing material expansive using RSCS, it's advisable to utilize its electrical sensitivity as a control parameter. However, for collapsible soils, finding a suitable control parameter remains challenging.

A potential issue with this new system is the contamination of soil samples with kerosene and brine. Proper disposal and treatment of test residues need to adhere to environmental regulations, a capability not commonly found in standard soil mechanics laboratories.

ACKNOWLEDGEMENTS

We extend our gratitude to National Council of Humanities, Science and Technology (CONAHCyT) for their support in this research through the Graduate Scholarship Program. We also appreciate the assistance provided by the academic and student community of the Department of Research and Graduate Studies at the Autonomous University of Querétaro. Special thanks to ROMA SOL Ingeniería S. de R.L. de C.V., Ingeum Engineering S.A. de C.V., and EPGC S. de R.L. de C.V. for granting us access to their laboratories.

REFERENCES

Ali, M.M. (2011) Identifying and Analyzing Problematic Soils. *Geotech Geol Eng* 29, pp. 343-350 (2011). https://doi.org/10.1007/s10706-010-9380-y.

ASTM. (2003). "Standard Test Method for Measurement of Collapse Potential of Soils" ASTM D5333, West Conshohocken, PA.

ASTM. (2010). "Standard test methods for laboratory determination of water (moisture) content of soil and rock by mass" ASTM D2216, West Conshohocken, PA.

ASTM. (2014a). "Standard Test Methods for Specific Gravity of Soil Solids by Water Pycnometer" ASTM D854, West Conshohocken, PA.

ASTM. (2014b). "Standard Test Methods for One-Dimensional Swell or Collapse of Soils" ASTM D4546, West Conshohocken, PA.

Ayadat, T., and Hanna, A. (2007). "Identification of Collapsible Soil Using the Fall Cone Apparatus." ASTM International. *Geotech. Test. J.* July 2007; 30(4): 312–323. https://doi.org/10.1520/GTJ14193.

Barman, D., and Dash, S. K. (2022). Stabilization of expansive soils using chemical additives: A review. *Journal of Rock Mechanics and Geotechnical Engineering*, Vol. 14(4), pp. 1319-1342. https://doi.org/10.1016/j.jrmge.2022.02.011.

Basma, A. A., & Tuncer, E. R. (1992). Evaluation and control of collapsible soils. *Journal of Geotechnical Engineering*, 118(10), 1491-1504. https://doi.org/10.1061/(ASCE)0733-9410(1992)118:10(1491).

BSI (1990). Methods of test for soils for civil engineering purposes. BS 1377-2, London, UK.

Castro, G. M., Park, J., and Santamarina, J. C. (2023). Revised soil classification system: implementation and engineering implications. *Journal of Geotechnical and Geoenvironmental Engineering*, 149(11), 04023109. https://doi.org/10.1061/JGGEFK.GTENG-10447.

Chew, S. H., Kamruzzaman, A. H. M., and Lee, F. H. (2004). Physicochemical and engineering behavior of

cement treated clays. *Journal of geotechnical and geoenvironmental engineering*, 130(7), 696-706. https://doi.org/10.1061/(ASCE)1090-0241(2004)130:7(696).

Denosov N. Y. (1951) The engineering properties of loess and loess loams, Gosstroiizdat, Moscow. Osnov Fudam Mech Grunt 5:5–8.

Fonseca, G. G., Cuello, C. M., Chávez, M. E., and Vaca, J. C. L. (2014). Identificación de los suelos dispersivos y colapsables del valle del río Verde, en Rioverde SLP, México. *Revista Digital del Cedex*, (176), 85-85 (in Spanish). https://ingenieriacivil.cedex.es/index.php/ingenieria-civil/article/view/506.

Jang, J., and Santamarina, J. C. (2016). "Fines classification based on sensitivity to pore-fluid chemistry." *J. Geotech. Geoenviron. Eng.* Vol. 142(4) https://doi.org/10.1061/(ASCE)GT.1943-5606.0001420.

Jang, J. and Santamarina, J. C. (2017). "Closure to "Fines classification based on sensitivity to pore-fluid chemistry" by Junbong Jang and J. Carlos Santamarina." *J. Geotech. Geoenviron. Eng.* Vol. 143(7), https://doi.org/10.1061/(ASCE)GT.1943-5606.0001694.

Jang, J., Cao, S. C., Stern, L. A., Jung, J., and Waite, W. F. (2018). "Impact of pore-fluid chemistry on fine-grained sediment fabric and compressibility." *J. Geophys. Res: Solid Earth.* Vol. 123(7), pp. 5495-5514, https://doi.org/10.1029/2018JB015872.

Mitchell, J. K., and Soga, K. (2005*). Fundamentals of soil behavior* (Vol. 3, p. USA). New York: John Wiley & Sons.

Okkels, N. (2019). Modern guidelines for classification of fine soils. *In Geotechnical engineering, foundation of the future conference proceedings.* The Icelandic Geotechnical Society. https://doi.org/10.32075/17ECSMGE-2019-0651.

Park, J., and Santamarina, J. C. (2017). Revised soil classification system for coarse-fine mixtures. *Journal of Geotechnical and Geoenvironmental Engineering*, Vol. 143(8), 04017039. https://doi.org/10.1061/(ASCE)GT.1943-5606.0001705.

Rezaei, M., Ajalloeian, R., and Ghafoori, M. (2012). Geotechnical properties of problematic soils emphasis on collapsible cases. *International Journal of Geosciences*, 3(1), 105-110. http://doi.org/10.4236/ijg.2012.31012.

Santamarina, J.C., Klein, K.A., Wang, Y.H., and Prencke, E., 2002. Specific surface: determination and relevance. *Canadian Geotechnical Journal* Vol. 39, 233–241. https://doi.org/10.1139/t01-077.

Sridharan, A., and Prakash, K. (2000). Percussion and cone methods of determining the liquid limit of soils: controlling mechanisms. *Geotechnical Testing Journal*, Vol. 23(2), pp. 236-244, 236-244. https://doi.org/10.1520/GTJ11048J.

Verdín Reyes, B. A. (2022). Experimental application of porous rock structures to reduce soil expansion. Master's Thesis. Departamento de Investigación y Posgrado de la Facultad de Ingeniería de la Universidad Autónoma de Querétaro (in Spanish). http://ri-ng.uaq.mx/handle/123456789/3671.

Zepeda, J. A. (2004). *Mecánica de suelos no saturados*. Soc. Mex. Mecánica Suelos, AC, Universidad Autónoma de Querétaro (in Spanish).

Proceedings of the XVIII ECSMGE 2024
GEOTECHNICAL ENGINEERING CHALLENGES
TO MEET CURRENT AND EMERGING NEEDS OF SOCIETY
© 2024 the Authors
ISBN 978-1-032-54816-6
DOI 10.1201/9781003431749-229
Open Access: www.taylorfrancis.com, CC BY-NC-ND 4.0 license

ECSMGE 24
XVIII EUROPEAN CONFERENCE ON SOIL MECHANICS AND GEOTECHNICAL ENGINEERING

Rockburst conditions prediction based on a decision tree algorithm

Prédiction des conditions d'éclatement des rochers basée sur un algorithme d'arbre de décision

D. Owusu-Ansah*, J. Tinoco, J. Matos
Department of Civil Engineering/ISISE/ARISE/University of Minho, Guimaraes, Portugal

F. Lohrasb
Department of Mining Engineering/Isfahan University of Technology, Isfahan, Iran

**dominic@civil.uminho.pt*

ABSTRACT: This research article explores an innovative method for predicting rockbursts using Machine Learning (ML) algorithms. The study utilizes a decision tree (DT) algorithm and tests two distinct approaches: (1) utilizing a DT model for each rock type (DT-RT) and (2) developing a single DT model (Unique-DT) for all rock types. The dataset comprises 210 records from China, Canada, the United States, Japan, and Italy and includes five input variables for training and testing. The effectiveness of the DT models is compared to other ML algorithms, including Random Forest (RF) and Gradient Boosting (AdaboostM1). The results show that the Unique-DT model performs well and has an F1 score of 0.65 in predicting rockburst conditions. Although RF and AdaboostM1 with F1 (0.66) outperform the Unique-DT model slightly, the Unique-DT model is recommended due to its superior ease of use, effectiveness, and accuracy.

RÉSUMÉ: Cet article de recherche explore une méthode innovante pour prédire l'éclatement des roches à l'aide d'algorithmes d'apprentissage automatique. L'étude utilise un algorithme d'arbre de décision (DT) et teste deux approches distinctes: (1) l'utilisation d'un modèle DT pour chaque type de roche (DT-RT) et (2) le développement d'un modèle DT unique (Unique-DT) pour tous les types de roches. L'ensemble de données comprend 210 enregistrements provenant de Chine, du Canada, des États-Unis, du Japon et d'Italie et inclut cinq variables d'entrée pour la formation et les tests. L'efficacité des modèles DT est comparée à d'autres algorithmes de ML, notamment Random Forest (RF) et Gradient-Boosting (AdaboostM1). Les résultats montrent que le modèle Unique-DT est performant et a un score F1 de 0.65 pour prédire les conditions d'éboulement. Bien que RF et AdaboostM1 (F1 = 0.66) soient légèrement plus performants que le modèle Unique-DT, ce dernier est recommandé en raison de sa facilité d'utilisation, de son efficacité et de sa précision supérieure.

Keywords: Rockburst; decision tree; machine learning; metrics; prediction.

1 INTRODUCTION

Underground activities, such as mining, railway, and road constructions, are intricate geotechnical works. This complexity can be partly attributed to the limited understanding of the subsurface, which makes underground constructions challenging due to the variability of the geology. Although underground operations at depths of 2000 m have become increasingly common, and efforts have been made to perfect underground constructions, uncertainties still arise occasionally. These uncertainties can lead to the waste of resources such as time, money, and properties, and even loss of life. It is important to address these uncertainties in order to minimize risk and improve outcomes in underground construction. One such uncertainty is the instability of rock mass, caused by factors including the type of rock, its strength, and brittleness. External conditions also contribute to the instability of the rock mass (Askaripour et al., 2022; Meng et al., 2017; Owusu-Ansah et al., 2023). These include dynamic disturbances, the magnitude of in situ stresses, and the order of excavation (Owusu-Ansah et al., 2023).

Rockburst is regarded as a form of rock mass failure in deep excavations involving hard and brittle rocks subjected to high-stress conditions (Askaripour et al., 2022; Lu et al., 2018; Meng et al., 2017; Owusu-Ansah et al., 2023). Rockburst is defined as the sudden and intense movement, accompanied by rock failure, in underground spaces under high-stress conditions. It transpires due to overburdening the rock mass (unaltered, brittle rock) when the stresses exceed the material's compressive strength (Dietz et al., 2018; Kidybiński, 1981; Owusu-Ansah et al., 2023; Xu and

Yu, 2016). Since rockburst is an unforeseen phenomenon, it presents a range of issues including loss of life, property damage, and in some instances, financial and temporal setbacks. Therefore, comprehending this phenomenon and determining its triggers is critical to prevent such vulnerabilities. This paper applies a rockburst intensity or rockburst conditions (RBC) grading system, consisting of four predetermined classes built on rock displacement, damage, and failure characteristics, as demonstrated in Table 1 (Blake & Hedley, 2003; Liu et al., 2023; Owusu-Ansah et al., 2023; Russenes, 1974; Zhou et al., 2012, 2021). The prediction of rockburst mechanisms has been extensively researched over the years. Numerous authors have produced thoughtful and profound works that demonstrate successful outcomes.

Table 1. Classification of rockburst intensities.

Rockburst Condition	Failure Characteristics
None	No sound of rockburst and rockburst activities.
Light	The surrounding rock is deformed, cracked, or rib-spalled, there is a weak sound, and no ejection phenomenon.
Moderate	The surrounding rock is deformed and fractured, and there is a considerable number of rock chip ejections, loose and sudden destruction, accompanied by crisp cracking, and often presented in the local cavern of surrounding rock.
Strong	The surrounding rock is busted severely, and suddenly thrown out or ejected into the tunnel, accompanied by a strong burst and roaring sound, air spray, and storm phenomena, with continuity that rapidly expands to the deep, surrounding rock.

Recent studies on the application of Machine Learning (ML) algorithms for predicting rockburst have revealed notable effectiveness when given sets of input and output data from earlier rockburst cases. This success confirms their capability. Thus, the objective of this paper is to explore the use of decision trees (DT), a type of ML algorithm, to determine rockburst conditions in diverse rock types. The objective is to create a distinctive model that can competently forecast rockburst conditions, irrespective of the type of rock. Two decision tree-based methods have been developed and assessed using performance metrics. Moreover, ML algorithms, specifically Random Forest (RF) and AdaBoostM1, are used for comparison (Owusu-Ansah et al., 2023). The study relies on a rockburst dataset and a pre-defined four-level classification scale (see Table 1).

2 METHODOLOGY

The decision tree is an ML algorithm used for both classification and regression tasks. It is a tree-like model, where each internal node represents a test on an attribute, each branch represents the outcome of the test, and each leaf node represents a class label or a numeric value. The algorithm works by recursively splitting the data based on the most important attribute at each level of the tree, thus forming a decision path from the root of the leaf node.

This paper focuses on the implementation of decision trees (J48) with a nominal classification method. The R statistical environment, in conjunction with the Rweka package, is utilized to execute various algorithms throughout this study. A cross-validation technique with a K-fold value of 10 is implemented for validating the results.

Two decision tree approaches, DT-RT, and the Unique-DT, are utilized to forecast rockburst conditions. The former predicts rockburst conditions for each rock category using three distinct models, namely Igneous (IG), Metamorphic (MT), and Sedimentary (SD). The latter utilizes all datasets (210 occurrences) to predict rockburst conditions, thereby reducing analysis work and increasing accuracy. Both approaches aim to enhance the efficiency of the algorithm in predicting rockburst conditions. The alternative technique employs RF and AdaboostM1 algorithms to predict rockburst conditions by using a dataset that comprises 210 records. The goal is to create a comparison of performance metrics with other approaches.

2.1 Data characterization and evaluation

The rockburst condition database comprises 210 records from studies conducted by multiple authors. Table 2 summarizes the data distribution by rock category.

Table 2. Rock category distribution.

Rock category	Number of records
Igneous	103
Metamorphic	58
Sedimentary	49

The database comprises five input variables used for predicting rockburst conditions: depth, elastic

energy index (EEI), Brittle Index BI — (σ_c/σ_t), Stress Index SI — (σ_θ/σ_c), and Rocktype exclusively for Unique-DT approach. With σ_c, σ_t, and σ_θ denoting uniaxial compressive strength, tensile strength and maximum tangential stress. To evaluate model performance, the metrics employed are F1-score (F1) and Accuracy (ACC). The F1-score is regarded as a superior metric for evaluating the classifier's performance when compared to the standard accuracy measure. Accuracy represents the percentage of correctly placed data points. In both cases, the closer the metric value is to one, the better the prediction. Furthermore, a sensitivity analysis (relative importance) (Cortez & Embrechts, 2013) was also performed on the two DT approaches. The aim was to identify the pertinent input variables that contribute to the prediction of rockburst conditions.

3 RESULTS AND DISCUSSIONS

The performance metrics for the models are presented in Table 3. The DT algorithm trained to predict metamorphic rock type exhibited the best F1 score (0.74) and accuracy (0.86), demonstrating superior performance compared to the trained model for sedimentary rock type, which performed the poorest. This difference may be ascribed to the intricate geological material and the scarcity of data.

Table 3. Metrics for Algorithms.

Algorithms	**Metrics**	
	F1	**ACC**
DT-IG	0.62	0.81
DT-MT	**0.74**	**0.86**
DT-SD	0.35	0.72
Unique-DT	*0.65*	*0.82*
RF	*0.66*	*0.83*
AdaboostM1	*0.66*	*0.82*

NB.: Best Value in Bold and Italics are comparison values

The Unique-DT model, which covers all rock types, exhibited promising performance with an F1 score of 0.65 and an accuracy of 0.82. It must be emphasized that the two other DT-RT models (for IG and SD prediction) demonstrated poorer performances than the Unique-DT. Additionally, when comparing the performance metrics of RF and AdaboostM1, they were found to be similar to the Unique-DT, with RF showing a slight advantage based on ACC metric. The study indicates that the Unique-DT model presents a viable approach over other ML algorithms for predicting rockburst conditions.

Figure 1 summarizes the relative importance of model attribute, illustrating that the elastic energy index (EEI), with a percentage of 36.13%, has the greatest impact on the Unique-DT model. Additionally, Depth (25.84%), Brittle index (BI = 16.13%), and Stress Index (SI = 13.85%) are other input variables with a significant impact in rockburst prediction. The influence of the variables on rockburst due to the rock type varies among the three DT-RT models. The DT-RT model's significance in sedimentary research highlights EEI (43.01%) as the primary factor, followed by Depth (21.19%), BI (18.71%), and SI (17.09%). Similarly, the IG and MT models prioritize BI (27.37%) and SI (32.21%), respectively, with EEI ranking second in importance for both.

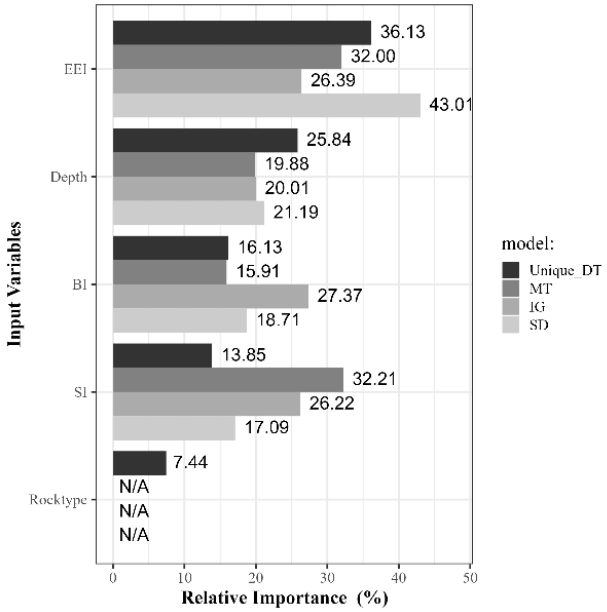

Figure 1. The relative importance of the two DT approaches for predicting rockburst condition.

These findings are consistent with previous studies on predicting rockburst conditions, stressing the significance of accurately identifying underlying factors by closely examining input data. It is worth noting that all models prioritize the elastic energy index (EEI), which aligns with the method presented by Owusu-Ansah et al. (2023) and Xu and Yu (2016) for predicting rockburst based on this index.

4 CONCLUSIONS

This paper proposes a novel model integrating rock type datasets to predict rockburst conditions using Machine Learning (ML) algorithms such as Decision Tree, Random Forest (RF), and AdaboostM1. Training and testing were conducted on a dataset comprising

210 records with 5 input variables, revealing that the Unique-DT model outperforms individual DT models for each rock type (DT-RT), achieving a promising F1 score of 0.65. RF and AdaboostM1 slightly outperformed Unique-DT with F1 scores of 0.66.

However, due to its simplicity and effectiveness, the unique-DT model is advised for rockburst prediction.

Based on this work, some future research should concentrate on improving the proficiency of ML models. Two viable approaches to explore are feature engineering which examine the formation of new features, or the transformation of existing features, to better capture the underlying patterns in rockburst conditions and hybrid models that integrate data-driven ML approaches with physics-based models. These hybrid models have the potential to improve prediction accuracy by leveraging the strengths of both approaches.

To summarise, this study highlights the potential of machine learning algorithms, specifically decision trees, in forecasting rockburst conditions by taking into account variables such as depth, elastic energy index, and rock strength parameters. Future research should focus on further enhancing the performance of machine learning models in this area.

ACKNOWLEDGEMENTS

This work was partly financed by FCT / MCTES through national funds (PIDDAC) under the R&D Unit Institute for Sustainability and Innovation in Structural Engineering (ISISE), under reference UIDB / 04029/2020 (doi.org/10.54499/UIDB/04029/2020), and under the Associate Laboratory Advanced Production and Intelligent Systems ARISE under reference LA/P/0112/2020.This work was also carried out under the "HILLS-AI" Project, by the "Tecminho-Spotlite" Consortium.

REFERENCES

Askaripour, M., Saeidi, A., Rouleau, A., & Mercier-Langevin, P. (2022). Rockburst in underground excavations: A review of mechanism, classification, and prediction methods. *Underground Space*, 7(4), 577–607, https://doi.org/10.1016/j.undsp.2021.11.008.

Blake, W., & Hedley, D. G. F. (2003). Rockbursts: Case Studies from North American Hard-rock Mines. Society for Mining, Metallurgy, and Exploration, Inc.: Littleton, CO, USA, 2003; ISBN 978-0-87335-232-1.

Cortez, P., & Embrechts, M. J. (2013). Using sensitivity analysis and visualization techniques to open black box data mining models. *Information Sciences*, 225, 1–17, https://doi.org/10.1016/j.ins.2012.10.039.

Dietz, M., Oremek, G. M., Groneberg, D. A., & Bendels, M. H. K. (2018). Was ist ein Gebirgsschlag? Zentralblatt für Arbeitsmedizin, *Arbeitsschutz und Ergonomie*, 68(1), 45–49, https://doi.org/10.1007/s40664-017-0215-z.

Kidybiński, A. (1981). Bursting liability indices of coal. *International Journal of Rock Mechanics and Mining Sciences & Geomechanics Abstracts*, 18(4), 295–304, https://doi.org/10.1016/0148-9062(81)91194-3.

Liu, H.; Zhao, Xiao, P.; Yin, Y. Ensemble Tree Model for Long-Term Rockburst Prediction in Incomplete Datasets. Minerals 2023, 13, 103. https://doi.org/10.3390/min13010103.

Lu, C.-P., Liu, Y., Zhang, N., Zhao, T.-B., & Wang, H.-Y. (2018). In situ and experimental investigations of rockburst precursor and prevention induced by fault slip. *International Journal of Rock Mechanics and Mining Sciences*, 108,86-95, https://doi.org/10.1016/j.ijrmms.2018.06.002.

Meng, F., Zhou, H., Wang, Z., Zhang, L., Kong, L., Li, S., Zhang, C., & Hu, S. (2017). Experimental study of factors affecting fault slip rockburst in deeply buried hard rock tunnels. *Bulletin of Engineering Geology and the Environment*, 76(3), 1167–1182, https://doi.org/10.1007/s10064-016-0926-y.

Owusu-Ansah, D., Tinoco, J., Lohrasb, F., Martins, F., & Matos, J. (2023). A Decision Tree for Rockburst Conditions Prediction. *Applied Sciences*, 13(11), 6655. https://doi.org/10.3390/app13116655.

Russenes, B. F. (1974). *Analysis of rock spalling for tunnels in steep valley sides*, Master Thesis, Trondheim: Norwegian Institute of Technology.

Xu, S., and Yu, S. (2016). A New Prediction Method of Rockburst in Underground Engineering Based on Elastic Energy Index. 271–274, https://doi.org/10.2991/i3csee-16.2016.52.

Zhou, J., Guo, H., Koopialipoor, M., Jahed Armaghani, D., & Tahir, M. M. (2021). Investigating the effective parameters on the risk levels of rockburst phenomena by developing a hybrid heuristic algorithm. *Engineering with Computers*, 37(3), 1679–1694, https://doi.org/10.1007/s00366-019-00908-9.

Zhou, J., Li, X., & Shi, X. (2012). Long-term prediction model of rockburst in underground openings using heuristic algorithms and support vector machines. *Safety Science*, 50(4), 629–644. https://doi.org/10.1016/j.ssci.2011.08.065.

Proceedings of the XVIII ECSMGE 2024
GEOTECHNICAL ENGINEERING CHALLENGES
TO MEET CURRENT AND EMERGING NEEDS OF SOCIETY
© 2024 the Authors
ISBN 978-1-032-54816-6
DOI 10.1201/9781003431749-230
Open Access: www.taylorfrancis.com, CC BY-NC-ND 4.0 license

ECSMGE 24
XVIII EUROPEAN CONFERENCE ON SOIL MECHANICS AND GEOTECHNICAL ENGINEERING

Combining slope satellite image analysis and artificial intelligence algorithms for highway service level assessment

Combinaison de l'analyse d'images satellites de pente et d'algorithmes d'intelligence artificielle pour l'évaluation du niveau de service des autoroutes

D. Owusu-Ansah*, J. Tinoco, J. Matos
Department of Civil Engineering/ISISE/ARISE/University of Minho, Guimaraes, Portugal

R. Cabral
Spotlite, Coimbra, Portugal

**dominic@civil.uminho.pt*

ABSTRACT: The study proposes an integrated approach using Artificial Intelligence (AI), satellite imagery analysis, and Machine Learning (ML) to address the global challenge of slope instabilities. It emphasizes the importance of comprehensive risk assessment frameworks, particularly focusing on Early Warning Systems (EWS) and decision-making tools. By structuring risk assessment around the hazard-exposure-vulnerability-damage model, the study aims to provide a systematic approach to slope instability management, especially in transportation networks. Additionally, the research evaluates ML algorithms, namely, Multiple linear Regression (MR) and Artificial Neural Networks (ANN), for displacement prediction, highlighting their promising performance while identifying areas for refinement in data preprocessing and model optimization. MR and ANN models consistently achieved high performance, with determinant coefficient (R^2) values of 0.93. This indicates that the model can explain approximately 93% of the variance in the target variable, reflecting strong predictive capability. Despite minor variations in other metrics, such as Mean Absolute Error, Mean Squared Error, and Root Mean Squared Error, the R^2 values remained consistent, emphasizing the robustness of the model in predicting displacements.

RÉSUMÉ: L'étude propose une approche intégrée utilisant l'intelligence artificielle (IA), l'analyse de l'imagerie satellitaire et l'apprentissage automatique (ML) pour relever le défi mondial des instabilités de pente. Elle souligne l'importance de cadres d'évaluation des risques complets, en mettant particulièrement l'accent sur les systèmes d'alerte précoce (SAP) et les outils de prise de décision. En structurant l'évaluation des risques autour du modèle danger-exposition-vulnérabilité-dommages, l'étude vise à fournir une approche systématique de la gestion de l'instabilité des pentes, en particulier dans les réseaux de transport. En outre, la recherche évalue les algorithmes de ML, à savoir la régression linéaire multiple (MR) et les réseaux de neurones artificiels (ANN), pour la prédiction des déplacements, mettant en évidence leurs performances prometteuses tout en identifiant les domaines à affiner dans le prétraitement des données et l'optimisation du modèle. Les modèles MR et ANN ont constamment atteint des performances élevées, avec des valeurs de coefficient déterminant (R^2) de 0,93. Cela indique que les modèles peuvent expliquer environ 93% de la variance de la variable cible, ce qui témoigne d'une forte capacité de prédiction. Malgré des variations mineures dans d'autres mesures, telles que l'erreur absolue moyenne, l'erreur quadratique moyenne et l'erreur quadratique moyenne racine, les valeurs R^2 sont restées cohérentes, soulignant la robustesse des modèles dans la prédiction des déplacements.

Keywords: Slope instability; artificial intelligence.

1 BACKGROUND

Slope instabilities, involving both natural and human-induced processes that alter slope shape, composition, or stability, give rise to a variety of potentially disastrous outcomes, including landslides, debris flow, rock falls, and avalanches (Casagli et al., 2016; Stavrou et al., 2011). These events pose significant threats to individuals, infrastructure, and the environment. Addressing these risks requires ongoing monitoring and the implementation of risk reduction measures. Various methodologies, including remote sensing techniques and Machine Learning (ML), have been explored to comprehend and mitigate slope instabilities (Casagli et al., 2016, 2023; Hammar-Klose & Thieler, 2001; Kuhn & Prüfer, 2014; Mihalić et al., 2015; Nhu et al., 2020; Owusu-Ansah, 2020; Segoni et al., 2018; Stanchev et al., 2013). This work

uses ML algorithms to develop predictive models for slope movement detection and stability level classification. The goal is to optimize these models to predict slope movement and classify stability levels accurately. Integrating satellite image analysis and AI algorithms offers promising opportunities for automating processes and enhancing decision-making in slope instability monitoring and risk assessment, addressing the urgent need for effective disaster risk reduction frameworks.

2 METHODOLOGY

The proposed framework integrates AI with satellite imagery to assess highway service levels by utilizing ML to detect slope movements and categorize them into four classes (A-D), with A representing the lowest risk and D indicating the most unstable conditions, through analysis of Interferometric Synthetic Aperture Radar (InSAR) data.

This framework specifically focuses on developing predictive models capable of detecting slope movements using InSAR data, which captures vertical and horizontal displacements on both road infrastructure and surrounding slopes. The data is segregated into two parts: one depicting displacements on the road infrastructure and the other showcasing displacements on slopes adjacent to it. This study particularly concentrates on the vertical displacements observed on the slopes, deliberately excluding other data sources to minimize noise.

The source dataset encompasses 5079 records of displacement values and dates spanning a 7-year period (2016-2023). To streamline the exploration of this dataset, a five-moving window technique is employed to transform it into a new dataset (training dataset) comprising five columns. This curated dataset is more manageable for analysis and serves as the foundation for model training. Table 1 and

Table *2* delineate the step-by-step process involved in processing the source dataset into the training dataset.

This report outlines an experiment for predicting slope movement, where data from the last four slope movements, specifically vertical displacement measurements, were condidered as inputs to forecast the subsequent movement (Next stage).

Table *2* illustrates the sampling strategy for the training data, providing insight into the methodology employed for model training and prediction.

Table 1. Sample of the source dataset (InSAR vertical displacements).

Date	PID1	PID2	PID3	PID4	PID5	PID6
04/10/2016	0	0	0	0	0	0
16/10/2016	2.65	3.08	1.72	1.18	0.55	1.9
28/10/2016	-1.91	-1.32	-1.77	-2.78	-2.5	-1.13
09/11/2016	-1.73	-1.58	-2.88	-3.44	-2.94	-2.02
21/11/2016	-8.23	-8.25	-9.58	-9.71	-8.5	-6.38
03/12/2016	-5.01	-4.22	-5.29	-6.28	-6.9	-5.69

Table 2. Sample of the new dataset (training dataset) produced by a sliding window of five.

FID	stage 1	stage 2	stage 3	stage 4	Next stage (Output)
1	0	2.65	-1.91	-1.73	-8.23
1	2.65	-1.91	-1.73	-8.23	-5.01
2	0	3.08	-1.32	-1.58	-8.25
2	3.08	-1.32	-1.58	-8.25	-4.22
3	0	1.72	-1.77	-2.88	-9.58
3	1.72	-1.77	-2.88	-9.58	-5.29
4	0	1.18	-2.78	-3.44	-9.71
4	1.18	-2.78	-3.44	-9.71	-6.28
5	0	0.55	-2.5	-2.94	-8.5
5	0.55	-2.5	-2.94	-8.5	-6.9
6	0	1.9	-1.13	-2.02	-6.38
6	1.9	-1.13	-2.02	-6.38	-5.69

2.1 Machine learning algorithms

The present study employs a data-driven approach to forecast displacements, utilizing two ML algorithms, namely Artificial Neural Network (ANN) and Multilinear Regression (MR). These algorithms were executed in the R statistical environment (Venables et al., 2024), employing the rminer package (Cortez, 2010). Under both algorithms, cross-validation (5-fold) was implemented for training and validation purposes.

The entire procedure was repeated five times (5 runs) for generalization.

2.2 Model evaluation

The complexity of ML algorithms poses a significant challenge, which can be addressed by evaluating the algorithms based on three primary criteria: accuracy, computational efficiency, and interpretability (Owusu-Ansah et al., 2022). To ensure accuracy, a set of metrics such as Mean Absolute Error (MAE), Mean Square Error (MSE), Root Mean Square Error

(RMSE), and determination Coefficient (R^2) are considered.

The smaller or closer MAE, MSE, and RMSE are to zero, the higher the accuracy of the predictive model. Similarly, a higher R^2 value indicates greater accuracy of the model. These metrics play a crucial role in assessing the algorithm's efficacy, so their importance must be recognized.

3 RESULTS

This section summarizes the results obtained from predicting the next stage using ANN and MR algorithms. The focus is on accuracy metrics, with *Table 3* presenting performance metrics for both iterations and algorithms. R^2 indicates a strong correlation, while low values of MAE, MSE, and RMSE emphasize their usefulness in predicting the next stage based on the preceding four stages and time intervals.

This study analyzed the correlation between experimental results and predicted outcomes using two ML algorithms. The correlation analysis, shown in Figure 1, indicated a promising overall performance. Metric values in Table 3 indicate that the results for both ML models perform well and similarly.

Accordingly, additional data pre-processing and the inclusion of other variables are being considered in further experiments aiming to develop more robust models.

Table 3. Models performance evaluations based on MAE, MSE, RMSE, and R^2.

Models	MAE	MSE	RMSE	R^2
MR (stage-MR)	2.19	8.14	2.85	0.93
ANN (stage-ANN)	2.19	8.14	2.85	0.93

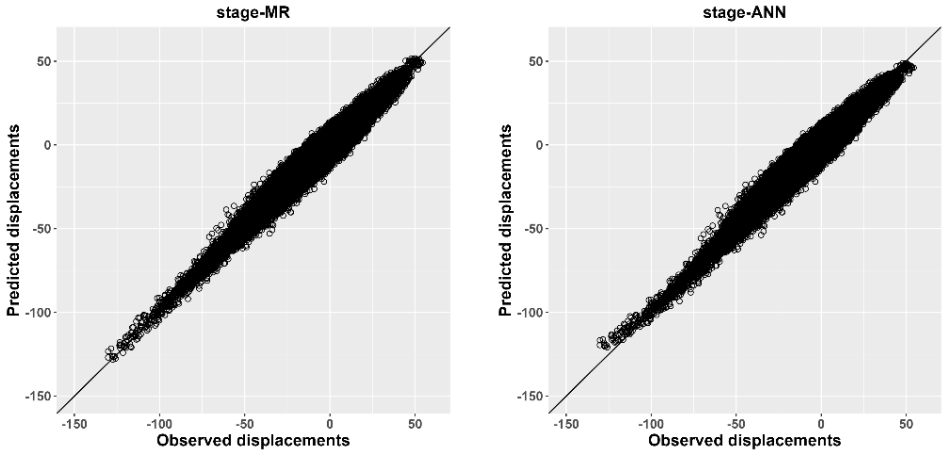

a) *b)*

Figure 1. Scatterplot of the proposed models: a) MR; b) ANN.

4 REMARKS

This study offers valuable insights into the predictive performance of Machine Learning (ML) algorithms for displacements. While the overall analysis shows promising results, there is a need for further refinement in data preprocessing techniques and model optimization to enhance prediction accuracy and reliability.

Correlation analysis, illustrated in Figure 1, reveals consistent and favorable performance trends for both ML algorithms, underscoring their effectiveness. The comparable metric values between the two algorithms suggest consistent performance.

Overall, this study contributes to advancing our understanding of ML-based displacement prediction and suggests avenues for future research, such as exploring additional input variables and refining model optimization techniques, to improve predictive outcomes for practical applications across various domains.

ACKNOWLEDGEMENTS

This work was partly financed by FCT / MCTES through national funds (PIDDAC) under the R&D Unit Institute for Sustainability and Innovation in Structural Engineering (ISISE), under reference UIDB / 04029/2020 (doi.org/10.54499/UIDB/04029/2020), and under the Associate Laboratory Advanced Production and Intelligent Systems ARISE under reference LA/P/0112/2020.This work was also carried out under the "HILLS-AI" Project, by the "Tecminho-Spotlite" Consortium.

REFERENCES

Casagli, N., Cigna, F., Bianchini, S., Hölbling, D., Füreder, P., Righini, G., Del Contse, S., Friedl, B., Schneiderbauer, S., Iasio, C., Vlcko, J., Greif, V., Proske, H., Granica, K., Falco, S., Lozzi, S., Mora, O., Arnaud, A., Novali, F., & Bianchi, M. (2016). Landslide mapping and monitoring by using radar and optical remote sensing: Examples from the EC-FP7 project SAFER. Remote Sensing Applications: Society and Environment, 4, 92–108. https://doi.org/10.1016/j.rsase.2016.07.001

Casagli, N., Intrieri, E., Tofani, V., Gigli, G., & Raspini, F. (2023). Landslide detection, monitoring and prediction with remote-sensing techniques. Nature Reviews Earth & Environment, 4(1), 51–64. https://doi.org/10.1038/s43017-022-00373-x

Cortez, P. (2010). Data Mining with Neural Networks and Support Vector Machines Using the R/rminer Tool. In P. Perner (Ed.), Advances in Data Mining. Applications and Theoretical Aspects (Vol. 6171, pp. 572–583). Springer Berlin Heidelberg. https://doi.org/10.1007/978-3-642-14400-4_44

Hammar-Klose, E. S., & Thieler, E. R. (2001). Coastal vulnerability to sea-level rise: A preliminary database for the U.S. Atlantic, Pacific, and Gulf of Mexico coasts. U.S Geological Survey Publication. https://doi.org/10.3133/ds68

Kuhn, D., & Prüfer, S. (2014). Coastal cliff monitoring and analysis of mass wasting processes with the application of terrestrial laser scanning: A case study of Rügen, Germany. Geomorphology, 213, 153–165. https://doi.org/10.1016/j.geomorph.2014.01.005

Mihalić Arbanas, S., & Arbanas, Z. (2015). Landslides: A Guide to Researching Landslide Phenomena and Processes (pp. 474–510). https://doi.org/10.4018/978-1-4666-7336-6

Nhu, V.-H., Mohammadi, A., Shahabi, H., Ahmad, B. B., Al-Ansari, N., Shirzadi, A., Geertsema, M., R. Kress, V., Karimzadeh, S., Valizadeh Kamran, K., Chen, W., & Nguyen, H. (2020). Landslide Detection and Susceptibility Modeling on Cameron Highlands (Malaysia): A Comparison between Random Forest, Logistic Regression and Logistic Model Tree Algorithms. Forests, 11(8), Article 8. https://doi.org/10.3390/f11080830

Owusu-Ansah, D. (2020). *The Use of Fibre Optic Sensors for Landslide Stability Monitoring: Experimetnal Tests for the Detection Of Acoustic Emissions,* Master Thesis, Politecnico Di Milano, Milan, Italy.

Owusu-Ansah, D., Tinoco, J., Correia, A. A. S., & Oliveira, P. J. V. (2022). Prediction of Elastic Modulus for Fibre-Reinforced Soil-Cement Mixtures: A Machine Learning Approach. Applied Sciences, 12(17), 8540. https://doi.org/10.3390/app12178540

Segoni, S., Piciullo, L., & Gariano, S. L. (2018). Preface: Landslide early warning systems: monitoring systems, rainfall thresholds, warning models, performance evaluation and risk perception. Natural Hazards and Earth System Sciences, 18(12), 3179–3186. https://doi.org/10.5194/nhess-18-3179-2018

Stanchev, H., Young, R., & Stancheva, M. (2013). Integrating GIS and high resolution orthophoto images for the development of a geomorphic shoreline classification and risk assessment—A case study of cliff/bluff erosion along the Bulgarian coast. Journal of Coastal Conservation, 17(4), 719–728. https://doi.org/10.1007/s11852-013-0271-2

Stavrou, A., Lawrence, J. A., Mortimore, R. N., & Murphy, W. (2011). A geotechnical and GIS based method for evaluating risk exposition along coastal cliff environments: A case study of the chalk cliffs of southern England. Natural Hazards and Earth System Sciences, 11(11), 2997–3011. https://doi.org/10.5194/nhess-11-2997-2011

Venables, W. N., Smith, D. M., & R core Team. (2024). An Introduction to R. 4.40, 103.

Proceedings of the XVIII ECSMGE 2024
GEOTECHNICAL ENGINEERING CHALLENGES
TO MEET CURRENT AND EMERGING NEEDS OF SOCIETY
© 2024 the Authors
ISBN 978-1-032-54816-6
DOI 10.1201/9781003431749-231
Open Access: www.taylorfrancis.com, CC BY-NC-ND 4.0 license

ECSMGE 24
XVIII EUROPEAN CONFERENCE ON SOIL MECHANICS AND GEOTECHNICAL ENGINEERING

Stabilization of excavation slopes between km 0+000 and km 2+000 of the EN337, in the municipality of Vouzela

Stabilisation des pentes d´excavation entre le km 0+000 et le km 2+000 de l´EN337, dans la commune de Vouzela

F. Paulino*, E. Fernandes, A. Dinis
Geovia, S.A., Lisbon, Portugal

**fpaulino@geovia.pt*

ABSTRACT: With this paper it is intended to present a case study referring to the cut slopes that occur between the kilometric points 0+000 and 2+000 of the EN337 national road, whose stabilization is within the scope of the intervention foreseen for the infrastructures and municipal equipment which were affected by the great fire that occurred in Portugal's Centre region. This fire, which broke out in June 2017, affected around 75% of the area in the municipality of Vouzela, having burned around 85% of the forest area, causing 8 deaths, losses of more than 8 million euros in agriculture and 4,75 million euros in infrastructure and municipal equipment. The occurrence and characteristics of this type of fire was aggravated by the extreme phenomena (fire) associated with climate change. It is assumed that the elimination of the vegetation area had the immediate consequence of aggravating the phenomena of the local geological formations (fracturing), thus increasing the risk of rock falls onto the road.

RÉSUMÉ: Cette communication entend présenter une étude de cas de pentes coupées qui se produisent de long de 2 km de l´EN337, conformément à l´intervention prévue par les infrastructures et équipements municipaux touchés par le grand incendie dans la région Centre. Cet incendie, qui s´est déclaré en juin 2017, a touché environ 75% de la superficie de la commune de Vouzela, ayant brûlé environ 85% de la superficie forestière, causant 8 morts, des pertes de plus de 8 millions d´euros in infrastructures et équipements municipaux. La survenue et les caractéristiques de ce type d´incendie ont été aggravées par les phénomènes extrêmes liés au changement climatique. Il est supposé que la suppression de la zone de végétation a eu pour conséquence immédiate d´aggraver les phénomènes des formations géologiques locales, augmentant ainsi les risques de chutes de pierres sur la route.

Keywords: Slopes; fire; deaths; climate; risk; rehabilitation; rock fall.

1 INTRODUCTION

As a consequence of the large fire which occurred in the municipality of Vouzela in June 2017, and the deforestation that has followed, the existing slopes' vulnerability to the erosive processes was increased. Ultimately, this led to the decrease of the slopes' stability in the affected area which. This paper's case study corresponds to the EN337 cut slopes that are present between km 0+000 and 2+000, and it is based on the slope stabilization project elaborated by this paper's authors (Elsamex, 2019).

Based on surface recognition, it was found that the existing geology at the site essentially comprise granite rock with degrees of alteration varying essentially between slightly weathered to moderately weathered (W2) and moderately altered (W3) and slope deposits, formed by the alteration of the rock mass, chaos of boulders and topsoil.

By analysing the existing situation, it was verified the existence of zones of block chaos at different heights of the slope and areas of outcrop of the rock mass that were slightly weathered and highly jointed, giving rise to discontinuity planes unfavourable to stability.

In order to reduce the increased risk of falling rock blocks, stabilization solution were defined for it, which include measures to prevent falling rock blocks and consolidation of the rock mass also prevents rockfalls, namely:

- Controlled removal of rock blocks;
- Application of mortared stone wall;
- Application of rockbolts;
- Installation of triple torsion wire mesh (Figure1);
- Installation of HEA panels (High Energy Absorption Panel) (Figure 2).

2 GEOLOGY

According to the explanatory notice on sheet 17-A (Viseu) of the Geological Chart of Portugal, the area under study is characterized exclusively by the presence of magmatic rocks, more specifically by Hercynian granitoids. The identified granitoid facies was framed within the deformation features of the surrounding rocks, taking as a reference the 3rd phase of Hercynian deformation, with which the granites of the region are related. Therefore the granites present in EN337 are late to post-tectonic (relative to D3). In relation to mineralogical composition, they are considered as granites with 2 micas.



Figure 1. View of the slope showing the heavily fractured rock mass at a high elevation with potential for instability.

3 SURFACE RECOGNITION AND DESCRIPTION OF THE EXISTING SITUATION

In order to accurately describe the existing conditions, a geological survey was performed between the kilometric points 0+000 and 2+000 of the EN337 road. The referred survey concerned the cut slopes that are present on the right side of the road.

The weathering grade of the rock mass, according to what was observed, varies essentially between little altered (W2) and moderately altered (W3) along the slope.

Between km 0+950 and 0+980, the rock massif is visible only at a height of around 10m, in a sub vertical structure (Figure 1). The massif appears much fractured, with loose blocks of medium large size with potential for instability.

Between approximately km 1+020 and km 1+090, a scenario similar to the previous one was observed, with the difference that the outcrop of the granite outcrop is visible from area adjacent to the road, i.e., it emerges at a higher elevation, low, extending in height (Figure 2).

To support the work developed, a topographic survey was carried out using a drone. This allowed a perception not only of the position and size of the blocks, as well as, the elevation at which the rock blocks are located in relation to the EN337 (Figure 3).



Figure 2. Slope featuring loose blocks with kinematic potential.



Figure 3. General aerial view of the site under study.

4 STABILIZATION SOLUTIONS

The controlled removal of rock blocks becomes necessary due to different facts, namely:

- Proximity to the road;
- Location at great heights, allowing the gain of kinetic energy;
- Subvertical slope of the massif where the rock blocks are located;
- Degradation of local friction conditions at the base of the blocks, due to weather or fires.

The recommended solutions include measures to prevent the potential fall of blocks along the slope, particularly in areas where highly fractured granite emerges, and active measures to consolidate the slope in areas of the granite mass with unfavourable discontinuity planes.

The application of triple-twist metal mesh (Figure 4) was defined for areas of the granite massif that present simultaneously a low degree of alteration and a high degree of fracture, which could consequently imply the detachment of blocks of different dimensions and subsequent fall to the road.

The solution for applying HEA panels (Figure 5) was defined only for areas where the isolated removal of blocks is unfeasible, due to steeper slopes and more significant slope heights. This solution aims to maintain rock blocks of considerable size in their position.

With the purpose of consolidating rock masses in areas where unfavourable joint planes are present, it was recommended to install localised rockbolts in exposed granitic masses with a low weathering grade (Figure 6). With its application, it was intended to prevent further development of the existing failure's surfaces and therefore increase stability.

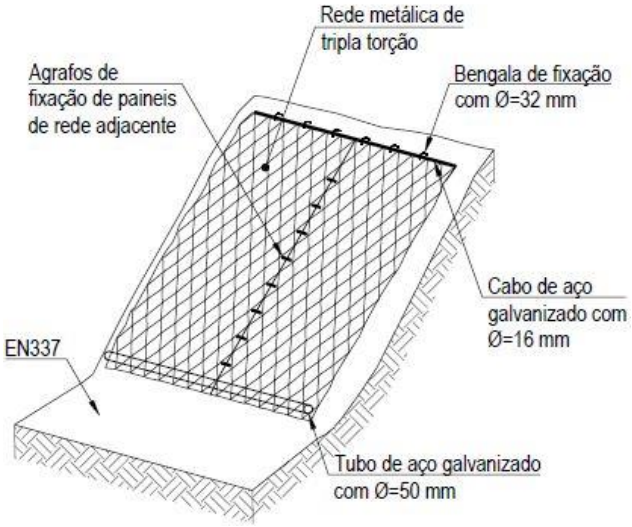

Figure 4. Triple twist wire mesh fastening diagram.

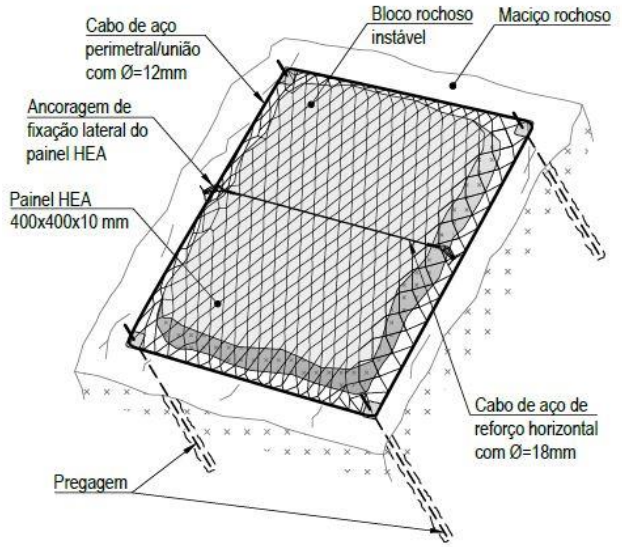

Figure 5. HEA panel fixing diagram.

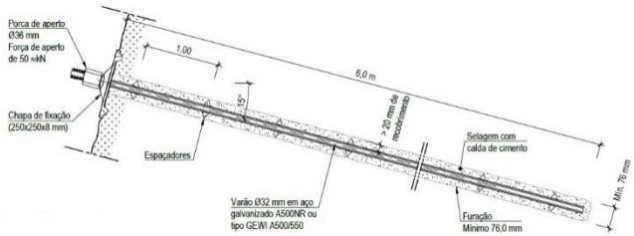

Figure 6. Rockbolt detail.

5 IMPLEMENTATION SOLUTIONS

Below, some photographs of the on-site works carried out within the scope of the solutions implemented are presented (see Figures 7 to 9).



Figure 7. Application of triple twist net and nailing in excavation slope.



Figure 8. Application of HEA panels and nailing in excavation slopes.



Figure 9. Application of punctual nailing in excavation slopes.

6 CONCLUSIONS

Following the large fire, which occurred in the municipality of Vouzela in June 2017, and the consequent deforestation, thus accelerating the erosion process and increasing the instability of slopes the need arose to carry out of the Execution Project for "Stabilization of Excavation Slopes of EN337 between km 0+000 and km 2+000".

In order to reduce the increased risk of falling rock blocks, stabilization solutions were defined, which include measures to prevent falling rock blocks and consolidate the rock mass, namely:

- Application of specific nails;
- Installation of metal mesh and triple twist;
- Installation of HEA panels (High Energy Absorption panel).

Triple wired mesh was applied in the most critical areas, whose locations comprised: i) Slopes that present clear signs of instability; ii) The steepest slopes and; iii) The higher slopes. In these areas, in addition to the triple wire mesh, it is also recommended to apply HEA panels whenever large and loose rock blocks are present.

ACKNOWLEDGEMENTS

The authors are grateful for the documentation support provided by municipality of Vouzela.

REFERENCES

Elsamex, S.A. (2019). Estabilização de Taludes de Escavação da EN337 entre o km 0+000 e o km 2+000, Lisboa, Portugal, 94 p.

Proceedings of the XVIII ECSMGE 2024
GEOTECHNICAL ENGINEERING CHALLENGES
TO MEET CURRENT AND EMERGING NEEDS OF SOCIETY
© 2024 the Authors
ISBN 978-1-032-54816-6
DOI 10.1201/9781003431749-232
Open Access: www.taylorfrancis.com, CC BY-NC-ND 4.0 license

ECSMGE 24
XVIII EUROPEAN CONFERENCE ON SOIL MECHANICS AND GEOTECHNICAL ENGINEERING

ReSist - A municipal policy to increase awareness on seismic risk

ReSist - Une politique municipale pour accroître la sensibilisation au risque sismique

C. Pinto*
Câmara Municipal de Lisboa, Lisbon, Portugal

M.A. Ferreira
IST/CERIS, Lisbon, Portugal

C. Almeida, M. Inácio, P. Pacheco, C. Pousada, C.S. Ferreira, A. Ferreira
Câmara Municipal de Lisboa, Lisbon, Portugal

**claudia.pinto@cm-lisboa.pt*

ABSTRACT: Lisbon has a dense urban occupation with more than half a million inhabitants, not accounting for the daily commutes of workers and students who enter the municipality, which increases this value up to 70%. Since most of the national economic and political decision-making centres are in Lisbon, the emergency response could be constrained in case of a high-impact event. The risk factor is further aggravated due to an old building stock. Considering this context, a municipal program was implemented to assess and promote seismic resilience. Within the scope of the ReSist framework, the City Council intends to carry out assessment campaigns aiming at achieving seismic resistance of the city's buildings and infrastructures. Implementing these targeted actions can accelerate the achievement of the United Nations 2030 Agenda for Sustainable Development, particularly the goal nr. 11 - to make cities and communities inclusive, safe, resilient, and sustainable, while improving people's well-being. Several studies and risk mitigation activities are being conducted by several action plans in different sectors, bringing together stakeholders from academic and research institutions, national administration entities, professional orders and associations, real estate, consultancy and insurance companies, and citizens. Dissemination strategies and workshops were also promoted, to raise awareness and prepare civil society for a seismic event.

RÉSUMÉ: Lisbonne présente une occupation urbaine dense, avec une population de plus d'un demi-million d'habitants, sans compter les déplacements quotidiens des travailleurs et des étudiants qui entrent dans la municipalité, augmentant ainsi cette valeur jusqu'à 70%. La plupart des centres de décision économique et politique nationaux se trouvent à Lisbonne. En cas d'événement à fort impact, la réponse d'urgence pourrait être entravée. Ce risque est exacerbé par un parc immobilier vieillissant. Dans ce contexte, un programme municipal a été lancé pour évaluer et promouvoir la résilience sismique. Dans le cadre du projet ReSist, le conseil municipal prévoit une évaluation rapide de la résistance sismique des bâtiments et infrastructures de la ville. La mise en œuvre de ces actions peut accélérer l'atteinte des objectifs de l'Agenda 2030 des Nations Unies pour le développement durable, en particulier l'objectif 11 de rendre les villes et les communautés inclusives, sûres, résilientes et durables, tout en améliorant le bien-être des habitants. Plusieurs études et mesures d'atténuation des risques sont menées dans le cadre de plans d'action et de formations impliquant divers secteurs, réunissant des acteurs issus d'établissements académiques, d'entités administratives centrales, d'ordres et d'associations professionnelles, d'entreprises immobilières, de cabinets de conseil et d'assurances, ainsi que des citoyens. Des stratégies de diffusion et des ateliers visant à sensibiliser et à préparer la société civile à un événement sismique ont également été promus.

Keywords: ReSist program; seismic resilience; retrofitting; inter-municipal communities.

1 INTRODUCTION

Lisbon's high exposure to active seismogenic sources, combined with the high population density in an urban context and the services located here, make the city extremely vulnerable to the impacts of earthquakes, also leading to a very high-risk factor.

It is recognized that the intense rehabilitation of buildings recorded over the past decade has improved the general conservation state of the city's buildings. Nonetheless, these might not have considered the necessity to maintain or reinforce the structure's resistance to damage during a near-future seismic event. Furthermore, according to the most recent

census data (INE, 2021), 60% of existing houses were built prior to seismic-resistant regulations, which coincidentally are in the most populated areas. In 1958, Portugal introduced its first design codes that explicitly included seismic provisions (RSCCS, 1958).

The context presented above led to the necessity of defining and applying a local strategy leading to the creation of the ReSist Program, a municipal program aiming at the promotion of seismic resilience to the private and municipal buildings and municipal urban infrastructures.

2 FRAMEWORK

The ReSist Program stems from the need to respond to the various programs and strategies of the city as part of a broader effort to promote Lisbon's seismic resilience.

Given the importance of the subjects approached by the program, in June of 2021 the Lisbon City Council unanimously approved it and set up a Project Team with the mission of implementing and monitoring the execution of the municipal program. In addition to the permanent members, the team has the support of the Advisory Structure (AS), the Technical-Scientific Council (TSC), and an Inter-municipal Technical Structure (ITS). The AS is composed by municipal technicians representing different services, while the TSC is composed by external entities or individuals with expertise in this domain, whose function will be the guidance and optimisation of the actions to be developed. The most recent addition to the project team was the establishment of the ITS (which is ongoing), aims to share knowledge and good practices between other municipalities through the intermunicipal communities.

2.1 ReSist Project main goals

The project is based in specific main goals materializes in 47 actions to be implemented, which will be presented generically throughout this article:

- Methodology development to define the criteria and tools to support preventive inspection and seismic vulnerability assessment to private and public buildings;
- Tools to support the prior control of urban planning operations and the subsequent execution of successive inspection actions;
- Submission of proposals for incentives or support, particularly at a technical level, to encourages owners to promote technical inspection in order to identify vulnerabilities and, therefore, adopt measures to buildings structural reinforcement;
- Development of information platform for monitoring purposes and to inform citizens;
- Development of methodologies and support tools that allow the assessment of the seismic vulnerability of the city's infrastructures (road network, artworks and sewage);

2.2 ReSist base vectors

These ReSist actions will be developed according to three base vectors (Figure 1).

2.2.1 Knowledge and modelling infrastructure

This vector frames the actions regarding acquisition, compilation, and data processing to define the most vulnerable areas in the city. A seismic resistance index of the private and public buildings and infrastructures will be proposed, as well as the definition of models and actions to enable the adoption of mitigation, prevention, and adaptation measures.

2.2.2 Society engagement

This vector comprises actions regarding the creation of municipal incentive programs aimed at involving private owners to provide technical or financial support in the inspection and reinforcement of the structural safety of private buildings.

Communication strategies and actions for the involvement of society are also included, as well as the participation in research and development projects.

The establishment of external partnerships will help guide the actions to be materialized.

2.2.3 Regulation and supervision

This vector integrates actions regarding the update of municipal regulations and territorial management instruments, procedure optimization, project quality evaluation, and the definition of standards that will regulate municipal inspection actions.

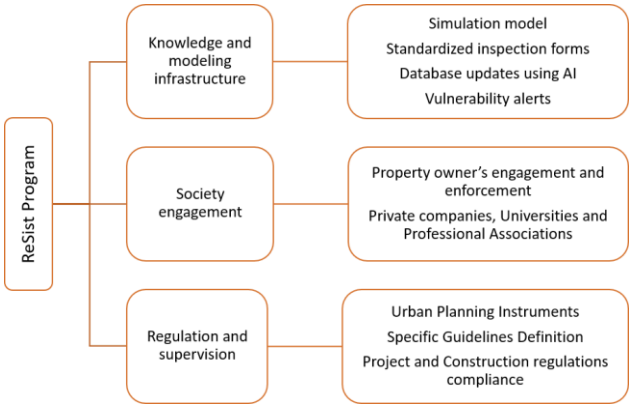

Figure 1. Base vectors of the ReSist Program.

3 RESULTS AND DEVELOPMENTS IN PROGRESS

3.1 Knowledge and modeling infrastructure

3.1.1 Development of seismic vulnerability assessment methodologies

The prompt assessment of the seismic vulnerability of the building stock was conducted by Instituto Superior Técnico (IST) and led to the production of a macroscale risk map for identify the most vulnerable areas and the early damage assessment. It also allowed the development of a methodology for assessing the seismic resistance of single buildings on a microscale approach. This methodology includes a visual inspection of the buildings to determine its typology, structural irregularities, and state of conservation. Posterior work will involve an information update about retrofitted buildings. The municipal building inspection program was conducted along 100 inspections realized in residential and equipment buildings, in close collaboration with Gebalis, an entity that manages municipal neighbourhoods. The sample selection considered the different architectural and structural typologies, intending to replicate the results obtained in the buildings evaluated by those with identical construction characteristics. (Figure 2). Using this methodology we were able to asses around 1600 buildings.

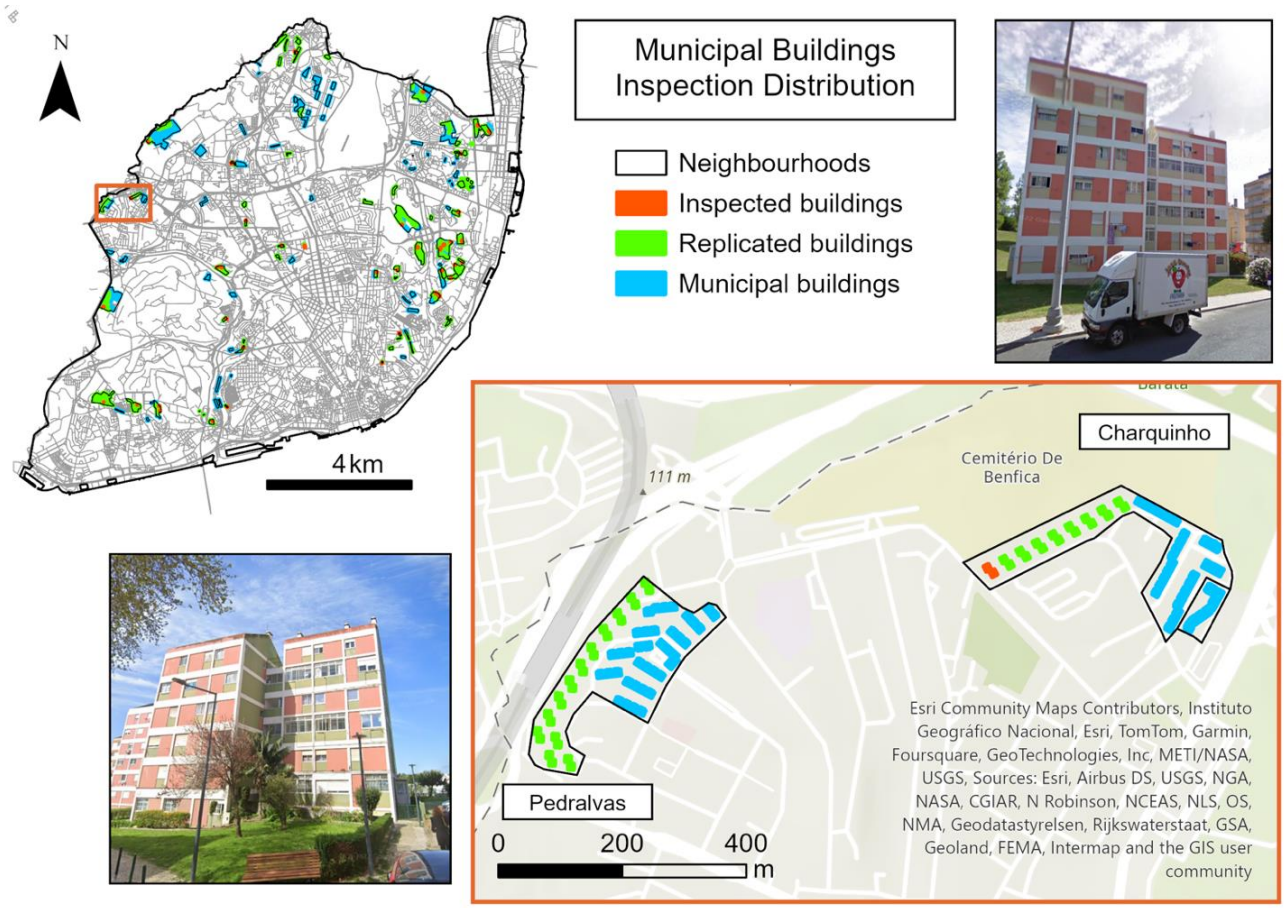

Figure 2. Map of Lisbon with distribution of municipal neighbourhoods. Example of building replication based on construction characteristics, in the Pedralvas neighbourhood based on an inspection made in the Charquinho neighbourhood.

The production and map updating, namely the geotechnical map of Lisbon and the natural and anthropic risks map available in Lisbon Master Plan, respectively, are taking place in parallel with other work, such as identifying complementary sources of information to supplement the gaps in the databases.

Other actions include a soil liquefaction and cyclic mobility study in partnership with the National Laboratory of Civil Engineering (LNEC), and the development of an application for managing inspection processes.

3.1.2 Development of a data management application

The development of a mobile application can standardize inspection surveys by allowing field technicians to do them based on observation. On the other hand, the LxReSist website will allow citizens to get relevant information about where they live according to the inputs they provide (Figure 3).

Process digitalization and incorporation into databases facilitates access to archived information.

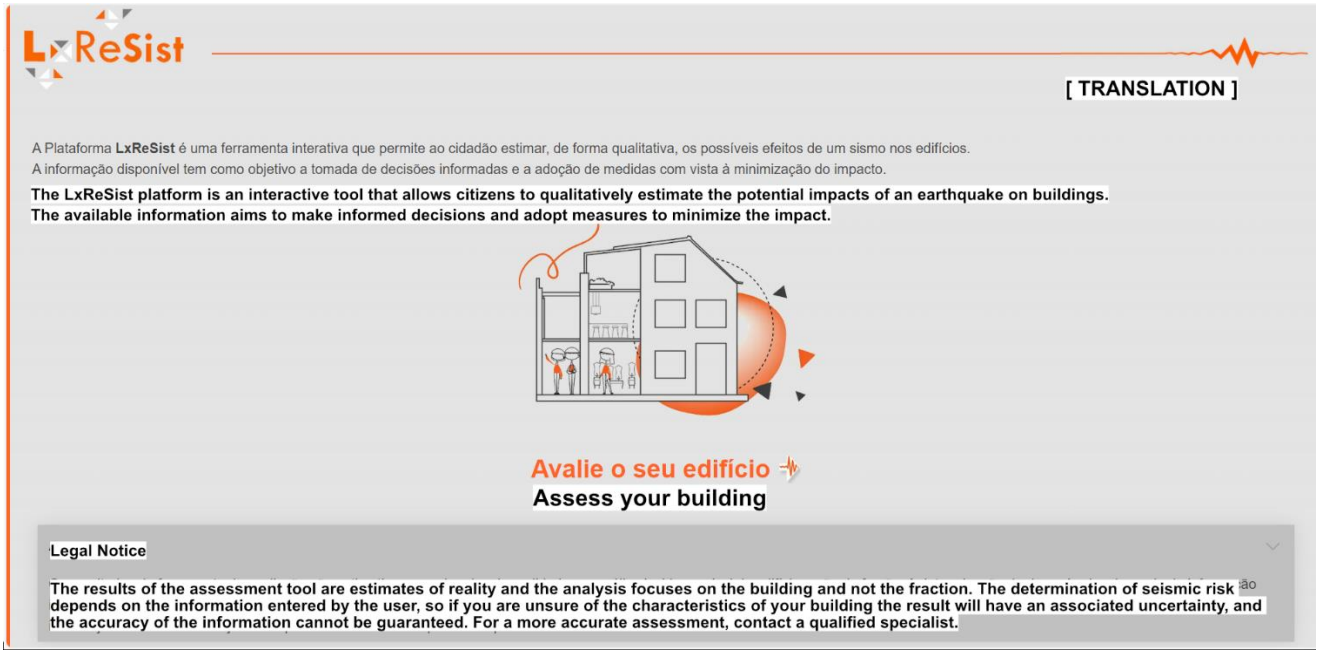

Figure 3. LxReSist platform front page.

3.2 Society engagement

Since its first public presentation in March 2022, the project team attended several events. The ReSist Journeys were developed and divided into three cycles: an Explanatory Cycle, a Capacitation Cycle, and a Training Cycle, with a total of 1183 participants. The explanatory and capacitation cycles reached diverse target audiences, while the training cycle was aimed at engineers, architects, designers and technicians in the inspection area. At the same time, some actions were carried out in schools, reaching a total of 2461 students (Figure 4), and others where 200 teachers participated.

Dissemination actions directed to the general population allowed the acquisition of skills that will lead to more efficient reactions when confronted with an earthquake, and these should be held periodically to sustain their desired effect. Concerning technical personnel, raising awareness of good practices will lead to the definition of better projects and safer buildings, with the help of methodology guides in development. Still within the scope of sharing good practices, the involvement of other municipalities located in the regions north to east of Lisbon and south of the Tagus basin is of great significance for everyone involved.



Figure 4. Actions developed in schools.

Communication strategies involved the production of several materials such as emergency kits for the students, roll-ups, flyers, as well as short and informative videos. Other dissemination and training actions are being developed, and the “Do it yourself” initiative is under expansion to raise public awareness (Figure 5).

As part of the intervention programs, the feasibility of installing gas seismic valves in new constructions is under review in partnership with the Gas Technological Institute (ITG) and General Direction of Energy and Geology (DGEG).



Figure 5. Flyer developed as part of the "Do it yourself" program. Adaptation of the original Portuguese flyer to show the icons designed and the main titles.

3.3 Regulation and supervision

In the context of standard development, a proposal for the structure and content to be included in the seismic vulnerability assessment report (RAVS) was prepared, and a procedural flow was developed to support urban management. In April 2023, the delivery of the RAVS (Figure 6) was introduced during the approval phase of the Architectural Project to ensure that structural safety is considered at an early stage of the urban licensing process.

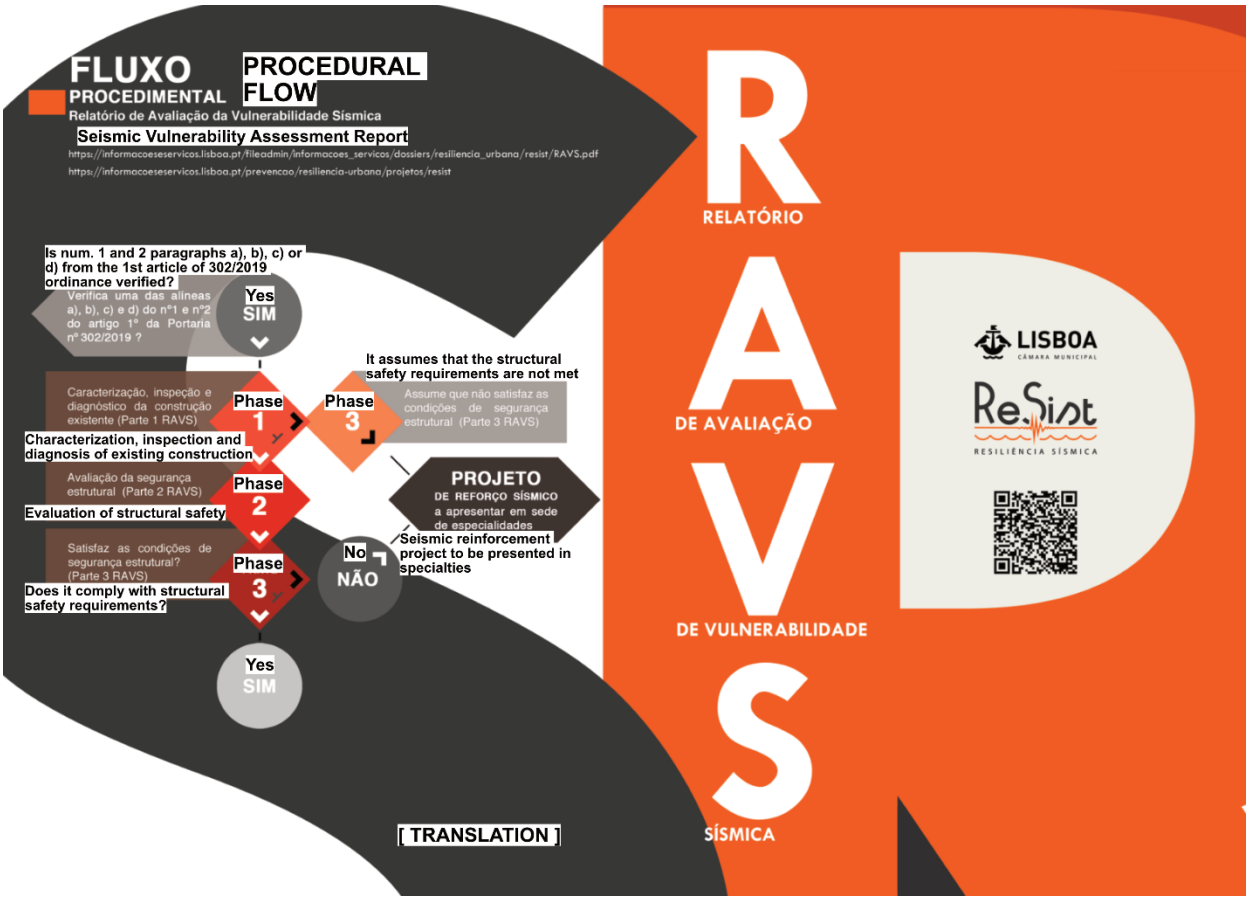

Figure 6. Seismic vulnerability assessment report: application and procedural flow (translation).

The regulation of the occupation of priority road axes and the operationalization of emergency plans are being developed with the Municipal Civil Protection Service and the Fire Department (RSB). To assess the viability and maintenance of the functionality of the road axes identified in the emergency plans, considering the collapse of the building stock after an earthquake, the development of a building collapse model (ÉRRE LRB, 2022), was contracted which will later be crossed with the sewage infrastructures. This measure also aims to identify the axes of access roads to critical infrastructures where seismic reinforcement intervention should be prioritized. The results will also lead to the definition of evacuation routes and definition of meeting points for population, serving as a support tool for planning actions.

Measures to be implemented in territorial management instruments require specific standards to be included in their regulation, accessible through the "Planning a Resilient City" guide.

4 CONCLUSIONS

The program's implementation relies on a governance model that emphasizes centralized management and coordination, with the ability to facilitate communication between municipal organic units, leading to flexibility and effectiveness in management. It combines technical knowledge with political and social engagement, appropriate regulation, incentive allocation, and technical support, which materialize the three fundamental aspects of the program.

ACKNOWLEDGEMENTS

The project presented in this article is grateful for the support provided by the partners and their availability to cooperate whenever required by the project team. Mónica Amaral Ferreira is grateful for the Foundation for Science and Technology's support through funding UIDB/04625/2020 from the research unit CERIS.

REFERENCES

ÉRRE LRB. (2022). Modelação do colapso do parque edificado em caso de sismo – Programa ReSist. Project Final Report. Braga, Portugal, LRB.RF.001.2022.CML01 (Modeling building collapse in an earthquake event - ReSist Programme in Portuguese).

INE (2021). Instituto Nacional de Estatística | Statistics Portugal CENSOS 2021, Available at: www.ine.pt, accessed: 21/09/23.

RSCCS (1958). Regulamento de Segurança das Construções Contra Sismos: Decreto-Lei nº41658, Imprensa Nacional, Lisboa, Portugal (Regulations for Building Safety Against Earthquakes: Decree-Law no. 41658 in Portuguese).

Proceedings of the XVIII ECSMGE 2024
GEOTECHNICAL ENGINEERING CHALLENGES
TO MEET CURRENT AND EMERGING NEEDS OF SOCIETY
© 2024 the Authors
ISBN 978-1-032-54816-6
DOI 10.1201/9781003431749-233
Open Access: www.taylorfrancis.com, CC BY-NC-ND 4.0 license

ECSMGE 24
XVIII EUROPEAN CONFERENCE ON SOIL MECHANICS AND GEOTECHNICAL ENGINEERING

The Citizens Observatories as a tool to manage geohazards. Lisbon Multihazards CO case study

Les Observatoires Citoyens comme outil de gestion des géorisques. Étude de cas de le Observatoire Multirisques de Lisbonne

C. Pinto*, A. Frias, P. Leonardo, C.S. Oliveira, M. Inácio
Lisbon Municipality, Lisbon, Portugal

R. Carrilho Gomes, M. Ferreira
Instituto Superior Técnico, University of Lisbon, Lisbon, Portugal

**claudia.pinto@cm-lisboa.pt*

ABSTRACT: As part of the Lisbon Multihazards Citizens Observatory, which is integrated in the AGEO Project - Platform for Atlantic Geohazard Risk Management, Lisbon Municipality has developed a platform to receive information by citizens - Citizen Observatory. The platform's interface, aiming to simplify the report, is based on graphic content and uses simple language, enabling ordinary citizens to give information about situations related with geotechnical risk in Lisbon. This solution allows citizens to play an active role in risk management systems and facilitates the monitoring of situations in which Lisbon Municipality technicians have increased difficulties due to lack of access. Ultimately, it allows Lisbon Municipality to anticipate problems that may arise in some parts of the city, such as settlements in buildings, enabling a proactive response and not a reactive one, as it happens today. In addition to the platform, educational contents were also developed aiming to raise population's awareness to geological risks, allowing the implementation of preventive measures.

RÉSUMÉ: Dans le cadre de l'Observatoire Citoyen Multirisques de Lisbonne, intégré à la Plateforme AGEO pour la Gestion du Risque Géohazard Atlantique, la municipalité de Lisbonne a développé une plateforme pour recevoir des informations des citoyens - l'Observatoire Citoyen. L'interface de la plateforme, visait à simplifier le rapport, est basé sur un contenu graphique et utilise un langage simple, permettant aux citoyens de donner des informations sur des situations liées au risque géotechnique à Lisbonne. Cette solution permettra aux citoyens de jouer un rôle actif dans les systèmes de gestion des risques et facilitera le suivi des situations où les techniciens de la Municipalité de Lisbonne rencontrent des difficultés accrues en raison du manque d'accès. En fin de compte, cet outil permettra à la Municipalité d'anticiper les problèmes qui pourraient survenir dans certaines parties de la ville, comme les affaissements dans immeubles, permettrant une réponse proactive et non réactive, comme c'est le cas aujourd'hui. En plus de la plateforme, des contenus pédagogiques ont également été développés visant à sensibiliser la population aux risques géologiques permettant la mise en œuvre de mesures préventives.

Keywords: Citizens observatory; geotechnical risk; educational contents; AGEO app.

1 INTRODUCTION

The Atlantic region is exposed to a range of low-probability/high-impact events and various hazard risk scenarios, which, due to the low likelihood of occurrence and/or the high cost of mitigating actions, lack the level of preparation for effective monitoring and response. It is in this context that the AGEO Project emerges. The aim was to implement several citizen observatories pilots aiming to test a new form of engagement between civil society and local authorities for geohazards-related local capacity building, also encouraging the local use of innovative Earth observation products and services provided by European data infrastructures.

Lisbon is located at the confluence of the Tagus River with the Atlantic Ocean, which gives the city a prominent geostrategic position, but also a high exposure to natural and climatic hazards, such as earthquakes, tsunamis, coastal and urban floods, landslides, and an increasing occurrence of extreme weather events. The city presents a high population density and hosts most of the government and services buildings, which, in case of a disruptive event, could directly impact the decision chain. Many of these city buildings, as well as the infrastructures, are aged, so urban improvement is required to reduce the impact of natural phenomena.

Lisbon is already preparing for other threats by integrating responsive services which increase

efficiency, but developments are required to have a more effective planning for larger, more severe events brought on by geohazards and climate changes. Considering this, it is fundamental to prepare the society to better respond to disasters and to guarantee that citizens, properly oriented towards a problem, can provide valuable data about a specific event in their area of residence and play an active role in risk management systems.

This was the proof of concept demonstrated in the Lisbon Pilot, managed by the Lisbon Municipality, on the behalf of AGEO Project, which addresses seismic risk, urban floods, landslides, and geotechnical risk, and has the particularity of being developed in an urban context.

One of the key objectives of a Citizen Observatory is to assure citizen engagement, building awareness and involving specific groups of stakeholders, from the common citizen to specialized professionals. To achieve that, it is critical to provide the appropriate means for active citizens to participate. One of the easiest ways is to create a direct information channel for citizens, allowing them to easily communicate events related with natural risks or geohazards, when they witness one. In the Lisbon pilot, this communication channel was materialized in a mobile application, considering the different levels of expertise and accessible to everyone by smartphone.

The stakeholder groups were selected considering their respective area of activity and ability to promote efficient monitoring of risk situations. In this case, local civil protection groups, municipal services (firefighters, sewage and pavement brigades), the scientific community, schools, senior university students and scout groups were involved.

Using the app, the citizens can report geohazards events easily and, in this way, play an active role in risk management systems, allowing for a more informed decision, and ultimately contribute to the implementation of proactive measures rather than reactive responses in terms of risk management.

2 COMMUNICATION STRATEGY / PUBLIC AWARENESS

Given that geological hazards constitute a type of risk whose concept not all people understand and are not aware of the relevance that such risks may have on their daily routine, it was considered necessary to develop an easy and direct communication strategy, which in this case began with the creation of the project's mascot, RISKA (Figure 1), a geologist who travels around the city of Lisbon, and became the communication identity of the Lisbon Pilot.



Figure 1. RISKA, the Lisbon pilot mascot.

Using RISKA, several communication materials were developed to support the work with stakeholders, particularly with educational community, such as flyers, posters, tray napkins with crosswords about AGEO and other games, bookmarks, rulers and keychains (Figure 2). These materials were distributed through several dissemination actions carried out in Lisbon schools, in which around 2500 students participated.



Figure 2. Educational Contents.

Aiming the engagement of the common citizen, a partnership with Delta Cafés (portuguese coffee company) was promoted, resulting in a campaign carried out to disseminate the AGEO Project through sugar packets distributed in the city of Lisbon (Figure 3). For this purpose, 10 layouts were developed regarding the risks managed by the Lisbon Pilot.



Figure 3. Two examples of sugar packets.

In addition to these materials, other contents were developed, including educational videos, in which RISKA explains, teaches and alerts to some of the daily problems that occur in the city, explaining how to prevent them and how to react in different situations. The videos are available on Youtube and at the Lisbon Municipality web page (https://informacoeseservicos.lisboa.pt/prevencao/resiliencia-urbana/projetos/ageo).

Given the diversity of the target audience, it was decided that communication on social media should be informal, explanatory, educational and with low

technical complexity, for easy understanding by the general population. Social networks, such as Facebook and Instagram, were widely used as communication platforms and more than 50 posts related to specific days were published during the Project (https://www.facebook.com/ageoatlantic; https://www.instagram.com/ageoatlantic).

3 LISBON AGEO APP

To assure citizen engagement and obtain as much data as possible, the Lisbon pilot developed a mobile application, accessible to everyone in every smartphone, available in iOS and Android formats, through which citizens can report situations related to geological risks, in particular earthquakes, landslides, floods, and geotechnical risk in the city of Lisbon, in a straightforward and standardized manner.

However, reporting geohazard events can be a tricky task. As the primary goal is to receive inputs from the biggest audience possible, the main target user is the regular citizen, that is, people with no technical expertise in the matters concerned. Still, it is expected that even a non-specialized citizen, if effectively directed, can provide meaningful and information about the witnessed events, allowing technical staff to analyse the reported data and to take better and informed decisions, even before visiting the site. This will optimize risk management systems and allow more informed decision-making, ultimately contributing to the implementation of proactive measures rather than reactive.

Taking these aspects into consideration, careful thought was put into the design of the geohazard reporting app, developing mock-ups of the app's user interface, and idealizing the user flow experience.

As the need for an easy, fast and low-cost implementation solution was evident, it was decided to use the technology available in Lisbon's spatial data infrastructure. Among the various applications available in the ESRI software, the ArcGis Survey 123 solution stood out, as it is free of access, it does not require any registration from the user and is accessible from the AppStore and Google Play. So, before using the AGEO application, citizens must install ArcGis Survey 123 on their mobile device, available on the Lisbon Municipality page.

3.1 Designing the user interface and application workflow

To provide a visual overview of the expected user interface for the report app, a set of mock-ups were developed. The layouts were designed focusing on the expected user experience and intending to provide an easy way to use and a visually attractive interface, with graphic buttons that facilitate the user's perception of the required information.

After installing the platform, the user has access to the interface. The main steps of the application workflow while reporting an event are:

A. Choosing the type of event to report.

In this step, the user is presented with a grid of graphic buttons representing the different types of events (Figure 4). An option of "Other events" was added, to facilitate the usage by those citizens who don't know which event to choose or are not comfortable in identifying the specific event type.

B. Taking photos of the event and providing some additional descriptive info.

C. Defining the location and date of the event and indicating the major elements at risk (people, animals and/or assets).

To define the location, the user can choose to use the device location info or, manually, pick the correct location in an interactive map available.

D. Reporting specific event information.

In this step, the user will be presented with distinct interfaces, according to the event type, helping the user provide meaningful information about the event.

Careful consideration was taken when defining the input interfaces for the user to provide information about the event, favouring self-explanatory graphic buttons that allow him to visually interpret what is expected and quickly report the information. When asking for measurement units, scales of measure with physical objects were provided so the citizen could easily visualize and identify the correct amount, even if he is not used to the standardized unit measuring systems. For instance, when asking the user to indicate the volume of land mass displaced in a landslide event, a graphic scale using vehicles was used, as shown in Figure 5. The flow of a report ends with Submission.



Figure 4. Graphic buttons representing the event types.



Figure 5. Examples of the interfaces for step D for two event types: subsidence and landslides.

In complement to reporting events, the citizen can check all the reported events through the app. Using a map-based interface, the user can download the information related with the events reported in each location. Filtering or ordering the reported events by type of event or occurrence date is also available.

3.2 Dealing with the reported data

Reports made by citizens via the AGEO App are always received by The ReSist team of Lisbon Municipality, which is focused on the urban resilience sector. Once the reports have been received, they are forwarded to the services responsible for dealing with each situation. In addition, if there are people at risk (a situation that can be flagged directly in the app), the report is automatically sent to the municipality's fire department occurrence management system, in order to ensure that the rescue services can act more quickly. All communication between the app and the services, including reporting to the regiment, is based on ESRI technology and it is always possible to locate the incident.

While considering individually each of the reported events, it can be hard to envision if the driving forces behind it are of geological nature or if they are related to some other site-specific circumstances. But when the reports are analysed altogether, evidence of more complex and systemic "problems" can emerge.

This ability to globally analyse the reports of several occurrences spatially related is one of these great advantages behind multihazards citizens' observatories (Figure 6). Despite that, if a concerned citizen reports a hazard of any kind, local governments and authorities must assure that no immediate security concerns are in place and must take measures to correct any reported damages.

To achieve this, it is fundamental to guarantee that the reported information reaches the local authorities responsible for the first response operations, in case of an emergency and/or the services responsible for the maintenance of public space. With this objective in mind, Lisbon municipality is implementing an automatic workflow that forwards the information reported by the citizens to the adequate entities according with the circumstances reported through the geohazards report app.

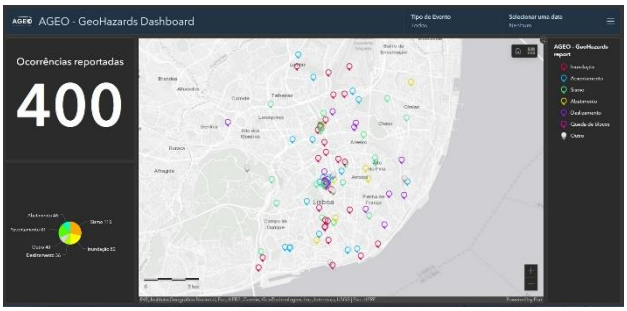

Figure 6. Dashboard for reports visualization and global analysis (data reflects simulated occurrences).

4 CONCLUSIONS

As part of the Lisbon Multihazards Citizen's Observatory, which is integrated in the AGEO Project – Platform for Atlantic Geohazard Risk Management, Lisbon Municipality developed a communication strategy based on a mascot called RISKA. Educational contents were also developed aiming to raise the population's awareness to geological risks and allowing the implementation of preventive measures.

To receive information by citizens a platform was developed. The platform's interface aimed to simplify the report using simple language and based on graphic content, to enable ordinary citizens to give information about situations related with geohazards in Lisbon. The simplicity of the app and the visual presentation of the screens had an excellent receptivity by the test public. This solution will allow citizens to play an active role in the risk management system and will facilitate the monitoring of situations in which Lisbon Municipality technicians have increased difficulties due to lack of access. Ultimately, this tool will allow Lisbon Municipality to anticipate problems that may arise, such as settlements in buildings, enabling a proactive response and not a reactive one, as it happens today.

The implemented proof of concept allowed to demonstrate that a citizen properly aware of a certain problem can contribute to a more efficient risk management in the city of Lisbon.

ACKNOWLEDGEMENTS

The authors would like to thank to all the municipality technicians that supported the tasks developed, as well as the stakeholders who participated in the several dissemination actions and who introduced the AGEO app in their daily work.

This work has been undertaken in the framework of the INTERREG Atlantic Area AGEO Project (EAPA_884/2018 – AGEO)

Proceedings of the XVIII ECSMGE 2024
GEOTECHNICAL ENGINEERING CHALLENGES
TO MEET CURRENT AND EMERGING NEEDS OF SOCIETY
© 2024 the Authors
ISBN 978-1-032-54816-6
DOI 10.1201/9781003431749-234
Open Access: www.taylorfrancis.com, CC BY-NC-ND 4.0 license

ECSMGE 24
XVIII EUROPEAN CONFERENCE ON SOIL MECHANICS AND GEOTECHNICAL ENGINEERING

An early warning procedure based on coupling short-time weather forecasting and numerical slope analysis

Un système de early warning basé sur le couplage prévision météo à court-terme - analyse numérique du comportement de la pente

M. Pirone*, G. Forte, A. Santo, G. Urciuoli
Università degli Studi di Napoli "Federico II", Naples, Italy

L. Picarelli
Centro Euro-Mediterraneo per i Cambiamenti Climatici, Italy

**marianna.pirone@unina.it*

ABSTRACT: Rainfall-induced debris flows and avalanches represent an impending hazard in some densely populated areas of Campania Region, Italy, which are mantled by loose air-fall volcanic ashes. The development of reliable early warning systems is then a strong need. The studies that have been carried out in the last twenty years, which include the long-lasting monitoring of some well instrumented slopes, have allowed to obtain a good knowledge about the hydraulic and mechanical properties of these soils. A further step should be now the assessment in real time of their response to expected rainfall aimed at setting up reliable early warning systems. A procedure that exploits the available short-term weather forecasts and a numerical analysis of the potential slope response to rainfall based on field monitoring of the initial conditions, is proposed.

RÉSUMÉ: Les coulées de debris induites par les précipitations représentent un risque permanent dans certaines zones densément peuplées de la Region Campanie, en Italie, qui sont caractérisées par des couvertures de cendres volcaniques lâches de déposition aérienne. Le développement de fiables systèmes de early warning est donc un impératif. Les études qui ont été conduits dans les vingt dernières années, qui ont inclus la surveillance à long terme de quelques pentes bien instrumentées, ont permis de obtenir une bonne connaissance du comportement hydraulique et mécanique du sol. Une nouvelle étape maintenant devrait être l'évaluation en temps réel de leur réponse aux précipitations prévues, dans le but de développer des fiables systèmes de early warning. Dans cet article on propose un processus qui utilise les prévisions météo à court-terme disponibles et l'analyse de la réponse potentielle de la pente aux précipitations sur la base de la surveillance sur site des conditions hydrauliques initiales.

Keywords: Unsaturated volcanic ash; rainfall forecasting; field monitoring; numerical analysis.

1 INTRODUCTION

Sudden and destructive rainfall-induced debris flows and avalanches represent an impending hazard in some densely populated areas of Campania Region, Italy, which are mantled by loose air-fall volcanic ashes. The development of reliable early warning systems is then a strong need. The studies which include in depth hydraulic and mechanical characterization of the soil and long-lasting monitoring of some well instrumented slopes, have allowed to obtain a good knowledge about the properties (Lampitiello, 2004; Nicotera et al., 2015; Dias et al., 2022) and behaviour of these soils (Comegna et al., 2016; Picarelli et al., 2020; Pirone et al., 2023). In order to protect people and infrastructure, a further step should be now the assessment in real time of their response to expected rainfall aimed at setting up reliable early warning systems. This paper describes a novel procedure based on the numerical analysis of the potential slope response to expected rainfall in the next hours by exploiting official weather forecasts and data provided by field monitoring, which can provide the initial hydraulic conditions. Here, first, the soil properties and the numerical model employed, with a focus on model validation, are presented; then, in order to assess if the proposed approach can be effectively used within early warning systems, results of some blinded analyses carried out in a monitored site in Campania, are shown.

2 THE INVESTIGATED AREA AND THE MAIN SOIL PROPERTIES

The proposed approach is applied in the area of Pagani (SA), 35 km South-East from Naples, in a site where some debris flows have occurred in the past. The stratigraphic setting consists of a 2 m deep succession of thin air-fall pyroclastic soil layers covering a

fractured carbonate bedrock (Santo et al., 2021). Bottom upward in the considered section (Figure 1a), the succession includes 20–60 cm thick silty sands (C1), overlaid by brown silty sands rich in pumices (A2), which have a thickness of 30–130 cm. The top soil consists of a highly weathered vegetated volcanic ash (A1); its thickness spans from 20 to 80 cm, with a mean value around 35 cm. The average slope angle is 35°.

The instrumentation consists of four tensiometers and four TDR probes installed in pairs at the same depth (Figure 1a). Matric suction and volumetric water content are being measured hourly since November, 2020. The site is also equipped with a rain gauge that records rainfall every ten minutes.

The pyroclastic cover is partially saturated over the entire year. Figure 1b shows the grain-size curves obtained from a number of samples; the curves fall within the envelopes of the pyroclastic soils of the whole Lattari chain (Santo et al. 2021) and of the Faito Mt. test site (Pirone et al., 2023). Considering that the Mt. Faito soils have the same geological history, stratigraphy and porosity as the Pagani soils, here we have assumed also the same friction angle (Table 1). The hydraulic properties have been obtained by processing field data collected at the Pagani test site and are summarized in Figures 2a, b. The solid lines in Figure 2a show the Water Retention Curves (WRCs) obtained by interpolating hourly field data, provided by tensiometers and TDR probes over the first part of the year 2021, by the Van- Genuchten model (crossed lines).

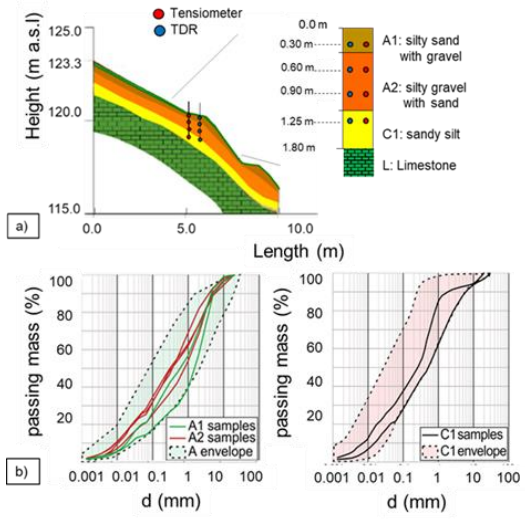

Figure 1. a) Longitudinal section of the slope, simplified stratigraphic soil profile, the instruments installed in the Test Site; b) Grain-size curves of soils A1, A2 and C1 along with the envelopes of the other samples collected on Lattari Mts.

Table 1. Mean physical and mechanical properties of soils sampled in Mt. Faito (γ_d: dry unit weight; n: soil porosity; φ':friction angle at critical state).

Soil	γ_d (kN/m^3)	n (-)	φ' (°)
A1	7.70	0.70	38.4
A2	8.19	0.65	38.4
C1	7.35	0.70	35.4

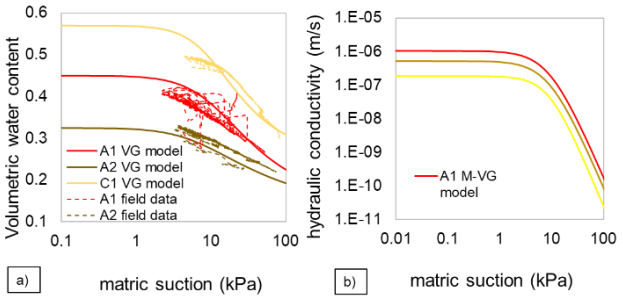

Figure 2. a) WRCs of single layers, as adopted in the analysis, compared to field data; b) HCs of single layers. In the figure M-VG means Mualem Van Genuchten.

The corresponding Hydraulic Conductivity curves (HCs, Figure 2b) have been obtained according to the modified Mualem-Van Genuchten function (Mualem, 1976). For what concerns the saturated permeability of layers A2 and C1, it has been assumed to be equal to the average value measured at the Monte Faito test site through constant head permeameter tests. Finally, the saturated permeability of layer A1 has been taken as a calibration parameter for the numerical model, adopting the value that best replicates the in-situ measurements of suction and water content.

3 RELIABILITY OF THE NUMERICAL ANALYSIS

The hydraulic slope response to precipitation has been investigated by means of the Richards' equation implemented in the FEM code SEEP/W using the WRCs and the HCs (Figs. 2a-b).

The longitudinal slope section shown in Figure 1a has been modeled through a mesh with element sizes of 0.05 m. In order to test the model's effectiveness, the effects of some rainy events recorded from winter 2021 to winter 2022, have been simulated by applying at the upper boundary the hourly rainfall measured by the rain gauge installed at the Test Site and neglecting evapotranspiration. The numerical simulations focus solely on rainstorm duration, adopting hourly time steps. The matric suction values measured in the pyroclastic cover before rainstorms have been assigned as initial conditions. It is useful to outline that the initial suction retains a memory of the slope's past hydraulic history. In all the analyses, the lower

boundary and the edges of the domain have been modeled as potential seepage faces, which keep null flux for pore pressure < 0 kPa, and convert the boundary condition to a head-type, with the total head, H, equal to the y-coordinate (which means assuming u = 0 kPa) when u > 0 kPa. Several numerical analyses have been carried out as the saturated hydraulic conductivity of layer A1 varies in the range of $5{\cdot}10^{-7}$ - $5{\cdot}10^{-6}$ m/s, which represents a reasonable interval of variation for the hydraulic conductivity of pyroclastic soils. The value of $1{\cdot}10^{\wedge-6}$ m/s resulted in the lowest mean error, *e*, defined as the difference between the measured and calculated value. Field vs calculated values of matric suction and volumetric water content at depths of 0.30 m and 1.25 m during four selected rainfall events are plotted in Figure 3 along with the values of *e* and of standard deviation of *e*, noted as dev.st (*e*). The good match between recorded and calculated values, which are characterized by *e* lower than 1 kPa for matric suction and equal to 0.015 for average volumetric water content, is encouraging. However, as expected, a greater standard deviation has been calculated for the topsoil (0.30 m) due to the difficulty to replicate the complex phenomena related to the soil-atmosphere interaction by means of this simple numerical model.

This indicates that, in principle, both the numerical approach and the soil properties used in the analysis allow to properly predict the slope response to rainfall.

4 THE PROPOSED EARLY WARNING PROCEDURE

The proposed procedure has been tested using the weather forecast provided by 3Bmeteo.com for April 16, 2023, rainfall, made 48h and 24h before respectively, i.e., on April, 14, and April, 15. Calculated and measured values of matric suction and volumetric water content are plotted in Figures 4a-d. Figures 4e and f, in turn, show the factor of safety (FS) calculated by uploading the predicted suction distribution in the code SLOPE/W that implements the limit equilibrium method (LEM). The contribution of matric suction to shear strength has been obtained through the equation proposed by Vanapalli et al. (1996). The critical shear surface has been determined by imposing the entry and exit option. The minimum thickness of the zone, within which the sliding surface may develop, has been set at a depth of 0.5 m based on evidence. The safety factors corresponding to rainfall forecast 48h and 24h before the selected day (April, 16) are compared to the safety factors determined under the rainfall that has been actually recorded.

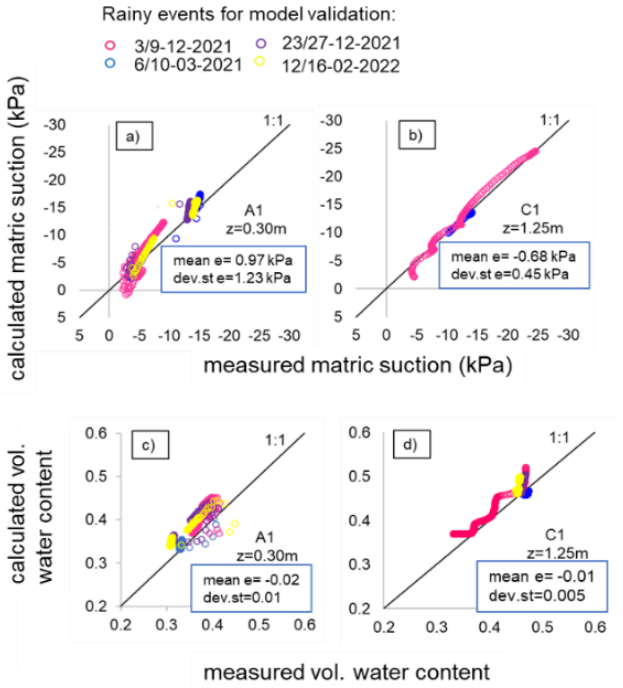

Figure 3. a), b) Measured vs calculated values of matric suction at depths of 0.30 m and of 1.25m; c), d) volumetric water content at the same depths.

As field readings show, almost the entire soil cover is subjected to suction decrease due to both the amount of rainfall and the high hydraulic conductivity of the soil in such a wet period. It is worth noting that suction at 0.30 m continues to increase even after rainfall stops. The corresponding factor of safety (FS) along with the critical slip surface are shown in Figures 4e and 4f. The maximum thickness of the involved soil body is 0.90 m (within the soil A2), and FS reflects the suction trend of the uppermost half part of the pyroclastic cover.

The daily rainfall forecasted 48h and 24h before April, 16, were 19 mm and 35.2 mm respectively, less than the value that was actually measured at the Test Site (42 mm). The analysis shows that rainfall forecast 24h before can provide a better prediction of the hydraulic slope response (Figure 4b,d), leading to FS values closer to those that have been determined under the recorded rainfall (Figure 4f). In contrast, the rainfall forecast 48h in advance underestimates the decrease in matric suction by providing FS values about 40% higher (FS=1.50 against FS=1.22) than those calculated for the actual rainfall distribution (Figure 4a, c, e). Since the capability to correctly assess the suction distribution from measured rainfall appears to be quite good (Figure 3), these results show that, at the moment, a major problem concerns the reliability of weather forecast, which strongly depends on the selected time interval in advance.

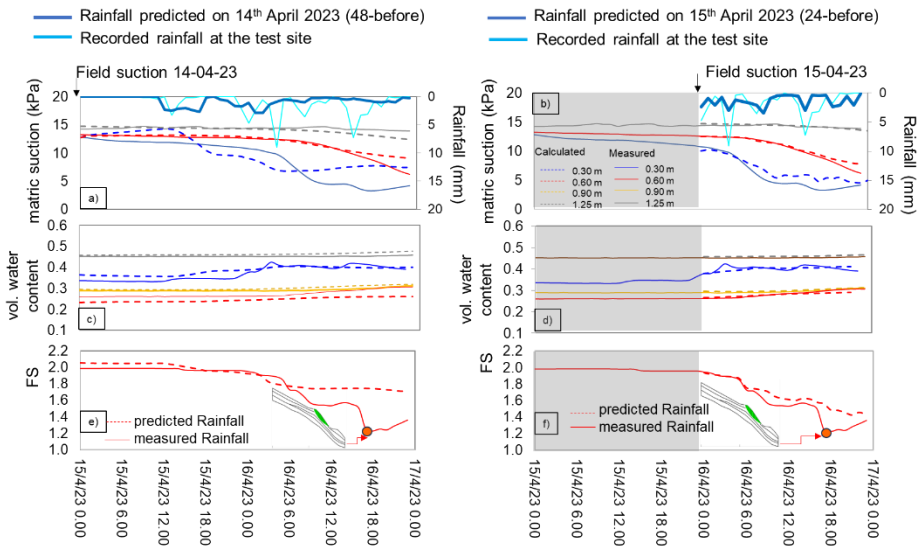

Figure 4. a), b), c), d) Measured (solid line) and predicted values (dashed line) of suction (a and b) and of volumetric water content (c and d) on April, 16, 2023, based on rainfall forecast 48 h and 24h in advance; e), f) safety factor, FS, calculated from measured and forecasted Rainfall along with the picture of critical slip surface determined for FS corresponding to measured Rainfall.

5 CONCLUSIONS

A numerical procedure for early warning of fast flow-like rainfall-induced landslides in unsaturated pyroclastic soils based on weather forecast and field monitoring of the initial soil conditions, is being tested in an area susceptible to slope failure. The first results are encouraging showing that the reliability of the approach strongly depends on a correct forecast of the rainfall amount and distribution. At the moment, further in-depth analyses are needed to have a clear understanding about the reliability and effectiveness of the procedure proposed.

REFERENCES

Comegna, L., Damiano, E., Greco, R., Guida, A., Olivares, L., Picarelli, L. (2016). Field hydrological monitoring of a sloping shallow pyroclastic deposit. *Can. Geotech. J.,* 53: 1125–1137. https://doi.org/10.1139/cgj-2015-0344.

Dias, A.S., Pirone, M., Nicotera, M.V., Urciuoli, G. (2022). Hydraulic hysteresis of natural pyroclastic soils in partially saturated conditions: experimental investigation and modelling. *Acta Geotech.,17*:837–855. https://doi.org/10.1007/s11440-021-01273-y.

Lampitiello, S. (2004). *Resistenza non drenata e suscettività alla liquefazione di ceneri vulcaniche della Regione Campania.* PhD Thesis, Seconda Università di Napoli.

Mualem, Y. (1976). A new model for predicting the hydraulic conductivity of unsaturated porous media. *Water Resour. Res.,* 12(3): 513–522. http://dx.doi.org/10.1029/WR012i003p00513.

Nicotera, M.V., Papa, R., Urciuoli, G. (2015). The hydro-mechanical behaviour of unsaturated pyroclastic soils: an experimental investigation. *Eng.Geol.*,195:70–84. https://doi.org/10.1016/j.enggeo.2015.05.02.3

Picarelli, L., Olivares, L., Damiano, E., Darban, R., and Santo, A. (2020). The effects of extreme precipitations on landslide hazard in the pyro clastic deposits of Campania region: A review. *Landslides,* 17 (10): 2343–2358. https://doi.org/10.1007/s10346-020-01423-5.

Pirone, M., Di Maio, R., Forte, G., De Paola, C., Di Marino, E., Salone, R., Santo, A., Urciuoli, G. (2023). Study of the groundwater regime in unsaturated slopes prone to landslides by multidisciplinary investigations: Experimental study and numerical modelling. *Eng. Geol.,* 315, 107045. https://doi.org/10.1016/j.enggeo.2023.107045.

Santo, A., Pirone, M., Forte, G., De Falco, M., Urciuoli, G. (2021). Slope Stability Assessment of the Test Site in Pagani (Campania, Southern Italy). *Lecture Notes in Civil Engineering*, 156:359–365. https://doi.org/10.1007/978-3-030-74258-4_23.

Vanapalli, S.K., Fredlund, D.G., Pufahl, D.E., Clifton, A.W. (1996). Model for the prediction of shear strength with respect to soil suction. *Can. Geotech.* J., 33:379–392. https://doi.org/10.1139/t96-060.

Proceedings of the XVIII ECSMGE 2024
GEOTECHNICAL ENGINEERING CHALLENGES
TO MEET CURRENT AND EMERGING NEEDS OF SOCIETY
© 2024 the Authors
ISBN 978-1-032-54816-6
DOI 10.1201/9781003431749-235
Open Access: www.taylorfrancis.com, CC BY-NC-ND 4.0 license

ECSMGE 24
XVIII EUROPEAN CONFERENCE ON SOIL MECHANICS AND GEOTECHNICAL ENGINEERING

Ground investigation methods used in high-speed railway for mitigation of dissolution features risk in chalk

Méthodes d'études de sol utilisées dans les chemins de fer à grande vitesse pour atténuer le risque de dissolution dans la craie

S. Pryce, M. Black
COWI UK

H. Saroglou*
Eiffage Keir Ferrovial BAM (EKFB) JV

G. Katsigiannis
Ferrovial Construction UK

S. Muniyasamy
Eiffage UK

**Harry.Saroglou@ekfb.com*

ABSTRACT: Chalk is known to have a potential risk for natural cavities (solution features) and documenting the location and nature of these geohazards is important to infrastructure projects. North Chilterns Area, one of the five projects within the HS2 Main Works Civils Contract, C23 includes cuttings, embankments and viaducts which will be designed and constructed in the formation of Chalk. The risk of presence of dissolution features in this area is high, either as infilled features near formation level in cuttings and embankments or void or infilled features, being present immediately below the toe of foundation piles, along their shafts, or below shallow footings. This paper discusses the risk from dissolution features for selected high-speed railway assets and presents the approach to investigate their presence based on various ground investigation methods, which were employed on the project. These include LiDAR surveys, surface geophysics (electromagnetic, electrical resistivity, microgravity surveys), intrusive ground investigation (boreholes, CPT probing), use of borehole cameras and downhole surveys. The limitations and advantages of these methods are discussed, highlighting the importance of the combined interpretation of ground investigation data to design appropriate mitigation works.

RÉSUMÉ: La craie est connue pour présenter un risque potentiel de présence de cavités naturelles (phénomènes de dissolution); ainsi, documenter l'emplacement et de la nature de ces aléas géologiques est important pour les projets d'infrastructure. La région de North Chilterns, l'un des cinq projets parmi le Contrat HS2 section C23, comprend des déblais, des remblais et des viaducs qui seront conçus et construits dans la craie. Le risque de présence d'éléments de dissolution dans cette zone est élevé, soit sous forme de cavités remplies près du niveau de formation dans les déblais et les remblais, soit sous forme de zones vides ou remplis, étant présentes immédiatement sous la base des pieux de fondation, le long de leur longueur, ou sous des semelles de foundation peu profondes. Cet article discute le risque de dissolution pour certains actifs de ligne de chemin de fer à grande vitesse et présente les démarches pour évaluer leur présence sur la base de diverses méthodes d'études de sol, qui ont été utilisées dans le cadre du projet. Il s'agit notamment des relevés LiDAR, de méthode géophysique de surface (relevés électromagnétiques, de résistivité électrique, de microgravité), d'études de sol intrusives (forages, sondages CPT), de l'utilisation de caméras de forage et de relevés géophysiques de fond. Les limites et les avantages de ces méthodes sont discutés, soulignant l'importance de l'interprétation combinée des données des diverses études de terrains pour soutenir la prise de décision et concevoir des travaux d'atténuation appropriés.

Keywords: Chalk; dissolution features; ground model; geohazard.

1 INTRODUCTION

The High Speed Two (HS2) project is a High-Speed Railway Line currently under construction in the UK. Phase 1 of HS2 runs between London and Birmingham across the English Midlands. This scope is part of the HS2 Main Works Civils Contract C23, awarded to Eiffage Keir Ferrovial Bam (EKFB) JV in partnership with the design JV of Arcadis Setec COWI (ASC). The North Chilterns Area (NCA) section covers an approximate length of 11km; of which approximately 8km is underlain by Chalk bedrock, namely Lewes Nodular Chalk, Holywell Nodular Chalk, New Pit

Chalk, Zig Zag Chalk and West Melbury Marly Chalk. This section of the route is the subject of this paper, as the chalk bedrock has an inherent risk of dissolution features and chalk mining features. These features present a risk to the project and require a strategic and coordinated approach to investigation, risk assessment and treatment.

2 GEOLOGICAL CONTEXT

Dissolution features are a common geohazard in karst geology and occur when slightly acidic rainwater is allowed to infiltrate into calcium carbonate rich bedrock, such as chalk. Features may occur in a variety of forms, as illustrated in Figure 1.

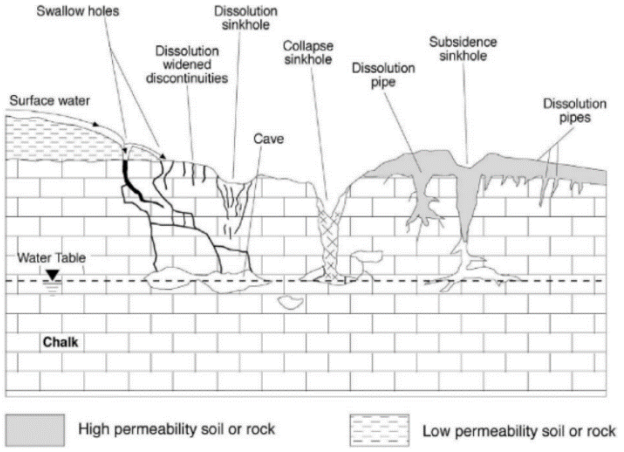

Figure 1. Schematic cross-section of common dissolution feature types (Lord et al, 2002).

Typically, these dissolution features present themselves as localised undulations in the bedrock profile at the interface of the chalk, which are infilled by loose superficial materials. Across the NCA section of the route, these superficial materials generally comprise cohesive Head deposits or Clay with flints.

Risk also exists associated with chalk mining. Historically, chalk was mined and used for spreading on heavy clays or in agricultural lime production, therefore the risk of chalk mines is particularly prevalent in areas where clay overburden is present, which covers most of the study area. It should be noted however in the works undertaken to date that chalk mining features have not been identified across the NCA route.

3 GROUND INVESTIGATION STRATEGY

3.1 Detailed design investigations

An initial phase of ground investigation works was undertaken across the NCA package as part of the detailed design phase. This generally included a suite of boreholes, CPTs and trial pits. As these were undertaken as part of the detailed design, they were not specifically targeted to investigate potential dissolution features. It was determined that these investigations should be undertaken as part of the construction programme to expedite the design works and subsequent approval processes.

However, as part of the detailed design investigation works, a preliminary programme of surface geophysics was undertaken. This comprised microgravity, electromagnetic and electrical resistivity surveys and covered approximately 52% of the total development footprint. The purpose of these works was to inform a preliminary qualitative assessment of the possible extent of dissolution features at each asset, in order that the targeted investigation works during the construction phase could be undertaken.

3.2 Dissolution features investigations

Given the risk of dissolution features extends over an area approximately 8km long, careful planning was required to optimise the ground investigations. This was particularly relevant to ensure best value was obtained from intrusive investigations. A phased approach was adopted utilising ground profiling and geophysics in advance of committing to intrusive investigations. The general phasing and rationale is summarised in Table 1.

Table 1. Summary of ground investigation phases.

Stage No.	Technique (s)	Rationale
1	Phase 1 Geophysics and LiDAR	Preliminary qualitative assessment of risk per asset
2	Phase 2 Geophysics	100% earthworks footprint coverage to identify anomalies for targeted intrusive GI
3	Dynamic probing / boreholes	'Ground truthing' of geophysical anomalies to identify features of concern.

3.3 Geophysical Surveys

The success of surface geophysics across this alignment was aided by the characteristics of the land; as this was largely open pasture uninterrupted by significant development and/or services, these works have yielded generally good results.

Three key geophysical techniques have been adopted. Electromagnetic and electrical resistivity surveys were utilised; these are generally reliable to 3-4mbgl and are therefore most useful in areas of shallow overburden. The focus of the geophysical works was microgravity surveying which is generally

reliable to 20-25mbgl and can therefore identify most features of concern; this technique was specified to cover 100% of the development footprint.

The results of the geophysical surveys were reviewed to identify areas where the results indicate a varying response of the surrounding ground (Figure 2).

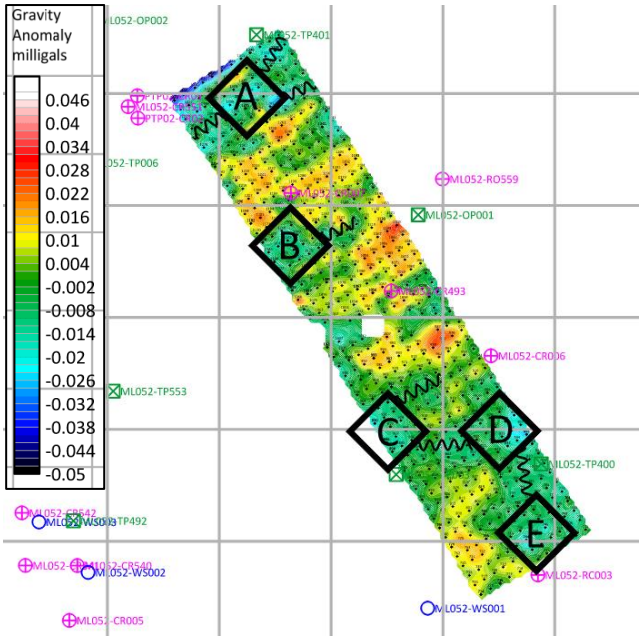

Figure 2. Interpreted microgravity results showing features of concern.

3.4 Targeted intrusive investigations

Where features of concern were identified from the Phase 2 geophysical surveys, intrusive investigations were scoped and targeted to these features as a means of 'ground truthing' the anomalies.

The intrusive investigations comprised a linear array of 9no. dynamic probing positions spanning the direction of the perceived feature of concern at 1.5m centres. The purpose of these was to identify perceived changes in in-situ density at the interface of the chalk materials that may indicate a possible dissolution feature. Following this, a rotary open-holed borehole with down-hole televiewer was targeted adjacent to the dynamic probing positions to confirm the geological interpretation of the probing results. An example of the distribution of these positions is presented in Figure 3.

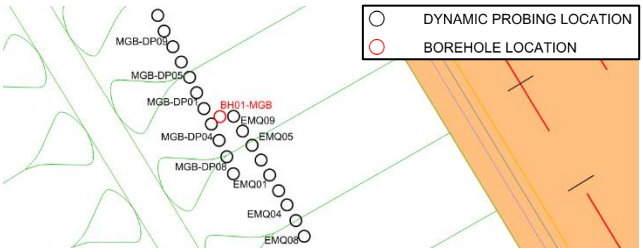

Figure 3. Distribution of intrusive GI at feature 'MG-B / EM-Q'

3.5 Interpretation of results

A review of the findings of the intrusive works was undertaken to assess the features of concern. The stratigraphy determined from the detailed design investigation was firstly superimposed onto the dynamic probing logs to determine the chalk interface profile/level. The probing results were then reviewed to identify zones of low blow counts, which was defined as three or more consecutive results with blow counts between 0-3.

An analysis of the data showed that between 15-25% of the geophysical anomalies could be correlated to solution features; the others could be attributed to other geological reasons including naturally occurring loose zones or localised boulders within the superficial deposits. The overriding principal of the interpretation of these results was to 'prove the negative', i.e., where a feature could not be proven, some interpretation had to be provided as to why the geophysical anomaly was recorded. This analysis fed into a feedback loop with the geophysics review to refine these assessments for each subsequent asset.

Following initial interpretation of the dynamic probing logs, a rotary-open holed borehole with down-hole televiewer was scheduled adjacent to these positions to allow a visual assessment of the chalk and verify the ground model assumptions (see Figure 4).

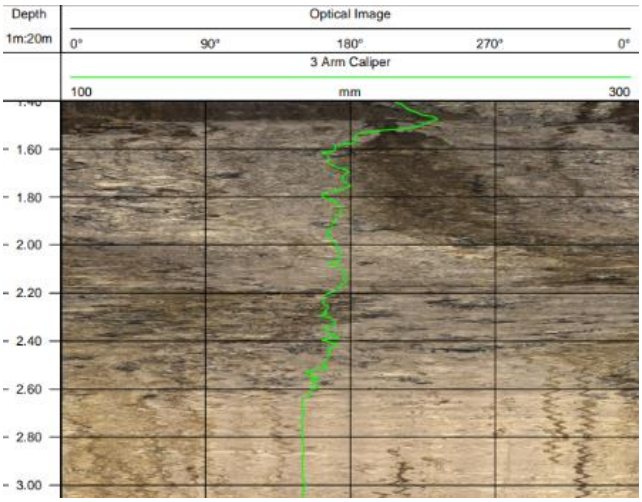

Figure 4. Extract from televiewer log from feature 'MG-B / EM-Q' showing overburden/chalk interface.

An example of an interpreted row of dynamic probing logs for feature 'MG-B' is presented in Figure 5. Characteristically, each of the perceived features identified a zone of low blow counts at chalk interface. Also apparent was a shallower zone of low blow counts within the superficial materials; interpreted as propagated loose material above the feature at an approximate draw angle of ~45-60° away from the edge of the feature.

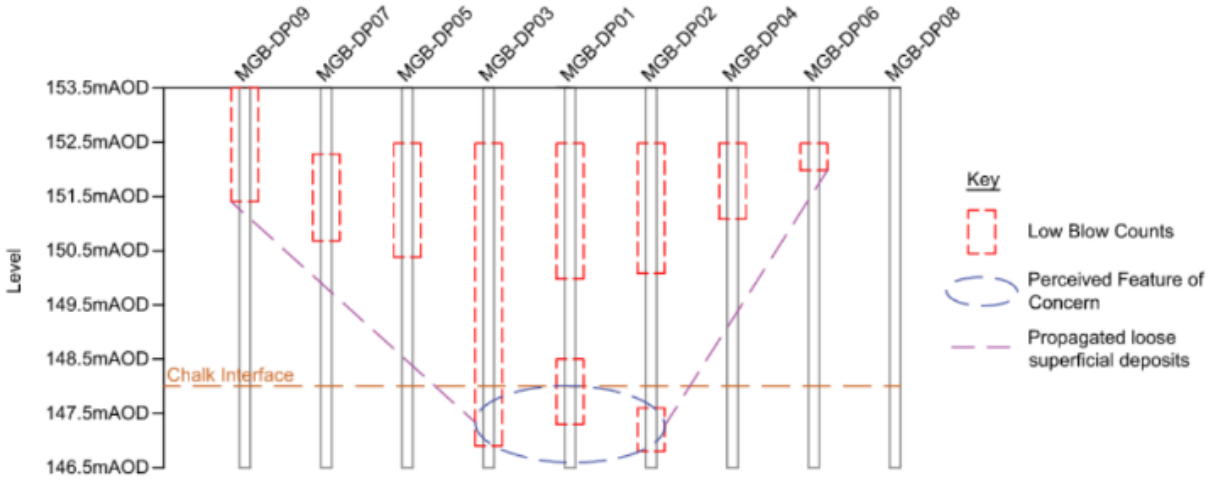

Figure 5. Interpretation of dynamic probing results at feature 'MG-B'.

3.6 Investigation strategy per asset type

The investigation strategy and sequence detailed in the foregoing sections describes the process adopted for earthworks assets (i.e., embankments and cuttings), with Small Dean South Embankment being used as a case study. These earthworks assets account for the majority of the development; however a number of structural assets including viaducts and underbridges are present across the alignment which have adopted a slightly different investigation approach.

The investigation requirements for each structural asset have been determined on an individual basis. To use Small Dean Viaduct as an example, it was determined that due to the relatively small footprint of the abutment foundations as well as significant programme constraints at this asset, Phase 2 geophysical works were replaced with an array of dynamic probes at 1.5m centres across the abutment footprints. The advantage of this approach was that the programme was expedited. No features of concern were identified from these works.

4 RISK ASSESSMENT AND TREATMENT

Where features of concern were identified by investigation, a risk assessment was undertaken to determine if treatment was required. The strategy determined that features were only deemed to require treatment where they were below the high-speed railway or were within the support zone for earthworks/foundations.

4.1 Rock cover ratio assessment

An initial risk assessment was undertaken on features of concern to determine if a suitable rock cover thickness was present above the feature so as to not present a risk to the development. This used a modified version of guidance for treatment of coal mine workings (R.J Piggot and P. Eynon, 1978). For the purposes of the risk assessment, Class 1A1 granular materials to be filled as part of 'excavate and replace' at the formation of earthworks assets were considered to contribute to this competent cover thickness, given the stringent control over the parameters of the placed materials.

As part of this risk assessment process, it was identified that a zone of uncertainty existed between the depth range of geophysical surveys and the depth of features considered to be tolerable within the design. This was particularly relevant to features relating to historic chalk mining (i.e., deeper than the chalk interface level) and is illustrated in Figure 6. This inherently led to some residual risk in the assessment.

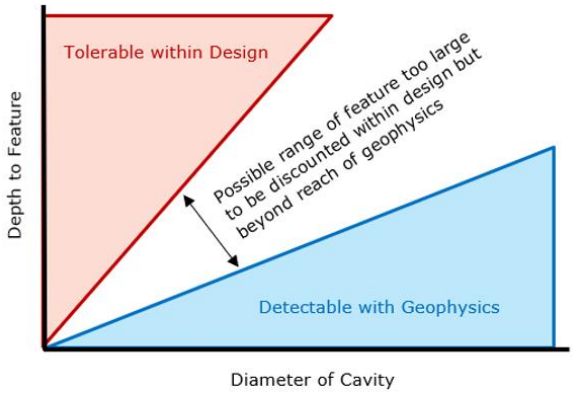

Figure 6. Schematic relationship between feature size and geophysics range.

The rock cover assessment method shown in Figure 7 utilised existing studies regarding collapse mechanisms in chalk (Z.E. Jeffrey et al, 2020, C.N. Edmonds, 2008, T. Waltham, 2008). The relationship was developed considering a conical failure mechanism for chalk grades A-D.

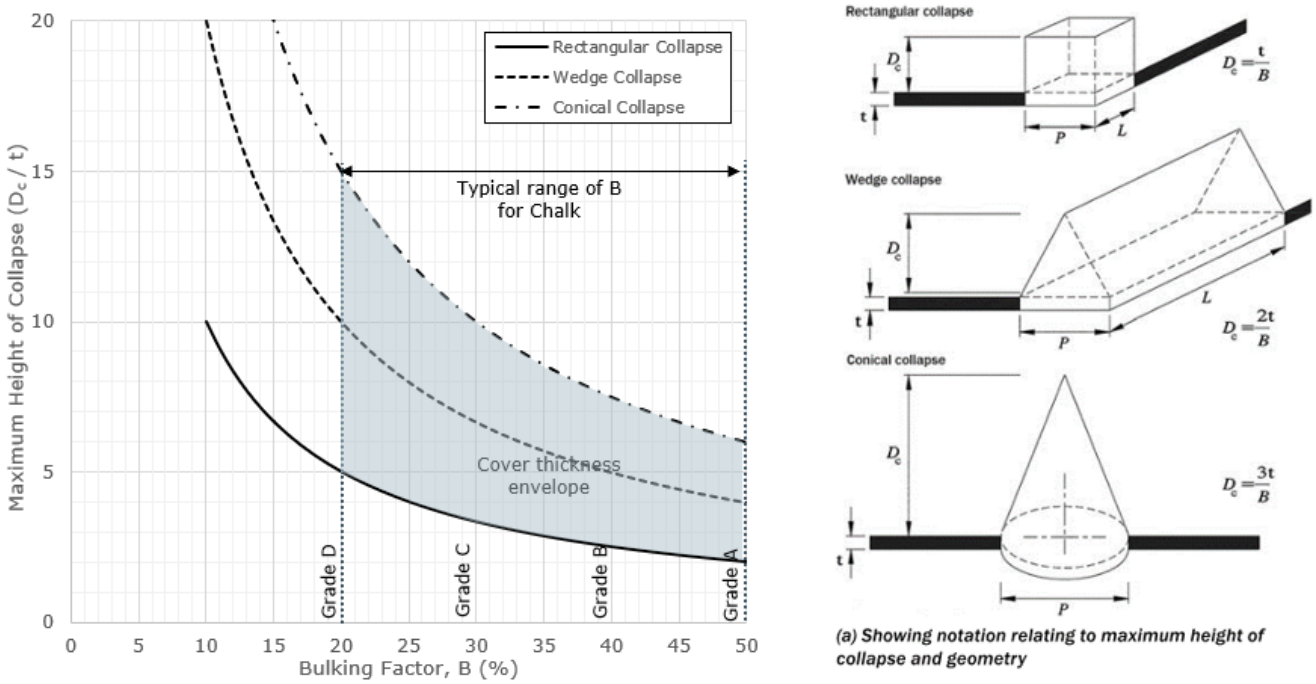

Figure 7. Modified cover assessment method for chalk grades A-D (after Piggot and Eynon, 1978).

This assessment model gives relationships for the cover thickness for each chalk grade, as summarised below:

$$Grade\ A = 6t \quad (1)$$

$$Grade\ B = 7.5t \quad (2)$$

$$Grade\ C = 10t \quad (3)$$

$$Grade\ D = 15t \quad (4)$$

Where *t* is the ratio of feature size versus the thickness (m) of competent cover materials above.

4.2 Treatment Options Hierarchy

Within the overarching strategy, a hierarchy of treatment options was developed between the designer and the contractor which informed the extent of the ground investigations required (see Table 2).

Where the depth to the base of the feature was sufficiently shallow (≈6m below earthworks formation level), the excavate and replace solution was seen as the preferred option, as by nature, this could be implemented under a semi-observational approach. This could therefore minimise the scope of intrusive ground investigations as the extents of the feature could be confirmed during treatment.

Grouting techniques were considered to be less effective at shallow depth due to the complexity of the method in comparison to excavation and replacement. For treatment to depths greater than 6m, grouting would be considered on a case-by-case basis considering the need for additional investigation works and regulatory requirements.

Table 2. Hierarchy of treatment solutions.

Solution	Prog-ramme	Cost	Residual Risk
1. Sufficient cover – no physical treatment	Very low	Very low	Low
2. Excavate & Replace using Class 1A1 fill / concrete plug	Low	Moderate	Very Low
3. Drill and Grout (cavity infill) or compaction grouting	High	Moderate / High	Low
4. Spanning / bridging solutions	Low	Low	Moderate

5 TREATMENT IMPLEMENTATION

To illustrate the application of the investigation, risk assessment and treatment strategy detailed within this paper, the implementation of the site works at Small Dean South Embankment is discussed below.

Within the first 500m of the asset, 3no. features of concern were identified, each at the interface of the chalk deposits. Of these, one was situated outside of the support zone for the high-speed railway and embankment therefore did not require treatment. The

two remaining features ('MG-B / EM-Q' and 'EM-S') required treatment by excavate and replace.

Figure 8 below shows the excavation to the base of the feature at 'EM-S'. The depth and extent of the feature extended far beyond what was anticipated. It was therefore concluded that the intrusive investigation works at 'EM-S' identified only the outer edge of the feature. This further reinforced the benefit of implementing the excavate and replace under a semi-observational approach. For 'MG-B / EM-Q', the extent of the feature correlated well to the interpretation of the dynamic probing results.



Figure 8. Excavation to base of feature at 'EM-S'.

As part of the backfilling of the feature, a concrete plug was installed at the approximate interface of the natural chalk level. This was to provide an impermeable interface to prevent further long-term deterioration of the chalk, bearing in mind that the mechanism for the initial creation of these features is through infiltration of slightly acidic rainwater. The installation of this concrete plug is shown in Figure 9.



Figure 9. Installation of concrete plug at 'EM-S'.

6 CONCLUSIONS

This paper discusses the approach to the ground investigation, risk assessment and treatment of chalk dissolution features covering an approximate length of 8km of high-speed rail development.

Given the extensive area within which these geohazards exist, the systematic phasing of investigations, firstly comprising geophysics then including targeted intrusive works, has allowed the risk to be effectively managed whilst optimising the extent of the intrusive investigations and programme.

The development of a treatment options hierarchy and tailoring of the investigation strategy per asset type (i.e., cutting / embankment / structure) has further allowed optimisation of the investigation scope. Further, the implementation of excavate and replace earthworks solutions under a semi-observational approach for earthworks assets has allowed the scope of intrusive investigations to be reduced significantly.

ACKNOWLEDGEMENTS

The authors are grateful for the support of HS2 Ltd. in the preparation of this paper.

REFERENCES

Edmonds, C.N. (2008). Karst and mining geohazards with particular reference to the chalk outcrop, England. *Quarterly Journal of Engineering Geology and Hydrogeology*. 41. https://doi.org/10.1144/1470-9236/07-206.

Jeffrey, Z.E., Penn, S., Giles, D.P. and Hastewell, L. (2020). Identification, investigation and classification of chalk dissolution features using integrated LiDAR and geophysical methods. *Quarterly Journal of Engineering Geology and Hydrogeology*. 53. https://doi.org/10.1144/qjegh2019-098.

Lord, J.A, Clayton, C. R. I. and Mortimore, R. N. (2002). CIRIA C574 – Engineering in Chalk. CIRIA, UK.

Parry, D. and Chiverrell, C. (2019). CIRIA C758D – Abandoned Mine Workings Manual. CIRIA, UK.

Piggot, R.J. and Eynon, P. (1978). Ground movements arising from the presence of shallow abandoned mine workings. *Proceedings of the 1st International Conference on Large Ground Movements and Structures*, J.D. Geddes (ed.). Pentech Press, London, UK, pp. 749-780.

Waltham, T. (2008). Sinkhole hazard case histories in karst terrains. *Quarterly Journal of Engineering Geology and Hydrogeology*. 41. https://doi.org/10.1144/1470-9236/07-211.

Proceedings of the XVIII ECSMGE 2024
GEOTECHNICAL ENGINEERING CHALLENGES
TO MEET CURRENT AND EMERGING NEEDS OF SOCIETY
© 2024 the Authors
ISBN 978-1-032-54816-6
DOI 10.1201/9781003431749-236
Open Access: www.taylorfrancis.com, CC BY-NC-ND 4.0 license

ECSMGE 24
XVIII EUROPEAN CONFERENCE ON SOIL MECHANICS AND GEOTECHNICAL ENGINEERING

Sensitivity analysis of the effects of liquefiable soil deposits on differential settlement of buildings by numerical modelling

Analyse de sensibilité des effets des dépôts de sols liquéfiables sur le tassement différentiel des bâtiments par modélisation numérique.

J. Quintero*
Construct GEO - Faculdade de Engenharia da Universidade do Porto, Porto, Portugal

M. Millen
Dept. of Civil and Natural Resources Engineering, Faculty of Engineering, University of Canterbury, Christchurch, New Zealand

A. Viana da Fonseca
Construct GEO - Faculdade de Engenharia da Universidade do Porto, Porto, Portugal

julieth@fe.up.pt

ABSTRACT: Differential settlement is one of the key causes of damage to buildings on liquefiable soil deposits. Although important technical developments in geotechnical earthquake engineering have provided significant insights into the performance of buildings on liquefiable soil, the current solutions for the mitigation of the associated damages are based on expensive mat foundations. While buildings with isolated footings are unexpensive, they are more susceptible to differential settlements. Differential settlement can not only make a building unusable and irreparable, but also introduce large stresses into a building that can result in damage and collapse of the superstructure. The main objective of this work is to investigate the key parameters that influence building differential settlements and tilting through nonlinear effective stress fully-coupled dynamic numerical simulations in PLAXIS-2D®. In this paper, 1-bay and 2-bays buildings on a mat foundation will be compared with an equivalent building on isolated footings.

RÉSUMÉ: Le tassement différentiel est l'une des principales causes de dommages aux bâtiments sur des dépôts de sols liquéfiables. Bien que d'importants développements techniques dans l'ingénierie géotechnique sismique aient fourni connaissances significatives sur la performance des bâtiments sur des sols liquéfiables, les solutions actuelles pour atténuer les dommages associés reposent sur des coûteuses fondation en radier. Alors que les bâtiments avec des semelles isolées sont peu coûteux, ils sont plus susceptibles aux tassements différentiels. Le tassement différentiel peut non seulement rendre un bâtiment inutilisable et irréparable, mais également introduire de grandes contraintes dans un bâtiment qui peuvent entraîner des dommages et l'effondrement de la superstructure. L'objectif principal de ce travail est d'étudier les paramètres clés qui influencent les tassements différentiels et l'inclinaison des bâtiments par simulations numériques dynamiques, non linéaires, contraintes effectives et entièrement couplées dans PLAXIS-2D®. Dans cet article, les bâtiments à 1 et 2 travées sur une fondation en radier seront comparés à un bâtiment équivalent sur des semelles isolées.

Keywords: Effective stress analysis; liquefaction; differential settlements; isolated footings.

1 INTRODUCTION

Earthquake-induced liquefaction can lead to significant damage in buildings and huge economic and social costs to communities. Although important technical achievements in liquefaction mitigation have been accomplished in the last decades in the field of earthquake geotechnical engineering, significant damage still occurs in seismic areas around the world.

Settlements and tilting of structures that are not supported by deep foundations are the main types of liquefaction-induced damage (Yoshimi and Tokimatsu, 1977; Acacio et al., 2001) and, due to that, several methodologies have been developed to study the performance of buildings with shallow foundations on liquefiable soil deposits (Yoshimi and Tokimatsu, 1977; Liu and Dobry, 1997; Karamitros et al., 2013; Millen et al., 2018; Viana et al., 2018). These methodologies have been based on field observations, centrifuge experiments, numerical simulations, or a combination of them.

The ability to easily vary key parameters within a numerical simulation has led to several new approaches to estimating the settlement of raft foundation buildings (Karamitros et al., 2013; Bray and Macedo, 2017). These new approaches have focused on the settlement of buildings with strong mat foundations while buildings with isolated footings, which represent a large part of the European building stock, are more susceptible to differential settlements.

This work intends to analyse the performance of isolated footings compared to mat foundations to start investigating more complex systems and provide key insights for extending the existing methods to estimate settlements in the future. This comparison was performed in PLAXIS-2D a finite element software, through nonlinear dynamic soil-structure interaction effective stress analyses.

2 DESCRIPTION OF THE NUMERICAL MODEL

Two identical soil profiles were modelled using two different buildings, one with a mat foundation (Building 1) and the other with isolated footings (Building 2) as shown in Figure 1. Both buildings were modelled considering 1-bay (with two columns) and 2-bays (with three columns).

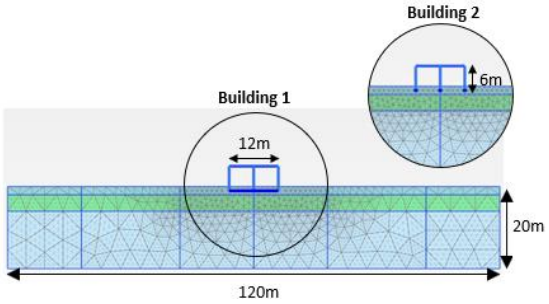

Figure 1. Numerical model with mat foundation and isolated footings for 2-bays buildings.

The finite element sizes were defined using the automated meshing algorithm selecting a 'Fine' mesh. Additionally, mesh refinement was adopted below the building. The soil profile was 20 m deep and the total model width was 10 times the building width, the lateral boundaries were tied together and the base boundary was a compliant base (absorbing) where the Northridge-01 motion in Figure 2 was entered as a horizontal displacement. This motion was recorded at the LA-Baldwin Hills station and was obtained from the NGAWest database. A scale factor of 1.22 was used to achieve a PGA of 0.612g to fit the acceleration response spectra of the selected ground motion with the acceleration response spectra of the reference seismic design action defined by the Portuguese National Annex to Eurocode 8 (PNAEC8) for the Greater Lisbon region.

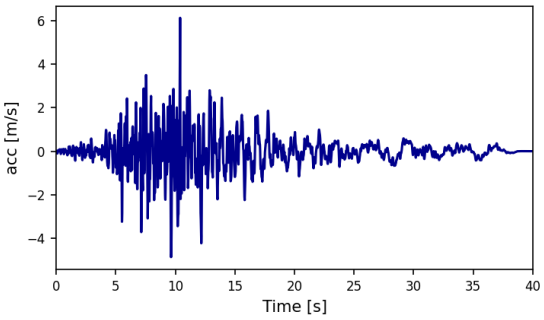

Figure 2. Input motion time series.

The soil profile consisted of a top layer of 2 m thick clay (L1), a 4 m thick liquefiable sand (L2) and a 14 m thick clay on the bottom (L3). The ground water table was set at 2 m. Prior to the dynamic loading phase, soil layers were modelled using the Hardening Soil (HS) constitutive model for the definition of initial stress states and the subsequent structural loading phases. The soil model for the liquefiable layer was switched to the PM4Sand constitutive model when the dynamic loading phase started. The parameters defining the HS model for the soil layers are listed in Table 1. Rayleigh damping was set at 2% at 0.5 Hz and 10 Hz to mitigate numerical instability. The type of calculation used in PLAXIS was a dynamic analysis with consolidation.

Table 1. Input parameters of the HS model.

Parameter	L1	L2	L3
H (m)	2	4	14
γ (kN/m^3)	15.6	19.6	20.2
e_0	0.70	0.65	0.60
E_{50}^{ref} (kN/m^2)	108x10^3	99x10^3	540x10^3
E_{oed}^{ref} (kN/m^2)	108x10^3	99x10^3	540x10^3
E_{ur}^{ref} (kN/m^2)	324x10^3	296x10^3	1620x10^3
m	1.0	0.5	1.0
c_{ref}	40	0	200
ϕ	0	33	0
k (m/s)	1x10^{-7}	1x10^{-5}	1x10^{-9}

The liquefiable layer was also assigned the additional PM4Sand properties of relative density of D_r=50%, normalised shear modulus of G_o=611, and contraction rate parameter, h_{po}=0.25 (Boulanger and Ziotopoulou, 2017). The contraction rate parameter was calibrated by performing numerical element tests using the subroutines provided by the authors of the PM4Sand model and adjusting the parameter to obtain a cyclic resistance ratio (CRR) of 0.126 for 15 cycles (15 cycles represent an earthquake with a magnitude of 7.5). The CRR value was estimated based on the relative density.

The height of the structure was 6 m and the bay length was 6 m, resulting in a total building width of 12 m. The beams and columns of the building were 0.45 m × 0.45 m. The foundation was located at a depth of 1 m. The footings of building 2 were 1 m length. A distributed load of 59.3 kN/m was applied in the beams and no self-weight or load was added to the columns and foundation elements. The structural elements were modelled as 'Plate' elements, which can only simulate elastic behaviour. They were modelled with the provided dimensions and a Young's modulus of 28 GPa. The secant-to-yield stiffness of the beams and columns was modelled according to the proposal of Haselton et al. (2016), which reduces the gross stiffness to simulate the effect of cracking and accounts for the axial force level. The secant-to-yield stiffness of the members considered was 50% of their gross stiffness. The interface between the base of the foundation elements and surrounding soil was fixed.

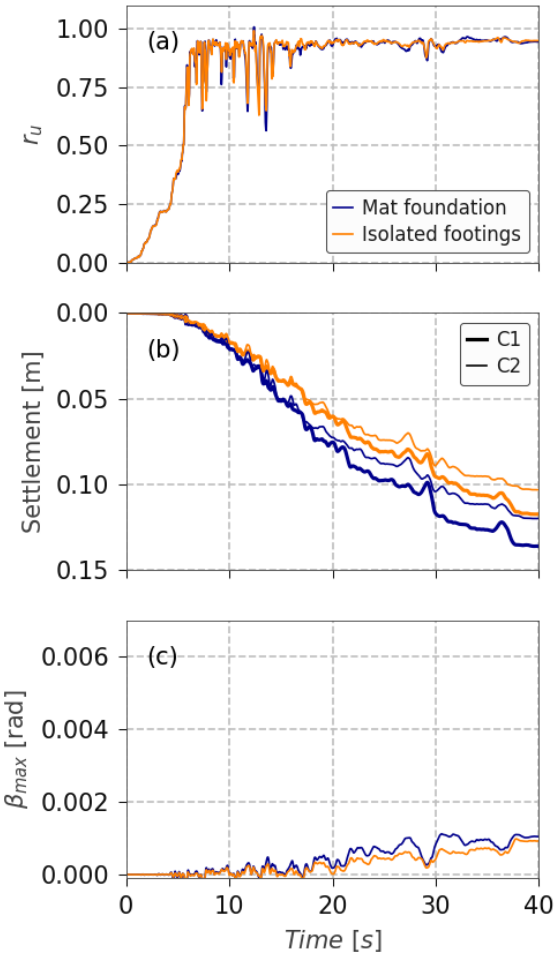

Figure 3. Comparison between the two 1-bay buildings numerical models: (a) excess pore pressure ratio in the middle of the liquefiable layer in free-field; (b) settlements at columns; and (c) maximum angular distortion.

3 RESULTS

1-bay and 2-bays buildings were modelled to analyse two different configurations of buildings, with mat foundation and isolated footings.

Figure 3 presents the results obtained from 1-bay building models and Figure 4 from 2-bay buildings model. In Figure 3(a) and Figure 4(a), the pore pressure ratio in the middle of the liquefiable sand layer for free-field conditions is shown. In both cases the pore pressure build up reached a state of total liquefaction at near 6 seconds.

When 1-bay buildings were modelled, Figure 3(b) shows that the total settlements in the building with mat foundation are higher when compared with the building with isolated footings, but the maximum angular distortion is similar using both types of foundations as observed in Figure 3(c).

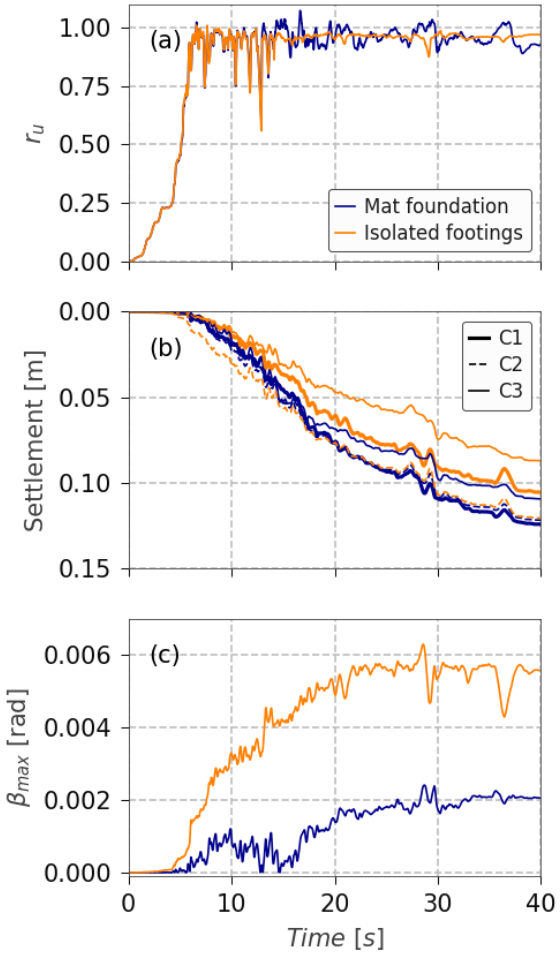

Figure 4. Comparison between the two 2-bay buildings numerical models: (a) excess pore pressure ratio in the middle of the liquefiable layer in free-field; (b) settlements at columns; and (c) maximum angular distortion.

When 2-bay buildings were modelled, Figure 4 (b) shows that the total settlements in the building with the

mat foundation are higher in the external columns (1 and 3) but almost the same in the central column when compared with the building with isolated footings. When the mat foundation was used the column on the left and the central column settled the same and more than the column on the right. When isolated footings were used the central column settled more than the external columns. Also, Figure 4 (c) shows that the maximum angular distortion is much greater when isolated footings were used.

If both buildings, 1-bay and 2-bays buildings, with mat foundation are compared, the external columns had more settlements when 1-bay building was modelled. Regarding the buildings with isolated footings, the external columns also had more settlements when 1-bay building was modelled.

A recent simplified approach (Bray and Macedo, 2017) that was developed for structures with mat foundation was used to estimate the settlements and compare them with the maximum settlement from numerical analyses. Foundation settlements of 0.024 m and 0.021 m were obtained for mat foundation buildings with 1-bay and 2-bay respectively. These settlements are very low when compared with the numerical results. If the simplified approach is used just considering the load in each footing, average values of 0.119 m and 0.140 m were obtained for buildings with 1-bay and 2-bay respectively. These settlements are similar with the numerical results.

4 CONCLUSIONS

This work provides the first key insights for extending the existing methods considering more complex systems such as buildings on shallow isolated footings. The numerical models presented in this paper allowed to observe the difference between total settlements and differential settlements when mat foundations and isolated footings are used. The results also showed the importance of considering the number of footings in the settlements of a building. The future analyses to complement this work should include additional parameters to quantify the mechanisms related to isolated footings, such as stiffness of the building and footing spacing.

ACKNOWLEDGEMENTS

This work was financially supported by UIDB/04708/2020 and UIDP/04708/2020 of CONSTRUCT – Institute of R\&D in Structures and Construction, Portugal funded by the national funds through the FCT/MCTES (PIDDAC). The first author acknowledges the support of Portuguese Foundation for Science and Technology (FCT) I.P./MCTES through the grant SFRH/BD/143817/2019.

REFERENCES

Acacio, A.A., Kobayashi, Y., Towhata, I., Bautista, R., and Ishihara, K. (2001). Subsidence of building foundation resting upon liquefied subsoil: case studies and assessment. *Soils and Foundations*, 41(6): 111-128. https://doi.org/10.3208/sandf.41.6_111.

Bentley. (2021). Plaxis2D ultimate, 2D geotechnical engineering software v21.01.00.479 [online]. Available at: https://www.bentley.com/software/plaxis-2d/, accessed: 22/10/2023.

Boulanger, R., and Ziotopoulou, K. (2017). PM4Sand (Version 3.1): A sand plasticity model for earthquake engineering applications. Report. No.UCD/CGM-17/01. University of California, Davis.

Bray, J., and Macedo, J. (2017). 6th Ishihara lecture: Simplified procedure for estimating liquefaction induced building settlement. *Soil Dyn. Earthquake Eng*, 102 (Nov): 215–231. https://doi.org/10.1016/j.soildyn.2017.08.026.

Haselton, C. B., Liel, A. B., Taylor-Lange, S. C. and Deierlein, G. G. (2016). Calibration of model to simulate response of reinforced concrete beam-columns to collapse. *ACI Struct. J*, 113 (6): 1141–1152. https://doi.org/10.14359/51689245.

Karamitros, D. K., Bouckovalas, G. D. and Chaloulos, Y. K.. (2013). Seismic settlements of shallow foundations on liquefiable soil with a clay crust. *Soil Dyn. Earthquake Eng*, 46 (3): 64–76. https://doi.org/10.1016/j.soildyn.2012.11.012.

Liu, L. and Dobry, R. (1997). Seismic response of shallow foundation on liquefiable sand. Journal of geotechnical and geoenvironmental engineering, 123(6):557-567. https://doi.org/10.1061/(ASCE)1090-0241(1997)123:6(557.

Millen, M., Viana da Fonseca, A. and Romão, X. (2018). Preliminary displacement-based assessment procedure for buildings on liquefied soil. *Proceedings of the 16th European Conference on Earthquake Engineering*. Springer (eds.). Thessaloniki, Greece.

Viana da Fonseca, A., Millen, M., Romão, X., Quintero, J., Rios, S., Cristiana, F., Fabrizio, P., Azeredo, C., Pereira, N., Logar, J., Oblak, A., Dolsek, M., Kosik, M., Kuder, S., Logar, M., Oztoprak, S., Kelesoglu, K., Sargin, S., Oser, C., Bozbey, I., Flora, A., Billota, E., Prota, A., Di Ludovico, M., Chiaradonna, A., Modoni, G., Paolella, L., Spacagna, R., Lai, C., Shinde, S. and Bozzoni, F. (2018). Methodology for the liquefaction fragility analysis of critical structures and infrastructures: description and case studies. Technical report: Deliverable 3.2. LIQUEFACT Project, Horizon 2020. Available at: www.liquefact.eu, accessed: 26/10/2023.

Yoshimi, Y. and Tokimatsu, K. (1997). Settlements of building on saturated sand during earthquakes. *Soil and Foundations*, 17(1): 23-38. https://doi.org/10.3208/sandf1972.17.23.

Proceedings of the XVIII ECSMGE 2024
GEOTECHNICAL ENGINEERING CHALLENGES
TO MEET CURRENT AND EMERGING NEEDS OF SOCIETY
© 2024 the Authors
ISBN 978-1-032-54816-6
DOI 10.1201/9781003431749-237
Open Access: www.taylorfrancis.com, CC BY-NC-ND 4.0 license

ECSMGE 24
XVIII EUROPEAN CONFERENCE ON SOIL MECHANICS AND GEOTECHNICAL ENGINEERING

A new, durable micropile for the foundation of rockfall protection structures

Un nouveau micropieu durable pour la fondation d'ouvrages de protection contre les chutes de pierres

M.J. Rebhan*, H.-P. Daxer, R. Marte
Graz University of Technology, Institute of Soil Mechanics, Foundation Engineering and Computational Geotechnics, Graz, Austria

M. Schuch
ÖBB Infrastruktur AG, Vienna, Austria

S.L. Burtscher
burtscher consulting GmbH, Vienna, Austria

**rebhan@tugraz.at*

ABSTRACT: The erection of protective structures is necessary to ensure the safety of infrastructure facilities such as roads and railways as well as settlement areas. Especially for rockfall protection structures, foundations in the form of micropiles are often used to transfer dynamic or impact-like loads into the subsoil. In addition to the requirements regarding the installation, the demands for a durable and sustainable foundation design of such structures have increased in recent years. In the course of a research project, a micropile system that can meet these requirements has been developed. It consists of a hollow bar that can be installed in a self-drilling manner and additionally has a corresponding durability due to a factory-applied resin coating. The advantages of such a system are the simple and fast installation process, which can be carried out with a wide range of equipment. This allows the system to be installed in areas that are difficult to access, as it is the case with protective structures. In addition, the resin coating has a high wear resistance in order to withstand the rough installation process during rotary percussive drilling and ensures the required corrosion protection layer for a durable geotechnical element. On the one hand, this paper presents findings from investigations on current corrosion protection methods for micropiles. On the other hand, the developed micropile system is introduced, which has already been tested and validated in a series of field tests. In addition, ongoing developments such as spacers and post grouting possibilities are presented.

RÉSUMÉ: La mise en place d'ouvrages de protection est nécessaire pour assurer la sécurité des infrastructures telles que les routes et les voies ferrées, ainsi que des zones d'habitation. En particulier pour les ouvrages de protection contre les chutes de pierres, des fondations sous forme de micropieux sont souvent utilisées pour transférer des charges dynamiques ou des charges d'impact dans le sous-sol. Outre les exigences relatives à l'installation, les demandes de conception de fondations durables pour de telles structures ont augmenté ces dernières années. Dans le cadre d'un projet de recherche, un système de micropieux capable de répondre à ces exigences a été développé. Il s'agit d'une barre creuse qui peut être installée de manière autoperceuse et qui présente en outre une durabilité correspondante grâce à un revêtement en résine appliqué en usine. Les avantages d'un tel système sont la simplicité et la rapidité du processus d'installation, qui peut être réalisé à l'aide d'un large éventail d'équipements. Cela permet d'installer le système dans des zones difficiles d'accès, comme c'est le cas pour les structures de protection. En outre, le revêtement en résine présente une résistance élevée à l'usure afin de supporter le processus d'installation brutal pendant le forage rotatif à percussion et assure la couche de protection contre la corrosion requise pour un élément géotechnique durable. D'une part, cet article présente les résultats d'études sur les méthodes actuelles de protection contre la corrosion pour les micropieux. D'autre part, il présente le système de micropieux développé, qui a déjà été testé et validé dans une série d'essais sur le terrain. En outre, les développements en cours, tels que les entretoises et les possibilités de post-encastrement, sont présentés.

Keywords: Rockfall-protection, durability, micropiles, impact-like loads.

1 FOUNDATION OF ROCKFALL PROTECTION STRUCTURES

Protective structures such as rockfall protection nets are an essential part of Austrian railways and roads and along settlement areas. Due to the topography, such structures are necessary and are currently becoming more frequent due to the effects of climate change. Rockfall protection structures can be designed in different forms and variants (Bergmeister, 2009). In addition to dam structures (Mölk & Hofmann, 2018), rockfall protection nets are often erected, as shown in Figure 1. These consist of a superstructure formed by posts and a net placed in between.



Figure 1. Rockfall protection net next to a support road of a railway line.

The (inclined) posts are connected to an appropriate foundation (e.g. slab) and can also be supplemented – depending on the energy level – by an additional upstream and downstream cable. Therefore, next to counterweights, micropiles are necessary for the foundation of protective structures in order to transfer the cable forces into the subsoil and to ensure the load-bearing capacity of the post foundations. Consequently, these are to be installed in the surrounding subsoil along the axis of the protective structure, which means that they are installed in mostly inaccessible areas.

As an installation method either solid rod systems or self-drilling systems can be used. The first are installed by means of a cased drilling with the advantage of a wide range of usability and the disadvantage of low performance in installation and correspondingly high costs. The second type can be installed easier and therefore offers a quite high performance under the constraints of the location of these structures.

2 CORROSION PROTECTION MEASURES & MICROPILE DCP-SBZ

In order to ensure the necessary (or expected) durability and the planned service life (ÖNORM B 1997-1-, 2021 & ONR 24810, 2017), appropriate corrosion protection of the micropiles is required. This generally applies to all buildings and structures, although protective structures usually have a shorter service life. A large part of the structural elements can be examined for damage of degradation in the course of visual tests and inspections. The foundation elements, however, are installed within the subsoil and therefore cannot be inspected visually. For this reason, attention must be paid to the corrosion protection of the tension elements.

Typical corrosion protection measures for micropiles are defined in the respective regulations (e.g. ÖNORM EN 14199, 2015) and have recently been specified more comprehensively in ÖNORM B 4456 (2021). Within this Austrian standard, a distinction is made between single corrosion protection (SCP), double corrosion protection (DCP see Figure 2 bottom) and material related corrosion protection (MCP). The first – and most frequently used SCP – can be further subdivided into sacrificial corrosion allowance (STA), coating corrosion protection (CCP), zinc corrosion protection (ZCP see Figure 2 top right) and grout cover protection (GCP see Figure 2 top left).



Figure 2. Types of corrosion protection, top left: grout cover protection (GCP), top right: uinc corrosion protection (ZCP) and double corrosion protection (DCP).

In the course of a research project (DAT, 2022), improvements on the corrosion protection of micropiles used as a foundation of protective structures has been investigated. The results of this project are described below and show a first basic concept while the field testing and application if given in chapter 3.

The basic concept was to develop a permanent and durable micropile, that fulfils both the requirements

for durability and load-bearing capacity and also offers easy installation. A system based on a self-drilling tensile element was used as the basis for this, which was supplemented by an appropriate coating to ensure durability. This corrosion protection system is based on the DCP, which is widely used for pre-stressed anchors (ÖNORM EN 1537, 2015) and other tensile elements, but is not yet used for self-drilling elements such as micropiles and soil nails. A schematic structure of an initial prototype is shown in Figure 3.

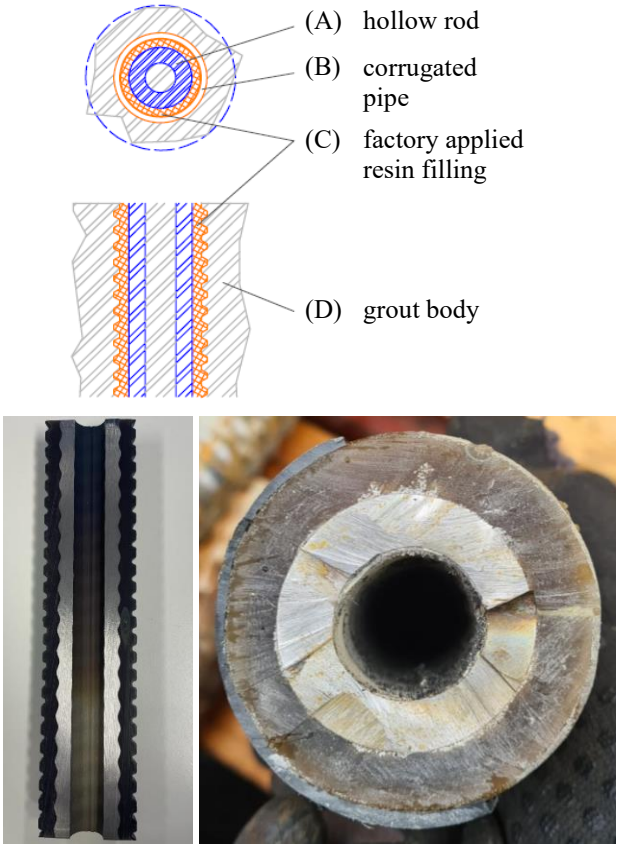

Figure 3. Developed double-corrosion-protection self-drilling tension element (DCP-SBZ), top: schematic, bottom: longitudinal and sectional cross section.

Rotary driven micropiles – using a hollow rod (A in Figure 3 top) – represent one of the cheapest installation methods in terms of equipment, making this system particularly suitable for the use in inaccessible areas. To prevent corrosion and furthermore fulfil the requirements of a planned service-life of more than 30 years, the metal rod was supplemented with a corrosion protection similar to a double corrosion protection DCP. However, this could not be achieved by using a cement-filled corrugated pipe (B in Figure 3 top), as it would not withstand the impact and abrasiveness due to the rotary percussive installation process. Consequently, the cement was replaced by a resin body (C in Figure 3 top) with a thickness of 4 to 7 mm depending on the shape of the rod.

The first results of this development have shown that a uniform and full-surface coating of the metal rod (see Figure 3 bottom) can be achieved during manufacturing, providing a continuous corrosion protection barrier.

3 FIELD TESTING, APPLICATION AND FURTHER DEVELOPMENT

In a series of field tests (DAT, 2022), investigations were carried out to determine whether the applied resin layer can withstand the installation process of rotary percussive drilling. These were carried out under a wide range of geological boundary conditions, from compact rock to soft, uncompacted fills and boulder dumps. The aim was to determine the applicability of the system and the influence of the subsoil on the installation. Figure 4 shows the installation process of aforementioned micropiles in a slope using a mounting carriage on an excavator.



Figure 4. Installation of DCP-SBZ (self-boring tensile element) micropiles for testing purposes.

These tests and a subsequent deinstallation of the micropiles showed, that over a large part of the pile length both the resin body and the corrugated pipe were still intact. On the one hand, micropiles installed were pulled out of the subsoil before the grout body hardened (Figure 5 left) and, on the other hand, the micropiles were uncovered after hardening (Figure 5 rigth) and the performance of tensile load tests.

In addition to the condition of the corrosion protection, a comparison of the load-bearing capacity with classic micropiles was also carried out. This showed no significant difference in either the load-deformation behaviour or the load-bearing capacity.

With respect to the corrosion protection only the head area near the drilling bit and in the area of fittings and joints small damages were observed when test bodies in (gravely and sandy) soil were exhumed after installation. These damages can be attributed to entrapment of coarse-grained fractions. However, such damage can be eliminated by further developing drill bits and also coupling devices, which provide protection for the transition zones.



Figure 5. Examples for exhumed micropiles.

The concept described and tested shows the development of a new type of micropile, which has considerable advantages due to the resin-based corrosion protection barrier and the simple self-drilling installation process. These range from the low installation effort to ensuring the required durability due to the double corrosion protection. The disadvantages at present are the high costs – due to the expensive resin that has to be used – and the fact that the application of the corrosion protection layer results in a significant increase in weight, which limits the handling by the site personnel.

Furthermore, the concept of this micropile additionally offers the possibility of post grouting (due to the core of the hollow rod), which can lead to an increase in the load bearing capacity and subsequently to a reduction in the required pile lengths. In addition to cost savings, this can result in a reduction in installation time, which can be a clear advantage given the difficult installation conditions for protective structures, as mentioned above.

Furthermore, this micropile system can also be used in other areas of geotechnics in addition to rockfall protection nets. Particularly in the construction and installation of soil nailing, the use of this type of system can create a permanent and therefore sustainable form of construction for cuttings and slope stabilisation.

4 CONCLUSIONS

This paper gives a brief insight into developments in the field of the foundation of protective structures through the use of micropiles.

A new type of micropile was presented, which is based on the application of a corrosion protection barrier to self-drilling tensile elements. The required corrosion protection can be ensured by a resin coating, which is factory-applied to the metal rod and therefore offers an easy and well-known installation process. This layer offers sufficient strength and abrasiveness to allow rotary percussive installation even in coarse-grained soils.

This article shows that there is a comprehensive potential for optimisation and improvement in the field of protective structures. Such developments are necessary to ensure the requirements for durability and thus a sustainable operation of the infrastructure, while still guaranteeing sufficient safety of the structures. Taking into account the increase in climate change-related effects, it can be assumed that there will be an increased need for such constructions in the future.

ACKNOWLEDGEMENTS

The authors are grateful for the financial support provided by the Austrian Research Promotion Agency FFG within the research project DAT – Durability in Anchor Techniques. The project presented in this article was additionally supported by the Austrian Federal Railways and Keller Grundbau GmbH.

REFERENCES

Bergmeister, K. (2009). *Protective structures against torrential hazards (In German).* Ernst & Sohn: Berlin.

DAT. (2022). Final report research project *DAT - Durability in anchor technology.* (In German) Technische Universität Graz. Institut für Bodenmechanik, Grundbau und Numerische Geotechnik. Graz.

Mölk, M. and Hofmann, R. (2018). *Protective structures against rockfall according to ONR 24810*. (In German). In. Berichte der Geologischen Bundesanstalt (125). P. 66 – 89.

ONR 24810. (2017). *Technical protection against rockfall*. ASI. Vienna.

ÖNORM B 1997-1-1. (2021). *Eurocode 7: Geotechnical design - Part 1: General rules - National specifications concerning ÖNORM EN 1997-1 and national supplements*. Austrian Standards International, Vienna.

ÖNORM B 4456. (2021). *Geotechnic – Durability of anchorages*. ASI. Vienna.

ÖNORM EN 1537. (2015). *Execution of Geotech-nical works – Ground anchors*. ASI. Vienna.

ÖNORM EN 14199. (2015). *Execution of geotechnical works – Micropiles*. ASI. Vienna.

Proceedings of the XVIII ECSMGE 2024
GEOTECHNICAL ENGINEERING CHALLENGES
TO MEET CURRENT AND EMERGING NEEDS OF SOCIETY
© 2024 the Authors
ISBN 978-1-032-54816-6
DOI 10.1201/9781003431749-238
Open Access: www.taylorfrancis.com, CC BY-NC-ND 4.0 license

ECSMGE 24
XVIII EUROPEAN CONFERENCE ON SOIL MECHANICS AND GEOTECHNICAL ENGINEERING

Landslide susceptibility map of the southern slope of the municipality of Odivelas using the AHP method

Carte de susceptibilité aux glissements de terrain du versant Sud de la municipalité d'Odivelas à l'aide de la méthode AHP

A.J. Roque*, M.J. Coelho
Laboratório Nacional de Engenharia Civil, Lisboa, Portugal
aroque@lnec.pt

ABSTRACT: The Laboratório Nacional de Engenharia Civil has produced a Landslide Susceptibility Map (LSM) of the Southern Slope of the municipality of Odivelas. Regarding the Portuguese legislation in force for the prevention of risks in potentially unstable areas, the main goal of this map is to support the ongoing urban planning on the site (155 ha), occupied by illegal constructions. Based on the information obtained about the characteristics of the ground in the study area, as well as on the consulted bibliography, six conditioning factors for landslides were selected, which in order of decreasing importance are as follows: slope, soil thickness, lithology, curvature, land use, and aspect. For each factor, classes with different degrees of susceptibility were used. The Analytic Hierarchy Process (AHP), a multicriteria analysis method, was used to structure, hierarchise and calculate the weights of those factors. Using these weights and the degrees of susceptibility assigned to the classes of each factor, a landslide susceptibility index was calculated, whose values and a susceptibility scale consisting of five classes have allowed generating the LSM.

RÉSUMÉ: Le Laboratório Nacional de Engenharia Civil a réalisé une Carte de Susceptibilité aux Glissements de Terrain (CSGT) du Versant Sud de la commune d'Odivelas. Concernant la législation portugaise en vigueur pour la prévention des risques dans les zones potentiellement instables, l'objectif principal de cette carte est de soutenir l'aménagement urbain en cours sur le site (155 ha), occupé par des constructions illégales. Sur la base des informations obtenues concernant les caractéristiques du terrain dans la zone d'étude, ainsi que sur la bibliographie consultée, six facteurs conditionnant les glissements de terrain ont été sélectionnés, qui par ordre d'importance sont les suivants: pente, épaisseur du sol, lithologie, courbure, l'utilisation du terrain, et l'exposition. Pour chaque facteur, des classes présentant différents degrés de susceptibilité ont été utilisées. L'Analytic Hierarchy Process (AHP), une méthode d'analyse multicritère, a été utilisée pour structurer, hiérarchiser et calculer les poids de ces facteurs. En utilisant ces poids et les degrés de susceptibilité attribués aux classes de chaque facteur, un indice de susceptibilité aux glissements de terrain a été calculé, dont les valeurs et une échelle de susceptibilité composée de cinq classes ont permis de générer la CSGT.

Keywords: Urban planning; unstable areas; conditioning factors; analytic hierarchy process; susceptibility mapping.

1 INTRODUCTION

To watch out and reduce risks in areas with potentially unstable slopes and contributing to the safety of people and property, Portuguese legislation has, since 2008, included them in a group of areas that are subject to special protection. The area shown in Figure 1 (approximately 155 ha), known as the Southern Slope (SS) of Odivelas, falls into this category. In a previous period, between the beginning of the 1960s and the end of the 1980s, most of this area was occupied by illegal construction. To proceed with its urban redevelopment it is intended to apply to the competent Portuguese regional authority for the detachment of the areas where potentially unstable slopes are low enough not to put urban occupation at risk. It was in this context that the National Laboratory for Civil Engineering and Odivelas Town Council signed a scientific and technical cooperation agreement to produce the Landslide Susceptibility Map (LSM) here presented.

Based on the geomorphological, geological-geotechnical and hydrogeological information obtained in the study area and on the bibliography collected and analysed, six conditioning factors for the mass movements of the SS of Odivelas were selected, which in descending order of importance are as follows: slope, soil thickness, lithology, curvature, land use, and aspect. Each of these factors was assigned various classes with different degrees of susceptibility. In order to structure, prioritise and calculate the weights for each factor, a multi-criteria analysis method, called the Analytic Hierarchy Process (AHP) was used (Saaty, 1980). Based on the

weights obtained for each factor and the degrees of susceptibility assigned to the classes of each factor, the landslide susceptibility index, I_S, was calculated for the square cells (or pixels) of 5 m side, into which the study area was divided. Considering the I_S value calculated for each cell and the five classes of susceptibility used (very high, high, moderate, low and very low), the areas of the LSM where the probability of landslides occurring is similar were generated.

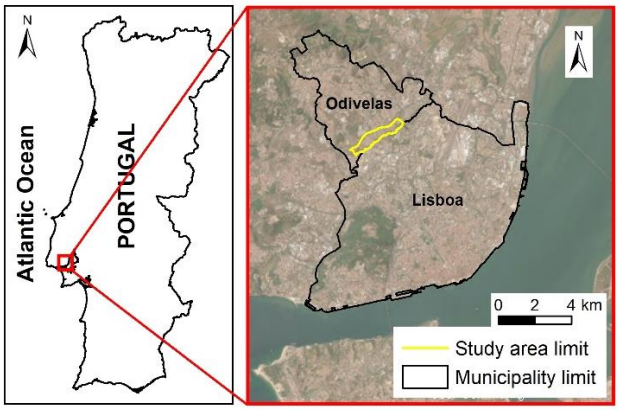

Figure 1. Location of the Southern Slope of Odivelas.

2 CHARACTERISTICS OF THE SOUTHERN SLOPE OF ODIVELAS

The SS of Odivelas is located on a very steep slope, which varies, in less than 500 metres, between plane areas (slope < 5%), to the north and steep areas (slope ≥ 50%), to the south. The areas occupied by these two classes are the most expressive compared to the others (5-15%, 15-30% and 30-50%). This morphology is due to the presence of a monoclinal structure, which dips moderately (10º to 25º) towards the SE, and the occurrence of lithologies (conglomerates or limestones) that are more competent at the top than in the concave part, where sandstones and claystones occur. The plane areas are occupied by the alluvium deposited by a local river, which has, approximately, the same orientation as the SS of Odivelas, i.e. SW-NE.

The geological-geotechnical and hydrogeological characterisation of the SS of Odivelas has been carried out on the basis of surface geological reconnaissance and, mainly, using information obtained from the following site investigation: i) 174 boreholes, of which 144 were located in the study area and the rest in the immediate vicinity, ii) 15 pits, iii) 8 seismic refraction profiles, and iv) 3 electrical resistivity profiles. Seventeen inclinometer tubes and 41 piezometers were installed in the boreholes to monitor the occurrence of horizontal ground displacement and groundwater level fluctuations.

From a geological-geotechnical point of view, the subsoil has been classified into two units. The superficial formations correspond to backfill, alluvium, colluvium and bedrock with a number of blows of the Standard Penetration Test (N_{SPT}) less than 30. The total thickness of these formations varies between 0 m, when the bedrock outcrops, and 18.2 m. The bedrock formations, individualised according to lithology and/or N_{SPT}, are as follows: a) sandstones and claystones, with $30 \leq N_{SPT} < 50$, b) claystones, siltstones and marls, with $N_{SPT} \geq 50$, c) clayey sandstones and marls, with $N_{SPT} \geq 50$, and d) fractured limestone and compact calcareous marls.

The variations in the groundwater level measured in the piezometer were less than 3 m for about 85% of the total, so there were no significant variations in the subsoil hydrogeological regime.

3 SELECTED CONDITIONING FACTORS FOR LANDSLIDES

The selection of conditioning factors to the occurrence of landslides in the SS of Odivelas took into account the provisions of the current Portuguese legislation, according to which "(...) at least (...) slope, slope aspect, slope curvature (cross-sectional profile), lithology and vegetation cover/land use should be considered. In addition, other relevant factors such as soils, superficial formations, Wetness Index and geological structure can be used.". Moreover, eight internationals (Jade and Sarkar, 1993; Irigaray et al., 2007; Jiménez-Perálvarez et al., 2009; Thanh and De Smedt, 2012; Faria and Fialho, 2013, Souza and Sobreira, 2014, Torres et al., 2015; Guedjeo et al., 2017) and four Portuguese (Garcia, 2002; Zêzere, 2002; ANPC, 2009; Policarpo, 2012) studies, were also considered. The selected conditioning factors are shown in Table 1. The legislation dealing with the "delimitation of areas of slope instability" does not establish classes for conditioning factors, so the classes shown in were defined on the basis of the authors' experience, knowledge of the geological-geotechnical characteristics of the study area and the bibliography consulted.

Based on the classes assigned to each conditioning factor, the corresponding factor maps were generated (Figure 2). All the maps were calculated or converted to raster format, with 5x5 m^2 cells, using ArcGIS 10.2.

Table 1. Selected conditioning factors and their classes.

Factor	Classes
Slope (%)	≥ 50; 40 – 50; 30 – 40; 15 – 30; < 15
Soil thickness (m)	≥ 5.0; 3.0 – 5.0; 1.5 – 3.0; < 1.5
Lithology	Backfill, alluvium, colluvium (superficial units) and bedrock with N_{SPT} < 30; Bedrock, or bedrock with a covering < 1.5 m
Curvature	Cc / Cv; Cc / P; Cc / Dv; P / Cv; P / P; P / Dv; Cx / Cv; Cx / P; Cx / Dv; HP
Land use	Built-up area; Agricultural area; Tree and forest area; Herbaceous and shrub area; Special infrastructure area
Aspect	North; East; West; South; HP

Cc – Concave; Cx – Convex; Cv – Convergent; Dv – Divergent; P – Planar; HP – Horizontal Plane.

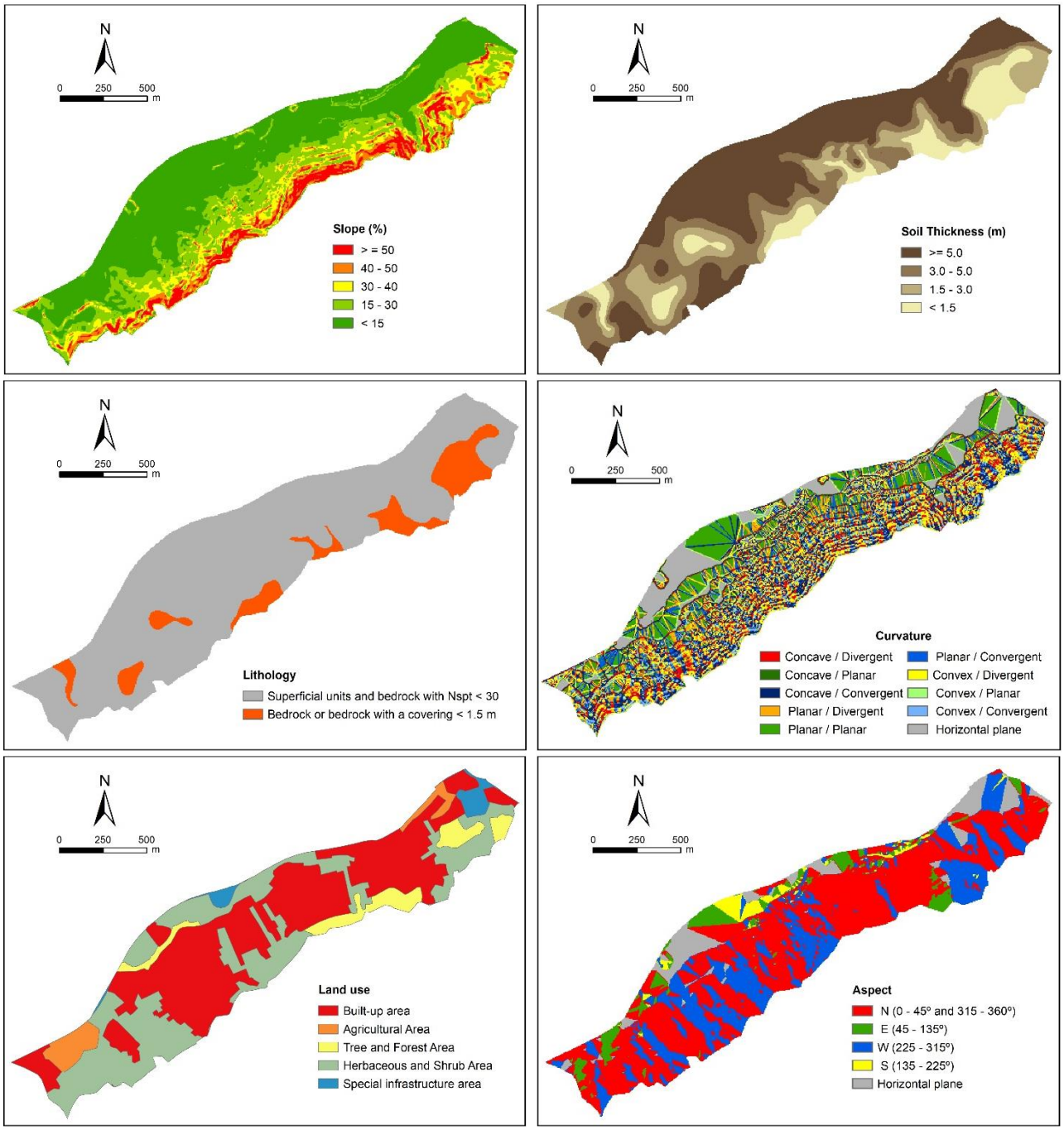

Figure 2. Conditioning factor maps used in the Southern Slope of Odivelas.

4 SUSCEPTIBILITY INDEX TO LANDSLIDES IN THE SOUTHERN SLOPE OF ODIVELAS

The methodology adopted for the calculation of the index of susceptibility, I_S, in the SS of Odivelas comprised two stages.

In the first stage, the AHP allowed to evaluate the weights (W_1 to W_6) of the six conditioning factors, which were used to calculate the susceptibility index, I_S (LNEC, 2018, Roque et al., 2023). The weights obtained were: W_1 = 48.902% for "Slope", W_2 = 20.367% for "Soil thickness", W_3 = 11.775% for "Lithology", W_4 = 8.155% for "Curvature", W_5 = 7.514% for "Land use", and, lastly, W_6 = 3.287% for "Aspect".

In the second stage, to each class listed in Table 1, some of which were regrouped into one class, was assigned a degree of susceptibility, $G_i(F_i)$, as shown in Table 2. These degrees vary between a minimum value of 1 (corresponding to the lowest susceptibility) and a maximum value of 5 (corresponding to the highest susceptibility). The degrees of susceptibility were assigned taking into account the relative importance of the classes in terms of ground movements. The full range of susceptibility degrees was only applied to the "Slope" factor. In the "Soil thickness", "Curvature" and "Aspect" factors, the range of values was between 1 and 4 and in the "Lithology" and "Land use" factors between 1 and 3.

Table 2. Degrees of susceptibility $G_i(F_i)$ assigned to the classes of each factor (F_i).

F_i	Class	$G_i(F_i)$	F_i	Class	$G_i(F_i)$
Slope	≥ 50%	5	Curvature	Cc / Cv or Cc / P	4
	40 – 50%	4		Cc / Dv or P / Cv or P / P	3
	30 – 40%	3		P / Dv or Cx / Cv	2
	15 – 30%	2		Cx / P or Cx / Dv or HP	1
	< 15%	1			
Soils thickness	High (≥ 5 m)	4	Land use	Built-up or agricultural area	3
				Tree and forest area	2
	Moderate (3 – 5 m)	3		Heraceous and shrub area or special infrastuctrures area	1
	Low (1.5 – 3 m)	2			
	Superficial (< 1.5 m)	1			
Lithology	Backfill, alluvium, colluvium (superficial units) and bedrock with N_{SPT} < 30	3	Aspect	N (0 – 45º and 315 – 360º)	4
	Bedrock or bedrock with a covering < 1.5 m	1		E (45º – 135º) or W (225º – 315º)	2
				S (135º – 225º) or HP	1

Cc – Concave; Cx – Convex; Cv – Convergent; Dv – Divergent; P – Planar; HP – Horizontal Plane.

Using the weights, W_i, obtained for each factor, F_i, and the degree of susceptibility, $G_i(F_i)$, assigned to each class of F_i, the I_S was calculated through the weighted sum of the weights W_i and the degrees of susceptibility $G_i(F_i)$, as follows:

$$I_S = \sum_{i=1}^{6} W_i \, G_i(F_i), \qquad (1)$$

with $\sum_{i=1}^{6} W_i = 1$ e $0 < W_i < 1$ $(i = 1, \cdots, 6)$

The minimum and maximum values that I_S can take are 1.00 and 4.30, respectively.

5 LANDSLIDE SUSCEPTIBILITY MAP OF THE SOUTHERN SLOPE OF ODIVELAS

The Landslide Susceptibility Map (LSM) of the SS of Odivelas (Figure 3) was obtained by dividing the study area into square cells of 5 m side and calculating the susceptibility index, I_S, value for each cell. As mentioned before, I_S varies between a minimum of 1.00 and a maximum of 4.30.

The ArcGIS 10.2 Natural Breaks classification method was applied to the distribution of I_S values in the cells of the study area, in order to obtain five classes, which corresponding to the same number of classes of the applied susceptibility scale: very high, high, moderate, low and very low. Areas represented by the same class are considered to be of the same order of magnitude in terms of susceptibility to landslides.

In the areas classified as very low (29.7 ha, 19%) to low (68.6 ha, 44%) susceptibility classes, the ground is generally plane or slightly sloping, with poor drainage and with the possibility of flooding. The hazard of ground movement in areas belonging to these classes is very low, making them favourable for

land use. In areas of moderate susceptibility (31.2 ha, 20%), the hazard of ground movement is low, although occasional interventions in existing buildings may be required to reduce the risk. Future local interventions must be carried out in such a way as not to affect the existing ground stability, in order to keep the risk at an acceptable level. In the areas of high susceptibility (16.7 ha, 11%), the anthropogenic interventions that were observed have increased the hazard of ground movement, given the existing geological-geotechnical and geomorphological conditions, which are not favourable to the occupation of these areas. In areas that have already been built on, local interventions may be necessary to reduce the risk and new building should not be allowed. Urban occupation of areas with very high susceptibility (9.0 ha, 6%) should clearly be avoided, as the hazard of ground movement is very high. The ground movements that have already occurred in the SS are almost always in this susceptibility class, as shows Figure 3. In built-up areas, intervention may be necessary to reduce the risk.

These results show that the areas of very low to moderate susceptibility represent approximately 83% of the total area. In these areas, the hazard of ground movement was considered to be acceptable and did not pose its occupation by people and goods at risk.

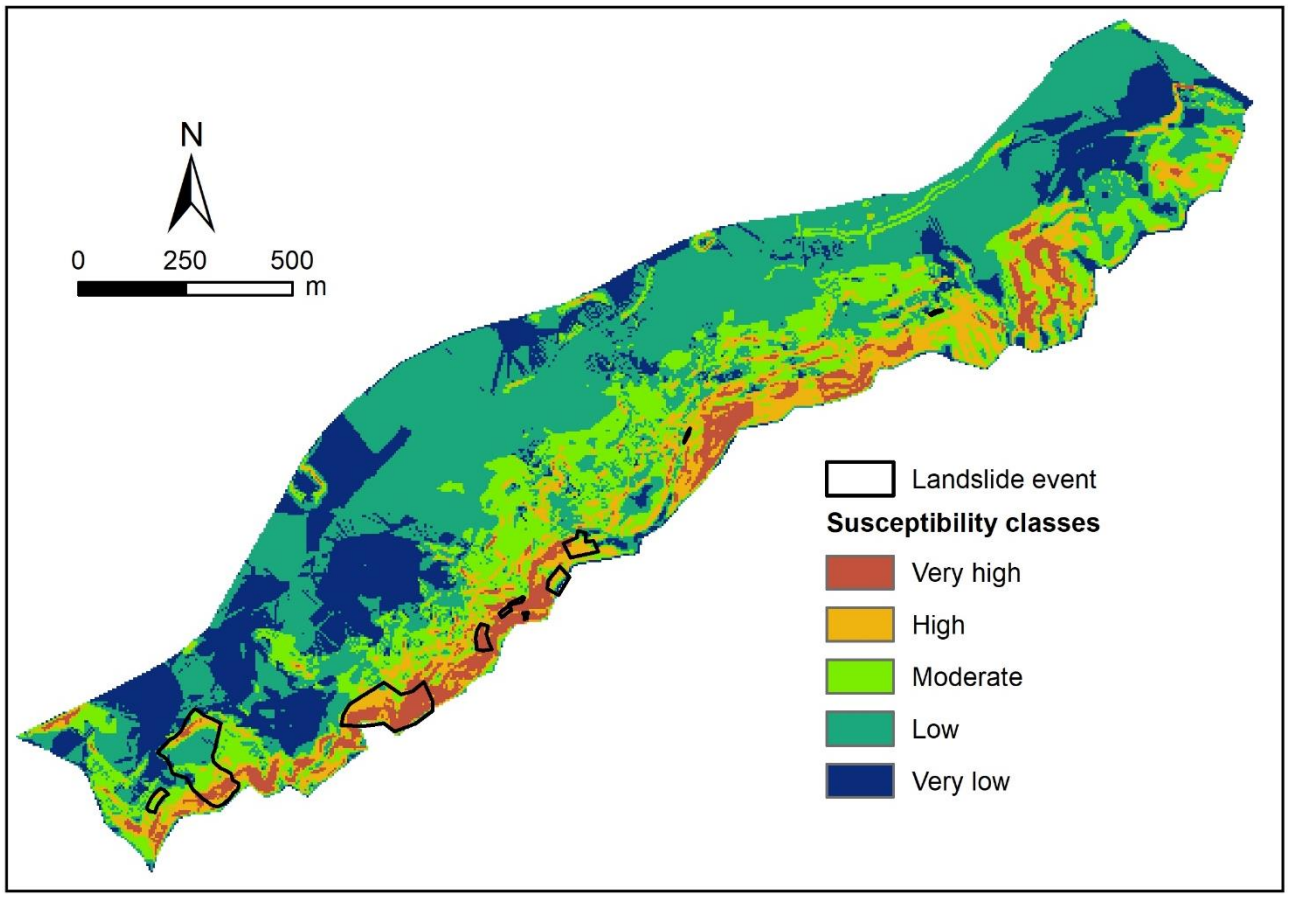

Figure 3. Landslide Susceptibility Map of the Southern Slope of Odivelas with depiction of past landslide events.

6 CONCLUDING REMARKS

Under current Portuguese legislation, the SS of Odivelas is classified as an area of potentially unstable slopes where the risks to the safety of people and property must be safeguarded and reduced. For Odivelas Town Council to proceed with the urban redevelopment of the SS, which has been occupied by illegal constructions since the early 1960s, it is necessary to apply to the competent Portuguese authorities for the de-annexation of areas where the hazard of ground movement occurring is acceptable. It was with the aim of mapping the areas of the SS of Odivelas that comply with this requirement, that the study presented in this communication was developed.

The obtained Landslide Susceptibility Map (LSM), based on six conditioning factors to landslides (slope, soil thickness, lithology, curvature, land use, and aspect) and a susceptibility scale with five classes (very high, high, moderate, low and very low), shown that the areas of very low to moderate susceptibility represented around 83% of the SS. In these areas, the risk to urban occupation was considered acceptable.

ACKNOWLEDGEMENTS

The authors are grateful to the Odivelas Town Council for permission to use and disseminate the work carried out to produce the Landslide Susceptibility Map of the Southern Slope of Odivelas.

REFERENCES

ANPC (2009). *Methodological guide for the production of municipal risk cartography and for the creation of municipal-based Geographic Information Systems (GIS)*. Autoridade Nacional de Proteção Civil (ANPC), Lisboa (in Portuguese).

Faria, D. G. M. and Fialho O. A. (2013). Landslide hazard mapping in Brazilian poor and slum urban areas with the application of the AHP method. *Revista Geotecnia*: 129, pp. 17-42 (in Portuguese). https://doi.org/10.14195/2184-8394_129_2.

Garcia, R. A. C. (2002). *Assessment of the risk of slope movements in the Abadia depression (Torres Vedras)*. Master's Thesis, Universidade de Lisboa, Lisboa (in Portuguese).

Guedjeo, C. S., Kagou Dongmo, A., Wotchoko, P., Nkouathio, D. G., Chenyi, M. L., Wilson Buma, G. and Kamgang, K. V. (2017). Landslide Susceptibility mapping and risk assessment on the Bamenda Mountain (Cameroon Volcanic Line). *Journal of Geosciences and Geomatics*, 5(4): 173-185. https://doi.org/10.12691/jgg-5-4-2.

Irigaray, C., Fernández, T., Hamdouni, R. El and Chacón, J. (2007). Evaluation and validation of landslide-susceptibility maps obtained by a GIS matrix method: examples from the Betic Cordillera (Southern Spain). *Natural Hazards*, 41: 61-79. https://doi.org/10.1007/s11069-006-9027-8.

Jade, S. and Sarkar, S. (1993). Statistical models for slope instability classification. *Engineering Geology*, 36(1-2): 91-98. https://doi.org/10.1016/0013-7952(93)90021-4.

Jiménez-Perálvarez, J. D., Irigaray, C., Hamdouni, R. El and Chacón, J. (2009). Building models for automatic landslide-susceptibility analysis, mapping and validation in ArcGIS. *Natural Hazards*, 50(3): 571-590. http://dx.doi.org/10.1007/s11069-008-9305-8.

LNEC (2018). *Geological-geotechnical study on construction capability in the hillsides of the Southern Slope of Odivelas municipality (Phase II). Revision of the Landslide Susceptibility Map*. LNEC Report 412/2018 – DG/NGEA, Laboratório Nacional de Engenharia Civil, Lisboa (in Portuguese).

Policarpo, N. O. S. G. (2012). *Susceptibility to slope movements and vulnerability in the municipality of Funchal*. Final Internship Report, Universidade de Lisboa, Lisboa (in Portuguese).

Roque, A. J., Coelho, M. J. and Murtinha, L. (2023). Susceptibility to mass movements on the Southern Slope of Odivelas: methodology and factors to produce the map. *Proceedings of the 18th Portuguese Geotechnics Congress*, I. Duarte, J. Marcelino, A. Pinho, P. Faria, L. Lopes and P. Pereira (eds), Portuguese Geotechnical Society, pp. 1137-1146 (in Portuguese).

Saaty, T. L. (1980). *The analytic hierarchy process*. McGraw-Hill International Book Company, New York.

Sousa, F. (2013). *Analysis of constraints to construction on a slope with instabilities*. Master's Thesis, Universidade de Lisboa, Lisboa.

Souza, L. A. and Sobreira, F. G. (2014). *Guide for preparing geotechnical maps of suitability for urbanization after natural disasters: Case study of Ouro Preto – 2013*. L. A. de Souza and F. G. Sobreira (eds), Brasília.

Thanh, L. N. and De Smedt, F. (2012). Application of an analytical hierarchical process approach for landslide susceptibility mapping in A Luoi district, Thua Thien Hue Province, Vietnam. *Environmental Earth Science*, 66(7): 1739-1752. https://doi.org/10.1007/s12665-011-1397-x.

Torres, F. S. M., Coutinho, R. Q., Duarte, C. C., Menezes, J. B., Fonsêca, D. N. and Pfaltzgraff, P. A. S. (2015). Charter of susceptibility to erosion and mass movements of the city of Ipojuca-PE. *Revista Geotecnia*, 135: 67-88 (in Portuguese). https://doi.org/10.24849/j.geot.2015.135.04.

Zêzere, J. L. (2002). Landslide susceptibility assessment considering landslide typology. A case study in the area north of Lisbon (Portugal). *Natural Hazards and Earth System Sciences*, 2: 73-82. https://doi.org/10.5194/nhess-2-73-200.

Proceedings of the XVIII ECSMGE 2024
GEOTECHNICAL ENGINEERING CHALLENGES
TO MEET CURRENT AND EMERGING NEEDS OF SOCIETY
© 2024 the Authors
ISBN 978-1-032-54816-6
DOI 10.1201/9781003431749-239
Open Access: www.taylorfrancis.com, CC BY-NC-ND 4.0 license

ECSMGE 24
XVIII EUROPEAN CONFERENCE ON SOIL MECHANICS AND GEOTECHNICAL ENGINEERING

Numerical and theoretical investigation on the triggering mechanisms of rainfall-induced landslides

Étude numérique et théorique des mécanismes de déclenchement des glissements de terrain provoqués par les précipitations

G.M. Rotisciani*
Università degli Studi Niccolò Cusano, Rome, Italy

A. Desideri, A. Amorosi
Università degli Studi di Roma Sapienza, Rome, Italy

**giada.rotisciani@unicusano.it*

ABSTRACT: In unsaturated shallow deposits, rainfall infiltration is the most common cause of landslides. This paper focuses on landslides involving coarse-grained soils and, in particular, analyses the mechanisms that cause the evolution of slides into flow-slides. This study provides an alternative explanation for the initiation of these phenomena, suggesting that they may result from a combination of two unstable processes: the first occurring when the soil is still in the unsaturated regime, the second taking place when full saturation is reached. This hypothesis is based on the analysis of the numerically observed response of an ideal infinite slope to rainfall events. Beyond illustrating the initiation of the unstable process, the study investigates its causes and provides an analytical criterion for capturing the onset of the instability and monitoring local slope stability.

RÉSUMÉ: Dans les dépôts peu profonds non saturés, l'infiltration des pluies est la cause la plus fréquente des glissements de terrain. Cet article se concentre sur les glissements de terrain impliquant des sols à gros grains et, en particulier, analyse les mécanismes qui causent l'évolution des glissements en glissements d'écoulement. Cette étude fournit une explication alternative pour l'initiation de ces phénomènes, suggérant qu'ils peuvent résulter d'une combinaison de deux processus instables: le premier se produisant lorsque le sol est encore dans le régime non saturé, le second se produisant lorsque la saturation complète est atteinte. Cette hypothèse est basée sur l'analyse de la réponse observée numériquement d'une pente infinie idéale lors d'événements pluvieux. Au-delà de l'illustration de l'initiation du processus d'instabilité, l'étude examine ses causes et fournit un critère analytique pour capturer la zone d'instabilité et surveiller la stabilité locale de la pente.

Keywords: Flow-slides; triggering mechanism; infinite slope; water infiltration; stability criterion.

1 INTRODUCTION

Rainfall-induced landslides are natural hazards that cause large numbers of casualties and economic losses every year. Due to the continuous climatic and environmental changes, the landslide risk has been increasing over time, especially that posed by extremely rapid movements, such as flow-slides. In recent years, failure and propagation mechanisms of flow-slides have been widely studied (Wang and Sassa, 2001; Olivares and Damiano, 2007, Cascini et al, 2010). These phenomena generally involve coarse-grained soils and are often triggered by the unstable soil behaviour under undrained conditions.

This study investigates the triggering mechanism of flow-slides and provides an alternative explanation for their initiation. According to this interpretation, flow-slides can stem from the combination of two instabilities: the first occurs in the unsaturated regime and leads to a rapid transition from unsaturated to saturated conditions; the second originates from the first one and occurs under undrained conditions. This interpretation is supported by the results of the numerical study presented in the following section, concerning the effects of water infiltration in an ideal infinite slope.

2 CASE OF STUDY

The study was conducted by analysing the response of an ideal infinite slope to rainfall events. The slope consists of an unsaturated cover 1.2 m thick, resting on a rigid and impervious bedrock inclined at 30° to the horizontal (Figure 1). The material is a lightly over-consolidated coarse-grained soil with low plasticity fine fraction (soil unit weight γ=19 kN/m^3).

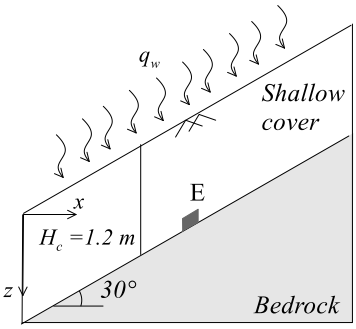

Figure 1. Ideal infinite slope.

The hydro-mechanical soil behaviour is described by combining the WR2-Unsat model (Rotisciani et al., 2021) and the Van Genuchten water retention model. The suction of 10 kPa is uniformly distributed within the shallow cover. Such value is typically observed during rainy seasons in the Campania region, where landslides evolving into flow-slides are frequent.

2.1 Constitutive laws for solid and fluid phases

The WR2-Unsat model is a single-surface hardening plastic model developed by extending the WR2-model (Boldini et al., 2019) to unsaturated conditions. The model is formulated in terms of Bishop's effective stress σ_{ij}': $\sigma'_{ij} = \sigma_{ij} + S_r\, s\, \delta_{ij}$, where σ_{ij} is the net stress, S_r the degree of saturation, s the matrix suction and δ_{ij} the Kronecker delta. The model can reproduce the main features of the mechanical behaviour of structured unsaturated soils under monotonic loading paths.

The model formulation presented below is a simplified version since it neglects *i*) the influence of the Lode angle on the yield surface, which is assumed to be circular in the deviatoric section, *ii*) the terms in the hardening law describing the destructuration phenomena since the shallow cover consists of an uncemented soil.

The yield surface F delimiting the elastic domain follows the expression proposed by Bigoni and Piccolroaz (2004):

$$-Np_c\sqrt{(\Phi - \Phi^{\mathrm{m}})\,[2(1-\alpha)\Phi + \alpha]} + q = 0 \quad (1)$$

where Φ is defined as: $\Phi = p'/p_c$, p' and q are the mean effective and deviatoric stress invariants, α, m and N define the shape of the curve in the stress invariants plane, and p_c is the hardening variable.

In the elastic domain, the material behaviour is hyperelastic, and the evolution laws of the stiffness moduli with effective stress are a function of the dimensionless parameters n_e, k, and g and the reference pressure p_a.

In the q-p' plane, the plastic potential function G follows an equation similar to the one adopted for the yield surface:

$$-N_g\hat{p}_c\sqrt{\left(\Phi_g - \Phi_g^{m_g}\right)\left[2\left(1-\alpha_g\right)\Phi_g + \alpha_g\right]} + q = 0 \quad (2)$$

where Φ_g is defined as: $\Phi_g = p'/\hat{p}_c$, $\hat{p}_c$ identifies the dimension of the G-locus passing through the current stress state, α_g, m_g, and N_g control the shape of the curve in the q-p' plane. In the deviatoric section, G always coincides with F.

The yield locus changes in size with the development of plastic strains and/or any variation in saturation. The isotropic hardening law is given by:

$$\dot{p}_c = p_c\left[\frac{1}{\lambda^*}\dot{\varepsilon}_v^p - b\dot{S}_r\right] \quad (3)$$

where $\dot{\varepsilon}_v^p$ is the volumetric plastic strain rate, $\dot{S}_r$ the increment of the degree of saturation, λ^* is the modified compression index evaluated in the bi-logarithmic compressibility plane, and b controls the mechanical effects induced by the variations of the degree of saturation.

The non-hysteretic uncoupled retention behaviour is described by the well-known Van Genuchten Water Retention Curve (WRC):

$$S_r = S_{r,res} + \frac{(1-S_{r,res})}{[1+(\alpha_w\, s)^{n_w}]^{m_w}} \quad (4)$$

where α_w, n_w and m_w control the shape of the curve and $S_{r,res}$ defines the residual degree of saturation.

The set of constitutive parameters adopted in the numerical study is listed in Table 1. The model was calibrated based on the literature data related to silty sands following the procedure described in Rotisciani et al. (2023). The selected class of materials is the one most involved in landslides evolving into flow-slides.

The yield surface has a distorted shape in the q-p' plane with the stress ratio at the maximum deviatoric stress η_p equal to 0.9 (Figure 2). The plastic potential function coincides with the ellipse of the Modified Cam Clay model, where N_g defines the slope of the Critical State Line (CSL) in the q-p' plane. The WRC is characterized by a low air-entry value, small slope, and negligible residual degree of saturation. The curve adopted is the one typically observed in coarse-grained soils (Rotisciani et al., 2014).

2.2 Wetting-induced instability

The effects of water infiltration were investigated, focusing on a soil element located at the base of the shallow cover (element E in Figure 1). This area is generally the first to be involved in the instability mechanism. Water infiltration was modelled by imposing an inflowing water flux of constant intensity, keeping unchanged the geostatic total stresses. Figure 2 shows the wetting-induced stress path in the q-p' plane. The reduction in suction leads to a reduction in the isotropic stress component under constant deviatoric stress. The test ends before reaching the CSL, suggesting no shear failure occurs.

Figure 3 shows the evolution of the pore water pressure u_w and volumetric strain ε_v with the water ratio e_w, defined as the ratio of water to solid volume. The simulation ends before attaining full saturation. The similarity of the curves u_w-e_w and ε_v-e_w suggests a mutual interaction between the two variables. Indeed, in water-content controlled tests, the degree of saturation and the volumetric deformations are interdependent: the increase in S_r causes the volumetric collapse of the solid skeleton, which in turn provokes a further increase in the saturation level. This process can give rise to an instability mode, as is the case here.

The instability is pointed out by *i*) uncontrolled increase of u_w and thus S_r that prevents the injection of further water volumes; *ii*) continuous changes in volume of the solid skeleton that reveals the inability of the soil to sustain the applied loadings.

Table 1. Constitutive parameters.

Elastic parameter		F and G shape parameters		WRC parameter	
Par.	Value	Par.	Value	Par	Value
n_e	0.5	α	0	α_w	0.2 kPa^{-1}
p_a	1 kPa	m	2	m_w	0.23
k	6666.7	N	1.1	n_w	1.3
g	5000	α_g	1	$S_{r,res}$	0.073
		m_g	2		
		N_g	1.33		

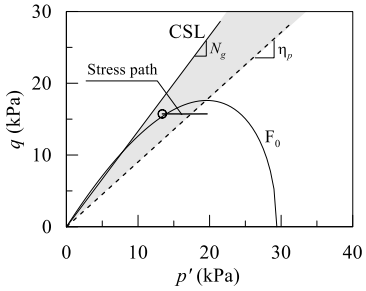

Figure 2. Wetting-induced stress path.

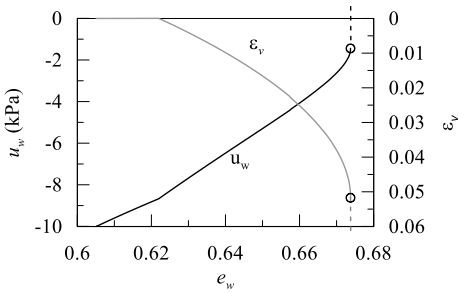

Figure 3. Evolution of pore water pressure and volumetric strains with water ratio.

It is important to note that the final stress state lies within the undrained failure domain coloured by pale grey in Figure 2. The latter is included between the straight lines with slope η_p and N_g (Rotisciani et al., 2021). This outcome reveals the possibility that the observed instability triggers a second instability, once attained full saturation. The latter can occur, provided that the soil yields under undrained conditions.

3 STABILITY CRITERION

The numerical results show the onset of an unstable process when the soil is still in the unsaturated regime. This instability mode is due to the strong coupling between solid and fluid phases and manifests as an uncontrolled growth of u_w, S_r, and ε_v. When the instability takes place, the combined effect of the volumetric collapse and the rapid increase in pore saturation prevents carrying on the injection of water volume. Therefore, the onset of the instability can be found by imposing the condition:

$$\dot{e}_w \leq 0 \tag{5}$$

Taking into account the definition of e_w, Eq. (5) can be rewritten in the form:

$$-\frac{\dot{e}_w}{1+e} = S_r\dot{\varepsilon}_v - n\dot{S}_r \geq 0 \tag{6}$$

where e is the void ratio, n the soil porosity, and $\dot{\varepsilon}_v$ the volumetric strain rate. The latter can be deduced by expressing the constitutive laws in the stress-based form:

$$\dot{\boldsymbol{\varepsilon}} = \left[\boldsymbol{C^e} + \frac{1}{H}\left(\frac{\partial G}{\partial \boldsymbol{\sigma'}} \otimes \frac{\partial F}{\partial \boldsymbol{\sigma'}}\right)\right]\dot{\boldsymbol{\sigma}}' + \left[\frac{1}{H}\frac{\partial F}{\partial p_c}\frac{\partial p_c}{\partial S_r}\frac{\partial G}{\partial \boldsymbol{\sigma'}}\right]\dot{S}_r \tag{7}$$

where $\boldsymbol{C^e}$ is the elastic compliance matrix, $\partial F/\partial \boldsymbol{\sigma'}$ and $\partial G/\partial \boldsymbol{\sigma'}$ are the partial derivative of F and G with respect to $\boldsymbol{\sigma'}$; $\partial F/\partial p_c$ is the partial derivative of F with

respect to p_c, H is hardening modulus defined as: $H = -\frac{\partial f}{\partial p_c}\frac{p_c}{\lambda^*}\frac{\partial G}{\partial p'}$.

Taking into account the imposed boundary conditions ($\dot{q} = 0$; $\dot{p} = 0$), $\dot{\varepsilon}_v$ is given by:

$$\dot{\varepsilon}_v = \left(C_{pp}^e - \frac{\lambda^*}{p_c}\frac{\partial F}{\partial p'}/\frac{\partial F}{\partial p_c}\right)\left(\frac{ds}{dS_r}S_r + s\right)\dot{S}_r + b\lambda^*\dot{S}_r \quad (8)$$

where the term $(ds/dS_r\, S_r + s)\dot{S}_r$ defines the increment of p', C_{pp}^e is equal to the inverse of the bulk modulus K. Substituting Eq (8) in Eq (6), the latter becomes:

$$\left[\left(\frac{1}{K} - \frac{\lambda^*}{p_c}\frac{\partial F}{\partial p'}/\frac{\partial F}{\partial p_c}\right)\left(\frac{ds}{dS_r}S_r + s\right)\dot{S}_r + b\,\lambda^*\dot{S}_r\right]S_r - n\dot{S}_r \geq 0 \quad (9)$$

By dividing for $\dot{S}_r$ (that is greater than 0) and placing:

$$n_{lim} = \left[\left(\frac{1}{K} + \frac{\lambda^*}{p_c}\frac{\partial F}{\partial p'}/\frac{\partial F}{\partial p_c}\right)\left(\frac{ds}{dS_r}S_r + s\right) + b\lambda^*\right]S_r \quad (10)$$

Eq. (9) can be simplified in the following form:

$$n \leq n_{lim} \quad (11)$$

where n_{lim} is the threshold porosity separating stable to unstable states.

The validity of the stability criterion (Eq. (11)) was checked by monitoring the evolution of n and n_{lim} in the above mentioned wetting test (Figure 4). The injection of water volume causes *i*) a small reduction in soil porosity due to the collapse of the solid skeleton; *ii*) a significant increase in n_{lim} taking place when full saturation is approached. According to the proposed criterion, the simulation ends when n is equal to n_{lim}.

4 CONCLUSIONS

The study inspects the stability of an ideal infinite slope during rainfall events, focusing on a soil element located at the base of the shallow cover. The numerical results show that the instability *i*) can occur before full saturation is reached, *ii*) manifests itself as an uncontrolled growth of soil strains and hydraulic variables, and *iii*) takes place when n=n_{lim}. These results suggest an alternative mechanism for the activation of flow-slides, according to which the rapid transition from unsaturated to saturated conditions is the triggering factor of the instability. Such instability can lead to a flow-slide, provided that *i*) the soil yields under undrained conditions and *ii*) the stress state is within the undrained failure domain.

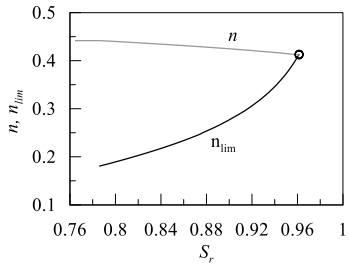

Figure 4. Evolution of n and n_{lim} with degree of saturation.

REFERENCES

Bigoni, D., Piccolroaz, A. (2004). Yield criteria for quasibrittle and frictional materials. *Int J Solids Struct.* 41: 2855–2878. https://doi.org/10.1016/j.ijsolstr.2009.06.006.

Boldini, D., Palmieri, F., Amorosi, A. (2019). A new versatile constitutive law for modelling the monotonic response of soft rocks and structured fine-grained soils. *Int J Numer Anal Methods Geomech*. 43(15): 2383–2406. https://doi.org/10.1002/nag.2975.

Cascini, L., Cuomo, S., Pastor, M., Sorbino, G. (2010). Modelling of rainfall-induced shallow landslides of the flow-type. *J. Geotech. Geoenviron. Eng* 136(1):85-98. https://doi.org/10.1061/(ASCE)GT.1943-5606.0000182.

Olivares, L., Damiano, E. (2007). Postfailure mechanism of landslides: laboratory investigation of flowslides in pyroclastic soils. *J. Geotech. Geoenviron. Eng*. 133(1): 51-62. https://doi.org/10.1061/(ASCE)1090-0241(2007)133:1(51).

Rotisciani, G.M., Desideri, A., Amorosi, A. (2021). Unsaturated structured soils: constitutive modelling and stability analyses. *Acta Geotech*. 16: 3355-3380. https://doi.org/10.1007/s11440-021-01313-7.

Rotisciani, G.M., Desideri, A., Amorosi, A. (2023). Wetting-induced instabilities: triggering mechanism and predisposing factors. *E3S Web of Conf.* 382: 10006.

Rotisciani, G.M., Sciarra, G., Desideri, A., Casini, F. (2014). Modeling rainfall infiltration through coarse and fine-grained unsaturated geomaterials. in *Unsaturated Soils: Research & Applications*, CRC Press, 521 – 528.

Wang, G., Sassa, K. (2001). Factors affecting rainfall-induced flowslides in laboratory flume tests. *Geotechnique*. 51(7): 587-599. https://doi.org/10.1680/geot.2001.51.7.587.

Proceedings of the XVIII ECSMGE 2024
GEOTECHNICAL ENGINEERING CHALLENGES
TO MEET CURRENT AND EMERGING NEEDS OF SOCIETY
© 2024 the Authors
ISBN 978-1-032-54816-6
DOI 10.1201/9781003431749-240
Open Access: www.taylorfrancis.com, CC BY-NC-ND 4.0 license

ECSMGE 24
XVIII EUROPEAN CONFERENCE ON SOIL MECHANICS AND GEOTECHNICAL ENGINEERING

Innovations in liquefaction mitigation: Modelling the mechanical cyclic behavior of biocemented soils

Innovations dans l'atténuation de la liquéfaction: Modélisation du comportement mécanique cyclique des sols biocimentés

Z.N. Sahlab*, D. Terzis, L. Laloui
Swiss Federal Institute of Technology – EPFL, Laboratory of Soil Mechanics, Lausanne, Switzerland
**ziad.sahlab@epfl.ch*

ABSTRACT: Liquefaction remains a major geotechnical hazard in seismically active zones. Traditional mitigation methods while effective, frequently have significant environmental and economic impacts and may not be suitable for existing structures. Biogeotechnical methods, notably Microbially Induced Calcite Precipitation (MICP), offer a sustainable alternative. Experiments reveal that MICP enhances liquefaction resistance, even at low calcite contents. However, the lack of models capturing this behavior hinders the design and adoption of these techniques. This study presents Hujeux-BC, a mechanical constitutive model for the cyclic behavior of biocemented soils. It independently incorporates the main characteristics of biocementation, densification and interparticle bonding. This is done by modifying the materials elastic parameters and relative density, as well as the addition of a bonding parameter. Using the measured calcite content and change in shear wave velocity, the model is able to simulate the cyclic behavior of biocemented soils. Notably, in an undrained cyclic direct simple shear (DSS) test, the model can simulate the porewater pressure generation, accurately estimating the number of cycles needed to trigger liquefaction. This accuracy and the model's straightforward calibration process provide a powerful tool for designing and optimizing MICP-based mitigation techniques, leading to more targeted and sustainable solutions.

RÉSUMÉ: La liquéfaction demeure un risque géotechnique majeur dans les zones sismiques. Les méthodes d'atténuation traditionnelles, malgré leur efficacité, ont des impacts environnementaux et économiques et ne conviennent pas toujours aux structures existantes. Les méthodes biogéotechniques, comme la Précipitation de Calcite Induite par Microbes (MICP), représentent une alternative durable. Les essais montrent que la MICP augmente la résistance à la liquéfaction, même à faible teneur en calcite. Cependant, l'absence de modèles constitutifs adéquats limite leur adoption. Cette étude introduit Hujeux-BC, un modèle constitutif pour le comportement cyclique des sols biocimentés. Il intègre séparément les caractéristiques principales de la biocimentation : la densification et la liaison entre particules. Ceci est fait en modifiant les paramètres élastiques du matériau, la densité relative, et en ajoutant un paramètre de liaison. En se basant sur la teneur en calcite et la vitesse des ondes de cisaillement, le modèle reproduit le comportement des sols biocimentés. Notamment, dans un essai cyclique non-drainé de cisaillement simple il permet de simuler la génération de la pression interstitielle, estimant le nombre de cycles nécessaires pour déclencher la liquéfaction. Cette précision, et la calibration simple des paramètres du modèle, en font un outil essentiel pour optimiser les techniques basées sur la MICP, menant à des solutions plus ciblées et durables.

Keywords: Liquefaction; biocementation; constitutive model; cyclic loading.

1 INTRODUCTION

Despite our increased understanding of liquefaction and the developed prevention methods, recent earthquake events highlight that liquefaction remains a threat to infrastructure (Cubrinovski et al., 2012), emphasizing the ongoing need to explore liquefaction mechanisms and preventative measures.

Traditional mitigation methods such as compaction, drainage, and grouting while effective, are often costly and invasive making them unsuitable for many existing structures. The need for more environmentally conscious, low-cost and non-invasive methods is therefore ever-present (Towhata, 2008). Biogeotechnical methods have emerged as a possible solution for this persistent hazard, particularly Microbially Induced Calcite Precipitation (MICP).

To assess the effectiveness of MICP based techniques, a combination of experiments and models is essential. Numerous experiments were conducted to observe the dynamic behavior of biocemented sands showing that biocementation greatly increased the liquefaction resistance, with highly cemented soils

becoming virtually un-liquefiable (Montoya et al., 2013; Sasaki and Kuwano, 2016; Zamani et al., 2021; Lee et al., 2022). Yet, the shortage of models for biocemented soils' cyclic behavior limits the technique's widespread use.

This study introduces Hujeux-BC, a cyclic elastoplastic constitutive model for biocemented soils. The model is based on the Hujeux (1985) cyclic model framework and integrates the observed changes in behavior of biocemented soils under both monotonic and cyclic loading. This is done by the addition of new biocementation parameters that are calibrated through the measured calcite content and the change in the shear wave velocity.

The model uniquely considers biocementation's mechanical effects, densification and inter-particle bonding, separately which enables it to simulate the bond degradation and the lasting densification impact of biocementation independently making it a valuable tool for studying the long-term behavior of biocemented sands subjected to repeated cyclic loading.

The following sections present the model formulation and performance in simulating an undrained cyclic DSS test on biocemented soils at varying cementation levels under different Cyclic Stress Ratios (CSR).

2 MODELLING FRAMEWORK

2.1 Theoretical background

The model development draws from observations of the physical mechanisms that govern the behavior of biocemented soils under both monotonic and cyclic loading. The main characteristics of the monotonic mechanical behavior of biocemented soils as detailed in numerous review papers (Terzis and Laloui, 2019; Fu et al., 2023) can be summarized as: i) increased soil stiffness, ii) increased soil strength and softening post peak, iii) dilatant behavior. Experimental data consistently attribute this behavior to two mechanisms: i) densification and ii) interparticle bonding(Nafisi and Montoya, 2018; Harran et al., 2023). Densification occurs due to the presence of calcite in the pore space which can be easily determined through acid washing or thermos-gravimetric analysis among other methods. Bonding on the other hand is more difficult to quantify. While it can be detected using advanced techniques like scanning electron microscopy or X-ray micro-tomography, it remains difficult to accurately identify the "active" bonds. Alternatively, these bonds can be estimated using indirect methods such as the shear wave velocity V_s (Nafisi and Montoya, 2018).

The cyclic behavior of biocemented has been investigated through different laboratory and scaled model tests where it was found that even low levels of cementation result in a dramatically increased liquefaction resistance (Montoya et al., 2013; Sasaki and Kuwano, 2016; Zamani et al., 2021; Lee et al., 2022). These studies identify the effects of biocementation on the cyclic behavior as: i) increased resistance, ii) reduced porewater pressure generation, iii) increased stiffness and iv) delayed onset of liquefaction. These observations align with the change in behavior under monotonic loading implying that the physical mechanisms inducing these changes are the same.

2.2 The effects of biocementation

2.2.1 Densification

A densification parameter for the elastic behavior is introduced as:

$$\xi_{den} = \frac{\rho_{cc}(G_s + eSr) + m_{cc}(G_s - Sr)}{\rho_{cc}(G_s + eSr)} \qquad (1)$$

where G_s is the specific gravity, Sr is the degree of saturation, e is the untreated void ratio, $m_{cc} = \frac{m_c}{m_s}$ is the calcite content, and $\rho_{cc} = \frac{\rho_c}{\rho_s}$ is the calcite density ratio.

The effect of densification on the yield surface is introduced through the parameter ψ_{den} expressed as:

$$\psi_{den} = \exp\left(\frac{e - e^*}{\lambda}\right) \qquad (2)$$

here, λ is the coefficient of compressibility obtained as the slope of the critical state line (CSL) in the $v - \ln(p')$ plane.

2.2.2 Bonding

The effect of active calcite bonds on the elastic behavior is obtained through the change in shear wave velocity and is estimated as:

$$\xi_{bon} = \frac{(V_s^2)^*}{V_s^2} = \frac{(V_s + \Delta V_s)^2}{V_s^2} \qquad (3)$$

where V_s^* and V_s are the shear wave velocities before and after calcite precipitation.

The effect of bonding on the yield surface is introduced through the parameter ψ_{bon} expressed as:

$$\psi_{bon} = \left(\psi_{bon_0}\right)^R \quad (4)$$

where ψ_{bon_0} is the initial degree of bonding and R is a debonding function given by:

$$R = \exp\left(-\omega \cdot \varepsilon_v^p\right) \quad (5)$$

Here, ω is the debonding rate and ε_v^p is the plastic volumetric strain. This expression was inspired by the work of Koliji et al. (2010) on structured soils since it was observed that their evolution during loading closely resembles that of biocemented soils.

3 MODEL FORMULATION

The model presented in this study is based on the work of Hujeux (1985) where the full elasto-plastic relationships are described. The following presents the changes due to biocementation.

The effect of biocementation on the elastic moduli is expressed as a combination of the densification and bonding parameters into a cementation factor CF_E given by:

$$CF_E = \xi_{den} \cdot \xi_{bon} \quad (6)$$

The elastic moduli are then expressed as:

$$K(p') = CF \cdot K_{ref}\left(\frac{p'}{p_{ref}}\right)^n \quad (7)$$

$$G(p') = CF \cdot G_{ref}\left(\frac{p'}{p_{ref}}\right)^n \quad (8)$$

where K_{ref} and G_{ref} are the reference bulk and shear moduli, p_{ref} is the mean effective pressure at which the moduli were estimated, p' is the current mean effective pressure, and n is an elastic exponent.

The change in the yield surface is done through the mean pressure at the critical state p'_{cs} which governs the strength response of the soil. p'_{cs} evolves to:

$$p'_{cs}{}^* = CF_S \cdot p'_{cs} \quad (9)$$

where $CF_S = \psi_{den} \cdot \psi_{bon}$ is the cementation factor for strength.

4 MODEL PERFORMANCE

The model's performance was tested against a series of undrained cyclic DSS tests conducted by Lee et al. (2022) on Ottawa sand F65 with light cementation levels.

The model was calibrated on the untreated results to determine the main model parameters and then the biocementation parameters were estimated from the reported calcite content and change in V_s. The results shown in Figure 1 align well with the experimental ones, accurately simulating the trends and the cycles needed to reach an excess pore water pressure (r_u) value of 0.95, highlighting the model's potential in predicting liquefaction under cyclic loading. Using the same model parameters calibrated on the tests shown in Figure 1, the model was used to simulate tests at all of the cyclic stress ratios used in the experiment to construct the CSR – N curves for the untreated soil and the two selected cementation levels shown in Figure 2. The simulated curves closely match the experimental ones for high CSRs but underestimate the cycles to liquefaction for lower CSRs. Given the inherent variability of cemented soils, however, the results offer a reasonable estimation showcasing the model's potential for evaluating MICP based mitigation techniques.

5 CONCLUSIONS

This study introduces the Hujeux-BC model, tailored for biocemented soils, that integrates biocementation's effects using the calcite mass content and shear wave velocity as input parameters. The model uniquely represents densification and inter-particle bonding independently, giving it the potential to simulate the long-term soil behavior as bonds degrade. When benchmarked, the model effectively mirrored biocemented soils' response under cyclic loading, particularly producing accurate CSR – N curves for biocemented soils at different levels of cementation.

Despite the complexities involved in modelling biocemented soils, this study shows that by using the reference, untreated state of sands as a starting point and incorporating parameters that reflect the densification and bonding effects, the cyclic behavior of biocemented sands can be understood and replicated, and as experimental observations increase, model calibration can be improved leading to a more robust framework.

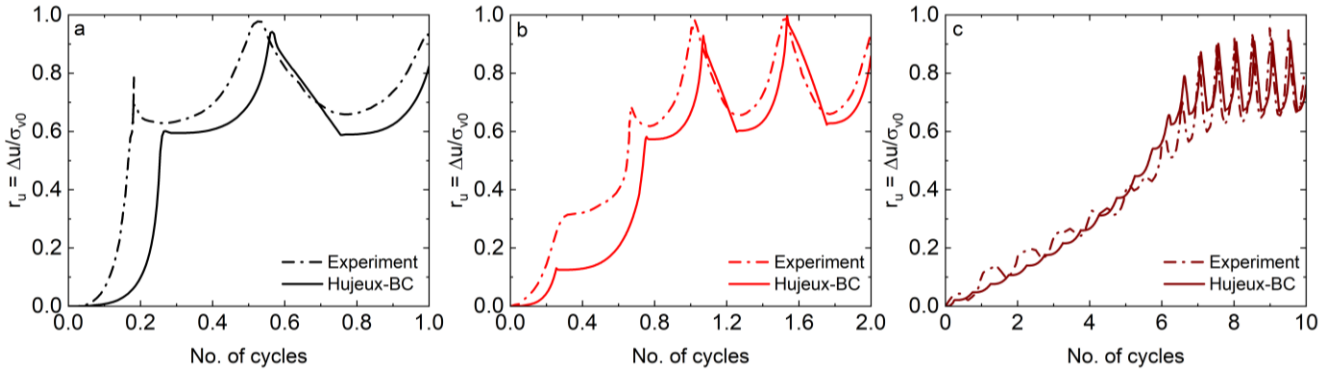

Figure 1. Comparison between experimental and simulations results for an undrained cyclic DSS on MICP-treated sands using Hujeux-BC a) untreated, b) $m_{cc} = 0.14\% - \Delta V_s = 16\ m/s$, c) $m_{cc} = 0.43\% - \Delta V_s = 36\ m/s$ (experimental data from (Lee et al., 2022)).

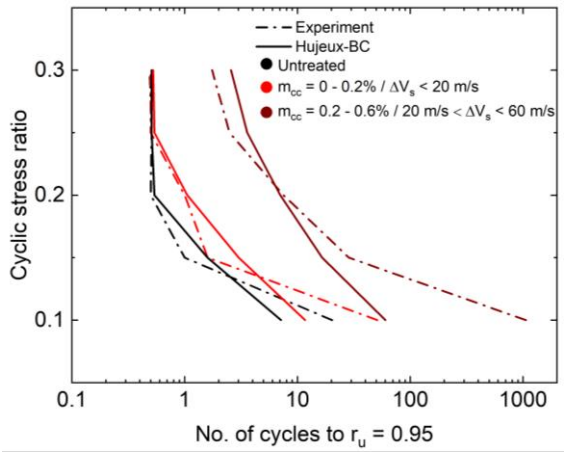

Figure 2. Comparison between simulated and experimental CSR – N curves (experimental data from (Lee et al., 2022))

ACKNOWLEDGEMENTS

The authors wish to thank the European Research Council (ERC) for the financial support under the European Union's Horizon 2020 research and innovation program (Grant Agreement No.: 788587). The work was also supported by the Swiss State Secretariat for Education, Research and Innovation (SERI).

REFERENCES

Fu, T., Saracho, A.C., Haigh, S.K., 2023. Microbially induced carbonate precipitation (MICP) for soil strengthening: A comprehensive review. Biogeotechnics 100002. https://doi.org/10.1016/j.bgtech.2023.100002.

Harran, R., Terzis, D., Laloui, L., 2023. Mechanics, Modeling, and Upscaling of Biocemented Soils: A Review of Breakthroughs and Challenges. International Journal of Geomechanics 23, 03123004. https://doi.org/10.1061/IJGNAI.GMENG-8446.

Hujeux, J.-C., 1985. Une loi de comportement pour le chargement cyclique, in: Genie Parasismique. Presse de l'ENPC, Paris, pp. 287–302.

Koliji, A., Laloui, L., Vulliet, L., 2010. Constitutive modeling of unsaturated aggregated soils. International Journal for Numerical and Analytical Methods in Geomechanics 34, 1846–1876. https://doi.org/10.1002/nag.888.

Lee, M., Gomez, M.G., El Kortbawi, M., Ziotopoulou, K., 2022. Effect of Light Biocementation on the Liquefaction Triggering and Post-Triggering Behavior of Loose Sands. J. Geotech. Geoenviron. Eng. 148, 04021170. https://doi.org/10.1061/(ASCE)GT.1943-5606.0002707.

Montoya, B. m., Dejong, J. t., Boulanger, R. w., 2013. Dynamic response of liquefiable sand improved by microbial-induced calcite precipitation. Géotechnique 63, 302–312. https://doi.org/10.1680/geot.SIP13.P.019.

Nafisi, A., Montoya, B.M., 2018. A New Framework for Identifying Cementation Level of MICP-Treated Sands 37–47. https://doi.org/10.1061/9780784481592.005.

Sasaki, T., Kuwano, R., 2016. Undrained cyclic triaxial testing on sand with non-plastic fines content cemented with microbially induced CaCO3. Soils and Foundations 56, 485–495. https://doi.org/10.1016/j.sandf.2016.04.014.

Terzis, D., Laloui, L., 2019. A decade of progress and turning points in the understanding of bio-improved soils: A review. Geomechanics for Energy and the Environment 19, 100116. https://doi.org/10.1016/j.gete.2019.03.001.

Towhata, I., 2008. Mitigation of Liquefaction-Induced Damage, in: Towhata, I. (Ed.), Geotechnical Earthquake Engineering, Springer Series in Geomechanics and Geoengineering. Springer, Berlin, Heidelberg, pp. 588–642. https://doi.org/10.1007/978-3-540-35783-4_26.

Zamani, A., Xiao, P., DeJong, J.T., Boulanger, R.W., Wilson, D.W., Carey, T.J., 2021. MICP Treatment to Mitigate Soil Liquefaction-Induced Building Settlements 308–317. https://doi.org/10.1061/9780784483411.030.

Proceedings of the XVIII ECSMGE 2024
GEOTECHNICAL ENGINEERING CHALLENGES
TO MEET CURRENT AND EMERGING NEEDS OF SOCIETY
© 2024 the Authors
ISBN 978-1-032-54816-6
DOI 10.1201/9781003431749-241
Open Access: www.taylorfrancis.com, CC BY-NC-ND 4.0 license

ECSMGE 24
XVIII EUROPEAN CONFERENCE ON SOIL MECHANICS AND GEOTECHNICAL ENGINEERING

Performance design of shallow foundations interacting with liquefiable soils

Performance design des fondations superficielles sur sols liquéfiables

I. Sarao Mannelli*, V. Minardi, G. Canetta
CEAS S.r.l., Milan, Italy

B. Becci
IN.SPE. S.r.l., Bergamo, Italy

**irene.saraomannelli@ceas.it*

ABSTRACT: Dealing with foundation soils that are likely prone to liquefaction, or at least cyclic mobility during Ultimate Limit State earthquakes, some relevant uncertainties may arise in selecting appropriate remedial schemes. While it is a most common practice to consider soil improvement works, in some practical scenarios such ordinary policy may result in unreasonable choices under both engineering and economical points of view. A typical case is the design of spread foundations or buried caissons of limited size, in moderately liquefaction prone soils. A case history is discussed in this contribution, related to a touristic infrastructure installation in a reclaimed area, at the seashore of Northern Adriatic Coast, Italy. Ordinary free-field, one-dimensional liquefaction analyses have been compared with results from numerical models based on Flac3D, implementing P2PSand constitutive model (Cheng and Detournay, 2021), capable of reproducing pore pressure build up. The seismic response has been predicted and maximum displacements as well as design stresses for the structure have been evaluated; consequently, the Performance Based Design Approach has allowed to assess the minimum countermeasures required, ensuring an appropriate safety level even without the need of huge soil improvement works.

RÉSUMÉ: Dans le cas de sols susceptibles à la liquéfaction, ou au moins à la mobilité cyclique en cas de séisme à l'état limite ultime, certaines incertitudes pertinentes peuvent survenir lors de la sélection des programmes de remédiation appropriés. Bien qu'il soit courant d'envisager des travaux d'amélioration du sol, dans certains scénarios pratiques, cette politique ordinaire peut aboutir à des choix déraisonnables d'un point de vue technique et économique. Un cas typique est la conception de fondations étalées ou de caissons enterrés de taille limitée, dans des sols modérément sujets à la liquéfaction. Dans cet article est explique un cas type, lié à une installation d'infrastructure touristique dans une zone de remise en état, au bord de la mer au nord de la côte Adriatique, en Italie. Les analyses de liquéfaction unidimensionnelles ordinaires en champ libre ont été comparées aux résultats numériques du logiciel Flac3D, en mettant en œuvre le modèle constitutif P2PSand (Cheng et Detournay, 2021), capable de reproduire l'accumulation de la pression interstitielle. La réponse sismique a été prédite et les déplacements maximaux ainsi que les contraintes de conception pour la structure ont été évalués; par conséquent, l'approche de méthodes de conception fondées sur la performance a permis d'évaluer les mesures minimales requises, afin de garantir un niveau de sécurité approprié même sans la nécessité d'énormes travaux d'amélioration du sol.

Keywords: Liquefaction phenomenon; performance design.

1 INTRODUCTION

The liquefaction phenomenon is a quite common issue concerning the reduction or the loss of soil stiffness and strength caused by earthquake shaking.

It takes place in loosely packed, water-saturated sediments at or near the ground surface. Liquefaction occurring beneath buildings and other structures can cause major damage during earthquakes.

Therefore, in order to mitigate the liquefaction hazards several techniques have been implemented. The ordinary methods include vibroflotation, compaction grouting, stone columns. The objective is to improve the strength, the density of the soil so that soil skeleton will not collapse under rapid loading and possibly improve the drainage characteristics of soils.

These common practices, in some scenarios, may result in unreasonable choices under both engineering and economical points of view. This is the case for lightweight buildings. In this respect, this proceeding provides a case history in which a different approach has been adopted based on Performance Design Approach. Following this procedure, as done by many researchers such as Murashev, Keepa et Tai, (2015) and Liu, Macedo et Candia (2021), the soil is not improved while the structure is designed to resist the

effects of liquefaction, in terms of internal forces due to settlements.

The evaluation of those settlements, in the state of practice still largely involves using empirical procedures developed to calculate post-liquefaction consolidation settlement in the free-field. This approach cannot possibly capture shear-induced and localized volumetric induced deformations in the soil underneath shallow foundations. Two dimensional or three dimensional soil structure interaction nonlinear effective stress dynamic analysis can provide a reliable estimates of building movement. Lopez-Caballero and Farahmand-Razavi (2008), Shakir and Pak (2010), Adrianopoulos et al. (2006), Dashti and Bray (2013), and Karimi and Dashti (2016a,b) perform numerical analysis in this field.

2 CASE STUDY

The effect of liquefaction on ancillaries, lightweight buildings, related to a touristic infrastructure installation in a reclaimed area, at the seashore of Northern Adriatic Coast, Italy, will be examined in this study.

At this purpose, several numerical analyses were carried out, starting from stratigraphic column model and comparing it with simplified models. The stratigraphic column was compared with a subsequent two-dimensional model under free-field conditions. And finally, the influence of the light building on the soil layer was analysed.

The aims of the seismic numerical analyses are, therefore, to:

- check the triggering of the phenomenon and compare the results obtained with the results of the empirical methods;
- assess the interaction between the liquefaction phenomenon and the foundation structures, in terms of maximum displacement and stresses acting on the foundation.

2.1 FLAC3D analysis: procedure

Analyses were carried out with the Flac3D finite difference code, implementing the 'P2PSand' constitutive model (Cheng and Detournay, 2021). The model is specially formulated and calibrated to reproduce main experimental evidences of the liquefaction phenomenon. It defines the deformability of the material, in terms of shear modulus, as a function of relative density by means of the following expression:

$$G = G_0 \, P_{atm} \left(\frac{p'}{P_{atm}}\right)^{0.5} \qquad (1)$$

$$G_0 = g_0 \left(D_R + C_{D_r}\right) P_{atm} \left(\frac{p'}{P_{atm}}\right)^{0.5} \qquad (2)$$

where, for clean and uniform sands, it is possible to assume: $g_0 = 1240$ e $C_{D_r} = 0.01$ ($P_{atm} = 101.3\ kPa$).

The main calibration parameters of the constitutive model are the relative density D_R and the shear modulus multiplier g_0. These parameters were calibrated to reproduce the design shear modulus along depth.

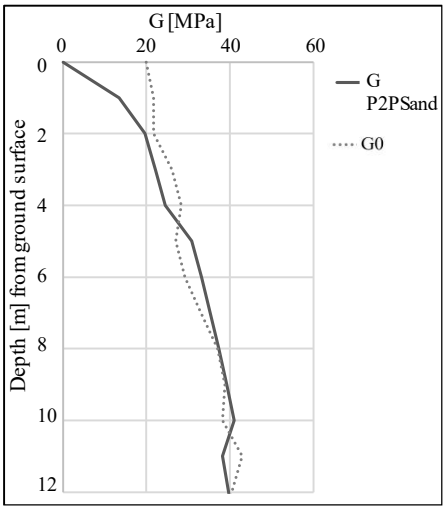

Figure 1. Calibration of shear modulus with P2PSand model.

The stratigraphy at the site can be modelled by four geotechnical units, defined as “R”, “A”, “B” and “C”. The liquefaction prone sandy sediments of geotechnical units R and A are modelled with the P2PSand constitutive model. Whereas Mohr-Coulomb model is used for geotechnical units B and C. The bottommost meter at the base of the model is modelled as elastic material in order not to have input wave distortion or noise in the application of seismic stress.

The main geotechnical input parameters are reported in Table 1 and Table 2. Water table is 2m below the ground surface.

Table 1. Geotechnical input parameters: P2PSand.

Unit	z [m]	γ [kN/m³]	φ [°]	Dr [%]	Vs [m/s]
R	0 ÷ 5	19	30	30	125
A	5 ÷ 10	19	30	35	161

Table 2. Geotechnical input parameters: Mohr-Coulomb.

Unit	z [m]	γ [kN/m³]	φ [°]	c' [kPa]	E [MPa]
B	10 ÷ 29	19	25	5	25
C	29 ÷ 39	20	33	30	70

REXEL, the database provided by ITACA, was used to define the seismic input: seven seismocompatible and spectrum-compatible accelerograms.

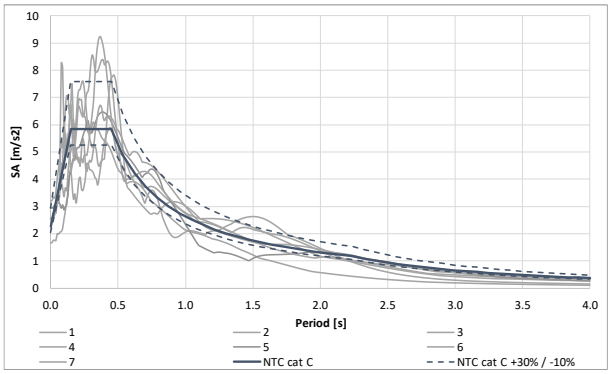

Figure 2. Response spectra of accelerograms extracted from REXEL. Comparison with NTC2018 spectrum.

The boundary conditions imposed on lateral sides of the numerical model are of the free-field kind. They consist of inserting a small column of soil at the extremes of the model to prevent both the distortion and the reflection of the seismic waves.

At the base of the model the following conditions were applied:

- The compliant base boundary conditions, which are implemented with independent dashpots in the normal and shear directions. They dampen the seismic wave, preventing its reflection within the model;
- the design velocity history, applied as time-dependent tangential stress:

$$\tau(t) = -\rho\, V_s\, v(t) \qquad (3)$$

where ρ and V_s are the density and shear wave velocity of the soil at the base of the model. v(t) is the seismic velocity diagram, obtained by integrating the deconvoluted design accelerograms.

The potential for liquefaction can be assessed by analysing the R_u coefficient, defined as the ratio of pore pressure increment Δu to geostatic vertical effective stress:

$$R_u = \frac{\Delta u}{\sigma'_{v0}} \qquad (4)$$

Soil is considered not subject to liquefaction if R_u<0.95.

The calculation phases implemented in the model are as listed below:

1. Initialisation of the geostatic stress state with the Mohr-Coulomb constitutive model;
2. Application of the P2PSand constitutive model on the geotechnical units R and A;
3. Dynamic analysis by applying the history of τ(t) of the 7 design accelerograms at the base of the model.

2.2 1D model: stratigraphic column

The numerical model is defined by a column with planimetric dimensions 2.0 m x 2.0 m (X and Y axes), and a height of 40.0 m (Z axis).

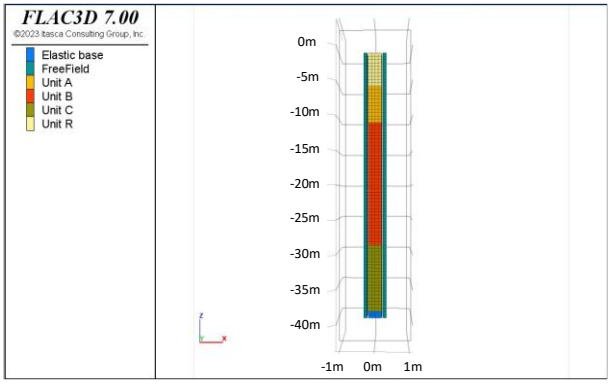

Figure 3. 1D model.

Figure 4, on the left, illustrates the 7 profiles of the R_u envelopes with depth, related to the 7 design accelerations; the profiles are sampled at the centre of the column. On the right, shows results from a common empirical approach (Robertson, 2009) for CPTus conducted in the same site. The factor of safety (F_s) against liquefaction is assessed by CRR (Cyclic Resistance Ratio) and CSR (Cyclic Stress Ratio) ratio.

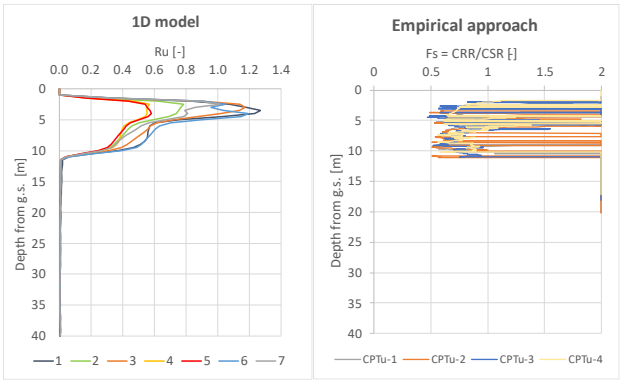

Figure 4. Results from numerical model (left) and empirical approach (Robertson, 2009).

It is noticeable that, by the empirical approach, geotechnical Unit R and A are prone to liquefaction (F_s <1), while the 1D model indicates probability of liquefaction just for Unit R, associated with a R_u>0.95 factor.

2.3 2D model: free field

The numerical model is defined by a two-dimensional block with planimetric dimensions 40.0 m x 0.5 m (X and Y axes), and a height of 40.0 m (Z axis).

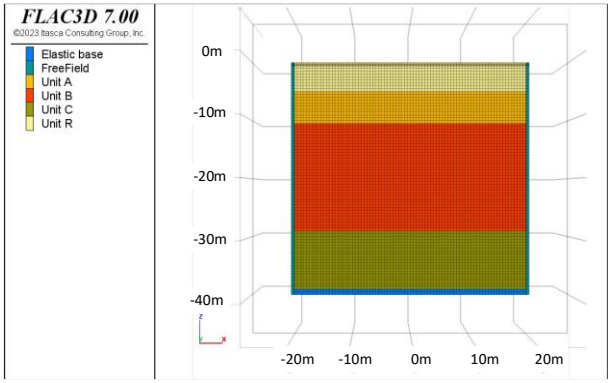

Figure 5. 2D model in free field conditions.

The 2D free field model confirm results observed in 1D model: soil belonging to unit R, as shown in Figure 6, when subjected to the seismic design stresses, induced by accelerograms 1, 3, 6 and 7, is liquefiable.

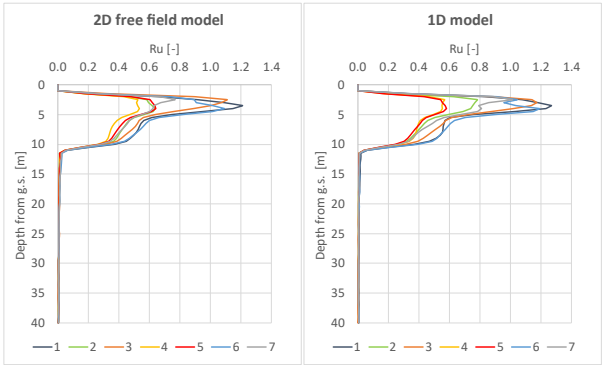

Figure 6. Comparison of free field 2D model (left) and stratigraphic column (right).

2.4 2D model: interaction with the shallow foundation

Based on free-field analyses, which reveal the occurrence of the liquefaction phenomenon, it is deemed necessary to further investigate the problem by modelling the on-site condition associated with the presence of some light buildings.

The building slab dimensions are B=9.5m and H=0.6m. It is modelled with elastic solid elements, having a specific weight equal to that of concrete (γ=25 kN/m^3), and a stiffness 20 times that of the surrounding soil (E=300 MPa).

The presence of the superstructure is simulated with elastic solid elements of equivalent weight and stiffness equal to that of the surrounding soil. The load due to the superstructure is 7.1 kPa, corresponding to an equivalent specific weight of 23.6 kN/m^3.

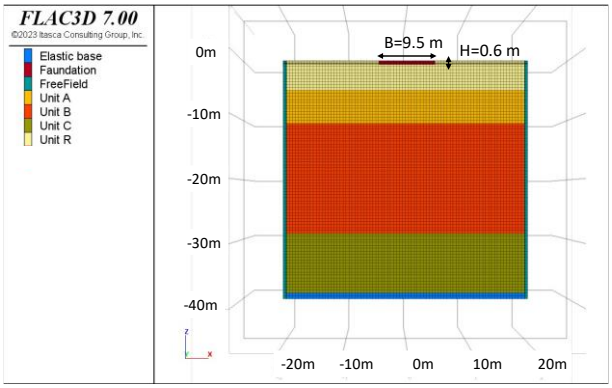

Figure 7. 2D model with shallow foundation.

In addition to the stages previously mentioned, three further stages run before phase 3: i) modelling the foundation slab; ii) applying the loads coming from the superstructure; iii) resetting the displacements before carrying out the dynamic analysis.

Obtained R_u profiles with ancillary building are compared with free-field profiles.

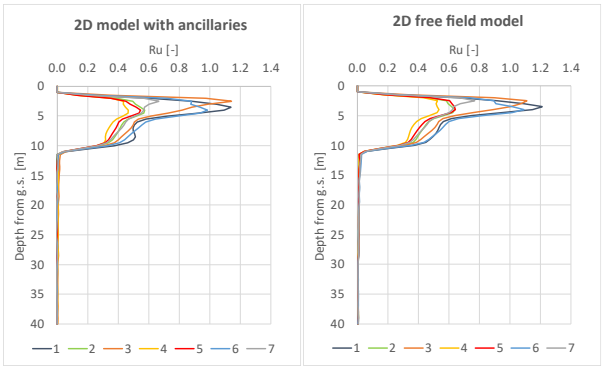

Figure 8. Comparison of model with ancillaries (left) and free-field model (right).

The presence of the building reduces the maximum value of R_u: this result is consistent with the fact that the building load increases the effective stresses near the foundation, reducing R_u ratio.

The results of the analysis in terms of displacement histories, associated with accelerogram 3, are shown in Figure 9. The upper Figure shows the vertical displacements of: the left end side of the foundation, in green; the point at the centre, in brown; and the right end side, in red. While the bottom one shows the horizontal displacements, which are uniform within the slab, which behaves as a rigid body.

The maximum horizontal displacement, experienced during the earthquake, is of the order of ± 5cm. While the residual one is close to 1 cm. To the contrary, vertical settlements tends to increase with

time, gathering some millimiters at mid axes as residual values.

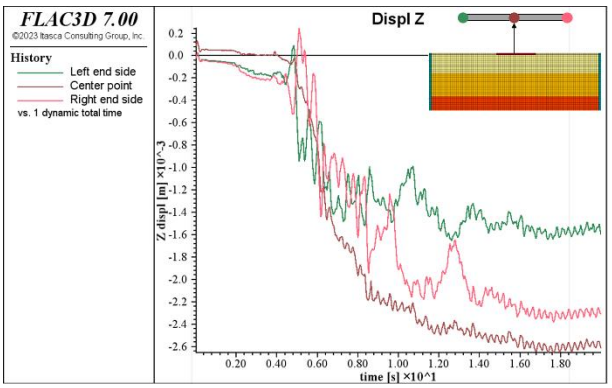

Figure 9. Time history of vertical displacements - accelerogram 3.

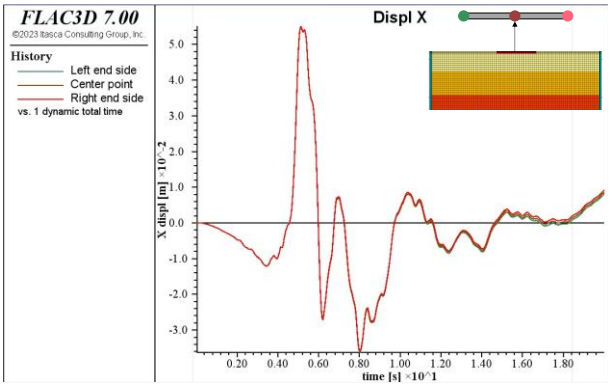

Figure 10. Time history of horizontal displacement - accelerogram 3.

The profile of the seven vertical displacements along the slab, associated to the design accelerations, are shown in Figure 11:

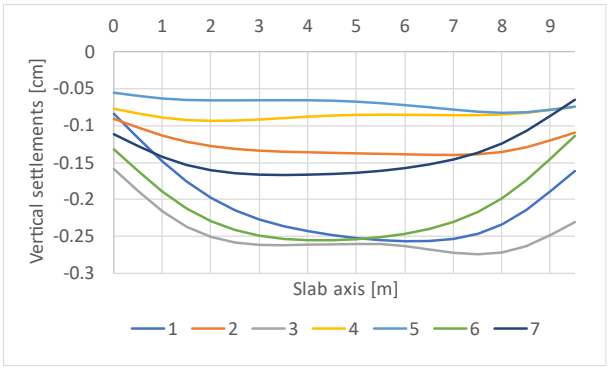

Figure 11. Vertical settlements along the slab.

The maximum vertical displacement is of the order of 0.27cm, associated with accelerogram 3. While the maximum differential settlement is of the order of 0.2cm associated with accelerogram 5.

Considering that the liquefaction phenomenon occurs without leading to excessive horizontal displacements and settlements, it has been decided to design foundations in such a way as to resist the additional stresses induced by liquefaction with a Performance Based Design approach.

2.5 Performance based design approach

The structure should be designed to resist the effects of liquefaction.

As a result of the analyses, the profiles of the horizontal minimum and maximum σ_{xx} stresses and the shear σ_{xz} stress acting in the slab elements were obtained.

Hence, the maximum bending moment and shear force were computed. These actions have to be added to the static design actions of the foundation as an additional loading condition due to soil liquefaction. In this way, the designed foundation will be able to resist to the envelope of the maximum expected deformations coming from the liquefaction phenomenon.

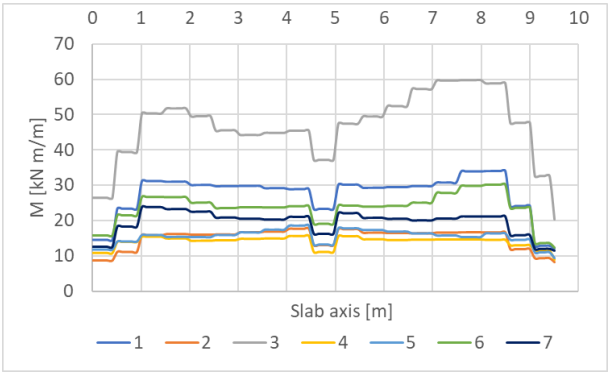

Figure 12. Bending moment along the slab.

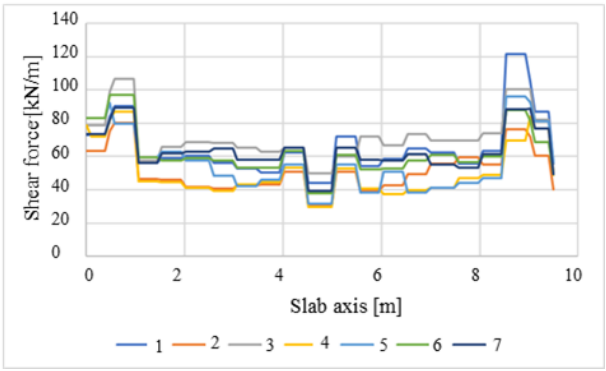

Figure 13. Shear force along the slab.

These supplementary actions, in the current project, are moderate. This is due to shallow setting of the foundation and to an R_u factor not far above unity.

Horizontal and vertical displacements of the foundation, due to the liquefaction phenomenon, are therefore compatible with design requirements.

3 CONCLUSIONS

FLAC 3D analyses confirmed the risk of soil liquefaction in same soil region where conventional calculations, based on empirical correlation, reported these issues.

However, such numerical approach is providing a relevant added value represented by a more accurate prediction of soil and foundation deformations occurring during seismic event. Such additional result is very important in the light of a Performance Based Design approach. In fact, according to this approach, the design of the foundation has the purpose to resist the effects of liquefaction in terms of deformations and supplementary actions, that are the results of the FLAC 3D analyses.

In the authors' opinion, such improvement in analysis results well counterbalances the increased efforts in terms of computational time and analysis complexities.

A further output of the numerical analysis, not dealt with in this contribution, is the evaluation of the increase of water pressures at the interface between foundation and soil. In case such overpressures may cause instability problems, such as uplift, appropriate countermeasures could be reliably assessed.

REFERENCES

Andrianopoulos, K., Bouckovalas, G., Karamitros, D., Papadimitriou, A. (2006) Effective stress analysis for the seismic response of shallow foundations on liquefiable sand, In: *6th European Conference on Numerical Methods in Geotechnical Engineering*, Graz, Austria. Available at: https://www.researchgate.net/publication/253795767_Effective_Stress_Analysis_for_the_Seismic_Response_of_Shallow_Foundations_on_Liquefiable_Sand.

Cheng, Z., Detournay, C. (2021) Formulation, validation and application of a practice-oriented two-surface plasticity sand model, *Computers and Geotechnics,* 132, https://doi.org/10.1016/j.compgeo.2020.103984.

Dashti, S., Bray, J.D. (2013) Numerical Simulation of Building Response on Liquefiable Sand, *Journal of Geotechnical and Geoenvironmental Engineering*, 139(8), https://doi.org/10.1061/(ASCE)GT.1943-5606.0000853.

Flora, A., Bilotta, E., Lirer, S., Mele, L., Modoni, G. (2023) Liquefaction mechanisms and mitigation techniques, *Rivista Italiana di Geotecnica,* 2, pp. 33-88 https://doi.org/10.19199/2023.2.0557-1405.033.

Karimi, Z., and Dashti, S. (2016) Numerical and Centrifuge Modeling of Seismic Soil-Foundation-Structure Interaction on Liquefiable Ground, *Journal of Geotechnical and Geoenvironmental Engineering*, 142(1) https://doi.org/10.1061/(ASCE)GT.1943-5606.0001346.

Itaca - ITalian ACcelerometric Archive - INGV. REXELweb. Available at: https://itaca.mi.ingv.it/ItacaNet_32/#/rexel.

Itasca Consulting Group, Inc. (2023) FLAC3D — Fast Lagrangian Analysis of Continua in Three-Dimensions, Ver. 7.0. Minneapolis: Itasca.

Liu, C., Macedo, J., Cambria, G. (2021) Performance-based probabilistic assessment of liquefaction-induced building settlements, *Soil Dynamics and Earthquake Engineering,* 151, https://doi.org/10.1016/j.soildyn.2021.106955.

Lopez-Caballero, F., and Farahmand-Razavi, A. M. (2008) Numerical Simulation of Liquefaction Effects on Seismic SSI, *Soil Dynamics and Earthquake Engineering*, 49, pp. 2-38. https://doi.org/10.1016/j.soildyn.2007.05.006.

Murashev, A. K., Keepa, C., Tai, A. (2015) Performance Based Design of a Structural Foundation on Liquefiable Ground with a Natural Soil Crust, In: *6th International Conference on Earthquake Geotechnical Engineering*, Christchurch, New Zealand. Available at: https://www.issmge.org/uploads/publications/59/60/39.00_Murashev.pdf.

Robertson, P. K. (2009) Interpretation of cone penetration tests — a unified approach, *Canadian Geotechnical Journalx,* 46(11), https://doi.org/10.1139/T09-065.

Shakir, H. and Pak, A. (2010). Estimating Liquefaction-Induced Settlement of Shallow Foundations by Numerical Approach, *Computer and Geotechnics*, 37(3), pp. 267-279. https://doi.org/10.1016/j.compgeo.2009.10.001.

Proceedings of the XVIII ECSMGE 2024
GEOTECHNICAL ENGINEERING CHALLENGES
TO MEET CURRENT AND EMERGING NEEDS OF SOCIETY
© 2024 the Authors
ISBN 978-1-032-54816-6
DOI 10.1201/9781003431749-242
Open Access: www.taylorfrancis.com, CC BY-NC-ND 4.0 license

ECSMGE 24
XVIII EUROPEAN CONFERENCE ON SOIL MECHANICS AND GEOTECHNICAL ENGINEERING

Effects of temperature, pore fluid composition and rate of shearing on the residual shear strength of soils

Effets de la température, de la composition du fluide interstitiel et de la vitesse de cisaillement sur la résistance résiduelle des sols

G. Scaringi*, O.P. Dhakal, M. Loche
Institute of Hydrogeology, Engineering Geology and Applied Geophysics, Faculty of Science, Charles University, Prague, Czech Republic

gianvito.scaringi@natur.cuni.cz

ABSTRACT: The residual shear strength is a crucial parameter in the post-failure behaviour of landslides. Many studies have shown that this parameter depends on the rate of shearing according to the normal stress and soil composition. Some researchers have shown that the composition of the pore fluid, which in landslide shear zones is typically an aqueous solution containing various dissolved ions, also can affect the residual shear strength. Smectites, in particular, can exhibit dramatic strengthening upon exposure to a concentrated salt solution. Few researchers have begun to evaluate the residual shear strength while also controlling the temperature during testing. Results demonstrated both strengthening and weakening upon heating, depending on soil composition. Owing to the coupled nature of hydraulic, thermal, chemical, and mechanical processes in soil, coupled effects also are expected; however, these effects are largely unexplored. We performed ring-shear experiments on pure clays and natural soils to obtain some insight into these coupled effects. We observed, for instance, that the effect of temperature fades away as the rate of shearing increases or the clay fraction decreases. We also observed some relationship between the shear rate effect and pore fluid composition. Understanding coupled processes in soils remains challenging; however, experiments may help improve our understanding of field-scale events, such as landslide reactivation and runout upon complex changes in boundary conditions.

RÉSUMÉ: La résistance résiduelle est un paramètre crucial dans le comportement post-rupture des glissements de terrain. De nombreuses études ont montré que ce paramètre dépend de la vitesse de cisaillement en fonction de la contrainte normale et la composition du sol. Chercheurs ont montré que la composition du fluide interstitiel, qui dans les zones de cisaillement est généralement une solution aqueuse contenant divers ions dissous, peut également affecter la résistance résiduelle. Les smectites, en particulier, peuvent montrer une augmentation considérable de la résistance si elles sont exposées à une solution saline concentrée. Peu de chercheurs ont commencé à évaluer la résistance résiduelle tout en contrôlant également la température pendant les tests. Les résultats ont démontré un renforcement ou un affaiblissement sous des températures élevées, en fonction de la composition du sol. En raison de la nature couplée des processus hydrauliques, thermiques, chimiques et mécaniques dans le sol, des effets couplés sont également attendus; cependant, ces effets sont largement inexplorés. Nous avons réalisé des expériences de cisaillement annulaire sur des argiles pures et des sols naturels pour obtenir un aperçu de ces effets couplés. Nous avons observé, par exemple, que l'effet de la température s'estompe lorsque la vitesse de cisaillement augmente ou que la fraction d'argile diminue. Nous avons également observé une certaine relation entre l'effet de la vitesse de cisaillement et la composition du fluide interstitiel. La compréhension des processus couplés dans les sols reste difficile; cependant, des expériences peuvent aider à améliorer notre compréhension des événements à l'échelle du terrain, tels que la réactivation des glissements de terrain et leur propagation lors de changements complexes des conditions aux limites.

Keywords: Residual shear strength; rate effect; thermo-hydro-mechanical coupling; chemo-mechanical coupling; clay.

1 INTRODUCTION

The residual shear strength is the minimum resistance that a soil can offer to shearing under a given effective normal stress (Scaringi and Di Maio, 2016). It is typically the only available resistance in regular landslide shear zones after large displacements and has been found to depend on the mineral composition of the solid skeleton as well as on that of the pore fluid (Di Maio, 2004; Di Maio and Scaringi, 2016). The residual shear strength also depends on the rate of shearing, and exhibits rate-strengthening, rate-weakening, or rate-neutral behaviours mainly according to the soil's mineral composition and grain-size distribution (Tika et al., 1996; Scaringi and Di Maio, 2016; Duque et al., 2023). Recent experiments

have demonstrated a dependence of the residual shear strength on the soil temperature during shearing (Loche and Scaringi, 2023). The residual shear strength and its controlling factors have been receiving increasing attention from researchers owing to the importance of this parameter in the behaviour (reactivation, runout) of landslides moving on clay-bearing shear zones. Understanding such behaviour has become even more critical under the ongoing, rapid climatic changes that many clay-rich regions are experiencing worldwide (Scaringi and Loche, 2022).

Here, we report on some recent ring-shear experiments that we conducted to begin quantifying how the aforementioned factors can condition the available shear resistance in the residual condition.

2 MATERIALS AND METHODS

2.1 Materials

We used commercial clays (kaolin, bentonite) as well as a number of natural soils in our experiments. Specifically, we used a Malaysian kaolin containing 46% of kaolinite and 48% of muscovite in dry weight. This kaolin exhibited a liquid limit of 63% and a plastic limit of 40%, with a granulometric clay fraction of 28% (< 2 μm), consistent with the typical large size of kaolinite stacks. Consequently, it had an activity of 0.82 and was classified as MH (inorganic, elastic silt) in the USGS classification. Further details on this material can be found in Duque et al. (2023).

The other commercial clay was a Ca-Mg bentonite named B75 and extracted from a deposit in the Czech Republic, containing 85% of montmorillonite and exhibiting a liquid limit and a plastic limit of 217% and 51%, respectively. Through sieve-sedimentation analysis, a clay fraction of 61% was evaluated, conferring the material an activity of 2.7 and resulting in a CH (fat clay) denomination in the USGS classification. Further details on this material can be found in Roháč et al. (2020) and Sun et al. (2022).

Additionally, samples of natural landslide soil (denominated A31, A68, A69, and A71) taken from the Melamchi catchment in Nepal were used. This Himalayan area experienced many landslides during a large-scale disaster in 2012. Owing to the limited accessibility of the site to heavy machinery, sampling was done using manual tools, down to depths of 0.5–1 m. The samples exhibited different index properties and mineral compositions. In general, they were characterized by low clay fraction (< 20%) and plasticity (< 20%), and by a dominance of kaolinite among the clay minerals. To explore the role of the clay component in determining the controlling factors of the residual shear strength, reconstituted samples (using distilled water or a concentrated NaCl solution) were prepared only from the fine fraction through successive sieving (< 125 μm, < 62 μm, < 20 μm).

2.2 Ring-shear device with temperature control

A Bromhead-type ring-shear device was employed (Wykeham Farrance, now Controls group). The device consists of a rotating base lined with a roughened brass porous platen, accommodating an annular sample 5 mm deep and 30 mm wide (outer diameter: 100 mm; inner diameter: 70 mm; area: 40 cm^2; volume: 200 cm^2). A top cap, also lined with a roughened porous platen, transfers the normal load to the sample and is prevented from rotating by two load cells contrasting a torque arm bolted to the cap.

The device was modified to gain control of the temperature of the water bath in which the sample is immersed. This was done by placing a closed water circuit made of a heat-conductive pipe, connected to an external thermostatic bath. Monitoring of the device's water bath was ensured by a thermocouple transmitting data to a computer, which was also receiving data from the device's controller (two load cells to determine the shear force and one sensor to monitor vertical displacements). Notably, we recorded a significant difference between the temperature measured in the device's bath and that set in the thermostatic bath owing to insufficient insulation of the device; therefore, we were unable to explore temperatures above ~55 °C even though we could reach ~90 °C in the thermostatic bath. The procedure for temperature-controlled experiments is described in Loche and Scaringi (2023). A sketch of the experimental setup is shown in Figure 1.

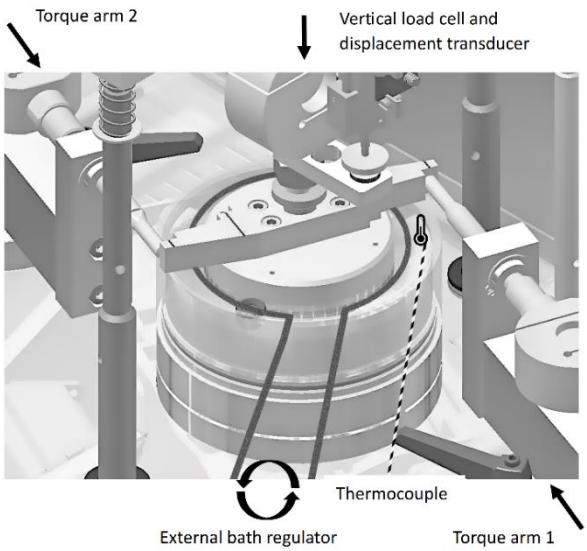

Figure 1. Sketch of the modified ring-shear device for temperature controlled experiments.

To evaluate the effect of the pore fluid composition we compared results using a conventional testing procedure (samples reconstituted with distilled water and immersed in a bath of distilled water during the whole test) with those evaluated on samples reconstituted with a concentrated (1 mol/L) NaCl solution and sheared while immersed in a bath of the same solution. The quality of the distilled water was ensured by measuring its electric conductivity (<1 µS/cm at 20 °C).

Finally, to evaluate the effect of the rate of shearing, we conducted experiments under various rates, exploiting the entire range available in the device. To preserve a smooth shear surface for as long as possible, we preferred a single-stage over a multi-stage procedure (Tiwari and Marui, 2004). We followed the protocol described by Stark and Eid (1994) to minimise the lateral friction by ensuring sample thicknesses above 4 mm before the start of the shearing phase. This required successive stages of consolidation with addition of material and overconsolidation to a normal load of 600 kPa prior to shearing under 50–150 kPa (i.e., OCR ≥ 4).

3 RESULTS AND DISCUSSION

The major role of the pore fluid composition in controlling the residual shear strength has been demonstrated extensively in various studies (see Di Maio and Scaringi, 2016). This was done with reference, in particular, to the role of inorganic salt solutions under landslide stress levels and very slow shearing (50–200 kPa; 0.005–0.018 mm/min). Less attention has been devoted to the coupled effect of pore fluid composition and rate of shearing. In Figure 2, we show an example of result using samples of kaolin, where the rate-strengthening behaviour and the (negligible) weakening effect of the salt solution are both visible. These effects are consistent with knowledge from the literature (Di Maio and Fenelli, 1994; Scaringi and Di Maio, 2016). Some enhanced rate-strengthening can be noticed in the samples in salt solution, but this is heavily masked by the wide error bars, which prevent a statistically-significant conclusion. The result suggests that a more refined device is necessary for a multivariate analysis.

More extensive studies on the shear-rate effects are reported in the literature, with a stress on the roles of the normal stress and mineral composition of the solid skeleton, that is, without specific attention to the influence of pore fluid composition and temperature. Nevertheless, important insights have been gained, for instance, concerning the predominant rate-strengthening behaviour of pure clays and clay-rich soils under rates of shearing corresponding to very slow to rapid landslides (Scaringi and Di Maio, 2016; Duque et al., 2023). Notably, under much larger displacement rates, shear-rate weakening is systematically observed independently of the soil nature. Various reasons for this phenomenon have been put forward, which entail frictional, acoustic, and thermo-chemical weakening mechanisms (Hu et al., 2018; Scaringi et al., 2018; Deng et al., 2020).

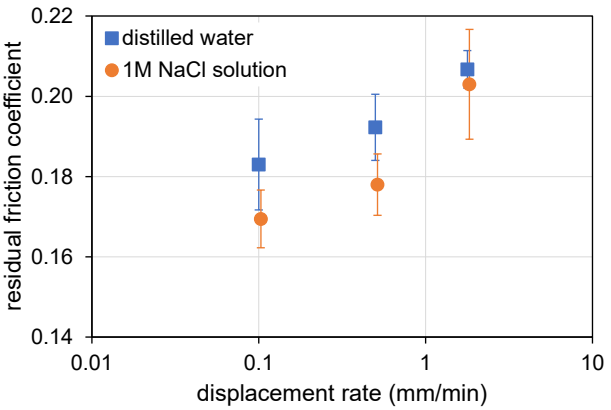

Figure 2. Residual friction coefficient (residual shear strength divided by the normal stress) of kaolin samples, prepared with and tested in a bath of distilled water or 1M NaCl solution, sheared under various displacement rates at 20 °C. The values correspond to the slopes of regression lines with zero intercept obtained from tests under 50, 100, and 150 kPa of normal stress (one test per normal stress). The error bars inform on the variability of the friction coefficient with the normal stress.

The effect of temperature on the residual shear strength of two pure clays was highlighted by Loche and Scaringi (2023), where considerations on a possible shear rate – temperature coupled effect were made, and implications in terms of possible changes in (shallow) landslide mobility under climate change were discussed. In Figure 3, a key result obtained on bentonite is reported, showing important strengthening upon heating during slow shearing (0.018 mm/min), which fades away upon faster shearing (0.5 mm/min) as the rate-strengthening behaviour dominates over the temperature-dependent one. This may be related to a change in the mode of shearing, from laminar to transitional or turbulent as the rate increases, which may result in a much less temperature-sensitive material. In fact, while laminar shearing is dominated by face-to-face interactions of clay particles, controlled by physico-chemical forces that are markedly sensitive to temperature, in a turbulent shearing condition, where particle arrangement is more chaotic, a role of pore fluid viscosity should prevail, which however varies little in the explored range of temperatures.

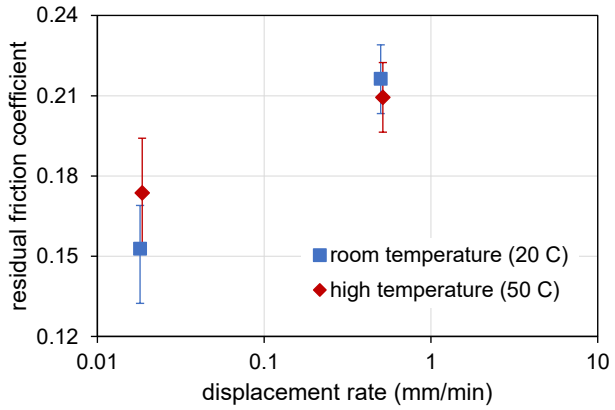

Figure 3. Temperature effects in ring-shear experiments on bentonite samples under various normal stresses, shear rates, and temperatures.

The experiments we conducted on natural soil, mainly aimed at identifying possible temperature effects, pointed out the crucial role of clay minerals in determining such effects, as evidenced by experiments carried out on the finest fraction of the samples. Figure 4 suggests that this can be evidenced by changing the cut-off grain size of the material submitted to the experiments. Obviously, by doing so, interpretation of field behaviours on the basis of experimental results becomes more difficult. However, in case of clay-enriched shear zones, it seems reasonable to hypothesise an enhanced role of the finest soil fraction in the process of shearing and in determining its controls.

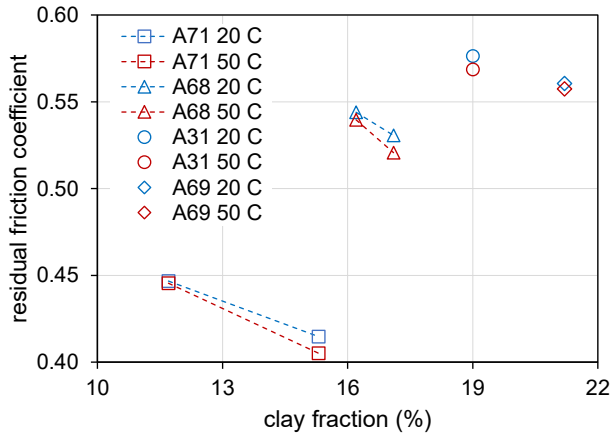

Figure 4. Temperature effects in ring-shear experiments on natural soil samples, sieved to enrich them in clay fraction. The experiments were conducted under 50–150 kPa of normal stress and 0.1 mm/min of rate of shearing.

4 CONCLUSION

We reported on ring-shear experiments aimed at evaluating the effects of pore fluid composition, temperature, and rate of shearing on the residual shear strength of various soils under stress conditions that are relevant in soil landslides. While many more experiments are needed to draw meaningful conclusions, we argue that the aforementioned effects should be studied comprehensively because coupled effects may arise. Furthermore, the role of grain size and/or mineralogical clay fraction, as well as that of the normal stress should be considered. Moreover, to study these effects, precise and accurate device setups providing highly repeatable results are essential to ensure that statistically significant conclusions can be reached.

ACKNOWLEDGEMENTS

The authors acknowledge financial support by the Ministry of Education, Culture and Sport of the Czech Republic (ERC CZ grant No. MŠMT-2853/2023-LL2316).

REFERENCES

Deng, Y., Yan, S., Scaringi, G., Liu, W., He, S. (2020). An empirical power density-based friction law and its implications for coherent landslide mobility. *Geophys. Res. Lett.* 47, e2020GL087581, https://doi.org/10.1029/2020GL087581.

Di Maio, C. (2004). Shear Strength of Clays and Clayey Soils: the Influence of Pore Fluid Composition. In: *Chemo-Mechanical Couplings in Porous Media Geomechanics and Biomechanics*, B. Loret, J.M. Huyghe (eds.), pp. 45–55. Springer, Vienna.

Di Maio, C., Fenelli, G.B. (1994). Residual strength of kaolin and bentonite: the influence of their constituent pore fluid. *Géotechnique* 44, 217–226, https://doi.org/10.1680/geot.1994.44.2.217.

Di Maio, C., Scaringi, G. (2016). Shear displacements induced by decrease in pore solution concentration on a pre-existing slip surface. *Eng. Geol.* 200, 1–9, https://doi.org/10.1016/j.enggeo.2015.11.007.

Duque, J., Loche, M., Scaringi, G. (2023). Rate-dependency of residual shear strength of soils: implications for landslide evolution. *Géotechnique Lett.* 13, 1–8, https://doi.org/10.1680/jgele.23.00004.

Hu, W., Scaringi, G., Xu, Q., Van Asch, T.W.J., Huang, R., Han, W. (2018). Suction and rate-dependent behaviour of a shear-zone soil from a landslide in a gently-inclined mudstone-sandstone sequence in the Sichuan basin, China. *Eng. Geol.* 237, 1–11, https://doi.org/10.1016/j.enggeo.2018.02.005.

Loche, M., Scaringi, G. (2023). Temperature and shear-rate effects in two pure clays: Possible implications for clay landslides. Results Eng. 20, 101647, https://doi.org/10.1016/j.rineng.2023.101647.

Roháč, J., Scaringi, G., Boháč, J., Kycl, P., Najser, J. (2020). Revisiting strength concepts and correlations with soil

index properties: insights from the Dobkovičky landslide in Czech Republic. *Landslides* 17, 597–614, https://doi.org/10.1007/s10346-019-01306-4.

Scaringi, G., Di Maio, C. (2016). Influence of Displacement Rate on Residual Shear Strength of Clays. *Procedia Earth Planet. Sci.* 16, 137–145, https://doi.org/10.1016/j.proeps.2016.10.015.

Scaringi, G., Hu, W., Xu, Q., Huang, R. (2018). Shear-Rate-Dependent Behavior of Clayey Bimaterial Interfaces at Landslide Stress Levels. *Geophys. Res. Lett.* 45, 766–777, https://doi.org/10.1002/2017GL076214.

Scaringi, G., Loche, M. (2022). A thermo-hydro-mechanical approach to soil slope stability under climate change. *Geomorphology* 401, 108108, https://doi.org/10.1016/j.geomorph.2022.108108.

Stark, T.D., Eid, H.T. (1994). Drained residual strength of cohesive soils. *J. Geotech. Eng*. 120, 856–871.

Sun, H., Scaringi, G., Mašín, D., Najser, J. (2022). An experimental investigation on the swelling behavior of compacted B75 bentonite. *Eng. Geol.* 296, 106452, https://doi.org/10.1016/j.enggeo.2021.106452.

Tika, T.E., Vaughan, P.R., Lemos, L.J.L.J. (1996). Fast shearing of pre-existing shear zones in soil. *Géotechnique* 46, 197–233, https://doi.org/10.1680/geot.1996.46.2.197.

Tiwari, B., Marui, H. (2004). Objective Oriented Multistage Ring Shear Test for Shear Strength of Landslide Soil. J. Geotech. Geoenvironmental Eng. 130, 217–222.

Proceedings of the XVIII ECSMGE 2024
GEOTECHNICAL ENGINEERING CHALLENGES
TO MEET CURRENT AND EMERGING NEEDS OF SOCIETY
© 2024 the Authors
ISBN 978-1-032-54816-6
DOI 10.1201/9781003431749-243
Open Access: www.taylorfrancis.com, CC BY-NC-ND 4.0 license

ECSMGE 24
XVIII EUROPEAN CONFERENCE ON SOIL MECHANICS AND GEOTECHNICAL ENGINEERING

Sand stabilization with colloidal silica for protection from liquefaction caused by dynamic loads

Stabilisation du sable avec de la silice colloïdale pour la protection contre la liquéfaction causée par les charges dynamiques

R.F. Sharafutdinov*, D.P. Kuznetsova, V.S. Morozov, Y.I. Stolyarov
Gersevanov Research Institute of bases and underground structures (NIIOSP)/JSC Research Center of Construction/Moscow/Russia

linegeo@mail.ru

ABSTRACT: Dynamic loads may cause liquefaction of the saturated sandy soil. The colloidal silica grouting is the most advanced and effective sand stabilization method. Higher permeability of the colloidal silica gives the method an advantage over other soil stabilization methods. Due to its water-like density and viscosity, the highly dispersive colloidal silica with the particle size less than 15 nm (up to 15-30 nm) is capable to penetrate into sands of various grain size. It forms gel in soil pores after being mixed with activator, thereby stabilizing the soil. The paper presents results of the study on gel time, permeability properties and dynamic strength of sand against concentration of the colloidal silica and sand density. It has been obtained that with increasing colloidal silica content and activator concentration, as well as with increasing temperature, the gel time significantly reduces. The defined and therefore recommended for use colloidal silica concentration ranges from 5% to 10%, which provides gel hardening within 10 days at the activator concentration of 1-2%. It has been found that dynamic strength of sand increases by 1.5-5 times when sand is grouted with minimum concentration of 5%. The performed study has shown that the colloidal silica concentration of 5% is sufficient for stabilizing the soil subjected to earthquakes of the intensity up to 9 (on the base of MSK-64 scale). The dependency of gel time on concentration resulted from the study can be applied in design practice. Due to its permeability, colloidal silica is a promising material for strengthening clayey or silty sand.

RÉSUMÉ: Les charges dynamiques peuvent provoquer la liquéfaction du sol sableux saturé. Le jointoiement de silice colloïdale est la méthode de stabilisation du sable la plus avancée et la plus efficace. Une perméabilité plus élevée de la silice colloïdale confère à la méthode un avantage par rapport aux autres méthodes de stabilisation du sol. En raison de sa densité et de sa viscosité semblables à l'eau, la silice colloïdale hautement dispersive avec une granulométrie inférieure à 15 nm (jusqu'à 15-30 nm) est capable de pénétrer dans des sables de différentes granulométries. Il forme du gel dans les pores du sol après avoir été mélangé avec un activateur, stabilisant ainsi le sol. L'article présente les résultats de l'étude sur le temps de gel, les propriétés de perméabilité et la résistance dynamique du sable contre la concentration de la silice colloïdale et la densité du sable. Il a été obtenu qu'avec l'augmentation de la teneur en silice colloïdale et de la concentration de l'activateur, ainsi qu'avec l'augmentation de la température, le temps de gel diminue considérablement. La concentration de silice colloïdale définie et donc recommandée pour une utilisation varie de 5% à 10%, ce qui permet un durcissement du gel en 10 jours à la concentration d'activateur de 1-2%. Il a été constaté que la résistance dynamique du sable augmente de 1,5 à 5 fois lorsque le sable est jointoyé avec une concentration minimale de 5%. L'étude réalisée a montré que la concentration de silice colloïdale de 5% est suffisante pour stabiliser le sol soumis à des séismes d'intensité jusqu'à 9 (sur la base de l'échelle MSK-64). La dépendance du temps de gel sur la concentration résultant de l'étude peut être appliquée dans la pratique de la conception. En raison de sa perméabilité, la silice colloïdale est un matériau prometteur pour renforcer les sables argileux ou limoneux.

Keywords: Ground improvement; colloidal silica; gelling time; dynamic strength.

1 INTRODUCTION

The earthquake hazard of more than 25 % of the Russian territory is classified as high. Sandy water-saturated soil of these regions is most liable to liquefaction. The dynamic strength improvement of liquefiable sands is necessary to use these soils as base of structures. However, the traditional grout improvement techniques (such as cement, microfine cement, epoxy or silica grouting) are often not applicable due to poor penetrability of materials into the granular soils (Semkin and Ibragimov, 2016).

The colloidal silica can be used for stabilizing saturated sand and protecting it against liquefaction. The advantage of the method is high penetrability of

colloidal silica. It is capable to penetrate into granular soil due to solution's finely dispersed particles of less than 15 nm in size and its density and viscosity are close to water. Soil stabilization is result of colloidal silica gelling caused by activator.

However, well-known laboratory tests on colloidal silica application have been conducted at a room temperature ~20˚C which differs from the natural soil temperature of 0-10˚C.

The article presents results of laboratory analysis of gel time and permeability of colloidal silica at the temperature ranging from 20 to 25°C and close to a natural temperature range from 0 to 10°C. The results of dynamic strength analysis of soil grouted by colloidal silica are presented. The optimal colloidal silica concentration on the basis of gel time, permeability and dynamic strength of the stabilized soil is determined.

2 METHODS

2.1 Gel time in relation to the temperature

The dependency of gel time on colloidal silica content at different the temperatures was studied in laboratory. For the purpose, a colloidal silica sol was taken with initial concentration of $K_{initial}$ = 30%. Gel time was analyzed at the temperature range from 5 to 25 ˚C. To maintain the required temperature, colloidal silica mixtures were prepared in a refrigeration chamber equipped with temperature controllers.

Series of tests were performed with:

- Colloidal silica concentration of 2.5, 5, 10 and 15%;
- *NaCl* activator concentration of 0.25, 0.5 1 and 2%;
- The temperature of 5, 10 and 25˚C.

Each test was repeated at least three times.

Testing technique was as follows:

At the first stage, NaCl was introduced into a desired volume of distilled water, thoroughly mixed until the required concentration of the activator was reached.

At the second stage, the required volume of colloidal silica was introduced into the *NaCL* solution, thoroughly mixed, hermetically sealed in the glass container and left at rest until the gelation started.

At the third stage, the gel was visually examined. A stage of the hard gel formation, at which no deformations of gel surface were observed, was taken as a gel time.

2.2 Permeation of colloidal silica

Permeation of colloidal silica was studied in tests on filtration soil properties, when soil was saturated with distilled water or colloidal silica of various concentrations. A series of test on medium and fine sands was carried out at:

- Colloidal silica concentration of 0, 2.5, 5, 10 and 15%;
- The temperature of 5; 10 и 25˚C;
- Minimum (I_D=0), medium (I_D=0,5) and maximum (I_D=1) density degree of sands.

Each test was repeated at least three times.

The components were kept at a given temperature in the refrigerator chamber for at least a day for further experiments. Testing and processing of results were carried out in accordance with the stationary filtration mode scheme prescribed by GOST 25584-2016.

2.3 Dynamic strength of soils grouted with colloidal silica

Dynamic triaxial test (Voznesensky, 1997) was used for assessing strength of sandy soil grouted with colloidal silica. Strength characteristics under dynamic loading were estimated for both grouted and clean sand. The tests were performed via GDS ELDYN (Figure 1).



Figure 1. Dynamic triaxial test system GDS ELDYN.

Tests were performed on medium and fine sands (Figure 2) at:

- Initial void ratio e=0,7; 0,6 and 0,5;
- Colloidal silica concentration of 5, 10 and 15%.

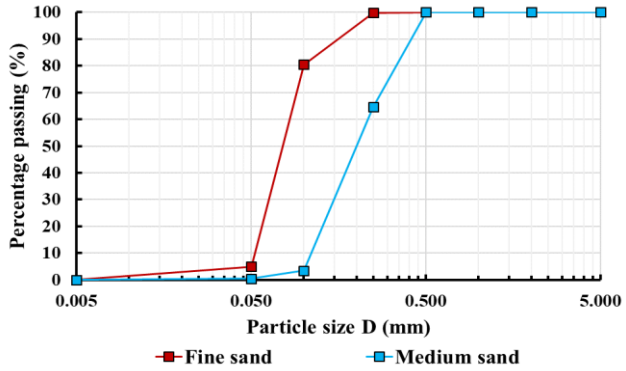

Figure 2. Cumulative curve of the grain size distribution.

Each test involved the following sequences:

At the first stage, a specimen was prepared in a special split mold by tamping dry soil in layers.

At the second stage, the specimen was grouted with colloidal silica through the bottom side (Figure 3) under the pressure of 10 kPa. When the specimens became saturated, the molds were removed and specimens were kept at rest until the gel stabilized.

At the third stage, after gel stabilization, the specimens were placed under water to prevent contact with the air and they were left so to gain strength.



Figure 3. Saturation device.

At the fourth stage, the specimens were loaded under anisotropic consolidation at a given initial stress and then were subjected to dynamic loading. The tests were repeated at least six times with a shear stress taken depending on soil strength. The dynamic load was applied until the specimens failed.

Changes in cyclic resistance ration *CRR* of specimens were assessed with a method of equivalent cycles. A critical number of cycles N_{cr}, at which the specimens failed, was determined for each test and a relation $CRR = f(N_{cr})$ was then generated.

3 RESULTS

Gel time. It has been defined that minimum colloidal silica SiO_2 concentration is 5%, inasmuch that with minimum temperature of 5 ˚C and minimum activator concentration of 1 % it was possible to fix moment of gelation within the optimum waiting period (Figure 4). At lower concentration, gel time increases significantly and gelation in laboratory conditions has not fixed.

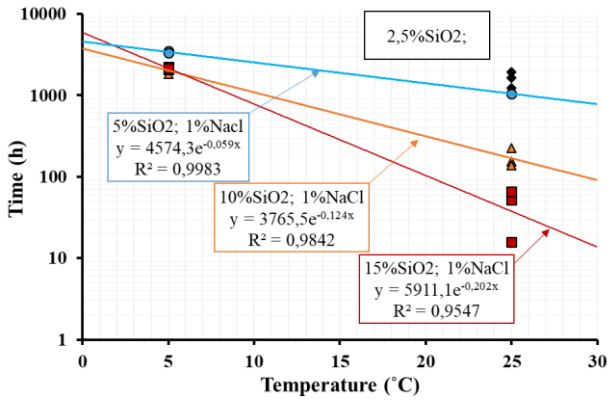

Figure 4. The relationship between gel time and temperature at activator concentration of 1%

Concentration of colloidal silica has a significant effect on its permeability. As the concentration increases from 0 to 15%, the hydraulic conductivity of sands decreases by average 2 times regardless of sands density, particles distribution and temperature conditions. It was observed, that for the concentration of colloidal silica $C_{SiO2} \leq 5\%$ the difference in the rate of colloidal silica delivery and water infiltration was less than 10%. This indicated the high permeability of low-concentrated grout (Figure 5).

The temperature drop by *5* times lowered the rate of grout delivery by 1,2 – 2,2 times, whatever density and particle distribution of sand were.

The hydraulic conductivity of sand decreased by 1,8 – 3,6 times with the increasing density degree I_D from 0 to 1. In this case, the influence of the density degree of medium sand was more significant than that of fine sand due to the pore size and the roundness of the particles of the soils considered (Figure 5).

Dynamic strenght of soils grouted with colloidal silica. Figure 6 shows the results of dynamic triaxial tests on fine sand (6a, 6b) and medium sand (6c, 6d) at different concentration of colloidal silica. It was observed that strength properties of fine sand increased significantly as compared to medium sand. Grouting smaller fractions was approximately 55% more effective.

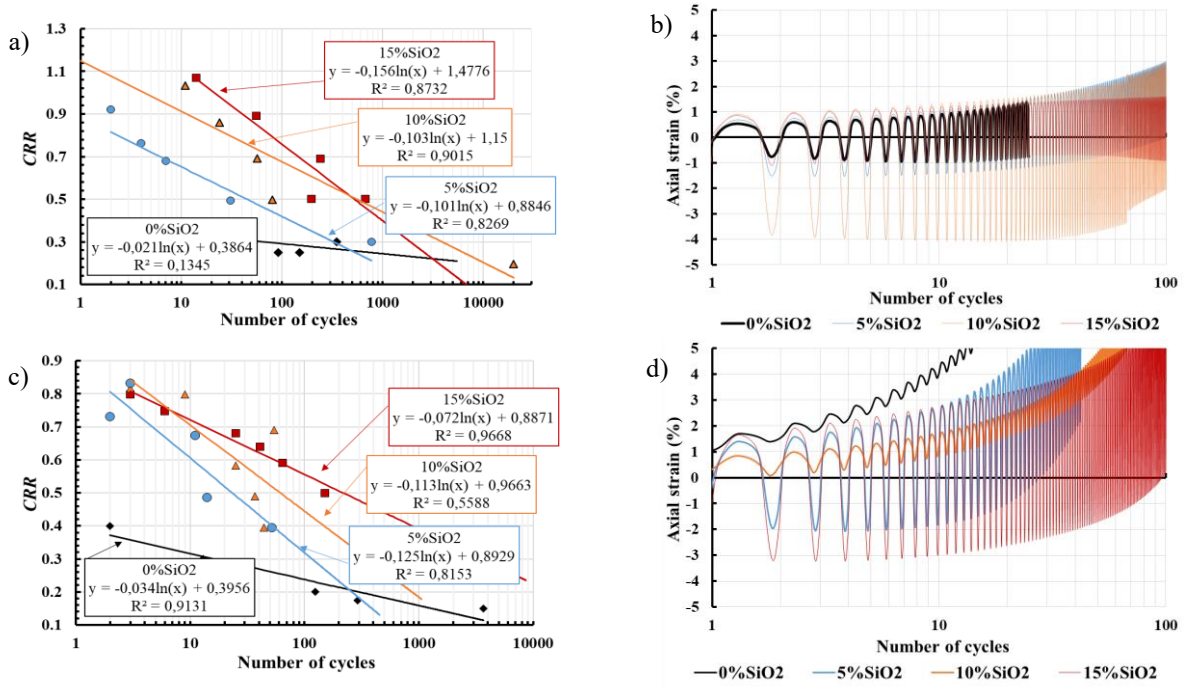

Figure 6. Results of dynamic triaxial tests: a - cyclic resistant ration (CRR=0,6) of fine sand (e=0,7) versus a number of loading cycles; b – fine sand axial strain under cyclic loading for different concentration of colloidal silica SiO_2 ; c- cyclic resistant ration (CRR=0,6) of medium sand (e=0,7) versus a number of loading cycles; d - medium sand axial strain under cyclic loading for different concentration of colloidal silica SiO_2.

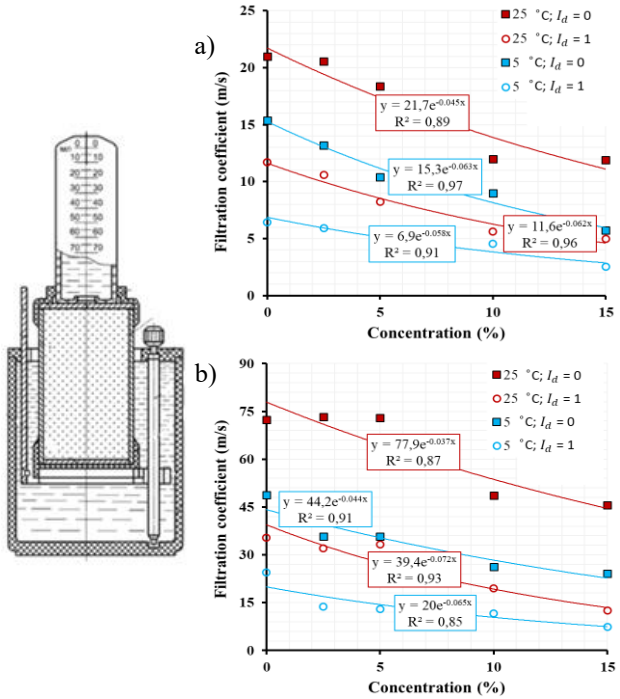

Figure 5. Installation scheme for testing filtration of sand at a constant pressure level: permeability of colloidal silica versus concentration in fine sand (a) and in medium sand (b).

On the base of regression analysis the following empirical dependence was proposed:

$$CRR = a_1 \lg N + a_2 \lg C_{SiO_2} + a_3 \qquad (1)$$

where, N – a number of dynamic triaxial loading cycles; C_{SiO_2} – concentration of the colloidal silica; a_1, a_2, a_3 – empirical coefficients derived from tests.

Overall, based on the total results published (Gallagher, 2002, 2009; Sharafutdinov and Kuznetsova, 2023), it can be noted that 5% colloidal silica content is enough to protect sandy soil from earthquakes with intensity up to 9 (on MSK intensity scale). However, most existing studies do not make a direct correlation between soil density and minimum colloidal silica concentration required. A content of 5% colloidal silica was defined for particular sands (including particle roundness, mineralogy etc.) and, therefore, could not be recommended for practical application (Figure 7).

Moreover, most existing publications assess the influence of colloidal silica content on stiffness and deformation of soil specimens prepared in laboratories. The benefits of colloidal silica grouting needs to be studied more thoroughly in-situ.

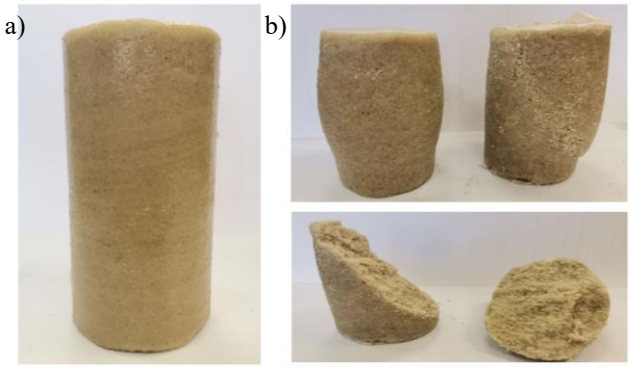

Figure 7. Specimens of sand grouted with colloidal silica: before (a) and after (b) dynamic testing.

4 CONCLUSIONS

Minimum concentration of colloidal silica needed to stabilize soils was defined as 5%, since with this concentration gel formed at minimum temperature of 5 ˚*C* and minimum activator concentration of 1%.

The permeability of colloidal silica has a significant influence on stabilization process. The research performed by the authors shows that with concentration of colloidal silica increasing from 0 to 15% its permeability reduces by 2 times. It is obvious that activator influences the results. While permeating, the colloidal silica forms gel and a real size of the grouted area is changing (Gallagher, 2007). Nevertheless, for the concentration of colloidal silica $C_{SiO2} \leq 5\%$ the difference in the rate of colloidal silica delivery and water infiltration is less than 10%. This indicates the high permeability of low-concentrated grout.

Temperature conditions are also of great importance. Notwithstanding the density degree of sand, hydraulic conductivity reduces by average 1,2-2,2 times when temperature falls by 5 times (from 25 ˚C to 5 ˚C). This factor should be taken into account when soil massive is grouted with colloidal silica in-situ.

On the base of the study performed, relations for estimating soil stiffness with regard to the concentration of colloidal silica, sand density and particle size distribution has been derived. Overall, based on the total results received, it can be noted that 5% colloidal silica content is enough to stabilize sandy soils, protecting them from dynamic impact. Strength properties of grouted fine sands are better if compared with medium sands. Grouting of fine fractions gives approximately 55% more effective results. The cyclic resistance ration can be estimated with relation (1), depending on concentration of the colloidal silica. However, the resulting empirical coefficients may be subjective, which requires additional research.

The performed study on gel time, permeability of colloidal silica and dynamic stiffness of sandy soil allows authors to conclude with carefulness that 5% concentration of colloidal silica may be recommended for grouting soils subjected to dynamic loading including seismic impact. According to the authors, benefits of colloidal silica grouting needs to be studied more thoroughly in-situ.

REFERENCES

Gallagher, P.M., Conlee, C.T., Rollins, K.M. (2007). Full-scale field-testing of colloidal silica grouting formitigation of liquefaction risk. *J. Geotech. Geoenviron*. Eng. 133(2), 186–196. https://doi.org/10.1061(ASCE)1090-0241(2007)133:2(186).

Gallagher, P.M., Lin,Y. (2009). Colloidal silica transport through liquefiable porous media. *J. Geotech. Geoenviron*. Eng. 135(11), 1702–1712. https://doi.org/10.1061/(ASCE) GT.1943-5606.000012.

Ibragimov, M.N., Semkin, V.V. & Shaposhnikov, A.V. Soil Solidification by Micro-Cements. Soil Mech Found Eng 53, 412–419 (2017). https://doi.org/10.1007/s11204-017-9421-0.

Sharafutdinov R.F. and Kuznetsova D.P. (2023) Colloidal silica as a medium for increasing sandy soil resistance to dynamic loading. *Foundations*, No 3, pp 74-76 (in Russian).

Voznesensky E.A. (1997). *Soil behavior under dynamic loading,* MSU, Moscow, The Russian Federation (in Russian).

Proceedings of the XVIII ECSMGE 2024
GEOTECHNICAL ENGINEERING CHALLENGES
TO MEET CURRENT AND EMERGING NEEDS OF SOCIETY
© 2024 the Authors
ISBN 978-1-032-54816-6
DOI 10.1201/9781003431749-244
Open Access: www.taylorfrancis.com, CC BY-NC-ND 4.0 license

ECSMGE 24
XVIII EUROPEAN CONFERENCE ON SOIL MECHANICS AND GEOTECHNICAL ENGINEERING

Landslide monitoring: comparative analysis of long-term automated systems in Brazil and the UK

Surveillance des glissements de terrain: analyse comparative des systèmes automatisés à long terme au Brésil et au Royaume-Uni

A. Silva*
Measurand, São Paulo, Brazil

C. Levesque
Measurand, Fredericton, Canada

B. Norberto, S. Holloway, D. Fornelli
Geotechnical Observations, London, UK

**andre.silva@measurand.com*

ABSTRACT: Long-term landslide monitoring is essential for understanding landslides and implementing mitigation strategies. Case studies in Brazil and the UK used automatic systems for this purpose. In Brazil, since 2013, a geotechnical sensor system has been monitoring soil movement, water pressure, and rainfall. In the UK, a project since 2012 has been using various instruments to monitor a highway's slope slippage. Both systems allow for early warnings and corrective actions. The current paper will also discuss the challenges and advantages of implementing such systems and also show the benefits of using the right instruments to provide long term monitoring of unstable assets in different regions and contexts.

RÉSUMÉ: La surveillance à long terme des glissements de terrain est essentielle pour comprendre ces phénomènes et mettre en œuvre des stratégies d'atténuation. Des études de cas au Brésil et au Royaume-Uni ont utilisé des systèmes automatiques à cet effet. Au Brésil, depuis 2013, un système de capteurs géotechniques surveille les mouvements du sol, la pression interstitielle et les précipitations. Au Royaume-Uni, un projet utilise divers instruments depuis 2012 pour surveiller le glissement de pente d'une autoroute. Les deux systèmes permettent des alertes précoces et des actions correctives. Le présent document exposera également les défis et avantages de la mise en œuvre de tels systèmes et montrer également les avantages de l'utilisation des bons instruments pour assurer le suivi à long terme des actifs instables dans différentes régions et contextes.

Keywords: Geotechnical monitoring; instrumentation; observational method; inclinometers; piezometers.

1 INTRODUCTION

Continuous monitoring systems aid risk management by understanding landslides and enabling timely responses to reduce casualties. They enhance risk reduction strategies and ensure infrastructure safety by using advanced technology for data acquisition and analysis. Monitoring enables informed decisions and timely interventions to mitigate landslide impacts.

Long-term monitoring of landslides is essential in regions like UK and the Brazil for understanding their dynamics and implementing mitigation measures. Both countries have adopted automatic systems for this purpose. For instance, a project in Lancashire, UK, initiated in 2012, employs ShapeArrays, water level recorders, rain gauges, and tiltmeters to monitor slope movements on a highway. Likewise, in Campos de Jordão, Brazil, a geotechnical sensor system has been operational since 2013, gathering real-time information on soil movement, water pressure, and rainfall. This system aids in early warnings and taking timely corrective actions. The current paper will expose the challenges and advantages of both long-term monitoring case studies.

The objective of the paper is not to provide an analysis and description of the failure mechanisms, or to undertake a back analysis of the data, but to stress the benefits of using the right instruments to provide long term monitoring of unstable assets in different regions and contexts.

2 UK CASE STUDY – SOUTHBOUND HIGHWAY

The United Kingdom has an extensive road network totalling approximately 400,000 km. The Strategic Road Network of England is the economic core of the country's road network and is made up of motorways and major A-roads, with a length of over 15,000 km. 80% of these (approx. 13,000 km) are comprised of cuttings and embankments.

An ageing infrastructure (mostly built in the 1960s and 1970s) and an increased volume of traffic (up approximately 80% between the 1980s and the early 2000s) have continuedly contributed to the deterioration of a significant number of geotechnical assets along the network.

The site presented in this paper is in Lancashire, United Kingdom and comprises a cutting approximately 250m long along the Southbound carriageway of a dual carriageway road part of the Strategic Road Network. The cutting features a sheet piled retaining wall spanning approximately 90m at the toe of the slope, raising approximately 1m above ground level, with a layer of rockfill behind it.

A ground investigation campaign was carried out in the Summer of 2011 which was used to install monitoring along the slope, comprised of piezometers and inclinometers. Initial readings of inclinometers were taken end of September 2011. In a manual monitoring campaign carried out early January 2012, cumulative displacements of up to 80mm had already been recorded, with a shear zone clearly identified in all the instruments. As it can be seen in Figure 1, the inclinometer measurements allow not only to understand the cumulative displacement of the slope, but also the rate of displacement and the width of the "shearing zone" within the soil; in the case of Figure 1, it is apparent how the soil deformation is concentrated within a "band" which is approx. 3m thick.

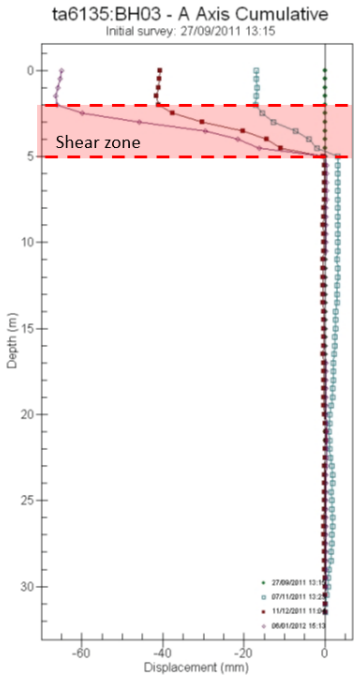

Figure 1. Manual inclinometer results for BH03 Jan/2012.

2.1 Automation monitoring

In April 2012, given the rate of displacement and the fact it wasn't possible to traverse the inclinometer casings with an inclinometer probe due to excessive bending, the slope monitoring was automated with ShapeArrays (Figure 3) and water level recorders. To complement this, a rain gauge was also installed on site in June 2012 and wireless tiltmeters were installed on the sheet pile wall in August 2012 (Figure 2).



Figure 2. Wireless tiltmeter in a sheet pile wall.

Data was collected using four independent networks of dataloggers connected via radio link. On each network, a main hub with a mobile network modem allows for remote data collection, with data being made available to the asset owner automatically via a web-based data visualisation and analysis platform.



Figure 3. Automatic inclinometers (ShapeArray) installation.

Since the installation of the automated monitoring in 2012, displacements have been registered up to a maximum of 995mm downslope, with an average displacement of ~86mm/year (Figure 4).

Based on the continuous monitoring of the asset, over the last 10 years, the client was able to assess the stability of the slope, implement any required safety measures, and guarantee the safety for the road users throughout the year.

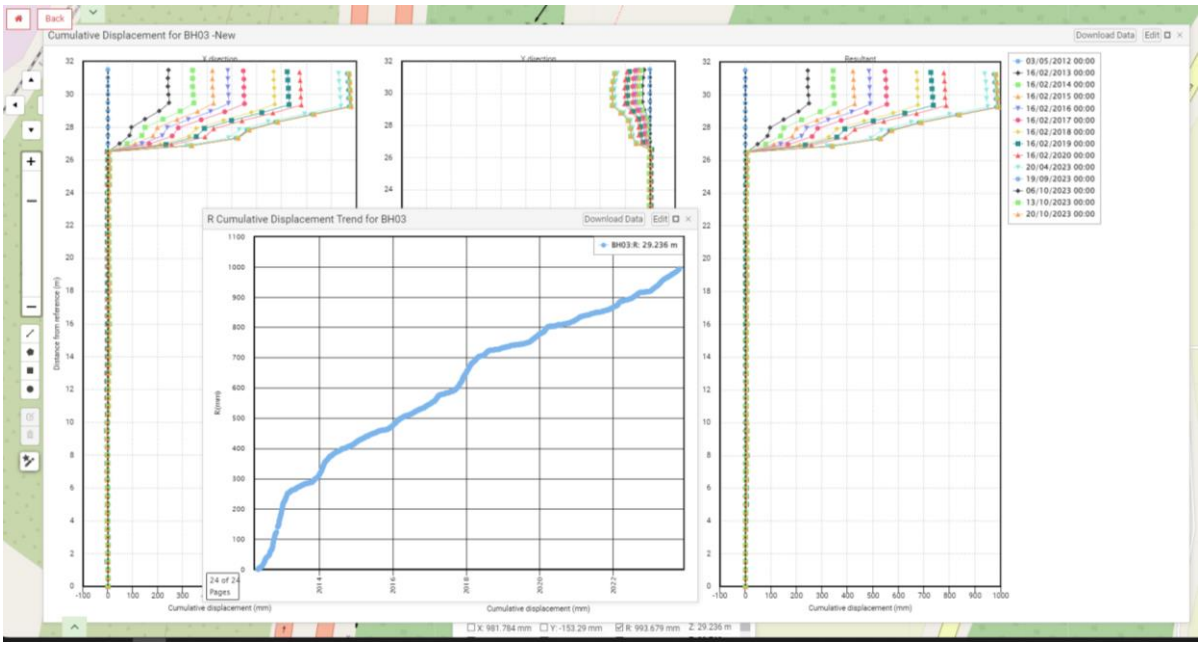

Figure 4. Cumulative displacement at BH03 in October 2023 and cumulative displacement trend.

The automation of the site allowed the monitoring to continue without costly re-drilling works, with increased frequency of data acquisition if/when required, reducing the presence of staff on site with only one/two maintenance visits throughout the year required to keep the system running.

Figure 5 shows how the thickness of the soil "band" interested by the deformations has been keeping consistent during the monitoring period. This kind of information could crucially inform the back analysis and the (consequent) optimisation of the maintenance strategy and maintenance interventions on the slope.

The slope stability analysis and any potential stabilisation/remedial works have been and are being carried out by a specialist engineering consultancy employed by the client. The authors are not involved in this process.

Recently, works were carried out to improve the drainage along the slope and the sheet pile wall was extended North for approximately 100m. The client and the engineering consultant are now assessing the impact of these works in the overall stability of the slope.

Over the years some of the equipment (mainly piezometers) started failing, which prompted the client to consider a refurbishment of the monitoring system. The ShapeArrays continued performing over the years, even when measuring significant deformations over very short lengths.

Due to the rate of movement over the years, manual data acquisition with an inclinometer probe and the required additional works to keep the monitoring going would render this option unsustainable. The ability to retrofit ShapeArrays into existing inclinometer casings that had suffered extreme bending proved to be a game changer for this project, allowing the monitoring of the slope to continue without costly additional works or disturbance of the slope with heavy drilling equipment.

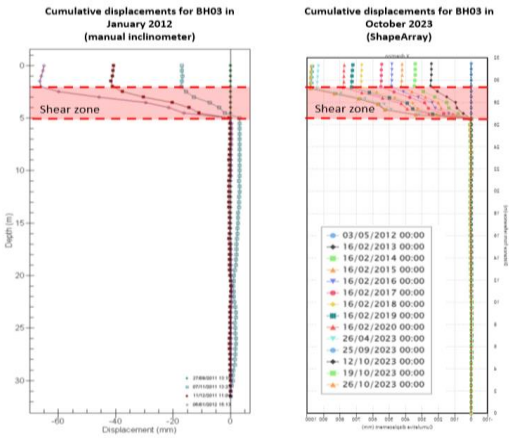

Figure 5. Comparison of cumulative displacement profiles between Jan/2012 and Oct/2023.

3 BRAZIL CASE STUDY – CAMPOS DO JORDÃO PILOT PROJECT

Brazil annually contends with floods and landslides affecting over 4 million people across 14,000 highly susceptible areas. During the rainy season (December-March), catastrophic events claim lives and cause substantial damage. In January 2023, flooding and landslides in São Paulo killed 65 and displaced 3,500. In the previous year, Petropolis saw 235 fatalities and 4,000 displaced due to intense rainfall. Despite recognizing the importance of geotechnical instrumentation, its inadequate implementation persists.

In 2013, a pilot project was initiated to monitor a slope in São Paulo, Brazil, using two ShapeArray inclinometers and two vibrating wire piezometers. The fully automated system has been operational for around 10 years with hourly data collection. The project aims to:

- Establish a remote monitoring system.
- Measure key variables.
- Ensure reliable, continuous data delivery.
- Enhance risk management in an area prone to landslides.

3.1 Geometric, geological, and geotechnical characterization

The slope is about 50m long and 10m wide from the top to its base. The water table varies between 2m from the surface at the base of the slope and about 5m at the top of it (Figure 6).

The stratigraphy obtained through the boreholes provided indicates the existence of a surface landfill stratum (brown clay silt) and an underlying layer with low, predominantly clayey resistance characteristics (Gray organic clay with 1 to 2 blows Nspt), followed by a saprolite soil (young residual soil) to saprolite (transition from residual soil to altered rock) typical of tropical regions.

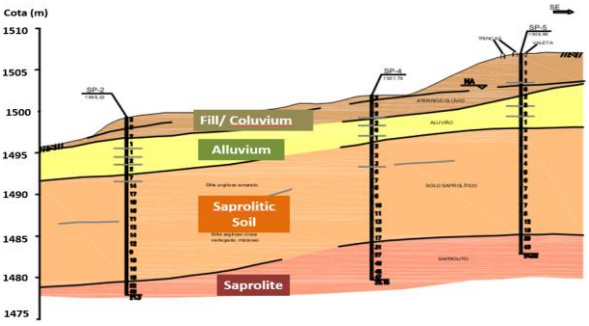

Figure 6. Geological profile of the study area (from top to bottom – Fill/Coluvium, Alluvium, Saprolitic soil, Saprolite.

Before installation, a Morgenstern-Price Method limit equilibrium analysis assessed slope stability (Figure 7). Despite moderate steepness, geological and hydrogeological factors favour mass movement. The analysis highlighted the importance of the alluvial layer (yellow layer in Figure 6 and Figure 7) in slope stability, with its characteristics directly influencing the overall safety factor. Rupture surfaces with safety factors near 1 are concentrated in this layer, indicating deeper landslide potential. Furthermore, stability worsens with heavy rainfall and loads on the upper slope. This limit equilibrium analysis was useful to understand the potential failure mechanism and define the instrumentation plan such as: type of instruments, location and data collection frequency.

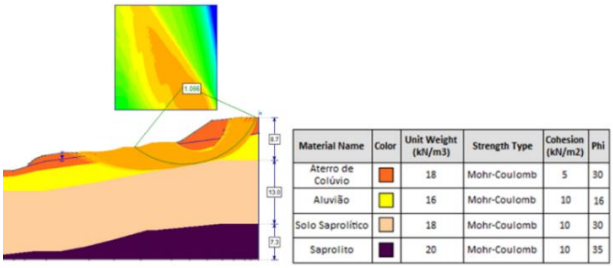

Material Name	Color	Unit Weight (kN/m3)	Strength Type	Cohesion (kN/m2)	Phi
Aterro de Colúvio		18	Mohr-Coulomb	5	30
Aluvião		16	Mohr-Coulomb	10	16
Solo Saprolítico		18	Mohr-Coulomb	10	30
Saprolito		20	Mohr-Coulomb	10	35

Figure 7. Results of the stability analysis (Morgenstern-Price Method - FS [1 to 1.5]. Material names translation from top to bottom: Fill/Colluvium, Alluvium, Saprolitic soil, Saprolite).

3.2 Instrumentation plan

The instrumentation project involved integrating two ShapeAccelArrays (SAAs) and two vibrating wire piezometers at a geological site. They were strategically placed based on-site features. A detailed assessment identified critical factors including horizontal displacements and pore pressures. Two SAAs (18m and 22m) measured displacements at various depths, while two piezometers (at 5m and 8m depths) monitored pore pressures. The data collection occurred at one-hour intervals.

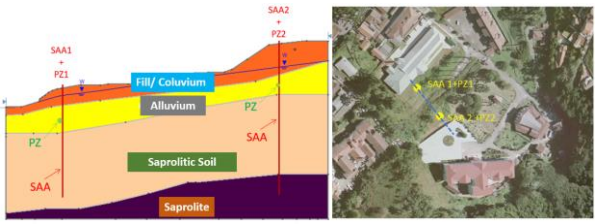

Figure 8. Cross-section with the location of the instruments (from top to bottom – Fill/Coluvium, Alluvium, Saprolitic soil, Saprolite.

As illustrated in Figure 8 there was a concern about anchoring the automated inclinometers in competent locations of the saprolitic or saprolite layers. The piezometers in the middle of the alluvial layer to verify the possible change in the pore pressure regime in this soft clay soil were identified as critical in the limit equilibrium stability analysis.

3.3 Analysis and data interpretation

It is important to note that although the monitoring has been taking place since 5/10/2013, there is a gap without data due to the lack of project funding funds that prevented the data from continuing to be transmitted, being only kept in the physical datalogger. However, due to the frequency adopted, the datalogger's ring memory was filled every three months, and the older data were overlaid as new data were collected. Continuous data collection resumed in July 2022. Even so, after diagnostic tests and sensor integrity checks, the equipments remain in good working condition.

Automated inclinometers demonstrate displacements in the shallowest strata of colluvium and alluvium. In SAA1, a clear-cut surface is defined about 3.5 m from the surface, while for SAA2, this surface is delineated from the surface 6 m, as illustrated in Figure 9. The results are consistent with the geological profile of the site, showing a creep phenomenon (Figure 11) that mobilizes slowly the surface layer of colluvium and part of the alluvium due to its characteristics of magnitude and velocity (1mm/year), with the latter showing more variation of around 2mm in periods of greater rainfall (Figures 9B and 10B).

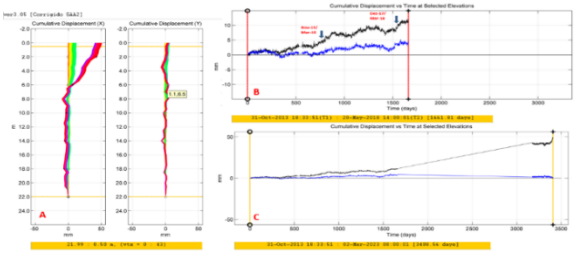

Figure 9. A) Cumulative displacements in the X (preferred direction of displacement) and Y axes of SAA2; B) Cumulative displacements in X (black) and Y (blue) axes over time at 1.0m depth, emphasizing acceleration during heavy rainfall; C) Cumulative displacements in X (black) and Y (blue) axes over time at 1.0m depth from 2013 to 2023.

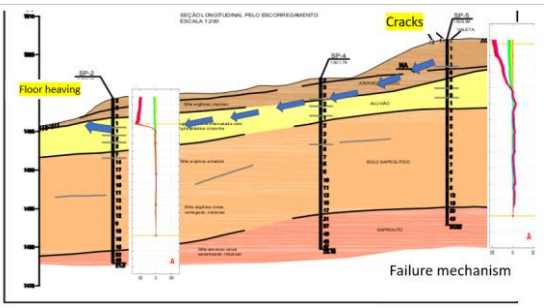

Figure 10. Illustration of the cumulative displacements in both ShapeArrays (left/right) according to the geological profile and installation site. Pathologies (cracks at the top and school floor heaving at the bottom). Location of vibrating wire piezometers and assumed position of the water table (NA) according to piezometric results. Understanding of the failure mechanism. (blue arrows).

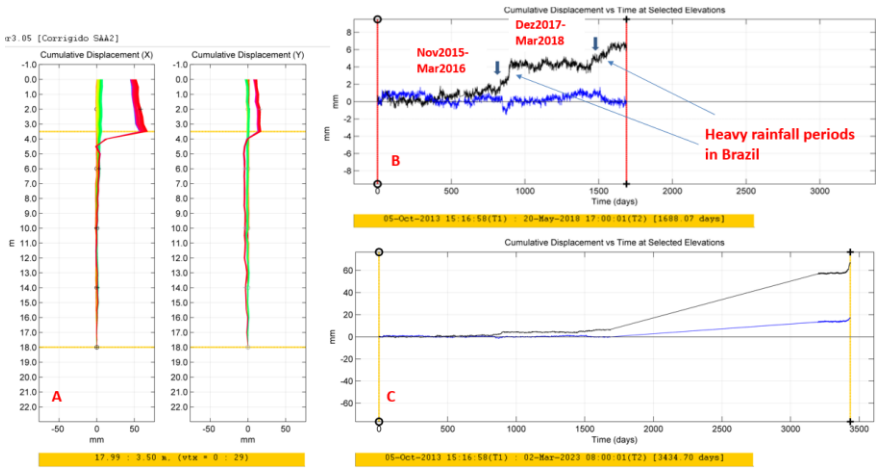

Figure 11. A) Cumulative displacements in the X (preferred direction of displacement) and Y axes of SAA1; B) Cumulative displacements in X (black) and Y (blue) axes over time at 3.5m depth, emphasizing acceleration during heavy rainfall; C) Cumulative displacements in X (black) and Y (blue) axes over time at 3.5m depth from 2013 to 2023.

3.3.1 Vibrating wire piezometers

The vibrating wire piezometers had a brief operational period due to technical issues. Data collected during this time was accurate. PZ1 and PZ2 showed consistent values with assumed groundwater levels from geotechnical investigations (Figure 12). Despite the short period, PZ1 detected minor variations during the initial high rainfall period (Nov/2013 to Mar/2014), indicating increased pore pressures during peak rainfall and subsequent decrease. This is likely due to colluvium layer saturation, increasing self-weight and loading on adjacent alluvium layer.

Barometric variations may also influence these changes.

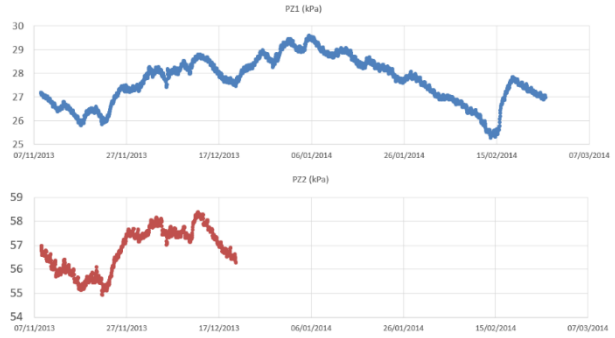

Figure 12. Pore pressure data recorded by vibrating wire piezometers (while operational).

3.3.2 Rain gauges

Rain gauge data from CEMADEN, a governmental institute tracking environmental data and natural disasters nationwide, was integrated with geotechnical monitoring from the pilot project. This enhanced landslide risk forecasting by correlating rainfall with soil stability. The data reveals annual rainfall and temperature patterns over 30 years (Figure 13), aiding in identifying regional wettest/driest and hottest/coldest periods.

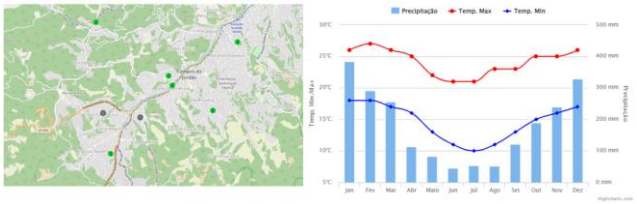

Figure 13. Left- Rain Gauge location (Green circles); Right - the average behaviour of rainfall (blue histogram) and temperature (min-blue line/max- red line) throughout the year at Campos de Jordão city– Source: CEMADEN.

4 CONCLUSIONS

1. Geological Behaviors in Brazil and the UK: Despite similar monitoring principles, distinct geological responses and context were observed.
   - Brazil: Revealed slow, 'creep' type landslide characterized by discrete movements.
   - UK: Showed high-magnitude displacements and faster landslide evolution.

2. Role of Automated Monitoring: Automated systems efficiently correlate rainfall with displacement rates, crucial in both cases.
   - Correlation with Rainfall: established over multiple seasonal cycles, illustrates the critical role of prolonged and intense rainfall as triggers for landslides.

3. Decision-making between Manual and Automated Monitoring: Hinges on project-specific factors.
   - Cost-effectiveness of Automation: Automated monitoring emerged as more cost-effective despite challenges faced (importation fees and taxes in the Brazilian case)

4. Integration of Geotechnical and Meteorological Data: Enhances effectiveness of preventive and corrective actions.
   - Improvement in Data Collection: Facilitates better correlation with rainfall, surpassing limitations of manual methods.

5. Challenges and Maintenance: Vulnerability of instruments and financial constraints emphasize the need for ongoing management.

6. Importance of Integrated Data for Understanding Geological Events: Integration of geotechnical and meteorological data crucial for comprehending slope stability dynamics.
   - Advancement in Research: Enables further exploration of rainfall, infiltration, and soil suction dynamics, expanding understanding of slope stability.

7. Contribution to Risk Management and Future Projects: Insights gained contribute significantly to risk management in slope stability, informing approaches for future projects in different regions and scenarios.

Proceedings of the XVIII ECSMGE 2024
GEOTECHNICAL ENGINEERING CHALLENGES
TO MEET CURRENT AND EMERGING NEEDS OF SOCIETY
© 2024 the Authors
ISBN 978-1-032-54816-6
DOI 10.1201/9781003431749-245
Open Access: www.taylorfrancis.com, CC BY-NC-ND 4.0 license

ECSMGE 24
XVIII EUROPEAN CONFERENCE ON SOIL MECHANICS AND GEOTECHNICAL ENGINEERING

Assessment of geotechnical properties using optimisation methods

Évaluation des propriétés géotechniques par des méthodes d'optimisation

M. Stãnciucu*, I. Mircea
University of Bucharest, Romania
**stanciucumihaela@yahoo*

ABSTRACT: The paper presents the results of the complex geotechnical evaluation of two sites situated on the alluvial plain of the Dâmbovita River in Bucharest, Romania, where geotechnical investigations were completed with the geophysical survey. Despite short distances between sites, the results illustrate significant variabilities of sedimentary layers and consequently of geotechnical properties. To obtain local representative correlations, we applied in the first instance several well-known formulas, but the degree of fitness was inferior. In the second stage, we developed several evolutionary polynomial regression algorithms (EPR), a method of solving optimization problems, when the objective function is nonlinear. The new predicted values were analyzed using statistical parameters and residual analysis. Thus, we obtain new formulas for each layer, allowing more precise correlations of geotechnical and geophysical parameters inside the sedimentary alluvial structure, by reporting to the relations proposed in the literature.

RÉSUMÉ: L'article présente les résultats de l'évaluation géotechnique complexe de deux sites situés sur la plaine alluviale de la rivière Dâmbovita à Bucarest, en Roumanie, où les études géotechniques ont été complétées avec l'étude géophysique. Malgré de courtes distances entre les sites, les résultats illustrent des variabilités significatives des couches sédimentaires et par conséquent des propriétés géotechniques. Pour obtenir des corrélations représentatives locales, nous appliquons en premier lieu plusieurs formules bien connues, mais le degré de fitness était très faible. Dans un second temps, nous avons développé plusieurs algorithmes de régression polynomiale évolutive (EPR) qui est une méthode de résolution de problèmes d'optimisation, lorsque la fonction objective est non linéaire. Les nouvelles valeurs prédites ont été analysées à l'aide de paramètres statistiques et d'analyses résiduelles. Ainsi, nous obtenons de nouvelles formules pour chaque couche, permettant des corrélations plus précises des paramètres géotechniques et géophysiques à l'intérieur de la structure alluviale sédimentaire, par rapport aux relations proposées dans la littérature.

Keywords: Evolutionary polynomial regression; alluvial deposits; lacustrine.

1 INTRODUCTION

The two sites we refer to (A and B, North and South) are located in the alluvial plain at small distances from the canalized course of the Dâmboviţa River the middle of Bucharest City.

In this research we considered three of the superficial layers, starting from the surface of the terrain, as:

(I) the upper cohesive (7-9m thickness) composed mainly on silty clays;

(II) the middle noncohesive, consisting of sands and fine gravel of 13-30m thickness with thin cohesive intercalations, and

(III) the deeper lacustrine clays, which were partially opened on 15m to 40m.

On each site geotechnical investigations (boreholes and laboratory analyses) were executed in tandem with geophysical survey works (cross-hole and down-hole).

2 CURRENT CORRELATIONS

Estimation of the density layers based on geotechnical usual practices is a very difficult task in case of under consolidate cohesive and noncohesive sedimentary deposits.

In consequence, realistic assessment of relative density through correlation with various in situ investigation results represent the only path to evaluate this important geotechnical parameter. One of the very few such correlations is given by Mayne and Schneider, (1999), which evaluates the relative density of soils ρ (g/cm^3) as a function of shear wave velocities Vs (m/s) and depth z (m):

$$\rho = 0.85\, log(V_s) - 0.16\, log(z) \qquad (1)$$

We apply this correlation for both sites A and B, but the fitting of results with measured data is poor considering the coefficient of correlation $0.2 \leq R^2 \leq 0.3$, fact that may be visually observed also in Figure 1.

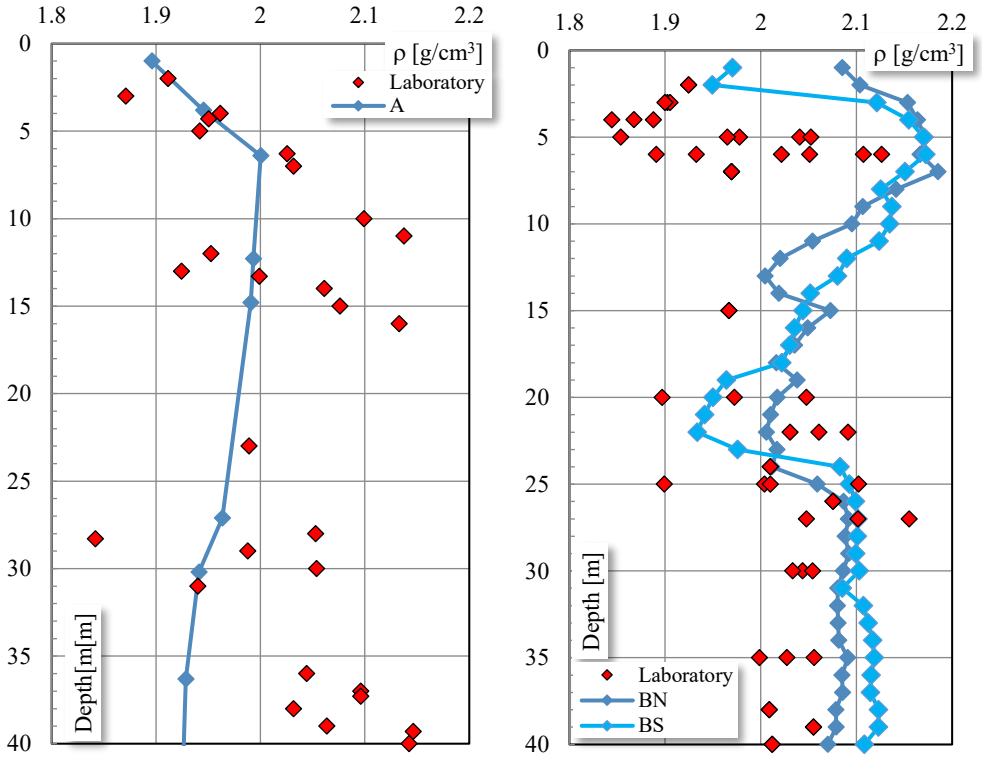

Figure 1. Variation in depth of measured and calculated values of relative density of soils, formula (1).

3 EPR MODEL CONSTRUCTION

3.1 Theoretical frame of EPR models

The mathematical model proposed for this paper is based on evolutionary polynomial regression (EPR) which is a method intensely used in geotechnics in order to find polynomial structures with an output-dependent variable Y and a set of independent variable X (Clegg et al, 2005; Keramati et al, 2014; Rezania et al, 2009).

The function can be written as:

$$Y_{N\times 1} = F(\alpha_{1xk}, X_{N\times m}) \quad (2)$$

where F is a function that will be determined using input – output data and $\alpha_{1\times k} = [a_0\ a_1\ a_2\ \dots\ a_n]$ is a vector with $k = n + 1$ parameters. For a matrix of inputs considered as $X_{N\times m} = [X_1\ X_2\ \dots\ X_m]$ and a matrix of exponents whose elements can take values within user–defined bounds, $E_{n\times m}$, can be defined n vectors whose elements are products of independent inputs X as:

$$Z^i_{N\times 1} = X_1^{E(i,1)} \cdot X_2^{E(i,2)} \cdot \dots \cdot X_m^{E(i,m)}, \quad i = 1, \dots, n \quad (3)$$

Thus, a matrix equation results:

$$Y_{N\times 1}(\alpha, Z) = Z_{N\times k} \times \alpha^T_{k\times 1} \quad (4)$$

where $Y_{N\times 1}(\alpha, Z)$ is the least squares estimate vector of the N target values.

To successfully determine the optimal values of the exponents, the genetic algorithm is recommended. This algorithm represents a method of solving optimization problems, especially when the objective function is nonlinear. The process consists of generating a population of individuals who are used as parents to produce a new generation through mutations and crossover techniques. The algorithm is used to obtain an equation that ensure the best possible fit of the data. Then, adjustable parameters a_i, $i = 0, 1, \dots, n$, can be determined by the linear square's method. The estimated equation of regression will be evaluated using the determination coefficient expressed as:

$$R^2 = \frac{\sum_i (\hat{y}_i - \bar{y})^2}{\sum_i (y_i - \bar{y})^2} \quad (5)$$

where $\hat{y}_i$ is the estimated value of the output of the process, y_i is the value of a dependent variable and $\bar{y}$ is the mean of the variable y. As R^2 it increases with the inclusion of several variables, the coefficient of determination is adjusted accordingly:

$$\bar{R}^2 = \frac{n-1}{n-p} R^2 - \frac{p-1}{n-p} \quad (6)$$

where n is the number of observations and p is the number of independent variables.

Another statistically important parameter is the residual standard error which is a measure used to assess the precision of the predictions. Regression testing consisted of studying the dispersion analysis, the *F - test* of global significance and the t-test. Thus, if *Significance F* has a value lower than the established significance threshold, then the null hypothesis of the statistic F is rejected. Also, for the *t - test*, a value of *P-value* lower than the significance threshold leads to the rejection of the nullity hypothesis (Clocotici, 2007). Residue analysis assumes the validity of an error normal distribution. This can be verified by studying the diagrams predicted values – residues, $(\hat{y}_i\ ,\ d_i)$, $i = 1, \dots, n$, where the normalized residuals d_i is given by (Montgomery et al., 2003; Pimpan and Suwattee, 2009):

$$d_i = \frac{e_i}{s(e_i)} \tag{7}$$

in which $e_i = y_i - \hat{y}_i$ and $s^2(e_i)$ is the dispersion of the residue e_i, $i = 1, \dots, n$.

If there is an observation i with a large standardized residual ($|d_i| > 3$) then that observation is a potential outlier and can be excluded from the data set or analyzed in another subject of interest.

3.2. EPR models used for geotechnical data

In the next step, several EPS models have been developed and analyzed according to the procedure described above for all three layers, on both sites.

For the upper cohesive layer (I), the EPR model is given in Eq. 8. Specific values of the coefficients $a_{i, i=0,1,2..6}$, as the statistical parameters of regression model are exposed in Table 1 (Figure 2).

$$\rho = a_0 + a_1 \frac{{V_s}^2}{z} + a_2 \frac{1}{z^2 {V_s}^2} + a_3 \frac{1}{z} + a_4 \frac{V_s}{z^2} + a_5 \frac{V_s}{z} + a_6 z V_s \tag{8}$$

Table 1. Regression coefficients and statistical parameters for layer (I), Eq. 8.

Coef-ficients	Value	Regression Statistics		Condi-tions
a_0	20.442344	MR	0.993737	
a_1	-0.000650	R Sq.	0.987513	
a_2	16341302	Ad. R Sq	0.965661	
a_3	-268.4582	St.Err	0.012176	2m<z<8m
a_4	0.108107	SS Res	0.000593	
a_5	0.693340	F	0.001202	
a_6	-0.002579			

For the second layer (II - the middle noncohesive), the regression equation is presented in Eq. 9, and Table 2 (Figure 3) contain the specific values of the coefficients and statistical parameters.

$$\rho = a_0 + a_1 \frac{1}{z {V_s}^2} + a_2 \frac{V_s}{z^2} + a_3 \frac{1}{z^2 V_s} + a_4 \frac{1}{\sqrt{z}} + a_5 z^2 + a_6 \frac{1}{z^2} + a_7 z^2 V_s \tag{9}$$

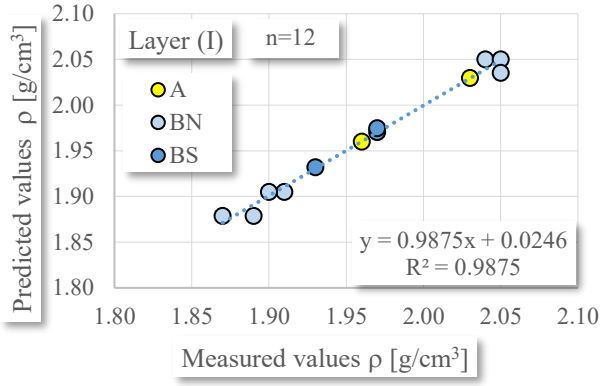

Figure 2. Results of EPR model of layer (I), Eq. 8.

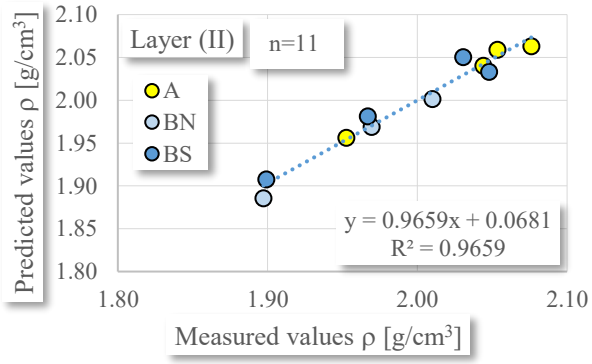

Figure 3. Results of EPR model of layer (II), Eq. 9.

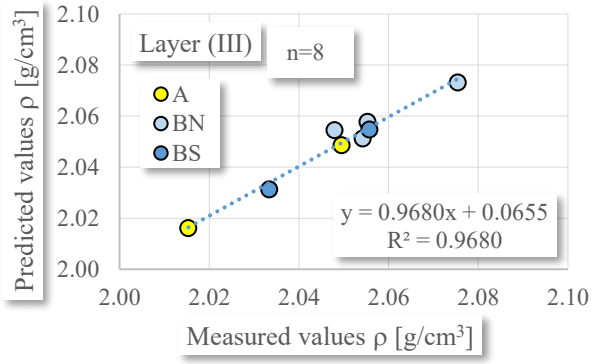

Figure 4. Results of EPR model of layer (III), Eq. 10.

Table 2. Regression coefficients and statistical parameters for layer (II), Eq. 9.

Coef-ficients	Value	Regression Statistics		Cond-itions
a_0	8.532624	MR	0.98278	5m<z<40m
a_1	17639312	R Sq.	0.96586	
a_2	-15.4535	Ad. R Sq	0.88619	
a_3	-3543866	St. Err	0.02099	
a_4	-55.7057	SS Res	0.00132	
a_5	-0.00728	F	0.03254	
a_6	15173.55			
a_7	0.000018			

Finally, for the deeper lacustrine clays (III) the regression equation is given in the following equation (Figure 4. Table 3):

$$\rho = a_0 + a_1 \frac{V}{z} + a_2 V^2 + a_3 \frac{1}{z} \qquad (10)$$

Table 3. Regression coefficients and statistical parameters for layer (III), Eq. (10).

Coef-ficients	Value	Regression Statistics		Condi-tions
a_0	1.016192	MR	0.983889	25m<z<50m
a_1	-0.142700	R Sq.	0.968038	
a_2	0.000004	Ad. R Sq.	0.944066	
a_3	76.770632	St. Err.	0.004179	
		SS Res.	0.000070	
		F	0.001895	

4 CONCLUSIONS

Depositional and spatial variability of recent alluvial deposits of the rivers could often mislead the assessment of geotechnical and geophysical parameters based on general correlation equations available in the literature. For this reason, the establishment of such particular relationships at the local scale of a geological or geomorphological formation is an important task in order to obtain precise and reliable results of investigations. Regardless of the quality, the amount or the diversity of investigations, the accuracy and the representativeness of such correlations are strongly influenced by the mathematical tool used for this purpose.

In this paper we examined geotechnical and geophysical investigations of two sites situated on the alluvial plain of Dâmboviţa River, Bucharest City. For the assessment of relative density based on shear wave velocity we elaborated an EPR model for every layer of the geological structure.

Using the genetic algorithm tool and the multidimensional linear regression method, equations were obtained that accurately describe the mathematical relationship of one of the most important geotechnical parameters (ρ) for every specific encountered layer. Finally, this may lead to a more precise approach in such regions where general relations are not relevant to the field situation

In these new EPR models statistical parameters extended between the limits exposed in Table 4, proved to be much appropriate than the well-known correlation formula ρ - Vs used in such situations.

Due to the fact that the accuracy of all mathematical models depends among other attributes, on the volume and density of the data used, it appears that it would be of scientific interest to elaborate a communitarian database associated with large geological and geomorphological units, in order to obtain a proper and realistic assessment of geotechnical parameters, which are the most important key parameters of serious and safe design of all civil or industrial projects.

Table 4. Limits of statistical parameters of the EPR models obtained for layers (I-III), Eqs. 8-9-10.

Regression Statistics	EPR models		Previous models
	Minimum value	Maximum value	
Multiple R	0.9828	0.9937	0.2-0.3
R Square	0.9659	0.9875	
Adjusted R Square	0.8862	0.9657	
Standard Error	0.0042	0.0210	
SS Residual	0.0001	0.0013	
Significance F	0.0012	0.0325	

REFERENCES

Clegg, J., Dawson, J.F., Porter, S.J. and Barley, M.H. (2005). The Use of a Genetic Algorithm to Optimize the Functional Form of a Multi-dimensional Polynomial Fit to Experimental Data, *Conference Evolutionary Computation. The 2005 IEEE Congress* on Volume 1. DOI: 10.1109/CEC.2005.1554782.

Clocotici, V. (2007). *Introducere in statistica multivariata*, Editura Universitatii Alexandru Ioan Cuza – Iasi (in Romanian). ISBN: 978-973-703-322-2.

Keramati, M., Reshad, S.K., Asgarpour, S. and Tutunchian, M.A. (2014). Predicting Shear Strength of Municipal Waste Material by Evolutionary Polynomial Regression (EPR). *Electronic Journal of Geotechnical Engineering*, 19, pp. 53-62.

Mayne, P.W. and Schneider, J.A. (1999). Small and large strain soil properties from seismic flat dilatometer tests. *Proceedings of the Pre-failure Deformation Characteristics of Geomaterials*, Jamiolkowski et al. editors, Torino, pp. 419-426. ISBN 90 5809 075 2.

Montgomery, D. C., Peck, E. A. and Vining, G. G. (2003). *Introduction to Linear Regression Analysis*, 3rd ed.

New York: John Wiley & Sons, 672 pag. ISBN-10: 0471315656.

Pimpan, A. and Suwattee, P. (2009). A comparative study of outlier detection procedures in multiple linear regressions. *Proceedings of the International Multi-Conference of Engineers and Computer Scientists*. Vol. 1. IMECS 2009, March 18 - 20, Hong Kong. ISBN: 978-988-17012-2-0.

Rezania, M., Javadi, A.A. and Giustolisi, O. (2009). Evaluation of liquefaction potential based on CTP results using evolutionary polynomial regression, *Computers and Geotechnics* 37, pp. 82-92. DOI: 10.1016/j.compgeo.2009.07.006.

Proceedings of the XVIII ECSMGE 2024
GEOTECHNICAL ENGINEERING CHALLENGES
TO MEET CURRENT AND EMERGING NEEDS OF SOCIETY
© 2024 the Authors
ISBN 978-1-032-54816-6
DOI 10.1201/9781003431749-246
Open Access: www.taylorfrancis.com, CC BY-NC-ND 4.0 license

ECSMGE 24
XVIII EUROPEAN CONFERENCE ON SOIL MECHANICS AND GEOTECHNICAL ENGINEERING

Comparative assessment of liquefaction susceptibility of unconsolidated deposits

Évaluation comparative de la sensibilité à la liquéfaction des dépôts non consolidés

M. Stãnciucu*, I. Dogaru
University of Bucharest, Romania
**stanciucumihaela@yahoo.com*

ABSTRACT: Liquefaction may be considered one of the most dangerous physical-geological processes associated with the seismic hazard that affects almost all granular deposits as the fine ones, of low plasticity. The triggering mechanism depends on many factors that vary in space and time and may be clustered into three classes: two related to the soil properties (general settings of soil layers and geomechanical features) and one defined by earthquake characteristics. In this frame, determining the cyclic resistance of soils through in situ tests becomes an important and sensitive issue in assessing liquefaction susceptibility. This paper presents the evaluation of this seismic characteristic through several semiempirical correlations based on the most important in situ test: the Standard Penetration Test, executed on one of the most vulnerable structures which are the Holocene sedimentary alluvial deposits encountered all over the world in the proximity of every river or stream.

RÉSUMÉ: La liquéfaction peut être considérée comme l'un des processus physico-géologiques les plus dangereux associés à l'aléa sismique qui affecte presque tous les dépôts granulaires comme les plus fins, de faible plasticité. Le mécanisme de déclenchement dépend de nombreux facteurs qui varient dans l'espace et le temps et peuvent être regroupés en trois classes: deux liées aux propriétés du sol (paramètres généraux des couches de sol et caractéristiques géomécaniques de ses) et une définie par les caractéristiques sismiques. Dans ce cadre, la détermination de la résistance cyclique des sols par des essais in situ devient un enjeu important et sensible dans l'évaluation de la sensibilité à la liquéfaction. Cet article présente l'évaluation de cette caractéristique sismique à travers plusieurs corrélations semi-empiriques basées sur le test in situ le plus important: Test de Pénétration Standard, qui a été réalisé sur l'une des structures les plus vulnérables qui sont les dépôts alluviaux sédimentaires holocènes rencontrés partout dans le monde à proximité de chaque rivière ou ruisseau.

Keywords: Liquefaction, cyclic resistance, alluvial deposits.

1 INTRODUCTION

Presently, assessment of liquefaction susceptibility may be performed in several different ways (Anwar et al, 2016), either through: (i) probabilistic methods which evaluate the probability of liquefaction (PL), which is a quantitative measure of the severity of this possible phenomenon; (ii) artificial neural networks (ANN) which are conceptual models that estimates the relationships between the earthquake characteristics and the soil with liquefaction potential or, more common, (iii) deterministic methods which provide an alternative verdict of "liquefiable" or "un-liquefiable" based on the computed values of the safety factor against liquefaction (Fsliq).

In this paper we will approach the third method of research and we will assess the factor of safety against liquefaction (Fs_{liq}) as defined by Ishihara (1993) and Seed and Harder (1990):

$$Fs_{liq} = \frac{CRR}{CSR} = \frac{CRR_{7.5}MSF}{CSR} K_\sigma K_\alpha \qquad (1)$$

where the significance of terms is: *CRR* - cyclic resistance ratio; $CRR_{7.5}$ - cyclic resistance ratio for an earthquake with 7.5 magnitude; *CSR* - cyclic stress ratio induced by the seismic shake; *MSF* - magnitude scaling factor; K_s - overburden stress correction factor and K_a - correction factor for sloping ground.

Due to the fact that the estimation of both *CRR* and *CSR* may be done through numerous semiempirical correlations with in situ test results, we chooses to perform comparative calculations based on the investigations results of three formulas of Standard Penetration Test (*SPT*), which is not only the older in situ test, but also the most widespread.

2 GENERAL FRAME OF THE SITE

The triggering mechanism of liquefaction depends on (Youd and Perkins, 1978): (i) factors related to geo-mechanical properties of soil: grain size distribution (percent of fines-*FC*, median diameter - D_{50}) and properties derived from it (hydraulic conductivity, plasticity of fines), relative density - *Dr*, frictional skills of soils; (ii) factors related to general settings of deposits: depth of the layer, thickness, overburden pressure, confining stress, nature of bed and roof layers, underground water level, and (iii) factors related to earthquake characteristics: magnitude, peak ground acceleration, intensity and duration, the distance from epicenter. In this view, alluvial layers, especially the newest Holocene ones, are the most prone to this very damaging phenomenon (Giardini et al, 2013; Ranguelov et al, 2007).

The site we refer to is located at the plain of Danube river, at short distances (less than 100km) from one of the stronger European seismic areas - namely Vrancea Seismic Zone. The specific sedimentary structure for this fluvial system consists mainly in cross-laminated fine sands, silts and mud with thin peat lenses, alternated with massive fine sandy silts and gravel bars. On selected site, these Holocene deposits in fluvial facies extend from surface to 80m up to 120m depth, and have been investigated by eight geotechnical boreholes situated at distances that do not exceed 50m one from other, in continuous rotary dry drilling system, with temporary metal casing protection, due to the fact that the water table level is very close to the terrain surface.

3 THE SUITABLE ASSESEMENT METHODS

3.1 Determination of CSR

CSR is defined as the average cyclic shear stress induced by shear waves normalized by the initial vertical effective stress (Seed and Idriss, 1971), or "the seismic demand on a soil layer" (Youd et al., 2001) is usually expressed using the well-known formula:

$$CSR = 0{,}65\left(\frac{a_{max}}{g}\right)\left(\frac{\sigma_v}{\sigma_v'}\right)r_d \qquad (2)$$

where the significance of terms is: a_{max} - maximum horizontal ground surface acceleration, g (m/s^2) - gravitational acceleration, σ_v (kPa) - total overburden pressure at depth z (m), σ'_v (kPa) - effective overburden pressure at depth z and r_d (-) is the stress reduction factor. The latest term, r_d, may be obtain through several analytical methods (Liao and Whitman, 1986; Idriss, 1999; Cetin et al, 2004). In this application we used the relation of Youd et al. (2001), as follows:

$$\begin{aligned} r_d &= (131 - z)/131, \text{ for } z \le 9.15\text{m};\\ r_d &= (44 - z)/37, \text{ for } 9{,}15\text{m} \le z \le 23\text{m};\\ r_d &= (93 - z)/125, \text{ for } 23\text{m} \le z \le 30\text{m};\\ r_d &= 0{,}50, \text{ for } z \ge 30\text{m} \end{aligned} \qquad (3)$$

3.2 Determination of CRR

The calculations of CRR were performed through three deterministic methods, all based on SPT resistance, expressed as functions of corrected and normalized values $(N_1)_{60}$ and of clean sand corrected N-value $(N_1)_{60cs}$.

(I) In the first set of relations Seed et al. (1984) and Youd et al. (2001) expressed the cyclic resistance ratio for an earthquake with 7.5 magnitude, based on the following equation:

$$CRR_{7.5} = \frac{1}{34-(N_1)_{60cs}} + \frac{(N_1)_{60cs}}{135} + \frac{50}{[10(N_1)_{60cs}+45]^2} - \frac{1}{200} \qquad (4)$$

According to Youd et al. (2001), $(N_1)_{60cs}$ may be obtained as a function of fine content (*FC*) from:

$$(N_1)_{60cs} = \alpha + \beta(N_1)_{60} \qquad (5)$$

in which for $FC \le 5\%$, $\alpha = 0$ and $\beta = 1.0$; for $5\% < FC < 35\%$, $\alpha = exp\left[1.76 - \left(\frac{190}{FC^2}\right)\right]$ and $\beta = \left[0.99 + \left(\frac{FC^{1.5}}{1000}\right)\right]$, and finally, for $FC \ge 35\%$ $\alpha = 5.0$ and $\beta = 1.2$.

(II) In the second set of relations, Idriss and Boulanger (2004) express $CRR_{7.5}$ from equation (6):

$$CRR_{7.5} = exp\left(\frac{(N_1)_{60cs}}{14.1} + \left(\frac{(N_1)_{60cs}}{126}\right)^2 - \left(\frac{(N_1)_{60cs}}{23.6}\right)^3 + \left(\frac{(N_1)_{60cs}}{25.4}\right)^4 - 2.8\right) \qquad (6)$$

in which $(N_1)_{60cs}$ has been calculated based on Idriss and Boulanger (2008), formulas (7).

$$(N_1)_{60cs} = (N_1)_{60} + \Delta(N_1)_{60}$$
$$\Delta(N_1)_{60} = exp\left(1.63 + \frac{9.7}{FC+0.01} - \left(\frac{15.7}{FC+0.01}\right)^2\right) \qquad (7)$$

(III) Finally, Japanese Bridge Code-JR (1990) attests that $CRR_{7.5}$ is affected by the median diameter of grain size distribution curve (D_{50}) as follows for $0.05\text{mm} \leq D_{50} \leq 0.6\text{mm}$ (8):

$$CRR_{7.5} = 0.0882\sqrt{\frac{(N_1)_{60cs}}{\sigma'_v+0.7}} + 0.255log\left(\frac{0.35}{D_{50}}\right) + R_3 \quad (8)$$

in which dimensionless coefficient $R_3=0$ for $FC<40\%$ and $R_3=0.004FC-0.16$ for $FC \geq 40\%$.

In this third calculation, $(N_1)_{60cs}$ has been used based on Idriss and Boulanger (2008) formulas.

4 RESULTS

In the first instance, we performed a single calculation of CSR as described in paragraph 3.1., considering a value $a_{max}=0.30g$, according to Romanian Seismic Code, for the depths where simultaneously grainsize distribution tests and SPT tests has been made.

We continued by applying the three variants of calculation of $CRR_{7.5}$ as described in paragraph 3.2. After normalization of SPT values, with the aim of calculation of the equivalent clean-sand corrected blow count $(N_1)_{60cs}$, we applied the relations (5) and (7), which proved to offer similar results on the first 10m, and slightly to significant different from 10m to 30m depth.

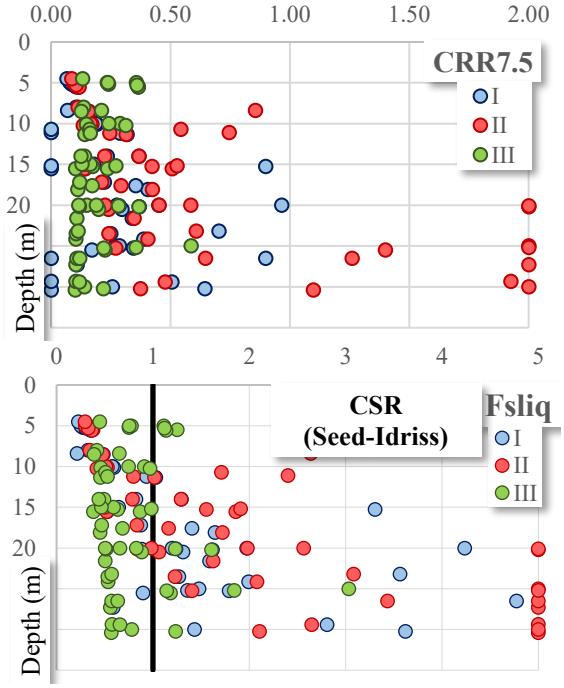

Figure 1. Comparative assessment of variation in depth of $CRR_{7.5}$ (up); factor safety against liquefaction according to Seed-Idriss (down).

In the following, we applied relations (4), (6) and (8), considering an event of magnitude 7.5, for which consequently the magnitude scaling factor is $MSF=1$, and a value of $K_\alpha=1$ for level ground. As for overburden stress correction factor K_s, we applied recommendations of Youd et.al (1996). The results are graphically presented in Figure 1.

In second instance, we recalculate CSR according to Eurocode 8, Part 5 and reevaluate the main parameter Fsliq through relations (4), (6) and (8), in the same conditions. The results are graphically presented in Figure 2, in which the differences ΔFsliq is given by the formula:

$$\Delta Fs_{liq} = Fs_{liq}^{Seed-Idriss} - Fs_{liq}^{Eurocod\ 8} \quad (9)$$

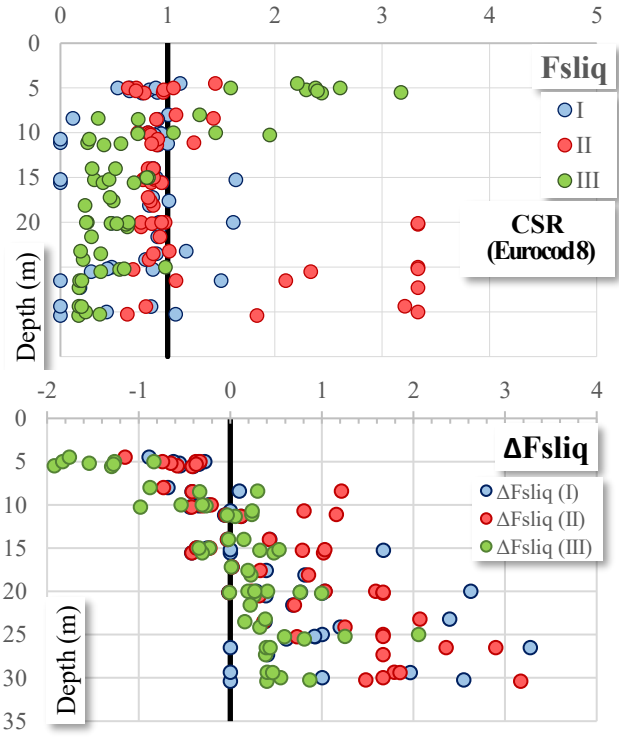

Figure 2. Factor safety against liquefaction according to Eurocod 8 (up); differences ΔFsliq between calculations (down).

5 CONCLUSIONS

A. Regarding the comparative calculation of the cyclic resistance ratio (CRR):

- as is presented in Figure 2 (up), the procedure II, Idriss and Boulanger (2004), provide the most overrated values compared to the other two set of results, while the Japanese Bridge Code-JRA (1990) - procedure III, offers the most conservative results;

- these ranges of values conducted at a safety profile against liquefaction mainly secure bellow 15m depth, according to procedures (I) and (II), while relations (III) extend the unsafety of the ground up to 30m depth;
- consequently, authors consider that procedures (I) or (II) are more suitable for shallow foundations, and procedure (III) is more appropriate for deep foundations.

B. Regarding the comparative calculation of the cyclic shear stress (CSR):

- the range of values resulting from Seed and Idriss formulas (Eq. 2) is strongly decreasing in depth and in consequence, the values Fsliq will directly increase in the same direction;
- on the other hand, the evaluation of CSR according to Eurocod 8 is influenced primarly by the fines percents and subservient by depth; this dependency makes that for the same set of data, the values Fsliq will decrease in the depth for most calculations;
- differences between these two procedures of calculation of CSR (Eq. 9), drive to large differences in term of factor of safety, wich varies $-2 < \Delta Fsliq < 3$, with prevalent negative values recorded above the depth of 15m (Figure 2 down).

REFERENCES

Anwar, A., Ahmad, S., Jamal, Y. and Khan, M.Z. (2016). Assessment of Liquefaction Potential of Soil Using Multi-Linear Regression Modeling, *International Journal of Civil Engineering and Technology*, 7 (1), 373-415.

Cetin K.O., Seed R.B., Der Kiureghian A., Tokimatsu K., Harder L.F. Jr, Kayen R.E. and Moss R.E.S. (2004). SPT-based probabilistic and deterministic assessment of seismic soil liquefaction potential, *Journal of Geotechnical and Geoenvironmental Engineering*, ASCE, 130 (12), 1314-1340. doi.org/10.1061/(ASCE)10900241(2004)130:12(1314).

EN 1998-5 (2004): Eurocode 8: Design of structures for earthquake resistance – Part 5: Foundations, retaining structures and geotechnical aspects.

Giardini D., Woessner J., Danciu L., Cotton F., Crowley H., Grünthal G., Pinho R., Valensise G., Akkar S., Arvidsson R., Basili R., Cameelbeck T., Campos-Costa A., Douglas J., Demircioglu M. B., Erdik M., Fonseca J., Glavatovic B., Lindholm C., Makropoulos K., Meletti C., Musson R., Pitilakis K., Rovida A., Sesetyan K., Stromeyer D. and Stucchi M. (2013). *Seismic Hazard Harmonization in Europe*: Online Data Resource, doi:10.12686/SED-00000001-SHARE.

Idriss, I. M. (1999). An update to the Seed-Idriss simplified procedure for evaluating liquefaction potential in *Proceedings, TRB Workshop on New Approaches to Liquefaction,* Publication No. FHWA-RD-99-165, Federal Highway Administration, January.

Idriss, I.M. and Boulanger, R.W. (2004). Semi-empirical procedures for evaluating liquefaction potential during earthquakes. *Proceedings of 11th International conference on soil dynamics and earthquake engineering, and 3rd International conference on earthquake geotechnical engineering*, vol. 1. Stallion Press. 32–56.

Idriss, I. M., and Boulanger, R. W. (2008). *Soil liquefaction during earthquakes*. Monograph MNO-12, Earthquake Engineering Research Institute, Oakland, CA, 261 pp.

Ishihara, K. (1993). Liquefaction and Flow Failure during Earthquake. *Géotechnique*, 43, 351-415. doi.org/10.1680/geot.1993.43.3.351.

JRA (1990). *Specification for Highway Bridges*: Part V- Seismic Design. Japan Road Association, Tokyo.

Liao, S.S.C. and Whitman, R.V. (1986). Overburden correction factors for SPT in sand. *Journal of Geotechnical Engineering*, 112, (3), 373-377. doi.org/10.1061/(ASCE)07339410(1986)112:3(37).

Ranguelov, B., Jelínek, R., Wood, M. and Hervás J., (2007). Risk Mapping of Earthquakes in New Member States. *JRC Scientifc and Technical Reports*, 38pp, ISSN 1018-5593.

Seed, H. B., and Idriss, I. M. (1971). Simplified Procedure for Evaluating Soil Liquefaction Potential, *Journal of the Soil Mechanics and Foundations Division*, ASCE, Vol. 97, No SM9, Proc. Paper 8371, September 1971, 1249-1273.

Seed, H. B., Tokimatsu, K., Harder, L. F. and Chung, R. M. (1984). The Influence of SPT Procedures in Soil Liquefaction Resistance Evaluations, *Earthquake Engineering Research Center Report No. UCB/EERC-84/15*, Univ. of California at Berkeley.

Seed, R.B. and Harder, L.F. (1990). SPT-based analysis of cyclic pore pressure generation and undrained residual strength. In *Proceedings of the H. Bolton Seed Memorial Symposium*, Berkeley, Calif. Edited by J.M. Duncan. BiTech Pub- lishers Ltd., Vancouver. Vol. 2. 351-376.

Youd, T. L. and Perkins, D.M. (1978). Mapping liquefaction-induced ground failure potential. *Journal of the Geotechnical Engineering Division.* ASCE,104, GT4, Proc. Paper 13659, April, 1978, 433-446.

Youd, T.L., Idriss, I.M., Andrus, R.D., Arango, I., Castro, G., Christian, J.T., Dobry, R., Finn, W.D.L., Harder, L.F., Hynes, M.E., Ishihara, K., Koester, J.P., Liao, S.S.C., Marcuson, W.F., Martin, G.R., Mitchell, J.K., Moriwaki, Y., Power, M.S., Robertson, P.K., Seed, R.B. and Stokoe, K.H. (2001) Liquefaction Resistance of Soils: Summary Report from the 1996 NCEER and 1998 NCEER/NSF Workshops on Evaluation of Liquefaction Resistance of Soils. *Journal of Geotechnical and Geoenvironmental Engineering*, 127, 297-313. dx.doi.org/ 10.1061/ (ASCE)1090-0241(2001)127:4(297).

Proceedings of the XVIII ECSMGE 2024
GEOTECHNICAL ENGINEERING CHALLENGES
TO MEET CURRENT AND EMERGING NEEDS OF SOCIETY
© 2024 the Authors
ISBN 978-1-032-54816-6
DOI 10.1201/9781003431749-247
Open Access: www.taylorfrancis.com, CC BY-NC-ND 4.0 license

ECSMGE 24
XVIII EUROPEAN CONFERENCE ON SOIL MECHANICS AND GEOTECHNICAL ENGINEERING

Liquefaction risk assessment of airport infrastructure using geological data and remote sensing techniques

Évaluation des risques de liquéfaction des infrastructures aéroportuaires à l'aide de données géologiques et de techniques de télédétection

M. Taftsoglou*, S. Valkaniotis
Department of Civil Engineering, Democritus University of Thrace, Xanthi, Greece

G. Papathanassiou
Department of Geology, Aristotle University of Thessaloniki, Thessaloniki, Greece

S. Argyroudis
Department of Civil and Environmental Engineering, Brunel University London, London, UK

mtaftsog@civil.duth.gr

ABSTRACT: Airport infrastructure plays a crucial role in regional and national economies, as well as during emergencies such as after major earthquakes. However, its functionality remains vulnerable to disruption caused by secondary earthquake effects, such as soil liquefaction. Hence, assess the risk posed to airport facilities by these phenomena becomes paramount for ensuring airport resilience and preparedness in the face of seismic events. This study, introduces a practical and rapid assessment tool for the risk analysis of airport infrastructure located in liquefaction-prone areas. Focusing on the Nestos delta in Greece, where the Kavala International Airport (KVA) is placed, a new methodology is proposed, which combines geological and remote sensing data to assess and map liquefaction susceptibility at local scale. The results reveal that a significant section of KVA's runway and taxiways are located on highly susceptible soils of abandoned meanders. Using FEMA's HAZUS methodology the study quantifies the impacts of liquefaction for a given seismic scenario. The analysis estimates a 49% probability of liquefaction for the highly susceptible class, with ground settlements predicted to reach 30cm. The results of the liquefaction hazard analysis are used for the risk assessment of the airport infrastructure, estimating a total direct loss of €22,2 million. The analysis is validated using datasets from three international airports that sustained extensive seismic damage in the past. This research serves toward safeguarding airport infrastructure in liquefaction-prone regions.

RÉSUMÉ: Les infrastructures aéroportuaires jouent un rôle crucial dans les économies régionales et nationales, ainsi que lors de situations d'urgence comme après des tremblements de terre majeurs. Cependant, sa fonctionnalité reste vulnérable aux perturbations causées par les effets secondaires des tremblements de terre, tels que la liquéfaction du sol. Par conséquent, évaluer le risque que ces phénomènes font peser sur les installations aéroportuaires devient primordial pour garantir la résilience et la préparation des aéroports face aux événements sismiques. Cette étude présente un outil d'évaluation pratique et rapide pour l'analyse des risques des infrastructures aéroportuaires situées dans des zones sujettes à la liquéfaction. En se concentrant sur le delta du Nestos en Grèce, où se trouve l'aéroport international de Kavala (KVA), une nouvelle méthodologie est proposée, qui combine des données géologiques et de télédétection pour évaluer et cartographier la susceptibilité à la liquéfaction à l'échelle locale. Les résultats révèlent qu'une partie importante de la piste et des voies de circulation du KVA est située sur des sols très sensibles de méandres abandonnés. À l'aide de la méthodologie HAZUS de la FEMA, l'étude quantifie les impacts de la liquéfaction pour un scénario sismique donné. L'analyse estime une probabilité de liquéfaction de 49 % pour la classe très sensible, avec des tassements au sol qui devraient atteindre 30 cm. Les résultats de l'analyse du risque de liquéfaction sont utilisés pour l'évaluation des risques de l'infrastructure aéroportuaire, estimant une perte directe totale de €22,2 millions. L'analyse est validée à l'aide d'ensembles de données provenant de trois aéroports internationaux qui ont subi d'importants dommages sismiques dans le passé. Cette recherche sert à sauvegarder les infrastructures aéroportuaires dans les régions sujettes à la liquéfaction.

Keywords: Liquefaction; airports; runways; risk analysis; remote sensing.

1 INTRODUCTION

Earthquakes pose a significant threat to vital infrastructure and communities, as they can induce damage due to ground shaking and ground failure. A common form of failure is soil liquefaction, a phenomenon in which granular material transforms

from a solid state into a liquefied state, as a result of decreased effective strength and increased pore pressure during seismic shaking (Youd, 1973). Generally, liquefaction occurs in fluvial and coastal regions and filled land areas, that contain shallow layers of low density, saturated and granular sediments (Youd and Hoose, 1978; Holzer, 1998; Tinsley et al., 1985). Ground settlement and cracking, lateral spreading and foundation failure caused by soil liquefaction have led to extensive damage to transport infrastructure and other lifelines in the past.

Airports are one of the most critical infrastructure, especially in the aftermath of devastating natural disasters, as they play a pivotal role in emergency response and recovery efforts. Previous seismic events in Niigata (Japan) in 1964, Loma Prieta (USA) in 1989, Nisqually (USA) in 2001, Tohoku in 2011 and the most recent one in Turkey-Syria in 2023 revealed the vulnerability of airports to both ground shaking and secondary earthquake effects like soil liquefaction. These factors can lead to damage and disrupt the normal operation of the airport. In particular, runways, taxiways, and ramp areas are susceptible to sinking or shifting, similarly to roadways, leading to substantial discontinuities or pavement cracking. Moreover, air traffic control, navigation, piping and fuel storage facilities, may incur damage from ground deformation or differential settlement. Given that most of the airport infrastructure has low tolerance to deformations, such damage can impede the transport of people and supplies, and result to destructive effects on the regional economy (Grogan and Vallerga, 2000). Therefore, it is crucial to have a comprehensive understanding of liquefaction mechanisms and their impact on airport environments, for ensuring that efficient mitigation measures are taken.

This paper introduces a practical and rapid tool for facilitating the risk analysis of airport infrastructure located in liquefaction prone areas. A new methodology is proposed for local-scale liquefaction assessement and mapping, which combines geological data and remote sensing techniques. This is applied on the Nestos delta in Greece, where the Kavala International Airport (KVA) is located. The results are utilised to estimate the permanent ground displacement (PGD), such as vertical displacements and lateral spreadings, due to liquefaction. Subsequently, PGD is used as the intensity measure for the risk analysis of the infrastructure. The liquefaction susceptibility and vulnerability assessment are validated using datasets from Oakland, King County (USA) and Hatay (Turkey) international airports.

2 METHODOLOGY

Considering the significant influence of depositional processes on the susceptibility of sediments to liquefaction, we have developed a methodology that enables the identification of surface geological units prone to liquefaction. This method involves creating a geomorphologically oriented map by integrating geological and remote sensing data, as outlined in the study by Taftsoglou et al. (2022). This procedure includes four phases (Figure 1).

In phase 1 geological and historical maps of the area, orthophotos and satellite images are collected in order to examine the geological formations and the geomorphological evolution of the plain. By combining these layers of information with the local topography (DEM) the mapping of geomorphological features is conducted in phase 2. Geomorphological formations, such as abandoned stream/meanders, point bars, oxbow lakes, dunes and lagoons are detected and traced during this step and a new geomorphological map is compiled. In phase 3 the classification of surficial geological units susceptible to liquefaction is performed. In particular, data provided by the geological maps and the new geomorphological map are used to define the age (<500yr, Holocene, Pleistocene) and the depositional environment of the geological units. Subsequently, the criteria by Youd and Perkins (1978) are applied to classify the geological units according to their susceptibility to liquefaction. In phase 4, a liquefaction susceptibility map is compiled, including four classes (Low, Moderate, High and Very High), where coastal and fluvial deposits are classified as high to very high susceptible units.

2.1 Liquefaction Susceptibility of KVA

KVA is located in the west side of Nestos delta plain in Thrace, Greece. The location of the airport along with the deposition of recent Holocene sediments and the presence of high potential onshore and offshore active faults capable to trigger large earthquakes in the area, were the motivational factors for this application.

By employing the proposed methodology, we noted a deficiency in the geological maps (HSGME) with regard to accurately representing Pleistocene and Holocene deposits. Using historical orthophoto maps dated before 1945 and Declassified Satellite images (KH-4) from 1960 and 1968 we were able to examine the geomorphological evolution of the plain and enrich the original classification of geological formations, mainly with the addition of fluvial and coastal deposits, such as abandoned river channels, oxbow lakes, point bars, dunes and deltaic deposits.

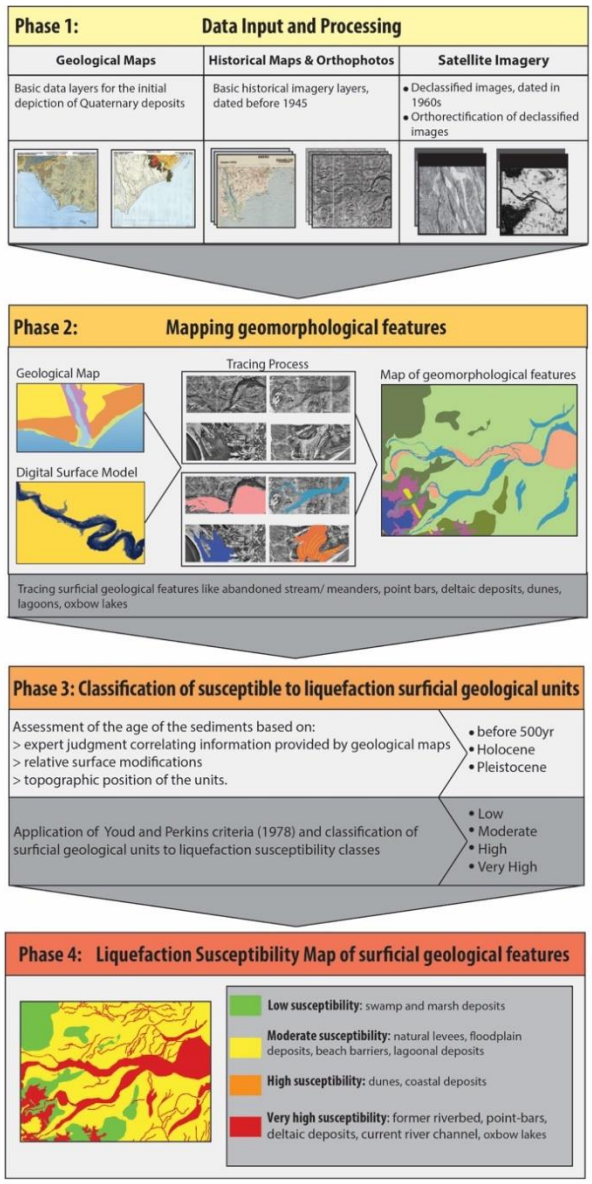

Figure 1. Methodology for assessing liquefaction susceptibility (Taftsoglou et al. 2022).

Another important observation was the extensive river network in the west side of Nestos plain, where old estuaries of Nestos river were formed. The airport was built during 1980s in this area, where land reclamation and modifications had already been occurred. Focusing on this location, the new geomorphological map reveals that a significant part of the airport's facilities and runway were built on an abandoned river branch of old estuaries and deltaic deposits (Figure 2). After the application of Youd and Perkins criteria, it was clear that part of the runway, taxiways and apron are located on a very high susceptible zone.

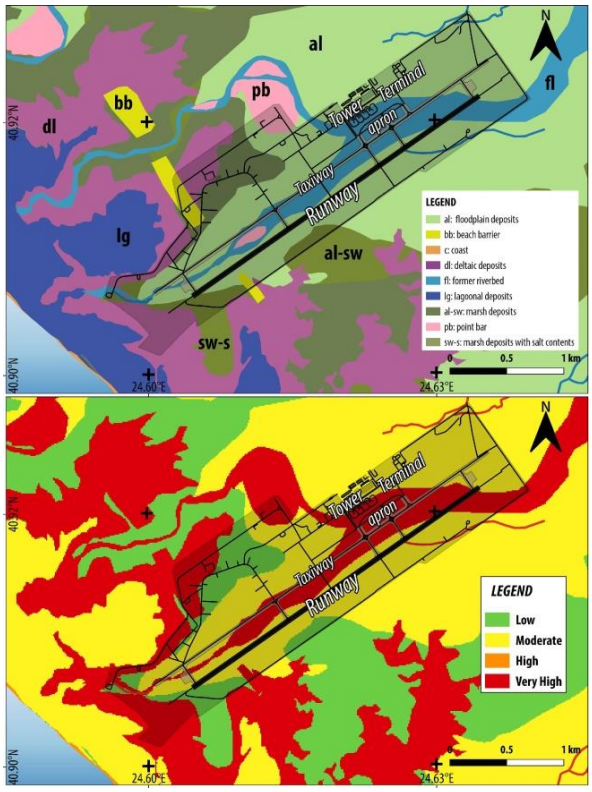

Figure 2. New geomorphological map and liquefaction susceptibility map of KVA.

2.2 Risk Analysis of KVA airport

The HAZUS (FEMA, 2022) methodology was adopted to evaluate the probability of liquefaction and the PGD based on the results described in section 2.1 and a representative seismic scenario based on SHARE and GreDaaS databases of seismogenic sources (Caputo et al, 2012; Giardini et al, 2013). An event of Mw 6.3 in the closest seismogenic source of Kavala-Xanthi-Komotini fault was selected and the ground motion map (PGA) was produced using REDAS software (Papatheodorou et al., 2023). Subsequently, the probability of liquefaction was assessed for each susceptibility category, taking also into account the amplitude of the ground shaking at the airport location (PGA=0.36g) and a groundwater depth of less than 6m. In particular, the probabilities for high and very high susceptibility classes were estimated to be 30 % and 49%, respectively (Figure 3).

The PGD in terms of ground settlements were evaluated following the criteria outlined by Tokimatsu and Seed (1987), while the lack of extended waterways in the vicinity of the infrastructure limited the expectations of lateral spreading phenomena. It is projected that areas classified as highly susceptible will experience ground settlement up to 15.2 cm, while those

categorised as very highly susceptible can reach 30.4 cm of settlement.

The vulnerability of the runway (3,000x45m), taxiways (4,000x35m) and apron (96,000m^2) is assessed based on the fragility functions that are included in HAZUS methodology (Figure 4). The probabilities of exceeding slight/moderate, extensive, and complete damage level were assessed for PGD values of 5.08 cm and 30.4 cm, as the runway, taxiways and apron are located on the moderate and very high susceptibility classes. Based on the probabilities of exceeding each damage state and a repair ratio of 0.1 for slight/moderate, 0.4 for extensive, and 0.8 for complete damage, average loss ratios of 0.125 and 0.590 were calculated for the two PGD values (Argyroudis, 2022). The reconstruction cost was considered equal to 180€/m^2 for the runway and 160€/m^2 for the taxiway and apron (Markovich, 2011). By multiplying the construction cost, average loss ratio and the corresponding area, the direct losses were estimated (Table 1). The total loss for this seismic scenario is assessed equal to €22,2 m. Yet, this is a conservative estimation assuming that liquefaction affects the entire runway, taxiway and apron. In reality, it is expected that ground failure due to liquefaction will likely be more localised, resulting in damage to a portion of these infrastructure.

Table 1. Estimation of direct losses for KVA.

Header	PGD (cm)	Area (m^2)	Loss ratio	Loss (million €)
Runway	5.08	122,247	0.125	2,8
	30.4	12,753	0.590	1,4
Taxiway	5.08	45,513	0.125	0,9
	30.4	99,489	0.590	9,3
Apron	5.08	17,605	0.125	0,4
	30.4	78,468	0.590	7,4

3 VALIDATION DATASETS

The liquefaction susceptibility assessment and risk analysis for the KVA airport are validated in the case studies of Oakland (OAK), Hatay (HTY) and King County (BFI) international airports, where the most extended liquefaction-related damages occurred to the runways areas. The estimated probabilities of liquefaction and PGD according to HAZUS-FEMA methodology, are consistent with the liquefaction occurrences after the earthquakes of Loma Prietta (1989), Turkey-Syria (2023) and Nisqually (2001) in the three airport locations (Table 2).

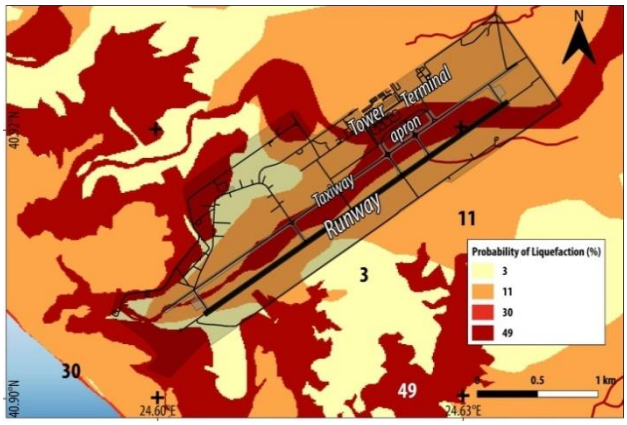

Figure 3. Probability of liquefaction in KVA area.

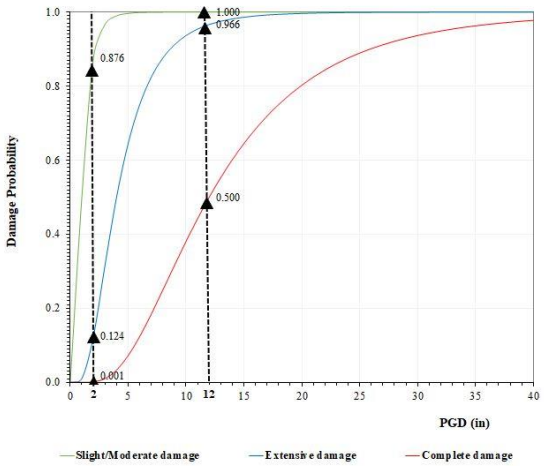

Figure 4. Fragility curves for the runway, taxiways and apron as a function of PGD (FEMA, 2022).

OAK is located on the eastern shore of the San Francisco Bay in western Alameda County. On the northeastern field is located the original part of the airport, built on a tidal marshland with deltaic and stream deposits of San Leandro Creek and fine-grained marsh sediments. The southwestern younger section was constructed on fill over tidal flats and shallow bay areas (Lajoie and Helley, 1975; Witter et al., 2006). During the 1989 Loma Prieta earthquake the extensive liquefaction induced damage resulted in property loss of at least $99 million (Holzer, 1998). According to the FEMA methodology, OAK predominantly falls within the very high susceptibility class, with a probability of 22.3% for liquefaction occurrences, corresponding to PGD of 30.4 cm (Table 2). Validation confirms the consistency between these estimations and the observed damage. Particularly, 900 m of the north-western runway was damaged by sand boils, together with cracking and buckling of the pavement and lateral spreading, while in the adjacent taxiway pavement cracks of 30 cm width and 15 cm vertical displacement were detected. Moreover, the west part of the runway shifted around 0.6 m to the south.

Liquefaction also occurred at the main terminal buildings and taxiways at the south end with pavement settlements up to 8 cm (Holzer, 1998; Seed et al. 1991).

HTY is located in the western part of Amik plain; on the formerly Amik Lake. During the 2023 earthquake doublet of Mw 7.7 and Mw 7.6 on East Anatolian Fault Zone (EAF) extensive liquefaction was observed over the former Amik lake floor, striking also HTY. In particular, the eastern part of the airport was affected by liquefaction shaking deformation phenomena (ground oscillation-lateral spreading) and or possibly triggered shallow slip of pre-existing neotectonic fault traces (Taftsoglou et al., 2023). Ground cracks and soil craters were detected on the runway and its closer area leading to closure of the airport for six days. In contrast to the east side, ground cracks of significant length in the western part of the airport were observed, related to surface fault ruptures of an unknown EAF segment, which cross Amik plain through this area. The results of FEMA's are consistent with the observed damages in this area, with almost all airport infrastructure classified to as highly susceptible to liquefaction, with probability of 98% and PGD of 15.2 cm (Figure 5).

The last case study is the BFI airport. After the 2001 earthquake of Mw6.8 in Nisqually valley, extensive liquefaction was observed at BFI (Nisqually Earthquake Clearinghouse Group, 2001; Bray and others, 2001), which is predominantly situated within an area highly susceptible to liquefaction, with a substantial portion of its runway built upon deposits from abandoned meanders that exhibit an extremely high susceptibility to these phenomena. The extensive liquefaction primarily affected the eastern runway, leading to the formation of ejecta-covered zones extending approximately 90 m in length. Ground surface settlements of up to 20 cm were occurred in this area. While a few isolated sand boils were observed along the western runway, a significant sinkhole measuring 1.2 m in width and 1.8 m in depth was reported at the northern end of the western runway. These phenomena were attributed to apparent ground oscillations, which resulted in the development of cracks in the pavement joints along both runways. Along the west edge of the western runway, a longitudinal crack measuring roughly 3 km in length and ranging from 1.2-2.5 cm in width was noted. Interestingly, the distribution of sand boils and pavement cracking appeared to align with the path of an ancient meander of the Duwamish River. As per HAZUS, the probability values for areas categorized as highly susceptible and very highly susceptible are 7.5% and 16.6% respectively, with estimated PGD of 15.2 cm and 30.4 cm. The observed damaged areas align closely with these estimations, indicating the accuracy in identifying the affected zones.

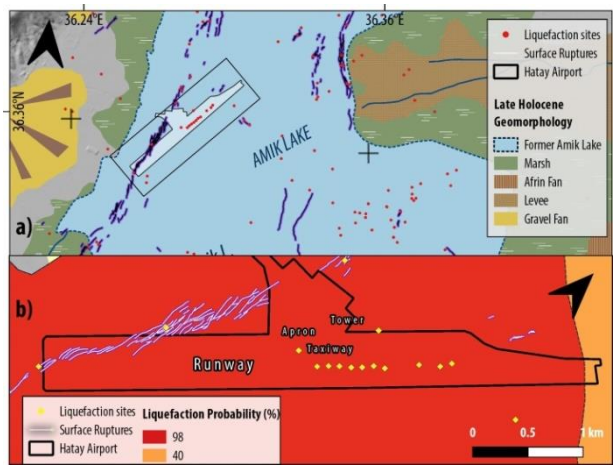

Figure 5. Liquefaction manifestations at HTY, after the 2023 earthquake doublet.

Table 2. Estimation of liquefaction probability (%) and PGD (cm) according to FEMA (2022) for different susceptibility classes (SC).

Airport	KVA	OAK	BFI	HTY	
PGA (g)	0.36	0.20	0.18	0.80	
Mw	6.3	6.9	6.8	7.7	
SC		**Probability (%)**			**PGD (cm)**
VH	49	22.3	16.6	100	30.4
H	29	11	7.5	98	15.2
M	11	3	1.6	41	5.1
L	3	0	0	15.5	2.5

4 CONCLUSIONS

This paper presents an efficient and rapid evaluation tool for assessing the risk of airport infrastructure located in liquefaction-prone areas, using geological and remote sensing data. The methodology is applied to the area where the Kavala International Airport (KVA) in Greece is built to produce a liquefaction susceptibility map. Subsequently, the probability of liquefaction and ground settlements are estimated for a representative seismic event. The direct losses for the runway, taxiways and apron are estimated to €22,2m. However, in reality, the ground failure caused by liquefaction is expected to be more localized, leading to damage in specific sections of this infrastructure and consequently resulting in reduced losses. The methodology is validated using three cases study airports which sustained damage due to liquefaction. The results show a good agreement between the observed and estimated damaged areas confirming the accuracy of the

proposed approach in identifying the susceptibility of areas prone to liquefaction. This research can inform decision making for mitigating risks due to liquefaction hazard in airports, and hence allow for continuous or very quick return to operations following seismic events.

REFERENCES

Argyroudis, S.A. (2022). Resilience metrics for transport networks: a review and practical examples for bridges. *Proc of the ICE-Bridge Engineering,* 175(3), 179-192).

Basili, R., Kastelic V., Wössner J. (2013). The European Database of Seismogenic Faults (EDSF) compiled in the framework of the Project SHARE.

Beetham, D., Beattie, G., Earl, B., Duncan, D. (2001). NZ society for earthquake engineering reconnaissance team to Seattle, USA: The February 28, 2001 Nisqually earthquake. *Bull New Zealand Soc Earthq Eng,* 34(4),253–275.

Bray, J.D., et al. (2001). Some observations of geotechnical aspects of the February 28, 2001, Nisqually earthquake in Olympia, South Seattle, and Tacoma, Washington, A NSF-PEER sponsored reconnaissance effort: http://peer.berkeley.edu/nisqually/geotech/.

Caputo, R., Chatzipetros, A., Pavlides, S., Sboras, S. (2012). The Greek Database of Seismogenic Sources (GreDaSS): state-of-the-art for northern Greece. *Annals of Geophysics*, 55(5), 859-894. https://doi.org/10.4401/ag-5168.

FEMA (2022). Hazus Earthquake Model Technical Manual, Hazus 5.1, FEMA US.

Giardini et al. (2013). Seismic Hazard Harmonization in Europe (SHARE): Online Data Resource, doi: 10.12686/SED-00000001-SHARE.

Grogan, W., Vallerga, B. (2000). Earthquake Damage and Repair of Oakland Airport Runway. *Journal of Performance of Constructed Facilities*. 14.

Holzer, T.L. (1998). The Loma Prieta, California, Earthquake of October 17, 1989 - Liquefaction: U.S. GSPP 1551-B, 314 p.

Lajoie, K.R., Helley, E. J. (1975). Differentiation of sedimentary deposits for purposes of seismic zonation. Studies for seismic zonation of the San Francisco Bay region: U.S. GSPP, A39-A51.

Markovich, M. (2011). Airport Costs. Transportation Costs Report: Florida DoT.

Nisqually Earthquake Clearinghouse Group (2001). The Nisqually, Washington, earthquake of February 28, 2001: EERI, 2001-01, 26 p.

Papatheodorou K, et al., (2023) Rapid Earthquake Damage Assessment and Education to Improve Earthquake Response Efficiency and Community Resilience. Sustainability. 2023; 15 (*in review*).

Pavlides S., Caputo R., Sboras S., Chatzipetros A., Papathanasiou G. and Valkaniotis S. (2010). The Greek catalogue of active faults and database of seismogenic sources, *Bulletin of the Geological Society of Greece,* XLIII (1), 486-494.

Seed, R.B., Riemer, M., Dickenson, S.E., (1991). "Liquefaction of Soils in the 1989 Loma Prieta Earthquake" *Int Conf on Recent Advances in Geotech Earthq Eng and Soil Dynamics*. 9.

Taftsoglou, M., Valkaniotis, S., Papathanassiou, G., Karantanellis E. (2023). Satellite Imagery for Rapid Detection of Liquefaction Surface Manifestations: The Case Study of Türkiye–Syria 2023 Earthquakes. *Remote Sensing*. 15(17):4190.

Taftsoglou, M., Valkaniotis, S., Papathanassiou, G., Klimis, N., Dokas I. (2022). A Detailed Liquefaction Susceptibility Map of Nestos River Delta, Thrace, Greece Based on Surficial Geology and Geomorphology. *Geosciences.* 2022; 12(10).

Tinsley, J.C., Youd, T.L., Perkins, D.M., Chen, A.T.F, (1985). Evaluating Liquefaction Potential, in Ziony, J.I., ed., Evaluating earthquake hazards in the Los Angeles Region an earth-science perspective: U.S. GSPP 1360, p. 263-316.

Washington Division of Geology and Earth Resources, 2016, Surface geology, 1:100,000-GIS data, November 2016: DS-18, ver 3.1.

Witter, R.C., et al. (2006). Maps of Quaternary deposits and liquefaction susceptibility in the central San Francisco Bay region, California: U.S. Geological Survey Open-File Report 2006-1037, scale 1:100,000.

Youd, T.L. (1973). Liquefaction, Flow and Associated Ground Failure; No. 688; U.S. Geological Survey, Washington, D.C.

Youd, T.L., Hoose, S.N. (1978). Historic ground failures in Northern California triggered by earthquakes: U.S. GSPP 993.

Youd, T.L., Perkins, D.M. (1978). Mapping of liquefaction induced ground failure potential. *J Geotech Eng Div*, 104, 433–446.

Proceedings of the XVIII ECSMGE 2024
GEOTECHNICAL ENGINEERING CHALLENGES
TO MEET CURRENT AND EMERGING NEEDS OF SOCIETY
© 2024 the Authors
ISBN 978-1-032-54816-6
DOI 10.1201/9781003431749-248
Open Access: www.taylorfrancis.com, CC BY-NC-ND 4.0 license

ECSMGE 24
XVIII EUROPEAN CONFERENCE ON SOIL MECHANICS AND GEOTECHNICAL ENGINEERING

Sand boil observations and geotechnical characterization of river embankments for the development of a backward erosion piping database

Observations de terrain et caractérisation géotechnique pour la mise en place d'une base de données des phénomènes d'érosion régressive

L. Tonni*, M. Marchi, I. Bertolini
DICAM, University of Bologna, Italy

A. Bassi, A. Rosso
Interregional Agency for the Po River (AIPo), Parma, Italy

**laura.tonni@unibo.it*

ABSTRACT: Sand boil formation at the toe of river embankments is the typical manifestation of initiation and progression of an internal erosion process known as backward erosion piping, which is recognized to be a major concern in many river systems worldwide. In Italy, more than 130 sand boils have been detected along the Po River, many of them experiencing recurrent reactivations during high-water events. As a consequence of such widespread occurrence and the risk for the safety of the surrounding territory and human activities, the development of a sand boil database has been increasingly seen as an essential tool for identifying triggering conditions and giving priorities for the implementation of mitigation measures. In recent years, as part of the activities of the European Project LIFE SandBoil, a GIS-based web application was developed in order to catalogue the sand boils observed along the Po River. The database allows keeping records of a comprehensive set of information, e.g. geometry of the river embankments, subsoil stratigraphy, data on the sand boils, and characteristics of high-water events. Taking a piping-prone cross-section along the Po River as reference, the paper aims at describing the main features of this versatile and flexible tool, which is meant to help in understanding the conditions causing initiation and the sand boil dynamics, as well as to support flood risk management against backward erosion piping.

RÉSUMÉ: Les phénomènes de boulance à l'aval des digues fluviales sont le signe d'initiation et progression d'un processus d'érosion interne qui se développe au sein des fondations, dans les couches de sables. Ce mécanisme, qui est connu sous le nom d'érosion régressive, est de loin le mécanisme le plus dangereux pour la stabilité des systèmes d'endiguement de plusieurs grands fleuves européens. En Italie, plus de 130 cas de boulance ont été recensés le long du fleuve Pô, lors des crues enregistrées pendant les trente dernières années. En raison des fréquentes manifestations d'érosion discernables en surface et des dégâts très importants, tant matériels qu'humains, qui pourraient être générés par la rupture des digues, le développement d'une base de données est de plus en plus considéré comme un outil fondamental pour identifier les conditions d'initiation du processus et donner des priorités pour la mise en œuvre de mesures de mitigation. Cet article vise à décrire les principales caractéristiques d'une application Web basée sur un SIG, qui a été récemment développée dans le cadre des activités du projet européen LIFE SandBoil afin de cataloguer toutes les amorces d'érosion régressive identifiées le long du Pô. La base de données permet de stocker une grande quantité d'informations, telles que la géométrie de la digue, la stratigraphie du sous-sol, la charge hydraulique, ainsi que les principaux indices alertant sur le mécanisme d'érosion.

Keywords: Backward erosion piping; sand boils; river embankments; Po River; piping database.

1 INTRODUCTION

Backward erosion piping is a major concern for the stability of many river embankment systems worldwide (Van Beek, 2015), during high-water events. The initiation and progression of this phenomenon is typically revealed by the presence of one or multiple sand boils, landward of the river embankment. Indeed, when the hydraulic head difference across the water retaining structure increases so much as to result in excessive underseepage and high local gradients in the underlying aquifer, uplift of the blanket layer may occur and erosion initiates at the exit point. A bubbling spring of fluidized sand is thus observed on the ground surface, most often accompanied by ejection of eroded soil particles to form a sand volcano around the exit zone: sand basically looks like a boiling fluid, hence

the name "sand boil". Once started, the erosion within the aquifer develops progressively in the upstream direction, i.e. towards the river, resulting in shallow pipes beneath the river embankment that cause in turn settlements, with a significant risk for the structure stability. The different phases of the backward erosion piping process, from boiling phase to failure of the water-retaining structure, have been investigated and described by various authors and a detailed description can be found in Van Beek (2015).

In Italy, sand boils are very commonly detected near the toe of the Po River embankments. Indeed, over the last 30 years, more than 130 sand boils have been catalogued: most of them have been mapped in the main course of the river and suffer from recurrent reactivations during high-water events, but those located in the delta area reactivate also at relatively moderate water levels. It is also worth mentioning that sand boils observed along the Po River may be of remarkable size, with some sand volcanoes having an external diameter greater than 3 m. In such cases, abundant and continuous erosion is very likely to occur beneath the river embankment, thus posing a major threat to the structure integrity.

In the last few years, the Interregional Agency for the Po River (AIPo), the Italian authority in charge of flood protection and flood damage reduction in the Po River basin, has been very active in collecting as much data as possible in river segments exhibiting ground manifestation of backward erosion piping. Indeed, the synergic use of a wide variety of data, including geometric features, stratigraphic arrangement, geotechnical and hydraulic characteristics of the foundation subsoil, together with groundwater flow models and records of hydraulic loads in past activations, may undoubtedly help in identifying triggering conditions of piping phenomena, assigning hazard classes to the different river embankment sections, enabling the identification of priorities for mitigation interventions. As a result, a piping database may serve as a useful tool to effectively support flood risk management.

Following early attempts of systematic collection carried out by both the Po River Basin District Authority (AdBPo) and AIPo (Aielli et al., 2019), a GIS-based web application has been recently developed as part of the activities devised in the European project LIFE SandBoil (2020).

This paper describes the main features of this flexible and versatile tool, making reference to a representative cross-section of the Po River, which experienced repeated reactivations of a so-called "historical sand boil".



Figure 1. (a) Satellite view of the Po River basin and location of the selected cross-section; (b) Reactivation of a sand boil in Guarda Ferrarese, during the 2018 high-water event.

2 THE SELECTED RIVER SECTION

In order to provide a meaningful example of the typical stratigraphic features encountered in Po River embankments prone to piping, the cross-section located near Guarda Ferrarese (Figure 1(a)), in the lower catchment of the watercourse, is described herein. This river stretch has indeed a well-known history of internal erosion and sand boil activity, hence over the last years it has been selected to conduct field studies and numerical models for underseepage research (e.g. García Martínez et al., 2020a, 2020b; Marchi et al., 2021; Bertolini et al., 2022). According to the available records, the first evidence of piping was reported in 1994, when it caused severe damage to the road embankment running parallel to the river; more recent sand boil reactivations observed in this segment date back to 2014, 2018 and 2020.

During the 2014 high-water event, in particular, evidence of major underseepage, in the form of a high energy sand boil, was observed, with the throat of the sand boil moving outside the sandbag ring and thus requiring re-ringing alongside, as also shown in Figure 1(b).

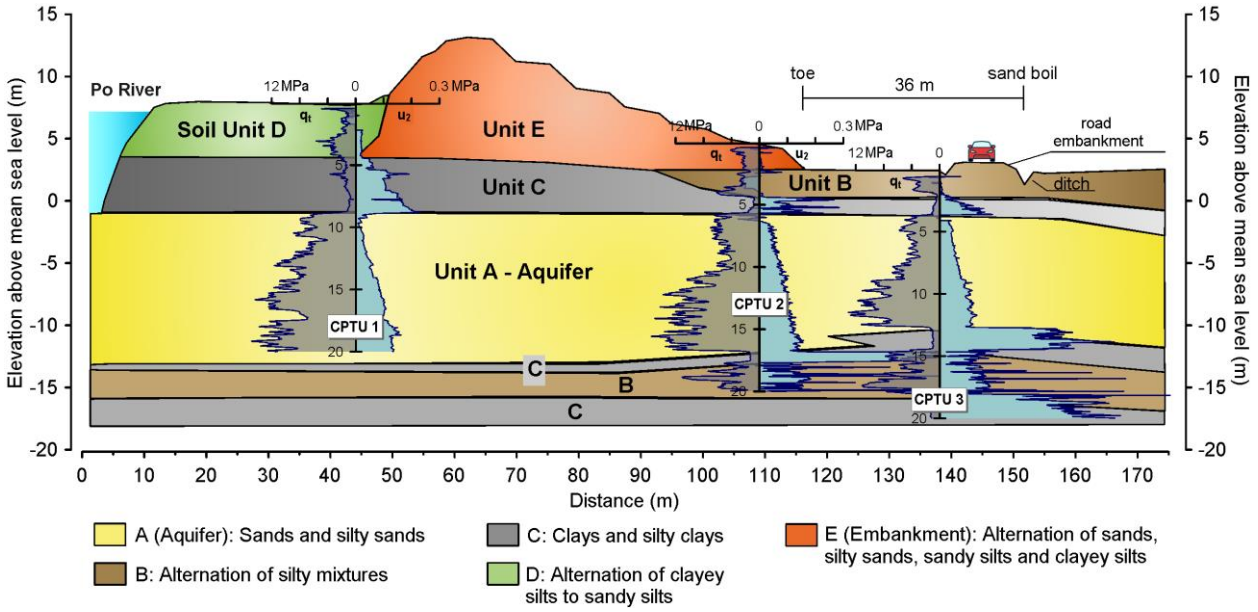

Figure 2. Stratigraphic model of the investigated cross-section in Guarda Ferrarese, with CPTU log profiles (vertical scale magnified). Modified from García Martínez et al., 2020a.

Table 1. Field measurements (net head on the river embankment, ΔH, and length of the vertical pipe, L) and local hydraulic gradients in the fluidized vertical pipe (i_{pipe}) during the monitoring period.

Date (d/m/year)	ΔH (m)	L (m)	i_{pipe} (-)
7/11/2018	4.65	1.46	0.53
9/11/2018	5.12	1.51	0.51
11/11/2018	5,82	1.54	0.50
20/11/2018	2.01	0.73	0.46

In 2018, despite a moderate flood intensity, a sizeable sand boil, having a 1m external diameter volcano, was recorded in a collector ditch as in previous activations. While the flood event was still underway, a comprehensive set of field measurements could be collected, encompassing sand boil geometry, grain size characteristics of the ejected sand, concentration of the sand–water mixture in the sand boil throat, together with a number of relevant hydraulic parameters, such as head loss in the vertical pipe, flow velocity, water discharge, all then interpreted in relation to the water level reached in the river (Marchi et al., 2021). Such field observations turn out to be key pieces of information when predictive models of piping initiation or progression (e.g. Robbins et al., 2020) are used. A selection of the collected hydraulic and geometrical data, namely the head loss ΔH between the river and the landside ditch, the length L of the vertical pipe, and the average gradient in the vertical pipe, i_{pipe}, is shown in Table 1. The vertical pipe was found to have a funnel shape, with a diameter of about 20 cm at the bottom to approximately 35 cm near the exit.

Figure 2 shows the stratigraphic model of the river embankment and the underlying subsoil, as obtained from interpretation of continuous coring boreholes and piezocone tests (CPTU) carried out along a cross-section drawn through the sand boil area. It is worth noting that the stratigraphic arrangement includes a 9–12 m thick sandy aquifer (Unit A), fed upstream by the river and overlain by a clayey soil unit (labelled as *C*) and a predominantly silty layer (Unit B), both forming a fine-grained soil cap typically referred to as *blanket* layer. The thickness of the blanket appears to reduce in proximity of the sand boil location, creating favorable conditions for backward erosion piping initiation. The susceptibility to backward erosion piping was also increased by the excavation of a ditch parallel to the road embankment, as shown in Figure 2.

The grain size analysis of the eroded soil, carried out on samples either collected in the volcano crater or obtained from the fluidized sand in the vertical pipe, provided evidence of a fine, uniform sand, with d_{10} and d_{50} in the ranges of 0.100–0.138 and 0.178–0.228 mm, respectively (Marchi et al., 2021).

Recent geotechnical campaigns carried out in this area have been especially meant to provide a better insight into the hydraulic parameters of the soil units forming the river embankment system, the attention being especially focused on the blanket layer and the aquifer involved in piping effects. Different experimental strategies and methods have been adopted (Lefranc tests, dissipation tests, CPTU-based empirical correlations) in order to obtain an accurate description of the subsoil permeability (k) and its spatial variability through the cross-section. Table 2

summarizes a few representative data for *k*. Details on this subject can be found in Bertolini et al. (2022).

Groundwater level monitoring through a few piezometers located landside (close to the toe, in proximity to the sand boil and approximately 400 m from the river embankment) revealed that the sub-artesian confined aquifer, corresponding to Unit A, is well synchronized with the river, whereas the phreatic surface in Unit B is governed by rainfall and evapotranspiration.

Table 2. Mean values of soil permeability k, as deduced from Lefranc tests and CPTU interpretation.

Soil units	Lefranc test *k* (m/s)	CPTU dissipation *k* (m/s)	CPTU correlation *k* (m/s)
A	8.9E-07	1.9E-06	9.1E-06
B	1.6E-06		1.0E-06
C		4.7E-09	4.6E-09
D			1.6E-07
E			1.2E-05

3 THE SAND BOIL DATABASE

The database described in this paper has been developed within the ongoing European project LIFE SandBoil, whose main objective is the development of an innovative and sustainable technology for the mitigation of backward erosion piping in river embankments. The project is coordinated by the University of Bologna and involves the Interregional Agency for the Po River, Officine Maccaferri Italia, and the North Transdanubian Water Directorate as project beneficiaries.

The database is a web application, built in a geographic information system (GIS). The design of the database was coordinated by AIPo, who is also responsible for data collection and uploading. The application has been designed in such a way that it can easily accommodate data from various river basins, in addition to the Po, and thus become an international database of backward erosion piping phenomena observed worldwide.

3.1 The Database Structure

The database (Hortus, 2021) is basically organized into two main sections, corresponding to the river and the sand boil, respectively. The first section allows specifying the different rivers for which sand boils are defined and the relevant hydrometric stations where river water levels are measured. These measurements are then used as input data by the flood simulation algorithm to obtain the river levels in cross-sections where piping evidences are detected during flood events.

The sand boil section allows uploading a wide variety of information about each river segment affected by piping, with respect to the following items:

- the river embankment, in terms of geometric profile, embankment components, subsoil stratigraphic arrangement;
- the flood event causing the activation/reactivation of a sand boil, described in terms of duration, maximum discharge, data from nearby piezometers;
- the sand boil itself, in terms of geolocation, geometrical features of the sand boil, type of activity, characteristics of the ejected sand, and details on adopted emergency actions.

Figure 3 shows a GIS digital map of the Po River basin, with green dots representing the sand boil locations currently entered into the database.

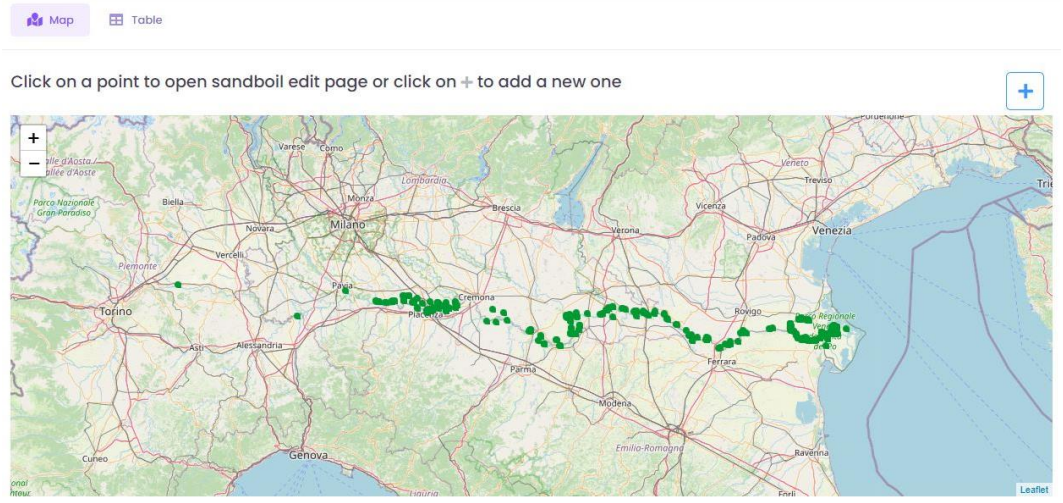

Figure 3. Map showing the location (green symbols) of the sand boils detected along the Po River (downloaded from the database).

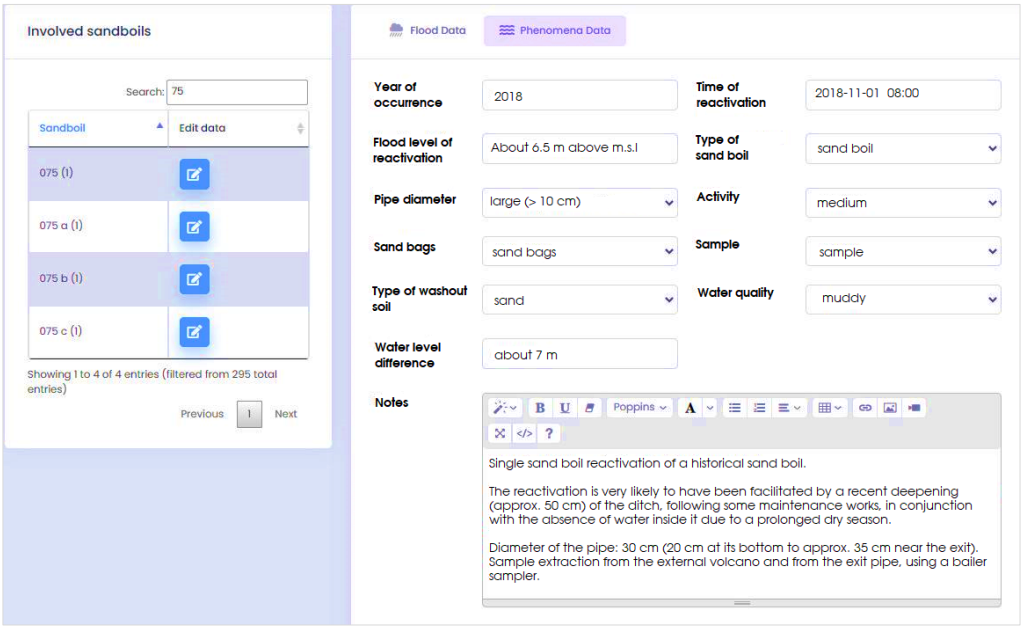

Figure 4. Example of data entry window in the web application, with reference to the sand boil No. 75 located in Guarda Ferrarese, reactivation of November 2018.

An example of the adopted interface for entering data and information is provided in Figure 4, with reference to the window containg data fields on sand boil geometry and piping activity during a high-water event. The entered data refers to the 2018 reactivation of the sand boil in Guarda Ferrarese.

3.2 Database Query

The data stored in the database can be easily exported or interpreted through graphs that allow analysing the effect of different flood events on a selected section along the Po River or comparing the response of different piping-prone river embankments during a specific high-water event. The sand boil management tool allows indeed creating two different types of graphs, referred to as "river graphs" and "historical graphs". The first type consists in a profile of the maximum high-water level reached along the watercourse during a flood event, with the indication of the river embankment sections that experienced some piping activity.

An example of historical graph is given in Figure 5, which provides an overview of the activations/non-reactivations observed at Guarda Ferrarese, for the flood events occurred from 2000 to 2020. The red bars are used to indicate activations or reactivations of the sand boil, the green ones are adopted when no evidence of piping was detected. In Figure 5, the horizontal red line reveals that the minimum water level causing past reactivations is equal to H_{min} = 7.63 m above m.s.l., whereas the maximum hydrometric level (H_{max} = 9.42 m above m.s.l.) for which no activation was observed is shown by the green line.

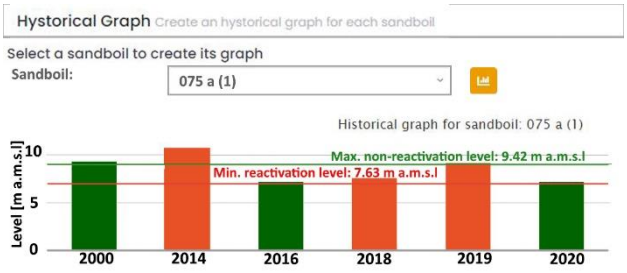

Figure 5. Example of data extraction in the form of "historical graph", with reference to the sand boil No. 75 detected in Guarda Ferrarese.

4 CONCLUSIONS

The paper has described the main features of a database that has been recently developed in order to catalogue the sand boils detected along the main Italian watercourse, i.e. the Po River. The database fields have been presented with respect to a well-documented river embankment section, located in the lower stretch of the Po River, which has experienced recurrent reactivations of a so-called historical sand boil. This flexible and versatile tool appears to be capable of providing an effective assessment of backward erosion piping hazard along the Po River and thus supporting flood risk management against this phenomenon.

ACKNOWLEDGEMENTS

The database presented in this paper was developed as part of the activities of the LIFE SandBoil project

"Natural-based solution to mitigate flood risk due to sand boils reactivations along the Po River" (Grant Agreement no. LIFE19 ENV/IT/000071), funded by the European Commission.

REFERENCES

Aielli, S., Pavan, S., Parodi, S., Rosso, A., Tanda, M.G., Marchi, M., Vezzoli, G., Pantano, A., Losa, D. and Sirtori, M. (2019). Collection and analysis of the reactivation data of the historical sand boils in the Po river levees. In: *Internal Erosion in Earthdams, Dikes and Levees*, *Lecture Notes in Civil Engineering,* S. Bonelli, C. Jommi and D. Sterpi (eds), pp. 327-335, Springer, Switzerland. https://doi.org/10.1007/978-3-319-99423-9.

Bertolini, I., Gottardi, G., Marchi, M., Tonni, L., Bassi, A. and Rosso, A. (2022). Application of CPT to the evaluation of permeability in a Po river embankment prone to backward erosion piping. *Proc. 5th International Symposium on Cone Penetration Testing (CPT'22)*, G. Gottardi and L. Tonni (eds), CRC Press, The Netherlands, pp. 300-305. https://doi.org/10.1201/9781003308829.

García Martínez, M.F., Tonni, L., Marchi, M., Tozzi, S. and Gottardi, G. (2020a). A numerical tool for the prediction of sand boil reactivations near river embankments. *Journal of Geotechnical and Geoenvironmental Engineering*, 146, e02380. https://doi.org/10.1061/(ASCE)GT.1943-5606.0002380.

García Martínez, M.F., Gottardi, G., Marchi, M. and Tonni, L. (2020b). On the reactivation of sand boils near the Po River major embankments. In: *Research for Land Protection and Development*, *Proceedings of CNRIG 2019*, F. Calvetti, F. Cotecchia, A. Galli and C. Jommi (eds), Vol. 40, pp. 328-337. Springer, Switzerland. https://doi.org/10.1007/978-3-030-21359-6.

Hortus (2021). Sand boil management: User manual, Hortus, Italy.

LIFE SandBoil (2020). Natural-based solution to mitigate flood risk due to SAND BOILS reactivations along the Po River, https://lifesandboil.eu/.

Marchi, M., García Martínez, M.F., Gottardi, G. and Tonni, L. (2021). Field measurements on a large natural sand boil along the river Po (Italy). *Quarterly Journal of Engineering Geology and Hydrogeology*, 54(4), qjegh2020-097. https://doi.org/10.1144/qjegh2020-097.

Robbins, B. A., Stephens, I.J., Van Beek, V.M., Koelewijn, A.R. and Bezuijen, A. (2020). Field measurements of sand boil hydraulics. *Géotechnique*, 70(2), pp. 153–160. https://doi.org/10.1680/jgeot.18.P.151.

Van Beek, V.M. (2015). *Backward erosion piping. Initiation and progression*, PhD thesis, Delft University of Technology.

Proceedings of the XVIII ECSMGE 2024
GEOTECHNICAL ENGINEERING CHALLENGES
TO MEET CURRENT AND EMERGING NEEDS OF SOCIETY
© 2024 the Authors
ISBN 978-1-032-54816-6
DOI 10.1201/9781003431749-249
Open Access: www.taylorfrancis.com, CC BY-NC-ND 4.0 license

ECSMGE 24
XVIII EUROPEAN CONFERENCE ON SOIL MECHANICS AND GEOTECHNICAL ENGINEERING

Thermo-hydro-mechanical analysis of soil strata suffered from desiccation cracking

Analyse thermo-hydro-mécanique des couches de sol souffrant de fissuration par la dessiccation

S. Tourchi*
Department of Civil and Environmental Engineering, University of Luxembourg, Luxembourg

M. Jabbarzadeh, H. Sadeghi
Department of Civil Engineering, Sharif University of Technology, Tehran, Iran

**saeed.tourchi@uni.lu*

ABSTRACT: Understanding the complex behaviour of cracked ground surface resulting from the desiccation process in swelling soils has received significant attention in recent years. The formation of these cracks is attributed to the complicated interplay between soil comprising of plastic nature and atmospheric conditions; in some cases, the influencing depth of cracking can be extended to several meters below the ground surface. Therefore, the main goal of this research is to investigate the thermo-hydro-mechanical (THM) behaviour of cracked soil strata using CODE-BRIGHT. Results indicated that crack presence led to heterogeneous moisture distribution during the drying process with more significant desiccation in crack edges and walls. In addition, the inclusion of crack into an initially homogeneous soil stratum enhanced the heterogeneous ground deformations, with the most pronounced effects observed near the cracks. Remarkably, the findings indicate that cracks display varying behaviour under diverse climatic conditions. They tend to widen more in warmer climates, and conversely, they exhibit a tendency to close during rainy periods, which can be attributed to soil swelling.

RÉSUMÉ: La compréhension du comportement complexe de la surface du sol fissurée résultant du processus de dessiccation dans les sols gonflants a suscité beaucoup d'attention ces dernières années. La formation de ces fissures est attribuée à l'interaction complexe entre un sol de nature plastique et les conditions atmosphériques ; dans certains cas, la profondeur d'influence des fissures peut s'étendre à plusieurs mètres sous la surface du sol. Par conséquent, l'objectif principal de cette recherche est d'étudier le comportement thermo-hydro-mécanique (THM) des strates de sol fissuré à l'aide de CODE-BRIGHT. Les résultats indiquent que la présence de fissures entraîne une distribution hétérogène de l'humidité pendant le processus de dessiccation, avec une dessiccation plus significative au niveau des bords et des parois des fissures. De plus, l'intégration de fissures dans un substrat de sol initialement homogène a renforcé les déformations hétérogènes du sol, les effets les plus prononcés étant observés près des fissures. Remarquablement, les résultats indiquent que les fissures présentent un comportement variable en fonction des conditions climatiques diverses. Elles ont tendance à s'élargir davantage dans les climats plus chauds, et inversement, elles montrent une tendance à se refermer pendant les périodes de pluie, ce qui peut être attribué au gonflement du sol.

Keywords: THM analysis; soil-atmosphere interaction; desiccation crack; heterogeneous deformation; geohazard.

1 INTRODUCTION

Soil deformation is a complex phenomenon influenced by various factors, including environmental conditions and soil properties. The behaviour of soils in response to changes in moisture content plays a crucial role in numerous engineering applications, from geotechnical engineering to infrastructure design (Yazdani et al., 2024). Cracks that develop within the soil matrix introduce an additional layer of complexity, altering the deformation patterns and redistributing of soil moisture and mechanical stresses (Wang et al., 2022). Understanding the deformation behaviour of soils under wetting and drying conditions is essential for predicting potential subsidence, swelling, and subsequent structural damage (Ghorbani et al., 2023). In this context, the presence of cracks further complicates the deformation mechanism, as cracks provide preferential paths that intensify evaporation and facilitate infiltration (Luo et al., 2023).

In recent years, advanced computational techniques and experimental methods have enabled researchers to delve deeper into soil desiccation cracking (Sanchez et al., 2014; Wei et al., 2016; Guo et al., 2023). Numerical simulations provide insights into the complex interplay between crack geometry, soil

properties, and environmental factors. Moreover, laboratory experiments involving controlled environmental conditions contribute valuable empirical data for the validation and calibration of numerical models. Integrating these approaches facilitates a comprehensive understanding of the soil desiccation cracking mechanisms and their influencing factors. Prior studies have mainly focused on crack initiation and propagation, overlooking the complexities of how these cracks and soil surface deform under actual climate fluctuations. Hence, key aspects such as heterogeneous subsidence and swelling during warm and wet periods, induced by surface layer shrinkage and expansion, were not addressed. Furthermore, most researchs have focused on smaller scales, conducting controlled experiments on soil samples to observe crack behaviour, while larger field-scale cracks are influenced by significant climatic shifts affecting surface topography.

This study seeks to establish a more profound comprehension of the cracked soil deformation and moisture dynamics under the influence of real climate changes with THM analysis using the CODE_BRIGHT finite element program.

2 MATERIALS AND METHODS

2.1 Balance and constitutive equations

The THM model's equations employed in this study are rooted in the theoretical framework introduced initially by Olivella et al. (1994). Therefore, the model contains solid mass, water mass, energy, and momentum balance to consider the changes in soil porosity, liquid pressure, temperature, and displacements, respectively. Moreover, Fourier's and Darcy's laws are used as fundamental thermal and hydraulic constitutive equations of the model. The van Genuchten's model is also utilised to define the soil-water retention curve. In order to incorporate non-advective species fluxes within liquid phases, encompassing phenomena like water vapour diffusion in the gas phase and air diffusion in water, Fick's law is defined.

Regarding the mechanical aspect of the model, the Barcelona Expansive Model (BExM) is employed (Alonso et al., 1999). This advanced model, rooted in the Barcelona Basic Model (BBM) (Alonso et al., 1990), offers an encompassing framework to capture the sequential dynamics of soil shrinkage and swelling in response to wetting and drying cycles (Sadeghi and Ng, 2018; Ghandilou et al., 2023a, 2023b). This model can consider two levels of structure: micro and macrostructure. High suction changes experienced by fine-grained soils during climate variations induce notable alterations in both the micro and macrostructural arrangement of the soil, leading to volumetric changes. These alterations are primarily driven by the soil's response to fluctuations in moisture content (Ng et al., 2017).

At the micro level, fine-grained soils like clays have complex pore networks. As moisture declines, capillary forces dominate, leading to tighter particle packing and shrinkage. On the macrostructural scale, the cumulative microstructural modifications lead to volumetric variations. During hot, dry periods, the soil experiences notable shrinkage and subsidence, causing surface settlement. Conversely, when wet conditions return, the soil swells upon absorbing moisture, leading to surface elevation changes (Sadeghi, 2016; Ng et al., 2017).

2.2 Soil-atmosphere interactions

Soil-atmosphere interactions refer to the exchange of heat and moisture between the soil and the surrounding environment. Transfer of the moisture involves the movement of water vapour due to factors such as moisture content, temperature, and pressure gradients. The exchange of thermal energy occurs through conduction, convection, and radiation (Hemmati et al., 2012).

In analysing soil-atmosphere interactions, the fundamental theoretical framework involves gas, water, and energy fluxes. Evaporation is calculated using an aerodynamic diffusion equation, and the movement of water vapour in soil pores is induced by this evaporation. Hence, the advective flux of vapour by the gas phase is defined. Additionally, thermal energy exchanges are considered by determining sensible and convective heat flux to account for the transfer of thermal energy and internal energy of each phase (Jabbarzadeh et al., 2023; Tourchi et al., 2024).

2.3 THM model

THM analyses are conducted using the finite element program CODE_BRIGHT (Olivella et al., 1996). To cover all input parameters, the Boom clay is considered as geomaterial of the model as its THM parameters were widely reported (Alonso et al., 1998; Delahaye and Alonso, 2002; Sanchez et al., 2005; Gens et al., 2007). In addition, the meteorological data of Qom city from 2015 to 2017, including temperature, wind speed, precipitation, relative humidity, and radiation, are also used to consider climate changes effect on cracked soil deformation. This region was selected because of its vulnerability to significant subsidence caused by its arid and warm climate (Sadeghi et al., 2023).

Recent studies have provided a limited dataset regarding the dimensions of crack geometry observed in the field. While there are other experimental and numerical investigations available, they are not suitable for this study as small cracks are beyond the scope of this research. To make the most of the available data, a dimensionless parameter known as the crack ratio (C_R), which represents the ratio of crack width (C_W) to crack depth (C_D), is introduced. This parameter allows us to utilise crack dimensions from previous experimental and numerical studies as well as field observations. To select modeling scenarios, a crack depth of 1 m is chosen. The deeper desiccation cracks up to 6 m are also reported by Morris et al. (1992). To accurately determine the crack geometry, statistical analyses were conducted using a dataset of crack dimensions reported in previous studies, considering crack ratios ranging from 1% to 42%. The results of these statistical analyses indicate that the distribution of crack ratios follows a lognormal distribution, as depicted in Figure 1(a). This insight has enabled the creation of a probability density function (PDF) for the crack ratios, visualized in Figure 1(b).

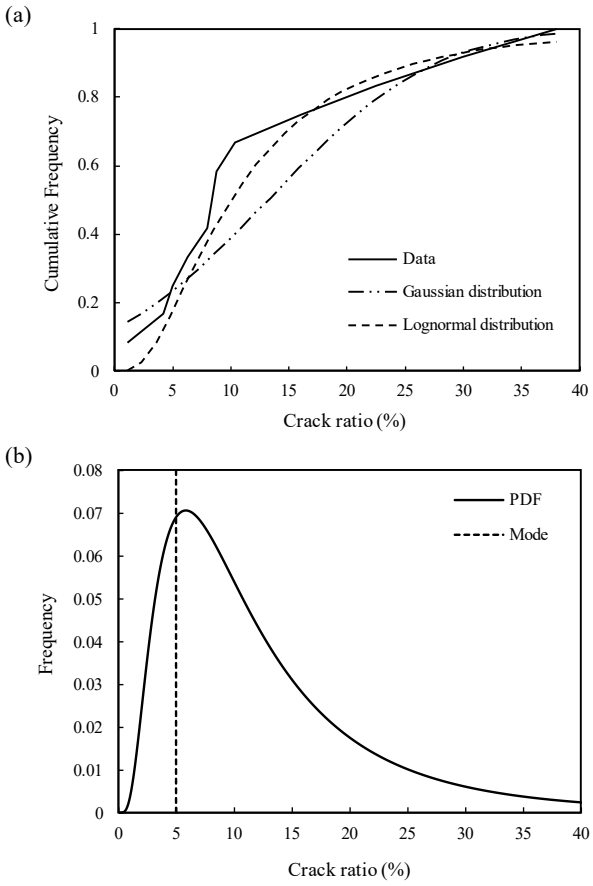

Figure 1. Statistical analysis of the crack ratio data.

Finally, the modeling scenario in terms of crack geometry was developed based on the obtained results. This scenario involves a crack with a depth of 1 m and a crack ratio of 5%, which is the peak of the PDF and shows a mode of data with the highest frequency. Once the crack shape has been established, the identified scenario is integrated into the numerical model to perform the THM analysis. This is accomplished by assigning the appropriate material properties, initial and boundary conditions. In this regard, the initial porosity is assumed to be 0.487, and the initial suction at the soil surface is set at 10 MPa. The suction value decreases linearly to a depth of 50 m, reaching a value of 0.4 MPa. Beyond this point, it declines with a different slope until it reaches the groundwater table at a depth of 90 m. To provide a visual representation, the schematic diagram of the crack geometry is depicted in Figure 2.

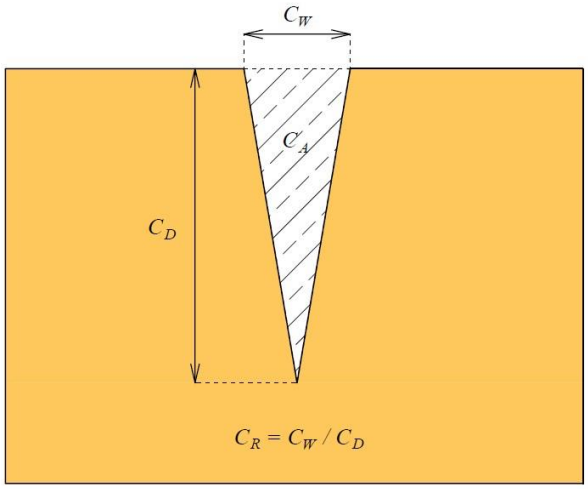

Figure 2. Schematic definition of parameters describing the crack geometry.

3 RESULTS AND DISCUSSION

3.1 Moisture distribution in the cracked soil

The soil maintains ongoing thermo-hydraulic interactions with its surrounding environment, a phenomenon that can be significantly intensified by the presence of cracks within the soil matrix. These cracks can act as conduits, amplifying processes such as water infiltration during rainfall and evaporation on warmer days. Therefore, the distribution of the degree of saturation (S_r) is visually represented in Figure 3 at three distinct time points: 100, 500, and 1000 days. These three selected days correspond to periods during the year when the weather is relatively warm, indicating the drying trend. However, the consecutive wetting-drying cycles before the chosen days have also influenced the moisture variations.

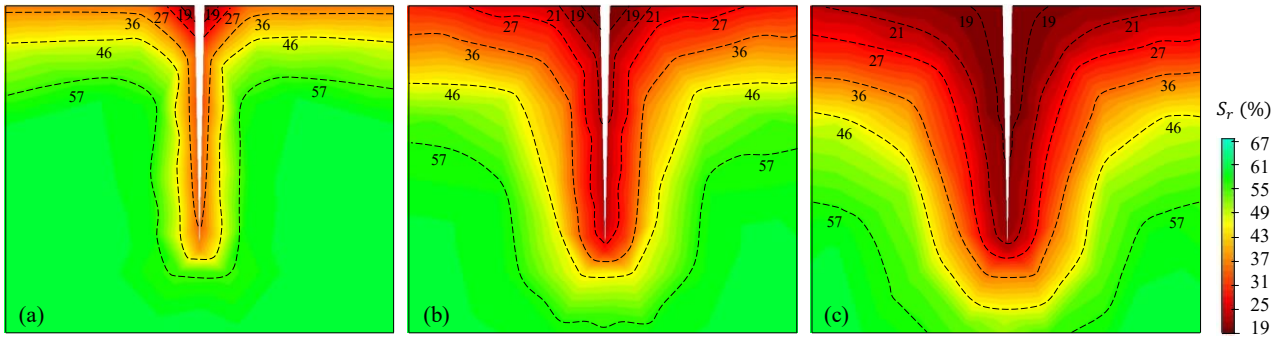

Figure 3. Spatial distribution of degree of saturation in cracked soil after (a) 100 days, (b) 500 days, and (c) 1000 days.

The results indicate that the presence of cracks leads to a heterogeneous S_r distribution, even within a homogeneous and isotropic soil layer. As illustrated in Figure 3(a), during the initial stages of the drying process, the cracked soil exhibits heightened desiccation along the edges of the cracks, while a relatively marginal drying effect is observed along the crack walls. With the progression of the drying period to the 500th day (see Figure 3(b)), the desiccation phenomenon intensifies, particularly within the cracked regions of the soil. This pattern underscores a key insight that within cracked soil, the edges and walls of the cracks are more susceptible to experiencing intensified desiccation under drying conditions. As observed, with the progression of desiccation, the contour lines deviate both horizontally and vertically away from the crack wall. This indicates that the presence of the crack exacerbates the reduction in soil moisture, both at the soil surface and in depth.

3.2 Heterogeneous deformation of the cracked soil under climate changes

The trend of moisture distribution in cracked soils can result in its non-uniform deformation under climatic variations, especially the uneven subsidence triggered by climatic warming. To explore this phenomenon, the deformed geometry of cracked soil is presented in Figure 4 for three distinct time intervals, after 100, 500, and 1000 days, compared to its initial state. As evident, the effect of soil desiccation and the consequent increase in evaporation lead to soil shrinkage and subsidence in the context of drying. This drying-induced subsidence not only affects the soil surface but also induces deformation within the crack geometry.

Notably, the findings demonstrate that the most substantial subsidence occurs along the crack edges, while the subsidence experienced by the soil surface diminishes with increasing distance from the cracks. These observations parallel the results of the moisture distribution within cracked soil, where the edges of cracks exhibited the most pronounced desiccation. Furthermore, as the drying process progresses, cracks widen and experience internal area expansion. This dynamic evolution of cracks' width and internal area alterations is visualised in Figure 5 with 100 days intervals. As evident from the results, the deformation of cracks is influenced by climatic variations in such a way that the crack deformation responds to changes in soil moisture content. With increasing soil moisture, cracks tend to expand, resulting in a reduction in their width and area. Conversely, decreasing soil moisture causes ground shrinkage, leading to their widening and increased area. As depicted in Figure 5, the changes in crack width exhibit a similar trend to those of crack area, although the variation in crack area is also influenced by the deformation of the crack walls. Consequently, this factor has contributed to a broader range of changes in crack area.

A noteworthy observation is that due to the soil's tendency to an equilibrium state, gradually the rate of the deformation diminishes. As evident, the rate of change in crack area exhibits a nonlinear relationship with time, following the trend line plotted in a logarithmic function. This proves that the deformation rate decreases nonlinearly over time. Given that the behaviour of crack width follows a similar trend as crack area, it can be inferred that the change in crack width may also follow this trend. According to Figure 5, crack with an initial width and area of 50 mm and 25000 mm^2 respectively, undergoes deformation. After 900 days, it reaches its maximum values of 114.5 mm and 55230 mm^2, indicating an increase of over twice the initial measurements. This substantial growth highlights the distinct deformation mechanism of cracked soil in comparison to uncracked soil. Coupled with climatic

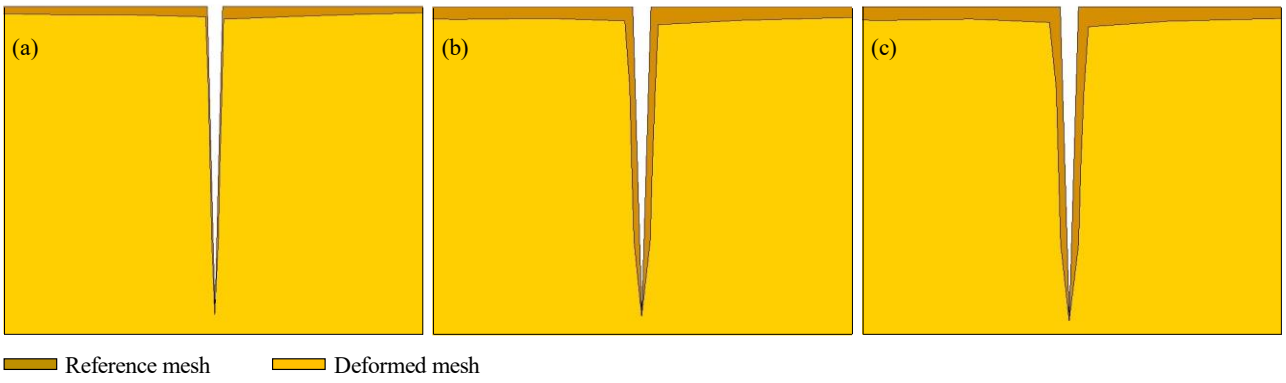

Figure 4. Heterogeneous subsidence of cracked soil under the influence of climate warming after (a) 100 days, (b) 500 days, and (c) 1000 days.

variations and global warming, which induce greater desiccation of surface soil layers, the phenomenon of soil cracking intensifies. This can result in heterogeneous subsidence of the soil surface, potentially leading to structural damages such as tilting, differential settlement, and structural cracks.

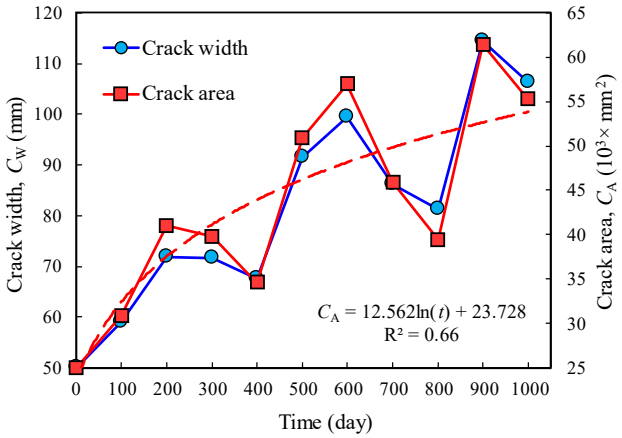

Figure 5. Variations in crack width and area with time under the influence of climate conditions.

4 CONCLUSIONS

This study focused on the THM analysis of desiccation cracked clayey strata, taking into account soil-atmosphere interaction by using real climate data from Qom between 2015 and 2017. The model incorporated various meteorological parameters like temperature, wind speed, precipitation, relative humidity, and radiation to investigate the effect of cyclic wetting-drying cycles on cracked soil behaviour. The characterization of crack geometry was achieved through statistical analysis of existing datasets from prior studies, which revealed a lognormal distribution for crack ratios. The examination of moisture distribution within cracked soil revealed a heterogeneous degree of saturation distribution. Notably, crack edges and walls experienced more pronounced desiccation, with a S_r of 19%. The behaviour of cracks under changing climatic conditions exhibited their sensitivity to moisture levels, impacting both their width and area. The findings highlighted a logarithmic trend in the changes of crack area and width, indicating a tendency toward an equilibrium state in deformation rates. Furthermore, the results underscored that cracked regions were more vulnerable to subsidence compared to uncracked areas, resulting in heterogeneous subsidence patterns in the cracked soils. Significantly, the study revealed substantial increases, exceeding twofold, in both crack width and area due to prolonged climate fluctuations.

REFERENCES

Alonso, E.E., Gens, A. and Josa, A. (1990). A constitutive model for partially saturated soils. *Géotechnique*. 40, 405-430. https://doi.org/10.1680/geot.1990.40.3.405.

Alonso, E.E., Lloret, A., Delahaye, C.H., Vaunat, J., Gens, A. and Volckaert, G. (1998). Coupled analysis of a backfill hydration test. *International Journal for numerical and analytical methods in Geomechanics*. 22, 1-27. https://doi.org/10.1002/(SICI)1096-9853(199801)22:1<1::AID-NAG906>3.0.CO;2-P.

Alonso, E.E., Vaunat, J. and Gens, A. (1999). Modelling the mechanical behaviour of expansive clays. *Engineering geology*. 54, 173-183. https://doi.org/10.1016/S0013-7952(99)00079-4.

Delahaye, C.H. and Alonso, E.E. (2002). Soil heterogeneity and preferential paths for gas migration. *Engineering geology*. 64, 251-271. https://doi.org/10.1016/S0013-7952(01)00104-1.

Gens, A., Vaunat, J., Garitte, B. and Wileveau, Y. (2007). In situ behaviour of a stiff layered clay subject to thermal loading: observations and interpretation. *Géotechnique*. 123-144. https://doi.org/10.1680/ssc.41080.0011.

Ghandilou, M.J., Tourchi, S. and Sadeghi, H. (2023a). Numerical Investigation of Cyclic Wetting and Drying of Boom Clay Based on the Barcelona Expansive Model. In *84th EAGE Annual Conference & Exhibition*.

No. 1, 1-5. https://doi.org/10.3997/2214-4609.202310400.

Ghandilou, M.J., Tourchi, S., Darzi, A.G. and Sadeghi, H. (2023b). Numerical modeling of volumetric behavior of unsaturated expansive soil under wetting and drying cycles. In *5th Iranian Conference on Geotechnical Engineering*. https://www.researchgate.net/publication/377265206.

Ghorbani, Z., Darzi, A. G., Sadeghi, H., & Garakani, A. A. (2023). Field reconnaissance and InSAR investigation of subsidence-induced damage to electricity dispatch centers–A case study in Tehran. In *Smart Geotechnics for Smart Societies* (pp. 1200-1203). CRC Press. https://doi.org/10.1201/9781003299127-171.

Guo, L., Chen, G., Ding, L., Zheng, L. and Gao, J. (2023). Numerical simulation of full desiccation process of clayey soils using an extended DDA model with soil suction consideration. *Computers and Geotechnics*. 153, p.105107. https://doi.org/10.1016/j.compgeo.2022.105107.

Hemmati, S., Gatmiri, B., Cui, Y.J., Vincent, M. (2012). Thermo-hydro-mechanical modelling of soil settlements induced by soil-vegetation-atmosphere interactions. *Engineering Geology*. 139, 1-6. https://doi.org/10.1016/j.enggeo.2012.04.003.

Jabbarzadeh, M., Sadeghi, H., Tourchi, S. and Darzi, A.G. (2023). Thermo-hydraulic analysis of desiccation cracked soil strata considering ground temperature and moisture dynamics under the influence of soil-atmosphere interactions. https://doi.org/10.31223/X58Q38.

Morris, P.H., Graham, J. and Williams, D.J. (1992). Cracking in drying soils. *Canadian Geotechnical Journal*. 29, 263-277. https://doi.org/10.1139/t92-030.

Ng, C. W. W., Baghbanrezvan, S., Sadeghi, H., Zhou, C., & Jafarzadeh, F. (2017). Effect of specimen preparation techniques on dynamic properties of unsaturated fine-grained soil at high suctions. *Canadian Geotechnical Journal*, 54(9), 1310-1319. https://doi.org/10.1139/cgj-2016-0531.

Ng, C. W. W., Sadeghi, H., & Jafarzadeh, F. (2017). Compression and shear strength characteristics of compacted loess at high suctions. *Canadian Geotechnical Journal*, 54(5), 690-699. https://doi.org/10.1139/cgj-2016-0347.

Olivella, S., Carrera, J., Gens, A. and Alonso, E.E. (1994). Nonisothermal multiphase flow of brine and gas through saline media. *Transport in porous media*. 15, 271-293. https://doi.org/10.1007/BF00613282.

Olivella, S., Gens, A., Carrera, J., Alonso, E.E. (1996). Numerical formulation for a simulator (CODE_BRIGHT) for the coupled analysis of saline media. *Engineering computations*. 13, 87-112. https://doi.org/10.1108/02644409610151575.

Sadeghi H. (2016). A micro-structural study on hydro-mechanical behavior of loess (*Doctoral dissertation, Hong Kong University of Science and Technology*). https://doi.org/10.14711/thesis-b1627816.

Sadeghi, H., Darzi, A. G., Voosoghi, B., Garakani, A. A., Ghorbani, Z., & Mojtahedi, S. F. F. (2023). Assessing the vulnerability of Iran to subsidence hazard using a hierarchical FUCOM-GIS framework. *Remote Sensing Applications: Society and Environment*, 31, 100989. https://doi.org/10.1016/j.rsase.2023.100989

Sadeghi, H., Ng, C.W.W. (2018). Shear behaviour of a desiccated loess with three different microstructures. In *The 7th international conference on unsaturated soils*. https://hdl.handle.net/1783.1/96575.

Sánchez, M., Gens, A., do Nascimento Guimarães, L. and Olivella, S. (2005). A double structure generalized plasticity model for expansive materials. *International Journal for numerical and analytical methods in geomechanics*. 29, 751-787. https://doi.org/10.1002/nag.434.

Sánchez, M., Manzoli, O.L. and Guimarães, L.J. (2014). Modeling 3-D desiccation soil crack networks using a mesh fragmentation technique. *Computers and Geotechnics*. 62, 27-39. https://doi.org/10.1016/j.compgeo.2014.06.009.

Tourchi, S., Jabbarzadeh, M., Sadeghi, H., Lavasan, A.A. (2024). Thermo-hydro-mechanical modelling of rock cliff-atmosphere interaction: the case of the Pozary test site in Czechia. In *EGU General Assembly Conference Abstracts.*

Wang, X., Yu, J., Li, Q., Yu, Y., & Lv, H. (2022). Study on the crack evolution process and stress redistribution near crack tip in soil. *International Journal of Geomechanics*, 22(1), 04021255. https://doi.org/10.1061/(ASCE)GM.1943-5622.0002236.

Wei, X., Hattab, M., Bompard, P. and Fleureau, J.M. (2016). Highlighting some mechanisms of crack formation and propagation in clays on drying path. *Géotechnique*. 66, 287-300. https://doi.org/10.1680/jgeot.14.P.227.

Yazdani, F., Sadeghi, H., AliPanahi, P., Gholami, M. and Leung, A.K. (2024). Evaluation of plant growth and spacing effects on bioengineered slopes subjected to rainfall. *Biogeotechnics*, p.100080. https://doi.org/10.1016/j.bgtech.2024.100080.

Proceedings of the XVIII ECSMGE 2024
GEOTECHNICAL ENGINEERING CHALLENGES
TO MEET CURRENT AND EMERGING NEEDS OF SOCIETY
© 2024 the Authors
ISBN 978-1-032-54816-6
DOI 10.1201/9781003431749-250
Open Access: www.taylorfrancis.com, CC BY-NC-ND 4.0 license

ECSMGE 24
XVIII EUROPEAN CONFERENCE ON SOIL MECHANICS AND GEOTECHNICAL ENGINEERING

Prediction of water content under climatic actions. A method based on spectral analysis and soil transfer functions

Prédiction de la teneur en eau sous actions climatiques. Une méthode basée sur l'analyse spectrale et les fonctions de transfert du sol

Y.F. Vargas-Alzate*, J. Vaunat, A.M. Zapata-Franco
Universitat Politècnica de Catalunya, BarcelonaTech (UPC)/International Centre for Numerical Methods in Engineering (CIMNE), Barcelona, Spain

A. Di Mariano
International Centre for Numerical Methods in Engineering (CIMNE)/Universitat Politècnica de Catalunya · BarcelonaTech (UPC), Barcelona, Spain

**yeudy.felipe.vargas@upc.edu*

ABSTRACT: Changes in water content and suction under climatic actions is one important process in several geotechnical issues, such as earth-structures deformation, foundation heave/settlement or slope failures seated in the vadose zone. In addition, under certain conditions, these changes may act as a forcing condition for the underlying saturated water column and control cyclic pore pressure changes at higher depths. The deterministic modelling of these effects requires considering soil-atmosphere thermo-hydro-mechanical interactions under long time high-frequency series. Associated computational cost appears quickly to be a limitation to this type of simulations, particularly when going to large geometry or regional analyses.This article shows two strategies to estimate the soil hydraulic response in time under climatic series handled by Fourier decomposition. These strategies present similarities with techniques used to analyse soil response under seismic actions and propose to define soil transfer functions relating the input (climatic time series) to the output (water content or suction/pore pressure variation at several depths).

RÉSUMÉ: Les changements dans la teneur en eau et la succion sous les actions climatiques sont un processus important dans plusieurs problèmes géotechniques, tels que la déformation des structures en terre, le soulèvement/affaissement des fondations ou les ruptures de pente situées dans la zone vadose. De plus, dans certaines conditions, ces changements peuvent agir comme une condition de forçage pour la colonne d'eau saturée sous-jacente et contrôler les changements cycliques de pression interstitielle à des profondeurs plus élevées. La modélisation déterministe de ces effets nécessite de considérer les interactions thermo-hydro-mécaniques sol-atmosphère dans des séries longues et hautes fréquences. Le coût de calcul associé apparaît rapidement comme une limitation à ce type de simulations, notamment lorsqu'il s'agit de grandes géométries ou d'analyses régionales. Cet article présente deux stratégies pour estimer la réponse hydraulique du sol dans le temps sous des séries climatiques traitées par décomposition de Fourier. Ces stratégies présentent des similitudes avec les techniques utilisées pour analyser la réponse des sols sous actions sismiques et proposent de définir des fonctions de transfert du sol reliant l'entrée (séries temporelles climatiques) à la sortie (teneur en eau ou variation de succion/pression interstitielle à plusieurs profondeurs).

Keywords: Water content, Fourier Transformation, Climatic variables, Soil properties.

1 INTRODUCTION

Expected scenarios of climate change point to a modification of the Intensity-Duration-Frequency curves (IDR) of precipitations, in which long periods of dryness will be suddenly interrupted by very intensive rainfalls (Heidari et al. 2020). This extreme phenomenon would rapidly increase the water content within a dry soil mass, leading to major failure probabilities. Modification of IDR may also play a significant role in earthquake-induced soil phenomena such as liquefaction and seismic slope stability (Keefer, 2002; Roback et al., 2018). Accounting for such effects requires estimation of water pressures or water contents within soil masses, under the whole climatic histogram.

Variations of pore pressures or water contents are governed by the mass balance of water, which results mathematically in a convection-diffusion equation. Under climatic actions, it is moreover coupled with the heat equation to model water phase changes and evaporation. These equations describe various diffusion processes of water, vapour and heat in porous

media (Stępniewski et al. 2011), which translate into an attenuation and shift of phase at the depth of surface fluctuations. Under simplifying assumptions, they can be reduced to a system of two diffusion equations that can be solved using classical techniques, avoiding direct-integration schemes (Canuto et al., 2007). For instance, spectral methods by mode decomposition, potentially involving the use of the Fast Fourier Transform (FFT, Cooley and Tukey, 1965). These techniques can be used to reduce the order of the problem by assessing, in the frequency domain, problems unmanageable within the limit of the current computational capacity (long time-periods – predictions under climate change – and large areas – city, hydrological basins). They also present the advantage of handling input defined as a frequency spectrum, avoiding working with time series of climate change scenarios.

Reduction of the computational cost by suppression of the time dimension allows to develop a computational framework to estimate the probability of occurrence of water pressure/water content above thresholds related to soil failure, for a prescribed spectrum of climatic variables. Moreover, computational effort reduction allows considering uncertainties involved, for instance, in the soil mechanical properties, acting loads, climate-related variables, etc.

This article examines two approaches to develop reduced order models capable to predict the evolution of water content in soils, denoted as θ, with time. The first approach is based on the development of transfer functions between climatic variables and θ. These functions are obtained as the ratio between the Fourier amplitude spectra of both θ and the climatic variables. The second approach has been oriented to study the capabilities to predict θ by means of a parametric transfer function. The latter has been developed by considering specific boundary conditions in terms of flux.

2 CLIMATIC VARIABLES AND WATER CONTENT IN THE SOIL

Records of a monitoring campaign carried out in an upper horizontal soil layer during seven years (max. depth 1 m, Calvet et al., 1999) have been analysed. They contain the time-history evolution of the soil water content at several depths. In addition, a series of climatic variables of the area have also been recorded.

2.1 Water content in the soil

Figure 1 shows the time evolution of θ with depth, in the analysed soil profile. Specifically, θ has been recorded at ten depths, the shallowest being at 5 cm from the surface whilst the deepest is at 95 cm.

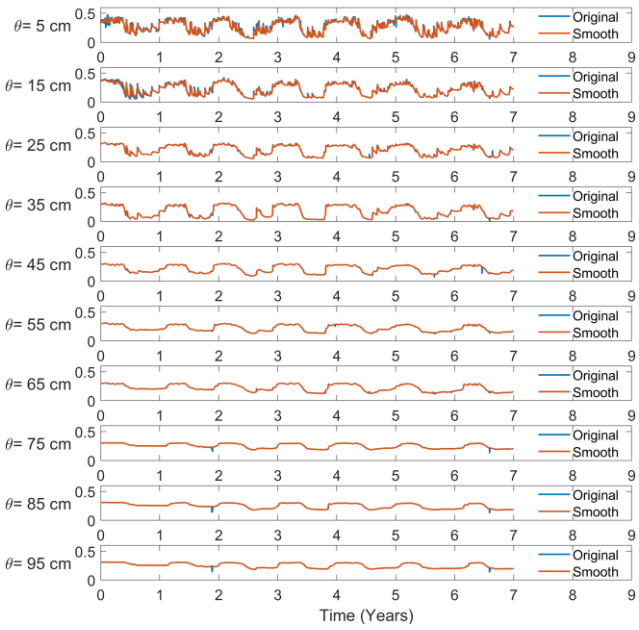

Figure 1. Water content in soils.

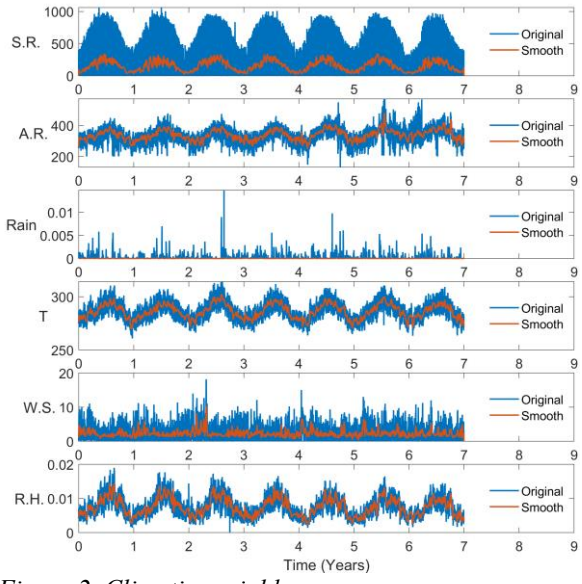

Figure 2. Climatic variables.

Due to some problems with the recording devices, some gaps in the data have been observed. They have been interpolated using a smooth function around a given data gap.

2.2 Climatic variables

Data on solar and atmospheric radiation (S.R. and A.R., respectively), rainfall intensity, temperature (T), wind speed (W.S.) and relative humidity (R.H.) have been collected in the aforementioned campaign (Climate-related variables); Figure 2 shows the time-history evolution of them. This figure also shows data

smoothing to analyse how the mean evolves over time. Data smoothing has not been applied to the time-history climate data.

3 TRANSFER FUNCTION ANALYSIS

The previous records can be seen as input (Climatic variables) and output variables (water contents at depth), namely I/O variables. Based on this perspective, these records have been used to develop TFs capable of making forecasts considering climatic variables as input. These transfer functions have been obtained as ratios between the Fourier's transform of the recorded I/O variables. Specifically, this approach seeks to characterize θ from a transfer function, *TF*. This function is obtained by considering the Fast Fourier transform (FFT) of θ and the Fast Fourier transform of a single climatic variable. The following equation shows the mathematical form that characterizes a *TF*:

$$TF_{i,j}(\omega) = \frac{f_{i,j}(\omega)}{g_j(\omega)} \quad (1)$$

where $f_{i,j}(\omega)$ is the Fourier amplitude spectrum of θ_i; $g_j(\omega)$ is the Fourier amplitude spectrum of the climatic variable g; subscripts i and j stand for a specific depth and a given climatic variable, respectively. The main hypothesis is that, given the time history of θ and a specific climatic variable, g_j, the *TF* obtained through Equation (1) can be used to approximate the Fast Fourier Transform of the Soil Response Parameter (SPR) to another record, g_k:

$$f_{i,k}(\omega) \approx TF_{i,j}(\omega) * g_k(\omega) \quad (2)$$

To validate this approach, the recorded data have been divided into two subsets: $(f_{i,j},g_j)$ and $(f_{i,k},g_k)$. The first one is used to develop the *TFs* whilst the second to evaluate the consistency of the results. It is worth mentioning that both subsets have data for 3 years. The seventh year has not been considered in the analysis to ensure balance between learning and validation time periods while maintaining signal stationarity.

The efficiency of a variable to predict the dynamic response of a system, using a transfer function, depends on the correlation between both (the variable and the response of the system). Therefore, at a first stage, the causality between I/O variables was evaluated. Specifically, a series of correlation analyses were performed to identify the variables that most influence the prediction of θ (Wagener and Pianosi, 2019). First, the bivariate distribution between pairs of I/O variables was studied. The efficiency (predictive capacity) of the input variables was measured in terms of the coefficient of determination, R^2. As a product of this analysis, a ranking based on the efficiency of the input variables was performed. Table 1 presents the R^2 values between I/O variables. The data show that T and R.H. have a strong correlation with θ, which emphasizes the main role of evaporation in water content changes at that site.

Table 1. R^2 between climatic variables and water content.

Z (cm)	S.R.	A.R.	Rain	T	W.S.	R.H.
5	-0.18	-0.44	0.07	-0.58	0.07	-0.55
15	-0.15	-0.45	0.05	-0.55	0.11	-0.54
25	-0.14	-0.45	0.04	-0.55	0.10	-0.55
35	-0.12	-0.45	0.03	-0.53	0.11	-0.55
45	-0.11	-0.44	0.03	-0.51	0.11	-0.53
55	-0.07	-0.39	0.02	-0.43	0.11	-0.44
65	-0.04	-0.36	0.03	-0.37	0.11	-0.37
75	0.02	-0.27	0.02	-0.25	0.11	-0.25
85	0.01	-0.29	0.02	-0.27	0.09	-0.26
95	0.04	-0.23	0.02	-0.18	0.11	-0.18
Mean	**-0.07**	**-0.38**	**0.03**	**-0.42**	**0.10**	**-0.42**

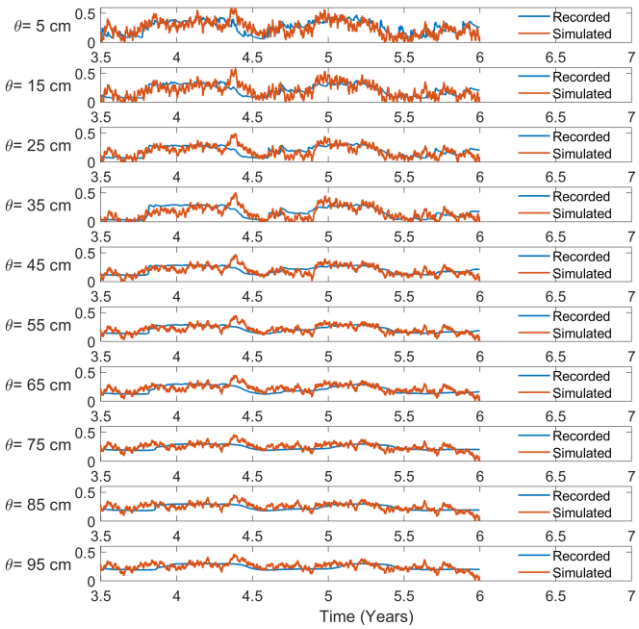

Figure 3. SRP's prediction by using TFs.

Based on the results presented in Table 1 and employing the first approach, a prediction of θ was performed and T was used to develop the transfer functions. Figure 3 shows the obtained results. There is good agreement between predicted and recorded data in terms of maximum values for all the analysed depths. Simulated data of θ show high frequency fluctuations which are not observed in recorded data.

4 PARAMETRIC TRANSFER FUNCTION

Another approach to predict θ by means of spectral methods is to develop a parametric transfer function. To do so, special boundary conditions need to be considered. In this case, the flux ($\frac{d\theta}{dt}$) at a given depth, L'_z, was set at zero and the θ value recorded at a depth of 5 cm was imposed at the surface (See Figure 1, top). In this manner, the analytical solution of the diffusion equation provides the expression of θ at depth z:

$$\theta = \delta_i * A_i \sum_{i=1}^{n} \sin(\omega_i t + \alpha_i * (z - L'_z) + \varphi_i + \frac{\pi}{2}) \quad (3)$$

where $\delta_i = \frac{e^{\alpha_i z} - e^{-\alpha_i z}}{e^{\alpha_i L'_z} - e^{-\alpha_i L'_z}}$; $\alpha_i = \sqrt{\frac{\omega_i}{2\kappa}}$; k is the diffusion coefficient, in a mathematical sense; A_i and φ_i are the amplitude and the phase of the harmonic with frequency ω_i, extracted from the Fourier's amplitude spectrum, respectively; $\bar{\theta}$ is the mean of the water content during the period taken into account.

Equation (3) has allowed estimating, at all the depths, the pair (κ, L'_z) that minimizes the mean square error (MSE) with respect to the recorded data. This was achieved by means of the Monte Carlo method. It is worth mentioning that the estimation provided by Equation 3 depends on the number of harmonics. Thus, the Monte Carlo minimization was performed using 100 harmonics. Figure 4 shows the evolution of the MSE as a function of κ and L'_z.

-3-3

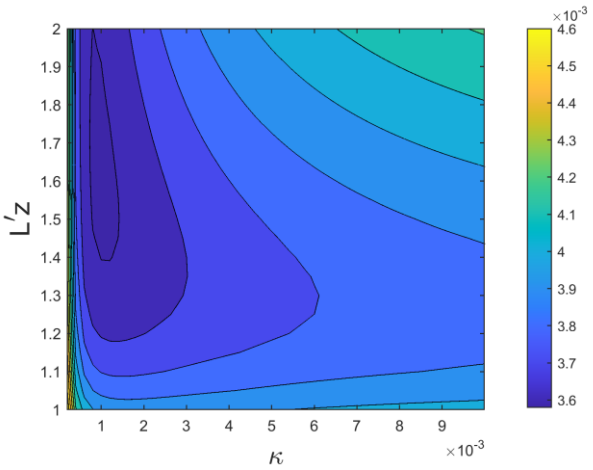

Figure 4. MSE as a function of κ and L'_z.

From Figure 4, it can be inferred that the optimal pair (κ, L'_z) is κ= 0.001 and L'_z= 1.6 m. By using these values, θ has been estimated for all depths; Figure 5 shows a comparison of both simulated and recorded data, using 100 harmonics in Equation 3. Simulated and recorded data are in good agreement for all depths. Simulated results do reproduce well both the attenuation with depth of the water change amplitudes and the disappearance of the higher frequency modes. This is consistent with the characteristics of the diffusion equation underlying the infiltration/ evaporation process and indicates that the sensitivity of water content changes to atmospheric fluctuations decays with depth.

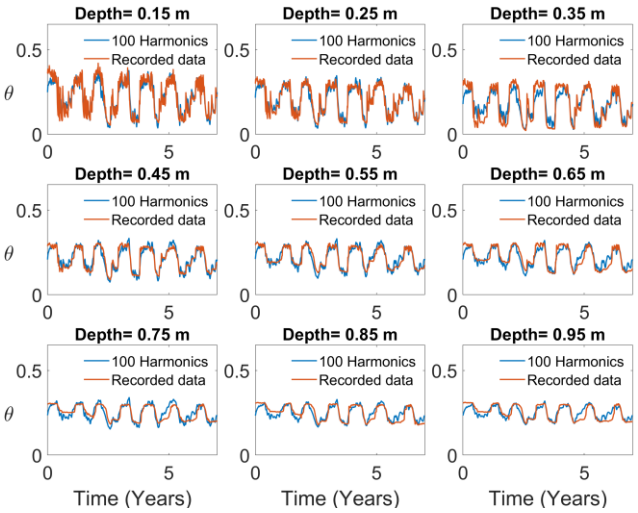

Figure 5. θ prediction considering 100 harmonics.

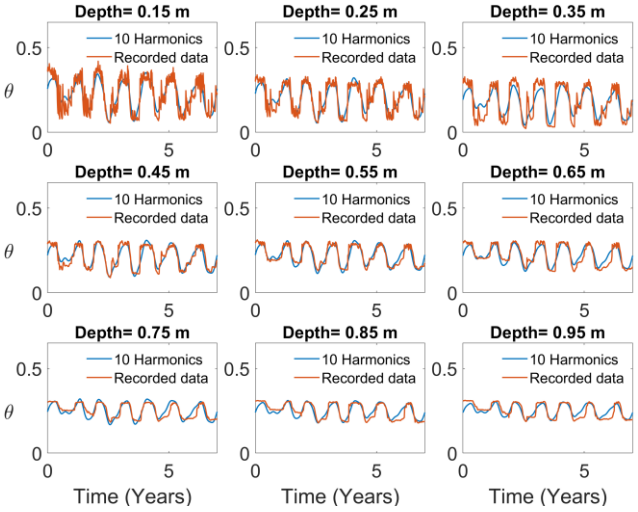

Figure 6. θ prediction considering 10 harmonics.

To study possible reduction of the computational cost, another analysis was conducted using the same pair (κ, L'_z) that minimizes the MSE and considering only the 10 harmonics (Figure 6) provided with the higher amplitudes. The agreement between simulated and recorded data is similar to the one observed for the analysis with 100 harmonics. This provides information about the most relevant modes to be used in future predictions of water content under climatic actions, at this site. The number of harmonics to be used decreases with depth as the result of the

attenuation of the fluctuations of higher frequencies with the distance to atmospheric boundary conditions.

5 CONCLUSIONS

This article presents two approaches based on spectral methods, for estimating soil water contents at different depths. The attractiveness of both methods relies mostly on the reduction of computational times. Data from a monitoring campaign carried out in an upper horizontal soil layer (max. depth 1 m, Calvet et al., 1999) were considered. These records implicitly contain information on the interaction of complex physical processes that trigger highly random variability. They provide an opportunity to conduct causality studies aimed at analysing which climate variables (input) have the highest explanatory capacity to predict soil water content, θ (output variable).

In the first approach, transfer functions connecting variables that influence climate (Solar and atmospheric radiation, rainfall intensity, temperature, wind speed, atmospheric pressure and relative humidity) and θ at several depths were operated. Data show that temperature and relative humidity are the atmospheric variables with the highest predictive capacity of θ. The correlation between these climatic variables and θ can increase if a multi-regression model composed of sub-groups of climatic variables is employed (See Vargas-Alzate et al., 2022). One of the main shortcomings of the first approach is that simulated data tend to fluctuate more than recorded series, over short time periods. However, these fluctuations can be mitigated if filters that act on the resulting signals are considered. Future research should be conducted to this end.

With regard to the second approach, a deterministic transfer function was employed, based on specific boundary conditions. Predictions based on this method are better than those based on the first approach, provided that parameters are previously estimated by back-analysis on sub-sets of data series. As depth increases, it is possible to consider fewer harmonics than close to the soil surface. Estimating the optimal number of harmonics as a function of depth would help improving the model efficiency. The use of a specific parameter that varies with depth would help addressing the intrinsic non-linearity of the diffusion coefficient.

ACKNOWLEDGEMENTS

This research has been funded by the Spanish Research Agency (AEI) through the project with reference: TED2021-132559B-I00 – J-02970.

REFERENCES

Calvet J.-C., P. Bessemoulin, J. Noilhan, C. Berne, I. Braud, D. Courault, N. Fritz, E. Gonzalez-Sosa, J.-P. Goutorbe, R. Haverkamp, G. Jaubert, L. Kergoat, G. Lachaud, J.P. Laurent, P. Mordelet, A. Olioso, P. Péris, J.L. Roujean, J.-l. Thony, C. Tosca, M. Vauclin and D. Vignes, 1999: Murex: a land surface field experiment to study the annual cycle of the energy and water budgets. Ann. Geophys., 17, 838-854. https://doi.org/10.1007/s00585-999-0838-2.

Canuto, C., Hussaini, M. Y., Quarteroni, A., and Zang, T. A. (2007). Spectral methods: evolution to complex geometries and applications to fluid dynamics. Springer Science & Business Media.

Cooley, J. W., and Tukey, J. W. (1965). An algorithm for the machine calculation of complex Fourier series. Mathematics of computation, 19(90), 297-301.

Heidari, H., Arabi, M., Ghanbari, M., and Warziniack, T. (2020). A probabilistic approach for characterization of sub-annual socioeconomic drought intensity-duration-frequency (IDF) relationships in a changing environment. Water, 12(6), 1522. https://doi.org/10.1023/A:1021274710840.

Keefer, D. K. (2002). Investigating landslides caused by earthquakes–a historical review. Surveys in Geophysics, 23(6), 473-510. https://doi.org/10.1023/A:1021274710840.

Roback, K., Clark, M. K., West, A. J., Zekkos, D., Li, G., Gallen, S. F., and Godt, J. W. (2018). The size, distribution, and mobility of landslides caused by the 2015 Mw7. 8 Gorkha earthquake, Nepal. Geomorphology, 301, 121-138. https://doi.org/10.1016/j.geomorph.2017.01.030.

Stępniewski W., Sobczuk H. and Widomski M. (2011) Diffusion in Soils. In: Gliński J., Horabik J., Lipiec J. (eds) Encyclopedia of Agrophysics. Encyclopedia of Earth Sciences Series. Springer, Dordrecht. https://doi.org/10.1007/978-90-481-3585-1_273.

Vargas-Alzate, Y. F., Hurtado, J. E., and Pujades, L. G. (2021). New insights into the relationship between seismic intensity measures and nonlinear structural response. Bull Earthquake Eng. 20, 2329–2365. https://doi.org/10.1007/s10518-021-01283-x.

Wagener, T., and Pianosi, F. (2019). What has Global Sensitivity Analysis ever done for us? A systematic review to support scientific advancement and to inform policy-making in earth system modelling. Earth-science reviews, 194, 1-18. https://doi.org/10.1016/j.earscirev.2019.04.006.

Proceedings of the XVIII ECSMGE 2024
GEOTECHNICAL ENGINEERING CHALLENGES
TO MEET CURRENT AND EMERGING NEEDS OF SOCIETY
© 2024 the Authors
ISBN 978-1-032-54816-6
DOI 10.1201/9781003431749-251
Open Access: www.taylorfrancis.com, CC BY-NC-ND 4.0 license

ECSMGE 24
XVIII EUROPEAN CONFERENCE ON SOIL MECHANICS AND GEOTECHNICAL ENGINEERING

Managing uncertainties in the geotechnical design of climate change resilient infrastructures

Gérer les incertitudes dans la conception géotechnique d'ouvrages résilientes au changement climatique

P. Vitale*, Z.Q. Liu
Norwegian Geotechnical Institute, Oslo, Norway
**patrizia.vitale@ngi.no*

ABSTRACT: The design of geotechnical infrastructures is the outcome of a qualitative interpolation of a series of factors, from the feasibility study to the final design phase. It is good practice to start the geotechnical assessment from the geo-morphological data available at the studied area. This is combined afterwards with available information from surrounding projects, additional geotechnical investigations and professional experience. The overall outline of the design is provided by technical standards, other than by the needs of customers and society. One of the challenges that the geotechnical engineer encounters during the design is to find the correct balance between those decision factors, especially in areas where the risk for geohazards may be relevant both for the project itself and for the socio-economic development of the area. Furthermore, it is more and more acknowledged that uncertainties in geotechnical design also need to be addressed in relation to the impact of climate change on structures. This paper presents an overview of the current climate change adaptation strategies for geo-structures in Europe, highlighting the need for scientific research for the implementation of methodologies centred on geotechnical engineering practice and design. Hence, it invites to discuss at a more practical level about the future needs for conceiving geotechnical infrastructures resilient to the effects of climate change.

RÉSUMÉ: La conception des infrastructures géotechniques est le résultat d'une interpolation qualitative d'une série de facteurs, depuis l'étude de faisabilité jusqu'à la phase de conception finale. Il est de bonne pratique de démarrer l'évaluation géotechnique à partir des données géomorphologiques disponibles dans la zone étudiée. Ceci est ensuite combiné avec les informations disponibles sur les projets environnants, des enquêtes géotechniques supplémentaires et l'expérience professionnelle. Le cadre de la conception est défini par des normes techniques, autres que par les besoins des clients et de la société. L'un des défis de l'ingénieur géotechnique est de trouver le bon équilibre entre ces facteurs de décision, en particulier dans les zones où les géorisques peuvent être pertinents à la fois pour le projet lui-même et pour le développement socio-économique de la zone. Ensuite, il est de plus en plus évident que les incertitudes dans la conception géotechnique doivent également être prises en compte en ce qui concerne l'impact du changement climatique sur les structures. Cet article présente un aperçu sur les actuelles stratégies d'adaptation au changement climatique pour les géostructures en Europe, en soulignant le besoin de faire de la recherche pour la mise en œuvre de méthodologies centrées sur la pratique et la conception géotechnique. Ainsi, il invite à discuter des besoins futurs pour concevoir des infrastructures géotechniques résilientes aux effets du changement climatique.

Keywords: Climate change adaptation; reliability; sustainability; uncertainties; geotechnical design.

1 INTRODUCTION

Climate change is the greatest global health threat facing humanity in the 21st century, as stated by the World Health Organization in Health and Climate Change (2018). The European Commission has committed to be climate-neutral by 2050, by establishing a set of measures through the European Green Deal (2019) and in line with the long-term strategies in the Paris Agreement (2015). The European Commission adopted its new strategy to become climate resilient by 2050 in the EU Climate Adaptation Strategy (2021).

Despite the international commitment to cut net global emissions to zero by 2050, average global temperature will increase because of a raising concentration of greenhouse gas emissions in the atmosphere and governments are challenged to limiting the global temperature rise to 1.5°C (International Energy Agency, 2021). In this context, the outlined decarbonization roadmap needs to be addressed faster and with more efficient solutions.

Climate change signals (i.e., a general increase in temperature and a changing precipitation pattern) have been observed in Europe, with a different degree of

impact on geo-structures throughout the region (Insana et al., 2021; IPCC, 2023). To deal with the changing frequencies and intensities of environmental hazards induced by climate change, geotechnical engineers need to rationally consider climate change when designing a new structure. However, it remains a challenge to assess and quantify the impact of climate change on geo-structures. In this view, reliability and risk-based approaches that account for uncertainties in climatic loads and soil strengths are useful tools for engineering recommendations and final decisions.

This paper provides a panoramic of the alternative strategies and methodologies to tackle climate change effects on geo-structures. Relying on a "factor of safety" design approach and conservative assumptions (especially when in lack of geotechnical and environmental data) is not considered a viable way in the actual environmental situation. Thus, this short review aims at enhancing the discussion on the future needs of the industry to design climate change resilient geotechnical infrastructures.

2 CLIMATE CHANGE ADAPTATION OF GEO-STRUCTURES

2.1 Causal chain mapping of climate change impacts on geotechnical infrastructures

Concern for environmental issues in Europe arose in the second half of the 19th century, when people became more and more aware of environmental pollution and damages to nature following the Industrial Revolution. This is also the background of the first United Nations Conference on the Human Environment, held in Stockholm in 1972 (UN Chronicle, 2007). Protecting ecological integrity became the core of the discussion and, hence, economic and social development happened to be constrained by environmental limits. This led to the concept of sustainable development and, hence, to environmental sustainability (Our Common Future, 1987, From One Earth to One World §I-3 and Part I §2-I). The latter was, then, defined as the ability to maintain an ecological balance in our planet's natural environment and conserve natural resources to support the wellbeing of current and future generations (Our Common Future, 1987; Paris Agreement, 2015).

Insana et al. (2021) presented an overview of research and literature review studies conducted in the last three decades on climate change impact on geo-structures. Their research shows that, in Europe and in most parts of the world, the concern is mostly focused on natural and engineered slopes, and far outnumbers those dealing with geo-structures. However, the concern over the impact of climate change on onshore geotechnical infrastructures has been rising in the last decade, especially in Europe. This is shown in the analysis carried out by Gariano et al. (2016) and updated by Insana et al. (2021). Geoscientists and engineers are analysing and mapping the causal chain of climate change impacts on geo-structures.

An in-depth study was conducted by Insana et. al. (2021) with regards to European regions. The research shows how climate change signals can have multiple effects on geotechnical and geological properties. Hence, the instability of slopes is just the visible output of a series of processes in the ground, groundwater, and vegetation, which leads to soil properties degradation. The survey conducted in this research shows that the most relevant impacts of climate change for geo-structures in Europe are the following: instability of natural and engineered slopes, damage/failure of engineered structures from flooding, and overtopping/breaching of dikes and levees.

There are many climate change features that have been identified in the context of climate change scenarios. Vardon (2015) and Vahedifard et al. (2016) provide an overview of climate change impacts on geotechnical infrastructures.

2.2 Climate change adaptation strategies related to geo-structures

Strategic documents on climate change adaptation (CCA), such as national adaptation plans (NAPs) and related action plans, have been initiated and drafted by most of the countries all over the world, as recommended in COP 16 (Conference of the Parties to the United Nations Framework Convention on Climate Change at its 16th Session, 2021). NAPs and related actions drafted by European countries are aligned one to another, and they refer to CCA of geo-structures with regards to damages of infrastructures (roads and rails) as a cause of instability of slopes, soil erosion, soil subsidence, and flooding. However, as highlighted by Insana et. al. (2021), specific strategies for geotechnical CCA are lacking. Put differently, strategies developed for adaptation of geo-structures are not centred on geotechnical engineering practice and design, but more on the consequences of climate change on natural hazards.

In the actual context of climate change, risk assessment and monitoring have become the most common adaptation strategies. In this regard, early warning systems, hazard and vulnerability mapping, and improved drainage are common management tools for climate change associated risks (Insana et al., 2021; IPCC, 2023). The implementation of these strategies is

mainly in relation to slope stability (Insana et al., 2021).

In the future, it is crucial to give attention also to other geo-structures, while enhancing slope stability. In this context, other measures such as reliability theory and probabilistic approach, adaptation of technical standards for the design of geotechnical infrastructures, the observational method and pre-mortem analyses, need to be assessed and implemented further in daily engineering practice.

3 THE EFFECT OF UNCERTAINTIES ON THE PERCEIVED FACTOR OF SAFETY

3.1 Uncertainties in design from climate change

The question that the geotechnical engineer needs to address during the design is how safe the structure is under the applied loads and given the assessed geotechnical conditions. Furthermore, the geotechnical assessment needs to include the impact of climate change on all loads and geotechnical factors.

As a response to a changing climate, it is necessary to adapt the geotechnical design to the mutation of uncertainties associated with a geotechnical problem. The uncertainties identified in the prediction of the response of geo-structures (i.e., spatial variation, limited site exploration and observation, soil parameters, various testing methods, loads, calculation model) need to be re-assessed in terms of altered environmental load and remodeled soil parameters due to climate change (i.e., soil drying, soil suction, soil dessication, soil erosion and flooding, soil saturation).

The upcoming second generation of Eurocodes may respond to some extension to such imminent demand.

3.2 Safety factor and reliability-based design

The factor of safety is a deterministic approach to a safety assessment, and it embodies a quantification of the margin of safety (M). As elaborated by Lacasse et al. (2019), the uncertainty in the safety margin can be addressed as a spectrum of failure probabilities (P_f). The risk analysed in a safety assessment will never be zero, because there will always be a certain level of uncertainty (i.e., a finite probability that a failure may occur). Silva et al. (2008) summarised in a diagram the correlation between safety factor and failure probability, based on experience, engineering judgement and historical statistics. One of the take-aways of the diagram is that for a certain factor of safety there is a wide range of perceived failure probability, depending on the uncertainties in the analysis. Lacasse et al. (2019) shows well this concept for slope stability issues in *Figure 1*.

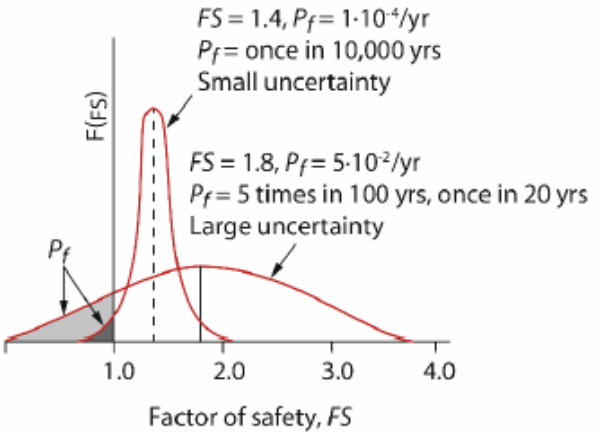

Figure 1. Variation of the safety factor of a slope with regards to failure probability (Lacasse et al., 2019).

A reliability-based approach accounts for the uncertainties in the analysis and their correlation, hence leading to a more rational assessment of safety of geotechnical structures. Such approach should, therefore, be used as a complement to the deterministic analysis, to provide a more robust design (Lacasse et al., 1998, 2019).

A simplification of the full reliability-based design is given through the LRFD (load and resistance factor design) approach. The partial safety factors in the LRFD approach reflect the uncertainty encountered in the design. The partial safety factors can also be calibrated such that a targeted safety level is ensured for determined levels of uncertainty in the geotechnical problem. However, uncertainties may be different from those assumed in the calibration phase, especially in the current environmental context. So, it is fundamental to couple such approach with a full reliability analysis using a target reliability index, to improve resilience to climate change effects in geotechnical design. Several examples of application of the reliability approach to actual case studies on- and off- shore are described by Farrokh (2017).

4 CONCLUSIONS

This short review shows that there is an increasing need for adapting the geotechnical design of geo-structures to the effects of climate change.

Our planet is undergoing an environmental adaptation to climate change. This process is happening fast, and it is affecting geotechnical infrastructures. It is difficult for geotechnical engineers to quantify such uncertainties and to take them into account in the design phase.

The interest for implementing efficient strategies to tackle climate change effects on geo-structures is increasing in Europe.

There are many different strategies which are assessed and developed in the European region (i.e., adaptation of technical standards, implementation of monitoring systems and of the observational method, implementation of reliability-based methodologies). The main challenge that geotechnical engineers face nowadays is how to combine those strategies and tools into practical solutions for a sustainable and climate change resilient design. Furthermore, such difficult task needs to be contextualized in interdisciplinary projects and with a holistic approach to design. In the future, there is the need to increase the connection between research and practice in geotechnical engineering for a climate change resilient design.

ACKNOWLEDGEMENTS

The authors would like to express their sincere gratitude to main contributors and mentors S. Lacasse, S. Feizi and J. Langford. We also acknowledge the support from NGI for making this work possible.

REFERENCES

European Commission (2019). The European Green Deal. Available at: The European Green Deal.

European Commission (2021). EU Adaptation Strategy. Available at: EU Adaptation Strategy.

Farrokh, N. (2017). Suzanne Lacasse Lecture: Reliability-based approach for robust geotechnical design. *Proceedings of the XIX ICSMGE, Seoul, South Korea*. Available at: Suzanne Lacasse Lecture | ISSMGE.

Gariano, S.L. and Guzzetti, F. (2016). Landslides in a Changing Climate. *Earth-Science Reviews*. 162. 10.1016/j.earscirev.2016.08.011.

Insana, A., Beroya-Eitner, M.A., Barla, M., Zachert, H., Žlender, B., van Marle, M., Kalsnes, B., Bračko, T., Pereira, C., Prodan, I., et al. Climate Change Adaptation of Geo-Structures in Europe: Emerging Issues and Future Steps. *Geosciences*, 2021, 11(12):488. https://doi.org/10.3390/geosciences11120488.

International Energy Agency (2021). Net zero by 2050, report. Available at: Net Zero by 2050 | IEA

Intergovernmental Panel on Climate Change (IPCC). Climate Change 2023: Synthesis Report. *Contribution of Working Groups I, II and III to the Sixth Assessment Report of the Intergovernmental Panel on Climate Change, Geneva, Switzerland*, 184 pp. 10.59327/IPCC/AR6-9789291691647.

Lacasse, S. and Nadim, F. (1998). Risk and reliability in geotechnical engineering. *Proceedings of the Fourth International Conference of Case Histories in Geotechnical Engineering*. 11. Missouri. Available at: https://scholarsmine.mst.edu/icchge/.

Lacasse, S., Nadim, F., Liu, Z.Q., Eidsvig, U.K., Le, T.M.H. and Lin, C.G. (2019). Risk assessment and dams – Recent developments and applications. *Proceedings of the XVII ECSMGE, Reykjavík, Iceland.* 10.32075/17ECSMGE-2019.

Silva, F., Lambe, W. and Marr, W.A. (2008). Probability and Risk of Slope Failure. *Journal of Geotechnical and Geoenvironmental Engineering*. 134. 1691. https://doi.org/10.1061/.

United Nations (2007). UN Chronicle: From Stockholm to Kyoto: A Brief History of Climate Change. Available at: UN Chronicle 2007 | UN.

United Nations (2015). Climate action - Paris Agreement. Available at: The Paris Agreement | UN.

United Nations (2021). Conference of the Parties (COP) to the United Nations Framework Convention on Climate Change at its 16th Session. Available at: COP21 | UNFCCC.

United Nations General Assembly (1987). Report of the World Commission on Environment and Development: Our Common Future. Transmitted to the General Assembly as an Annex to document A/42/427 – Development and International Co-operation: Environment. Oxford University Press. p. 27. Available at: Our common future | UN.

Vahedifard, F., Robinson, J. D., & AghaKouchak, A. (2016). Can protracted drought undermine the structural integrity of California's earthen levees?. *Journal of Geotechnical and Geoenvironmental Engineering*. 142(6). 10.1061/(ASCE)GT.1943-5606.0001465.

Vardon, P. J. (2015). Climatic influence on geotechnical infrastructure: a review. *Environmental Geotechnics*, 2(3), 166-174. 10.1680/envgeo.13.00055.

World Health Organization (2018). Health and Climate Change. Available at: Health and climate change | WHO.

Proceedings of the XVIII ECSMGE 2024
GEOTECHNICAL ENGINEERING CHALLENGES
TO MEET CURRENT AND EMERGING NEEDS OF SOCIETY
© 2024 the Authors
ISBN 978-1-032-54816-6
DOI 10.1201/9781003431749-252
Open Access: www.taylorfrancis.com, CC BY-NC-ND 4.0 license

ECSMGE 24
XVIII EUROPEAN CONFERENCE ON SOIL MECHANICS AND GEOTECHNICAL ENGINEERING

Shear strength of sand under different range of confining stresses using various shearing devices

Résistance au cisaillement du sable sous différentes plages de contraintes de confinement à l'aide de divers dispositifs de cisaillement

M. Vivoda Prodan*, J. Peranić, V. Jagodnik, D. Marušić, D. Štiberc, N. Kamenar, Ž. Arbanas
Faculty of Civil Engineering University of Rijeka, Rijeka, Croatia

**martina.vivoda@gradri.uniri.hr*

ABSTRACT: Small-scale slope modelling is being conducted at the Faculty of Civil Engineering, University of Rijeka, to investigate various aspects of landslides triggered by rainfall, such as effects of initial soil moisture and soil hydraulic properties, the characteristics and patterns of rainfall on the hydro-mechanical response of slopes, and the physical processes and mechanisms driving the initiation and propagation of rainfall-induced landslides, as well as the effectiveness of various remediation measures. Understanding the test results of the physical slope model requires, among others, knowledge of the shear strength properties of the soil(s) forming the model. This study comprises a series of laboratory tests to investigate the shear strength of clean sand used as a base soil material for the construction of slope models. A series of laboratory shear tests were performed using conventional direct shear, triaxial and ring shear devices under a wide range of confining stresses, including low confining stresses typically present in 1g model tests. The strain-controlled tests were performed on sand samples installed at the same density conditions representative to the sand material used in the small-scale slope physical models and under stress conditions representative in small-scale and real slopes.

RÉSUMÉ: Une modélisation des pentes à petite échelle est actuellement menée à la Faculté de génie civil de l'Université de Rijeka pour étudier divers aspects des glissements de terrain déclenchés par les précipitations, tels que l'effet de l'humidité initiale du sol et de ses propriétés hydrauliques, les caractéristiques et les régimes des précipitations sur le sol, la réponse hydromécanique des pentes et, les processus, les mécanismes physiques à l'origine de l'initiation et de la propagation des glissements de terrain induits par les précipitations, ainsi que l'efficacité des diverses mesures d'assainissement. Comprendre les résultats des tests du modèle physique de pente nécessite, entre autres, la connaissance des propriétés de résistance au cisaillement du ou des sols formant le modèle. Cette étude comprend une série d'essais en laboratoire visant à étudier la résistance au cisaillement du sable propre utilisé comme matériau de base pour la construction de modèles de pente. Une série d'essais de cisaillement en laboratoire ont été réalisés à l'aide de dispositifs conventionnels de cisaillement direct, triaxial et annulaire sous une large gamme de contraintes de confinement, y compris les faibles contraintes de confinement généralement présentes dans les essais sur modèle 1g. Les tests de déformation contrôlée ont été effectués sur des échantillons de sable installés dans les mêmes conditions de densité représentatives du matériau sableux utilisé dans les modèles physiques de pente à petite échelle et dans des conditions de contrainte représentatives des pentes à petite échelle et réelles.

Keywords: Landslides; laboratory testing; shear strength; low effective confining stresses.

1 INTRODUCTION

Landslides are among the greatest geohazards and are being studied in a variety of fields worldwide, including landslide modelling and landslide remediation.

A research project funded by the Croatian Science Foundation entitled "Physical modelling of landslide remediation constructions behaviour under static and seismic actions" was a part of extensive research on small-scale slopes. The main task of the project was to compare the responses of scaled slope models from different soil types and geometric conditions with and without remediation measures subjected to different loading conditions - static (rainfall-triggered landslide) and seismic (earthquake-triggered landslide) instrumented with geodetic and geotechnical monitoring equipment. More on the tests performed on the physical model can be found in Jagodnik & Arbanas (2022); Pajalić et al. (2021); Peranić et al. (2022); Vivoda Prodan et al. (2023).

The shear strength of sand at low confining stresses present in small-scale slope physical model needs to be investigated. One of the pioneering researches on the shear strength of sands at low confining stresses

was done by Ponce & Bell (1971). The authors have registered the dilatative behaviour of loose sands at low confining stresses, similar to dense sands' behaviour at moderate confining stresses. General shear strength and dilatative characteristics of saturated sands at low confining stress were further investigated and presented by Fukushima & Tatsuoka (1984). Shaoli et al. (2003) studied the undrained behaviour of sand under low confining stresses, and found that static liquefaction in such conditions is dominantly governed by the sand's relative density. Laurent et al. (2006) showed in their research that at low confining stresses, the sands' friction and dilatancy angle are stress-dependent. Finally, Chakraborty & Salgado (2010) used a series of triaxial compression and plane-strain compression data results to analyze the dependence of dilatancy and friction angle on sand specimens' relative density and confining stress. Winters et al. (2016) found that a better representation of the relationship between shear stress and normal stress can be found by curving the failure envelope at low confining pressures.

Based on an extensive literature showing the differences between the results that can be obtained with different devices (Castellanos & Brandon, 2013; Cuomo et al., 2016; Vivoda Prodan et al., 2016), different test devices were used in this study.

The ring shear tests were conducted using the ICL-1 ring shear device, (Marui & Co., Ltd., Osaka, Japan) developed in 2010 (Figure 1a), which can simulate the formation of the landslide sliding surface with the following post-failure motion, observe the consequence of mobilized shear resistance and the post-failure shear displacement as well as the generated pore water pressure. The ICL-1 can perform stress (monotonic, dynamic, seismic), strain and pore water pressure controlled tests in drained or undrained conditions. It can maintain a pore water pressure of up to 1 MPa and apply a normal stress of up to 1 MPa, making it suitable for investigation of large-scale and deep-seated landslides. The cylindrical sample has an inner and outer diameter of 10 and 14 cm, respectively and a maximum height of 5.2 cm. The maximum and minimum shear rate is 5.4 and 0.01 cm/s, respectively and cyclic torque control tests can be performed at a maximum frequency of 1.0 Hz (Oštrić et al., 2014). Vivoda Prodan et al. (2016); Vivoda Prodan & Arbanas (2020) investigated the influence of the weathering process on the shear strength of siltstones from a flysch rock mass on the northern Adriatic coast of Croatia using the ICL-1.

Direct shear tests were performed using the Back Pressured Shear Box (GDS Instruments Ltd., London, United Kingdom), (Figure 1b). The device enables the testing of square soil samples in a saturated or partially saturated state with the dimensions 100x100x30 mm at a maximum normal force of 10 kN and a maximum shear force of 5 kN. The maximum shear displacement is ±12.5 mm, while the maximum working back pressure that can be applied is 1 MPa. The device was used by Peranić et al. (2020) to perform standard, strain-controlled tests on undisturbed samples of residual soil from flysch rock mass in unsaturated (i.e. suction-controlled) and saturated conditions. Peranić & Arbanas (2020) used the same device to investigate the behaviour of the soil when undergoing the wetting process.

Static triaxial tests were performed using the Wykeham Farrance static triaxial system (Figure 1c). Tests were performed on a sample with a height to diameter ratio of 100/50 mm. The maximum pressure capacity of the static triaxial system is 1 MPa, the load cell used had a maximum force of 25 kN. The maximum axial displacement is 50 mm (Jagodnik et al., 2020).

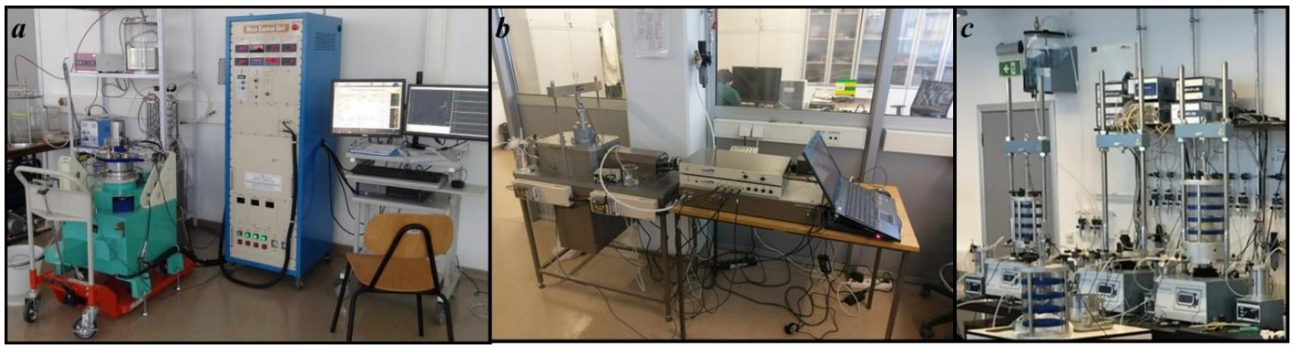

Figure 1. Devices at the Geotechnical laboratory at the Faculty of Civil Engineering University of Rijeka to determine shear strength of sand: a) ring shear (RS) device, b) back pressurized direct shear (DS) device for soil testing in saturated and unsaturated conditions, c) triaxial (TX) device.

The focus of this study is to investigate the shear strength properties of a uniformly graded fine sand used in physical slope modelling. So far, a series of laboratory tests were carried out using direct shear,

triaxial and ring shear devices under a wide range of confining stresses, including relatively low values of stresses representative for the 1g modelling tests.

2 LABORATORY TESTING

Barotropy, i.e. the dependence of the mechanical behaviour of the soil on the stress level, is known to be one of the greatest limitations in a use of small-scale physical models under 1g conditions. The main objective of conducted laboratory tests is to establish relationships between soil material behaviour in a small-scale model and a prototype, i.e., a real slope in a field.

2.1 Sand properties

The fine-grained (0–1 mm) Drava River sand was selected as the base material to represent cohesionless slopes. Figure 2 shows the physical model after the installation of the material and monitoring equipment. The basic physical properties of the described material are given in Table 1.



Figure 2. View of the small-scale physical model.

Table 1. Basic physical properties of the sand material built in the small-scale model.

Parameters	Values
Specific gravity, G_s	2.70
Dry density, ρ_d (g/cm^3)	1.52
Effective particle size	
D_{10} (mm)	0.19
D_{60} (mm)	0.37
Uniformity coefficient, c_u	1.947
Coefficient of curvature, c_c	1.092
Minimum void ratio, e_{min}	0.641
Maximum void ratio, e_{max}	0.911

2.2 Testing devices and methodology

Laboratory tests included direct shear (DS) tests, ring shear (RS) tests, and triaxial (TX) tests on the sandy material performed at the Geotechnical laboratory in the Faculty of Civil Engineering University of Rijeka, Croatia (Figure 1).

The samples were prepared under the same initial conditions as in the physical model, i.e. initial relative density of 50%, initial porosity equal to 0.44, and initial water content equal to 2%. Based on the known conditions related to the desired porosity, and an initial moisture of the tested samples, the mass of mixed sand and water installed in the devices was determined. After installation, samples were consolidated under a range of effective vertical stresses from 4 up to 200 kPa. The strain-controlled tests were performed under drained conditions with different strain rates, as presented in Table 2.

The ring shear box was filled with wet sand samples and then circulated with CO_2 and deaired distilled water. After consolidation at the effective vertical stresses in the range of 30 to 200 kPa with a back pressure of 15 to 50 kPa, shearing was performed at a shear rate of 0.01 cm/s.

Sand material was compacted in the shear box to achieve the sample height of 3 cm and the targeted porosity. Once the sample was installed, the chamber was filled with the deaired water and the sample was left to saturate in the following 24 hours period. After the saturation, the samples were consolidated under a range of confining stresses between 4 and 120 kPa. Finally, the samples were sheared at a low shear rate of 0.0087 mm/min to ensure drained response of the soil.

The samples for testing in the triaxial device were prepared using the undercompaction method, developed by Ladd (1978). The degree of undercompaction was 5%. To achieve faster saturation, the sample was percolated with CO_2 before water percolation. This assures that the Skemptons' *B* coefficient reaches value of 0.97, in average, after back pressurising. The rate of axial strain was 0.6 mm/min.

Table 2. List of the performed strain-controlled laboratory tests.

Device	Effective vertical stress (kPa)	Shear rate (cm/s)
RS	30, 60, 120, 200	0.01
DS	4, 8, 16, 30, 60, 120	1,44676E-05
TX	*16, 30, 60	**≈0.001

*** isotropic confining stress; ** rate of axial strain**

2.3 Test results

This section presents the results of performed drained tests with ring shear (RS), direct shear (DS) and triaxial (TX) devices on the uniform sand material. Figure 6 presents the peak and shear strength envelopes for steady-state conditions obtained in all

devices. The results are fitted using the Mohr-Coulomb strength criteria in σ'-τ plane.

Samples tested in the ring shear device show a tendency for compaction and then dilatation. The material experiences a sudden pronounced peak shear resistance followed by strain softening to the steady state (Figure 3). The residual shear strength envelope (Figure 6a) was obtained for the shear stress values corresponding to the maximum shear displacement reached during the tests, which could be infinite.

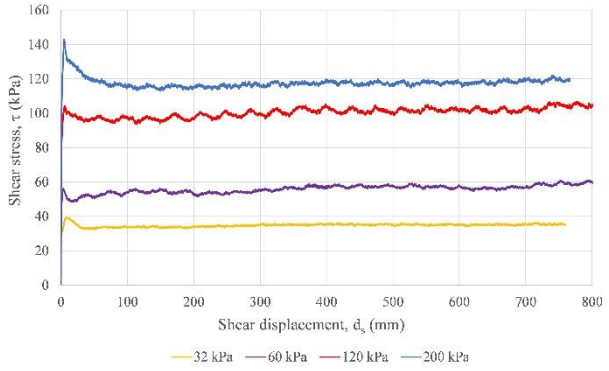

Figure 3. Shear stress-shear displacement of the RS tests.

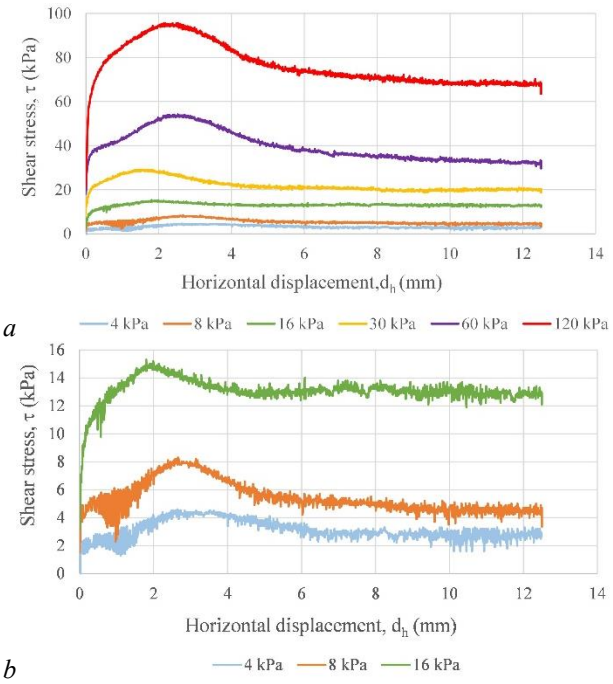

Figure 4. Shear stress- shear displacement results of the DS tests at a) all range of vertical effective stresses, b) low vertical effective stresses.

All direct tests show a clearly pronounced shear resistance peak and subsequent strain softening (Figure 4). The higher the effective vertical consolidation stress, the higher the peak and residual shear resistance. Figure 4b shows shear strength at low effective normal stresses from 4 to 16 kPa. The values of the test results for peak and residual conditions show a non-linear relationship, over the entire stress range of effective normal stresses (Figure 6b).

The test results obtained using triaxial tests are presented in Figure 5. Mean effective stress and deviatoric stress are calculated according to MIT principle (Lambe, 1967). For better comparison with the results obtained with DS and RSA, peak and residual values of shear strength obtained through triaxial tests (Figure 6c) were converted to the equivalent vertical and shear stress that would correspond to shear state obtained using the equipment with predefined shear surface.

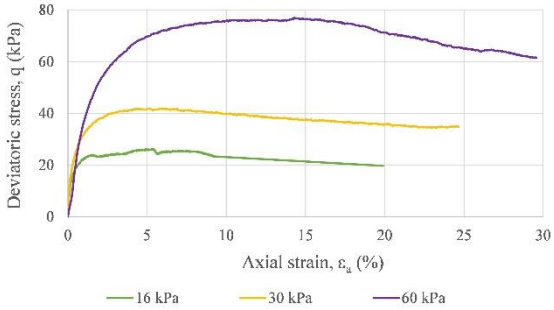

Figure 5. Deviatoric stress- axial strain results of the TX tests.

Figure 7 shows the peak and residual shear strength values for different vertical effective stresses according to the test results for all testing devices. The peak shear strength values obtained with the TX and RSA devices are close to each other, while the highest values were obtained with the DS device. The highest value of residual shear strength was obtained with the RSA device, while the values for the TX and DS devices were close to each other. Regardless of the testing device, the tests have the mean square error (R^2) greater than 0.87 (Figure 6).

The calculated effective friction angle for the peak and critical state obtained with different devices is analysed. The peak and residual friction angles obtained with the DS were 44° and 35° respectively for low effective normal stresses and reduced to 40° and 28° for higher stresses. The peak friction angle obtained with the DS is the highest, while the residual friction angle is the lowest among the used devices.

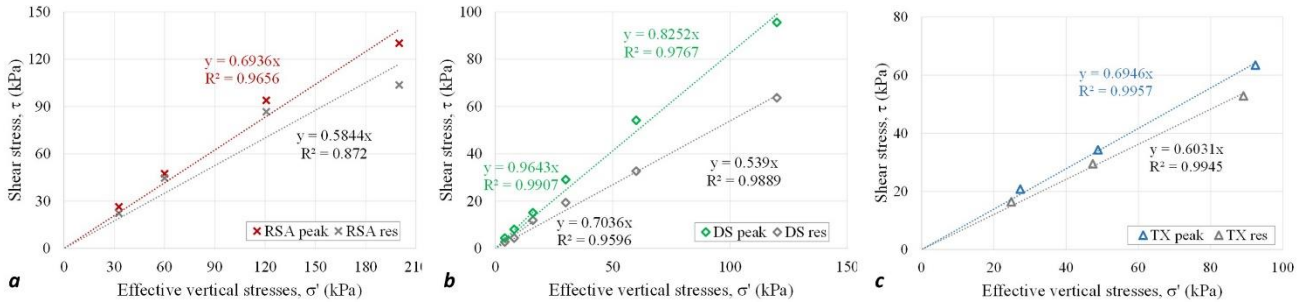

Figure 6. Mohr-Coulomb saturated shear strength envelope of sand obtained in the: a) ring shear tests, b) direct shear tests, c) triaxial tests.

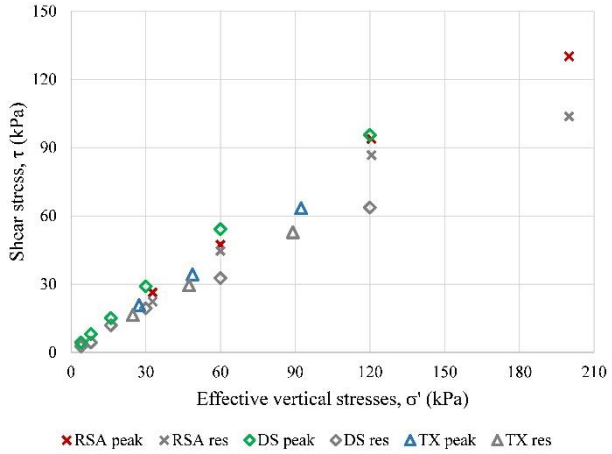

Figure 7. Peak and critical shear strength values of sand for different vertical effective stresses according to test results on all testing devices.

The peak value of the effective friction angle is between 40° and 35°, while the residual value is between 31° and 28° for higher stresses for the different devices.

It should be noted that the soil critical state is reached at different displacements depending on the type of the testing device (Figures 3, 4, and 5). For the DS and RSA tests, the critical state is reached in the range of 3 to 9 mm depending on the effective vertical stress value.

3 CONCLUSIONS

The paper dealt with the characterization of the sandy soil shear strength used in the small-scale physical models. Ring shear, direct shear, and triaxial tests were performed to investigate the differences in terms of friction angle under a range of stresses corresponding to the overburden stresses in the small-scale model and the real slope.

The paper showed that the experimental tests are fully reproducible as it concerns both the specimen preparation procedure and the testing technique.

The comparison between the results obtained with the different devices was made based on the residual and peak shear strength obtained and by calculating the effective friction angle. The test results indicate that the higher the effective vertical consolidation stress, the higher the peak and residual shear strength. The preliminary results of the tests indicate that the shear strength depends on the magnitude of the effective stresses and that as the stress level increase, the friction angle decreases. The ring shear device and triaxial devices show similar peak stress envelope while residual envelope is closer for direct shear and triaxial devices. A difference was found between the friction angle of sand at small normal stresses and at large normal stresses, indicating the need to use different values for the friction angle in the numerical modelling of the small-scale model and the real slope.

The results obtained in this study will be implemented in the future numerical modelling activities: while the shear strength characteristics obtained at relatively low confining pressures will be useful for a better understanding of small-scale slope models, the results obtained under higher stresses will be useful for numerical studies of real-size slopes.

ACKNOWLEDGEMENTS

The research presented in this paper was supported by Croatian Science Foundation under the Project IP-2018-01-1503. This work has been supported in part by the Ministry of Science, Education and Sports of the Republic of Croatia under the project Research Infrastructure for Campus-based laboratories at the University of Rijeka, number RC.2.2.060001. The project has been co-funded from the European Fund for Regional Development (ERDF). This paper was funded by the University of Rijeka under the project ZIP-UNIRI-1500-1-22 and partially supported by the project uniri-mladi-tehnic-22-62. This paper has been supported by the International Consortium on Landslides under the IPL-256 and IPL-265 projects. These supports are gratefully acknowledged.

REFERENCES

Castellanos, B. A., & Brandon, T. L. (2013). A Comparison Between the Shear Strength Measured with Direct Shear and Triaxial Devices on Undisturbed and Remolded Soils. *18th International Conference on Soil Mechanics and Geotechnical Engineering (Paris)*.

Chakraborty, T., & Salgado, R. (2010). Dilatancy and Shear Strength of Sand at Low Confining Pressures. *Journal of Geotechnical and Geoenvironmental Engineering*, *136*(3), 527–532. https://doi.org/10.1061/(ASCE)GT.1943-5606.0000237.

Cuomo, S., Foresta, V., & Moscariello, M. (2016). Shear strength of a pyroclastic soil measured in different testing devices. In *Volcanic Rocks and Soils* (1st Edition, p. 25).

Fukushima, S., & Tatsuoka, F. (1984). Strength and Deformation Characteristics of Saturated Sand at Extremely Low Pressures. *Soils and Foundations*, *24*(4), 30–48. https://doi.org/https://doi.org/10.3208/sandf1972.24.4_30.

Jagodnik, V., & Arbanas, Ž. (2022). Cyclic Behaviour of Uniform Sand in Drained and Undrained Conditions at Low Confining Stress in Small-Scale Landslide Model. *Sustainability*, *14*(19). https://doi.org/10.3390/su141912797.

Jagodnik, V., Kraus, I., Ivanda, S., & Arbanas, Ž. (2020). Behaviour of Uniform Drava River Sand in Drained Condition—A Critical State Approach. *Applied Sciences*, *10*(17). https://doi.org/10.3390/app10175733.

Ladd, R. S. (1978). Preparing Test Specimens Using Undercompaction. *Geotechnical Testing Journal*, *1*, 16–23.

Lambe, W. T. (1967). Stress Path Method. *Journal of the Soil Mechanics and Foundations Division*, *93*(6), 309–331. https://doi.org/10.1061/JSFEAQ.0001058.

Laurent, L., Isam, S., & Marwan, A. M. (2006). Failure and Dilatancy Properties of Sand at Relatively Low Stresses. *Journal of Engineering Mechanics*, *132*(12), 1396–1399. https://doi.org/10.1061/(ASCE)0733-9399(2006)132:12(1396).

Oštrić, M., Sassa, K., Ljutić, K., Vivoda, M., He, B., & Takara, K. (2014). Manual of transportable ring shear apparatus, ICL- 1. *Proceedings of 1st Regional Symposium on Landslides in the Adriatic-Balkan Region "Landslide and Flood Hazard Assessment,"* 1–4.

Pajalić, S., Peranić, J., Maksimović, S., Čeh, N., Jagodnik, V., & Arbanas, Ž. (2021). Monitoring and Data Analysis in Small-Scale Landslide Physical Model. *Applied Sciences*, *11*(11). https://doi.org/10.3390/app11115040.

Peranić, J., & Arbanas, Ž. (2020). Impact of the wetting process on the hydro-mechanical behavior of unsaturated residual soil from flysch rock mass: preliminary results. *Bulletin of Engineering Geology and the Environment*, *79*(2), 985–998. https://doi.org/10.1007/s10064-019-01604-0.

Peranić, J., Čeh, N., & Arbanas, Ž. (2022). The Use of Soil Moisture and Pore-Water Pressure Sensors for the Interpretation of Landslide Behavior in Small-Scale Physical Models. *Sensors*, *22*(19). https://doi.org/10.3390/s22197337.

Peranić, J., Moscariello, M., Cuomo, S., & Arbanas, Ž. (2020). Hydro-mechanical properties of unsaturated residual soil from a flysch rock mass. *Engineering Geology*, *269*, 105546. https://doi.org/https://doi.org/10.1016/j.enggeo.2020.105546.

Ponce, V. M.-, & Bell, J. M. (1971). Shear Strength of Sand at Extremely Low Pressures. *Journal of the Soil Mechanics and Foundations Division*, *97*(4), 625–638. https://doi.org/10.1061/JSFEAQ.0001578.

Shaoli, Y., Sandven, R., & Grande, L. (2003). Liquefaction of sand under low confining pressure. *Journal of Ocean University of Qingdao*, *2*(2), 207–210. https://doi.org/10.1007/s11802-003-0053-9.

Vivoda Prodan, M., & Arbanas, Ž. (2020). Analysis of the Possible Reactivation of the Krbavčići Landslide in Northern Istria, Croatia. In *Geosciences* (Vol. 10, Issue 8). https://doi.org/10.3390/geosciences10080294.

Vivoda Prodan, M., Mileusnić, M., Mihalić Arbanas, S., & Arbanas, Ž. (2016). Influence of weathering processes on the shear strength of siltstones from a flysch rock mass along the North Croatian Adriatic Coast. *Bulletin of Engineering Geology and the Environment*, *in press*.

Vivoda Prodan, M., Peranić, J., Pajalić, S., & Arbanas, Ž. (2023). Physical Modelling of Rainfall-Induced Sandy and Clay-Like Slope Failures. *Advances in Materials Science and Engineering*, *2023*, 3234542. https://doi.org/10.1155/2023/3234542.

Winters, K. E., Taylor, O.-D. S., Berry, W. W., Rowland, W. R., & Antwine, M. D. (2016). Cohesionless Soil Fabric and Shear Strength at Low Confining Pressures. In *Geo-Chicago 2016* (pp. 212–221). https://doi.org/10.1061/9780784480151.022.

Proceedings of the XVIII ECSMGE 2024
GEOTECHNICAL ENGINEERING CHALLENGES
TO MEET CURRENT AND EMERGING NEEDS OF SOCIETY
© 2024 the Authors
ISBN 978-1-032-54816-6
DOI 10.1201/9781003431749-253
Open Access: www.taylorfrancis.com, CC BY-NC-ND 4.0 license

ECSMGE 24
XVIII EUROPEAN CONFERENCE ON SOIL MECHANICS AND GEOTECHNICAL ENGINEERING

Simulation of responses of a Tender Net Foundation on silty ground subjected to consecutive earthquakes

Simulation des réponses d'une Fondation Tender Net sur sol limoneux soumis à des séismes consécutifs

H. Vo-Cong*, K. Takeuchi, Y. Tomono
Takeuchi Construction Inc., Hiroshima, Japan

T. Matsumoto
Kanazawa University, Ishikawa, Japan

**han@takeuchi-const.co.jp*

ABSTRACT: Liquefaction induced by earthquakes causes instability of buildings such as large settlements resulting in damage to the building structures. Usually, when an earthquake occurs, the saturated loose sandy ground is most susceptible to liquefaction. Even for the saturated silty ground with small SPT *N*-values, the possibility of liquefaction needs to be considered in the design process. Tender Net Foundation (TNF) is a kind of shallow foundation with a combination of grid-shaped soil improvement to depths of 2 to 3 meters, concrete slab, and concrete single footings. In this paper, the dynamic analysis of an actual TNF on the silty ground subjected to three consecutive earthquakes is conducted. Measurements of the settlements of the TNF were made after the second earthquake. The silty ground is modeled by the UBC3D-PLM model. Ground accelerations recorded about 10 km away from the site area are used as the input accelerations in dynamic analyses. The responses of the TNF as well as the ground during and after the earthquakes are analyzed. The numerical analyses simulated well the measured settlements.

RÉSUMÉ: La liquéfaction induite par les tremblements de terre provoque une instabilité des bâtiments tels que de grandes agglomérations, entraînant des dommages aux structures des bâtiments. Habituellement, lorsqu'un tremblement de terre se produit, le sol sablonneux meuble et saturé est le plus susceptible de se liquéfier. Même pour les sols limoneux saturés avec de faibles valeurs SPT *N*, la possibilité de liquéfaction doit être prise en compte dans le processus de conception. Tender Net Foundation (TNF) est une sorte de fondation peu profonde combinant une amélioration du sol en forme de grille jusqu'à des profondeurs de 2 à 3 mètres, une dalle de béton et des semelles simples en béton. Dans cet article, l'analyse dynamique d'un TNF réel sur un sol limoneux soumis à trois tremblements de terre consécutifs est réalisée. Des mesures des tassements du TNF ont été réalisées après le deuxième séisme. Le sol limoneux est modélisé par le modèle UBC3D-PLM. Les accélérations du sol enregistrées à environ 10 km de la zone du site sont utilisées comme accélération d'entrée dans l'analyse dynamique. Les réponses du TNF ainsi que du sol pendant et après les séismes sont analysées. L'analyse numérique a bien simulé les tassements mesurés.

Keywords: TNF system; liquefaction; settlement; silty ground; FEM.

1 INTRODUCTION

Tender Net Foundation (TNF) is a kind of shallow foundation with a combination of grid-shaped soil improvement, concrete slab and concrete single footings (see Figures 1 and 2). The original soil is improved by blending with cement as a solidification material using a backhoe. Cement powder with lower elution of hexad chrome is mixed with the original soil at the site for environmental friendliness. The mass of cement per unit soil volume is varied so that the improved soil has an unconfined compression strength q_u of 300 to 450 kPa in common. Cong et al. (2022) analyzed the TNF system subjected to vertical loading and demonstrated that the TNF system is an efficient foundation for reducing settlement and volume of soil improvement compared to the conventional shallow soil improvement method.

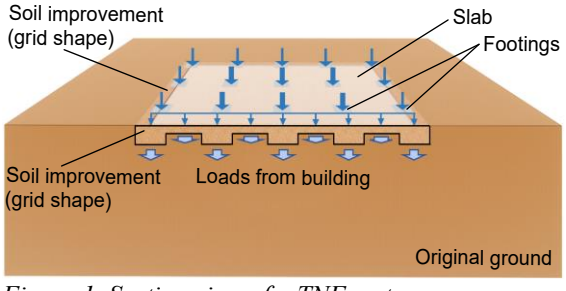

Figure 1. Section view of a TNF system.

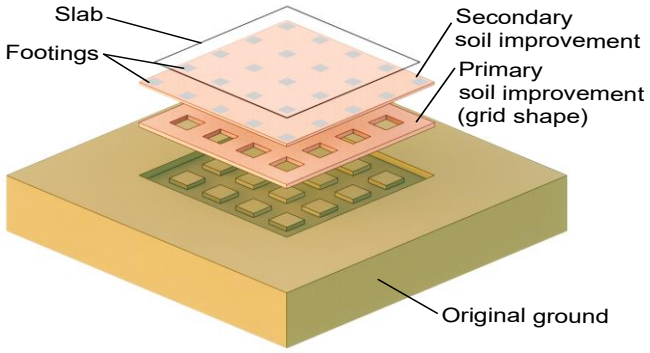

Figure 2. Composition of a TNF system.

By improving the surface layer to depths of 2 to 3 meters in a grid shape, the TNF may be an efficient foundation for suppressing the damage to buildings when liquefaction occurs.

In this paper, the dynamic analysis of an actual TNF on silty ground subjected to three consecutive earthquakes is conducted. Measurements of the settlements of the TNF were made after the second earthquake.

PLAXIS 3D FEM software (Bentley, 2022) is used for simulation analysis. The silty ground is modeled by the UBC3D-PLM model. The time histories of ground accelerations during three earthquakes recorded about 10 km away from the site area are used as the input accelerations in the dynamic analyses of the TNF. The responses of the TNF as well as the ground during and after the earthquakes are calculated. The analysis shows that liquefaction occurs in the silty ground. The calculation simulated well the measured settlements. To demonstrate the efficiency of the TNF for suppressing the settlements induced by liquefaction, a similar analysis of a conventional shallow foundation is also carried out for comparison purposes.

2 OUTLINE OF BUILDING

Figure 3 shows the plan view of the construction site and two boreholes (BHs). The target of this analysis is a TNF for the foundation of a factory constructed in Japan. The factory is a 1-story building with a floor area of 30 × 19.5 m and a height of 5.7 m.

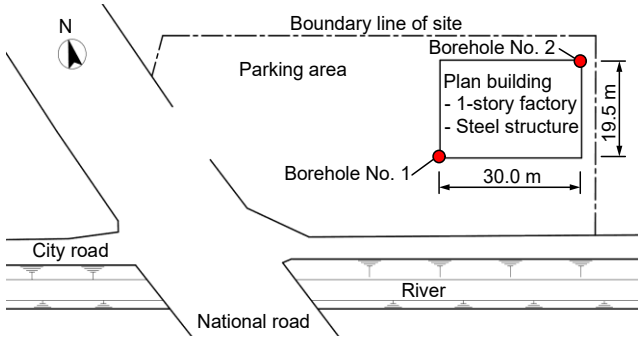

Figure 3. Plan view of the construction site and boreholes.

Figure 4 shows the profiles of soil layers and SPT *N*-values. The ground at each borehole consists of 7 soil layers. The sandy silt layer ② (N = 1) exists at depths 0.5 to 2.7 m (2.2 m thick) at BH No. 1, and at depths 1.0 to 2.9 m (1.9 m thick) at BH No. 2. The silt layer ④ (N = 0) exists at depths 3.7 to 13.5 m (9.8 m thick) at BH No. 1, and at 3.7 to 14.6 m (10.9 m thick) at BH No. 2. The groundwater level is 0.9 m at BH No. 1 and 0.65 m at BH No. 2 below the ground surface.

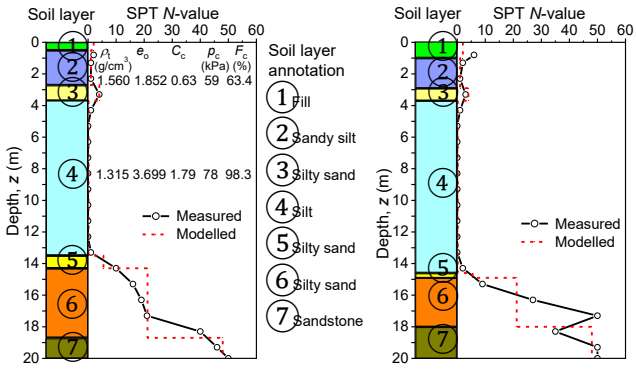

(a) Borehole No.1. *(b) Borehole No.2.*

Figure 4. Profiles of soil layers and SPT N-values.

Figure 5 shows the plan view of the TNF system considered in the design process. The size of the TNF system is 33.7 m × 25.6 m having a primary soil improvement layer with a thickness of 1.5 m, and a secondary soil improvement layer with a thickness of 0.75m. The thickness of the concrete footings is 0.4 m, and the thickness of the concrete slab is 0.2 m.

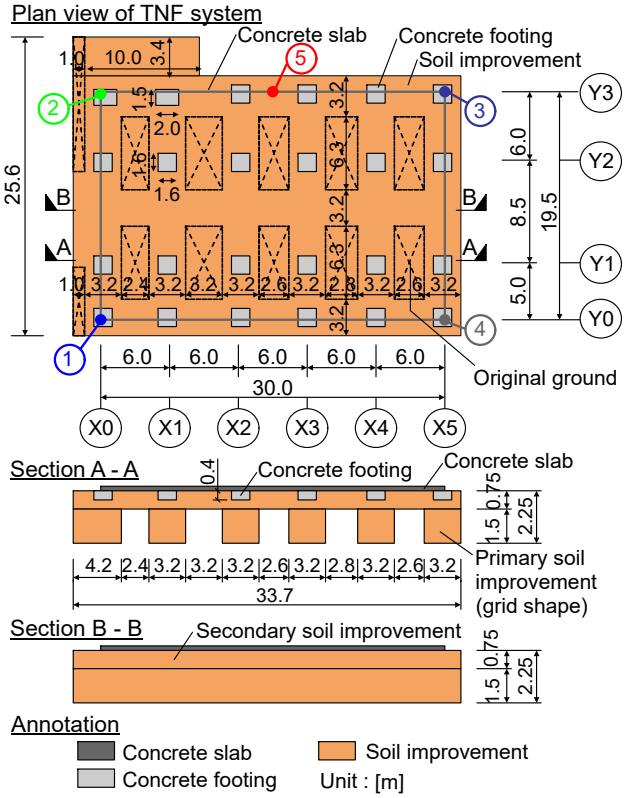

Figure 5. Plan view of the TNF system.

Figure 6 shows the construction progress, earthquakes history, and measured settlements at the five points of the TNF (see Figure 5). The settlement measurements were started just after the earthquake with Japan Meteorological Agency (JMA, 2023) Seismic Intensity scale (*SI* scale) of 5- on 2017-02-28. For example, an earthquake with *SI* scale of 5- is one in which many people are frightened and feel the need to hold onto something stable. Hanging objects such as lamps swing violently. Dishes in cupboards and items on bookshelves may fall. Small cracks may form and liquefaction may occur in the ground. Refer to JMA (2023) for more details on *SI* scales.

It is seen that the differential settlement Δw occurred. Interestingly, large ground settlements were measured after the occurrence of earthquakes having *SI* scale of 5- or higher.

Hence, the influence of earthquakes is strongly suspected as the cause of the differential settlement.

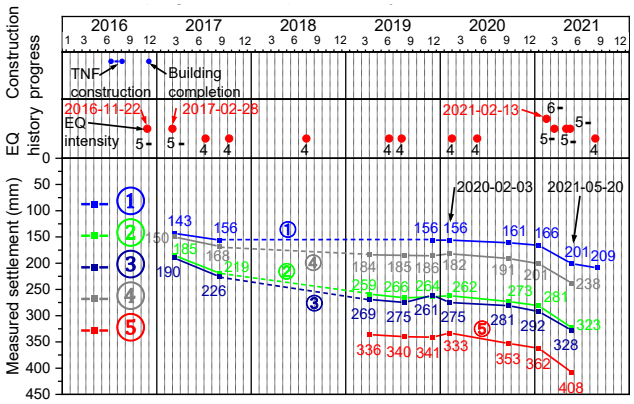

Figure 6. Construction progress, earthquakes history, and measured settlements.

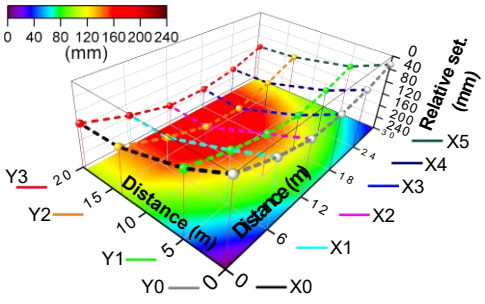

(a) on 2020-02-03.

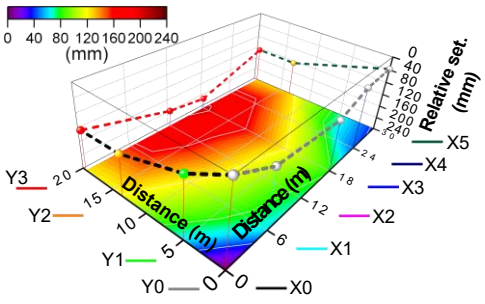

(b) on 2021-05-20 (after the EQ on 2021-02-13).

Figure 7. Measured relative settlements of the TNF.

Figure 7 shows the distributions of relative settlements of the TNF measured on 2020-02-03 and on 2021-05-20, respectively. The measured relative settlements were defined as the difference between the settlement at given points and the settlement at point ① (X0, Y0). It is seen that the maximum Δw and the average settlement w_{ave} on 2021-05-20 increased compared with those on 2020-02-03. That is, the maximum Δw was 186 mm and settlement at the reference point ① was 156 mm in Figure 7(a). Those were 207 mm and 201 mm in Figure 7(b).

To investigate the cause of settlements of the TNF, the dynamic FEM analysis is conducted.

3 DYNAMIC ANALYSIS CONDITIONS

Figure 8 shows the PLAXIS 3D FEM analysis model. The ground was modeled by 7 soil layers. The thickness of fill layer ① is 0.65 m at BH No.1 and 1.19 m at BH No.2. The vertical loads of the building were applied as the point loads on the footings and as the uniform surface load on the slab. The earthquake loads were applied to the bottom of the ground.

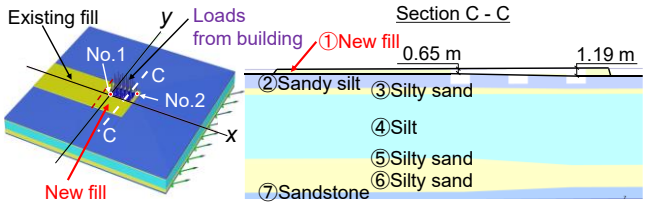

Figure 8. PLAXIS 3D FEM analysis model.

Figure 9 shows the analysis phases. The analysis phases were set following the construction progress and earthquake history.

In this research, earthquakes with seismic intensity scale *SI* of 5- or higher on 2016-11-22 (1st EQ, *SI* = 5-), on 2017-02-28 (2nd EQ, *SI* = 5-), and on 2021-02-13 (3rd EQ, *SI* = 6-) were considered. The seven earthquakes with *SI* of 4 between 2017-02-28 and 2021-02-13 were omitted in this particular analysis because the settlements caused by these earthquakes were considered negligible.

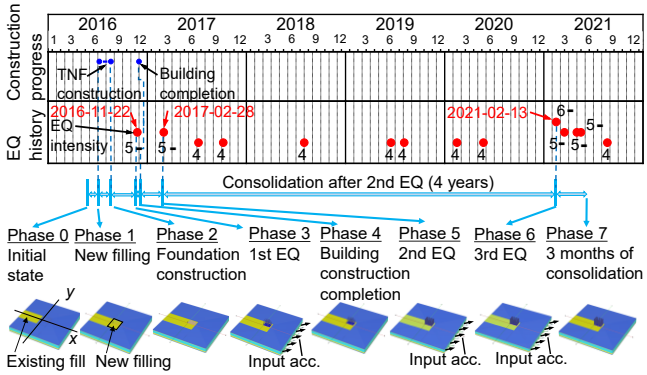

Figure 9. Analysis phases.

The ground accelerations of the earthquakes recorded about 10 km away from the site area were used as input accelerations of the three earthquakes in the dynamic analyses at Phases 3, 5 and 6. The other phases were set by consolidation analysis.

Undrained conditions were set for the ground below the groundwater level, while drained conditions were set for the ground above the groundwater level.

Figure 10 shows the input acceleration data used in the dynamic analyses. The acceleration data were obtained from K-NET strong-motion seismograph network (2022) and were converted to acceleration data into *x*- and *y*-directions.

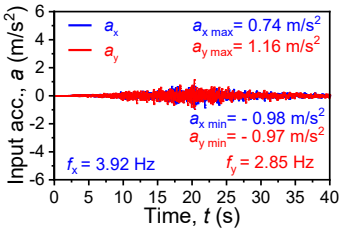

(a) 1st EQ on 2016-11-22.

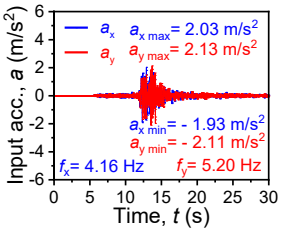

(b) 2nd EQ on 2017-02-28.

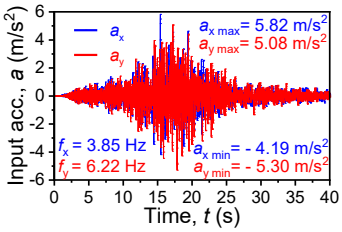

(c) 3rd EQ on 2021-02-13.

Figure 10. Input acceleration data.

Table 1 shows the physical and mechanical properties of each soil layer.

The averaged *N*-value in each layer was used for estimating V_s using Eq. (1) specified in Japan Road Association (2012):

$$V_s\ (\mathrm{m/s}) = \begin{cases} 100N^{1/3} & \text{for clay} \\ 80N^{1/3} & \text{for sand} \end{cases} \quad (1)$$

Shear modulus G was calculated using Eq. (2):

$$G = \frac{\gamma_t}{g} V_s^2 \quad (2)$$

Young's modulus E was calculated using Eq. (3):

$$E = 2(1+\nu)G \quad (3)$$

Poisson's ratio ν and coefficient of permeability k of each soil layer were assumed as shown in Table 1.

Table 2 shows the parameters of the UBC3D-PLM model for each soil layer. The relative density D_r was estimated according to Tokimatsu and Yoshimi (1983). The fine grain content ratio F_c is needed for estimating D_r. F_c of sandy silt layer ② and silt layer ④ was obtained from soil test results (see Figure 4), while F_c of other soil layers was assumed to be 10 %.

The cohesion c of the silt layer (layer ④, $N = 0$) was estimated to be 0 using $c = 6.25N$ kPa (BCJ, 2019). The c of sandy silt and silty sand layers was set to 0.

The other parameters of the UBC3D-PLM model in Table 2 were obtained using D_r following PLAXIS 3D Manuals (Bentley, 2022).

Table 1. Physical and mechanical properties of each soil layer.

No.	Soil layer type	Soil model	t_1 (m)	t_2 (m)	SPT N	γ_t (kN/m³)	V_s (m/s)	G (kPa)	E (kPa)	ν	k (m/day)
1	Fill	Linear elastic	0.65	1.19	2	17.00	100.8	1.76×10^4	4.23×10^4	0.2	8.64
2	Sandy silt	UBC3D-PLM	2.20	1.90	1	15.29					3.2×10^{-4}
3	Silty sand	UBC3D-PLM	1.00	0.80	4	17.00					8.6×10^{-3}
4	Silt	UBC3D-PLM	9.80	10.90	0	12.89					1.7×10^{-4}
5	Silty sand	UBC3D-PLM	0.80	0.30	5.5	17.00					8.6×10^{-3}
6	Silty sand	UBC3D-PLM	4.40	3.10	21.2	17.00					8.6×10^{-3}
7	Sandstone	Linear elastic	1.15	1.81	48	16.00	363.4	2.16×10^5	5.18×10^5	0.2	0

t_1 = Thickness of soil layer in Borehole No. 1, t_2 = Thickness of soil layer in Borehole No. 2, γ_t = Total unit weight, V_s = Shear wave velocity, G = Shear modulus, E = Young's modulus, ν = Poisson's ratio, k = Coefficient of permeability

Table 2. Parameters of UBC3D-PLM model used for each soil layer.

No.	D_r (%)	e_0	k_B^e	k_G^e	k_G^p	m_e	n_e	n_p	φ_{cv} (deg.)	φ_p (deg.)	c (kPa)	f_{dense}	f_{Epost}	R_f
2	59.70	1.575	763	1090	921	0.5	0.5	0.4	21.7	23.3	0	1.00	1.00	0.73
3	54.12	0.919	715	1021	619	0.5	0.5	0.4	24.6	25.9	0	1.00	1.00	0.75
4	64.50	1.947	803	1148	1277	0.5	0.5	0.4	18.4	20.2	0	1.00	1.00	0.71
5	62.82	0.936	789	1128	1141	0.5	0.5	0.4	25.0	26.8	0	1.00	1.00	0.72
6	67.28	0.791	826	1180	1533	0.5	0.5	0.4	27.6	29.6	0	1.00	1.00	0.70

D_r = Relative density, e_0 = Initial void ratio,
k_B^e = Elastic bulk modulus factor, k_G^e = Elastic shear modulus factor, k_G^p = Plastic shear modulus factor,
m_e = Rate of stress dependency of elastic bulk modulus, n_e = Rate of stress dependency of elastic shear modulus,
n_p = Rate of stress dependency of plastic shear modulus, φ_{cv} = Constant volume friction angle,
φ_p = Peak friction angle, c = Cohesion, f_{dense} = Densification factor, f_{Epost} = Post-liquefaction factor, R_f = Failure ratio

Table 3. Material parameters of concrete and soil improvement used for the TNF system.

Material	Soil model	Total unit weight, γ (kN/m^3)	Shear wave velocity, V_s (m/s)	Shear modulus, G (kPa)	Young's modulus, E (kPa)	Poisson's ratio, ν
Concrete (Slab, Footing)	Linear elastic	24	2001	9.79×10^6	23.50×10^6	0.2
Soil improvement	Linear elastic	17	271	1.28×10^5	3.20×10^5	0.25

The parameters of soil improvement of the TNF in Table 3 were estimated using Eqs. (1), (2) and (3) with *N*-value assumed as 20.

4 ANALYSIS RESULTS

Figure 11 shows the calculated settlement curves of the TNF at Points A, B, C, D. Large settlements occurred during each earthquake. Settlements were largest in the 3rd EQ with *SI* = 6-. It is seen that the earthquakes also caused differential settlements of the TNF.

The analysis of no earthquake was also conducted to evaluate the influence of the earthquakes. The calculated settlement curve at Point C of no earthquake is added in Figure 11. It is seen that the earthquakes were the main cause of large settlements of the TNF.

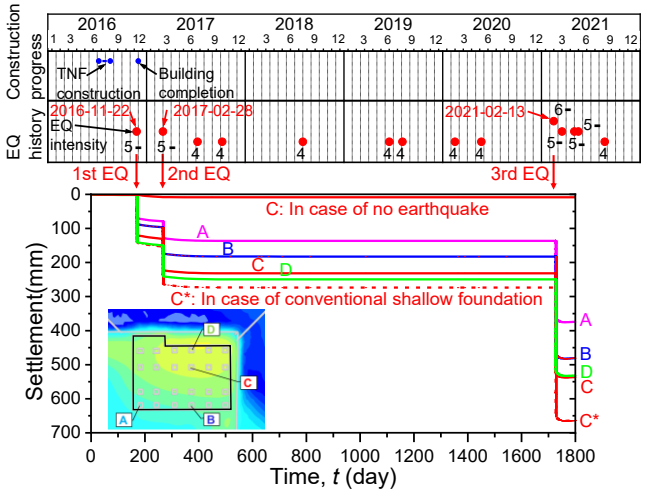

Figure 11. Calculated settlement curves of TNF.

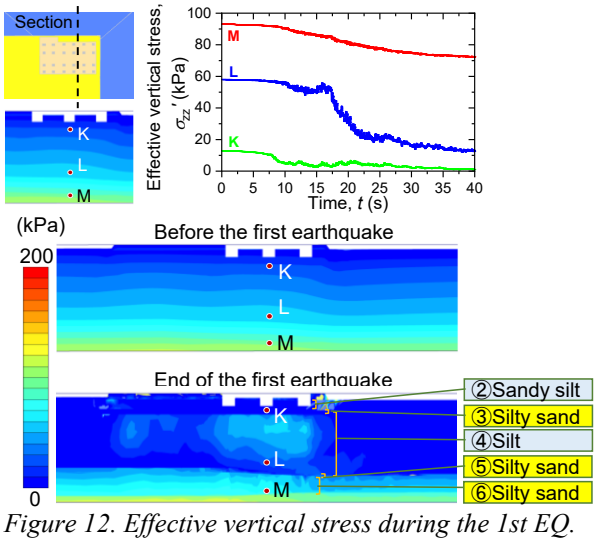

Figure 12. Effective vertical stress during the 1st EQ.

Figure 12 shows the effective vertical stress σ_{zz}' during the 1st EQ. The σ_{zz}' of all soil layers of the ground decreased during the EQ. At the end of the 1st EQ, the σ_{zz}' of silty layers (layers ② and ④) and sandy ground (layer ③) decreased nearly to 0 kPa. It is seen that liquefaction occurs even in the silty ground.

Figure 13 shows the excess pore water pressure p_{excess} during the 1st EQ. The p_{excess} of the whole ground increased during the EQ, and p_{excess} at the end of the 1st EQ was much larger than those before the earthquake. p_{excess} at the end of the 1st EQ caused consolidation settlements of the TNF and the surrounding ground after the earthquake as shown in Figure 11.

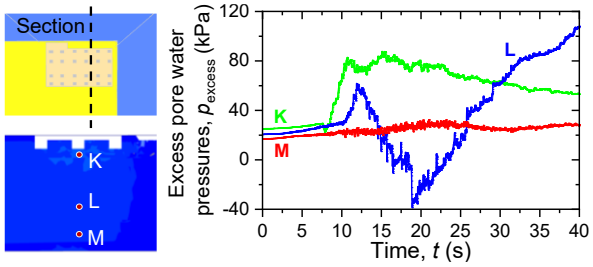

Figure 13. Excess pore water pressure during the 1st EQ.

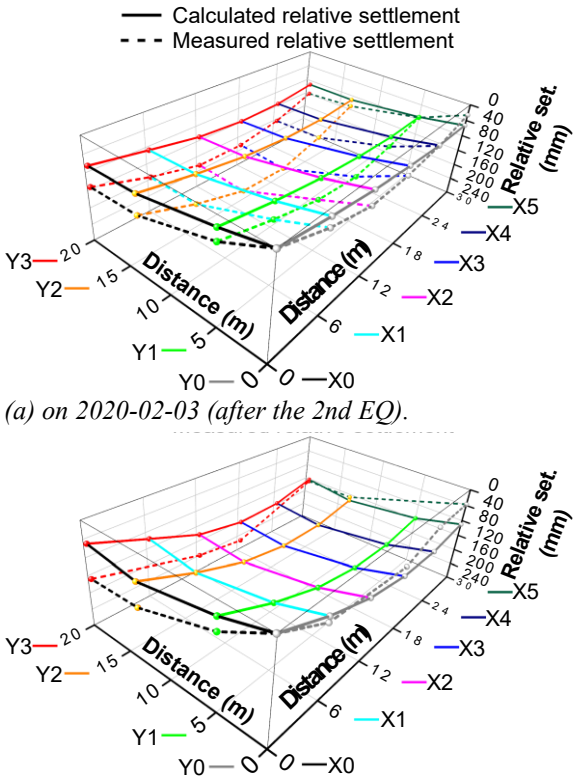

(a) on 2020-02-03 (after the 2nd EQ).

(b) on 2021-05-20 (after the 3rd EQ).

Figure 14. Comparison of calculated relative settlement and measured relative settlement of the TNF.

Figure 14 compares the calculated relative settlement and measured relative settlement of the TNF on 2020-02-03 and 2021-05-20, respectively.

As shown in Figure 14(a), the distributions of relative settlement in the measurement and the calculation are almost the same although the calculated settlement is a little bit smaller than the measured settlement. In Figure 14(b), although the number of measurement points is less, the calculated results are close to the measured results again.

Figure 15 shows the comparison of the calculated and measured settlements on 2021-05-20 (after the 3rd EQ). It is seen that the calculation simulated well the measured settlements. Along the Y-axis direction (Figure 15a), maximum settlement occurred at the center points (X3 axis) in both the measurement and the calculation, and the settlement gradually decreased toward the edges. Along the X-axis direction (Figure 15b), the measured and calculated maximum settlements occurred at the Y2 axis. Although there were only two measurement points along the X3 axis, it is inferred that a similar trend occurred.

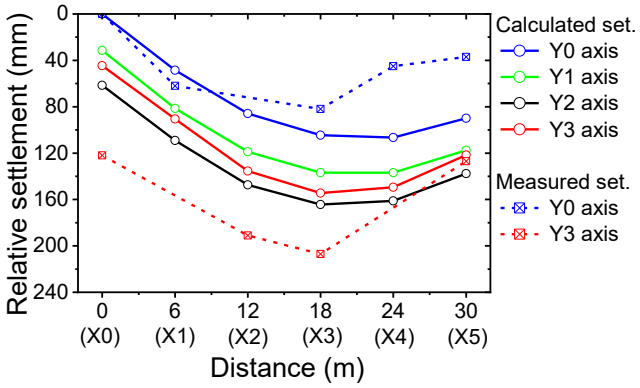

(a) along the Y-axis direction.

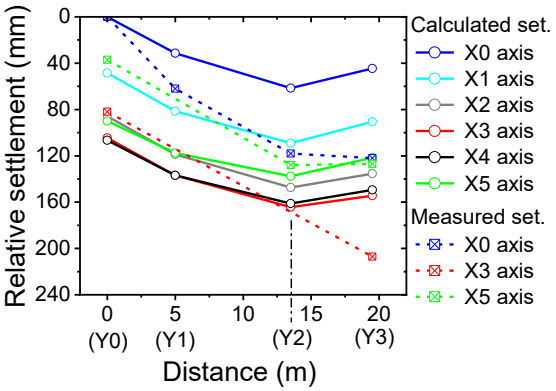

(b) along the X-axis direction.

Figure 15. Comparison of calculated settlements and measured settlements on 2021-05-20 (after the 3rd EQ).

To demonstrate the efficient performance of the TNF for suppressing the settlements induced by liquefaction, a similar analysis of a conventional shallow foundation shown in Figure 16 was conducted.



Figure 16. Section view of conventional shallow foundation.

The settlement curve of the conventional shallow foundation at Point C has been indicated in Figure 11 to compare with the TNF. It is seen that the settlement of the TNF is much suppressed compared to the settlement of the conventional shallow foundation, especially in the 3rd EQ (*SI* = 6-).

5 CONCLUSIONS

The dynamic analysis of the actual TNF on the silty ground subjected to three consecutive earthquakes was conducted. The responses of the TNF as well as the ground during and after the earthquakes were calculated to investigate the occurrence of liquefaction in the silty ground. Furthermore, a similar analysis of a conventional shallow foundation was carried out. From comparisons between the measured and calculation results, the main conclusions are drawn as follows:

1) The calculation simulated well the measured settlements.
2) Earthquakes were the main cause of settlements and differential settlements of the TNF in this project.
3) Liquefaction occurs even in the silty ground.
4) The TNF is an efficient foundation for suppressing the settlements induced by liquefaction compared to the conventional shallow foundation.

REFERENCES

Bentley (2022). PLAXIS 3D Manuals.

Cong, H.V. et al. (2022). Parametric numerical study on deformation of the Tender Net Foundation subjected to vertical loading. *The 11th Int. Conf. on Stress Wave Theory and Design and Testing Methods for Deep Foundations*, Rotterdam, 6p. http://doi.org/10.5281/zenodo.7142087.

Japan Meteorological Agency (JMA) (2023). https://www.jma.go.jp/jma/en/Activities/inttable.html.

Japan Road Association (JRA) (2012). Specifications for highway bridges V: Seismic design (in Japanese).

K-NET strong-motion seismograph network (2022). https://www.kyoshin.bosai.go.jp/.

The Building Center of Japan (BCJ) (2019). Recommendations for design of building foundations (in Japanese).

Tokimatsu, K. and Yoshimi, Y. (1983). Empirical correlation of soil liquefaction based on SPT *N*-value and fines content. *S and F*, 23(4): 56-74. https://doi.org/10.3208/sandf1972.23.4_56.

Proceedings of the XVIII ECSMGE 2024
GEOTECHNICAL ENGINEERING CHALLENGES
TO MEET CURRENT AND EMERGING NEEDS OF SOCIETY
© 2024 the Authors
ISBN 978-1-032-54816-6
DOI 10.1201/9781003431749-254
Open Access: www.taylorfrancis.com, CC BY-NC-ND 4.0 license

ECSMGE 24
XVIII EUROPEAN CONFERENCE ON SOIL MECHANICS AND GEOTECHNICAL ENGINEERING

Enhancing landslide anomaly detection in aerial imagery through pre-processing and GANomaly deployment

Amélioration de la détection d'anomalies de glissements de terrain dans l'imagerie aérienne grâce au pré-traitement et au déploiement de GANomaly

C.H. Wang*
Dept. of Civil Engineering, Chung Yuan Christian University, Taoyuan City, Taiwan (R.O.C.)

K.C. Lo
Dept. of Public Works, Taoyuan City, Taiwan (R.O.C.)

C.Y. Hu
Dept. of Civil Engineering, Chung Yuan Christian University, Taoyuan City, Taiwan (R.O.C.)

P.H. Wang
Dept. of Information and Computer Engineering, Chung Yuan Christian University, Taoyuan City, Taiwan (R.O.C.)

**chwang@cycu.edu.tw*

ABSTRACT: The application of aerial imagery for landslide anomaly detection encapsulates a promising avenue for early geohazard identification. This study utilizes GANomaly, a model built upon Generative Adversarial Networks (GAN), to identify anomalies by learning to reconstruct normal data and measuring reconstruction errors to discern anomalies. Initially, a pre-processing process was developed to enhance the clarity and quality of images, thereby facilitating more effective training and testing by GANomaly. This pre-processing process encompasses several steps: image RGB channels adjustments, image slicing into tiles, tile classifications, and tile rotations. The GANomaly model is then employed, trained on a substantial dataset derived from the pre-processing stage, and tested to evaluate its efficacy in detecting landslide anomalies within the aerial imagery. The entire process involved the selection and analysis of over 120,000 tiles, each acting as a data point to feed the robust anomaly detection framework. The results highlight the potential of integrating advanced pre-processing techniques with GAN-based anomaly detection models, forging a framework for real-time geohazard monitoring and early-warning systems. The results were verified from the confusion matrix parameters to ensure the potential of integrating advanced pre-processing techniques with GAN-based anomaly detection models.

RÉSUMÉ: L'utilisation de l'imagerie aérienne pour repérer les anomalies de glissements de terrain offre une méthode prometteuse d'identification précoce des risques géologiques. GANomaly, un modèle sur les réseaux GAN, apprend à identifier les anomalies en reconstruisant et analysant les erreurs des données normales. Un prétraitement améliore la qualité des images pour un entraînement et test efficaces de GANomaly, incluant l'ajustement RGB, le découpage en tuiles, leur classification, et rotation. Testé sur un grand ensemble de données prétraitées, GANomaly évalue son aptitude à détecter les anomalies de glissements. L'analyse de plus de 120 000 tuiles démontre l'intégration réussie de prétraitement avancé et de détection d'anomalies par GAN, établissant une méthode pour le suivi des géorisques et l'alerte précoce. Les résultats, validés via la matrice de confusion, confirment l'efficacité de cette approche.

Keywords: landslide; aerial imagery; artifical intelligence; anomaly detection.

1 INTRODUCTION

Generative Adversarial Networks (GANs) represent a groundbreaking advancement in the field of artificial intelligence, particularly within the domain of deep learning. Developed by Goodfellow et al. (2014), GANs have improved the way machines understand and generate data. At their core, GANs consist of two neural networks, the generator and the discriminator, engaged in a continuous competition. The generator creates data that is indistinguishable from real data, while the discriminator evaluates this data, differentiating between the authentic and the artificial. This dynamic results in the generator becoming increasingly proficient at producing realistic data, making GANs highly effective for tasks in image generation(Salimans et al., 2016; Zhao et al., 2020), industry(Yan, 2021), and medical purposes(Skandarani et al., 2023; Struski et al., 2023).

GANomaly (Akcay et al., 2018), a variant of GAN, is specifically tailored for anomaly detection. It extends the conventional GAN architecture by introducing an additional encoder network. This setup allows the model not only to generate new data but also to reconstruct input data. In the context of anomaly detection, GANomaly works by training on a dataset of 'normal' instances. The model learns to recreate these instances, and when presented with an anomalous instance, it struggles to reproduce it accurately. This discrepancy in reconstruction is then used as a signal for anomaly detection.

Utilizing aerial imagery for detecting landslide anomalies introduces a transformative method in geohazard analysis. Traditional techniques often emphasized on the diverse appearances of landslides(Bui et al., 2020; Prakash et al., 2021; Syifa et al., 2019). Here, GANomaly's application marks a significant advancement. Unlike conventional methods that depend on labeled datasets, GANomaly excels in unsupervised learning environments. It learns from unlabeled data, detecting anomalies by their deviation from 'normal' patterns. This is especially beneficial in contexts where anomalies are infrequent or ambiguous(Ferrari et al., 2023; Han & Chang, 2023; Li et al., 2020; Madzia-Madzou & Kuijf, 2022). GANomaly's sophisticated pattern recognition abilities are adept at identifying early indicators of land shifts or unusual terrain features, enabling proactive risk mitigation and timely response in landslide management.

This study aims to apply GANomaly, an advanced variant of Generative Adversarial Networks (GANs), in the analysis of aerial imagery for detecting landslide anomalies. The approach is structured into two key phases: an extensive training phase and a subsequent testing phase. The training phase emphasized on preparing the GANomaly model to accurately identify and distinguish normal terrain from potential landslide anomalies. It began with the RGB Adjustment of the aerial images, where the color channels were tuned to enhance the consistancy on overall RGB characteristics. Following this, the images were segmented into smaller tiles. Further, these tiles were classified where they were categorized based on distinct terrain features. This step aids in training the model the various characteristics of normal terrain. To augment the dataset and enhance the model's ability to recognize patterns from different perspectives, these tiles were then subjected to rotations. This rotational variation ensures that the model is robust and can accurately identify anomalies irrespective of the orientation of the features in the imagery. The testing phase was designed to rigorously evaluate the model's effectiveness. This phase employs a smaller batch of normal tiles to ensure the model's accuracy in recognizing normal terrain patterns without raising false positives. Additionally, the model is tested with known abnormal tiles, which contain features characteristic of landslide anomalies. This step is pivotal in verifying the model's capability to detect deviations from normal terrain patterns.

2 METHODOLOGY AND RESULTS

2.1 Description of aerial images

The aerial images utilized in this study were specifically sourced from the mountainous regions within the Fuxing District of Taoyuan City, Taiwan. This area, known for its complex terrain and susceptibility to landslides, presents an ideal location for analysing the capabilities of GANomaly in detecting terrain anomalies.

The aerial images for this study were captured using aerial remote sensing aircraft, operated by the Aerial Survey and Remote Sensing Branch of the Forestry and Nature Conservation Agency, under the Ministry of Agriculture. These aircraft were flown at an altitude of 35,000 feet. The orthophoto images obtained were corrected by ground control points, and adjusted by digital orthoimage mosaicking and toning, ensuring a consistent scale and an accurate representation of the earth's surface. Each image possesses a resolution of 25 cm, which is an essential benefit for the detailed and precise identification of potential landslide anomalies in the complex terrain of the study area.

2.2 Procedure for image pre-processing

In this study, an image pre-processing procedure was employed to prepare aerial images for the training and testing of the GANomaly model, focusing on landslide anomaly detection. The procedure commenced with an step of RGB profile adjustment. The aerial images, containing three channels, were standardized against a base image chosen for its optimal RGB balance. This involved a comparison of the RGB histograms of all images against the base image. The mean values of these histograms were then adjusted to align with those of the base image, ensuring a consistence on RGB profile representation across the dataset. This step aims to establish a consistent coloration for the accurate identification and analysis of terrain features. Figure 1 presents the base image (Image 1) along with its corresponding RGB histograms and mean values. Figure 2 and Figure 3 illustrate the images before (Image 2) and after (Image 3) RGB adjustment, respectively.

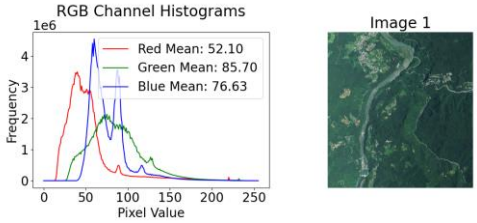

Figure 1. Plot of RGB histograms of the base image.

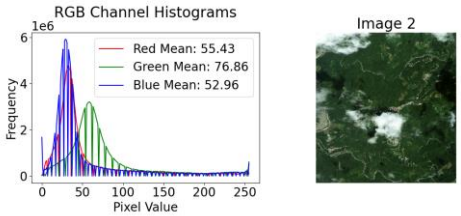

Figure 2. Plot of RGB histograms of the image required adjustment.

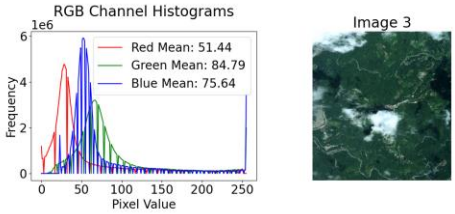

Figure 3. Plot of RGB histograms of the image after RGB adjustment.

Following the RGB profile adjustment, the images were sliced into tiles, each measuring 128×128 pixels. This slicing step allowed for a more granular examination of the terrain, enabling the GANomaly model to focus on specific areas and detect subtle anomalies that might be indicative of potential landslide risks. The smaller size of the tiles ensures that even minor variations in the terrain are captured and analysed.

To further refine the dataset, a classification of tiles was implemented. Tiles were categorized based on prominent terrain features visible in images, such as trees, agricultural land, buildings, roadways, rivers, and riverbanks. This classification allowed for a detailed characterization of normal terrain, establishing a baseline for the model to identify deviations that signify anomalies.



Figure 4. Examples of tiles classified as trees.



Figure 5. Examples of tiles classified as agricultural land.

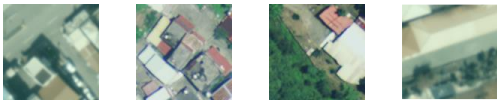

Figure 6. Examples of tiles classified as buildings.

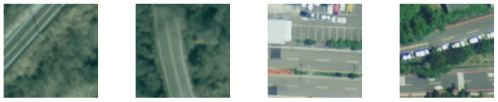

Figure 7. Examples of tiles classified as roadways.



Figure 8. Examples of tiles classified as rivers.

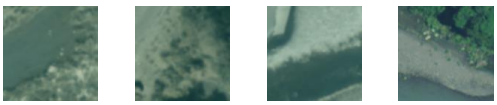

Figure 9. Examples of tiles classified as riverbanks.

The final step in the preparation process was the rotation of tiles. Each tile underwent rotations at angles of 90, 180, and 270 degrees, as shown in Figure 10. This step was particularly important for addressing the disparity in the number of tiles available for certain categories. Notably, the categories of agricultural land, buildings, roadways, rivers, and riverbanks were underrepresented compared to the number of tiles depicting trees. By rotating the tiles, the study effectively augmented the dataset for these less represented categories, ensuring a more balanced and comprehensive training set for the GANomaly model.

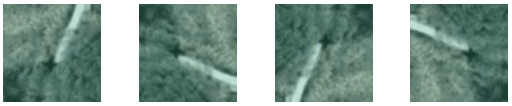

Figure 10. Examples of tiles after rotation.

2.3 Training

The training stage of the GANomaly model is designed to equip the model with the ability to accurately identify potential landslide anomalies in aerial imagery. The primary purpose of this training was to enable GANomaly to learn and differentiate between various terrain features, particularly focusing on patterns that deviate from what is typically observed in normal landscapes. For the training process, a substantial dataset comprising approximately 120,000 tiles was used in the training stage. This large number of tiles ensured that the model was exposed to a wide range of terrain features and conditions, thereby improving its learning and accuracy.

A significant portion of this dataset, about 100,000 tiles, represented areas covered with trees. Trees often dominate aerial imagery in mountainous regions, making them an component of the dataset for the model to understand and recognize as part of normal terrain. The remaining 20,000 tiles were evenly distributed among other crucial categories, namely agricultural land, buildings, roadways, rivers, and riverbanks. This equal division of the remaining tiles among these categories was strategically implemented to provide a balanced representation of various terrain types.

Among the mountainous regions, given the lower availability of tiles in these categories compared to those depicting trees, the approach of rotation tiles ensured that the model was not overly biased towards tree-covered areas and could effectively recognize and analyze a diverse range of terrain features. This balanced training approach was pivotal in preparing GANomaly for the task of landslide anomaly testing and detection, ensuring it could operate effectively across the varied landscapes present in the mountainous aerial imagery.

2.4 Testing and results

For the testing stage of the GANomaly model, a database comprising both normal and abnormal tiles was used. The normal tiles, amounting to 5,800 in total, were selected from the same aerial imagery of the mountainous areas in the Fuxing District. However, these tiles were distinct from those used in the training dataset, ensuring a rigorous testing process. In the distribution of these normal tiles, about half, or approximately 2,900 tiles, represented tree-covered areas. The remaining half was evenly divided among other categories: agricultural land, buildings, roadways, rivers, and riverbanks. This distribution was designed to mirror the diverse landscape features of the region and provide a comprehensive basis for testing the model's accuracy in differentiating normal terrain features. The number of 100 abnormal tiles were collected through visual inspections of landslide-affected areas. These tiles were used in evaluating the model's efficacy in detecting anomalies that are characteristic of landslide occurrences. Some example tiles in abnormal class are shown in Figure 11.

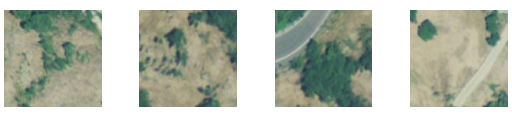

Figure 11. Examples of abnormal tiles in testing stage.

During the testing procedure, a receiver operating characteristic (ROC) curve was generated to determine the effectiveness of the model in distinguishing between normal and abnormal tiles, as shown in Figure 12. Two threshold determination approaches were employed: Youden's J statistic(Youden, 1950) and the closest to top-left threshold method. These approaches yielded the best threshold values of 0.0047 and 0.0048, respectively.

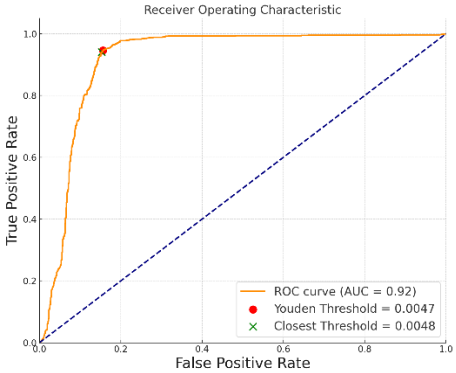

Figure 12. ROC curve in testing stage.

Adopting a threshold value of 0.00475 for the final analysis, the results were quantified using a confusion matrix. The metrics derived from this analysis were: an area under the curve (AUC) of 0.917, an accuracy rate of 0.895, an F1 score of 0.900, a precision of 0.857, and a recall of 0.947. These results indicated a high level of efficacy of the GANomaly model in detecting landslide anomalies, demonstrating its potential as a powerful tool in geohazard monitoring and risk assessment. The combination of high accuracy, precision, and recall underscores the model's reliability in identifying both the presence and absence of landslide-related anomalies in the aerial imagery.

3 CONCLUSIONS

In this study, we demonstrated the potential of employing GANomaly, an advanced Generative Adversarial Network model, for detecting landslide anomalies in aerial imagery of Fuxing District's mountainous terrain. Our methodology involved an training database of around 120,000 tiles, predominantly featuring tree-covered areas, balanced with a variety of other terrain types. This diverse dataset ensured a comprehensive and effective learning process for the GANomaly model. The testing phase, using 5,800 normal and 100 visually-inspected abnormal tiles, validated the model's precision in anomaly detection. The application of ROC curve analysis and optimal threshold determination through Youden's J statistic and closest to top-left threshold methods resulted in performance metrics: an AUC of 0.917, an accuracy of 0.895, and an F1 score of 0.900.

These results feature the potential of artifical intelligence in enhancing geohazard monitoring and risk assessment. The integration of GANomaly in high-resolution aerial imagery analysis marks a significant advancement in environmental monitoring, paving the way for more sophisticated, real-time monitoring systems.

ACKNOWLEDGEMENTS

The project presented in this article was supported by Office of Road and Accessary Maintenance, Taoyuan City.

REFERENCES

Akcay, S., Atapour-Abarghouei, A., & Breckon, T. P. (2018). GANomaly: Semi-Supervised Anomaly Detection via Adversarial Training. https://doi.org/10.48550/ARXIV.1805.06725

Bui, T.-A., Lee, P.-J., Lum, K.-Y., Loh, C., & Tan, K. (2020). Deep Learning for Landslide Recognition in Satellite Architecture. IEEE Access, 8, 143665–143678. https://doi.org/10.1109/ACCESS.2020.3014305

Ferrari, N., Fraccaroli, M., & Lamma, E. (2023). GRD-Net: Generative-Reconstructive-Discriminative Anomaly Detection with Region of Interest Attention Module. International Journal of Intelligent Systems, 2023, 1–18. https://doi.org/10.1155/2023/7773481

Goodfellow, I. J., Pouget-Abadie, J., Mirza, M., Xu, B., Warde-Farley, D., Ozair, S., Courville, A., & Bengio, Y. (2014). Generative Adversarial Networks. https://doi.org/10.48550/ARXIV.1406.2661

Han, Y., & Chang, H. (2023). XA-GANomaly: An Explainable Adaptive Semi-Supervised Learning Method for Intrusion Detection Using GANomaly. Computers, Materials & Continua, 76(1), 221–237. https://doi.org/10.32604/cmc.2023.039463

Li, Z., Zhao, G., Yin, A., Wang, T., Chen, H., Guo, L., Yang, H., Yang, J., & Lin, C. (2020). CS-GANomaly: A Supervised Anomaly Detection Approach with Ancillary Classifier GANs for Chromosome Images. 2020 IEEE 3rd International Conference of Safe Production and Informatization (IICSPI), 492–499. https://doi.org/10.1109/IICSPI51290.2020.9332331

Madzia-Madzou, D. K., & Kuijf, H. J. (2022). Progressive GANomaly: Anomaly detection with progressively growing GANs. https://doi.org/10.48550/ARXIV.2206.03876

Prakash, N., Manconi, A., & Loew, S. (2021). A new strategy to map landslides with a generalized convolutional neural network. Scientific Reports, 11(1), 9722. https://doi.org/10.1038/s41598-021-89015-8

Salimans, T., Goodfellow, I., Zaremba, W., Cheung, V., Radford, A., & Chen, X. (2016). Improved Techniques for Training GANs. https://doi.org/10.48550/ARXIV.1606.03498

Skandarani, Y., Jodoin, P.-M., & Lalande, A. (2023). GANs for Medical Image Synthesis: An Empirical Study. Journal of Imaging, 9(3), 69. https://doi.org/10.3390/jimaging9030069

Struski, Ł., Urbańczyk, T., Bucki, K., Cupiał, B., Kaczyńska, A., Spurek, P., & Tabor, J. (2023). MeVGAN: GAN-based Plugin Model for Video Generation with Applications in Colonoscopy. https://doi.org/10.48550/ARXIV.2311.03884

Syifa, M., Kadavi, P., & Lee, C.-W. (2019). An Artificial Intelligence Application for Post-Earthquake Damage Mapping in Palu, Central Sulawesi, Indonesia. Sensors, 19(3), 542. https://doi.org/10.3390/s19030542

Yan, K. (2021). Chiller fault detection and diagnosis with anomaly detective generative adversarial network. Building and Environment, 201, 107982. https://doi.org/10.1016/j.buildenv.2021.107982

Youden, W. J. (1950). Index for rating diagnostic tests. Cancer, 3(1), 32–35. https://doi.org/10.1002/1097-0142(1950)3:1<32::AID-CNCR2820030106>3.0.CO;2-3

Zhao, S., Liu, Z., Lin, J., Zhu, J.-Y., & Han, S. (2020). Differentiable Augmentation for Data-Efficient GAN Training. https://doi.org/10.48550/ARXIV.2006.10738.

Proceedings of the XVIII ECSMGE 2024
GEOTECHNICAL ENGINEERING CHALLENGES
TO MEET CURRENT AND EMERGING NEEDS OF SOCIETY
© 2024 the Authors
ISBN 978-1-032-54816-6
DOI 10.1201/9781003431749-255
Open Access: www.taylorfrancis.com, CC BY-NC-ND 4.0 license

ECSMGE 24
XVIII EUROPEAN CONFERENCE ON SOIL MECHANICS AND GEOTECHNICAL ENGINEERING

Development and experimental calibrations of a multifunction slope monitoring device - Smart Pole

Développement et étalonnages expérimentaux d'un dispositif de surveillance multifonctionnel de pente - Mât Intelligent

C.H. Wang*
Dept. of Civil Engineering, Chung Yuan Christian University, Taoyuan City, Taiwan (R.O.C.)

S.Y. Jeng, B.J. Hou
Dept. of Electronic Engineering, Chung Yuan Christian University, Taoyuan City, Taiwan (R.O.C.)

Y.T. Hu
Dept. of Civil Engineering, Chung Yuan Christian University, Taoyuan City, Taiwan (R.O.C.)

**chwang@cycu.edu.tw*

ABSTRACT: Slope failures pose a significant threat to infrastructure and human safety, primarily influenced by factors such as rainfall, surface runoff, changing soil water content, and slope movement. However, most of the existing technologies rely on separate devices with limited integration capabilities. This study addresses these limitations by developing the Smart Pole, a multifunctional slope monitoring device. Equipped with sensors including a rain gauge, humidity and temperature sensor, surface water runoff sensor, camera, soil moisture content sensor, and an Inertial Measurement Unit (IMU), the Smart Pole offers versatility in assembling and disassembling sensors to meet specific monitoring needs. The device incorporates a power supply system and a Microcontroller Unit (MCU) for data collection, processing, and transmission using LoRa technology. This article introduces the purpose, functional requirements, and components of the Smart Pole. Additionally, laboratory calibration and field testing were conducted to validate the Smart Pole's performance. The testing process presents the calibration process of the device's soil water content measurements. The final performance presents the integration of the Smart Pole.

RÉSUMÉ: Les glissements de terrain représentent une menace significative pour l'infrastructure et la sécurité humaine, influencés principalement par des facteurs tels que les précipitations, le ruissellement de surface, la variation de la teneur en eau du sol, et les mouvements de pente. Cependant, la plupart des technologies existantes reposent sur des dispositifs séparés avec des capacités d'intégration limitées. Cette étude aborde ces limitations en développant le Mât Intelligent, un dispositif de surveillance de pente multifonctionnel. Équipé de capteurs tels qu'un pluviomètre, un capteur d'humidité et de température, un capteur de ruissellement d'eau de surface, une caméra, un capteur de teneur en humidité du sol, et une Unité de Mesure Inertielle (IMU), le Mât Intelligent offre une polyvalence dans l'assemblage et le désassemblage des capteurs pour répondre aux besoins spécifiques de surveillance. Le dispositif intègre un système d'alimentation et une Unité de Microcontrôleur (MCU) pour la collecte, le traitement et la transmission des données via la technologie LoRa. Cet article présente l'objectif, les exigences fonctionnelles et les composants du Mât Intelligent. De plus, une calibration en laboratoire et des tests sur le terrain ont été réalisés pour valider les performances du Mât Intelligent. Le processus de test illustre la calibration de l'appareil pour les mesures de la teneur en eau du sol. La performance finale met en avant l'intégration du Mât Intelligent.

Keywords: Slope stability; monitoring device; laboratory calibration.

1 INTRODUCTION

In landscapes susceptible to the repercussions of vigorous meteorological events, understanding and analysing rainfall-induced slope failures become crucial. The failure of slopes due to excessive rainfall has a sequence of occurring in stages, initiating with the saturation of the slope surface and followed by infiltration into the interior of the slope. This process can induce several potential slope failure conditions, such as deformations, cracks, sliding, and in dire situations, complete slope collapse. It's noteworthy that the acceleration in the severity of deformation is often directly related to increasing rainfall amount, thus necessitating a deeper examining monitoring and mitigation strategies in the context of these phenomena. To effectively manage and potentially

curtail the progression of failure phenomena, a diligent monitoring framework is indispensable.

To accomplish the objective of gathering field data for subsequent data analysis, Karunarathne et al. (2020) illustrated the use of an Internet of Things (IoT) device equipped with wireless communication capabilities for monitoring landslides. This research highlighted the evolution of IoT technology for data collection, curation, and presentation, with the potential for future machine learning applications. Accompany with the landslide susceptibility assessment, Jeong et al. (2020) utilized wireless sensor network technology to connect multiple individual sensors to monitor a potential slope failure threatened by rainfall events. With the assistance of diverse monitoring sensors, Bai et al. (2020) constructed a microservices architecture incorporating a web service to enhance the provision of early warning services for landslide hazards. Li et al. (2021) developed a risk assessment methodology that leveraged 5G and IoT technology to measure potential landslide indicators, including surface displacement, rainfall, and ground cracks. This early warning system was implemented and validated using an actual project as an example. To explore the failure mechanism of shallow landslides, research by Bovolenta et al. (2020) has revealed that the water content of the slope surface serves as a important indicator for reliably illustrating the slope failure process. Chen et al. (2020) presented the calibration and filed performance of the tilting measurements on a underground structure in a landslide area.

Monitoring is important for tracking slope failures, collecting data for future models, and enhancing safety and sustainability. This study presents the Smart Pole device, equipped with sensors for soil water content, runoff, humidity, temperature, tilt, camera, and rain gauge, plus a MCU, storage, and power. This article presents calibrating the soil water content sensor and the camera's trigger mechanism, activating at excessive tilt.

2 DESIGN AND METHODOLOGY

An effective monitoring system comprehensively incorporates multiple factors that contribute to potential failure, with rainfall amount being at the forefront. However, merely observing rainfall quantities is not sufficient. Analysing the soil water content of the slope surface offers insight into the amount of infiltration, which is a key element influencing slope stability. Once surface runoff is initiated, the velocity of water runoff and the volume of water accumulating on the slope during flow can affect the stability and erosion of the slope.

When slopes begin revealing signs of failure, observing and recording of the slope inclination can provide important indications regarding possible initiation and progression of failure. Employing on-site cameras, which can be triggered when certain failure criteria are met, can offer visual documentation of the failure process. Additionally, considering environmental factors like humidity and temperature is also crucial, as these can influence the micro-environmental conditions of the slope.

As illustrated in Figure 1, the distinct levels of the Smart Pole were each equipped with sensors meticulously tailored to gauge different parameters and facets of slope stability. Among the various sensors, there are two functional blocks. Each block has its own memory storage and MCU. A key distinction lies in the triggering logic for the camera. As illustrated in Figure 1, when IMU records a tilting angle surpassing a specific threshold—such as exceeding 15°—the camera is triggered to capture a picture.

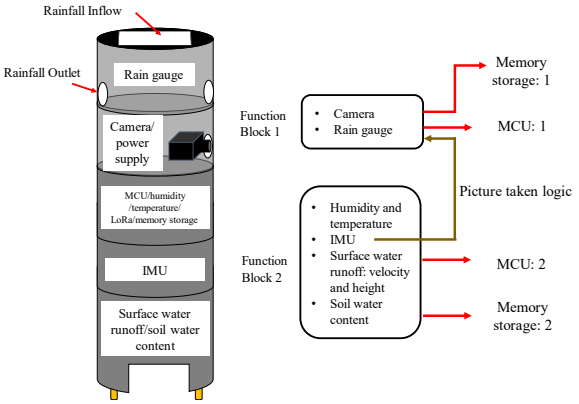

Figure 1. Scheme of Smart Pole device.

3 CALIBRATION AND PROTOTYPE ASSEMBLY DEMONSTRATION

3.1 Calibration of soil moisture measurement

The function of measuring soil moisture was utilized by the YL-69 hydrometer sensor. Three distinct soil types were meticulously prepared for calibration purposes: reddish laterite clay (typical to the local soil), Ottawa sand, and a 1:1 weight mixture of reddish laterite and Ottawa sand. Utilizing the Harvard Miniature Compaction approach, soil samples were produced with a height of 71mm and a diameter of 33mm. Soil samples were compacted using a combination of diverse of dry soils and water. Water content within the soil samples was determined by calculating the weight of the water added to the dry

soils. As indicated in Figure 2, The YL-69 sensor was inserted into each soil sample, and analogue readings were recorded. Note that, to prevent loss of water content during measurement, the sample with the YL-69 was sealed inside a plastic bag, which is not shown in Figure 2.



Figure 2. Calibration process of soil water content sensor.

In the scope of this study, both the volumetric water content (VWC) and gravimetric water content (GWC) were calibrated with sensor, providing a holistic view of the moisture within the soil samples. The calibration results are depicted in Figures 3 and Figure 4, which also display the calibration equations for the reddish laterite. These equations will subsequently be utilized in the following demonstration step.

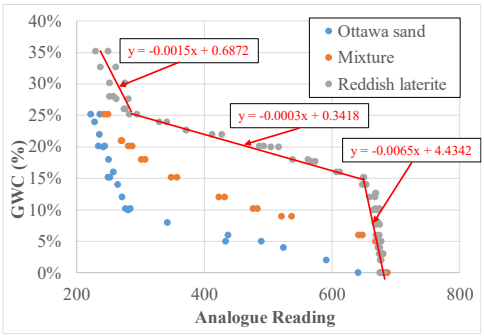

Figure 3. Calibration results of gravimetric water content (GWC) versus YL-69 analogue readings for 3 types of soils.

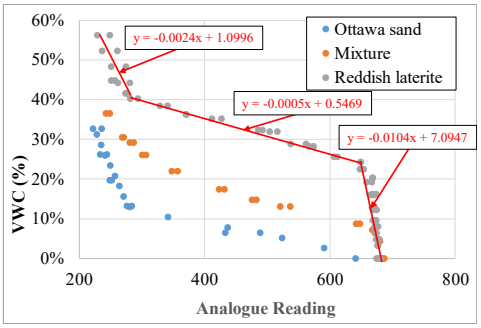

Figure 4. Calibration results of volumetric water content (VWC) versus YL-69 analogue readings for 3 types of soils.

3.2 Prototype assembly demonstration

Figure 5 displays the prototype of the Smart Pole device, with the left side illustrating the inner levels with various sensors, and the right side depicting the finished exterior. Figure 6 illustrates the field setup for measuring soil water content. On the left side of Figure 6, picture shows that the YL-69 sensor was inserted on the surface of the local soil (reddish laterite), while the right side demonstrates a laptop computer used for data collection via LoRa. The initial soil condition was dry; by pouring water from a bottle, as indicated in Figure 7, the measured analogue reading indicates increasing GWC. Figure 7 demonstrates a good agreement when compared to the calibrated data presented in Figure 3.

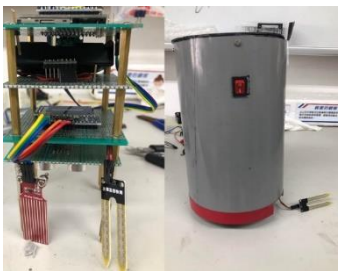

Figure 5. Smart Pole device.



Figure 6. Field testing on measuring water content.

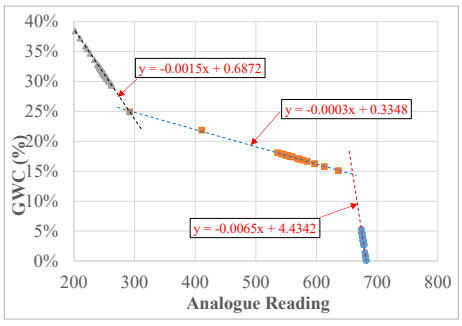

Figure 7. Field testing on gravimetric water content (GWC) versus YL-69 analogue readings.

Figure 8 displays the setup for triggering the camera action based on the tilting angles measured by the IMU (model: MPU6050). As shown in Figures 9 and 10, when the measured tilting angles exceed 15° in the X direction, a picture was taken to show the surroundings, as picture shown on the right side of Figure 8. The angle of 15 degrees was chosen arbitrarily for a functional test with taking only a single image. In future developments, the tilting angle can be set more purposefully according to specific requirements, with multiple pictures captured as

needed. For further exploration, since central MCU processes all the signals within devise, additional data could serve as criteria for triggering picture capture, such as the amount of rainfall accumulation, rainfall intensity, a combination of tilting on different directions measured by the IMU, surface water runoff conditions, and soil water content.



Figure 8. Field testing on camera action triggering.

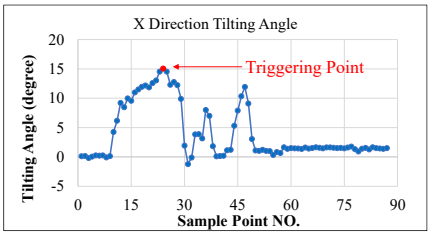

Figure 9. Field testing on camera action triggering.

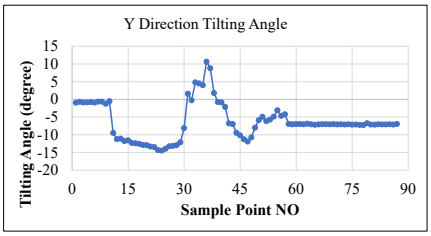

Figure 10. Field testing on camera action triggering.

4 CONCLUSIONS

This study introduces the Smart Pole device, aiming to address the challenges associated with slope failures, particularly those prone to occur during rainfall events. The primary objective of this device is to meticulously monitor and gather physical data related to the various factors affecting slope stability. The Smart Pole incorporates an array of sensors, encompassing measurements such as soil water content (e.g., GWC and VWC), surface runoff velocity and depth, slope tilting angle, humidity, temperature, camera, and a rain gauge. Each of these sensors was tailored to capture distinct micro-environmental parameters crucial for assessing slope stability.

Empowered by its self-contained power source and data transmission capability via LoRa, the Smart Pole was proficient in providing real-time data for in-depth analysis of rainfall-induced slope failures. Additionally, it served the purpose of an early warning system. To showcase the capabilities of this device, the study conducted laboratory calibrations for GWC and VWC using three different soil types: Ottawa sand, reddish laterite clay, and a 1:1 mixture of Ottawa sand and reddish laterite clay. Furthermore, a field test demonstrated the measurement of GWC in the field, with data collected and transmitted through LoRa. The Smart Pole's triggering mechanism, which activated a built-in camera based on measured tilting angles from an IMU sensor, was also showcased. This feature allowed the device to potentially record immediate environmental changes during critical slope movements.

In summary, the Smart Pole, along with its comprehensive design, calibration methods, and validated functionalities, not only enriches existing academic and practical knowledge but also lays the foundation for future research and field applications in this domain.

ACKNOWLEDGEMENTS

The authors are grateful for the financial support provided by John Su Foundation.

REFERENCES

Bai, D., Tang, J., Lu, G., Zhu, Z., Liu, T., & Fang, J. (2020). The design and application of landslide monitoring and early warning system based on microservice architecture. *Geomatics, Natural Hazards and Risk*, *11*(1), 928–948. https://doi.org/10.1080/19475705.2020.1766580.

Bovolenta, R., Iacopino, A., Passalacqua, R., & Federici, B. (2020). Field Measurements of Soil Water Content at Shallow Depths for Landslide Monitoring. *Geosciences*, *10*(10), 409. https://doi.org/10.3390/geosciences10100409.

Chen, I.-H., Lin, Y.-S., & Su, M.-B. (2020). Computer vision–based sensors for the tilt monitoring of an underground structure in a landslide area. *Landslides*, *17*(4), 1009–1017. https://doi.org/10.1007/s10346-019-01329-x.

Jeong, S., Ko, J., & Kim, J. (2020). The Effectiveness of a Wireless Sensor Network System for Landslide Monitoring. *IEEE Access*, *8*, 8073–8086. https://doi.org/10.1109/ACCESS.2019.2960570.

Karunarathne, S. M., Dray, M., Popov, L., Butler, M., Pennington, C., & Angelopoulos, C. M. (2020). A technological framework for data-driven IoT systems: Application on landslide monitoring. *Computer Communications*, *154*, 298–312. https://doi.org/10.1016/j.comcom.2020.02.076.

Li, Z., Fang, L., Sun, X., & Peng, W. (2021). 5G IoT-based geohazard monitoring and early warning system and its application. *EURASIP Journal on Wireless Communications and Networking*, *2021*(1), 160. https://doi.org/10.1186/s13638-021-02033-y.

Proceedings of the XVIII ECSMGE 2024
GEOTECHNICAL ENGINEERING CHALLENGES
TO MEET CURRENT AND EMERGING NEEDS OF SOCIETY
© 2024 the Authors
ISBN 978-1-032-54816-6
DOI 10.1201/9781003431749-256
Open Access: www.taylorfrancis.com, CC BY-NC-ND 4.0 license

ECSMGE 24
XVIII EUROPEAN CONFERENCE ON SOIL MECHANICS AND GEOTECHNICAL ENGINEERING

The A83 Loch Shira landslide, Scotland

Le glissement de terrain A83 du Loch Shira, en Écosse

M.G. Winter*
Winter Associates, Kirknewton, Scotland, United Kingdom

T. Waaser, G. Fiddes
Transport Scotland, Glasgow, United Kingdom

**mwinter@winterassociates.co.uk*

ABSTRACT: The A83 Loch Shira landslide has been active since the early-1990s, and this paper will present a brief history of this mass movement. Significant movements are evident in the bund immediately adjacent to the road, narrowing the verge from around 2m in 1995 to effectively zero in places. Movement is also apparent in the cut slope above the bund and evidenced clearly by the significant distortion of a catch pit, the date of installation of which, while post-1995, is unknown. The movement of the landslide is driven by groundwater, specifically water from rockhead at the interface with the superficial deposits. This drives movement downslope to the stiffer complex formed by a retaining wall, the road and the rockfill bund adjacent to the road. In 1995 it was postulated that this stiffer complex could store energy and potentially lead to a catastrophic failure. The movement of the bund and the cut slope above seems likely to be a manifestation of a limited pressure (or energy) release and the current state of the landslide is of concern. The potential adverse influences of climate change on the landslide include increased water in the system from both direct rainfall and recharged groundwater, storm effects on the retaining wall and erosion of the slope above the retaining wall from increased road runoff.

RÉSUMÉ: Le glissement de terrain A83 du Loch Shira est actif depuis le début des années 1990, et cet article présentera un bref historique de ce mouvement de masse. Des mouvements importants sont évidents dans la digue immédiatement adjacente à la route, rétrécissant l'accotement d'environ 2 m en 1995 à effectivement zéro par endroits. Le mouvement est également apparent dans la pente coupée au-dessus de la digue et mis en évidence par la déformation importante d'un puisard dont la date d'installation, bien que postérieure à 1995, est inconnue. Le mouvement du glissement de terrain est entraîné par les eaux souterraines, en particulier l'eau de la tête rocheuse à l'interface avec les dépôts superficiels. Cela entraîne un mouvement vers le bas de la pente vers le complexe plus rigide formé par un mur de soutènement, la route et la digue en enrochement adjacente à la route. En 1995, il a été postulé que ce complexe plus rigide pourrait stocker de l'énergie et potentiellement conduire à une défaillance catastrophique. Le mouvement de la digue et de la pente de coupe au-dessus semble être la manifestation d'une libération de pression (ou d'énergie) limitée et l'état actuel du glissement de terrain est préoccupant. Les influences négatives potentielles du changement climatique sur le glissement de terrain comprennent l'augmentation de l'eau dans le système à partir des précipitations directes et des eaux souterraines rechargées, les effets des tempêtes sur le mur de soutènement et l'érosion de la pente au-dessus du mur de soutènement due à l'augmentation du ruissellement routier.

Keywords: Landslide; instability; drainage road; infrastructure.

1 INTRODUCTION

Loch Shira is located approximately 65 km to the northwest of Glasgow (Figure 1) and the A83 trunk (strategic) road to mid-Argyll follows its shoreline on the approach to Inverary.

Since the earliest history of the landslide in the 1970s, only relatively minor works have been undertaken to reduce instability. The site was highlighted as high risk in the Scottish Road Network Landslides Study (Winter et al., 2005, 2008, 2013).

In this paper we examine the history of the landslide and indicate the likely approach to remediation.

2 HISTORY

In the mid-1970s a 1 m high masonry retaining wall that showed signs of distress was removed and the toe of the slope cut back. Soon after, what was described as a major slip occurred and, following emergency works to clear the road, a 2m high gabion basket wall was installed with rockfill behind.

In 1992 the stability of the gabion basket wall was questioned. The wall showed signs of bulging, the baskets were rounded in shape and the fill seemed to be loose. There was no evidence of any compromise to the overall stability of the wall.

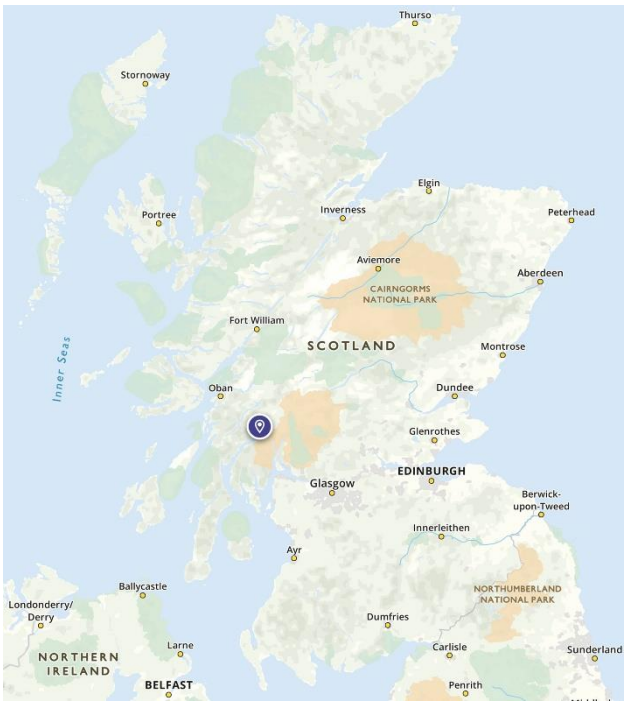

Figure . Map of Scotland (excluding Orkney and Shetland) showing the location of the Loch Shira landslide.

At this time the slope was inspected and multiple shallow slip circles and scarps up to 300 mm in height identified. Trees with vertical trunks of 3 m to 5 m height were [erroneously] cited as evidence of a lack of movement. Monitoring pins were established on the road, the top of the wall and on the slope; no movement of the pins was recorded between December 1992 and March 1994.

In April 1994, 15 mm to 20 mm of rotational movement was recorded [it remains unclear how this was determined to be rotational movement]. An emergency contract was let to remove the gabion wall and trim the cut slope to 1:2. During the contract there was a slope failure at the southern end of the works and remedial works were extended 20 m in this direction. Movement began at the northern end of the works and a 0.5 m rockfill blanket was installed at the toe of the cut slope. The contract was completed in June 1994 and the surface of the cut slope left exposed to allow visual detection of water flow. In September 1994 slope filter drains were installed and a minor slope failure repaired.

In December 1994, exceptionally heavy rainfall caused two minor slips above the surface water cut-off drain at the top of the cut slope. Further emergency works were carried out to repair the drainage system and to install a 6 m high rockfill bund extending 80 m along the toe of the slope. During these works extensive cracking was observed in the area above the cut slope. Extensive monitoring using wooden surface pegs was established and this minor downslope movement over the next six to 12 months.

Contemporaneous, local rainfall data is not available. The nearest current gauge is at Loch Restil which gives an average annual rainfall for 2013 to 2022 of 3,341 mm with a range of 2,613 to 4,110 mm. However, the distance (approximately 12 km) from and relative elevation (around 250 m higher) of this gauge to Loch Shira does perhaps question whether this is entirely representative. In addition, Inverary is anecdotally known for having something of a microclimate with unverified sources suggesting annual average rainfall closer to 1,600 mm.

In April 1995, the first author and a colleague undertook an assessment of the slope (Figure 2). The primary conclusion of that work was that the failure was most likely controlled by water pressure at rockhead. Both old and new scarps were identified, recent slips in the regraded cut slope were observed and the entire area of the landslide was wet with some areas being identified as particularly boggy. Streams, both active and ephemeral were encountered, some of which fed into tension cracks and/or scarps. Other slips were identified in the area outside the landslide as might be expected.

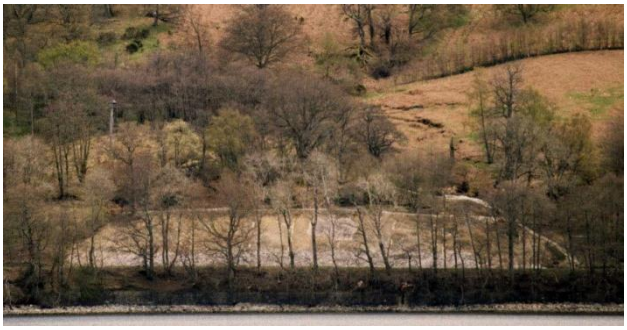

Figure 2. The Loch Shira landslide in 1995.

The depth to the Phyllite rockhead (Anon., 1897; Hill et al., 1905) at road level was, to some degree, uncertain (see Figure 3) and fundamental to the likely behaviour of the landslide. While only minor movements had been observed since the December 1994 rainfall, it was considered that further such rainfall could initiate further significant movement. The prevalence of an extensive network of drainage ditches talking water from a former forestry plantation to the head of the landslide and the removal of the trees were considered to be contributory factors. A full ground investigation was recommended and designed and supervised in summer 1995 by the first author.

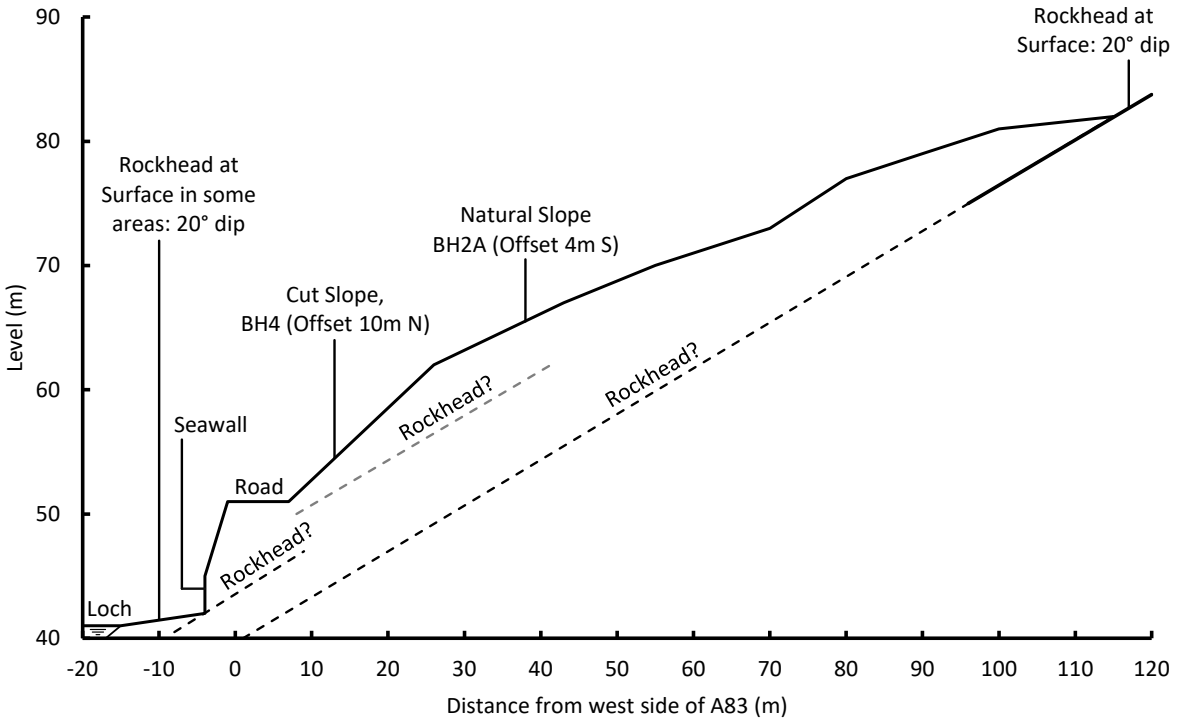

Figure 3. East-west section through the Loch Shira slope: the landslide is approximately 100m at road level.

The investigation comprised 10 boreholes sunk primarily by cable percussion, although four were sunk into bedrock by rotary drilling, and eight trial pits were sunk to depths of between 2.8 and 5.2 m with the extensive use of benching and trench support. Fifteen standpipe piezometers were installed (11 single installations and two twin installations) in the boreholes and trial pits to enable the long-term monitoring of groundwater; inclinometer tubes were installed in boreholes at the outer edge of the road to allow the long-term monitoring of subsurface lateral displacements.

The piezometer in the centre of the landslide regularly exhibited hydrostatic pressures in excess of 2.5 m above ground level. This broadly confirmed the hypothesis that high water pressures at the soil-rock interface were a major cause of instability.

Rockhead was originally conjectured in three locations but the ground invcestigation conformed the deeper location with daylighting at the loch shore.

3 RECENT CONDITION

Following the ground investigation, a remedial design was developed to stabilise the landslide. This involved the removal of ground water and the effective capture of surface water in order to reduce the water content of the soils and increase their strength and therefore the stability of the landslide mass. The design comprised:

- A pattern of downslope drainage on the natural slope consisting of well points to access water entering the landslide linked by a series of deep, lined rockfill trench drains linked to an external drainage system alternating with less deep, lined rockfill trench drains (without well points) on the body of the landslide with adjacent trench drains linked by herringbone drains.
- On the cut slope a system of counterfort drains linked by herringbone drains was proposed.

This preliminary design was not taken forward and there followed a period of almost two decades of irregular inspections which revealed relatively little movement at road level other than a significant degree of distortion to the rockfill bund immediately above the road. This occurred post-1998 when the first author's observations indicate that the rockfill bund remained planar, while by mid-1999 a sinusoidal shape could be observed along its length.

In the early-2010s the inspections recognised that the existing post-1995 drainage provision was in poor condition, effectively failed, and key elements of the drainage system were replaced, and additional drains installed to supplement the existing design in early-2016.

In 2022 (14 April, 18 and 26 October) the site was inspected by the authors as part of Transport Scotland's Vulnerable Locations Operations Group activities, which inter alia include identifying assets that need adaptation to provide adequate resilience to the effects of climate change. It was immediately apparent that there had been significant outward movement of the rockfill bund (Figure 4); as late as 1999 the distance from the toe to the edge of the

running surface was 2m whereas by 2022 the bund was, in places, touching the edge of the running surface.

Inspection of the 2016 drainage scheme revealed measured strains of up to 15% in the downslope direction and up to 10% orthogonally (Figure 5).



Figure 4. The original distance of the toe of the bund from the edge line of the carriageway was approximately 2m, by April 2022 the distance had reduced to zero in places.

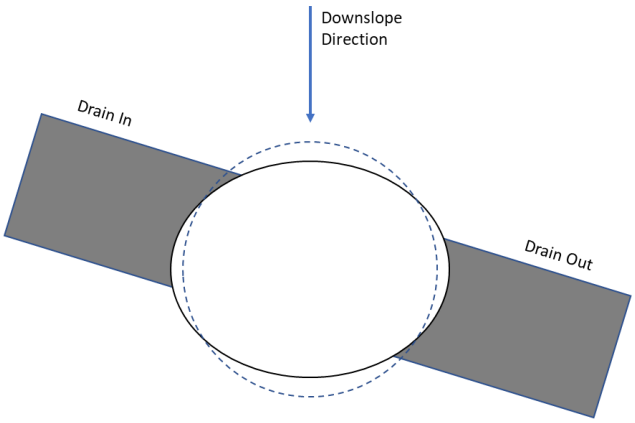

Figure 5. Catch pit plan view showing the original circular shape (600mm diameter, dashed blue line) the current shape of the ellipse (minor axis 510mm, major axis 660mm as a solid black line), the inflow and outflow pipes, and the downslope direction.

4 WAY FORWARD AND CONCLUSIONS

The A83 Loch Shira landslide has been of concern for around three decades.

Recent observations suggest that significant downslope movement is occurring within the landslide mass and that this is manifesting at road level in downslope movement and distortion of the rockfill bund. The major concern is that if the movements are occurring at rockhead then energy is being stored behind the mass formed by the seawall, the road and the slope between, leading to the potential for a brittle failure of those components.

The existing design is heavily predicated towards the use of deep and surface drains to capture groundwater and surface water, as would be expected for a landslide such as that at Loch Shira that is driven by water. These in turn rely on filter drains, including counterfort, herringbone and deep well points and trench drains. Recent work on the longevity of such drains (Nettleton et al., 2022) strongly suggest that significant maintenance of such drains, amounting to renewal of the filtration and drainage media, would be required approximately every 15 to 25 years. This is supported by the fact that the drains installed in the early-1990s had failed and were replaced and supplement in 2016, slightly more than 20 years after installation.

A review of potential remedial solutions is currently underway, but it is difficult to envisage a solution that does not involve large scale drainage features.

ACKNOWLEDGEMENTS

The authors are grateful to Transport Scotland for funding and permission to publish this article.

REFERENCES

Anon. (1897). Inverary. Scotland Sheet 37, One-Inch Series, Drift Edition. Institute of Geological Sciences, Edinburgh.

Hill, J B, Peach, B N, Clough, C T, Kynaston, H, Teall, J J H & Flett, J S. (1905). The geology of Mid-Argyll (Explanation of Sheet 36). Memoir of the Geological Survey, Scotland. British Geological Survey, Edinburgh.

Nettleton, I M, Winter, M G & Duffy-Turner, M. 2022. Forensic examination of Critical Special Geotechnical Measures: Counterfort Drain Information Note. Published Project Report PPR 1034. Transport Research Laboratory, Wokingham.

Winter, M G, Macgregor, F & Shackman, L (Eds.). (2005). *Scottish Road Network Landslides Study*, 119p. Trunk Roads: Network Management Division Published Report Series. The Scottish Executive, Edinburgh.

Winter, M G, Macgregor, F & Shackman, L (Eds.). (2008). *Scottish road network landslides study: implementation*, 278p. Transport Scotland Published Report Series. Transport Scotland, Edinburgh.

Winter, M G, Harrison, M, Macgregor, F & Shackman, L. (2013). Landslide hazard assessment and ranking on the Scottish road network. *Proceedings, Institution of Civil Engineers (Geotechnical Engineering)*, 166(GE6), 522-539. https://doi.org/10.1680/geng.12.00063.

Proceedings of the XVIII ECSMGE 2024
GEOTECHNICAL ENGINEERING CHALLENGES
TO MEET CURRENT AND EMERGING NEEDS OF SOCIETY
© 2024 the Authors
ISBN 978-1-032-54816-6
DOI 10.1201/9781003431749-257
Open Access: www.taylorfrancis.com, CC BY-NC-ND 4.0 license

ECSMGE 24
XVIII EUROPEAN CONFERENCE ON SOIL MECHANICS AND GEOTECHNICAL ENGINEERING

Back analysis of flexible barrier response following an open hillslope landslide impact at Pa Mei, Hong Kong

Analyse rétrospective de la réponse d'une barrière flexible suite à un impact de glissement de terrain sur une pente ouverte à Pa Mei, Hong Kong

E.K.L. Wong*, J.W.C. Lau
Geotechnical Engineering Office, Civil Engineering and Development Department, Hong Kong, China
J.-W. He, Z.-H. Zhou, S.L. Chan
Formerly Hong Kong Polytechnic University, Hong Kong, China
**eugeneklwong@cedd.gov.hk*

ABSTRACT: An open hillslope landslide occurred above Ma Wan New Village at Pa Mei on Lantau Island, Hong Kong in October 2021, involving a total debris volume of approximately 240 m^3. About half of the debris was deposited on the hillside while the rest travelled further downslope to hit the edge panels of two flexible rockfall barriers, which had a rated energy capacity of 3,000 kJ. The debris was stopped and retained by the barriers with limited observable damage to the barriers. This paper documents the back analysis of the response of the flexible barriers using the finite element program LS-DYNA. A numerical simulation was first conducted to replicate a full-scale rockfall test to calibrate the flexible rockfall barrier model. The landslide impact process was then reconstructed numerically and calibrated against field observations. The impact velocity and energy were estimated from free-field debris mobility analysis and coupled debris-barrier interaction. Using the calibrated numerical model, a hypothetical landslide debris impact event close to the energy rating of the barrier system is also investigated. Future work on the design of flexible rockfall barrier systems subjected to landslide debris impact is discussed.

RÉSUMÉ: Un glissement de terrain à pente ouverte s'est produit au-dessus du Nouveau Village de Ma Wan à Pa Mei sur l'île de Lantau, à Hong Kong, en octobre 2021, impliquant un volume total de débris d'environ 240 m^3. Environ la moitié des débris ont été déposés sur le flanc de la colline, tandis que le reste s'est déplacé plus loin vers le bas de la pente pour heurter les panneaux de bord de deux barrières pare-pierres flexibles, d'une capacité énergétique nominale de 3,000 kJ. Les débris ont été arrêtés et retenus par les barrières, avec des dommages visibles limités sur les barrières. Cet article documente l'analyse rétrospective de la réponse des barrières flexibles à l'aide du programme d'éléments finis LS-DYNA. Une simulation numérique a d'abord été réalisée pour reproduire un test de chute de pierres à grande échelle afin de calibrer le modèle de barrière anti-chute flexible. Le processus d'impact du glissement de terrain a ensuite été reconstruit numériquement et calibré par rapport aux observations sur le terrain. La vitesse et l'énergie d'impact ont été estimées à partir d'une analyse de la mobilité des débris en champ libre et de l'interaction couplée débris-barrière. À l'aide du modèle numérique calibré, un événement hypothétique d'impact de débris de glissement de terrain proche de la cote énergétique du système de barrière est également étudié. Les travaux futurs sur la conception de systèmes de barrières anti-pierres flexibles soumis à l'impact des débris de glissements de terrain sont discutés.

Keywords: Flexible barrier; landslide; debris impact; back analysis; LS-DYNA.

1 BACKGROUND

An open hillslope landslide occurred above Ma Wan New Village at Pa Mei, Lantau Island in October 2021. Approximately 110 m^3 of landslide debris impacted on two flexible rockfall barriers (3000 kJ model). The debris was successfully stopped and retained by the flexible barriers with limited observable damage to the barriers. This incident provided a good opportunity for studying the behaviour of rockfall barriers subjected to impact from debris consisting primarily of granular soil.

It was estimated that the landslide occurred in the evening of 9 October 2021 (Fugro, 2022). The shallow landslide was probably rain-induced and was attributed to the development of transient elevated pore water pressures within the colluvium and completely decomposed tuff layers above the shallow bedrock. The landslide source measured approximately 20 m long by 13.5 m wide by 1.5 m deep. The failure volume at the source area was

estimated at 220 m^3. The length of the landslide trail between the crown of the landslide scar and the barriers was approximately 40 m. A debris volume of 20 m^3 was estimated to have been entrained along the landslide path. About a third (80 m^3) of the total landslide debris was observed to have deposited upslope of flexible barrier FW-1A, of which approximately 20 m^3 was retained by the south-eastern edge panel of barrier FW-1A. After impact, the maximum net elongation (outward deflection) of FW-1A was found to be about 2.3 m measured from the barrier axis (i.e. line connecting base of barrier posts) from hand-held LiDAR scanning. The residual height of the barrier net was 84% of the original minimum net height of 4.9 m. The rest of the debris (160 m^3) deposited upslope of lower barrier FW-1B, of which approximately 90 m^3 was retained behind the barrier net in its north-western edge panel. The maximum net elongation of FW-1B after impact measured 2.8 m from the barrier axis. The residual height of the barrier net was 78% of the original minimum net height.

2 FLEXIBLE BARRIER SYSTEM

Six separate flexible barriers totalling approximately 388 m in length, were constructed in 2012 to protect the downslope area against boulder fall and open hillslope landslide hazards originating from the natural hillside.

A general view of the flexible barriers is shown in Figure 1. The barriers hit by landslide debris, FW-1A and FW-1B, were located in a largely planar natural hillside sloping at about 30°. FW-1A comprised five net panels while FW-1B comprised four net panels. All panels were approximately 12 m wide. The steel posts in the barriers consisted of 5.5 m high HEB 200 beams. Two top longitudinal "suspension cables" suspended the principal nets in alternate spans (Figure 2). Brake elements were provided to each suspension cable in alternate spans. A third longitudinal cable, the "brake cable", ran parallel to the two suspension cables. The brake cable was provided with brake elements at the centre of each span. The arrangement of the bottom longitudinal "ground cables" followed a similar arrangement, i.e. two ground cables and one brake cable. The principal net consisted of a diagonal net made up of 10 mm diameter wire ropes arranged in a 140 mm × 140 mm square pattern. The wire ropes were 6×7 IWRC stranded ropes with breaking force of 72 kN. The energy-dissipating devices (brake elements) are mobilised through friction developed as cable loads cause the wire ropes to slip through the openings in each brake plate, tightening and taking up the available length in the wire rope loop (Figure 2). After mobilisation, the force in each brake element stays relatively constant before the maximum elongation is reached. No major signs of movement were noted in the brake elements after the incident, although signs of abrasion in the stranded ropes to the extent of 1-2 cm were observed. A more detailed description of the components and the working mechanism of the barrier system is given in Wong and Lau (2022).



Figure 1. General view of barriers FW-1A (left) and FW-1B (right) after installation in 2012.



Figure 2. Longitudinal cables and brake elements.

3 NUMERICAL MODEL

3.1 Material models and properties

The material models used in the numerical model of the 3000 kJ flexible barrier and the main input parameters are summarised in Table 1. The steel posts were modelled as elastic-perfectly plastic beam elements. Wire ropes, including those making up the diagonal net, were modelled as elastic cables which develop no internal forces in compression or bending. A typical value of the elastic modulus for stranded wire ropes was used. For stranded wire ropes, the range of the modulus of elasticity has been given as between approximately 100 and 130 GPa (e.g. DIN, 1984; Feyrer, 2000; Boroška et al., 2014). The nominal

metallic cross sectional area was used with typical values from EN 12385-2 (BSI, 2008).

Brake elements were modelled as inelastic springs with fully specified force-elongation relationships as shown in Figure 3.

Table 1. Material models and input parameters used in numerical model.

Component and element type	LS-DYNA material model	Key input parameters
Boulder (solid)	RIGID	ρ = 2478 kg/m^3
Landslide debris (solid)	SOIL_AND_FOAM	ρ = 2000 kg/m^3 G = 6 MPa B = 12 MPa (bulk modulus) ν = 0.3 c' = 1 kPa ϕ_1' = 30°
Posts (beam)	PLASTIC_KINEMATIC	ρ = 7850 kg/m^3 E = 205 GPa ν = 0.3 p_y = 235 MPa
Wire ropes (beam)	CABLE_DISCRETE_BEAM	ρ = 7900 kg/m^3 E = 120 GPa
Net (beam)		
Brake elements (beam)	SPRING_INELASTIC	See Figure 3

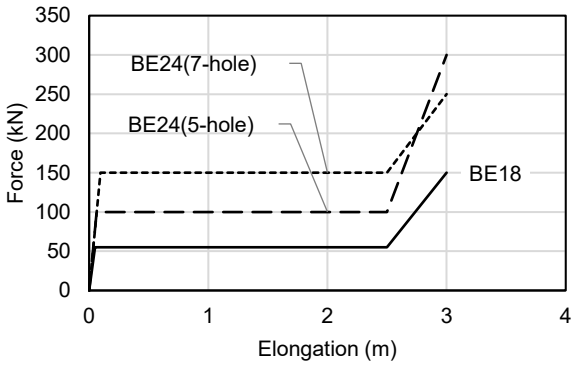

Figure 3. Force-elongation relationship of brake elements.

3.2 Replication of full-scale rockfall test

The diagonal net was tied to the suspension cables through seam ropes. It is expected that the friction between the diagonal net and suspension cables could be greater than that in ring-net type barrier nets, in which the principal net consists of ring-nets suspended from longitudinal cables directly or through shackles. Koo and Kwan (2016) carried out numerical simulation of a punching rockfall test using a coefficient of friction of $\mu = 0.1$ for the sliding contact between shackles and steel cables, with good agreement with physical test results. To model the sliding contact between the diagonal net and suspension cables through seam ropes under the present study, different values of the coefficient of friction was attempted.

The deformed shape of the barrier is shown in Figure 4. The deceleration and location of the block was consistent between measurement and simulation results. The difference in maximum elongation of the barrier net was within 5%. The overall mode and magnitude of deformation were well reproduced in the simulation. Overall, a value of $\mu = 0.9$ returned simulation results most consistent with the physical test. The average anchorage forces for the top longitudinal cables were within about ±10% of the measured values in the physical test while the anchorage forces in the bottom longitudinal cables were smaller than measured values by 13%. The simulated net elongation and residual height were also within 1 to 3% of physical test results.

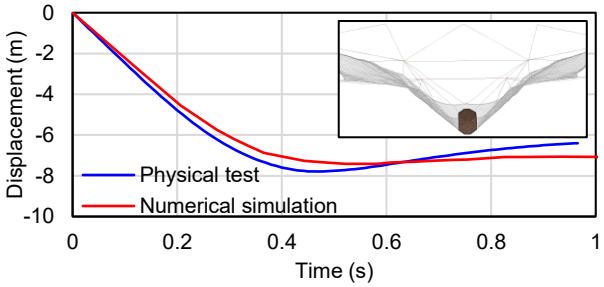

Figure 4. Displcaement of test block after impact.

3.3 Model setup for coupled analysis

The setup of the numerical model is shown in Figure 5. As-built coordinates of the barrier posts and anchorages were used to construct the numerical model. Shell elements were used to construct the three-dimensional topography from airborne LiDAR data obtained in 2020 at 0.5 m resolution. Following the landslide event, hand-held LiDAR scanning of the source area was carried out. The 2020 topography was locally modified to take into account the depression at the source area resulting from the landslide. A "landslide source container" was constructed following the outline of the landslide source area delineated from field investigations. The container was topped by a "lid", which was identical to the pre-landslide topography shell elements but offset vertically by a prescribed distance to make up the target landslide source volume. The landslide source was generated in the space enclosed by the container, the topography and the lid. The debris was released by lifting the landslide source container. A regular array comprising of regular tetrahedral solid elements ("the ALE mesh") was set up to define the largest possible extent of the debris.

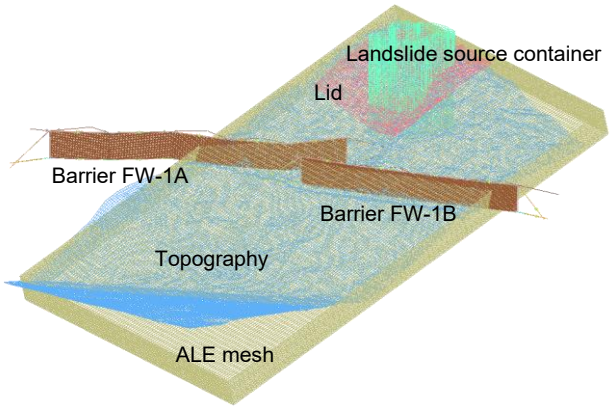

Figure 5. Numerical model setup.

Koo (2017) carried out back analysis of notable open hillslope landslides and channelised debris flows in Hong Kong using LS-DYNA. The back-calculated internal friction angle ϕ_i of landslide debris was found to be in the range of 25° to 30° for open hillslope landslides. The back-calculated apparent basal friction angle ϕ_a was found to be 20° for the Sham Wan Road landslide (GEO and Knill, 1995), which had occurred in a similar open hillslope setting. GEO (2012) recommends that ϕ_a = 25° and 20° should be used in mobility assessments for open hillslope landslides with source volume small than or equal to 500 m^3 and larger than 500 m^3, respectively.

The Drucker-Prager yield criterion was used for modelling the landslide debris (Table 1). An internal friction angle of 30° was adopted as a first estimate, while values between 27° to 32° were also attempted. The derivation of input parameters for the Drucker-Prager criterion from ϕ_i followed the procedure in Koo (2017). It is known that modelling results are not sensitive to the values of shear modulus, bulk modulus and Poisson's ratio and that sufficiently low stiffness values may be used for computational efficiency (Koo, 2017). A basal friction angle ϕ_a of 25° to 28° were attempted.

4 RESULTS OF COUPLED ANALYSIS

4.1 Barrier deformation

The frontal impact velocity, barrier deformation and debris geometry are presented in Table 2 for the case of internal friction angle of 30° and basal friction angles of 27°. The impact process is shown in Figures 6(a) and (b). The debris largely came to a stop at the end of the simulation as evidenced by the velocity contour shown in Figure 6(c). The total kinetic energy of the entire debris also reached a residual level (Figure 6(d)).

The deformation of the barriers was in general consistent with field observations (Figures 6(e) and (f)). For the upper barrier, the net elongation and the residual height were consistent with field measurements. In the simulation, a gap of about 1.5 m developed between the edge post and the net, as a result of the net elongation and sliding of the net along the longitudinal cables under the force of the oblique impact. Measurements using hand-held LiDAR scanning indicated that the opening was about 2 m wide.

4.2 Retained volume

There were uncertainties as to the relative proportions of debris depositing along the debris trail and of the debris directly retained by the barriers, given that the debris body was a continuum in the simulation. Nevertheless, the volume of debris at the upper barrier was largely consistent with field observations. Although the net elongation and the residual height of the lower barrier were also replicated reasonably well in the simulation, the debris volume was smaller than field observations. This is evidence of the challenging nature of modelling the behaviour of multiple-barrier systems, especially one involving edge impacts.

Table 2. Results of debris-barrier interaction.

	Upper barrier		**Lower barrier**	
	Numerical simulation	**Field observation**	**Numerical simulation**	**Field observation**
Debris frontal velocity at impact (m/s)	5.5	-	5.8	-
Maximum elongation of principal net (m)	2.3	2.3	2.1	2.8
Normalised residual height	82%	84%	81%	78%
Width of retained debris (m)	12	8	12	12
Volume of retained debris (m^3)	21	20	62	90

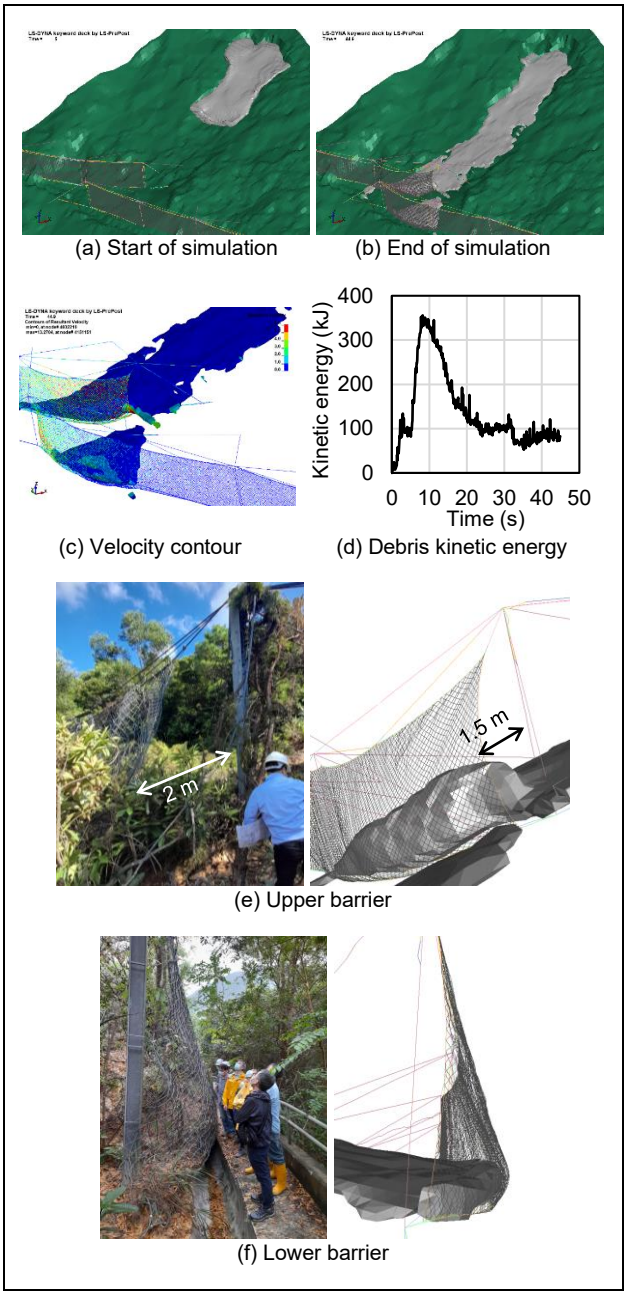

Figure 6. Results of coupled analysis.

4.3 Mobilisation of brake elements

The elongation of brake elements in the simulation was up to about 20% of the available length of the brake loops. As will be discussed later, the characteristics of the friction type brake elements make it difficult to achieve a close match between numerical and field results in terms of brake mobilisation under low energy impacts. Nevertheless, the overall deformation of the barriers was reasonably replicated in the numerical simulation. There was no overloading of wire ropes or brake elements.

4.4 Hypothetical impact scenario

Following the validation of the debris-barrier numerical model against field observations, an alternative impact scenario was studied by removing the upper barrier to investigate the condition if the lower barrier alone was subjected to a hypothetical 500 m^3 event, which gives rise to an impact energy close to the energy rating of the barrier.

Without the upper barrier, the lower barrier was able to resist the 500 m^3 debris impact, with greater net elongation (2.8 m) and lower residual height (77%) than either of the two barriers in the original twin-barrier layout. The brake element at the ground cable anchorage would also be mobilised to a far greater extent (30% as opposed to 17%). Nevertheless, a substantial reserve capacity was evident in terms of the utilisation of structural capacity of components and displacement limits of brake elements.

5 DISCUSSION

5.1 Impact energy

Three-dimensional debris mobility modelling using the numerical program 3d-DMM (Law et al., 2022), based on the SPH technique, was used to estimate the cumulative kinetic energy passing through the barrier locations under free-field conditions. In Hong Kong, this free-field cumulative kinetic energy is used for estimating the debris impact energy sustained by an energy-rated rockfall barrier. Although LS-DYNA could be used to perform debris mobility modelling (e.g. Koo, 2017), the computational demand is high. In this study, the frontal velocity from LS-DYNA was found to be close to 3d-DMM results, considering that the same 3D ground profile derived from LiDAR data was used in both programs. This confirms that it is reasonable to estimate the flow kinematics and impact energy using 3d-DMM.

It could therefore be estimated from 3d-DMM that the impact energy of the debris at barriers FW-1A and FW-1B was approximately 568 kJ and 421 kJ, respectively, accounting for approximately 15% to 20% of the energy capacity of the barrier. The relatively low impact energy resulted in relatively small deformations (i.e. high residual height).

Results of the present study indicate that a single barrier installed at Pa Mei would be able to resist an open hillslope landslide with a source volume of 500 m^3. Results from 3d-DMM give an impact energy of about 3100 kJ, i.e. close to the energy rating of the barrier. The barrier was able to sustain the impact without overloading of structural components or excessive deformation of brake elements.

5.2 Dynamic characteristics of brake elements

For brake elements which dissipate energy by plastic deformation, studies have shown that the forces developed and hence the amount of energy dissipated are marginally greater under dynamic condition than under static condition (Lam and Sze, 2021).

The behaviour for friction type brake elements used at the Pa Mei flexible barriers appears to be different. The mobilised forces in the brake elements are consistently lower under dynamic loading. This is consistent with the general rule that static friction is greater than dynamic friction. The use of force-elongation relationships obtained from static load tests may therefore overestimate the energy dissipation capacity of a friction type brake element. Nevertheless, landslide debris generally travels at a much lower velocity than a rockfall impact with the same kinetic energy. The use of static relationships is generally considered acceptable.

6 CONCLUSION AND FUTURE WORK

The response of the flexible barriers affected by the open hillslope landslide at Pa Pei has been back analysed using LS-DYNA. The numerical model was able to reproduce the barrier deformation and debris distribution to a reasonable extent.

This back analysis has enabled the development and validation of a coupled numerical model to investigate debris-barrier interaction. It has been demonstrated that the barrier system would be able to sustain a hypothetical impact event at or above its rated energy capacity.

The validated numerical model of flexible barriers and terrain under this study would enable a supplementary study on the assessment of the energy capacity of flexible rockfall barriers subjected to landslide debris impacts. This would also allow further optimisation of the design of flexible debris-resisting barriers by fully utilising the rated energy capacity of flexible rockfall barriers and by providing guidance on the appropriate residual height to be adopted for the assessment of retention capacity.

ACKNOWLEDGEMENTS

This paper is published with the permission of the Head of the Geotechnical Engineering Office and the Director of Civil Engineering and Development, the Government of the Hong Kong Special Administrative Region, China.

REFERENCES

Boroška, J., Pauliková, A. and Ivančo, V. (2014). Determination of Elastic Modulus of Steel Wire Ropes for Computer Simulation. *Applied Mechanics and Materials*, 683, pp. 22-27, https://doi.org/10.4028/www.scientific.net/AMM.683.22.

BSI (2008). BS EN 12385 2:2002+A1:2008 Steel Wire Ropes – Safety – Part 2: Definition, Designation and Classification. British Standards Institute, UK.

DIN (1984). DIN 15018-1 Cranes – Steel structures verification and analysis. Deutsches Institut Fur Normung, Germany.

Feyrer, K. (2000). *Drahtseile – Bemessung, Betrieb, Sicherheit* (2nd Ed.). Springer Vieweg Berlin, Heidelberg, Germany. https://doi.org/10.1007/978-3-642-54296-1.

Fugro (2022). Detailed Study of the October 2021 Landslide on the Natural Hillside above Ma Wan New Village, Pa Mei, Tung Chung. Geotechnical Engineering Office, Hong Kong, Landslide Study Report No. LSR 2/2022.

GEO and Knill, J. (1995). Report on the Shum Wan Road Landslide of 13 August 1995. Geotechnical Engineering Office, Hong Kong.

GEO (2012). Guidelines on Assessment of Debris Mobility for Open Hillslope Failures. Geotechnical Engineering Office, Hong Kong, GEO Technical Guidance Note No. 34.

Koo, R.C.H. and Kwan, J.S.H. (2016). A Numerical Study of Dynamic Responses of Two Selected Flexible Rockfall Barriers Subject to Punching and Areal Loads. Geotechnical Engineering Office, Hong Kong, GEO Report No. 323.

Koo, R.C.H. (2017). 3D Debris Mobility Assessment Using LS-DYNA. Geotechnical Engineering Office, Hong Kong, GEO Report No. 325.

Lam, H.W.K. and Sze, E.H.Y. (2021). Pilot Experimental Study on Brake Elements at High Strain Rate. Geotechnical Engineering Office, Hong Kong, GEO Discussion Note No. DN 2/2021.

Law, R.P.H., Kwan, J.S.H. and Ko, F.W.Y. (2022). Validation of Geotechnical Computer Program "3d-DMM (SPH Version 2.0)". Geotechnical Engineering Office, Hong Kong, GEO Report No. 353.

Wong, E.K.L. and Lau, J.W.C. (2022). Back Analysis of Flexible Barrier Response following Impact from the October 2021 Open Hillslope Landslide at Pa Mei, Lantau Island. Geotechnical Engineering Office, Hong Kong, Special Project Report No. SPR 3/2022.

Proceedings of the XVIII ECSMGE 2024
GEOTECHNICAL ENGINEERING CHALLENGES
TO MEET CURRENT AND EMERGING NEEDS OF SOCIETY
© 2024 the Authors
ISBN 978-1-032-54816-6
DOI 10.1201/9781003431749-258
Open Access: www.taylorfrancis.com, CC BY-NC-ND 4.0 license

ECSMGE 24
XVIII EUROPEAN CONFERENCE ON SOIL MECHANICS AND GEOTECHNICAL ENGINEERING

Technical aspects and remediation work for hazardous landslides: Tskneti example, Georgia

Les aspects techniques et les travaux de remédiation pour les glissements de terrain dangereux: exemple de Tskneti, Géorgie

T. Yildiz*
Assystem, Ankara, Turkey

D. Kuparadze, D. Pataridze
Caucasian Institute of Mineral Resources / Tbilisi State University, Tbilisi, Georgia

**tahir.yildiz88@gmail.com*

ABSTRACT: This study seeks to elucidate technical facets of the Tskneti landslide occurred in June 2015, Tbilisi, Georgia. Unfolding during an extraordinary intense storm on 13-14 June 2015, the landslide originated 10 km west-southwest of Tbilisi. The event resulted in the catastrophic destruction of a significant segment of the Tskneti-Betania highway and a portion of the Akhaldaba road. Subsequently, massive debris flow temporarily obstructed Vere river, leading to the formation of an artificial berm along the riverbed. Due to the substantial hydrostatic pressure resulting from the accumulated water mass, this berm collapsed. Debris flow transportation along the riverbed towards to Tbilisi city centre lead to flash flood and 22 fatalities ensued. The technical underpinnings of the landslide and landslide-induced flood will be evaluated by geological, topographical and hydrological aspects. The remediation approach for the damaged roads will be assessed in geotechnical engineering perspective.

RÉSUMÉ: Cette étude vise à élucider les aspects techniques du glissement de terrain de Tskneti survenu en juin 2015 à Tbilissi, en Géorgie. Survenant lors d'une tempête extraordinairement intense les 13 et 14 juin 2015, le glissement de terrain a pris naissance à 10 km à l'ouest-sud-ouest de Tbilissi. L'événement a entraîné la destruction catastrophique d'un segment significatif de l'autoroute Tskneti-Betania et d'une partie de la route d'Akhaldaba. Par la suite, un écoulement de débris massif a temporairement obstrué la rivière Vere, conduisant à la formation d'une digue artificielle le long du lit de la rivière. En raison de la pression hydrostatique substantielle résultant de la masse d'eau accumulée, cette digue s'est effondrée. Le transport des écoulements de débris le long du lit de la rivière vers le centre-ville de Tbilissi a conduit à des inondations soudaines et à 22 décès. Les fondements techniques du glissement de terrain et des inondations induites par le glissement de terrain seront évalués en tenant compte des aspects géologiques, topographiques et hydrologiques. L'approche de remédiation pour les routes endommagées sera évaluée dans une perspective de génie géotechnique.

Keywords: Landslide; remediation; MSE wall.

1 INTRODUCTION

This paper aims to define the technical aspects of the Tskneti landslide which was occurred on June 2015 in Tbilisi. On 13-14 June 2015, during an intense storm, the landslide developed at 10 km west-southwest of Tbilisi (Kuparadze and Pataridze, 2019). Located on the south side of the Vere River watershed in the Lesser Caucasus Mountains, the landslide catastrophically destroyed a big portion of the Tskneti - Betania Highway and a portion of the Akhaldaba Road. Due to the heavy rainfall and storm, approximately 65 landslides are detected around the region with small to minor scale. The major Landslide caused a massive debris with 1.2 cubic millions of soil and rock fragments while the 60000 cubic meters of plant roots and trees are dislocated from the upper edges of the Tskneti-Betania Road. This massive debris flow has temporarily blocked the Vere River and caused to an artificial berm along the riverbed. By the effect of the enormous hydrostatic pressure caused by the water mass, berm failure was occurred, and debris flow went through to the Tbilisi City Center. As a result of flood, 22 people dead in the disaster.

The technical background of the disaster will be summarized in the sections by evaluating geological, topographical, hydrological facts. The remediation plan for the damaged roads will be expressed by geotechnical perspective.

The general layout for area of interest is given in Figure 1.

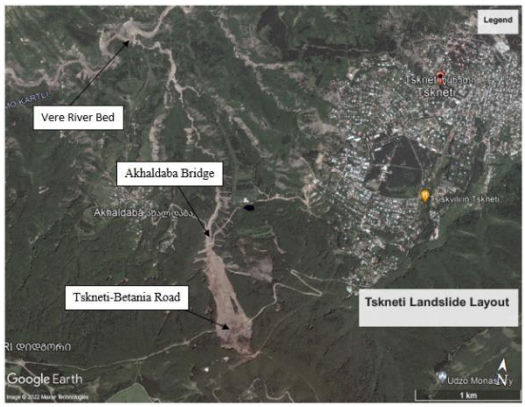

Figure 1. General layout of the area.

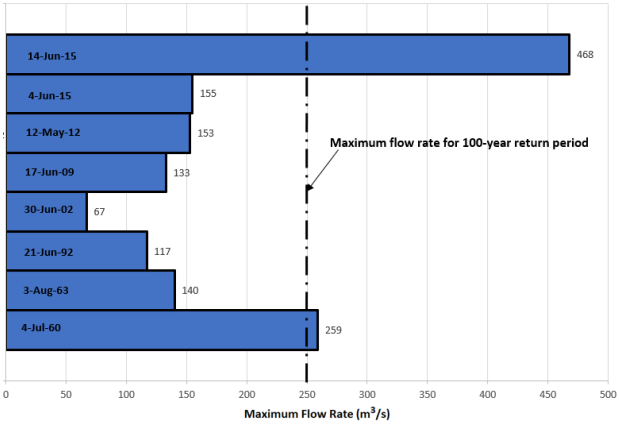

Figure 2. Maximum flow rates of Vere river.

2 TECHNICAL BACKGROUND

Geological, hydrological and meteorological conditions of the site are presented in this chapter.

2.1 Geological conditions

The territory of Georgia, as a part of the Caucasus, is located within the collision zone of the Eurasian and Afro-Arabian plates, in the Mediterranean (Alpine-Himalayan) belt, at the interface of European and Asian segments. (UNDP 2015).

The landslide zone is located to the South-East from Tskneti village at an altitude of 1180-1300 meters composing of Oligocene and lower Miocene clays, sandstones, conglomerates (Maikop series), marine molasse. The landslide zone is located in the central part of the Adjara-Trialeti fold system – on the northern flank of the Telety anticline (Gamkrelidze et. al.,2021). The western slopes are steeper, and the eastern slopes are flatter showing the monoclinic form of the Telety anticline (Kuparadze and Pataridze, 2019).

2.2 Hydrological conditions

Based on the local database for Vere River, the annual rate flow of river ranges between 0.26 m^3/s to 1.22 m^3/s. The maximum flow rate with 100 year return period is assumed as 240 m^3/s. The peak flow rates are reported as 259 m^3/s and 153 m^3/s in 1960 and 1972, respectively (UNDP, 2015).

The study of Gorum and Fidan (2021) claims that majority of the fatal rainfall-induced landslides occurred by following the extreme peak summer rainfalls, not during the rainiest periods. The hydrological portrait of the disaster fits with this approach while the landslide occured after the maximum flow rate measured in summer season. The maximum flow rate is measured as 468 m^3/s, almost double the maximum design flow (i.e. 240 m^3/s) for 100-year return period (Figure 2).

3 SITE INVESTIGATIONS

As a part of rehabilitation works, geophysical investigations including vertical electrical sounding (VES) and magnetometer surveys were performed to identify the landslide characteristics (Kuparadze and Pataridze, 2019). The scope of investigation covers 2 individual sections of the damaged road called as Site W-1 and T-1 including the drilling of 9 boreholes and 10 sets of VES alignment.

Magnetometer survey results show that, sandstone layers composed of large blocks with intercalations of argillite has high values of magnetic fields (>49530 nanoTesla) while thin-grained sandstones have relatively low magnetic field values (i.e. <49500 nanoTesla).

VES results identify two individual layers along the survey depth as follows:

Geoelectric layer with specific electrical resistance 100-170 Ohm · m – intensively weathered fractured sandstones with interlayer's of argillite and conglomerates.

Geoelectric layer with specific electrical resistance of 175-330 Ohm · m – slightly weathered fractured sandstones with interlayer's of argillite and conglomerates.

As a summary of geophysical survey results, western part of the investigation zone is estimated as the zone of crushing (fracture), contact zone between coarse and thin-layered sandstone. It has been stated that, potential landslide may have been occurred in the past by the movement of individual blocks at this section.

Groundwater was encountered in all boreholes. Drill holes indicate temporary presence of groundwater. Groundwater levels were measured between 1285 m to 1325 m located nearby the bedrock elevation.

Site investigation layout and potential fracture alignments are given in Figure 3.

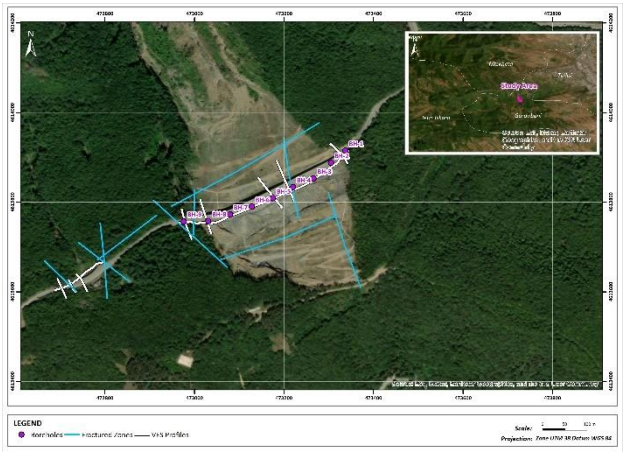

Figure 3. Site investigation layout & fracture zones.

4 REMEDIATION WORKS

Within the scope of remediation studies of damaged roads, different solutions have been evaluated. Remediation sections called T1, G1 and W1 are to support the Tskneti-Samadlo road platform while the A1 places at the Akhaldaba road which was completely destroyed (See Figure 4).

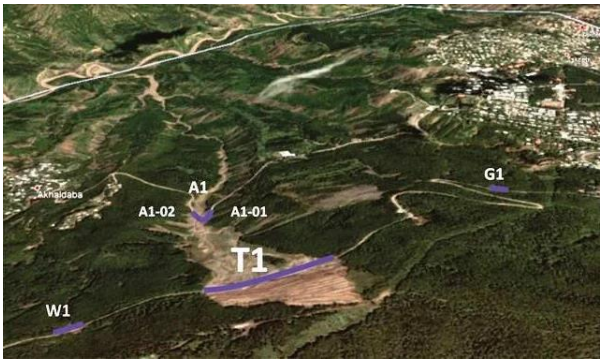

Figure 4. Remediation sections.

The remediation classification for sections referring Holtz and Schuster (1996) approach is listed in Figure 5.

Section	Category	Procedure
G1	1 - Avoid Problem	Remove unstable materials
	4- Increase Internal Strength	Use reinforced backfill (MSE Wall)
A1	1 - Avoid Problem	Install bridge / remove unstable materials
	4- Increase Internal Strength	Reinforced backfill (MSE Wall)
W1/T1	1 - Avoid Problem	Remove unstable materials
	3 - Use structural systems / anchor installation	Reinforced concrete walls with injection piles / Anchor installation for back-face stabilization of trimmed slope
	4- Increase Internal Strength	Reinforced backfill (MSE Wall) above RC wall

Figure 5. Method of rehabilitation per section (Adapted from Holtz and Schuster (1996)).

T1 area is placed at the center of landslide-zone where the inclination angle of sliding slope is measured as 40° with the maximum elevation difference between the natural ground and new road level is ≈ 15.0 m.

4.1 Hybrid Solution for W1 and T1 Sections

W1 and T1 sections are very close to the main landslide zone leading complexity in remediation system. The remediation method has been identified as a combination of anchors, reinforced concrete retaining wall and Mechanically Stabilized Earth (MSE) wall.

Even if the MSE walls are not common in landslide stabilization (Holts and Schuster, 1996). Turner (2005) provided as a good reference of using a hybrid retaining structure system a combination of soil nailing and MSE walls in landslide remediation.

T1 and W1 is a kind of modified version of the section advised by Turner (2005). First component of the system; Reinforced concrete wall with soil nails are used to stabilize the fill slope. This component also provides an adequate spacing for construction of second component: MSE wall (Figure 7).

The key notations for composite retaining system are given as follows:

Prior mission of reinforced concrete base wall is to stabilize the toe section.

Reinforced concrete base wall is helpful to reduce the strip lengths of the MSE wall.

Minimizing the MSE wall height helps to reduce the amount of earthwork and prevent new landslides during construction, triggered by earthwork operations.

The MSE wall is founded on the compacted coarse-grained structural fill behind the reinforced concrete wall. Foundation soil with good mechanical characteristics is sufficient to use shorter strips at the bottom of MSE wall. (FHWA).

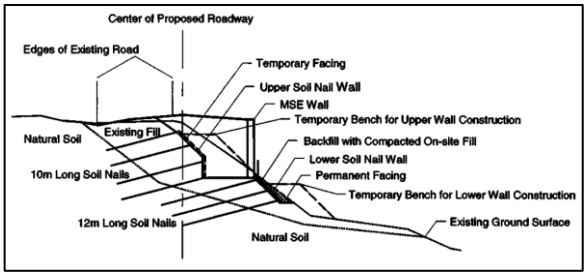

Figure 6. Hybrid wall section advised by Turner (2005).

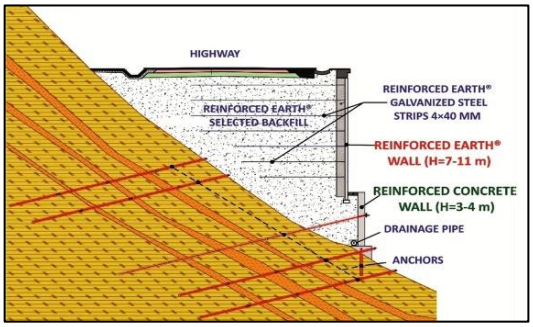

Figure 7. Typical section for W1 and T1.

The pictures showing the site conditions before and after construction presented in Figure 8 and Figure 9 for W1 and T1.



Figure 8. Rehabilitation works for W1 section.



Figure 9. Rehabilitation works for T1 section.

5 CONCLUSIONS

In this study, the technical background of Tskneti landslide occurred in 13-14 June 2015 is examined for significant engineering aspects. The geological and hydrological facts of the disaster are evaluated. Scope of site investigation ana remediation studies of the damaged roads are ezplained in detail.

The landslide zone is located to the South-East from Tskneti village at an altitude of 1180-1300 meters composing of Oligocene and lower Miocene clays, sandstones, conglomerates (Maikop series), marine molasse.

Per hydrological perspective, the maximum flow rate with 100 year return period is assumed as 240 m^3/s for Vere River. In 13-14 June 2015, the maximum flow rate reaches to 468 m^3/s, almost 2 times higher than the maximum design flow for 100 year return period.

The geophysical methods including vertical electrical sounding and magnetometer survey was used to describe the possible fractured zones of the area. As a summary of geophysical survey results, western part of the investigation zone can be defined as the zone of crushing (fracture), contact zone between coarse and thin-layered sandstone. It has been indicated that, potential landslide may have been occurred in the past by the movement of individual blocks at this section.

The technical details of the remediation method for damaged roads are presented in Section 4. A hybrid solution for critical W1 and T1 sections, combining soil nails, reinforced concrete toe wall and mechanically stabilized earth (MSE) was explained in detail with technical advantages.

In brief, landslide stabilization projects shall be classified as a multidisciplinary study including geology, hydrology, meteorology, geotechnical perspective. A remediation project shall not be limited to construct the damaged structures in a very short time. The simple reconstruction procedure without any action plan ignoring the possible reasons of the disasters will not be the proper solution. A comprehensive study of related engineering fields is mandatory: Both for the detecting the possible reasons and proper engineering solutions.

REFERENCES

Berg, R.R., Christopher, B.R., Samtani, N.C., (2009). "FHWA-NHI-10-024: Design of Mechanically Stabilized Earth Walls and Reinforced Soil Slopes-Volume:I" Technical Manual , Woodbury USA.

Gamkrelidze, Okrostsvaridze, Koiava, Maisadze, (2021). Geological Structure of Georgia. http://dx.doi.org/10.1007/978-3-030-62966-3_2.

Görüm, T., Fidan, S. (2021) Spatiotemporal variations of fatal landslides in Turkey. Landslides 18, 1691–1705 https://doi.org/10.1007/s10346-020-01580-7.

Gudjabidze, G. E. (2003): Geological Map of Georgia 1: 500.000. Georgian State Department of Geology and National Oil Company "Saqnavtobi".

Holtz, R. D., and Schuster, R. L. (1996). "Stabilization of soil slopes." Chap. 17 in Landslides: Investigation and mitigation, Special Report 247, A. K. Turner and R. L. Schuster, eds., Transportation Research Board, National Academy Press, Washington, D.C., 439–473.

Kuparadze D., Pataridze D., (2019), "Engineering Solution of the Catastrophic Landslide Areas (By the example of Georgia)" Proceedings of the IX International Scientific and Practical Conference International Trends in Science and Technology,– Vol.1 pp:9-17, Warsaw, Poland.

Turner, John P., and Wayne G. Jensen. (2005) "Landslide stabilization using soil nail and mechanically stabilized earth walls: case study." Journal of Geotechnical and Geoenvironmental Engineering 131.2 pp: 141-150.https://doi.org/10.1061/(ASCE)1090-0241(2005)131:2(141).

UNDP—United Nations Development Programme (2015a) Tbilisi disaster needs assessment 2015. Part 1 (Final draft), 59 pp

UNDP—United Nations Development Programme (2015b) Towards a multi-hazard early warning system for Georgia, 25 pp.

Proceedings of the XVIII ECSMGE 2024
GEOTECHNICAL ENGINEERING CHALLENGES
TO MEET CURRENT AND EMERGING NEEDS OF SOCIETY
© 2024 the Authors
ISBN 978-1-032-54816-6
DOI 10.1201/9781003431749-259
Open Access: www.taylorfrancis.com, CC BY-NC-ND 4.0 license

ECSMGE 24
XVIII EUROPEAN CONFERENCE ON SOIL MECHANICS AND GEOTECHNICAL ENGINEERING

Towards improved earthquake preparedness: Site effects considering multiple seismic zones

Vers une meilleure préparation aux tremblements de terre: effets sur le site compte tenu de la multiplicité des zones sismiques

A.M. Zapata-Franco*, Y.F. Vargas-Alzate, J. Vaunat
Universitat Politècnica de Catalunya, BarcelonaTech (UPC)/International Centre for Numerical Methods in Engineering (CIMNE), Barcelona, Spain

A. Di Mariano
International Centre for Numerical Methods in Engineering (CIMNE)/Universitat Politècnica de Catalunya · BarcelonaTech (UPC), Barcelona, Spain

**ana.maria.zapata@upc.edu*

ABSTRACT: Site response analysis is a key aspect in the quantification of seismic risk. Parameters defining the main dynamic properties that characterize a specific site mainly depend on the ground motion at the bedrock level and the soil features close to the ground surface. Integrating both, ground motion and soil features, within a probabilistic framework that considers the randomness of the mechanical properties of existing civil infrastructures is challenging, especially because of the computational effort involved. In addition, the dynamic properties of the soil tend to be affected at very low shear strains. These limits mainly depend on the duration and intensity of the ground motion. This study aims to apply a recently developed computational framework that allows for probabilistic considerations of the dynamic interaction between the ground and the surrounding structures during seismic events. Specifically, a set of ground motion records has been selected to propagate through random soil profiles. The resulting signals at the ground surface are transmitted to building models of varying heights, and their dynamic behaviour is evaluated. Then, using the cloud analysis approach, intensity measures, vibration periods of the degraded soil profile and structures have been used to search for the best-fit model that minimizes errors in predicting the influence of the site. The results of this study are expected to have significant practical applications in earthquake engineering and risk prevention.

RÉSUMÉ: L'analyse de la réponse du site est un aspect essentiel de la quantification du risque sismique. Les paramètres définissant les principales propriétés dynamiques qui caractérisent un site spécifique dépendent principalement du mouvement du sol au niveau du socle rocheux et des caractéristiques du sol à proximité de la surface du sol. L'intégration du mouvement du sol et des caractéristiques du sol dans un cadre probabiliste qui prend en compte le caractère aléatoire des propriétés mécaniques des infrastructures civiles existantes est un défi, notamment en raison de l'effort de calcul nécessaire. En outre, les propriétés dynamiques du sol ont tendance à être affectées par de très faibles contraintes de cisaillement. Ces déformations dépendent principalement de la durée et de l'intensité du mouvement du sol. Cette étude vise à appliquer un cadre de calcul récemment développé qui permet des considérations probabilistes de l'interaction dynamique entre le sol et les structures environnantes pendant les événements sismiques. Plus précisément, un ensemble d'enregistrements de mouvements du sol a été sélectionné pour se propager à travers des profils de sol aléatoires. Les signaux résultants à la surface du sol sont transmis à des modèles de bâtiments de différentes hauteurs, et leur comportement dynamique est évalué. En utilisant une approche d'analyse de nuage, les mesures d'intensité, les périodes de vibration du profil de sol dégradé et des structures ont été utilisées pour rechercher le meilleur modèle d'ajustement qui minimise les erreurs dans la prédiction des effets du site. Les résultats de cette étude devraient avoir des applications pratiques significatives dans le domaine du génie sismique et de la prévention des risques.

Keywords: Seismic risk, probabilistic model, dynamic interaction, cloud analyses approach.

1 INTRODUCTION

Soil-structure interaction is a fundamental factor in seismic risk estimation, where soil acts as a filter amplifying or damping harmonics based on its dynamic properties (Cruz and Miranda, 2021). Structures may resonate with the soil, leading to a rethinking of seismic risk paradigms, as observed during the 1985 earthquake in Mexico City (Beck and Hall, 1986). Therefore, understanding the dynamic response of the soil beneath a civil structure is crucial

for seismic risk studies. Advanced nonlinear models, such as 3D finite element method representations, offer insights into this complexity. However, for computational efficiency, simplified 1D models like Kelvin-Voigt solids, which effectively approximate soil dynamics, are often used (Hardin and Scott, 1967).

This article employs a computational framework (Zapata-Franco et al., 2023) to analyse steadfastness in intensity measures (IMs) for predicting nonlinear building responses. This statistical property allows grouping results stemming from different building models without losing efficiency. This is of particular interest since new tendencies for seismic hazard characterization are evolving from 'Uniform Hazard Spectrum' to 'Uniform Risk Spectrum'. This enhanced approach is influenced by collapse fragility functions that should represent a large variety of buildings for consistent collapse probabilities across regions.

The framework has been originally developed for Reinforced Concrete structures, RC, which were modelled by considering Multi-Degree-of-Freedom systems. However, it has proven to be adaptable to a variety of structures, providing insights on seismic risk predictions (Vargas-Alzate et al., 2022). Particularly, in this article, simplified proxies built from Single-Degree-of-Freedom systems, SDoFs, have been employed to model RC buildings.

Bogotá has been chosen as a study site due to soft soil deposits and a comprehensive soil profile database, providing valuable data for seismic risk assessment (Pagliaroli et al., 2014). Regression analyses, comparing Scalar-based and Vector-valued IMs with building responses, indicate efficiency gains when grouping buildings by similar height ranges. This research provides insights into improving seismic risk predictions, particularly for cities with diverse building heights like Bogota.

2 PROBABILISTIC SOIL MODEL

A probabilistic soil model is generally used in geotechnical applications to consider the spatial and temporal variability of soil properties, and their effects on civil structures. These models rely on statistics and probability theory to simulate soil features such as strength and stiffness, which can vary with location and time. In this article, the probabilistic soil model presented in Zapata-Franco et al. (2023) has been employed. Figure 1 is a sketch of this computational framework. The variables represented within the soil profile scheme (shear modulus, density, damping parameter and layer thickness, G_i, ρ_i, ξ_i and h_i, respectively) determine the dynamic features of the modelled soil.

In summary, the probabilistic framework presented in Zapata-Franco et al. (2023) allows for:

i. Introducing a ground motion record at the bedrock level of a soil profile.
ii. Estimating the stiffness degradation and increase of damping in each soil layer based on the equivalent linear method.
iii. Calculating the resulting ground motion at the surface after propagation through the soil profile, taking into account the degradation of soil properties.
iv. Considering the resulting ground motion estimated in the previous step, by applying it at the base of one of the probabilistic building models.

These steps have been implemented after generating random samples of both soil profiles and structures, which are affected by ground motion records selected from a seismic database. These records have been acquired in seismic stations located on hard-soils.

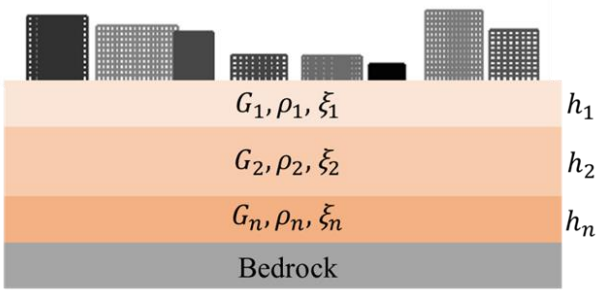

Figure 1. Schematic representation of the complete model.

2.1 Case of study: Bogotá Microzonation

This study focuses on Lacustrine soils that compose a critical deposit in Bogotá city, which is characterized by soft clays with high compressibility, interspersed with lenses of loose sand, volcanic ash, and peat up to 1m in thickness. The sediment width for this deposit varies from 50m to 500m.

2.2 Probabilistic generation of soil profiles

The probabilistic framework used in this research employs the Toro's model to generate soil profiles. (Silva et al., 1996). In brief, this probabilistic model consists of three main elements: i) a model describing the random stratigraphy at the site; ii) the median wave velocity profile; iii) a model considering both the deviation of the velocity from the median and its correlation with respect to the layer above. In the following, the elements of the Toro's model, applied to the lacustrine data for Bogotá city, are described.

2.2.1 Random stratigraphy at the site

For soil parameterization, 10 lacustrine profiles of the city have been employed (FOPAE, 2011). The random stratigraphy is characterized by using the "Layering Model" (Silva et al., 1996). This allows to consider that, often, as the soil layer deepens, it becomes thicker. Accordingly, the following power law is adopted:

$$\lambda(h) = C_3[h + C_1]^{-C_2} \quad (1)$$

where λ is the layer boundary rate (1/m) and h is the depth in meters. The estimation of the values C_1, C_2 and C_3 is carried out by using the capabilities of the Monte Carlo method to minimize multi-dimensional functions (Kucherenko et al., 2015).

2.2.2 The median wave velocity profile at the site

Due to the cumulative process associated to the creation of sedimentary deposits, it has been observed that a log-normal distribution adequately parametrizes the aleatory character of shear wave velocities (Toro, 2022). This parametric distribution has been adopted in the sampling process of the shear wave velocity. Note that, according to the Toro's model, the velocity is estimated at the layer midpoints.

2.2.3 Deviations of the velocity in each layer

Another important aspect observed in soil profiles is related to the spatial correlation between closer layers. The closer the layers the higher the correlation (Angelini and Heuvelink, 2018). This implies that widely separated layers tend to be less correlated. It has been assumed that the correlation between adjacent soil layers decreases with distance by means of the following model:

$$\rho_{i,j} = \begin{cases} i = j & \rho_{i,j} = 1 \\ i = j \pm k & \rho_{i,j} = 1 - \frac{k}{r} \geq 0 \end{cases} \quad (2)$$

where k is a number related to the position of a layer belonging to the same profile; r is a coefficient associated to the rate of correlation between adjacent layers. In this research, r has been fixed to 100/3.

2.3 Probabilistic simulation of soil profiles

Based on the description of the probabilistic features that soil profiles must meet, statistic models have been obtained via Monte Carlo simulations. The resulting soil profiles can be seen in Zapata-Franco et al. (2023). They all correspond to low shear strains.

3 SEISMIC HAZARD

3.1 Colombian seismic database

A compilation of ground motions recorded in Colombia between 1993 and 2017 has been considered, with a magnitude greater than 4.0 Mw. Accordingly, a total of 1992 records have been extracted from the SGC (SGC, 2020). From this set, 1236 ground motion recorded at hard soils have been used in this research.

3.2 Ground motion identification and scaling

In order to obtain a more precise representation of the seismogenic environment of Bogotá, the proximity algorithm developed in Zapata-Franco et al. (2023) has been employed. Bogotá has been regarded as a reference point, considering a radius of 400 km around the city. A set of 1023 ground motions recorded on hard-soils have been identified. 1000 of them have been employed to perform the calculations in this research.

There are several methods for scaling ground motions from a database (Haselton C.B., 2012). Typically, the aim is to have enough records leading the buildings to different performance levels. However, in current databases, there are often no strong ground motion records with high intensity values. This leads to excessive scaling, which may introduce bias in the structural response (Haselton C.B., 2012). To address this issue when using cloud analysis (Jalayer et al., 2015), the method proposed by Vargas-Alzate et al. (2022b) to select and scale ground motion records has been used. Figure 2 shows the total set of scaled ground motions acting at the bed rock level.

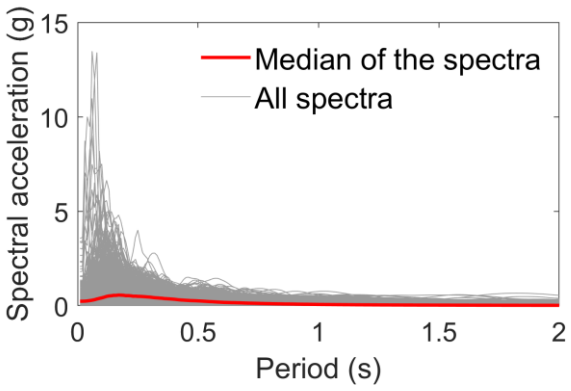

Figure 2. Spectra of ground motion records acting at bedrock level.

4 SEISMIC WAVE PROPAGATION

Seismic wave propagation leads to the degradation of soil stiffness and an increase in material damping in each layer. These alterations are dependent on the maximum shear strain experienced by the soil during seismic events. Several methods address this effect, one of the most widely used being the linear equivalent method (Kumar and Mondal, 2017).

This method iteratively estimates physical properties of a compatible soil profile using linear approximations, emulating the dynamic response obtained through computationally expensive non-linear analyses. The equivalent linear method considers stiffness degradation and increased material damping, utilizing normalized shear modulus and hysteretic damping curves. Reference curves from a geotechnical report (FOPAE, 2011) have been considered in this research to estimate the nonlinear response of probabilistic soil profiles. To do so, the ground motions have been scaled following the description presented in section 3.2. The resulting spectra of the ground motion at the surface, once applied the equivalent linear approximation, are shown in Figure 3.

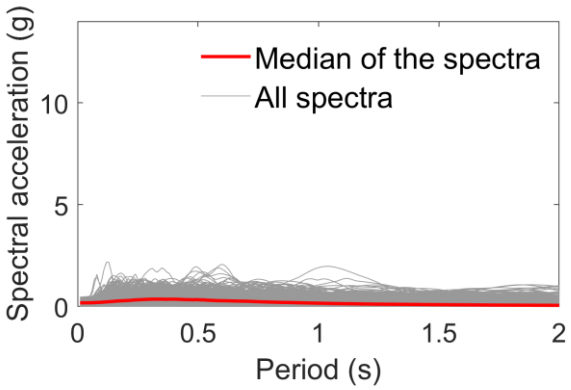

Figure 3. Spectra of ground motion records at the surface.

5 STRUCTURAL MODELLING

Simplifying structural models is crucial for efficient computations, allowing faster analyses of multiple buildings. The Single Degree of Freedom (SDoF) system is commonly used for dynamic calculations, offering easy time-history responses based on the fundamental period and damping. However, SDoF responses overlook stiffness loss due to plastic damage and the effect of higher modes. To address both issues, a proposed approach involves approximating the dynamic behaviour of Reinforced Concrete (RC) structures by averaging the time-history response of a set of SDoF systems within the interval ($0.1T$, $1.8T$), where T is the fundamental period of the analysed building in the main direction.

The dynamic response associated with each oscillator has been estimated by means of the dynamic equilibrium equation for SDoF systems:

$$m\ddot{u}(t) + c\dot{u}(t) + ku(t) = -m\ddot{u}_g(t) \quad (3)$$

where $\ddot{u}(t)$, $\dot{u}(t)$ and $u(t)$ are the spectral acceleration, velocity and displacement time history responses of the SDoF, respectively; $\ddot{u}_g(t)$ is the acceleration ground motion; m, c, and k represent the mass, damping, and stiffness of the system, respectively. Thus, the spectral time history response of a building in terms of displacements, $\bar{u}(t)$, is estimated as follows:

$$\bar{u}(t) = \frac{1}{p}\sum_{i=1}^{p} u_{(i)}(t, T_i) \quad (4)$$

where $u_{(i)}(t, T_i)$ is the response of the SDoFs with period T_i within the interval ($0.1T$, $1.8T$).

Several engineering demand parameters (EDPs) can be extracted from the averaged time-history responses described above. For example, the maximum global drift ratio of a structure, MGDR, which is an EDP widely used in seismic risk estimations employing the capacity spectrum method (Freeman, 1998), can be estimated according to the following equation:

$$MGDR = PF_1 \frac{max\ (u_{(x,y)})}{\mathrm{H}} \quad (5)$$

where PF_1 is the load participation factor (Applied Technology Council, 1996); H is the height of the building. Regarding PF_1, it has been assumed that this variable is a function of the number of stories. In this research, $PF_1 = (\frac{7}{460}N_{st} + \frac{123}{115})$, where N_{st} represents the number of stories. In this manner, the higher the structure the larger PF_1.

Due to the probabilistic approach followed in this article, a set of fundamental periods has been generated to represent the analysed typology. Classical relationships between the evolution of this period and the height of the structure can be used (Goel and Chopra, 1997). For the case of study, it has been employed the following formula to relate the fundamental period vs the height of the structure (AIS, 2010):

$$T_1 = C_h * H^{0.9} \quad (6)$$

where C_h is a random regression coefficient which depends on the type of structure. This allows to

consider possible uncertainties in the characterization of T_1. In the case of RC typologies, the average C_h is 0.047; it has been assumed a coefficient of variation equal to 0.12.

Three different structural typologies have been simulated. The difference between them is the number of stories. Thus, Low-, Medium- and High-Rise RC structures are composed of buildings whose number of stories varies from 2-6, 7-15 and 16-25, respectively.

6 CLOUD ANALYSIS

Cloud analysis requires to calculate the best fit curve between a set of IM-EDP simulations in the log-log space. In the following, the efficiency in terms of the coefficient of determination, R^2, has been calculated considering two approaches: i) using the ground motion records acting at bedrock levels to estimate IMs; ii) develop a multi-regression model that allows combining information provided by the soil profile and the IMs calculated in the previous approach. The IMs described in Zapata-Franco et al. (2023) have been employed to find the best correlated arrangements to predict the MGDR in both approaches. In addition to IMs, the following set of soil variables have been employed in the multi-regression model (Approach 2):

Table 1. Soil information variables.

Variables	Equation	Description
T_{S_L}	$\sum_{i=1}^{nlayer} T_{S_{L,i}}$	Fundamental period of the soil profile
$\bar{\xi}_L$	$\frac{\sum_{i=1}^{nlayer} \xi_{L,i}}{nlayer}$	Average linear damping of the soil profile
$\bar{\xi}_{NL}$	$\frac{\sum_{i=1}^{nlayer} \xi_{NL,i}}{nlayer}$	Average nonlinear damping of the soil profile
$\overline{Vs}_L$	$\frac{\sum_{i=1}^{nlayer} Vs_{L,i}}{nlayer}$	Average shear wave velocity of the soil profile
ΔT_L	$\lvert T_{S_L} - T_B \rvert$	Absolute difference between the fundamental period of the soil profile and fundamental period of the building (T_B)

6.1 Approach 1

After assessing the bivariate distribution between IMs and the MGDR, Zapata-Franco et al. (2023) show that AvSd is the best correlated IM to predict the MGDR. Accordingly, in approach 1 the authors focus on this IM for the statistical analysis. Results are summarized in Figure 4 for Low, Medium, and High-rise structures; results for a combination of the three typologies (All) have also been included.

6.2 Approach 2

The multi-regression model described in (Vargas-Alzate et al., 2022) has been used to identify the optimal combinations between IMs and soil parameters to predict the MGDR. Arrangements of three information variables have been assessed. Results are summarized in Figure 4 for Low, Medium, and High-rise structures; results for a combination of the three typologies (All) have also been included.

As Figure 4 indicates, for all types of structures, approach 2 shows higher regression coefficients than approach 1.

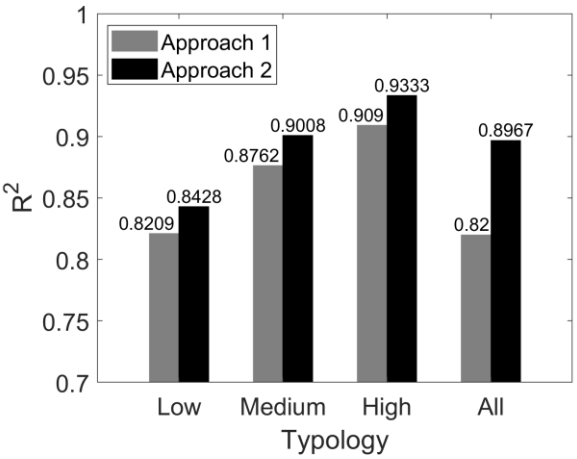

Figure 4. Regression coefficient Approach 1 and 2.

7 CONCLUSIONS

This article delves into the efficiency to predict the seismic response of simplified building models by considering inelastic responses of soils. These models are based on the average response of SDoFs around the fundamental period of each building. By employing the equivalent linear method to address the non-linear behaviour of soils, this study has integrated probabilistic soil profiles, structural models, and ground motion records into a Monte Carlo-based framework. Specifically, random samples of soil profiles have been generated and subjected to a set of accelerograms extracted from a Colombian database. The resulting motions at the ground surface have been employed to perform calculations on structural SDoF-based models.

At a first stage, it has been investigated the causal relationship between scalar-based IMs at the base of soil profiles and the resulting MGDR of structural models (Approach 1). The main conclusion is that AvSd is the most robust scalar-based IM for predicting the buildings response, when considering the interferences produced by the propagation of seismic

waves through soil media. This conclusion holds when structural models are grouped by their number of stories or not. Note also that grouping buildings results in a significant increase in R^2, compared to a regression performed with the total amount of data. In general, the correlation increases when the number of storeys making up a subgroup also increases. This may be related to the fact that as the height of the buildings increases, the periods of both the structure and the ground profiles become more similar.

The objective of the second approach has been to analyse the increase in efficiency when considering vector-valued IMs. These IMs consider information of both the ground motion acting at the bedrock level and soil profiles. Again, AvSd has placed a central role in the regression analysis. This IM appears in all statistical regressions performed. In terms of the soil profile parameters, variables related to damping, velocity and period are the ones producing the highest increase in efficiency. These results highlight the importance of considering both structural and geotechnical factors to improve design and assessment of structures.

Future research should investigate the IM behaviour considering different soil types, seismogenic environments and structural typologies. Also, it would be usefully to extend the computational framework to 3D soil models.

ACKNOWLEDGEMENTS

This research has been funded by the Spanish Research Agency (AEI) through the project with reference: TED2021-132559B-I00 – J-02970.

REFERENCES

AIS (2010). *Reglamento Colombiano de Construcción Sismo Resistente NSR-10*.

Angelini, M.E. and Heuvelink, G.B.M. (2018). Including spatial correlation in structural equation modelling of soil properties, *Spat Stat* 25, 35–51. https://doi.org/10.1016/j.spasta.2018.04.003.

Applied Technology Council (1996). *ATC-40 Seismic evaluation and retrofit of concrete buildings*, Applied Technology Council, Redwood City, California.

Beck, J.L. and Hall, J.F. (1986). Factors contributing to the catastrophe in Mexico City during the earthquake of September 19, 1985. *Geophys Res Lett* 13, 593–596. https://doi.org/10.1029/GL013i006p00593.

Cruz, C. and Miranda, E. (2021). Insights into damping ratios in buildings. *Earthq Eng Struct Dyn* 50, 916–934. https://doi.org/10.1002/eqe.3356.

FOPAE (2011). *Procesamiento e interpretación de señales de la red de acelerógrafos de Bogotá 2009 - 2011*. Bogotá.

Freeman (1998). Development and Use of Capacity Spectrum Method. *Proc. of the 6th U.S. National Conf. on Earthquake Engineering*, Seattle, Oakland, USA. Scientific Research Publishing.

Goel, R.K. and Chopra, A.K. (1997). Period Formulas for Moment-Resisting Frame Buildings. *Journal of Structural Engineering* 123, 1454–1461. https://doi.org/10.1061/(ASCE)0733-9445(1997)123:11(1454).

Hardin, B.O. and Scott, G.D. (1967). Erratum for "Generalized Kelvin-Voigt Used in Soil Dynamics Study." *Journal of the Engineering Mechanics Division* 93, 79–79. https://doi.org/10.1061/JMCEA3.0000830.

Haselton C.B., Whittaker A.S., Hortacsu A., Baker J.W., Bray J. and Grant D.N. (2012). Selecting and Scaling Earthquake Ground Motions for Performing Response-History Analyses. *15th World Conference on Earthquake Engineering*, Lisboa, Portugal.

Jalayer, F., De Risi, R. and Manfredi, G. (2015). Bayesian Cloud Analysis: Efficient structural fragility assessment using linear regression. *Bulletin of Earthquake Engineering* 13, 1183–1203. https://doi.org/10.1007/S10518-014-9692-Z.

Kucherenko, S., Albrecht, D. and Saltelli, A. (2015). Exploring multi-dimensional spaces: a Comparison of Latin Hypercube and Quasi Monte Carlo Sampling Techniques. *arXiv - University of Cornell (USA); arXiv - University of Cornell (USA). JRC98050*.

Kumar, A. and Mondal, J.K. (2017). Newly Developed MATLAB Based Code for Equivalent Linear Site Response Analysis. *Geotechnical and Geological Engineering* 35, 2303–2325. https://doi.org/10.1007/s10706-017-0246-4.

Pagliaroli, A., Lanzo, G., Tommasi, P. and Di Fiore, V. (2014). Dynamic characterization of soils and soft rocks of the Central Archeological Area of Rome. *Bulletin of Earthquake Engineering* 12, 1365–1381. https://doi.org/10.1007/s10518-013-9452-5.

SGC (2020). *Sistema de Consulta de la Amenaza Sísmica de Colombia,* Colombian geological survey. https://amenazasismica.sgc.gov.co/.

Silva, W.J., Abrahamson, N., Toro, G. and Constantino, C. (1996). *Description and validation of the stochastic ground motion model*, Pacific Engineering and Analysis.

Toro, G.R. (2022). Uncertainty in Shear-Wave Velocity Profiles. *J Seismol* 26, 713–730. https://doi.org/10.1007/s10950-022-10084-x.

Vargas-Alzate, Y.F., Hurtado, J.E. and Pujades, L.G. (2022). New insights into the relationship between seismic intensity measures and nonlinear structural response. *Bulletin of Earthquake Engineering* 20, 2329–2365. https://doi.org/10.1007/s10518-021-01283-x.

Zapata-Franco, A.M., Vargas-Alzate, Y.F., Pujades, L.G. and Gonzalez-Drigo, R. (2023). Improved intensity measures considering soil inelastic properties via multi-regression analysis. *Front Earth Sci* (Lausanne) 11. https://doi.org/10.3389/feart.2023.1214536.

C - Risk analysis and safety evaluation
C - Analyse des risques et évaluation de la sécurité

Proceedings of the XVIII ECSMGE 2024
GEOTECHNICAL ENGINEERING CHALLENGES
TO MEET CURRENT AND EMERGING NEEDS OF SOCIETY
© 2024 the Authors
ISBN 978-1-032-54816-6
DOI 10.1201/9781003431749-260
Open Access: www.taylorfrancis.com, CC BY-NC-ND 4.0 license

ECSMGE 24
XVIII EUROPEAN CONFERENCE ON SOIL MECHANICS AND GEOTECHNICAL ENGINEERING

FEM parametric analyses of the seismic behaviour of tunnel-soil-overstructure systems

Analyses paramétriques FEM du comportement sismique des systèmes tunnel-sol-surstructure

G. Abate, M.R. Massimino*
Department of Civil Engineering and Architecture, University of Catania, Italy
**maria.massimino@unict.it*

ABSTRACT: Nowadays, the urgent need to achieve high levels of environmental sustainability motivates researchers to look at solutions to solve the environmental pollution generated by road traffic, and so to improve the quality of life. Surely, tunnels represent one solution for urban areas and so they are in continuous development. In their design it is extremely important to assess the possible damage that can occur during an earthquake to the tunnel and to the aboveground structures, to provide adequate mitigation measures. Very care must be devoted to this evaluation because the presence of tunnels close to aboveground structures may modify the response of these structures, and, at the same time, the presence of aboveground structures may modify the dynamic response of tunnels. Furthermore, the dynamic properties of the soil "involved" by the aboveground and underground structures play an important role. The present paper deals with a tunnel-soil-aboveground building system, whose studies are still very few. The focus is the evaluation of the effects of the tunnel on the seismic response of the aboveground building and vice versa; this study was performed by different parametric FEM analyses. Starting from a cross-section of the recently built underground network in Catania (Italy), involving heterogenous soils and including an aboveground building, the tunnel's depth, the aboveground building's position, and the seismic inputs were changed, analysing their effects in terms of lining forces on the tunnel and seismic horizontal forces on the aboveground structures.

RÉSUMÉ: Aujourd'hui, le besoin d'atteindre des niveaux élevés de durabilité environnementale motive les chercheurs scientifiques à chercher des solutions pour résoudre la pollution environnementale générée par le trafic routier et donc améliorer la qualité de vie. Les tunnels représentent sûrement une solution pour les zones urbaines et en fait ils sont en développement continu. Lors de leur conception, il est extrêmement important d'évaluer les dommages possibles aux tunnels et aux structures surélevées qui peuvent survenir lors d'un tremblement de terre et donc fournir des mesures d'atténuation adéquates. Une grande attention doit être apportée à cette évaluation car la présence de tunnels à proximité de structures peut modifier la réponse de ces structures et, en même temps, la présence de structures peut modifier la réponse dynamique des tunnels. De plus, les propriétés dynamiques du sol jouent un rôle important. Le présent article traite d'un système tunnel-sol-structure, sur lesquels il existe encore peu d'études. L'accent est mis sur l'évaluation des effets des tunnel sur la réponse sismique du bâtiment surélevé et vice versa. Cette étude a été réalisée par différentes analyses paramétriques FEM. A partir de la section transversale d'un réseau souterrain récemment construit à Catania (Italie), impliquant des sols hétérogènes et un bâtiment surélevé, la profondeur du tunnel, la position du bâtiment surélevé et les inputs sismiques ont été modifiés, analysant leurs effets en termes de forces sur les tunnels, de forces sismiques horizontales sur les structures surélevées.

Keywords: Tunnel depth; building location; seismic tunnel lining forces; acceleration response spectra.

1 INTRODUCTION

Today, underground structures play a crucial role in transportation and utility networks in urban areas. Their static design has achieved a high level of accuracy. Instead, tunnels' efficient seismic design is not yet completely gotten.

The present paper deals with a tunnel-soil-aboveground building system, whose studies are still very few (Vassilis et al., 2014; Abate & Massimino, 2017). The effects of a tunnel crossing heterogeneous soils on the response of the aboveground building and vice versa are analysed by means of 2D FEM parametric analyses. Starting from a cross-section of the recently built underground network in Catania (Italy), the tunnel's depth, the aboveground building's position, and the seismic inputs were changed, analysing their effects in terms of lining forces on the tunnel and seismic horizontal forces on the aboveground building.

2 THE REFERENCE CASE-STUDY

The cross-section of the underground network in Catania (Italy) is shown in Figure 1.a. The tunnel is a reinforced concrete structure, with a diameter equal to 10 m and a tunnel cover equal to 17 m. The building is a typical reinforced concrete structure, with foundation beams; its symmetry axis is shifted of a distance equal to 20 m in respect of the vertical symmetry axis of the tunnel. As for the soil, Figure 1.b shows the V_s profiles: achieved by HVSR tests, hypothesized to find the conventional bedrock (found at 80 m where V_s = 800 m/s, neglecting the rock layer present at z = 5-20 m). For more details see Abate et al. (2023).

3 THE FEM MODELLING

For developing the parametric analyses, the tunnel's depth, the aboveground building's position, and the seismic inputs were changed. Three different accelerograms were used: one recorded during the 1990 earthquake at the Sortino station (Eastern Sicily); two synthetic accelerograms reproducing the 1693 and 1818 scenario earthquakes for the city of Catania (Azzaro & Barbano, 2000). The three inputs were scaled to PHA = 0.383g (the average expected value at the bedrock for the reference case study; NTC2018). They differ in the frequency content: f_{input} = 2 Hz for the 1990 seismic input, $f_{1,input}$ = 0.7 Hz and $f_{2,input}$ = 5 Hz for the 1693 seismic input, f_{input} = 0.6 Hz for the 1818 seismic input. Indicating with ΔZ the tunnel cover and with ΔY the distance between the building symmetry axis and the tunnel symmetry axis, the values ΔZ = 17 m, 12 m, 7 m, and ΔY = 20 m, 5 m, 0 m were chosen (ΔZ = 17 m and ΔY = 20 m were the values of the reference case-study). Combining them, nine different 2D FEM models were performed by the ADINA FEM code (ADINA, 2008). They consisted of a soil 80 m deep (see Figure 1.b), and 300 m wide, to reduce the boundary effects (Figure 2.a). The soil was divided into 8 horizontal layers (see Figure 1.b). The nodes of the soil vertical boundaries were linked by "constraint equations" that imposed the same displacements at the same depths. The nodes at the base were constrained only in the vertical direction; moreover, in the horizontal direction, dashpots were implemented to simulate the elastic bedrock according to Kuhlemeyer & Lysmer (1973). The seismic inputs were applied through these dashpots. Contact surfaces were defined at the soil-structure interface to model probable uplifting and/or sliding phenomena, assuming the Coulomb friction coefficient $\mu = 2/3\ \phi$. As for the soil-tunnel interface, the condition for which soil and tunnel cannot slide relative to each other was assumed (μ = 1). The tunnel and the building were modelled by linear visco-elastic constitutive models, assuming: E_l = 36283 MPa and ν_l= 0.2 for the tunnel; E_b = 30000 MPa and ν_b = 0.2 for the building; γ = 25 kN/m^3 and D = 5% for both the structures. The soil was modelled by a linear-equivalent-visco-elastic constitutive model, for considering its soil nonlinearity. So, according to the achieved shear strains for each soil layer and for each seismic input, evaluated by iterative procedures using the $G(\gamma)$ and $D(\gamma)$ curves shown in Figure 2.b (concerning the Catania volcanic soil; Cavallaro et al., 2006), the operative values of G_s and D_s were estimated. The Rayleigh coefficients α e β were adopted for simulating the material viscosity according to (1), where D are the damping ratios and ω the natural angular frequencies of the involved systems:

$$\alpha = 2 \cdot \frac{D \cdot \omega_i \cdot \omega_j}{\omega_i + \omega_j};\ \beta = 2 \cdot \frac{D}{\omega_i + \omega_j} \qquad (1)$$

The soil's natural angular frequencies were evaluated as $\omega_i = \omega_1 = (V_{s,av}/4H)\cdot 2\pi$ and $\omega_j = 3\cdot\omega_1$ (Kwok et al., 2007), with H heigh of the soil deposit and $V_{s,av}$ weighted average of the shear wave velocities of the soil deposit. The tunnel's frequencies were assumed equal to those of the soil, because tunnel and soil respond approximately in agreement to the movement induced by the earthquake. The structure's frequencies were computed by means of modal analyses.

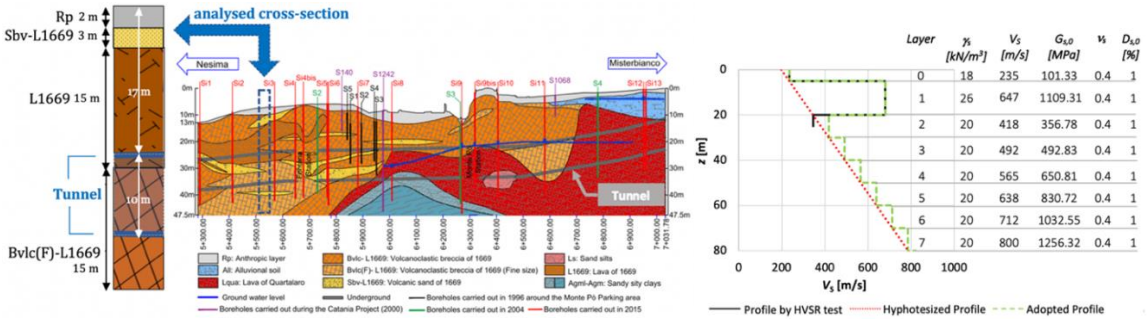

Figure 1.a Soil profile along the Nesima-Misterbianco segment of the underground network in Catania and zoom on the analysed cross-section next to borehole Si3 (after Abate et al. 2023); 1.b $V_s(z)$ profile (after Abate et al. 2023).

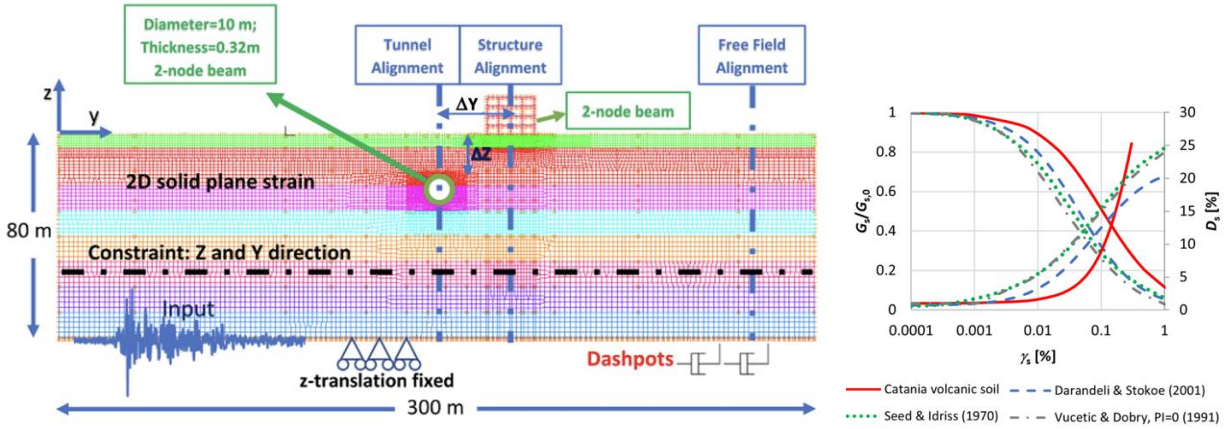

Figure 2.a FEM Model of the configuration for the reference case-study: ΔZ = 17 m and ΔY = 20 m. (after Abate et al. 2023). 2.b Adopted $G_s/G_{s0}(\gamma)$ and $D_s(\gamma)$ curves (after Abate et al. 2023).

4 THE MAIN RESULTS

The seismic response of the tunnel was investigated in terms of lining internal forces, evaluated both numerically and analytically (Wang, 1993; Penzien, 2000). Nevertheless, these analytical solutions refer to a circular tunnel inside a homogeneous soil. So, for using them, the authors fit them for the analysed heterogeneous soil (for details see Abate et al. 2023).

Figure 3 shows the comparison between the numerical and analytical maxima ΔM and ΔN.

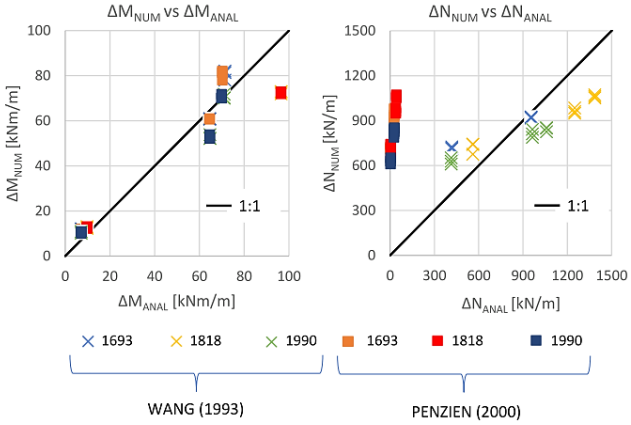

Figure 3. Comparison between numerical and analytical dynamic bending moments and dynamic axial forces.

Wang (1993) reproduced quite well the numerical results; Penzien (2000) drastically underestimates ΔN. The best agreement was achieved for ΔZ = 7 m, for which the tunnel crossed a homogeneous soil; furthermore, the lowest ΔM were obtained, because of the lack of strong impedance ratio, that led to small strains which in turn produced low ΔM. For ΔZ = 17 m, the highest ΔM were obtained, because the tunnel crossed a major thickness of more deformable soil layer. Similar results concerned the ΔN, even if the tunnel cover had a minor influence. The position of the aboveground structure had a low influence on the lining internal forces; in fact, similar values were achieved for all the three hypothesized ΔY. Finally, the highest values of lining forces were generally obtained for the 1818 seismic input. This was due to probable resonance. The closer the input predominant frequency f_{input} was to the soil natural frequency f_{soil}, the higher the strains were and so the higher the forces were, too.

The seismic response of the structure was investigated in terms of horizontal forces. The numerical ones were compared with the values achieved by the expression furnished by NTC2018:

$$F_{hi} = F_h \cdot z_i \cdot \frac{w_i}{\sum_j z_j w_j} \qquad (2)$$

where $F_h = S_e(T_1) \cdot W \cdot \lambda / g$; w_i and w_j are the weights of the ith and j^{th} floors, respectively; z_i and z_j are the heights of the masses from the foundation level; $S_e(T_1)$ is the spectral acceleration value at the first natural period of the structure; W is the weight of the whole aboveground structure; λ is a coefficient equal to 0.85 because $T_1 < 2T_C$ and the aboveground structure has more than three floors; g is the gravity acceleration (9.81m/s^2).

Figures 4 shows that NTC2018 furnished values three times higher than the numerical ones. So, numerical analyses should be always recommended for avoiding too expensive designs. The seismic forces varied slightly with ΔY and ΔZ, recording a minimal improvement for ΔY = 0 and ΔZ = 7 m. Different responses were found to the different seismic inputs, due to probable resonance: the higher F_h achieved for the 1693 input motion can be due to the ratio f_{input}/f_{stru} very close to the unit value, where f_{stru} = 3.7 Hz is the first natural frequency of the structure resting on the soil including the tunnel, evaluated as ratio between the Fourier spectra computed at the top and at the bottom of the structure.

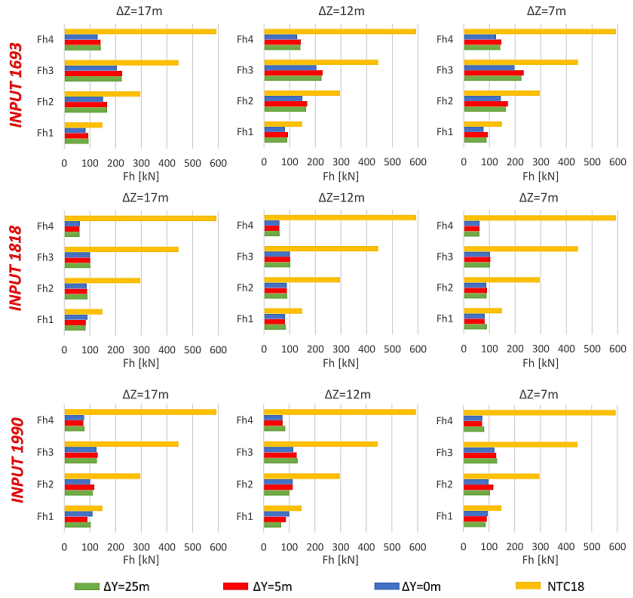

Figure 4. Horizontal seismic forces on the structure.

5 CONCLUSIONS

Starting from a typical cross-section of the underground network in Catania (Italy), the paper deals with FEM parametric analyses of the seismic response of a full-coupled tunnel-soil-aboveground building system. Tunnel cover, aboveground building's position, and seismic inputs were varied. The main results can be summarised as follows.

The lowest values of dynamic lining forces were obtained for the tunnel completely inside a homogeneous soil layer, as well as the highest ones were obtained when the tunnel crosses a greater portion of the more deformable soil layer. These results highlight the importance of evaluating the exact soil profile and eventual heterogeneities.

The seismic forces on the building recorded a minimal improvement for aligned tunnel-structure and the shallow tunnel. Strong differences were achieved between the numerical values and the values suggested by NTC2018. This because the numerical modelling considered uplifting and sliding phenomena at the soil-structure interface, that led to a decrease in seismic forces on the aboveground structure.

REFERENCES

Abate, G. and Massimino, M.R. (2017). Parametric analysis of the seismic response of coupled tunnel–soil–aboveground building systems by numerical modelling. *Bull Earthq Eng*, 15(1), 443–67.

Abate, G., Grasso, S. and Massimino, M.R. (2023). Effect of soil heterogeneity on seismic tunnel lining forces. *Soil Dynamics and Earthquake Engineering*, 168, Article number 107849. ISSN 02677261. DOI 10.1016/j.soildyn.2023.107849.

ADINA (2008). *Automatic dynamic incremental nonlinear analysis. Theory and modelling guide*. USA: ADINA R&D, Inc. Watertown.

Azzaro, R. and Barbano, M.S. (2000). *Seismogenetic features of SE Sicily and scenario earthquakes for Catania.* The Catania project: earthquake damage scenarios for a high-risk area in the Mediterranean, part I: seismotectonic framework and earthquake scenarios. Roma: CNR-Gruppo Nazionale per la Difesa dai Terremoti; 2000. 9–13.

Cavallaro, A., Grasso, S. and Maugeri, M. (2006). Volcanic soil characterization and site response analysis in the city of Catania, In: *8th Nat. Conf. on Earthquake Engineering Proceedings*, 18–22 April 2006, San Francisco, California, USA.

Kuhlemeyer, R.L., Lysmer, J. (1973). Finite element method accuracy for wave propagation problems. *Journal of the Soil Mechanics and Foundations Division, ASCE,* 99(5), 421-427. https://doi.org/10.1061/JSFEAQ.0001885.

Kwok, A.L., Stewart, J.P., Hashash, Y.M., Matasovic, N., Pyre, R., Wang, Z. and Yang, Z. (2007). Use of exact solutions of wave propagation problems to guide implementation of nonlinear seismic ground response analysis procedures. *J. Geotech. Eng.*, 133, 1385-1398. DOI:10.1061/(ASCE)1090-0241(2007)133:11(1385).

NTC2018, D.M. 17/01/18 - *Updating of technical standards for buildings*, Official Journal of the Italian Republic, 17th January 2018 (In Italian).

Penzien, J. (2000). Seismically-induced racking of tunnel linings, *Int. Earthquake Eng. Struct. Dyn.* 29, 683-691. DOI:10.1002/(SICI)1096-9845(200005)29:5<683:AID-EQE932>3.0.CO;2-1.

Vassilis, K., Papanikolaoua, A.J. and Kappos. (2014). Practical nonlinear analysis of unreinforced concrete tunnel linings. *Tunn Undergr Space Technol*, 40, 127–40. https://doi.org/10.1016/j.soildyn.2023.107849.

Wang, J.-N. (1993). *Seismic Design of Tunnels: A State-of-the-Art Approach*, Monograph, monograph 7. Parsons, Brinckerhoff, Quade and Douglas Inc, New York.

Proceedings of the XVIII ECSMGE 2024
GEOTECHNICAL ENGINEERING CHALLENGES
TO MEET CURRENT AND EMERGING NEEDS OF SOCIETY
© 2024 the Authors
ISBN 978-1-032-54816-6
DOI 10.1201/9781003431749-261
Open Access: www.taylorfrancis.com, CC BY-NC-ND 4.0 license

ECSMGE 24
XVIII EUROPEAN CONFERENCE ON SOIL MECHANICS AND GEOTECHNICAL ENGINEERING

A novel framework to evaluate the influence of seismic performance of geotechnical systems on the resilience of road networks

Un nouveau cadre pour évaluer l'influence de la performance sismique des systèmes géotechniques sur la résilience du réseau routier

C. Amendola*
Aristotle University of Thessaloniki, Thessaloniki, Greece

R. Conti
University of Rome Tor Vergata, Rome, Italy

P. Zimmaro
University of Calabria, Arcavacata di Rende, Italy / University of California, Los Angeles, Los Angeles, USA

M. Marinelli
University of Sannio, Benevento, Italy

L. Pariota, L. Di Costanzo, F. de Silva
University of Naples Federico II, Naples, Italy

**chiaamen@civil.auth.gr*

ABSTRACT: A proper evaluation of the seismic performance of geotechnical systems is a fundamental step for assessing the functionality of a transportation network after the occurrence of an earthquake. This paper illustrates the preliminary results of a novel methodology aimed at identifying geotechnical systems characterized by an unsatisfactory seismic performance, resulting in a compromised functionality of the overall road network. The proposed framework is applied to an ideal case study using gravity retaining walls as an illustrative example of more complex geotechnical systems. The potential damage to each retaining wall is quantified through *ad-hoc* generated fragility curves, starting from a scenario ground motion map. A new scale of functionality loss is proposed by exploiting existing damage scales. Information on partial or complete road closures is incorporated as part of a standard transportation engineering framework. Such framework is used to estimate variations in the performance of the road network by means of specific indicators, e.g. active accessibilities and path generalized costs. The analysis of these indexes is used to quantify the effects of loss of functionality of the retaining walls and the resulting actions on the overall performance of the transportation network. The versatility of the proposed framework allows it to be applied to any transportation network and geotechnical system.

RÉSUMÉ: Une évaluation rigoureuse de la performance sismique des systèmes géotechniques est une étape fondamentale pour évaluer la fonctionnalité d'un réseau de transport après un tremblement de terre. Cet article illustre les résultats préliminaires d'une nouvelle méthodologie visant à identifier les systèmes géotechniques caractérisés par une performance sismique insatisfaisante, ce qui compromet la fonctionnalité de l'ensemble du réseau routier global. Le cadre proposé est appliqué à une étude de cas idéale, utilisant des murs de soutènement gravitaires comme exemple illustratif de systèmes géotechniques plus complexes. Les dommages potentiels à chaque mur de soutènement sont quantifiés à l'aide de courbes de fragilité ad-hoc, à partir d'une carte de mouvement du sol scénarisée. De nouvelles échelles de perte de fonctionnalité sont proposées en exploitant les échelles de dommages existantes. Les informations sur les fermetures partielles ou complètes de routes sont incorporées dans un cadre standard d'ingénierie des transports. Ce cadre est utilisé pour estimer les variations de la performance du réseau routier au moyen d'indicateurs spécifiques (e.g., accessibilités actives et les coûts généralisés des chemins). L'analyse de ces indices permet de quantifier les effets de la perte de fonctionnalité de chaque système individuel, et des actions qui en découlent, sur la performance globale du réseau de transport. La polyvalence du cadre proposé permet son application à tout réseau de transport et système géotechnique.

Keywords: geotechnical systems, fragility curve, seismic resilience, road infrastructure, transportation networks.

1 INTRODUCTION

Transportation networks represent a crucial civil infrastructure in developed nations, playing a vital role in the advancement of interconnected communities, and aiding in the recovery process during and/or after natural disasters such as earthquakes. Transportation networks comprise several critical components, such as viaducts, tunnels, embankments, and retaining structures (key components). While the seismic performance is studied through fragility curves for systems like viaducts and tunnels, there is a lack for embankments and retaining walls. Retaining walls are among the most frequent key components in transportation networks providing critical support to slopes, embankments, and various infrastructural elements. Damage or failure of these structures can impact the entire network's functionality.

Existing literature on this topic (Argyroudis et al., 2013, Zamiran et al., 2018, Cosentini et al., 2019) highlighted the dependence of the performance on the amplitude and frequency content of the input motion, but they often deal with specific case studies and consequently lack generality.

Starting from the initial outcomes of ongoing research on the topic (Amendola et al. 2023, 2024) this paper employs fragility curves derived using a novel approach for a comprehensive quantification of seismic fragility, applicable to all types of retaining walls founded on whatever soil type.

These fragility curves are then utilized to assess the resilience of road networks by looking at the decrease in functionality (such as reduced speed, partial or full closure) caused by the failure of key components. Additionally, it evaluates the network's resilience by comparing its performance before and after an earthquake.

The methodology is fully described by Amendola et al. (2023). In the following, its application to a case study is presented.

2 CASE STUDY

The proposed framework has been applied herein for demonstration purposes to the case of a simple road network with a distribution of 27 retaining wall (Figure 1).

This network layout is inspired by the existing road infrastructure in Basilicata, Italy, and comprises three distinct road categories (namely Road class A, B, and C) adhering to the specifications stipulated by the Italian National Regulation (MIT, 2001) with specific geometric characteristics and speed limits. The distinctions in these attributes are incorporated into the analysis through the utilization of the Bureau of Public Roads (BPR) link performance function (Cascetta, 2013).

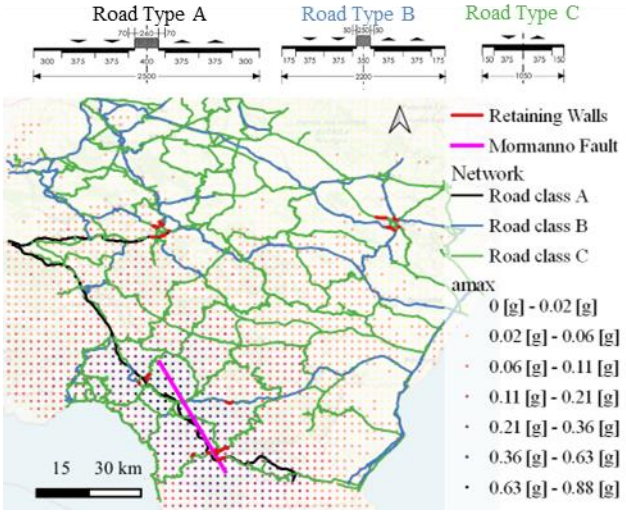

Figure 1. Analysed road network on the map of peak ground acceleration (a_{max}) at bedrock for the simulated earthquake scenario and cross sections of the road classes.

Within the proposed framework, the pre- and post-event performance of the transportation system is assessed incorporating an estimation of travel demand levels within the region. The analysis is conducted considering the typical morning peak hour of a working day at the regional scale considering data from the Italian National Institute of Statistics (ISTAT). Link flows for each simulated scenario are computed using the software PTV Visum, which assigns the estimated demand levels to the transportation network (Cascetta, 2013).

The post-earthquake network analysis was executed considering the occurrence of a seismic event with a moment magnitude of M=6.6 originating from the Rimendiello-Mormanno normal fault (Figure 1).

The distribution of retaining walls along the network was chosen to be on the main important links (i.e., close to main cities and to the epicentre). One typology is selected corresponding to a critical acceleration of the wall, a_c=0.15g, associated with a sliding failure mechanism. This prototype is inferred from recurrent retaining walls along Italian roads and it is designed according to the Italian Building Code (NTC, 2018). More details are provided in Amendola et al. (2023).

3 FRAGILITY CURVES AND FUNCTIONALITY LOSS

Starting from the peak ground acceleration (a_{max} in Figure 1) on the location of each retaining wall, its

probability of failure was estimated through fragility curves by Amendola et al. (2024).

These curves were derived by employing a nonlinear single degree of freedom (SDoF) oscillator (Conti and Caputo, 2019) based on the capacity model proposed by Callisto (2019). The nonlinear response of the system was modelled through a hyperbolic capacity curve, as depicted in Figure 2. This curve correlates the horizontal seismic coefficient (k_H) with the normalized horizontal displacement at the top of the wall (u/H), where H is the height of the wall. The maximum of this curve denotes the critical acceleration coefficient, $k_c=a_c/g$, with a_c denoting the critical acceleration, achieved at a normalized displacement (s_F) associated with the initiation of a plastic mechanism within the soil-wall system. Table 1 presents the parameters of the capacity curve employed in this study, including ξ_{ur}, which stands for the damping ratio during unloading-reloading cycles, and k, representing the ratio between k_c and the actual asymptote of the hyperbolic function (Caputo et al., 2023).

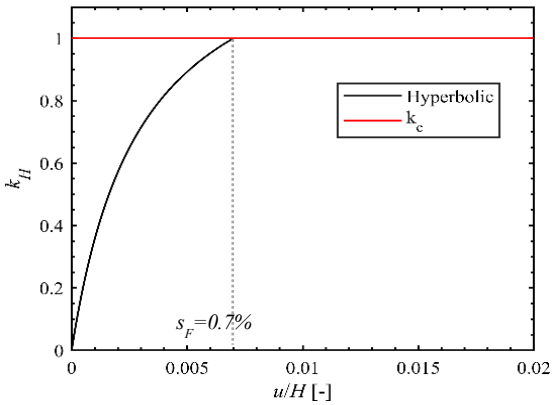

Figure 2. Hyperbolic approximation of the wall capacity curve obtained with the model parameters reported in Table 1(modified after Callisto, 2019).

Table 1. Parameters defining the capacity curve (Callisto, 2019) and the considered prototypes of retaining walls.

Type	ξ_{ur}	k	s_F	H [m]	a_c	Soil Class
Gravity	5%	0.7	0.7%	2,4,6	0.1, 0.2,0.3	A,B,C,D

To provide a comprehensive fragility model, systems with different height and capacity (i.e. different critical acceleration coefficient, $k_c=a_c/g$) were considered for the analyses. Finally, this simplified SDoF model was excited by free-field motions of natural earthquakes (Pitilakis et al., 2013), recorded on different soil classes (i.e. Soil Class A, B, C and D as defined in the EC8, CEN, 2005) following the so-called Cloud method (Jalayer et al. 2017). The results of nonlinear dynamic analyses provided the seismic-induced horizontal permanent displacement at the top of the wall, u. The results are displayed in Figure 3 as a function of a_{max}/a_c for the considered input motions.

As expected, displacements increase with increasing the ratio a_{max}/a_c. To compute fragility curves, the results are fitted using a unique linear regression on the whole set of analyses, thus disregarding the soil class and the wall type. The regression line is superimposed to Figure 3 along with the defining parameters, i.e. slope, b, intercept, a and the value of the standard deviation, σ.

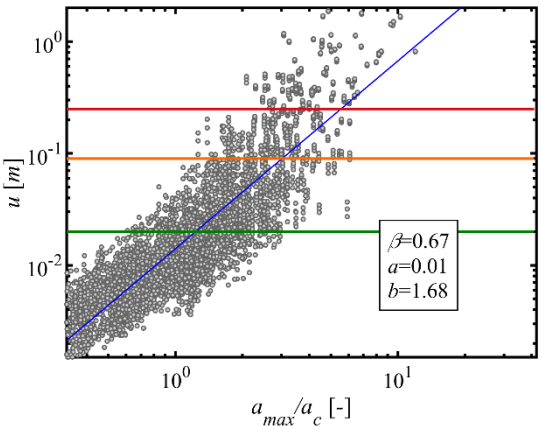

Figure 3. Regression law calculated on the horizontal wall displacements derived from the analyses as a function of a_{max}/a_c.

The so-calculated fragility models are reported in Figure 4 and they are expressed in terms of an intensity measure IM=a_{max}/a_c. They refer to three different damage states (DS): minor, moderate, and extensive/complete. The latter are associated with horizontal displacement thresholds (see Figure 3) obtained from the typical vertical displacements directly impacting the accessibility of the road lane (Argyroudis et al., 2013) . In detail, when the retaining wall is employed for supporting road, embankments or bridge abutments, the horizontal permanent displacement at the top of the wall results in simultaneous cracks and vertical displacements, denoted as 'v', across the lanes of the road. Following the criteria outlined by Argyroudis et al. (2013), low damage is categorized for displacements falling within the range of 2 cm < v < 8 cm, moderate damage for 8 cm < v < 22 cm, and substantial damage for 22 cm < v < 58 cm. This study adopts a conservative approach by considering the displacement thresholds equal to 2 cm, 9 cm and 25 cm respectively.

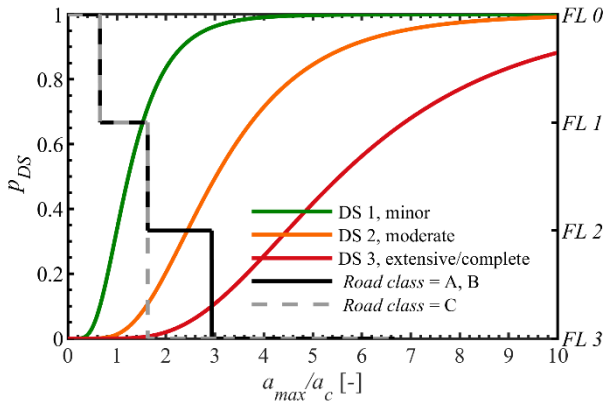

Figure 4. Fragility curves and functionality loss function adopted in this study.

The attainment of the different DS produces a functionality loss (FL) of the road above the wall (right axis in Figure 4), that is a speed reduction (FL 1); a speed reduction and a partial closure (FL 2); and the full closure (FL 3). In this study, FL 2 is not considered for the road class C. The link is assumed to suffer the FL(i) if the DS(i) overcomes a probability of failure equal to 10%. The functionality loss step function is overlapped with the fragility curves in Figure 4. showing that full closure (FL 3) is estimated starting from moderate a_{max}/a_c values.

4 RESILIENCE ASSESSMENT

An examination of the functional analysis of the 27 retaining walls within the network revealed that the seismic event impacted only 12 of them. To gauge the resilience of the road network, a concurrent assessment was conducted utilizing two indices: Traffic Flow Betweenness (TFB) of a link "*l*" (Li et al., 2020), and Accessibility Loss (AL) of the road network resulting from the failure of a subset of links (Maltinti et al., 2012).

Traffic Flow Betweenness serves as a link-based metric for evaluating the significance of a link, irrespective of specific events. This metric can be seen as a measure of the link importance in the network, and proves advantageous when formulating strategies to bolster the network's resilience. AL, on the other side, is related to a specific event, and represents the loss of accessibility by evaluating the increase in travel costs associated with the consequences of the seismic event (e.g. with road closures). The findings of the resilience evaluation show that: (i) the seismic event and ensuing road closures induce a redistribution of traffic flows across the network, potentially without causing increased congestion; (ii) the reshuffling of traffic flows and deterioration in traffic conditions, if any, may extend beyond the immediate vicinity of the affected link; (iii) the traffic load on links subjected to actions, such as speed or capacity reduction, may not necessarily decrease.

The phenomena described in (i) and (ii) arise because variations in the link cost impact the costs associated with all routes using that link. Specifically, such changes may affect routes connecting origins and destinations situated far from the link itself. Variations in route cost can heighten the probability of travellers opting for alternative routes, thereby influencing other segments of the network.

Conversely, in certain scenarios (e.g., links characterised by the highest value of TFB among those computed), elevating route costs may prove insufficient to prompt a switch to alternative routes. In such cases, described in (iii), the flow on the link could potentially increase as a consequence of the same mechanisms triggered by actions, such as road closures, applied to other links. This circumstance is particularly pronounced in a network resembling the one exemplified in this case study, characterized by relatively low road density.

As a consequence of the event, it is estimated a reduction of accessibility conditions of 11.4% with reference to the value of the initial accessibility index *A(0)* and to the accessibility index excluding closed links *A(e)* are $7.9 \cdot 10^7$ and $8.8 \cdot 10^7$, respectively. It is worth noting that this severe reduction results from actions taken on the only 12 links actually affected by the event, which represent a tiny percentage of the link of the network.

5 CONCLUSIONS

The aim of the present study is to introduce and apply a framework for assessing the network impacts of disruptive events, focusing specifically on geotechnical systems exposed to seismic actions. The modelled network is derived from the actual infrastructure in the Basilicata region, Southern Italy, featuring a realistic estimation of traffic flows and subjected to a hypothetical seismic event. In this investigation, only one type of retaining wall is examined as a geotechnical key component. However, it is essential to note that such simplified assumptions can be relaxed, and this constitutes an ongoing research focus for the authors.

The case study analysis reveals that an effective prediction of the consequences of a disruptive earthquake requires a combined application of approaches from diverse engineering disciplines.

Detailed knowledge of the geotechnical system's characteristics is crucial for estimating specific event

effects and the subsequent necessary actions. Simultaneously, a profound understanding of traffic patterns across the broader area, along with the network's structure, is essential for forecasting the overall post-event network functionality.

ACKNOWLEDGEMENTS

The research activities discussed in the paper were funded by the European Union - Next Generation EU, M4C2 mission of the Italian National Recovery and Resilience Plan, investment 1.1-, through the research project of relevant national interest Framework to Assess the Infrastructure Resilience and Management Operations In Roads After Earthquake, FAIR MOIRAE (Project Code: P202224T7S).

REFERENCES

Amendola, C., Conti, R., and de Silva, F. (2024). Influence of the Seismic Performance of Geotechnical Systems on the Resilience of a Road Network. In *ICEGE* (pp. 662-670). Cham: Springer Nature Switzerland.

Amendola, C., Conti, R., Zimmaro, P., Pariota, L., Marinelli, M., and de Silva, F. (2023). Influence of the Seismic Performance of Geotechnical Systems on the Resilience of a Road Network. In *National Conference of the Researchers of Geotechnical Engineering* (pp. 662-670). Cham: Springer Nature Switzerland.

Argyroudis, S., Kaynia, A. M., and Pitilakis, K. (2013). Development of fragility functions for geotechnical constructions: application to cantilever retaining walls. Soil dynamics and earthquake engineering, 50, 106-116. https://doi.org/10.1016/j.soildyn.2013.02.014.

Callisto, L. (2019). On the seismic design of displacing earth retaining systems. EarthProc. 7th International Conference on Earthquake Geotechnical Engineering, pp. 239–255.

Caputo G., Conti R., Viggiani, G.M.B. (2023). Displacement-based seismic design of anchored walls: performance and limitations of newly developed methods. J Geotech Geoenviron Eng., 149(11). https://doi.org/10.1061/JGGEFK/GTENG-11442.

Cascetta, E. (2013). Transportation systems engineering: theory and methods (Vol. 49). Springer Science & Business Media.

CEN. (2005). Eurocode 8: Design of structures for earthquake resistance-part 1: general rules, seismic actions and rules for buildings. European Standard EN 1998-1:2004. Brussels, Belgium: European Committee for Standardisation.

Conti, R., and Caputo, G. (2019) A numerical and theoretical study on the seismic behaviour of yielding cantilever walls. Géotechnique. 69(5), 377-390. https://doi.org/10.1680/jgeot.17.P.033.

Cosentini, R. M., Bozzoni, F., Conca, D., and Lai, C. G. (2019). Developing fragility curves for earth-retaining walls along the Italian roadway network. In Earthquake Geotechnical Engineering for Protection and Development of Environment and Constructions (pp. 1878-1886). CRC Press.

NTC (2018). D.M. 17/01/2018. Norme Tecniche per le Costruzioni. Gazzetta Ufficiale, n. 42 del 20/02/2018, Supplemento ordinario n.8.

ISTAT, https://www.istat.it/it/archivio/139381.

Jalayer, F., Ebrahimian, H., Miano, A., Manfredi, G., and Sezen, H. (2017). Analytical fragility assessment using unscaled ground motion records. Earthquake Engineering & Structural Dynamics, 46(15), 2639-2663. https://doi.org/10.1002/eqe.2922.

Li, F., Jia, H., Luo, Q., Li, Y. and Yang, L. (2020). Identification of critical links in a large-scale road network considering the traffic flow betweenness index. PLoS ONE, 15, e0227474.

Maltinti, F., Melis, D., and Annunziata, F. (2012). Road network vulnerability: A review of the literature. In ICSDC 2011: Integrating Sustainability Practices in the Construction Industry; American Society of Civil Engineers: Reston, VA, USA, pp. 677–685.

MIT. (2001). Ministero delle Infrastrutture e dei Trasporti. Norme funzionali e geometriche per la costruzione delle strade. In G.U. n 3, 4-1-2002.

Pitilakis, K., Riga, E., and Anastasiadis, A. (2013). New code site classification, amplification factors and normalized response spectra based on a worldwide ground-motion database. Bulletin of Earthquake Engineering, 11(4), 925-966. https://doi.org/10.1007/s10518-013-9429-4.

Zamiran, S., and Osouli, A. (2018). Seismic motion response and fragility analyses of cantilever retaining walls with cohesive backfill. Soils and Foundations, 58(2), 412-426. https://doi.org/10.1016/j.sandf.2018.02.010.

Proceedings of the XVIII ECSMGE 2024
GEOTECHNICAL ENGINEERING CHALLENGES
TO MEET CURRENT AND EMERGING NEEDS OF SOCIETY
© 2024 the Authors
ISBN 978-1-032-54816-6
DOI 10.1201/9781003431749-262
Open Access: www.taylorfrancis.com, CC BY-NC-ND 4.0 license

ECSMGE 24
XVIII EUROPEAN CONFERENCE ON SOIL MECHANICS AND GEOTECHNICAL ENGINEERING

Experimental landfill of filtered iron ore flotation tailings at Minas-Rio system

Digue expérimentale de résidus de flottation de minerai de fer filtrés au système Minas-Rio

D.G. Amorim*
University of Brasilia, Brasília, Brazil

L.F. Silva, F.F. Rezende, T.A. Nicoli, U. Albino, F. Saliba
Anglo American and TEC3 Engenharia, Belo Horizonte, Brazil

R.C. Silva
University of Brasilia, Brasília, Brazil

**daniela.amorim@aluno.unb.br*

ABSTRACT: An experimental landfill was built at Serra do Sapo Mine using filtered iron ore flotation tailings. The main purpose was to evaluate the constructive methodology regarding the equipment, layers thickness and geotechnical evaluation of the material behaviour in order to support the development of a filtered tailings pile design. The landfill consists of eleven layers: eight of them with 0.50m and three with 0.70m thickness. After each layer completion, sand replacement method tests were carried out to determine the in-situ density and verify the material compaction. In addition, samples were also collected in all layers to obtain the water content and compaction using oven-drying method and Standard Proctor tests. According to tests results, the material was compacted with a water content below the optimum moisture content and a greater in-situ density due to higher compaction energy. In the 2nd, 5th, 9th and 11th layers, geotechnical characterization, drained and undrained triaxial tests were conducted. Regarding geotechnical characterization, the material is a fine silty sand and does not present variations on the particle size distribution. In order to monitor the pore pressures during the landfill implementation, three piezometers were installed and there is no significant variation in data results and low values of increase in pore water pressure during the layers construction.

RÉSUMÉ: Une digue expérimentale a été construite en la mine de Serra do Sapo en utilisant des résidus de flottation de minerai de fer filtrés. L'objectif principal était d'évaluer la méthodologie constructive en ce qui concerne l'équipement, l'épaisseur des couches et l'évaluation géotechnique du comportement des matériaux afin de soutenir le développement de la conception d'un tas de résidus filtrés. La décharge est composée de onze strates: huit d'entre elles d'une épaisseur de 0,50 m et trois d'une épaisseur de 0,70 m. Après l'achèvement de chaque couche, des essais de remplacement de sable ont été effectués pour déterminer la densité in situ et vérifier le compactage du matériau. En outre, des échantillons ont également été collectés dans toutes les couches pour obtenir la teneur en eau et le compactage par séchage au four et par essais Proctor standard. Selon les résultats des essais, le matériau a été compacté avec une teneur en eau inférieure à la teneur en eau optimale et une densité in situ plus élevée en raison d'une énergie de compactage plus élevée. Dans les 2e, 5e, 9e et 11e couches, des essais de caractérisation géotechnique, triaxiaux drainés et non drainés ont été réalisés. En ce qui concerne la caractérisation géotechnique, le matériau est un sable limoneux fin et ne présente pas de variations dans la distribution granulométrique. Afin de surveiller les pressions interstitielles pendant la mise en place de la décharge, trois piézomètres ont été installés. Il n'y a pas de variation significative dans les résultats des données et les valeurs d'augmentation de la pression interstitielle sont faibles pendant la construction des couches.

Keywords: Filtered flotation tailings; experimental landfill; tailings characterization.

1 INTRODUCTION

Filtered tailings disposal in piles has become popular in recent years, however, without many experiences and acquired knowledge, applicable legal regulations and studies focused on this method. Piles can reach hundreds of millions of cubic meters and considerable heights, which requires a specific monitoring plan and a consistent design.

The evaluation of the geotechnical behaviour of tailings piles considering geotechnical parameters, construction process, quality control and operating mode is substantial to ensure a safe and sustainable

operation of these structures (Ulrich and Coffin, 2013). In this scenario, the construction of experimental landfills is required for assessing the performance of the filtered tailings during and after layers compaction. Performance must be verified both in terms of geotechnical properties and material workability. For the pile design, the geotechnical properties identified in the experimental landfill will be used in the geotechnical model.

This paper covers the construction of an experimental landfill of filtered iron ore flotation tailings. This landfill represents an important first step in the development of tailings filtration process in Minas-Rio Iron Ore Operation, at Anglo American mine site, located in Conceição do Mato Dentro, Minas Gerais, Brazil.

The purpose of the experimental landfill was to provide a preliminary assessment of filtered tailings pile in terms of equipment, compaction degree and eventual lamination issues, cracks, or those related to excess pore pressure generation. During construction, geotechnical investigation was performed, including field tests and disturbed and undisturbed samples collection for laboratory tests. Furthermore, electrical piezometers were installed to monitor the excess pore pressure generation.

2 METHODOLOGY

The experimental landfill was built from January to August 2022 and it is 20m wide, 85m long and 5.9m high. The landfill was prepared in eleven layers: eight of them with 0.5m and three with 0.7m thickness. To reproduce the operating conditions, equipment commonly used for this type of construction was used: trucks, backhoe loader, bulldozer, compactor roller, moto grader, loader and water tank truck were used. The layers were constructed in order to present a minimum value of 98% compaction. The general arrangement of the area is presented in Figure 1.

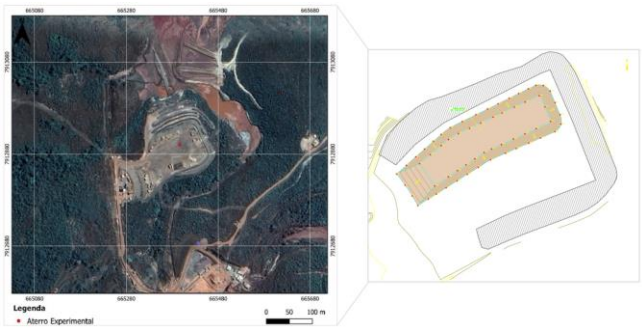

Figure 1. Experimental landfill location.

2.1 Compaction control

After each layer completion, tests were carried out to obtain the situ density using the sand replacement method to verify the material compaction. Additionally, samples were collected to obtain the moisture content using the oven method and to conduct Standard Proctor test.

Field tests were carried out by Fugro company from January to August 2022 and, in total, 96 sand replacement method test were performed in the 11 layers of the experimental landfill. In addition to sand replacement method test, 11 samples were collected for Standard Proctor test, 30 samples for over-drying method and 4 disturbed and undisturbed samples for laboratory tests.

2.2 Tailings characterization

Laboratory tests were performed using samples collected in the 2nd, 5th, 9th and 11th layers of the experimental landfill. The particle-size distribution was defined by sieve and hydrometer analysis in accordance with ABNT NBR 7181 standard.

Over-drying method was used to obtain the natural moisture content of the soil (w) in accordance with ABNT NBR 645 standard. The specific gravity of soil solids was obtained by pycnometer method in accordance with ABNT NBR 6458 standard. Atterberg limits tests were also carried out as recommended by the ABNT NBR 6459 standard and ABNT NBR 7180 standard.

The maximum void ratio was obtained by Method B (ABNT NBR 16840:2020 Corrected Version:2021) and the minimum void ratio by Method B.1 (vibrating table for sieving and dry material; ABNT NBR 16843:2020). Standard Proctor tests were conducted according to ABNT NBR 7182. Each of the points of the compaction curves was obtained without material reuse.

2.3 Monitoring system

The experimental landfill geotechnical instrumentation consisted of three electrical piezometers installed at the base of the landfill. Monitoring data was obtained from February to June 2022 during construction. The automated instruments recorded readings over a 24-hour period.

3 RESULTS AND DISCUSSION

The disturbed samples used for compaction tests are represented as S21012, S21020, S21064 e S21079. Undisturbed samples were also collected for triaxial tests and they are identified in Table 1.

Table 1. Samples identification.

Samples	Layer	Samples
S21010	2ª	Undisturbed
S21012		Disturbed
S21018	5ª	Undisturbed
S21020		Disturbed
S21062	9ª	Undisturbed
S21064		Disturbed
S21077	11ª	Undisturbed
S21079		Disturbed

The Standard Proctor tests results are presented in Figure 2. An average value of maximum dry density of 1.87 g/cm³ (1.79 g/cm³ < dry density < 1.96 g/cm³) and optimum moisture content, with an average value of 13% (11.50% < moisture content < 14.20%).

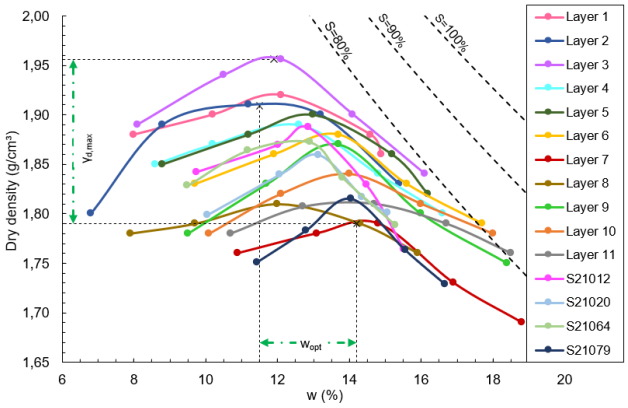

Figure 2. Compaction tests results.

According to tests results (Figure 3), the material was compacted with a water content below the optimum moisture content and a greater in-situ density due to higher compaction energy.

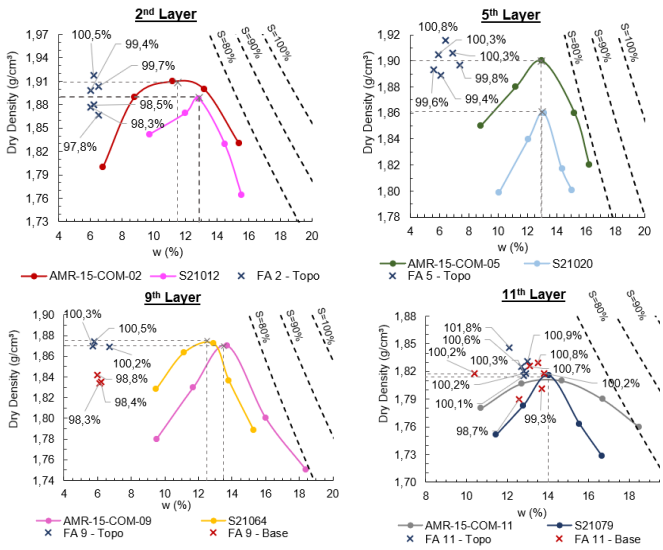

Figure 3. Comparison between sand replacement method and compaction curves.

Technical specification has considered 98% of the Proctor density. Besides that, moisture content correction was not carried out in the initial layers. There is also a discrepancy between the optimum moisture content carried out on samples collected in different layers. This behaviour could be explained due to the higher compaction energy close to 100%.

Laboratory tests results including specific gravity, moisture content, void ratio and Atterberg Limits are presented on Table 2 and 3.

Table 2. Specific gravity and moisture content.

Samples	Gs (g/cm³)	Moist. Content (%)
S21010	-	4,76
S21012	2,97	-
S21018	-	6,60
S21020	2,97	-
S21062	-	5,93
S21064	2,97	-
S21077	-	7,10
S21079	2,90	-

Table 3. Void ratio and Atterberg Limits.

Samples	e_{min}	e_{max}	IP
S21012	0,55	0,95	NP
S21020	0,52	0,91	NP
S21064	0,52	0,97	NP
S21079	0,57	1,02	NP

Particle-size distribution curves are indicated in Figure 4. The results indicated that filtered flotation tailings does not present significant grain size variability and are defined as fine silty sand.

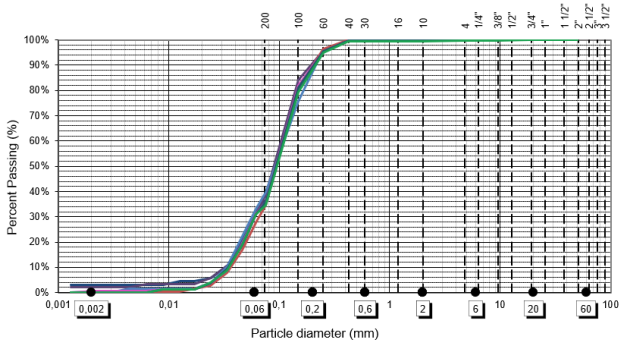

Figure 4. Grain size distribution.

Consolidated-drained test (CID) and consolidated-undrained test (CIU) were performed and the results indicate a high shear stress and friction angle ranging from 32° to 40° and null cohesion intercept (Figure 5 and Figure 6).

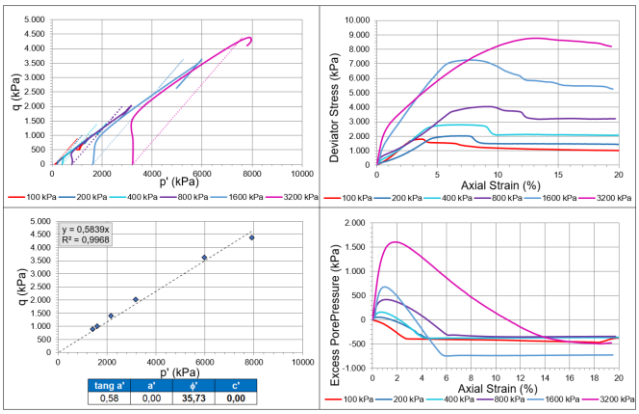

Figure 5. CIU results – 9th layer.

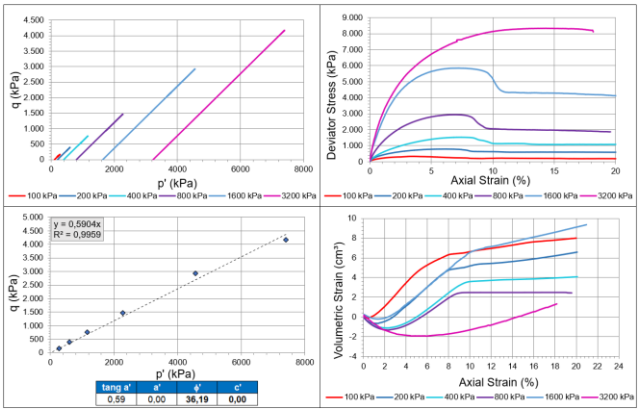

Figure 6. CID results – 9th layer.

Regarding geotechnical monitoring system, piezometers monitoring data was obtained from February to June 2022 during construction. The results (Figure 7) confirms that there was no significant variation in readings during this period, therefore, the development of excess pore pressures was very low. This behaviour may be due to the fact that the experimental landfill layers were compacted with moisture content significantly below the optimum content.

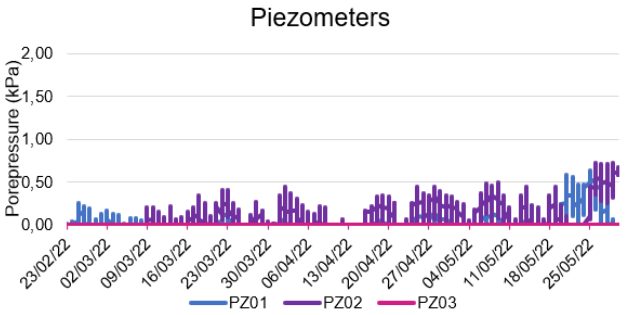

Figure 7. Monitoring data.

4 CONCLUSIONS

The experimental landfill construction was a remarkable step in order to provide data regarding geotechnical parameters and also material workability. According to field tests results, the material achieved the required degree of compaction (98%) and the average maximum dry density was 1.87g/cm³ with optimum moisture content with an average value of 13%. The filtered flotation tailings were compacted with a water content below the optimum moisture content and a greater in-situ density due to a higher compaction energy during construction.

The material does not present variability in particle size distribution and is defined as a fine silty sand. Triaxial tests indicates high shear stress and friction angle ranging from 32° to 40° and null cohesion. It was not identified excess pore pressure generation during construction according to electrical piezometers data.

ACKNOWLEDGEMENTS

The authors are grateful for the support provided by Anglo American, TEC3 Engenharia and F&Z Consultoria engineers.

REFERENCES

Ulrich, B. and Coffin, J. (2013). Considerations for tailings facility design and operation using filtered tailings. *16th international seminar on paste and thickened tailings*, Belo Horizonte, Brazil. https://doi.org/10.36487/ACG_rep/1363_15_Ulrich.

Proceedings of the XVIII ECSMGE 2024
GEOTECHNICAL ENGINEERING CHALLENGES
TO MEET CURRENT AND EMERGING NEEDS OF SOCIETY
© 2024 the Authors
ISBN 978-1-032-54816-6
DOI 10.1201/9781003431749-263
Open Access: www.taylorfrancis.com, CC BY-NC-ND 4.0 license

ECSMGE 24
XVIII EUROPEAN CONFERENCE ON SOIL MECHANICS AND GEOTECHNICAL ENGINEERING

Monitoring and analyzing vibrations from tunnel boring machine in urban areas

Suivi et analyse des vibrations générées par les tunneliers en zones urbaines

Y. Aslan*, A. Rallu, D. Branque
Université de Lyon, ENTPE, LTDS - UMR CNRS 5513, Vaulx-en-Velin, France

N. Berthoz
Centre d'Études des Tunnels (CETU), Bron, France

C. Chatzigogos, T. Makrypidi
Géodynamique et Structure, Montrouge, France

**yara.aslan@entpe.fr*

ABSTRACT: To enhance safety during the excavation phase of the urban tunnel construction using a Tunnel Boring Machine (TBM), we conducted an experimental study focused on the vibratory impact of excavating Line 18 of the Grand Paris Express in France, particularly at the Orly site. Our experimental setup involved strategically placing geophones and accelerometers along the tunnel route: on the surface, in the ground near the TBM, and inside the TBM itself. This article presents and analyzes the outcomes of the experiments, encompassing measurements of characteristic velocities and the identification of frequency ranges with elevated energy levels. The results not only illustrate the distribution of vibration energy linked to the excavation process but also offer insights into how the ground responds to these vibrations.

RÉSUMÉ: Afin d'améliorer la sécurité lors de la phase d'excavation au tunnelier (TBM) de la construction de tunnels urbains, nous avons réalisé une campagne expérimentale visant à étudier l'impact vibratoire du creusement de la Ligne 18 du Grand Paris Express (France) sur le site d'Orly. Le dispositif expérimental incluait des géophones et des accéléromètres positionnés sur le tracé du tunnel à la fois en surface, dans le sol proche du tunnelier et à l'intérieur du tunnelier. Cet article présente et analyse les résultats expérimentaux, qui englobent des mesures de vitesses caractéristiques et l'identification de plages de fréquences présentant des niveaux d'énergie élevés. Les résultats mettent en évidence non seulement la distribution de l'énergie vibratoire liée au processus de creusement, mais fournissent également des informations sur la réponse du sol à ces vibrations.

Keywords: Ground-borne vibrations; tunnel boring machine; in-situ measurements; dynamic characterization; frequency domain decomposition.

1 INTRODUCTION

Urban tunneling operations employing tunnel boring machines (TBMs) have become increasingly common. The analysis of vibrations generated by these excavations is deemed essential, given their impact on public safety and nearby structures. The selection of TBMs, whether earth pressure balanced shield (EPBS), slurry shield (SS), or open/hard rock TBMs, is contingent on geological conditions and project requirements. To advance our comprehension of these vibrations' behavior, their characterization can be achieved through the application of analytical methods and numerical models. Nevertheless, it is imperative to have these models validated using experimental data collected from various locations. Vibrations resulting from TBM excavations have been researched, with some studies conducted within the TBM itself and others concentrating on surface measurements, such as (non-exhautive list, a deeper review can be found in (Rallu et al., 2023)): Flanagan (1993) for the Buffalo metro (USA) and Hiller and Crabb (2000) for the London JLE metro (UK). A time-domain and frequency-domain analysis of vibrations measured simultaneously inside the TBM and on the surface had been performed on four tunnel projects in different geological contexts in Rallu et al. (2023). Moreover, Lu et al. (2022) conducted vibration measurements at different depths in a tunnel cover during the excavation phase in order to characterise the influence of geometric and geological parameters.

This study aims to compile data from various positions, including inside the TBM, within the ground, and on the surface, at the Orly, France, Metro Line 18 tunnel project. Various sensor types and

analyses are employed to enhance our understanding of the vibrations' behavior.

2 CASE STUDY OVERVIEW: METRO LINE 18

2.1 Study area description

The investigation was carried out at the metro Line 18 project, affiliated with the Grand Paris Express initiative and situated in the vicinity of Paris' Orly Airport. Covering a total distance of 35 kilometers, Line 18 comprises both an elevated and an underground segment, with a specific focus on the latter for this study. This metro line employs an earth pressure balance shield boring machine with a diameter of 9.15 m and features 10 stations along its route.

To understand the soil composition at the site, cross-hole in situ tests were conducted, and soil core samples were collected, providing insights into its characteristics. It is important to note that the site is saturated with water. In the studied site, overburden is around 28 m, see Figure 1.

A diverse range of sensors, including the Tromino from the Moho brand and 3D geophones with high precision (10^{-7}mm/s) capable of measuring ambient noise, were implemented on the construction site. The sensor has the option of being affixed to the soil using its three small pointed legs or simply placed on the surface. The coordination of these sensors involved the utilization of the global positioning system (GPS), with its limitations in underground areas recognized. To address this, all sensors were synchronized at a central surface location to collect GPS time data before being deployed to their respective positions.

The Soil Spy Rosina sensor, comprising vertical 1D geophones that can be positioned in the ground or on the surface, was also used. These geophones are connected to a central computer for data acquisition, and each Soil Spy Rosina sensor is characterized by an accuracy level of about 4×10^{-8} mm/s.

In this scenario, cylindrical 3D accelerometers from Syscom, featuring an impressive measurement range of up to $\pm$4g, were employed. These sensors are intricately connected to their dedicated central acquisition unit via a lengthy 50-meter cable. Despite their primary role in measuring acceleration, it is noteworthy that the transformation of this data into velocity is achievable through the integration of the acceleration data. This transformation process includes additional steps, such as filtering the data, to enhance accuracy.

Depth interval(m)	Geological Layer	Vs(m/s)
[0 – 3]	LP: plateau silt	353
[3 – 6]	TB: Brie and Sannois limestone	462
[6 – 14.42]	GV:Green clays	230
[14.42 – 25]	MSGp: Supragypsous marls of Pantin	418
[25 – 33.5]	MSGa: Supragypsum marls of Argenteuil	469
[33.5 – 39.5]	MFL: Masses and marls of gypsum	616

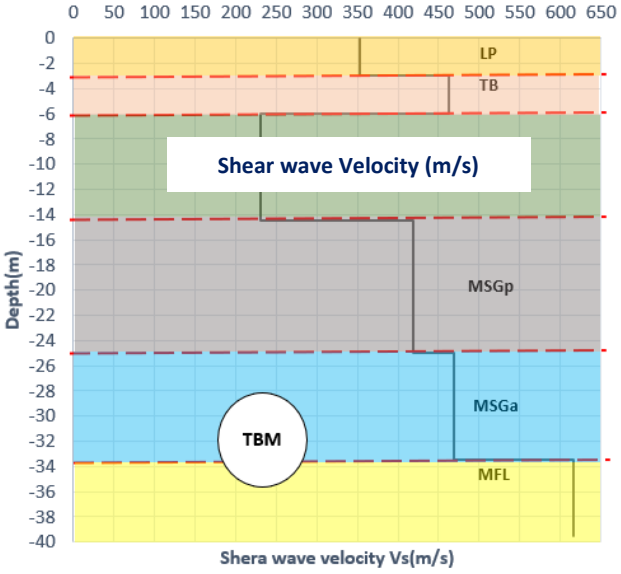

Figure 1. Site geological profile (scale not represented).



Figure 2. Types of sensors: Tromino, Rosina, and Syscom (from left to right).

At the construction site, two boreholes, namely T1 and T2, were employed, spaced 10 meters apart and possessing diameters of 80 mm. The lengths of these boreholes were 26 m and 38.8 m for T1 and T2, respectively. These boreholes played a pivotal role in the precise positioning of our sensors, adhering to the experimental setup illustrated in Figure 3:

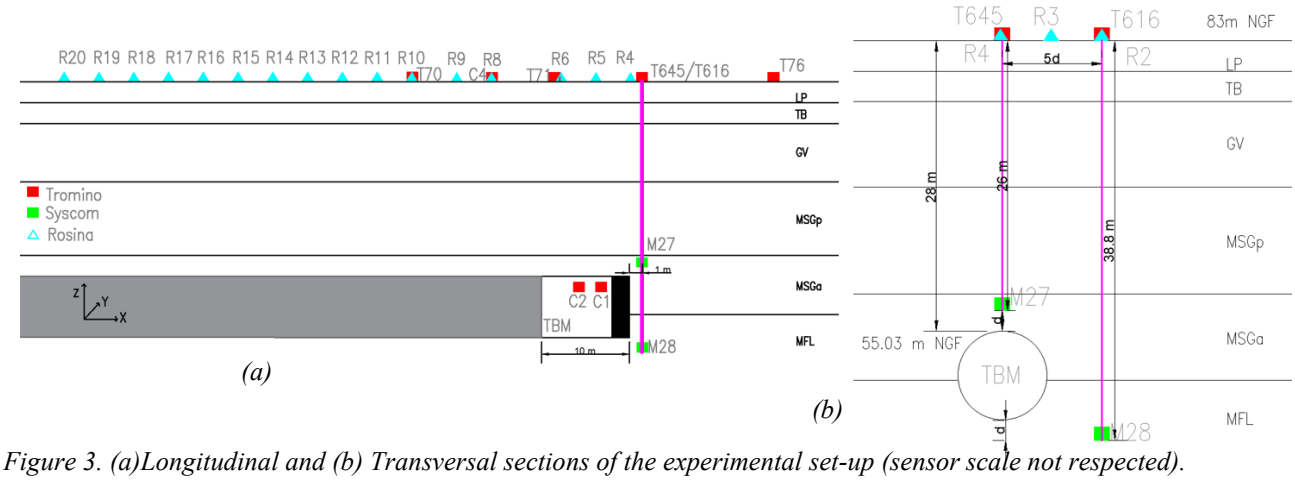

Figure 3. (a)Longitudinal and (b) Transversal sections of the experimental set-up (sensor scale not respected).

- On the surface, seven Trominos were strategically placed with a 10m separation between each (C4/T70/T71/T75/T76/T616/T645);
- Within the TBM's manlock, two Trominos (C1/C2) were positioned, with distances of 2.5 m and 4.5 m from the cutter wheel, respectively;
- On the surface, an L-shaped array consisting of 18 Rosina sensors (R2-R20) was organized, with a 5 m gap between each sensor;
- At the bottom of each borehole, two Syscom sensors were positioned: M27 and M28. M27 was installed d = 2 m above the tunnel crown, while M28 was installed d = 2 m below the tunnel raft. Both sensors were situated at the same longitudinal distance of 1 m from the face of the TBM, as illustrated in Figure 3.

3 DATA PROCESSING METHODOLOGY

Two distinct field campaigns were undertaken in this research. The first, conducted in January 2023, aimed to collect data in the presence of normal mechanical noise conditions. The second campaign, executed in April 2023 upon the arrival of the TBM at our site, centered on synchronized data collection from all designated sensors. This phase was dedicated to capturing data during the TBM's specific operational conditions to assess the vibrations emitted by the tunnel.

3.1 Data pre-processing

The primary aim at this stage is to ensure the reliability and quality of collected sensor data. To achieve this, a series of procedures were implemented to clean, improve, and prepare the data for further analysis. These procedures involve:

- restricting time traces to a relevant interval showing stationary behaviour;
- iltering signals within the frequency range 0-160 Hz, aligning with typical frequencies in building engineering;
- ensuring a zero-mean value for the time-histories.

By applying these steps, the data is refined enabling more dependable analysis in subsequent stages.

3.2 Data post-processing

Two primary methods were employed for data analysis in our research: Time Domain Analysis (TDA) and Frequency Domain Analysis (FDA). In the TDA, the characteristic vibratory level was measured using characteristic velocity per channel. This value corresponds to the absolute velocity within a 0.5% probability of being exceeded and captures the majority of signal energy, effectively eliminating non-representative peaks. On the other hand, FDA involved signal transformation to reveal its spectral content, allowing the understanding of how energy is distributed across different frequency components. These two approaches were employed in synergy, contributing to the overall improvement of signal characterization.

4 RESULTS AND DISCUSSION

4.1 Temporal analysis

Conducting a TDA with data from sensors strategically placed within the TBM, within the ground, and on the surface, the evaluation aimed to precisely measure the vibrations generated by the TBM during excavation and their subsequent propagation into the surrounding environment.

Figure 4 provides a detailed depiction:

- The time history for sensor C2 (blue color) in the Z direction reveals a characteristic velocity, as indicated by the envelope of the data, measuring around 1 mm/s;
- The time history for sensor M27 (orange color) in the Z direction exhibits a characteristic velocity of approximately 0.1 mm/s, noticeably lower compared to those observed inside the TBM.

As a result, it is relevant to consider that the signals acquired within the ground and inside the TBM are quasi-stationary. Additionally, the velocity magnitude inside the TBM is approximately 10 times larger than that within the ground (as measured by the Syscom sensor): $v_{k,TBM} \approx 10\, v_{k,soil}$. This indicates that not all the energy generated by the TBM is transferred to the surrounding area.

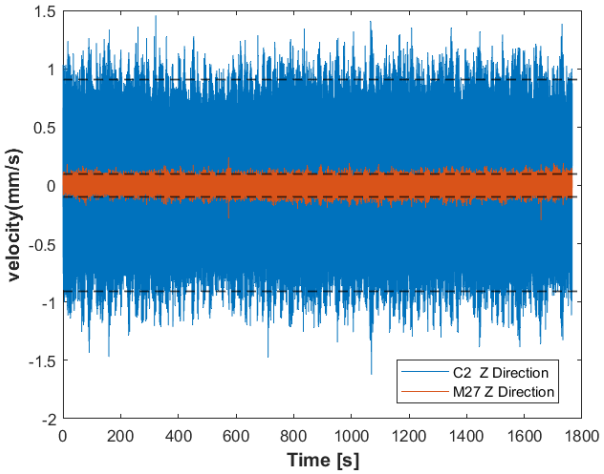

Figure 4. Time histories of sensors C2 (inside the TBM) and M27 (inside the ground) in the direction Z. Horizontal dashed lines represent the characteristic velocities.

The characteristic velocities of the sensors in the Tunnel Boring Machine (TBM), within the ground, and on the surface are depicted in Figure 5 for each acquisition direction. These velocities are presented as a function of their distance from the center of the cutting wheel, calculated based on the Pythagorean norm $\sqrt{x^2 + y^2 + z^2}$. The plot in Figure 6 illustrates the change in characteristic velocity (mm/s) for the Z direction across all sensor locations. Notably, Figure 5 reveals the similarity in amplitudes for all three directions at each sensor position. Furthermore, the vibration levels exhibit high comparability among the TBM (1 mm/s), within the soil (0.1 mm/s), and at the surface (0.01 mm/s). As a result, it can be inferred that the total energy is not entirely transferred to the surroundings. Instead, there is dissipation within the TBM itself and through the geological layers.

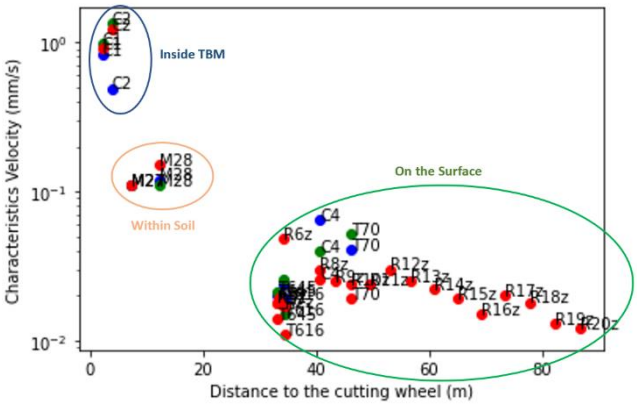

Figure 5. Characteristic velocities in function of the distance of the sensor to the cutting wheel, in the three directions of acquisition (X, Y, Z) for sensors located inside the TBM, on the surface and within the ground.

4.2 Frequency analysis

The distinct contributions of the signal at specific frequencies are revealed by the frequency analysis, often characterized using Fourier analysis. The vibration source's frequency characteristics are clarified, and the relationship between this frequency representation and its impact on the surface is established as primary objectives.

A method to estimate a signal's frequency spectrum involves the calculation of its power spectral density (PSD) through the Welch method, which combines the concept of Fourier transform and averaging to provide a more robust and reliable estimate of the PSD. In this method, the input signal is divided into overlapping segments, and a periodogram (an estimate of the signal's spectrum) is computed for each segment. These periodograms are then averaged to obtain a smoother and more accurate estimate of the PSD.

Detecting the relevant frequency ranges representing both the excitation level of the source and the ground's response is challenging when employing individual spectrum analysis from each sensor. To address this challenge, an approach inspired by the Frequency Domain Decomposition (FDD) technique was employed. Dominant frequency content in groups of synchronized sensors is identified by this technique, enhancing the representation of correlated frequencies across all signals and eliminating isolated peaks.

It is important to note that the traditional FDD plot often involves multiple Singular Value Decompositions (SVDs). In this case, the focus is on visualizing the first singular value (σ). This approach, introduced in the research conducted by Rallu et al. (2023), aims to evaluate the energy levels of signals concerning their frequencies in various underground

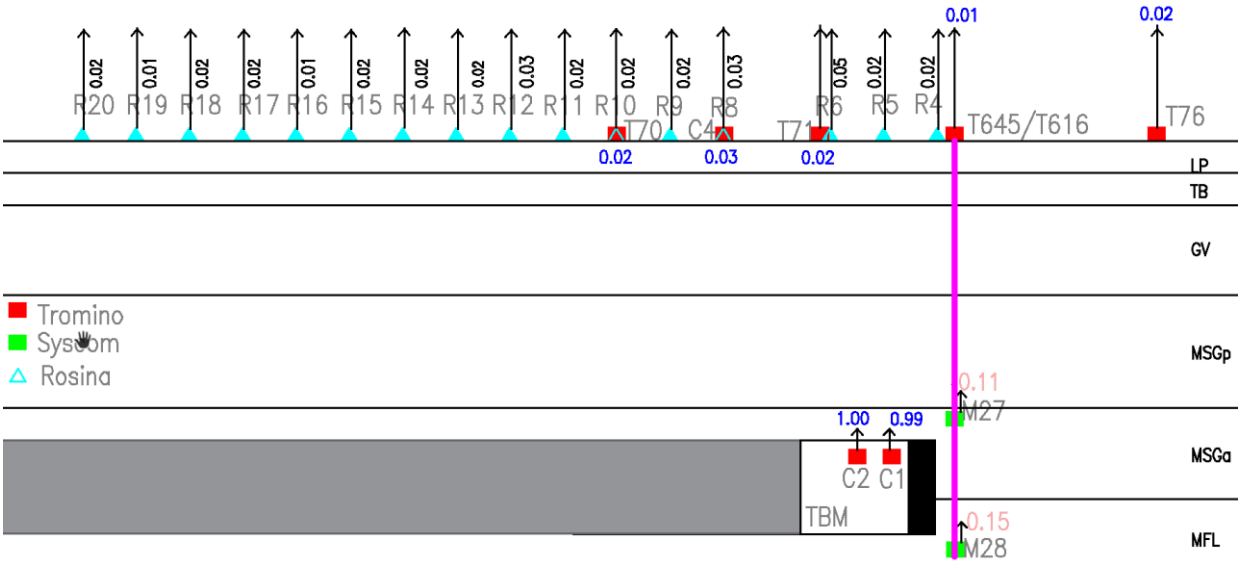

Figure 6. Depiction of vertical (Z) characteristic velocities in mm/s across all sensors throughout the excavation phase in a longitudinal section.

projects. Notably, it reveals the frequency coherence between signals recorded within the Tunnel Boring Machine (TBM) and those captured on the surface during excavation.

Two scenarios were employed in the study, encompassing the measurement of ambient noise before excavation and measurements during excavation, which included on-surface, within the soil (utilizing Syscoms), and inside the Tunnel Boring Machine (TBM). Examining the scenario of surface sensors capturing mechanical ambient noise, energetic peaks in the site spectra corresponded to frequency bands around the soil's eigenfrequencies. The initial singular value (σ) derived from the Power Spectral Density (PSD) matrix serves as an indicator of signal energy across diverse situations and orientations. This visual representation facilitates a comprehensive exploration of connections and correlations between these signals. The lack of strong intercorrelation between two signals may result from weak values in one or both signals or a feeble correlation between them. Conversely, if two signals contribute energetically in the same frequency band, a robust intercorrelation in that band occurs. Referring to Figure 7, irrespective of the sensor's position during the excavation phase, the overall trend of the first singular value across frequencies remains consistent, displaying identical local peaks with varying amplitudes.

Figure 7 illustrates a significant difference in energy levels at three positions during excavation: approximately $10^{-2}(mm/s)^2$ inside the TBM, $10^{-5}(mm/s)^2$ within the soil, and $10^{-6}(mm/s)^2$ on the surface. This disparity supports the conclusion that energy transfer is not uniform towards the surface.

Additionally, it shows the consistent evolution of the three directions for the three sensor positions is observed during the excavation phase. In contrast, under ambient noise, differences emerge, with a peak at a higher frequency in the Z direction, attributed to the terrain's anisotropy.

Upon comparing the spectra in Figure 7, it becomes evident that peaks around 85 Hz and 175 Hz, present inside the tunnel boring machine, are also observed in the ground and on the surface during excavation. Consequently, the excavation phenomenon is characterized by the presence of two peaks: 85 Hz and 175 Hz.

In the frequency range below 70 Hz, the soil, exposed to ambient noise, displays an energetic frequency band typical of classical soil eigenfrequencies. This results in a robust response significantly influenced by the TBM, generating energetic reactions on the surface that extend beyond the vicinity of the tunnel axis. However, beyond 100 Hz, the site-spectrum under ambient noise functions as a transfer function. Therefore, the response on the surface and within the soil under TBM influence corresponds to the convolution between the TBM and ambient noise. Identical local peaks observed on both the surface and near the tunnel axis represent the frequencies of the source.

5 CONCLUSION

Extensive vibration measurements were undertaken as an integral component of the Metro Line 18 Grand Paris project. These measurements encompassed

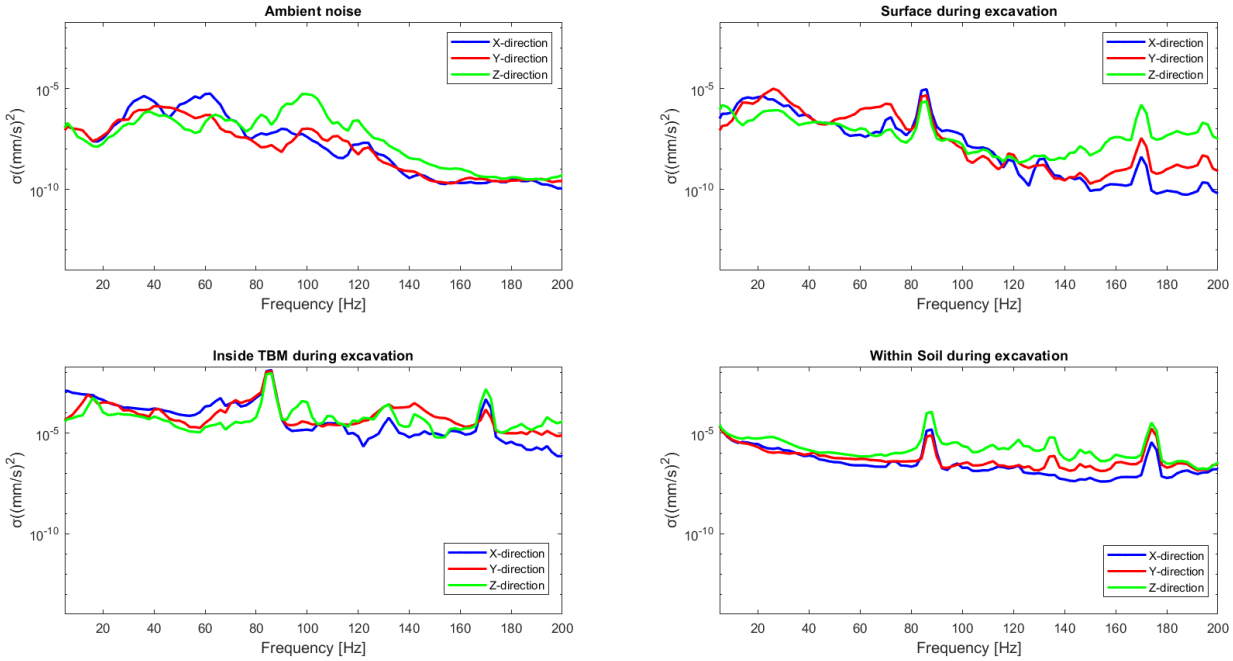

Figure 7: Representation of the intercorrelation between 3 sensor positions: (at the surface, within the soil and inside the TBM) for the 2 cases: (ambient noise and during excavation).

sensors strategically positioned on the surface, within the ground, and inside the Tunnel Boring Machine (TBM), both during excavation and ambient noise conditions. The analyses focused on assessing characteristic velocity amplitudes and frequency characteristics of the recorded signals, leading to several key findings:

- Surface velocity vibrations (10^{-2} mm/s) were significantly lower than those inside the TBM (100 times);
- Velocity amplitudes within the TBM were ten times higher than those within the ground via Syscom sensors which is 1 m apart from the TBM face, indicating energy dissipation within the TBM ;
- Energy dissipation was confirmed by analysing the highest singular values of spectral density matrices from all sensors, with three levels of energy recorded: approximately $10^{-2}(mm/s)^2$ inside the TBM, $10^{-5}(mm/s)^2$ within the soil, and $10^{-6}(mm/s)^2$on the surface.
- During the excavation phase, two frequencies, namely 85Hz and 175Hz, were observed within the Tunnel Boring Machine (TBM), within the ground, and on the surface. Notably, these frequencies were absent under ambient noise conditions, indicating their association with the excavation phenomenon.

ACKNOWLEDGEMENTS

The authors are grateful for the assistance provided by CETU and Me2i for establishing the geological profile as well as for the support provided by the Société du Grand Paris. Results presented in this paper have been obtained within the framework of the French research Project E-PILOT (Evaluation of the impact on Piles response during Tunnelling).

REFERENCES

Rallu A., Berthoz N., Charlemagne S. and Branque D. (2023), Vibrations induced by tunnel boring machine in urban areas: In situ measurements and methodology of analysis, Journal of Rock Mechanics and Geotechnical Engineering, Volume 15,Issue1,pp.130145.(https://doi.org/10.1016/j.jrmge.2022.02.014).

Flanagan RF (1993), Ground vibration from TBMs and shields. Tunnels and Tunnelling 25(10):30-33(https://link.springer.com/article/10.1007/s00603-015-0887-7).

Hiller, D.M., Crabb, G.I. (2000), Groundborne Vibration Caused by Mechanised Construction Works, vol. 429. Transport Research Laboratory report, United Kingdom, 52 p.

Lu Z., Wang X., Zhou G., Feng L., Jiang Y. (2022), Investigation on vibration influence law of double shield tbm tunnel construction, Applied Sciences (Switzerland),12. (https://doi.org/10.3390/app12157727).

Proceedings of the XVIII ECSMGE 2024
GEOTECHNICAL ENGINEERING CHALLENGES
TO MEET CURRENT AND EMERGING NEEDS OF SOCIETY
© 2024 the Authors
ISBN 978-1-032-54816-6
DOI 10.1201/9781003431749-264
Open Access: www.taylorfrancis.com, CC BY-NC-ND 4.0 license

ECSMGE 24
XVIII EUROPEAN CONFERENCE ON SOIL MECHANICS AND GEOTECHNICAL ENGINEERING

Evaluation of slope safety during pile driving in clay

Évaluation des risques lors du battage de pieux dans des pentes argileuses

Y. Attari*, E. Sørlie
Multiconsult AS, Oslo, Norway

H.P. Jostad
Norwegian Geotechnical Institute, Oslo, Norway

G.R. Eiksund
Norwegian University of Science & Technology (NTNU), Trondhiem, Norway

**Yeganeh.attari@multiconsult.no*

ABSTRACT: Pile driving adjacent to or in slopes can trigger landslides, specifically in marginally stable slopes and in the presence of sensitive soil deposits. Slope failure incidents due to pile driving have been reported in countries such as Norway, Sweden and Canada where soft sensitive clay deposits are prevalent. However, the failure mechanisms involved in such incidents are not well studied nor understood. Furthermore, the methods currently used to estimate the reduction in the slope's factor of safety during pile driving lack scientific consensus. This paper describes how pile driving can reduce slope stability by means of empirical relations and analytical solutions from soil mechanics as well as numerical analysis.

RÉSUMÉ: Le battage de pieux à proximité ou dans des pentes argileuses peut déclencher des glissements de terrain, particulièrement dans des pentes peu stables et en présence de sols mout et sensible. Des glissements de terrain dus au battage de pieux ont été répertoriés dans différents pays comme la Norvège, la Suède et le Canada, pays dans lesquels les argiles sensibles. Cependant, les mécanismes de rupture qui explique ces incidents ne sont pas clairement identifiés ni compris. De plus, les méthodes actuellement disponibles pour quantifier les coefficients de sécurité des pentes durant le battage de pieux manque de précision scientifique. Cet article décrit comment le battage de pieux peut affecter la stabilité de la pente.

Keywords: Pile driving; slope stability; excess pore pressure; strain softening; numerical modelling.

1 INTRODUCTION

Pile driving generates stresses, strains, excess pore pressures and vibrations in the soil (Seed and Reese, 1957). Pile driving in clay is an undrained type of loading where multiple hammer-blows generate excess pore pressure in the adjacent soil which may lead to cyclic degradation of the soil (Randolph and Gourvenec, 2011). These effects are visually depicted in Figure 1. As a result, characteristics of the soil (such as plasticity index and strength among others) in the vicinity of the pile change during and for a period after the pile driving. These changes are usually temporary, and the soil regains its initial strength to some extent (Karlsrud and Nadim 1990). But this process can take many months depending on the properties of the soil, mainly permeability and stiffness of the soil material.

In some cases, these temporary changes in the soil can lead to a reduction in the factor of safety of a slope and lead to excessive movements or initiate a landslide. Understanding the mechanisms involved and methods to account for this reduction in the safety factor can help reduce risks related to pile driving conducted in slopes.

There are not many reported and documented cases of landslides due to pile driving in the literature (Attari et al., 2023). Reviewing the few numbers of reported cases shows that this type of slope failure is more common in Norway, Sweden and Canada where sensitive and brittle clay materials are present in the soil (Attari et al., 2023). For instance, a large landslide occurred in 1950 in the Gota river valley area, located nearby Gothenburg city in Sweden. The landslide affected 240,000 m^2 of the area and swept away 31 family houses and resulted in a loss of life (Bernander, 2011). At the time of the landslide, pile driving was being conducted at the top of the slope. A landslide took place in 1966 a few hours after completion of driving 50 wooden piles into soft sensitive clay (Broms and Bennemark, 1967). Another landslide occurred in Quebec, Canada in 1978 while pile driving was in operation for an electrical tower (Carson, 2011). The results of grain size analysis and drilling

reports indicated lenses of sand and silt in the deposit and the investigating committee report concluded that the vibrations induced by pile driving have resulted in the liquefaction of these sand lenses, causing the surrounding clay to lose part of its shear strength, resulting in continuation of the movements even after pile driving had stopped (Carson, 2011).

A list of slope failure incidents due to pile driving is provided in Attari et al. (2023). In some of these cases, noticeable rise in pore pressure was observed prior or after the landslide and a lot of the soil investigation reports indicate lenses of silt and sand between the clay layers. Despite the significance of this problem, there is still not a standard method developed to accurately account for the reduced stability of a slope due to pile driving (Langford et al., 2021).

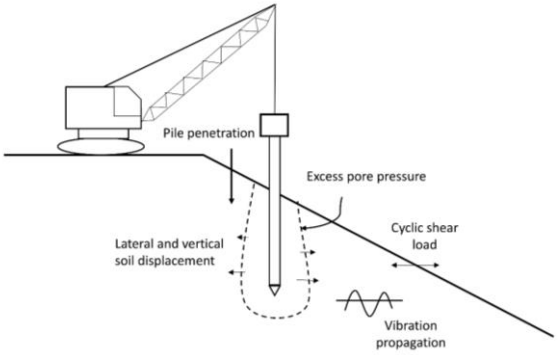

Figure 1. Effects of pile installation in a slope (Attari et al., 2023).

Common practice in Norway to account for reduced stability of a slope during pile driving, is to monitor pore pressures during construction. Limits are set on maximum allowable pore pressure levels to avoid slope failure. Piling operations are stopped when these limits are exceeded and are continued where pore pressures return to allowable rates (Tefera et al., 2013). However, the basis for obtaining these limiting values is not accurate. Moreover, the costs for waiting time or for moving pile-driving machines to different locations to allow for pore pressure dissipation can be large and there are a lot of uncertainties in the installation/construction phase, which usually infers extra costs. Therefore, there is a strong need for further research to develop an approach to account for pile installation effects on slope stability in a more reliable manner.

2 REVIEW OF THE BASIS OF THE TRADITIONAL METHODS

The basis for the currently used methods in practice together with measuring of pore pressures is that soil strength is dependent on effective stresses (Ladd & Foott, 1974). The SHANSEP technique which assesses the effect of stress history on the shear strength of soil was developed by Ladd & Foott (1974). This concept is based on a series of laboratory tests which establish undrained shear strength as a function of Overconsolidation Ratio (OCR) and accordingly, calculates the undrained shear strength based on the in-situ vertical effective stress, using Equation (1).

$$S_u = S.OCR^m.P' \quad (1)$$

$$P' = P - \Delta u \quad (2)$$

where S_u is the undrained shear strength, P is the *in-situ* vertical stress, P' is the *in-situ* vertical effective stress, Δu is pore pressure, S is undrained shear strength ratio in normally consolidated state (OCR=1) and m is a constant dependent on the type and Plasticity Index of clay. Using the SHANSEP principle in a pile driving scenario will provide reduced shear strength values (Kirkebø et al., 2008) due to the reduction in P' given by Equation (2). The methods assume that the excess pore pressure results in reduced effective stresses in the soil adjacent to the pile, and as given by the SHANSEP formula, the undrained shear strength reduces. Accordingly, the reduced Su results in a lower safety factor of the slope.

However, these assumptions do not consider that pile driving is an undrained loading mechanism in clay (considering the low permeability of clays) which increases the total stresses. Thus, according to equation (2), which is the basis of the effective stress concept by Terzaghi (1943), the change in effective stresses is dependent on both total stress and excess pore pressure which are both increasing. A more in-depth evaluation of these methods can be found in Attari et al. (2023).

3 NUMERICAL ANALYSIS

It is a complex task to simulate pile driving using Finite Element Analysis (FEA). For the purpose of this study, it was deemed suitable to only take into account the effect of the lateral push that is generated due to driving a pile in the slope, assuming the row of piles are installed simultaneously to full depth. For this reason, pile driving was simulated using the prescribed

volumetric strain feature in the finite element code Plaxis, where in a 2D setting, lateral strains are applied to a wished-in-place pile modelled as a soil cluster. This volumetric strain feature expands or contracts a soil cluster equal to the applied strain (Brinkgreve et al., 2021). This change in strains will then affect the surrounding soil until equilibrium is reached between all clusters. Application of prescribed volumetric strains on the pile cluster, generates lateral displacements in the soil similar to the expansion of a cylindrical cavity in a soil medium, which is widely used in combination with a constitutive soil model to simulate the effects of pile driving in soil (Hunt, 2000). Although this method disregards the changes in vertical stresses during pile driving, it still provides good estimates of stresses, displacements and excess pore pressures in the soil due to pile penetration (Hunt, 2000). The accuracy of the results in these analyses are highly dependent on the choice of the constitutive soil model. For instance, a simple soil model such as Mohr-Coulomb cannot simulate several important effects of pile driving (stress dependent stiffness, strain softening) and are therefore not able to capture the reduction of the safety factor of the slope. More advanced constitutive models such as Soft Soil can provide better estimates of, for example, the excess pore pressure and, accordingly, provide a better understanding of the extent of undrained shear strength mobilization in the soil after pile driving.

More advanced constitutive models that can take into account strain-softening of the clay are further employed in FEA. Sensitive clays show a reduction in their undrained shear strength after the peak strength is reached in undrained conditions. This characteristic is referred to as strain-softening. A gradual progression of strain-softening behavior throughout the slope could ultimately lead to a global failure (Urciuoli et al., 2007). This type of failure is defined as progressive failure in sensitive deposits where a local disturbance may trigger a landslide Bernander (2011). The NGI-ADPSoft model is an elastoplastic constitutive soil model that can be used in total stress analysis of soils and can simulate the strain softening behaviour of sensitive clays and hence, can capture the reduction of the undrained shear strength in the soils as a function of strain level in undrained conditions. This could be used to calculate a representative factor of safety in the sensitive clay slope (see Figure 2). This representative factor of safety is obtained by increasing the unit weight of the soil int the analysis (instead of reducing the soil strength) until failure is reached. More information about this soil model can be found in Jostad et al. (2014) as well as Grimstad & Jostad (2012).

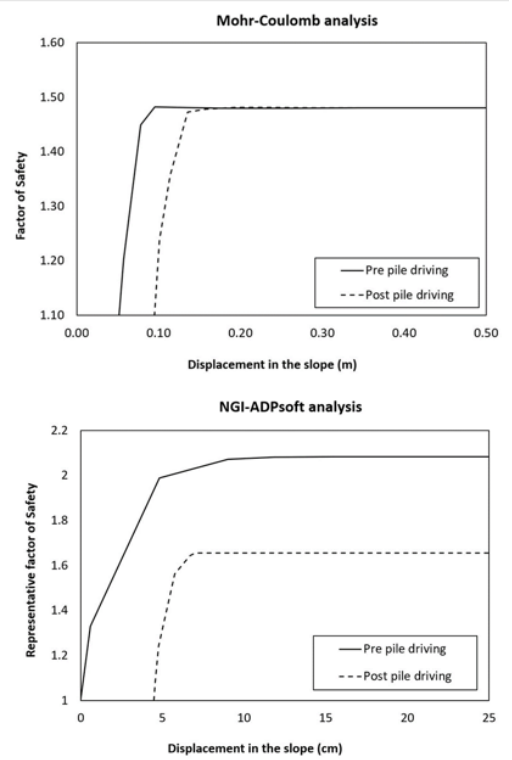

Figure 2. Comparison of factor of safety using different constitutive soil models in Plaxis (Attari et al., 2023).

4 CYCLIC SOIL DEGRADATION DUE TO PILE DRIVING

Soil response to cyclic loading is substantially different from the soil response under monotonic loading and depends on the mode, amplitude and frequency of the cyclic loading. To investigate if the cyclic loading generated due to pile driving can influence the stability of slopes due to cyclic degradation of the soil strength the following methodology is being investigated. A pile driving analysis is conducted to provide pile displacements in time by means of 1D stress wave analysis using the GRLWEAP software. The displacement versus time output can be used in a dynamic finite element analysis to estimate the extent and magnitude of the changes in stresses, strains and excess pore pressures due to the cyclic loading. These results can be used in combination with cyclic degradation contour diagrams developed by Andersen (2009) to determine the reduction in shear strength. These diagrams are developed for a great range of soils and are based on large numbers of laboratory tests on block samples (Andersen, 2009). The result of this study is planned to be included in future articles by the authors.

5 CONCLUSIONS

Throughout this study, changes occurring in clay due to pile driving have been briefly explained and their possible effect on the reduction of soil strength was pointed out. Subsequently, methods currently used by geotechnical engineers to take into account the reduction in the stability of a slope during pile driving were presented. It was pointed out that these methods lack theoretical consensus. Furthermore, examples of how numerical analysis can contribute to better understanding of this problem were outlined.

ACKNOWLEDGEMENTS

This study was done within BegrensSkade (REMEDY) II research project financed by the Norwegian Research Council (grant 267674). The authors acknowledge the support of the research project leader, Dr. Jenny Langford at the Norwegian Geotechnical Institute.

REFERENCES

Andersen, K. H. (2009). Bearing capacity under cyclic loading—offshore, along the coast, and on land. The 21st Bjerrum Lecture presented in Oslo, 23 2007. *Canadian Geotechnical Journal*, *46*(5), 513 November –535.

Attari, Y., Jostad, H.P., Grimstad, G. et al. (2023) Evaluation of Pile Driving Effects on Slope Stability in Clay. Geotechnical and Geological Engineering. https://doi.org/10.1007/s10706-023-02636-w

Bernander, S. (2011) Progressive Landslides in Long Natural Slopes: Doctoral Thesis. Luleå University of Technology.

Brinkgreve, R. B. J., Engin, E., & Swolfs, W. M. (2017). Plaxis 2D manual. Rotterdam, Netherlands.

Broms, B. B. and Bennemark, H. (1967). Session 1 - Free discussion, sensitive clay landslides. In PROCEEDINGS OF THE GEOTECHNICAL CONFERENCE, Oslo.

Carson M.A. (2011) On the retrogression of landslides in sensitive muddy sediments: reply. Can Geotech J16(2):431–444. https://doi.org/10.1139/t79-047

Grimstad, G. & Jostad, H. (2012). Stability analyses of quick clay using FEM and an anisotropic strain softening model with internal length scale. 675-680.

Hunt, Christopher (2000). Effect of pile installation on static and dynamic soil properties. Doctoral Dissertation, University of California, Berkley.

Jostad, H. and Fornes, P. and Thakur, V. (2014). Effect of Strain-Softening in Design of Fills on Gently Inclined Areas with Soft Sensitive Clays. https://doi.org/10.1007/978-94-007-7079-9_24

Karlsrud, K. and Nadim, F. (1990) 'Axial capacity of offshore piles in clay', in Offshore technology conference. Offshore Technology Conference.

Kirkebø, S., Athanasiu C. & Tvedt G. (2008). Stabilitetsmessige utfordrigner i forbindelse med peleramming langs trange elveløp. 15th Nordic Geotechnical Meeting (NGM), Sandefjord, Norge.

Ladd, C. C. and Foott, R. (1974) 'New design procedure for stability of soft clays', Journal of Geotechnical and Geoenvironmental Engineering, 100 (Proc Paper 10064).

Langford J, Lande EJ, Sandene T, Kahlstrom M, Nadim F, Noren-Cosgriff K, Piciullo L, Ritter S, Hauser C, Lysdahl A, Attari Y, Formreide R (2021) BegrensSkade II–REMEDY–risk reduction of groundwork damage: an overview. In: IOP conference series: earth and environmental science Vol. 710, No. 1, p. 012058. IOP Publishing.

Randolph, M. and Gourvenec, S. (2011). Offshore geotechnical engineering / Mark Randolph and Susan Gourvenec; with contributions from David White and Mark Cassidy. Spon Press, Abingdon, Oxon; New York.

Seed HB and Reese LC (1957) The action of soft clay along friction piles. Trans American Soc Civil Eng 122(1):731–754.

Tefera T, Tvedt G, Oset F (2013) Control of excess pore pressure development during pile installations in soft sensitive clay. Install Eff Geotech Eng Procee Int Conf Install Eff Geotech Eng ICIEGE 2013:140–145. https://doi.org/10.1201/b13890-22

Terzaghi, K. (1943). *Theoretical Soil Mechanics.* John Wiley & Sons.

Urciuoli, G., Picarelli, L., and Leroueil, S. (2007). Local soil failure before general slope failure. Geotechnical and Geological Engineering, 25(1):103-122.

Proceedings of the XVIII ECSMGE 2024
GEOTECHNICAL ENGINEERING CHALLENGES
TO MEET CURRENT AND EMERGING NEEDS OF SOCIETY
© 2024 the Authors
ISBN 978-1-032-54816-6
DOI 10.1201/9781003431749-265
Open Access: www.taylorfrancis.com, CC BY-NC-ND 4.0 license

ECSMGE 24
XVIII EUROPEAN CONFERENCE ON SOIL MECHANICS AND GEOTECHNICAL ENGINEERING

Effect of increased vertical stress on the state of grains in tailings

Effet de l'augmentation du stress vertical sur l'état des grains dans les résidus miniers

S. Aulestia*, V. Wiklund, M. Dossey, R. Knutsson, J. Laue
Luleå University of Technology, Luleå, Sweden

**shane.aulestia@ltu.se*

ABSTRACT: The mining industry has experienced rapid growth, leading to the accumulation of substantial mine waste, commonly referred to as tailings. Tailings are typically stored in tailings storage facilities, conventionally consisting of an impoundment surrounded by tailings dams. The construction of tailings dams can involve various methods, with the upstream method being commonly used in the industry. It is crucial to comprehend the long-term mechanical and geochemical behavior of deposited tailings to ensure the safety of upstream constructed tailings dams. The mineral composition, particle size distribution, and particle shape all affect the susceptibility to particle breakage or physical alteration. Therefore, there is an interest in understanding how grain size and grain shape relate to mineral composition and potential particle breakage to ensure the understanding of the long-term mechanical behavior. This study focuses on characterizing deposited tailings from various depths and investigates the impact of increased vertical stress on tailings, particularly examining the potential for crushing effects. The findings highlight the importance of considering these factors for a comprehensive understanding of tailings behavior and their implications for the long-term safety of tailings dams.

RÉSUMÉ: L'industrie minière a connu une croissance rapide, entraînant une accumulation substantielle de rejets de concentrateur, communément appelés résidus miniers. Les résidus sont généralement stockés dans des parcs à résidus, traditionnellement constituées d'un bassin entouré de digues construites de résidus. La construction de digues avec des résidus se fait avec différentes méthodes, la méthode amont étant couramment utilisée dans l'industrie minière. Il est crucial de comprendre le comportement mécanique et géochimique à long terme des résidus déposés pour garantir la sécurité des digues de résidus. La composition minéralogique, la distribution granulométrique et la forme des particules ont toutes une influence sur la susceptibilité des particules à se briser. Par conséquent, il est essentiel de comprendre comment la variation de taille et de forme des grains est liée à la composition minéralogique et à la possibilité de rupture des particules afin de garantir le comportement mécanique des digues à long terme. Cette étude se concentre sur la caractérisation des résidus déposés à différentes profondeurs dans la digue et examine l'impact de l'augmentation de la contrainte verticale sur les résidus, en particulier en ce qui concerne le potentiel d'effets de broyage. Les résultats mettent en évidence l'importance de prendre en compte ces facteurs pour une compréhension complète du comportement des résidus et de leurs implications pour la sécurité des digues de résidus à long terme.

Keywords: Tailings; mineralogy; particle size distribution; particle shape.

1 INTRODUCTION

The mining industry, vital for modern life, has seen rapid growth and thereby increasing notably the mine waste (Lyu et al., 2019). One type of mine waste is tailings and this leftover material is typically stored within impoundments surrounded by tailings dams, which are often built and raised up using tailings itself (Villavicencio et al., 2014).

Tailings dam construction can be classified into three main methodologies: upstream, centreline and downstream construction methods. Traditionally many tailings dams have been built by the upstream method and in this approach, embankments are placed on top of previous deposited tailings, implying that the tailings impoundment will eventually become part of the dam body and foundation for future embankments. Many upstream facilities have demonstrated satisfactory performance; however, this construction method is generally considered the least reliable (e.g., Fourie et al., 2022).

Intuitively, it is essential to understand both the mechanical and geochemical behavior of tailings to be able to perform safety assessments of upstream tailings dams over time (e.g., Vick, 1990).

According to Vick (1990), there could be a potential change among some of the intrinsic

properties of the tailings related to the long-term behavior, which thereby likely modifies the mechanical behavior. Some changes could be related to particle size distribution (PSD) and particle shape, as they adapt to new state properties (stress state and void ratio). Potentially crushing, particle breakage or degradation can occur implying a change in the PSD and particle shape. Zhang et al. (2020) emphasize that the magnitude of change in PSD and particle shape is strongly dependent of the mineralogic composition.

Bhanbhro (2017) looked at the crushing for uniform sized tailings (i.e. tailings sorted out in different group gradations) and exposed them to stepwise increased vertical stress from oedometer test making a comparison of the strength parameters, particle shape and breakage analysis.

The aim of this paper is to investigate the potential for particle breakage or physical alternations in form of change in the PSD on a whole tailing gradation, exposed to increased vertical stress (i.e., from slow and stepwise increased overload due to continued deposition). By conducting a comparative analysis, the study provides inputs that may enhance the understanding of tailings behavior under increased vertical load, although from the results presented herein it is understood and highlighted how mineralogical analysis must be merged into the analyses of PSD and particle shape analyses for better understanding.

2 METHODOLOGY

This study involved the analysis of disturbed samples extracted from a borehole within a tailings impoundment in northern Sweden, reaching a depth of approximately 40 m. Laboratory work was conducted on 4 samples collected from the borehole at varying depths, separated by approximately 10 meters each. These samples were designated as A (4.2 – 4.5 m), B (15.0 – 15.4 m), C (24.5 – 25.0 m), and D (33.5 – 34.0 m) as shown in Figure 1.

The samples underwent initial characterization, including PSD, particle shape and mineralogy. Subsequently, they were subjected to vertical stepwise loading through oedometer testing up to 640 kPa. Finally, another PSD characterization was performed on the oedometer tested samples.

The samples exhibited a PSD of sand and silt grains, with a fines content (<0.063 mm) ranging between 10 and 30%. The maximum grain size identified within the samples was 2.00 mm.

Samples were reconstituted using tamping methodology and the non-linear undercompaction method by Jiang et al. (2003). Additionally, one sample (D) was also prepared as a slurry to investigate possible effects of soil fabric and particle arrangement in the oedometer results.

For particle shape and mineralogical analyses, a qualitative assessment was done for particles greater than 0.063 mm through imaging using reflected light and scanning electron microscopy (SEM), respectively. SEM analysis was performed only in 2 out of 4 samples (A and B) since it was not possible to complete the test in all samples as expected due to some technical equipment problems.

Initial PSD samples were determined through wet sieving and sedimentation methods, while a dynamic image analysis was executed after oedometer testing using a Camsizer XT equipment. This equipment uses LED light sources and high-resolution cameras to scan particle collective injecting compressed air. This approach emerged as an alternative due to the limited amount of sample obtained after oedometer testing and potential uncertainties in the results when employing traditional sieving.

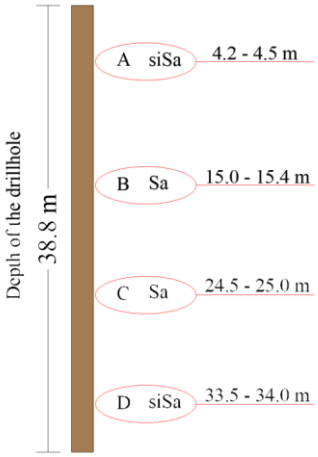

Figure 1. Drillhole and sampling schema.

3 RESULTS

3.1 Particle size distribution

The study presented herein focus on the changes in particle size distribution comparing before and after oedometer testing. The findings showed that the incremental stepwise loading produced minor and, in some cases, negligible variations in PSD. These variations were primarily observed in the coarser particles, leading to an increase in fines content. The most noticeable deviations occurred between sieves with apertures of 1.00 mm and 0.063 mm. Figure 3 and Figure 2 displays the PSD for sample A and D, correspondingly. Samples B and D showed the most prominent changes at the 0.125 mm sieve size with an

increase of 2.93% and 3.83% compared to their original PSD, and belonging to decrement at the 0.5 mm sieve size about 0.48% - 1.71%. Sample A displayed the lowest variation in fines after testing, with a maximum deviation of 0.46% at the 0.125 mm sieve.

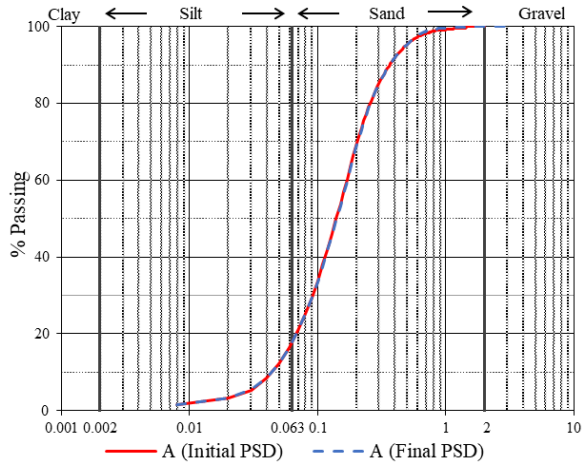

Figure 2. PSD sample A before and after testing.

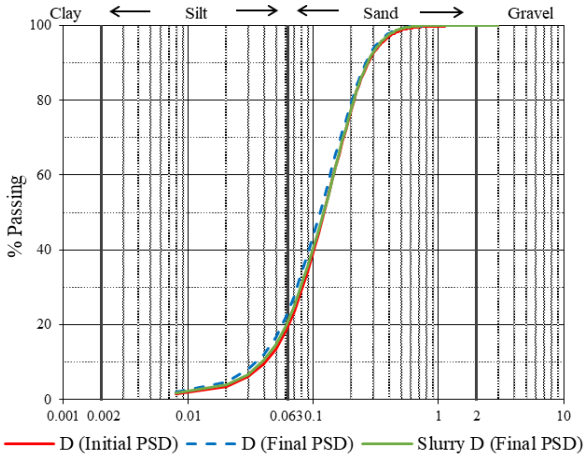

Figure 3. PSD sample D before and after testing.

In this study the change of PSD before and after oedometer testing are relatively small. However, the results are consistent in that all samples exhibited an increment of finer particles after oedometer testing. These results agree with the findings of Bhanbhro (2017), who for the tailings with the same origin showed that in uniform gradings coarser particles are more prone to breakage than finer particles. The uniform gradings of large particles (1-0.5 mm) in Bhanbhro (2017) exhibited a decrement around 14% at the 0.5 mm sieve. Thereby, it is clear that the uniform particles showed a more distinct physical alteration than the whole gradation tested samples in this study. If magnitude of alteration in PSD is disregarded all samples (from both studies) indicate that larger particles are more prone to physical alterations under vertical loading. This may be attributed to the presence of internal fractures and stress concentration at particle edges, that are more present at larger particles. The reason to only a small change in PSD for the whole grading samples in this study are likely attributed to finer particles filling out the voids between the coarser particles.

Slurry sample D (green in Figure 2) exhibits reduced susceptibility to potential physical alteration of particles, with a maximum deviating increment of 1.31%, compared to its initial PSD at sieve 0.063 mm. Corresponding deviating increment for tamped sample D was 3.58% (blue in Figure 2). This result suggests that slurry samples display another interlocking behavior between particles, where finer particles protect the larger ones more effectively than tamped samples.

3.2 Mineralogy

The mineralogical composition of particles is generally similar among the analyzed samples, but variations in element concentrations are evident as shown in Figure 4 and Figure 5. Assessing the elements concentration on particles, the most common minerals identified in both samples include mica, feldspar, plagioclase, and quartz. However, other residual minerals are also found. Sample A exhibited gangue minerals such as sorosilicate, K-feldspar, and apatite, while sample B contained iron, hematite, pyrite, illite, and biotite.

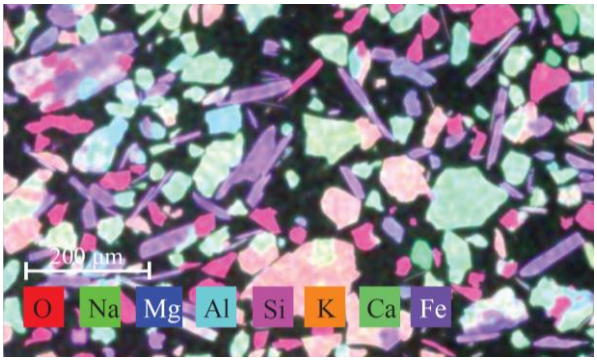

Figure 4. SEM analysis of sample A, depth 4.2 – 4.5 m.

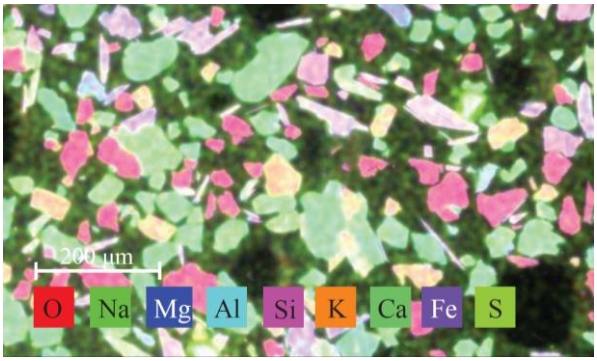

Figure 5. SEM analysis of sample B, depth 15.0 – 15.4 m.

3.3 Particle shape

Qualitative analysis of the results obtained from reflective light imaging and SEM analysis was performed using the roundness qualitative scale developed by Powers (1953). The tailings in this study have particles with a low sphericity shape where larger tailings particles are mostly subangular. Meanwhile the smaller the particles become, the shape turns into a combination of subangular and very angular. The black holes observed in Figure 4 and Figure 5 are voids that became trapped during sample preparation; however, they did not affect the interpretation.

4 CONCLUSIONS

This study shows that change in PSD of silty-sandy tailings tested in oedometer are evident, although the changes are small to neglectable. Tamped samples were found to be more susceptible to changes in PSD after oedometer testing compared to slurry samples. Furthermore, the magnitude of the change in PSD are smaller in this study than the similar, but uniform graded, tailings tested by Bhanbhro (2017).

Consequently, this implies that the characteristics of the soil fabric is important when consider the potential for physical alterations of particles due to increased vertical stress. The presence of fine particles and the manner they fill the voids and confine the larger particles clearly influence the vulnerability for particle breakage or physical alterations of particles. To some extent this is intuitive, if one considers that the particle-to-particle contact, stress distribution as well as the possibility of particle rearrangements directly are affected by how and to what extent the fine particles connect to the larger particles.

It is essential to assess the entire particle size distribution when evaluating susceptibility to breakage in a particular tailings sample. In addition, this study has shown that soil fabric can affect susceptibility to particle breakage or other physical alterations due to increased vertical stress. Neither tamped nor slurry prepared soil fabric in the laboratory might be the accurate replicate of field conditions. It is a complex topic and among several factors the in-situ soil fabric varies due to deposition methods, sedimentation, consolidation, saturation conditions, geochemical processes, etc.

Depending on tailings mineralogy and particle shape composition, there might or might not exist risk of change in PSD due to particle breakage or physical alterations which in the end likely will influence the mechanical behavior. Quantification and detailed analysis of the potential for particle breakage is complex. A step forward is believed to link the particle shape and particle size to the mineralogic composition as differences in hardness will affect the change in PSD. This, then can increase the understanding for the potential to physical alterations of particles and thereby the susceptibility of tailings to suffer from change in mechanical behavior over time.

5 ACKNOWLEDGMENTS

The Centre of Advanced Mining and Metallurgy at Luleå University of Technology supported the use of the Camsizer XT equipment and acknowledgement to Samarthkumar Pachchigar at the research subject of Energy Engineering at Luleå University for assisting with the Camsizer XT equipment.

REFERENCES

Bhanbhro, R. (2017). *Mechanical Behavior of Tailings: Laboratory Tests from a Swedish Tailings Dam*. Luleå University of Technology, Mining and Geotechnical Engineering.

Fourie, A., Verdugo, R., Bjelkevik, A., Torres-Cruz, L. A., & Znidarcic, D. (2022, October). *20ICSMGE State of the Art - Tailings*.

Jiang, M. J., Konrad, J. M., & Leroueil, S. (2003). An efficient technique for generating homogeneous specimens for DEM studies. *Computers and Geotechnics*, *30*(7), 579–597. doi.org/10.1016/S0266-352X(03)00064-8

Lyu, Z., Chai, J., Xu, Z., Qin, Y., & Cao, J. (2019). A Comprehensive Review on Reasons for Tailings Dam Failures Based on Case History. *Advances in Civil Engineering*, *2019*, 1–18. doi.org/10.1155/2019/4159306

Powers, M. C. (1953). A new roundness scale for sedimentary particles. *Journal of Sedimentary Research*, 23(2), 117-119. doi.org/10.1306/D4269567-2B26-11D7-8648000102C1865D

Vick, S. G. (1990). *Planning, Design, and Analysis of Tailings Dams*. BiTech Publishers Ltd. doi.org/10.14288/1.0394902

Villavicencio, G., Espinace, R., Palma, J., Fourie, A., & Valenzuela, P. (2014). Failures of sand tailings dams in a highly seismic country. *Canadian Geotechnical Journal*, *51*(4), 449–464. doi.org/10.1139/cgj-2013-0142

Zhang, X., Baudet, B. A., & Yao, T. (2020). The influence of particle shape and mineralogy on the particle strength, breakage and compressibility. *International Journal of Geo-Engineering*, *11*(1). doi.org/10.1186/s40703-020-0108-4

Proceedings of the XVIII ECSMGE 2024
GEOTECHNICAL ENGINEERING CHALLENGES
TO MEET CURRENT AND EMERGING NEEDS OF SOCIETY
© 2024 the Authors
ISBN 978-1-032-54816-6
DOI 10.1201/9781003431749-266
Open Access: www.taylorfrancis.com, CC BY-NC-ND 4.0 license

ECSMGE 24
XVIII EUROPEAN CONFERENCE ON SOIL MECHANICS AND GEOTECHNICAL ENGINEERING

Spatial vulnerability of levees to cascading hazards

Vulnérabilité spatiale des digues aux aléas en cascade

M. Bačić, N. Rossi*, L. Librić, M.S. Kovačević
University of Zagreb, Faculty of Civil Engineering, Zagreb, Croatia
*nicola.rossi@grad.unizg.hr

ABSTRACT: Levees are vulnerable to a multitude of hazards which may cause their partial or complete failure, thus leading to loss of their main purpose of protection against floods. As earthen structures, levees are also highly susceptible to earthquakes. A major concern arises in the unlikely case that these two events occur at the same time with extreme magnitudes. A similar situation occurs when an earthquake damages upstream components of the same flood protection network, such as dams, causing water waves to propagate downstream. The loads are not simultaneous, but within the short delay the damage to the levees would not have yet been identified/repaired to prevent flooding of the surrounding area. This paper analyses cascading scenarios of strong earthquakes followed by water waves resulting from damaged dams, acting upon the downstream levees. The levees in the cross-border area of Croatia and Slovenia, sharing the seismic and flooding hazards, are selected for validation of the vulnerability assessment methodology. The vulnerability of levees was modelled considering the influence of earthquakes on both the levee network and the upstream hydropower plant. Probabilities of failure are derived, enabling the categorization of the levee network, and giving valuable information to infrastructure managers and first responders on the criticality of the network whose overall efficiency is controlled by the weakest link.

RÉSUMÉ: Les digues sont vulnérables à une multitude d'aléas qui peuvent provoquer leur rupture partielle ou totale, entraînant ainsi la perte de leur fonction principale de protection contre les inondations. En tant que struct. en terre, les digues sont également très sensibles aux tremblements de terre. Une préoccupation majeure surgit dans le cas peu probable où ces deux événements se produiraient en même temps avec des ampleurs extrêmes. Une situation similaire se produit lorsqu'un tremblement de terre endommage les composants en amont du même réseau de protection contre les inondations, tels que les barrages, provoquant la propagation des vagues d'eau en aval. Les charges ne sont pas simultanées, mais dans un court laps de temps, les dommages causés aux digues n'auraient pas encore été identifiés/réparés pour éviter l'inondation des zones environnantes. Cet article analyse des scénarios en cascade de forts tremblements de terre suivis de vagues d'eau résultant de barrages endommagés, agissant sur les digues en aval. Les digues de la zone transfrontalière de la Croatie et de la Slovénie, partageant les risques sismiques et d'inondation, sont sélectionnées pour la validation de la méthodologie d'évaluation de la vulnérabilité. La vulnérabilité des digues a été modélisée en tenant compte de l'influence des tremblements de terre à la fois sur le réseau de digues et sur la centrale hydroélectrique en amont. Les probabilités de défaillance sont dérivées, permettant la catégorisation du réseau de digues et fournissant des informations précieuses aux gestionnaires d'infrastructure et aux premiers intervenants sur la criticité du réseau dont l'efficacité globale est contrôlée par le maillon le plus faible.

Keywords: Probability of failure; cascading effect; levees; point estimate; categorization.

1 INTRODUCTION

Throughout history, humans have been continuously trying to establish control over rivers, both for resources and for containing and regulating damaging floods. This is done by altering the watercourse by constructing hydraulic structures such as dams, levees, weirs, culverts, etc., at which point the river loses its natural flow regime. The more regulating structures are constructed, the more potential failure points there are, which are subject to many uncontrollable conditions which may deteriorate their stability, resulting with a lot of variability and uncertainty in risk management. Such uncertainty is usually addressed by conducting probabilistic analyses where probabilities of failure or unwanted behaviour are calculated, which serve as a basis for conducting maintenance works. The considered loads can be diverse, mostly high river discharges, rainfall, and earthquakes, or a combination of loads such as the one analysed in this study.

2 PROBLEM DESCRIPTION

This paper presents a case study pertaining to the categorization of a stretch of levees along the river Sava, between the hydropower plant (HPP) in Brežice (Slovenia) and the Jankomir bridge in Zagreb (Croatia), an area of mutual interest for flood protection (Figure 1). At the same time, this cross-

border area is extremely prone to earthquakes due to its position in a seismically active area.

The categorization also includes levees along the 6 tributary rivers, for a total length of 51 km. It consists of determining the probability of failure of the levees, induced by the cascading effect of high river discharges due to partial failure of the HPP Brežice dam caused by an earthquake. Two earthquakes are considered, one occurring near Brežice, and the other near Zagreb, both with 2475-year return periods. As a starting assumption, we take it that both earthquakes will surely lead to a partial failure of the dam, which is defined through 5 scenarios that generate different hydrographs (Rak et al., 2023). Due to the relatively large area of interest, a simplified methodology is used to efficiently assess the stability of the levees.

3 METHODOLOGY

3.1 Cross-section selection

To categorize a large stretch of levees with limited resources, optimizing the number of considered cross-sections is necessary. To discretize the levees, they are divided into reaches, which ideally would not only be defined by similar geometrical, physical, and mechanical properties, but also by equal consequences (flooded area) in the case of failure of any of the sections along the reach. However, to simplify the selection of relevant sections in accordance with the available data, both sides of each tributary river's levees are deemed one reach (6 reaches), and the river Sava's levees are divided into reaches where breaks in their continuity occur on each side of the river, such as bridges, tributaries, etc., resulting in 7 reaches. One of the seven Sava reaches was further divided due to geometrical differences, which finally resulted in 14 reaches total. Each reach is defined by one section, whose positions are shown in Figure 1. For a division into reaches, however detailed it is, the safety of the whole reach is defined by its most critical section (the weakest link). The sections' geometries are assessed through LiDAR data shown in Figure 1, provided by courtesy of the International Sava River Basin Commission (ISRBC), as well as from the respective projects of the levees not covered by the LiDAR.

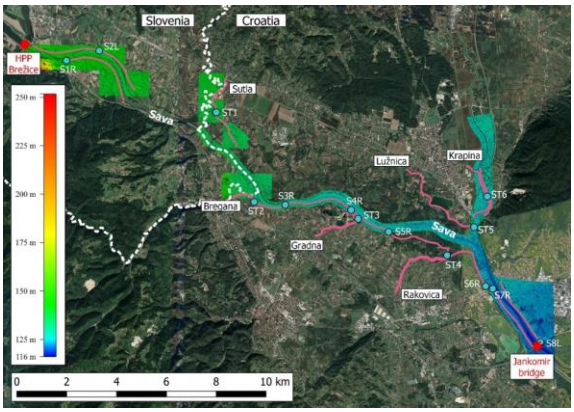

Figure 1. Situational view of the study area, with LiDAR.

3.2 Site characterization

The soil profiles and the geotechnical parameters are determined from existing borehole logs with SPTs, used to check the validity of the division into reaches, and supplementary CPTu data on the exact section locations. The necessary parameters for the analyses $(c, \varphi, \gamma, k, n)$ are thus determined separately for each selected cross-section. The foundation soil throughout the whole area is relatively similar, due to all the levees being constructed on the Sava river-terraces and floodplain, which consist predominantly of gravels and sands, with some clay content. Local differences are found mostly in thin, fine-grained, surface layers.

3.3 Conducted analyses

The analyses need to consider the previously described cascading effect. However, when an earthquake occurs, it will not only damage the dam but also the levees. To consider this effect, we would first need to quantify the earthquake-damage on the levees, before moving on to the stability during the water waves from the five scenarios. This type of damage includes soil liquefaction, subsidence, slope failures, longitudinal and perpendicular cracks, as seen in (Sasaki et al., 2012), and is unfeasible to quantify as an effect on the mechanical properties of soil. Thus, we need to introduce some assumptions and disregard all earthquake effects except slope failure. That way, we can compare the damage caused by earthquakes with the damage expected from high-water events. This is done in two stages. The first is analysing the slope stability during the earthquake, and if the levee fails at this stage, then further analyses are irrelevant, i.e., stability is determined by the earthquake alone. This means that the earthquake would give us a lower bound for the stability measure. If the levee holds (i.e., has satisfactory stability during the earthquake), then the oncoming water wave might bring it to failure. As we did not consider the effect of the damage on mechanical properties, the next stage consists of a simultaneous occurrence of the earthquake and the high-water, which is not realistic is this situation due to the source of the water wave but can give us a higher bound to the stability measure. Thus, the true stability measure should be found in between the two analysed cases. GeoStudio is used, with finite-element and limit equilibrium (Morgenstern-Price) methods for transient seepage and stability analyses, respectively.

An example of a model is shown in Figure 2, for the ST2 cross-section. The initial water table in each model is set to the corresponding hydrograph's starting elevation and is modelled as dependent of the water wave. After creating the models for each section, and assigning the five corresponding hydrographs, it is found that many hydrographs do not raise the water levels enough to even reach the levees' toes. In cases where the water does rise over the toe, the relatively short durations of the water waves (about 12 hours) are not enough to generate any meaningful seepage through the bodies. For this reason, only the water side stability is considered (during drawdown).

The analysed levees vary in sizes, and thus not all are vulnerable to slope failures of the same magnitude (depth, volume). To account for that, the slip surfaces are limited to a minimal depth which varies depending on the geometry of each section. For very small levees the limit is 0.5 m, for most sections the limit is 1 m, and for one section (S6R) the limit is set to 3 m.

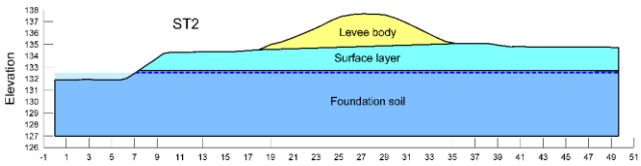

Figure 2. Example of a calculation model.

3.3.1 Probability of failure

The results of the described analyses are deterministic factors of safety (FS). To calculate the stability measure as the probability of failure (p_f), multiple LE analyses are required, and to optimize the required number of calculations on each section Rosenblueth's Point Estimate Method (PEM) (Christian and Baecher, 1999) is employed. It is assumed that the factors of safety are functions of only one random variable, the PGA, while all the others are deterministically known. In such case, this method requires only three analyses to estimate the distribution of the FS, assumed to be normal. The PGA follow a lognormal distribution, meaning that in the logarithmic space it is symmetric and approximately Gaussian. By evaluating the FS at the mean PGA and at two more values symmetrically spaced around the mean ($\mu_x \pm \sqrt{3}\sigma_x$), we can estimate the mean and standard deviation of the FS from its expected value raised to the power of m (Eq. 1).

$$E[Y^m] \approx P_-(y_-)^m + P\left(y_\mu\right)^m + P_+(y_+)^m \quad (1)$$

where y are the FS estimates, and P are weights at the corresponding points ($2/3$ for the mean, and $1/6$ for the rest). From this we estimate the mean and standard deviation as in Equations 2 and 3.

$$\mu \equiv E[Y] \quad (2)$$

$$\sigma \equiv \sqrt{E[Y^2] - (E[Y])^2} \quad (3)$$

Considering failures occur at FS equal to unity, the reliability index (β) can be calculated, and from it the p_f. This procedure is performed twice, first for the Zagreb earthquake, then for the Brežice earthquake.

4 RESULTS

The results are shown in Table 1. Along the scenarios 1-5 defined by 5 hydrographs resulting from different partial failure modes of the dam, an additional scenario designated 0 is introduced to indicate the earthquake acting on the levee alone. The blank cells show the scenarios where the water level did not rise over the levee toe. The scenarios which yield the highest increase in p_f are highlighted in red for each section. The increase might be interpreted as the maxium effect that the high water corresponding to the specific scenario has on increasing the probability of failure, after the slope being damaged by an earthquake, where the slope failure caused by the earthquake is further propagated by the water wave.

According to USACE (1997), the probability of slope failure deemed hazardous corresponds to 16%, which is far exceeded by many sections. However, two aspects are to note. First, the calculated probabilities relate to slope failure, and do not equal the probability of breaching, i.e., failure of the whole section. Thus, these calculated probabilities may be interpreted as total damage instead of failure. Global failure may be eventually achieved by propagation of the developed failure surface during future hazards, if not mended in the meantime. Second, in most cases the p_f values stem from the earthquake, with only a small percentage added due to the water wave, while only in a handful of cases the water wave has a major effect on increasing the p_f. This is because the analysed scenarios luckily generate such hydrographs that raise the water level not much over the toe, so even if complete failure would occur, the consequences are not expected to be great, other than the damaged levees. More so for the fact that failure is calculated during the receeding period of the water wave (RDD). Finally, a categorization is conducted based on the probabilities, shown in Figure 3. The reaches are divided into 5 categories, where the first two correspond to the values reported by USACE (1997) for „high" to „above average" behaviour ($p_f \leq 0.1\%$) and „above average" to „hazardous" behaviour ($p_f \leq 16\%$), while the rest all fall into the „hazardous"

category, but are still arbitrarily divided into three groups. Even if whole reaches are categorized by one section, this does not mean that whole levees will fail, due to the variations in local conditions.

Table 1. Probability of failure (%) for all analysed sections.

	S0		S1		S2		S3		S4		S5	
	Z	B	Z	B	Z	B	Z	B	Z	B	Z	B
S1R	72.7	99.1	73.1	99.1	76.5	99.1	74.1	99.1	71.0	98.9	89.9	99.7
S2L	1.80	69.7	-	-	3.90	77.1	-	-	-	-	10.2	87.3
S3R	98.0	94.1	98.8	94.2	98.5	96.0	97.8	94.4	98.9	94.5	99.0	96.8
S4R	40.7	1.61	59.0	6.62	58.6	6.24	64.0	9.80	58.9	6.39	59.0	6.76
S5R	34.7	0.30	35.7	0.51	35.0	0.50	-	-	-	-	35.6	0.40
S6R	58.5	0.05	-	-	-	-	-	-	-	-	-	-
S7R	43.1	<0.01	-	-	-	-	-	-	-	-	-	-
S8L	55.5	0.05	-	-	-	-	-	-	-	-	67.5	0.33
ST1	1.51	8.14	-	-	-	-	-	-	1.51	8.14	3.67	15.7
ST2	24.9	19.1	-	-	-	-	-	-	-	-	27.6	21.5
ST3	82.2	19.5	83.6	21.3	84.3	23.3	-	-	-	-	87.0	26.8
ST4	71.8	0.71	-	-	77.5	1.07	-	-	-	-	78.3	1.17
ST5	27.2	≪0.01	-	-	-	-	-	-	-	-	45.9	<0.01
ST6	77.7	0.51	-	-	-	-	-	-	-	-	77.7	0.51

Z – Zagreb, B – Brežice

5 CONCLUSIONS

The categorization of levees in the cross-border area of Croatia and Slovenia, resulting from the presented methodology, shows very high probabilities of slope failure (or damage), which are mostly attributed to the effect of the earthquake, and not so much to the water discharge scenarios, with the exception for a handul of scenarios. This means that even if slope failures do occur at certain sections, they may not propagate much further to cause a breach, and if they do, the water level is mostly too low to cause substantial consequences. For the damaged levees to breach and cause consequential floods, future hazards should occur. Finallly, it is more likely that the Brežice earthquake, closer to the HPP, will cause the partial failure of the dam, in which case the reported probabilities are much more acceptable. If the Croatian earthquake does indeed not fail the dam, then the high p_f still remains, but with no fear of flooding.

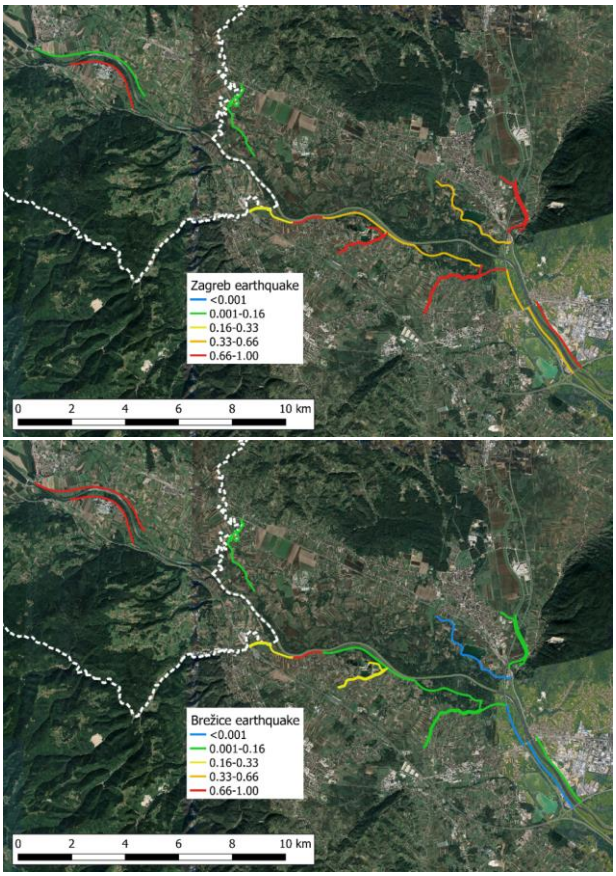

Figure 3. Levee categorization for both earthquakes.

ACKNOWLEDGEMENTS

The authors are grateful for the financial support provided by European Union Civil Protection Mechanism, GA no. 101048395, CROSScade project.

REFERENCES

Christian, J.T., Baecher, G.B., 1999. Point-Estimate Method as Numerical Quadrature. J. Geotech. Geoenviron. Eng. 125, 779–786. https://doi.org/10.1061/(ASCE)1090-0241(1999)125:9(779).

Rak, G. et al., 2023. CROSScade Deliverable 3.2 - Cross-border cascading hazard events and scenarios (Deliverable No. D3.2.).

Sasaki, Y. et al., 2012. Reconnaissance report on damage in and around river levees caused by the 2011 off the Pacific coast of Tohoku earthquake. Soils and Foundations, 52(5), 1016–1032. https://doi.org/10.1016/j.sandf.2012.11.018.

USACE, 1997. Introduction to probability and reliability methods for use in geotechnical engineering (No. 1110-2-547), Engineering and Design. USACE, Washington, D.C.

Proceedings of the XVIII ECSMGE 2024
GEOTECHNICAL ENGINEERING CHALLENGES
TO MEET CURRENT AND EMERGING NEEDS OF SOCIETY
© 2024 the Authors
ISBN 978-1-032-54816-6
DOI 10.1201/9781003431749-267
Open Access: www.taylorfrancis.com, CC BY-NC-ND 4.0 license

ECSMGE 24
XVIII EUROPEAN CONFERENCE ON SOIL MECHANICS AND GEOTECHNICAL ENGINEERING

Insights from the implementation of levelAMS, a geotechnical asset management software, on Brisa's network

Aperçu de la mise en œuvre de levelAMS, un logiciel de gestion des actifs géotechniques, sur le réseau de Brisa

J. Barros*, M. Pinheiro
Level company, Braga, Portugal

M. Cruz, I. Gonzalez
Brisa, SA, Lisboa, Portugal

T. Miranda
University of Minho, Guimarães, Portugal

julianabarros@level-gam.com

ABSTRACT: LevelAMS is a cutting-edge asset management software designed for extensive geotechnical assets networks. This cloud-based platform integrates a comprehensive suite of services and features aimed at optimizing daily operations and resources for concessionaires. Its primary objectives include enhancing safety measures and minimizing geotechnical hazard risks. In addition to maintaining an inventory of assets, LevelAMS offers a user-friendly experience by enabling visual inspections, work scheduling, and comprehensive data storage for registered occurrences and accidents. The platform goes beyond basic functionalities by providing users with access to risk maps and a condition index.This study provides initial insights into the utilization of LevelAMS within the Brisa geotechnical network, encompassing 11,837 slopes (embankments and cuts) and 570 retaining walls of diverse types. The vast and heterogeneous nature of this network, spanning over 1,100 km, underscores the imperative for advanced asset management software and risk mitigation tools. Noteworthy advantages of LevelAMS include the ability to categorize asset conditions, identify urgent intervention needs, and closely monitor assets on a daily basis.

RÉSUMÉ: LevelAMS est un logiciel de gestion d'actifs de pointe conçu pour les vastes réseaux d'actifs géotechniques. Cette plateforme basée sur le cloud intègre une suite complète de services et de fonctionnalités visant à optimiser les opérations quotidiennes et les ressources des concessionnaires. Ses principaux objectifs consistent à améliorer les mesures de sécurité et à minimiser les risques géotechniques. En plus de maintenir un inventaire des actifs, LevelAMS offre une expérience conviviale en permettant des inspections visuelles, la planification des travaux et le stockage complet des données pour les occurrences et les accidents enregistrés. La plateforme va au-delà des fonctionnalités de base en offrant aux utilisateurs l'accès à des cartes de risques et à un indice de condition. Cette étude fournit des premières impressions sur l'utilisation de LevelAMS au sein du réseau géotechnique de Brisa, comprenant 11 837 pentes (remblais et coupes) et 570 murs de soutènement de différents types. La nature vaste et hétérogène de ce réseau, s'étendant sur plus de 1 100 km, souligne l'impératif d'un logiciel de gestion d'actifs avancé et d'outils de mitigation des risques. Les avantages notables de LevelAMS comprennent la possibilité de catégoriser les conditions des actifs, d'identifier les besoins d'interventions urgentes et de surveiller de près les actifs au quotidien.

Keywords: Geotechnical asset management; risk mitigation tools; asset's condition; Brisa's network.

1 INTRODUCTION

LevelAMS is a sophisticated geotechnical asset management software designed for daily use, providing decision-makers with optimized tools to effectively manage their assets. The management of linear assets, which often constitutes a substantial number, requires a standardized and streamlined process to mitigate geotechnical accidents resulting from asset degradation. In response to this need, levelAMS offers a comprehensive and integrated solution for the monitoring and management of such assets.

This work aims to provide a detailed overview of the asset management software, outlining its features, advantages, and its practical application within a real motorway network.

Brisa, a private motorway concession company based in Portugal, boasts an extensive network of over

1100 km of motorways. Despite the meticulous management of various assets, geotechnical assets are frequently lacking a fully assessed management process. Recognizing this gap, there is an imperative to digitize and integrate the management of these assets for enhanced efficiency and comprehensive oversight.

2 BRISA'S NETWORK

Brisa's Motorway Concession (BCR) is a private Portuguese company within the Brisa Group, tasked with overseeing the management of an extensive motorway network spanning over 1100 km. The network comprises 12 highways that traverse from the north to the south of Portugal, encompassing critical road axes in major cities such as Lisbon and Porto (Figure 1).

Within the scope of Brisa's geotechnical assets, there exists a total of 12,406 assets, categorized into slopes and retaining walls with 11,836 and 570 assets, respectively. Approximately 60% of the slopes consist of cuts, while the remaining 40% are embankments, varying in length from 6 m to 2200 m and reaching a maximum height of 50 m. Notably, around 10% of the slopes are protected with shotcrete.

In terms of retaining walls, they exhibit diverse characteristics, with a maximum length of 1400 m and a height of 24 m. The various types of retaining walls include gabion, cantilever, gravity walls, and a few reinforced soil or concrete walls, with or without anchors.

The lithology of the network is notably heterogeneous. In the northern region, slopes are predominantly composed of granite and schist, while the central region features mainly sandstones and limestones. In the southern region, the prevalent geological composition consists mostly of sands and limestones.

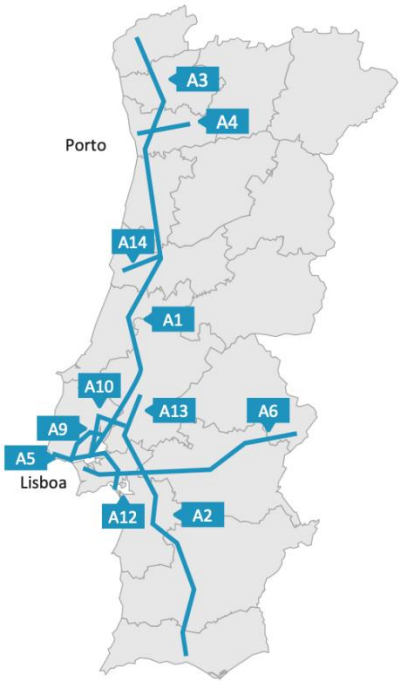

Figure 1. Brisa's motorway network.

3 GEOTECHNICAL ASSET MANAGEMENT

3.1 LevelAMS description

LevelAMS is a comprehensive software solution designed for the management and risk assessment of geotechnical assets, specifically focusing on retaining walls and slopes. This innovative solution encompasses a range of features, including a database with an inventory of geotechnical assets, mobile platforms for on-site inspections and incident recording, interactive risk maps utilizing a 5-level scale, and a customizable dashboard presenting network analytics for retaining walls and slopes.

This geotechnical asset management software effectively addresses the primary requirements of asset management, including inventory management, risk assessment, documentation of visual inspections, recording of occurrences, and the planning of conservation and maintenance efforts. The efficiency of this management is facilitated through a georeferenced database that houses both inventory information and data collected during visual inspections and incident recording. The standardization and centralization of these processes contribute to enhanced asset management effectiveness and improved cost control.

LevelAMS employs a qualitative and quantitative classification system for assets, utilizing a condition index developed as part of an academic research project (Pinheiro et al., 2015). This condition index,

informed by various factors directly and indirectly linked to asset stability and condition, enables the establishment of risk levels and identifies geotechnical assets requiring closer monitoring or conservation actions. The outcome is a more streamlined and economically efficient management approach for geotechnical assets.

It is worth noting that the system and its associated processes are flexible and can be tailored to the specific needs and realities of road management companies, accommodating diverse characteristics and complexities within their road networks.

3.2 LevelAMS main features

In addition to the previously highlighted features, the key functionalities of levelAMS are summarized in Table 1. These core functionalities comprehend a customizable dashboard, an extensive assets database, a module for warnings and inspections lists, risk maps with filter options based on risk levels, and a financial analysis module. The financial analysis module serves to compare the annual budget with the actual execution, providing valuable insights into budgetary performance. This comprehensive set of features ensures that levelAMS offers a versatile and robust solution for the efficient management and assessment of geotechnical assets.

Table 1. levelAMS main features description.

	Modulus	General Description
1	Dashboard	Analytical representation of the most relevant data of the assets network: number of assets by condition index, number and type of inspections, work and incidents carried out or registered, and the severest inspections results
2	Assets	Georeferenced inventory database, which contains all the information for each of the geotechnical assets (retaining walls and slopes)
3	Warnings	Alert system for all assets network that is triggered whenever: an incident is registered; a given instrument registers a value higher than the predefined threshold; and the condition index exceeds a predefined value
4	Risk maps	Depending on the condition index, assets are classified according to their level of risk on a qualitative scale (very low; low; moderate; high; very high) and quantitative ranging from 1 to 5. Risk maps are georeferenced using a colour scale to identify the associated asset risk
5	Continuous Monitoring	Optional functionality. Allows you to visualize through a map the assets that include continuous monitoring
6	Financial analysis	It allows an annual economic control of the network of assets, through the direct comparison of the budget value versus the real cost per road and concession for the different actions available
7	Reporting	Contains all the reports that summarizes all data and changes made about the asset or the assets network during a period of time to be selected
8	Inspections	Stores and show all inspections forms and details performed on the network

3.3 Asset condition index (CI)

The qualitative and quantitative classification of assets through a condition index was developed by Pinheiro et al. (2015) as part of a comprehensive scientific investigation conducted over several years in collaboration with the University of Minho. This condition index serves as a fundamental tool for characterizing and diagnosing the condition of retaining walls and slopes within the asset network.

During the operational phase, the utilization of this condition index proves invaluable in providing insights into the overall health of the assets network. The Condition Index (CI) allows users to classify slopes on a scale ranging from 1 to 5, where 1 indicates very good condition and 5 reflects a very poor condition. The index is based on various factors and parameters directly or indirectly linked to the stability of retaining walls and slopes. Each group of parameters is assigned different weights based on its relevance to slope and wall stability.

Importantly, these weights are adaptable to the specific characteristics and geographical nuances of road networks managed by concessionaires. Users have the flexibility to adjust the weights assigned to each factor and the parameters of the CI for each type of asset. Such customization enables a tailored approach, allowing for the incorporation of diverse network characteristics. Any adjustments made by the user will subsequently impact the calculation of the CI. For a detailed understanding of the CI calculation methodology, please refer to the publication by Pinheiro et al. (2015).

3.4 Risk Map

Based on the outcomes of the condition index, assets undergo classification according to their risk level on both a qualitative (very low, low, moderate, high, very high) and a quantitative scale ranging from 1 to 5. This dual-scale approach enables the identification of assets at the highest risk, pinpointing those requiring urgent interventions and specifying the type of necessary action.

Moreover, it facilitates the examination of the proposed monitoring plan, as outlined in Table 2, to be

implemented strategically in response to the assessed risk levels.

Table 2. Recommendation and indications to be adopted according to the risk level of the geotechnical asset.

Risk Levels	Inspections	Recommended actions	Temporal Space
Low	Routine inspections up to every 2 years Principal Inspections up to every 8 years	Only needs preventive or current maintenance actions	No relevant actions except for current maintenance
Moderate	Routine inspections up to every 2 years Principal Inspections up to every 4 years	Requires current maintenance actions and, possibly, conservation actions with the need for a design project	Medium Term Intervention
High	Routine inspections up to every 1 year Principal Inspections up to every 2 years	Dedicates a need for rehabilitation or replacement actions. However, complementary diagnostic actions (e.g., monitoring) may be necessary to mitigate associated risks	Short to Medium Term Intervention
Very high	Principal Inspections up to every 1 year	Requires immediate implementation of additional monitoring/diagnostic measures and conditioning for continued use	Short Term Intervention Immediate Mitigating Measures and Conditioning to Circulation

3.5 Degradation models

Utilizing the evolution of the Condition Index (CI) over time enables the visualization of the degradation curve for each asset, as can be seen in the example shown in Figure 2-a)). With real-time updates for every new entry in the software, users can observe the dynamic changes in the CI, providing insights into the asset's condition evolution.

Given that the CI is categorized into groups, users gain the ability to analyze the performance of each group and its contribution to the overall condition of the asset. This categorization facilitates a detailed examination of which specific aspects may be underperforming, offering valuable information to guide interventions and improve the overall CI of the asset. In the example shown in Figure 2-b), environmental conditions, visual inspections results and geological characteristics are the ones contributing to a poorer CI.

In essence, this feature empowers users with actionable insights, guiding them on where interventions are most needed to enhance the condition of the asset.

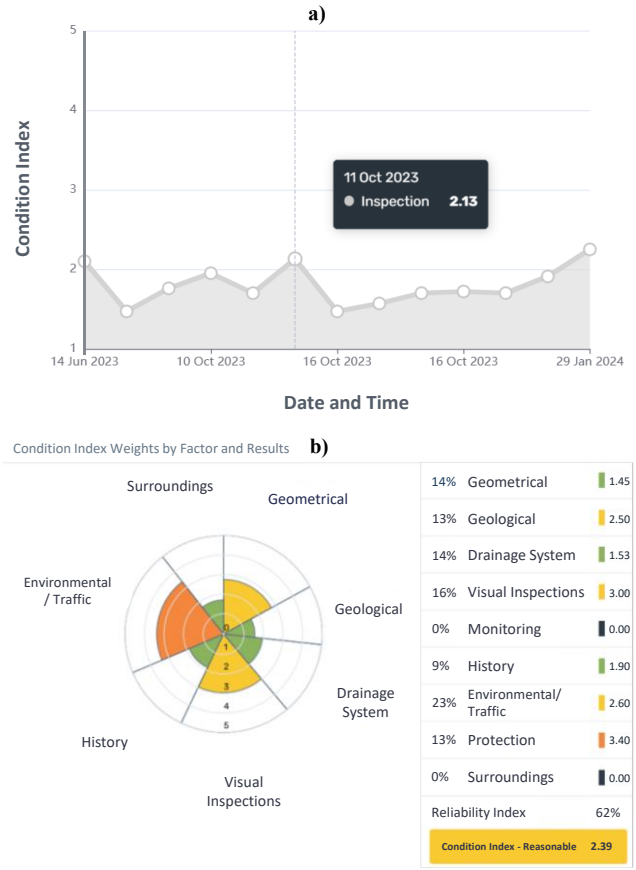

Figure 2. Degradation model graphic (a)) and details of group classification (b)).

4 RESULTS

The entire network of geotechnical assets has been successfully integrated into levelAMS, resulting in the classification of their condition into two classes: reasonable (8,396) and good (4,010), as illustrated in Figure 3. Despite the software 5 classes classification, most of the uploaded information are geometrical and traffic related. Moreover, environmental information remains the same for each asset. Therefore, the 5 classes are not fully represented by this initial set of assets. Regarding the parameters group that presents a relevant weight for the CI, namely geological and visual inspections there are no information uploaded. Although, it is important to mention that as more visual inspection are done, incidents and monitoring are registered, the assets group should obtain a more unfavourable class, mainly 4 or even 5.

The liability index, based on the amount of field information available, ranges from 48% to 66%. Notably, the reliability of the Condition Index (CI) increases with more comprehensive information.

Consequently, certain factors such as details about the surroundings, structural specifics, or geological data remain empty due to insufficient information. It is important to highlight that due to the lack of information, the amount of data imported for each asset is almost the same, therefore, the liability index remain quite stable. As more actions are done on levelAMS, meaning works or inspections added, this index should present a higher variation. According to maintenance actions, levelAMS provides a summary of the visual inspection helping decision makers to correct any pathologies observed. Since CI evaluates several parameters additional to visual inspections, the classes variation is reduced and controlled.

Following the initial campaign of inspections, some of the assets introduced in levelAMS have undergone assessment and monitoring. Critical assets that are instrumented can benefit from continuous monitoring using levelAMS, as depicted in Figure 4. Using the icon and colour scale it is possible to quickly identify the status of the monitoring system and understand if an alert or alarm threshold is reached (yellow and red, respectively). The software provides users with a user-friendly interface, offering real-time status updates of the assets and serving as a graphical display for the installed sensors. Additionally, warnings can be triggered and displayed if an asset surpasses a specified CI threshold.



Figure 3. 5-classes distribution of Brisa's network of geotechnical assets.



Figure 4. Critical asset network of sensors using icons (TM-tiltmeters, I-Inclinometers, P-Piezometers, O-Other) and colours (Green-sensors are OK, Red-alarm threshold and Gray-no connection).

5 CONCLUSIONS

This study provides initial insights into the newly developed geotechnical asset management software, levelAMS, implemented within Brisa's network. In addition to facilitating inventory management, the software enables the classification of assets based on their condition, utilizing the Condition Index developed by Pinheiro et al. (2015).

Centralizing all asset information within a single platform and enabling seamless processes for inspections, work registrations, and incident recording stand out as primary advantages of the software. To further comprehend the full spectrum of benefits, additional inspection campaigns are warranted. The platform's potential for risk assessment emerges as a significant advantage, particularly for the management of extensive asset networks.

This comprehensive mapping capability holds the promise of fostering a more strategic approach to short and long-term intervention planning. It also offers the ability to analyse the individual or macro-level condition evolution of slopes, thereby contributing to more informed and rational decision-making processes in geotechnical asset management.

ACKNOWLEDGEMENTS

The authors thank the Brisa Concessão Rodoviária for the provided information. The levelAMS results used on this work were obtained from levelAMS software, a cloud-based platform from level company.

REFERENCES

Level (2021). Level AMS- Asset Management Software v1 [cloud-based platform].

Pinheiro et al. (2015). A new empirical system for rock slope stability analysis in exploitation stage. International Journal of Rock Mechanics & Mining Sciences 76 (2015) 182–191. http://dx.doi.org/10.1016/j.ijrmms.2015.03.015.

Proceedings of the XVIII ECSMGE 2024
GEOTECHNICAL ENGINEERING CHALLENGES
TO MEET CURRENT AND EMERGING NEEDS OF SOCIETY
© 2024 the Authors
ISBN 978-1-032-54816-6
DOI 10.1201/9781003431749-268
Open Access: www.taylorfrancis.com, CC BY-NC-ND 4.0 license

ECSMGE 24
XVIII EUROPEAN CONFERENCE ON SOIL MECHANICS AND GEOTECHNICAL ENGINEERING

Distributed strain, settlement and temperature sensing in geotechnical earth embankments

Détection distribuée de la déformation, du tassement et de la température dans les remblais géotechniques

Ł. Bednarski
AGH University of Science and Technology in Kraków, Kraków, Poland

T. Howiacki*, R. Sieńko
Faculty of Civil Engineering, Cracow University of Technology, Kraków, Poland

K. Zuziak
SHM System / Nerve-Sensors, Kraków, Poland

**tomasz.howiacki@pk.edu.pl*

ABSTRACT: Distributed fibre optic sensing (DFOS) is more and more applicable in civil and geotechnical engineering to monitor the structural performance during construction and operation. The main advantage of this approach is the ability to measure selected physical quantities continuously over the entire length of the sensor – from few millimetres to hundreds of kilometres. This makes DFOS particularly useful for monitoring linear structures such as tunnels, roads, highways, bridges, pipelines, dams or embankments. The article describes the principles of this technique, including its main advantages and limitations, and then focuses on practical applications in several road embankments, including one of the highest in Poland. Depending on the project requirements, the type of the DFOS sensor and the configuration of the whole system, distributed strains, displacements (settlements) and temperatures can be extracted from measurements and analysed in detail. The article summarises a number of good practices and lessons learned on practical issues like selection of the sensor and optical device, installation method, thermal compensation, post-processing algorithms and data visualisation to facilitate its engineering interpretation.

RÉSUMÉ: La détection distribuée par fibre optique (DFOS) est de plus en plus utilisée en génie civil et géotechnique pour surveiller les performances structurelles pendant la construction et l'exploitation. Le principal avantage de cette approche est la possibilité de mesurer des quantités physiques sélectionnées en continu sur toute la longueur du capteur - de quelques millimètres à des centaines de kilomètres. La DFOS est donc particulièrement utile pour la surveillance des structures linéaires telles que les tunnels, les routes, les autoroutes, les ponts, les pipelines, les barrages ou les remblais. L'article décrit les principes de cette technique, y compris ses principaux avantages et limites, puis se concentre sur des applications pratiques dans plusieurs remblais routiers, dont l'un des plus hauts de Pologne. En fonction des exigences du projet, du type de capteur DFOS et de la configuration de l'ensemble du système, les déformations réparties, les déplacements (tassements) et les températures peuvent être extraits des mesures et analysés en détail. L'article résume un certain nombre de bonnes pratiques et d'enseignements tirés sur des questions pratiques telles que la sélection du capteur et du dispositif optique, la méthode d'installation, la compensation thermique, les algorithmes de post-traitement et la visualisation des données afin de faciliter leur interprétation technique.

Keywords: Distributed fibre optic sensing; earth embankment; strain; temperature; settlement.

1 INTRODUCTION

Distributed fibre optic sensing (DFOS) is finding increasing applications in civil (Bado and Casas, 2021) and geotechnical (Shi et al., 2021) engineering. The characteristic feature of that measurement technology and, at the same time, its main advantage, the ability to measure different physical quantities continuously over the entire length of the sensor. These quantities include strain, stress, crack, temperature displacement (Piątek et al., 2023) or vibration (Zhu et al., 2022). Distributed sensing capabilities can directly address one of the main goals and challenges of structural health monitoring (SHM), namely direct local event (or damage) detection. Local events along the measurement path can include, among other things, cracks in concrete, (Howiacki, 2022), leakages in pipelines (Bednarz et al., 2021), sinkholes and settlements in geotechnical structures (Bednarski et

al., 2021) or different types of third-party intrusions (Tanimola and Hill, 2009). The distance range can be from a few millimetres to hundreds of kilometres, making DFOS particularly useful for monitoring linear structures (Popielski et al., 2021) such as tunnels, roads, highways, bridges, pipelines, dams or embankments. However, it must be stressed that this is not a plug-and-play solution. The configuration of the system and the measurement parameters should always be tailored to the expectations and requirements of a particular project. The remainder of the article briefly describes the general assumptions and discusses three practical examples of geotechnical embankment applications. Each of the selected case studies concerns the DFOS-based measurement of different physical quantities: strains, temperatures and settlements.

2 SYSTEM CONFIGURATION

In general terms, the DFOS-based system consists of the sensor and the interrogator unit (optical data logger) – Figure 1. Usually, interrogators utilise three main physical phenomena, which are Rayleigh (Palmieri et al., 2022), Brillouin (Bastianini et al., 2019) and Raman (Li and Zhang, 2022) scattering. The first two enable measuring strains (which are the sum of mechanical and thermal effects), while Raman approach is sensitive only to thermal changes. It can be used to compensate the strain results or as an independent diagnostics solution to detect events related to temperature change (e.g. fires or leakages).

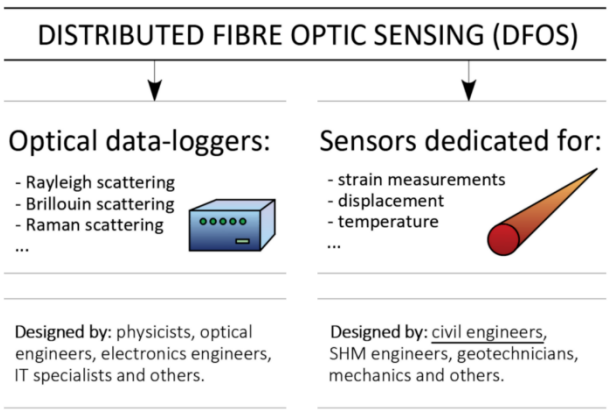

Figure 1. Design of DFOS-based measurement system.

When designing the system, interrogator parameters such as distance range, special resolution, accuracy, sampling frequency or acquisition time should be considered. Although they have a significant impact on the quality of the measurements, the sensors remain the key component of the overall system. Firstly, their long-term interaction with the structure must allow correct interpretation of the results. Secondly, if a data logger fails, it is technically easy to replace. However, this is not possible with long sensors that are permanently integrated into the structure (e.g. embedded in an earth embankment).

The design of the sensor should provide the best possible strain transfer from the structure to the internal optical fibre, which is always the main sensing element. Despite the fact that many commercial solutions are sold for the same purpose (strain measurement), the results obtained may be significantly different (Howiacki et al., 2023). The research shows, that the best performance in Rayleigh-based detection of local events is shown by the monolithic DFOS sensors, in which optical fibre is integrated into composite core without intermediate layers – Figure 2.

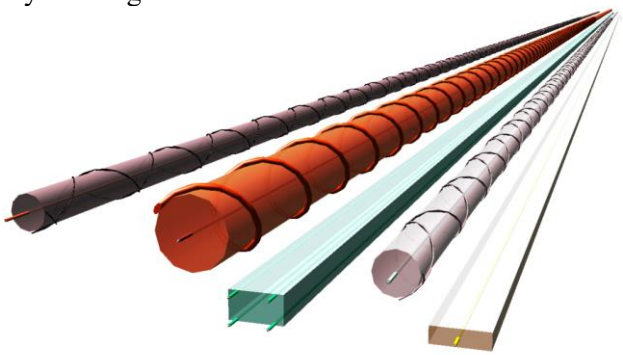

Figure 2. Visualisation of different monolithic sensors.

Although the general idea of monolithic sensors remains the same, some of their parameters can be adapted to the application (Bednarski et al., 2022). These include the shape and size of the cross-section, the stiffness, the number of fibres or the presence of an external braid. For example, in geotechnical applications, high stiffness and robustness are of great importance, whereas for laboratory research, softer and more flexible sensors are desired.

In addition to the interrogators and sensors, other aspects should be considered when designing and creating an efficient DFOS-based measurement system. The most important of these are the installation methods, the thermal compensation approach, the acquisition system, the post-processing algorithms, the data visualisation methods, the interpretation and, finally, the procedures to be followed if an anomaly is detected in the operation of a structure.

In the practical examples of installations and experiences described below, distributed monolithic sensors were used for strain (Nerve-Sensors - EpsilonRebar, 2023) and displacement (Nerve-Sensors - 3DSensor, 2023) measurements.

3 CASE 1 – STRAIN SENSING

The first example concerns an innovative earth embankment that was reinforced at its base with composite rebars. Some of these have been replaced by rigid monolithic sensors, which in this particular case have a dual function in the structure: both sensing and reinforcing.



Figure 3. Monolithic sensor delivered on site in coil.

The sensors were delivered to site in coils (Figure 3) and then stabilised in their intended positions. It should be noted that the installation conditions within the geotechnical structure are very often more challenging for the sensors to survive than those during normal operation - Figure 4. The sensor must therefore be sufficiently robust.



Figure 4. Challenging field conditions during embankment construction.

Figure 5 shows the arrangement of all the DFOS sensors installed within the mesh of the composite reinforcement. There are 6 longitudinal sections (along the embankment axis) of 20 m each and 8 transverse sections (in the lower and upper aggregate layers) of 62 m each. Their exact positions were documented with a geodetic survey immediately after installation.

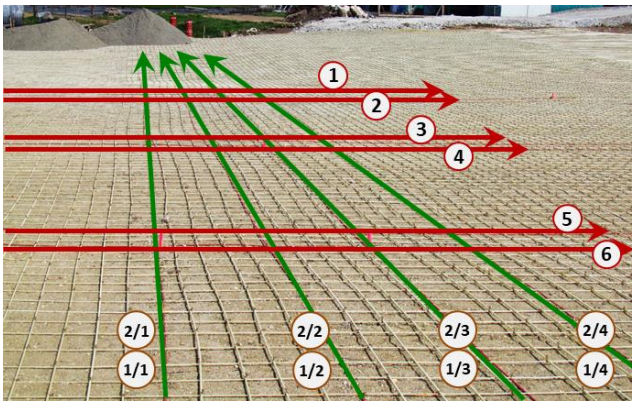

Figure 5. View of the DFOS strain sensors arrangement.

The distributed measurements were carried out as planned during the construction of the subsequent soil layers and after the road embankment had been commissioned. One of the objectives was to estimate strain-based stresses in the reinforcement to assess its effectiveness and compare it with theoretical predictions. Figure 6 shows selected strain profiles measured by one of the longitudinal sensors at subsequent construction stages. The profiles are not uniform along the length and local extremes (stress concentrations) can be clearly observed. These are caused by the uneven substrate and the random stiffness of the heterogeneous aggregate layer.

The strain results were compensated for the thermal changes, which were measured by both a Raman-based device and spot thermistors.

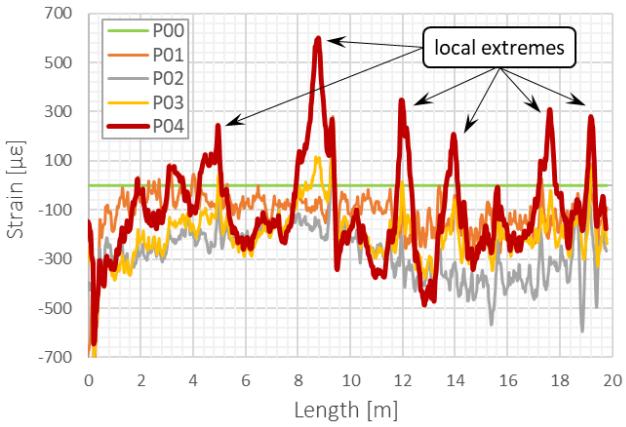

Figure 6. Example DFOS strain results from longitudinal section in subsequent sessions.

It should be noted that the costs of DFOS-based monolithic sensors are negligible compared to the cost of the structure. However, the sensors become an integral part of the earth embankment and can be read at any time. The comprehensive strain results can be valuable during the warranty period and also for long-term assessment of structural condition and health. The durability of the composite sensors is comparable to the lifetime of the structure itself.

4 CASE 2 – TEMPERATURE SENSING

The second case refers to one of the highest road embankments in Poland, exceeding 30 m in some locations – Figure 7.



Figure 7. The view of the road embankment in question during construction.

It was therefore essential to control its deformation during construction in order to ensure efficient work and the earliest possible commissioning. In order to achieve this goal, it was decided to install vertical inclinometers as well as horizontal measurement lines at the base of the embankment, equipped with the following techniques: horizontal inclinometers, hydraulic profilers to measure vertical displacements and, finally, monolithic DFOS-based sensors for temperature distribution control. A typical cross section of the embankment equipped with selected measurement solutions is shown in Figure 8.

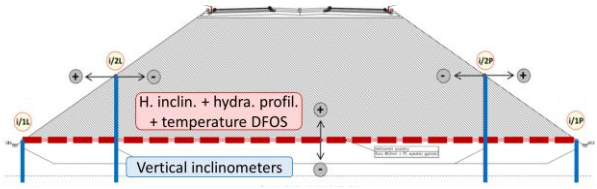

Figure 8. Typical cross-section of the embankment equipped with selected measurement solutions.

The temperature data was used, among other things, to compensate for the readings from two other settlement measurement techniques. All solutions were installed within the HDPE pipe filled with cement-bentonite injection, as shown in the spatial visualisation in Figure 9. The reason for this was that the installation was carried out when some of the soil layers had already been built and compacted. Special cross boreholes were made to allow the installation of the measurement system.

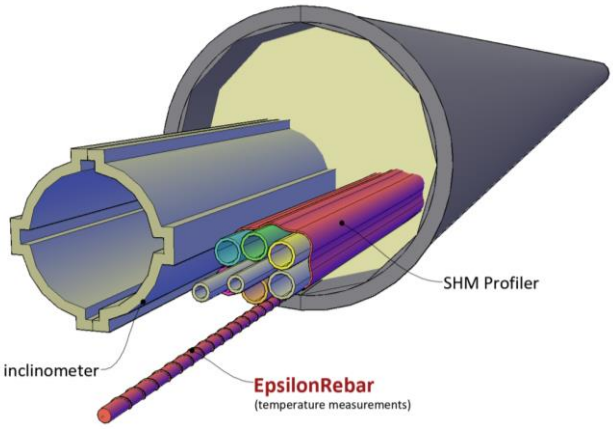

Figure 9. Spatial visualisation of horizontal inclinometer casing, hydraulic profiler and DFOS temperature sensor.

Figure 10 shows example temperature profiles recorded in 20 subsequent readings during one of the measurement sessions. The temperature gradients over length are strictly related to the embankment geometry and they reach more than 10°C along the first 15 m on both sides (influence of slopes). Such large differences can affect the results of settlement measurement techniques and require compensation for correct physical interpretation.

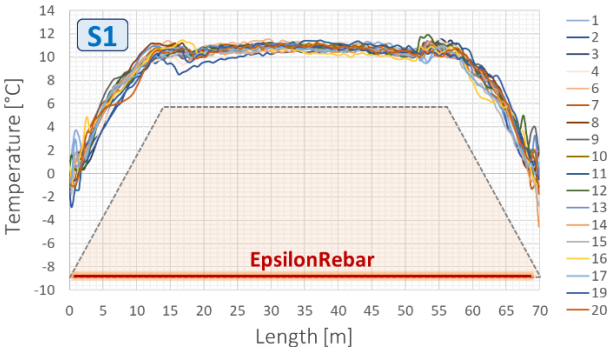

Figure 10. Example temperature distributions in subsequent measurements in reference to the embankment geometry.

Besides the geometry itself, the temperature distribution is also influenced by the current weather conditions, the solar exposure of the slopes and the location of the measurement sections – Figure 11.



Figure 11. Selected locations of measurement cross-sections (S1 – S5) within the embankment - top view.

5 CASE 3 – SETTLEMENT SENSING

The last example focuses on the road earth embankment built over the substrate strenghtened with Controlled Modulus Columns (CMC), as shown in spatial visualisation in Figure 12.

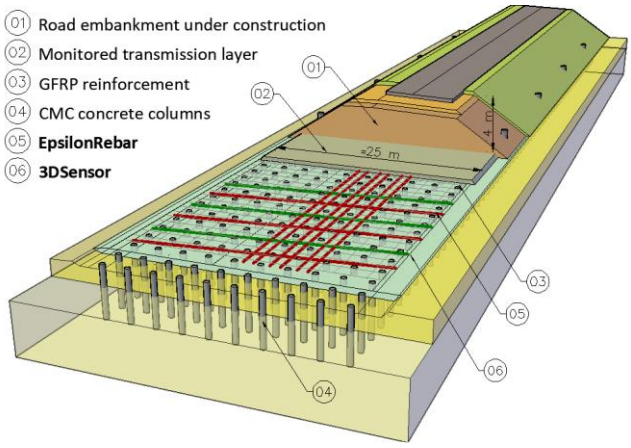

Figure 12. Spatial visualization of the embankment over the substrate strengthened with concrete columns.

Distributed strain and displacement sensors were installed within the transmission layer, both in longitudinal and transverse direction (Figure 13), as a part of GFRP reinforcement mesh. It is worth noting that the transverse sections are not perfectly perpendicular and run through areas directly above the column range as well as between the column ranges.

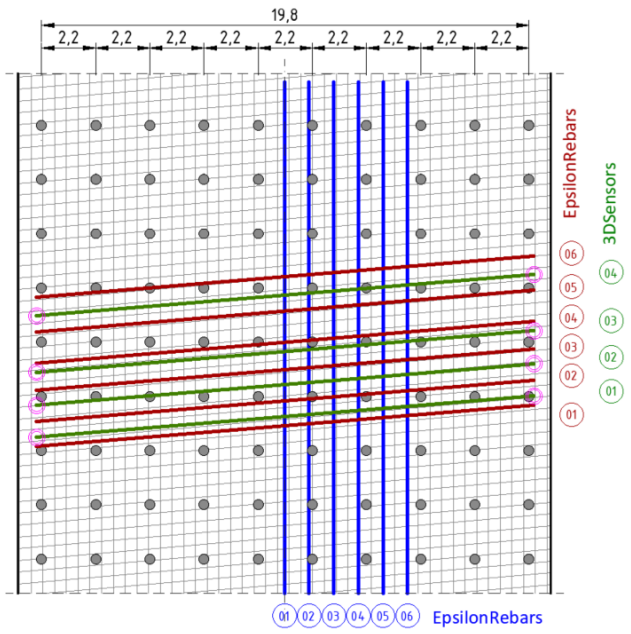

Figure 13. The arrangement of GFRP reinforcement and optical sensors within transmission layer.

The sensors were placed on the ground during construction and then backfilled with successive layers of soil. The installation stage is shown in Figure 14.

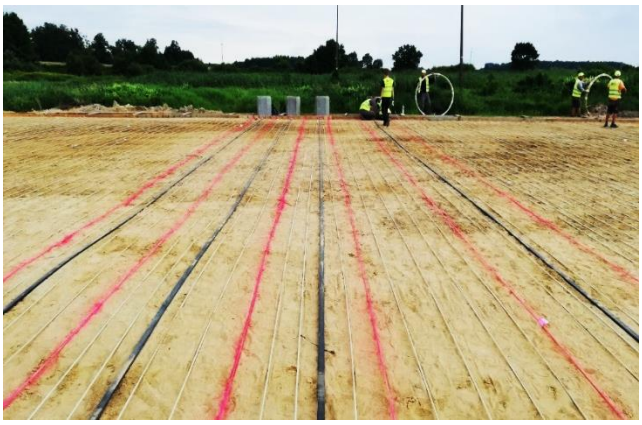

Figure 14. Installation of EpsilonRebars and 3DSensors at the base of the embankment.

The readings were taken during the construction of the embankment according to the planned schedule. An example of the vertical displacements (settlements) of 3DSensor no. 2 is shown in Figure 15. The area between the columns, where the graphs are smooth, and the area immediately above the columns with their local influences on the displacement profiles, can be clearly observed. The boundary conditions (start and end displacement values) were measured by geodetic survey. The 3DSensor internal design allows self-compensation due to the temperature changes in time and length (Bednarski et al., 2021).

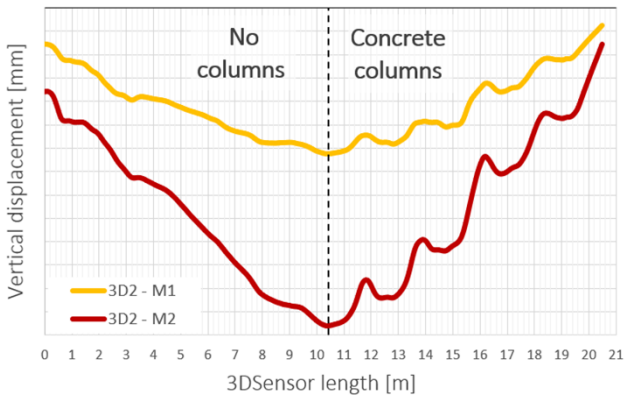

Figure 15. DFOS settlement results from 3DSensor no. 2 in two subsequent measurement sessions M1 and M2.

6 CONCLUSION

The case studies briefly described in the article confirm the versatility of the DFOS technique in monitoring various physical quantities such as strain, temperature or displacement. The ability to acquire distributed profiles makes it suitable and increasingly used for monitoring civil engineering and geotechnical structures. Key challenges include automation and the development of data processing and analysis software.

FUNDING

Selected works presented in this paper were supported by the projects "*Innovative fibre optic sensor for measuring strain and temperature*" (POIR.01.01.01-00-1154/19) and "*Development of the new fibre optic sensor allowing for the determination of the vertical and horizontal displacements of the studied objects at the distances of up to 120 km*" (POIR. 01.01.01-00-0550/15) funded by the National Centre for Research and Development within the Intelligent Development Operational Program 2014-2020. Both projects were realised by SHM System, Krakow, Poland (SHM System, n.d.).

REFERENCES

Bado, M.F. and Casas, J.R. (2021). A Review of Recent Distributed Optical Fiber Sensors Applications for Civil Engineering Structural Health Monitoring. *Sensors*. 21(5): 1818. https://doi.org/10.3390/s21051818.

Bastianini, F., Di Sante, R., Falcetelli, F., Marini, D. and Bolognini, G. (2019). Optical Fiber Sensing Cables for Brillouin-Based Distributed Measurements. *Sensors*. 19(23): 5172. https://doi.org/10.3390/s19235172.

Bednarski, Ł., Sieńko, R., Grygierek, M. and Howiacki, T. (2021). New Distributed Fibre Optic 3DSensor with Thermal Self-Compensation System: Design, Research and Field Proof Application Inside Geotechnical Structure. *Sensors.* 21(15): 5089. https://doi.org/10.3390/s21155089.

Bednarski, Ł., Sieńko, R., Kanty, P. and Howiacki, T. (2021). New Hydraulic Sensor for Distributed and Automated Displacement Measurements with Temperature Compensation System. *Sensors.* 21(14): 4678. https://doi.org/10.3390/s21144678.

Bednarski, Ł., Sieńko, R., Howiacki, T. and Zuziak, K. (2022). The Smart Nervous System for Cracked Concrete Structures: Theory, Design, Research, and Field Proof of Monolithic DFOS-Based Sensors. *Sensors* 22(22): 8713. https://doi.org/10.3390/s22228713.

Bednarz, B., Popielski, P., Sieńko, R., Howiacki, T. and Bednarski, Ł. (2021). Distributed Fibre Optic Sensing (DFOS) for Deformation Assessment of Composite Collectors and Pipelines. *Sensors*. 21(17): 5904. https://doi.org/10.3390/s21175904.

Howiacki, T. (2022). Analysis of cracks in concrete structures with the use of distributed optical fibre measurements. PhD thesis, Faculty of Civil Engineering, Cracow University of Technology, Poland.

Howiacki, T., Sieńko, R., Bednarski, Ł. and Zuziak, K. (2023). Crack Shape Coefficient: Comparison between Different DFOS Tools Embedded for Crack Monitoring in Concrete. *Sensors.* 23(2): 566. https://doi.org/10.3390/s23020566.

Li, J. and Zhang, M. (2022). Physics and applications of Raman distributed optical fiber sensing. *Light Science & Applications*. 11(1):128. https://doi.org/10.1038/s41377-022-00811-x.

Nerve-Sensors (2023). EpsilonRebar - the world's first monolithic strain DFOS sensor designed for direct embedding into the structural member, concrete or soil. Available online at: https://nerve-sensors.com/product/epsilonrebar/, accessed: 24/08/2023.

Nerve-Sensors (2023). 3DSensor - the world's first shape DFOS sensor for geotechnics and civil engineering, measuring displacements of the structure in 3d space along its entire length. Available online at: https://nerve-sensors.com/product/3dsensor/, accessed: 24/08/2023.

Palmieri, L., Schenato, L., Santagiustina, M. and Galtarossa, A. (2022). Rayleigh-Based Distributed Optical Fiber Sensing. *Sensors*. 22(18): 6811. https://doi.org/10.3390/s22186811.

Piątek, B., Howiacki, T., Kulpa, M., Siwowski, T., Sieńko, R. and Bednarski, Ł. (2023). Strain, crack, stress and shape diagnostics of new and existing post-tensioned structures through distributed fibre optic sensors. *Measurement.* 113480. https://doi.org/10.1016/j.measurement.2023.113480.

Popielski, P., Bednarz, B., Sieńko, R., Howiacki, T., Bednarski, Ł., and Zaborski, B. (2021). Monitoring of Large Diameter Sewage Collector Strengthened with Glass-Fiber Reinforced Plastic (GRP) Panels by Means of Distributed Fiber Optic Sensors (DFOS). *Sensors*. 21(19): 6607. https://doi.org/10.3390/s21196607.

Shi, B., Zhang, D., Zhu, H., Zhang, C., Gu, K., Sang, H., Han, H., Sun, M., & Liu, J. (2021). DFOS Applications to Geo-Engineering Monitoring. *Photonic Sensors*. 11(2): 158–186. https://doi.org/10.1007/s13320-021-0620-y.

Tanimola, F. and Hill, D. (2009). Distributed fibre optic sensors for pipeline protection. (2009) *Journal of Natural Gas Science and Engineering*. 1(4-5): 134–143. https://doi.org/10.1016/j.jngse.2009.08.002.

Zhu, H.-H., Liu, W., Wang, T., Su, J.-W. and Shi, B. (2022). Distributed Acoustic Sensing for Monitoring Linear Infrastructures: Current Status and Trends. *Sensors*. 22(19): 7550. https://doi.org/10.3390/s22197550.

Proceedings of the XVIII ECSMGE 2024
GEOTECHNICAL ENGINEERING CHALLENGES
TO MEET CURRENT AND EMERGING NEEDS OF SOCIETY
© 2024 the Authors
ISBN 978-1-032-54816-6
DOI 10.1201/9781003431749-269
Open Access: www.taylorfrancis.com, CC BY-NC-ND 4.0 license

ECSMGE 24
XVIII EUROPEAN CONFERENCE ON SOIL MECHANICS AND GEOTECHNICAL ENGINEERING

Effect of suction and preparation method on the compressibility of Stava silty tailings

Effet de la succion et de la méthode de préparation sur la compressibilité des terrains résidus limoneux de Stava

G. Bella*
Pini Group SA, Lugano, Switzerland

D. Czerski, S. Ghezzi, M. Giani, M. Lüscher, C. Ambrosi
University of Applied Sciences and Arts of Southern Switzerland (SUPSI), Mendrisio, Switzerland

**gianluca.bella@pini.group*

ABSTRACT: Tailing storage facilities are complex geotechnical structures to safely store the waste products resulting from mining processes. Proper knowledge of the hydro-mechanical behaviour of tailing wastes under unsaturated conditions allows for assessing reliable stability analysis of tailing dams. This research provides the preliminary results of an experimental campaign carried out on silty tailings to analyze their pre-shearing state of stress. The experiment was performed on statically compacted and remoulded samples through oedometric tests under saturated and unsaturated conditions. The dependency of the 1d-Normal Compression Line (1d-NCL) on suction and sample preparation technique is investigated, with the suction level evaluated based on the water retention tests performed on the same soil. The compressibility and the occurrence of a transitional behaviour depending on the suction level and preparation method were finally analyzed based on the Basic Barcelona Model.

RÉSUMÉ: Les installations de stockage des terrains résidus sont des structures géotechniques complexes destinées à stocker en toute sécurité les déchets résultant des processus d'exploitation minière. Une bonne connaissance du comportement hydromécanique des résidus dans des conditions non saturées permet d'évaluer une analyse fiable de la stabilité des digues à résidus. Cette recherche fournit les résultats préliminaires d'une campagne expérimentale menée sur des résidus limoneux afin d'analyser leur état de contrainte avant cisaillement. Les essais œdométriques ont été réalisés sur des échantillons statiquement compactés et reconstitués dans des conditions saturées et non saturées. La dépendance de la 1d-NCL par rapport à la succion et à la technique de préparation de l'échantillon est étudiée, le niveau de succion étant évalué sur la base des tests de rétention d'eau effectués sur le même sol. La compressibilité et l'apparition d'un comportement transitoire en fonction du niveau de succion et de la méthode de préparation ont été analysées sur la base du Basic Barcelona Model.

Keywords: Unsaturated soil; oedometric test; 1d-NCL; compressibility; water retention curve.

1 INTRODUCTION

Tailing storage facilities ('TSF') are complex disposal systems mainly consisting of an embankment and a basin. They contain the waste products of the mining industry ('tailings') composed of a slurry mixture made of soil, rock and water that remain after the mineral values have been extracted from the ore. Owing to the complexity and high rate of failure of TSF, a deep knowledge of tailings response under unsaturated conditions represents an essential tool for reliably assessing the stability of tailing storage facilities (Bella and Musso 2024; Bella *et al*., 2023; Girardi and Bella, 2023; Deng *et al.,* 2020; Tarantino and Mountassir 2013; Zanardin *et al*., 2009). This research provides the preliminary results of an experimental campaign aimed at investigating the mechanical behaviour of the Stava silty tailings collected from the lower portion of the upper embankment which remained in place after the collapse occurred in 1985 in Stava, Italy. The pre-shearing state of stress under nearly saturated and unsaturated conditions is investigated by performing oedometric and water retention tests. The effects of the sample preparation method and suction level on the compressibility and 1d-NCL of Stava tailings are investigated. The outcomes are then compared to those obtained by the same soil tested under fully saturated conditions.

2 MATERIAL CHARACTERIZATION

The experimental campaign was carried out at the soil testing laboratory of the University of Applied Sciences and Arts of Southern Switzerland (SUPSI)

and Politecnico di Torino. Silty samples passing through a 0.074 mm sieve were tested since they represent the finer tailings fraction deposited into Stava basins (Bella *et al.,* 2024). According to Carrera (2008), liquid limit, plastic limit, and plasticity index, are w_L=27.4%, w_P=18.0%, PI=9.4%, while the specific gravity and hydraulic conductivity are G_S=2.83 and k=10^{-7} m/s. X-ray diffraction analysis showed that Stava tailings were predominantly made of quartz, with a relevant amount of calcite and fluorite (Bella, 2017; Bella and Musso 2023).

3 EXPERIMENTAL TECHNIQUES AND TESTING APPARATUS

3.1 Oedometric tests

Oedometric tests were performed to investigate the dependency of the compressibility on the degree of saturation (and in turn the matric suction level) of the Stava tailings. Specimens 50mm diameter, 20 mm in height are prepared by imposing different void ratio, degrees of saturation, or preparation methods:

- the static compaction outside the oedometer cell (SC) is the procedure adopted to create unsaturated samples (Sr≤90%) and nearly saturated samples in the current research (90%<Sr<100%). The same technique was adopted by previous studies performed by Carrera (2008) on Stava silty samples under fully saturated conditions (Sr=100%). All samples were prepared by hand-mixing a certain amount of dry soil with the required amount of demineralized, de-aired water to obtain the desired initial water content. The mixture was then put into a hermetic cylindrical mold and statically compacted by gradually applying an axial force until the desired volume was reached.
- The remoulded specimen (RS) edo_0.76-100 was prepared inside the oedometer cell by mixing a known quantity of dry soil with a certain amount of demineralized, de-aired water to obtain a slurry sample (water content equal to the liquid limit). Back analysis then allowed to evaluate the initial degree of saturation and void ratio of the sample.

All tests were carried out by using a conventional oedometer cell (Figure 1). Constant water content conditions were imposed for testing the unsaturated samples, indeed a mass-based analysis performed at the end of each test showed no water content variations during the entire test. An axial loading sequence was imposed, followed by an unloading path. The axial displacements experienced by the samples were measured by using an external linear variable differential transducer (LVDT). Table 1 lists the RS sample and the SC tested in the current research together with the initial state of the SC-saturated samples tested by Carrera (2008).

Table 1. Initial state: initial void ratio, degree of saturation, saturation state, sample preparation method.

Sample	e_0 (-)	Sr (%)	Prep. Meth.	Authors
edo_0.510-093	0.510	93	SC	Current research
edo_0.593-091	0.593	91	SC	
edo_0.528-078	0.528	78	SC	
edo_0.568-074	0.568	74	SC	
edo_0.650-066	0.650	66	SC	
edo_0.760-100	0.760	100	RS	Bella *et al.*, 2021
edo_028	0.772	100	SC	Carrera, 2008
edo_020	0.885	100	SC	
edo_019	0.925	100	SC	
edo_018	0.750	100	SC	
edo_017	0.930	100	SC	

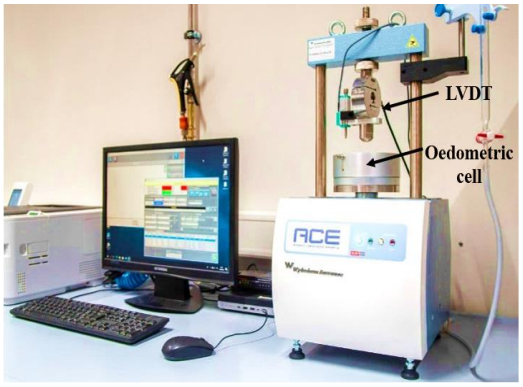

a)

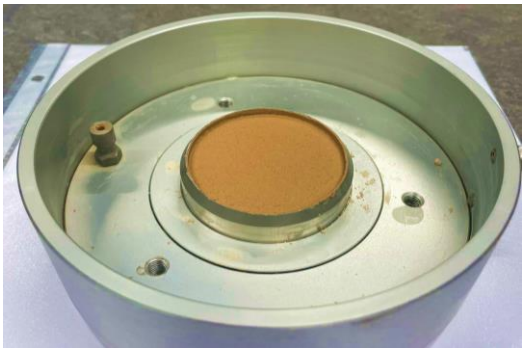

b)

Figure 1. a) Conventional oedometer apparatus; b) detail of the sample inside the oedometer cell.

3.2 Water retention tests

The suction level reached by the samples during the loading phase was estimated by carrying out water retention tests based both on techniques where the suction was imposed and the water content was

measured ('axis translation technique' ATT, 'vapor equilibrium technique' VET), and on tests where the water content was imposed and the suction was measured ('dew point technique' DPT). The axis translation technique was applied into a suction-controlled oedometer cell on samples 50mm diameter and 20mm height (Figure 2). The vapor equilibrium and dew point measurements were performed, respectively, into a relative humidity-controlled sealed box and by using a chilled-mirror psychrometer on samples 20mm diameter, 10mm height. More details are provided in Bella, 2021.

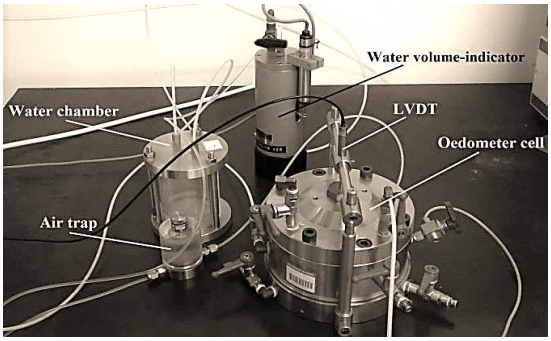

Figure 2. Suction-controlled oedometric cell (Bella, 2021).

4 EXPERIMENTAL RESULTS AND INTERPRETATION

4.1 Estimation of the matric suction levels

The experimental results obtained by the water retention tests on a silty sample (e_0=0.60) are provided on the (e_w–s) plane in Figure 3, where the water ratio is evaluated as e_w=Sr·e. The green squares represent the outcomes given by applying the axis translation technique; blue circles are the results obtained from the vapor equilibrium technique, while red triangles stand for the experimental points obtained by the dew-point technique. To account for the variation of the void ratio experienced during the oedometric loading phase, the experimental points were fitted by applying the model proposed by Gallipoli *et al.* (2003):

$$Sr = \frac{1}{\left(1+\left[\Phi(v-1)\psi s\right]^{n}\right)^{m}} \qquad (1)$$

where v is the specific volume, and dimensionless parameters n, m, ψ, and Φ (kPa^{-1}) are soil constants to be calibrated (Tab.2).

Table 2. List of the Gallipoli retention parameters.

Main drying branch				Main wetting branch			
n (-)	**m (-)**	**Φ (1/kPa)**	**Ψ (-)**	**n (-)**	**m (-)**	**Φ (1/kPa)**	**Ψ (-)**
1.67	0.40	0.28	5.32	1.50	0.33	5.40	7.81

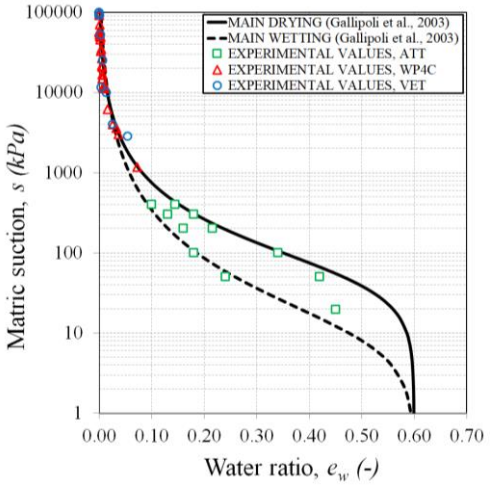

Figure 3. Experimental points and fitting curve for the three applied techniques.

Then, knowledge of the water ratio allowed to define a vertical hydraulic path (Figure 4, red arrow) because of the constant water content conditions. The hydraulic path crosses the main wetting branches of the WRC evaluated at void ratio e_i and e_f reached by the compression curve (1d-NCL), so the suction level can be obtained as the average value. A suction level equal to 13kPa was estimated for unsaturated sample edo_0.650-066 as shown in the figure below.

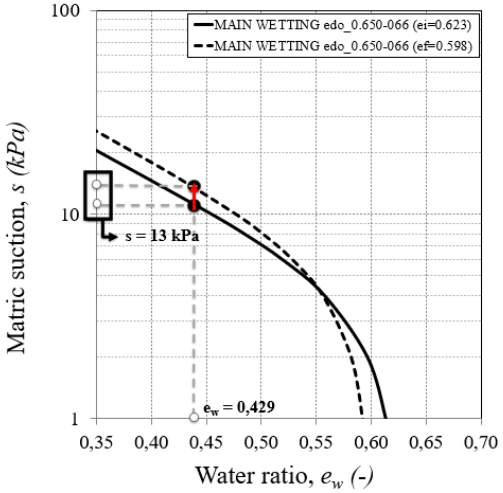

Figure 4. Evaluation of the matric suction level for sample edo_0.650-066.

The same procedure allowed the estimation of the matric suction level reached by all unsaturated samples (Tab.3). It is worth noting that the Stava silt is an inorganic soil with low plasticity, so the osmotic suction represents a small amount of the total suction. Therefore, the total suction can be assumed equal to the matric suction.

4.2 Pre-shearing state of stress of Stava tailings

The oedometric tests performed by Carrera on SC saturated samples (black lines) and the test carried out on the RS saturated sample (red line) are given in Figure 5a. All the curves converge toward a unique 1d-NCL regardless of the preparation method (compressibility index λ approx. 0.104). According to Carrera (2008), the uniqueness of the 1d-NCL of Stava silty tailings under fully saturated conditions seems to confirm the absence of a "transitional behaviour". On the other hand, the saturation state of the sample seems to influence the behaviour of Stava tailings. Indeed, oedometric tests performed on fully saturated samples (grey lines) and tests carried out on SC nearly saturated samples (blue lines) are given in Figure 5b. A little transitional behaviour is observed for the latter ones with the 1d-NCL moving up with initial void ratio and maintaining the same slope because of similar suction levels reached during the loading phase.

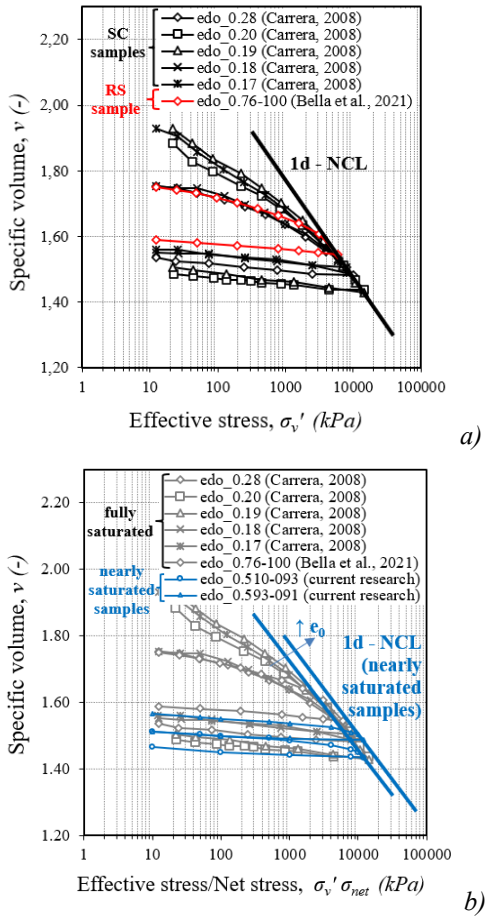

Figure 5. Compression curves and 1d-NCL: a) RS fully saturated sample and SC fully saturated samples; b) fully saturated samples and nearly saturated samples.

Some research has shown that transitional behaviour can be expected also for tailings (Al-Tarhouni *et al.*, 2011; Coop, 2015), but there is still some debate about whether the initial fabric has a relevant effect on the behaviour of soils (Li *et al.*, 2019). The normal compression lines for different suction levels are given in Figure 6. It is worth noting that the suction levels, estimated by the WRCs, are derived from the combined effect of the water content and the void ratio of the samples during the oedometric compression. Indeed, the retention properties of Stava tailings were found to largely depend on the void ratio (Bella and Musso 2024; Bella, 2021). For this reason, the denser sample edo_0.528-078 shows a suction level higher than those of looser samples edo_0.568-074 and edo_0.650-066. According to Alonso *et al.* (1990), a reduction of the compressibility index can be observed as the matric suction increased and this is due to the increase of the soil stiffness with the degree of saturation reduction. Indeed, the higher λ=0.059 was obtained for the SC sample edo_0.650-066 (green line) associated with the lower suction values s=13kPa. On the other hand, the lower compressibility index λ=0.052 was obtained for the SC sample edo_0.528-078 (red line) associated with the higher suction values s=35kPa. A summary of the suction level reached by Stava samples is provided in Table 3.

Table 3. List of matric suction level and compressibility index of Stava silty tailings.

Sample	s (kPa)	λ (-)	Authors
edo_0.510-093	1.0	0.090	Current research
edo_0.593-091	2.0	0.088	
edo_0.528-078	35.0	0.052	
edo_0.568-074	25.0	0.055	
edo _0.650-066	13.0	0.059	
edo_0.760-100	≈ 0	0.096	Bella *et al.*, 2021
edo_028	≈ 0	0.104	Carrera, 2008
edo_020			
edo_019			
edo_018			
edo_017			

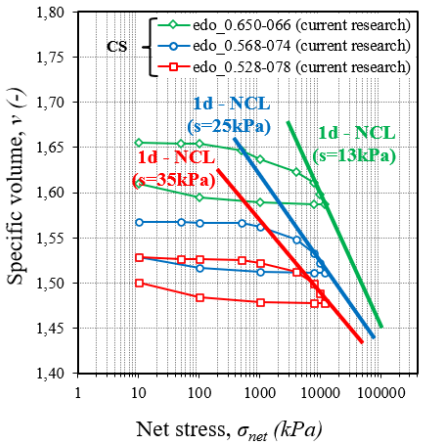

Figure 6. Influence of the suction level on the 1d-NCL.

The Basic Barcelona Model (BBM) is then adopted to interpret the experimental data, so the compression index with suction is estimated:

$$\lambda(s) = \lambda(0)\cdot\left[(1-r)e^{-\beta s} + r\right] \qquad (2)$$

where $\lambda(0)$ is the compressibility index under fully saturated conditions, s is the matric suction, while r and β are model parameters calibrated based on the experimental data (r = 0.49, β = 0.12). As shown by the solid line in Figure 7a, an increase in stiffness (decrease of the compressibility index) is observed with a suction increase, suggesting that the minimum value could be achieved at suction greater than 40-50 kPa. An additional formulation was proposed by Alonso *et al.* (1990) to evaluate the compression index with suction (dotted line, Figure 7a):

$$\lambda(s) = b + d\cdot ln(s) \qquad (3)$$

where b and d are dimensionless parameters to be calibrated (b = 0.087, d = -0.0102).

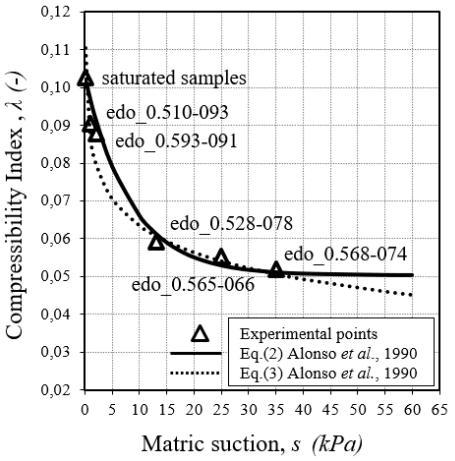

a)

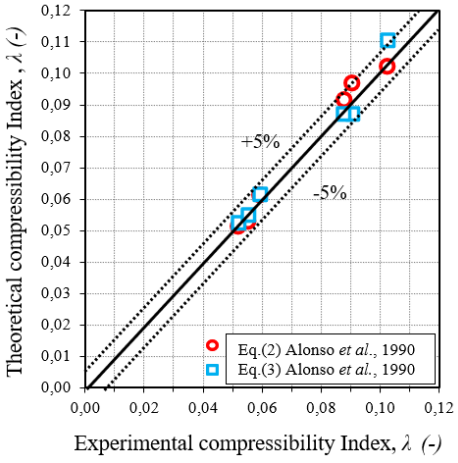

b)

Figure 7. a) Dependence of the compression index from suction level according to Eq.(2) and Eq.(3). b) Experimental compressibility index and theoretical compressibility index as predicted by Eq.(2) and Eq.(3).

Both Eq.(2) and Eq.(3) well predict the compressibility index with suction but it is worth noting that, according to Alonso *et al.* (1990), results provided by Eq.(3) are less realistic than those given by Eq.(2). Indeed, also for Stava silty tailings, Eq.(3) predicts an unlimited increase in soil stiffness ($\lambda \rightarrow 0$) for increasing s and this may be a limitation for wide ranges of suction variations. As shown in Figure 7b, the two formulations are finally compared with the experimental results providing reliable prediction (max error approx. 5%) within the suction range under investigation.

5 CONCLUSIONS

The effect of the matric suction on the hydro-mechanical response of Stava silty tailings is investigated. Based on the experimental test results, the following considerations can be drawn:

- The sample preparation method seems not to affect the occurrence of the transitional behaviour, while the saturation state little affects the uniqueness of the 1d-NCL;
- The compression index decreased with suction because the soil stiffness increases with matric suction;
- Water retention tests were performed on Stava silt by applying different techniques and not-conventional apparatus, such as a suction-controlled oedometer cell, vapor equilibrium technique, and chilled-mirror psychrometer;
- Water retention tests allowed to estimate the WRC of the soil under investigation, thus providing the suction level reached by the samples during the oedometric tests;
- The formulations proposed by the Basic Barcelona Model were adopted to estimate the compression index with suction. An increase of the soil stiffness with matric suction was observed within the suction range investigated.

Following the above outcome, additional investigations may be performed to better reproduce the real environment of tailing dams. At this scope, the aging effects (i.e. rearrangements, macro-interlocking or the cementation of the particles), together with the effect of the temperature could be considered for further investigations.

ACKNOWLEDGEMENTS

The authors are grateful to Prof. Guido Musso (Politecnico di Torino) for his valuable inputs, suggestions and support while analyzing the experimental data.

REFERENCES

Al-Tarhouni, M., Simms, P., Sivathayalan, S. (2011) Cyclic behaviour of reconstituted and desiccated-rewet thickened gold tailings in simple shear. *Canadian Geotechnical Journal*, 48(7), 1044-1060. https://doi.org/10.1139/t11-022.

Alonso, E., Gens, A. Josa, A. (1990) A constitutive model for partially saturated soils. *Geotechnique,* 40 (3), 405‑430, https://doi.org/10.1680/geot.1990.40.3.405.

Bella, G. (2021) Water retention behaviour of tailings in unsaturated conditions, *Geomechanics and Engineering, An Int'l Journal*, 26(2),117-132, http://doi.org/10.12989/gae.2021.26.2.117. https://doi.org/10.1016/j.sandf.2019.04.004.

Bella, G. (2017) *Hydro-Mechanical Behaviour of Tailings in Unsaturated Conditions*, Doctoral dissertation, Politecnico di Torino.

Bella, G., Musso, G. (2024) Liquefaction Susceptibility of Silty Tailings Under Monotonic Triaxial Tests in Nearly Saturated Conditions, *Geomechanics and Engineering, An Int'l Journal*. 36(3), pp.247-258. https://doi.org/10.12989/gae.2024.36.3.247.

Bella, G., Ghezzi, S., Czerski, D., Ambrosi, C., Lüscher, M., Giani, M. (2024) Preliminary Evaluation of the Effects of the Unsaturated Conditions on the Pre-Shearing State of Stress of Quarzitic Tailings, In: *9th International Conference on Geotechnical Research and Engineering (ICGRE 2024)*, London, UK, pp. 1-8.

Bella, G., Freire, C., Lameiras, F., Giani, M. (2023) Numerical Investigation on Tailing Dams Stability: a Preliminary Parametric Analysis of some Key Factors, In: *8th International Conference on Geotechnical Research and Engineering (ICGRE 2023)*, Lisbon, Portugal, pp. 1-8.

Bella, G., Musso, G. (2023) Hydro-mechanical behaviour and Critical State Conditions of unsaturated silty tailings, In: *8th International Conference on Geotechnical Research and Engineering (ICGRE 2023)*, Lisbon, Portugal, pp. 9-16.

Bella, G., Nocera, E. (2021) Influenza del grado di saturazione sulla compressibilità e sulla 1d-NCL della frazione limosa dei tailings di Stava, In: *X Incontro Annuale dei Giovani Ingegneri Geotecnici (IAGIG 2021)*, Pisa, Italy, pp. 23-26.

Carrera, A. (2008) *Mechanical Behaviour of Stava Tailings*, Doctoral dissertation, Politecnico di Torino.

Coop, M.R. (2015) Limitations of a critical state framework applied to the behaviour of natural and "transitional" soils. In: *6th International Symposium on Deformation Characteristics of Geomaterials*, Buenos Aires, Argentina, pp. 115-155.

Deng, D., Wen, S., Lu, K., Li, L. (2020) Calculation model for the shear strength of unsaturated soil under nonlinear strength theory, *Geomechanics and Engineering, An Int'l Journal*, 21(3), 247-258. https://doi.org/10.12989/gae.2020.21.3.247.

Gallipoli, D., Wheeler, S.J., Karstunen, M. (2003) Modelling the variation of degree of saturation in a deformable unsaturated soil, *Geotechnique*, 53(1), 105-112. https://doi.org/10.1680/geot.2003.53.1.105.

Girardi, V., Bella, G. (2023) Application of Material Point Method to tailing dams failure due to static liquefaction, In: *VIII Convegno Nazionale dei Ricercatori di Ingegneria Geotecnica (CNRIG 2023)*, Palermo, Italy, pp. 435-443.

Li, W., Coop, M.R. (2019) Mechanical behaviour of Panzhihua iron tailings. *Canadian Geotechnical Journal*, 56(3), 420‑435. https://doi.org/10.1139/cgj-2 018-003.

Tarantino, A. Mountassir, G. (2013) Making unsaturated soil mechanics accessible for engineers: Preliminary hydraulic–mechanical characterisation & stability assessment, *Engineering Geology*, 165(24), 89-104. https://doi.org/10.1016/j.enggeo.2013.05.025.

Zanardin, M.T., Oldecop, L.A., Rodriguez, R., Zabala, F. (2009) The role of capillary water in the stability of tailing dams, *Engineering Geology*, 105 (1-2), 108-118. https://doi.org/10.1016/j.enggeo.2008.12.003.

Proceedings of the XVIII ECSMGE 2024
GEOTECHNICAL ENGINEERING CHALLENGES
TO MEET CURRENT AND EMERGING NEEDS OF SOCIETY
© 2024 the Authors
ISBN 978-1-032-54816-6
DOI 10.1201/9781003431749-270
Open Access: www.taylorfrancis.com, CC BY-NC-ND 4.0 license

ECSMGE 24
XVIII EUROPEAN CONFERENCE ON SOIL MECHANICS AND GEOTECHNICAL ENGINEERING

Extension of the Lisbon subway between Santos station and the Terminal of the Cais do Sodré station - assessment of excavation induced damage in buildings

Extension du métro de Lisbonne entre la Gare Santos et le Terminal de la gare Cais do Sodré – evaluation des dommages causés pour les travaux d'excavation sur les constructions

F. Bernardo*, S. Ferreira, R. Pistone
COBA, Consultores de Engenharia e Ambiente, S.A., Lisboa, Portugal

R. Pina
Metropolitano de Lisboa E.P.E., Lisboa, Portugal

A. Tavares
Metro Santos Sodré ACE, Linda-a-Velha, Portugal

**f.bernardo@cobagroup.com*

ABSTRACT: The expansion of Lisbon's Underground network through the Yellow and Green lines extension project is taking place in a densely urbanized area of Santos and Cais do Sodré. The area, close to the Tagus River, combines challenging ground conditions and a large diversity of vulnerable assets, including heritage listed buildings, residential buildings and major utilities companies' assets. The project comprises the construction of the new Santos station and adjacent tunnels using the Conventional Method. The construction works will employ a sequential excavation method through poor ground conditions and low ground cover, including sections with less than one diameter of ground cover between the tunnels and the surface. In order to reduce the risk of damage to the buildings located in the zone of influence of the excavation works, a comprehensive damage assessment study was carried out in the initial stage of the project to assist the design of the tunnel primary lining and cut & cover retaining walls. This article will present the key challenges faced by the design team and the adopted solutions to reduce the risk of damaging the existing assets.

RÉSUMÉ: L'expansion du Métro de Lisbonne comprend d'extension de la lignes Jaune et Vert se développe dans une zone densément urbanisée de Santos et Cais do Sodré. La zone, proche du Tage, combine des conditions de sol difficiles et une grande diversité d'actifs vulnérables, particulièrement, édifices historiques, des édifices résidentiels et des actifs de services publics. Le projet comprend la construction de la nouvelle gare de Santos et des tunnels adjacents selon le méthode conventionnelle NATM (New Austrian Tunneling Method). Les travaux de construction utiliseront une méthode d'excavation séquentielle dans un massif avec faible résistance, y sections avec moins d'un diamètre de couverture entre les tunnels et la surface. Afin de réduire le risque de dommages aux édifices situés dans la zone d'influence des travaux souterrains, une étude complète d'évaluation des dommages a été réalisée dès la phase initiale du projet pour aider à la conception du tunnel, à la séquence d'excavation et au soutènement primaire. et calcul des structures de soutènement. Cet article présentera les principaux défis rencontrés par l'équipe de projet et les solutions adoptées pour réduire le risque de dommage des édifices.

Keywords: Building damage assessment; ground movements; damage assessment model and mitigation measures.

1 INTRODUCTION

The extension of the Yellow and Green lines is the most significant upgrade to Lisbon's subway network in the last decade. By creating a new connection between two existing lines (Green and Yellow), this project will form a circle line which will enhance the usability of public transportation services in the city centre (Figure 1). Construction works started in 2021 and passenger services are planned to start in 2025.

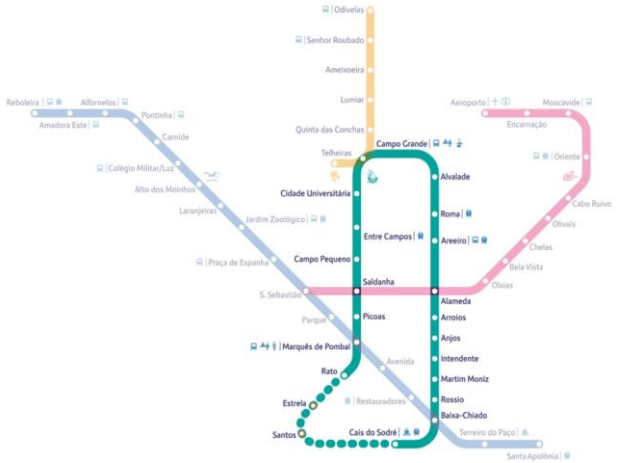

Figure 1. Lisbon's subway network (Metropolitano de Lisboa).

The project comprises a total of 1984 metres of running tunnels, two new underground stations, station upgrades at Rato and Cais do Sodré stations and a new flyover at Campo Grande. Works are divided into four lots, with Lots 1 and 2 splitting the civil works, Lot 3 includes the Campo Grande Flyover and Lot 4 includes all Mechanical, Electrical, Public Health and Architectural works.

This paper provides an overview of the building damage assessment analysis carried-out for Lot 2. This lot comprises 664 metres of new railway tunnels, running from the new underground station at Santos to the existing Cais do Sodré station (Figure 2).

The ground conditions change significantly along the route of the project, with Miocénic and Lisbon's Vulcanic formations at Santos' station, gradually changing to Tagus' River Alluvium Deposits at Cais do Sodré station.

The excavation works comprise deep shaft excavation, NATM/SCL tunnelling for the station platform tunnels, running tunnels and Cut and Cover excavations.

The zone of influence of the excavation works is a medium density urbanised area of Lisbon's downtown area. As part of the damage assessment analysis, 104 assets were analysed, comprising residential buildings, commercial buildings, listed buildings, railway lines and utilities. This paper will only cover the building damage assessments.



Figure 2. Plan view of Lot 2 (Yellow and Green lines extension project).

The damage assessment analysis provided essential information regarding the expected response of structures to ground movements induced by the excavation works. This allowed the design team to effectively adjust the construction methodology and, where required, to design ground movement mitigation measures. The requirement for ground movement mitigation measures to be implemented was identified by the damage assessment analysis. The efficiency of these measures was also confirmed by the damage assessment analysis. The ground movement mitigation measures included modifications to the construction methodology, underpinning of buildings, ground movement reduction barriers and structural bracing of buildings.

In areas where vulnerable buildings were located, the construction methodology for tunnels was adjusted to reduce the ground movements to the required magnitude to avoid damage.

The monitoring plan also was developed considering the output from the damage assessment analysis.

This paper provides an overview of the methodology adopted by the design team to develop the building damage assessment and how its output was used to assist on decisions regarding the construction methodology, the application of ground movement mitigation measures and the monitoring plan. An example of the implementation of this methodology to one of the buildings is presented in this paper.

2 METHODOLOGY

2.1 Building damage assessment model

The damage assessment analysis was part of the detailed design for the civil works. The analysis started

with the development of a damage assessment model using specific software (Oasys Xdisp Pro). This software automates building damage assessments based on Burland's (1995) assessment method. The model covered the full length of the project, including all the assets and excavation works (Figure 4).

In parallel, condition surveys were conducted to assess the condition of each building in the zone of influence of the excavation works. The condition surveys provided the design team with valuable information reg to understand the structure type (i.e. concrete framed or masonry), the type of foundation (i.e. shallow or deep foundations) and preexisting damages.

Each asset was defined in the model considering its generic dimensions (layout, foundation level, height, and structure type).

The building damage assessment analysis followed the staged risk assessment approach (Burland, 1995), which includes a preliminary assessment, a second stage assessment and detailed evaluation.

A total of sixty-eight buildings were damage assessed and ten required a combination of ground movement mitigation measures and more precise instrumentation and monitoring equipment (Figure 3).

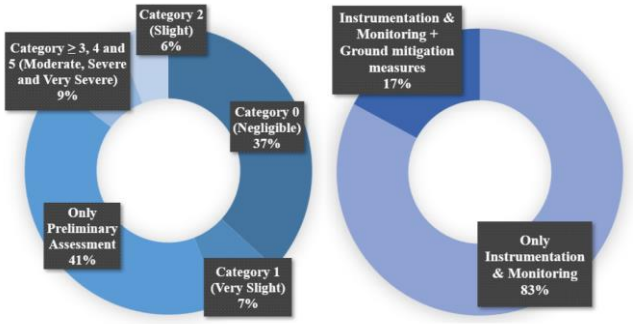

Figure 3. Assessed building damage categories (Burland, 1995) and ground movement mitigation measures.

2.2 Ground movement curves

The ground movements were calculated for each building and along each of its walls. The curves were obtained from bi-dimensional and tri-dimensional finite elements models (FE) (Figure 5). The curves were obtained for surface and sub-surface ground movements (vertical and horizontal).

The FE models were used to design the shaft support, retaining walls and the tunnel primary lining. These included the geotechnical model of the ground, the excavation support, surcharges of adjacent structures and the construction stages. The ground movement curves obtained from the FE models were compared with empirical curves from Peck (1969) and CIRIA 760 for reference.



Figure 4. 3D view of the damage assessment model.

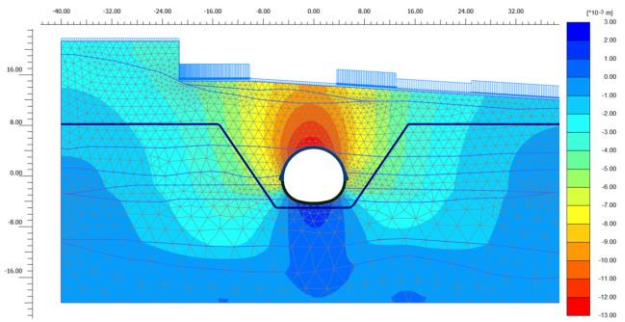

Figure 5. Example of a bi-dimensional finite element model.

2.3 Buildings

To assess damage categories in accordance with Burland's (1995) assessment method, a set of properties were required to be assigned to each building wall. These properties are representative of the building's geometry and the type of structure so that the maximum resulting tensile strains can be calculated and compared to the damage category limits.

In order to consider the vulnerability of listed buildings, the obtained damage category was increased by up to two levels, depending on preexisting damage and architectural features.

3 RESULTS

For the purpose of presenting an example of the building damage assessment work carried-out for this project, the following points describe the results to assess damage on a vulnerable listed building near Santos' station excavation works. Ground movement mitigation measures were implemented in this building to ensure that the resulting damage category was kept within the project's requirement (equal or below Damage Category 2).

3.1 Description of the building

This building was dated to the sixteenth century and it was part of a larger monastery where it was used as a lower choir. Over the centuries this building experienced several modifications to its architecture and to its use. However, the original columns, arches and ceiling paintings are still preserved (Figure 6 and Figure 7).



Figure 6. Low Choir (building's exterior view).



Figure 7. Low Choir (building's interior view) (Left) and Ceiling paintings (right).

3.2 Building damage assessment results

Due to its proximity to Santos' station excavation works, the ground movements estimated at the location of this building were in exceedance of 40 mm (Figure 8).

It was estimated that if no ground mitigation measures were implemented at this building, it could reach damage category 3 (Moderate), and considering the vulnerability of its architectural features, it would reach damage category 5 (Very Severe).

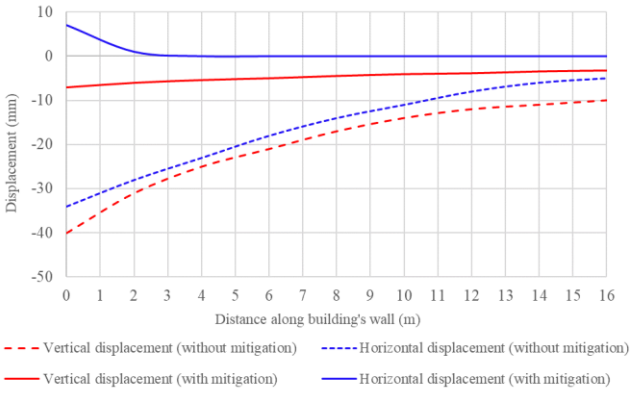

Figure 8. Ground movement profile along the most critical wall (with and without ground movement mitigation measures).

3.3 Ground movement mitigation measures

A desk study was carried-out to determine the most viable, safe and efficient ground movement mitigation measures. It was determined that the measures would be the installation of a ground movement reduction barrier, consisting of a bored piled wall (0,8 metre diameter piles, spaced at 1,0 centres) (Figure 9). and internal bracing of the building's structure (Figure 10).

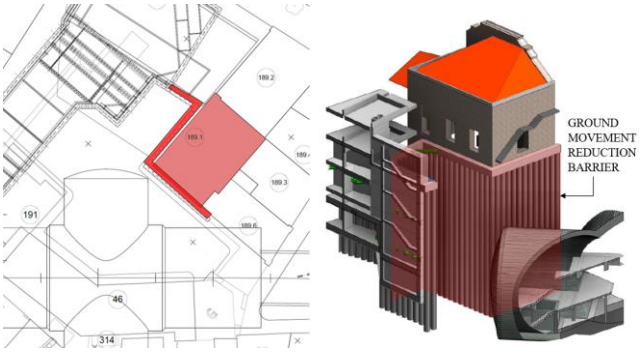

Figure 9. Location of the ground movement barrier.



Figure 10. Internal bracing of the building's structure.

3.4 Assessment of the effectiveness of ground movement mitigation measures

A detailed analysis based on 3D finite element modelling (3D FEM) was carried-out to assess the effectiveness of the ground movement reduction barrier (Figure 11).

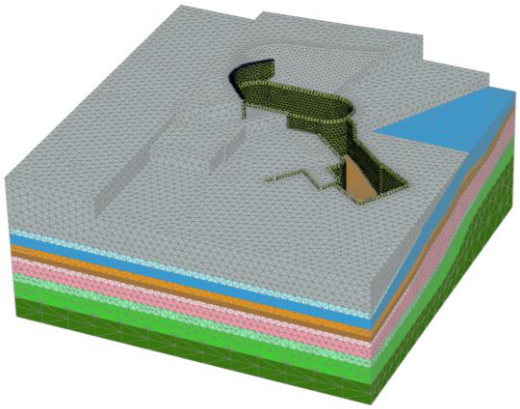

Figure 11. 3D FE model for Santos station (southern side).

The 3D FE model was developed to perform safety check calculations for all identified failure mode mechanisms. In order to reduce the calculation time, Santos station was analysed using two 3D FE models, one 3D FE model for the northern part and another 3D FE model for the southern part of the station. To assess the effectiveness of the ground movement reduction barrier, the southern 3D FE model was used. This model considered the heterogeneity of geological and geotechnical ground conditions, the groundwater conditions, the soil-structure interaction conditions, the construction sequence and the reinforcement elements, such as the primary lining and retaining walls (Figure 12).

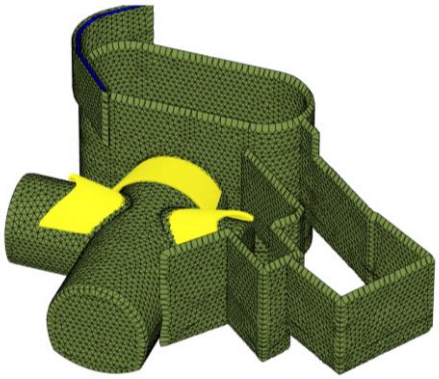

Figure 12. 3D FE model for Santos station (southern side) including primary lining and retaining walls elements.

The ground movement reduction barrier was modelled as a plate element and its stiffness and soil-structure interaction parameters, were assigned accordingly. The presence of the Low Choir building was modelled as a distributed load at ground level. The ground displacements were obtained from the 3D FE model (Figure 13).

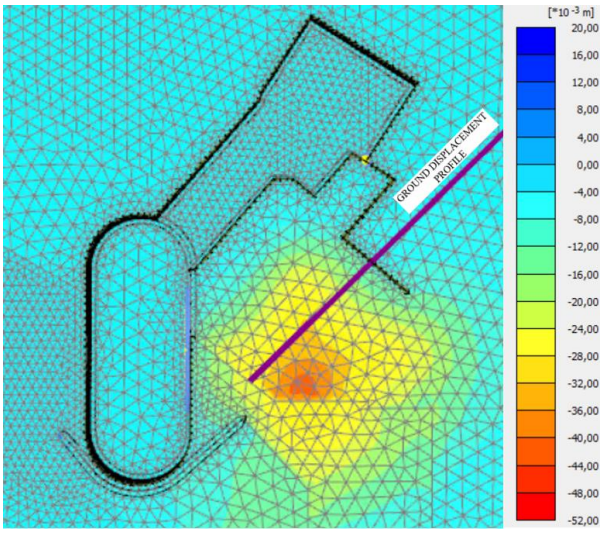

Figure 13. Estimated total displacements with ground movement mitigation measures (3D FEM).

The ground displacements were processed (Figure 14) and its analysis indicated that the inclusion of ground movement mitigations reduced the damage category to category 0 (Negligible), and considering the vulnerability of its architectural features, the damage category was estimated at damage category 2 (Slight).

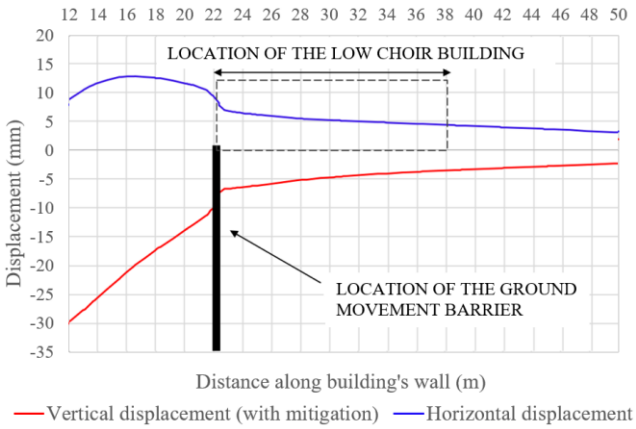

Figure 14. Ground displacement profile with ground movement mitigation measures (ground settlement profile).

4 CONCLUSIONS

This paper provides an overview of the building damage assessment work carried-out to assist the design team on the design of the excavation works for Lot 2 of the extension of the Yellow and Green lines.

The building damage assessment is an essential part of a large infrastructure project including excavation works in an urban environment.

The ability to combine in a damage assessment model multiple sources of ground movement, provides the opportunity to analyse the combined effects of various works. The opportunity to automate this analysis is critical to provide timely input to the design development so that efficient mitigation measures can be introduced, and adjustments can be made to the excavation methodology.

REFERENCES

Burland, J. 1995. Assessment of risk of damage to buildings due to tunnelling and excavation. Earth. Geot. Eng., Balkema, 1189-1202.

Gaba, A, Hardy, S, Doughty, L, Powrie and W, Selemetas, D, 2017, CIRIA 760 - Guidance on embedded retaining wall design, CIRIA, London.

Oasys Xdisp Manual, 2019, Oasys Software, London

Peck, R. 1969. Deep excavations and tunnelling in soft ground. Proc. 7th ICSMFE, State of-the-art Volume, 225-290.

Proceedings of the XVIII ECSMGE 2024
GEOTECHNICAL ENGINEERING CHALLENGES
TO MEET CURRENT AND EMERGING NEEDS OF SOCIETY
© 2024 the Authors
ISBN 978-1-032-54816-6
DOI 10.1201/9781003431749-271
Open Access: www.taylorfrancis.com, CC BY-NC-ND 4.0 license

ECSMGE 24
XVIII EUROPEAN CONFERENCE ON SOIL MECHANICS AND GEOTECHNICAL ENGINEERING

Eurocode 7 – Second Generation: Retaining structures – Looking beyond the partial factors for safety in design

Eurocode 7 – Deuxième génération – Ouvrages de soutènement – Au-delà des facteurs partiels de sécurité dans la conception

W. Bogusz*
Jacobs, Warsaw, Poland
**witold.bogusz@jacobs.com*

ABSTRACT: The second generation of Eurocode 7 brings many changes to various aspects of geotechnical design. The new Clause 7 "Retaining structures" of EN 1997-3 is one of the updated elements of this standard. As code-compliance in design is often associated with ultimate limit state verification and application of partial factors, there are less obvious improvements, which ensure the reliability of design involving ground-structure interaction and improved harmonisation of design rules between different Eurocode parts. In geotechnical design, it is vital to identify the relevant design situations, to formulate design assumptions, and to understand their underlying uncertainties. Application of the safety factors and verification of limit states is only one of the last steps in ensuring that the design is safe and fit-for-purpose. The paper presents the major elements related to design of retaining structures in the new Eurocode 7.

RÉSUMÉ: La deuxième génération de l'Eurocode 7 apporte de nombreux changements à divers aspects de la conception géotechnique. Le nouvel article 7 « Structures de soutènement » de l'EN 1997-3 est l'un des éléments mis à jour de cette norme. Comme la conformité aux codes dans la conception est souvent associée à la vérification de l'état limite ultime et à l'application de facteurs partiels, il existe des améliorations moins évidentes, qui garantissent la fiabilité de la conception impliquant une interaction sol-structure et une meilleure harmonisation des règles de conception entre les différentes parties de l'Eurocode. En conception géotechnique, il est essentiel d'identifier les situations de conception pertinentes, de formuler des hypothèses de conception et de comprendre leurs incertitudes sous-jacentes. L'application des facteurs de sécurité et la vérification des états limites ne constituent que l'une des dernières étapes permettant de garantir que la conception est sûre et adaptée à son objectif. L'article présente les principaux éléments liés à la conception des structures de soutènement dans le nouvel Eurocode 7.

Keywords: Eurocode 7; standardisation; retaining structures; partial factors, safety.

1 INTRODUCTION

Retaining structures, included in Part 1 of the first generation of Eurocode 7 (CEN, 2004), were moved to Clause 7 of the second generation EN 1997-3 (CEN, 2024b). As no revolutionary changes were introduced in regard to their design, the main improvements are the results of general changes to the entire set of the Eurocodes. This evolution resulted in overall increase of harmonisation of general rules for structural and geotechnical design (CEN, 2023a) as well as across all the new Eurocodes. More importantly, within the Eurocode 7 itself (CEN, 2024a, 2024b), design rules for all geotechnical structures are aligned to a greater extent. In the case of retaining structures (Clause 7), the design is strongly interrelated with other structures, most significantly, with slopes and cuttings (Clause 4), as well as anchors (Clause 8). Figure 1 presents, as an example, a schematic view of a retaining structure, where different Eurocode parts are involved. The main guidance of Clause 7 on retaining structures covers basis of design, geotechnical analysis, limit state verification, and quality assurance of:

- Gravity walls;
- Embedded walls;
- Composite retaining structures - composed of elements of gravity and embedded walls.

The normative content of Clause 7 is further supplemented by the informative Annex D, containing additional guidance on aspects such as estimation of earth pressures. The use of this annex and its content is subject to the choice of each CEN member country in their National Annex.

The main advantage of the new version of the code is the improvement in more holistic view on the design process. The verification of limit states is only one of the aspects of Eurocode 7 design.

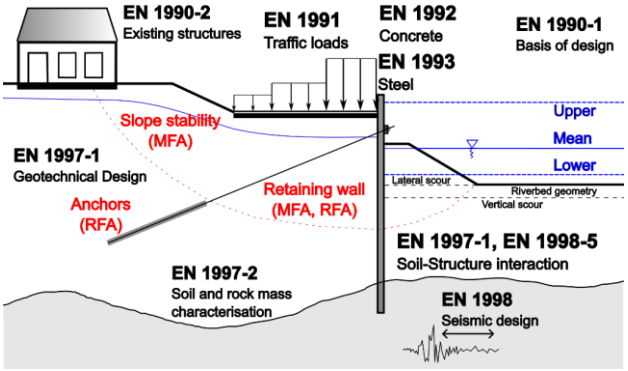

Figure 1. Interrelation of various design aspects covered by different Eurocodes.

The partial factors prescribed by the code are only part of the way of providing sufficient margin of safety. Their importance is often overestimated, as the real challenge is to identify relevant design situations, adopting realistic but cautious design assumptions, selecting representative values of actions and parameters, as well as prescribing quality assurance requirements for execution and maintenance. The updated version of the code addresses all of those aspects, but some still cannot be fully covered by standardisation.

The paper presents some of the major aspects and design requirements relevant for retaining structures that are introduced by the second generation of the Eurocode 7 Part 1 and 3 (CEN, 2024a, 2024b).

2 BASIS OF DESIGN

The basic elements affecting the design of retaining structures that have to be considered are:

- Zone of influence – including impact on existing structures;
- Consequences of failure, Geotechnical Complexity Class, Geotechnical Category;
- Robustness, durability and sustainability requirements for the given service life;
- Ground model, with representative stratigraphy and groundwater conditions;
- Design situations and geometrical properties;
- Actions and environmental influences;
- Groundwater conditions;
- Identification and verification of relevant limit states with reliable calculation models;
- Representative ground properties for each limit state considered;
- Quality management requirements.

Due to the limited scope of this paper, only some of those aspects are discussed, but all of them are covered in sufficient detail in the new Eurocode 7 (CEN 2024a, 2024b). Although the standard now offers the guidance for all the elements of design process, it is not intended to replace sound engineering judgement, but to supplement it.

The second generation of Eurocode 7 (CEN, 2024a) improves the concept of the "zone of influence". To ensure that the assumed Ground Model accounts for all the relevant strata that might affect the behaviour of the structure, the extent of site investigation is directly related to it. Next, a Geotechnical Design Model has to be developed, based on the Ground Model, for each geotechnical design situation, with corresponding combinations of actions and associated relevant limit states. Loads within the zone of influence may be considered as concentrated or uniform, depending on their nature and proximity to the retaining structure. In that regard, significant improvement is provided in EN 1991-2 Eurocode 1 (CEN, 2023b), where traffic load models specific for geotechnical applications are introduced. However, it is still the role of the designer to identify the relevant design situations and load combinations taken under consideration.

After the publication of the first generation of Eurocode 7, Simpson et al. (2011) highlighted the need for careful evaluation of a full range of credible scenarios based on engineering expertise, which cannot be simply substituted by requirements of a standard. In practice, the limit state analysis should cover situations considered as the worst credible conditions. For example, the design has to account for future anticipated excavations, and possible scour or erosion in front of the retaining structure, even if it might occur post-construction.

This also requires understanding of construction sequence and its effects on distribution of ground and water pressures. However, it is important to understand the difference between prediction of behaviour, serviceability limit state (SLS) analysis, and ultimate limit state (ULS) verification. Their level of conservatism in assumptions of representative parameters (material, geometrical, pressures, etc.) might differ.

3 GROUNDWATER

Significant consideration has been given to groundwater and water pressures in the process of the second generation of Eurocode 7 development. It is commonly recognised that effects of water pressures are very important in geotechnical design, especially for retaining structures. Usually, appropriate selection of the representative water levels (pressures) for each relevant design situation is considered as more important than application of partial factors in

providing safety in design. Consideration has to be given to a number of different factors in the selection process. Among them, climate change influence should be considered, as well as variation with time.

If there is sufficient data to derive the representative value of groundwater pressure on the basis of the annual probability of exceedance, it can be assumed in two ways, as:

- Upper ($G_{wk,sup}$) or lower ($G_{wk,inf}$) single characteristic permanent value (Figure 1) – the more adverse for the given limit state;
- Permanent mean value with variable amplitude.

Moreover, design situations can be divided into persistent, transient, and accidental situations, which can further influence the selection of the representative values.

However, if there is insufficient data to derive the values based on statistics, which often is the case in practice, upper and lower values should be selected as cautious estimates of the most adverse values likely to occur. The main point is to determine the most critical design scenarios and the water pressures associated with them. In practice, the analysis might consider various design situations, with different possible combinations of upper and lower estimate values, in front and behind the retaining wall.

The design value of groundwater level (pressure) for ULS can be obtained by:

- Direct assessment,
- A deviation to the representative value,
- Applying a partial factor to the representative groundwater pressures or their action effects.

In many cases, the most appropriate and most robust way of providing prescribed margin of safety will be to apply an offset of water pressures from their representative values, i.e. raising or lowering of the water levels. However, engineering judgement has to be used in that process.

Groundwater pressures arising from a common source of groundwater or surface water should be considered as a single action. However, upper- and lower-estimates should be considered if the water pressures can have both favourable and unfavourable effects. Furthermore, potential obstruction of natural groundwater flow caused by embedded retaining walls has to be considered. This applies to the possible increase of water level (dam effect) as well as the possibility of considering the pressures as coming from a single source. In some cases, detailed consideration has to be given to water levels on both sides of the retaining wall, especially in case of waterfront and flood protection structures.

Additional guidance on groundwater control measures has been also presented in Clause 13 of part 3 (CEN, 2024b). Its content is particularly important for cases where temporary or permanent drainage might be provided, or where an embedded wall acts as a cut-off barrier.

4 GEOTECHNICAL ANALYSIS

The geotechnical analysis of retaining structures is mostly related to the determination of earth pressure distribution and its impact on effects of actions. It has to take account of the expected failure mechanisms and deformations at the limit state under consideration. In general, three kinds of models can be used in the analysis:

- Analytical models - including limit equilibrium models and limit analysis.
- Semi-empirical models - including earth pressure envelopes.
- Numerical models - including beam-on-spring or continuum models.

Eurocode 7 Part 3 (CEN, 2024b) gives detailed description how to determine limiting values of earth pressure analytically for active, passive, and at-rest values of earth pressures. Intermediate values of earth pressure have to be determined considering the wall movement and its direction relative to the ground. Moreover, earth pressures due to backfill compaction have to be considered.

For embedded retaining structures, aside from the simplest of design cases, ground-structure interaction with numerical methods might be advisable. In such cases, all the relevant components (ground, retaining wall, support elements, etc.) have to be modelled in a realistic manner for the range of expected behaviour; an appropriate ground model and properties are key to obtaining reasonable estimates of performance (Haberfield, 2017).

The most critical geotechnical failure mechanism or combination of failure mechanisms may be determined by numerical continuum models using shear strength reduction approach. Although all the relevant failure modes not always can be checked in a single numerical analysis, a continuum numerical model can be used concurrently for overall stability calculations as well as to verify rotational resistance, stability of excavations, and structural failure.

5 ULTIMATE LIMIT STATES

Ultimate limit states specific to all retaining structures, in addition to those given in EN 1997-1 (CEN, 2024a) for all geotechnical structures, include but are not limited to:

- Failure of structural elements, their connections or their interfaces;

- Combined failure in the ground and structural element;
- Excessive movement of the retaining structure (potential collapse of the structure, nearby structures or services that rely on it).

For gravity retaining walls, additional ULS are to be considered:

- Bearing failure;
- Failure by sliding along the base;
- Failure by overturning or by toppling.

On the other hand, for embedded walls, verification includes:

- Failure by rotation or translation of the wall;
- Failure by lack of vertical equilibrium.

In addition, in the presence of hydraulic gradients, it shall be verified that limit states due to uplift, hydraulic heave, and internal erosion or piping, or bottom failure mechanisms, i.e. basal heave due to ground unloading, are not exceeded.

The verification of ultimate limit state by partial factor method can take two forms (CEN, 2023a). It can typically be considered in terms of effects of actions as forces and stresses (eq. 1), or in some cases in terms of deformations or strains (eq. 2):

$$E_d \leq R_d \quad (1)$$

$$E_d \leq C_{d,ULS} \quad (2)$$

where: E_d is the design value of effects of actions; R_d is the design value of the corresponding resistance; $C_{d,ULS}$ is the limiting design value for ULS of the excessive deformation that is considered to cause an ULS.

As alternative to verification by partial factor method, retaining structures may be verified using the Observational Method.

For structural resistance analysis, Eurocodes relevant for a given material should be used. Resistance shall be verified considering all geotechnical failure mechanisms that can interfere with the retaining structure. For advanced analysis, when elasto-plastic behaviour of structural elements is considered and load redistribution is allowed for non-linear problems, the input values of structural resistances may already be factored.

5.1 Overall stability

The problem of overall stability of retaining structures is often connected to the slope stability covered by Clause 4 of EN 1997-3 (CEN, 2024b). For retaining structures in sloped ground, where additional thrust on the wall would be induced by the slope deformation, one of the three possible approaches should be used:

- a continuum numerical model to check effects of actions on the retaining structure;
- a limit equilibrium method to check failure surfaces intercepting the retaining structure;
- a limit equilibrium method with an additional model factor to check failure surfaces not intercepting the retaining structure;

In such case, using continuum numerical methods offers an advantage of checking both the wall and the overall stability using a single model. However, the structural elements should have the properties defined as either:

- Elastic - forces in these structural elements have to be checked based on the Eurocode relevant for a given material.
- Elasto-plastic - verification is conducted based on Eurocode 7 Part 1 (CEN, 2024a), with structural ultimate resistance based on other relevant Eurocode.

5.2 Partial factors

In general, partial safety factors should be applied to where the major uncertainty exists, and when applied, to drive the solution towards reaching the ULS. When ULS verification by partial factor method is considered, two approaches for retaining structures are possible (Table 1), with corresponding sets of factors:

- Material Factor Approach (MFA) – where actions and material properties are factored;
- Resistance Factor Approach (RFA) – where actions and resistances are factored.

The sets of partial factors for actions or effects of actions are based on Verification Cases (VC) given in EN 1990 (CEN, 2023a) - Annex A. The partial factors for material properties (set M) are given in EN 1997-1 (CEN, 2024a).

In the case of RFA, the possibility of using partial factors for actions (VC1) or effects of actions (VC4) exists. Factoring the effects of actions (VC4), in a similar manner to DA2* approach from the first generation Eurocode 7, may be especially useful when applying continuum numerical methods, and for problems where water pressures have dominant impact on design.

For structural design of the wall, effects of actions in terms of structural forces should be factored to obtain their design values for verification of the relevant limit states.

Table 1. Partial factors for retaining structures for fundamental design situations.

Verification of	Partial factor on	Symbol	Material Factor Approach both (a) and (b) or only (c)			Resistance Factor Approach	
			(a)	(b)	(c)	(d)	(e)
Overall stability	Based on Clause 4 (Slopes, cuttings, and embankments)						
Gravity walls	Actions, Effects of actions	γ_F, γ_E	VC4	VC3	VC1	VC1	VC4
	Ground properties	γ_M	M1	M2	M2	Not factored	
	Bearing resistance	γ_{RN}	Not factored			1,4	
	Sliding resistance	γ_{RT}				1,1	
Embedded walls	Actions, Effects of actions	γ_F, γ_E	VC4	VC3	Not used	VC1	VC4
	Ground properties	γ_M	M1	M2		Not factored	
	Vertical resistance, basal heave	γ_R	Not factored			1,4	
	Passive earth resistance	γ_{Re}				1,4	

As retaining structures are often designed as part of slope stabilising measures (Figure 1), it is worth highlighting that for slope stability problems (Clause 4) only MFA (sets VC3 and M2) is allowed. On the other hand, for anchors, often used as support elements, only RFA approach is possible.

The new Eurocodes (CEN, 2023a, 2024a, 2024b) allow for consistent ULS verification of multiple problems with the same sets of partial factors, even for solutions combining more than one retaining wall or geotechnical structure. This is especially important when continuum numerical methods are used. Those methods are gaining popularity as designers generally prefer to conduct design limit state verifications, both ULS and SLS, with as few models as possible. The verification of ULS with the use of continuum numerical methods in the context of Eurocode 7 has been a subject of interest for a long time, e.g. by Bauduin et al. (2005) or Simpson et al. (2011). However, a lack of formal guidance on the code-compliant procedure of partial factors implementation has been often considered as a problem. The new code (CEN, 2024a) finally provides that guidance, explicitly offering following possibilities:

- Approach 1 (preferred) with two verifications:
  1. Output factoring - factoring effects of actions (VC4), e.g. bending moments.
  2. Input factoring - factoring primarily material properties (sets VC3 and M2).
- Approach 2 (alternative) – factoring effects of actions (VC4) and resistances, without the reduction of ground properties (set M1).

5.3 Supporting elements

Supporting elements for retaining structures include, but are not limited to: walls, piles, anchors, props, soil nails, and rock bolts. They have to resist the design values of the effects of actions E_d from the structure given for VC1 and VC3 (eq. 3), or VC4 (eq. 4), as:

$$E_d = \gamma_{Sd} max\{F_{ULS,d}; \gamma_F F_{SLS,rep}\} \quad (3)$$

$$E_d = \gamma_{Sd} max\{\gamma_E F_{ULS,rep}; \gamma_E F_{SLS,rep}\} \quad (4)$$

where: $F_{ULS,d}$ and $F_{ULS,rep}$ are respectively the design and representative values of action that supporting element shall provide to prevent ULS; $F_{SLS,rep}$ is the representative value of action that supporting element shall provide to prevent SLS; γ_{Sd} is a model factor; γ_F and γ_E are partial factors converting forces to their design values.

To maintain consistency of design, Clause 8 on anchors does not include partial factors on actions or effects of actions, as those will be transferred from the supported structure. Furthermore, the equations in Clause 4 for supporting elements of slopes, cuttings, and embankments, have a similar form. However, in their case, the wall itself can be a supporting element.

6 SERVICEABILITY LIMIT STATES

Serviceability limit states specific to retaining structures, in addition to those given in EN 1997-1 (CEN, 2024a) for all geotechnical structures, include but are not limited to:

- Movements of the retaining structure that cause damage or affect the appearance or the use of the structure, or nearby structures or services.
- Unacceptable leakage through or beneath the structure.
- Unacceptable change in the groundwater conditions induced by the retaining structure.

The impact on adjacent structures and services is now explicitly included and emphasised. It is often one of the factors governing the design of retaining walls

in an urban environment. The tolerance to displacements of supported structures and utilities within the zone of influence should be considered in selection of limiting values of ground movements around the retaining wall. The serviceability criteria may be defined as proportion of the limiting values of the deformations of the affected structures.

When assessing the serviceability limit states, which should be based on reasonably anticipated worst case situations, the SLS verifications should not be confused with prognosis of behaviour, which will depend on the most probable baseline scenario (calculations with best-estimate values).

7 IMPLEMENTATION OF DESIGN

Significantly more attention is now given to implementation of design in execution, which covers: inspection, monitoring, maintenance, testing, and reporting requirements. The need for specific plans, as part of the design, is now dependent on the Geotechnical Category of the structure. Furthermore, the importance and levels of validation of adopted calculation models with their assumptions are also emphasised. They might often involve checking the calculations against alternative methods and comparable experience.

The monitoring of a retaining structure should be planned based on identified mode of deformation. It should be specified, which aspects of the behaviour of the geotechnical structure shall be monitored to confirm compliance with the serviceability criteria. Moreover, limiting as well as threshold values should be established in design.

When the safety and the serviceability of the retaining structure depend on the successful performance of a drainage system, a Maintenance Plan has to be prepared.

To increase transparency of design process and to allow for third-party verification of design and the construction process, detailed reporting requirements are provided in the Eurocode 7. They cover not only the design documentation, but also Geotechnical Construction Record and Geotechnical Test Reports, prepared during execution, when implementing the design.

8 CONCLUSIONS

The new Eurocode 7 in terms of requirements for retaining structures offers an evolution rather than a revolution compared to the first generation. The main improvements are due to greater harmonisation between different Eurocode parts and across different geotechnical structures. In many aspects, the requirements are just aligned with the current state-of-the-art industry's practices and guidelines. However, the standard still maintains sufficient flexibility for modification and supplementation at the national level through National Annexes. Therefore, the designers should not find it overly challenging to implement the second generation of Eurocode 7 for the design of retaining structures.

ACKNOWLEDGMENTS

I would like to acknowledge the contribution of the members of the Task Group CEN TC250/SC7 TG-D1 on "Slopes, Retaining Structures, and Anchors", which I had the privilege of leading from 2020 to 2023. The group provided a significant contribution to the development and improvement of the Clauses 4, 7, and 8 of EN 1997-3 on geotechnical structures.

REFERENCES

Bauduin, C., Bakker, K.J. and Frank, R. (2005). Use of Finite Element Methods in Geotechnical Ultimate Limit State Design, *Proc. 16th Int. Conf. Soil Mech. And Geotech. Eng.*, IOS Press, pp. 2775-2779. http://doi.org/10.3233/978-1-61499-656-9-2775.

CEN (2004). EN 1997-1 Eurocode 7: Geotechnical design - Part 1: General rules, CEN-CENELEC.

CEN (2023a). EN 1990-1 Eurocode – Basis of structural and geotechnical design – Part 1: New structures, CEN-CENELEC.

CEN (2023b) EN 1991-2 Eurocode 1 — Actions on structures – Part 2: Traffic loads on bridges and other civil engineering works, CEN-CENELEC.

CEN (2024a). EN 1997-1 Eurocode 7: Geotechnical design - Part 1: General rules, CEN-CENELEC.

CEN (2024b). EN 1997-1 Eurocode 7: Geotechnical design - Part 3: Geotechnical structures, CEN-CENELEC.

Haberfield, C. (2017). Practical application of soil structure interaction analysis. *Proc. 19th Int. Conf. on Soil Mech. and Geotech. Eng.*, Korea Geotechnical Society, Seoul, pp. 81-99.

Simpson B., Vogt, N. and Van Seters, A.J. (2011). Geotechnical safety in relation to water pressures, ISGSR, *Proc. 3rd Int. Symp. on Geotechnical Safety and Risk*, Bundesanstalt für Wasserbau, Germany, pp. 501-517.

Proceedings of the XVIII ECSMGE 2024
GEOTECHNICAL ENGINEERING CHALLENGES
TO MEET CURRENT AND EMERGING NEEDS OF SOCIETY
© 2024 the Authors
ISBN 978-1-032-54816-6
DOI 10.1201/9781003431749-272
Open Access: www.taylorfrancis.com, CC BY-NC-ND 4.0 license

ECSMGE 24
XVIII EUROPEAN CONFERENCE ON SOIL MECHANICS AND GEOTECHNICAL ENGINEERING

Excavation and tunnelling impact on existing structures in the context of the second generation Eurocodes

Impact des travaux d'excavation et des tunnels sur les constructions existants dans le contexte des Eurocodes de deuxième génération

W. Bogusz*
Jacobs, Warsaw, Poland
**witold.bogusz@jacobs.com*

ABSTRACT: Ground deformations due to construction of deep excavations and tunnels, often affecting serviceability and causing damage to existing buildings, are important considerations in the design of underground structures. While the first generation of Eurocode 7 has not covered those aspects in much detail, the updated standard indirectly offers a design framework where this issue can be addressed in a code-compliant way. The paper presents some of the requirements implemented in second generation of the Eurocodes, relevant in the context of excavation-related impact assessment, as well as supplement them with information extending this guidance to tunnelling-induced deformations. Although tunnel design is still not officially covered even under the updated Eurocode framework, European standards are often used also for those applications. With ongoing efforts to officially bring underground structures under the scope of these standards, a general proposal is provided on how existing code can cover assessment in the case of tunnelling.

RÉSUMÉ: Les déformations du sol dues à la construction d'excavations et de tunnels profonds, affectant souvent la fonctionnalité et causant des dommages aux bâtiments existants, sont des considérations importantes dans la conception des structures souterraines. Bien que la première génération de l'Eurocode 7 n'ait pas couvert ces aspects de manière très détaillée, la norme mise à jour offre indirectement un cadre de conception dans lequel ce problème peut être résolu de manière conforme au code. Le document présente certaines des exigences mises en œuvre dans la deuxième génération des Eurocodes, pertinentes dans le contexte de l'évaluation des impacts liés aux excavations, et les complète par des informations étendant ces lignes directrices aux déformations induites par les tunnels. Bien que la conception des tunnels ne soit toujours pas officiellement couverte, même dans le cadre des Eurocodes mis à jour, les normes européennes sont souvent également utilisées pour ces applications. Dans le cadre des efforts continus visant à soumettre officiellement les structures souterraines au champ d'application de ces normes, une proposition générale est fournie sur la manière dont le code existant peut couvrir l'évaluation dans le cas des tunnels.

Keywords: Eurocode 7; impact assessment; deep excavations; tunnels, serviceability.

1 INTRODUCTION

Impact of underground construction works on existing structures is one of major problems associated with execution of deep excavations and tunnels. The second generation of the Eurocodes offers now a sufficiently detailed framework to address this problem in a code-compliant way. Basis of design aspects for new structures (CEN, 2023a) has been supplemented with requirements for assessment of existing structures (CEN, 2023b). Moreover, Eurocode 7 (CEN, 2024a) explicitly highlights the concept of the zone of influence of geotechnical structures and the need of assessing the impact on existing structures and utilities within that zone. The detailed guidence, relavant for underground construction activities, is mostly provided in Clause 7 on retaining structures of the new Part 3 (CEN, 2024b). However, together with the general provisions of the Eurocodes, it can easily be applied also for tunnelling-induced ground deformations and their impact on buildings, other structures, and utilities. Even though the development of tunnelling specific guidance is underway (Athanasopoulou et al., 2022), the Eurocodes are already commonly applied to different aspects of tunnel design (Figure 1). In this light, the existing Eurocode framework, based on its second generation, already provides a good basis for code-compliant impact assessment to be used.

2 ZONE OF INFLUENCE

A zone of influence is defined as a zone where construction works or the geotechnical structure can adversely affect the safety and serviceability of the

geotechnical structure, other structures, utilities, ground, or groundwater (CEN, 2024a).

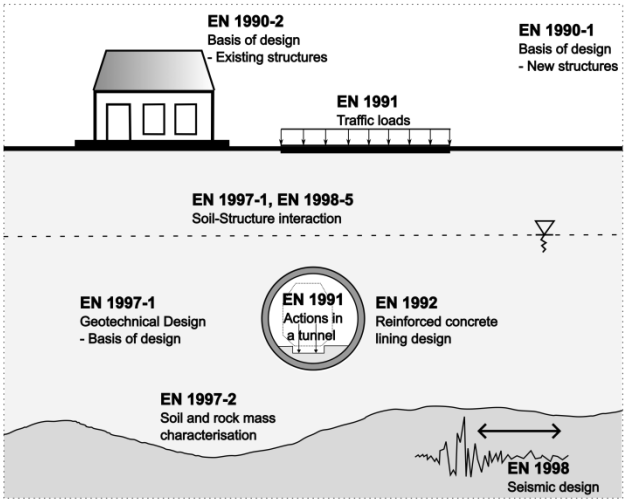

Figure 1. Applicability of Eurocodes to underground structures (adopted after Bogusz et al., 2023).

This zone is also related to the extent of potential failure surfaces and occurrence of significant ground displacements that have to be determined in design. The impact on ground, existing structures, and utilities within this zone should be investigated.

3 EXISTING STRUCTURES

All the existing structures within the zone of influence should be identified and assessed. The assessment of an existing structure should be carried out following a stepwise process with increasing levels of detail and accuracy (CEN, 2023b). It should include:

- Condition survey;
- Preliminary stage of assessment;
- Detailed stage of assessment.

Based on the assessment, the serviceability criteria for the existing structures, utilities, and ground within the zone of influence should be defined.

Furthermore, as the importance of existing structures and potential consequence of their failure cannot be ignored, their presence should be taken into account when deciding on the selection of Geotechnical Category in design.

4 EXCAVATION-INDUCED GROUND MOVEMENTS

Prediction of displacement due to deep excavations or tunnelling is needed to assess their influence on adjacent structures. Viable methods of prediction, in the case of impact assessment, include:

- Prescriptive rules;
- Empirical methods;
- Numerical methods;
- The Observational Method.

The current state-of-the-art approach in most cases of impact assessment is to implement empirical methods and 2D numerical models. When considering the use of empirical models, it is necessary to consider the conditions under which they were established and for which they are applicable. Despite that limitation, there is no restriction to use those models in the context of limit state design or probabilistic analysis that fulfils the requirements of the standard. However, Eurocode 7 does not provide a specific calculation model for prediction of ground movements in vicinity of structures; such models would have to be supplemented by additional guidelines. In the case of numerical models, their level of complexity for the impact analysis can vary, ranging from relatively low for 2D analysis to highly complex 3D modelling as summarised in Table 1.

Table 1. Model complexity levels for tunnelling impact assessment.

Model complexity level[1)]		Extent of required information[2)]	Geometry	Tunnel construction modelling	Adjacent structures
1	Low	Medium[3)]	2D	Volume loss method or Convergence-confinement method	Greenfield conditions
2	Normal				Equivalent load
3					Equivalent load and stiffness[4)]
4					
5	High	High	3D		Structural elements explicitly modelled
6		Very high		Detailed sequence	

[1)] Complexity levels 1 to 3 are typical for normal assessment, while levels 4 to 6 for detailed assessment.
[2)] For simplifies (prescriptive) and semi-empirical methods, the extent of required input information can be considered as very low and low, respectively.
[3)] Constitutive modelling of the ground will often need to account for non-linear stiffness for realistic prediction.
[4)] For plane-strain analysis (2D), stiffness of adjacent structures may be represented by consideration of simplified structural elements (e.g. foundation slabs, floors, walls, columns, piles, etc.) or structure with equivalent stiffness.

Loads within the zone of influence may be considered as concentrated or uniform depending on their nature and proximity to the retaining structure or a tunnel. However, it is often impractical to perform a detailed evaluation of loads for each adjacent building, unless benefits of such detailed assessment justify the effort. For practical applications, simplified representation is often sufficient. For example, in Polish practice, depending on the type and the use of a building, an assumption of uniformly distributed load of 10÷15 kN/m² per floor or 2.5÷3.0 kN/m² per one meter of height of the building is considered as a sufficient approximation, assuming sufficient distance from the new structure.

Ground movement around retaining structures, as well as tunnels, and their effects on supported structures and services, always have to be checked against comparable experience.

5 IMPACT ON EXISTING STRUCTURES

When the deformations imposed on surrounding ground by the excavation are predicted, their impact on the existing structure can be verified. This can be done based on limit state design framework of the Eurocodes, with distinction between serviceability (SLS) and ultimate (ULS) limit states.

States prior to structural collapse may be treated as ULS related to excessive movement that may cause collapse of the nearby structure or services. Movements that cause damage that can affect the appearance or inhibit the use of the nearby structure or services are considered as SLS. Limiting values of ground movements, as the serviceability criteria, have to consider the tolerance to displacements of supported structures and utilities within the zone of influence. Those criteria should be established for serviceability limit states (SLS) concerning:

- the functioning of the structure or structural members under normal use;
- the comfort of people;
- the appearance.

In general, serviceability requirements for each project should be specified individually. For protecting the historical, cultural or societal value of the structure, more restrictive serviceability criteria should be considered.

To limit the adverse impacts on existing structures, serviceability criteria may be defined as a proportion of the limiting value of the deformation of the affected existing structures. Although it is not explicitly stated, the limiting values of deformations may be established for performance-based design, where different values of deformations are assigned to specific performance levels or categories of damage.

The new version of the Eurocode (CEN, 2023a) already allows for verifications of both SLS and ULS in terms of deformations or strains using inequalities:

$$E_d \leq C_{d,SLS} \quad (1)$$

$$E_d \leq C_{d,ULS} \quad (2)$$

where: E_d is the design value of effects of actions; $C_{d,SLS}$ is limiting design value of the relevant serviceability criterion – it may be different for different serviceability considerations or level of damage (Figure 2); $C_{d,ULS}$ is limiting design value for ULS of excessive deformation.

Depending on which limit state is considered, not only the limiting design values should be differentiated, but also the considered actions resulting in ground displacements. The analysis has to be based on the representative values of actions and properties, appropriate for the considered limit state, usually considered as cautious (SLS) or worst credible (ULS) estimates. However, for prognosis of behaviour during execution, calculation with best-estimate values may be used.

In the case of tunnelling, usually volume loss associated with specific tunnelling method and ground conditions will be the major design assumption. Ideally, the choice of a representative value of volume loss should be based on the statistical analysis of prior tunnelling experiences in the considered area. Values for different probabilities of exceedence may be assumed in design for different limit states, based on risk tolerance level adopted. In case of lack of sufficient well documented experience to establish a statistical basis, a nominal value based on expert judgement can be selected.

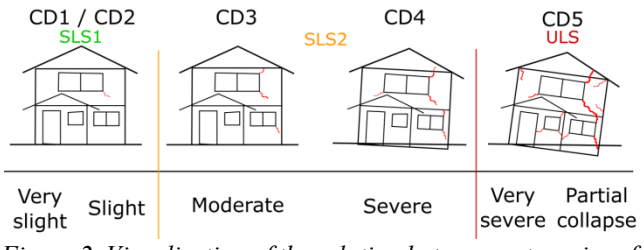

Figure 2. Visualisation of the relation between categories of damage (CD) and limit states (Bogusz, 2021).

6 EXAMPLE

As a short example, Figure 3 shows possible approach to selection of representative values of a tunnelling-related volume loss for Earth Pressure Balance Tunnel

Boring Machine (EPB-TBM) construction method, based on prior experience from M2 metro line construction in Warsaw (Bogusz, 2021). On the basis of that experience, representative values were adopted for impact assessment of new tunnels designed in similar ground conditions (Figure 4). The assessment has been conducted with both the empirical (preliminary assessment; Figure 5) and numerical (detailed assessment; Figure 6) methods. Due to the limitations of this paper, the full version of the design example is not presented here; however, it can be found in the annex to the JRC Report (Athanasopoulou et al., 2022) published online in open access.

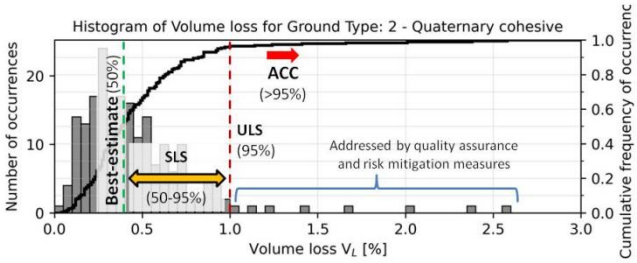

Figure 3. Selection of representative values of tunnelling volume loss based on statistical data.

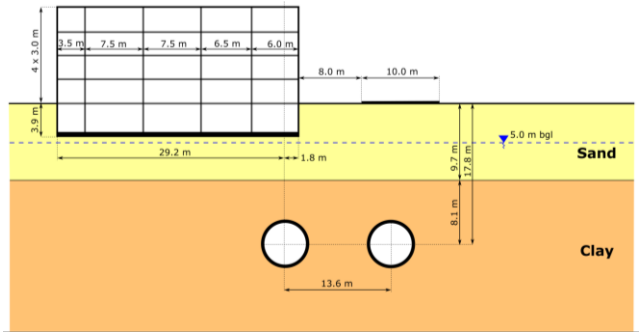

Figure 4. Conceptual model for impact assessment (Athanasopoulou et al., 2022).

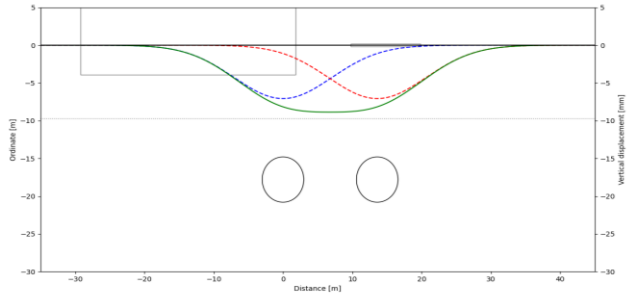

Figure 5. Ground displacement distribution from semi-empirical model (Athanasopoulou et al., 2022).

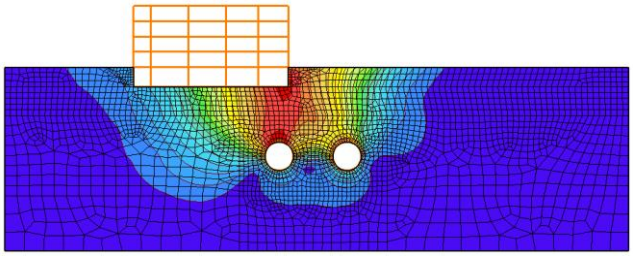

Figure 6. Ground displacement distribution from numerical model (Athanasopoulou et al., 2022).

7 CONCLUSIONS

The second generation of the Eurocodes does not solve all the issues associated with the impact of underground works on adjacent structures. However, it provides a good framework for impact assessment to be conducted in a code-compliant way. Additional supplementation with relevant calculation models and specific guidance would be useful; however, this can be easily provided by national or industrial guidelines and in the future by an additional Eurocode part, which is intended to be developed.

REFERENCES

CEN (2023a). EN 1990-1 Eurocode – Basis of structural and geotechnical design – Part 1: New structures, CEN-CENELEC.

CEN (2023b) EN 1990-2 Eurocode — Basis of structural and geotechnical design – Part 2: Assessment of existing structures, CEN-CENELEC.

CEN (2024a). EN 1997-1 Eurocode 7: Geotechnical design - Part 1: General rules, CEN-CENELEC.

CEN (2024b). EN 1997-1 Eurocode 7: Geotechnical design - Part 3: Geotechnical structures, CEN-CENELEC.

Athanasopoulou, A. et al. (2022). JRC Report: Prospects for designing tunnels and other underground structures in the context of the Eurocodes, Publications Office of the European Union, Luxembourg, JRC130784. https://publications.jrc.ec.europa.eu/repository/handle/JRC130784.

Bogusz, W. et al. (2023). Standardisation of tunnel design in Europe – Past practice, current situation and prospects, In: *Underground Construction*, Prague, Czech Republic.

Bogusz, W. (2021). *Prediction of tunneling-induced ground movements*, PhD thesis, Building Research Institute. Available at: http://dx.doi.org/10.13140/RG.2.2.36666.11205/1.

Proceedings of the XVIII ECSMGE 2024
GEOTECHNICAL ENGINEERING CHALLENGES
TO MEET CURRENT AND EMERGING NEEDS OF SOCIETY
© 2024 the Authors
ISBN 978-1-032-54816-6
DOI 10.1201/9781003431749-273
Open Access: www.taylorfrancis.com, CC BY-NC-ND 4.0 license

ECSMGE 24
XVIII EUROPEAN CONFERENCE ON SOIL MECHANICS AND GEOTECHNICAL ENGINEERING

Pile response to the effect of basement construction in soft clay

Réponse des pieux à l'effet de la construction de sous-sols dans de l'argile molle

T. Boonyarak*, A.Y. Aung
Department of Civil Engineering, King Mongkut Institute of Technology Ladkrabang, Bangkok, Thailand
Z.Z. Aye
Seafco Public Company Limited, Bangkok, Thailand
**thayanan.bo@kmitl.ac.th*

ABSTRACT: Basement construction and deep excavation in very soft clay could induce excessive ground movements and cause adverse effects on piles located inside the excavation area. The research was conducted using data from field monitoring on the instrumented pile inside the basement and three-dimensional numerical back-analysis to evaluate the pile-soil interaction under various basement construction techniques. The key factors investigated in this study include the influence of the basement construction method, system stiffness, pile-soil stiffness, and duration of construction period. Moreover, the influence of soil consolidation, pore pressure dissipation, and time-dependent soil behaviour on pile response is thoroughly investigated. Field measurements are conducted at selected construction sites in Bangkok, where retaining structures include jet-grouted retaining walls and cut-slope excavation. The diameter bored pile ranges from 0.6 m to 1.5 m and the depth of the pile tip is 50 m. The fully coupled three-dimensional finite element method using a hardening soil model with small strain stiffness is utilized to simulate the complex soil-structure interaction, considering the time-dependent behavior of soft clay to provide insights into observed behavior. A series of numerical parametric studies are carried out to identify the impact of each investigated factor affecting pile movement. The key results highlight the importance of system stiffness of the retaining structure that strongly impacts pile movement inside the basement. The time-dependent behaviour can cause larger pile movement in retaining systems with smaller stiffness, such as cut-slope excavation, than those with rigid retaining walls.

RÉSUMÉ: La construction de sous-sols et les excavations profondes dans des argiles très molles pourraient entraîner des mouvements excessifs du sol et avoir des effets néfastes sur les pieux situés à l'intérieur de la zone d'excavation. Cette étude a utilisé des données de surveillance sur le terrain sur le pieu instrumenté à l'intérieur du sous-sol et une analyse numérique tridimensionnelle pour évaluer l'interaction sol-pieu sous diverses techniques de construction de sous-sols. Les principaux facteurs étudiés incluent l'influence de la méthode de construction du sous-sol, la rigidité du système de structure de retenue, la rigidité sol-pieu, et la durée de la période non contreventée. De plus, l'impact de la consolidation du sol, de la dissipation de la pression interstitielle, et du comportement du sol dépendant du temps sur la réponse des pieux est examiné en détail. Les mesures sur le terrain sont réalisées à Bangkok, où les structures de retenue comprennent des murs de soutènement injectés au jet et des excavations en pente. La méthode des éléments finis tridimensionnels est utilisée pour simuler l'interaction sol-structure, en tenant compte du comportement dépendant du temps de l'argile molle.

Keywords: Pile-soil interaction; basement construction; soft clay; case history; three-dimensional numerical analysis.

1 INTRODUCTION

The construction of basements in soft clay environments significantly influences the behavior and response of bored piles inside the excavation area, rendering it a topic of substantial interest and study within geotechnical engineering. Soft clay presents unique challenges for constructing basements, primarily due to its low stiffness, high compressibility, and susceptibility to significant deformation under load.

In many cases, the excavation contractors inadvertently damage piles within the excavation area, the integrity of the pile, safety considerations, and project timeline may all be affected. Thus, it is crucial to understand the causes, and implementing appropriate necessary measures are essential steps in preventing such incidents.

Pile lateral movement due to excavation has been investigated and reported by Poulos & Chen (1997), Leung et al. (2003), Elkady (2013), and Aye et al. (2016). However, the in-depth response of the pile caused by excavation in soft clay is still not fully understood.

For many practical engineers, pile movement caused by basement construction is not fully aware. Figure 1a shows inclined bored piles caused by excavation works using cut-slope excavation and unbraced sheet pile walls. This pile movement causes pile integrity problem that requires remedial work.

To avoid disputes between the piling contractor and the excavation works contractor, survey markers are installed on the pile head to collect the initial location of the pile after piling works as shown in Figure 1b. When the excavation of the basement started, the pile location was measured to compare the movement of the pile caused by basement construction.

The objective of this paper is to provide a better understanding of pile behavior subjected to lateral movement caused by excavation works for basement construction. Parameters affecting the lateral movement of the pile, induced bending moment, and time-dependent movement are investigated.

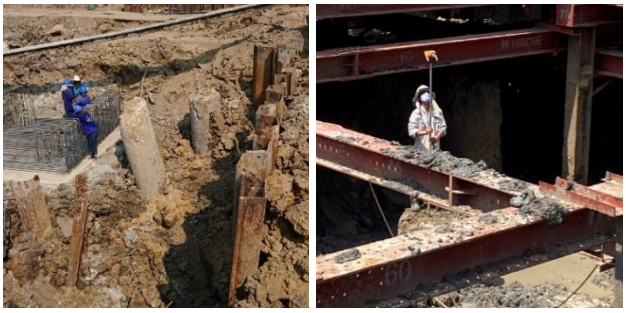

(a) (b)

Figure 1. (a) Deviated pile induced by excavation; (b) Pile location measurements using survey method.

2 GEOTECHNICAL INFORMATION

To understand the ground response due to excavation, typical geotechnical data of Bangkok is described below.

2.1 Typical soil profile

Bangkok's typical soil profile is shown in Figure 2a. A thick Bangkok soft marine clay layer (about 12-18 m thick) is located at the top followed by a thin layer of medium clay underlying alternating layers of stiff clay and dense sand. The undrained shear strength of soft clay ranges between 10 and 25 kPa. In stiff and hard clay, undrained shear strengths are about 150 and 200 kPa, respectively. The angles of internal friction (ϕ') of dense sands are estimated to be from 31˚ to 33˚.

2.2 Piezometric level

Apart from the geotechnical parameters, the distribution of measured pore water pressure and estimated trend line is given in Figure 2b. For Bangkok aquifers, there was a decrease in pore water pressure from 1988 to 1997 due to excessive underground water pumping. This effect of pore pressure decrease caused land subsidence. Thus, underground water pumping has been prohibited since 1997. This policy resulted in a recovery in the pore water pressure until 2011. Since 2011, the depth of the groundwater table has been stable at 13 m.

3 OBSERVED PILE MOVEMENT DUE TO EXCAVATION WORKS

Data from two case studies of pile movement due to basement construction is interpreted and presented in this paper.

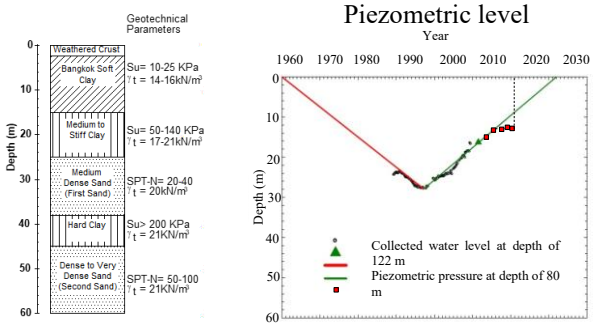

(a) (b)

Figure 2. (a) Typical Bangkok soil profiles; (b) Piezometric level of Bangkok.

3.1 Case Study 1: Excavation with jet-grout column retaining wall

The basement excavation of Case Study 1 is shown in Figure 3. Excavation depth to the pile head is varying from 3.35 m to 7.75 m. The deep foundation to support the building is bored piles diameter 1.0 with a depth of 50 m. The retaining system comprises three rows of 0.6 m with a depth of 15 m jet-grout column and an I-section driven pile with a dimension of 400 by 400 mm with a depth of 15 m. One and two layers of bracing are used for excavation depths of 3.35 m and 7.75 m, respectively.

According to the measured data, pile movement with the range from 25 to 35 mm was recorded for a pile head level of -3.35m. These movements were

induced by jet-grout installations, pile-driving activities, and basement excavations.

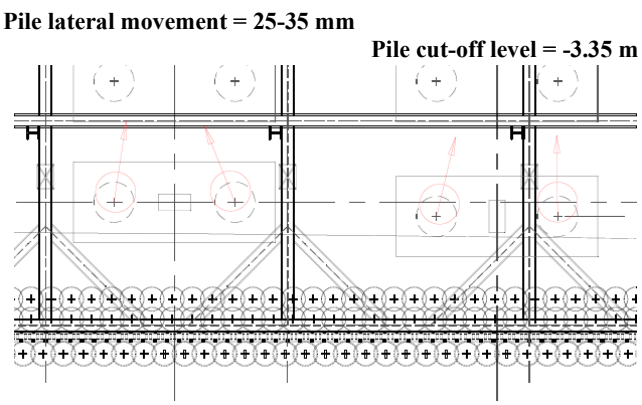

Figure 3. Case study 1: Pile movement due to excavation works using jet-grout column wall.

3.2 Case Study 2: Excavation with jet-grout column wall

Construction of the Case Study 2 is shown in Figure 4a. The pile cut-off level of this project is -7.5 m. The excavation method of this project was the cut slope with a horizontal to-vertical distance ratio of 2:1. Inclinometer tubes installed at the crest of the slope are used to monitor the soil movement as shown in Figure 4b. The soil movement induced by excavation works when reaching the maximum excavation depth is 110 mm. After leaving the slope unbraced for 2 months, the maximum soil lateral movement became 122 mm.

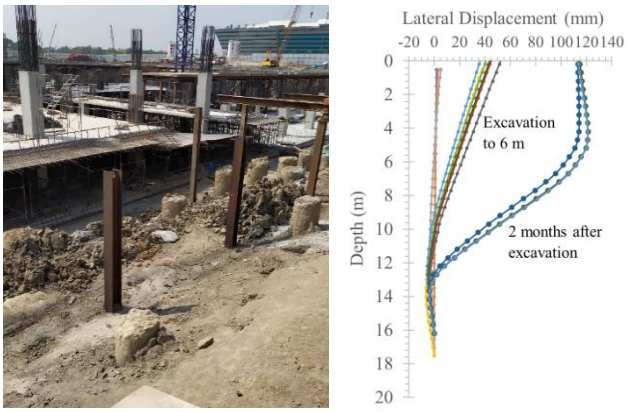

(a) *(b)*

Figure 4. Case study 2: (a) Excavation works using slope; (b) Inclinometer measurement in the soil in the slope crest.

Measured data on the pile markers show that slope excavation caused pile movement from 120 to 140 mm toward the toe of the slope.

4 NUMERICAL ANALYSIS

To assess the effects of excavation on the bored pile inside the excavation area, a three-dimensional numerical back-analysis and parametric study were carried out using the finite element program PLAXIS 3D 2023.

4.1 Mesh and boundary conditions

The finite element mesh used for back-analysis of the monitored results of Case Study 1 is shown in Figure 5a. For brevity of the paper, the mesh of Case Study 2 is not shown. The dimension of the mesh is set to the location near the retaining wall only to minimize the calculation time for three-dimensional analysis. Note that the distance from the wall to the boundary is larger than 3.5 times the excavation depth as reported as influence distance by Wang et al. (2010).

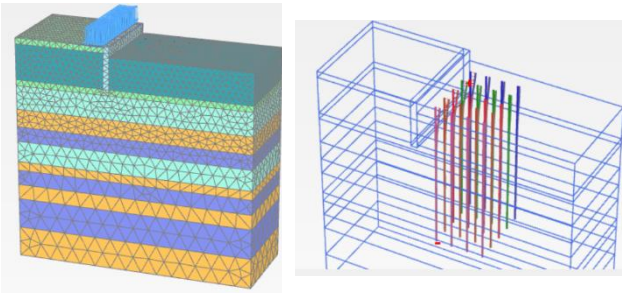

(a) *(b)*

Figure 5. (a) Mesh of three-dimensional numerical analysis; (b) Model piles of the Case study 1.

The boundary conditions of the four vertical sides were roller support while hinge support was applied to the bottom boundary as it is expected no lateral movement at the base. The boundary conditions for water flow are open for all sides and closed for the bottom of the model.

The jet-grout column wall was simulated as soil elements. Bored piles (as shown in Figure 5b) were simulated using embedded beams where friction and end bearing of each pile were taken into account. Fixed-end anchor was used for the temporary bracing. The surcharge simulated in the analysis is 15 kPa.

4.2 Model parameter and sequence of analysis

To back-analyze the result and carry out the parametric study, the Hardening Soil model with Small strain stiffness (HSS) considered (Schanz et al., 1999; Benz et al. 2009) was adopted. Unlike the conventional elastic-perfectly plastic soil model, the HSS model can simulate soil stiffness dependency on stress, strain, and path. Input parameters for Bangkok soil were adopted and modified by Surasak et al. (2012), Likitlersuang et

al. (2013), and Aye et al. (2016). All parameters are summarized in Table 1.

The sequence of numerical analysis is as follows. First, generate the initial conditions of stress in soil and pore water pressure. Construct retaining wall and bored pile. Apply surcharge and excavate soils in undrained conditions. For time-dependent behavior, perform consolidation analysis, which is a fully hydro-mechanically coupled analysis, for 60 days to simulate the actual time of construction on site.

4.3 Numerical parametric study

To extend a better understanding of pile behavior due to excavation activity, a series of three-dimensional numerical parametric studies were carried out.

Factors affecting the pile movement including pile diameter, distance of the pile to the retaining wall, and depth of excavation are investigated.

Table 1. Summary of input parameters.

Part 1

Soil Type	From (m)	To (m)	c' (kPa)	ϕ' (°)	Ψ' (°)	E_{50}^{ref} (kPa)	E_{oed}^{ref} (kPa)
Medium stiff clay	0	2	5.0	27	0	5,150	6,425
Soft clay	2	14	1.0	27	0	800	850
Medium stiff clay	14	16	5.0	27	0	5,150	6,425
Stiff to very stiff clay	16	24	11.5	28	0	5,150	6,425
Dense sand	24	30	0.1	31	5	27,000	27,000
Hard clay	30	42	11.5	28	0	9,500	12,000
Dense sand	42	50	0.1	31	5	27,000	27,000
Hard clay	50	55	11.5	28	0	9,500	12,000
Very dense sand	55	65	0.1	31	5	27,000	27,000

Part 2

Soil Type	E_{ur}^{ref}	R_f	m	K_o^{nc}	k (m/s) x10^{-7}	$\gamma_{0.7}$ (%)	G_{max} (kPa)
Medium stiff clay	19,000	0.9	1.0	0.74	5.5	0.0010	16,000
Soft clay	8,000	0.9	1.0	0.74	6.0	0.0005	5000
Medium stiff clay	19,000	0.9	1.0	0.74	5.5	0.0010	16,000
Stiff to very stiff clay	19,000	0.9	1.0	0.5	0.55	0.0010	48,000
Dense sand	162,000	0.9	0.5	0.5	400	0.0140	200,000
Hard clay	30,000	0.9	1.0	0.5	0.55	0.0015	124,000
Dense sand	162,000	0.9	0.5	0.5	400	0.0140	200,000
Hard clay	30,000	0.9	1.0	0.5	0.55	0.0015	124,000
Very dense sand	162,000	0.9	0.5	0.5	400	0.0140	200,000

Note: ν_{ur} is 0.2 for all soils

5 INTERPRETATION OF RESULTS

According to the measured results and three-dimensional numerical analysis, the findings are interpreted as described below.

5.1 Effect of pile diameter and pile distance from the retaining wall

Pile head lateral displacements due to excavation using jet-grout retaining wall is shown in Figure 6. The measured pile movement is taken from Case Study 1 (refer to Subheading 3.1 and Figure 3). The measured movement of 1.0 m diameter bored piles ranges from 25 to 35 mm (2.5 – 3.5% Pile diameter, D).

The computed movement of pile diameter 1.0 at the same distance from the retaining wall (X) as in Case Study 1 (X/excavation depth, H of 1.0) is 3.1%D, which is similar to the measured results. It suggests that the 3D numerical model and its parameters can be used to investigate pile response due to basement construction.

For the effects of pile diameter on the induced movement, as expected, the smaller piles are subjected to higher movement than the larger piles. Although the pile head displacements are normalized by their diameter, the normalized movement is still not identical. This is because of pile-soil stiffness interaction. The smaller piles are subjected to larger shear strain, thus the soil stiffness becomes smaller. Also, the flexural rigidity of the smaller pile is much smaller than that of the larger pile.

The pile movement reduces with increasing distance from the retaining wall. At X/H of about 4, the pile lateral movement reduces to about half of that at X/H of 1. It suggests that the major influence of excavation effects on pile movement is about four times the excavation depth.

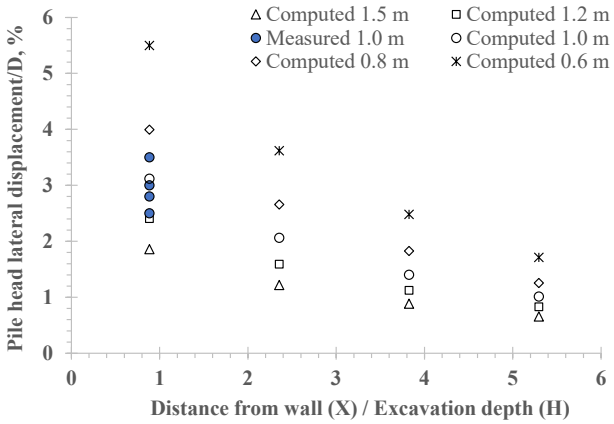

Figure 6. Pile movement for soil-cement column wall.

5.2 Effect of system stiffness on pile lateral movement

For excavation in soft clay, the system stiffness of a retaining system plays a critical role in maintaining the stability of the excavation. The stiffness of the system is important for controlling wall deflection, minimizing ground movements, and ensuring the safety of adjacent structures. Figure 7 shows system stiffness and normalized pile lateral movement with the excavation depth (H). Clough et al. (1989) defined a parameter for system stiffness as $EI/\gamma_w s^4$, where E, I, γ_w, and s are Young's modulus of retaining wall, a second moment of inertia, unit weight of water, and average vertical spacing of strut, respectively.

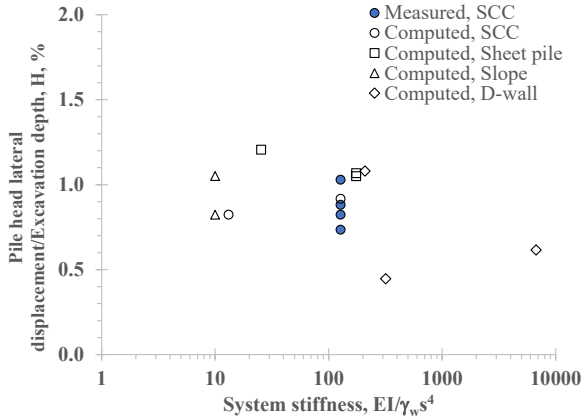

Figure 7. Effect of system stiffness on pile lateral movement.

The results in this figure include that from measured (from Figure 3) and numerical parametric study that varies excavation depth (3.35 m and 6.0 m) and type of retaining system (jet-grouted wall, sheet pile wall, slope excavation, and diaphragm wall).

The general trend suggests that normalized pile lateral displacement decreases with increasing system stiffness. The lateral movement of the pile significantly reduces if the system stiffness is larger than 300. The flexible wall induced significantly larger pile lateral movement than the rigid wall (diaphragm wall). However, when the diaphragm wall is in cantilever condition, the pile movement is still large (1.1%H). This is because no lateral bracing is provided to control the pile movement.

It appears that the excavation depth can be used as the normalizing factor as there is no significant difference in normalized pile movement between the excavation depth of 3.35 m and 6 m.

5.3 Time-dependent pile behavior

The measured data of time-dependent behavior of the pile response due to basement construction and numerical analysis is from Case Study 2 (refer to Figure 4). Figure 8a shows the measured and computed lateral displacement of 0.8 m diameter piles after the excavation depth reached 7.5 m and two months before the casting of the base slab. The location of the piles is on the crest of the slope, where the soil movement measured by the inclinometer was about 122 mm (refer to Figure 4b).

The displacements of the piles are between 85-92 mm and 120 to 140 mm, for the former and the latter, respectively. The computed back-analysis results mainly capture the pile response due to the excavation works.

The extent of depth of pile movement is about 15 m from the existing ground, which is the base of a soft to medium stiff clay layer (refer to Table 1). The lower soil layers (stiff clay, hard clay, and dense sand) provide much larger soil stiffness than the former.

Due to the excavation of the slope, a bending moment was induced in the bored pile as shown in Figure 8b. The maximum bending moment was 230 kN.m on the crest side of the slope. The depth of the maximum bending moment when the excavation reached the maximum depth was 15 m. This depth is the boundary between the soft soil and the stiffer soil. After two months, the depth of the maximum bending moment shifted to 9 m. This is because of the excess pore water pressure dissipation.

To further investigate the time-dependent behavior, excess pore water pressure (Δu) computed from soil elements along the 0.8 m pile at the slope crest is shown in Figure 8c. At depths from 0 to 3 m, the positive Δu up to 120 kPa was induced. This is because of shearing behavior due to soil movement at the slope crest. From a depth of 3 to 8 m, negative Δu occurs. This is due to unloading from excavation works. Two months after the final excavation, the Δu was fully dissipated. This caused the shift in the depth of the maximum bending moment of Figure 8b.

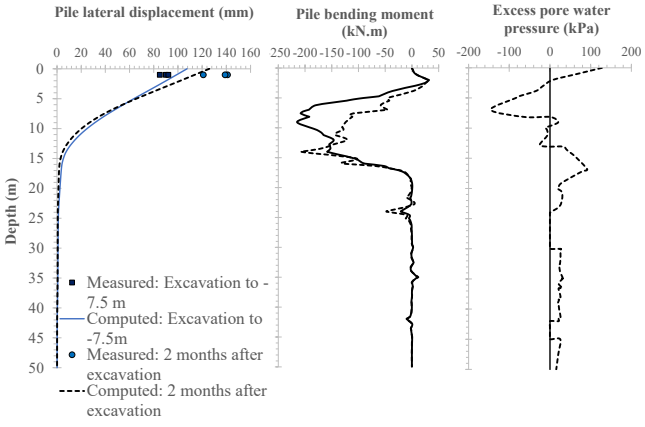

(a) (b) (c)

Figure 8. Time-dependent behavior (a) Pile lateral movement; (b) Bending moment in pile; (c) Excess pore water pressure.

6 CONCLUSIONS

Based on field monitoring, numerical back-analysis, and numerical parametric study results, the following conclusions may be drawn.

(a) The smaller piles are subjected to higher movement than the larger piles, as expected. Although the pile head displacements are normalized by their diameter, the normalized movement is still not identical. This is because the smaller piles are subjected to larger shear strain, thus the soil stiffness becomes smaller. Also, the flexural rigidity of the smaller pile is much smaller than that of the larger pile.

(b) The induced pile movement reduces with increasing distance from the retaining wall. At the distance from the retaining wall to excavation depth ratio (X/H) of 4, the pile lateral movement reduces to about half of that at X/H of 1. It suggests that the major influence of excavation effects on pile movement is about four times the excavation depth.

(c) In general, normalized pile lateral displacement decreases with increasing system stiffness. The lateral movement of the pile significantly reduces if the system stiffness is larger than 300. The flexible wall induced significantly larger pile lateral movement than the rigid wall (diaphragm wall). However, when the diaphragm wall is in cantilever condition, the pile movement is still large (1.1%H). This is because no lateral bracing is provided to restrain the pile head movement.

(d) Pile lateral movement increases by 35% after two months of reaching the maximum depth of excavation. The extent of the pile movement depth is at the boundary between soft soils (soft to medium stiff clays) and stiffer soils (stiff to hard clays).

(e) The soil at the top part (from 0 to 3 m) of the pile registered positive excess pore water pressure. This is because of shearing behavior due to soil movement at the slope crest. From a depth of 3 to 8 m, negative excess pore water pressure occurs. This is due to unloading from excavation works. Two months after the final excavation, the excess pore water pressure was fully dissipated. It caused the shift in the depth of maximum bending moment in the pile from 15 m to 9 m.

ACKNOWLEDGEMENTS

The Authors would like to acknowledge the executives and staff of Seafco Public Company Limited and EDE Company Limited for supporting measured data and technical support for this paper.

REFERENCES

Aye, Z. Z., Boonyarak, T., Thasnanipan, N. and Chea, S. (2016). Effects of cut-and-cover tunnel construction on adjacent piles of an overpass in Bangkok soft clay. *Fourth Geo-China International Conference*, 25-27 July, Shantong, China. https://doi.org/10.1061/978078448003 8.034.

Benz, T., Schwab, R., and Vermeer, P. (2009). Small-strain stiffness in geotechnical analyses. *Bautechnik* 86(S1): 16-27. https://doi:10.1002/ bate.200910038.

Elkady T. (2013). Effect of Excavation Induced movement on Adjacent Piles. *18th Int. Conf. on Soil Mechanics and Geotechnical Engineering*, Paris, France,707-710.

Leung, C. F., Lim, J. K., Shen, R. F., Chow, Y. K. (2003). Behavior of pile groups subject to excavation-induced soil movement. *J. Geotech. Geoenviron. Eng.*, 129(1), pp. 58-65. https://doi.org/10.1061/(ASCE)1090-0241(2003) 129:1(58).

Likitlersuang, S., Teachavorasinskun, S., Surarak, C., Oh, E. and Balasubramaniam, A. (2013). "Small Strain Stiffness and Stiffness Degradation Curve of Bangkok Clays". *Soils and Foundations.* 53(4): 498–509. https://doi.org/10.1016/j.sandf.2013.06. 003.

Poulos, H. G. and Chen L. T. (1997). Pile Response Due to Excavation-Induced Lateral Soil Movement. *J. Geotech. Geoenviron. Eng.*, 94-99. https://doi.org/10.1061/(ASCE)1090-0241(1997) 123:2(94).

Schanz, T., Vermeer, P. A. and Bonnier, P. G. (1999). Formulation and verification of the Hardening soil model, In: *Beyond 2000 in Computational Geotechnics*, A.A. Balkema, Rotterdam, Netherlands, pp. 281-290. https://doi:10.1201/ 9781315138206-27.

Surarak, C., Likitlersuang, S., Wanatowski, D., Balasubramaniam, A., Oh, E., Guan, H., (2012). Stiffness and strength parameters for hardening soil model of soft and stiff Bangkok Clays. *Soils and Foundations.* 52(4), 682–697. https://doi.org/ 10. 1016/j.sandf.2012.07.009.

Wang, J. H., Xu, Z. H. and Wang, W. D. (2010). Wall and ground movements due to deep excavations in Shanghai soft soils. *J. Geotech. Geoenviron. Eng.*, 136 (7), 985-994. https://doi.org/10.1061/ (ASCE) GT.1943-5606.0000299.

Proceedings of the XVIII ECSMGE 2024
GEOTECHNICAL ENGINEERING CHALLENGES
TO MEET CURRENT AND EMERGING NEEDS OF SOCIETY
© 2024 the Authors
ISBN 978-1-032-54816-6
DOI 10.1201/9781003431749-274
Open Access: www.taylorfrancis.com, CC BY-NC-ND 4.0 license

ECSMGE 24
XVIII EUROPEAN CONFERENCE ON SOIL MECHANICS AND GEOTECHNICAL ENGINEERING

Assessment of displacements and deformation mechanisms in a rockfill dam: case study of Cerro da Mina reservoir

Évaluation des déplacements et des mécanismes de déformation dans un barrage en enrochement: étude de cas du réservoir Cerro da Mina

L. Bottaro*, G. Tavares
TPF Consultores de Engenharia e Arquitetura, Lisbon, Portugal

M. Oliveira, A. Rodrigues
Somincor - Sociedade Mineira de Neves Corvo, Castro Verde, Portugal

**lucas.bottaro@tpf.pt*

ABSTRACT: Reservatório Cerro da Mina is an industrial water reservoir, consisting of rockfill lined by an impervious HDPE membrane. Monitoring showed that the rockfill experienced a few moments of sudden deformation in the first years of operation. The assessment of the environmental conditions in the periods of interest revealed that these more abrupt displacements coincided with periods of intense rainfall, rise in the water level in the reservoir and low evaporation. Both vertical and horizontal deformations of the rockfill showed a tendency of sudden increase when a new maximum in the precipitation record occurred and the precipitation values exceeded the potential evaporation, indicating that the increase in humidity in the rockfill voids led to a significant decrease in the rock pore suction, causing wet-induced collapses in the rockfill. Additionally, except potentially for the first load due to filling, the influence of the oscillation of the water level in the reservoir was not considerable for the vertical displacements, but significant in the horizontal direction.

RÉSUMÉ: Le Reservatório Cerro da Mina est un réservoir d'eau industrielle, constitué d'un remblai en enrochements recouverts d'une membrane imperméable en PEHD. L'auscultation a montré que l'enrochement a connu quelques instants de déformation brusque au cours des premières années d'exploitation. L'évaluation des conditions environnementales au cours des périodes d'intérêt a révélé que ces déplacements plus brusques coïncidaient avec des périodes de précipitations intenses, d'élévation du niveau de l'eau dans le réservoir et de faible évaporation. Les déformations verticales et horizontales de l'enrochement ont montré une tendance à une augmentation soudaine lorsqu'un nouveau maximum dans l'enregistrement des précipitations se produisait et que les valeurs des précipitations dépassaient l'évaporation potentielle, ce qui indique que l'augmentation de l'humidité dans les vides de l'enrochement a conduit à une diminution significative de la succion des pores des blocs rocheux, provoquant des effondrements due au mouillage de l'enrochement. De plus, hormis potentiellement la première charge due au remplissage, l'influence de l'oscillation du niveau d'eau dans le réservoir n'était pas considérable pour les déplacements verticaux, mais significative dans les horizontales.

Keywords: Wet-induced collapse; impervious rockfill dam; rockfill deformations.

1 INTRODUCTION

Reservatório Cerro da Mina (RCM) experienced a few moments of relatively small, yet sudden settlements on the rockfill embankment during the first years of operation. Under constant load, the largest post-constructive settlements are normally anticipated at the beginning of the operation of the dam, and the rates in which strains occur are expected to reduce over time (Oldecop and Alonso, 2007, Kermani et al., 2017). In this case, however, superficial settlement markers, vertical extensometers and inclinometers installed in the rockfill recorded peaks of movements some years after the end of construction and first load due to filling. The moments of increase in the settlement rates coincided with periods of large pluviosity, when the water level in the reservoir and the moisture in the rockfill tend to rise.

The relation between shift in environmental conditions and change in deformation rates are quite known in geotechnical monitoring, and assessing the mechanisms involved can enhance the understanding of the structure's behaviour and provide a better prediction of future movements. This study aims to present monitoring data of the rockfill, correlate with the conditions existent in the moments of sudden deformation and, based on that assessment, explain the mechanisms involved.

2 ROCKFILL CHARACTERISTICS

RCM is a 1,45 hm^3 industrial water reservoir located in Castro Verde, Portugal. The embankment consists, on the west side, of a main embankment with a maximum height of approximately 30 m, and on the north side, of a saddle embankment of 11 m on its highest section. Due to chemical activity of the industrial water stored, the reservoir is operated considering zero discharge to the environment. A double lining system was installed, consisting of a 2,5 mm HDPE membrane, lying on a geocomposite clay liner. The embankment was constructed with sound or moderately weathered greywackes excavated from the pond area, according to the zoning in Figure 1:

- Type A: support material for the lining system. Only sound greywacke rock used. Less than 5% of fines, 40 mm ≤ D100 ≤ 60 mm; 3,3 mm ≤ D50 ≤ 12 mm.
- Type B: filter for materials type A and C. Only sound greywacke rock used.
- Type C: good quality material, well compacted rockfill with high deformability modulus. Only sound greywacke rock used. Less than 5% of fines, 300 mm ≤ D100 ≤ 600 mm; 20 mm ≤ D50 ≤ 150 mm.
- Type D: random finer rockfill. Use of moderate weathered greywacke rock allowed. Less than 5% of fines, 60 mm ≤ D100 ≤ 280 mm; 7 mm ≤ D50 ≤ 55 mm.
- Type E: protection layer. Blocks between 50 mm and 800 mm.

The geomechanical characterization of the rockfill was executed in two phases. For the design, samples from not so fresh greywacke were tested. In the beginning of construction, fresh greywacke from the experimental fills was tested to validate the design assumptions. The main results are shown in Table 1.

3 DISPLACEMENT MONITORING

The monitoring plan of RCM was conceived according to the Portuguese dam safety regulation and specificities of the reservoir. Regarding the assessment of displacements on the rockfill, there are 25 superficial survey beacons installed on the crest, 17 of which located on the main embankment and 8 on the saddle embankment. There are 3 inclinometer casing tubes, each one associated to vertical extensometers (consisting of magnetic rings) in different elevations of the rockfill. Additionally, the water level on the reservoir is recorded daily and a meteorological station measures precipitation and evaporation potential.

Table 1. Index-properties of greywacke rockfill (mean ± standard deviation [number of samples]).

Parameter	Design phase	Construction
Apparent density (kgm^{-3})	2581 ± 17 [10 samples]	2588 ± 33 [6 samples]
Porosity	4.81 ± 0.83 [10 samples]	4.25 ± 0.71 [6 samples]
Uniaxial compr. (MPa)	40.0 ± 4.4 [10 samples]	-
Crushing – Pa_{50} air dried (kgf)	1219 ± 378 [4 samples]	1033 [1 sample]
Crushing – Pa_{50} saturated (kgf)	690 ± 218 [4 samples]	506 [1 sample]
Los Angeles abrasion test	39.0 ± 5.7 [2 samples]	27 [1 sample]
Slake durability – 7th cycle, dry	2.5 ± 0.3 [4 samples]	-
Slake durability – 7th cycle, wet	7.2 ± 2.7 [4 samples]	-
Maximum water content (%)	1.86 ± 0.35 [10 samples]	1.65 ± 0.27 [6 samples]

This study will present the analysis of the inclinometer and extensometers installed in the centre of tallest section of the rockfill, IB3. Table 2 presents the initial elevation of the extensometers.

Table 2. Initial elevation of extensometers in section IB3.

Extensometer	Initial elevation (m)
IB 3 – Ring 9	238.215
IB 3 – Ring 8	235.079
IB 3 – Ring 7	232.088
IB 3 – Ring 6	228.959
IB 3 – Ring 5	225.859
IB 3 – Ring 4	222.731
IB 3 – Ring 3	219.654
IB 3 – Ring 2	216.541
IB 3 – Ring 1	213.465
Datum	211.920

Figure 2 presents the total vertical displacements measured and Figure 3 the post-construction vertical displacements measured in the extensometers IB3. As expected, the readings suggest that the largest deformations occurred during the construction and initial months after its completion. The form of the vertical displacement curves in the first year (between the end of 2013 and November of 2014) was similar to the expectations, with the general shape resembling a logarithmic relation in time, steeper in the beginning,

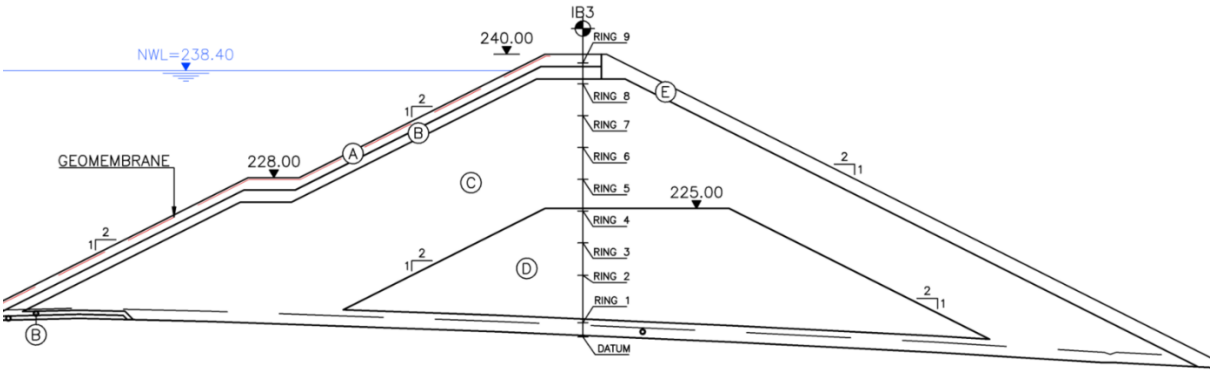

Figure 1. Typical cross section of RCM (adapted from Cenor, 2010).

reducing inclination after the first few months and showing a tendency to future stabilization. In addition to these predictable significant movements recorded in 2014, it is possible to notice though three moments of abrupt settlement: in the last months of 2014 and the first months of 2017 and 2018.

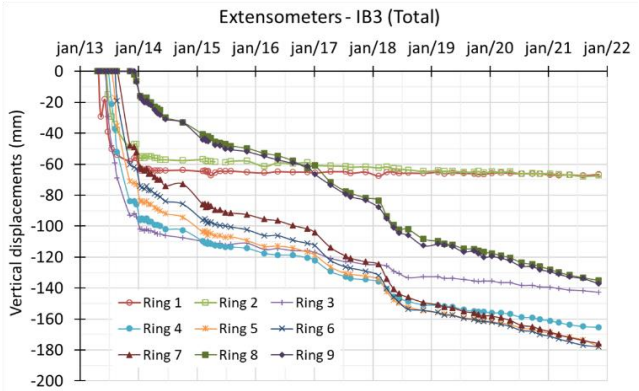

Figure 2. Total vertical displacements at IB3.

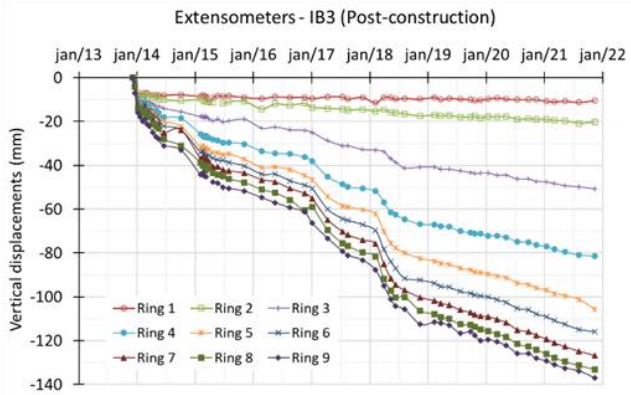

Figure 3. Post-construction vertical displacements at IB3.

Figure 4 presents the horizontal displacements in the main axis of inclinometer IB3. To associate the displacements in the vertical and horizontal directions of the rockfill, Figure 5 depicts the evolution of horizontal movements in the points of the inclinometer at the closest elevations of the magnetic rings. These readings suggest a significant increase in the horizontal displacement at the three moments previously identified in the vertical direction. Additionally, these instruments also show the tendency of a periodic horizontal movement of the embankment, superposed with those discussed moments of abrupt displacement and with long-term deformations. These fluctuating movements are significant smaller than the recorded in the moments of abrupt vertical deformation, but still evident.

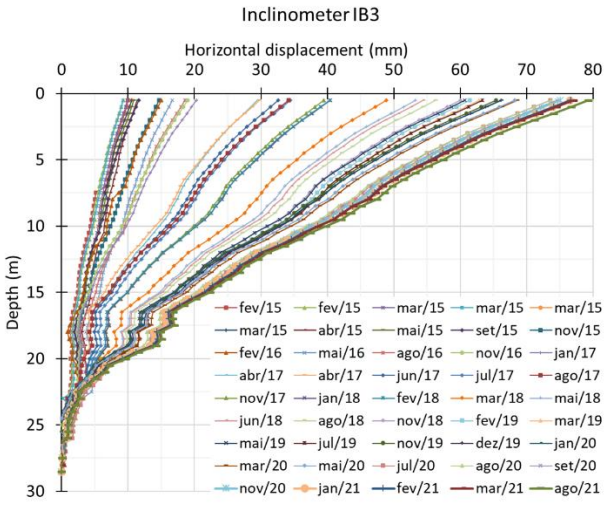

Figure 4. Horizontal displacements at inclinometer IB3.

Figure 6 presents the relations between post-constructive vertical and horizontal displacements for the extensometers on IB3. In terms of this relation, an interesting aspect is that the ratio in which the displacement of the rings occurred did not show any tendency of shift caused by the collapses. Except for the extensometers located at the lowest elevation (Rings 1 and 2), which did not exhibit clear tendencies in any direction, the trends of the ratio of vertical and horizontal displacements remained virtually unchanged after the collapses, suggesting that these events affected the movements in both directions in a similar manner. It is also noticeable that the ratio between vertical and horizontal displacement tends to increase with depth.

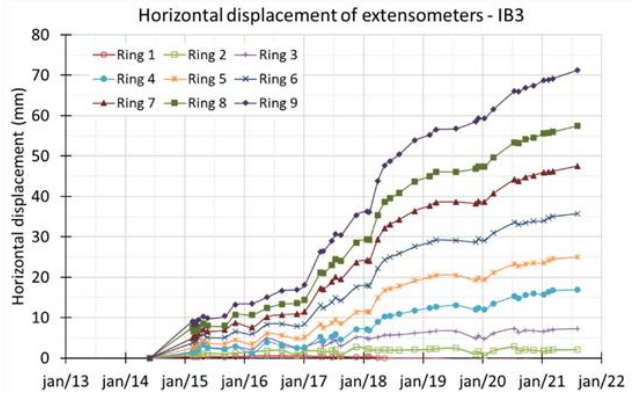

Figure 5. Horizontal displacements elevations equivalents to the vertical extensometers at IB3.

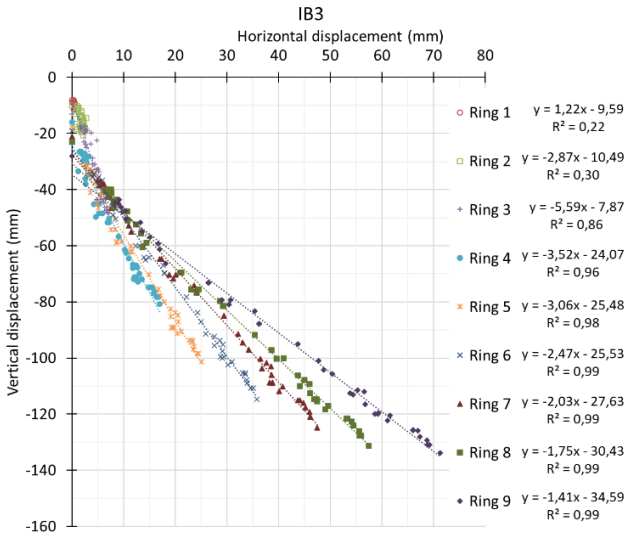

Figure 6. Relation between vertical and horizontal post-constructive displacements on IB3 section.

4 ENVIRONMENTAL CONDITIONS AND DEFORMATION MECHANISMS

Figure 7 presents the monthly measurements of precipitation and potential evaporation. The moments of abrupt movements recorded in the displacements monitoring devices coincide with intense pluviosity and low potential evaporation. The sudden deformation due to intense wetting of a rockfill mass can be often linked to the well-known phenomenon of wet-induced collapse, which is associated to the increase of humidity in the rockfill voids, causing a reduction of suction in the pores of the rock particles (Alonso and Cardoso, 2010, Alonso and Tapias, 2019). This loss of suction permits the fractures of the rock elements to suddenly propagate at a much higher velocity, causing rapid particle breakage, leading to rearrangement of these fractured elements and consequent reduction of the rockfill voids. This phenomenon is expected to occur every time a new lowest value of suction is reached in the rock pores, until zero suction is reached for the first time (Alonso et al., 2005).

All 3 moments of abrupt increase in displacement rates correspond to the highest record of accumulated precipitation until that moment. In addition, no historical maximum occurred without an abrupt settlement, causing this interesting one-to-one relation. Furthermore, in every moment of abrupt settlement, the amount of precipitation surpassed the potential evaporation, which occurred only a few times (17 of 108 months) in the period of monitoring. It should be acknowledged, though, that the excess precipitation for the second collapse does not correspond to a new maximum. It is consistent, however, to the largest period recorded in which the balance of rainfall is positive: 3 consecutive months. These observations indicate that wet-induced collapse is probably the mechanism responsible for the abrupt settlements recorded in the rockfill.

Figure 8 presents the variation of water level in the reservoir. Despite acknowledging pluviosity as the main cause for the deformations, it is possible that the variations of the water level in the reservoir have also affected the deformations of the rockfill, and therefore their influence should be assessed as well. Since RCM has an impervious HPDE membrane internally, the influence of the water level is restricted to the load on the embankments, without any percolation on the rockfill or foundation directly associated to the pond. Table 3 presents the variation in the cartesian stresses calculated by a stress-strain model of the section of inclinometer IB3, estimated in points halfway between the rings, comparing before and after the filing of the reservoir. The results show that the variation in the vertical stress due to filling is practically negligible in the vertical direction, but significant on the horizontal direction.

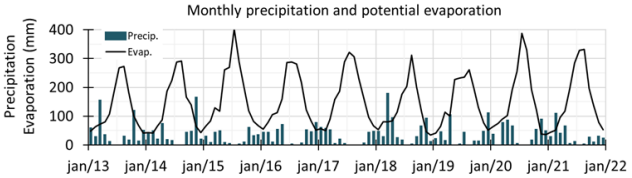

Figure 7. Monthly precipitation and potential evaporation.

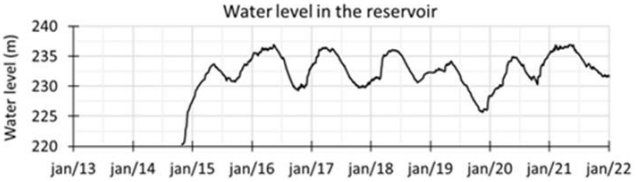

Figure 8. Water level in the reservoir.

Table 3. Variation of vertical and horizontal stresses with filing of the reservoir.

Elevation	Variation on effective stress	
	Vertical	Horizontal
Datum - Ring 1	+2,7%	+1,9%
Ring 1 - Ring 2	+2,5%	+5,2%
Ring 2 - Ring 3	+2,2%	+10,0%
Ring 3 - Ring 4	+2,0%	+17,4%
Ring 4 - Ring 5	+1,7%	+25,4%
Ring 5 - Ring 6	+1,1%	+31,7%
Ring 6 - Ring 7	+0,8%	+36,1%
Ring 7 - Ring 8	+0,4%	+28,0%
Ring 8 - Ring 9	+0,3%	+9,2%

Another relevant aspect regarding the variation of the reservoir level is that none of the 3 moments of collapse corresponded the maximum level recorded in the reservoir. In that matter, in the first semesters of 2016 and 2021 water levels were higher than in any of the moments of abrupt deformation, and on these occasions the movement rates did not show significant increase.

Besides the small effect on the vertical stress underneath the centre of the crest and the fact that the moments with the highest water level do not correspond to the highest settlement rates, two other relevant aspects support the conclusion that variation of water load does not play a key role in the abrupt vertical displacements. First, the extensometers and superficial settlement beacons did not exhibit any clear tendency of swell associated to the partial drawdowns of the reservoir. If those increases in vertical stress were the main cause for additional compression of the rockfill, decreases should produce some level of extension – or at least significant reduction in the settlement rate –, which did not happen. The second point relates to the fact that after the maximum load was reached for the first time, the rockfill would be subject to unload-reload cycles, in which the stiffness of the material would be substantially higher. Therefore, the deformations associated to the fluctuation in the reservoir level following that moment should be much smaller than the associated to the first filling, differently from what really occurred.

Concluding that collapse due to wetting is the main mechanism responsible for the abrupt settlements recorded in RCM suggests that Rings 1 and 2 of all extensometers, which did not show clear pattern shift for their deformation trends through time, probably have reached very low values of suction (perhaps even zero) at least once, probably during construction were seepage may have happened before the lining installation. There are no measurements to confirm that proposition, but these are the rings located at the lowest elevation in the rockfill, placing them closer to the bedrock seepage and further from the atmosphere, thus less subject to evaporation in dry periods than the more superficial rings.

Regarding the association with environmental conditions and measurements of the inclinometers, substantial increases in the horizontal displacements were recorded concomitantly to the abrupt settlements. In the moments of wet-induced collapse, the horizontal movements essentially follow the same behaviour registered for the vertical displacements. Therefore, all considerations made regarding the association of settlements and pluviosity is valid for the horizontal movements as well. The moments of the 2nd and 3rd collapses are quite evident, and although before the 1st collapse there was only the initial measurement 8 months earlier, the horizontal displacements registered next are substantial, suggesting that a collapse could have happened.

On the other hand, the important influence of the water level in the reservoir on the horizontal stress acting on the rockfill is fairly noticeable on the displacements recorded in the inclinometers, contrasting with the reduced impact seen in the vertical direction. Occurring simultaneously with long-term deformations, the oscillation of horizontal movements related to the fluctuation on the water level is very clear. The superposition of these two phenomena produces a curve that resembles a periodic relation (due to the variation in the water level) around an inclined axis (due to the time dependent deformations). Rises on the reservoir levels tend to produce larger horizontal movements, while partial drawdowns generates slowing or even recuperation of those displacements. Nevertheless, the influence of wet-induced collapses still is much more prominent in terms of total displacements, with a substantial portion of all horizontal measurements being caused by them.

5 CONCLUSIONS

The analysis of the instruments monitoring movements of the embankment in association with the environmental conditions allowed to conclude that the mechanism responsible for the unexpected abrupt settlement registered in the embankment was wet-induced collapse, a very well-known post-construction deformation mechanism for rockfill. The main arguments to support this proposition are based on the fact that all collapses recorded were associated to a new maximum in the precipitation historical series, and every time a new maximum was registered, a collapse occurred. Also, every collapse occurred in months in which precipitation exceeded potential evaporation, suggesting that an increase in humidity in the rockfill was probable. The analysis of the

fluctuations of the water level in the reservoir permitted to conclude that these oscillations represented a small change in the vertical stress underneath the centre of the crest, making improbable the association of these events to the rapid settlements. Moreover, no abrupt deformation was recorded when the water level reached its maximum, and the extensometers and superficial beacons never registered swell associated to the reduction of load due to partial drawdowns of the reservoir.

All these evidences support the conclusion that the influence of the variations of the water level in the reservoir is probably very reduced and, if existent, restricted to the first filling. In addition to that, the general behaviour registered by the extensometers and superficial settlement beacons in RCM were very similar to typical deformation curves of rockfill upon wetting (Justo, 1990, Alonso et al., 2005, Alonso and Cardoso, 2010, Oldecop and Alonso, 2007).

The inclinometers demonstrated substantial increases in the horizontal movements in the same moments that abrupt settlements were recorded in the extensometers, suggesting that wet-induced collapse causes deformation in both directions. However, differently from what happened with vertical displacements, measurements in the inclinometers showed that fluctuations in the water level have impact in the horizontal movements of the rockfill. Rises in the reservoir are coincident with increases in the horizontal displacements rates, as well partial drawdowns are followed by reduction in the movements rates, eventually even indicating some recuperation in the displacements. Nevertheless, this influence is only perceptible in the periods when no collapses occur, since when the mechanisms overlap the displacements due to plastic strains are considerably larger.

ACKNOWLEDGMENTS

The authors would like to acknowledge Somincor and Lundin Mining for allowing the publication of the data in this study.

REFERENCES

Alonso, E., Olivella, S. and Pinyol, N. (2005). A review of Beliche Dam. *Géotechnique*, 55(4): 267-285. https://doi.org/10.1680/geot.2005.55.4.267.

Alonso, E., Cardoso, R. (2010). Behaviour of materials for earth and rockfill dams: Perspective from unsaturated soil mechanics. *Frontiers of Architecture and Civil Engineering in China*, 4: 1-39. https://doi.org/10.1007/s11709-010-0013-6.

Alonso, E., Tapias, M. (2019). Suction and time effects in rockfill deformation. *Intenational Journal for Numerical and Analytical Methods in Geomechanics*, 43: 1032-1050. https://doi.org/10.1002/nag.2916.

Cenor (2010). Somincor – Reservatório Cerro da Mina – Projecto de execução – Reservatório – Cortes transversais (1/2), Cenor Consulting Engineers, Lisbon, Portugal.

Cetin, H., Laman, M., Ertunc, A. (2000). Settlement and slaking problems in the world's fourth largest rock-fill dam, the Ataturk Dam in Turkey. *Engineering Geology*, 56(3-4): 225-242. https://doi.org/10.1016/S0013-7952(99)00049-6.

Charles, J. (1990). Laboratory compression tests and the deformation of rockfill structures. *In Advances in rockfill structures, edited by E. Maranha das Neves*, 1st ed., Kluwer Academic Publishers, Dordrecht, The Netherlands, 664p.

Chávez, C., Romero, E., Alonso, E. (2009). A rockfill triaxial cell with suction control. *Geotechnical Testing Journal*, 32(3): 1-13. https://doi.org/10.1520/GTJ101590.

Hunter, G., Fell, R. (2003). Rockfill modulus and settlement of concrete face rockfill dams. *Journal of Geotechnical and Geoenvironmental Engineering*, 129(10): 909-917. https://doi.org/10.1061/(ASCE)1090-0241(2003)129:10(909).

Justo, J. (1990). Collapse: its importance, fundamentals and modelling. *In Advances in rockfill structures, edited by E. Maranha das Neves*, 1st ed., Kluwer Academic Publishers, Dordrecht, The Netherlands, 664p.

Kermani, M., Konrad, J., Smith, M. (2017). An empirical method for predicting post-construction settlement of concrete face rockfill dams. *Canadian Geotechnical Journal*, 54(6): 755-767. https://doi.org/10.1139/cgj-2016-0193.

Oldecop, L., Alonso, E. (2003). Suction effects on rockfill compressibility. *Géotechnique*, 53(2): 289-292. https://doi.org/10.1680/geot.53.2.289.37265.

Oldecop, L., Alonso, E. (2007). Theoretical investigation of the time-dependent behaviour of rockfill. *Géotechnique*, 57(9): 289-301. https://doi.org/10.1680/geot.2007.57.3.289.

Proceedings of the XVIII ECSMGE 2024
GEOTECHNICAL ENGINEERING CHALLENGES
TO MEET CURRENT AND EMERGING NEEDS OF SOCIETY
© 2024 the Authors
ISBN 978-1-032-54816-6
DOI 10.1201/9781003431749-275
Open Access: www.taylorfrancis.com, CC BY-NC-ND 4.0 license

ECSMGE 24
XVIII EUROPEAN CONFERENCE ON SOIL MECHANICS AND GEOTECHNICAL ENGINEERING

Eurocode 7 – second generation reinforced fill structures

Eurocode 7 - seconde génération remblais renforcés

G. Bräu*
Technical University of Munich, Chair and Testing Institute of Soil Mechanics and Foundation Engineering, Rock Mechanics and Tunneling, Munich, Germany

N. Denies
Buildwise, Limelette, Belgium

**gerhard.braeu@tum.de*

ABSTRACT: The reinforced fill structures are well-known and established worldwide as an economic and ecological valuable construction method. In many countries, standards and recommendations exist for reinforcing steep slopes, walls, and other applications. On the European level until now, there was only a standard for the execution of such construction available, but no standard for the design. With the second generation of Eurocode 7 (EN 1997), this gap is filled. Specific requirements for reinforcing materials (geosynthetics, steel, polymeric coated steel woven wire meshes) and specific requirements for the reinforcing elements due to the environment and their interaction with the fill material are provided with basic design approaches and appropriate partial factors.

RÉSUMÉ: La technique des remblais renforcés est reconnue dans le monde entier comme une méthode de construction économique et écologique. Dans de nombreux pays, il existe des normes et des recommandations pour le renforcement des pentes raides, des parois, et d'autres applications. Au niveau européen, il n'existait jusqu'à présent qu'une norme pour l'exécution de ce type de construction, mais aucune norme pour leur dimensionnement. La seconde génération de l'Eurocode 7 (EN 1997) comble cette lacune. L'Eurocode 7 fournit des règles spécifiques pour les matériaux de renforcement (géosynthétiques, acier, treillis métalliques enduits de polymères) ainsi que des exigences spécifiques pour les éléments de renforcement tenant compte de leur durabilité et de leur interaction avec le matériau de remplissage avec des approches de dimensionnement et des facteurs partiels appropriés.

Keywords: Reinforced fill structures; soil reinforcement; geosynthetics; steel; polymeric coated steel woven wire meshes.

1 BACKGROUND

Reinforced fill structure is a well-known technique and established worldwide. In many countries, standards and recommendations exist for reinforcing steep slopes, walls, and other applications. On the European level, there is only a standard for the execution of such construction: EN 14475, but no standard for the design. With the new generation of Eurocode 7 (EN 1997) a clause is introduced, developed from the various national design standards, to fill this gap.

Reinforcement materials such as geosynthetics and steel are used for decades and the material properties and their testing are regulated in different European standards. Combined products such as polymeric coated steel woven wire meshes are currently difficult to use in practice or cannot be used with an equivalent level of safety and robustness because they cannot be clearly assigned to known material groups and because they do not have appropriate standards. This situation is solved with the new EN 1997 by specific rules for these products.

The clause "Reinforced Fill Structures" (EN 1997-3, Clause 9) is part of EN 1997 and the design principles are defined elsewhere in the code (EN 1990, EN 1997-1 and -2). Also is the calculation of overall stability of slopes and embankments (EN 1997-3, Clause 4), of the bearing and sliding resistance (EN 1997-3, Clause 5) and of the static equilibrium (EN 1997-3, Clause 7) defined in the aforementioned clauses. EN 1997-3, Clause 9 therefore concentrates on the effect of the reinforcement used and the special features of the interaction between fill material and reinforcement and their consideration in the design.

This publication does not intend to go into details of EN 1997-3, Clause 9, but tries to highlight the important topics.

2 FIELD OF APPLICATION

EN 1997-3, Clause 9 deals with all kinds of applications where engineered fill (not asphalt) is reinforced. Reinforcing of ground (not engineered

fill) is dealt in other clauses (e.g. Clause 8 Anchors, 10 Soil nailed structures, 11 Rock bolts and rock surface support, 12 Ground improvement).

Especially mentioned are reinforced walls and abutments, reinforced slopes, basal reinforcement for embankments (including load transfer platforms over inclusions and areas prone to development of voids) and reinforcement along slope surface (veneer reinforcement) (see Figure 1).

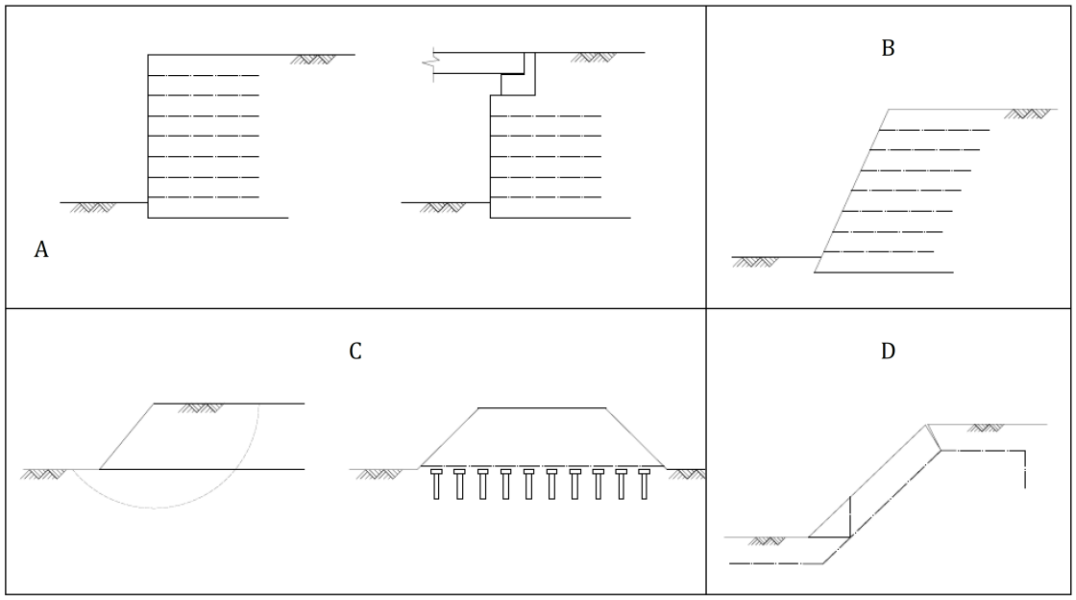

Figure 1. Reinforced fill structures: A - reinforced wall and abutments, B - reinforced slope, C - basal reinforcement for embankments (including load transfer platforms over inclusions and areas prone to development of voids), D - Veneer reinforcement (EN 1997-3, Clause 9).

Geotextile encased columns are covered in EN 1997-3, Clause 12 “Ground Improvement”.

3 BASIS OF DESIGN

General design principles (e.g. design situation, geometrical properties, zone of influence, actions), given in EN 1997-1, are also valid for reinforced fill structures.

3.1 Environmental influences

An exception are the environmental influences as they may affect the reinforcing material directly. Chemical components of ground (soil outside the reinforced construction) or groundwater may influence the durability of all reinforcement as well as ultra violet exposure and high temperature especially for polymeric based reinforcement. Therefore their properties have to be tested in the appropriate extent.

3.2 Ultimate limit states

The ultimate limit states are described and defined by EN 1997-3, Clause 9 in detail. On the one hand, they refer to other clauses when the reinforcement has no influence (e.g. failure entirely outside of the reinforced fill structure):

- calculation of overall stability of slopes and embankments (EN 1997-3, Clause 4);
- calculation of the bearing and sliding resistance (EN 1997-3, Clause 5);
- calculation of the static equilibrium (EN 1997-3, Clause 7).

On the other hand, they are specific whenever the reinforcement is involved in the failure mechanism, mainly:

- rupture of the reinforcing element;
- rupture of any connection between a reinforcing element and a facing element of the structure (reinforcement at the connection, facing element at the connection, connector);
- rupture of any seam or joint between the reinforcements themselves;
- failure along slip surfaces that pass wholly or partially through the reinforced block, either through the fill or along a reinforcement (sliding);
- failure at the interface between the fill and the reinforcing element (pullout).

Besides other aspects also the topic “excessive deformation” of the reinforced fill structure is mentioned as an ultimate limit state (and not as a serviceability limit state), because this might cause failure of nearby structures. Many published

measurements however show that the deformations of well-designed reinforced structure are at no risk and that the structures are ductile due to the reinforcement used.

A particular concern in the drafting of this clause was the clear separation of failure mechanisms that affect the reinforced fill body and those that exclusively affect the facing and the connection of the reinforcement there. Therefore, possible ultimate limit states for the facing system are mentioned, mainly:

- structural and equilibrium failure of the facing element;
- connection failure between reinforcement and facing units;
- shear failure between face elements i.e. bulging;
- shear failure between face elements and reinforcements.

It is obvious that the most critical failure mechanism (whichvere ULS it originates from) has to be found wherever it occurs in the reinforced fill structure.

3.3 Serviceability limit states

The serviceability limit states deal with the different deformations that might occur. The consideration of the following main topics are listed:

- deformations of the reinforced fill structure itself;
- differential settlement along the facing due to subsoil deformation;
- differential movement between facing and reinforcing elements;
- deformation of the reinforced fill structure, which can cause serviceability limit states of nearby structures or services that rely on it;
- deformations of the facing system.

Although the items are obvious, the calculation with analytical methods is often not possible. The calculation of the settlement of a structure is standard, but horizontal deformations depend on the interaction of reinforcement and fill material and soil. The behaviour can, if at all, generally only be determined using numerical methods or estimated using measurements on existing monitored structures.

4 MATERIALS

The chapter “Materials“ deals with all materials involved, whereas for “engineered fill“ material within the reinforced zone and the “ground“ (soil outside the reinforced zone) only references are also given. Specific requirements are given for the materials used as reinforcement or for the facing system.

4.1 Geosynthetics

For geosynthetics, a lot of European standards are available. The most relevant standard is EN 13251 which deals with the characteristics of geotextile-related products required for use in earthworks, foundations and retaining structures and the marking of these products. Relevant tests needed for reinforcements are referred, mainly for the determination of their characteristic tensile strength (T_k) based on EN ISO 10319. In order to use this value T_k for the design service life, reduction factors (well known in most national standards) must be taken into account for the:

- tensile creep rupture or excessive deformation due to sustained static load at the design temperature;
- mechanical damage during transportation, installation and execution;
- weathering;
- chemical and biological degradation at the design temperature;
- intense and repeated loading (fatigue);
- joints and seams between geosynthetic reinforcing elements.

Reference is especially made to ISO/TS 20432 for the determination of these reduction factors, which may mean adjustments to the partial safety factors discussed later when implemented in national standards (e.g. National Annex to EN 1997).

4.2 Steel

For reinforcement made of steel (strips, bars or rods, wire meshes, etc.) the appropriate material standards are referred as well as the standards for galvanization. The main issue with steel is corrosion which is introduced by using the net reduced cross-sectional area of the reinforcing element, allowing for the effects of potential corrosion. For determining this value, requirements are given based on electro-chemical properties (cf. EN 14475:2006) by corrosion parameters for galvanized and non-galvanized steel with or without water and corrosion concentration factors taking into account the geometry and dimensions of the steel reinforcement.

Long-term effects of sustained load in reinforcement (creep), long-term changes in fill properties, and potential damage of the reinforcement during transport, storage and installation shall be considered anyhow.

4.3 Polymeric coated steel woven wire meshes

Polymeric coated steel woven wire meshes as reinforcement material are a mixture of the above-

mentioned steel and polymeric components. This leads to confusion in the practice, because often not appropriate rules for steel or geosynthetics are used leading to an economical benefit of the polymeric coated steel woven wire meshes. Here EN 1997-3, Clause 9 is attempting for the first time to specify a clear procedure for this specific material. As for the other materials, reduction factors are defined for the effects of mechanical damage to the steel during transportation, installation, and execution and for the adverse effects of degradation of the element by corrosion over the design service life of the structure. The latter factor is to be determined due to the local loss of protection caused by mechanical and chemical damage to the polymeric coatings in the long term. The loss of strength of the material for the service life of the structure has to be determined due to the long-term effects of sustained load in reinforcement (creep) and long-term changes in fill properties.

4.4 Material for facings

There is a great variety of materials for the facings. The main materials (concrete, steel, masonry, timber) are mentioned with their appropriate Eurocode or material standards.

4.5 Other materials

For all reinforcement and facing materials, an opening phrase is given to allow the use of not-mentioned materials and to allow the development of new materials. They have to follow appropriate material standards, that might be defined in national standards (e.g. National annex to EN 1997).

5 GEOTECHNICAL ANALYSIS AND ULTIMATE LIMIT STATES

For the calculation of external and compound failure mechanisms in a reinforced fill structure, the references are given to other clauses whereas the benefits of the reinforcing elements are described in Clause 9.

For internal failure mechanisms and for design procedures specific to the application, different approaches exist in Europe. They are mentioned with references to the national standards and recommendations, mainly (in alphabetic order):

- ASIRI, Recommandations pour le dimensionnement, l'exécution et le contrôle de l'amélioration des sols de fondation par inclusions rigides;
- BS 8006-1, Code of practice for strengthened / reinforced soils and other fills;
- CUR 226 Design guideline basal reinforced piled embankments;
- EBGEO, Recommendations for design and analysis of earth structures using geosynthetic reinforcements;
- NF P 94 270 Calcul géotechnique - Ouvrages de soutènement - Remblais renforcés et massifs en sol cloué.

Reinforced slopes, walls, and bridge abutments should be verified using one or more of the following:

- coherent gravity method;
- tie-back wedge method;
- multiple wedge method or;
- slope stability methods.

Basal reinforcement for embankments, load transfer platforms over discrete ground improvement, overbridging systems and veneer stability are also listed in EN 1997-3, Clause 9 with their essential requirements. Detailed design approaches still have to be defined or developed by national bodies.

The effect of a reinforcing element for the calulation is based on the tensile resistance (determined specific for each type of reinforcing material), the pull-out resistance and the resistance in direct shear. The latter two resistance values are determined in EN 1997-3, Clause 9 for sheet and discrete reinforcement elements. Each value gets assigned a partial factor of safety that are presented in Table 1. The table shows in the first three lines the references to the design procedures in the basic clauses for the aforementioned failure mechanisms. For the internal failure mechanisms, the references to EN 1990:2023 and the Verification Cases (VCs) are given.

The following lines of the table present the partitial factors to be adopted for the reinforcing and the facing elements whenever such an element is impacted by a failure mechanism. The presented values are the result of a european compromise leading to higher and lower values compared to the actual national standards. They are selected in such a way that a design with them enables a safe construction taking into account that the reduction factors are derived based on the procedure described in the “Material“ section (e.g. for geosynthetics especially according to ISO/TS 20432).

As the table is NDP (national determined parameter), each country has the possibility to define other values in national standards. They can be defined e.g. by comparative calculations ensuring the continuity of their current level of safety.

Table 1. Partial factors (NDP) for the verification of resistance of reinforced fill structures for fundamental (persistent and transient) design situations from EN 1997-3, Clause 9.

Verification of	**Partial factor on**		**Symbol**	**Material Factor Approach**	**Resistance Factor Approach**
Overall and compound failure mechanisms	See Clause 4				
Bearing resistance and sliding	See Clause 5				
Overturning	See Clause 7				
Internal failure mechanisms	Actions, Effect of actions		γ_F, γ_E	VC3[a]	VC1 [a]
	Ground properties		γ_M	M2[b]	Not factored
Pull-out and direct shear	Pull-out resistance of reinforcement		$\gamma_{R,po}$	Not factored	1,25
	Resistance to direct shear along interface		$\gamma_{R,ds}$	Not factored	1,25
Rupture of reinforcing element	Tensile resistance of	geosynthetic reinforcement	$\gamma_{M,gs}$	1,25	
		structural steel per EN 10025-2 or EN 10025-4	γ_{M0}	specified in EN 1993-1-1	
			γ_{M2}	specified in EN 1993-1-1	
		reinforcing steel per EN 10080	γ_S	specified in EN 1992-1-1	
			γ_t	1,25	
		polymeric coated steel wire mesh reinforcement	$\gamma_{M,pwm}$	1,25	
Rupture of connections to facing	Tensile resistance at connection	Reinforcement	$\gamma_{R,con,el}$	As specified above for rupture of reinforcement	
		Connector	$\gamma_{R,con,c}$	As specified in the relevant material Eurocode	
		Facing element	$\gamma_{R,con,f}$	As specified in the relevant material Eurocode	

a Values of the partial factors for Verification Cases (VCs) 3 and 4 are given in EN 1990:2023, Annex A.

b Values of the partial factors for sets M1 and M2 are given in FprEN 1997-1:2024, Table 4.8.

6 GEOTECHNICAL ANALYSIS AND SERVICABILITY LIMIT STATES

The clause about serviceability limit states simply refers to previous clauses 4, 5 and 7. As the modelling of the system “fill material/reinforcement“ is still not finally solved, it is rarely possible to use analytical methods. With numerical methods the behaviour could be modelled in some cases, but have to be verified with site experience. As this is often not possible or cost- and time-consuming, EN 1990:2023 allows the omission of the verification of serviceability limit states of reinforced fill structures provided that ultimate limit states are verified.

7 FINAL CHAPTERS AND ANNEX

The last chapters in EN 1997-3, Clause 9 are following the general structure of EN 1997-3 and give general hints and references for the implementation of design (inspection, monitoring and maintenance), testing and reporting.

The (informative) annex to this Clause 9 has a long history from a short version via a version as a handbook back again now to a very short version. The final consideration of the involved countries was that each country will prepare its own annex. Countries that want to adopt the annex directly should be warned that a design of reinforced structures with this standard and its default annex version will still require additional contribution from other guidelines regarding the details of design. The standard aims to provide only a general framework for design.

8 CONCLUSIONS

With the 2nd generation of EN 1997-3 a widely recognized, often already nationally standardised, economic and sustainable construction method is harmonised at the European level and makes it available to a wider range of users. This is a major step, but one that has also involved many years of work. The base for the design is now given in the 2nd generation of EN 1997, although details and checks of the safety levels to be achieved are still pending at the beginning of 2024. Also updates of related standards have to follow (e.g. EN 14475).

ACKNOWLEDGEMENTS

The present clause "Reinforced Fill Structures" of EN 1997-3 2nd Generation is based on preliminary work in various working groups since 2011 under the leadership of my predecessors Martin Vanicek (Czech Republic) and Nicolas Freitag (France). The active members of all working groups until now have been consistently active over many years with great commitment, great tenacity and a strong desire for agreement and harmonization. I want to take this opportunity to express my sincere thanks to all of them!

The text of this paper contains many phrases derived from EN 1997-3, Clause 9 which is the nature of things. Many thanks to CEN/TC 250/SC 7 for their understanding and support.

REFERENCES

EN 1990:2023, Eurocode - Basis of structural and geotechnical design (under development).

EN 1997-1 Eurocode 7 - Geotechnical design - Part 1: General rules (under development).

EN 1997-2 Eurocode 7 - Geotechnical design - Part 2: Ground properties (under development).

EN 1997-3 Eurocode 7 - Geotechnical design - Part 3: Geotechnical structures (under development, basis for this paper: CEN/TC 250, N1739 prEN 1997-3:2023 CIB draft, 12/2023).

EN ISO 10319: 2015. Geosynthetics – Wide-width tensile test.

EN 13251, Geotextiles and geotextile-related products - Characteristics required for use in earthworks, foundations and retaining structures.

EN 14475:2006, Execution of special geotechnical works - Reinforced fill.

ISO/TS 20432:2022, Guidelines for the determination of the long-term strength of geosynthetics for soil reinforcement.

ASIRI (2012), Recomandations pour le dimensionnemant, l'exécution et le controle de l'amélioration des sols de foundation par inclusions rigides., Presse de Ponts. ISBN 978-2-85978-462-1.

BS 8006-1, Code of practice for strengthened/ reinforced soils and other fills.

CUR226 van Eekelen, S.J.M. and Brugman, M.H.A. editors (2016), Design guideline basal reinforced piled embankments (CUR226). CRC press, Delft, the Netherlands (English translation). ISBN 9789053676240.

EBGEO, Recommendations for design and analysis of earth structures using geosynthetic reinforcements, (English Translation) Deutsche Gesellschaft für Geotechnik, Ernst & Sohn, München, Germany, 2011.

NF P 94 270 Calcul géotechnique - Ouvrages de soutènement - Remblais renforcés et massifs en sol cloué.

Proceedings of the XVIII ECSMGE 2024
GEOTECHNICAL ENGINEERING CHALLENGES
TO MEET CURRENT AND EMERGING NEEDS OF SOCIETY
© 2024 the Authors
ISBN 978-1-032-54816-6
DOI 10.1201/9781003431749-276
Open Access: www.taylorfrancis.com, CC BY-NC-ND 4.0 license

ECSMGE 24
XVIII EUROPEAN CONFERENCE ON SOIL MECHANICS AND GEOTECHNICAL ENGINEERING

The implications of poor leadership on geotechnical risk

Les implications d'un mauvais leadership sur le risque géotechnique

C.A. Bridges*
Queensland University of Technology, Brisbane, Australia
**chris.bridges@hdr.qut.edu.au*

ABSTRACT: Major infrastructure projects require that a wide range of design and construction specialists be fully integrated in order to achieve the project goals. Of critical importance to these projects are the geotechnical engineers who work on the project from investigation through design and onto construction. The failure of geotechnical teams and engineers to adequately integrate into a wider team can result in greater risks being taken by the project. Through a case study of a major infrastructure project, this paper discusses how issues can arise and the consequences that can result. It then presents thoughts on how they can be overcome with appropriate leadership and management.

RÉSUMÉ: Les grands projets d'infrastructure nécessitent qu'un large éventail de spécialistes de la conception et de la construction soient pleinement intégrés afin d'atteindre les objectifs du projet. Les ingénieurs géotechniques qui travaillent sur le projet depuis l'enquête en passant par la conception et jusqu'à la construction sont d'une importance cruciale pour ces projets. L'incapacité des équipes géotechniques et des ingénieurs à s'intégrer adéquatement dans une équipe plus large peut entraîner une prise de risques plus importante pour le projet. À travers une étude de cas d'un projet d'infrastructure majeur, cet article explique comment les problèmes peuvent survenir et les conséquences qui peuvent en résulter. Il présente ensuite des réflexions sur la manière de les surmonter grâce à un leadership et une gestion appropriée.

Keywords: Leadership; risk.

1 INTRODUCTION

Geotechnical risks can result in failures on projects when they are not effectively communicated by geotechnical engineers or understood by non-geotechnical engineers. For risks to be appreciated by non-geotechnical engineers, they have to have confidence in the geotechnical engineers communicating those risks.

On a major infrastructure project in Eastern Australia, the geotechnical design team was identified as having issues of poor performance. This resulted in a lack of confidence in the ability of that team. Once these issues were addressed, the geotechnical site team was identified as having similar concerns. This paper presents an analysis of the team, what caused the poor performance issues, and how these were resolved. The paper concludes with some recommendations for team leaders on similar projects.

2 THE PROJECT

The project consisted of the widening 11 km of an existing motorway from four-lanes to six-lanes. This involved major earthworks, new bridges, ground treatment and new pavements. The project cost over AUD 1.1 bn.

The works were undertaken under a Design and Construct contract for the State Road Authority with a major contractor (the Contractor) undertaking the construction supported by two design consultancies who formed a Design Joint Venture (DJV).

3 THE GEOTECHNICAL TEAM

The Geotechnical Team (GT) was made up from the two DJV companies and a specialist sub-consultant (SSC).

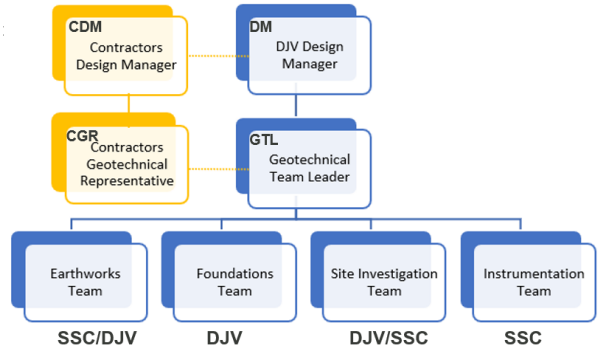

Figure 1. Geotechnical Team structure.

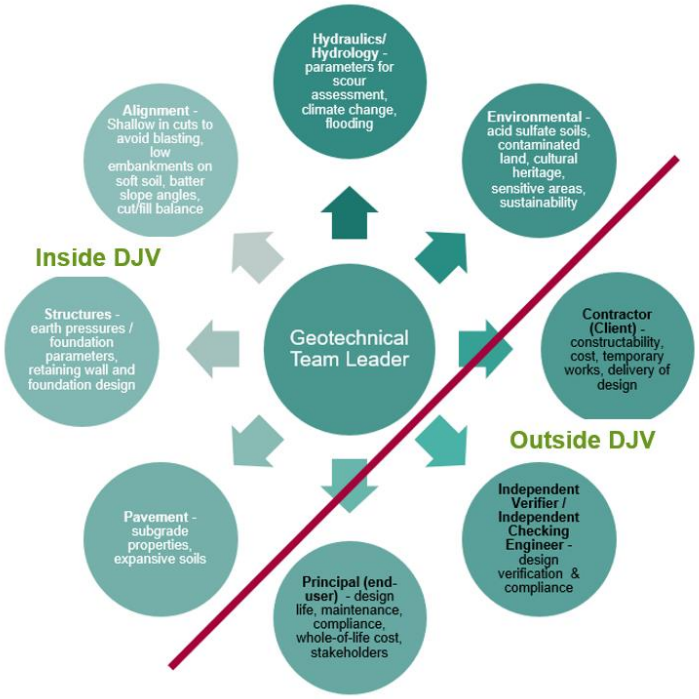

Figure 2. Geotechnical Team Leader interactions (after Bridges (2019)).

Table 1. Assessment of Geotechnical Team performance.

Input	Process	Output
Individuals: • engineers / geologists from different companies • variable levels of motivation • different levels of competencies • some diversity in the team • some pre-existing social connections • different team members working on flexible work arrangements (i.e. 4 days per week, 9-day fortnight) **Team:** • functional based • low team spirit • task focused • independent team • team chosen based on availability not ability • some tasks based on company **Environment / Context:** • large scope of work (multiple deliverables) • complicated technical task • high pressure environment • difficult client representative • tight deadlines and budget • interface with other teams	**Leadership Process:** • weak leader • developed a culture of "us vs. them" with respect to Client Representative • task-focused • poor delivery • no coaching **Team process:** • poor coordination of tasks • lack of empowerment • uneven work load and budget responsibility • diverse levels of commitment • lack of team spirit • bunker attitude • uncommunicative • lack of cohesion • no team learning or mentoring • no team building opportunities • keeping certain tasks within individual companies	**Individual:** • mental and physical fatigue • feeling of unfairness / resentment • loss of motivation **Team:** • failure to deliver on budget (4 x over budget) • low performance team • damaged reputation • siloed team **Project:** • delays due to late deliverables • design over budget • constant complaints from contractor • poor solutions

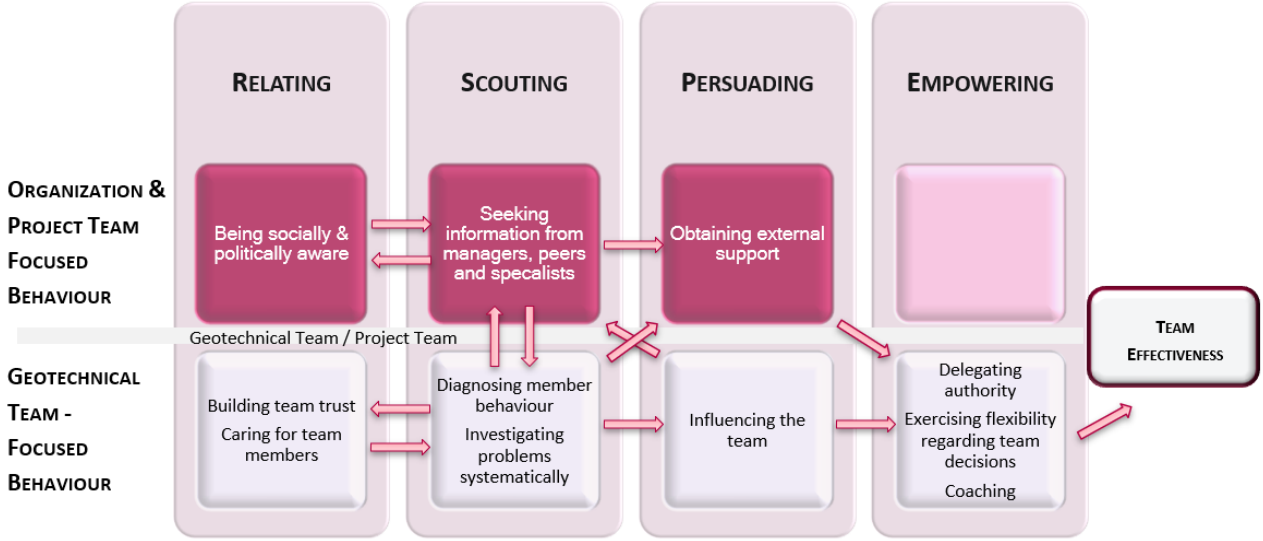

Figure 3. Team Leaders should be focused internally and externally (after Druskat and Wheeler, 2004).

During the tender phase the geotechnical support had been provided solely by the SSC, however, unable to agree terms with the Contractor after project award, the DJV took over the geotechnical design and the SSC was retained as a sub-consultant.

Starting the detailed design phase of the project, therefore, the GT had some underlying complexity around structure (Figure 1) and incorporating an unhappy SSC. Unfortunately, some of the tasks were separated by company – for example, the use of certain proprietary software - which meant that even if someone wasn't busy, they were restricted to limited tasks.

Like most major projects the GT Leader reported to a Design Manager - in this case of the DJV – who liaised with the Contractors Design Manager (CDM). The GT Leader also liaised with multiple stakeholders within the design team and externally of the DJV, including the Independent Verifier and the Principal (the State Road Authority) (Figure 2).

Both internally, within the DJV, and externally by the CDM, concern was raised about the poor performance of the GT, particularly with respect to delivery of reports and designs. This led to the CDM appointing an external Geotechnical Representative (CGR) to oversee the GT.

4 ANALYSIS

An analysis of the GT was undertaken using an Input-Process-Output assessment (Mathieu et al., 2009) and this is presented in Table 1. Outward signs of problems included poor delivery, and observations that there was no communication between the geotechnical team members – everyone quietly working at their desks all day and not speaking to each other. The GT Leader was noted especially for not delivering any of her design reports and having an incredibly fractious relationship with the CGR.

Druskat and Wheeler (2004) identify that team effectiveness increases if the team leader undertakes *boundary spanning* activities (going outside the team to get support, influence and information) and *empowers* the team through delegating, coaching and mentoring (Figure 3).

4.1 Boundary spanning

It is important to understand the political environment within a project. It is not uncommon for the geotechnical team to be accused of poor delivery or of conservatism in design – ultimately without any justification.

Building relationships within the wider design team and externally with a client or contractor and understanding the drivers of critically important individuals will, therefore, enable the GT Leader to ensure that these can be addressed – for example, programme or procurement constraints, or poor experiences on previous projects. The advantage of having trusted relationships will enable feedback early to avoid or address problems early. Unfortunately, this was not undertaken by the GT Leader on this project, and this led to GT being devoid of external support when problems arose.

As with this project, the team may not have the experience that is needed. Even if they do, it is always important that the geotechnical team is supported by others such as: reviewers, verifiers and experienced individuals from who advice can be sought. Again, the GT Leader needs to build these relationships to ensure

the right resources are available at the right time to enable delivery targets to be met.

4.2 Team focused behaviour

Working on projects has become more complex over time. Instead of one company, geotechnical teams are typically made up from engineers and geologists from different companies, including subconsultants and subcontractors. In the post-Covid19 environment, many individuals may work from home, from another state or from multiple local offices.

The GT Leader on this project did not really engage with her team which caused the dysfunction that resulted. Especially given the fact they came from different companies and were under a lot of pressure to perform. Although difficult, the GT Leader needs to be open, supportive and communicative with a sense of humour. The positivity of the GT Leader is important and likely to improve team performance (Avey et al., 2011; Balkundi et al., 2011). Each person will have different needs and expectations that will have to be met in some way (Jiang et al., 2015; Kerns, 2019) and creating a unified team culture is ultimately critical in maintaining an effective team (Ammeter and Dukerich, 2002; Druskat and Wheeler, 2004; Jiang et al., 2015; Jordan et al., 2015; Kerns, 2019; Sharma and Bhatnagar, 2017). Having the right behaviour and creating the right environment can create an engaged team.

5 CONCLUSIONS AND RECOMMENDATIONS

The performance of the GT Leader severely impacted the team and impacted the project through increased risk by late communication of project risks due to deliverable delays, which undermined the value of the geotechnical advice, and caused project delays.

In order to improve the GT Leader's performance and maintain an effective project team, the following are recommended:

- Network within your team and within the wider project team – build trusted relationships
- Minimise your own deliverables – do not get distracted from the bigger picture
- Delegate, but support (coaching)
- Provide a focus for the team – be empathetic to the client's needs
- Have a team that is adequately experienced for the task
- Obtain senior resources for review and advice on an "*as needed basis*".

REFERENCES

Ammeter, A. P., and Dukerich, J. M. (2002). Leadership, team building, and team member characteristics in high performance project teams. *Engineering Management Journal*, *14*(4), 3-10. https://doi.org/10.1080/10429247.2002.11415178.

Avey, J. B., Avolio, B. J., and Luthans, F. (2011). Experimentally analyzing the impact of leader positivity on follower positivity and performance. *The Leadership Quarterly*, *22*, 282-294. https://doi.org/10.1016/j.leaqua.2011.02.004.

Balkundi, P., Kilduff, M., and Harrison, D. A. (2011). Centrality and Charisma: Comparing How Leader Networks and Attributions Affect Team Performance. *Journal of Applied Psychology*, *96*(6), 1209-1222. https://doi.org/10.1037/a0024890.

Bridges, C. (2019). Geotechnical risk: it's not only the ground. *Australian Geomechanics*, *54*(1), 27-38.

Druskat, V. U., and Wheeler, J. V. (2004). How to Lead a Self-Managing Team. *MIT Sloan Management Review*, *45*(4), 65-71.

Jiang, W., Gu, Q., and Wang, G. G. (2015). To Guide or to Divide: The Dual-Side Effects of Transformational Leadership on Team Innovation. *Journal of Business and Psychology*, *30*(4), 677-691. https://doi.org/10.1007/s10869-014-9395-0.

Jordan, P. J., Werner, A., and Venter, D. (2015). Achieving excellence in private intensive care units: The effect of transformational leadership and organisational culture on organisational change outcomes. *SA Journal of Human Resource Management*, *13*(1). https://doi.org/10.4102/sajhrm.v13i1.707.

Kerns, C. D. (2019). Managing Teamwork: a key leadership practice. *Journal of Leadership, Accountability and Ethics*, *16*(1), 40-53.

Mathieu, J., Maynard, M. T., Rapp, T., and Gilson, L. (2009). Team Effectiveness 1997-2007: A review of recent advancements and a glimpse into the future. *Journal of Management*, *34*(3), 410-476. https://doi.org/10.1177/0149206308316061.

Sharma, A., and Bhatnagar, J. (2017). Emergence of team engagement under time pressure: role of team leader and team climate. *Team Performance Management: An International Journal*, *23*(3/4), 171-185. https://doi.org/10.1108/tpm-06-2016-0031.

Proceedings of the XVIII ECSMGE 2024
GEOTECHNICAL ENGINEERING CHALLENGES
TO MEET CURRENT AND EMERGING NEEDS OF SOCIETY
© 2024 the Authors
ISBN 978-1-032-54816-6
DOI 10.1201/9781003431749-277
Open Access: www.taylorfrancis.com, CC BY-NC-ND 4.0 license

ECSMGE 24
XVIII EUROPEAN CONFERENCE ON SOIL MECHANICS AND GEOTECHNICAL ENGINEERING

Designing a pre-load embankment for the construction of a stage over a sanitary landfill founded in soft soils

Conception d'un remblai de précharge pour la construction d'une scène au-dessus d'une décharge sanitaire fondée sur des sols meubles

A. Brito*, J. Carreto
Laboratório Nacional de Engenharia Civil, Lisbon, Portugal
**andreabrito@lnec.pt*

ABSTRACT: For World Youth Day event in 2023 (JMJ), the organizing committee selected an area in *Parque das Nações* that met the imposed requirements, notably in terms of area (for 1 million spectators) and proximity to the Lisbon center. This area, on the other hand, has the distinction of being a sanitary landfill, which was sealed in 1997 as part of the EXPO98 interventions, and which previously, in 1995, experienced a large-scale landslide in the direction of the river, with a front of 300 m of extension, enveloping the foundation up to significant depths. The fundamental cause of the landslide, according to studies undertaken at the time, was the low undrained strength of the foundation's soft soils that were still in the sub-consolidation phase, particularly at the deepest levels. Considering this scenario, LNEC performed limit equilibrium stability analyses as well as three-dimensional stress and strain finite-element analyses to estimate the magnitude and evolution of the settlements of the JMJ stage to be built in the southern area. The analyses carried out, the results of which are presented in the article, revealed the need of a pre-load embankment and were used to define criteria for the constructive phasing of the work, which was inherently dynamic and based on the outcomes of the monitoring system installed on site. Finally, values obtained from the monitoring system installed during the construction phase are compared to the values estimated during the design phase.

RÉSUMÉ: Pour les Journées Mondiales de la Jeunesse 2023 (JMJ), le comité d'organisation a sélectionné une zone du *Parque das Nações* qui répondait aux exigences imposées, notamment en termes de superficie (pour 1 million de spectateurs) et de proximité avec le centre de Lisbonne. Cette zone, en revanche, a la particularité d'être une décharge contrôlée, qui a été scellée en 1997 dans le cadre des interventions EXPO98, et qui auparavant, en 1995, avait connu un glissement de terrain à grande échelle en direction de la rivière, avec un front de 300 m d'extension, enveloppant la fondation jusqu'à des profondeurs importantes. La cause fondamentale du glissement de terrain, selon les études réalisées à l'époque, était la faible résistance non drainée des sols meubles des fondations, encore en phase de sous-consolidation, en particulier aux niveaux les plus profonds. À la lumière de ce scénario, le LNEC a réalisé des analyses de stabilité statique ainsi que des analyses par éléments finis de contraintes et de déformations tridimensionnelles pour estimer l'ampleur et l'évolution des tassements de l'étage JMJ à construire dans la zone sud. Les analyses réalisées, dont les résultats sont présentés dans l'article, ont révélé la nécessité d'un remblai de précharge et ont permis de définir des critères pour le phasage constructif des travaux, par nature dynamique et basé sur les résultats du système de surveillance installé sur place. Une comparaison est effectuée entre les valeurs obtenues dans le système de surveillance et l'estimation réalisée lors de la phase de conception.

Keywords: Sanitary landfill; pre-load embankment; soft soils; slope stability; consolidation.

1 INTRODUCTION

The use of an old sanitary landfill in the Lisbon area for the Catholic Youth World Event in August 2023 required some adjustments of the landfill. The first involved modelling the landfill in the northeast, expanding it north, and flattening the slopes. The second intervention was the construction of a stage in the southeast part of the area.

Given the history of instability of the landfill and the geological-geotechnical characteristics of its foundation, as described in the second chapter of this document, numerical analyses were performed using the limit equilibrium method to verify the global static stability of the landfill after the construction of the South stage. Given the short duration of the event, no seismic stability check was carried out.

Based on numerical analysis utilising three-dimensional finite element models and resorting to the PLAXIS 3D software, Chapter 3 presents an estimate of the magnitude and evolution of settlements and their impacts on the foundation caused by the stage load. These settlements are compared to the actual settlements measured during construction, as covered

in Chapter 4, which also covers a number of other aspects of construction.

Some final considerations are made in Chapter 5.

2 GEOLOGICAL-GEOTECHNICAL FRAMEWORK

Extensive field testing was carried out in the Beirolas sanitary landfill site, since 1984 to 2020, including boreholes, field vane tests and cone penetration tests (Figure 1). According to this geotechnical investi-gation (Figure 2), beneath the deposit of contami-nated soil and municipal waste that reaches a maximum height of 20 m is a layer of heterogeneous landfill containing silt-clay materials mixed with sand and rubble, dumped on site in the 1980s. The average thickness of this "artificial" landfill is 4 to 5 metres but decreases closer to the river until it disappears in the area covered by the tide. In some localized areas the thickness of the landfill was discovered to be higher, probably as a result of prior instability.

An alluvial deposit made of compressible silt soils with very variable thickness occurs beneath the "artificial" landfill layer. The depth of the muddy soils in the south stage area increases towards the river from 2 m to 25 m but remains constant from north to south. After the large-scale landslide in 1995, studies revealed that these soft soils had a low undrained strength and were still in the sub-consolidation phase, particularly at the deepest levels. At the base of the alluvial deposit a layer of sand and pebbles ranging in thickness from a few centimetres to 2 m have been discovered. Immediately underneath, the Miocene formation includes sandstones, calcarenites, and limestones, that are more or less marly.

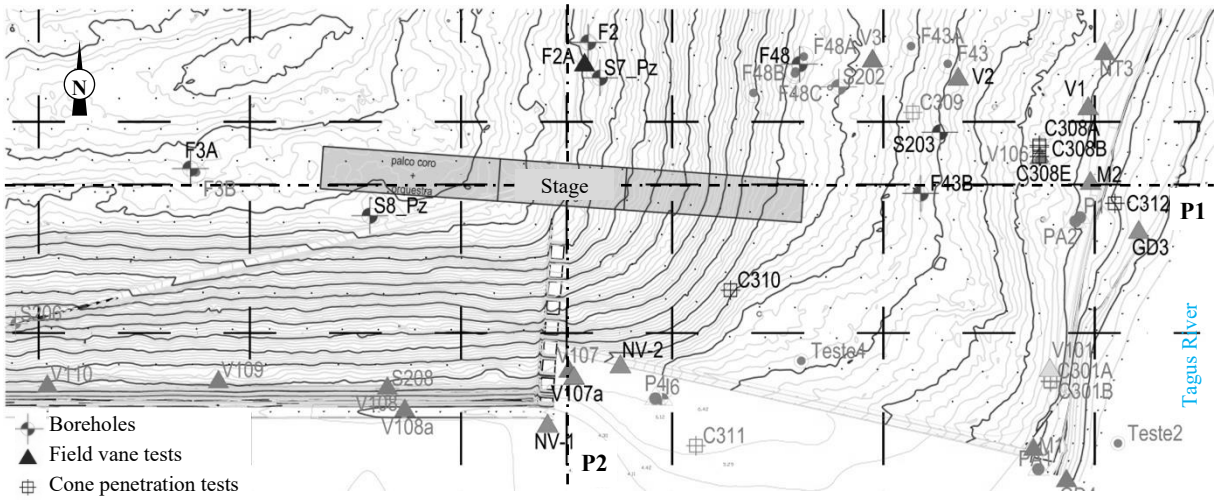

Figure 1. Ground investigations conducted around the southern stage's site.

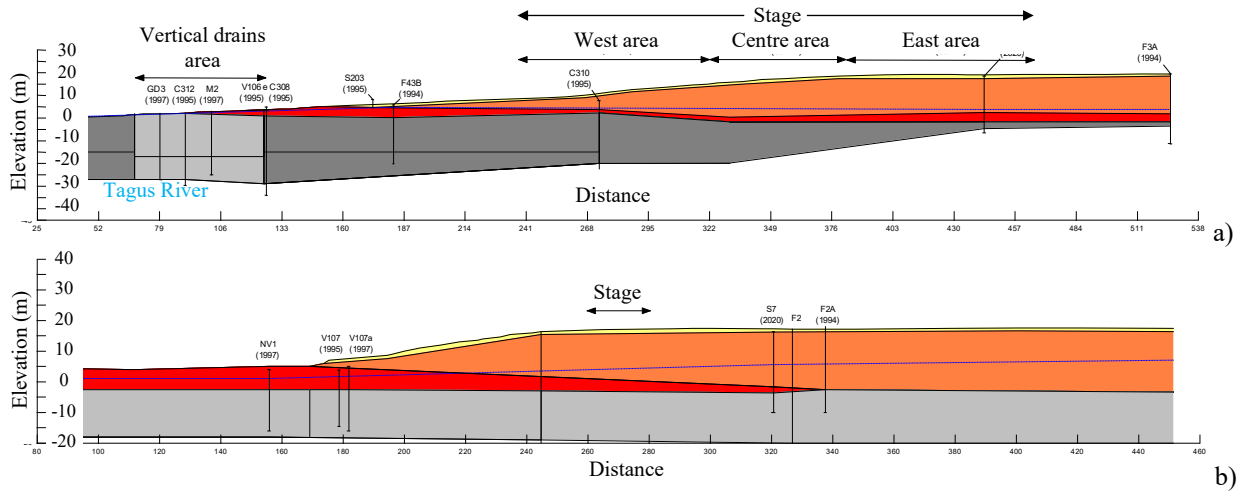

Figure 2. Geological-geotechnical cross-sections at the south stage site: a) P1; b) P2.

The sanitary landfill itself includes urban waste deposited in 1991 and layers of compost and contaminated soil deposited in cells and other areas from 1995 to 1997. Its thickness varies from about from 16 m to the west to about 4 m at the east end of the stage layout. It turned out to be a very heterogeneous landfill made up of layers of different materials with varying compressibility.

3 SETTLEMENTS ASSESSMENT IN THE SOUTH STAGE AREA

3.1 Calculation model description

The width of the calculation model illustrated in Figure 3 is equal to the width of the stage + 30 m on each side (1.5 times the width of the stage), to reduce the influence of the borders on the results. The base of the model is in the top of the Miocene formation, at -24 m. Due to calculating software constraints, the topography of the terrain was simplified by neglecting the slope in the south-north direction.

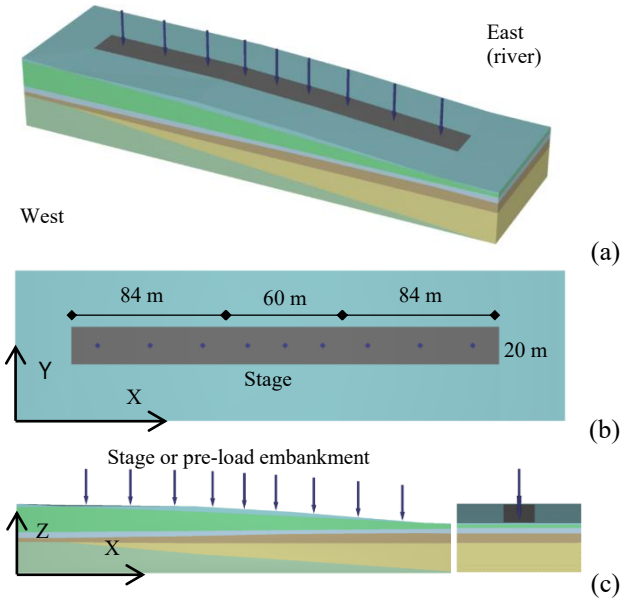

Figure 3. Calculation model geometry: (a) perspective; (b) plant; (c) elevations.

The preload embankment and stage were simulated by applying distributed loads on the area designated for the South stage. In the central and western areas, a value of 60 kPa was considered, whereas in the eastern area, a lower value, of 50 kPa, was used to ensure the overall stability of the landfill and its foundation. Calculations were carried out in two phases. Settlements caused by the construction of the stage were evaluated in the first phase. According to the JMJ organizing committee, the load imposed to the foundation due to the construction of this stage, would be 50 kN/m^2. In a second phase, a pre-load embankment was built prior to the stage, with a height of 3 m in the central and western areas. Due to stability issues, the height of this pre-load embankment was limited to 2.5 m on the east side.

Two options were considered in this second calculation. In the first option, the pre-load embankment would be removed one year after it was constructed, and the stage would be built immediately afterwards. The second option calls for the embankment to be removed six months after it is constructed and the stage to be built six months after the pre-load embankment is removed.

3.2 Materials characterization

The "soft soil" constitutive model (Bentley, 2020) was used to integrate the effect of consolidation process on the behaviour of muddy materials (superficial and deep clayey mud) as well as on the behaviour of the materials that form the sanitary landfill and the "artificial" landfill.

The elasto-plastic constitutive model with the Mohr-Coulomb failure criterion was used for the cover landfill, and the elasto-linear model was used for the Miocene formation.

Table 1 provides the values for the physical and mechanical parameters of the soft soil constitutive model materials, whereas Table 2 shows the values for the cover embankment and the Miocene formation. These parameters were based on laboratory tests conducted to date and prior LNEC studies (LNEC, 1996a, 1996b, 1997, 1999).

3.3 Calculation model results

Table 3 presents the settlement values of the stage for the most critical phases, assuming no pre-load embankment is built beforehand. The points in the table are fictious points at the top of the embankment, in the centre of each of the three regions of the stage, as shown in Figure 4. The time required to attain a consolidation degree of 95 % and 98 % is also provided in the same table. Table 4 presents the total settlement of the foundation considering the pre-load embankment construction.

According to Table 3, stage settlements can achieve significant values of the order of 0.29 m, but with reduced relevance in terms of differential settlements, although with the potential to affect its serviceability if built one year before the JMJ event.

Table 1. Parameters adopted for materials with soft soil constitutive model.

Description	γ (kN/m³)	e_0	Cc	Ce	ϕ'(º)	c' (kPa)	k (m/day)
Sanitary landfill	15,4	0,5	0,2	0,02	25º	10	0,086
"Artificial" landfill	18,0	0,3	0,1	0,04	25º	0,3[1]	1,64 x 10^{-4}
Superficial clayey mud (up to -5 m)	18,8	1,2	0,2	0,09	28º	0,3	2,25 x 10^{-5}
Deep clayey silt	16,5	1,8	0,2	0,04	28º	0,3[1]	1,11 x 10^{-5}

γ – unit weight; e_0 – initial void ratio; C_C – compression index; Ce – swelling index; ϕ` – effective friction angle; c` – effective cohesion intercept; k – permeability coefficient.

Table 2. Parameters adopted for materials with elasto-plastic and linear-elastic constitutive models.

Description	γ (kN/m³)	E (MPa)	ν	ϕ' (º)	c'(kPa)	k (m/day)
Cover landfill	20	25	0,35	30	0,3	3,456
Miocene Formation	21	100	0,33	-	-	0,864 x 10^{-3}

γ – unit weight; E – deformation modulus; ν – Poisson ratio; ϕ` – effective friction angle; c` – effective cohesion intercept; k – permeability coefficient.

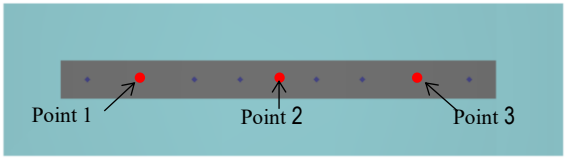

Figure 4. Location of calculation points.

Table 3. Stage settlements and time to attain a consolidation degree (without a pre-load embankment).

Point	δ_i (m)	δ_{1y} (m)	δ_{max} (m)	T_{95} (years)	T_{98} (years)
1	0.113	0.211	0.219	1,5	2
2	0.112	0.175	0.203	11	92
3	0.164	0.233	0.316	30	92
Max	0.213	0.290	0.407	-	-

δ_i – initial settlement; δ_{1y} – settlement 1 year after construction; δ_{max} – maximum settlement; T_{95} – time required to attain a consolidation degree (CD) of 95 %; T_{98} – time required to attain a CD of 98 %.

Table 4. Accumulated settlement of the foundation considering pre-load embankment construction.

Point	δ_{1y} (m)	δ_{3m} (m)	δ_{6m} (m)
1	0.256	0.245	0.246
2	0.213	0.205	0.206
3	0.227	0.235	0.239
Max	0.298	0.297	0.302

δ_{1y} – foundation settlement after 1 year of pre-load; δ_{3m} – accumulated settlement of the foundation 3 months after stage construction; δ_{6m} – accumulated settlement of the foundation 6 months after stage construction.

Because equal compressibility was assumed for both materials, stage settlement increases as the sum of the thickness of the sanitary landfill and the muddy soils increases. This explains why point 1 has a higher settlement than point 2 and point 3 has a higher settlement than point 1. However, results show that the closer the river, the slower the evolution of the settlements, i.e., the time necessary to achieve the same consolidation degree (CD). Therefore, even though the maximum settlement (considering a CD equal to 98 %) of point 3 is 40 % greater than that of point 1, this relationship is only 1.1 times at the end of one year.

Considering the magnitude of the settlements obtained in these calculations, as well as the fact that the consolidation of the muddy soils under the action of that load is still far from complete in a significant area of the stage at the time of the event, a method to reduce stage settlement, without causing environmental impacts was investigated. This approach entails constructing a pre-load embankment prior to the construction of the stage and leaving it *in situ* for 6 months to one year to allow the foundation ground to be consolidated. Table 4 shows the results of the model that simulates this solution. Figure 5 shows the distribution of settlements along a longitudinal profile of the stage and along three cross sections that include points 1, 2, and 3.

Table 5. Stage settlement after one year of pre-load.

Point	δ_i (m)	δ_{3m} (m)	δ_{6m} (m)
1	0.029	0.031	0.032
2	0.030	0.032	0.033
3	0.042	0.047	0.051

di – initial settlement; d_{3m} – settlement 3 months after construction; d_{6m} – settlement 6 months after construction.

According to the study's results, the highest foundation settlement caused by the pre-load embankment occurs in the west area, where the soft soil thickness is lower, and the sanitary landfill thickness is higher. This occurs because the time required to consolidate landfill materials is substantially shorter than the time required to consolidate muddy soils.

Six months after the construction of the pre-load embankment, the rate of settlement of the alluvial

formation is already very low, which explains the reduced increase in settlements (in the range of 1 to 8 %) after an additional six months of pre-load. The removal of the pre-load embankment causes an expansion, which is followed by ground settlement with the construction of the stage. Since the stage load is lower than the load of the embankment in its central and western areas, the accumulated settlement of the foundation is smaller than that recorded before the removal of the pre-load embankment. Due to the process of consolidation of the foundation ground, the longer the stage's lifespan, the greater the settlements it will suffer.

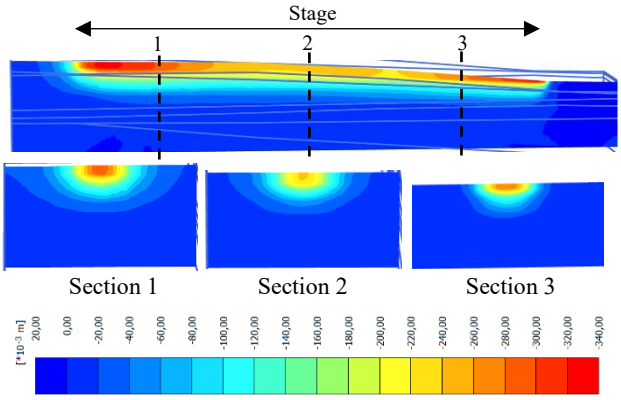

Figure 5. Foundation settlements, 6 months after stage construction (one year of pre-load).

Figure 5 also shows that the settlements of the sanitary landfill are small from a distance of the order of 25 m from the centre of the stage and that this distance decreases to the east.

4 CONSTRUCTION OF THE PRE-LOAD EMBANKMENT

Construction of the pre-load embankment began on July 7, 2022, following the installation of two multi-point magnetic extensometers on the foundation, near point 2 of Figure 4, 12 topographic marks, distributed by the stage area, and 4 topographic marks in its surrounding region.

It should be noted that the final location and layout of the stage were changed during construction, with the western half being eliminated and the stage being enlarged to 40 m in the north-south direction.

Figure 6 exhibits the evolution of the settlements measured in one of the extensometer installed at the site during pre-load embankment construction and thereafter, until its complete removal on January 4, 2023. Figure 7 presents the accumulated settlement of the same extensometer at different depths after 4 months of pre-load.

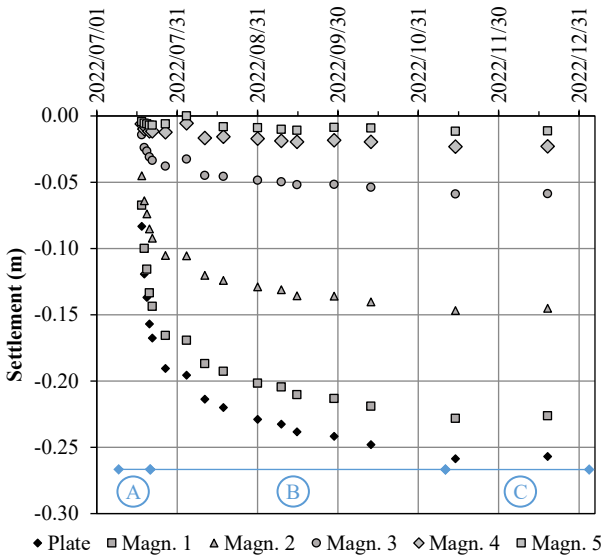

A – Construction of the pre-load embankment.
B – Consolidation period.
C – Removal of the pre-load embankment.
Figure 6. Settlement of the extensometer magnets over time.

The following conclusions can be drawn from Figures 6 and 7:

- The settling rate fell significantly six days after the completion of the pre-load embankment, on 27 July. 75% of the total settlement took place during these first 20 days, which included the pre-load embankment construction.
- By mid-August the rate at which settlements occurred was gradually decreasing. At the time of removal of the pre-load embankment, settlement occurred at an approximately constant average rate of 3 mm/week.
- The total settlement recorded by the two extensometers was of the same order of magnitude as the adjacent topographic marks. At the end of 3.5 months, the greatest value of settlement was 0.26 m.
- Figure 7 demonstrates that the total settlement of the pre-load embankment was caused by the sanitary landfill settling up to 13.5 m depth. The clayey mud layer had just a minor effect, most likely because its compressibility was lower than predicted.
- The extensometer settlement was 18 % higher than calculated at the nearest point (0.22 m) at the end of six months, but less than the maximum calculated value (0.30 m). An explanation could be related with the higher consolidation rate of the sanitary landfill.
- The removal of the pre-load embankment was anticipated since a lighter structure than the modelled one (with half the load) was adopted for the stage during the works.

- As shown in Figure 6, a minor expansion occurred when the pre-load embankment was removed.

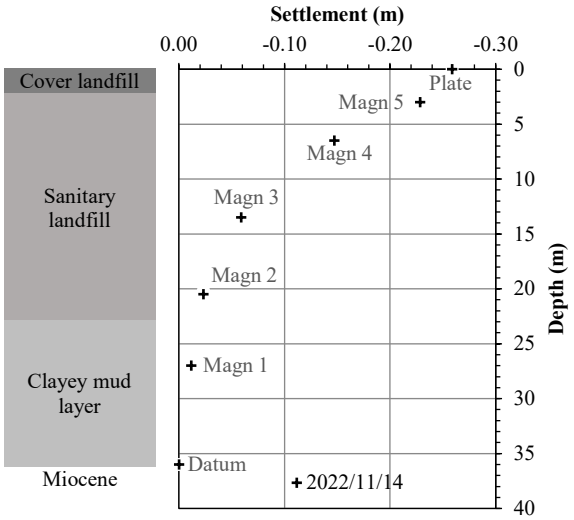

Figure 7. Accumulated settlement at different depths after 4 months of pre-load.

5 CONCLUSIONS

Given the history of instability at the Beirolas sanitary landfill and the geological-geotechnical characteristics of its foundation, numerical analyses were performed to verify the global static stability of the slopes and estimate the settlements caused by the construction of the JMJ stage.

Using a finite element model, it was also determined that stage settlements could reach an amount that would jeopardise its serviceability. Taking this into consideration, as well as the fact that the consolidation of the muddy soils under the action of that load could still be far from complete at the time of the event, a strategy to limit settlements without producing adverse environmental effects was investigated. This method entailed constructing a pre-load embankment prior to the construction of the stage, which would stay in place long enough for the consolidation of the sanitary landfill and the soft soils in the foundation to occur.

Data collected from the extensometers and topographic markers placed on the foundation and the pre-load landfill built at the forthcoming stage's location confirmed the results reached during the design phase. The use of a lighter structure for the stage, together with a small settlement rate observed by the monitoring system, allowed the pre-load embankment to be removed ahead of schedule. The stage was built without any sign of differential settlement.

ACKNOWLEDGEMENTS

The authors are grateful to *Lisboa Ocidental SRU - Sociedade de Reabilitação Urbana E.M., S.A.* for granting permission to disseminate the study's findings.

REFERENCES

Bentley (2020). PLAXIS 3D Reference Manual.

LNEC (1996a). Analysis of the solution presented by the Designer for the final coverage of the Beirolas landfill. Process. 056/1/12477. Report 77/1996 – DG/GEA (in Portuguese).

LNEC (1996b) – Addendum to the analysis of the solution presented by the Designer for the final coverage of the Beirolas landfill - Proc. 056/1/12477. Report 209/1996 – DG/GEA. (in Portuguese).

LNEC (1997) – Analysis of the area treated with vertical drains in the eastern expansion of the Beirolas landfill - Proc. 056/1/12477. Report 237/1997 – DG/GEA. (in Portuguese).

LNEC (1999) – Technical assistance to Parque Expo in the review of projects surrounding the Beirolas landfill - Proc. 056/1/13360. Report 286/1999 – DG/GEA. (in Portuguese).

Proceedings of the XVIII ECSMGE 2024
GEOTECHNICAL ENGINEERING CHALLENGES
TO MEET CURRENT AND EMERGING NEEDS OF SOCIETY
© 2024 the Authors
ISBN 978-1-032-54816-6
DOI 10.1201/9781003431749-278
Open Access: www.taylorfrancis.com, CC BY-NC-ND 4.0 license

ECSMGE 24
XVIII EUROPEAN CONFERENCE ON SOIL MECHANICS AND GEOTECHNICAL ENGINEERING

Eurocode 7 – second generation - numerical methods

Eurocode 7 – deuxième génération – méthodes numériques

S. Burlon*
Terrasol - Setec, Paris, France

H. Walter
Salzburg, Austria

C.C. Smith
Department of Civil and Structural Engineering, University of Sheffield, Sheffield, UK

**sebastien.burlon@setec.com*

ABSTRACT: The development of the second generation of EN1997 has reached its final stage. The formal vote will take place in autumn 2024. Numerical methods are now largely considered for the design of geotechnical structures both for SLS and ULS verifications in terms of mechanical and hydraulic issues. This paper presents how numerical methods are now implemented in EN 1997 and three main topics are dealt with:
- (i) SLS verifications with the importance of the choice of constitutive models in line with the geotechnical design model. Representative values of the ground properties shall account for all these situations based on the derived values presented in the ground model,
-(ii) ULS verifications with the input and ant the output factoring approaches: several examples are discussed in order how to choose and implement these two approaches. The verification of structural elements including nonlinearities is highlighted. Other approaches where geotechnical resistances may be calculated by numerical models by forcing geotechnical structures to fail by particular mechanisms are also presented.
-(iii) hydraulic verifications where numerical modelling can help the designer to check the hydraulic gradient and the variation of pore water pressures as proposed now by EN 1997 regarding hydraulic issues.

RÉSUMÉ: Le développement de la deuxième génération d'EN1997 a atteint sa phase finale. Le vote formel aura lieu à l'automne 2024. Les méthodes numériques sont désormais largement envisagées pour la conception des ouvrages géotechniques tant pour les vérifications des ELS que des ELU en termes de problématiques mécaniques et hydrauliques. Cet article présente comment les méthodes numériques sont maintenant mises en œuvre dans l'EN 1997 et trois sujets principaux sont traités:
- (i) Vérifications des ELS avec l'importance du choix des modèles de comportement en lien avec le modèle de dimensionnement géotechnique. Les valeurs représentatives des propriétés du sol doivent tenir compte de toutes ces situations sur la base des valeurs dérivées présentées dans le modèle de terrain,
-(ii) Vérifications des ELU avec les approches de factorisation d'entrée et de sortie: plusieurs exemples sont discutés afin de choisir et de mettre en œuvre ces deux approches. La vérification des éléments structuraux, y compris les non-linéarités, est mise en évidence. D'autres approches où les résistances géotechniques peuvent être calculées par des modèles numériques en forçant des mécanismes de rupture particuliers sont également présentées.
-(iii) des vérifications hydrauliques où la modélisation numérique peut aider le concepteur à vérifier le gradient hydraulique et la variation des pressions interstitielles comme proposé maintenant par le nouvel Eurocode 7 concernant les questions hydrauliques.

Keywords: Eurocode; numerical methods; partial factor; constitutive law.

1 USE OF NUMERICAL METHODS IN EN 1997-1

At the end of 1990's, when the first generation of Eurocode 7 was drafting, the use of numerical methods was at its beginning mainly due to the low computational power available. Meshes including very few elements and only 2D analysis were possible in practice. This first draft provided very limited information for geotechnical design assisted by numerical methods.

During the last 20 years, the use of numerical modelling has increased significantly with the reduction of computation time and the commercial development of many software packages (see Figure 1). In order to provide appropriate responses to this

new context, in comparison to this previous draft of EN 1997-1, the new draft deals with the use of numerical methods for the design of geotechnical structures by providing useful and applicable recommendations for the verifications of SLS (serviceability limit states) and ULS (ultimate limit states). This paper aims to address specifically three main issues: the SLS verifications, the ULS verifications and the hydraulic verifications.

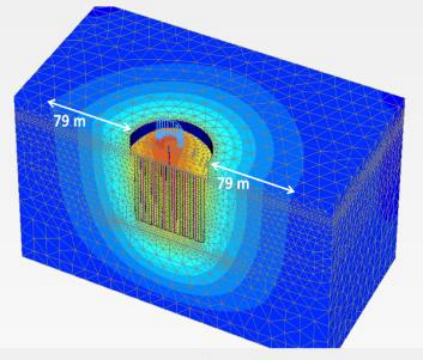

Figure 1. Example of a 3D typical mesh for a piled-raft foundation.

2 SLS VERIFICATIONS

SLS verifications are a fundamental part of the geotechnical design as they allow justification of a structure regarding its functioning under normal use, the comfort of people and the appearance of the construction works. These issues require a relevant choice of constitutive models in line with the geotechnical design model considering for each verification case the amplitude and the frequency of the loading as well as the strain or the stress range and the failure mechanism taking into account stress paths. Representative values of the ground properties shall account for all these situations based on the derived values presented in the ground model. prEN 1997-2 provides some recommendations regarding both strain and strength parameters: the complexity of the models shall be consistent with the available data and the verifications to be carried out. Ground parameters are also presented for coupled calculations (consolidation, thermos-mechanical analysis, etc.). Based on these different issues, the main issue is the selection of the ground parameters (Figure 2) from the derived values presented in the Ground Investigation Report (GIR) to generate the representative values that form the basis of the Geotechnical Design Model (GDM). Back-analysis can also be used in this way.

3 ULS VERIFICATIONS

3.1 Principles

In the second generation of the Eurocodes partial factors on actions γ_F and action effects γ_E are grouped in four Verification Cases (VC1 to VC4) in prEN 1990 (CEN 2022) for all types of structures and are partly listed in Table 1. (The tables in this paper contain considerable simplifications and omissions, refer to the tables in prEN 1990, prEN 1997-1 and prEN 1997-3 for all de-tails, Smith and Walter, 2023).

For geotechnical structures, partial factors on material strength parameters γ_M and resistances γ_R are supplied in prEN 1997-1 if they are valid for all types of geotech-nical structures, and in prEN 1997-3 if they are specific for certain types of geotechnical construction. Partial factors on material strength parameters are listed and grouped in sets M1 and M2 in prEN 1997-1 and are partly listed in Table 2.

Whether partial factors on material strength parameters (Material Factor Approach, MFA) or partial factors on resistances (Resistance Factor Approach, RFA) are used, the choice of the Verification Case and of set M1 or M2 and suggested values for partial factors on resistances are specified in prEN 1997-3 for the different types of geotechnical structure. National standards bodies may modify these specifications, including the val-ues of the partial safety factors.

A specific procedure is given in prEN 1997-1 for numerical methods. Two approaches are described and the more unfavourable of the two governs the design, currently without a distinction between different types of geotechnical construction:

- Input factoring using VC3 and M2,
- Output factoring using VC4 and M1.

These approaches are given to facilitate the straightforward use, and to take full advantage of the power of numerical methods. However, it is also clear that design check outcomes may differ if using factors for numerical methods compared to using factors for specific design calculation methods as listed in prEN 1997-3. prEN 1997-3 allows to perform ULS verifications by focusing on specific failure mechnisms: Geotechnical resistances may be calculated by numerical models by forcing geotechnical structures to fail by particular mechanisms.

Table 1. Table of values for verification cases for persistent design situations (where k_F is a consequence factor).

Type	Resulting effect	VC1	VC3	VC4
Permanent action (G_k)	unfavourable (all)	1.35 k_F	1.0	G_k is not factored
	unfav. (water)	1.2 k_F	1.0	
	favourable	1.0	1.0	
Variable action (Q_k)	unfavourable (all)	1.5 k_F	1.3	1.1
	unfav. (water)	1.35 k_F	1.15	1.0
Effects of action (E)	unfavourable	γ_E is not applied		1.35 k_F
	favourable			1.0

Table 2. Table of values for material sets for soil and fill (where K_M is a consequence factor).

Ground property	M1	M2
Shear strength in effective stress analysis (τ_F)	1.0	1.25 K_M
Coefficient of peak friction (tan ϕ'_p)	1.0	1.25 K_M
Peak effective cohesion (c'_p)	1.0	1.25 K_M
Coefficient of friction at critical state (tan ϕ'_{cs})	1.0	1.1 K_M
Shear strength in total stress analysis (c_u)	1.0	1.4 K_M

3.2 Input factoring

This approach is now mainly based on the use of shear strength reduction procedures that are fully available in many softwares. prEN 1997-1 recommends:

- (i) to reach the value γ_M 1.25 to check the geotechnical verifications,
- (ii) to check the structural forces that are obtained from this calculation with strength reduction to γ_M without or with the use of elastoplastic structural elements.

For each phase, the calculation is performed with representative values of the loads and the ground properties. Each phase can be used for SLS verifications (ignoring the results with strength reduction). The calculations can be organised according to Figure 2.

Instead of using a strength reduction procedure, the shear strength parameters can also be reduced ab initio or after previous steps with representative values of the strength parameters. One has to keep in mind that these variants can result in different displacements and different forces on the structural elements.

3.3 Output factoring

For each phase, the calculation is performed with representative values of the loads and the ground properties. Using VC4, the representative values of the action effects are multiplied by 1.35 in order to obtain the design values. When it is possible, the mobilized resistance that can be calculated and then evaluated and compared to the ultimate resistance determined by a separate calculation. In the case of a retaining wall for which a subgrade reaction approach is used, Figure 3 presents the typical results.

3.4 Coupling input and output factoring approaches

Input and output factoring approaches can be combined in the same calculation as proposed by Figure 5.

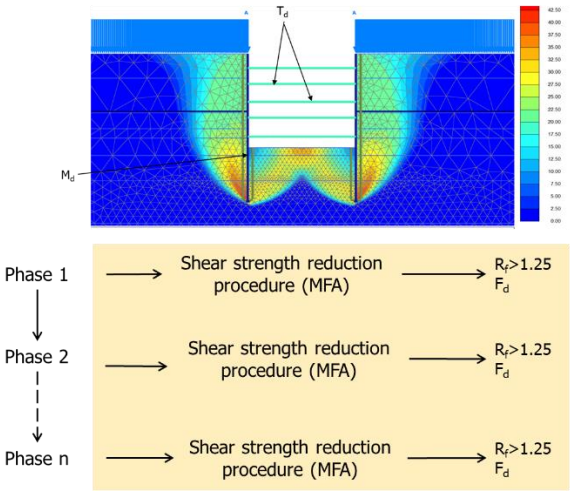

Figure 2. input factoring with shear strength reduction procedure.

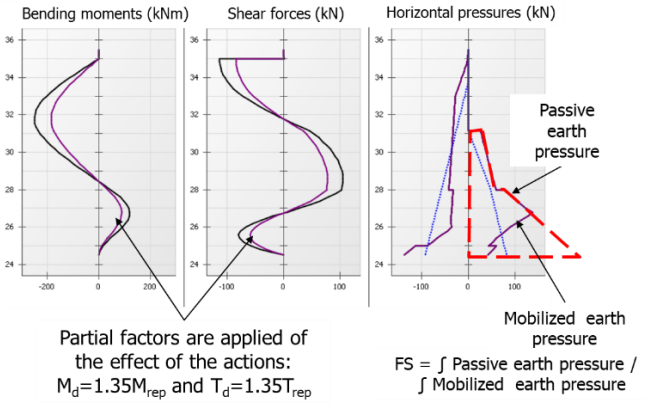

Figure 3. Output factoring with subgrade reaction methods.

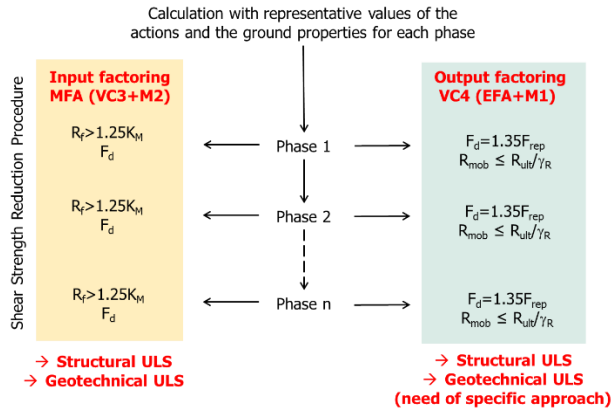

Figure 4. Coupling of input and output factoring.

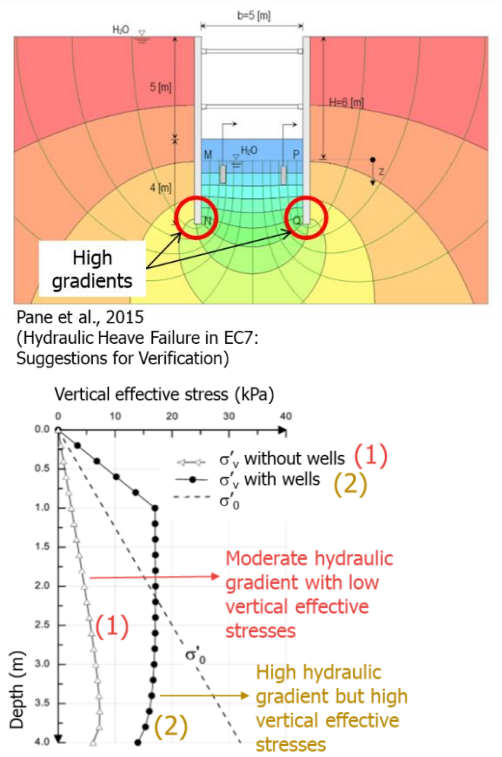

Pane et al., 2015
(Hydraulic Heave Failure in EC7: Suggestions for Verification)

Figure 5. Hydraulic verifications.

3.5 Identifying particular mechanisms

Identifying particular failure mechanisms is sometimes very useful for the design of foundations. Two options can be performed:

- Option 1: calculate the ultimate resistance R_{ult} by means of a numerical method and check that:
$$1.35G + 1.5Q \leq R_{ult}/\gamma_R$$
- Option 2: Increase the load to show that it induces low settlement:
$$\alpha.V < R_{ult} \text{ (with low settlements)}$$

and α can be written as: $\alpha = (1.35 \text{ to } 1.5).\gamma_R$ then:

$(1.35 \text{ to } 1.5).\gamma_R.V \leq R_{ult} \leftrightarrow 1.35G + 1.5Q \leq R_{ult}/\gamma_R$

4 HYDRAULIC VERIFICATIONS

Numerical methods are also very useful to perform hydraulic verifications required by prEN 1997-1. Two failure mechanisms are presented: the first one is related with the hydraulic gradient and corresponds to a local verification while the second one deals with the equilibrium between the vertical stresses and the groundwater pore pressures and corresponds to a global verification. An example taken from a paper published by Pane et al. (2015) illustrates these two verifications. These calculations do not require any partial factors as input, which simplifies the analysis (the worst case hydraulic conditions are adopted).

5 CONCLUSIONS

The new subclause on numerical methods in prEN 1997-1 paves the way for using numerical methods as a standard tool for verifying ULS and SLS in geotechnical design for both mechanical and hydraulic mechanisms. A variety of geotechnical constructions can be tackled using this tool as has been demonstrated at the hand of three construction types. The list of requirements in prEN 1997 is sufficiently open, both for following more traditional paths of verification and for making full use of nonlinear constitutive laws for ground and supporting elements. Engineering judgement is still required, especially in case of strong soil-structure-interaction, where the stiffnesses of ground and structure may be affected as a side effect of strength reduction.

ACKNOWLEDGEMENTS

The authors have been involved at various stages in the development of the second generation of Eurocode 7, serving on a range of evolution and working groups or project teams. They are grateful to their colleagues for all the fruitful discussions. However, the content of the paper reflects the opinion of the authors and does not reflect the official opinion of SC7.

REFERENCES

CEN 2022. Eurocode - Basis of structural and geotechnical design, FprEN 1990:2022. Comité Européen de Normali-sation, Brussels.

CEN 2022a. Eurocode 7: Geotechnical design — Part 1: General rules, prEN 1997-1:2022, document CEN/TC 250/SC 7, N 1662. Comité Européen de Normalisation, Brussels.

CEN 2022b. Eurocode 7: Geotechnical design — Part 3: Ge-otechnical structures, prEN 1997-1:2022, document CEN/TC 250/SC 7, N 1670. Comité Européen de Normalisation, Brussels.

Pane, V., Cecconi, M. and Napoli, P. (2015) Hydraulic Heave Failure in EC7: Suggestions for Verification, Geotechnical and Geological Engineering volume 33, pages739–750.

Smith, C. and Walter, H. (2023) Integration of numerical methods in the second generation of Eurocode EN 1997. Proceedings 10th NUMGE 2023 10th European Conference on Numerical Methods in Geotechnical Engineering Zdravković L, Konte S, Taborda DMG, Tsiampousi A (eds).

Proceedings of the XVIII ECSMGE 2024
GEOTECHNICAL ENGINEERING CHALLENGES
TO MEET CURRENT AND EMERGING NEEDS OF SOCIETY
© 2024 the Authors
ISBN 978-1-032-54816-6
DOI 10.1201/9781003431749-279
Open Access: www.taylorfrancis.com, CC BY-NC-ND 4.0 license

ECSMGE 24
XVIII EUROPEAN CONFERENCE ON SOIL MECHANICS AND GEOTECHNICAL ENGINEERING

Tensile strength of rocks: Comparison of different testing methods

Résistance à la traction des roches: Comparaison de différentes méthodes d'essai

J. Castro*, J. Justo, M.H. Olson, M. Miranda
Universidad de Cantabria, Santander, Spain

**castrogj@unican.es*

ABSTRACT: While direct tensile testing is widely acknowledged as the most accurate method of determining tensile strength, indirect methods are frequently employed, due to the problems and the precision required to obtain viable results with the direct method. Accurate values of tensile strength are very important, especially for design purposes. Thus, values obtained from the direct tensile test are beneficial and they should be compared to other experimental values measured with different methods. This study compares experimental results of standard methods of indirect tensile testing, such as the Brazilian (splitting tensile) test and three and four point bending flexural tests with the ones obtained from direct tensile testing performed following the ASTM standard. For the comparison, a highly isotropic and uniform rock, namely a Moleanos limestone, is used. Results show that bending tests produce higher values than those obtained using the Brazilian test, and in turn, the latter produces also slightly higher values than direct tensile testing.

RÉSUMÉ: L'essai de traction directe est généralement considéré comme la méthode la plus précise pour déterminer la résistance à la traction ; cependant, les méthodes indirectes sont souvent utilisées en raison de la difficulté et de la précision requises pour obtenir des résultats viables avec la méthode directe. Il est important d'obtenir des valeurs de résistance à la traction précises, en particulier pour la conception, c'est pourquoi les valeurs obtenues à partir de l'essai de traction directe sont utiles, pour pouvoir les utiliser et les comparer à d'autres valeurs expérimentales et à d'autres méthodes. Cette étude compare les résultats expérimentaux des méthodes standard d'essais de traction indirects, tels que l'essai brésilien (traction par fendage) et les essais de flexion à trois et quatre points, avec ceux obtenus à partir d'essais de traction directs réalisés conformément à la norme ASTM. Pour la comparaison, une roche hautement isotrope et uniforme, à savoir un calcaire du Moleanos, est utilisée. Les résultats montrent que les essais de flexion produisent des valeurs plus élevées que celles obtenues à l'aide de l'essai brésilien et, ces dernières produisent également des valeurs plus élevées que celles obtenues avec de l'essai de traction directe.

Keywords: Tensile strength, Brazilian test, direct tensile test, three-point bending test.

1 INTRODUCTION

Measuring the tensile strength of rocks is critical due to their sensitivity to tensile loading, which is a common cause of failure. However, accurately measuring this strength is challenging due to the low tensile strength of rocks and various factors that affect the stress state during testing. The direct tensile (DT) test (Figure 1) is the common method for many construction materials, such as steel, but it may not always be feasible or accurate enough for rocks.

The difficulties associated with conducting direct uniaxial tensile tests on rocks have resulted in the development of different variations of the test, such as using dog-bone specimens or indirect methods (Table 1). These indirect methods involve experimental configurations that create inhomogeneous stresses in the specimen. However, when interpreting the results from these indirect methods, the multi-axial stress state and the influence of other components of the stress tensor are usually not considered. Additionally, linear elastic behavior is typically assumed.

Table 1. Summary of tensile testing methods.

Name	***Reference***
Glued end caps	ISRM (1978); ASTM (2020)
Split grips	Hawkes and Mellor (1970)
Confined biaxial ext.	Brace (1964)
Comp.-tension convert	Gorski (1993)
Brazilian splitting test	ISRM (1978); ASTM (2008)
3-point bending test	Franklin and Dusseault (1989)
4-point bending test	Franklin and Dusseault (1989)
Sleeve fracturing test	Franklin and Dusseault (1989)
Modified tension test	Luong (1990)

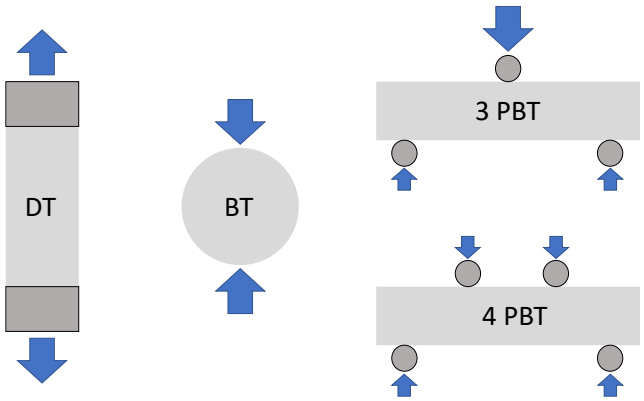

Figure 1. Summary of performed tests to measure Moleanos limestone tensile strength.

Among the indirect tensile tests, the bending of prismatic bars with circular or rectangular cross sections is widely used in mechanical and civil engineering to assess the tensile strength of various materials, such as ceramic materials, rocks, mortars... Three (3PT) and four (4PBT) points bending tests (Fig. 1) are adopted as a standard (e.g., ASTM C99: 2018, ASTM C880: 2018).

In rocks, the so-called Brazilian (splitting tensile) test (BT) (ASTM D3967: 2008) is commonly used due to the cylindrical shape of specimens. This test is preferred as it is relatively easy to prepare specimens, the testing method is straightforward, and the results obtained from the test exhibit low variability (Coviello et al., 2005). Detailed discussions on the Brazilian test have been presented by various authors (e.g., Colback, 1966), emphasizing its relevance in rock testing.

In recent years, with the development of high resistance glues that make easier using glued end caps, the direct tensile test is being revisited (e.g., Jensen, 2016; Zhang et. al., 2021; Pérez-Rey et al., 2023). In this way, the direct tensile test has recently been developed and implemented at the Geotechnical Engineering Laboratory of the University of Cantabria (Spain), following the ASTM standards with glued end caps (Castro et al., 2023).

Using the variety of tensile testing methods available (Figure 1), the different results obtained in a sample material, namely Moleanos limestone, are here compared and analysed, complementing existing comparisons between different testing methods to obtain the tensile strength (e.g., Coviello et al. 2005, Perras & Diederichs 2014).

2 LITERATURE REVIEW

Several authors have compared different methods to measure the tensile strength of rocks in the laboratory. For example, Coviello et al. (2005) compared tensile strength values measured with different tests, namely direct tensile test, Brazilian test, ring test, three and four-point bending tests and the Luong test (LT). They tested an artificial building stone (Gasbeton) and a natural calcarenite of the Gravina di Puglia geological formation. DT tests were perfomed using glued end steel caps and spherical joints in both ends. Good aligment was ensured and inclinometers were mounted on the lateral surface of the specimens. This is likely the reason to the fact that measured tensile strength using DT tests was higher than usual. Bending tests provided higher tensile strengths than those measured using the BT, and LT provided the lowest values.

On the other hand, Wang et al. (2020) performed tests on a granite from China and obtained that BT provided the higher tensile strength values in comparison to other methods, such as hydraulic fracturing hollow-cylinder, LT and DT tests.

Tensile strength obtained using bending tests relies on the linear elastic behaviour of the rock until failure. Thus, tensile strength is usually overestimated when using bending tests, unless a large thickness specimen is used (e.g., Biolzi et al., 2001).

For the DT test, some authors (e.g., Biolzi et al., 2001; Rabat et al., 2023) introduce a notch at the mid-section, but that could concentrate stresses and give overconservative tensile strength values.

As a brief summary, Table 2 compares the DT/BT ratio measured by different authors. More complete information and comparisons may be found for example in Perras and Diederichs (2014) or Rabat et al. (2023).

Table 2. Literature review of the relative tensile strength measured using direct tensile tests and Brazilian tests.

DT/BT ratio	***Rock***	***Reference***
0.98-1.07	Calcarenite	Coviello et al. (2005)
1.60	Gasbeton	Coviello et al. (2005)
0.84	Granites	Perras & Diederichs (2014)
0.69-0.93	Dataset	Perras & Diederichs (2014)
0.99-1.10	Schist	Ramana and Sarma (1987)
0.96-1.21	Granite	Ramana and Sarma (1987)
0.85	Quartz	Ramana and Sarma (1987)
0.71-0.84	Granite	Wang et al. (2020)

3 LABORATORY TESTING

3.1 Moleanos limestone

Moleanos limestone may be classified as an intrasparitic-pelsparitic limestone or grainstone. The most abundant components are pellets and intraclats, comprising 51% and 43% of the grains, respectively, with an additional 6 % of bioclasts. This limestone has been previously analyzed by the authors (e.g., Justo et

al. 2017, 2021) and it is predominantly isotropic and relatively homogeneous from a microstructural point of view, which simplifies the analysis.

3.2 Indirect tensile tests

6 BT tests were performed (Table 2) on disc-shaped specimens with a diameter of 64 mm and a thickness of 32 mm (Figure 2). The tests were performed under displacement control at 2.5 mm/min following ASTM standards (ASTM D3967: 2008).

For the bending tests, parallelepiped 180x30x30 mm specimens were used. A repetitiveness of 3 was used for both 3 and 4 PBT (Table 3). It is worth noting that both specimen size and repetitiveness are low and larger specimens and more tests should be used for an improved accuracy. The support span at the base was 150 mm and the upper loading span for the 4PBT was 50 mm.

All the tested specimens failed as expected (i.e., along a vertical central plane).

Table 3. Summary of performed laboratory tests.

Type	***Number***	***Result, σ_t (MPa)***
BT	6	7.8, 7.7, 7.1, 7.0, 6.8, 4.8
3PBT	3	10.8, 9.5, 9.2
4PBT	3	11.0, 10.1, 9.1
DT	15	7.9, 7.7, 7.6, 7.5, 7.3, 7.3, 6.4, 6.3, 6.3, 5.5, 5.3, 5.2, 5.2, 5.1, 4.4

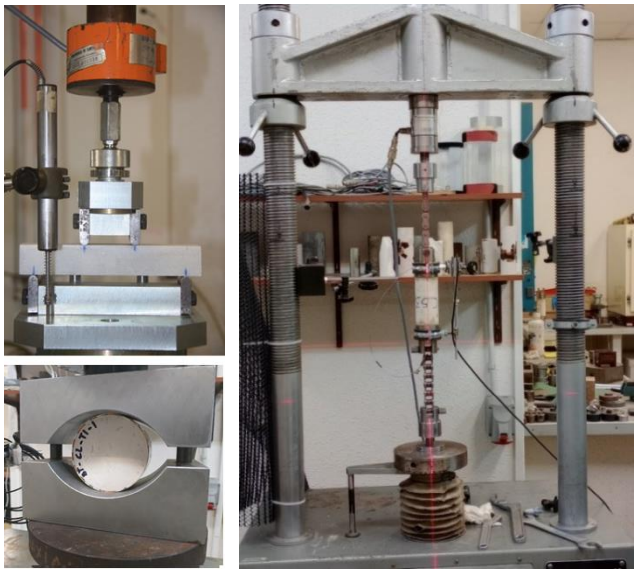

Figure 2. Test set-up of the different tests.

3.3 Direct tensile tests

DT tests were implemented at the Geotechnical Engineering Laboratory of the Univerisity of Cantabria mainly following the ASTM D2936: 2020. Samples of 50 mm diameter with a length diameter ratio of 2.5 were employed. They were glued to the metallic caps of 300 mm thickness and same diameter. Efforts were made to achieve a good alignment and failure of DT samples was reached in any area of the central part and was approximately horizontal. Detailed description of the DT tests may be found in Castro et al. (2023).

4 COMPARISON OF RESULTS

The interpreted tensile strength, σ_t, measured in each test is presented in Table 3 and plotted in Figure 3. The dispersity of the results for the DT is slightly higher than that of the BT (standard deviation of 1.15 vs 1.08 MPa).

The tensile strength predicted by the DT is the lowest. This is attributed to the fact that any misalignment introduces bending moments that reduce the theoretically calculated value. Nevertheless, the difference between the DT and the BT is not large (mean value of 6.3 vs. 6.9 MPa, respectively). Trying to discard the low values affected by possible misalignments, a truncated mean value (mean value of the 2/3 higher values) is shown in Figure 3. The truncated mean is slightly more similar, 7.0 vs 7.4 MPa for DT and BT, respectively.

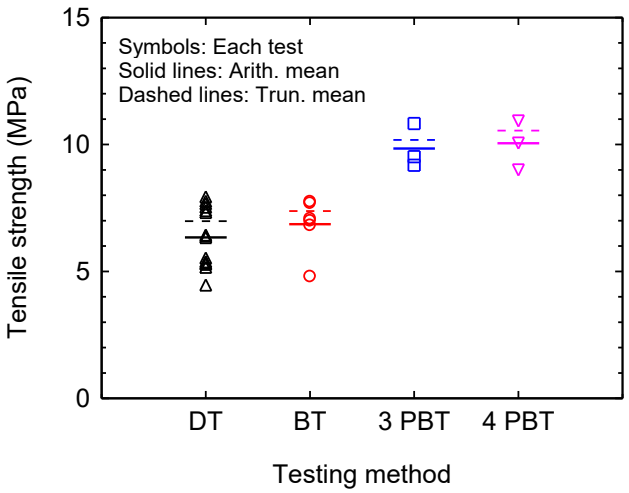

Figure 3. Tensile strength of Moleanos limestone obtained using different testing methods.

Bending tests give a much higher tensile strength, 10.2 and 10.5 MPa for the 3PBT and 4PBT, respectively. This is attributed to the stress gradient effect (e.g., Coviello et al. 2005), which is more notable in these samples of low thickness (30 mm of thickness). The 4 PBT has a zone of constant bending moment in the central part, while the 3 PBT reaches the maximum bending only in the central cross section. On the other hand, the application of the load in the 3 PBT may introduce some damage.

5 CONCLUSIONS

Measuring the tensile strength of rocks is crucial due to their susceptibility to tensile loading, a common cause of failure. Direct tensile testing, although the most accurate method, can be challenging and require precise conditions. Factors such as sample preparation, gripping, misalignments and stress concentrations tend to reduce the measured value. Therefore, indirect methods are often employed and several authors have presented comparisons between different methods.

The comparison presented here shows that DT results had slightly higher dispersity than BT, but the DT mean value was only a bit lower than that measured using BT (6.3 vs 6.9 MPa, a ratio of 0.91). On the other hand, bending tests yielded much higher tensile strength values (over 9 MPa in all the cases), highlighting the impact of the stress gradient effect, especially in low-thickness samples and when using linear elasticity until failure for the interpretation. In summary, while direct and indirect methods provide insights into rock tensile strength, careful consideration of specimen characteristics and testing conditions are essential for reliable results.

ACKNOWLEDGEMENTS

This work is part of the R&D project “Strain energy density in rock strength at different temperatures (EnergyRock)” (Ref.: PID2020-116138GB-I00) funded by MCIN/ AEI /10.13039/501100011033.

REFERENCES

ASTM C880. (2018). Standard Test Method for Flexural Strength of Dimension Stone. ASTM International, West Conshohocken, USA.

ASTM C99. (2018). Standard Test Method for Modulus of Rupture of Dimension Stone. ASTM.

ASTM D2936. (2020). Standard Test Method for Direct Tensile Strength of Intact Rock Core Specimens. ASTM International, USA.

ASTM D3967. (2008). Standard Test Method for Splitting Tensile Strength of Intact Rock Core Specimens. ASTM International, USA.

Brace, W. (1964). Brittle fracture of rocks. *Proc. Int. Conf. State Stress Earth’s Crust*, pp. 111-174.

Biolzi, L., Cattaneo, S. and Rosati, G. (2001). Frexural/Tensile strength ratio in rock-like materials. *Rock Mech Rock Eng.* 34(3): 217-233.

Castro, J., Miranda, M., Olson, M.H. and J. Justo. (2023). Direct tensile testing of Moleanos limestone. Proc. Eurock 2024, Alicante, Spain.

Colback, P. (1966). An analysis of brittle fracture initiation and propagation in the Brazilian test. *Proc. 1st Conf. ISRM*, Lisbon, pp. 385-391.

Coviello, A., Lagioia, R. and Nova, R. (2005). On the measurement of the tensile strength of soft rocks. *Rock Mech. Rock Eng.* 38(4): 251-273.

Franklin, J. and Desseault, M. (1989). *Rock Engineering*. New York, McGraw-Hill.

Gorski, B. 1993. Tensile testing apparatus. United States Patent nº 5193396.

Hawkes, I. and Mellor, M. 1970. Uniaxial testing in rock mechanics laboratories. *Eng. Geol.* 4(3): 179-285. DOI: 10.1016/0013-7952(70)90034-7.

ISRM. (1978). Suggested methods for determining tensile strength of rock materials. *Int. J. Rock Mech. Min. Sci.* 15(3): 99-103.

Jensen, S. S. (2016). *Experimental study of direct tensile strength in sedimentary rocks*. Master Thesis. NTNU, Trondheim, Norway.

Justo, J., Castro, J., Cicero, S., Sánchez-Carro, M. A. and Husillos, R. (2017). Notch effect on the fracture of several rocks: Application of the Theory of Critical Distances. *Theor. App. Fract. Mech.* 90, 251-258. DOI: 10.1016/j.tafmec.2017.05.025.

Justo, J., Castro, J. and Cicero, S. (2021). Application of the Theory of Critical Distances for the fracture assessment of a notched limestone subjected to different temperatures and mixed mode with predominant mode I loading conditions. *Rock Mech. Rock Eng.* 54: 2335-2354.

Pérez-Rey, I., Muñoz-Ibañez, A., González-Fernández, M. A., Muñiz-Menéndez, M., Herbón Penabad, M., Estévez-Ventosa, X., Delgado, J. and Alejano, L. R. (2023). Size effects on the tensile strength and fracture toughness of granitic rock in different tests. *J. Rock Mech. Geotech. Eng.* 15: 2179-2192. DOI: 10.1016/j.jrmge.2022.11.005.

Perras, M. A. and Diederichs, M. S. (2014). A review of the tensile strength of rock: concepts and testing. *Geotech. Geol. Eng.* 32: 525–546.

Rabat, A., Tomas, R. and Cano, M. (2023). Assessing water-induced changes in tensile behaviour of porous limestones by means of uniaxial direct pull test and indirect methods. *Eng. Geol.* 313: 106962.

Ramana, Y.V. and Sarma, L.P. (1987). Split-collar, tensile test grips for short rock cores. *Eng. Geol.* 23: 255-261. DOI: 10.1016/0013-7952(87)90092-5.

Wang, C., Gao, G., Jia, Q. and Wang, C. (2020). Investigation of optimum sample shape for the Luong core tension test. *Bull. Eng. Geol. Environ.* 79: 831-844. DOI: 10.1007/s10064-019-01607-x.

Zhang, Y., Zhang, Q.-Y., Zhou, X.-Y. and Xiang, W. (2021). Direct tensile test of red sandstone under different loading rates with the self-developed centering device. *Geotech. Geol. Eng.* 39: 709-718.

Proceedings of the XVIII ECSMGE 2024
GEOTECHNICAL ENGINEERING CHALLENGES
TO MEET CURRENT AND EMERGING NEEDS OF SOCIETY
© 2024 the Authors
ISBN 978-1-032-54816-6
DOI 10.1201/9781003431749-280
Open Access: www.taylorfrancis.com, CC BY-NC-ND 4.0 license

ECSMGE 24
XVIII EUROPEAN CONFERENCE ON SOIL MECHANICS AND GEOTECHNICAL ENGINEERING

Probability-based hybrid landslide assessment system integrating landslide susceptibility and numerical modeling

Système d'évaluation hybride des glissements de terrain basé sur la probabilité intégrant la susceptibilité aux glissements de terrain et la modélisation numérique

Y.-H. Chen*, K.-W. Liao
Department of Bioenvironmental Systems Engineering, National Taiwan University, Taipei, Taiwan
**r12622015@ntu.edu.tw*

ABSTRACT: Landslides have emerged as a critical disaster type due to the increasing frequency of extreme rainfall events attributed to climate change. In recent years, research on landslide analysis and slope stability has grown. The most common research methods in landslide studies fall into two categories: numerical modeling and machine learning models. Both approaches hold potential for contributing to landslide disaster management, although research combining these methods remains limited. Therefore, the primary objective of this study is to harness the strengths of both approaches, which involves the establishment of landslide susceptibility maps and the subsequent development of probability-based numerical model, providing valuable insights for disaster prevention on high-risk areas. The results from this preliminary phase indicate that the categorization boundaries in the machine learning-based landslide susceptibility maps are primarily influenced by the proportion of historical landslide areas. However, given that this factor does not represent the main characteristics of the target objects, it should be excluded in future research. The forthcoming stages will emphasize the examination of slope and dip slope area proportions while incorporating additional landslide-related geomorphic and hydrological factors and enhancing data resolution to improve predictive model accuracy. In the context of probability-based numerical model, the research highlights the sensitivity of cohesion and the internal friction angle to the probability of slope system failure. Real-world slope and soil parameter experiments are planned for the next phase to establish a more realistic probability-based numerical model.

RÉSUMÉ: Les glissements de terrain ont émergé comme un type de catastrophe critique en raison de l'augmentation de la fréquence des événements pluvieux extrêmes attribués au changement climatique. Ces dernières années, la recherche sur l'analyse des glissements de terrain et la stabilité des pentes a augmenté. Les méthodes de recherche les plus courantes dans les études sur les glissements de terrain se répartissent en deux catégories : la modélisation numérique et les modèles d'apprentissage automatique. Les deux approches ont le potentiel de contribuer à la gestion des catastrophes liées aux glissements de terrain, bien que la recherche combinant ces méthodes reste limitée. Par conséquent, l'objectif principal de cette étude est de tirer parti des forces des deux approches, ce qui implique l'établissement de cartes de susceptibilité aux glissements de terrain et le développement ultérieur de modèle numérique basés sur la probabilité, fournissant des informations précieuses pour la prévention des catastrophes dans les zones à haut risque. Les résultats de cette phase préliminaire indiquent que les limites de catégorisation dans les cartes de susceptibilité aux glissements de terrain basées sur l'apprentissage automatique sont principalement influencées par la proportion de zones de glissements de terrain historiques. Cependant, étant donné que ce facteur ne représente pas les principales caractéristiques des objets cibles, il devrait être exclu des recherches futures. Les prochaines étapes mettront l'accent sur l'examen des proportions de pentes et de zones de pentes inclinées tout en incorporant des facteurs géomorphologiques et hydrologiques supplémentaires liés aux glissements de terrain et en améliorant la résolution des données pour améliorer la précision du modèle prédictif. Dans le contexte des modèle numérique basés sur la probabilité, la recherche met en évidence la sensibilité de la cohésion et de l'angle de frottement interne à la probabilité de défaillance du système de pente. Des expériences sur le terrain réel des paramètres de pente et de sol sont prévues pour la prochaine phase afin d'établir un modèle numérique basé sur la probabilité plus réaliste.

Keywords: Landslide management; susceptibility maps; reliability analysis; sensitivity analysis

1 INTRODUCTION

Landslides pose a significant threat to human life and property, making them one of the most critical disaster types. Moreover, with the increasing frequency of extreme rainfall events due to climate change, landslides triggered by heavy precipitation demand more attention and management (Crozier, 2010). Over

the years, there has been a multitude of research in slope stability analysis and landslide disaster mitigation. The most common research methods fall into two categories: (1) numerical modeling and (2) machine learning models. In this study, the term "numerical models" refers to methods based on a deterministic approach. These methods rely on complex mathematical computations that require computer calculations. Examples include Limit Equilibrium Methods (LEMs), Finite Element Method (FEM), and the Material Point Method (MPM). Numerical models can simulate the movement of slopes and study the mechanisms of failure, but typically limited to relatively small areas. On the other hand, machine learning models use geospatial and hydrological data to generate risk assessment maps on a broader scale, employing a data-driven approach. This method offers the advantage of identifying areas with potential high risk (Merghadi et al., 2020).

Both machine learning and numerical models have their merits and can significantly contribute to landslide disaster management. However, there is limited research that combines both methods for analysis. Hence, the ultimate aim of this study is to leverage the strengths of both approaches. Initially, a machine learning model will be used to establish landslide susceptibility maps. Subsequently, probability-based numerical model using a probability of failure approach will be constructed for areas with a potential high risk, offering valuable insights for disaster prevention.

The research consists of three phases. The first phase involves creating preliminary machine learning and probability-based numerical model for simpler cases. Factors affecting landslide susceptibility will be analysed, and adjustments made based on their impact. The future direction for model complexity will also be discussed.

In the second phase, the most suitable combination of factors identified in the first phase will be incorporated into more complex model designs, considering additional real-world conditions in the study area. The representative model will be employed to identify hazard zones and conduct probability-based numerical model analysis. Finally, the third phase involves model validation and optimization and an attempt to generalize this hybrid model for landslide disaster applications in other regions.

This draft paper primarily focuses on the outcomes of the first phase and presents specific plans for future research work based on these results.

2 METHODS

2.1 Study area

The Jhuoshuei River is Taiwan's longest river, approximately 187 km in length, and it flows through the central region of Taiwan, spanning four counties and cities. Its upper and middle reaches are characterized by fractured bedrock and heavy rainfall in mountainous areas, resulting in high sediment content in the river. The lower reaches are densely populated and heavily involved in agricultural activities. Taking into account slope vulnerability and the considerations for resident safety, this area was chosen for the first phase of the study.

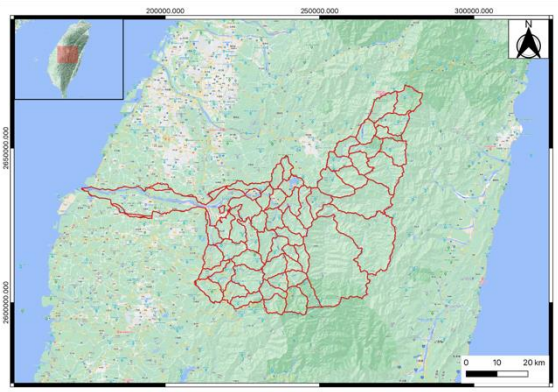

Figure 1. Study watersheds and their slope units.

2.2 Establishment of Machine Learning Models

The study area was divided into 53 sub-watersheds using watershed analysis methods (Figure 1). Three major extreme rainfall typhoons in recent years, namely, Typhoons Saola, Soulik, and Meranti, were selected as the main events for landslide analysis. Geospatial and hydrological factors were chosen as parameters for building the machine learning models and included slope, dip slope area proportion, historical landslide area proportion, and rainfall from individual typhoon events.

Using the landslide records corresponding to the selected typhoon events as known landslide outcomes, Support Vector Machine (SVM) was employed to create landslide prediction machine learning models. The dataset was divided into a training set (3/4 of the data) and a testing set (the remaining 1/4). Two types of classification boundaries, linear and non-linear (RBF), were utilized to compare the classification performance of the two SVM models.

2.3 Identification of key factors in machine learning models

As a classification model, visual representation of SVM classification boundaries can be created by pairwise combinations of factors. This allows for a comparison of the determinative impact of different factors on landslide classification outcomes. For instance, if the classification boundary appears to be vertical, it signifies that the classification results are entirely dependent on the horizontal-axis factor. Conversely, if the boundary is horizontal, it implies that the classification results are solely dependent on the vertical-axis factor.

By comparing the pairwise combinations, it is possible to rank and assess the significance of each factor in determining landslide prediction outcomes within this model. ranking is instrumental in determining the level of emphasis to be placed on each factor.

2.4 Establishment of probability-based numerical model

This research focuses on landslides with large displacement, and traditional slope stability analysis methods like the Limit Equilibrium Method (LEM) and Finite Element Method (FEM) have limitations in simulating large displacements and cannot describe the motion processes adequately (Kaur and Sharma, 2016; Soga et al., 2016). In contrast, the Material Point Method (MPM) can provide better simulations of the motion processes and offer in-depth insights into the physical mechanisms of slope failure (Wyser et al., 2020).

In this study, Anura3D software was chosen for the MPM analysis of slope stability. To simplify the problem in the initial stages of the research, a basic geometric scenario was selected for analysis (Anura3D MPM Research Community, 2022a). The geometric is illustrated in Figure 2.

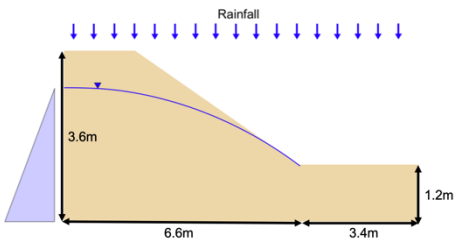

Figure 2. Geometric of selected problem (Anura3D MPM Research Community, 2022a).

To quantitatively assess the slope's safety level, this study introduces reliability analysis. This involves using AK-PSO-HHs (Thedy and Liao, 2023) to calculate failure probabilities under various conditions based on the MPM results. Note that the accuracy of this method has been validated, for details, please refer to Thedy and Liao, 2023.

In reliability analysis, it is essential to provide a clear definition of „failure“. As the shear stress-based safety factor cannot fully represent the occurrence of large landslides, this study chooses to define failure in terms of „displacement“, which is a more direct indicator of landslide occurrence. In practical management, displacement or displacement rates are often used to establish warning thresholds.

2.5 Identification of key factors in probability-based numerical model

This study analyses seven factors, encompassing cohesion (C), internal friction angle (ϕ), wet density (ρ), Young's modulus (E), along with hydrological parameters, including infiltration rate (I_R), groundwater level (H), and the correlation coefficient between cohesion and internal friction angle (r). These parameters are selected within reasonable ranges, their respective probability distribution types and statistical parameters are detailed in Table 1.

A sensitivity analysis of the system's failure probability concerning various factors is conducted following established methodologies (Malkawi et al., 2000). By adjusting the coefficients of variation (COV) for these seven factors within their reasonable ranges, the impact of each factor's variability on the system's failure probability is explored. This comparative analysis identifies the sensitivity of each parameter, and parameters demonstrating sensitivity within the system are considered as key factors of interest.

Table 1. Parameter information.

Parameter	Probability distribution	Mean	Range
C (kPa)	Lognormal	2.5	1.1~5.3
ϕ (°)	Lognormal	27	19.2~41.2
E (kPa)	Lognormal	30000	8450~11540
ρ (kg/m^3)	Lognormal	2650	2175~3250
I_R (m/s)	Uniform	0.0002	0.0001~ 0.0004
H (m)	Beta	2.2	1.5~2.5
r (-)	–	0	-0.9~0.9

3 RESULTS

3.1 SVM model performance

Performance assessment of the models includes confusion matrices for both linear and non-linear

classification boundaries (Table 2, Table 3). Three primary validation indices, True Positive Rate (TPR), True Negative Rate (TNR), and Accuracy, are utilized to gauge model effectiveness. The findings consistently favour the linear model over the non-linear one across all metrics. Subsequently, emphasis will be placed on the superior linear model in the ensuing discussion.

Table 2. Linear SVM Model performance.

	Actual landslides	Actual no landslides
Predicted Landslides	11	6
Predicted no landslides	2	21
TPR	84.6%	
TNR	77.8%	
Accuracy	80%	

Table 3. Nonlinear SVM Model performance.

	Actual landslides	Actual no landslides
Predicted Landslides	9	8
Predicted no landslides	8	15
TPR	52.9%	
TNR	65.2%	
Accuracy	60%	

3.2 Factor analysis in the SVM model

To establish a landslide prediction model, the factors used are combined pairwise. A linear classification boundary model is employed to visualize the relationships between the classification boundary and various factors, aiming to compare the significance of each factor in predicting „landslide occurrence“, as shown in Figure 3.

In the combination of dip slope area proportion and slope, the model categorizes all data points as „no landslide“ (Figure 3a), resulting in an overall accuracy of only 57.5%. Conversely, when combining historical landslide area proportion with dip slope area proportion (Figure 3b), the overall accuracy reaches 75%.

However, the classification boundary is solely dependent on historical landslide area proportion, as one factor. A similar situation is observed in the combination of historical landslide area proportion with slope (Figure 3c).

Finally, by combining rainfall of each event and historical landslide area proportion, the overall predictive accuracy reaches 77.5% (Figure 3d), approaching the predictive accuracy of the model with four integrated factors (80%). Nevertheless, the classification boundary remains primarily influenced by historical landslide rates, with only slight adjustments based on rainfall.

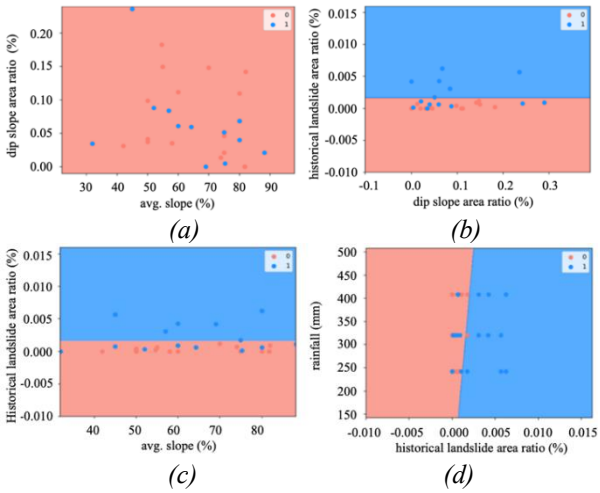

Figure 3. Pairwise comparison SVM classification boundaries. (a) Combination of dip slope area proportion and slope. (b) Historical landslide area proportion and dip slope area proportion. (c) Historical landslide area proportion and slope. (d) Rainfall of each event and historical landslide area proportion.

3.3 Factor sensitivity in the probabilistic numerical model

In this section, the approach outlined by Malkawi et al. (2000) is employed to create sensitivity assessment plots of the variation in failure probability concerning each parameter.

The results of this simulation exhibit a linear relationship in all cases, except for the negative correlation between friction angle and cohesion. The sensitivity of each parameter can be assessed by examining the slope of the regression line. In this research case, the most influential factors in terms of their impact on the system's failure probability are COV($\emptyset$) with a slope of 0.3077 and COV(C) with a slope of 0.2492. Following these are the positive correlation (r_+) between cohesion and friction angle with a slope of 0.028, COV(H) with a slope of 0.0175, and COV(I_R) with the smallest slope of 0.0023. COV(ρ) and COV(E) exhibit minimal sensitivity in this context.

4 DISCUSSION

4.1 Factors of interest in the SVM model

The impact of slope and dip slope area proportion on classification boundaries, as observed in pairwise evaluations, seems to be minimal (Figure 3).

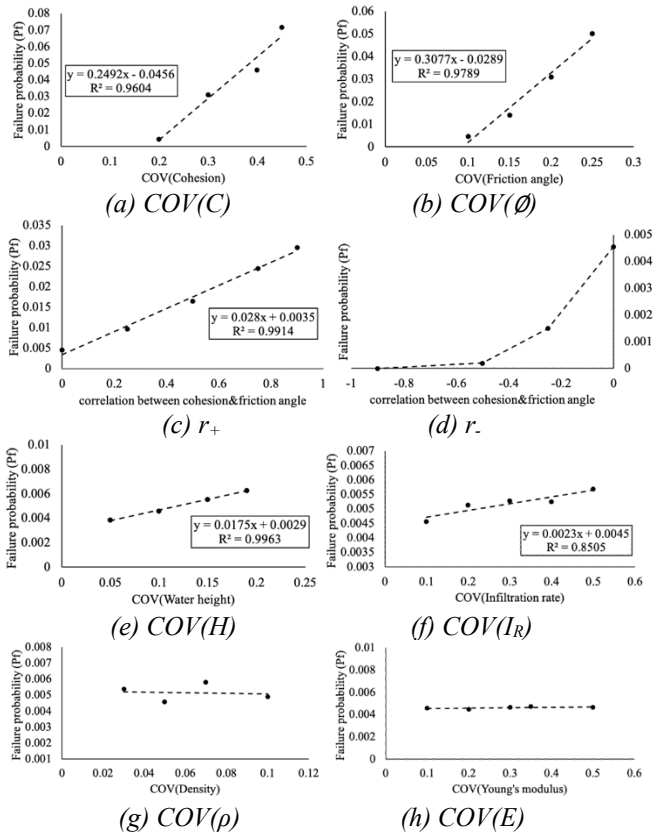

Figure 4. Sensitivity analysis of each parameter.

However, it is essential not to draw conclusions regarding the insignificance of these two geomorphic factors. The historical landslide area proportion, which takes precedence, represents the proportion of landslide-prone areas within sub-watersheds. Disasters tend to recur in regions where critical conditions exist, making the „historical landslide area proportion“ an integrative measure that accounts for all contributing landslide factors. Thus, incorporating it along with natural background conditions, such as slope and dip slope area proportion, as predictive factors in the model, can dilute the effects of individual natural conditions and potentially lead to misleading conclusions about their importance.

In the final phase of this study, the primary objective is to identify high-potential landslide areas that have been previously overlooked. These areas typically lack significant historical landslide records. While the historical landslide area proportion predominantly influences the classification in this research phase, considering its impact on other factors, along with its misalignment with the target characteristics, suggests its exclusion from the list of factors of interest in subsequent research phases. Moreover, the predictive performance highlights the need to incorporate additional landslide-related geomorphic and hydrological factors, such as rock type, rock fragmentation, and groundwater levels, as factors of interest. This comprehensive approach will provide a more complete understanding of the influence of various spatial factors on landslide occurrence.

4.2 SVM model refinement directions

Based on the current phase's results, recommendations for enhancing the machine learning model in the next phase are: (1) Continue investigating rainfall of each event, and focusing on diluted factors like slope and dip slope area proportion while diversifying relevant factors for improved predictions; (2) Increasing the spatial resolution of factors to better represent sub-watershed characteristics; (3) Considering a smaller study area, focusing on a few key sub-watersheds due to enhanced data resolution.

4.3 Factors of interest in the probability-based numerical model

Based on the results of parameter sensitivity analysis (Figure 4), cohesion (C), the internal friction angle ($\emptyset$), and their correlation were identified as the most sensitive factors influencing system failure probability. Therefore, they have been included as attention factors.

While groundwater level (H) and infiltration rate (I_R) showed some sensitivity in the model, their impact on slope stability, particularly the influence of „water“ in the context, is not as significant as expected.

Hence, their exact implications require further investigation, and they will be retained as attention factors for subsequent stages of research.

On the other hand, soil moisture density (ρ) and Young's modulus (E), which were found to be insensitive in this stage, may be excluded from the attention factors in sensitivity analysis during the subsequent phases.

4.4 Further discussion on the groundwater level in the numerical model

This study examines the sensitivity of groundwater levels in slope safety evaluation, essentially altering the soil submerged range. The changes in groundwater level arises from alterations in excess pore water pressure, leading to a reduction in effective stress and, consequently, triggering slope instability. The material properties adopted in this study are single point two-phase. Specifically, pore water and the acceleration of soil is set as unknowns to solve the governing equations. Ultimately, this calculation yields the physical behavior of saturated soil (Anura3D MPM Research Community, 2022b). The effectiveness of analyzing the impact of groundwater level changes on landslides using the MPM has been validated through the study by Troncone et al., 2020.

Our founding here is that the sensitivity of groundwater level is relatively smaller than soil strength parameters. However, this doesn't imply its insignificance to landslides. Since the Mohr-Coulomb criterion directly relies on soil strength parameters, it is reasonable for these two parameters to exhibit the highest sensitivity. Besides these two parameters, groundwater level is the most significant factor affecting slope stability, where soil infiltration naturally also becomes an important factor influencing slope stability. Thus, in a situation where a slope undergoes rainfall infiltration without soil strength parameter changes, groundwater level demonstrates the highest sensitivity to slope stability.

4.5 Probability-based numerical model refinement directions

The initial phase of this research focused on simplifying the analysis of case study, primarily applicable to artificial slopes with a height of 3.6 meters or less. Caution is needed when extending this model to slopes exceeding this range. Hence, future phases should focus on making the numerical model's geometry more complex, resembling real-world scenarios or directly conducting motion analyses for specific slope conditions. Regarding parameter values, using actual soil experiment data from the analysis area is essential to realistically reflect the impact and sensitivity of various considerations on slope failure mechanisms.

5 CONCLUSIONS AND FUTURE WORKS

This study is the initial phase of the three-tiered objectives, concentrating on simpler scenarios to establish initial machine learning and probabilistic-numerical model. Based on these findings, the second phase should consider the following adjustments:

1. Enrich the factors in the landslide prediction machine learning model. In addition to the factors explored in this phase, such as rainfall of each event, slope and dip slope area proportion, incorporate more landslide-related geophysical and hydrological factors to enhance predictive performance.
2. Narrow down the research scope of the landslide prediction machine learning model for improved spatial data resolution.
3. Refine the probability-based numerical model by real-world slope geometry and soil parameters. In sensitivity analyses, emphasize discussions about the variation in soil strength parameters (C, ϕ) and the sensitivity of hydrological factors (H, I_R) within the system.

REFERENCES

Anura3D MPM Research Community. (2022a). *Anura3D MPM Software Tutorial Manual*, [online] Available at: https://github.com/Anura3D/Anura3D_OpenSource/tree/main/manuals, accessed: 02/02/2024.

Anura3D MPM Research Community. (2022b). *Anura3D MPM Software, Scientific Manual*, [online] Available at: https://github.com/Anura3D/Anura3D_OpenSource/blob/main/manuals/ScientificManual_2022.pdf, accessed: 02/02/2024.

Crozier, M.J. (2010) Deciphering the effect of climate change on landslide activity: A review, *Geomorphology*, 124(3–4), pp.260-267, https://doi.org/10.1016/j.geomorph.2010.04.009.

Kaur, A. and Sharma, R.K. (2016) Slope stability analysis techniques: A review. *International Journal of Engineering Applied Sciences and Technology*, 1(4), pp. 52-57, Available at: https://www.ijeast.com/papers/52-57,Teasma104,IJEAST.pdf , accessed: 02/02/2024.

Malkawi, A.I.H., Hassan, W.F and Abdulla, F.A. (2000) Uncertainty and reliability analysis applied to slope stability. *Structural Safety*, 22(2), pp. 161-187, https://doi.org/10.1016/S0167-4730(00)00006-0.

Merghadi, A., Yunus, A. P., Dou, J., Whiteley. J., ThaiPham, B., Bui, D. T., Avtar, R. and Abderrahmane, B. (2020) Machine learning methods for landslide susceptibility studies: A comparative overview of algorithm performance. *Earth-Science Reviews*, 207, 103225, https://doi.org/10.1016/j.earscirev.2020.103225

Soga, K., Alonso, E., Yerro, A., Kumar, K. and Bandara, S. (2016) Trends in large-deformation analysis of landslide mass movements with particular emphasis on the material point method. *Géotechnique*, 66(3), pp. 248-273, https://doi.org/10.1680/jgeot.15.LM.005

Thedy, J. and Liao, K. W. (2023) Adaptive Kriging adopting PSO with Hollow-Hypersphere space in structural reliability assessment. *Probabilistic Engineering Mechanics*, 74, 103513, https://doi.org/10.1016/j.probengmech.2023.103513

Troncone, A., Pugliese, L., and Conte, E. (2020) Run-Out Simulation of a Landslide Triggered by an increase in the Groundwater Level Using the Material Point Method. *Water*, 12(10), 2817, https://doi.org/10.3390/w12102817

Wyser, E., Alkhimenkov, Y., Jaboyedoff, M. and Podladchikov, Y.Y. (2020) A fast and efficient MATLAB-based MPM solver: fMPMM-solver v1.1. *Geoscientific Model Development*, 13(12), pp. 6265-6284, https://doi.org/10.5194/gmd-13-6265-2020

Proceedings of the XVIII ECSMGE 2024
GEOTECHNICAL ENGINEERING CHALLENGES
TO MEET CURRENT AND EMERGING NEEDS OF SOCIETY
© 2024 the Authors
ISBN 978-1-032-54816-6
DOI 10.1201/9781003431749-281
Open Access: www.taylorfrancis.com, CC BY-NC-ND 4.0 license

ECSMGE 24
XVIII EUROPEAN CONFERENCE ON SOIL MECHANICS AND GEOTECHNICAL ENGINEERING

Large-scale soil investigations for greenfield railways using airborne geoscanning: A case study from Mato Grosso, Brazil

Études de sol à grande échelle pour de nouvelles voies ferrées à l'aide de la géoscanographie aérienne: Une étude de cas du Mato Grosso, Brésil

C.W. Christensen*, B.R. Bloss, A.A. Silva, E.J. Harrison
EMerald Geomodelling AS, Oslo, Norway

M.S. Gomes, R.W.M. Ferraz
Rumo Logística SA, Curitiba, Brazil

cch@emrld.no

ABSTRACT: We present large-scale ground investigations along 170 km of the Lucas do Rio Verde railway, a new, 730-km-long railway being planned in Mato Grosso, Brazil through airborne geoscanning. We combe airborne geophysical data with limited intrusive ground data to generate 3D ground models, with the help of machine learning algorithms. These rapidly acquired data and generated models allowed us to quickly characterize geological heterogeneity in the area, predict the depth to the soil-rock interface, and identify key groupings of soil types. While some results were limited by poor geophysical contrast between sand and sandstone in some portions of the survey area, they allowed to focus the next phase of ground investigation on critical areas. We show that we reduce the uncertainty in estimating rock excavation costs by 30% compared to a conventional, borehole-only workflow. This case study is the first successful example of airborne geoscanning in an infrastructure project in a tropical climate.

RÉSUMÉ: Nous présentons des études de terrain à grande échelle le long de 170 km de la voie ferrée Lucas do Rio Verde, une nouvelle voie ferrée de 730 km de long en cours de planification dans le Mato Grosso, au Brésil en utilisant la géoscanographie aérienne. Nous combinons des données géophysiques aéroportées avec des données terrestres intrusives limitées pour générer des modèles 3D terrestres, à l'aide d'algorithmes d'apprentissage automatique. Ces données rapidement acquises et ces modèles générés nous ont permis de caractériser rapidement l'hétérogénéité géologique de la région, de prédire la profondeur de l'interface sol-roche et d'identifier des groupements principaux de types de sol. Bien que certains résultats aient été limités par le faible contraste géophysique entre le sable et le grès dans certaines parties de la zone d'étude, ils ont permis de concentrer la phase suivante d'investigations sur les zones critiques. Nous montrons que nous réduisons l'incertitude liée à l'estimation des coûts d'excavation de roches de 30 % par rapport à un flux de travail conventionnel, uniquement constitué de forages. Cette étude de cas est le premier exemple réussi de géoscanographie aérienne dans un projet d'infrastructure dans un climat tropical.

Keywords: Railway; geological risks; site investigation; geophysics; machine learning.

1 INTRODUCTION

Site investigations using traditional intrusive techniques have limitations in mitigating geological risk in large infrastructure projects. They are relatively slow, costly, and only provide information at a single point. Airborne electromagnetics (AEM) is a geophysical method with complementary strengths: low unit cost, rapid acquisition, continuous data coverage. In a workflow we call *airborne geoscanning*, we combine both AEM and traditional geotechnical soundings using machine learning to generate geological models that take advantage of the strength of both data types. This new case study presents airborne geoscanning results from the Lucas do Rio Verde Project, a 730-km-long railway being planned in Mato Grosso state, Brazil. Our aims were to (1) understand large-scale geological trends; (2) map different soil and rock types, and (3) optimize future drilling campaigns. This text focuses on the first 130 km of the railway of the planned railway.

2 METHODS

2.1 Airborne electromagnetics

Airborne electromagnetic (AEM) systems allows one to map differences in the electrical resistivity of the subsurface, and have been widely used in mineral

exploration, hydrogeology, and, more recently, infrastructure applications (Auken et al., 2017). In 2021, EMerald Geomodelling and Rumo Logística used the RESOLVE EM system by Xcalibur Multiphysics to survey 170 km of railway, collecting 5 parallel flightlines in a 200-m-wide corridor centred on railway alignments.

Pre-processing of these data was consisted of four main tasks: (1) removing data adversely affected by nearby man-made, metallic structures; (2) removing measurements taken outside of acceptable flight parameters (roll, pitch, altitude); (3) averaging of consecutive sounding points to improve signal to noise ratio; and (4) removing measurements with low signal amplitude, usually due to highly resistive geology. We then used inversion modelling to transform this dataset into a model of electrical resistivity, which formed the basis for subsequent geological interpretation. All these steps were executed using a combination of in-house software and AarhusGeoSoftware's Aarhus Workbench.

2.2 Geotechnical data

At the time of the survey, 104 standard penetration tests (SPs), 68 auger borings (STs) and 14 combined SPs and rock core drillings (SMs) were available as ground trust training data. Data was logged at intervals of 1 m in most cases, meaning the vertical precision of these data is assumed to be 1 m. Materials were classified using two different schemes. First, we used the Brazilian Geological Association's (ABGE) criteria for classifying sandstones by friability (Pastore et al. 2015), separating unconsolidated sediments (Category 1) from partly weathered rock (Cat. 2) and intact rock (Cat. 3). (Too few instances of Category 2 material were encountered to determine a meaningful correlation with electrical resistivity, so Categories 2 and 3 were merged for our interpretation.) Second, five broad categories of material were parsed from the textual descriptions of material recording during field observations: clay, silt, sand, rock, and laterite. Where multiple materials were mentioned, only the primary constituent (e.g., the "silt" in a "clayey silt") was used.

2.3 Data Integration and modelling

We use three techniques to analyse the field data. First, we use a hierarchical clustering algorithm on the electrical resistivity model to group locations with similar results in the uppermost 30 m of the subsurface. Second, we use an artificial neural network

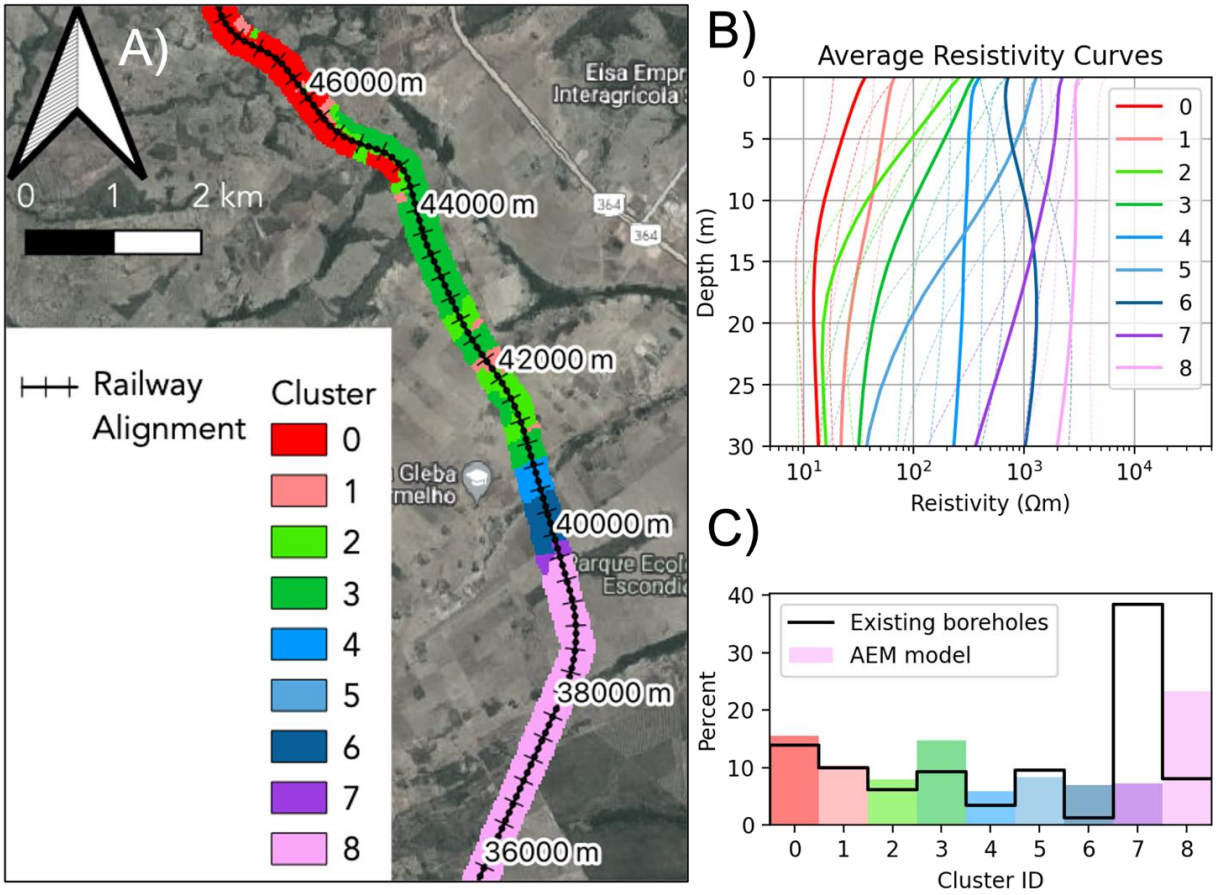

Figure 1. Outputs of the cluster analysis: A) Map view of a portion of the survey; B) Average resistivity curves of each cluster; C) Proportion of clusters within the resistivity model and the existing geotechnical soundings. Adapted from Christensen et al. 2023.

(ANN) approach based on Lysdahl et al. (2022) to predict the depth to the interface between Category 1 and Category 2/3 material. Lastly, we use a supervised machine-learning algorithm based on Christensen et al. (2021) to generate a volumetric model of material types. Whereas clustering only uses the resistivity model, the latter two techniques combine electrical resistivity and geotechnical data.

3 RESULTS

The resultant geophysical clusters (Figure 1), interface model (Figure 2A) and material classification model (Figure 2B) provided information on not only the expected ground conditions, but also where there was variability, and where there was uncertainty or a lack of data. For instance, we compared the relative proportion clusters among AEM and geotechnical sounding location and note that medium-resistivity (Clusters 2, 4, and 6) and the highest-resistivity cluster (8) are undersampled by existing drillings. In the interface model, median depth of 6.0 m, the 75th percentile was 8.7 m, and a few isolated cases of depths exceeding 20 m in some tall hills. Uncertainties had a median value of 3.4 m. Lastly, the material classification model showed that there are long stretches with a very high probability of sandy materials and multiple shorter stretches that are clearly fine-grained. High uncertainties occur at the transitions between these major, uniform zones and in isolated instances of local heterogeneity.

To assist with planning of subsequent ground investigations, we used these models to divide the survey area into high-, medium-, and low-priority zones (Figure 3). High-priority zones highlight areas with one of or multiple of the following: elevated uncertainty in the interpreted geological models, undersampled clusters, elevated heterogeneity, poor correlation between geophysics and geological targets, intersections between geological targets and the planned railway alignment or unexplained/unsampled features in the geophysical models. In all, 50% of the railway alignment is assigned as high priority, 38% as medium, and 12 % as low priority.

4 DISCUSSION

Airborne geoscanning has led to reductions in time and direct cost in this phase of this project. We estimate that 33% fewer geotechnical soundings were needed to adequately characterize these railway alignments, a similar magnitude to past projects in Norway (Christensen et al. 2020). This is achieved reduction comes from targeting regions with higher geological uncertainty and avoiding redundant holes where resistivity models can be explained by existing data.

Quantifying risk is challenging, but one way we attempt to do so is to compare estimated excavation costs from the ANN-based interface model to a boreholes-only one. Standard practice in Brazil is to perform a linear interpolation (i.e., triangulation) of depth. Uncertainty estimation is not common, so we use variogram modelling and ordinary kriging to estimate uncertainties. While the median estimated excavation costs from either model do not vary by more than 3 %, the confidence range for the borehole-only method (R$74-231 million) is 30% wider than that of the ANN-based on (R$86-210 million) due the fact that uncertainties in the ANN-based interface model are lower. This shows that airborne geoscanning reduced the worst-case scenario by R$21 million. Though difficult to quantify, we expect other indirect, long-term benefits such as reduced exposure risk for field personnel, reduced risk of work stoppage and litigation from unforseen ground conditions, and avoidance of overcommitment to suboptimal design thanks to a more rapid investigation.

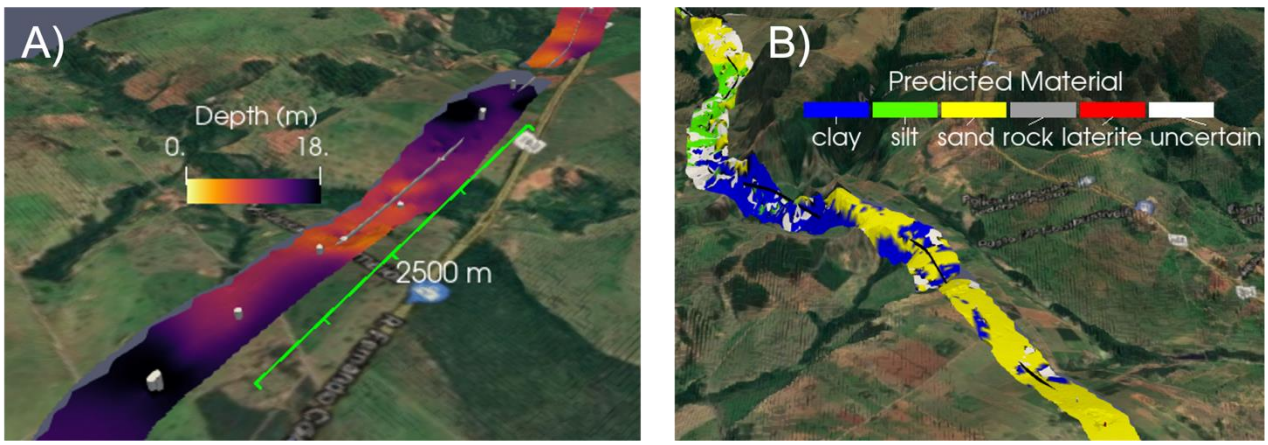

Figure 2. 3D renderings of the interface (A) and material classification (B) models. Adapted from Christensen et al. (2023).

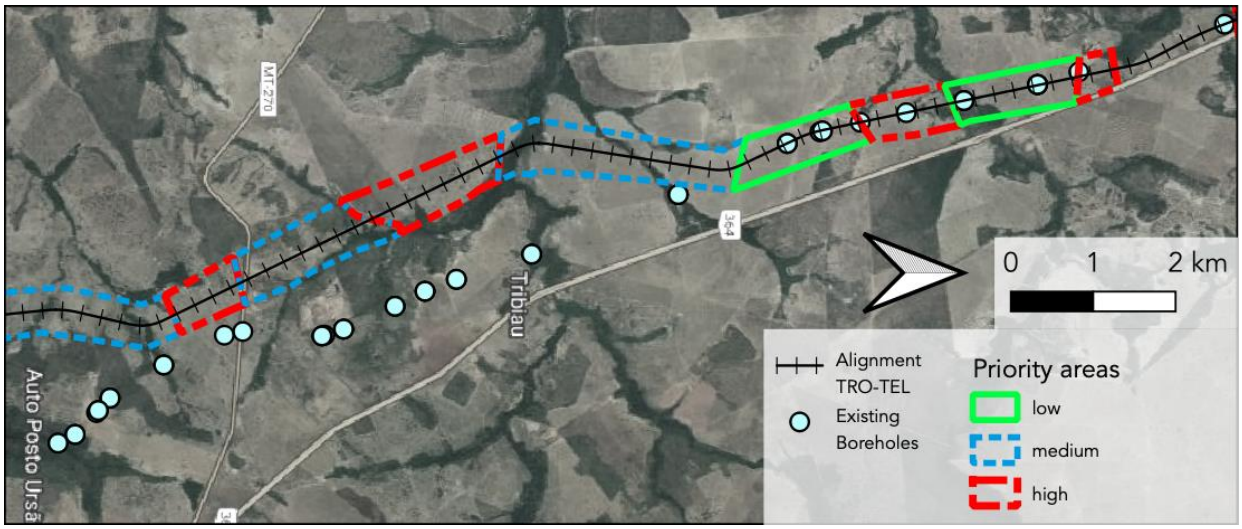

Figure 3. Example of mapped priority zones along a 14-km segment. Adapted from Christensen et al. (2023).

This technology is not without limitations. For one, there are some sections where there is limited electrical resistivity contrast, notably between some sands and sandstones. Boreholes are still necessary to identify the soil-rock interface within these zones. In addition, past case studies have shown that the main benefit from airborne geoscanning comes from optimizing linear infrastructure alignment, an impact that far exceed beyond direct savings of a reduced number of drillings (Christensen et al. 2020). Nonetheless, this case study adds to the growing body of literature on airborne geoscanning and its versatility as a ground investigation tool for large infrastructure projects.

5 CONCLUSIONS

This case study demonstrated that airborne geoscanning is a valuable tool for performing more efficient, large-scale site investigations in infrastructure projects. Though resultant ground models had some uncertainties and were not available early enough in the project‘s lifetime to be used for route optimizations, there were significant benefits in short-term cost and time savings and long-term benefits by reducing risk. This study exapnds on the literature on airborne geoscanning by being the first example from Brazil and the first example in an infrastructure project in a tropical climate.

6 REFERENCES

Auken, E., Boesen, T., Christiansen, A. V. (2017) A Review of Airborne Electromagnetic Methods With Focus on Geotechnical and Hydrological Applications From 2007 to 2017. In *Advances in Geophysics,* 58, pp. 47–93. Elsevier. https://doi.org/10.1016/bs.agph.2017.10.002.

Christensen, C. W., Bloss, B. R., Rassmussen, A. H., Silva, A. A., Silva Filho, J. C., Gomes, M. S., Ferraz, R. W. M. (2023) Large-scale soil investigations for greenfield railways using airborne geoscanning: A case study from Mato Grosso, Brazil, In :*12th International Heavy Haul Association Conference 2023,* Rio de Janeiro, Brazil.

Christensen, C.W., Harrison, E.J., Pfaffhuber, A.A., Lund, A.K. (2021), A machine learning–based approach to regional-scale mapping of sensitive glaciomarine clay combining airborne electromagnetics and geotechnical data. *Near Surface Geophysics*, 19, pp. 523-539. https://doi.org/10.1002/nsg.12166.

Christensen, C.W., Skurdal, G.H., Pfaffhuber, A.A., Rønning, S., Lindgard, A. and Sellgren, K.C. (2020) Airborne geoscanning and efficient geotechnical ground investigation workflows: a road-building case study from Central Norway. *18th Nordic Geotechnical Meeting,* Helsinki, Finland.

Lysdahl, A.K., Christensen, C.W., Pfaffhuber, A.A., Vöge, M., Andresen, L., Skurdal, G.H., Panzner, M. (2022) Integrated bedrock model combining airborne geophysics and sparse drillings based on an artificial neural network. *Engineering Geology*, 297, 106484. https://doi.org/10.1016/j.enggeo.2021.106484.

Pastore, E.L, da Cruz, P.T., Freitas, M.S. Jr. (2015) Fundações de barragens e estruturas em arenitos: natureza dos maciços e controle de fluxo e erosões. *XXX Seminário Nacional de Grandes Barragens*, Foz de Iguaçu, Brazil.

Proceedings of the XVIII ECSMGE 2024
GEOTECHNICAL ENGINEERING CHALLENGES
TO MEET CURRENT AND EMERGING NEEDS OF SOCIETY
© 2024 the Authors
ISBN 978-1-032-54816-6
DOI 10.1201/9781003431749-282
Open Access: www.taylorfrancis.com, CC BY-NC-ND 4.0 license

ECSMGE 24
XVIII EUROPEAN CONFERENCE ON SOIL MECHANICS AND GEOTECHNICAL ENGINEERING

The use of dynamic load tests for execution control of driven precast piles in logistic warehouses

L'utilisation d'essais de charge dynamique pour le contrôle d'exécution de pieux préfabriqués battus dans les entrepôts logistiques

J. Costa*
KELLER Cimentaciones - Sucursal em Portugal, Agualva-Cacém, Portugal

J.M. Díaz, J.C. Sanchez
KELLER Cimentaciones, Alcalá de Henares, Spain

**joel.costa@keller.com*

ABSTRACT: Execution control during and after driving precast concrete piles is a critical issue for work validation and acceptance. This is especially important due to the high compressive stresses usually expected to be resisted by precast piles, taking advantage of the high-resistant concrete used on its manufacture and given the effects of driving and lateral displacement of the soil on increasing geotechnical bearing capacity. Among others, refusal measure is one of the main aspects of the execution control of every driven piles, and the refusal criterion is defined using pile driving formulas, usually conservative. Dynamic load tests play a key role in the execution control process, testing a sample of piles, driven with the refusal criterion, to a maximum axial load defined with a given Safety Factor. The results of the Dynamic Load Tests are then used to check and set the refusal driving criterion or calibrate it if needed. In this paper is presented a description of the execution control process used by KELLER in major piling works for logistic warehouses, and a preliminary study comparing the allowable loads deducted from Dynamic Load Tests results and the allowable loads estimated through refusal measurement.

RÉSUMÉ: Le contrôle de l'exécution pendant et après le battage des pieux en béton préfabriqués est une question critique pour la validation et l'acceptation des travaux. Ceci est particulièrement important en raison des fortes tensions de compression auxquelles les pieux préfabriqués s'attendent généralement à résister, en tirant parti du béton à haute résistance utilisé pour sa fabrication et compte tenu des effets du battement et du déplacement latéral du sol sur l'augmentation de la capacité portante géotechnique. Entre autres, la mesure de refus est l'un des principaux aspects du contrôle d'exécution de chaque pieu battu, et le critère de refus est défini à l'aide de formules du battage des piex, généralement conservatrices. Les essais de charge dynamique jouent un rôle clé dans le processus de contrôle de l'exécution, en testant un échantillon de pieux, battus avec le critère de refus, à une charge axiale maximale définie avec un facteur de sécurité donné. Les résultats des tests de charge dynamique sont ensuite utilisés pour vérifier le critère de refus du battage ou pour le calibrer si nécessaire. Dans cet article, nous présentons une description du processus de contrôle d'exécution utilisé par KELLER dans les grands travaux de battage pour les entrepôts logistiques, et une étude préliminaire comparant les charges admissibles déduites des résultats des essais de charge dynamique et les charges admissibles estimées par mesure de refus.

Keywords: Driven piles; execution control; pile driving formulas; dynamic load tests.

1 INTRODUCTION

Driven precast concrete piles have been a foundation technique widely used in logistic warehouse projects in the Iberian Peninsula.

Execution control during and after driving precast piles is a critical issue for work validation and acceptance. This is especially important due to the high compressive stresses usually expected to be resisted by precast piles, taking advantage of the high-resistant concrete used on its manufacture and given the effects of driving and lateral displacement of the soil on increasing geotechnical bearing capacity.

A description of the execution control process, used by KELLER for driven piles works, is presented in this paper, including driving and loading data from some major logistic warehouse projects performed in Portugal.

2 EXECUTION CONTROL PROCESS

2.1 Refusal driving criterion

Quoting Lawton et al. (1986): "dynamic pile-driving formulas have been available for more than 160 years to predict the static bearing capacity of piles. In the early 1960s the editors of Engineering News-Record had 450 dynamic pile formulas on file. All these formulas are based on the assumption that the ultimate capacity of the pile under static loading is directly related to the driving resistance of the pile in its last stages of embedment.

The stress-strain relationship in a pile during driving is extremely complicated, making on exact theoretical treatment impractical. A small percentage of the available pile-driving formulas are empirical in their entirety; however, most formulas are based on Newton's law of impact and conservation of energy principles and are modified to account for energy losses during impact and during the propagation of stresses."

There are around 20 (more or less) dynamic pile driving formulas commonly used world wide, and the Dutch formula is one of them.

In Portugal and Spain, KELLER uses the Dutch formula to set the refusal criterion, which is a pile driving formula widely used in the Iberian peninsula because of its easy application and easy refusal measurement on site.

The Dutch formula correlates the penetration of the pile, at the end of the driving process, with an estimated allowable axial compression load on the pile ($N_{allowable}$), in order to achieve the following:

$$N_{allowable} \geq N_{SLS} \qquad (1)$$

where N_{SLS} is the maximum axial compression load for Serviceability Limit State.

$N_{allowable}$ is estimated with the Dutch formula as follows:

$$N_{allowable} = \frac{M^2 \times H}{(FS \times e \times (M+P))} \qquad (2)$$

where M is the weight of the mass of the driving hammer, H is drop height of the hammer, FS is the safety factor (6.0 for pile lengths ≥ 12m and 7.0 to 10.0 for pile lengths < 12m), e is the pile penetration per blow, and P is the pile weight.

The refusal driving criterion is finally set as the maximum penetration for the last 10 blows of the driving process ($e \times 10$) for each kind of pile, equalizing $N_{allowable}$ to the respective maximum N_{SLS}.

This is an empirical way to ensure the $N_{allowable}$ needed for every driven pile, and it comes with some uncertainty. Nevertheless, it's known as a conservative approach because of the high safety factors used (6 to 10) and the expected increase of piles bearing capacity in the following days after the driving end and set-up, especially due to the soil rearrangement along the shaft in clayey soils.

2.2 Dynamic load tests

In addition to the refusal driving criterion, dynamic load tests are performed on at least 5% of the piles, 24 or 48 hours (minimum) after the driving end. These are non-destructive tests, consisting in re-driving the piles with the same equipment, and previously installing 2 accelerometers and 2 extensometers at the pile's head. An example is shown in Figure 1.



Figure 1. Instrumentation and load application during a dynamic load test.

The instruments are connected to a PDR unit (data acquisition recorder) which sends the stress wave signals to the monitoring field computer, where curves for force and velocity x impedance are registered for further processing. Later, a FEM software is used for signal-matching, and after that a static calculation of the model is performed, obtaining the total axial compression load applied in the pile test and estimating the shaft load and the base load separately.

Maximum compression stresses, tension and displacements are also obtained.

As part of the execution control process, with these dynamic load tests on a sample of piles the following objectives can be achieved:

- Confirm the $N_{allowable}$ of each kind of pile, applying a maximum test load in order to check the following:

$$Max.Test\ Load \geq N_{SLS} \times FS_{EC7} \qquad (3)$$

where FS_{EC7} is the combination of the partial safety factors and model factor, as defined in the Eurocode 7 (usually around 2.0m for SLS).

- Confirm and calibrate (if needed) the refusal driving criterion.
- Verify the structural integrity of the tested piles.
- Verify hammer efficiency.

3 REFUSAL MEASUREMENT VS. DYNAMIC LOAD TEST

As a preliminary study, data from dynamic load tests (DLT) has been collected from 4 sites of logistic warehouses piling projects in Portugal, and the $N_{allowable_DLT}$, has been considered equal to the maximum test load divided by a FS of 2.0.

At the same time, the respective $N_{allowable_REFUSAL}$ for each tested pile has been estimated using the Dutch formula with a FS between 6.0 and 10.0 depending on the driven length of the piles.

The time after the pile installation has been registered for each pile tested.

The sites have been chosen in order to have 2 sites of clayey soils and 2 sites of sandy soils.

The tested precast concrete piles have square sections, from 270, 300 and 350mm, with concrete class ≥ C50/60.

The pile lengths vary between 12.0 and 15.3m for site 1; 24.9 and 25.9m for site 2; 10.4 and 16.4m for site 3; and between 5.7 and 6.0 for site 4.

The graphics summarizing the results are presented in the Figures 2 to 5, showing in the horizontal axis the penetration of the piles for the last 10 blows at the end of the installation process, and in the vertical axis the ratio ($N_{allowable_DLT}$ / $N_{allowable_REFUSAL}$).

If this ratio is near 1.0, it means that there is a good correlation between the axial allowable compression load of the pile, deducted from the dynamic load test and from the refusal measurement. It would indicate that the applied execution control process is safe and nearly optimal.

If the ratio is much lower than 1.0, it means that the applied execution control process is safe but conservative. This usually occurs when the penetration of the pile during refusal control is very small (with very high $N_{allowable_REFUSAL}$), but the maximum test load of the DLT is only the needed to verify the serviciability load ($N_{SLS} \times FS_{EC7}$).

If the ratio is higher than 1.0, it means that the there will be a doubt during the refusal measurement, related to a low $N_{allowable_REFUSAL}$ value, but if the maximum test load of the DLT is enough to verify the serviciability load ($N_{SLS} \times FS_{EC7}$), then the doubt will be cleared, preserving the safety of the applied execution control process. If this kind of situation happens consistently in a site, then calibration of the refusal driving criterion would be advisable.

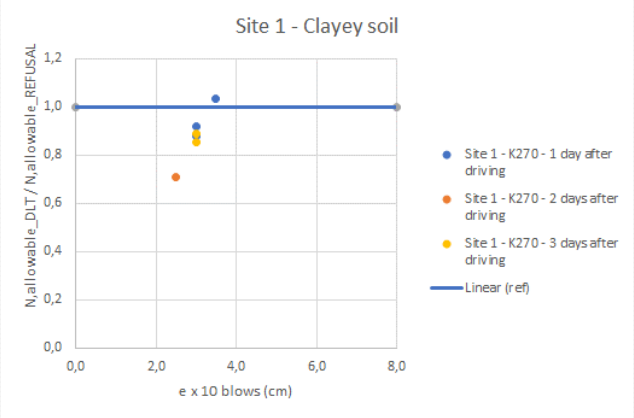

Figure 2. Site 1_Clayey soil - $N_{allowable}$ comparison DLT / REFUSAL.

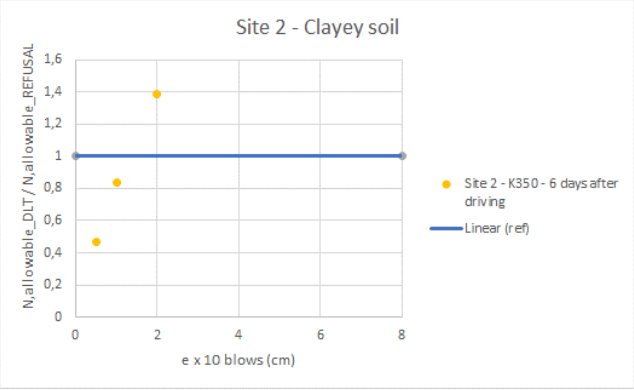

Figure 3. Site 2_Clayey soil - $N_{allowable}$ comparison DLT / REFUSAL.

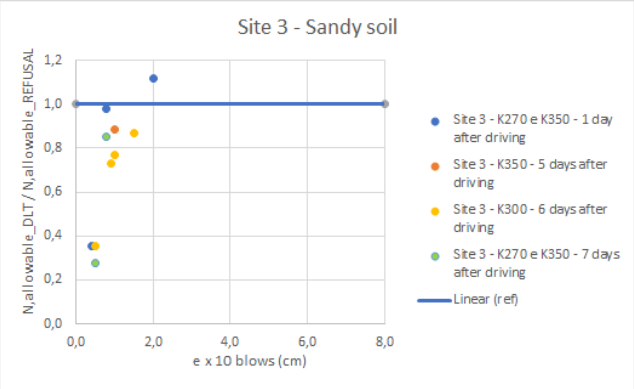

Figure 4. Site 3_Sandy soil - $N_{allowable}$ comparison DLT / REFUSAL.

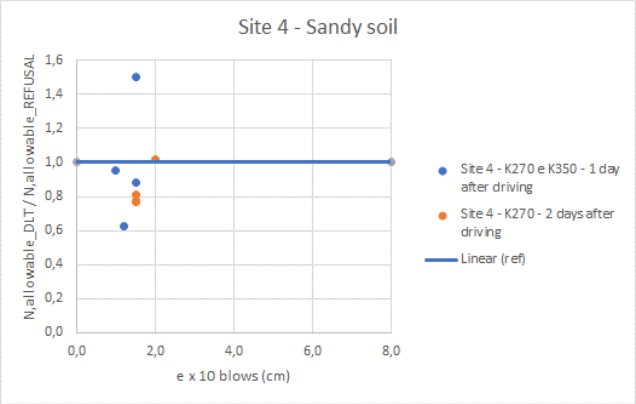

Figure 5. Site 4_Sandy soil - $N_{allowable}$ comparison DLT / REFUSAL.

Analyzing the results presented in the figures above, it is possible to observe that the ratio ($N_{allowable_DLT}$ / $N_{allowable_REFUSAL}$) is usually between 0.8 and 1.0, but sometimes hits low values (minimum of 0.3) and also values higher than 1.0 (maximum os 1.5).

Influence of the soil type and/or time after pile installation hasn‘t been clearly noticed in this results.

4 CONCLUSIONS

The execution control process proposed and applied by KELLER for pile driving works, combining the refusal driving criterion from the Dutch formula, in all piles, with dynamic load tests in a sample of them, has been proved to be safe and robust. Nevertheless, it’s important to ensure that the process isn’t too conservative, optimizing it if possible.

The preliminary study presented in this paper aims this objective, and within the limits of the analised data it seems that, in general, the execution control process has been nearly optimal, and when it isn‘t it has been proved safe.

Seeking the optimization of the process, it will be necessary to extend the analysed sites and data as much as possible, in order to identify the situations where calibration of the refusal criterion could be advisable and to clarify the theoretical influence of the soil type and/or time lag after pile installation.

ACKNOWLEDGEMENTS

The authors are grateful to KELLER Cimentaciones for the motivation and support provided for the preliminary study presented in this article.

REFERENCES

Lawton, E. C., Fragaszy, R. J., Higgins, J. D., Kilian, A. P. and Peters, A. J. (1986). Review of methods for estimating pile capacity, *Transportation Research Record*, 1105(004), pp. 32-40, Available at: 1105-004.pdf (trb.org), accessed: 22/12/2023.

CEN (2009). EN 1997-1:2004 + AC:2009, CEN, Brussels.

Likins, G. E., Fellenius, B. H. and Holtz, R. D. (2012). Pile driving formulas – Past and present, In: *Full-Scale Testing in Foundation Design*, Hussein, M. H., Holtz, R. D., Massarsch, K. R. and Likins, G. E. (eds.), Geotechnical Special Publication 227, Geo-Congress Oakland March 25-29, USA, pp. 737-753, Available at: Discussions on Pile Driving Formulas (windows.net), accessed: 22/12/2023.

Proceedings of the XVIII ECSMGE 2024
GEOTECHNICAL ENGINEERING CHALLENGES
TO MEET CURRENT AND EMERGING NEEDS OF SOCIETY
© 2024 the Authors
ISBN 978-1-032-54816-6
DOI 10.1201/9781003431749-283
Open Access: www.taylorfrancis.com, CC BY-NC-ND 4.0 license

ECSMGE 24
XVIII EUROPEAN CONFERENCE ON SOIL MECHANICS AND GEOTECHNICAL ENGINEERING

Review of SPT-undrained shear strength correlation for UK soil deposits

Examen de la corrélation entre la résistance au cisaillement SPT et non drainée pour les dépôts de sol britanniques

J.J. Crispin
University of Oxford, Oxford, UK

C.E.L. Gilder
Arcadis, Bristol, UK

P.J. Vardanega*
University of Bristol, Bristol, UK

**p.j.vardanega@bristol.ac.uk*

ABSTRACT: The Standard Penetration Test (SPT) is a ubiquitous test undertaken during ground investigations in the UK (and worldwide). In UK geotechnical practice the Stroud relationship is often used to estimate undrained shear strength using the plasticity index and the SPT blow count. Increasingly geotechnical engineering is adapting to the presence of open-data which can be used to re-evaluate and update design rules. This paper makes use of data from various literature sources and data obtained from archived AGS files, which store digital ground investigation information in an industry standard format. AGS files were obtained from the British Geological Survey's (BGS) National Geoscience Data Centre (NGDC) to compare test results with the original Stroud relationship. This work quantifies the potential parameter variation that may be encountered when estimating undrained shear strength using the SPT across six geological deposits. This allows for improved risk mitigation during the design process and, while the existing relationship remains in line with the new results, this highlights the possibility of material specific correlations.

RÉSUMÉ: L'essai au pénétromètre dynamique (SPT) est un essai omniprésent lors des études du sol au Royaume-Uni (et dans le monde entier). Dans la pratique géotechnique britannique, la relation de Stroud est souvent utilisée pour estimer la résistance au cisaillement non drainé en utilisant l'indice de plasticité et le nombre de coups du SPT. L'ingénierie géotechnique s'adapte de plus en plus à la présence de données ouvertes qui peuvent être utilisées pour réévaluer et actualiser les règles de conception. Cet article s'appuie sur des données provenant de diverses sources de littérature et sur des données obtenues à partir de fichiers AGS archivés, qui stockent des informations numériques sur l'étude du sol dans un format standard industriel. Les fichiers AGS ont été obtenus auprès de l'Institut d'études Géologiques Britannique (BGS) du Centre National de Données Géoscientifiques (NGDC) afin de comparer les résultats des tests avec la relation originale de Stroud. Ce travail quantifie la variation potentielle des paramètres qui peut être retrouvée lors de l'estimation de la résistance au cisaillement non drainé à l'aide du SPT dans six gisements géologiques. Cela permet d'améliorer l'atténuation des risques au cours du processus de conception et, bien que la relation existante reste conforme aux nouveaux résultats, cela met en évidence la possibilité de corrélations spécifiques aux matériaux.

Keywords: Standard penetration test; undrained shear strength; soil variability; correlations.

1 INTRODUCTION

Many geotechnical design parameters are difficult to obtain directly during routine design work due to the need for complex and/or time-consuming field or laboratory tests. Therefore, practitioners often use published correlations to estimate more complex parameters (e.g. undrained shear strength, s_u; shear modulus, G) from those parameters which are more readily available. The Standard Penetration Test (SPT) is commonly used in this context (e.g. Terzaghi *et al.* 1996, Reid and Taylor, 2010) and a number of authors have attempted to obtain correlations which relate plasticity index (I_P) and SPT blow count (N) to the s_u parameter for fine-grained soils.

1.1 Skempton (1954)

Skempton (1954) presented the following empirical correlation for s_u measured with field vane ($s_{u,FV}$) normalised by the effective overburden pressure (σ'_{v0}):

$$s_{u,FV}/\sigma'_{v0} = 0.11 + 0.0037(I_P, \%) \quad (1)$$

In Skempton (1957) further data were added, and Mayne (2013) gave the following regression coefficients proving similar to the original regression result (R^2 = 0.946, n = 19):

$$s_{u,FV}/\sigma'_{v0} = 0.1006 + 0.0038(I_P, \%) \quad (2)$$

As detailed in Wood (1990, pp. 302-305) data from Bjerrum (1973) were used by Mesri (1975) to question the dependence of s_u/σ'_{v0} on I_P. Mayne (2013) showed regressions fitted to data from Ladd and DeGroot (2003) showing weaker correlations linking s_u/σ'_{v0} to I_P (%) for other shear modes (e.g. direct simple shear, DSS; triaxial compression, TC; and triaxial extension, TE). The significance of I_P on s_u parameters for fine-grained soils will be discussed in this paper.

1.2 Stroud (1974)

Past studies (e.g. Sowers 1954 and de Mello 1971) had linked soil strength parameters to SPT-*N*. Stroud (1974) then proposed the following estimation for the s_u of insensitive clays and soft rocks, mostly from unconsolidated undrained triaxial compression tests (therefore expressed here as $s_{u,UU}$):

$$s_{u,UU} = f_1 N \quad (3)$$

where f_1 is an empirical factor that Stroud (1974, p. 369) noted 'is a constant essentially independent of depth and of discontinuity spacing, although it may vary in some way from site to site according to the characteristics of the material being tested'. The parameter f_1 ranges from 3.1 to 7.6 for the soils studied by Stroud (1974) and Stroud and Butler (1975), who showed that f_1 varies with I_P for the studied clays. However, the lack of a statistically derived trend was noted by Reid and Taylor (2010).

Further studies using the SPT to estimate s_u include Hara *et al.* (1974), Terzaghi *et al.* (1996), Sivrikay and Toğrol (2006) and Tan and Ramli (2023). The SPT has also been used to estimate various other geotechnical design parameters, e.g. soil stiffness (e.g. Hara *et al.* 1974, Rocha *et al.* 2023) and stress ratios that result in liquefaction (e.g. Seed *et al.* 1985). Seed *et al.* (1985) recommended using a standardized energy ratio to 'correct' raw SPT-*N* values: a value of 60% was advised. This corrected SPT parameter (N_{60}) was also supported by Skempton (1986) who also recommended a correction for overburden pressure denoted as $(N_1)_{60}$. Stroud (1989) then recast the plot from Stroud and Butler (1975) with $f_1 = s_u/N_{60}$.

Following Stroud (1974), Stroud and Butler (1975) and Stroud (1989), f_1 is essentially a 'site' parameter which is derived site-by-site by assuming the s_u with depth trend has the same gradient as the SPT-*N* versus depth data. This means that f_1 is averaged and that individual locations on a site may deviate from the site value. Also, the I_P value may not be available at each SPT-*N*:s_u test pair and hence the f_1 value is related to a representative I_P value in the original work of Stroud (1974) and Stroud and Butler (1975).

White *et al.* (2019) recently presented a revised method for the calculation of f_1; essentially f_1 values are calculated for specific pairs of s_u and SPT-*N* values which can then be arithmetically averaged across a geological unit. However, White *et al.* (2019) retained the method of averaging these f_1 values for each site. The analysis of nine sites presented in White *et al.* (2019) suggested an increase in average representative f_1 values for London Clay from 4.4 to 5.7, the cause of which was attributed to changes in the SPT test since the original Stroud (1974) paper.

1.3 Open data sources

The challenges of data sharing in the geotechnical community have been reviewed in Gilder *et al.* (2021). Considerable open data is available from the British Geological Survey's (BGS) National Geoscience Data Centre (NGDC), which has been used in various UK research projects (e.g. Thorpe and Terrington 2023).

The BGS NGDC provides archived files in AGS format (described in AGS 2017) detailing the results of ground investigations across the UK. So far, 54 projects have been found with SPT-*N*, s_u and I_P data (project references are not reported here for brevity).

1.4 Study Aims

Following the observations in Reid and Taylor (2010) regarding the lack of detailed statistical analysis in the UK studies reviewed in Section 1.2, the authors have used open AGS data from the BGS NGDC to investigate if:

- this data can be used to calculate f_1 values for UK soils to verify the proposed range provided by past studies and provide statistical measures;
- the increased f_1 for modern SPTs in White *et al.* (2019) can be extended to other deposits;
- the data statistically supports the link between f_1 and I_P over geological deposits (rather than project sites); and
- alternative parameters, such as depth, show a more statistically significant correlation with f_1.

This paper presents the preliminary results of this study, focussed on the first two points listed above.

2 DATA PROCESSING

Python software was used to combine AGS data files from multiple projects. Following White *et al.* (2019), each triaxial test result was paired with the nearest SPT test from the same borehole to form an SPT-N:s_u pair. These were then used to calculate f_1 values, and the nearest I_P value was assigned to this result. Additionally, the SPT was required to be in the same geological unit and undertaken within 1.5m of the triaxial test and the I_P value had to be obtained from a sample within 3m. Note that these preliminary results do not include investigation into the sensitivity of the proximity between SPT-N, s_u and I_P values; suitable SPT corrections could not be applied; and no outliers were excluded.

A significant proportion of the data was sourced from linear infrastructure projects such as the A14 Cambridge to Huntington project and the Thames Tideway Tunnel. In these cases, it was not intuitive to average values over a whole project or split them into sites. This highlights the problems with performing a statistical analysis based on data grouped by sites with different amounts of information. Instead, this data has been grouped only by geological deposit. Excluding non-glacial superficials, six deposits were found to have enough data to analyse using this approach.

3 RESULTS

Table 1 shows the summary statistics for the f_1 and I_P values obtained in each of the six geological deposits. The mean values are plotted in Figure 1 and compared to the tabulated UK data from Stroud (1974), Stroud and Butler (1975) and White *et al.* (2019). Note that the Mercia Mudstone data were not based on triaxial tests and were therefore excluded, and the geological deposits were renamed according to BGS (2023).

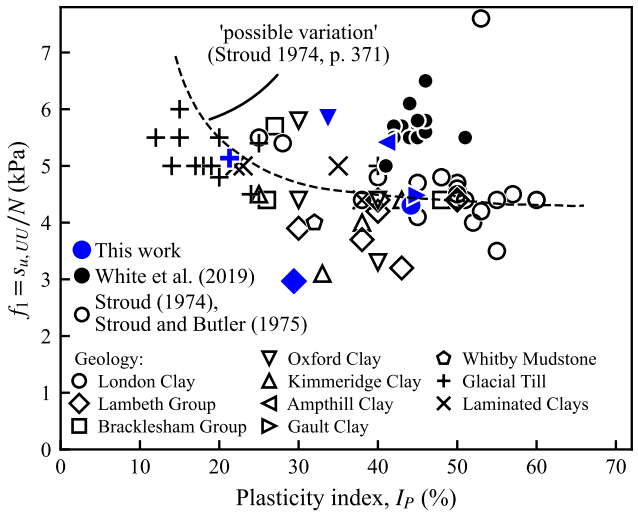

Figure 1. f_1 vs. I_P values compared to tabulated UK data.

Table 1. f_1 and I_P summary statistics by geological deposit. n=number of points, μ=mean value, P_{25}= 25th percentile, and P_{75}=75th percentile, COV=Coefficient of Variation.

Geology	n	param.	P_{25}	μ	P_{75}	COV (%)
London Clay	283	f_1 (kPa)	3.0	4.3	5.4	46
		I_P (%)	40	44	49	16
Lambeth Group	89	f_1 (kPa)	1.3	3.0	3.7	100
		I_P (%)	22	29	36	35
Oxford Clay	94	f_1 (kPa)	2.9	5.8	6.7	83
		I_P (%)	29	34	37	18
Ampthill Clay	36	f_1 (kPa)	3.8	5.4	6.4	47
		I_P (%)	38	41	45	13
Gault Clay	31	f_1 (kPa)	2.6	4.5	5.0	62
		I_P (%)	43	45	48	8
Glacial Till	72	f_1 (kPa)	3.3	5.1	6.6	57
		I_P (%)	16	21	25	31

The following observations are made from these preliminary results: (a) the mean f_1 values show a similar range to the original dataset by Stroud (1974) and Stroud and Butler (1975); (b) the coefficient of variation for f_1 is relatively high in each deposit; (c) the mean f_1 = 4.3kPa for London Clay is notably lower than in White *et al.* (2019); and (d) no strong evidence of the correlation between f_1 and I_P was found.

4 SUMMARY AND CONCLUSIONS

This paper presented the preliminary results of a study investigating f_1 values for UK soil deposits. In total, 54 projects were analysed to obtain 605 suitable datapoints in six geological deposits. A similar variation of f_1 values to that indicated in the Stroud (1974) and Stroud and Butler (1975) results was found. Summary statistics were provided quantifying the variation by deposit. The f_1 values for London Clay were generally closer to those from Stroud (1974) than the newer results from White *et al.* (2019), suggesting that the proposed higher values should be supported with site-specific data before use. The methodology presented here can be refined further to investigate the suitability of correlating f_1 with I_P and other parameters. However, due to the inherent variability of SPT and UU triaxial tests, significant scatter is expected and engineers should exercise caution when relying on correlations between these parameters.

This study shows how open data can be used to re-examine the variability of geotechnical design parameters and highlights the importance of increased data sharing (Gilder *et al*. 2021). This correlation is in common use in UK geotechnical practice and improved confidence could represent considerable cost savings and sustainability gains.

ACKNOWLEDGEMENTS

The authors thank Garry Baker and Martin Nayembil for their help obtaining data from the BGS NGDC and Dr Ahmad EL Hajjar for his assistance with the translation of the abstract into French. *Data availability:* the project references are available from the first author upon request.

REFERENCES

AGS (2017). *Electronic Transfer of Geotechnical and Geoenvironmental Data*, Ed. 4.0.4. Association of Geotechnical and Geoenvironmental Specialists, Kent, UK.

BGS (2023). The BGS Lexicon of Named Rock Units. www.bgs.ac.uk/lexicon/ [accessed: 27/11/23].

Bjerrum, L. (1973). Problems in soil mechanics and construction on soft clays and structurally unstable soils (collapsible, expansive and others). In: *Proc. 8th ICSMFE,* Moscow, USSR, vol. 3, pp. 111-159.

de Mello, V.F.B. (1971). The Standard Penetration Test. In: *Proc. 4th PCSMGE*, San Juan, Puerto Rico. Vol. 1, pp. 1-86.

Gilder, C.E.L., Geach, M., Vardanega, P.J., Holcombe, E.A. and Nowak, P. (2021). Capturing the views of geoscientists on data sharing: a focus on the geotechnical community. *Q. J. Eng. Geol. Hydrogeol.*, 54(2). doi:10.1144/qjegh2019-138.

Hara, A., Ohta, T., Niwa, M., Tanaka, S. and Banno, T. (1974). Shear modulus and shear strength of cohesive soils. *Soils Found.*, 14(3): 1-12. doi:10.3208/sandf1972.14.3_1.

Ladd, C.C. and DeGroot, D.J. (2003). Recommended practice for soft ground site characterization. In: Whittle, A.J. *et al.* (eds.) *Proc. 12th PCSMGE*. Cambridge, MA, USA, vol. 1, pp. 3-57.

Mayne, P.W. (2013). Discussion: Laboratory measurement of strength mobilisation in kaolin: link to stress history. *Géotech. Lett.*, 3(1): 16-17. doi:10.1680/geolett.13.00005.

Mesri, G. (1975). Discussion of "New Design Procedure for Stability of Soft Clays". *J. Geotech. Eng. (ASCE)*, 10(4): 409-412. doi:10.1061/AJGEB6.0005026.

Reid, A. and Taylor, J. (2010). The misuse of SPTs in fine-grained soils and the implications for Eurocode 7. *Ground Engineering*, 43(7): 28-31.

Rocha, A., da Silva, B.C. and Giacheti, H.L. (2023). Maximum shear modulus estimative from SPT for some Brazilian tropical soils. *Soils and Rocks*, 46(1). doi:10.28927/SR.2023.005222.

Seed, H.B., Tokimatsu, K., Harder, L.F. and Chung, R.H. (1985). Influence of SPT Procedures in Soil Liquefaction Resistance Evaluations. *J. Geotech. Eng. (ASCE)*, 111(12): 1425-1445. doi:10.1061/(ASCE)0733-410(1985)111:12(1425).

Sivrikaya, O. and Toğrol, E. (2006). Determination of undrained strength of fine-grained soils by means of SPT and its application in Turkey. *Eng. Geol.*, 86(1): 52–69. doi:10.1016/j.enggeo.2006.05.002.

Skempton, A.W. (1954). Discussion of the structure of inorganic soil. *Proc. ASCE*, 80 (Separate 478): 19-22.

Skempton, A.W. (1957). Discussion: The planning and design of the new Hong Kong Airport. *Proc. of the Institution of Civil Engineers*, 7(2): 305-307. doi:10.1680/iicep.1957.2568.

Skempton, A.W. (1986). Standard penetration test procedures and the effects in sands of overburden pressure, relative density, particle size, ageing and overconsolidation. *Géotechnique*, 36(3): 425-447. doi:10.1680/geot.1986.36.3.425.

Sowers, G.F. (1954). Modern procedures for underground investigations. *Proc. ASCE*, 80 (Separate 435), 11pp.

Stroud, M.A. (1974). The Standard Penetration Test in insensitive clays and soft rocks. In: *Proc.. European Symposium on Penetration Testing*, Stockholm, Sweden, vol. 2, pp. 367-375.

Stroud, M.A. and Butler, F.G. (1975). The Standard Penetration Test and the Engineering Properties of Glacial Material. *Proc. Sym. on the Eng. Behav. of Glacial Mat.*, University of Birmingham, Birmingham, UK. pp. 124-135.

Stroud, M.A. (1989). The Standard Penetration Test – Its applications and interpretation: part 2. In: *Penetration testing in the UK*. Thomas Telford, London, UK, pp. 29-49.

Tan, J.J. and Ramli, H. (2023). Effect of Standard Penetration Test Correlations on the Estimation of Undrained Shear Strength. *J. Civ. Eng. Manag.*, 29(6): 501-515. doi:10.3846/jcem.2023.18441.

Terzaghi, K., Peck, R.B. and Mesri, G. (1996). *Soil Mechanics in Engineering Practice*, Third Edition. John Wiley & Sons Inc., NY, USA.

Thorpe, S. and Terrington, R. (2023). Improving data accessibility and application for underground climate research at the British Geological Survey. *Sym. on Energy Geo.: Acc. the Energy Transition,* Delft, the Netherlands. doi:10.59490/seg.2023.513.

White, F., Ingram, P., Nicholson, D., Stroud, M. and Betru, M. (2019). An update of the SPT-c_u relationship proposed by M. Stroud in 1974. In: *Proc. of ECSMGE-2019*, Reykjavík, Iceland. doi:10.32075/17ECSMGE-2019-0500.

Wood, D.M. (1990). *Soil behaviour and critical state soil mechanics*. Cambridge University Press, Cambridge, UK.

Proceedings of the XVIII ECSMGE 2024
GEOTECHNICAL ENGINEERING CHALLENGES
TO MEET CURRENT AND EMERGING NEEDS OF SOCIETY
© 2024 the Authors
ISBN 978-1-032-54816-6
DOI 10.1201/9781003431749-284
Open Access: www.taylorfrancis.com, CC BY-NC-ND 4.0 license

ECSMGE 24
XVIII EUROPEAN CONFERENCE ON SOIL MECHANICS AND GEOTECHNICAL ENGINEERING

Why geotechnical engineering isn't ready yet for machine learning?

Pourquoi l'ingénierie géotechnique n'est-elle pas encore prête pour l'apprentissage automatique?

T. Daktera*, L. Janodet
SoilCloud SAS, Le Mesnil-le-Roi, France

**tomasz.daktera@soilcloud.fr*

ABSTRACT: Data science technologies are universally known, but only some people understand the foundations and how to implement them operationally on real projects. "Data science" is the common ground between business knowledge (in our case geotechnical engineering), computer science, and advanced mathematics. The example of geotechnics is a typical case, as soil data is a significant part of construction projects. So why is it not common to use those algorithms in geotechnical engineering in 2023? This article describes the current state of the art in which geotechnical engineers, designers, and contractors manage the transfer of geotechnical data in Poland, France, and the Anglo-Saxon world. The authors of this article believe that the solution for implementing data science in geotechnical engineering is first to address the issue of data transfer. This involves providing a specially designed software that will allow companies, at first, to build their own geotechnical database. It is only at this point that one can begin to think about going further, by processing the data and using geostatistical and artificial intelligence techniques.

RÉSUMÉ: Les technologies de la science des données sont universellement connues, mais seules certaines personnes en comprennent comment les mettre en œuvre de manière opérationnelle sur des projets réels. La « science des données » est le terrain commun entre les connaissances commerciales (dans notre cas l'ingénierie géotechnique), l'informatique et les mathématiques avancées. L'exemple de la géotechnique est un cas typique, car les données sur les sols constituent une part importante des projets de construction. Alors pourquoi n'est-il pas courant d'utiliser ces algorithmes en géotechnique en 2023 ? Cet article décrit l'état actuel de l'art dans lequel les géotechniciens gèrent le transfert de données géotechniques en Pologne, en France et dans le monde anglo-saxon. Les auteurs de cet article estiment que la solution pour mettre en œuvre la science des données en ingénierie géotechnique consiste d'abord à aborder la question du transfert de données. Il s'agit de fournir un logiciel spécialement conçu qui permettra aux entreprises, dans un premier temps, de constituer leur propre base de données géotechniques. C'est seulement à ce stade que l'on peut commencer à réfléchir à aller plus loin, en traitant les données et en utilisant les techniques géostatistiques et d'intelligence artificielle.

Keywords: Geotechnical engineering; cloud database; artificial intelligence; machine learning.

1 INTRODUCTION

The current era is witnessing an unprecedented surge in data science applications across diverse industries. However, despite its wide-ranging capabilities, the integration of data science within specialized fields like civil engineering and going even more into details, geotechnical engineering, remains limited.

It is important to distinguish AI (artificial Intelligence) from ML (Machine Learning). AI is a broader field that relates to intelligent systems. ML on the other hand is much more specific where the focus is on developing algorithms that learn from data and improve their performance over time. The key is the data quality. If the data quality one has in hand is poor, the ML algorithm will be unsatisfactory and therefore it will not be widely used by professionals.

In geotechnical engineering, building a database becomes the problem, as all documentation for small to medium projects are transferred between the parties in the PDF format. For large projects, such as infrastructure (roads, tunnels etc.) we are witnessing a change - engineers realized that it is impossible to manage the related risks with thousands of pages of data (graphs and tables) in PDF. Consequently, before tackling AI/ML related applications, the whole industry needs to "play the game" of structuring geotechnical data and transferring the data in digital, organized formats (PDF isn't considered as a digital format). This article will show a couple of approaches,

with their advantages and disadvantages, to solve this data structuring and transfer problem.

2 POSSIBILE AI/ML APPLICATIONS IN GEOTECHICAL ENGINEERING

This paragraph is a non-exhaustive list of possible AI/ML applications in geotechnical engineering:

1. Image recognition can be used for example to recognize the size distribution of grains in a sieve analysis test. After taking a picture of the strewed soil grains, the AI algorithm, will be able to scale all grain sizes, draw conclusions and get a grain size distribution curve.
2. Image recognition can be used for soil description applications where the soil descriptions would be made automatically (hopefully verified by engineers/geologists).
3. Image recognition can be used during cone penetration test (with a camera use) to be able to interpret the results on more than just the qc and fs parameters.
4. A classic application of ML would be the interpretation of the Menard pressuremeter test (PMT). This case is very specific as a large database of PMT's would be needed. A geotechnical management system called SoilCloud (used mostly in France) has the largest PMT dataset verified by humans (over 400,000 PMT's with datasets at each of the interpretation steps made by a human). Such a database would suffice to have conclusions on PMT interpretations and perhaps replace the human factor which would greatly decrease the risk related to PMT data interpretation (it is greatly dependent on the person doing the interpretation).

This list is not exhaustive and many other AI or ML applications in geotechnical engineering are possible and will be available to engineers in the future.

3 STATE OF THE ART ON NATIONAL GEOTECHNICAL DATA INFORMATION SYSTEMS

Without going too much into detail, there are very interesting national initiatives in many countries to gather geological and geotechnical data.

As an example, for France, the BRGM (the French Geological Survey) works on gathering geological and geotechnical data since it was founded in 1959. Among their large range of initiatives, one of them called la Banque du Sous-Sol (BSS) covers now the whole French territory with over 2 million exploratory holes and its data in PDF format. The quality of the data remains questionable by professionals. According to the code minier (French mining code), all geotechnical data have to be transferred to the BRGM so it can be imported to the BSS (on real projects it doesn't happen very often and soil investigation companies are not eager to transfer the data).

For Poland, the Panstwowy Instytut Geologiczny (Polish geological survey) is working on similar initiatives but are focuing much more on geological data and not geotechnical data – there is a clear separation and no foundation design parameters are stored in the database.

For the UK, the BGS (British geological survey) has smiliar initiatives with a very large comunity of geologists and engineers woring around these projects.

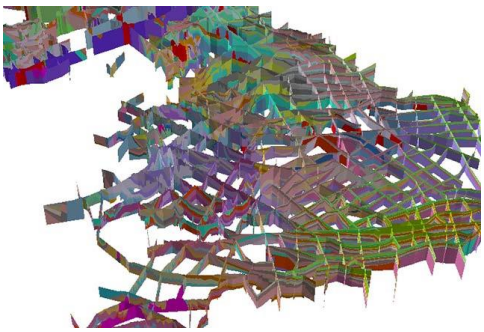

Figure 1. BGS geotechnical cross-sections (source: bgs.as.uk).

Figure 1 shows geotechnical cross-sections based on thousands of borehole data used for foundation design projects.

A last example worth mentioning is the one for the Netherlands: Basisregistratie Ondergrond (BRO), i.e. the underground database, was created for a system of 26 geotechnical input data types. According to general knowledge, as a public initiative, this system compiling such an extensive scope of geotechnical research is the most advanced system in the world. The system was opened in 2020 (Source: Basisregistratie Ondergrond).

4 STATE OF THE ART ON DATA TRANSFER IN GEOTECHNICAL ENGINEERING

This paragraph describes the current state of art of geotechnical datasets being transferred between civil engineers during the life of a project across three European countries: France, Poland and the UK. The advantages and disadvantages of each transfer method are presented for each of the three countries with the names of the leading software companies that provide geotechnical data management software. For all three countries, more than 50% of all geotechnical data (all borehole, in-situ and

laboratory tests performed in each country) is/was being imported on these software packages.

4.1 Transfer of geotechnical data in France

In France, there is no obligation to transfer data in any digital format. The NF P 94-500 standard: Geotechnical engineering projects specifies the sequence of geotechnical projects/missions. This standard only requires the transmission of an inseparable engineering report but without specifying its format. Thus, the transmission of geotechnical data in France was done using reports in paper and/or PDF format. This was until about 2019, the SoilCloud company proposed a very innovative way to share the geotechnical data for a project. The users can export the data in many digital formats or share dynamic links. The exports have been used over 45 thousand times since on over 35 thousand projects (over 350 thousand boreholes with their in-situ and laboratory tests information).

It is important to note that depending on the country, geotechnical investigations are based on different geotechnical tests which has an impact on data transfer. In France, most of the structural designs (shallow and deep foundations or deep excavations) are based on the PMT where the final interpreted results (pressure and module) are discreet values every (most often) 1.5m. Before the technology proposed by SoilCloud, during the design stage of a project, the design engineer was retyping the PMT data from PDF to a tabular type format (Excel for example).

4.2 Transfer of geotechnical data in Poland

Geotechnical reports in Poland are managed by the Ministerial Decree 463 of April 25, 2012. This decree refers to Parts 1 and 2 of the Eurocode 7. The Polish Geological Institute has published a guide to use of project owners and contractors, Wytyczne badań podłoża budownlanego na potrzeby budownictwa drogowego, indicating the content of soil investigation campaigns. This guide also discusses data transfer and storage issues. However, in practice, the use of this guide is considered complex and ultimately, the recommendations regarding the transfer of digital data are not followed.

In Poland, the tests carried out on infrastructure projects are mainly CPT (Cone Penetration Test) and laboratory tests. For CPTs, their interpretation is almost impossible without prior transfer of the data in digital format. Thus, CPT data are sometimes appended, in csv (comma separated values) digital format, to geotechnical engineering reports. This data transfer only applies to CPT, the other data being transmitted directly in non-digital format in the engineering PDF report.

The transmission of CPT data in digital format is therefore not motivated by a desire to manage the geotechnical project, but by practical common sense. This practical common sense brings, despite everything, the advantage of having data in digital format but has the disadvantage of neglecting the digital transfer of other geotechnical data of the project, in particular laboratory tests or the coordinates of the survey points.

At the beginning of the century, a company called Geostar proposed a database solution to manage the data for geotechnical projects (only borehole data). Today, this software seams to encrypt the database, on purpose which means that the users of this software cannot open their own database in any other software.

4.3 Transfer of geotechnical data in the UK and the .ags format file

In the UK, the content of geotechnical engineering reports is defined in BS5930, the code of practice for site investigations. Chapter 62 of this standard specifies "The data generated from the ground investigation should be put into a format which allows data communication between all parties and data manipulation at various stages throughout the life of the works". In NOTE 2, of the same chapter 62, the .ags format is mentioned. Thus, although recommended, no transfer of data in digital format is imposed.

However, the experience of the authors of this publication on large infrastructure projects in Great Britain shows that geotechnical data is commonly transferred using .ags format files. This format, written and worked on since the end of the 1990s by the Association of Geotechnical & Geo-environmental Specialists, was designed to respond to the problem of standardized transmission of geotechnical data with the aim of reducing geotechnical risk. An .ags format file is a text file containing only ASCII (American Standard Code for Information Interchange) characters. The .ags file contains all the digital data of the project structured around headers defined in the standard. In particular, the .ags file contains the location information of the surveys (latitude, longitude, altitude), the dates of completion, the lithological descriptions, the raw results of the tests carried out, the references of the samples taken, etc.
The use of .ags files allows immediate transfer of geotechnical data between the different stakeholders in a project, which is a real advantage. However, each time the project is updated, in the case of an additional campaign for example, the transmission of a new .ags

file is necessary. This therefore requires discipline from all project stakeholders so that each geotechnical engineer has access to new data, which represents the main drawback of using .ags files.

In the UK, a software called Holebase was used since the beginning of the century and was structured around the .ags format. This means, that it has all the advantages of the .ags format but also its disadvantages. Being a very well documented and complete text format is its largest advantage. At the same time, being a text file and not a database format file (for example .xml) is its disadvantage as error in the file are very probable (data repetitions in the files and no direct links in the file, just text).

Additionally, the use of the .ags files is often limited to the duration of the project. Thus, once the project is completed, these files are "forgotten" because current software does not allow centralized storage and visualization. Over the years, this represents a loss of value for all stakeholders in geotechnical projects.

5 ADVANTAGES OF A CENTRALIZED AND COLLABORATIVE GEOTECHNICAL DATA MANAGEMENT SYSTEM

As discussed above, the use of interoperable files, such as the .ags format files, provide better control of geotechnical data, but, however, has the drawback of requiring discipline from each of the parties involved in transferring these files. Therefore, a centralized solution on a project and enterprise scale is more relevant. Today, IT technologies provide tools for centralized exchange of data. The Internet/web is a modern way to exchange, store and visualize geotechnical data, as well as providing specially designed applications. The web technology allows collaborative work. Thus, as soon as a stakeholder adds or modifies data from a project, all the other stakeholders have immediate access to it. The discipline effort mentioned previously is therefore reduced to nothing.

6 CONCLUSIONS

The following conclusions come to mind to answer the question asked in the title:

1. AI/ML algorithms require organized and verified datasets to give expected results. In geotechnical engineering, such datasets can be created once the engineers use digital data formats when working on civil engineering projects. Such formats are for example .ags format files or database format files.

2. A verified technology for transferring of geotechnical data is the web technology with centralized and collaborative data management systems.

3. Although none of the countries discussed previously legally require digital geotechnical data transfer, an exchange of geotechnical data in digital format improves the quality of engineering and reduces geotechnical risk. National initiatives led by the national survey institutes are important to educate and spread the knowledge about the importance of digital files.

An additional reflexion on this topic would be: The technologies for AI/ML algorithms already exist but using such technologies mean a deep change in the way the geotechnical engineers presently work. Might the geotechnical engineers' habits and resistance to change be the main obstacle to generalisation of AI/ML?

REFERENCES

Association of Geotechnical & Geoenvironmental Specialists (2020). Electronic Transfer of Geotechical and Geoenvironmental Data.

BS 5930 (2015). Code of practice for ground investigations.

Daktera, T. and Janodet L. (2022). Discussion sur le transfert des données géotechniques en France. *11èmes journées nationales de géotechnique et de géologie de l'ingénieur, Institut National des Sciences Appliquées de Lyon [INSA Lyon], CFMS, CFMR, CFGI, Jun 2022, Lyon, France.* hal-03719813.

NF EN 1997-1. Eurocode 7 : Calcul géotechnique – Partie 1 : Règles générales. (1997).

NF EN 1997-2. Eurocode 7 : Calcul géotechnique – Partie 2 : Reconnaissance des terrains et essais. (1997).

NF P 94-500. Missions d'ingénierie géotechnique (2013).

Polish Geological Institute (2019). Soil investigation guidelines for road construction. Translated from Polish: Wytyczne badań podłoża budowlanego na potrzeby budownictwa drogowego.

Proceedings of the XVIII ECSMGE 2024
GEOTECHNICAL ENGINEERING CHALLENGES
TO MEET CURRENT AND EMERGING NEEDS OF SOCIETY
© 2024 the Authors
ISBN 978-1-032-54816-6
DOI 10.1201/9781003431749-285
Open Access: www.taylorfrancis.com, CC BY-NC-ND 4.0 license

ECSMGE 24
XVIII EUROPEAN CONFERENCE ON SOIL MECHANICS AND GEOTECHNICAL ENGINEERING

Geotechnical parameters estimation in iron ore tailings piles via Bayesian models

Estimation des paramètres géotechniques dans les haldes de résidus de minerai de fer via des modèles Bayésiens

B.M. de Lacerda*
Simplelab Tecnologia, Minas Gerais, Brasil

R. Chammas
Chammas Engenharia, Minas Gerais, Brasil

T.C.O. Fonseca
UFRJ, Rio de Janeiro, Brasil

T.B. dos Santos
UFOP, Minas Gerais, Brasil

**bianca.lacerda@simplelabtech.com.br*

ABSTRACT: As a result of the several events involving dams around the world, the construction of upstream dams was banned, new regulations have been established, and revisions to waste disposal norms have been made. New technologies were developed for the tailings treatment, allowing alternatives for their disposal, such as the construction of different stacking methodologies. Several measures are taken in order to assure the structures safety, such as carrying out geotechnical tests throughout the construction and technological control, which ensure that the project technical specifications are complied. Some tests must be carried out in the laboratory and require a long execution time, reducing the information number of materials physical and geomechanical parameters. In this way, important geotechnical parameters for the complete understanding of the behaviour of the tailings are restricted to a few points of the structures, and with deterministic results. Despite to work with a distribution of samples that represent the structure in a significant way, as they may be subjected to different levels of stresses, humidity, granulometry, among other conditions, using values from specific locations to assure the safety of the whole construction can lead to erroneous estimates in unsampled locations. In this article, data from piles of different locations in MG/Brazil extracted of Geolabor, an ecosystem of applications for managing geotechnical data, were used to estimate different geotechnical parameters from the technological control at non-tested points. Multiple spatial and non-spatial regressions were implemented, and the results obtained were satisfactory, showing the importance of the methodology developed and implemented with Geolabor.

RÉSUMÉ: En raison des nombreux événements impliquant des barrages dans le monde entier, la construction de barrages en amont a été interdite, de nouvelles réglementations ont été établies et des révisions des normes de traitement des déchets ont été effectuées. De nouvelles technologies ont été développées pour le traitement des résidus miniers, permettant des alternatives à leur élimination, telles que la construction de différentes méthodologies d'empilement. Plusieurs mesures sont prises pour assurer la sécurité des structures, telles que la réalisation de tests géotechniques tout au long de la construction et le contrôle technologique, qui garantissent que les spécifications techniques du projet sont respectées. Certains tests doivent être effectués en laboratoire et nécessitent un temps d'exécution long, réduisant le nombre d'informations sur les paramètres physiques et géomécaniques des matériaux. De cette manière, d'importants paramètres géotechniques pour la compréhension complète du comportement des résidus miniers sont restreints à quelques points des structures, et avec des résultats déterministes. Malgré le travail avec une distribution d'échantillons représentant la structure de manière significative, étant donné qu'ils peuvent être soumis à différents niveaux de contraintes, d'humidité, de granulométrie, entre autres conditions, l'utilisation de valeurs provenant de points spécifiques pour garantir la sécurité de toute la construction peut conduire à des estimations erronées dans les emplacements non échantillonnés. Dans cet article, des données extraites de Geolabor, un écosystème d'applications pour la gestion des données géotechniques, provenant de tas de différentes localités de MG/Brésil, ont été utilisées pour estimer différents paramètres géotechniques à partir du contrôle technologique aux points non testés. Des régressions spatiales et non spatiales multiples ont été mises en œuvre, et les résultats obtenus étaient satisfaisants, montrant l'importance de la méthodologie développée et mise en œuvre avec Geolabor.

Keywords: Piles and Dams; technological control; geostatistics; statistical geotechnics; parameter prediction.

1 INTRODUCTION

In soil study, there are uncertainties in the calculations of the physical and geomechanical materials properties, possibly associated with the limited number of samples in the structure, the tests carried out and the geological field conditions (Flores, 2008). Statistical studies in mining geotechnics have as main objective to considere these uncertainties, searching for results that are more coherent with reality. The practical applications of the statistical analyzes in mining geotechnics have been growing and gaining prominence in recent years, but they still constitute a study with a restricted approach (Ferreira, 2022).

Literature authors, such as Azevedo (2019), Badaró (2022) and Ferreira (2022), discuss different ways of applying statistics in mining geotechnics, these being, respectively: The study of outliers for identification discrepant readings in piezometers when monitoring dams; The use of statistical analyzes to compare the performance of different methods of obtaining moisture for the technological control of filtered waste disposal structures; And the comparison of deterministic and probabilistic analyzes to determine the safety factor in the study of dam stability. In this article, a case study will be carried out with real data from iron ore tailings piles, applying statistical techniques to predict geotechnical variables from technological control.

As emphasized by Phoon (2020), one of the greatest difficulties in carrying out statistical analyzes in geotechnics is the small amount of data available. This problem is not caused by the lack of soil studies in geotechnical constructions, but by the lack of a database that can be used for future analyses, enabling relationships between different parameters, types of materials and interpretations of data in relation to the regions under study.

Despite being recognized for years in the literature, the importance of working with a data management system has been gaining prominence in recent years, and there are currently many mining companies that carry out geotechnical processes on physical paper, writing results for digitizing information (de Lacerda and Chammas, 2023). In order to meet this need, Geolabor was developed, an intelligent geotechnical data management system, aimed at the mining field. Acting in all engineering processes, from planning, operation, data processing and approval of results, Geolabor builds a structured database, automatically updated with its use for field investigations, laboratory and technological control.

By using Geolabor data, it is possible to compile data from different structures to carry out a complete statistical analysis. In this article, data from two iron ore tailings piles from different locations in Minas Gerais/Brazil will be used to estimate geotechnical parameters of technological control, via Bayesian geostatistical models. Totaling more than two thousand samples collected, the main objective of this article is to predict the missing values of geotechnical variables obtained in tests carried out in the technological control of the structures under study.

Spatial and non-spatial analyzes will be carried out in order to understand the importance of taking into account spatial effects for this type of material. In that way, this work validates the possibility of using data from different piles together, resulting in analyzes with a greater quantity of observed data and enabling, for example, the future estimation of the material's physical and geomechanical parameters obtained from triaxial tests in the laboratory and carried out less frequently than those resulting from other tests from technological control.

2 MISSING DATA

The three main types of missing data are Missing Completely At Random (MCAR), Missing At Random (MAR) and Missing Not At Random (MNAR), where: MCAR applies when there is no need to treat missing data, since the data observed in the sample are representative of the population; MAR applies to cases where the missing data is not random, however, there is information in the other variables in the sample that can be used to complete the data; and MNAR, which will deal with samples where the reason for the existence of missing data is related to the variable of interest, resulting in the possibility of biased analyzes (Little and Rubin, 2019).

In this paper, the missing data will be characterized as MAR, since the geotechnical variables can be explained by the other variables observed from the same material. The analyzes will be carried out in R, by using the averages of the nearest neighbors; the MissForest packages (Stekhoven and Bühlmann, 2012), a non-parametric method that allows interactive effects and no linear, working with data of mixed types; and MICE package (Van Bureen and Karin, 2011), a method that works with imputation under the multivariate normal and log-linear distribution, specifying a multivariate distribution for the missing data and imputing the values from MCMC (Markov Chains Monte Carlo).

3 ANALYSIS

In this article, predictions were made of the following geotechnical parameters, obtained from HILF tests:

Ground Moisture (w_{med} – %); Maximum Dry Density (γ_{dmax} – g/cm³); Optimum Moisture (w_{opt} – %); Degree of Compaction (Dc – %); Moisture Degree (Dw – %). As the work is being carried out with real information, the missing data is, in fact, unknown. Thus, in order to enable compare the predicted values with the real ones, ramdom points were removed, for subsequent verification of results. Table 1 presents the number of points analyzed, along with the percentage of missing data for each variable studied in each pile.

Table 1. Missing data percentage of each covariate.

Pile	Pile 1	Pile 2	Pile 1 and Pile 2
Total Samples	1823	655	2478
Removed Samples	182	57	239
Missing w_{med} (%)	9.98	20.15	12.67
Missing γ_{dmax} (%)	10.09	9.47	9.93
Missing w_{opt} (%)	10.04	9.47	9.89
Missing Dc (%)	10.20	21.83	13.66
Missing Dw (%)	10.04	20.15	13.59

The histograms of each geotechnical variable observed in Pile 1 and Pile 2 together are shown in Figure 2.

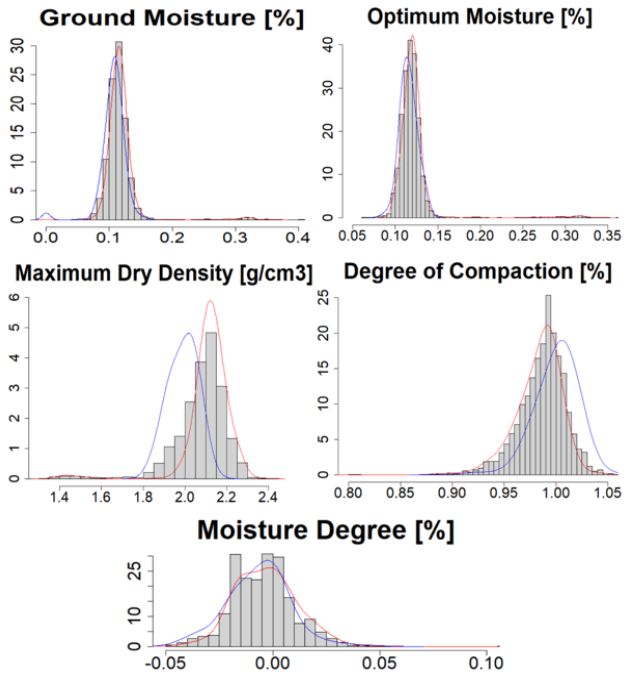

Figure 1. Histograms of each geotechnical variable observed in Pile 1 and Pile 2 together, along with the density curves of Pile 1, in red, and Pile 2, in blue.

Figure 2 presents the two-by-two relationships between the geotechnical variables observed in Pile 1, in red, and in Pile 2, in blue.

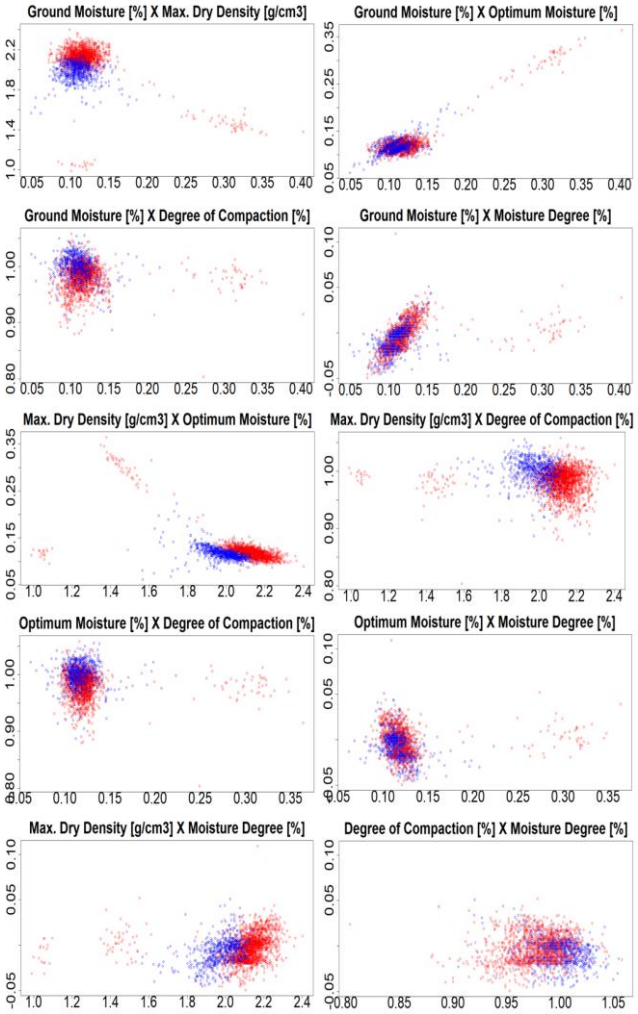

Figure 2. Two-by-two relations between the variables in analyse (red are referred to Pile 1 and blue to Pile 2).

It can be observed, from the histograms presented in Figure 2 and the graphics presented in the Figure 3, that the geotechnical variables present a similar behavior, with a slightly greater discrepancy in values for the Maximum Dry Density. This similarity is due to the same type of material being studied, despite coming from different mineral activities, and arranged in different structures.

Table 2 contains the percentage errors of the predictions made from the missing data imputation. The percentages of points where the error obtained was less than 5% and 10% are also presented. The results are obtained by comparing the value predicted by the above methodologies with the real values that were initially artificially removed for verification. An1 is refer to Close Neighbouhood; An2 to MissForest R Package; and An3 to MICE R Package. All results in Table 1 are given as percentages (%).

Table 2. Errors from analysis, with the best results in bold.

Error	w_{med}	γ_{dmax}	w_{opt}	Dc	Dw
Pile 1: Error <= 5%	31.87	89.56	58.79	94.51	4.4
	89.01	**92.86**	**89.01**	**96.7**	26.92
	85.16	84.62	86.81	88.46	**37.36**
Pile 1: Error <= 10%	57.14	99.45	84.07	**100**	6.59
	92.31	**100**	**96.7**	99.45	40.66
	91.21	98.9	95.05	99.45	**50**
Pile 1: Average Error	10.4	2.46	6.23	1.81	170.26
	2.4	**1.96**	**2.21**	**1.64**	**41.72**
	2.81	2.74	2.67	2.2	47.74
Pile 2: Error <= 5%	26.92	75.44	36.84	97.83	9.43
	73.08	**96.49**	**80.7**	**100**	**22.64**
	36.54	85.96	49.12	95.65	11.32
Pile 2: Error <= 10%	46.15	98.25	64.91	100	11.32
	92.31	**100**	**91.23**	**100**	**37.74**
	63.46	98.25	73.68	100	13.21
Pile 2: Average Error	12.76	3.12	8.4	1.43	142.45
	3.41	**1.95**	**3.57**	**1.05**	**35.09**
	9.17	2.92	6.2	1.88	133.09
Piles 1 and 2: Error <= 5%	31.47	75.21	50	**96.92**	5.56
	86.64	**81.93**	**86.97**	96.48	**35.04**
	83.62	64.71	74.37	88.11	32.48
Pile 1 and Pile 2 Together: Error <= 10%	61.21	94.96	76.47	**99.56**	5.56
	94.4	**97.06**	**98.32**	**99.56**	**50.43**
	92.24	94.12	91.6	99.12	**50.43**
Pile 1 and Pile 2 Together: Average Error	10.32	3.82	7.01	1.79	123.69
	2.37	**2.87**	**2.05**	**1.74**	**35.7**
	4.22	4.3	3.92	2.53	45.41

4 CONCLUSIONS AND NEXT STEPS

Based on the results presented in Table 2, the methodology that presented the best results in most analyzes was the MissForest R package. It is possible to state that the implemented methodologie is mostly satisfactory, achieving predictions with percentage errors lower than 4% for all geotechnical variables analyzed, but to the Moisture Degree. The error quality analysis corroborates this statement, by presenting at least 73% of results with a percentage error of less than 5% and at least 91% than 10%. The domain of the moisture deviation variable is very close to zero, which may be affecting the predictions or the calculation of errors. This in-depth analysis will be carried out later.

So far, no multivariate imputation methodology that takes spatial effects into account has been implemented, nor has the existence and influence of potential outliers been analyzed. Analyzing the results presented, it is possible to verify that the reduction in error quality is not significant when data from the same material and different locations are combined in the analyses. Thus, the development of the work so far suggests that it is feasible and makes practical sense to combine information from different stacks to make predictions of values that would not be possible in a single structure due to insufficient data. Following the development, the same analyses presented in this article will be performed with the geotechnical variables obtained in the CPN, GPS, MES, and CIUsat tests, considering outliers and spatial effects.

ACKNOWLEDGEMENTS

The authors are thankful for the support of the Institute of Mathematics and Statistics at UFRJ and the team at Simplelab Tecnologia, for the Geolabor data.

REFERENCES

Azevedo, A. G. (2019). Statistical analysis to identify discrepant piezometry readings: case study in an earthen dam. Available in: <monografias.ufop.br/>.

Badaró, J. V. O. (2022). Statistical analysis as a decision-making tool: case study in determining moisture in the technological control of a filtered waste disposal structure. Available in: <ufop.br>.

de Lacerda, B. M. and Chammas, S. C. (2023). The Importance of Geotechnical Data Management in Pile and Tailings Dam Works. SNGB, Dams Week, Foz do Iguaçú. Available in: <https://cbdb-web>.

Ferreira, P. M. (2022). Assessment of the reliability of the safety factor obtained by probabilistic analysis in relation to deterministic analysis in mining dams. Available in: <monografias.ufop.br/>.

Flores, E. A. F. (2008). Probabilistic analyses of slope stability considering the spatial variability of the soil. Rio de Janeiro. Available in: <abge.org.br/>.

Little, Roderick JA; Rubin, Donald B. Statistical analysis with missing data (2019). Vol. 973.

Phoon, K. K. (2020). *The story of statistics in geotechnical engineering*. Georisk: Assessment and Management of Risk for Engineered Systems and Geohazards, 14(1), 3-25. https://doi.org/10.1080/17499518.2019.1700423.

Stekhoven, D. J., & Bühlmann, P. (2012). MissForest non-parametric missing value imputation for mixed-type data. Bioinformatics, 112-118. https://doi.org/10.1093/bioinformatics/btr597.

Van Bureen, Stef; G.O., Karin. *Mice: Multivariate imputation by chained equations in R*. Journal of statistical software (2011). v. 45, p. 1-6. https://doi.org/10.18637/jss.v045.i03.

Proceedings of the XVIII ECSMGE 2024
GEOTECHNICAL ENGINEERING CHALLENGES
TO MEET CURRENT AND EMERGING NEEDS OF SOCIETY
© 2024 the Authors
ISBN 978-1-032-54816-6
DOI 10.1201/9781003431749-286
Open Access: www.taylorfrancis.com, CC BY-NC-ND 4.0 license

ECSMGE 24
XVIII EUROPEAN CONFERENCE ON SOIL MECHANICS AND GEOTECHNICAL ENGINEERING

Interactive three-dimensional management of data from technological control of stacks and dams – case study

Gestion tridimensionnelle interactive des données du contrôle technologique des pieux et des barrages – étude de cas

B.M. de Lacerda*, S.C. Chammas
Simplelab Tecnologia, Belo Horizonte, Brasil

W. Silva, V. Rezende
Samarco, Belo Horizonte, Brasil

**bianca.lacerda@simplelabtech.com.br*

ABSTRACT: Innovations in geotechnics in the mining field have been constant, aiming to evolve construction techniques and the management of the generated information throughout the work. In order to provide a practical, fast and efficient methodology for data management of stacks and dams, it was developed the first interactive 3D model focused at the technological control of these structures. Geotechnical constructions are dynamic and complex, in addition, they are large constructions, new layers are compacted every day and several tests are carried out, which must be in accordance with the norms and technical specifications of the project. In this way, the importance of the possibility of critical analysis in real time is evident, making it able to avoid future problems. By integrating the project implemented with the Cesium geospatial model platform into the Geolabor, geotechnical data management system, a complete three-dimensional view is generated, which associates geometry with information. The 3D model is updated in real time, automatically and without the need for any programming or modeling skills from the user. The geometry of the as-built model is associated with the information that is registered in Geolabor throughout the construction, allowing the visualization in scales of colors of the evolution of the work, of the samples, tests and their respective geotechnical parameters and the compliance with the project technical specifications. This article presents a case study carried out in a waste and tailings stacks of the mining company Samarco, presenting the practical advantages of using the 3D model integrated to Geolabor.

RÉSUMÉ: Les innovations géotechniques dans le domaine minier sont des techniques de construction et une gestion des informations générées sur site constantes et en évolution. Dans le but de fournir une méthodologie pratique et efficace pour la gestion des données des pieux et des barrages, le premier modèle 3D interactif axé sur le contrôle technologique de ces structures a été développé. Les constructions géotechniques sont dynamiques et complexes, en plus d'être des constructions à grande échelle et chaque jour de nouvelles couches sont compactées et divers tests sont effectués, qui doivent répondre aux normes et spécifications techniques du projet. De cette manière, l'importance de la possibilité d'une analyse critique en temps réel devient évidente, contribuant ainsi à éviter de futurs problèmes. En intégrant le projet mis en œuvre avec la plateforme de modèles géospatiaux Césio dans le système de gestion des données géotechniques Geolabor, une vue tridimensionnelle complète est générée, combinant la géométrie et l'information. Le modèle 3D est mis à jour en temps réel, automatiquement et sans aucune connaissance en programmation ou modélisation de la part de l'utilisateur. La géométrie du modèle as-built est associée aux informations enregistrées dans Geolabor tout au long de la construction, permettant la visualisation en échelles de couleurs de l'évolution de la structure, des échantillons, des tests et des paramètres géotechniques respectifs et du respect des spécifications techniques du projet. Cet article présente une étude de cas réalisée sur une décharge et une halde à déchets Samarco, présentant les avantages pratiques de l'utilisation du modèle 3D intégré à Geolabor.

Keywords: Three-dimensional model; data management; stacks and dams; mining geotechnics; technological control.

1 INTRODUCTION

Despite essential for the safety, geotechnics did not always follow clear regulations regarding the practice of its exercise (Araújo, E. R., 2016). Over the past few years, the search for innovation in the mining geotechnical field has been growing, seeking to develop new methodologies, norms and good practices that help prevent possible new disasters involving stacks and dams around the world. With technological progress, this process of evolution becomes constant, in order to guarantee the safety and compliance of the constructions.

In this scenario, the importance of carrying out careful technological control and the use of a

centralized and structured data management system has been gaining prominence in the geotechnics practice (de Lacerda, B. M., 2023). Technological control is the process that ensures that technical design specifications are met throughout construction. In order to optimize this process and assist in critical decision-making, the first interactive three-dimensional model aimed at managing geotechnical data for the technological control of stacks and dams was implemented by de Lacerda, B. M. (2022).

The 3D model was implemented using the Cesium platform, a complete tool for developing spatial models of different types. Using Cesium JS, all internal programming of the model was performed, automating the entire creation of the geometry of the geotechnical structure, based solely on the data collected during technological control. Without the need for user knowledge in modeling or programming, this model is an innovation for the geotechnical area.

The main objective of this article is to present the integration of the 3D model developed into a geotechnical data management system, Geolabor, enabling automatic and real-time updating of geometry and associated information, in accordance with the construction of the structure. Geolabor operates in all engineering processes, from planning, execution, and conducting analyses to issuing reports. Geolabor is a software in constant development, which seeks evolution and innovation daily, pioneering the practice of different methodologies that increase the safety of geotechnical constructions, guaranteeing the quality of the works.

After integrating the 3D model into the Geolabor system, both the geometry and the information associated with the structure are now updated in real time, according to the natural use of Geolabor in the technological control. To make use of the 3D model, nothing different from the routine of technological control needs to be done, as the system utilizes the information registered in the data management system to create and update the geometry and information contained in the 3D model. The 3D as-built model allows a practical visualization of the progress of the work, facilitating the control of geometry, samples, compliance with the technical design specification criteria and geotechnical parameters obtained in tests carried out throughout construction.

2 CASE STUDY

In order to put into practice the three-dimensional data management model integrated in Geolabor, a case study was developed with the mining company Samarco. The 3D model was implemented at PDER Alegria Sul (Tailings Storage Facility – TSF Alegria Sul), located at Mine Alegria Sul of Samarco (Mariana, MG/Brazil); a shared disposal stack of waste rock and filtered tailings, where the layers of landfill are built following thickness and compaction controls (Simplelab, T., 2022). The main objectives of this study are to highlight the practical importance of using the 3D model developed in the day-to-day life of a geotechnical construction, using real data.

The Samarco team uses Geolabor to manage technological control at PDER Alegria Sul and used Geolabor's 3D module for a month to carry out analyzes of this case study. Figure 1 presents the three-dimensional visualization of the stack under study.



Figure 1. PDER Sul Three-dimensional as built model.

It is possible to observe in Figure 1 that the model developed has no restrictions on the geometry of the structure, following the normally irregular shapes of tailing stacks. The model is built based on a methodology that takes into account the information that is collected throughout construction, as layers thickness and topographic data. The input of the coordinates (E, N, and Z) of the polygonal of the layers can be done manually or from a .csv file, with no need for any drone flights or point cloud file.

To create the initial model of a project that was already in progress before the start of implementation of the 3D module, only information relating to the last two compacted layers is required. The coordinates of the subsequent layers are inferred by the system, building the complete model with all layers registered in the Geolabor. Throughout the construction, it is not mandatory to register the coordinates of all built layers, as these are inferred by the system and automatically created in the 3D model. However, the more layers have their coordinates registered; the closer to reality the visualization will be, although the inference of coordinates does not affect the use, efficiency and interactivity of the 3D model for technological control.

All geometry is associated with information, constituting a complete model for managing the

geotechnical data of stacks and dams. Being completely interactive, when clicking on a certain layer, its respective information is displayed, such as elevation, start and end dates, status, volume, and acceptance criteria, as shown in Figure 2 below.



Figure 2. Visualization of information registered in Geolabor for a specific layer, when selected in the 3D model.

In addition to visualize the layers and their information, it is also possible to view all the samples collected throughout the construction and registered in Geolabor, as shown in Figure 3. Without losing interactivity in any of its features, when clicking on a specific sample, they information relating to the selected sample are displayed, also including the tests that were carried out on this sample and the geotechnical parameters obtained in each test.



Figure 3. Representation in the 3D model of samples registered in Geolabor for the PDER Alegria Sul stack.

From Figure 3, it is possible to observe, in a practical and immediate way, that there is at least one sample with its coordinates registered with some error, since there is a point outside the space of the structure. This type of verification is one of the direct advantages of using the 3D module, where it becomes possible to guarantee the conformity of construction records, with complete management of construction technological control data.

Geolabor allows areas and subareas to be specified in the system, so that technological control can be carried out in a personalized way for each project, as makes the most sense for the user. In the 3D model, it is possible to view and filter each of these areas or make horizontal cuts in the structure, by elevation or by layer, enabling a careful view of the division of the structure and the construction progress, as shown in Figure 4 below.

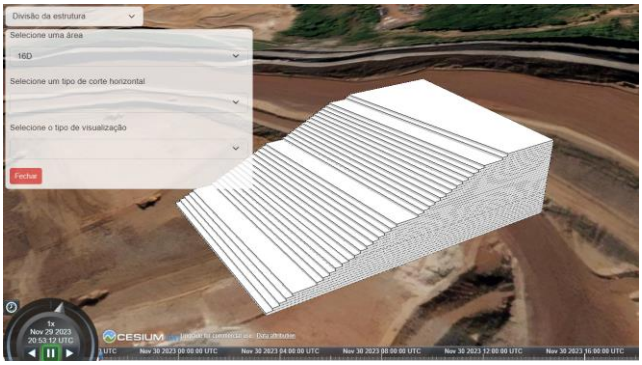

(a)



(b)

Figure 4. (a) Representation of a specific subdivision of the stack; (b) Horizontal cut to visualize a specific layer or elevation.

Once the technical project specifications are registered in the system, upon completing a test, it is calculated whether the geotechnical parameters obtained are within the previously specified limits, and the acceptance of the project criteria is presented in Geolabor. It is then possible to visualize these results in color scales on the 3D model, and filter the areas and layers according to what is registered, as shown in Figure 5.

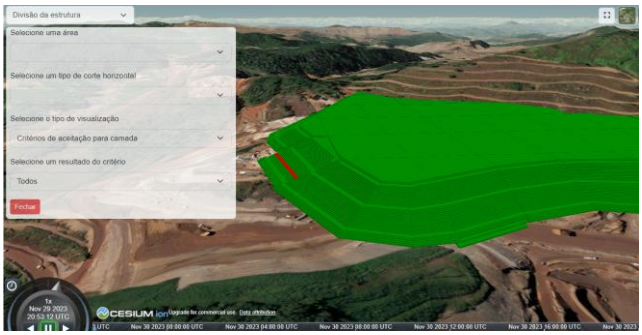

(a)



(b)

Figure 5. (a) Color scale visualization of compliance with technical specifications; (b) Filtering to visualize layers that did not meet the requirements of the registered technical specifications.

With the 3D model use, it was possible for the Samarco team to verify that there were typing errors in the registration of some layers. As can be seen in Figure 4, the layers in red would have the status of "did not comply", as they did not comply with the acceptance criteria, however, carrying out a critical analysis, registration errors were found. It was also possible, just by using the model, to verify that there were obsolete or duplicate criteria registered in the system. Previously, all this information was compiled in Excel spreadsheets, which are no longer necessary on a day-to-day basis with the full use of Geolabor and its features.

3 CONCLUSIONS

The case study carried out allowed to verify the practical usefulness of the 3D model integrated into Geolabor, presenting satisfactory results. The Samarco team was satisfied with the use of the functionality, and excited for future implementations, which are already in the development phase.

In the next work, the Heatmap will be implemented, allowing the visualization of the results of the geotechnical parameters obtained in the tests carried out, in a color scale and in the form of a three-dimensional graph. The functionalities to be developed later will be defined according to the practical needs of geotechnics, always seeking innovation, practicality and quality in the process of technological control of stacks and dams.

ACKNOWLEDGEMENTS

The authors would like to thank the team at Simplelab Tecnologia, for the work carried out on Geolabor, and the Samarco team, for their availability to carry out the case study and for seeking to use all of Geolabor's functionalities in the best way as possible, contributing to the constant improvement of the system.

REFERENCES

Araújo, E.R., Fernandes F.R.C. (2016) – Mining in Brazil: Economic growth and environmental conflicts. In portuguese: "Mineração no Brasil: Crescimento econômico e conflitos ambientais". In: Guimarães, P.E., Cebada, J.D.P. (eds) "Environmental Conflicts in the Mining and Metallurgical Industry: The past and the presente" In portuguese: Conflitos Ambientais na Indústria Mineira e Metalúrgica: O passado e o presente. Évora, CETEM, CICP, Rio de Janeiro, p.65–88.

de Lacerda, B. M. and Chammas, S. C. (2023) – The Importance of Geotechnical Data Management in Pile and Tailings Dam Works. In portuguese: "A Importância da Gestão de Dados Geotécnicos em Obras de Pilhas e Barragens de Rejeitos". SNGB, Dams Week, Foz do Iguaçú. Available in: cbdb.

de Lacerda, B. M., Chammas, S. C. (2022) – Interactive Three-Dimensional Data Management of Technological Control for Piles and Dams. In portuguese: "Gestão Tridimensional Interativa de Dados do Controle Tecnológico para Pilhas e Barragens". In: Anais do XX COBRAMSEG, Campinas. Available in: cobramseg-2022/.

Simplelab Tech (2022) – Geolabor Technological Control at Alegria Sul Samarco's Mine. In portuguese: "Geolabor Controle Tecnológico na Mina Alegria Sul da Samarco". Available in: https://www.youtube.com/.

Proceedings of the XVIII ECSMGE 2024
GEOTECHNICAL ENGINEERING CHALLENGES
TO MEET CURRENT AND EMERGING NEEDS OF SOCIETY
© 2024 the Authors
ISBN 978-1-032-54816-6
DOI 10.1201/9781003431749-287
Open Access: www.taylorfrancis.com, CC BY-NC-ND 4.0 license

ECSMGE 24
XVIII EUROPEAN CONFERENCE ON SOIL MECHANICS AND GEOTECHNICAL ENGINEERING

A method for the prediction of greenfield 3D settlement troughs around deep excavations

Une méthode de prédiction des tassements en 3D dans des conditions greenfield autour d'excavations profondes

M. De Luca, G. Russo, M.V. Nicotera, I. Esposito*
Università degli studi di Napoli Federico II, Naples, Italy

**ilaria.esposito3@unina.it*

ABSTRACT: The evaluation of ground movements induced by deep excavations is a topic of considerable importance, especially in the context of urbanized environments. Semi-empirical 2D methods, aimed at a first approximation of the problem, have been developed and widely used in literature to evaluate the settlement profile along retaining wall perpendicular direction whilst less attention has been paid to describe the profile along parallel direction. Recently, a 3D semi-empirical closed-form function, obtained by modifying existing 2D solutions, has been proposed to better grasp the three-dimensional effects induced by excavation. The four independent parameters that define the shape of the settlements and the scale parameter constituting the 3D subsidence function were calibrated through least squares regression of data sets from 3D FEM analyses. This calibration, in the context of a first comparison with real cases, has led to satisfactory and encouraging results revealing dependencies of the parameters on the excavation geometry. This paper is dedicated to the application of this three-dimensional subsidence function to additional real cases of open pit excavations to evaluate the applicability and the possible generalization of the method. Correlations between some of the four independent shape parameters and geometry of the pit are simply outlined.

RÉSUMÉ: L'évaluation des mouvements du sol induits par les excavations profondes est d'une grande importance, surtout dans le contexte des environnements urbanisés. Des méthodes semi-empiriques en 2D, visant une première approximation du problème, ont été développées et largement utilisées dans la littérature pour évaluer le profil de tassement le long de la direction perpendiculaire au mur de soutènement, tandis que moins d'attention a été accordée à la description du profil le long de la direction parallèle. Récemment, une fonction semi-empirique en 3D sous forme fermée, obtenue en modifiant les solutions existantes en 2D, a été proposée pour mieux appréhender les effets tridimensionnels induits par l'excavation. Les quatre paramètres indépendants qui définissent la forme des tassements et le paramètre constituant la fonction de subsidence en 3D ont été calibrés par régression des ensembles de données issus des analyses par la méthode des éléments finis en 3D. Cette calibration, dans le cadre d'une première comparaison avec des cas réels, a conduit à des résultats encourageants révélant les dépendances des paramètres vis-à-vis de la géométrie de l'excavation. Cet article est dédié à l'application de cette fonction de subsidence tridimensionnelle à des cas réels d'excavations à ciel ouvert pour évaluer l'applicabilité et la possible généralisation de la méthode. Des corrélations préliminaires entre les quatre paramètres indépendants de forme et plusieurs facteurs additionnels sont simplement esquissées.

Keywords: Deep excavations; 3D shape function; settlements troughs; semi-empirical; prediction.

1 INTRODUCTION - 3D SETTLEMENT FIELD AROUND A DEEP EXCAVATION

Settlements induced by deep excavations in urban settings can generate structural damage to neighbouring buildings. Two approaches for the prediction of ground movements around excavations are commonly used: the semi-empirical and numerical methods. The latter exploits advanced computational techniques like finite element method (FEM) or discrete element method (DFM) software to accurately model geometries, materials and construction sequences. The semi-empirical approach leverages geometric parameters such as excavation depth, bedrock depth, and plan dimensions to predict settlements troughs. Various empirical methods have been proposed by different researchers, including Ou (2006), Clough and O'Rourke (1992), Bowles (1996), and Roboski and Finno (2006). A novel analytical framework for describing three-dimensional subsidence around deep excavations has recently been introduced by Russo and Nicotera (2022). The function, which combines modified two-dimensional semi-empirical methods, resulting in a two-variable subsidence function, has the following form:

$$\frac{\delta_v(x,y)}{\delta_{v,max}} = f(y) \cdot g(x) \qquad (1)$$

where *g(x)* represents the 2D settlement pattern in the direction parallel to the supporting wall (i.e., x direction) while *f(y)* represents the 2D shape function for transversal settlement pattern (i.e., along y direction). The first member of Eq. 1 is the ratio between the function $\delta_v(x,y)$, which describes the 3D settlement trough, and the maximum measured settlement, $\delta_{v,max}$.

The proposed framework has been validated through meticulous 3D FEM nonlinear analyses conducted on practical urban soil profiles, where the influence of various factors such as the distribution of support props, excavation depth, and the presence of openings, was indagated. As clearly shown by the eq. 1, the two combined functions describe a shape while the exact subsidence profile is scaled on the basis of the maximum vertical settlement $\delta_{v,max}$. On the transversal shape governed by *f*(y) the above-mentioned literature offers many suggestions which Russo and Nicotera (2022) have summarized and validated with reference to the maximum value of *f*(y) and its first derivative at y=0.

On the other hand, the longitudinal shape *g*(x) has been first proposed by Russo and Nicotera (2022) in its actual form and a graphical representation is given in Figure 1:

$$g(x) = \frac{1}{2} erfc\left[2.8 \frac{|x/L| - (1/2 - A/L)}{(1/2 - A/L) - \Delta/L}\right] \qquad (2)$$

with x representing the distance from the center of the excavation, L the excavation length and A the distance of the function inflection point from the corner of the excavation, as already proposed Roboski and Finno (2006). Russo et al. (2019) introduced the new coefficient Δ to simulate different longitudinal settlement profiles: very smooth (i.e., large Δ) to very sharp ones (i.e. small and even negative Δ).

Correlations between A and Δ and geometry of the pit have been explored on the basis of 3D FEM non-linear analysis (Russo and Nicotera, 2022). The proposed two variable function was also experimented for best fitting exercises on case studies in the city of Napoli where a huge development of the existing underground network is going on since a couple of decades and mainly in sandy profiles. Here in the following, case studies in clay are used to further validate and calibrate the proposed semi-empirical method. In both cases the results showed a promising alignment between the proposed analytical framework and the observed settlement patterns, affirming its potential applicability in practical scenarios.

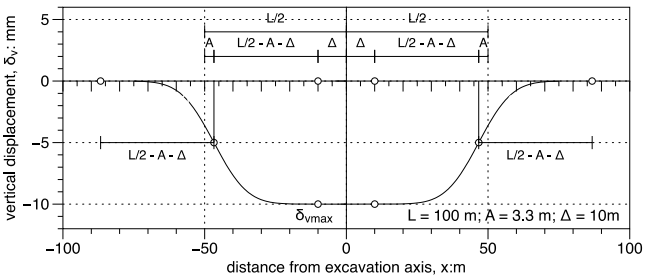

Figure 1. Longitudinal settlement trough – example case Δ =+10 > 0.

2 CASE STUDY

In the present paper the results in terms of ground settlement of six case studies of deep excavations are used and compared with the previously described shape function proposed by Russo and Nicotera (2022), derived for excavations in sand. The cases taken into account are: Chicago Robert H. Lurie Medical Center (CRHLM); Chicago and State Subway expansion (CSSE); Hangzhou Metro Basement (HMB); Taipei National Enterprise Center (TNEC); South Qilianshan Road Station (SQRS); Tokyo excavation (TKY).

Both the excavations in Chicago are about 12 m deep and the involved stratigraphy crosses granular soils overlying clays of stiffness increasing with depth (Roboski and Finno, 2006). The CRHLM excavation is 68x80 m in plan and the retaining system is made by sheet pile walls supported by two or three levels of tie-back prestressed anchors. Along three out four sides of the excavation 200 survey points were installed to monitor ground movements (Finno and Roboski, 2005). In the CSSE, secant pile walls anchored both with struts and tieback anchors were used as a retaining structure for the shaft, whose plan dimensions are 24×47 m. On a building adjacent to the pit instruments aimed to monitor ground movements were installed (Roboski and Finno, 2006). The excavation in clay silt, for the HMB, is 190×20m in plan and 17.5 m deep.

The retaining system is composed by 37 m long diaphragm walls supported by five strut levels. 10 monitoring lines were arranged on both sides of the basement, orthogonally to its axis, allowing surface settlements control during different stages of the excavation (Ying et al., 2022). The 107×45 m in plan excavation for the construction of the TNEC, 19.7 m deep, was conducted through subsequent layers of silty clays and silty sands with increasing shear strength, overlying a gravel formation 46 m below ground level (b.g.l.). Concrete floor slabs (constructed in top -down) sup-

ported the perimeter diaphragm walls and the settlements were monitored along a 36 m stretch of the 107 m excavation side (Roboski and Finno, 2006). The SQRS shaft has 188×26 m dimensions in plan, and a depth varying between 17 and 26 m. A perimeter wall supported by struts and waterproofed by a jet grouting treatment forms the retaining structure for the excavation. Due to the large dimensions of the pit, twelve monitoring sections were provided, orthogonal to the principal axis of the excavation, installing level instruments on the surrounding buildings (Tan et al., 2014). The deepest excavation (28 m) here considered is the one carried out in Tokyo in a two-layers stratigraphy: silt overlying fine sand, separated by a thin layer of peat. There is no information about the support system. Settlements data were collected along the 30 m side of the excavation for two reached depths: 20 and 28 m (Roboski and Finno, 2006).

3 DATA FITTING

The settlement data collected in the literature database and summarized in the paragraph 2 were fitted using the two-variable subsidence function to further calibrate and validate the proposed semi-empirical method. All the mentioned case studies are propped deep excavations in different soil conditions, but all characterized by enough monitoring data in a nearly greenfield condition to support a 2D fitting operation.

In the paper by Russo and Nicotera (2022) both propped and unpropped cases in sand were analysed by using 3D FEM. The obtained fitted surfaces are generally satisfactory, and the quality of the fitting synthetically represented by the value of the coefficient of determination, R^2 is indeed promisingly high as reported in Table I.

Table I. Coefficient of determination, R^2 for all the cases.

Case	Samples	Soil type	Range of R^2
CRHLM	1	Clay	0.80
CSSE	1	Clay	0.84
HMB	2	Clay silt	0.83-0.84
SQRS	2	Clay	0.75-0.91
TNEC	3	Silty Clay-Sand	0.94-0.97
TKY	2	Silty sand	0.95-0.98

Some cases have provided more settlement trough samples to be fitted with reference to different level of intermediate excavation or to different sides of the shaft.

The transversal profile f(y) is fully described by the parameters f_0 (f value at y=0), f'_0 (inclination of the settlement trough at the excavation edge) and f_I (f value at y equal to the extension PIZ of the "primary influence zone" as defined by Ou, 2006), while the longitudinal one is described by A and Δ (Russo and Nicotera, 2022). In the context of this study, we focus on the longitudinal profile parameters and the relationship between these last ones and the dimensionless depth of the excavation. As shown in Russo and Nicotera (2022) the parameters A and Δ show different trends in propped and unpropped excavations. For propped cases, like the ones analysed in this study, A depends linearly on the ratio H/L between depth (H) and length (L) of the excavation parallel to the settlement trough regardless of openings presence in the slabs used as props. As regards the parameter Δ, it depends linearly on the natural logarithm of the ratio H/L.

The following equations represent the relationship between A, Δ and the excavation depth H for propped excavations:

$$\frac{A}{L} = -0{,}1 \cdot \left(\frac{H}{L}\right) - 0{,}02 \quad (3)$$

$$\frac{\Delta}{L} = -\frac{1}{3} \cdot ln\left(\frac{H}{L}\right) - 0{,}59 \quad (4)$$

Figures 2 and 3 show the above described linear relationships between A, Δ and the ratio H/L, together with the FEM results (see legend) used in the best fitting exercise. The linear realationships 3) and 4) are drawn as dotted lines and represent a sort of either a lower or an upper bound of all the data for the parameter A and Δ respectively.

The results referred to the newly added case studies, togheter with the case studies SPS (i.e. San Pasquale Station) and MTD (i.e. Monte di Dio car park) in sand already used and discussed by Russo and Nicotera (2022), are also reported in both Figures. All the available data are included within the shaded areas bounded by two dotted lines: in each figure one of them represents Eq. 3) or 4), the other one was obtained by enveloping all the available data.

Only two values of Δ/L from Tokyo case study are not inclued in the shaded area because they appear as a sort of outliers compared to the overall population of data. Furthermore this case reports settlement profiles measured on a buried pipe whose stiffness is likely to bridge and thus to modify the concave shape of the observed settlement longitutindal profile. Finally the full line reported in the plot represent a tentative new linear correlation whose inclination is kept equal to the numerical derived equations (3) and (4) while the intercept is accodomated to fit only the experimental

data. The experimetally based intercepts are thus 0.06 and -0.79 for A/L and Δ/L respectively.

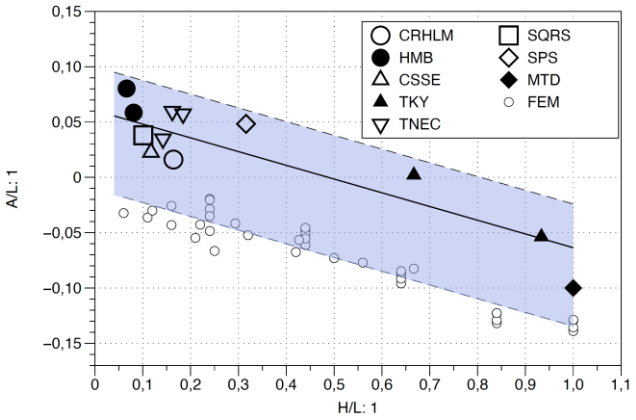

Figure 2. A/L as a function of the dimensionless depth of excavation H/L.

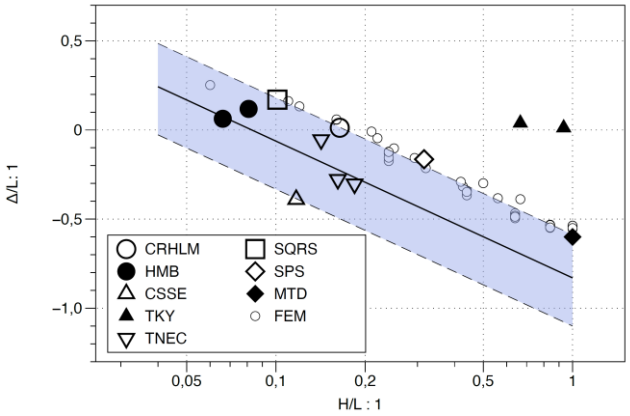

Figure 3. Δ/L as a function of the dimensionless depth of excavation H/L.

4 CONCLUDING REMARKS

The addition of case studies has reinforced some findings of previous studies about the 3D subsidence trough around a deep excavation based on 3D FEM computations of propped and unpropped excavations in sand. For space reason focus has been kept only on the longitudinal trough:

a) The inclination of the relationships of A and Δ with the depth of excavation H is confirmed;
b) As already anticipated by Roboski and Finno (2006) for increasing values of H/L the inflexion point tends to move outside the excavation (i.e. A<0);
c) The new parameter Δ introduced by Russo and Nicotera (2022) has a similar trend with the natural logarithm of the H/L ratio.

Further well documented case studies are needed to improve the reliability of the semi-empirical method.

ACKNOWLEDGEMENTS

This study was partially funded by the European Union - NextGenerationEU_, in the framework of the _GRINS -Growing Resilient,INclusive and Sustainable_ project (MUR: GRINS PE00000018 – CUP E63C22002140007) and partially funded by the National center for Sustainable Mobility CN4, spoke7 – CCcam and Smart Infrastructure (MUR: CN00000023- CUP Unina: E63C22000930007). The views and opinions expressed are solely those of the authors and do not necessarily reflect those of the European Union, nor can the European Union be held responsible for them.

REFERENCES

Bowles, J.E. (1996). Foundation analysis and design. The Mac Graw Hill Comp. Inc.

Clough, G. W. and O'Rourke, T. D. (1992) Construction induced movements of insitu walls. J. Geotech. Eng https://doiorg/10.1061/(ASCE)07339410(1992)118:4(665).

Finno, Richard J., and Roboski, Jill F. (2005).Three-Dimensional Responses of a Tied-Back Excavation through Clay. Journal of Geotechnical and Geoenvironmental Engineering, 131(3), 273-282. doi:10.1061/(ASCE)10900241(2005)131:3(273).

Ou, C.Y. (2006). Deep excavation theory and practice. Taylor and Francis, London.

Roboski, J., and Finno, R. J. (2006). Distributions of ground movements parallel to deep excavations in clay. Canadian geotechnical journal, 43(1), 43-58. https://doi.org/10.1139/t05-091.

Russo, G. and Nicotera, M.V. (2022). A closed form shape function describing 3D settlement field around a deep excavation in sand. Sci Rep 12, 18528 (2022). https://doi.org/10.1038/s41598-022-22003-8.

Russo, G., Nicotera, M.V. and Autuori, S., (2019). Three-Dimensional Performance of a Deep Excavation in Sand. Journ. Geotech Geoenv. Eng. 2019;145. https://doi.org/10.1061/(ASCE)GT.19435606.0002037.

Tan, Y., Wei, B., Diao, Y., and Zhou, X. (2014). Spatial corner effects of long and narrow multipropped deep excavations in Shanghai soft clay. Journal of Performance of Constructed Facilities, 28(4), 04014015.https://doi.org/10.1061/(ASCE)CF.1943-5509.0000475.

Ying, H., Cheng, K., Liu, S., Xu, R., Lin, C., Zhu, C., and Gan, X. (2022). An efficient method for evaluating the ground surface settlement of Hangzhou metro deep basement considering the excavation process. Acta Geotechnica, 17(12),5759-5771. https://doi.org/10.1007/s11440-022-01549-x.

Proceedings of the XVIII ECSMGE 2024
GEOTECHNICAL ENGINEERING CHALLENGES
TO MEET CURRENT AND EMERGING NEEDS OF SOCIETY
© 2024 the Authors
ISBN 978-1-032-54816-6
DOI 10.1201/9781003431749-288
Open Access: www.taylorfrancis.com, CC BY-NC-ND 4.0 license

ECSMGE 24
XVIII EUROPEAN CONFERENCE ON SOIL MECHANICS AND GEOTECHNICAL ENGINEERING

Monitoring of soil deformations induced by deep mixing using an FME-based data analysis tool

Suivi des déformations du sol induites par un mélange profond à l'aide d'un outil d'analyse de données basé sur FME

F. Deckner*, V. Enbom, A. Kriege, K. Borgström, T. Forsberg
GeoMind, Stockholm, Sweden

**fanny.deckner@geomind.se*

ABSTRACT: A vast land reclamation project is under construction in Sweden, within a bay of the Baltic Sea. To enclose the area from the bay, a 600 m long rubble mound of crushed rock founded on deep mixing is constructed. The area has previously been prone to slides with its very soft clay. This paper focuses on the design and execution of the rubble mound in the western land connection, where the rubble mound serves as a temporary working platform. A rigorous control program was developed to ensure a safe work progress. To process all the data and facilitate analysis an FME-based tool was developed providing instant feedback for the designer. This paper describes the design process and the monitoring during execution as well as the measures taken when deformations exceeded alarm values. The paper also presents measured soil displacement and provides practical tips for future deep mixing projects where deformations are of concern.

RÉSUMÉ: Un vaste projet de poldérisation est en cours de construction en Suède, dans une baie de la mer Baltique. Pour entourer la décharge, un remblais de gravier de 600 m long, composé de roches concassées, fondé sur mélange profond. La zone était auparavant sujette aux glissements de terrain en raison de son argile très molle. Cet article se concentre sur la conception et l'exécution du remblais de gravier dans la connexions terrestre ouest, où le remblais sert de plate-forme de travail temporaire. Un programme de contrôle rigoureux a été élaboré pour garantir une progression sécurisée des travaux. Pour traiter toutes les données et faciliter l'analyse, un outil basé sur FME a été développé, fournir un retour instantané au concepteur. Cet article décrit le processus de conception et le suivu pendant l'exécution ainsi que les mesures prises lorsque les déformations dépassent les valeurs d'alarme. Le document présente également le déplacement mesuré du sol et fournit des conseils pratiques pour les futurs projets de mélange en profondeur où les déformations sont préoccupantes.

Keywords: Monitoring; deep mixing; soil displacement; soft clay; FME-programming.

1 INTRODUCTION

In the middle of Sweden, a vast land reclamation project is under construction. The planned area consists of an onshore and an offshore area within Skönviken, a bay of the Baltic Sea. To enclose the area, a 600 m long rubble mound of crushed rock founded on deep mixing is constructed, see Figure 1. The deep mixing consists of both dry soil mixing (DSM) and wet soil mixing. The DSM is conducted as overlapping columns with a coverage rate of approximately 96%.

This paper focuses on the design and execution of the DSM and the rubble mound in the western land connection. At the western connection the shallow water depths meant that the columns had to be installed from land, where the filled area (i.e the rubble mound) will serve as a working platform, as the installation progresses eastward. In order to ensure a safe work progress, a rigorous control program and active design was needed. To process all the data and facilitate analysis an FME-based tool was developed.

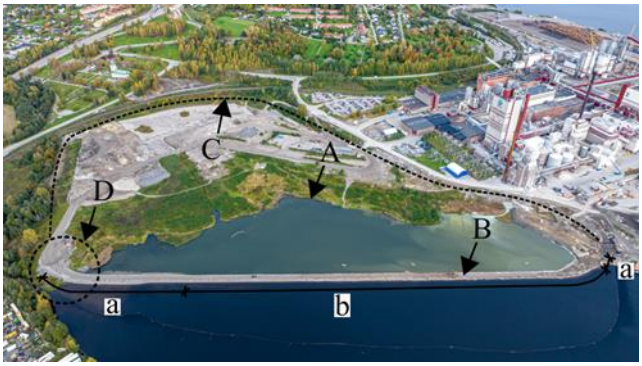

Figure 1. Overview of the project. (A) Existing shoreline, (B) New shoreline consisting of rubble mound on deep mixing, (a) dry soil mixing and (b) wet soil mixing, (C) Onshore boundary, (D) Western land connection. Photo: Håkan Sjödin.

Installation of DSM can cause relatively large ground movements due to the mixing and the addition of binder in the soil (Porbaha et al., 2001, Larsson, 2005 and Dong & Whittle, 2018). This mass displacement disturbs the soil and temporarily reduces its' strength (Shen et al., 2008). The aim of the developed data analysis tool is to collect and present data of mass displacement caused by the column installation. To avoid slope failure, this is important information for the designer. With the tool, it is possible to check the soil mass displacement effect of the column installation at different distances to the column front. Hence, it is possible to decide a likely distance in front of the DSM installation that is disturbed and model a strength reduction of the soil in this area. This provides a good basis for safe progress in the project.

The aim of this paper is to describe the challenges in the design process and the monitoring during execution as well as the measures taken when deformations exceed alarm values. The measured soil displacements are analysed based on distance from the DSM front and are also compared with previous measured displacement providing generalized conclusions regarding soil displacement induced by deep mixing.

2 GEOTECHNICAL CONDITIONS

The soil in the area consists generally of very soft to soft clay on silt and sand upon till on bedrock. The clay has an undrained shear strength varying from 3 to 20 kPa. In some areas, the clay is classified as quick clay. The thickness of the clay stratum varies between 10 to 20 m. During a backfill operation in the early 1980's, a landslide occurred and the area close to the shoreline has since been prohibited from any construction activity.

The shear strength of the clay is an important parameter for the design. The undrained shear strength of the clay has been investigated through CPT, direct shear tests, active undrained triaxial tests and fall cone test. Any disturbance of the clay will reduce its' strength; hence, it is highly important that any disturbance is accounted for.

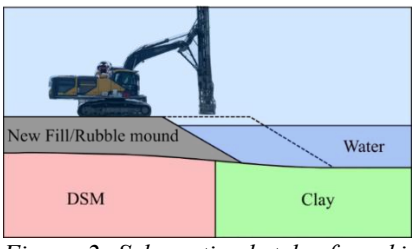

Figure 2. Schematic sketch of working order for western land connection.

3 DESIGN PROCESS

The planned working order was to perform DSM in sections and then fill with 0,5-2,0 m of crushed rock on the stabilized area. After certain curing time of the columns the DSM rig could advance out onto the newly filled area and commence with the subsequent section of further DSM installation. A schematic sketch of the working order is shown in Figure 2.

Initial stability calculations were made to ensure the rig's advancement. As the rig relies on the capacity of the relatively young DSM columns before advancing, a reduced shear strength of 30 kPa was chosen for the stabilized material, whereas the original design shear strength after 28 days is set to 100 kPa. The calculations and the availiable machine park gave that the rig was able to install columns 5 m in front of the reinforced area and needed to wait for 12 hours until it could advance to ensure enough aging of the DSM. 5 m ahead of the rig's working platform a new future platform was filled. As this fill was placed on non-reinforced soil and was not loaded by machines, a lower safety factor was accepted. However, the safety factor under the rig was satisfactory, as can be seen in Figure 3, as a minimum safety factor of 1,5 was required.

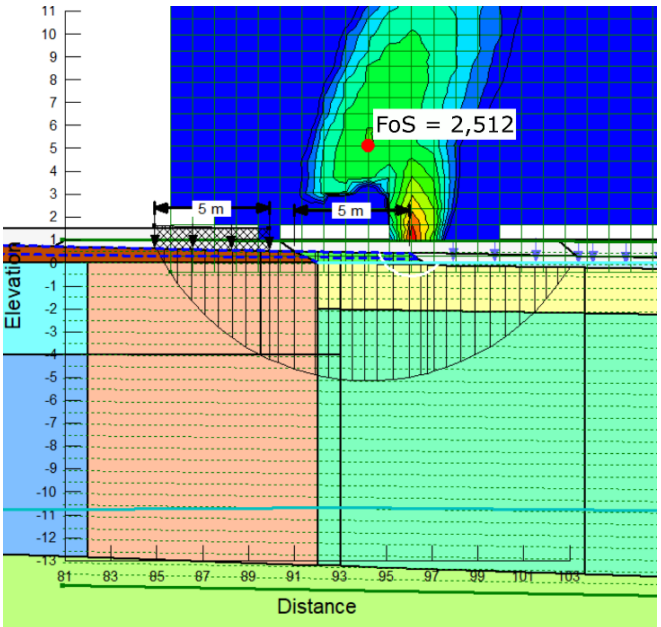

Color	Name	γ/γ' (kN/m³)	c_u (kPa)	c' (kPa)	ϕ' (°)
	Sand	17,0/19,0	-	0	32
	DSM	17,0/17,0	30	-	-
	Clay 1	15,5/15,5	3+1/m	-	-
	Clay 2	16,8/16,8	5+1,3/m	-	-
	Clay 3	17,0/17,0	10	-	-
	Clay 4	17,0/17,0	10+1,5/m	-	-
	Clay, dry crust	18,0/18,0	30	-	-
	Sandy Silt	18,0/20,0	-	0	32

Figure 3. Stability calculation for installation of the DSM.

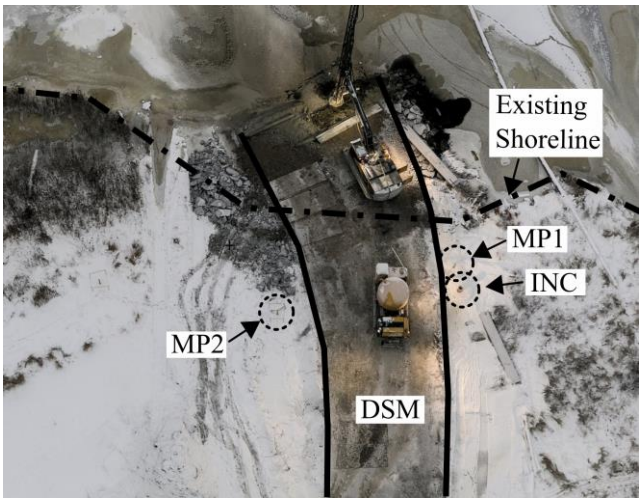

Figure 4. Location of instrumentation in plan.

4 MEASUREMENTS AND CONTROL PROGRAM

To monitor soil displacement during installation of the DSM, a control program was implemented. The control methods included instrumentation in the form of an inclinometer (INC) and two prisms (MP1 and MP2). For location of measurement equipment see Figure 4. In the INC the horizontal displacement with depth was monitored, whereas in MP1 and MP2 both vertical and horizontal displacements were measured at the surface.

To monitor the location of installed columns machine control with GPS was used for exact location of the columns.

Instrumentation was installed prior to DSM installation. From the start of DSM installation, the prisms were measured manually every second day, except weekends, until the end of installation. The inclinometer had automatic logging every 60 minutes. Both the construction management and the designer had access to the inclinometer data at a web-based platform.

The alarm values for horizontal displacement were set to 50 mm based on previous reported deformations stated in Larsson (2005). No alarm values were set for vertical displacements, these were monitored for follow-up and to gain understanding of the soil mass displacement. In the control program the first action point to be taken if the above set alarm value was exceeded was to stop production and perform updated stability calculations based on the assumed shear strength reduction considering the measured displacements.

5 DATA PROCESSING

Follow-up of column installation and inclinometer movements has been carried out using FME Desktop and Excel. FME has been used to manage the raw data from inclinometer measurements, prisms, and information of executed columns. The inclinometer data is read from an Excel sheet and is transformed and reordered to be better adapted to the purpose of the survey. For columns, as-built DSM pdfs are read to extract information such as coordinates and installation time and then fit to appropriate structure. When new data is received, the already established FME runs easily, and no other measures are required regarding formatting or manual input.

The Excel file reports the result in the form of graphs for installed columns and inclinometer results at a given time, which is selected with a slider (upper left corner), see Figure 5. The deflection of the inclinometer is then reported at the time where installed (reported) columns are located. The difference from the previous day is also reported. In our model, the stage is increased in days, but it is also possible to analyse in narrower intervals.

The plan graph is an xy dot graph where the column coordinate list is read, together with other coordinated objects (inclinometer, shoreline). The coordinate list is in a separate sheet designed to check if the column exists at the searched date. Then the coordinate values are reported, otherwise they are not reported. The inclinometer data is in another sheet designed to use one more search function to look for the searched date and return the corresponding deformations.

6 ACTIVE DESIGN

During installation of DSM from the western land connection, vertical and horizontal displacements were closely monitored. After 17 days of DSM installation, the horizontal displacements of the inclinometer passed the set alarm value of 50 mm.

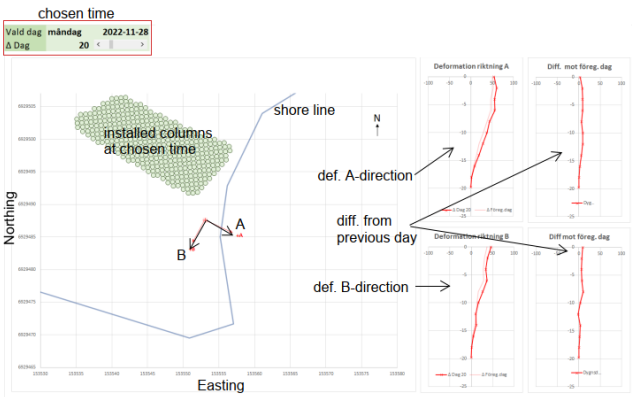

Figure 5. Example of results presented in the Excel file.

According to the actions in the control program, production was stopped, and new stability calculations were performed to ensure that the soil displacement would not endanger the previous assumptions. In the new calculations, the clay 10 m ahead of the DSM front was reduced to 50% of the initial shear strength. This lowered the overall safety factor to 2,186, but it was still satisfactory, see Figure 6.

During the production stop, the soil displacement in the INC remained constant, hence there was a clear correlation between displacement and DSM installation. Due to the poor stability and the risk for loss of strength in the clay, there was a planned break in production every 12 hours. During these breaks, the same correlation between soil displacement and DSM column installation was observed. Hence, it was decided that installation could be recommenced, with the restriction that no increase in recorded displacement during the planned breaks occurred.

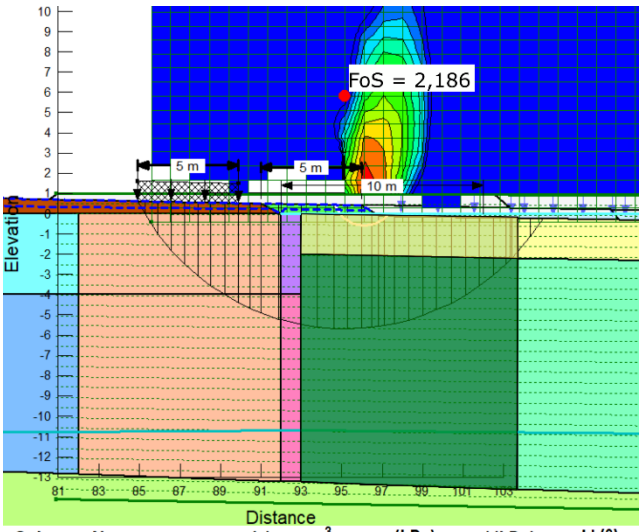

Color	Name	γ/γ' (kN/m³)	c_u (kPa)	c' (kPa)	ϕ' (°)
	Clay 1, red 50%	15,5/15,5	1,5+0,5/m	-	-
	Clay 2, red 50%	16,8/16,8	2,5+0,65/m	-	-
	Clay 3, red 50%	17,0/17,0	5	-	-
	Clay 4, red 50%	17,0/17,0	5+0,75/m	-	-

Figure 6. Updated stability calculation with decreased shear strength in the clay ahead of the DSM front. For previously used materials see legend in Figure 3.

7 ANALYSIS AND DISCUSSION

The soil displacement induced by deep mixing within this project was correlated with previous experiences. Both Porbaha et al. (2001) and Larsson (2005) has presented graphs showing horizontal soil displacement against the distance from DSM installation. Larsson (2005) has compiled the results from Uchiyama (1996), Masuda et al. (1996), Hirai et al. (1996) and Kakihari et al. (1996). A comparison with the measured soil displacement at the ground surface in the INC, MP1 and MP2 within this project is shown in Figure 7. As can be seen there is good correlation between the current measurement data and the previously reported in Larsson (2005). That the soil displacement within this project is at the upper boundary can be related to the high coverage rate of approximately 96%.

Analysing the soil displacement at the ground surface, measured displacements in the INC show a direction that is almost always perpendicular to the point of installation, see Figure 8 where the measured displacement in the beginning, when the distance (x) from the DSM front is large in comparison to its' depth (L), is purely in the A-direction. Whereafter the displacement increases more rapidly in the B-direction as x/L decreases. The horizontal soil displacement at the ground surface reached a limit value of 55 mm in the A-direction and 64 mm in the B-direction resulting in a total soil displacement of 84 mm.

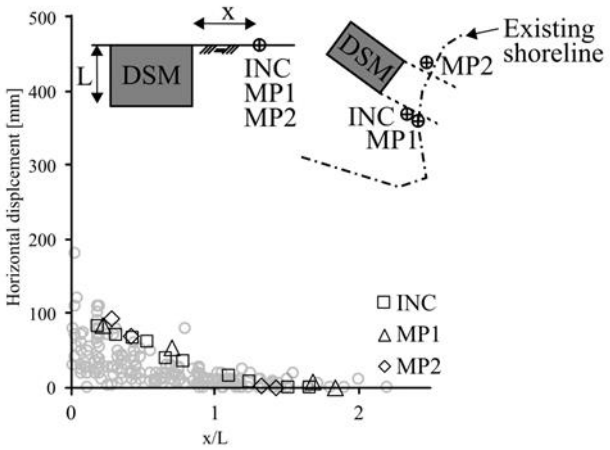

Figure 7. Horizontal displacement of INC, MP1 and MP2 plotted against distance from DSM (x/L), compared to data presented in Larsson (2005) in grey.

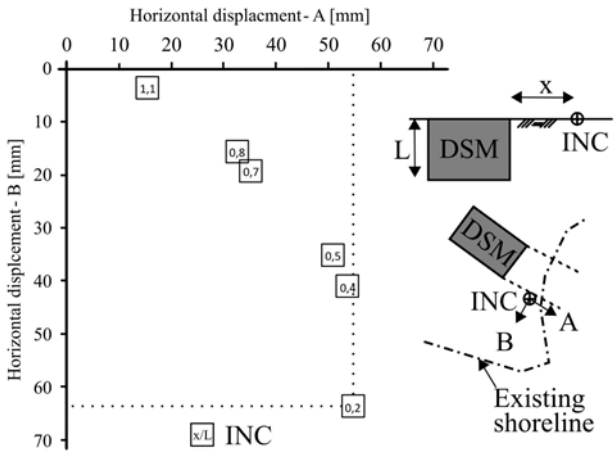

Figure 8. Horizontal displacement of INC in plan view plotted for different distances from DSM (x/L).

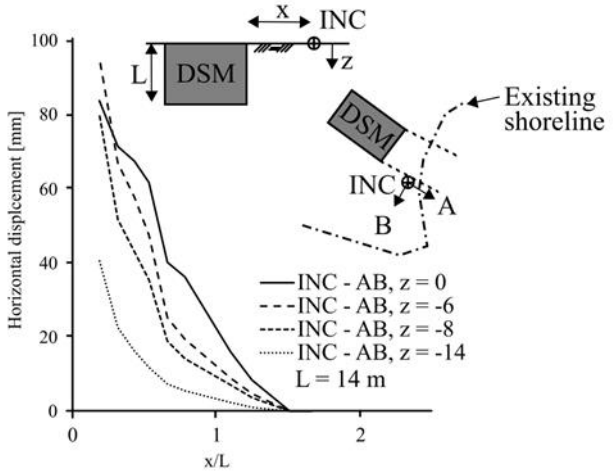

Figure 9. Horizontal displacement of INC for direction AB (resultant) with depth "z" below the ground surface plotted against distance from DSM (x/L).

With the INC as well the development of the soil displacement with depth could be monitored and analysed, see Figure 9. The displacements show over all depth a close to exponential increase as the distance between the installation and the measurement point decreases. Comparing the horizontal soil displacement with depth it can be observed that the maximum soil displacement does not occur at the ground surface at closest distance to the measurement point. The maximum value of 95 mm is measured at a depth of 6 m from the ground surface, which approximately coincides with the slip surface indicated in Figure 3 and Figure 6.

8 CONCLUSIONS

In a land reclamation project in Sweden an FME-based data analysis tool was developed to enable reliable and efficient monitoring of soil displacement due to installation of deep mixing columns. The tool provided the designer with easy access to measurement data that was used in the decision-making process to minimize the risk for slope failures and ensure a safe work progress during installation of DSM.

The main conclusions from the measurement of horizontal displacement were:

- The displacements are mainly perpendicular to the point of installation.
- The increase of displacement shows an exponential increase as the distance between installation and measurement point decreases.
- Maximum soil displacement does not occur at the ground surface closest to the DSM front, but at a depth of 6 m from the ground surface.
- Soil displacement related to DSM installation was instant.
- The horizontal ground displacements in the current project align well with previous observed displacements during DSM installation.

For future projects, with comparable geotechnical conditions, where ground deformations in relation to DSM installation is of importance, the presented graphs of displacement in relation to distance from installation can be used to predict a likely horizontal displacement.

ACKNOWLEDGEMENTS

The authors are grateful for the support provided by the project owner SCA and Biorefinery Östrand.

REFERENCES

Dong, Y.P. and Whittle, A.J. (2018). Effects of deep soil mixing and jet grouting on adjacent retaining walls and ground. *Proceedings of the 9th International Symposium on Geotechnical Aspects of Underground Construction in Soft Ground*, Negro, A. and Cecilio Jr, M.O. (eds.), pp. 91-96.

Hirai, T., Ise, J., Kusakari, T., Gotou, M and Hibi, Y. (1996). Development and application of deep mixing soil stabilization method to control displacement of adjacent ground. *Proceedings of the IS-Tokyo'96*, Yonekura, R., Terashi, M. and Shibazaki, M. (eds.), Vol 1, pp. 485-490.

Larsson, S. (2005). State of Practice Report – Execution, monitoring and quality control. *Proceedings of the International Conference on Deep Mixing – Best Practice and Recent Advances*, Svensk Djupstabilisering Report 13, Vol. 1, pp.732-788.

Masuda, T., Shimizu, M. and Aizawa, F. (1996). Evaluation of ground deformation due to deep mixing in adjacent construction activities. *Proceedings of the IS-Tokyo'96*, Yonekura, R., Terashi, M. and Shibazaki, M. (eds.), Vol 1, pp. 515-520.

Porbaha, A., Raybaut, J-L. and Nicholson, P. (2001). State of the art in construction aspects of deep mixing technology. *Ground Improvement*, 5(3): 123-140. https://doi.org/10.1680/grim.2001.5.3.123.

Shen, S-L., Han, J. and Du, Y-J. (2008). Deep mixing induced property changes in surrounding sensitive marine clays. *Journal of Geotechnical and Geoenvironmental Engineering*, 134(6): 845-854. DOI: 10.1061/(ASCE)1090-0241(2008)134:6(845)

Uchiyama, K. (1996). Prevention of displacement while using DJM method. *Proceedings of the IS-Tokyo'96*, Yonekura, R., Terashi, M. and Shibazaki, M. (eds.), Vol 1, pp. 675-680.

Proceedings of the XVIII ECSMGE 2024
GEOTECHNICAL ENGINEERING CHALLENGES
TO MEET CURRENT AND EMERGING NEEDS OF SOCIETY
© 2024 the Authors
ISBN 978-1-032-54816-6
DOI 10.1201/9781003431749-289
Open Access: www.taylorfrancis.com, CC BY-NC-ND 4.0 license

ECSMGE 24
XVIII EUROPEAN CONFERENCE ON SOIL MECHANICS AND GEOTECHNICAL ENGINEERING

Calibration of a numerical model for the investigation of piled rafts under dynamic loading

Étalonnage d'un modèle numérique pour l'étude des radeaux de pieux sous chargement dynamique

Y. Degu*
Department of Geotechnical Engineering, University of Kassel, Kassel, Germany and Faculty of Civil; Water Resources Engineering, Bahir Dar University, Bahir Dar, Ethiopia

O. Reul
Department of Geotechnical Engineering, University of Kassel, Kassel, Germany

A. Worku
School of Civil and Environmental Engineering, Addis Ababa University, Addis Ababa, Ethiopia

F. Tschuchnigg
Institute of Soil Mechanics, Foundation Engineering and Computational Geotechnics, Graz University of Technology, Graz, Austria

yideg@uni-kassel.de

ABSTRACT: Limited knowledge available on the soil-structure interaction of piled rafts under cyclic and dynamic loading together with gaps in national building codes frequently prevents the design of technically and economically optimised foundations for sensitive structures, such as foundations for high-rise buildings or bridges. As the first step in a research project to investigate the bearing behaviour of piled rafts under dynamic loading, existing model tests and in-situ measurements are evaluated to provide a database for the calibration of numerical models. This paper focuses on the numerical back-analysis of the centrifuge model tests on piled rafts by Horikoshi et al. (2003a; 2003b). The 3D finite element model employs the Hardening Soil model with small-strain stiffness (HSsmall) to simulate the material behaviour of the Toyoura sand used in the model tests. In the scope of this work, the calibration process of the material parameters and the results of the back-analysis of the model tests are presented.

RÉSUMÉ: Les connaissances limitées disponibles sur l'interaction sol-structure des radeaux de pieux sous charge cyclique et dynamique, ainsi que les lacunes des codes de construction nationaux, empêchent souvent la conception de fondations techniquement et économiquement optimisées pour les structures sensibles, telles que les fondations des immeubles de grande hauteur ou des ponts. Dans le cadre de la première étape d'un projet de recherche visant à étudier le comportement des radeaux de pieux sous charge dynamique, les essais sur modèle et les mesures in situ existants sont évalués afin de fournir une base de données pour l'étalonnage des modèles numériques. Cet article se concentre sur la rétro-analyse numérique des essais en centrifugeuse effectués sur des radeaux de pieux par Horikoshi et al. (2003a ; 2003b). Le modèle d'éléments finis 3D utilise le sol durcissant avec une rigidité à faible déformation (HSsmall) pour simuler le comportement du matériau du sable de Toyoura utilisé dans les essais sur modèle. Dans le cadre de ce travail, le processus d'étalonnage des paramètres matériels et les résultats de la rétro-analyse des essais sur modèle sont présentés.

Keywords: Piled raft; dynamic loading; centrifuge test; numerical analysis; HSsmall soil model.

1 INTRODUCTION

The piled raft is a well established foundation system especially for tall buildings (e.g. O'Neill et al, 1996, Poulos, 2001, Reul and Randolph, 2003) under predominantly vertical static loading. For this load case a guideline for design, dimensioning and construction already exists (ISSMGE Technical Committee 212, 2013) with piled rafts designed according to this guideline termed Combined Pile-Raft Foundations (CPRF). Also, piled rafts are applied frequently for bridge foundations (e.g. Hecht and Dürrwang, 2001, Comodromos et al., 2016) where lateral loads generally are of more importance. However, in contrast to piled rafts under predominantly vertical loading, comparatively few in-situ measurements on completed structures and large-scale model tests (field

investigations) have been documented for piled rafts under combined vertical and horizontal loading, regardless of whether monotonic, cyclic or dynamic actions are involved. To investigate the bearing behaviour of piled rafts under complex loading conditions small scale model tests as well as centrifuge model tests have been carried out by different researchers (e.g. Horikoshi et al., 2003a; 2003b; Sawada and Takemura, 2014; Unsever et al., 2014; Hamada et al., 2015).

In some recent studies, the behaviour of piled rafts under dynamic loading conditions was studied numerically using model tests as a means of validation (e.g. Eslami et al., 2011; Kumar et al., 2016; Bhaduri and Choudhury, 2019; Akbari et al., 2021). However, frequently the capability to realistically capture main aspects of soil-structure-interaction is limited by the use of linear elastic-perfectly plastic soil models, which generate only elastic strains upon small strain load reversals. Evidently, more advanced constitutive models are vital to model for example hysteretic damping.

The current research projects aims on providing a better understanding of the bearing behaviour of piled rafts under lateral monotonic and dynamic loading by means of numerical simulations with the finite element method (FEM) applying the Hardening Soil model with small-strain stiffness. This paper presents the results of the first phase of the project with the calibration of the material parameters of HSsmall model for dry Toyoura sand by means of the back-analysis of the centrifuge model tests employing of 3D finite element analysis (FEA).

2 CALIBRATION OF THE HSSMALL MODEL

The HSsmall model (Benz, 2007) is an extension of the standard Hardening Soil (HS) model (Schanz et al., 1999) incorporating two additional parameters: the shear modulus at a very small strain G_0^{ref} and the threshold shear strain $\gamma_{0.7}$, the shear strain at which the secant shear modulus G_s^{ref} is degraded to $0.72 \cdot G_0^{ref}$. Thus, the model accounts for the small strain stiffness, which can be related to a degrading secant stiffness with an S-shaped characteristics curve according to the formulation of Santos and Correia (2001) and an accompanying increasing damping ratio with increasing strain amplitudes. As a result, it reproduces hysteretic elastic soil behaviour in loading-reloading cycles leading to hysteretic damping.

Most of the model parameters of the HSsmall model for Toyoura sand were calibrated using the tool Plaxis SoilTest for simulating element tests where the hypoplastic parameters for Toyoura sand provided by Herle and Gudehus (1999) and Ng et al. (2013) were used as a reference.

Due to the limited space available, in the following, the description of the calibration procedure is restricted to the two parameters mainly controlling the material behaviour at small strains, namely G_0^{ref} and $\gamma_{0.7}$. The reference small strain shear stiffness modulus G_0^{ref} was estimated by means of three different approaches which all yielded similar values. In the first approach, an initial tangent slope of a hysteretic loop of a cyclic triaxial test simulation was evaluated. Alternatively, G_0^{ref} was determined by making use of the secant shear stiffness at a very small shear strain, where the secant shear stiffness in turn was determined from the deviatoric stress and shear strain values of standard triaxial test simulation. In the third approach, the initial Young's modulus E_0^{ref} of the standard triaxial test was used to determine the small strain shear stiffness from

$$G_0^{ref} = E_0^{ref} / \left(2 \cdot (1 + \nu_{ur})\right) \qquad (1)$$

where $\nu_{ur} = 0.2$ was employed as suggested by Benz (2007). Additionally, the obtained result was compared with the values extracted from charts by Alpan (1970) and Benz (2007), showing reasonable agreement.

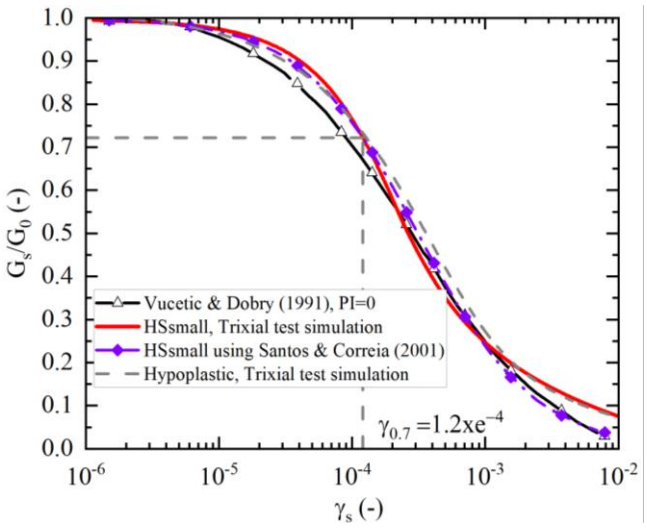

Figure 1. Shear stiffness degradation curves.

The second small strain parameter, the threshold shear strain $\gamma_{0.7}$, was calibrated using an iterative curve fitting procedure with reference to the secant shear modulus degradation and damping ratio curves of the reference hypoplastic model. The degradation curves were generated from deviatoric stress and small strain values of the triaxial simulation results and using the approach by Santos and Correia (2001). The result

was further refined by fitting with the secant shear modulus reduction curves of Vucetic and Dobry (1991) for a zero plasticity index value. As shown in Figure 1, the shear stiffness degradation curves of the current study are in good agreement with the hypoplastic reference model result and the curve presented by Vucetic and Dobry (1991).

The basic parameters defining the HSsmall model and their calibrated values, as determined from the calibration process, are listed in Table 1. It has to be noted that a cohesion was introduced for the reason of increasing numerical stability (in the dynamic FEA). This approach appears to be legitimate since the focus of the research project is on the serviceability rather than the ultimate capacity of foundations.

Table 1. Calibrated HSsmall model parameters.

Parameters		Description	Values
E_{50}^{ref}	MPa	reference secant stiffness at 50% of q_f	42.1
E_{oed}^{ref}	MPa	Tangent oedometric stiffness	30.2
E_{ur}^{ref}	MPa	unloading-reloading stiffness	126.9
ν_{ur}	-	unloading-reloading Poisson's ratio	0.2
m	-	power for stress-level dependency of stiffness	0.65
p^{ref}	kPa	reference stress for stiffness	100.0
G_0^{ref}	MPa	reference shear stiffness at very small strain	149.0
$\gamma_{0.7}$	-	threshold shear strain at which $G_s = 0.722 \cdot G_0$	$1.20 \cdot 10^{-4}$
c	kPa	cohesion	5.8
φ	°	angle of internal friction	35.6
ψ	°	angle of dilatancy	8.7
K_0^{nc}	-	at rest earth pressure coefficient for NC soil	0.47
R_f	-	failure ratio (q_f/q_a)	0.9

3 NUMERICAL MODEL

The numerical simulation of the centrifuge tests by Horikoshi et al. (2003a; 2003b) was carried out with the program PLAXIS 3D in prototype scale applying the appropriate scaling laws (e.g. Muir Wood, 2004). The dimensions of piles and raft as well as the material properties applied in the 3D FEA are summarised in Table 2. The piles were installed "wished-in-place" in the FE model which is considered to capture the installation process in the centrifuge tests reasonably well where the sand was poured around the piles at 1g level.

The soil as well as the piles and the raft were modelled with 10-node tetrahedral volume elements. Between soil and piles, respectively between soil and raft 12-node interface elements, with $R_{int} = 0.59$, are located. The piles and the raft are rigidly connected. The finite element mesh is shown in Figure 2 together with the boundary conditions applied at the lateral and bottom surfaces of the model for both static and dynamic loading conditions, reflecting the situation in the centrifuge model tests. For dynamic loading conditions, energy dissipation is reproduced by introducing free field boundary conditions at the side boundaries in the direction of loading and by using Rayleigh damping in addition to the hysteretic damping considered in the chosen constitutive model.

In FEA, careful selection of the mesh size plays a vital role in ensuring the accuracy of the numerical analysis at an optimum computational time. Accordingly, the size of the model and the discretisation were systematically varied to check and minimise their effect on the analysis. Based on convergence of the results and computing time criteria, a fine-sized mesh with additional refinement in the vicinity of the foundation was generated. For dynamic loading, the mesh size should be smaller than one-eighth of the wavelength associated with the maximum frequency component of the input motion, as suggested by Kuhlemeyer and Lysmer (1973). A typical model comprising 82698 elements and 131867 nodes with an average element size of 0.68 m fulfills this criteria.

Table 2. Model dimensions and additional parameters.

Parameter		Loading types	
		Vertical (Static)	Horizontal (Static/ Dyn*)
Pile (Solid)			
Length	m	8.5	9.0
Diameter	m	0.5	0.5
Unit weight	kN/m^3	9.72	9.72
Young's modulus	GPa	41.7	41.7
Raft			
Thickness	m	1.25	2.00
Width	m	4	4
Unit weight	kN/m^3	27	27
Young's modulus	GPa	71	71
Soil			
Width	m	20	20
Length	m	35	35
Depth	m	23.5	23.0/16.0*
Unit weight	kN/m^3	15.2	15.2
Initial void ratio	-	0.75	0.75
Interface			
Interface str., R_{int}	-	0.59	0.59

* dynamic loading

The loads were applied similar to the procedure followed in the centrifuge test. For the monotonic loading conditions, the loads were employed in two stages. In the first stage, the vertical load was applied

as a raft weight plus an additional vertical pressure. Whereas in the subsequent stage, the monotonic loads were applied by means of prescribed displacement cycles in their respective directions. Similarly, for the dynamic loading case, the vertical load was induced by making use of an increased unit weight of the raft, and the horizontal dynamic load was excited at the bottom of the soil model by applying harmonic loading of 1 m/s^2 amplitude and frequency of 1 Hz for 20 s with an additional 5 s steady- state (zero amplitude) condition before and after the main excitation. For both the static and dynamic lateral loading cases, a total vertical load of 5751 kN was applied, equalling a total mass of 4.69 kg in the model scale. Moreover, Rayleigh damping was introduced by employing damping coefficients $\alpha = 0.52,$ and $\beta = 0.0027,$ at a damping ratio of 5%.

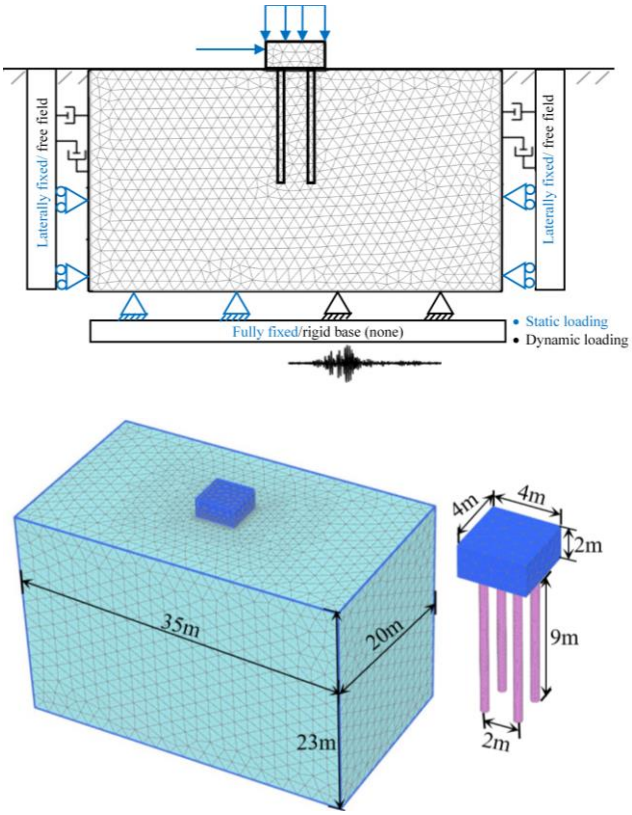

Figure 2. Schematic illustration and FE mesh of the model for static lateral loading case.

4 COMPARISON OF CENTRIFUGE TESTS AND NUMERICAL SIMULATIONS

4.1 Static vertical and horizontal loading

To validate the numerical model and verify the suitability of the selected constitutive model and its model parameters the results of 3D FEA are compared to the respective centrifuge test results on piled rafts. The results for the vertical monotonic load test are presented in Figure 3 and Figure 4 showing a very good agreement between centrifuge model tests and numerical simulation.

The minor difference in the vertical load share is probably related to software limitations in extraction of the structural forces of the piles. The vertical settlement is also compared with numerical analysis result provided by Alnuaim et al. (2017) using a linear elastic-perfectly plastic soil model with a Mohr Coulomb's failure criteria.

The variation of the horizontal displacement and the horizontal stiffness, defined by the ratio of the horizontal load to the horizontal displacement, is compared and presented in Figure 5 and Figure 6, respectively.

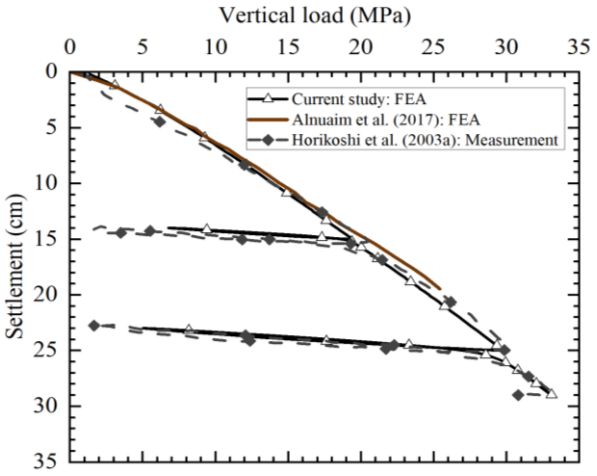

Figure 3. Vertical loading: Variation of settlement with load.

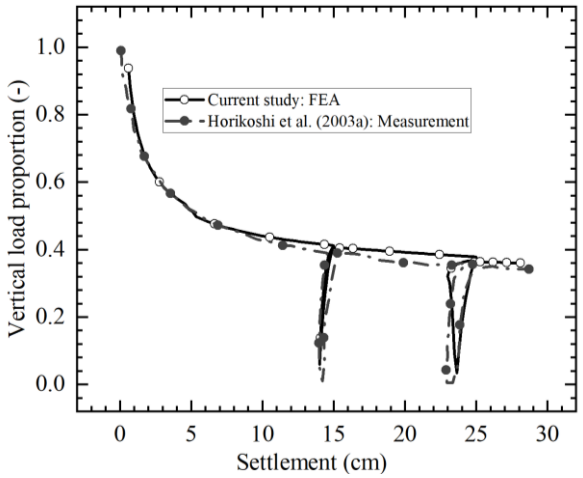

Figure 4. Vertical loading: Variation of pile load share with settlement.

4.2 Dynamic horizontal loading

Back analyses conducted for dynamic loading conditions also revealed a reasonable agreement with the test results. For example, the measured and simulated acceleration and settlement time histories at the top of the raft are compared in Figure 7 and Figure 8,

respectively. The maximum acceleration response at the top of the raft was also compared with the numerical results of Eslami et al. (2011) and Kumar et al. (2016), where a linear elastic-perfectly plastic soil model was used. The comparison indicates that the results achieved with the HSsmall model is in better agreement with the measurements than the two models justifying the application of this more advanced model, particularly for dynamic loading cases.

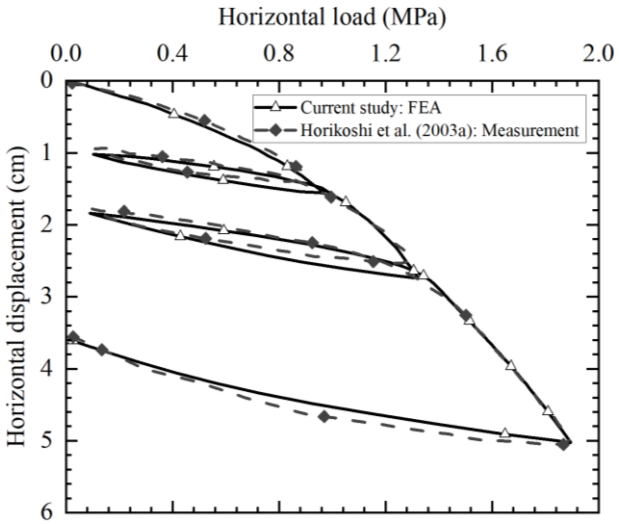

Figure 5. Horizontal loading: Variation of horizontal displacement with load.

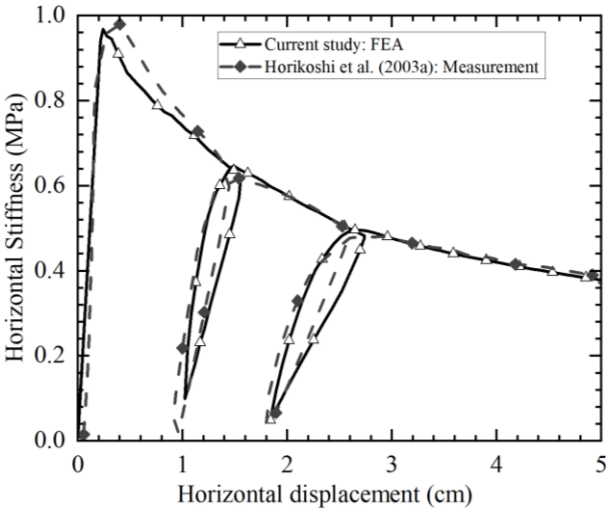

Figure 6. Horizontal loading: Variation of horizontal stiffness with horizontal displacement.

5 CONCLUSIONS

In this work, the calibration of the parameters of the HSsmall model and the validation of 3D numerical model by means of back-analysing centrifuge model tests on piled rafts in sand were presented. Most of the calibrated material parameters were derived by more than one method obtaining similar results. From the validation process, it can be concluded that the 3D numerical model in combination with the HSsmall constitutive model are reasonably well suited for the analysis of piled rafts under static as well as dynamic conditions.

In the next step of the research project the calibrated and verified numerical model will be used for an extensive study investigating piled rafts subjected to different loading conditions.

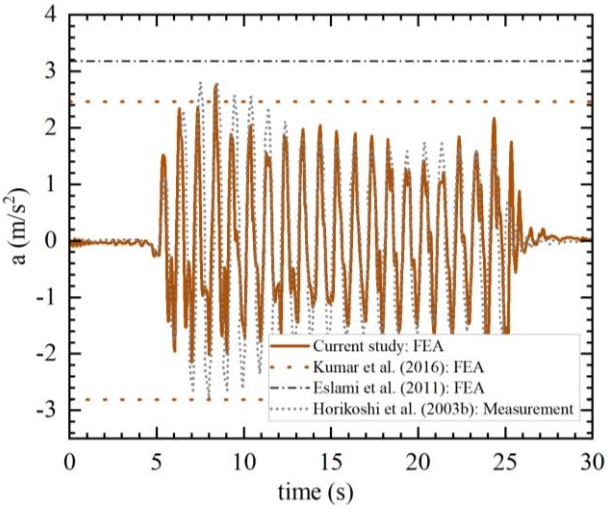

Figure 7. Dynamic loading: Comparison of variation of acceleration at the top of the raft with time.

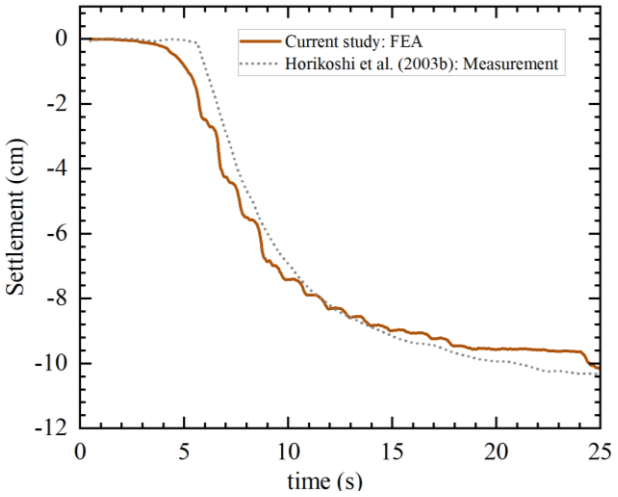

Figure 8. Dynamic loading: Comparison of settlement with time from FEA and test result.

ACKNOWLEDGMENTS

This work is financially supported by Bahir Dar University, the Catholic Academic Exchange Service, the Ethiopian Ministry of Education, the German Academic Exchange Service, and the University of Kassel. The authors are grateful for the financial support.

REFERENCES

Akbari, A., Eslami, A. and Nikookar, M. (2021). Influence of soil stiffness on the response of piled raft foundations under earthquake loading, *Transp. Infrastruct. Geotech.* 8(4), pp. 590–606. https://doi.org/10.1007/s40515-021-00157-8.

Alnuaim, A. M., El Naggar, H. and El Naggar, M. H. (2017). Evaluation of piled raft performance using a verified 3D nonlinear numerical model, *Geotech. Geol. Eng.* 35(4), pp. 1831–1845. https://doi.org/10.1007/s10706-017-0212-1.

Alpan, I. (1970). The geotechnical properties of soils, *Earth-Science Reviews* 6(1), pp. 5–49. https://doi.org/10.1016/0012-8252(70)90001-2.

Benz, T. (2007). *Small-strain stiffness of soils and its numerical consequences,* PhD thesis, Universität Stuttgart, Institut für Geotechnik, Stuttgart.

Bhaduri, A. and Choudhury, D. (2019). Influence of connection rigidity on combined pile-raft foundation under seismic loading. In *Earthquake Geotech. Eng. for Protection and Development of Envir. and Const.,* Rome, Italy, pp. 1437–1444.

Brinkgreve, R., Bonnier, P. and Kappert, M. (2007). Hysteretic damping in a small-strain stiffness model, X, Pande, G. N., Pietruszczak, S. (Eds.). In *Numerical Models in Geomechanics,* Rhodes, Greece, pp. 737–742. https://doi.org/10.1201/NOE0415440271.ch106.

Comodromos, E. M., Papadopoulou, M. C. and Laloui, L. (2016). Contribution to the design methodologies of piled raft foundations under combined loadings, *Can. Geotech. J.* 53(4), pp. 559–577. https://doi.org/10.1139/cgj-2015-0251.

Eslami, M. M., Aminikhah, A. and Ahmadi, M. M. (2011). A comparative study on pile group and piled raft foundations (PRF) behavior under seismic loading, *Comp. Meth. Civil Eng.,* 2(2), pp. 185–199.

Hamada, J., Tsuchiya, T., Tanikawa, T. and Yamashita, K. (2015). Lateral loading tests on piled rafts and simplified method to evaluate sectional forces of piles, *Geotech. Eng. J. of the SEAGS and AGSSEA,* 46(2), pp. 29–42.

Hecht, T. and Dürrwang, R. (2001). Optimierung der Gründung der Reichenbachtalbrüke mit der Kominierten Pfahl-Plattengrüdung, In *Pfahl-Symposium*, Braunschweig, Germany, 65, pp. 21–34. (in German).

Herle, I. and Gudehus, G. (1999). Determination of parameters of a hypoplastic constitutive model from properties of grain assemblies, *Mech. Cohes.-Frict. Mater.* 4(5), pp. 461–486. https://doi.org/10.1002/(SICI)1099-1484(199909)4:5<461::AIDCFM71>3.0.CO;2-P.

Horikoshi, K., Matsumoto, T., Hashizume, Y., Watanabe, T. and Fukuyama, H. (2003a). Performance of piled raft foundations subjected to static horizontal loads, *Int. J. of Physical Modelling in Geotech.* 3(2), pp. 37–50. https://doi.org/10.1680/ijpmg.2003.030204.

Horikoshi, K., Matsumoto, T., Hashizume, Y. and Watanabe, T. (2003b). Performance of piled raft foundations subjected to dynamic loading, *Int. J. of Physical Modelling in Geotech.* 3(2), pp. 51–62. https://doi.org/10.1680/ijpmg.2003.030205.

ISSMGE Technical Committee 212 (2013). ISSMGE combined pile-raft foundation guideline, Katzenbach, R. and Choudhury, D. (Eds.), Darmstadt, Germany.

Kuhlemeyer, R. L. and Lysmer, J. (1973). Finite element method accuracy for wave propagation problems, *J. Soil Mech. and Found. Div.* 99(5), pp. 421–427. https://doi.org/10.1061/JSFEAQ.0001885.

Kumar, A., Choudhury, D. and Katzenbach, R. (2016). Effect of earthquake on combined pile–raft foundation, *Int. J. Geomech.* 16(5), pp. 04016013: 1–16. https://doi.org/10.1061/(ASCE)GM.1943-5622.0000637.

Muir Wood, D. (2004). *Geotechnical Modelling*. 1st ed., CRC Press, London. https://doi.org/10.1201/9781315273556.

Ng, C. W., Shi, J. and Hong, Y. (2013). Three-dimensional centrifuge modelling of basement excavation effects on an existing tunnel in dry sand, *Can. Geotech. J.* 50(8), pp. 874–888. https://doi.org/10.1139/cgj-2012-0423.

O'Neill, M. W., Caputo, V., De Cock, F., Hartikainen, J. and Mets, M. (1996). Case histories of pile-supported rafts (Report for ISSMFE-Technical Committee TCl8, University of Houston, Texas).

Poulos, H. G. (2001). Piled raft foundations: design and applications, *Géotechnique* 51(2), pp. 95–113. https://doi.org/10.1680/geot.51.2.95.40292.

Reul, O. and Randolph, M. F. (2003). Piled rafts in overconsolidated clay: comparison of in situ measurements and numerical analyses, *Géotechnique* 53(3), pp. 301–315. https://doi.org/10.1680/geot.2003.53.3.301.

Santos, J. A. and Correia, A. G. (2001). Reference threshold shear strain of soil. Its application to obtain an unique strain-dependent shear modulus curve for soil. In *15th Int. Conf. on Soil Mech. and Geotech. Eng.,* Istanbul, Turkey. Vol. 1, pp. 267–270.

Sawada, K. and Takemura, J. (2014). Centrifuge model tests on piled raft foundation in sand subjected to lateral and moment loads, *Soils and Foundations* 54(2), pp. 126–140. https://doi.org/10.1016/j.sandf.2014.02.005.

Schanz, T., Vermeer, P. A. and Bonnier, P. G. (1999). The hardening soil model: formulation and verification. In *Beyond 2000 in Computational Geotechnics*, Ronald B.J. Brinkgreve (Ed.), pp. 281–296. https://doi.org/10.1201/9781315138206-27.

Unsever, Y. S., Matsumoto, T., Shimono, S. and Ozkan, M. Y. (2014). Static cyclic load tests on model foundations in dry sand, *Geotech. Eng. J. of the SEAGS & AGSSEA,* 45(2), pp. 40–51

Vucetic, M. and Dobry, R. (1991). Effect of soil plasticity on cyclic response, *J. of Geotech. Eng.*117(1), pp. 89–107. https://doi.org/10.1061/(ASCE)0733-9410(1991)117:1(89).

Proceedings of the XVIII ECSMGE 2024
GEOTECHNICAL ENGINEERING CHALLENGES
TO MEET CURRENT AND EMERGING NEEDS OF SOCIETY
© 2024 the Authors
ISBN 978-1-032-54816-6
DOI 10.1201/9781003431749-290
Open Access: www.taylorfrancis.com, CC BY-NC-ND 4.0 license

ECSMGE 24
XVIII EUROPEAN CONFERENCE ON SOIL MECHANICS AND GEOTECHNICAL ENGINEERING

Eurocode 7 – Second generation. Design of ground improvement works

Eurocode 7 - Seconde génération Dimensionnement des travaux d'amélioration de sol

N. Denies*
Buildwise, Limelette, Belgium

C. Bohn, P. Pandrea, M. Topolnicki
Keller, Germany and Poland

C. Plomteux, K. Trybocka
Menard, France and Poland

**nicolas.denies@buildwise.be*

ABSTRACT: The purpose of Ground Improvement (GI) works is to create usable grounds whose original properties are too weak to meet the design conditions required by the specific construction project. Well-designed ground improvement schemes are being increasingly applied as an alternative to conventional foundation solutions in order to lower construction costs, shorten construction time and reduce CO_2 emissions. The current Eurocode 7 does not cover ground improvement. This will change significantly with the introduction of the second generation of Eurocode 7, which includes a new clause for the design of such geotechnical works. One of the main difficulties of including ground improvement works in the standard was the wide variety of techniques used for this purpose and considering their specific features. Some of them involve soil densification or drainage, while others require installation of various inclusions or treatment of the soil in place using binders. Therefore, it was necessary to establish a comprehensive design methodology that aligns with the philosophy of partial factors in Eurocode 7 and accommodates this versatility. This article presents the adopted concept and highlights the main challenges encountered.

RÉSUMÉ: L'objectif des travaux d'amélioration du sol est de rendre constructibles des terrains dont les propriétés d'origine sont trop faibles pour être utilisés dans les conditions de conception requises par un projet de construction spécifique. Des projets d'amélioration de sol bien conçus sont de plus en plus utilisés comme alternative aux solutions de fondations conventionnelles afin de réduire les coûts de construction, de raccourcir les délais de construction et de réduire les émissions de CO_2. L'Eurocode 7 actuel ne couvre pas l'amélioration du sol. Cette situation changera de manière significative avec l'introduction de la deuxième génération de l'Eurocode 7, qui comprend une nouvelle clause pour la conception de ces travaux géotechniques. L'une des principales difficultés pour inclure les travaux d'amélioration du sol dans la norme était la grande variété des techniques utilisées à cette fin et la prise en compte de leurs spécificités. Certaines d'entre elles impliquent la densification ou le drainage du sol, tandis que d'autres nécessitent l'installation d'inclusions ou le traitement du sol en place à l'aide de liants. Il était donc nécessaire d'établir une méthodologie de dimensionnement globale conforme à la philosophie des facteurs partiels de l'Eurocode 7 qui s'adapte à cette polyvalence. Cet article présente le concept adopté et souligne les principaux défis rencontrés.

Keywords: Second generation Eurocode 7; ground improvement; design methodology.

1 GROUND IMPROVEMENT (GI) CLASSIFICATION AND DEFINITIONS

A wide range of different ground improvement methods are used in practice. An exemplary classification of them was presented by Mitchel (1981), among others. A more recent proposal was also elaborated by TC211 of the ISSMGE (Chu et al., 2009). Both of these and similar classifications take into account executional aspects only and concentrate on the specific techniques used for carrying out the works. However, such a breakdown is not useful regarding the design of ground improvement. A new classification scheme had to be developed taking into account how the ground improvement is applied and also modelled. According to prEN 1997-3, ground improvement shall be classified according to Table 1 considering the diffused or discrete character of the GI and the possibility to measure the unconfined compressive strength (UCS) of the improved ground.

Very important is the definition of rigid inclusions, which represent structural elements with stiffness and strength both significantly higher than the ground in which they are installed. In order to clearly distinguish them from conventional piles, one of the following conditions should be satisfied for Class BII applications, as illustrated in Figure 1:

- structural loads are transferred from the slab and spread foundations or embankment through a Load Transfer Platform (LTP) into the improved ground;
- in absence of a LTP, there is no structural connection between the rigid inclusions and the slab or spread foundation.

2 SELECTION OF THE GROUND IMPROVEMENT TECHNIQUE

The ground improvement technique should be selected considering the following:

- the design situation and load variation;
- thickness and properties of the ground or fill material;
- water pressure in the various strata;
- nature, size and position of the structure to be supported by the ground;
- prevention of damage to adjacent structures or services during execution;
- whether the ground improvement is temporary or permanent;
- in terms of anticipated deformations, the relationship between the ground improvement technique and the construction sequence;
- the effects on the environment including pollution by deleterious substances or changes in groundwater level or properties;
- the durability of the improved ground; and
- any long-term deterioration of the ground.

The actions and ground model shall be assessed according to Parts 1 and 2 of Eurocode 7, respectively: prEN 1997-1 and prEN 1997-2.

3 GROUND INVESTIGATION

The second generation of Eurocode 7 includes a concept of the zone of influence, where construction works or the geotechnical structure can adversely affect the safety, serviceability, robustness, durability or sustainability of the geotechnical structure to be built, other structures, utilities, ground, or groundwater. The depth and horizontal extent of ground investigation shall be sufficient to determine the ground conditions within this zone. The maximum spacing and the minimum number of investigation locations for different types of structures are given in Annex H of EN 1997-2. Unless the National Annex (NA) gives another value, the minimum depth of field investigation below treatment depth is set to 5 m for GI Classes AI and AII, and to the maximum value of 5 m or three times the equivalent diameter of the non-rigid/rigid inclusion for Classes BI and BII. prEN1997-2 specifies that this value should be increased in the case of unfavourable ground conditions and may be reduced in competent ground if sufficient comparable experience exists to allow the determination of its properties throughout the zone of influence.

Table 1. Classification of ground improvement adopted in the second generation of Eurocode 7 (prEN 1997-3).

Class	A-Diffused	B-Discrete
I	**AI – Diffused with no measurable unconfined compressive strength (UCS)** The improved ground has an increased shear strength or stiffness higher than that of the original ground. The improved ground can be modelled as a ground with improved properties. *e.g., deep vibration, dynamic compaction, vertical drains and surcharge, compaction grouting, soil replacement, mass soil mixing.*	**BI – Discrete with non-rigid inclusions** Inclusions, installed in the ground, with higher shear capacity and stiffness compared to the surrounding ground. The unconfined compressive strength of the inclusion is not measurable. *e.g., stone or sand columns, dynamic replacement, geosynthetic encased columns.*
II	**AII – Ground improvement zone with measurable unconfined compressive strength** The improved ground is modified from its original natural state, has a measurable unconfined compressive strength and is significantly stiffer than the surrounding ground. Usually, it comprises a composite of a binder and ground. *e.g., permeation grouting, jet grouting, ground freezing, mass soil mixing with measurable UCS.*	**BII – Discrete with rigid inclusions** Rigid inclusions, installed in the ground, with unconfined compressive strength and significantly higher stiffness than the surrounding ground. The inclusions can be an engineered material such as timber, concrete/grout or steel or a composite of a binder and ground. *e.g., jet grouting and soil mixing columns/panels, concrete or grout columns, steel or timber inclusions.*

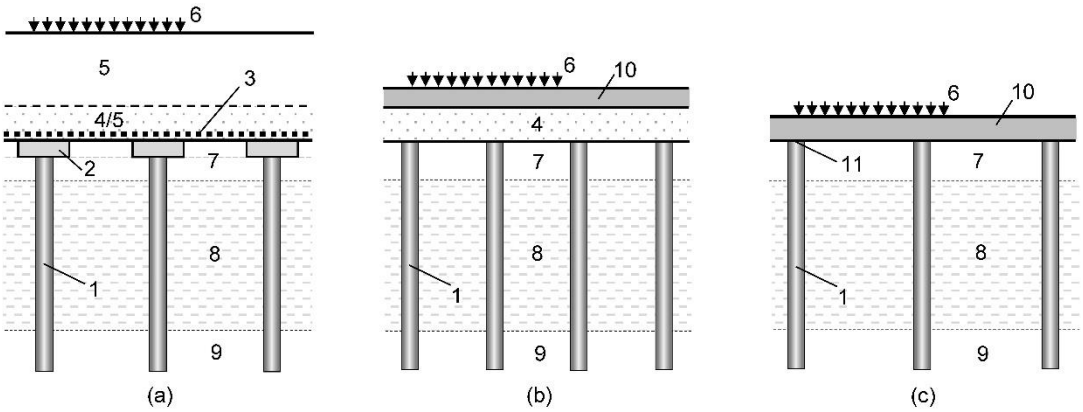

Figure 1. Class BII concepts: a) embankment, b) slab or spread foundation with a LTP, c) slab or spread foundation without a LTP. Key: 1 – rigid inclusions, 2 – optional caps, 3 – optional basal reinforcement, 4 – Load Transfer Platform (LTP), 5 – embankment, 6 – load, 7 – working platform, 8 – weak soil, 9 – load bearing ground, 10 – slab or spread foundation, 11 – no structural connection between 1 and 10 (Figure 1c).

4 GEOMERICAL PROPERTIES AND EXECUTION TOLERANCES

A challenging aspect of the design methodology of the second generation of Eurocode 7 was the consideration of geometrical properties in relation to various GI techniques. According to EN 1990, the design value of a geometrical property (a dimension) is its value including any possible deviation from a predetermined nominal value. Further to what EN 1990 states, acceptable deviations of the geometrical properties shall be considered in GI design.

In geotechnical practice, construction deviations often result from execution tolerances. These are the geometrical imperfections that can occur during the works even with the highest standards of workmanship, corresponding to the best execution practice for a given GI technique. In other words, they are inherent to the construction process selected, and can be maintained by a competent contractor adhering to the state of practice. Moreover, they should not be arbitrarily adjusted to meet specific design requirements, and subsequently enforced on the contractor. Consequently, if consideration of execution tolerances does not allow the design requirements to be met, the extent of works should be increased or a different GI technique or foundation method should be considered.

In accordance with the prEN1997-3, acceptable deviations of the geometrical properties of the GI shall be as specified in the relevant execution standards. In the absence of a relevant execution standard, acceptable deviations of the geometrical properties can be specified in the National Annex. When no national choices are made, the values of these acceptable deviations can be specified by a relevant authority.

For verification of limit states using the partial factor method, the deviation of a geometrical property that is within a specified tolerance is assumed to be catered for by the partial factors γ_F, γ_M, γ_E, and γ_R (cf. EN 1990).

5 GEOTECHNICAL ANALYSES AND DESIGN VERIFICATIONS

Analyses of the interaction between a structure, improved ground and ground should be carried out to verify that the ultimate and serviceability limit states (ULS, SLS) are not exceeded, and should take into account the stiffness ratio of discrete inclusions to the surrounding ground.

For ground improvement the following ULS shall be verified in particular:

- failure of the ground improvement inclusion or zone in compression, tension, bending, buckling or shear;
- failure in the ground due to transverse loading of the improved ground zone;
- uplift or insufficient tensile resistance of the ground improvement zone;
- combined failure in the ground and in the ground improvement inclusion or zone;
- bearing resistance failure below the ground improvement inclusion or zone;
- limit states caused by changes in groundwater conditions or groundwater pressure;
- failure at the edges of the improved ground zone.

Design of Class A ground improvement is similar to the design of structures without the use of any ground improvement technique, and the resulting improved ground or material properties are used in the verification of limit states for the corresponding geotechnical structure. The behaviour of the improved

ground can be conveniently modelled by conventional ground models.

Where Class B ground improvement is used to support or retain a structure, the calculation model shall include:

- the consideration of the interaction effects between the ground, discrete inclusions, and the overlying structure, embankment, or LTP; and
- for Class BII ground improvement a verification of the structural resistance of the individual inclusions.

Interaction effets for Class BII ground improvement are similar to those relevant for a piled raft, whereby a LTP additionally impacts the load distribution between rigid inclusions and supporting ground, leading to the development of negative skin friction in the upper part of the inclusions (Figure 2).

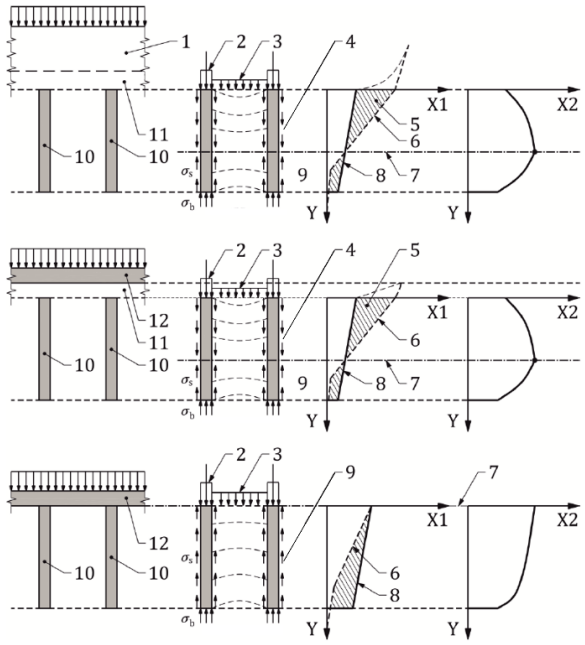

Figure 2. Interaction effects of a ground improvement with rigid inclusions. Key: X1 – settlement, X2 – inclusion axial force, Y – depth, 1 – embankment, 2 – load transmitted to the inclusion, 3 – load transmitted to the ground, 4 – negative skin friction, 5 – differential settlement, 6 – settlement of the ground, 7 – neutral plane, 8 – settlement of the inclusion, 9 – positive skin friction, 10 – inclusion, 11 – load transfer platform, 12 – structure (e.g. slab or spread foundation), σ_s – mobilised shaft friction along inclusion, σ_b – mobilised tip resistance of the inclusion.

5.1 Design resistance of Class B ground improvement

The design resistance of a Class BI ground improvement $R_{sys,d}$ may be determined from the representative value of the total resistance of the ground improvement system with inclusions $R_{sys,rep}$ using a partial factor $\gamma_{R,sys}$ and a model factor $\gamma_{Rd,sys}$, i.e.:

$$R_{sys,d} = \frac{R_{sys,rep}}{\gamma_{R,sys}\,\gamma_{Rd,sys}} \quad (1)$$

For Class BII applications, the design resistance $R_{sys,d}$ may be determined by adding two components:

- the sum of the representative values of the vertical resistance of the i-th rigid inclusion $R_{ri,i}$ with a model factor $\gamma_{Rd,ri}$ and a partial resistance factor for the rigid inclusion system $\gamma_{R,ri}$; and
- the representative value of the vertical resistance of the ground after installation of inclusions R_g with a partial factor γ_{Rg}, i.e.:

$$R_{sys,d} = \frac{\sum_i^n R_{ri,i}}{\gamma_{Rd,ri}\,\gamma_{R,ri}} + \frac{R_g}{\gamma_{Rg}} \quad (2)$$

The representative resistance of a rigid inclusion R_{ri} shall be determined as for piles, depending on the installation technique and taking into account group and further interaction effects, as shown in Figure 2. Consequently, the ultimate geotechnical resistance of a group of rigid inclusions is not the same as the sum of that of the individual inclusions.

The verification of geotechnical limit states for individual inclusions may be omitted provided it is verified that the system is able to redistribute loads without itself exceeding an ultimate or serviceability limit state.

Serviceability limit states of geotechnical structures on improved ground shall be verified according to other relevant clauses of prEN1997-3.

5.2 Unconfined compressive strength (UCS) of Class II ground improvement material

The representative values of the properties of concrete, steel, and timber inclusions shall be determined in accordance with EN 1992-1-1, EN 1993-1-1, and EN 1995-1-1, respectively.

For the treated ground material (e.g. with jet grouting, soil mixing…), provided that at least N samples of the material are tested, the representative value of the unconfined compressive strength $q_{u,imp,rep}$ shall be determined from:

$$q_{u,imp,\mathrm{rep}} = \eta_c \eta_t q_{u,imp,k} \quad (3)$$

where: η_c is a reduction factor accounting for long-term effects, η_t is a factor accounting for the difference in time between testing (typically 28 days) and when the material is exposed to the design stresses and $q_{u,imp,k}$ is the characteristic value of the UCS of the Class II ground improvement material.

$q_{u,imp,k}$ should be determined, according to prEN 1997-1, as the P fractile of the dataset of the relevant

statistical distribution (where recommended values for the parameters N and P are 10 and 10%, respectively, unless the National Annex gives different values). Soils treated with binders typically correlate with the lognormal distribution (Topolnicki and Pandrea, 2012). The P fractile can also be determined from the cumulative frequency curve of the dataset.

If fewer than N samples are tested, $q_{\mathrm{u,imp,rep}}$ shall be determined from:

$$q_{u,imp,\mathrm{rep}} = \eta_c \eta_t q_{u,imp,\mathrm{nom}} \quad (4)$$

where $q_{\mathrm{u,imp,nom}}$, the nominal value of the UCS, should be determined, after execution, as the minimum of the following values:

- the minimum value of all the UCS test results;
- the arithmetic average value of all the UCS test results multiplied by a reduction value k;
- a maximum value $q_{u\,max}$.

Before execution, nominal value can be taken as a cautious estimate of the UCS based on comparable experience, cf. prEN1997-1.

The recommended values of k and $q_{u\,max}$ are 0.7 and 12 MPa, respectively, unless the National Annex gives different values.

For hydraulic binders and cement-based materials, the value of $\eta_c = 0.85$ for geotechnical structures and 1.0 for temporary geotechnical structures (cf. prEN 1997-1) unless the National Annex gives a different value.

The value of η_t should be determined directly from testing for the specific type of Class II ground improvement material, for the specific ground and the specific hydraulic binder or cement-based material. An indicative range of η_t for curing periods $t \leq 28$ days is given in the Annex I to prEN1997-3 (Figure 3).

It is noted that stabilised soils often exhibit significant strength increase with extended curing time over 28 days. This property can also be accounted for in the design by taking $\eta_t > 1$. For example, UCS after 60 days is commonly used in practice. Recommended values for η_t can be found in Topolnicki (2021) with η_t in the range of 1.15 to 1.25.

The design value of the UCS of Class II ground improvement material shall be determined from the representative value as follows:

$$q_{ud} = \frac{q_{u,imp,rep}}{\gamma_M} \quad (5)$$

where $\gamma_M = 1.5$ is a partial material factor for persistent and transient design situations.

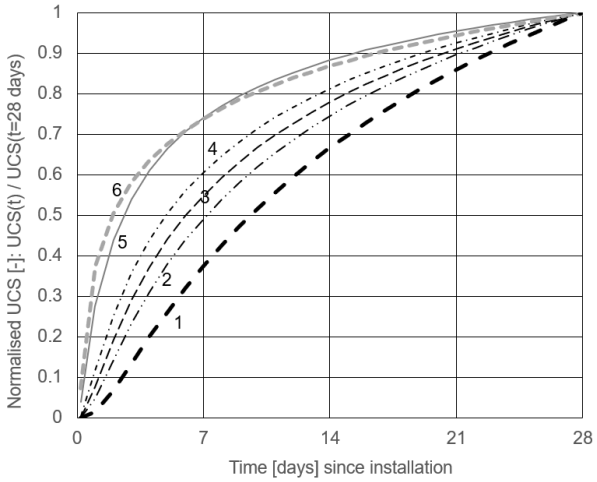

Figure 3. Indicative range for the strength development of Class II ground improvement material over time.
Key: 1− loam-cement (BBRI/SBRCURnet, 2017), 2− sand-cement (BBRI/SBRCURnet, 2017), 3− prEN 1992-1-1 Class CS cement f_{ck} < 35 MPa, 4− prEN 1992-1-1 Class CN cement f_{ck} < 35 MPa, 5− prEN 1992-1-1 Class CR cement f_{ck} < 35 MPa, 6− FHWA Design Manual 2013

5.3 Structural resistance of rigid inclusions

The structural resistance of rigid inclusions shall be verified according to the relevant standard for the material installed. If no such standard exists, for materials of Class II ground improvement, ultimate limit states shall be verified by demonstrating that design effects of actions do not exceed the stress envelope of the material used (Figure 4). When normal stresses and shear stresses are verified separately, the design value of the normal stresses and of the shear stresses shall not exceed $0.7q_{\mathrm{ud}}$ and $0.2q_{\mathrm{ud}}$, respectively.

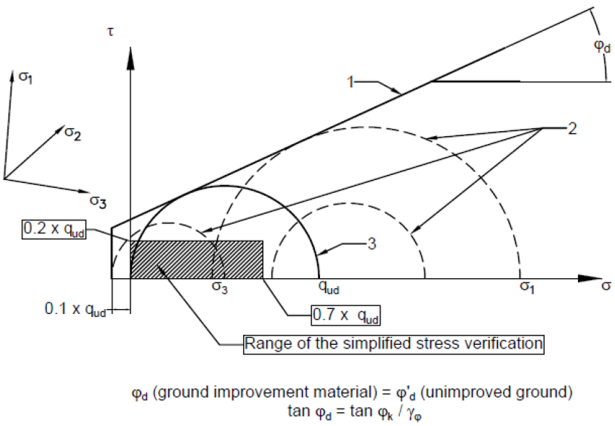

Figure 4. Allowable stresses in ground improved material with UCS.
Key: 1 – envelope for allowed states of stress, 2 – examples for allowed states of stress σ_1, σ_3, 3 – state of stress in uniaxial compression test: σ_3=0, $\sigma_1 = q_{ud}$.

For rigid inclusions subject to compression, buckling shall be verified. When one of the following

conditions is met, verification of buckling of Class BII inclusions may be omitted:

- inclusion diameter $B_{ri} > B_{ref}$;
- thickness of the soft layers, where $c_u < c_{u,ref}$, is smaller than h_{ref}.

The reference values are: B_{ref} = 0.3 m, $c_{u,ref}$ = 15 kPa and h_{ref} = 1.0 m, unless other values are given in National Annex.

5.4 Load transfer platform

The Load Transfer Platform (LTP) and the possible reinforcing elements are designed to transfer the load from the structure or the embankment to the improved ground. ULS verification may be omitted for a LTP where it can be demonstrated that the loads can be redistributed within the confined system, provided that the load transfer platform does not fail at its edges. A confined system can be assumed inside a grid of inclusions in a GI zone (ASIRI, 2012; Bohn, 2016). The tensile resistance of the reinforcements possibly installed in the LTP should be verified according to Clause 9 of prEN 1997-3. In the absence of a LTP, additional verifications may be considered during the design, such as verifications of the stress concentrations at the top of the inclusions and internal forces within the slab or spread foundation.

6 TESTING OF GROUND IMPROVEMENT

The types of testing should be determined according to the GI technique. The minimum frequency and type of control test should be given by the relevant execution standard or, when no relevant execution standard is available, by the relevant authority or, where not specified, as agreed by the relevant parties for a specific project. Typical control tests may include for:

- Class AI: investigations of treated ground as for the original ground in accordance with prEN1997-2, with possible field and laboratory tests and monitoring where relevant (for example, for preloading and vertical drains);
- Class AII: tests on extracted samples of treated ground to verify UCS and other properties;
- Class BI: field testing inside and/or in between inclusions, dummy foundation test on improved ground (individual inclusion and surrounding ground), zone load test on a group of inclusions (group of inclusions and surrounding ground);
- Class BII: load test on isolated rigid inclusions, zone load test on a group of inclusions (group of rigid inclusions and surrounding ground), UCS test of inclusion material.

Material control tests shall be performed to verify that the determined representative values of the improved ground are achieved. The minimum number of control test should be determined based on local experience, ground conditions and the applied ground improvement technique. Sampling should be performed according to relevant execution standard. If undisturbed sampling is impractical, the strength may be determined from documented correlations with other in-situ tests. The stiffness of ground improvement materials should be determined either from laboratory tests on undisturbed samples, documented correlations, or by monitoring of deformations.

The unconfined compressive strength should be determined on undisturbed cylindrical samples with a height to diameter ratio of two. After conducting all UCS tests on suitable samples, the results of the test specimens with unmixed soil inclusions larger than one-sixth of the diameter of the test specimen may be excluded. In addition, no more than 15% of the UCS results of the tested specimens from one specific site may be excluded. In absence of a material standard and unless the National Annex gives different values, the recommended testing frequency is:

- for Class AII ground improvement, 1 test per 125 m³ (minimum of 4 tests) per treated geotechnical unit (volume of ground defined as a single material), conducted on samples representative of the whole treatment depth;
- for Class BII ground improvement, 1 test per 125 m³ (minimum of 4 tests) of rigid inclusion volume, conducted on samples representative of the whole treatment depth.

REFERENCES

ASIRI (2013). Recommendations for the design, construction and control of rigid inclusion. Presse des Ponts, Paris, ISBN: 9782859784706.

BBRI/SBRCURnet. (2018). Handbook Soil mix walls. Design and execution. ISBN: 9780367733964.

Bohn, C. (2016). Serviceability and safety in the design of rigid inclusions and combined pile-raft foundations. *Ph D thesis*, Technical University Darmstadt, Germany.

Chu, J., Varaksin, S., Klotz, U. and Mengé, P. (2009). SoA Report. Construction processes. *XVII ICSMGE,* 132p.

Mitchell, J.K. (1981). Soil improvement – SoA report. *X ICSMFE, Stockholm, 4: 509-565.*

Topolnicki M., Pandrea P. (2012): Design of in-situ soil mixing, Proc. Int. Symp. of ISSMGE TC211, Recent research, advances & execution aspects of ground improvement works, Brussels, Belgium, vol. III, pp. 309-316.

Topolnicki, M. (2021). 20-Years of Deep Soil Mixing in Poland and Lessons Learned, Int. on-line Conf. Deep Mixing, www.researchgate.net/publication/353261051.

Proceedings of the XVIII ECSMGE 2024
GEOTECHNICAL ENGINEERING CHALLENGES
TO MEET CURRENT AND EMERGING NEEDS OF SOCIETY
© 2024 the Authors
ISBN 978-1-032-54816-6
DOI 10.1201/9781003431749-291
Open Access: www.taylorfrancis.com, CC BY-NC-ND 4.0 license

ECSMGE 24
XVIII EUROPEAN CONFERENCE ON SOIL MECHANICS AND GEOTECHNICAL ENGINEERING

Estimation of permeability coefficient using machine learning algorithms on the example of AdaBoost and Artificial Neural Network algorithms

Estimation du coefficient de perméabilité à l'aide d'algorithmes d'apprentissage automatique sur l'exemple des algorithmes AdaBoost et Artificial Neural Network

J. Dzięcioł*, W. Sas
Warsaw University of Life Sciences – WULS, Warsaw, Poland
**justyna_dzieciol@sggw.edu.pl*

ABSTRACT: The development of the Construction sector in recent decades and the systematic reduction of natural aggregate (NA) resources oblige the search for alternatives and substitutes for these important construction materials. The use of anthropogenic aggregates as replacements for natural aggregates provides an opportunity to reduce the number of landfills and recycle waste materials from construction and demolition (CDW), which can be successfully used in Civil Engineering. It may also involve risks that undoubtedly include estimating geotechnical parameters based on solutions developed to date for natural aggregates. A major factor affecting these estimates is that anthropogenic aggregates could have different properties and chemical compositions. This study analyzed the possibility of estimating the coefficient of permeability for Concrete Aggregate (RCA) using Machine Learning algorithms - AdaBoost and Artificial Neural Networks. The obtained results were compared with each other and with the previously used empirical formulas for estimating the coefficient of permeability in non-cohesive materials. Based on the results received, an attempt was made to interpret the physical characteristics of the aggregate that have a significant impact on the estimation of the model by the Machine Learning algorithm. The analysis carried out will allow the formulation of conclusions for further application of Machine Learning algorithms as a tool to support the prediction of the coefficient of permeability.

RÉSUMÉ: Le développement du secteur de la construction au cours des dernières décennies et la réduction systématique des ressources en granulats naturels obligent à rechercher des alternatives et des substituts à ces importants matériaux de construction. L'utilisation de granulats anthropogéniques pour remplacer les granulats naturels permet de réduire le nombre de décharges et de recycler les déchets de construction et de démolition (CDW), qui peuvent être utilisés avec succès en génie civil. Elle peut également comporter des risques, notamment en ce qui concerne l'estimation des paramètres géotechniques sur la base des solutions développées à ce jour pour les granulats naturels. L'un des principaux facteurs influençant ces estimations est le fait que les agrégats anthropogéniques peuvent avoir des propriétés et des compositions chimiques différentes. Cette étude a analysé la possibilité d'estimer le coefficient de perméabilité pour les granulats de béton (RCA) en utilisant des algorithmes d'apprentissage automatique - AdaBoost et les réseaux neuronaux artificiels. Les résultats obtenus ont été comparés entre eux et avec les formules empiriques précédemment utilisées pour estimer le coefficient de perméabilité des matériaux non cohésifs. Sur la base des résultats obtenus, on a tenté d'interpréter les caractéristiques physiques de l'agrégat qui ont un impact significatif sur l'estimation du modèle par l'algorithme d'apprentissage automatique. L'analyse effectuée permettra de formuler des conclusions pour l'application ultérieure des algorithmes d'apprentissage automatique en tant qu'outil d'aide à la prédiction du coefficient de perméabilité.

Keywords: Permeability coefficient; machine learning; AdaBoost; artificial neural network.

1 INTRODUCTION

Sustainability is the improvement of the quality of life in a healthy environment, positively affecting social, economic and environmental conditions for present and future generations. Growing awareness of environmental degradation caused by human activity is motivating stricter regulations and innovative recycling methods (Kumar Mehta, 2001; McNeil & Kang, 2013). Life cycle analysis of a material begins with its potential reuse, which shapes the sustainable nature of the material. This includes stages such as raw material acquisition, processing, use, preservation and disposal or recycling. Sustainable manufacturing seeks

to reduce waste through a closed-loop economy (Cassiani et al., 2021; Vieira et al., 2016).

An example is the recycling of concrete from demolition, which becomes a valuable concrete aggregate that replaces natural aggregates in many applications, including road construction.

The use of recycled concrete aggregates in construction is a developing technique. According to Buck (Buck, 1973), after World War II, when the demolition of buildings and roads generated large amounts of waste and Europe needed to be rebuilt, the use of these aggregates began to be widely used. The process of obtaining recycled concrete aggregates involves crushing concrete, excluding rebar, bricks and soft materials (wood, glass, polystyrene), and obtaining material with fractions from 0 to 63 mm (Oikonomou, 2005). Physical properties of recycled concrete aggregates include density, moisture content, porosity, water absorption, grain shape, fractional composition and filtration properties. In road construction and dam design, the filtration coefficient is crucial. For cost reduction and waste management, the filtration coefficient can be predicted based on physical properties instead of performing costly field or laboratory tests. Machine Learning is employed to more effectively amalgamate concealed details within datasets. The objective of machine learning involves utilizing algorithms to unveil connections between attributes present in datasets, and these revelations can subsequently enhance the procedure of making informed decisions. The purpose of this publication is to demonstrate the predictive capabilities of AdaBoost and Artificial Neural Network algorithms for estimating the filtration coefficient for recycled concrete aggregates (RCA).

2 MATERIAL

The concrete aggregate used in the study came from the demolition work of a repaired road surface. The grain size curves are presented below in Table 1.

Table 1. A summary of the material's grain size range.

	Minimum	**Maximum**
Particle size (d_5), [mm]	0.15	0.17
Particle size (d_{10}), [mm]	0.28	0.30
Particle size (d_{17}), [mm]	0.60	0.80
Particle size (d_{20}), [mm]	0.98	1.30
Particle size (d_{30}), [mm]	1.90	2.20
Particle size (d_{50}), [mm]	3.30	3.90
Particle size (d_{60}), [mm]	5.50	7.80
Particle size (d_{90}), [mm]	9.80	12.50

Figure 1 presents the results of the coefficient of permeability tests with a compaction energy of 0.59 J/cm^3 and 2.65 J/cm^3.

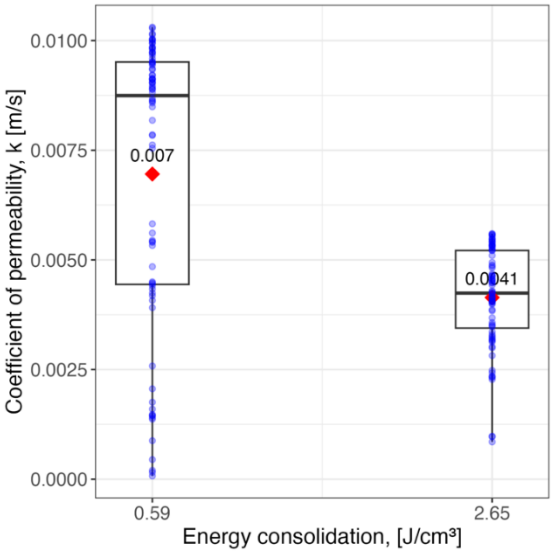

Figure 1. The results of the coefficient of permeability tests.

3 METHOD

A constant head method was applied to test the coefficient of permeability. Artificial Neural Networks and the newer boosting method, AdaBoost, were used for testing and predictive analysis. A brief overview of both Machine Learning algorithms is presented below.

Artificial Neural Networks, often referred to as ANNs or neural networks, represent a widely adopted technique in the realm of machine learning, employed to scrutinize and comprehend data by utilizing an intricate network of decision-making layers. These networks are essentially composed of interconnected decision-making entities, known as nodes, which collaborate through connections akin to the synapses of biological neurons. The arrangement of these nodes takes the form of layers, with the initial layer usually being fed with a comprehensive dataset. This initial layer constitutes raw input data, encompassing a spectrum of information formats such as numerical values, textual data, and even visual or auditory components like image pixels or sound waveforms. In the functioning of an ANN, each input node functions as a transmitter of information, conveying its input to the subsequent layer of nodes via the network's interconnections. This process enables the network to progressively synthesize and process data, capturing intricate relationships among diverse attributes (Lagaros, 2023; Shahin et al., 2021).

The core objective of AdaBoost is the amalgamation of numerous weak learning attributes into a singular potent learning attribute. This technique centers its

attention on these weak learning attributes, often taking the form of decision trees with minimal partitions, akin to what is colloquially known as decision trunks. The primary emphasis lies in enhancing the performance of these less complex learning components and fusing them into a formidable collective force, capable of achieving more robust and accurate outcomes (Lin et al., 2006; Zhou & Yu, 2009).

Cross-validation serves as a fundamental tool within the realm of Machine Learning, aiming to assess a model's capacity for predicting data outcomes. The process involves a parameter known as "k," which signifies the number of partitions in which the dataset is to be segregated. Upon selecting a specific value for "k," it can be directly utilized to characterize the model; for instance, when k equals 10, it transforms into a 10-fold cross-validation (Browne, 2000).

In practical terms, cross-validation entails utilizing a limited dataset to gauge how proficiently the model is likely to perform when making predictions on new, previously unseen data. This practice is particularly advantageous as it mitigates the risk of overestimating the model's predictive prowess, which can occur when using other evaluation techniques (Fushiki, 2011).

This methodology is especially appealing due to its simplicity and comprehensibility. It contributes to the creation of a more dependable model, fostered by the learning and testing phases of its development. The cumulative outcome of k-fold cross-validation is distilled through the computation of the average skill scores exhibited by the model. To gain a comprehensive understanding, it is advisable to incorporate a measure of the fluctuation within these skill scores, which can be conveyed by parameters such as the standard deviation or standard error. The results were verified with the use of error analysis, for individual models were estimated:

- Root Mean Square Error (RMSE):

$$RMSE = \sqrt{\frac{1}{N}\sum_{i=1}^{N}(y_i - \hat{y})^2} \quad (1)$$

- Mean Squared Residuals (MSR):

$$MSR = \frac{\sum_{i=1}^{n}(\hat{y}_i - y_i)^2}{n} \quad (2)$$

- Mean Absolute Error (MAE):

$$MAE = \frac{1}{n}\sum_{i=1}^{n}|y_i - y_t^P| \quad (3)$$

- Coefficient of determination (R^2):

$$R^2 = \frac{\sum_{i=1}^{N}(\hat{y}_i - \bar{y})^2}{\sum_{i=1}^{N}(y_i - \bar{y})^2} \quad (4)$$

SHAP analysis was also performed.

4 RESULTS

4.1 Analysis of prediction results

Table 2 presents the prediction results of the permeability coefficient for both algorithms.

The following physical characteristics of the investigated Recycled Concrete Aggregate (RCA) were used to determine models based on AdaBoost and Neural Network algorithms: grain sizes at selected percentage content, including smaller sizes (d_5, d_{10}, d_{17}, d_{20}, d_{30}, d_{50}, d_{60}, d_{90}), grain size curvature index (C_C), and uniformity coefficient (C_U), volumetric density of the skeletal gravel structure, porosity index, and degree of compaction. In addition to material properties, the prediction also included the gradient at which the test was performed. It was decided to include the gradient as an important parameter of the study.

In the case of the training sample, better results of fitting to the observation data were obtained for the AdaBoost algorithm, in its case the R^2 was 0.959, for Neural Network the R^2 was 0.682.

Table 2. Evaluation of training set.

Model	RMSE	MSR	MAE	R^2
AdaBoost	0.001	3.04×10^{-7}	3.62×10^{-4}	0.959
Neural Network	0.002	2.39×10^{-6}	1.26×10^{-3}	0.682

In the test sample (Table 3) the R^2 results obtained for the algorithms were lower for AdaBoost the coefficient of determination was 0.886, and for Neural Network it was 0.640.

Table 2. Evaluation of test set.

Model	RMSE	MSR	MAE	R^2
AdaBoost	0.001	8.07×10^{-7}	6.34×10^{-4}	0.886
Neural Network	0.002	2.53×10^{-6}	1.30×10^{-3}	0.640

The results of the prediction of the filtration coefficient versus the results from the observations are presented in the figures below. For the AdaBoost algorithm for the training sample in Figure 2, for the test sample in Figure 4, the Neural Network algorithm in Figure 3 for the training sample and Figure 5 for the test sample. The R^2 results for both algorithms translate into a distance of the individual results from the reference line, and thus larger values of the residuals. Comparing all the graphs, one can notice a greater concentration of results around the reference line in the case of the AdaBoost algorithm, which harmonizes with the obtained high R^2 results and low error results for this algorithm.

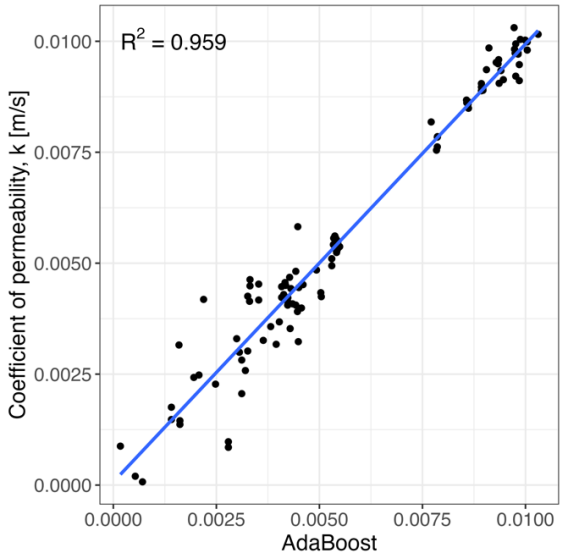

Figure 2. Training set – AdaBoost.

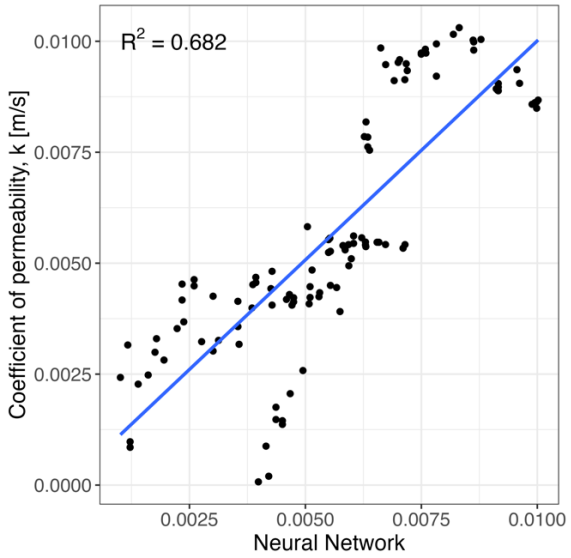

Figure 3. Training set – Neural Network.

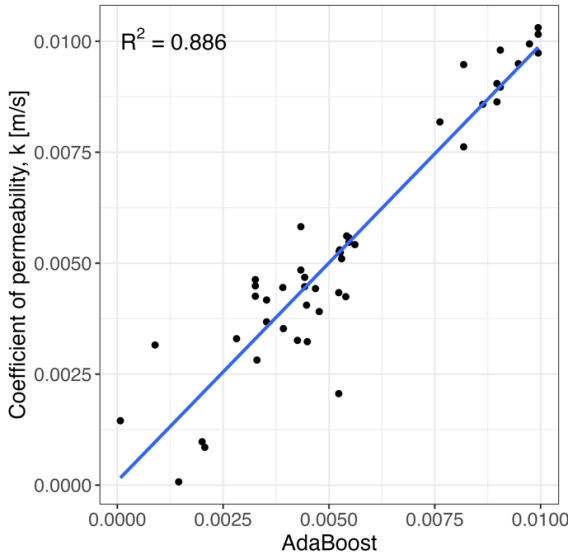

Figure 4. Test set – AdaBoost.

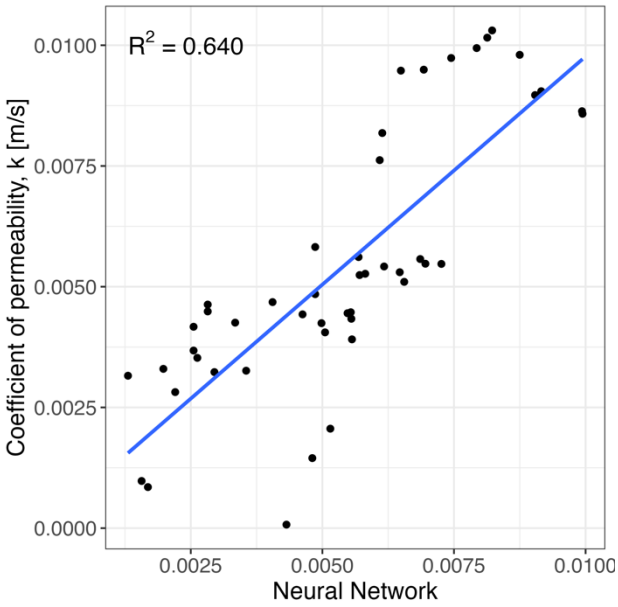

Figure 5. Test set – Neural Network.

Significant discrepancies in the results obtained by the various algorithms should be attributed to their different operating model. Adaboost and Artificial Neural Networks are two distinct approaches to machine learning, each with its characteristics and applications.

Adaboost is an ensemble learning method, specifically a boosting algorithm that combines multiple weak learning algorithms to create a strong learning algorithm. The algorithm sequentially matches these weak learning algorithms to the data, with each successive learning algorithm paying more attention to instances misclassified by previous ones. Artificial Neural Networks are a type of machine learning model inspired by the structure and functioning of the human brain. The process of learning an algorithm is usually done through backpropagation, in which errors are propagated backward through the network, updating the weights to minimize the error. Neural networks require significant amounts of labeled data to train, especially for tasks involving high-dimensionality inputs. Increasing the number of analyzed results may lead to reduced errors.

4.2 Interpretation of results using the SHAP technique

Explanatory methods for predictive models generated by machine learning algorithms offer crucial insights into the inner workings of these algorithms, enabling comprehension of the relationships among dataset features and their impact on model outcomes. Efforts to combine prediction and interpretation models give rise to an unavoidable trade-off between prediction

accuracy and the ease of model interpretation. To address this, the concept of explainable artificial intelligence (XAI) comes into play. In XAI models, such as local interpretable model-agnostic explanations (LIME) and Shapley additive explanations (SHAP), prediction and interpretation models are developed independently. These models enhance interpretability without compromising prediction accuracy.

Interpreting the decisions made by machine learning models like Artificial Neural Networks and Adaboost can be challenging due to their complex structures and opaque decision-making processes. The SHAP technique assigns specific scores to input features in the dataset based on their relevance in predicting the target value. Additionally, it is commonly applied for feature selection and dimensionality reduction, enhancing machine learning model performance by removing less pertinent features.

Applied to ANNs, the SHAP value method helps reveal which input features have the greatest impact on the network's predictions. By studying SHAP values for different features across multiple instances, patterns can be identified and insights can be gained into how the network processes information.

SHAP values can be applied to Adaboost by considering the contribution of each weak learner to the ensemble prediction for a particular instance. This involves evaluating how a change in input features affects the predictions made by each weak learner and aggregating these effects to calculate SHAP values for the ensemble's predictions. Unlike ANNs, Adaboost models are more interpretable because they consist of a collection of simpler models. Therefore, interpreting the contribution of individual weak learner models using SHAP values can provide simpler insights into model behavior.

Figures 6 and 7 in this paper employ SHAP to elucidate the role of features in prediction models, with SHAP calculating the impact of each feature on the predictions made by the learned model.

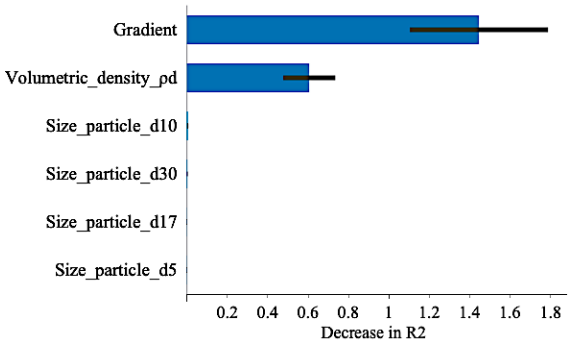

Figure 6. Feature Importance – AdaBoost.

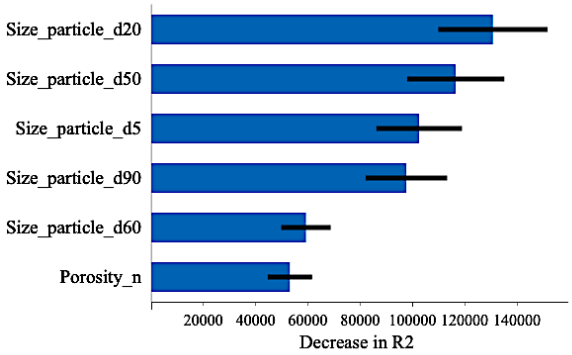

Figure 7. Feature Importance – Neural Network.

The RCA features that turned out to be particularly relevant to the model determined using the AdaBoost algorithm were gradient and volumetric density, in the second place the model took into account particle size in the case of the Neural Network where particle size d_{20}, d_{50} and d_5.

5 CONCLUSIONS

This study explores sustainable practices in recycling concrete aggregates, particularly in predicting the filtration coefficient for recycled concrete. Using machine learning techniques, AdaBoost and Neural Network algorithms were employed and compared. AdaBoost outperformed in the training sample (R^2 = 0.959), and testing sample (R^2=886). The SHAP technique enhanced interpretability, highlighting key features like gradient and volumetric density for AdaBoost and particle size (d_{20}, d_{50}, and d_5) for Neural Network. Overall, the study emphasizes the potential of machine learning in sustainable material practices.

REFERENCES

Browne, M. W. (2000). Cross-Validation Methods. *Journal of Mathematical Psychology*, *44*(1), 108–132. https://doi.org/10.1006/JMPS.1999.1279.

Buck, A. D. (1973). Recycled Concrete. *Highway Research Report*, 1–8. https://onlinepubs.trb.org/Onlinepubs/hrr/1973/430/430-001.pdf.

Cassiani, J., Martinez-Arguelles, G., Peñabaena-Niebles, R., Keßler, S., & Dugarte, M. (2021). Sustainable concrete formulations to mitigate Alkali-Silica reaction in recycled concrete aggregates (RCA) for concrete infrastructure. *Construction and Building Materials*, *307*, 124919. https://doi.org/10.1016/J.CONBUILDMAT.2021.124919.

Fushiki, T. (2011). Estimation of prediction error by using K-fold cross-validation. *Statistics and Computing*,

21(2), 137–146. https://doi.org/10.1007/S11222-009-9153-8/METRICS.

Kumar Mehta, P. (2001). Reducing the Environmental Impact of Concrete. *Concrete International*, *23*(10), 61–66.

Lagaros, N. D. (2023). Artificial Neural Networks Applied in Civil Engineering. *Applied Sciences 2023, Vol. 13, Page 1131*, *13*(2), 1131. https://doi.org/10.3390/APP13021131.

Lin, G., Feng, G., Xiaohong, G., Dianmin, Z., & Jie, L. (2006). A regression algorithm based on AdaBoost. *Proceedings of the World Congress on Intelligent Control and Automation (WCICA)*, *1*, 4400–4404. https://doi.org/10.1109/WCICA.2006.1713209.

McNeil, K., & Kang, T. H. K. (2013). Recycled Concrete Aggregates: A Review. *International Journal of Concrete Structures and Materials*, *7*(1), 61–69. https://doi.org/10.1007/S40069-013-0032-5/FIGURES/6.

Oikonomou, N. D. (2005). Recycled concrete aggregates. *Cement and Concrete Composites*, *27*(2), 315–318. https://doi.org/10.1016/j.cemconcomp.2004.02.020.

Shahin, M. A., Jaksa, M. B., & Maier, H. R. (2021). Artificial neural network applications in geotechnical engineering. *Australian Geomechanics*, *36*(1), 49–62.

Vieira, D. R., Calmon, J. L., & Coelho, F. Z. (2016). Life cycle assessment (LCA) applied to the manufacturing of common and ecological concrete: A review. *Construction and Building Materials*, *124*, 656–666. https://doi.org/10.1016/J.CONBUILDMAT.2016.07.125.

Zhou, Z.-H., & Yu, Y. (2009). AdaBoost. *The Top Ten Algorithms in Data Mining*, 141–164.

Proceedings of the XVIII ECSMGE 2024
GEOTECHNICAL ENGINEERING CHALLENGES
TO MEET CURRENT AND EMERGING NEEDS OF SOCIETY
© 2024 the Authors
ISBN 978-1-032-54816-6
DOI 10.1201/9781003431749-292
Open Access: www.taylorfrancis.com, CC BY-NC-ND 4.0 license

ECSMGE 24
XVIII EUROPEAN CONFERENCE ON SOIL MECHANICS AND GEOTECHNICAL ENGINEERING

Probabilistic stability assessment of deforested steep slopes using 3D finite element method

Étude probabiliste de la stabilité de pentes raides défrichées en utilisant la méthode des éléments finis 3D

A. Ebener*, K. Lesny
University of Siegen, Siegen, Germany
**andra.ebener@uni-siegen.de*

ABSTRACT: Not all effects of climate change can be described directly; changing boundary conditions bring a multitude of indirect consequences. As an example, the droughts of recent years have caused large-scale forest dieback, also in Germany, and thus led to extensive areas of calamity in the Siegerland, a region in Germany's central low mountain range. The slopes, some of which are very steep here, are no longer covered with trees, so that the root system, the natural reinforcement of the soil, begins to rot. In particular, increasing extreme events such as persistent precipitation and heavy rainfall in combination with the lack of trees raise the question of the stability of the now bare slopes. Due to the variability of soil properties and the uncertainties related to the hydrological boundary conditions as well as to vegetation rooting, a reliability-based approach is deemed to be an appropriate tool to assess the stability of deforested slopes. This paper presents the reliability assessment procedure for slopes with vegetation and discusses the challenges when practically applied to a 3D Finite Element model as compared to an analytical Limit Equilibrium model of the slope.

RÉSUMÉ: Tous les effets du changement climatique ne peuvent pas être décrits directement; les changements des conditions limites entraînent une multitude de conséquences indirectes. À titre d'exemple, les sécheresses des dernières années ont également entraîné un dépérissement des forêts à grande échelle en Allemagne et, par conséquent, de vastes zones de calamité dans le Siegerland, une région du massif montagneux central de l'Allemagne. Les pentes, dont certaines sont très raides ici, ne sont plus couvertes d'arbres, de sorte que le système racinaire, le renforcement naturel du sol, commence à pourrir. En particulier, l'augmentation des événements extrêmes tels que les précipitations persistantes et les fortes pluies combinées au manque d'arbres soulève la question de la stabilité des pentes désormais dénudées. En raison de la variabilité des propriétés du sol et des incertitudes liées aux conditions limites hydrologiques ainsi qu'à l'enracinement de la végétation, une approche basée sur la fiabilité est considérée comme un outil approprié pour évaluer la stabilité des pentes déboisées. Cet article présente la méthode d'évaluation de la fiabilité des pentes avec végétation et examine les défis liés à l'utilisation d'un modèle 3D par éléments finis par rapport à un modèle analytique d'équilibre limite de la pente.

Keywords: Slope stability; probabilistic analysis; failure probability; vegetation; Monte Carlo Simulation.

1 INTRODUCTION

Initial stability investigations of calamity areas on steep slopes in the Siegerland, a German low mountain region, which were caused by the drought of past years, made clear that purely deterministic considerations may not be sufficient to represent the uncertainties of the factors influencing slope stability. Probabilistic approaches instead are suitable to take into account the variability of relevant input parameters and uncertainties in their determination.

The future generation of Eurocode 7 (FprEN 1997-1:2024) will explicitly allow the verification of limit states by reliability-based methods other than the conventional semi-probabilistic approach with partial factors. It further includes explicit recommendations for limit state verification using numerical methods.

This article, therefore, illustrates how to practically represent random variables in a stability assessment of a natural slope considering the effect of tree roots in a Finite Element (FE) analysis. The challenges associated to the reliability-based stability assessment using FE modelling are discussed in comparison to the application of an analytical Limit Equilibrium (LE) model. For this purpose, the geometry and the selection of soil parameters for the slope model have been deliberately kept simple.

2 CONSIDERATION OF VEGETATION IN THE STABILITY ANALYSIS

Especially in naturally formed slopes and hillsides, vegetation generally, but not exclusively, has a positive impact on slope stability (e.g. Schwarz et al., 2013; Rickli et al., 2002), which is expressed in two ways: mechanical effects and hydrological effects, whereby the hydrological effects are not addressed here. Among the mechanical effects is the reinforcement of the soil by the roots, increasing the shear strength of the soil. Roots can also anchor themselves in deeper layers, thus supporting the uphill soil mass against sliding. However, weight of vegetation and its associated downhill forces increase the load on the slope but also the resistance forces.

The enhancement of soil shear strength is a result of the high tensile strength of the roots and the density of the plant root system. However, due to the natural and somewhat random orientation of roots, the influence on the friction angle is assumed to be minor (Gray et al., 1982). Instead, the increase in shear strength through the root system is typically be represented by an increase in soil cohesion, known as root cohesion (c_r). The root cohesion can thus be integrated into the Mohr-Coulomb failure criterion to describe the soil's shear strength as follows:

$$\tau = c' + c_r + \sigma' \cdot tan\,(\varphi') \qquad (1)$$

where τ (kPa) represents the shear strength of the soil, c' (kPa) is the effective cohesion, c_r (kPa) is the root cohesion, σ' (kPa) is the normal stress, and φ' (°) is the effective friction angle (e.g., Chok et al. 2015).

The positive influence of tree roots will be considered accordingly in the following stability analysis, considering the fact that the calamity areas are primarily in coniferous forests on steep slopes. The influence of grasses and shrubs will be neglected, even though it is commonly acknowledged that they may also contribute to slope stability (e.g., Ali & Osman, 2008).

3 3D-FE SLOPE STABILITY MODEL CONSIDERING VEGETATION

In the assessment of slope stability using the Finite Element Method, the linear-elastic ideal-plastic Mohr-Coulomb model is often deemed sufficient to describe material behavior (EANG, 2014). The so-called φ-c reduction is used in this approach. In this process, the shear parameters tan(φ) and c in the FE model are gradually reduced until the limit equilibrium is reached. This is indicated by termination of the FE analysis because the system can no longer achieve equilibrium.

According to FprEN 1997-1:2024, the φ-c reduction starts with representative values of the shear parameters. The safety of the analysed slope is defined as the ratio of available shear strength to the shear strength, below which slope stability is no longer guaranteed, expressed as the safety factor (SF):

$$SF = \frac{c}{c_f} = \frac{tan(\varphi)}{tan\,(\varphi_f)} \qquad (2)$$

where the shear parameters c_f and tan(φ_f) describe the shear strength at the limit state (f: failure).

To illustrate the practical approach of a reliability assessment based on numerical analysis of the ultimate limit state of the slope within this paper, the geometry of the 3D FE-model has deliberately kept simple. The investigated slope is 5 m high and has an inclination of 30°. To consider the effect of vegetation in the stability analysis, a distinct soil layer is defined as a rooted zone, where the cohesion is increased by the root cohesion c_r (see Figure 1). The thickness h_r (m) of the rooted soil depends on the typical rooting depth of the existing vegetation and is subject to both spatial and temporal variations. However, the influence of the variation of h_r is not part of the investigations in this paper. Hence a constant value of h_r = 1 m is assumed. In addition, no groundwater was taken into account at this point. The mesh was created with 10-noded elements and a medium element distribution. In general, a finer mesh may lead to a more accurate solution, but a finer mesh also increases the calculation time. Therefore, a medium mesh with low computation time was used for the purpose of this generic study.

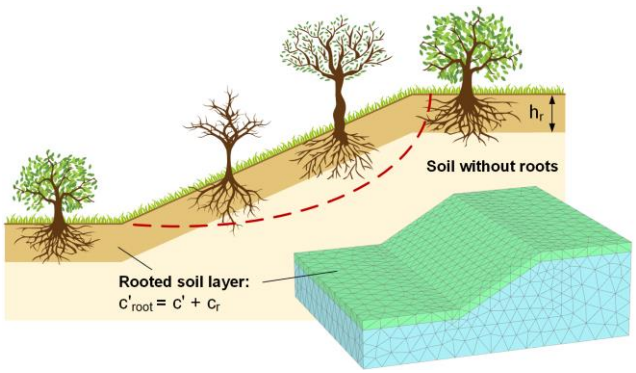

Figure 1. Consideration of vegetation in the FE model by a simplified rooted soil zone.

4 DESCRIPTION OF SCATTERED VARIABLES AND THEIR EFFECTS

Both the material properties of the soil and vegetation exhibit a high degree of variability, leading to

significant uncertainties in their determination. To account for these uncertainties in geotechnical analysis and design, probabilistic approaches are utilized. In the future generation of Eurocode 7 (FprEN 1997-1:2024), these methods are explicitly recognized as an alternative to the traditional design approach involving partial safety factors, aiming to verify a sufficient safety of a geotechnical structure.

Probabilistic approaches rely on the use of probability distributions to model uncertainties in soil properties, geometry, load assumptions, and calculation models. In contrast to semi-probabilistic methods, which rely on a single estimate of parameters, probabilistic approaches allow for the direct consideration of uncertainties and their impacts on the reliability of a system. One fundamental investigation is the probabilistic sensitivity analysis, which can be used to analyse the effect of parameter variability and detect the parameters with the greatest influence on the failure mechanism under study. Based on this, the relevant variables can be modeld as random variables in further reliability studies. Ebener & Lesny (2023) illustrate the performance of a probabilistic sensitivity analysis for the example addressed in this paper.

In the slope model presented here, the parameters c', c'_{root}, and φ' were modeled as random variables represented by probability distribution functions. For the implementation, appropriate distribution functions had to be chosen. Figure 2 displays the selected distribution functions of the soil and vegetation parameters, which are a normal distribution for the friction angle φ' and a log-nomal distribution for the cohesion c' and the root cohesion c'_{root}. Both the associated parameters mean and variance as given in Figure 2, as well as all other deterministic soil parameters were adopted from the literature (e.g., Uzielli et al., 2006; Keller, 2017) and are typical for soils at natural hillsides in the region of the Siegerland.

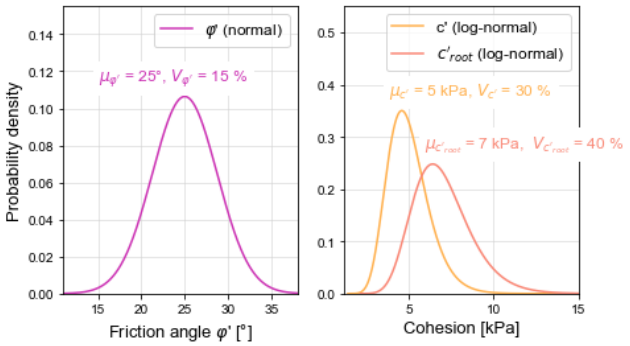

Figure 2. Distribution functions of the random variables assumed in the model.

Accordingly, the deterministic parameter were set to soil unit weight $\gamma = 20$ kN/m³ and Young's modulus $E = 10^4$ kN/m². The poisson's ratio ν was assumed to be 0,35 and the dilation angle ψ to 0° (also EANG, 2014).

5 CALCULATING THE PROBABILITY OF FAILURE

5.1 General application

To assess the probability of failure (P_f) or the reliability index (β), the structural performance is characterized by a limit state function g(X). This function is defined so that g(X) = 0 delineates a limit state separating undesirable ($g < 0$) from desirable ($g \geq 0$) conditions (TC250/SC7/TG-C3 2023). For the slope in the FE model, the limit state function is defined as:

$$g = SF - 1, \tag{3}$$

from which the following can be deduced for the assessment of slope stability in a similar manner:

$$SF \begin{cases} < 1, & unstable\ slope \\ \geq 1, & stable\ slope \end{cases} \tag{4}$$

If the slope stability is now considered as a function of random variables, the slope stability can be assessed for each possible parameter combination (sample). The results of the computational runs, resulting in a safety factor SF for each sample which can then be used in the limit state equation, can be presented as a density function with the corresponding probabilities of occurrence or frequencies. The area under the function less than 0 corresponds to the probability of failure P_f of the slope, which is displayed as failure region in Figure 3.

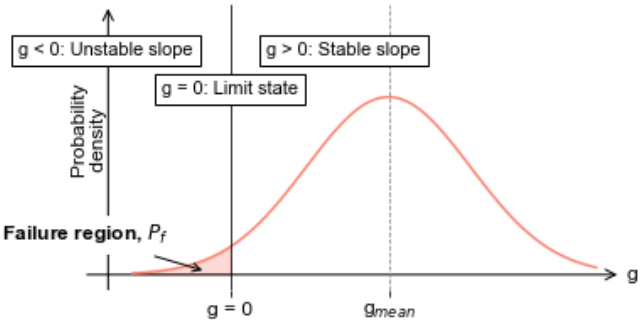

Figure 3. Distribution function of the limit state function, calculated with the resulting safety factor SF for each sample; shaded area represents the failure region corresponding to the probability of failure P_f.

5.2 Target reliability

The selection of a target reliability is crucial in geotechnical design as it forms the basis for ensuring the safety and reliability of geotechnical structures. It allows engineers to assess the probability of failure and its potential impacts on the environment, society, and the economy, ensuring the long-term stability and sustainability of such projects. In accordance with ISO 2394:2015, the selection of target failure probabilities should take into consideration various factors such as the severity and type of failure, economic consequences, societal disruptions, environmental impacts, sustainable use of natural resources, and the associated costs and efforts required to mitigate the risk of failure. EN 1990 Annex C outlines specific reliability index values (β values) for a reference period of 50 years. It is worth noting that different target reliability levels for various reference periods can be established through the National Annexes. A report from JRC (2023) sheds light on the origins of these target values, originally designed for use in buildings and bridges. However, the reliability calibration study within the same report suggests that these target values may also be applicable to geotechnical structures, as exemplified in the case of spread foundations and piled foundations (TC250/SC7/TG-C3, 2023).

5.3 Basic analysis – crude Monte Carlo simulation

In order to approximate the density function of, in this case, SF, sampling methods are widely used. Monte Carlo simulation (MCS) in its simplest form (crude Monte Carlo) is a sampling method, which collects a defined number of random samples from the probability distributions of the random variables involved in a process or system under study. For the calculation of the probability of failure with the MCS, a total of n_{total} samples are generated based on the underlying distribution functions (sampling). The evaluation involves determining which randomly generated parameter combinations result in failure (n_f) when evaluating the corresponding limit state function (in this case Equation 3). The estimator of the probability of failure P_f is the ratio of the number of realizations resulting in failure (n_f) and the total number of realizations or samples (n_{total}):

$$P_f \approx \frac{n_f}{n_{total}} \tag{5}$$

The accuracy of the estimate depends on the number of (failed) realizations, which can be expressed in terms of the coefficient of variation of the estimated probability of failure:

$$V_{Pf} = \sqrt{\frac{1-P_f}{n_{total} \cdot P_f}} \tag{6}$$

A coefficient of variation (V_{Pf}) ranging from 5 to 10% is deemed adequately precise for assessing structural reliability. Consequently, V_{Pf} can serve as a convergence or termination criterion for the Monte Carlo simulation and serves as the foundation for determining the uncertainty bounds of the estimated values. Equation 7 suggests that the required sample size n_{req} can be determined using a prior estimate of the probability of failure (TC250/SC7/TG-C3, 2023):

$$n_{req} \approx \frac{1}{V_{pf}^2 \cdot P_f} \tag{7}$$

5.4 Implementation and problems

To obtain reliable statements regarding the failure probability of a slope or any other geotechnical structure, a high number of MCS is required to represent the overall population of possible parameter combinations as realistically as possible. For example, according to Table C.3 (prEN 1990:2022) for a structure assigned to Consequence Class 2 the target reliability index is $\beta = 3.8$ which corresponds to a failure probability of $P_f = 1 \cdot 10^{-4}$. With Equation 7 this means that one million (10^6) samples would be required to obtain a sufficiently reliable result with a coefficient of variation of 10%. The presented simple model in Plaxis 3D has a computation time of about 3 minutes with a medium mesh coarseness, resulting in a total computation time of 3,000,000 minutes ≈ 2,083 days on the available computer for a required number of simulations with randomly generated parameter combinations of one million. This, of course, is unrealistic for practical applications.

For comparison and to illustrate the need for large sample sizes, MCS for the model slope was performed using a limit equilibrium method of slices with Plaxis 3D LE. The method chosen here was the General Equilibrium Method (GLE) according to Fredlund & Krahn (1977). For a sample size of one million using this model the total computation time was about 2,000 minutes.

Figure 4 shows the results of the MCS for sample sizes n = 100; 1,000; 10,000; 100,000 and $1 \cdot 10^6$. The safety factors, along with their associated relative frequencies for the MCS with various sample sizes n, illustrate the necessity of large sample sizes. With small sample size, a failure probability of 0.00% was calculated, meaning that no combination resulted in a

safety factor less than 1.0 in the randomly generated samples. Only sample sizes starting from $n \sim 3{,}000$ or larger contained parameter combinations that can lead to failure (which is shown in the blue ellipse in Figure 4). Thus, a smaller sample size implies a 100% safety, albeit solely due to the random absence of parameter combinations resulting in failure. While the probability of failure for the MCS in this example is no longer 0 from $n \sim 3{,}000$, it varies between the sample sizes up to about $n \sim 250{,}000$ and slowly converges to an approximately constant value of $P_f \approx 0.03\%$ ($= 3 \cdot 10^{-4}$) with increasing sample size. The limits mentioned here are an outcome of a unique implementation of the MCS with the specified sample sizes n. However, these limits may differ when the MCS is repeated with the same sample sizes, especially in the case of small numbers of samples which only represent a limited number of randomly selected parameter combinations. On the other hand, the results converge if the sample sizes are large enough, as a significantly broader range of possible parameter combinations is represented, thus approximating the overall population. In the case of large sample sizes, it can thus be assumed that even less probable and potentially destabilizing parameter combinations will be considered in the safety assessment.

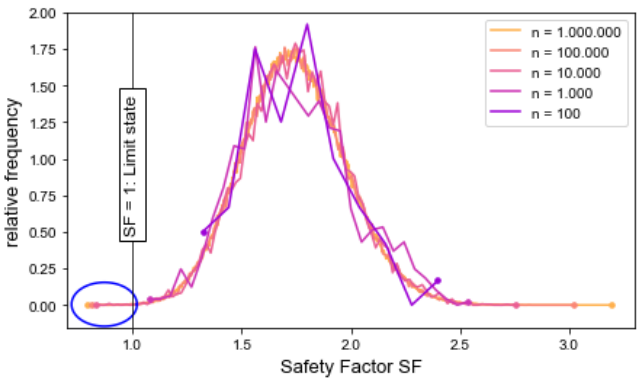

Figure 4. Results of MCS, distribution of the safety factor SF for different sample sizes n; lowest and highest values of each distribution are market with dots.

6 FURTHER STEPS FOR RELIABILITY ANALYSIS OF NATURAL SLOPES

In order to evaluate the reliability of natural slopes using FE, the Monte-Carlo Simulation is not practicable and other methods are needed, for example, surrogate modeling, where the system response to the random variables can be predicted without modelling the real process itself. Surrogate models can provide results within seconds and can be used for MCS (e.g., Furtney et al., 2022). Furthermore, other sampling methods can be used, such as importance sampling, a variance reduction technique that use additional prior information about the failure region for sampling only close to the failure/safe boundary (e.g. TC250/SC7/TG-C3, 2023).

Another relevant aspect of modeling and reliability assessment of natural slopes, which has not been addressed here, is the representation of external influences such as precipitation in particular which can have a significant impact on stability and thus on reliability. In addition, natural and vegetated slopes in particular are subject to high spatial variability in terms of topography and soil stratification as well as soil properties and vegetation. The spatial variability can be taken into account e.g. using various geostatistical methods (e.g., Chilès & Delfiner, 2012). Further, by including vegetation in the slope model, it is possible to study the effects of cleared forests, i.e., the influence of root systems that are no longer present on the reliability of a slope.

In addition, studies have shown that the probability of failure is sensitive to the correlation between shear parameters which as well should be considered in the probabilistic analysis (e.g., Wang & Akeju, 2016).

REFERENCES

Ali, F. H. & Osman, N. (2008): Shear strength of a soil containing vegetation roots. Soils Found Tokyo, 48(4):587–596; DOI: 10.3208/sandf.48.587.

Chok, Y.H.; Jaksa, M.B.; Kaggwa, W.S. & Griffiths, D.V. (2015): Assessing the influence of root reinforcement on slope stability by finite elements. Internatioal Journal of Geo-Engineering (2015) 6:12; DOI: 10.1186/s40703-015-0012-5.

Chilès, J.-P. & Delfiner, P. (2012): Geostatistics: Modeling Spatial Uncertainty, Wiley Seriesin Probability and Statistics. John Wiley & Sons, Inc., Hoboken, NJ, USA; DOI: 10.1002/9781118136188.

EANG (2014): Empfehlungen des Arbeitskreises „Numerik in der Geotechnik“. Deutsche Gesellschaft für Geotechnik e.V. (Hrsg.).

Ebener, A. & Lesny, K. (2023): Investigation of landslide-prone slopes under consideration of scattering influencing variables (in German); Fachsektionstage Geotechnik - Interdisziplinäres Forum 2023, Congress Centrum Würzburg, 12. - 13. September 2023; ISBN: 978-3-946039-10-5.

EN 1990-10:2021, Eurocode 0: Basis of structural design.

Fredlund, D. G. & Krahn, J. (1977): Comparison of slope stability methods of analysis; Canadian Geotechnical Journal, 14: 429-439; DOI: 10.1139/t77-045.

Furtney, J. K.; Thielsen, C., Fu, W. & Le Goc, R. (2022): Surrogate Models in Rock and Soil Mechanics: Integrating Numerical Modeling and Machine Learning; Rock Mechanics and Rock Engineering (2022) 55:2845–2859; DOI: 10.1007/s00603-021-02720-8.

Gray D.H, & Leiser, A.T. (1982): Biotechnical slope protection and erosion control. Van Nostrand Reinhold Co., New York; ISBN: 9780442212223.

ISO 2394:2015: General principles on reliability for structures.

JRC (2023). Reliability backgrounds of the Eurocodes. JRC Technical Report produced by CEN/TC250/SC10 Basis of structural and geotechnical design. Joint Research Council of the European Commission, draft version, final version expected date: 2024.

Keller, B. (2017): The influence of root cohesion on the stability of steep colluvium slopes using the example of gravitational processes on the Sonnenberg near Lucerne (in German); Weiterbildungsseminar 17 (2017), Forschungs-stelle Rutschungen. ISSN 2196-2863.

FprEN 1997-1:2024, Eurocode 7: Geotechnical design – Part 1: General rules, CEN/TC 250/SC 7 draft for Formal Vote.

Rickli, C.; Zürcher, K.; Frey, W. & Lüscher, P. (2002): Effects of the forest on near-surface landslide processes (in German). Schweiz. Z. Forstwes. 153 (2002) 11: 437–445; DOI: 10.3188/szf.2002.0437.

Schwarz, M.; Giadrossich, F. & Cohen, D. (2013): Modeling root reinforcement using a root-failure-Weibull survival function. Hydrol. Earth Syst. Sci., 17, 4367–4377, 2013; DOI: 10.5194/hess-17-4367-2013.

TC250/SC7/TG-C3 (2023): Reliability-based methods for geotechnical design and assessment; guideline document for the next-generation Eurocodes. Working draft TC250/SC7/TG-C3, version May 2023.

Uzielli, M.; Lacasse, S.; Nadim, F. and Phoon, K.-K. (2006): Soil variability analysis for geotechnical practice. In Proceedings of the second international workshop on characterisation and engineering properties of natural soils, Singapore. Balkema, The Netherlands, 1653-1752.

Wang, Y. & Akeju, O.V. (2016). Quantifying the cross-correlation between effective cohesion and friction angle of soil from limited site-specific data. Soils and Foundations 56 (6), 1055-1070; DOI: 10.1016/j.sandf.2016.11.009.

Proceedings of the XVIII ECSMGE 2024
GEOTECHNICAL ENGINEERING CHALLENGES
TO MEET CURRENT AND EMERGING NEEDS OF SOCIETY
© 2024 the Authors
ISBN 978-1-032-54816-6
DOI 10.1201/9781003431749-293
Open Access: www.taylorfrancis.com, CC BY-NC-ND 4.0 license

ECSMGE 24
XVIII EUROPEAN CONFERENCE ON SOIL MECHANICS AND GEOTECHNICAL ENGINEERING

Development of database of monitoring results for retaining walls of deep excavations

Développement d'une base de données des résultats de surveillance des murs de soutènement des excavations profondes

A. Ene*
Technical University of Civil Engineering of Buharest and Popp & Asociatii Inginerie Geotehnica Co., Buharest, Romania

I. Ciocaniu, D. Marcu
Popp & Asociatii Inginerie Geotehnica Co., Buharest, Romania

H. Popa
Technical University of Civil Engineering of Buharest, Buharest, Romania

**alexandra.ene@p-a.ro*

ABSTRACT: This paper presents several results obtained from the monitoring process of multiple deep excavations performed in Bucharest area. These projects comprised several retaining structures for deep excavations in Bucharest with 2 basement levels or more (more than 6 m in depth), using top – down method or supported by struts or ground anchors. The retaining walls for the deep excavation were monitored during the works for wall deformations (inclinometers), ground settlements, neighbouring building settlements, groundwater level variation etc. The database was started by the authors several years ago for Bucharest specific lithology and geotechnical characteristics, and through this paper supplementary data available is considered. Thus, the previously evaluated indices and ratios, such as the ratios between the excavation depth and length and thickness of the retaining wall, or the ratio between vertical displacement of the ground outside the excavation and horizontal displacement at the top of the retaining wall are reanalysed and updated values are provided. These data and the comparisons made between the projects are very useful to designers for future similar works.

RÉSUMÉ: Ce papier présente plusieurs résultats obtenus à partir du processus de surveillance de multiples fouilles profondes effectuées dans la région de Bucarest. Ces projets comprenaient plusieurs structures de soutènement pour des excavations profondes à Bucarest avec 2 niveaux de sous-sol ou plus (plus de 6 m de profondeur), en utilisant la méthode top-down ou soutenues par des butons ou des ancrages. Les parois de soutènement pour les excavations profondes ont été surveillés pendant les travaux pour détecter les déformations des parois (inclinomètres), les tassements du sol, les tassements de bâtiments voisins, la variation du niveau de la nappe phréatique, etc. La base de données a été créée par les auteurs plusieurs années auparavant pour la lithologie et les caractéristiques géotechniques spécifiques de Bucarest et, dans le présent document, des données supplémentaires disponibles sont prises en compte. Ainsi, les indices et ratios précédemment évalués, tels que les rapports entre la profondeur d'excavation et la longueur et l'épaisseur des parois de soutènement, ou le rapport entre le déplacement vertical du sol à l'extérieur de l'excavation et le déplacement horizontal en tête de la paroi sont réanalysés et des valeurs actualisées sont fournies. Ces données et les comparaisons faites entre les projets sont très utiles aux concepteurs pour de futurs travaux similaires.

Keywords: Monitoring; deep excavations; database creation.

1 INTRODUCTION

Deep excavations in urban areas are works that can affect neighbouring buildings and involve relatively high risks related to their structural integrity. In these conditions, monitoring of the retaining walls of deep excavations, as well as of the neighbouring constructions, is not only indicated, but even mandatory, in order to identify an alert or damage situation, and also to compare the previously calculated efforts and deformations with the real situation (Ciocaniu et al., 2023, Popa, 2010).

In recent years, the calculation models of the retaining walls for deep excavations have evolved a lot. However, the complexity of the characteristic interaction parameters, related especially to the terrain, but also to the configuration of the site in terms of existing constructions nearby, lead to a high degree of uncertainty in the results obtained through

calculations, especially in terms of displacements and the deformations of the supporting work and its surroundings.

The only way to verify the results and validate the calculation models used is monitoring throughout the execution works and sometimes during the service life.

The data obtained through monitoring, however, become really useful by synthesizing the measurements in a database that allows a quick evaluation, even in the preliminary design phase, of the behavior of a retaining wall according to different characteristics: its length in relation to the depth of excavation, lateral displacements related to the free height of the wall, neighboring settlements related to the support system of the wall, etc.

For this reason, the creation of such a database (Marcu et al, 2015) was started many years ago. This database currently has reached over 30 retaining walls for deep excavations over 3 m in urban areas, which were monitored.

The paper presents some aspects of this database and makes some remarks regarding its use.

2 FEATURES OF THE DATABASE

As it was presented in the previous paper (Marcu et al, 2015) the database includes the following features:

- general project information;
- geometric data: excavation depth, retaining wall thickness and length, cantilever height, free height etc.
- main design results: maximum efforts in the retaining wall, horizontal displacements of the retaining wall at characteristic points, vertical displacements;
- measurements from the monitoring process: values of the horizontal and vertical displacements of the retaining wall and of the neighboring constructions, efforts in props or anchors;
- processing area: the evaluation of some behavior indices, such as the ratio between the depth of the excavation and the length or thickness of the wall, the ratio between calculated and measured values, the ratio between vertical and horizontal displacements etc.

In Table 1 are shortly presented the general data of the analyzed works and the geometrical characteristics of the retaining structures.

Table 1. Information of the analysed works and geometric data.

No.	D-wall solution	Support System	H [m]	L [m]	t [cm]
1-6	SW	TD	13-16.4	21-30	60/80
7-9	SW	IS	6-9.4	16.8-20	60
10-17	TP	IS	5.8-11.5	10-20.1	60
18	SP	HS	9.3	17	90
19	SW+SP	3 lvs p-s HS	13.2	19.5	60/90
20	SW	3 lvs A	16	24	80
21	SW	A	12	18	60
22-26	SW	clv	4.8-6	15-19	60
27-33	TP	clv	3-6.6	7.5-13.7	60

SW- Slurry Walls; SP - Secant Piles; TP – tangent piles; TD – Top-Down; HS – Horizontal Struts; IS – Inclined struts; A – Anchorages; p-s – pre-stressed; clv – cantilevel; H - excavation depth; L- DW length (depth); t – DW thickness

Some supplementary remarks should be made to the information given in Table 1:

- the buildings have 2-5 basements;
- when the retaining wall consists of slurry walls or secant piles, it indicates that the hydrostatic level is high (5-9m) and the length of the wall might have been dimensioned for watertightness condition;
- in the cases the top-down technology was chosen or three levels of pre-stressed steel struts were used, the displacements needed to be limited to protect the neighbouring buildings.

3 PROCESSING AND ANALYSIS OF DATABASE VALUES

By using the values measured in the monitoring process and/or by relating them to the values obtained through calculations, a series of indicative indices can be obtained regarding the behaviour of a retaining wall of a deep excavation, depending on the technological solution (diaphragm wall, secant piles, etc.), by the support system (cantilever wall or supported with props or anchors, the top-down system) and by the geometric characteristics of the work.

It should be noted that these observations are indicative, but extremely useful, especially in the initial design phase. It should also be remembered that monitoring on the ground is subject to a certain degree of uncertainty, on the one hand related to the precision of the instruments, on the other hand to the correctness of the monitoring process (for example, the identification of a correct stage of execution of the excavation at the time of the measurements or the limitation of the inclinometric tube at the level of the tip of the wall considered fixed, etc.).

3.1 The ratio between the maximum depth of the excavation and the total length of the retaining wall

Most of the cases indicated values between 0.3 and 0.7 for the ratio between the maximum excavation depth and the total length of the retaining wall.

If the analysis is made by types of wall supports, in the case of cantilever walls this interval is 0.3-0.5, in the case of walls supported on a single level, the interval is 0.33-0.6, and in the case of walls supported on 2 or more levels, the interval is 0.4-0.7.

Of course, these intervals, depending on the lithological characteristics of the site (the presence of weak or hard layers) and the presence of underground water (which requires dewatering works), can be exceeded, in one sense or the other.

But the values of this index can be successfully used for a preliminary assessment of the total required length of a retaining wall, including the number of temporary supports.

3.2 The ratio between the maximum depth of the excavation and the thickness of the retaining wall

The values of the ratio between the maximum depth of the excavation and the thickness of the supporting wall (reinforced concrete walls, panels or drilled piles) are in the range of 7...25. The average value is 16, while the most frequent value is between 10 and 12 for the analysed works.

It must be stated, however, that the thickness of the retaining walls, especially for diaphragm walls, is directly related to the execution technology, which is normally modulated to a value of 20 cm, starting from a minimum of 60 cm. Even in the case of walls made of drilled piles, there is no greater availability in terms of diameters, although in their case atypical diameters can occasionally be found.

The index values serve to choose the thickness that corresponds both from an economic point of view (ratio between the amount of reinforcement and concrete), but also to ensure a good behavior of the wall in terms of movements.

3.3 The evolution of the maximum values of the bending moments in the retaining wall

The bending moment determined from calculations is analysed against the total excavation depth for cantilever and against the maximum free span between two supports (or between support and excavation depth), as shown in Figure 1.

For the analysis of this evolution, the bending moment was normalized by referring to the linear deformation modulus of the wall and to the maximum free span, and the excavation depth was related to the maximum length of the retaining wall (Figure 1).

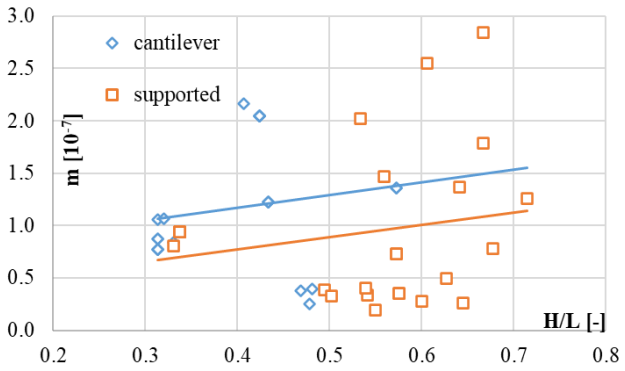

Figure 1. The variation of the bending moment with the maximum depth.

A trend of increase in the bending moment with the excavation depth is observed, as expected, but it should be noted that there is a significant spread of the data due to different ground conditions, but also for the ratio of the excavation depth and the wall length, the last being dictated by the condition of embeddment for groundwater control and not for stability.

3.4 The ratio between the maximum measured values of the horizontal displacements of the retaining wall and the depth of the excavation

For the evaluation of this index, the normalization of the values was used again in the following way: the horizontal displacements were normalized by the excavation depth, and the excavation depth by the length of the wall (Figure 2).

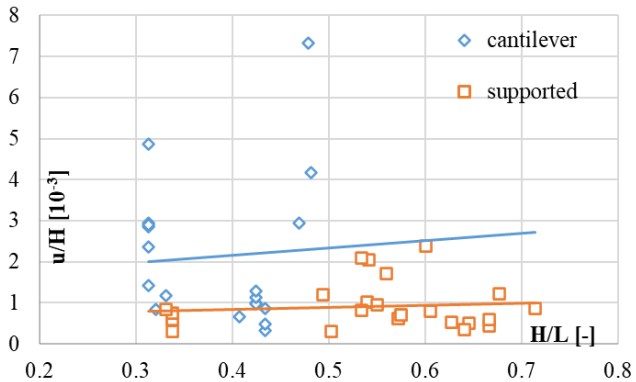

Figure 2. The variation of the wall maximum horizontal displacement with the excavation depth.

The same data spread can be observed and for this case also more because there were different displecements measured for cases where the design conditions were appreciated as similar (Ene et al.,

2019). Still, the same trend of increase in the wall displacment with the excavation depth is observed, as expected.

3.5 The relation between the settlements of the neighbouring constructions and the maximum measured values of the horizontal displacement of the wall

Again, taking into account the variables involved in this dependence, the normalization of the values was resorted to. Thus, the settlement was normalized by the distance to the excavation and the horizontal displacement of the wall was normalized by the excavation depth (Figure 3).

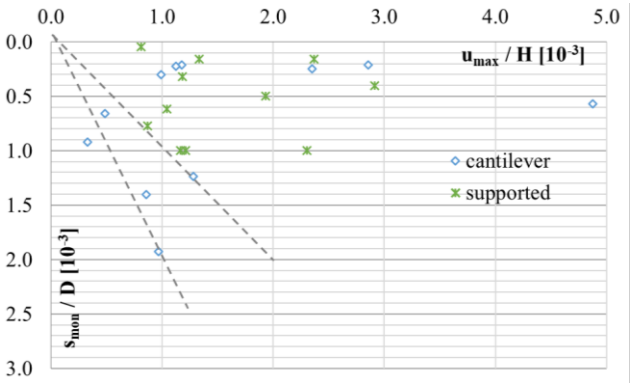

Figure 3. The variation of the settlement of the neighbouring constructions with the maximum displacement of the retaining wall.

It is observed that there is a great spread of the data, justified by the diversity of the neighbouring buildings in terms of loading, height, foundation level, but also because the values of the measured values are small and thus leading to a sensitive ratio. However, it can be concluded that for all the cases the ratio between the normalized settlement and horizontal displacement of the wall is below 1 for supported systems and below 2 for catilever structures.

3.6 The ratio between the measured and calculated values of the horizontal displacements of the retaining wall

For most cases, the values of this ratio fall within the range of 0.3 to 1. The sub-unit value of the ratio indicates a correct and comprehensive calculation in terms of horizontal displacements, corresponding to a typical SLS evaluation.

It should be noted that only the calculation values from the design were filled in the database and not values from back-analysis calculations that seek to obtain the most probable displacement values.

Also, there were cases when the ratio was higher than 1, meaning that the measured values were greater than those estimated for SLS, but that was mostly due to the fact that for very small values, this ratio is very sensitive.

4 CONCLUSIONS

Creating a database with calculated and measured values regarding the behaviour of deep excavation retaining walls is extremely useful in design work or even execution of these structures. Based on these records, different trends of evolution of movements related to the geometric characteristics of the retaining walls and their supported systems can be created and analysed.

Considering the influence that the retaining walls of deep excavations have on the built neighborhoods, such analyzes lead to the choice of technical solutions that meet both the necessary safety criteria and the economic ones, which ultimately means a more efficient design.

Last but not least, it represents a way of validating calculation models or a possible warning in case of behaviors that may pose a risk to the built neighborhoods.

REFERENCES

Ciocaniu, I., Ene, A. and Popa, H. (2023). Analysis and correlations between design estimations and monitoring works for a deep excavation in Bucharest. *Proceedings of 17DECGE*, Bucharest, Romania, pp. 841-848.

Ene, A., Carașca O., Ionescu, I., Marcu, D. and Popa, H. (2019). Comparisons between design estimations and measurements on several design sections of a deep excavation in Bucharest, In: *Proceedings of the XVII ECSMGE-2019*, Reyjkavik, Iceland. http://doi.org/10.32075/17ECSMGE-2019-1067.

Marcu, D., Ene, A. and Popa, H. (2015). Monitoring measurements on retaining walls for deep excavations in similar sites – database creation, In: *Proceedings of the XVI ECSMGE*, Edinburgh, Scotland, Vol. 6, pp. 3577-3582. http://doi.org/10.1680/ecsmge.60678.

Popa, H. (2010). Deep excavations in urban areas – influence on the neighbouring structures; measurements and calculation, *Mathematical Modeling in Civil Engineering* 1, 19-26.

Proceedings of the XVIII ECSMGE 2024
GEOTECHNICAL ENGINEERING CHALLENGES
TO MEET CURRENT AND EMERGING NEEDS OF SOCIETY
© 2024 the Authors
ISBN 978-1-032-54816-6
DOI 10.1201/9781003431749-294
Open Access: www.taylorfrancis.com, CC BY-NC-ND 4.0 license

ECSMGE 24
XVIII EUROPEAN CONFERENCE ON SOIL MECHANICS AND GEOTECHNICAL ENGINEERING

Eurocode 7 – Second generation: determination of representative values

Eurocode 7 - Deuxième génération: détermination des valeurs représentatives

J. Estaire*
Laboratorio de Geotecnia – CEDEX, Madrid, Spain

J. Sorgatz
Federal Waterways Engineering and Research Institute, Hamburg, Germany

T. Orr
Trinity College, Dublin, Ireland

**jose.estaire@cedex.es*

ABSTRACT: This paper explains the concepts behind the different terms involved in the determination of ground properties within the framework of the Second Generation Eurocode 7. The process begins with the derived values that are collected in the ground investigation activities: desk study, site inspection, design investigation and monitoring. It continues to the determination of the "representative value" that is the value that affects the occurrence of the limit state. This value is either used directly in Resistance Factor Approach (RFA) verifications or factored by the partial material factor to obtain the "design value" that will be used in Material Factor Approach (MFA) verifications of the different ultimate limit states of the geotechnical structures. The future Eurocode 7 establishes two possible ways to determine such a "representative value" of a ground property: selecting the value from a limited number of test results, based on engineering judgment and comparable experience in similar cases, being in this case termed a "nominal value"; or evaluating the value by statistical methods, being in this case termed a "characteristic value". Additionally, the paper gives a brief outline of a statistical method to determine the characteristic value of a ground property that accounts for spatial variability.

RÉSUMÉ: Ce document explique les concepts qui sous-tendent les différents termes impliqués dans la détermination des propriétés du sol dans le cadre de la deuxième génération de l'Eurocode 7. Le processus commence par les valeurs dérivées qui sont collectées dans les activités d'investigation du sol : étude documentaire, inspection du site, investigation de la conception et surveillance. Il se poursuit par la détermination de la "valeur représentative", c'est-à-dire la valeur qui affecte l'occurrence de l'état limite. Cette valeur est soit utilisée directement dans les vérifications RFA, soit pondérée par le facteur matériel pour obtenir la "valeur de conception" qui sera utilisée dans les vérifications MFA des différents états limites ultimes des structures géotechniques. Le futur Eurocode 7 établit deux manières possibles de déterminer cette "valeur représentative" d'une propriété du sol : la sélection de la valeur par le jugement de l'ingénieur et l'expérience comparable dans des cas similaires, étant dans ce cas appelée "valeur nominale" ; ou l'évaluation de la valeur par des méthodes statistiques, étant dans ce cas appelée "valeur caractéristique". En outre, le document donne un bref aperçu de la méthode statistique pour déterminer la valeur caractéristique d'un terrain.

Keywords: Representative value; Nominal value; Characteristic value, Eurocode 7, Spatial variability

1 INTRODUCTION

The determination of material property values to be used in geotechnical designs is covered in Part 1/Section 4.3.2 of the 2nd generation Eurocode 7 (FprEN 1997-1:2023). Some of its paragraphs will be used in this paper to explain some of the concepts behind them.

The committee responsible for Eurocode 7 (TC250/SC7) decided in 2020 to establish four "Task Groups" (TGC1 to TGC4) to draft the following four guideline documents to help designers in the understanding, implementation, and use of EC7 in geotechnical designs, with scopes and objectives that are very related to this paper. The tittles of those guidelines are: "Determination of representative values from derived values for verification of limit states with EN1997", "Assembling the Ground Model and the derived values"; "Reliability-based methods for geotechnical design and assessment" and "Implementation of Design during Execution and Service Life". These guidelines will be published by

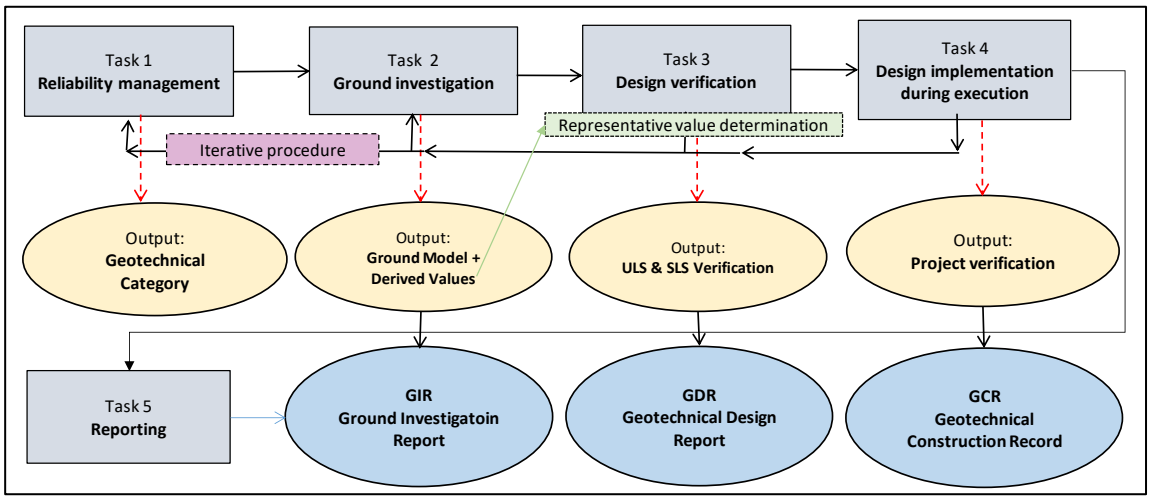

Figure 1. Tasks in the design of a geotechnical structure.

the JRC (Joint Research Centre of the European Commission) probably in 2024.

2 REPRESENTATIVE VALUE DETERMINATION IN THE DESIGN OF GEOTECHNICAL STRUCTURES

According to EN1997, the process of designing a geotechnical structure involves five major tasks, as shown in Figure 1:

1 Reliability management: a series of classifications aimed to place the geotechnical structure into a single Geotechnical Category that can be changed at each stage of design. The Geotechnical Category combines the uncertainty and complexity of the ground and ground-structure interaction with the consequence of failure of the structure.
2 Ground investigation: whose main output is the Ground Model that "comprises the geological, hydrogeological, and geotechnical conditions at the site" and it also includes the derived values.
3 Design verification: covering all the procedures to verify that no limit states are exceeded in any design situations that the structure may encounter during its service life.
4 Design implementation: ensuring that the structure is constructed while meeting the design assumptions and other detailed plans developed during the design phase.
5 Reporting: the work performed during the design and execution of the geotechnical structure must be documented by carrying out the following reports: Ground Investigation Report, Geotechnical Design Report, and Geotechnical Construction Record.

In this design process, the determination of representative values of ground properties is performed at the beginning of the "Design verification" task, when the designer analyses the derived values presented in the Ground Investigation Report, as shown in Figure 1.

3 CHAIN OF CONCEPTS RELATED TO GROUND PROPERTY VALUES: FROM DERIVED TO DESIGN VALUES

3.1 Introduction

Parallel to these different tasks, there is a set of interrelated concepts relative to the following values of the ground properties that appear in the design process: "Measured values", "Derived values, "Nominal value", "Characteristic value", "Representative values" and "Design value".

This section explains the links between such values and concepts that are adopted throughout the design process depending on the design stage. Figure 2 shows the path that a ground property value must travel from when it is obtained during the ground investigation stage to when it is used in a calculation model at the design stage to verify a limit state, either an ultimate limit state (ULS) or serviceability limit state (SLS).

3.2 Ground Investigation and Measured values

The purpose of a ground investigation is to determine the ground properties for design. Part 2 of the new Eurocode 7 gives the requirements for ground investigation, which involve the following types of investigation: a) Desk study; b) Site inspection; c) Performance of field and laboratory tests; and d) Geotechnical monitoring. The upper part of Figure 2 shows the different types of values that can be obtained during these types of investigation, which are: historical values, assessed values, measured values

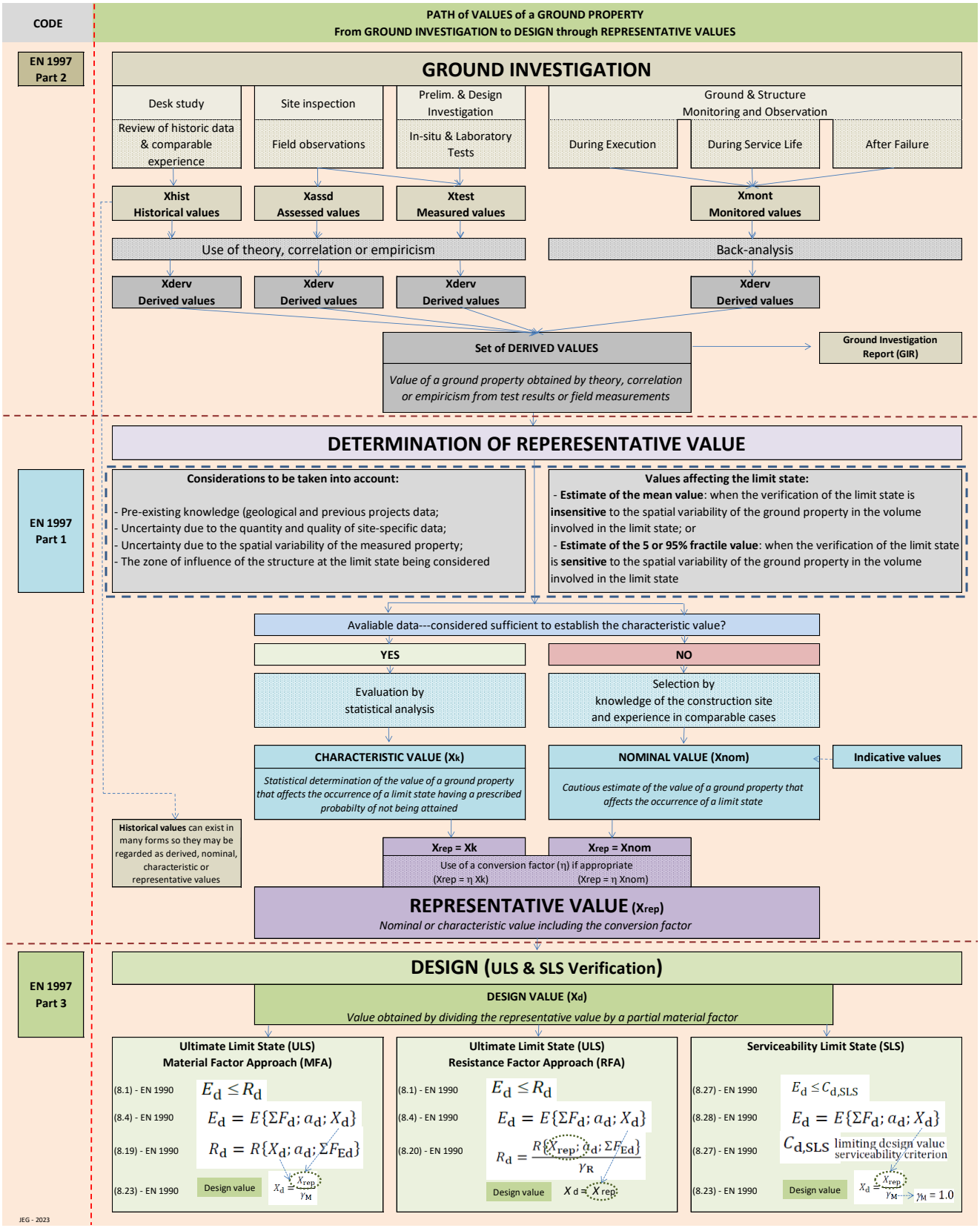

Figure 2. Path of values: From Ground Investigation to Design Stage.

and monitored values. The only value referred to explicitly in the new Eurocode 7 is the measured value, which is defined in FprEN 1997-2/3.1.2.2 as "*the value of a ground property recorded during a test*", while the others appear for the sake of explanation.

3.3 Derived values

The derived value of a ground property is defined in FprEN 1997-1/3.1.3.2, as the "*value of a ground property obtained by theory, correlation or empiricism from test results or field measurements*" and, as shown in Figure 2, may be obtained from historical values, assessed values, measured values and monitored values. Derived values are used to establish the Ground Model that, according to FprEN 1997-2:4.1(5) *"shall reference the derived values of ground properties for encountered geotechnical units*". FprEN 1997-1:3.1.6.5 states that a geotechnical unit is *"the volume of ground that is defined as a single material".*

3.4 Representative value

The representative value of a ground property (X_{rep}) is defined in FprEN 1997-1/3.1.3.5 as a "*nominal or characteristic value…*" while 4.3.2.1 states "*Representative values of ground properties to be used in ultimate and serviceability limit state verifications shall be determined from derived values presented in the Ground Investigation Report*". Consequently, "*the representative value refers to a particular ground property of a single geotechnical unit.".*

According to FprEN 1997-1:4.3.2.1(6) when available data are considered sufficient to establish the characteristic value (X_k), the representative value of a ground property (X_{rep}), should be determined from Formula 1(a). However, according to 4.3.2.1(7), when the available data are insufficient to establish the characteristic value of a ground property, the representative value should be determined from Formula 1(b), where X_{nom} is the nominal value of the ground property:

$$a)\ X_{rep} = X_k\ ; \qquad (1)$$
$$b)\ X_{rep} = X_{nom}$$

The designer needs to decide whether to determine the representative value as a characteristic or a nominal value, based on their understanding of the sufficiency of the available data, i.e. a) its quantity and quality, b) its spatial distribution, c) the extent of the zone of influence, and d) the need to avail of and take into account pre-existing knowledge in the form of comparable experience. These four considerations that need to be considered when determining the representative value are extensively explained in the TGC1 document (JRC, 2024).

While the use of statistics is not extensive in current geotechnical design practice in Europe, it is anticipated that, in the future, as ground investigation methods develop and more data become available, there will be a tendency for an increased use of statistics and of characteristic values. Nationally determined practices may also have an influence on whether the representative value is determined as a characteristic or a nominal value.

On other hand, according to 4.3.2.1(3), "*The representative value of a ground property shall be determined for each limit state, according to its sensitivity to spatial variability of the ground property in the volume of ground involved*". In 4.3.2.1(4) it is stated that "*If the limit state is insensitive to spatial variability of the ground, the representative value of the ground property shall be determined as an average value*", while in 4.3.2.1(5) it is stated that "*If the limit state is sensitive to spatial variability of the ground, the representative value of the ground property shall be determined as an inferior or superior value*".

The significance of the sensitivity of the limit state to the spatial variability of the ground leads to the three "Types of estimates" of the representative value shown in Figure 3. Selecting the appropriate representative value corresponding to Type A, B or C is a function of the designer's understanding of the extent of limit state that mobilises the ground property and the magnitude of the ground spatial variability, represented by the extent of the failure mechanism or zone of influence, L compared to the magnitude of the scale of fluctuation of the ground property (θ), as explained in subsection 3.6 of this paper. Note Type C is introduced in the TGC1 document and is not in FprEN 1997-1.

3.5 Nominal value

The nominal value of a ground property (X_{nom}) is defined in EN 1990-1/3.1.2.29 as the "*value fixed on a non-statistical basis; for instance, on acquired experience or on physical conditions*". FprEN 1997-1/ 4.3.2.3(1) elaborates this by stating that "*the nominal value of a ground property (X_{nom}) shall be selected as a cautious estimate of the (average, inferior or superior) value affecting the occurrence of the limit state (based on the knowledge of the construction site and comparable experience)*".

The nominal value is selected by the designer based on derived values, knowledge of the construction site, consideration of the design situation and limit state, and comparable experience. It is a cautious estimate of the property value chosen to represent the behaviour of the volume of ground involved in the limit state being considered.

The selection of the nominal values also follows the three types of estimates, shown in Figure 3: Type A, a cautious estimate of an average value; Type B, a more cautious estimate of an inferior or superior value and Type C, an estimate of an intermediate value between the Type A and B values.

TYPE	CONCEPT	SCALE FLUCTUATION v REFERENCE LENGTH(1)	REPRESENTATIVE VALUE
A	[In EN1997-1 // 4.3.2.1 – Paragraph (4)] (4) If the limit state is "very" **INSENSITIVE** to ground spatial variability, the Representative Value shall be determined as an **AVERAGE** value	L >> θ	Value: Nominal (Cautious) => Estimate of an AVERAGE VALUE Or Characteristic (Statistical) => Estimate of an MEAN VALUE
B	[In EN1997-1 // 4.3.2.1 – Paragraph (5)] (5) If the limit state is "extremely" **SENSITIVE** to ground spatial variability, the Representative Value shall be determined as an **INFERIOR** (or superior) value	L ≤ θ	Value: Nominal (Cautious) => Estimate of an INFERIOR / SUPERIOR Or Characteristic (Statistical) => 5% / 95% FRACTILE
C	[In TG-C1 Document // Chapter 4] If the limit state has an **INTERMEDIATE** sensitivity to ground spatial variability such that: • Type A is considered **not to be adequately cautious** and • Type B is seen **to be overly cautious**, the Representative Value shall be determined as an **INTERMEDIATE** value between the average and inferior (or superior) value	L > θ	Value: Nominal (Cautious) => Estimate of an INTERMEDIATE VALUE between Average and Inferior / Superior value Or Characteristic (Statistical) => Mean Value and 5% / 95% Fractile
Note (1): Reference length (L) = dimension of the failure surface for the limit state upon consideration			

Figure 3. Types of estimates of the representative values.

3.6 Characteristic value

The definition of the characteristic value of a ground property given in FprEN 1997-1/3.1.3.4 is the "*statistical determination of the value of a ground property that affects the occurrence of a limit state having a prescribed probability of not being attained*".

According to FprEN 1997-1/4.3.2.2(4), the characteristic value should be determined statistically from Formula 2, when a normal distribution is assumed and taking account of the number (n) of derived values:

$$X_k = X_{mean}[1 \mp k_n V_X] \qquad (2)$$

where X_{mean} is the mean value of the ground property X from a number n of derived values, V_X is the coefficient of variation of the ground property; $\mp$ denotes that $k_n V_X$ should be subtracted or added depending on whether a lower or upper value of X_k is required; k_n is a coefficient that depends on the number of derived values used to calculate X_{mean}, the level of knowledge regarding V_X, and the type of characteristic value being determined.

Formulae for k_n for different V_X cases and types of estimates (A, B or C) are given in Figure 4 (inspired by FprEN1997- 1/Table A.3), while Table A.2 gives indicative values of V_X for various ground properties.

Three different cases are identified regarding the knowledge of V_X. According to FprEN 1997-1/Annex A.4 Case 1 - V_X known - *"should be used when the coefficient of variation of the ground property is known from prior knowledge"*; Case 2 - V_X unknown – *"should be applied when the coefficient of variation of the ground property being determined is unknown ab initio*" and Case 3 - V_X assumed – "*should be applied when indicative values are used for ground properties, or for test parameters*".

In addition, FprEN 1997-1/Annex A provides formulae to determine the characteristic value for lognormally distributed data.

Cases with different knowledge concerning V_X	Types of estimates of the characteristic value		
	Type A: Estimate of the mean value ($\Gamma^2 = 0$)	Type B: Estimate of the inferior (5%) or superior (95%) fractile value ($\Gamma^2 = 1$)	Type C: Estimate of the intermediate value when $\Gamma^2 = \theta/L$
Case 1: V_X known and Case 3: V_X assumed	$N_{95}\sqrt{\frac{1}{n}}$ (A1)	$N_{95}\sqrt{1+\frac{1}{n}}$ (B1)	$N_{95}\sqrt{\Gamma^2+\frac{1}{n}}$ (C1)
Case 2: V_X unknown	$t_{95-1}\sqrt{\frac{1}{n}}$ (A2)	$t_{95,n-1}\sqrt{1+\frac{1}{n}}$ (B2)	$t_{95,n-1}\sqrt{\Gamma^2+\frac{1}{n}}$ (C2)

Figure 4. Formulae for k_n for different combinations of types of estimates and V_x cases

To account for the sensitivity of the limit state to the variability of the ground regarding the extent of the volume of ground involved in the limit state, in the TGC1 document (JRC,2024) a more general form of the formulae for k_n that those given in FprEN1997-1/Annex A is proposed for Type C. This Type C formulae includes the sensitivity index (Γ^2), defined by Formula 3, that can only take values between 0 and 1:

$$\Gamma^2 = \theta/L \qquad (3)$$

where θ is the scale of fluctuation, i.e., magnitude of the ground property variability, and L is the extent of the volume of ground involved in the limit state.

Indicative values of the horizontal and vertical scales of fluctuation (θ_h and θ_v) can be found in the literature (e.g. Cami et al, 2020). These indicative values, relative to sedimentary materials not involved in tectonic movements, show that the θ_h values are

much greater than the θ_v values. In addition, examination of these numbers shows that, for normal design situations, θ_v values range mainly from 1 to 1,5 m while θ_h values range from 15 to 50 m.

3.7 Design value

According to FprEN 1997-1/4.4.1.3(3), for inferior values of X_{rep}, the design values of a ground property (X_d), should be calculated from Formula 4:

$$X_d = X_{rep}/\gamma_M \quad (4)$$

where γ_M is the material partial factor, whose values for persistent, transient, and accidental design situations are given in FprEN 1997-1/Table 4.8. This design value of a ground property is used in Material Factor Approach (MFA) design verifications.

When using the MFA, EN 1990-1/8.3.5.2(1) states that the design value of the resistance (R_d) for design verifications should be determined using Formula 5:

$$R_d = R\{X_d; a_d; \sum F_{Ed}\} \quad (5)$$

where a_d denotes the design values of geometrical properties and ΣF_{Ed} is the design value of actions.

Note that in Resistance Factor Approach (RFA) design verifications, X_{rep} is used, as shown in Formula 6, where γ_R is the resistance partial factor:

$$R_d = R\{X_{rep};\ a_d;\ \sum F_{Ed}\}/\gamma_R \quad (6)$$

4 FURTHER CONSIDERATIONS

It is worth highlighting that the TGC1 document (JRC ,2024) also presents guidance on the use of statistic to select the characteristic value of ground properties in four very common situations in design:

- Situations in which there are few derived values. Six different criteria are presented to assess the least number of derived values required for the use of statistics.
- Situations in which properties are depth-dependent. The background and statistical formulae to account for depth-dependency are presented.
- Situations in which the properties are mutual dependent parameters so they cannot be determined independently of each other (for instance, Mohr-Coulomb parameters: cohesion and friction angle).
- Situations in which derived values come from different sources. Three methods, that can be easily applied in practice, are presented to determine representative values from multiple data sources.

Additionally, TGC1 document (JRC, 2024) contains five design cases that cover various aspects: different geotechnical structures and limit states, different number of derived values, different distribution functions, and depth- dependent and independent ground properties.

5 CONCLUSIONS

This paper addresses the determination of representative values of ground properties according to the new Eurocode 7. Overall, it can be stated that this topic has considerably improved in comparison to the current version of the code, since now there is a clear conceptual distinction between the nominal value, where designers select the value according to their knowledge and experience, and the characteristic value, where designers determine the value with the aid of statistics. Also, the factors to be considered when selecting the representative value: the quantity and quality of the geotechnical data; its spatial distribution; the extent of the zone of influence; and the need to avail of and take into account pre-existing knowledge in the form of comparable experience, have been elaborated. Additionally, the procedure to determine the characteristic value taking account of the quality and quantity of the data and the spatial variability, described in FprEN 1997- 1/Annex A, will help to extend the use of characteristic values in design verification.

ACKNOWLEDGEMENTS

The authors are grateful for the collaboration and hard work provided by their colleagues in Task Group TG- C1 during the drafting of the TGC1 document.

REFERENCES

Cami B; Javankhoshdel S, Phoon KK and Ching J (2020): Scale of Fluctuation for Spatially Varying Soils: Estimation Methods and Values, State-of-the-Art Review, ASCE Journal of Risk and Uncertainty in Engineering Systems, Part A: Civil Engineering, 6:4, 2020.

FprEN 1997-1:2023. Eurocode 7: Geotechnical design - Part 1: General rules. Draft for Formal Vote, August 2023. CEN-TC 250-SC 7_N172.

JRC (2024) Guideline document: Determination of representative values from derived values for verification of limit states with EN1997. Report drafted by CEN TC250/SC7/TGC1, published by JRC, Joint Research Centre of the European Commission.

Proceedings of the XVIII ECSMGE 2024
GEOTECHNICAL ENGINEERING CHALLENGES
TO MEET CURRENT AND EMERGING NEEDS OF SOCIETY
© 2024 the Authors
ISBN 978-1-032-54816-6
DOI 10.1201/9781003431749-295
Open Access: www.taylorfrancis.com, CC BY-NC-ND 4.0 license

ECSMGE 24
XVIII EUROPEAN CONFERENCE ON SOIL MECHANICS AND GEOTECHNICAL ENGINEERING

Behaviour of stabilizing piles arranged with different layouts

Comportement des pieux stabilisateurs disposés selon différents schémas

L. Fantera
Tecne, Autostrade per l'Italia S.p.a. Group, Rome, Italy

S. Lirer*
Dept. of Engineering Sciences, University Guglielmo Marconi, Roma, Italy

A. Desideri, S. Rampello
Dept. of Geotechnical and Structural Engineering, University of Rome La Sapienza, Italy

s.lirer@unimarconi.it

ABSTRACT: Stabilizing piles can be designed to increase the safety factor of a landslide (acting as a stabilization countermeasure) or to reduce slope displacements (acting as a protection countermeasure). Equally spaced piles are usually installed, in one or more rows transversal to ground movements, adopting a linear arrangement. Since piles must be designed to ensure adequate safety factors for both slope stability and pile structural integrity, the paper focuses on a different plane layout, namely a staggered array, that can be an alternative design choice. A 2D and 3D numerical study has been developed, with the aim to compare the overall behaviour of a two-layer slope reinforced with one row of piles arranged with linear or staggered layouts: soil arching effect, ground movements and resisting forces are analysed and discussed in the paper.

RÉSUMÉ: Les pieux de stabilisation peuvent être conçus pour augmenter le facteur de sécurité d'un glissement de terrain ou pour réduire les déplacements de la pente. Les pieux sont généralement installés en une ou plusieurs rangées ou de manière orthogonale par rapport aux mouvements du sol, en adoptant une disposition linéaire. Étant donné que les pieux doivent être conçus de manière à garantir des critères de sécurité adéquats à la fois pour la stabilité des pentes et pour l'intégrité structurelle des pieux, l'article se concentre sur une disposition plane différente, à savoir la disposition en quinconce, qui peut constituer un choix de conception alternatif. Une étude numérique en 2D et 3D a été développée dans le but de comparer le comportement global d'une pente à deux couches renforcées par une rangée de pieux disposés linéairement ou en quinconce : la voûte du sol, les mouvements du sol et les forces de résistance ont été analysés.

Keywords: Stabilizing piles; soil arching; piles arrangements.

1 INTRODUCTION

The use of rows of vertical piles is a well-developed engineering practice to improve slope stability providing a resisting force to unstable soil masses.

Equally spaced piles are generally used in shallow and slow landslides and are installed transversally to soil movement adopting different arrangements (Figure 1). The well-known "soil arching", allows adjacent piles to act as a linear continuous retaining structure able to transfer part of soil pressure from the unstable layer to the lower stable one. The stabilizing rows of piles must be designed keeping piles spacing (s) as large as possible for cost effectiveness, but not so large to make them unable to generate sufficient soil arching.

In order to guarantee the development of soil arching effect, Durrani *et al.* (2006) suggest adopting a pile spacing ratio (s/D, where D is the pile diameter) less than a critical value $(s/D)_{cr} = k_p^2/(k_p\text{-}k_a)$, where k_p and k_a are the Rankine earth pressure coefficients. For gentle slopes in fine to medium grained soils, the critical spacing ratio is in the range $2.5 < (s/D)_{cr} < 4.0$.

The effects of some relevant parameters (i.e., pile spacing, pile stiffness and embedded length, row position, mechanical soils properties, slope inclination, pile top restrain, soil displacements) on the efficiency of equally spaced piles have been investigated by many authors over the years (Lirer, 2012; Chen and Martin, 2002; Liang and Zeng, 2002; Kourkoulis *et al*., 2011; Muraro *et al*., 2014; Pirone and Urciuoli, 2018, Fantera *et al*. 2022).

Regarding piles arrangement, some authors (Kourkoulis *et al*. 2011, Pham *et al*. 2019; Shangguan *et al*. 2023) highlighted that the staggered (or quincunx) array can be an effective design choice because it reduces the "shadow effect" created by the rear piles to the front ones in a double row layout (Figure 1), also developing a "multiple" soil arch (one between piles

of the rear row and the other one between the front pile and the adjacent rear pile, Figure 1).

Analysing the ultimate lateral resistance of stabilizing piles arranged in linear or quincunx layouts, Pham *et al*. (2019) verified that for cohesive soils the effect of piles arrangement becomes negligible for pile spacing ratio $s/D \geq 3$ (Figure 2b).

Since the ULS condition is generally attained for soil displacements larger than 0.3÷0.4 times the pile diameter, this paper focuses on the stages far away from the ultimate condition, analysing through 2D and 3D numerical models the performance of elastic piles installed with linear and quincunx layouts in a shallow translational landslide in fine-grained soils.

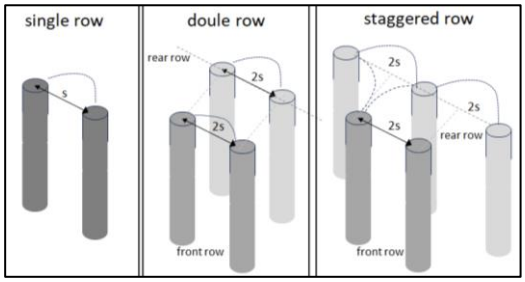

Figure 1. Pile arrangements.

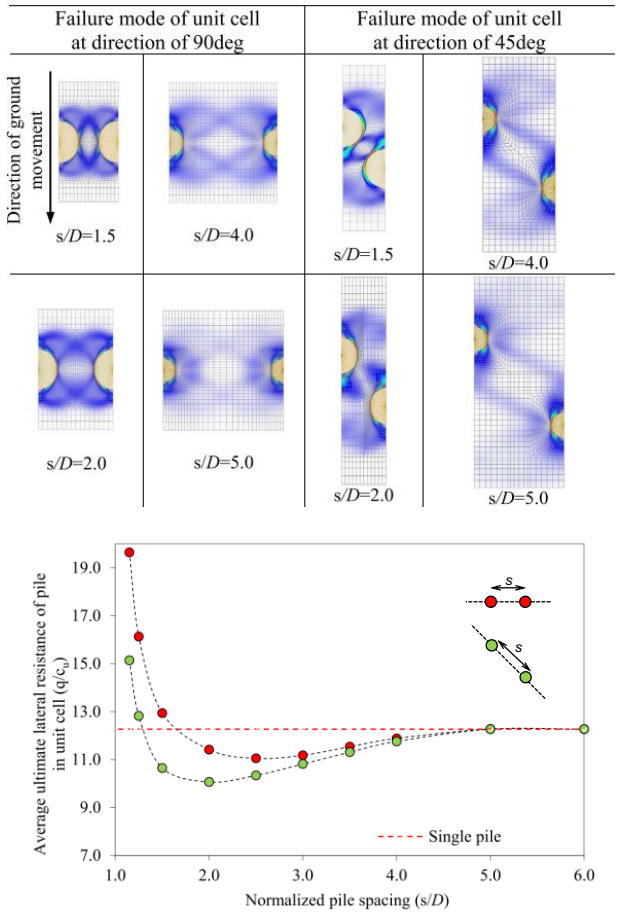

Figure 2. Average ultimate lateral resistance of an infinite row of piles arranged in a linear and staggered layout (Pham et al. 2019) within a cohesive slope.

2 FD NUMERICAL MODELLING

The numerical study (Finite Difference code FLAC) refers to a two-layer slope reinforced with an infinite line of piles shown in Figure 3 (thickness of sliding layer H = 6m). Specifically, a row of piles (length L) is located in the middle of the model (y = ±12D from the vertical boundaries) and two planes of symmetry are introduced through the pile midplanes. An increasing uniform displacement ($u_{y,inp}$) was applied in the analyses at the uphill boundary to simulate soil sliding over the shear band. Soils behaviour (unstable, shear band and stable layer) has been described using an elastic–perfectly plastic soil model obeying the Mohr–Coulomb failure criterion.

A wide three-dimensional parametric study has been developed (Fantera *et al*., 2022) in order to investigate piles efficiency considering the achievement of both force-based and displacement-based requirements within the slope: the influence of the main parameters affecting the complex soil–pile interaction mechanism (pile spacing s, pile embedded length L_2, soil mechanical properties, slope inclination, pile shaft constrains) has been considered (Figure 4). For the simple scheme of infinite slope in fine grained soils, the numerical study permitted to evaluate the non-dimensional resisting contribution given by piles arranged in a linear layout as a function of the spacing ratio s/D and the displacement ratio $u_{y,dw}/u_{y,inp}$, the latter representing the desired reduction of downhill slope movement.

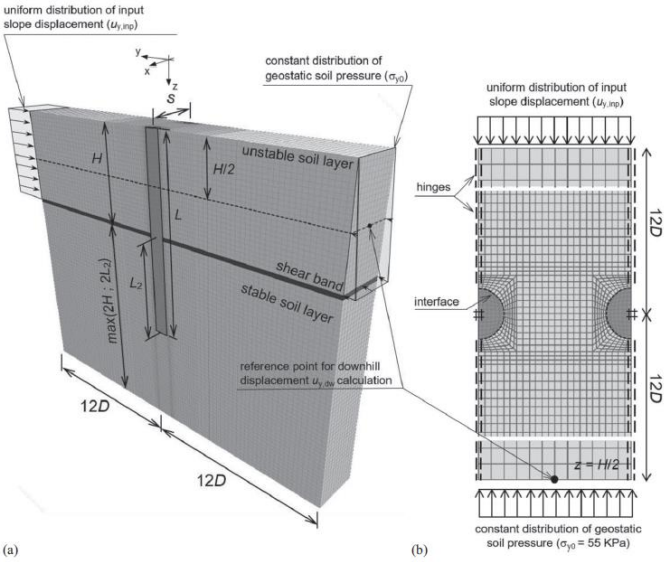

Figure 3. Grids and boundary conditions used in the numerical study (Fantera et al. 2022) of piles arranged in a linear array: a) 3D and b) 2D models (z=H/2=3m).

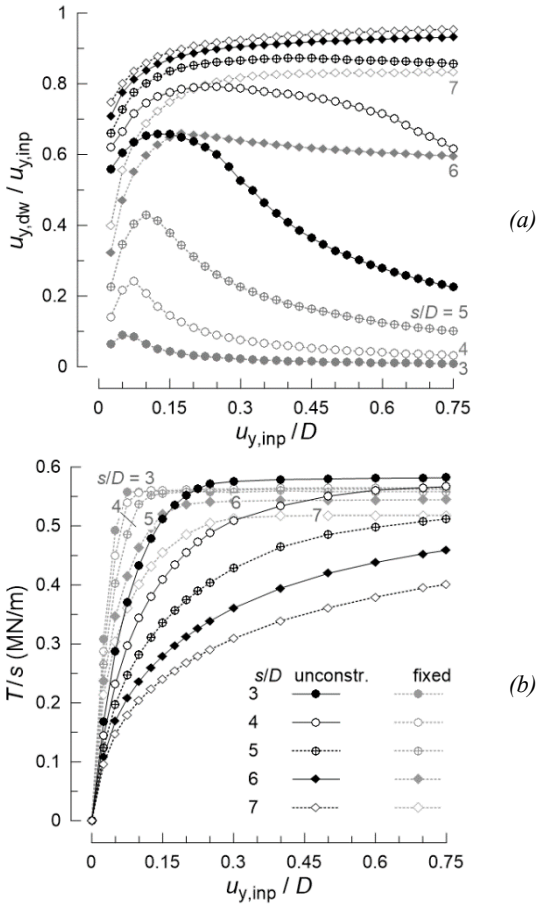

Figure 4. Normalised downhill displacements (a) and resisting contribution (T/s) provided by a line of fixed and unconstrained piles (L_2/H=1, E_p = 30GPa) versus input displacements $u_{y,inp}/D$ (Fantera et al. 2022). Soil properties in Tab.1.

2.1 Soil arching development (2D and 3D models)

Soil arching around the piles has been studied by means of plane strain (2D) and three-dimensional numerical analyses, assuming fixed piles installed in a linear or staggered arrangements, with a spacing ratio $s_x = 3D$ (Figure 5). The adopted soil properties are reported in Table 1.

Soil-pile interaction mechanism has been analysed by examining:

- evolution of principal stresses direction and normal stresses σ_n acting on the piles shaft (2D model, Figure 6);
- evolution of normalised horizontal stress increments ($\Delta\sigma'_{yy}/\sigma'_{yy,0}$) computed uphill of the piled line within the sliding soil mass ($0 < z < 6$m) (3D model, Figures 7-8).

The results from plane strain analyses (Figure 6) show that in both arrangements, the normal stresses acting on the piles (σ_n) move away from the initial (k_0) stress distribution as the imposed slope displacements $u_{y,inp}/D$ increase, as a result of arching-induced stress transfer.

Furthermore, it can be observed that in a staggered layout, the 2D normal stresses acting on the rear and front piles are different (Figure 6b): according to the previous research studies (Pham *et al*., 2019), the front piles are much less loaded than the rear ones, for which the normal stresses are very similar (up to $u_{y,inp} = 3D$) to the ones observed for the linear array (Figure 6a).

The contours of the normalised horizontal stress increments ($\Delta\sigma'_{yy}/\sigma'_{yy,0}$) computed in the 3D model at the same depth (z = 3m) have been plotted in Figure 7 for a given value of the soil movements (i.e., $u_{y,inp} = 0.1$D): the stress contours clearly show the arching effect developing between the rear and the front piles (Shangguan *et al*. 2023; Pham *et al*., 2019).

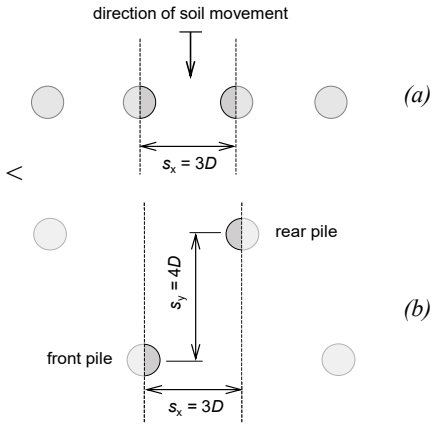

Figure 5. Pile arrangements adopted in the numerical study: (a) linear and (b) staggered layout.

Table 1. Soil properties (Figure 3).

Soil	Unstable	Shear band	stable
γ (kN/m³)	18.5	18.5	18.5
E′(MPa)	30	3000	60
ν	0.2	0.2	0.2
c′ (kPa)	2	0	20
φ′ (°)	28	0.1	28
ψ (°)	0	0	0

The evolution of the resulting horizontal 3D stress increments (integral extended to the thickness of the sliding layer H) with the imposed slope movements (Figure 8), confirms the outcomes of the plane strain models: slope movements mainly act on the piles belonging to the first row, inducing larger loads on the rear fixed piles. Considering that the ratio between the shear force over the pile spacing (T/s) is the resisting contribution provided by the line of piles, it is worth noting that the earth pressure acting on the pile belonging to the liner array is very close to the average value

of the actions acting on the two piles of the quincunx array. This means that the same overall contribution on the slope stability for the two schemes is expected.

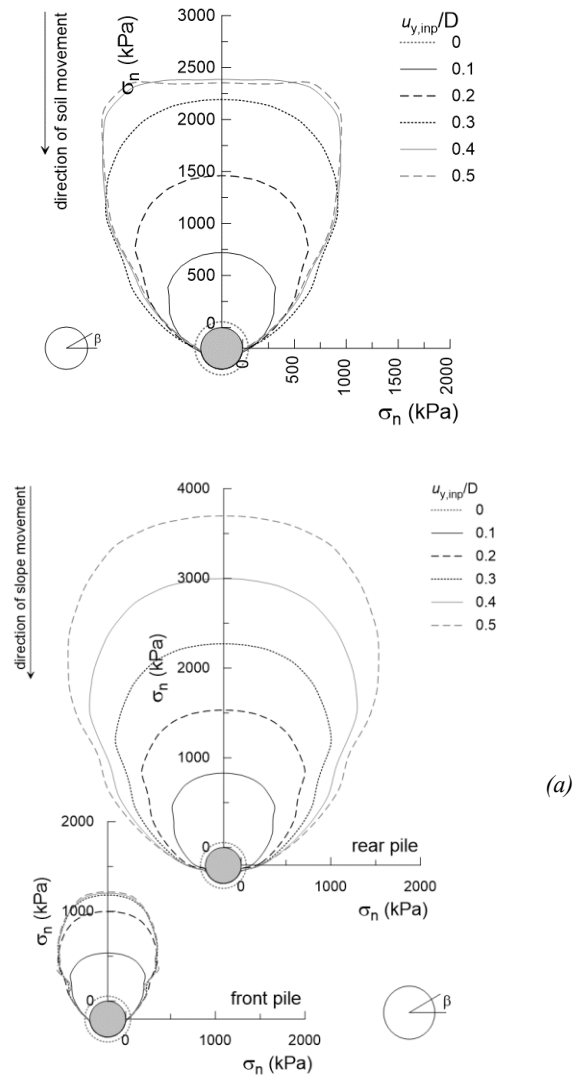

Figure 6. Contours of normal stress computed in 2D models (z=H/2=3m) in linear (a) and staggered (b) arrangements for different normalised input displacement $u_{y,imp}/D$.

2.2 Soil displacements and resisting force (3D models)

The most convenient plane layout should be defined considering the achievement of both force-based and displacement-based requirements, that is, the shear resisting force provided by the piles at the depth of the sliding surface (T) and the reduction of downhill slope displacements ($u_{y,dw}/u_{y,inp}$). For such a reason, a three-dimensional model has been adopted considering unconstrained elastic piles (E_p = 30GPa) in both arrangements and comparing the numerical results in terms of:

- percentage of horizontal displacements transferred from the uphill to the downhill sides of the model, where the downhill displacement ($u_{y,dw}$) was computed in the middle plane between the piles ($x = s/2$, y=+12D, Figure 3), at a depth z = 3 m from the ground surface (Figure 9);
- evolution of the shear force T provided by the piles at the depth of the sliding surface (Figure 10).

For 3D models the profiles of bending moment $M(z)$ and shear forces $T(z)$ have been computed using the profiles of pile displacement u(z):

$$M(z) = E_p I \frac{d^2u(z)}{dz^2} \quad (1a)$$

$$T(z) = E_p I \frac{d^3u(z)}{dz^3} \quad (2a)$$

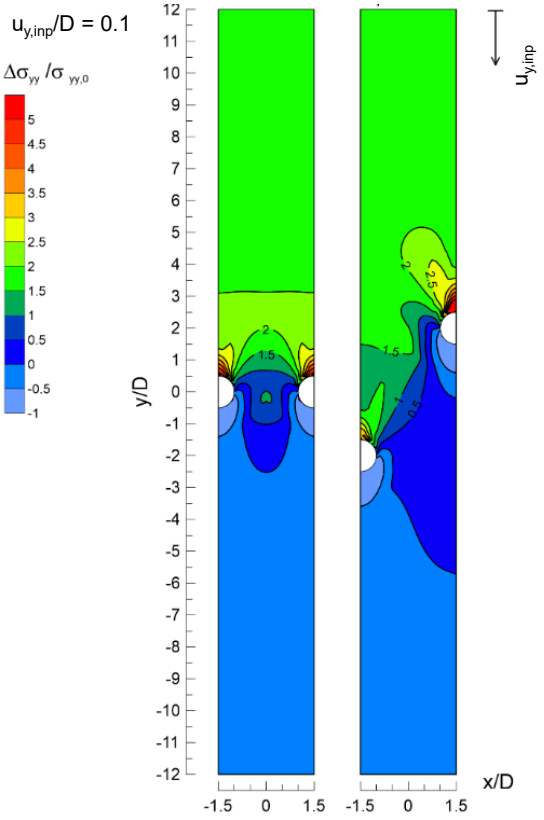

Figure 7. Contours of horizontal stress increments ($\Delta\sigma'_{yy}/\sigma'_{yy,0}$) computed at z= 3m in 3D models in linear and staggered arrangements for $u_{y,inp}/D$=0.1 (fixed piles).

It can be noted (Figure 9) that the two arrangements have the same containment effect, with a reduction of slope displacement of at least 20% to 35%, for $u_{y,inp}/D \approx 0.15$. Since the two schemes have the same effect on the overall displacements of the slope, they are expected to develop the same resisting contribution T/s along the sliding surface. In fact, it can be noted (Figure 10) that the overall piles response is the same: the computed shear force (T) sharply increases in both arrangements with $u_{y,inp}/D$, attaining the maximum

value when soil arching fully develops ($u_{y,inp}/D \approx 0.2$): further soil movements do not affect stress redistribution, and the load acting on the piles remains constant (Figure 10).

The performance of each pile within the group has been also analysed in more detail by plotting the evolution with $u_{y,inp}/D$ of the pile internal forces (bending moments M and shear forces T) normalized to the ones measured in the linear layout (Figure 11). The results show that some differences exist for the two schemes up to $u_{y,inp}/D < 0.25$, with the rear pile slightly more loaded than the front one. For larger soil movements, the difference in shear force T becomes negligible and both the front and rear piles in the quincunx array behave as the ones in the linear array ($T_{quincunx}/T_{linear} \approx 1$). The evolution of the normalized bending moment also stops beyond this threshold, with both the front and the rear piles exhibiting bending moments M lower than the ones computed for a infinite line of piles ($M_{quincunx}/M_{linear} < 1$).

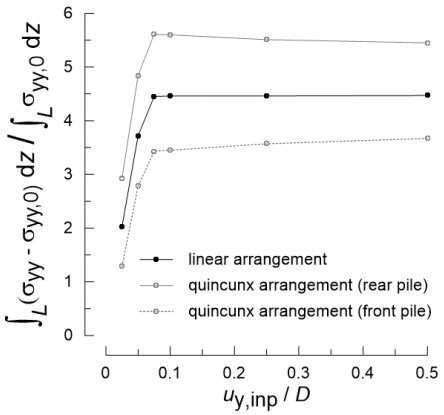

Figure 8. Evolution with $u_{y,inp}/D$ of the integral of the normalised 3D horizontal stress increments ($\Delta\sigma'_{yy}/\sigma'_{yy,0}$) computed uphill of the pile line y=+0.5D (fixed piles).

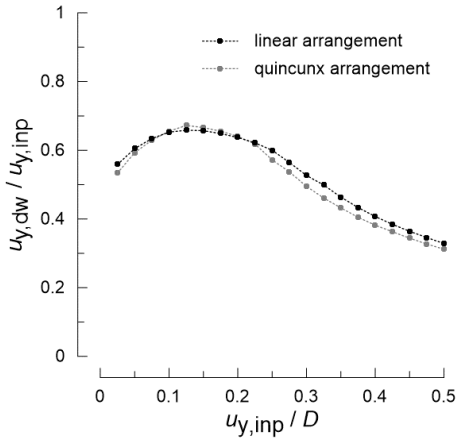

Figure 9. 3D numerical results (unconstrained piles): normalized downhill soil displacements $u_{y,dw}/u_{y,inp}$ versus input slope movements for linear and quincunx arrangements.

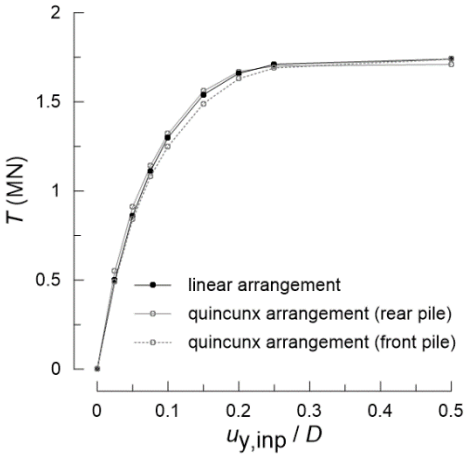

Figure 10. 3D numerical results (unconstrained piles): shear forces T versus input slope movements for linear and quincunx arrangements.

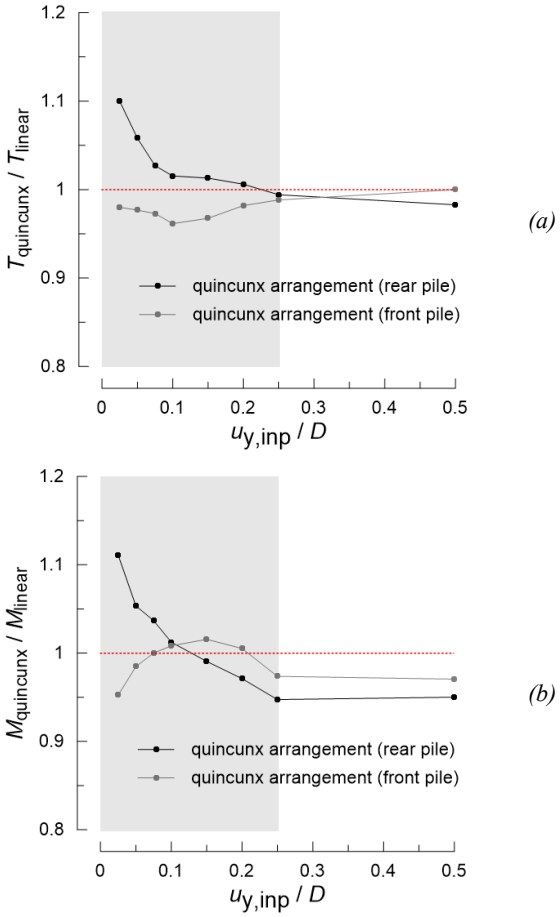

Figure 11. 3D numerical results (unconstrained piles): shear forces T(a) and bending moments M (b) acting in the piles at the depth of the sliding surface in the quincunx array, normalised to the ones measured in the linear array.

3 CONCLUDING REMARKS

Numerical results obtained for unconstrained piles show that, for the adopted pile spacing ($s_x = 3D$) and pile embedded length ($L_2/H = 1$), the linear and quincunx arrangements have the same effectiveness in terms of reduction of soil movements of a shallow translational landslide in fine-grained soils. It is evident that this outcome is strictly related to the chosen pile spacing in the direction of the ground movement (s_y in Figure 4b), between the rear and the front rows: the 2D and 3D numerical results highlighted that for $s_y = 4D$ the "multiple" arching effect makes the two schemes equally effective. On the other side, comparing the performance (shear force T and bending moment M) of each pile within the group, some differences have been observed between the rear and front piles of the quincunx layout. This result seems to indicate that the choice of a different piles arrangement is more related to pile response than slope stability, perhaps allowing a less conservative design of the front piles of the row.

Both aspects (piles effectiveness and performance) will have to be analysed in more detail through a broader 3D parametric study, considering different values of the ratio s_y/s_x in order to identify the threshold that guarantees the formation of the beneficial "multiple" soil arching effect and, at the same time, reduces the internal forces within the front piles.

REFERENCES

Chen C.Y. and Martin G.R. (2002). Soil-structure interaction for landslide stabilizing piles. *Computer and Geotechnics*, 29: 363-386. DOI: 10.1016/S0266-352X(01)00035-0.

Durrani I.K., Ellis E. and Reddish D.J. 2006. Modelling lateral pile-soil interaction for a row of piles in a frictional soil. Proc. 4th International FLAC Symposium in Numerical Modelling in Geomechanics, 231-238.

Fantera L. Lirer S., Desideri A and Rampello S. (2022). Effect of piles Stabilizing Slopes in Fine-Grained Soils. *International Journal of Geomechanics* 22 (9). DOI: 10.1061/(ASCE)GM.1943-5622.000247.

FLAC 2D, version 7.0, User Manual.

FLAC 3D, version 6.0, User Manual.

Kourkoulis R., Gelagoti F., Anastasopoulos I. and Gazetas G. (2011). Slope stabilizing piles and pile groups: parametric study and design insights. *Journal of Geotechnical and Geoenvironmental Engineering*, 137 (7): 663-677. DOI: 10.1061/(ASCE)GT.1943-5606.0000479.

Lirer, S. (2012). Landslide stabilizing piles: Experimental evidences and numerical interpretation. *Engineering Geology* 149–150: 70–77. DOI: 10.1016/j.enggeo.2012.08.002.

Liang R. and Zeng S. (2002). Numerical study of soil arching mechanism in drilled shafts for slope stabilization. *Soils and Foundations*, 42 (2): 83-92. DOI: 10.3208/sandf.42.2_83.

Muraro S., Madashi A. and Gajo A. (2014). On the reliability of 3D analyses on passive piles used for slope stabilization in frictional soils. *Géotechnique*, 64 (6): 486-492. DOI: 10.1680/geot.13.T.016.

Pham Q.N., Ohtsuka S., Isobe K., Fukumoto Y. (2019). Group effect on ultimate lateral resistance of piles against uniform ground movement. *Soils and Foundations* 59(2019): 27-40. DOI: 10.1016/j.sandf.2018.08.013.

Pirone M. and Urciuoli G. (2018). Analysis of slope stabilising piles with the shear strength reduction technique. *Computers and Geotechnics*, 102: 238-251. DOI: 10.1016/j.compgeo.2018.06.017.

Shangguan Y., Xue D., Wang G. Li D., Bao S. and Wang W (2023). A study on soil arching effect of anti -slide pile considering different pile arrangements. *Frontiers in Earth Science*. DOI: 10.3389/feart.2023.1195552.

Proceedings of the XVIII ECSMGE 2024
GEOTECHNICAL ENGINEERING CHALLENGES
TO MEET CURRENT AND EMERGING NEEDS OF SOCIETY
© 2024 the Authors
ISBN 978-1-032-54816-6
DOI 10.1201/9781003431749-296
Open Access: www.taylorfrancis.com, CC BY-NC-ND 4.0 license

ECSMGE 24
XVIII EUROPEAN CONFERENCE ON SOIL MECHANICS AND GEOTECHNICAL ENGINEERING

Safety assessment of a gravity dam using a hydromechanical model: fracture propagation at the dam/foundation interface

Evaluation de la sécurité d'un barrage-poids à l'aide d'un modèle hydromécanique: propagation des fractures à l'interface barrage/fondation

M.L.B. Farinha*, N.M. Azevedo, S. Oliveira
Laboratório Nacional de Engenharia Civil, Lisbon, Portugal

**lbraga@lnec.pt*

ABSTRACT: Most gravity dam failures occur due to sliding along the dam/foundation interface, rock mass discontinuities, or rock mass layers of lower strength. The possibility of sliding of a dam is usually evaluated based on simplified limit equilibrium techniques. In this study an explicit time-stepping small displacement algorithm, Parmac2D-Fflow, is used to assess the safety of gravity dams. This algorithm is based on a discrete representation of discontinuities, simulates the hydro-mechanical interaction, and considers softening constitutive laws that are closer to the actual behaviour of the dam/foundation interface. Seepage flow along the dam/foundation interface is only allowed to occur after contact failure, making it possible to model a coupled propagation failure along the dam/foundation interface due to a hypothetical dam overtopping scenario. For two gravity dams with different heights, the numerical results predicted with a coupled/fracture propagation model are compared with those obtained with a coupled/fully fractured model and with an uncoupled analysis. The results presented highlight the relevance of taking into account a coupled hydro-mechanical for dam safety and show that with coupled-fracture propagation model slightly higher safety factors are predicted.

RÉSUMÉ: La plupart des ruptures de barrages-poids sont dues à un glissement le long de l'interface barrage/fondation, des discontinuités de la masse rocheuse ou des couches de masse rocheuse de moindre résistance. La possibilité de glissement d'un barrage est généralement évaluée sur la base de techniques simplifiées d'équilibre limite. Dans cette étude, un algorithme explicite de petits déplacements à pas de temps, Parmac2D-Fflow, est utilisé pour évaluer la sécurité des barrages-poids. Cet algorithme est basé sur une représentation discrète des discontinuités, simule l'interaction hydromécanique et considère des lois constitutives d'adoucissement qui sont plus proches du comportement réel de l'interface barrage/fondation. Le flux d'infiltration le long de l'interface barrage/fondation n'est autorisé qu'après la rupture de contact, ce qui permet de modéliser une rupture par propagation couplée le long de l'interface barrage/fondation en raison d'un scénario hypothétique de débordement du barrage. Pour deux barrages-poids de hauteurs différentes, les résultats numériques prédits avec un modèle de propagation couplé/fracture sont comparés à ceux obtenus avec un modèle couplé/entièrement fracturé et avec une analyse non couplée. Les résultats présentés mettent en évidence la pertinence de la prise en compte d'un modèle hydro-mécanique couplé pour la sécurité des barrages et montrent qu'avec un modèle couplé de propagation des fractures, des facteurs de sécurité légèrement plus élevés sont prédits.

Keywords: Gravity dam; hydromechanical coupled model; fracture propagation; safety assessment.

1 INTRODUCTION

The hydro-mechanical behaviour of concrete dam foundations must be considered, and the behaviour of the discontinuities must be represented by realistic constitutive models. Studies have been carried out to characterise the properties and failure mechanisms of the concrete/rock interface and its effect on the stability of dams (Dong et al., 2016; Krounis et al. 2015; Tian et al., 2015). The safety of concrete dams is often quantified by a factor, which can be obtained by reducing the resistant characteristics of the discontinuities involved in the failure mechanism or by increasing the hydrostatic pressure on the upstream face of the dam (Azevedo et al., 2021; Farinha et al., 2017; Enzell et al., 2023).

This study uses a hydromechanical model to assess the stability of gravity dams, which consider the opening/closing movements of discontinuities and the water pressures in the dam foundation discontinuities and in the dam/foundation interface, considering a contact model with weakening of cohesion and tensile strength of the concrete/concrete and concrete/rock interfaces. Stability analyses are carried out on two gravity dams of different heights. Using the gradual load amplification method, the sliding safety factors are determined considering a softening model for the

joint elements that simulates the discontinuities (concrete / concrete and concrete / rock) (Azevedo et al., 2010, 2015). Two hypotheses for the foundation rock mass behaviour are considered: linear elastic or brittle failure. A critical analysis of the results is presented in relation to the sliding safety assessment.

2 HYDROMECHANICAL MODEL AND SOFTENING MODEL

This study was carried out with Parmac2D-Fflow (Azevedo et al., 2021; Farinha et al., 2017), which allows fully coupled hydromechanical analysis. The mechanical domain is divided into blocks, which are internally divided into a mesh of plane triangular elements, in order to simulate their deformability. The interaction between these deformable blocks, which simulate both the dam and the foundation, is done using joint finite elements in small displacements. The hydraulic model is superimposed on the mechanical model and thus for each joint element there is a corresponding seepage channel.

An interface contact model with softening was adopted for the behaviour of both concrete/concrete and concrete/rock discontinuities, based on a joint model with bilinear softening in the normal and shear directions. This model has been applied to particle models (Azevedo et al. 2010, 2015). From the moment the maximum strength values (tensile and cohesion) are reached, the maximum strength tensile force and/or the maximum cohesion are reduced based on the damage value, which varies between 0 (no damage) and 1 (contact considered cracked, only working in pure friction). The strength parameters of this contact model are: the ultimate tensile stress (σ_t), the maximum cohesion (C), the friction coefficient (μ_c), and the tensile (G_I) and shear (G_{II}) fracture energies.

3 STABILITY ANALYSIS OF GRAVITY DAMS

3.1 Model description

3.1.1 Geometry and boundary conditions

Four models were considered in this study, representing two large gravity dams of different heights (15 m and 30 m) with their foundations on rock masses with two fracture geometries. Figure 1 shows the schematically geometry of the models, with all the dimensions represented as a function of the height of the dam (H) and the thickness of the construction at the top (a).

The construction joints in the dam body were simulated by a family of discontinuities with a spacing of 3.0 metres (Figure 2 and Figure 3). The foundation rock masses were represented with two families of discontinuities. One model, called "reg", was considered, with a family of continuous horizontal discontinuities with a spacing of 5.0 metres and a family formed by vertical discontinuities with an average spacing of 5.0 metres and a standard deviation of 1.0 metre. Another model was considered, called "dip", with families of continuous orthogonal discontinuities that make angles of 15º and 105º with the horizontal. In the latter case, the orientation and the fact that the families of discontinuities are continuous and flat favours the formation of failure mechanisms, with the formation of wedges that can slide under the dam.

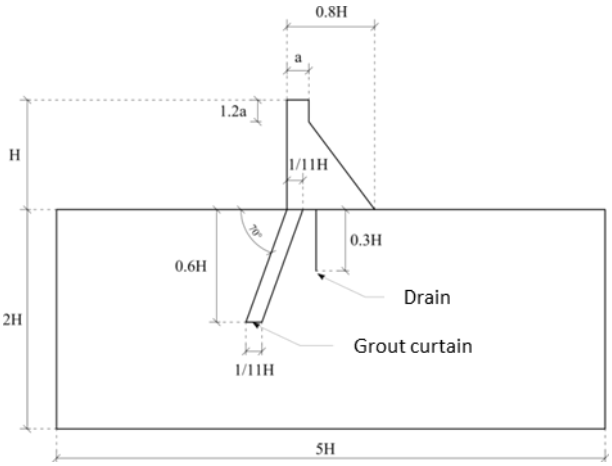

Figure 1. Model geometry.

Table 1 shows the number of mechanical and hydraulic elements used in the four models. It should be noted that the average size of the edges of the triangular elements is 0.6 metres.

Table 1. Model characteristics (number of different elements)

Model	**a***	**b***	**c***	**d***	**e***
15-reg	6531	9629	1420	1322	1379
15-dip	8063	10058	2550	2299	2509
30-reg	25883	38549	5843	5367	5659
30-dip	31784	40178	10221	9115	10037

***a**: mechanical nodal points; **b**: triangular elements; **c**: joint elements; **d**: hydraulic nodal points; **e**: seepage channels

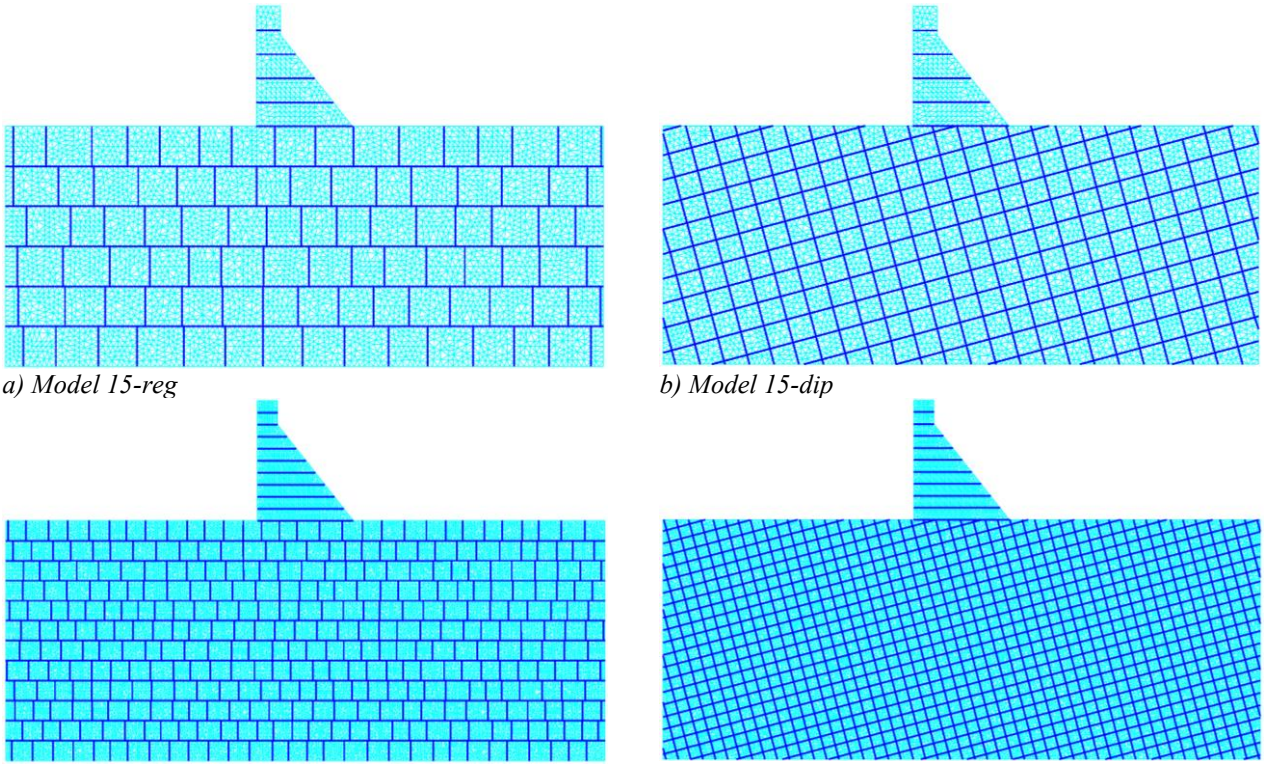

a) Model 15-reg *b) Model 15-dip*

c) Model 30-reg *d) Model 30-dip*

Figure 2. Discontinuum models of the dam/foundation system. a) and b) 15 m high gravity dam; c) and d) 30 m high gravity dam. Each block is discretized using triangular plane finite elements.

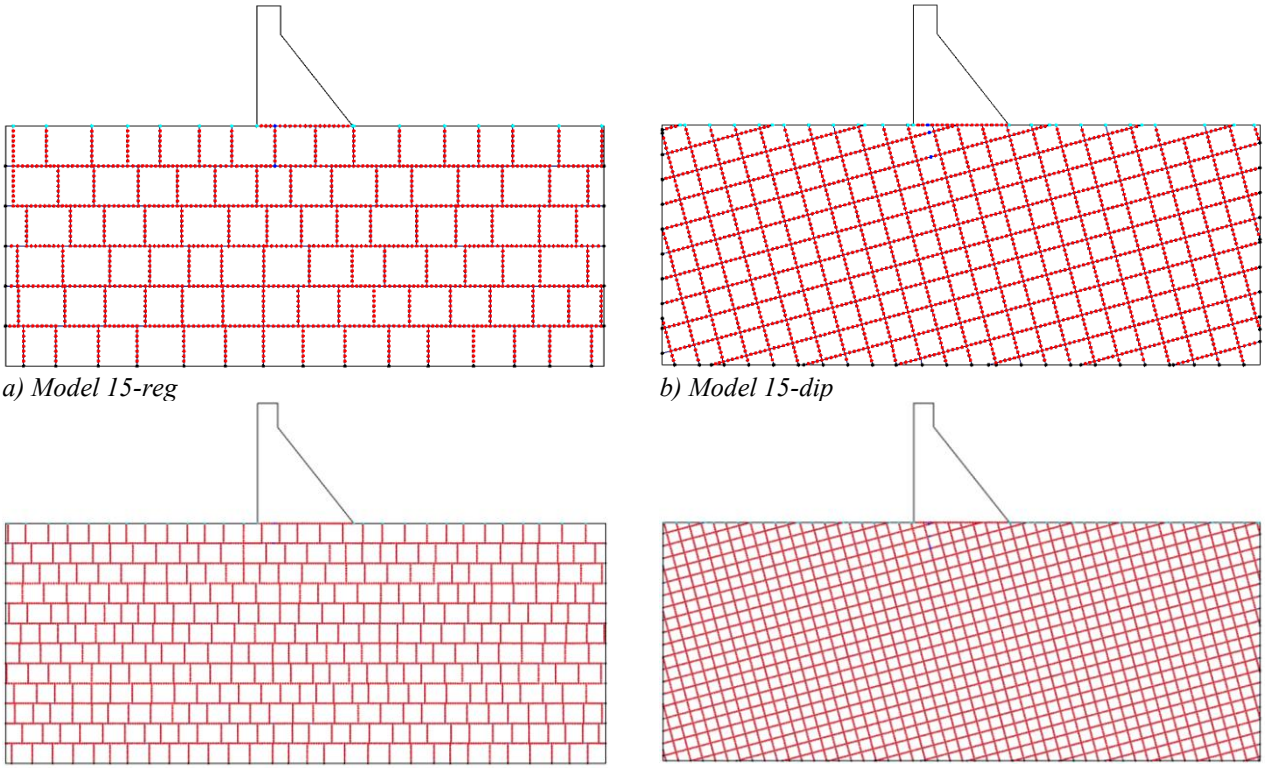

a) Model 15-reg *b) Model 15-dip*

c) Model 30-reg *d) Model 30-dip*

Figure 3. Hydraulic models. Hydraulic head assumed on the rock mass surface upstream and downstream from the dam (light blue dots); hydraulic head assumed at the drainage system (dark blue dots); hydraulic channels (red dots); impervious lateral and bottom model boundaries (black dots).

Concerning mechanical boundary conditions, the base of the model was fixed and horizontal displacements on the lateral boundaries were prevented. As hydraulic boundary conditions, zero permeability was assumed at the base and lateral boundaries of the model and the drainage system was simulated by assigning a water pressure along the drain axis equal to 1/3 of the hydraulic head upstream from the dam.

3.1.2 Material properties

The dam concrete and the blocks of the foundation rock mass are assumed to have linear elastic behaviour, with the properties shown in Table 2. At the joints in the concrete zone, the normal stiffness (k_n) is equal to 60.6 GPa/m and the shear stiffness (ks) is equal to 24.2 GPa/m. At the dam/foundation interface and at the rock mass discontinuities, k_n = 120.8 GPa/m and k_s = 51,5 GPa/m. In the rock mass discontinuities, when non-linear behaviour is considered, zero cohesion and traction and a friction angle of 45º are assumed.

Table 2. Material mechanical properties (after Dong et al., 2016).

Material	E [GPa]	ν [-]	ρ [kg/m^3]
Dam concrete	30.3	0.24	2400
Rock mass	64.4	0.20	2700

Regarding the hydraulic apertures of the seepage channels, $a_0 = 1.668\times10^{-4}$ m, $a_{res} = 1/3 \times a_0$ and $a_{max} = 5 \times a_0$ were assumed. It was assumed that the permeability of the dam/foundation interface was half that of the discontinuities in the foundation. The grout curtain permeability is 2.5 times lower than that of the rock mass. The dam construction joints are impervious.

Table 3 shows the softening interface contact model parameters.

Table 3. Softening model parameters for the two different discontinuities: concrete/rock and concrete/concrete.

σ_t	G_I [Nm/m^2]	C [kg/m^3]	G_{II} [Nm/m^2]	tan φ
2.9	250	8.0	2500	1

3.2 Stability analysis

The models developed were used to assess the sliding safety of the dam/foundation system, assuming that sliding can occur not only at the dam/foundation interface but also at the rock mass discontinuities. The analysis was carried out in two phases: first, a hydro-mechanical calculation was carried out, taking into account the weight of the dam, assuming that the water table was at ground level and that the ratio between horizontal and vertical effective stresses in situ was equal to 0.5; then the hydrostatic pressure was applied at the upstream face of the dam and at the base of the reservoir, assuming all the discontinuities had linear elastic behaviour. In this second phase, a mechanical analysis was carried out first, followed by a hydromechanical analysis. In cases where non-linear behaviour of the discontinuities was assumed, this was only considered after equilibrium had been reached. In all calculations, the reservoir was assumed to be at the dam crest level. Figure 4 shows the hydraulic head contours, where the effect of the drainage system can be clearly identified.

For each gravity dam the results obtained with a coupled/fracture propagation model are compared with those obtained with a coupled/fully fractured model and with an uncoupled analysis, where the pressures remained constant and equal to those obtained in the initial equilibrium situation (no hydraulic calculation was carried out in this model). In the coupled analyses, the hydraulic head upstream from the dam was gradually increased given the water height above the dam crest. In the fracture propagation model, seepage along the dam/foundation interface was just allowed after damage initiation at each joint element.

Table 4 shows the safety factors obtained for the four different models carrying out numerical analysis assuming three different hypotheses: uncoupled (UCP), coupled (CP) and coupled with fracture propagation due to water pressure (CP-FP) and two different foundation behaviors: elastic (E) and brittle model (F). Figure 5 shows the horizontal crest displacement during the process of amplification of water pressure for the dam with 30 m height. As shown, with a fractured foundation a higher crest displacement is obtained when compared with an elastic foundation.

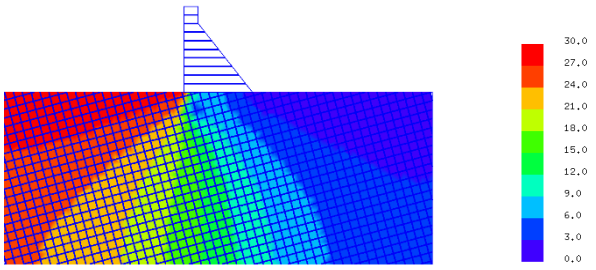

Figure 4. Hydraulic head contours (model 30-dip).

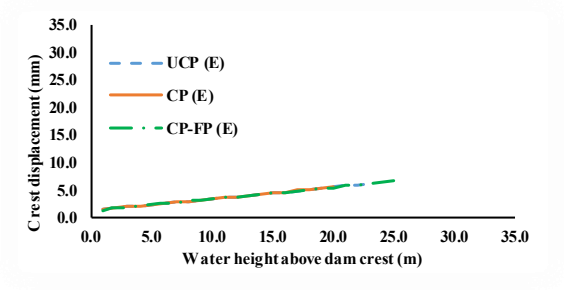

a) Model 30-reg (E)

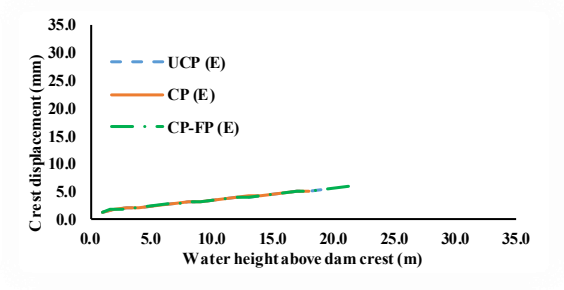

b) Model 30-dip (E)

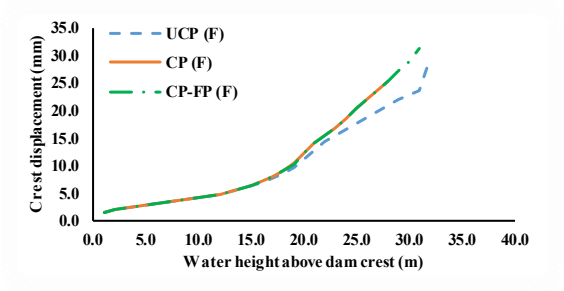

c) Model 30-reg (F)

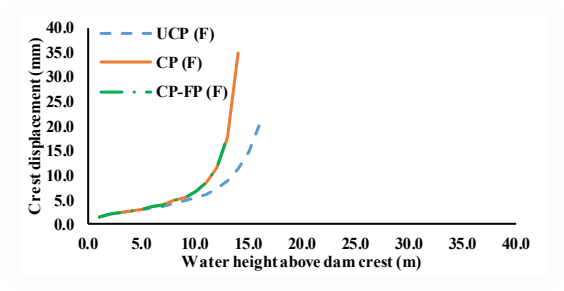

d) Model 30-dip (F)

Figure 5. Horizontal crest displacement during the process of amplification of water pressure.

In the elastic foundation model (E) the simplified uncoupled model (UCP) always predicts a higher safety factor than that obtained with a coupled model (CP), that considers a permeable dam/foundation interface from the beginning of the load amplification process. With a coupled model taken into account fracture propagation (CP-FP) at the dam/foundation interface, the predicted safety factors are, as expected, higher than those predicted with a coupled model, and are also higher than those predicted with a simplified uncoupled model (UCP).

In the fractured foundation model (F) the simplified uncoupled model (UCP) always predicts a higher safety factor. The coupled model with fracture propagation (CP-FP) at the dam/foundation interface leads, when compared with the coupled model (CP) that considers a permeable dam/foundation interface from the beginning of the load amplification process, with the exception of model 30-dip, to a higher safety factor.

As expected, for a fractured foundation (F), the geometry with discontinuity families with an orientation that favours the formation of failure mechanisms (15-dip and 30-dip), the predicted safety factors are, for all calculation hypothesis, always lower than those predicted with a regular foundation.

Overall the results here presented indicate that with an uncoupled model (UCP) the safety factor predicted may be higher than that obtained with a coupled fracture propagation model (CP-FP). The results presented also show that the coupled model (CP) that considers the dam/foundation interface permeable from the start of the safety factor calculation leads to a value in the range or lower than the value predicted with the coupled fracture propagation model (CP-FP).

Table 4. Safety factors: Elastic foundation (E) and fractured foundation (F).

Model	***15-reg***	***15-dip***	***30-reg***	***30-dip***
UCP (E)	4.60	4.73	2.53	2.27
CP (E)	4.33	4.33	2.33	2.20
CP-FP (E)	4.87	4.87	2.67	2.47
UCP (F)	5.80	3.00	3.13	2.07
CP (F)	5.13	2.47	2.87	1.93
CP-FP (F)	5.67	2.47	3.07	1.87

Figure 6 presents the predicted failure modes for a fractured foundation, for the 30 m high dam using both the coupled model (CP) and the coupled model taking into account fracture propagation (CP-FP). As shown, by taking into account fracture propagation due to the water pressure at the dam/foundation interface, the failure modes are slightly different and occur for a smaller deformation even if for the maximum amplification factor the dam/foundation is fully damaged allowing water to flow along the dam/foundation discontinuity. Figure also shows that the sliding of the dam is accompanied by rotation with an axis at the downstream foot and that failure involves opening of discontinuities in the foundation mass near the upstream toe of the dam.

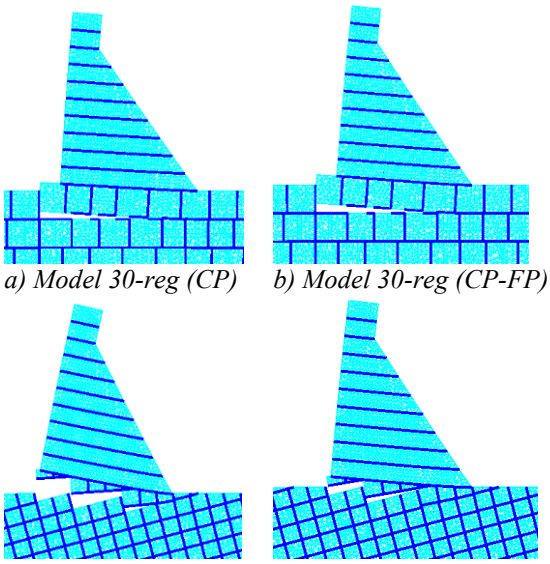

a) Model 30-reg (CP) *b) Model 30-reg (CP-FP)*

c) Model 30-dip (CP) *d) Model 30-dip (CP-FP)*

Figure 6. Failure modes for the 30 m high dam with fractured foundation for the maximum load amplification factors (block deformation magnified 200 times for the reg model and 50 times for the dip model).

4 CONCLUSIONS

The results of safety analyses of existing dams for situations of overtopping, due to floods greater than foreseen in the design phase and/or due to climate changes, and for seismic actions, will enable the definition of alert levels to be used in the prediction models, in order to anticipate failure scenarios and the production of a database of failure analyses.

The safety assessment of gravity dams should be carried out using a coupled hydromechanical model, with proper material properties and behaviour following a load amplification approach. When compared with the simplistic strength reduction approach, typically applied in foundation design and proposed in current dam safety design guidelines, more realistic safety factors and failure modes can be obtained.

Within a coupled analysis the consideration of an initial impervious dam/foundation interface may be a more realistic scenario. The results presented show that slightly higher safety factors are predicted taking into account fracture propagation during the load amplification process.

Further work is underway in order to assess the coupled model with fracture propagation performance for a large set of material properties (concrete, rock mass and corresponding interfaces), material behaviour, including nonlinear behaviour at both the dam and foundation areas, dam geometries and the consideration of a downstream rock wedge that contributes to the stability of the dam.

ACKNOWLEDGEMENTS

The study presented here is part of the research project StepDam: A step forward for the ability to anticipate and prevent failures of concrete dam foundations, supported by LNEC.

REFERENCES

Azevedo, N. M., Farinha, M. L. B., Sá, M., Almeida, J. (2021) Modelos descontínuos na análise tridimensional do comportamento hidromecânico de fundações de barragens de betão, *Geotecnia*, 151: 5-32 https://doi.org/10.24849/j.geot.2021.151.02.

Azevedo, N. M., Lemos, J., Almeida, J. (2010). A discrete particle model for reinforced concrete fracture analysis, *Structural Engineering and Mechanics*, 36(3): 343-361. https://doi.org/10.12989/sem.2010.36.3.343.

Azevedo, N., Candeias, M., Gouveia, F. (2015). A rigid particle model for rock fracture following the Voronoi Tessellation of the grain structure: formulation and validation, *Rock mechanics and Rock Engineering*, 48 (2): 535-557 https://doi.org/10.1007/s00603-014-0601-1.

Dong, W., Wu, Z., Zhou, X. (2016). Fracture mechanisms of rock-concrete interface: experimental and numerical. *Journal of Engineering Mechanics*, 142: 04016040-1 to 11. https://doi.org/10.1061/(ASCE)EM.1943-7889.0001099.

Enzell, J.; Nordström, E.; Sjölander, A.; Ansell, A.; Malm, R. Physical Model Tests of Concrete Buttress Dams with Failure Imposed by Hydrostatic Water Pressure (2023). *Water*, 15(20), 3627. https://doi.org/10.3390/w15203627.

Farinha, M. L. B., Azevedo, N. M., Candeias, M. (2017). Small displacement coupled analysis of concrete gravity dam foundations: static and dynamic conditions. *Rock Mechanics and Rock Engineering*, 50(2): 439-464. https://doi.org/10.1007/s00603-016-1125-7.

Krounis, A.; Johansson, F.; Larsson, S. (2015). Effects of spatial variation in cohesion over the concrete-rock interface on dam sliding stability. *Journal of Rock Mechanics and Geotechnical Engineering*, 7(6): 659-667. https://doi.org/10.1016/j.jrmge.2015.08.005.

Tian, H.M.; Chen, W.Z.; Yang, D.S.; Yang, J.P. (2015). Experimental and numerical analysis of the shear behaviour of cemented concrete–rock joints. *Rock Mechanics and Rock Engineering*, 48(2): 213-222. https://doi.org/10.1007/s00603-014-0560-6.

Proceedings of the XVIII ECSMGE 2024
GEOTECHNICAL ENGINEERING CHALLENGES
TO MEET CURRENT AND EMERGING NEEDS OF SOCIETY
© 2024 the Authors
ISBN 978-1-032-54816-6
DOI 10.1201/9781003431749-297
Open Access: www.taylorfrancis.com, CC BY-NC-ND 4.0 license

ECSMGE 24
XVIII EUROPEAN CONFERENCE ON SOIL MECHANICS AND GEOTECHNICAL ENGINEERING

Analysis of subsidence problems on a highway section in Valencia (Spain) with the help of satellite radar interferometry

Analyse de problèmes d'affaissement sur un tronçon d'autoroute à Valence (Espagne) à l'aide de l'interférométrie radar par satellite

A. Fernández Eusebio, J. Moreno Robles, F. Pardo de Santayana*, D. Mora Cejudo
Laboratorio de Geotecnia-CEDEX/Madrid/Spain

A. Parrilla Alcaide
Dirección General de Carreteras-MITMA/Madrid/Spain

D. Carrasco Díaz, A. Mendizabal
Hisdesat Servicios Estratégicos S.A./Madrid/Spain

J. Duro, D. Monells, R. Iglesias
Dares Technology S.L./Barcelona/Spain

**f.pardo.s@cedex.es*

ABSTRACT: The General Directorate of Roads of the Spanish Ministry of Transports requested the Geotechnical Laboratory of CEDEX technical assistance for the study of some pathologies detected in A-33 highway in La Font de la Figuera, province of Valencia (Spain). In 2022, after six years in service, anomalous settlements, up to 10 cm, and some longitudinal cracks on the pavement on both carriageways were detected at several zones around station 85+000 of the highway, all of them located in embankment cross sections. Initially, several possible causes of the pathologies were considered: malfunction of the underground drainage of the pavement structure; presence of an abandoned railway tunnel under the embankment; and the existence of collapsible soils at the embankment foundation. An inspection visit to the area was carried out and a site investigation campaign comprising dynamic penetration tests, execution of boreholes with core recovery and installation of micrometric pipe and piezometers, and hydrogeological tests with tracers has been proposed to determine the cause of the detected pathologies. Meanwhile, measurements of ground surface movements obtained by interferometric processing of 46 high resolution radar images, taken by the Paz satellite, have been used to help analyse the cause of anomalous settlements, pointing out that the most likely cause is the existence of collapsible soils at the embankment foundation, what shall be confirmed by the results of the site investigation campaign. The paper presents the results of the study carried out so far.

RÉSUMÉ : La Direction Générale des Routes du Ministère des Transports espagnol a demandé au Laboratoire Géotechnique de l'Assistance technique CEDEX pour l'étude de certaines pathologies détectées dans l'autoroute A-33 à La Font de la Figuera, province de Valence (Espagne). En 2022, après six ans de service, des tassements anormaux, jusqu'à 10 cm, et des fissures longitudinales sur la chaussée des deux chaussées ont été détectés dans plusieurs zones autour du point kilométrique 85+000 de l'autoroute, toutes situées dans des sections transversales de remblai. Initialement, plusieurs causes possibles des pathologies ont été envisagées : dysfonctionnement du drainage souterrain de la structure de la chaussée ; présence d'un tunnel ferroviaire abandonné sous le remblai; et l'existence de sols affaissables au niveau de la fondation du remblai. Une visite d'inspection a été effectuée dans la zone et une campagne d'étude du site comprenant des tests de pénétration dynamique, l'exécution de forages avec récupération du cœur et installation de tuyaux micrométriques et de piézomètres, ainsi que des tests hydrogéologiques avec traceurs a été proposée pour déterminer la cause des pathologies détectées. Entre-temps, les mesures des mouvements de la surface du sol obtenues par traitement interférométrique de 46 images radar à haute résolution prises par le satellite Paz ont été utilisées pour aider à analyser la cause des tassements anormaux, soulignant que la cause la plus probable est l'existence de sols affaissables sur la fondation du remblai, ce qui sera confirmé par les résultats de la campagne d'étude du site. Le document présente les résultats de l'étude réalisée jusqu'à présent.

Keywords: Subsidence; highway; interferometry; collapsible soils.

1 DESCRIPTION OF THE PROBLEMS

The General Directorate of Roads of the Spanish Ministry of Transports requested the Geotechnical Laboratory of CEDEX technical assistance for the study of some pathologies detected around station 85+000 of A-33 highway in La Font de la Figuera, province of Valencia (Spain). During the first half of 2022, and after six years in service, the A-33 conservation team detected five zones with anomalous settlement and some longitudinal cracks on the pavement on both carriageways of the highway (Figure 1, 2 and 3). The settlement zones are a few hundreds of meters apart one from another and are all located in embankment cross sections. The maximum settlement is about 10 cm.

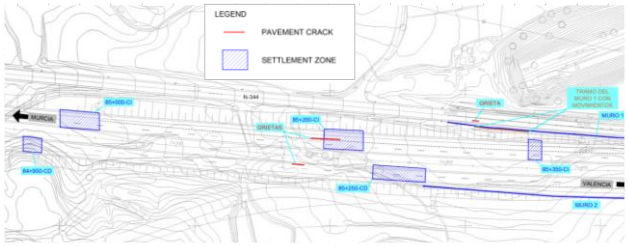

Figure 1. Distribution of zones with cracks and anomalous settlements around station 85+000.

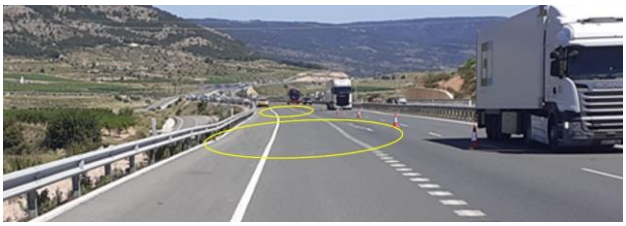

Figure 2. Settlement zone at stations 85+200 and 85+350, (left carriageway, June 2022. View towards Valencia.



Figure 3. Settlement zone at station 85+350, left carriageway, June 2022. View towards Murcia.

In the case of zone 85 + 200-left carriageway, in addition to the settlement, a longitudinal crack of around ten meters appeared. It had an opening of 1-2 cm with no unevenness between lips, see Figure 4.



Figure 4. Longitudinal crack in area 85+200-left carriageway, April 2022.

2 POSSIBLE CAUSES OF THE DAMAGES

Several causes for these pathologies were initially considered:

- Malfunction of the underground drainage of the pavement structure.
- The presence of an abandoned railway tunnel under the section of the highway with the pathologies.
- The existence of collapsible soils in the embankment foundation.

Though the first of the aforementioned possible causes is one of the most frequent when an early bad performance of the pavement is detected, in this case, however, has been discarded: both the superficial and underground drainage systems seem to be well designed, built, and maintained and, up to the moment, there were not anomalies reported or observed regarding this issue. The remaining two are discussed next.

The abandoned railway tunnel is about 1500 m long and was built in the late nineteenth century (1885). The areas with pathologies are relatively close to the tunnel north portal (see Figures 5, 6 and 7).

In a section of the tunnel, about 80 m long and located about 40 m from the north portal (see Figure 7) there are significant water infiltrations, contrarily to the rest of the tunnel. It seems that the section of tunnel with leaks is acting as a general drain of the area and, therefore, causing a hydraulic gradient and a depression of the water table (see Figure 8). The corresponding flow lines towards the tunnel are carrying material to its interior.

As it can be seen inside the tunnel, this transportation process includes two mechanisms: salt dissolution and precipitation and soil drag. This process must have been occurring, with greater or lesser intensity, since the tunnel construction, and could be causing subsidences at the ground surface level.

If the amount of material transported towards the tunnel is large enough there would be a risk of sinkhole formation at the highway carriageways. This could, therefore, cause fatal traffic accidents. During an inspection visit in August 2022, that is, in the driest time of the year and after a long period without rain, the water flow observed at the north portal was of around 0.5-1.0 l/s. It is believed that it could be significantly higher in the rainiest periods. The infiltrations seem to drag a significant amount of material with their flow, consisting of brown clayey-silty soils with a very soft consistency, due to their high humidity. There is also a very intense precipitation of salts (carbonates). This is not observed in the "dry" tunnel areas located further south.



Figure 5. North access to Mariaga tunnel (August 2022).

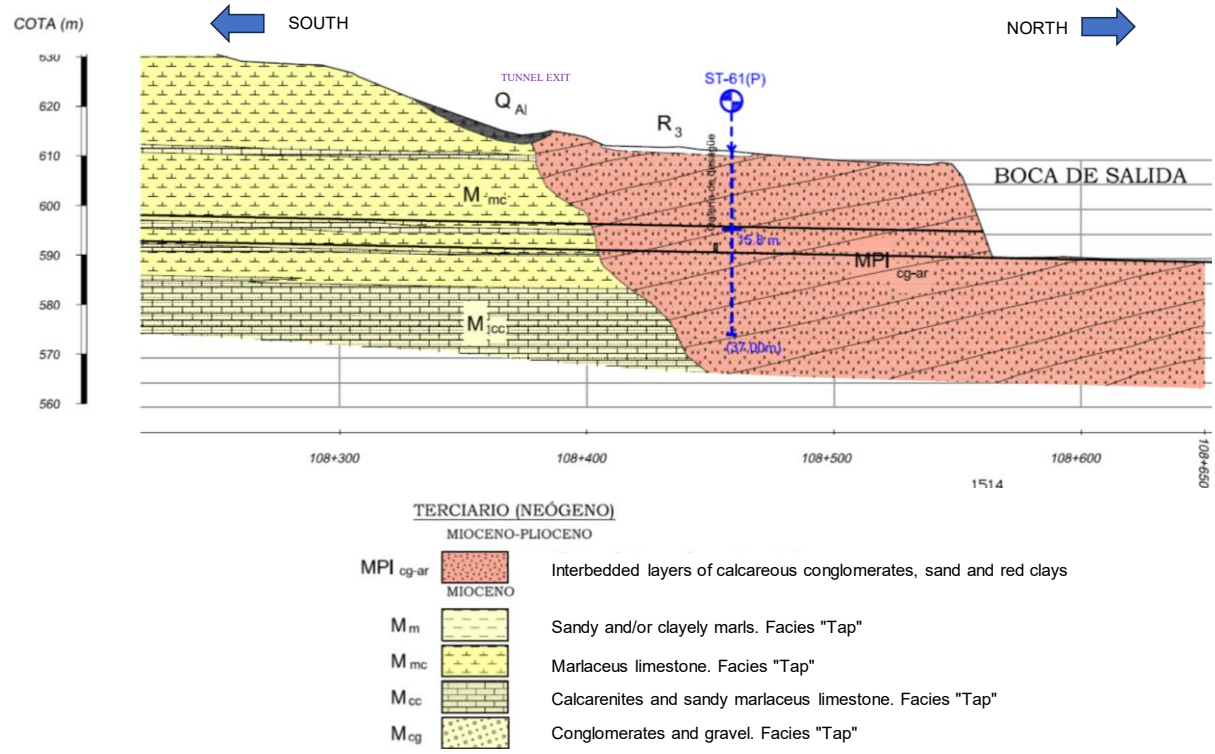

Figure 6. Longitudinal geological profile of Mariaga tunnel north end, showing contact between Miocene-Pliocene MPL (calcareous conglomerate, sands and red clays) and Miocene M (marls and limestones).

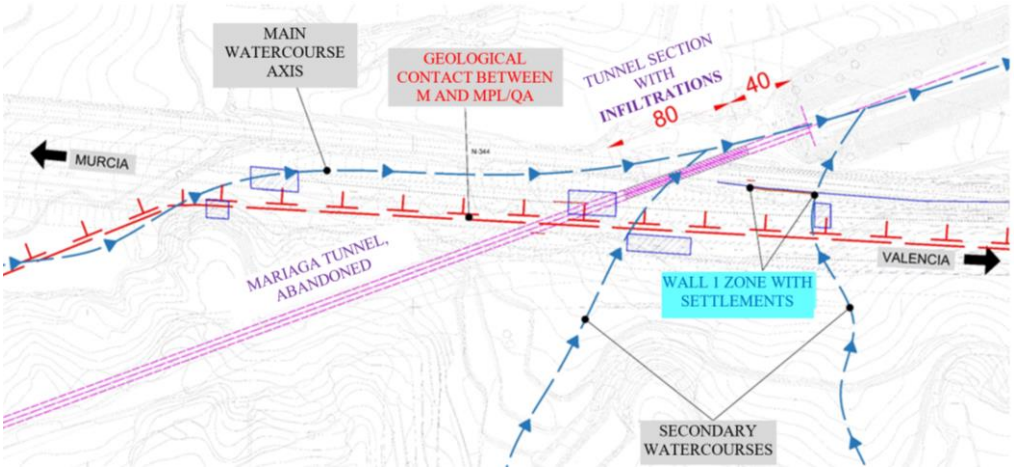

Figure 7. Plan scheme showing location of the geological contact between formations MPL/M and of streambeds.

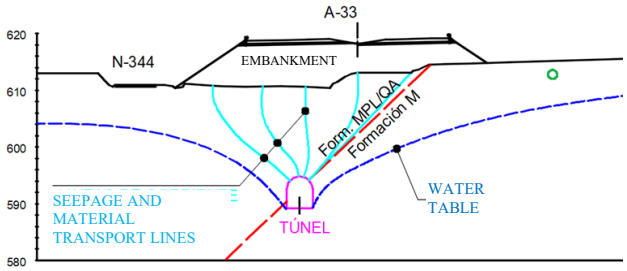

Figure 8. Schematic cross section of seepage towards tunnel (note: this section comes from assumptions).

To help analyze the cause of anomalous settlements, a site investigation campaign comprising dynamic penetration tests, execution of boreholes with core recovery and installation of sliding deformeters and piezometers, and hydrogeological tests with tracers was proposed. Meanwhile, measurements of ground surface movements obtained by interferometric processing of high-resolution SAR images from PAZ satellite have been used. This technology (Mora et al., 2001; Mora et al., 2002) has proved to be very useful to identify the most probable cause of the settlement and will be briefly discussed below.

3 SATTELLITE DATA AND INTERPRETATION OF RESULTS

The lnSAR analysis was carried out using 46 SAR images acquired by PAZ satellite in High Resolution SpotLight mode (1m x 1m resolution), covering the period between 02/02/2021 and 19/09/2022. The analysis provided high quality results and was of the utmost importance for the determination of the cause of the damage.

SAR sensors are sensitive to motion in the LOS direction (Line of Sight direction). Therefore, the displacements measured in the LOS represent a projection of the actual movement. In this context, the lnSAR measurement points are represented by colorations ranging from red to blue (Figure 9) to be interpreted as follows:

- Green-yellow-red: moving away from the radar sensor (subsidence if the motion is assumed to be mainly vertical). Negative values are used to represent this type of movement.
- Blue: stability (meaning no movement)

Sectors without measurement points correspond to areas where the quality of the measurements is not sufficient to ensure the reliability of the results (due to the presence of vegetation or changes on the ground surface).

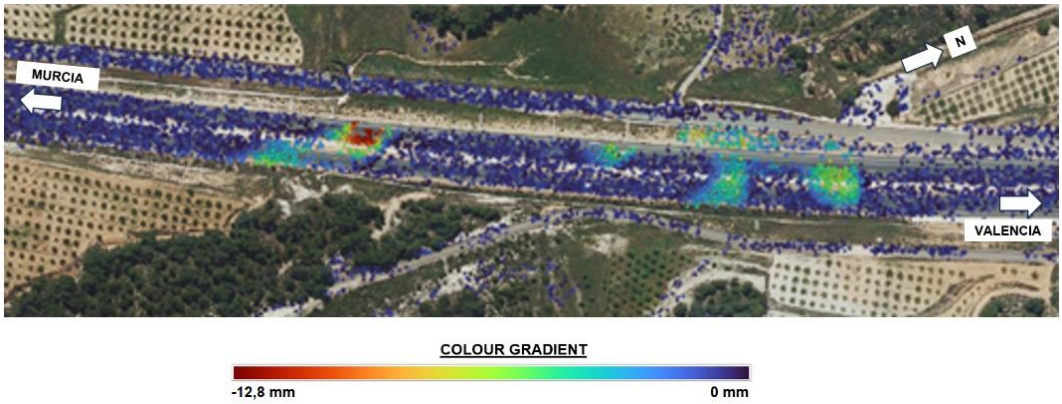

Figure 9. Ground movements obtained by interferometric processing of high-resolution radar images taken by the PAZ satellite around station 85+000. General view.

The precision of the movements obtained by this InSAR procedure is millimetric (2-3 mm, as it is a fraction of a half of the band X radar wavelength, which in this case is 31/2 = 16 mm).

With the aid of the satellite, anomalous settlements in the area around station 85+000 have been compared with those measured in another nearby zone, also with pathologies, at station 86+800 (Figures 10 and 11).



Figure 10. Location of zones with pathologies at station 85+000 and at station 86+800.

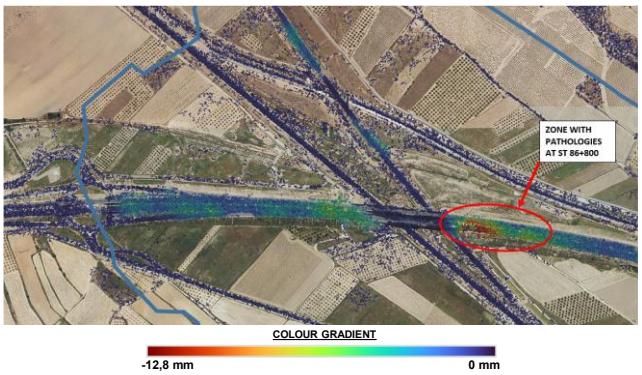

Figure 11. General plan view of the InSAR settlements within the Hoya Manuel basin around station 86+800.

The 86+800 zone is located inside the Hoya Manuel endorheic basin, where rainwater may accumulate creating a temporary lake. This has caused deposition of alluvial soils during its geological history. As known, the finest grained soils are deposited towards the center of this kind of topographical depressions and the coarse soils near the borders. Within this basin, settlements are observed in embankment sections of the A-33 highway and the railway lines, all of them built in the last 6-7 years, but not in cut or at grade sections. The evolution in time of settlements measured in both areas (85+000 and 86+800) is very similar, showing a sharp increase after periods of heavy rain (Figure 12 and 13). Because of that it is thought that the cause of the settlements could be the same.

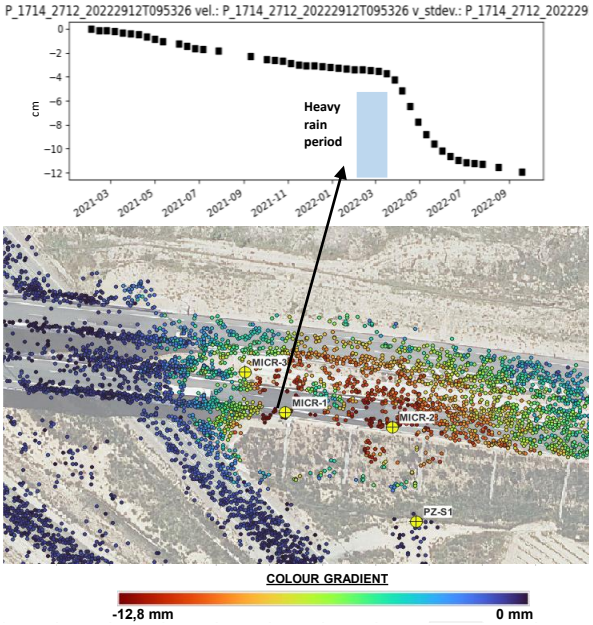

Figure 12. General plan location (below) and displacement time series (top) obtained by InSAR of one representative point at the 86+800 zone (note: see a more detailed rainfall time evolution in Figure 16).

Figure 14 shows the results of vertical displacement measurements obtained from sliding deformeters and the corresponding geotechnical profile at a borehole installed around station 86+800. In Figure 15 it is shown a schematic cross section representing the ground model interpreted according to the boreholes and other relevant information. As can be seen in Figure 14, settlements occur at a depth between 16 and 23 m (from the embankment top and 0-9 m from the general terrain surface), corresponding to a lake deposits layer (Formation QL) consisting of collapsible clayey soils. Under the QL soils there are dense to very dense granular soils (Glacis Formation) that do not settle.

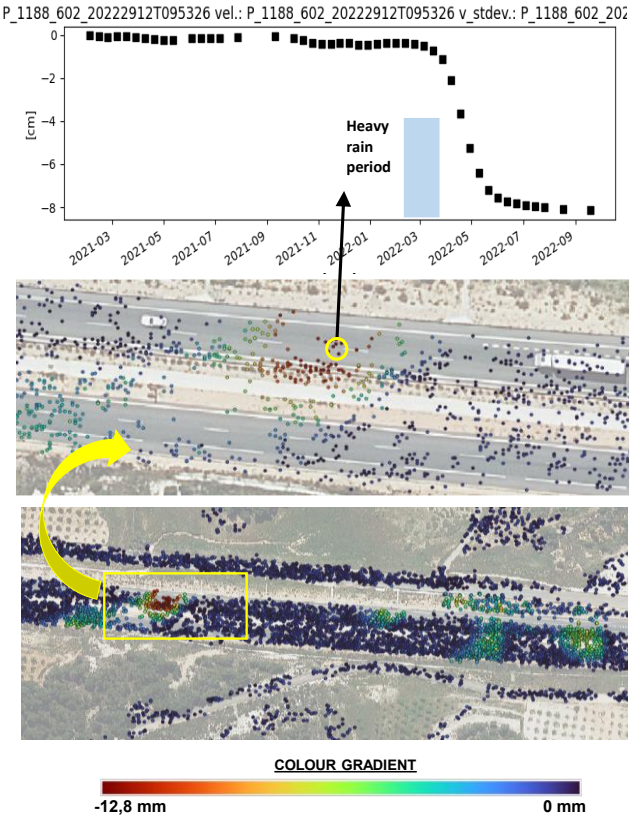

Figure 13. General plan location (below), detailed plan location (middle) and displacement time series (top) obtained by InSAR of one representative point at the 85+000 zone (note: see a more detailed rainfall time evolution in Figure 16).

The existence of the QL deposits, the seasonal humidity variations in them (because they are in general at the ground surface and therefore are directly affected by the rainfall), and the loads imposed by the embankment own weight seems to be the cause of the pathologies in the 86+800 station zone.

Because of that it is thought that in the 85+000 zone the presence of collapsible soils, similar in nature to the ones found at the center of the Hoya Manuel endorheic basin (86+800), and the existence of

recently build embankments could also be the cause of the problems. At the 85+000 the collapsible soils would only appear near the three streambeds that are crossed by the highway in this area (see Figure 7). Also, to be noted is the absence of settlements outside areas loaded with recent embankments.

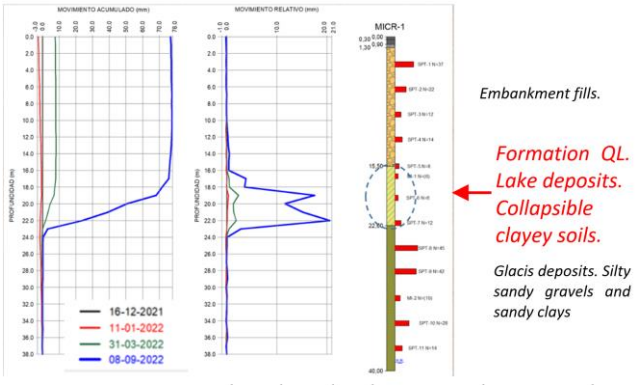

Figure 14. Accumulated and relative settlements obtained from the sliding micrometer MICR-1 located in zone 86+800, and corresponding borehole.

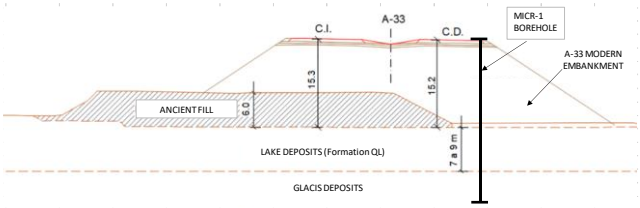

Figure 15. Schematic ground model cross section at the position of the sliding micrometer MICR-1 in zone 86+800.

In the Figure 16 a comparison of the ground settlements time-series at the location of the sliding deformeter MICR-1, using InSAR and sliding deformeter measurements is shown. The vertical movement it also compared with rainfall regime (quarterly precipitations measured at the Fuente la Higuera meteorological station from AEMET). Similar comparisons have been made using other sliding deformeters installed nearby with similar results. As it can be seen the movements obtained by the two methods match reasonably well both in magnitude and in temporal evolution.

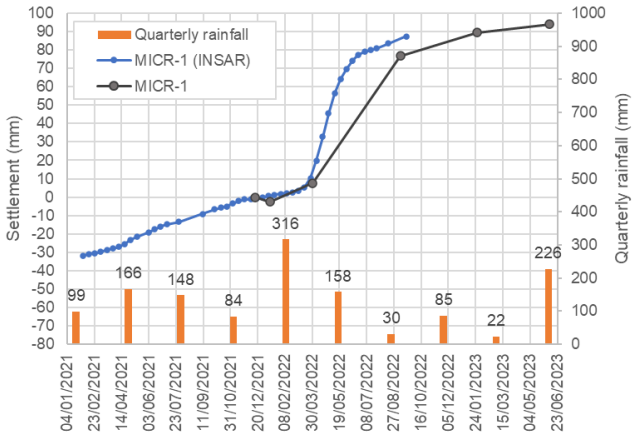

Figure 16. Comparison of the ground settlements time-series at the location of the sliding deformeter "MICR-1" using InSAR (blue) and sliding deformeter measurements (black) and evolution of rainfall regime. (Note: In the figure the InSAR settlements have been forced to be zero at the date when the sliding deformeters measures start. Negative values of settlements of the InSAR time-series indicate only values measured before that date).

4 CONCLUSIONS

The causes of anomalous settlement in a highway section have been analysed with the help of interferometric high resolution radar images. It seems that the most probable cause of these settlements is the existence of collapsible soils at the highway embankment foundation. Another cause, related to the material transportation towards the interior of an abandoned railway tunnel crossing below the highway platform, by salts dissolution or soil dragging, was also considered but does not seem to be the main cause, as there is not subsidence, or at least, it has not been observed, outside the areas occupied by the highway embankments. A site investigation campaign will help to confirm this conclusion.

REFERENCES

Mora, O., Mallorqui, J. J., Duro, J. and Broquetas, A. (2001). Long-term subsidence monitoring of urban areas using differential interferometric SAR techniques, *Proc. IGARSS*, Vol. 3, Sydney, Australia, July, pp. 1104–1106.

Mora, O., Mallorqui, J. J. and Duro, J. (2002). Generation of deformation maps at low resolution using differential interferometric SAR data, *Proc. IGARSS*, Vol. 5, Toronto, ON, Canada, July, pp. 2696–2698.

Proceedings of the XVIII ECSMGE 2024
GEOTECHNICAL ENGINEERING CHALLENGES
TO MEET CURRENT AND EMERGING NEEDS OF SOCIETY
© 2024 the Authors
ISBN 978-1-032-54816-6
DOI 10.1201/9781003431749-298
Open Access: www.taylorfrancis.com, CC BY-NC-ND 4.0 license

ECSMGE 24
XVIII EUROPEAN CONFERENCE ON SOIL MECHANICS AND GEOTECHNICAL ENGINEERING

Characterization of a highway reinforced earth wall pathology with the help of a terrestrial laser scanner model, analyses of the causes and proposal of remediation measures

Caractérisation d'une pathologie de mur de terre armé d'autoroute à l'aide d'un modèle de scanner laser terrestre, analyses des causes et proposition de mesures correctives

A. Fernández Eusebio, J. Moreno Robles, F. Pardo de Santayana*, D. Mora Cejudo
Laboratorio de Geotecnia-CEDEX, Madrid, Spain

A. Parrilla Alcaide
Dirección General de Carreteras-MITMA, Spain

f.pardo.s@cedex.es

ABSTRACT: The General Directorate of Roads of the Spanish Ministry of Transports asked the Geotechnical Laboratory of CEDEX for technical assistance for the study of a pathology detected at a section, between stations 12+625 and 12+860, of the Burgos ring highway (BU-30). Just after the inauguration of this highway section in 2016, some longitudinal cracks appeared on the right carriageway. Here, the highway runs on embankment which is contained on its right side by earth reinforced wall that in some sections is founded on a stone wall. The cracks reached a vertical gap of about 5-10 cm and were coincident with the vertical plane where the reinforcement strips of the existing reinforced earth wall ended. To prevent accidents these cracks were fixed several times by sealing, milling, and replacing the pavement, but reappeared shortly after. The evolution of movements has been controlled by topographic procedures and by auscultation devices (inclinometers and sliding deformeters). A terrestrial laser scanner (TSL) has also been used to analyse the wall movements, showing a substantial tilting of the wall face, exceeding 0.5 m at wall crest. From the monitoring results it was inferred that the reinforced earth wall has been tilting at a constant rate of up to 60 mm/year, without tendency to stabilize over time. In this paper the highway pathologies, and the methods to characterize them, are described. The analyses of the probable causes and the recommended remedial actions are also presented.

RÉSUMÉ : La Direction Générale des Routes du Ministère espagnol des Transports a demandé au Laboratoire géotechnique du CEDEX une assistance technique pour l'étude d'une pathologie détectée sur la section entre les stations 12+625 et 12+860 de l´autoroute périphérique de Burgos (BU-30). Juste après l'inauguration de ce tronçon autoroutier en 2016, des fissures longitudinales sont apparues sur la chaussée droite. Ici, l'autoroute passe sur un remblai qui est contenu sur son côté droit par un mur mixte de terre armée au-dessus d'un mur d'enrochement. Les fissures ont atteint une ouverture verticale d'environ 5 à 10 cm et coïncidaient avec le plan vertical où se terminaient les bandes de renforcement du mur de terre armé existant. Pour éviter les accidents, ces fissures ont été réparées plusieurs fois par scellement, fraisage et remplacement de la chaussée, mais sont réapparues peu de temps après. L'évolution des mouvements a été contrôlée par des procédures topographiques et par des dispositifs d'auscultation (inclinomètres et déformètres de forage). Un modèle de scanner laser terrestre (TSL) a également été utilisé pour analyser les mouvements des murs, montrant une inclinaison importante de la face du mur, supérieure à 0,5 m à la crête du mur. Les résultats de la surveillance ont permis de déduire que le mur de terre armé s'inclinait à un rythme constant allant jusqu'à 60 mm/an, sans tendance à se stabiliser avec le temps. Dans cet l'article, les pathologies routières et les méthodes pour les caractériser sont décrites. Les analyses des causes probables et les mesures correctives recommandées sont également présentées.

Keywords: Reinforced wall; tilting; highway; terrestrial laser scanner.

1 DESCRIPTION OF PATHOLOGY

Just after the inauguration of this section of the BU-30 highway in 2016 (Burgos, Spain), some longitudinal cracks appeared between the stations 12+625 and 12+860 (construction stations 3+675 to 3+910) on the right carriageway (river side), Figures 1 and 2. Here, the highway runs on embankment which is contained on its right side by a reinforced earth wall that in some sections is founded on a stone wall. The cracks

reappeared soon after the various repair works carried out (consisting of milling and replacement of mixtures bituminous). At some point the cracks have reached a step of about 10 cm of height and separations between lips of up to 6 cm, which has forced to close to traffic the right lane of the right carriageway on several occasions. The location of the cracks was coincident with the vertical plane where the reinforcement strips of the existing reinforced earth wall ended.



Figure 1. Longitudinal cracks on the right carriageway.

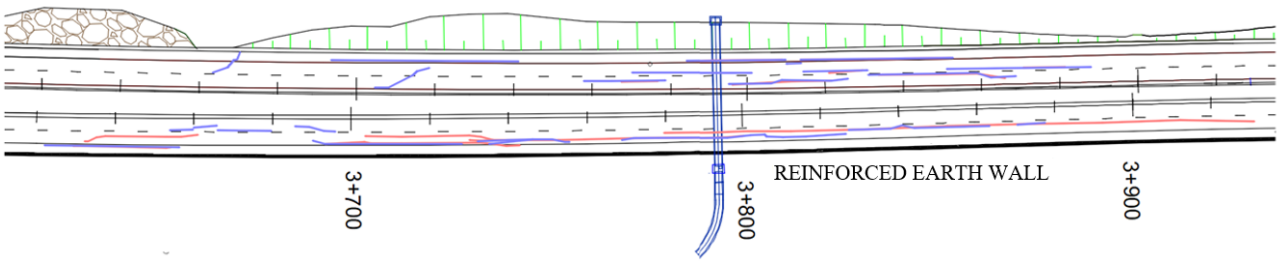

Figure 2. Plan view of the main cracks. In red, October 2019. In blue, September 2020.

The geological-geotechnical cross section of the natural ground, as in the original design project, is shown in Figure 3. The fills and walls that support the platform of the highway in the area of study sit in the lower part of a natural slope, about 90 m high and with an average inclination of 20-25º, which consists of tertiary formations, arranged according to sub horizontal strata, with alternating predominance of clayey or sandy materials.

In the affected area, the reinforced earth wall has variable heights (H) between 6.0 and 13.9 m and reinforcement strip lengths (L) that vary between 0.5· H (in the section with the highest height) and 0.67· H (therefore, between 4 and 7 m). The wall face is made up of reinforced concrete cross-shaped plates of 1.5 m side whose thickness is 14 cm (Figure 4).

The highest movements of the platform and wall occur near the station 3+800, where the embankment/wall height of the highway section is the biggest, on both roads, and also where the drainage cross culvert DCC-3 + 790 is located, see Figure 5.

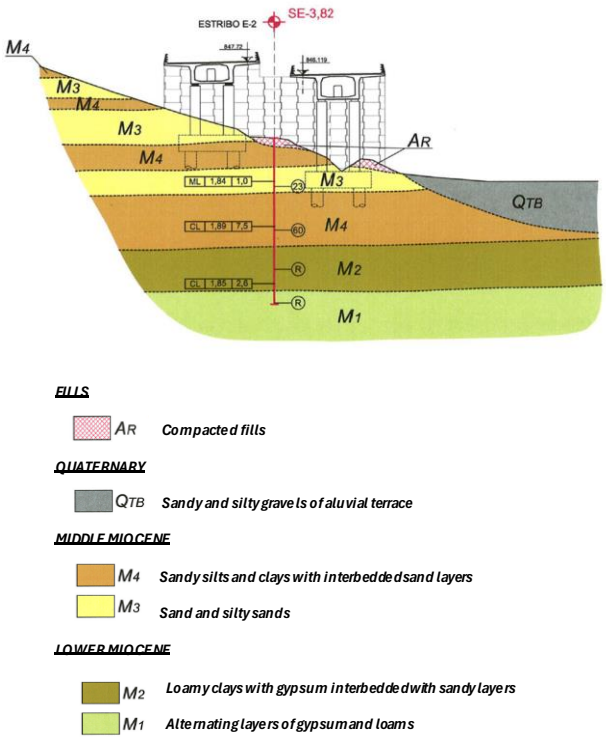

Figure 3. Geological-geotechnical cross section from the original design.



Figure 4. Lateral view of the walls and outlet of drainage cross culvert, DCC-3+790.

The DCC-3+790 consists of a concrete tube, 1.80 m in diameter, which connects both sides of the highway and seems to sit directly on the tertiary substrate. There is also a secondary tube, made of polyethylene and 0.80 m in diameter, which connects the median with the left side of DCC (mountain side inlet) through the core of the embankment fill and under the left carriageway.

Several visual inspections were carried out inside the 1.80 m tube. These inspections showed the DCC is in a general good condition, without failures or loss of alignment due to eventual settlements. This indicated that the foundation of the fill was behaving well. An important issue to note is that in rainy periods it has been observed how jets of pressurized water enter the tube through some of the joints between the tube sections, see Figure 6. This is an indication that there is an accumulation of water, and a saturation of the materials, at the base of fills, which is being evacuated in an uncontrolled manner by the aforementioned "jets".

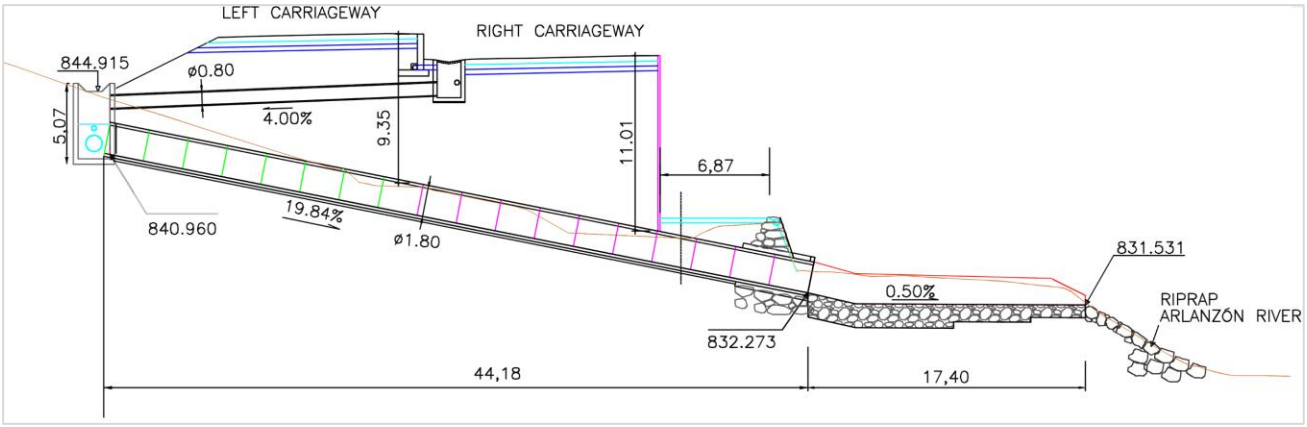

Figure 5. Cross section of the DCC-3+790.



Figure 6. Inside view of DCC-3+790 (October 2020); and view of water entering into the pipe under pressure through one of the joints during a rainy season.

With regard to the face of the reinforced earth wall, there were no significant plate breaks or anomalous joint openings, meaning that there are no significant differential settlements (or angular distortions) longitudinally along the wall. However, transversely considerable tilting of the wall can be seen with the naked eye.

Another aspect to highlight is that neither in the longitudinal vertical profile of the road nor in the barriers or road markings there are losses of alignment, or anomalous undulations, of importance. This is another indication that the pathologies experienced by the road do not produce significant differential movements in the longitudinal direction.

The evolution of movements in the area has been controlled by topographic procedures and by auscultation elements (4 inclinometers/sliding deformeters installed in boreholes drilled in the median). A terrestrial laser scanner model (TSL) has also been used to analyze the wall movements (Figures 8 to 10), showing a substantial tilting of the wall face, exceeding 0.5 m at wall crest. The TLS model showed that the wall tilting varies from 30 to 50 cm, which is equivalent to a loss of verticality of approximately 2.5% to 4%.

It has been found that the reinforced earth wall was tilting with speeds of up to 60 mm/year (wall crest

horizontal displacement) without show a tendency to stabilize over time. Settlements are also recorded, although of lesser magnitude, so it is interpreted that the movement of the wall is fundamentally horizontal.

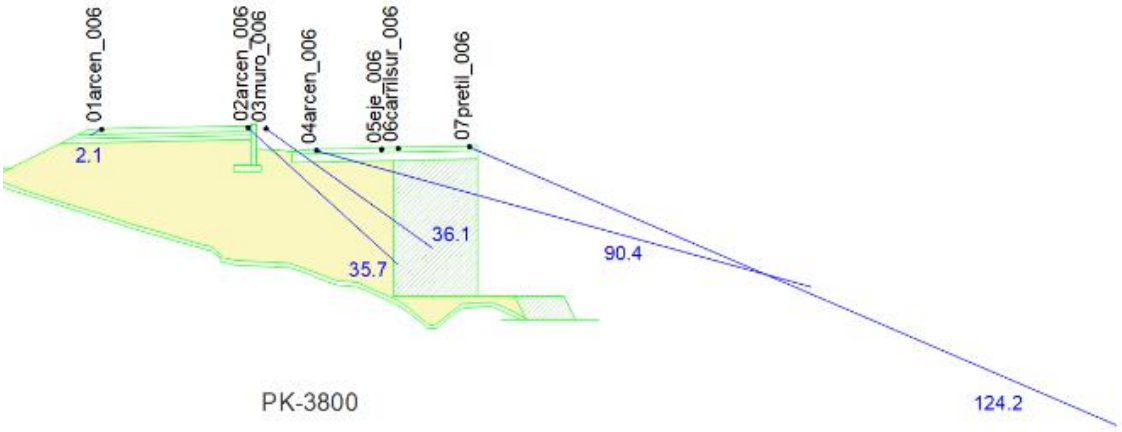

Figure 7. Transversal displacements vectors (in mm), obtained by classical topography and with a total station, between January 2019 and July 2021.



Figure 8. View of the TLS 3D model.

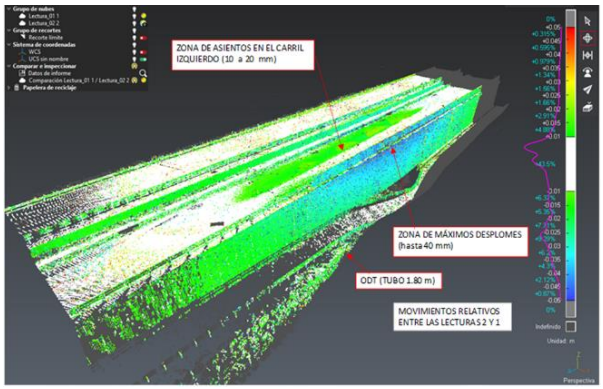

Figure 9. Relative displacements obtained by comparing TLS point clouds from model 1 (taken on October 2020) and model 2 (taken on March 2021).

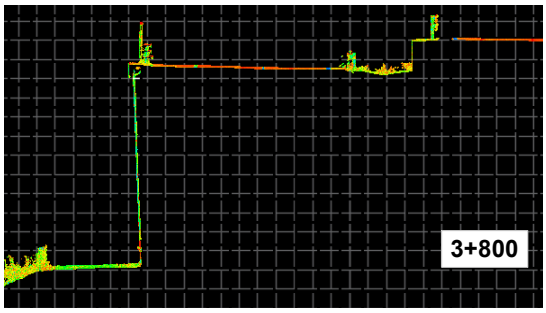

Figure 10. Cross section at station 3+800 obtained from the TLS model (grid on the images is 1 m long).

The movements and movement speeds obtained by the three procedures (TLS, topography and auscultation) have been reasonably consistent.

2 CAUSES OF THE PATHOLOGIES

It is considered that the causes of the pathologies can be the following:

- The existence of earth pressures at the back of the reinforced earth wall greater than expected due to: strength parameters (friction angle) of the retained fill lower than those considered in the design; existence of water pressures on the back of the reinforced earth fill not taken into account in the calculations; and saturation of the lower portion of retained and reinforced fill, or their foundation, by groundwater flows coming from the most pervious layers of the natural slope (sandy soils) or by leakages from the superficial drainage system.
- Inadequate construction details to avoid pavement cracking when a reinforced earth fill partially occupies the road platform (no extension of reinforcement strips in the upper zone of the reinforced earth fill until complete the whole width of the platform).

3 CORRECTIVE MEASURES

The wall has been tilting at a constant speed, that is, without showing a tendency to stabilization. The accumulated horizontal displacement observed at the wall crest ranges from 30 to 50 cm. As the wall had been tilting, at the mentioned rate, at least for around

5 years, it is considered that most of the accumulated displacement took place after construction.

Considering these circumstances, it was recommended to carry out some type of remedial actions. The measures should focus directly on the causes of the problem, that is, on reducing the pressure on the back of the reinforced earth wall and on avoiding saturation of the foundation of the retained and reinforced fill.

Therefore, it was proposed to act in two ways: improvement of strength of the retained fill and improvement of the general underground drainage. A required condition was that any remedial action should be undertaken always allowing the traffic to pass through at least one of the carriageways of the highway.

To improve the underground drainage, a longitudinal alignment of drainage wells located upstream the retained fill and the wall was proposed, see Figure 11. The wells are interconnected at their bottom, by horizontal drills with the adequate slope (2-5%), to allow the drained water to flow towards the central well. From the central well a longer and greater diameter drill hole carries all water drained by the well system to the river.

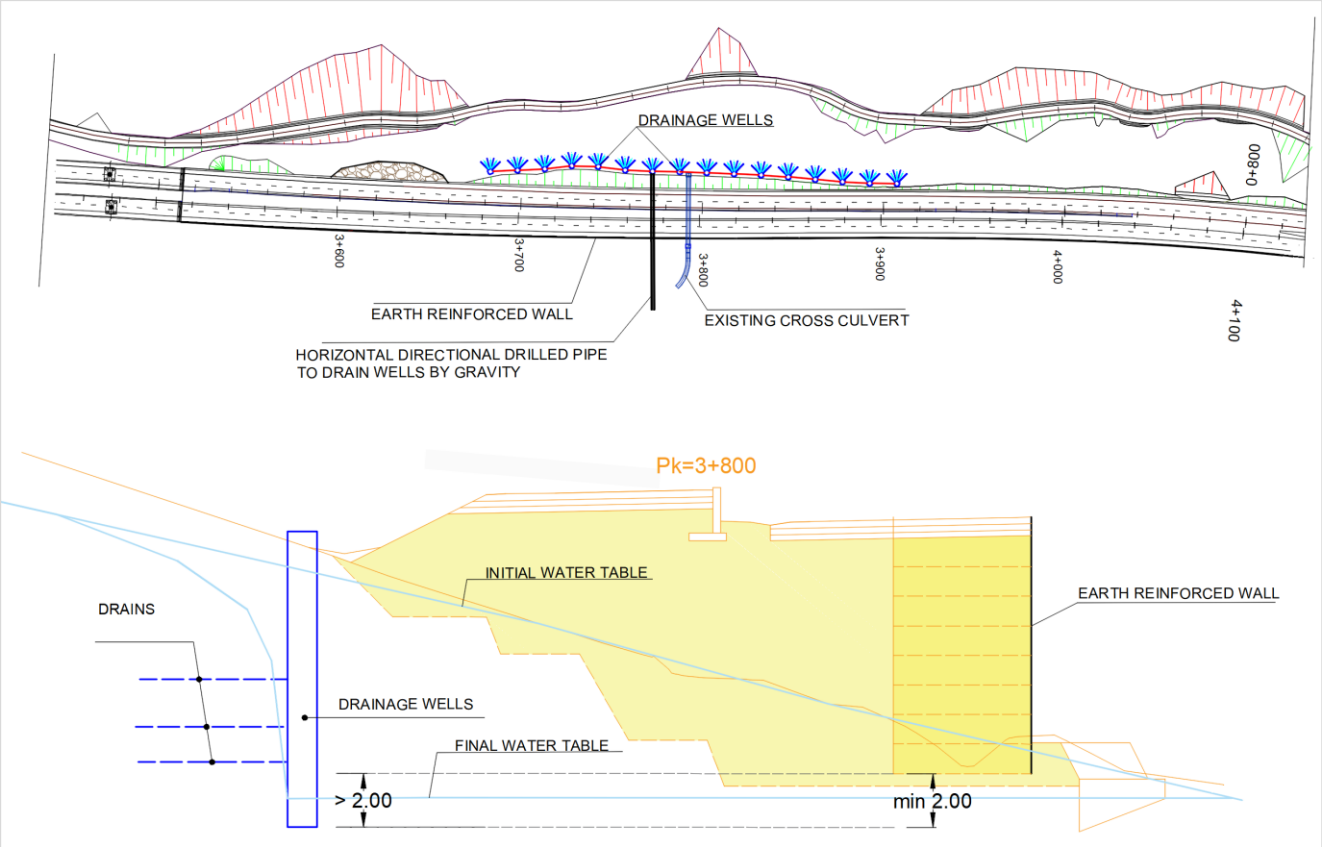

Figure 11. Schematic plan and cross section of the proposed draining wells (the water table position is an assumption).

To improve the retained backfill strength, the construction of transversal mortar (or deep mixed soil) diaphragm walls, 0.6 m thick and 7 m long, placed each 5 m in the longitudinal direction, were recommended. Each diaphragm wall module will act as a buttress of improved soil to reduce earth pressures on the wall, see Figure 12.

Finally, a reinforcement of the pavement structure was also proposed, as shown in Figure 13.

The construction works to implement these corrective measures ended in september 2022. Until now, january 2024, the inclinometer monitoring control of the wall indicates that the tilting movements have ceased. On the other hand, there are no new cracks reported on the pavement surface.

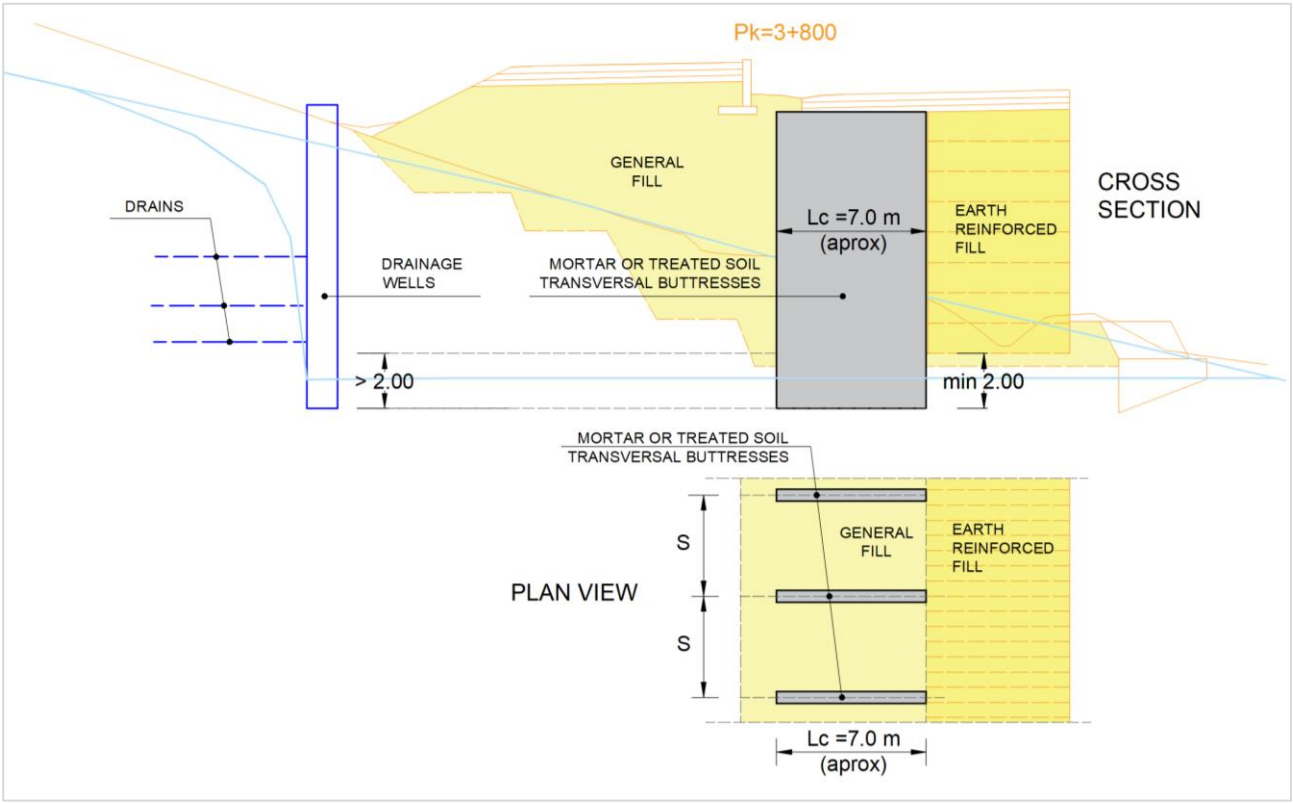

Figure 12. Schematic cross section and plan of proposed backfill improvement.

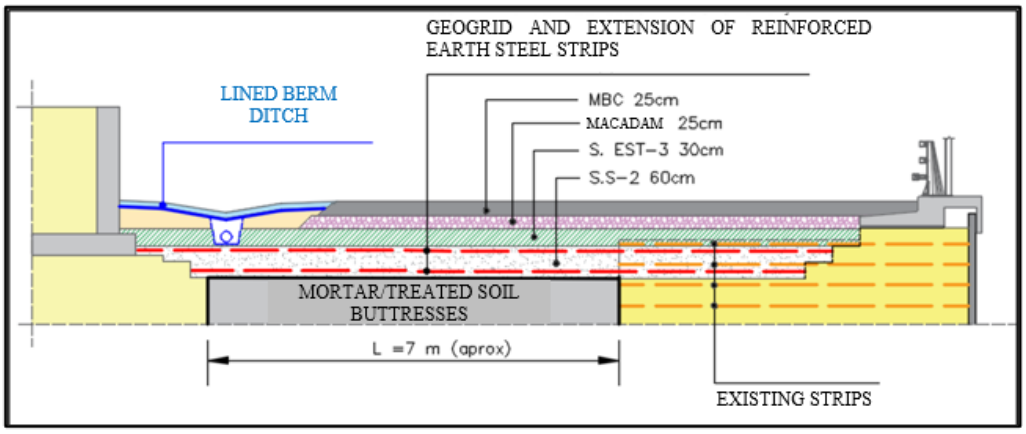

Figure 13. Cross section of proposed pavement structure.

4 CONCLUSIONS

A case of on-going tilting of a reinforced earth wall in a Spanish highway embankment has been presented. In order to analyse the problem, besides traditional monitoring system, a terrestrial laser scanner model (TSL) has also been used. It resulted very useful to analyse and quantify the wall movements. The causes of the pathology have been identified, and remedial measures have been proposed to correct the problem.

REFERENCES

ATC (2021). *Patologias en estribos y muros de suelo reforzado de puentes y estructuras de carreteras*, 1st ed., Asociación Técnica de la Carretera. Madrid, Spain.

SETRA (1994). *Les ouvrages en terre armee*, 1st ed., Service d'études tecniques des routes et autoroutes. Bagneux Cedex, France.

Proceedings of the XVIII ECSMGE 2024
GEOTECHNICAL ENGINEERING CHALLENGES
TO MEET CURRENT AND EMERGING NEEDS OF SOCIETY
© 2024 the Authors
ISBN 978-1-032-54816-6
DOI 10.1201/9781003431749-299
Open Access: www.taylorfrancis.com, CC BY-NC-ND 4.0 license

ECSMGE 24
XVIII EUROPEAN CONFERENCE ON SOIL MECHANICS AND GEOTECHNICAL ENGINEERING

Comparison between biocementation and a traditional cover solution to avoid ravines in slopes caused by water flow

Comparaison entre biocementation et une solution de couverture traditionnelle pour éviter les ravins dans les pentes causées par l'eau

R. Fernández Rodríguez*, R. Cardoso
CERIS/IST/University of Lisbon, Lisbon, Portugal

**roman.fernandez@tecnico.ulisboa.pt*

ABSTRACT: The occurrence of intense rainfalls with high erosion potential in roads is expected under a climate change scenario. Malfunction or defective discharge systems may cause downslope soil erosion through scour and runoff, and therefore it is important to increase slope resilience by adopting adequate protection solutions. This paper presents an experimental study where the effectiveness of biocementation through enzymatically induced carbonate precipitation (EICP) was investigated as an alternative to a traditional solution consisting in adopting a riprap cover. Two identical small-scale slopes were built with dry uniform grading size sand in the laboratory. The first slope was treated with enzyme and the second with a calcareous rip rap cover. Both were subjected to a water thread of 0.13 l/min simulating a culvert outflow. For the enzyme-treated slope no scour or runoff erosion have occurred under this concentrated water jet, while resistance to runoff erosion was observed but scour erosion has occurred for the slope where the traditional solution was adopted. Both tests ended when the first signs of instability appeared after saturation. The two methods have prevented runoff erosion of the slopes, but only EICP prevented scour erosion, proofing the efficiency of this treatment against ravine formation. The paper ends discussing the main practical aspects of both solutions, presenting advantages and limitations.

RÉSUMÉ: Dans le cadre du scénario de changement climatique, on s'attend à des précipitations intenses avec un fort potentiel d'érosion sur les routes. Un mauvais fonctionnement ou des systèmes d'évacuation défectueux peuvent entraîner une érosion du sol en aval par affouillement et ruissellement, et il est donc important d'accroître la résistance des pentes en adoptant des solutions de protection adéquates. Cet article présente une étude expérimentale dans laquelle l'efficacité de la biocimentation par précipitation de carbonate induite par voie enzymatique (EICP) a été étudiée en tant qu'alternative à une solution traditionnelle consistant à adopter une couverture en enrochement. Deux pentes identiques à petite échelle ont été construites en laboratoire avec du sable sec de granulométrie uniforme. La première pente a été traitée avec une enzyme et la seconde avec une couverture d'enrochement calcaire. Toutes deux ont été soumises à un débit d'eau de 0,13 l/min simulant l'écoulement d'un ponceau. Pour le talus traité à l'enzyme, aucun affouillement ou érosion par ruissellement ne s'est produit sous ce jet d'eau concentré, tandis qu'une résistance à l'érosion par ruissellement a été observée, mais une érosion par affouillement s'est produite pour le talus où la solution traditionnelle a été adoptée. Les deux essais ont pris fin lorsque les premiers signes d'instabilité sont apparus après la saturation. Les deux méthodes ont empêché l'érosion par ruissellement des pentes, mais seul l'EICP a empêché l'érosion par affouillement, ce qui prouve l'efficacité de ce traitement contre la formation de ravins. L'article se termine par une discussion sur les principaux aspects pratiques des deux solutions, en présentant leurs avantages et leurs limites.

Keywords: Slope; biocemention; riprap; ravine.

1 INTRODUCTION

Road construction often results in the creation of bare slopes. To prevent their erosion, drainage systems are designed to collect runoff water and discharge it downhill through culverts, as shown in Figure 1. However, these concentrated outflows can result in scour and ravine formation (Bochet and García-Fayos, 2004; LaMarche and Lettenmaier, 1998), leading to significant soil losses and high maintenance costs, especially in non-cohesive soils (Chehlafi et al., 2019).

A common countermeasure adopted to avoid this problem, is to cover the slope with rock or gravel blocks. This simple solution is known as riprap and acts as an energy dissipation structure (Price, 2021). The material used in riprap construction should preferably be angular and resistant to weathering, their size being determined by the velocity of water flow (Lagase e al., 2006).

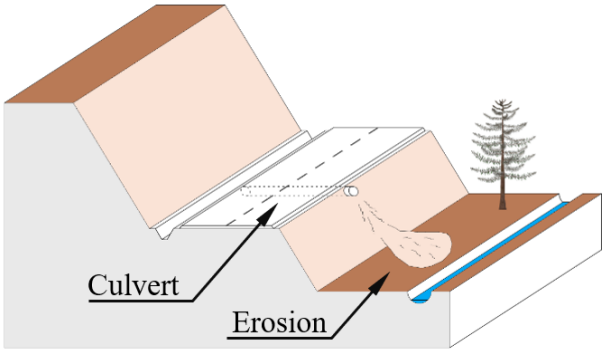

Figure 1. Slope erosion due to culvert discharge (adapted from Fu et al., 2010).

Enzyme Induced Carbonate Precipitation (EICP) is an environmentally friendly technique that can be an effective alternative to riprap, with the advantage of eliminating the visual impact of covering the slope with rocks. This technique is also known under the generic name of biocementation and is based on the use of enzyme urease that is introduced into the soil pores, together with urea ($CO(NH_2)_2$) and a calcium source (ions Ca^{2+}), to promote the precipitation of calcium carbonate ($CaCO_3$). The hydrolysis of urea (Equation 1) is 10^{14} times faster in the presence of the enzyme:

$$CO(NH_2)_2 + 2H_2O \rightarrow 2NH_4^- + CO_3^{2-} \quad (1)$$

The precipitated calcium carbonate (Equation 2) acts as a natural cement binding the soil particles together and thus increasing their strength and stiffness, while reducing permeability due to pore clogging:

$$C_a^{2+} + CO_3^{2-} \rightarrow C_aCO_3 \quad (2)$$

This paper compares these two techniques (biocementation vs. riprap). For this purpose, two small slopes were built in the laboratory. One was treated with enzymes to promote the precipitation of calcium carbonate and the other was covered with gravel to simulate a riprap. Then, both were subjected to a constant flow of water for the same period, simulating the discharge of a culvert.

2 MATERIALS AND METHODS

A commercial fine river sand with mean diameter (D_{50}) 0.3 mm, and coefficient of uniformity (C_u) of 2 was used to build the slopes. It classifies as poorly graded sand (SP) according to the Unified Soil Classification System. Its mineral composition is mainly quartz and feldspar.

For building the slopes, the sand was pre-dried in an oven and then placed carefully in a transparent methacrylate box to have a final porosity of 44%, which corresponds to the void ratio (e) 0.8. The slopes formed, with the horizontal dimension twice the vertical dimension (inclination 30º), were 15 cm high, with 30 cm long and 30 cm wide.

For the enzyme-treated slope, the treatment was carried out in two phases. In the first, 100 ml of distilled water and powdered urease enzyme solution (from the plant *Canavalia ensiformis*) was sprayed on the surface of the slope. In the second phase, 30 minutes later, 200 ml of a 0.5 M equimolar solution of urea and calcium chloride (source of calcium) and 1:10 diluted growth medium were applied. This treatment was repeated for five days. The water content was 10% before the start of the erosion test.

For the second slope, a limestone gravel with a mean diameter (D_{50}) of 4 mm and a coefficient of uniformity (C_u) of 2.2 was used to form a riprap. The soil cover was 100% in the central area of the slope, forming a layer 10 cm wide and 7 mm thick. The size of the riprap particles was compatible with laboratory scale and was tested to ensure that the water jet to be applied would not transport them, such as in real scale solutions.

During the construction of the second slope, a layer of red sand was placed under the riprap, to increase the colour contrast between the sand and the gravel, thus facilitating the observation of possible erosive phenomena.

3 EROSION TEST

3.1 Experimental setup

A water tank was used to ensure a constant water head, being the desired flow rate regulated with a tap. The flow rate of 0.13 l/min was established based on preliminary tests, which showed that this streamflow has energy enough to cause an erosion channel in less than 15 minutes when applied to an untreated slope.

The outlet pipe has a diameter of 5 mm and was positioned at a height of 1 cm above the highest part of the slope in its middle part. The duration of the test was 15 minutes for both slopes.

3.2 Results

The amount of biocement precipitated in the surface area of the enzyme-treated slope was 1.7 %. This percentage was sufficient to prevent scour erosion. Furthermore, runoff erosion was practically negligible, as can be observed in Figure 2. It is worth

to note that the permeability of the treated slope surface remained high, as water continued to infiltrate.

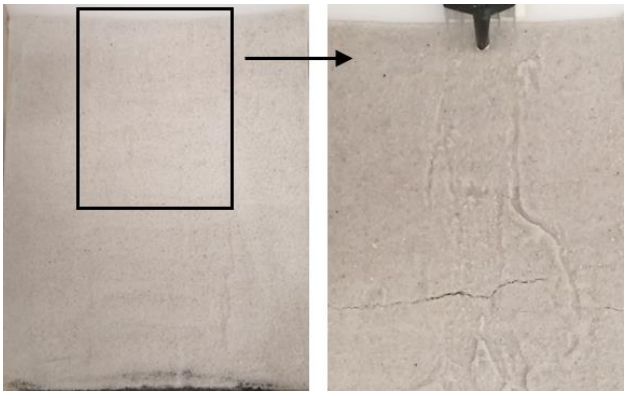

Figure 2. Enzyme-treated slope before (left) and after the test (right). Top view.

For the slope protected by a riprap, the weight of the limestone particles prevented them from being moved by the water jet, thus contributing to dissipate its energy. At the same time, this highly pervious layer acts as a drain, favouring water infiltration and reducing runoff (Li et al., 2022). However, as the test progressed, the particles under the impact zone of the water jet began to move slightly, which favoured the penetration of the water and the undermining of the soil below. This scour is evidenced during the test by the appearance of eroded sand (pink in colour) around some gravel blocks (see Figure 3).

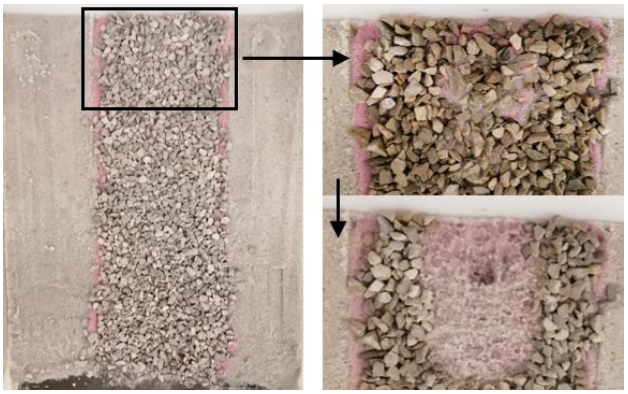

Figure 3. Riprap slope before (left) and after the test (right). Top view. Scour erosion can be seen in the area where the water discharge occurred.

Once the test was completed, the gravel blocks were removed one by one, taking care not to disturb the slope surface. Once this cover was removed, no signs of runoff erosion were visible. However, a small pit or scour of approximately 1 cm in depth can be observed in the water discharge area (see Figure 3). This is the evidence that riprap can be an effective measure to prevent runoff erosion, but it does not eliminate scour erosion.

Regardless of the effectiveness of both techniques in protecting the slope from erosion by runoff and scour, slope instability phenomena occurred in both cases. These were due to the fact that during the test, the soil becomes progressively saturated with water.

Saturation of the slopes resulted in increased water pressure and, as a consequence, reduced shear strength. In addition, once the slope was completely saturated, water started to flow through the bottom interface, between the permeable (sand) and impermeable (methacrylate) material, which also favoured the failure (Li and Mo, 2019).

Although this explanation is satisfactory for both tests, the failure developed was different in each case. In the EICP slope, tension cracks formed because the superficial layer of the slope was cemented. Once broken, this rigid layer moved with the underlying saturated sand in a manner similar to the ground movements known as soil spreading.

In the slope protected with riprap, there was a failure at the foot of the slope due to liquefaction, without the development of cracks such as those in the EICP slope.

Figure 4 shows the frontal view of both slopes at the end of the tests, where the cracks developed are visible.



Figure 4. Failure in the EICP treated (left) and riprap covered (right) slopes. Front view.

4 DISCUSSION

Many are the solutions adopted to protect slopes against erosion caused by concentrated water flow. Figure 5 presents some examples, namely the protection using projected cement, a riprap cover and the used of geotextiles with seeds to promote vegetation growth and root fixation. All these solutions can be used in sandy geological formations.

Not only the mechanical behaviour of such covers to resist to erosion mut be considered, but also their hydraulic characteristics, being both usually linked. Indeed, the adoption of a stiff solution such as when using cement requires drain installation to allow internal drainage because it is impervious. Failure in such case may be caused by the accumulation of water pressure below the protection cover. The use of rip rap

masks also introduces some stiffness, ensuring both drainage and infiltration. Failure in this case may be caused by slope surface instability caused by weight or by heavy water flow during extreme rain events.

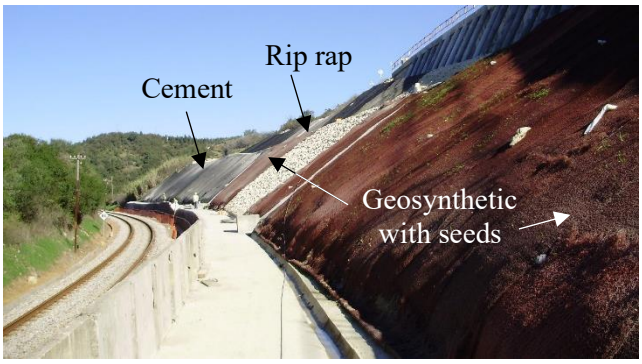

Figure 5. Several solutions adopted for slope protection (from back to front: cement projection, vegetal cover seeded in geosynthetics, gravel mask and vegetal cover seeded in geosynthetics).

It is well known the favourable contribution of vegetation for shallow slope stabilization, ensuring water infiltration. Howevwer, the vegetal cover is not continuous in the entire surface, or the roots may not be deep enough to resist to heavy water flow during extreme rain events. The entire protection of the slope area is ensured when a geosynthetic cover is installed, being this a pervious solution with very low stiffness. The drawbacks of such solution are mainly the time necessary for vegetation to grow, anchor durability and need for some maintenance.

Biocementation is a solution that joins the characteristics of all. In terms of particle cementation and consequent creation of a stiff cover, it is similar to a cement cover but with much lower stiffness than cement. The soil permeability remains high, therefore infiltration (and drainage) still can occur, as for rip rip and vegetation covers. Although further vegetation growth is limited to some species, this treatment solution offers the advantage of ensuring an homogeneous protection of the entire slope area.

5 CONCLUSIONS

The study performed at laboratory scale has shown that biocementation can be a good solution to protect slopes against erosion, introducing some stiffness but keeping the permeability of the soil. These characteristics are desirable for slope protection solutions as discussed. The adoption of a riprap cover did not performed as well because there was some scour erosion below this pervious cover. Biocementation is a promising solution, which must be applied in real cases to evaluate better its performance.

ACKNOWLEDGEMENTS

The authors would like to thank to the Foundation for Science and Technology (FCT, I.P.) of Portugal for funding through projects BIOSOIL (Ref PTDC/ECI-EGC/32590/2017) and CALCITE (Ref PTDC/ECI-EGC/1086/2022).

REFERENCES

Bochet, E., García-Fayos, P. (2004) Factors controlling vegetation establishment and water erosion on motorway slopes in Valencia, Spain, *Restor Ecol,* 12, pp. 166-174. https://doi.org/10.1111/j.1061-2971.2004.0325.x.

Chehlafi, A., Kchikach, A., Derradji, A., Mequedade, N. (2019) Highway cutting slopes with high rainfall erosion in Morocco: Evaluation of soil losses and erosion control using concrete arches, *Eng Geol,* 260:105200. https://doi.org/10.1016/j.enggeo.2019.105200.

Fu, B., Newham, L. T. H., Ramos-Scharrón, C. E. (2010) A review of surface erosion and sediment delivery models for unsealed roads, *Environ Model Softw*, 25, pp. 1-14. https://doi.org/10.1016/ j.envsoft.2009.07.013.

Lagase, P. F., Clopper, P. E., Zevenbergen, L. W., Ruff, J. F. (2006). Riprap design criteria, recommended specifications, and quality control, NCHRP Transportation Research Board, Washington DC, USA, Rep. 5682006.

LaMarche, J., Lettenmaier, D. P (1998). Forest road effects on floods flows in the Deschutes river basin, Water Resources Series University of Washintong, Washintong, USA, Rep. 158.

Li, X., Fu, S., Hu, Y., Liu, B. (2022) Effects of rock fragment coverage on soil erosion: Differ among rock fragment sizes?, *Catena*, 214:106248. https://doi.org/10.1016/j.catena.2022.106248.

Li, Y., Mo, P. (2019) A unified landslide classification system for loess slopes: A critical review, *Geomorphology*, 340, pp. 67-83. https://doi.org/10.1016/j.geomorph.2019.04.020.

Price, K. (2021) Advancing Australian Riprap Sizing Approaches, In *Digital Water: Hydrology and Water Resources Symposium*, pp. 978-979. https://search.informit.org/doi/10.3316/informit.344070779690239.

Proceedings of the XVIII ECSMGE 2024
GEOTECHNICAL ENGINEERING CHALLENGES
TO MEET CURRENT AND EMERGING NEEDS OF SOCIETY
© 2024 the Authors
ISBN 978-1-032-54816-6
DOI 10.1201/9781003431749-300
Open Access: www.taylorfrancis.com, CC BY-NC-ND 4.0 license

ECSMGE 24
XVIII EUROPEAN CONFERENCE ON SOIL MECHANICS AND GEOTECHNICAL ENGINEERING

Risk analysis of decommissioning design of tailings dams

Analyse des risques liés au projet du déclassement des barrages de stériles

J.S. Figueira, C. Mata, G. Tavares*
TPF Consultores, S.A., Lisbon, Portugal

A. Brito, J. Marcelino, L. Caldeira
Laboratório Nacional de Engenharia Civil, Lisbon, Portugal

**Goncalo.Tavares@tpf.pt*

ABSTRACT: The mining industry usually resorts to dams as tailings storage facilities, and these structures represent a significant risk to the environment and surrounding communities if inadequate solutions are implemented. Several failures of such structures have happened before resulting in disastrous consequences, which has made society aware of the need for proper governance of tailings dams based on risk assessment and safety evaluations. After the most recent tailings dam failures, the concern associated with upstream tailings dams intensified, leading, in some cases, to the need for decommissioning design of these structures in order to prevent further failures. Within the process of improving tailings management systems, risk analysis methodologies have become an important tool. This paper resorts to a set of upstream tailings dam decommissioning designs to identify key aspects related to risk management of such structures before, during and after decommissioning. The application of the Failure Modes Effects and Criticality Analysis (FMECA) allowed to identify the main risks associated with the decommissioning of the dams and to define preventive and mitigation actions as well as controls to be implemented in order to minimize the risk, consistent with the principles of Global Industry Standard on Tailings Management.

RÉSUMÉ: L'industrie minière a généralement recours à des barrages comme installations de stockage de stériles, et ces structures représentent un risque important pour l'environnement et les communautés environnantes si solutions inadéquates sont utilisez. La défaillance de telles structures s'est déjà produite et a entraîné des conséquences désastreuses, ce qui a fait prendre conscience à la société de la nécessité d'une bonne gouvernance des barrages de stériles basée sur l'évaluation des risques et de la sécurité. Après les ruptures les plus récentes des barrages de stériles, les préoccupations associées aux barrages réalisent dan méthode en amont se sont intensifiées, ce qui a conduit à la nécessité, dans certain cas, au démantèlent de ces structures afin de prévenir de futures ruptures. Dans le cadre du processus d'amélioration des systèmes de gestion des résidus, les méthodologies d'analyse des risques sont devenues un outil important. Cet article recourt à un ensemble de projets de démantèlement de barrages de stériles réalisent dan méthode en amont pour identifier les aspects clés liés à la gestion des risques de ces structures avant, pendant et après le démantèlement. L'application de l'Analyse des Modes de Défaillance, de leurs Effets et de leur Criticité (AMDEC) a permis d'identifier les principaux risques associés au démantèlement des barrages et de définir les actions et contrôles de prévention et d'atténuation à mettre en œuvre afin de minimiser le risque, conformément aux principes de la Norme industrielle mondiale sur la gestion des résidus.

Keywords: Risk analysis; decommissioning of tailings dams; tailings dam design.

1 INTRODUCTION

The mining industry has been seizing from technology evolution which made it economically feasible to mine lower-grade ores and significantly increase the excavated volumes (Piciullo et al., 2022; Bowker and Chambers, 2016), leading to significant increase on tailings production over the past 100 years. In 2010, the production of tailings by the mining industry was estimated to be 14 billion tonnes (Jones and Boger, 2012). Being the by-product of the mining activity, tailings are a mixture of granular material with significant content of metals, chemical reagents and process water from extractive industrial processes, considered to be waste after the extraction of valuable minerals, metals, mineral fuels or coal (Kossof et al., 2014). Tailings represent a hazardous material. Its composition is complex and can display dangerous characteristics (corrosive, volatile, acidic and other characteristics related to the mined material), and it has to be safely managed, for its release can pose a threat to the surrounding environment and communities. Tailings management have been done using several approaches which include riverine disposal, submarine disposal, wetland retention, backfilling, dry stacking, and storage in dams (Lottermoser, 2007). Currently, tailings are commonly stored in dams. Typically, these

dams are not built to meet full capacity, instead they follow the production and are raised as storage volume demand increases, commonly heightened upstream, centreline, or downstream. Of these three methods, the upstream raising is the cheapest (Soares et al., 2000) and represents 37% of the total existing facilities, being the most common construction raising method. Although its construction has been greatly decreasing due to its safety issues, active upstream tailings dams report higher incidence of stability problems (Franks et al., 2021).

Tailings dams are among the largest engineered structures and its management is primarily focused on risk reduction strategies, to avoid potential hazard exposure. Historically, there has been some tailings dam failures which resulted in disastrous consequences, e.g. Mount Polley (Canada, 2014), Samarco (Brazil, 2015), Brumadinho (Brazil, 2019), Luming (China, 2021) and Catoca (Angola, 2021). These ocurrences led to a renewed attention to tailings management practices and tailings dam maintenance by government and mining companies (Franks et al., 2021).

This paper highlights the importance of adoption of risk reduction strategies for managing upstream tailings dams. Based on several upstream tailings dam risk analysis regarding its decommissioning design and deconstruction processes, the intention is to identify key aspects of the risk management in decommisioning design.

2 DECOMISSIONING OF TAILINGS DAMS

At the end of available storage volume, tailings dams are either raised further or decommissioned. The decommissioning of tailings dams typically involves the rearrangement of the geometry of the structure to significantly decrease long-term stability risks and hazardous events, e.g. by creating a gentler slope, and ensuring the proper management of the water inflow, alongside with landscape remediation.

Due to the high frequency and consequences of dam failures and upstream tailings dam stability concerns, upstream raised dams have been banned in Chile (1970), Peru (2014) and Brazil (2019) (Franks et al., 2021). Moreover, after the most recent tailings dam failures, the concern associated with upstream tailings dams intensified, leading to specific attention regarding safety, monitoring and decommissioning of these structures. Furthermore, in some countries it is mandatory to decommission all the active upstream tailings dams, in order to prevent future failures. Nonetheless, the decommission of such structures is complex and requires the understanding of the risks acting on the structure before, during and after the decommission process. Additionally, it is important to involve all the stakeholders in this process, understand possible failure modes and make recommendations to prevent them.

3 KEY ASPECTS OF DECOMMISSIONING TAILINGS DAMS

Tailings dams are complex and risky, as they involve numerous risk factors that can provoke catastrophic consequences. The identification of risks and their characteristics is an important part of the system safety management (Zheng et al., 2022). By priorly identifying the failure modes and their causes, safety management of tailings dams can focus on prevention and/or mitigation of its consequences. Consequently, within the process of improving tailings management systems, including decommissioning tailings dam design, risk analysis methodologies have become an important tool (Schaffer, 2021). To identify the key aspects of decommissioning of tailings dams, the present paper resorts to a set of risk analyses previously made to several upstream tailings dams in decommissioning design phase. The analysed dams consist of internal dikes (heights between 10 and 20 m) of a big tailings dam. They were built over tailings and then heightened by the upstream method. The decommissioning design phase considered the need of deconstructing all the internal dikes and leave the main dam intact. The risk analyses were developed by using FMECA methodology (Failure mode, effects, and criticality analysis). This methodology has been widely used for risk analysis of geotechnical structures including embankment dams (Santos et al., 2008).

Decommissioning of tailings dams involves an existing structure with specific characteristics, a defined monitoring system, and a maintenance processes. The decommission is normally related with an existing failure risk, most of the times, associated with some important uncertainties regarding the tailings, the as-built structure (namely method of construction), and the possible consequences in case of failure. Naturally, the risk analyses carried out allowed the conclusion that the failure risk reduces substantially after decommissioning. However, it was verified that during the process itself, the risk could increase if the decommissioning design is not sufficiently robust and could even increase the probability of failure with respect to the situation prior to decommissioning. It was also verified that the decommissioning design must detail construction sequence for each phase, as well as to improve the

monitoring system for most critical phases that could constitute triggers for specific failure modes. By going through the risk analyses during the decommissioning design phase, it was possible to properly adapt the design to decrease the risk associate with failure.

The decommissioning design must take into account several aspects when defining the long-lasting residual structure and also the decommissioning processes to minimise/prevent failure modes and mitigate its consequences. These key aspects are presented further in the next sections.

3.1 Tailings characteristics and its vulnerability to stability problems

Being the byproduct of the mining activity, tailings have an inherent level of uncertainty regarding its properties, for example, in terms of grain size (within a certain range specific to the processing method), saturation level and chemical composition (within a certain spectrum related to the nature of the tailings and industrial process involved). These uncertainties and the heterogeneities of the material make it hard to predict its behaviour. This aspect gains relevance when tailings are used as foundation for heightening of tailings dams. Since there are uncertainties regarding its behaviour, it is risky for the integrity of the structure to be dependent on the mechanical properties of tailings and its response to loading/unloading.

Some recent upstream tailings dam failures were related to liquefaction of the tailings serving as foundation for the dam raised structure. Moreover, the state and saturation conditions of tailings, which normally are difficult to evaluate, add to the uncertainty regarding its mechanical behaviour. This implies that these uncertainties must be taken into consideration when raising a tailings dam but also when decommissioning these structures.

It is important to control and register the deposition process and the properties of the tailings during active deposition phase and create a robust archive of all the information of the structure, to create a basic knowledge and as-built information to diminish these uncertainties.

3.2 Water management

Typically, when contained in dams, tailings are disposed with high water content. Normally, taking into consideration the characteristics and chemical composition of the tailings, the water released during deposition and the contact water cannot be freely discharged in the surrounding environment. So, throughout the lifetime of the dam, there must be a water management system to control the tailings saturation, the inflow of water into the facility and its containment or its diversion to treatment plants to be discharged into the environment (if possible).

During decommissioning, the structure generally evolves from a containment barrier to a stable slope, losing its capacity to contain water. This transition must be very well designed in order to reduce the risk associated with overtopping, erosion and release of untreated/contact water.

This implies that decommissioning design must consider a solution for the management of water inflow at all stages of the decommissioning processes. Special attention must be given to the specific stage where the water inflow is no longer contained but, instead, directed downstream.

Since decommissioned dams have no longer the objective of containing tailings and water inflow, its design must consider a way to divert and/or safely conduct the inflow towards downstream. In this way, decommissioning design must incorporate long-lasting water management systems to diminish infiltration and containment of the water, including drainage structures, both internal and external, with sufficient flow capacity.

3.3 Deconstruction processes

Decommissioning of tailings dams may involve several processes with significant earthworks. When dealing with tailings, an additional concern must be taken into consideration related to the excavation rhythm and type of equipment used. Heavy and invasive vibrations can trigger liquefaction of the tailings (Liew et al., 2020) and endanger the integrity of the structure.

The construction processes should minimise the vibrations to prevent liquefaction. Since there are some limitations in simulate the behaviour of tailings to construction induced vibrations, experimentation and in situ testing may be a good approach to define specific safety criteria and assess the effect of vibration. Besides, it is important to also consider the installation of monitoring equipment to measure the tailings response to vibrations, for example, with geophones. Additionally, measuring the excess of porewater pressure (with vibrating wire piezometers, for example) and its correlation to vibrations can be important to obtain information regarding the behaviour of the tailings in response to the earthworks, especially tailings on the foundation of upstream tailings dams.

3.4 Permanent closure and monitoring

Since the decommissioning objective is to prepare the structure for a long-lasting residual state where its

conditions are maintained throughout the rest of its life, guaranteeing its structural integrity, chemical stability, and resistance to external actions (such as erosion agents, earthquakes, among others) is crucial.

The decommissioning design must take into consideration the objective of turning the structure into a long-lasting safety condition with no need of significant maintenance. In order to have confidence on the general stability of the solution throughout its lifetime, a long-lasting smart monitoring system is needed to measure the evolution of the structure characteristics (e.g., the degree of saturation, ground movement, superficial erosion, among others).

4 CONCLUSIONS

Tailings dams may present high risk of failure during the decommissioning process, if not properly designed and implemented. The risk management of these processes is complex and, based on several risk analysis of decommissioning designs of tailings dams, four main aspects were identified:

- Tailings heterogeneity and behaviour uncertainties can pose additional concerns on safety when decommissioning tailings dams and designing the long-lasting structure;
- By decommissioning tailings dams, one of the concerns is to guarantee an effective water management system. This refers to the effective water diversion to ensure that it does not accumulate in the decommissioned structure and not deteriorate its stability;
- During decommissioning, the earthworks that are involved must take into consideration the triggering of tailings liquefaction. Thus, construction rhythm and type of equipment to be used must be compatible with tailings response to load/unloading;
- The long-lasting residual structure must be considered stable and inert, and so requiring effective and resilient smart monitoring system with low maintenance needs.

Having considered these key aspects, risk and safety management on decommissioning design of tailings dams can provide crucial guidance to successful projects. Additionally, risk analyses during the design phase can significantly contribute to adapt the design and include preventive measures that can decrease failure risk.

REFERENCES

Bowker, L.N., Chambers, D.M. (2016). Root Causes of Tailings Dam Overtopping: The Economics of Risk & Consequence. *Proc. 2nd Intern. Sem. on Dam Protection Against Overtopping*, Colorado, USA, 7-9 September 2016.

Franks, D.M., Stringer, M., Torres-Cruz, L.A., Baker, E., Valenta, R., Thygesen, K., Matthews, A., Howchin, J., Barrie, S. (2021). Tailings facility disclosures reveal stability risks. *Sci. Rep.* 11, 5353. https://doi.org/10.1038/s41598-021-84897-0.

Jones, H., Boger, D.V. (2012). Sustainability and waste management in the resource industries. *Ind. & Engin. Chemistry Research*, 51: 10057-10065. https://doi.org/10.1021/ie202963z.

Kossof, D., Dubbin, W.E., Alfredsson, M., Edwards, S.J., Macklin, M.G., Hudson-Edwards, K.A. (2014). Mine tailings dams: Characteristics, failure, environmental impacts, and remediation. *Applied Geochemistry*, 51: 229-245. https://doi.org/10.1016/j.apgeochem.2014.09.010.

Liew, M., Xiao, M., Liu, S., Rudenko, D. (2020). In Situ Seismic Investigations for Evaluating Geotechnical Properties and Liquefaction Potential of Fine Coal Tailings. *Jour. of Geotechnical and Geoenvironmental Engineering*, 146 (5). https://doi.org/10.1061/(ASCE)GT.1943-5606.0002228.

Lottermoser, B. (2007). *Mine Wastes: Characterization, Treatment and Environmental Impacts*. Springer, Berlin, Heidelberg, New York.

Piciullo, L., Storrosten, E.B., Liu, Z., Nadim, F., Lacasse, S. (2022). A new look at the statistics of tailings dam failures. *Engineering Geology*, 303. https://doi.org/10.1016/j.enggeo.2022.106657.

Santos, R., Caldeira, L., Serra, J. (2008). Case Study of an application of FMEA/FMECA to a Tailing Dam. Sociedade Portuguesa de Geotecnia, *Geotecnia,* 114: 113-142. https://doi.org/10.14195/2184-8394_114_6.

Schaffer, H.L., Beier, N.A., Macciotta, R. (2021). A Failure Modes and Effects Analysis Framework for Assessing Geotechnical Risks of Tailings Dam Closure. *Minerals* 2021, 11, 1234. https://doi.org/10.3390/min11111234.

Soares, L., Arnez, F.I., Hennies, W.T. (2000). Major causes of accidents in tailing dam due to geological and geotechnical factors. In: *Mine Planning and Equipment Selection*, 1st edition. Routledge, London, UK.

Zhen, Z., Wu, X., Ma, B. et al. (2022). Propagation network of tailings dam failure risk and the identification of key hazards. *Sci. Rep.* 12, 5580. https://doi.org/10.1038/s41598-022-08282-1.

Proceedings of the XVIII ECSMGE 2024
GEOTECHNICAL ENGINEERING CHALLENGES
TO MEET CURRENT AND EMERGING NEEDS OF SOCIETY
© 2024 the Authors
ISBN 978-1-032-54816-6
DOI 10.1201/9781003431749-301
Open Access: www.taylorfrancis.com, CC BY-NC-ND 4.0 license

ECSMGE 24
XVIII EUROPEAN CONFERENCE ON SOIL MECHANICS AND GEOTECHNICAL ENGINEERING

Comparison of floating and end-bearing pile wall barriers for tunnelling in layered soil

Comparaison des barrières de parois de pieux flottants et porteurs pour le creusement de tunnels dans un sol stratifié

A. Franza*
Aarhus University, Aarhus, Denmark
**anfr@cae.au.dk*

ABSTRACT: The construction of an embedded pile wall between the excavation and the foundation, before tunnelling, is a possible mitigation measure against excessive movements. This paper presents a three-dimensional interaction model, using the two-stage approach, the layered half-space theory, and the beam theory for the barrier, to study the efficiency of pile walls in layered grounds. In particular, a two-layer undrained ground model is considered which is key to capturing the fundamental differences between barriers of floating and end-bearing piles (as long as the approximation of linear soil behaviour applies). Results illustrate that, when possible, end-bearing barriers (with tips embedded in stiffer bottom layers) should be preferred to floating pile walls with their tips embedded below the tunnel invert depth to maximise the reduction of surface and subsurface settlements; contrarily, the effects of the barrier on lateral ground movements are minor for both floating and end-bearing barriers.

RÉSUMÉ: La construction d'un mur de pieux encastrés entre l'excavation et la fondation, avant le creusement du tunnel, est une mesure possible d'atténuation contre les mouvements excessifs. Cet article présente un modèle d'interaction tridimensionnel utilisant l'approche en deux étapes, la théorie du demi-espace en couches et la théorie des poutres pour la barrière, afin d'étudier l'efficacité des murs de pieux dans des terrains stratifiés. En particulier, un modèle de sol à deux couches non drainé est considéré, ce qui est essentiel pour saisir les différences fondamentales entre les barrières de pieux flottants et celles à appui (tant que l'approximation du comportement linéaire du sol s'applique). Les résultats montrent que, lorsque c'est possible, les barrières à appui (avec leurs pointes encastrées dans des couches inférieures plus rigides) devraient être préférées aux murs de pieux flottants dont les pointes sont encastrées sous la profondeur du tunnel pour maximiser la réduction des tassements en surface et sous la surface. En revanche, les effets de la barrière sur les mouvements latéraux du sol sont minimes pour les barrières flottantes et à appui.

Keywords: Tunnelling; ground movements; mitigation; barrier; pile wall.

1 INTRODUCTION

The excavation of tunnels can detrimentally affect near foundations of buildings, monuments, and infrastructure. Embedded barriers, either pile or diaphragm walls, are a passive, low-cost, low-impact mitigation measure of tunnelling-induced movements.

The use of embedded barriers has been successfully tested in important tunnelling projects in the urban environment (Di Mariano et al. 2007; Losacco et al. 2019). While the underlying mechanisms governing their behaviour have been thoroughly investigated for uniform soil (Bilotta and Russo 2001; Ledesma and Alonso 2017; Song et al. 2023), Franza et al. (2021a) indicated substantial differences in the barrier performance in layered ground (Di Mariano et al. 2007; Rampello et al. 2019). Despite recent analytical studies considering the relative soil stiffness between shaft and tip of piles (Cao et al. 2022), yet there is no design guideline to distinguish between floating and end-bearing pile barriers. For instance, the barrier's efficiency in reducing settlements is currently only related to the embedment of the barrier beneath the tunnel invert level (e.g. Ledesma and Alonso 2017).

This paper studies the shielding mechanism of tip-bearing and floating walls in a two-layered clay deposit using both a three-dimensional linear-elastic two-stage continuum-based interaction model. A parametric study quantifies the barrier's mitigation effects in terms of vertical and horizontal displacement reduction. Finally, the conclusions discuss the implications of linear elasticity in the design context.

2 STUDIED SCENARIOS

Figure 2 summarises the considered tunnelling and barrier scenarios in undrained soil. The study investigates a tunnel with a radius R =5 m and axis depth H = 15 m being excavated into three possible ground cases: namely, *case U* for uniform soft clay; *case S* for a stratigraphy consisting of a soft clay up to 25 m above a stiff clay layer (interface depth H_i = 25 m, giving H_i/H = 1.7); *case D* in which the stiff clay is deeper than Case S and located at the depth of 35 m (interface depth H_i = 35 m, giving H_i/H = 2.3). For all cases, the bedrock is 90 m below the surface. The soft clay has a Young's modulus E_s = 7.5 MPa whereas E_s = 300 MPa for the stiff clay, giving a stiffness ratio of 40 between the strata of the layered cases. For both clayed grounds, undrained conditions are considered (Poisson's ratio ν_s = 0.5).

Barriers of 11 bored reinforced concrete piles are analysed with Young's modulus E_p = 30 GPa, diameter d_p = 1 m, spacing in the tunnel longitudinal direction of S_p = 2 m (S_p/d_p = 2), an offset from the tunnel centreline of X_w =7.5 m (X_w/H = 0.5), and all having a tip level below the tunnel depth H. These tip locations are considered ($L_p > H$) because piles adjacent to and extending below the tunnel lead to efficient protective actions. To investigate the impact of layered grounds on the barrier performance, three possible embedment depths are considered, L_p = 22 m, 30 m, 40 m ($L_p/H \approx$ 1.3, 2.0, 2.7) to cover a variety of floating and end-bearing piles. In particular, floating piles are entirely located in a uniform soil stratum (case U or cases S and D with $L_p < H_i$) while end-bearing piles have their tip embedded in the stiffer bottom layer (cases S and D with $L_p > H_i$).

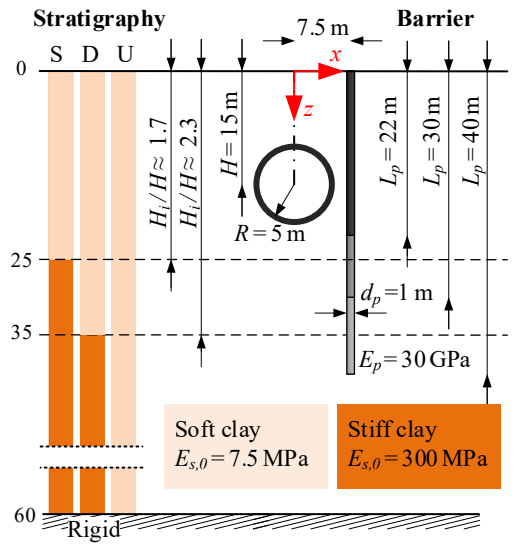

Figure 1. Scenarios of the parametric study.

3 INTERACTION MODEL

The COMPILE model is adopted for the linear elastic continuum-based two-stage analysis of tunnel-soil-barrier interaction (Franza et al. 2021a; 2021b). It allows the analysis of the soil-pile foundation interaction induced by ground movements in either homogeneous or layered ground.

As displayed in Figure 2, this interaction model accounts for the three-dimensional geometry of a pile row aligned along the tunnel longitudinal direction. This model assumes elastic Euler-Bernoulli beams for piles, thus considering pile axial vertical, horizontal, and rotational degrees of freedom. The homogeneous or layered isotropic half-space (referred to as a *continuum*) is adopted for the ground, characterised by Young's modulus $E_{s,i}$ and Poisson's ratio $\nu_{s,i}$ of each stratum. This is done by computing the flexibility functions of the soil (i.e. describing the soil displacements to loads in the three directions (x, y, z) along the pile axes) from integration at the pile boundary, without accounting for the presence of the tunnel. In the elastic solution, perfect compatibility is assumed between the pile axes and the half-space. As detailed by Franza et al. (2023), these functions are used to describe pile-soil interaction, pile-soil-pile interaction, as well as the shielding effect of the barrier on tunnelling-induced movements (the latter to propagate the local variation in displacements induced by the barrier across the half-space).

In this model the excavation is modelled using greenfield ground movements; considering steady-state conditions, the analytical displacement field of Loganathan and Polous (1998) for tunnelling in clay is adopted, as the tunnel invert is distant from the bedrock or stiff clay.

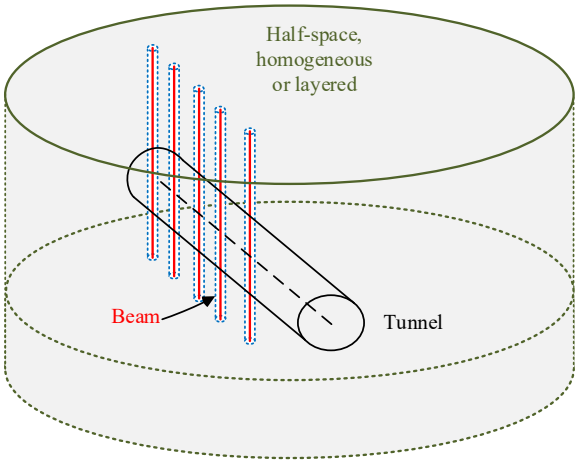

Figure 2. Elements of the three-dimensional interaction model.

4 RESULTS

Figures 3–5 show the results of the parametric study consisting of nine analyses (three barriers with $L_p/H = [1.3; 2.0; 2.7]$ and at an offset $x_w/H = 0.5$, three ground condition). Greenfield movements (GF) are compared with soil–structure interaction elastic results (SSI EL). As the interaction model is three-dimensional, results are at the transverse plane $x - z$ located at the centre of the barrier (in the tunnel longitudinal direction), which is of greatest interest. In particular, sub-plots (a) and (b) show horizontal and vertical displacements at two horizons (surface and subsurface at mid-depth to the tunnel axis), respectively; sub-plots (c) and (d) display, respectively, the horizontal and vertical displacements along the vertical at an offset of 1 pile diameter behind the barrier (for a normalised offset from the tunnel centreline $x/H = (x_w + d_p)/H = 0.57$). In the latter plots, a dashed line is used to indicate the interface depth H_l between soft and stiff clays. Also, displacement results are normalised by $u_{norm} = \Delta V/(\pi H) = V_{l,t}R^2/H$, where ΔV is the ground loss while $V_{l,t}$ the tunnel volume loss (as discussed by Franza et al. (2021a) to focus on the variation in the shape of the displacement field).

Results at surface and subsurface horizons indicate that the floating barriers have a limited capability to reduce settlements (both for the uniform soil case U, as well as for the layered cases S and D), whereas nearly null settlements are obtained behind the wall for barriers embedding in the stiff bottom later. Interestingly, the reduction in settlements extends to both sides of the barrier (consistently with previous analytical elasticity-based works). Contrarily, for all types of barriers, shielding of tunnelling-induced horizontal movements is minimal. Finally, for both pile types, note that settlements are reduced across the entire surface and subsurface horizons (i.e. both behind and on the front sides), as the pile-induced reduction in the greenfield settlement propagates according to the half-space flexibility functions.

The vertical *local wall efficiency* η_w is considered, defined as the complementary to unity of the relative reduction in the ground settlement behind the barrier (at $x/H = 0.57$). For floating barriers with tip at invert level ($L_p/H = 1.3$) the local efficiency is limited to 50–70% across all cases, whereas the embedment of end-bearing piles in the stiff clay layer determines the greatest efficiency (nearly 100%). Therefore, engineers should consider in design if the embedment of the pile tips into stiff deep layers (when present) could improve the barrier performance, as a function of the ratio between the depths of the tunnel invert and stiff layer.

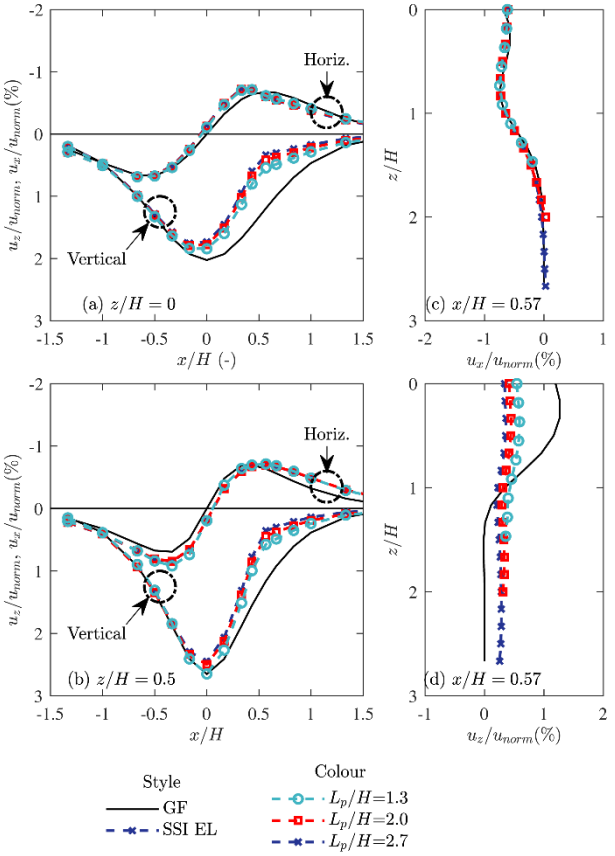

Figure 3. Effects of the barrier embedded in the uniform soil (case U) on surface and subsurface ground displacements.

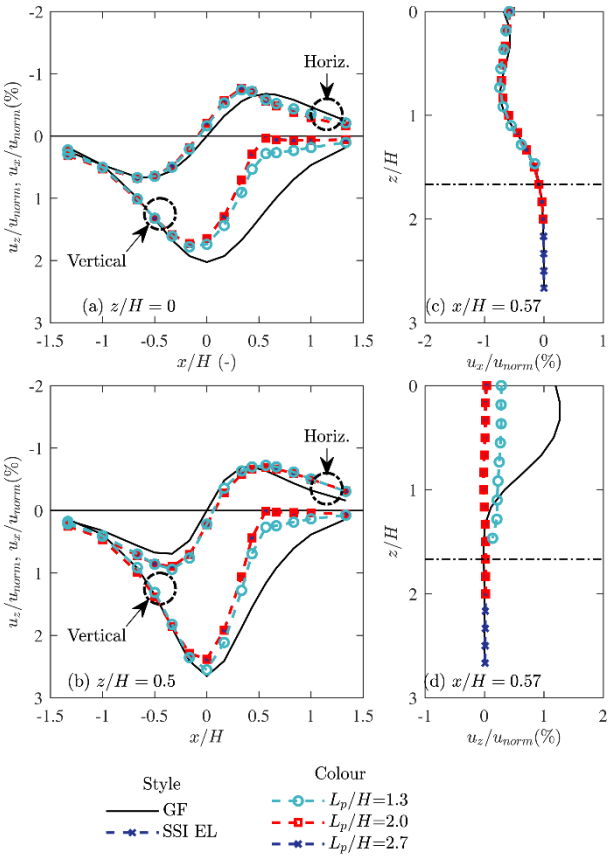

Figure 4. Effects of the barrier embedded in the layered soil (case S) on surface and subsurface ground displacements.

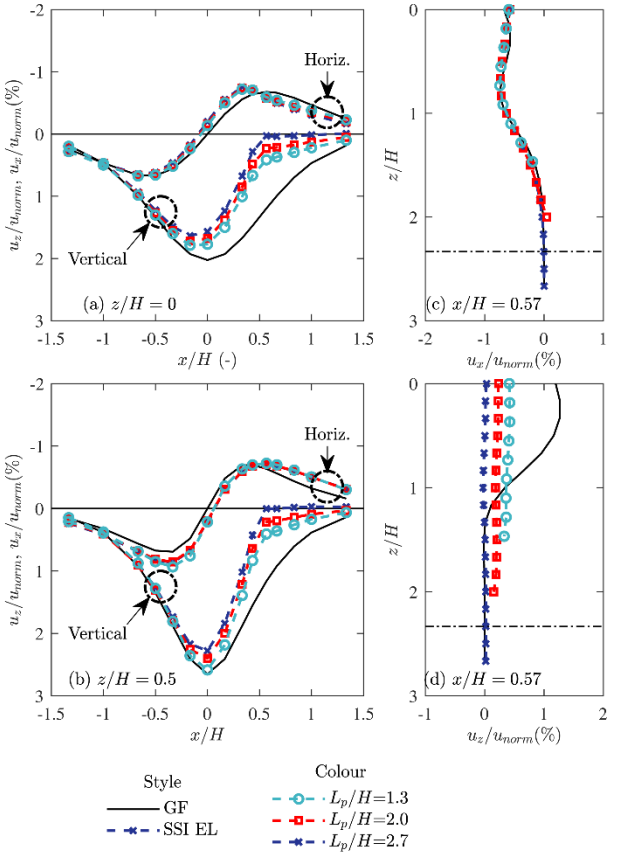

Figure 5. Effects of the barrier embedded in the layered soil (Case D) on surface and subsurface ground displacements.

5 CONCLUSIONS AND DISCUSSION

This paper presented an elasticity-based study of floating and end-bearing pile wall barriers next to a new tunnel in undrained layered soil. The following conclusions are drawn.

End-bearing barriers nearly prevented tunnelling-induced settlements behind the barrier (with local efficiency > 95%). On the other hand, when there is a significant distance between the stiff layer and the barrier tip, floating barriers extending up to or below the tunnel invert could only approximately halve the tunnelling-induced settlements.

For both pile types, as the soil behaviour is linear elastic, ground settlements were reduced both behind and on the front sides. However, literature results indicated that this mechanism may not apply when soil yielding plays an important role. Ongoing research is addressing this aspect.

Both end-bearing and floating barriers had a small shielding action on horizontal movements, despite the high bending stiffness of the considered piles. Therefore, the embedment in a stiff deep layer may not be beneficial if the aim is to limit horizontal ground movements.

REFERENCES

Bilotta, E., and Russo, G. (2011). Use of a line of piles to prevent damages induced by tunnel excavation. *Journal of Geotechnical and Geoenvironmental Engineering*, 137(3): 254–262. https://doi.org/10.1061/(ASCE)GT.1943-5606.000042.

Cao, L., Chen, X., Shen, X., Zhang, D., Su, D., and Fang, H. (2022). Theoretical analysis of the barrier effect of embedded isolation piles on tunneling-induced vertical ground displacements. Computers and Geotechnics, 144: 104609. https://doi.org/10.1016/j.compgeo.2021.104609.

Di Mariano, A., Gesto, J.M., Gens, A., and Schwarz, H. (2007). Ground deformation and mitigating measures associated with the excavation of a new Metro line. *Proceedings of the XIV ECSMGE*.

Franza, A., Losacco, N., Ledesma, A., Viggiani, G.M.B., and Jimenez, R. (2021a). Protecting surface and buried structures from tunnelling using pile walls: a prediction model. *Canadian Geotechnical Journal*, 58(10): 1590–1602. https://doi.org/10.1139/cgj-2020-0476.

Franza, A., Zheng, C., Marshall, A. M., and Jimenez, R. (2021b). Investigation of soil-pile-structure interaction induced by vertical loads and tunnelling. *Computers and Geotechnics*, 139: 104386. https://doi.org/10.1016/j.compgeo.2021.104386.

Ledesma, A., and Alonso, E.E. (2017). Protecting sensitive constructions from tunnelling: the case of World Heritage buildings in Barcelona. *Géotechnique*, 67(10): 914–925. https://doi.org/10.1680/jgeot.SiP17.P.155.

Losacco, N., Romani, E., Viggiani, G. M. B., and Di Mucci, G. (2019). Embedded barriers as a mitigation measure for tunnelling induced settlements: A field trial for the Line C in Rome. *Proceedings of the WTC 2019*. https://doi.org/10.1201/9780429424441-618.

Rampello, S., Fantera, L., and Masini, L. (2019). Efficiency of embedded barriers to mitigate tunnelling effects. *Tunnelling and Underground Space Technology*, 89: 109–124. https://doi.org/10.1016/j.tust.2019.03.027.

Song, G., Xu, J., and Marshall, A. M. (2023). Numerical study on the effect of protective wall depth in reducing structure deformations caused by tunnelling. *Computers and Geotechnics*, 158: 105374. https://doi.org/10.1016/j.compgeo.2023.105374.

Proceedings of the XVIII ECSMGE 2024
GEOTECHNICAL ENGINEERING CHALLENGES
TO MEET CURRENT AND EMERGING NEEDS OF SOCIETY
© 2024 the Authors
ISBN 978-1-032-54816-6
DOI 10.1201/9781003431749-302
Open Access: www.taylorfrancis.com, CC BY-NC-ND 4.0 license

ECSMGE 24
XVIII EUROPEAN CONFERENCE ON SOIL MECHANICS AND GEOTECHNICAL ENGINEERING

A holistic risk sensitivity analytical approach for assessing flood protection infrastructure

Une méthode globale d'analyse des risques pour évaluer les infrastructures de protection contre les inondations

H.K. Fung, V. Nyambayo*
AtkinsRéalis, Epsom, United Kingdom

**vincent.nyambayo@atkinsrealis.com*

ABSTRACT: Many UK regions are flood-prone, with thousands of kilometres of flood defences having been installed to protect communities and infrastructure. Failure of flood defences usually results in huge socio-economic costs and occasionally human life. Since asset owners have limited resources to maintain infrastructure health, they often prioritise renewal and maintenance to assets that are nearing their 'end of life' based on risk analysis. This paper presents a methodology that was used to holistically evaluate the residual life of an existing 400m anchored sheet pile flood defence wall along a major river in UK. The approach included sensitivity analyses to understand risks more broadly and enabled further investigations or planned works to be informed, with awareness of how activities would impact on budget and programme constraints. Studies by previous consultants had concluded that the wall no longer had residual life. Sensitive factors which affect the anchor and sheet pile stability were identified, with the most sensitive factors being combined into models which represent the current and potential future conditions of the wall. A decision tree was then created, combining the critical sensitivity scenarios with the decision options which led to proportionate responses. The resultant benefits enabled the client to optimise resource deployment across their flood defence portfolio.

RÉSUMÉ: De nombreuses régions du Royaume-Uni étant sujettes aux inondations, des milliers de kilomètres de dispositifs de protection contre les inondations ont été installés pour protéger les communautés et les infrastructures. L'échec des défenses contre les inondations entraîne généralement d'énormes coûts socio-économiques et parfois des pertes humaines. Les propriétaires d'actifs disposant de ressources limitées pour maintenir les infrastructures, ils donnent priorité au renouvellement et à l'entretien des actifs proches de leur « fin de vie », selon les analyses de risques. Cet article présente une méthodologie utilisée pour évaluer de manière globale la durée de vie résiduelle d'un mur de protection contre les inondations en palplanches ancrées de 400 m, le long d'une rivière principale au Royaume-Uni. Des analyses de sensibilité ont permis de comprendre les risques de manière plus générale, et de permettre des enquêtes plus approfondies ou des travaux organisés, en tenant compte de l'impact des activités sur les contraintes budgétaires et de planification. Des études précédentes avaient conclu que le mur n'avait plus de durée de vie résiduelle. Les facteurs sensibles qui affectent la stabilité des ancrages et des palplanches ont été identifiés, les plus sensibles étant combinés dans des modèles représentant les conditions actuelles et futures potentielles du mur. Un arbre de décision a ensuite été créé, combinant les scénarios de sensibilité critique avec les options de décision qui ont conduit à des réponses proportionnées. Les avantages issus de cette étude ont permis au client d'optimiser le déploiement des ressources dans son portefeuille de défense contre les inondations.

Keywords: Sensitivity analysis; flood defence; decision tree; WALLAP.

1 INTRODUCTION

This paper demonstrated the application of a novel holistic risk sensitivity analytical approach for assessing the health of infrastructure asset, with an example of a flood protection sheet pile located in the UK. This differs from the traditional deterministic approach that only considers the central most likely case.

The flood defence is in South West England, UK. Following a long history of flooding recorded in the 1980s, a steel sheet pile wall with a reinforced concrete upstand and anchor was constructed in 1992 to protect properties along the riverbank. The wall is 400m long with a maximum retained height of 2.3m. A typical cross section is shown in Figure 1.

Previous studies and condition inspections had been carried out to investigate the residual life of the flood defence wall. Inspections identified possible leakages and extensive corrosion on the exposed riverward steel, which raised a concern regarding stability of the sheet pile wall.

The client requested the undertaking of additional studies prior to any further inspection, maintenance or

anchor lift off tests suggested in previous report recommendations by other consultants. The scope included a sensitivity analysis of factors affecting the stability of the wall, in order to understand the likely stability and risks associated with various possible scenarios. A decision tree was produced to inform the risk assessment to ensure that proportionate measures would be identified taking into consideration the safety, cost, and other key factors.

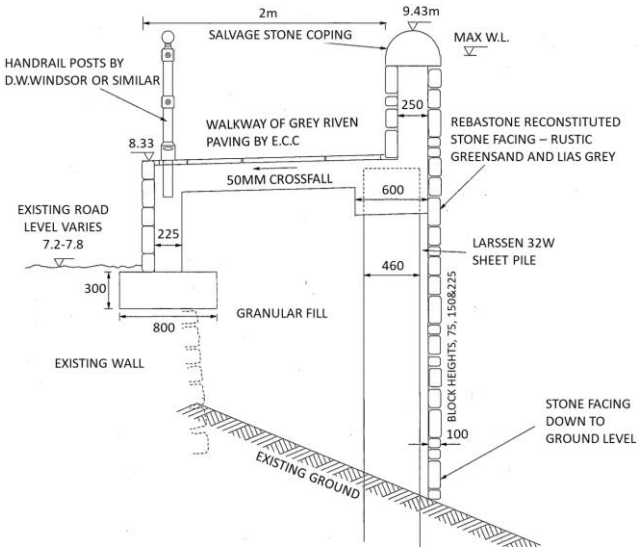

Figure 1a. As-built drawing showing typical cross section.

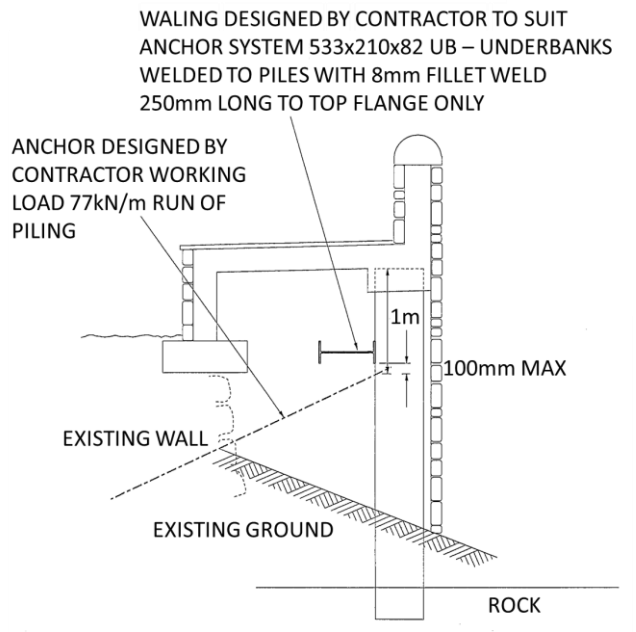

Figure 1b. As-built drawing showing anchorage details.

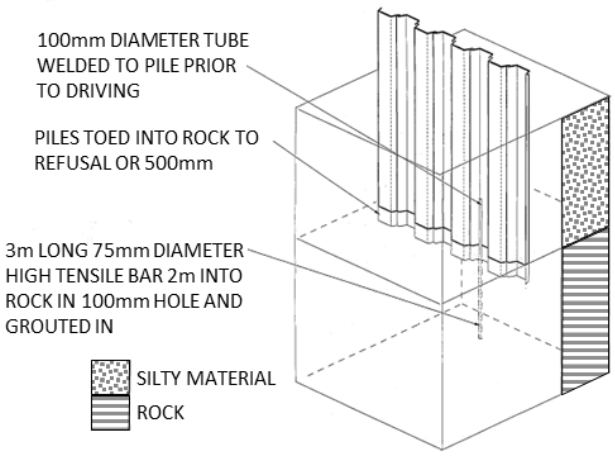

Figure 2. As-built drawing showing the sheet pile details.

2 METHODOLOGY

The following ground model was adopted in the sensitivity analyses:

Table 1. Ground model adopted in WALLAP.

Stratum	Top of Strata (m AOD)
Made Ground	+7.23
Alluvium	+4.93
Conglomerate	-0.07

2.1 Sensitivity Analyses

This study utilizes uses the limit state equilibrium method, as implemented in WALLAP version 6.06. A series of sensitivity analyses were carried out to understand and assess the consequences of different scenarios, based on the available as-built drawings. The presumed construction sequence was modelled in WALLAP (Borin, 2010) as follows:

i) insert Larssen 32W pile sheet piles;
ii) add Made Ground granular fill up to the elevation of the anchors;
iii) insert anchor force, setting the head plates into the sheet piles and adding pre-stress;
iv) complete the filling of the Made Ground to just under the pavement elevation.

Steel properties were adopted from relevant guidance (ArcelorMittal, 2008), with the loading regime being conceptualised as shown in Figure 3.

2.2 Selected sensitivity case types

A central case (Scenario A below) was based on historic design drawings.

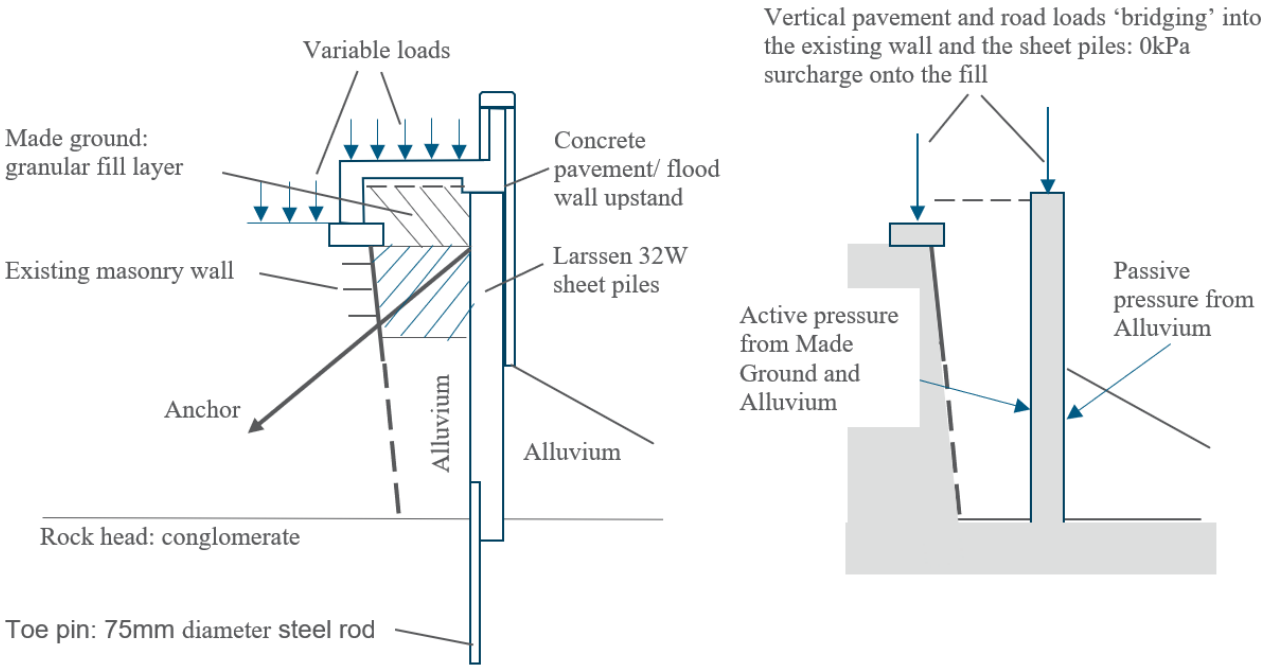

Figure 3. Conceptualised cross section.

In addition, the following cases were also modelled, varying the sensitivity parameters as specified:

- A Base model, as shown in as-built drawings
- B Riverward Alluvium berm at +3.26m AOD and steepened 1 in 1.5 to assess the limiting condition
- C Riverward Alluvium reduced to +1.83m AOD with an assumed gradient of 1 in 3.6
- D Riverward Alluvium reduced to +1.83m AOD with a gradient of 1 in 3.5 to test for the limit of stability (critical factor of safety (FoS) case)
- E Base model except alluvium friction angle adjusted +/- 2 degrees
- F Same as Case C but with extensive corrosion of the sheet piles
- G Base model except raised groundwater on landward side, and reduction in level of Alluvium in Riverside, berm gradient was set in 1 in 3
- H Base model except varying toe fixity and embedment
- I Base model except the riverward Alluvium is reduced to +2.20m AOD and no rod.
- J Base model except assuming pile refusal at top of rock head causing the rod to be lifted
- K Loss of anchor and riverward Alluvium

3 RESULTS

The results, calculated in accordance with Eurocode guidance (British Standards Institution, 2013) and the accompanying National Annex (British Standards Institution, 2009), demonstrated that several mechanisms exist by which the modelled wall section might become unstable, as shown in the table below:

Table 2. WALLAP result ranges for each case type.

Case Type	Factor of Safety	Bending moment (kNm/m)	Shear Force (kN/m)	Anchor Force (kN)	Maximum deflection (mm)
A	2.172	56	27	196	8
B	1.086	156	107	386	16
C	1.012	170	121	406	17
D	0.996	No results – wall stability failure			
E	2.075 to 2.273	55 to 57	23	196	8
F	1.023	172	68	407	19
G	1.012	241	107	646	27
H	1.330 to 2.484	17 to 63	4 to 6	129 to 203	8 to 25
I	1.066	160	64	392	23
J	1.045	81	39	265	16
K	1.021	83	24	No anchor	51

3.1 Overview of Results

Various scenarios have differing levels of probability and different outcomes for wall stability, including structural failure or excessive deflection. The relative probabilities of each scenario are determined qualitatively, based on literature and engineering judgment (Burland, 1987). The implications from the sensitivity cases modelled are listed below:

Low likelihood scenarios

- Case G - extreme retention of elevated groundwater on the landward side combined with riverward Alluvium at +2.75m AOD can exceed the designated strength of the anchor, leading to only marginal stability in the model. This level of lag is considered very low probability, given the granular fill used behind the upper part of the wall;
- Case H - toe fixity and embedment changes are only important to stability when combined with a loss of Alluvium on the riverward side. Loss of toe fixity can be identified as a large deflection along the bank elevation;
- Case K - failure of a single anchor makes the model unstable if combined with riverward Alluvium below +4.40m AOD. The riverbank elevation is already observed as +3.26m AOD, and if an anchor had failed, a larger deflection of the wall at the failure location would be apparent. This is because the waling transfers the load sideways to neighbouring anchors. Since there is no current observation of excessive deflection of the wall, the failure of an anchor remains a low probability.

Moderate likelihood scenario

- Case E - Variable frictional strength of the Alluvium is a moderate probability but does not have a significant impact on the model;

Higher likelihood scenarios

- Case B, C, D, or I - Loss of riverward Alluvium reduces the model stability FoS < 1. Both the elevation of the top of the Alluvium and its slope gradient control the stability.
- Case F - modelling indicates the corrosion of exposed piles impacts wall stability significantly, as corrosion will affect the long term thin section buckling resistance;

In terms of how this affects the future management of the flood defence, the results demonstrate both short and longer term high risks. The short term risk is the loss of an additional 1.43m of Alluvium from the riverward side which will lead to instability. If riverward erosion was controlled but some portion of the sheet piles were permitted to remain exposed, concentrated corrosion of the outpan combined with less rapid corrosion of the flange will eventually lead to a long term thin section buckling failure (Breakell et al., 2015).

4 DECISION TREE

4.1 Background

With any historical structural asset, there is a general risk around obtaining sufficient certainty regarding its current condition and stability. Part of the process of constructing a decision tree involves understanding the current condition of structural elements and making reasonable predictions about their future condition. These aspects were addressed in various ways in the earlier studies of the structure but needed further considerations as follows:

- What manner of corrosion is occurring on the exposed sheet pile faces, what corrosion rate should be projected forward, and on which parts of the pile should this rate be applied?
- Is there a stability risk to the highest retained height along the wall and its supports due to riverbank erosion and sheet pile corrosion?
- Is there a reasonable justification to carry out standard investigations on the anchors (anchor lift of tests) and will testing these anchors make a difference to the overall assessment?
- Is there an optimal cost/benefit option?
- The following summarise the information relating to each of the problems listed above and provide the basis of the decision tree. The decision tree is presented in Figure 4.

4.2 Maintenance aspects

It is understood that periodically during high water events, there is ponding of water accumulating to the western part of the flood defence and to the southern end of the underbanks defence. All stakeholders agreed that the most likely cause of the ponding water is that one or more of the flap valves cannot close properly. The cause of the underbanks ponding is not sufficiently investigated. Part of the decision tree will include remediation of the flap valves that are not working properly and investigation of the underbanks area of concern.

4.3 Decision tree process

The decision tree is constructed as a set of options for the client to consider as ‘do nothing’, ‘do minimum’ and ‘do refurbish / replace / improve’. Information from the sensitivity analysis crosses into the decisions and indicates what risk is attached to the selected

decision. Where text is highlighted red, the risk is considered high that the option could lead to instability of the wall. The amber text indicates that wall stability failure is averted but there are other maintenance tasks which, if not carried out, will lead to deterioration of the asset. The green text indicates decisions which mitigate the stability risk and control deterioration of the wall.

To summarise, the 'Do refurbish' emerges as the optimal technical solution. Whether it is taken forward as the preferred option will be dependent on the economic/carbon benefit delivered in comparison to the Do Minimum / Do Nothing baseline options. The extent of refurbishment would be subject to the cost-benefit / carbon analysis carried out as part of the Outline Business Case.

The analysis indicates a 'Do nothing' option has a limited time frame dependent on the rate of erosion in front of the wall. The overall rate of erosion is currently unknown. It is recommended that the Alluvium level in front of the wall be monitored as part of the ongoing monitoring that has recently started for the wall.

5 SUMMARY

A risk sensitivity analysis methodology to holistically evaluate the residual life of an existing anchored sheet pile flood defence wall in UK has been presented. The approach allows asset owners with finite resources to understand the risks and consequences affecting their asset more broadly, thereby enabling better informed investigations and planned management works to be undertaken. Sensitivity and parametric studies must consider risk, reliability, and public expectations, to better inform the decision process.

REFERENCES

ArcelorMittal (2008). Piling Handbook, 8th Edition, ArcelorMittal, Luxembourg.

Borin, D. L. (2010). WALLAP Propped, anchored and Cantilever Retaining Wall Analysis Program, Geosolve, United Kingdom.

Breakell, J. E. et al. (2005). C634 Management of accelerated low water corrosion in steel maritime structures, CIRIA, United Kingdom, ISBN: 978-0-86017-634-3.

British Standards Institution (2013). BS EN 1997-1:2004+A1:2013 Eurocode 7 Geotechnical design - General rules, British Standards Institute, United Kingdom, ISBN: 978 0 580 80773 2.

British Standards Institution (2009), UK National Annex to Eurocode 3: Design of steel structures – Part 5: Piling, British Standards Institute, United Kingdom, ISBN 978 0 580 54962 5.

Burland, J. (1987). The teaching of Soil Mechanics: a personal view, In: *Volume 3: Proceedings of the 9th European conference on soil mechanics and foundation engineering*, Dublin, Republic of Ireland, pp. 1427-1447.

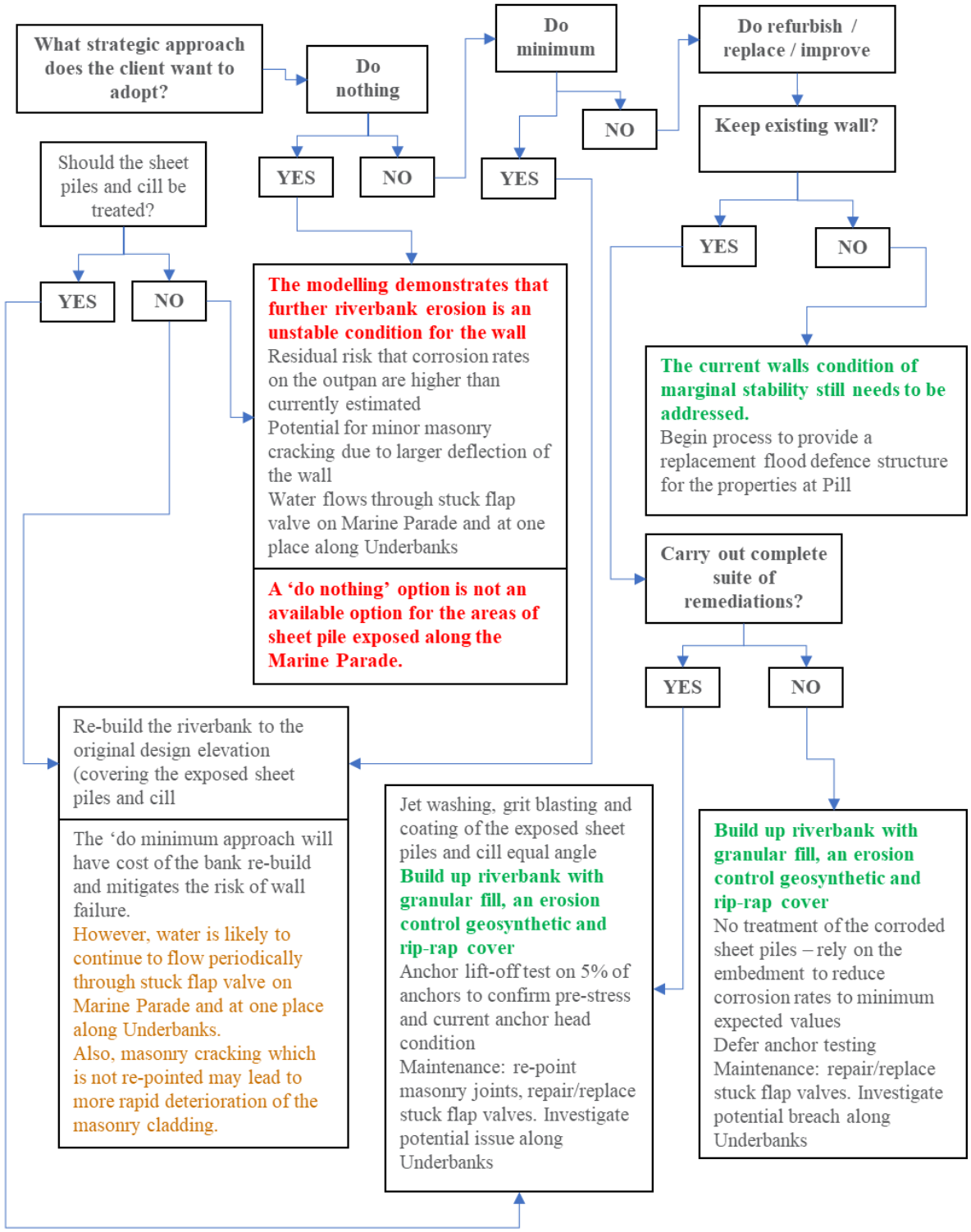

Figure 4. Decision tree diagram.

Proceedings of the XVIII ECSMGE 2024
GEOTECHNICAL ENGINEERING CHALLENGES
TO MEET CURRENT AND EMERGING NEEDS OF SOCIETY
© 2024 the Authors
ISBN 978-1-032-54816-6
DOI 10.1201/9781003431749-303
Open Access: www.taylorfrancis.com, CC BY-NC-ND 4.0 license

ECSMGE 24
XVIII EUROPEAN CONFERENCE ON SOIL MECHANICS AND GEOTECHNICAL ENGINEERING

Eurocode 7 – second generation - ground model

Eurocode 7 - deuxième génération - modèle géotechnique

H. Garin*
GeoVerkstan, Kungsbacka, Sweden

M. Baldwin
Independent Consultant, Leeds, United Kingdom

P. Reiffsteck
Université Gustave Eiffel, Champs-sur-Marne, France

K-J. van der Made
Wiertsema & Partners, Tolbert, Netherlands

R. Wudtke
University of Applied Sciences Nordhausen, Germany

**hakan.garin@geoverkstan.se*

ABSTRACT: The Ground Model is defined in the second generation of Eurocode as a *'site-specific outline of the disposition and character of the ground and groundwater based on results from ground investigations and other available data'*. The Ground Model is a compilation of data including maps, plans, sections, and reports that capture objective information regarding the soil, rock types and groundwater conditions across the zone of influence (ZOI). The Ground Model should cover the site and the surrounding area to provide the geotechnical and geological context, potential sources of materials for construction, and the surrounding conditions that may influence the groundworks. Since the Ground Model is an illustration (including the distribution of the geotechnical units within the zone of influence) based on interpolation between factual data and derived values, the model itself can be considered the most likely representation based on the available data during that phase of a project. Uncertainties inherent to such Ground Models may be quantified and reduced during subsequent project phases when more data becomes available.

RÉSUMÉ: Le modèle géotechnique est défini dans la deuxième génération de l'Eurocode comme un "*aperçu spécifique au site de l'arrangement et de la nature des terrains et des eaux souterraines sur la base des résultats des reconnaissances de sol et d'autres données disponibles*". Le modèle géotechnique est une compilation de données comprenant des cartes, des plans, des coupes et des rapports qui contiennent des informations objectives concernant les types de sol et de roche et les conditions des eaux souterraines dans la zone d'influence. Le modèle géotechnique doit couvrir le site et la zone environnante afin de fournir le contexte géotechnique et géologique, les sources potentielles de matériaux de construction et les conditions environnantes susceptibles d'influencer les travaux de terrassement. Étant donné que le modèle géotechnique est une illustration (y compris la distribution des unités géotechniques dans la ZOI) basée sur des valeurs dérivées et une interpolation entre les données factuelles et les valeurs dérivées des essais, le modèle lui-même peut être considéré comme la représentation la plus probable basée sur les données disponibles au cours de la phase en cours d'un projet. Les incertitudes inhérentes à ces modèles géotechniques peuvent être quantifiées et réduites au cours des phases ultérieures du projet, lorsque davantage de données sont mises à disposition.

Keywords: Ground model; Eurocode 7; EN 1997.

1 INTRODUCTION

One of the new requirements in the second generation of Eurocode 7 is the need to prepare a Ground Model. Since the concept of a Ground Model may not be familiar to many practising geotechnical engineers, the Guideline – Assembling the Ground Model and derived values (JRC, 2024) has been prepared to explain the concept of the Ground Model and forms the basis for this paper.

The Ground Model for a project is defined in the Eurocode as a *'site-specific outline of the disposition and character of the ground and groundwater based on results from ground investigations and other available data*'.

There are two distinct models in the current revision of Eurocode 7. The Ground Model (in FprEN

1997-2:2024) includes geology and presentation and evaluation of test results. The Geotechnical Design Model (in FprEN 1997-1:2024) covers the design of the structure, and so includes the selection of the geotechnical design parameters.

A Ground Model is a representation of the geological, hydrogeological and geotechnical conditions, for which we can sensibly read the 'engineering ground conditions', which includes the presentation and evaluation of the test results into derived values. However, the inclusion and selection of design parameters develop this into the next step, which is a 'Geotechnical Design Model'.

The Ground Model is a compilation of data including maps, plans, sections, and reports that capture objective information regarding the soil, rock types and groundwater conditions across the zone of influence (ZOI). The Ground Model should cover the site and the surrounding area to provide the geotechnical and geological context, potential sources of materials for construction, and the surrounding conditions that may influence the earthworks and engineering structure".

It is intended that the Ground Model will make use of the distribution of the geotechnical units within the ZOI, together with an interpolation of factual data, and where appropriate derived values, to produce the most likely indication of the ground and groundwater conditions for this phase of a project.

Uncertainties inherent in the compilation of Ground Models must be quantified. A review of the results, limitations, uncertainties, discrepancies and gaps in data should be recorded as part of the Ground Model development process. It is intended that uncertainties will be reduced during subsequent phases of a project when more data becomes available.

The Ground Model includes, but is not limited to, the following components within the ZOI:

- rockhead and structural geology;
- the geometry of the layers;
- superficial geology and geomorphology;
- seismicity;
- hydrogeological conditions; and
- geotechnical and geochemical conditions.

Within the above list of components, seismicity brings unique and complex issues to the design of structures.

Development of the Ground Model should be commenced as early as possible, but in any case as part of the desk study, using existing geological maps, previous investigations, reports, satellite imagery, photogrammetric and/or LiDAR data, site reconnaissance, and consideration of the site's geological history and geomorphology. The Ground Model captures the general composition and assembly of the soil and rock types and forms the basis of the field and laboratory investigation planning. The Ground Model must be verified with additional geotechnical, geological and hydrogeological data during the life of the project.

The Ground Model should be developed alongside the compilation of the Ground Investigation Report (GIR). The horizontal blue dotted line in Figure 1 shows the delineation between the Ground Model and the Geotechnical Design Model (GDM). All of the data and information relating to the ground and groundwater conditions for the Ground Model area should be captured and presented within the GIR.

2 THE PURPOSE AND PROCESS OF THE GROUND MODEL

The Ground Model is a verbal, graphical and schematic tool and process that is used to advance knowledge of the ground and groundwater characteristics of the ZOI of the structure (or structures), and to help identify the corresponding risks.

The assembling and use of the Ground Model should be a fundamental activity for any geotechnical project. The Ground Model is an essential tool for engineering quality control and provides a transparent way of identifying project-specific, critical ground and groundwater risks and properties.

Any Ground Model must consider the ZOI since they are intrinsically linked. The initial ZOI should be defined at the same time as the Ground Model is first considered.

The following aspects should be reported regarding the selected ZOI:

- the location and type of geotechnical structure(s) that is the origin of the ZOI;
- potential construction methods considered; and
- considerations that have influenced the selection of the ZOI.

Figure 1 shows the transition from the Ground Model to the Geotechnical Design Model. Although not shown in this figure, it is implicit that the Ground Model is developed alongside the Ground Investigation Report (GIR) and indeed much of the data accumulated in the GIR, will help develop the Ground Model.

3 THE EXTENT OF THE GROUND MODEL

It is critical to the success of any project, that the extent of the Ground Model is appropriate to the project and

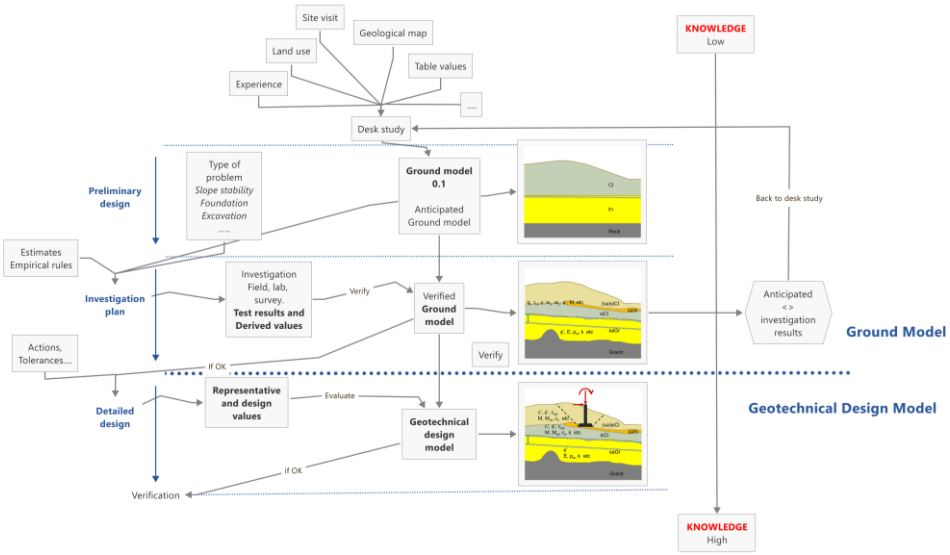

Figure 1. Relationship of Ground Model to Geotechnical Design Model. Source: Guideline - Assembling the Ground model and the derived values.

the ground and groundwater conditions. Whilst the complexity of the Ground Model will vary depending on the phase and nature of the project being considered, in every case, the Ground Model should match the ZOI that has been identified as relevant to the project as a whole.

Initially, as noted in FprEN 1997-1:2024, 4.1.2.1 (4), the extent of the ZOI and by extension, the extent of the Ground Model, shall be estimated before the ground investigation is planned.

4 STAGES

It is advisable to update the Ground Model at each key stage described in the EN 1997 and reproduced in flow chart form in Figure 2. The stages of development of the Ground Model should correspond to the Geotechnical Category and in particular, the Geotechnical Complexity Class into which the ground is classified as the level of detail increases.

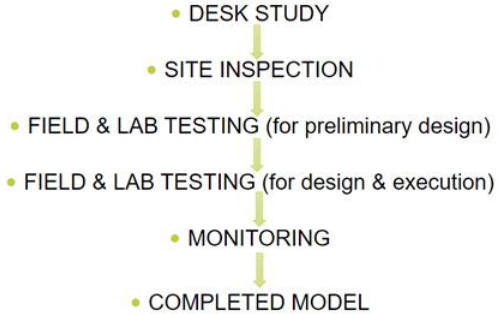

Figure 1. Key Stages for the development and updating of the Ground Model.

It is possible to identify several critical stages where the Ground Model should be assessed and updated as necessary. Whilst the development of the Ground Model is an ongoing activity that will last for the life of the project, the stages shown in Figure 2 are clear milestones at which additional data should be gathered and the model reassessed.

A preliminary version of the Ground Model must be prepared at the desk study/site inspection stage. This will consist of topographical, geomorphological, geomechanical and stratigraphical information obtained from available maps or previous survey campaigns. The preliminary model will allow for optimising and planning site and/or laboratory geotechnical investigations and concentrate them where needed, ensuring a level of detail and a spatial extent of investigations appropriate to the ZOI of the structure. Subsequently, it will be improved iteratively as data are collected.

5 ASSEMBLING THE GROUND MODEL

The identification of the lithology that can be matched between the ground investigation locations (GIL) according to the identification of the ground layers and the mechanical parameters depends on the distance between the GILs and the difference in level between the layers compared. A good correspondence suggests a stratigraphic link between the layers.

Various techniques may be used to form a decision tree (chart, tables, etc.), or the 'Random Forest' technique, depending on the regional practice, projects, expertise, national rules, etc.

Once the description, classification or mechanical characterisation is achieved at a particular 1D location (i.e. borehole), the graphical representation needs to fill the gap by interpolation techniques:

- IDW: Inverse Distance Weighting;
- minimum curvature method;
- irregular triangulation with smoothing;
- rectangular interpolation;
- local polynomial; or
- Kriging.

In practice, these Individual 1D stratigraphies may be jointly interpreted with diverse geophysical surveys to derive a single model of the investigated subsurface region. This approach is, however, largely qualitative and hence the outcome depends heavily on the background, experience and preconceptions of the interpreter.

Interpolation is also a need for:

- Determination of the zones of higher risk
- Determination of areas where more ground investigation is needed
- Volume calculation of excavation

However, in most practice, interpolation shall not be used for determining the layering used in the geotechnical design calculation. In the Ground Model, a clear distinction should be made between the locations where the ground layering was measured and the areas between measurements.

Figure 3 shows the different stages in developing a 3D model.

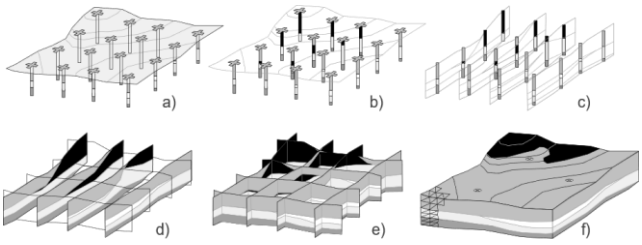

Figure 3. Schematic example of the process to develop the 3D model.

6 GROUND MODEL UNCERTAINTIES

The Ground Model should include the derived values of the relevant ground properties for all the geotechnical units encountered in the ZOI. Several sources of uncertainty appear during the process of assembling the Ground Model and the derived values. Therefore, throughout the process, care must be taken to minimise these uncertainties.

The sources of uncertainties in assembling the detailed Ground Model in the ZOI are related to:

- The accuracy of the information in already available ground investigation including desk-study and site-inspection.
- The accuracy of available geological descriptions, hydrological and geological information, and geological 3D models.
- The accuracy of existing 3D models used as a basis in new 3D models.
- The position and depth measurement of the new ground investigations.
- The interpretation of the results from new ground investigations:
  - CPT, FVT, SPT, PMT, etc;
  - Borehole data: determination of geological formations with intrinsic dependency on the experience of the interpreter (geologist); and
  - Water pressure measurements, piezometer readings, etc.
- The unknown shape of the boundary between measurements (2 points): straight lines, curved lines.
- The presence of manmade hard inclusions (historical foundations, cables, sewerage pipes, etc.)

Other hidden uncertainties may exist such as the one that originates from a too-large adaptation of the investigation program to the shape of the ZOI. The spatial heterogeneity of the investigations may then be a problem, especially in the case of linear infrastructures, which leads to longitudinal over-information.

The definition and treatment of uncertainties encountered during ground investigation testing to obtain derived values are detailed in the test standards.

ACKNOWLEDGEMENTS

The guideline, which is the basis of this paper, has been prepared by Task Group C2 within CEN/TC 250/SC 7/WG 1 as a result of European cooperation. Member countries in Task Group C2 have been Belgium, Estonia, Finland, France, Germany, Italy, Latvia, Luxembourg, Netherlands, Norway, Poland, Portugal, Romania, Slovakia, Spain, Sweden, Switzerland, and the United Kingdom.

The authors would like to thank the members of TG C2 for their cooperation and the parallel task groups C1, C3 and C4. All valuable contributions have made it possible to compile and agree on the guideline.

REFERENCES

Guideline - Assembling the Ground Model and the derived values (2024). Technical report by the Joint Research Centre (JRC), CEN/TC 250/SC 7.

FprEN 1997-1:2024 Eurocode 7: Geotechnical design — Part 1: General rules.

FprEN 1997-2:2024 Eurocode 7: Geotechnical design — Part 2: Ground properties.

Proceedings of the XVIII ECSMGE 2024
GEOTECHNICAL ENGINEERING CHALLENGES
TO MEET CURRENT AND EMERGING NEEDS OF SOCIETY
© 2024 the Authors
ISBN 978-1-032-54816-6
DOI 10.1201/9781003431749-304
Open Access: www.taylorfrancis.com, CC BY-NC-ND 4.0 license

ECSMGE 24
XVIII EUROPEAN CONFERENCE ON SOIL MECHANICS AND GEOTECHNICAL ENGINEERING

Influence of lateral stress on soil-structure interface tests in a hollow cylinder apparatus

Influence de la contrainte latérale sur les expérience d'interface sol-structure dans un appareil à cylindre creux

S. Gehring*, H.H. Stutz, T. Lohrmann, Ph. Förschler
Institute of soil mechanics and rock mechanics, Karlsruhe, Germany

**sabine.gehring@kit.edu*

ABSTRACT: The contact shear behaviour between the soil and a structure has a significant impact on the load transfer of geotechnical structures. In the past, several different approaches to test and quantify this soil-structure interface behaviour have been conducted using e.g. modified ring-shear, direct-shear or simple-shear devices. In most experimental studies, the lateral deformation is restricted to zero (stiff frames of direct shear and simple shear devices) and the lateral stress is unknown. To gain insights on the influence of an anisotropic stress state on the interface, contact shear tests on ring-shaped samples with various lateral stresses are presented in this work. Therefore, a modified hollow cylinder apparatus with a contact plate and short sample geometries was used. The first results indicate, that neither the anisotropy of the stress state can be neglected, nor the interface behaviour follows straight the soil shearing behaviour for the test setup used here.

RÉSUMÉ: Le comportement de cisaillement de contact entre le sol et une structure a un impact significatif sur le transfert de charge des structures géotechniques. Dans le passé, plusieurs approches différentes pour tester et quantifier le comportement de l'interface sol-structure ont été menées en utilisant, par exemple, des dispositifs de cisaillement annulaire modifié, de cisaillement direct ou de cisaillement simple. Dans la plupart des études expérimentales, la déformation latérale est limitée à zéro (cadres rigides des dispositifs de cisaillement direct et de cisaillement simple) et la contrainte latérale est inconnue. Pour mieux comprendre l'influence d'un état de contrainte anisotrope sur l'interface, des essais de cisaillement par contact sur des échantillons en forme d'anneau avec différentes contraintes latérales sont présentés dans ce travail. Pour ce faire, un appareil à cylindre creux modifié avec une plaque de contact et des géométries d'échantillons courtes a été utilisé. Les premiers résultats indiquent que l'anisotropie de l'état de contrainte ne peut pas être négligée et que le comportement de l'interface ne suit pas directement le comportement de cisaillement du sol pour la configuration d'essai utilisée ici.

Keywords: Interface tests; contact shear behaviour; anisotropic stress state.

1 INTRODUCTION

In many geotechnical projects, interfaces occur, as they include rigid structures such as piles, walls and foundations. The contact shear behaviour between the soil and the structure has a significant impact on the load transfer of geotechnical structures. For instance, the surface roughness of the structural element has a considerable influence on the behaviour of the entire system. This inspired several authors to experimental investigations and modelling approaches for interface shearing behaviour (e.g. Wernick 1978; Uesugi and Kishida 1986; Stutz and Martinez 2021). Some interface models depend only on the normal stress on the interface (e.g. Ghionna and Mortara 2002) while others use existing soil models for derivation and therefore take the whole stress tensor into account. The last-mentioned attempts for contact modelling are based on different assumptions concerning the stress state at the interface: while Arnold and Herle (2006) suppose all normal stresses to be equal ($\sigma_{11} = \sigma_{22} = \sigma_{33}$) for simplicity, Stutz et al. (2017) make another assumption. They assume the in-plane deformation to be negligible and allow the in-plane stress to take other values than the stress normal to the interface ($\sigma_{11} \neq \sigma_{22} = \sigma_{33}$). The approach of Staubach et al. (2022) couples neither the in-plane stresses nor the in-plane deformations directly with each other but with the neighbour soil (in FEM) so all normal stresses can be different ($\sigma_{11} \neq \sigma_{22} \neq \sigma_{33}$). Most previous experimental studies on interfaces have been conducted using modified ring-shear, direct-shear or simple-shear devices. In these cases, the frames restrict the lateral deformation to zero and the lateral stress is unknown. Therefore, important information to characterize interface shear behaviour under different stress conditions is raw (Dumitrescu et al. 2009).

One step towards understanding the influence of the 3D stress state was taken by Dumitrescu et al. (2009). They developed an interface shearing device with one adjustable normal stress on a plane orthogonal to the interface. A cylinder with a contact surface is rotated in a hollow cylinder sample, while the normal stress on the interface is applied through a membrane (radial stress) and the normal stress on one of the planes orthogonal to the interface is applied by a piston (axial stress). The experimental results indicate that the anisotropy of the initial stress state should be considered in the description of contact shear behaviour.

In this work, another device for interface tests with different normal stresses was developed. Therefore, a modified hollow cylinder triaxial device with a contact plate and short samples is used. This allows to control four independent stress or strain components and to take more complex stress states into account. First experiments with Karlsruhe fine sand are presented and compared to simple existing boundary surfaces for soils (section 3.2, Figure 6 and Figure 7).

2 TEST DEVICE AND METHODS

2.1 Test device

In the modified hollow cylinder apparatus (see Figure 1), a hollow cylinder shaped soil sample is tested in a pressure cell. The sample is separated from the cell fluid by membranes on the outer and inner curved surface areas. A plate with glued sand on the bottom of the sample ensures a fully rough contact with a full force transfer. In this modified device, the top plate is a changeable contact plate, so different roughness properties can be tested (see Figure 2). By rotating the bottom plate, torsion can be applied to the sample and shear deformation is induced at the interface.

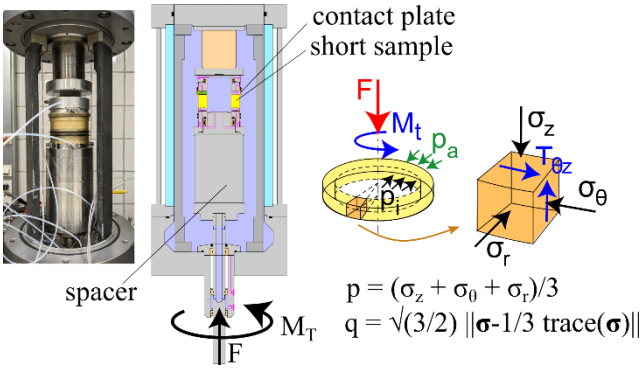

Figure 1. Modified hollow cylinder apparatus to control three independent normal stresses in interface shearing tests (one on shear plane, two on orthogonal planes).

The normal stress at the interface is controlled by an axial load. Additionally, the pressure on the outer cell (p_a) and in the inner cell inside the hollow sample (p_i) can be controlled independently. Thereby, an anisotropic initial stress state can be generated and with different pressures on the outer and the inner membranes, three different normal stresses can be applied (one on the shear plane and two on the planes orthogonal to the shear plane).



Figure 2. Different rough contact plates: with glued sand (left), coarse sandblasted (center), fine sand blasted (right).

2.2 Sample preparation and soil properties

The experiments were conducted on medium dense samples of Karlsruhe fine sand (Figure 3). For preparation, the membranes are placed in a mould and the sand was pluviated between the membranes (Figure 3). The sample has an outer and inner diameter of 100 mm and 60 mm with a height of 20 mm.

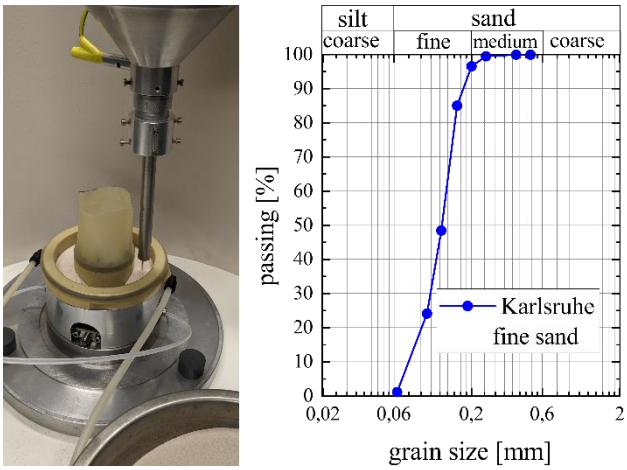

Figure 3. Sample preparation with air pluviation (left) and grain size distribution of Karlsruhe fine sand (right).

2.3 Influence of membrane stiffness

The membranes are fixed at the bottom and top caps hence they are deformed in the same way as the sample and contribute to the measured forces. Especially for the short sample height of 20 mm and a tangential shear deformation up to 30 mm, the influence of the membrane stiffness cannot be neglegted: The measured moment during torsion tests results not only from the mobilised friction on the sample but also from membrane forces. In the literature, dummy tests with water-filled membranes are used to develop correction formulas for the membrane forces in hollow cylinder

tests (e.g. Koseki, Yoshida and Sato 2005). In these tests, unrealistic membrane deformations occur when it comes to large rotation angles. For an enhanced correction, in the present work, tests on soil samples with different membranes were used to capture the actual membrane (or sample) deformation and a mathematical correction was developed. Example test data with the membrane correction is shown in Figure 4.

3 RESULTS

3.1 Loading path

All tests were driven with a constant vertical stress σ_z of 100 kPa (normal stress on the shear plane), except the tests in Figure 5. The normal stresses on the planes orthogonal to the shear plane (radial stress σ_r and tangential stress σ_θ, see Figure 1) were 50 kPa, 100 kPa or 150 kPa and identical in the presented tests. After reaching the test specific initial stress state, the drained contact shearing phase was started by rotating the bottom end plate.

For the medium dense samples ($I_D \approx 0.6$), the corrected shear stress (see Figure 4) increases until an asymptotic state is reached. In the test series a rough contact plate with glued grains and less rough contact plates of fine and coarse sandblasted steel were used.

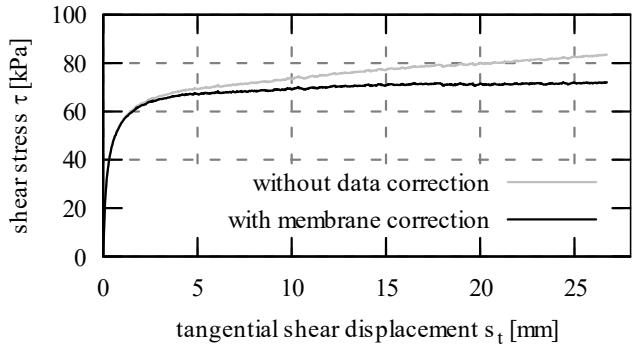

Figure 4. Drained contact shearing phase (torsion) after isotropic initial state (p = 100 kPa) with medium dense Karlsruhe fine sand and a rough contact plate.

3.2 Shear strength

The tests with isotropic initial stress states (Figure 5) show a proportional relation between the shear strength and the mean stress as well as between the shear strength and the normal stress on the shear plane and therefore act in the framework of common yield criteria, e.g. the Mohr-Coulomb criterion.

This behaviour changes for the test series including anisotropic initial states: Figure 6 and Figure 7 show the deviatoric stress in the sample (colored) and the shear stress on the shear plane (grey) during tests with a contact plate with glued grains and one of fine sandblasted steel. Note, that the largest reached deviatoric stress q appears not necessary at the same test as the largest shear stress on the shear plane $\tau_{\theta z}$. The maximum deviatoric stresses do not match with the critical deviatoric stress q_{crit} calculated with the Mohr-Coulomb criterion and the corresponding Lode angle (value at asymptotic state is marked with x). A hypothesis for the explanation is the occurrence of a forced horizontal failure plane. The geometry and

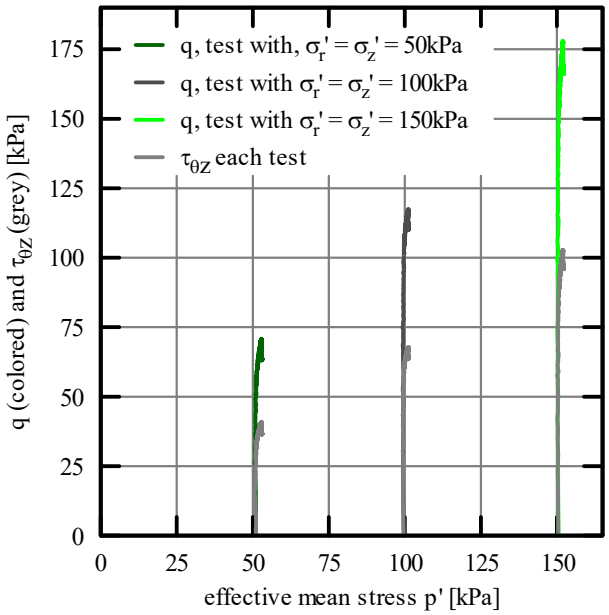

Figure 5. Interface tests with isotropic initial state: $\sigma_z = \sigma_r = \sigma_\theta = p$, rough contact plate of coarse sandblasted steel.

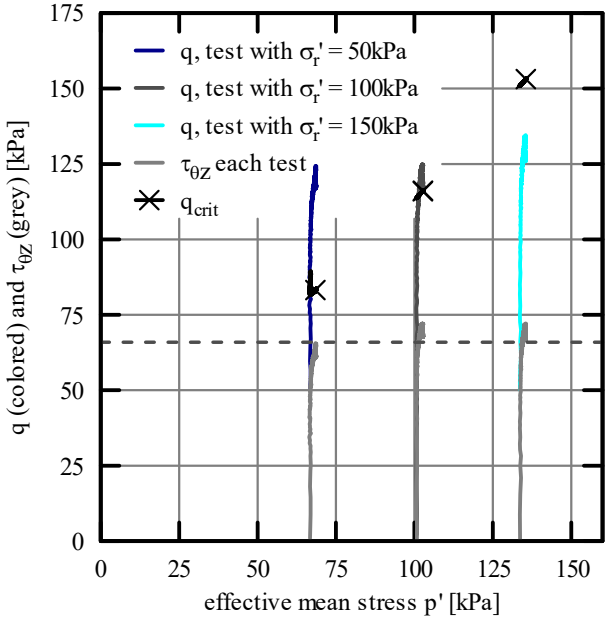

Figure 6. Interface tests with anisotropic confinement and rough contact plate with glued grains.

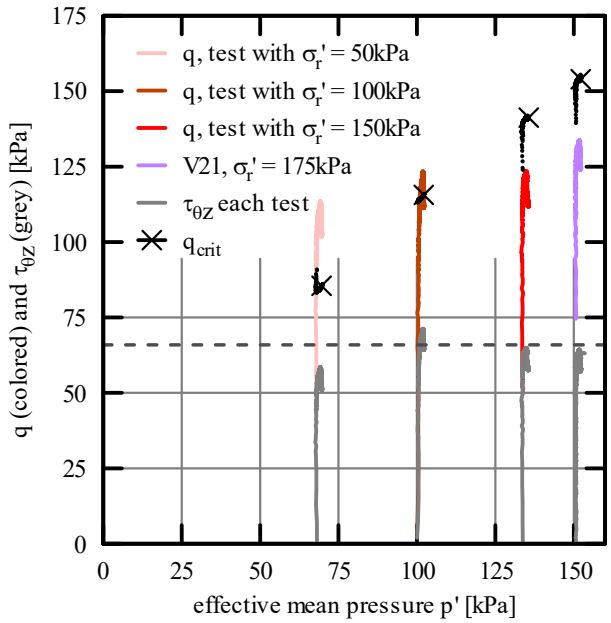

Figure 7. Interface tests with anisotropic confinement and less rough contact plate of fine sandblasted steel.

end plates might constrain the decisive failure plane to be horizontal. Following this assumption and looking at the vector on the shear plane, only the stress components σ_z and $\tau_{\theta z}$ are contributing. As the normal stress is equal in all tests in Figure 6 and Figure 7, the maximum shear stress $\tau_{\theta z}$ should be a constant value (dashed line: calculated with Mohr-Coulomb on horizontal failure plane).

The experimental data diverge from this line and hence indicate, that the anisotropic confining stress influences the shear strength. The different values of lateral stress change the state of the soil above the contact plate and render the shear strength of the interface. These results confirm the findings of Dumitrescu et al. (2009), who reported an influence of the normal stresses on the plane orthogonal to the shear plane (anisotropic confinement).

4 CONCLUSIONS

The presented experiments contribute to the understanding of soil-structure interface behaviour.

- A hollow cylinder apparatus was modified that three independent normal stresses can be controlled during interface shear tests.
- Due to boundary and interface conditions, the maximum deviatoric stress did not match with failure criteria in pure soil shearing. This might result from a predefined failure plane.
- The maximum shear stress on the horizontal (failure) plane is potentially influenced by anisotropic confinement states, as the normal stresses on the planes orthogonal to the shear plane render the state of the soil on the contact and so the shear strength of the interface.
- Further investigations should be conducted on the influence of sample geometry to separate possible effects during monotonic and cyclic shearing.

REFERENCES

Arnold, M. and Herle, I. (2006). *Hypoplastic description of the frictional behaviour of contacts.* Graz, Austria, Taylor & Francis, pp. 101-106.

Dumitrescu, A. I., Corfdir, A., and Frank, R. (2009). Influence of the anisotropy of confining stress on the sand/steel interface behaviour in a cylinder shear apparatus. *Soils and foundations*, 49(2), pp. 167-174. http://doi.org/10.3208/sandf.49.167.

Ghionna, V. N. and Mortara, G. (2002). An elastoplastic model for sand–structure interface behaviour. *Géotechnique*, 52(1), pp. 41-50. https://doi.org/10.1680/geot.2002.52.1.41.

Koseki, J., Yoshida, T., and Sato, T. (2005). Liquefaction properties of Toyoura sand in cyclic tortional shear tests under low confining stress. *Soils and Foundations*, 45(5), pp. 103-113. https://doi.org/10.3208/sandf.45.5_103.

Staubach, P., Machaček, J. and Wichtmann, T. (2022). Novel approach to apply existing constitutive soil models to the modelling of interfaces. *International Journal for Numerical and Analytical Methods in Geomechanics*, Band 46, pp. 1241-1271. https://doi.org/10.1002/nag.3344.

Stutz, H. H., and Martinez, A. (2021). Directionally dependent strength and dilatancy behavior of soil–structure interfaces. *Acta Geotechnica*, *16*(9), 2805-2820. https://doi.org/10.1007/s11440-021-01199-5.

Stutz, H. H., Mašín, D., Sattari, A. S., and Wuttke, F. (2017). A general approach to model interfaces using existing soil constitutive models application to hypoplasticity. *Computers and Geotechnics*, 87, pp. 115-127. https://doi.org/10.1016/j.compgeo.2017.02.010.

Uesugi, M., and Kishida, H. (1986). Frictional resistance at yield between dry sand and mild steel. *Soils and foundations*, *26*(4), pp. 139-149. http://doi.org/10.3208/sandf1972.26.4_139.

Wernick, E. (1978). Skin friction of cylindrical anchors in noncohesive soils. In *Symp. on Soil Reinforcing and Stabilising Techniques*, pp. 201-219.

Proceedings of the XVIII ECSMGE 2024
GEOTECHNICAL ENGINEERING CHALLENGES
TO MEET CURRENT AND EMERGING NEEDS OF SOCIETY
© 2024 the Authors
ISBN 978-1-032-54816-6
DOI 10.1201/9781003431749-305
Open Access: www.taylorfrancis.com, CC BY-NC-ND 4.0 license

ECSMGE 24
XVIII EUROPEAN CONFERENCE ON SOIL MECHANICS AND GEOTECHNICAL ENGINEERING

Numerical investigation of the interaction between existing tunnels and driven pile installation

Enquête numérique sur l'interaction entre les tunnels existants et l'installation de pieux battus

L. Hai*, P. Yensri, A. Faramarzi, N. Metje
University of Birmingham, School of Engineering, Edgbaston, Birmingham, UK
**lxh224@student.bham.ac.uk*

ABSTRACT: The advancement of urbanisation in large cities yields an increased use of piles to support high-rise buildings and critical infrastructure. Compared to bored piles, the impact on existing buried assets and infrastructure including tunnels is often more pronounced for driven pile construction. However, the evolution of the deformation of segmental lined tunnels, which affects the operation and safety of tunnel, during pile installation, has not received significant attention. This study investigated tunnel deformation during pile installation using finite element analysis adopting the Arbitrary Lagrangian Eulerian (ALE) method, which was validated against published data. Three cases with a circular pile of 0.6 m in diameter and 20 m in length near a concrete-continuous-lined tunnel with a diameter of 6 m and a burial depth of 12 m in sandy ground were studied. In these cases, the tunnel cross-section changes from circular to vertical oval with the horizontal contraction being around 0.02% - 0.03% *D* with *D* being the tunnel's outer diameter. The results showed that the deformation varies approximately linearly with respect to the distance between the tunnel and the pile. Additionally, the centre of the tunnel moves away horizontally while it settles first and then uplifts vertically at a certain pile insertion depth. The section begins to heave at a smaller pile insertion depth when the clearance between pile and tunnel is larger. The results showed that the simulation method can accurately capture the behaviour of the tunnel during the pile installation. The results provide more insight with respect to pile design when the pile installation occurs in the vicinity of a tunnel.

RÉSUMÉ: L'avancement de l'urbanisation dans les grandes villes entraîne une utilisation accrue de pieux pour soutenir les immeubles de grande hauteur et les infrastructures critiques. Comparé aux pieux forés, l'impact sur les actifs enterrés existants et les infrastructures, y compris les tunnels, est souvent plus prononcé lors de la construction de pieux battus. Cependant, l'évolution de la déformation des tunnels à revêtement segmentaire, qui affecte le fonctionnement et la sécurité, pendant l'installation des pieux n'a pas reçu une attention significative. Cette étude a examiné la déformation du tunnel pendant l'installation des pieux en utilisant la méthode Lagrangien Eulerien Arbitraire (ALE), qui a été validée par rapport à des données publiées. Trois cas avec un pieu circulaire de 0,6 m de diamètre et de 20 m de longueur près d'un tunnel revêtu en continu de béton avec un diamètre de 6 m et une profondeur d'enterrement de 12 m dans un sol sablonneux ont été étudiés. Dans ces cas, la section transversale du tunnel passe d'une forme circulaire à une forme ovale verticale avec une contraction horizontale d'environ 0,02% à 0,03% D, D étant le diamètre extérieur du tunnel. Les résultats ont montré que la déformation varie approximativement de manière linéaire par rapport à la distance entre le tunnel et le pieu. De plus, le centre du tunnel s'éloigne horizontalement tout en s'installant d'abord, puis en se soulevant verticalement à une certaine profondeur d'insertion du pieu. Plus le pieu est éloigné du tunnel, moins la profondeur d'insertion du pieu à laquelle la section commence à se soulever est importante. Les résultats ont montré que la méthode de simulation peut capturer avec précision le comportement du tunnel pendant l'installation des pieux. Les résultats fournissent davantage d'informations concernant la conception des pieux lorsque l'installation des pieux se produit à proximité d'un tunnel.

Keywords: Driven pile construction; existing tunnel; ALE method; pile-soil-tunnel interaction.

1 INTRODUCTION

Urbanisation and population growth stimulate more and more exploitation of underground space in many big cities (Schroeder et al., 2002; Shen et al., 2014; Wu et al., 2018). New construction and reconstruction projects are expected to use pile foundations extending to competent strata, because many cities sit on top of soft soil, in order to support the significant surface loads from large structures. The installation of piles will inevitably induce disturbances to the surrounding soil which will be transferred to adjacent buried infrastructures and assets including tunnels. These tunnels are used for transportation, water conveyance and as utility pipelines. The disturbance induced by pile installation potentially influences the operation

and serviceability of the existing tunnels. Previous studies have shown that the impact of driven pile installations on the surrounding soil is more pronounced compared to bored piles (Huang et al., 2018; X. Liu et al., 2019). However, the way the tunnel section deformation develops as a result of the installation of driven piles has not been fully investigated.

During the past years, studies have focused on the interaction between pile installation and existing tunnels. In contrast to bored piles though, studies on driven pile installations are limited (Salim and Lafta, 2020). Physical tests have been conducted to explore the strain and stress distribution along the tunnel induced by nearby pile insertion, and the influence of the clearance between the pile and tunnel (Kong et al., 2021; Standing & Leung, 2005), as well as the soil properties (Salim and Lafta, 2017), were considered. However, the scaling law was not fully considered in these experiments which can impact the accuracy of the results. On the other hand, theoretical deduction based on a beam model with elastic foundation to consider the effect of pile groups has been carried out. However, it is difficult to incorporate many critical conditions in these simplified theoretical models such as the failure of soil and the tunnel section distortion. This will lead to differences between modelling results and real observations. Numerical simulation techniques provide opportunities to account for more complex interactions between a pile and a tunnel. Ding and Zhang (2019) and Liu et al. (2019) incorporated Finite Element Modelling (FEM) and cavity expansion theory (CET) to investigate the effect of soil compaction induced by pile insertion on an existing tunnel in clay. However, these simulations ignored the friction between the pile and the soil. Also, the development of the tunnel deformation could not be explored based on these simulations. Fall et al. (2021) coupled the Arbitrary Lagrangian Eulerian (ALE) method and the element deletion technique to investigate the impact of vibration induced by the pile installation on an existing tunnel. In their study, the soil failing around the pile was ignored which is in contrast to the real contact between the soil and the pile. Additionally, the development of tunnel deformation was also ignored. Above all, previous studies have not fully considered the contact between the soil and the pile resulting in less reliable results. Furthermore, the development of tunnel deformation has not received sufficient attention.

This study aims to investigate the development of tunnel deformation during a nearby single pile installation in sandy soil. A more realistic strategy coupling ALE and CET is developed to develop the numerical simulation of the pile installation. The effectiveness of the strategy is validated by published physical tests. A parametric study is carried out to investigate the influence of clearance between the tunnel and the pile on the deformation of the existing tunnel.

2 NUMERICAL MODELS

2.1 Model's details

The ALE method has been proven to be an effective and efficient numerical method to cope with potential mesh distortion in geotechnical problems involving large deformations (Fu et al., 2023). Figure 1 shows the FEM mesh and layout of the numerical model for the focused problem where the pile installation happens next to an existing tunnel with continuous lining. The model is developed based on physical tests from Arshad et al., (2014) to validate the numerical simulation strategy.

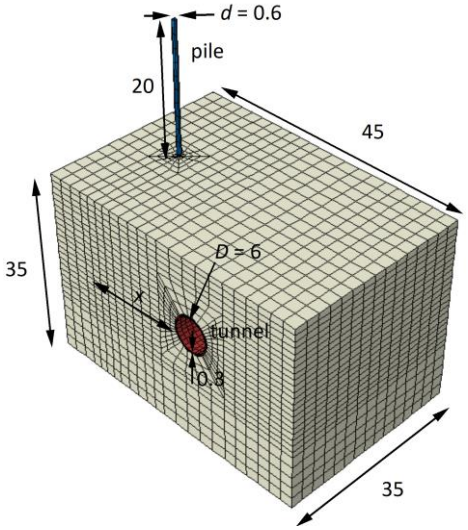

Figure 1. Geometry of the numerical model (units: m).

The model is 45 m in length, 35 m in width and 35 m in height. The outer diameter and the thickness of the tunnel lining are D = 6 m and t = 0.3 m, respectively. The depth of the tunnel axis is $H_t = 2D$ to the centre of the tunnel. The pile diameter is d = 0.6 m. The pile length is 20 m. A square area around the pile with a length of 10 d is assigned as the ALE region. The remeshing frequency is set at 1 per increment and the remeshing sweep is set at 25 per increment, which means the mesh in the ALE region will be remapped every increment and the mesh will be remapped 25 times per increment.

The properties of the soil and the tunnel are shown in Table 1.

C3D8R (8-node linear hexahedral reduced integration) elements are employed for the soil mass

and the existing tunnel while R3D4 elements are adopted for the pile. Besides, hourglass control is adopted for the ALE region to avoid elements without stiffness in numerical calculations. The soil mass and the tunnel are defined using solid elements while the pile are defined using shell elements. The soil is modelled as linear elastic-perfectly plastic with Mohr Coulomb strength and non-associative flow. The tunnel is modelled as linear elastic and the pile is modelled as discrete rigid elements.

*Table 1. Parameters used in the model (Note, * from Arshad et al., 2014).*

Header	Parameter	Unit	Value
soil	Density*	kg/m^3	1680
	Young's modulus *	MPa	60
	Poisson's ratio *		0.25
	Friction angle *		39
	Dilation angle *		5
	Cohesion *	Pa	0
Tunnel lining	Density	kg/m^3	2450
	Young's modulus	GPa	30
	Poisson's ratio		0.25

The surface-to-surface contact is used to simulate the interface between the pile and the soil. The surfaces of pile are master face while the surface of the soil is the slave surface. The contact between the pile and soil is defined as 'hard contact' in the normal direction with a friction coefficient of 0.2 in the tangential direction.

2.2 Simulation of the pile installation

The strategy to simulate the pile installation is derived from the work by Carter et al. (1979) where it is stated that expanding a cavity with the radius from a_0 to $2a_0$ can be used to give an adequate approximation to what happens in soil when a cavity expands from 0 to r occurs.

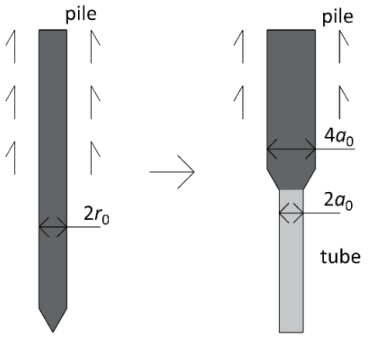

Figure 2. demonstration of the pile installation strategy in numerical modelling.

To achieve this, in the numerical model, a pre-installed virtual tube is installed ahead of the pile where the radius of the tube is a_0 while the diameter of the pile is refined as 2 a_0, as shown in Figure 2. The relationship between the real pile diameter d and a_0 is:

$$d/2 = \sqrt{3}\, a_0 \qquad (1)$$

In the numerical model, the tube is modelled as discrete rigid elements and the contact between the soil and tube is defined as frictionless.

2.3 Validation of the pile installation strategy

To test the reliability of the simulation strategy of the pile installation, another numerical model was developed with a penetrometer insertion into the sandy soil where the properties of the materials and geometry are exactly the same as those in the well-instrumented CPT (cone penetration test) tests (Arshad et al., 2014).

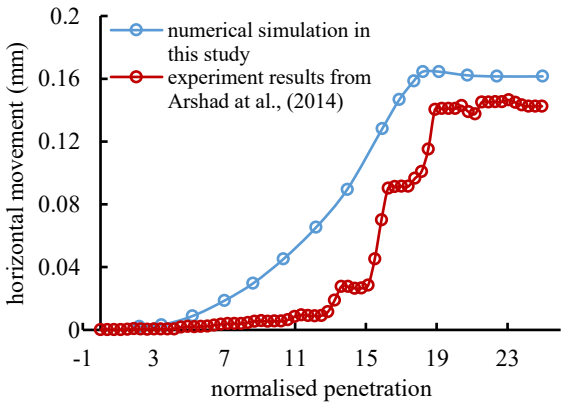

Figure 3. Comparison of the results from the numerical simulations and experimental data for the horizontal movement of the soil particles.

As shown in Figure 3, the numerical simulation results for the horizontal movement of the monitored point (The depth of the point is 18.5 r_c while the distance from pile centre is 3 r_c with r_c be the penetrator radius) can capture the trend of the observation from physical tests in spite of differences. The ultimate difference between the results is 13% with the numerical simulation predicting slightly larger values. According to the simulation results, it is indicated that the simulation strategy for pile installation is reliable enough to replicate the soil movement induced by pile penetration.

3 DEVELOPMENT OF TUNNEL DEFORMATION

Three cases are considered in this study with different clearances x between the tunnel and the pile: 2 D, 2.5

D and 3 *D* while all other parameters remain the same. The focus will be on the deformation of the middle of the tunnel.

3.1 Deformation of the tunnel circumference

Figure 4 to Figure 6 demonstrate the development of the tunnel section shape during the nearby pile installation with different clearances between the tunnel and the pile. The final aggregated displacements (u_x, u_y) of the tunnel crown, spring line and invert are marked with u_x the horizontal and u_y the vertical displacement. To facilitate the presentation of the results, the displacements are multiplied by 100. Besides, the normalised pile insertion depth, H_r, is defined as:

$$H_r = (H - H_t)/D \qquad (2)$$

with H the pile tip depth and H_t the tunnel centre depth.

Figure 4, Figure 5, and Figure 6 demonstrate the evolution of the tunnel section shape during the pile installation when the separation is 2 *D*, 2.5 *D*, and 3 *D*. In these cases, the tunnel section keeps moving horizontally away from the pile with the procedure of pile installation. The final horizontal deformation is the largest at the left springline while it is smallest at the right springline and is nearly the same at the crown and the invert. The vertical deformation is relatively small compared with the horizontal deformation, especially at the right springline. The crown keeps moving upward while the invert keeps moving downward. The resultant horizontal contraction and vertical extension of the tunnel section keep increasing during the pile installation. The horizontal contraction is prone to be slightly more than the vertical extension.

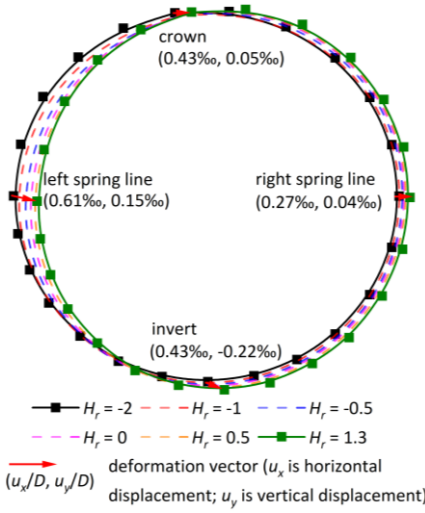

Figure 4. Progressive change in tunnel section shape with a pile clearance of 2 D with D = tunnel diameter. Note: the displacements are multiplied by 100 for visualisation.

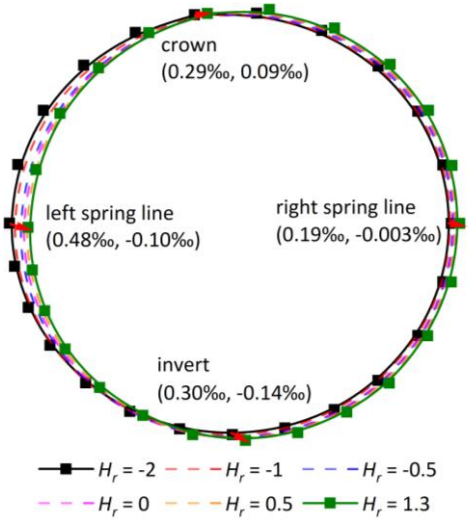

Figure 5. Progressive change in tunnel section shape with a pile clearance of 2.5 D with D = tunnel diameter. Note: the displacements are multiplied by 100 for visualisation.

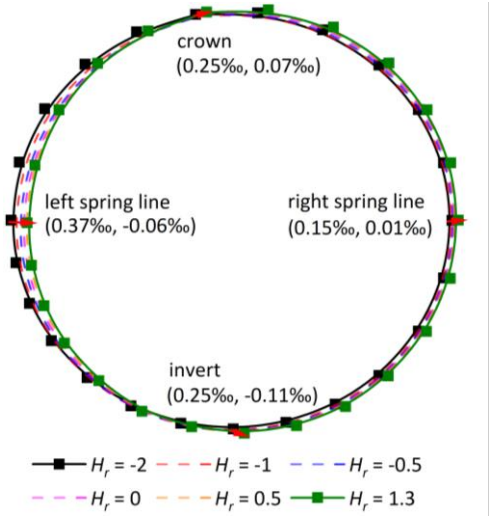

Figure 6. Progressive change in tunnel section shape with a pile clearance of 3 D with D = tunnel diameter. Note: the displacements are multiplied by 100 for visualisation.

The horizontal tunnel axis keeps contracting while the vertical axis continues to extend. The final changes of the horizontal and vertical diameters are shown in Table 2. As the clearance between the tunnel and the pile decreases, the diameter change tends to get larger.

Table 2. Diameter change in horizontal and vertical directions.

Header	Horizontal direction	Vertical direction
Clearance = 2 *D*	0.34‰ *D*	0.27‰ *D*
Clearance = 2.5 *D*	0.27‰ *D*	0.23‰ *D*
Clearance = 3 *D*	0.22‰ *D*	0.18‰ *D*

3.2 The displacement of the centre of the tunnel section

Figure 7 demonstrates the displacement of the tunnel section centre for the three different separations between the tunnel and the pile. The square markers represent the position change of the centre when H_r equals -2 *D*, -1.7 *D*, -1.3 *D*, -1 *D*, -0.7 *D*, -0.5 *D*, -0.3 *D*, 0 *D*, 0.3 *D*, 0.5 *D*, 0.7 *D*, 1. *D*, 1.3 *D*.

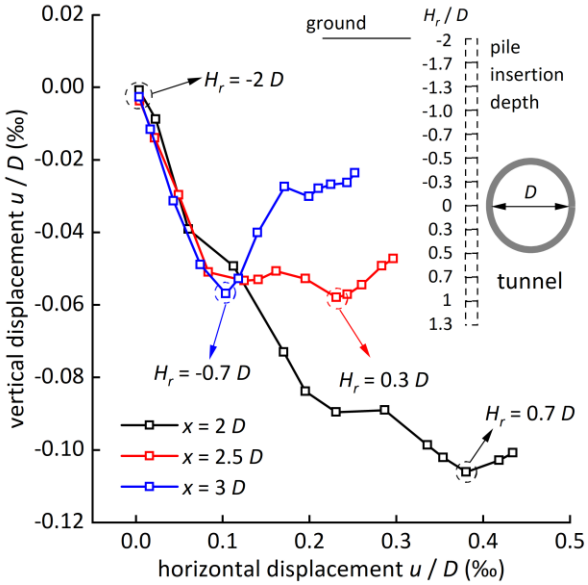

Figure 7. Movement of the tunnel section centre for pile clearances of 2 D, 2.5 D and 3 D with H_r = normalised pile depth.

It can be observed that the section centre continues to move away from the pile horizontally with final displacements of 0.43‰ *D*, 0.29‰ *D* and 0.25‰ *D* with clearances for 2 *D*, 2.5 *D* and 3 *D* respectively. With respect to the vertical displacement, the centre settles downward first and then uplifts until the pile tip reaches a certain depth. The critical pile tip depth is H_r = 0.7, H_r = 0.3 and H_r = -0.7 with clearances of 2 *D*, 2.5 *D* and 3 *D* respectively. The maximum settlement is 0.11‰ *D*, 0.06‰ *D* and 0.06‰ while the final settlement is 0.10‰ *D*, 0.05‰ *D* and 0.02‰ with clearances of 2 *D*, 2.5 *D* and 3 *D* respectively.

The horizontal displacement of the tunnel section centre is more than the vertical displacement at each pile installation depth. The tunnel tends to settle first and then heave. The pile tip depth changes from 0.7 D to -0.7 D at which tunnel begins to heave with the increase in clearance between the tunnel and the pile. During the design stage of a pile installation next to an existing tunnel, it is not sufficient to focus on the final stage of the pile installation. The maximum vertical displacement of the tunnel section may happen the pile tip at a certain depth.

Above all, despite the low magnitudes, the non-uniform displacement may potentially impact on the facilities inside the tunnel. In the case with clearance being 2 *D*, the horizontal displacement of sectional centre is 2.58 mm, which exceeds the limit for a train tunnel with the ballastless track structure (Liu et al., 2022). As a result, it may induce disturbance of the serviceability of the tunnel.

4 CONCLUSIONS

This study developed a numerical model to investigate the development of the deformations of an existing circular tunnel lining during the installation of a single circular driven pile in close proximity. A numerical strategy to simulate pile insertion into soil was developed based on the ALE method and CET. The main conclusions are as follows:

- The numerical model developed for the pile installation captured the behaviour of the surrounding soil well in terms of soil displacement.
- The pile installation caused the section at the middle of the tunnel to keep moving away from the pile horizontally. The maximum deformation happens at the left spring line. The crown keeps moving upward while the invert keeps moving downward.
- The horizontal contraction and vertical extension happen due to the pile installation. The contraction and extension keep increasing as the pile installation processes. The final horizontal contraction and vertical extension are 0.34‰ *D*, 0.27‰ *D*, 0.22‰ *D* and 0.27‰ *D*, 0.23‰ *D* and 0.18‰ *D* when the clearance is 2 *D*, 2.5 *D* and 3 *D*. It is indicated that the deformation is relatively small compared with the case in Liu et al., (2019), which is due to the single pile in this study instead of pile group and the lining of the tunnel is simplified as contiunous where the joints are not considered.
- The section centre keeps moving away from the pile with a final horizontal deformation of 0.43‰ *D*, 0.29‰ *D* and 0.25‰ *D* when the clearance is 2 *D*, 2.5 *D* and 3 *D*. While the centre moves downward first and then upward when the pile tip reaches a certain depth. The farther the pile is away from the tunnel, the less the pile insertion depth at which the section begins to uplift. The maximum settlement is 0.11‰ *D*, 0.06‰ *D* and 0.06‰ while the resultant final settlement is 0.10‰ *D*, 0.05‰ *D* and 0.02‰ when the clearance is 2 *D*, 2.5 *D* and 3 *D*.

- The tunnel tends to settle first and heave at a certain pile installation depth where the maximum tunnel settlement happens.

ACKNOWLEDGEMENTS

The authors are grateful for the support and funding provided by the Chinese Scholarship Council, the National Buried Infrastructure Facility, School of Engineering, The University of Birmingham. The project presented in this article is supported by the National Buried Infrastructure Facility, School of Engineering, The University of Birmingham.

REFERENCES

Arshad, M. I., Tehrani, F. S., Prezzi, M., and Salgado, R. (2014). Experimental study of cone penetration in silica sand using digital image correlation. *Geotechnique*, 64(7), 551–569. https://doi.org/10.1680/geot.13.P.179.

Carter, J. P., Randolph, M. F., and Wroth, C. P. (1979). Stress and pore pressure changes in clay during and after the expansion of a cylindrical cavity. *International Journal for Numerical and Analytical Methods in Geomechanics*, 3(4), 305–322. https://doi.org/10.1002/nag.1610030402.

Ding, Z., and Zhang, X. (2019). Numerical analysis of influence of pile foundation construction on adjacent metro tunnel. *Journal of Central South University (Science and Technology)*, 50(2), 390–399.

Fall, M., Gao, Z., and Ndiaye, B. C. (2021). Safety evaluation of existing tunnel nearby driving pile using two different standards. *International Journal of Geomechanics*, 21(3), 1–11. https://doi.org/10.1061/(asce)gm.1943-5622.0001948.

Fu, S., Yang, Z. X., Jardine, R. J., and Guo, N. (2023). Large-deformation finite-element simulation of deformation and strain fields resulting from closed-end displacement pile installation in sand. *Journal of Geotechnical and Geoenvironmental Engineering*, 149(6). https://doi.org/10.1061/JGGEFK.GTENG-10480.

Huang, Z., Fu, H., Chen, W., Zhang, J., and Huang, H. (2018). Damage detection and quantitative analysis of shield tunnel structure. *Automation in Construction*, 94(February), 303–316. https://doi.org/10.1016/j.autcon.2018.07.006.

Kong, S. M., Oh, D. W., Lee, S. W., Kim, C. Y., and Lee, Y. J. (2021). Effects of pile installation on existing tunnels using model test and numerical analysis with medium density sand. *Applied Sciences (Switzerland)*, 11(15). https://doi.org/10.3390/app11156904.

Liu, X., Sang, Y., Zhao, F., Shi, G., and Heng, Y. (2019). Evaluation of effects of static pile driving on existing metro tunnel structure. *Journal of Performance of Constructed Facilities*, 33(4), 1–11. https://doi.org/10.1061/(asce)cf.1943-5509.0001309.

Liu, Y., Song, H. L., Sun, X. D., Xing, H. P., Feng, C. Y., Liu, J. F., and Zhao, G. T. (2022). Characteristics of rail deformation caused by tunnel floor heave and corresponding running risk of high-speed train. *Construction and Building Materials*, 346, 128385. https://doi.org/https://doi.org/10.1016/j.conbuildmat.2022.128385.

Salim, N., and Lafta, S. (2020). Effect of a driven pile on an existing tunnel. *Journal of Engineering and Sustainable Development*, 24, 94–109. https://doi.org/10.31272/jeasd.24.1.7.

Schroeder, F. C., Addenbrooke, T. I., and Potts, D. M. (2002). A numerical investigation into the impact of pile group loading on tunnels. *Planning and Engineering for the Cities of Tomorrow. Second International Conference on Soil Structure Interaction in Urban Civil EngineeringSwiss Federal Inst of Technology, Zurich; European Commission COST; Swiss Federal Office for Education and Science*.

Shen, S. L., Wu, H. N., Cui, Y. J., and Yin, Z. Y. (2014). Long-term settlement behaviour of metro tunnels in the soft deposits of Shanghai. *Tunnelling and Underground Space Technology*, 40(2014), 309–323. https://doi.org/10.1016/j.tust.2013.10.013.

Standing, J., and Leung, W. (2005). Investigating stresses around tunnels and piles using photo-elasticity techniques. *Proc., 5th Int. Symp. on Geotechnical Aspects of Underground Construction in Soft Ground*, 171–177.

Wu, H. N., Shen, S. L., Yang, J., and Zhou, A. (2018). Soil-tunnel interaction modelling for shield tunnels considering shearing dislocation in longitudinal joints. *Tunnelling and Underground Space Technology*, 78(April), 168–177. https://doi.org/10.1016/j.tust.2018.04.009.

Proceedings of the XVIII ECSMGE 2024
GEOTECHNICAL ENGINEERING CHALLENGES
TO MEET CURRENT AND EMERGING NEEDS OF SOCIETY
© 2024 the Authors
ISBN 978-1-032-54816-6
DOI 10.1201/9781003431749-306
Open Access: www.taylorfrancis.com, CC BY-NC-ND 4.0 license

ECSMGE 24
XVIII EUROPEAN CONFERENCE ON SOIL MECHANICS AND GEOTECHNICAL ENGINEERING

Earth mounds construction in York's Norman castles: Implications for current performance and protection

Construction de monticules de terre dans les châteaux normands de York: Implications pour les performances et la protection actuelles

A. Heitor*
University of Leeds, Leeds, UK

P. Winslow, E. Yenne
Formerly, University of Leeds, Leeds, UK

C. MacRae, S. Gandolfi
City of York Council, York, UK

**a.heitor@leeds.ac.uk*

ABSTRACT: This paper aims to review the construction technologies that would have likely been adopted in motte and bailey type of castles, in particular those adopted in construction of earth mounds of the Clifford tower and Baile Hill, built circa the 11th century. While Norman builders having presumably rudimentary knowledge of soil behaviour built these structures, their durability compares favourably with more recently built uncontrolled geostructures using heavier plant (e.g., Victorian earth retaining structures and embankments). This seems to suggest that the level of expertise of building with soil may have been greater than it is typically assumed for these periods. A comparison with modern construction techniques adopted in earthworks and influence of vegetation cover is also included in a bid to explain its remarkable durability. Results of a recent non-destructive site investigation campaign carried out at Baile Hill are also included to assist in the assessments of their current performance and evaluate its vulnerability. Some insights on the use of protection measures for enhanced resiliency against climate change are also included.

RÉSUMÉ: Cet article vise à passer en revue les technologies de construction qui été adoptées dans les châteaux de type motte et bailey, en Clifford et de Baile Hill, construits vers le 11ème siècle. Bien que les Norman constructeurs ayant vraisemblablement une connaissance rudimentaire du comportement du sol ont construit ces structures, leur durabilité se compare avantageusement à celle des géostructures non contrôlées construites plus récemment utilisant des installations plus lourdes (par exemple, les structures de soutènement et les remblais de l'époque victorienne). Cela semble suggérer que le niveau d'expertise en matière de construction avec du sol pourrait avoir été supérieur à ce qu'on suppose généralement pour ces périodes. Une comparaison avec les techniques de construction modernes adoptées dans les travaux de terrassement et l'influence de la couverture végétale est également incluse dans le but d'expliquer sa remarquable durabilité. Les résultats d'une récente campagne d'investigation non destructive du site menée à Baile Hill sont également inclus pour faciliter l'évaluation de leurs performances actuelles et évaluer leur vulnérabilité. Certaines informations sur l'utilisation de mesures de protection pour renforcer la résilience face au changement climatique sont également incluses.

Keywords: Heritage; geostructures; Norman castles; compacted soils.

1 INTRODUCTION

Heritage geostructures across the UK are being subjected to increasingly erratic environmental and climatic conditions due to climate change. This is predicted to worsen in the future which could lead to a higher risk of failure and collapse. This is mainly because the modern principles of compaction were not employed at the time of construction and thus it is likely that these geostructures were placed in a relatively loosely compacted condition. This in turn increases their vulnerability to climatic action, i.e., sudden wetting proceeding intense periods of rainfall and drying causing the onset of desiccation cracking (e.g., Heitor et al., 2015, and Walker et al, 2023).

2 CONSTRUCTION OF MOUNDS IN NORMAN CASTLES

During the Norman invasion, the motte and bailey was a common design geometry adopted in the

construction of castles by Norman builders (Pounds, 1994). Much like the castles in York there were numerous similar structures built across England during that time to support the Norman invasion effort and deal with local uprisings. Mottes were large conical earth mounds that were constructed by pilling layers of soils and stones and flattened on top. The top of the mound typically accommodated a tower or keep either constructed in wood or stone to enhance the castle defensibility (Toy, 1985). Some were also built over older man-made geostructures, such as Bronze Age barrows or Roman infrastructure (Kenyon, 2005).

In England and Wales, only 7% of mottes were taller than 10 metres high; 24% were between 10 and 5 metres, and 69% were less than 5 metres tall (King, 1972). The motte was often protected by a moat, i.e., a channel dug a few meters deep which usually surrounded the castle perimeter which provided further protection. The excavation of the moat would have typically been a source of the soil for constructing the mound itself. Considering the likely manpower and construction tools available during that period, i.e., rudimentary picks and shovels (Figure 1), it is estimated that the larger mottes might have taken up to a year to build (Kenyon, 2005).



Figure 1. Building of the Motte at Hastings (modified after Bayeux Tapestry, source: City of Bayeux).

The type of soil available locally would have largely governed the design of the motte (DeVries, 2003). Those built from fine grained soils (e.g. clays and silts) could support a steeper slope as the soil would be pilled and lightly compacted in unsaturated condition (i.e. greater magnitude of capillary stresses), whilst coarse grained soils (e.g. gravel, sands) would exhibit a gentler incline typically controlled by their angle of repose. Several accounts after their construction, report that these geostructures required frequent maintenance (e.g. Pounds, 1994). The main issues reported were associated with superficial erosion and washouts during flooding, particularly with steeper mounds. This is consistent with the placement of soils in a relatively loose condition. Over time however, some mottes suffered from subsidence and localised damage caused by flooding, which required repairs and stabilisation work (Cooper, 1911). Nonetheless, despite these specific localised issues most of these geostructures are in remarkable condition, compared to those built in Victorian time. Figure 1 depicts the construction of a mound and indicates that the mound would have been built in layers which is similar to the practices adopted today compared to Victorian times when fills were just tipped (Walker et al, 2022). In addition, the soil is represented as a particulate material which may indicate the level of expertise of building with soil would have been greater than typically assumed. In this paper, the site investigation works undertaken at Baile Hill mound conducted as part of pilot study to support a preliminary engineering assessment of the stability of a motte and bailey mound are showcased.

3 SITE INVESTIGATION

3.1 Baile Hill site

The site is currently a steep vegetated mound present to the south of Cromwell Road and the east of Baile Hill Terrace, roughly centred around 460266E, 451274N (British National Grid). Neither the bailey nor the ditch at the base of the hill are still present. Baile Hill is one of two castles constructed by William the Conqueror in 1069 in York (Figure 2).

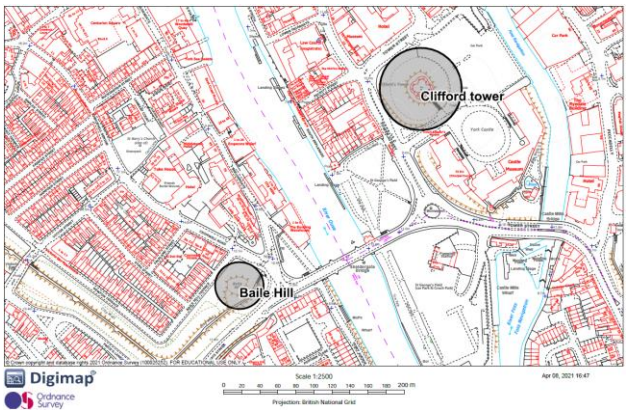

Figure 2. Ordnance map from York (Source: Digimap Ordnance survey collection, 2021).

The encircling ditch at the base of the hill, which is no longer present, is considered to have been 21m wide and 12m deep based on findings obtained by excavations undertaken during the 1960s. Addyman and Priestley (1977) speculated that the ditch is filled with soil (glacial till from the York Moraine member)

that may have washed out or resulted from localised shallow landslides from the Baile Hill mound. However, it is also likely that it may have been backfilled to support the rapid expansion of the town of York during Victorian times (Winslow and Heitor, 2024).

3.2 Methods

A combination of destructive and non-destructive methods were used. Georadar was proposed for an initial survey to identify the main composition layers within the mound and for identifying any buried structures. Advanced Continuous Surface Wave (ACSW) relies on the measurement of subsurface propagation of surface waves. The velocity of Rayleigh waves is monitored over a range of frequencies; starting at higher wave frequencies (shallow) to low frequencies (deep). The velocity of the Rayleigh waves (V_R) can be used to derive the velocity of shear waves (Vs) considering Poisson ratio (ν) as follows (Heymann, 2007):

$$\frac{V_R}{V_s} = \frac{0.874 + 1.117\nu}{1+\nu} \quad (1)$$

Electrical Resistivity Tomography (ERT) was undertaken to assist with the identification of moisture in the mound. While moisture content cannot be directly extracted from the ERT, their values are generally proportional (e.g. Archie's law). In addition, ERT is also sensitive to variation in soil density and grain size thus where the moisture regime is likely to be similar (at the same depth), lateral changes in density can be identified. A borehole was also drilled on the top of the Baile Hill to a depth of 5.45mbgl with window sampling and follow-on by dynamic Probe to 10.00mbgl.

4 RESULTS AND DISCUSSION

The Baile Hill site geology is dominated by the deposits of the York Moraine member consisting of clay, sand and gravel formed during the quaternary period. There are also alluvium deposits approximately 10m to the east of the site (British Geological Survey viewer), thus it is also possible that alluvium deposits underlie the base of the mound.

The quality of the results obtained by Georadar is relatively poor because the mound readily absorbed the radar energy. This behaviour is typically observed in clay rich formations, which indicates the mound consists of mainly clayey soils. Unfortunately, no stratification details or features were identified.

At the top of the hill the values of shear wave velocity obtained are generally between 200 and 300m/s with occasional outliers over 300m/s that may represent either areas that are denser or drier (Figure 3). These results indicate that the soils in the hill are considerably better compacted compared to the ground in the surrounding area (maximum values around 200m/s). The larger shear wave velocities can be the result of compression due to the self-weight of the fill material over time and some degree of ageing.

The ERT data is displayed in Figure 4. Generally, the electrical resistivity increases as the water content of a soil decreases and as the air voids increase (i.e., poorly compacted). On the top of the mound (0 to 19m), higher resistivity values were observed typically above 300 Ω.m for depths up to 2.5m (dry or perhaps loosely compacted). From the shear wave velocity surveys, it would seem the resistivity values may be combination of both, as shear wave velocities of about 200m/s (Figure 3) are typically considered relatively low for compacted materials.

The overall high resistivity region identified from 16-19m chainage is likely due to the moisture deficit caused by root water uptake and evapotranspiration processes of a nearby mature tree. The area of low resistivity between chainage 16 to 19 is anecdotally the location of the archaeological excavation (Addyman and Priestley, 1977). Similar values of electrical resistivity were also detected at the top of the mound at a depth of 3mbgl, which is likely the same material. At this level, the intrusive works at the top of the mound revealed the presence of a gravelly sandy clay layer with a high water content. It is likely that the beyond this depth the material is stiffer and has a high-water content as expected given the clay large water retention capacity. This is in line with the very low electrical resistivity levels recorded (below 30 Ω.m). It should be noted that while the gravelly sandy clay observed beyond 3mbgl appeared to be stiffer it is still likely made ground constructed with local glacial tills from the York Moraine member considering local geomorphology.

At chainage of 38 to 40m, a bulb of high resistivity is noted. As the line of ERT electrodes traversed a Rowan tree at this location, it is likely that the bulb indicates the presence of an area of low moisture content caused by root water uptake. These contours are also in agreement with field studies for direct moisture measurements conducted by Biddle (1998).

5 POTENTIAL PROTECTION MEASURES

The results from ERT indicated that high resistivity values were obtained in the vicinity of mature trees. At

the moment the mound is well vegetated and that may be the reason for its remarkable condition, i.e. no apparent deep seated failures. This seems to indicate that the use of well managed vegetation could be a cost effective and environmentally friendly protection measure for these geostructures. The vegetation use in this context can have multiple purposes, i.e. surface erosion mitigation, physical reinforcement of the superficial layers that are less compacted and increase in the soil shear strength driven by root water uptake (e.g., Pallewatta et al., 2019 and Pathirage et al., 2019). Where slope failures are frequent the use of capillary barrier system together with vegetation (e.g. grasses) could be effective in managing increased risk due to climate change (e.g. Scarfone et al., 2020).

Nonetheless, while the use of vegetation is attractive from a geotechnical standpoint, it should be noted that from an archaeological perspective it can hinder the conservation efforts as roots can damage buried heritage artifacts. In addition, for urban areas such as Baile Hill, the use of vegetation can have an unintented negative impact of the social landscape of the site (e.g. antisocial behaviour).

6 CONCLUSIONS

The results of this preliminary study, show that the shear wave velocity values measured and observations from the borehole, that the fill material in the mound may be loose to moderately compacted.

This is not surprising considering historical accounts of the construction methods employed and soil ageing and compression during the past 10 centuries. It is postulated that despite some localised evidence of soil movement, the vegetation via root reinforcement and moisture deficit induced by root water uptake may be playing a critical role to ensure the stability of the mound. However, more detailed investigations are required to ascertain the level of moisture deficit and the changes in stability between seasons driven by differences in the evapotranspiration processes in the vegetation.

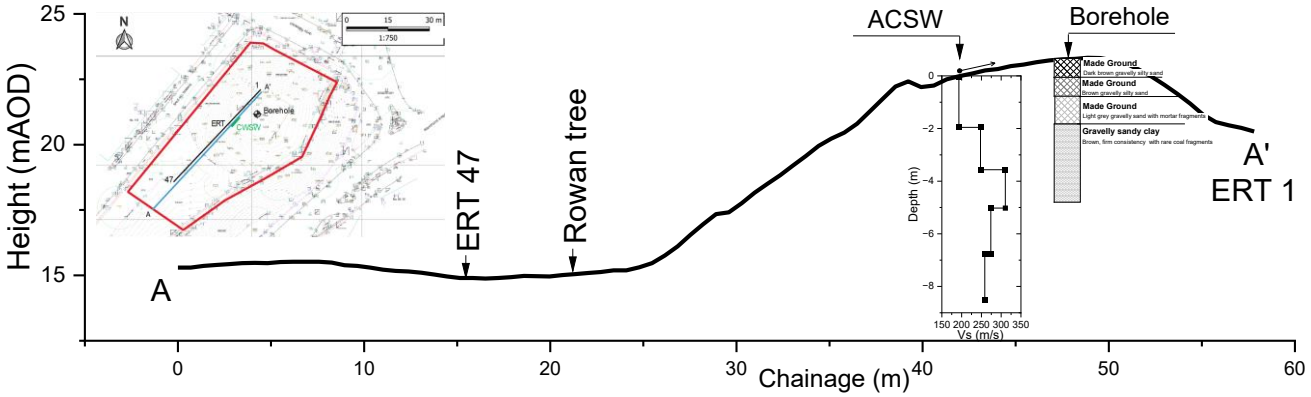

Figure 3. Shear wave velocity and borehole log profile obtained on top of the mound.

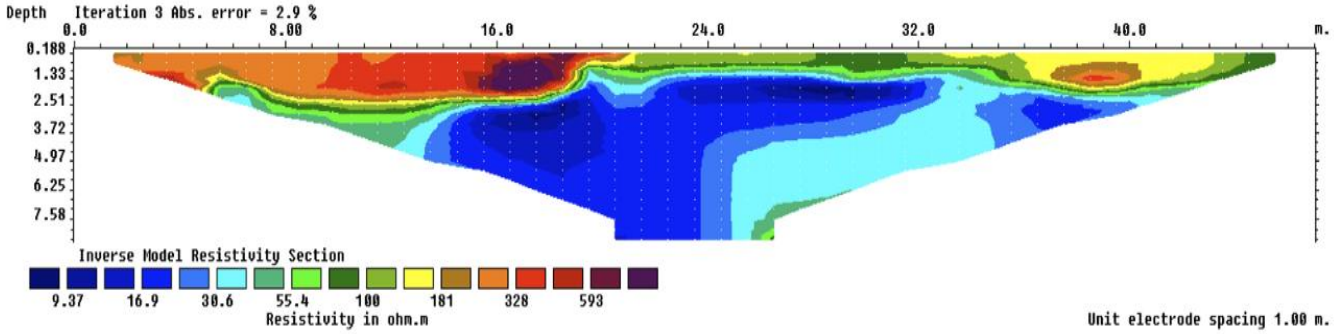

Figure 4. Electrical Resistivity values with depth section noted in Figure 3 (top of the mound 0 to 19m, inversion by RES2D).

ACKNOWLEDGEMENTS

Financial support provided by the Worshipful Company of Constructors Sir Ian Dixon scholarship awarded to P. Winslow is gratefully acknowledged. Technical assistance with geophysical techniques provided by Dr Adam Booth (Georadar) and James Blyth (ACSW, Soil safe) is appreciated. Assistance provided by Keith Emerick (Historic England) and by

York Archaeological Trust (archaeological watching brief) are also gratefully acknowledged.

REFERENCES

Addyman and Priestley (1977) Baile Hill, York. The Archaeological Journal, Volume 134.

Biddle. P. J. (1998) Tree Root Damage to Buildings, Willowmead Publishing Ltd, 676 p., ISBN: 9780953308606.

Cooper, Thomas Parsons. (1911) The History of the Castle of York, from its Foundation to the Current Day with an Account of the Building of Clifford's Tower. London: Elliot Stock. OCLC 4246355.

DeVries, Kelly. (2003) Medieval Military Technology. Toronto, Canada: University of Toronto Press. ISBN 978-0-921149-74-3.

Heitor, A., Indraratna, B. and Rujikiatkamjorn, C. (2015) The role of compaction energy on the small strain properties of a compacted silty sand subjected to drying-wetting cycles Géotechnique. Vol. 65 (9), pp. 717-727.

Heymann, G. (2007) Ground stiffness measurement by the continuous surface wave test, J. South Africa Ints. Civil Eng., 49 (1), 25–31, Paper 631.

Loffman, G. (2022) Archaeological Investigations at Baile Hill, York, YAT Report YA/2022/92.

Kenyon, John R. (2005) Medieval Fortifications. London: Continuum. ISBN 978-0-8264-7886-3.

King, D. J. Cathcart. (1972) "The field archaeology of mottes in England and Wales: eine kurze übersichte," in Château Gaillard: études de castellologie médiévale. V, pp. 107–111.

Official digital representation of the Bayeux Tapestry – 11th century. Credits: City of Bayeux, DRAC Normandie, University of Caen Normandie, CNRS, Ensicaen, Photos: 2017 – La Fabrique de patrimoines en Normandie.

Pallewattha, M., Indraratna, B., Heitor, A. and Rujikiatkamjorn C. (2019) Shear strength of a vegetated soil incorporating both root reinforcement and suction, *Transportation Geotechnics*, 18, pp. 72-82.

Pathirage, U., Indraratna, B., Pallewattha, M., Heitor, A. (2019) A theoretical model for total suction effects by tree roots, *ICE Journal of Environmental Geotechnics*, (6) 6 pp. 353-360. http://dx.doi.org/10.1680/jenge.15.00065.

Pounds, Norman John Greville. (1994) The Medieval Castle in England and Wales: a social and political history. Cambridge: Cambridge University Press. ISBN 978-0-521-45828-3.

Toy, S. (1985) Castles: Their Construction and History. ISBN 978-0-486-24898-1.

Scarfone R, Wheeler SJ and Lloret-Cabot M (2020). Conceptual hydraulic conductivity model for unsaturated soils at low degree of saturation and its application to the study of capillary barrier systems. *Journal of Geotechnical and Geoenvironmental Engineering*, 146(10), 04020106.

Walker, C., Heitor, A., Clarke. B. G. (2022). Influence of Weather-Driven Processes on the Performance of UK Transport Infrastructure with Reference to Historic Geostructures, *Applied Sciences,* 12(15), 7461. https://doi.org/10.3390/app12157461.

Walker, C., Heitor, A. and Clarke, B. G. (2023). Impact of drying-wetting cycles on the small strain behaviour of compacted clay. *Transportation Geotechnics*, 42, p.101063.

Winslow, P. and Heitor A. (2024) Non-intrusive Investigation and Slope Modelling of Compacted Soil in Heritage Geostructures in Geo-Resilience 2023 Conference, Cardiff, Wales D.G. Toll & M.G. Winter (Eds) British Geotechnical Association, London. https://doi.org/10.53243/Geo-Resilience-2023-7-10.

Proceedings of the XVIII ECSMGE 2024
GEOTECHNICAL ENGINEERING CHALLENGES
TO MEET CURRENT AND EMERGING NEEDS OF SOCIETY
© 2024 the Authors
ISBN 978-1-032-54816-6
DOI 10.1201/9781003431749-307
Open Access: www.taylorfrancis.com, CC BY-NC-ND 4.0 license

ECSMGE 24
XVIII EUROPEAN CONFERENCE ON SOIL MECHANICS AND GEOTECHNICAL ENGINEERING

Seismic response of the Kathmandu basin from 3D physics-based numerical simulations

Réponse sismique du bassin de Katmandou à partir de simulations numériques 3D basées sur la physique

V.M. Hernández-Aguirre*, R. Rupakhety
Earthquake Engineering Research Center – University of Iceland, Selfoss, Iceland
**vmh5@hi.is*

ABSTRACT: During the 2015 Mw7.8 Gorkha earthquake, which is the largest to have struck Kathmandu in the last 80 years, the ground motion inside the basin exhibited a notable amplification at low frequencies (<0.9 Hz). Different factors, including source, path as well as site effects, were responsible for the unusual recorded ground motion characteristics. To shed light on the site effects contribution, we study the seismic response of the Kathmandu basin by means of 3D physics-based numerical simulations of some of the aftershocks of the Gorkha earthquake, using the open-source high-performance spectral element code SPEED. To this aim, we developed a large 3D numerical model for the central part of Nepal, including the most recent data for the Kathmandu basin geometry and soil stratigraphy. With the ever-increasing computational power, 3D numerical simulations are becoming increasingly appealing to study the seismic response of complex tectonic and geological systems. The 3D model presented here could support future studies on the seismic response of the Kathmandu basin.

RÉSUMÉ: Lors du tremblement de terre de Gorkha de 2015 (Mw7.8), qui est le plus important à avoir frappé Katmandou au cours des 80 dernières années, le mouvement du sol à l'intérieur du bassin a présenté une amplification notable aux basses fréquences (<0.9 Hz). Différents facteurs, dont la source, la trajectoire et les effets de site, sont responsables des caractéristiques inhabituelles des mouvements du sol enregistrés. Pour mettre en lumière la contribution des effets de site, nous étudions la réponse sismique du bassin de Katmandou au moyen de simulations numériques 3D basées sur la physique de certaines répliques du tremblement de terre de Gorkha, en utilisant le code d'éléments spectraux haute performance SPEED. À cette fin, nous avons développé un vaste modèle numérique en 3D pour la partie centrale du Népal, incluant les données les plus récentes sur la géométrie du bassin de Katmandou et la stratigraphie du sol. Avec l'augmentation constante de la puissance de calcul, les simulations numériques en 3D deviennent de plus en plus attrayantes pour étudier la réponse sismique de systèmes tectoniques et géologiques complexes. Le modèle 3D présenté ici pourrait servir de support à de futures études sur la réponse sismique du bassin de Katmandou.

Keywords: Kathmandu basin; Wave propagation; Site effects; Physics-based simulations; Gorkha earthquake.

1 INTRODUCTION

Kathmandu is located on an oval intermontane valley of approximately 30 km long in the east-west direction and approximately 25 km wide in the north-south direction. The valley floor is overlain by soft, thick fluvial, fluvio-lacustrine, and fluvio-deltaic sediments, that reach thicknesses of around 600 m in the central part of the valley (Moribayashi & Maruo, 1980; Sakai, 2001).

Given the characteristics of the Kathmandu basin, the ground motion from the 25 April 2015 Mw7.8 Gorkha earthquake, that broke the bottom portion of the locked zone of an eastern segment of the Main Himalayan Thrust (Avouac et al., 2015), and from some of the aftershocks, was strongly amplified at low frequencies (e.g., Asimaki et al., 2017; Rupakhety et al., 2017) due to site effects arising from the basin geometry and soil stratigraphy. The ground motion in the Kathmandu basin from the mainshock (Takai et al., 2016) and from some of the aftershocks (Shigefuji et al., 2022) was recorded by a network installed by the Hokkaido University in collaboration with the Department of Geology from Tribhuvan University.

In the recent years, 3D numerical simulations of the 2015 Gorkha mainshock, and/or some aftershocks, have been carried out (e.g., Bijukchhen, 2018; Shen et al., 2022; Sreejaya & Raghukanth, 2022; Wei et al., 2018), however, these studies were limited to very low frequencies (<0.5 Hz), or modelled the 3D structure of basin in a simplified way.

In this work we present a 3D numerical model for the central part of Nepal that includes the surface topography and the most recent data for the Kathmandu basin geometry and soil stratigraphy. Moreover, we compare the results from 3D physics-based numerical simulations of some of the aftershocks with the respective recorded motion.

2 SETUP OF THE 3D NUMERICAL MODEL FOR CENTRAL NEPAL

2.1 The spectral element code SPEED

Three-dimensional physics-based numerical simulations were carried out using the open-source computer code SPEED (http://speed.mox.polimi.it), suitable for the simulation of seismic wave propagation problems including the coupled effects of the seismic source and the propagation path through heterogeneous Earth's media (Mazzieri et al., 2013). SPEED allows treating different seismic sources, including kinematic (either double couple point source or extended fault) and dynamic rupture models, as well as incoming plane waves.

2.2 Crustal structure

The adopted crustal structure (Table 1) is the 1D model developed by Mahesh et al. (2013), which has been used in locating local events and tested against more complex structures, with the addition of a layer of approximately 600 m thickness (H) with a lower stiffness at the top of the model.

Table 1. Crustal model adopted in the 3D model.

H [km]	ρ [kg/m^3]	Vs [m/s]	Vp [m/s]	Qs	Qp
0.6	2400	2200	4000	200	400
15.4	2530	3200	5500	320	640
4.0	2690	3500	6000	350	700
6.5	2830	3700	6450	370	740
10.0	2900	3850	6650	385	770
5.0	3070	4150	7200	415	830

2.3 Velocity model for the basin

Recently, Gilder et al. (2020) collected databases of ground conditions, in situ and laboratory geotechnical tests, and geophysical tests carried out in Kathmandu. Based on this information they created a 3D model of the sediment/bedrock boundary.

Based on a modified version of the sediment/bedrock boundary model of Gilder et al. (2020), and on the 3D velocity structure for Kathmandu defined by Bijukchhen (2018), we created a 3D model for the basin that has a linearly increasing Vs with depth. The shear-wave velocity at the ground surface decreases from 300 m/s at the edges of the basin, to 200 m/s at the locations where the basin thickness is larger than 100 m. For the whole basin Vs at the contact with the first crustal layer is 550 m/s. Figure 1 shows an E-W cross section of the velocity model for the basin.

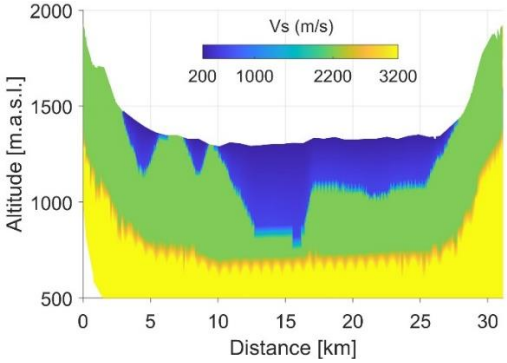

Figure 1. Cross section showing the shear-wave velocity model used for the basin. The location of the cross section is shown with a blue dashed line in Figure 2.

2.4 Numerical model

The mesh, shown in Figure 2, was created using the software CUBIT. It extends over a volume of about 196x98x42 km^3, and it is discretized using an unstructured hexahedral conforming mesh. The mesh is designed so that simulations are accurate up to about f_{max} = 0.9 Hz, to limit the computational load. The order of the spectral polynomials (N) is 4. Overall, the mesh consists of 614'752 spectral elements, resulting in approximately 40.4x10^6 degrees of freedom. The numerical simulations were performed on the Elja cluster from the University of Iceland. A linear viscoelastic model was used for all the materials present in the model.

3 RESULTS FROM THE 3D PHYSICS-BASED SIMULATIONS

Two aftershocks were simulated using point sources, the 25/04/2015 6:53 M4.9 and the 12/05/2015 7:36 M6.1, with depths of 8 and 9 km, respectively. Their epicenters are shown in Figure 2. For the sake of brevity, just some results for the M4.9 simulation are presented here.

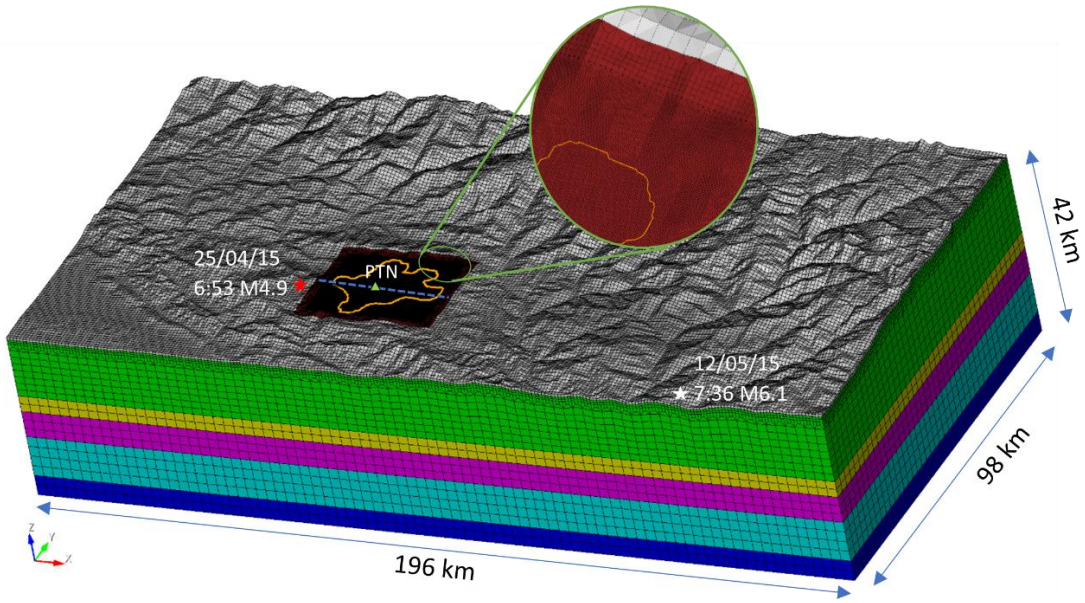

Figure 2. Three-dimensional mesh for Nepal. The contour of the Kathmandu basin is highlighted with an orange line. The blue dashed line represents the location of the cross section presented in Figure 1. For reference the location of station PTN is shown with a green triangle.

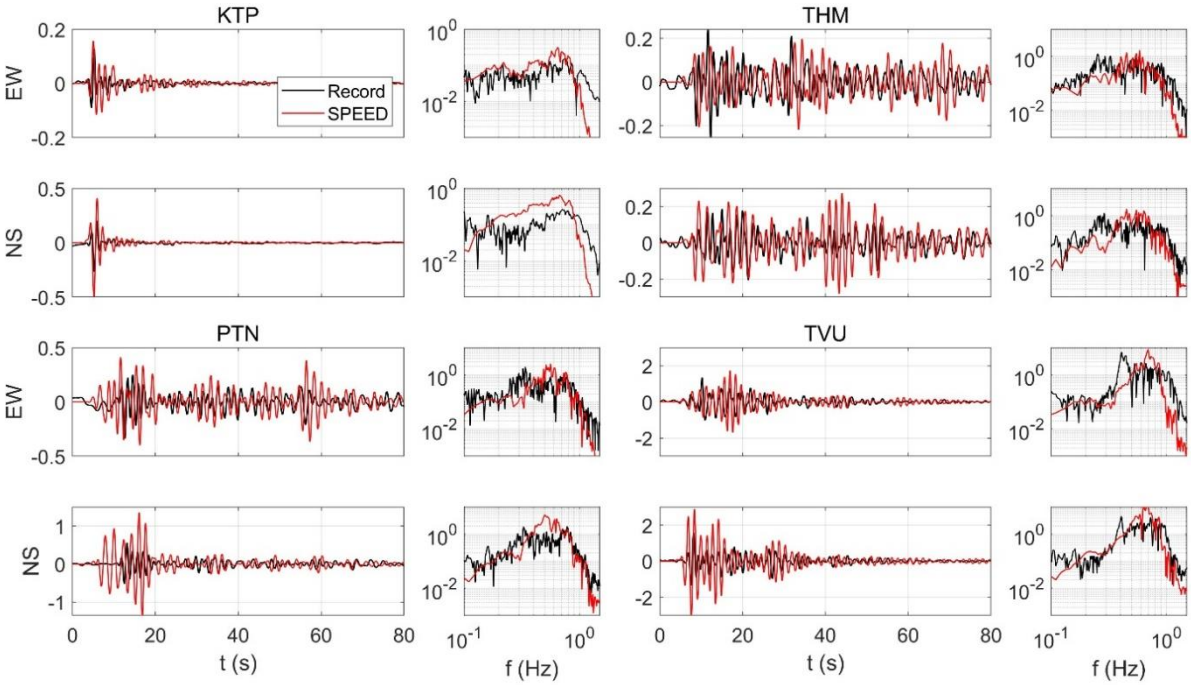

Figure 3. Comparison between recorded (black lines) and simulated (red lines) velocity waveforms (in cm/s) and their corresponding FAS (in cm) for the 25/04/2015 6:53 M4.9 earthquake.

In Figure 3 velocity waveforms are presented. The locations of the stations are shown in Figure 4. Synthetics and records have been low-pass filtered at 0.9 Hz, for consistency with the spatial resolution of the mesh While there is an overall good agreement between simulated and recorded ground motion, the peaks in the Fourier spectra (FAS) of the simulated motions appear at slightly higher frequencies. It is interesting to note the differences in strong ground motion duration; for instance, at station KTP, located in outcropping bedrock, the duration is of less than 10 s, while for station THM, located in a deeper part of the basin, the duration is of more than 50 s.

In order to highlight the effect of the basin on the ground motion, Figure 4 shows a map of geometric mean of horizontal peak ground velocity (PGV), from which the amplification of ground motion is evident inside the basin. Moreover, it's clear that for this case, PGVs are larger at the western part of the basin, since the simulated earthquake is located to the west. Using simple 1D simulations it is not possible to obtain the observed spatial variation of the ground motion.

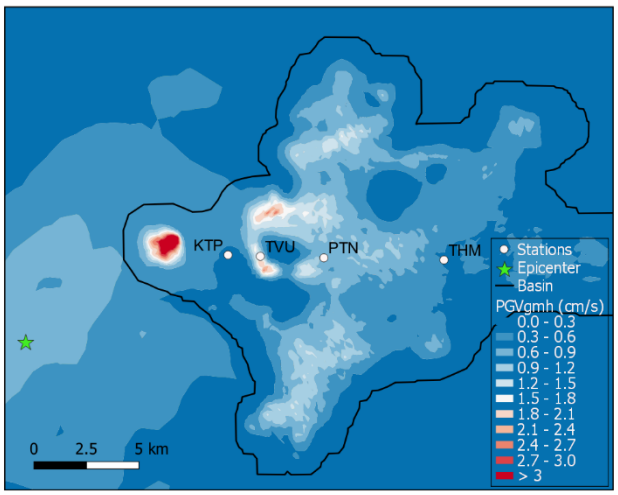

Figure 4. Ground motion map of PGV for GMH (geometric mean of horizontal) components.

4 CONCLUSIONS

Three-dimensional physics-based numerical simulations of two aftershocks of the 2015 Gorkha earthquake were produced by the open-source spectral element code SPEED. A 3D numerical model covering an area of 196x98 km^2 was constructed, based on the geological and geophysical investigations available, with special emphasis on the Kathmandu basin. While the maximum frequency that our model is able to propagate is relatively low (0.9 Hz), we were able to realistically simulate the basin effects, evident in the long-duration ground motion inside the basin with strong amplification at low frequencies.

At this point we did not attempt to simulate the Mw7.8 mainshock or the largest aftershock, since it has been shown that for these events soil non-linearity was present, and the model used here is linear viscoelastic. However, in the near future we expect to simulate also the mainshock.

ACKNOWLEDGEMENTS

The authors are grateful for the financial support provided by the SERICE project funded by the Icelandic Centre for Research (RANNIS), Grant Number: 218149-051. RR acknowledges support from the University of Iceland Research Fund.

REFERENCES

Asimaki, D., Mohammadi, K., Mason, H. B., Adams, R. K., Rajaure, S., & Khadka, D. (2017). Observations and simulations of basin effects in the Kathmandu valley during the 2015 Gorkha, Nepal, Earthquake Sequence. *Earthquake Spectra*, *33*(Special issue 1), S35–S53. https://doi.org/10.1193/013117EQS022M.

Avouac, J.-P., Meng, L., Wei, S., Wang, T., & Ampuero, J.-P. (2015). Lower edge of locked Main Himalayan Thrust unzipped by the 2015 Gorkha earthquake. *Nature Geoscience*, *8*(9), 708–711. https://doi.org/10.1038/ngeo2518.

Bijukchhen, S. (2018). *Construction of 3-D velocity structure model of the Kathmandu Basin, Nepal, based on geological information and earthquake ground motion record.* PhD Thesis, Hokkaido University.

Gilder, C. E. L., Pokhrel, R. M., Vardanega, P. J., De Luca, F., De Risi, R., Werner, M. J., Asimaki, D., Maskey, P. N., & Sextos, A. (2020). The SAFER geodatabase for the Kathmandu Valley: Geotechnical and geological variability. *Earthquake Spectra*, *36*(3), 1549–1569. https://doi.org/10.1177/8755293019899952.

Mazzieri, I., Stupazzini, M., Guidotti, R., & Smerzini, C. (2013). SPEED: SPectral Elements in Elastodynamics with Discontinuous Galerkin: a non-conforming approach for 3D multi-scale problems. *International Journal for Numerical Methods in Engineering*, *95*, 991–1010. https://doi.org/10.1002/nme.4532.

Moribayashi, S., & Maruo, Y. (1980). Basement Topography of the Kathmandu Valley, Nepal. *Journal of the Japan Society of Engineering Geology*, *21*(2).

Rupakhety, R., Olafsson, S., & Halldorsson, B. (2017). The 2015 Mw 7.8 Gorkha Earthquake in Nepal and its aftershocks: analysis of strong ground motion. *Bulletin of Earthquake Engineering*, *15*(7), 2587–2616. https://doi.org/10.1007/s10518-017-0084-z.

Sakai, H. (2001). Stratigraphic division and sedimentary facies of the Kathmandu Basin Group, central Nepal. *Journal of Nepal Geological Society*, *25*, 19–32.

Shen, W., Yang, D., Xu, X., Yang, S., & Liu, S. (2022). 3D simulation of ground motion for the 2015 M w 7.8 Gorkha earthquake, Nepal, based on the spectral element method. *Natural Hazards*, *112*(3), 2853–2871. https://doi.org/10.1007/s11069-022-05291-1.

Shigefuji, M., Takai, N., Bijukchhen, S., Ichiyanagi, M., Rajaure, S., Dhital, M. R., Paudel, L. P., & Sasatani, T. (2022). Strong ground motion data of the 2015 Gorkha Nepal earthquake sequence in the Kathmandu Valley. *Scientific Data*, *9*(1). https://doi.org/10.1038/s41597-022-01634-6.

Sreejaya, K. P., & Raghukanth, S. T. G. (2022). Hybrid Broadband Ground Motion Simulation for 2015 Mw 7.9 Nepal Earthquake. *Journal of Earthquake and Tsunami*, *16*(5). https://doi.org/10.1142/S1793431122500154.

Takai, N., Shigefuji, M., Rajaure, S., Bijukchhen, S., Ichiyanagi, M., Dhital, M. R., & Sasatani, T. (2016). Strong ground motion in the Kathmandu Valley during the 2015 Gorkha, Nepal, earthquake 4. Seismology. *Earth, Planets and Space*, *68*(1). https://doi.org/10.1186/s40623-016-0383-7.

Wei, S., Chen, M., Wang, X., Graves, R., Lindsey, E., Wang, T., Karakaş, Ç., & Helmberger, D. (2018). The 2015 Gorkha (Nepal) earthquake sequence: I. Source modeling and deterministic 3D ground shaking. *Tectonophysics*, *722*, 447–461. https://doi.org/10.1016/j.tecto.2017.11.024.

Proceedings of the XVIII ECSMGE 2024
GEOTECHNICAL ENGINEERING CHALLENGES
TO MEET CURRENT AND EMERGING NEEDS OF SOCIETY
© 2024 the Authors
ISBN 978-1-032-54816-6
DOI 10.1201/9781003431749-308
Open Access: www.taylorfrancis.com, CC BY-NC-ND 4.0 license

ECSMGE 24
XVIII EUROPEAN CONFERENCE ON SOIL MECHANICS AND GEOTECHNICAL ENGINEERING

Revisit a landslide in Boulder clay at Selset, Yorkshire: Insights from probabilistic analysis

Réexaminer un glissement de terrain dans l'argile de Boulder à Selset, Yorkshire: Perspectives issues d'une analyse probabiliste

W. Huang*
Teesside University, Middlesbrough, United Kingdom

S. Bulolo
Kyambogo University, Kampala, Uganda

W. Zhang
Durham University, Durham, United Kingdom

M. Zhang
Zhengzhou University of Aeronautics, Zhengzhou, China

**w.huang@tees.ac.uk*

ABSTRACT: Skempton and Brown (1961) presented a well-documented landslide case study involving a heavily overconsolidated boulder clay deposit in Selset, Yorkshire, UK. While the laboratory testing program revealed significant inherent variability in soil parameters, their analyses were limited to deterministic approaches. This study revisits their work within the framework of probabilistic analysis. We employed Monte Carlo Simulations (MCS) alongside Random Field Finite Element Limit Analysis (RF-FELA), which explicitly accounts for spatial variability. Additionally, we conducted MCS using a closed-form solution, implicitly neglecting spatial variability, i.e., assuming a scale of fluctuation tending towards infinity. Our analysis revealed that neglecting spatial variability can lead to an overestimation of the probability of failure. Nevertheless, MCS with the closed-form solution substantially reduces the computational time required by RF-FELA from hours (or even days) to minutes, making it an efficient tool for preliminary probabilistic analysis. The case study also demonstrate that probabilistic slope stability analysis provides more profound insights, offers a more transparent means of quantifying slope risk, and better captures the rapid increase in risk as the verge of failure is approached.

RÉSUMÉ: Skempton et Brown (1961) ont présenté une étude de cas bien documentée sur un glissement de terrain impliquant un dépôt d'argile à blocs fortement surconsolidée à Selset, Yorkshire, Royaume-Uni. Alors que le programme d'essais en laboratoire a révélé une variabilité inhérente significative des paramètres du sol, leurs analyses se limitaient à des approches déterministes. Cette étude réexamine leur travail dans le cadre de l'analyse probabiliste. Nous avons utilisé des simulations de Monte Carlo (MCS) en conjonction avec l'Analyse de Limite d'Éléments Finis de Champ Aléatoire (RF-FELA), qui prend explicitement en compte la variabilité spatiale. De plus, nous avons effectué des MCS en utilisant une solution en forme fermée, négligeant implicitement la variabilité spatiale, c'est-à-dire en supposant une échelle de fluctuation tendant vers l'infini. Notre analyse a révélé que le fait de négliger la variabilité spatiale peut conduire à une surestimation de la probabilité de défaillance. Néanmoins, les MCS avec la solution en forme fermée réduisent considérablement le temps de calcul nécessaire par RF-FELA, passant de heures (voire jours) à quelques minutes, en en faisant un outil efficace pour une analyse probabiliste préliminaire. L'étude de cas démontre également que l'analyse probabiliste de la stabilité des pentes offre des perspectives plus approfondies, fournit un moyen plus transparent de quantifier le risque de pente et capture mieux l'augmentation rapide du risque à l'approche de la défaillance.

Keywords: Slope stability; deterministic analysis; probabilistic analysis; Monte Carlo Simulation; Spatial variability.

1 INTRODUCTION

Soils are naturally occurring materials and exhibit inherent variability. When addressing slope stability issues, deterministic analysis is a commonly employed method. However, deterministic analysis falls short in adequately addressing the inherent uncertainties and variations in soil properties. The key advantage of employing probabilistic analysis lies in its ability to effectively quantify parameter uncertainties.

In this research, we revisit a well-documented landslide case that occurred in Selset, Yorkshire, UK,

using a probabilistic approach. This paper is structured as follows. First, we present a closed-form solution suitable for integrated deterministic and probabilistic analysis. Following this, we provide a brief overview of the Selset slope failure, and subsequently, we delve into both deterministic and probabilistic analyses.

2 CLOSED FORM SOLUTIONS FOR SLOPE STABILITY ANALYSIS

Taylor (1937) found that solutions of homogeneous slopes can be presented as dimensionless charts. Since then a large number of slope stability charts have been presented in the literature (e.g., Bishop and Morgenstern, 1960; Barnes, 1991; Michalowski, 2002; Steward et al. 2011). Slopes are rarely homogeneous. However, site investigation is often limited at early design stage or for analyses at regional and network scales. For such situations, simplification and assuming homogeneous ground condition become necessary. For the Selset slope failure revisited in this study, the slope is relatively simple and homogenous, use of stability charts gives accurate stability assessment (Skempton and Brown, 1961).

Slope stability charts are a product of 20th century, and it does not comply with the digital design workflow in the 21st century (Huang, 2023a). Instead of presenting dimensionless stability solutions as charts, Huang (2018, 2023b) further carried out regression analyses and innovatively developed a series of closed form solutions for dry, saturated and unsaturated slopes. The closed form solution for saturated slopes, which can be used to back analyse Selset slope failure, is given below:

$$F = A\left(\frac{c'}{\gamma H \tan\phi'}\right)^{B} \tan\phi' + \frac{\tan\phi'}{\tan\alpha} - \left(\frac{c'}{\gamma H}\frac{1}{\tan\alpha} + \frac{\tan\phi'}{\sin\alpha\cos\alpha}\right) r_u \quad (1)$$

where F = factor of safety, c' = effective cohesion, ϕ' = friction angle, γ = soil unit weight, H = slope height, α = slope angle. Parameters A and B are the two curve-fit parameters in regression analyses and they can be calculated as

$$A = 10.50\exp(-0.009\alpha) \quad (2)$$

If $0 \le \frac{c'}{\gamma H \tan\phi'} \le 1$:

$$B = 0.72 - 3.5\times10^{-5}\alpha^2 + 0.0031\alpha \quad (3a)$$

If $1 < \frac{c'}{\gamma H \tan\phi'} \le 3$:

$$B = 0.83 - 2.2\times10^{-5}\alpha^2 + 0.0026\alpha \quad (3b)$$

The slope angle α should be input as degree in Eq. (2) and (3). The applicable range of Eq. (1) is α = 11°~65° and $\frac{c'}{\gamma H\tan\phi'}$ = 0~3, which should cover most slopes encountered in practice. Closed form solution for α > 65° is also provided by Huang (2023b).

The advantages of closed form solutions over slope stability charts are (Huang, 2023a):

- The slope parameters are continuous within the defined range (rather than being restricted to discrete values necessarily dictated by the use of stability charts), therefore the user has more flexibility on the choice of parameter value.
- Closed form solutions can easily be incorporated into modern digital design workflows, such as Excel spreadsheets.
- Closed form solutions can be used for both deterministic and probabilistic slope stability analyses, as demonstrated in Sections 4 and 5.

3 SELSET SLOPE FAILURE

Skempton and Brown (1961) presented a case study on a slip at the river valley side in Selset, Yorkshire, UK. Figure 1 illustrates a cross-section of the landslide, with a slope height of H = 12.8 m and a slope angle of α = 28°. The slip occurred in Boulder clay, a heavily overconsolidated clay (OC) that likely deposited about 45,000-50,000 years ago during an early stage of the Last Glaciation. Alongside the hill slope's toe, a river has been flowing for at least a century, potentially causing erosion during floods. As per Skempton and Brown (1961), the slope may have remained in or near a state of limiting equilibrium for an extended period.

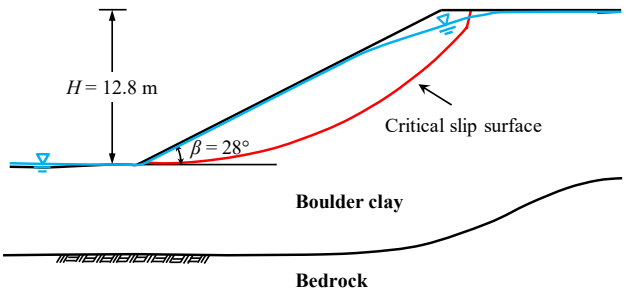

Figure 1. Cross-section of Selset slope failure.

The site investigation revealed the following basic soil properties: natural water content = 12%, clay fraction (< 2μ) = 25%, liquid limit w_L = 26, plastic limit w_P = 13, plasticity index I_P = 13. Eight samples were collected from the site, and consolidated drained

triaxial tests were conducted on these samples. Each sample had a diameter of 38mm and a height of 76 mm. The soil parameters are summarised in Table 1. Figure 2 displays the statistical distributions of the soil properties as presented by Skempton and Brown (1961), along with the Normal and Lognormal fits. Due to the limited amount of data, no consideration was given to the correlation between the random variables.

Table 1. Summary of soil properties.

	Mean (μ)	**Standard deviation (σ)**	**Coefficient of variation (COV)**
Saturated unit weight (γ)	21.8 kN/m^3	0.44 kN/m^3	2.0%
Cohesion intercept (c')	8.7 kPa	3.1 kPa	35.6%
Friction angle (ϕ')	32.0°	1.8°	5.5%

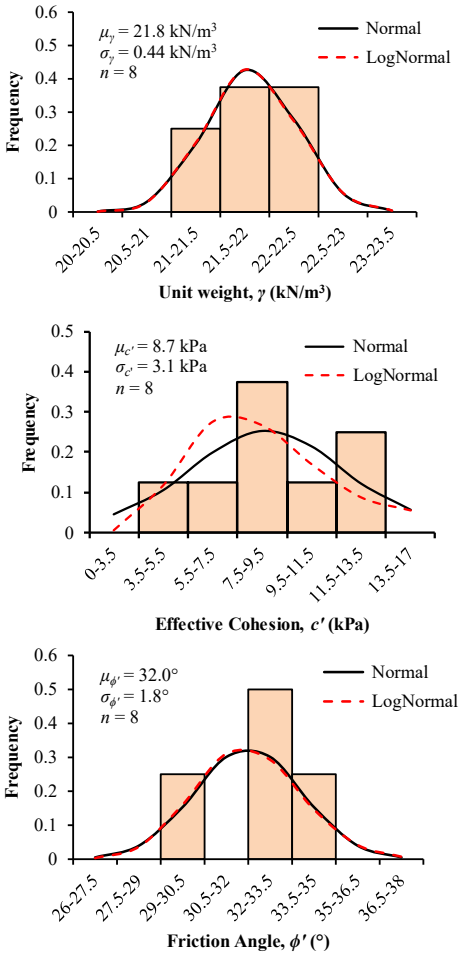

Figure 2. Statistical distribution of the soil properties for Selset Slope (data from Skempton and Brown, 1961).

The slip surface passes through intact Boulder Clay. Consequently, the field value of the cohesion intercept c' is approximately equal to the laboratory value measured in drained triaxial test. This observation stands in stark contrast to the outcomes typically observed in long-term slips occurring in overconsolidated fissured clays, where cohesion diminishes over time and eventually tends towards zero (Skempton, 1970).

4 DETERMINISTIC ANALYSIS

The highest water level measured at winter months, as shown in Figure 1, is practically at the ground surface except at the top of the slope. If the water level is simply taken as at the ground surface, preliminary analyses can be carried out at two extreme pore-water pressure conditions (Skempton and Brown, 1961): 1) hydrostatic condition, pore-water pressure ratio $r_u = \frac{\gamma_w}{\gamma} = \frac{9.81}{21.8} = 0.45$; and 2) steady state seepage with flow parallel to the slope surface, $r_u = \frac{\gamma_w}{\gamma}\cos^2\beta = 0.35$. Given the water level depicted in Figure 1 and in accordance with the two-dimensional critical slip surface presented by Skempton and Brown (1961), the area of the failure mass is about 103 m^2 and the submerged failure mass is about 96 m^2. Therefore, the pore-water pressure ratio can be approximated as $r_u = \frac{96}{103}\frac{\gamma_w}{\gamma} = \frac{96}{103} \times \frac{9.81}{21.8} \approx 0.42$ at hydrostatic condition.

Table 2. Deterministic analysis results.

	Factor of safety			
	r_u = 0.35	**r_u = 0.42**	**r_u = 0.45**	**Method**
Skempton and Brown (1961)	1.14	1.05	0.99	Stability chart
Miller and Hamilton (1989)	1.14	1.02	0.97	UBLA
This study	1.12	1.01	0.96	by Eq. (1)

Back analyses of Selset slope failure have been carried out by Skempton and Brown (1961), Miller and Hamilton (1989) and in this study. Deterministic analyses were carried out with mean values of soil parameters given in Table 1. The results are summarised in Table 2. The geometry of the Selset slope is relatively simple and critical slip surface in a relatively uniform material. Therefore, slope stability analysis can be carried out accurately with slope stability charts, and the charts developed by Bishop

and Morgernstern (1960) was used by Skempton (1961) in back analyses. Miller and Hamilton (1989) reanalysed the Selset slope failure using upper bound limit analysis with rigid-body rotation mechanism. In this study, Eq. (1) is used for the back analyses. Factors of safety reported in the literature and obtained by Eq. (1) are remarkably consistent, with F = 1.12~1.14 at r_u = 0.35, F = 1.01~1.05 at r_u = 0.42, and F = 0.96~0.99 at r_u =0.45. The low safety margin or with F < 1 has, to some extent, explained the slope failure. However, laboratory testing of the soil, as shown in Figure 2, reveals soil variability and uncertainty. Yet, this is not captured by deterministic analysis. Therefore, probabilistic analysis would be carried out to bring additional insights.

5 PROBABILISTIC ANALYSIS

5.1 Random Field Finite Element Limit Analysis

Random field finite element limit analyses (RF-FELA) were carried out using the software Optum G2 (version 2021 2.1.6). Finite element limit analyses can be carried out by lower or/and upper bound. Agbaje et al. (2022) showed that the difference in probability of failure calculated by lower/upper bound is generally less than 2%. Therefore, lower bound limit analysis, which is slightly on the conservative side, is adopted in this study. Variability of the soil properties (Table 1), quantified by coefficient of variation (COV), is explicitly modelled. As COV of cohesion is 35.6%, the soil parameters are assumed to follow Lognormal distribution to avoid negative inputs (physically impossible). The spatial variation/random field modelling was generated using the Karhunen-Loeve (KL) expansion method. Huang et al. (2022) investigated vertical scale of fluctuation (δ_y) of London Clay with CPT data, and reported that δ_y ranges from 0.24 to 1.01 m with a mean of 0.48 m. No analysis has been found on Boulder clay. In this study, δ_y of Boulder clay is simply taken as 0.5 m. For the soils that have gone through normal deposition process, horizontal scale of fluctuation (δ_x) is generally much greater than δ_y, but the values of δ_x are rarely reported due to the scarcity of site investigation data collected at closely spaced horizontal intervals. Therefore, parametric studies are carried out with δ_x =1 m, 5 m, 50 m, respectively. The number of element of the finite element mesh is set to 1000, and mesh adaptivity is enabled with 3 adaptive iterations, so that the mesh is automatically refined along the critical slip surface. A typical set of results is shown in Figure 3(a) for δ_x = 1 m, δ_y = 0.5 m, and Figure 3(b) for δ_x = 50 m, δ_y = 0.5 m.

Probabilistic analysis was completed using the Monte Carlo Simulation (MCS). Probability of failure (P_f) is calculated as the ratio of the number of slope failures (F < 1) to the total number of simulations. The number of simulations is set to be 1000, which is considered as sufficient when the probability of failure is relatively high and used by Agbaje et al. (2022). The results are presented in Section 5.3.

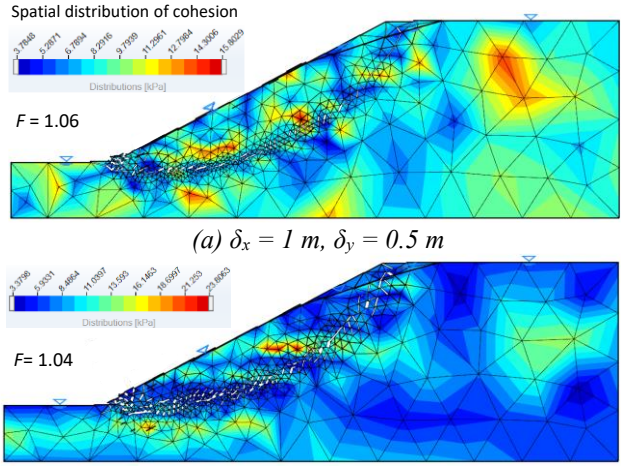

(a) δ_x = 1 m, δ_y = 0.5 m

(b) δ_x = 50 m, δ_y = 0.5 m

Figure 3. Illustration of random field finite element analysis (the contours show spatial distribution of cohesion).

The time required for 1000 simulations with RF-FELA takes about 7.4 hours on a computer with i7-9750H CPU@2.60GHz and 16 GB of RAM. In cases involving slopes with lower P_f, greater number of simulations would be required to ensure accuracy of MCS. Though MCS is widely regarded as a superior approach, the computational time requirement limits its application in industry practice.

5.2 Efficient Probabilistic analysis with closed form solutions

With the closed form solution Eq. (1), Monte Carlo simulation with 1,000,000 simulations can be completed in 3 minutes on a computer with i7-9750H CPU@2.60GHz and 16 GB of RAM. This stands in sharp contrast to the 7.4 hours required for 1000 simulations using RF-FELA. Probabilistic analysis with first-order reliability method (FORM) and first-order second moment (FOSM) method can be completed instantly. Excel spreadsheets and VBA scripts used to implement MCS, FORM and FOSM has been provided by Huang (2023a, 2023b). They are adapted for the back analysis of Selset landslide in this study. The results are summarized in Section 5.3.

5.3 Probabilistic analysis results

The results of MCS by RF-FELA, where δ_x varies from 1 m to 50 m (with δ_y held at 0.5 m), are shown in **Error! Reference source not found.**. Additionally, MCS with Eq. (1) are presented. In the case of MCS using Eq. (1), in each simulation the slope is homogenous, therefore it is equivalent to assume $\delta_x = \delta_y = +\infty$. The cumulative probability increases with the increase in F and shows a "S" shape. For each cumulative probability curve, the cumulative probability at $F = 1$ represents the probability of failure, as summarised in **Error! Reference source not found.**. For the MCS with RF-FELA, P_f increases with the increase in scale of fluctuation, from 5.2% to 27.7%. It should be noted that this observation is made when $P_f < 50\%$, and P_f may decrease with the increase in scale of fluctuation when $P_f > 50\%$ (Huang, 2020). The solution obtained by MCS with Eq. (1) should be viewed as an approximate solution, and a 20% is reasonable compared to those reported by MCS with RF-FELA.

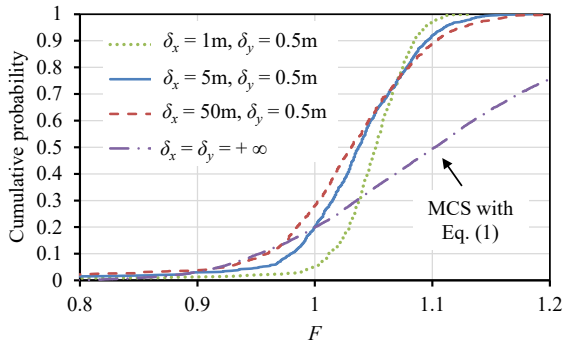

Figure 4. Cumulative probability of failure of Selset slope considering spatial variability (r_u = 0.35, Lognormal distribution).

Use of MCS with RF-FELA is limited to Lognormal distribution of the soil parameters and steady state seepage of water pressure (r_u is about 0.35). Further analyses were carried out using MCS with Eq. (1) considering both Normal and Lognormal distributions and r_u ranging from 0.35 to 0.45. The results are summarised in Table 4. The P_f obtained with Lognormal distribution is very closed to or slightly greater than Normal distribution. The P_f is about 20% at $r_u = 0.35$, increase to about 50% at $r_u = 0.42$, and further increase to more than 60% at $r_u = 0.45$.

With the closed form solution Eq. (1) parametric studies can readily be carried out for various r_u for both deterministic and probabilistic analyses, as illustrated in Figure 5. The P_f obtained by FORM and MCS with Normal and Lognormal distributions are almost identical (only those for Lognormal distribution are shown). Factor of safety F decrease linearly with the increase in r_u. When $r_u \leq 0.25$, P_f is practically zero, and P_f increase exponentially with the further increase in r_u. It can be concluded that probabilistic analysis better capture the increment of risk level of the slope.

Table 3. Effect of spatial variability on probability of failure (r_u = 0.35, Lognormal distribution).

Method	**Monte Carlo Simulation (MCS) with Random Field Finite Limit Analysis**			**MCS with Eq. (1)**
Scale of fluctuation	δ_x = 1 m, δ_y = 0.5 m	δ_x = 5 m, δ_y = 0.5 m	δ_x = 50 m, δ_y = 0.5 m	$\delta_x = +\infty$ $\delta_y = +\infty$
Probability of failure (P_f)	5.2%	19.8%	27.7%	20.0%

Table 4. Probabilities of failure by Monte Carlo Simulation with Eq. (1) ($\delta = +\infty$).

Distribution	**r_u = 0.35**	**r_u = 0.42**	**r_u = 0.45**
Lognormal	20.0%	52.8%	66.4%
Normal	20.3%	47.2%	61.0%

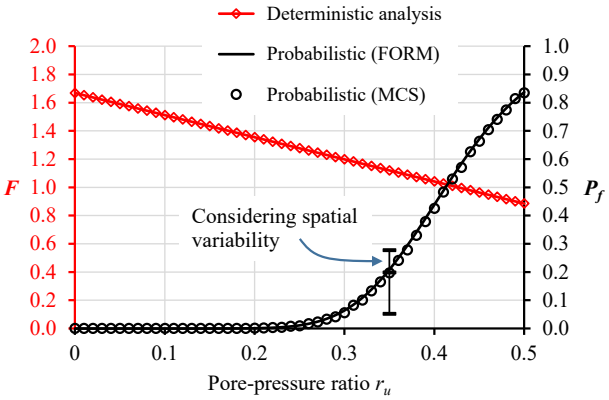

Figure 5. Comparison of deterministic and probabilistic analysis for Selset slope failure.

6 CONCLUSION

This study revisited the Selset slope failure. Despite the soil being situated within a single soil layer and consisting of relatively uniform Boulder Clay, it exhibits inherent variability. To address this, probabilistic analyses were conducted using Monte Carlo Simulation, employing Random Field Finite Element Limit Analysis, and a closed-form solution as defined in Eq. (1). The results from these back analyses demonstrate that probabilistic analysis provides a more accurate reflection of the slope's risk level through directly quantifies parameter variability

and more effectively captures the increase in slope risk with the change of triggering factors (e.g., pore-water pressures).

REFERENCES

Agbaje, S., Zhang, X., Ward, D., Dhimitri, L., & Patelli, E. (2022). Spatial variability characteristics of the effective friction angle of Crag deposits and its effects on slope stability. *Computers and Geotechnics*, 141, 104532. https://doi.org/10.1016/j.compgeo.2021.104532.

Barnes, G. E. (1991). A simplified version of the Bishop and Morgenstern slope stability charts. *Canadian Geotechnical Journal*, 28(4), 630–637. https://doi.org/10.1139/t91-076.

Bishop, A. W., and Morgenstern, N. (1960). Stability coefficients for earth slopes. Géotechnique, 10(4), 129–153. https://doi.org/10.1680/geot.1960.10.4.129.

Huang, W. (2018). *Stability of unsaturated soil slopes under rainfall and seismic loading*. PhD thesis, Nanyang Technological University, Singapore.

Huang, W. (2020). Discussion of "Probabilistic seismic slope stability analysis and design". *Canadian Geotechnical Journal*, 57(7), 1099–1101. https://doi.org/10.1139/cgj-2019-0486.

Huang, W. (2023a). Efficient analytical approach for stability analysis of infrastructure slopes. *Proceedings of the Institution of Civil Engineers – Geotechnical Engineering*, 176(2), 194-207. https://doi.org/10.1680/jgeen.21.00106.

Huang, W. (2023b). Stability of homogeneous slopes: from chart to closed-form solutions and from deterministic to probabilistic analysis. *International Journal of Geomechanics*, 23(9), 04023136. https://doi.org/10.1061/IJGNAI.GMENG-8258.

Huang, W., Dijkstra, T., Loveridge, F., Hughes, P., Blake, A., Dobbs, M., Gonzalez, Y. G. (2022). Spatial variability of London Clay using CPT and SPT data. *Proceedings of the 8th International Symposium on Geotechnical Safety and Risk (ISGSR)*, 14th – 16th December 2022, Newcastle, Australia.

Michalowski, R. L. (2002). Stability charts for uniform slopes. *Journal of Geotechnical and Geoenvironmental Engineering*, 128(4), 351–355. https://doi.org/10.1061/(ASCE)1090-0241(2002)128:4(351).

Miller, T. W., & Hamilton, J. M. (1989). A new analsis procedure to explain a slope failure at the Martin Lake mine. *Géotechnique*, 39(1), 107-123. https://doi.org/10.1680/geot.1989.39.1.107.

Skempton, A. W. (1970). First-time slides in over-consolidated clays. *Géotechnique*, 20(3), 320-324. https://doi.org/10.1680/geot.1970.20.3.320.

Skempton, A. W., & Brown, J. D. (1961). A landslide in boulder clay at Selset, Yorkshire. G*éotechnique*, 11(4), 280-293. https://doi.org/10.1680/geot.1961.11.4.280.

Steward, T., Sivakugan, N., Shukla, S. K., and Das, B. M. (2011). Taylor's slope stability charts revisited. *International Journal of Geomechanics*, 11(4), 348–352. https://doi.org/10.1061/(ASCE)GM.1943-5622.0000093.

Taylor, D. W. (1937). Stability of earth slopes. *Journal of Boston Society of Civil Engineers*, 24(3), 197–246.

Proceedings of the XVIII ECSMGE 2024
GEOTECHNICAL ENGINEERING CHALLENGES
TO MEET CURRENT AND EMERGING NEEDS OF SOCIETY
© 2024 the Authors
ISBN 978-1-032-54816-6
DOI 10.1201/9781003431749-309
Open Access: www.taylorfrancis.com, CC BY-NC-ND 4.0 license

ECSMGE 24
XVIII EUROPEAN CONFERENCE ON SOIL MECHANICS AND GEOTECHNICAL ENGINEERING

Flash floods in Lisbon – Local scale mitigation and adaptation measures

Crues soudaines à Lisbonne - Mesures d'attenuatión et d'adaptation à l'échelle locale

M. Inácio*, C. Pinto, C. Almeida, P. Leonardo, M. Morais
CML, Lisbon, Portugal

**ext.miguel.inacio@cm-lisboa.pt*

ABSTRACT: The common approaches to flood risk management are based on a top-down view, which, from our perspective, does not allow the adoption of effective solutions considering the different origins of this problem, such as insufficient drainage systems, surface water level, and impermeabilization. With this bottom-up approach, the idea is to consult the information available in municipal services to identify and delimit flooded areas. This mapping will allow the definition of flood zones in which subsequent actions will be promoted. An integrated analysis can be carried out for each affected area, which should include a definition of mitigation and/or adaptation measures to be implemented at a local scale. In some locations, given the constraints, it will only be possible to develop adaptation strategies, such as the placement of anti-flood barriers at the doors of affected buildings, which will allow for proactive rather than reactive actions. As a proof of concept, a street in the floodable area will be selected, barriers will be purchased, and an evaluation will be made in the next event. After this analysis and definition, the areas adjacent to the floodable areas should be analyzed to narrow the systems contributing to flooding in each location.

RÉSUMÉ: Les approches courantes de la gestion des risques d'inondation sont basées sur une vision descendante, qui, selon notre perspective, ne permet pas l'adoption de solutions efficaces en tenant compte des différentes origines de ce problème, par exemple les systèmes de drainage insuffisants, le niveau des eaux de surface, et l'imperméabilisation. Dans cette approche ascendante, l'idée est de consulter les informations disponibles dans les services municipaux pour identifier et délimiter les zones inondées. Cette cartographie permettra de définir des zones d'inondation sur lesquelles des actions ultérieures seront promues. Une analyse intégrée peut être proposée pour chacune des zones touchées, qui devrait inclure la définition de mesures d'atténuation et/ou d'adaptation à mettre en œuvre à l'échelle locale. Dans certains endroits, compte tenu des contraintes, il ne sera possible de développer que des stratégies d'adaptation, comme la mise en place de barrières anti-inondation aux portes des bâtiments affectés, ce qui permettra des actions proactives plutôt que réactives. Pour preuve de concept, une rue dans la zone inondable sera sélectionnée, des barrières seront achetées et une évaluation sera effectuée lors du prochain événement. Après cette analyse et définition, les zones adjacentes aux zones inondables devraient être analysées afin de réduire les systèmes contribuent aux inondations dans chaque localisation.

Keywords: Flood; risk management; bottom-up approach; precipitation; adaptation.

1 INTRODUCTION

The city of Lisbon, located at the confluence of the Tagus River with the Atlantic Ocean, is a major economic center in Portugal with a high population density. This location has given the city a prominent geostrategic position but also exposes it to natural and climatic hazards such as urban floods and an increasing occurrence of extreme weather events.

Whenever episodes of intense precipitation occur, exceeding the normal levels, parts of the city become completely flooded, with several centimeters of water, causing partial paralysis of the city and significant financial losses for both Lisbon and the country because many people are unable to go to their workplaces. During intense rainfall events, most urban flooding is caused by overflow in former watercourses that are occupied by buildings roads and pavements. These structures act as obstacles to the unimpeded flow of water, obstructing and hindering its movement and thereby creating a barrier-like effect.

According to a study conducted by Antunes et al. (2017), assessing vulnerability of sea level rising (MSL) in urban areas is crucial for defining and adopting strategies for climate change adaptation.

Based on the records of the Cascais tide gauge, in operation since 1882, it can be concluded that the MSL on the Portuguese coast has already risen about 22 cm

since the second decade of the 20th century, with 8 cm of this increase occurring in the last 25 years. The hypothesis that the MSL is in a process of increasing its rate of rise is supported by the most recent ocean observation data from satellites, altimetry, gravimetry, and the network of floats measuring the evolution of the average temperature of the top 300 m layer of the oceans, showing an acceleration in the rise of MSL in the last 10 years (Antunes, 2019).

Despite the uncertainty about the evolution of CO_2 and greenhouse gas emissions into the atmosphere, coupled with the complex dynamics of the oceans, a continuous rapid rise in MSL is expected. Global warming is the main contributor to the increase in melting of the largest continental ice reservoirs located in Antarctica and Greenland (Antunes et al., 2017).

With the increasing frequency of these intense precipitation episodes, 2022 was a critical year for the city, with December being an extremely warm month in terms of air temperature and very rainy in terms of precipitation. Classified in Portugal mainland as the warmest December in the last 92 years, the average value of the air temperature was 2.76ºC above normal. The average minimum air temperature was 9.58ºC, representing an anomaly of +3.53ºC. Meanwhile, the average maximum air temperature reached 15.87ºC, which is higher than the average value with an anomaly of +1.99ºC, being the second-highest value since 1931. The extreme precipitation value in 24 hours was 110.7 mm in Lisbon (Gago Coutinho on the 13th of December). The total average precipitation in December was 250.4 mm, which corresponds to 174% of the normal value, ranking as the 10th highest since 1931 and the 2nd highest since 2000 (IPMA, 2022).

In December, there were several instances of heavy precipitation, particularly on the 4th, 5th, 7th, 8th, 12th, and 13th, and at the end of the month. The two most extreme episodes of precipitation, on the 7th-8th and 12th-13th, accounted for approximately half of the total monthly precipitation.

2 METHODOLOGY, RESULTS AND DEVELOPMENTS IN PROGRESS

The work began with consulting operational services to identify and delineate the flooded areas during the floods in December of 2022. These floods prove to have a high return period, so their occurrence is comparable to those that happen every 100 years. Undertaking the drafting of this map will facilitate the delineation of the various zones in which the actions to be taken will take place. It is proposed that each of the affected areas be analyzed in an integrated manner, including the definition of a strategy with mitigation and adaptation measures to be adopted in the building or along the block. As this is on a local scale, it is recommended that measures be implemented at the level of urbanization plans and detailed plans, but also at the level of green areas and unoccupied public spaces.

2.1 Mapping occurrences

The Fire Department records all flooding incidents within the municipality. This record was made available to the authors of this work so that they could use this information as a basis for identifying vulnerable areas. The aim of this task was to identify the periods of flooding corresponding to the centennial rainfall values (with a return period or recurrence of 100 years). To this end, the events were filtered to periods that met these requirements, namely the rainfall events of December 7, 8, 12, and 13 of 2022 that affected Lisbon (Figure 1).

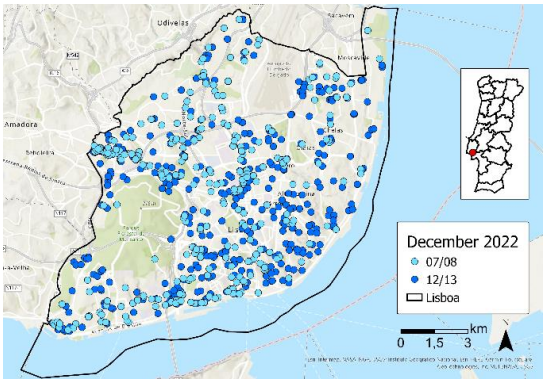

Figure 1. Flooding incidents reported to the Lisbon Fire Department Regiment on December 7, 8, 12 and 13 of 2022.

In addition, the tide values recorded during these periods were checked, and it was identified that the periods with the highest number of occurrences corresponded to high-tide periods. Thus, at the end of this phase, it was possible to obtain a list of events that occurred during the hours of greatest rainfall and with the highest tides, which were likely occurrences of centenary rainfall events. Duplicate occurrence records were also checked and excluded (sometimes the same occurrence was recorded twice, which is normal because firefighters receive information from more than one data source).

2.2 Mapping of flood-prone areas

Case studies:

- December 7-8: The weather in Portugal mainland was conditioned by the presence of a depression centered to the east of the Azores Island. This rainfall led to several flash floods in various urban areas of the Lisbon metropolitan

area, and two daily rainfall maximums were recorded by Instituto Geofísico (83.3 mm) and Gago Coutinho (78.9 mm) weather stations.

- December 12-13: The weather was conditioned by an intense SW flow associated with the passage of warm, humid, and unstable air masses with a high content of precipitable water. There was persistent rain, which was sometimes heavy, and caused flash floods, particularly in Greater Lisbon. During this period, there was an extremely high 3-hour rainfall at the Gago Coutinho (76.9 mm) and Relógio (73.5 mm) stations between 03:10 and 06:10 on December 13. As for the 24-hour figures, it is worth noting that the rainfall is close to the typical climatological values for the month at three weather stations.

The occurrences provided by the Lisbon Fire Department) are recorded on their platform in a point geometry. The analysis of the areas where the incidents were recorded depends on many factors, and the consideration of theoretical factors, such as soil type or geomorphology, proved to be ineffective in delimiting the areas of expected flooding, since Lisbon is a city that has most of its area sealed off and where water infiltration is essentially done through the sewage structure. It was therefore decided to meet with the firefighters who attended each event to find out which area was affected in each event. Additionally, it will be ascertained how high the water level reached at the stage of greatest flooding.

This information will be obtained from the fire brigade, and further data can be obtained from the residents of the affected areas by working with volunteers from the city's parish councils and filling in the information in the AGEO App, an application developed by the Lisbon Municipality as part of the AGEO Project, which aims to report occurrences related to risks of geological origin. This empirical process, which is currently underway, allows for the delimitation of the areas affected by the extreme rainfall events that occurred in Lisbon and is a reliable and credible way of transforming the occurrences in point geometry into areas that were actually flooded (polygons).

2.3 Flood map cartography

Once the relevant events are identified, corresponding to rainfall periods with a return period of 100 years, and the affected areas are delimited, it will be possible to create a new flood-vulnerability map. This map will identify the flood-prone areas based on the previously flooded ones, as well as define a level of susceptibility based on the height that the water has reached in the various locations.

2.4 Geological and geotechnical framework

Lisbon's geological formations range from the Cretaceous to the Holocene period. The Cretaceous formations are hard rocks, composed of limestone and basalts from the Lisbon Volcanic Complex, both of which with geotechnical aptitude. Above, there is a detritic Oligocene formation of continental origin, which is heterogeneous from a geological and geotechnical perspective. Most of Lisbon's urbanized area was raised above a sequence of Miocene formations classified as hard soils, composed of thick alternation of sandstone, limestone and claystone, reaching around 200m. These formations are generally geotechnically competent, except for the decompressed surface layers. Finally, the Holocene formations are made up of alluvium, which are distributed along the water courses (streams) and on the city's riverfront, where they can be up to 40 m thick. In addition, there are landfills of anthropogenic origin. The landfills and alluvial fans are poorly geotechnically competent and do not offer the capacity to support structural elements with prior improvement.

The city is heavily impermeabilized by anthropogenic action (except in the Monsanto area). Even so, the Cretaceous limestones have high permeability values (fracturing), while the volcanic complex and the Oligocene formation have lower permeability. In the Miocene system, permeability is quite variable, being lower in the clay formations and higher in the sand formations. Finally, the alluvial fans have very variable permeability values depending on the main lithologies, although they tend to be high.

2.5 Identification of the type of measures to be implemented in each area

Lisbon Municipality is implementing the Lisbon General Drainage Plan 2016-2030, in which large collectors are being built so that the water drains into the river. In addition, increasing the acceptable flow rate of the drainage network is another action that should be taken to mitigate the impacts of extreme rainfall events. It is also recommended that actions be taken to clean the gutters, thus facilitating water infiltration. Studies are also underway to create water-retention basins.

Nevertheless, even when considering these measures, there are areas whose characteristics reduce the effectiveness of the planned mitigation measures. The riverside area of the city is affected by the presence of water at near-surface levels due to its proximity to the river. This effect is even more evident at high tide, as the water inside the estuary is still significantly affected by this phenomenon.

2.6 Development of a solution

In this work, the priority is to identify the most vulnerable areas for which it is estimated that general mitigation measures may be insufficient or ineffective. Therefore, the Lisbon Municipality is conducting a study to identify which adaptation solutions are available for the population to purchase, namely, anti-flooding barriers that can be implemented without technical knowledge or specialized material.

Flood barriers are designed to protect every room in a building and prevent water from entering through doors, garages, windows, gates, and/or underground floors. As well as homes, they can be used in public areas, stores, shopping centers, industrial buildings, churches, museums, historic buildings, and storage buildings. One of the models of this type allows one to adjust the width of the barrier, whereas another allows one to adjust its height. They do not require invasive construction work because they fit into the existing wall next to the access point frame and are secured by moving the lever or by inflating the seals on the sides and base of the structure (depending on the type of barrier, you will usually have one of two mechanisms). Installation is quick, easy, and accessible to anyone, and has been tested under extreme conditions. If it is necessary to protect a larger area in which the entry exceeds the maximum measures of applicability of a single barrier, several barriers can be joined together because of a removable element when unnecessary, leaving the anchoring base covered. There are also measures to be adopted to prevent theft and extend the life of the equipment. This type of solution allows the population living in areas frequently affected by flooding to adapt to areas where mitigation measures have proved ineffective. The idea is that whenever warnings are issued forecasting heavy rainfall events, people will be able to put up these barriers, avoiding flooding in their homes, with consequent material losses and their safety at risk. This is the definition of the type of reaction that the population is supposed to be able to acquire: proactive, rather than reactive.

2.7 Implementation

The effective implementation of adaptation solutions that protect everyone's home is ultimately the responsibility of everyone. However, the Lisbon Municipality, as a public management and governance body that cuts across the entire city, plays a role in supporting populations that are often affected by flooding caused by extreme rainfall events. Thus, the implementation of the products studied is up to everyone, but there are lists of options for solutions that can be purchased at reasonable prices, which everyone can install in their homes. A list will also be provided of the most effective solutions to be implemented in each area, depending on its level of vulnerability, as well as the effectiveness of the mitigation solutions currently being implemented. The evaluation of the success of the solutions implemented will be carried out by Lisbon Municipality after heavy rainfall events, again by collecting data on the level of water reached and the damage, namely the damage caused and the areas of the property or establishment affected, and this data will be entered and forwarded via the AGEO app.

3 CONCLUSIONS

The work in progress involves a micro-scale analysis, starting with the information obtained through access to the first responders' records of occurrences, which will then evolve into a macro-scale analysis so that it can be included in Lisbon's Municipal Master Plan. This will result in a map highlighting the areas that have flooded and are frequently impacted by it. For future reference, the ideal would be to have a dynamic map that is updated as more recent data comes in.

ACKNOWLEDGEMENTS

The authors are grateful for the support provided by internal and external partners and their availability to cooperate whenever required by the project team.

REFERENCES

Antunes, C., Catita, C., Rocha, C. (2017). Estudo de Avaliação da Sobrelevação da Maré. Determinação da Cartografia de Inundação e Vulnerabilidade da área Ribeirinha de Lisboa afetada pela Sobrelevação da Maré como consequência da futura subida do Nível Médio do Mar. EMAAC - Estratégia Municipal de Adaptação às Alterações Climáticas da Câmara Municipal de Lisboa. Instituto Dom Luiz, Faculty of Sciences, University of Lisbon. Lisbon, Portugal, Technical Report (Study on Assessment of Tidal Elevation – Determination of Flood Mapping and Vulnerability in Lisbon's Riverside Area Affected by Tidal Elevation due to Future Sea Level Rise in Portuguese).

Antunes, C. (2019). Assessment of Sea Level Rise at West Coast of Portugal Mainland and Its Projection for the 21st Century. *J. Mar. Sci. Eng.*7(3), 61. https://doi.org/10.3390/jmse7030061.

IPMA (2022). Boletim Climático Portugal Continental – Dezembro 2022. Instituto Português do Mar e da Atmosfera, I.P. Divisão de Clima e Alterações Climáticas, Lisboa, Portugal, ISSN 2183-1076 (Mainland Portugal Climate Bulletin – December 2022 in Portuguese).

Proceedings of the XVIII ECSMGE 2024
GEOTECHNICAL ENGINEERING CHALLENGES
TO MEET CURRENT AND EMERGING NEEDS OF SOCIETY
© 2024 the Authors
ISBN 978-1-032-54816-6
DOI 10.1201/9781003431749-310
Open Access: www.taylorfrancis.com, CC BY-NC-ND 4.0 license

ECSMGE 24
XVIII EUROPEAN CONFERENCE ON SOIL MECHANICS AND GEOTECHNICAL ENGINEERING

Climate change impacts on safety of levees: A Review

Impacts du changement climatique sur la sécurité des digues: un examen

J.K. Janga, K.R. Reddy*, J. Schulenberg
University of Illinois Chicago, Chicago, USA

**kreddy@uic.edu*

ABSTRACT: Levees are an important part of infrastructure, whose failure can have severe socio-economic consequences including loss of life. Levee failure can be due to various reasons including overtopping, erosion, structural, or geotechnical failures. Many of these failures can be associated with the magnitude and frequency of the occurrence of extreme flooding events. Given the wide-ranging factors affecting the safety of levees, a risk-based-approach accounting for various stability factors should be adapted. In most cases, risk-based analysis of the safety of levees, considers existing data on extreme weather events assuming stationary climatic conditions. However, it was proven that extreme weather events can become more frequent than usual because of climate change. The assumption of stationarity would no longer be valid. Hence, adaptation strategies for levee remediation must be designed based on realistically predicted future weather events considering the non-stationarity of climate. One can employ techniques such as downscaled general circulation models (GCMs) using static or dynamic downscaling, and considering time-varying exceedance probabilities of return levels in order to realistically model future weather patterns. These climate predictions, coupled with detailed hydro-mechanical analyses of levees, can be an effective way to design levee remediation strategies that are adaptive and resilient to future climate change.

RÉSUMÉ: Les digues sont une partie importante de l'infrastructure, dont la défaillance peut avoir de graves conséquences socio-économiques, y compris la mort. La défaillance d'une digue peut être due à diverses raisons, notamment le dépassement, l'érosion, les défaillances structurelles ou géotechniques. Bon nombre de ces défaillances peuvent être associées à l'ampleur et à la fréquence de survenue d'inondations extrêmes. Compte tenu du large éventail de facteurs affectant la sécurité des digues, une approche basée sur les risques tenant compte des différents facteurs affectant leur stabilité devrait être adaptée. Dans la plupart des cas, l'analyse de la sécurité des digues basée sur les risques tient compte des données existantes sur les phénomènes météorologiques extrêmes en supposant des conditions climatiques stationnaires. Mais il a été prouvé que les phénomènes météorologiques extrêmes peuvent devenir plus fréquents que d'habitude en raison du changement climatique, et l'hypothèse de stationnarité ne serait plus valide. Par conséquent, les stratégies d'adaptation pour l'assainissement des digues doivent être conçues sur la base d'événements météorologiques futurs prédits de manière réaliste, compte tenu de la non-stationnarité du climat. On peut utiliser des techniques telles que les MCG à échelle réduite utilisant une réduction d'échelle statique ou dynamique et en tenant compte des probabilités de dépassement des niveaux de retour variant dans le temps, afin de modéliser de manière réaliste les modèles météorologiques futurs. Ces prévisions climatiques, associées à des analyses hydromécaniques détaillées des digues, peuvent constituer un moyen efficace de concevoir des stratégies d'assainissement des digues qui s'adaptent et résistent aux futurs changements climatiques.

Keywords: Weather extremes; climate change adaptation; risk identification; risk attribution; levee resilience.

1 INTRODUCTION

Levees, also known as dikes or embankments, are structures built adjacent to lakes or rivers, to protect communities, agricultural lands, and other business areas from flooding. Although floodwalls, sheet pile walls, and other concrete structures can also serve as levees, levees are primarily earthen structures made of compacted soils. According to the National Levee Database, there are more than 24,500 miles of levees recorded. The National Levee Database (NLD) of the United States estimates that these levees safeguard approximately $2.3 trillion worth of property and a large portion of the country's critical infrastructure systems. However, with an average age of 57 years, most of the country's levees are in poor condition, below standard, with many components nearing the end of their service life. Many of these levees were constructed decades ago, and lack proper design guidelines, leaving them vulnerable to failure, in the face of severe weather events. In addition, the impact of climate change-induced weather extremes has become a significant threat to the infrastructure of the country. Therefore, there is a pressing need to focus on the development of climate-resilient infrastructure (ASCE 2018). Similarly, with an increase in the

frequency of heavy rainfall events, breaches in levees have become a frequent occurrence. There have been several instances of devastating levee breaches, such as the ones caused by Hurricane Katrina in New Orleans, which resulted in over $150 billion worth of property damage. Other notable examples include the levee breaches during the 2008 Midwest floods and 2011 Mississippi river floods, as well as more recent floods along the Salinas river in California. Given, the economic and social impacts that could result from a levee breach, it is crucial to prioritize the development of resilient levee systems capable of withstanding the effects of climate change (Wenger 2015).

Resilience is a critical attribute of systems, requiring the system's capacity to rapidly recover from damage and restore functionality while also adapting to future extreme events. Achieving such resilience in levee design necessitates a comprehensive risk-based approach, involving four essential steps: identifying potential disastrous extremes, assessing the risk of their impact, conducting site-specific vulnerability assessment, and developing an adaptation strategy based on the risk assessment (Reddy et al., 2019). Such risk-based strategies, which utilize probabilistic methods for determining the stability of earthen levees, generally make use of levee fragility curves to assess the vulnerability of a levee with respect to flood levels. Fragility curves are tailored to specific failure modes by taking into account the factors influencing that particular mode of failure (Rossi et al. 2021, and Mazzoleni et al. 2015). However, many of these strategies developed for levees consider stationary climatic conditions. It is widely acknowledged, based on recent events, and an abundance of scientific research that human-induced climate change is leading to an increase in the frequency and severity of extreme weather events (Arnbjerg-Nielsen, K et al. 2013), and the assumption of stationarity in climate is no longer valid (Reid 2022). Therefore, there is a pressing need to adopt a more comprehensive and realistic approach to modeling climatic conditions and incorporating them into risk-based strategies to mitigate levee risks.

2 RISK-BASED APPROACH FOR REMEDIATION OR DESIGN OF LEVEE SYSTEMS

Given that most levee systems have exceeded their intended lifespan, and are prone to various modes of failures such as overtopping, external erosion, slope instability, slump slides, and under-seepage or through-seepage (Hui et al. 2016, and Richards and Reddy 2014), using traditional deterministic methods to evaluate their stability may not accurately account for the risk of failure. Therefore, the use of probabilistic methods, which takes the uncertainties in the levee material properties and weather patterns into account, is desired in order to be more realistic (Wang et al. 2018). However, the uncertainties in the properties of a levee material are not easy to determine. To accurately model the uncertainty, a periodic comprehensive geodetic survey, which includes the determination of the shape and dimensions of a levee, as well as the measurement of material properties through geotechnical testing and identification of potential threats to stability is essential (Mirosław-Świątek et al. 2021).

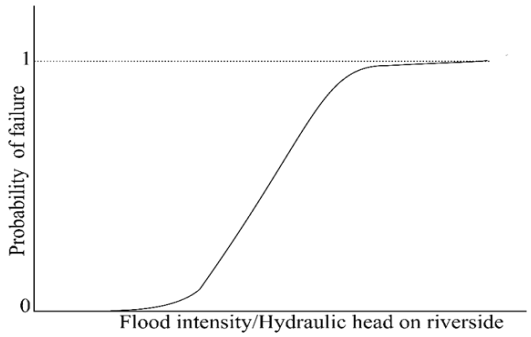

Figure 1. Typical levee fragility curve.

A fragility curve, as shown in Figure 1, is constructed by plotting the results of probabilistic analyses at different levels of river flow intensity, as represented by varying hydraulic heads, which are used to show the vulnerability or resilience of a levee structure, or system under different flow conditions. The steeper the curve, the more susceptible the structure is to failure, with increased flow. Furthermore, fragility curves are generated for each mode of failure in order to provide a comprehensive understanding of the system's vulnerability to failure (Hui et al. 2016, Rossi et al. 2021, and Mazzoleni et al. 2015). Several Researchers have integrated multiple failure modes together in order to consider the combined effects of various failure methods leading to a more comprehensive risk assessment (Fu et al. 2018, and Rahimi and Shafieezadeh 2020).

When performing the risk assessment of levees, both the vulnerability quantified through fragility curves, as well as the potential consequences and costs of failure should be accounted for. A risk-based approach to levee remediation involves a comprehensive risk assessment, prioritizing critical issues, and developing long-term maintenance plans for optimal resource allocation and levee sustainability. Given that levees can fail in multiple ways, such as overtopping or through intermediate geotechnical failures like through-seepage, a risk assessment is usually conducted by evaluating the

likelihood of failure for each mode of failure, and assessing the potential impacts and consequences resulting from it (Hui et al. 2016). A general risk assessment framework adapted for levees is shown in Figure 2. From an engineering standpoint, the most vital components of this risk assessment include forecasting the maximum hydrological load and its likelihood of occurring, as well as evaluating the condition of a levee and identifying potential weaknesses.

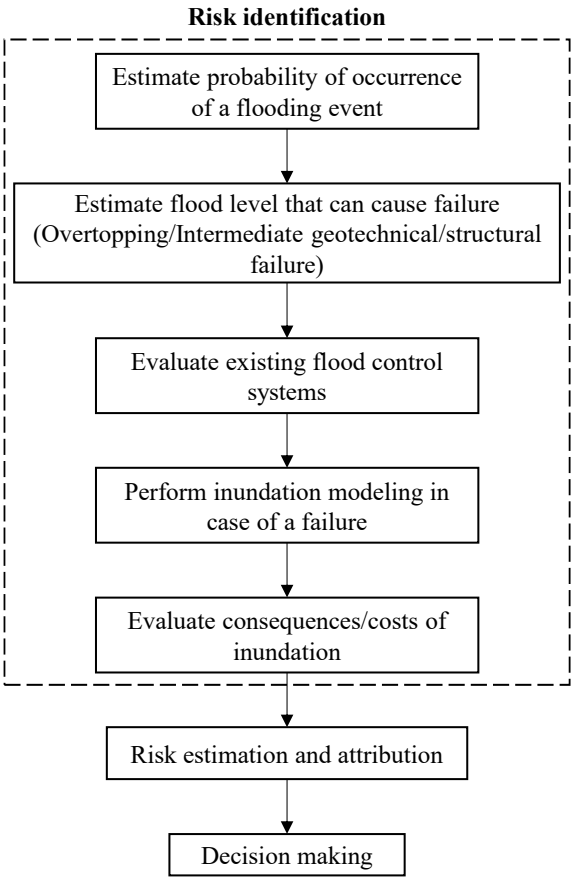

Figure 2. A general risk assessment framework for safety of levees and levee-protected systems (Steps inside the dotted box indicate steps for risk identification).

3 PREDICTION OF PEAK HYDROLOGICAL LOADS USING CLIMATE MODELS

Floods can be understood as the loads to which levees are subjected to, and are designed to withstand. These loads are typically characterized by a peak flood level, and an associated returning period (T), and are often related to the inflow hydrographs or the runoff into a river (Fluixá-Sanmartín 2018). In order to generate flood hydrographs, gridded hydrological models are used which divide an area into a grid of cells of specific size. These models use weather data such as temperature, wind, and precipitation to simulate the amount of runoff that is generated from each cell of the grid, taking into account variations in topography and other factors (Arheimer, and Lindström 2015, Dankers and Feyen 2008, and Herbozo *et al*. 2022). Multivariate hydrological models can also be used in order to address the interdependence of hydrological variables such as peak discharge and flood duration in order to consider issues such as long-term erosion, and fatigue induced weakening of levee systems leading to a potential breach (Balistrocchi *et al*. 2019). A general framework for predicting the peak hydrological load on a levee is presented in Figure 3.

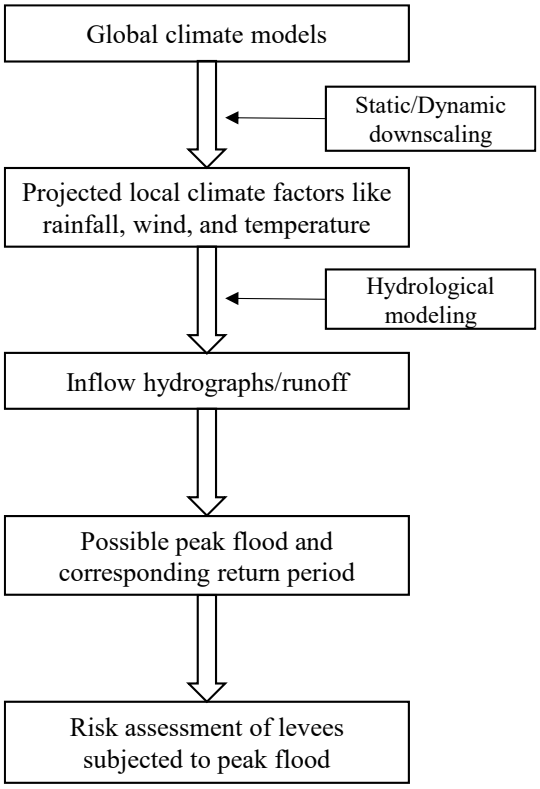

Figure 3. Example flowchart for determination of flood frequency under different climate scenarios based on downscaled projections.

General circulation models (GCM) are commonly downscaled and bias-corrected to generate more accurate local weather information, for use in hydrological models, and forecasting future weather patterns. The Inter-government Panel on Climate Change (IPCC) in its latest assessment report (IPCC 2014) recommends using 4 different representative concentration pathways (RCPs) to simulate future weather patterns. These RCPs include RCP 2.6, RCP 4.5, RCP 6, and RCP 8.5, and each one is based on a set of assumptions about the driving forces for greenhouse gas emissions, such as policies and socio-economic factors (Wayne 2013). For example, RCP 2.6 assumes that stringent policies will be

implemented to reduce emissions, resulting in a peak radiative forcing of 3 W/m^2 at some time before 2100, and it will reduce to 2.6 W/m^2 by 2100. On the other hand, RCP 8.5 assumes no change in the rate of emissions, and relatively lenient guidelines, resulting in an increase in radiative forcing up to 8.5 W/m^2 by 2100. The other two scenarios are intermediate stabilization scenarios. These scenarios can be used by researchers and engineers to realistically predict future weather patterns (Fluixá-Sanmartín 2018).

4 ACCOUNTING FOR NON-STATIONARITY IN CLIMATE FOR RISK ASSESSMENTS

The current practice for developing fragility curves to assess levee risk assumes a stationary climate. In other words, it is assumed that although the frequency and intensity of extreme events will increase, it will remain constant at the increased level for the design life of the levee. However, owing to the changes in climate patterns it is understood that climate cannot be considered stationary (ASCE 2018). Consequently, the probability of occurrence of a T-year flood cannot be accurately estimated using a simple 1/T probability model for the design life of a levee. To address this issue, it is crucial to consider the non-stationarity of climate when assessing the risk of levees. Several researchers have proposed frameworks for estimating non-stationary and time-varying return levels, return periods, and risks of climatic extremes in the face of changing climate (Cheng *et al.* 2014, Mentaschi *et al.* 2016, and Renard *et al.* 2013). These frameworks can inform levee remediation strategies based on the design life by estimating the change in exceedance probability of a standard return level with time. Alternatively, the non-stationarity of climate can be accounted for by dividing the design life into reasonable time periods and determining the return levels and exceedance probabilities of climate parameters for each period, which can be incorporated into the risk-analysis (Dhanai et al. 2022). Several researchers suggest that the structures should be designed for temporary conditions and then be flexible enough to be adjusted after a few years, depending on the climatic conditions at that point of time (Reid 2022). Hence, it is imperative to consider non-stationarity of climate into risk-based remediation strategies in order to truly achieve resilience.

5 CLIMATE CHANGE IMPACTS ON STRUCTURAL INTEGRITY OF LEVEES

Global warming and climate change have proven to increase the frequency and duration of extreme weather events. While some areas are experiencing frequent floods as a result of extreme precipitation, other areas are experiencing drought-like conditions, and higher temperatures. For instance, the State of California, in the US, has experienced extreme drought conditions for almost three years until recent rains. Such prolonged droughts can challenge and deteriorate the structural integrity of earthen embankments by reducing their strength, causing desiccation cracks, and ground subsidence due to drawdown of water levels (Robinson and Vahedifard 2016, and Vardon 2015). According to Dettinger et al. 2016, as a result of climate change, droughts can become longer, and rainfall due to storms can become more intense, which can result in larger peak discharges in rivers, when the levees are at their most vulnerable state. Levees subjected to such wet and dry cycles can get weakened, and their structural integrity might get compromised, leading to slope instability, seepage induced piping, earth subsidence, external and internal erosion and other forms of deterioration. Hence, a need arises for constant monitoring of levees, using technologies like LiDAR, and PoISAR to scan for structural deformities in the levee systems (Liu et al. 2020, and Sehat et al. 2014).

In view of the possible deterioration, a comprehensive stability analysis, including the hydro-mechanical response of the levee systems to extreme droughts or floods, needs to be modeled and performed periodically. Several studies (Dwornik et al. 2016, and Tracy et al. 2020) have focused on coupled 2D modeling for transient seepage analysis at extreme flood loads, and it was observed that the climate change impacts the performance of levee systems significantly. Therefore, a thorough examination that incorporates climate change projections to calculate future flood loads/drought conditions, combined with a thorough analysis of the probability of failure due to seepage, uplift, and slope instability, when subjected to those extreme loads, can be an effective method for conducting a comprehensive risk assessment.

If the levee systems were found to be unstable under any projected future flood event, remedial measures might be required in order to keep the levees from breaching. According the United States Army Corps of Engineers Manual on Design and Construction of Levees (USACE, 2000), there are several methods to control excessive seepage, and prevent piping or uplift failures. The following remedial measures can be adopted, based on site-

specific conditions: cutoff walls, riverside blankets, landside seepage berms, pervious toe trench, pressure relief wells, pervious toe drains, and horizontal/inclined drainage layers. If the slope stability analysis gives a factor of safety less than the acceptable standards, at any future weather extremes, slopes can be stabilized either by flattening the slopes or by using stability berms. In order to protect the riverside slope from erosion, various slope protection measures like grass cover, articulated concrete mat, concrete paving, among others, might have to be undertaken to avoid slope instability.

6 CONCLUSION

The study aimed to address the limitations of traditional risk assessment strategies for levees and propose a more comprehensive approach to enhance the resilience of these crucial infrastructure systems against climate change. Conventional risk assessment methods typically assume stationary climatic conditions to determine the likelihood of a levee failure and associated risks. However, given the changing climate, this approach may not be adequate. Therefore, this study suggests utilizing global climate models (GCMs), for different representative concentration pathways (RCP) scenarios, as an alternative approach to predict future weather patterns. As GCMs often have coarse spatial resolution (250-500 km), localized predictions require downscaling techniques. Climate indicators such as precipitation, wind, humidity, among others, obtained from these downscaled models, can then be used to develop flood hydrographs that correspond to specific levees.

The resulting peak flood levels can be utilized to assess the vulnerability of the levee to failure utilizing coupled hydro-mechanical analyses for greater reliability and a more realistic risk assessment. The study suggests that relying solely on a stationary return period to forecast future extremes might be inadequate, and instead recommends taking into account the non-stationarity of climate when evaluating the risk associated with levees. Finally, the study discussed the vulnerability of levee systems when subjected to extreme weather conditions to emphasize the importance of considering climate change in risk assessments. Various remedial measures were then listed to remediate vulnerable levees, and make them resilient to climate change.

Overall, this study provides a comprehensive approach to evaluating the risk of extreme weather events on levee systems. It emphasizes the significance of incorporating the effects of climate change in the design and maintenance of these critical infrastructure assets. By doing so, we can better safeguard communities and assets from potential damage caused by climate change induced levee failures.

7 REFERENCES

American Society of Civil Engineers (ASCE), *Climate-Resilient Infrastructure: Adaptive Design and Risk Management*. Ed. Ayyub, B.M. ASCE, VA, USA. https://doi.org/10.1061/9780784415191.

Arheimer, B., and Lindström, G., *Climate Impact on Floods: Changes in High Flows in Sweden in the Past and the Future (1911–2100)*, Hydrol. Earth Syst. Sci., 19, 771–784, 2015. DOI: 10.5194/hessd-11-7551-2014.

Arnbjerg-Nielsen, K., Willems, P., Olsson, J., Beecham, S., Pathirana, A., Bülow Gregersen, I., and Nguyen, V. T. V., *Impacts of Climate Change on Rainfall Extremes and Urban Drainage Systems: A Review*, Water science and technology, 68(1), 16-28, 2013. DOI: 10.2166/wst.2013.251.

Balistrocchi, M., Moretti, G., Orlandini, S., and Ranzi, R., *Copula-Based Modeling of Earthen Levee Breach Due to Overtopping*, Advances in Water Resources, 134, 103433, 2019. DOI: 10.1016/j.advwatres.2019.103433

Cheng, L., AghaKouchak, A., Gilleland, E., and Katz, R. W., *Non-stationary extreme value analysis in a changing climate*, Climatic change, 127, 353-369, 2014. DOI: 10.1007/s10584-014-1254-5.

Dankers, R., and Feyen, L., *Climate Change Impact on Flood Hazard in Europe: An Assessment Based on Highresolution Climate Simulations*, J. Geophys. Res., 113, D19105, 2008. DOI: 10.1029/2007JD009719.

Dettinger, M. D., Anderson, J., Anderson, M. L., Brown, L. R., Cayan, D., and Maurer, E. P., *Climate Change and the Delta,* San Francisco Estuary and Watershed Science, USGS Publications Warehouse, 14(3), 1-26, 2016.

Dhanai, P., Singh, V. P., and Soni, P., *Rainfall Triggered Slope Instability Analysis with Changing Climate,* Indian Geotechnical Journal, 52(2), 477-492, 2022. DOI: 10.1007/s40098-021-00581-0.

Dwornik, M., Krawiec, K., Franczyk, A., and Leśniak, A., *Numerical Modelling of Levee Stability Based on Coupled Mechanical, Thermal and Hydrogeological Processes*. In E3S Web of Conferences, Vol. 7, 03021, EDP Sciences, 2016. DOI: 10.1051/e3sconf/20160703021.

Fluixá-Sanmartín, J., Altarejos-García, L., Morales-Torres, A., and Escuder-Bueno, I., *Climate Change Impacts on Dam Safety*, NHESS, 18(9), 2471-2488, 2018. DOI: 10.5194/nhess-18-2471-2018.

Fu, Z., et al., *Multiple Failure Modes-Based Practical Calculation Model on Comprehensive Risk for Levee Structure*. Stoch Environ Res Risk Assess, 32, 1051–1064, 2018. DOI: 10.1007/s00477-017-1448-2.

Groeneweg, J., Caires, S., van Nieuwkoop, J., and Bottema, M., *A First Assessment of the Effect of Storm Climate Trends and Uncertainties on Dutch Levee Design*.

Journal of Flood Risk Management, 15(3), e12808, 2022. DOI: 10.1111/jfr3.12808.

Herbozo, J.E., et al., *Non-Stationary Hydrological Regimes Due to Climate Change: The Impact of Future Precipitation in the Spillway Design of a Reservoir, Case Study: Sube y Baja Dam, in Ecuador*. Atmosphere 2022, 13, 828, 2022. DOI: 10.3390/atmos13050828.

Hui, R., Jachens, E., and Lund, J., *Risk-based Planning Analysis for a Single Levee*. Water Resources Research, 52(4), 2513-2528, 2016. DOI: 10.1002/2014WR016478.

Intergovernmental Panel on Climate Change (IPCC), *Climate Change 2014: Mitigation of Climate Change. Contribution of Working Group III to the Fifth Assessment Report of the Intergovernmental Panel on Climate Change*, Edenhofer, O. R., et al. (eds.), Cambridge Univ. Press, Cambridge, UK and NY, USA, 2014.

Kandalai, S., John, N.J., and Patel, A., *Effects of Climate Change on Geotechnical Infrastructures — State of the Art*. Environ Sci Pollut Res, 2023. DOI: 10.1007/s11356-022-24788-7.

Liu, Q., et al., *Storm Surge Hazard Assessment of the Levee of a Rapidly Developing City-Based on LiDAR and Numerical Models*, Remote Sensing, 12(22), 3723, 2020. DOI: 10.3390/rs12223723.

Mazzoleni, M., Barontini, S., Ranzi, R., and Brandimarte, L., *Innovative Probabilistic Methodology for Evaluating the Reliability of Discrete Levee Reaches Owing to Piping*, Journal of Hydrologic Engineering, 20(5), 04014067, 2015. DOI: 10.1061/(ASCE)HE.1943-5584.0001055.

Mentaschi, L., et al., *The Transformed-Stationary Approach: A Generic and Simplified Methodology for Non-Stationary Extreme Value Analysis*, Hydrol. Earth Syst. Sci., 20, 3527–3547, 2016. DOI: 10.5194/hess-20-3527-2016.

Mirosław-Świątek, D., et al., *Analysis of Factors Influencing Levee Safety Using the DEMATEL Method*, PLoS ONE, 16(9), e0255755, 2021. DOI: 10.1371/journal.pone.0255755.

Pk, S., Bashir, R., and Beddoe, R., *Effect of Climate Change on Earthen Embankments in Southern Ontario, Canada*, Environmental Geotechnics, 8(2), 148–169, 2021. DOI: 10.1680/jenge.18.00068.

Rahimi, M., and Shafieezadeh, A., *Coupled Backward Erosion Piping and Slope Instability Performance Model for Levees*. Transportation Geotechnics, 24, 100394, 2020. DOI: 10.1016/j.trgeo.2020.100394.

Reid, R. L., *How to Make Infrastructure more Resilient against Climate Change,* Asce.org, January 3, 2022. Retrieved from https://www.asce.org/publications-and-news/civil-engineering-source/civil-engineering-magazine/issues on April 12, 2023.

Renard, B., Sun, X., and Lang, M., *Bayesian Methods for Non-stationary Extreme Value Analysis*, In: AghaKouchak, A. *et al*. (eds) Extremes in a Changing Climate. Water Science and Technology Library, Vol 65. Springer, Dordrecht, 2013. DOI: 10.1007/978-94-007-4479-0_3.

Reddy, K.R., Cameselle, C., and Adams, J.A., *Disaster Resiliency*, In Sustainable Engineering: Drivers, Metrics, Tools, and Applications, John Wiley andSons, Inc., Hoboken, New Jersey, 103-127, 2019.

Richards, K. S., and Reddy, K. R., *Kinetic Energy Method for Predicting Initiation of Backward Erosion in Earthen Dams and Levees*. Environmental & Engineering Geoscience, 20(1), 85-97, 2014. DOI: 10.2113/gseegeosci.20.1.85.

Robinson, J.D., and Vahedifard, F., *Weakening Mechanisms Imposed on California's Levees under Multiyear Extreme Drought*, Climatic Change, 137, 1–14, 2016.

Rossi, N., Bačić, M., Kovačević, M. S., and Librić, L., *Development of Fragility Curves for Piping and Slope Stability of River Levees*. Water, 13(5), 738, 2021. DOI: 10.3390/w13050738.

Sehat, S., et al., *Using In-Situ Soil Measurements for Analysis of a Polarimetric SAR-Based Classification of Levee Slump Slides in the Lower Mississippi River*, Engineering geology, 181, 157-168, 2014. DOI: 10.1016/j.enggeo.2014.07.007.

Tracy, F. T., et al., *Monte Carlo Simulations of Coupled Transient Seepage Flow and Compressive Stress in Levees*. Scalable Computing: Practice and Experience, 21(1), 2020. DOI: 10.12694/scpe.v21i1.1629.

USACE, *Design and Construction of Levees*. Engineer Manual No. EM 1110-2-1913. Washington DC: USACE, 2000.

Vahedifard. F., et al., *Levee Fragility Behavior under Projected Future Flooding in a Warming Climate*, Journal of Geotechnical and Geoenvironmental Engineering, 146(12), 04020139, 2020. DOI: 10.1061/(ASCE)GT.1943-5606.0002399.

Vardon, P. J., *Climatic Influence on Geotechnical Infrastructure: A Review*. Environmental Geotechnics, 2(3), 166-174, 2015. DOI: 10.1680/envgeo.13.00055.

Wang, L., Powers, M., Studiner, M., Fallatah, M., and Gong, W., *Geotechnical Stability Analysis of Earthen Levees in the Face of Uncertainty*. In IFCEE 2018, 247-256, 2018. DOI: 10.1061/9780784481608.024.

Wayne, G., *The Beginner's Guide to Representative Concentration Pathways*, Skepticalscience.com, August, 2013. Retrieved from https://skepticalscience.com/rcp.php?t=3 on December 27, 2022.

Wenger. C., *Better Use and Management of Levees: Reducing Flood Risk in a Changing Climate*, Environmental Reviews, NRC Research Press, 23 (2): 240-255, 2015. DOI: 10.1139/er-2014-0060.

Proceedings of the XVIII ECSMGE 2024
GEOTECHNICAL ENGINEERING CHALLENGES
TO MEET CURRENT AND EMERGING NEEDS OF SOCIETY
© 2024 the Authors
ISBN 978-1-032-54816-6
DOI 10.1201/9781003431749-311
Open Access: www.taylorfrancis.com, CC BY-NC-ND 4.0 license

ECSMGE 24
XVIII EUROPEAN CONFERENCE ON SOIL MECHANICS AND GEOTECHNICAL ENGINEERING

Evaluation of unsaturated slope stability under rainfall infiltration based on experimental and numerical modeling

Évaluation de la stabilité des pentes non saturées sous infiltration de pluie basée sur une modélisation expérimentale et numérique

J. Josifovski*, B. Susinov
Ss. Cyril and Methodius University in Skopje, Faculty of Civil Engineering, North Macedonia
**jjosifovski@gf.ukim.edu.mk*

ABSTRACT: The presented paper contributes to the definition of the hydro-mechanical behavior of unsaturated soils while evaluating the problem of rainfall-induced slope instabilities. The slope instabilities in the Western Balkan countries have significantly increased in the past couple of years, due to climate change effects and its influence on the slope stability. Besides the arid climate, the increased manifestations of intense rainfalls often equal to monthly precipitation are the main contributing factors. Therefore, in North Macedonia, an assessment study has been initiated to re-evaluate the safety and define the risk level of the engineered slopes. To define the slope stability of such a system, the phenomenon of soil-atmosphere interaction is necessary to be analyzed. The slope stability will be governed by a coupled system's thermal, hydro, and mechanical conditions. Moreover, the vegetation as a factor that has additional effects on rainfall infiltration water and evapotranspiration is not considered in this study. The paper presents an analysis of an ideal slope example subjected to intense rainfall, for which both physical and numerical models were employed. The aim was to assess the impact of infiltrated water on moisture and suction as the main factors that lead to instability. The sandy soil slope with an angle of 51 degrees is subjected to a rainfall intensity of 30mm/h until the failure occurs. The comparison of the experimental and numerical results has shown very good agreement. In conclusion, the results have shown that intensive rainfalls might have a significant impact on the surface layers of the slopes causing serious erosion and local instability which after a prolonged duration is transformed into a global slope failure mechanism.

RÉSUMÉ: L'article présenté contribue à la définition du comportement hydromécanique des sols non saturés tout en évaluant le problème des instabilités de pente induites par les précipitations. Les instabilités des pentes dans les pays des Balkans occidentaux, ont considérablement augmenté ces dernières années, en raison des effets du changement climatique et de son influence sur la stabilité des pentes. Outre le climat aride, les manifestations accrues de précipitations intenses, souvent égales à des précipitations mensuelles, sont considérées comme les principaux facteurs contributifs. C'est pourquoi, en Macédoine du Nord, une étude d'évaluation a été lancée dans le but de réévaluer la sécurité et de définir le niveau de risque des pentes aménagées. Pour définir la stabilité de pente d'un tel système, il est nécessaire d'analyser le phénomène d'interaction sol-atmosphère. La stabilité des pentes sera régie par les caractéristiques thermiques, hydroélectriques et mécaniques dans un système couplé. De plus, la végétation comme facteur ayant des effets supplémentaires sur l'eau d'infiltration des précipitations et l'évapotranspiration n'est pas prise en compte dans cette étude. L'article présente une analyse d'un exemple de pente idéale soumise à des précipitations intenses, pour lequel des modèles physiques et numériques ont été utilisés. L'objectif était d'évaluer l'impact de l'eau infiltrée sur l'humidité et la succion comme principaux facteurs conduisant à l'instabilité. La pente du sol sableux avec un angle de 51 degrés est soumise à une intensité de pluie de 30 mm/h jusqu'à ce que la rupture se produise. La comparaison des résultats expérimentaux et numériques a montré un très bon accord. En général, les résultats ont montré que les pluies intensives ont un impact significatif sur les couches superficielles des pentes, provoquant une grave érosion et une instabilité locale qui, après une durée prolongée, se transforment en un mécanisme global de rupture des pentes.

Keywords: Unsaturated soil; rainfall; slope stability; physical model; numerical model.

1 INTRODUCTION

The intense rainfalls due to climate variations and change are more often seen as a triggering factor for instabilities, such as soil sliding and erosion of natural and engineering slopes. This phenomenon widely known as soil-atmospheric interaction is very often neglected by the engineers during the design. This interaction is realized through the wetting or drying of soil as a result of atmospheric, thermal, and hydraulic, conditions. In the case of rainfall, the water infiltrates through the surface of the slope thus causing an

increase in the soil water content and pore pressure, while reducing the suction, thereby reducing the shear strength, and increasing the probability of sliding.

Figure 1 shows slope sliding and erosion that occurred on the Miladinovci – Shtip highway in the central part of Macedonia after heavy rainfall on 29 May 2022 (Susinov and Josifovski, 2022). The nearest weather station measured 52 and 43mm/h for two consecutive 12-hour periods. The national weather monitoring station measured 25.2mm in one hour and 40.1mm in two hours.



Figure 1. Erosion on the slopes between the 2 extreme rainfall events on May 29, 2022.

The rise in the soil water content significantly influences the behavior of soils to the extent that the classical theory of soil mechanics is no longer appropriate. Hence, to understand the behavior of unsaturated or partially saturated soils it is necessary to introduce additional parameters, dependencies, and theories. Moreover, for a comprehensive solution to the problem of rainfall-induced slope instabilities, coupled thermo-hydro-mechanical analyses need to be performed.

2 MATERIALS AND METHODS

To properly address the problem under consideration, it is necessary to use transient analysis which considers the mechanical and hydraulically soil models defining time-dependent material behavior. The most reliable and comprehensive method would be the so-called coupled flow-deformation analysis which is used in the present study. Successful application of this method requires knowledge of soil shear strength parameters, hydraulic parameters, and rainfall characteristics (Zhang et al., 2018). Then, not only the mechanical model but also the hydraulic model should be selected. It uses the relationship between soil suction and water content or saturation degree (Sr), the so-called soil water retention curve – SWRC, and the suction-relative permeability relationship.

A sandy soil material was used in the present study (Susinov and Josifovski, 2018) defined with the Mohr-Coulomb model for the mechanical part (γ=18.2kN/m^3, φ=30˚ and c=0kPa) and the user-defined (Spline) model for the hydraulic part. The SWRC and permeability function defining the relationship between the degree of saturation (S_r) – suction (ψ) and relative hydraulic conductivity (K_r) – suction (ψ) have to be determined with specific hydraulic laboratory testing.

A physical model representing an ideal slope subjected to intense rainfall with more than 30 mm/h intensity was adopted in this study (Susinov et al., 2019). An explanatory photo is shown in Figure 2. In particular, a large-scale model with the following dimensions 400 × 200 × 200 cm was instrumented with three sensors (volumetric water content, pore water pressure, suction) on five different locations in the slope. Additionally, the deformations were scanned by LIDAR equipment and camera (Figure 3).

The aim was to assess the role of infiltrated water on moisture and suction through installed sensors as the main factors that lead to instability.



Figure 2. Photo of the physical model.

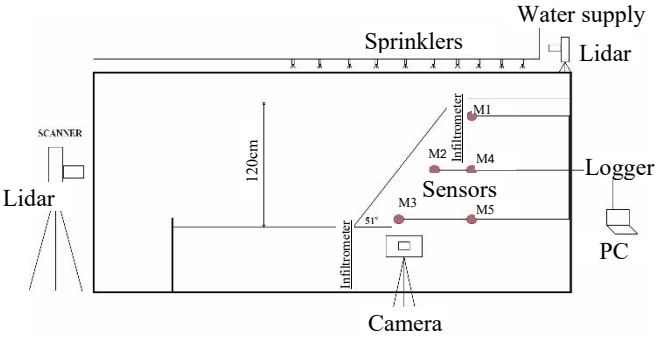

Figure 3. Schematic of the physical model and measuring sensors.

The change in volumetric water content (VWC) and suction during the rainfall event are presented in Figures 4 and 5, respectively.

Change in VWC was observed firstly at the M1 and M2 sensors placed near the slope surface. The value at the end of the test is lower in comparison with M3 and

M5 sensors which are placed near the phreatic level. It means that it is far from full saturation due to drainage of the infiltrated water into the lower layers. The lowest registered initial VWC is 0.050 m^3/m^3, while the highest at the end of the test is 0.422 m^3/m^3.

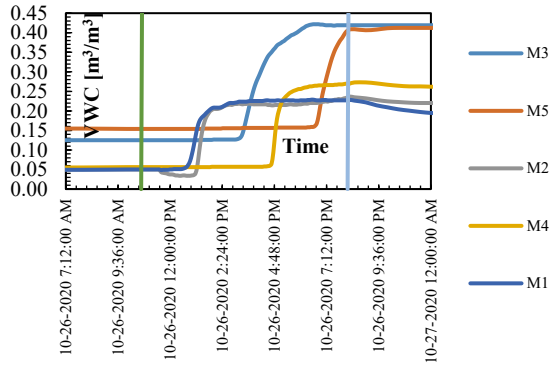

Figure 4. Changes in VWC during the rainfall event.

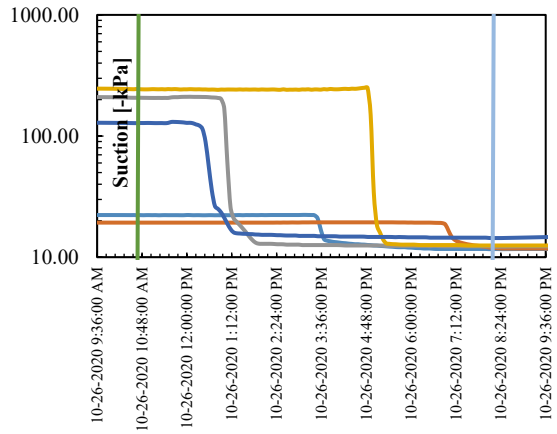

Figure 5. Changes in suction during the rainfall event.

The initial value of suction depends on the degree of saturation of the soil before the test. The sensors placed in the upper half of the slope (M1, M2, and M4) show the highest initial suction. A significant change – a drop in suction is observed when the infiltrated water reaches the sensor location. The largest registered initial suction is 244.7 kPa, while the lowest at the end of the test is 11.7 kPa. It can be concluded that the material loses suction relatively quickly during saturation.

3 NUMERICAL MODEL

Based on the data measured on the physical model during the rainfall test, a calibration of a numerical model subjected to constant rainfall was performed using FEM analyses by way of the PLAXIS code. For simulation purposes, a fully coupled flow-deformation analysis was adopted using the relationships presented in Figure 6.

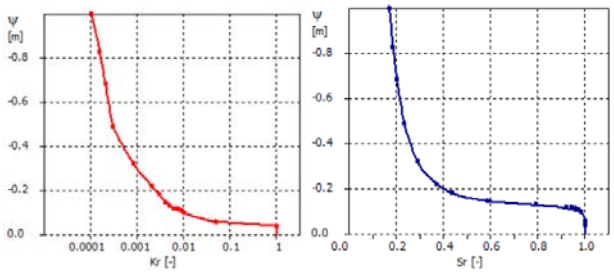

Figure 6. Used relationship for Spline model in PLAXIS.

In Figures 7 and 8 profiles of the saturation degree and suction before and after 3 hours of rainfall are respectively presented. The obtained results show a very good agreement with the measured ones.

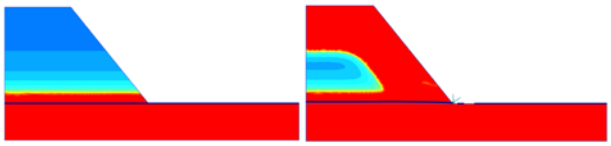

Figure 7. Degree of saturation before (left) and after (right) 3 hours of rainfall.

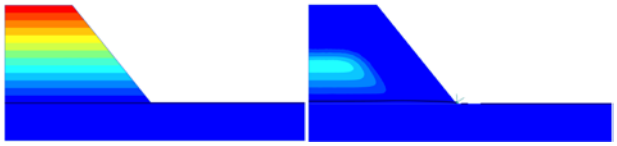

Figure 8. Suction before (left) and after (right) 3 rainfall.

The change in the saturation degree begins immediately after the beginning of rainfall as a result of the infiltration. In particular, the saturation zone increases and the suction decreases as the infiltration increases. The maximum saturation degree and suction changes were observed on the slope surface where the rainfall influence is the highest (Fredlund et al., 2012). The minimum value of the initial saturation degree at the top of the slope is 16.89%. As infiltration increases, the unsaturated zone decreases and matches that of the physical model. At the end of the test, the minimum value level of the saturation degree is 24.2%. The suction in PLAXIS is defined as negative pressure above the GWL and is related to the degree of saturation through the previously defined function which means that it cannot be compared directly.

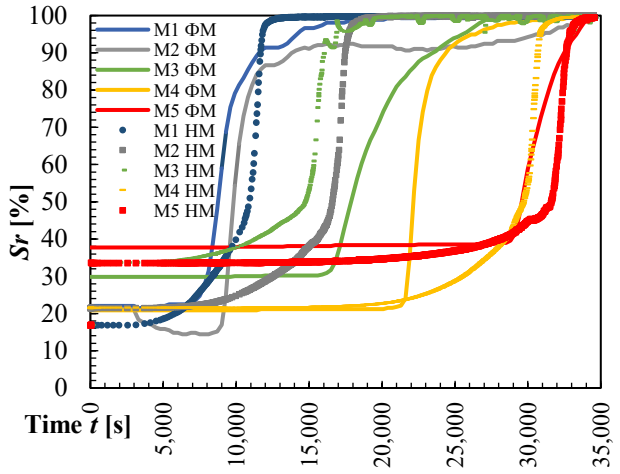

Figure 9. Comparison of S_r between the physical and numerical model.

Figure 9 presents the saturation degree value for both models. The initial degree of saturation in the characteristic points M1, M2, and M4 is lower compared to that in M3 and M5 where there is an influence from the groundwater due to the capillary effect. Compared over time, the degree of saturation at points M1 and M5 at the top of the slope and the lower part, respectively, show the best matching results. In points M2, M3, and M4, a minimal deviation is observed in the time when the change starts, although a sudden change is observed in both models. At the end of the analysis, all measuring points are completely saturated (S_r=100%).

Another aspect of the comparison between both models is the deformations and the geometry of the potential failure surface. Thus, in Figure 10 the slope deformations with the ultimate global Factor of safety (FoS) are presented. The maximum calculated deformations are 6.62 cm and the minimum FoS equals 1.037, which is very close to the slope limit equilibrium.

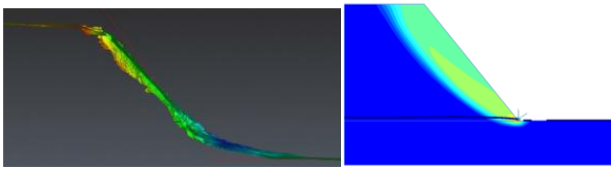

Figure 10. Slope deformation in physical (left) and numerical (right) models.

4 CONCLUSIONS

Comparing the measured data from the test on the physical model and results obtained with numerical analysis of slope stability, it can be concluded that there is very good agreement between them. In the initial phase of numerical analysis, the slope is partially saturated above the groundwater level, where the saturation is close to that in the physical model. From the influence of rainfall in the coupled analysis, the distribution of the degree of saturation and suction changes. The maximum suction occurs at the part above the groundwater level in the middle of the model, which is expected. Over time, maximum deformations develop in the lower part of the slope initiating its destabilization, as in the physical model.

If we compare the saturation degree value for both models, it can be concluded that the hydraulic behavior of the material in the physical model is similar to that of the numerical model.

Regarding the deformations, it can be concluded that there is very good agreement with the measured and calculated displacement although the soil erosion cannot be simulated by FEM.

The forecasting of future climate change scenarios is challenging, thus the prediction of slope-atmosphere interaction effects represents a demanding engineering task. Nevertheless, the presented successfully tests a concept that can re-evaluate the stability and reliability of the existing slopes on prescribed rainfall intensities, which are expected to be even more frequent in the future, thus more slope instabilities are eminent.

REFERENCES

Galavi, V. (2010). *Groundwater flow, fully coupled flow deformation and undrained analyses in PLAXIS 2D and 3D, Plaxis report*, [PLAXIS].

Susinov, B. and Josifovski, J. (2018). Investigation of the hydro-mechanical properties of silty sand material from Topolnica tailings dam, In *ce/papers*, Skopje, R.N.Macedonia, pp. 797-802

Susinov, B. Josifovski, J. and Naumovski, M. (2019). Hydrological analysis of high-intensity rainfalls over Topolnica tailing dam, In *Ss. Cyril and Methodius University, Civil Engineering Faculty – Skopje*, Skopje, R.N.Macedonia.

Susinov, B. and Josifovski, J. (2022). Slope instabilities caused by atmospheric influences, In *Macedonian Association for Geotechnics*, Ohrid, N.Macedonia, pp. 669-678, *ISBN 978-9989-2053-5-4*

Zhang, L., LI, J., Li, X., Zhang, J., Zhu, H. (2018). *Rainfall-induced soil slope failure: stability analysis and probabilistic assessment*, Ist ed., CRC Press, Boca Raton.

Proceedings of the XVIII ECSMGE 2024
GEOTECHNICAL ENGINEERING CHALLENGES
TO MEET CURRENT AND EMERGING NEEDS OF SOCIETY
© 2024 the Authors
ISBN 978-1-032-54816-6
DOI 10.1201/9781003431749-312
Open Access: www.taylorfrancis.com, CC BY-NC-ND 4.0 license

ECSMGE 24
XVIII EUROPEAN CONFERENCE ON SOIL MECHANICS AND GEOTECHNICAL ENGINEERING

Impact of a spacing reduction in a fall cone test

Technique d'essai répétée du cone de chute

R. Khalili, C. Jommi
Department of Civil and Environmental Engineering, Politecnico di Milano, Milan, Italy
W.T. Sołowski*
Department of Civil Engineering, Aalto University, Espoo, Finland
**wojciech.solowski@aalto.fi*

ABSTRACT: The paper investigates an adjustment to the fall cone test, where the same soil sample is reused for four extra tests. The analysis shows that the fall cone test inaccuracies are much higher than the effect of reusing the sample. Therefore, the proposed procedure may help to establish the soil properties more accurately without much extra effort and reduce the number of samples needed for testing.

RÉSUMÉ: L'article étudie un ajustement au test du cône de chute, où le même échantillon de sol est réutilisé pour quatre tests supplémentaires. L'analyse montre que les imprécisions du test du cône de chute sont bien supérieures à l'effet de la réutilisation de l'échantillon. Par conséquent, la procédure proposée peut aider à établir les propriétés du sol avec plus de précision sans trop d'effort supplémentaire et à réduire le nombre d'échantillons nécessaires aux tests.

Keywords: Fall cone test; statistical analysis; marine clay; sensitive clay.

1 INTRODUCTION

The fall cone test was initially devised by the Swedish state railways during the period from 1914 to 1922 and subsequently gained widespread adoption in Scandinavian countries (Hansbo, 1957). Currently, the ISO 17892-6:2017 standard contains the details of the procedure.

In general, the fall cone test requires that before its release the metallic cone is in direct contact with the surface sample. After the release, the cone penetrates the specimen. The undrained shear strength is correlated with the measured depth of penetration. The test relies on the lack of friction in the apparatus, hence the apparatus should be lubricated to minimise friction. The test accuracy is related to a number of factors, the interested reader may see Llano-Serna & Contreras (2020) for discussion on cone roughness influence and further references.

2 RESEARCH HYPOTHESIS

The ISO 17892-6:2017 standard requires that the test points should be distributed so that the distance between the outer boundaries of the cone penetration in two tests is at least 14mm, and the cone penetration closest to the perimeter is at least 7mm. For soft marine clays, for 60 deg 60g cone the penetration can reach 9mm, leading to the spacing requirement of 24,4 mm between centres of penetration and 12,2 mm from the sample perimeter. For common core diameters 50, 54 and – used in this study – 58 mm, these limitations lead to 3 sampling points on the single cross-section of the sample. Three points are the minimum required by ISO 17892-6:2017. However, ISO 17892-6:2017 requires that any test result deviating from the mean penetration by more than 0.5mm should be excluded. This means that often an extra point is needed, however, due to distance restriction, no more sampling points are allowed on the sample and another sample for testing should be taken. This may be difficult and affects the testing programme.

Recent research (e.g Mohapatra *et al*., 2023a; Mohapatra *et al.*, 2023b; Tran & Sołowski, 2019), has indicated that the impact of the fall cone penetration into a soft sensitive clay is contained to approximately double the radius of the 60-degree fall cone penetration mark, see Figure 1. Furthermore, the results have shown little sensitivity to lateral support, with no changes for full lateral support or lack of it. Based on those results we decided to check the hypothesis that a reduction of the spacing of the sampling points to double the radius of the penetration mark may have no influence on the results, while it allows for the increase of the number of sampling points on a standard 50 to 58mm sample cross-section, potentially increasing the accuracy of the findings. Additionally, the work aims to evaluate whether the

results of the test are statistically influenced by removing the lateral support. If the denser spacing or lack of lateral support has an effect, the depth of the penetrations closer to the sides of the sample should be higher compared to the first penetration in the middle of the sample.

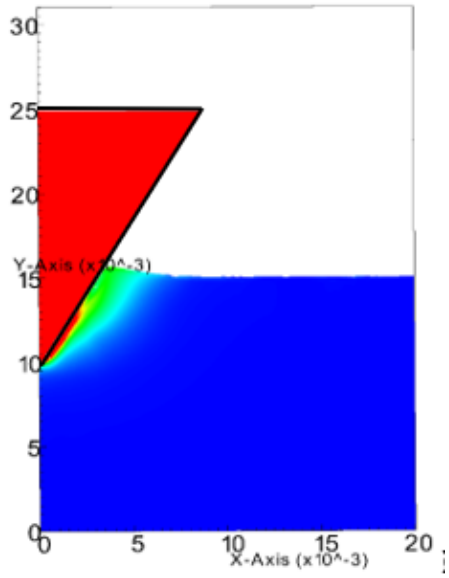

Figure 1. Numerical replication of a fall cone test in soft marine clay showing localised deformations around the cone, Mohapatra et al. (2023b).

3 CLAY SAMPLES

In this research, tested soil samples had a diameter of 58 mm and a height of 10 cm. The penetration test was conducted using a cone with a 60° angle and a mass of 60 grams. The observed penetration depths across all samples range approximately from four to 12 mm.

In this study, a total of 39 normally consolidated marine clay samples were tested with a fall cone. The samples came from four locations at the offshore Kytö site: KU2 (with depths ranging from 0.1 to 3.87 meters), KU3 (with depths ranging from 0 to 3.48 meters), KU1 (with depths ranging from 0 to 3.1 meters), and KU4 (with depths ranging from 0.15 to 3.75 meters). For a more detailed site description see Saresma *et al.* (2023), while for more details on properties and tests see Li *et al.* (2023).

The composition of these marine sediments exhibits some variations primarily attributed to the different stages of the Baltic Sea's evolutionary history. However, the stratification of these sediments is relatively weak and the samples were very similar. The clays are structured and sensitive. Their intact undrained shear strength varies, mainly due to differences in depth from which the samples originate.

4 METHODS

4.1 Fall cone test procedure

Figure 2 shows the position of each penetration for each sample in the testing programme, with numbers indicating the penetration sequence, leading to the spacing between the sampling points smaller than required by ISO 17892-6:2017. The sample used had a 58 mm diameter and the points 2-5 were positioned at least 10 mm from the side of the sample, with the impact point approximately in the middle of the line connecting the edge of the penetration 1 mark and sample perimeter, i.e. around 10-14mm from the sample perimeter. This means that the distance between the edge of the penetration mark was around 5-8mm to the sample perimeter, but there could be only about 8 mm between the edges of the penetration mark at test 1 and the subsequent test, instead of the required 14mm. Nonetheless, the spacing always was approximately 2 penetration radii, complying with the condition identified in numerical analyses. Besides the spacing, the testing procedure followed ISO 17892-6:2017, with tests done on thick 10cm extruded from plastic tubes. There was no lateral support at the sides.

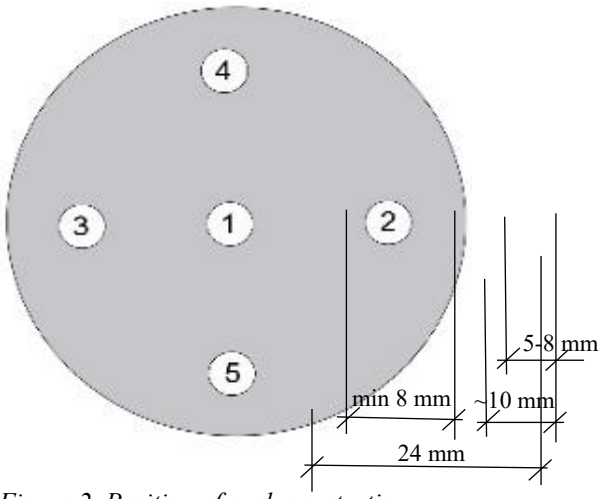

Figure 2. Position of each penetration.

4.2 Discussion of the testing procedure

An alternative would be to perform 3 tests according to ISO 17892-6:2017 and then one extra test in the middle with smaller distances to the other tests. However, that would lead to a distance between the middle test mark and any other test as low as 5mm, in which case the penetration distortion zones would likely overlap.

4.3 Statistical analysis

In case the spacing of the points was too close, the subsequent penetrations should be affected due to the disturbance of soil and the associated reduction in the

undrained shear strength. Hence, in case the soil is disturbed, we expect that there will be a statistically significant difference between the results obtained in the first penetration (middle point) and the subsequent 4 penetrations. Similarly, in case the lack of lateral constraint affects the penetration depth, the statistical analysis should reveal that.

Even though ISO 17892-6:2017 decides on the acceptance or rejection of the test based on penetration, in this contribution we decided to concentrate on the statistical analysis of the undrained shear strength. This is because the undrained shear strength is the key value obtained in the test and the important value for engineering. The results of the analysis performed based on the penetration depths are similar, but not included in this paper.

To analyse the data, first, all the undrained shear strengths were normalised with respect to the 'correct' penetration in the middle of the sample.

$$s_{n,i} = \frac{s_i}{s_1} \qquad i = 2,3,4,5 \qquad (1)$$

where $s_{n,i}$ is the normalised value of the undrained shear strength obtained from the i-th penetration with respect to the value s_1 obtained from the first penetration. This assumes the middle point is the correct one, with the four subsequent penetrations possibly deviating from it. First, we tried analysing the data for each penetration. Then, as the number of tests was small, we decided to pool the data together.

In this case, all the tests besides the first one are treated the same, leading to 39 sets of 4 deviating data points. Then, we first assessed whether the obtained data follows a normal distribution. Later, we checked whether the undrained shear strengths from the subsequent 4 penetrations deviated from the undrained shear strength obtained from the test done at the centre of the sample using the Student's t-test. The null hypothesis for the test is that the differences in the averages obtained from the other penetrations are not statistically significant when compared to the first penetration.

Finally, we also assessed whether the data with outliers removed (defined as data points with undrained shear strength deviating from the value obtained in the middle point by a certain percentage) would lead to any statistically significant result. The outlier cut-offs were 250% and 40% (marked 2.5), 200% and 50% (marked 2), 150% and 66.7% (marked 1.5) and 125% and 80% (marked 1.25).

We also assessed the data with tests following the acceptance/rejection strategy similar to that in ISO 17892-6:2017. In this case, if in the first three penetrations, there was a value deviating by more than 0.5mm, the value most deviating from the average was discarded (excluding the test from the middle of the sample) and another value was taken to compute the average.

5 RESULTS

5.1 Statistical distribution of the normalised data and testing of the hypothesis

The data is first normalized with respect to the data from the first penetration. Assuming a normal distribution for data, data obtained for each penetration has a very high standard deviation, see Table 1. The difference in mean value, vs the middle penetration, is between 0,68% to 7.84%, while the standard deviation is between 30,76% to 78.08%. These are very high values, indicating much scatter in the data. In this case, for each penetration point, we had 39 tests. The results of the Student's t-test show that the differences in obtained undrained shear strengths for each test point location are not statistically significant. The t-test suggests that the mean values differences are not statistically meaningful and cannot be taken as evidence that the adjusted test procedure leads to differences in the obtained values of undrained shear strength. Unfortunately, the amount of data points for each penetration location is not sufficiently large to make a meaningful discussion about whether the assumption of normal distribution is correct.

Table 1. Mean value, standard deviation and t-test result for each penetration location.

Location	Mean	Standard deviation	T-test	Significant?
2	1,0186	0,3869	0,3005	NO
3	1,0784	0,7808	0,6267	NO
4	0,9932	0,3076	0,1389	NO
5	1,0730	0,4614	0,9874	NO

To increase the amount of data, we decided to pool the data from all the points together, leading to 155 data points, due to cutting one outlier (see Figure 3). This full data, as well as data with cut outliers, is assessed for the normal distribution based on histograms and QQ plots, see Figures 4 and 5. The plots are similar and suggest that the normal distribution is an acceptable assumption. The results of a statistical analysis based on the assumption that the data follows normal distribution are in Table 2. The same table contains also mean and standard deviation values, as well as the Student's t-test values.

An alternative is to use lognormal distribution, with the QQ plots, see Figure 6. Both distributions are visually confirmed based on histograms, see Figure 7,

with perhaps lognormal distribution being a slightly better assumption.

The full data, as well as data prepared according to ISO 17892-6:2017, and data with outliers cut, were tested against the null hypothesis using Student's t-test. We checked both normal and lognormal distributions for statistical significance for the hypothesis that the undrained shear strength results obtained from tests done at the sides of the sample are statistically meaningfully different to the undrained shear strength values obtained from the tests done in the middle of the sample, Tables 1-3 contain the analysis results.

Table 2. Mean value, standard deviation and t-test values for the combined data, normal distribution assumption.

Cut-off	Data points	Mean	Standard deviation	T-test	Significant?
No	155*	1.041	0.5127	0.3221	No
ISO	77	1.033	0.2349	0.2150	No
2.5	153	1.001	0.3389	0.0505	(No)
2	146	0.979	0.2713	0.0114	No
1.5	121	1.007	0.1881	0.5530	No
1.25	88	1.006	0.1153	0.6464	No

*Cutoff – preparation of the data, with the cut-off indicating cut-off values – 2.5- values below 40% and above 250% of the average value cut, 2 – 50% and 200%, 1.5 – 150% and 66,7%, ISO – according to ISO standard/ N- assumed normal distribution, L – lognormal. T-test confirms the hypothesis when p<0.05. *one point cut out, see Figure 3 for an explanation.*

5.2 Analysis of the results

The results confirm that there is no statistically meaningful effect indicating that the undrained shear strength obtained for the samples at the sides is different from those in the middle. The confirmation of the hypothesis for the cut-off value of 2.0 is due to the different number of points cut from both sides of the distribution. The results for this case, see Figure 5, indicate that the penetration depths at the sides are smaller than in the middle, which has no physical sense. This perhaps shows how tricky it is to cut the outliers in the data and that such action should be avoided, as it may lead to incorrect results.

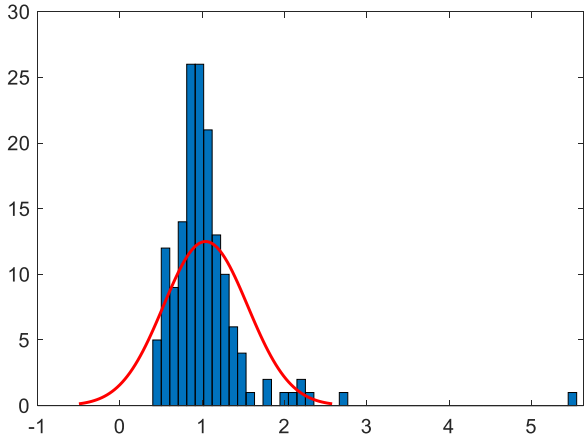

Figure 3. Histogram of all the data. The outlier pointed out by the arrow is cut off for analysis, as it is a clear testing error (insufficient penetration due to excessive friction in the apparatus).

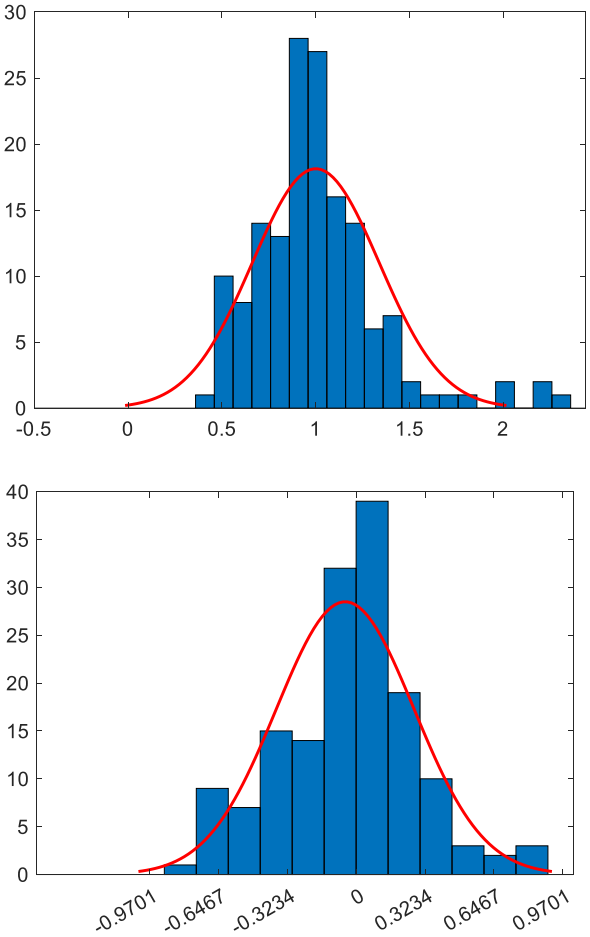

Figure 4. Histogram of data with outliers cut off (cut of value 40% and 250% of the average value), shown vs normal distribution (top) and lognormal distribution (bottom) In lognormal distribution numbers correspond to standard deviations.

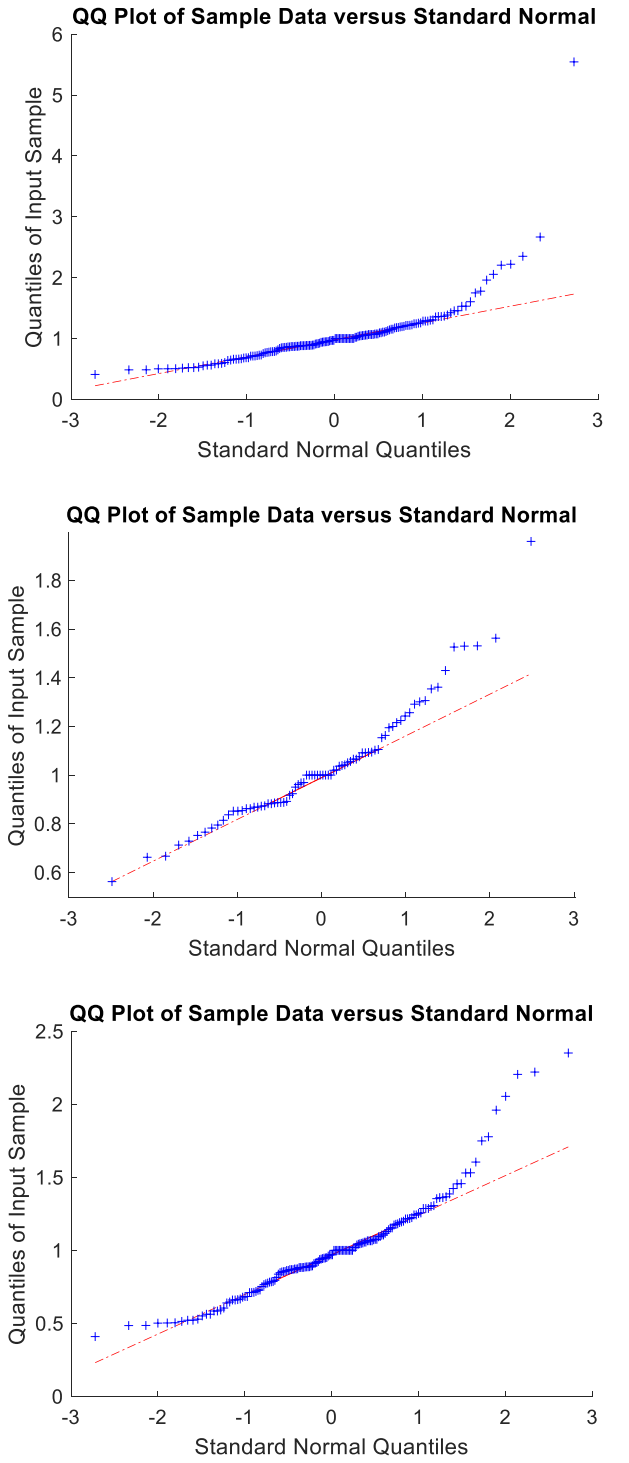

Figure 5. QQ plots of data assuming normal distribution: full data (top), data prepared according to ISO 17892-6:2017 (middle) and with outliers cut off (cut of value 40% and 250% of the average value)(bottom).

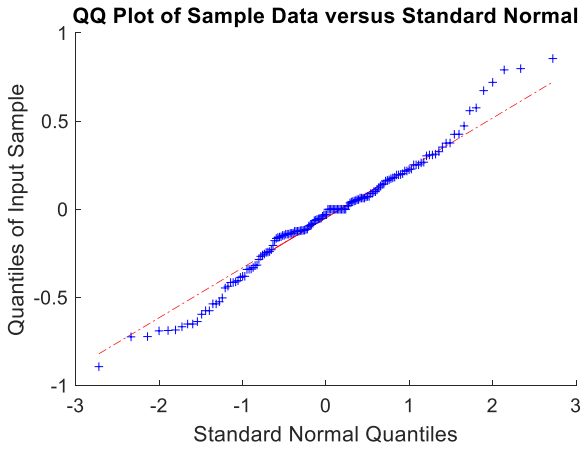

Figure 6. QQ plot of data vs lognormal distribution line with outliers cut off (cut of value 40% and 250% of the average value).

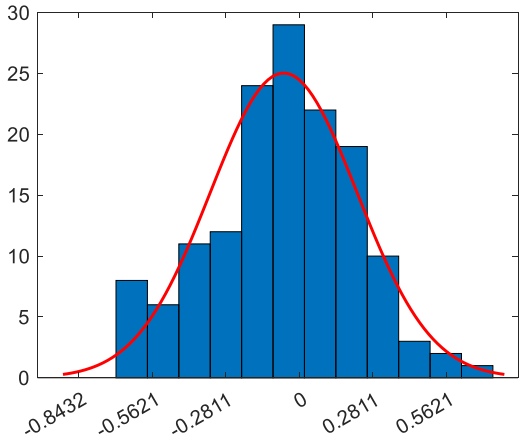

Figure 7. Histogram of data with outliers cut off at 50% and 200% of the average value, shown vs lognormal distribution, with numbers indicating standard deviations. Data is skewed towards lower values of undrained shear strength due to the cut-off value selected.

Table 3. Student's t-test values, lognormal distribution.

Cut-off	t-test p-value	Confirmed (Y/N)
No	0.2484	N
ISO	0.7120	N
2.5	0.0505	(N)
2	0.0114	**Y**
1.5	0.5530	N
1.25	0.9479	N

Cutoff – preparation of the data, with the cut-off indicating cut-off values – 2.5- values below 40% and above 250% of the average value cut, 2 – 50% and 200%, 1.5 – 150% and 66,7%, ISO – according to ISO standard/ N- assumed normal distribution, L – lognormal. T-test confirms the hypothesis when $p<0.05$.

6 CONCLUSIONS

The data we have does not support the hypothesis that the undrained shear strength values from tests on the

sides of the sample are different to the undrained shear strength values obtained from the tests in the middle of the sample, even when the distances of the penetrations are smaller than those required by ISO 17892-6:2017. Instead, the statistical analysis of the data indicates that there is no meaningful difference between the results of the tests in the middle and on the sides of the samples. The data used is still small in the statistical sense (a total of 39 tests, with each test giving 5 data points), and the test results for each sample are quite scattered. As such, in the future, the analysis may be redone with a larger set of data, ideally with data which exhibits smaller variation. Such analysis may give a more definite answer to the posed hypothesis. Additionally, the tests may also be extended to plastic limit tests.

The proposed approach is very convenient and may improve the uncertainty of the testing results, due to the larger amount of obtained values of undrained shear strength. Further investigations and comparisons to other methods of obtaining undrained shear strength will give further arguments on whether the proposed approach is beneficial, and what is the best strategy to obtain the accurate undrained shear strength values based on fall cone tests.

ACKNOWLEDGEMENTS

This project has received funding from the European Union – NextGenerationEU instrument and is funded by the Academy of Finland under grant number 347602.

REFERENCES

Hansbo, S. (1957). New approach to the *determination of the shear strength of clay by the fall-cone test: Vol. No 14*. Royal Swedish Geotechnical Institute Proceedings, lvnr Hoeggstroms Boktryckeri AB.

ISO 17892-6:2017 Geotechnical investigation and testing - Laboratory testing of soil-Part 6: Fall cone test. (2017).

Li, Z.-S., Mohapatra, D., Sołowski, W. T., Saresma, M., Virtasalo, J. J., & Khalili, R. (2023). Geological, Geophysical, and Mechanical Identification of Marine Deposits From the Gulf of Finland. *9th International SUT Offshore Site Investigation and Geotechnics Conference*, 874–882.

Llano-Serna, M. A., & Contreras, L. F. (2020). The effect of surface roughness and shear rate during fall-cone calibration. *Géotechnique*, *70*(4),332–342. https://doi.org/10.1680/jgeot.18.P.222.

Mohapatra, D., Li, Z., Saresma, M., Virtasalo, J., & Sołowski, W. (2023a). Replication of fall cone test on marine clay with a Generalized Interpolation Material Point Method simulation. In Zdravkovic L, Kontoe S, Taborda DMG, & Tsiampousi A (Eds.), *10th European Conference on Numerical Methods in Geotechnical Engineering*.
https://doi.org/https://doi.org/10.53243/NUMGE2023-289.

Mohapatra, D., Saresma, M., Virtalaso, J., & Sołowski, W. (2023b). Numerical Simulation of a Laboratory-Scale Free Fall Cone Penetrometer Test in Marine Clay with the Material Point Method. *VIII International Conference on Particle-Based Methods*. https://doi.org/10.23967/c.particles.2023.032.

Saresma, M., Virasalo, J. J., Li, Z.-S., Mohapatra, D., & Sołowski, W.T. (2023). In Situ Free-Fall Penetrometer (FF-CPT) and Laboratory Fall Cone Characterisation of Soft Marine Sediments in the Gulf of Finland, Baltic Sea. *9th International SUT Offshore Site Investigation and Geotechnics Conference*, 1911–1918.

Tran, Q.-A., & Sołowski, W. (2019). Generalized Interpolation Material Point Method modelling of large deformation problems including strain-rate effects – Application to penetration and progressive failure problems. *Computers and Geotechnics*, *106*, 249–265. https://doi.org/10.1016/j.compgeo.2018.10.020.

Proceedings of the XVIII ECSMGE 2024
GEOTECHNICAL ENGINEERING CHALLENGES
TO MEET CURRENT AND EMERGING NEEDS OF SOCIETY
© 2024 the Authors
ISBN 978-1-032-54816-6
DOI 10.1201/9781003431749-313
Open Access: www.taylorfrancis.com, CC BY-NC-ND 4.0 license

ECSMGE 24
XVIII EUROPEAN CONFERENCE ON SOIL MECHANICS AND GEOTECHNICAL ENGINEERING

Probabilistic analysis for the design of a Vienna metro shaft using Monte Carlo simulation

Analyse probabiliste pour la conception d'un puits de métro à Vienne à l'aide de la simulation de Monte Carlo

O. Kichaieva*
TU Wien, Institute of Geotechnics, Vienna, Austria; O. M. Beketov National University of Urban Economy in Kharkiv; Dept. of Geotechnics, Underground Structures and Hydrotechnical Construction, Kharkiv, Ukraine

D. Adam
TU Wien, Institute of Geotechnics, Vienna, Austria

**oksana.kichaieva@tuwien.ac.at*

ABSTRACT: This paper describes a method of using Monte Carlo simulation for the probabilistic analysis of the shaft structure of a projected metro line in Vienna. The paper presents a discussion of the quality of the input data in the context of their probabilistic variability and their influence on the stress-strain state of the structures. A variant of the problem using the Hardening Soil (HS) and Hardening Soil Small (HSS) models and representing an improved elastic-plastic model was selected for statistical modelling. As a result of multiple variational modelling of the initial data of the soil in which the considered reinforced concrete structures of the tunnel are located, coefficients of variation for the main package of forces and deformations occurring in the reinforced concrete structures and in the soil mass were obtained. These coefficients of variation can then be used in the design process of reinforced concrete structures of this type. The probability of failure according to the criterion of additional settlement for buildings located near the construction site was determined. The degree of influence of certain initial data on the stress-strain state of the structure was also determined using regression analysis.

RÉSUMÉ: Cet article décrit une méthode d'utilisation de la simulation Monte Carlo pour l'analyse probabiliste de la structure d'un puits d'accès d'une ligne de métro projetée à Vienne. L'article présente une discussion sur la qualité des données d'entrée dans le contexte de leur variabilité probabiliste et de leur influence sur l'état de contrainte-déformation des structures. Une variante du problème utilisant les modèles Hardening Soil et Hardening Soil Small et représentant un modèle élastique-plastique amélioré a été sélectionnée pour la modélisation statistique. La modélisation variationnelle multiple des données initiales du sol dans lequel se trouvent les structures en béton armé du tunnel a permis d'obtenir des coefficients de variation pour les principaux ensembles de forces et de déformations se produisant dans les structures en béton armé et dans la masse du sol. Ces coefficients de variation peuvent ensuite être utilisés dans le processus de conception des structures en béton armé de ce type. La probabilité de rupture selon le critère du tassement additionnel pour les bâtiments situés à proximité du site de construction a été déterminée. Le degré d'influence de certaines données initiales sur l'état de contrainte et de déformation de la structure a également été déterminé à l'aide d'une analyse de régression.

Keywords: Probability approach; reliability; Monte Carlo simulation; regression analysis.

1 INTRODUCTION

In solving the problems of reliability theory, it is particularly difficult to determine the value of the risk of reaching a limit state on the basis of solving the corresponding statistical dynamics task. To solve such a problem today, the following methods are used: numerical integration techniques, Monte Carlo simulations, and First and Second Order Reliability Methods (FORM/SORM). The Monte Carlo statistical testing method (Monte Carlo Simulation) is a numerical method for solving mathematical problems based on modelling random variables and performing a significant number of statistical tests using random variables according to known distribution laws. The statistical test method is quite universal and is used to assess the reliability and safety of building structures and bases when solving reliability theory problems based on modelling random variables and constructing statistical estimates, as well as to develop possible (probable) processes or results using various random number generation methods, which are then applied to a real model. The Monte Carlo method is successfully implemented in geotechnical design practice (Pereira and Caldeira, 2011; Griffiths and Fenton, 2007,

Chalermyanont and Benson, 2004; Baecher and Christian, 2003, etc.).

The reliability of structural and geotechnical systems, as well as individual structures, cannot be fully assessed by neglecting the probabilistic nature of external loads and impacts, as well as the properties of structural materials and soils. This is especially true for structures that are located in an aggressive environment – for buried structures in contact with wet soil and water.

Description, modelling, calculation and analysis of the results of these processes is a complex task, the solution of which is impossible without the use of numerical methods and construction of correct calculation schemes. For structures operating in conditions of significant ground contact, the choice of ground model must be justified to a sufficiently high degree. In turn, obtaining adequate results is impossible without thorough geotechnical surveys and appropriate soil tests. This paper describes the experience of using probabilistic-statistical apparatus (Monte Carlo simulation) in determining and analysing the stress-strain state (SSS) of the geotechnical system of the underground construction site in Vienna – Schacht Triester Straße (U2/18 Matzleinsdorfer Platz, Figure 1).

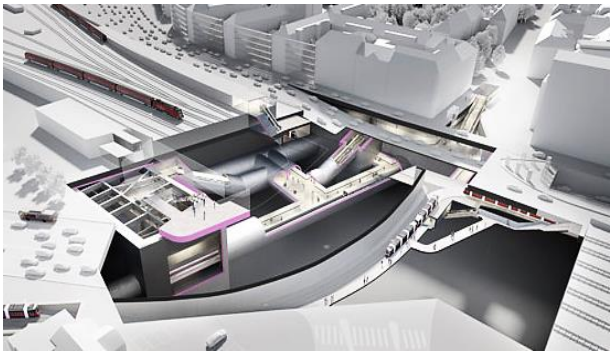

Figure 1. Visualization of Matzleindorfer Platz station (© OLN – Office Le Nomade 2018).

2 MODELING AND CALCULATION

2.1 Soil model

Adequate choice of the ground model is one of the important components in modelling complex technical systems. For statistical modelling, a variant using the Hardening Soil (HS) and Hardening Soil Small (HSS) models was chosen to represent an advanced elastic-plastic model. The actual stiffness characteristics are calculated by PLAXIS software from the achieved stresses, taking into account the development of the stress-strain state of the soil according to a hyperbolic relationship. The coefficients of variation for the varied characteristics were adopted according to the JCSS Probabilistic Modelling Code and in accordance with the scientific studies of Phoon and Kulhawy, 1999, and Griffiths and Fenton, 2007.

2.2 Calculation scheme

The calculation scheme of the system "underground structure – soil" of the metro section was performed and calculated in the PLAXIS programme (Figure 2).

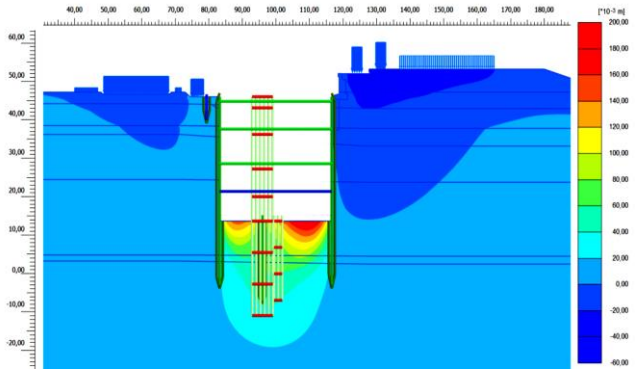

Figure 2. The calculation scheme of the system "underground structure – soil" and one the calculation variant (vertical displacement distribution).

The specified distributions for loads and materials are mainly taken from the Probabilistic Model Code, draft Eurocode 7 prEN 1997-1:2022 (E), and from some other sources of scientific literature (Griffiths and Fenton, 2007; Misra and Roberts, 2007; etc.). Geometric dimensions of building structures and their physical and mechanical characteristics are accepted in accordance with the design data.

2.3 Calculation algorithm

The conducted numerical experiment determines all the parameters of the stress-strain state of the system using Finite Element method and Monte Carlo method in the following order.

1. Values of some parameters of the soils used in the calculation (γ, φ, c, E_{50}^{ref}, E_{oed}^{ref}, E_{ur}^{ref}) and laws of distribution of values are shown in Table 1. The SSS random values of the system are fixed.

2. In the design and construction of underground structures in dense urban areas, one of the main requirements is to ensure the preservation of the surrounding buildings. This requirement is more stringent than the usual assignment of the subsidence level (SLS), as the deformations allowed for the surrounding buildings are always smaller than for

Table 1. Parameters of soils accepted for calculation.

Parameters	Desig-nation	Distri-bution	COV	Mean (1 layer)	Mean (2 layer)	Mean (3 layer)	Mean (4 layer)	Mean (5 layer)	Units
Weight density	γ	normal	0.05	19	21	20	20	20	kN/m^3
Angle of friction	φ	normal	0.1	25	35	25	25	25	°
Specific cohesion	c	normal	0.1	1	1	30	30	30	kPa
Secant stiffness modulus	E_{50}^{ref}	log-normal	0.2	10	60	20	20	20	MPa
Oedometer tangent stiffness modulus	E_{oed}^{ref}	log-normal	0.2	10	60	25	25	25	MPa
Young´s modulus for unloading and reloading	E_{ur}^{ref}	log-normal	0.2	40	240	100	100	100	MPa

new construction. Therefore, when designing underground structures, design solutions must be adopted that ensure not only the reliability of the structure itself, but also the safety of the neighbouring development. In this case, as a quantitative expression of the risk measure for existing buildings, we can use a criterion that limits the additional settlement of urban buildings to a certain permissible level: the value of additional deformations should not exceed the maximum permissible value. To determine the probability of exceeding additional deformations, it is advisable to adopt the method of statistical tests (Monte Carlo method) using the calculation results obtained by means of the PLAXIS program.

3. In this case, the following laws of distribution of input parameters are adopted: 1) distribution of the random variable $P_{S_{add}} = P_{S_{add}}(S_{add})$ additional vertical deformations, adopted with the normal distribution law with mean value $m_{S_{add}}$ = 0.03 m and standard deviation $\sigma_{S_{add}}$ = 0.003 m. The values of this parameter are determined by analysing FEM calculations. 2) The distribution of the random variable $P_s = P_s(s)$ of the limiting additional deformations, which is assumed with the normal law of distribution respectively with m_s and σ_s. The mean value is taken based on the analysis of monitoring of buildings and structures, literature and common sense.

4. According to this method, N statistical tests (N = 10^5) are conducted according to this algorithm. 1) Determination of random values of vertical deformation s (FEM). 2) In each case the condition $s \leq S_{add}$. 3) After conducting all N tests, the probability of exceeding the limit additional deformations during the design life is calculated as the ratio of the number of tests at which $S_{add} - s < 0$ to the number of all tests. Figure 3 shows the probability density functions of estimated additional settlement and allowable additional settlement.

5. It is highly likely that the surrounding development is mainly in the CC2 impact class, for which the minimum value β is 2.9 for a time period of 1 year and β = 1.5 for a time period of 50 years (Table C2 of EN1990:2002).

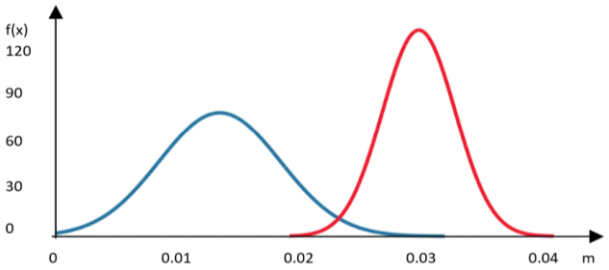

Figure 3. Density functions of the distribution of calculated additional settlement s (blue curve) and allowable additional settlement S_{add} (red curve).

2.4 Results

1. So, according to the results of FEM calculations with varying initial data, all characteristics of the stress-strain state of the "underground structure – soil" system were obtained, as well as the coefficients of variation of these characteristics, which are as follows:

- for longitudinal forces $N - v = 0.08$ (8%);
- for bending moments $M - v = 0.09$ (9%);
- for shear forces Q – $v = 0.11$ (11%);
- for vertical displacement $u_y - v = 0.237$ (≅24%);
- for horizontal displacements $u_x - v = 0.2$ (20%).

2. After checking the obtained values of all aforementioned parameters by the criterion of agreement at the significance level of 0.05, it was determined that they have normal distribution.

3. Probabilistic calculations performed in the Mathcad Prime software package showed that the probability of system failure by the criterion of additional vertical deformations is p_f = 0.002, and corresponds to the safety index β = 3.0, which is quite

acceptable and complies with the normative document "Probabilistic Model Code".

2.5 Regression Analysis

Regression analysis of the influence of varying factors on the main parameters of the stress-strain state obtained from the FEM calculation was performed. Regression analysis is a set of statistical methods to assess the relationship between variables and the degree of this relationship, as well as modelling of future dependence. Linear, multilinear and nonlinear models are the most common models of analysis. In this case, the first two models were used, and regression analysis was carried out on the basis of the least squares method.

After enumerating many variations, an interesting pattern was identified – the magnitude of the longitudinal force N in the shaft wall can be satisfactorily described by a linear regression model, as 90.1% of the percentage variability of the longitudinal force values is explained by this model. In this two-factor experiment, the independent variables were the specific gravity of the soil γ and the angle of internal friction of the soil φ, and the dependent variable was the value of the longitudinal force N. Further calculations were carried out only to establish the relationship between soil specific gravity and longitudinal force values, and it was found that 86% of the variability of longitudinal force values can also be described by a linear regression model.

An experiment was also conducted to establish the relationship between the vertical strain values and the values of soil specific gravity γ and elastic modulus E_{50}^{ref}. It was found that the percentage of variability of vertical deformation values also depends linearly on these two independent variables, but only 54.2% of the variability of values is described by a linear model.

3 CONCLUSIONS

Modelling of empirical distributions of initial data parameters of the system "underground structure – soil" was carried out, after which multiple variation calculations of this system were performed in the PLAXIS software package. As a result, the values of variation coefficients for the main set of forces and deformations were obtained, which can be used in reliability calculation after selection of cross-section and reinforcement of reinforced concrete structures of similar type.

The range of displacement values of the buildings during construction was also obtained and the reliability calculation was carried out using Monte Carlo numerical modelling using the criterion of additional settlement of the buildings surrounding the Schachtes Triester Straße (Baulos U2/18 Matzleinsdorfer Platz). The probability of failure was 0.002 and the reliability index β = 3.0, which are quite acceptable values for the SLS condition.

Regression analysis of the influence of changing soil characteristics on the main parameters of the stress-strain state was carried out. Regression analysis of the influence of varying soil characteristics on the main parameters of the stress-strain state has been performed. Correlation dependences between some parameters were established.

REFERENCES

Baecher, G., Christian, J. (2003). *Reliability and Statistics in Geotechnical Engineering*. John Wiley & Sons Inc. Ltd, The Atrium, Southern Gate, Chichester, England. ISBN: 978-0-471-49833-9.

Chalermyanont, T., Benson, C. (2004). Reliability-based design for internal stability of mechanically stabilized earth walls. *Journal of Geotechnical and Geoenvironmental Engineering*, Vol. 128(5), pp. 381-390. https://doi.org/10.1061/(ASCE)1090-0241(2004)130:2(163).

Griffiths, D., Fenton, G. (2007). Probabilistic Methods in Geotechnical Engineering, Vol. 491, Serie CISM International Centre for Mechanical Sciences, Springler Vienna. ISBN 3211100741, 9783211100745.

Duncan, J. (2000). Factors of Safety and Reliability on Geotechnical Engineering. Journal of Geotechnical and Geoenvironmental Engineering. ASCE, Vol. 126, Issue 4, pp. 307-316. https://doi.org/10.1061/(ASCE)1090-0241(2000)126:4(307).

Misra, A., Roberts, L.A. (2007) Reliability-Based Design of Shallow Foundation Based on Elastic Settlement. *Proc. of the First International Symposium on Geotechnical Safety & Risk,* Shanghai, Tongji University, China, pp. 471 - 483.

Pereira, C., Caldeira, L. (2011) Shallow Foundation Design through Probabilistic and Deterministic. *Proc. of the 3rd Intern. Symposium on Geotechnical Safety and Risk (ISGSR2011)*. Munich, Germany. pp. 199-207. ISBN 978-3-939230-01-4.

Phoon, K., Kulhawy, F. (1999) Characterization of Geotechnical Variability. *Canadian Geotechnical Journal* 36, pp. 612-624, https://doi.org/10.1139/t99-038.

Probabilistic Model Code (2001) Part I – Basic of Design. JCSS. ISBN 978-3-909386-79-6. https://www.jcss-lc.org/jcss-probabilistic-model-code/.

Proceedings of the XVIII ECSMGE 2024
GEOTECHNICAL ENGINEERING CHALLENGES
TO MEET CURRENT AND EMERGING NEEDS OF SOCIETY
© 2024 the Authors
ISBN 978-1-032-54816-6
DOI 10.1201/9781003431749-314
Open Access: www.taylorfrancis.com, CC BY-NC-ND 4.0 license

ECSMGE 24
XVIII EUROPEAN CONFERENCE ON SOIL MECHANICS AND GEOTECHNICAL ENGINEERING

Effect of flood duration on levee stability

Effet de la durée de l'inondation sur la stabilité d' une digue

E. Koch*, R.P. Ray
Széchenyi István University, Győr, Hungary
**koche@sze.hu*

ABSTRACT: During the last decades, flood events in Hungary and other European countries have become an unprecedented challenge to geotechnical engineering due to the increase in frequency and severity. Construction of the flood protection system has been started in the middle of the 19th century. Their construction materials and methods do not meet current standards and require constant inspection and maintenance. The three most significant historic floods (i.e., characterized by the largest yield) along the main Hungarian Rivers have occurred in the last 20 years. During these events, soil instability and embankment failure occurred along the levees at several locations. The paper focuses on the effect of water levels on levee stability at a selected site along the Tisza River that failed during the 2006 flood events. To model the failure induced by extremely high water level, transient seepage analysis was carried out. The input parameters were determined based on the results of site investigations and laboratory tests. The study showed that with increasing water levels and time of flood, the stability of the levees decreased.

RÉSUMÉ: Au cours des dernières décennies, les inondations en Hongrie et dans d'autres pays européens sont devenues un défi sans précédent pour l'ingénierie géotechnique en raison de l'augmentation de leur fréquence et de leur gravité. La construction du système de protection contre les inondations a commencé au milieu du 19ème siècle. Les matériaux et les méthodes de construction ne répondent pas aux normes actuelles et nécessitent une inspection et un entretien constants. Les trois inondations historiques les plus importantes (c'est-à-dire caractérisées par le plus grand débit) le long des principales rivières hongroises se sont produites au cours des 20 dernières années. Au cours de ces événements, l'instabilité du sol et la rupture des digues se sont produites à plusieurs endroits. L'article se concentre sur l'effet des niveaux d'eau sur la stabilité des digues sur un site sélectionné le long de la rivière Tisza qui s'est rompu lors des inondations de 2006. Pour modéliser la rupture induite par un niveau d'eau extrêmement élevé, une analyse transitoire des infiltrations a été réalisée. Les paramètres d'entrée ont été déterminés sur la base des résultats des enquêtes sur le site et des tests en laboratoire. L'étude a montré que la stabilité des digues diminuait avec l'augmentation des niveaux d'eau et du temps d'inondation.

Keywords: Flood duration; levee; slope stability; transient seepage analysis; numerical simulation.

1 INTRODUCTION

Flooding is a natural hazard that probably has the highest occurrence in time and space worldwide, causing considerable damage in terms of loss of life and property every year (Loat, 2009).

There are many reasons and triggering processes that may cause levee failure. For flood risk reduction, CIRIA (2013) defines failure as the inability to achieve a defined performance threshold for a given function.

A levee can fail through structural or hydraulic mechanisms or both. Structural failure occurs by a breach in the levee system that results from damages affecting at least one system segment. Hydraulic failure (non-structural) occurs if water ingress into the leveed area (by through-flow, overflow or overtopping of the levee) before the planned protection level is reached and without prior damage to the system element. Structural failure can induce hydraulic failure and vice versa.

Slope failure occurs when the driving loads applied on the levee (weight of the materials, hydraulic forces) exceed the shear strengths of the materials in the embankment body and foundation (Tourment et al., 2019). Sliding can occur both on the inner slope and on the outer slope, the latter typically occurs after a high-water event when the water level falls but pore water pressures in the levee remain high.

Nagy and Toth (2005) conducted an extensive study of levee breaches in Hungary during the last 50 years (1954-2004). Based on analyses of 117 breaches, they determined that 98% of all breaches were caused by overtopping, piping and loss of slope stability (Figure 1).

Flooding due to hydraulic loading is often the result of the interaction of multiple phenomena, which may follow different failure paths. Engineers designing embankments consider separate, individual failure paths. However, back analysis of failure events often

indicates that flooding resulted from a combination of phenomena and that site-specific characteristics play a significant role in the occurrence of different events.

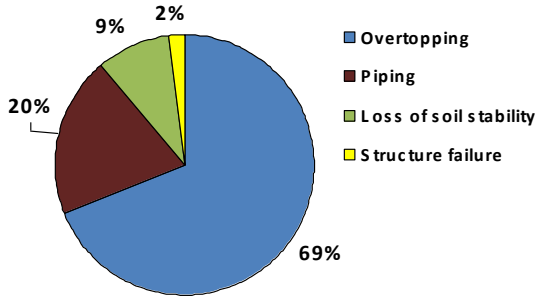

Figure 1. Distribution of failure mechanisms for levee breaches in Hungary between 1954-2004 (Nagy and Toth (2005).

This paper presents a back-analysis of a slope failure induced by the April 2006 flood near the Tisza River. The failure occurred on the landside of the levee (Figure 2) and required immediate stabilization by a sandbag revetment at its toe.



Figure 2. Stability problem along the Tisza River.

2 STUDY AREA

The Tisza River (catchment area: 157,000 km2) in Central Europe drains the eastern half of the Pannonian Basin, where river systems have a long history of evolution. The oldest fluvial deposits date back to the Late Miocene. The courses of the rivers, including the Tisza, are influenced by several sinking grabens. One of the most active ones is the South Tisza Graben, where approximately 700-m-deep fluvial sediments have accumulated. Until the Late Pleistocene, the graben subsidence was continuous but fluctuating; during the Holocene, it terminated as Early Holocene floodplain forms were not buried by younger sediments (Sheishah et al., 2023).

The original length of the Tisza River was 1.400 km from its spring in the north-eastern Carpathian Mountains in Ukraine to its mouth at the Danube. During the second half of the 19th century, extensive measures on the river and flood control were undertaken along the river. As a result of these works, the river's total length was shortened by approximately 30%, and today, it is 966 km.

Constructed in the 1880s, artificial levees (length = 2940 km) created flood-safe areas and decreased flood duration. They confined the floodplain width to 0.4–5 km. Over time, their further construction raised their heights to counteract higher flood levels (Lóczy et al., 2009). A typical levee cross-section reveals many different zones (Figure 3).

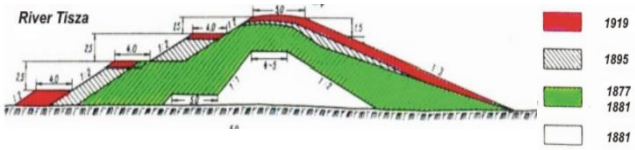

Figure 3. Typical cross-section along the Tisza River (Sheishah, 2023).

The groundwater elevation follows the river elevation changes and is close to the surface; as a result, the foundation soils are almost always saturated.

Figure 4 shows the water level elevation during the flood event in 2006. The typical zero water elevation reading on the river at Csongrád is ~75 m above the Baltic Sea level. During the 2006 spring flood, the peak level reached 1062 cm. The flood wave started at the end of March and peaked four weeks later. The figure also shows the flood warning levels I., II., and III. (650, 750, 850 cm).

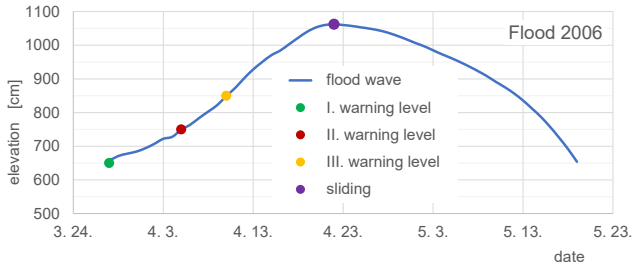

Figure 4. Water elevations during the 2006 April flood wave along the Tisza River.

3 MODELING APPROACH

Due to the levee evolution, the cross-section is inhomogeneous and anisotropic. PLAXIS 2D geotechnical software can analyse the time-dependent water level raising and the stability of the levee. Design approach 3 has been selected in the Hungarian national annexe of Eurocode 7 (EC7) for overall stability problems as in other countries. The choice is exceptionally reasonable for levees because design actions should receive no partial factor. The partial

factor for shear strength parameters for resistance is 1.35 (Szepesházi et al., 2015).

Geotechnical finite element software performs stability analysis using the ϕ-c reduction method, also called Safety Analysis by Plaxis, corresponding to design approach 3. The resulting safety factor must be compared with the partial factors defined by the standard, $\gamma_{\phi,c}$=1.35.

An extensive geotechnical investigation of ten boreholes determined soil stratification and parameters. The geotechnical laboratory of Széchenyi University tested disturbed and undisturbed samples to determine their physical and mechanical characteristics. Figure 5 shows the results of the triaxial test and shear tests of the high-plasticity clay. The figure also represents the characteristic shear stress value of the clay material.

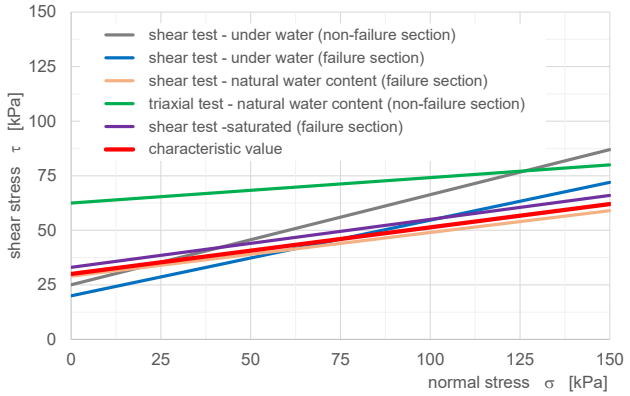

Figure 5. Results of the laboratory tests.

The soil properties are summarized in Table 1. The top layer was modeled as low-plasticity clay, the foundation and core as high-plasticity clay, and the bottom layer as silt and sandy soils.

The measured levee's present height is 6.5 m, and the base width is 45 m, with a crest 4.5 m wide. The landside slope of the levee is 1:3, and at 2/3 of the height, there is a 3.5 m wide berm.

We applied a fully coupled flow-deformation analysis to simulate the water level raising and followed by the overall stability using phi-c reduction method. The applied constitutive model was Mohr-Coulomb. The finite element mesh is shown in Figure 6. Stability was modeled with four water levels: warning levels I, II, and III, and the maximum water level (max) (Figure 6).

Before the flood, the levee was in good condition, showing overall stability MSF=2.6, much higher than the required value by the EC-7, MSF=1.35. Figure 7. shows the possible failure mechanism related to the condition without flood.

Observations of field performance pointed to the apparent failure mechanism where seepage helped to generate reduced effective stress and strength. The slope (berm) moved just as the water level peaked, rising 1.5 m in about a week. The water seeped over the lower, less permeable black clay material and through the upper, more permeable yellowish-brown zone. This process weakened the strength of the black clay interface and, to some extent, the yellowish-brown layer. At the same time, seepage gradients almost parallel to the downslope direction increased the sliding forces.

Table 1. Soil properties

parameters	Sand	Silt	HP Clay	LP Clay
γ_{unsat} [kN/m^3]	20.0	20.0	18.5	21.0
ν [–]	0.3	0.3	0.35	0.35
E_{oed} [MN/m^2]	15.0	7.0	5.0	3.0
c_{ref} [kN/m^2]	1.0	25.0	30.0	50.0
ϕ [°]	32.0	23.0	10.0	10.0
k [m/day]	1.5	8E-3	2E-4	8E-4

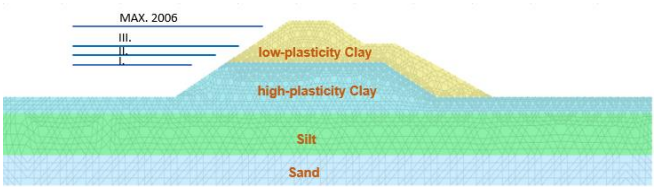

Figure 6. Finite element mesh and water elevation at the outer side of the levee.

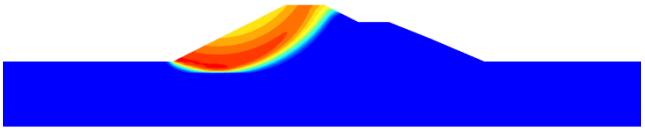

Figure 7. Possible failure mechanism before the flood (blue is no deformation; red maximum).

4 RESULTS

The stability of the levee was evaluated as a function of water level elevation and duration of rising water level. After 10 days of water level rising to 450 cm, the slope safety factor was MSF=2.3. During the next 10 days, reaching I. warning level (650 cm), the safety factor decreased to 1.88. With another 100 cm increase in water elevation (II. warning level=750 cm), it decreased to MSF=1.56. On the 35th day of the flood, reaching the III. warning level (850 cm), the safety factor decreased to MSF=1.32. With an additional 200 cm increase in water level elevation (MAX=1062 cm) the levee became unstable.

The factor of safety for stablity of the levee decreased with time and increasing water elevations. Figure 8. shows the failure mechanism at the peak water level with the safety factor MSF=1.03. The modelled slip surface matches the real failure observed

at the site. The factor of safety was plotted as a function of water levels and duration of the flood (Figure 9).

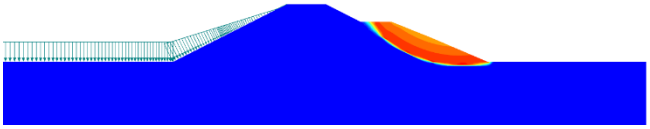

Figure 8. Possible failure mechanism at peak water level during flooding.

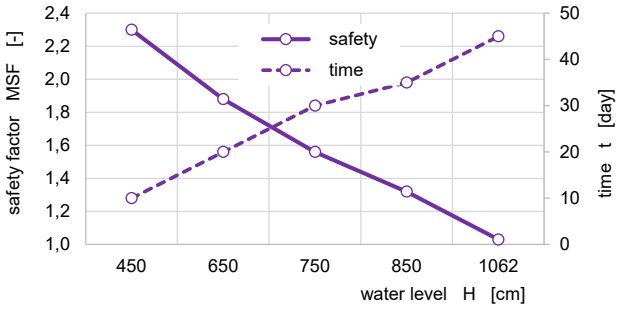

Figure 9. Factor of safety as a function water level and time of flooding.

After the flood, the failed slope was reinforced using a revetment on the land side. The applied material was coarse-grained and a drainage system was also constructed along the landside levee toe. After simulation of a longer, 60 day flood with the same peak water level (1062 cm), the stability shows MSF=1.37. The possible failure mechanism is shown in Figure 10. The slip surface seems similar to the surface related to the failure, but due to the coarse-grained revetment and the drainage system at the levee toe, the water flow through the levee had accelerated. Reducing the shear strength of the levee foundation and core might be avoided.

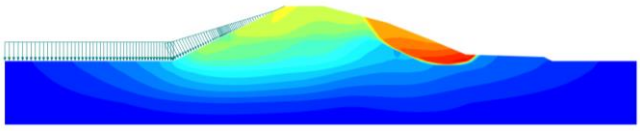

Figure 10. Failure mechanism after reinforcement.

5 CONCLUSIONS

Levee breaches are decreasing due to recent improvements in the levee systems. However, the safety of the levees can decrease because of other problems, such as instability due to the increase in the frequency of floods and longer and higher flood waves. Our study showed that with increasing water levels and the duration of rising water level, the stability of the levees decreased.

For the past 15 years, flood water elevations in the Tisza River have exceeded the previously determined maximum water levels. Higher levels have destabilized levees at unpredictable locations. Other new improvements are necessary since former solutions, such as increasing the crest and the width of the levee, can lead to structural problems. Thoroughly evaluating stability under the new flooding conditions and their impact on effective stress and strength of slopes during transient seepage loads represents a new challenge to the geotechnical engineer. Accurately modeling the transient seepage regime, global, and local stability is necessary to evaluate the performance of the levee system and any proposed improvements.

REFERENCES

Brinkgreve R.B.J. and Vermeer P.A. (2014). PLAXIS 2D Finite element code for soil and rock analyses, Part 3. Material Models Manuals, Delft University of Technology & Plaxis bv, The Netherlands.

CIRIA (2013). International levee handbook (C731), Section 2. CIRIA, London.

EN 1997-1 (2004). Eurocode 7: Geotechnical design - Part 1: General rules [Authority: The European Uni-on Per Regulation 305/2011, Directive 98/34/EC, Directive 2004/18/EC].

Loat R. (2009). Flood mapping in Europe – EXCIMAP. UNECE workshop on transboundary flood risk management, Genova.

Lóczy, D., Kis, É., Schweitzer, F. (2009). Local flood hazards assessed from channel morphometry along the Tisza River in Hungary. Geomorphology, 113, pp. 200-209. https://doi.org/10.1016/j.geomorph.2009.03.013.

Nagy, L. and Tóth, S. (2005). Detailed Technical Report on the collation and analysis of dike breach data with regards to formation process and location factors, Tech. rep., H-EURAqua Ltd., Hungary.

Sheishah, D., Kiss, T., Borza, T. et al. (2023). Mapping subsurface defects and surface deformation along the artificial levee of the Lower Tisza River, Hungary. Nat Hazards 117, 1647–1671. https://doi.org/10.1007/s11069-023-05922-1.

Sheishah, D. (2023). Mapping and Evaluating the Condition of Artificial Levees. Ph.D Dissertation, University of Szeged.

Szepesházi, R, Koch, E. and Wolf, Á. (2015). Numerical modeling of levees according to Eurocode 7, XVI European Conference on Soil Mechanics and Geotechnical Engineering, Edinburgh.

Tourment, R., Beullac, B., Berthelier, E., Boulay, A., Maurin, J., and Queffelean, Y. (2019). Inondations-Analyse de risque des systèmes de protection-Application aux études de dangers. Lavoisier.

Proceedings of the XVIII ECSMGE 2024
GEOTECHNICAL ENGINEERING CHALLENGES
TO MEET CURRENT AND EMERGING NEEDS OF SOCIETY
© 2024 the Authors
ISBN 978-1-032-54816-6
DOI 10.1201/9781003431749-315
Open Access: www.taylorfrancis.com, CC BY-NC-ND 4.0 license

ECSMGE 24
XVIII EUROPEAN CONFERENCE ON SOIL MECHANICS AND GEOTECHNICAL ENGINEERING

Deformations assessment of phosphogypsum waste heap in Wiślinka after 15 years of its reclamation

L'évaluation de la déformation du terril de phosphogypse à Wiślinka après 15 ans de remise en état

A.P. Korzec*, W. Świdziński
Institute of Hydro-Engineering/Polish Academy of Sciences, Gdańsk, Poland
*a.korzec@ibwpan.gda.pl

ABSTRACT: The article presents an analysis of the long-term response of the phosphogypsum waste heap in Wiślinka, Poland, almost 15 years after its reclamation. The behaviour of such heaps is an important issue since phosphogypsum has no industrial application so far and, consequently, such structures will become a part of the landscape or even a substructure. The heap deformations are assessed based on the results of two monitoring systems consisting of survey markers and inclinometers installed at various periods. In the analysis, available historical records combined with the most current records obtained in the course of the ongoing project are implemented. The crest of the slope of the oldest part of the heap settled by 2.5 m over the last 20 years. The settlement progresses with rate of up to 66 mm/year, which is 75% lower than in 2007. Horizontal displacements of the heap slope are also observed with the rate 11 mm/year and have remained constant since at least 2019. Based on these results and further investigations being currently carried out, the hypothesis concerning the existence of 3 different mass movements of some parts of the heap has been stated. To verify the hypothesis, a monitoring system has been developed and new results will be analysed during the course of the project that is still ongoing.

RÉSUMÉ: Cet article présente une analyse de la réponse à long terme du terril de phosphogypse localisé à Wiślinka en Pologne, près de 15 ans après sa remise en état. Le comportement de tels amas est une question importante puisque le phosphogypse n'a jusqu'à présent aucune application industrielle et, par conséquent, de telles structures deviendront une partie du paysage ou même une sous-structure. Les déformations du tas sont évaluées sur la base des résultats de deux systèmes de surveillance installés à différentes périodes de temps, constitués de balises d'enquête et d'inclinomètres installés à différentes périodes de temps. Dans l'analyse, les enregistrements historiques disponibles combinés avec des enregistrements actuels obtenus au cours du projet en cours sont mis en œuvre. La crête du talus de la partie la plus ancienne du terril s'est tassée de 2,5 m au cours des 20 dernières années. La sédimentation continue de se produire à un rythme pouvant atteindre 66 mm/an et est 75% inférieur à celui de 2007. Des déplacements horizontaux de la pente du tas sont également observés à raison de 11 mm/an et sont restés constants depuis 2019. Sur la base de ces résultats et d'autres investigations en cours, l'hypothèse concernant l'existence de 3 mouvements de masse différents de certains des parties du tas ont été indiquées. Un système de suivi a été développé et de nouveaux résultats seront analysés au cours du projet qui est toujours en cours afin de vérifier l'exactitude de l'hypothèse.

Keywords: Heap; landslides; mass movement; deformations; monitoring systems.

1 INTRODUCTION

The paper regards the performance of the reclaimed phosphogypsum heap located in Wiślinka, in Pruszcz Gdański district, Poland, Figure 1. The heap belongs to the Azoty Group Fosfory, Gdańsk, a producer of mineral fertilizers widely used in agriculture. The phosphogypsum is a by-product of the phosphoric acid made of phosphate rock. As such it is not considered as hazardous waste and can be utilized by its deposition. The location decision issued in 1969 defined the area occupied by the heap to be 26 ha. In 1983, it was established that a maximum of 16.6 Mt of chemical industry waste could be stored on the heap, and its height could not exceed 41 m. In order to facilitate the transportation process of phosphogypsum (Ph) using a waterway, the heap has been located nearby *Martwa Wisła* River. The deposition of phosphogypsum in the heap was carried out in the years 1972-2009.

The closure of the heap had been performed based on the detailed documentation. Reclamation works were carried out in 2008-2009. The main goal of the procedure of heap closure was to define its final geometry which minimises the negative impact of the heap on surface and ground waters, neighbouring agriculture lands and air as well as to assure lifetime

stability of the heap's slopes. The long-term behaviour of such heaps is an important issue since phosphogypsum has no industrial application so far (Bilal et al., 2023). According to Polish law, the behaviour of the heap should be monitored for 50 years after closure.

The essential part of the closure documentation consisted of the project and implementation of the monitoring system to follow the response of the heap in time and to assess its environmental impact and stability. The monitoring system, intended for stability assessment, consisted of 33 benchmarks to monitor the surface deformations accompanied by 2 inclinometers for investigation of deeper earth movements. On-site inspection revealed that 5 survey markers installed in 2004, before heap reclamation, still exist. Since the measurement records are also available, in this paper, the heap deformations monitored for almost 20 years are analysed.



Figure 1. Southern Slope of Wiślinka heap (October 2022).

2 GENERAL CHARACTERISTICS

2.1 Heap geometry and material

The base of the heap has an irregular shape. For the sake of the analysis, four parts of the heap corresponding to the cardinal directions have been distinguished, Figure 2. Next, based on satellite technology characteristic cross-sections of the heap slopes together with current geometry have been defined, Figure 3 and Figure 4. The maximum elevation of the heap's top plateau is 42.3 m asl. The heap is surrounded by dikes with a crest at the elevation of 5.8 m asl. The ground level from is 2.5 m asl from the *Martwa Wisła* river side and 0.5 m asl from the south side. Currently, the Western Slope is the most inclined slope of the heap. Its inclination is 37° (*V:H* = 1:1.3). The Eastern and Southern Slopes have similar geometry with a 10 m wide intermediate bench located at the elevation of 11 m asl and the average inclination of the upper slope 35° ± 5% (1:1.4). The Northern Slope has the lowest inclination of 25° (1:2.1). The original steep slope was reconstructed to form technical access road and to improve its stability.

Based on documentation analysis, site interviews and analysis of boreholes made in 2022, the method of phosphogypsum deposition has been concluded. Initially, the phosphogypsum (of white colour) had been deposited in a basin formed between surrounding dikes which resulted in the formation of laminations of mineral soil (Phl). After reaching the elevation of 2.5 m, phosphogypsum was deposited as a dry stack in 5 to 15 m thick layers without any compaction.

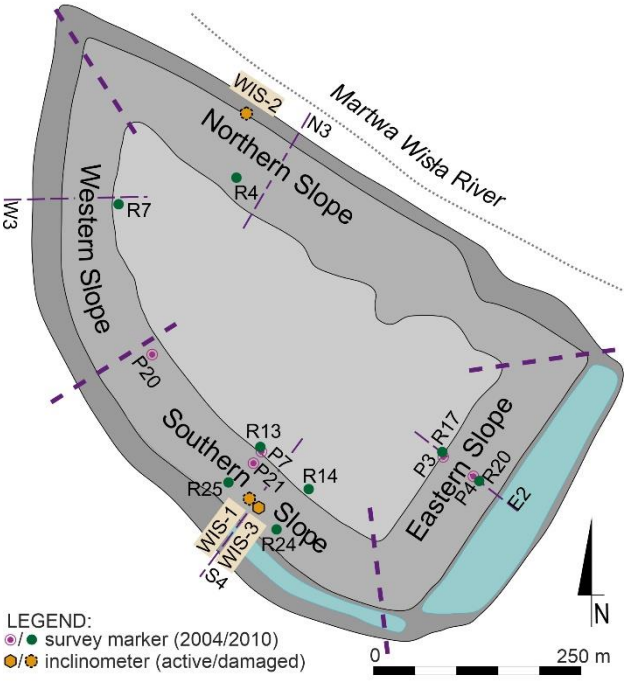

Figure 2. Scheme of Wiślinka waste heap.

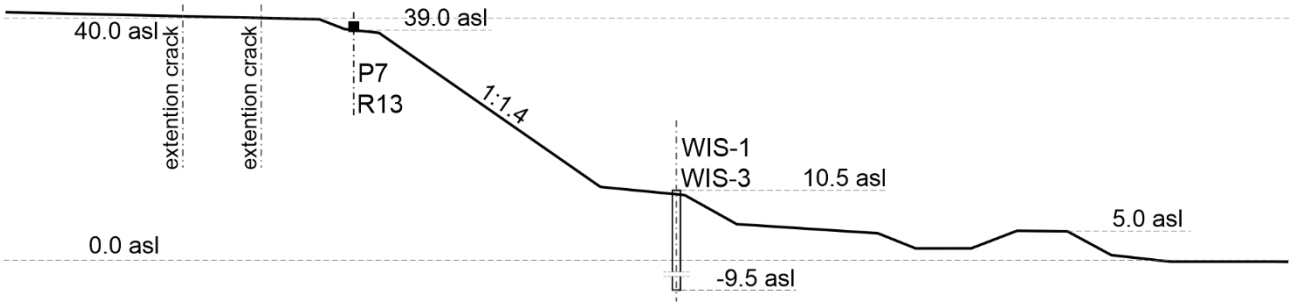

Figure 3. S4 profile of Southern Slope of Wiślinka waste heap.

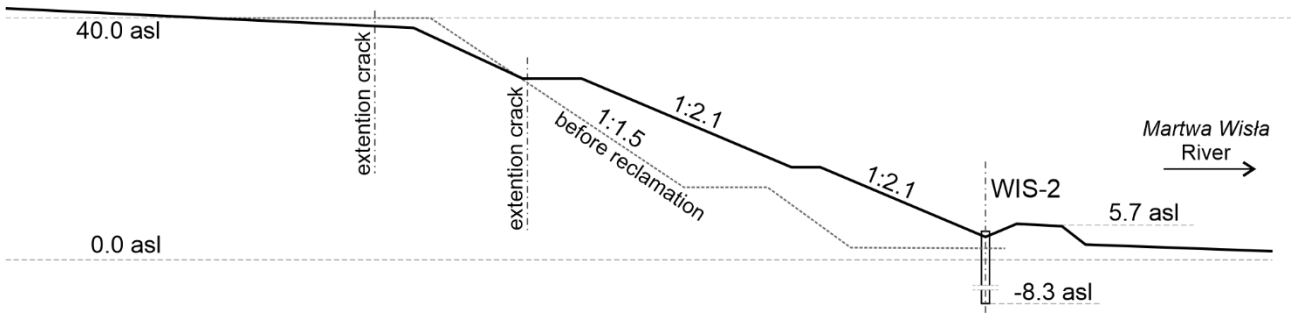

Figure 4. N3 profile of Northern Slope of Wiślinka waste heap.

The initial angle of external slopes might have reached even 63°, which has been confirmed by the photogrammetric measurements carried out in 1996. The variety of colours identified in phosphogypsum cores (from yellow-grey by grey to brown-grey), as well as their consistency (from very firm to loose) and moisture content, allows us to conclude that the raw material and the superphosphate production process had been changing over the years. The final elevation of the deposition was first reached in the eastern and southern parts of the structure (1999) whereas the rest of the heap was formed just prior to the closure.

2.2 Subsoil characteristic

The foundation under the heap, to the depth of the recognition carried out in the course of the ongoing project (19.6 m bsl), is strongly stratified. Such a stratification is characteristic of alluvial regions located near the rivers. Finally, three layers of organic soils interbedded by mineral soils have been identified. The first two organic layers are composed of mud and peat. The second, 3.1 m thick organic layer, seems to be decisive from the slope stability point of view. It consists of loose organic silts underlain by plastic clays.

3 DEFORMATION MONITORING SYSTEM

3.1 Surface deformations

Historically, the monitoring of the heap deformations measured during the development of the structure practically served to control its top elevation. In 2004, 21 benchmarks were installed in order to monitor the heap deformations in those parts which have been assumed to be completed. The surveying was carried out up to 2007 using an electronic tachometer with ±3 cm accuracy. The inventory of the existing monitoring infrastructure performed in the course of the project and initiated by the Authors of the paper showed that there are only 5 benchmarks left: three are located at the Western Slope (1 on the crest and 2 on the slope) whereas remaining two at the Eastern Slope (on the crest and slope, respectively), Figure 2. In the paper, these benchmarks are marked by the letter P. Measurements have been resumed since the autumn of 2022.

In 2010, a new monitoring system of heap deformation, consisting of 33 benchmarks, was installed. Benchmarks from that system are marked by the letter R. Measurements were initially carried out once every half a year, then once a year. The accuracy of the horizontal displacements was ±2 cm, whereas for vertical ones ±3 cm.

Initially, the surveying was carried out with reference to the Gdańsk70 coordinate system and the Kronsztadt86 elevation system. Since 2010, measurement has been performed using the 2000 and the Kronsztadt86 reference systems. Therefore, to obtain a continuous history of heap deformation, measurement data from the years 2004-2007 and 2010-2021 were converted to reference systems currently legally permitted in Poland, i.e. 2000 and EVRF2007 (Amsterdam 2007).

In three locations, the benchmarks from both above-mentioned systems are located close to each other; P3-R17 pair on the crest of the Eastern Slope, while P7-R13 and P4-R20 pairs on the crest and bench of the Southern Slope, respectively. Combining the results of geodetic measurements from both systems allowed us to obtain the deformation pattern over a longer period. It also enables the identification of possible displacements and their rates that might have occurred in parts of the heap formed later.

Starting from 2004, the top of the Eastern Slope settled by 2.32 m. Currently, the rate of subsidence is 66 mm/year. The vertical displacement u_Z rate in the period of 2004-2007 was as high as 260 mm/year. Similar values regard the Southern Slope i.e. u_Z = -2.52 m, Δu_Z = 40 mm/year, Figure 5. Over such, relatively long, observation periods some kind of stabilisation can be identified.

In Figure 6 the settlement's time-histories of four R benchmarks representing the crest of each slope were compared. The R7 benchmark settled 2.59 m since 2012. The settling rate of the youngest part of the heap

is 160 mm/year. Thus, some settlements are still expected to occur. A large settlement was recorded on the reconstructed northern part of the heap. However, if we ignore the first increment of the settlement, R4 behaves quite similarly to the older part of the heap.

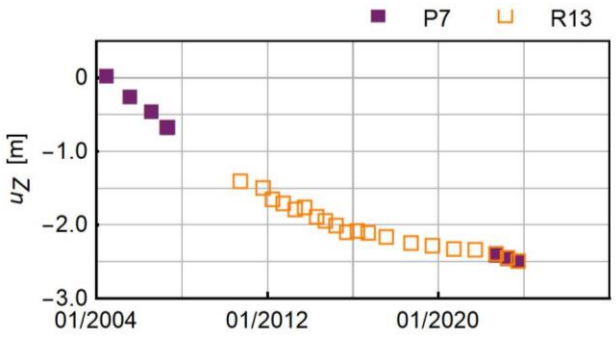

Figure 5. Settlements of P7 and R13 control points located at Southern Slope.

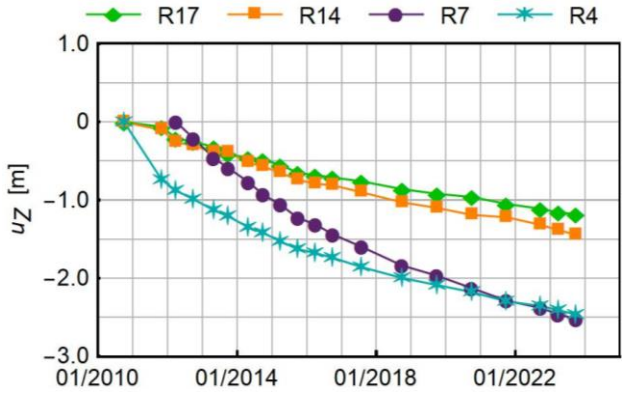

Figure 6. Settlements of control points installed in 2010 (R) representative for each slope.

The directions of horizontal displacement vectors of benchmarks installed in 2010 indicate an occurrence of mass motions observed along three slopes. Only the Eastern Slope has not been moving horizontally. It can be noticed that the values of displacements, as well as, their rates are different which mainly results from the different times of the construction of the heap parts.

The total horizontal displacements u_{XY} of Eastern Slope (P3-R17) recorded from 2004 reached merely 0.08 m and currently, the changes fall below measurement accuracy. In the same period, the top of the Southern Slope moved downstream by 0.47 m, Figure 7. The current displacement rate is 11 mm/year. In the time-history plot, the reduction of displacements u_{XY} can be observed in 2008. It is an effect of the construction of 2.5 m high embankments on the heap's top during the reclamation process.

The highest rates of horizontal displacements are observed along the Western and the Northern Slopes which from the start of the measurements reached the value of 0.9 m, (Figure 8) with the average rates of 30 mm/year and 50 mm/year, respectively.

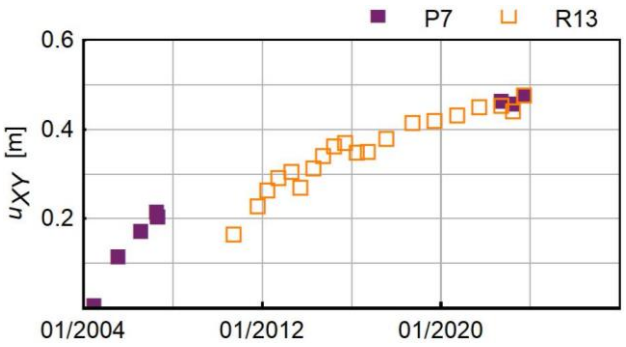

Figure 7. Horizontal displacements of P7 and R13 control points located at Southern Slope.

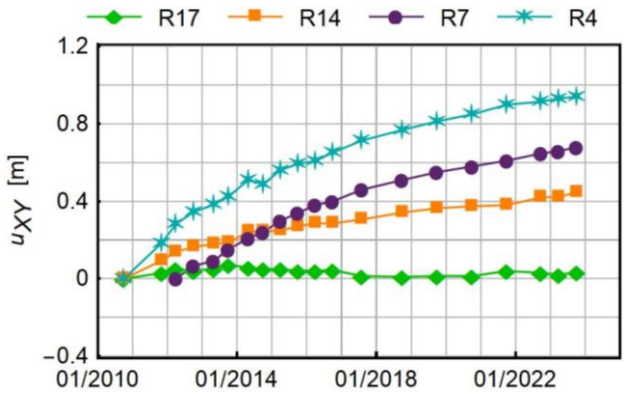

Figure 8. Horizontal displacements of control points installed in 2010 (R) representative for each slope.

Horizontal displacements u_{XY} of the R24 benchmark located along the Southern Slope were 198 mm at the rate of 9.98 mm/year, observed between 2016 and 2023. In previous years the rate was almost twice as high, reaching 18.2 mm/year with much notable fluctuations, Figure 9. The deformations that occurred in periods 2010-2016 (0.10 m) and 2019-2023 (0.03 m), have been confronted with the deformations of inclinometer WIS-1 and inclinometer WIS-3 which will be a subject of discussion presented in the next section of the paper.

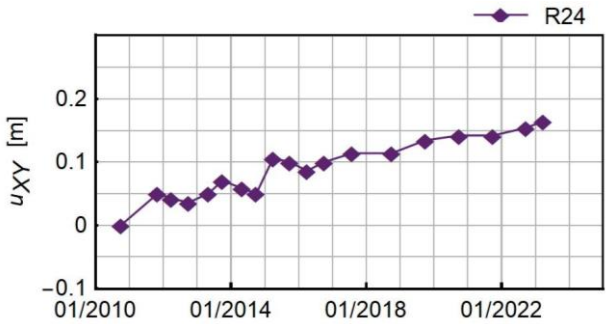

Figure 9. Horizontal displacements of R24 control poins located at Southern Slope.

3.2 Inclinometers

In 2007 two inclinometers for monitoring the potential mass movement were installed, one within the inland

side and the other on *Martwa Wisła* riverside (see WIS-1 and WIS-2 in Figure 2). The grooves of the inclinometer housing were orientated to directly measure the main direction of potential mass movement (Cornforth, 2005). Periodic measurements, at least once a year, have been carried out using a two-directional probe with an accuracy of ± 0.13mm/rm.

16 m long inclinometer WIS-1 was installed at the bench on the Southern Slope. In the fall of 2016, it was found damaged by the probe which was blocked at a depth of 8 m. Total cumulative displacements Δu_A of the inclinometric pipe at this depth were 173 mm. The records revealed a linear trend of this displacement over 9 years. The estimated displacement rate was 18.4 mm/year. In the period from fall 2010 to fall 2016 the displacement of the inclinometer head was 86.5 mm.

In 2019, a new 20 m deep inclinometer was installed in close vicinity to the sheared one (marked as WIS-3). The first measurement was taken in June 2019. Since 2020, the measurement of inclinometric displacements has been performed by another company with a similar two-directional probe equipped with a MEMS gauge. In both cases, the measurement error was ± 0.08 mm/rm. Fortunately, the raw data from all these measurements were available. Therefore, an attempt was made to assemble the data. Firstly, the measurements carried out in December 2022 by two different companies were compared. The maximum difference was 0.184 mm along 0.5 m of pipe length, whereas the cumulative difference of the head was 0.422 mm. It was deemed, that such a difference would not affect the conclusions.

The cumulative displacement obtained from all measurements relative to the very first one from 2019 is shown in Figure 10. The maximum values of horizontal displacements of the order of 50 mm occur at a similar elevation as in the case of damaged inclinometer WIS-1 with a practically constant deformation rate of 11.1 mm/year, Figure 11. According to the Cruden and Varnes classification (Zabuski, 2022), movement with this rate of displacement is classified as extremely slow. Cumulative horizontal displacement as a sum of total displacements recorded in both inclinometers WIS-1 and WIS-3 was estimated to be 232 mm (164.5 mm since 2010).

In the period 2019-2023, the horizontal displacements of WIS-3 inclinometer head were 27.4 mm whereas the observed corresponding displacement of the benchmark located on the bench was 30 mm. Therefore, it can be assumed that displacements of both inclinometers WIS-1 and WIS-3 reflect the main deformation mechanism of the Southern Slope.

The rotational character of the movement can be assumed from the cumulative displacement curve. The displacements of the inclinometer head are almost 40% lower than at 7 m depth. The largest pipe deformations occur in the organic soil and laminated phosphogypsum (Phl), (soil profile in Figure 10).

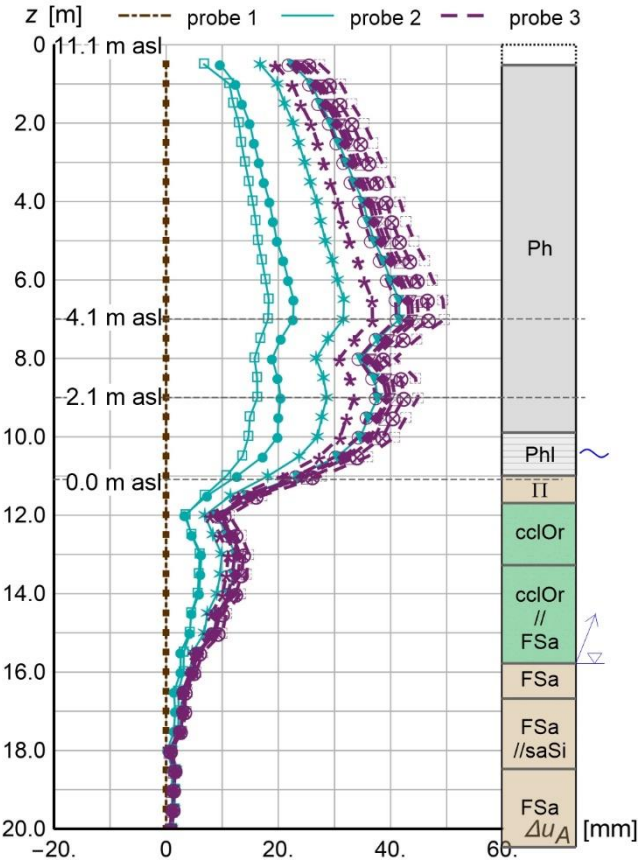

Figure 10. Cumulative displacement in A direction of WIS-3 inclinometer in relation to measurement of 27th June 2019.

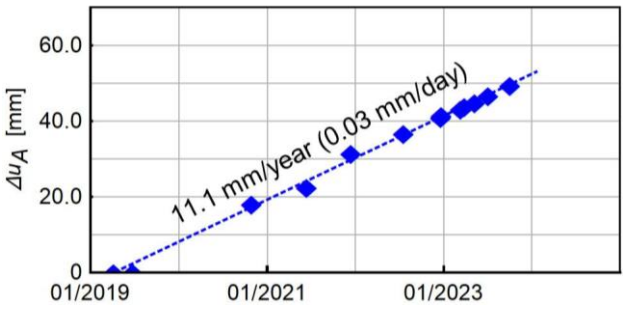

Figure 11. Cumulative displacement at 7 m of WIS-3 inclinometer in relation to measurement of 27th June 2019.

The second inclinometer from those two installed in 2007 was unfavourably installed in the internal trench of the Northern Slope, Figure 1. The largest displacements of the inclinometer casing were cumulated in the second layer of organic soils, with the maximum at the depth of 11 m. This movement practically disappeared in 2012 after dissipation of excess pore pressures which were generated during construction of the buttress. In the years 2012-2017,

the displacement rate was merely 1.4 mm/year. In 2021, the pipe was clenched at the depth of 2.5 m. No raw data from the period of 2012-2023 are available which could help to understand the slope displacement revealed by geodetic measurements.

4 CONCLUSIONS

In the paper, the results of the analysis of long-term deformation measurements of the phosphogypsum waste heap are presented and discussed. A trivial, however important, conclusion coming from such analyses is the importance of preserving the continuity of measurements and archiving data. In the presented case, the implementation of the original procedures for combining historical data obtained by various companies made it possible to extend the time window of the analysed deformations.

20 years after reaching the final height of the Eastern and the Southern Slope of the heap, continuous settlements at the rate of 66 mm/year are still observed. The current settlement rate is 75% lower than that observed in 2004-2007. As far as horizontal displacements are concerned, creep mass movements at the rate of 11 mm/year are recorded along the Southern Slope. From comparison of geodetic and inclinometric results, it was concluded that the WIS-1 and WIS-3 describe the main deformation mechanism of the Southern Slope.

The Eastern Slope does not move horizontally, however settlement occurs.

The rates of both horizontal and vertical displacements are the highest along Western Slopes which is due to the latter time of its formation.

The displacements observed in the inclinometer installed at the base of the Northern Slope did not contribute to the explanation of horizontal slope displacements. In order to reliably assess the stability of the Western and the Northern slopes, it was necessary to develop a monitoring system. Four inclinometers were installed, among other devices, to collect more data required for detailed identification of failure mechanisms driving the observed deformations.

ACKNOWLEDGEMENTS

The authors are grateful for the financial support for the project *'Safety assessment of phosphogypsum waste heap in Wiślinka, Poland'* provided by the Provincial Fund for Environmental Protection and Water Management (Gdansk, PL). www.wfos.gdansk.pl).

The authors are grateful to companies *GEOTEKO*, Warszawa and *GEO-EKSPERT*, Gdansk for providing raw data from inclinometer measurements.

REFERENCES

Bilal E. et al. (2023). Phosphogypsum circular economy considerations: A critical review from more than 65 storage sites worldwide. *Journal of Cleaner Production*, 414 (137561): 438–483. https://doi.org/10.1016/j.jclepro.2023.137561.

Cornforth, D. (2005). *Landslides in Practice: Investigation, Analysis, and Remedial/Preventative Options in Soils*. John Wiley & Sons.

Zabuski, L. (2022). *Mechanics of landslide* processes – modelling, stability, stabilisation. IBW PAN. (in Polish).

Proceedings of the XVIII ECSMGE 2024
GEOTECHNICAL ENGINEERING CHALLENGES
TO MEET CURRENT AND EMERGING NEEDS OF SOCIETY
© 2024 the Authors
ISBN 978-1-032-54816-6
DOI 10.1201/9781003431749-316
Open Access: www.taylorfrancis.com, CC BY-NC-ND 4.0 license

ECSMGE 24
XVIII EUROPEAN CONFERENCE ON SOIL MECHANICS AND GEOTECHNICAL ENGINEERING

Representative values of geotechnical parameters derived from dynamic penetration test

Valeurs représentatives des paramètres géotechniques dérivées de l'essai de pénétration dynamique

E. Kucova*, M. Kuvik
Department of Geotechnics, Faculty of Civil Engineering, Slovak University of Technology in Bratislava, Slovakia

*eliska.kucova@stuba.sk

ABSTRACT: Dynamic penetration test is a relatively simple field test, which is frequently used for testing of soil resistance. From the results of this test, it is possible to derive physical and mechanical geotechnical parameters of coarse-grained soils, namely relative density, angle of shear strength and deformation modulus. The representative values of these parameters can be furthermore used in design of geotechnical structures. The new Eurocode 7 provides a set of equations that should be followed to establish the characteristic value if the data is considered sufficient. In this article the results of dynamic penetration tests, performed in the locality of the capital city of Slovakia, were used for determination of mechanical properties of Danube gravels. Afterwards, results were statistically processed, and characteristic value was estimated according to Eurocode 7. The characteristic values of geotechnical parameters were compared with traditional evaluation procedures, where the average value is determined for each soil layer.

RÉSUMÉ: Le test de pénétration dynamique est un test sur le terrain relativement simple, fréquemment utilisé pour tester la résistance du sol. A partir des résultats de cet essai, il est possible de déduire des paramètres géotechniques physiques et mécaniques des sols à gros grains, à savoir la densité relative, l'angle de résistance au cisaillement et le module de déformation des graviers et des sables. Les valeurs représentatives de ces paramètres peuvent en outre être utilisées dans la conception de structures géotechniques. Le nouvel Eurocode 7 donne des lignes directrices pour l'estimation de la valeur représentative en tant que valeur caractéristique. Dans cet article, les résultats de tests de pénétration dynamiques, réalisés dans la localité de la capitale de la Slovaquie, ont été utilisés pour déterminer les propriétés mécaniques des graviers du Danube. Ensuite, les résultats ont été traités statistiquement et la valeur caractéristique a été estimée selon l'Eurocode 7. Les valeurs caractéristiques des paramètres géotechniques ont été comparées aux procédures d'évaluation traditionnelles, où la valeur moyenne est déterminée pour chaque couche de sol.

Keywords: Representative value of geotechnical parameter; coarse-grained soil; dynamic penetration test; statistics.

1 INTRODUCTION

In Slovak geotechnical practice the dynamic penetration test (DP) is frequently used in engineering geological surveys. The test is primarily intended for testing of coarse-grained soils due to less skin friction on the rod. The penetration rod is driven into the ground by dynamic force and the resistance of soil is measured.

From the measured data, it is possible to determine specific physical and mechanical properties of sands and gravels. These properties can be determined by using correlations of international and national significance (EN 1997-2:2008, DIN 4094-3:2002, EN ISO 22476-2, PN-B-04552:2002, STN 72 1032: 1997, Matys et al., 1990). The given literature offers both direct and indirect correlations to choose from.

Standards (EN 1997-2:2008, DIN 4094-3:2002, EN ISO 22476-2, PN-B-04552:2002, STN 72 1032: 1997) mention mainly direct correlations for the relative density (I_D) of sands and gravels that are directly derived from number of blows (*N)* measured during the penetration test. The indirect correlation is expressed for the angle of internal friction, that is evaluated based on the relative density of coarse-grained soil (Schnaid, 2009; Carter, Bentley, 2016; Sanglerat, 1972, Bolton, 1979; Robertson, and Hughes 1986, EN 1997-2:2008).

More direct correlations for the determination of coarse-grained soil geotechnical parameters are published in regional (Slovak) literature. These correlations are based on the results of dynamic penetration resistance (q_{dyn} in MPa).

From the derived geotechnical parameters, it is possible to determine a representative value, which is essential for the design of geotechnical structure. The new generation of Eurocode 7 (prEN 1997-1:2024) defines that the representative value can be either nominal or characteristic value.

In the previous Eurocode 7 (EN 1997-2:2008) the the characteristic value was referred to as cautious estimate of the value affecting the limit state and the statistical procedure for its estimation was not precisely specified. This assessment was analysed by various authors (e.g. Schneider 2010, Orr 2019, Prästings et al. 2019). The conclusion of these studies was that procedure did not consider the uncertainty of geotechnical properties. Authors also pointed out that the statistical procedure was not clearly defined and the same statistical rules as for man-made materials cannot be followed.

Therefore, in the new Eurocode 7 (prEN 1997-1:2024) the characteristic value is defined using a statistical procedure that includes basic statistical characteristics as mean, standard deviation, and coefficient of variation.

In our research we used the statistical procedure from the new EC 7 to determine the characteristic value as a representative value of the angle of internal friction. The angle of internal friction was derived from the results of dynamic penetration resistance using Slovak correlations for Danube gravels.

The obtained results were compared with other foreign correlations and nominal values used in Slovakia with the intention to investigate appropriateness and accuracy of the regional correlations.

2 METHODOLOGY

To determine the representative value of the angle of internal friction we analysed 120 heavy dynamic penetration tests performed in gravels near the Capital of Slovakia.

2.1 Material

Investigated gravels belong to Quaternary sediments of Danube River. The river has in the region accumulative and sedimentary activity, due to which the gravel particles are fine, smooth, well rounded with size of 1 – 5 centimetres.

In this article we focused on the analysis of the poor-graded gravel (G2/GP) which is together with gravels G3/G-F, the most represented gravel class in the area. Poor-graded gravels of the investigated area consist of 54 – 77% of gravel fraction. Grading of gravel particles at d_{60} is from 5 – 15 millimetres (Figure 1).

2.2 Determination of the angle of internal friction and its characteristic value

The angle of internal friction (φ_{eff}) was derived from results of dynamic penetration test. Its values were derived from the number of blows (N_{10}) using correlation from to Slovak standard (STN 721032:1997) and dynamic penetration resistance using correlations according to Švasta (Matys et al., 1990). The mentioned correlations are summarized in Table 1 and Table 2.

The characteristic value of the angle of internal friction was determined by following recommended approach from the second generation of Eurocode 7 (prEN 1997-1:2024).

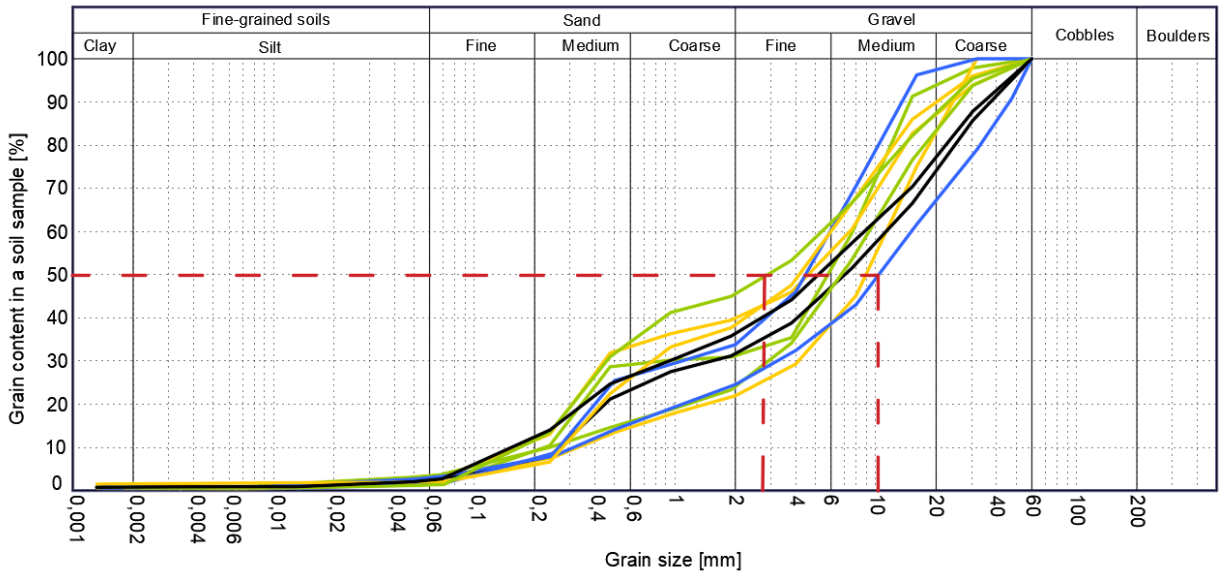

Figure 1. Grading curves of poor-graded gravel (G2/GP).

Table 1. Correlation between φ_{eff} and N_{10}.

Reference	Soil	Correlation	
		N_{10}	φ_{ef} (°)
STN 72 1032	Gravels	< 3	< 30
		3 – 6	30 – 35
		6 – 17	35 – 40
		17 – 30	40 – 45
		> 30	> 45

Table 2. Correlation between φ_{eff} and q_{dyn}.

Reference	Soil	Correlation	
Švasta	Gravels & Sands	$\varphi_{ef} = p\,(q_{dyn})^{r}$	[°]

Note: unitless coefficient p equals to 24
unitless coefficient r equals to 0,16

The characteristic value, denoted as X_k, corresponds to a specific quartile of the assumed statistical distribution of assessed soil parameter.

The second generation of Eurocode 7 recommends determining the characteristic value according to given formula:

$$X_k = X_{mean}[1 \mp k_n V_x] = X_{mean}\left[\frac{1 \mp k_n s_x}{X_{mean}}\right] \qquad (1)$$

where X_{mean} is an average of measured values of soil parameter, V_x is coefficient of variation of the measured values of soil parameter, k_n is the coefficient depending on the number of the measured values (n) of the soil parameter and s_x is the standard deviation of the measured values of soil parameter.

The procedure is applicable for both, known and unknown coefficient of variation, which is decisive when evaluating the coefficient k_n (prEN 1997-1:2024).

3 RESULTS

The values of the angle of internal friction obtained from the results of dynamic penetration are shown in Figure 2. The values of φ_{ef} were categorized according to relative density to three categories - φ_{ef} of loose, medium dense and dense poor-graded gravels. For each category the corresponding characteristic value was evaluated (Figure 2, Table 3).

Compering the results the difference between the two correlations is approximately 2° for medium and dense gravels while correlation according to STN 72 1032 being more optimistic. The difference between the two correlations for loose gravels is bigger.

The results in Table 3 are furthermore compared with other foreign correlations and nominal values published in cancelled Slovak standard, which are still in use as comparable experience.

Analysing Table 3 we can see that in regional (Slovak) literature there is no recommendation of nominal values for loose gravels. But European standards (BS 8002, Eurocode 7, DIN 4094-3) recommend an indicative value of 30° for φ_{ef} of loose gravels. This value is higher than our characteristic value derived by regional correlations.

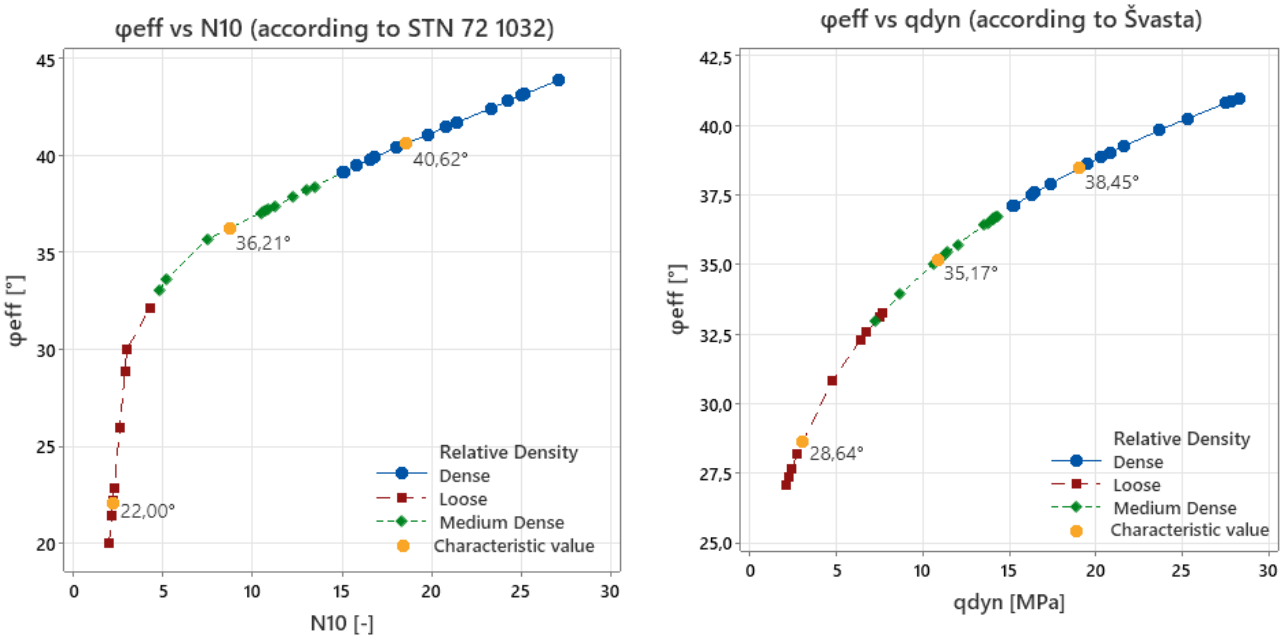

Figure 2. Evaluation of the angle of internal friction G2/GP according to regional correlations.

Table 3. Comparison of the characteristic and nominal values of φ_{eff}.

Soil	Relative density	φ_{eff} [°]				
		Characteristic values		Nominal values		
		Švasta	STN 72 1032	BS 8002	EC7/ DIN 4094-3	STN 73 1001
G2/GP	Loose	28,64	22,00	30,00	30,00	-
	Medium dense	35,17	36,21	32,50	34,00	35,50
	Dense	38,45	40,62	35,00	38,00	38,50

The characteristic values for medium dense gravels are in accordance with used nominal values and are more optimistic than the foreign correlations.

Dense G2/GP were also tested in laboratory using large-scale shear box machine, where we measured the values of φ_{eff} in range of 41,00° – 48,50°. Comparing the results, we can see that the British standard indicates the lowest value, and the laboratory tests designates the highest values for the angle of internal friction.

4 CONCLUSIONS

The article analyses the representative values of angle of internal friction for poor-graded river gravel.

Results of φ_{ef} were categorized according to the relative density of the soil and were compared with the laboratory test results, other correlations and nominal values used as comparable experience in Slovakia.

Characteristic values of φ_{ef} for loose G2/GP reaches according to Slovak correlations lower values than those specified by European standards. Moreover, there is no recommendation for nominal values in the Slovak standard.

Correlated results (according to Švasta in Matys et al. 1990, and STN 72 1032:1997) of medium dense and dense gravel show a good match with nominal values. Dense poor-graded gravels were also tested in laboratory and the results shows higher values of angle of internal friction. This can indicate that even higher values of φ_{eff} could be used as nominal values for Danube gravels in Slovakia.

To optimize regional correlations and suggest nominal values for the national appendix of new EC 7 the research will be complemented with the data from other localities in Slovakia by studying the coarse-grained soils of another genesis.

ACKNOWLEDGEMENTS

This article was supported by the Grant Agency of the Ministry of Education, Science, Research and Sport of the Slovak Republic, VEGA, grant project No. 1/0745/21.

REFERENCES

BS 8002:1994: Code of practice for Earth retaining structures.

Bolton M.D. (1979). A guide to soil mechanics. Macmillian Press, London, 439 pp.

Carter, M. - Bentley, P. S. (2016). Soil properties and their correlations. Second Edition. United Kingdom: John Wiley & Sons, Inc., ISBN 9781119130901.

DIN 4094-3:2002: Subsoil. Field testing. Part – 3: Dynamic probing.

prEN 1997-1:2024 Geotechnical design – General rules, (final draft), CEN, 2024.

EN 1997-2:2008: Eurocode 7. Geotechnical design. Part 2: Ground investigation and testing.

EN ISO 22476-2:2005: Geotechnical investigation and testing - Field testing - Part 2: Dynamic probing.

Matys, M. – Ťavoda, O - Cuninka, M. (1990). Field soil testing. Bratislava: Alfa 1990. 304 pp. ISBN 80-05-00647-0.

Orr, T. (2019). Development in selection of characteristic geotechnical parameters in Eurocode 7. Proceedings of the 7th International Symposium on Geotechnical Safety and Risk. Taipei. Taiwan.

Prästings, A. - Spross, J. - Larsson, S. (2019). Characteristic values of geotechnical parameters in Eurocode 7. Proceedings of the Institution of Civil Engineers: Geotechnical Engineering. 172(4), 301–311. https://doi.org/10.1680/jgeen.18.00057.

Sanglerat, G. (1972). The penetrometer and soil exploration, Interpretation of penetration diagrams – theory and practice. Amsterdam. Elsevier Publishing Company. ISBN 0-444-40976-9.

Schnaid, F. (2009). In Situ Testing in Geomechanics. The main tests. London. New York: Taylor & Francis. 328 p. ISBN 0-203-93133-5.

Schneider, H., R. (2010). Characteristic Soil Properties for EC7: Influence of quality of test results and soil volume involved. Proc. 14th Danube-European Conference on Geotechnical Engineering. STU Bratislava.

STN 72 1032: 1997: Dynamic penetration test.

STN 73 1001:1987: Foundations. Base soil under the spread foundations.

Proceedings of the XVIII ECSMGE 2024
GEOTECHNICAL ENGINEERING CHALLENGES
TO MEET CURRENT AND EMERGING NEEDS OF SOCIETY
© 2024 the Authors
ISBN 978-1-032-54816-6
DOI 10.1201/9781003431749-317
Open Access: www.taylorfrancis.com, CC BY-NC-ND 4.0 license

ECSMGE 24
XVIII EUROPEAN CONFERENCE ON SOIL MECHANICS AND GEOTECHNICAL ENGINEERING

3-D geotechnical modelling contributing to the risk management in a road construction project - a case study

Modélisation géotechnique tridimensionnelle contribuant à la gestion des risques dans un projet de construction routière - une étude de cas

R. Kudou-Wada*, K. Takahashi, C. Konishi, R. Ito, K. Sakurai
OYO Corporation, Tokyo, Japan

**kudou-rie@oyonet.oyo.co.jp*

ABSTRACT: A case study of reliable 3-D geotechnical modelling based on drilling and geophysical survey data is presented. In this study, the distribution of a soft alluvial clay deposit having the risk of consolidation/deformation/subsidence was required for a new road planning. It was first estimated based only on drilling data. Then, a 2-D microtremor survey was conducted for more detailed modelling and resulted in the detection of a deeply buried valley filled with soft sediments, which have potential risks. The buried valley was confirmed by the additional drilling. The scale and direction were detected using a 3-D microtremor array measurement. The direction of the buried structure was oblique to the planning line of the road. It means that only drilling and a geophysical survey in 2-D were insufficient, and a 3-D survey was necessary to capture the geometry of the buried structure. These investigation results have been reflected in the 3-D geotechnical model. This study demonstrated the effectiveness of the geophysical survey for geotechnical modelling. The updated model, including the risk information, can be handed over to the owner and designers and planned to be used as a BIM model.

RÉSUMÉ: Une étude de cas de modélisation géotechnique tridimensionnelle fiable basée sur des données de forage et d'étude géophysique est présentée. Dans cette étude, la distribution d'un dépôt d'argile alluviale molle présentant un risque de consolidation/déformation/affaissement était nécessaire pour la planification d'une nouvelle route. Elle a d'abord été estimée sur la base des seules données de forage. Ensuite, une étude de microtremor 2-D a été menée pour une modélisation plus détaillée et a permis de détecter une vallée profondément enfouie remplie de sédiments mous, qui présentent des risques potentiels. La vallée enfouie a été confirmée par des forages supplémentaires. L'échelle et la direction ont été détectées à l'aide d'un réseau de mesure microtremor tridimensionnel. La direction de la structure enfouie était oblique par rapport à la ligne de planification de la route. Cela signifie que le forage et l'étude géophysique en 2−D étaient insuffisants et qu'une étude en 3-D était nécessaire pour saisir la géométrie de la structure enfouie. Les résultats de cette étude ont été pris en compte dans le modèle géotechnique tridimensionnel. Cette étude a démontré l'efficacité de l'étude géophysique pour la modélisation géotechnique. Le modèle mis à jour, y compris les informations sur les risques, peut être remis au propriétaire et aux concepteurs et il est prévu de l'utiliser comme modèle BIM.

Keywords: 3-D geotechnical model; geophysical survey; 3-D microtremor array measurement; risk information; BIM.

1 INTRODUCTION

Geological and geotechnical model of the underground plays an important role throughout all the phases of a construction project and is relevant for decisions and design solutions. This is because some types of risks are associated with geological conditions and uncertainties of predicting the ground conditions and have a significant impact on the cost of construction projects (Anan, 2021). However, in Japan, there have been a number of accidents during and after construction due to the models that does not satisfactorily represent geological/geotechnical uncertainties and risk information, or the underestimation of information by designers and builders (PWRI, 2017).

BIM (Building Information Modelling) is a process to achieve the improvement in productivity, safe construction, quality control and reduction of total cost over the lifecycle of a structure. BIM has been partly mandatory for public works since 2023 in Japan. In this process, digital models consisting of physical representations of the shape of the objects and semantics, like functions, dimensions, strength, and price, are created and shared to support decision-making and management from planning through design to construction and operation. Recommended data exchange standards for BIM have been

established by buildingSMART International (bSI), a non-profit international organization, and those for geotechnical data are under development (Rives, 2023). Demonstrations of various successful examples of risk management using 3-D geotechnical modelling can help to reduce the number of accidents caused by geotechnical conditions during the life of a structure and promote BIM in the geotechnical field.

In this paper, we present an example of successful risk management in road construction work in which a combination of borehole surveys and geophysical exploration resulted in a more reliable model, which in turn contributed to reducing the risk of rework and accidents in the projects.

2 PROJECT OVERVIEW

A new bypass was planned to run straight through a winding valley in a lowland where there are agricultural fields and residential areas. The construction of road embankments and soil reinforcement walls was planned in some sections of the bypass, and the site investigations were carried out for the preliminary design in order to reveal the distribution and thickness of the soft alluvial deposits such as cohesive and humic soils.

The survey locations are shown in Figure 1 and the survey sequence is shown in Figure 2 (Ito et al., 2023). First, two boreholes were drilled in each of the areas A and B shown in Figure 1. Then, 2-D microtremor surveys were conducted to evaluate the geotechnical conditions around two boreholes.

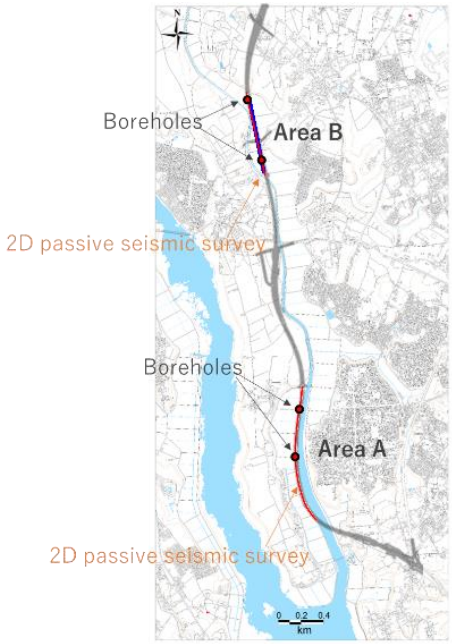

Figure 1. The survey locations.

In Area A, the geophysical survey detected a valley-shaped concavity with low-velocity, so additional drilling and a 3-D microtremor array measurement (Hayashi et al., 2021) were carried out to determine its detailed 3-D structure, following the flow shown in Figure 2.

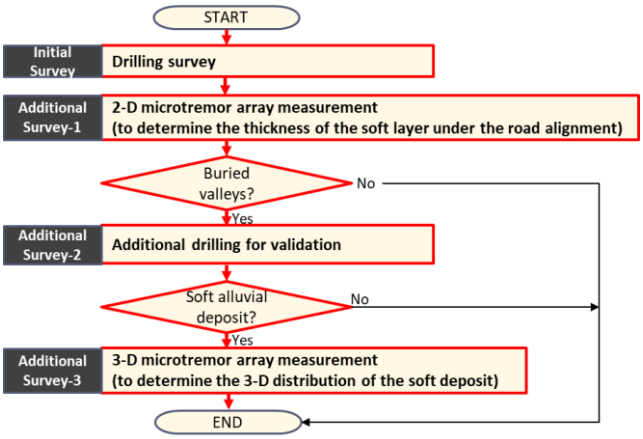

Figure 2. The survey sequence.

3 SURVEY RESULTS AND ESTIMATION OF UNDERGROUND STRUCTURE

The results of the investigation in Area A, where the buried valley was found, are described in detail. The locations of the boreholes, 2D and 3D geophysical surveys in Area A are shown in Figure 3 (Ito et al., 2023).

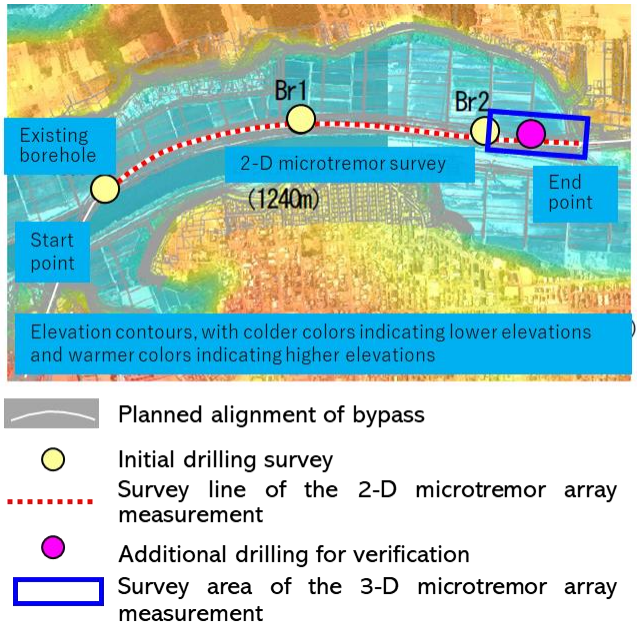

Figure 3. The survey locations in Area A.

The thickness of the soft alluvial deposits, shown in light blue, decreases towards the end of the cross-section (right side), as shown in Figure 4(a). Next, a 2-

D microtremor survey was carried out. The obtained S-wave velocity cross-section is shown in Figure 4(b). The relationship between N-value and S-wave velocity (Vs) suggests that Vs less than 100 m/s corresponds to alluvial layers, and the geological cross-section estimated on this basis is shown in Figure 4(c). A buried valley was expected to exist in the area in concave shape with a low S-wave velocity, where the stiff ground consisting of diluvial sand had been estimated in Figure 4(a). A borehole survey was therefore carried out at the location for verification. The results showed that the depression was filled with alluvial clay with an *N*-value close to 0-1, demonstrating the existence of a buried valley as shown in Figure 5. A 3-D geotechnical model was constructed based on the results of the investigations up to that point, as shown in Figure 6(a) and (b).

A 3-D microtremor survey was then carried out in the area indicated by the blue rectangle in Figure 3 to reveal the 3-D geometry of the buried valley and to accurately determine the extent of the ground improvement.

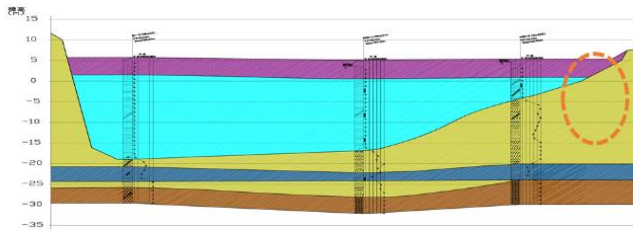

(a) Geological section based only on drillings (initial survey).

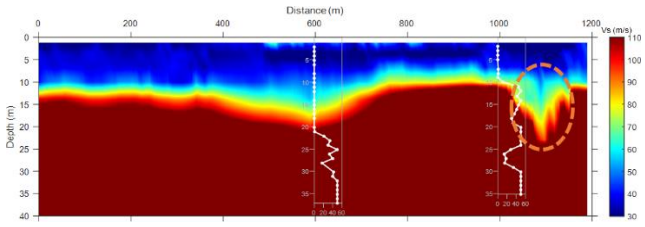

(b) S-wave velocity section (additional survey-1).

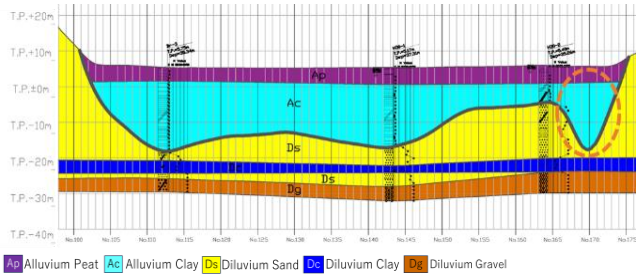

(c) Geological section based on a combination of drillings and microtremor survey (additional survey-1).

Figure 4. The cross sections obtained by the surveys shown in Figure.2.

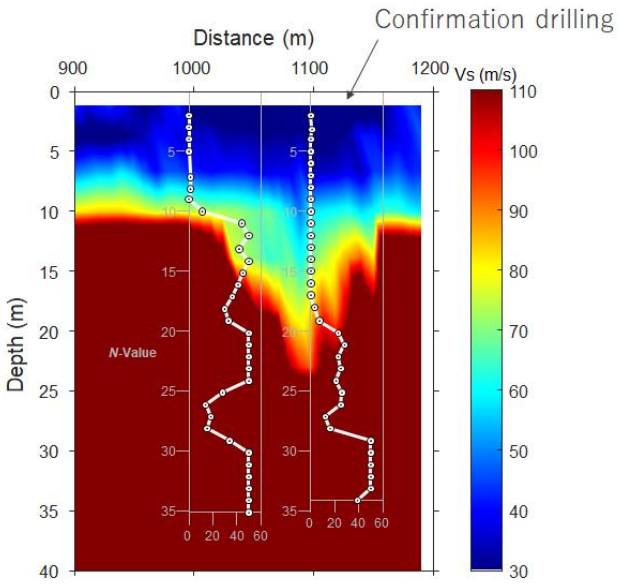

Figure 5. The burried valley confirmed by additional drilling (additional survey-2 in Figure 2).

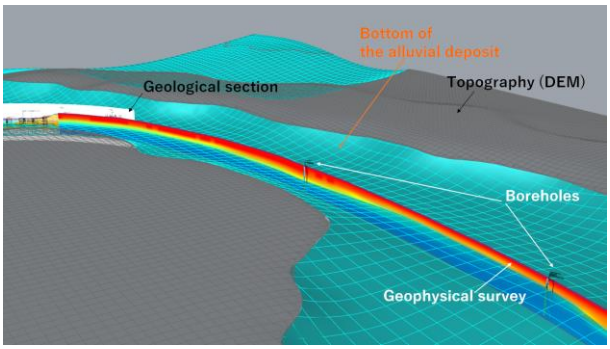

(a) The surface model of each layer.

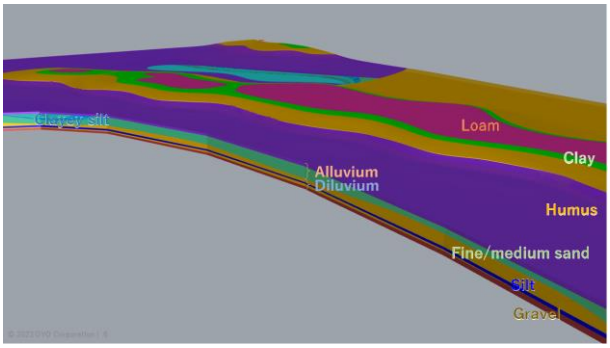

(b) The solid model.

Figure 6. The 3-D geotechnical model of entire survey area of the project.

The distribution of depths at Vs = 80 m/s estimated from the 3-D velocity model is shown in Figure 7. The survey result indicated that the direction of the buried valley would intersect the planned road. Since this direction agrees with the distribution of the floodplain of the small river, it could be an old river channel. Based on this result, the 3-D geotechnical model was updated for use in the design.

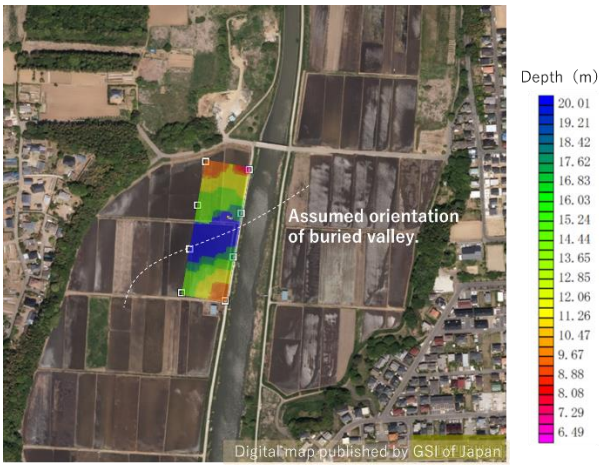

Figure 7. The distribution of depths at Vs = 80 m/s by 3-D microtremor survey.

4 CONSIDERATION

In this project, borehole investigations were combined with geophysical surveys in order to obtain continuous and accurate information on the subsurface in and around the vicinity of the linear structure. The detection of the buried valley filled with soft alluvial deposit resulted in a reduction in the risk of business such as unequal settlement after road fill construction, pavement cracks and their countermeasures. The 3-D model of the survey results also makes it easier to visually understand the positional relationship between the structure, ground conditions and potential risks, and simplifies communication and risk sharing between the parties involved.

One of the difficulties of applying geotechnical models in BIM is that models cannot be treated as a whole, as they are interpreted models and contain uncertainties, whereas the structure model shows the substance. Improving the reliability of geotechnical models by considering the results of geophysical surveys would contribute to the application and spread of geotechnical models in BIM.

5 CONCLUSIONS

The combination of borehole investigations and geophysical surveys detected a buried valleys that was not identified by borehole investigations alone. It resulted in a reduction in project risks such as rework during construction and unequal settlement and deformation of structures after construction. Furthermore, the improved reliability of the geotechnical model incorporating geophysical exploration must contribute to the application and dissemination of the geotechnical model in BIM.

REFERENCES

Anan, S. (2021). 地質・地盤リスクマネジメントについて,Management of Geo-risk in Civil Engineering Works. *Journal of JG,* 69(7), pp.13-16. (in Japanese).

Hayashi, K., Craig, M., Tan, S., Konishi, C., Suzuki, H., Tahara, M., Falkenstein, K., He, B., and Cheng, D. (2021), Common-midpoint spatial autocorrelation analysis of seismic ambient noise obtained from spatially unaliased sensor distribution, *Geophysics*, 86, EN51-EN62, https://doi.org/10.1190/geo2020-0467.1.

Ito, R., Konishi, C., Terada, Y., and Nakajima, I. (2023), 微動アレイ探査による埋没地形の検出と考察, Detection of buried valley using microtremor array survey, Available at: [https://www.zenchiren.or.jp/forum/pdf/2023/2023_gr003.pdf], accessed: 30/10/2023. (in Japanese).

PWRI (2017), 福岡地下鉄七隈線延伸工事現場における道路陥没に関する検討委員会報告書, Report of the Study Committee on Road Cave-ins at the Fukuoka Subway Nanakuma Line Extension Construction Site, Public Work Research Institute, Japan, Rep.95. (in Japanese).

Rives, M (2023), buildingSMART International IFC-for-Tunnelling (Ifc4.4) deployment update, buildingSMART International Standards Summit-Lillestrøm 2023.

Proceedings of the XVIII ECSMGE 2024
GEOTECHNICAL ENGINEERING CHALLENGES
TO MEET CURRENT AND EMERGING NEEDS OF SOCIETY
© 2024 the Authors
ISBN 978-1-032-54816-6
DOI 10.1201/9781003431749-318
Open Access: www.taylorfrancis.com, CC BY-NC-ND 4.0 license

ECSMGE 24
XVIII EUROPEAN CONFERENCE ON SOIL MECHANICS AND GEOTECHNICAL ENGINEERING

Evaluation of the reliability of pressuremeter tests using a multi-criteria analysis

Évaluation de la fiabilité de l'essai pressiométrique à travers une analyse multicritères

L. Lachérade*
BRGM, Orléans, France / Université de Bordeaux, CNRS, Arts et Métiers Institute of Techology, Bordeaux INP, INRAE, I2M Bordeaux, Talence, France

A. Marache, A. Denis
Université de Bordeaux, CNRS, Arts et Métiers Institute of Techology, Bordeaux INP, INRAE, I2M Bordeaux, Talence, France

I. Halfon, J. Rohmer, L. Closset, F. Quesnel
BRGM, Orléans, France

**l.lacherade@brgm.fr*

ABSTRACT: In the context of the Grand Paris Express (GPE) metro project, a large number of pressuremeter tests were collected to improve knowledge of subsoil properties and to design underground structures. Despite the standardized nature of pressuremeter testing, many factors can influence the quality and reliability of the results. This article proposes a multi-criteria analysis methodology to assess the reliability of pressuremeter tests by calculating a reliability index for the pressuremeter modulus. Applying the evaluation process to 300 GPE pressuremeter tests, we classify them into different rating groups, identify suspicious tests and establish characteristic curves that can be extremely useful to the geotechnical profession.

RÉSUMÉ: Dans le cadre du projet de métro du Grand Paris Express (GPE), un grand nombre d'essais pressiométriques ont été collectés afin d'améliorer la connaissance des propriétés du sous-sol et dans un but de conception des ouvrages souterrains. Malgré la procédure standardisée de l'essai pressiométrique, de nombreux facteurs peuvent influencer la qualité et la fiabilité des résultats. Ainsi, une méthodologie d'analyse multicritères est proposée dans cet article afin d'évaluer la fiabilité des essais pressiométriques en calculant un indice de fiabilité du module pressiométrique. L'application du processus d'évaluation à 300 essais pressiométriques du GPE permet une classification en différents groupes de notations, l'identification des essais suspicieux et l'établissement de courbes caractéristiques qui peuvent s'avérer être très utiles à la profession géotechnique.

Keywords: Pressuremeter test; pressuremeter modulus; Reliability index; characteristic curves.

1 INTRODUCTION

In the context of large-scale underground projects such as the Grand Paris Express (GPE), a huge amount of data is collected to better characterize the underground, design structures and minimize risks. Within these high-volume databases, the quality and reliability of the data is very often heterogeneous, and it is not always easy to identify the suspicious data.

In engineering geology, it is common practice to establish borehole quality assessment systems to screen out poor-quality boreholes (Gunnink et al., 2013; Jørgensen et al., 2015). Nevertheless, concerning geotechnical information and more specifically pressuremeter testing, reliability rating systems are scarce or even absent.

The aim of the work presented in this paper is to develop and propose a reliability rating system for pressuremeter testing, a highly strategic geotechnical test for underground projects such as the GPE.

First, a description of the pressuremeter test and the pressuremeter data available is given. A step-by-step presentation of the multi-criteria pressuremeter modulus evaluation system is then undertaken and applied to 300 tests from a specific sector of the GPE. Finally, the reliability results obtained are analyzed, and characteristic curves for pressuremeter modulus reliability are presented.

2 PRESSUREMETER TEST AND AVAILABLE DATA

2.1 Pressuremeter test and parameters

Firstly introduced by Louis Ménard in 1955, the pressuremeter test is a static loading *in-situ* test in soil, in which a cylindrical probe is expanded in a borehole to measure the expansion of the borehole wall due to the pressure applied by the probe (Gambin et al., 2005). It has the advantage of characterizing both soil deformability and rupture. This distinction enables it to provide an estimate of soil properties for geotechnical studies (Clarke, 1994), while also being useful for the design of geotechnical structures (Arscop, 2023).

The pressuremeter test is performed by applying a loading program that progressively expands the pressuremeter probe within the borehole in successive pressure steps. The pressures applied to the wall and the volumes injected into the probe are recorded at 30 and 60s to construct two curves: the pressuremeter curve for volume variations at 60s as a function of applied pressures (Figure 1, blue curve) and the creep curve, plotting the volume variation measured between 30 and 60s at pressure steps (Figure 1, orange curve). Analysis of both experimental test curves should enable us to distinguish three distinct phases: contact between the pressuremeter probe and the borehole wall, the pseudo-elastic phase and the plastic phase. Test curves can be used to determine two main soil parameters:

- The pressuremeter modulus Em: derived from the pseudo-elastic phase;
- The limit pressure Pl: determined from the plastic phase.

These soil parameters are very useful for tunnel design (e.g. dimensioning), characterization of the spatial variability of the soils crossed (e.g. geostatistical interpolation, see Lachérade et al. 2023) and risk analysis (e.g. settlement prediction).

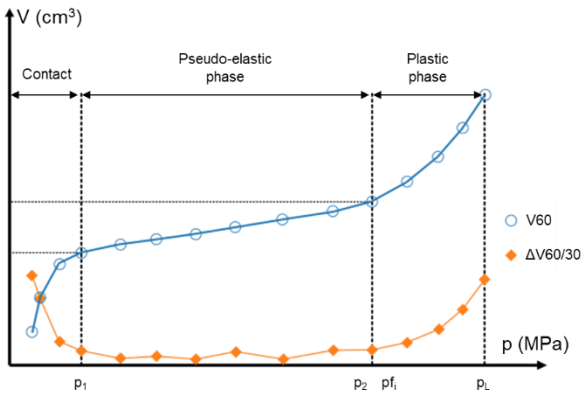

Figure 1. Representation of pressuremeter test results.

2.2 Available pressuremeter data

This study focuses on a specific sector of the Grand Paris Express project. Within the framework of this tunneling project, more than 6,000 pressuremeter tests were carried according to the European standard NF EN ISO 22476-4. Preliminary checking test are used to identify suspicious tests and eliminate outliers (Thierry et al., 2009; Dong et al., 2015, Lachérade et al., 2023). However, these controls are insufficient to detect all unreliable assays. This is the case, for example, with Plastic Clays, whose swelling behavior can result in Em values of a satisfactory order of magnitude when, in reality, the Em given is not correctly determined (Bergere and Ropers, 2018). These findings raise the need to better quantify the reliability of pressuremeter parameters. For this purpose, in this study we have chosen to focus on the Em.

3 METHODOLOGY OF RELIABILITY ASSESSMENT

Reliability criteria are established from the recommendations for good practice in pressuremeter testing provided by standard NF EN ISO 22476-4. For the Em, the criteria are determined by checking the content of the test reports, and in particular the pressuremeter/creep curves, more specifically the contact phase and the pseudo-elastic one (cf. §2.2.). Each criterion is scored binary according to its achievement, with two possible combinations: (0)/(+1) or (-1)/(0) depending on the criterion's positive or negative impact.

The general shape of the test to be assessed must first be analyzed to determine whether or not assessment can be started. If the test shows a pressuremeter curve with large variations in volume at low pressures, it is classified as incorrect, rejected and the rating process is not started.

The contact phase, which determines the quality and reliability of the parameters determined later, covers 4 criteria:

- Significant increase in volumes at 60s (V60) on first pressure steps (+1);
- High creep values (ΔV60/30) (> 5 cm³) with a peak at the beginning of the curve (+1);
- Contact made in a single step (+1);
- The p1 point, which materializes the transition to the pseudo-elastic phase, if found on the first step, means that the contact phase is not distinguished (-1).

The pseudo-elastic phase combines 6 criteria:

- Visible linear part, progressive evolution of volume with pressure increase (+1);
- Number of steps >= 2 (+1);
- End of linear part materialized by p2, if not before the beginning of the increasing part (-1);
- Operator indicates doubtful Em (-1);
- Creep low and close to 0 with +50% bearings with creep less than 10 cm^3 (+1);
- Recurrent negative creep (i.e., +50% steps < 0 cm^3) (-1).

These criteria are grouped together to create a pressuremeter module reliability rating scale (Figure 2), which results in a maximum Em rating of 6 points.

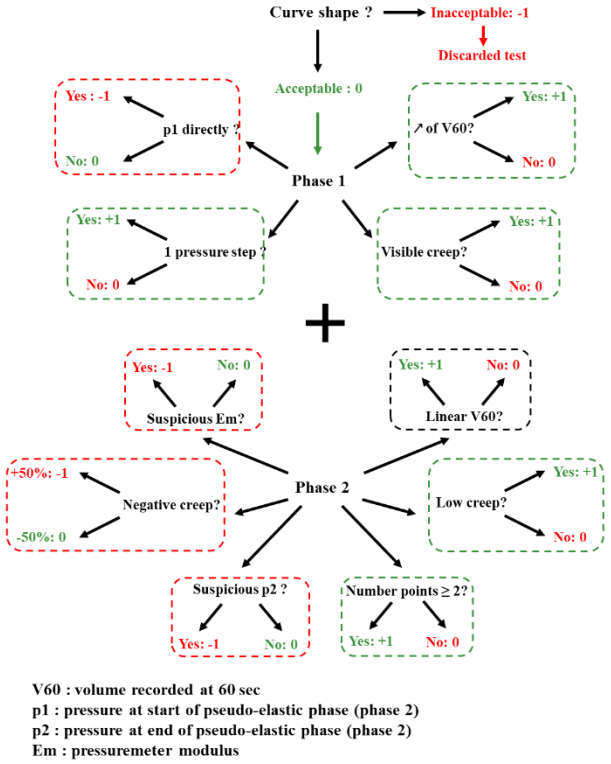

Figure 2. Pressuremeter modulus rating system workflow.

4 RELIABILITY RESULTS AND ABACUSES

4.1 Reliability results

The rating scale is applied manually to 300 tests randomly selected on the metro line, in order to check the consistency of the rating system and analyze the scores obtained.

The range of scores is from 2 to 6, and the distribution of the 300 tests within the scores is shown in Table 1. The reliability index for Em scores corresponds as follows:

- Em score = 2: very unreliable Em;
- Em score = 3: not very reliable Em;
- Em score = 4: moderately reliable Em;
- Em score = 5: reliable Em;
- Em score = 6: very reliable Em.

Tests with an "extreme" Em reliability rating, i.e. very unreliable and very reliable, are poorly represented, with proportions of 6.7% and 7% respectively. If scores 2 and 3 are combined to form a single unreliable score, and scores 5 and 6 to form a reliable score, then 33% of tests are unreliable and 44% reliable.

Table 1. Number of tests within reliability scores.

	Score 2	**Score 3**	**Score 4**	**Score 5**	**Score 6**
Proportion	6.7%	26.3%	22.7%	37.3%	7%

An example of a test for score Em = 3 and score Em = 6 is shown in Figure 3. A high degree of heterogeneity is observed between the pressure and creep curves for both scores. The contact phase is very well represented on score Em = 6 which is not the case for score Em = 3. Based on these observations of heterogeneity on individual tests, the relevance of developing a system of characteristic curves per note is raised.

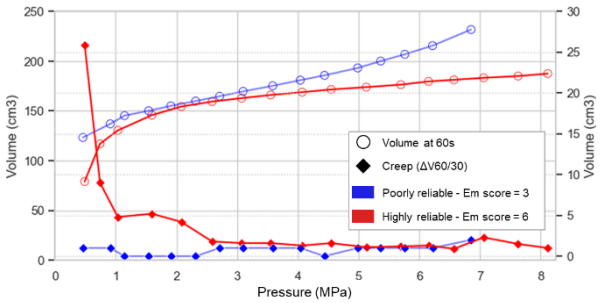

Figure 3. Experimental curves examples of tests of poor reliability (Em score = 3) and high reliability (Em score = 6).

4.2 Characteristic curves

Characteristic curves are built independently for each Em score group by dividing the 300 tests into their respective score groups. Three main steps are involved in constructing the characteristic curves:

- A min-max normalization of pressures and volumes;
- Homogenization and densification of pressure levels to obtain 100 steps of regular increments;
- Aggregation of curves by score group.

The results of the process of constructing characteristic curves by note group are shown in Figure 4. The differences between the curves for each note are clearly shown for both V60 and ΔV60/30.

Characteristic curves of low reliability (Em scores = 2 and 3) show no vertical part on the first part of the V60 curve and have a non-linear second part on pressure close to 1, meaning that the plastic phase has undoubtedly already begun. With regard to ΔV60/30, the creep peak normally expected at the start of the test is not always observed, and creep is not low during the pseudo-elastic phase. The opposite is true of curves with good reliability (Em rating = 5 and 6). The Em = 4 curves, perfectly localized between the two groups described, offer intermediate reliability. These characteristic curves can be a powerful tool for quickly assessing the reliability of a test by superimposing its standardized test curves.

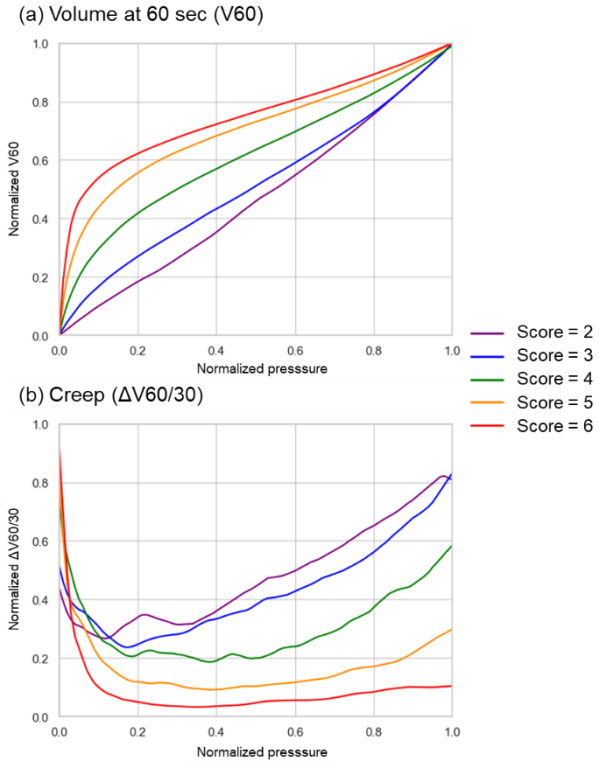

Figure 4. Characteristic curves for normalized (a) Volume at 60 sec (V60) and (b) Creep (ΔV60/30).

5 CONCLUSION

The aim of this study was to develop a system for assessing the reliability of Em from pressuremeter testing. This was achieved through the presentation of a multi-criteria scoring approach, which results in a reliability score for the pressuremeter modulus Em. Applying the evaluation process from 300 pressuremeter tests collected on a section of the Grand Paris Express, we were able to provide an overview of test reliability on the overall scale of the metro line. The results highlight the heterogeneity of test reliability, with a significant proportion of tests considered unreliable: 43% reliable and 33% unreliable. The scoring results have also been used to build characteristic curves for each group of scores, which can be assimilated to reliability "abacuses".

Prospects for improvement have been identified, in particular by extending the scoring system to the plastic phase of the pressuremeter test, in order to obtain a limit pressure rate. The time-consuming of the notation method also prompts reflection on automating the process, to help generalize it to new data. Questions are also being raised about the integration of reliability information into the geotechnical design and risk analysis processes. Finally, with regard to the characteristic curves, a study on the influence of the lithology may prove useful, as despite the diversity of the geological units represented by the selected tests, their distribution within them is not homogeneous.

ACKNOWLEDGEMENTS

We would like to thank the Société du Grand Paris for the access to its database and the interest shown in this work, as well as the Bureau de Recherches Géologiques et Minières (BRGM) for its financial support for this research project.

REFERENCES

Arscop, (2023). Accueil, Eléments de contexte. Available at: https://www.arscop.fr/, accessed: 27/11/2023 (in French).

Bergere, A., Ropers, F. (2018). Les Argiles Plastiques de L'Yprésien et leur comportement capricieux, The Argiles Plastiques Fm of Ypresian and their capricious behaviour. In: *Journées Nationales de Géotechnique et de Géologie de l'Ingénieur* (in French).

Clarke, B. G. (1994). *Pressuremeters in geotechnical design*. 1st Edition, Tailor and Francis, London, UK. https://doi.org/10.1201/9781482269345.

Dong, M., Neukum, C., Hu, H., Azzam, R. (2015). Real 3D geotechnical modeling in engineering geology: a case study from the inner city of Aachen. Germany, *Bull Eng Geol Environ*, 74, pp. 281-300. https://doi.org/10.1007/s10064-014-0640-6.

Gambin, M., Magnan, J.P., Mestat, P. (2005). *ISP5 – Pressio 2005, Symposium International – 50 ans de pressiomètre, ISP5 – Pressio 2005, Symposium International – 50 years of pressuremeter*. Volume 1, Presses de l'ENPC/LCPC, Paris, France (in French).

Gunnink, J. L., Maljers, D., van Gessel, S. F., Menkovic, A., Hummelman, H. J. (2013). Digital Geological Model (DGM): a 3D raster model of the subsurface of the Netherlands. *Netherlands Journal of Geosciences*, 93(1), pp. 33-46. https://doi.org/10.1017/S0016774600000263.

Jørgensen, F., Høyer, A-N., Sandersen, P. B.E., He, X., Foged, N. (2015). Combining 3D geological modelling techniques to address variations in geology, data type

and density – An example from Southern Denmark. *Computers & Geosciences*, 81, pp. 53-63. https://doi.org/10.1016/j.cageo.2015.04.010.

Lachérade, L., Marache, A., Denis, A., Halfon, I., Rohmer, J., Closset, L., Quesnel, F. (2023) A sectorisation-based method for geostatistical modeling of pressuremeter test data: Application to the Grand Paris Express project (France). *Engineering Geology,* 324, 107270. https://doi.org/10.1016/j.enggeo.2023.107270.

NF EN ISO 22476-4. (2015). Reconnaissance et essais géotechniques – Essais en place - Partie 4 : essai au pressiomètre Ménard, Geotechnical investigation and testing – In situ testing – Part 4: Ménard pressuremeter test (in French).

Thierry, P., Prunier-Leparmentier, A-M., Lambezat, C., Vanoudheusden, E., Vernoux, J-F. (2009). 3D geological modeling at urban scale and mapping of ground movement susceptibility from gypsum disssolution: The Paris example (France). *Engineering Geology*, Vol(105), 51–64. https://doi.org/10.1016/j.enggeo.2008.12.010.

Proceedings of the XVIII ECSMGE 2024
GEOTECHNICAL ENGINEERING CHALLENGES
TO MEET CURRENT AND EMERGING NEEDS OF SOCIETY
© 2024 the Authors
ISBN 978-1-032-54816-6
DOI 10.1201/9781003431749-319
Open Access: www.taylorfrancis.com, CC BY-NC-ND 4.0 license

ECSMGE 24
XVIII EUROPEAN CONFERENCE ON SOIL MECHANICS AND GEOTECHNICAL ENGINEERING

Finite element modelling of a tailings dam using the Clay and Sand Model

Modélisation par éléments finis des barrages de retenue de résidus miniers à l'aide du Clay And Sand Model

A. Laera*
Seequent, the Bentley Subsurface Company, Milan, Italy

V.H. Miranda
Civil Engineering & Geo-Sciences, Delft University of Technology, Delft, The Netherlands

R.J N. Azeiteiro
Seequent, the Bentley Subsurface Company, London, United Kingdom

T. Bui, S. Brasile
Seequent, the Bentley Subsurface Company, Delft, The Netherlands

R.B.J. Brinkgreve
Civil Engineering & Geo-Sciences, Delft University of Technology, Delft, The Netherlands

**anita.laera@seequent.com*

ABSTRACT: Tailings dam failures are one of the most destructive phenomena, both in terms of number of victims and of generated environmental impact. Over the years, different causes have been identified, with flow liquefaction being a prominent factor to consider when assessing the stability of tailings deposits. Due to the complexity of these events, numerical models are crucial for the analysis and design phases, where appropriate advanced soil constitutive models must be selected to reproduce the relevant features of the soil behaviour. In this paper, the Clay And Sand Model (CASM), originally proposed by Yu (1998) and later modified by Arroyo and Gens (2021) and Manica et al. (2021), has been adopted for the simulation of flow liquefaction of tailings deposits. The model incorporates the state parameter concept (Been and Jefferies, 1985) and has been implemented as a User-Defined Soil Model (UDSM) into the finite element code PLAXIS; thereby, it becomes generally applicable to a wide range of geotechnical applications. Due to its versatile yield surface and plastic potential formulations, CASM can be used to model the behaviour of a wide range of soils, from fine-grained (e.g., clays) to coarser-grained soils (e.g., silts and sands). This paper shows the capability of the model, as well as the robustness of the finite element formulation, to reproduce the soil flow liquefaction observed in boundary value problems.

RÉSUMÉ: Les ruptures de barrages de résidus miniers sont l'un des phénomènes les plus destructeurs, tant en termes de nombre de victimes que d'impact environnemental généré. De différentes causes ont été identifiées, parmi eux la liquéfaction statique étant un facteur important pour l'évaluation de la stabilité des dépôts de résidus miniers. En raison de la complexité de ces événements, les modèles numériques sont cruciaux pour les phases d'analyse et de dimensionnement, où des modèles constitutifs avancés doivent être utilisés pour reproduire les caractéristiques pertinentes du comportement du sol. Dans cet article, le Clay And Sand Model (CASM), proposé originalement par Yu (1998) et modifié par Arroyo et Gens (2021) et Manica et al. (2021), a été adopté pour la simulation de la liquéfaction statique des résidus miniers. Le modèle intègre le concept de paramètre d'état (Been et Jefferies, 1985) et a été implémenté en tant que User-Defined Soil Model (UDSM) dans le code des éléments finis PLAXIS; de ce fait, il devient généralement applicable à un grand nombre d'applications géotechniques. Grâce à la flexibilité de la formulation de la surface de charge et du potentiel plastique, CASM peut être utilisé pour modéliser le comportement de plusieurs types de sols, des sols à grain fin (comme les argiles) aux sols à grain plus grossier (comme les limons et les sables). Cet article montre la capacité du modèle, ainsi que la robustesse de la formulation par éléments finis, à reproduire la liquéfaction statique du sol observée dans les structures géotechniques.

Keywords: CASM; flow liquefaction; static liquefaction; tailings dams.

1 INTRODUCTION

Over the last 50 years, several failures of tailings facilities have been recorded around the world, resulting in hundreds of fatalities, and damage to infrastructures and environment. Static (or flow) liquefaction has often been identified as either the main cause of failure, as in the case of the Fundão tailings dam (Morgenstern et al., 2016), or as the major contributor to the devastating consequences of failure, as in the case of the Aznalcóllar dam (Alonso and Gens, 2006). The mechanism underlying flow liquefaction is undrained softening, which occurs when the soil undrained strength reduces significantly after a peak (instability point). This phenomenon is observed in tailings and, more in general, in hydraulic fills that are deposited in a loose state, and may be caused by different triggering mechanisms, such as undrained loading, drained lateral stress reduction, or a change in the hydraulic conditions.

To back-analyse known failure events, evaluate the status of existing tailings dams, or design new tailings facilities, advanced numerical analysis accounting for large deformations, soil non-linearity and softening should be performed. A key element in the numerical simulation of flow liquefaction is the choice of the constitutive model. The Clay And Sand Model (CASM) has been developed by Yu (1998) in the framework of Critical State Soil Mechanics (Schofield and Wroth, 1968) as a versatile constitutive model able to simulate the behaviour of both clays and sands. CASM can simulate static liquefaction and has been successfully employed to analyse the Brumadinho (Arroyo and Gens, 2021) and Merriespruit dam failures (Mánica et al., 2022).

CASM has been implemented as a User-Defined Soil Model (UDSM) in PLAXIS (Bentley Systems Inc, 2023). Compared to the original formulation, this version of CASM includes Lode's angle dependency, an alternative plastic potential equation (Arroyo and Gens, 2021) and the possibility to use it as either a rate-independent plastic model or as an elasto-viscoplastic model accounting for time-dependency (Manica et al., 2021).

In this paper, the Tar Island Dyke failure (Plewes et al., 1989) has been chosen as a case study to be modelled using the rate independent CASM model. After describing the constitutive equations, the finite element model is presented together with the strategy adopted to calibrate the model parameters and the results of the numerical analysis.

2 CONSTITUTIVE EQUATIONS

In the following, soil mechanics convention is used, i.e. stresses are positive in compression. Vectorial and tensorial quantities are denoted in bold, while scalars are in normal character.

2.1 Main concepts

As in the classical elasto-plasticity theory, the total strain rate is decomposed into an elastic $\dot{\boldsymbol{\varepsilon}}^{\boldsymbol{e}}$, and a plastic part $\dot{\boldsymbol{\varepsilon}}^{\boldsymbol{p}}$:

$$\dot{\boldsymbol{\varepsilon}} = \dot{\boldsymbol{\varepsilon}}^{\boldsymbol{e}} + \dot{\boldsymbol{\varepsilon}}^{\boldsymbol{p}} \tag{1}$$

Both strain rate tensors consist of a volumetric part $\dot{\varepsilon}_v$, and a deviatoric part $\dot{\boldsymbol{e}}$:

$$\dot{\boldsymbol{\varepsilon}} = \frac{1}{3}\dot{\varepsilon}_v\boldsymbol{\delta} + \dot{\boldsymbol{e}} \tag{2}$$

where $\boldsymbol{\delta}$ is the second-order identity tensor.

Similarly, the effective stress tensor $\boldsymbol{\sigma'}$ can be decomposed into a hydrostatic part p', and a deviatoric part $\boldsymbol{s}$:

$$\boldsymbol{\sigma'} = \frac{1}{3}p'\boldsymbol{\delta} + \boldsymbol{s} \tag{3}$$

The model has been derived from a reformulation of the original Cam-Clay model in terms of the state parameter ξ, defined as the difference between the specific volume υ at the current state and the specific volume on the critical state line at the same mean pressure p'. A positive value of the state parameter indicates a loose material that, under shearing, shows a volume contraction in drained conditions or an increase in pore pressure and a reduction of p', leading to flow liquefaction, in undrained conditions. The distance between the critical state line (CSL) and the reference consolidation line corresponds to the reference state parameter ξ_R.

2.2 Model formulation

CASM adopts a general stress-state relation to describe the yield surface for a variety of soils:

$$f = \left(\frac{q}{M_\theta p'}\right)^n + \frac{\xi}{\xi_R} - 1 \tag{4}$$

where q is the deviatoric stress, n is a parameter that controls the shape of the yield function, and M_θ is the stress ratio at critical state, dependent on Lode's angle θ according to (Sheng et al., 2000):

$$M_\theta = M\left(\frac{2\alpha^4}{1+\alpha^4+(1-\alpha^4)\sin 3\theta}\right)^{1/4} \quad (5)$$

In Equation 5, M is the critical stress ratio in triaxial compression and α is a parameter controlling the shape of the yield function in the deviatoric plane, both depending on the friction angle φ:

$$M = \frac{6\sin\varphi}{3-\sin\varphi}; \qquad \alpha = \frac{3-\sin\varphi}{3+\sin\varphi} \quad (6)$$

Finally, $\sin 3\theta$ is equal to:

$$\sin 3\theta = -\left(\frac{3\sqrt{3}}{2}\frac{J_3}{J_2^{3/2}}\right) \quad (7)$$

where J_2 and J_3 are the second and third invariant of the deviatoric stress tensor $\boldsymbol{s}$, respectively.

In the model implementation, it is preferred to use an alternative equivalent equation for the yield surface:

$$f = \left(\frac{q}{M_\theta p'}\right)^n + \frac{1}{\ln r}\ln\frac{p'}{p'_0} \quad (8)$$

where r is the spacing ratio and p'_0 is the preconsolidation pressure (Figure 1).

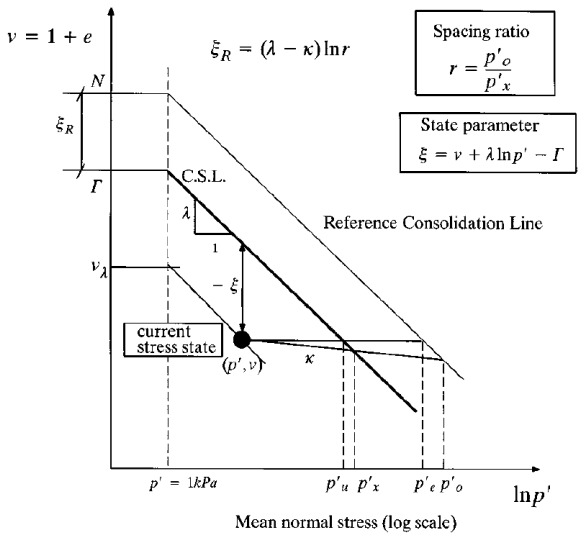

Figure 1. Definitions of state parameter, critical state constants, and reference state parameter (Yu, 1998).

Inside the yield surface, the behaviour is elastic and isotropic, defined by the bulk stiffness K', and the shear stiffness G. K' depends linearly on the mean effective pressure p', while G is a function of the bulk modulus and the coefficient of Poisson ν' (constant):

$$K' = \frac{p'(1+e_0)}{\kappa}; \qquad G = \frac{3(1-2\nu')}{2(1+\nu')}K' \quad (9)$$

where e_0 is the initial void ratio and κ is the slope of the swelling line in the ($\ln p'$, υ) space.

Instead, the plastic strains are calculated based on a non-associated flow rule. The plastic potential g can be described by either the original equation derived from Rowe's stress-dilatancy relationship (Rowe, 1962), or by the one introduced by Arroyo and Gens (2021), overcoming the limitations of the first one for stress paths with low stress ratios. The latter (Eq. 10) has been adopted in this paper:

$$g = \left(\frac{q}{M_\theta p'}\right)^m + m - \frac{p'_c(m-1)}{p'} - 1 \quad (10)$$

where m is a parameter controlling the shape of the plastic potential and p'_c must be solved for the current stress state such that the plastic potential passes through it.

Finally, the same isotropic volumetric hardening rule as in the Cam-Clay models is adopted:

$$\dot{p}'_0 = \frac{\upsilon\,\dot{\varepsilon}_v^p}{\lambda-\kappa}p'_0 \quad (11)$$

where λ is the slope of the CSL and reference line in the ($\ln p'$, υ) space, and $\dot{\varepsilon}_v^p$ is the plastic volumetric strain increment.

3 FINITE ELEMENT MODELLING OF THE TAR ISLAND DYKE

The Tar Island Dyke is a tailings structure built to retain sand tailings for the Suncor oil sand mine in Canada. Plewes et al. (1989) describe that, after an initial construction phase with the centreline method, the upstream construction method with compacted sand has been used for the subsequent phases. Adjacent to it, sand beaches were formed by discharging tailings from the upstream dyke crest.

Failure events of different entities have been registered during the construction, with the largest one occurring in 1974 due to flow liquefaction. When this slump occurred, a compacted cell 12.8 m high and about 36 m wide with a front slope of 1V:1H, was being placed on an approximately 9 m thick layer of loose sand recently deposited. The cell was placed in five lifts over the period from May 14 to August 22, 1974. During the construction of the first four lifts, no failure signals were observed, while the slump started near the completion of the last lift when the final compaction works were being carried out. The compacted cell did not liquefy and behaved as a rigid slab, while the beach sand below the cell liquefied and flowed out into the pond, generating a rapid failure. According to Plewes et al. (1989), the increased

construction rate and the considerable height of the compacted cell may have been the reasons for inducing static liquefaction.

The geometry of the model is shown in Figure 2, with the water table indicating the pond level on the upstream and falling within the dyke due to the downstream drainage system (Shuttle et al., 2021b). The bottom of the model is fully fixed, while the two lateral boundaries are normally fixed.

The finite element model has been discretised using a very fine mesh with 15-noded triangular elements, and with different degrees of local mesh refinement where significant changes in stresses and strains are expected during the analysis (i.e. in the loose beach sand below the compacted cell).

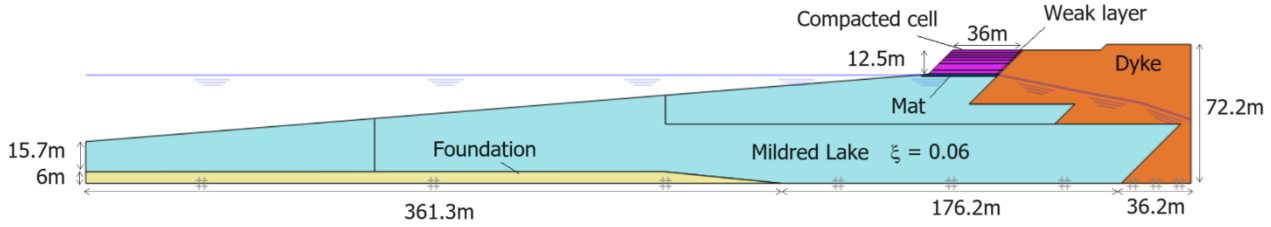

Figure 2. Model geometry in PLAXIS 2D.

The compacted dyke embankment, the compacted cell and the foundation layer have been modelled using drained Mohr-Coulomb model (Table 1).

Table 1. Parameters values for Mohr-Coulomb model.

γ_{unsat}	γ_{sat}	G	ν'	c'	φ'
18.6	19.6	33.3	0.2	5	48
kN/m^3	kN/m^3	MPa	-	kPa	°

For the foundation layer, an increased stiffness (G equal to 80 MPa) and strength (cohesion equal to 1 MPa) were assumed to simulate a rigid bedrock. The influence of a tension crack was considered by including a weak layer in between the compacted cell and the dyke, with a tension cut-off of 10 kPa and a friction angle of 5° (Shuttle et al., 2021b).

In this paper, the beach sand is assumed to consist entirely of loose material, modelled using CASM with a state parameter ξ of 0.06, while the mat at the bottom of the compacted cell consists of the same material but characterised by ξ equal to -0.1 (Shuttle et al., 2021b).

Since there were no investigations at that location at the time, Shuttle et al. (2021b) have selected the Mildred Lake data among test results available for tailings from existing mines in the area, determining the slope λ equal to 0.02826, the specific volume Γ of the CSL at a mean effective stress of 1 kPa equal to 1.89, and the stress ratio M equal to 1.29, i.e. a friction angle of about 32°. Additionally, the value of κ has been estimated equal to 0.004, based on the experimental data reported by Shuttle et al. (2021b).

The remaining model parameters characterising the shape of the yield surface and of the plastic potential should be calibrated based on laboratory tests. However, no tests are available for loose Mildred Lake material, which would be required for the calibration of CASM in problems involving flow liquefaction. For this reason, the calibration of the CASM parameters has been performed comparing the triaxial tests simulation results with those obtained with the NorSand (Jefferies, 1993) data set calibrated for the same application (Shuttle et al., 2021b). This results in a value of 20.4 for the spacing ratio r, 2 for n and 2.05 for m.

The initial stress state is generated assuming a coefficient of earth pressure at rest K_0 equal to 0.6, based on self-bored pressuremeter data at other tailings facilities, representing the case of normally consolidated tailings (Shuttle et al., 2021a, Shuttle et al., 2021b). The CASM parameters values are summarised in Table 2.

Table 2. CASM parameters values.

γ_{unsat}	γ_{sat}	λ	κ	ν'	φ
18.6	19.6	0.02826	0.004	0.2	32
kN/m^3	kN/m^3	-	-	-	°
n	r	m	Γ	ξ	K_0
2	20.4	2.05	1.89	0.06	0.6
-	-	-	-	-	-

The numerical analysis consists of six phases. In this study, we focus on reproducing the reported failure during the construction of the last tailings layer of which the increased of construction rate (Plewes et al., 1989) might be a contributing factor to flow liquefaction. Therefore, after the stress initialisation, the first four compacted layers are built in drained conditions, while the last one is built in undrained conditions. Considering the large strains expected in flow liquefaction problems, large deformation theory is taken into account in the construction phases through the Updated Lagrangian formulation (Bathe, 1982). Additionally, the arc-length control procedure

is adopted to improve the robustness of the analysis when dealing with failure in non-linear problems.

Three stress points have been selected to show the stress path evolution in the last phase, at the locations shown in Figure 3.

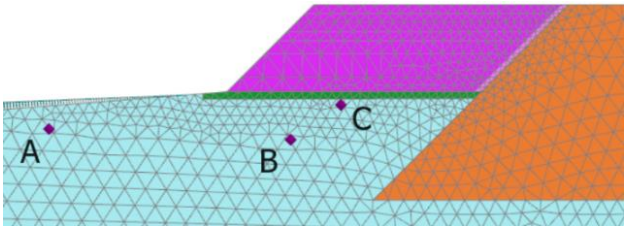

Figure 3. Selected stress points.

4 RESULTS

The first four construction stages are completed successfully while failure is detected during the activation of the top layer in undrained conditions.

During the last phase, prior to the occurrence of liquefaction, very small values of the deviatoric strain increment (in the order of 10^{-3}) are shown in Figure 4a. As expected, at the same step, the state parameter is positive in the loose beach sand, ranging from 0.04 to 0.06, approximately (Figure 4b).

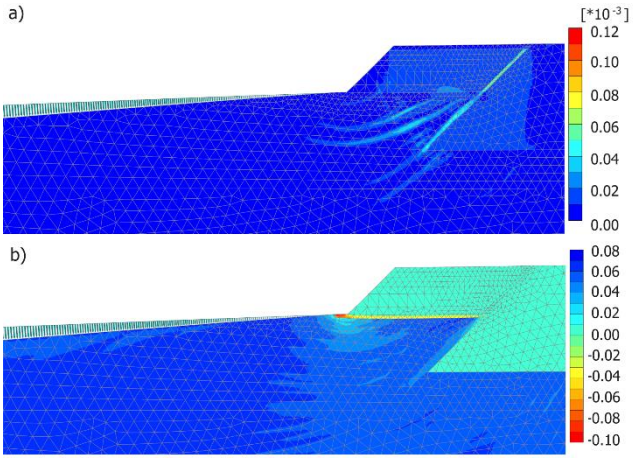

Figure 4. Contours prior to liquefaction occurrence: a) Deviatoric strain increment; b) State parameter.

In a subsequent step, shear bands develop (Figure 5a), along which the value of the state parameter approaches zero (Figure 5b), indicating that flow liquefaction has occurred.

Finally, at a later stage of liquefaction propagation, the deviatoric strain increment contours show multiple shear bands that extend to larger areas in the beach sand below the cell (Figure 6a). The state parameter is approximately zero in the same area (Figure 6b), showing that critical state has been reached. At the same step, the total displacement contours (Figure 6c) show that the compacted cell moves downwards, and that the depth of the collapsing mechanism extends to about 30 m below the cell.

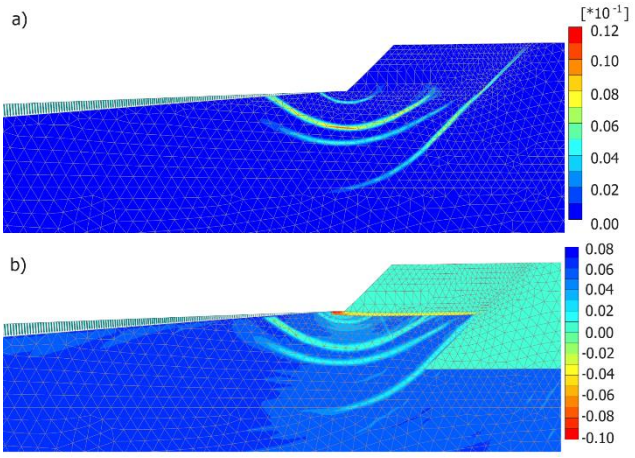

Figure 5. Contours at an early stage of liquefaction propagation: a) Deviatoric strain increment; b) State parameter.

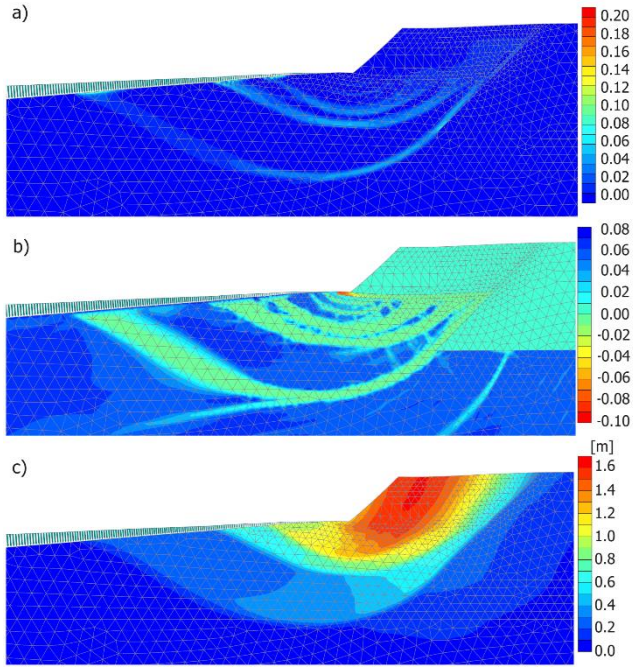

Figure 6. Contours at a later stage of liquefaction propagation: a) Deviatoric strain increment; b) State parameter; c) Total displacements.

A sharp decrease in terms of both deviatoric stress and mean pressure is observed along the shear bands, as shown by plotting the stress paths of the preselected stress points (Figure 7a). Starting from a relatively high value of p' and q, both stresses reduce, even to a value close to zero for point A, and reach the critical state line with a typical path indicating flow liquefaction. In the stress-strain plot (Figure 7b), undrained softening can be observed after a peak deviatoric stress is reached in each point.

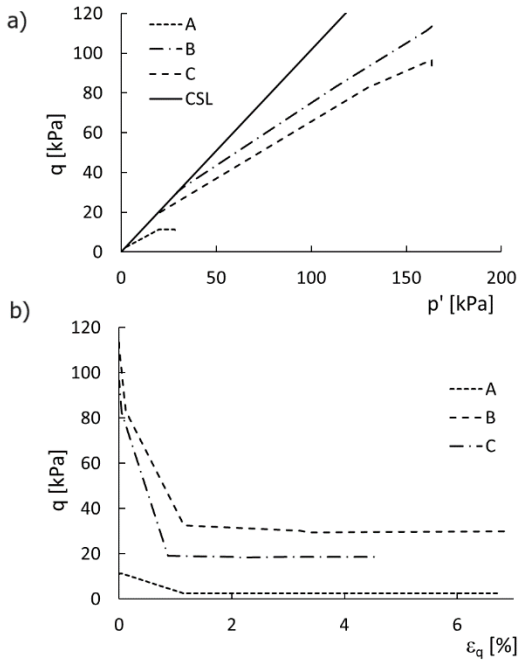

Figure 7. Results in preselected stress points: a) Stress paths; b) Stress-strain response.

5 CONCLUSION

This paper shows the capabilities of CASM to simulate undrained softening and reproduce the behaviour of soils susceptible to flow liquefaction. The model has been implemented as a user-defined soil model in PLAXIS and includes some improvements with respect to the original formulation, such as Lode's angle dependency, an alternative plastic potential equation and the possibility to account for creep effects.

In this paper, CASM has been calibrated based on available data and triaxial tests simulations on loose tailings. The Tar Island Dyke has been selected as a case study, where a major failure event caused by flow liquefaction of loose beach sand has been recorded in 1974. The results of the finite element analysis are consistent with the observations and show that CASM is capable of reproducing the behaviour of loose tailings in both drained and undrained conditions. In particular, the model is suitable for applications in which flow liquefaction may occur.

REFERENCES

Alonso, E. E., and Gens, A. (2006). Aznalcóllar dam failure. Part 3: Dynamics of the motion. *Géotechnique*, 56(3), pp. 203-210. https://doi.org/10.1680/geot.2006.56.3.203.

Arroyo, M., and Gens, A. (2021). Computational analyses of Dam I failure at the Corrego de Feijao mine in Brumadinho. Final report to VALE S.A.

Bathe, K.J. (1982). Finite element nonlinear analysis in solid and structural mechanics, In: *Finite element analysis in engineering analysis.* Prentice-Hall, New Jersey, United States.

Been, K., and Jefferies, M. (1985). A state parameter for sands. *Géotechnique*, 35(2), pp. 99-112. https://doi.org/10.1680/geot.1985.35.2.99.

Bentley Systems Inc. (2023). PLAXIS 2D (23.02). Available at: https://www.bentley.com/software/ plaxis-2d, accessed: 30/11/2023.

Jefferies, M. (1993). Nor-Sand: A simple critical state model for sand. *Géotechnique*, 43(1), pp. 91-103. https://doi.org/10.1680/geot.1993.43.1.91.

Mánica, M.A., Arroyo, M. and Gens, A. (2021). Effects of tailings viscosity on liquefaction triggering analyses. In: *Tailings and mine waste '21: proceedings of the twenty-fifth international conference on tailings and mine waste.* pp. 372-381. University of Alberta, Banff, Canada.

Mánica, M. A., Arroyo, M., Gens, A., and Monforte, L. (2022). Application of a critical state model to the Merriespruit tailings dam failure. *Proceedings of the Institution of Civil Engineers-Geotechnical Engineering*, 175(2), pp. 151-165. https://doi.org/10.1680/jgeen.21.00001.

Morgenstern, N. R., Vick, S. G., Viotti, C. B., and Watts, B. D. (2016). Report on the Immediate Causes of the Failure of the Fundão Dam. Fundão Tailings Dam Review Panel.

Plewes H.D., O'Neill H.D., McRoberts E.C., and Chan W.K. (1989). *Liquefaction considerations for Suncor Tailings Ponds.* Second Alberta Dam Safety Seminar, Edmonton, Alberta, Canada.

Rowe, P. W. (1962). The stress-dilatancy relation for static equilibrium of an assembly of particles in contact. *Proceedings of the Royal Society of London. Series A. Mathematical and Physical Sciences*, 269(1339), pp. 500-527. https://doi.org/10.1098/rspa.1962.0193.

Schofield, A. N., and Wroth, P. (1968). Critical state soil mechanics. Vol. 310. McGraw-Hill, London, United Kingdom.

Sheng, D., Sloan, S.W., and Yu, H.S. (2000). Aspects of finite element implementation of critical state models. *Computational mechanics*, 26, pp. 185-196. https://doi.org/10.1007/s004660000166.

Shuttle, D., Martens, S., and Jefferies, M. (2021a). Geostatic stress in oilsand tailings. *Proceedings of the Institution of Civil Engineers–Geotechnical Engineering*. https://doi.org/10.1680/jgeen.21.00114.

Shuttle, D., Marinelli, F., Brasile, S., and Jefferies, M. (2021b). Validation of computational liquefaction for tailings: Tar Island slump. *Geotechnical Research*, 9(1), pp. 32-55. https://doi.org/10.1680/jgere.21.00007

Yu, H.S. (1998). CASM: A unified state parameter model for clay and sand. *International journal for numerical and analytical methods in geomechanics,* 22(8), pp. 621-653.

Proceedings of the XVIII ECSMGE 2024
GEOTECHNICAL ENGINEERING CHALLENGES
TO MEET CURRENT AND EMERGING NEEDS OF SOCIETY
© 2024 the Authors
ISBN 978-1-032-54816-6
DOI 10.1201/9781003431749-320
Open Access: www.taylorfrancis.com, CC BY-NC-ND 4.0 license

ECSMGE 24
XVIII EUROPEAN CONFERENCE ON SOIL MECHANICS AND GEOTECHNICAL ENGINEERING

Brief insights: In-situ permeability test in weathered and poorly-graded rockfill

Essai de perméabilité in-situ dans un enrochement altéré et mal calibré

C. Laina-Gómez*, D. Escudero-Merino, E. Asanza-Izquierdo
CEDEX Geotechnics Laboratory, Madrid, Spain

*carlos.laina@cedex.es

ABSTRACT: Rockfills safeguard the core of engineered earth structures, enhancing strength and mitigating pore pressure accumulation. Factors such as significant thermal oscillations, severe frost/thaw, wetting/drying cycles, and shifts in rainfall patterns are likely to speed up the weathering of in-place rockfill particles. Throughout the past decade, investigations at CEDEX have revealed signs of particle alteration, including potential crumbling in aged dams, harbors, and embankments. These alterations result in significant changes in particle size distributions, consequently leading to a decline in drainage efficiency and overall structural strength. While large-scale laboratory tests such as permeameter, triaxial tests, or Rowe's cell, are able to assess the permeability of coarse-grained soils, in-situ tests performed on a larger scale appear to yield even more reliable results. These tests replicate natural conditions, including porosity, compaction, true grain-size distribution, and boundary conditions. This paper presents a case study on the in-situ measurement of permeability in a weathered, poorly-graded rockfill, providing valuable insights into real-world conditions.

RÉSUMÉ: L'enrochement protège le noyau des structures en terre, offrant de la résistance et minimisant l'accumulation de pression interstitielle. Les grandes oscillations thermiques, les cycles sévères de gel/dégel et de mouillage/séchage et les changements dans les régimes de précipitations sont des facteurs susceptibles d'accélérer l'altération des particules de l'enrochement. Ainsi, au cours de la dernière décennie, les cas de barrages, de ports et de remblais vieillissants étudiés au CEDEX ont montré une tendance à l'altération des particules (même d'effritement), entraînant des changements notables dans leur distribution granulométrique et, par conséquent, une dégradation de l'efficacité du drainage et de la résistance du matériel. Bien que des équipements d'essai de laboratoire soient disponibles pour évaluer la perméabilité des sols à grains grossiers (perméamètre, test triaxial ou cellule de Rowe), les essais à grande échelle in-situ semblent fournir des résultats encore plus fiables, car ils testent les conditions naturelles, c'est-à-dire la porosité, le compactage, la distribution granulométrique réelle et les conditions aux limites. Cet article traite d'une étude de cas de la mesure in-situ de la perméabilité dans un enrochement altéré mal gradué.

Keywords: In-situ; measurement; permeability; trench; weathered; rockfill.

1 INTRODUCTION

This communication presents a singular in-situ test carried out by CEDEX Geotechnics Laboratory, whose purpose was to assess how much the weathering and breakdown of the rockfill particles of an earth structure reduces its permeability. The rockfill basically consists of cobbles and gravels from a nearby quarry in a dolomite rock with sugary (saccharoidal) texture, yet partially dedolomitized into a somehow sandstone-like.

The study of the degradation of its particles, that had been addressed by CEDEX in the past, did not lead to sound conclusions regarding frost/thaw and wetting/drying cycles; however, those laboratory test that entailed direct mechanical stresses, showed that the particles were highly prone to crumble (into sugary sand). It was apparent that the mere rough mechanical handling at the lab led to fine production. For instance, dropping a particle onto the concrete floor might cause its crumbling.

After four decades as the upstream slope that protected the clay core of a large dam, a keen eye could recognize certain weathering features in the rockfill (bulgy profile, dying dusty, sandy patches). Since an expert assessment after on-site inspection had stated that the current bulk permeability of the rockfill could be as low as k≈0.01cm/s and that, therefore, the upstream slope stability during a rapid drawdown might be at risk due to excess pore pressures, CEDEX Geotechnics Laboratory engineered a full-scale test aimed at measuring the permeability on site.

2 THEORETICAL FRAMEWORK

2.1 On the in-situ measurement of permeability

Some formulations and tables the compute permeability based on non-comprehensive soil features (grain size and size distribution) can be found in the literature, such as the classical equations of Hazen (1911 and 1930) or Sherard (1984). Note that many of them neglect the degree of soil packing (void ratio), thereby the permeability of a shallow normally consolidated soil would erroneously remain constant until its maximum dry density.

Thus, such desk appraisal fails to take into account in-situ conditions (dry density, particle degradation and boundary conditions). Unfortunately, laboratory permeability tests with coarse soils fail again to reproduce the in-situ conditions, not to mention the drawbacks concerning the maximum grain size (a few inches) to meet standards. Soil resampling would force the coarse fraction to be excluded, changing the natural soil structure and, therefore, its porosity, which is a key issue in this study.

On the contrary, in-situ tests hardly disturb the natural conditions and allow a large mass of material to be tested, so its representativeness is much more reliable. In-situ measurements of permeability can be divided into two groups: tests carried out inside a borehole (Gilg-Gavard, Lugeon and Lefranc tests) and percolation tests on the surface through a trench in the soil (Haefeli and Matsuo tests).

In-situ measurements of the permeability inside a borehole were discarded, due to the major difficulties of placing a drilling machine on a steep slope and drilling into a coarse granular material. Additionally, a standard drilling diameter is not large enough in relation to the pore size of the rockfill skeleton. Furthermore, taking into account that the particles are prone to crumble, drilling works would likely produce an undesired amount of fines.

According to Fell et al. (2015), drilling works in such materials tend to cause the soil pore structure to close and become clogged, leading to highly biased permeability results, one or two orders of magnitude lower than that of the original soil.

2.2 Vedernikov´s solution (1934)

The percolation tests carried out on the surface through a trench seem to be an appropriate alternative when it comes to coarse materials. The State of the Art on percolation tests refers to several geometry arrangements of the trench or pit, but all of them assume a deep impermeable layer, are based on the Vedernikov's solution (1934), a 2D percolation model (q) from trapezoidal canal, given by Equation 1:

$$q = k \cdot (W + A \cdot y) \qquad (1)$$

where: q, is the flow rate [$L^2 \cdot T^{-1}$]; k, the permeability coefficient [$L \cdot T^{-1}$]; W, the width of the free water surface (L); y, the height of the trench from the discharge level; and A, a parameter that accounts for the maximum widening experienced by the downward flow [-].

As the close-form solution for the parameter A is rather complex, Vedernikov presented a chart for a wide range of shapes of trapezoidal canal (Figure 1).

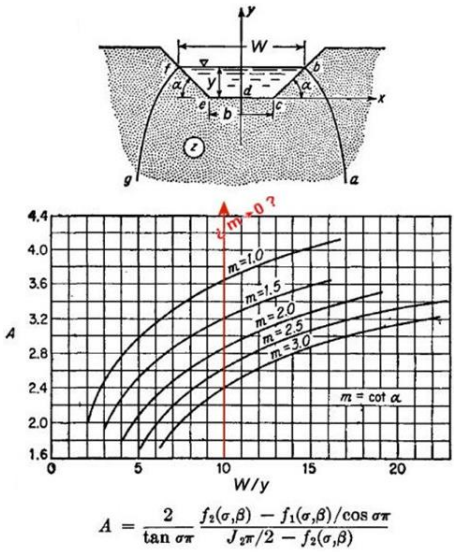

Figure 1. Percolation from a trapezoidal canal, Vedernikov's model (Harr, 1990).

However, this chart falls short to solve upper or lower bound cases, thereby vertical face (m = 0), perhaps the simplest, the geometry selected by the CEDEX Geotechnics Laboratory. For this reason, the article by Chahar (2001) has been used, which extends this abacus for extreme geometries (Figure 2).

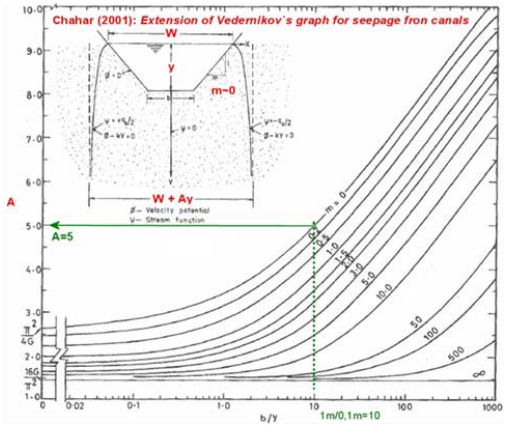

Figure 2. Chahar's chart (2001); generalization of Vedernikov's chart for obtaining A.

3 IN-SITU MEASUREMENT OF THE PERMEABILITY

3.1 Definition and scope

Figure 3 is a general layout of the in-situ permeability test that the Laboratory drew up. The aim was to measure the permeability of a large mass of the rockfill in the upstream slope, preferably in a zone with clear evidence of crumbling a weathering.

Vedernikov's model was taken on as the reference theoretical framework. In fact, it has been proven that percolation tests are in close agreement with theory as long as $H>3W$.

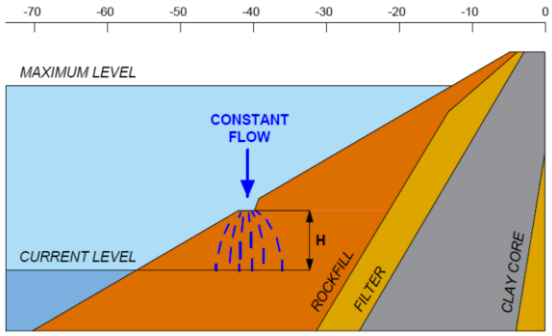

Figure 3. Layout of in-situ measurement of the permeability.

In this case, CEDEX set the base of the trench 3m above the discharge level, considering a trench width of W=1, due to constrains by the limited number and capacity of the available pumps. It is worth pointing out that in-situ tests long enough ($L>>W$) to meet 2D conditions turn out impractical for many other reasons. Thus, CEDEX concluded that even a square shallow pit would result cost-effective, regardless of minor fitting to match a 2D model with a 3D.

Bearing in mind the available pumps, pressure losses and preliminary judgement on the permeability expected, the in-situ test carried out by CEDEX was based on digging a shallow trench (W = 1m, y = 10cm), reaching total area between 1 and 3m².



Figure 4. Equipment calibration in CEH Laboratory.

3.2 Equipment calibration and mock test at CEH Laboratory

Due to the novelty of the test design, the large volume and flow rates of water and the specific devices (4 pumps operating in parallel, electronic flowmeters and connecting elements), the calibration, setting up and even a mock permeability test were carried out at CEDEX Hydraulics Laboratory (CEH), with ample resources and expertise in this field (Figure 4).

3.3 Description, details, and results of the in-situ test

The first preliminary works consisted of clearing and levelling a trail through the upstream slope with a backhoe to the approved testing spot. Next, CEDEX technicians contoured and prepared manually the trench. Finally, they proceeded to fix the pumps and the hoses, with special care with the intake from the reservoir, as well as the rest of the elements (Figure 5).

The design included the trench be lined with a macro-perforated sheet, in order to avoid potential erosion from the water squirting from the hose without loss of percolation capacity.

First test: Trench 1m x 3m in size.

A rectangular trench was meant to reduce somehow the 3D effect. Thus, the principle of the test was to adjust a flow of water just capable of maintaining a target height of water (10cm) in the trench.

However, it was soon recognized that with a size of 3m² the array of pumps at its maximum water flow rate ~ 13.6 l/s (~ 820 l/min) failed to fill the trench at all. In any case, the percolation capacity (permeability) in those 3m² exceeded 820 l/min. These results made possible to set a lower bound of the permeability of the rockfill (it was an order of magnitude higher than assumed, of k = 0.01cm/s), and therefore, dissipating all the doubts raised about the hypothetical loss of permeability due to the material "sanded".

Second and final test: Trench of 1m x 1m.

The technicians of the CEDEX Geotechnics Laboratory dissatisfied with the results, decided to repeat the test in a smaller trench (1m x 1m), even though this geometry maximized the three-dimensional effect.

Finally, following a very similar methodology this test was completed successfully. The main advantage was to obtain the order of magnitude flow rate associated with a steady height of water, which was maintained for several minutes in the trench.

The final flow rate of water, using three of the four available pumps, was 8.7 l/s (520 l/min).



Figure 5. Stages of testing; A) access road into the rockfill; B) installation of the 4 hydraulic pumps; C) preparation of the trench of 3m x 1m; D) preparation of the trench of 1m x 1m; E) detail of the trench of 1m x 1m; F) Trench of 1m x 1m with the level of water stabilized in 10cm.

4 ANALYSIS RESULTS

4.1 Approach

The difference in level between the trench and the water surface of the reservoir (about 3m) is sufficient to accept that the widening of the percolating flow is very close to its asymptotic value; in other words, the flow is almost vertical when it reaches the reservoir level.

The flow rate required to obtain a steady percolation flow in the trench of 1m x 1m was about 520 l/min. It is a three-dimensional flow and very similar to the case of an axil-symmetric problem (assuming a circular surface of area 1m²).

An approximation with the two-dimensional flow model could also be accepted, understanding that the asymptotic border does not influence whether it is a square trench or one of infinite length of equal width.

4.2 In-situ measurement

If there were a two-dimensional flow in a trench with vertical faces ($m = 0$), width (W) of 1m and water depth (y) of 0.1m, the flow would widen to an asymptotic value ($L_{asymptote}$) of:

$$L_{asymptote} = W + A \cdot y = 1m + A \cdot 0.1m$$

As seen in the above Figure 2, the present case it results that $A = 5$. Then:

$$L_{asymptote} = W + Ay = 1m + 5 \cdot 0.1m = 1.5m$$

It can be accepted that the flow is already practically vertical once it has descended the 3m difference between the trench and the reservoir's water surface, with a width equal to its asymptotic value.

As it is a square trench, three assumptions can be made about the dimensions and shape of the flow section when it intersects the level of the reservoir. The three options are represented in Figure 6.

Hypothesis 1: (upper bound) it is a square section with side $L_{asymptote} = 1.5m$.

$$S_{max} = 1.5m \cdot 1.5m = 2.25m^2$$

Then, the apparent speed for 520 l/min flow is:

$$v = 0.52m^3/min / 2.25m^2 = 0.39cm/s$$

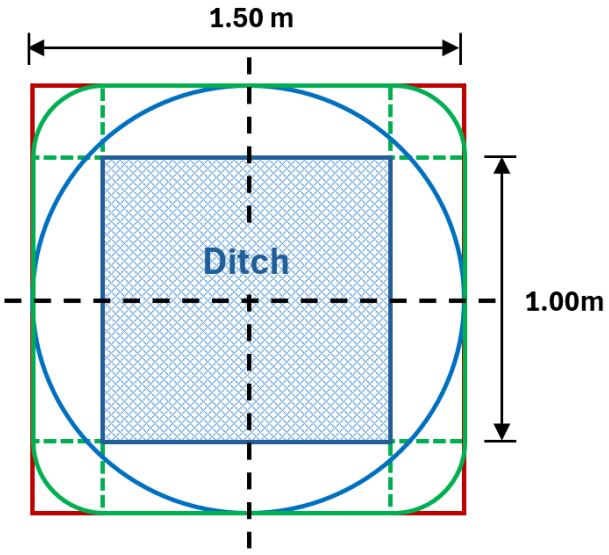

Figure 6. Possible sections formed by the flow when it intercepts the reservoir level.

Hypothesis 2: (intermediate bound) it is a square section with side $L_{asymptote} = 1.5m$ and the corners rounded.

$$S_{max} = 1.5m \cdot 1.5m - 4 \cdot 0.25^2 + \pi \times 0{,}25^2 = 2.20m^2$$

Then, the apparent speed for the same flow is:

$$v = 0.52m^3/min / 2.20m^2 = 0.39cm/s$$

Hypothesis 3: (lower bound) it is a circle section with a diameter of $L_{asymptote} = 1.5m$.

$$Smax = 0.25 \cdot \pi \times 1.5^2 = 1.77m^2$$

Then, the apparent speed for the same flow is:

$$v = 0.52m^3/min / 1.77m^2 = 0.49cm/s$$

It can be accepted with reasonable approximation that the area of the flow, when it reaches the level of the reservoir, will be that of the intermediate value between the different hypotheses raised. Therefore, it can be considered valid to approximate the apparent velocity to 0.4cm/s.

As the gradient in this percolation problem is $i = 1$, according to Darcy's law ($v = k \cdot i$), permeability is equal to the flow rate: $k \sim 0.4cm/s$.

5 CONCLUSIONS

The CEDEX Geotechnics Laboratory suggested this purpose-built permeability test in the poorly-graded weathered rockfill at upstream slope of the earthfill

dam, since an expert assessment had stated that its current permeability could be as low as $k \approx 0.01$cm/s.

For this purpose, the Laboratory took the Vedernikov solution, described by Harr (1990). In these “percolation" problems the gradient reaches i ~1 and the seepage turns soon downwards and tends to a constant "seepage area".

The setting up of this novelty model needed prior levelling and pumps capable of supplying a flow rate that would maintain the water level at the ditch. This calibration was carried out at CEDEX Hydraulics Laboratory under the support of its staff.

Although, an attempt was made to carry out the test as planned: a 3x1m ditch, it was soon recognized that the array of pumps at its maximum water flow rate failed to fill the trench at all. Finally, test was completed successful in a smaller trench of 1x1m with a final flow rate of water of 520 l/min.

As a conclusion and assuming a laminar flow (the true permeability would be higher than that derived from the test, as inertial loses are neglected), permeability equals the flow rate results: k ~0.4cm/s, and accordingly all the doubts raised about the hypothetical loss of permeability due to the material "sanded" were dissipated.

REFERENCES

Chahar, B.R. 2001. Extension of Vedernikov's graph for seepage from canals. Groundwater, 39: 272- 275.

Darcy, H. (1856). Les fontaines publiques de la ville de Dijon. Paris: Dalmont.

Fell, R., MacGregor, P., Stapledon, D., Bell, G., & Foster, M. 2015. Geotechnical engineering of dams. CRC Press.

Gilg, B. & Gavard, M. 1957. Calcul de la perméabilité par des essais d'eau dans les sondages en alluvions, Bulletin technique de la Suisse romande.

Gonzalez de Vallejo, L., Ferrer, M., Ortuño, L., & Oteo, C. 2002. Ingeniería Geológica. Prentice Hall.

Harr, M. 1990. Groundwater and seepage, Dover Publications, New York.

Hazen, A. 1911. Discussion on Dams on sand foundations. Trans ASCE 73:199.

Hazen, A. 1930. Water supply. American Civil Engineers Handbook. Wiley, New York.

Matsuo, S., Hanmachi, S. & Akai, K. 1953. A field determination of permeability. Zurich. 3rd ICSMFE (Vol. 1). 268-271.

Sherard, J. L., Dunnigan, L. P., & Talbot, J. R. 1984. Filters for silts and clays. Journal of Geotechnical Engineering, 110(6): 701-718.

Proceedings of the XVIII ECSMGE 2024
GEOTECHNICAL ENGINEERING CHALLENGES
TO MEET CURRENT AND EMERGING NEEDS OF SOCIETY
© 2024 the Authors
ISBN 978-1-032-54816-6
DOI 10.1201/9781003431749-321
Open Access: www.taylorfrancis.com, CC BY-NC-ND 4.0 license

ECSMGE 24
XVIII EUROPEAN CONFERENCE ON SOIL MECHANICS AND GEOTECHNICAL ENGINEERING

Eurocode 7 – Second generation: rock engineering

Eurocode 7 – Deuxième génération: ingénierie des roches

L. Lamas*
Portuguese National Laboratory for Civil Engineering, Lisbon, Portugal

J. Estaire
CEDEX – Laboratorio de Geotecnia, Madrid, Spain

J.P. Harrison
University of Toronto, Toronto, Canada

N. Maca
Titan Polska, Kraków, Poland

P. Pinto
University of Coimbra, Coimbra, Portugal

H. Walter
Salzburg, Austria

**llamas@lnec.pt*

ABSTRACT: Developing the second generation of the structural Eurocodes is now reaching its final steps. The title of the revised Eurocode EN 1990 ("Basis of structural and geotechnical design") reflects the specific identity of geotechnical problems. While the original version of the geotechnical Eurocode EN 1997 ("Geotechnical design") was developed largely based on soil mechanics, the aim is that the revised version treats soil and rock on an equal basis. Thus, rock engineering aspects have been substantially revised and expanded. The paper presents the main changes to the Eurocodes as far as they affect rock engineering design and lists improvements that will still be necessary after this critical revision.

RÉSUMÉ: Le développement de la deuxième génération des Eurocodes structurels atteint désormais ses dernières étapes. Le titre de l'Eurocode EN 1990 révisé ("Bases du calcul structurel et géotechnique") reflète l'identité spécifique des problèmes géotechniques. Alors que la version originale de l'Eurocode géotechnique EN 1997 ("Conception géotechnique") a été développée en grande partie sur la base de la mécanique des sols, l'objectif était que la version révisée traite le sol et la roche sur un pied d'égalité. Ainsi, les aspects de l'ingénierie des roches ont été considérablement révisés et élargis. L'article présente les principales modifications apportées aux Eurocodes dans la mesure où elles affectent la conception technique des roches et répertorie les améliorations qui seront encore nécessaires après cette révision critique.

Keywords: Eurocode; geotechnical structures; rock engineering; design.

1 INTRODUCTION

This paper addresses new developments and changes in the forthcoming second generation of Eurocode 7 Geotechnical design with a focus on rock engineering, based on the nearly final drafts available in January 2024. It is based on a series of six papers published in a special issue of "Geomechanics and Tunnelling" (Lamas *et al*., 2023; Walter *et al*., 2023; Estaire *et al*., 2023; Stille *et al*., 2023; Maca *et al*., 2023; Harrison *et al*., 2023) and on the presentations at the workshop "The second generation of Eurocode 7 and the integration of rock engineering" organised in conjunction with the 15th International Congress on Rock Mechanics of the ISRM, in October 2023.

The Structural Eurocodes are a suite of European standards (EN 199x) for the design of buildings and civil engineering works, whose implementation started in 2010 when contradictory national standards were withdrawn. EN 1990:2002 sets the basis of structural design, with the other Eurocodes dealing with different materials and specific aspects of design. Geotechnical aspects of design are covered by EN 1997 Eurocode 7: Geotechnical design, with two parts: EN 1997-1:2004 General rules and EN 1997-2:2007 Ground investigation and testing.

The revision of the Eurocode system was initiated in 2012 by the European Committee for Standardization (CEN), after an invitation by the

European Commission, and responsibility for the revision of Eurocode 7 was assigned to sub-committee CEN/TC250/SC7.

The primary objectives of the evolution of the Eurocodes are to incorporate improvements that reflect the state-of-the-art in engineering design and the needs of the civil engineering market; to improve the ease-of-use of the standards; and to harmonize practice between countries. With regard to Eurocode 7, plans were laid to make the following changes:

- Restructuring to make it more consistent with other Eurocodes, easier to understand and navigate, more comprehensive in its technical coverage and easier to add new topics.
- Improve guidance on selecting characteristic ground parameters and design water pressures, application to numerical methods, rock engineering and dynamic design.
- Improve ease-of-use by clarifying existing clauses, removing repetitions and removing unnecessary information.

The need for enhancing support for rock engineering in Eurocode 7 was explicitly recognized. While the original version was developed largely based on soil mechanics, without involvement of rock mechanics experts, the aim was that the revised version of Eurocode 7 would treat engineering in soil and rock on an equal basis.

Successive working groups of rock engineering experts were formed to give input and accompany the development of the revision, and to comment on the successive drafts. These groups organised a workshop in 2014 in Vigo and published three collective papers. The current group is the Rock Engineering Platform (REP), which is formed by all experts working in the Eurocode 7 revision process with interest in rock engineering design. All authors of this paper are both co-authors on the series of six papers mentioned in the introductory paragraph and members of the REP.

2 RESTRUCTURING OF THE SECOND GENERATION OF EN 1997

The first generation of EN 1997 has two parts:

- Part 1 – General Rules (EN 1997-1:2004).
- Part 2 – Ground investigation and testing (EN 1997-2:2007).

For improved ease-of-use the second generation of the EN 1997 is organized in three parts:

- Part 1 – General rules (EN 1997-1).
- Part 2 – Ground properties (EN 1997-2),
- Part 3 – Geotechnical structures (EN 1997-3).

The contents of the current Part 1 (EN 1997-1:2004) are reconfigured in the following way:

- The basis of geotechnical design was moved to the revised EN 1990.
- The general rules that affect all geotechnical designs remains in Part 1 (EN 1997-1).
- The specific rules for particular geotechnical structures form the new Part 3 (EN 1997-3).

An important aspect of this restructuring is that the revised EN 1997-1 only covers aspects of geotechnical design that are common to all geotechnical structures. EN 1997-3 covers all aspects specific for the particular types of geotechnical structures. The existing Part 2 focusses primarily on data collection methods for laboratory and field data, while the revised EN 1997-2 focusses on obtaining ground properties of engineering interest. Calculation models based on tests presented in Annexes to the existing Part 2 have been moved to EN 1997-3. It is expected that this will improve the everyday usefulness of the code to practitioners, particularly to those working on rock engineering projects. EN 1997, as well as all the other Eurocodes, shall be read in conjunction with EN 1990.

3 GENERAL CHANGES CONCERNING ROCK ENGINEERING

Profound changes and additions have been made to EN 1997 with regard to rock engineering, namely:

- accepted definitions of rock, rock masses and discontinuities, as well as requirement to consider the discontinuous nature of a rock mass;
- recognition that rock mass geometrical properties (e.g. discontinuity spacing and orientation) may be considered probabilistically.
- recognition that ground properties (i.e. of rock masses) must consider the geometrical properties of the discontinuities when they affect the mechanical behaviour of the ground;
- recognition that reliability-based methods may be used in design situations not covered by the partial factor design format, due to the specific nature of actions and design scenarios, and in ground conditions such as rock, strongly affected by discontinuities and other geometrical phenomena;
- an understanding that risk-informed approaches may apply in design situations where uncertainties or consequences are outside common ranges;
- rock mass classification systems;
- the physical, and chemical properties relevant to rock, including relevant laboratory and field tests, and testing standards;

- the potential need to determine the *in situ* stress state and methods for its determination;
- specific strength envelopes for rock, rock masses and discontinuities and methods to determine their parameters, as well as specific aspects of rock and rock mass deformability;
- failure mechanisms relevant for rock masses;
- values of partial factors on ground properties to be used for rock, rock mass and discontinuities;
- increased attention given to the observational method and prescriptive rules for the design of rock engineering structures;
- rock anchors, rock bolts and surface support;
- groundwater control measures.

Table 1 shows the number of occurrences of the terms "rock", "rock mass" and "discontinuities" in the existing and revised versions of EN 1997. The increase in the use of "rock mass" and "discontinuities" is 36%, 412% and 522%, respectively. This is a clear sign of more material on rock issues, a better understanding of the discontinuous nature of rock masses and the relevance of discontinuities. With EN 1990 the corresponding numbers are modest: the occurrence of "rock" increased from 2 to 4, there is no occurrence of "rock mass", and the term "discontinuities" was not present but now occurs twice.

Table 1. Occurrence of rock related terms in the existing and the revised EN 1997.

	Rock	Rock mass	Discontinuities
prEN 1997-1:2023	52	10	27
prEN 1997-2:2023	284	91	105
prEN 1997-3:2023	278	76	35
Total	614	177	167
EN 1997-1:2004	136	22	18
EN 1997-2:2007	316	21	14
Total	452	43	32

Tunnels and other underground structures are not covered by the revised EN 1997-3, because they are complex geotechnical structures, where ground-structure interaction is critical, and involve different materials such as concrete and steel. However, steps in this direction are being taken by CEN/TC250/SC7.

4 DETAILED CHANGES CONCERNING ROCK ENGINEERING

4.1 General rules

The basis for ensuring reliability is distributed between EN 1990 and EN 1997-1. To facilitate straightforward application of the reliability model, three classifications have been introduced: Consequence Classes (CC) dealing with the consequences of a failure, Geotechnical Complexity Classes (GCC) that take into account the difficulties and uncertainties in obtaining ground conditions and parameters and modelling the ground behaviour, and Geotechnical Categories (GC) which combine the first two classifications. CC is introduced in EN 1990, where failure probabilities and modifications of partial factors depending on the CC of a (geotechnical) structure are specified. Examples of geotechnical structures in each CC are given in EN 1997-1.

GCC and GC are detailed in EN 1997-1, and are essential for appropriate handling of rock mass complexity. Tables are provided and aid in selecting the appropriate GCC and obtaining the resulting GC. The GC of a geotechnical structure (or part of it) has multiple consequences on the design. It shall be used to specify measures that cover the aspects of design and construction that are essential in ensuring the appropriate level of reliability, namely:

- appropriate extent of ground investigation;
- validation of ground investigation information;
- validation of the geotechnical design model;
- validation of calculation models;
- minimum designer qualifications and experience;
- minimum design checking level;
- appropriate implementation of design.

In EN 1990 and EN 1997-1 verification of ultimate limit states (ULS) using the partial factor method is dominant. However, in rock engineering, the observational method and prescriptive rules are also commonly used. Thus, the expression "validation of calculation models" should be interpreted more generally as "evaluation of verification method and of calculation models, and checking the applicability of the prescriptive rules".

For the verification of limit states of geotechnical structures by the partial factor method, so-called Design Approaches were used in the first generation of the Eurocodes. In the new EN 1990, which now contains all the partial factors on actions and action effects, four Verification Cases (VC) are defined.

Table 2 is an excerpt of Table 4.8 of EN 1997-1 with partial factors on material properties for persistent and transient design situations. Partial factors for rock mass, rock material and discontinuity properties have been added. τ_f is the effective shear strength, $\tan\phi'_p$ and $\tan\phi'_{cs}$ are the peak and critical state coefficients of friction, c_u is the shear strength in total stress, q_u is the unconfined compressive strength and $\tan\phi'_{dis,r}$ is the coefficient of residual friction. The values of γ are the partial factors of these material properties. The factor k_M is a consequence factor which depends on the

consequence class. For comparison, values for soil and fill are also presented. Which set (M1 or M2) of factors and which verification case have to be combined is specified in EN 1997-3 for the different types of geotechnical structures.

Table 2. Partial factors on material properties.

	Ground property	Symbol	Set M1	Set M2
Soil and fill	τ_f	$\gamma_{\tau f}$	1.0	1.25 k_M
	$\tan\phi'_p$	$\gamma_{\tan\phi,p}$	1.0	1.25 k_M
	$\tan\phi'_{cs}$	$\gamma_{\tan\phi,cs}$	1.0	1.1 k_M
	c_u	γ_{cu}	1.0	1.4 k_M
Rock material and rock mass	τ_f	$\gamma_{\tau f}$	1.0	1.25 k_M
	q_u	γ_{qu}	1.0	1.4 k_M
Rock discontinuities	τ_f	$\gamma_{\tau dis}$	1.0	1.25 k_M
	$\tan\phi'_{dis,r}$	$\gamma_{\tan\phi,dis}$	1.0	1.1 k_M

From a rock engineering perspective, one must be aware that application of the partial factor method according to the Eurocode may result in a false impression of safety, because actions and material strengths and resistances are factored, but geometry is not. In rock engineering geometric properties of discontinuities are frequently crucial in determining the probability of failure, and the uncertainties related to the geometric properties of discontinuities must be considered by alternative methods. This can be done by sensitivity analyses, namely considering different discontinuity orientations and spacings, or even using probabilistic descriptions of the discontinuities (and using partial factors or other method for the actions and the strengths and resistances). The use of discontinuity fracture networks (DFN) based on probabilistic descriptions of the geometric properties of discontinuity networks is one such methods.

4.2 Ground properties

Ground properties are dealt in the new EN 1997-2. In Clause 4 the concept of Ground Model (GM) is introduced, which comprises the geological, hydro-geological, and geotechnical conditions at the site, as well as the derived values of the properties of the geotechnical units, based on the ground investigation results. Clause 5 is organized to support the designer's need to obtain this information through the tasks accomplished during the ground investigation phases: desk study, site inspection, preliminary and design investigation, using field and laboratory tests.

Clauses 6 to 12 are focused on obtaining the ground properties of the geotechnical units included in the GM. They cover the main properties required to address all geotechnical materials, from soil and rock, such as: state, physical and chemical properties; strength, stiffness, compressibility and consolidation properties; cyclic, dynamic and seismic properties; geohydraulic and thermal properties.

EN 1997-2 presents the methods for determining those properties directly, by means of field or laboratory tests, and indirectly, using correlations. Direct and indirect methods are compiled in tables, with additional information on the applicable EN standards and the minimum quality class of the samples to be used, in the case of soils.

Besides the new contents concerning rock presented in section 3, reference is made in EN 1997-2 to the standard EN ISO-14689 for the description and classification of rock and its weathered profile, as well as to the ISRM Suggested Methods for laboratory testing of rocks and *in situ* testing of rock masses.

4.3 Slopes, foundations and retaining structures

The overall and local stability of slopes, cuttings and embankments in rock are addressed in Clause 4 of EN 1997-3. The following topics are included: rock excavation techniques and sequence; damaging effects of excavation by blasting; influence on local stability within slopes and cuttings of rock discontinuities and weathered zones; influence of strength anisotropy of the rock material; possible effect of local instability on the overall stability. Calculation models for analysing the stability of rock mass are provided in Annex A.4.

Prescriptive rules, often used in rock engineering, as well as methods based on classification systems, are referred to in EN 1997-3.

Spread foundations are considered in Clause 5, where the minimum extent of field investigation is specified, noting the influence of the presence of rock masses. Bearing resistance on rock is introduced and two cases are considered: either the rock mass behaves as a discontinuous or as an equivalent continuous medium. Recommendations regarding the type of analysis to be performed are included.

Clause 6 is devoted to piled foundations, with most of the provisions regarding piles on rock that deal with shaft and base resistance calculations included as suggested methods in Annex C. Model factors γ_{Rd} for verification of axial pile resistance by testing or assisted by testing, for piles installed in rock, are provided in this clause.

The design of retaining structures is the subject of Clause 7, but is also interconnected with nearly all the other clauses in EN 1997-3: among other aspects, it requires foundation design, supporting elements such as anchors and rock bolts, and groundwater control. This clause is written mainly for soils and fills. In order to incorporate rock, it is stated that the term earth

pressure shall be interpreted as ground pressure and also includes acting pressure from rock cuttings and slopes behind the retaining structure. It is also emphasized that rock pressure shall account for strength anisotropy of the rock material and that arising from the presence of the discontinuities.

4.4 Anchors, rock bolts, rock support and groundwater control

Anchors are addressed in Clause 8 of EN 1997-3. As the design rules for anchors were thoroughly revised in 2014, the changes mostly express the general changes within the Eurocodes and harmonization with other clauses. Crucially, there is no distinction in design principles between anchors in soil and rock.

One element of completely new content in EN 1997-3 is soil nailed structures, to which Clause 10 is dedicated entirely. Soil nails are used in weak or weathered rock masses, or in mixed ground conditions. The basic approach of resistance determination follows the concept of piles in tension. Further, the basis of design, as well as materials and testing are provided for commonly used rock engineering facing systems, such as wire mesh and sprayed concrete.

The inclusion of rock bolts and rock surface support are additions to the content, being the subject of Clause 11, focused on rock bolts for stabilization of slopes and excavations, but not covering underground structures. Clause 11 deals with the design of single rock bolt elements, and is thus strongly interconnected with other clauses of EN 1997-3 that deal with aspects of overall limit states. The verification of limit states for rock bolts is based on calculation, testing or prescriptive measures, giving the broad flexibility to use the most suitable method in any given conditions. The importance of the geometric relation of rock bolts to the orientation and location of discontinuities is highlighted. Rock surface support is to be verified by prescriptive rules. Additionally, materials and corrosion specifications concerning considering the nature of the rock mass are given. Finally, the clause provides the requirements regarding testing.

Groundwater control measures, relevant for all geotechnical structures, are dealt with in a new Clause 13. Generally, the limit states of structures requiring groundwater control measures are verified according to those clauses applicable to them. Criteria for serviceability limit states are presented, and Clause 13 indicates that verification of these criteria is primarily by the observation method or field tests. As for aspects of groundwater control specific to rock engineering, elements of ground investigation and rock testing methods for the design of rock grouting are provided.

5 PERSPECTIVES ON THE EVOLUTION TO THE THIRD GENERATION

The current Eurocode revision process has sought to improve EN 1997 for application to rock engineering, while including only techniques and procedures that are in widespread customary use. Unsurprisingly, this required detailed examination of customary rock engineering techniques in the context of limit state design (LSD) as implemented in the Eurocodes.

This work revealed many discrepancies between customary rock engineering practice and the basis of design implemented in the Eurocodes. Crucially, this in turn led to the germination of many ideas about how rock engineering practice may need to develop and evolve in order to embrace the principles on which the Eurocodes are based. In particular, aspects of determining the properties of rock masses, and design verification by observational methods, partial factors, numerical modelling, and prescriptive rules are all thought to require significant improvement or fundamental modification.

In the context of the Eurocodes, rock engineering practice is unique in terms of its reliance on classification schemes for obtaining design values. All rock mass classification schemes currently in general use require subjective qualitative assessments. Such assessments are unavoidably always biased, and generate ordinal data (*i.e.*, numeric values that are labels with a meaning of order). This latter point is crucial, as ordinal data cannot be used in the statistical sense needed for LSD. Also, no rock mass classification schemes have been calibrated against rock mass conditions or performance. This state of affairs suggests that the current classification schemes have no role to play in design verification by calculation. This is an immense challenge, as many design techniques and formulae traditionally used in rock engineering involve rock mass classification parameters: prediction of rock mass strength and stiffness are perhaps the two most common. Without doubt rock mass classification schemes will continue to play a significant role in rock engineering practice, but in the context of the Eurocodes this may need to be as input to prescriptive rules. Perhaps Eurocode 7 will need to evolve to better embrace the combined use of prescriptive rules, design verification by calculation and application of observational methods.

The fundamental geometrical and mechanical complexity of discontinuous rock masses presents an immense challenge to the application of LSD to rock engineering practice. Because of this, the authors hold the opinion that attaining perfection in the application of LSD to rock engineering is not feasible, but strongly believe that with a concerted effort by the rock

engineering community, the necessary developments can be made to ensure the potential future EN 1997:2035 (the tentatively, and cheekily suggested date for the next revision is 2035!) will contain rules that are both useful and good for rock engineering practice. Thus, the immediate challenge is one of mobilising this community to ensure this is the case.

6 CONCLUSIONS

Many changes were introduced in the forthcoming second generation of Eurocode 7 with regard to rock engineering, as a result of overall improvement to Eurocode 7: the restructuring into three parts, the introduction of an improved reliability model and the inclusion of a new EN1997-2 offering improved ease-of-use, but also enhanced guidance on obtaining properties for rock, rock masses and discontinuities, exemplify these.

Of particular value for rock engineering are clauses which recognise that partial factor approaches may be inappropriate or insufficient when occurrence of the limit state is governed by the geometry of discontinuities. Similarly, many clauses now recognise aspects particular to rock engineering, such as specific strength criteria, the necessity to use the observational method, and the common use of rock mass classification systems.

The revision process has revealed much about the discrepancies between customary rock engineering practice and the basis of limit state design as implemented in the Eurocode suite. In the coming years rock engineers will start gaining experience applying the Eurocodes for design and providing information on the advantages and the difficulties encountered, so that the targets for a subsequent revision can be defined.

An immediate challenge is that of mobilising the rock engineering community to develop techniques which will reduce any discrepancies. We expect the REP will play a central role in mobilising and coordinating this effort over the next few years.

7 ACKNOWLEDGEMENTS

Since the Eurocode 7 evolution, and then revision process began in 2011, well over 100 experts in rock mechanics and rock engineering from across Europe have contributed to the work. The authors of the present paper are immensely grateful to all of these colleagues for their contributions to this effort.

REFERENCES

CEN (2002). EN 1990:2002, Eurocode: Basis of structural design, CEN, Brussels.

CEN (2004). EN 1997-1:2004, Eurocode 7: Geotechnical Design – Part 1: General rules, CEN, Brussels.

CEN (2007), EN 1997-2:2007, Eurocode 7: Geotechnical Design – Part 2: Ground investigation and testing, CEN, Brussels.

CEN (2023). EN 1990:2023, Eurocode: Basis of structural and geotechnical design, CEN, Brussels.

CEN (2023). prEN 1997-1:2023, Eurocode 7: Geotechnical design – Part 1: General rules, CEN, Brussels.

CEN (2023). prEN 1997-2:2023, Eurocode 7: Geotechnical design – Part 2: Ground properties, CEN, Brussels.

CEN (2023). prEN 1997-3:2023, Eurocode 7: Geotechnical design – Part 3: Geotechnical structures, CEN, Brussels.

Estaire, J.; Heintz, R.; Johansson, E.; Muralha, J.; Nuijten, G.; Segalini, A. (2023) Rock engineering design in tomorrow's geotechnical toolbox: Eurocode 7 – Ground properties (EN 1997-2:2024). *Geomechanics and Tunnelling*, 16(5), pp. 510–523, https://doi.org/10.1002/geot. 202300023.

Harrison, J.; Burbaum, U.; Lamas, L.; Spross, J.; Stille, H. (2023) Rock engineering design in tomorrow's geotechnical toolbox: Eurocode 7 – Perspectives of the evolution to the 2035 third generation. *Geomechanics and Tunnelling*, 16(5), pp. 560–572, https://doi.org/10.1002/geot. 202300027.

Lamas, L.; Burbaum, U.; Estaire, Harrison, J.P.; Nuijten, G.; Pereira, R. (2023) Rock engineering design in tomorrow's geotechnical toolbox: Eurocode and the basis of structural and geotechnical design (the second generation of EN 1990 and EN 1997). *Geomechanics and Tunnelling*, 16(5), pp. 469–490, https://doi.org/ 10.1002/geot.202300021.

Maca, N.; Dietz, K.; Stille, H.; Virely, D. (2023) Rock engineering design in tomorrow's geotechnical toolbox: Eurocode 7 – Geotechnical structures: anchors, reinforced fill structures, ground reinforced elements, ground improvement and groundwater control (EN 1997-3:2024). *Geomechanics and Tunnelling*, 16(5), pp. 53.6–559, https://doi. org/10.1002/geot.202300026.

Stille, H; Ashcroft, B.; Boley, C.; Labiouse, V.; Pinto, P. (2023). Rock engineering design in tomorrow's geotechnical toolbox: Eurocode 7 – Geotechnical structures: slopes, spread and piled foundations and retaining structures (EN 1997-3:2024). *Geomechanics and Tunnelling*, 16(5), pp. 524–535, https://doi.org/10.1002/geot. 202300025.

Walter, H.; Lamas, L.; Labiouse, V.; Nuijten, G.; Spross, J.; Stille, H. (2023) Rock engineering design in tomorrow's geotechnical toolbox: Eurocode 7 – General rules (EN 1997-1:2024). *Geomechanics and Tunnelling*, 16(5), pp. 491–509, https://doi.org/10.1002/geot.202300019.

Proceedings of the XVIII ECSMGE 2024
GEOTECHNICAL ENGINEERING CHALLENGES
TO MEET CURRENT AND EMERGING NEEDS OF SOCIETY
© 2024 the Authors
ISBN 978-1-032-54816-6
DOI 10.1201/9781003431749-322
Open Access: www.taylorfrancis.com, CC BY-NC-ND 4.0 license

ECSMGE 24
XVIII EUROPEAN CONFERENCE ON SOIL MECHANICS AND GEOTECHNICAL ENGINEERING

Analysis and simulation of a rainfall-induced landslide on Enna Area (Italy)

Analyse et simulation des glissements de terrain induits par les précipitations dans la région d'Enna (Italie)

V. Lentini*, K. Pinargote, F. Castelli
Faculty of Engineering and Architecture, University Kore of Enna, Enna, Italy
**valentina.lentini@unikore.it*

ABSTRACT: One of the most dangerous effects of climate change is heavy rainfall, often responsible for the triggering of natural phenomena, such as floods or landslides. In recent years, landslides and alluvial events had a strong impact on the road networks, creating the need to define criteria for management and mitigation of hydrogeological risk related with transport infrastructure systems. The reliability of transport infrastructures plays a key role since, in many cases, their inefficiency has caused serious damage to the anthropic system. In the paper the modelling of a debris flow occurred in the Enna area in the south of Italy is described. The area is prone to landslides, often consisting in shallow movements induced by rainfall. Starting from the study of the geological framework and the historical background for landslides of the Enna district, the research has focused on the causes triggering the landslides. In particular, the real case of 1st-2nd February 2014 which affected Enna city has been modelled. The event caused damage to private buildings and the interruption of the main infrastructure connecting Enna city to the motorway, due to the material on the road. The characterization of soil properties along the slope is based on a detailed geotechnical investigation in addition to a collection of topographical and hydrogeological data. The second part reports the results of the numerical analysis simulating the landslide event to assess the appropriate mitigation works, to reduce the damages to structures and infrastructures located in the area.

RÉSUMÉ: L'un des effets les plus dangereux du changement climatique est la forte pluie, souvent responsable de déclencher des phénomènes naturels tels que des inondations ou des glissements de terrain. Ces dernières années, les glissements de terrain et les événements alluviaux ont eu un impact important sur les réseaux routiers, créant ainsi la nécessité de définir des critères pour la gestion et l'atténuation des risques hydrogéologiques liés aux systèmes d'infrastructures de transport. La fiabilité des infrastructures de transport joue un rôle clé, car dans de nombreux cas, leur inefficacité a causé de graves dommages au système anthropique. Dans cet article, la modélisation d'une coulée de boue survenue dans la région d'Enna, dans le sud de l'Italie, est décrite. La région est sujette aux glissements de terrain, souvent dus à des mouvements superficiels induits par les précipitations. À partir de l'étude du cadre géologique et du contexte historique des glissements de terrain du district d'Enna, la recherche s'est concentrée sur les causes déclenchant les glissements de terrain. En particulier, le cas réel du 1er-2 février 2014, qui a touché la ville d'Enna, a été modélisé. Cet événement a causé des dommages aux bâtiments privés et l'interruption de l'infrastructure principale reliant la ville d'Enna à l'autoroute, en raison des matériaux sur la route. La caractérisation des propriétés du sol le long de la pente repose sur une enquête géotechnique détaillée en plus de la collecte de données topographiques et hydrogéologiques. La deuxième partie présente les résultats de l'analyse numérique simulant l'événement du glissement de terrain afin d'évaluer les travaux d'atténuation appropriés pour réduire les dommages aux structures et aux infrastructures situées dans la région.

Keywords: Landslides; debris flow; geo-hydrological.

1 INTRODUCTION

Landslides can be triggered by various factors, such as meteorological events and tectonic forces. In Italy, frequent landslides, often deadly and economically destructive, are primarily triggered by rainfall.

Evaluating landslide risk involves analysing the spatial and temporal likelihood of specific landslides occurrence. This includes assessing rainfall patterns, triggering factors, event dynamics, propagation areas, and rheology. Efforts over the past decades have focused on developing numerical models to create reliable landslide inventory maps. The information on hazard, elements at risk, vulnerability, as well as geological and geotechnical data is essential.

The aim of this paper is to present the results of the numerical analysis simulated with the model in the FLO-2D (Wu et al., 2013; Stancanelli and Foti, 2015) of the landslide event that struck Enna, Italy, on

February 1st-2nd, 2014, with the goal of evaluating debris flow behaviour.

2 LANDSLIDE INVENTORY IN ENNA AREA

A crucial component of landslide zonation is the creation of a landslide inventory map, which details the information. This inventory serves as a prerequisite for conducting analyses to establish relationships between landslide distribution and various influencing factors. The creation of a comprehensive landslide inventory map, as in Figure 1 (Castelli et al., 2016) in whiche the case study is highlighted in yellow, is pivotal for effective landslide zonation.

In the context of Enna (Sicily – Southern Italy region), a series of landslides triggered by rainfall events (Table 1) were examined and categorized, including the movement data, movement types and soil involved.

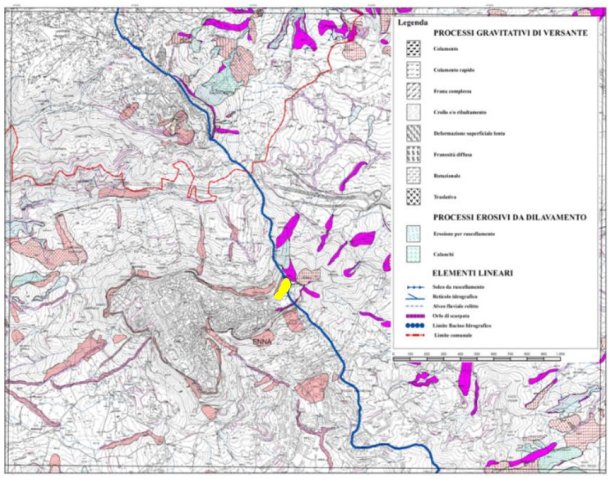

Figure 1. Landslide inventory map in the area of Enna, Sicily (Castelli et al., 2016).

Table 1. Cumulative rainfall, critical value and alert period for the landslides analysed and classified.

Event	Date of occurence
1	13/10/1991
4 - 5 - 6 - 7	08/09/1999
9 - 10	16/10/2003
12 - 13	12/12/2003
14 - 15′- 15′′ - 15′′′ - 16 - 17	06/03/2005
18 - 19	12/04/2005
20	15/01/2010
24	31/01/2011
25	02/02/2014

3 CASE STUDY OF ENNA

Italy, particularly Sicily (Castelli and Lentini, 2013) is marked by a complex landscape and geology that results in a variety of potential instabilities. Enna, situated in the heart of Sicily, exhibits steep hill slopes (Castelli et al., 2016). The geological composition comprises the Numidian Flysch and Holocene-age river alluvium (Castelli et al., 2017). On the night of February 1st to 2nd of 2014, Enna experienced a heavy downpour that resulted in significant damage to structures. It took place in a basin covering 0.158 km², leading to a debris flow. The impact of the rainfall event can be assessed by comparing photos taken before and after the event (Figure 2).

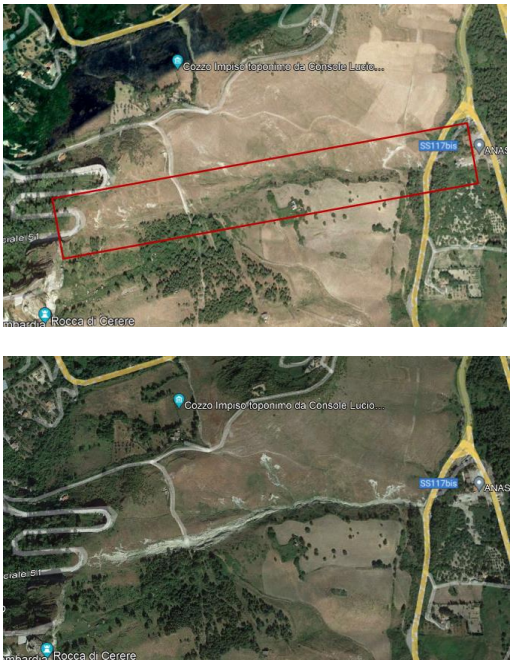

(a)

(b)

Figure 2. (a) the area before the debris flow; (b) the area after the debris flow.

4 RAINFALL DATA

The focus is on identifying rainfall thresholds as potential triggers for landslides, and their significance in mitigating geo-hydrological risks. By continuously monitoring meteorological, hydrological, and geotechnical parameters and combining them with predefined threshold values.

Information of rainfall data collected by Enna Meteorological Station was used. Figure 3 presents the rain intensity of the event on February 2, 2014 in Enna. The landslide associated with this event was initiated after intense rainfall, with precipitation exceeding 116.6 mm in less than one hour.

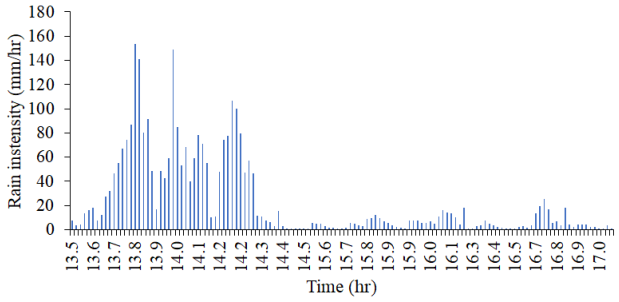

Figure 3. Rain intensity of the event of the 1st – 2nd February 2014 in Enna.

5 GEOTECHNICAL CHARACTERIZATION

The characterization of the foundation soil is an important key in the geotechnical study. That´s why the geotechnical parameters of silty clay (unsaturated soil), such as soil unit weight γ *(kN/m³)*, water content $w_{n\ (\%)}$, strength parameters in terms of friction angle $\phi'(°)$, cohesion $c'(kN/m^2)$, and undrained cohesion c_u *(kN/m²)* were obtained from in-situ tests and geotechnical laboratory tests, which have been used to subsequently define the geotechnical properties such as the consistence index I_C, presented in Table 2 (Castelli et al., 2017).

Table 2. Geotechnical parameters (Castelli et al., 2017).

Sample	γ $\left(\frac{kN}{m^3}\right)$	w_n (%)	c' $\left(\frac{kN}{m^2}\right)$	φ' (°)	c_u $\left(\frac{kN}{m^2}\right)$	I_c
S1C1	20.1	21.0	-	-	-	-
S1C2	20.9	20.4	39.44	25	-	1.50
S1C3	19.5	20.0	-	-	223.0	1.23
S1C5	20.2	26.0	25.36	24	255.0	0.67

6 NUMERICAL MODELLING AND RESULTS

The primary aim of the present numerical analyses is: to assess the ability of computational models to replicate the dynamics of debris flow.

To model the debris flows, it is required: a digital terrain model (DTM), hydrological data, and the rheological properties. The DTM was constructed using a grid system in FLO-2D, developed by O´Brien (1986). For this case, it assumed a single-phase modeling approach. The hydrological input was applied where the debris flow initiation was observed (Armanini et al., 2009).

In the simulations based on the literature reference (O´Brien and Julien, 1988; Bertolo and Wieczorek, 2005; Boniello et al., 2010; Wu et al., 2013) utilizing the FLO-2D model, specific parameter values of the rheological coefficients have been chosen from those available in the literature of Stancanelli and Foti (2015) that are closely resembling of the geomorphological and lithological characteristics of the study area α1= 0.006032, β1= 19.9, α2= 0.000707, and β2= 29.8.

A reconstructed representation of the area was yielded (Figure 4). The following important data were obtained:

- The maximum flow depths observed during the event, derived from the FLO-2D simulation, are presented in Figure 4a, with the highest predicted flow depth reaching approximately 1.10 meters.
- Figure 4b illustrates the final flow depths, with the highest predicted value at around 0.20 meters.
- Furthermore, Figure 4c displays the predicted maximum velocities, indicating that the greatest velocities were recorded in the upper regions of the basins, where the slopes were steeper, ranging from 4 to 6 m/s.

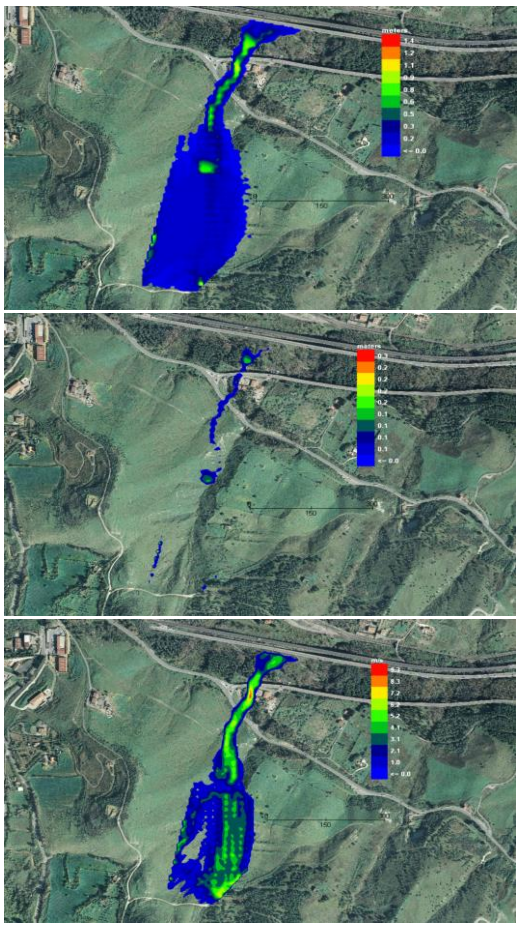

Figure 4. The simulation model carried out with the FLO-2D: (a) maximum flow depth; (b) final flow depth and (c) maximum velocity.

7 CONCLUSIONS

The results presented from a geological, geomorphological, and geotechnical survey of a real case in Enna, demonstrating that predicted values align closely with observed data and were reported in terms of the maximum flow depth, final flow depth and maximum velocity.

The study utilizes FLO-2D to simulate the case of the 1st-2nd of February 2014 create reliable numerical models for debris flows (Figure 4), which aid in assessing the set of variable direct infiltration of intense rainfall and runoff into cover materials. Likewise, was also possible to appreciate the key role that pore water pressure plays for the propagation stage, making dispersion patterns more complex. Ultimately, a precise representation of the topography in the system being a needed step to obtain a rational replication of the observed deposition patterns and to be able to carry out specific mitigation work for the area.

ACKNOWLEDGEMENTS

This study was carried out within the RETURN Extended Partnership and received funding from the European Union Next-GenerationEU (National Recovery and Resilience Plan - NRRP, Mission 4, Component 2, Investment 1.3 - D.D. 1243 2/8/2022, PE0000005).

REFERENCES

Armanini, A., Fraccarollo, L., and Rosatti, G. (2009). Two-dimensional simulation of debris flows in erodible channels. Computers and Geosciences, 35(5), 993–1006. https://doi.org/10.1016/j.cageo.2007.11.008.

Bertolo, P., and Wieczorek, G. F. (2005). Calibration of numerical models for small debris flows in Yosemite Valley, California, USA. Natural Hazards and Earth System Sciences, 5(6), 993–1001. https://doi.org/https://doi.org/10.5194/nhess-5-993-2005, 2005.

Boniello, M. A., Calligaris, C., Lapasin, R., and Zini, L. (2010). Rheological investigation and simulation of a debris-flow event in the Fella watershed. Natural Hazards and Earth System Science, 10(5), 989–997. https://doi.org/10.5194/nhess-10-989-2010.

Castelli, F., Castellano, E., Contino, F., and Lentini, V. (2016). A Web-based GIS system for landslide risk zonation: the case of Enna area (Italy). Proceedings 12th International Symposium on Landslides, 2, 595–603.

Castelli, F., Freni, G., Lentini, V., and Fichera, A. (2017). Modelling of a Debris Flow Event in the Enna Area for Hazard Assessment. Procedia Engineering, 175, 287–292. https://doi.org/10.1016/j.proeng.2017.01.026.

Castelli, F., and Lentini, V. (2013). Landsliding events triggered by rainfalls in the Enna area (South Italy). Proc. 2nd World Landslide Forum WLF2, 3–7.

O´Brien, J. S. (1986). Physical process, rheology and modeling of mudflows [PhD thesis]. Colorado State University.

O´Brien, J. S., and Julien, P. Y. (1988). Laboratory analysis of mudflow propierties. Journal of Hydraulic Engineering, 114(8), 887–887. https://doi.org/https://doi.org/10.1061/(ASCE)0733-9429(1988)114:8(877).

Stancanelli, L. M., and Foti, E. (2015). A comparative assessment of two different debris flow propagation approaches - Blind simulations on a real debris flow event. Natural Hazards and Earth System Sciences, 15(4), 735–746. https://doi.org/10.5194/nhess-15-735-2015.

Wu, Y. H., Liu, K. F., and Chen, Y. C. (2013). Comparison between FLO-2D and Debris-2D on the application of assessment of granular debris flow hazards with case study. Journal of Mountain Science, 10(2), 293–304. https://doi.org/10.1007/s11629-013-2511-1.

Proceedings of the XVIII ECSMGE 2024
GEOTECHNICAL ENGINEERING CHALLENGES
TO MEET CURRENT AND EMERGING NEEDS OF SOCIETY
© 2024 the Authors
ISBN 978-1-032-54816-6
DOI 10.1201/9781003431749-323
Open Access: www.taylorfrancis.com, CC BY-NC-ND 4.0 license

ECSMGE 24
XVIII EUROPEAN CONFERENCE ON SOIL MECHANICS AND GEOTECHNICAL ENGINEERING

Eurocode 7 – second generation – spread foundations

Eurocode 7 - deuxième génération – fondations superficielles

K. Lesny*
University of Siegen, Siegen, Germany

T. Orr
Trinity College, Dublin, Ireland

**kerstin.lesny@uni-siegen.de*

ABSTRACT: In the new second generation version of Eurocode 7, Part 3 the limit state design for various geotechnical structures is outlined. Spread foundations are covered in Clause 5 of this part where requirements for the verification of ultimate and serviceability limit states are provided. In comparison to the current version of Eurocode 7 the requirements have been improved first by revising the structure of this clause so that it is now unified and consistent with the other clauses in this part and follows the design-path defined in Part 1. In addition, various aspects addressing the limit state design of spread foundations have been complemented or modified such as the inclusion of the well-known Terzaghi-Buisman method for calculating the bearing resistance in the main text, the explicit consideration of rock mass as well as various calculation models provided in Annex B, e.g. models for punching failure and foundation settlement evaluation. The present paper provides an overview of the design of spread foundations according to the new Eurocode 7. A simple design example illustrates the design procedure.

RÉSUMÉ: Dans la nouvelle version de deuxième génération de l'Eurocode 7, partie 3, la conception des états limites pour diverses structures géotechniques est décrite. Les fondations superficielles sont traitées par la clause 5 de cette partie, où les exigences relatives à la vérification des états limites ultimes et d'aptitude au service sont fournies. Par rapport à la version actuelle de l'Eurocode 7, les exigences ont été améliorées tout d'abord en révisant la structure de cette clause afin qu'elle soit désormais unifiée et cohérente avec les autres clauses de cette partie et qu'elle suive le chemin de conception défini dans la partie 1. En outre, divers aspects relatifs à la conception à l'état limite des fondations superficielles ont été complétés ou modifiés, comme l'inclusion de la méthode bien connue de Terzaghi-Buisman pour le calcul de la résistance à l'appui dans le texte principal, considération explicite des masses rocheuses ainsi que divers modèles de calcul fournis dans l'annexe B, par exemple des modèles pour la rupture par poinçonnement et l'évaluation du tassement de la fondation superficielle. Le présent document donne un aperçu de la conception des fondations superficielle selon le nouvel Eurocode 7. Un exemple simple de conception illustre la procédure de conception.

Keywords: Second generation Eurocode 7; spread foundations; design; ultimate limit state; serviceability limit state.

1 INTRODUCTION

The design of spread foundations is covered in Part 3, Clause 5 of the new second generation Eurocode 7 (prEN 1997-3:2023). Clause 5 is organized with design provisions following the unified structure of all the clauses in Part 3 which reflects the design requirements in Part 1 (prEN 1997-1:2023) as illustrated in Figure 1. Clause 5 also refers to Part 2 (prEN 1997-2:2023) for required derived ground properties.

The scope of Clause 5 is the limit state design of spread foundations, i.e. of pad, strip and raft foundations. Compared to the current version of Eurocode 7 (EN 1997-1:2004 + AC:2009 + A1:2013) the scope has been extended to include unreinforced working platforms.

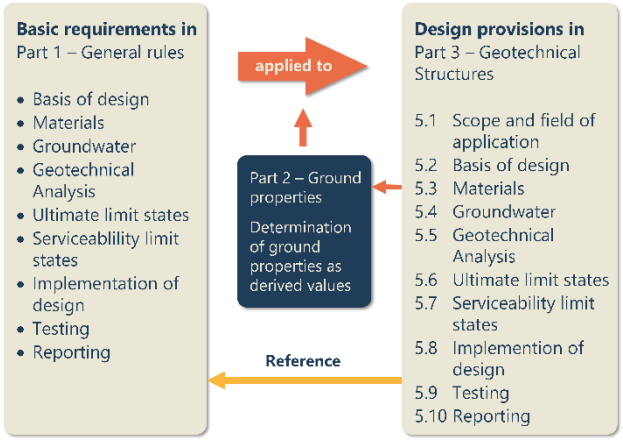

Figure 1. Structure of clause 5 – spread foundations.

While the design of load transfer platforms over rigid inclusions is covered in Clause 11 of Part 3,

Clause 5 is applicable to certain aspects as well. Furthermore, it is applicable to deep foundations such as caissons, which behave as spread foundations.

The present paper addresses the most important changes compared to the current version of the code with a focus on the basis of design, the geotechnical analysis and the verification of the ultimate and serviceability limit states. The procedure of design verification is illustrated using a simple design example at the end of this paper.

2 PHILOSOPHY AND DESIGN BASICS

2.1 Design philosophy

The head Eurocode EN 1990 (EN 1990:2023), Basis of structural and geotechnical design, states that the reliability required for structures within the scope of this document shall be achieved by design in accordance with all parts of the Eurocodes. Thus, the overall design goal is achieved if a design follows the requirements provided in Eurocode 7, Parts 1 to 3 together with those in EN 1990.

The new Eurocode 7, Part 1 provides a set of measures to achieve this reliability goal. These measures address not only the representation of design parameters and the accuracy of calculation models used, but also the prevention of errors in design and execution. They are defined at different levels, depending on the Geotechnical Category of the structure. The Geotechnical Category reflects the relationship between the Geotechnical Complexity Class, describing ground and groundwater conditions as well as ground-structure interaction, and the Consequence Class, considering the consequences of failure of the structure or the foundation. The provisions in Clause 5 address these requirements.

2.2 Basis of design

Clause 5, Subclause 5.2 summarizes the basic design information such as the design situations, geometrical properties, actions and environmental influences, limit states and ground investigations, which are spread over several subclauses in the current version of the code. Reliability, as outlined in 2.1, is addressed by reference to Part 1 only, so no specific provisions are given for spread foundations. However, the minimum extent (depth) of ground investigations defined here is one of the measures to achieve the required reliability. Table 1 shows the minimum depth values given for spread foundations. These values reflect the zone of influence of different types of spread foundations and are comparable to the recommendations in Annex B of the current Eurocode 7, Part 2. The width B is either the width of a single foundation or the width of a foundation group, depending on the considered system. The content of the table can be modified in the National Annexes.

Table 1. Minimum depth of ground investigations from Table 5.1 of prEN 1997-1:2023.

Types of spread foundations	Minimum depth
Square or circular footing	d_{min} = max (3B; 6m)
Strip footing	d_{min} = max (5B; 6m)
Raft or structure supported by a group of foundations	d_{min} = max (1.5B; 6m)

2.3 Materials and groundwater

Subclause 5.3 addresses the materials used in design. It mainly refers to Part 2 for the determination of ground properties and to Part 1, Clause 5.5 for concrete foundations. It further points out the use of effective or total stress ground properties, depending on the design situation.

Subclause 5.4 on groundwater demands explicitly the consideration of groundwater levels and pressures, which could affect the bearing behaviour of a spread foundation. Capillary rise inducing possible deterioration of footing material is mentioned as well.

3 GEOTECHNICAL ANALYSIS

The calculation models for verifying the limit states of spread foundations are the content of Subclause 5.5. The main changes compared to the current version of Eurocode 7 are related to the calculation of the bearing resistance. The well-known general Terzaghi-Buisman formulae for the bearing resistance of soils and fills for drained and undrained analysis (Terzaghi, 1943) are now presented in the code text of the new Eurocode 7. The parameters for the bearing resistance formulae are defined in Annex B.4.

The bearing resistance formulae for soil and fill were extended by depth factors and ground inclination factors. For the depth factors the formulae proposed by Brinch Hansen (1970) and adopted by Vesic (1973) and for the ground inclination factors the formulae provided by Vesic (1975) were adopted. More changes include the deletion of the cohesion term in the load inclination factors and a modification of the bearing capacity factor N_γ. For the latter the formulation provided by Caquot & Kérisel (1953) and Vesic (1973) was selected, which is slightly different from the formulae used in Annex D of the current Eurocode 7, i.e. $N_\gamma = 2(N_q + 1)\cdot\tan\varphi'$ instead of $N_\gamma = 2(N_q - 1)\cdot\tan\varphi'$. Figure 2 illustrates the effect of this modification and of the consideration of depth factors on the

foundation design width, B for a simplified design situation.

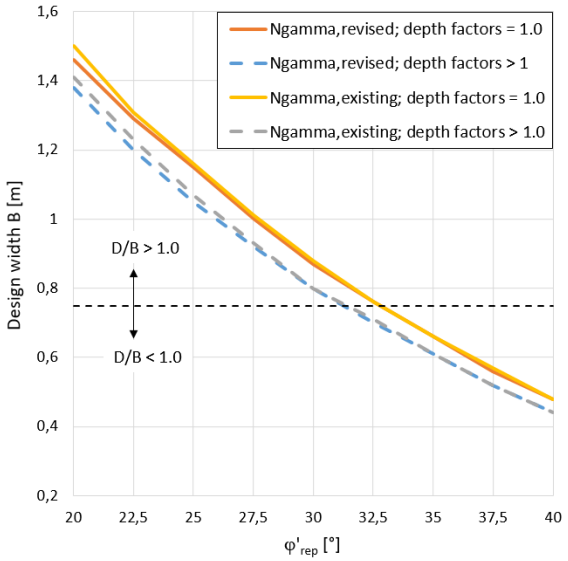

Figure 2. Design width B for a square foundation with 250 kN vertical load calculated using RFA for a dry coarse soil with γ = 18 kN/m³ and an embedment depth of D = 0.75 m (modified from M515/CEN/TC250/SC7/PT4, 2020).

Clearly, the modification of N_γ has negligible effect on B for φ‘ ≥ 27.5°. For φ‘ < 27.5° it results in widths B which are slightly smaller than with the existing formulation. No cohesion was considered here, which soils with small friction angles typically exhibit and which would increase the bearing resistance. In view of the scatter generally associated with the factor N_γ (see e.g. Paikowsky et al., 2010) the consequences of using the new N_γ formula are acceptable.

Compared to this, the effect of the depth factors is more significant. However, the depth factors should only be used with great care as the soil within the embedment zone is often disturbed. Consequently, the code states that they should only be used when the strength of the soil or fill in the embedment zone is equal to or greater than the strength of the soil below foundation level.

A further addition is that Subclause 5.5 includes some guidance on how to verify the bearing resistance of rock mass. It also allows the derivation of the bearing resistance from empirical models, provided comparable experience has shown their successful use. Annex B includes additional calculation models, e.g. for punching, a more detailed model for bearing resistance from pressuremeter test results and a model for bearing resistance of rock mass based on wedge equilibrium.

Regarding the calculation of sliding resistance and settlement or heave, no major changes have been made. Annex B provides various calculation models for settlement evaluation, e.g. based on the adjusted elasticity method and on pressuremeter or cone penetration test results.

Subclause 5.5 also includes recommendations for selecting appropriate distributions of bearing pressures for structural analysis.

4 DESIGN VERIFICATION WITH PARTIAL FACTORS

4.1 Limit states

According to Subclause 5.2.5 the design verification shall consider primarily the ultimate limit states (ULS) and serviceability limit states (SLS) shown in Figure 3.

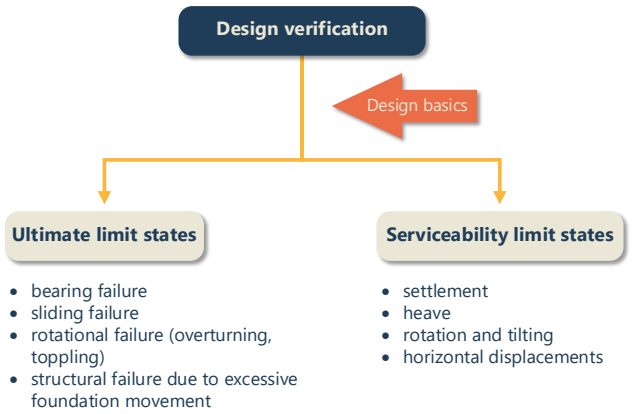

Figure 3. Ultimate and serviceability limit states of spread foundations.

Figure 3 also mentions failure by excessive deformations. However, Clause 5 does not provide recommendations on how to verify this limit state. Instead, this topic is addressed in Part 1.

4.2 Verification of the ultimate limit state

The new Eurocode 7 allows the material factor approach (MFA) and the resistance factor approach (RFA) to be used for ULS design verification. The partial resistance factors to obtain the RFA design resistances of spread foundations are provided in Subclause 5.6 of Part 3, Table 5.2, whereas the partial material factors to obtain the design MFA ground properties are given in Part 1, Table 4.8. The partial factors on actions and effects of actions are defined for different verification cases (VC) in EN 1990, Table A.1.8. The National Annexes will specify the factoring approach and partial factors to be used. The two approaches result in the combinations (a) to (c) for MFA and (d) and (e) for RFA (see Table 2). However,

combination (e) should be used only if the representative load inclination is not larger than 0.2.

Table 2. Partial factors for the ULS verification of spread foundations for persistent and transient design situations (Table 5.2, prEN 1997-3:2023).

Verification of	Partial factor on	Symbol	Material factor approach (MFA), either both combinations (a) and (b) or the single combination (c)			Resistance factor approach (RFA), either combination (d) or (e)[c]	
			(a)	(b)	(c)	(d)	(e)
Overall stability	See Clause 4						
Bearing and sliding resistance	Actions effects-of-actions	γ_F ,γ_E	VC1[a]	VC3[a]	VC1[a]	VC1[a]	VC4
	Ground properties	γ_M	M1[b]	M2[b]	M2[b]	Not factored	
	Bearing resistance	γ_{RN}	Not factored			1,4	
	Sliding resistance	γ_{RT}	Not factored			1,1	
	Passive resistance	$\gamma_{RT,face}$	Not factored			1,4	

[a] Values of the partial factors for Verification Cases (VCs) 1, 3, and 4 are given in prEN 1990:2023 Annex A.
[b] Values of the partial factors for Sets M1 and M2 are given in prEN 1997-1:2023, Table 4.8.
[c] Use combination (d) except where specified otherwise in 5.6.6 (2)

Combinations (a) and (b) correspond to the current DA1 Combination 1 and DA1 Combination 2, (d) corresponds to DA2, (e) to DA2* and (c) to DA3 with VC3 partial factors on structural actions. The new Eurocode 7 offers the possibility of reducing the partial material and partial resistance factors for transient design situations by multiplying them by a reduction factor, k_{tr} provided the products are not less than 1.0 and any constraints on its use are satisfied. It should also be noted that all tables with partial factors are Nationally Determined Parameters (NDPs) and therefore can be adjusted based on national practices and given in National Annexes.

Overall, the verification procedures for undrained and drained bearing and sliding resistances have not changed. Nevertheless, in addition to verification of the undrained sliding resistance in MFA and RFA, it still has to be checked that $R_{tud,base} \leq 0.4 \cdot N_{rep}$ ($R_{tud,base}$: design undrained base resistance; N_{rep}: representative value of the force acting normal to the foundation base (considered as favourable action)). This condition limits the load inclination when there is an irregular bearing surface with poor contact between the base of the foundation and the ground and, thus a reduced contact area, to ensure that simultaneous shearing and bearing failure does not occur. This limit corresponds to a maximum load inclination angle of 21.8° in such a design situation.

In case of eccentrically loaded spread foundations the new Eurocode 7 clearly distinguishes between the limit states of overturning and toppling. Overturning involves failure of the ground caused by rotation of the footing, whereas toppling describes a pure loss of static equilibrium without failure of the ground.

According to Subclause 5.6 the verification against overturning is covered by the bearing resistance verification. It is stated further on that the designer should note the following:

- Reduction of the plan area A to the effective plan area A' should be limited so that rotation does not cause a limit state in the foundation or the overlying structure;
- National Annexes can provide limiting values for the design eccentricity in the ULS;
- Precautions should be taken in the design if the eccentricity exceeds 1/3 of the footing width (or length) or 0.59 times the foundation radius.

It is also indicated that numerical methods can be more appropriate than the conventional bearing resistance formulae if the eccentricity is large.

For verification of the limit state of toppling reference is made to Part 1 and EN 1990. The verification includes a comparison of design stabilizing and destabilizing moments.

Finally, Subclause 5.6 provides guidance on ULS verification by prescriptive rules, testing and the observational method.

4.3 Verification of the serviceability limit state

Not many changes have been made to the verification of the serviceability limit state, which is covered in Subclause 5.7. Nevertheless, a clear distinction is now made between settlement and tilting caused by load eccentricity.

For eccentrically loaded foundations it shall also be verified that the load eccentricity remains within certain limits to confine the occurence of a physical gap at the edge of the foundation (see Table 3).

Table 3. Limits of the representative load eccentricity in SLS verification (Table 5.3, prEN 1997-3:2023).

Loading effects	Strip foundation	Circular foundation	Rectangular foundation
Permanent action effects only (No tension gap)	$\frac{e_B}{B} \leq \frac{1}{6}$	$\frac{e}{R} \leq \frac{1}{4}$	$\frac{e_L}{L} + \frac{e_B}{B} \leq \frac{1}{6}$
Permanent and variable action effects	$\frac{e_B}{B} \leq \frac{1}{3}$	$\frac{e}{R} \leq 0{,}59$	$\left[\frac{e_L}{L}\right]^2 + \left[\frac{e_B}{B}\right]^2 \leq \frac{1}{9}$

5 DESIGN EXAMPLE

The application of the design procedure outlined above will be illustrated using the example of a spread foundation under combined loading embedded in sand. For this purpose Example A2 prepared by CEN/TC250/SC7TG B2 in the course of analysing the applicability of the new Eurocode 7 (Bogusz, 2022) was selected and slightly modified. Figure 4 shows the design situation. In the following, only the ULS verification is presented.

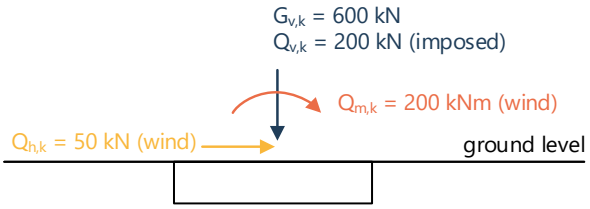

Figure 4. Design situation of a spread foundation on sand according to TG B2 example A2 by Bogusz (2022).

The cast-in-place square footing (weight density 25 kN/m³) has a width of 1.45 m and a thickness of 1.0 m which is equal to the embedment depth. The ground comprises a medium dense silty sand to significant depth and the groundwater level is located at the footing base. The representative weight density of the soil is 19 kN/m³ above and 9 kN/m³, the buoyant weight density, below groundwater level. The peak effective angle of internal friction of the silty sand is 39°. The foundation carries a vertical central permanent load of 600 kN, an imposed central vertical variable load of 200 kN, a horizontal wind load of 50 kN and a moment due to wind of 200 kNm. In the following, the ULS of the foundation is verified for Consequence Class 2 (CC2).

Table 4 summarizes the partial factors adopted in the various MFA and RFA approaches recommended for CC2 (see Section 4.2). In Combination (e) (RFA/VC4) the factor γ_Q results from $\gamma_Q = \gamma_Q/\gamma_E = 1.5/1.35 = 1.11$ (see EN 1990, Table A.1.8).

Table 4. Partial factors for the design example for the different combinations.

	MFA			RFA	
	a	b	c	d	e
	VC1	VC3	VC1	VC1	VC4
γ_G	1.35	1.0	1.35	1.35	1.0
$\gamma_{G,fav}$	1.0	1.0	1.0	1.0	1.0
γ_Q	1.5	1.3	1.5	1.5	1.11
γ_E	1.0	1.0	1.0	1.0	1.35
$\gamma_{\tan\varphi,p}$	1.0	1.25	1.25	1.0	1.0
$\gamma_{\tan\delta}$	1.0	1.25	1.25	1.0	1.0
γ_{RN}	1.0	1.0	1.0	1.4	1.4
γ_{RT}	1.0	1.0	1.0	1.1	1.1

To determine the representative load, combination factors according to Table A.1.7 of EN 1990 need to be considered, which are $\psi_0 = 0.7$ for imposed loads on buildings and $\psi_0 = 0.6$ for wind actions. With that, the following two load combinations were considered here for the bearing resistance verification: LC1 when the imposed load is the leading variable action and LC2 when wind effects are the leading variable actions (horizontal load and moment resulting from the same source). For the sliding resistance, load case LC3 is used with the permanent load assumed to act favourably ($\gamma_{G,fav}$ = 1.0 for all combinations). Since only wind effects are considered, the imposed load must be neglected.

Table 5 presents the resultant design loads for bearing and sliding resistance verification. For bearing resistance only the LC2 design loads are provided. The table also indicates which value (representative or design, unfactored or factored) of the soil shear strength (tan φ') and the strength in the footing interface (tan δ) must be considered. Note that the footing is cast-in-place so tan δ = tan φ'.

Table 5. Design loads for bearing resistance (LC2 only) and for sliding resistance (LC3) verification and relevant strength parameters for soil and footing interface (all numbers are rounded).

	MFA			RFA	
	a	b	c	d	e
	VC1	VC3	VC1	VC1	VC4
Design loads for bearing resistance [kN] or [kNm]					
$G_{v,d}$	881	653	881	881	653
$Q_{v,d}$	300	260	300	300	222
$Q_{h,d}$	45	39	45	45	33
$Q_{m,d}$	225	195	225	225	167
Design load for sliding resistance [kN]					
T_d	75	65	75	75	75
Relevant shear strength [-]					
$\tan\varphi'_{rep}$	-	-	-	0.81	0.81
$\tan\varphi_d$	0.81	0.65	0.65	-	-
$\tan\delta_{rep}$	-	-	-	0.81	0.81
$\tan\delta_d$	0.81	0.65	0.65	-	-

Table 6 shows the results of the design verifications for the assumed footing width of 1.45 m. Figure 5 illustrates these results by comparing the utilization achieved by the different combinations (a) to (e). The utilization is defined as the ratio of N_d/R_{Nd} and T_d/R_{Td}.

The results indicate that for this design example the RFA, with combinations (d) and (e), leads to consistent results for both the bearing and sliding resistance verification. For MFA, combination (a), in which the shear strength is not factored, leads to a much lower utilization than combination (b), in which the strength and the variable actions are factored, and so combination (b) controls the design in this case. Combination (c), in which both the strength and all the actions are factored and which can be used alternatively to (a) and (b) (see Table 2), leads to the highest utilization in MFA and hence to more conservative designs.

Table 6. Design values of effects of actions and resistances as well as resultant utilization for bearing resistance and sliding resistance verifications (all numbers are rounded).

	MFA			RFA	
	a	b	c	d	e
	VC1	VC3	VC1	VC1	VC4
Bearing resistance verification					
N_d	1181	913	1181	1181	1181
R_{Nd}	3738	1634	1744	2670	2670
N_d/ R_{Nd}	**0.32**	**0.56**	**0.68**	**0.44**	**0.44**
Sliding resistance verification					
T_d	75	65	75	75	75
R_{Td}	528	423	423	480	480
T_d/ R_{Td}	**0.14**	**0.15**	**0.18**	**0.16**	**0.16**

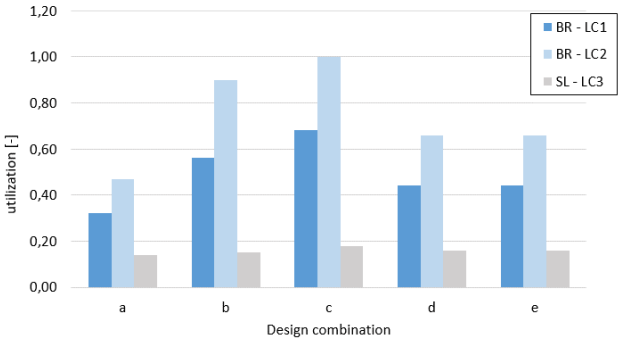

Figure 5. Comparison of the utilization achieved for the different combinations of partial factors for bearing resistance (BR) and sliding resistance (SR).

6 CONCLUSIONS

This paper addresses the design of spread foundations according to the new Eurocode 7. Overall, it can be stated that the design methodology has not changed in comparison to the current version of the code. On the other hand, improvements have been reached e.g. by a clear and unified structure of the code, by an increased harmonization in regard to the calculation of the bearing resistance, by the explicit distinction between soil/fill and rock and by a significantly extended informative Annex B including more calculation models.

Also the new code allows sufficient flexibility to accommodate national design practices and traditions through modification of existing or inclusion of additional tables with NDP values. However, the design example showed that the different alternatives of combining the partial factors lead to significant differences in the design results. So, these factors need to be defined with great care reflecting national design requirements and experiences.

REFERENCES

Bogusz, W. (2022). Report on the design example A2: Spread foundation on sand. Internal report for CEN/TC250/SC7/TGB2. Unpublished.

Brinch Hansen, J. (1970). A revised and extended formula for bearing capacity. Bulletin No. 28, pp. 5-11. The Danish Geotechnical Institute, Copenhagen.

Caquot, A. and Kerisel, J. (1953). Sur le terme de surface dans le calcul des fondations en milieu pulvérulent, *Proceedings 3rd International Conference on Soil Mechanics and Foundation Engineering*, Zurich, Vol. 1, pp. 336-337.

EN 1990-1:2023. Eurocode - Basis of structural and geotechnical design - Part 1: Design of new structures. Draft May 2023. CEN/TC250/SC10.

EN 1997-1:2004 + AC:2009 + A1:2013. Eurocode 7: Geotechnical design - Part 1: General rules. CEN/TC250/SC10.

M515/CEN/TC250/SC7/PT4 (2020). Background document on Clause 5: Spread Foundations. Unpublished.

prEN 1997-1:2023. Eurocode 7: Geotechnical design - Part 1: General rules. Draft for Formal Vote, August 2023. CEN/TC 250/SC 7/WG 1 "Evolution of 1997 series".

prEN 1997-2:2023. Eurocode 7: Geotechnical design - Part 2: Ground properties. Draft for Formal Vote, August 2023. CEN/TC 250/SC 7/WG 1 "Evolution of 1997 series".

Paikowsky, S. G.; Canniff, M. C.; Lesny, K.; Kisse, A.; Amatya, S.; Muganga, R. (2010). LRFD Design and Construction of Shallow Foundations for Highway Bridge Structures. NCHRP Report 651, National Cooperative Highway Research Program Transportation Research Board. Washington, D.C., National Academies Press.

prEN 1997-3:2023. Eurocode 7 - Geotechnical design - Part 3: Geotechnical structures. Draft May 2023 after Formal Enquiry. CEN/TC250/SC10.

Terzaghi, K. (1943). *Theoretical Soil Mechanics.* John Wiley & Sons.

Vesic, A. S. (1973). Analysis of ultimate loads of shallow foundations. *Journal of Soil Mechanics and Foundation Division*, 99(1): 45-76.

Vesic, A.S. (1975) Bearing capacity of shallow foundations. In *Foundation Engineering Handbook*, H.F Winterkorn and H.Y. Fang (eds.), pp.121-147. Van Nostrand Reinhold Co..

Proceedings of the XVIII ECSMGE 2024
GEOTECHNICAL ENGINEERING CHALLENGES
TO MEET CURRENT AND EMERGING NEEDS OF SOCIETY
© 2024 the Authors
ISBN 978-1-032-54816-6
DOI 10.1201/9781003431749-324
Open Access: www.taylorfrancis.com, CC BY-NC-ND 4.0 license

ECSMGE 24
XVIII EUROPEAN CONFERENCE ON SOIL MECHANICS AND GEOTECHNICAL ENGINEERING

A new interpretation method of rapid pile load testing: verification through comparison with static load test

Une nouvelle méthode d'interprétation des essais rapides de charge sur pieux: vérification par comparaison avec un essai de charge statique

S. Lin*, S. Kamei, I. Yamamoto
Jibanshikenjo Co. Ltd., Tokyo, Japan

K. Watanabe
Aichi Institute of Technology, Nagoya, Japan

T. Matsumoto
Kanazawa University, Kanazawa, Japan

N. Shkodrani
Polytechnic University of Tirana, Tirana, Albania

s_rin@mail.jibanshikenjo.co.jp

ABSTRACT: Hybridnamic Rapid Load Test (Hybridnamic RLT) and Static Load Test (SLT) were carried out on three identical open-ended steel pipe piles (SPPs), named Piles No. 2, No. 4 and No. 5, in the Jibanshikenjo test yard at Sashima, Ibaraki Prefecture, Japan. The test piles had an outer diameter of 318.5 mm, a wall thickness of 6.6 mm and an embedment length of 11.0 m. In the RLTs, the classic UnLoading Point Connection (ULPC) method and a new interpretation method: UnLoading Point Connection method invoking Case Method (ULPC_CM) proposed by the authors, were used to obtain "static" load-displacement curves. According to the Japanese RLT standards, the relative loading duration $T_r = t_L/(2L/c)$ (t_L is loading duration, L is pile length, c is bar wave velocity in the pile) shall be greater than 5. In Pile No. 4, RLTs with T_r = 5 were caried out after SLT. In Pile No. 2, RLTs with T_r = 3 were carried out intentionally prior to SLT. In Pile No. 5, RLTs with T_r = 3 were caried out after SLT. In this paper, test conditions and test results are presented in detail. It will be shown that the static load-displacement curves from the ULPC method overestimate the SLT results, while the static load-displacement curves from the ULPC_CM method conform to the SLT results well even if T_r decreased to 3.

RÉSUMÉ: Des tests de charge rapide Hybridnamic (Hybridnamic RLT) et des tests de charge statique (SLT) ont été réalisés sur trois pieux en acier à extrémité ouverte identiques (SPP), nommés Pieux n°2, n°4 et n°5, dans la cour d'essai de Jibanshikenjo à Sashima, préfecture d'Ibaraki, au Japon. Les pieux d'essai avaient un diamètre extérieur de 318,5 mm, une épaisseur de paroi de 6,6 mm et une longueur d'enfouissement de 11,0 m. Dans les RLT, la méthode classique de Connexion du Point de Déchargement (ULPC) ainsi qu'une nouvelle méthode d'interprétation, la méthode de Connexion du Point de Déchargement invoquant la Méthode de Case (ULPC_CM) proposée par les auteurs, ont été utilisées pour obtenir des courbes de charge-déplacement "statiques". Conformément aux normes japonaises en matière de RLT, la durée relative de chargement T_r doit être supérieure à 5. Dans le Pieu n°4, des RLT avec T_r = 5 ont été effectués après le SLT. Dans le Pieu n°2, des RLT avec T_r = 3 ont été intentionnellement réalisés avant le SLT. Dans le Pieu n°5, des RLT avec T_r = 3 ont été effectués après le SLT. Dans cet article, les conditions d'essai et les résultats sont présentés en détail. Il sera démontré que les courbes de charge-déplacement statiques obtenues par la méthode ULPC surestiment les résultats du SLT, tandis que les courbes de charge-déplacement statiques obtenues par la méthode ULPC_CM sont en bonne concordance avec les résultats du SLT, même lorsque T_r est réduit à 3.

Keywords: Rapid load test; static load test; steel pipe pile; interpretation method; case study.

1 INTRODUCTION

The first standards for the method for Rapid Load Test (RLT) of single piles were published in 2002 (JGS, 2002). In the standards, load test with relative loading duration $T_r \geqq 5$ is defined as RLT, because it is thought that the wave propagation phenomena can be negligible. In the conventional interpretation method, UnLoading Point Connection method (ULPC), the pile body is modelled as a rigid single mass.

Aiming at widening the range of application of RLT, a new signal interpretation method, the

UnLoading Point Connection method invoking Case method (ULPC_CM) was proposed (Lin et al., 2023).

In this study, RLTs were carried out on three steel pipe piles (SPPs) with different relative loading durations, T_r = 5 and 3. Furthermore, Static Load Test (SLT) and RLT were carried out in different order. Load-displacement curves obtained from SLT and RLT using two interpretation methods, ULPC and ULPC_CM, were compared to examine the advantages and reliability of the new interpretation method over the conventional ULPC method.

2 OUTLINE OF PILE LOAD TESTS

2.1 Site conditions

Load tests were carried out in Sashima test yard of Jibanshikenjo Co. Ltd., Japan. Figure 1 shows the arrangements of soil investigations and test piles. One Standard Penetration Test (SPT) and Electric Cone Penetration Tests (CPTs) were carried out at just points of test piles.

Figure 2 shows the results of soil investigations, and embedment of the instrumented test piles. SPT *N*-values from the ground level to a depth z = 5 m are 1 to 3. Below this depth, *N*-value increases with depth. Below z = 10 m, a sand layer with $N \approx 33$ exists. The test piles were driven to z = 11 m. Groundwater table is at z =3.5 m. It can be seen from the distributions of SPT-*N* and CPT q_t (cone resistance corrected for pore pressure at filter) that ground conditions are similar in each test pile location.

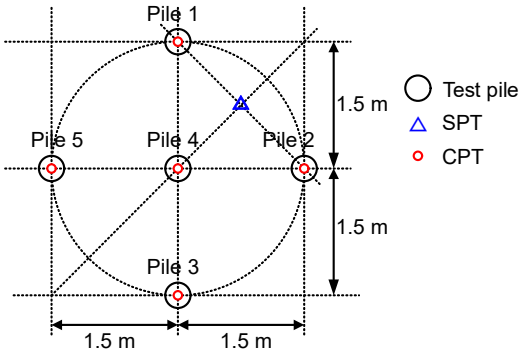

Figure 1. Locations of SPT, CPTs and test piles.

2.2 Test piles

Table 1 shows the specifications of 5 test steel pipe piles (SPPs). Channel steels were welded on the outer surface of the test SPPs for protecting strain gages and accelerometers.

Table 1. Specifications of test piles.

Item	Value	
	Original	with protection
Pile length, L (m)	11.8	
Embedment length, L_d (m)	11.0	
Outer diameter, D_o (mm)	318.5	
Inner diameter, D_i (mm)	305.3	
Wall thickness, t_w (mm)	6.6	
Cross-sectional area, A (m^2)	0.00651	0.00926
Young's modulus, E (GPa)	205	
Density, ρ (ton/m^3)	7.81	
Bar wave velocity, c (m/s)	5123	
Mass, m (ton)	0.610	0.819

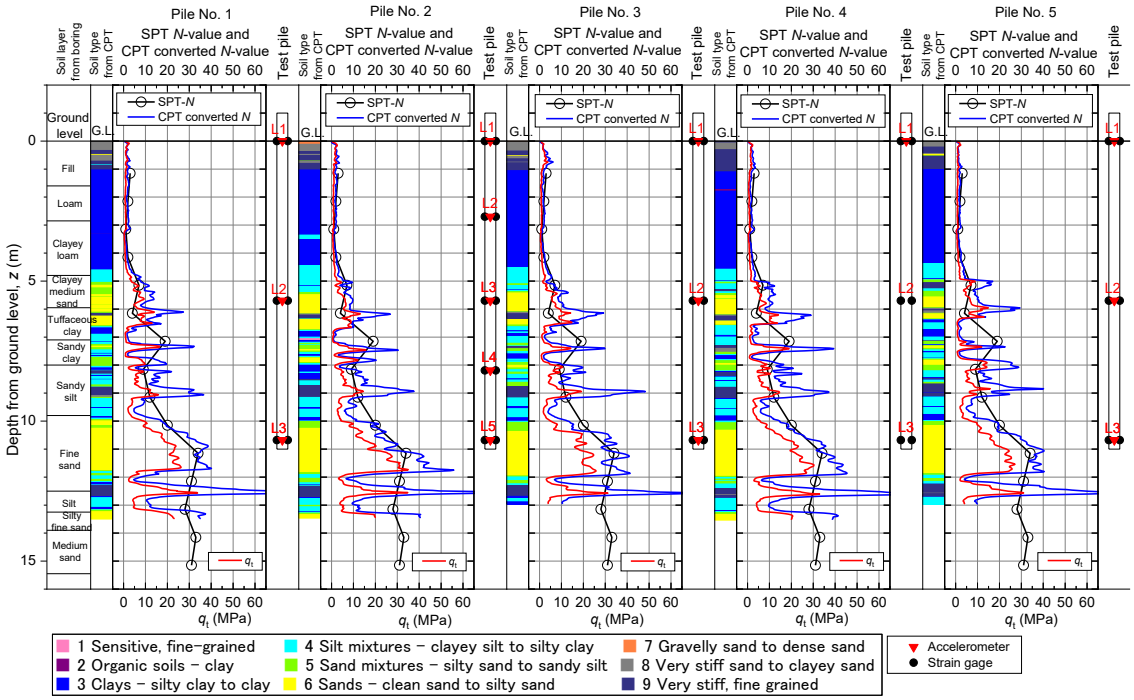

Figure 2. Profiles of soil layers, SPT N-values and CPT q_t, together with instrumented test piles.

Table 2. List of test sequence.

Pile No.	Driving date (DLT)	Curing (day)	DLT	Curing (day)	Load test		Curing (day)	Load test	
1	2022/05/11	1	2022/05/12	30	RLT (T_r = 5)	2022/06/11	---	---	
2	2022/05/11	1	2022/05/12	33	RLT (T_r = 3)	2022/06/14	184	SLT	2022/12/15
3	2022/05/12	---	---	32	RLT (T_r = 4)	2022/06/13	---	---	
4	2022/05/12	---	---	25	SLT	2022/06/07	8	RLT (T_r = 5)	2022/06/15
5	2022/05/12	---	---	279	SLT	2023/02/15	140	RLT (T_r = 3)	2023/07/05

2.3 Test cases

Table 2 shows the test sequence of each test pile. Dynamic Load Tests (DLTs) were carried out during initial pile driving. After curing period of 1 day, DLTs were carried out again on Pile No. 1 and Pile No. 2 to grasp "set-up" phenomena. RLTs with the relative loading duration $T_r = t_L/(2L/c) = 5$ (t_L is the loading duration, L is pile length, c is bar wave velocity in the pile) were carried out on Pile No. 1 and Pile No. 4, according to the JGS standards (JGS, 2002) in which $T_r \geqq 5$ is required. RLTs with $T_r = 3$ were carried out on Piles No. 2 and No. 5 intentionally. If RLT with shorter T_r is reasonable, it will be possible to apply RLT to piles with longer length and greater bearing capacity using the current RLT devices.

3 INTERPRETATION METHODS OF RLT

In this section, interpretation methods of RLT signals used in this research are described.

3.1 ULPC method

The ULPC method is an extension method of UnLoading Point (ULP) method. In ULPC, the pile is treated as a rigid single mass. To obtain soil resistance R_{soil}, the pile inertial force $R_a = m\alpha$ (m = the pile mass and α = acceleration at pile head) is subtracted from the rapid load F_{rapid}. ULP is the point of R_{soil} at the maximum pile displacement w, where pile velocity v = 0. Hence, R_{soil} at ULP is equal to the static soil resistance R_w. By connecting ULPs from multiple blows, static load-displacement relation is easily obtained.

3.2 ULPC_CM method (Lin et al., 2023)

The Case method (Raushe et al., 1985) is a method based on the one-dimensional stress-wave theory, in which the penetration resistance R_t (= R_{soil}) of a pile during driving is estimated.

First, the downward traveling wave F_d and the upward traveling wave F_u are calculated from the measured dynamic signals (axial force F and pile velocity v) by means of Eqs. (1) and (2), respectively; then, by using Eq. (3), the time variation of R_t (= R_{soil}) is obtained (Figure 3):

$$F_d(x_m,t) = \frac{F(x_m,t) + Z \cdot v(x_m,t)}{2} \quad (1)$$

$$F_u(x_m,t) = \frac{F(x_m,t) - Z \cdot v(x_m,t)}{2} \quad (2)$$

$$R_t(x_m,t) = F_d\left(x_m, t - \frac{L_m}{c}\right) + F_u\left(x_m, t + \frac{L_m}{c}\right) \quad (3)$$

where, x = coordinate along the pile axis (pile head = 0), x_m = measurement position, L_m = pile length from x_m to pile tip, Z = impedance (=EA/c).

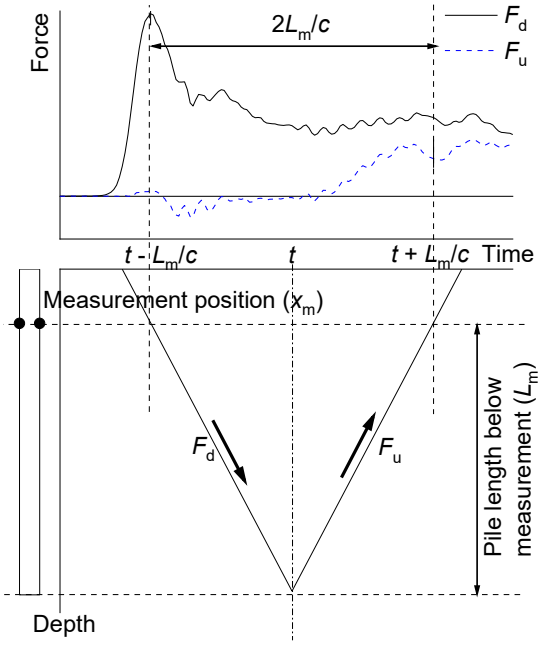

Figure 3. Case method (Raushe et al. 1985).

The Case method evaluates the penetration resistance of the pile during driving, but the load-displacement relationship of the pile cannot be obtained by this method alone. Since the Case method is based on the one-dimensional wave theory, the penetration resistance of the pile can be evaluated correctly regardless of the pile length.

In the ULPC_CM method, multiple blows (rapid load tests) are applied to a pile. The time variation of soil resistance R_{soil} is obtained from the Case method, and the time variation of pile displacement w is directly measured. Hence, $R_{soil} - w$ relation is easily obtained. R_{soil} at the maximum pile displacement can be regarded as the static resistance R_w. Similar to the ULPC method, static load-displacement curve is constructed by connecting ULPs from the multiple blows.

As the ULPC_CM method is based on the one-dimensional stress-wave theory, it has the advantage of not requiring correction for pile inertia R_a. Hence, the ULPC_CM method would be applied to RLTs on piles with $T_r < 5$.

4 COMPARISON OF RESULTS OF SLT AND RLT

4.1 SLT

SLTs were carried out on Piles No. 4, No. 2 and No. 5. The results of SLT will be shown in comparison with the RLT results later.

4.2 RLT (Pile No.4, $T_r = 5$)

In Pile No. 4, RLTs were carried out after SLT. In RLTs, a hammer mass m_h = 3.5 ton was used and 8 blows (RLTs) were applied to the pile with increasing drop height h from 0.03 to 0.83 m. Loading duration t_L was adjusted by changing the stiffness of cushion placed on the pile head to have $T_r \geqq 5$.

Figure 4 shows the measured dynamic signals, rapid load F_{rapid}, pile head displacement w, velocity v and acceleration α, in the RLT at h = 0.83 m (8th blow). In the figure, soil resistance R_{soil} (ULPC) from the ULPC method, R_{soil} (ULPC_CM) from the ULPC_CM method are shown together with F_{rapid}. Furthermore, F_d and F_u are also shown.

R_{soil} (ULPC_CM) at the maximum w where $v = 0$ is defined as the static resistance R_w (R_{ULP}) in a similar way to the ULPC method. Static load-displacement relation can be obtained by connecting R_{ULP} from ULPC_CM from multiple blows (RLTs).

Figure 5 shows the static load-displacement relations from ULPC and ULPC_CM compared with the SLT result. It is seen from the RLT results that the static soil resistance R_w from ULPC is larger than that from ULPC_CM. The load-displacement relation from ULPC_CM matches with the SLT result very well.

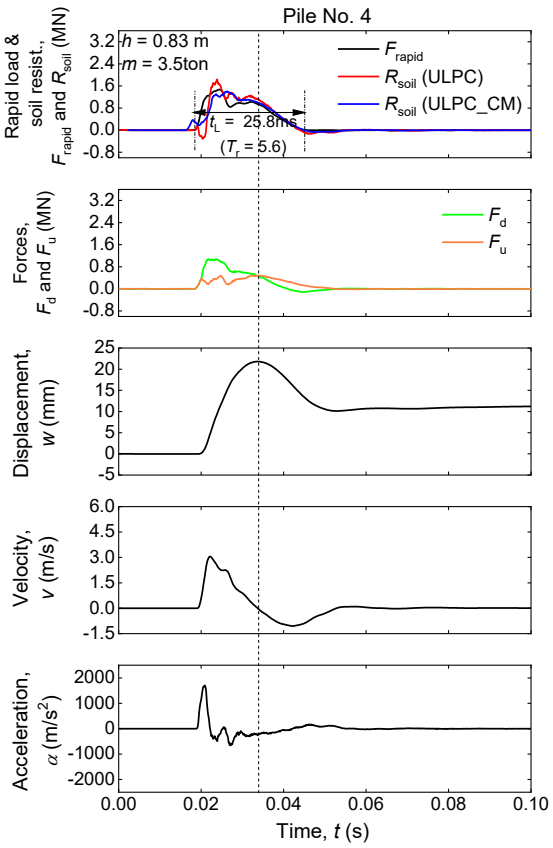

Figure 4. RLT signals (Pile No. 4, h = 0.83 m).

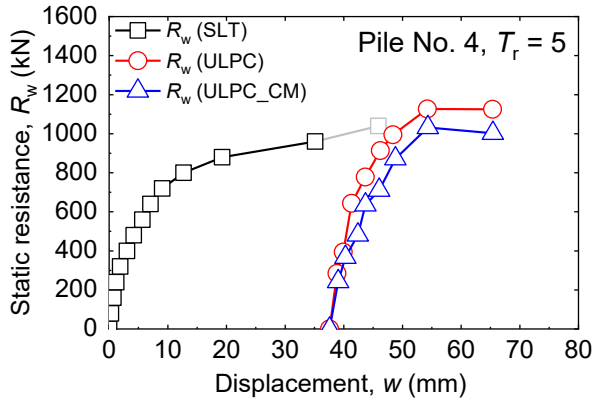

Figure 5. Comparison of load-displacement curves from SLT, RLTs with ULPC and ULPC_CM (Pile No. 4).

4.3 RLT (Pile No.2, $T_r = 3$)

In Pile No. 2, SLT was carried out after RLTs. In RLTs, a hammer mass m_h = 0.95 ton was used and 12 blows (RLTs) with $T_r = 3$ were applied to the pile with increasing drop height h from 0.02 to 3.84 m.

Figure 6 shows the measured F_{rapid}, w, v and α in the RLT in the 8th blow (h = 1.35 m) with T_r = 3.2. In the figure, R_{soil} (ULPC) and R_{soil} (ULPC_CM) are

shown together with F_{rapid}. Furthermore, F_d and F_u are also shown.

Figure 7 shows the static load-displacement relations from ULPC and ULPC_CM compared with SLT result. The load-displacement relation from ULPC_CM matches with the SLT result very well again, even for a shorter $T_r \approx 3$.

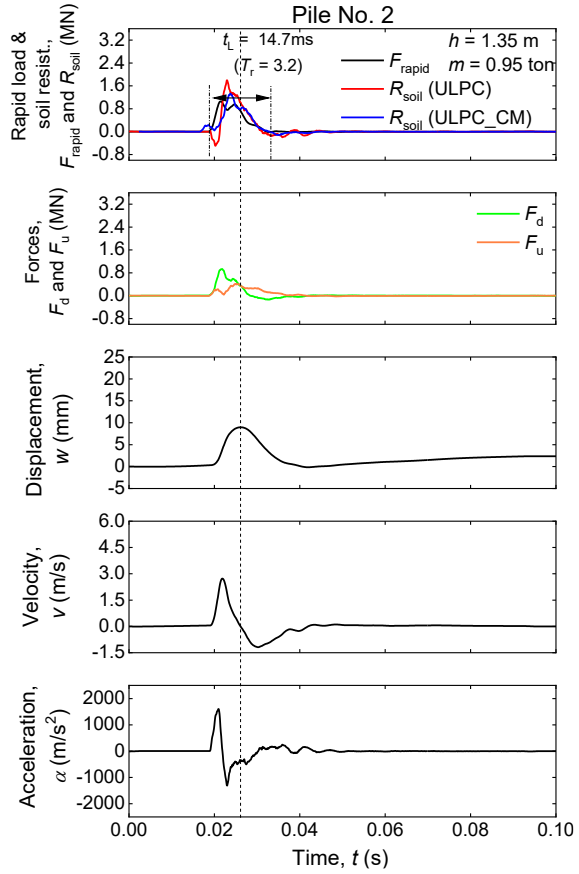

Figure 6. RLT signals (Pile No. 2, h = 1.35 m).

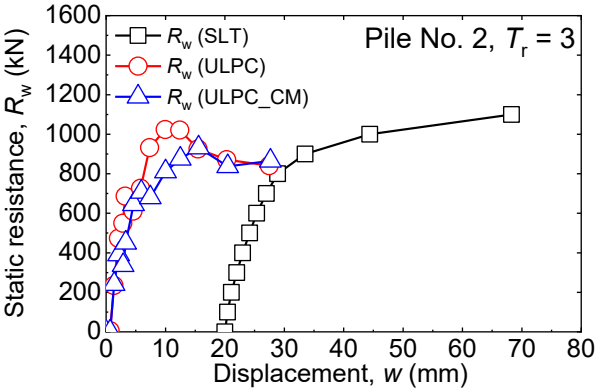

Figure 7. Comparison of load-displacement curves from SLT, RLTs with ULPC and ULPC_CM (Pile No. 2).

4.4 RLT (Pile No.5, T_r = 3)

In Pile No. 5, RLTs were carried out after SLT. In RLTs, a hammer mass m_h = 0.95 ton was used and 13 blows (RLTs) with T_r = 3 were applied to the pile with increasing drop height h from 0.02 to 3.84 m.

Figure 8 shows the measured F_{rapid}, w, v and α in the RLT in the 13th blow (h = 3.84 m) with T_r = 3.5.

Figure 9 shows the static load-displacement relations from ULPC and ULPC_CM compared with SLT result. The load-displacement relation from ULPC_CM matches with the SLT result very well again, even for $T_r \approx 3$.

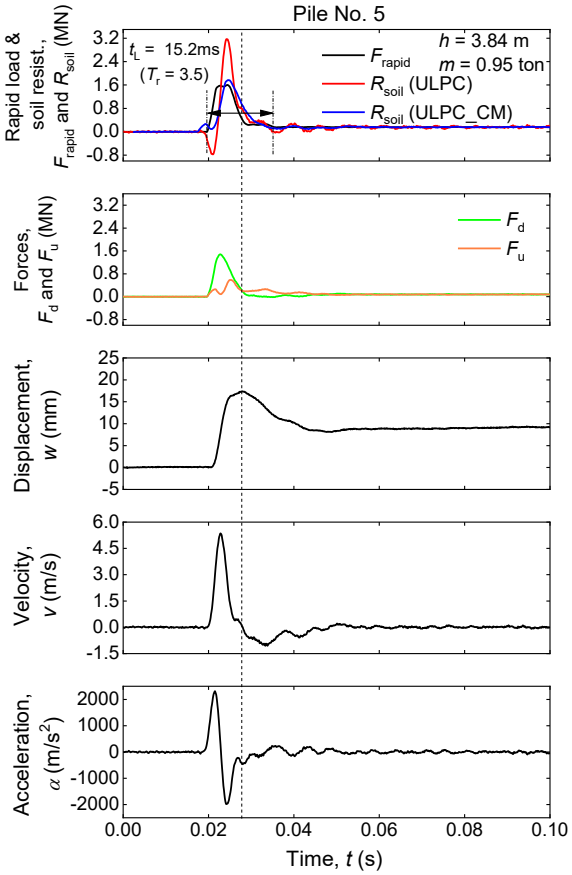

Figure 8. RLT signals (Pile No. 5, h = 3.84 m).

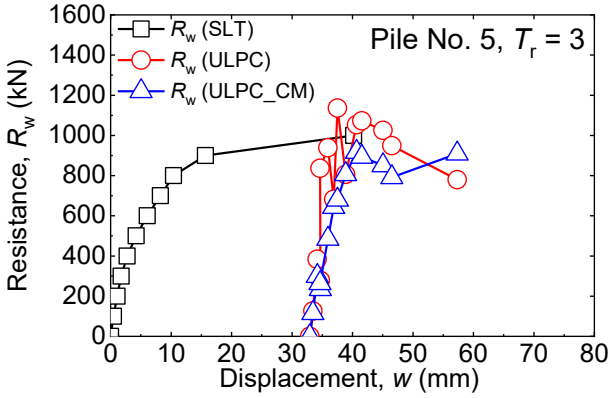

Figure 9. Comparison of load-displacement curves from SLT, RLTs with ULPC and ULPC_CM (Pile No. 5).

4.5 Comparison of results of RLTs having different relative loading durations

Figure 10 shows the comparison of load-displacement curves from SLT and RLTs with ULPC interpretation for the three test piles. ULPC result in case of $T_r = 5$ is consistent with the SLT result. However, the results in cases of $T_r = 3$ fluctuate and overestimate the SLT result. This suggests that ULPC is applicable for RLTs with $T_r \geqq 5$ as specified in the JGS standards.

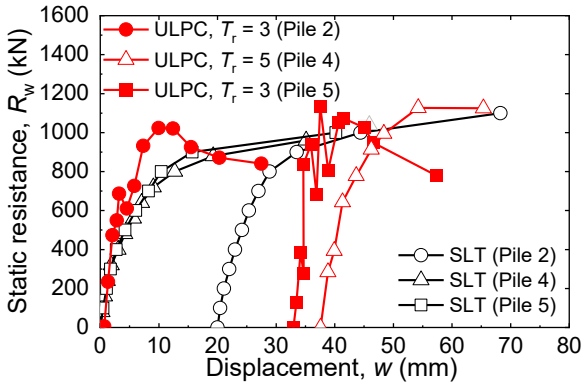

Figure 10. Comparison of load-displacement curves from SLT, RLTs with ULPC.

Figure 11 shows the comparison of load-displacement curves from SLT and RLTs with ULPC_CM interpretation for the three test piles.

Despite a slight underestimation, the load-displacement curves in both cases of $T_r = 3$ and 5 are comparable to the SLT results.

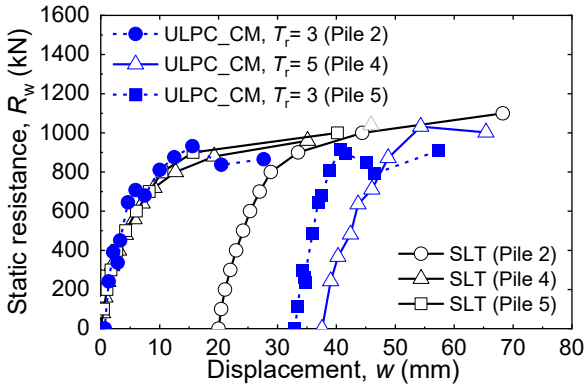

Figure 11. Comparison of load-displacement curves from SLT, RLTs with ULPC_CM.

Figure 12 shows an example of application ranges of RLTs with different T_r in case of m_h = 100 ton and h = 3.00 m. The stiffness of the cushion is varied so that required T_r is satisfied.

With the widened range of application of RLT by decreasing T_r in RLT with ULPC_CM method, it is possible to apply RLTs to a longer and higher capacity pile with the same loading device. On the other hand, it is possible to carry out RLT with the same load by using a lighter hammer, providing a more economical and convenient testing option.

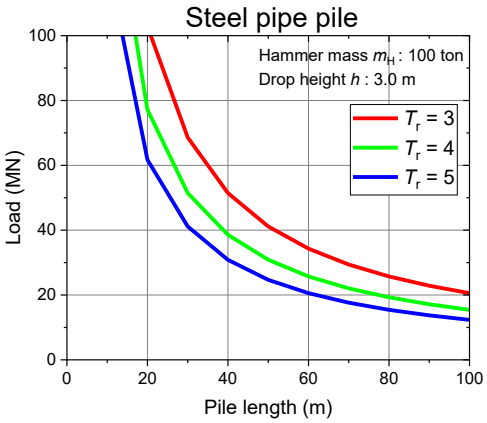

Figure 12. Application ranges of RLTs with different T_r.

5 CONCLUSIONS

In this study, comparative RLTs and SLTs were carried out on driven steel pipe piles to examine the validity of the new interpretation methods: ULPC_CM.

RLTs with $T_r = 5$ were carried out according to the JGS Standards in which T_r is required to be equal or greater than 5. Furthermore, RLTs with $T_r = 3$ were carried out to widen the application of RLT.

The static load-displacement relations from the ULPC_CM method matched with the SLT results very well even in cases of $T_r = 3$, regardless of order of SLT and RLT.

It can be said that it is possible to apply the RLT with ULPC_CM method to piles with longer length and greater bearing capacity using the current RLT devices.

The authors are planning to conduct similar comparisons between RLTs and SLT for different types of piles to examine the applicability of ULPC_CM method in the near future.

REFERENCES

Japanese Geotechnical Society (JGS) (2002) JGS 1815-2002 Method for Rapid Load Test of Single Piles.

Lin, S., Kamei, S., Yamamoto, I. and Matsumoto, T. (2023). Hybridnamic rapid load testing with UnLoading Point Connection method invoking Case method. *Proc. the 17th Asian Regional Conference on Soil Mech. and Geotech. Engineering 2023 (Smart Geotechnics for Smart Societies)*, Nur-Sultan, pp. 1425-1429.

Raushe, F., Goble, G. and Likins, G. E. Jr. (1985). Dynamic determination of pile capacity. *ASCE Jour. Geotech. Div.*, 111(3), pp. 367-383. DOI:10.1061/(ASCE)0733-9410(1985)111:3(367).

Proceedings of the XVIII ECSMGE 2024
GEOTECHNICAL ENGINEERING CHALLENGES
TO MEET CURRENT AND EMERGING NEEDS OF SOCIETY
© 2024 the Authors
ISBN 978-1-032-54816-6
DOI 10.1201/9781003431749-325
Open Access: www.taylorfrancis.com, CC BY-NC-ND 4.0 license

ECSMGE 24
XVIII EUROPEAN CONFERENCE ON SOIL MECHANICS AND GEOTECHNICAL ENGINEERING

Various approaches to derive state of tailings materials on the basis of shear wave velocity measurement

Différentes approches pour dériver l'état des matériaux de résidus sur la base de la mesure de la vitesse des ondes de cisaillement

M.J. Lipiński*, M. Wdowska
Warsaw University of Life Sciences-WULS, Institute of Civil Engineering, Warsaw, Poland

I. Puspitaningrum
Warsaw University of Life Sciences-WULS, Doctoral School, Warsaw, Poland

**miroslaw.lipinski@wp.pl*

ABSTRACT: Undrained response of cohesionless soils to cyclic or monotonic loading might lead to liquefaction phenomenon, especially when material is in relatively loose or medium dense state. Such situations are often encountered in case of tailings storage facilities with special reference to those constructed by upstream method. High sensitivity of tailings material to sample disturbance create strong promise to look for alternative approaches than conventional sampling. The method based on laboratory measurement of shear wave velocity (V_S) on reconstituted sample and combined with relevant V_S values determined on undisturbed material *in situ* deserves special attention since V_S reflects changes in state of stress and void ratio as well. The important issue of such approach is a formula which links shear wave velocity, void ratio and state of stress. The paper presents a three conceivable formulae which were derived on basis of comprehensive triaxial test program carried out on two batches of tailings with various amount of fines. Logarithm and various power function regressions were considered. After a brief explanation of the derivation basis for all the considered formulas, the results of projecting the correlation for the tailings profile were shown for selected granulation.

RÉSUMÉ: La réponse non drainée des sols sans cohésion à une charge cyclique ou monotone peut conduire à un phénomène de liquéfaction, en particulier lorsque le matériau est relativement lâche ou moyennement dense. De telles situations sont souvent rencontrées dans le cas d'installations de stockage de résidus, en particulier celles construites par la méthode en amont. La grande sensibilité du matériau des résidus à la perturbation de l'échantillon incite fortement à rechercher des approches alternatives à l'échantillonnage conventionnel. La méthode basée sur la mesure en laboratoire de la vitesse des ondes de cisaillement (*Vs*) sur l'échantillon reconstitué et combinée avec les valeurs VS pertinentes déterminées sur le matériau non perturbé in situ mérite une attention particulière puisque la *Vs* reflète également les changements dans l'état de contrainte et d'indice de vides. La question importante de cette approche est une formule qui relie la vitesse de l'onde de cisaillement, d'indice de vide et l'état de contrainte. L'article présente trois formules concevables qui ont été dérivées sur la base d'un programme d'essais triaxiaux complet réalisé sur deux lots de résidus avec différentes quantités de fines. Des régressions logarithmiques et diverses fonctions de puissance ont été prises en compte. Après une brève explication de la base de dérivation de toutes les formules considérées, les résultats de la projection de la corrélation sur le profil des résidus ont été montrés pour une granulation sélectionnée.

Keywords: Soil liquefaction; state of tailings material; shear wave velocity; fines content.

1 INTRODUCTION

Liquefaction of soil is one of the most challenging issues in geotechnical engineering. Accumulated experience concerning this subject during the last sixty years has shown that mechanism of liquefaction is similar in case of cyclic and monotonic loading (e.g. Casagrande, 1975). This might be one of the reasons why critical state approach to soil liquefaction is so popular among engineers. This concept assumes that initial state prior to undrained loading determines the type of response of cohesionless materials to undrained loading – dilative (safe) or contractive (unsafe) response associated with liquefaction. Laboratory experience proves that in case of coarse sand characterized by relatively small slope of steady state line (SSL) the third type of response can be noticed i.e. limited strain softening also associated with liquefaction of soil. Strain rate during load controlled tests in which such a response of material appears is very high, as in the case of full collapse behaviour. In Figure 1 this type of response is shown

in the form of stress-strain diaphragm, stress paths and excess pore pressure charts. The same characteristics are shown for comparison for sample that revealed slightly dilative response. It is worth to emphasize the very small difference in value of void ratio (Δe= 0.011) between the samples. This proves how important is accuracy of void ratio determination in liquefaction problems. Sampling of cohesionless soils is inevitably associated with sample disturbance resulting in change in void ratio which might convert response of soil. Therefore, there is a need to look for an alternative approach to get soil of representative state.

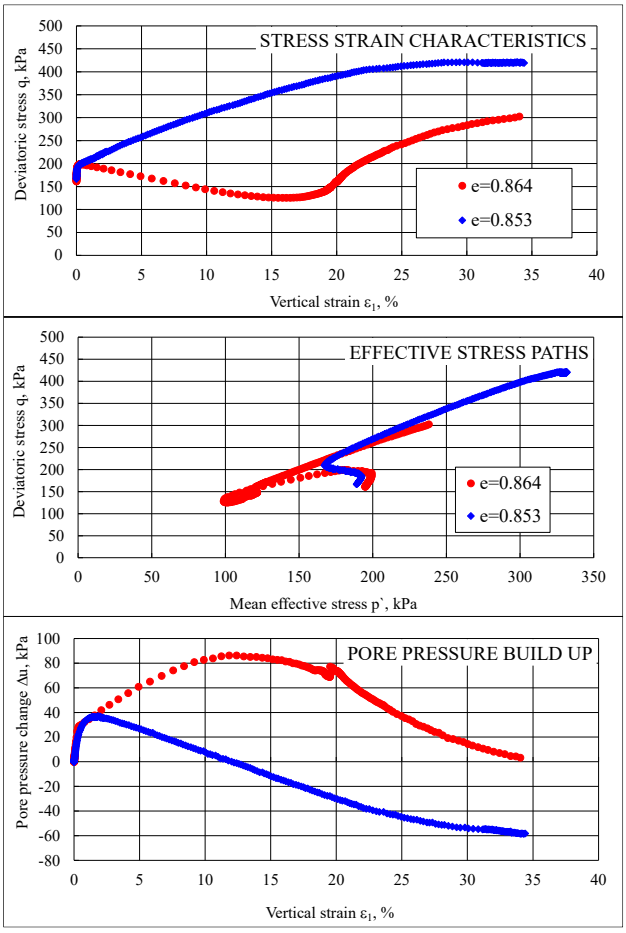

Figure 1. Sensitivity of undrained response of coarse sand to monotonic loading to small change in void ratio.

One of the conceivable solution of bypassing problems with sample disturbance is based on shear wave velocity measurement. The major argument for use of shear wave velocity (V_S) is that its value depends mainly on components of stress state and void ratio value i.e. both variables contributing to state of material. In addition shear wave velocity can be measured in the laboratory and in situ as well so that correlation obtained in the triaxial apparatus may be projected on a soil profile. Such combination of laboratory and field measurement is usually referred to as “hybrid method”. This approach is very convenient to use in case of tailings dams constructed by upstream method where liquefaction hazard is a major concern and high quality undisturbed sampling is not feasible. Additional difficulty associated with such constructions is considerable spatial variability of tailings materials containing various amount of fines. The latter controls compressibility characteristics and position of steady state lines which strictly contribute to the value of state parameter ψ (Been and Jefferies, 1985).

The procedure of evaluating void ratio distribution in the tailings profile on the basis of hybrid approach can be found in other authors' papers (e.g. Lipinski et al., 2023). It should be pointed out that relations between shear wave velocity and state of stress can be described by various formulae. In the further paragraphs of the paper application of hybrid method is presented with the use of three different relations among shear wave velocity, void ratio and stress components. At first, the results of most popular approach based on normalized shear wave velocity with respect to vertical effective stress are presented. Next, shear wave velocities were approximated against mean effective stress by logarithm and power function regressions.

2 LABORATORY TEST PROCEDURE

Triaxial tests were carried out on reconstituted specimens which were 50 mm in diameter and 100 mm in height. Triaxial cell with internal linking bars and high resolution proximity transducers for internal measurement of deformation were used for the test (Lipinski et al. 2020). Specimens were prepared by moist tamping by undercompaction method which enables preparation of samples in a wide range of void ratio, especially for loose state. When a triaxial cell was assembled, a specimen was saturated by back pressure until Skempton's parameter B exceeded value 0.96. After saturation specimens were consolidated anisotropically with zero lateral strain. When consolidation was terminated, shear wave velocity was measured. Piezoelectric transducer of bender type was used for sending and receiving the signals.

Two kinds of predominantly silicious tailings batches were tested which represented sand like behaviour and transition zone material. The batches contained respectively 10% and 36% of fines content i.e. material passing sieve diameter 0,075 mm.

Shear wave velocity $V_{S(VH)}$ in the field was measured during seismic cone tests (SCPTu).

2 NORMALIZED SHEAR WAVE VELOCITY

Most popular approach allowing to extract components representing void ratio and soil structure from measured value of shear wave velocity is its normalization with respect to vertical effective stress (Robertson et al., 1992). The following formula was proposed:

$$V_{S1} = V_S \left(\frac{Pa}{\sigma_v'}\right)^{0.25} \quad (1)$$

where:

V_{S1} - normalized shear wave velocity (m/s)

V_S - shear wave velocity (m/s)

σ'_v - vertical effective stress (kPa)

Pa - reference pressure (usually 100 kPa)

By normalization of V_S with respect to vertical effective stress a unique relationship between normalized shear wave velocity and void ratio can be achieved. Normalization can be done with respect not only to vertical effective stress but also with respect to both components of principal effective stress. The results of both approaches with characteristics showing relationship between normalized shear wave velocity and void ratio were presented in paper (Lipinski et al., 2017). The formulae linking void ratio with shear wave velocity and vertical effective stress were the following:

for tailings with 10% of fines:

$$e = \frac{343.57 - V_S\left(\frac{100}{\sigma_v'}\right)^{0.25}}{189.02} \quad (2)$$

for tailings 36% of fines:

$$e = \frac{472.38 - V_S\left(\frac{100}{\sigma_v'}\right)^{0.25}}{432.69} \quad (3)$$

The comparison of measured and calculated values of void ratio on the basis of the above formulae for both kinds of tailings is shown in Figure 2.

The obtained comparison reveals significant difference between two kinds of soil. For sandy materials with 10% of fines the values of void ratio predicted by trend line are in a good agreement with the measured ones. For tailings with 36% of fines the calculated values are substantially higher than the measured ones, especially for denser state.

4 APPROACH BASED ON FIT CURVES

The analysis of the laboratory test results allowed us to determine that the relationship between the shear wave velocity Vs and the mean effective stress p' can be reflected by a power function of the form:

$$V_s = Ap'^B \quad (4)$$

or a logarithmic function of the form:

$$V_s = Alnp' + B \quad (5)$$

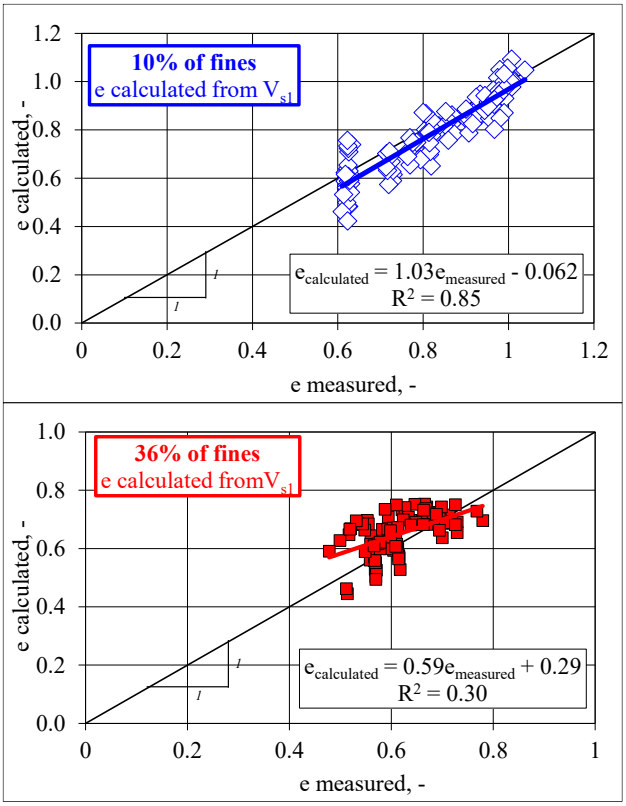

Figure 2. Calculated against measured values of void ratio on the basis of normalized shear wave velocity for material containing 10% and 36% of fines.

In order to show the differences between the two solutions, each of the above functions was determined for several ranges of void ratio and presented on a linear and logarithmic scale of the mean effective stress p'. Both types of regression have a high R-squared value - above 0.89 for the power function and above 0.92 for the logarithmic function. The data and the procedure for derivation of the formulae was presented in detail in authors' papers for power function (Lipinski and Wdowska, 2020) and for the logarithmic function (Lipinski and Wdowska, 2019), respectively. There is no clear answer to the question which function is better suited; function fit varies in different void ratio ranges. Due to the fact that the coefficient of the independent variable is proportional

to the void ratio, it is possible to obtain a procedure for determining the relationships enabling the calculation of the void ratio value. The procedure is shown in the diagram in Figure 3.

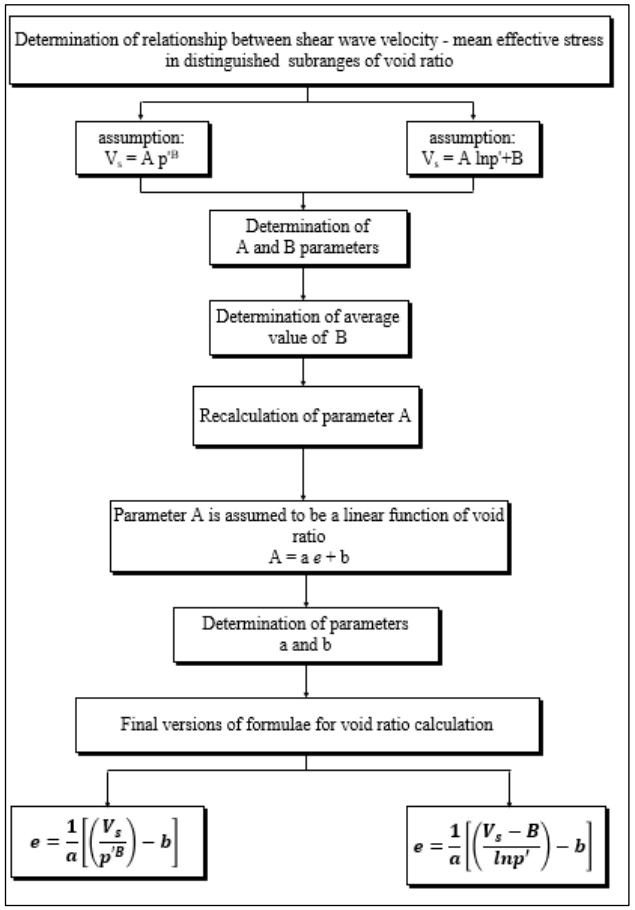

Figure 3. Procedure for determination of formulae for void ratio calculation based on logarithmic and power functions fit curves $V_s = f(p')$.

The derived formulae are the following:
for power function:

$$e = \frac{1}{a}\left[\left(\frac{V_S}{p'^B}\right) - b\right] \quad (6)$$

$$e = \frac{1}{a}\left[\left(\frac{V_S - B}{\ln p'}\right) - b\right] \quad (7)$$

Similarly, in the case of normalized shear wave velocity, the charts comparing void ratio calculated on the basis of both above formulae against the measured values were prepared. They are showed in Figure 4 for tailings with 10% of fines and in Figure 5 for finer material with 36% of fines.

For sandy materials R-squared values are high, (approximately 0.87 for both chars), although trend line in case of logarithmic function better fits the equal value line. In case of both formulae void ratio for loose material is better predicted.

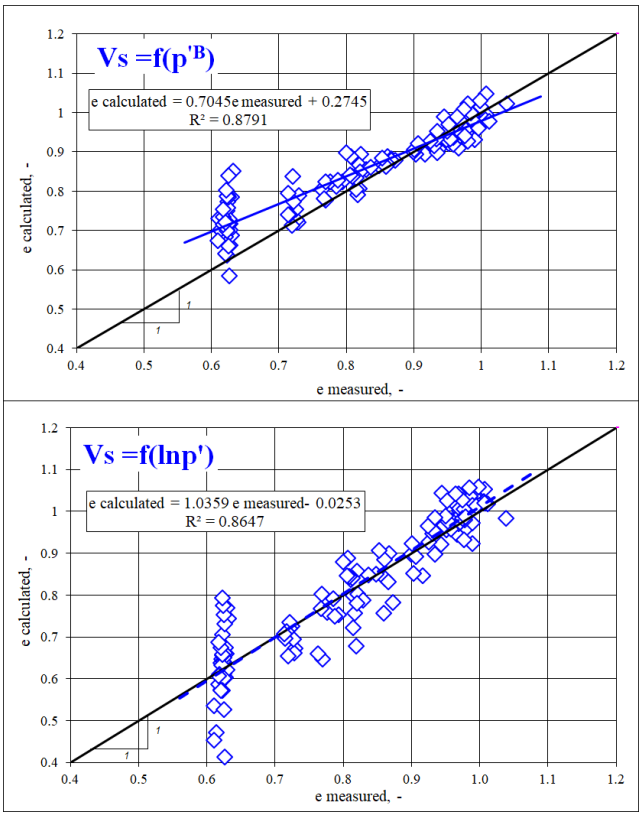

Figure 4. Comparison of measured and calculated (with both formulae) void ratio values for soils containing 10% of fines.

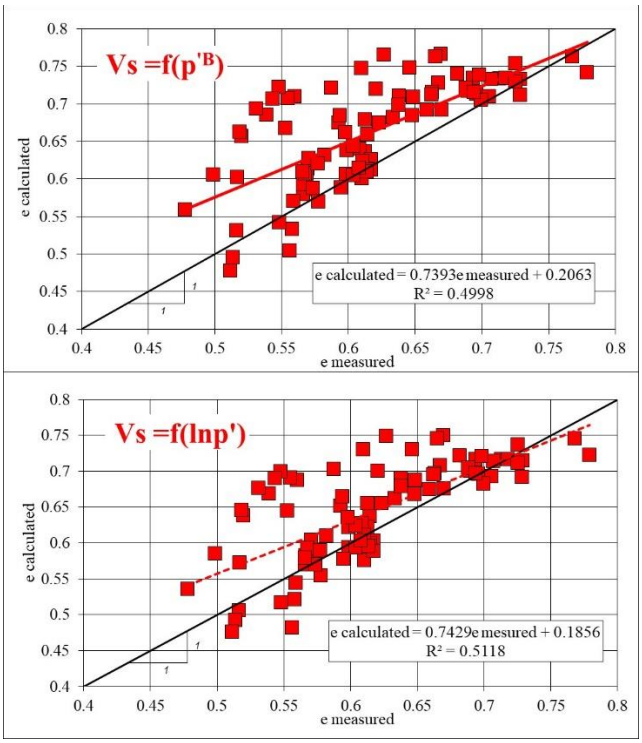

Figure 5. Comparison of measured and calculated (with both formulae) void ratio values for soils containing 36% of fines.

For transition zone material with 36% of fines content, the values predicted by both formulae are not

as good as in case of sandy material. The points on the both charts are more scattered. R-squared values are in the same order (approximately 0.50) with slightly higher coefficient for logarithmic function. In both cases predicted values of void ratio overestimated the measured ones, although, similarly as in the case of normalized shear wave velocity, convergence of trend lines is higher for loose state. It is worth to emphasize that R-squared values for that kind of soil for fit curves solutions are considerable higher (0.50) than for normalization procedure.

5 VOID RATIO DISTRIBUTION IN SITU

As it was aforementioned in the first paragraph, void ratio distribution was determined on the basis of hybrid method which assumes that various formulae derived from laboratory test results assuming different relations among void ratio, shear wave velocity and effective stress components, create the input for evaluation of void ratio values determined on the basis of the measurement of shear wave velocity carried out in non-homogeneous tailings profiles.

In order to compare results of all methods there is a need to notify an assumption concerning effective stress components contribution to the final results. In case of normalization procedure only vertical effective stress is considered in this research. However, for fit curves approaches mean effective stress p' is taken. This requires assumption concerning coefficient of earth pressure at rest. In case of tailings material deposited by discharge of slurry, the values of K_0 are in the range of 0.40-0.50, depending on granulation and void ratio. It was verified that maximum void ratio variation assuming extreme values of K_0 is 0.02 for sandy material and less than 0.01 for silty tailings. Therefore for further analysis fixed value of $K_0 = 0.4$ was assumed.

In order to compare effectiveness of all three approaches, the correlations obtained in the laboratory were projected on real profile of tailings. Thus one profile of shear wave velocity measured in the field generated six profiles of void ratio (3 formulae x 2 granulation). The results are shown in Figure 6.

The data shown in Figure 6 can be analysed according to various criteria. At first, general remarks concerning obtained values of void ratio can be presented.

- Void ratio values are less scattered than *e* values determined on cores retrived by Mostap sampler and void ratio distribution determined on the basis of CPT results.
- Profiles reflect the upper (approximately 5 m deep) zone densified by bulldozers forming the beach. Next, starting from the depth of 11 m, effect of densification caused be verical effective stress coming from gravitation is visible.
- Void ratio values for each tailings batch are approximately in the range observed during compressibility tests in the laboratory.
- Variability of void ratio value in a profile is bigger for material containing 10% of fines than in case of tailings having 36% of fines.

With regard to the three methods compared and the role of fines content, it is quite clear from the chart shown in Figure 6 that the change in fines content from 10 to 36% influences much more void ratio value than the differences resulting from applied method of data reduction. The differences of void ratio between the applied methods are smaller in case of sandy material.

For material with 36% of fines the biggest void ratio values in a profile are obtained for normalized shear wave velocity method and the smallest one for logarithmic function. However, even for that batch the difference between extreme values of void ratio is the range of 0.010-0.052 with average not exceeding 0.038.

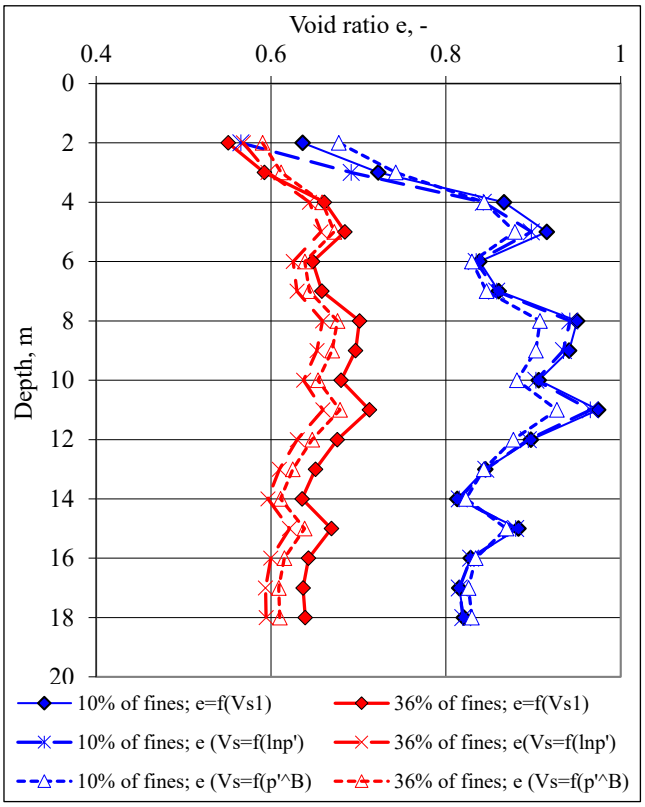

Figure 6. Comparison of void ratio profiles calculated on the basis of various approaches for tailings containing 10 and 36% of fines.

6 CONCLUSIONS

The high quality triaxial tests results combined with internal measurement of sample deformation and shear wave velocity measured in the laboratory and in the field make it possible to evaluate soil state for unaged and uncemented sands and silts with fines content up to 36%. Such approach delivers much more consistent results than any other based on static or dynamic probes, especially in case of tailings dams where non-homogeneous material containing various amount of fines prevails.

The relations among void ratio, effective stress components and shear wave velocity were obtained on the basis of laboratory tests results with use of three different approaches. One of them used very popular concept of normalized shear wave velocity and the other two were based on fit curves to relate shear wave velocity and mean effective stress p' approximated by logarithm or power function with distinguished void ratio categories. Although all three methods delivered good results for sandy material with 10% of fines, the methods based on fit curves better predict void ratio values for material with 36% of fines. Void ratio projected on field profile of tailings has shown that void ratio predicted on the basis of shear wave velocity measured in the laboratory and in the field has large potential to evaluate state of tailings in materials where undisturbed sampling of satisfactory quality is not feasible. The next step to improve void ratio prediction in a real tailings profile is associated with accounting for better reconstruction of laboratory specimen structure (slurry instead of moist tamping by undercompaction) and account for a real fines content change in a tailings profile.

REFERENCES

Been, K. and Jefferies, M. G. (1985). A state parameter for sands. *Géotechnique*, 35(2): 99-112. https://doi.org/10.1680/geot.1985.35.2.99.

Casagrande, A. (1975). Liquefaction and cyclic deformation of sands: A critical review. *Proceedings of the Fifth Pan-American Conference on Soil Mechanics and foundation Engineering*, Buenos Aires, ArgentinaVol.5, pp. 79-133.

Lipinski, M. J. and Wdowska, M. (2019). Evaluation of void ratio of sands with various amount of fines on the basis of shear wave velocity measurement. *IOP Conference Series: Materials Science and Engineering,* Vol. 471. DOI:10.1088/1757-899X/471/4/042026.

Lipinski, M. J. and Wdowska, M. (2020). Evaluation of State of Fine Sands on the Basis of Shear Wave Velocity. *Archives of Civil Engineering*, 66(2): 135-146. DOI:10.24425/ace.2020.131801.

Lipinski, M. J., Wdowska, M. and Jaroń Ł. (2017). Shear wave velocity for evaluation of state of cohesionless soils with fines. *IOP Conference Series: Materials Science and Engineering*, Vol. 245(3). DOI:10.1088/1757-899X/245/3/032083.

Lipinski, M. J., Wdowska, M. and Wudzka, A. (2020). Capability of Triaxial Apparatus with Respect to Evaluation of Nonlinearity of Soil Stiffness. *Archives of Civil Engineering*, 66(1): 69-80. DOI:10.24425/ace.2020.131775.

Lipiński, M.J., Wdowska, M. and Puspitaningrum I. (2023). Applicability of shear wave velocity to evaluate state of granular materials with fines. *Proceedings of the 8th International Symposium on deformation characteristics of geomaterials*, Porto, 3rd - 6th September 2023.

Robertson, P. K., Woeller D. J. and Finn W. D. L. (1992). Seismic cone penetration test for evaluating liquefaction potential under cyclic loading. *Canadian Geotechnical Journal*, 29(4): 686-695. https://doi.org/10.1139/t92-075.

Proceedings of the XVIII ECSMGE 2024
GEOTECHNICAL ENGINEERING CHALLENGES
TO MEET CURRENT AND EMERGING NEEDS OF SOCIETY
© 2024 the Authors
ISBN 978-1-032-54816-6
DOI 10.1201/9781003431749-326
Open Access: www.taylorfrancis.com, CC BY-NC-ND 4.0 license

ECSMGE 24
XVIII EUROPEAN CONFERENCE ON SOIL MECHANICS AND GEOTECHNICAL ENGINEERING

Analysis of risk associated with failures of tailings storage facility

Analyse du risque associé à la rupture de digues à résidus

Z.Q. Liu*, S.S. Nagula, L. Piciullo, S. Lacasse
Norwegian Geotechnical Institute, Oslo, Norway

**zhongqiang.liu@ngi.no*

ABSTRACT: In view of the recent failures of tailings storage facilities (TSF) caused by static liquefaction, there is need for (1) a critical evaluation of the methodologies used for quantifying uncertainties and (2) increased use of advanced approaches to assess failure probability and consequences. The failure probability combined with the expected consequences will provide an estimate of the risk associated with the unsatisfactory performance of the TSF. A risk-informed framework was developed to analyse potential breaches of a TSF induced by static liquefaction of the tailings. The framework and the tools to estimate hazard and consequences are briefly discussed in the paper. The framework is then used to determine the probability distribution of instability, predict the mobility flow downstream, assess the vulnerability of buildings in the influence area and do a consequence assessment.

RÉSUMÉ: Compte tenu des récentes ruptures de barrages à résidus dues à la liquéfaction statique, il est nécessaire de faire une évaluation critique des méthodologies utilisées pour quantifier les incertitudes et d'utiliser davantage les approches pour évaluer la probabilité de défaillance et les conséquences d'une telle défaillance.. La probabilité de défaillance combinée aux conséquences fournit une estimation du risque associé à une défaillance d'un part à résidus. Une approche «risque-informé» générique est proposée pour des défaillances dues à une liquéfaction statique des résidus. L'approche et certains outils probabilistes pour estimer les dangers et les conséquences sont discutés dans l'article. L'usage de la méthodologie est démontrée pour une digue à résidus: on y démontre la probabilité d'instabilité, la prévision de la mobilité de résidus en aval, la vulnérabilité des bâtiments dans la zone d'influence et l'évaluation des conséquences et du risque.

Keywords: Failure probability; vulnerability; risk; tailings storage facility.

1 INTRODUCTION

Currently, thousands of tailings storage facilities (TSFs) exist around the world. The stored tailings are often highly toxic and the failure of a tailings dam and the uncontrolled release of the impounded waste can have disastrous consequences for the public, the environment and the owner or operator. Keeping the TSFs safe is one of the biggest challenges of the mining industry. A correct approach to long-term TSF management is crucial to the successful operation of facilities and for the reputation of the mining industry. Guidelines have been issued (e.g., ICMM, 2020), but few give details on how to do qualitative or quantitative risk assessment.

Tailings dam failures can occur due to several reasons: for example, foundation failure due to the raising of the dam; slope instability; internal erosion within the dam; earthquake-induced or static liquefaction of the tailings; and lack of or wrongful maintenance or operation. Examples of recent failures include the Fundão Tailings Dam in Minas Gerais, Brazil, on November 4, 2015, causing at least 19 deaths, destruction of 158 homes and contamination of three large rivers; and collapse of the decommissioned Córrego do Feijão dam in Minas Gerais in January 2019, causing 270 fatalities and destroying large sections of agricultural land.

A systematic approach to do the risk assessment of potential TSF failures is urgently needed as there are many active TSFs and many closed facilities with unknown risk conditions. The current approaches of TSF safety need to be critically evaluated and the procedures for risk assessment need to be improved. This paper proposes an integrated framework for the risk assessment of TSFs that includes new methods to analyse the stability and the mobility of tailings.

2 NEW RISK-INFORMED FRAMEWORK FOR TAILINGS STORAGE FACILITIES

Traditionally, the geotechnical design of a TSF has been based on a deterministic Factor of Safety (FoS).

The FoS is meant to implicitly account for all the uncertainties in external loads and resistance (strength) of the tailings, but it does not address the uncertainties in the analysis explicitly. Such approach is insufficient today. Two tailings storage facilities with nominally the same FoS can have vastly different safety margin and failure probability because of the different inherent uncertainties in the analyses (Lacasse and Höeg, 2019). Risk assessment is needed to assess the actual safety margin. The conventional design methods are also rapidly being transformed by advances in numerical analysis, constitutive modelling, real-time remote monitoring, data interpretation with machine learning and an increased ability to model and interpret deformation and seepage. These advances help reduce the uncertainties, thereby reduce the limitations of an overall FoS.

Figure 1 presents the integrated risk management framework for TSFs that brings together the required information and enables risk-informed decision-making. It systemizes the risk assessment and management in four parts: (1) gathering and assessing the information required for deterministic and probabilistic hazard and consequence assessment (green zone); (2) carrying out the risk assessment, qualitatively or quantitatively or both (yellow zone); (3) making risk-informed decisions on reducing risk (blue zone); and (4) regular and frequent re-assessment of risk loop (grey zone). The framework also requires layers of review, recurrent risk assessment and performance-based validation through the life of the facility, and can be described as "performance-based risk-informed TSF management". This study focuses on probabilistic methods used to assess hazard, vulnerability, and consequence in the yellow zone.

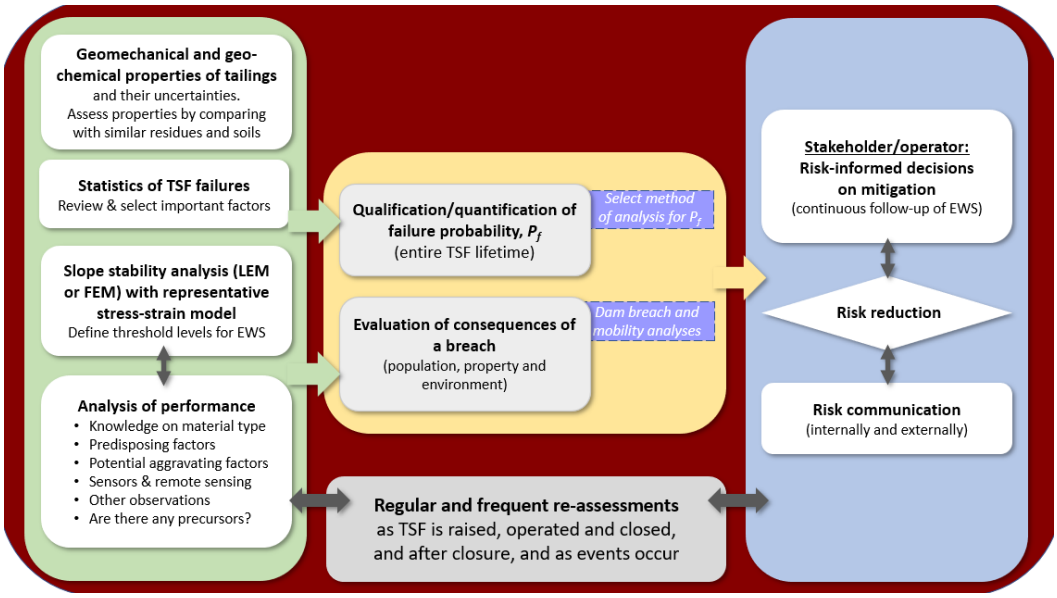

Figure 1. Proposed integrated framework for risk-informed management of tailings storage facilities.

3 PROBABILISITIC STABILITY ANALYSIS

For stability evaluation during the life of a TSF and safe tailings dams, it is necessary to consider the complete stress-strain behaviour of the soils, using appropriate and reliable constitutive models. For example, if the tailings are subjected to a shear stress higher than the undrained shear strength, the material becomes unstable, and a small pore pressure change can cause a progressive failure or static liquefaction. This failure mode can easily be overlooked if stability is assessed by conventional limit equilibrium analyses. The preferred approach is to use numerical modelling with the finite element method (FEM) and a constitutive model simulating softening and hence, the initiation of static liquefaction in tailings dams and provide an estimate of FoS against failure. However, significant uncertainties exist in the input parameters because of existing conditions in situ and in the way we calculate the factor of safety against failure. In such cases, probability-based approaches provide more insight than deterministic analyses.

3.1 Numerical modelling in PLAXIS

An idealised geometry for a TSF was numerically simulated (Reid and Fourie, 2023). The stability analyses were carried out in Plaxis 2D, using the NorSand model (Jefferies, 1993), as presented in Figure 2. The slope was 50 m high with 1V:3H side slope. A 10-m wide bench was included at a height of 25 m, making the overall average slope 1V:3.2H.

The model was divided into four layers of tailings to account for the variability in state parameter and variation of phreatic line (Figure 2). The bottom boundary of the model is fixed, and the vertical boundaries are fixed in the lateral direction. An initial phreatic line commencing from 30 m upstream of the toe till 26 m height as shown in Figure 1.

The state parameters ($\psi = e - e_c$, where e is the in-situ void ratio and e_c is the critical void ratio at same mean pressure p) were evaluated using the CPTU data, using the correlation after Been and Jefferies (1992). The mean and standard deviation for each layer are shown in Table 1. The standard deviation of ψ is very high in all four layers, and extremely high in Layer 1, making it difficult to determine whether is contractive or dilative. This reemphasises the need to analyse TSFs in a probabilistic framework.

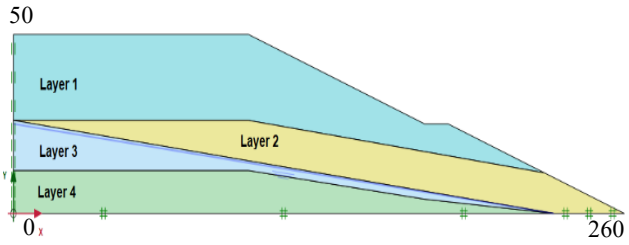

Figure 2. PLAXIS 2D model of tailings dam with 4 layers of tailings. Phreatic line is between Layers 2 and 3.

Table 1. Mean and standard deviation of state parameter for each layer.

Layer	Mean ψ (M)	Std. Dev. Ψ (D)
Layer 1 (x1)	-0.01756	0.04513
Layer 2 (x2)	0.05206	0.03794
Layer 3 (x3)	0.07968	0.02977
Layer 4 (x4)	0.07968	0.02977

3.2 Probability of failure

The first- and second-order reliability methods (FORM and SORM), enhanced with response surface method (RSM) modelling, were utilized to estimate failure probability.

Figure 3 describes the change in the failure probability for the idealized geometry and the highly uncertain state parameters in Table 1 as a function of the elevation of the phreatic surface at centreline of the modelled TSF. The results show that the failure probability increases from 1% to 32 % as the phreatic line rises from 26 to 50 m. Figure 4 illustrates with the FORM sensitivity coefficients (a^2 in the mini-table) that the state parameter in Layer 4 (a = 0.94) has the most influence on the calculated failure probability.

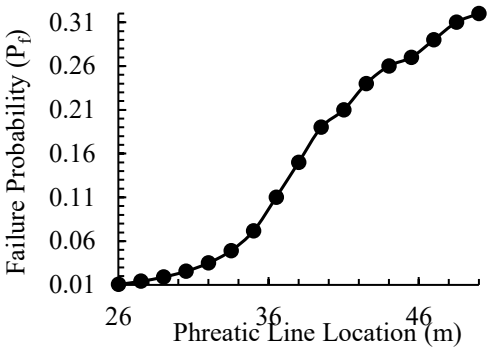

Figure 3. Variation of P_f with normally distributed state parameters for all layers as a function of the elevation of the phreatic line at the centreline of the Model (FORM results).

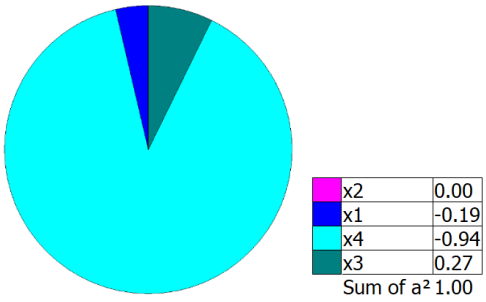

Figure 4. Alpha variables (a) for state parameters in each layer (SORM analyses).

4 RUNOUT AND CONSEQUENCES: MOBILITY ANALYSIS

4.1 Numerical simulations of runout

If a TSF fails, the tailings can travel long distances, posing a risk to life and health, infrastructure, and the environment. Modelling the mobility of tailings is a challenging, yet essential, task for estimating the elements at risk and consequences of a TSF failure. A flow slide following a static liquefaction event can be modelled by non-Newtonian fluid mechanics models, in particular the Herschel-Bulkley model. In the present study, the BingClaw model was used to predict the mobility of the Feijão Mine tailings dam.

The BingClaw model is a visco-plastic model with Herschel-Buckley rheology (Liu et al. 2021). The model is an extension of the Bing model (Imran et al. 2001) in Eulerian coordinates in two horizontal dimensions. Figure 5 presents an example of a BingClaw simulation of the runout distance of the Feijão Mine tailings dam.

Estimating the released volume for analyses that aim to predict the runout is a fundamental issue. Empirical correlations (e.g., Piciullo et al. 2022) can be useful for preliminary release volume estimation. In this study, the released volume was estimated by interpreting from satellite data the topography before

and after the failure. Figure 5 superposes the periphery of the deposited material at the end of the sliding with the simulated runout. The agreement between the simulated and observed runout distance and its spatial distribution after failure is excellent.

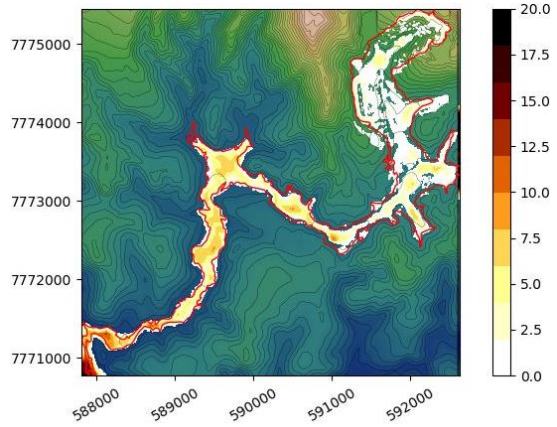

Figure 5. Tailings runout 133 minutes after failure of the Feijão Mine tailings dam: red curve is the mapped runout extent; white area is the calculated runout with BingClaw; scale on right is debris thickness in m.

4.2 Consequence analysis

The quantitative modelling of vulnerability and consequence is a central part of the quantitative risk assessment for a TSF. Vulnerability assessment for TSFs should consider the magnitude of potential failures and the variable nature of the elements at risk. Figure 6 presents an example of a simulation of the velocity of the Feijão Mine tailings dam and the buildings affected by the failure.

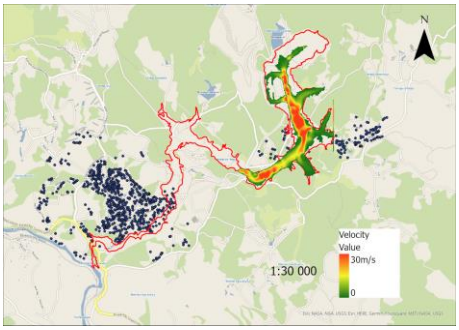

Figure 6. Simulated velocity of the Feijão Mine tailings at 10 minutes after dam failure and the mapped buildings affected by the failure.

Consequence analysis can be conducted based on the velocity and the exposure of buildings. Number of fatalities can be estimated from the path of the flow and the thickness of the wave and debris.

5 CONCLUSIONS

The paper outlines a risk-informed decision-making framework to estimate the failure probability and the consequence of tailings storage facilities. The recent catastrophic tailings dam failures necessitate the use of reliability-based methods to adhere to new regulations and make risk informed, and thereby more robust decisions.

REFERENCES

Been, K. and Jefferies, M.G. (1992). Towards systematic CPT interpretation. Predictive soil mechanics: Proceedings of the Wroth Memorial Symposium, 121-134.

ICMM (2020). Global industry standard on tailings management. August 2020.

Imran, J., Parker, G., Locat, J., Lee, H. (2001). 1-D numerical model of muddy subaqueous and subaerial debris flows. *J. Hydraul. Eng.* 127: 959-968. doi:10.1061/(ASCE)0733-9429(2001)127:11 (959).

Jefferies, M. G. (1993). Nor-Sand: a simple critical state model for sand. *Géotechnique*, 43(1): 91-103. https://doi.org/10.1680/geot.1993.43.1.91.

Liu, Z. Q., L'Heureux, J.-S., Glimsdal, S., Lacasse, S. (2021). Modelling of mobility of Rissa landslide and following tsunami. *Computers and Geotechnics*, 140: 104388. https://doi.org/10.1016/j.compgeo.2021.104388.

Piciullo, L., Storrøsten, E. B., Liu, Z., Nadim, F. and Lacasse, S. (2022). A new look at the statistics of tailings dam failures. *Engineering Geology*, 303, 106657. https://doi.org/10.1016/j.enggeo.2022.106657.

Reid, D. and Fourie, A.B. (2023). Development and outcomes of a tailings slope stability comparative design exercise. *Canadian Geotechnical Journal*, https://doi.org/10.1139/cgj-2022-0065.

Proceedings of the XVIII ECSMGE 2024
GEOTECHNICAL ENGINEERING CHALLENGES
TO MEET CURRENT AND EMERGING NEEDS OF SOCIETY
© 2024 the Authors
ISBN 978-1-032-54816-6
DOI 10.1201/9781003431749-327
Open Access: www.taylorfrancis.com, CC BY-NC-ND 4.0 license

ECSMGE 24
XVIII EUROPEAN CONFERENCE ON SOIL MECHANICS AND GEOTECHNICAL ENGINEERING

Hydro-Mechanical response of a shale subjected to gas transport in the context of radioactive waste disposal

Réponse hydromécanique d'un schiste soumis au transport de gaz dans le contexte du stockage de déchets radioactifs

Q. Llabjani*, A. Ferrari, L. Laloui
Swiss Federal Institute of Technology Lausanne (EPFL), Laboratory of Soil Mechanics, Lausanne, Switzerland
P. Marschall
Nationale Genossenschaft für die Lagerung radioaktiver Abfälle (NAGRA), Wettingen, Switzerland
**qazim.llabjani@epfl.ch*

ABSTRACT: In the context of deep geological radioactive waste disposal, significant amount of generated gas is expected to migrate from the repositories into the surrounding host rock, affecting its hydro-mechanical state. In Switzerland, Opalinus Clay is the selected host geological formation and requires a comprehensive understanding of the relevant phenomena that characterize its behaviour associated with gas transport regarding the long-term safety assessment of the repository. In this context, water and gas injection tests were performed using a high pressure oedometer cell. The results suggest that gas-induced porewater displacement is a key feature during gas invasion processes in clay-rich host rock. Furthermore, water permeability was not impacted by gas transport and consistently found in the order of 10^{-21} (m^2) before and after the gas invasion tests. The experimental outcome of the study provided unique observations of the hydro-mechanical behaviour of Opalinus Clay when subjected to gas transport in the short-term and long-term.

RÉSUMÉ: Dans le contexte de l'enfouissement géologique profond des déchets radioactifs, une quantité significative de gaz sera générée et migrera vers la roche hôte environnante, influençant son état hydromécanique. En Suisse, l'argile à Opalinus a été choisie comme formation géologique hôte et nécessite une compréhension approfondie des phénomènes caractérisant son comportement lorsqu'elle est associée au transport de gaz, en vue de l'évaluation à long terme de la sécurité du dépôt. Dans ce contexte, des essais d'injection d'eau et de gaz à haute pression ont été réalisés à l'aide d'une cellule œdométrique spécialement développée. Les résultats suggèrent que le déplacement de l'eau interstitielle induit par le gaz est une caractéristique clé lors de l'invasion de gaz. De plus, la perméabilité de l'eau n'a pas été impactée par le transport de gaz avec des valeurs mesurées l'ordre de 10^{-21} (m^2) avant et après l'invasion de gaz. Les résultats expérimentaux de l'étude ont fourni de nouvelles observations sur le comportement hydromécanique de l'argile d'Opalinus lorsqu'elle est soumise au transport de gaz à court et à long terme.

Keywords: Radioactive waste; opalinus clay; hydro-mechanical behaviour; gas transport.

1 INTRODUCTION

Regardless of the national strategies concerning nuclear energy production, there is an urgent need to address the problem of disposing high-level nuclear waste produced by power plants. Switzerland foresees a deep geological repository which relies on a multi-barrier system to isolate the waste from the biosphere for dozens of thousands of years. However, uncertainties still exist about the late stage of the repository when a significant amount of gas will be produced due to various processes. This gas production may cause gas pressure build-up with a potential propagation of the gas front into the host rock. Those circumstances can result in the loss of the mechanical integrity of the multi-barrier system and may impact the long-term safety of the repository (Levasseur et al., 2021).

In Switzerland, Opalinus Clay has been selected as the host geomaterial for the underground disposal of radioactive waste. More experimental evidence for a comprehensive understanding of the relevant phenomena that characterize the hydro-mechanical (H-M) behaviour of Opalinus Clay (OPA) when subjected to gas invasion is thus required.

In this paper we are showing the results of an experimental campaign on OPA conducted with a high-pressure oedometer apparatus allowing the performance of water and gas injection tests while assessing the vertical deformation of the tested

material with the aim to better observe and understand the involved phenomena.

2 MATERIAL AND METHODS

2.1 Tested material

Opalinus Clay is a fine-grained sedimentary geomaterial with a mineral composition mainly consisting of silicates, carbonates and quartz. The tested material was retrieved from the deep borehole in Trüllikon in the Zürich Northeast siting region in Switzerland (Ammen and Palten, 2021) and was sourced at a depth of about 848 (m). Complete geotechnical characterization has been performed and included: bulk density ρ=2.50 (g/cm^3), density of solid particles ρ_s=2.78 (g/cm^3), water content w=0.05, void ratio e=0.15, degree of saturation Sr=0.63, initial total suction ψ=66 (MPa).

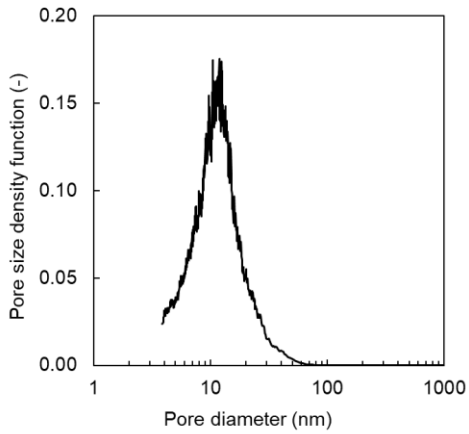

Figure 1. MIP test results.

The pore structure of Opalinus Clay was studied by Mercury Intrusion Porosimetry (MIP), using the freeze-drying technique for sample preparation. To overcome the conformance effect and the compressibility of the sample below the entry pressure of mercury, a correction was applied to the MIP data according to (Comisky et al., 2011). As depicted in Figure 1, a unimodal pore size distribution was obtained in the range of 8 to 16 (nm) with a peak value at about 12 (nm). The size of the detected porosity was from 4 to 60 (nm); 4 (nm) being the smaller pore size detectable with the apparatus. The results are in good agreement with values from the literature on the same material (e.g., Crisci et al., 2019; Minardi et al., 2021). From the larger detected pores, air is expected to enter the pore space of the initially saturated porous medium at a capillary pressure of about 5 (MPa) according to the Young-Laplace equation.

2.2 Experimental set-up and procedure

The experimental work used a high-pressure oedometer cell, as depicted in Figure 2, that allowed to apply a vertical total stress up to 100 (MPa) with the possibility to perform water and gas injection from the bottom and top side of the specimen with a fluid pressure up to 16 (MPa) and 20 (MPa), respectively (Minardi et al., 2021). The vertical deformation was assessed using three LVDTs with 0.2 (μm) resolution. The height and diameter of the specimen were 12 and 35 (mm), respectively. The specimen was tested with the vertical load and fluid injection perpendicular to the bedding planes (S-sample).

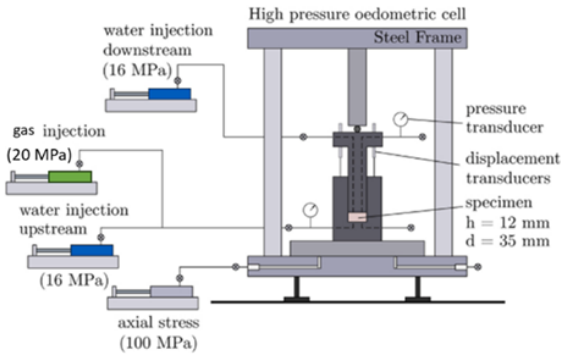

Figure 2. High pressure oedometer test set-up.

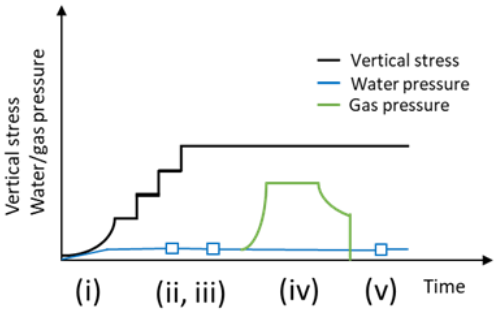

Figure 3. Sequences for the water and gas injection tests.

The experimental procedure was composed of five test sequences (phases i to v) which are illustrated in Figure 3 and described hereafter. (i) The experimental procedure included first a water resaturation in isochoric conditions with synthetic water mimicking the in-situ porewater (Aschwanden et al., 2021). (ii) Mechanical loading up to the target vertical effective stress was performed to simulate in situ conditions. To do so, constant water pressure of 1 (MPa) was applied at the bottom ($u_{w,bot}$) and top ($u_{w,top}$) and the vertical total stress (σ_v) was increased in steps up to 15 (MPa). (iii) Constant head water permeability tests were performed at different vertical effective stresses by applying a differential pressure of 1 (MPa). Then, in order to perform the gas injection test (iv), the water pump connected at the bottom side of the specimen

was replaced by the gas pump filled with nitrogen pressurized at 3 (MPa). The sequence comprised then a constant rate gas injection period (0.2 (ml/min) for an initial gas volume of 500 (ml) in the reservoir) during which gas pressure was increased from 3 MPa to 10 MPa. Gas pressure was then kept constant until steady state conditions were observed for both gas flow and volumetric response of the tested specimen. Finally, a shut-in phase was performed where the gas pump was stopped, ensuring constant gas volume at the inlet, and gas pressure decay was monitored. Water back-pressure at the top side of the specimen was kept constant during the entire phase at $u_{w,top}$=1 (MPa). (v) After the gas injection phase, water resaturation was performed under constant vertical total stress, followed by a second water permeability test in order to assess the evolution of the intrinsic permeability due to gas transport.

3 RESULTS

3.1 Hydro-mechanical results (phases i to iii)

During the resaturation phase, the vertical total stress was progressively increased ensuring isochoric conditions and minimizing damage due to swelling. The swelling pressure, S_p, developed during this phase was 3 (MPa) as shown in Figure 4.

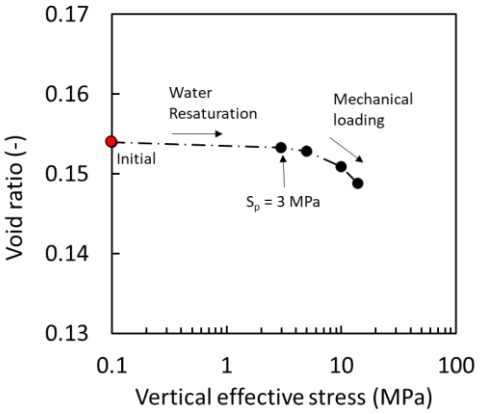

Figure 4. Oedometer curve for tested specimen.

The mechanical compression up to the target vertical effective stress allowed an assessment of the relationship between void ratio and the applied stress. The deformation of the oedometer system was accounted for every loading step (Ferrari et al., 2016). Figure 4 shows the compression of the specimen with increasing vertical effective stress. The water intrinsic permeability was computed from the constant head tests performed at different vertical effective stresses. The water intrinsic permeability was obtained in the range of $2\text{-}3\cdot10^{-21}$ (m^2) and is in good agreement with values reported in the literature for the same material (Crisci et al., 2019; Minardi et al., 2021).

3.2 Gas injection test (phase iv)

The gas injection test was performed at fast gas pressure build-up rate with the intention to favour an undrained response of the material. The applied boundary conditions, such as vertical stress and fluids pressures are shown in Figure 5 (top).

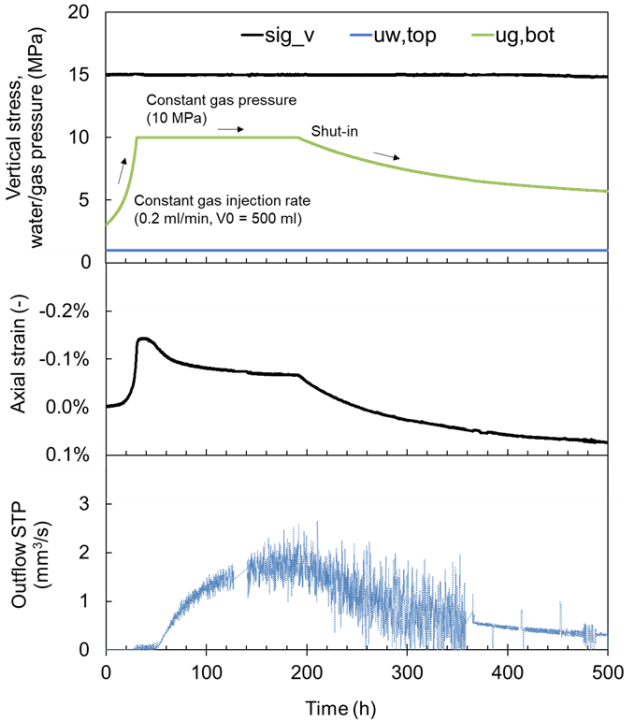

Figure 5. Gas injection test results.

The global axial strain of the specimen computed from the measurement of the vertical deformation, shown in Figure 5 (middle), indicates that almost no deformation was observed at the early phase as gas pressure was likely below the entry pressure and had not yet invaded the pore space. Once gas reached a pressure of about 5 (MPa) at t=17 (h), expansion of the specimen was observed, indicating the start of gas invasion, which was associated with porewater displacement and development of capillary pressure. The air entry value was consistent with the estimation from the MIP test. Expansion continued as gas pressure increased further. Once gas pressure was kept constant at 10 (MPa) from t=30.5 (h), expansion continued to slightly increase and reached a strain of -0.14% and was followed by a slow reduction and stabilization at about -0.07% until t=193 (h). As gas pressure decreased during the shut-in phase, t > 193 (h), the specimen experienced compression. Gas pressure after shut-in was measured at 5.7 (MPa).

The observed mechanical response was consistent with the measured outflow from the specimen. Gas breakthrough was observed only after the maximum gas pressure was reached (t = 50 h). This suggests that gas movement was impaired by the low permeability of the specimen. With time, as gas further invaded the pore space, the measured outflow increased until steady state conditions were observed at about t=193 (h). The gas outflow at standard temperature and pressure (STP) conditions was about 2 (mm^3/s). During the shut-in, gas outflow decreased until almost no flow was observed anymore.

3.3 Hydro-mechanical results (phase v)

No significant strain (less than 0.01%) due to water uptake was observed during resaturation at constant vertical stress. The water intrinsic permeability after resaturation was found very similar to prior to the gas injection, $2\text{-}3 \cdot 10^{-21}$ (m^2), suggesting that gas transport did not impair the intrinsic permeability of the tested material.

4 CONCLUDING REMARKS

In this study, the hydro-mechanical response of Opalinus Clay associated with gas transport was investigated. Water and gas injection tests have been performed using a high-pressure oedometer cell to replicate the in-situ stress conditions. In particular, the short- and long-term responses to gas invasion were assessed during fast gas pressure build-up.

The interpretation of the results in terms of drained/undrained behaviour is consistent with the general deformation behaviour of clayey geomaterials. If the tested material is subjected to fast gas pressure build-up, it is more likely that gas transfer is initially associated with larger deformation due to generation of excess porewater pressure during the transient phase. The results suggested that gas-induced porewater displacement is a key feature during gas invasion processes in clay-rich host rock.

Furthermore, the consistent water permeability values obtained before and after the gas injection test suggest that the involved gas transport processes are unlikely to impact the long-term barrier function of the host rock.

The experimental outcome of the study provided additional observations of the hydro-mechanical behaviour of Opalinus Clay associated with gas transport in the short-term and the long-term. Further experimental investigation, as well as numerical analysis, are required to better understand the involved processes, such as the development of non-uniform and localized strains associated with gas invasion.

ACKNOWLEDGEMENTS

The authors are grateful to the Swiss agency for radioactive waste management (NAGRA) for the financial support (NAGRA order 18'713). Furthermore, the acknowledgements are extended to the European Joint Programme on Radioactive Waste Management (EURAD WP-GAS) within the European Union's Horizon 2020 research and innovation programme under grant agreement No 847593.

REFERENCES

Ammen, M., Palten, P.-J. (2021). TBO Trüllikon-1-1: Drilling, NAB 20-09, Nagra, Wettingen, Switzerland.

Aschwanden, L., Camesi, L., Gimmi, T., Jenni, A., Kiczka, M., Mäder, U., Mazurek, M., Rufer, D., Waber, H.N., Wersin, P., Zwahlen, C., and Traber D. (2021). TBO Trüllikon-1-1: Rock Properties, Porewater Characterisation and Natural Tracer Profiles, NAB 20-09, Nagra, Wettingen, Switzerland.

Comisky, J. T., Santiago, M., McCollom, B., Buddhala, A., & Newsham, K. E. (2011) Sample Size Effects on the Application of Mercury Injection Capillary Pressure for Determining the Storage Capacity of Tight Gas and Oil Shales, *Unconventional Resources Conference, SPE*, https://doi.org/10.2118/149432-ms.

Crisci, E., Ferrari, A., Giger, S. B., & Laloui, L. (2019) Hydro-mechanical behaviour of shallow Opalinus Clay shale, *Engineering Geology*, 251, 214– 227, https://doi.org/10.1016/j.enggeo.2019.01.016.

Ferrari, A., Favero, V., & Laloui, L. (2016) One-dimensional compression and consolidation of shales. *International Journal of Rock Mechanics and Mining Sciences*, 88, 286–300, https://doi.org/10.1016/j.ijrmms.2016.07.030.

S. Levasseur, F. Collin, K. Daniels, M. Dymitrowska, J. Harrington, E. Jacops, O. Kolditz, P. Marschall, S. Norris, X. Sillen, J. Talandier, L. Truche, J. Wendling, (2021). Deliverable D6.1 of the project EURAD, Work Package Gas.

Minardi, A., Stavropoulou, E., Kim, T., Ferrari, A., Laloui, L. (2021) Experimental assessment of the hydro-mechanical behaviour of a shale caprock during CO2 injection, *International Journal of Greenhouse Gas Control*, 106, 103225, https://doi.org/10.1016/j.ijggc.2020.103225.

Proceedings of the XVIII ECSMGE 2024
GEOTECHNICAL ENGINEERING CHALLENGES
TO MEET CURRENT AND EMERGING NEEDS OF SOCIETY
© 2024 the Authors
ISBN 978-1-032-54816-6
DOI 10.1201/9781003431749-328
Open Access: www.taylorfrancis.com, CC BY-NC-ND 4.0 license

ECSMGE 24
XVIII EUROPEAN CONFERENCE ON SOIL MECHANICS AND GEOTECHNICAL ENGINEERING

Relevance of correlation length in geotechnical engineering

Pertinence de la longueur de corrélation en ingénierie géotechnique

M. Lloret-Cabot*, K. Zhang, W. Zhang, D. Toll
Durham University, Durham, United Kingdom

**marti.lloret-cabot@durham.ac.uk*

ABSTRACT: Soils are heterogeneous in nature and as such, their properties inherently exhibit a distinct spatial variation that reveals past information of their geological history. This spatial variability is an important source of geotechnical uncertainty and hence its proper characterisation is of importance to geotechnical design. Random field theory provides a consistent mathematical framework to account for this soil's heterogeneity and it is a powerful computational tool to perform reliability analyses of geotechnical structures when combined with the finite element method. A key parameter in these stochastic analyses is the correlation length (or sometimes also referred to as scale of fluctuation) because it controls variations of a soil property in a given spatial direction. This spatial statistic can be estimated from in-situ data (e.g., cone penetration test CPT) and the quality of such estimation is the main question tackled in this paper.

RÉSUMÉ: Les sols sont de nature hétérogène et, en tant que tels, leurs propriétés présentent intrinsèquement une variation spatiale distincte qui révèle des informations passées sur leur histoire géologique. Cette variabilité spatiale est une source importante d'incertitude géotechnique et sa caractérisation appropriée est donc importante pour la conception géotechnique. La théorie des champs aléatoires fournit un cadre mathématique cohérent pour tenir compte de l'hétérogénéité de ce sol et constitue un outil informatique puissant pour effectuer des analyses de fiabilité des structures géotechniques lorsqu'il est combiné avec la méthode des éléments finis. Un paramètre clé dans ces analyses stochastiques est la longueur de corrélation (ou parfois également appelée échelle de fluctuation) car elle contrôle les variations d'une propriété du sol dans une direction spatiale donnée. Cette statistique spatiale peut être estimée à partir de données in situ (par exemple, test de pénétration du cône CPT) et la qualité d'une telle estimation est la principale question abordée dans cet article.

Keywords: Correlation length; scale of fluctuation; uncertainty; soil variability.

1 INTRODUCTION

Due to the geological/engineering processes by which soil is formed/deposited, its property values vary with position, meaning that soil is not homogenous. More interestingly, if a given direction within a soil domain is considered, higher correlation values are likely to be found in the geotechnical property values (e.g., undrained shear strength, S_u) measured at points that are closer to each other (small lag distance τ) because the soil conditions at these closer points are likely to be quite similar. In contrast, values of such property measured at points that are further away from each other (larger lags τ) will likely show bigger differences, because of a lower correlation. This decay of correlation in the property values at pairs of points along a given direction is described by the correlation function $\rho(\tau)$ and the sharpness of such decay is controlled by a key statistical parameter known as the correlation length, θ, (or also referred to as scale of fluctuation, SOF).

Such representation of the spatial variation of a geotechnical property in a given direction is useful because it facilitates a consistent approach able to capture the spatial heterogeneous nature of a soil property. It is also useful because it allows to incorporate in a relatively easily way the spatial variability of a soil property in geotechnical design via the random finite element method (RFEM) (e.g., Fenton and Griffiths, 2003) which combines the finite element method with the random field generator LAS (Local Average Subdivision method proposed by Fenton & Vanmarcke, 1990).

The RFEM has been used extensively in the literature to assess the structural response of a geotechnical system (Fenton and Griffiths, 2003; Hicks and Spencer, 2010; Griffiths et al., 2011). Interestingly, using the RFEM in any of these geotechnical problems facilitates a probabilistic assessment of their structural performance because, rather than solving the problem for a single realisation (considering an homogeneous soil), the same problem can be solved for a finite number of realisations within a Monte Carlo approach, so that the response of the geotechnical system can be assessed in probabilistic terms, allowing for the description of failure in terms

of a probability of failure (and not in terms of a single factor of safety, as historically done). In doing such probabilistic assessment, all these works above confirm the relevance of incorporating the spatial variation of soil properties in the geotechnical design of these structures and, more specifically, the relevance of the correlation length. Perhaps due to this importance, many studies in the literature have studied the concept of the correlation length (e.g., DeGroot and Baecher, 1993; Phoon and Kulhawy, 1999; Fenton, 1999ab; Jaksa, 1995; Uzielli et al., 2005; Cami et al., 2020; Lloret-Cabot et al., 2013, Ching et al. 2023) estimated from available in situ or artificially generated information (most commonly cone penetration test data, CPT). These studies, however, do not all use the same estimation method (not even the same theoretical correlation model), they often treat the trend in the data in different ways and they do not all estimate θ using the same specific in situ test or, if they do, the sampling interval is not necessarily the same. These differences in the available literature make challenging the comparison between the different estimated θs. Against this background, the current paper aims to provide some further insight (in terms of accuracy) of the computational performance of the most common estimation method of θ which consists in minimising the error between an assumed theoretical correlation model $\rho(\tau)$ (see Table 1) and the estimated experimental correlation function $\hat{\rho}(\tau)$ (calculated from the in-situ or artificially generated data). Various theoretical correlation models $\rho(\tau)$ are available in the literature but due to space constraints only the most common two are considered in this research. Their definition is given in Table 1.

Table 1. Most common theoretical correlation models.

Name	Expression
Markovian	$\rho(\tau) = \exp\left\{\frac{-2\lvert\tau\rvert}{\theta}\right\}$
Gaussian	$\rho(\tau) = \exp\left\{-\pi\left(\frac{\lvert\tau\rvert}{\theta}\right)^2\right\}$

Note: θ is the correlation length in a given direction and the τ lag distance

According to the method of moments, the experimental correlation function takes the following form:

$$\hat{\rho}(\tau_j) = \sum_{i=1}^{k-j} \frac{(X_i-\hat{\mu})(X_{i+j}-\hat{\mu})}{(X_i-\hat{\mu})^2}, \quad for\ j = 0, \dots k-1 \tag{1}$$

where $\hat{\rho}(\tau_j)$ is the experimental correlation function between two points separated by a lag distance τ_j, $\hat{\mu}$ is the experimental mean, k is the total number of measurement points and i is the total number of pairs of points (separated by τ_j).

Equation 1 can be re-written in terms of the experimental variance $\hat{\sigma}^2$ in the following two forms depending on wether an unbiased (Equation 2) or biased (Equation 3) estimator of the experimental variance $\hat{\sigma}^2$ is considered:

$$\hat{\rho}(\tau_j) = \frac{1}{\hat{\sigma}^2(k-j)} \sum_{i=1}^{k-j} (X_i - \hat{\mu})(X_{i+j} - \hat{\mu}), \quad for\ j = 0, \dots k-1 \tag{2}$$

$$\hat{\rho}(\tau_j) = \frac{1}{\hat{\sigma}^2 k} \sum_{i=1}^{k-j} (X_i - \hat{\mu})(X_{i+j} - \hat{\mu}), \quad for\ j = 0, \dots k-1 \tag{3}$$

Traditionally, Equation 2 has been most commonly used in the geotechnical literature. However, recent work by Cami et al. (2020) proposes using Equation 3 instead to prevent negative eigenvalues in the correlation matrices. In the context of the work presented here (primarily focussed on the estimation of the correlation length in the vertical direction from artificially generated CPT data), any of the three equations is likely to give very similar estimates because a CPT typically has a large number of data points available in the vertical direction (and the value of the experimental mean should be close to zero, when using de-trended and normalised data, Lloret-Cabot et al., 2014). This research has used Equation 3.

2 ACCURACY ASSESSMENT

The main goal of this investigation is to assess the accuracy of using two of the most common theoretical correlation models to estimate the vertical correlation length from CPT data (see Table 1). This section aims to address this issue by using an equivalent numerical strategy to that proposed in Lloret-Cabot et al. (2014). Rather a two-dimensional (2-D) random fields as used in Lloret-Cabot et al. (2014), this work uses LAS to generate 1-D random fields as a suitable representation of de-trended and normalised CPT tip resistances with known zero mean ($\mu = 0$) and unit variance ($\sigma^2 = 1$), and with a vertical correlation length of $\theta_v = 1.5$m (e.g, Fenton, 1999b). The total length considered is D = 20m and the sampling distance d_y is 0.1m. A typical example is illustrated in Figure 1.

From this random field data, the experimental correlation function $\hat{\rho}(\tau)$ can be estimated using Equation 3 as illustrated in Figure 2. The optimal value $\widehat{\theta_v}$ can be then estimated by best fitting $\hat{\rho}(\tau)$ to a theoretical correlation structure $\rho(\tau)$. A number n of estimated $\widehat{\theta_v}$ are obtained by repeating this process from j = 1 to n, (where n = 1,000 corresponds to the

number of realisations considered here). In order to assess the accuracy of the correlation model used, the obtained value of $\widehat{\theta_v}$ (averaged over the n estimated correlation lengths) is compared against the known value of θ_v used to generate each CPT.

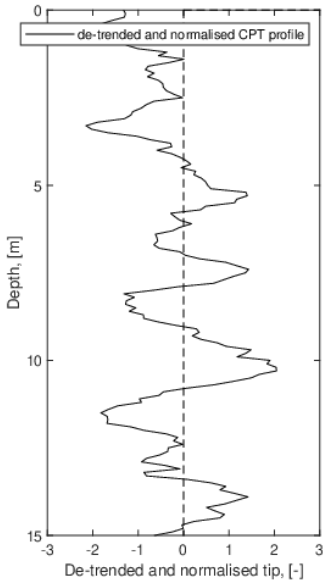

Figure 1. Typical CPT profile generated using LAS.

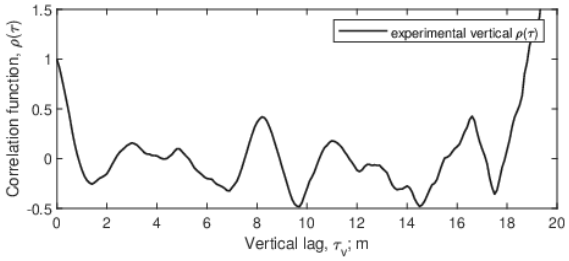

Figure 2. Typical experimental correlation structure.

The accuracy of estimating θ_v when using the approach discussed earlier with a Markovian or a Gaussian correlation structure is illustrated in Figures 3 and 4 respectvely. Each figure includes results for n = 1,000 realisations. In the figures, the representation of $\rho(\tau)$ with the corresponding optimized θ_v is represented as a thick solid line whereas the averaged experimental correlation model is indicated by a dashed thick line. The thinner continuous lines represent each of the individual $\hat{\rho}(\tau)$ estimated for each CPT. It is perhaps worth noting here that practically the same result for the optimal $\widehat{\theta_v}$ is obtained by best fitting the averaged experimental correlation structure and the theoretical one. Inspection of the figures shows that a very similar performance is achieved by the two correlation structures assumed, with an optimal $\widehat{\theta_v}$ of 1.55m and 1.54m for Markovian and Gaussian, respectively, corresponding to relative errors of 3.33% and 2.67%, which are values in line with similar analysis published in the literature (e.g., Lloret-Cabot et al., 2014). This similarity suggests that both theoretical correlation functions are equally valid for tackling this problem.

In addition to investigating the convergence of the estimation method to the true value of the vertical correlation length (Figures 3 and 4), it is also convenient to study the response of each individual estimated value of θ_v, as illustrated in Figure 5 in the form of a histogram.

Figure 5 includes also the true and estimated values of the vertical correlation length which are indicated, respectively, by a solid and a dashed line. For completeness the 90% confidence interval of LogNormal probability distribution fit is also plotted in the figures showing a reasonably good representation of the estimated θ_v. Inspection of the figure confirms that both approaches provide very similar results and, in particular, both show a right-skewed distribution which, interestingly, resembles well the histograms obtained from estimations of θ_v using real CPT data (e.g., Cami et al. 2020). Finally, it is worth noting that about two thirds of the estimated values of θ_v below the true value (1.5m) in agreement with the results from Nie et al. (2015) which illustrates well the challenge in estimating this parameter (as, clearly, the number of CPTs available in a specific site will be much less and hence the magnitude of the error might become quite important).

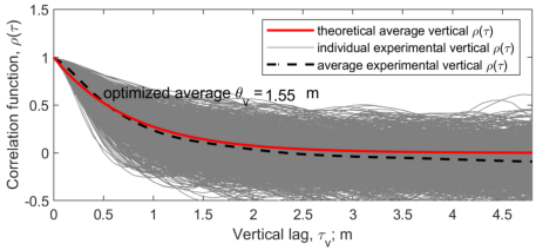

Figure 3. Estimation of the vertical correlation length with Markovian correlation structure and n = 1,000 realisations.

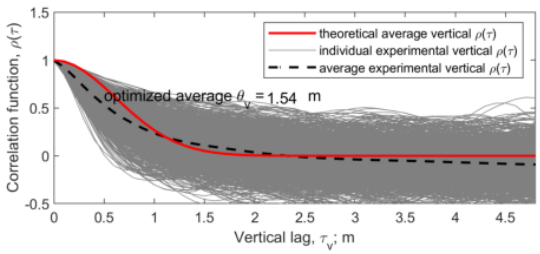

Figure 4. Estimation of the vertical correlation length with Gaussian correlation structure and n = 1,000 realisations.

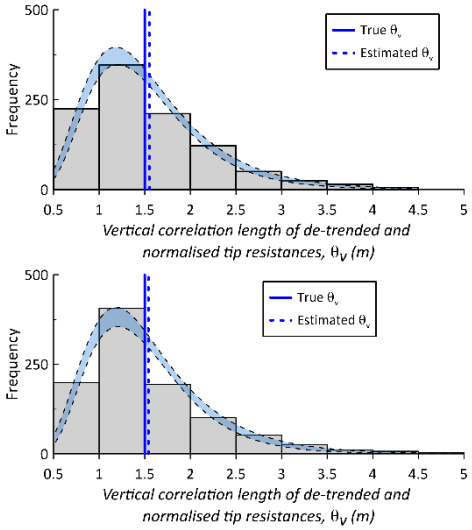

Figure 5. Histogram of estimated correlation lengths Markovian (top) or Gaussian (bottom).

3 CONCLUSIONS

The importance of the correlation length has been discussed in the context of probabilistic geotechnical analyses and its estimation has been assessed through a numerical investigation using artificially generated CPT data. The analyses showed that a very good accuracy is generally achieved when using a substantial number of realisations (1,000) demonstrating the applicability of the methods. However, a more detailed analysis on the individual estimated values of θ_v showed great variability which highlights the challenge and the potential error involved in the estimation process.

REFERENCES

Cami, B., S. Javankhoshdel, K. K. Phoon, and J. Ching. (2020). Scale of fluctuation for spatially varying soils: Estimation methods and values. *ASCE-ASME J. Risk Uncertainty Eng. Syst. Part A: Civ. Eng.*, 6(4): 03120002. https://doi.org/10.1061/AJRUA6.0001083.

Ching, J., M. Uzielli, K. K. Phoon and X. Xiaojun. (2023). Characterization of Autocovariance Parameters of Detrended Cone Tip Resistance from a Global CPT Database. *J. Geotech. Geoenviron. Eng.*, 149(10): 04023090. https://doi.org/10.1061/JGGEFK.GTENG-11214.

DeGroot, D. J., and G. B. Baecher. (1993). Estimating autocovariances of in-situ soil properties. *J. Geotech. Eng.*, 119(1):147–166. https://doi.org/10.1061/(ASCE)0733-9410(1993)119:1(147).

Fenton, G. A. and E. H. Vanmarcke. (1990). Simulation of random fields via local average subdivision. *J. Engineering Mechanics*, 116:(8), 1733-1749. https://doi.org/10.1061/(ASCE)0733-9399(1990)116:8(1733).

Fenton, G. A. (1999a). Estimation for stochastic soil models. *J. Geotech. Geoenviron. Eng.*, 125 (6): 470–485. https://doi.org/10.1061/(ASCE)1090-0241(1999)125:6(470).

Fenton, G. A. (1999b). Random field modeling of CPT data. *J. Geotech. Geoenviron. Eng.*, 125(6): 486–498. https://doi.org/10.1061/(ASCE)1090-0241(1999)125:6(486).

Fenton, G. A., and D. V. Griffiths. (2003). Bearing capacity prediction of spatially random c-φ soils. *Can. Geotech. J.*, 40(1): 54–65. https://doi.org/10.1139/t02-086.

Griffiths, D. V., J. Huang, and G. A. Fenton. (2011). Probabilistic infinite slope analysis. *Comput. Geotech.*, 38(4): 577–584. https://doi.org/10.1016/j.compgeo.2011.03.006.

Hicks, M. A., and W. A. Spencer. (2010). Influence of heterogeneity on the reliability and failure of a long 3D slope. *Comput. Geotech.*, 37 (7–8): 948–955. https://doi.org/10.1016/j.compgeo.2010.08.001.

Jaksa, M. (1995). The influence of spatial variability on the geotechnical design properties of a stiff, overconsolidated clay. *Ph.D. dissertation*, Dept. of Civil and Env. Engineering, Univ. of Adelaide.

Lloret-Cabot, M., G. A. Fenton, and M. A. Hicks. (2014). On the estimation of scale of fluctuation in geostatistics. *Georisk: Assess. Manage. Risk Eng. Syst. Geohazards*, 8(2): 129–140. https://doi.org/10.1080/17499518.2013.871189.

Lloret-Cabot, M., M. A. Hicks, and J. D. Nuttall. (2013). Investigating the Scales of Fluctuation of an Artificial Sand Island. In *Proceedings of the Int. Conf. GEO-INSTALL*, Hicks et al. (eds.), Rotterdam: CRC Press Taylor and Francis Group 192–197

Nie, X., Huang, H., Liu, Z., et al. (2015). Scale of fluctuation for geotechnical probabilistic analysis. In Schweckendiek et al. (eds.), Proc. *ISGSR2015: Geotechnical Safety and Risk V*, IOS Press, 816-821.

Phoon, K. K., and F. H. Kulhawy. (1999). Characterization of geotechnical variability. *Can. Geotech. J.*, 36(4): 612–624. https://doi.org/10.1139/t99-038.

Uzielli, M., G. Vannucchi, and K. K. Phoon. (2005). Random field characterisation of stress-normalised cone penetration testing parameters. *Géotechnique*, 55(1): 3–2. https://doi.org/10.1680/geot.2005.55.1.3.

Proceedings of the XVIII ECSMGE 2024
GEOTECHNICAL ENGINEERING CHALLENGES
TO MEET CURRENT AND EMERGING NEEDS OF SOCIETY
© 2024 the Authors
ISBN 978-1-032-54816-6
DOI 10.1201/9781003431749-329
Open Access: www.taylorfrancis.com, CC BY-NC-ND 4.0 license

ECSMGE 24
XVIII EUROPEAN CONFERENCE ON SOIL MECHANICS AND GEOTECHNICAL ENGINEERING

Challenges in the geotechnical characterisation of bauxite tailings (Red Mud)

Défis dans la caractérisation géotechnique des résidus de bauxite (Red Mud)

I. Lopes*, M. Garcia, G. Tavares
TPF Consultores de Engenharia e Arquitetura, Lisbon, Portugal

**isabel.lopes@tpf.pt*

ABSTRACT: The geotechnical characterisation of tailings from mining operations is a current challenge of great relevance. The geotechnical behaviour of tailings accumulation is very variable and depends on many factors, among others, the original mineralogy, the process used to obtain the ore, and the deposition form. Authors have studied tailings of various mineralogical origins, dealing with their geotechnical and geochemical particularities. The data presented in this paper comes from the study of Bauxite tailings, known as Red Mud. Tailings geotechnical characteristics are also a function of their disposal method, which depends on the percentage of solids, i.e. whether they were disposed as slurry (<50%), thickened (50% to 65%), paste (65% to 70%), or filtered (>70%), and if compaction processes were used. In this paper, the main Red Mud aspects and its geotechnical characteristics (obtained from literature) are presented, and the differences in the mechanical behaviour depending on the disposal method are discussed.

RÉSUMÉ: La caractérisation géotechnique des résidus miniers est un défi actuel de grande importance. Le comportement géotechnique des accumulations de résidus est très variable et dépend de nombreux facteurs, notamment de la minéralogie d'origine, du processus utilisé pour obtenir le minerai et de la forme du dépôt. Les auteurs ont étudié des résidus de diverses origines minéralogiques, en traitant leurs particularités géotechniques et géochimiques. Les données présentées dans cet article proviennent de l'étude des résidus de bauxite, connus sous le nom de *Red Mud*. Les caractéristiques géotechniques des résidus sont également fonction de leur processus de dépôt, qui dépend du pourcentage de solides, c'est-à-dire s'ils ont été déposés sous forme de boue (<50%), épaissis (50% à 65%), pâte (65% à 70%), ou filtrés (>70%), et si des processus de compactage ont été utilisés. Dans cet article, les principaux aspects de Red Mud et ses caractéristiques géotechniques (tirées de la littérature) sont présentés et les différences de comportement mécanique en fonction de la méthode de dépôt sont discutées.

Keywords: Tailings geotechnical behaviour; red mud; disposal method; CPTu.

1 INTRODUCTION

Red Mud results from the processing of bauxite ore to obtain alumina. To introduce and explain the site observations, based on literature, the main aspects, that are specific of the composition and behaviour of red mud are presented and are, also, described the different tailings disposal methods.

To show the differences in behaviour that will be presented in this case study, the results of CPTu tests will be used, as for the *in situ* geotechnical characterisation of tailings, is one of the tests established. One of the methods used for the separation between contractive and dilative behaviour is based on the Robertson (2016) charts.

In this paper is presented the separation between the different observed behaviours in the same red mud TSF, depending of the disposal method and are discussed the challenges felt on the TSF characterization and analysis.

2 RED MUD

2.1 Origin and composition

Red mud is a waste industrial product (tailing) from aluminium industries which is produced during the extraction of alumina from the bauxite ore. Bauxite is a weathered rock, typically with a soft structure (hardness between 1-3), containing two forms of hydrated aluminium oxide, in a quantity usually between 30-65%. These oxides are either predominantly monohydrate [AlO(OH)] or trihydrate [$Al(OH)_3$], represented by the minerals Gibbsite, Boehmite and/or Diaspore, which have a specific gravity (Gs) between 2.6-3.5. This ore has additional Fe_2O_3 as the main impurity. Although the minerals that compose bauxite ore have high Gs, the rock has a dry bulk density between 1.5 and 2.5 t/m^3 due to its high porosity.

The Bayer process is the commonly used process for the purification of this ore and it involves digesting the bauxite in a solution of NaOH at temperatures between 140 and 280°C (function of the mineralogy), under pressure. During the digestion process, aluminium reacts with the NaOH to form soluble sodium aluminate, leaving behind the Fe_2O_3 and other impurities. The process results in a highly alkaline pH=11-13 waste material, whose mineral components can include hematite, goethite, gibbsite, rutile, calcite, sodalite, and complex silicates. Notably, there is usually absence of quartz or clay minerals in this waste. The quantities of each mineral in the red mud are very variable and depend on the source bauxite and the original mineralogical composition of the ore is one of the most important factors influencing the red mud tailings properties (Table 1).

Table 1. Examples of chemical composition of different red muds produced in the world (adapted from Reddy et al., 2021).

Location	% Composition (by dry weight)										
	Fe_20_3	**Al_2O_3**	**TiO_2**	**CaO**	**SiO_2**	**Na_2O**	**MgO**	**P_2O_5**	**MnO**	**K_2O**	**LOI**
Brazil	19.85	19.87	2.66	4.61	14.34	7.35	-	-	-	-	27.20
China (1)	10.63	22.31	6.64	20.46	18.92	5.72	-	-	-	-	-
China (2)	29.79	22.96	1.83	2.03	21.24	8.93	-	-	-	0.03	12.19
China (3)	11.60	7.34	5.36	44.69	27.99	0.58	2.01	-	-	0.43	-
Greece	46.70	18.10	5.80	8.50	7.30	2.80	-	-	-	-	8.50
Hungary	31.63	10.50	5.90	11.66	12.20	6.09	0.53	0.55	0.34	0.05	-
India (1)	35.00 - 37.00	18.10 - 21.00	17.00 - 22.50	1.70 - 2.20	6.00 - 6.84	5.20 - 5.50	-	-	-	-	11.80 - 14.00
India (2)	44.00 - 47.00	17.80 - 20.10	8.20 - 10.40	1.00 - 3.00	7.50 - 8.50	3.50 - 4.60	-	-	-	-	10.80 - 14.00
India (3)	40.00 - 45.17	18.00 -27.00	2.50 - 5.15	1.50 - 2.50	5.70 - 16.00	3.64 - 4.50	-	-	-	-	11.00 - 15.00
Iran	22.17	13.98	7.17	24.25	13.00	4.20	2.01	0.16	0.06	0.42	9.55
Jamaica	49.50	16.50	7	5.50	3.00	2.30	-	-	-	-	11.60
Spain (1)	37.22 ± 0.33	12.40 ± 1.07	20.10 ± 0.59	6.30 ± 0.20	3.81 ± 0.16	4.64 ± 0.41	0.14	0.51	0.06	0.05	11.34
Spain (2)	31.80	20.10	22.60	4.78	6.10	4.70	0.20	-	-	0.03	-
Turkey	35.04	20.20	4.00	5.30	17.29	9.40	0.33	-	-	-	8.44

2.2 Geotechnical properties

Due to the high variability of combinations found it is difficult to generalize about red mud geotechnical behaviour. Both the original mineralogy, as the disposal method, strongly influence its behaviour. Nonetheless, some aspects are specific to its nature and can be found in literature (among others Newson et al., 2006 and Reddy et al., 2021):

- It is usually found in two grades: fine-grained "red mud" and coarse "red sand", being the "red mud" the more common type;
- Typical gradings show up to 20–30% clay sized, with most particles in the silt range, reason why some authors prefer the term *ferrosilt* to classify these materials, because of the high amount of red iron oxide and dominance of the silt size fraction. Despite that, some have been found with ≥50% of particles with less than 2 μm (clay sized), but it is a function of the digestion process used and of the characteristics of the ore body;
- Clay fraction grains microscopic analysis show equidimensional polyhedric grains with slightly rounded edges. Minerals of flat shape, typical of clay minerals, can hardly be found;
- They tend to have low plasticity (e.g., WL≈39-45%, IP≈10-15%) and are mainly ML in UCS. In spite of their IP and lack of clay minerals, they show many geotechnical properties similar to clayey tailings found in other mineral processing e.g. gold tailings;
- The specific surface area (BET) is between 10-30 m^2/g and the CEC (Cation Exchange Cap.) is comparable with kaolin or illite minerals;
- They present relatively high specific gravity (Gs=2.8-3.3), function of the strong presence of

iron minerals. Red mud tailings Gs is highly dependent on its mineralogical and chemical composition;

- Consolidation and settling has been found to be a function of the type and quantity of iron minerals i.e., Al-goethite, goethite, and hematite. In particular, very fine goethite can cause problems due to its relatively high Gs (=3.2) and high BET compared to the other oxide minerals;
- 1D compression tests indicate compression indices Cc=0.27-0.39, permeabilities k=(2-20)×10^{-7} cm/s and coefficients of consolidation c_v=(3-50)×10^{-3} cm^2/s and are therefore similar to silty-clay soils;
- Very high friction angles (ϕ') of 38-42° are also found for these materials, which are more typical of sandy soils;
- In situ undrained shear strengths are typically very high compared to uncemented clayey soils at equivalent liquidity indices (i.e. Su≥2 kPa for I_L>1) and sensitivities from 5 to 15 are commonly found (i.e. very low residual Su). Thixotropy has been observed with these materials and apparent preconsolidation pressures in excess of actual overburden pressures are found (apparent overconsolidation). Hence there is a strong indication that some red muds are cemented or aggregated;
- Leaching by freshwater and acid neutralization has been found to reduce in situ void ratios and compression indices.

Some examples values obtained for geotechnical properties and parameters, in different locations, are presented in Table 2, as extracted from literature. These values should only be used as reference as there is details about the tests made, and without indication, for instance, on the type of shear tests performed or on the disposal method used. This last point, as will be presented, has a big influence on the red mud tailings behaviour. To use the data here presented, or to obtain more information about the results and thier origins, it is strongly recommended to consult the original paper (Reddy et al., 2021).

Table 2. Examples of geotechnical parameters observed in different red muds produced in the world (adapted from Reddy et al., 2021).

Location		India (a)	India (b)	UK	Guinea	Spain	China	Jamaica
Physical property								
Specific gravity, Gs		2.85 - 3.45	2.85 - 2.97	3.05	3.20 – 3.70	3.44	2.77	2.70 - 3.70
pH		10.7 – 11.5	10.2 - 11.0	11.6	13.1 - 13.5	10.2	-	11.3 - 12.5
Surface area (m^2/g)		20.4 - 47.2	-	-	-	23.7	-	-
Consistency limits	**WL**	21 - 45	40 - 45	54	44 - 66	39±2	64	45
	WP	16 - 36	30 - 35	40	33 - 36	31±2	42	36
	IP	5 - 7	5 - 14	14	11 - 26	8	22	9
% Grain. fraction	**Gravel**	0	0	0	0	0	0	0
	Sand	5 - 15	10 - 14	0	36	12	5	20 - 30
	Silt	43 - 76	43 - 57	80	44	50	75	50
	Clay	22 - 35	29 - 39	20	20	38	20	20 - 30
USCS		ML	ML	MH	ML-CL	ML	MH	ML
Compaction	**γ_{dmax} (kN/m^3)**	12.5 - 17.0	14.5 - 16.4	17.5	15.5	16.9	17.0	-
	w_{opt} (%)	22 - 34	33	-	30	7 - 35	50	-
Consolidation	**c_v (cm^2/s)**	3 - 50×10^{-3}	-	-	-	-	-	7.5×10^{-4} to 3×10^{-2}
	c_c	0.093	-	0.41	0.28 - 0.38	-	-	0.268
	ϕ(°)	34 - 42	26 - 28	38 - 42	30 - 35	-	28 - 33	37 - 45
Strength	**Cohesion (kPa)**	7 - 28	10 - 20	10 - 20	-	-	11 - 35	-
	q_u (kPa)	102 - 136	143	130	-	-	-	20 - 175
Hydraulic conductivity	**k (cm/s)**	5.832×10^{-4} to $.13\times10^{-8}$	2 - 30×10^{-6}	2 - 10×10^{-7}	1.4 - 6.7×10^{-6}	-	4.5×10^{-6}	10^{-5} to 10^{-7}
Swelling property	**Free swell index (%)**	No swell	No swell	No swell	No swell	Very low	-	-

Other specific information is found in literature that is important to understand the red mud behaviour. For instance, Newson et al. (2006) observed the microstructure of a red mud specimen from a site in the UK and found that it is composed of a collection of small, apparently aggregated particles. Closer inspection shows a layer of material coating most of the particle surfaces (cementation?), composed of crystals with a cubic habit. X-ray analysis suggests that the coating is composed largely by hydroxysodalite (feldspar). Cementation can help to justify the high peak Su and the cohesion values obtained in shear testing.

Another important characteristic is red mud dispersivity. According with Rout et al. (2013), the results of the crumb tests, double hydrometer tests and turbidity tests made on red mud samples show that it is highly to extremely dispersive, with a dispersion ratio of 94% in the double hydrometer test.

One of the main parameters used to understand the tailings geotechnical behaviour is the void ratio (e), even though the huge difficulties in characterizing it in situ. In literature are found values for red mud bulk and dry densities, as being the parameter that gives the idea of their in situ state, but due to the high Gs of its grains, these parameters can be misleading. Newson et al. (2006), for the UK red mud analysed, obtained e values, both for intact and reconstituted specimens, varying between 1.76-1.45, but Carrier III et al. (1983) refers the value of 9 for the e_0 of red mud. Also here, the disposal method is very important for the void ratios obtained/observed.

3 TAILINGS DISPOSAL

Generally, tailings are the combination of the fine-grained solid materials (usually silt-sized), remaining after extraction from the ore of metals and minerals, with the water used in the recovery process. Depending on solid/liquid ratio of the tailings, they can be disposed (Figure 1 and Figure 2) as slurry (with the higher water content), as thickened tailings and paste, or as cake (often called dry stacking), that can be "wet" or "dry". The disposal can also be made in co-disposal with coarse wastes. The different solids concentrations are achieved by dewatering, and the concentrations vary for different tailings, since particle size distributions, clay mineral content, particle shape, mineralogy, electrostatic forces and flocculant dosing vary considerably and deeply influence the final result (Australian Government, 2016).

Tailings are commonly pumped as a slurry in a pipeline and discharged sub-aerially into a surface Tailings Storage Facility (TSF). The consistency of the slurry (% solids by mass) depends on the type of tailings, the particle size distribution and specific gravity, and the extent of thickening at the processing plant (Figure 1). Upon discharge (Figure 2), tailings slurry segregates, being the coarser and higher Gs particles deposited on the upper beach after which remains substantial supernatant water that carries finer and lower Gs particles forward into the decant pond. The segregation and settling of the tailing particles result in a significant curvature of the beach profile, i.e. more steep near the point of discharge and becoming flatter further down the beach profile. Thickened tailings still show some segregation, settling and bleed on placement, accompanied by some curvature of the beach profile, while paste tailings have a non-segregating, non-settling consistency that releases only small quantities of water after placement.

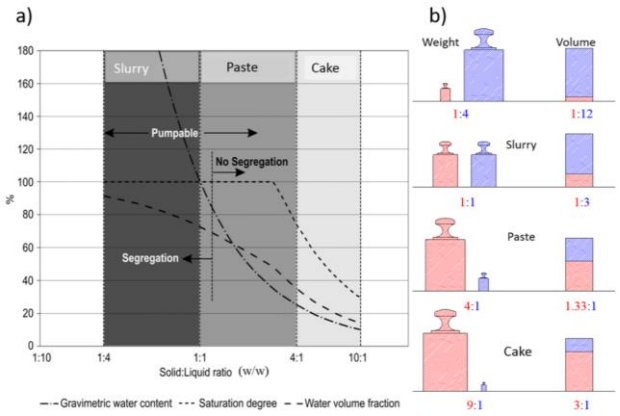

Figure 1. a) Types of mine tailings according to its solid/liquid ratio. including profiles for gravimetric water content. saturation degree. and water volume fraction and b) comparison between w/w and v/v ratios for a particle density of 3g/cm³ (Pacheco, 2018).

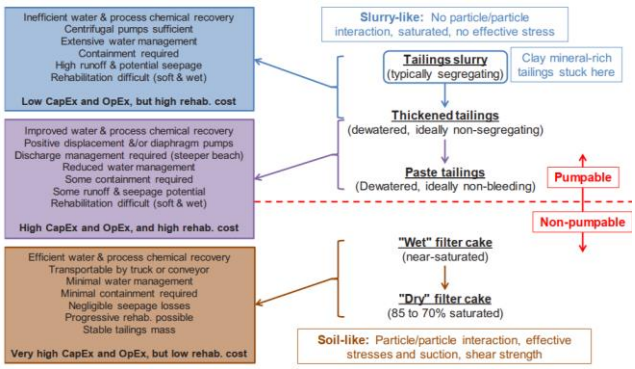

Figure 2. Tailings Continuum (Australian Government, 2016).

Thickening tailings reduces the quantity of water delivered to the TSF, which reduces the risks of overtopping, reduces seepage, evaporation losses, and reduces the risk of TSF embankment failure by

lowering the pond level and reducing the phreatic surface within the embankment. Thickening of tailings in the processing plant before disposal also enables process water to be recycled directly back to the plant, reducing water losses and reducing plant raw water demand.

Tailings can be also brought to a 'solid-like' state by centrifuging or filtration, producing a consistency that is potentially transportable by truck or conveyor. True dry stacking requires that the flocculated tailings be filtered, usually under pressure or possibly under vacuum to produce a product that is transportable and stackable using 'dry' material transportation and disposal techniques. In this state they may then be placed, spread and compacted to form an unsaturated, dense and stable tailings 'dry stack'.

4 SITE OBSERVATIONS

4.1 Site tailings disposal description

The site in analysis is a red mud TSF where there were 3 stages of deposition, one overlapping the other. At first, the operation started with the deposition of tailings in slurry form with 30% solids. During this 1st deposition stage, tailings were in liquid state and were pumped as a wet slurry through a pipeline and discharged sub-aerially. Due to the high specific gravity of the grains, the solid phase sedimented and there was supernatant water remaining ("pond").

In the 2nd deposition stage, after introduction of the use of drum filter and dumper in the installation, the red mud was transported in cake form, with a solid content of around 65-70%, but the discharge of the tailings was made by trucks into a "pond" (Beach Below Water Disposal - BBW).

When the surface of the TSF achieved a dry situation (without supernatant water), the 3rd deposition stage has started. At this stage, a almost dry material with 70 to 75% solids was transported using trucks and stacked, spreading and compacted using a bulldozer.

4.2 CPTu results

Two CPTu campaigns were made in the site, in different years. The CPTu data were processed following the state-of-the-art methodologies, one of which is detailed in Roberston (2016).

The results obtained were similar, allowing to separate the different stages. Nonetheless, as they were made in different moments of deposition, the number of points sampled in the red mud tailings of the different deposition stages is different, i.e. 53% in the 1st dep. stage, 31% in the 2nd and only 16% in the 3rd. An example of the results, separating the different stages of tailings deposition, above the natural soil, is presented in Figure 3.

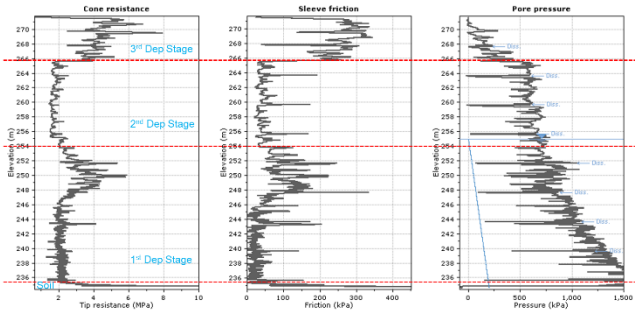

Figure 3. Example of a CPTu test made in study site, showing the division between the different deposition stages.

Being the grain size distribution of the red mud tailings, in the different deposition stages, similar, the main differences in the site are due to the disposal method and to the installed water level (WL), observed to be slightly above the top of the tailings of the 1st deposition stage.

When looking to the points plotted in the Robertson (2016) SBTn classification charts (Figure 4) it is evident the difference in the behaviour between the 1st dep. stage (slurry below the water table), where the data appear in the clay contractive (CC) area of the chart, but expanding to the CCS sensitive materials, and the dilative behaviour of the 3rd dep. stage (stacked filtered dry tailings above the WL). To note is the observed behaviour of the red mud tailings of the 2nd dep. stage, that were deposited with high solids content, but in BBW. These tailings, even though are not below the WL, are clearly close to saturation and present low resistance. When ploting in the SBTn chart they appear with a behaviour very close to the one observed in the slurry, mainly with clay contractive behaviour type.

As in all tailings, analysing and interpreting the behaviour od red mud, depends not only on the results of the site investigation tests, but also on understanding the TSF history.

5 CONCLUSIONS

Tailings studies are very challenging, and the difficulties start, frequently, with the difficulty to build the initial ground model, due to lack of data from construction period, and to define the TSF history. In the case of red mud, the challenges continue due to: its mineralogical content, that promotes cement mineral neoformation; the dominant silt fraction, that promotes partial drainage when tested; high Gs; sometimes high

e_0; and high sensitivity, with the observation of high peak strength and very low residual strength.

From the site, the results show that, as expected, the dry stacking presents mainly dilative behaviour and that slurry tailings present contractive behaviour. To note, in this site, is the clear evidence that the disposal of tailings in BBW conditions, even if they are filtered, fully saturates the materials resulting in contractive behaviour, showing the importance of the deposition on the geotechnical behaviour.

It is also important to note that, while the 3rd dep. stage materials are dilatant, there are no guarantees for the TSF stability, as stacking materials (with lower *e* and high unit weight) above contractive materials may induce excess pore pressures, being the contractive materials, the ones ruling the overall stability of the facility.

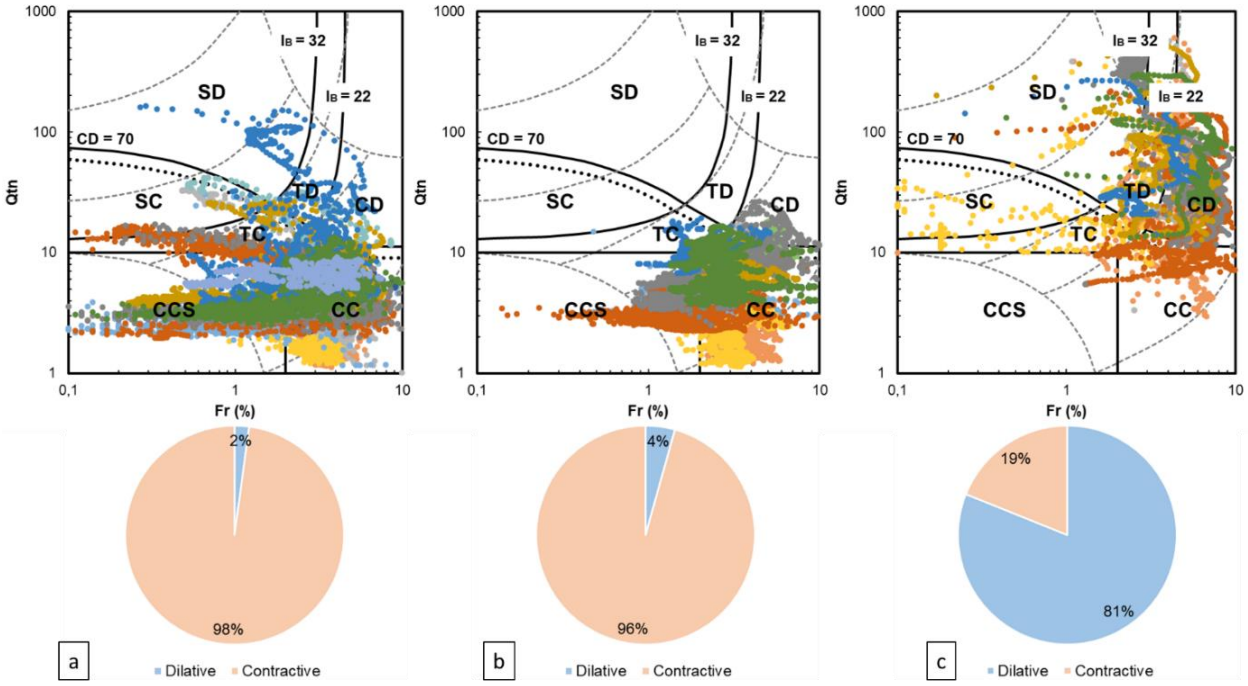

Figure 4. Red mud updated SBTn classification (Roberston, 2016) and percentage of points showing contractive or dilative behaviour in tailings disposed, in the same TSF, as: a. slurry (30% solids); b. filtered tailings (65% solids) disposed in beach below water; c. filtered tailings (70% solids) dry stacking.

REFERENCES

Carrier, II, W.D.; Bromwell, L.G.; Somogyi, F. (1983). Design capacity of slurried mineral waste ponds, *J. Geotechnical Engrg*, 109, pp. 699-716.

Newson, T.; Dyer, T.; Adam, C.; Sharp, S. (2006). Effect of structure on the geotechnical properties of bauxite residue, *Journal of Geotechnical and Geoenvironmental Engrg*, 132 (2), pp.143-151, DOI:10.1061/(ASCE)1090- 0241(2006)132:2(143).

Rout, S.K.; Sahoo, T.; Das, S.K. (2013). Design of tailing dam using red mud, *Central European Journal of Engineering*, 3(2), pp. 316-328, DOI:10.2478/s13531-012-0056-7.

Pacheco, R.L.R. (2018). Static liquefaction in tailing dam and flow failure. *Sem. Riesgos Geotécnicos*. Master en Ing. Geológica. UCM 29/11/2018. 12p.

Australian Government (2016). Tailings Management: Leading practice sustainable development program for the Mining Industry.

Reddy, P.S; Reddy, N.G.; Serjun, V.Z.; Mohanty, B.; Das, S.K.; Reddy, K.R.; Rao, B.H. (2021) Properties and assessment of applications of red mud (bauxite residue): Current status and research needs, *Waste and Biomass Valorization* 12, pp 1185–1217, DOI:10.1007/s12649-020-01089-z.

Robertson, P.K. (2016). Cone penetration test (CPT)-based soil behaviour type (SBT) classification system — an update. *Can. Geotech. J.* 00: 1–18, https://doi.org/10.1139/cgj-2016-0044.

Proceedings of the XVIII ECSMGE 2024
GEOTECHNICAL ENGINEERING CHALLENGES
TO MEET CURRENT AND EMERGING NEEDS OF SOCIETY
© 2024 the Authors
ISBN 978-1-032-54816-6
DOI 10.1201/9781003431749-330
Open Access: www.taylorfrancis.com, CC BY-NC-ND 4.0 license

ECSMGE 24
XVIII EUROPEAN CONFERENCE ON SOIL MECHANICS AND GEOTECHNICAL ENGINEERING

Assessment of shear stiffness and damping variations in undrained cyclic triaxial tests of iron ore tailings

Évaluation des variations de la rigidité au cisaillement et de l'amortissement dans des essais triaxiaux cycliques non drainés de résidus de minerai de fer

J.C. Lourenço*
University of Coimbra and TPF Consultores, Portugal

D.L.D. Camacho, P.A.L.F. Coelho
University of Coimbra, Coimbra, Portugal

jclourenco@uc.pt

ABSTRACT: Tailings dams pose severe risks to society and to the environment. Many failures occur worldwide, suggesting that their behaviour remains poorly understood. This is particularly true in the case of tailings dams built in seismically active regions, where the ability to properly understand and model the behaviour of ore tailings under cyclic loading is critical. This paper aims to clarify the undrained cyclic behaviour of iron ore tailings observed in triaxial tests on reconstituted samples of mining waste obtained from Torre de Moncorvo Iron Mine. Firstly, the undrained cyclic behaviour of this unconventional geomaterial is compared with that of other typical soils, including loose granular soils. Secondly, the degradation of the shear stiffness and the increase in the damping ratio with the number of loading cycles are assessed using suitable software created to compute the values of these properties relative to each hysteretic loading cycle automatically. In addition, the challenges in analysing real undrained cyclic triaxial tests on iron ore tailings are discussed in detail. Based on the results presented in the paper, the authors expect to shed further light on the undrained cyclic response of ore tailings under seismic loading and the degradation of the mechanical properties, namely the stiffness and the damping, caused in each loading cycle.

RÉSUMÉ: Les barrages de résidus miniers présentent des risques graves pour la société et pour l'environnement. De nombreuses défaillances surviennent dans le monde entier, suggérant que leur comportement reste mal compris. Cela est particulièrement vrai dans le cas des barrages de résidus miniers construits dans des régions sismiquement actives, où la capacité à comprendre et modéliser correctement le comportement des résidus de minerai sous chargement cyclique est cruciale. Cet article vise à clarifier le comportement cyclique non drainé des résidus de minerai de fer observé dans des essais triaxiaux sur des échantillons reconstitués de déchets miniers obtenus de la mine de fer de Torre de Moncorvo. Tout d'abord, le comportement cyclique non drainé de ce géo-matériau non conventionnel est comparé à celui d'autres sols typiques, y compris des sols granulaires lâches. Deuxièmement, la dégradation de la rigidité au cisaillement et l'augmentation du rapport d'amortissement avec le nombre de cycles de chargement sont évaluées à l'aide d'un logiciel approprié créé pour calculer automatiquement les valeurs de ces propriétés par rapport à chaque cycle de chargement hystérétique. De plus, les défis liés à l'analyse des essais triaxiaux cycliques non drainés réels sur les résidus de minerai de fer sont discutés en détail. Sur la base des résultats présentés dans l'article, les auteurs espèrent apporter davantage d'éclairage sur la réponse cyclique non drainée des résidus de minerai sous chargement sismique et la dégradation des propriétés mécaniques, à savoir la rigidité au cisaillement et l'amortissement, causée à chaque cycle de chargement.

Keywords: Tailings; earthquakes; cyclic liquefaction; stiffness degradation; damping variation.

1 INTRODUCTION

Tailings dams are enormous geotechnical structures built to contain the waste resulting from mining activities. Recently, due to significant failures around the world (e.g., Robertson et al., 2029), the safety of these structures has been under strict review. When tailings dams are built in seismically active regions, accidents are also common (e.g., Vergudo et al., 2012), not only due to the possible occurrence of cyclic liquefaction but also due to the inertial forces imposed by wave propagation within the dam. Thus, the degradation of tailings properties imposed during undrained cyclic loading must be assessed to ensure the safety of tailings dams under dynamic loading. As limited data exist in this field, this paper discusses interpreting the undrained cyclic behaviour of iron ore tailings collected from a Portuguese mine.

2 EXPERIMENTAL PROGRAM

Research Project GeoSusTailings aims to improve tailings management's safety and sustainability, applying a geotechnical approach to characterise and numerically model tailings behaviour. Herein, the cyclic behaviour of iron ore tailings is discussed.

2.1 Torre de Moncorvo iron tailings

Torre de Moncorvo iron tailings are used in this paper to assess the cyclic undrained behaviour of mining waste. The mine is in the North of Portugal (Figure 1) and was reactivated under the concession of Aethel Mining. Table 1 lists the main properties of the low plasticity iron-rich tailings from an old deposit with particles having dimensions in the silty-sand range. The unusually high values of G and γ_d are remarkable and result from the significant presence of high-density iron particles, which increases the risk of particle segregation during reconstitution.

2.2 Sample reconstitution of studied tailings

Slurry-based reconstituted samples of the studied iron ore tailings were tested and used for the analysis. The sample reconstitution method and the capability of reconstituted samples to qualitatively replicate the behaviour of undisturbed samples collected from the site are depicted by Coelho et al. (2022). Overall, the reconstituted samples obtained through consolidation of a uniform liquid slurry could avoid segregation and replicate the field behaviour satisfactorily.

2.3 Cyclic triaxial testing

Undrained cyclic triaxial tests are commonly used to address the behaviour of granular saturated soils under the effects of dynamic loading, namely if earthquake-induced liquefaction is a relevant phenomenon. Strain-controlled undrained cyclic triaxial tests with fixed deviator stress peaks were performed on reconstituted samples isotropically consolidated at 200 kPa. These were loaded and unloaded in each cycle between the fixed predefined minimum and maximum deviatoric stress values, imposing variable cyclic stress ratios.



Figure 1. Location of Torre de Moncorvo Iron Mine.

Table 1. Physical and identification properties of Torre de Moncorvo iron tailings.

Property	In situ range
γ_d [kN/m^3]	27~29
G [-]	4.4~5.1
e [-]	0.60~0.70
D_{50} (mm)	0.05~0.06
D_{10} (mm)	0.012~0.23
P.L. [%]	14~16
L.L. [%]	19~21
P.I. [%]	4~6

2.4 Undrained cyclic triaxial behaviour of Torre de Moncorvo iron tailings

The undrained cyclic triaxial behaviour of the studied tailings is similar to that of granular materials under similar loading conditions. In particular, the concepts of critical state and phase transformation lines (Ishihara et al., 1975) are valid for describing tailings' stress paths and stress-strain responses under undrained cyclic loading. More importantly, the progressive reduction of the effective confining stress up to near-zero values and the ensuing degradation of the tailings' mechanical behaviour in each cycle can be identified (Figure 2). This degradation is often assessed through the reduction of the shear stiffness and the variation of damping with the shear strain, as Seed et al. (1986) proposed. Even if the so-called degradation curves are more popular for describing the behaviour of natural granular materials, these can also be used for natural soils with variable plasticity (e.g., Okura & Ansal, 2007) or tailings (e.g., Urbano et al., 2017) under undrained cyclic loading causing liquefaction. However, some practical difficulties arise when evaluating the stiffness and damping of soils under cyclic loading, namely for large deformations. It is also true for the iron ore tailings tested, which motivated the creation of a numerical tool to calculate the stiffness and damping consistently for each cycle.

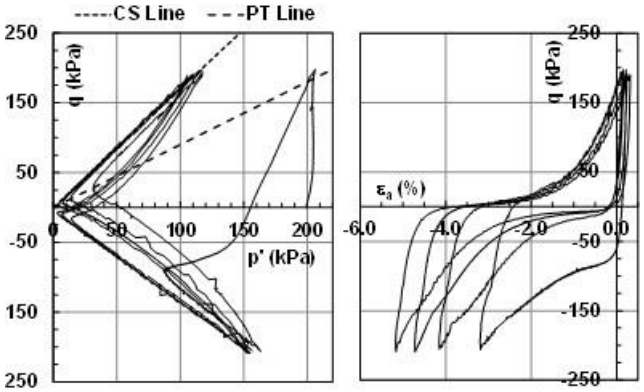

Figure 2. Undrained cyclic triaxial behaviour of Torre de Moncorvo Iron Tailings.

3 TOOL TO ASSESS THE STIFFNESS AND DAMPING RATIO VARIATIONS

The secant shear modulus (G) and damping ratio (ξ) for each cycle, defined in Figure 3, exhibit significant variation with the shear strain. A GNU/Octave script, detecting and individualising all the cycles, was developed to assess these variations. As the cyclic stress-strain responses are not closed, symmetrical, or as well-defined as the example shown in Figure 3, some processing is required in each cycle.

3.1 Numerical procedures

In undrained triaxial tests, no volumetric strain exists (1), and the shear strain relates to the axial strain, as described in (*2*). Moreover, the shear modulus (G) relates the shear stress with the shear strain (*3*):

$$\epsilon_v = \epsilon_a + 2\epsilon_r = 0 \quad (1)$$

$$\gamma = (\epsilon_a - \epsilon_r) = \frac{3}{2}\epsilon_a \quad (2)$$

$$G = \frac{\tau}{\gamma} = \frac{\frac{q}{2}}{\frac{3}{2}\epsilon_a} = \frac{q}{3\epsilon_a} \quad (3)$$

The script has the following sections:

i) detection of the global maximum and minimum values of deviatoric stress (q) for each cycle ($q_{max,i}$ and $q_{min,i}$), local extremes being discarded, in order to individualise all the cycles by detecting the starting point for the extension and compression stress paths;

ii) for the ith cycle, the script calculates the deviatoric strains that correspond to $q_{max,i}$, $q_{min,i}$ and $q_{end,i}$ (i.e., $\varepsilon_{d,qmax,i}$, $\varepsilon_{d,qmin,i}$ and $\varepsilon_{d,end,i}$); the extension path starts in $q_{max,i}$ point and ends at $q_{min,i}$ point, and the compression path starts in $q_{min,i}$ and ends in $q_{end,i}$;

iii) the extension closed cycle is built; the cycle deviatoric strain ($\varepsilon_{d,ext,i}$) for the extension section is given by $\varepsilon_{d,qmax,i}$ - $\varepsilon_{d,qmin,i}$; an extension symmetry line is formed by connecting points ($\varepsilon_{d,qmax,i}$, $q_{max,i}$) and ($\varepsilon_{d,qmin,i}$, $q_{min,i}$), the closed cycle results from mirroring the original extension path around the symmetry line; the cycle is translated to centre it in $\varepsilon_{d,i} = 0$ (Figure 4);

iv) the compression closed cycle is built; for the compression section, the cycle deviatoric strain ($\varepsilon_{d,comp,i}$) is determined by $\varepsilon_{d,qend,i}$ - $\varepsilon_{d,qmin,i}$; an extension symmetry line is formed connecting the points ($\varepsilon_{d,qmin,i}$, $q_{min,i}$) and ($\varepsilon_{d,qend,i}$, $q_{end,i}$), and the closed cycle is formed by mirroring the original compression path around the symmetry line; the cycle is translated to have its centre in $\varepsilon_{d,i} = 0$;

v) the shear stiffness (G) and the damping ratio (ξ) for the ith cycle are determined (Figure 4).

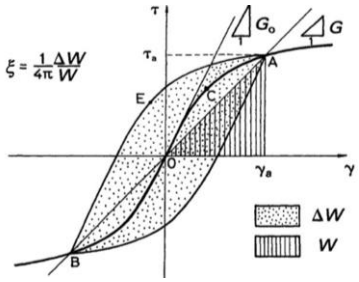

Figure 3. Definition of elastic (G_0) and secant (G) shear moduli and damping ratio (ξ), relating dissipated (ΔW) and elastic stored (W) energies (adapted from Ishihara, 1996).

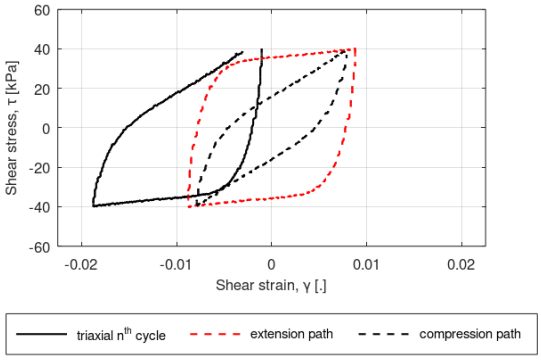

Figure 4. Extension and compression closed cycles, defined after a generic triaxial cycle.

3.2 Results obtained

Figure 5 illustrates the cyclic shear stress- shear strain responses for several cycles obtained after processing using the script, showing that the stiffness degradation resulting from the compression and extension sections is similar. On the contrary, the damping ratio depends more on the section of the curve considered during processing. Figures 6 and 7 highlight this qualitative assessment, the stiffness and damping values for all the cycles registered in the test being plotted against shear strain. In fact, the stiffness degradation with the shear strain (Figure 6, G_0 not available) has a shape typically observed in natural soils (e.g., Okura and Ansal, 2007) and is quite independent of the selected curve path.

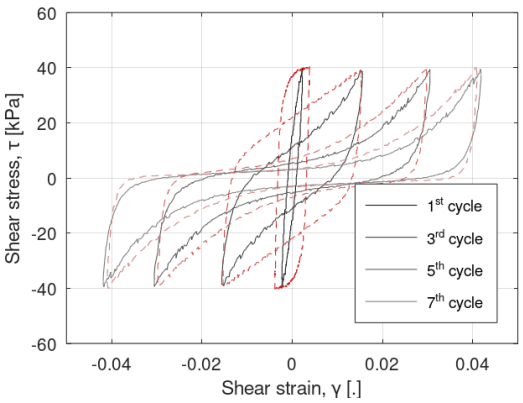

Figure 5. Cyclic shear stress- shear strain derived from the compression and extension sections after processing.

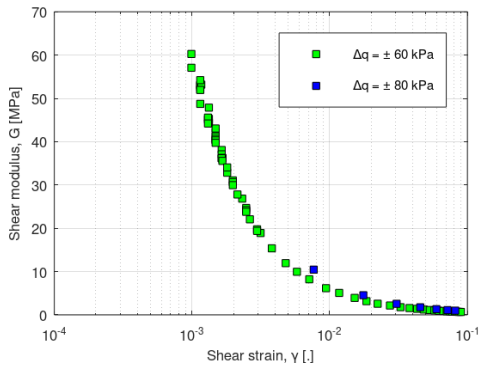

a) extension path

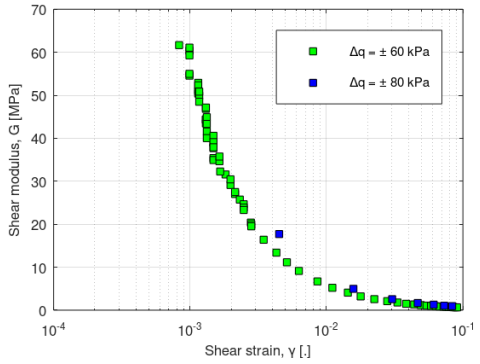

b) compression path

Figure 6. Shear modulus evolution with shear strain.

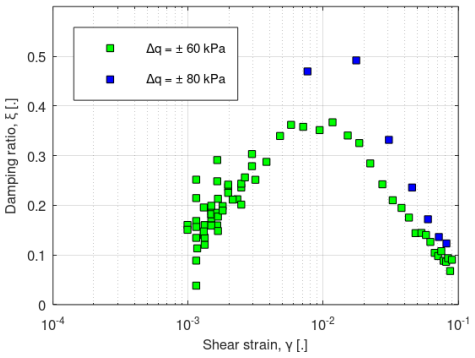

a) extension path

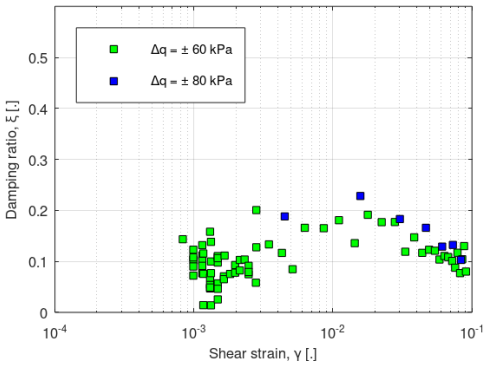

b) compression path

Figure 7. Damping ratio evolution with shear strain.

In contrast, the variation of damping with the shear strain has two parts: firstly, some scatter is observed at low strains, possibly due to calculation challenges; secondly, after reaching a peak at around 10^{-2} of shear strain, the damping decreases with shear strain. This latter behaviour is physically doubtful but may find some support in Okura and Ansal (2007), as damping stabilizes at 10^{-2} of shear strain. But as the shape of the stress-strain curves observed differs from usual curves (Figure 3), normal calculation methods may not apply.

4 CONCLUSIONS

A script is proposed to assess the shear modulus and damping ratio variation with shear strain observed in undrained cyclic triaxial tests on iron tailings. The results show that degradation curves match those observed in natural soils (e.g., Okura and Ansal, 2007) while damping variation is physically debatable and requires further validation through alternative tests.

ACKNOWLEDGEMENTS

This research is funded through F.C.T.'s Research grant PTDC/ECI-EGC/4147/2021.

REFERENCES

Coelho, P.A.L.F., Camacho, D.L.D., Gobbi, F.S. & Araújo Santos, L.M. (2022) Sample reconstitution for evaluating the cyclic liquefaction resistance of iron ore tailings, *20th ICSMGE*, Sydney, Australia.

Ishihara, K., (1996). *Soil behaviour in earthquake geotechnics*. Oxford Univ. Press, 1996. https://doi.org/10.1093/oso/9780198562245.001.0001.

Ishihara, K., Tatsuoka, F. & Yasuda, S. (1975). Undrained deformation and liquefaction of sand under cyclic stresses. *Soils & Foundations*, 15(1). https://doi.org/10.3208/sandf1972.15.29.

Okura, D. V.; Ansal, A. (2007). Stiffness degradation of natural fine-grained soils during cyclic loading, *Soil Dynamics & Earthq. Eng.*, 27(9): 843–854. http://dx.doi.org/10.1016/j.soildyn.2007.01.005.

Robertson, P. K., Melo, L., Williams, D. & Wilson, G. W. (2019) *Report of the Expert Panel on the Technical Causes of the Failure of Feijão Dam I*.

Seed, H.B., Wong R.T., Idriss, I.M. & Tokimatsu K. (1986) Moduli and Damping Factors for Dynamic Analyses of Cohesionless Soils, *JGE ASCE*, 112(11). https://doi.org/10.1061/(ASCE)0733-9410(1986)112:11(1016).

Urbano, S., Puma, D., Ovalle, C. & Sáez, E. (2017) Monotonic and cyclic behavior of thickened copper tailings, *19th Intern. Conference on Soil Mechanics and Geotechnical Engineering*, Seoul 2017.

Verdugo R. et al (2012) Seismic Performance of Earth Structures during the February 2010 Maule, Chile Eq.,*Eq. Sp. 28* https://doi.org/10.1193/1.4000043.

Proceedings of the XVIII ECSMGE 2024
GEOTECHNICAL ENGINEERING CHALLENGES
TO MEET CURRENT AND EMERGING NEEDS OF SOCIETY
© 2024 the Authors
ISBN 978-1-032-54816-6
DOI 10.1201/9781003431749-331
Open Access: www.taylorfrancis.com, CC BY-NC-ND 4.0 license

ECSMGE 24
XVIII EUROPEAN CONFERENCE ON SOIL MECHANICS AND GEOTECHNICAL ENGINEERING

Eurocode 7 – Second generation: anchors, rock bolts and soil nailed structures

Eurocode 7 – Deuxième generation - Ancrages, boulons de roche et structures clouées au sol

N. Maca*
TITAN POLSKA Sp. z o.o., Krakow, Poland
**natalia.maca@titan.com.pl*

ABSTRACT: Among the objectives of the second generation of Eurocode 7 was to consider developments in the industry, including the introduction of common geotechnical structures so far not covered in the Eurocodes, aiming towards harmonising geotechnical design. Among the new structures introduced in the EN 1997-3 are rock bolts and soil-nailed structures, which are the paper's focus. To complement the discussion on tension-supporting elements, the paper also briefly describes the anchor clause's revision. It provides an overview of significant aspects of geotechnical design, considering limit states, material and durability requirements and demonstrates verification methods. As the reliability of the structures in question in the whole process, from design through execution to testing, is to be harmonised, some guidance to the compulsory supplement standards is also provided.

RÉSUMÉ: L'un des objectifs de la deuxième génération de l'Eurocode 7 était de prendre en compte les développements dans l'industrie, y compris l'introduction de structures géotechniques communes jusqu'à présent non couvertes par les Eurocodes, dans le but d'harmoniser la conception géotechnique. Parmi les nouvelles structures introduites dans l'EN 1997-3 figurent les boulons de roche et les structures clouées au sol, qui font l'objet du présent document. Pour compléter la discussion sur les éléments de support de tension, le document décrit également brièvement la révision de la clause sur les ancrages. Il donne un aperçu des aspects importants de la conception géotechnique, en tenant compte des états limites, des exigences en matière de matériaux et de durabilité, et démontre les méthodes de vérification. Étant donné que la fiabilité des structures en question doit être harmonisée tout au long du processus, de la conception aux essais en passant par l'exécution, des indications sur les normes complémentaires obligatoires sont également fournies.

Keywords: Eurocode 7; standardisation; anchors; rock bolts; soil nails.

1 INTRODUCTION

The second generation of Eurocode 7 will consist of three parts, denoted here as prEN 1997-1 (CEN 2024a), prEN 1997-2 (CEN 2024b) and part 3 which contains design rules specific to a particular type of geotechnical structures prEN 1997-3 (CEN 2024c).

Among the objectives of the second generation of Eurocode 7 was to take account of developments in the industry, including the introduction of new chapters addressing commonly used geotechnical structures so far not covered in the Eurocodes, aiming towards the harmonisation of geotechnical design. It should be noted that even if the structures in the new content are widely used in Europe, a common design approach has yet to be available and national practices are considerably different. Thus, drafting the new clauses was challenging and ended with the current form of consensus.

The paper focuses on anchors, rock bolts and soil nailed structures. While anchors are familiar to the reader and the design requirements within their scope have been slightly revised, the remaining ones are entirely new content barely mentioned in the first generation of Eurocode 7 (CEN, 2004).

As a consequence of the changes in the entire set of Eurocodes and prEN 1997-3 itself, as well as the harmonisation of the general rules for structural and geotechnical design, the design aspects of geotechnical elements within the scope of the paper are closely linked to other parts of Eurocode 7, which should therefore be considered together.

2 COMMON ASPECTS OF DESIGN

2.1 Design concept in prEN 1997-3

One of the significant features in prEN 1997-3 is that it contains many references to the other two parts (CEN, 2024a, 2024b) and other structural Eurocodes, as well as the execution and testing standards. This is an effect of the increase of harmonisation of structural and geotechnical design, as well as the close linking of all stages of construction from design through to execution and testing.

Within the new Eurocode 7 itself, the design principles for all geotechnical structures are more consistent. Thus, in prEN 1997-3 anchors in Clause 8 and rock bolts in Clause 11 are described as single supporting elements being a part of a larger structure. Therefore, the load acting on these elements and general aspects of the design of the structures supported by these elements are defined in different clauses: Clause 4 (Slopes, cuttings, and embankments), 5 (Spread foundations), 7 (Retaining structures) and in some cases Clauses 6 (Piled foundations) or 9 (Reinforced fill structures). Soil nailed structures are defined in Clause 10, but general design aspects are referenced in the corresponding clause where the soil nails are used. Also, as structures in the scope are often rely on groundwater control, the guidance on its measures is given in Clause 13.

2.2 Different tension supporting elements – definitions and clarification

One of the aims of the revision of Eurocode 7 was to include and clarify all standard tension supporting elements, addressing their specifics in the design. As they can be constructed and executed in the same way and often in the same ground condition, clear distinction is necessary so that the proper design path for this application is used. Thus, the elements distinguishing features are defined as:

- Tension piles in Clause 6 are piles transferring axial tension force by friction between the surface of the pile and the adjacent ground;
- Anchors in Clause 8 are elements transmitting a tensile load from the anchor head through a free length to into the ground (soil, rock or fill);
- Soil nails in Clause 10 are reinforcing elements mobilising resistance with the ground along the entire length, working mainly in tension, creating composite soil nailed structures;
- Rock bolts in Clause 11 are reinforcing elements for stabilising rock excavations and slopes, transferring load from the unstable exterior to the confined interior of the rock mass, including doweling to prevent shear failure through discontinuities.

The summary of the mode of operation with the referenced standards is presented in Figure 1. Corresponding verification methods with regulations regarding execution and tests result in diverse safety factors of the given element.

element	anchor	micropile	soil nail	rock bolt
design	Clause 8	Clause 6	Clause 10	Clause 11
execution	EN 1537	EN 14199	EN 14490	[future EN 14490]
testing	EN ISO 22477-5	EN ISO 22477-2	prEN ISO 22477-6	prEN ISO 22477-6
mode of operation	individual effect	individual effect	group effect	individual effect
	tension	tension	tension (doweling negligable)	tension/ doweling
	free length	no free length	no free length	no free length
	active (prestressed)	passive	passive (may be pre-loaded)	passive (may be pre-stressed)
	without slope deformation	with slope deformation	with slope deformation	with slope deformation
	100% tested (NDP)	3% tested (NDP)	2-3% tested (NDP)	0-2% tested (NDP)

Figure 1. Comparison of tension supporting elements.

2.3 Transition between soil and rock

Following the above discussion on the definitions, one common question in the drafting process was whether the stabilised rock mass slope should be designed according to the rock bolt or soil nail clause and, consequently, which verification methods and partial factors are allowed. This question is justified as the structures in the scope of the paper could be applied in the whole spectrum of ground conditions: from soil (also fill) and weak to hard rock mass. In many cases, a clear distinction between soil and rock is impossible, and we can observe a smooth transition in the continuum between of soil and rock. Thus, if the precise categorisation of the ground condition is not feasible, the Eurocode leaves it up to the designer to choose what ground model and element behaviour, either rock bolt or soil nail, should be applied.

2.4 Material and durability

One of the improvements in the second generation of Eurocode 7 is the compilation and clarification of requirements for materials used for geotechnical structures. As the reliability of the structures, which are mostly covered underground, may be highly influenced by the durability issue, this aspect is also highlighted in the code. Consequently, information about assessing the corrosive potential based on the chemical properties of the ground and the ground water as well as the climate conditions, are provided.

Thus, for anchors, the current regulations have been maintained; however, they have mostly been moved from EN 1537 (CEN, 2012) to prEN 1993-5 (CEN, 2021). New clauses for soil nails and rock bolts introduce in an orderly fashion the various regulatory texts dealing with material and corrosion protection for steel soil nails and rock bolts, following the rules for

tension piles as in prEN1993-5), primarily consistent with the current EN 14490 (CEN, 2010). Moreover, the a set of requirements for facing are provided, with a particular focus on wire mesh including an exhaustive list of referenced standards and EADs (European Assessment Documents) is provided.

3 ANCHORS

The anchors clause was already completely revised in 2014. Thus, in prEN 1997-3, it was only slightly edited to fit the general changes of the entire set of the Eurocodes and further details and harmonisation with interdependent standards were introduced. The informative Annex E further supplements the content of Clause 8 with some practical guidance on the design considerations.

The calculation models to determine the required anchor force to prevent an ultimate or serviceability limit states are given in prEN 1997-3 Clauses 4 and 7 for supporting elements or prEN 1997-1 for uplift. It should be noted, that the effect of action E_{d} used in the design of anchors is the maximum result from ULS or SLS during the design service life of the supported structure.

In prEN 1997-3, the design path for geotechnical resistance determination has not been changed compared to the current version of Eurocode 7. The geotechnical design and construction are obligatorily verified by testing according to EN ISO 22477-5 (CEN, 2018), with the possibility of verification by comparable experience in the National Annex. The requirements to determine the geotechnical resistance are now clearly stated for both grouted and non-grouted anchors.

The partial factors for verifying geotechnical resistance and limiting criteria remain the same as in the current version, but are supplemented with the values for temporary anchors. It can be noted that Method 2 as specified EN ISO 22477-5 is no longer used in the design.

The structural resistance of the anchor shall comply with prEN 1993-5 and has to be checked for the proof load according to EN ISO 22477-5.

Regarding testing prEN 1997-3 addresses aspects of types of tests, proof load values, acceptance criteria and the number of tests, while EN ISO 22477-5 is referenced for the testing procedures.

4 SOIL NAILED STRUCTURES

4.1 General

prEN 1997-3 includes a new Clause 10 devoted entirely to soil nailed structures, which is intended to cover the requirements and design procedures comprehensively. It standardises different design methods used in the EU countries and takes over design-related aspects from EN 14490. Clause 10 is supplemented with informative annex G providing guidance on verification of pull-out resistance.

Clause 10 applies to "soil nailed structures - cutting, slope, or existing structure reinforced with soil nails" which form a composite structure usually including facing elements. There are no limitations regarding the technique or material of the soil nails. Facing systems in the scope of the clause are: wire mesh, plain and reinforced concrete, sprayed concrete, concrete panels and other facing elements.

As soil nailed structures are basically a reinforced cut or slope, embankment or retaining structure, the basis of desing follows the rules of Clauses 4, 5, or 7, respectively, Clasue 10 defines additionally only the requirements specific for the given elements in clause, as below.

4.2 Geotechnical analysis

The geotechnical analysis of a soil nailed structure is mainly related to pull-out resistance of soil nails and structural resistance of wire mesh and sprayed concrete, described in section 4.3.

The stability of a soil nailed structure should be verified using limit equilibrium methods (slope stability or multiple wedge methods) and/or numerical models. The details regarding the calculation models for stability analysis, are given in Clause 4 and Annex A. prEN 1997-3 allows verification using one design method, if it adequately addresses all relevant limit states, which is beneficial for the efficiency of designing, especially when using numerical models.

4.3 Ultimate limit states

The general limit states of soil nailed structures are to be analysed according to Clauses 4, 5, or 7, as appropriate, considering the beneficial effect of soil nails. Clause 10 focuses on ultimate limit states related to the single supporting element, which are necessary to analyse, among others:

- failure at the interface between the ground and the soil nail (pull-out) and/or between the soil nail and the grout (if present);
- structural failure of soil nails or any facing element and their connections.
- bearing failure beneath a head plate
- loss of force or resistance by deformation or loss of ground behind the soil nailed structure.

All verification methods are allowed to design the soil nailed structure:

- verification by the partial factor method;

- verification using prescriptive rules;
- verification by testing;
- verification using the Observational Method.

For soil nails the minimum of pull-out resistance $R_{po;d}$ (in the active and passive zone), structural resistance $R_{el;d}$ and the resistance of connection to the facing $R_{con;d}$ shall be verified against the effects of actions E_d:

$$E_{\mathrm{d}} \leq \min\left\{R_{\mathrm{po,d}}; R_{\mathrm{el,d}}; R_{\mathrm{con,d}}\right\} \qquad (1)$$

The basic approach of pull-out resistance $R_{po;d}$ determination is consistent with other tension elements, introducing verification by testing and by calculation based on the ground model method or model pile method, as defined in Clause 6 (Piled foundations). Additionally, design based on comparable experience allows continuing the current practice used in different countries. To ensure the proper reliability level, different methods are related to different sets of model and correlation factors and additional requirements regarding testing. For given methods the corresponding sets of factors for both Material Factor Approach MFA (sets VC3 and M2) or Resistance Factor Approach RFA (with VC1) are determined, conveniently allowing using wide range of design methods for the whole structure. The summary of the verification methods and safety factors as well as corresponding requirements regarding testing in the given method, is presented in Table 1.

Regarding the structural resistance the soil nail and resistance of the connection to the facing shall comply with prEN-1993, considering any anticipated loss of strength with time.

As currently dimension of the wire mesh is not standardised, Clause 10 gives the formulas for determining the tensile and puncture resistance, consistent with the general EC7 design philosophy and the current practice. A vague guidance regarding determining the loads acting on a facing element is also given with additional references to BS 8006-2 or FHWA.

Table 1. Summary of design verification methods for soil nails pull-out resistance determination

Method	The formula and factoring approach	Factors	Testing
By testing	RFA $R_{po;d} = \frac{1}{\gamma_{\mathrm{R,po}} \times \gamma_{\mathrm{Rd}}} \min\left\{\frac{R_{\mathrm{test;mean}}}{\xi_{mean}}; \frac{R_{\mathrm{test;min}}}{\xi_{min}}\right\}$	$\gamma_{\mathrm{Rd}} = 1.0, \xi = 1.0 - 1.4,$ $\gamma_{\mathrm{R,po}} = 1.25$	Recommendation for acceptance tests
By calculation - Model Pile method	RFA $R_{po;d} = \frac{1}{\gamma_{\mathrm{R,po}} \times \gamma_{\mathrm{Rd}}} \min\left\{\frac{R_{\mathrm{calc;mean}}}{\xi_{mean}}; \frac{R_{\mathrm{calc;min}}}{\xi_{min}}\right\}$	$\gamma_{\mathrm{Rd}} = 1.4, \xi = 1.0 - 1.4,$ $\gamma_{\mathrm{R,po}} = 1.25$	
By calculation – Ground model method	MFA for effective stress analysis: $R_{\mathrm{po;d}} = \frac{1}{\gamma_{Rd}} \int_0^{L_{\mathrm{po}}} P(x) \cdot \frac{\mu_{\mathrm{po}}}{\gamma_{\tan\varphi}} \cdot \sigma'_r(\mathrm{x}) \cdot dx$	$\gamma_{\mathrm{Rd}} = 1.2 - 1.6$ $\gamma_{\tan\varphi}$=1.25 γ_{cu}=1.40	Recommendation for verification by suitability tests
	MFA for total stress analysis: $R_{\mathrm{po;d}} = \frac{1}{\gamma_{Rd}} \int_0^{L_{\mathrm{po}}} P(x) \cdot \frac{c_u}{\gamma_{cu}} \cdot \alpha \cdot dx$		For GC3 $R_{po;d}$ shall be determined from investigation tests and verified by suitability tests only
	RFA for effective stress analysis: $R_{\mathrm{po;d}} = \frac{1}{\gamma_{\mathrm{R,po}} \times \gamma_{\mathrm{Rd}}} \int_0^{L_{\mathrm{po}}} P(x) \cdot \mu_{\mathrm{po}} \cdot \sigma'_r(\mathrm{x}) \cdot dx$	$\gamma_{\mathrm{Rd}} = 1.2 - 1.6$ $\gamma_{\mathrm{R,po}} = 1.25$	
	RFA for total stress analysis: $R_{\mathrm{po;d}} = \frac{1}{\gamma_{\mathrm{R,po}} \times \gamma_{\mathrm{Rd}}} \int_0^{L_{\mathrm{po}}} P(x) \cdot c_u \cdot \alpha \cdot dx$		Recommendation for acceptance tests
	with RFA for comparable experience: $R_{po;d} = \frac{1}{\gamma_{\mathrm{R,po}} \times \gamma_{\mathrm{Rd}}} \int_0^{L_{\mathrm{po}}} P(x) \cdot \tau_{\mathrm{po}}(x) \cdot dx$	$\gamma_{\mathrm{Rd}} = 1.2 - 1.6$ $\gamma_{\mathrm{R,po}} = 1.25$	

4.4 Serviceability limit states

In addition to general serviceability limit states (SLS) given in EN 1997-1 (CEN, 2024a) the specific ones for soil nailed structures are, among others:

- bulging and deformation of the facing;
- deformation adversely affecting the function or appearance of the structure or causing damage to existing structures;
- cracking or spalling of any concrete facing.

What is important, especially with calculation models based on limit equilibrium methods, the permission is given to omit SLS verification, provided that ultimate limit states are verified and there are no explicit serviceability criteria.

4.5 Testing

prEN 1997-3 addresses testing of the soil nails in terms directly related to design, particularly verification methods. The new soil nail content is primarily consistent with the current EN 14490, adding more guidance and ensuring compatibility with future prEN ISO 22477-6 (ISO, 2023) which will regulate the

testing procedures. Compared to EN 14490 the terminology and essential requirements regarding testing are harmonised for all tension elements.

According to the approach used in the design, soil nails should be tested using Investigation, Suitability, Acceptance tests with the minimum number of tests depending on the geotechnical category and type of the test. A per the design method, not all types of tests are obligatory. Values of proof load are also proposed. Acceptance criteria for tests are analogous to the ones for anchors with the addition of the new criteria for test methods with constant displacement rate.

5 ROCK BOLTS AND ROCK SURFACE SUPPORT

5.1 General

Clause 11 describes another new content to Eurocode 7: rock bolts and rock surface support. The text is supplemented with informative annex H providing guidance on verification of interface resistance.

According to the definition, rock bolts are used to stabilise rock mass. They primarily work in tension but also through open discontinuities to prevent shear failure through discontinuities with a dowelling effect. Rock surface support, such as wire mesh or sprayed concrete, "prevents potential rock falls and ravelling of the rock surface ".

At this stage, prEN 1997-3 does not cover rock bolt applications in tunnelling or other underground structures.

Rock bolts and the rock surface support in Clause 11 are considered as individual elements. The design questions for overall supported structures are considered in Clauses 4, 5 or 7.

5.2 Geotechnical analysis

The rock bolts shall be analysed considering the interaction between them and the rock mass, with particular attention on geometrical properties including any discontinuities and weathered zones with the direction of the action imposed on the supported structure.

It should be noted that tension and shear load development is governed by complex interaction between bolt and rock. However, it can be shown in particular geometrical arrangements between rock bolt and discontinuity that the effect of shear stresses on steel material's structural resistance can be ignored.

The geotechnical analysis of rock bolts also determines the interface resistance for two parts of the rock bolt: the anchoring length behind the discontinuity (in the stable zone) and the pick-up length in the zone in front of the discontinuity object of the reinforcement.

5.3 Ultimate limit states

The general limit states of structures supported by rock bolts are to be analysed according to Clauses 4, 5, or 7, respectively. The limit states to consider specifically for rock bolts and rock surface support are, among others:

- Rupture of the rock bolt cross section, the connection to the head plate or the plate itself;
- Failure at the interface between the ground and the rock bolt (for non-grouted bolts) or between the ground and the grout and between the grout and the rock bolt (for grouted bolts);
- Loss of force in the bolt or surface support owing to deformation or loss of ground behind the head plate;
- Rupture of the surface support and between the surface support and its fixing into or onto the rock mass.

Limit states of rock bolts may be verified by: calculations, testing or prescriptive rules, while the design of rock surface support shall be based on prescriptive rules. Regarding the complete supported structure, the observational method is in most cases the preferred approach.

As prescriptive rules are commonly used for rock bolt verification, it should be recalled that they must be used within their known limitations and that they are suitably conservative and justified by comparable experience. Examples of this method are the rules based on rock mass classification system.

For rock bolts it shall be verified that the design value of the effects of actions E_{d} satisfies:

$$E_{\mathrm{d}} \leq \min\{R_{\mathrm{ri,d}}, R_{\mathrm{el,d}}, R_{\mathrm{ro,d}}\} \qquad (2)$$

where $R_{\mathrm{ri,d}}$ and $R_{\mathrm{ro,d}}$ are respectively the design value of a rock bolt interface resistance for the pick-up and anchoring part and $R_{el;d}$ is the structural resistance.

The determination of the interface resistance follows the principles of other tension elements, introducing verification by testing and by calculation based on comparable experience. Specific verification methods are associated with strictly defined sets of safety factors and additional requirements. The summary of the verification methods and safety factors as well as corresponding requirements regarding testing in the given method, is presented in Table 2. It should be noted that while for overall stability verification only MFA is allowed, the rock bolts may be verified using only RFA approach.

Table 2 Summary of design verification methods for rock bolts interface resistance determination

Method	The formula and factoring approach	Factors	Testing
By testing	$\left.\begin{matrix}R_{\mathrm{ri,d}}\\R_{\mathrm{ro,d}}\end{matrix}\right\} = \frac{1}{\gamma_{\mathrm{Rr}}}\min\left\{\frac{R_{\mathrm{r,mean}}}{\xi_{mean}};\frac{R_{\mathrm{r,min}}}{\xi_{min}}\right\}$	$\xi = 1.0 - 1.4$ $\gamma_{\mathrm{Rr}} = 1.25$	In GC3, τ_f (the interface resistance) should be determined from investigation tests or verified by suitability tests. Recommendation for acceptance tests.
By calculation	$\left.\begin{matrix}R_{\mathrm{ri,d}}\\R_{\mathrm{ro,d}}\end{matrix}\right\} = \frac{1}{\gamma_{\mathrm{Rr}} \times \gamma_{\mathrm{Rd}}}\int_0^{L_{\mathrm{po}}} P(x)\cdot\tau_{\mathrm{f}}(x)\cdot dx$	$\gamma_{\mathrm{Rd}} = 1.5$ $\gamma_{\mathrm{Rr}} = 1.25$	In GC1 or GC2 τ_f may be determined from comparable experience, in GC 3 should be based on calculations.
Prescriptive rules	Prescriptive rules according to prEN 1997-1, 4.5;		Control tests shall be performed and inspection plan is required

For structural resistance, design shall comply with prEN 1993-1-1, considering tension and shear stresses and making corrosion allowance.

The details regarding special considerations of design in rock are discussed in (Maca et al., 2023).

5.4 Serviceability limit states

Serviceability limit states specifically for the rock bolt or surface support are, among others, deformation of the rock bolt or surface support that adversely affects the function or appearance of the supported structure or causing damage to existing structures, utilities, or ground in the zone of influence.

5.5 Testing

The approach for testing rock bolts in prEN 1997-3 is analogical to the ones described for soil nails with differences in the number of tests. For rock bolts the load testing according to prEN ISO 22477-6 is not obligatory. However, if design by prescriptive rules is used, the control tests, such as visual inspection grouting process, acoustic or ultrasonic testing or Rock Bolt Tester shall be performed. Control tests for rock bolts and rock surface support can be specified in the National Annex or agreed for a specific project.

6 CONCLUSIONS

The introduction of elements such as rock bolts and soil nailed structures, with the in-depth reorganisation and harmonisation of design rules for different geotechnical structures (including revision of the Anchors Clause) in the second generation of the Eurocode 7 provides a significant improvement. Even if, due to the complex challenge of compromising diverse national practices across the EU, the new content does not solve all the issues, it provides a solid framework for the design. The open character of the requirements enables the national standardisation bodies to decide on the preferred verification methods or calculation models and the designers to use the design tools according to the actual needs, conditions and experience. It also means that commonly used guidelines and manuals can be used after some adaptation with the second generation Eurocode.

ACKNOWLEDGEMENTS

Many people have contributed to developing the second generation of the Eurocodes. I am especially indebted to the members of Task Group CEN TC250/SC7 TG-D3, with whom I was privileged to work together from 2021 to 2023 and who provided a significant contribution to the development of the Clauses 10 and 11 of EN 1997-3.

REFERENCES

CEN (2004) EN 1997-1 Eurocode 7: Geotechnical design - Part 1: General rules, CEN-CENELEC.

CEN (2010) EN 14490:2010 (2010) Execution of special geotechnical works – Soil nailing. CEN-CENELEC.

CEN (2018) ISO 22477-5 Geotechnical investigation and testing — Testing of geotechnical structures — Part 5: Testing of grouted anchors, CEN-CENELEC.

CEN (2021) prEN 1993-5 Eurocode 3 – Design of steel structures – Part 5: Piling. CEN-CENELEC.

CEN (2024a). EN 1997-1 Eurocode 7: Geotechnical design - Part 1: General rules, CEN-CENELEC.

CEN (2024b). EN 1997-1 Eurocode 7: Geotechnical design - Part 2: Ground properties, CEN-CENELEC.

CEN (2024c). EN 1997-1 Eurocode 7: Geotechnical design - Part 3: Geotechnical structures, CEN-CENELEC

ISO (2023) prISO 22477-6 Geotechnical investigation and testing — Testing of geotechnical structures — Part 6: Testing of soil nails and rock bolts, ISO.

Maca, N., Dietz, K., Stille, H. and Virely, D. (2023), Rock engineering design in tomorrow's geotechnical toolbox: Eurocode 7 – Geotechnical structures: Anchors, rock bolts soil nails, and groundwater control (EN 1997-3:2024). *Geomechanics and Tunnelling*, 16: 536-558. https://doi.org/10.1002/geot.202300026.

Proceedings of the XVIII ECSMGE 2024
GEOTECHNICAL ENGINEERING CHALLENGES
TO MEET CURRENT AND EMERGING NEEDS OF SOCIETY
© 2024 the Authors
ISBN 978-1-032-54816-6
DOI 10.1201/9781003431749-332
Open Access: www.taylorfrancis.com, CC BY-NC-ND 4.0 license

ECSMGE 24
XVIII EUROPEAN CONFERENCE ON SOIL MECHANICS AND GEOTECHNICAL ENGINEERING

Failure in cohesive soil due to hydraulically induced fractures

Rupture d'un sol cohésif due à des fractures d'origine hydraulique

H. Machacek*, B. Odenwald
Federal Waterways Engineering and Research Institute, Karlsruhe, Germany

K.J. Witt
Bauhaus University Weimar, Weimar, Germany

**helen.machacek@baw.de*

ABSTRACT: According to Eurocode 7 the verification against hydraulic heave on the downstream side of a sheet pile wall must be fulfilled independent from the ground properties. The mechanism of hydraulic heave is based on the soil behaviour of non-cohesive soil, in which the upward directed seepage forces on the downstream side can cause liquefaction if the effective stress is reduced to zero. However, other failure mechanisms are expected in cohesive soil due to additional binding forces. Laboratory experiments have shown, that the alternative failure mechanism in cohesive soil is triggered by the formation of fractures at the foot of the sheet pile where high hydraulic gradients occur. To further investigate the mechanisms of these hydraulically induced fractures in cohesive soils, a new triaxial test has been developed, in which the pore water pressure in the centre of the specimen is increased until failure by fracturing occurs. The pore water pressure at fracture initiation, the fracturing pressure, is a measure for the soil resistance against hydraulic induced fractures. In an extensive laboratory study the influencing factors on the fracturing pressure have been determined by variation of the sampling material, the rate of the pore water pressure increase, the stress and drainage conditions. Further insight into the stress state at fracture initiation could be gained by numerical calculations. It could be concluded, that the failure by fracture differs significantly from the failure mechanisms in cohesionless soil. Therefore new concepts are required to ensure the safety against hydraulic failure.

RÉSUMÉ: Selon l'Eurocode 7, la vérification contre le soulèvement hydraulique du côté aval d'un mur de palplanches doit être réalisée indépendamment des propriétés du sol. Le mécanisme de soulèvement hydraulique est basé sur le comportement du sol non cohésif, dans lequel les forces d'infiltration dirigées vers le haut sur le côté aval peuvent provoquer une liquéfaction si la contrainte effective est réduite à zéro. Cependant, d'autres mécanismes de rupture sont attendus dans les sols cohésifs en raison de forces de liaison supplémentaires. Des expériences en laboratoire ont montré que l'autre mécanisme de rupture dans un sol cohésif est déclenché par la formation de fractures au pied de la palplanche, là où les gradients hydrauliques sont élevés. Pour étudier plus avant les mécanismes de ces fractures d'origine hydraulique dans les sols cohésifs, un nouvel essai triaxial a été mis au point, dans lequel la pression de l'eau interstitielle au centre de l'échantillon est augmentée jusqu'à ce qu'une rupture par fracturation se produise. La pression de l'eau interstitielle à l'initiation de la fracture, la pression d'initiation, est une mesure de la résistance du sol aux fractures induites par l'hydraulique. Dans le cadre d'une étude approfondie en laboratoire, les facteurs influençant la pression d'amorçage ont été déterminés par la variation du matériau d'échantillonnage, le taux d'augmentation de la pression de l'eau interstitielle, la contrainte et les conditions de drainage. Des calculs numériques permettraient de mieux comprendre l'état de contrainte au moment de l'initiation de la fracture. On peut conclure que la rupture par fracture diffère considérablement des mécanismes de rupture dans un sol sans cohésion. Par conséquent, de nouveaux concepts sont nécessaires pour garantir la sécurité contre les ruptures hydrauliques.

Keywords: Hydraulic failure; fractures; cohesive soil; laboratory study.

1 INTRODUCTION

When dimensioning sheet piles for excavations in groundwater or along canals, the verifications against hydraulic failure mechanisms are often decisive for the required embedment depth. The current standardisation according to EC7 requires among other the verification against hydraulic heave, which is to be carried out on the basis of a force equilibrium from the soil's deadweight under buoyancy and the upward flow force, almost independent from the existing ground. However, this verification concept is based on the hydraulic failure mechanism in non-cohesive soils, where the flow force can cause soil liquefaction in the downstream area. Only in highly cohesive soils is it common practice to dispense with

the verification against hydraulic heave and instead to perform the verification against uplift. The actual hydraulic failure mechanisms in fine-grained soils have been little studied, which is why both verifications are not very accurate.

Laboratory tests by (Wudtke, 2014) on a wall in silt and clay conducted by undercurrent have shown that the hydraulic failure mechanism in fine-grained soils is triggered by hydraulically induced fractures at the base of the wall. Since the subsequent sequence of failure ending in the loss of the earth abutment can proceed quickly and unnoticed, the hydraulically induced fracture initiation is decisive for the design.

But currently there is neither practical experience nor sufficient theoretical basis to determine the resistance to hydraulic fracture failure in fine-grained soils. Although various fields of geotechnics and geomechanics have been dealing with the formation and propagation of hydraulically induced fractures in rock or sand for decades, no study has yet comprehensively considered a greater number of potentially relevant influencing factors on fracture formation in fine-grained subsoil (Günther, 2019). In order to formulate a design concept against hydraulically induced fractures in fine-grained soils, it is essential to investigate the main factors influencing fracture resistance of these soils experimentally.

2 EXPERIMENTAL STUDY

To fill this knowledge gap, a laboratory study was carried out in a new type of triaxial test. In this test, the failure of the cylindrical sample (height= diameter=100mm) is not caused by shearing, but by an excess pore water pressure applied in its centre. For this purpose, a cannula with a filter tip was attached to the top plate of the triaxial device, where the pore water pressure is increased until fracture occurs. As fractures initiate at flaws in the material (Jaworski et al., 1981), the samples must be as homogeneous as possible to ensure reproducible test results.

The test setup, test procedure and sample preparation are described in detail in (Günther, 2019), (Machacek, 2024) and (Machacek and Odenwald, 2023). The resistance of a sample to hydraulically induced fractures is determined by the pore water pressure at the filter tip required for the first fracture to form. This pressure is referred to as the fracturing pressure $p_{w,fr}$. At the moment of fracture initiation there is a significant pressure drop at the controller of the pore pressure at the filter tip and at simultaneously a sharp increase in the volumes flowing in and out of the sample at the top and bottom plate (in case of drained boundary conditions). This is exemplified in Figure 1 with diagrams of the pressure curves over the time for the filter tip and the end plates (left) and the corresponding volume curves over the pressure at the filter tip (right) during the hydraulic loading.

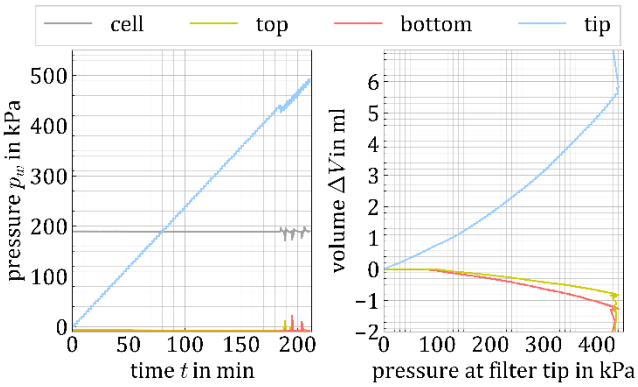

Figure 1. Typical results of the triaxial test with hydraulic loading. Left: pressure vs time for a pressure controlled loading phase with open drainage at the end plates, the pressure drop at the filter tip indicates the fracturing pressure. Right: volume change vs the pressure at the filter tip. The in- and outflowing volumes increase suddenly as the fracturing pressure is reached.

2.1 Variations

In order to investigate the soil-mechanical parameters influencing the resistance to hydraulic fractures and the fracturing pressure numerous variations with different initial and boundary conditions were carried out as part of the laboratory study.

To analyse the influence of the soil type and structure, test samples made of silt, kaolin or bentonite were loaded until fracture failure. These were either consolidated as described in (Günther, 2019) or produced by static compaction, whereby the compaction, in contrast to the consolidation, produces a soil structure with clear aggregate formation.

To vary the initial stress state, the samples were consolidated to different initial mean effective stresses p at isotropic ($\sigma_h = \sigma_v$) or anisotropic stress ratios ($K = \sigma_h/\sigma_v \neq 1$) prior to hydraulic loading. The effect of preloading by a consolidation pressure p_c was investigated by different overconsolidation ratios $OCR = p_c/p$. With regard to the hydraulic loading, variations were made between pressure and volume controlled loading with different pressure rates or volume flows. This rate of hydraulic loading must always be related to the hydraulic permeability of the sample material, so that the ratio between the flow velocity v and the permeability coefficient k is decisive.

Furthermore, tests were carried out with and without drainage at the end plates during the loading phase and the backpressure was varied during the

loading phase, which influences the speed of pore water pressure propagation.

To ensure the reproducibility of the tests with hydraulic loading each variation was repeated at least two to four times under identical conditions.

2.2 Results

The fracturing pressure $p_{w,fr}$ is reproducible. Depending on the test variant, the coefficient of variation is a maximum of 17.2% and, with a mean value of 5.7%, is below the coefficient obtained in undrained triaxial shear tests carried out on the same samples.

The fracture pattern and the expansion of the fracture surfaces can be visualised by injecting potassium permanganate into the cannula after removing the sample from the triaxial cell. However, no regularity with regard to the fracture formation can be determined. Yet Figure 2 shows some fractured samples to give a better idea of the failure patterns. Fracture propagation is very complex an depends on numerous factors, which is why the following investigation focusses exclusively on factors influencing the fracturing pressure $p_{w,fr}$.

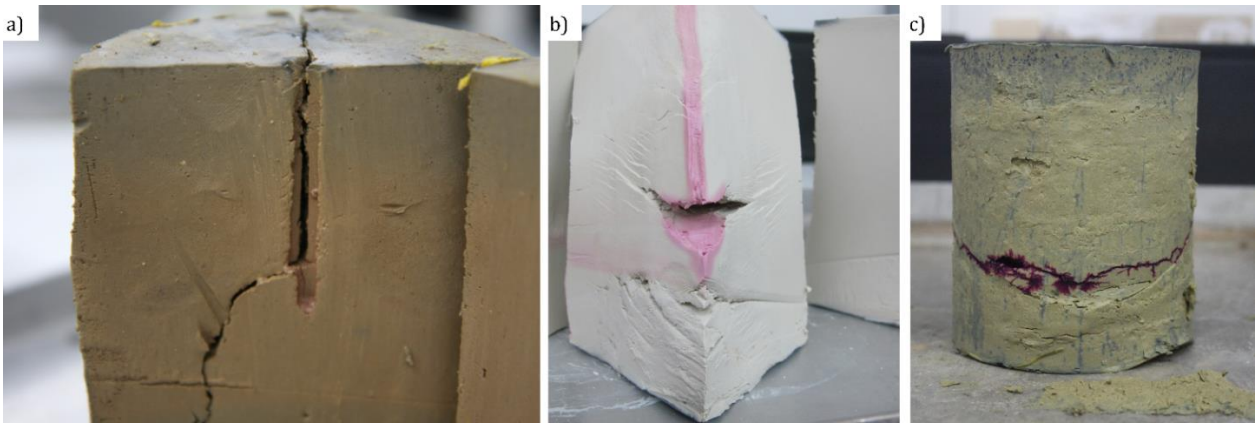

Figure 2. Examples of the fracture patterns observed by injecting potassium permanganate (purple) after removing the sample from the cell. a) A vertical fracture in a silt sample. b) Slightly horizontal fractured kaolin sample. c) A diagonal fracture through a bentonite sample.

The variations in the laboratory study showed that the magnitude of $p_{w,fr}$ was mainly influenced by the material, the initial stress state, the overconsolidation ratio OCR and the rate of the loading pore pressure (or the v/k-ratio). The other variations had minor influence on $p_{w,fr}$.

Regarding the sample material $p_{w,fr}$ increased with the amount of fines in the material. Hence the lowest fracturing pressures were observed in the silt samples and the highest in the bentonite samples. Only consolidated samples show reproducible results, in compacted samples the range of the fracturing pressures was comparatively large due to the larger aggregates and variation in pore size. Though under the same testing conditions the consolidated samples clearly show higher fracturing pressures than the compacted samples.

Further the fracturing pressure increases with the initial effective mean stress p and the overconsolidation ratio OCR. For the isotropic stress state there is an almost linear relationship between p and the fracturing pressure. The variation of the initial stress ratio K for normally consolidated samples ($OCR = 1$) shows that the fracturing pressure does not depend solely on the smaller principal stress σ_h, but on the stress state.

To compare the fracturing pressures resulting from tests with different OCR, $p_{w,fr}$ is normalised by p. The normalised fracturing pressure increases asymptotically and reaches a maximum value of $p_{w,fr}/p \sim 4$ at $OCR \sim 8$.

One of the most important influence factors is the pressure rate or the v/k -ratio. The higher the v/k -ratio, the higher the fracturing pressure. From the test results it can be assumed that the injected water does not infiltrate into the pores of the sample if the v/k -ratio is very high. Instead the soil around the filter tip is displaced and the expanding cavity is filled with the injected water.

A more detailed description of the quantitative results of the study would go beyond the scope of this article and therefore reference is made here to (Machacek, 2024).

3 NUMERICAL ANALYSIS

For the fracture failure by hydraulic loading from the centre of the sample, only the local stress state around

the filter tip where the fracture first occurs is of interest. So far no analytical can describe the stress changes around the filter tip due to the pore pressure increase regarding all the influence factors observed in the laboratory study. Hence, to analyse the stress state which leads to the fracture failure a numerical analysis is required which considers the transient coupling between soil as a continuum and pore water.

3.1 Numerical model

An axisymmetric FE-model of the sample was created to simulate the tests in the laboratory study. Thereby only the stress state in the soil as a continuum until the first fracture occurs was regarded. It is not the intention to model the fracture initiation or propagation. For the material behaviour the Modified Camclay-Model (MCC) was chosen and the material parameters were calibrated from standard compression and triaxal tests. The dimensions, the (loading) boundary conditions and the mesh are shown Figure 3. To start from realistic stress states, not only the hydraulic loading but also the consolidation phases were simulated.

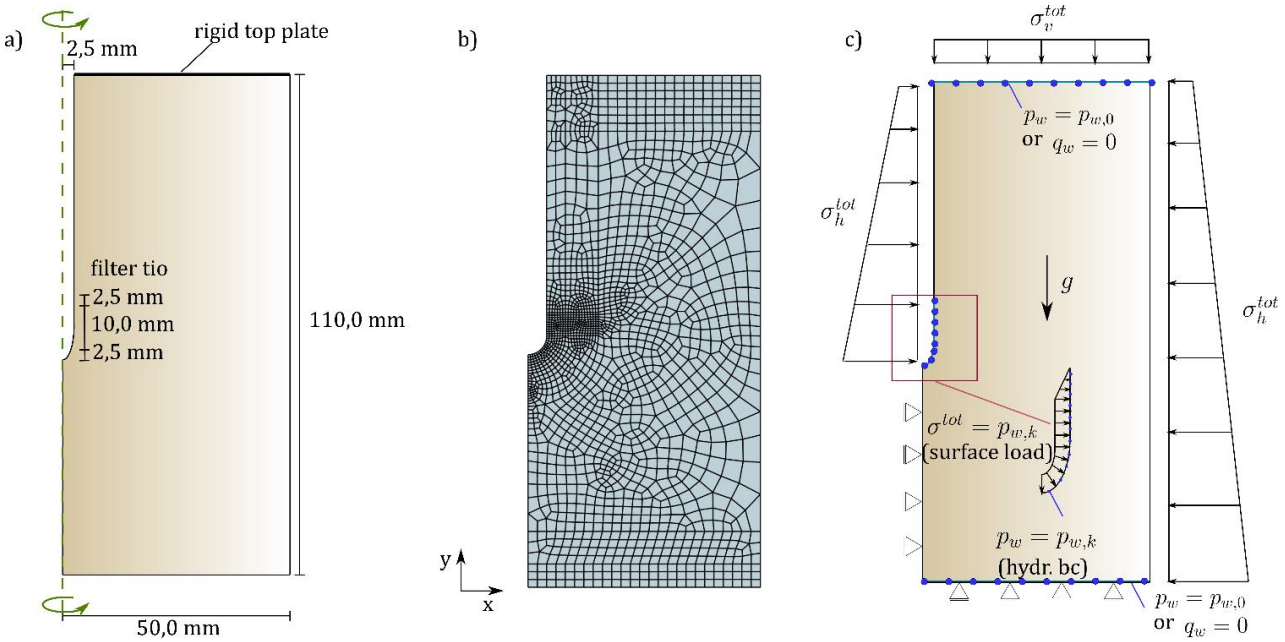

Figure 3. Axisymmetric FE-model of the triaxial test with hydraulic loading. a) Dimensions of the modelled sample. b) Mesh of the model. c) Boundary conditions (bc) and loading of the sample to model all phases of the triaxial test in different variations, e.g. pressure or volume controlled loading and drained or undrained conditions at the end plates.

To analyse the stress state around the filter tip at the moment the fracture occurs, the simulations were evaluated at the corresponding point of time t_{fr} at which the fracturing pressure was reached in the laboratory test variation.

3.2 Critical stress states

In the numerical calculations no failure criteria were given as the fracture criteria for fine-grained soil is unknown. But by using the MCC model the critical state line (CSL) is included. Fractures can be triggered by tensile and or shear stresses, hence in the postprocessing both were analysed at the moment of fracture initiation t_{fr}. The numerical analysis of the tests on consolidated samples show, that at $t = t_{fr}$ an area around the filter tip exists in which the minor principal stress σ_{min} becomes tensile stress or in which the shear stress ratio $\eta = q/p$ with the deviator stress q reaches the CSL. In the following these areas are called critical stress zones. The size of these zones as well as the maximum tensile or shear stress intensity within the zone correlate primarily with the sample's material and the overconsolidation ratio. In other words, the stress analysis of test variations with the same material and OCR show almost identical critical stress zones independent from the drainage condition, the backpressure and the v/k -ratio. Even the initial stress state has in fact little influence on these critical areas. This is demonstrated in Figure 4 by field plots of the stress ratio η at $t = t_{fr}$ for the test series on silt with different initial mean stresses of $p = 100$ kPa, 200 kPa and 300 kPa. The critical zones in which the stress ratio reaches the CSL of silt with $\eta \geq M_c = 1{,}4$ is displayed in grey. The size of the grey zone grows only slightly with p. In contrast Figure 5 shows the field plots of the test series on silt with $OCR = 1, 2$ and 4.

The grey zones of the c critical shear stress with $\eta \geq 1{,}4$ and of tensile stress $\sigma_{min} \leq 0$ kPa grow with the increase of OCR.

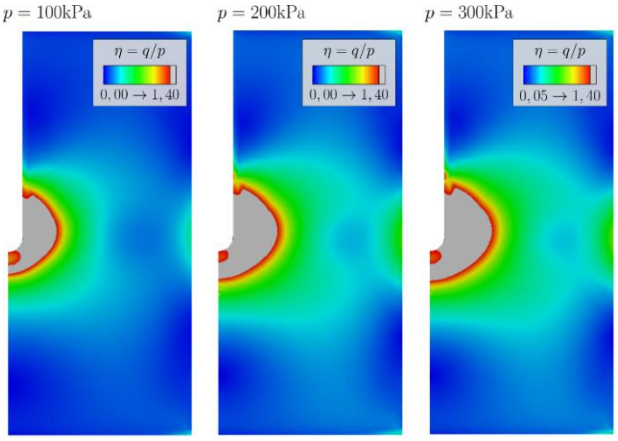

Figure 4. Stress ratio η at the moment of fracturing for test variations with different initial mean stresses p. The grey zone where the maximum stress ratio of $M_c = 1{,}4$ is reached increases only slightly with p.

The conclusion from this numerical analysis was drawn with a view on the basics of fracture mechanics.

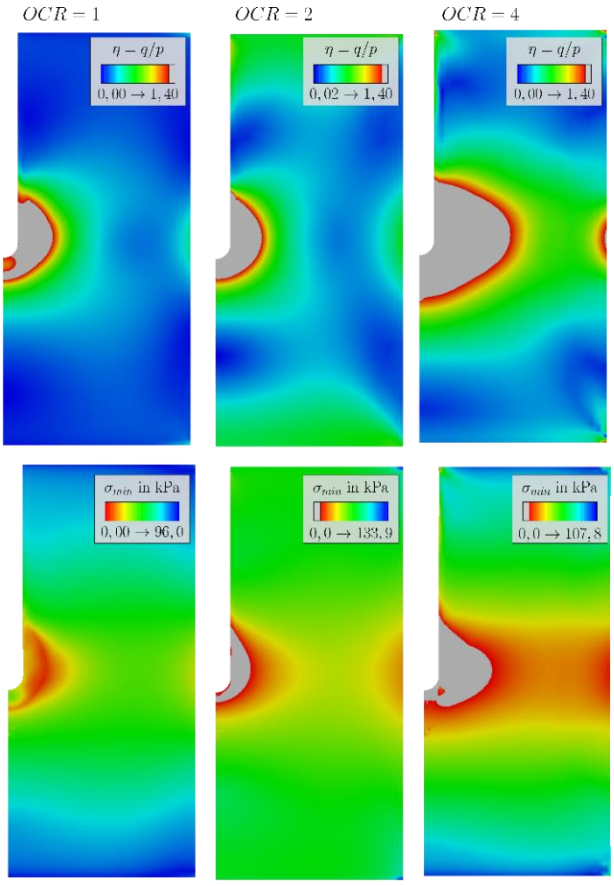

Figure 5. Stress ratio η (upper row) and minimum principal stress σ_{min} (lower row) at the moment of fracturing for test variations with different overconsolidation ratios OCR. The grey zone where the maximum stress ratio of $M_c = 1{,}4$ is reached or the σ_{min} is tensile increases with OCR.

According to these fractures initiate at an imperfection in the material, where high tensile or shear stress loads occur. If these stress intensities at an imperfection reach the materials specific critical value, the fracture extends from the imperfection. If the pore structure of a homogenous material in which larger pores, extraneous inclusions or little fissures represent imperfections, then the fracture initiates if in the critical stress zone around the filter tip the material strength is reached at one of these imperfections.

This results in a probabilistic issue: as the pore water pressure at the filter tip increases, the critical stress zone grows and with it the probability that there is an imperfection in this area where the material strength is exceeded. If this zone varies in its size when fracture occur, the material will either differ in strength or in the amount and size of imperfections.

4 CONCLUSIONS

With the newly developed triaxial test for hydraulic induced fractures in soil reproducible results regarding the fracturing pressure in consolidated fine-grained samples can be obtained. In an extensive laboratory study the material of the samples, the initial stress state, the overconsolidation ratio and the rate of the hydraulic loading were identified as the decisive factors influencing the fracturing pressure. A numerical analysis of the stress state at the time of fracture initiation in the test variations of the study show that there are similar zones of high tensile or shear stress around the filter tip. The size of this zone and the level of tension or shear depends only on the material, the overconsolidation ratio and slightly on the initial stress state.

Based on this numerical analysis and the fundamentals of fracture mechanics, it can be hypothesised that the hydraulically induced fractures in the samples are only influenced by three factors: the material resistance, the effective stress state and the defects in the material.

REFERENCES

Eurocode 7 – Geotechnical design – Part1: General rules; German version EN 1997-1:2004+AC:2009+A1:2013. 2014. Beuth.

Günther, H. (2019) Development of a triaxial test for hydraulic loading of fine-grained soil. In *Proceedings of the XVII ECSMGE-2019 Geotechnical Engineering foundation of the future,* Reykjavik, Iceland. https://doi.org/10.32075/17ECSMGE-2019-0055.

Machacek, H. (2024) *Analyse von Einflussfaktoren des Widerstands feinkörniger Böden bei hydraulischer Belastung*. Phd-Thesis Bauhaus Universität Weimar.

Machacek, H. and Odenwald, B. (2023). Nachweise bei umströmten Wänden in bindigen Böden – Ansätze und experimentelle Untersuchungen, In: *Kolloquium Geohydraulische Aspekte bei Baumaßnahmen des Verkehrswasserbaus,* Karlsruhe, Germany, pp. 69-79.

Jaworski, G.W., Seed, H.B. and Duncan, J. M. (1981) Laboratory study of hydraulic fracturing. *Journal of the Geotechnical Engineering Division,* 107(6), pp. 713-732, https://doi.org/10.1061/AJGEB6.0001147.

Wudtke, R.-B. (2014) *Hydraulischer Grundbruch in bindigem Baugrund*. Phd-Thesis Bauhaus Universität Weimar.

Proceedings of the XVIII ECSMGE 2024
GEOTECHNICAL ENGINEERING CHALLENGES
TO MEET CURRENT AND EMERGING NEEDS OF SOCIETY
© 2024 the Authors
ISBN 978-1-032-54816-6
DOI 10.1201/9781003431749-333
Open Access: www.taylorfrancis.com, CC BY-NC-ND 4.0 license

ECSMGE 24
XVIII EUROPEAN CONFERENCE ON SOIL MECHANICS AND GEOTECHNICAL ENGINEERING

Mine tailings properties and its hypoplastic predictions

Propriétés des résidus miniers et leurs prédictions hypoplasiques

H.R. Manaviparast*, T. Miranda
University of Minho, Guimarães, Portugal

G. Medicus
University of Innsbruck, Innsbruck, Austria

N. Cristelo
University of Trás-os-Montes e Alto Douro, Vila Real, Portugal

*id8028@alunos.uminho.pt

ABSTRACT: Copper mine tailings (CMT) are the waste material that remains after the economic fraction is extracted from the mineral ore and consist of a slurry of ground rock, water, and chemical reagents that remain after metallurgical processing. These tailings are considered toxic to the environment, so controlling their environmental toxicity and improving their mechanical properties are crucial. However, only a few studies have focused on assessing such performance by establishing the constitutive behaviour of the CMT. In this paper, we describe mine tailings properties and perform laboratory tests to calibrate clay hypoplasticity. Hypoplasticity is a constitutive model that includes concepts from Critical State Soil Mechanics, as a stress-dependent critical void ratio and a critical stress cone, according to Matsuoka-Nakai. The results show that hypoplasticity can well predict the mine tailings triaxial test behaviour.

RÉSUMÉ: Les résidus miniers de cuivre (CMT) sont les déchets qui restent après l'extraction de la fraction économique du minerai minéral et consistent en une boue de roche broyée, d'eau et de réactifs chimiques qui restent après le traitement métallurgique. Ces résidus sont considérés comme toxiques pour l'environnement, il est donc crucial de contrôler leur toxicité environnementale et d'améliorer leurs propriétés mécaniques. Cependant, seules quelques études se sont concentrées sur l'évaluation de ces performances en établissant le comportement constitutif du CMT. Dans cet article, nous décrivons les propriétés des résidus miniers et effectuons des tests en laboratoire pour calibrer l'hypoplasticité de l'argile. L'hypoplasticité est un modèle constitutif qui inclut des concepts de la mécanique des sols à l'état critique, comme un indice de vide critique dépendant de la contrainte et un cône de contrainte critique, selon Matsuoka-Nakai. Les résultats montrent que l'hypoplasticité peut bien prédire le comportement des essais triaxiaux des résidus miniers.

Keywords: Mine tailings; waste material; constitutive model; hypoplasticity.

1 INTRODUCTION

Mine tailings are the materials left over after the process of separating the valuable fraction of mined ores from the uneconomic fraction of the ore. Tailings can contain a variety of materials depending on the ore being mined. They often include finely ground rock particles, chemicals used in the extraction process, and water (Sarker et al., 2022).

Mine tailings pose significant environmental concerns. Proper storage in dams is crucial to mitigate their impact on surrounding ecosystems and water sources. The necessity of determining the behaviour of mine tailings is essential to design how it is deposited, which will influence their potential environmental impact and their management strategy (Cacciuttolo and Atencio, 2023). This assessment helps safeguard ecosystems, water sources, and communities from potential hazards such as acid mine drainage and other health risks, not to mention their mechanical stability (Rezaie and Anderson, 2020).

Constitutive models are indispensable for understanding and predicting the mechanical behavior of materials. Their importance extends beyond academic study to practical engineering solutions that drive innovation. Determining the behavior of mine tailings with constitutive models involves using mathematical representations to describe how these materials respond to various mechanical conditions (Qiu et al., 2018). These models are based on fundamental principles of material behavior, which are also determined through triaxial tests and can help predict stress-strain relationships, peak and critical shear strength, among other important aspects that control the overall response of tailing deposits. By applying constitutive models, users can simulate and

analyse the performance of mine tailings in different scenarios, aiding in the design of safe storage and containment systems (Bursa et al., 2023).

2 EXPERIMENTAL WORK

To assess the behaviour of copper tailings from the Neves Corvo mine located in Portugal, triaxial compression undrained tests (CU) were conducted to determine the shear strength characteristics of mine tailings. According to the ASTM unified classification (2006), the copper mine tailing was designated as CL—lean clay with liquid and plastic limits of 23% and 11%, respectively (Manaviparast et al., 2022).

For the purpose of simulating the deposition of mining waste in landfills and simulating deposition in layers, each test sample was molded in 6 layers, with a pre-established amount of mixture introduced into each layer and compacted. The compaction process of each layer was important since each layer was compacted with a different degree of compaction; as the layers progressed, the greater degree of compaction applied. However, in theoretical terms, all layers will have the same density due to the adjustments that the material makes with the different degrees of compaction applied to each of the layers.

According to the BS 1377-7 (1990) standard, tests were performed through three distinct phases of saturation, consolidation, and shear under confining stresses of 97 kPa, 188 kPa, and 277 kPa in normally to slightly overconsolidated conditions to be utilized as a pivotal foundation for the calibration of model parameters. The experimental results, including the trajectory of stress paths, deformation characteristics, the stress-strain relationship, and the evolution of pore pressure with axial strain, are shown in Figures 1 to 4, respectively.

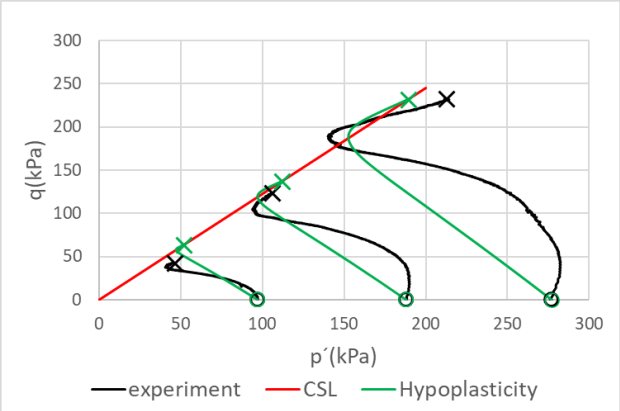

Figure 1. Experimental and hypoplastic stress paths observed in the q-p' plane for triaxial tests (CU) on mine tailing samples under slightly overconsolidated conditions.

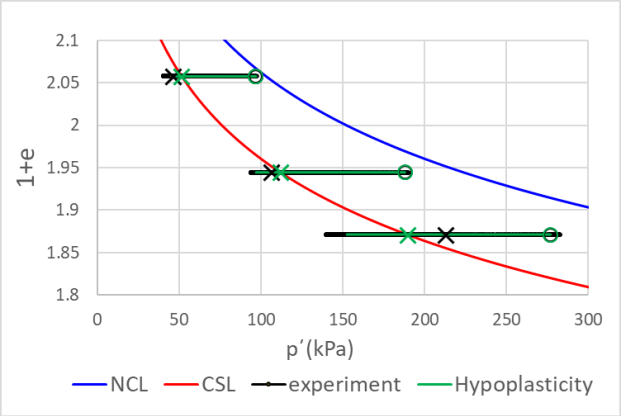

Figure 2. Experimental and predicted hypoplastic paths observed in the (1+e)-p' plane for triaxial tests (CU) on mine tailing samples under slightly overconsolidated conditions.

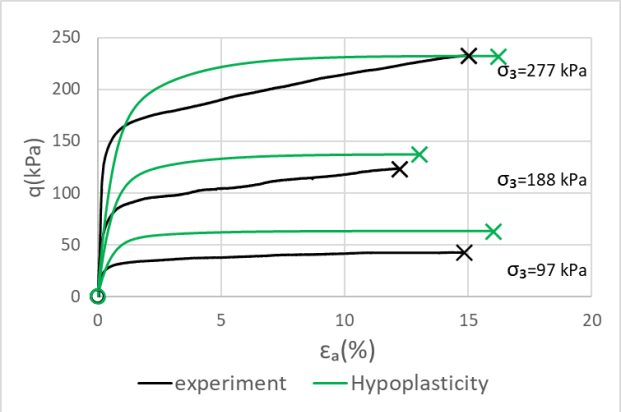

Figure 3. Experimental and predicted hypoplastic relation between deviatoric stress and axial strain.

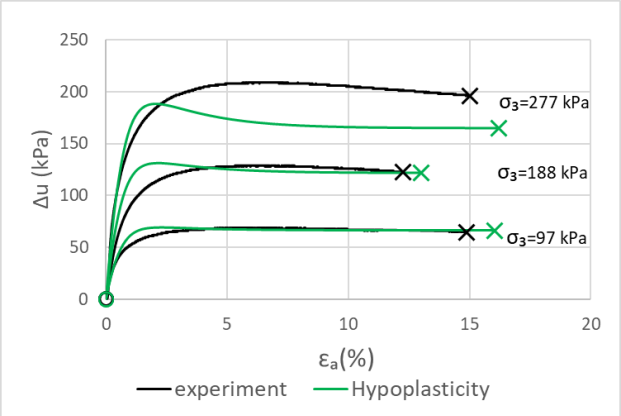

Figure 4. Evolution of pore pressure with axial strain in the experiments and the hypoplastic predictions.

3 PREDICTIONS WITH CLAY HYPOPLASTICITY

Clay hypoplasticity (Mašín, 2013) is a constitutive model in which the stress rate is formulated as a tensorial function of the current stress **σ**, void ratio *e*, and strain rate.

Hypoplasticity incorporates concepts from critical state soil mechanics, such as the critical stress cone, according to Matsuoka-Nakai, and a stress-dependent critical void ratio e_c, i.e., the critical state line (CSL) in the void ratio vs the mean effective stress plane. The strength and stiffness response is, therefore, dependent on the stress level and the overconsolidation ratio. Figure 5 shows the so-called asymptotic state boundary surface (ASBS) of clay hypoplasticity in the *p'-q-e* space (left) and in the *p'-q* and *e-p'* projections. All feasible states lie within the ASBS. In the *(1+e)-p'* projection, the Normal Compression Line (NCL), as well as the CSL are defined as follows:

$$\text{NCL: } ln(1+e) = N - \lambda^* ln\, p' \qquad (1)$$

$$\text{CSL: } ln(1+e) = N - \lambda^* ln(2p') \qquad (2)$$

The slope of the CSL in the *p'-q* projection is

$$M = \frac{6sin\,\varphi_c}{3-sin\,\varphi_c} \qquad (3)$$

for axisymmetric triaxial compression.

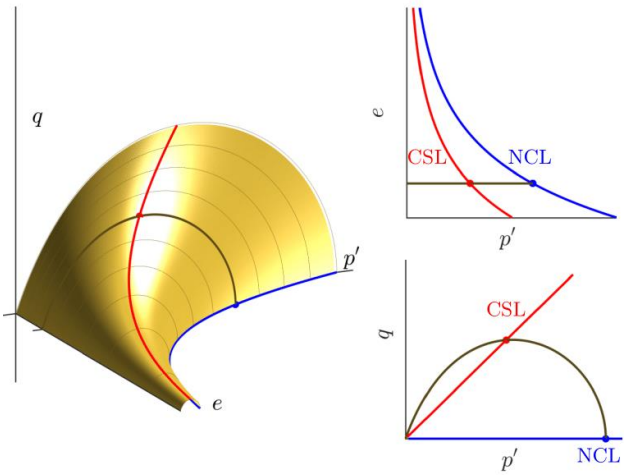

Figure 5. Clay hypoplasticity: Concepts from Critical State Soil Mechanics are included in the model. Left: Asymptotic state boundary surface (ASBS) of clay hypoplasticity in p'-q-e space, above right: e-p' projection, below right: p'-q projection [Link].

3.1 Calibration

For the calibration of some of the model's parameters, the automatic calibration software Excalibre, soilmodels.com/excalibre-en, developed by Kadlíček et al. (2022a, 2022b), available on the platform SoilModels (Gudehus et al., 2008) was used.

Due to the lack of compression data, the parameters to define the NCL have been estimated based on the initial states of the normally to slightly overconsolidated initial states of the CU tests, see Figures 1 and 2. The slope of the CSL in the *p'-q* plane is governed by the critical friction angle φ_c according to equation (3). The parameter ν was calibrated by parametric study to capture the shape of the undrained stress paths, see Figure 1. In the absence of isotropic unloading data, κ^* was set to the typical value of 0.1 (Mašín, 2013). All parameters of clay hypoplasticity are provided in Table 1.

Table 1. Calibrated model parameters.

Parameters	Value
Ordinate intercept of the NCL (N)	1.06
Slope of the NCL (λ^*)	0.073
Slope of unloading line under isotropic compression (κ^*)	0.01
Critical friction angle (φ_c)	30.6°
Poisson's ratio (ν): controls the shear modulus and affects the shape of undrained stress paths	0.25

3.2 Predictions with hypoplasticity

The samples are initially normally to slightly overconsolidated, with the initial states marked with o in Figures 1-4.

The critical strength q_c equals $M \cdot p'_c$, where p'_c follows from the location of the CSL in *(1+e) - p'* plane, see Figure 2. In hypoplasticity the position of the CSL in relation to the NCL is fixed by $p'_e/p'_c=2$, where p'_e is the so-called Hvorslev's equivalent pressure on the NCL and p'_c is the mean effective stress at critical state on the CSL. The final states of the simulations, as well as the experiments, are marked with x. The pore water pressure and the deviatoric stress of the experiments are not yet constant. This means that the samples are still approaching the critical state and have not yet reached it. The final points of the simulations already lie on the CSLs in Figures 1 and 2. Deviatoric stress *q* as well as the pore pressure at a given axial strain are well predicted by the model, see Figures 3 and 4. In order to predict the undrained strength of samples with different initial densities, it is necessary to use a constitutive model that incorporates the framework of critical state soil mechanics.

4 CONCLUSION

Understanding the behavior of mine tailings is of paramount importance for the safe and responsible management of these waste materials. Triaxial tests provide invaluable insights into the mechanical properties and stability of mine tailings under varying

stress conditions, offering essential data for the design of secure containment systems. Furthermore, employing constitutive models enhances our ability to predict and analyse the response of mine tailings, enabling informed decision-making in engineering practices. By leveraging both experimental testing and mathematical representations, we can effectively address environmental concerns and minimize potential risks associated with the disposal of mine tailings. This comprehensive approach underscores the significance of adopting responsible mining practices that prioritise the protection of ecosystems, water sources, and surrounding communities.

ACKNOWLEDGEMENTS

This work was partly financed by FCT/MCTES through national funds (PIDDAC) under the R&D Unit Institute for Sustainability and Innovation in Structural Engineering (ISISE), under reference UIDB/04029/2020, and under the Associate Laboratory Advanced Production and Intelligent Systems ARISE under reference LA/P/0112/2020. This work was also partly funded by the research project MINECO—New Eco-Innovative Materials for Mining Infra, with reference ERA-MIN/0001/2018, funded by Portuguese State Budget through the FCT/MCTES.

This research was funded in part, by the Austrian Science Fund (FWF) V 918. For the purpose of open access, the authors have applied a CC BY public copyright licence to any Author Accepted Manuscript version arising from this submission. G.M. gratefully acknowledges financial support of the FWF.

This work was partly financed by Project "NGS - New Generation Storage", with reference C644936001-00000045, financed by the Recovery and Resilience Plan and the Next Generation EU European Funds.

REFERENCES

Bursa, B., Stefaniak, P., & Kakogiannos, I. (2023). Applying Model-Based Systems Engineering to Tailings Storage Facility Structures. *Materials Proceedings*, 15(1), 12. https://doi.org/10.3390/materproc2023015012.

Cacciuttolo, C., & Atencio, E. (2023). In-Pit Disposal of Mine Tailings for a Sustainable Mine Closure: A Responsible Alternative to Develop Long-Term Green Mining Solutions. *Sustainability*, 15(8), 6481. https://doi.org/10.3390/su15086481.

Gudehus, D., D., Amorosi A., Gens, A., Herle, I., Kolymbas, D. Mašín, D., Muir Wood, D., Nova, R., Niemunis, A., Pastor, M., Tamagnini, C., Viggiani, G. 2008. The soilmodels.info project. *International Journal for Numerical and Analytical Methods in Geomechanics*, 32:1571–1572. https://doi.org/10.1002/nag.675.

Kadlíček, T., Janda, T., Šejnoha, M., Mašín, D., Najser, J. & Beneš, Š. 2022a. Automated calibration of advanced soil constitutive models. Part II: hypoplastic clay and modified Cam-Clay. *Acta Geotechnica,* 17:3439-3462. https://doi.org/10.1007/s11440-021-01435-y.

Kadlíček, T., Janda, T., Šejnoha, M., Mašín, D., Najser, J. & Beneš, Š. 2022b, Automated calibration of advanced soil constitutive models. Part I: hypoplastic sand. *Acta Geotechnica,* 17:3421-3438. https://doi.org/10.1007/s11440-021-01441-0.

Manaviparast, H. R., Pinheiro, J., Najafi, E. K., Abreu, C., Araújo, N., Cristelo, N., & Miranda, T. (2022). Mechanical Behavior of a Mine Tailing Stabilized with a Sustainable Binder. *Applied Sciences*, 13(7), 4103. https://doi.org/10.3390/app13074103.

Mašín, D. 2013. Clay hypoplasticity with explicitly defined asymptotic states, *Acta Geotechnica*, 8, 481-496. https://doi.org/10.1007/s11440-012-0199-y.

Mašín, D. 2013. Clay hypoplasticity with explicitly defined asymptotic states. *Acta Geotechnica*, 07(5):481–496. https://doi.org/10.1007/s11440-012-0199-y.

Qiu, J. P., Yang, L., Xing, J., & Sun, X. G. (2018). Analytical solution for determining the required strength of mine backfill based on its damage constitutive model. *Soil Mechanics and Foundation Engineering*, 54, 371-376. https://doi.org/10.1007/s11204-018-9483-7.

Rezaie, B., & Anderson, A. (2020). Sustainable resolutions for environmental threat of the acid mine drainage. *Science of The Total Environment*, 717, 137211. https://doi.org/10.1016/j.scitotenv.2020.137211.

Sarker, S. K., Haque, N., Bhuiyan, M., Bruckard, W., & Pramanik, B. K. (2022). Recovery of strategically important critical minerals from mine tailings. *Journal of Environmental Chemical Engineering*, 10(3), 107622. https://doi.org/10.1016/j.jece.2022.107622.

Proceedings of the XVIII ECSMGE 2024
GEOTECHNICAL ENGINEERING CHALLENGES
TO MEET CURRENT AND EMERGING NEEDS OF SOCIETY
© 2024 the Authors
ISBN 978-1-032-54816-6
DOI 10.1201/9781003431749-334
Open Access: www.taylorfrancis.com, CC BY-NC-ND 4.0 license

ECSMGE 24
XVIII EUROPEAN CONFERENCE ON SOIL MECHANICS AND GEOTECHNICAL ENGINEERING

The use of physically based methods to locate the in-site surveys in areas prone to rapid landslides

L'utilisation de méthodes physiques pour localiser les études sur place dans les zones sujettes aux glissements de terrain rapides

M.C. Mandaglio*
Department DICIV/University of Salerno, Salerno (SA), Italy

N. Moraci
Department DICEAM/University of Reggio Calabria, Reggio Calabria (RC), Italy

M. Ciurleo
Research Institute for Geo-Hydrological Protection (CNR-IRPI)/ Rende (CS), Italy

mmandaglio@unisa.it

ABSTRACT: The application of physically based methods to areas affected by landslides requires the knowledge of geometric, geotechnical and rainfall input data. Once the geometric and rainfall data have been acquired, the geotechnical data are of relevant importance for the results obtained by method implementation. Indeed, if significant geotechnical properties on the soil involved by landslides are not available, any methodological application is a simplistic exercise. To overcome this issue, in the preliminary stage, data from the literature – for soils similar to those involved in the landslides – can be used in order to localize the in-site investigations in areas potentially affected by landslides. The paper shows an application of the physically based method TRIGRS to an area affected by rapid debris flows for the susceptibility assessment. Firstly, TRIGRS has been applied using as input geotechnical parameters those available in literature and the zones potentially affected by similar landslides have been identified. Detailed in-site investigations have been located and carried out in the so identified zones. By means of the results of in-site surveys and laboratory tests a reliable geotechnical slope model for the area has been created. Therefore, TRIGRS has been applied again to the study area using as input geotechnical parameters those obtained from the survey. The last application of the method provided the susceptibility zoning map of the area. The achievement of these results has been favored by the limited extension of the area and by availability of literature data for the involved soils.

RÉSUMÉ: L'application de méthodes physiques aux zones touchées par les glissements de terrain nécessite la connaissance des données géométriques, géotechniques et pluviométriques. Une fois les données géométriques et pluviométriques acquises, ces données géotechniques sont d'une importance pertinente pour les résultats obtenus par la mise en œuvre de la méthode. En effet, si des données géotechniques significatives sur les sols impliqués par les glissements de terrain ne sont pas disponibles, toute application méthodologique est un exercice simpliste. Pour surmonter ce problème, au stade préliminaire, les données de la littérature sur les sols - similaires à celles impliquées dans les glissements de terrain - peuvent être utilisées afin de localiser les enquêtes sur place dans les zones potentiellement touchées par les glissements de terrain. L'article montre une application de la méthode physique TRIGRS à une zone affectée par des écoulements rapides pour l'évaluation de la susceptibilité. Tout d'abord, TRIGRS a été appliqué en utilisant comme paramètres géotechniques d'entrée ceux disponibles dans la littérature et les zones potentiellement affectées par des glissements de terrain similaires ont été identifiées. Des enquêtes détaillées sur place ont été localisées et effectuées dans les zones ainsi identifiées. Grâce aux résultats des études sur site et des essais en laboratoire, un modèle géotechnique fiable de pente a été créé pour la région. Par conséquent, TRIGRS a été appliqué à nouveau à la zone d'étude en utilisant comme paramètres géotechniques d'entrée ceux obtenus à partir du levé. La dernière application de la méthode a fourni le tableau de zonage de sensibilité de la région. L'obtention de ces résultats a été favorisée par l'extension limitée de la zone et par la disponibilité de données documentaires pour les sols concernés.

Keywords: Shallow landslides; TRIGRS; in situ investigations; laboratory tests.

1 INTRODUCTION

In the wider frame of shallow landslide risk assessment, this paper is aimed to show the ability of a physically based model both to locate in a coherent scientifically based manner the in-situ investigations and to assess the susceptibility to shallow landslides in an area.

For this purpose, the "Transient Rainfall Infiltration and Grid-based Slope-Stability" (TRIGRS) deterministic model is applied to a study area periodically affected by rainfall-induced shallow landslides, located in Calabria (Southern Italy).

The implementation of TRIGRS needs of several data including rainfall, topographical and geomorphological data, mechanical and hydraulic properties of soils, pore water pressure regime. The database can be created starting from the data available from scientific literature on soils similar, for genesis and stress history, to those of the studied area (literature data) and it can be upgraded every time that a new data is available.

TRIGRS is applied twice, firstly using literature geotechnical data and secondly using in-site survey and laboratory test results. Particularly, literature data have been initially used to implement TRIGRS in order to individuate slopes potentially affected by shallow landslides. In these slopes in situ investigations, that included sampling and subsequent geotechnical laboratory tests, have been located on.

Once geotechnical data have been gathered, a reliable geotechnical slope model has been obtained and TRIGRS has been applied again to assess shallow landslide susceptibility of the area.

2 MATERIALS AND METHOD

2.1 Study area and landslide inventory

The study area, approximately 1 km^2, is located within the Costa Viola zone between Scilla and Bagnara Calabra (Reggio Calabria, Southern Italy).

From a geological point of view, the paleozoic basement of the area is manly made up of para- and ortho-gneiss, strongly tectonised and intensely weathered. Consequently, residual, colluvial and detrital soils (gneiss of Class VI according to Gioffrè et al., 2016) cover about 60% of the study area.

In the study area, several types of landslides periodically occur. The paper focuses on shallow landslides, involving class VI soils, that frequently propagated as debris flows affecting the urbanized area and transportation infrastructures. Two typical examples are debris flows occurred on 12 May 2001 and on 31 March 2005 (Figure 1).

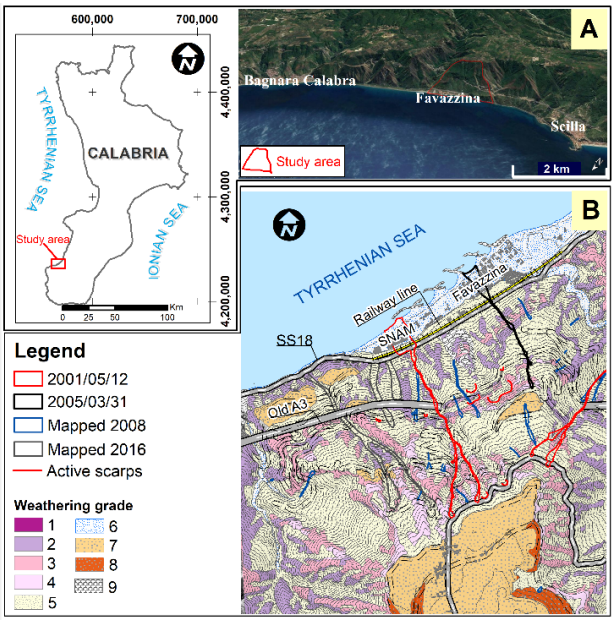

Figure 1. View of study area with debris flow location and weathering grade map (modified from Gioffrè et al., 2016). Legend of weathering grade: 1, gneiss of class II; 2, gneiss of class III; 3, gneiss of class IV; 4, gneiss of class V; 5, gneiss of class VI (colluvial and detrital soils); 6, coastal and alluvial deposits; 7, terraced marine deposits; 8, marine coarse sandstone deposits; 9, landslide debris.

The soil volumes triggered in source areas with sliding surfaces not exceeding 2 meters in depth rapidly moved along steep channels with strong entrainment of material and water; the deposition occurred on debris fans and the mass partially reached and deposited in the sea (Ciurleo et al., 2019a, 2019b).

The landslide inventory (Figure 1) has been made by combining these debris flows, the landslides mapped in 2008, the landslide inventory provided by the Calabria Region (dated 2016) and the landslide scarps identified by Moraci et al. (2017).

From a hydrological point of view, the Scilla rain gauge recorded rainfall of 20 mm over two consecutive days (on 12 May 2001) and 13.6 mm over two consecutive days (on 31 March 2005).

2.2 The methodology

The methodology consisted of two stages (I and II), in both stages, the method used to simulate shallow landslide triggering has been TRIGRS. It is a spatially distributed slope stability model coupled with a one-dimensional rainfall infiltration model. The input data of TRIGRS are: rainfall, topographical data, soil thickness, initial ground water table depth and mechanical and hydraulic properties of soils.

Referring to rainfall intensity, a rainfall of 20 mm over two consecutive days was considered because of it is the highest known value.

Referring to topographical data, a digital elevation model (DEM) of the study area with 5 m cell resolution has been used.

TRIGRS analysis is sensitive to initial steady state groundwater conditions, soil depths and geotechnical properties of soils (Godt et al., 2008; Salciarini et al., 2006; Sorbino et al., 2007, 2010).

To this regard, in stage I, TRIGRS was implemented using as input geotechnical parameters those available in literature. The aim of this stage has been the location of in-site investigations, included sampling, in slopes recognised as the most susceptible to the occurrence of shallow landslides (Ciurleo et al., 2019b, 2022).

By means of the results of in situ investigations and laboratory tests, a reliable geotechnical slope model of the study area has been obtained and used in the stage II.

In stage II, TRIGRS has been implemented again to assess shallow landslide susceptibility of the study area.

In this stage, owing to the lack of data on the initial steady state ground water position, several parametric analyses were performed in order to quantify the role of partially saturated conditions on the slope stability.

The performance of the model has been assessed by the true positive rate (TPR), also called sensitivity, and by the area under the receiver operating characteristic (ROC) curve (Swets, 1988).

3 RESULTS

3.1 Stage I

The input data used by TRIGRS in stage I are slope gradient and flow direction maps, derived by DEM, reported in Figure 2A and 2B. Referring to weathering grade map, gneiss of class VI (SOIL 1) and gneiss not involved by shallow landslides of slide type (SOIL 2) were identified (Figure 2C). Referring to ground water table location, according to Ciurleo et al. (2018), two different zones (Zone “A” and Zone “B”) with two different depths of ground water table were considered in the study area. Particularly, in Zone “A” (near the landslide source area) the water table was located at the ground surface, in the remain part of the study area (Zone “B”), it was considered at 1.5 m of depth from the ground surface (Figure 2D).

From a geotechnical point of view, in stage I, literature data have been used to carry out several parametric analyses in the Favazzina hamlet (Figure 2) with the aim to identify the combination of geotechnical parameters that best fit the available multi-temporal shallow landslide inventory.

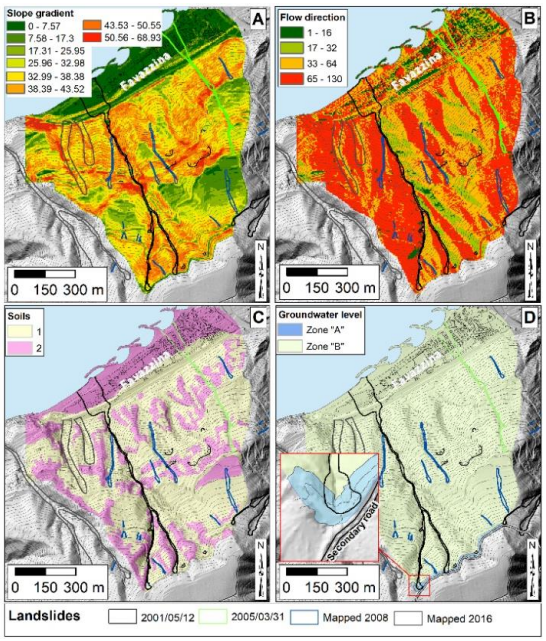

Figure 2. TRIGRS input data maps: (A) slope gradient; (B) flow direction; (C) weathered gneiss; (D) initial groundwater table depth (modified from Ciurleo et al., 2022).

The best obtained map in terms of sensitivity (TPR) is shown in Figure 3. It has been obtained using the literature mean values of hydraulic parameters (i.e., the saturated conductivity K_{sat} equal to 1.79E−05 m/s, the soil diffusivity D_0 equal to 7.92E−05 m^2/s, and the saturated water content θ_{sat} equal to 0.4); a constant value of soil cover thickness equal to 1.5 m; a value of cohesion (c') equal to 2.5 kPa and a value of shear strength angle (φ') equal to 30°. Several maps have been obtained changing the above mentioned geotechnical parameters but these maps did not fit the triggering areas mapped in landslide inventories.

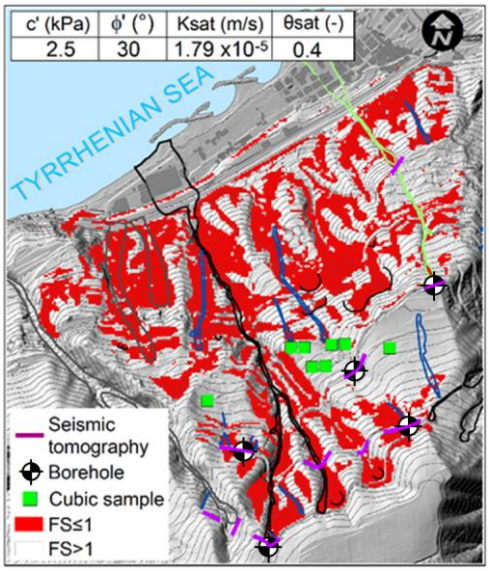

Figure 3. Map used to locate in situ investigations (modified from Ciurleo et al., 2022).

Starting from this map, in the slopes most susceptible to landslides, 10 seismic refraction tomographies, 5 boreholes with undisturbed samples have been located and performed (Figure 3). Cubic samples, due to the procedures of sampling, have been located in areas simply reachable by men and equipment (Figure 3). Tomographies and boreholes allowed us to identify the main soil cover thickness (gneiss of class VI) and confirmed that, in shallow landslide source areas, it is less than 2.0 m (about 1.5 m in most cases).

In order to develop a more detailed analysis, the results obtained by geotechnical laboratory tests performed on undisturbed specimens retrieved from the boreholes and the cubic samples have been considered in the following analyses.

The class VI gneiss involved in the shallow landslides have been classified, according to the Unified Soil Classification System (USCS), as silty sand (SM) and clayey sand (SC) with uniformity coefficient U = 76.05, 76.83, 113.51 and inorganic fine fraction of medium compressibility and not active. The value of LL ranged from 30.23 to 33.36% and PI from 3.25% to 11.36%. These soils have a solid unit weight (γ_s) varying from 25.9 to 26.1 kN/m^3; void ratio (e) variable from 0.9 to 1.17 and porosity (n) varying from 0.47 to 0.54.

Regarding the hydraulic properties of these soils, permeability tests have been performed in oedometer at different consolidation stresses ranging from 50.00, to 196.45 kPa, the obtained values of hydraulic saturated conductivity vary respectively from 3.64E-07 to 1.63E-08 m/s. The value of the hydraulic conductivity equal to 3.64E-07 m/s has been used for the analyses due to the expected (shallow) depths of the studied landslides.

The soil water characteristic curve has been obtained by a suction controlled oedometer test, and the laboratory data have been fitted with the Gardner model with a value of saturated volumetric water content (Θ_s) equal to 0.51, residual volumetric water content (Θ_r) equal to 0.23 and α parameter equal to 0.69 (Ciurleo et al., 2022).

Referring to mechanical properties, shear strength parameters have been obtained by drained triaxial compression tests on the undisturbed saturated specimens previously classified (i.e. SM) and they have been equal to c' = 1 kPa and $\varphi' = 35°$.

3.2 Stage II

In stage II several TRIGRS analyses have been performed in saturated and unsaturated conditions using the geotechnical input data obtained in stage I.

Regarding pore water pressure regime, different positions of the initial ground water table have been considered (Table 1). The first column of Table 1 shows a progressive identification number with the letter U, in case of unsaturated soil conditions, or S in case of saturated soil conditions. Cases 1U, 2U and 3U have been performed considering for the whole study area three different position of ground water table, respectively equalling 3.0 m, 2.5 m and 2.0 m.

Case 4S has been performed considering an initial steady state water table located at 1.5 m in the whole study area.

In case 5S the study area has been divided in two zones (Figure 2D): in zone "A" the depth of water table has been located at 0 m from the ground surface and in zone "B" a steady state ground water table at 1.5 m of depth has been considered.

Table 1. Ground water table location used in saturated and unsaturated soil conditions.

Case	Zone "A"	Zone "B"
1U	3.0	3.0
2U	2.5	2.5
3U	2.0	2.0
4S	1.5	1.5
5S	0	1.5

The simulation performed in unsaturated conditions with an initial water table located at 3.0 m (Figure 4 A) showed that only some cells of the study area are computed as unstable by the model and this initial configuration did not allow to simulate the real source areas mapped by multi-temporal landslide inventory.

When the position of the water table rose (Figure 4 B and C), the number of cells computed as unstable by the model increased even if the overall computed instability has been still very far from the simulation of the triggering areas mapped by the multi-temporal landslide inventory. This consideration has been supported by values of TPR equal to 0.08 and 0.14 for 1U and 2U cases. At the initial ground water table location of 2 m of depth, the value of TPR started to increase, reaching 0.45 (case 3U).

In saturated conditions, case 4S (Figure 4D) showed that the areas computed as unstable by the model well fitted the real source areas mapped by multi-temporal landslide inventory except the triggering area A_{01} that is one of the source areas that was triggered in the 2001 debris flow.

On the contrary, considering an initial ground water table located as reported in case 5S (Table 1, Figure 4E), TRIGRS has been able to correctly back-analyse the landslide source areas mapped by the inventory including the triggering area A_{01}.

The highest value of TPR, equal to 0.86, was reached for Case 5S that had a value of AUC equal to 86.4% so testifying a good ability of the model to back-analyse shallow landslide source areas.

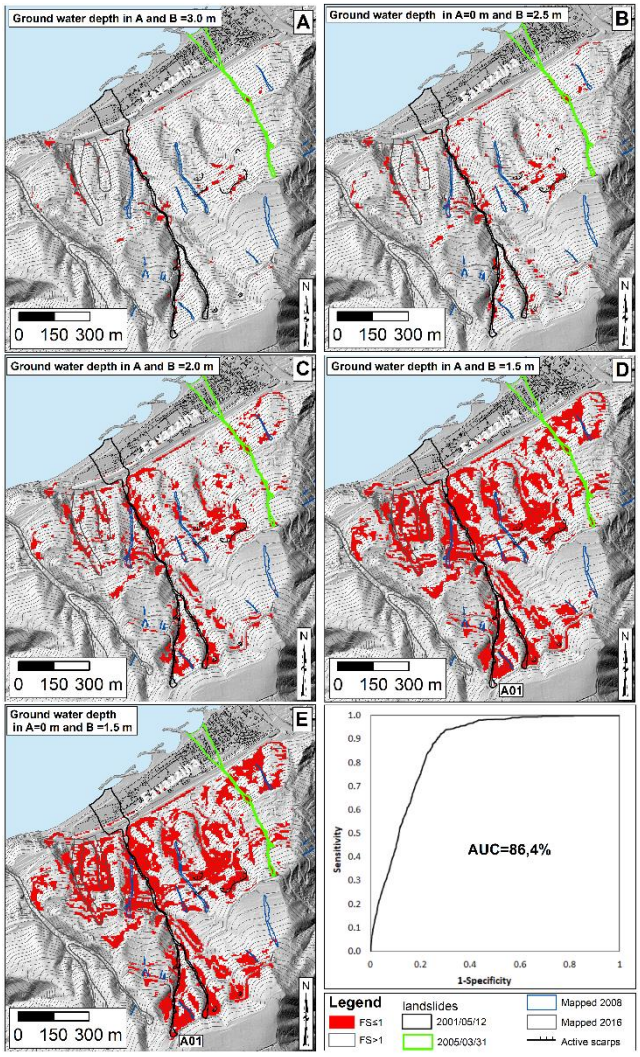

Figure 4. TRIGRS results in unsaturated and saturated soil conditions.

4 CONCLUSIONS

The paper showed for the first time in scientific literature the application of TRIGRS as tool to locate in-site investigation and laboratory tests.

The obtained results also show a good performance of the model in predicting shallow landslide occurrence.

Starting from the consideration that TRIGRS is a free software and the required input data can be found on literature, it is author opinion that the proposed methodology could become the common practice in landslide susceptibility assessment by using physically based models to locate in-site investigations so allowing the characterization of the soils potentially involved by landslides.

REFERENCES

Ciurleo, M., Ferlisi, S., Foresta, V., Mandaglio, M.C., Moraci, N. (2022) Landslide Susceptibility Analysis by Applying TRIGRS to a Reliable Geotechnical Slope Model. *Geosciences*, 12, 18 https://doi.org/10.3390/geosciences12010018.

Ciurleo, M., Mandaglio, M.C., Moraci, N., Pitasi, A. (2019a) A method to evaluate debris flow triggering and propagation by numerical analyses. In *Geotechnical Research for Land Protection and Development*. CNRIG 2019, Calvetti, F., Cotecchia, F., Galli, A., Jommi, C. (eds), Lecture Notes in Civil Engineering; vol 40. Springer, Cham.

Ciurleo M., Mandaglio M.C., Moraci N. (2019b) Landslide susceptibility assessment by TRIGRS in a frequently affected shallow instability area. *Landslides* 16:175‑188. https://doi.org/10.1007/s10346-018-1072-3.

Gioffrè D., Moraci N., Borrelli L., Gullà G. (2016) Numerical code calibration for the back analysis of debris flow runout in southern Italy. Landslides and Engineered Slopes. Experience, Theory and Practice: Proceedings of the 12th International Symposium on Landslides (Napoli, Italy, 12-19 June 2016), Vol. 3, pp 1339‑1344.

Moraci N., Mandaglio M.C., Gioffrè D., Pitasi A. (2017) Debris flow susceptibility zoning: an approach applied to a study area. *Riv Ital Geot* 2:47–62. DOI: 10.19199/2017.2.0557-1405.047.

Godt J.W., Baum R.B., Savage W.Z., Salciarini D., Schulz W.H., Harp E.L. (2008) Transient deterministic shallow landslide modeling: requirements for susceptibility and hazard assessments in a GIS framework. *Eng Geol* 102:214–226. https://doi.org/10.1016/j.enggeo.2008.03.019.

Salciarini D., Godt J.W., Savage W.Z., Conversini P., Baum R., Michael J.A. (2006) Modeling regional initiation of rainfall induced shallow landslides in the eastern Umbria region of Central Italy. *Landslides* 3:181–194. https://doi.org/10.1007/s10346-006-0037-0.

Sorbino G., Sica C., Cascini L., Cuomo S. (2007) On the forecasting of flowslides triggering areas using physically based models. In: *Proceedings of 1st North American Landslides Conference*, vol. 23. AEG Special Publication, pp. 305–315.

Sorbino G., Sica C., Cascini L. (2010) Susceptibility analysis of shallow landslides source areas using physically based models. *Nat Hazards* 53:313–332. DOI: 10.1007/s11069-009-9431-y.

Swets J.A. (1988) Measuring the accuracy of diagnostic systems. *Science* 240:1285–1293. DOI: 10.1126/science.3287615.

Proceedings of the XVIII ECSMGE 2024
GEOTECHNICAL ENGINEERING CHALLENGES
TO MEET CURRENT AND EMERGING NEEDS OF SOCIETY
© 2024 the Authors
ISBN 978-1-032-54816-6
DOI 10.1201/9781003431749-335
Open Access: www.taylorfrancis.com, CC BY-NC-ND 4.0 license

ECSMGE 24
XVIII EUROPEAN CONFERENCE ON SOIL MECHANICS AND GEOTECHNICAL ENGINEERING

A comparative study of European and Japanese pile design codes based on a test site data

Une étude comparative des codes de conception de pieux européens et japonais basée sur les données d'un site d'essai

K. Mandal, S. Lin
Jibanshikenjo Co. Ltd., Tokyo, Japan

G. Belokas*
University of West Attica, Athens, Greece

N. Shkodrani
Polytechnic University of Tirana, Tirana, Albania

T. Matsumoto
Kanazawa University, Kanazawa, Japan

**gbelokas@uniwa.gr*

ABSTRACT: Pile Static Load Test (SLT) and Rapid Load Test (RLT) results at the Jibanshikenjo test site in Sashima were compared to the empirical pile resistances estimated based on SPT and CPT measurements proposed by different European (EC7 National Annexes) and Japanese codes. RLT requires an interpretation, however, it is quick to perform and for this case it was in close agreement with SLT. The empirical pile resistance calculations from SPT and CPT vary in terms of methodology, gave different results and no consistent trend, especially for the tip resistance. Concerning the shaft resistance BS code for shaft resistance from SPT and Unified CPT, AFNOR and DIN codes from CPT gave good results. SLT and RLT must be considered more accurate, while the empirical methods should always consider local experience and preferably be compared to SLT or RLT results.

RÉSUMÉ: Les résultats des tests de charge statique et des tests de charge rapide sur le site d'essai de Jibanshikenjo à Sashima ont été comparés aux résistances empiriques des pieux estimées sur la base des mesures SPT et CPT proposées par différents codes européens (annexes nationales EC7) et japonais. RLT nécessite une interprétation, cependant, elle est rapide à réaliser et pour ce cas elle a été en étroit accord avec SLT. Les calculs empiriques de résistance des pieux de SPT et CPT varient en termes de méthodologie, ont donné des résultats différents et aucune tendance cohérente, en particulier pour la résistance aux pointes. Concernant la résistance à l'arbre BS pour la résistance à l'arbre du SPT et du CPT Unifié, l'AFNOR et le DIN du CPT ont donné de bons résultats. SLT et RLT doivent être considérés comme plus précis, tandis que les méthodes empiriques doivent toujours tenir compte de l'expérience locale et être de préférence comparées aux résultats SLT ou RLT.

Keywords: Pile resistance; design codes; representative value; empirical methods; Rapid Load Test.

1 GENERAL

The ultimate limit state (ULS) bearing capacity check of a single pile includes the calculation of the Ultimate Pile Load (UPL) representative value (R_{rep}), which corresponds to the pile bearing resistance failure (according to EN 1997-1:2004) or to the failure of the ground surrounding the piles (according to the upcoming 2nd generation EN 1997-3). In most cases, the bearing capacity calculation is based on static load tests, or on dynamic impact tests, or on ground tests results (e.g. EN 1997-1:2004) and these three alternatives result in different computational models, i.e. methods of calculation.

The static load test provides a direct estimation of the in situ total bearing resistance (R_c) or separately base (R_b) and shaft (R_s) resistances (EN 1997-1:2004). The dynamic impact test provides R_c, R_b and R_s after an interpretation and according to EN 1997-1:2004 "the validity of the result shall have been demonstrated by previous evidence of acceptable performance in static load tests on the same pile type of similar length and cross-section and in similar ground conditions".

Regarding methods to be incorporated based on ground tests the calculation results "shall have been established from pile load tests and from comparable experience" EN 1997-1: 2004. Ground test results may be either laboratory or in-situ tests. In Europe each country may propose a different calculation methodology, which is influenced by the local experience, for instance the DIN 1054, AFNOR NF P 94-262 and BS 8004 National Annexes (NAs) for EN 1997-1. For instance, the BS 8004, adopts the α-method if laboratory determined undrained shear strength (s_u) is available, or the β-method if drained shear strength (Mohr – Coulomb effective cohesion c' and effective angle of shearing resistance φ') is available. Notably, in Japan a variance of methods are prescribed in different Japanese Codes adopted by different authorities for their applications (Architectural Institute, Road Association, Ports and Harbours Bureau and Railway TRI). Concerning the use of in situ results all codes propose totally different methodologies.

The calculation of the UPL design value (R_d) differs on the way the design codes apply the factors of safety: a) Material Factor Approach (MFA), in which partial factors of safety are applied to the material strength constants or b) the Resistance Factor Approach (RFA), in which overall factors of safety are applied to the representative UPL.

This work performs a comparative analysis of the EC7 DIN, EC7 AFNOR, EC7 BS and four Japanese Codes with regards to in situ tests results carried out at the Jibanshikenjo test yard in Sashima Japan (Lin et al., 2023b).

2 ULTIMATE PILE LOAD

A general definition of the Ultimate Pile Load (UPL) representative value ($R_{c;rep}$) is presented in to Equation (1). The design value ($R_{c;d}$) depends whether the MFA or RFA approaches are adopted, or Equations (2) and (3) respectively. Equation (3) directly relates to Equation (1) by the overall factor of safety on the resistance. The EN 1997 signs have been adopted, while $X_d = X_{rep} / \gamma_M$ and $F_d = \gamma_F F_{rep}$ correspond to the design values of strength and loads respectively.

$$R_{c;rep} = R\left(F_{rep}, X_{rep}\right) \quad (1)$$

$$R_{c;d} = R\left(\gamma_F F_{rep}, X_{rep}/\gamma_M\right) \quad (2)$$

$$R_{c;d} = R_{c;rep}/\gamma_R = R_{c;rep}/\gamma_t \quad (3)$$

If bearing capacity is further analysed into the base (R_b) and the shaft (R_s) resistances, then:

$$R_{c;d} = R_{b;rep}/\gamma_b + R_{s;rep}/\gamma_s \quad (4)$$

The selection of MFA (Equation (2)) or RFA (Equation (3)) relates closely on the methodolody applied to estimate the single pile bearing capacity:

- Static Load Test (SLT) or Dynamic Impact Test: If it determines $R_{c;rep}$ applies RFA. If it determines $R_{b;rep}$ and $R_{s;rep}$ apply MFA or RFA (Equations (4) and (3) respectively).
- Ground Tests (GT): $R_{b;rep}$ and $R_{s;rep}$ are determined (Equations (5) and (6)). Empirical correlations are applied to laboratory results (soil strength constants) or in situ results (CPT, SPT), to calculate the representative base bearing capacity ($q_{b;rep}$) and shaft unit bearing capacity ($q_{s;rep}$, or $q_{s;i;rep}$ for ith layers). Either MFA or RFA (Equastions (4) and (3) respectively) can be applied.

$$R_{b;rep} = A_b q_{b;rep} \quad (5)$$

$$R_{s;rep} = \sum_{i=1}^{n} A_{s;i} q_{s;i;rep} \quad (6)$$

The MFA and RFA for pile $R_{c;d}$ calculation will give similar results for calculations from GT because the computational models are practically linear functions of the soil strength (c_u or c' and $\tan\varphi'$) or the in situ measurements (corrected cone resistance q_t, or blow counts N_{SPT}). This is in strong contrast with the shallow foundation case under drained conditions (e.g. Kovaiou & Belokas, 2023), where the bearing capacity equation is non-linear function of $\tan\varphi'$. Next, the European and Japanese methodologies for R_{rep} calculation of steel pipes are compared based on SLT (Static Load Test), RLT (Rapid Load Test) and in situ GT (SPT and CPT) results.

3 CALCULATION METHODS

DIN 1054 applies model factors $\eta_b < 1$ and $\eta_s < 1$ on Eqs. (5) and (6), i.e. $R_{b;rep} = \eta_b A_b \; q_{b;rep}$ and $R_{s;rep}=\sum \eta_{si} A_{si} q_{s;i;rep}$. Bearing capacities estimations are based on a representative resistance-settlement curve, which uses empirical limit settlements for $q_{b;rep}$ and $q_{s;rep}$ full mobilization and empirical correlations for ultimate $q_{b;rep}$ and $q_{s;rep}$ values that depend on limit settlements and CPT or c_u values.

AFNOR: NF P 94-262 classifies Close-ended Pipe Piles (CPP) to "class 4" and Open-ended Pipe Piles (OPP) to "class 5". It employs $q_{b;rep} = k_c \; q_{ce}$ and $q_{s;rep} = \alpha f_{soil} \leq q_{smax}$, where q_{ce} is an equivalent CPT value, k_c varies according to soil type, pile geometry and pile class, while $0.2 \leq \alpha \leq 2.25$ and q_{smax} vary according to soil type and pile class.

BS 8004 classifies CPP to "high displacement class" and OPP to "low displacement class", which refer to the degree of installation disturbance. It allows calculation from SPT, CPT (both used herein) or soil strength data. The CPT calculation is $R_{b;rep(0.1)} = A_b c_{b;0.1} q_{c;b;rep}$ and $R_{s;rep}=\sum c_{s;i} A_{s;i} q_{c;i;rep}$, where $q_{b;0.1}$ is the measured cone resistance over 1.5D depth below base, $q_{c;i}$ is the measured cone resistance within the layer, while $c_{b0.1}$ and $c_{s;i}$ are empirical coefficients that depend on soil pile type and can be estimated from Tables. The SPT calculation is $R_{b;rep(0.1)} = A_b n_{b;0.1} p_{ref} N_b$ and $R_{s;i} = A_s n_{s;i} p_{ref} N_i$, where $p_{ref} = 100$ kPa, $n_{b;0.1}$ and $n_{s;i}$ empirical coefficients that depend on soil and pile type (typical tabulated values are given), N_b and $N_{s;i}$ the uncorrected N_{SPT} at the base and in layer i respectively.

Tables 1 and 2 summarise the Japanese codes AIJ (2019) of Architectural Institute, JRA (2017) of Road Association, MLIT (2020) of Ports and Harbours Bureau and RTRI (2012) of Railway TRI.

Table 1. q_b and q_s based on Japanese codes (in kPa) (1/2).

Code	Type	Soil type: Sand	Soil type: Clay
Railway	q_b	$210N$ (≤10000)	6.3c or $75N$ (≤20000)
		CPP: N = mean N-value $3D_o$ below pile tip	
		$175N$ (≤ 8000)	$55N$ or $5.5s_u$ (≤16000)
		OPP with w/ $D_o \leqq 0.8$ m and $l/D_o > 5$: N = N-value of ground at pile tip, l = equivalent embedment length into bearing stratum, $l = [5\ D_o\ (N_1+N_2)/2]/N$, N_1 = N-value at $5D_o$ above pile tip, N_2 = N-value of ground at pile tip, D_o = outer pile diameter	
		$35(l/D_o)N$ (≤8000)	$11(l/D_o)N$ or $1.1(l/D_o)s_u$ (≤16000)
		OPP with w/ $D_o \leqq 0.8$ m and $l/D_o \leqq 5$: N = N-value of ground at pile tip	
		$(140/D_o)N$ (≤8000)	$(44/D_o)N$ or $(4.4/D_o)s_u$ (≤16000)
		OPP with w/ $D_o > 0.8$ m and $l/D_o > 5$: N = N-value of ground at pile tip	
		$(28/D_o)(l/D_o)N$ (≤8000)	$(8.8/D_o)(l/D_o)N$ or $(0.88/D_o)(l/D_o)s_u$ (≤16000)
		OPP with w/ $D_o > 0.8$ m and $l/D_o \leqq 5$: N = N-value of ground at pile tip	
	q_s	$3N$+30 (≤150)	$6N$ or $0.4s_u$ (≤120)
		$3N$ (≤120)	$6N$ or $0.4s_u$ (≤120)

Table 2. q_b and q_s based on Japanese codes (in kPa) (2/2).

Code	Type	Soil type: Sand	Soil type: Clay
Port	q_b	$300\eta N$ (≤15000)	$6s_u$
		$N = (N_1+N_2)/2$, N_1 = N-value of ground at pile tip, N_2 = mean N-value $4D_o$ above pile tip, η = plugging efficiency	
	q_s	$2N$ (≤100)	$1s_u$ (≤100)
Archi.	q_b	$300\eta N$ (≤18000)	$6s_u$ (≤18000)
		$\eta = 0.16(L_B/D_i)$ for $2 \leq L_B/D_i \leq 5$; $\eta = 0.8(L_B/D_i)$ for $L_B/D_i > 5$; L_B = embedment into bearing stratum, D_i = inner pile diameter	
	q_s	$2N$ (≤100)	$0.8s_u$ (≤100)
Road	q_b	$130N$ (≤6500)	$90N$ (≤4500)
	q_s	$5N$ (≤100)	$6N$ or $1s_u$ (≤70)

4 COMPARISON OF PILE RESISTANCES

Results from an open-ended steel pipe pile (SPP) at Jibanshikenjo test site in Sashima, Ibaraki Prefecture, Japan are considered. It had an outer diameter of 318.5 mm, a wall thickness of 6.6 mm and an embedment length of 11.0 m. The Static Load Test (SLT) and Rapid Load Tests (RLTs) carried out are summarized in Figure 1. The RLT instrumentation is shown in Figure 2. To estimate the soil resistance R_{soil} (= static soil resistance R_w + dynamic soil resistance R_d) and R_w from the measured values of applied load F_{rapid} and pile head acceleration α, UnLoading Point Connection Method invoking CASE method (ULPC_CM) (Lin et al., 2023a) was used. The relative loading duration $T_r = t_L/(2L/c)$ (t_L= loading duration, L = pile length, c = bar wave velocity in pile) in RLTs was about 5 according to JGS (2002).

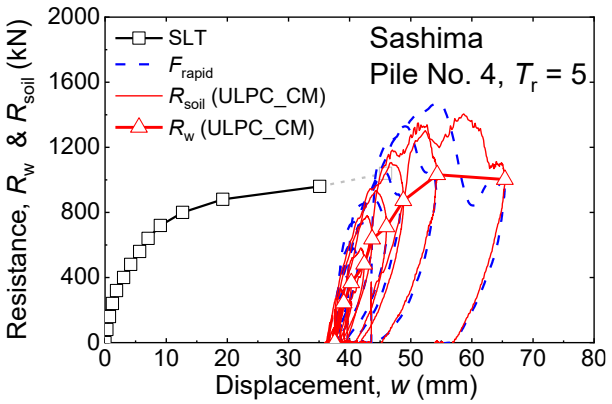

Figure 1. Static load-displacement relations from SLT and RLTs.

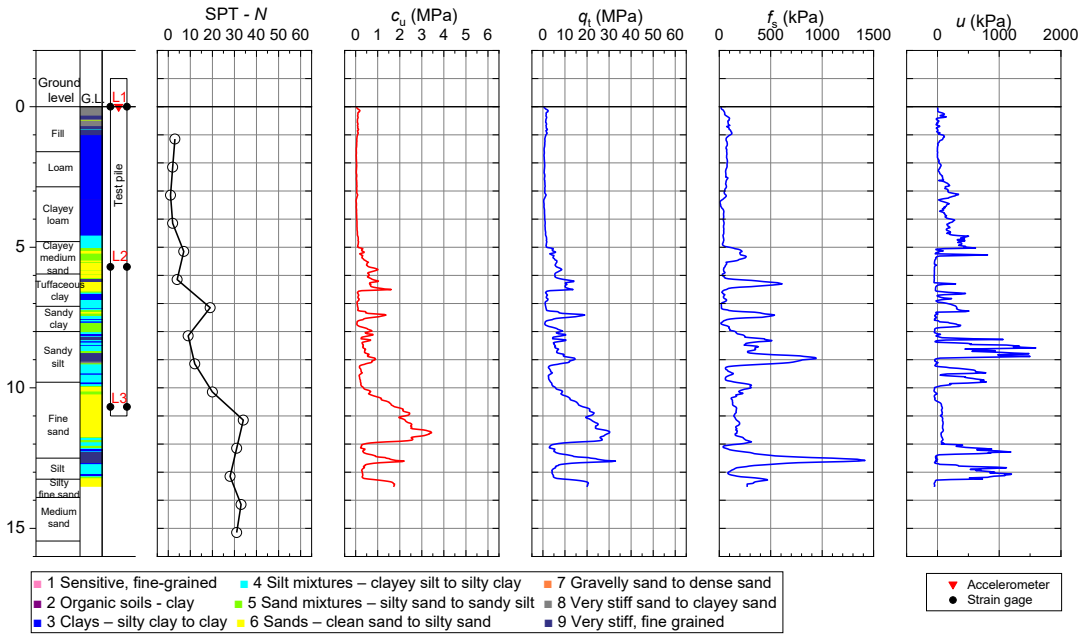

Figure 2. Site soil profile (undrained strength c_u is computed from q_t).

Figure 2 presents the soil profile and the in-situ results: a) SPT N-values obtained at 1 m intervals and b) electric Cone Penetration Test (CPT) measurements of corrected cone tip resistance q_t, sleeve friction f_s and pore water pressure u at 20 mm intervals. The undrained shear strength c_u was estimated using q_t. Notice that the estimated c_u is valid for only clayey soil layers.

Three EN 1997 National Annexes, namely DIN (including "Recommendations on Piling", DGGT (2013)), AFNOR and BSI and four Japanese codes, are applied to the test site results.

4.1 Calculation by SPT N-value

Four Japanese codes and EN 1997 Annex BS have been used. Figure 3 shows the distributions with depth of shaft resistance τ_f (or $q_{s;rep}$) from static Load Tests (SLT), Rapid Load Tests (RLT) with ULPC_CM and SULPC interpretations (Lin et al., 2023b), and various design codes. SULPC is an extension of ULPC. If the dynamic signals are measured at several levels of a pile, the pile is divided into several pile segments. ULPC interpretation is applied to each pile segment to obtain the static force-displacement relation of the segment. Response of the whole pile subjected to static pile head load is then calculated through a one-dimensional FEM using the static response of pile segments previously obtained (Kamei et al., 2023).

Notice that when the empirical equation using only cohesion (undrained shear strength) c is specified in the Japanese codes, $c = 6.25N$ (kPa) was assumed.

In Figure 3, the dotted lines are the shaft resistance τ_f estimated from the various design codes. The solid lines indicate the average values of τ_f along the pile segment, specifically Seg. 1 and Seg. 2. The thick solid lines are the measured τ_f in SLT and RLTs.

Concerning RPL, to estimate the soil resistance on each pile segment, ULPC_CM interpretation analysis was carried out using the measured signals at each measurement level (L1, L2 and L3). When the signal measured at L1 are used, the soil resistance below L1 is obtained. Similarly, when the signals measured at L2 are used, the soil resistance below L2 is obtained. When signals measured at L3 are interpreted, the soil resistance is the pile tip resistance. Hence, the soil resistance acting on each segment was obtained.

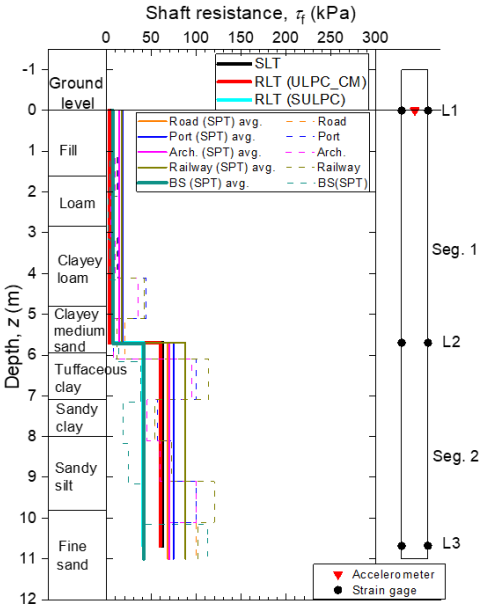

Figure 3. Distributions of shaft resistance τ_f from SLT, RLT and design codes (SPT).

Figure 4 shows the comparison of shaft resistance τ_f of two pile segments from SLT, RLT and the design codes. While Japanese codes show no significant differences, they tend to overestimate the SLT result. On the other hand, the shaft resistance τ_f from BS and RLTs are almost equal to the SLT result.

Figure 5 shows the comparison of maximum total shaft resistance Q_s and maximum total tip resistance Q_b from SLT, RLT and the design codes. The trend of Q_s is similar to that described in Figure 4. There is a wide variation in Q_b from the design codes. The plugging efficiency $\eta = 1$ in Port code and Road code, while $\eta = 0.52$ in Architectural code for this particular test pile condition. Q_b from RLT is the most reasonable estimation for the SLT result.

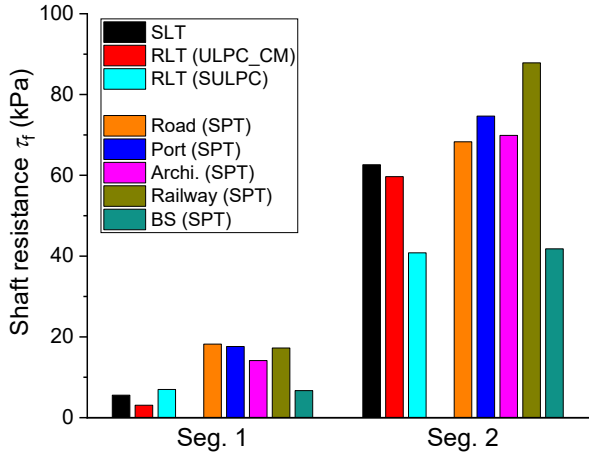

Figure 4. Comparison of average shaft resistance τ_f of two pile sections from SLT, RLT and design codes (SPT).

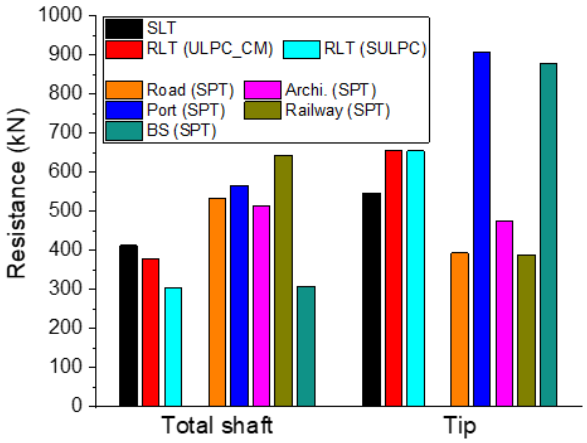

Figure 5. Comparison of maximum shaft resistance Q_s and maximum tip resistance Q_b from SLT, RLT and design codes (SPT).

4.2 Calculation by CPT

The Unified CPT method (Lehane et al., 2022a, b) and three EN 1997 Annexes (BSI, AFNOR, DIN) are applied to compare them to shaft resistances and tip resistance from SLT and RLT. The shaft resistances are estimated at 0.02 m intervals of CPT measurements. When CPT-based methods were used, soil classification from the borehole investigation (SPT) (Fig. 2) was used. Loam, clayey loam, tuffaceous clay and sandy clay were classified as "clay", and the other soil layers were classified as "sand".

Figure 6 shows the distributions with depth of shaft resistance τ_f from the SLT, RLT with ULPC_CM and SULPC interpretations (Lin et al., 2023b) and the various CPT codes (dotted lines). The solid lines indicate the average values of τ_f along the pile Seg. 1 and Seg. 2. Notice a coefficient F_{st} was set as 0.3 in the Unified CPT method.

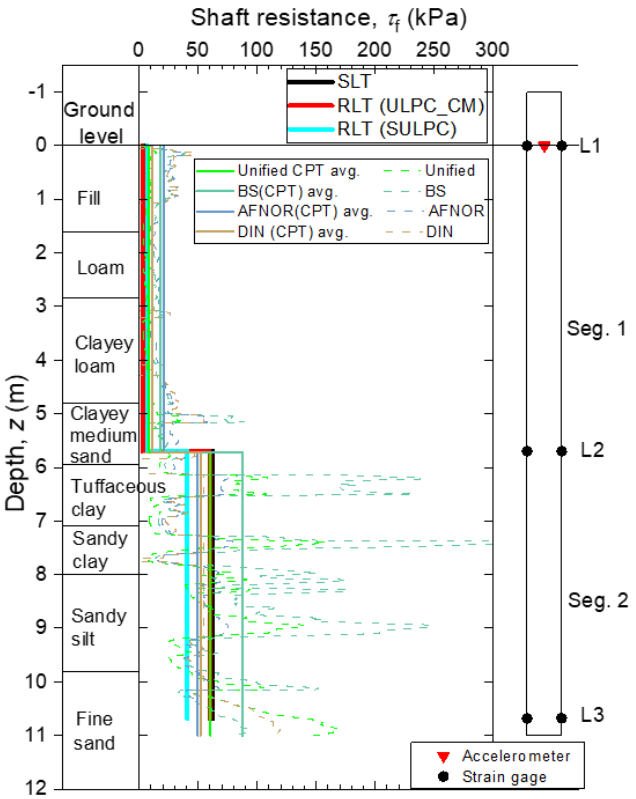

Figure 6. Distributions of shaft resistance τ_f from SLT, RLT and design codes (CPT).

Figure 7 shows the comparison of shaft resistance τ_f of two pile segments from SLT, RLT and the design codes. Shaft resistance from BS tends to overestimate the result of SLT. The shaft resistance τ_f from Unified CPT, DIN and RLT are almost equal to the SLT result.

Figure 8 shows the comparison of maximum total shaft resistance Q_s and maximum total tip resistance Q_b from SLT, RLT and the CPT codes. The Q_s of RLT, Unified CPT, AFNOR and DIN are almost equal to the SLT result. However, all the Q_b from CPT code underestimate the SLT result.

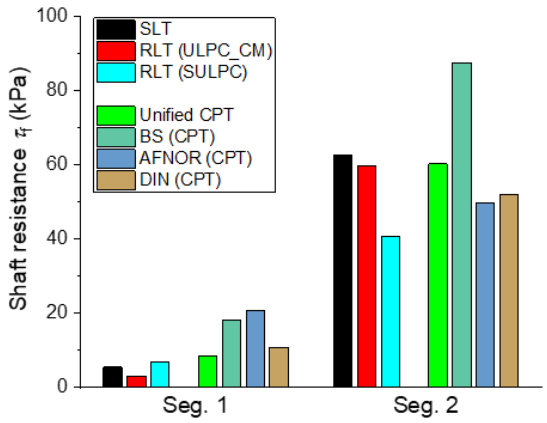

Figure 7. Comparison of average shaft resistance τ_f of two pile sections from SLT, RLT and design codes (CPT).

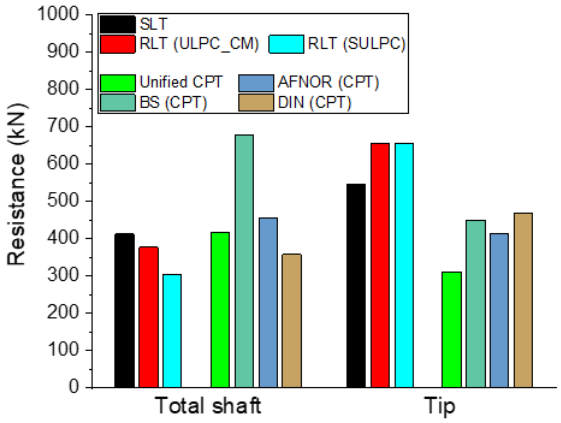

Figure 8. Comparison of maximum shaft resistance Q_s and maximum tip resistance Q_b from SLT, RLT and design codes (CPT).

5 CONCLUSIONS

Pile SLT and RLT results at the Jibanshikenjo test site in Sashima were compared to the pile resistance estimated based on SPT and CPT measurements for different European and Japanese codes. Test piles SLT and RLT showed close agreement. The different empirical pile resistance estimations from SPT and CPT varied considerable. Despite that some methods gave good results, e.g. BS for shaft resistance from SPT, Unified CPT, AFNOR and DIN for shaft resistance from CPT, there was not any consistent trend, especially for the tip resistance. SLT and RLT must be considered more accurate, while the empirical methods should always consider local experience and preferably be compared to SLT or RLT results.

REFERENCES

AFNOR (2012). *NF P 94-262 Justification of geotechnical structures National Enforcement Standards Eurocode 7 – Deep Foundations*. French Association of Normalization (AFNOR).

AIJ (2019). Guidelines for Building Foundation Structures. Archit. Inst. of Japan (in Japanese).

BSI (2015). BS 8004:2015 Code of practice for foundations. British Standards Institution.

DGGT (2013). *Recommendations on Piling (EA Pfähle)*. Deutsche Gesellschaft für Geotechnik (Johnson, A Translation). Wiley.

DIN (2021) *DIN 1054:2021-04 Subsoil - Verification of the safety of earthworks and foundations - Supplementary rules to DIN EN 1997-1*. DIN.

EN 1997-1:2014 (2014). Eurocode 7: Geotechnical design - Part 1: General Rules

JRA (2017). Specification for Highway Bridges: Part IV Substructures. Japan Road Association.

Japanese Geotechnical Society (JGS) (2002) JGS 1815-2002 Method for Rapid Load Test of Single Piles.

Kamei, S., Lin, S., Yamamoto, I. & Matsumoto, T. (2023). Hybridnamic rapid load testing with an extended interpretation method of dynamic signals. *Proc. the 17th Asian Regional Conference on Soil Mech. and Geotech. Engineering 2023*, Nur-Sultan, pp. 1420-1424.

Lehane, B., Igoe, D., Gavin, K. & Bittar, E. (2022a). Application of the Unified CPT method to assess the driving resistance of pipe piles in sand. *Proc. 11th Int. Conf. on Stress Wave Theory and Design and Testing Methods for Deep Foundations*, The Netherlands, 10.5281/zenodo.7148654.

Lehane, B. M., Liu, Z., Bittar, E., Nadim, F., Lacasse, S., Bozorgzadeh, N., Jardine, R., Ballard, J. C., Carotenuto, P., Gavin, K., Gilbert R. B., Bergan-Haavik, J., Jeanjean, P. & Morgan, N. (2022b). CPT-based axial capacity design method for driven piles in clay. *Jour. of Geotech. and Geoenv. Eng.*, 148 (9): 04022069.

Lin, S., Kamei, S., Yamamoto, I. and Matsumoto, T. (2023a). Hybridnamic rapid load testing with UnLoading Point Connection method invoking Case method. *Proc. the 17th Asian Regional Conference on Soil Mech. and Geotech. Engineering 2023*, Nur-Sultan, pp.1425-1429.

Lin, S., Watanabe, K., Kamei, S., Yamamoto, I. and Matsumoto, T. (2023b). Comparative static and rapid load tests on steel pipe piles: A case study at Sashima test yard. *Proc. 5th Int. Conf. on Geotechnics for Sustainable Infrastructure Development*, Hanoi (to be published).

MLIT (2020). Technical Standards and Commentaries for Port and Harbour Facilities in Japan. Ports and Harbours Bureau, Ministry of Land, Infrastructure, Transport and Tourism.

RTRI (2012). Design Standards for Railway Structures and Commentary: Substructures. Railway Technical Research Inst. (in Japanese).

Proceedings of the XVIII ECSMGE 2024
GEOTECHNICAL ENGINEERING CHALLENGES
TO MEET CURRENT AND EMERGING NEEDS OF SOCIETY
© 2024 the Authors
ISBN 978-1-032-54816-6
DOI 10.1201/9781003431749-336
Open Access: www.taylorfrancis.com, CC BY-NC-ND 4.0 license

ECSMGE 24
XVIII EUROPEAN CONFERENCE ON SOIL MECHANICS AND GEOTECHNICAL ENGINEERING

Control of technological processes during underground construction in the historical centre of megacities in weak soils using interactive geotechnical monitoring

Contrôle des processus technologiques lors de la construction souterraine dans le centre historique des mégapoles dans des sols faibles à l'aide d'une surveillance géotechnique interactivedu

R.A. Mangushev, A.I. Osokin*, I.P. Diakonov
Saint- Petersburg State University of Architecture and Civil Engineering (SPbGASU), Saint-Petersburg, Russia
**geostroy-osokin@mail.ru*

ABSTRACT: The development of historical cities naturally consists in the development of underground space. The article considers an integrated approach to the preservation of buildings - monuments on the example of the city of St. Petersburg, which has a large capacity of weak soils in its geological structure and a significant building area, which is a World Heritage Site protected by UNESCO. The article analyzes the experience of using various geotechnologies to minimize the impact of underground construction on the surrounding buildings. The high role of geotechnical monitoring for the preservation of monuments located near the site of underground construction is noted. The use of modern laser scanning systems and traditional methods of assessing deformations of buildings allow us to take into account the features of a unique object during monitoring. Prospects for the use of high-precision spatial monitoring of architectural monuments suggest the introduction of a new tool for monitoring the state and risk analysis of historical heritage. The data on the implementation of the described studies are confirmed by the successful implementation of the construction of an underground space on weak soils in the historical districts of the city of St. Petersburg.

RÉSUMÉ: Le développement des villes historiques consiste naturellement en l'aménagement de l'espace souterrain. L'article considère une approche intégrée de la préservation des bâtiments - monuments sur l'exemple de la ville de Saint-Pétersbourg, qui a une grande capacité de sols faibles dans sa structure géologique et une zone de construction importante, qui est un site du patrimoine mondial protégé par l'UNESCO. L'article analyse l'expérience de l'utilisation de diverses géotechnologies pour minimiser l'impact de la construction souterraine sur les bâtiments environnants. Le rôle important de la surveillance géotechnique pour la préservation des monuments situés à proximité du site de construction souterraine est noté. L'utilisation de systèmes de balayage laser modernes et de méthodes traditionnelles d'évaluation des déformations des bâtiments nous permet de prendre en compte les caractéristiques d'un objet unique lors de la surveillance. Les perspectives d'utilisation de la surveillance spatiale de haute précision des monuments architecturaux suggèrent l'introduction d'un nouvel outil de suivi de l'état et d'analyse des risques du patrimoine historique. Les données sur la mise en œuvre des études décrites sont confirmées par la mise en œuvre réussie de la construction d'un espace souterrain sur des sols faibles dans les quartiers historiques de la ville de Saint-Pétersbourg.

Keywords: Additional deformations; historical building; geotechnical monitoring; geotechnics; plaxis.

1 INTRODUCTION

The development of historical cities naturally consists in the development of underground space. Consider the option of creating predominantly pedestrian streets, while developing transport infrastructure under existing roads, canals, buildings. Using the example of a city with a large capacity of weak soils and widespread existing buildings in the status of objects of cultural significance, geotechnical construction involves the study of not only complex soils, but also the structures of palaces and monasteries built hundreds of years ago. Under these conditions, over the past 10 years, experience has been accumulated and analyzed in the application of various technologies for the construction of piles, enclosing structures and strengthening the foundation soils (Mangushev and Nikiforova, 2017).

At the same time, significant expenditures of the construction budget were spent on measures aimed at ensuring the safety of historical buildings. The laws of construction in such areas require a practical lack

of impact from new construction. So, the additional sediment should not exceed 0.5 cm. On weak thixotropic clay soils, any construction work leads to the risk of destruction of the existing building (Mangushev et al., 2018). The answer to each of the technological challenges of underground space development is the appearance of a new technology on the construction equipment market, which allows solving a new range of tasks taking into account the requirements and peculiarities of local ground conditions. In this regard, we are convinced that even the most advanced technological methods should be adapted to local geotechnical conditions. For example, in the conditions of weak thixotropic clay soils of St. Petersburg, the modulus of deformation of which can be 2...3 MPa, the role of control of technological operations is enhanced. An example of such development can be considered the accumulation of research experience on the construction of pit fences by the "Wall in the ground" method and the immersion of the sheet pile by static and vibration method. Within the framework of these studies, criteria for the technological performance of work were determined, such as speed, sequence of operations and calculation method for a preliminary analysis of the safety of work.

In this regard, the role of monitoring the behavior of the object of protection and the instrument of operational control of its structures is being strengthened. At the same time, the role of soil surveys and structures of the cultural heritage object becomes a priority, determining the principles of modeling and implementation of construction. Improving the quality of risk assessment at the stage of project development is also ensured by improving the methods of monitoring spatial deformations of the building and its parts. Traditional monitoring systems monitor only certain points on the object. At the same time, an increase in the number of points will lead to an increase in the cost of geodetic works. The use of scanning systems to obtain a point cloud, as well as a digital double of an object, can be a useful tool that allows you to present a complete picture of deformation, including the presence of defects and cracks in the structure.

In addition, the building of historical buildings requires an individual approach both in design and monitoring. The use of laser scanning systems in interaction with scanning drones, and traditional methods for assessing movements and efforts in the structure, allow you to take into account all the details of a unique object when monitoring its safety.

Comparable modeling and monitoring capabilities of the facility allow for operational control of the stress-strain system. In addition, spatial monitoring using laser scanning provides an analysis of the impact of construction on cultural heritage sites, and the accumulation of such experience makes it possible to develop models of materials of load-bearing structures and verify the method of their modeling based on the results of comparison with actual deformations. In order for the scanning in the monitoring system to meet the requirements for measurement accuracy, it was necessary to develop a survey methodology that includes new types of geodetic signs (spherical prisms), the use of unmanned aerial vehicles to build an additional point cloud, as well as a method for processing a point cloud. The prospects of using high-precision spatial monitoring of architectural monuments suggest the introduction of a new tool for monitoring the condition and risk analysis of historical heritage. The data on the implementation of the described studies are confirmed by the successful implementation of the construction of an underground space on weak soils in the historical districts of the city of St. Petersburg.

2 LITERATURE REVIEW

Reducing the amount of additional deformations in the building of the surrounding building naturally leads to the choice of an enclosing structure of greater rigidity. At the same time, we are increasing the technological component of additional precipitation. A number of authors (Mangushev et al., 2020, Sapin, 2014) under the guidance of Professor Mangushev were engaged in studies of the nature and methods of calculating technological sediments in the construction of pit fences. In his research, D.A. Sapin (Sapin, 2015) showed that the technological component of the toughest enclosing structure – the trench wall in the ground reaches 80% of the total additional deformation of the building of the surrounding development. The results of field and laboratory modeling of static immersion of steel sheet piling, performed by A.V. Gursky, (Mangushev and Gursky, 2016), allowed us to conclude that additional technological deformations of the tongue-and-groove device will be less than in the case of a trench wall in the ground, however, the subsequent additional deformations of the building caused by the horizontal movement of the flexible retaining tongue-and-groove wall are comparable, and even exceed the technological risks from the trench wall in the ground. The main problem that forms these risks is a large thickness of weak clay soils, during the operation of equipment in which thixotropic structural disturbances begin to occur and are always

accompanied by large movements (Mangushev and Osokin, 2019). Under these conditions, the deformations of the surrounding historical buildings can be 150...600 mm (Ulitskiy et al., 2013, Paramonov, 2009). As we noted earlier, the permissible amount of precipitation is 5...20 mm. The negative effects of these values of deformations are always enhanced by the presence of a large unevenness of deformations, which leads to the formation of cracks and the destruction of the building.

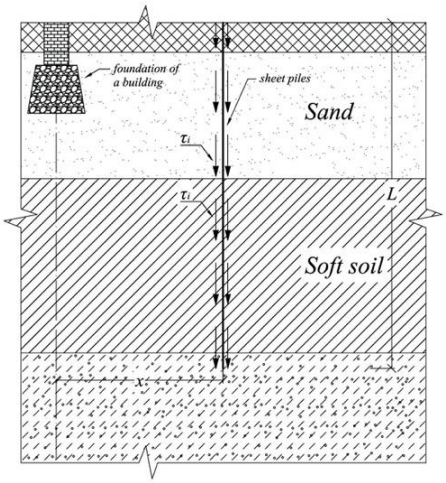

Figure 1. Additional settlement of an existing building under the technological influence of the device of the enclosing structure.

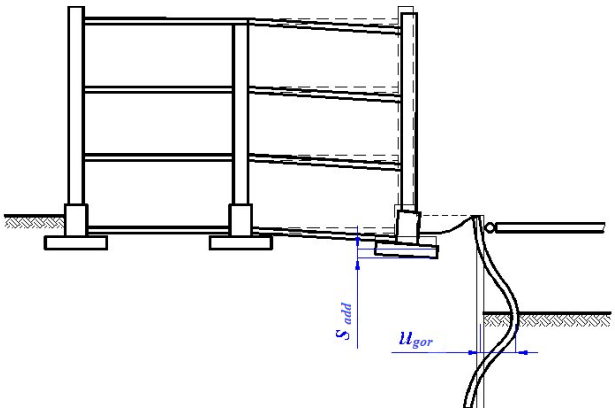

Figure 2. Additional settlement of the existing building from the horizontal displacement of the fence during excavation of the pit

In the case under consideration, a comprehensive solution is proposed, which consists in the construction of a fence structure "wall in the ground" of drill-cut piles d = 350 mm, performed under the protection of a geotechnical barrier with preliminary multi-stage reinforcement of the foundations and foundations of existing historical buildings (Osokin et al., 2019). Thus, at the stage of fencing construction, technological precipitation of manufacture was minimized. And in order to avoid negative consequences when digging a pit, jet–grouting technology was proposed as a spacer plate below the bottom of the pit.

Geotechnical monitoring plays an important role in assessing the effectiveness of the technology, operational adjustment of the speed and sequence of work. At the same time, the main role should be given to geodetic spatial observations of aboveground structures and structures of the pit fence, which can be performed using both classical equipment (leveling, total station) and modern scanning systems and aerial photography. Spatial monitoring allows you to get an interconnected field of points. The area where the field of points is built can include both the building itself and adjacent territories with structures and structures. Long-term satellite positioning of the points system can improve the accuracy of scanning with a measurement error of vertical deformations of 1...2 mm, horizontal displacements of 2...5 mm. This technology is indispensable in conditions of difficult accessibility to the object of observation. The complexity of the information obtained allows us to evaluate complex deformations of individual structures, the development of cracks. The basis for ensuring the accuracy of measurements by laser scanners and unmanned aerial vehicles (UAVs) is always the measurement procedure, the rules of which come out of geodetic standards. However, a significant increase in productivity can be considered the use of a list of equipment that allows you to get a point cloud of good quality, which will require less time for in-house processing. One of such developments is a new type of stamp developed by researchers of the Department of Geodesy of the St. Petersburg University of Architecture and Civil Engineering made on a polymer 3D photo printer that provides the necessary surface quality of the stamp. The effectiveness of the use of this type of stamps, which also consists in increasing the scanning speed, has been demonstrated in laboratory conditions, at research sites and has already been successfully implemented by us in construction production at the stages of spatial monitoring.

The results and application of spatial monitoring are increasingly in demand with the increasing use of joint calculations of the "building-base" system. In this situation, you can monitor the complex deformation of the entire building, with further comparison and refinement of the design model. For existing historical buildings built hundreds of years ago, only such an approach is possible, which can compensate for the lack of complete detailed design documentation, as is the case with new construction.

3. METHODS

The above design scheme of the excavation enclosure was used in the construction of an underground structure in the center of St. Petersburg. At the same time, the construction under construction was erected in close proximity to 6 buildings - objects of cultural heritage.

At the same time, the engineering and geological conditions of the construction site are represented by a significant thickness of weak clay soils. The construction project involved the development of a 3.5 m deep excavation in close proximity to existing cultural heritage sites. To ensure their safety, taking into account the above data, a device for fencing the pit using the technology of boring piles was chosen. This technology involves the construction of fencing from drilling piles under the protection of bentonite mortar. From the point of view of the preservation of buildings of the surrounding development, a significant advantage of this technology over the technology of trench wall in the ground is a significantly smaller amount of excavation for the device of one section of fencing, and before the technology of the device of tongue–and-groove fencing - the absence of transmission to the ground base of static or dynamic loads during immersion.

At the same time, a significant disadvantage of this technology can be called a significantly lower bending stiffness of the enclosing structure than in the cases of sheet piling and trench wall in the ground. To compensate for the insufficient rigidity of the fence, at the design stage, it was provided for the installation of a ground-cement jet-diaphragm below the bottom of the pit, contributing to an increase in the overall rigidity of the enclosing structure. The general scheme of the pit enclosure is shown in Figure 3.

The experience of the construction of pit fences using this technology in the conditions of St. Petersburg shows that the technological precipitation of the surrounding buildings, even when they are directly adjacent to the construction site, does not exceed 1 mm. In this regard, when assessing additional sediments of cultural heritage objects, only additional sediments caused by the excavation were evaluated.

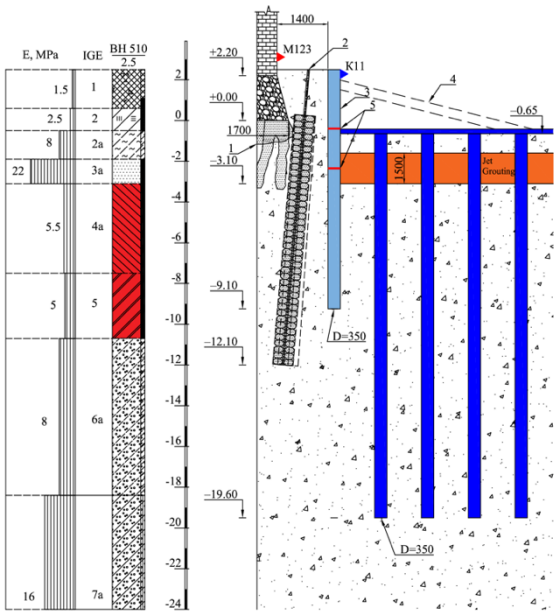

Figure 3. Applied structures of fencing, fixing of the pit, reinforcement of the existing building and geotechnical barrier device.



Figure. 4. The spacer system of the pit at the stage of excavation to the bottom of the pit.

When performing a computational analysis of the development of additional sediments, the following factors were taken into account (Kuznetsov et al., 2023):

1. The stage of work.
2. Nonlinear behavior of the foundation soils (using the Hardening Soil model).
3. Undrained behavior of weak clay soils (drainage type – undrained B).
4. Reinforcing effect of a pile field made for the projected building (using Embedded Beams elements)
5. Nonlinear behavior of reinforced concrete of the enclosing structure and the pile foundation (using the M-k diagram).

Due to the complexity of sampling of sufficiently high quality in the conditions of St. Petersburg, the specific resistance to undrained shear of weak clay soils was determined on the basis of static sounding

data according to the formula: $s_u=q_c / 19$ (Shashkin, 2014).

Construction of a graph of the dependence of the bending stiffness of reinforced concrete piles was performed numerical simulation of the cross section, taking into account the peculiarities of the work of concrete in tension and compression (Osokin et al., 2023). The calculated cross-section of the reinforced concrete pile and the obtained dependence of the bending stiffness on the acting bending moment are shown in Figure 5.

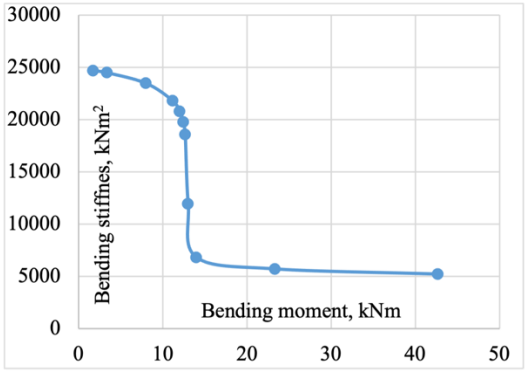

Figure 5. Dependence of the bending stiffness of the pit fence on the acting bending moment.

Below, Figures 6-7 presents the results of numerical modeling of the impact of the development of the pit on the buildings of the existing development.

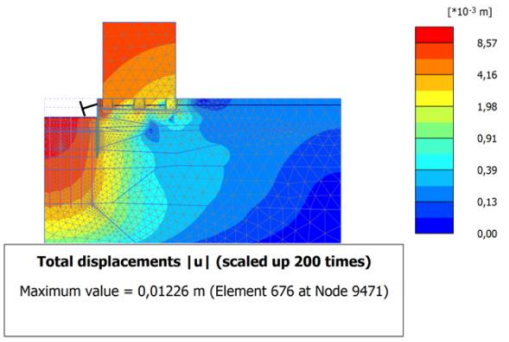

Figure 6. Isofields of complete displacements of the soil mass.



Figure 7. Diagram of deformations of the settlement of surrounding buildings.

4. CONCLUSIONS

1) The development of underground space is an integral part of the development of urban space in the central part of historical cities;

2) In the conditions of complex engineering and geological conditions, represented by a significant capacity of weak clay soils, one of the most important aspects of the preservation of historical buildings is the correct choice of technology for the construction of enclosing structures of the pit;

3) In order to ensure the preservation of the surrounding historical buildings, when developing pits up to 5 m deep in close proximity to existing buildings, a structural scheme of the enclosing structure is proposed, which is a combination of small diameter borehole piles, a spacer system and a deep jet diaphragm;

4) On the example of a real object in the conditions of the historical center of St. Petersburg, the effectiveness of this variant of the enclosing structure is shown;

5) To predict the development of additional sediments of the existing development, a design scheme is proposed that takes into account the undrained behavior of the foundation soils, the preliminary arrangement of the pile field within the contour of the pit, the nonlinear behavior of the soil mass and reinforced concrete enclosing structures.

REFERENCES

Ku, A., Bashmakov, I., Murashova, D., & Savikov, R. (2023). Taking into account technological features of the diaphragm wall for deep pits. *E3S Web of Conferences, 371, 02013.*

Mangushev, R.A., Gursky, A.V. (2016) Impact assessment of indentation of steel piles on additional settlements of adjacent buildings. *Geotechnics,* 2, pp.34-41.

Mangushev, R.A., Gursky, A.V., Polunin, V.M. (2020) Taking into account the influence of technological precipitation of buildings of the surrounding development when installing sheet piling fences of neighboring ditches. *Housing construction*, 9, pp. 9–19. http://doi.org/10.31659/0044-4472-2020-9-9-19.

Mangushev R.A., Nikiforova N.S. (2017) *Technological precipitation of buildings and structures in the zone of influence of underground construction*, Publishing House of the DIA, Moscow, Russia.

Mangushev, R.A, Osokin, A.I. (2019) Foundations of unique buildings and structures of St. Petersburg in difficult soil conditions, *Proc. of the XVII ECSMGE-Reykjavik,*p.p.1-5 http://doi.org/10.32075/17ECSMGE-2019-1097.

Osokin, A.I., Kalach, F.N., Diakonov, I.P., Remisova N.V. (2019) Value of additional vertical deformations of foundations depend on injection grouting conditions. *IOP Conf.Series: Materials Science and*

*Engineering775,CAEST,*9p. http:/doi.org/10.1088/1757-899X/775/1/012144.

Osokin, A., Paramonov, M., Dyakonov, I., & Bashmakov, I. (2023). Determination of the Bending Moment in the Diaphragm Wall by Inclinometric Observations. *E3S Web of Conferences, 371, 02015*. https://doi.org/10.1051/e3sconf/202337102015.

Paramonov V.N. (2009) Risk factors in the construction of underground structures in complex engineering and geological conditions. *Housing construction*, 2, 2009 – pp.35-37.

Sapin, D.A. (2014) Settlement of the adjoining development during construction of trench slurry wall. *Bulletin of civil engineers*., 6, pp.133-139.

Sapin, D.A. (2015) Settlements of foundations of adjacent buildings when arranging the trench "slurry wall". *Housing construction*. No. 4, pp.8-13.

Shashkin A.G. (2014) *The design of buildings and underground structures in the complex engineering and geological conditions of St. Petersburg* - M.: Academic Science - Geomarketing, Moscow, Russia p. 352. ISBN 978-5-905138-10-2.

Ulitsky, V.M., Shashkin, A.G., Sashkin, K.G., Vasenin V.A., Lisyuk M.B., Dashko R.E. (2013) Interaction between structures and compressible subsoils considered in light of soil mechanics and structural mechanics// *Proc.of the 180th Int. Conf. on Soil Mech. and Geotech. Eng. «Challenges and Innovation in Geotechnics».* Vol.1, Paris, France, p.p. 825-828.

Proceedings of the XVIII ECSMGE 2024
GEOTECHNICAL ENGINEERING CHALLENGES
TO MEET CURRENT AND EMERGING NEEDS OF SOCIETY
© 2024 the Authors
ISBN 978-1-032-54816-6
DOI 10.1201/9781003431749-337
Open Access: www.taylorfrancis.com, CC BY-NC-ND 4.0 license

ECSMGE 24
XVIII EUROPEAN CONFERENCE ON SOIL MECHANICS AND GEOTECHNICAL ENGINEERING

Structural health monitoring and inspection of dams based on Unmanned Aerial Vehicles photogrammetry with image 3D reconstruction

Surveillance de l'état structural et inspection des barrages basées sur la photogrammétrie par des véhicules aériens sans pilote avec reconstruction d'images en 3D

J. Marcelino*, J. Manso, D. Leite
National Laboratory of Civil Engineering, Lisbon, Portugal

N.C. Marques, O. Freire
NOVA LINCS/NOVA School of Science and Technology, Lisbon, Portugal

**marcelino@lnec.pt*

ABSTRACT: The introduction of new technologies applied in unmanned aerial vehicles (UAV), to monitor civil engineering structures, substantially developed inspection techniques and deformation measurements in embankment dams. The use of UAV allows the acquisition of essential data on the behaviour of a structure, at a reduced cost. During a UAV flight, aerial photographs are recorded following a pre-defined route. They can be easily converted to orthophotos after processing. The quality of those orthophotos depends on many factors, namely, the photographs' quality (resolution, noise, distortion), their overlap, and the identification of enough control points, among other factors. To improve the accuracy of the orthophoto, and allow georeferencing, enough control points must be defined to allow for a high-quality orthophoto. Such control points, also called Ground Control Points (GCP), are positioned in situ with high-precision coordinates. Due to the great amount of aerial photographs recorded on each flight, it is essential to increase efficiency in GCPs identification in each photograph. This paper describes an open-source algorithm, developed by National Laboratory for Civil Engineering (LNEC) and NOVA University Lisbon, within the scope of a master's thesis, which automatically identifies GCPs and prepares data for processing in the WebODM platform.

RÉSUMÉ: L'introduction de nouvelles technologies appliquées aux véhicules aériens sans pilote (UAV) pour surveiller les structures de génie civil a considérablement développé les techniques d'inspection et de mesure de déformation dans les barrages en remblai. L'utilisation d'UAV permet d'acquérir des données essentielles sur le comportement d'une structure à moindre coût. Lors d'un vol d'UAV suivant un itinéraire prédéfini, des photographies aériennes sont enregistrées. Elles peuvent être facilement enregistrées avec des orthophotos après traitement. La qualité de ces orthophotos dépend de nombreux facteurs, notamment la qualité des photographies (résolution, bruit, distorsion), leur chevauchement, l'identification d'un nombre suffisant de points de contrôle, entre autres facteurs. Pour améliorer la précision de l'orthophoto et permettre la géoréférencement, un nombre suffisant de points de contrôle peut être défini pour permettre l'enregistrement, ainsi que le calcul de la proximité de l'ajustement obtenu dans le processus d'enregistrement. De tels points de contrôle, également appelés points de contrôle au sol (GCP), sont positionnés in situ avec des coordonnées de haute précision. En raison de la grande quantité de photographies aériennes enregistrées lors de chaque vol, il est essentiel d'augmenter l'efficacité de l'identification des GCP dans chaque photographie. Cet article décrit un algorithme open source, développé par le Laboratoire National de l'Ingénierie Civile (LNEC) et l'Université NOVA de Lisbonne, dans le cadre d'une thèse de maîtrise, qui identifie automatiquement les GCP et prépare les données pour le traitement dans la plateforme WebODM.

Keywords: UAV; dam; monitoring; safety; WebODM.

1 INTRODUCTION

The monitoring of civil engineering structures plays a fundamental role in analysing their behaviour and safety and predicting future performance. It also contributes to the development of new design methods. In the case of dams, given its high potential risk resulting from a dam failure, monitoring plays an increased role in safety control.

Monitoring essentially comprises two components: instrumental measurements and visual observations. Instrumental measurements involve collecting data

from instruments installed inside or on the surface of the dam observing specific aspects of the structure. The combination and integration of these two components with conceptual, statistical, and mathematical models provide decision support for ensuring dam safety.

In the context of visual inspections, it is important to underscore that numerous anomalies may manifest on dams, such as cracks, settlements, and seepages, often eluding detection, particularly in their early stages. Nevertheless, early detection of these anomalies can prove pivotal for remedial measures, safeguarding the structural integrity and safety of dams.

In this context, the application of Unmanned Aerial Vehicles (UAVs) and laser scanning in monitoring dams has seen a notable increase, primarily due to reduced costs in acquisition, development, and dissemination (Leite et al., 2020). This cost-effectiveness allowed the development of new monitoring techniques and displacement measurements. However, the quality of the data collected by UAVs relies on factors, such as, the quantity and quality of ground control points (GCPs). GCPs play a crucial role in correcting the position of objects in the three-dimensional model during the post-processing process. This paper presents an algorithm developed to enhance the efficiency of GCP identification and data preparation for processing on the WebODM platform (Freire, 2022).

2 THE USE OF UAVS FOR VISUAL OBSERVATIONS

The importance of visual observations in dam security is paramount, and UAVs can play a crucial role in the development and implementation of innovative visual observation methodologies. By collecting data from UAVs, it is possible to generate a dam model from a point cloud and subsequently reconstruct its geometric representation. Point clouds result from processing georeferenced images captured during the flight. These three-dimensional models exhibit geometric precision and enable the comprehensive modelling of the entire object to a certain extent. They provide the unique advantage of analysing perspectives of the dam that are typically inaccessible, such as views from above and upstream.

Beyond the evident benefit of capturing the entire geometry during the flight survey, these models, in an ideal scenario, promote a more thorough and phased inspection over time. Moreover, the data derived from the geometric model closely resembles that obtained through instrumental monitoring, offering a numerical representation stored in a database, devoid of subjectivity. The approach is not limited to the visible spectrum; alternative systems capturing data outside this range (thermal, infrared or ultraviolet) can also be employed. While the current study focuses on visible spectrum data, the developed technique can be applied for any sensor, as long as the maps obtained refer to the same positions in the image.

2.1 Developed technique

Regardless of the type of sensor, ensuring high geometric accuracy is essential to enhance the quality and efficiency of the model. To achieve this, in each data collection survey, points with known coordinates (GCPs) are used. These points, visible in a large number of photographs, provide each photograph with a set of GCP coordinates in pixels, aligning them accurately with the real-world coordinates. This procedure significantly enhances the model's quality. These points are used in object reconstruction algorithms that use photographs to correct the geometry.

In this study, an Open-Source Software (OSS) was used to apply UAV technologies in dam observation, since it allows for the development of applications avoiding dependencies on a specific supplier. The Open Drone Map (ODM) software was used in its version with a web interface (WebODM). WebODM serves as an GUI application interface for ODM, which, in itself, comprises a collection of open-source tools designed to process and convert aerial images captured by drones into various georeferenced outputs, including maps, point clouds, digital elevation models, and 3D textured models. When processing images, ODM performs a sequence of six operations: Structure from Motion (SFM), Multi View Stereo (Point Cloud Densification), Meshing, Texturing, Georeferencing, Orthophoto Processing, and Generation.

2.2 GCP finder

In SFM, when photographs are georeferenced, ODM uses this information to determine the camera's position at the time of capture. In the absence of this metadata, the camera's position can still be deduced approximately, albeit with some errors. However, even with georeferencing, factors such as image size, granularity, optical quality, or minor variations during the UAV's flight can induce considerable errors. This is where GCPs come into play. An effective GCP should be easily identifiable from a high altitude, possess shapes or colours that distinguish it from the surrounding environment, and feature a well-defined point for convenient GPS placement. Regardless of the GCP format, a matte non-reflective target is essential

to prevent light reflection, ensuring ease of identification in the photographs (Freire, 2022).

Creating a manual list of coordinates is a relatively straightforward task for a small number of photographs, but it becomes highly time-consuming and prone to errors when dealing with a large volume of images, as often encountered in real surveys. Thus, the developed algorithm is essential for the SFM phase, as it enables the automatic and high-quality generation of a comprehensive list of GCP coordinates in each image (Marcelino et al., 2022). The algorithm is freely accessible on the GitHub (t.ly/EhGIQ - in the console version) and on the web interface for server installations, found at (t.ly/quv7U). The platform provides the source code, installation instructions, and a practical application example.

3 CASE STUDY

3.1 Description of Lapa Dam

Lapa is an embankment dam with a maximum height of 24 m and a crest level at 174.0 m, as presented in Figure 1. The full reservoir level (FRL) is set at 170.0 m, while the Maximum Flood level (MFL) is positioned at 171.92 m and the dead storage level (dSl) is located at 162.2 m. The reservoir has a relatively modest volume (0.64 hm^3), and a flooded area of 9.5 ha. The upstream and downstream slopes exhibit ratios of 1:3.25 (V:H) and 1:2.5 (V:H), respectively. Additionally, the downstream slope incorporates a 2.5 m wide bench, positioned at 164.0 m.

3.2 UAV surveys carried out

Two UAV surveys of the Lapa dam were conducted in 2021 (Figure 1) and in 2022 (Figure 2). GCP were employed in both surveys, and in 2022, the GCP finder algorithm was used for their automatic detection.



Figure 1. Textured model of the Lapa dam, survey of 2021.



Figure 2. Textured model of Lapa dam and UAV positions, survey of 2022.

Figure 3 presents an image derived from the 2022 orthophoto, showcasing two different types of GCP: one traditional and one with a QR Code (Aruco marker). These GCPs are automatically identified by the GCP Finder and immediately classified, as the pattern of each GCP corresponds to its assigned number. For example, in the figure, the visible GCPs are numbered 3 and 11 (https://chev.me/arucogen/).



Figure 3. View of GCP – Aruco marker nº 3 and nº 11.

The disparity in the crest between the two surveys was assessed using point cloud visualization tools and algorithms (Figure 5). According to the figure, settlements occur at the base of the dam downstream and in the spillway channel.

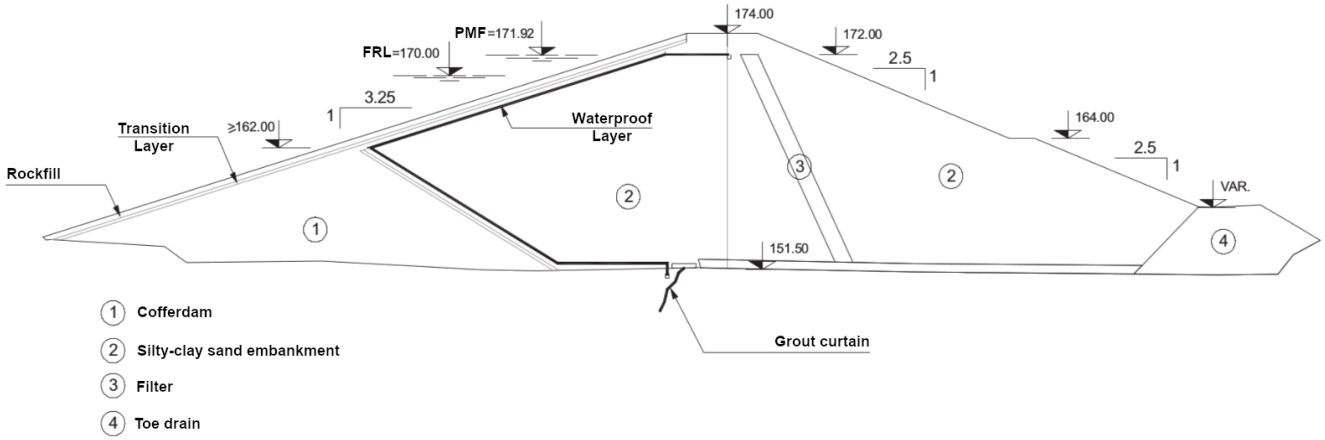

Figure 4. Cross-section of the Lapa dam.

Occasionally, there are also some movements on the downstream face, but these cases may correspond to errors due to deforestation (partial in 2021 and total in 2022). In the case of settlements in the spillway channel, it is necessary to take into account that the visualization of this area is less precise due to its geometry, so the displacement values obtained from the survey will be less accurate.



Figure 5. Settlements increments (2021-2022) in Lapa dam obtained by photogrammetric processing of high-resolution UAV images

4 CONCLUSIONS

The use of UAVs to support visual inspections of geotechnical structures has been increasingly significant, driven either by cost reduction or the development of more efficient post-processing software.

The quality of surveys and models obtained through post-processing depends heavily on various factors, such as the quality of the optics, image resolution, ambient light during photography, and also the existence of reference points with known coordinates that allow correction of the reconstructed model.

This paper outlines the development of an important tool designed to automate the identification of GCP in photographs derived from photogrammetric surveys. This tool was developed as part of a master's thesis at Universidade Nova de Lisboa, under the guidance of LNEC, is now accessible to any user under an open-source license, allowing unrestricted use.

In further developments, GCPs could incorporate GPS positioning modules, eliminating the necessity for individual position determination. Instead, these targets could communicate with each other, transmitting their positions to a centralized server for data consolidation.

REFERENCES

Leite, D., Marcelino J., & Gonçalves, (2020). Application of drones and oss for mapping and visual inspection of embankment dams. In Proceedings of the Fourth International DAM WORLD Conference (Vol. 1, pp. 527-532). LNEC.

Freire, O. (2022). Open Source Software (WebODM) Automation for Dam Modeling and Mapping with Drones. "Autonomização de software open source (WebODM) para modelação e mapeamento de barragens com drones". Msc Thesis. Universidade Nova de Lisboa.

Marcelino, J., Freire, O., Manso, J., Leite, D., & Marques N. (2022). GCP FINDER – Automatic Control Point Detection for Photogrammetric Models. "Deteção automática de pontos de controlo para modelos fotogramétricos". 6as Jornadas Portuguesas de Engenharia de Estruturas.

Proceedings of the XVIII ECSMGE 2024
GEOTECHNICAL ENGINEERING CHALLENGES
TO MEET CURRENT AND EMERGING NEEDS OF SOCIETY
© 2024 the Authors
ISBN 978-1-032-54816-6
DOI 10.1201/9781003431749-338
Open Access: www.taylorfrancis.com, CC BY-NC-ND 4.0 license

ECSMGE 24
XVIII EUROPEAN CONFERENCE ON SOIL MECHANICS AND GEOTECHNICAL ENGINEERING

The use of vane shear tests in granular materials for shear strength measurement

Utilisation d'essais de cisaillement à palettes dans des matériaux granulaires pour la mesure de la résistance au cisaillement

J. Meng, J. Laue*
Department of Civil, Environmental and Natural Resources Engineering, Luleå University of Technology, Luleå, Sweden
**jan.laue@ltu.se*

ABSTRACT: The field vane shear test offers a convenient way for assessing the undrained shear strength of fine soils. However, various factors, including the rotation rate, vane insertion disturbances, vane shape, soils' organic content and strength anisotropy, can affect the test results. Its application is largely limited to clays, and its suitability for other granular materials like tailings is questionable. Nonetheless, due to its simplicity and ease of use, ongoing theoretical developments and increased data reporting for other granular materials have become available. In the author's opinion, reviewing and summarising recent developments in the vane shear test for granular materials can help interested readers to find out the relevant papers on a specific topic and aid engineers in interpreting the available measured results.

RÉSUMÉ: L'essai de cisaillement à la girouette offre un moyen pratique d'évaluer la résistance au cisaillement non drainé des sols fins. Cependant, divers facteurs, notamment le taux de rotation, les perturbations d'insertion des aubes, la forme des aubes, la teneur en matières organiques du sol et l'anisotropie de résistance, peuvent affecter les résultats des tests. Son application est largement limitée aux argiles et son adéquation à d'autres matériaux granulaires comme les résidus est discutable. Néanmoins, en raison de sa simplicité et de sa facilité d'utilisation, des développements théoriques en cours et une augmentation des rapports de données pour d'autres matériaux granulaires sont devenus disponibles. De l'avis de l'auteur, passer en revue et résumer les développements récents dans l'essai de cisaillement aubes pour les matériaux granulaires peut aider les lecteurs intéressés à trouver les articles pertinents sur un sujet spécifique et aider les ingénieurs à interpréter les résultats mesurés disponibles.

Keywords: Vane shear tests; shear strength; field tests.

1 INTRODUCTION

The vane shear test is a commonly used field method for testing undrained shear strength. While sampling disturbance effects are avoided, the vane insertion causes excess pore pressure and changes the original stress conditions. Moreover, research has identified several factors that impact the test results: failure modes (Flaate, 1966), rotation rate (Sharifounnasab and Ullrich, 1985), anisotropy (Silvestri and Aubertin, 1988), waiting time (Watson et al., 2000) and organic content (Andersland et al., 1980). Nevertheless, despite these concerns, the vane shear test remains a common choice for geotechnical site investigations.

While its validity in clays is well recognized, recent studies have also applied the vane shear test to other granular materials, such as tailings (Reid, 2016), organic mud (Schlue et al., 2010) and Peat (Landva, 1980), and even to measure the friction angle of sands (Park et al., 2018). Furthermore, the vane device has seen development with new vane shapes and measurement systems and automation.

In this study, we will review the use of vane shear tests in granular materials for shear strength. Specifically, we will examine the main factors that influence test results and explore recent advancements in both theory and hardware related to this testing method. The objective is to help to assess its result reliability by considering its test conditions and assumptions and to encourage its further developments for broader applications in geotechnical field investigations.

2 FACTORS INFLUENCING THE TEST RESULTS

The principle of the vane shear test is described briefly in Figure 1. It assumes a cylindrical failure surface around the vane's perimeter, with uniform shear stress

along this surface. The torque necessary to rotate the vane under undrained conditions is measured to calculate the shear strength (ASTM, 2008). While the concept is straightforward, assumptions are made to interpret the results and reviewed here.

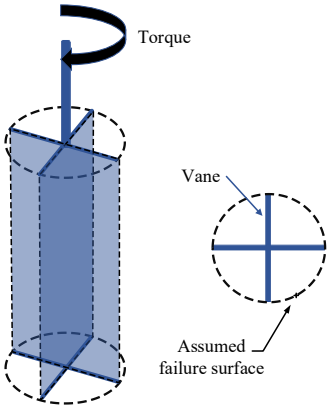

Figure 1. Sketch of the vane shear test.

2.1 Failure modes

Gylland et al. (2012) have performed experimental and numerical studies on soft sensitive clay finding the rounded square failure surfaces instead of the previously assumed circular shape. Numerical studies, employing a Eulerian approach is used to model the large deformation of clays, further supported these findings (Kundu et al., 2021, Shen et al., 2023). The circular failure shape is finally formed after peak torque with a large rotation. This implies a underestimation of 6-7% when using the assumed circular failure surface (Gylland et al., 2013).

Progressive failure in sensitive clay is another critical concern regarding the reliability of results given that the materials is assumed to reach their shear strength simultaneously. The finite element model is developed using an elasto-plastic constitutive law with strain-softening (De Alencar et al., 1988). The numerical results show the strength is mobilised non-uniformly and the stress is not uniform at peak torque.

2.2 Soil disturbance by vane insertion

The insertion of a vane into soils causes soil fabric disturbance and strength degradation (Chandler, 1988). The effect of vane insertion on the measured undrained strength exhibits a positive correlation with soil sensitivity and is also influenced by vane geometry factors. Moreover, experimental studies show that even a very slow vane insertion can generate high excess pore pressure (Kimura and Saitoh, 1983). As pore pressure dissipates, the consolidation can enhance the strength. To ensure fully undrained conditions, a delay time of no longer than 1 minute is advised to be used (Wilson et al., 2016).

2.3 Rotation rate

The measured shear strength is affected by the rotation rate due to the interplay of two conflicting factors: drainage and soil viscosity effects. The effect varies depending on soils' properties and test conditions, resulting into not unique relationship between the shear strength and rotation rate. Numerous experimental studies have been conducted on this effect such as in (Sharifounnasab and Ullrich, 1985, Peuchen and Mayne, 2007). A conceptional chart is proposed to illustrate this effect in (Quinn and Brown, 2011), defining mechanical responses of soils in four zones across a wide range of rotation rates.

2.4 Correction factor

After obtaining field vane shear strength data, it is important to correct the measured value before practical use. A correction factor is normally used as follows (ASTM, 2008):

$$\tau_u = \mu(S_u)_{fv} \quad (1)$$

where μ is the empirical correction factor, and its value depends on test conditions and soil parameters such as plasticity index (PI) and liquid limit (w_L). While many choose plasticity index based correction factors (Bjerrum, 1972, Chandler, 1988), the Swedish Geotechnical Institute recommends a correction factor based on the liquid limit (Larsson et al., 1984):

$$\mu = \left(\frac{0.43}{w_L}\right)^{0.45} \quad (2)$$

Recently, vane shear testing has been conducted to determine correction factors. For example, the values are presented for Swedish fine-grained sulphide soils (Westerberg et al., 2015), harbor mud with an emphasis on the rotation rate effect (Schlue et al., 2010) and certain fine-grained soils based on the liquidity index (Kayabali et al., 2015).

3 VANE SHEAR TESTS IN VARIOUS GRANULAR MATERIALS

While the vane shear test is usually used to measure the strength of clays, research has been conducted to explored its potential for being used in other granular materials. Typical examples include but are not limit to peat and organic soil (Andersland et al., 1980, Landva, 1980, Schlue et al., 2010, Boylan et al., 2011, Boylan and Long, 2014), silty soils (Long et al., 2010, Reid, 2016, Jana and Stuedlein, 2022) and even snow (Diamond and Hansen, 1956, Domine et al., 2011).

When applying the vane shear tests on intermediate permeability soils, partial drainage can occur at the standard rotation rate. Blight (1968) developed a model, validated with experimental data, that is widely accepted for practical applications in estimating drainage conditions (Chandler, 1988). Its pore pressure assumption for vane insertion is later corrected in a revision model (Morris and Williams, 2000). Recently, a theoretical model is developed for assessing partial drainage effects (Forcelini et al., 2020), drawing from the poromechanical theory of consolidation induced by the vane shearing process (Dienstmann et al., 2018). The model allows for the quantification of the rotation rate effect, enabling the prediction of undrained shear strength at standard rotation rate.

There are also a few studies on the application of vane shear tests in coarse granular materials (Park et al., 2016, Park et al., 2018). Laboratory vane tests are performed in sands, in which the torque and horizontal stresses are used to calculate the friction angle.

4 DEVICE DEVELOPMENT

The vane shear device has also seen further developments to enhance its usability. Changing the vane blade shape is likely the most straightforward concept to consider. Silvestri et al. (1993) proposed eighteen vane blade configurations including rectangular, rhomboidal, triangular and elliptic shapes. A so-called advanced vane shear test system is developed that can measure torque underground, directly above the vane, to minimize errors associated with rod friction (Peuchen and Mayne, 2007, Selänpää et al., 2017). Most recently, an automated vane shear tool is integrated into an unmanned ground vehicle for remote field tests, aiming to lower cost and reduce risks to workers (Olmedo et al., 2020).

5 CONCLUSIONS

The field vane shear test is a commonly used tool for testing the undrained shear strength of clays, relying on certain assumptions. There have been numerous studies on the use of vane shear test in granular materials involving field tests, numerical simulations, analytical equations, and device developments in the literature. These studies collectively enhance our understanding of the test's underlying assumptions, aiming for higher result accuracy and expand its applicability to a broader range of granular materials.

ACKNOWLEDGEMENTS

The authors are grateful for the financial support by Svenskt vattenkraftcentrum, SVC.

REFERENCES

Andersland, O., A. Khattak and A. Al-Khafaji (1980). Effect of organic material on soil shear strength. *Laboratory shear strength of soil*, Chicago, ASTM.

ASTM (2008). Standard test method for field vane shear test in cohesive soil, ASTM International.

Bjerrum, L. (1972). Embankments on soft ground: State of the Art Report. *Performance of Earth and Earth-Supported Structures*, Purdue University, ASCE.

Blight, G. (1968). "A note on field vane testing of silty soils." *Canadian Geotechnical Journal* 5(3): 142-149.

Boylan, N. and M. Long (2014). "Evaluation of peat strength for stability assessments." *Proceedings of the Institution of Civil Engineers-Geotechnical Engineering* 167(5): 421-430.

Boylan, N., M. Long and F. A. Mathijssen (2011). "In situ strength characterisation of peat and organic soil using full-flow penetrometers." *Canadian Geotechnical Journal* 48(7): 1085-1099. https://doi.org/10.1139/t11-023.

Chandler, R. J. (1988). *The in-situ measurement of the undrained shear strength of clays using the field vane*, ASTM International West Conshohocken, PA, USA.

De Alencar, J. A., D. H. Chan and N. R. Morgenstern (1988). "Progressive failure in the vane test." *Vane shear strength testing in soils: field and laboratory studies, ASTM STP* 1014: 150-164.

Diamond, M. and B. L. Hansen (1956). "Use of a shear vane in snow."

Dienstmann, G., F. de Almeida, A. Fayolle, F. Schnaid and S. Maghous (2018). "A simplified approach to transient flow effects induced by rigid cylinder rotation in a porous medium." *Computers and Geotechnics* 97: 134-154. https://doi.org/10.1016/j.compgeo.2017.11.014.

Domine, F., J. Bock, S. Morin and G. Giraud (2011). "Linking the effective thermal conductivity of snow to its shear strength and density." *Journal of Geophysical Research: Earth Surface* 116(F4). https://doi.org/10.1029/2011JF002000.

Flaate, K. (1966). "Factors influencing the results of vane tests." *Canadian Geotechnical Journal* 3(1): 18-31.

Forcelini, M., S. Maghous, F. Schnaid and F. Schaedler de Almeida (2020). "Simplified model for interpretation of undrained shear-strength from field-vane tests in transient soils." *Journal of Geotechnical and Geoenvironmental Engineering* 146(6): 04020043. https://doi.org/10.1061/(ASCE)GT.1943-5606.0002272.

Gylland, A., H. P. Jostad and S. Nordal (2012). Failure geometry around a shear vane in sensitive clays. *Proceedings of the 16th Nordic geotechnical meeting*.

Gylland, A. S., H. P. Jostad, S. Nordal and A. Emdal (2013). "Micro-level investigation of the in situ shear vane failure geometry in sensitive clay." *Geotechnique*

63(14): 1264-1270. https://doi.org/10.1680/geot.13.P.011.

Jana, A. and A. W. Stuedlein (2022). "Dynamic, in situ, nonlinear-inelastic response and post-cyclic strength of a plastic silt deposit." *Canadian Geotechnical Journal* 59(1): 111-128. https://doi.org/10.1139/cgj-2020-0652.

Kayabali, K., O. Akturk, M. Fener, O. Dikmen and F. H. Harputlugil (2015). "Revisiting the Bjerrum's correction factor: Use of the liquidity index for assessing the effect of soil plasticity on undrained shear strength." *Journal of Rock Mechanics and Geotechnical Engineering* 7(6): 716-721. https://doi.org/10.1016/j.jrmge.2015.07.003.

Kimura, T. and K. Saitoh (1983). "Effect of disturbance due to insertion on vane shear strength of normally consolidated cohesive soils." *Soils and foundations* 23(2): 113-124.

Kundu, P., B. Hawlader and R. Karmaker (2021). Two-dimensional finite element modelling of field vane shear test in sensitive clay. *Proceedings of the 74th Canadian Geotechnical Conference, Niagara, ON, Canada*.

Landva, A. O. (1980). "Vane testing in peat." *Canadian Geotechnical Journal* 17(1): 1-19.

Larsson, R., U. Bergdahl and L. Eriksson (1984). *Evaluation of shear strength in cohesive soils with special referens to Swedish practice and experience*, Statens geotekniska institut.

Long, M., G. Gudjonsson, S. Donohue and K. Hagberg (2010). "Engineering characterisation of Norwegian glaciomarine silt." *Engineering geology* 110(3-4): 51-65. https://doi.org/10.1016/j.enggeo.2009.11.002.

Morris, P. H. and D. J. Williams (2000). "A revision of Blight's model of field vane testing." *Canadian geotechnical journal* 37(5): 1089-1098. https://doi.org/10.1139/t00-035.

Olmedo, N. A., B. Fisseha, W. Wilson, M. Barczyk, H. Zhang and M. G. Lipsett (2020). "An automated vane shear test tool for environmental monitoring with unmanned ground vehicles." *Journal of Terramechanics* 91: 53-63. https://doi.org/10.1016/j.jterra.2020.05.003.

Park, S.-S., D.-R. Kim and S.-B. Lee (2018). "Measurement of Friction Angle of Sand from Horizontal Stress and Torque Acting on Vane." *KSCE Journal of Civil and Environmental Engineering Research* 38(1): 63-71. https://doi.org/10.12652/Ksce.2018.38.1.0063.

Park, S.-S., A. Zhou and D.-R. Kim (2016). "Vane shear test on nakdong river sand." *KSCE Journal of Civil and Environmental Engineering Research* 36(3): 463-470. https://doi.org/10.12652/Ksce.2016.36.3.0463.

Peuchen, J. and P. Mayne (2007). Rate effects in vane shear testing. *SUT Offshore Site Investigation and Geotechnics*, SUT.

Quinn, T. and M. Brown (2011). Effect of strain rate on isotropically consolidated kaolin over a wide range of strain rates in the triaxial apparatus. *Fifth International Symposium on Deformation Characteristics of Geomaterials*, IOS Press.

Reid, D. (2016). Effect of rotation rate on shear vane results in a silty tailings. *5th International Conference on Geotechnical and Geophysical Site Characterisation* Queensland, Australia, The Australian Geomechanics Society.

Schlue, B. F., T. Moerz and S. Kreiter (2010). "Influence of shear rate on undrained vane shear strength of organic harbor mud." *Journal of geotechnical and geoenvironmental engineering* 136(10): 1437-1447. https://doi.org/10.1061/(ASCE)GT.1943-5606.0000356.

Selänpää, J., B. Di Buò, T. Länsivaara and M. D'Ignazio (2017). Problems Related to Field Vane Testing in Soft Soil Conditions and Improved Reliability of Measurements Using an Innovative Field Vane Device. *Landslides in Sensitive Clays: From Research to Implementation*. V. Thakur, J.-S. L'Heureux and A. Locat. Cham, Springer International Publishing**:** 109-119.

Sharifounnasab, M. and C. R. Ullrich (1985). "Rate of shear effects on vane shear strength." *Journal of Geotechnical Engineering* 111(1): 135-139.

Shen, J., X. Wang, Q. Chen, Z. Ye, Q. Gao and J. Chen (2023). "Numerical Investigations of Undrained Shear Strength of Sensitive Clay Using Miniature Vane Shear Tests." *Journal of Marine Science and Engineering* 11(5): 1094. https://doi.org/10.3390/jmse11051094

Silvestri, V. and M. Aubertin (1988). "Anisotropy and in-situ vane tests." *Vane shear strength testing in soils. STP* 1014: 88-103.

Silvestri, V., M. Aubertin and R. P. Chapuis (1993). "A study of undrained shear strength using various vanes." *Geotechnical Testing Journal* 16(2): 228-237.

Watson, P., N. Suemasa and M. Randolph (2000). Evaluating undrained shear strength using the vane shear apparatus. *ISOPE International Ocean and Polar Engineering Conference*, ISOPE.

Westerberg, B., R. Müller and S. Larsson (2015). "Evaluation of undrained shear strength of Swedish fine-grained sulphide soils." *Engineering Geology* 188: 77-87. https://doi.org/10.1016/j.enggeo.2015.01.007.

Wilson, L., G. Kouretzis, J. Pineda and R. B. Kelly (2016). "On the determination of the undrained shear strength from vane shear testing in soft clays." *Australian Geomechanics Society, Sydney*.

Proceedings of the XVIII ECSMGE 2024
GEOTECHNICAL ENGINEERING CHALLENGES
TO MEET CURRENT AND EMERGING NEEDS OF SOCIETY
© 2024 the Authors
ISBN 978-1-032-54816-6
DOI 10.1201/9781003431749-339
Open Access: www.taylorfrancis.com, CC BY-NC-ND 4.0 license

ECSMGE 24
XVIII EUROPEAN CONFERENCE ON SOIL MECHANICS AND GEOTECHNICAL ENGINEERING

Practical application of non-linear dynamic soil-structure interaction analysis. Case study in the Groningen field, The Netherlands

Application pratique de l'analyse dynamique non linéaire de l'interaction sol-structure. Étude de cas dans le champ de Groningen, aux Pays-Bas

C. Merino
Ove Arup & Partners SAU, Madrid, Spain

J.M. Torres*
Ove Arup & Partners SAU, Madrid, Spain
Universidad Politécnica de Madrid, Madrid, Spain

**josemanuel.torres@arup.com*

ABSTRACT: This paper presents a comprehensive seismic assessment of an existing building subject to induced seismicity in the Groningen region, a location with unique geological characteristics that pose significant safety concerns for building occupants. To assess the seismic response of the building more accurately, we incorporate non-linear dynamic soil-structure interaction (DSSI) through response-history analysis using a finite element global model. Our study demonstrates the importance of accounting for non-linear soil-structure interaction in the seismic assessment of combinations of rigid buildings and soft soils and highlights the need for more comprehensive approaches to building safety in such regions. We also show that the use of a holistic dynamic soil-structure interaction performance-based approach can improve the reliability of seismic assessments for existing structures and ensure cost-effective retrofit solutions with quantifiable levels of performance. Our results have important implications for building design and safety in the Groningen region and contribute to the broader field of seismic engineering by improving the understanding of the complex interactions between buildings and soil.

RÉSUMÉ: Cet article présente une évaluation sismique complète d'un bâtiment existant soumis à une sismicité induite dans la région de Groningen, un endroit présentant des caractéristiques géologiques particulières qui posent d'importants problèmes de sécurité pour les occupants du bâtiment. Pour évaluer plus précisément la réponse sismique du bâtiment, nous incorporons l'interaction dynamique no linéaire sol-structure (DSSI) par le biais d'une analyse temporelle à l'aide d'un modèle global à éléments finis. Notre étude démontre l'importance de la prise en compte de l'interaction non linéaire sol-structure dans l'évaluation sismique des combinaisons de bâtiments rigides et de sols mous et met en évidence la nécessité d'approches plus globales de la sécurité des bâtiments dans ces régions. Nous montrons également que l'utilisation d'une approche holistique de l'interaction dynamique sol-structure basée sur la performance peut améliorer la fiabilité des évaluations sismiques pour les structures existantes et garantir des solutions de réhabilitation économiques avec des niveaux de performance quantifiables. Nos résultats ont des implications importantes pour la conception et la sécurité des bâtiments dans la région de Groningen et contribuent au domaine plus large de l'ingénierie sismique en améliorant la compréhension des interactions complexes entre les bâtiments et le sol.

Keywords: Existing building; non-linear dynamic soil-structure interaction; performance based seismic design.

1 INTRODUCTION

Dynamic soil-structure interaction (DSSI) occurs when a structure and the soil on which it is founded interact during a dynamic event such as an earthquake. In the last decades, there is increasing evidence in literature that this interaction may induce unavoidably nonlinearities both in the soil around the foundation and at the soil-foundation interface (Kutter et al., 2003, Pecker et al., 2012, Gazetas, 2015). This fact, especially when we talk about rigid structures on soft soils, requires design engineers to include these nonlinearities in their analyses.

Traditional substructuring techniques rely on the superposition theorem (Kausel et al., 1978) and, consequently, are limited to linear elastic or viscoelastic domain. They can account for some nonlinearities, in particular those related to the

propagation of the seismic waves (equivalent linear soil behavior), but there is no possibility to introduce the nonlinearities specifically arising from DSSI.

This calls for other techniques, allowing nonlinearities to be captured in the vicinity of the foundation. A practical way to include them is the use of the direct approach through a 3D nonlinear finite element global model, which allows you to analyze in a single step the complete soil-foundation-structure system. These models can capture different nonlinearities in the structure and in the soil as long as the soil, the structure and the soil-structure interfaces are modeled appropriately.

Finite-element analysis programs such as LS-DYNA® (ANSYS, 2023) offer an integrated environment for complete soil-structure system analysis which enables the study in a single model of all the energy dissipation phenomena that take place in a seismic event.

This paper presents the case study of the dr. Aletta Jacobs College in Hoogezand, a village 10 km southeast of Groningen, sitting on soft soil and how different nonlinear mechanisms in the soil-foundation interface are activated during the analysis, leading to a more realistic seismic response characterization.

2 ANALYSIS APPROACH AND SEISMIC MODELLING

A wide range of analysis approaches, with differing degrees of reliability and conservatism, are available to the earthquake engineer. State of the art approaches to assess the seismic performance of structures use response history analysis, which requires solving the equation of motion at each time step for the structure (and soil) when excited by a ground-motion time series. Thanks to the improvement in the computational capabilities of cloud computing, advanced numerical dynamic simulations are catching on as an alternative approach to conventional approaches, eliminating the need for unrealistic simplifications.

A nonlinear response history analysis is thus carried out to assess the seismic performance of the system. The following sections describe the modelling strategy adopted to model all the elements necessary for conducting this type of analysis.

2.1 Bedrock motions development

The first step is to develop a suite of ground motion time histories representative of a sufficiently stiff layer beneath the surface where nonlinearities due to earthquake wave propagation are considered to be limited. It was defined in this case as a soil layer with a shear wave velocity equal to 300 m/s. The depth at which this layer appears is referred to as the reference depth and corresponds to 20 m below ground level.

This procedure involved selection and spectral matching of seed records to a target acceleration response spectrum at the reference depth, developed through a site-specific probabilistic seismic hazard assessment (PSHA).

A suite of eleven 2475-year input motions was applied at the base of the soil block underlying the structure.

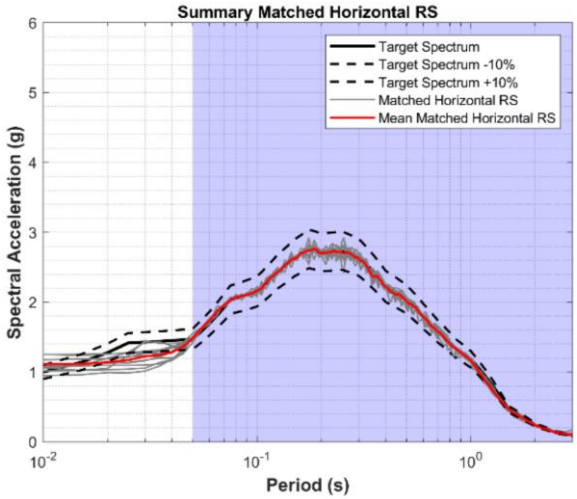

Figure 1. Horizontal spectrally matched components of the 11 earthquake acceleration time signals.

2.2 3D soil domain definition

Since the shallow soil layers in the Groningen region are typically soft and relatively weak, the response of the soil when subjected to significant earthquake shaking in performance-based analysis can be highly non-linear. Soil was modelled with 3D solid elements using a nested bounding surface plasticity model, which is suitable to reproduce the hysteretic, nonlinear behaviour of soils. At a minimum, it requires: density, bulk modulus, Poisson's ratio and a backbone curve of shear strain versus shear stress. These curves were derived using site-specific soil information and a shear strength matching routine at large strains using the hyperbolic fitting procedure provided in Groholski et al., 2016. The model follows the extended unload-reload Masing rules (Masing, 1926) to reproduce hysteretic behaviour.

In the near field domain (i.e., soil zone where localized shear induced nonlinearities due to soil-structure interaction are concentrated), the mesh was refined enough to explicitly capture local soil-foundation flexibility, bearing failure for shallow foundations, soil yielding and geometrical nonlinearities.

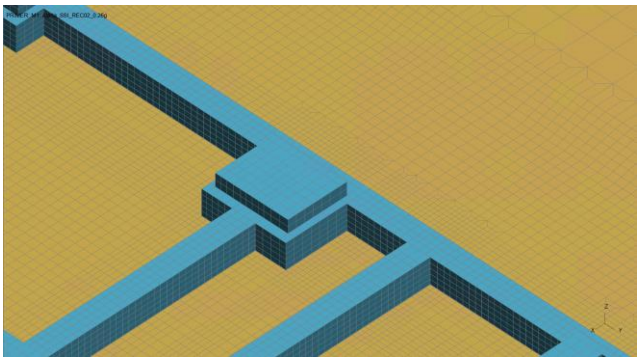

Figure 2. Soil mesh refinement in the vicinity of shallow foundations.

However, for piles, this would increase the computational cost of the model dramatically and thus, the interaction between the soil and the pile elements is modelled using nonlinear springs (see section 2.5).

2.3 Above-grade structure definition

The building is a 3 storey school (dimension in plan is about 80x66m) with a fully concrete structure, where some elements are cast in situ while others are precast, like columns and part of the floor system. The lateral stability system (mainly conceived for wind loads) consists of concrete shear walls located in 4 areas of the building, in both the principal directions. Finally, within the building, some steel structures are present (mezanine floor and staircases) together with several masonry non load bearing walls.

A detailed model of the structure was created (figure 3) to perform the as-built seismic assessment and to develop proposals for the seismic strengthening. In this case, the main retrofit measure was to add circular hollow steel bracings in some locations along the internal and external facade with an inverted V-shape layout. The upgraded building was also assessed to ensure this retrofit could effectively provide seismic stability and meet the target performance objective.

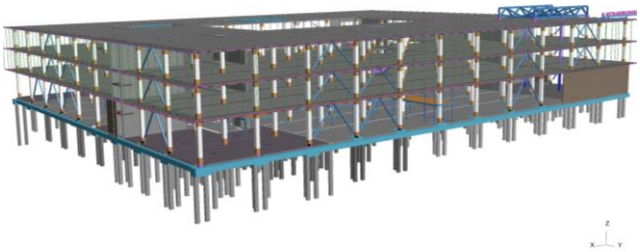

Figure 3. Building perspective view.

2.4 Below-grade structures definition

Foundation pads and beams are supported on groups of 1-to-4 piles, transferring the loads to a stiffer deeper sandy layer. Pads and beams are modelled using 3D solid elements.

1D beam elements are used to define the piles. These are 0.55m diameter concrete piles ranging from 3.5 to 7.5 m in length. A lumped-plasticity material model is used, which is able to capture axial-bending and axial-shear interaction.

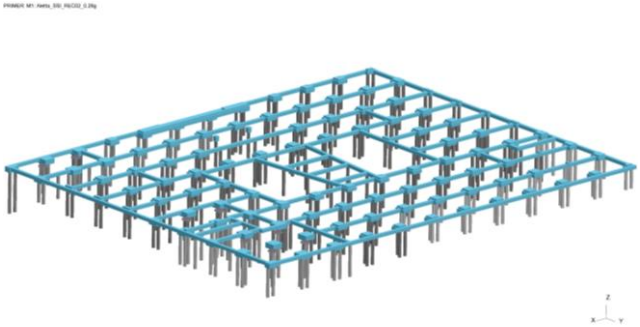

Figure 4. Foundation layout. Shallow and deep elements.

2.5 Soil-structure interfaces

Special attention was paid to the soil-structure interface modelling strategy. Different techniques, which are situation-dependent, can be applied.

The interaction between the footings and the soil is modelled using zero-thickness contact elements that allow relative shear displacements (sliding) and separation between the soil and foundation (gapping). Moreover, this does not require congruous meshes, allowing on each side of the contact different size of elements on the soil and on the foundation. The tangential behaviour of these contacts adopts a classical Coulomb model where the tangential frictional stress is taken proportional to the normal stress. A penalty algorithm is adopted for the contact behavior.

The soil-pile interaction, in place of using any joint element strategy to model the interface, uses a penalty-based coupling between the 1D beam elements (piles) and 3D solid elements (soil). The nodes of the 1D element are rigidly connected to a ring of nodes situated at the true diameter of the pile.

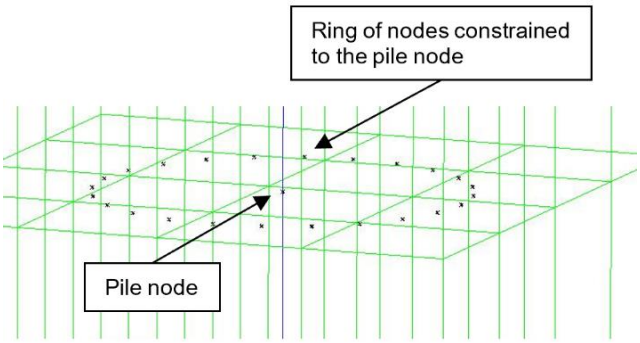

Figure 5. Pile nodes and surrounding soil elements.

These are constrained to the pile node translationally and rotationally. For each node in the ring of nodes, a new initially coincident "point" is created that will be constrained to move with the soil element within which it lies. The pile and soil move independently of each other during the analysis, so the new points (fixed within the soil element) will no longer be coincident with the nodes in the ring (figure 6). The difference in displacement between the pile node and the new point controls the stress on the soil/pile interface. Forces (equal to stress times area) are applied to the pile node and reacted onto the nodes of the soil element.

These nodes are attached to the soil mesh through nonlinear springs that are previously calibrated through separate soil-structure interaction analyses to obtain the desired lateral (p-y), skin friction (t-z) and end bearing (Q-z) behaviour.

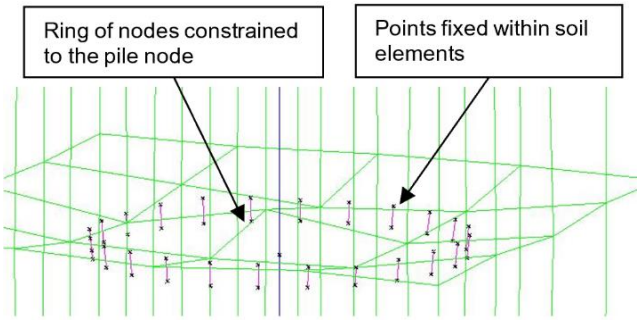

Figure 6. Ring of nodes and the new soil-constrained nodes.

The load on the base of the pile is spread over the pile area. The number and positions of points on the base was automatically defined by the software, with a spacing roughly equal to the spacing of points around the outer circumference.

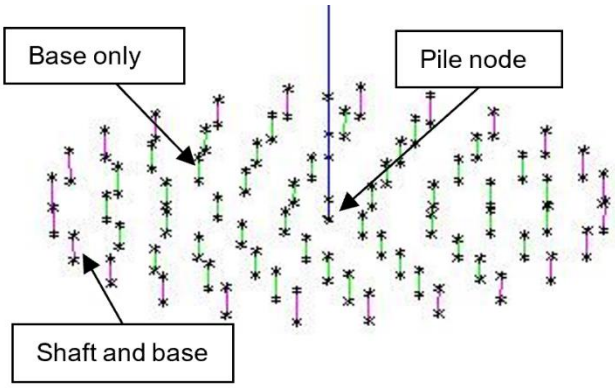

Figure 7. Base points created at the toe pile node level.

2.6 Boundary conditions

When using a global FE model, one of the cautions to be taken is that the boundaries used do not introduce spurious reflections in the model that may alter the results of the simulations.

For this purpose, we included absorbing boundaries (Lysmer dampers) at the base of the soil block. Lateral boundary nodes are tied together without relative movement and are located more than four times the distance from the surface to the reference depth away. This approach mitigates boundary effects at the edges and thus, avoids the need of transmitting boundaries at the lateral sides of the model.

3 NONLINEAR DSSI MECHANISMS

Due to the direct modelling approach of the nonlinear soil-structure interaction described in the previous section, all these sources of nonlinearities at the foundation level were included in the response of the system: soil (and structural) yielding, sliding and gapping of foundations. In the following, we give evidence of such mechanisms.

3.1 Residual displacements

At the end of the time history application, part of the deformation is not recovered, giving rise to residual displacements in the foundation. Figure 8 shows the horizontal displacement time histories of all pile heads, indicating that piles and surrounding soil undergo plastic deformations during the earthquake.

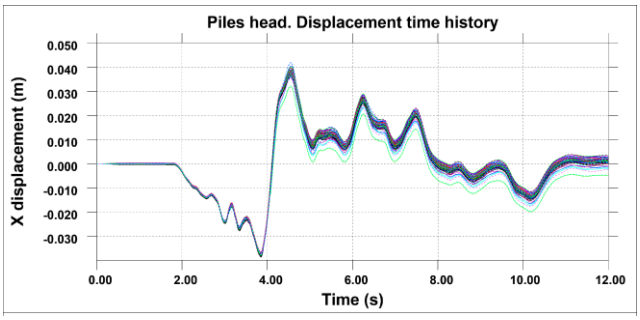

Figure 8. Residual foundation X displacements: pile heads.

3.2 Sliding and gapping of shallow foundations

Relative displacement between foundation elements and soil is the main geometric nonlinearity occurring at the foundation level. It can take place without losing contact between the soil-foundation system (sliding) or with separation of the two surfaces (gapping). Therefore, two nodes near each other, one in each element, may not show the same history of displacements.

3.2.1 Sliding

An important sliding occurs between the soil layer and the foundation pads and beams close to the areas where the concrete shear walls are concentrated. Due to the important shear loads attracted by the shear walls, the piles in these zones fail in shear at 4.2s, causing the pads and beams to work only as shallow foundations. This conservative design assumption increases vertical and differential settlements of these shallow elements, but it doesn't lead the building to collapse because foundation beams and pads are able to support the structure after the pile failure (with additional settlement). This unusual situation allows us to check the capacity of the soil-foundation interface to develop a nonlinear response. Figure 9 shows the Y displacement of the foundation element and the soil, showing the relative displacement between two nodes initially in contact.

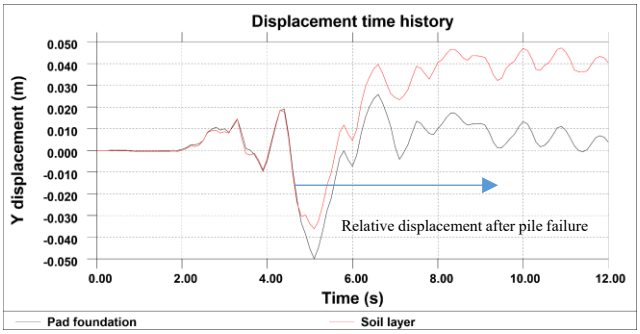

Figure 9. Sliding at the "new" shallow foundations.

3.2.2 Gapping

Another complex phenomenon known to be a potential source of energy dissipation is gapping, allowed between the soil and the foundation beams. In the same areas, concrete walls move almost as rigid blocks (sliding and rocking), deforming the soil around them. This induces high horizontal forces to soil embedding the footings and plastic deformations occur. Having defined a tensionless interface, lateral soil cannot follow the foundation movement and detachment occurs.

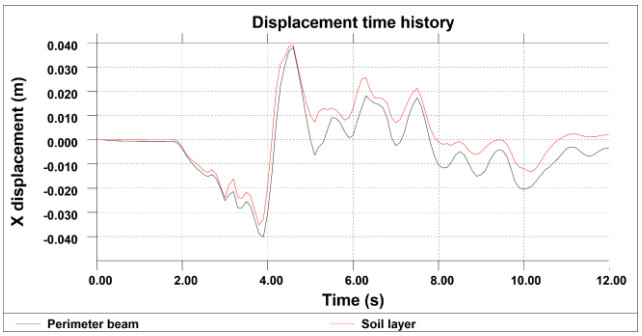

Figure 10. Gapping at perimeter foundation beam.

In addition, it is also noted how the distance between soil and foundation slightly increases over time, suggesting a progressive yielding of the embedding soil.

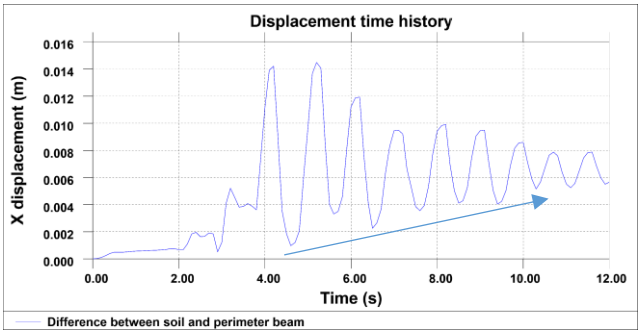

Figure 11. Differential horizontal displacement.

4 CONCLUSIONS

A case study where the nonlinear soil-structure interaction has been modeled explicitly in a global FE model is presented. Key results proving the existence of nonlinear mechanisms in the foundation-soil interface are also shown.

The paper aims to show that for a comprehensive and integrated performance-based oriented seismic design approach of rigid buildings on soft soils, in addition to the structural nonlinear behavior, we must consider that the foundation participates in the energy dissipation process during earthquake loading. This helps to achieve a more realistic seismic behavior of

this type of buildings, including explicitly in the system response the geometrical and material nonlinearities developed in the near field.

In addition to a more accurate representation of seismic response, there is mounting analytical and experimental evidence that material and geometric nonlinearities in the soil and soil-foundation interface may play a beneficial role (Gajan and Kutter, 2008, Anastasopoulos et al., 2010, Liu et al., 2013, Gazetas et al., 2014, Sakellariadis et al. 2021) boosting its inclusion in the design phases of structures. The effort in modeling these phenomena could be thus justified, for the sake of designing more cost-effective structures and enhancing resilience.

ACKNOWLEDGEMENTS

The authors would like to acknowledge colleagues at Arup who participated in the project described in this paper, especially Paolo Fici who also contributed to the preparation of Section 2. We would also like to thank our client Nationaal Coördinator Groningen (NCG) for the opportunity to work on this project.

REFERENCES

Anastasopoulos, I., Gazetas, G., Loli, M., Apostolou, M. and Gerolymos, N. (2010). Soil failure can be used for seismic protection of structures. *Bulletin of Earthquake Engineering*, 8, 309-326, https://doi.org/10.1007/s10518-009-9145-2.

ANSYS (2023). Keyword User's Manual, LS-DYNA R.14. https://lsdyna.ansys.com/.

Gajan, S., and Kutter, B.L. (2008). Capacity, settlement, and energy dissipation of shallow footings subjected to rocking. *Journal of Geotechnical and Geoenvironmental Engineering*, 134, 1129-1141, https://doi.org/10.1061/(ASCE)1090-0241(2008)134:8(1129).

Gazetas, G. (2015). 4th Ishihara lecture: Soil-foundation-structure systems beyond conventional seismic failure thresholds. *Soil Dynamics and Earthquake Engineering*, 68, 23-39, https://doi.org/10.1016/j.soildyn.2014.09.012.

Gazetas, G., Anastasopoulos, I. and Garini, E. (2014). Geotechnical design with apparent seismic safety factors well-below 1. *Soil Dynamics and Earthquake Engineering*, 57, 37-45, https://doi.org/10.1016/j.soildyn.2013.10.002.

Groholski, D., Hashash, Y., Kim, B., Musgrove; M., Harmon, J. and Stewart, J. (2016). Simplified model for small-strain nonlinearity and strength in 1D seismic site response analysis. *Journal of Geotechnical and Geoenvironmental Engineering*, 142, 04016042 https://doi.org/10.1061/(ASCE)GT.1943-5606.0001496.

Kausel, E., Whitman, A., Morray, J. and Elsabee, F. (1978). The spring method for embedded foundations. *Nuclear Engineering and Design*, 48, 377-392, https://doi.org/10.1016/0029-5493(78)90085-7.

Kutter, B.L., Martin, G., Hutchinson T.C., Harden, C., Gajan, S. and Phalen, J.D. (2003). Status report on study of modeling of nonlinear cyclic load-deformation behavior of shallow foundations. In: *PEER workshop*, University of California Davis, USA, March 5.

Liu, W., Hutchinson, T. C., Kutter, B. L., Hakhamaneshi, M., Aschheim, M. A. and Kunnath, S. K. (2013). Demonstration of compatible yielding between soil-foundation and superstructure components. *Journal of Structural Engineering*, 139, 1408-1420, https://doi.org/10.1061/(ASCE)ST.1943-541X.0000637.

Masing, G. (1926). Eigenspannungen und verfestigung beim messing. In: *2nd International Congress on Applied Mechanics*, Zurich, Switzerland, pp. 332-335.

Pecker, A., Paolucci, R., Chatzigogos, C., Correia, A. and Figini, R. (2012). The role of non-linear dynamic soil-foundation interaction on the seismic response of structures. In: *2nd International Conference on Performance-Based Design in Earthquake Geotechnical Engineering*, Taormina, Italy, May 28-30, Keymote lecture.

Sakellariadis, L., Alber, S., Fehr, M. and Anastasopoulos, I. (2021). Unconventional retrofit design of bridge pile groups: Benefits & limitations. In: *Proc. Of the 4th International Conference on Performance-based Design in Earthquake Geotechnical Engineering*, Beijing, China, pp. 1222-1230, https://doi.org/10.1007/978-3-031-11898-2_102.

Proceedings of the XVIII ECSMGE 2024
GEOTECHNICAL ENGINEERING CHALLENGES
TO MEET CURRENT AND EMERGING NEEDS OF SOCIETY
© 2024 the Authors
ISBN 978-1-032-54816-6
DOI 10.1201/9781003431749-340
Open Access: www.taylorfrancis.com, CC BY-NC-ND 4.0 license

ECSMGE 24
XVIII EUROPEAN CONFERENCE ON SOIL MECHANICS AND GEOTECHNICAL ENGINEERING

Influence of permeability on the behaviour of tailings storage facilities by hydromechanical numerical analysis

Influence de la perméabilité sur le comportement des installations de stockage de résidus par analyse numérique hydromécanique

C. Midão
Faculdade de Engenharia da Universidade do Porto, Porto, Portugal

A. Viana da Fonseca, S. Rios*
CONSTRUCT – GEO - Faculdade de Engenharia da Universidade do Porto, Porto, Portugal

**sara.rios@fe.up.pt*

ABSTRACT: Given the catastrophic accidents seen in the last decade at tailings storage facilities (TSF's), there is a growing consensus that a better understanding of the behaviour of these structures is needed including different approaches to analyse their stability. In that sense, the use of numerical tools allowing coupled hydromechanical stress-strain analysis has been encouraged. This paper presents the results of PLAXIS 2D® numerical analysis conducted on a simple slope where the water head was increased in the upstream boundary and a seepage flow was established. A parametric study was developed for different slope heights, water heights, and soil permeability, where the minimum time required for a steady-state seepage flow stabilization was identified. A mathematical formulation is proposed that relates the normalized water height, the soil permeability, and the steady-state time.

RÉSUMÉ: Compte tenu des accidents catastrophiques observés au cours de la dernière décennie dans les installations de stockage de résidus (TSF), il existe un consensus croissant selon lequel une meilleure compréhension du comportement de ces structures est nécessaire, notamment différentes approches pour analyser leur stabilité. En ce sens, l'utilisation d'outils numériques permettant une analyse couplée hydromécanique contrainte-déformation est nécessaire. Cet article présente les résultats de l'analyse numérique PLAXIS 2D® menée sur une pente simple où la hauteur d'eau a été augmentée dans la frontière amont et un écoulement d'infiltration a été établi. Une étude paramétrique a été développée pour différentes hauteurs de pente, hauteurs d'eau et permeabilité du sol, où le temps minimum requis pour une stabilisation à l'état stable d'un écoulement d'infiltration à travers la pente a été identifié. Une formulation mathématique est proposée qui relie la hauteur d'eau normalisée, la perméabilité du sol et le temps d'équilibre.

Keywords: Tailings; PLAXIS 2D®; liquefaction; seepage flow; permeability.

1 INTRODUCTION

Advances in mining technology allowed the exploitation of lower-quality deposits, leading to the generation of more tailings, the discarded material after ore extraction. This has created an increasing pressure on tailings storage facilities which need to be larger in a shorter time. Moreover, the rupture of these structures often involves the release of material downstream, with catastrophic consequences for populations, the environment, and the economy. The triggering causes of failure in these structures are numerous which can be summarized in the following: the existence of defects in the structure, problems in the foundation, unusual weather events, seismic events, overtopping, subsidence, and lack of maintenance during operation and after its closure.

The analysis of several case studies identified static liquefaction and cyclic liquefaction in most cases (Mánica et al., 2022). In practice, static liquefaction phenomena occur much less frequently than cyclic liquefaction phenomena, but their effects are generally much more serious.

The term liquefaction, which was originally created by Mogami and Kubo (1953), has historically been used with a variety of phenomena involving soil deformations caused by monotonic, transient, or repeated disturbances of saturated, cohesionless soils under undrained conditions. The generation of excess pore pressures under undrained loading conditions is common to all liquefaction phenomena. When cohesionless soils are saturated, however, rapid loading occurs under undrained conditions, so that the

tendency toward densification causes excess pore pressure to increase and effective stresses to decrease.

Ledesma et al. (2022) presented a procedure to assess the vulnerability of a tailings dam due to flow liquefaction. The procedure required the development of a numerical model with the complete definition of the contour boundaries of the dam under study, where the tailings had to be modeled using a constitutive model capable of capturing the onset of liquefaction and the subsequent loss of strength for complex stress values and the ability to change from drained to undrained loading or fully coupled flow deformation loading without changing material parameters.

This requires a thorough characterization of the tailing material for the proper identification of critical state and instability locus (Viana da Fonseca and Cordeiro, 2022) as well as the influence of stress induced anisotropy (Viana da Fonseca et al., 2023). Delgado et al. (2023) highlighted that this geomechanical characterization needs to be performed up to high stress levels to simulate the stress state at the bottom of large embankments. In some cases, the embankments need to be reinforced with cemented berms (Meneses et al., 2023) where more sustainable binders may be used (Caetano et al., 2023).

This paper aims to summarize the main conclusions drawn from a parametric study with hydromechanical stress-strain numerical analysis in tailings storage facilities to assess their stability with the progressive rise of water. For the analysis, the PLAXIS 2D® software and the Mohr-Coulomb constitutive model were used to evaluate which parameters influence the stability of the water flow. Subsequently, a correlation was established to determine the time necessary to promote a stable/permanent flow regime in tailings storage facilities (TSFs).

2 NUMERICAL ANALYSIS

2.1 Model geometry

In the developed study, two types of embankment sections were used. The first one consists of a 30º slope with a height of 35 m in the upstream boundary and 8 m in the downstream boundary. The second model has the same slope but twice the dimensions of the first one. A larger embankment was used to evaluate the effect of embankment dimensions on the steady-state seepage flow stabilization time. The geometry of the first model can be seen in Figure 1.

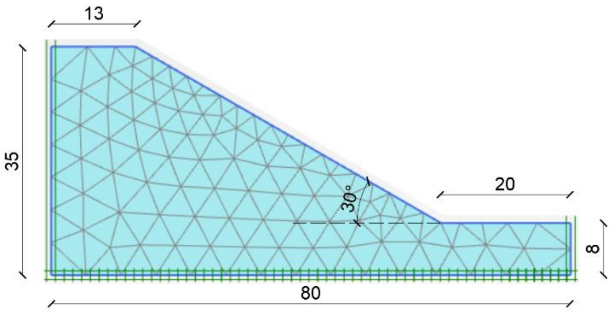

Figure 1. Geometry and dimensions of the first numerical model.

2.2 Material parameters

The constitutive model used was the linear elastic perfectly plastic Mohr-Coulomb model. The parameters for the material were determined through a significant set of monotonic compression triaxial tests, conducted in the Geotechnical Laboratory of FEUP (Table 1).

Table 1. Soil parameters (Mohr-Coulomb).

Parameter		Value	Unit
Unit weights	γ_{sat}	18.00	kN/m^3
	γ_{unsat}	20.00	kN/m^3
Initial void ratio	e	0.800	-
Young Modulus	E	44 000	kN/m^2
Poisson ratio	ν	0.30	-
Friction angle	ϕ'	33.40	º
Cohesion	c'	2	kN/m^2
Coef. earth pressure at rest	K_0	0.45	-
Permeability	k_x=k_y	10^{-5} *to* 10^{-8}	m/s

2.3 Mesh and boundary conditions

The PLAXIS® plane strain numerical model has finite elements with triangular 15-node elements. The generated mesh comprises 1493 nodes in 174 triangular elements.

In terms of mechanical boundary conditions, the bottom boundary was fixed in both directions, while the left and right boundaries were only fixed horizontally. As for hydraulic boundary conditions during the hydromechanical analysis, a constant head was imposed in the left boundary (which changes depending on the analysis), and on the right bottom border a null head was imposed to simulate downstream drainage.

The numerical analysis comprises two consecutive phases: i) an initial phase to activate the stress state (Gravity Loading); ii) a second stage where the hydraulic boundaries were activated and a hydromechanical numerical analysis (fully coupled flow-deformation analysis) was developed.

These analyses were repeated for the two model heights (H=35 m and 70 m), seven water heads on the left boundary (H_w=5m, 10m, 15m, 20m, 25m, 30m to 35m), four soil permeabilities (k=10^{-5}, 10^{-6}, 10^{-7}, and 10^{-8} m/s), and different seepage times (from a couple of months to several years). The seepage time is imposed as the time factor of the fully coupled flow-deformation analysis.

3 RESULTS

3.1 Identification of steady-state flow condition

For all the analyses where the stability of the embankment was assured, the maximum groundwater flow was recorded for each seepage time, water height, and soil permeability, as illustrated in Figure 2. Therefore, it was possible to plot the relation between water flow and seepage time. Figure 3 shows an example of such graph, where it's clear that after some time the seepage flow stabilises. The minimum time to the groundwater flow stabilization was considered the time to steady-state.

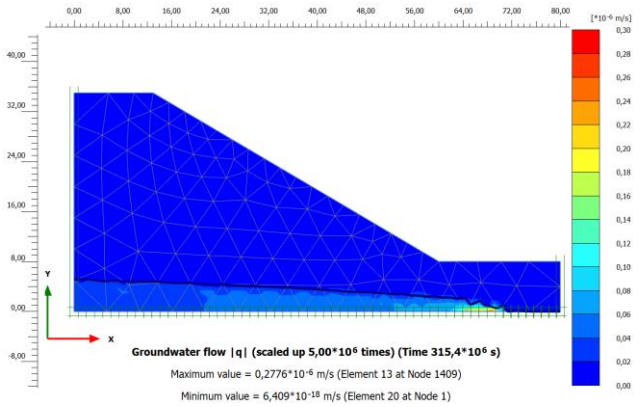

Figure 2. Groundwater flow (m/s) for the first embankment section, with Hw=5m, k=10-6 m/s and seepage time=10years.

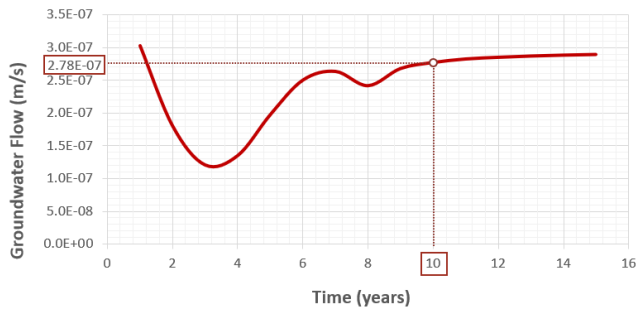

Figure 3. Groundwater flow recorded for each seepage time, and minimum flow time obtained (First embankment section with H_w=5m and k=10^{-6} m/s).

For water heights of 25m, 30m, and 35m in the first embankment section of 35 m, and for water heights of 50m, 60m, and 70m in the second model of 70 m, the slope collapsed without groundwater flow stabilization.

3.2 Results of the parametric study

To compare all the analyses performed in the two model geometries, the water weight was normalized by the slope height (H_w/H) leading to the following ratios: 0.143, 0.286, 0.429, and 0.571. Figure 4 presents the minimum flow time obtained for each height ratio (H_w/H), demonstrating that it does not change much with the height ratio but it varies significantly with soil permeability.

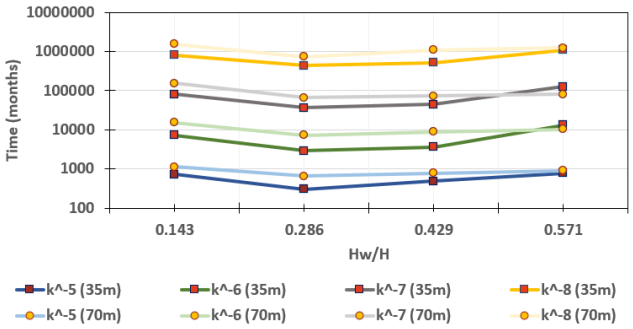

Figure 4. Minimum flow time for each height ratio (H_w/H) and soil permeability for the two model geometries.

3.3 Proposed interpretation model

Considering all the 32 data points obtained, a relation was pursued between the three variables: height ratio, soil permeability, and minimum flow time. Figure 5 shows the 3D graph obtained with the data points used for its generation. To improve the visualisation of the data, logarithms were applied to the two variables: soil permeability and minimum flow time. So, instead of a permeability of 10^{-5} m/s it only appears -5.

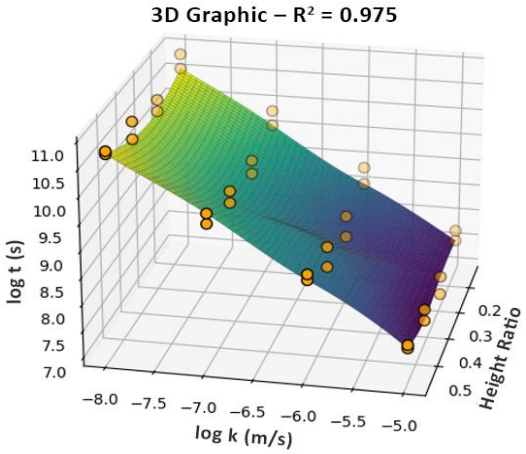

Figure 5. 3D Graphic, with the variables Time (log t (s)), Permeability (log k(m/s)), and Height Ratio.

After creating the 3D graph relating the three variables, a mathematical function that could represent that graph was formulated – equation (1)

$$t = a + b(\frac{H_w}{H}) + c(k) + d\left(\frac{H_w}{H}\right)^2 + e(k)^2 + f(\frac{H_w}{H})(k) \quad (1)$$

where t is the flow time, k is the soil permeability, H_w is the water height, H is the embankment height, and a, b, c, d, e, and f are correlation coefficients. For these later, the following values provided the best adjustment to the data points: a = 3.1639, b = -4.8535, c = -0.9772, d = 6.7779, e = 0.0038, f = -0.0116.

Including the coefficient values in equation (1) the following complete function was obtained, for which a correlation coefficient (R^2) of 0.975 was obtained:

$$t = 3.164 - 4.853(\frac{H_w}{H}) - 0.977(k) + 6.778\left(\frac{H_w}{H}\right)^2 + 0.004(k)^2 - 0{,}012(\frac{H_w}{H})(k) \quad (2)$$

4 CONCLUSIONS

A numerical study was performed to demonstrate the influence of soil permeability, embankment height, and water head on the minimum time for the stabilization of seepage flow. For this purpose, hydromechanical stress-strain numerical analysis were performed in PLAXIS 2D® with Mohr-Coulomb constitutive model. For higher water heads the slope was unstable, but for the other conditions, it was possible to identify the minimum flow time for each case. It was concluded that for a certain soil permeability (k) there is not much variation in the minimum flow time with the height ratio (ratio of water head by embankment height, H_W/H). The paper finishes with a mathematical expression to obtain the minimum flow time depending on the given variables (k and H_W/H).

ACKNOWLEDGEMENTS

This work was financially supported by national funds through the FCT/MCTES (PIDDAC), namely the CONSTRUCT - Instituto de I&D em Estruturas e Construções, Base Funding UIDB/04708/2020 https://doi.org/10.54499/UIDB/04708/2020, the research project INPROVE-2022.02638.PTDC (https://doi.org/10.54499/2022.02638.PTDC), and by scholarship of the last author CEECIND/04583/2017 (https://doi.org/10.54499/CEECIND/04583/2017/CP1399/CT0003).

REFERENCES

Caetano, I., Rios, S., Delgado, B., Viana da Fonseca, A. (2023). Stabilisation of Iron Tailings with alkali activated binders, *Proc. 1st Int. Conference on Geotechnics of Tailings and Mine Waste, GeoMin 2023*, 24-26 Out., Ouro Preto, Brasil https://geominouropreto.com.br/2023/icgtmw2023

Delgado, B., Viana da Fonseca, A., Bitter, R. J., Castilho, B.M., Coelho, D. (2023). Geomechanical behaviour of an iron ore tailings under high-stress levels for disposal by dry stacking, *Proc. 1st Int. Conference on Geotechnics of Tailings and Mine* Waste - GeoMin, 24-26 Out., Ouro Preto, Brasil https://geominouropreto.com.br/2023/icgtmw2023

Ledesma, O., Sfriso, A., Manzanal, D. (2022) Procedure for assessing the liquefaction vulnerability of tailings dams. *Computers and Geotechnics*, 144, https://doi.org/10.1016/j.compgeo.2022.104632.

Mánica MA, Arroyo M, Gens A and Monforte L. Application of a critical state model to the Merriespruit tailings dam failure. *Proceedings of the Institution of Civil Engineers – Geotechnical Engineering*, https://doi.org/10.1680/jgeen.21.00001.

Meneses, B., Rios, S., Viana da Fonseca, A. (2023). Stacking with Cemented Tailings Berms: A Parametric and Limit Equilibrium Analysis. *The XLIV Ibero-Latin American Congress on Computational Methods in Engineering. Mini-Symposium on Computational Geotechnics*, 13-16 novembro, Porto, Portugal (https://cilamceporto2023.pcoabreu.com/).

Mogami T., Kubo K. (1953). The behaviour of soil during vibrations. *Proc. 3rd Int. Conf. on Soil Mechanics and Foundations Engineering*, Vol. 1, 152-155, Switzerland.

Viana da Fonseca, A., Cordeiro, D. (2022). Critical state and instability locus of a silty-sand iron tailing, *Proc. 20th ICSMGE International Conference on Soil Mechanics and Geotechnical Engineering*, Vol. 2, pp. 4429-4434, https://www.issmge.org/publications/online-library, Sydney, Australia.

Viana da Fonseca, A., Molina-Gomez, F., Besenzon, D., Coelho, D. (2023). The influence of stress induced anisotropy in undrained yield and ultimate shear strengths in brittle loose deposited silts, *IS-Porto 2023, Proc. 8th Int. Symposium on Deformation Characteristics of Geomaterials*, (https://www.issmge.org/publications/online-library/conferences/isdcg2023).

Proceedings of the XVIII ECSMGE 2024
GEOTECHNICAL ENGINEERING CHALLENGES
TO MEET CURRENT AND EMERGING NEEDS OF SOCIETY
© 2024 the Authors
ISBN 978-1-032-54816-6
DOI 10.1201/9781003431749-341
Open Access: www.taylorfrancis.com, CC BY-NC-ND 4.0 license

ECSMGE 24
XVIII EUROPEAN CONFERENCE ON SOIL MECHANICS AND GEOTECHNICAL ENGINEERING

Establishing the geotechnical category through analysis of difficult soils - a proposed procedure

Établissement de la catégorie géotechnique par l'analyse des sols difficiles - une procédure proposée

E. Milutinovici*, G. Dragomir, D. Mihailescu
Prospect Technical Studies, Bucharest, Romania

**emiliamilutinovici@gmail.com*

ABSTRACT: Establishing the geotechnical category for a site is an important result of the geotechnical investigation process. According to it, the design and execution characteristics are established, which directly influence the costs of a construction. The most influential factor in establishing the geotechnical category is the type of foundation ground, specifically if this is considered as difficult soil. The procedure developed in the paper involves the analysis of such difficult soils; thus, for each individual borehole, the type of difficult soils is established, based on the geotechnical properties determined by field and laboratory tests. Depending on the foundation solution, although the soils where the future construction is to be founded may be part of the category of difficult soils, it is possible that they will not negatively influence the way of execution or exploitation of the future construction. As a result, the score given to this risk factor can be reduced, thus reducing the final score for establishing the geotechnical category. This paper presents a detailed procedure to allow the standardization of setting the geotechnical category for several types of constructions and geological areas, intending to optimize the method of establishing the geotechnical category and the geotechnical risk.

RÉSUMÉ: L'établissement de la catégorie géotechnique d'un site est un résultat important du processus d'étude géotechnique. Selon lui, les caractéristiques de conception et d'exécution sont établies, ce qui influence directement les coûts d'une construction. Le facteur le plus influent dans l'établissement de la catégorie géotechnique est le type de sol de fondation, en particulier s'il est considéré comme un sol difficile. La procédure développée dans l'article implique l'analyse de ces sols difficiles; ainsi, pour chaque forage individuel, le type de sols difficiles est établi, sur la base des propriétés géotechniques déterminées par des essais sur le terrain et en laboratoire. Selon la solution de fondation, bien que les sols où la future construction doit être fondée puissent faire partie de la catégorie des sols difficiles, il est possible qu'ils n'influencent pas négativement le mode d'exécution ou d'exploitation de la future construction. En conséquence, la note attribuée à ce facteur de risque peut être réduite, réduisant ainsi la note finale pour l'établissement de la catégorie géotechnique. Cet article présente une procédure détaillée pour permettre la standardisation de la définition de la catégorie géotechnique pour plusieurs types de constructions et de zones géologiques, dans le but d'optimiser la méthode d'établissement de la catégorie géotechnique et du risque géotechnique.

Keywords: Difficult soils; geotechnical category.

1 INTRODUCTION

In recent years, Romania, with the help of the European cohesion fund, has invested heavily in road infrastructure. Thus, in order to complete and integrate into the structure of TEN-T (The Trans-European Transport Network), the competent state institutions have promoted and financed numerous road infrastructure projects: highways, express roads, road rings. For each of these projects, one of the most important steps in achieving a feasible design is the geotechnical study. In order to carry out the geotechnical study, the standards and technical norms are aligned with the European norms. However, there are typical conditioning according to the natural and engineering characteristics specific to Romania.

The main technical norm that establishes the way of carrying out geotechnical studies and interpreting the obtained data, is NP074 "Normative regarding technical documentation for constructions". In accordance with this technical norm, both geotechnical investigations and design are carried out according to the geotechnical category of the work established according to the criteria described in the norm.

2 LEGISLATIVE PROVISION

The geotechnical category is a notion that appears in geotechnical design standards and norms. In Eurocode 7, part 1, one of the principles stated is that "in order to establish minimum requirements regarding the volume and content of field research, calculations and control verifications, the complexity of each geotechnical design and the associated risks must be identified" (ASRO, 2008). The geotechnical categories in which geotechnical designs/works can fit are 3: category 1, 2 and 3.

In order to establish the geotechnical category, 5 criteria will be applied. These are: land conditions, groundwater, classification of buildings by importance, neighborhoods and seismic area. (MDLPA, 2023). For each criterion, a score is given according to its characteristics. The lower the score obtained after evaluating all the criteria, the lower the geotechnical category of the design/work, so the associated risks are fewer. Also, the higher the score awarded, the higher the geotechnical category and the associated risk is also considered major (MDRAP, 2014).

3 PRESENTATION OF METHOD

In calculating the geotechnical category, the criterion of ground conditions can have the greatest influence, due to the variation of the score from 1 point for good foundation soils to 6 points for difficult foundation soils. No other criterion is given such a high score as that given for difficult foundation soils. As a result, it becomes extremely important to classify as difficult foundation soils, to be done very carefully considering the design and financial implications.

The working method involves a detailed study of the conditions under which a ground can be considered being a difficult soil or not. As a result, the authors consider that the spliting into categories of terrain conditions must take into account both the classification of a land as an intrinsic characteristic in the category of difficult lands and the circumstantial characteristic that can make the award of the maximum score different. Thus, while for a certain constructive situation, the existence of a difficult soil within the foundation ground can be considered a difficult ground condition, for another constructive situation, the influence of the difficult soil is minimal, so the ground condition is no longer considered difficult and can be considered medium or good. The two characteristics that lead to the establishment of field conditions are, in the authors' view: a. the type of soil (foundation ground) and b. the type of interaction between foundation ground and construction (mainly type of foundation: shallow or pile foundation). It is necessary to study in parallel the both characteristics.

Road infrastructures such as motorways, expressways, bypass, ringsare mainly linear constructions, developed over long lengths and having complex objectives. Projects that are ongoing in Romania and subject to the procedure in this article can have lengths between 10 and 100 km. Such work can not only take place in areas where geology/geomorphology can change (hence the types of soil/foundation land), but also the construction characteristics of a road infrastructure can be very different.

3.1 Determining the type of difficult soil/foundation ground

In the category of difficult foundation soils / lands belong to the following types (MDLPA, 2023):
1-sandy soils, including loose silty soil. It is considered to be loose soils, those soils for which the results obtained from performing in situ investigations of the Standard Penetration Test type, have N30<9 values (ISPIF, 1988); 2-saturated sandy soils susceptible to liquefaction under seismic actions. They are considered to be liquefiable soils, those soils which constitute themselves as "extensive layers or thick lenses of loose sand, with or without silty or clayey particles, below the level of the groundwater, or where the level of the underground water is close to the surface of the land" (ASRO, 2006); 3-fine soils with consistency index CI<0.5, are those soils that fall into the category of soft plastic soils (ASRO, 2018); 4-sensitive soils (loess, loessoidic soils), are those soils whose structure and mechanical behavior change substantially and irreversibly in contact with water (MDRT, 2011); 5-soils with high swelling and contraction (expansive soils) , with high and very high activity are those clay soils active in relation to water, which have the property of significantly changing their volume as a result of moisture variation (MDRT, 2012); 6-soils with a high content of organic matter, are those soils formed relatively recently (as geological age) and which include organic matter, such as banks, silts, peatlands, gyttja and dy (ISPIF, 1988), (ASRO, 2018); 7-sloping lands with sliding potential, are those lands that have a hazard coefficient with values that show a medium or high landslide hazard, with a very high probability of landslides. (Guvernul Romaniei, 2003); 8-uncontrolled earth fillings less than 10 years old, are those lands that belong to the category of anthropogenic lands (ASRO, 2018) and which can be identified when crossing existing old roads or platforms, or crossing controlled or uncontrolled warehouses; 9-fillings from household

waste, regardless of age, belong to the category of anthropogenic lands, located near urban areas, having a controlled character, where the contours are clearly defined or uncontrolled, constituting illegal landfills, whose contours are undefined and not fully identifiable at the time of geotechnical investigations; 10-Freezing sensitive soils (difficult soil category mentioned in the 2014 version of NP074) are those soils that are sensitive to frost identified in the depth range between the land surface and the depth of freezing (ICPTT, 1990); (IRS, 1977).

The authors suggest the following methodology: a.for each geotechnical drilling performed, difficult soils are identified throughout its depth, thus classified according to the criteria mentioned above; b. based on the investigations carried out, the thickness of the identified layer is established, but also its extension in space, especially along the investigated linear structure, but also transversely, where they exist. In the case of infrastructure works carried out over long distances, most investigations are carried out axially, in longitudinal profile; c. It also identifies the depth at which difficult earth appears, as well as the depth at which it is no longer identified.

Thus, one by one, the types of soil encountered in geotechnical drilling (in each drilling performed) are analysed if they fall into the categories of difficult soils mentioned.

3.2 Establishing the type on interaction between the foundation soils/ground and the construction (foundation type)

In a very simplist way, the highways structures are divided in road structures and bridge structures. In functie de modul de realizare, road structures se impart in embankments, cuttings and mixt profiles. Depending on the foundation mode, bridge structures are direct (shallow) foundation or indirect (usually piles) foundation and the road structure are made in embankment, in cutting or in mixed profile.

In order to know the type of interaction with the foundation ground, the authors recommend dividing the studied route of the motorways into objects to be treated separately and unitarily. These can be: a. Indirect foundations structures (viaducts, bridges, overpasses); b. shallow foundations structures (viaducts, bridges, overpasses); c. Facilities, shallow foundation: administrative buildings, footbridges, lighting poles; d. directly founded road structures: highway/expressway body, parking lots, built in cutting conditions, in embankment conditions or in mixed profile conditions. Can be add as many objectifs are needed.

3.3 Concomitant analysis of the two criteria

For each type of difficult soil identified, the type of structure is also analyzed.

As an example, the situation of marlys soils can be considered a paradox. The same type of marly soil can be considered within a linear structure of highway/expressway type, as good foundation condition or difficult foundation condition.

When we consider the marlys soils as being at surface in the depth of moisture vatiation during the changing season, the marly soils are part of the category of difficult soils, because they significantly change their volume due to moisture variation. In this case the score for ground conditions is 6.

Thus, if a marly soil is identified in depth, as bedrock (almost incompressible, prequaternary) and is constituted as foundation ground for indirect foundations, the marly soils are part of the category of good or medium foundation ground conditions, the score granted being 2 points or 3 points. In the Table 1, the authors shows an example of how the dual character of marly soils as ground foundation condition can be interpreteted.

4 RESULTS

The results are expressed in tabular form, both for classification in the category of difficult lands and for establishing the geotechnical category.

Table 1. Exemplification of marly soil duality characterisation.

Criterion	**Hypothesis 1**	**Hypothesis 2**
Objective	Road structure in cutting area	bridge
Borehole no.	BH35	BH36
Depth interval (m)	3-30	3-30
Soil type	Marly clay	Marly clay
Foundation type	Direct (shallow)	Indirect (piles)
Foundation depth (m)	6.00	25.00
Soil category	3-difficult	2-medium
Soil subcategory	5	5
Score	6	3
Total score from other factors	10	10
Total score	16	13
Category of risk	high	medium

5 CONCLUSIONS

The paper aims to present a procedure for determining the land conditions for framing a design/construction in a geotechnical category and is based on practical engineering, taking into account Romanian standards and norms. It is intended to be constituted as a description of a way of practice in Romania.

In order to determine the geotechnical category, the most important criterion that influences the score awarded is ground conditions (type of soils). Although the standards and norms in force consider that ground conditions are defined only by the types of soils / foundation lands encountered (good, medium, difficult), the authors consider that besides this intrinsic feature, the circumstantial characteristic related to the interaction between the foundation earth / ground and the construction (type of foundation) must be taken into account.

The concomitant analysis of the two characteristics influences the correctness of scoring for the criterion of ground conditions, there being situations in which a foundation soil / land that can fall into the category of good or medium foundation soils, to enter the category of difficult soils, if the circumstantial characteristic is modified.

The transition from the overall study of the criterion of ground conditions to its detailed study, taking into account the type of soils but also the characteristics of the interaction between soils and construction, entails a higher precision in the classification in the geotechnical category, therefore an increase in the safety of the future construction.

ACKNOWLEDGEMENTS

The authors are grateful for possibilities to work in such a big geotechnical project with the unconditional support of Prospect Technical Studies and Search Corporation.

REFERENCES

ASRO. (2006). Eurocod 8: Proiectarea structurilor pentru rezistenta la cutremur. Partea 5: Fundatii, structuri de sustinere si aspecte geotehnice. ASRO Standard Roman, Bucharest.

ASRO. (2008, July). SR EN 1997-1 Eurocode 7: Geotechnical design; Part 1: General rules. ASRO Roman Standard, Bucharest.

ASRO. (2018). Geotechnical investigations and tests. Identification and classification of land. Part 2: Principles for a classification. ASRO Standard Roman, Bucharest.

Government of Romania. (2003, 05 07). Decision no. 447 of 10 April 2003 approving the methodological norms regarding the elaboration and content of natural risk maps for landslides and floods. Official Gazette, Bucharest.

ICPTT. (1990). The action of the freeze-thaw phenomenon at road works. Prevention and remediation of degradation from frost - thaw. Technical prescriptions. State Standard, Bucharest.

IRS. (1977). Foundation ground. Maximum freezing depths. Zoning of the territory of the Socialist Republic of Romania. State Standard, Bucharest.

ISPIF. (1988, 09 01). Foundation ground. Classification and identification of land, STAS 1243-88. State Standard, Bucharest.

MDLPA. (2023). Normative on geotechnical documentation for construction, indicative NP074-2022. Official Gazette of Romania, Bucharest.

MDRAP. (2014). Normative regarding geotechnical documentation for constructions - NP074-2014. Official Gazette, Part I, Bucharest.

MDRT. (2011, 03 04). Normative regarding the foundation of constructions on wet-sensitive soils, NP125:2010. Official Gazette of Romania, Part I, Bucharest.

MDRT. (2012, 06 13). Normative regarding the foundation of constructions on lands with large swelling and contractions, indicative NP126:2010. Official Gazette of Romania, Part I, Bucharest.

Proceedings of the XVIII ECSMGE 2024
GEOTECHNICAL ENGINEERING CHALLENGES
TO MEET CURRENT AND EMERGING NEEDS OF SOCIETY
© 2024 the Authors
ISBN 978-1-032-54816-6
DOI 10.1201/9781003431749-342
Open Access: www.taylorfrancis.com, CC BY-NC-ND 4.0 license

ECSMGE 24
XVIII EUROPEAN CONFERENCE ON SOIL MECHANICS AND GEOTECHNICAL ENGINEERING

Numerical assessment of the ongoing settlements of the western tower of Terreiro do Paço, in Lisbon, Portugal

Évaluation numérique des affaissements en cours à la tour ouest de Terreiro do Paço, à Lisbonne, Portugal

L. Miranda*, J. Carreto
LNEC, Lisboa, Portugal

**lmiranda@lnec.pt*

ABSTRACT: The development of Terreiro do Paço Square began after the 1755 Lisbon earthquake, with the construction of the eastern side buildings. On the western side, an embankment had to be built first, in an area previously occupied by the river, overlying the existing soft soils. The western tower was constructed later, overlooking the Tagus River, and was not completed until the mid-nineteenth century. In 1941, a Portuguese historian reported that this tower had suffered a settlement of more than 0.5 m. Between 1956 and October 2019, the southeast and northeast corner's settlement increased by 0.15 m and 0.11 m, respectively. Interestingly, no damage was found on the external walls or the arched ceiling of the first storey, indicating a rigid body movement. More recently, the Lisbon Municipality sought to extend the Lisbon Museum by placing one of its modules in the newly vacant western tower. Using the finite elements approach and a three-dimensional numerical model, stress and strain studies were carried out with the purpose of analysing the effect of the rehabilitation works on its safety and functionality. Because of the period since the tower's completion and the permeability of the muddy soils in its foundation, a soft soil constitutive model with creep was used to simulate the ongoing settlements, with satisfactory results. This allowed for a more reliable prediction of future settlements caused by the tower's new usage.

RÉSUMÉ: Le développement de la place du Terreiro do Paço a commencé après le séisme de Lisbonne de 1755, avec la construction des bâtiments du côté est. Du côté ouest, il a fallu d'abord construire un remblai, dans une zone précédemment occupée par la rivière, sur les sols mous existants. La tour ouest a été construite plus tard, surplombant le Tage, et n'a été achevée qu'au milieu du XIXe siècle. En 1941, un historien portugais rapportait que cette tour avait subi un affaissement de plus de 0,5 m. Entre 1956 et octobre 2019, l'affaissement des coins sud-est et nord-est a augmenté respectivement de 0,15 m et 0,11 m. Il est intéressant de noter qu'aucun dommage a été constaté sur les murs extérieurs ou sur le plafond voûté du premier étage, ce qui indique un mouvement rigide du corps. Plus récemment, la Municipalité de Lisbonne a cherché à agrandir le musée de Lisbonne en plaçant un de ses modules dans la tour ouest nouvellement vacante. En utilisant l'approche des éléments finis et un modèle numérique tridimensionnel, des études de contraintes et de déformations ont été réalisées dans le but d'analyser l'effet des travaux de réhabilitation sur sa sécurité et sa fonctionnalité. En raison de la période écoulée depuis l'achèvement de la tour et de la perméabilité des sols boueux de ses fondations, un modèle constitutif de sol mou avec fluage a été utilisé pour simuler les affaissements en cours, avec des résultats satisfaisants. Cela a permis une prévision plus fiable des futurs affaissements provoqués par la nouvelle utilisation de la tour.

Keywords: Settlements; foundation; numerical modelling; historic building.

1 HISTORIC FRAMEWORK

The development of Terreiro do Paço Square began after the 1755 Lisbon earthquake, with the construction of the eastern side buildings. On the western side, an embankment had to be built first, in an area previously occupied by the river, overlying the existing soft soils. The western tower was constructed later, overlooking the Tagus River, and was not completed until the mid-nineteenth century. Its structure consists of exterior walls of stone masonry, a 1st floor supported by stone arcades and vaults, resting in 16 stone columns, being the remaining floors and the roof supported by the exterior walls and four steel pillars, circular and hollow, at the centre of the building. Its foundation comprises a "massive 7 m thick masonry block, resting on a wooden grid" (Castro, 1966), to which pine piles are connected.

Concerning the geological-geotechnical scenario at the tower site, the survey campaign carried out by the Rodio company, in 1965 (Castro, 1966), revealed the presence of heterogeneous landfills, with remains of ancient foundations, to depths of 5 to 10 m. Under the landfill, a layer of clayey mud appears, with increasing thickness towards the river, followed by a layer of

sand, also with a slope towards the river and a thickness varying between 5 and 10 m. Then, another mud formation follows, but with a siltier component, and a thickness (under the tower) of around 8 m, which becomes more clayey in contact with the Miocenic formation, which occurs at around 40 m depth (Figure 1). The water table was found at elevation +1.0 m.

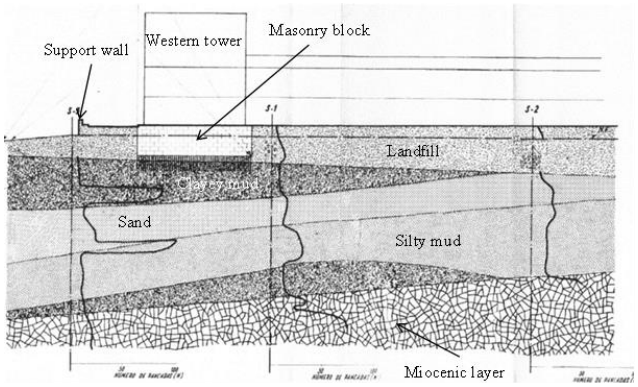

Figure 1. Geological-geotechnical profile at the zone of the western tower, adapted from Castro (1966).

In 1941, a Portuguese historian reported that this tower had suffered a settlement of more than 0.5 m. These significant settlements are explained by the high deformability of the materials in the tower's foundation and its thickness. Regarding the higher settlements of the tower when comparing with the other western wing buildings, this is explained by an increase in the thickness of the muddy soil from north to south, but also by the south area having been gained from the river through the construction of an embankment, after the 1755 earthquake, constituting an additional load on the compressible foundation.

From 1956 onwards, LNEC began measuring the vertical displacements of 8 topographic marks installed in the western wing buildings of Terreiro do Paço. The records are shown in Figures 2 and 3 (Braz, 2019). Between 1956 and 2019, the additional settlement was of 0.153 m, in the southeast corner of the tower (mark N8), and of 0.114 m, in the northeast corner (mark N7). The settlement profile (Figure 2) resembles the deformation of a cantilever beam, fixed at the north end and loaded at the south end. The greatest curvature of the settlement profile was recorded between the N4 and N6 marks, in an area where cracks were identified in the arcade and façade of the Ministry of Agriculture building.

There is an absence of readings between 1989 and 1999. The increase in settlement (66 mm, at the N8 mark) and settlement rate might have been due to an embankment construction, in 1995, as part of the Blue Line of the Lisbon Subway, located at a minimum distance of 35 m from the tower, and due to the TBM passage, from December 1997. In 2009, there was also an increase in the settlement rate, which could be attributed to the construction of a reinforced concrete pile curtain near the south and east façades of the tower. From 2010-2012, the settlement rate reduced at the N6, N7 and N8 marks, remaining practically constant until 2019.

A relevant fact, which is in line with a rigid body type movement of the tower, is the absence of cracks in the exterior walls or in the vaults supporting the 1st floor (Valente and Mesquita, 2017).

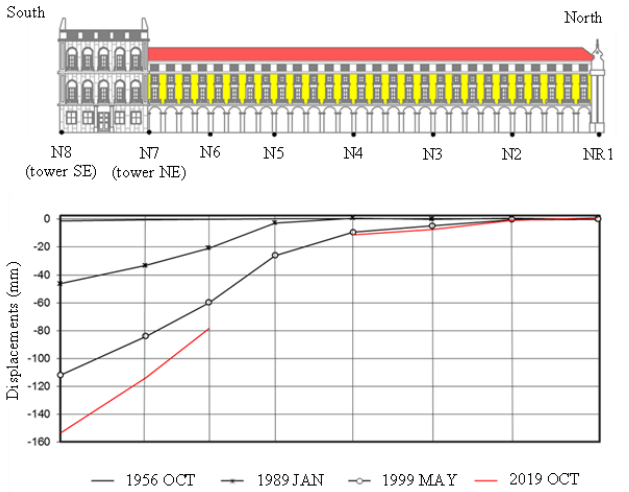

Figure 2. Settlements of the 8 marks installed in the buildings of the western wing of Terreiro do Paço, in October 1956, January 1989, May 1999 and October 2019.

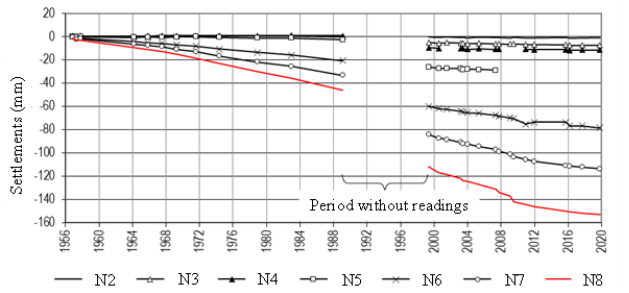

Figure 3. Evolution of the settlements in the marks installed in the buildings of the western wing of Terreiro do Paço.

2 NUMERICAL MODELLING

2.1 Goals

Recently, the Lisbon Municipality sought to extend the Lisbon Museum by placing one of its modules in the newly vacant western tower. Using the finite elements approach and a 3D numerical model, stress and strain studies were carried out with the purpose of analysing the effect of the rehabilitation works on its safety and functionality. In this model, the evolution of the settlements since the tower's construction was simulated, considering: the mechanical and geometric properties of the masonry block foundation; the

temporary embankment, built as part of the Lisbon Subway Blue Line construction; and the distribution and magnitude of the permanent and live loads, in the current situation, and after rehabilitation of the tower, to serve the new Museum functions, including the construction of new floors and the removal of the 4 central pillars above the 1st floor.

2.2 Calculation model

2.2.1 Model geometry

The width of the model is equal to the width of the masonry block plus 50 m on each side, to minimize the borders' influence on the results. A depth of 50 m was considered in the z-direction, to reach the Miocenic formation. A support wall, at 16 m distance from the south façade of the tower, was also considered (Figure 4). The tower was assumed to be nearly square in plan, with 24.6 m sides. An extra width of 1.4 m, in the x-direction, and of 1.7 m, in the y-direction, was adopted for the masonry block, with an average depth of 7 m.

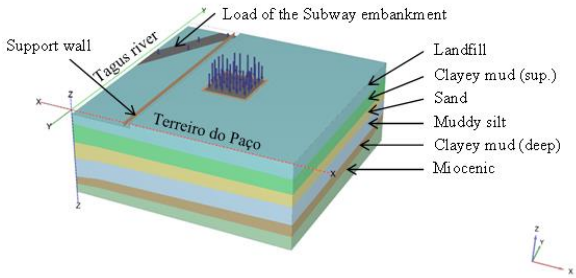

Figure 4. Geometry, geological layers, loads and axes of the calculation model.

The real arrangement of the geological layers is reproduced in Figure 5. Interfaces were introduced between the landfill and the support wall, and between the former and the masonry block, and assigned half the resistance of the adjacent soil. The finite element mesh was generated in *Plaxis 3D* and refined to have a greater density of elements around the masonry block and under the applied loads (Figure 6).

2.2.2 Modelling of the foundation loading

The simulation of the tower's structure, and of the respective permanent and live loads, was carried out through the application of distributed loads at the top of the masonry block, both in the current situation and in the situation of future use. Globally, the tower's requalification project will lead to a 6 % increase on the foundation loading and the removal of the 4 central pillars implies additional loading of the outer walls.

The Lisbon Subway embankment was simulated by a distributed load of 105 kPa, corresponding to a height of 5 m, applied in a width similar to the tunnel diameter.

2.2.3 Foundation materials characterization

A soft soil constitutive model with creep was adopted for the muddy materials, with the aim of integrating the effect of time on their behaviour. Given the period since the construction of the tower and the typical permeability of these soils, it was considered likely that the occurring settlements were due to secondary consolidation of the soil, or creep.

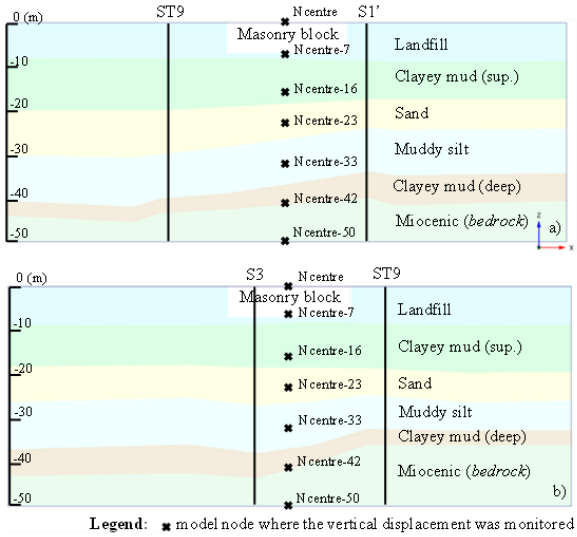

Figure 5. Cross-sections of the geological layers, passing through the centre of the tower: a) x-z and b) y-z.

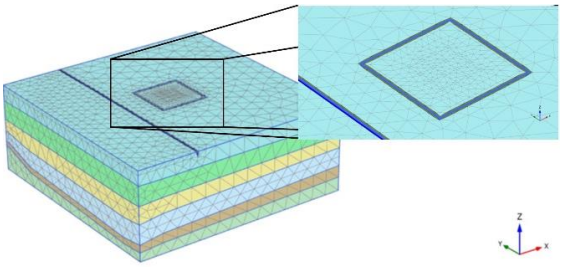

Figure 6. Finite element mesh.

For the remaining materials an elasto-plastic constitutive model with a Mohr-Coulomb failure criterion was implemented, including the muddy silt, since this material presents physical characteristics closer to a silt than to a mud. For the masonry, the linear, single-phase elastic model was adopted, as the voids between masonry blocks were filled with mortar.

In Tables 1 to 3, the parameters that simulate the physical and mechanical properties of the materials are presented. Regarding the muddy materials, the value of the initial void index (e_0) was based on the density of the solid particles, equal to 2.75, and on the water content, obtained from Castro (1966). The modified

compressibility, λ^*, and expansibility, k^*, indexes' values were based on LNEC's knowledge of the typical characteristics of these materials in the area. The value of the modified creep index, μ^*, was adjusted to obtain, in the southeast corner of the tower (N8), a similar settlement to the one obtained from 1956 to 2019 (Braz, 2019), while keeping the value in the usual range for organic soils.

The parameters for the remaining materials were defined considering the work of Castro (1966).

2.2.4 Calculation model stages

The calculation model encompassed several phases, namely:

- Initial phase, to establish the initial stresses.
- Phase 1, in which the ground on the south side of the tower was modelled, simulating a fictitious excavation near the river and the construction of the south wall. An elastoplastic analysis was performed, without consideration of consolidation. The displacements at the end of this stage were nullified, so it only influenced the "in situ" stresses.
- Phase 2, in which the masonry foundation block was built and the loads from the tower were applied almost instantly (1 day), allowing the soil to consolidate in the remaining period. This phase went from 1840, when the tower was built, to 1956, when the settlement monitoring campaign began. The calculated values of the settlements are due to the tower's construction.
- Phase 3, which ran from 1956 to 1995. At this stage, only consolidation of the foundation ground occurred.
- Phase 4, which began in 1995, the year when a temporary embankment was placed over the Blue Line tunnel of the Lisbon Subway, and ended in 2007, the year when the embankment was removed. From 1989 to 1999, no geodetic campaigns were carried out by LNEC. With the resumption of measurements, a very significant increase of the tower settlement rate was noted. Thus, this phase was introduced to evaluate the influence of the embankment construction on the behaviour of the tower.
- Phase 5, which began in 2007 and ended in 2021. In this phase, only consolidation of the ground was considered.

To perform a comparative study of the estimated settlements between 2001 and 2100, 3 distinct scenarios were considered, specifically:

- Scenario 6a, in which the current loading situation was maintained.
- Scenario 6b, in which the loading corresponded to the new structure and tower functions.
- Scenario 6c, theoretical situation in which permanent and live loads remained the same until 2100, and 1 m of the masonry block was excavated, reducing its weight and, consequently, the load on the foundation ground. This situation was simulated in the model through reducing the volumetric weight of the masonry from 24 kN/m^3 to 20.6 kN/m^3.

The reinforced concrete pile curtain, built to mitigate the effects of soil liquefaction on the tower, wasn't modelled, as its construction, in 2009, didn't have a significant effect on the settlements of the tower (Figure 3).

Table 1. Parameters adopted for muddy materials.

	Clayey mud (sup.)	**Clayey mud (deep)**
γ (kN/m^3)	17.6	19
e_0	1.24	0.96
λ^*	0.0757; 0.15	0.0757; 0.15
κ^*	0.0371	0.0371
μ^*	0.018	0.018
ϕ'(º)	20	25
c'(kPa)	0.3	0.3
k (m/day)	0.432x10^{-3}	0.0432 x10^{-3}

γ - saturated soil unit weight; ϕ' – effective friction angle; c' – effective cohesion; k – permeability coefficient.

Table 2. Parameters adopted for the remaining materials.

	Landfill	**Sand**	**Muddy silt**	**Miocenic layer**
γ (kN/m^3)	21	21	19.5	20
E (MPa)	10	14	14	100
ν	0.3	0.3	0.3	0.25
ϕ'(º)	30	35	28	30
c'(kPa)	0.3	0.3	0.3	250
k (m/day)	4.64	4.64	0.0864 x10^{-3}	0.0432 x10^{-3}

E – deformability modulus; ν - Poisson's ratio.

Table 3. Parameters adopted for the masonry block.

	γ (kN/m^3)	E (MPa)	ν
Masonry	24	2000	0.2

2.3 Calculation model results

2.3.1 Model results from construction to 2021

In the model, the vertical displacements are monitored at the 4 corners of the tower (N8, N7, M8, M7) and at its centre: at the surface (Ncentre), at -7 m (Ncentre-7, base of the masonry block), at -16 m (Ncentre-16, shallow clayey mud), at -23 m (Ncentre-23, sand), at -33 m (Ncentre-33, muddy silt), at -42 m (Ncentre-42,

deep clayey mud) and at -50 m (Ncentre-50, Miocenic) (Figures 5 and 7).

Figure 7 shows the vertical displacement over time for each of the nodes mentioned above. After the immediate settlement of the layers of sand and muddy silt, there is an initial phase of relatively higher settlement rate, up to approximately 5000 days, which gradually reduces as a result of the primary consolidation of the shallow and deep clayey mud layers. It is estimated that this phase would be almost completed 65 years after the construction of the tower, giving way to the secondary consolidation (through creep) of these layers, with a lower settlement rate and a tendency of stabilization.

The largest settlement occurs in the tower's southwest corner, followed by the southeast corner, which is in accordance with the observations made by Valente and Mesquita (2017). The accumulated settlement at point N8, from 1956 until 2019, attained 153 mm. This value, and the differential settlement between nodes N8 and N7, are in accordance with the accumulated settlements recorded by Braz (2019).

Despite the foundation of the subway embankment having suffered a settlement of 1.15 m, its construction, between 1989 and 1999, seems to have an insignificant effect on the behaviour of the tower.

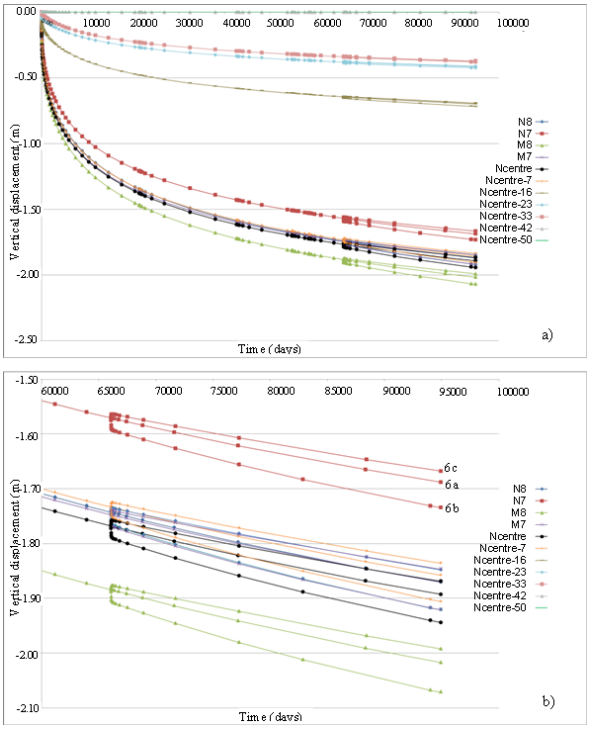

Figure 7. Evolution of the vertical displacement: a) since the beginning of the tower's construction; b) evolution of settlements in phases 6a, 6b and 6c.

Additionally, the vertical displacement at the base of the tower's foundation block (Ncentre-7) is very similar to the one at its top (Ncentre), in accordance with the high stiffness of the block. Moreover, the masonry block rotates like a rigid body, as can be seen in Figure 8.

The vertical displacement of the shallow clayey mud layer is around 33 to 40 % of the settlement of the masonry block and the layers of muddy silt and sand are responsible for around 20 to 25 % of the total settlement of the tower's foundation.

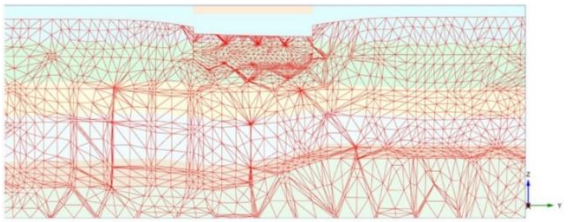

Figure 8. Displacements of the masonry block in 2021 (increased 5 times)

2.3.2 Model results after 2021

The 3 distinct scenarios, from 66078 days (2021) on, are shown in Figure 8: the settlement rate remains the same if the current situation continues (6a); it increases slightly with the increase in loading after the requalification of the tower (6b); and it decreases faintly when 1 m of the masonry block is excavated (6c), after expected bulking from load removal.

Maintaining the current loading, a settlement of 128 mm is obtained in the southeast corner of the tower (N8), between 2021 and 2100, which corresponds to an average rate of 1.6 mm/year (Table 4), a value higher than the rate measured from 2012 onwards (1 mm/year). A differential settlement between N7 and N8 of just 11 mm is calculated with the numerical model.

Table 4. Settlement and average settlement rate, between 2021 and 2100, in N7 / N8, for the current loading situation.

	$\delta_{(2021\text{-}2100)}$ (mm)	$\delta_{(2021\text{-}2100)}/\Delta t$ (mm/year)
N8	128	1.6
N7	117	1.5

$\delta_{(2021\text{-}2100)}$ – settlement; Δt – time period (79 years).

Changing the loading, after requalification of the tower, a settlement of 174 mm is obtained in the southeast corner of the tower (N8), between 2021 and 2100, which corresponds to an average rate of 2.2 mm/year (Table 5). A differential settlement between N7 and N8 of 14 mm is calculated. The increase in the average settlement rate, compared to the previous situation, results from the mud's primary consolidation, due to the increase of load on the foundation (around 6 %).

Considering a 1 m deep excavation of the masonry block, a settlement of 107 mm is obtained in the

southeast corner of the tower (N8), between 2021 and 2100, which corresponds to an average rate of 1.4 mm/year (Table 6). A differential settlement between N7 and N8 of 9 mm is estimated.

Table 5. Settlement and average settlement rate, between 2021 and 2100, in N7 / N8, for changing the loading, after requalification of the tower.

	$\delta_{(2021\text{-}2100)}$ (mm)	$\delta_{(2021\text{-}2100)}/\Delta t$ (mm/year)
N8	174	2.2
N7	160	2.0

Table 6. Settlement and average settlement rate, between 2021 and 2100, in N7 / N8, for the situation after a 1 m deep excavation of the masonry block.

	$\delta_{(2021\text{-}2100)}$ (mm)	$\delta_{(2021\text{-}2100)}/\Delta t$ (mm/year)
N8	107	1.4
N7	98	1.2

2.4 Comparative analysis of the modelled cases

Comparing the situation with increased loading, after requalification of the tower, with the current loading situation, there is a difference in the accumulated settlement in 2100, in the southeast corner of the tower (N8), of 46 mm, and, in the northeast corner of the tower (N7),of 42 mm (Table 7). In terms of differential settlement, between N7 and N8, the change in loading leads to a negligible increase of 4 mm.

Comparing the situation of 1 m deep excavation of the masonry block with the current loading situation, there is a reduction in settlement in 2100, in the southeast corner of the tower (N8), of 21 mm, and, in the northeast corner of the tower (N7), of 19 mm (Table 7). The reduction of the differential settlement, between N7 and N8, compared to the current situation, does not exceed 2 mm and is insignificant.

Table 7. Settlement difference in 2100, between scenarios.

	$\Delta\delta_{req\text{-}current\ (2100)}$ (mm)	$\Delta\delta_{exc\text{-}current\ (2100)}$ (mm)
N8	46	-21
N7	42	-19

$\Delta\delta_{req/exc\text{-}current\ (2100)}$ – settlement difference in 2100, between the current situation and after requalification / after a 1 m deep excavation of the masonry block, respectively.

In a nutshell, the excavation of the masonry block has a limited effect on reducing the settlement of the tower in 2100 and has virtually no effect on the differential settlement. This happens because the settlement of the tower, at this stage, is caused by secondary consolidation of the mud layers. The effect of the change in loading, due to requalification, on the differential settlement between N7 and N8 is also reduced, although an increase in accumulated settlement of around 40 mm is expected in 2100, in N7 and N8, in relation to the current loading settlement.

3 CONCLUSIONS

Given the settlement history of the western tower of Terreiro do Paço, and for the purpose of evaluating the consequences of the loading changes on its foundation, three-dimensional stress and strain analyses were carried out, assuming different scenarios.

If the current situation continues, it is expected that the tower will suffer an increase in settlement, in 2100, of 0.12 m in the southeast corner, while the settlement difference between the southeast and northeast corners will only increase by 0.01 m.

With requalification of the tower, load changes will result in an increase in accumulated settlement in the southeast and northeast corners of the tower of around 0.04 m in 2100, in relation to the current scenario, but without significant change in differential settlement.

The possibility of minimizing future settlements of the tower, by removing 1 m in height of the masonry block, has a limited effect, especially with regard to the differential settlements, and requires the reinforcement of the façade and columns foundation. It is, therefore, a complex and low-efficiency solution.

In view of these results, it is considered that the requalification of the tower will not significantly deteriorate its safety and functionality conditions. In fact, after its construction, the tower has already suffered an estimated settlement greater than 0.65 m, with no consequences in terms of its stability.

ACKNOWLEDGEMENTS

The authors are grateful for the support to publish this article, given by the Lisbon City Council.

REFERENCES

Braz, N. (2019). West section of Praça do Comércio. Results of a geodetic survey conducted in October 2019, LNEC, Lisboa, Portugal (in Portuguese).

Castro, G. (1966). Settlements of the west section tower of Praça do Comércio, LNEC, Lisboa, Portugal (in Portuguese).

Valente, R. and Mesquita, C. (2017). West tower building, located in Praça do Comércio, in Lisbon. Preliminary study on the tower's structural and constructive characteristics and on its state of conservation, Oz, Lisboa, Portugal (in Portuguese).

Proceedings of the XVIII ECSMGE 2024
GEOTECHNICAL ENGINEERING CHALLENGES
TO MEET CURRENT AND EMERGING NEEDS OF SOCIETY
© 2024 the Authors
ISBN 978-1-032-54816-6
DOI 10.1201/9781003431749-343
Open Access: www.taylorfrancis.com, CC BY-NC-ND 4.0 license

ECSMGE 24
XVIII EUROPEAN CONFERENCE ON SOIL MECHANICS AND GEOTECHNICAL ENGINEERING

An energetic approach to the soil mechanical behaviour description in a zero-dimensional formulation

Une approche énergétique de la description du comportement mécanique du sol dans une formulation à dimension zéro

A. Yu. Mirnyy*
Lomonosov Moscow State University, Moscow, Russian Federation
**MirnyyAY@mail.ru*

ABSTRACT: Geotechnical risks assessment in limit state design involves the use of mathematical models to predict the stress-strain state of the soil under the external loads. Most of these models are based on continuum mechanics solutions and rely on the concepts of "moduli" as parameters of stress-strain curve. For dispersed media, these concepts are devoid of physical meaning, since the mechanism of resistance to volumetric compression, shear strain and plastic yielding are fundamentally different, and are not caused by the rigidity of the bonds between the crystal lattice elements. The proposed energy approach allows to estimate the energy spent on each process occurring in a dispersed soil under mechanical action. The change in porosity, internal friction, hardening due to dilatancy and the increase in pore pressure are expressed by separate energy parameters, each of which in turn is described by a nonlinear stress state function. User defined threshold strain levels allow to turn on and off various mechanisms. The proposed approach better corresponds to the physical meaning of the processes. The method can be easily applied to adapt the theory of plasticity solutions. The development of a mathematical model based on the proposed approach will improve the quality of forecasting the occurrence of limit states in the soil bases.

RÉSUMÉ: L'évaluation des risques géotechniques dans la conception à l'état limite implique l'utilisation de modèles mathématiques pour prédire l'état de contrainte-déformation du sol sous les charges externes. La plupart de ces modèles sont basés sur des solutions de mécanique des milieux continus et reposent sur les concepts de "modules" comme paramètres de la courbe contrainte-déformation. Pour les milieux dispersés, ces concepts sont dépourvus de signification physique, car le mécanisme de résistance à la compression volumétrique, à la déformation par cisaillement et à la déformation plastique est fondamentalement différent et n'est pas causé par la rigidité des liaisons entre les éléments du réseau cristallin. L'approche énergétique proposée permet d'estimer l'énergie dépensée pour chaque processus se produisant dans un sol dispersé sous action mécanique. Le changement de porosité, le frottement interne, le durcissement dû à la dilatance et l'augmentation de la pression interstitielle sont exprimés par des paramètres énergétiques distincts, chacun étant à son tour décrit par une fonction d'état de contrainte non linéaire. Les niveaux de contrainte seuil définis par l'utilisateur permettent d'activer et de désactiver divers mécanismes. L'approche proposée correspond mieux à la signification physique des processus. La méthode peut être facilement appliquée pour adapter la théorie des solutions de plasticité. Le développement d'un modèle mathématique basé sur l'approche proposée améliorera la qualité de la prévision de l'occurrence des états limites dans les bases du sol.

Keywords: Energy approach; triaxial compression; dispersed soil; mathematical model.

1 INTRODUCTION

Dispersed soils mechanical properties study is largely complicated by the parallel flow of various processes. During volumetric strain compaction occurs, which, in turn, leads to the formation of additional contacts, changes in shear resistance conditions. In plasticity theory this process is described by hardening – an increase in the yield strength as plastic straining occurs.

At the same time, during the shear, phenomena due to the discreteness of the structure are observed – dilatancy and contraction – which cause a change in the volume of the pore space. As a consequence, the direct determination of the stress-strain state parameters mutual dependence is difficult. Various researchers have obtained dependence data for certain values of third-party factors, for example, the degree of density, water saturation, drainage regime, etc. A comprehensive analysis of these data, in fact, has not yet been carried out: most of the laws of soil mechanics are phenomenological in nature, and do not

explain the physical nature of the processes taking place.

In addition to the multifactorial nature of the processes under study, the fundamental description of the dispersed soils mechanical behaviour laws is complicated by the limited capabilities of the test equipment. In no other field of materials science or, in a broader sense, solid mechanics, such a large number of devices of various designs are used. This is due to practical difficulties when trying to implement a homogeneous stress-strain state in the sample, but since most of the stress-strain state components are vector quantities, the resulting deviations lead to an increase in the discrepancy between the exact analytical solution and the actual experiment. Together with the change in the sample structure (and, as a consequence, the physical and mechanical properties) during the experiment, this does not allow for unambiguous interpretation of the test results.

2 THEORETICAL ANALYSIS

The solutions to the mechanics of granular media appear to be the direct method of describing dispersed soils mechanical behaviour, taking into account the discreteness of their structure (Kandaurov, 1966). Based on the characteristic particle size, a calculation scheme can be constructed that allows us to consider the equilibrium of individual particles, taking into account their mutual location. Unfortunately, as the number of particles increases, the number of equations in the solution also increases, and the introduction of different sized particles or deviations from the idealized packaging into the scheme leads to a stochastic solution, the result of which coincides in the limit with the solutions of solid mechanics.

The most well-known generalizing theory linking shear resistance parameters with physical characteristics is the critical state theory (Roscoe et. al, 1958). This theory assumes that each value of the average stress corresponds to its own value of the porosity coefficient, and the porosity coefficient, in turn, determines the amount of resistance to plastic yielding. Despite the active development of this theory in literary sources, in most implementations it is impossible to describe hardening or softening, as well as shear straining with its help.

In most cases, physical characteristics are completely excluded from the problems of soil mechanics, and the solution is carried out for an idealized solid body, the parameters of which are moduli, linking stresses and strains with linear or nonlinear laws. These parameters are obtained by laboratory tests and comparison of experimental values of stress-strain state components. At the same time, a significant number of studies have been carried out linking the values of these parameters with physical characteristics, in particular density, consistency, and granulometric composition (Goldin and Rasskazov, 2001; Kryzhanovsky et. al., 1985). The correlations obtained in these studies do not allow us to describe the causes of dependence, but only quantify it.

An alternative method of interpreting the results of laboratory tests can be the energy method, which is widely used in the mechanics of deformable solids and, in particular, in the theory of plasticity (Drucker and Prager, 1952). A change in the stress-strain state of some medium at a point is accompanied by energy transformations. On the one hand, external forces acting on this medium do the work. On the other hand, the energy expended is partially stored by elastic forces, and partially spent on overcoming internal friction and irreversible structural changes. Taking into account that in the conditions of a laboratory experiment the system can be considered as closed, the energy approach can be confidently applied as an additional method of interpreting the results.

The pioneers in the application of the energy method were specialists in the field of the plasticity theory of metals. The hypothesis of internal energy constancy during plastic yielding allowed to formulate the von Mises failure criterion. Most theories of plastic yielding (first of all, Prandtl–Reissner, Saint-Venant–Mises, Hill) take into account the work of plastic strain or its power. For example, the analysis of the work of strains allows us to describe the hardening during plastic yielding on the basis of Prandtl diagram.

In relation to soil mechanics, this approach was first adapted in the law of unassociated flow and a specialized flow condition. Also known are the works of a group of researchers in the field of critical state theory (Roscoe et. al., 1958), the main provisions of which were derived from energy prerequisites. A group of researchers considered a method for determining the transition point to plastic yielding based on the work expended (Crooks and Graham, 1976). Currently, the energy approach is used in the study of soil properties under dynamic loading, which makes it possible to assess the degree of energy absorption by comparing the work of elastic strain and the energy dissipated during one loading cycle (Ishihara, 2006). Based on the work of strain, it is proposed to evaluate the so-called "strain instability" - the strain levels at which structural changes occur in dispersed soils (Voznesensky, 2018; Usov and Voznesensky, 2016). Also, energy methods are used to determine the history of loading (re-compaction parameters), among them the methods of pre-

consolidation pressure determination (Becker, 1987; Wang and Frost, 2004).

3 RESEARCH METHODOLOGY

In this paper, we propose a method for interpreting the test results of axisymmetric triaxial compression from the standpoint of the energy and work of strain. This test method was chosen as, on the one hand, quite widespread, and on the other – allowing measurements of all stress-strain components during the experiment.

Triaxial compression tests can be carried out in various modes that determine both the initial state of the sample and the drainage conditions during the experiment. If we do not consider the unconsolidated regime as highly specialized, then at the initial moment of the experiment, filtration consolidation in the sample is considered completed (there is no excess pore pressure, the density of the skeleton is constant and can be unambiguously determined). In the case of full water saturation in the undrained mode during loading, the volume of the pore space remains constant due to the incompressibility of the liquid. This means that only shear strain will occur in the soil skeleton, and the increment of the average stress will cause an increase in pore fluid pressure instead of volumetric strain. The pore pressure change will also be caused by an additional change in the pore volume during the shearing – the pressure will fall in dilating soils and grow in contracting ones. Consequently, in the course of undrained tests, energy will be spent on elastic shear strain, plastic shear strain and pore pressure changes.

In the drained mode, the pore space is open during the experiment, therefore, the pore pressure does not change, and an increase in the average stress p will cause volumetric strain. This usually happens when using the standard stress trajectory (CTC) where an increase in the maximum main stress also causes an increment in the average stress. The processes of dilatancy and contraction proceed freely. Energy is spent on elastic and plastic shear and volumetric strain, and the plastic volume strain consists of the action of medium stress and dilatancy/contraction.

The implementation of the loading trajectory with a constant average stress (TC) leads to the fact that any volumetric strain in the experiment occurs solely due to dilatancy/contraction. Energy is spent on elastic and plastic shear strains, and volume strains are exclusively plastic and are caused by dilatation/contraction. Thus, in the presence of a series of experiments in different modes, with different loading trajectories and at different average stresses, parallel processes can be divided and the work expended on them can be compared.

The total work can be determined through the vertical force F and the movement of the rod Δh (1). The resulting value should be attributed to the volume of the sample in order to proceed to the specific work of strain.

$$\Delta W_{tot} = \Delta F \cdot \Delta h \quad (1)$$

where ΔW_{tot} (J/m^3) is the specific work of strain, ΔF (N) is the vertical force increment, Δh (m) is the rod displacement.

4 EXPERIMENTAL STUDIES

As an experimental basis, this paper considers the results of triaxial compression tests of model soils (quartz grains of 2-5 mm fraction), performed in a stabilometer with a sample diameter of 300 mm, manufactured by NPP Geotek LLC for the Moscow State University of Civil Engineering. The tests were performed at an average stress of 200, 400 and 800 kPa. All tests were performed in kinematic mode with a constant strain rate. As a result, the dependences of vertical strain on the stress deviator, as well as volumetric strain on the vertical, were obtained, taking into account all the necessary corrections due to the design of the device. The resulting data set allows you to build any dependencies for other stress-strain state components.

The simplest analysis is performed for tests along the TC trajectory. If we select the last section corresponding to the constant slope of the dependence graph $W(\gamma)$, then we can assume that only plastic strain develops in this section (Fig. 1). At the same time, both shear strains and volume strains develop due to dilatancy. Considering that the energy costs in this case are caused solely by overcoming friction, the ratio of linear approximation equations can be considered as a function of internal friction, which is confirmed by the linear dependence of this ratio on the cell pressure. This ratio corresponds in meaning to the plastic ratio λ between the increment of plastic strain and the intensity of tangential stresses in the theory of plastic flow (2):

$$d\lambda = \frac{dA_p}{2\tau^2} \quad (2)$$

Where $\Delta\lambda$ is the specific work of strain, ΔA_p (J) is the work increment, τ (Pa) is the shear stress.

It is noteworthy that these lines intersect the ordinate axis at almost the same point corresponding to the shear strain γ = 0.0108-0.0129. Such shear strain corresponds to axial strain ε = 0.007, which in absolute

terms is 4.2 mm – approximately the average particle size in the samples studied.

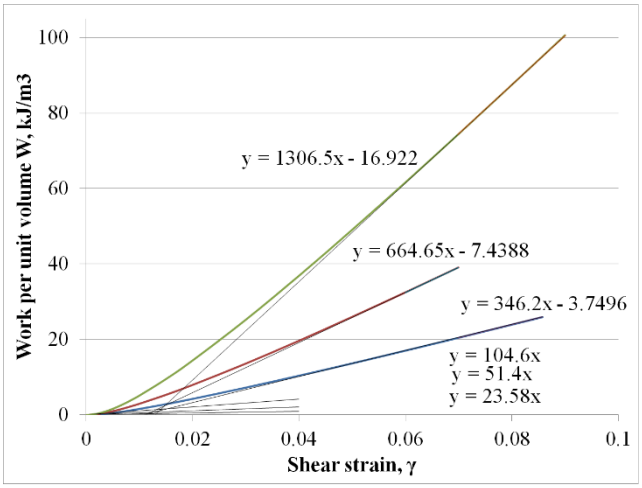

Figure 1. Dependences of the specific work of strain on the shear strain for tests at a pressure in the chamber of 200, 400 and 800 kPa with the correlation equations of the initial and final linear sections.

For tests performed at different average stresses, these ratios are obtained differently, since the resistance to plastic flow is determined mainly by internal friction. If we plot the obtained values of $d\lambda$ on a graph depending on the average stress, then these values are well approximated by a linear function (3) reflecting the dependence of the resistance to plastic flow on the average stress:

$$d\lambda(p) = 1.6p + 25 \qquad (3)$$

where $\Delta\lambda$ is the specific work of strain, p (Pa) is the mean stress.

The threshold shear strain at which the transition to plastic flow occurs is γ = 0.03-0.05 for all tests.

If we correlate the obtained rate of work change to the shear strain and the work performed by the loading device, then we can identify a discrepancy – for example, for a sample tested at a pressure in a chamber of 800 kPa, the work of shear strain is 77.1% of the total work of the loading device. The remaining 22.9% of the energy is spent on friction in the elements of the device, deformation of the membrane and – mainly – on plastic volume strain. This observation gives grounds to consider the dependence of volumetric strain on the stress deviator, and similarly to obtain the amount of energy spent on plastic volume strain. Given that the tests were carried out in kinematic mode, the resulting percentage ratio directly allows to determine the dilatancy angle (4):

$$\psi = arcsin\frac{22.9}{77.1} = 17.3°. \qquad (4)$$

Where ψ (°) is the dilatancy angle.

On the other hand, the construction of approximating lines from the origin allows us to obtain the energy consumed for elastic strain. Their slope is also proportional to the cell pressure, while these points are approximated by a power function. This correlates well with the power law of the dependence of stiffness on stress, repeatedly described for various conditions (Benz, 2007; Janbu, 1963; Schanz et. al., 1999).

In the test along the trajectory of deviatory crushing (CTC), these processes will overlap with each other, while ceasing to be linear, since during the experiment the average stress increases (which means there is an increase in stiffness and shear resistance). This means that both elastic and plastic strains with increasing stresses will require more energy. But, given that the tests are carried out on the same material, the dependencies obtained earlier will be partially valid.

5 RESULTS AND DISCUSSION

Based on the analysis of the results of the triaxial compression test with a constant average stress, the following patterns were determined:

- specific work of elastic shear strain W_e^s (5):

$$W_e^s = 0.0803p^{1.075}; \qquad (5)$$

- specific work of plastic shear strain W_p^s (6):

$$W_p^s = 1.6p + 25; \qquad (6)$$

- specific work of plastic volume strain W_p^v (7):

$$W_p^v = 0.297W_p^s; \qquad (7)$$

Taking into account that the values of threshold strainss can be determined from the end points of the linear approximation sections, using these parameters it is possible to reproduce the shape of the original experimental curve. The modelling method is quite simple – for a certain step of shear strain (for example, 0.1%), the value of the stress deviator is calculated. In this case, the specific work of strain is calculated by (4-6), depending on the average stress. When the threshold strains are reached, individual terms are turned on or off. The dependencies obtained as a result of modelling are shown in Fig. 2.

It follows from the simulation results that the proposed approach allows reproducing experimental dependencies with high accuracy. The simulation result consists of separate fairly simple mathematical patterns (4-6), each of which acts in the appropriate

range of strains: up to the level of 0.007, it is exceptionally elastic, then elastic and plastic, after 0.03 - plastic. At the same time, part of the energy consumed is spent on volumetric plastic strain.

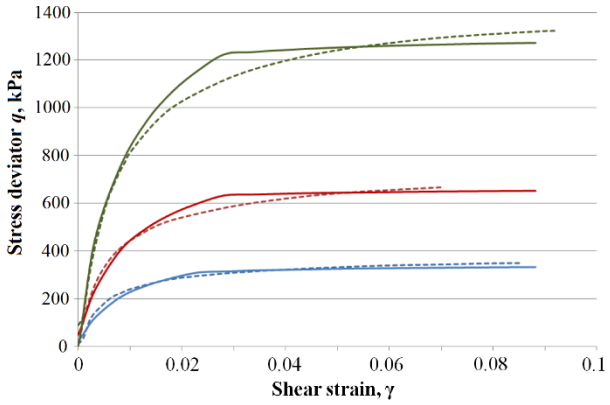

Figure 2. The result of modelling experimental curves. The dotted line shows experimental data, the solid line shows modelling.

The greatest discrepancy is observed at the transition site from elastic-plastic deformation to plastic flow. This is probably due to the smooth development of dilatancy in the real sample, which can be taken into account when processing the test results in more detail.

Based on the joint analysis of tests on two different trajectories, it is possible to separately describe all the ongoing deformation processes.

6 CONCLUSION

The method proposed in this paper for interpreting the results and modelling mechanical behaviour has a number of advantages in relation to solid mechanics.

- the theories of stresses and strains are used separately, the connection between them is established using energy parameters reflecting the physical meaning of the processes occurring during deformation;
- the resulting parameters are scalar quantities, and are represented as simple functions of the average stress;
- threshold strain values can be determined experimentally and correlated with the granulometric composition of samples.
- the proposed method of analysing the results of triaxial compression tests can be applied to other types of laboratory tests (simple shear, oedometric compression), provided that the stress-strain state is constant during the experiment.

REFERENCES

Becker, D.E. [et al.] (1987). Work as a criterion for determining yield stresses in situ in clays. *Canadian Geotechnical Journal*. 24: 549-564. https://doi.org/10.1139/t87-070.

Benz, T. (2007). *Soil stiffness under small deformations and its numerical consequences*, Stuttgart: Institut fur Geotechnik, Germany.

Crooks, J. H. A. and J. Graham. (1976). Geotechnical properties of Belfast estuarine deposits. *Géotechnique,* 20 (3): 293-315. https://doi.org/10.1680/geot.1976.26.2.293.

Drucker, D. S. and W. Prager. (1952). Soil mechanics and plastic analysis or ultimate design. *Journal of Applied Mathematics*. 10: 157-165. https://doi.org/10.1090/qam/48291.

Goldin, A. L. and L. N. Rasskazov. (2001). *Проектирование грунтовых плотин. Soil damb design*. ASV. (in Russian).

Ishihara, K. (1996). *Soil behavior in earthquake geotechnics*. Clarendon press.

Kandaurov, I. I. (1966). *Механика зернистых сред и ее применение в строительстве. Granular material mechanics and its application in construction.* Stroyizdat. (in Russian).

Kryzhanovsky, A. L., T. D. A. Mendoza and E. Ukibaev. (1985). Сопротивление сдвигу смеси сыпучих грунтов. Shear resistance of a mixture of loose soils. *Engineering geology*. 2: 35-41. (in Russian).

Roscoe, K. H., A. N. Schofield and C. P. Wroth. (1958). On the Yielding of Soils. *Géotechnique*, 8: 22-53. http://doi.org/10.1680/geot.1958.8.1.22.

Schantz, T., P. A. Vermeer and P. G. Bonnier. (1999). Model of hardening soil: formulation and verification. *Beyond 2000 in Computational Geotechnics*. Balkema.

Van, L. B., and J. D. Frost. (2004). Method of strain energy dissipation for determining pre-compaction pressure. *Canadian Geotechnical Journal*. 41 (4): 760-768. https://doi.org/10.1139/t04-013.

Usov, A. N. and E. A. Voznesensky. (2016). Деформационная неустойчивость в глинистых грунтах. Возникновение и идентификация. Deformation instability in clay soils. Occurence and identification. *Engineering geology*. 2: 14-21. (in Russian).

Voznesensky, E. A. (2018). Пороговые деформации в грунтах. Threshold strain in soils. *Geotechnics*. 5-6 (10): 6-16. (in Russian).

Yanbu, N. (1963). Compressibility of soil determined using an edometer and triaxial tests. *Proceedings of European Conference on Soil Mechanics and Foundation Engineering (ECSMFE)*, Wiesbaden, Vol. 1, p. 19-25.

Proceedings of the XVIII ECSMGE 2024
GEOTECHNICAL ENGINEERING CHALLENGES
TO MEET CURRENT AND EMERGING NEEDS OF SOCIETY
© 2024 the Authors
ISBN 978-1-032-54816-6
DOI 10.1201/9781003431749-344
Open Access: www.taylorfrancis.com, CC BY-NC-ND 4.0 license

ECSMGE 24
XVIII EUROPEAN CONFERENCE ON SOIL MECHANICS AND GEOTECHNICAL ENGINEERING

Eurocode 7 – second generation – piled foundations

Eurocode 7 – deuxième génération – pieux

Ch. Moormann*
University of Stuttgart, Institute of Geotechnical Engineering, Stuttgart, Germany

S. Burlon
Terrasol - Setec, Paris, France

**christian.moormann@igs.uni-stuttgart.de*

ABSTRACT: Eurocode 7 is known as the European standard for geotechnical engineering design and is widely considered as a great success story. The second generation of the standard recently being finally drafted by CEN/TC250 SC7 will be published 2024/2025 and will represent a significant step forward towards further harmonization and efficient guidance for geotechnical design. Besides other geotechnical structures this is the case also and especially for piled foundations. In comparison to the first generation the clause on piled foundations in EN 1997-3 ´Geotechnical Structures´ has been fundamentally revised and improved including new rules for pile design. For example, in the second generation pile groups and piled rafts will be covered equivalently to single piles. Detailed guidance is provided to consider actions due to ground displacements like downdrag. Revised sets of correlation, model and partial factors were specified. The design approaches for axial and lateral loaded piled foundations were harmonized. As the authors have been involved in the evolution of the revised clause on pile foundations since 2011 this paper aims to inform first-hand about the upcoming changes and to present the improvements and challenges.

RÉSUMÉ: L'Eurocode 7 en tant que norme européenne pour la conception géotechnique est largement considéré comme une grande réussite. La deuxième génération de la norme récemment rédigée par le CEN/TC250 SC7 sera publiée en 2024/2025 et constituera une avancée significative vers une harmonisation plus poussée avec des orientations efficaces pour la conception géotechnique: c'est notamment le cas des fondations sur pieux. Par rapport à la première génération, le chapitre relatif aux fondations sur pieux a été fondamentalement révisé et amélioré, avec de nouvelles règles pour la conception des pieux. Par exemple, dans la deuxième génération, les groupes de pieux et radiers dur pieux seront traités avec un niveau de détails similaire à ceux des pieux isolés. Des recommandations détaillées sont fournies pour prendre en compte les actions dues aux déplacements du sol comme le frottement négatif. Les ensembles de facteurs de corrélation, de modèle et partiels ont été révisés. Les approches de conception pour les fondations sur pieux chargés axialement et latéralement ont été harmonisées. Comme les auteurs ont été impliqués dans l'évolution de la clause révisée sur les fondations sur pieux au cours des 12 dernières années, cet article vise à présenter simplement les changements à venir ainsi que les améliorations et les défis qui se profilent.

Keywords: Eurocode 7; piled foundations; pile groups; piled rafts; partial factor; axial and transversal loading.

1 EURCODE 7, PART 3 (2025)

In its second generation the new Eurocode 7 comprises three parts as illustrated in Figure 1. The contents of the existing Eurocode 7, Part 1 ´General rules´ (EN 1997-1:2004) have been split between EN 1990 ´Basis of structural and geotechnical design´, a revised Part 1 (EN 1997-1:2024) ´General rules´; and a new Part 3 (EN 1997-3:2025) ´Geotechnical structures´.

The new Part 3 comprises text from Sections 5-9 and 11-12 of the original Part 1 together with new Clauses on reinforced fill structures, ground reinforcing elements, ground improvement and groundwater control (Bond et al. 2019). In this context the Section 7 ´Pile foundation´ of EN 1997-1:2024 formed the basis for the new Clause 6 ´Piled foundations´.

The contents of the existing Eurocode 7, Part 2 ´Ground investigation and testing´ (EN 1997-2:2007) are also being revised to focus in the new Part 2 ´Ground parameters´ (EN 1997-2:2024) on derivation of design parameters. Calculation models that currently reside in Annexes to EN 1997-2:2007, e.g. on CPT-based calculation of axial pile resistances, have been moved to the new Part 3, as illustrated in Figure 1.

Relevant for the design of piled foundations according to the second generation of Eurocodes are therefore mainly EN 1990, EN 1997-1 and EN 1997-3 whereby the relevant design aspects are illustrated in Figure 1.

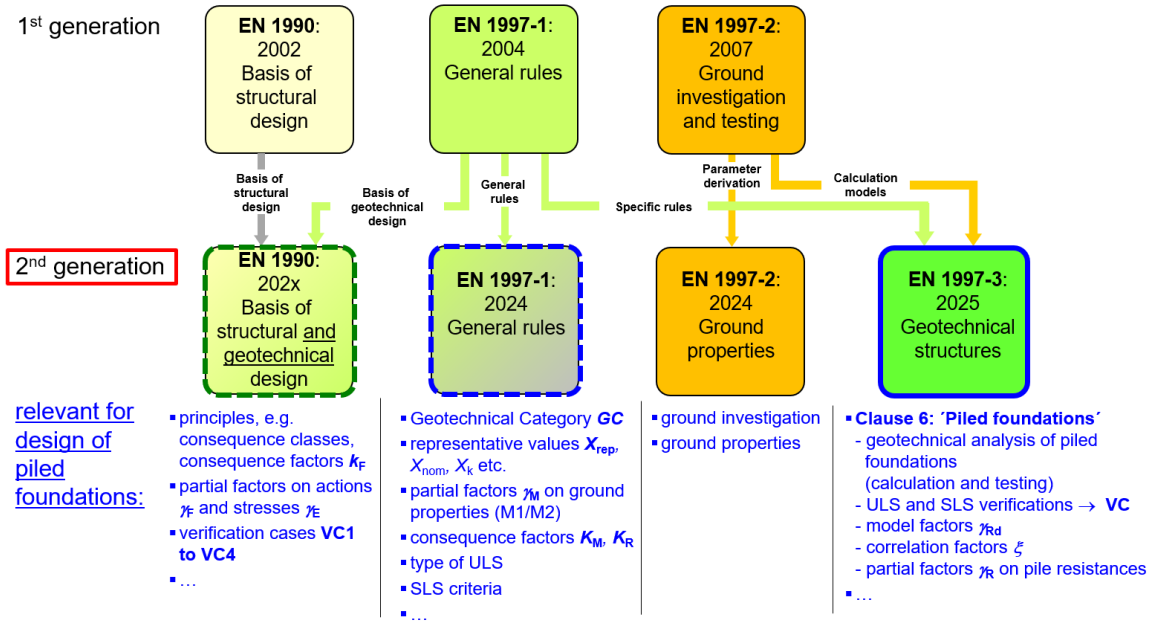

Figure 1. Division and redistribution of the 1st generation of Eurocode 0 and Eurocode 7 into the standards of the second generation; at the bottom: contents of these standards being relevant for design of piled foundations.

2 CLAUSE 6: PILED FOUNDATIONS

2.1 Introduction

Relevant for the design of piled foundations is predominantly Clause 6 'Piled foundations' of EN 1997-3:2025 which was elaborated on basis of Section 7 'Pile foundation' of EN 1997-1:2024 whereby the previous regulations were fundamentally revised, improved and supplemented including new resp. additional rules for pile design. Fundamentally, in the second generation pile groups and piled rafts will be covered equivalently to single piles whereby the regulation of the first generation focused solely on single piles. Detailed guidance is provided to consider actions on piles due to ground displacements like downdrag. Revised sets of correlation, model and partial factors were specified. The design approaches for axially and laterally loaded piled foundations were harmonized.

As each Clause of EN 1997-3 (Clauses 4 to 12) follows a common structure, also Clause 6 comprises the following sub-sections which have the same order as the Clauses in EN 1997-1:2024 and which provide structure-specific rules in addition to the general rules specified in Part 1 of Eurocode 7:

6.1 Scope
6.2 Basis of design
6.3 Materials
6.4 Groundwater
6.5 Geotechnical analysis
6.6 Ultimate limit states
6.7 Serviceability limit states
6.8 Execution
6.9 Testing
6.10 Reporting

These sections of Clause 6 provide specific regulations for the analysis and design of piled foundations. In this context the detailed information documented in Clause 6 includes for example the following aspects:

- requirements on the minimum extent of ground investigations;
- analysis of piled foundations due to structural loads and effects of ground displacements;
- design of piled foundations by testing, calculation, prescriptive measures;
- the specification of ultimate limit state (ULS) and serviceability limit state (SLS) verifications for single piles, pile groups and piled rafts including a definition of the verification cases (VC) being relevant for those verifications;
- the specification of the sets of model factors γ_{Rd}, correlation factors ξ as well as partial factors γ_R for the evaluation of the design value of pile resistances.

Besides the structure-specific regulations documented in Clause 6 of EN 1997-3, information needed for the design of piled foundations are provided also by EN 1990 and EN 1997-1 as illustrated in Figure 1.

EN 1990 specifies the principles of classification of structures according to consequences classes and the consequences factors k_F for actions as well as the principles of limit state design and of the verification by the partial factor method including specification of partial factors on actions γ_F and stresses γ_E. EN 1990

also specifies the ´Verification Cases´ VC1 to VC4 being relevant for different design situations like structural resistance, static equilibrium and geotechnical design and the related sets of partial factors. The partial factors can either be applied on material properties, i.e. the ´Material Factor Approach´ (MFA), or to resistances, i.e. the ´Resistance Factor Approach´ (RFA).

EN 1997-1 as well provides relevant specifications and regulations needed for the design of piled foundations. Besides specifications of the Geo-technical Category (GC) which should be determined by a combination of the Consequence Class (CC) of the structure and the Geotechnical Complexity Class (GCC), the evaluation of representative values X_{rep} as well as partial factors γ_{M} on ground properties and consequence factors both on ground properties k_{M} and resistances k_{R} are specified in Part 1 of Eurocode 7.
In the following some of the most relevant modifications for the design of piled foundations according to second generation of Eurocode 7 are explained in more detail.

2.2 Ground investigations

In addition to EN 1997-2:2024 which includes fundamental requirements on ground investigation and evaluation of ground properties section 6.2 of EN 1997-3 provides additional specific regulations, e.g. specifications on the minimum depth d_{min} of field investigation on piled foundations (Table 1).

Table 1. Minimum depth of ground investigation for piled foundations.

Application	Minimum depth
Single piled foundation	d_{min} = max (5 m; 3·$B_{\mathrm{n,eq}}$)
Pile groups or piled rafts in soils and in very weak and weak rock masses	d_{min} = max (5 m; 3·$B_{\mathrm{n,eq}}$; p_{group})
Pile groups or piled rafts in strong rock masses	d_{min} = max (3 m; 3·$B_{\mathrm{n,eq}}$)

d_{min} is the minimum investigation depth beneath pile base level.

$B_{\mathrm{n,eq}}$ is the equivalent size of the pile base, equal to B_{b} (for square piles), D_{b} (for circular piles), or p_{b}/π (for other piles);

B_{b} is the base width of the pile with the largest base (for square piles);

D_{b} is the base diameter of the pile with the largest base (for circular piles);

P_{group} is the smaller dimension of a rectangle circumscribing the group of piles forming the foundation, limited to the depth of the zone of influence.

2.3 Verification of axial resistance of single piles (ULS)

For axially loaded single piles the axial (compression) resistance shall be verified using:

$$F_{cd} \leq R_{cd} \tag{1}$$

Thereby, the verification for axial loaded piles (single piles, pile groups and piled rafts) could be harmonized as solely the Resistance Factor Approach (RFA), where the partial factors are applied on the pile resistance, shall be used in combination with Verification Case VC1, where the partial factors are applied on the actions. Thus, the design value of actions is defined as follows:

$$F_{cd} = 1.35G_{rep} + 1.5Q_{rep} \tag{2}$$

with Q_{rep} as caractersitic value, combination value, frequent value or quasi-permanent value.

The design value of the axial pile resistance is defined as follows:

$$R_{\mathrm{cd}} = \frac{R_{\mathrm{c,rep}}}{\gamma_{\mathrm{Rc}} \cdot \gamma_{\mathrm{Rd}}} \; or \; \left(\frac{R_{\mathrm{b,rep}}}{\gamma_{\mathrm{Rb}} \cdot \gamma_{\mathrm{Rd}}} + \frac{R_{\mathrm{s,rep}}}{\gamma_{\mathrm{Rs}} \cdot \gamma_{\mathrm{Rd}}}\right) \tag{3}$$

where γ_{Rc}, γ_{Rb}, γ_{Rs} are partial factors for pile resistrances and γ_{Rd} is a model factor.

The representative values of the pile resistance in axial compression $R_{\mathrm{c,rep}}$ resp. of the base and shaft resistance $R_{\mathrm{b,rep}}$ and $R_{\mathrm{s,rep}}$ can be obtained by testing, by calculation or by prescriptive rules. The use of prescriptive rules is very rare for piles. For the determination of the axial resistances of single piles by calculation either the ´Ground Model Method´ or the ´Model Pile Method´ can be applied. In case of the Ground Model Method the axial resistance of a single pile is calculated based on ground properties determined from both field and laboratory tests, accounting for horizontal variability of the ground in the piled area. The Model Pile Method is a calculation method to determine the axial resistance of a single pile based on individual pile resistance profiles determined from correlations with field test results or ground properties from field or laboratory tests. Methods of calculating base and shaft resistance are included in Annex C of EN 1997-3 for ground parameters as well as for cone penetration methods and for pressuremeter methods. Figure 2 provides an overview about these calculation methods.

The axial resistance of a single pile at ultimate and serviceability limit state may be also determined from the results of static load tests. Dynamic impact and rapid load tests may be used to determine the ultimate limit state of a single pile in compression.

Pile resistance based on ground parameters

$q_{s,rep}$ with $\alpha \cdot c_u$ or $\beta \cdot \sigma'_v$

$q_{b,rep}$ with N_c or N_q

Pile resistance based on CPT or PMT data

$q_{s,rep}$ = f (soil type, pile type, q_c or p^*_{LM})

$q_{b,rep}$ = f (soil type, pile type, q_c or p^*_{LM})

pile resistance based on CPT profiles:

$q_{s,rep}$ with $c_s \cdot q_c$

$q_{b,rep}$ with $c_b \cdot k_{shape} \cdot q_c$

pile resistance from PMT profiles:

$q_{s,rep}$ with $\alpha_{pile\text{-}ground} \cdot f(p^*_{LM})$

$q_{b,rep}$ with $k_{b,PMT} \cdot p^*_{LM}$

Pile resistance based on empirical tables

Example: Representative values of unit shaft resistance $q_{s,rep}$ for bored piles in soils

Fine soils		Coarse soils	
Undrained shear strength c_u (kPa)	**$q_{s,rep}$ (kPa)[a, b]**	**Mean cone resistance q (MPa)**	**$q_{s,rep}$ (kPa)[a,b]**
60	30-40	7,5	55-80
150	50-65	15	105-140
≥ 250	65-85	≥ 25	130-170

[a] The lower value represents the 10 % quantile and the upper value the 50 % quantile

[b] Intermediate values can be obtained by linear interpolation

Figure 2. Available calculation methods for evaluation of axial pile resistances.

Table 2 specifies the evaluation of representative values of axial pile resistances from calculated or measured values.

Table 2. Evaluation of representative axial resistances of single piles based on calculation or testing.

Ground Model Method: R_{calc} from ground parameters (c_u, φ′ and c′, p_{LM}*, q_c, N_{SPT}, etc.)	$R_{rep} = R_{calc}$
Model Pile Method: R_{calc} from N field test profiles (N CPTs, N PMTs, N SPTs, etc.)	$R_{rep} = \min\left\{\frac{R_{calc,mean}}{\xi_{mean}}; \frac{R_{calc,min}}{\xi_{min}}\right\}$
Pile tests: R_{test} from static, dynamic impact or rapid load tests	$R_{rep} = \min\left\{\frac{R_{test,mean}}{\xi_{mean}}; \frac{R_{test,mean}}{\xi_{min}}\right\}$

Figure 3 visualizes the possible procedures to evaluate design values of axial pile resistances from testing and calculation. Tables 3 and 4 document the model factors γ_{Rd} for verification of axial pile resistance assisted by testing and calculations.

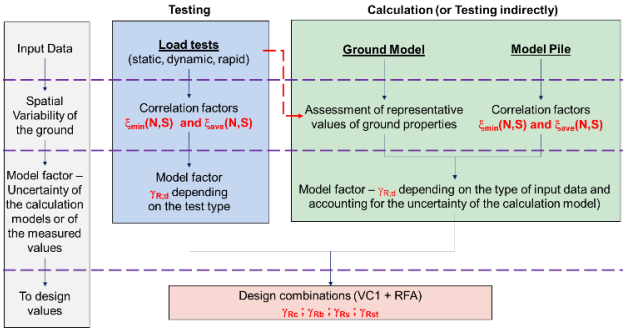

Figure 3. Calculation procedures for piles.

Correlation factors ξ allows to consider the spatial variability of the ground alternatively to the selection of the representative values of the ground parameters which is always related to subjective interpretation. Correlation factors ξ as documented in section 6.2.4 of EN 1997-3 continues to be dependent form number of executed pile tests or ground profiles. The correlation factors given reflect an average uncertainty corresponding to a coefficient of variation of about 12%; other approaches are therefore acceptable if spatial variation is lower or higher.

The correlation factors for the Model Pile Method can be adjusted according to the density of the field test profiles (CPTs, PMTs, etc.) considering the ratio of the average horizontal spacing d_{avg} between the N

Table 3. Model factors γ_{Rd} for verification of axial pile resistance assisted by testing.

Verification by		**Model factor γ_{Rd}**		
		Fine soils	Coarse soils	Rock mass
Static load tests		1.0	1.0	1.0
Rapid load tests (multiple load cycles)		1.4	1.1	1.2
Rapid load tests (single load cycle)		1.4	1.1	1.2
Dynamic impact tests (signal matching)	Shaft bearing	1.5	1.1	1.2
	End bearing	1.4	1.25	1.25
Dynamic impact tests (multiple blow)	Shaft bearing	1.5	1.1	1.2
	End bearing	1.4	1.2	1.2
Dynamic impact tests (closed form solutions)	Shaft bearing	Not permitted	Not permitted	Not permitted
	End bearing	Not permitted	1.3	1.3
Wave equation analysis		Not permitted	1.6	1.5
Pile driving formulae		Not permitted	1.8	1.7

Table 4. Model factors γ_{Rd} for verification of axial pile resistance by calculation.

Verification by	**Based on**	**Model factor γ_{Rd}**	
Ground Model Method	Ultimate pile tests	1.15	
	Extensive comparable experience without site-specific control tests	1.3	
	Serviceability pile tests	1.35	
	No pile load tests and limited comparable experience	1.55	
		Compressive resistance	Tensile resistance
Model Pile Method	Pressuremeter test	1.15	1.4
	Cone penetration test	1.1	1.1
	Profiles of ground properties based on field or laboratory tests	1.2	1.2

tests profiles located in the area S to a reference distance d_{ref} = 30 m:

$$\xi_{mean}(S) = 1 + \frac{d_{avg}}{d_{ref}}(\xi_{mean} - 1) \quad (4)$$

$$\xi_{min}(S) = 1 + \frac{d_{avg}}{d_{ref}}(\xi_{min} - 1) \quad (5)$$

2.4 Verification of axial resistance of pile groups and piled rafts (ULS)

As already mentioned Clause 6 of EN 1997-3:2025 covers not only single piles but equally also pile groups and piled rafts.

Pile group design shall consider that the resistance and load-displacement behaviour of single piles in a group might show significant variation compared to the behaviour of single piles due to pile-pile interaction. Calculation of pile group effects should consider the potential changes in stress and density of the ground resulting from pile installation together with the effects of group behaviour due to the structural loads taking the stiffness of the pile cap and the structure into account. The ultimate vertical resistance of a pile group R_{group} with n piles should be determined from:

$$R_{group} = \min\{\sum_i^n R_i ; R_{block}\} \quad (6)$$

where R_i is the ultimate axial resistance of the i-th pile in the pile group, taking full account of the effects of pile interaction, and where R_{block} is the ultimate vertical resistance of the block of ground bounded by the perimeter of the pile group. The design resistance of a pile group $R_{d,group}$ shall be verified using

$$F_d \leq R_{d,group} \quad (7)$$

with

$$R_{d,group} = \frac{R_{rep,group}}{\gamma_{R,group} \cdot \gamma_{Rd,group}} \quad (8)$$

where $\gamma_{R,group}$ is a resistance factor and $\gamma_{Rd,group}$ is a model factor for the pile group.

The design of piled rafts shall consider beside the pile-pile interaction the pile-raft interaction (Figure 4). Considering the compatibility of the displacements of the piles and the raft, the ultimate compressive resistance $R_{piled\text{-}raft}$ of a piled raft should be determined as

$$R_{piled-raft} = \left(\sum_i^n R_{c,i} + R_{raft}\right) \quad (9)$$

where R_{raft} is the additional bearing resistance from the raft. The design resistance of a piled raft $R_{d,piled\text{-}raft}$ shall be verified using

$$F_d \leq R_{d,piled-raft} \quad (10)$$

with

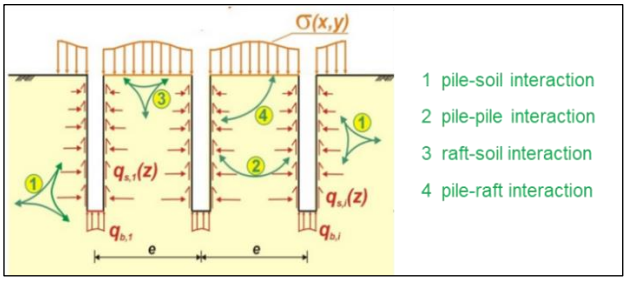

Figure 4. Interaction effects to be considered for the verification of piled rafts according to EN 1997-3, 6.5.6.

$$R_{d,piled-raft} = \frac{R_{rep,piled-raft}}{\gamma_{R,piled-raft} \cdot \gamma_{Rd,piled-raft}} \quad (11)$$

where $\gamma_{R,piled\text{-}raft}$ is a resistance factor and $\gamma_{Rd,piled\text{-}raft}$ is a model factor for the piled raft.

For the ULS-verification of axially loaded pile groups and piled rafts EN 1997-3 pretends the application of verification case VC1 in combination with RFA and partial factors of $\gamma_{R,group}$ = 1.4 resp. $\gamma_{R,piled\text{-}raft}$ = 1.4 leading to a comparable equivalent gloabal safety level as for spread foundations or single piles. For combined axial and transversal loaded pile groups and piled rafts both approaches, MFA or RFA, might be used for ULS-verficiations.

Verification of limit states for pile groups and piled rafts may be carried out by analytical or empirical, but preferential by numerical calculation methods.

2.5 Pile settlements and SLS verifications

Verification of the serviceability limit state for piled foundations should be based on modelling that accounts for non-linear stiffness of the ground, flexural stiffness of the structure, and interaction between the ground, structures, and piles. The non-linearity of the load-displacement curves of axially loaded piles should be considered for the verification of both geotechnical and structural limit states.

The settlement of a single pile may be determined from load tests or calculated using empirical or analytical methods or numerical modelling.

2.6 Downdrag (negative skin friction)

The adverse effects of a drag force caused by moving ground shall be included in the verification of serviceability *and* ultimate limit states of piled foundations when relevant. Thereby the drag force caused by downdrag should be classified as a permanent action. The effects of the downdrag should be modelled by carrying out a ground-pile interaction

analysis, to determine the depth of the neutral point L_{dd} corresponding to the point where the pile settlement s_{Pile} equals the ground settlement s_{ground}. This neutral point is different for SLS or ULS conditions as shown in Figure 5 which also illustrates the approach recommended to be used to calculate the neutral point and the dragforce owing to potential downdrag.

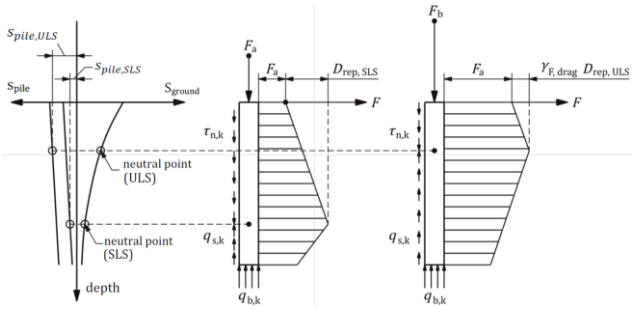

Figure 5. Force distribution for assessment of drag force on a pile subject to downdrag according to EN 1997-3, C.9.

The representative drag force D_{rep} should then be determined from

$$D_{rep} = p \int_0^{L_{dd}} \tau_s \cdot dz \qquad (12)$$

where p is the perimeter of the pile and τ_s is the (negative) unit shaft friction causing downdrag at depth z. EN 1997-3 provides in its Annex C a simplified approach for calculating the drag force by adopting a depth to the neutral plane L_{dd} that results in an upper value of the drag force.

2.7 Transversal loading

Clause 6 of EN 1997-3 provides also guidance on the verification of single piles, pile groups and piled rafts due to lateral loading. In Annex C.12 calculation models, mainly based on *p-y* curves from undrained and drained soil properties, are provided to calculate the behaviour of transversely loaded single piles. For the verification of the transverse resistance either the MFA or the RFA can be applied.

2.8 Buckling

The buckling resistance of a slender pile under compression and embedded in soil should be determined by a validated model, either analytic or numerical, according to second order theory considering the support of the soil and initial transverse deflection due to production imperfections, installation etc. EN 1997-3 provides detailed guidance to evaluate the buckling resistance by analytical methods even though other approaches, e.g. by numerical methods can be applied.

2.9 Cyclic effects

Cyclic and dynamic actions can result in reduced ground strength and stiffness leading to additional pile displacements and loss of resistance. Therefore, EN 1997-3 requests to consider the adverse effects of cyclic and dynamic actions on the long-term axial and transverse resistance of piled foundations. In Annex C.14 of EN 1997-3 the concept of ´stability diagram´ based on Poulos (1988) is provided to determine in a simple way whether the axial cyclic loads applied at the pile head can induce any degradation effects to reduce the axial pile resistance.

2.10 Further aspects

Clause 6 of EN 1997-3 provides guidance to many further aspects being relevant for piled foundations including further calculation and design issues but also execution, testing and reporting. Even aspects of sustainability are addressed as the thermal, geo-technical and structural design aspects of thermo-activated deep foundations are mentioned.

ACKNOWLEDGEMENTS

The authors have been involved at various stages in the development of the second generation of Eurocode 7, serving on a range of evolution and working groups or project teams. They are grateful to their colleagues for their contributions to the development of EN 1997-3.

REFERENCES

Bond, A.J., Jenner, C., Moormann, Ch. (2019): *Tomorrow's geotechnical toolbox: EN 1997-3: 202x Geotechnical structures*. Proc. XVIIth Europ. Conf. on Soil Mech. and Geotech. Eng., ECSMGE-2019, Reykjavik, ISBN 978-9935-9436-1-3.

CEN 2022. *Eurocode 0 - Basis of structural and geotechnical design*. prEN 1990:2022, Document N 576 of CEN/TC 250, The European Committee for Standardization, Brussels.

CEN 2023a. *Eurocode 7: Geotechnical design – Part 1: General rules*. prEN 1997-1:2023, prEN 1997-1:2023 CIB draft FV, Document N 1707 of CEN/TC 250/SC 7, The European Committee for Standardization, Brussels.

CEN 2023b. *Eurocode 7: Geotechnical design – Part 2: Ground properties*. prEN 1997-2:2023 CIB draft FV, Document N 1710 of CEN/TC 250/SC 7, The European Committee for Standardization, Brussels.

CEN 2023c. *Eurocode 7: Geotechnical design – Part 3: Geotechnical structures*. prEN 1997-3:2023 CIB draft FV, Document N 1739 of CEN/TC 250/SC 7, The European Committee for Standardization, Brussels.

Poulos, H.G. (1988): Cyclic stability diagram for axially loaded piles. Journal of Geotechn. Engineering, Vol. 114 (8), 877-895.

Proceedings of the XVIII ECSMGE 2024
GEOTECHNICAL ENGINEERING CHALLENGES
TO MEET CURRENT AND EMERGING NEEDS OF SOCIETY
© 2024 the Authors
ISBN 978-1-032-54816-6
DOI 10.1201/9781003431749-345
Open Access: www.taylorfrancis.com, CC BY-NC-ND 4.0 license

ECSMGE 24
XVIII EUROPEAN CONFERENCE ON SOIL MECHANICS AND GEOTECHNICAL ENGINEERING

Evaluation of seismic-induced crest settlement of earth dams

Évaluation du tassement de la crête des barrages en terre induit par les séismes

A. Nardo*, G. Biondi, E. Cascone
University of Messina, Contrada di Dio, Messina, Italy
**andrea.nardo@studenti.unime.it*

ABSTRACT: In this paper an original empirical formula for the prediction of the permanent crest settlement of earth dams is proposed starting from the results of a large set of 2D dynamic finite element analyses carried out with reference to an Italian zoned earth dam. Various seismic parameters, representative of the input motion, have been considered as possible predictive variables, individually or in combinations, and an original seismic parameter is introduced to reliably describe the variation of the crest settlement with the characteristics of the input motion in terms of amplitude, energy and frequency content. The proposed empirical formula has been checked using data available in the literature with reference to two other Italian earth dams, for which specific predictive formulas have been also derived. Finally, the use of the proposed seismic parameter to check the possible occurrence of earthquake-induced limit states in earth-dam is also explored.

RÉSUMÉ: Dans cet article, une formule empirique originale pour la prédiction du tassement permanent des barrages en terre est proposée à partir des résultats d'un grand ensemble d'analyses dynamiques 2D par éléments finis effectuées en référence à un barrage en terre zoné italien. Différents paramètres sismiques, représentatifs du mouvement d'entrée, ont été considérés comme des variables prédictives possibles, individuellement ou en combinaison, et un paramètre sismique original est introduit pour décrire de manière fiable la variation du tassement de la crête avec les caractéristiques du mouvement d'entrée en termes d'amplitude, d'énergie et de contenu fréquentiel. La formule empirique proposée a été vérifiée à l'aide des données disponibles dans la littérature en référence à deux autres barrages en terre italiens, pour lesquels des formules prédictives spécifiques ont également été dérivées. Enfin, l'utilisation du paramètre sismique proposé pour vérifier l'occurrence possible d'états limites induits par les tremblements de terre dans les barrages terrestres est également explorée.

Keywords: Earth dams; seismic performance; damage index; predictive correlations; dam crest settlements.

1 INTRODUCTION

The seismic performance of an earth dam and the possibly expected damage (freeboard loss, slope instability, cracking and erosion of water tightness elements, soil liquefaction) depend on several factors, such as the type of dam, the construction materials, the geometry, the foundation soils, the past loading history and the characteristics of the seismic-induced ground motion (e.g. USCOLD 1992, Adamo et al. 2020).

It is widely recognised (e.g. Swaisgood 2003, Aliberti et al. 2019, Nardo et al. 2024a) that the permanent crest settlement of earth dams represents a suitable index of their seismic performance and of the earthquake-induced level of damage.

Seismic-induced crest settlements can be evaluated by performing numerical dynamic analyses that allow simulating complex geometries, as well as reproducing the non-linear soil behaviour through advanced constitutive models; however, the simulation of other stages necessary to reproduce the pre-earthquake effective stress state can significantly increase the computational effort.

Swaisgood (2003) investigated the factors that influence crest settlement using 69 case histories of performance of dams during strong and weak earthquakes and proposed a relationship between crest settlements and the peak horizontal ground acceleration at the site of the dam. Although this approach is promising, it does not consider the mechanical characteristics of different dams. Therefore, relationship calibrated on individual dams may be more reliable.

As an alternative, some authors recently proposed original empirical formulas valid for a single dam giving the crest settlement as a function of an intensity measure representative of the characteristics of the input motion (e.g. Zefa et al 2022, Khalid et al. 2023, Nardo et al. 2023).

In this paper, 2D dynamic finite element analyses have been performed with reference to an Italian zoned earth dam for which an accurate geotechnical

characterization is available. Specifically, the seismic response of the San Pietro dam was investigated using to 58 rock outcropping earthquake records. In the analyses the soil behaviour has been simulated using an isotropic hardening elasto-plastic hysteretic model.

Several seismic parameters, representative of the amplitude, energy, frequency and duration of the input motion (Zefa et al., 2022) have been considered (individually or in combinations) to detect the proper variable for an accurate prediction of the permanent crest settlements of the dam.

As a result, an original intensity measure and a predictive formula (the latter valid for the San Pietro dam) has been proposed. Results available in the literature for two other Italian dams have been used to check the effectiveness of the predictive formula relating the proposed seismic parameter to the crest settlements.

Finally, the proposed intensity measure and the predictive formula developed for the San Pietro dam have been used to assess the occurrence of possible limit states induced by the ground motion and hence predict the seismic-induced level of damage expected at the dam.

2 DAMS EXAMINED IN THE ANALYSES

The dynamic analyses presented in the paper refer to the San Pietro dam. The results of dynamic analyses relative to two other earth dams have been also collected and analysed: namely, the Marana Capacciotti dam, examined by Elia and Rouainia (2013), and the Camastra dam, studied by Sica and Pagano (2009). Figure 1 schematically shows the main sections of these three dams.

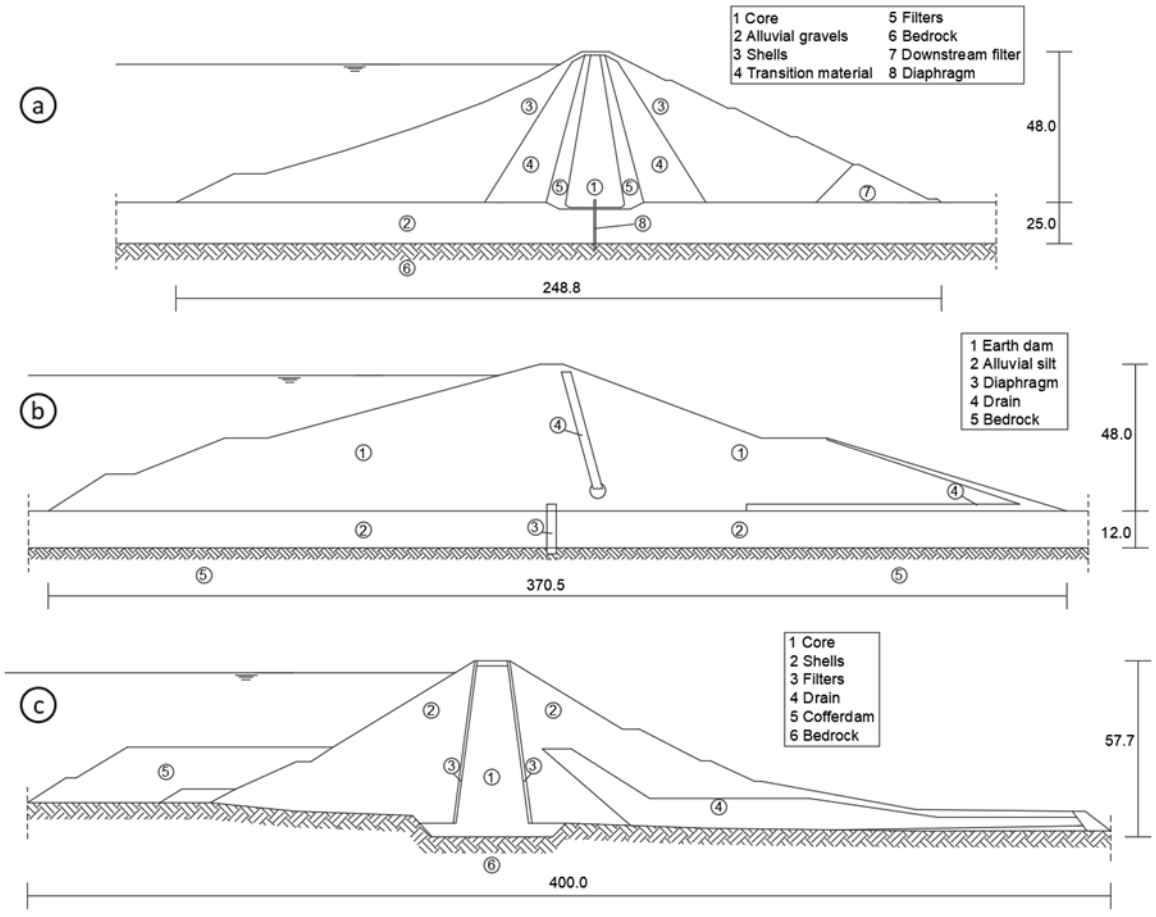

Figure 1. Object dams: a) San Pietro dam, b) Marana Capacciotti dam and c) Camastra dam.

2.1 San Pietro dam

The San Pietro dam is a zoned earth dam placed along the Osento river in Campania, in an area of high seismicity. It has a height of about 48 m (Figure 1a).

The geotechnical characterization of the dam embankment and of the foundation soils is based on the results of the investigations described by Calabresi et al. (2004). Data on the geotechnical soil properties and on the seismic hazard of the dam site can be found in Biondi et al. (2021) and Cascone et al. (2021).

The dam has been modelled using a finite element code, simulating the non-linear soil behaviour through the HSsmall model, an isotropic hardening elasto-plastic hysteretic model, available in the code library. The calibration of the constitutive model for the soils of the dam and of the foundation is described by Casablanca et al. (2022) and Nardo et al. (2024b).

The values of the small strain shear modulus G_0 adopted in the analyses have been evaluated starting from the small strain shear modulus profiles obtained interpreting the results of available cross-hole tests.

The model parameters have been calibrated on the results of oedometer tests, resonant column tests, drained and undrained triaxial compression tests carried out on undisturbed soil samples. The values of model parameters are summarized in Table 1.

The numerical analyses have been performed in plane strain conditions, discretizing the dam and the foundation soils in a finite element mesh of about 5000 triangular 15-noded elements. The FE numerical models used in the static and dynamic analyses are depicted in Figure 2.

To reproduce the pre-earthquake stress-strain state of the dam and foundation soils, under the static conditions, the staged construction of the dam and the subsequent impoundment of the reservoir have been preliminarily simulated.

In dynamic analyses the coarse-grained soils of the dam flanks below the phreatic line have been considered in undrained conditions, according to the Undrained A procedure implemented in the computer code Plaxis. The portion of the flank above the phreatic line is considered drained, neglecting the effect of suction on the shear strength of the flank. The previous assumption of a fully undrained flank was preliminarily checked according to the relationship provided by Zienkiewicz et al. (1980). Furthermore, several fully coupled dynamic analyses have been performed to verify the correctness of the fully undrained assumption for the saturated flanks. The results in terms of the excess pore water pressures and crest settlements are practically comparable, so, the assumption of fully drained behaviour of the saturated flank seems to be reasonable.

Two sets of acceleration records have been used for the dynamic analyses of the San Pietro dam:

- a set of 58 earthquake records, recorded on rock outcropping sites, encompassing wide ranges of amplitudes, energy and frequency contents with the aim of exploring the seismic behaviour of the dam at several intensity levels;
- a *validation set* of 7 earthquake records, recorded on rock outcropping sites, compatible with the seismicity of the dam site (Biondi et al. 2021, Nardo et al. 2024b).

The first set of accelerograms has been used as a *calibration set* for the development of a suitable formula to predict the crest settlement of the San Pietro dam. For this *calibration set*, the peak ground acceleration ($PGA = 0.096$ - $0.673g$) and the Arias Intensity ($I_A = 0.01$ - 2.01 m/s) vary within large intervals (Nardo et al. 2024b), thus representing a broad set of seismic motions, suitable to adequately explore the dam response in a wide range of strain levels. These intervals of PGA and I_A also comprise the values of the seismic parameters of the *validation set* of 7 earthquake records which was used to validate the proposed predictive formula.

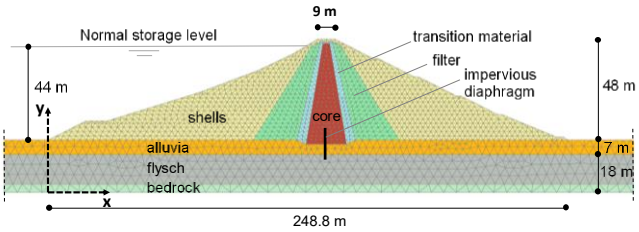

Figure 2. FEM adopted in the numerical analyses.

Table 1. Model parameters of the San Pietro dam.

Parameters	Core	Shell	Alluvia	Flysch
$E_{50\ ref}$ (MPa)	30	30	440	440
$E_{oed\ ref}$ (MPa)	30	17.5	440	440
$E_{ur\ ref}$ (MPa)	90	216	1320	1320
m	0.66	0.78	0	0
ν_{ur}	0.2	0.2	0.2	0.2
p'_{ref} (kPa)	100	100	100	100
$G_{0\ ref}$ (MPa)	170	450	1100	1100
$\gamma_{0.7}$ (%)	0.053	0.007	0.044	0.044
c_{ref}	25.4	1	1	1
φ	26.4	38	42	42
ψ	0	0	0	0
R_f	0.9	0.85	0.9	0.9

2.2 Marana Capacciotti dam

The Marana Capacciotti dam is a homogeneous earth dam located in southern Italy and built between 1970 and 1975. Its height is about 57 m (Figure 1b).

Elia and Rouainia (2013) calibrated an advanced kinematic hardening model (RMW model) to describe the non-linear behaviour of the dam and foundation soils in both static and cyclic loading conditions.

The FE analyses of the dam have been undertaken assuming plane strain free draining conditions. To minimize the lateral boundary effects, the mesh has been horizontally extended approximately to three times the width of the base of the embankment, and vertically down to 42 m from the ground surface, where a bedrock formation can be identified. Standard boundary conditions along the vertical and bottom sides of the mesh have been used during the static analyses.

The initial static stress state and the corresponding model internal variables have been obtained following the approach described by Elia et al. (2011). After the simulation of the embankment construction, in four layers, the subsequent reservoir impounding to the maximum serviceability conditions has been numerically reproduced through a coupled seepage analysis.

The initial shear modulus profile along the dam axis has been obtained as a result of the static analyses. Once the static stress state has been initialized, the dynamic simulations have been performed applying the input motions to the solid nodes at the base of the mesh as prescribed horizontal displacement time histories, with fixed vertical displacement. To avoid spurious wave reflections at the boundaries of the foundation layer, tied-nodes boundary conditions have been adopted along the lateral sides of the mesh.

The first natural frequency of the dam embankment is 1.28 Hz corresponding to a fundamental period of 0.78 s (Elia and Rouainia 2013).

The selection of the input motions was based on the seismic hazard study relative to the dam site. Specifically, 5 earthquake records were selected and scaled to two different *PGA* values, namely 0.127*g* and 0.425*g*, thus obtaining 10 input motions having Arias Intensity in the range I_A = 0.06 - 2.47 m/s.

2.3 Camastra dam

The Camastra Dam, built between 1963 and 1964, is a zoned earth dam located in Southern Italy, in a seismic prone area. It is characterized by a height of about 57 m (Figure 1c).

The constitutive model adopted to simulate the soil behaviour is the Hujeux model, characterized by both isotropic and kinematic hardening.

The determination of the hardening parameters was carried out by estimating a suitable G/G_0-γ curve for the soils at hand and then by back-analysing this trend through the Hujeux model. The shear modulus at small strains G_0 was obtained from the shear wave velocity measurements of the DH test and conventionally referred to a value of shear strain equal to 10^{-5} %. The model parameters have been set also considering the results of triaxial and oedometer tests, carried out on the core and shell materials during the design and the construction stage.

The first natural frequency of the dam embankment in the transversal direction is 3 Hz and was obtained by interpreting several weak motion events recorded by the Camastra Dam seismic network (Sica et al., 2008).

The seismic response was investigated by Sica and Pagano (2009) using 7 acceleration records as input motion, selected through a seismological study of the dam site. The values of *PGA* and I_A of the selected accelerograms vary in the intervals *PGA*=0.168-0.528*g* and I_A=0.02 – 4.44 m/s.

3 ANALYSIS OF RESULTS

The results presented in this paper have been obtained through dynamic analyses of the San Pietro dam, carried out under plane strain condition using the computer code *Plaxis*. Through the best-fit of the numerical results, a predictive formula has been calibrated to estimate the crest settlements of the dam as a function of a suitable set of seismic parameters. Specifically, screening analyses pointed out that the intensity measure $I_D = I_A \cdot T_m / PGV^{0.5}$, defined by Nardo et al. (2024b) as a suitable combination of the Arias intensity I_A, mean period T_m and peak ground velocity *PGV*, represents a proper predictive parameter to assess the dam crest settlement.

Using an integral definition of the mean period and the Parseval's theorem, the product of $I_A \cdot T_m$, can be expressed in the following form:

$$I_A \cdot T_m = \frac{\pi}{g} \int_0^{\omega_N} \omega^{-1} C^2(\omega) d\omega \quad (1)$$

where ω_N is the Nyquist frequency, $C(\omega)$ is the Fourier amplitude spectrum of the acceleration time-history, ω is the circular frequency and *g* is gravity acceleration. This form represents the area of the acceleration amplitude Fourier spectrum weighted with respect to the inverse of circular frequencies, thus implying that lower frequencies have a larger weight.

PGV describes the motion amplitude at the intermediate frequencies, providing a more accurate indication of damage potential than peak ground acceleration (Kramer 1996). Also, according to Trifunac and Brady (1975) and Housner and Jennings (1982), *PGV* can be correlated to the earthquake intensity since it is directly associated with the energy demand.

Thus, the use of the proposed intensity measure I_D allows accounting for the energy demand at both low and intermediate frequencies which are generally more relevant for geotechnical systems such as dams and embankments.

Figure 3 shows the results of the analyses carried out using the *calibration set* of accelerograms and the linear best-fit described by eq. 2. In the figure the results obtained using the *validation set* of accelerograms are also plotted, showing a good agreement with the proposed predictive formula.

Using results of dynamic analyses relative to the Marana Capacciotti (Elia and Rouainia 2013) and the Camastra (Sica and Pagano, 2009) dams, it has been confirmed that I_D is well related to the earthquake-induced crest settlement and two specific different predictive formulas, namely Eqs. 3 and 4, have also been derived.

The empirical predictive formulas proposed for the San Pietro (Eq. 2), Marana Capacciotti (Eq. 3) and Camastra (Eq. 4) are plotted in Figure 4 together with the values of the permanent crest settlements adopted in their derivation:

$$w_c = 2,67 \cdot I_D \quad (2)$$

$$w_c = 2,05 \cdot I_D \quad (3)$$

$$w_c = 0,92 \cdot I_D \quad (4)$$

Equations (2)-(4) provides w_c in cm as a function of the proposed intensity measure I_D given in $(cm \cdot s)^{0.5}$. As described by Nardo et al. (2024b), differences in the regression coefficients of the proposed formulas, representin the gradients of the linear best-fits plotted in Figure 4, can be ascribed to the factors affecting the dynamic response of the dam.

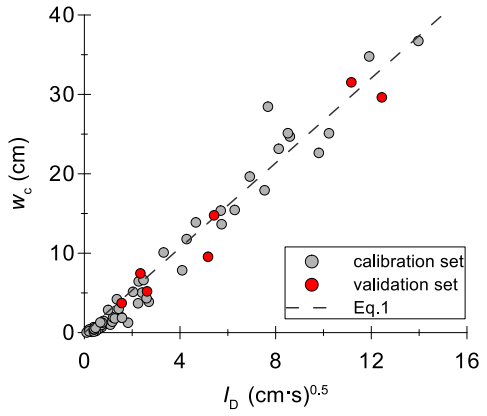

Figure 3. Crest settlements computed for the San Pietro Dam and predictive formula (eq.1).

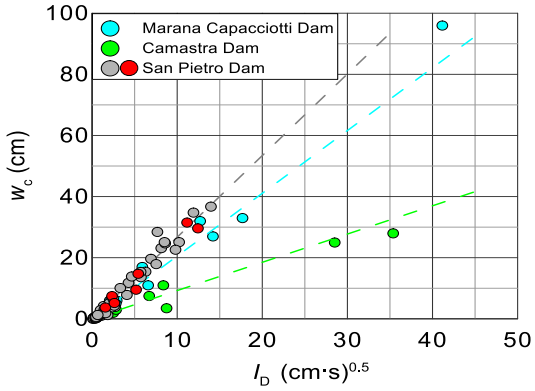

Figure 4. Crest settlements computed for three earth dams and relative linear best fits.

Recently, Nardo et al. (2024a) and Aliberti et al. (2019) proposed threshold values $w_{c,y}/H$ of the normalized crest settlement (i.e. the crest settlement normalized with respect to the total height H of the dam-foundation system) to check the possible occurrence of serviceability (*Operative limit states* OLS, *Damage limit states* DLS) or ultimate (*Life Safety limit states* LLS and *Collapse limit states* CLS) limit states. These threshold values were derived using a large set of well-documented case-histories and update those previously proposed by Swaisgood (2003).

According to Nardo et al. (2024b), the combined use of I_D and of the threshold values of the normalized permanent crest settlement allows a reliable evaluation of the earthquake-induced level of damage in earth dams. An example of this combined use is presented in Figure 5 with reference to the San Pietro, Marana Capacciotti and Camastra dams.

For the San Pietro dam it is apparent that accelerograms characterized by $I_D < 3$ do not induce any damage since it is $w_c/H < 0.1$; values of I_D in the range 3÷11 correspond to normalized crest settlements for which the OLS and DLS could be achieved; finally, the *Damage limit state* could be attained for $I_D > 12$.

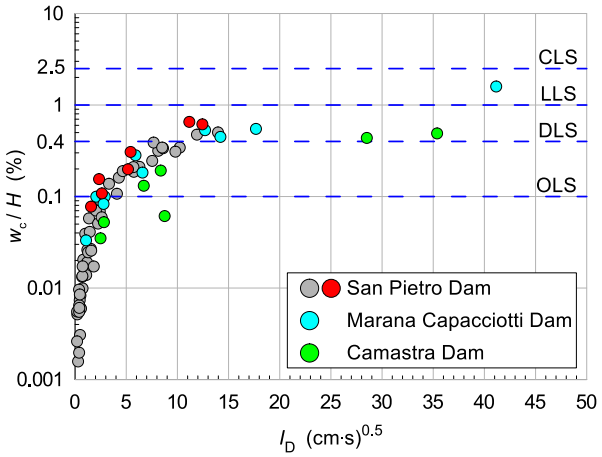

Figure 5. Evaluation of the expected level of damage for three earth dams.

Similar conclusions can be drawn for the Marana Capacciotti and the Camastra dams. It can be observed that, in the examined cases, the threshold value $w_c/H = 1\%$ is never reached (with only one exception relative to the Marana Capacciotti dam) implying that for the input motions considered herein these three dams can only suffer moderate damage.

4 CONCLUSIONS

The seismic performance of the San Pietro dam has been studied through a finite element analysis using

two set of input motions and the obtained results have been used to develop and verify a predictive formula for the assessment of the crest settlement.

Analysing data available in the literature, it has been verified that the proposed seismic intensity measure is well correlated to the crest settlements, also for other two Italian dams. Using a suitable combination of the intensity measure I_D and threshold values of the normalized crest settlement recently proposed by Nardo et al. (2024a) and Aliberti et al. (2019), a simplified evaluation of the expected level of earthquake-induced damage in the examined earth dams has been proposed.

ACKNOWLEDGEMENTS

This work is part of the research activities carried out in the framework of the research project of major national interest, PRIN n. 2017YPMBWJ, on "Risk assessment of Earth Dams and River Embankments to Earthquakes and Floods (REDREEF)" funded by the Italian Ministry of Education University and Research.

REFERENCES

Adamo, N., Ansari, N.A., Sissakian, V., Laue, J., Knutsson, S. (2020). Dam safety and earthquakes, *Journal of Earth Sciences and Geotechnical Engineering*, 10(6): 79–132.

Aliberti, D., Biondi, G., Cascone, E., Rampello, S. (2019). Performance indexes for seismic analyses of earth dams, *In Earthquake Geotechnical Engineering for Protection and Development of Environment and Constructions,* pp. 1066-1073.

Biondi, G., Cascone, E., Aliberti, D., Rampello, S. (2021). Screening-level analyses for the evaluation of the seismic performance of a zoned earth dam, *Engineering Geology*, 280, 105954. DOI: 10.1016/j.enggeo.2020. 105954.

Calabresi, G., Rampello, S., Callisto, L., Cascone, E. (2004). Diga S. Pietro sul fiume Osento. In: Verifica delle condizioni di stabilità e analisi del comportamento in condizioni sismiche, Research Report.

Casablanca, O., Nardo, A., Biondi, G., Di Filippo G., Cascone, E. (2022). Seismic performance of a zoned earth dam, *Proc. 4th Int. Conf. on Performance Based Design in Earthquake Geotechnical Engineering*, pp. 1929-1936. DOI: 10.1007/978-3-031-11898-2_176.

Cascone, E., Biondi, G., Aliberti, D., Rampello, S. (2021). Effect of vertical input motion and excess pore pressures on the seismic performance of a zoned dam, *Soil Dynamics and Earthquake Engineering*, 142, 106566. DOI: 10.1016/j.soildyn.2020.106566.

Elia, G., Amorosi, A., Chan, A.H.C., Kavvadas, M. (2011*).* Fully coupled dynamic analysis of an earth dam, *Geotechnique*, 61(7), 549–563.

Elia, G., Rouainia, M. (2013). Seismic Performance of Earth Embankment Using Simple and Advanced Numerical Approaches, *J. Geotechnical and Geoenvironmental Engineering,* 139(7): 1115–1129. DOI:10.1061/(ASCE) GT.1943-5606.0000840.

Housner, G.W., Jennings, P.C. (1982). Earthquake design criteria. EERI Monograph Series. Berkeley, CA: Earthquake Engineering Research Institute.

Khalid, M. I., Park, D., Fei, J., Nguyen, V., Nguyen, D., Chen, X. (2023). Selection of efficient earthquake intensity measures for evaluating seismic fragility of concrete face rockfill dam, *Computers and Geotechnics*, 163, 105721. DOI: 10.1016/j.compgeo.2023.105721.

Nardo, A., Casablanca, O., Di Filippo, G., Biondi, G., Cascone, E. (2023). Influence of vertical ground motion on the seismic performance of an earth dam, *Proc. of the VIII Italian Conference of Geotechnical Researchers CNRIG,* 679-686. DOI: 10.1007/978-3-031-34761-0_82.

Nardo, A., G., Biondi, G., Cascone, E. (2024a). Seismic performance indexes for dams, *submitted to Italian Geotechnical Journal.*

Nardo, A., Casablanca, O., Di Filippo, G., Biondi, G., Cascone, E. (2024b). Seismic intensity measures for the evaluation of earthquake – induced crest settlements of earth dams, *submitted to Earthquake Engineering and Structural Dynamics*.

Sica, S., Pagano, L., Vinale, F. (2008). Interpretazione dei segnali sismici registrati sulla diga di Camastra, *Italian Geotechnical Journal*, XLII(4): 97–111.

Sica, S., Pagano, L. (2009). Performance-based analysis of earth dams: procedures and application to a sample case, *Soils and Foundations*, 49(6): 921-939. DOI: 10.3208/sandf.49.921

Swaisgood, J.R. (2003). Embankment dam deformations caused by earthquakes, *Paper presented at: 7th Pacific Conference on Earthquake Engineering*, Christchurch, New Zealand.

Trifunac, M.D, Brady, A.G. (1975). A study of the duration of strong earthquake ground motion. *Bulletin of the Seismological Society of America*, 65:581-626.

USCOLD. (1992). *Observed Performance of Dams during Earthquakes*, Volume I.

Zefa, L., Zhenyu, W., Xiang, L., Jingren, Z., Jiankang, C., Lijun, L., Liang, P. (2022). Efficient seismic risk analysis of gravity dams via screening of intensity measures and simulated non-parametric fragility curves, Soil Dynamics and Earthquake Engineering, 152, 107040. DOI: 10.1016/j.soildyn.2021.107040.

Zienkiewicz, O.C., Chan, A.H.C., Pastor, M., Schrefler, B. A., Shiomi, T. (1999). Computational geomechanics with special reference to earthquake engineering, Wiley, Chichester, U.K.

Proceedings of the XVIII ECSMGE 2024
GEOTECHNICAL ENGINEERING CHALLENGES
TO MEET CURRENT AND EMERGING NEEDS OF SOCIETY
© 2024 the Authors
ISBN 978-1-032-54816-6
DOI 10.1201/9781003431749-346
Open Access: www.taylorfrancis.com, CC BY-NC-ND 4.0 license

ECSMGE 24
XVIII EUROPEAN CONFERENCE ON SOIL MECHANICS AND GEOTECHNICAL ENGINEERING

Slope failure cause evaluation based on earthworks management and meteorological conditions analyses

Évaluation de la cause de la défaillance du talus, basée sur l'analyse de la gestion des travaux de terrassement et des conditions météorologiques.

T.Q. Nguyen
Thuyloi University, Hanoi, Vietnam

D.B. Van, M.V. Nguyen, N.A. Do
Hanoi University of Mining and Geology, Hanoi, Vietnam

P. Osinski*, E. Koda
Institute of Civil Engineering, Warsaw University of Life Sciences - SGGW, Warsaw, Poland

**piotr_osinski@sggw.edu.pl*

ABSTRACT: Rainfall-triggered slope failures are a well-known cause of disasters. To increase the stability of slopes a retaining wall is often proposed. However, associated earthworks could bring the great danger of a landslide during the construction process, if not properly managed. The paper aims to investigate the collapse cause of residential buildings located at the edge of the slope in the northwest part of Vietnam, where engineering works were performed to prevent failure due to undercutting soil erosion. During the retaining wall construction works, significant vibrations and additional dynamic loads could have affected the building foundations' bearing capacity, leading to structural failure. Another cause is associated with heavy precipitation recorded at the site just after the excavation works down the slope. The paper consists of analyses allowing simulation of possible scenarios, including the effect of changing saturation conditions using the metrological data. The analyses concerned slope stability improvement to secure the remaining infrastructure.

RÉSUMÉ: Les glissements de terrain déclenchés par les précipitations sont une cause bien connue de catastrophes liées aux structures. Pour accroître la stabilité, la construction d'un mur de soutènement est souvent proposée. Cependant, de tels travaux peuvent également entraîner un danger élevé de glissement de terrain pendant la construction s'ils ne sont pas gérés correctement. L'objectif de l'article est d'investiguer la cause de l'effondrement des bâtiments résidentiels situés en bordure du talus dans le nord-ouest du Vietnam, où des travaux d'ingénierie ont été effectués pour prévenir les défaillances dues à l'érosion des sols causée par le sous-excavation. Pendant les travaux de construction du mur de soutènement, des vibrations importantes et des charges dynamiques supplémentaires auraient pu affecter la capacité portante des fondations des bâtiments, entraînant une défaillance structurelle. Une autre cause est liée aux fortes précipitations enregistrées sur le site juste avant le début des travaux d'excavation en descente du talus. L'article comprend des analyses permettant de simuler des scénarios possibles, y compris l'effet des conditions de saturation changeantes à l'aide des données météorologiques. Les analyses ont porté sur l'amélioration de la stabilité du talus afin de sécuriser les infrastructures restantes.

Keywords: Slope stability; rainstorm event; infrastructure failure; retaining wall.

1 INTRODUCTION

Slope stability issues are a common safety concern when it comes to development plans in urban areas. Landslides can occur due to natural processes and poor management of developing sites. The natural process like changing climate conditions, are very challenging to control. When it comes to human factor-triggered landslides most of the failures could be easily avoided by fully understanding the danger caused by the construction works and management of developing sites. The present study analyses triggering factors of the collapse of buildings located by the edge of the natural slope. The collapse is recognised to be associated with extreme precipitation events recorded at the site and poor drainage conditions after the retaining wall construction works.

Retaining walls are primarily designed to improve the structure stability but can also eliminate the soil erosion effect on the river banks or slopes located by the waterways, undercutting the slope at its toe. When considering the construction of the retaining wall in areas of high-risk failure due to the presence of associated infrastructure, the method of reinforcement

installation is crucial (Look, 2022). There are a number of case studies researching rainfall-triggered landslides (Lacroix et al, 2020; Maturidi et al, 2021) or slope failures due to poor execution of earthworks during the installation of reinforcements. Engineering practice shows that one of the most common causes of slope failures is the decrease of soil shear strength due to the development of groundwater pressure at the potential slip surfaces (Filho and Fernandes, 2019). Long-lasting precipitation is affecting dipper parts of a slope profile resulting in severe collapses (Patuti et al, 2017; Alsubal et al, 2019). The present paper aims to investigate the real cause of slope failure in the northwest part of Vietnam. The sequence of events recorded at the site, both natural and manmade, resulted in severe damage to the surrounding infrastructure, forcing the residents to evacuate. The authors tried to reconstruct the process by collecting available data and investigating mechanisms that could have caused the failure of the slope and the infrastructure.

2 STUDY SITE DESCRIPTION

The case study site is located in a mountainous district in the centre of Dien Bien province, in the northwest part of Vietnam (Figure 1). It is divided into two landform zones where the terrain elevation ranges from 350-1000 m a.s.l. The terrain is morphologically complex with a number of valleys and rivers crossing the entire region, where during the wet season the meandering streams are cutting the mountain toes. What is important for the case study is the presentation of the local climate condition that has a major effect on the working conditions of the infrastructure and causes of natural hazards. The conditions are typical for tropical monsoon climate. The annual rainfall ranges from 1,600 to 2,400 mm.

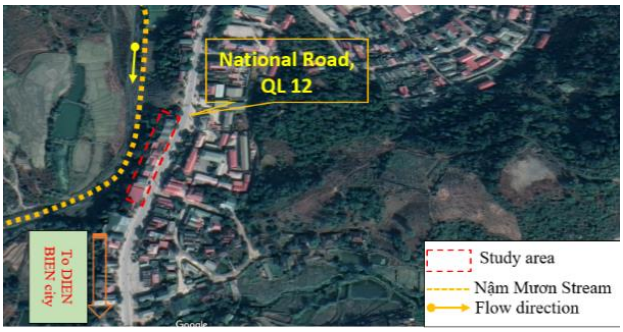

Figure 1. Location of study area.

The case study concerns a natural slope with extensive infrastructure developed at the top edge. The infrastructure development started with the construction of a local road near the edge and the design of the drainage system redirecting the runoff down the 25m high slope. Following the road construction number of storey buildings were constructed in the section between the road and the slope's edge. At the toe of the slope, there is a natural stream passing with the flow changing depending on the rainfall volume. In recent years, the local community's major awareness has been focused on the erosion effect due to the stream continuously cutting the toe of the slope. Thus, a retaining wall was constructed to control the water erosion and improve the slope's stability. After the works were accomplished significant rainfall events took place. The finger pipe drainage was installed at the back of the wall. A few weeks later the residents reported the first building cracking, which continued to develop until the next severe rainfall event that was followed by the slope failure and a collapse of buildings located at the study site. Figure 2 presents graphically the sequence of events leading to a final slope failure. The authors of the present paper aim to investigate events and the processes contributing to the failure occurrence. Based on the data collected from the site investigation report, meteorological report and the information gathered during the site visits, the analytical study was performed to reflect the in-situ conditions.

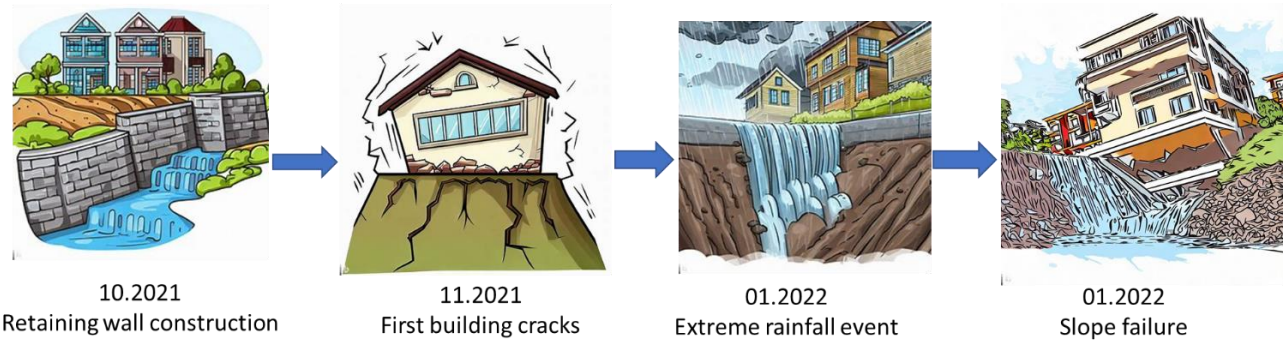

Figure 2. Graphical presentation of the sequence of events leading to a structural failure of residential buildings.

3 GEOTECHNICAL CONDITION

For analyses of the conditions at the study site, a geotechnical investigation was performed. During the site investigation, 11 core samples were collected and transported to the laboratory where physical and mechanical parameters were determined using triaxial tests. There were 4 main geotechnical layers determined, with the groundwater table investigated at 2,5m depth. The experimental results of physico-mechanical parameters are presented in Table 1.

Table 1. Physico-mechanical properties of soil layers.

Parameter	Soil type			
	Fill	Shale *	Shale **	Sandstone **
w (%)	23.9	28.2		
γ (g/cm^3)	1.96	1.90	2.2	2.50
e (%)	0.69	0.8		
Ip (%)	16.2	15.7		
c‘ (MPa)	0.0167	0.174	0.09	0.18
φ‘ (°)	17	20	32	46

*highly weathered; **moderately weathered

Since the rainfall events in the study were concerned with having a major effect on the failure, the precipitation data were also analysed. To allow further understanding of the failure cause the rainfall data was collected from the nearby monitoring station. Important for the study is the accumulative rainfall of 2000 mm recorded on 10.2021. Another crucial note for the study is that the finger pie drainage behind the retaining wall was found to be clogged during the site investigation.

4 RESULTS AND DISCUSSION

The authors attempted first to reflect the sequence of events by analysing all the circumstances at the site starting with matching the recorded rainfall data with the time of constructing the retaining wall, through observed cracks on the buildings and the time of the final failure of the slope. The graph presented in Figure 3, shows the chronologic sequence of events to give a better understanding of all the possible causes of the final failure of the slope, which eventually resulted in severe damage to the residential buildings. In late 2021, due to the alarming technical condition of the slope, the local authorities decided to support the toe by constructing the retaining wall, in the form of a concrete gravity wall, preventing potential failure. The excavation works that took place on 7-20.10.2021 caused heavy ground vibrations that were reported by the local citizens occupying the buildings located at the top of the slope. Soon after the retaining wall works were completed a significant rainfall event was recorded, reaching 30 mm on 22.10.2021. It is worth noting that the accumulation rainfall recorded for October is 2000 mm. A week later, the first cracks developing in the buildings were observed. It was only 2 months later, on 16.01.2022 when more damages to the building were reported and the slope failed after the rainfall event that reached nearly 45 mm in a single day. Through the analytical approach and detailed investigation of events, it is assumed that two major factors triggering the slope failure were the retaining wall earthworks and poor drainage conditions during the torrential precipitation.

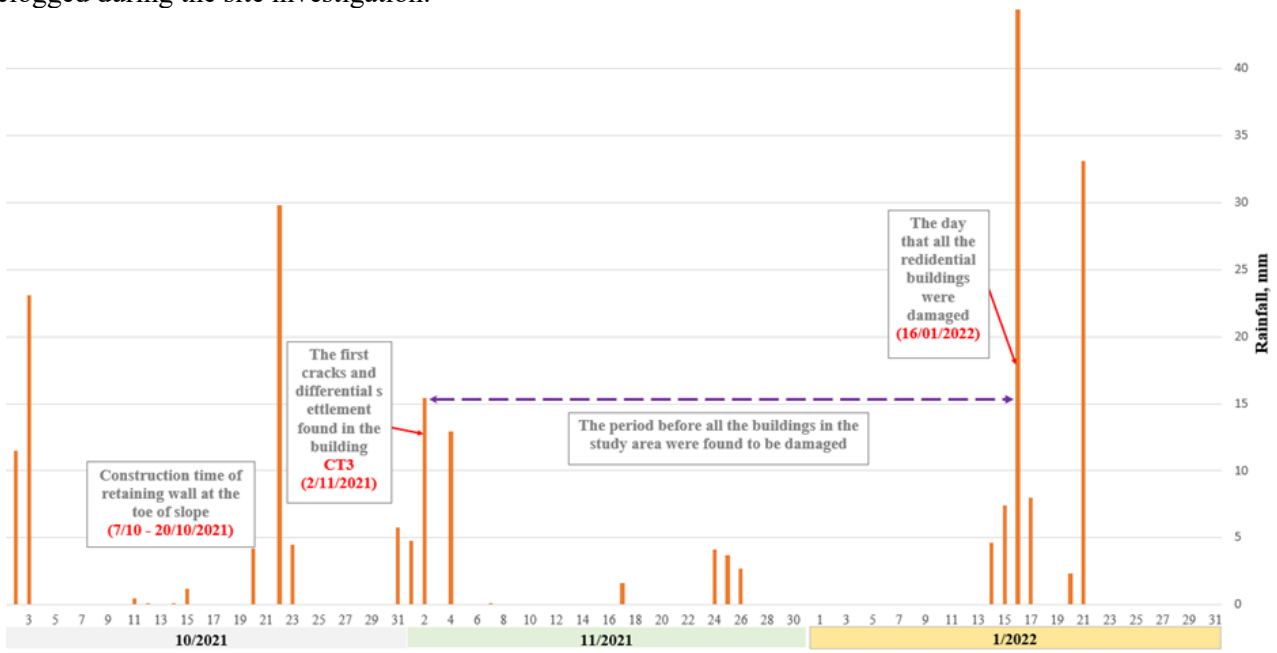

Figure 3. The sequence of events leading to a final failure with referencing rainfall data recorded in the study area.

During the earthworks, the dynamic loads loosened the soil material at the building foundation. The following rainfall could then easily penetrate the soil profile causing the decrease of the soil's mechanical parameters due to build-up of effective stress, also caused by poor drainage conditions. Based on geotechnical investigation data and rainfall volume the computations of geotechnical safety were performed to determine the failure mechanism and to reflect the sequence of the events. Based on the analyses the restoration works and computations of geotechnical safety were performed. The slope stability analyses were performed using the finite element method for the parameters obtained from the site investigation. The geotechnical model used for further analyses was based on the Mohr-Coulomb soil model, and the factor of safety was computed based on the shear strength reduction method. There were different scenarios for the analyses applied, depending on the changing groundwater level due to rainfall and infiltration. To ensure safety the entire slope was re-engineered and reinforcement such as MSE and gabion wall was proposed. The system allowed for minimising the excavation and earthworks' impact on the remaining infrastructure so as not to cause any more damage. Finding the optimum solution, the deformations and the factor of safety were computed as presented in Figure 4. The obtained factor of safety was 1.34 > [FS]=1.25 and maximum horizontal displacement did not exceed 4.25 cm < [δ]=H/200 = 7.5 cm, where H is the total height of the wall.

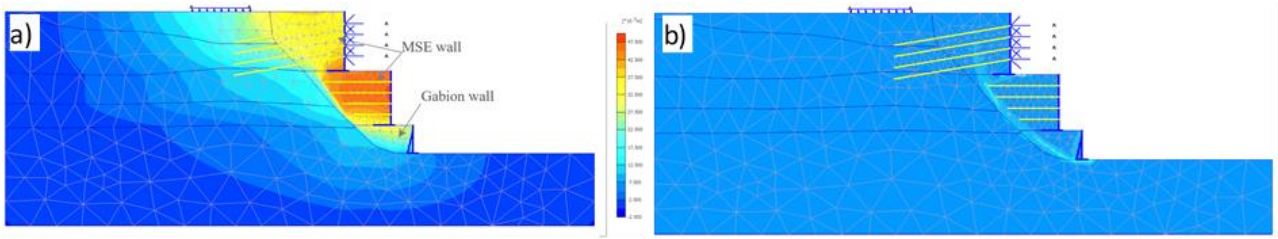

Figure 4. Computations of geotechnical safety a) displacements, b)FS and slip surface determination.

5 CONCLUSIONS

The study's objective was to investigate the on-site conditions and imitate the events that may have led to the residential building damage and eventually the slope failure. The site investigation data, meteorological monitoring reports, drainage conditions and the examination of earthworks during the construction of the retaining wall allowed comprehensive examinations of events that contributed to the slope's failure. Based on all the gathered information a reclamation plan was implemented and solutions for improving the geotechnical safety were proposed, by computing the factor of safety and total deformations of failed and then newly engineered slopes. The lesson learned from the case study is that the earthwork aiming at improving safety, in particular circumstances, when dealing with severe weather events could have the opposite, even damaging effect.

REFERENCES

Alsubal, S., Sapari, N., Harahap, S. and Al-Bared, M., (2019). A review on mechanism of rainwater in triggering landslide. In *IOP Conference Series: Materials Science and Engineering*. IOP, 513(1): 012009. https://doi.org/10.1088/1757-899X/513/1/012009.

Filho, O. and Fernandes, A. (2019). Landslide analysis of unsaturated soil slopes based on rainfall and matric suction data. *Bulletin of Engineering Geology and the Environment*, 78: 4167-4185. https://doi.org/10.1007/s10064-018-1392-5.

Lacroix, P., Handwerger, L. and Bièvre, G. (2020). Life and death of slow-moving landslides. *Nature Reviews Earth & Environment*, 1(8): 404-419. https://doi.org/10.1038/s43017-020-0072-8.

Look, G. (2022). *Earthworks: Theory to Practice-Design and Construction*. CRC Press. London. UK. https://doi.org/10.1201/9781003215486.

Maturidi, M., Kasim, N., Taib, A. and Azahar, N. (2021). Rainfall-induced landslide thresholds development by considering different rainfall parameters: A Review. *Journal of Ecological Engineering*, 22(10): 85-97. https://doi.org/10.12911/22998993/142183.

Patuti, M., Rifa'i, A. and Suryolelono, B. (2017). Mechanism and characteristics of the landslides in Bone Bolango regency, Gorontalo province, Indonesia. *Geomate Journal*, 12(29): 1-8. https://doi.org/10.21660/2017.29.79901.

Proceedings of the XVIII ECSMGE 2024
GEOTECHNICAL ENGINEERING CHALLENGES
TO MEET CURRENT AND EMERGING NEEDS OF SOCIETY
© 2024 the Authors
ISBN 978-1-032-54816-6
DOI 10.1201/9781003431749-347
Open Access: www.taylorfrancis.com, CC BY-NC-ND 4.0 license

ECSMGE 24
XVIII EUROPEAN CONFERENCE ON SOIL MECHANICS AND GEOTECHNICAL ENGINEERING

Effect of variability parameters on 3D probabilistic slope stability prediction

Impact des paramètres de variabilité sur la prédiction probabiliste de stabilité des pentes en 3D

E.A. Oguz*, T.M.H. Le
Norwegian Geotechnical Institute, Department of Geotechnics and Natural Hazards, Trondheim, Norway
**emir.ahmet.oguz@ngi.no*

ABSTRACT: Uncertainties in landslide assessment arise substantially from spatial variability of geotechnical and hydrological parameters. Spatially variable model parameters are often represented by a probability density function with a mean and a standard deviation, and a covariance function with a spatial correlation length. The variability parameters are frequently selected based on values in literature due to a lack of real data, thus not necessarily representing the true spatial variability characteristics of a given problem. Such a selection might lead to overestimated or underestimated safety levels. Therefore, there is a need to quantify how the choice of variability parameters affects the safety levels. This study addresses this need by studying the effect of variability parameters on the landslide slope stability predictions in terms of factor of safety using the 3-Dimensional Probabilistic Landslide Susceptibility model (3DPLS) on a simplified 2 m-thick inclined slope. Different sizes of an ellipsoidal sliding surface were analysed for a range of variability parameters over varying extent of problem domains. The results indicate that variability parameters significantly affect the safety levels depending on the extent of the problem domain and the size of the sliding surface. In addition, the critical spatial correlation length leading to the lowest safety level is found to have strong correlation with the size of the sliding surface.

RÉSUMÉ: Les incertitudes en évaluation des glissements de terrain résultent de la variabilité spatiale des paramètres géotechniques et hydrologiques. Ces paramètres modélisés, variables spatialement, s'appuient souvent sur des données littéraires, ne reflétant pas totalement la réalité spatiale par manque de données réelles. Cette sélection pourrait conduire à des niveaux de sécurité surestimés ou sous-estimés. Il est donc crucial d'évaluer son impact. Cette étude examine comment les paramètres de variabilité affectent les prédictions de stabilité des pentes de glissement à l'aide du 3DPLS sur une pente inclinée de 2 mètres d'épaisseur. Diverses tailles de surface de glissement ellipsoïdales ont été analysées sur différents domaines, montrant une forte influence des paramètres de variabilité sur les niveaux de sécurité, en fonction de l'étendue du domaine et de la taille de la surface de glissement. De plus, il est constaté une forte corrélation entre la longueur de corrélation spatiale critique, associée au niveau de sécurité le plus bas, et la taille de la surface de glissement.

Keywords: Probability; landslide; spatial variability; 3D slope stability.

1 INTRODUCTION

Slope stability predictions are subjected to a variety of sources of variability, including aleatory and epistemic uncertainties associated with the geotechnical and hydrological parameters, the uncertainty in input data, and the limitations of prediction models. One of the sources contributing substantially to the uncertainties of model predictions is natural spatial variability of the soil parameters. Geotechnical and hydrological parameters can vary significantly over short distances. This can lead to significant changes of parameters between adjacent areas, and results in different levels of slope stability (Fenton & Griffiths, 2008).

Spatially variable model parameters can be modelled by using a probability density function with a mean and a standard deviation, and a covariance function with a spatial correlation length representing the spatial dependence of the parameters. In the literature, many studies addressed the need for accounting for variability and showed the impact on stability predictions (e.g., Hu et al., 2022; Kasama & Whittle, 2016; Tabarroki et al., 2013; Zhu et al., 2019). The findings of these studies revealed that deterministic models or traditional probabilistic models without spatial variability might lead to unconservative estimates of failure probability.

The essentiality of accounting for the spatial variability in slope stability prediction over large areas was addressed in the literature (Arnone et al., 2016; Mergili et al., 2014; Oguz et al., 2022). Oguz et al. (2022) developed the 3-Dimensional Probabilistic Landslide Susceptibility, 3DPLS, model to account for spatial variability over large areas. 3DPLS model

utilizes random field approach for spatially variable soil parameters and performs 3D slope stability analyses over a landslide susceptible zone in a probabilistic framework. Using the 3DPLS model, Oguz et al. (2022) showed the significant impact of spatially variable soil parameters on landslide stability predictions.

In practice, variability parameters are primarily chosen based on the literature values due to insufficient data from the area susceptible to landslides. The selection of variability parameters can impact stability predictions, and the extent of this effect needs to be addressed. This study addresses this need by conducting a parametric study on a shallow, 2 m thick inclined slope. The current study expands the investigation on the impact of variability level and degree of spatial variability in Oguz et al. (2022) by further exploring the impact of varying dimensions of sliding surface and problem extents in a probabilistic framework.

2 THE 3DPLS MODEL

The 3DPLS model (Oguz et al., 2022) was developed to address the spatial variable model parameters in rainfall-induced landslide susceptibility assessment. The model couples a hydrological model relying on Iverson's solution of the Richards equation assuming tension saturation (Iverson, 2000) and a slope stability model employing the extension of Bishop's method of slope stability to 3D (Hungr, 1987). Spatial variable model parameters are modelled with 2D Gaussian and lognormal random fields (Fenton & Griffiths, 2008). Uncertainties in model parameters are propagated to the model output through Monte Carlo simulations, in each of which a new random field is generated for the spatial variable model parameters.

The 3DPLS model generates ellipsoidal sliding surfaces over a landslide-susceptible area discretized into grid units, i.e., cells. An ellipsoidal sliding surface characterized by the lengths of principal semi-axes $a_e - b_e - c_e$, and inclination and aspect of motion, respectively β and α. β and α are calculated by the 3DPLS model using the input data. While a_e is defined along the principal semi-axis in the direction of the steepest slope, b_e is the length along the semi-axis perpendicular to the steepest slope. c_e is the depth of the sliding surface defined perpendicular to the other two semi-axes (Oguz et al. 2022).

In the 3DPLS model, the spatial variability in the horizontal dimensions is modelled with 2D Gaussian and lognormal random fields. The spatial variability along the soil thickness/depth is not modelled for simplicity. The model, through Monte Carlo simulations, provides FS maps for each simulation, mean FS maps, and the probability of failure, P_f, map.

In this study, a global factor of safety, F_S^g, is defined for each simulation as the most critical sliding surface over the problem domain such that $F_S^g = \min[F_{Si}: i = 1, \dots, n]$ where n is the number of cells over the problem domain. Following Monte Carlo simulations, F_S^g values are averaged to calculate the mean global factor of safety, μ_g, such that $\mu_g = 1/N_S \sum(F_S^g)$ where N_S is the number of simulations. The effect of variability parameters on 3D probabilistic slope stability prediction was investigated considering the μ_g values for different problem domain extents, sliding surface dimensions, and varying variability levels. Current study utilized the up-to-date version, 3DPLS v1.0, (2022). The details of the model can be seen in Oguz et al. (2022).

3 PARAMETRIC STUDY

In this study, a simplified problem geometry has been examined where the soil layer has a thickness of 2 m with a 25° inclination over a varying size of the problem domain: 200 m x 200 m, and 50 m x 50 m. The ground water table is assumed at the ground surface with a surface parallel flow through the inclination. The problem domain was discretized into 2 m cell size. Different sizes of an ellipsoidal sliding surface were utilized assuming equal horizontal semi-axes, i.e., $a_e = b_e = \{10, 20, 40\}$ m, with a constant semi-axis along the depth, i.e., $c_e = 2$ m. β is calculated same as the inclination of the problem domain. A parametric study was conducted for drained case, i.e., effective stress based, with the unit weight of the soil and water being 20 and 10 kN/m^3, respectively. A frictional material is utilized with cohesion, c', and friction angle, ϕ', treated as spatially variable parameters (see Table 1). Varying spatial correlation lengths, l, from zero, i.e., no spatial dependence, to 1000 m where soil parameters are highly correlated over the problem domain were examined. Same correlation lengths in horizontal directions were assumed.

Table 1. Variability of parameters.

	c' (kPa)	ϕ' (°)
Mean value	6 (lognormal dist.)	40 (normal dist.)
*CoV	0.10, 0.20,0.30	0.05,0.10,0.15
l (m)	0,10,40,80,200,1000	

*Coefficient of variation for low, moderate, high levels

Deterministic model simulations were performed to have an idea of the safety level for different ellipsoidal sliding surfaces. The deterministic F_S^g for 10-10-2, 20-

20-2, and 40-40-2 m size ellipsoidal sliding surfaces are 1.57, 1.48, 1.45, respectively. Further increasing the size to infinity, i.e., infinite slope stability condition, leads to a F_S^g of 1.29. This study performed 3D probabilistic slope stability analyses for each combination of variability level and spatial correlation length with 1000 random field realizations and the results are presented in the following section.

4 RESULTS

4.1 Effects of parameter variability

Figure 1 presents how variability parameters, including variability levels and degree of spatial dependence, influence the 3D probabilistic slope stability predictions over 200 m x 200 m problem domain. The results show that the values of μ_g are lower than the corresponding values of the deterministic F_S^g regardless of variability levels. As the variability level increases at any correlation length, the values of μ_g decrease for each ellipsoidal sliding surface dimension.

For a given ellipsoidal sliding surface dimension, μ_g is significantly affected by correlation length. No spatial dependence, i.e., 0 m correlation length, leads to higher μ_g compared to the other values of the correlation length. This was attributed to the fact that cells with lower values of strength parameters are most likely to be adjacent to cells with high values. These low values of strength parameters are compensated by the high values in stability calculation, and higher μ_g is obtained.

The results reveal that an increase in correlation length at low range (approximately <80-100 m) resulted in a decrease in μ_g, but further increase beyond a threshold value leads to a subsequent rise in μ_g. A more substantial reduction was observed for larger variability levels. As the correlation length increases, the random field tends to smooth out the spatial variations over the field, and the spatial dependence between neighboring cells becomes stronger. The adjacent cells are more likely to have similar parameter values. Consequently, the probability of encountering a weak zone within the sliding surface would decrease. Therefore, further increasing the correlation length results in higher values of μ_g. Similar observations were made for 2D single slopes in the literature (e.g., Kasama and Whittle 2016; Tabarroki et al. 2013).

4.2 Critical correlation length and effect of problem domain extent

This study revealed that a particular correlation length leads to the lowest value of μ_g and will hereafter be referred to as the 'critical correlation length'. This study examined the critical correlation length for different sizes of the ellipsoidal sliding surface, extents of problem domain, and all variability levels. The results showed strong correlation between critical correlation length and length of the sliding surface in the direction of motion, i.e., $L = 2a_e$. The correlation coefficient was found to be in the range of 0.62-0.76 for 200x200, and 50x50 m extent of the problem domain, with an overall correlation of 0.59 for all analyses. Besides, linear regression revealed that the critical correlation length is approximately 1.8 times the length of the sliding surface in the direction of motion.

Figure 2 presents the effects of the extent of problem domain on the probabilistic slope stability predictions in terms of the μ_g for 10-10-2 m sliding surface and high variability level. It is observed that the μ_g decreases as the extent of the problem domain increases regardless of the ellipsoidal sliding surface dimension and correlation length. A larger problem extent results in increased parameter fluctuation across the domain, leading to a wider confidence interval by remaining nearly consistent mean value.

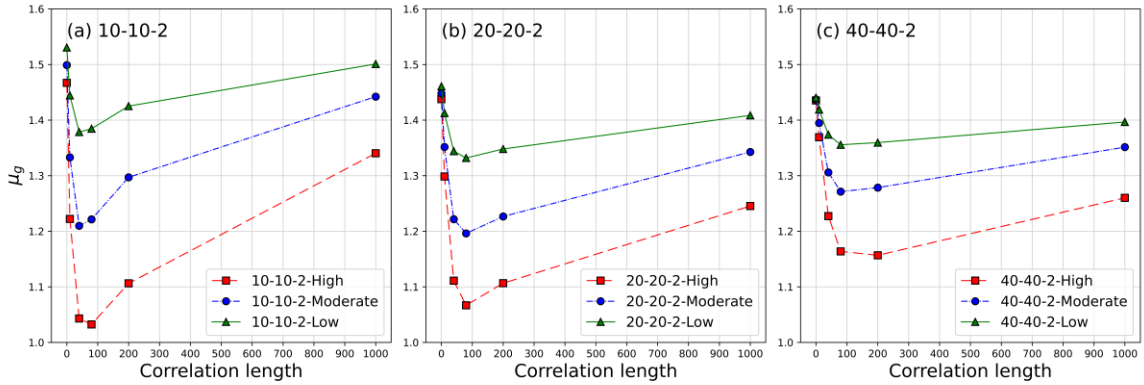

Figure 1. Effects of variability level and degree of spatial dependence on the values of μ_g for different sizes of sliding surface.

Wider confidence interval amplifies the influence of weak zones on F_S^g, consequently resulting in a progressive reduction of μ_g obtained through Monte Carlo simulations, see Figure 2.

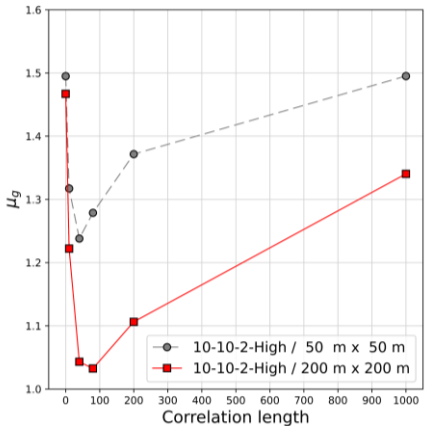

Figure 2. Effects of the problem domain extent for 10-10-2 m sliding surface and high variability level.

5 CONCLUSION

The current study investigated the impact of variability parameters on the 3D probabilistic slope stability prediction using the 3DPLSmodel. A simplified 2 m-thick 25° inclined slope was studied with spatial variable geotechnical strength parameter. Sliding surfaces of varying dimensions were used over varying extents of problem domain.

The results showed that 3D probabilistic slope stability predictions are substantially affected by the variability level and degree of spatial dependence. Accounting for variability in the analysis leads to lower safety levels compared to deterministic approach, regardless of problem domain extent or sliding surface dimension. The decrease in μ_g was found to be greater at a higher variability level. The degree of spatial dependence substantially affects the predictions. Significantly lower values of μ_g can be obtained depending on the correlation length. Additionally, a larger problem domain extent was found to be leading to lower values of μ_g for a given sliding surface dimension.

A critical value of correlation length resulting in the lowest μ_g was identified. A strong correlation between the critical correlation length and the sliding surface dimension was observed with an average correlation coefficient of 0.59. The critical correlation length was found to be approximately 1.8 times the length of the sliding surface. The relationship between critical correlation length and length of the sliding surface is of high importance in the absence of substantial information on the variability characteristics of the soil parameters, particularly in the context of design of critical infrastructures with slope stability.

ACKNOWLEDGEMENTS

The authors acknowledge support from the GEOLAB project (Horizon 2020, grant ID: 101006512).

REFERENCES

3DPLS v1.0. (2022, August). The 3-Dimensional Probabilistic Landslide Susceptibility (3DPLS) Model, version 1.0. Https://Github.Com/EmirAhmetOguz/3DPLS.Git.

Arnone, E., Dialynas, Y. G., Noto, L. V., & Bras, R. L. (2016). Accounting for soil parameter uncertainty in a physically based and distributed approach for rainfall-triggered landslides. Hydrological Processes, 30(6), 927–944. https://doi.org/10.1002/hyp.10609.

Fenton, G. A., & Griffiths, D. V. (2008). Risk assessment in geotechnical engineering (Vol. 461). John Wiley \& Sons New York.

Hu, L., Takahashi, A., & Kasama, K. (2022). Effect of spatial variability on stability and failure mechanisms of 3D slope using random limit equilibrium method. *Soils and Foundations*, *62*(6). https://doi.org/10.1016/j.sandf.2022.101225.

Hungr, O. (1987). An extension of Bishop's simplified method of slope stability analysis to three dimensions. *Geotechnique*, *37*(1), 113–117. https://doi.org/10.1680/geot.1987.37.1.113.

Iverson, M. R. (2000). Landslide triggering by rain infiltration. *Water Resources Research*, *36*(7), 1897–1910.

Kasama, K., & Whittle, A. J. (2016). Effect of spatial variability on the slope stability using Random Field Numerical Limit Analyses. *Georisk*, *10*(1), 42–54. https://doi.org/10.1080/17499518.2015.1077973.

Mergili, M., Marchesini, I., Alvioli, M., Metz, M., Schneider-Muntau, B., Rossi, M., & Guzzetti, F. (2014). A strategy for GIS-based 3-D slope stability modelling over large areas. *Geoscientific Model Development*, *7*(6), 2969–2982. https://doi.org/10.5194/gmd-7-2969-2014

Oguz, E. A., Depina, I., & Thakur, V. (2022). Effects of soil heterogeneity on susceptibility of shallow landslides. *Landslides*, *19*(1), 67–83. https://doi.org/10.1007/s10346-021-01738-x

Tabarroki, M., Ahmad, F., Banaki, R., Jha, S. K., & Ching, J. (2013). Determining the Factors of Safety of Spatially Variable Slopes Modeled by Random Fields. *Journal of Geotechnical and Geoenvironmental Engineering*, *139*(12), 2082–2095. https://doi.org/10.1061/(asce)gt.1943-5606.0000955.

Zhu, D., Griffiths, D. V., & Fenton, G. A. (2019). Worst-case spatial correlation length in probabilistic slope stability analysis. Geotechnique, 69(1), 85–88. https://doi.org/10.1680/jgeot.17.T.050.

Proceedings of the XVIII ECSMGE 2024
GEOTECHNICAL ENGINEERING CHALLENGES
TO MEET CURRENT AND EMERGING NEEDS OF SOCIETY
© 2024 the Authors
ISBN 978-1-032-54816-6
DOI 10.1201/9781003431749-348
Open Access: www.taylorfrancis.com, CC BY-NC-ND 4.0 license

ECSMGE 24
XVIII EUROPEAN CONFERENCE ON SOIL MECHANICS AND GEOTECHNICAL ENGINEERING

Application of the slurry deposition method to the reconstitution of samples of wolframite ore tailings

Application de la méthode de mise em moule pour la reconstitution d'échantillons de résidus de minerai de wolframite

J.P. Oliveira*
University of Coimbra, Coimbra, Portugal

P. Coelho
University of Coimbra, CITTA, Coimbra, Portugal

L. Araújo Santos
Polytechnic Institute of Coimbra, Coimbra Institute of Engineering, CITTA, SUScita, Coimbra, Portugal

*joaopsvo@uc.pt

ABSTRACT: Safer and more sustainable mining implies a better assessment of the mechanical behaviour of ore tailings under different realistic testing conditions. This paper addresses the issue of reconstituting samples for element testing of ore tailings from the Panasqueira mine, an important Portuguesa tungsten mine with suitable mining waste management. The paper discusses the capabilities of a slurry-base reconstitution method using ore tailings from this mine. To this end, the undrained triaxial behaviour of the reconstituted samples and the effects of the reconstitution method on the characteristics of samples with unusual geometries, such as those used in the Hollow Cylinder Apparatus, are discussed.

RÉSUMÉ: Une exploitation minière plus sûre et plus durable implique une meilleure évaluation du comportement mécanique des résidus de minerai dans différentes conditions d'essai réalistes. Cet article aborde la question de la reconstitution d'échantillons pour des essais élémentaires de résidus de minerai de la mine de Panasqueira, une importante mine de wolframite portugaise dont la gestion des déchets miniers est appropriée. Il examine les capacités d'une méthode de reconstitution à base de mise en moule en utilisant les résidus de minerai de cette mine. En vue de cela, le comportement triaxial non drainé des échantillons reconstitués et les effets de la méthode de reconstitution sur les caractéristiques des échantillons à géométrie inhabituelle, tels que ceux utilisés dans l'appareil à cylindre creux, sont examinés.

Keywords: Element testing; wolframite ore tailings; slurry-based reconstitution method, undrained triaxial compression.

1 INTRODUCTION

The last century has seen an increase in the volume of tailings produced, caused by the demand for minerals and metals. The behaviour of these unconventional geomaterials under different loading paths is still poorly understood, which may justify some of the serious disasters that have occurred all over the world (Wang et al. 2014). However, for laboratory testing to be successful, it is necessary to obtain intact samples or, when these are not available, to prepare suitable reconstituted samples. This article discusses the characteristics of reconstituted samples and the effects resulting from the preparation of reconstituted samples, with different sizes and shapes, of tungsten ore tailings using the slurry deposition method (Carraro & Prezzi, 2008, Tastan & Carraro, 2013). Reconstituted samples were prepared with different water contents to assess the effect on the sample's void ratio. Possible segregation problems in the preparation of each type of sample were also evaluated. Finally, some results of undrained triaxial compression tests are presented and compared in order to verify the repeatability of the sample preparation method.

2 SLURRY-BASED EXPERIMENTAL PROCEDURE TO PREPARATE RECONSTITUED SAMPLES

2.1 Studied Material

The tungsten ore tailings used in this study were collected at the Panasqueira´s mine in Portugal. Although there are no records of past accidents nor evidences of possible risks, these tailings were selected for the geotechnical investigation presented in this paper.

The basic physical and identification properties of the tungsten ore tailings were firstly determined. The liquid and plastic limits were measured as 23 and 15%, respectively, the density of the solid particles being 3.15. The void ratio of the intact samples taken were also determined, ranging from 0.62 to 0.75. Tungsten ore tailings, as well as other mining by-products, generally consist of irregular particles originating from the crushing and grinding of mined rock. Panasqueria´s tailings are composed of 16% clay-like, 73% of silt-like and 11% of sand-like, according to their sizes.

2.2 Reconstitution method at UC/ISEC

Based on the technique proposed by Carraro and Prezzi et al. (2008), an equipment was developed to mechanically mix the tailings with water and obtain a truly homogeneous mixture of the slurry. Operation consists in introducing the mine tailings and water into the metal mixing vat and running it for around 2 minutes, using a specially designed blade to deeply mix the mixture. After this time, the mixer is switched off and the tap located at the bottom of the metal vat is opened to pour the paste by gravity into the mould of the sample to be tested. This equipment facilitates the reconstitution of samples of different sizes and shapes, including cylindrical triaxial samples and hollow samples for the Hollow Cylinder Apparatus (HCA).

Once the slurry paste has been deposited in the mould, it is noticeable that the suspended particles tend to settle under the effect of gravity. The paste becomes denser and expels the water out of the tailing voids towards the surface. As the water dissipates, the soil particles tend to move closer together and the voids tend to shrink, as demonstrated in the tests carried out by Qin et al. (2021). To assess the settling time of the slurry paste after deposition, two 1000 ml graduated test tubes were used. Approximately 700 ml of slurry paste with a water content of 27% was placed in the test tubes. The water content defined to prepare the paste took into account two aspects: the liquidity limit (23%) and the warranty of a continuous deposition of the slurry. Approximately 2kg of tailings were placed in the mixer along with 540g of water. It should be noted that it is important that the weight remaining in the metal vat is sufficient to allow constant deposition rate of the paste. As deposition is gravitationally-driven, reducing the weight of the material in the container leads to changes in deposition speed and, as a result, variability throughout the sample, particularly in larger samples such as HCA ones. Once the deposition of the slurry is complete, readings were taken at 5-minute intervals until the end of the first 30 minutes and at 10-minute intervals until 60 minutes. Analysing Figure 1, which shows the settlement results over time, it can be seen that there is a more pronounced increase in settlement up to 30 minutes, which, then, tend to stabilise over time.

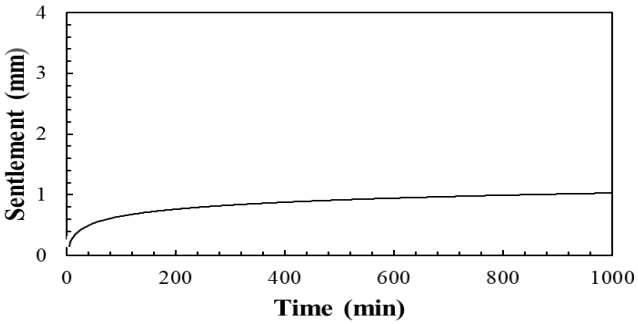

Figure 1. Settling of the surface of the paste over time.

2.3 Full section cylindrical triaxial samples

In order to study the settlement of the paste in full-section samples that could be used in triaxial tests, as well as possible segregation effects, three samples were prepared in metal moulds with a diameter of 50 mm and an average height of 70 mm with the same water content (27%) (Figure 2a). The height of the samples varies slightly due to the uncontrolled fitting of the impermeable base. Table 1 summarises the results obtained.

Table 1. Settlement the full section samples.

Sample	Settlement (mm)	DH/H (%)
A1	3,73	4,99
A2	4,25	5,44
A3	3,85	5,27

It should be noted that the sample preparation method developed shows very similar settlement values.

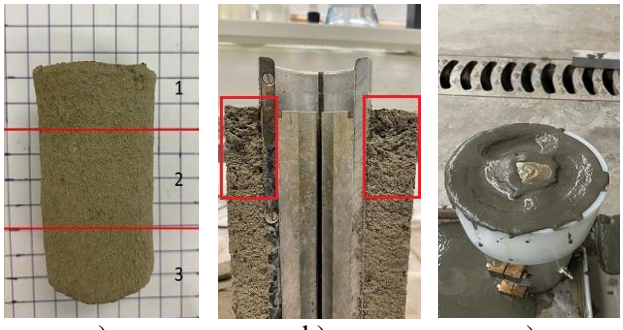

a) b) c)

Figure 2. Reconstituted samples: a) Sample division zones in the full section; b) Zone 1 sample hollow section.; c) Depositing the slurry with the collar.

This settlement should be taken into account when preparing samples in the triaxial equipment, by adding a surplus of slurry to compensate the variation in height (Qin et al. 2021). The results obtained for the full-section moulds indicated settlement values of around 4mm. for an initial average height of 70mm. It should be noted that all the moulds were left to rest for 30 minutes and then placed in an oven. The value of 4 mm is in line with that obtained in Figure 1 for the settlement after 30 minutes.

To assess possible particle segregation effects, the samples were removed from the mould after a drying process and divided in three parts, as shown in Figure 2a. Visual inspection did not detect any obvious particle segregation in any of the sample zones. This conclusion is corroborated by the determination of particle size curves for each of the three zones of the three samples produced. Similar grain size distribution curves were obtained, being also identical to those of the tailings before deposition, as it can be seen in Figure 3. However, it was possible to observe that for particles smaller than 0.06, zone 1 of the three samples analysed showed slightly higher percentages of finer particles when compared to the initial particle size curve. The analysis of the density of solid particles provides identical conclusions, with values ranging between 3.15 and 3.17.

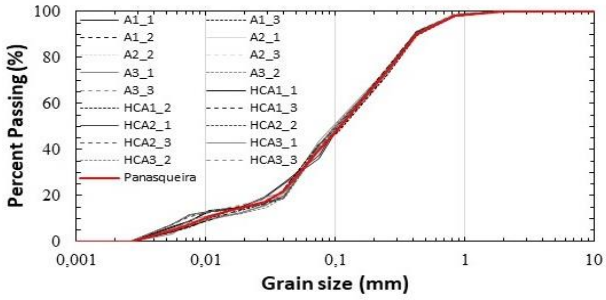

Figure 3. Particle size distribution curves of Panasqueira tailings and different zones of reconstituted samples.

In order to study the effect of different water contents used to prepare the slurry, particularly its influence in terms of void ratio (e), 5 samples were prepared using the same mould used previously, with water contents varying between 26 and 34 %. The values chosen were based on the liquidity limit and the homogeneous deposition of the sample, as well as the maximum limit for visible segregation in the sample. Figure 4 illustrates the results, showing the "theoretical" variation of e based on equation 1, which assumes an obviously invalid hypothesis that the soil is fully saturated and that no water is expelled from the voids after deposition:

$$e = G\ x\ w = 3{,}15\ .\ (w) \qquad (1)$$

where e is the void ratio and w the desired water content, both values deriving from the experiments. There is a clear difference, for each water content used, between the "theoretical" and the resulting values of void ratio, the latter being smaller due to the observed particle settlement. Still, the void ratio increases for more liquid slurries, but never as markedly as if the particles had not settled. It should be noted that all the samples had an equal deposition time of 30 minutes.

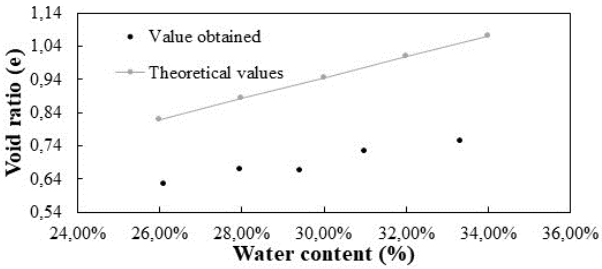

Figure 4. Variation of the void ratio (e) as a function of the water content of the slurry used in the reconstitution.

2.4 Hollow Section Samples for the HCA

Hollow cylindrical samples, with 60ID:100OD:200H mm (inner diameter:outer diameter:height) have also been prepared, aiming for future tests to be carried out in a HCA. Due to the hollow section, the slurry is deposited by means of circular movements along the circular crown of the sample.

Three samples have been prepared: i) HCA1: no collar (extension above the mould), no surplus soil in the vat; ii) HCA: no collar, with surplus soil in the vat; iii) HCA3 with collar, with surplus soil in the vat. For the HCA1 sample, it is visible that in zone 1, represented as an example in Figure 2b, there was some lack of material, showing a visibly porous surface. It was possible to determine a settlement of around 12 mm below the surface of the mould, corresponding to a relative settlement of 6.1%. By analysing the particle size curves, zone 1 of the HCA1 test shows a slightly higher percentage of fines compared to the other zones and the original particle size curve. The use of surplus soil (HCA2) makes it possible to achieve a completely filled surface in zone 1, while maintaining the settlement of 12 mm in relation to the top of the mould. Finally, with the use of a collar (HCA3) in addition to the soil surplus in the vat while preparing the mixture (Figure 2c), the entire mould is filled, with no settlement being observed, since the same occurs in the collar, and no variability being visually detected in the three zones. It should be noted that, due to the process of mounting the sample in a HCA, and unlike in a triaxial equipment, it is mandatory for the top of the sample to be flush with the top of the outer mould.

3 LABORATORY REPEATABILITY OF SLURRY SAMPLES

In order to assess the uniformity of the samples reconstituted using the sludge deposition method described above, 6 undrained triaxial compression tests were carried out with three different consolidation stresses (200, 800 and 1500 kPa). All the samples were prepared using the method described in Section 3.2 for full-section samples, with a water content of 27%. The tests were carried out under the same conditions and the results are illustrated in Figure 5. Independently of the initial consolidation stresses, all the samples show an initial contracting behaviour followed by a dilating behaviour for higher strains. Comparing the pairs of tests, similar behaviour can be identified, even if TX1_800 sample shows a slightly more rigid behaviour in comparison to TX2_800 test. Despite this difference, acceptable in laboratory testing, the results suggest that the technique used to reconstitute the samples shows good repeatability, although future improvements may be achieved.

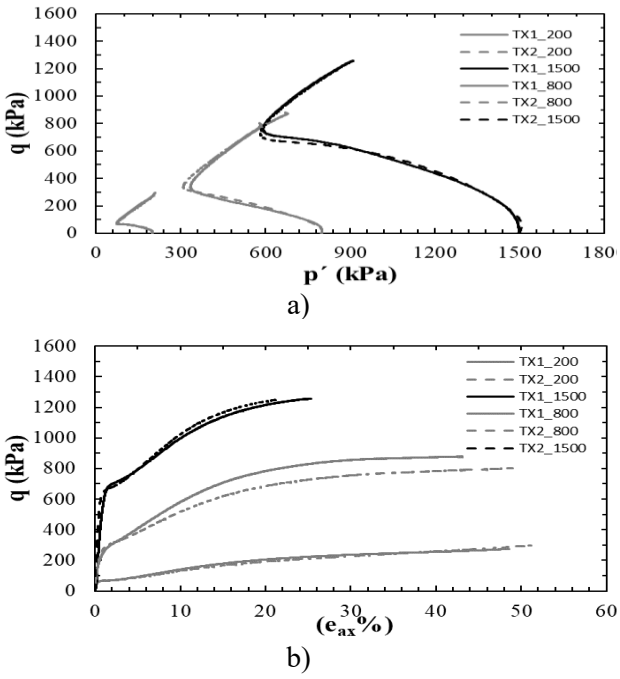

Figure 5. Undrained triaxial compression tests: a) Stress path in p´-q space; b stress-strain behaviour.

4 CONCLUSIONS

This paper discusses the preparation of reconstituted samples through the deposition of slurry paste, using samples of different sizes and geometries. The following aspects can be highlighted:

- The slurry-based sample preparation method proposed produces a homogeneous mixture with no obvious visual segregation effects.
- Sedimentation of the tailing's particles from the Panasqueira´s mine occurs initially in the first 30 minutes, showing a tendency to stabilise
- The samples top layers had a slightly higher percentage of fines compared to the other layers.
- The settlement process, after slurry deposition, causes a significant decrease in the void ratio.
- The increase in the slurry water content causes a less significant increase of the void ratio than expected from an ideal no-settlement condition.
- The preparation of reconstituted hollow-section samples for HCA requires a collar so that the paste settlement does not affect the next steps.
- The triaxial tests carried out show a good potential for repeatability of the samples produced by the technique presented.

ACKNOWLEDGEMENTS

The authors acknowledges the financial support of the Foundation for Science and Technology to GeoSusTailings Project through the Research Grant PTDC/ECI-EGC/4147/2021 and the support of the company Beralt Tin and Wolfram Portugal, S.A., which operates the Panasqueira mine concession in Portugal and collaborates with the research project by supplying the tungsten tailings for testing.

REFERENCES

Carraro, J. and Prezzi, M. (2008) A New Slurry-Based Method of Preparation of Specimens of Sand Containing Fines, *Geotechnical Testing Journal* 31(1): 111. https://doi.org/10.1520/GTJ100207.

Qin, J., Zheng, J., and Li, L. (2021). An analytical solution to estimate the settlement of tailings or backfill slurry by considering the sedimentation and consolidation. *International Journal of Mining Science and Technology*, 31(3): 463–471. https://doi.org/10.1016/j.ijmst.2021.02.004.

Tastan, E. O. and Carraro, J. A. H. (2013) A New Slurry-Based Method of Preparation of Hollow Cylinder Specimens of Clean and Silty Sands, *Geotechnical Testing Journal*, 36(6): 811-822. https://doi.org/10.1520/GTJ20130056.

Wang, C., Harbottle, D., Liu, Q., and Xu, Z. (2014). Current state of fine mineral tailings treatment: A critical review on theory and practice. *Minerals Engineering* 58: 113–131. https://doi.org/10.1016/j.mineng.2014.01.018.

Proceedings of the XVIII ECSMGE 2024
GEOTECHNICAL ENGINEERING CHALLENGES
TO MEET CURRENT AND EMERGING NEEDS OF SOCIETY
© 2024 the Authors
ISBN 978-1-032-54816-6
DOI 10.1201/9781003431749-349
Open Access: www.taylorfrancis.com, CC BY-NC-ND 4.0 license

ECSMGE 24
XVIII EUROPEAN CONFERENCE ON SOIL MECHANICS AND GEOTECHNICAL ENGINEERING

The use of InSAR to analyse ground displacement: the case study of Póvoa de Santa Iria industrial area

L'utilisation de InSAR pour l'analyse de déplacements du terrain: le cas d'étude de la zone industrielle de Póvoa de Santa Iria

M. Ormeche*, R.C. Gomes, A.P. Falcão
Instituto Superior Técnico, University of Lisbon, Portugal

**mariana.ormeche@tecnico.ulisboa.pt*

ABSTRACT: Riverside alluvium areas are prone to consolidation settlements that can induce serviceability and/or structural damage to construction. Several in-situ measurements can be used to monitor soil and structural displacement. However, the use of Synthetic Aperture Radar (SAR) images has been proven to be an accurate monitoring tool for ground and structural displacements, allowing regular displacement monitoring over wide areas, with approaches such as Interferometric SAR (InSAR). The applicability of SAR images in consolidation settlement monitoring is analysed in the case study of an industrial area in the northern part of Lisbon city (Portugal). The site has been used since de 1980s and several storehouses have been built ever since. The goal of this work is to compare the in-situ measurements with long-term InSAR time series acquired by Sentinel-1 between 2018 and 2022. From 2006 and 2014, a maximum vertical displacement of ~1 m was measured with *in situ* techniques. The Sentinel-1 data (2018-2022) measured displacement rates between 6 and 8 mm/year. This work presents the use of the European Ground Motion Service (EGMS) time series to complement *in situ* measurements of the industrial area. The evolution of SAR satellites is also analysed though the comparison of the image characteristics and their influence on consolidation subsidence monitoring.

RÉSUMÉ: Les zones d'alluvions riveraines sont sujettes à des tassements de consolidation qui peuvent entraîner des dommages de service et/ou structurels à la construction. Plusieurs mesures in situ peuvent être utilisées pour surveiller les déplacements du sol et des structures. Cependant, l'utilisation d'images de *Synthetic Aperture Radar* (SAR) s'est avérée être un outil de surveillance précis pour les déplacements du sol et des structures, permettant une surveillance régulière des déplacements sur de vastes zones, avec des approches telles que l'interférométrie SAR (InSAR). L'applicabilité des images SAR dans la surveillance des tassements de consolidation est analysée dans l'étude de cas d'une zone industrielle située dans la partie nord de la ville de Lisbonne (Portugal). Le site est utilisé depuis les années 1980 et plusieurs entrepôts ont été construits depuis. L'objectif de ce travail est de comparer les mesures in situ avec les séries temporelles InSAR à long terme acquises par Sentinel-1 entre 2018 et 2022. Entre 2006 et 2014, un déplacement vertical maximal de ~1 m a été mesuré avec des techniques in situ. Les données de Sentinel-1 (2018-2022) ont mesuré des taux de déplacement entre 5 et 8 mm/an. Ce travail présente l'utilisation de la série temporelle de le *European Ground Motion Service* (EGMS) pour compléter les mesures in situ de la zone industrielle. L'évolution des satellites SAR est également analysée à travers la comparaison des caractéristiques de l'image et leur influence sur la surveillance de l'affaissement de la consolidation.

Keywords: Settlement; ground movement monitoring; InSAR; EGMS.

1 INTRODUCTION

The Tagus river alluviums present several challenges for the construction and serviceability of structures, requiring the need for soil reinforcement (Falcão et al., 2000; Pinto et al., 2011, 2016; Sêco e Pinto et al., 2020). The Póvoa de Santa Iria industrial area ground was reinforced in 2002 using stone columns, allowing the growth of the industrial site. Nevertheless, in 2012, one of the storehouses started to show signs ground displacement.

In fact, displacements reaching 1.00 m were measured between 2006 and 2015 using topographical monitoring. Displacements were also captured using the remote sensing technique, Interferometric Synthetic Aperture Radar (InSAR). Between 2015 and 2022 displacements of ranging from 3.00 mm/year to 8.50 mm/year were captured in the European Ground Motion Service (EGMS) (Copernicus, 2023; Costantini et al., 2021).

The goal of this work is to combine *in situ* and remote sensing monitoring techniques to monitor and evaluate the ground displacement of the Santa Iria industrial area.

2 SITE DESCRIPTION

The Póvoa de Santa Iria industrial site is located north of Lisbon, near the Tagus river (Figure 1).

The site is built on top of the Tagus river alluviums, composed by sludge and sand and can reach depths up to 60 m. The alluviums are followed by "Areolas de Cabo Ruivo", a Mycenaean formation composed of clayey sands and sandstones with a thickness of about 21 m (LNEG, 2011). From the geotechnical survey conducted in 2015, the lithology observed is presented in Table 1.

Table 1. Lithology of the site.

Depth (m)	Description
2.00 – 3.00	**Landfill** Crushed aggregate limestone
18.80 – 27.00	**Alluvium** Sludge and sands
> 24.00	**"Areolas de Cabo Ruivo"** Silty clays

The area has been used as an industrial site since before 2002, when the soil was reinforced with stone columns. In fact, through the analysis of historical optical imagery (Google Earth Pro, 2023), a history of the construction could be established since 1985.

Prior to March 2002, only one storehouse is present on the site, closer to the river (Figure 2). This first storehouse was then demolished between 2004 and 2005, and replaced with the storehouse that we see today (Figure 1).



Figure 1. Póvoa de Santa Iria industrial site in April 2023 (adapted from Google Earth Pro, 2023).



Figure 2. Póvoa de Santa Iria industrial site in March 2002 (adapted from Google Earth Pro, 2023).

The construction evolution of the industrial site is presented in Figure 3. After the soil reinforcement in 2002, the industrial site grew exponentially, especially between 2002 and 2012.

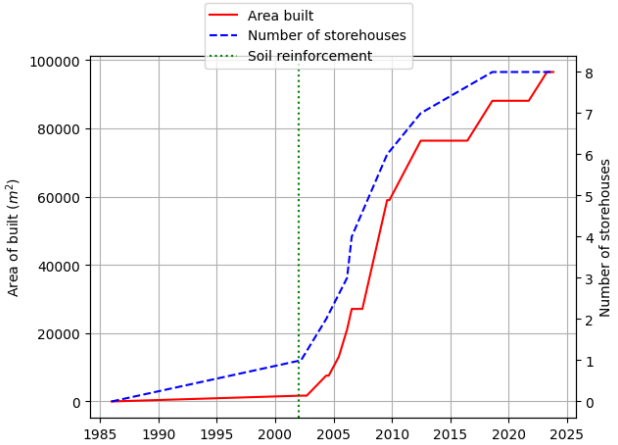

Figure 3. Construction evolution of the industrial site.

In 2012, one of the storehouses (SH1) built in 2006 showed signs of large ground displacement with cracks on the building. In 2014 another storehouse (SH2) also started to show signs of displacement on the ground surrounding the building.

The displacements of the storehouse were monitored between 2014 and 2015, and in 2023 using topography. These measurements were then complemented with the data from the EGMS between 2015 and 2022.

3 TOPOGRAPHICAL MONITORING

In 2014 six topographic targets were placed in SH1 (Figure 4), A1 to A3 in the North façade of the building, and A4 to A6 in the South façade. The targets were monitored between 2014 and 2015, and in 2023.

From the construction of SH1 in 2006 until 2014, the building registered a maximum displacement of 1.03 m in A5. It can be observed that the North and the South façades of SH1 behave differently. In fact, between 2006 and 2014, the North façade settled ~0.45 m, whereas the South façade settled ~0.98 m (Figure 5). The South façade settled the double of the North façade, this differential displacement is probably the reason cracks appears on the building.

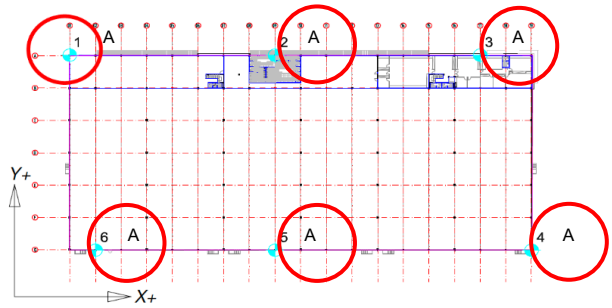

Figure 4. Location of the topographic targets.

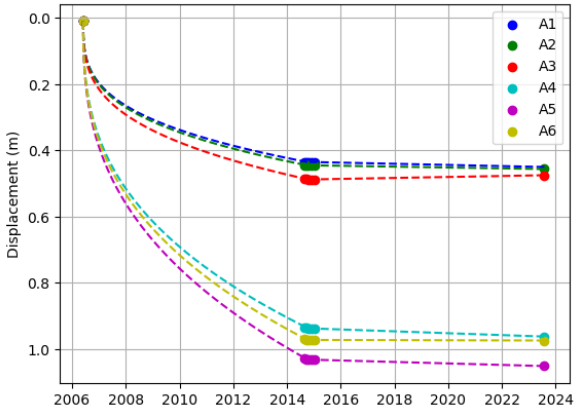

Figure 5. Displacement observed in SH1 with topographical monitoring.

In Figure 5, two types of displacement are distinguished. It is between 2006 and 2014 that the major displacements are observed, where a load settlement curve can be fitted. However, between 2014 and 2023, the movements seem to be linear, with rates ranging from 3.50 mm/year to 7.80 mm/year.

4 INSAR MONITORING

To complement the topographic monitoring, InSAR was used. InSAR is a technique that allows the analysis of long-term temporal series of displacements in the Earth's surface though the comparison of several SAR images (ASF, 2019; Bamler & Hartl, 1998; Crosetto et al., 2016; Earth Science Data Systems, 2020; Ferretti et al., 2007; Massonnet & Feigl, 1998).

SAR is an active imaging system that uses microwaves and records the backscattered signal. This system allows for all-day, all-nigth and all-weather measurements since the microwaves can penetrate clouds.

The InSAR technique can measure displacements through the difference of the phase registered in different images, called the interferometric phase, $\Delta\phi$. Considering ϕ_1 and ϕ_2 two phases registered at a given point by image 1 and image 2, respectively, the interferometric phase is given by the following equation:

$$\Delta\phi = \phi_2 - \phi_1 \quad (1)$$

The interferometric phase, $\Delta\phi$ is affected by displacement, topography, atmosphere, satellite orbit and noise. The interferometric phase is then given by:

$$\Delta\phi = \Delta\phi_{displacement} + \Delta\phi_{topography} + \Delta\phi_{atmosphere} + \Delta\phi_{orbit} + \Delta\phi_{noise} \quad (2)$$

The measurements points were obtained through the EMGS, that is a service that provides InSAR displacement time-series across Europe with the Sentinel-1 satellite (Copernicus, 2023; Costantini et al., 2021). Today the time series available are from 2018 to 2022 and provide measurements every 6 to 12 days. Two points were obtained in SH1, one on the North façade and another one on the South façade with displacement rates of 5.60 mm/year and 7.50 mm/year, respectively (Figure 6).

5 RESULTS AND DISCUSSION

The InSAR measurements confirmed the linear pattern of displacement observed with topography from 2014 onwards. In fact, similar movement rates are captured with both techniques, with displacement ranging from 3.50 mm/year to 7.80 mm/year and from 5.60 mm/year to 7.50 mm/year with topography and InSAR, respectively.

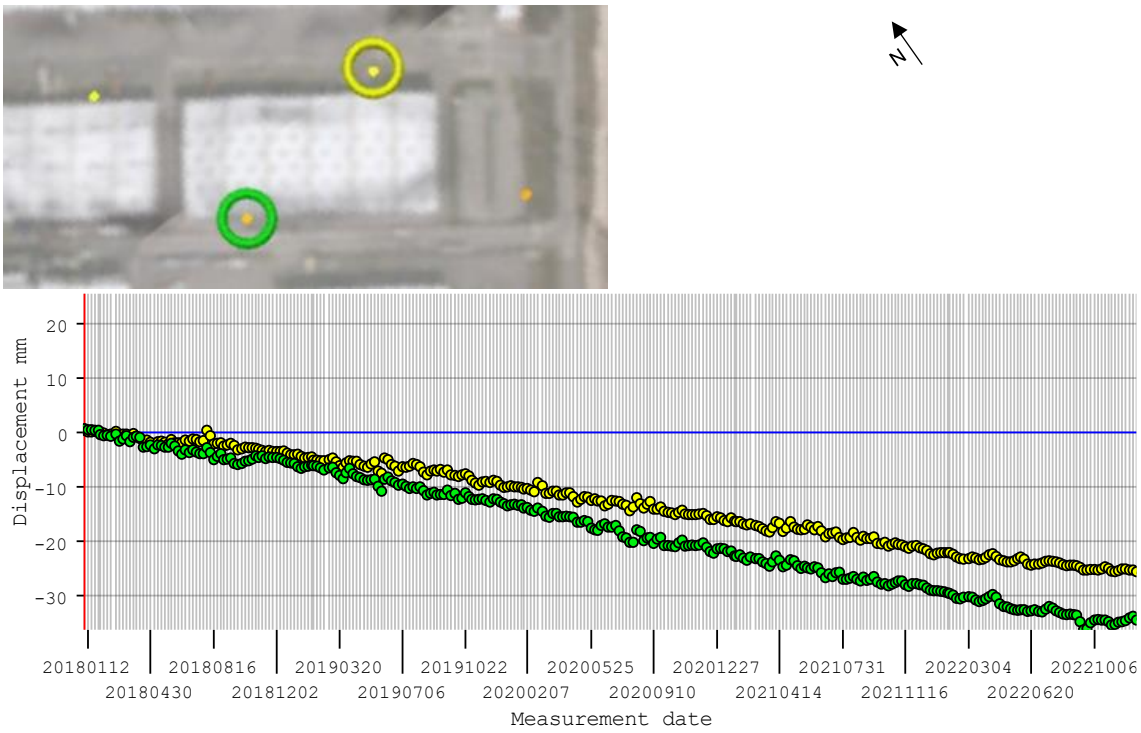

Figure 6. Vertical displacement of SH1 from 2018 to 2022 (adapted from Copernicus, 2023).

From 2014 onwards the settlement of SH1 seems to have stabilized and presents now a linear movement of a couple of millimetres per year. This behaviour is present not only in SH1 but in the whole industrial area, that presents linear movements, with larger displacements when approaching the Tagus River (South).

This study shows that InSAR can be a useful and reliable technique when monitoring displacement of structures. However, InSAR has its limitations, first the fact that measurement points limited to the backscatter registered, which makes man made structed good measuring points (Massonnet & Feigl, 1998) but not planar fields for example. Then, the measuring points are limited to the resolution of images, for Sentinel-1 the maximum resolution is 5 x 5 m. Lastly, the maximum displacement that can be measured with InSAR techniques is half the wavelength between image acquisition (Massonnet & Feigl, 1998), which in the case of Sentinel-1 is 27 mm every 6 to 12 days (ESA, 2023), i.e. ~1.60 m/year to ~0.80 m/year.

6 CONCLUSIONS AND FUTURE DEVELOPMENT

The Póvoa de Santa Iria industrial area presented settlements over time that seem to have reduced and is moving now at a rate of few millimeters per year.

In this case the EGMS, and InSAR, have proven to be effective tools to retrieve displacement time series over the last decade and the displacement trends over large areas.

Future developments of this analysis include the use of other SAR images to measure displacement over the Póvoa de Santa Iria industrial area to:

- Have better resolution results, i.e. more measuring points, with for example images of TerraSAR-X that has a 1 x 1 m resolution.
- Characterise the displacements that occurred between 2006 and 2014 with images of satellites that were flying during this time period. For example, ENVISAT (2002 – 2011) or ALOS-2 (2006 – 2013).

ACKNOWLEDGEMENT

The authors are grateful for the financial support provided by Fundação para a Ciência e Tecnologia through the PhD Studentship 2021.06437.BD.

REFERENCES

ASF. (2019, March 6). *What is SAR?* Alaska Satellite Facility (ASF). https://asf.alaska.edu/information/sar-information/what-is-sar/.

Bamler, R., & Hartl, P. (1998). Synthetic aperture radar interferometry. *Inverse Problems*, *14*(4), R1. https://doi.org/10.1088/0266-5611/14/4/001.

Copernicus. (2023). *European Ground Motion Service (EGMS)* [Online]. https://egms.land.copernicus.eu/.

Costantini, M., Minati, F., Trillo, F., Ferretti, A., Novali, F., Passera, E., Dehls, J., Larsen, Y., Marinkovic, P., Eineder, M., Brcic, R., Siegmund, R., Kotzerke, P., Probeck, M., Kenyeres, A., Proietti, S., Solari, L., & Andersen, H. S. (2021). European Ground Motion Service (EGMS). *2021 IEEE International Geoscience and Remote Sensing Symposium IGARSS*, 3293–3296. https://doi.org/10.1109/IGARSS47720.2021.9553562.

Crosetto, M., Monserrat, O., Cuevas-González, M., Devanthéry, N., & Crippa, B. (2016). Persistent Scatterer Interferometry: A review. *ISPRS Journal of Photogrammetry and Remote Sensing*, *115*, 78–89. https://doi.org/10.1016/j.isprsjprs.2015.10.011.

Earth Science Data Systems, N. (2020, April 10). *What is Synthetic Aperture Radar?* [Backgrounder]. Earthdata; Earth Science Data Systems, NASA. https://www.earthdata.nasa.gov/learn/backgrounders/what-is-sar.

ESA. (2023). *Sentinel Online*. European Space Agency (ESA). https://sentinels.copernicus.eu/web/sentinel/missions/sentinel-1/data-products.

Falcão, J. F., Pinto, A. L., & Pinto, F. D. (2000). *Case Histories of Ground Improvement Solutions Using Jet-grouting*. ISRM-IS-2000-343.

Ferretti, A., Monti-Guarnieri, A., Prati, C., Rocca, F., & Massonnet, D. (2007). Part A Interferometric SAR image processing and interpretation. In *InSAR Principles: Guidelines for SAR interferometry Processing and Interpretation* (p. A-3-A-40). ESA Publications.

Google Earth Pro. (2023). *Historical imagery* [Online].

LNEG. (2011). *Notícia explicativa da folha 34-B Loures*. Laboratório Nacional de Energia e Geologia (LNEG).

Massonnet, D., & Feigl, K. L. (1998). Radar interferometry and its application to changes in the Earth's surface. *Reviews of Geophysics*, *36*(4), 441–500. https://doi.org/10.1029/97RG03139.

Pinto, A., Tomásio, R., & Marques, G. (2016). Ground Improvement with Jet Grouting Solutions at the New Cruise Terminal in Lisbon, Portugal. *Advances in Transportation Geotechnics III*, *143*, 1495–1502. https://doi.org/10.1016/j.proeng.2016.06.176.

Pinto, A., Tomásio, R., Ravasco, J., & Marques, G. (2011). Fill of the "Terreiro do Trigo" Dockyard in Lisbon over Alluvial and Hard Soils. *Proceedings of the 15th European Conference on Soil Mechanics and Geotechnical Engineering*, 787–792. https://doi.org/10.3233/978-1-60750-801-4-787.

Sêco e Pinto, P. S., Oliveira, R., & Portugal, A. (2020). Understanding Pile Foundations Design Through Case Histories of New Tagus Bridge and Leziria Bridge. In P. Pinto, C.-Y. Ou, & H. Shehata (Eds.), *Innovative Solutions for Deep Foundations and Retaining Structures* (pp. 106–153). Springer International Publishing.

Proceedings of the XVIII ECSMGE 2024
GEOTECHNICAL ENGINEERING CHALLENGES
TO MEET CURRENT AND EMERGING NEEDS OF SOCIETY
© 2024 the Authors
ISBN 978-1-032-54816-6
DOI 10.1201/9781003431749-350
Open Access: www.taylorfrancis.com, CC BY-NC-ND 4.0 license

ECSMGE 24
XVIII EUROPEAN CONFERENCE ON SOIL MECHANICS AND GEOTECHNICAL ENGINEERING

Rehabilitation of overpass at Ch.19.978 of Fier-Vlora highway. Influence of time of consolidation in the performance of the overpass structure

Réhabilitation du passage supérieur du Ch.18.978 de l'autoroute Fier-Vlora. Influence du temps de consolidation sur la performance de la structure du viaduc

E. Paçi*, N. Shkodrani, A. Dervishaj
Polytechnic University of Tirana, Faculty of Civil Engineering, Tirana, Albania
ervin.paci@fin.edu.al

ABSTRACT: The overpass of Ch. 18.978 of the new highway Fier-Vlore in the West South of Albania less than one year after the opening to the traffic was closed due to excessive settlements of the abutments. This paper illustrates the work for analysing the causes of the problem and the design for the rehabilitation of the structure of the overpass. The abutments are constructed as an embankment of 8m on top of which was placed a RC raft with 4 piles 16m deep. From the geological re-study, it was seen that the geological layers, contrary to what was predicted, were a mixture of silty-clays and organic clays with very weak properties. To analyse the problem, consolidation analysis was carried out and for rehabilitation interventions of soil reinforcement by stone columns with vibro-compaction techniques and foundation reinforcement with additional piles were evaluated. Based on the detailed geotechnical analysis, it was estimated that the consolidation time for the soil-structure system was nearing its end. These analyses were verified by the monitoring in site and was decided for an intervention only to reposition the superstructure of the overpass and the replacement of the damaged supports and bearings. The article indicate the importance of a pre-consolidation process, the proper calculation of time of consolidation and monitoring influence to the performance of the overpass structure.

RÉSUMÉ: Le viaduc du Ch. 19.978 de la nouvelle autoroute Fier-Vlore dans l'ouest-sud de l'Albanie, moins d'un an après l'ouverture à la circulation, a été fermée en raison de tassements excessifs des culées. Cet article illustre les travaux d'analyse des causes du problème et la conception de la réhabilitation de la structure du viaduc. Les culées sont construites comme un remblai de 8 m au-dessus duquel a été placé un radier RC à 4 pieux de 16 m de profondeur. De la réétude géologique, il a été constaté que les couches géologiques, contrairement à ce qui était prévu, étaient un mélange d'argiles limoneuses et d'argiles organiques aux propriétés très faibles. Pour analyser le problème, une analyse de consolidation a été réalisée et, pour la réhabilitation, des interventions de renforcement du sol par des colonnes de pierre avec des techniques de vibro-compactage et de renforcement des fondations avec des pieux supplémentaires ont été évaluées. Sur la base de l'analyse géotechnique détaillée, il a été estimé que le temps de consolidation du système sol-structure touchait à sa fin. Ces analyses ont été vérifiées par le suivi sur site et il a été décidé une intervention uniquement pour repositionner la superstructure du viaduc et le remplacement des supports et appareils d'appui endommagés. L'article indique l'importance d'un processus de pré-consolidation, du calcul approprié du temps de consolidation et de l'influence de la surveillance sur la performance de la structure du viaduc.

Keywords: Consolidation; overpass structure rehabilitation.

1 INTRODUCTION

The overpass of Ch. 18.978 of the new highway Fier-Vlore in the west-south of Albania was closed less than one year after the opening to the traffic due to excessive settlements of the abutments. This paper illustrates the work for analysing the causes of the problem and the design for the rehabilitation of the structure of the overpass. The abutments are constructed as an embankment of 8m on top of which a RC raft with 4, 16m deep piles was placed. From the geological re-study, it was seen that the geological layers, contrary to what was predicted, were a mixture of silty-clays and organic clays with very weak properties. To analyse the problem, consolidation analysis was carried out and, for the overpass rehabilitation interventions solutions involving soil reinforcement by stone columns with vibro-

compaction techniques and foundation reinforcement with additional piles were evaluated. Based on a detailed geotechnical analysis, it was estimated that the consolidation time for the soil-structure system was nearing its end. These analyses were verified by monitoring in site and an intervention only to reposition the superstructure of the overpass and the replacement of the damaged supports and bearings was decided. The article indicates the importance of proper calculation of time of consolidation and monitoring on the performance of the overpass structure.

2 PROBLEMS IN THE VIADUCT

2.1 Description of the existing design

The viaduct at km 18.978 consists of two spans bridge structure facilitating passage across the service road (secondary) of the 'By-Pass Fier' highway. The Figure 1 gives the cross section of the overpass.

The structure is composed of 4 girder precast post-tensioned beams (20.75m) every 1.62m connected by a 20cm reinforced concrete slab and supported by elastomeric bearings at the abutments and at the cap-beam of the central pier. The width of the superstructure is 5m +2*0.6m=6.2m.

Abutments A and B consist of a plate supported on 4 piles (6+14m, D=80cm) with a 6m above-ground part to achieve the overpass level filled with granular material. The granular material substitute also the first 4m of the natural soil under the abutments.

The pier is a 4.8x1.2m reinforced concrete wall supported on 1.5m thick foundation plate with 6 piles (D=80cm).

The levelling of the super-structure with the filling of the abutments is done by means of a 10 cm expansion joint.

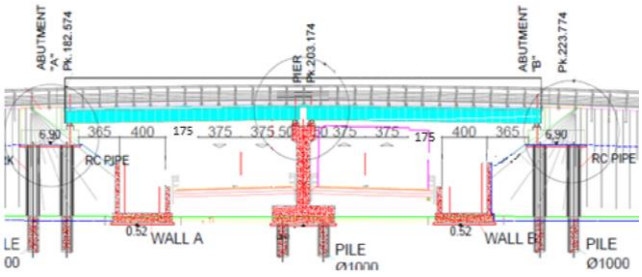

Figure 1. View of the viaduct structure.

2.2 Observed settlements

Approximately 10 months after opening to traffic, significant openings and unevenness were detected at the expansion joints. These deformations indicated settlements of the abutments. After this finding, the viaduct was closed for operation and benchmarks were placed in the abutments and in the central pier for periodic measurement of settlements. The first measurements have shown 35-40cm settlements.

Monitoring of settlements was carried out throughout the analysis, design and implementation of rehabilitative interventions.

2.3 Structural damages

Besides settlements, the structure exhibited cracks in the reinforced concrete walls of the abutments, accompanied by lateral deformations and initial signs of rubber cracks in the elastomeric bearings. The Figures 2 and 3 illustrate some of the damages.



Figure 2. View of elastomeric bearing damage.



Figure 3. View of RC abutment wall damage.

3 ANALYSIS OF THE EXISTING CONDITIONS

3.1 General for existing condition

In response to the investor's request, a comprehensive analysis was conducted to comprehend the issues and determine measures to restore the viaduct's functionality. The design geological study wasn't performed for the exact position of the viaduct, so a new detailed geological study was done.

3.2 Geological study

The recent study revealed exceedingly soft soils, particularly at depths of 9-12-24m, characterized by organic soil and extremely soft clays. The bedrock was at a depth of 44m. One of the borehole logs is given in the Figure 4.

#	Name	Thickness	Top Elevation	Bottom Elevation
1	Fill	1	0	-1
2	Clay 2	7	-1	-8
3	Sand 5	1	-8	-9
4	Clay MH OH 3	3	-9	-12
5	Clay 4 Prog.	12	-12	-24
6	Sand 5	1	-24	-25
7	Clay 5	2	-25	-27
8	Sand 5	1	-27	-28
9	Clay 5	5	-28	-33
10	Clay 6	5	-33	-38
11	Clay 6a	6	-38	-44
12	W clay rock 7	6	-44	-50

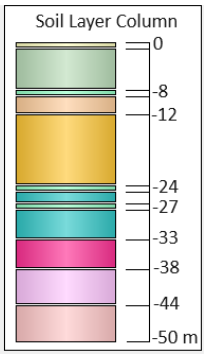

Figure 4. View of borehole 1-layers thickness.

The layer parameters used in the analysis are given in the Figure 5.

Material Name	Color	Unit Weight (kN/m3)	Sat. Unit Weight (kN/m3)	Es (kPa)	Eur (kPa)	Material Type	Cc	Cr	OCR	e0	Cv (m2/y)	Cvr (m2/y)
Fill		18	18	10000	10000	Non-Linear	0.3	0.1	1	1.1	1	1
Clay 2		13.13	18	7000	20000	Non-Linear	0.4	0.07	1	1.1	0.3	0.3
Clay ML OH 3		13.2	17	2650	8000	Non-Linear	0.75	0.11	1	0.8	3	1
Clay 4 progresive		11	17	7000	10000	Non-Linear	0.4	0.1	1	1	1	1
W clay rock 7		19	20	80000	200000	-	-	-	-	-	-	-
Sand 5		13.5	18.4	19000	50000	-	-	-	-	-	-	-
Clay 6		15	18.5	-	-	Non-Linear	0.3	0.1	1	1.1	0.35	0.5
Clay 5		17	18	7000	20000	Non-Linear	0.3	0.1	1	1	0.4	1
Clay 6a		15	19	17000	40000	Non-Linear	0.225	0.1	1	0.8	0.2	0.4

Figure 5. View of layers geotechnical parameters.

3.3 Analysis

Two types of analysis were performed: finite difference and finite element numerical analyses (Software Settle 3D and Plaxis 2D).

Figures 6 to 8 depict the mentioned models. In each model after the generation of the natural stress field are simulated the stages of construction by

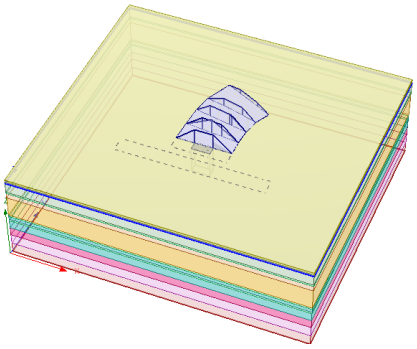

Figure 6. View of finite difference (FD) model. (Settle 3D).

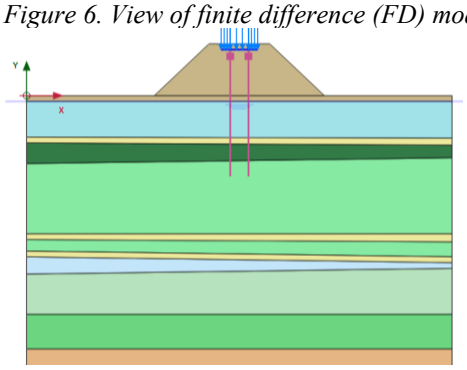

Figure 7. View of numerical FE cross section model. (Plaxis 2D).

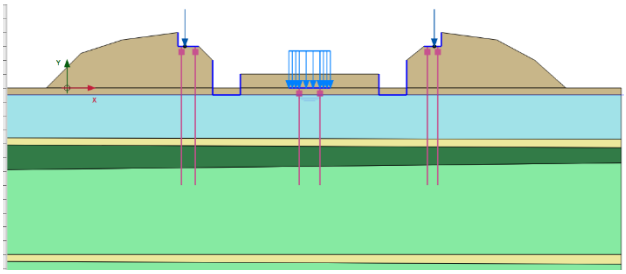

Figure 8. View of numerical FE longitudinal section model.

3.4 Results and conclusions for existing condition

Figures 9 to 11 show some results of the deformation analysis.

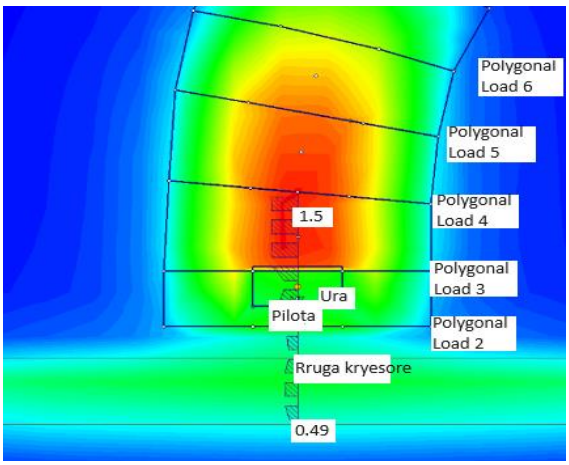

Figure 9. Settlement for the FD model.

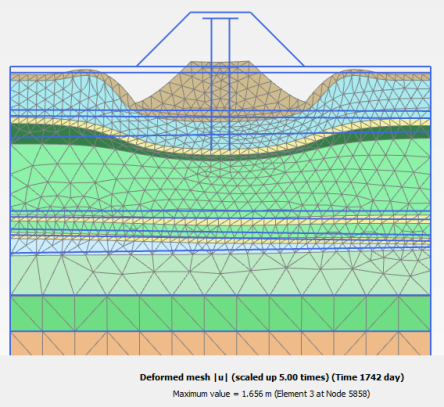

Figure 10. Deformed numerical cross section numerical model.

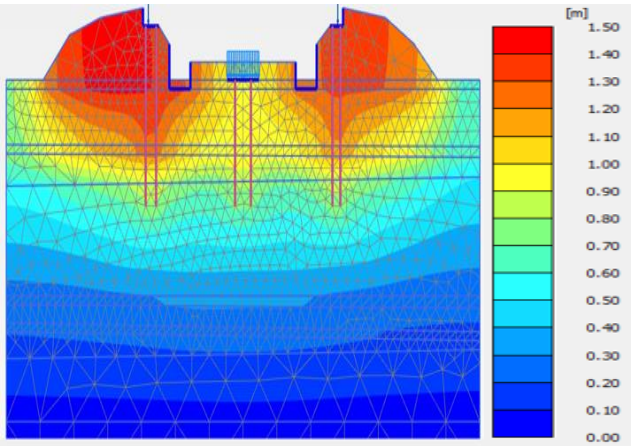

Figure 11. Settlement for the numerical longitudinal model.

The essential conclusions of the performed analyses may be summarized as follows.
The total settlements (immediate and consolidation) for the analytical model are 150cm. The time of 90% of consolidation is 5 years and 98% correspond to 50years.

The total settlements (immediate and consolidation) for the numerical model are 165/144cm. The time of 90% of consolidation is 1.8 years and 98% correspond to 4.9 years.

The values of settlements in both types of models are similar and only the time of consolidation differs indicating that the coefficients of compression given in the geological study were not calibrated.

This conclusion is proved also by the manual simplified calculations.

4 ANALYSIS OF INTERVENTION SCENARIOS

4.1 Identification of intervention scenarios

Based on the analysis results it's seen that the problems results from insufficient capacity of the viaduct foundations. So, structural and soil reinforcement methodologies have been identified for rehabilitaion intervention scenarios.

4.1.1 First Scenario of Interventions (I)

Scenario "I" consists in the following interventions.
1. Soil reinforcement and consolidation
This intervention consists in the execution of vertical drains (stone columns and wick drains) in a uniform manner and the system of removal of drained waters. The duration of the drainage is expected to be about 1 year until the majority of the consolidation is achieved, Then the overpass structure can be rehabilitated (repositioning of bearings and beams).
2. Widening of abutment A and B.
3. Repositioning of bearings and beams by jack or crane lifts.

4.1.2 Second Scenario of Interventions (II)

Scenario "II" consists in the following interventions.
1. Soil and structural foundation reinforcement.
This intervention consists in the execution of RC drilled piles connected with a widening foundation of the abutments and central pier.
2. Widening of abutment A and B and central Pier foundation.
3. Repositioning of bearings and beams by jack or crane lifts.

4.1.3 Third Scenario of Interventions (III)

Scenario "III" consists in the control of settlements and the following interventions.
1. Extension/elevation of abutment A and B by RC blocks that support the bearings.
2. Replacement of beam bearings by lifting with a jack or crane and placing new bearings.
3. Separation of the continuous slab in the middle pier.
4. Widening of the support of the beams in the middle pier.
5. Continuous monitoring and adjustment/restoration of the support of the abutments and pier every 6-9 months to adapt to the uniformity of the soil settlements. (The duration of this process is expected to be up to 3 years).

The adjustment and re-elevation of the support blocks will be done in case of deformations that cannot be accommodated by the connecting joints on the surface.

The jack-up of the superstructure will be carried out as in point 2.

4.2 Results for each scenario

Figures 12 to 16 give the main results of analyses.

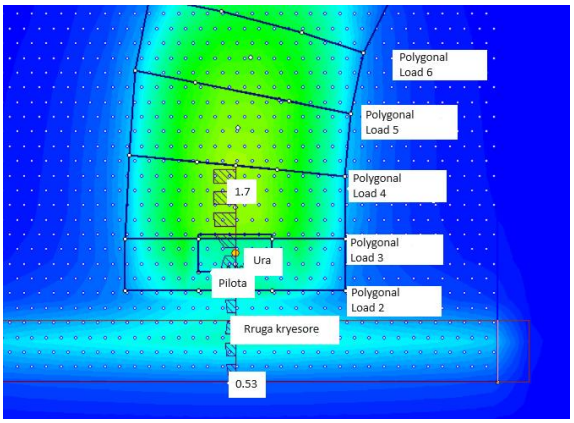

Figure 12. Settlements of abutment A for SC soil reinforcement. (u_{max}= 1.7m), Scenario I.

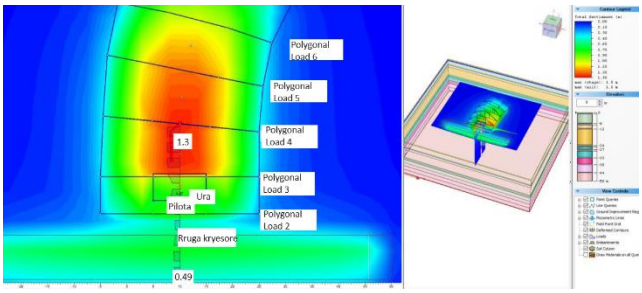

Figure 13. Settlements of abutment A for RC piles reinforcement. (u_{max}= 1.5m), Scenario II.

Settlements of Pier foundation for RC piles reinforcement has resulted u_{max}= 0.83m, Scenario II.

Scenario III will ensure the sequential stability of the overpass - soil system, but after the abutments we will again have settlements that will be uniform and reduced in time for a period of up to 3 years. Settlements can cause difficulties in circulation and must be considered during operation and maintenance. The settlements that the reinforced structure will suffer result from the difference between the current settlements and those at the time of the end of the consolidation.

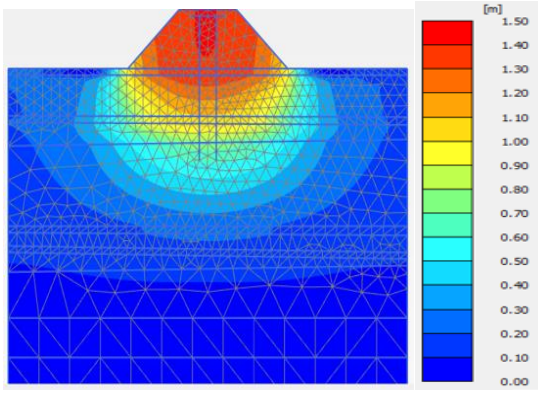

Figure 14. Settlements of abutment A for consolidation time 300 days. Plaxis 2D.

The total settlements in the model with detailed numerical analysis for a time 300 days are given in Figure 14. The max settlements are u_{max}=140cm.

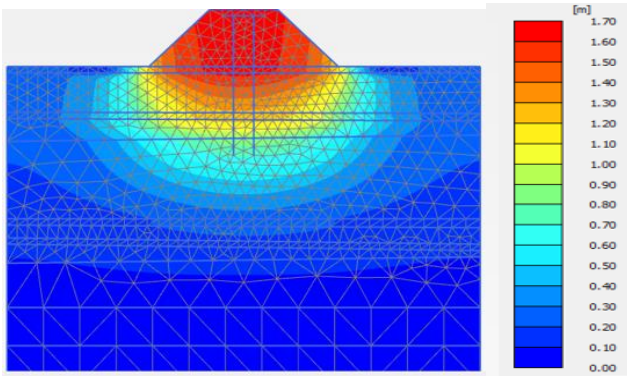

Figure 15. Settlements of abutment A for consolidation time 675 days.

Total settlements in the model with detailed numerical analysis for a time 675 days are given in figure 15. The max settlements are u_{max}=165.1cm.

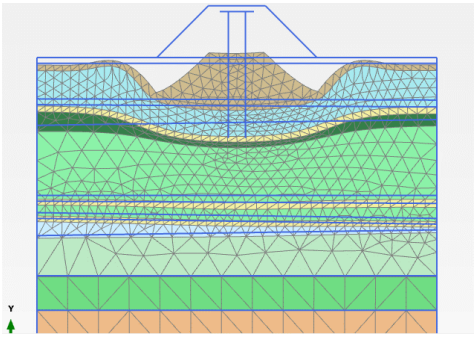

Figure 16. Settlements of abutment A for consolidation time 1742 days.

Total settlements in the model with detailed numerical analysis for a time 1742 days are given in Figure 16. The max settlements are u_{max}=165.6cm.

The differences in the settlements are about 25cm. So an increase/continuation of settlements of 25cm is expected for a period of 675-180= 495 days (1.35 years). In order to cope with these settlements, the project of changes to the structure of the abutments and the replacement of elastomeric bearings supports was made.

4.2.1 Analysis of the bridge structure

The calculation model for the bridge remains almost the same during the intervention phase and completely the same during the exploitation phase, therefore the intervention does not affect the bearing capacity of the superstructure for vertical loads and traffic loads.

Even for seismic loads, the intervention will not have effect during the exploitation phase of the work.

The capacity of the bridge for design loads remains unchanged as per the original project.

We have built a model given in Figure 17, to analyze the impact of the settlements and then to take the

forces in the supports and choose the suitable elastomeric bearings for the support of the superstructure and the accommodation of the continuation of the settlements.

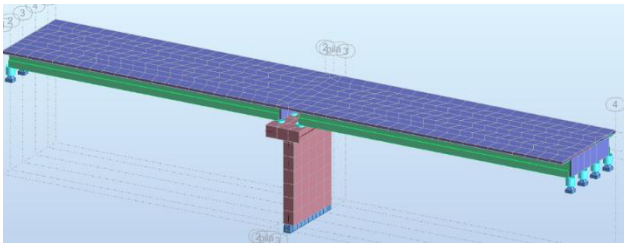

Figure 17. View of bridge structure model.

From the result, it is seen that the continuous slab in the middle support will be destroyed (0.017+0.008 rad – 4.5° for slab section above pier), and the bearings will suffer large residual transverse deformations, much larger than the deformations allowed during a calculated seismic event.

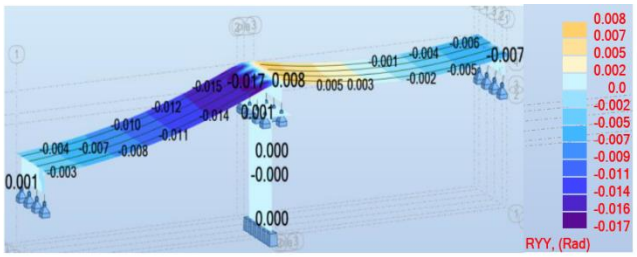

Figure 18. Rotations (Rad) in the slab bridge structure model for design seismic load.

For the internal forces from the result of the undamaged structure, new elastomeric bearings have been chosen and the support block of the bearings and the transversal diaphragm of the beams have been reinforced. The Figure 18 presents details of the strengthening intervention in the abutments.

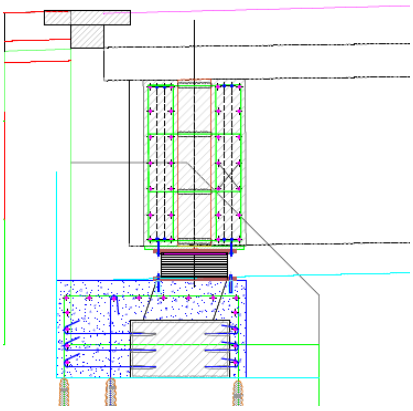

Figure 19. View of the interventions in the abutments.

The continuous slab on the pier has been replaced with a joint that will allow large deformations.

5 CONCLUSIONS

After ascertaining the problem from the Investor, a rehabilitative intervention was requested. Three possible interventions to perform structure rehabilitation of the bridge have been identified: (I) stone columns + structural rehabilitation, (II) RC piles + foundation and structural rehabilitation, (III) Evaluation of time of consolidation + structural bearings re-habilitation.

After detailed analyses and continous monitoring of settlements, it was seen that the settlements has reached about 80% of the total settlement and only 15-20cm are predicted to occur after bearings rehabilitations. Moreover, the differential settlements between abutments and the central pile are about 2-5cm.

So it was decided to rehabilitate only the structure and no intervention was foreseen for the foundations and abutment fillings. The results of continous monitoring up to now (+2cm for a period of one year) show the good judgement for the choice of analyses and intervention.

REFERENCES

Bentley Systems, United States, Plaxis 2D, V22. Software and Manual Theory, Home | Bentley | Infrastructure Engineering Software.

Rocscience. Settle 3D, Software and Manual Theory. 2D and 3D Geotechnical Software | Rocscience Inc.RN Yong, FC Townsend, (1986), *Consolidation of Soils: Testing and Evaluation*, ISBN-13: 978-0-8031-0446-4.

Proceedings of the XVIII ECSMGE 2024
GEOTECHNICAL ENGINEERING CHALLENGES
TO MEET CURRENT AND EMERGING NEEDS OF SOCIETY
© 2024 the Authors
ISBN 978-1-032-54816-6
DOI 10.1201/9781003431749-351
Open Access: www.taylorfrancis.com, CC BY-NC-ND 4.0 license

ECSMGE 24
XVIII EUROPEAN CONFERENCE ON SOIL MECHANICS AND GEOTECHNICAL ENGINEERING

Geotechnical pathologies of Spanish historical monuments adjacent to natural slopes. Case histories

Pathologies géotechniques des monuments historiques espagnols adjacents aux pentes naturelles. Études de cas

F. Pardo de Santayana*, J. González-Gallego, J.A. Díez
Laboratorio de Geotecnia-CEDEX, Madrid, Spain

f.pardo.s@cedex.es

ABSTRACT: The Centro de Estudios y Experimentación de Obras Públicas (CEDEX) is an autonomous body organically attached to the Ministry of Transport, Mobility and Urban Agenda of Spain, being the Laboratorio de Geotecnia one of its units. Although traditionally the activity of this Laboratory has been mainly aimed at the field of transport infrastructures, hydraulic works, and environmental geotechnics, throughout its history it has also carried out different works related to geotechnical pathologies of historical-artistic monuments and urban ensembles. Frequently, the cause of the pathology in these historical buildings or urban ensembles is the existence of an adjacent natural slope with special geological or geotechnical conditions. In these cases, the scope of the intervention of the Laboratorio de Geotecnia has been variable, from site investigation works, diagnosis, and proposal of corrective solutions to the accompaniment of the execution of repair work. Interesting examples are the following: a) works carried out to characterize the geotechnical problems of the "hanging houses" of the town of Frías (Burgos), declared a Historic-Artistic Site; b) studies carried out in the monumental complex of the Alhambra, in Granada; c) site investigation and reinforcement works at the historical building of the Parador Nacional de Turismo of Carmona, in Seville province. The objective of this communication is to offer an overview of some of these cases, not previously, or only poorly, published, in which the Laboratorio de Geotecnia has intervened in the past.

RÉSUMÉ: Le Centro de Estudios y Experimentación de Obras Públicas (CEDEX) est un organisme autonome organiquement rattaché au ministère des Transports, de la Mobilité et de l'Agenda urbain d'Espagne, étant l'une de ses unités. Bien que traditionnellement l'activité de ce laboratoire ait été principalement orientée vers le domaine des infrastructures de transport, des travaux hydrauliques et de la géotechnique environnementale, tout au long de son histoire, il a également réalisé différents travaux liés aux pathologies géotechniques des monuments historiques et artistiques et des ensembles urbains. Fréquemment, la cause de la pathologie dans ces bâtiments historiques ou ensembles urbains est l'existence d'une pente naturelle adjacente avec des conditions géologiques ou géotechniques particulières. Dans ces cas, la portée de l'intervention du Laboratorio de Geotecnia a été variable, des travaux d'étude de site, de diagnostic et de proposition de solutions correctives à l'accompagnement de l'exécution des travaux de réparation. Des exemples intéressants sont les suivants : a) travaux réalisés pour caractériser les problèmes géotechniques des « maisons suspendues » de la ville de Frías (Burgos), déclarée site historique et artistique; b) études réalisées dans le complexe monumental de l'Alhambra, à Grenade; c) étude du site et travaux de renforcement du bâtiment historique du Parador Nacional de Turismo de Carmona, dans la province de Séville. L'objectif de la présente communication est d'offrir une vue d'ensemble de certaines de ces affaires, non publiées ou pauvrement publiées auparavant, dans lesquelles le Laboratorio de Geotecnia est intervenu dans le passé.

Keywords: Historical building; geotechnical pathology; natural slope; site investigation.

1 RELEVANT STUDIES CARRIED OUT BY CEDEX

Numerous historic buildings in Spain are located in topographically elevated areas, next to the crest of slopes or cliffs, mainly because of defensive reasons. These slopes are made up of geological formations of different nature, and, in any case, are exposed to phenomena of degradation by erosion and instabilities that develop with greater or lesser speed depending on the type of material, geological structure, inclination and other factors. The result is the appearance of geotechnical pathologies that affect these buildings, and it is necessary to study and correct. Table 1 shows, in chronological order, some relevant cases in which the Laboratory of Geotechnics of CEDEX has intervened in relation to this kind of geotechnical problems in the past three decades, approximately. It is not intended to include all interventions of this type, but the most significant, due to the importance of the

building, the scope of the intervention or the uniqueness of the study. Two of them are summarized in subsequent sections: the case of Frías and that of the Parador de Carmona. The scope of the works has been variable, from soil investigation, diagnosis, and proposal of corrective solutions to the control of remedial works for the geotechnical pathologies detected.

Table 1. Most significant monuments and historical-artistic urban complexes adjacent to natural slopes with geotechnical problems in which the CEDEX Geotechnical Laboratory has intervened.

Building or urban complex	Pathology or cause of intervention	Date of intervention	Type of action
Monumental complex of Alhambra, Granada *(Santos et al., 1994) (Cuéllar et al. 1995)*	Stability of slopes, fall of rocks and stones. Differential movements in buildings, degradation of foundation support. Collapse of walls.	1989-1995	Inspections and mapping of cracks in buildings. Geological and geotechnical investigation. Auscultation of movements and deformations. Definition of foundation conditions. Boreholes, in situ and laboratory geotechnical tests and geophysical tests. Stability analysis. Study of structural elements. Seismic behavior.
"Hanging houses" of Frías, Burgos	Erosion processes at travertine rocky promontory cliffs adjacent to the "hanging houses" and other buildings of the old town.	1993	Study of slope degradation processes and their impact on buildings; proposals for solution and minimization of collapse and rock falls risks.
Citadel of Ibiza, Baleares *(Martínez et al., 2001)*	Deterioration of the cliff under the wall of the Citadel of Ibiza.	1996	Geological-geotechnical study of the cliff, and proposal of measures for wall underpinning.
Parador of Carmona, Sevilla	Detachment of a large block of calcarenite, created by a crack originated in the 1504´s earthquake, on which the south wing of the building rests.	1997-1998	Soil investigation, identification of the origin of the damage, design and control of the proposed underpinning works.
Hermitage of Bethlehem of Carrión de los Condes, Palencia	Stability problems of the slope adjacent to the hermitage, undermined at its foot by the Carrión river.	2009-2014	Study of the stability and control of execution of slope stabilization works at the left bank of the Carrión River.
Hermitage of San Tirso and San Bernabé in Ojo Guareña, Burgos *(González et al., 2019)*	Subsidence of the esplanade of access to the hermitage, excavated in karstic limestone. The esplanade is located on a slope 60 m above the Guareña river sinkhole.	2016	Geotechnical investigation, determination of the causes of the pathologies, related to plugging of the sinkhole and saturation of the colluvial.
Mudéjar tower of Coca, Segovia *(Pardo et al., 2021)*	Stability problems, due to fluvial erosion, of the natural slope next to whose crest the tower is located.	2018	Geotechnical study of the stability of the slope and proposals for reinforcement to protect the tower area.

Due to the importance of the monumental complex and the relevance of the work carried out, it is worth highlighting the actions carried out in the monumental complex of Alhambra and Generalife (Granada), where the geotechnical characterization of the foundation conditions of a series of buildings was performed for several years, as well as stability studies of the slopes surrounding the area (Santos et al., 1994). The triggers of these studies were the visible cracks in the buildings and the signals of instability that appeared on some of the slopes by the walls and towers of the complex. A long-range work plan was established aimed at the design of geotechnical actions for correction or reinforcement of slopes and foundations and the definition of a surveillance network for the monitoring of movements in the buildings to control their evolution.

Within this group of studies relating to the Alhambra palace, it is worth highlighting the work of characterizing the dynamic properties of the ground, foundations, and walls of the tower of Comares (Cuéllar et al., 1995). G_{max} values of the different materials were determined by seismic refraction, P waves transmission tomography and cross-hole and down-hole tests. Using data obtained from dynamic surface wave tests and static plate load tests carried out in two trenches dug in the vicinity of the palace, it was possible to determine the variation of the secant module G of the ground with the level of shear strain for the stress levels expected from earthquakes. In the rest of the materials this variation was determined using the data obtained from samples tested in the laboratory. The analysis of the response of the structure to earthquakes of magnitude M = 5, such as

those that had recently been recorded at the top and bottom of the tower, allowed to verify the goodness of the estimated dynamic parameters.

Another study was carried out for the General Directorate of Coasts in 1996, consisting of the geological-geotechnical characterization of the natural cliff located under the wall of the citadel of Ibiza. The conditions of the cliff and the wall were analysed using terrestrial photogrammetry (from a boat in this case) and corrective measures were proposed for the undermined areas of the wall (Martínez et al., 2001).

A frequent type of instability of historic building is the one that occurs when the building is situated at the crest of a slope whose foot is affected by river erosion. The cases of Ermita de Belén de Carrión de los Condes (Palencia) and the Mudejar Tower of Coca (Segovia) belong to this type of instability (see Table 1). The case of the Hermitage of San Tirso and San Bernabé de Ojo Guareña (Burgos), constructed in a cave in karst limestone, refers to subsidence of the platform of access to the hermitage due to saturation of colluvial soils when the sinkhole of the Guareña River, located at the same slope 60 m below the hermitage is blocked with detritus (see Table 1).

2 CLIFF EROSION PROCESSES BELOW MEDIEVAL TOWN OF FRÍAS

In 1993 CEDEX carried out a study of the geotechnical-geological problems that affected the old town of Frías, located on top of a carbonated rocky massif, of travertine origin, below which, especially on the southern slope, the rest of the town stretches out on loamy and clayey materials. The vertical cliffs surrounding the promontory have a height of between 15 and 20 m, being the area of the castle the highest point with a height of 30 m (Figure 1). A piedmont of 60 to 100 m in length and slope of 20º to 30º extends at the bottom of the cliffs. On the crest of the promontory, especially at the southern and southeastern sides, a line of houses, known as "hanging houses", are located. The promontory sides presented a certain state of deterioration due to erosion of the cliff materials. Given the irregular and chaotic growth that travertine had in its formation, a multitude of cracks and fractures appeared throughout the escarpment of the promontory. The geological-geotechnical risks were inscribed in the processes of alteration and geomechanical degradation and possible detachments of blocks of different sizes, risks supported by the large number of events over the centuries recorded in different bibliographic citations. When the study was carried out, three areas were considered the most dangerous: the castle, in relation to blocks located at the top of the rock; several areas of the southern cliff where the "hanging houses" are located; and the north side of the promontory below the main church of the town.

The study carried out by the CEDEX for the Junta de Castilla y León was based on two basic lines of work: on the one hand, the geological-geotechnical characterization of the rocky massif that forms the cliffs, and on the other, the determination of the general topographic and geometric characteristics of the site and affected buildings. It was considered of special importance to determine the state and structure of the rock, and in particular, the geometric definition of the sets of blocks and the mapping of the preferred directions of lithoclases of the tuffaceous formation, by means of both direct observation and photographs of different scales (Figure 2). This work was completed with the determination of the topography of the cliffs, by means of terrestrial photogrammetry, based on a general stereographic principle, in the vertical plane, whose restitution allowed to obtain the geometry and the contour lines of the cliff without optical deformation. Thus, a "topographical" plan of the vertical plane and the corresponding cross sections of the cliff were obtained (Figure 3). Besides, a planimetric and altimetric survey of the surroundings of the cliff at the nearby streets, at its crest and foot, as well as a detailed mapping of the plants and elevations of the affected houses was carried out. Likewise, the cracks observed in these buildings were mapped.

Once the pathology was described, the study proposed a series of stabilization actions (Figure 4), discarding those that, due to their volume or impact, could represent a substantial change in the existing heritage environment, and resorting to specific or local application systems that were, as far as possible, immersed inside the massif or masked their visual effects in the exposed areas. It was based on two basic principles: on the one hand, the safety conditions linked to the buildings next to the cliff should be completely guaranteed, and, on the other, the systems of stabilization assets (bolts, buttresses, etc.) were restricted to those large sizes of block, slabs, or stones, which due to their volume and weight could imply significant risks. In addition, the installation of a dynamic barrier to stop the fall of minor blocks at the foot of the slope was proposed. From these basic ideas, the conditions presented by the rocky massif and cliff were analysed, together with the adjoining buildings, establishing a differentiation by zones according to the specific typology of the existing problem in each case (unstable blocks, cantilevered cornice, etc.).

.



Figure 1. View of the southern cliff of the promontory of Frías with the "hanging houses", and detail of the castle.



Figure 2. Geotechnical zoning of the cliff (Frías).



Figure 3. Photogrammetric vertical contour map of the cliff (Frías).

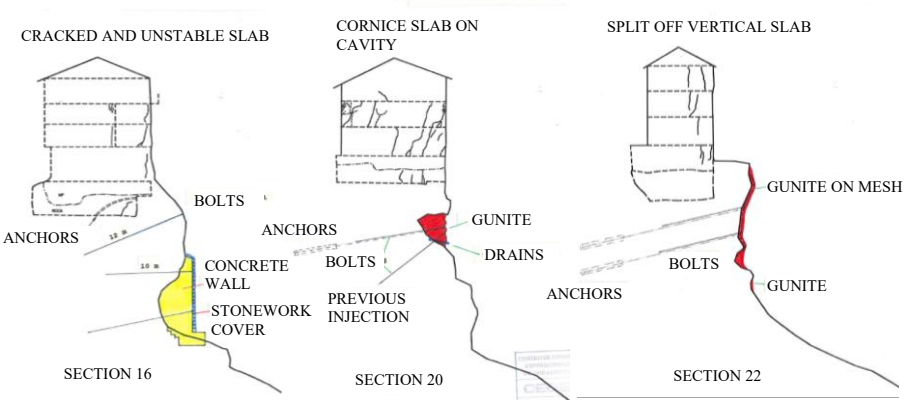

Figure 4. Photogrammetric profiles, crack mapping in party walls of the houses and proposed reinforcement actions (Frías).

Recommended treatments included bolting, preferably injected, of unstable wedges and blocks; selective sealing and protection with coloured gunite of soft rock levels; underpinning of blocks with gunite; filling of cavities with concrete or gunite with a shade closure face for camouflage and provision of drainage pipes; gunite on mesh, accompanied by anchors or bolts; and in some areas the execution of a concrete wall covered with masonry for landscape integration.

3 SLOPE INSTABILITY AFFECTING HISTORICAL BUILDING IN CARMONA

The Parador Nacional de Turismo de Carmona, built in 1970, on what had been the Parade Ground of the Alcázar of King Pedro the 1st of Castille, in the Sevillian town of Carmona, is located at the crest of a hillside, next to the meeting of two slopes of erosion, south and east. The stratigraphic profile of the terrain corresponds to a superficial platform of calcarenites lying on *albero* sandstone and underlying grey intercalations of sands, clays, and marly clays. The area of implantation of the south wing of the Parador was located on a large block of the calcarenite platform separated by a crack from the rest of it. This crack, with origin in the 1504's earthquake, caused horizontal and vertical displacements of the detached block greater than one meter. After an initial treatment of the platform under the Parador with injections in 1970 and two successive underpinnings: one with soil nailing in 1981 and the other with anchors in 1987, movements continued, forcing the closure of the south wing. Under these conditions, the Geotechnical Laboratory of CEDEX carried out a study of the ground to establish corrective measures.

Once the available data and the observed pathologies had been analysed, 10 triple-tub rotation boreholes were proposed, as a complement to those from previous campaigns, which made it possible to get a set of geological profiles of the foundation ground. Tests carried out on samples from the boreholes served to identify the natural state and evaluate the mechanical behaviour of the materials. The presence of horizontal movements in the Parador was clearly conditioned by the tilting of the calcarenite block whose movement was linked, on the one hand, to the progressive erosion of the materials underlying the calcarenite, and on the other, to the effect of the water infiltrated through the "crack" that broke off the block in the lower sandy levels. On the other hand, it was necessary to consider two basic mechanisms of instability of the slope: the first, with predominance of horizontal movements and possible emergence on the slope with mobilization of relatively small superficial sliding masses supported on soft soils. The second corresponded to deep landslides in very deformable areas of the lower loamy clays.

As a proposal to reinforce the south wing of the Parador, a stabilization of the movement of the broken calcarenite block was proposed through a treatment of armed injections. In the Parador de Carmona this treatment consisted mainly of the nailing and massing of the area of the crack that affected the south wing, in addition to the stabilization of the supporting levels located under the calcarenite block until reaching the relative elevation of -44 m, in relation to the level of entrance to the Parador (elevation ±0.00 m). The treatment was designed based on a series of buttresses, with separation of about 5 m, which were drilled and treated alternately, from the south and north areas of the south wing, by means of steel tube fans equipped with sleeve valves. The adoption of the buttress configuration in the treated ground was intended to prevent the formation of a barrier to groundwater seepage. The depth of the treatment up to 44 m, and its location on both sides of the crack allowed to also ensure stabilization for the differe mechanisms outlined. The previous treatment was completed with the execution of a drainage system of the hillside in three levels. For the execution of the work, a technical specification was established in which, among other aspects, the requirements of the injection mixtures and the operating procedure to be followed during the treatment were specified. Under the technical direction of CEDEX a Spanish company specialized in injections proceeded to execute the underpinning works, permanently controlling, during the four months that the works lasted (January to May of 1997) the vertical movements of the Parador with levels of precision and electro-levels and the horizontal movements with convergence tapes, extensometers, and crack gauges. In total, 33 armed injection fans were performed, with a total of 297 drills. In the cases in which the movements observed by the auscultation advised it, especially during the month of April, in which, due to the intensification of the injection works, a raising of the building began to be detected, the volumes and rate of injection were reduced, considerably decreasing these uplift movements. The injection was carried out by three pumps with two lines each, continuously recording pressure, flow rate and volume injected per sleeve.

About the drainage of the hillside, once the injection works were completed, a total of 43 horizontal drains were executed, with lengths of 20, 30, 40 and 44 m. The drains were completed with the execution of three perimeter ditches, placed at the supposed foot of the landslide.

Throughout the work, the state of the building was continuously monitored by means of auscultation,

with the aim of knowing the effect of the underpinning works and other factors (climatological) on it and be able to adopt appropriate corrective measures at any time. For the control of horizontal movements, 23 convergence sections were established distributed over two floors to alleviate, as much as possible, thermal conditions. Likewise, three instrumented sections with a large base extensometer were arranged. For the control of vertical movements, 90 m of electrolevels and a conventional precision levelling system were used, for which a fixed point was installed in the parade ground, anchored at elevation -41 m. In total, 34 INVAR levelling strips were placed, which were controlled with an accuracy of 0.2 mm. The analysis of the evolution of the vertical movements recorded by means of the levelling strips, from their installation in the Parador in mid-January until the end of June, allowed to verify how since the beginning of May the movements of all the points stabilized.

The subsequent monitoring of the behaviour of the ground on which the Parador lays, particularly in periods of heavy rain, indicated a correct functioning of the reinforcement executed, without any evidence of evolution of old damage or appearance of new damages that could question its validity.

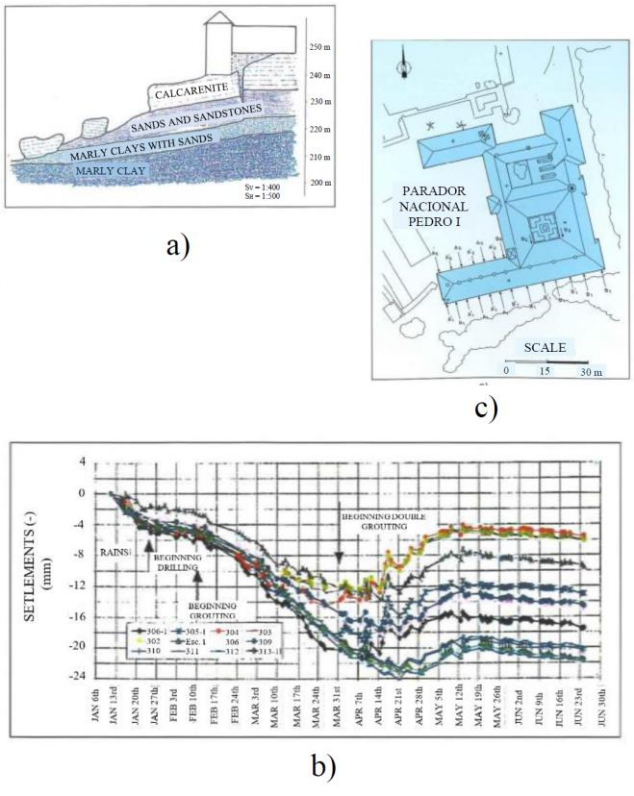

Figure 5. a) Geological profile N-S of the Parador de Carmona; b) vertical movements recorded on the south façade of the Parador; c) plan of Parador de Carmona.

4 CONCLUSIONS

An overview of some cases of geotechnical pathologies of Spanish historical monuments adjacent to natural slopes, in which the Laboratorio de Geotecnia of CEDEX has intervened in the past, has been presented. Two not previously published interesting case histories have been described in more detail.

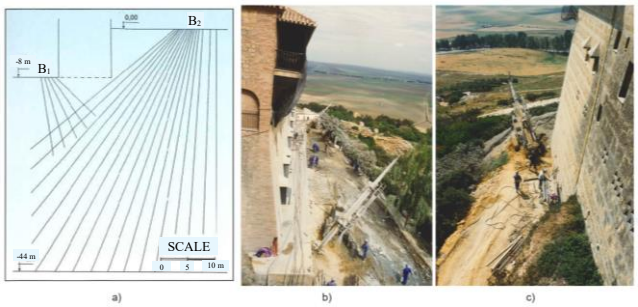

Figure 6. a) Scheme of injection fans B_2 (north) and B_1 (south) in the Parador de Carmona; (b) and (c) views of injection work.

REFERENCES

Cuéllar, V., Kausel, E., Monte, J.L., Roesset, J.M. and Valerio, J. (1995). Obtención mediante ensayos in situ de las características dinámicas del terreno, cimentación y muros del Palacio de Comares en la Alhambra. *Ingeniería Civil*, nº. 100, pp. 87-96. 163-95-005-7. CEDEX.

González-Gallego, J., García de la Oliva, J.L. and Tijera, A. (2019). Geotechnical issues on the access of the Ojo Guareña karst complex. *Proceedings of the XVII ECSMGE-2019*. ISBN 978-9935-9436-1-3. Reykjavik, Iceland.

Martínez Santamaría, J.M.; González-Gallego Rodríguez-Barbero, F.J. and Barea Luchena, J. (2001). Estudio geológico-geotécnico de un acantilado de difícil acceso en Ibiza. *V Simposio Nacional sobre Taludes y Laderas Inestables.* Vol. 1, 2001, pp. 75-86. ISBN 84-7790-365-4. Madrid.

Pardo de Santayana, F. Díez, J.A. and Perucho, A. (2021). Stability of a natural slope at left bank of Eresma river in the historical town of Coca, Spain. *Proceedings of the 20th International Conference on Soil Mechanics and Geotechnical Engineering*, pp. 2541-2546. Sydney, Australia. ISBN 978-0-9946261-4-1.

Santos, A., Martínez, J.M. and Salinas, J.L. (1994). Caracterización geotécnica de las condiciones de cimentación de los edificios y estabilidad de las laderas del conjunto monumental de la Alhambra y Generalife. *Ingeniería Civil*, nº 96, pp. 77-86. 163-94-001-6. CEDEX.

Proceedings of the XVIII ECSMGE 2024
GEOTECHNICAL ENGINEERING CHALLENGES
TO MEET CURRENT AND EMERGING NEEDS OF SOCIETY
© 2024 the Authors
ISBN 978-1-032-54816-6
DOI 10.1201/9781003431749-352
Open Access: www.taylorfrancis.com, CC BY-NC-ND 4.0 license

ECSMGE 24
XVIII EUROPEAN CONFERENCE ON SOIL MECHANICS AND GEOTECHNICAL ENGINEERING

Slope instability risk assessment along the Almada municipality coastline, Portugal

Évaluation des risques d´instabilité des pentes le long du littoral de la municipalité d´Almada, Portugal

F. Paulino*, E. Fernandes, A. Dinis
Geovia, S.A., Lisbon, Portugal

A. Aires, A. Godinho
Câmara Municipal de Almada, Almada, Portugal

**fpaulino@geovia.pt*

ABSTRACT: The Portuguese continental coastline extends for 987 km, centralizing around 75% of the national population in just 25% of the territory, generating 85% of the gross domestic product (GDP). Approximately 30% of the coastline is considered a protected area and included in the National Network of Protected Areas, with around 50% including areas belonging to the Rede Natura 2000. The exponential growth that has occurred in recent decades, resulting in increased demographic pressure on the coastal strip, has been promoting the occupation of dangerous zones subject to possible landslides. It is known that the adulteration of the physical landscape, in the name of development, has reached alarming proportions. The loss of territory and damage to coastal infrastructure are visible consequences of human intervention on the coast. As a result, it is crucial to investigate the mass movements of cliffs. This type of movement is difficult to predict due to its lack of warning signs and displacement speeds that occur in seconds. Once the movement begins, it is impossible to contain it, making it necessary to identify potential weaknesses in cliffs and minimize inherent risks by understanding rupture mechanisms. With this communication it is intended to present the geomechanical study of the stability of several cliffs of the municipality of Almada.

RÉSUMÉ: Le littoral portugais s´étend sur 987 km, centralisant environ 75% de la population nationale sur seulement 25% du territoire, générant 85% du produit intérieur brut (PIB). Environ 30% du littoral est considéré comme une zone protégée et inclus dans le réseau national des zones protégées, avec environ 50% comprenant des zones appartenant au Rede Natura 2000. La croissance exponentielle survenue au cours des dernières décennies, entraînant une pression démographique accrue sur la bande côtière, a favorisé l´occupation de zones dangereuses sujettes à d´éventuels glissements de terrain. On sait que la falsification du paysage physique, au nom du développement, a atteint des proportions alarmantes. Les conséquences de l´intervention humaine sur le littoral sont visibles, à savoir la perte de territoire et les dommages aux infrastructures de protection côtière. Cependant, les mouvements de masse sur les falaises doivent être considérés comme l´un des principaux axes d´étude en raison de leur irrégularité temporelle. Ce type de mouvement se caractérise par des vitesses de déplacement de l'ordre de la seconde, pas toujours précédées de signes avant-coureurs et, de ce fait, considérées comme difficiles à prévoir. Une fois de mouvement amorcé, il devient impossible de le contenir, ce qui nécessite de comprendre les mécanismes de rupture pour identifier les signes de faiblesse potentielle des falaises et minimiser le risque inhérent. Avec cette communication, il est prévu de présenter l'étude géomécanique de la stabilité des différentes falaises de la municipalité d´Almada.

Keywords: Risk assessment; rock cliffs; slope stability.

1 INTRODUCTION

The incorporation of stability studies of Portugal's coastline zones in land planning and urbanism policies is a recent development that started in the 90s. This change in mentality demonstrates an awareness of the potential risk to people and property caused by cliff movements. This is due to an increase of the Portuguese coast occupation rate.

Ten study locations were selected along the Almada municipality coastline for risk assessment, using information provided by the Almada municipality, namely:

- Olho-de-Boi (Poente)
- Banática
- Pica Galo
- Abas da Raposeira
- Foz do Rego

- Porto Brandão
- Arriba Fóssil da Costa de Caparica
- Arriba Fóssil do Bairro do Fóni
- Arriba Fóssil – Via Panorâmica Pablo Neruda
- Quinta da Arealva.

2 METHODOLOGY

Initially, the applied methodology consisted of a semi-quantitative risk assessment to promote a simple and quick prioritization of risks identified. This was achieved by determining the Risk Index (RI), using the following equation:

Risk Index (RI) = Probability of Occurrence (PO) x Magnitude (M) x Potential Damage (PD)/Response Capacity (RC) (1)

where (PO x M) defines the dangerousness (D) and (PD/RC) represents the vulnerability (V).

This methodology is adapted from Costa et al. (2009). Each term in the equation was categorized on a scale of 1 to 5 (respectively: not significant, reduced, average, high and very high). Equation (1) calculates the risk values associated with the hazard in question. The matrix used to calculate RI values for all possible scenarios was recalculated for the interval [0;1], instead of [0.2;1], for better perception of the obtained values. The calculated values were divided into 5 classes of equal amplitude.

The danger calculated by this methodology must be understood as an apparent danger, differing from the concept proposed by Varnes (1984). This is because it is not based on the probability of an occurrence, but rather on a weighted calculation that relies on available information and on the expert assessment of geological-geotechnical factors that affect cliff stability (refer to Figure 1). Even though this assessment has some degree of subjectivity, when well-founded, it is generally more valuable than mere numerical calculations, namely in Geotechnics (Schubert, 2004). Furthermore, an expedited initial assessment allows the concentration of more detailed studies in places that require priority intervention.

In the second phase, the behaviour was measured through geomechanical analysis of the cliffs wherever RI≥0.80 was obtained, based on the geotechnical characterization of the rock mass and on identifying rupture mechanisms (Brissos, 2013; Brissos et al., 2014).

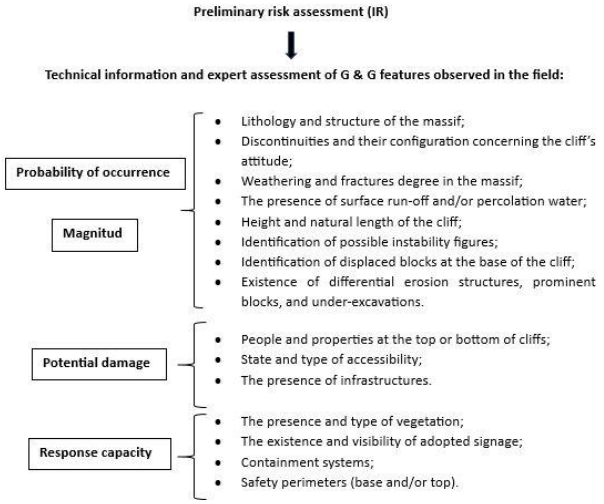

Figure 1. Schematization of the preliminary risk assessment methodology.

3 RESULTS

3.1 Preliminary risk assessment (1st phase)

Table 1 presents the values attributed to the different variables of equation (1), as well as the calculation of the Risk Index (RI) associated with the problem under analysis.

The cliffs in the Almada municipality represent a risk due to the lithological and weathering characteristics of the rock mass. These conditions can lead to frequent instabilities caused by differential erosion of the existing rock masses. Figure 2 shows the panoramic view of the fossil cliff in Bairro do Fóni, with houses adjacent to the cliff's crest, figure 3 shows a fallen limestone block from Banática cliff near two parked cars, figure 4 represents a panoramic view of the fossil cliff in Olho de Boi, with Almada Cemetery behind, and figure 5 shows the panoramic view of the cliff in Porto Brandão, with houses adjacent to the base of the cliff.

Table 1. Calculation of hazard, vulnerability and risk values for the identified locations.

Locals	Stations	Dangerousness			Vulnerability			Risk Index	
		PO	M	Final Value	PD	RC	Final Value	Preliminar RI	Classification
Olho de Boi	1	5	5	25	5	1	5	1,00	Very high
	2	5	4	20	3	3	9	0,16	Insignificant
	3	5	4	20	4	2	8	0,32	Reduced
	4	5	5	25	5	1	5	1,00	Very high
Quinta da Arealva	5	5	5	25	4	2	8	0,24	Reduced
	6	5	4	20	4	1	4	0,48	Moderate
Banática	7	5	4	20	5	1	5	0,80	Very high
	8	5	5	25	5	1	5	1,00	Very high
Porto Brandão	9	4	2	8	3	1	3	0,19	Insignificant
	10	4	4	16	1	2	2	0,06	Insignificant
	11	5	5	25	5	1	5	1,00	Very high
	12	3	2	6	5	2	10	0,12	Insignificant
	13	4	4	16	5	4	20	0,16	Insignificant
Abas da Raposeira	14	5	3	15	5	2	10	0,30	Reduced
	15	5	3	15	4	1	4	0,48	Moderate
	16	5	3	15	3	3	9	0,12	Insignificant
Pica Galo	17	5	4	20	5	1	5	0,60	High
	18	5	4	20	5	1	5	0,60	High
	19	1	1	1	5	5	25	0,01	Insignificant
	20	5	4	20	5	3	15	0,27	Reduced
	21	5	5	25	5	1	5	0,64	High
Arriba Fóssil Costa Caparica	22	5	5	25	2	2	4	0,20	Reduced
	23	5	5	25	4	2	8	0,40	Moderate
	24	5	5	25	2	2	4	0,20	Reduced
	25	5	5	25	3	1	3	0,20	High
Via Panorâmica Pablo Neruda	26	5	4	25	5	3	15	0,42	Moderate
	27	5	4	20	2	1	2	0,32	Reduced
	28	4	4	16	2	1	2	0,26	Reduced
	29	5	4	20	2	1	2	0,32	Reduced
	30	4	4	16	2	1	2	0,26	Reduced
Estrada da Foz do Rego	31	2	3	6	5	1	5	0,24	Reduced
	32	3	3	9	3	1	3	0,36	Reduced
	33	4	4	16	4	1	4	0,51	Moderate
	34	5	4	20	4	1	4	0,64	High
	35	4	3	12	5	1	5	0,48	Moderate
	36	4	3	12	5	1	5	0,48	Moderate
	37	4	3	12	5	1	5	0,48	Moderate
Arriba Bairro do Fóni	38	5	4	20	4	1	4	0,80	Very high
	39	5	4	20	5	1	5	0,80	Very high
	40	3	3	9	3	1	3	0,22	Reduced
	41	5	5	25	4	1	4	0,80	Very high
	42	2	2	4	2	1	2	0,06	Insignificant
	43	4	4	16	2	1	2	0,26	Reduced
	44	5	4	20	5	1	5	0,80	Very high



Figure 2. Panoramic view of the fossil cliff in Bairro do Fóni with houses adjacent to the cliff's crest (June, 2023).



Figure 3. Limestone block from Banática Cliff near parked cars (June, 2023).



Figure 4. Panoramic view of the fossil cliff in Olho de Boi with Almada Cemetery behind (June, 2023).

Table 1 shows that certain locations have a higher risk index due to the greater height of the cliffs, the history of incidents and the possibility of large blocks being mobilised from these locations (as shown in Figure 3).

This higher risk index, in specific cases like Olho-de-Boi, Banática, Porto Brandão and Bairro do Fóni, is associated with poor conditions caused by their close proximity to urban areas with constructed infrastructure both at the top and at the base of the cliffs.



Figure 5. Panoramic view of the cliff in Porto Brandão with houses adjacent to its base (June, 2023).

For example, the landslides and rock fall events observed at the Olho-de-Boi cliff occurred at the base of the slope, leading to an overhang at the top. This indicates that the layers with the least resistance are located at the bottom of the cliff, while the ones with the most resistance are at the top. It is obseved that the most weathered and the less weathered layers are divided by tension cracks parallel to the cliff and subvertical fractures visible at the top of the cliff.

In Banática, the houses are located near the slope (between 2.0m and 10.0m) and there is no protection against slope movements. This is a scenario of maximum damage potential and no response capacity.

In Porto Brandão, there are several residential and commercial buildings occupying the foot of the cliff with no safety distance. This represents a very high vulnerability, as there is minimum response capacity and maximum potential damage.

In Bairro do Fóni, there is a very sharp cliff retreat with evidence of significant ravines. There are buildings located on the top of the cliff, with emphasis to an overhanging reinforced concrete structure at risk of structural failure.

Considering the above, it became evident that stability studies must be conducted in these areas. This is necessary not only because of the geomechanical conditions that favour instability phenomena, but also due to the high vulnerability associated with human occupation at both the base and the top of these cliffs.

3.2 Reassessment of risk and proposal mitigation measures mitigation (2nd phase)

The preliminary risk evaluation in this study was reassessed based on the geological-geotechnical characterization of each cliff and the geotechnical zoning. The estimated retreat rates and the simulation of the trajectories of falling blocks from the studied cliffs also contributed to the reassessment of the preliminary risk.

The risk reassessment also considered the current and future of the areas of influence (crest and base), with the results presented in Table 2.

It appears that in general the values remained the same in practically all locations. The exception occurred at a station 38 on fossil cliff in Bairro do Fóni.

After the risk reassessment, the Risk Index (RI) is maintained based on the occurrence of falling blocks in the past, the number of people using the access paths to the top or base of the cliffs, and the annual retreat rate of the cliffs.

Table 2. Risk reassessment and comparison with the preliminary risk evaluation.

Locals	Stations	Dangerousness			Vulnerability			Risk Index		
		PO	M	Final Value	PD	RC	Final Value	Final RI	Preliminar RI	Classification
Olho de Boi	1	5	5	25	5	1	5	1,00	1,00	Very high
	4	5	5	25	5	1	5	1,00	1,00	Very high
Banática	7	5	4	20	5	1	5	0,80	0,80	Very high
	8	5	5	25	5	1	5	1,00	1,00	Very high
Porto Brandão	11	5	5	25	5	1	5	1,00	1,00	Very high
Arriba Bairro do Fóni	38	5	4	20	4	1	4	0,64	0,80	High
	39	5	4	20	5	1	5	0,80	0,80	Very high
	41	5	5	25	4	1	4	0,80	0,80	Very high
	44	5	4	20	5	1	5	0,80	0,80	Very high

Based on this reassessment, a proposal for a short-term risk mitigation plan was presented (Table 3). The adopted approach focuses on reducing long-term vulnerability by reinforcing appropriate signage and placing physical fences to prevent access to the top of the cliff.

The dismantling of some larger, potentially unstable blocks, must be considered using appropriate dismantling methodologies, as well as, the fixing of metal nets to control blocks that may detach from the cliff face.

Subsequently, nailing should be carried out, possibly associated with cables and steel mesh, pulled and anchored to the massif, to fix the larger volume consoles. The use of shotcrete, always accompanied by the execution of drainage holes, could be an alternative. The installation of ridge ditches allows the collection of runoff water, making infiltration and washing of fractures more difficult. The effective implementation of a monitoring plan is still considered necessary for long-term prevention perspective.

Table 3. Risk mitigation plan proposed for the case study.

Risk Mitigation				
Structural				
Stabilization measures		Protection measures	Drainage	Non-structural
Correction	Reinforcement			
Dismantling of rock blocks; Cliff re-profiling	Nails; Metal mesh associated with steel cables / shotcrete	Nailed/anchored metal mesh	Cliff crest ditch	Implementation of appropriate danger signs in clearly visible locations (foothills and crests); Restriction and prohibition lanes with respective signs and fences, at the base and on the crest and foothills; New Jersey-type barriers in areas that require protection against blocks that could roll from the top of the cliff to homes

4 CONCLUSIONS

The methodology used for instability risk assessment of the studied cliffs relies heavily on subjective methods, rather than quantitative analysis. However, this methodology demonstrates higher reliability in establishing a preliminary risk zoning. This allows to hierarchise the most critical cliffs, which are in need of detailed stability studies, implementation of risk stabilization and mitigation measures, and their respective monitoring.

ACKNOWLEDGEMENTS

The authors are grateful for the documentation support provided by Almada municipality.

REFERENCES

Brissos, J., 2013. Avaliação de risco de instabilidade de arribas no troço Sines-Zambujeira do Mar (SW Alentejo). Dissertação de mestrado, Universidade Nova de Lisboa (não publicada), 159 p.

Brissos, J., Lamas, P., Sá Caetano, P., 2014. Estabilidade e zonamento geomecânico das arribas da praia da Zambujeira do Mar em contexto da análise de risco. *Actas do XIV Congresso Nacional de Geotecnia*, Covilhã, Portugal, 12 p.

Costa, C., Sá Caetano, P., Brito, G., Vendas, D., 2009. Estudo Preliminar do risco associado à instabilidade de arribas no troço entre Cabo Espichel e Setúbal. Relatório Técnico não publicado), FCT-UNL, 33 p.

Schubert, P., 2004. Geotechnical Risk Management in Tunnelling. *Course on Geotechnical Risk in Rock Tunnels*. Aveiro, 12 p.

Varnes, D.L. (1984). *Landslide hazard zonation*: a review of principles and practice. *UNESCO – Landslides Hazards*, **Series 3**, Paris, 63 p.

Proceedings of the XVIII ECSMGE 2024
GEOTECHNICAL ENGINEERING CHALLENGES
TO MEET CURRENT AND EMERGING NEEDS OF SOCIETY
© 2024 the Authors
ISBN 978-1-032-54816-6
DOI 10.1201/9781003431749-353
Open Access: www.taylorfrancis.com, CC BY-NC-ND 4.0 license

ECSMGE 24
XVIII EUROPEAN CONFERENCE ON SOIL MECHANICS AND GEOTECHNICAL ENGINEERING

Strength resistance of sea dikes to increased wave overtopping due to the rise in sea levels

Résistance des digues à l'augmentation du déferlement des vagues due à l'élévation du niveau de la mer

M. Pohl*, T. Nuber
Federal Waterways Engineering and Research Institute (BAW), Hamburg, Germany

J. Moreno
Hannover, Germany (formerly BAW)

**martin.pohl@baw.de*

ABSTRACT: The predicted rise in sea levels due to climate change results in the requirement to increase the height of coastal dikes in order to maintain current safety levels. The extraction of suitable natural clay material for dike coverings is significantly restricted. Therefore, this study will consider dredged material as an alternative and if higher wave overtopping rates can be tolerated. Field tests with simulated water infiltration rates similar to those of a storm surge event at existing dikes were conducted. Soil samples were subsequently taken and examined in the laboratory, e.g. by triaxial tests. The results showed, that dredged material with a certain clay content is as suitable for dike coverings as glacial till and soft marsh soil, which are commonly used for dike coverings in estuaries resp. the Baltic Sea region. Measurements by vane tests directly after a storm surge event revealed different soil strengths across the dike, whereby the future highest hydraulicly loaded areas showed the lowest but still sufficient strength resistances. In an explicit numerical simulation model all field and laboratory test results were merged. For simulating the non-static wave overtopping at the dike crest, shear forces were applied at distinct dike surface areas. By defining a failure criterion for a progressing erosion process and high overtopping rates, a dike failure similar to observed ones in the past could be simulated.

RÉSUMÉ: L'élévation prévue du niveau de la mer en raison du changement climatique impose d'augmenter la hauteur des digues côtières afin de maintenir les niveaux de sécurité actuels. L'extraction de matériaux argileux naturels appropriés pour les revêtements de digues est considérablement limitée. Par conséquent, cette étude examinera les matériaux de dragage comme alternative et déterminera si des taux de débordement des vagues plus élevés peuvent être tolérés. Des essais sur le terrain ont été réalisés avec des taux d'infiltration d'eau simulés similaires à ceux d'une onde de tempête sur les digues existantes. Des échantillons de sol ont ensuite été prélevés et examinés en laboratoire. Les résultats ont montré que les matériaux de dragage ayant une certaine teneur en argile conviennent aussi bien aux revêtements de digues que le till glaciaire et le sol mou des marais, qui sont couramment utilisés pour les revêtements de digues dans les estuaires et dans la région de la mer Baltique. Les mesures effectuées à l'aide d'essais à la girouette directement après une onde de tempête ont révélé des résistances du sol différentes d'un bout à l'autre de la digue, les futures zones les plus chargées sur le plan hydraulique présentant les résistances les plus faibles, mais néanmoins suffisantes. Dans un modèle de simulation numérique explicite, tous les résultats des essais sur le terrain et en laboratoire ont été fusionnés. Pour simuler le débordement non statique des vagues sur la crête de la digue, des forces de cisaillement ont été appliquées à des zones distinctes de la surface de la digue.

Keywords: Sea dike; wave overtopping; dredged material; failure, soil mechanics.

1 MOTIVATION

Dikes in Germany and other countries consist in most cases of a sand core which is covered with a cohesive dike covering and a grass revetment. The purpose of the dike covering and the grass revetment is to resist the hydraulic loads by waves and currents and prevent erosion.

Due to the predicted sea level rise, the height of coastal dikes has to be increased in order to maintain current safety levels. One aspect hereby is the allowed overtopping rate at the dike crest and the landward slope.

Examinations by (Van Hoven et al, 2010) have shown, that higher overtopping rates, than actually allowed, do not damage the dike, if the grass revetment has a good quality and no singularities in the dike exist.

For a better understanding of these processes and the suitability-check of alternative cohesive materials, physical tests, i.e. field and laboratory tests in

conjunction with numerical simulations were conducted.

2 FIELD TESTS

2.1 Infiltration tests

The infiltration tests were performed to simulate a storm surge or heavy rainfall. The question to be answered is: how does the water content and thus the corresponding shear strength change over the depth of the dike covering in dependence of the infiltration time? This is of particular importance for the stability of the dike covering and thus its resistance against failure.

Therefore, tests at dike coverings consisting of glacial till, soft marsh soil and dredged material were conducted. The infiltration times were up to 38 hours, which is in good accordance with one of the heaviest storm surges at the Baltic Sea on 21/10/2023. After the distinct infiltration times, undisturbed soil samples were taken with a drilling rig (Figure 1).



Figure 1. Field test set up.

A direct test-result is the permeability of the examined dike section. Regarding the aging of a dike it can be concluded, that the permeability of a new constructed dike is lower than that of an older dike. This is due to cracks and fissures, which develop over time; initiated by weathering processes (drying out – wetting) and by burrowing animals. The permeability of an older dike can be taken to $5x10^{-5}$m/s. This is in good accordance with (TAW, 1996; Achmus et al, 2019) for soft marsh soil dikes and applies, thus also for glacial till and dredged material dikes.

2.2 Vane tests after storm surge

Vane tests at a section of a soft marsh soil dike near Wedel were executed immediately after the heavy storm surge event "Xaver" did occur. Due to the limited data, the findings are mere qualitatively.

The results (Table 1) are: at the seaside slope below driftline (i.e. level, where material was deposited by the storm surge) and at the dike crest, the strength tends to be higher than at the seaside slope above driftline and the landside slope. This might be explained by the maintenance and usage of the dike: vehicles move below the driftline to remove the deposited material and pedestrians walk on the dike crest. Both events lead to a recurring compaction. It has to be mentioned, that the inclination of the landside slope is 1:3 and at the seaside 1:6 to 1:10. Above the driftline more signs for burrowing animals were encountered. No overtopping did occur during Xaver.

At the landside slope the strength is the lowest, but still sufficient according to (EAK, 2002). But this also means, that in the area where wave overtopping occurs the resistance and strength of the dike is the lowest.

Table 1. Mean undrained shear strength cu [kPa].

Depth [cm]	Seaside below driftline	Seaside above driftline	Dike crest	Land-side
10	67	53	72	39
40	104	53	80	43
70	123	78	78	42

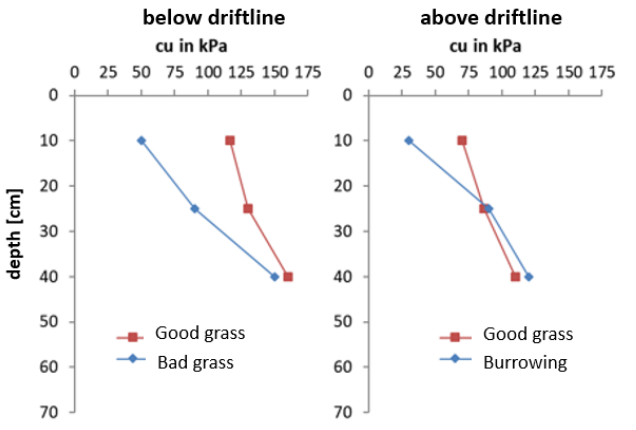

Figure 2. Influence of grass quality and burrowing.

Figure 2 illustrates that in sections with poor grass quality or evidence of burrowing activities, the strength is lower, reaching values comparable to a well-established grass quality revetment at a depth of approximately 30 cm. This implies that the resistance against near-surface slope sliding (Achmus et al, 2019) is evidently affected.

3 LABORATORY TESTS

3.1 Water contents

The undisturbed samples were analysed regarding the classifying properties. Additionally, the water content as caused by the infiltration tests were determined. No safe correlation between infiltration times, depths and water contents or levels of saturation is possible for all examined materials and dike sections (of different ages). The corresponding undrained shear strength values cu vary likewise between 30 (no infiltration) and 400 kPa (24h infiltration).

The results reflect the heterogeneity of the dike material in itself over a dike section and the locally different permeability due to cracks. Hence, the water applied by the infiltration tests does not infiltrate perfectly vertically but follows in the direction of cracks.

3.2 Soil mechanical tests

Soil mechanical tests: triaxial tests and compression tests were executed for determining the strength and the stress-strain-behaviour of the dike covering for the numerical model.

The stress-strain-curves varied quite widely. No safe correlation to the aspects mentioned above as well as classifying properties was possible. Hence, the stress-strain-curves were grouped and reference curves were developed therefrom.

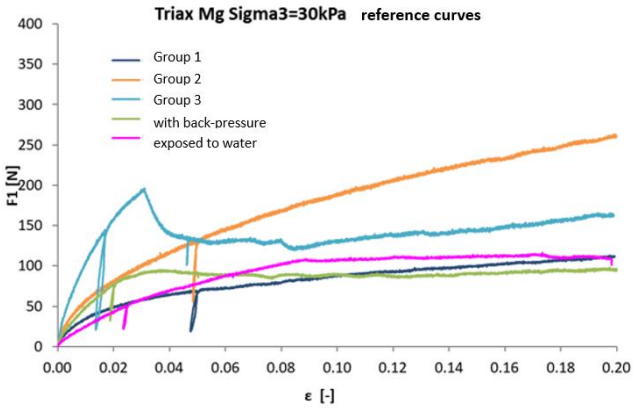

Figure 3. Stress-strain-curves of refence tests.

Figure 3 shows the reference stress-strain-curves for glacial till, which could be differentiated in 3 groups. The tests were performed with the water content of the soil samples as taken in situ. Additional test-series were done with samples which were exposed to water at the base and the top, and samples with back-pressure, i.e. full saturation.

The samples with back-pressure have a higher initial strength than the samples of group1 and water-exposed, but align at larger strains quite well. Therefore, and for an unequivocal handling at the numerical simulation, the results of the samples with back-pressure were used in the following.

4 NUMERICAL MODEL

4.1 Model and parameters

The software FLAC3D, Vers. 7.0 (Itasca, 2019) with the hardening soil model was used for the simulation of a dike section at a storm surge event. The finite difference method was chosen due to the expectable large deformations.

The derived model parameters for the examined dike materials are given in Table 2.

Table 2. Model parameters.

	Glacial till	**Soft marsh soil**	**Dredged material**
ρ_d [g/cm³]	1,83	1,54	1,35
φ' [°]	33,2	33,1	36,9
c'[kPa]	8,2	7,3	11,1
ψ [°]	5	3	3
ν [-]	0,3	0,3	0,3
p_{ref} [kPa]	25	25	25
E_{50ref} [kPa]	5445	4480	4720
E_{oedref} [kPa]	5025	2105	1290
E_{urref} [MPa]	30,3	24,55	18,55
m [-]	0,56	0,13	0,62

The comparison of the shear-strength highlights, that the difference of the 3 examined materials are quite similar. Regarding the compression it is noted, that the soft marsh soil and dredged material are softer than the glacial till.

4.2 Simulation of stability and erosion process due to wave overtopping

The results of the field and laboratory tests were implemented in a numerical model dike in which the material at the seaside above driftline and the landward slope were set to be 50% weaker than at the dike crest and the seaside below driftline (Table 1). At these conditions, the dike is stable, with a factor of safety of about 2.

For simulating the storm surge event, shear stresses due to overtopping according to (Weissmann, 2003) and the criteria for erosion according to (Hoffmans, 2009) were used. I.e. that at a deformation of 10 cm erosion occurs.

The shear stresses were applied at the seaside above driftline, dike crest and landward slope in a strip of 1m width. The limited strip reflects the investigations by (Van Hoven et al, 2010) with the overtopping

simulator, where the first damages occurred locally at weak zones of limited expansion.

At each grid point in the numerical model, the deformation velocities were measured. The critical value of 10 cm was at $5x10^{-6}$ m/s. At an overtopping rate of 100 l/(s m), i.e. shear stresses of 960 N/m², the dike started to fail. Therefore, it was assumed, that the surrounding soil of an eroded area softens to 20% of the initial strength, due to the consequent water infiltration. In this way a progressive dike failure developed (Figure 4). The numerically simulated dike-failure and a documented one (Achmus et al, 2019) fit quite well. The dashed lines indicate the initial dike geometry.

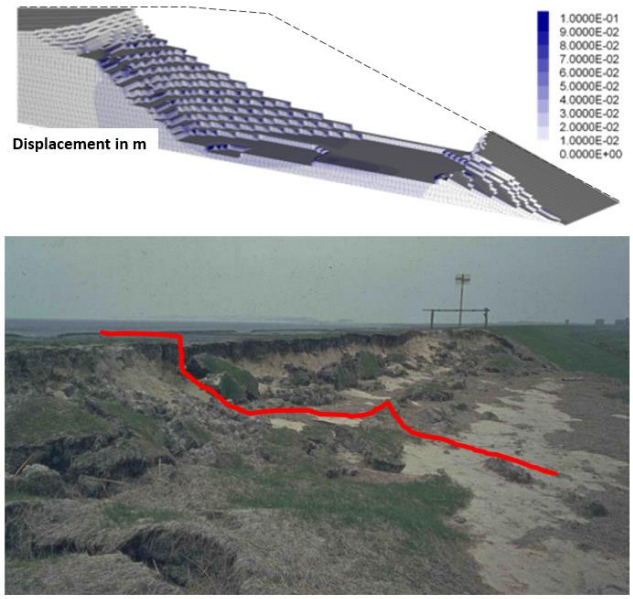

Figure 4. Numerical results and physical dike failure.

5 CONCLUSIONS

From the examinations and simulations the following conclusions can be drawn: The permeability of the examined cohesive dike coverings are about $5x10^{-5}$ m/s. For soil mechanical tests, a soil sample with back-pressure reflects the worst in-situ situations quite well. The seaside slope above drift line and the landward slope, which are exposed to wave overtopping are weaker than the other areas of a dike. A good grass quality and dike management are crucial for a high dike resistance. Dredged material is equivalent to commonly used materials, especially soft marsh soil. A realistic dike failure at high overtopping rates could be simulated.

Although higher overtopping rates as accepted could be applied in the numerical model, the authors want to emphasise, that the climate change leads to cracks and bad grass revetments due to droughts. Thus, the dike-resistance will be decreased, if not adequate actions will be taken.

ACKNOWLEDGEMENTS

The authors are grateful for the support by the state authorities of Schleswig-Holstein, Hamburg, Bremen and Mecklenburg–Western Pomerania at conducting the field tests and the waterways and shipping authority of Stralsund for the first fruitful discussions.

REFERENCES

Achmus, M., Pohl, M., Schüttrumpf, H. and Temmler, H. (2019). Infiltrationsbedingte Prozesse in der Abdeckung von See- und Ästuardeichen und deren Einfluss auf die Standsicherheit - Infiltration-related processes in the cover of sea and estuarine dikes and their influence on the stability (in german). *Die Küste*, *Heft 87* https://doi.org/10.18171/1.087113.

EAK (2002). Empfehlungen für die Ausführung von Küstenschutzwerken durch den Ausschuss für Küstenschutzwerke - Recommendations for the execution of coastal protection works by the Committee for Coastal Protection Works (in german). *Die Küste*, Heft 65. https://doi.org/10.18171/1.088100.

Hoffmans, G., Akkerman, G., Verheij, H., van Hoven, A. and van der Meer, J. (2009): The erodibility of grassed inner dike slopes against wave overtopping. *Proceedings of the 31st International Conference of Coastal Engineering (ICCE)*. Hamburg, Germany. https://doi.org/10.1142/9789814277426_0267

ITASCA (2019). Itasca Consulting Group, Inc. FLAC3D 7.0. Minneapolis, MN, USA.

TAW (1996). Technical Report „Clay for Dikes“. Technical Advisory Committee for Flood Defence in The Netherlands, Delft.

Van Hoven, A., Hardeman, B., van der Meer, J. W., Steendam, G. J. (2010). Sliding stability of landward slope clay cover layers of sea dikes subject to wave overtopping. *Proceedings of the International Conference of Coastal Engineering (ICCE)*, Shanghai/China. https://doi.org/10.9753/icce.v32.structures.5.

Weissmann, R. (2003). Die Widerstandsfähigkeit von Seedeichbinnenböschungen gegenüber ablaufendem Wasser - The resistance of inner dike slopes to run-off water (in german). *Mitteilungen aus dem Fachgebiet für Grundbau und Bodenmechanik, Heft 30.* Essen: Glückauf.

Proceedings of the XVIII ECSMGE 2024
GEOTECHNICAL ENGINEERING CHALLENGES
TO MEET CURRENT AND EMERGING NEEDS OF SOCIETY
© 2024 the Authors
ISBN 978-1-032-54816-6
DOI 10.1201/9781003431749-354
Open Access: www.taylorfrancis.com, CC BY-NC-ND 4.0 license

ECSMGE 24
XVIII EUROPEAN CONFERENCE ON SOIL MECHANICS AND GEOTECHNICAL ENGINEERING

Seepage in a flood protection dam – first centrifuge test results

Infiltration dans une digue de protection contre les crues – premiers résultats d'essais en centrifugeuse

G. Portmann*, A. Arnold
Lucerne University of Applied Sciences and Arts, Engineering and Architecture, Institute of Civil Engineering, Horw, Switzerland

Y. Zhang, A. Askarinejad
Delft University of Technology, Geoscience & Engineering, Delft, The Netherlands

**gregor.portmann@hslu.ch*

ABSTRACT: Many flood protection dams in Europe were built more than 100 years ago. These dams often do not meet current flood protection requirements due to increased level of safety requirements, higher damage potential in the valley plains and due to higher peak discharges or water levels expected with changing climatic conditions. A first series of centrifuge tests on an idealized cross-section of a flood protection dam has been carried out in the geotechnical centrifuge at TU Delft in order to study the seepage behaviour of a horizontally layered dam consisting of layers with coarse and fine-grained material. Main aspects of the testing equipment such as a specially manufactured test box which allows to simulate certain flood events of different durations and intensities are presented. Furthermore, measured values of the pore pressure during the investigated flood event, are presented and discussed in comparison to the results of finite element modelling of the dam. Finally, the influence of the hydraulic boundary conditions on the seepage behaviour in the physical and numerical modelling is critically discussed.

RÉSUMÉ: De nombreux digues de rivière en Europe ont été construites il y a plus de 100 ans. Souvent, ces digues en terre ne répondent plus aux exigences récentes en matière de protection contre les crues, en raison des besoins accrues en matière de sécurité, du potentiel de dommages plus élevé et de l'augmentation des niveaux d'eau attendus due au changement climatique. Une première série d'essais en centrifugeuse sur une coupe idéalisée d'une digue de terre a été réalisée dans la centrifugeuse géotechnique de l'Université technique de Delft afin d'étudier le comportement d'infiltration d'une digue stratifiée composée de couches de sol grossier et de sol fin. Les principaux aspects de l'équipement d'essai, tels qu'une boîte d'essai spécialement fabriquée qui permet de simuler certains événements de crue de durées et d'intensités différentes, sont présentés. En outre, les valeurs mesurées de la pression interstitielle pendant la crue étudiée sont présentées et discutées en comparaison avec les résultats de la modélisation par la méthode des éléments finis. Enfin, l'influence des conditions limites hydrauliques sur le comportement de l'infiltration dans la modélisation physique et numérique fait l'objet d'une discussion critique.

Keywords: Centrifuge modelling; seepage; flood protection dam; numerical modelling.

1 INTRODUCTION

Many flood protection dams no longer meet today's safety requirements, especially in the context of climate change. Higher water levels must be expected nowadays. This is illustrated by the example of the flood protection dams along the Alpine Rhine, which are currently being restored in sections. The original straightening and damming of the Rhine started in the 19th century (*Schweizerische Bauzeitung*, 1927) and no longer fulfils flood protection requirements.

A conservative engineering design approach assumes steady-state seepage flow through the dam and is often considered when investigating dam stability or developing measures against stability problems (CIRIA, 2013). However, it seems reasonable to consider transient seepage conditions, as flood events in alpine regions often only have a duration of 12 to 48 h. This could offer a potential for cost minimisation in project planning of remediation measures. Research results on a model river-embankment consisting of silty-sandy material in a geotechnical centrifuge by Giretti et al. (2022) show that the saturation front in the dam reaches the air side of the dam only after a long flood period. Mayor (2013) reports similar results in his large-scale tests at

the river Rhône dam, whereas it should be considered that the time until the saturation front reaches the air side depends directly on its permeability and its degree of saturation at the beginning of the flood.

However, if transient flow conditions are to be considered in the design, a more detailed understanding of the evolution of pore water pressure in the dam body is required to ensure safe design. Physical modelling under transient flow conditions can provide valuable data for better interpretation and potentially validation of numerical calculation methods.

A model-dam is used because the construction of a 1:1 scale model dam is complex and costly (Mayor, 2013; Toromanovic et al., 2020). A geotechnical centrifuge is used to increase the acceleration field and thus the effective stresses in the model to ensure comparable results of the model tests with the prototype (Madabhushi, 2014). A geometrically *n*-times smaller dam is subjected to an *n*-times larger *g*-level as the effective stresses are generally accepted to be linearly correlated with depth (Wood, 2004; Askarinejad et al., 2015).

2 METHOD

The focus of the herein described investigation on the flow behaviour and permeability within a layered flood dam lies on the physical centrifuge modelling. Subsequently, a numerical model was created – as would typically be the case in current engineering practise – in order to supplement the experimental results in the sense of a comparative investigation.

2.1 Centrifuge modelling

The experiments were conducted at 100 *g* in the geotechnical centrifuge at TU Delft which has a radius of 1.22 m and a basket size of 400x500x500 mm (Allersma, 1994; Zhang and Askarinejad, 2021). A testing strongbox was created for this purpose. A flood wave could be generated inflight with the help of a water tank and servo coupled valves. In addition, an overflow was placed on the air side of the dam to maintain a constant water level. The model box has outer dimensions of LxHxW = 615x200x120 mm, with 15 mm thick aluminium panels and a transparent front made of 15 mm thick acrylic glass. Figure 1 shows a model dam installed in the test box in the centrifuge basket. The water tank for the flood wave (1.6 litres) is situated on top of the test box. The model dam was constructed according to the prototype of a typical cross-section of the river Rhine dam. On top of the permeable Rhine gravel lies a less permeable layer of flood deposits on which the gravelly dams were built.

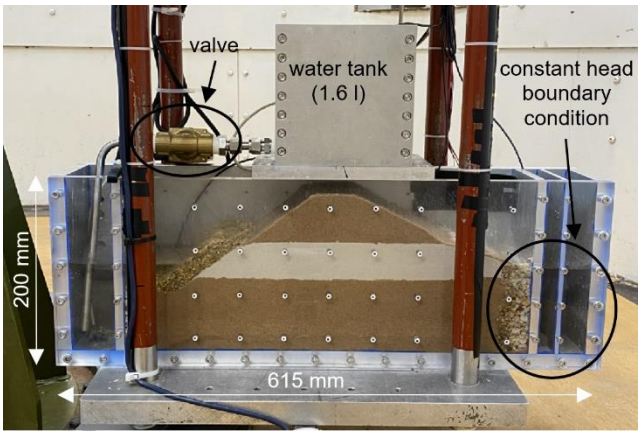

Figure 1. Modell Dam inside the strongbox.

The model dam was constructed at a scale of 1:100 as shown in Figure 2. The crest of the dam is 80 mm higher than the air side terrain and has a base width of approximately 350 mm. It is important that the underlying permeable Rhine gravel is modelled as well since it may influence the seepage behaviour. Geotechnical properties of the materials used in the model are summarised in Table 1. In prototype, the Rhine gravel and the Rhine dam have a similar permeability, so both materials are modelled with Baskarp B25 sand (Pol et al., 2021). For the less permeable layer of flood deposits a mixture of Geba Sand (Maghsoudloo et al., 2021) with 5% Kaolin Clay was used (Figure 2). The permeabilities were determined with constant head tests (Head & Epps, 2011). The values determined in the tests correspond to the vertical permeability k_v.

Table 1. Geotechnical properties of the dam materials used in the centrifuge test.

Soil type	$e^{1)}$	k_v [m/s]	φ'_{cv} [°]
Baskarp B25 Sand	0.69	$6 \cdot 10^{-5}$	32 - 34
Geba Sand with 5% Kaolin Clay	0.64	$2 \cdot 10^{-6}$	~ 31[2)]

[1)] voids ratio after compaction at w = 10%
[2)] value applies for Geba Sand without clay

The soil materials were placed in the model box in layers with a water content of 10% and compacted uniformly. After the entire box was filled, the dam was shaped by removing the excess material. At the same time, samples were taken to check the layer density.

Three Porewater-Pressure-Transducers (PPT) were installed at the bottom of the model (Figure 2) in order to record the propagation of pore water pressure in the dam. In order to check the boundary conditions, two PPTs were installed in the left inlet tank and in the right outlet tank, respectively. Figure 3 shows the planned flood characteristics in the prototype scale for the tests. The water levels refer to the heights from the

base of the strongbox (Figure 2). The riverbed accordingly lies at a height of 7.4 m. The goal was to model a flood wave consisting of a pre-wave (13 m), peak (15.4 m) and post-wave (12.3 m) by opening and closing the valves, starting from an initial river level at 9.4 m (steady state with 2 m high river, see Figure 2). Water was used as the fluid for the centrifuge experiments. The model time for seepage processes is therefore reduced by a factor of 1:100[2] (Garnier et al., 2007; Wood, 2004) since the model was tested at 100 *g*. This means that the entire flood event with a duration of 60 h at prototype scale translates to 21.6 s in the centrifuge experiment. The experiments were recorded through the acrylic glass using a digital camera.

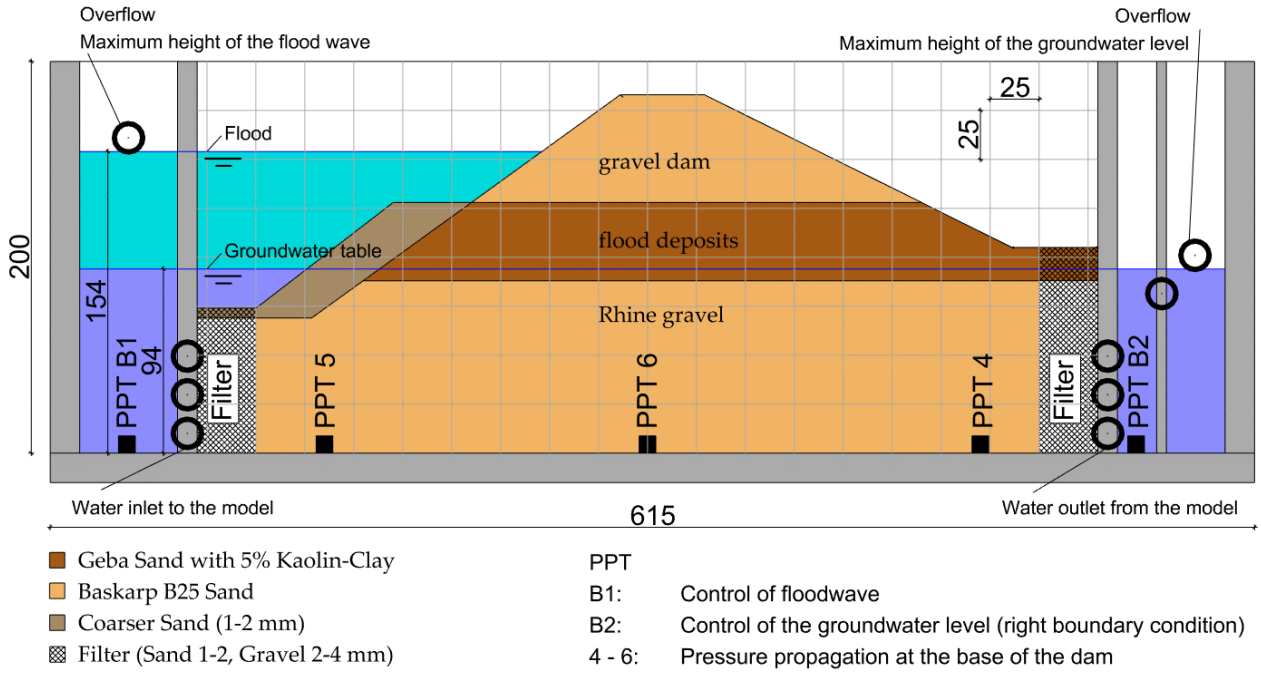

Figure 2. Geometry of the dam built into the test box including positions of PPTs. Dimensions in [mm].

The test procedure is described hereafter with the corresponding prototype time steps, model time is given in parentheses: After the centrifuge reaches 100 *g* (t = 0), the initial water level of 9.4 m (94 mm) is kept constant for 14 d (2 min) to allow stationary conditions to be established. Subsequently, the flood wave is applied stepwise within 60 h (21.6 s) as shown in Figure 3. Finally, the model is kept under 100 *g* for another 35 d (5 min) to restore initial conditions.

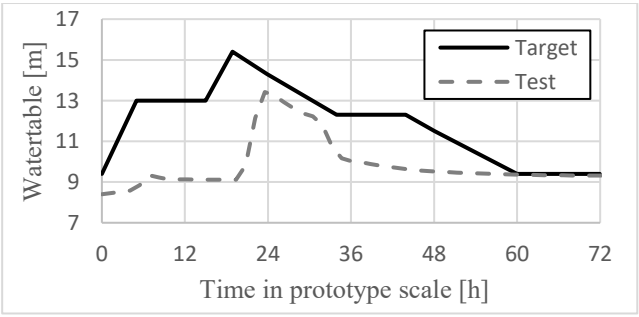

Figure 3. Target hydrograph of the flood wave in prototype scale compared to the actual flood wave achieved during the test (measurement of PPT B1, riverbed is located at 7.4 m).

After the centrifuge test, the model is checked for any signs of erosion, piping processes or stability problems. The initial water table is restored before starting the next test series. However, the desired flood wave could not be achieved because some of the valves could not be opened or closed properly at 100 *g* (Figure 3). Thus, it was difficult to maintain a constant water level with the water available in the tank due to the loss of water through seepage.

2.2 Comparative numerical model

A comparative numerical model of the dam is set at prototype scale in the program PlaxFlow2D from Plaxis with the same boundary conditions as given in the experiment. Special attention was paid to the following points:

- The flood wave is modelled according to the data measured in the centrifuge test (‘Test’ hydrograph in Figure 3).
- The permeable berm on the water side made of coarse sand is not modelled to minimise the computational effort. It is assumed that due to the higher permeability, it does not significantly influence the seepage behaviour.

- A constant head boundary condition is set on the air side as given in the centrifuge model test.
- The FEM model with the corresponding boundary conditions and the mesh is shown in Figure 4.

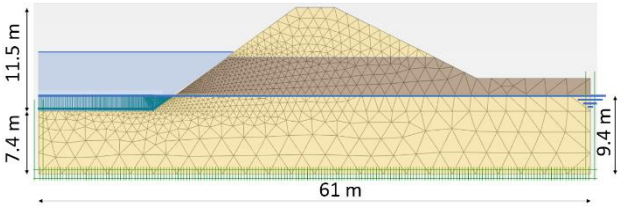

Figure 4. FEM model geometry with mesh and boundary conditions for the PlaxFlow calculation: The initial water level of the river is indicated with blue arrows and corresponds to the height of the constant head boundary condition on the right edge of the model (initially no hydraulic gradient). The variable water level is indicated in blue on the left.

The pressure conditions are compared at points that are always saturated (PPTs in Figure 2). However, it must be assumed that the modelling of the unsaturated dam area above has an influence on the results. For a comparative model, the unsaturated zones of the dam and their behaviour are described using the Van Genuchten (1980) model implemented in the software. Thus, with the help of the dimensionless water content Θ, the relative hydraulic permeability K_r of partially saturated soils can be described:

$$\Theta = \frac{(\theta - \theta_r)}{(\theta_s - \theta_r)} \quad (1)$$

$$K_r(\Theta) = \Theta^{\frac{1}{2}}\left[1 - \left(1 - \Theta^{\frac{1}{m}}\right)^{m}\right]^2 \quad (2)$$

In equation 1, θ describes the actual volumetric water content, θ_r is the residual and θ_s is the saturated volumetric water content. The parameter m is linked to the soil-water retention curve given in Equation 3 as m = 1-1/n:

$$\theta = \theta_r + \frac{(\theta_s - \theta_r)}{[1+(\alpha \cdot h)^n]^{(m)}} \quad (3)$$

In equation 3, α, n and m are model parameters describing the curvature of the water retention curve after Van Genuchten (1980) and h is the pressure head (suction is positive). However, no soil-water retention curves were available for the materials used. To be able to carry out an approximate calculation and compare it to the centrifuge tests, parameter sets stored in Plaxis were used, see Table 2. The parameter sets were selected on the basis of the particle size distribution in such a way that the numerical calculation models produced the best possible comparison to the centrifuge test results. Due to the chosen procedure, some general points must be emphasised:

- The calculations represent an initial estimate. The actual water retention curves and the associated parameters α and n may differ from those used in the present model.
- A difference between drying and wetting curves can be observed in reality (Benson et al., 2014). This is not taken into account in the numerical model.
- As there is no information on the ratio of saturated horizontal permeability k_h to vertical permeability k_v and a reliable estimate is difficult, no distinction was made.

Table 2. Input parameters for the transient seepage analysis.

	Geba Sand with 5% Kaolin Clay	**Baskarp B25 Sand**
$k_h = k_v$ [m/s]	$2.3 \cdot 10^{-6}$	$5.0 \cdot 10^{-5}$
e_{init}	0.64	0.69
θ_r	0.01	0.1
θ_s	0.34	0.32
α [1/m]	1.7	5.21
n	1.717	2.374

3 COMPARISON OF RESULTS

The dam did not exhibit any stability problems during the centrifuge tests. Furthermore, it became evident that the entire model (i.e. the centrifuge basket) tilts slightly during the experiments, which results in a water level that is inclined relative to the model box. This phenomenon occurs when the centre of gravity is not in the axis of the centrifuge basket's hinge. However, due to the flood wave and the seepage, the centre of gravity is constantly changing - which explains the phenomenon (the model was installed perpendicular to the flight direction to avoid curvature of the water surface). Thus, at the beginning of the test, the water table at PPT B1 was lower at about 8.4 m than at the end of the test at about 9.3 m (Figure 3). Nevertheless, the propagation of the flood wave through the dam during the centrifuge experiments could be analysed with the help of the PPT measurements, see Figure 5. It is noticeable that there is a significant damping of the flood wave upon entering the dam (see PPT5) and the propagation of the flood wave within the dam is significantly slower on the water side than towards the air side. This becomes clear by comparing the shifting of the pressure peaks over time. The delay between the flood wave and PPT5 is about 5.6 hours, whereas it is only about 3.3 hours between PPT6 and PPT4.

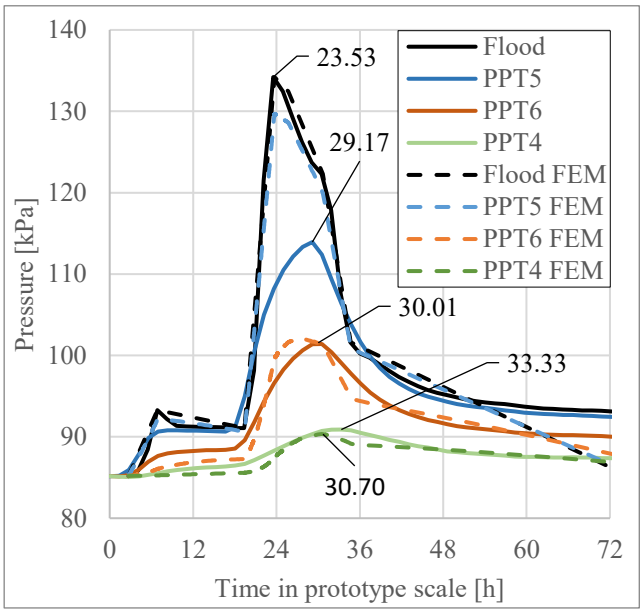

Figure 5. Results of the PPT measurement during the centrifuge tests and comparison with the FEM-simulation. The timestamps of the pressure peaks are indicated in the diagram.

By comparing the pressure changes from the centrifuge test with those from the comparative numerical model (FEM in Figure 5), the following observations can be made: The infiltration behaviour of the numerical model differs significantly from the physical model (PPT5 shows almost no damping in the numerical model compared to the data from the centrifuge test). Nonetheless, PPT6 and PPT4 show relatively good agreement at least in the damping of the pressure magnitude. In the centrifuge test it took about 10 hours to reach the maximum pore pressure at the air side of the dam (peak of PPT4 compared to peak of 'Flood'), whereas in the numerical model there are only about 7 hours in between.

4 CONCLUSION

A difference in time of rise and magnitude of the pore water pressure due to high water levels was observed between the physical model test and the comparative FEM simulation (Figure 5). The difficulties in predicting the pore water pressure distribution and the development of the saturation front in dams were already pointed out by Vaughan (1994) in his Rankine lecture, since most models do not take stress dependent permeability in terms of overburden pressure and heterogeneity of the material into account. In addition, there are considerable uncertainties in soil permeability measurements (anisotropy etc.). The largest deviations between the numerical model and the centrifuge test are found on the water side of the dam. The numerical model overestimates the speed at which the flood wave infiltrates the dam and underestimates the damping of the pore water pressures on the water side.

A further topic to be addressed is the influence of the hydraulic boundary conditions, as it is reasonable to assume, that the type of the air side boundary condition not only has an influence on the dam stability, but also on the overall seepage behaviour. This is particularly relevant as the centrifuge tests are intended to represent the conditions within the prototype dam in order to more realistically portray the behaviour under flood conditions. The tests presented in this paper are based on hydraulic boundary conditions on the air side of the dam corresponding to a constant hydrostatic water pressure (Figure 6 a).

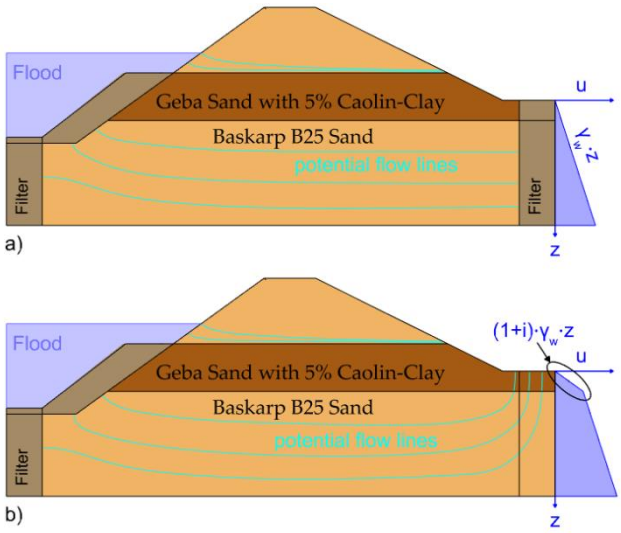

Figure 6. Variation of the boundary conditions on the air side of the dam and their potential influence: a) constant head boundary as modelled in the first test series; b) impermeable boundary – excess pore water pressure assumed below the interlayer as a result.

If the dam was constructed on a widespread fine-grained layer, as it is the situation in parts of the Alpine Rhine, some excess pore water pressures may develop beneath the bottom of the dam on the air side during a flood. As an extreme case, there could be a vertical impermeable boundary such as a construction pit closure in the dam footing area, see Figure 6 b. The pore water pressure distribution beneath the bottom of the dam on the air side therefore depends directly on the permeability and the distance of the air-side boundary condition (this applies to models as well as to prototypes) and must be carefully chosen.

The following observations may be considered to improve the results from further experiments:

- More PPTs should be installed on the water side of the dam to better quantify the flood wave propagation into the dam close to the riverbed. This is where the largest differences between

centrifuge tests and numerical simulation have been observed.

- The initial degree of saturation of the dam above the seepage line is unknown - but this significantly influences the infiltration time (Mayor, 2013). The installation of tensiometers to measure suction could therefore be advantageous.
- The intended flood wave, which is inspired by real flood events, could not be achieved due to the complexity of the test control. If the flood wave characteristics are to be simplified for further tests, possible saturation changes of the dam before the flood should be considered.
- It should be considered whether the test may be carried out with viscous fluid instead of water to reduce the time scaling factor (Wood, 2004). This could help to simplify the experimental control and data collection.

ACKNOWLEDGEMENTS

The authors would like to thank the Agency for Civil Protection (ABS) of the Principality of Liechtenstein, on whose behalf the centrifuge model tests could be carried out. The assistance of the technicians from TU Delft, Karel Heller, Kees van Beek, Roland Klassen and Ronald van Leeuwen greatly contributed to the successful execution of the tests.

REFERENCES

Allersma, H. G. B. (1994). The University of Delft geotechnical centrifuge. *Centrifuge '94: Proc. of the Int. Conf.*, 47-52.

Askarinejad A., Beck A., and Springman S.M. (2015). Scaling law of static liquefaction mechanism in geocentrifuge and corresponding hydromechanical characterization of an unsaturated silty sand having a viscous pore fluid. *Canadian Geotechnical Journal*. 52(6): 708-720. https://doi.org/10.1139/cgj-2014-0237.

Benson, C. H., Chiang, I., Chalermyanont, T., & Sawangsuriya, A. (2014). Estimating van Genuchten Parameters α and n for Clean Sands from Particle Size Distribution Data. *From Soil Behavior Fundamentals to Innovations in Geotechnical Engineering*, 410–427. https://doi.org/10.1061/9780784413265.033.

CIRIA (ed.). (2013). *The International Levee Handbook*. CIRIA, London.

Garnier, J., Gaudin, C., Springman, S. m., Culligan, P. j., Goodings, D., Konig, D., Kutter, B., Phillips, R., Randolph, M. f., & Thorel, L. (2007). Catalogue of scaling laws and similitude questions in geotechnical centrifuge modelling. *International Journal of Physical Modelling in Geotechnics*, 7(3), 01–23. https://doi.org/10.1680/ijpmg.2007.070301.

Giretti, G., Pirone, M., Ventini, R., Mancuso, C., Dodaro, E., Gragnano, G., Gottardi, G., Fioravante, V., & Gabrieli, F. (2022). Centrifuge modelling of a river embankment subjected to transient seepage conditions. *Proceedings of the 10th Int. Conf. on Physical Modelling in Geotechnics. ICPMGE 2024*, Daejeon, South Korea.

Head, K., & Epps, R. (2011). *Manual of soil laboratory testing. Volume 2: Permeability, Shear Strength and Compressibility tests* (3rd Ed.). Wiley, New York.

Madabhushi, G. (2014). *Centrifuge modelling for civil engineers*. Taylor & Francis, Boca Raton.

Maghsoudloo, A., Askarinejad, A., de Jager, R. R., Molenkamp, F., & Hicks, M. A. (2021). Large-scale physical modelling of static liquefaction in gentle submarine slopes. *Landslides*, 18(10), 3315-3335. https://doi.org/10.1007/s10346-021-01705-6.

Mayor, P., A. (2013). *Verhalten eines Flussdammes unter wiederholter Hochwasserbelastung.* Doctoral Thesis, ETH Zürich. https://doi.org/10.3929/ethz-a-010028707.

Pol, J.C., van Klaveren, W., Kanning, W., van Beek, V.M., Robbins, B., & Jonkman, Sebastiaan N. (2021). Progression Rate of Backward Erosion Piping: Small Scale Experiments. *Proceedings of the 10th Int. Conf. on Scour and Erosion*. ICSE-10, Arlington, Virginia, USA.

s.n. (1927). Zur Rhein-Hochwasserkatastrophe. *Schweizerische Bauzeitung*, 89/90 (Heft 16). ETH Zürich. https://doi.org/10.5169/seals-41789.

Toromanovic, J., Lagerlund, J., Viklander, P., & Laue, J. (2020). Geotechnical instrumentation of an experimental embankment dam. 171–176. *Proc. of the 4th Europ. Conf. on Physical Modelling in Geotechnics 2020*, Luleå, Sweden.

Vaughan, P. R. (1994). Assumption, prediction and reality in geotechnical engineering. *Géotechnique*, 44(4), 573–609. https://doi.org/10.1680/geot.1994.44.4.573.

Van Genuchten, M. Th. (1980). A closed-form equation for predicting the hydraulic conductivity of unsaturated soils. *Soil Sci. Soc. Am. J.* 44:892-898 https://doi.org/10.2136/sssaj1980.03615995004400050002x

Wood, D. (2004). *Geotechnical modelling*. Spon Press, London. https://doi.org/10.1201/9781315273556.

Zhang, W, Askarinejad, A. (2021). Centrifuge modelling of static liquefaction in submarine slopes: scaling law dilemma. *Canadian Geotechnical Journal.* 58(2): 200-209. https://doi.org/10.1139/cgj-2019-0417.

Proceedings of the XVIII ECSMGE 2024
GEOTECHNICAL ENGINEERING CHALLENGES
TO MEET CURRENT AND EMERGING NEEDS OF SOCIETY
© 2024 the Authors
ISBN 978-1-032-54816-6
DOI 10.1201/9781003431749-355
Open Access: www.taylorfrancis.com, CC BY-NC-ND 4.0 license

ECSMGE 24
XVIII EUROPEAN CONFERENCE ON SOIL MECHANICS AND GEOTECHNICAL ENGINEERING

Internal erosion initiation in gap-graded soils: A 3D microstructure assessment using convolutional autoencoders

Initiation de l'érosion interne dans les sols à granulométrie discontinue: Une évaluation de la microstructure 3D à l'aide d'autoencodeurs convolutifs

J. Qi, N. Yousefpour*, G. Narsilio
Department of Infrastructure Engineering, The University of Melbourne, Parkville, Australia

M. Pouragha
Department of Civil and Environmental Engineering, Carleton University, Ottawa, Canada

**negin.yousefpour@unimelb.edu.au*

ABSTRACT: Internal erosion in gap-graded soils is a major risk faced by earth dams and levees. However, the understanding of internal erosion mechanisms, especially at the particle scale, is still limited. This research couples the Discrete Element Method (DEM) with Computational Fluid Dynamics (CFD) to simulate the internal erosion (suffusion) process in gap-graded soil samples and further train Artificial Intelligence (AI)/Deep Learning (DL) algorithms to identify subtle patterns and anomalies related to internal erosion initiation. A time-lapse micro-structure visualisation approach is introduced using 3D voxelization of soil elements under internal erosion. Particle-scale parameters such as particle and flow velocity, number of contacts, contact forces etc are extracted from the CFD-DEM simulations throughout the internal erosion process forming time-series tensors used to train the AI models. The Autoencoder models with 3D Convolutional Neural Network (CNN) layers as encoder and decoder are developed to investigate the micro-scale patterns within the particle-fluid assembly together with the variations and anomalies throughout the erosion process. Using Sequential Training framework, anomalies within the data are detected by Convolutional Autoencoder models to identify the locus and time of internal erosion initiation. In addition, the micro-mechanisms during the initiation of internal erosion such as fine particle migration and contact loss are investigated. The 3D voxelization approach for internal erosion micro-mechanism visualisation can be integrated with advanced imaging techniques (e.g., micro-computed tomography) for early detection of internal erosion in future.

RÉSUMÉ: L'érosion interne dans les sols à granulométrie écartée représente un risque majeur pour les barrages en terre et les digues. Cependant, la compréhension des mécanismes d'érosion interne, en particulier à l'échelle des particules, reste limitée. Cette recherche couple la Méthode des Éléments Discrets (DEM) avec la Dynamique des Fluides Computationnelle (CFD) pour simuler le processus d'érosion interne (suffusion) dans des échantillons de sol à granulométrie écartée et pour entraîner davantage les algorithmes d'Intelligence Artificielle (IA)/Apprentissage Profond (AP) afin d'identifier des modèles subtils et des anomalies liées à l'initiation de l'érosion interne. Une approche de visualisation micro-structurale en accéléré est introduite en utilisant la voxelisation 3D des éléments de sol sous érosion interne. Des paramètres à l'échelle des particules tels que la vitesse des particules et du flux, le nombre de contacts, les forces de contact, etc., sont extraits des simulations CFD-DEM tout au long du processus d'érosion interne pour former des tenseurs en série temporelle utilisés pour entraîner les modèles d'IA. Des modèles d'Autoencodeurs avec des couches de Réseau Neuronal Convolutif (CNN) 3D comme encodeur et décodeur sont développés pour étudier les modèles microscopiques au sein de l'assemblage particule-fluide ainsi que les variations et anomalies tout au long du processus d'érosion. En utilisant le cadre de Formation Séquentielle, les anomalies dans les données sont détectées par des modèles d'Autoencodeur Convolutif pour identifier le lieu et le moment de l'initiation de l'érosion interne. De plus, les micro-mécanismes lors de l'initiation de l'érosion interne tels que la migration des particules fines et la perte de contact sont étudiés. L'approche de voxelisation 3D pour la visualisation des micro-mécanismes d'érosion interne peut être intégrée avec des techniques d'imagerie avancées (par exemple, la micro-tomographie informatisée) pour la détection précoce de l'érosion interne à l'avenir.

Keywords: DEM-CFD; internal erosion; convolutional neural networks (CNN); autoencoder; anomaly detection; deep learning; microstructure visualisation.

1 INTRODUCTION

Internal erosion is a typical issue faced by earth dams and levees, posing a significant risk to public safety and the economy. This phenomenon frequently occurs in gap-graded soils subjected to certain hydraulic and mechanical conditions. The initiation and development of internal erosion are mainly influenced by three factors: (a) particle gradation, (b) hydraulic condition, and (c) mechanical state (Brown & Bridle, 2009). In this context, the internal erosion has been studied through field monitoring (Cai et al., 2020; Chen et al., 2018), laboratory tests (Planès et al., 2016), numerical simulations (Tran et al., 2017), and data-driven analysis (Fisher et al., 2016; Yousefpour & Fazel Mojtahedi, 2023). Internal erosion usually initiates from imperceptible transport of fine particles at the pore scale with no evident signs and gradually develops into catastrophic dam breaches, which highlights the necessity of insight into the particle scale behaviours and their link to the macro-scale/field observations.

This study couples the Discrete Element Method (DEM) with Computational Fluid Dynamics (CFD) to simulate the internal erosion process in gap-graded soils, simulating the suffusion mechanism (Qi et al., 2022). 3D voxelization of the gap-graded soil was conducted with associated particle-scale parameters stored in the voxels as the input for the DL model. The Autoencoder models with 3D Convolutional Neural Network (CNN) layers as encoder and decoder are developed to investigate the micro-structure patterns within the particle-fluid assembly. A Sequential Training framework is introduced for Dl models to detect anomalies within the time-series of 3D particle-scale tensors for an assessment of locus and time of internal erosion initiation.

2 METHODOLOGY

2.1 CFD-DEM simulation

The coupled CFD-DEM simulations are performed to assess the internal erosion initiation process in gap-graded soil driven by a range of hydraulic gradients. A gap-graded sand sample with a Fine Content (FC) of 25% is selected for the simulation. The sample gradation and mass fractions for the grain sizes are provided in Table 1.

Table 1. Soil sample gradation and mass fractions.

Particle Group	Diameter	Finer %	Mass %
D1	3.43	62.5%	37.5%
D2	2.36	25.5%	37.5%
D3	0.36	12.5%	12.5%
D4	0.30	0	12.5%

The 3D CFD-DEM model of the gap-graded sand is created within a cylindrical shell (D=15mm, H=25mm). The time step of DEM is set to be 5e-7s for the stability of the calculation. For the first step, the particles are randomly generated at the top of the cylinder with predefined mass fractions and then settled to the bottom under gravity as shown in Figure 1. The generated dry samples are then compacted by a top plate to achieve a target sample density before saturation.

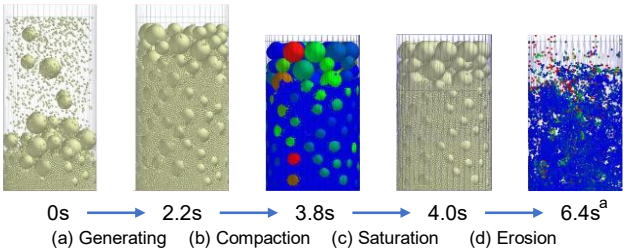

Figure 1. CFD-DEM model (a) Sample generating, (b) sample compaction to target porosity, (c) saturation and stabilization of compacted sample, (d) internal erosion.
[a] Coarse particles are hidden at t=6.0s for better visualization.

The compacted dry sample is then coupled with CFD under static hydraulic pressure for saturation. Both the DEM and CFD simulations continue to reach equilibrium during the saturation process. For the erosion stage, the plate on the top is replaced by a mesh that is only permeable to the fine particles. The hydraulic pressure of the outlet is set to 0, while that of the inlet is fixed to a value that applies a hydraulic gradient to the whole sample. The hydraulic pressure is linearly increased from 0kPa at t=4.0s to 100kPa at t=5.5s, during which fine particles are gradually eroded from the pore space between coarse particles. The eroded particles are deleted when they exit the top mesh.

2.2 Particle-scale data and 3D microstructure representation

The CFD-DEM simulation outputs are extracted in a high temporal resolution of 0.01s, which produces abundant particle-scale data. This data includes time-lapse tensor of particle velocity, contact force, contact number etc, which can reflect the subtle changes in interaction and migration of particles during internal erosion. However, this data could not require pre-processing before using as an input for DL models.

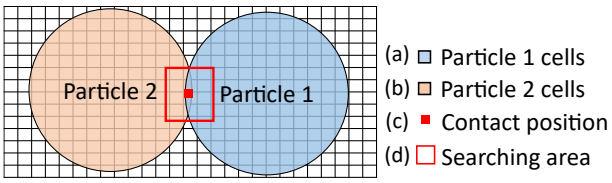

Figure 2. Particle data representation (a)&(b) cells with information from particle 1 &2, (c) contact position of two particles, (d) area to search for the contact cells.

To facilitate such purpose, a voxelization algorithm is developed to convert the particle-scale data into 3D matrix (tensor) representations. Voxels are defined using grids within the particle-fluid assembly domain. Each voxel is occupied by particles and fluid. The relevant particle-scale data are assigned to the respective DEM voxels, including particle velocity, contact force, contact number etc (Figure 2). As coarse particles are intact during suffusion, only fine particle parameters are considered in this process.

The voxels for storing the contact information are detected within a domain centred at the contact position by comparing the voxel-particle distance and the particle radius. With the particle information stored in the voxels, the constructed 3D matrices serve as the input for the subsequent Machine Learning models.

2.3 Deep learning approach

Convolutional Neural Networks (CNN) have been proven powerful in capturing/extracting features from image data (Tang et al., 2022). Also, Autoencoders have been successfully used for unsupervised anomaly detection for problems where normal (true) versus anomaly (fake) data is not known apriori (Yousefpour & Fazel Mojtahedi, 2023). Considering the 3D particle-scale data structure from CFD-DEM, a 3D Convolutional Autoencoder (CAE) architecture is deemed as a viable architecture to extract spatial-temporal patterns and anomalies related to subtle microstructure changes in the soil sample around the initiation of erosion. In this problem, the sample 3D microstructure is visualised by the generated particle-scale tensors. These time-series tensors are treated as image data for the CAE algorithm. The encoder compresses the input data into latent representations while the decoder reconstructs the input from the latent space. The encoder and decoder are constructed from 3D Convolutional layers and the necessary max pooling or deconvolutional layers as depicted in Figure 3. The CAE model learns the reconstruction error distribution over the training dataset and then detects anomalies within the test dataset using a set error threshold. A data point is recognised as an anomaly if its reconstruction error is larger than this threshold.

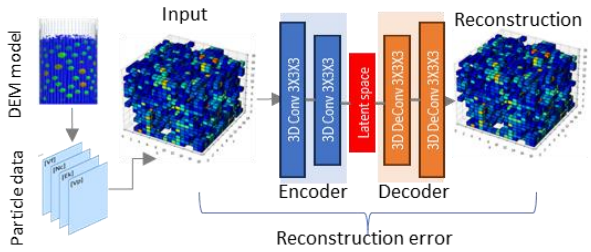

Figure 3. 3D CNN Autoencoder architecture.

2.4 Data division and sequential training

CFD-DEM outputs are extracted at a time step of 0.01sec, from 4.0sec to 6.4sec, generating a time-series of 240 tensors. Sequential Training is a systematic approach of Machine Learning (ML) training in consecutive steps, where the training database size grows linearly at each step, rather than using the entire dataset at once (Yousefpour & Fazel Mojtahedi, 2023). This approach has proven effective in detecting the initiation of internal erosion based on the evolution of the number and trend of anomalies. In this study, Sequential Training was conducted over eight stages. During each step, a distinct segment of the data was used for training followed by a non-overlapping segment for validation (see Figure 5).

3 RESULTS

3.1 Fine particle migration

To better capture the internal erosion process, only a fraction of the whole CFD-DEM located at the top of the sample where the most intensive migration of fine particles happened is incorporated to train the CAE model. The particle velocity tensors are converted to a binary scale, such that voxels with particle velocity are represented as 1. Visualizing two slices of the binary tensors at t=4.1s, shown in Figure 4(a) and t=6.2s, shown in Figure 4(b) reveals the patterns of fine particles migration. It's also observed that the scatter within the selected region gets denser as the fine particles gradually migrate from lower positions to the top. In particular, potential preferential erosion paths that fine particles take through the pore space between coarse particles are captured.

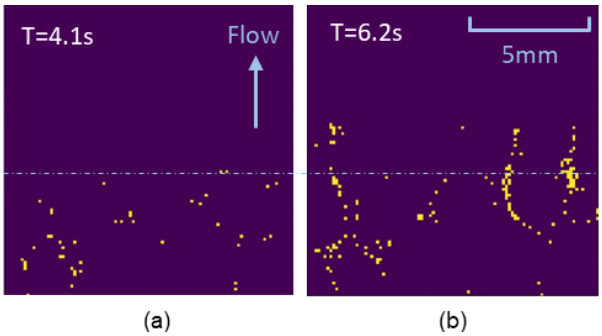

Figure 4. Binary particle velocity slices (a) before suffusion (T=4.1s) (b)after suffusion (T=6.2s).

3.2 Anomaly detection

The Convolutional Autoencoder model is trained using the binary particle velocity tensors prior to obvious internal erosion initiation in the sample (mass loss). The reconstruction errors are calculated for tensors within the test dataset after each training step. The number of detected anomalies from the testing data is recorded as the internal erosion evolves after the application of hydraulic gradient at t=4.0s as shown in Figure 5. The number of anomalies stays constant at the initial steps (from 4.0s to 5.2s) with all the test data being recognised as anomalies, meaning the fine particle velocity patterns during this stage are largely different from the test dataset and internal erosion did not happen at this stage. After t = 5.2s, the number of anomalies decreases abruptly, which can indicate a sudden pattern change of the fine particles. Between 5.2s and 5.6s, the number of anomalies starts to converge to a constant value. This trend shows that the training dataset is more representative of the test dataset patterns (therefore fewer anomalies are identified) and be an indicative of the approximate time of internal erosion initiation. Based on the above observations, it can be inferred that internal erosion initiated between 5.2s and 5.4s.

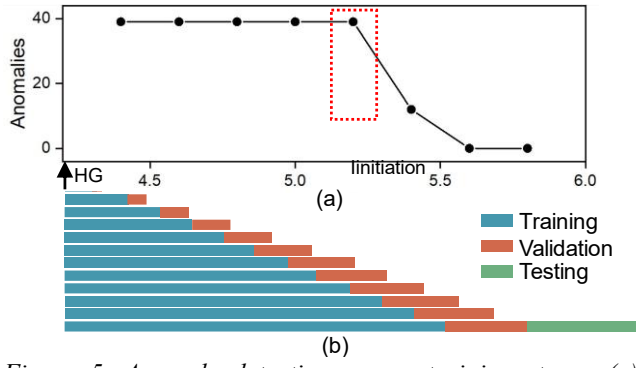

Figure 5. Anomaly detection across training stages (a) Number of anomalies detected from different training stages (b) sequential training stages.

4 CONCLUSIONS

This research investigates the initiation of internal erosion in gap-graded soils through a Convolutional Autoencoder deep learning algorithm trained using CFD-DEM simulations data.

Fine particle velocity data are visualized using a 3D voxelization method and converted to time-lapse binary tensors to assess the internal erosion patterns during the initiation phase. The subtle changes in the microstructure of the soil element and migration patterns of the fine particles are captured using this approach.

The CAE model trained with the time-series of particle-scale tensors based on the sequential training framework shows a sudden drop followed by the convergence trend close to the initiation of internal erosion. This shows that the 3D voxelisation approach for internal erosion micro-mechanism visualisation can be potentially integrated with advanced imaging techniques (e.g. micro-CT) for early detection of internal erosion in future studies.

ACKNOWLEDGEMENTS

The authors are grateful for the financial support of the University of Melbourne's Early Career Research Grant and the China Scholarship Council Scholarship.

REFERENCES

Brown, A., & Bridle, R. (2009). Report on the European working group on internal erosion, St. Petersburg. *Dams and Reservoirs*, *19*(3), 133–136. https://doi.org/10.1680/dare.2009.19.3.133.

Cai, Y., Cheng, H., Wu, S., Yang, Q., Wang, L., Luan, Y., & Chen, Z. (2020). Breaches of the Baige Barrier Lake: Emergency response and dam breach flood. *Science China Technological Sciences*, *63*(7), 1164–1176. https://doi.org/10.1007/s11431-019-1475-y.

Chen, C.-Y., Chen, S.-C., Chen, K.-H., & Liu, Z.-H. (2018). Thermal monitoring and analysis of the large-scale field earth-dam breach process. *Environmental Monitoring and Assessment*, *190*(8), 483. https://doi.org/10.1007/s10661-018-6869-y.

Fisher, W. D., Camp, T. K., & Krzhizhanovskaya, V. V. (2016). Crack Detection in Earth Dam and Levee Passive Seismic Data Using Support Vector Machines. *Procedia Computer Science*, *80*, 577–586. https://doi.org/10.1016/j.procs.2016.05.339.

Planès, T., Mooney, M. A., Rittgers, J. B. R., Parekh, M. L., Behm, M., & Snieder, R. (2016). Time-lapse monitoring of internal erosion in earthen dams and levees using ambient seismic noise. *Géotechnique*, *66*(4), 301–312. https://doi.org/10.1680/jgeot.14.P.268.

Qi, J., Yousefpour, N., Narsilio, G., & Pouragha, M. (2022). Initiation of Internal Erosion in Earth Dams: A Particle-

Scale Computational Approach. *Australian Geomechanics Society 2022 Victoria Symposium*.

Tang, P., Zhang, D., & Li, H. (2022). Predicting permeability from 3D rock images based on CNN with physical information. *Journal of Hydrology*, *606*. https://doi.org/10.1016/j.jhydrol.2022.127473.

Tran, D. K., Prime, N., Froiio, F., Callari, C., & Vincens, E. (2017). Numerical modelling of backward front propagation in piping erosion by DEM-LBM coupling. *European Journal of Environmental and Civil Engineering*, *21*(7–8), 960–987. https://doi.org/10.1080/19648189.2016.1248794.

Yousefpour, N., & Fazel Mojtahedi, F. (2023). Early detection of internal erosion in earth dams: combining seismic monitoring and convolutional AutoEncoders. *Georisk*.

Proceedings of the XVIII ECSMGE 2024
GEOTECHNICAL ENGINEERING CHALLENGES
TO MEET CURRENT AND EMERGING NEEDS OF SOCIETY
© 2024 the Authors
ISBN 978-1-032-54816-6
DOI 10.1201/9781003431749-356
Open Access: www.taylorfrancis.com, CC BY-NC-ND 4.0 license

ECSMGE 24
XVIII EUROPEAN CONFERENCE ON SOIL MECHANICS AND GEOTECHNICAL ENGINEERING

Geotechnical conditions of "Debelo brdo" tunnel construction on the highway E-80: Nis-Merdare-Pristina ("Peace Highway")

Conditions géotechniques de la construction du tunnel "Debelo brdo" sur l'autoroute E-80: Nis-Merdare-Pristina ("Autoroute de la Paix")

D. Rakic*, I.B. Ikodinovic, R. Lapcevic
University of Belgrade, Faculty of Mining and Geology, Belgrade, Serbia

D. Lukic
University of Novi Sad, Faculty of Civil Engineering, Subotica, Serbia

dragoslav.rakic@rgf.bg.ac.rs

ABSTRACT: The construction of the highway E-80 has begun in Serbia, which will represent the traffic hub of the Western Balkans and will be part of the main regional transport network of Southeast Europe. Its total length through Serbia is 77 km, and one part of the route is designed through a typical plain terrain, while a larger part of the route passes through hilly terrain. The construction of the tunnel "Debelo brdo" is planned partly in an open cut excavation with a length of 240 m, and partly with an underground excavation with a length of 190 m. The geotechnical conditions of tunnel construction in open cut excavation, and especially the geotechnical conditions of tunnel excavation, will be presented in the paper.

RÉSUMÉ: La construction de l'autoroute E-80 a commencé en Serbie, qui constituera la plaque tournante du trafic des Balkans occidentaux et fera partie du principal réseau de transport régional de l'Europe du Sud-Est. Sa longueur totale à travers la Serbie est de 77 km, et une partie de l'itinéraire est conçue sur un terrain plat typique, tandis qu'une plus grande partie de l'itinéraire traverse un terrain vallonné. La construction du tunnel „Debelo brdo" est prévue en partie avec une excavation à ciel ouvert d'une longueur de 240 m et en partie avec une excavation souterraine d'une longueur de 190 m. Les conditions géotechniques de construction de tunnels en fouille à ciel ouvert, et notamment les conditions géotechniques de creusement de tunnels, seront présentées dans l'ouvrage.

Keywords: „Debelo brdo" tunnel; temporary slopes; open cut excavation; tunnel excavation; piles.

1 INTRODUCTION

The construction of the E-80 Nis-Merdare-Pristina highway is of special economic and social interest for the Republic of Serbia. It represents the traffic hub of the Western Balkans and will be part of the main regional transport network of Southeast Europe (that's why it was called the "Peace Highway"). The total length of the highway is 77 km. The "Debelo Brdo" tunnel is located on the first 36.3 km long highway section. The construction of one tunnel tube with an approximate cross-section of about 85 m^2 is planned by the project. The height of the open part of the tunnel in relation to the pavement is about 8.3 m, while the structural height ranges from 10.9 - 11.9 m, not counting the protective support structure.

2 GENERAL GEOTECHNICAL CHARACTERISTICS OF THE TERRAIN

The geological structure at the location of the "Debelo brdo" tunnel consists of younger Neogene hilly terrains. The complex corresponds to the upper Miocene and lower Pliocene, so it is separated as a Mio-Pliocene complex of heterogeneous lithological composition. In the surface part, marly clays of the weathered zone dominate (in the tunnel zone, the thickness of the weathering crust is over 10 m), and the base consists of marls with rare layers of silt and fine-grained sand, while thinner layers of sandstone also occur occasionally. In the zone of the entrance portal of the tunnel, the occurrences of active sliding as well as conditionally unstable terrains, whose relief forms are characteristic of calmed landslides,

have been determined, so that inadequate cutting could cause new instabilities (Rakic et al., 2019).

Along the route of the tunnel with a total length of 430 m, two geotechnical quasi-homogeneous zones were separated: GTZ-1 and GTZ-2. The first geotechnical zone (GTZ-1) represents the weathering crust of marls and sandstones dominated by silty marly clays. This area is in the overburden area above the tunnel, with a thickness of 10-13 m, and its border approximately follows the surface of the terrain. It is a material of hard-plastic to semi-hard consistent state with extremely high plasticity. When it is exposed to atmospheric influence for a long time, it easily disintegrates, crushes and crumbles. Within this geotechnical zone, the tunnel excavation will be carried out in an open cut excavation. The second geotechnical zone (GTZ-2) is built of clayey marl, locally silty-sandy, and represents the basic rock mass in which the complete underground excavation for the tunnel will be carried out.

Piezometer constructions were installed in two exploration boreholes, in which regular observations were made. The piezometric level ranged from 5.5 to 13.5 m, which indicates that water filtration is carried out down the slope, and as the morphology of the terrain is variable, the GWL ranges from 300 to 307 m. At the time of field investigation works, the groundwater level was approximately at the level of the tunnel or just below it.

Geotechnical longitudinal section of the terrain, with separated geotechnical zones, conditionally stable slope, forecast groundwater level, position of tunnel level and proposed method of excavation, is shown in Figure 1.

3 DEFINING PHYSICAL-MECHANICAL PARAMETERS

Laboratory tests have shown that the Mio-Pliocene clay-marly complex is extremely plastic material with a yield strength of over 110% in some samples.

These are materials with I_c>1.0, so the uniaxial compressive strength is usually q_u>250 kPa. However, occasional occurrences of sandstone laminae and thinner marl laminae (thickness 10-20 cm), as well as zones of slightly weathered marl, had a significant impact on the increase in uniaxial compressive strength. The tests were performed in accordance with the appropriate standard (SRPS EN 1926), but a non-standard method was also applied, which involved several cycles of unloading and reloading at lower values of axial pressure. For these reasons, a significantly wider interval of q_u values was determined, which ranged from q_u= 243–774 kPa (Figure 2).

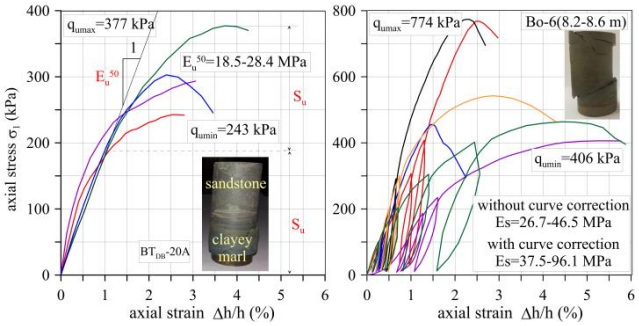

Figure 2. Characteristic diagrams for standard and non-standard uniaxial tests.

Due to significant heterogeneity of the environment, the value of undrained modulus of elasticity ranged in a very wide interval from E_s=26.7-95 MPa. In addition, the values of the undrained modulus of elasticity were also obtained based on correlations with the undrained shear strength (s_u) using the appropriate dependence and amounted to E_s=33.0-89.0MPa (Duncan and Buchignani,1976).

It should be noted that geophysical investigations were also carried out at the location of the tunnel, and that the values of the modulus of elasticity were obtained in the interval of E_s=35-82MPa.

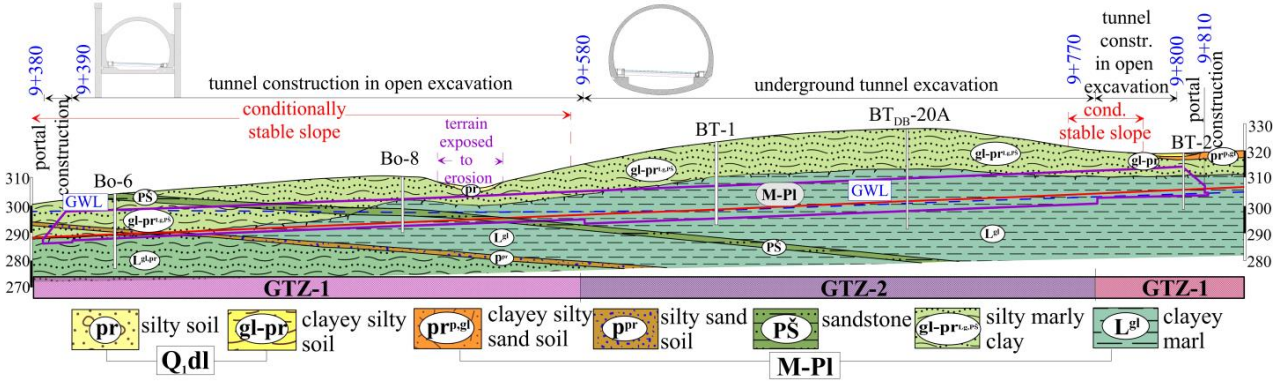

Figure 1. Geotechnical longitudinal section along „Debelo brdo“ tunnel.

When it comes to shear strength parameters, geotechnical characteristics have shown that it is necessary to propose parameters for two different excavation systems. The first one refers to the case that underground works and protection of slopes with supporting structures are carried out quickly in a short time interval after excavation. In that case, it is proposed to use "critical" shear strength parameters, which are defined at the appropriate displacement value. In the case that the construction of the tunnel cannot be carried out in a short period of time, the use of residual shear strength parameters is proposed, due to the fact that an active landslide has been identified in the immediate zone of the tunnel.

It is characteristic that on the basis of oedometer tests, all samples showed swelling potential, regardless of the soil from which they were taken (silty marly clays-gl-pr^{Lg} or locally silty clayey marls-L^{gl,pr}). In some samples, the swelling stress was higher of σ_{sw}>300 kPa.

Based on the observation of the field conditions and the summary analysis of all laboratory tests, the proper values of the physical-mechanical parameters, which were used during the geotechnical analysis, were adopted (Table 1).

Table 1. Proper values of physical-mechanical parameters.

GT layer	Physical-mechanical parameters						
	γ kN/m^3	c' kPa	φ' (°)	c_r kPa	φ_r (°)	E_s MPa	E_r MPa
(gl-pr^{Lg})	18.5	28	18	12	10	20	60
(L^{gl,pr})	19	40	20	12	11	25	75

4 GEOTECHNICAL CONDITIONS OF TUNNEL CONSTRUCTION

4.1 Tunnel construction on open excavation part

For the construction of tunnels in an open excavation, securing with piles is provided. Geotechnical analyses were conducted in two phases. In the first phase of the excavation, the top parts of the slope were covered, while in the second phase, the excavation for the construction of the tunnel structure was analysed.

The first phase involves the formation of a temporary slope and a working plateau for the installation of piles. As it is a conditionally stable slope, the analysis was first performed using the residual shear strength parameters, for the designed slope inclination of 1:2, and on that occasion the safety factor Fs<1.0 was obtained. Therefore, it was suggested that the excavation be carried out with one berm 4 m wide at a height of about 5 m in relation to the elevation of the working plateau. However, in the case that earthworks and slope protection with a supporting structure are carried out in a short period of time without the influence of atmospheric changes, the analysis was also performed with "critical" parameters of shear strength, so that a significantly higher factor of safety was obtained (Fs=1.747). Within the second phase of excavation, protective piles will be carried out secured by the brace beam.

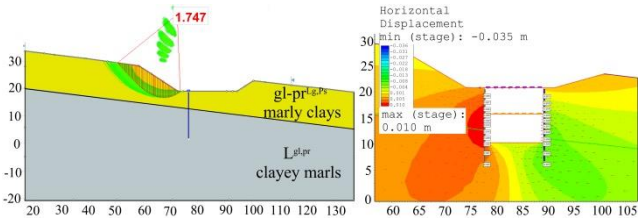

Figure 3. Geotechnical stability analyses (stability of temporal slope and horizontal displacement of piles).

4.2 Tunnel construction on underground excavation part

The underground excavation of the tunnel will be carried out according to the principles of NATM (New Austrian Tunnelling Method). Excavation is planned with phased development of the profile: calotte, abutments, and then the inverted arch. For the protection of the calotte excavation, a primary support is provided: pipe-roof shield, ribs, reinforcement mesh and layers of shotcrete. To prevent excessive settlements, an elephant foot, installation of micro piles and anchors, and construction of a temporary inverted arch are provided. To secure the excavation in the area of abutments and inverted arch, a construction made of ribs, reinforcement mesh, layers of shotcrete and anchors is planned. Also, at the level of the abutments, the construction of the second elephant foot, the installation of the second row of micro piles and the second temporary inverted arch is planned.

For the stress-strain analysis in different phases of construction in the tunnel support and the surrounding rock mass, tunnel stability calculations were performed using a 2D model with the indirect introduction of 3D effects. Simulating tunnel excavation and supporting was carried out in nine steps. By adopting certain assumptions about the properties, condition and behaviour of the rock masses (Coulomb-Moore failure criterion, different values of the modulus of elasticity for loading E_s and unloading E_r, the pipe shield is simulated with a material with equivalent properties, relaxation stress in the excavation phase by λ=0.3, was simulated by progressive softening of the rock, after installing the pipe shield, the stresses in the rock mass were relaxed to λ=0.7), geotechnical

analyses were conducted and the values of certain parameters were obtained, which are shown in Table 2.

Table 2. Values of parameters used during the simulation of the impact on the tunnel face excavation.

N_s	λ_{cr}	r_p	λ_0	r_{p0}	K_o
9.8	0.41	24.7	0.7	10.1	0.65

r_p-radius of the plasticization zone for the case of unsupported excavation

r_{p0}-radius of plasticization zone for the case of relaxation $\lambda_o = 0.7$

Verification of the tunnel support was performed using the software package *Phase2*. The phases of model creation followed the usual construction practice (excavation and application of security measures). The calculation results indicate that the excavation will cause significant displacements of the rock mass in the zone of the tunnel excavation, and certain displacements will be manifested on the surface of the terrain as well (Figure 4). Also, the plasticization zone of the rock mass occurs up to the surface of the terrain. The biggest stress-strain changes occur in the stage of the calotte excavation, under the pipe shield, in the area of the elephant feet. For these reasons, the possible effects of lowering the pipe shield to the floor of the calotte were considered on a modified model, without the elephant foot and micropiles at the level of the calotte. Calculation models with calculation results, which indicate the effects achieved by modifying the design solution, are shown in Figure 4.

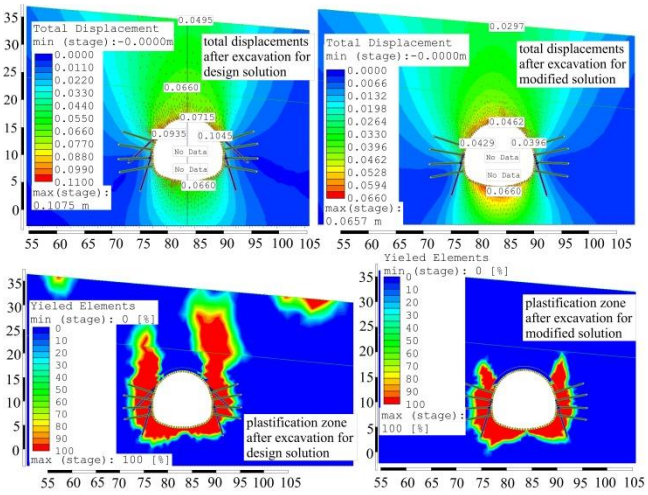

Figure 4. Stress-strain analyses for design and modified solution.

It is proposed that the excavation of the calotte be carried out by phase development of the face side, with the formation of a supporting body.

Summary of all displacements for the proposed design solution, as well as the solution with the proposed modification is shown in Figure 5.

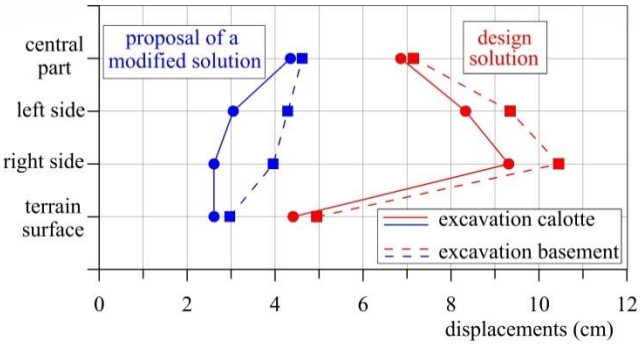

Figure 5. Summary of displacements of calotte and invert arch for design and modified solution.

5 CONCLUSIONS

For the construction of the "Debelo brdo" tunnel, the geotechnical conditions related to the excavation of the tunnel in the open excavation, and in the part of the underground excavation, were analysed separately.

For the construction of the tunnel in the open excavation, it is planned to secure the excavation by installing piles. Geotechnical analyses have shown that temporary slopes, above the level of the working plateau, can be performed with the proposed slope inclination of 1:2, but with a 4 m wide berm at a height of 5 m above the working plateau.

When it comes to the underground excavation, for the proposed design solution, geotechnical analyses obtained significant displacements of the rock mass, which are also manifested on the surface of the terrain. For these reasons, the analysis was also performed for a partially modified solution with an extended pipe shield, but without the application of the elephant foot and micropiles at the calotte level. With this variant, significantly smaller deformations around the tunnel excavation and negligible deformations on the terrain surface were obtained.

REFERENCES

Duncan, J. & Buchignani, A. (1976) An Engineering Manual for Settlement Studies. Department of Civil Engineering, University of California. Berkeley, USA.

Rakic, D.; Berisavljevic, Z.; Basaric, I.; Bogdanovic, S.; Jankovic, J. (2019). Geotechnical zoning of the terrain along the first section of E-80 highway in Serbia – SEETO route 7", *Proceedings of the XVII European Conference of Soil Mechanics and Geotechnical Engineering ECSMGE-2019,* Reykjavik, Iceland, http://doi:10.32075/17ECSMGE-2019-0393.

Proceedings of the XVIII ECSMGE 2024
GEOTECHNICAL ENGINEERING CHALLENGES
TO MEET CURRENT AND EMERGING NEEDS OF SOCIETY
© 2024 the Authors
ISBN 978-1-032-54816-6
DOI 10.1201/9781003431749-357
Open Access: www.taylorfrancis.com, CC BY-NC-ND 4.0 license

ECSMGE 24
XVIII EUROPEAN CONFERENCE ON SOIL MECHANICS AND GEOTECHNICAL ENGINEERING

Geotechnical structures stability: ULS calculations using the finite element method

Stabilité des ouvrages géotechniques: calculs aux ELU par la méthode des eléments finis

D. Remaud*
itech, Saint-Maurice, France

E. Bourgeois
Université Gustave Eiffel, Marne-la-Vallée, France

**d.remaud@itech-soft.com*

ABSTRACT: The new version of Eurocode 7 deals explicitly with the use of the finite element method for the design of geotechnical structures. The relevance of this method is widely recognized for Service Limit States (SLS) i.e. to assess the deformations of the structures (soil settlements, displacements induced by the progress of the work or even interactions with the neighbouring works). For Ultimate Limit State (ULS) verifications, so far in most cases the finite element method is used to performed two types of computations: search for a limit load (verification of a bearing capacity for example) or reduction of resistance properties of the ground, called "phi-c reduction". The new requirements elaborated in the future EC7 gives the opportunity to discuss more precisely how finite elements can be used for geotechnical stability analyses. The article presents the current possibilities of the CESAR software, and discusses additional functionalities that can be introduced to facilitate the verifications required by the new normative framework.

RÉSUMÉ: La nouvelle version de l'Eurocode 7 traite explicitement de l'utilisation de la méthode des éléments finis pour le dimensionnement des ouvrages géotechniques. La pertinence de cette méthode est largement reconnue pour les Etats Limites de Service (ELS) c'est-à-dire pour évaluer les déformations des ouvrages (tassements de la surface du sol, déplacements liés à l'avancement des travaux ou encore interactions avec les ouvrages voisins). Pour les vérifications aux Etats Limites Ultimes (ELU), jusqu'à présent dans la plupart des cas la méthode des éléments finis est utilisée pour effectuer deux types de calculs: recherche d'une charge limite (vérification d'une capacité portante par exemple) ou réduction des propriétés de résistance du sol («c-phi réduction»). Les nouvelles exigences du futur EC7 donnent l'opportunité de discuter plus précisément de la manière dont les éléments finis peuvent être utilisés pour les états limites ultimes. L'article présente les possibilités actuelles du logiciel CESAR, et discute des fonctionnalités supplémentaires qui peuvent être introduites pour faciliter les vérifications requises par le nouveau cadre normatif.

Keywords: ULS; stability; finite element method; phi-c reduction.

1 INTRODUCTION: EVOLUTIONS OF EUROCODE 7

The second generation of Eurocode 7, which should be finalized in a near future, introduces significant evolutions as regards the use of numerical methods for geotechnical design. Numerical modelling is recognized as an efficient tool for service limit states (SLS) provided that suitable constitutive models are used. For Ultimate Limit States (ULS), the future rules define more precisely how numerical tools can be used. They distinguish several factoring approaches: RFA (Resistance Factoring Approach), MFA (Material Factoring Approach) and EFA (Effect factoring approach). RFA is not generally applicable to numerical methods because the mode of failure and thus the available resistance is not known in advance; EFA consists in factoring outputs of the calculation and can be seen as a specific post-treatment of numerical results; last, MFA consists in factoring input data and can in most cases be treated using the familiar “phi-c reduction” procedures (Brinkgreve and Bakker, 1991, Griffiths and Lane, 1999).

One of the major evolutions lies in the fact that design approaches (DA) have been replaced by the notion of verification cases (VC), and that the verification of ULS by numerical methods is now explicitly twofold: it combines a geotechnical verification based of MFA, and a structural verification based on EFA.

This contribution discusses in what respect the usual numerical tools are fit to match the requirements of the rules, and how they should be adapted.

2 PRINCIPLES OF FINITE ELEMENT ASSESSMENT OF ULS

The principle of the so-called phi-c reduction procedures consists in initializing the stresses in a geotechnical structure, using a preliminary calculation that has led to a state of equilibrium. Then, the program reduces the strength properties of the soil (c and tan φ are divided by a given value F), and searches for the largest value of F for which the calculations conclude that stability is reached. Various softwares may adopt (very) different strategies to reach the final result, but they have in common the fact that the strength reduction results in a correction of the stress state, which is converted into out-of-balance nodal forces. It must be kept in mind that the computed displacements should be interpreted cautiously. Nevertheless, this type of procedure has been extensively discussed and is now widely accepted.

3 SOFTWARE ADAPTATIONS RELATED TO EVOLUTIONS OF DESIGN RULES

3.1 Construction stages

The construction of a geotechnical structure generally comprises several construction stages. From a numerical point of view, data are transmitted from one stage to the following. In the CESAR code, the user can define explicitly a "staged construction" model, which contains the successive construction stages.

The verification requires an MFA analysis is conducted for each construction stage. The sequence of *computation stages* is therefore no longer linear and parallel to the *construction stages*, but includes verification stages. This requires that suitable modifications be brought to the user interface. In the recent version of the software CESAR, the user is given the possibility to define sub-phases to answer this specific need (Figure 1).

3.2 Checking stability for a given reduction factor

For some structures, the safety factor is large and the phi-c reduction produces, often at high computational cost, a safety factor much larger than 1. Another perspective, which might be adopted in the future Eurocode 7, is to verify that the safety factor is larger than 1.25, in other words, that the structure is stable for strength properties reduced by a factor 1.25. It can be expected that this type of verification will be much faster in many cases. In practice, this should require only minor (if any) modification to the existing finite element codes implementing a phi-c reduction procedure; but this specific type of verification should be clearly identified in the interface of the software, because the result is no longer the value of the safety factor, but rather the fact that the structure is stable for a given value of the strength reduction factor. It can be expected that the final version of EC7 will define a clear terminology to describe the type of verification that is to be performed.

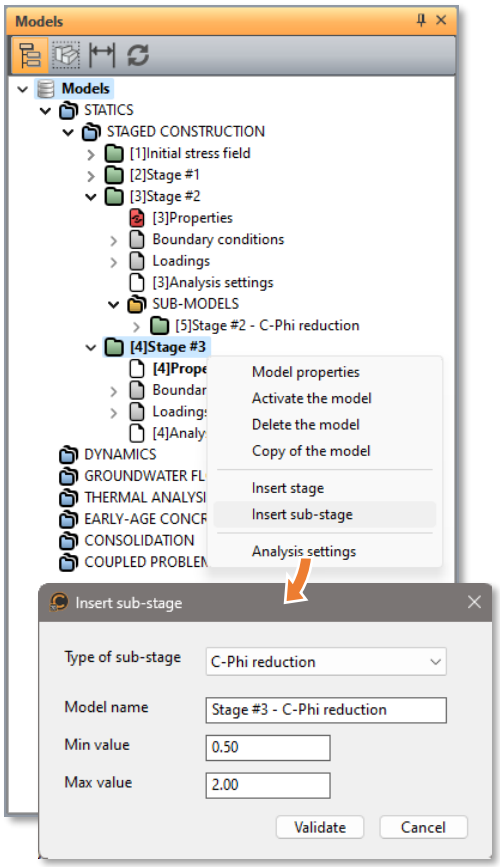

Figure 1. View of the stage sequence in the „Models "tree, and insertion of a sub-stage.

3.3 Accounting for the role of structural elements

Eurocode 7 requires to perform also EFA verifications to check the resistance of structural elements. Two possibilities can be considered:

- perform simulations in which structural elements have a linear elastic constitutive model and check if the computed forces and bending moments are compatible with the structure resistance characteristics,

- perform simulations with non-linear models (e.g. perfect plasticity) that include the possibility of failure.

The second solution corresponds to a higher level of complexity, and may resort to a wide variety of models, which means that the interpretation of the results may not be straightforward. This is why, even if the second approach may seem more complete, it is not necessarily preferable in the current state of ULS verifications.

3.4 Role of groundwater level

Groundwater level in the design is an important factor, yet difficult to determine and/or monitor. The Eurocode 7 makes the choice to use representative values, which means that no factoring is applied on the effects of water. Conversely, there is no need for specific evolutions of the software currently in use.

3.5 Interface shear strength

It is worth noting that shear strength of interfaces (between ground and structures) should be factored, which is not necessarily automatically supported in all FEA software. It is expected that the user understands how the software is implementing the material factoring approach, but it is preferable that the choices made regarding soil-structure interfaces be clear.

3.6 Limiting the area subjected to strength reduction

Some authors (for instance Magnan and Meyer, 2018) point out that in some situations, it can be advisable to reduce the strength properties only in certain parts of the ground. In the case of embedded walls for instance, reducing the strength properties on both sides of the wall leads to increase the active pressure on the wall, in a manner that is not necessarily realistic.

To this end, the user interface of the finite element code CESAR offers the possibility to exclude some areas of the mesh (bodies) from the strength reduction procedure.

4 EXAMPLES

4.1 Strength reduction method for MFA

In the scope of the MFA analysis, a robust phi-c reduction procedure is required. The one programmed in CESAR has been duly validated by comparison to analytical methods such a Bishop. In the scope of the Finite Element method, the German Soil Mechanics society has gathered results of several software answering to a benchmark problem (DGGT, 2019). The originality of the problem lies in the fact that the soil mass is made up of two different layers (sand and marls) and in the presence of the wall, assumed to be linear elastic. Soil-structure interfaces with friction behaviour are taken into account in the modelling and their resistance is factored (Figure 2).

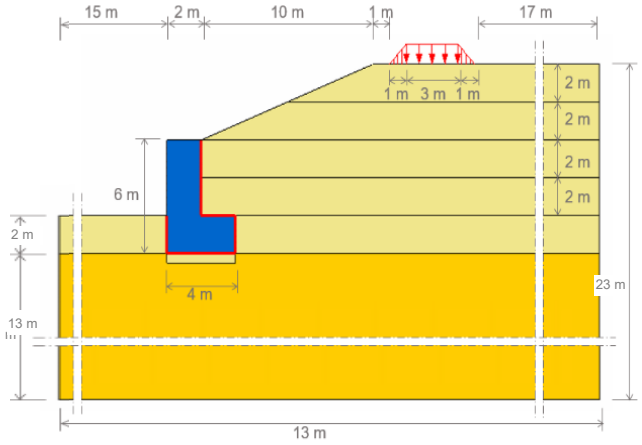

Figure 2. Scheme of the benchmark problem.

The Table 1 gives the safety factors reached by CESAR software, in both 2D and 3D. They show a very good agreement with the values of the benchmark. More, the mechanism of the failure is very well represented with the display of shear strains (Figure 3).

Table 1. Comparison of results.

	Sand	**Sand & Marls**	**Marls**
CESAR 2D	1.81	1.58	1.39
CESAR 3D	1.76	1.62	1.39
Benchmark	[1.74; 1.83]	[1.56; 1.63]	[1.36; 1.41]

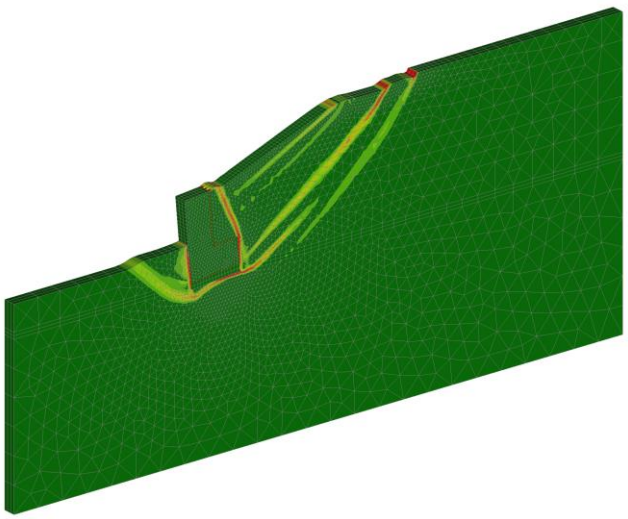

Figure 3. Example of failure mechanism (deformed mesh).

4.2 Strength reduction method with excluded areas

As an illustration of the influence of the restriction of the strength reduction to some areas in the ground, and more precisely of excluding the ground behind an embedded wall, a staged construction of an experimental sheet pile wall in Hochstetten has been modelled. This project has often been used as the support of a benchmark exercise and is therefore well documented (Von Wolffersdorff, 1994a, 1994b). To give only a general description, the final excavation depth was 5 m and the distance between the two walls was 4 m. The wall was built in sand. The construction comprises four excavation stages and a level of props; a load is applied at the ground surface behind the right wall.

Once the final state is reached, a phi-c reduction computation is performed either by reducing the strength in all the mesh (Figure 4), or by reducing the strength only in the ground located between both walls (Figure 5); the idea is to compare the active pressure on the wall with the available resistance. We do not discuss here the conditions in which this approach is relevant, but just show that numerical results give different failure mechanisms and factors of safety. The position of the shear band is a little modified and the factor of safety increases from 1.13 to 1.43.

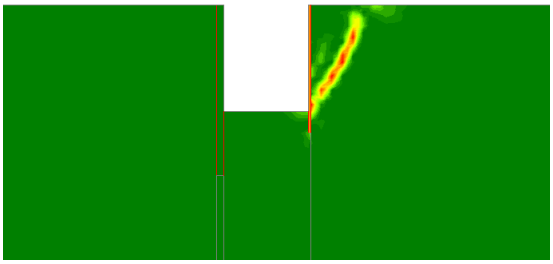

Figure 4. Failure mechanism for a homogeneous strength reduction (FOS = 1.13).

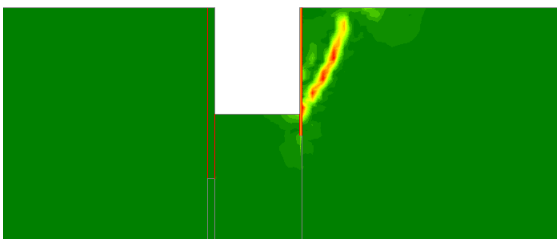

Figure 5. Failure mechanism for a strength reduction applied only to the ground between the walls (FOS = 1.43).

5 CONCLUSION

The preparation of the next version of Eurocode 7, has taken into account from the beginning the question of the use of numerical methods for the verification of geotechnical structures. This makes it necessary to rethink the ergonomics of the software used by engineering companies, in order to make verifications easier to perform – and numerical results easier to check. This communication is an attempt to identify the counterpart of the evolutions of the normative framework in terms of development of new procedures (or adaptation of existing procedures) in the existing computing software.

REFERENCES

DGGT Arbeitskreis 1. 6 (2019), Numerik in der Geotechnik: Berechnung der Standsicherheit mit der FEM durch Reduzierung der Festigkeitsparameter, *Geotechnik 2*, pp. 88-97. DOI: 10.1002/gete.201900006.

Brinkgreve RBJ, Bakker HL. (1991). Non-linear finite element analysis of safety factors. *Int. Conf. on Computer Methods and Advances in Geomechanics Proceedings*, Rotterdam, 1117-1122.

itech and Université Gustave Eiffel (2023). CESAR (version 2023.0), [computer program] Available at www.cesar-lcpc.com.

Griffiths, DV., Lane, PA. (1999). Slope Stability Analysis by Finite Elements. *Géotechnique*, Vol. 49, No. 3, 387-403.
DOI: 10.1680/geot.1999.49.3.387.

Magnan JP, Meyer G (2018). Domaines d'application de la réduction de c et phi dans les études géotechniques. In : *JNGG 2018 Proceedings*, Marne-la-Vallée, pp. DOI: 10.1051/geotech/2018002.

Von Wolffersdorff P.-A. (1994a). Spundwand-Feldversuch in Hochstetten / Sheetpile wall field test in Hochstetten. Part A: Presentation of the problem. Part B: Test results and predictions. *Workshop Sheet Pile Test Karlsruhe*, Delft University, October 6 and 7, 1994.

Von Wolffersdorff P.-A. (1994b). Results of field test and evaluation of the predictions and subsequent calculations, *Workshop Sheet Pile Test Karlsruhe*, Delft University.

Proceedings of the XVIII ECSMGE 2024
GEOTECHNICAL ENGINEERING CHALLENGES
TO MEET CURRENT AND EMERGING NEEDS OF SOCIETY
© 2024 the Authors
ISBN 978-1-032-54816-6
DOI 10.1201/9781003431749-358
Open Access: www.taylorfrancis.com, CC BY-NC-ND 4.0 license

ECSMGE 24
XVIII EUROPEAN CONFERENCE ON SOIL MECHANICS AND GEOTECHNICAL ENGINEERING

Iron tailings reclamation: Geotechnical analysis during emerged and submerged excavations

Réutilisation des résidus de fer: Analyse géotechnique lors de fouilles émergées et immergées

L. Rezende*, M. Ehrlich
Federal University of Rio de Janeiro, Rio de Janeiro, Brazil

A. Oliveira
Mines Paris Tech, Paris, France

**leonardo.rezende@coc.ufrj.br*

ABSTRACT: It is estimated that Brazil has around 570 Mt of iron ore stored in dams without a national reuse plan. This case study focuses on the Carajás Mine tailing dam, a reservoir with a volume of 100 Mm³ and iron ore content of 63%, located in the state of Pará. Regarding the geotechnical risk during excavations to remove the tailing, the present work identifies in depth the fine and coarse tailing through laboratory and field tests. Analyzes will be conducted to verify if the ruptures can represent a trigger that leads the tailing to liquefaction. The seismic piezocone tests (SCPTu) were reinterpreted considering perched water table, saturated specific weight equal to 30.1 kN/m³, cone factor (Nkt) equal to 15. Field seismic data were compared to laboratory seismic tests to determine the void ratio and shear modulus (G0) along the entire tailing profile, analyzing possible layers with liquefaction potential.

RÉSUMÉ: On estime que le Brésil possède environ 570 Mt de mineral de fer stocké dans des barrages sans plan national de réutilisation. Cette étude de cas concerne de la Carajás Mine résidus, un réservoir d'un volume de 100 Mm³ et d'une teneur en mineral de fer de 63%, situé dans l'État du Pará. Concernant le risque géotechnique lors des excavations pour éliminer les résidus, le présent travail identifie en profondeur les résidus fins et grossiers à travers des essais en laboratoire et sur le terrain. Des analyses seront menées pour vérifier si les ruptures peuvent représenter un déclencheur menant à la liquéfaction des résidus. Les essais sismiques au piézocône ont été (SCPTu) réinterprétés en considérant: nappe phréatique perchée, poids spécifique saturé égal à 30,1 kN/m³, facteur de cône (Nkt) égal à 15. Les données sismiques de terrain ont été comparées aux essais sismiques de laboratoire pour déterminer l'indice de vide et le module de cisaillement (G0) sur tout le profil du résidu, analyser les couches possibles ayant un potentiel de liquéfaction.

Keywords: Perched water table; iron ore tailings; seismic piezocone; bender element.

1 INTRODUCTION

In 2021, Brazil's National Mining Agency (ANM) issued Resolution No. 85, promoting and facilitating the reuse of tailings and waste generated from mining activities through innovative mineral processing techniques. The reuse of iron tailings, particularly from legacy deposits, contributes to reducing risks for society by eliminating materials with high liquefaction potential.

The best technique for recovering tailings deposited in reservoirs or dams made of this material depends on the characteristics of the deposit, composition, storage condition, transportation possibilities, handling and final use of the tailings (ENGELS et al, 2004).

Souza (2020) apud Muir et al. (2005) incorporate that topography and watercourses are preponderant in the analysis of technical and economic viability in mining and reusing the mineral asset present in the tailings. There are three primary methods for reclaiming materials from natural resources: hydraulic re-mining using high-pressure water monitor guns, mechanical reclamation, and dredging.

According to Souza (2020), it is necessary to guarantee geotechnical safety in tailings removal operations for the entrepreneur and other parties involved. In this sense, it is crucial to identify the heterogeneity of the tailings released into the reservoir, analyzing the history of disposal, resistance, deformation and pore pressures.

Becker (2022) et al, reassessing the work of Whittle et al. (2022) in dam B1 (Brumadinho), considers the presence of extensive horizontal layers of fine, clayey, plastic tailings, with a low density coefficient, which

led to the formation of several perched water tables. Stability analyzes using the limit equilibrium method proved to be satisfactory and consistent with failure, provided that adequate resistance, type of sliding surface, stratigraphy and pore pressure are used.

The identification of thin soils (plastic) through piezocone tests is well debated by Aguiar (2022), identifying normalized undrained resistance (Su/σ'v) in the order of 0.11, much lower than the value of 0.22 proposed by Mesri (1975) for soft clays.

In the case of the Fundão sandy tailings, the shear speed in the laboratory to obtain the undrained condition was estimated at 0.011 mm/min according to Coelho (2018). This makes it clear that ruptures in fine materials can be a trigger for liquefaction in thick materials, since the rupture speed in plastic materials can be greater than the dissipation time of non-plastic tailings.

Therefore, this work focuses on the importance of back-analyzing data from seismic piezocone tests in correctly determining the geotechnical profile, identifying tailings with liquefaction potential and how a good interpretation can help in decision-making when planning the removal of tailings in a dam reservoir, combining geotechnical and operational safety.

2 METHOD

2.1 Materials and testing

The tailings have iron contents of about 63%. Table 1 shows the performed geotechnical laboratory (physical characterization and bender element tests) and field studies (standart penetration, SPT, and seismic piezocone, SCPTu, tests) for the characterization and determination of geotechnical parameters of those tailings.

Table 1. Data survey.

Date	Survey	Quant	Test
2001	SPT	141	Granulometry; chemical characterization
2010	SPT	214	Granulometry; chemical characterization
2022	SCPTu	4	Physical characterization; bender element

2.2 Perched water table

Figure 1 shows layers of fine material influencing the position of the water table, generating a suspended water table (ICOLD, 2001). The term perched sheet is used in places where the pore pressures measured by tests and instruments differ from the hydrostatic pressures, this occurs when there are layers of low permeability materials and the water above this layer creates groundwater and below it may even be dry or governed by horizontal and vertical flows.

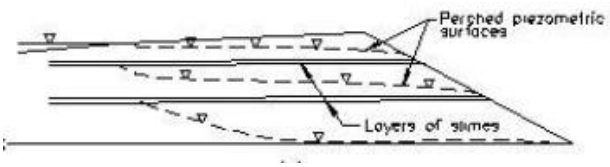

Figure 1. Perched water table around the slimes layers (ICOLD, 2001).

2.3 The problem of surface and subsurface flow

The permeability of tailings is influenced by two mechanisms during hydraulic disposal: segregation during discharge and consolidation. In this reservoir, the high rainfall in the region leads to particle transport by erosion and suspension. Submerged flow, which is complex, can initially transport coarse particles to areas occupied by fine particles. Figure 2 aims to illustrate these flow characteristics of the Carajás Mine tailings dam.

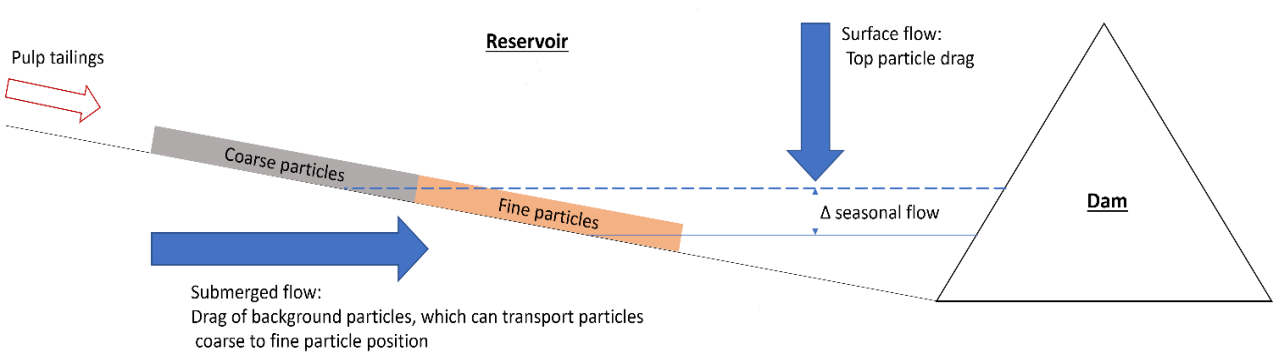

Figure 2. Hydraulic segregation of tailing over time of tailings of the Carajás Mine dam.

2.4 Criteria fine and coarse tailings

To determine the layers of fine (plastic) and sandy (non-plastic) tailings, data from the geotechnical investigation campaign and an analysis of the reservoir's history may be conducted, as follows:

- Analysis of the percussion survey campaign to identify the thickness of the tailings packages deposited in the reservoir;
- Understanding the history of tailings release based on the hydrocyclone and its underflow (sandy) and overflow (fine) discharge;
- Analysis of the SCPTu campaign and determination of the Ic behavior index (Jefferies and Been, 2006), suspended water table, vertical flow and dissipation of pore pressures;
- Analysis of the shear modulus (G_0) using the Bender element and seismic cone tests.

2.5 Criteria for evaluation of liquefaction potential in sandy tailings

The state parameter (ψ) can be obtained through correlation with the normalized cone resistance (Q_{tn}). According to Jefferies and Been (2016) ψ values below -0.05 tend to exhibit strain softening (contractile) behavior under undrained shear and indicate that the tailings may be prone to liquefaction.

Triaxial tests conducted on the Fundão dam in the fine tailings did not indicate liquefaction potential (Morgenstern, 2016).

Based on a large database of historical liquefaction cases suggested a correction factor to correct the normalized cone strength in silty sands to an equivalent value of clean sand (Qtn,cs). After the accident at the B1 dam in Brumadinho, Robertson (2021) updated Eq. 5.

$$Q_{tn} = \left[\frac{q_t - \sigma_v}{p_a}\right](p_a/\sigma'_{v0})^n \quad (1)$$

$$n = 0{,}381\left[I_{c(R\&W)}\right] + 0{,}05\left(\frac{\sigma'_{v0}}{p_a}\right) - 0{,}15 \quad (2)$$

$$Q_{tn,cs} = K_c\, Q_{tn} \quad (3)$$

$$K_c = 1{,}0 \qquad \text{if } I_c < 1{,}7 \quad (4)$$

$$K_c \approx 15 - \frac{14}{1+\left(\frac{I_c}{2{,}95}\right)^{11}} \qquad \text{if } I_c < 3{,}0 \quad (5)$$

$$\psi = 0{,}56 - 0{,}33\, log Q_{tn,cs} \quad (6)$$

where q_t is the corrected cone resistance, I_c is the soil behaviour type, K_c is the correction factor, p_a is the atmospheric pressure.

Schnaid and Yu (2007) propose the incorporation of the shear modulus (G0) to interpret the mechanical properties of sandy soils. The state parameter can be obtained through correlation (Eq. 7).

$$\psi = \alpha\left(\frac{\sigma'_{v0}}{p_a}\right)^{\beta} + \chi \ln\left(\frac{G_0}{q_c}\right) \quad (7)$$

where $\alpha = -0{,}520$, β =-0,07 and χ=0,18 average values obtained by calibration suggested by the authors.

3 RESULTS

3.1 Field investigation

Location of the piezocone tests is shown in figure 3 and results obtained from piezocone data of SCPTu-01 conducted at Carajás Mine tailing dam are presented in Figures 4 and 5. Analyses results indicated that, from the 4.5m to 12m depth, there is a layer of fine grained material, with plastic behavior.

This conclusion is based on both the direct and indirect results of the piezocone test, and is in line with historical information about the discharge of tailings into this reservoir. The SCPTu-01 piezocone is the most representative of the four tests carried out in the dam reservoir, which contains predominantly fine tailings combined with coarse tailings.

In Figure 5, the stiffness of fine soils is assessed using the rigidity index (Ir), defined as the ratio of the shear modulus (G_0) to the undrained soil strength (Su). This index is a relevant parameter for estimating the consolidation coefficient (ch) using the piezocone.

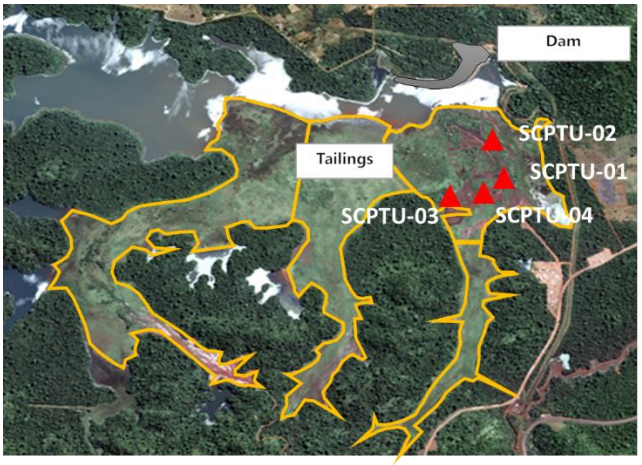

Figure 3. Site of reclamation iron tailings. Piezocone location SCPTu-01,02,03 and 4.

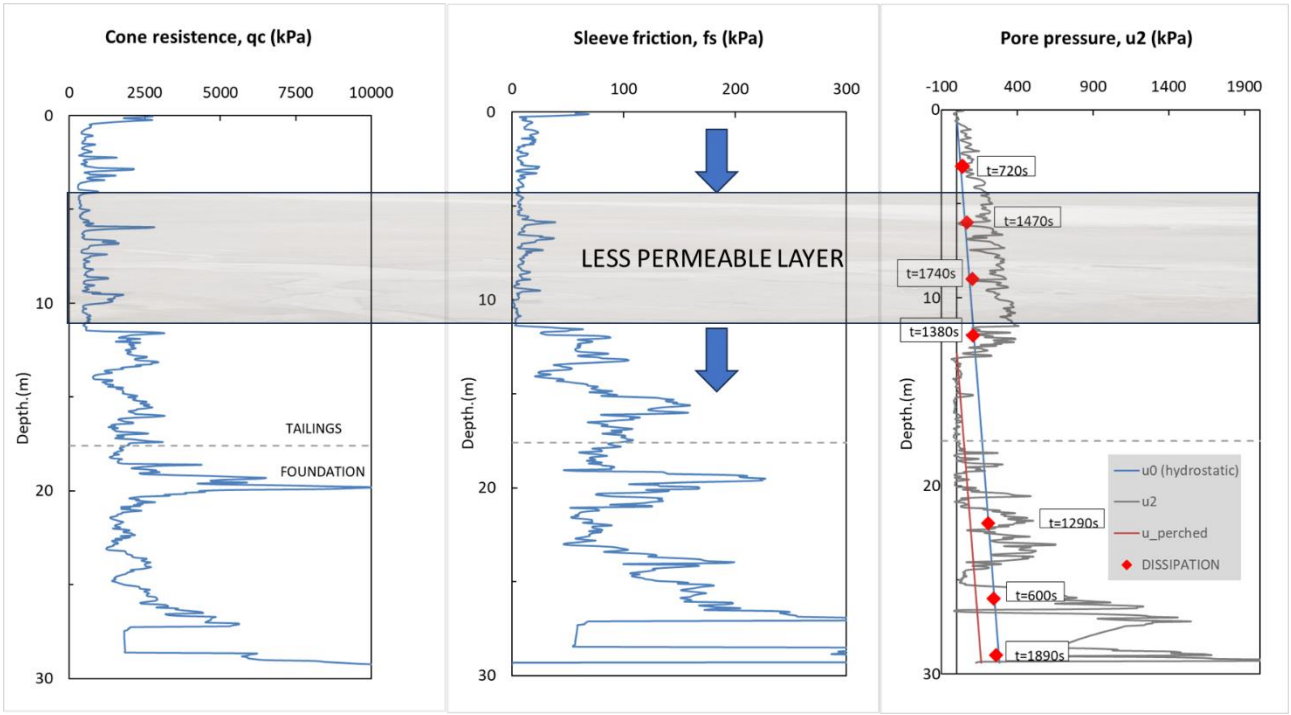

Figure 4. Direct piezocone data of SCPTu-01.

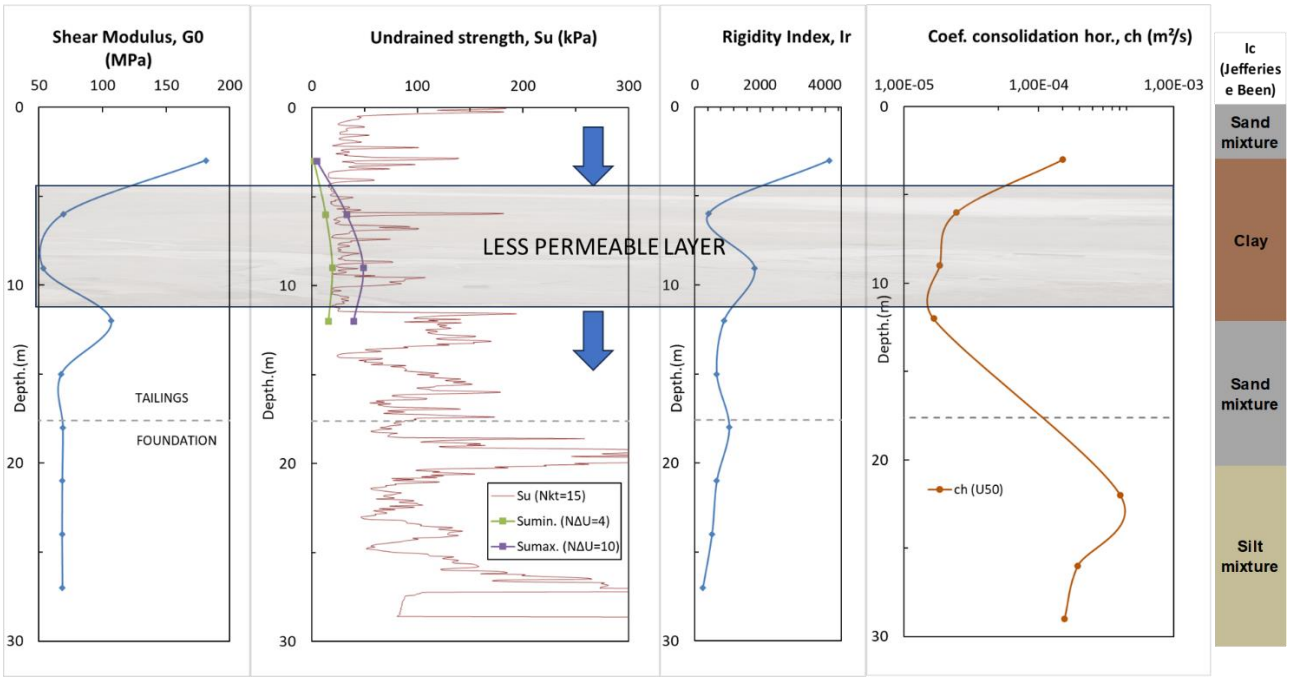

Figure 5. Indirect piezocone data of SCPTu-01.

3.2 Laboratory studies

3.2.1 Index properties

Table 2 present results of laboratory test for physical characterization of tailings from the Carajás Mine tailing dam. Figure 6 shows comparison of grain size distribution of the tailings from the Carajás Mine dam with the determined values for another iron tailings.

These laboratory tests results confirmed the geotechnical profile determined using the piezocone test, showing sandy grain size interspersed with a fine grain layer. The granulometry of the dredged tailings in the present study has a higher fines content in relation to the tailing samples from Brumadinho B1 (Viana, 2022) and Vargem Grande VG (Souza, 2020). It is essential to highlight that the percentage of iron varies depending on the granulometry of the tailings, being more concentrated in the fine grained material.

Table 2. Average values of physical characterization of the tailings from the Carajás Mine dam.

Test	Value
Moisture content (w)	17%
Particle density	4.80 g/cm³
Void ratio	0.83
Saturated density	3.03 g/cm³

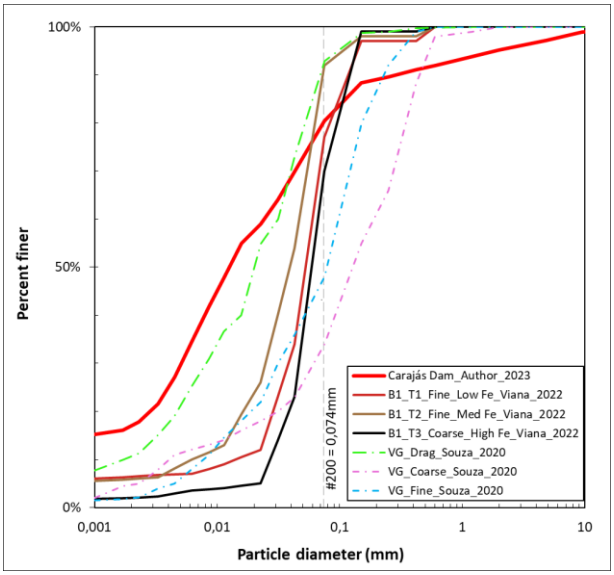

Figure 6. Comparison of grain size distribution of the tailings from the Carajás Mine dam with another iron tailings.

3.2.2 Bender element

For the Bender Element test, samples of the tailings of Carajás Mine dam was collected at 6 m depth from the top. In the laboratory, this sample was conditioned in a triaxial chamber, connected to end-to-end electrodes to measure the speed of the S wave (V_s) at each variation in effective stress consolidation (Fig. 7). The tests were conducted on the same sample, which initially had a relative density of 30%, and was subsequently tested at 50% and 75%. The samples were isotropically consolided for effective stresses of 25 kPa, 50 kPa, 100 kPa, 200 kPa, 400 kPa and 600 kPa. The shear modulus (G_0) can be obtained through correlation (Eq. 8).

$$G_0 = \rho . V_s^2 \qquad (8)$$

where ρ is a specific gravity (kg/m³)

Figure 8 show results of correlation between the shear modulus (G_0) and S wave velocity in the Bender Element test. With the results obtained in the field (V_s), it is possible to obtain the depth profile of the shear modulus (G_0). Notice that Silva (2022) carried out Bender element tests on fine and sandy tailings and the results were similar to the present work.

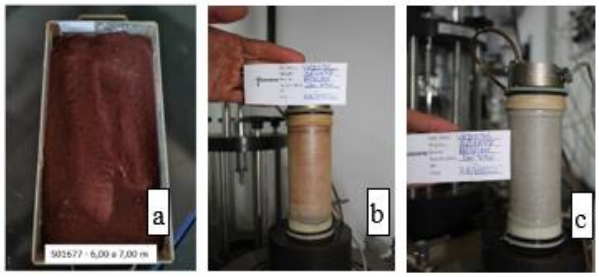

Figure 7. a) Sample; b) Bender element initial condition; c) Final condition.

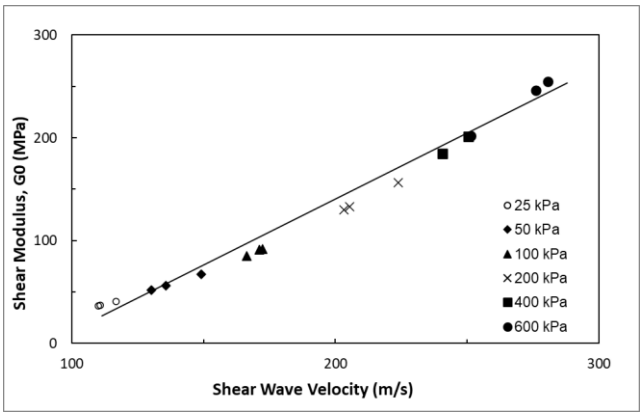

Figure 8. Correlation of shear modulus (G_0) and S wave velocity in the Bender Element test.

3.2.3 Comparison of determined results from Bender element and seismic piezocone tests

Figure 9 presents a comparison of the shear modulus of tailings from the Carajás Mine dam, determined using results from the Bender Element and seismic piezocone tests. These results validate the findings obtained from laboratory tests.

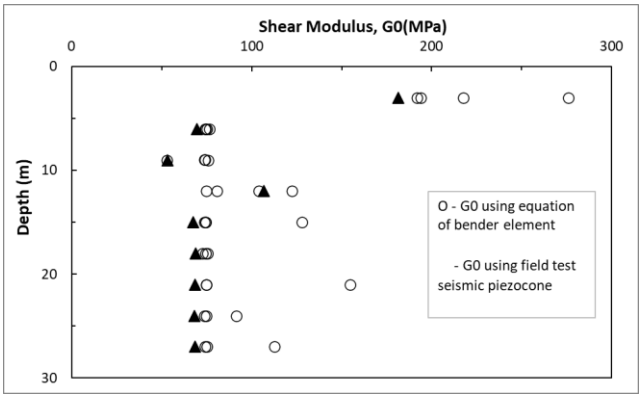

Figure 9. Comparison of results of shear modulus profile (G_0) with depth determined from the Bender Element and seismic piezocone tests.

3.2.4 Potential liquefaction

Figure 10 shows the profile of the state parameter obtained by the methodology of Robertson (2010/2021) and Schnaid and Yu (2007). Notice that the procedure for evaluation of the state parameter by

Schnaid and Yu (2007) is valid for sands and the determine values for the fine tailings using this methodology may not be representative. The results suggest that the sandy tailings near the surface do not exhibit liquefaction potential. However, the sandy tailings situated beyond the fine tailings show liquefaction potential, as indicated by positive state parameter values (ψ). According to Jefferies and Been (2016), materials exhibit contractive behavior when ψ exceeds -0.05.

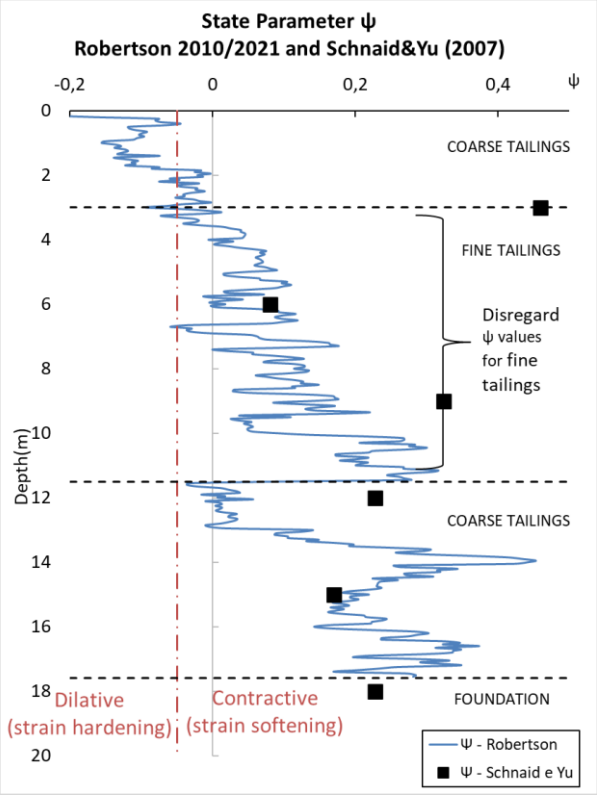

Figure 10. Profile of the state parameter obtained by the methodology of Robertson (2010/2021) and Schnaid and Yu (2007).

4 CONCLUSIONS

The performed geotechnical study indicate that certain tailings from the Carajás Mine dam may have liquefaction potential. It is noteworthy that the excavation process and potential ruptures in the fine tailings could trigger liquefaction. Based on these findings, both submerged and surface excavations were planned to commence from upstream to downstream of the dam reservoir. This approach aims to minimize the liquefied volume in the event of temporary instabilities, ensuring that it remains small enough to prevent overtopping of the structure. As coarse and fine tailings may undergo changes over time due to surface and subsurface flow, it is crucial to conduct investigation campaigns regularly to support stability analyses and potential geometry revisions for stabilizing the tailings. This is particularly important in regions with liquefaction potential.

ACKNOWLEDGEMENTS

The work presented in this paper is part of the main author's dissertation at COPPE/UFRJ.

The authors are grateful to Vale for providing data for this study.

REFERENCES

Aguiar, A.L.S. (2022). *Study of the variability of the undrained resistance of plastic tailings from the Germano dam through field tests*. MSc dissertation, Federal University of Rio de Janeiro, Rio de Janeiro, RJ, Brazil.

Becker, L.D.B.; Ehrlich, M.; Barbosa, M.C. (2022). *Discussion of Stability Analysis of Upstream Tailings Dam Using Numerical Limit Analyses.* Journal of Geotechnical and Geoenvironmental Engineering.149(3): 07023001. https://doi.org/10.1061/JGGEFK.GTENG-11272.

Coelho, A.S. (2018). *Behavior Assessment Undrained Sands*. MSc dissertation, PUC Rio de Janeiro, Rio de Janeiro, RJ, Brazil.

Morgenstern, N.R., Vick, S.G., Viotti, C.B. & Watts, B.D. (2016), *Fundão Tailings Dam Review Panel – Report on the Immediate Causes of the Failure of the Fundão Dam*, Belo Horizonte, MG, Brazil.

Viana da Fonseca, A., Cordeiro, D., Molina-Gómez, F., Besenzon, D., Fonseca, A., and Ferreira, C. (2022). *The Mechanics of Iron Tailings from Laboratory Tests on Reconstituted Samples Collected in Post-Mortem Dam I in Brumadinho*. Soils and Rocks 45 (2): 120. https://doi.org/10.28927/SR.2022.001122.

Silva, J.P.S (2022). *Mechanical behavior of mining tailings iron from the perspective of critical states*. PhD thesis, University of Brasilia, Brasilia, DF, Brazil.

Souza, G.M. (2020). *Proposal for a methodology for mining iron tailings dams constructed using the hydraulic embankment technique*. PhD thesis, Federal University of Ouro Preto, Minas Gerais, MG, Brazil.

Proceedings of the XVIII ECSMGE 2024
GEOTECHNICAL ENGINEERING CHALLENGES
TO MEET CURRENT AND EMERGING NEEDS OF SOCIETY
© 2024 the Authors
ISBN 978-1-032-54816-6
DOI 10.1201/9781003431749-359
Open Access: www.taylorfrancis.com, CC BY-NC-ND 4.0 license

ECSMGE 24
XVIII EUROPEAN CONFERENCE ON SOIL MECHANICS AND GEOTECHNICAL ENGINEERING

Accuracy of machine learning techniques in forecasting tunnelling-induced soil settlements with limited data

Fiabilité des techniques d'apprentissage automatique dans la prévision des tassements induits par les tunnels avec des données limitées

T. Richa*
Terrasol Setec, Paris, France

J.M. Pereira, L.-M. Guayacan-Carrillo
Navier, Ecole des Ponts, Univ Gustave Eiffel, CNRS, Marne-La-Vallée, France

G. Chapron
Terrasol Setec, Paris, France

F. Lanquette
Tpi Setec, Paris, France

**tatiana.richa@setec.com*

ABSTRACT: This article presents a comprehensive comparison of the predictive accuracy of 5 Machine Learning algorithms – Support Vector Machine, Decision Tree, Random Forest, Extreme Gradient Boosting (XGBoost) and Back-propagation Neural Network – in forecasting maximum settlements induced by earth pressure balance tunnel boring machines. The study evaluates those algorithms' performance using a dataset of 2,590 settlement measurements associated with soil parameters and shield operational parameters, collected from 13 km of the Grand Paris Express Project (line 15 South West and line 14 South). The analysis reveals that, for the small dataset used in this study, ensemble methods, specifically XGBoost and Random Forest, outperform artificial neural networks in predicting settlements. These methods remain reliable even with only 30% of the dataset used for training. The article further explores the regularization and optimization of hyperparameters for Random Forest and XGBoost, shedding light on their enhanced predictive capabilities. Furthermore, variations in the data split between training and testing sets are explored, highlighting the effectiveness of these Machine Learning algorithms in achieving accurate predictions with limited datasets.

RÉSUMÉ: Cet article présente une comparaison approfondie de la fiabilité de 5 algorithmes d'apprentissage automatique: Support Vector Machine, Decision Tree, Random Forest, Extreme Gradient Boosting (XGBoost) et Back-propagation Neural Network - dans la prévision des tassements maximaux induits par le creusement des tunnels au tunnelier, spécifiquement au tunnelier à pression de terre. L'étude évalue les performances des algorithmes en utilisant un ensemble de données de 2 590 mesures de tassements associées à des paramètres de sol et à des paramètres de pilotage du tunnelier, collectées auprès de 13 km du projet du Grand Paris Express (ligne 15 Sud-Ouest et ligne 14 Sud). L'analyse révèle que, pour le petit ensemble de données utilisées dans le cadre de cette étude, les méthodes ensemblistes, spécifiquement XGBoost et Random Forest, surpassent les réseaux neuronaux artificiels dans la prédiction des tassements. Ces méthodes restent fiables même avec seulement 30% de l'ensemble de données utilisé pour l'entraînement. L'article explore également la régularisation et l'optimisation des hyperparamètres pour Random Forest et XGBoost, mettant en lumière leurs capacités prédictives améliorées. De plus, des variations dans la répartition des données entre les ensembles d'entraînement et de test sont explorées, soulignant l'efficacité de ces algorithmes d'apprentissage automatique dans l'obtention de prédictions précises avec des ensembles de données limités.

Keywords: TBM; artificial intelligence; data analysis; optimization; surface settlements.

1 INTRODUCTION & SCOPE OF WORK

Tunnelling in dense urban areas and complex geologies generates significant risks, particularly in the form of surface settlements accompanying the tunnelling progress. Established techniques, including empirical formulas and numerical modelling, have traditionally served to predict these settlements. However, with the growing advancements in Machine Learning (ML), researchers are increasingly exploring its application for the prediction of tunnelling-induced

settlements (Kim et al., 2022; P. Zhang et al., 2020; W. Zhang et al., 2021; Zhou et al., 2023).

One pivotal consideration emerges: the quantity of data required to harness the full potential of ML methodologies, while avoiding the pitfalls of overfitting—a common challenge in adapting complex models to limited datasets. In this article, the authors address this critical question by proposing a methodology to determine the volume of data required for achieving acceptable predictive performance depending on the specificities of each project.

2 METHODOLOGY

The methodology employed in this study is designed to rigorously evaluate the performance of five selected Machine Learning (ML) algorithms in forecasting tunnelling-induced soil settlements.

2.1 Dataset description

The data used in this study originates from 2 metro lines of the Grand Paris Express (GPE), which is considered as the largest tunnelling project in Europe to date. The dataset contains parameters related to Tunnel Boring Machine (TBM) operations, as well as combined soil parameters following (Chen et al., 2019) and maximum settlement observed on top of the tunnel axis s_{max}. Soil parameters include layer thickness and location relatively to the tunnel section, and soil mechanical properties.

Ensuring the quality of the data is of utmost importance, requiring a meticulous preprocessing phase (Richa, 2023; Richa et al., 2022). This includes tasks such as handling missing values, managing outliers, and incorporating feature engineering among others. Through these measures, the dataset undergoes optimization, ensuring it is well-suited for the effective training of ML models.

The resulting dataset comprises 2,590 observations, providing a robust foundation for the subsequent analyses. Selected key variables include tunnel geometry, TBM operating parameters, and geological conditions. These variables are cover depth (D[m]), advance rate (R_A[mm/min]), torque of the cutting wheel (T_o[kN.m]), front pressure (P_f[bar]), thrust (T_h[kN]), pressure (P_g[bar]) and volume (V_g[m^3]) of grout, soil density (γ[kN/m^3]), pressuremeter modulus (E_M[MPa]) and soil rheological coefficient alpha (α[-]), earth pressure coefficient (K_0[-]), soil cohesion (c[kPa]), and soil friction angle (φ[°]).

To ensure data robustness, a statistical analysis is conducted on the selected variables, serving a dual purpose: validating data quality and enhancing comprehension. The results are presented in

Table 1.

2.2 Machine learning

2.2.1 Algorithms

This study relies on the utilization of five distinct ML algorithms: Support Vector Machine (SVM), Back-propagation Neural Network (BPNN), Extreme Gradient Boosting (XGBoost), Random Forest (RF) and Decision Trees (DT).

The choice was based on the findings of previous studies, such as Su et al., (2022), which compared the performance of SVM, BPNN and XGBoost using a dataset of 533 observations. The study concluded that XGBoost exhibits superior accuracy and interpretability compared to BPNN and SVM. Consequently, the primary focus of this study is on XGBoost, complemented by another ensemble method based on Trees: RF. DT algorithm is used to highlight the improvements achieved by RF and XGBoost.

It's crucial to note that each of these models comes with its own set of hyperparameters, which are key configurations influencing the model's behavior. As an example, one vital hyperparameter in XGBoost is "n_estimators", representing the number of trees in the ensemble. Optimizing these hyperparameters is a key aspect of the model training process.

Table 1. Statistical Description of selected features.

Unit	s_{max} *mm*	R_A *mm/min*	T_o *kN.m*	P_f *bar*	T_h *kN*	P_g *bar*	V_g *m^3*	D *m*	γ *kN/m^3*	E_M *MPa*	α	K_0	c *kPa*	φ °
Mean	-3.5	33	4687	1.2	20599	2.7	10	29.5	12	66.6	0.4	0.3	41.4	20
Std	2.4	8	1852	0.6	6726	0.8	3	8	1	30.2	0.1	0.1	19.2	3.1
Min	-17.5	10	0	0	3014	0	0	11.3	11	15.7	0.3	0.2	10	14.3
Median	-3.2	33	4387	1.2	19267	2.7	11	28.7	12	60.5	0.4	0.3	38.3	19.7
Max	-0.2	59	17540	2.6	43442	6.6	21	52.8	18	135.1	0.6	0.4	80.2	36.3

2.2.2 Model training and evaluation

The model training process involves a division of the dataset into training, validation, and testing sets. This partitioning ensures the assessment of model performance on distinct subsets of data, providing insights into generalization capabilities. To enhance robustness, cross-validation techniques are applied, mitigating the risk of model overfitting and ensuring a more reliable estimation of performance metrics.

Error metrics, including Root Mean Squared Error (RMSE) and R-squared (R^2), are employed to quantify the models' predictive accuracy. Lower RMSE values indicate better accuracy, and R^2 values closer to 1 means that the model effectively explains the variance in the data.

Learning curves offer an additional layer of insight, depicting how model performance evolves concerning the training size. These curves aid in identifying not only how much data is enough data to obtain a sufficient training score but also highlight potential issues related to overfitting.

2.2.3 Regularisation and optimisation

To enhance the predictive performance of the obtained models, two crucial techniques – regularization and optimization – are employed.

Regularization techniques control the complexity of models by adjusting hyperparameter values. This process helps strike a balance between bias and variance, preventing overfitting, where the model becomes too tailored to the training data, thereby improving its generalization to new, unseen data.

Optimization of Machine Learning algorithms aims to systematically adjust the model's hyperparameters for optimal performance. In this study, the Random Search technique is employed to explore different hyperparameter combinations, contributing to an iterative refinement process. The objective is to enhance the model's capacity to capture underlying patterns in the data.

Table 2. Model results for 5 ML algorithms using 80% of data for training.

	R^2		RMSE	
	Train	***Test***	***Train***	***Test***
SVM	0.91	0.84	0.73	0.86
BPNN	0.95	0.89	0.53	0.71
DT	1	0.82	0	1
RF	0.99	0.91	0.24	0.68
XGBoost	1	0.93	0.02	0.64

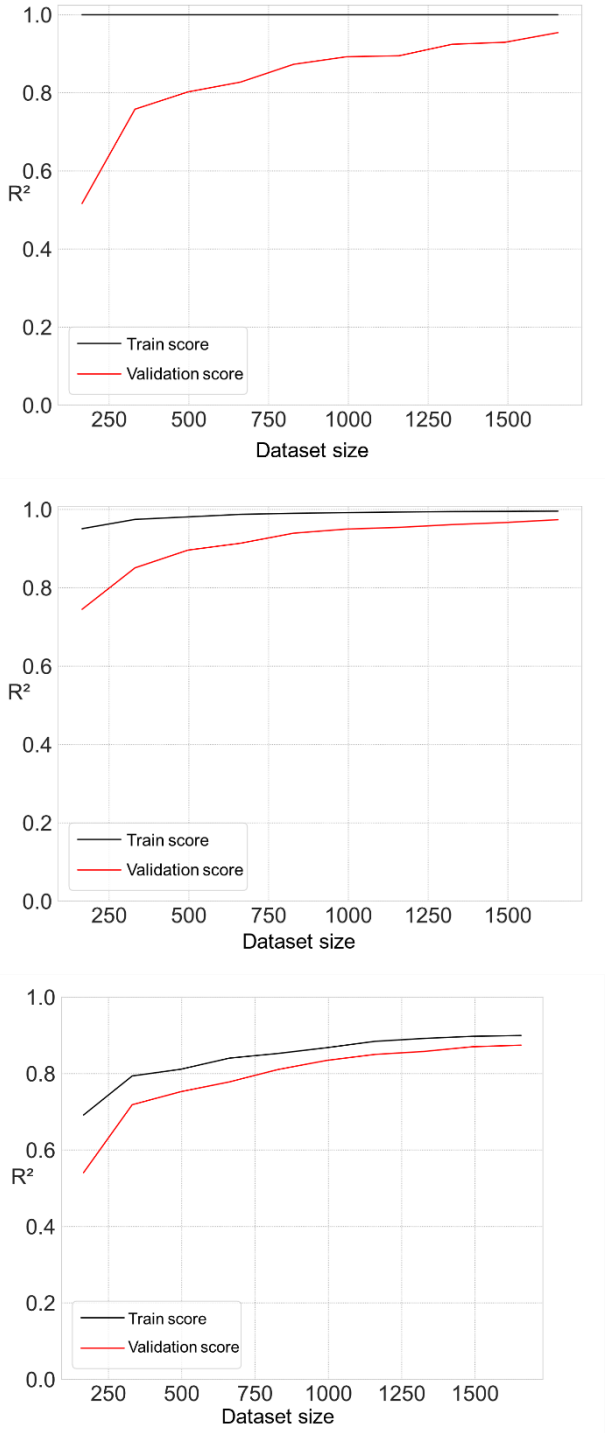

Figure 1. Learning curves of DT (top), RF (middle) and SVM (bottom).

3 RESULTS

3.1 Comparative assessment of algorithms

In the initial phase, the model is subjected to training and cross-validation using 80% of the dataset, with the remaining 20% reserved for testing. The findings, presented in Table 2., offer valuable insights.

Firstly, both RF and XGBoost showed superior predictive performance with higher R^2 and lower RMSE during testing. However, a notable observation unfolded regarding models based on tree structures, including DT, XGBoost, and RF. These models exhibit signs of overfitting, reaching maximal scores on the training datasets.

Moreover, analyzing the learning curves (Figure 1) showed that XGBoost and RF have exceptional performance with a relatively limited dataset size, approximately 600 observations, which represents 30% of the dataset.

3.2 Training with limited data

Building upon the earlier findings, the authors opted for a training set comprising 30% of the dataset, reserving the remaining 70% for testing. The outcomes affirm that 777 observations seem to provide enough data for the effective training of RF and XGBoost. Notably, the R^2 scores on the test set are impressive, standing at 0.91 and 0.93 for RF and XGBoost, respectively.

Despite their strong predictive performance, it's evident that both models show signs of overfitting. The R^2 score on the training set remains at the maximum value of 1, underscoring a tight fit to the training data. Consequently, the next crucial steps involve regularization techniques, followed by the optimization of hyperparameters for these models. These measures aim to enhance their generalization capabilities and fine-tune their predictive accuracy.

3.3 Dealing with overfitting

Addressing overfitting in these algorithms involves a strategic approach to regularization. For instance, this involves constraining the depth of the trees in the ensemble because excessively deep trees tightly adhere to the training data, resulting in overfitting. Various hyperparameters undergo regularization in this study, including the number of trees (n_estimators) in the ensemble, the maximum number of features considered for leaf division in RF, or for XGBoost, gamma, which acts as a regularization parameter.

Determining the optimal values requires a delicate balance between bias and variance, considering the range of values that minimizes both errors (Figure 2). To pinpoint the optimum value within this range, a Random Search is conducted. This method efficiently explores the parameter space, identifying the value that yields optimal results without succumbing to overfitting or underfitting.

Results show that, even after undergoing regularisation and optimisation, both algorithms continue to give remarkable performance in testing. XGBoost reaches an R^2 close to 0.9, while RF achieves 0.92, with the R^2 for the training set never reaching the maximum value of 1 (Figure 3).

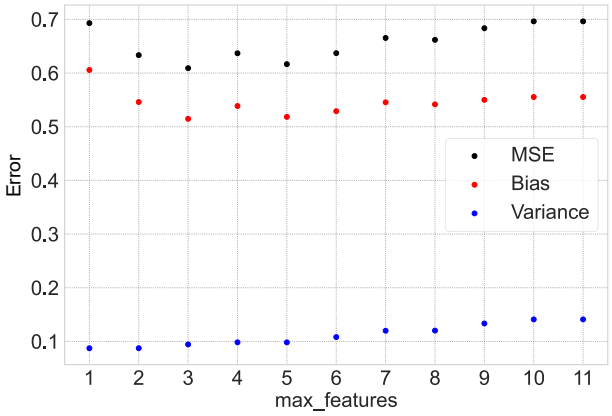

Figure 2. Example of bias and variance calculations for max_features hyperparameter in RF.

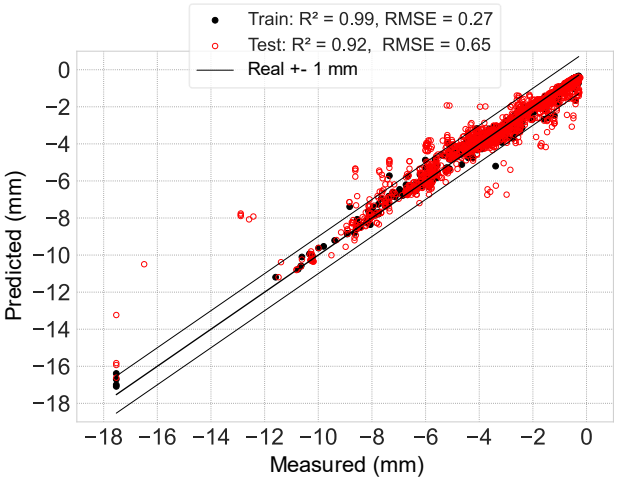

Figure 3. Results of RF after regularisation and optimisation.

4 CONCLUSIONS

This study compared 5 machine learning algorithms – Support Vector Machine, Decision Tree, Random Forest, Extreme Gradient Boosting, and Back-propagation Neural Network – giving valuable insights into their predictive accuracy for forecasting maximum settlements induced by earth pressure balance tunnel boring machines. Leveraging a dataset comprising 2,590 settlement measurements from the Grand Paris Express Project, the analysis uncovered the superior performance of ensemble methods, specifically XGBoost and Random Forest. These algorithms remain reliable even with only 30% of the dataset used for training. Furthermore, the investigation delved into the regularization and optimization of hyperparameters for Random Forest

and XGBoost, shedding light on their enhanced predictive capabilities. The exploration extended to variations in the data split between training and testing sets, emphasizing the effectiveness of these machine learning algorithms in achieving accurate predictions despite limited datasets.

REFERENCES

Chen, R.-P., Zhang, P., Kang, X., Zhong, Z.-Q., Liu, Y., & Wu, H.-N. (2019). Prediction of maximum surface settlement caused by earth pressure balance (EPB) shield tunneling with ANN methods. *Soils and Foundations*, *59*(2), 284–295. https://doi.org/10.1016/j.sandf.2018.11.005.

Kim, D., Pham, K., Oh, J.-Y., Lee, S.-J., & Choi, H. (2022). Classification of surface settlement levels induced by TBM driving in urban areas using random forest with data-driven feature selection. *Automation in Construction*, *135* (August 2021), 104109. https://doi.org/10.1016/j.autcon.2021.104109.

Richa, T. (2023). *Prévision des tassements induits par le creusement au tunnelier : construction d'une base de données et apprentissage automatique* [Ecole des Ponts ParisTech]. https://pastel.hal.science/tel-04221306.

Richa, T., Pereira, J.-M., Chapron, G., & Guayacán-Carrillo, L. M. (2022). Constitution d'une base de données des mesures obtenues lors du creusement de deux tunnels du Grand Paris Express. *JNGG*, 1093–1100.

Su, J., Wang, Y., Niu, X., Sha, S., & Yu, J. (2022). Prediction of ground surface settlement by shield tunneling using XGBoost and Bayesian Optimization. *Engineering Applications of Artificial Intelligence*, *114* (June), 105020. https://doi.org/10.1016/j.engappai.2022.105020.

Zhang, P., Wu, H. N., Chen, R. P., & Chan, T. H. T. (2020). Hybrid meta-heuristic and machine learning algorithms for tunneling-induced settlement prediction: A comparative study. *Tunnelling and Underground Space Technology*, *99* (May 2019), 103383. https://doi.org/10.1016/j.tust.2020.103383.

Zhang, W., Li, H. R., Wu, C. Z., Li, Y. Q., Liu, Z. Q., & Liu, H. L. (2021). Soft computing approach for prediction of surface settlement induced by earth pressure balance shield tunneling. *Underground Space (China)*, *6*(4), 353–363. https://doi.org/10.1016/J.UNDSP.2019.12.003.

Zhou, X., Zhao, C., & Bian, X. (2023). Prediction of maximum ground surface settlement induced by shield tunneling using XGBoost algorithm with golden-sine seagull optimization. *Computers and Geotechnics*, *154* (July 2022), 105156. https://doi.org/10.1016/j.compgeo.2022.105156.

Proceedings of the XVIII ECSMGE 2024
GEOTECHNICAL ENGINEERING CHALLENGES
TO MEET CURRENT AND EMERGING NEEDS OF SOCIETY
© 2024 the Authors
ISBN 978-1-032-54816-6
DOI 10.1201/9781003431749-360
Open Access: www.taylorfrancis.com, CC BY-NC-ND 4.0 license

ECSMGE 24
XVIII EUROPEAN CONFERENCE ON SOIL MECHANICS AND GEOTECHNICAL ENGINEERING

Centrifuge model tests to evaluate the stability of embankments in hydrodynamic conditions

Modélisation en centrifugeuse pour évaluer la stabilité de remblais dans conditions hydrodynamiques

S. Rios*, A. Viana da Fonseca, L. Ribeiro
Construct GEO - Faculdade de Engenharia da Universidade do Porto – FEUP – Porto, Portugal

C. Cengiz, S.J.M. van Eekelen
Deltares - Delft - Netherlands

**sara.rios@fe.up.pt*

ABSTRACT: Embankments associated with mine tailings storage facilities, levees, and earth dams have fine granular soils susceptible to liquefaction when their state is on the wet side of the critical state line. During periods of heavy rain or drainage system issues, a partially saturated material can become saturated after infiltration during rainfall. For low degrees of compaction, the response can be contractive, particularly at medium to high confining pressures. Therefore, centrifuge model tests were performed at Deltares, Netherlands, to assess the stability of a slope made of a silty fine sand subjected to seepage flow. An upstream water level was installed inside the slope, allowing a steady-state seepage flow through the model, while water was recovered on the downstream border where the water level was kept at a much lower level. This paper presents the centrifuge test results in terms of pore pressure evolution, which was then compared with numerical analysis performed in PLAXIS 2D®.

RÉSUMÉ: Les remblais associés aux installations de stockage de rejets miniers, aux digues, et aux barrages en terre sont composés de sols granulaires sensibles aux phénomènes de liquéfaction lorsque leur état se situe du côté humide de la ligne d'état critique. Lors des périodes de fortes pluies ou problèmes dans le système de drainage, un matériau partiellement saturé peut le devenir après infiltration. Pour de faibles niveaux de compactage la réponse peut être contractante, en particulier sous contraintes effectives moyennes à élevées. Par conséquent, des essais sur modèles en centrifugeuse ont été réalisés à Deltares, aux Pays-Bas, pour évaluer la stabilité d'une pente constituée d'un sable fin limoneux soumis à un écoulement d'infiltration. Un niveau d'eau est installé à l'intérieur de la pente permettant un débit d'infiltration stable à travers du modèle, tandis que l'eau est récupérée sur la bordure en aval où le niveau d'eau est maintenu à un niveau beaucoup plus bas. L'article présente les résultats des essais en centrifugeuse, notamment l'évolution de la pression interstitielle, qui est comparé aux résultats de l'analyse numérique réalisée dans PLAXIS 2D®.

Keywords: Seepage flow; liquefaction; slope stability; numerical analysis.

1 INTRODUCTION

There are different types of embankments, such as mine tailings storage facilities, levees, and earth dams, facing potential risks under adverse hydrodynamic conditions. These geotechnical structures often contain fine granular soils that can be sensitive to liquefaction when their state is on the wet side of critical state line. If liquefaction is not contained and propagates throughout the deposit, a flow slide results.

For instance, dry stacks are massive embankments of compacted filtered tailings. To construct these massive embankments, the tailings slurry obtained in the mining process passes through a filtering system to reduce its water content. However, the term "dry" stack can be misleading, as the state of the material forming the stack is not entirely dry. Davies (2011) suggests that it is a partially saturated material with a degree of saturation around 70-85%, but this depends on several factors (filtration process, type of material, transportation mode, climate conditions…).

Under inadequate draining conditions, a filtered dry stack in a partially saturated state can become fully saturated through infiltration during rainfall. When the degree of compaction is high (typically over than 95% of standard Proctor), filtered tailings show dilatant response under various confining stresses. Lower degrees of compaction result in a contractive response, particularly under medium to high confining pressures. Additionally, when the material is less compacted and/or on the wet of optimum, it may

become saturated under high effective stresses induced by embankment rise. Depending on the material's permeability, mineralogy, and loading rate (due to subsequent lifts), excess pore pressures may develop in the embankment. This can mobilize low undrained strength ratios far from critical state conditions eventually dropping to post-peak residual values, displaying non-Newtonian behaviour (Gens, 2019). In a climate change scenario, the increased frequency of heavy rain and storms poses additional challenges.

For these reasons, design must account for the fact that material strength depends on various factors, including the type of material, degree of saturation and compaction, drainage conditions, effective stresses due to loading, and/or excess pore pressure generation. Driven by the recognition of the brittle nature of liquefaction failure (Morgenstern et al., 2015; Jefferies et al., 2019, Arroyo and Gens, 2021), stress-deformation hydromechanical analyses of tailings dams are replacing the limit equilibrium methods that, until recently, were considered the best available practice for stability analyses (Garbarino et al., 2018, Mánica et al., 2022).

Nevertheless, it is recognised that effective use of these numerical models requires adequate calibration. Without this calibration, any attempt to simulate ground improvement technologies or more stable geometries will be seriously hampered. In a recent European Project, H2020-GEOLAB-SAFETY, simple slope models were tested in a geotechnical centrifuge. This paper presents some of the results obtained, together with hydromechanical numerical analyses.

2 CENTRIFUGE TESTS

The GeoCentrifuge at Deltares is a beam centrifuge with a 260 g-tonne capacity and a platform radius of 5.0 m. The experiment presented here comprises a homogeneous profile of a silty sand obtained with the mixture of two silica based natural soils: 56% of Geba sand and 44% of a fine fraction of Baskarp sand. This mixture allowed the simulation of the grain size distribution curve of an iron tailing material for which dry stacking is being studied. The obtained silty sand has the following physical properties: 47% of fines content, curvature coefficient Cc=0.74, uniformity coefficient Cu=2.94, mean effective diameter D_{50}=0.086 mm, maximum void ratio = 1.03, and minimum void ratio = 0.63. The model is initially prepared with unsaturated loose material by moist tamping (Figure 1), being placed in the centrifuge for an acceleration of 100g. The g-level is applied at the base of the model container corresponding to the base bottom layer of soil. After a permanent steady-state water flow is established, the hydraulic gradient is gradually increased by raising the water head on the left boundary while keeping a low water head at the right boundary. The model is instrumented with 10 pore pressure transducers (PPTs) from MEAS France (EPB-PW-7BS/Z0/PC0.5/L5M) with measuring range between -50 and 700kPa and accuracy of 0.5%FS.



Figure 1. Physical model inside the strongbox.

3 NUMERICAL MODELING

3.1 Geometry and scale factors

Numerical analysis using PLAXIS 2D® simulated the centrifuge experiment at prototype scale. Table 1 summarises the scale factors to convert the physical model results into prototype scale, so that they could be compared to the numerical data. The imposed acceleration was 100 g, although the conversion to the prototype scale used *N* values corresponding to the measured *g* level at each instance. The prototype geometry consists of a 30º slope with a height of 39 m in the upstream boundary and 8 m in the downstream boundary. There's a blanket drain at the bottom right corner of the model, extending 17.2 m from the right boundary (Figure 2).

Table 1. Scaling laws for centrifuge tests at Ng (Taylor, 1995).

Parameter	Scale (Model/Prototype)
Linear dimension (m)	1/N
Stress (kPa)	1
Time for water flow (s)	$1/N^2$

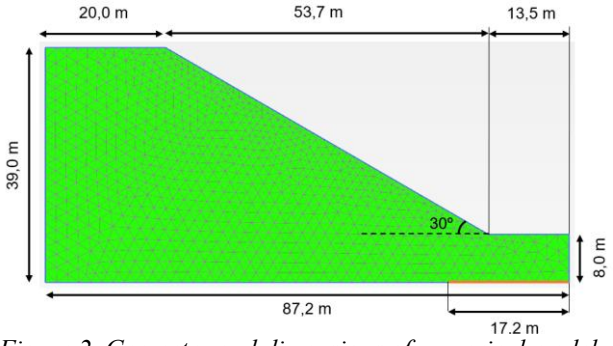

Figure 2. Geometry and dimensions of numerical model.

3.2 Material parameters

The constitutive model used was the linear elastic perfectly plastic Mohr-Coulomb model. The parameters for the material were determined through monotonic compression triaxial tests, conducted in the Geotechnical Laboratory of FEUP. To accurately simulate the unsaturated conditions above the water table, the van Genuchten parameters associated with the soil water retention curve were introduced in the groundwater parameters (Table 2).

Table 2. Soil parameters (Mohr-Coulomb).

Parameter		Value	Unit
Unit weights	γ_{sat}	18.10	kN/m^3
	γ_{unsat}	15.00	kN/m^3
Young Modulus	E	50 000	kPa
Poisson ratio	ν	0.31	-
Friction angle	ϕ'	33.32	º
Initial void ratio	e	0.800	-
Cohesion	c'	0	kPa
Coef. earth pressure at rest	K_0	0.4507	-
Permeability	k_x=k_y	$1x10^{-5}$	m/s
Van Genuchten parameters	S_r	0.00	-
	S_{sat}	1.00	-
	g_n	2.26	-
	g_a	1.82	-
	g_l	-0.66	-

3.3 Mesh and boundary conditions

The PLAXIS® numerical model has plane strain finite elements with triangular 15-node elements. The mesh created for this case is considered "very fine", comprising 13741 nodes in 1680 triangular elements. The bottom boundary was fixed in both directions, while the left and right boundaries were only fixed horizontally.

The numerical analysis comprises two phases: i) an initial phase to activate the stress state (Gravity Loading); ii) a hydromechanical numerical analysis (fully coupled flow-deformation analysis) where the head in the left boundary, and in the drain region were raised gradually, following the head evolutions measured in centrifuge test and shown in Figure 3.

So, the hydraulic boundary conditions during the hydromechanical analysis, comprise a null flux imposed in the bottom boundary, except for the drain region, where a head evolution (head function 1) was applied. In the left boundary, the other head evolution was applied, as indicated in Figure 3 (head function 2). These functions were created to represent the water table conditions observed in the centrifuge test.

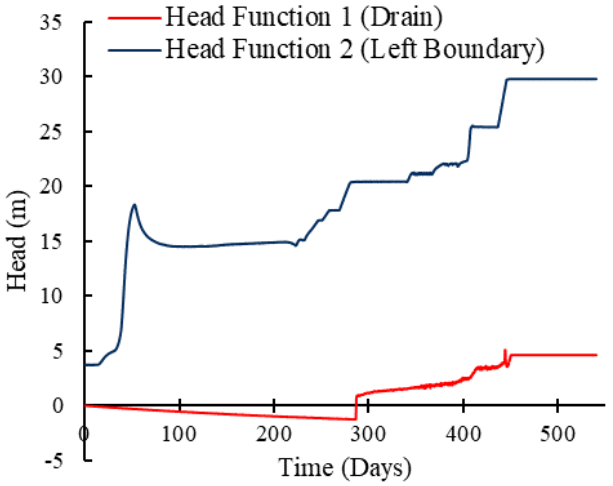

Figure 3. Water table elevation: head evolutions on the left boundary and in the drain region measured in the centrifuge test.

4 RESULTS

The physical and numerical model results are compared in terms of the pore pressures obtained in nine points of the model.

Figure 4 presents the pore pressures at the last phase of the numerical analysis, where a failure happened. The figure also shows the position of the PPTs as well as the position of the water table.

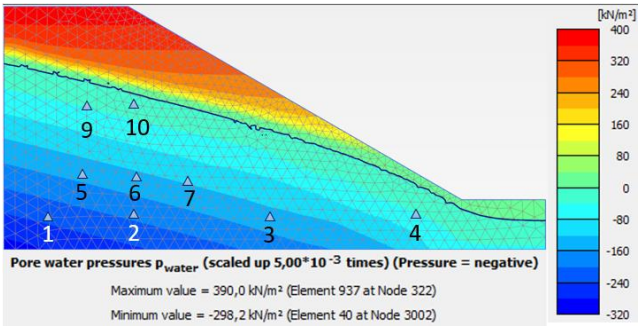

Figure 4. Pore pressure distribution and water table at the last phase of the numerical analysis, as well as the position of selected PPTs.

Figures 5 and 6 show the pore pressure evolution with time in six PPTs. Figure 5 shows that the measured values of the PPTs located close to the left boundary match the calculations well. However, Figure 6 shows that the values differ for the PPTs further away from the left boundary. This indicates that the slope failed faster in the centrifuge test than in the numerical model. This difference may be related to a small erosion at the slope toe that was noticed in the centrifuge test which may have resulted in a faster collapse of the slope than in the calculations.

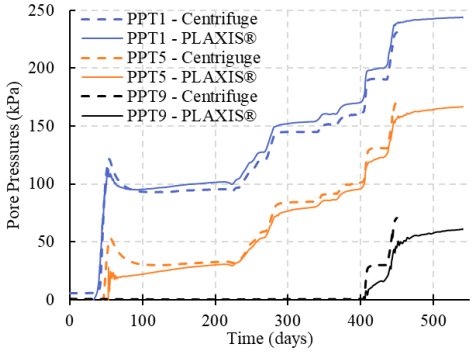

Figure 5. Pore pressures over time (PPTs 1, 5 and 9).

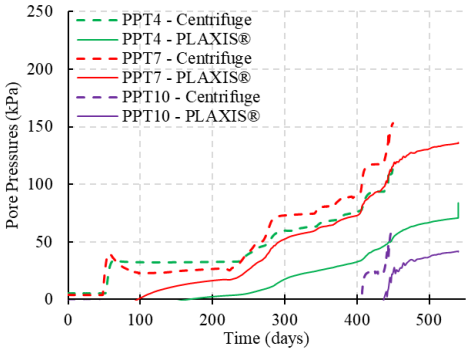

,

Figure 6. Pore pressures over time (PPTs 4, 7 and 10).

Indeed, the slope collapses at 540 days in the numerical model and at 450 days in the centrifuge experiment. This is shown by the sharp increase in pore pressure in all considered points at the failure moment. Be aware that the additional 90 days (540-450) corresponds to 13 min in the centrifuge test (model scale). Further studies are being performed on this data, namely to analyse post-mortem results obtained with a mini-CPT and with a laser scan of model surface.

5 CONCLUSIONS

A comparison of the pore pressures registered in the centrifuge test and calculated with the numerical model shows that their values match well for the points closer to the left boundary, showing that the numerical model is well-simulating the water percolation. Furthermore, a similar type of failure was observed in the experiment and the centrifuge test. Slope failure came earlier in the centrifuge test than in the numerical calculations, probably due to the relatively fast erosion of the slope in the centrifuge test. Future developments include the use of advanced numerical analyses capable of simulating soil liquefaction.

ACKNOWLEDGEMENTS

This work was financially supported by national funds through the FCT/MCTES (PIDDAC), namely the CONSTRUCT - Instituto de I&D em Estruturas e Construções, Base Funding UIDB/04708/2020 https://doi.org/10.54499/UIDB/04708/2020, the research project INPROVE-2022.02638.PTDC (https://doi.org/10.54499/2022.02638.PTDC), and by scholarship of the first author CEECIND/04583/2017 (https://doi.org/10.54499/CEECIND/04583/2017/CP 1399/CT0003). The centrifuge tests in Deltares were funded by a funding received from the European Union's Horizon 2020 research and innovation program under Grant Agreement No. 101006512 for the transnational GEOLAB project SAFETY.

REFERENCES

Arroyo, M. and Gens, A. (2021). Computational analyses of Dam I failure at the Corrego de Feijao mine in Brumadinho. Final Report from CIMNE to Vale S.A. (available to the public) http://www.mpf.mp.br/mg/sala-de-imprensa/noticias-mg/desastre-da-vale-relatorio-elaborado-por-universidade-da-espanha-aponta-causas-do-rompimento-da-barragem-em-brumadinho-mg.

Davies, M. (2011). Filtered Dry Stacked Tailings – The Fundamentals. Proc.Tailings and Mine Waste, Vancouver.

Garbarino, E., Orveillon, G., Saveyn, H. G., Barthe, P., and Eder, P. (2018). Best available techniques (BAT) reference document for the management of waste from extractive industries. JRC Science for policy Rep.

Gens, A. (2019). Hydraulic fills with special focus on liquefaction. In Proceedings of the XVII ECSMGE-2019: Geotechnical Engineering foundation of the future (pp. 1-31). DOI: 10.32075/17ECSMGE-2019-1108.

Jefferies, M., Morgenstern, N. R., Van Zyl, D. V., and Wates, J. (2019). Report on NTSF Embankment Failure. Technical report, Cadia Valley Operations for Ashurst Australia., South Orange, NSW.

Mánica MA., Arroyo M., Gens A., and Monforte L. (2022). Application of a critical state model to the Merriespruit tailings dam failure. Proceedings of the Institution of Civil Engineers – Geotechnical Engineering, 175(2), 151-165 https://doi.org/10.1680/jgeen.21.00001.

Morgenstern, N., Vick, S., Viotti, C., and Watts, B. (2015). Fundão Tailings Dam Review Panel: Report on the immediate causes of the failure of Fundao dam. http://fundaoinvestigation.com/.

Taylor, R.N., (1995). Geotechnical centrifuge technology. Blackie Academic and Professional, London.

Proceedings of the XVIII ECSMGE 2024
GEOTECHNICAL ENGINEERING CHALLENGES
TO MEET CURRENT AND EMERGING NEEDS OF SOCIETY
© 2024 the Authors
ISBN 978-1-032-54816-6
DOI 10.1201/9781003431749-361
Open Access: www.taylorfrancis.com, CC BY-NC-ND 4.0 license

ECSMGE 24
XVIII EUROPEAN CONFERENCE ON SOIL MECHANICS AND GEOTECHNICAL ENGINEERING

Distributed fibre optic sensing of stabilised soil

Détection distribuée par fibre optique d'un sol stabilisé

S. Ritter*
Norwegian Geotechnical Institute (NGI); Oslo Metropolitan University, Oslo, Norway

E.S. Rørvik
Norwegian University of Science and Technology (NTNU), Trondheim, Norway

H.J. Meland
NGI, Oslo, Norway

S. Hov, P. Paniagua
NGI & NTNU, Trondheim, Norway

**stefan.ritter@ngi.no*

ABSTRACT: A frequently adopted method to improve engineering properties of soft soils is the dry deep mixing method, where dry binders like lime and cement are mixed with the soil using a rotating mixing tool. To date, the properties of improved soil are predominantly measured using destructive methods and based on locally constrained methods. Latest sensing technologies such as distributed fibre optic sensing (DFOS) are promising tools to map temporal and spatial changes of geotechnical structures. However, the use of DFOS for stabilised soil has received scant attention. There is a lack of detailed investigations on monitoring curing temperature and detecting weakness zones in stabilised soil using distributed temperature sensing (DTS) and on the strain transfer mechanism between a fibre optical cable and the stabilised soil. This paper experimentally examines DFOS to quantify the integrity and the stress-strain relation of stabilised soil. Samples with layers of stabilised and remoulded clay were instrumented with a loose tube fibre optical cable to monitor changes in the curing temperature. The results indicate that untreated soil layers with a thickness of a few centimetres can effectively be identified when installing a fibre optical cable during the first hours after soil improvement. To address the strain transfer mechanism, composite fibre optical strain cables were directly embedded into stabilised soil samples and tested in unconfined compression tests. The obtained data show that the stiffness differences between the stabilised soil and the fibre optical cable resulted in a complicated strain transfer, which requires further investigation. The findings from this research suggest that DFOS can provide a means of evaluating the engineering performance and safety of stabilised soil.

RÉSUMÉ: Une méthode fréquemment adoptée pour améliorer les propriétés techniques des sols mous est la méthode du mélange sec en profondeur, où des liants secs comme la chaux et le ciment sont mélangés au sol à l'aide d'un outil de mélange rotatif. À ce jour, les propriétés des sols améliorés sont principalement mesurées à l'aide de méthodes destructives et basées sur des méthodes localement contraignantes. Les dernières technologies de détection, telles que la détection par fibre optique distribuée (DFOS), sont des outils prometteurs pour cartographier les changements temporels et spatiaux des structures géotechniques. Cependant, l'utilisation de la DFOS pour les sols stabilisés n'a reçu que peu d'attention. On manque d'études détaillées sur la surveillance de la température de durcissement et la détection des zones de faiblesse dans les sols stabilisés à l'aide de la détection de température distribuée (DTS) et sur le mécanisme de transfert de contrainte entre un câble à fibre optique et le sol stabilisé. Cet article examine expérimentalement la DTS pour quantifier l'intégrité et la relation contrainte-déformation du sol stabilisé. Des échantillons avec des couches d'argile stabilisée et remoulée ont été instrumentés avec un câble à fibre optique à tube lâche pour surveiller les changements de la température de durcissement. Les résultats indiquent que les couches de sol non traitées d'une épaisseur de quelques centimètres peuvent être efficacement identifiées lors de l'installation d'un câble à fibre optique au cours des premières heures suivant l'amélioration du sol. Pour étudier le mécanisme de transfert de contrainte, des câbles composites à fibres optiques ont été directement intégrés dans des échantillons de sol stabilisé et soumis à des essais de compression non confinée. Les données obtenues montrent que les différences de rigidité entre le sol stabilisé et le câble à fibres optiques ont entraîné un transfert de contrainte compliqué, qui nécessite une étude plus approfondie. Les résultats de cette recherche suggèrent que le DFOS peut fournir un moyen d'évaluer la performance technique et la sécurité des sols stabilisés.

Keywords: Distributed fibre optic sensing; ground improvement; deep dry mixing; observational method.

1 INTRODUCTION

The dry deep mixing (DDM) method has been widely employed in countries including Finland, Japan, Norway and Sweden. Traditionally, dry binders such as lime and cement have been mixed with soft soil to obtain stabilised soil columns with improved strength and deformability properties.

Current design procedures weigh the area of the improved and unimproved soil to obtain average strength estimates for the total soil volume (Norsk Geoteknisk Forening, 2012) and to evaluate settlements during loading (e.g., Broms, 1991; Alen et al., 2005; Baker, 2000). In this approach, the spatial variability of both the stabilised and virgin soil is neglected. Likewise, any interaction between the DDM columns and the surrounding clay is ignored. These limitations introduce considerable uncertainties in the design of DDM and often result in conservative estimates.

Field testing and full-scale trials have frequently been employed to improve adopted design solutions. However, traditional field-testing techniques such as sampling of the stabilised soil columns and penetration tests are destructive and often provide only locally constrained data at a specific time after the soil mixing. Reliable data about potential weakness zones in the stabilised soil is often lacking. Monitoring of full-scale field trials typically results in cumulative settlements or settlement data at specific depths. Spatially distributed data about the stress-strain response of stabilised soil remains missing.

A potential technique to obtain high resolution data about the field performance of DDM improved soil is distributed fibre optic sensing (DFOS). Recent research showed the successful application of DFOS in geotechnical engineering (Soga and Luo, 2018). For example, distributed temperature sensing (DTS) was used to quantify the integrity of a cast-in-place concrete pile (Rui et al., 2017). Another study showed that distributed strain sensing (DSS) can provide the full strain profiles of bored concrete piles (Pelecanos et al., 2018). So far, the application of DFOS to DDM has however received scant attention.

The hypothesis of this research is that DFOS can unlock the real performance of DDM improved soil. The specific research objectives were to experimentally investigate if DTS can detect weakness zones in stabilised soil, and if DSS can quantify the stress-strain response of stabilised soil.

2 METHODOLOGY

Two types of laboratory tests were carried out: so-called temperature and strain tests. For each test type, the used soil was a very sensitive clay from Tiller-Flotten, Norway. L'Heureux et al. (2019) provided a detailed description of this clay. The following sections discuss both test types in more detail.

2.1 Temperature tests

The DTS cable was a single-mode optical fibre (PureBandTM-PLUS from SUMITOMO ELECTRIC) within a hydraulic oil (Shell Tellus S3 M 46) filled plastic tube with an internal and external diameter of 2 and 3 mm. The cable was placed at the centre of an isolation box (Figure 1a), which replicated semi-adiabatic conditions (Bache et al., 2022). Two specimens with a diameter of 100 mm and a height of 200 mm with equal parts of stabilised and remoulded clay were prepared.

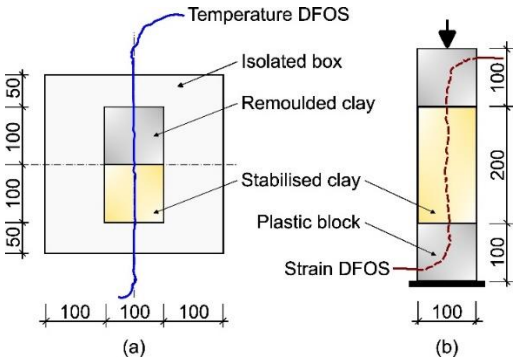

Figure 1. Experimental setups: (a) vertical cross-section of the temperature tests and (b) view of the strain tests. Dimensions in mm.

First, the Tiller-Flotten clay was manually remoulded. Then 50 kg/m^3 of dry burnt lime was added to half of the remoulded clay and mixed. The lime-clay mixture was then added to the isolation box and moulded using a tamping rod. This work was carried out with caution to avoid damage of the DTS cable while minimising the air content of the stabilised clay. The remoulded clay was then poured into the top half of the specimen to replicate a weakness zone in the stabilised soil.

An OBR4600 fibre optic interrogator from Luna Innovations and a spatial resolution of 1 cm was used. A reference measurement was carried out immediately after the sample preparation was finalised. Subsequently, measurements were taken about every 5 minutes until almost 40 hours.

2.2 Strain tests

Three stabilised soil specimens with a diameter of 100 mm and a height of 200 mm were prepared. Similar to the temperature tests, the Tiller-Flotten clay was first remoulded and then mixed with 50 kg/m^3 of dry burnt lime and 50 kg/m^3 of ordinary Portland

cement (CEM I 52.5 R). Then, the lime-cement-clay mixture was moulded in a plastic cylinder, in which an EpsilonSensor composite fibre optical core (Nerve-Sensors, 2023) was centrally placed. The EpsilonSensor had a diameter of 3 mm, an elastic modulus of 3 GPa and a strain measurement range of ±4%. The specimens were then wrapped in plastic and cured at room temperature (around 21°C).

After 19 to 27 days the specimens were tested in unconfined compression (UC) tests. Figure 1b shows the experimental setup including purpose-built slotted, rigid plastic blocks to guide the cable from the stabilised soil specimen. This setup ensured that the uniaxial load was only applied to the stabilised soil and not to the fibre optical cable. The UC tests were carried out with displacement rates between 0.2 to 0.4 mm/min and displacement increments between 0.1 to 0.4 mm. Fibre optic strain measurements were obtained before the loading started and after every displacement increment. Again, the OBR4600 with a spatial resolution of 1 cm was used.

3 RESULTS

3.1 Temperature tests

Figure 2 shows the DTS data during the first eight hours of the tests. In the stabilised clay section of the specimens, the measured temperature decreased with the experimental time. This is a result of the reference reading, which was conducted after the peak of the temperature increase had been reached. Consequently, all subsequent readings indicated a temperature reduction compared to the reference reading. By contrast, the temperature transferred to the untreated clay section and caused a temperature increase.

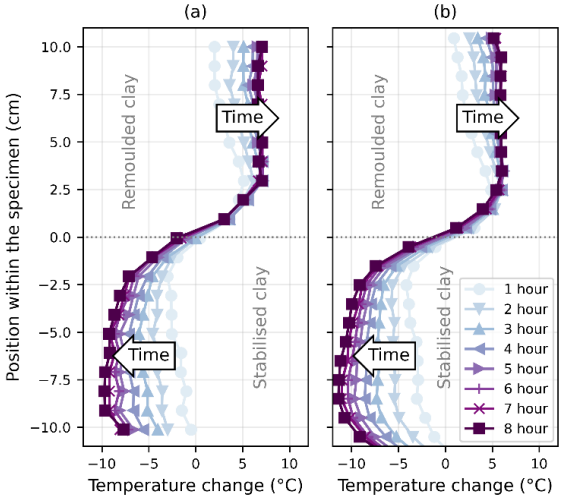

Figure 2. Distributed temperature sensing profiles within the first eight hours of the temperature tests: (a) first specimen and (b) second specimen.

The DTS data exhibited a signature temperature profile at the transition zone between the stabilised and untreated soil, see Figure 2. This suggests that zones with lower binder content in DDM can be detected using DTS. The data further indicate that notable temperature changes were obtained for the first five hours. This suggests that in the field a DTS cable should be installed directly after a DDM column is installed and immediate measurements should be taken.

3.2 Strain results

The three strain tests resulted in UC strength and stiffness values between 524 to 674 kPa and 27 to 54 MPa, respectively. These values agree with typical strength and stiffness values of laboratory improved soils (e.g., Hov and Larsson, 2023).

Figure 3 shows strain profiles obtained for the three different tests. Each strain profile relates to a specific axial strain, ε_{UC}, applied on the stabilised soil specimen. Interestingly, the strain data show a maximum strain value in the centre region of the specimens which differs from the theoretical axial strain profile of UC tests. The disagreement may be due to stiffness differences between the DSS cable and the stabilised soil affecting the associated strain transfer mechanism. Similar observations about complex strain transfer were reported when embedding DSS cables in both granular (Zhang et al., 2020) and cementitious material (Zhang et al., 2022).

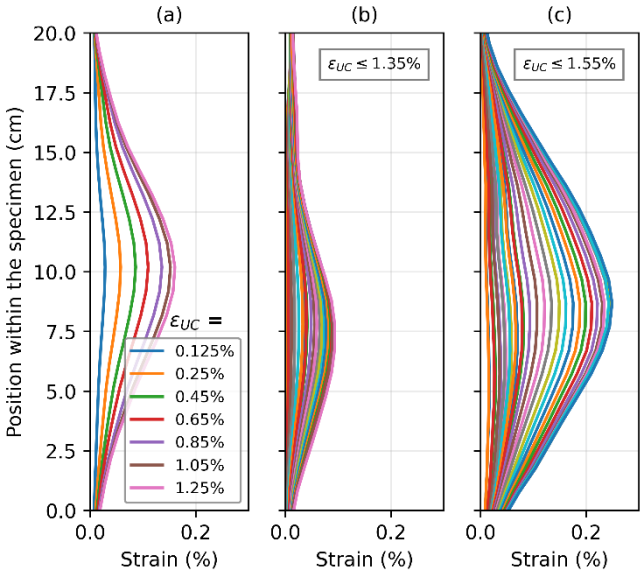

Figure 3. Distributed strain sensing profiles for the three tested specimens before the fibre optical cable noticeably slipped. For test (a), the applied axial strain in the unconfined compression test, ε_{UC}, are indicated. For tests (b) and (c), each strain profile corresponds to ε_{UC} increments of 0.05%.

In addition to the different strain profiles, the magnitude of the strains measured by the DFOS was considerably lower than the applied strain (compare measured strains with applied ε_{UC} in Figure 3). This observation indicates that the entire strain could not be transferred from the stabilised soil to the DSS cable. Again, this inconsistency may be due to the notable stiffness differences between the stabilised clay and the DSS cable and partial slippage. In addition, the length of the DSS cable was most likely too short to transfer the entire applied strain to the DSS cable.

The differences between the three strain tests are likely a result of how well the stabilised soil could be compacted in the vicinity of the DSS cable. Although great care was taken while preparing these specimens, good bond between the DSS and cable and the stabilised soil was difficult to achieve. This is especially true for the top of test (b) as can be seen from Figure 3b.

4 CONCLUSIONS

The objectives of this research were to examine if DTS can reveal anomalies in stabilised soil, and if DSS can quantify the stress-strain response of stabilised soil. This study can draw the following conclusions:

- During the first hours after mixing clay with lime, DTS exhibited a signature temperature profile at the interface between the stabilised and untreated soil. This implies that DTS may locate weakness zones with lower binder content of only a few centimetres in stabilised soil.
- DSS data resulted in notably different strain magnitudes and profiles compared to the axial strains in UC tests. The obtained disagreement could be attributed to stiffness differences between the stabilised clay and the fibre optical cable and the small length of the DSS cable in the stabilised soil specimen causing a complex strain transfer mechanism. This finding indicates that caution must be applied when interpreting the strain data from a DSS cable embedded in stabilised soil.

The obtained results support the hypothesis that DFOS can provide novel insight into the properties and performance of DDM improved soil. However, future studies are required to explore the interface behaviour between DSS cables and stabilised soil to better understand the associated strain transfer. In addition, full-scale tests are needed to study the installation of fibre optical cables in stabilised soil.

ACKNOWLEDGEMENTS

The authors are indebted to MSc Eiwind Solum Rørvik for his valuable contribution to this research while working on his MSc thesis (Solumn, 2023). The support of the staff of the NGI rock and soil mechanics laboratory of this experimental work is greatly appreciated. We also thank the Research Council of Norway (grant number 328767 "GOAL – Green soil stabilisation") for the financial support.

REFERENCES

Alén C., Baker S., Bengtsson P. E., Sällfors, G. (2005). Lime/Cement column stabilised soil – A new model for settlement calculation. In*: Deep Mixing '05 (1.2)*, Stockholm, Sweden, , pp. 205-212.

Baker, S. (2000). Deformation behavior of lime/cement column stabilized clay. *PhD thesis*, Chalmers University of Technology.

Broms, B. B. (1991). Stabilization of soil with lime columns. In: *Foundation engineering handbook*, Springer, New York, USA, pp. 833-855, https://doi.org/10.1007/978-1-4615-3928-5.

Bache, B. K. F, Wiersholm, P., Paniagua, P., Emdal, A. (2022). Effect of Temperature on the Strength of Lime–Cement Stabilized Norwegian Clays. *Journal of Geotechnical and Geoenvironmental Engineering*, 148(3), pp. 04021198 1-14, https://ascelibrary.org/doi/10.1061/%28ASCE%29GT.1943-5606.0002699.

Hov, S., Larsson, S. (2023). Strength and Stiffness Properties of Laboratory-Improved Soft Swedish Clays. *International Journal of Geosynthetics and Ground Engineering*, 9(1), pp. 1-15, https://doi.org/10.1007/s40891-023-00432-3.

L'Heureux, J. S., Lindgard, A., Emdal, A., (2019) The Tiller-Flotten research site: Geotechnical characterization of a very sensitive clay deposit. *AIMS Geosciences*, 5(4), pp. 831-868, https://www.aimspress.com/article/10.3934/ geosci.2019.4.831.

Nerve-Sensors (2023). EspilonSensor-1. Datasheet. https://nerve-sensors.com/wp-content/uploads/2021/04/EpsilonSensor-1.pdf, accessed: 05/07/2023.

Norsk Geoteknisk Forening (2012). Veiledning for grunnforsterkning med kalksementpeler. *Norwegian Geotechnical Society*, Oslo, Norway (in Norwegian).

Pelecanos, L., Soga, K., Elshafie, M. Z., de Battista, N., Kechavarzi, C., Gue, C. Y., Ouyang, Y., Seo, H. J. (2018). Distributed fiber optic sensing of axially loaded bored piles. *Journal of Geotechnical and Geoenvironmental Engineering*, 144(3), pp. 04017122 1-16, https://ascelibrary.org/doi/epdf/10.1061/%28ASCE%29GT.1943-5606.0001843.

Rui, Y., Kechavarzi, C., O'Leary, F., Barker, C., Nicholson, D., Soga, K. (2017). Integrity testing of pile cover using distributed fibre optic sensing. *Sensors*, 17 (2949), pp 1-21, https://www.mdpi.com/ 1424-8220/17/12/2949.

Zhang, C., Shi, B., Zhu, H., Wang, B., Wei, G. (2020). Toward Distributed Fiber-Optic Sensing of Subsurface Deformation: A Theoretical Quantification of Ground-Borehole-Cable Interaction. *J. Geophys. Res. Solid Earth,* 125, pp. 1-25, https://doi.org/10.1029/2019JB018878.

Soga, K., Luo, L. (2018). Distributed fiber optics sensors for civil engineering infrastructure sensing, *Journal of Structural Integrity and Maintenance*, 3:1, pp. 1-21, https://doi.org/10.1080/24705314.2018. 1426138.

Solum, E. R. (2023). Distributed Fiber Optic Sensing for monitoring stabilized clay, *NTNU MSc thesis*, Available at: https://hdl.handle.net/11250/3095069, accessed: 24/09/2023.

Zhang, S., Liu, H., Govindjee, S., DeJong, M. J. (2022). Strain Transfer Mechanisms and Mechanical Properties of Optical Fiber Cables. *Sensors,* 22 (99669), pp. 1-27, https://doi.org/10.3390/s22249966.

Proceedings of the XVIII ECSMGE 2024
GEOTECHNICAL ENGINEERING CHALLENGES
TO MEET CURRENT AND EMERGING NEEDS OF SOCIETY
© 2024 the Authors
ISBN 978-1-032-54816-6
DOI 10.1201/9781003431749-362
Open Access: www.taylorfrancis.com, CC BY-NC-ND 4.0 license

ECSMGE 24
XVIII EUROPEAN CONFERENCE ON SOIL MECHANICS AND GEOTECHNICAL ENGINEERING

Use of steel piles in the de-characterization process of tailings dams in Brazil

Utilisation de pieux métalliques pour la décaractérisation des digues à stériles au Brésil

R.F. Rodrigues* A.N. Milagres, M.M.M. Fontes, M.R. Petronilho, B.C. Novais, G. Hurtado
Fonntes Geotécnica Ltda., Belo Horizonte, Brazil

**rafael.rodrigues@fonntesgeotecnica.com*

ABSTRACT: The recent accidents involving tailings dams in Brazil have promoted significant changes in the current legislation and, consequently, have made the criteria and assumptions in projects related to mining tailings dams more restrictive. The short deadlines set by the inspection agents, the unavailability of areas, constructive restrictions and, mainly, the need for systematic operational controls during construction to eliminate possible triggers for the liquefaction process to which such structures are susceptible, made the application of steel pile walls as a reinforcement/containment element in dams to become technically feasible in comparison with conventional alternatives. The pile driving method associates the pressing method (Press in) to the rotation technique (Gyropress) and presents, among other advantages, low vibration levels, low noise levels, easy driving in different types of foundations and minimization of downstream damage. This paper presents the results of the application of the pile driving using the press in method to reinforcement as part of the process that dam decharacterization projects developed in Brazil by the applications of criteria and premises established by the International Press-in Association (IPA, 2019).

RÉSUMÉ: Les récents accidents impliquant des digues à stériles au Brésil ont entraîné des changements significatifs dans la législation actuelle et, par conséquent, ont rendu plus restrictifs les critères et les hypothèses dans les projets liés aux digues à stériles minières. Les délais courts fixés par les agents d'inspection, l'indisponibilité des zones, les restrictions constructives et, principalement, la nécessité de contrôles opérationnels systématiques pendant la construction afin d'éliminer les déclencheurs possibles du processus de liquéfaction auquel ces structures sont sensibles, ont fait que l'application de murs de pieux en acier en tant qu'élément de renforcement/confinement dans les barrages est devenue techniquement réalisable par rapport aux solutions de rechange conventionnelles. La méthode de battage des pieux associe la méthode de pressage (Press in) à la technique de rotation (Gyropress) et présente, entre autres avantages, de faibles niveaux de vibration et de bruit, un battage facile dans différents types de fondations et une minimisation des dommages en aval. Cet article présente les résultats de l'application du battage de pieux à l'aide de la méthode de pressage pour le renforcement dans le cadre du processus des projets de décaractérisation des barrages développés au Brésil par l'application des critères et des prémisses établis par l'Association internationale de pressage (IPA, 2019).

Keywords: Steel piles; dam, tailings, decharacterization.

1 INTRODUCTION

The last decade was marked by two accidents involving mining dam collapses in Brazil, which prompted significant changes in state and federal legislation, as well as in techniques for disposing of mining tailings. In this context, at the federal level, the National Mining Agency (ANM) published Resolution No. 95 of 2022, which covers the entire country and establishes precautionary regulatory measures to ensure the stability of mining dams.

In response to the new guidelines and criteria, the entrepreneurs had to update their geological-geotechnical information bases and gain a better understanding of the boundary conditions that control the geotechnical and hydraulic behavior of the structures, in operation or not. As part of this process, new field investigations and susceptibility studies of the materials that make up the dams (embankment, tailings, and foundation) were initiated, to evaluate of the undrained behavior of these materials. As a result, several structures were declared unstable, with safety factors below the requirements, resulting in the need to reinforce the structures.

The short deadlines established in the legislation for reinforcing the structures, as well as factors such as the unavailability of areas and construction restrictions, such as the generation of vibration and

noise that could be triggers for the process of liquefaction and cause instability dams, required the search for new alternatives to implement the reinforcements.

As a technically feasible alternative, studies using steel piles as a construction element and reinforcement have shown advantages over conventional solutions. Among the different technologies for driving piles, the press-in method stands out. This method is widely used in the construction of walls to protect against tsunamis in Japan, and in slope stabilization works in urban areas, mainly in Japan and Europe, according Dobrisan (2018). The Press in method consists of using hydraulic jacks attached to the pile installation equipment to press the piles into the ground. When compared to the other driving techniques used, the press in method stands out due to its fast execution and low noise and vibrations. This technique also determines the load capacity of the piles, since this driving is like a static load test (Tehrani et al., 2016). Installation by pressing uses static loading for its execution. Its design is based on using the tensile strength of piles previously installed in the ground to obtain the reaction force to press, with a static load, the new piles that will be driven into the ground. Depending on the resistance penetration of the foundation soil, it may be necessary to combine the Press in method with the Gyropress technique. In this case, the Gyropress method combines driving by pressing with the rotational movement of the pile, which results in the cutting of the ground by means of a cutting tool (drill) welded to the tip of the pile. Therefore, this combination allows them to be driven piles into resistant materials such as rocks or concrete structures (Ishihara, 2018) (Randolph, 2021).

According to Viel (2022), the advantages of this method are related to:

- low vibration levels, making possible the application in restricted areas like dams at risk or near homes,
- low noise levels;
- ease of driving in almost any type of terrain;
- minimizing damage downstream;
- reduced construction time
- facility with transportation and handling of construction materials;
- the possibility to vary the pile lengths;
- high resistance to compression, bending and cutting;
- high quality control during the construction stages.

In the case of a project using tubular piles installed by the press-in method, it is recommended to adopt the premises and criteria consolidated by the International Press-in Association (IPA), in the document Press-in retaining structures: a handbook (IPA, 2019).

In view of the advantages of using steel piles and the pressing method, the aim of this work is to present a technical feasibility analysis of the use of tubular steel piles to reinforce dams, enabling stabilization and reinforcement processes prior to the dam decommissioning process. A methodological proposal for sizing this type of structure in Brazil will be presented, addressing the particularities and adaptations required, and finally the application of the sizing of a fictitious reinforcement structure, designed according to the proposed methodology.

In order to design these reinforcements, some items deserve special attention, including the calculation of the forces on the pile, the moments and displacements acting on the piles, as well as the evaluation of the behavior of the foundation materials in the face of the demands imposed, and it is also important to note that the behavior of the groundwater after the piles are installed must be analyzed.

2 METHODOLOGY

The design of the steel piles will be based on the calculation methodology presented in the document Press-in retaining structures: a handbook prepared by the International Press-in Association (IPA). The stability of the retaining structure will be checked using the computer software Slide 2® and RS2®.

According to Santos and Futai (2021), for a structure in which one of the dimensions extends indefinitely in relation to the others the assumption of plane state of deformation of the reinforced soil is realistic. The beam element developed in the Timoshenko methodology, as pointed out in the work by Cheng et. al. (1997), adequately correlates principles of stress distribution in beams according to the mechanics of deformable solids and displacement behavior associated with shear forces, using geometric and deformability parameters of the retaining wall and boundary elements of the soil medium itself.

Considering the guidelines contained in the IPA manual, the analysis of tubular piles to be adopted in this study will consider equation (1) to define the tension yield stress adopted for the material:

$$\sigma_e = \frac{M_{max}}{Z} \qquad (1)$$

where Mmax is the maximum moment in the pile (kNm) and Z is the resistant moment area (m³).

It is important to note that the IPA recommends that σ_max should be lower than the steel's admissible

stress, so a safety factor of 1.50 will be used over the yield strength.

Equations (2) and (3) show the calculations developed to measure the area resistant moment, and there is a correction for the resistant moment per meter, dividing it by the diameter of the pipe plus the spacing between them:

$$Z_i = \frac{\pi \left({R_{ext}}^4 - {R_{int}}^4\right)}{4 * R_{ext}} \quad (2)$$

$$Z = \frac{Zi}{Dext + e} \quad (3)$$

For the maximum shear force developed in the pile, referring to the Plane State of Deformation, the Tresca failure criterion will be used in which, in the direction of the shear stress. Equations (4) and (5) express the equations evaluated:

$$\tau_{xy} = \frac{\sigma_e}{2} \quad (4)$$

$$F_{máx} = \tau_{xy} * A \quad (5)$$

where σ_e= tension yield stress adopted for the material (MPa); τ_xy= yield shear stress (MPa); A= effective area of the section (m²).

Although studies in Brazil take into account the determination of reference Safety Factors (SF) for stability studies, in this study, due to the use of the Press-in method, in addition to the SF, the criteria defined in Japan will be used, which prioritize the limit state of use according to the guidelines of the Japan Road Association (2009). Therefore, the maximum horizontal pile displacement is used as a design criterion:

- Less than 1% of the length the pile in the case of normal works;
- Less than 3% of the length the pile in the case of temporary works;

In addition to the displacement criterion presented, the pile's resistance to bending and shearing forces will also be checked. To do this, the maximum bending moment found in the piles in the simulations performed must be less than an allowable moment calculated for each pile or set of piles.

The piles are first inserted into the model embedded in competent material, and then the number of pile rows and embedment length are adjusted to meet the criteria for relative displacement, bending stresses, and safety factors. First, the maximum bending moment in the pile is observed to determine which pile configuration (number of rows, type of steel, and pile thickness) has a higher allowable moment and is closest to the maximum achieved. The analysis is then conducted for the most suitable configuration from the point of view of bending stresses. If necessary, the pile length is adjusted by increasing the embedment to reduce the relative displacement at the top of the pile until the relative displacement criterion is met, and then the pile length is adjusted if it is necessary to embed more than required to reduce the relative displacement at the top of the pile until the relative displacement criterion is met in the most optimized way. This length adjustment will be reflected in the bending moments generated, so it should be re-evaluated with respect to the allowable moments of the proposed pile configuration. It should be noted that this process can be repeated several times until the most optimized result is obtained, with relative displacements and maximum moments below and closer to the allowable ones.

In addition to the bending stresses and relative displacements, the yielding of the foundation materials and the shear deformations associated with yielding will also be observed, looking for the formation of a failure mechanism that could lead to the pile collapse. After this stage, the solution is validated using the safety factors obtained by limit equilibrium, according to Brazilian and international standards, demonstrating the effectiveness of the solution.

3 RESULTS

3.1 Definition of the boundary conditions for the design of the structure

This stage of the project consists of defining the position and alignment of the pile rows and checking the conditions of the containment structure's foundation.

The location of the containment must take into account the conditions of the subsoil and the geomorphology of the terrain. In order to better understand the subsoil, a campaign of geotechnical investigations should be carried out, including field and laboratory tests that will help validate the geotechnical parameters of the area, define the stratigraphic profile of the subsoil and identify the water level. In order to define the specifications for the necessary driving system, it is important to check the resistance parameters. For this study, a geotechnical profile of a fictitious foundation was proposed.The geotechnical parameters for the foundation and materials were defined using values from the literature and are shown in Table 1.

3.2 Taling Dam without reinforcement

Based on the resistance and deformability parameters established above, the structure was checked for the current condition, without the implementation of reinforcement. In this condition, it was found that the dam does not present favorable safety conditions for the liquefied (Figure 1) and pseudo-static (Figure 2), scenarios, thus justifying the implementation of reinforcement works for these conditions.

Table 1. Material strength and deformability parameters.

Material Name	Unit Weight (kN/m3)	Poisson's Ratio	Young's Modulus (kPa)	Failure Criterion	Material Type	Peak Friction Angle ( )	Peak Cohesion (kPa)	Vertical Stress Ratio	Minimum Shear Strength (kPa)
Sterile	21	0.25	50000	Mohr-Coulomb	Plastic	36	0		
Landfill - silty sand	20	0.4	30000	Mohr-Coulomb	Plastic	36	5		
Granodiorite A4/R1+	20	0.25	500000	Mohr-Coulomb	Elastic	35	105		
Granodiorite A4/R1-	20	0.25	300000	Mohr-Coulomb	Elastic	35	10.5		
Calcilutite A4/R1-	20	0.27	200000	Mohr-Coulomb	Elastic	35	10.5		
Tailings - clayey	19	0.33	8000	Vertical Stress Ratio	Plastic			0.3	5
Tailings - sandy silt with clay	19	0.3	160000	Vertical Stress Ratio	Plastic			0.25	5
Tailings - silty sand	19	0.35	25000	Mohr-Coulomb	Plastic	34	0		
Tailings - clayey silt	19	0.35	16000	Mohr-Coulomb	Plastic	24	0		
Compacted silty sand embankment	20	0.4	40000	Mohr-Coulomb	Plastic	35	0		
Peak tailings - clay	27	0.3	8000	Vertical Stress Ratio	Plastic			0.3	5
Peak tailings - sandy silt with clay	19	0.3	16000	Vertical Stress Ratio	Plastic			0.25	5
Peak tailings - silty sand	19	0.35	8000	Vertical Stress Ratio	Plastic			0.3	5
Peak tailings - clayey silt	27	0.3	20000	Mohr-Coulomb	Elastic	35	10.5		

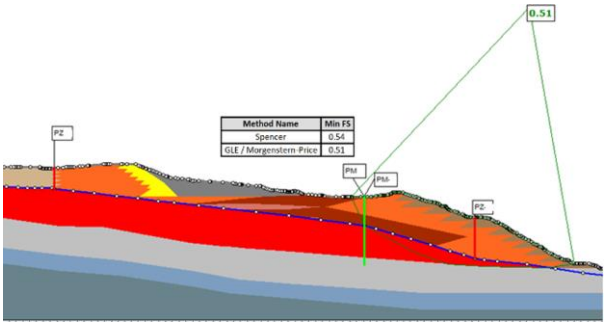

Figure 1. Stability analysis for the dam's base scenario - liquefied scenario.

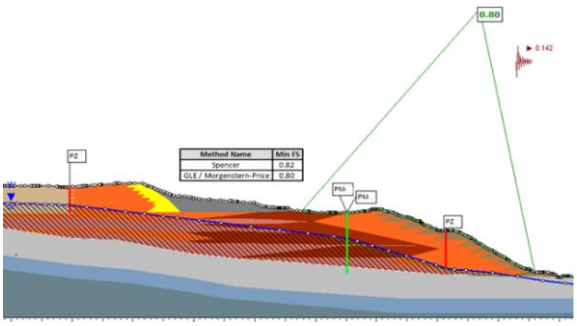

Figure 2. Stability analysis for the dam's base scenario - pseudo-static scenario.

3.3 Tailing dam with reinforcement

Bearing in mind that the project is presented as a definitive solution, the evaluation criterion for relative displacements is that they must be less than or equal to 1% of the total length of the pile. In this context, the section meets the established criterion with the greatest displacement occurring in axis 5 of the solution, at 0.94%. (Figure 3). As for the bending stresses, in the configuration defined for this section, in axes 1, 2 and 3, there is a solution with a 1200 mm pile, 21 mm thick and grade 50 steel, in which the maximum bending moment of 1926.8 kNm was verified in axis 2, which is lower than the 3516 kNm admissible for this configuration. For axes 4, 5 and 6, the solution is a 1500 mm pile, 25 mm thick and grade 50 steel, in which the maximum bending moment of 2171.9 kNm was verified. (Figure 4) in axis 6, which was lower than the 5446 kNm admissible for this configuration. Finally, as for the other evaluations, yielding and shear deformation, the section behaved satisfactorily and within expectations during the scenarios evaluated, undergoing yielding in some regions of the tailings. (Figure 5), with a maximum shear deformation of less than 5% near the piles (Figure 6), indicating that these regions where yielding occurs are not representative of a rupture wedge that could lead to the collapse of the structure. The results of the stress-strain study and the behavior of the piles in terms of permissible and acting moments are shown in Table 2. This fact was proven in the limit equilibrium analyses, which in the liquefied scenario the solution presents FS of 1.24 (Figure 7 higher than FS>1.1 and FS of 1.23 (Figure 8) for the pseudo-static scenario, higher than FS>1.1, both stipulated by the CDA (2019).

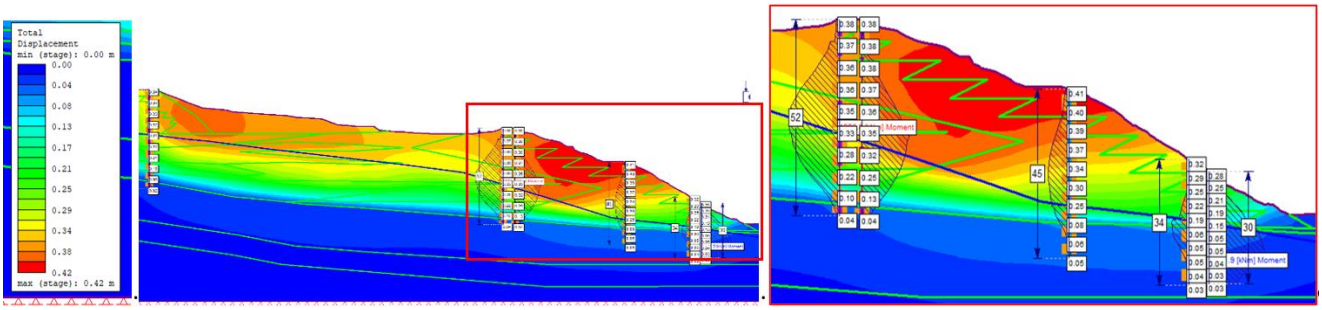

Figure 3. Total Displacement.

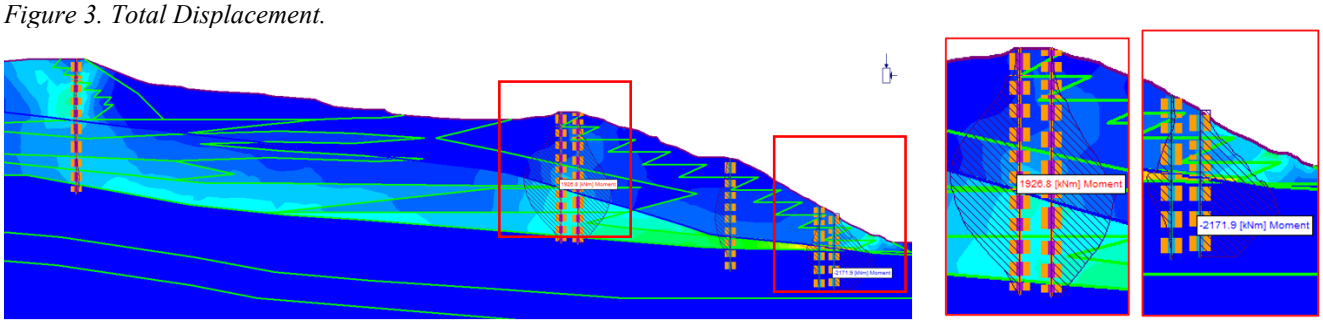

Figure 4. Bending Moment.

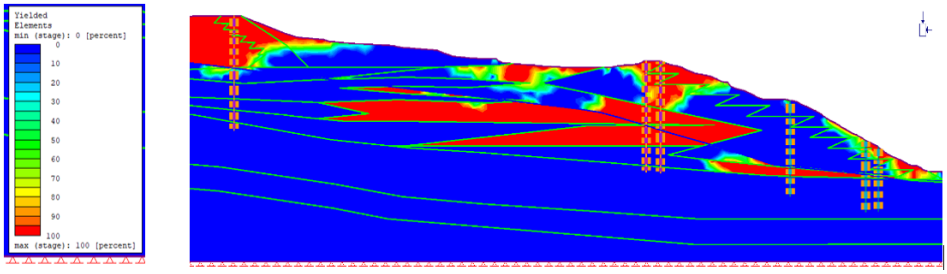

Figure 5. Yielded Elements.

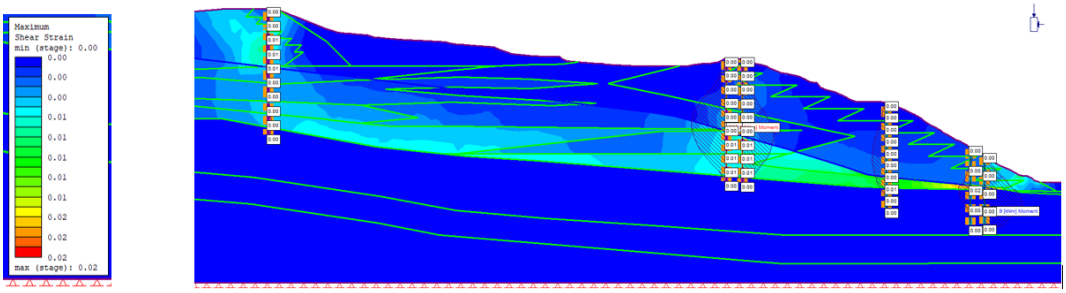

Figure 6. Maximum Shear Strain.

Table 2. Summary of the results of the stress-strain study.

Section	Maximum moment		Allowable moment (kNm)	Maximum deformation				Permissible deformation (%)	Piles
	Axis	Value (kNm)		Length	Displacement		%		
Section AA	1	166,7	**3516**	54	Top	0,34	0,63%	**1,00% of the length the pile (Japan Road Association, 2009)**	1200mm thickness 21mm and GRADE 50 STEEL
	2	1926,8		52	Top	0,38	0,73%		
	3	1806,2		52	Top	0,38	0,73%		
	4	797,56	**5446**	45	Top	0,41	0,91%		1500mm thickness 25mm and GRADE 50 STEEL
	5	668,27		34	Top	0,32	0,94%		
	6	2171,9		30	Top	0,28	0,93%		

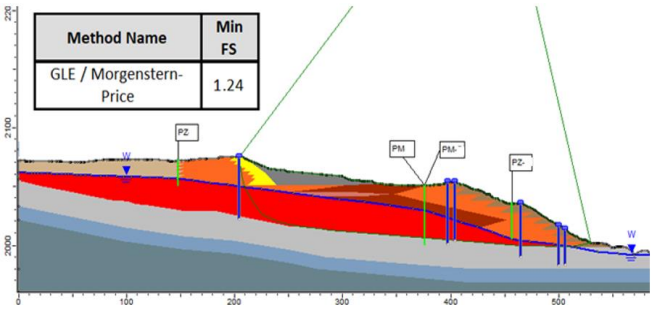

Figure 7 – Stability analysis for the dam's base case - liquefied scenario.

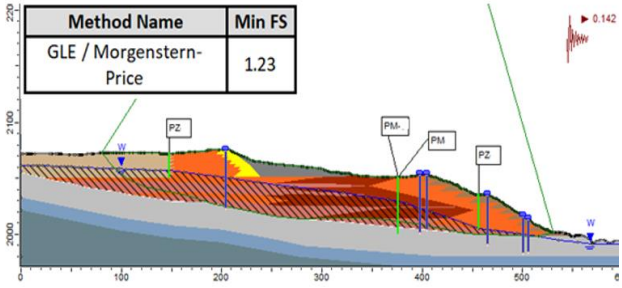

Figure 8 – Stability analysis for the dam's base scenario - pseudo-static scenario

4 CONCLUSIONS

As presented, there are technologies available that can promote the geotechnical improvement of upstream dams, to increase the safety conditions of the structure and carry out its de-characterization process. The innovative nature of using the press-in method to reinforce these structures susceptible to liquefaction stands out. In this application context, this methodology becomes viable due to the low levels of vibrations during driving, which, through full-time control and monitoring, can avoid triggering liquefaction during the construction of the reinforcement. Therefore, given the relevance and risk levels associated with such geotechnical structures, to conduct the reinforcement, a monitoring plan must be implemented with the installation of quick response piezometers associated with geophones. It is worth mentioning that control levels must be previously defined through the execution of tested areas.

ACKNOWLEDGEMENTS

The authors are grateful to Fonntes Geotécnica for having provided an environment that supports us in overcoming challenges, with the opportunity and incentive to develop innovative projects to serve our clients and to disseminate the results in scientific circles to promote knowledge in the geotechnical community.

REFERENCES

ANM. *Resolution No. 95*. (2022). Consolidates the normative acts that provide for the safety of mining dams. Brasília.

Dobrisan, A.; Haigh, S. K.; Ishihara, Y (2018). *Evaluating the efficiency of jacked-in piles as tsunami defences*. In: Proceedings of the First International Conference on Press-in Engineering. https://doi.org/10.50876/icpe.1.0_23.

IPA- International Press-In Association. (2019). *Press-in retaining structures: a handbook*. 2. ed. International Press-in Association. 392 p.

Ishihara, Y., Haigh, S. (2018). *Cambridge-Giken collaborative working on pile-soil interaction mechanisms.* In: Proceedings of the International Conference on Press-in Engineering First International Conference. International Press-in Association. p. 23-46. https://doi.org/10.50876/icpe.1.0_23.

Japan Road Association. (2009). Technical standard, ISBN-10: 488950415X, July 1, 2009. 道路土工一切土工・斜面安定工指針 (Guidelines for road embankment work and slope stabilization), [S. l.], 1 Jul.

Randolph, M. F. (2021). *Design considerations for piles jacked or driven into strong soil or weak rock*. In: Proceedings of the Second International Conference on Press-in Engineering 2021, Kochi, Japan. CRC Press. p. 3. https://doi.org/10.1201/9781003215226.

Santos, G. O. F., Futai, M. M. (2021). *Evaluation of deformability criteria for downstream retaining structures composed of tubular piles*. Proceedings of the Brazilian Conference on Slope Stability.

Tehrani, F. S. et al. (2016). *Comparison of Press-Replace Method and Material Point Method for analysis of jacked piles*. Computers and Geotechnics, [S.l.], v. 78, p.38-53.

Viel, I. N. (2022). *The use of tubular steel piles in protection structures for mining tailings dams*. Master's degree dissertation. Federal University of Ouro Preto - UFOP. https://doi.org/10.1016/j.compgeo.2016.04.017.

Proceedings of the XVIII ECSMGE 2024
GEOTECHNICAL ENGINEERING CHALLENGES
TO MEET CURRENT AND EMERGING NEEDS OF SOCIETY
© 2024 the Authors
ISBN 978-1-032-54816-6
DOI 10.1201/9781003431749-363
Open Access: www.taylorfrancis.com, CC BY-NC-ND 4.0 license

ECSMGE 24
XVIII EUROPEAN CONFERENCE ON SOIL MECHANICS AND GEOTECHNICAL ENGINEERING

Influence of the procedure for determining the characteristic values of strength parameters on the probability of failure of unsupported cuts

Influence de la procédure de détermination des valeurs caractéristiques des paramètres de résistance sur la probabilité de rupture des talus d'excavation

F.P.S. Rogério*
DEC/ISPTundavala, Lubango, Angola. NOVA School of Science and Technology, Almada, Portugal

N.M.C. Guerra, A.N. Antão, M. Vicente da Silva
UNIC, NOVA School of Science and Technology, Almada, Portugal

M. Matos Fernandes
FEUP, Porto, Portugal

**f.rogerio@campus.fct.unl.pt*

ABSTRACT: Estimating the characteristic value of strength parameters for design is an important matter in geotechnical practice. In this study, Latin Hypercube Sampling (LHS) is used to generate statistical meshes with the spatial variability of the friction angle and the true effective cohesion of the soil. For this, typical values of the coefficient of variation and of the horizontal and vertical scales of fluctuation of the friction angle and of the effective cohesion are adopted. Soil characterization is simulated in each of these statistical meshes. The characteristic values of the friction angle and effective cohesion are estimated following two procedures regarding the assumed knowledge of the soil properties. With these characteristic values, unsupported cuts are designed using the Load and Resistance Factor Design (LRFD) method. Slope stability analyses are performed with the software *mechpy*, using the Random Finite Element Limit Analysis (RFELA) and considering the above-mentioned meshes. Then, the probability of failure of the designed unsupported cuts is estimated using direct reliability analysis. The results show that adopting this procedure using simulation of site characterization has a substantial effect on the probability of failure.

RÉSUMÉ: L'estimation de la valeur caractéristique des paramètres de résistance pour le projet est une question importante pour la pratique géotechnique. Dans cette étude, l'échantillonnage hypercube latin (LHS) est utilisée pour générer des mailles statistiques avec la variabilité spatiale de l'angle de frottement et de la cohésion effective réelle du sol. Des valeurs typiques du coefficient de variation et des échelles horizontale et verticale de fluctuation sont adoptées pour caractériser le sol. Les valeurs caractéristiques de l'angle de frottement et de la cohésion effective sont estimés en suivant deux procédures en fonction de la connaissance supposée des propriétés du sol. Les talus d'excavation sont dimensionnés en utilisant la méthode *Load and Resistance Factor Design* (LRFD). Les analyses de stabilité des talus sont réalisées en utilisant le logiciel mechpy et le *Random Finite Element Limit Analysis* (RFELA) en prenant en compte les maillages statistiques. Enfin, la probabilité de rupture des talus d'excavation non soutenus est estimée à l'aide d'une analyse de fiabilité directe. Les résultats montrent que l'adoption de cette procédure utilisant la simulation de la caractérisation du site a un effet substantiel sur la probabilité de rupture.

Keywords: Characteristic value; simulated characterization; unsupported cut; probabilistic analysis; numerical limit analysis.

1 INTRODUCTION

The load and resistance factor design (LRFD) method uses representative values that can be taken as characteristic values, determined from the available data of soil characterization using statistical methods. When performing probabilistic analyses, it is important to take into account the spatial variability of soil properties to properly account for the inherent uncertainties, as it was shown in several studies that spatial variability has a significant effect on the probability of failure (Cho, 2007; Griffiths et al., 2009; Ji et al., 2012; Chok et al., 2015; Yang et al., 2022). The main objective of this study is to assess the influence of the procedure used for determining

the characteristic values of the effective cohesion, c', and the friction angle, ϕ', of soil on the probabilistic analysis of unsupported cuts under drained conditions, considering the effect of spatial variability. An adaptation of the Random Finite Element Method (RFEM) (Fenton & Griffiths, 2008), the Random Finite Element Limit Analysis (RFELA) is used for this purpose. A similar procedure can be applied to undrained conditions.

Latin Hypercube Sampling (LHS) is used to generate statistical meshes with the spatial variability of c', and ϕ' of soil in drained conditions, adopting typical values of the coefficient of variation, COV, and of the scales of fluctuation in the horizontal and vertical directions, θ_x, and θ_y (Phoon & Kulhawy, 1999; Cami et al., 2020; ISSMGE-TC304, 2021).

The characteristic values of the strength parameters are estimated through two scenarios regarding the knowledge of the soil properties. One where there's no prior knowledge of the mean value and COV of the soil properties, and the other where there's prior knowledge of these soil parameters. The first scenario is based on a site characterization simulated on the statistical meshes. Then, the characteristic value for each statistical mesh is estimated from the mean value and COV of c' and ϕ' therein obtained. In the second scenario, the characteristic value is estimated using the input parameters, the mean value, and the COV of c' and ϕ' used to generate the statistical meshes. The properties' design values are defined according to the principles of the Eurocode 7. The unsupported cuts are designed using deterministic stability analyses with Finite Element Limit Analysis (FELA). These stability analyses aim to evaluate the maximum unit weight γ_{EC7} for which the unsupported cuts with height h and inclination β verify safety.

The stability analyses of the designed unsupported cuts are then evaluated with RFELA. The probability of failure is estimated through the direct integration of the Probability Density Function (PDF) on the failure side of the limit state function (Huang & Griffiths, 2011). The limit state function is defined by the margin of safety, computed by the difference between the resistance and the loading (Baecher & Christian, 2003; Christian, 2004).

The generation of the statistical meshes, the simulation of site investigation, and the stability analyses of unsupported cuts are performed using the software *mechpy* (Vicente da Silva & Antão, 2013), developed at the Department of Civil Engineering of NOVA School of Science and Technology. This is a FELA software, where the kinematic and static theorems of limit analysis are implemented within a finite element analysis framework (Vicente da Silva et al., 2020). It has been applied by the authors to reliability analyses (Simões et al., 2014, 2020). The software uses a remesh procedure based on Martin's (2011) work. In this approach, the analyses are performed in 4 steps, in which the finite element meshes are progressively refined in the zones of higher plastic distortion.

2 DESCRIPTION OF THE PROBLEM

This paper considers a problem of an unsupported cut with h = 15 m, l = 12 m, L = 35 m, L_1 = 50 m, D = 22 m, and β = 45º, modelled in plane strain state, with the boundary conditions presented in Figure 1.

The shear strength parameters c' and $\tan\phi'$ (here regarded as uncorrelated random variables) with the mean values of 10 kPa and 27º, and COV of 0.2 and 0.08, respectively, are assumed to follow the lognormal distribution, with the scales of fluctuation θ_x (30, 50, 80, and ∞) and θ_y (1, 3, 80, and ∞), measured in meters. Hence, four cases are assessed, three of which with spatial variability [case 1 (θ_x = 30 m; θ_y = 1 m); case 2 (θ_x = 50 m; θ_y = 3 m); case 3 (θ_x = 80 m, θ_y = 80 m)], and one without spatial variability [case 4 ($\theta \to \infty$)].

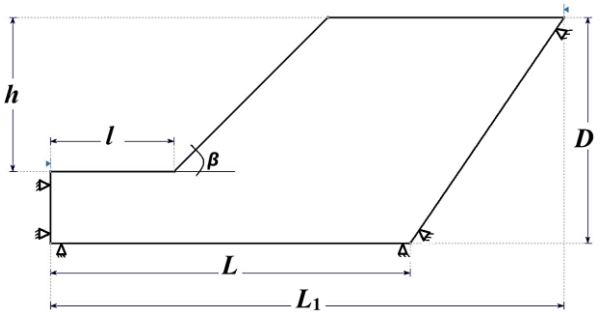

Figure 1. Geometry and boundary conditions of the numerical model.

The same values of scales of fluctuation are adopted for both c' and ϕ'. Cases 1 and 2 correspond to realistic situations, whereas case 3 is used for control and comparison with case 4. For cases 3 and 4, only the second scenario is considered.

3 GENERATION OF STATISTICAL MESHES

The generation of the random fields is achieved with LHS, a more efficient sampling technique than standard Monte Carlo (McKay et al., 1979;

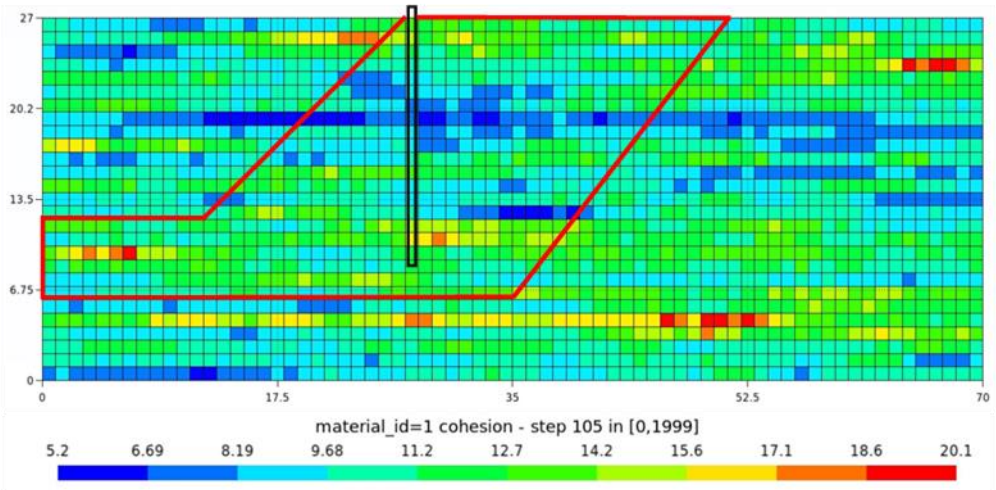

Figure 2. Example of a statistical mesh sample, of c' distribution, superposed with the geometry considered in finite element calculations.

Olsson et al., 2003). A two-dimensional ellipsoidal correlation function is used to describe the autocorrelation of the random variables (Fenton & Griffiths, 2008), from element to element, for a horizontal distance, Δ_x, and a vertical distance, Δ_y, from the centre of mass for the elements of the statistical mesh:

$$\rho(\Delta x, \Delta y) = \exp\left[-2\sqrt{\left(\frac{\Delta_x}{\theta_x}\right)^2 + \left(\frac{\Delta_y}{\theta_y}\right)^2}\right] \qquad (1)$$

in which ρ is the coefficient of correlation. An example of a statistical mesh is presented in Figure 2, with 70 m width and 27 m height, containing square statistical elements of 1x1 m^2 dimension. For this study, 2000 statistical meshes were generated for each of the cases 1 to 3 described in section 2.

4 SITE CHARACTERIZATION

The site characterization is simulated on both c' and ϕ' statistical meshes and provides the "exact" value of these spatially distributed random properties, although, in practice, measurement errors are inevitable (Yang et al., 2022). This simulation of site investigation is executed at the crest of the unsupported cut as shown in Figure 2 obtaining the values of c' and ϕ', from the top boundary down to $1.2h$. In this procedure, these values are collected at points situated 1 m from each other, assuming that such values could be obtained from site characterization, for each statistical mesh. The values of c' and ϕ' obtained in this way are used for determining the characteristic values of the parameters, for each sample, for the 1st scenario described in Section 1. In this scenario, 2000 characteristic values are calculated for each case, while in the 2nd scenario, only one characteristic value is computed for each case.

5 DESIGN

The characteristic value is defined from the values of the parameters of the statistical meshes using the following equation:

$$X_k = \exp[Y_m(1 - k_n.COV_{\ln X})] \qquad (2)$$

where Y_m is the mean value of the logarithms of individual parameters, and k_n is the statistical coefficient related to the type of distribution, confidence limit, and number of test values n. For the first scenario, k_n is calculated using the expression:

$$k_n = t_{n-1}^{0.95}\sqrt{1/n} \qquad (3)$$

in which $t_{n-1}^{0.95}$ is the student's t-value for n-1 degrees of freedom at a confidence level of 95% (Bond & Harris, 2006; Frank et al., 2004). In this scenario, n = 19, which corresponds to the number of values of c' and ϕ' collected in each characterization simulated.

As for the second scenario, k_n is estimated by:

$$k_n = N_{95}\sqrt{1/n} \qquad (4)$$

where N_{95} represents the Normal distribution, evaluated for a 95% confidence level and infinite degrees of freedom. For this scenario, k_n is computed by assuming n = 30.

The design value of the ground properties X_d is derived from the characteristic value by applying the Design Approach 1, Combination 2 (DA1 – C2) of the Eurocode 7 (EN 1997-1, 2004),

$$X_d = x_k/\gamma_M \quad (5)$$

in which γ_M is the partial factor of safety considered equal to 1.25 for c' and $\tan\phi'$.

6 STABILITY ANALYSIS

This process starts by mapping the values of c' and ϕ' from the statistical meshes into the finite element mesh with the geometry of the unsupported cut (Figure 2), as presented in the example in Figure 3 a). Subsequently, the stability analyses are performed, applying the kinematic and static theorems of limit analysis. The approximation of the unit weight that causes the collapse of the unsupported cut is obtained from both analyses and the average of the two, $\gamma_{RFELA,i}$, is determined for each statistical mesh sample. The failure mechanisms can be inferred from the mesh deformation and the maximum distortion (Figure 3 b)) in the case of the kinematic theorem calculations.

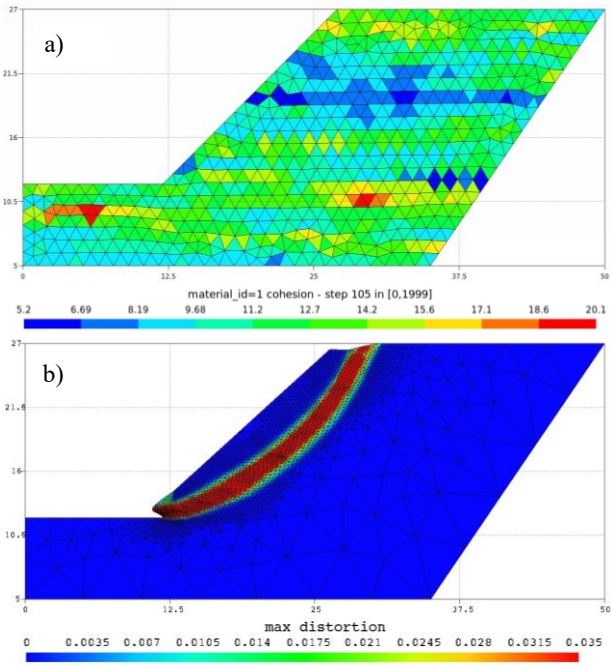

Figure 3. Example of a result of: a) mapping RFELA mesh values of c', and b) a deformed mesh with maximum distortion, determined from kinematic theorem calculations.

7 PROBABILITY OF FAILURE

For performing the direct reliability analysis, in this study, the margin of safety is computed as:

$$M = \gamma_{RFELA} - \gamma_{EC7}.(1 + COV.\Delta) \quad (6)$$

in which Δ is either zero or a random "noise" that follows the normal standard distribution, with a mean of 0 and a standard deviation of 1, assuming that COV is equal to 0.10. The implementation of the random "noise" seeks to simulate the effect of variability in the action.

The purpose is to find the probability of $M \leq 0$, and it is estimated using the cumulative distribution function of either the Normal or the Log-normal distribution.

For cases 1 and 2 it was found that the Normal distribution gave the best approximation to the data, and for cases 3 and 4 it was the Log-normal.

Figure 4 presents an example of the CDF of the margin of safety, for comparison of a situation with the random "noise" ($\mathbf{M\Delta} \rightarrow \Delta \neq 0$) and another without it ($\mathbf{M} \rightarrow \Delta = 0$). It is also possible to observe that the random "noise" has a significant effect on the probability of failure.

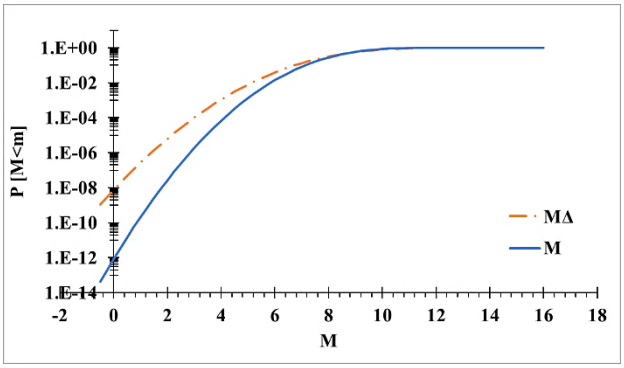

Figure 4. Cumulative distribution function of the margin of safety for case 1, with site characterization simulation.

Table 1 lists the results of the cases considered in this study. It shows that the probability of failure increases with the scale of fluctuation. There are clear differences in the results of the first (***1st sc.***) and the second (***2nd sc.***) scenarios considered. The probability of failure is substantially lower in the first scenario in both cases 1 and 2. The difference between the two scenarios is much greater when no random "noise" is considered.

Figure 5 presents the comparison between the curves of the cumulative relative frequency of cases 1 and 2, for $\Delta = 0$, 1st scenario. It shows how in the first case the values remain closer to the overall mean value of M, therefore with a lower probability of failure. This suggests that, with greater spatial variability (smaller θ), the mean values of ground properties along the slip surface in the generated statistical meshes are closer to its overall mean value. As the scale of fluctuation increases, the spatial distribution of ground properties approximates a

homogeneous state ($\theta \rightarrow \infty$). Therefore, the mean values of the properties in the statistical meshes along the slip surface exhibit a growing divergence from the overall mean value. When the spatial variability of shear strength properties is not considered in probabilistic analysis, the probability of failure is considerably higher (case 4).

Table 1. Results of the probabilistic analyses.

Case	θ_x	θ_y	p_f			
			$\Delta = 0^1$		$\Delta \neq 0^2$	
	(m)	(m)	*1st sc.*[3]	*2nd sc.*[4]	*1st sc.*[3]	*2nd sc.*[4]
1[5]	30	1	8.4×10^{-13}	2.2×10^{-9}	8.3×10^{-9}	3.8×10^{-7}
2[5]	50	3	5.8×10^{-8}	3.4×10^{-5}	2.0×10^{-6}	1.2×10^{-4}
3[5]	80	80	--	3.0×10^{-3}	--	4.6×10^{-3}
4[6]	∞	∞	--	2.7×10^{-3}	--	4.5×10^{-3}

[1]without random noise; [2]with random noise; [3]first scenario; [4]second scenario; [5]RFELA analysis; [6]FELA analysis.

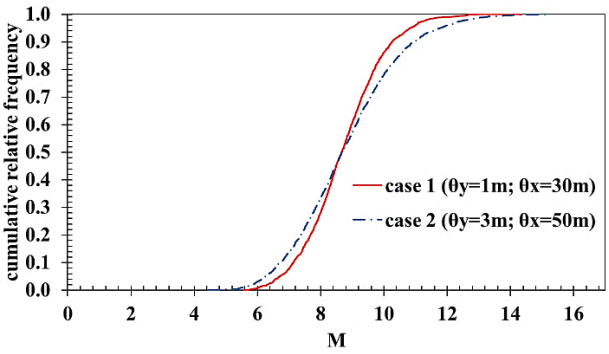

Figure 5. Example of the cumulative distribution function of the margin of safety, cases 1 and 2 (1st scenario; Δ=0).

When the scale of fluctuation is very high, $\theta = 80$ m (case 3), the probability of failure is of the same order of magnitude as the analysis with $\theta \rightarrow \infty$ (case 4). This is a consequence of the homogenization of the mesh caused by the low spatial variability.

These results demonstrate that when performing probabilistic analyses of unsupported cuts, it is important to consider the spatial variability of soil properties. It also shows the clear benefits of performing site characterization, for determining the characteristic value, rather than assuming complete knowledge of the grounds' properties, even in this case, where that knowledge was used to generate the samples themselves.

8 CONCLUSIONS

The degree of knowledge of a site's properties plays an important role in reliability analyses due to the influence of uncertainty on the probability of failure. The results show that the simulations of site characterization have a substantial effect on the probability of failure; in every case studied it decreased the value obtained. The use of the characteristic values obtained from the simulated site characterization has emphasized its importance in the probabilistic analysis of unsupported cuts, even when there is prior knowledge of the ground properties.

Uncertainty in the actions has a major impact on the probability of failure, as its effect resulted in a clear reduction of its value for both scenarios.

Spatial variability of ground properties, within a realistic range, has a considerable influence on the probability of failure. Neglecting it can lead to an overestimation of the probability of failure.

The significance of the correlation between c' and ϕ' in probabilistic analyses of unsupported cuts on spatially variable soils is an important aspect to ponder, and its effect is the subject of further study.

ACKNOWLEDGEMENTS

The first author acknowledges the support from FCT through the PhD scholarship with reference PRT/BD/151571/2021.

REFERENCES

Baecher, G. B. and Christian, J. T. (2003). *Reliability and Statistics in Geotechnical Engineering*. John Wiley & Sons. https://www.researchgate.net/publication/247385445.

Bond, A. and Harris, A. (2006). *Decoding Eurocode 7*. CRC Press. https://doi.org/10.1201/9781482265873

Cami, B., Javankhoshdel, S., Phoon, K.-K. and Ching, J. (2020). Scale of Fluctuation for Spatially Varying Soils: Estimation Methods and Values. ASCE-ASME *Journal of Risk and Uncertainty in Engineering Systems, Part A: Civil Engineering*, 6(4), 03120002. https://doi.org/10.1061/ajrua6.0001083.

Cho, S. E. (2007). Effects of spatial variability of soil properties on slope stability. *Engineering Geology*, 92(3–4), 97–109. https://doi.org/10.1016/j.enggeo.2007.03.006.

Chok, Y. H., Jaksa, M. B., Griffiths, D. V., Fenton, G. A. and Kaggwa, W. S. (2015). Probabilistic analysis of a spatially variable c'-ϕ' slope. *Australian Geomechanics Journal*, 50(2), 17–27. http://random.engmath.dal.ca/fenton/pubs/journal/2015/.

Christian, J. T. (2004). Geotechnical Engineering Reliability: How Well Do We Know What We Are Doing? *Journal of Geotechnical and Geoenvironmental Engineering*, 130(10), 985–1003. https://doi.org/10.1061/(ASCE)1090-0241(2004)130:10(985).

EN 1997-1. (2004). Eurocode 7: Geotechnical design - Part 1: General rules. CEN, European Committee for Standardization.

Fenton, G. A. and Griffiths, D. V. (2008). *Risk assessment in geotechnical engineering*. John Wiley & Sons.

Frank, R., Bauduin, C., Driscoll, R., Kavvadas, M., Krebs Ovesen, N., Orr, T., Schuppener, B. and Gulvanessian H. (2004). Designers' guide to EN 1997-1 Eurocode 7: Geotechnical design - General rules. Thomas Telford. https://www.icevirtuallibrary.com/doi/book/10.1680/dgte7.31548.

Griffiths, D. V., Huang, J. and Fenton, G. A. (2009). Influence of Spatial Variability on Slope Reliability Using 2-D Random Fields. *Journal of Geotechnical and Geoenvironmental Engineering*, 135(10), 1367–1378. https://doi.org/10.1061/(ASCE)GT.1943-5606.0000099.

Huang, J. and Griffiths, D. V. (2011). Observations on FORM in a simple geomechanics example. *Structural Safety*, 33(1), 115–119. https://doi.org/10.1016/j.strusafe.2010.10.001

ISSMGE-TC304. (2021). State of the art review of inherent variability and uncertainty in geotechnical properties and models. http://140.112.12.21/issmge/tc304.htm?=6.

Ji, J., Liao, H. J. and Low, B. K. (2012). Modeling 2-D spatial variation in slope reliability analysis using interpolated autocorrelations. *Computers and Geotechnics*, 40, 135–146. https://doi.org/10.1016/j.compgeo.2011.11.002.

Martin, C. M. (2011). The use of adaptive finite-element limit analysis to reveal slip-line fields. *Géotechnique Letters*, 1(2), 23–29. https://doi.org/10.1680/geolett.11.00018.

McKay, M. D., Beckman, R. J. and Conover, W. J. (1979). Comparison of three methods for selecting values of input variables in the analysis of output from a computer code. *Technometrics*, 21(2),239–245. https://doi.org/10.1080/00401706.1979.10489755.

Olsson, A., Sandberg, G. and Dahlblom, O. (2003). On Latin hypercube sampling for structural reliability analysis. *Structural Safety*, 25(1), 47–68. https://doi.org/10.1016/S0167-4730(02)00039-5.

Phoon, K.-K. and Kulhawy, F. H. (1999). Characterization of geotechnical variability. *Canadian Geotechnical Journal*, 36(4), 612–624. https://doi.org/https://doi.org/10.1139/t99-038.

Simões, J. T., Neves, L. C., Antão, A. N. and Guerra, N. M. C. (2014). Probabilistic analysis of bearing capacity of shallow foundations using three-dimensional limit analyses. *International Journal of Computational Methods*, 11(02), 1342008. https://doi.org/10.1142/S0219876213420085.

Simões, J. T., Neves, L. C., Antão, A. N. and Guerra, N. M. C. (2020). Reliability assessment of shallow foundations on undrained soils considering soil spatial variability. *Computers and Geotechnics*, 119, 103369. https://doi.org/10.1016/j.compgeo.2019.103369.

Vicente da Silva, M. and Antão, A. N. (2013). Programa mechpy. Available at: http://geocluster.dec.fct.unl.pt/mechpy/, accessed:22/10/2023.

Vicente da Silva, M., Deusdado, N. and Antão, A. N. (2020). Lower and upper bound limit analysis via the alternating direction method of multipliers. *Computers and Geotechnics*, *124*, 103571. https://doi.org/10.1016/j.compgeo.2020.103571.

Yang, R., Huang, J. and Griffiths, D. V. (2022). Optimal geotechnical site investigations for slope reliability assessment considering measurement errors. *Engineering Geology*, 297. https://doi.org/10.1016/j.enggeo.2021.106497.

Proceedings of the XVIII ECSMGE 2024
GEOTECHNICAL ENGINEERING CHALLENGES
TO MEET CURRENT AND EMERGING NEEDS OF SOCIETY
© 2024 the Authors
ISBN 978-1-032-54816-6
DOI 10.1201/9781003431749-364
Open Access: www.taylorfrancis.com, CC BY-NC-ND 4.0 license

ECSMGE 24
XVIII EUROPEAN CONFERENCE ON SOIL MECHANICS AND GEOTECHNICAL ENGINEERING

Exploring soil mechanics laboratory tests: accuracy, discrepancies, and implications

Exploration des tests de laboratoire de mécanique des sols: précision, écarts et implications

J. Rohac*
Charles University, Prague, Czech Republic; Czech Geological Survey, Prague, Czech Republic
**jakub.rohac@natur.cuni.cz*

ABSTRACT: In this paper, a summary of the study on the accuracy of routine soil mechanics laboratory tests and their implications for engineering geologists is presented. The shear strength and physical properties of soils, all material parameters, which should yield consistent results across different laboratories for a given soil were examined. The accuracy of laboratory test results can be influenced by various factors, including the thoroughness of reconstituted slurry preparation, the choice of the apparatus or test method, or discrepancies in the processing of tests by the laboratory itself. To investigate this issue, several samples of fine-grained soils were submitted to 3 different soil mechanics laboratories. The findings revealed significant discrepancies in the results obtained. For instance, the determination of the clay fraction through grain size distribution exhibited differences of up to 43% between two laboratories (22% versus 65%). Similarly, significant variations were observed in the determination of shear strength parameters, where the critical friction angle differed by 8° on a single soil (20.5° versus 28.5°). These discrepancies have practical implications, particularly when considering numerical modelling of slope stability what can lead to unrealistic conclusions. This was demonstrated through a parametric study of a model landslide, which yields varying results for the factor of safety between 1 to almost 3. Overall, this study emphasizes the importance of accurate and consistent laboratory test results in soil mechanics across different laboratories. By addressing the factors influencing accuracy increases the reliability and practical implications of soil mechanics testing. Furthermore, given the inconsistencies in the results, the utility of correlation equations as a valuable tool for estimating shear strength of soils is demonstrated.

RÉSUMÉ: Dans cet article, un résumé de l'étude sur la précision des tests de mécanique des sols réalisés en laboratoire et leurs implications pour les géologues du génie est présenté. La résistance au cisaillement et les propriétés physiques des sols, tous des paramètres matériels qui devraient fournir des résultats cohérents dans différents laboratoires pour un sol donné, ont été examinés. La précision des résultats des tests de laboratoire peut être influencée par divers facteurs, notamment l'exhaustivité de la préparation des suspensions reconstituées, le choix de l'appareil ou de la méthode d'essai, ou les écarts dans le traitement des tests par le laboratoire lui-même. Pour étudier cette question, plusieurs échantillons de sols fins ont été soumis à 3 laboratoires de mécanique des sols différents. Les résultats ont révélé des écarts significatifs dans les résultats obtenus. Par exemple, la détermination de la fraction argileuse par la distribution granulométrique présentait des différences allant jusqu'à 43 % entre deux laboratoires (22 % contre 65 %). De même, des variations significatives ont été observées dans la détermination des paramètres de résistance au cisaillement, où l'angle de frottement critique différait de 8° sur un seul sol (20.5° contre 28.5°). Ces écarts ont des implications pratiques, notamment lors de la modélisation numérique de la stabilité des pentes, ce qui peut conduire à des conclusions irréalistes. Cela a été démontré à travers une étude paramétrique d'un glissement de terrain modèle, qui donne des résultats variant entre un facteur de sécurité de 1 à presque 3. Dans l'ensemble, cette étude souligne l'importance de résultats précis et cohérents des tests de laboratoire en mécanique des sols dans différents laboratoires. En abordant les facteurs influençant la précision, on augmente la fiabilité et les implications pratiques des tests de mécanique des sols. De plus, étant donné les incohérences des résultats, l'utilité des équations de corrélation comme outil précieux pour estimer la résistance au cisaillement des sols est démontrée.

Keywords: Laboratory testing; soil mechanics; shear strength, estimation of friction angle.

1 INTRODUCTION

Shear strength parameters and physical index properties are key soil conditions for reliable stability analyses. This study is mainly focused on the accuracy of the results of basic soil mechanics tests in the everyday practice of commercial laboratories in Czech Republic. Specific cases that involve possibly different results obtained from testing the same soil samples in three different soil mechanics laboratories are discussed. The aim is to quantify the sources of

differences, which may be attributed to various factors such as the type of testing equipment used, the correctness and precision of the laboratory tests procedure, and/or the laboratory's ability to correctly process the data obtained from the tests. The determination of shear strength parameters in the laboratory is the preferred method, but in this case it's possible to estimate them or/and check their correctness based on the correlation equations with some of the soil index properties. Numerous correlations have been established to estimate shear strength of cohesive soil based on liquid limit w_L (e.g. Stark and Eid, 1994), on the plasticity index I_P (Kenney, 1959, Equation (1); Kanji, 1974, Equation (3); Wood, 1990, Equation (2)), or on the clay fraction percentage c.f. (Skempton, 1964). Rohac et al. (2020) concluded that the best predictor for estimating of both shear parameters is I_P and preliminary evaluation by empirical correlations can be useful in the engineering practice. The shear strength parameters results differences' impact is demonstrated through a parametric study of slope stability using the geotechnical software Geo 5 considering the limit values of shear strength parameters for the same sample from the shear zone.

2 MATERIAL AND METHODS

2.1 Laboratories

To assess the accuracy of the results 6 soil samples were sent to 3 selected soil mechanics laboratories in the Czech Republic. All these laboratories are widely used for commercial purposes, in this study labelled as lab A, B and C. Shear strength laboratory tests were also performed by the authors of the study for comparison and are labelled as *This study*.

2.2 Soil samples

The soil samples consisted of 2 natural clays and refined kaolin and bentonite. The natural samples (labelled 1002 and 1009) were taken from the landslide-prone area of Prackovice in the Czech Republic during borehole investigation. The goal was to study not only the variation in results between different laboratories but also the differences within the same laboratory. Therefore, we sent both natural clay samples in two forms as thoroughly homogenized reconstituted slurry labelled as sample M and the same soil as dried core pieces from the borehole labelled as sample S (see Figure 1). In the case of the dried core, each laboratory had to prepare the reconstituted samples themselves, while reconstituted slurry samples (M) were prepared by the authors according to Burland (1990). This way, any potential influence of sample preparation on the results of laboratory tests can be monitored. The second group of samples included refined kaolin from Kaolin Malaysia Sdn Bhd labelled as KAOL and refined bentonite from the Černý vrch locality from Keramost, a.s., Czech Republic, labelled as BENT. These soils were chosen based on their different and in literature well studied physical properties (e.g. Sun et al., 2019; Duque et al., 2022). These samples were sent to the laboratories as dry powder.



Figure 1. Natural clay samples, both in two forms: slurry (M) and dried core (S).

2.3 Properties and parameters

In the laboratories, the physical properties of soils were determined, such as the liquid limit (w_L, determined by Casagrande cup in lab A and B, by cone penetration test in lab C), plastic limit (w_P), from which the plasticity index ($I_P = w_L - w_P$) was derived. Additionally, the grain size curve and the percentage of clay fraction (c.f.), defined as particles <0.002 mm were analysed. The shear strength parameters were also determined by different apparatuses depending on laboratory. Authors and lab A determined φ'_{cr} by triaxial CIUP test, while lab A, B and C used direct shear test. In the case of φ'_r, the authors and laboratory A determined it by ring shear test, laboratories A and B by direct shear box test.

The values of I_P from laboratories were used for estimation and/or verification of critical friction angle and residual friction angles based on following correlation equations from literature:

$$\varphi'_{cr} = 0.81 - 0.223 \log I_p \quad (1)$$

$$\sin \varphi'_{cr} = 0.35 - 0.1 \ln(I_p/100) \quad (2)$$

$$\varphi'_r = 46.6 I_P^{-0.446} \quad (3)$$

where φ'_{cr} and φ'_r are the critical and residual friction angles and I_P (%) is the plasticity index. These corelations were selected because of their widespread use and large dataset over which they were calibrated. Results of these estimations are compared with results obtained thru determination in the laboratories.

2.4 Slope stability

The most controversial shear strength results obtained from the laboratories were used in stability analysis of the well-studied landslide that disrupted the D8 highway in the Czech Republic in 2013 (Roháč et al., 2020). The factor of safety (FS) was analysed with the Geo 5 Software (Fine Ltd.) using the Morgenstern-Price method. The landslide condition corresponds to post-collapse, with FS≈1, where the φ'_r was used (Skempton, 1964, Palladino and Peck, 1972). The mechanical and geological setting of the soil from the slip surface was analogous to soil samples used in this study (Valečka, 1989).

3 RESULTS

3.1 Properties and parameters

All laboratory results are shown in Figure 2. The results of c.f. within a single sample (1009-S) reached a difference of up to 41% (22 vs. 63%). A systematic error is evident in the values: Lab A consistently (5 out of 6 cases) determined the lowest c.f. value, while lab B consistently reported the highest c.f. value for the same sample. Similar discrepancies were also shown in the determination of w_L, where lab A always determined higher values than lab B, both using the Casagrande cup method, lab C uses the cone penetration test. These differences were also reflected in the results of the plasticity index.

Furthermore, variations were noted in the results even within the same laboratory for samples S and M. Samples S consistently yielded lower c.f. values, likely due to incomplete soil mixing in the given laboratory. Significant differences were also observed in the results related to soil shear strength. For example, φ'_{cr} for sample 1002 ranged from 20.5°to 28.5°. It was observed that the direct shear test provided the result of shear strength higher by up to 8° compared to the triaxial device. The tendency depending on the shear apparatus used is consistent with Kostkanová and Herle (2012).

In the case of φ'_r , it was observed that the ring shear test provided the lowest value for the residual friction angle (lower by up to 6° compared to the direct shear test, 8.7 vs. 14.7°), consistently with literature (e.g. Vithana et al., 2012).

In the case of strength determination in lab B, parameters with a non-zero cohesion were obtained for both, residual and critical state shear strength (e.g., for sample 1002-S: $\varphi'_r = 3.5°$, $c_r = 44$ kPa). Consequently, these erroneous results were re-evaluated by the authors of this study in all cases using the dataset from the laboratory test protocols (e.g., for sample 1002-S: $\varphi'_r = 11.6°$).

The results of I_P were used for estimating of φ'_{cr} and φ'_r. Figure 2 also shows these estimations and compares them with the laboratory-determined results. The shear strength estimates for φ'_{cr} closely aligned with the results of triaxial tests for both sets of samples. The estimates of φ'_r in both cases overestimated values obtained from ring shear tests. This can be explained by the fact that the used eq. (3) was calibrated on the data from direct shear tests only (Kanji, 1973).

3.2 Slope stability

Table 1 illustrates the impact of different φ'_r results on FS of the analyzed slope.

Table 1. Differences in factor of safety FS.

Lab. test	φ'_r (kPa)	c_r (kPa)	FS
Ring shear	8.3	0	1.08
Direct shear	11.6	0	1.46
Direct shear	3.5	44	2.84
Equation (3)	9.5	0	1.22

Since the landslide condition corresponds to post-collapse, with an approximate FS of 1, the FS value is taken as a basis for evaluating the accuracy of the laboratory results and estimates of φ'_r. The most reliable result is determined by ring shear apparatus (FS=1.08). Conversely, an erroneously evaluated direct shear test with non-zero cohesion offered an unusually high FS value (FS=2.84), confirming its unsuitability for application in slope stability analysis. Interestingly, upon re-evaluating the data from this same test in accordance with the theory of soil mechanics, a more meaningful result was obtained (FS=1.46). As expected, the direct shear test reached higher φ'_r compared to the result obtained from the ring shear test. Lastly, the use of correlation equations for strength estimation proved to be very beneficial in this case, resulting in an FS value of 1.22.

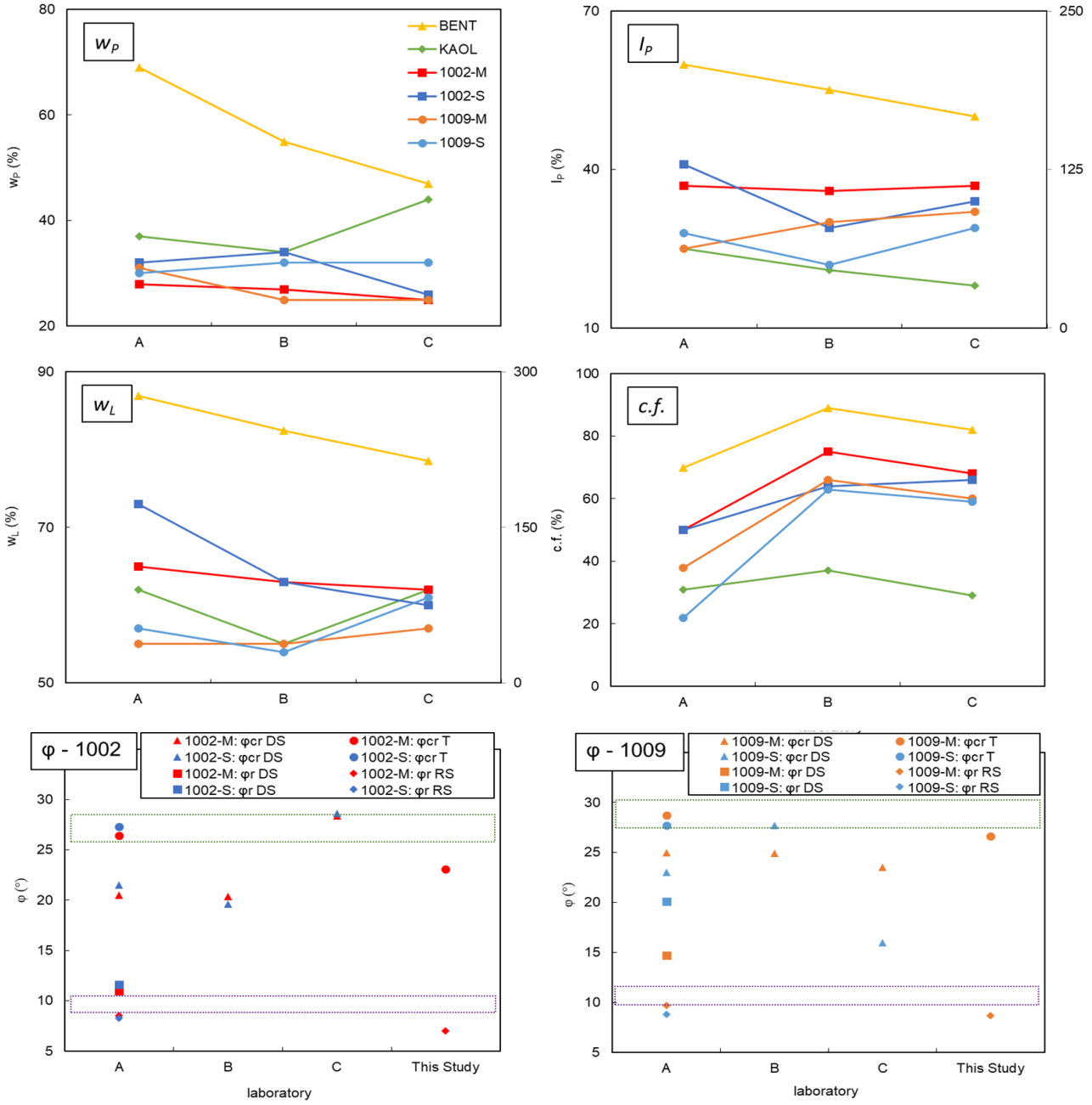

Figure 2. Results of all properties and parameters corresponding to the source laboratory (A, B, C) or This study; in graph for I_P and w_L – sample BENT (yellow) corresponds to the axis on the right side of the given graph; in graph for φ-1002 and φ-1009, results of Direct Shear tests (DS), Ring Shear tests (RS) and Triaxial CIUP tests (T); estimations of φ'_{cr} by combination of Equation (1) and Equation (2) labelled with green area, estimations of φ'_r by Equation (3) labelled with purple area.

4 CONCLUSIONS

- The slurry preparation process, specifically the level of thoroughness in mixing, significantly impacted the results obtained through subsequent research methods.
- A systematic error of laboratories in measurements was identified, particularly noticeable during the determination of clay fraction percentages and liquid limits.
- The selection of the shear test device type had a notable impact on the results of the internal friction angle.
- The inaccuracies in determining the internal friction angle had a significant impact on the factor of safety values for a landslide slope, potentially resulting in misleading conclusions in engineering geological surveys.

- Correlation equations can be a useful tool for verifying the results of the shear strength laboratory tests.

ACKNOWLEDGEMENTS

This research was supported by the Johannes Amos Comenius Programme (P JAC), project No. CZ.02.01.01/00/22_008/0004605, Natural and anthropogenic georisks and by Project RENS - Rock Environment and Natural Resources No. SS02030023 - TAČR (Technology Agency of the Czech Republic).

REFERENCES

Burland, J. B. (1990). On the compressibility and shear strength of natural clays, *Géotechnique* 40 (3), 329-378. https://doi.org/10.1680/geot.1990.40.3.329.

Duque, J., Roháč, J., Mašín, D., Najser, J. (2022). Experimental investigation on Malaysian kaolin under monotonic and cyclic loading: inspection of undrained Miner's rule and drained cyclic preloading, *Acta Geotechnica,* 17(11), 4953-4975. https://doi.org/10.1007/s11440-022-01643-0.

Kanji, M. A. (1973). *Resistência ao cisalhamento de contactos solo-rocha,* Doctoral Thesis, Universidade de São Paulo, Brazil. https://doi.org/10.11606/T.44.2016.tde-07072016-085900.

Kanji, M. A. (1974). The relationship between drained friction angles and Atterberg limits of natural soils, *Geotechnique*, 24(4), 671-674. https://doi.org/10.1680/geot.1974.24.4.671.

Kenney, T. C. (1959). Discussion of "geotechnical properties of glacial Lake clays", *Journal of the Soil Mechanics and Foundations Division*, 85(3), 67-79 https://doi.org/10.1061/JSFEAQ.0000201.

Kostkanová, V., Herle, I. (2012). Measurement of wall friction in direct shear tests on soft soil, *Acta Geotechnica,* 7, 333-342. https://doi.org/10.1007/s11440-012-0167-6.

Palladino, D. J., Peck, R. B. (1972). Slope failures in an overconsolidated clay, Seattle, Washington, *Geotechnique,* 22(4), 563-595. https://doi.org/10.1680/geot.1972.22.4.563.

Roháč, J., Scaringi, G., Boháč, J., Kycl, P., Najser, J. (2020). Revisiting strength concepts and correlations with soil index properties: insights from the Dobkovičky landslide in Czech Republic, *Landslides*, 17, 597-614. https://doi.org/10.1007/s10346-019-01306-4.

Skempton, A. W. (1964). Long-term stability of clay slopes, *Geotechnique*, 14(2), 77-102. https://doi.org/10.1680/geot.1964.14.2.77.

Stark, T. D., Eid, H. T. (1994). Drained residual strength of cohesive soils, *Journal of Geotechnical Engineering*, 120(5), 856-871. https://doi.org/10.1061/(ASCE)0733-9410(1994)120:5(856).

Sun, H., Mašín, D., Najser, J., Neděla, V., Navrátilová, E. (2019). Bentonite microstructure and saturation evolution in wetting-drying cycles evaluated using ESEM, MIP and WRC measurements, *Géotechnique,* 69(8), 713-726. https://doi.org/10.1680/jgeot.17.P.253.

Valečka, J. (1989). Základní geologická mapa ČSSR 1:25000 (Basic geological map of the CSSR 1:25000), pp. 02-233, Jílové, Czechoslovak Geological Survey, Prague, Czech Republic.

Vithana, S. B., Nakamura, S., Gibo, S., Yoshinaga, A., & Kimura, S. (2012). Correlation of large displacement drained shear strength of landslide soils measured by direct shear and ring shear devices, *Landslides*, 9(3), 305-314. https://doi.org/10.1007/s10346-011-0301-9.

Wood, D. M. (1990). *Soil behaviour and critical state soil mechanics*, Cambridge university press, United Kingdom. https://doi.org/10.1017/CBO9781139878272.

Proceedings of the XVIII ECSMGE 2024
GEOTECHNICAL ENGINEERING CHALLENGES
TO MEET CURRENT AND EMERGING NEEDS OF SOCIETY
© 2024 the Authors
ISBN 978-1-032-54816-6
DOI 10.1201/9781003431749-365
Open Access: www.taylorfrancis.com, CC BY-NC-ND 4.0 license

ECSMGE 24
XVIII EUROPEAN CONFERENCE ON SOIL MECHANICS AND GEOTECHNICAL ENGINEERING

Assessment of seismic ground amplification at the Chieti courthouse site

Évaluation de l'amplification sismique du sol au palais de justice de Chieti

N. Salvatore*
University of Catania, Italy

A. Pagliaroli, F. Di Buccio, A. Pizzi, S. Amoroso
University of Chieti-Pescara, Italy

**nadia.salvatore@phd.unict.it*

ABSTRACT: During the 2009 L'Aquila earthquake (M_W = 6.1), the Chieti courthouse was partially damaged by the ground shaking. To better understand the reasons why the damage affected essentially the southern portion of the structure, a study on local seismic response effects was carried out. The historical center of Chieti is located on the top of a hill (330 m a.s.l.), in the Periadriatic sector of Central Apennines, consisting of Pleistocene clays to sands and conglomerates deposits of the Mutignano formation (FMT), carved by Pescara and Alento rivers. The courthouse area is located above landfill deposits rich in historical artifacts, up to 10 m thick, covering sub-horizontal sandy-conglomerate deposits, about 30 m thick, which in turn overlay mostly pelitic lithofacies of the FMT several hundred meters thick. In this study, we reconstruct a geotechnical model of the Chieti hill mainly through *in-situ* (boreholes, SPT, DMT and SDMT) tests. Moreover, we performed a 2D FEM site response analysis to evaluate the ground motion spatial pattern in the courthouse site in terms of main ground motion parameters. An input motion representative of the 2009 L'Aquila earthquake was derived through a deconvolution of the 2009 recordings at the RAN accelerometric station of Chieti Scalo and applied at the seismic bedrock. Physical phenomena responsible for site effects are discussed by comparing 1D and 2D site response analyses at selected points.

RÉSUMÉ: Lors du séisme de 2009 à L'Aquila (M_W = 6.1), le palais de justice de Chieti a été partiellement endommagé par les secousses du sol. Pour mieux comprendre les raisons pour lesquelles les dommages ont affecté essentiellement la partie sud de la structure, une étude sur les effets de la réponse sismique locale a été réalisée. Le centre historique de Chieti est situé au sommet d'une colline (330 m d'altitude), composé d'argiles aux sables et aux dépôts de conglomérats, sculptés par les rivières Pescara et Alento. La zone du palais de justice est située au-dessus de dépôts d'enfouissement riches en artefacts historiques, jusqu'à 10 m d'épaisseur, couvrant des dépôts sub-horizontaux de conglomérat sableux, d'environ 30 m d'épaisseur, qui recouvrent à leur tour les lithofacies principalement pélitiques. Dans cette étude, nous avons procédé à une reconstruction du modèle géotechnique du col de Chieti obtenu par des essais in situ. De plus, nous avons effectué une analyse 2D FEM de la réponse du site pour évaluer le modèle spatial du mouvement du sol sur le site du palais de justice en termes de paramètres principaux du mouvement du sol. Un mouvement d'entrée représentatif du tremblement de terre de L'Aquila en 2009 a été obtenu par déconvolution des enregistrements de 2009 à la station accélérométrique RAN de Chieti Scalo et appliqué au socle rocheux sismique. Les phénomènes physiques responsables des effets sur le site sont abordés en comparant les analyses de réponse 1D et 2D du site à des points sélectionnés.

Keywords: 2009 L'Aquila earthquake; site response analysis; in-situ tests; numerical modelling.

1 INTRODUCTION

In 2009 a M_W 6.1 earthquake affected the area of L'Aquila, Central Italy, causing 309 victims and extensive damage to buildings and infrastructure. During this event, the courthouse of Chieti, an L-shaped masonry 3-storeys building, approximately 70 km far from the epicenter, was partially damaged. In this respect, a detailed site investigation of seismic dilatometer (SDMT) tests, foundation boreholes and cyclic laboratory tests were performed in 2011 on Chieti hill to restore this historical building. According to Amoroso et al. (2013), the geotechnical campaign allowed to detect weak zones in the Southern part of the building when compared to the Northern part of the structure in terms of constrained modulus and horizontal stress index in the upper 8 m of depth. This information resulted in agreement with the earthquake observations since the structure appeared to be considerably fissured in its Southern part, while approximately intact in the Northern area.

In this study, we reconstruct a geotechnical model of the Chieti hill mainly through the available in-situ (boreholes, SPT, DMT and SDMT) tests. Moreover,

we performed a 2D FEM site response analysis to evaluate the ground motion spatial pattern in the courthouse site. An input motion representative of the 2009 L'Aquila earthquake was derived through a deconvolution of the 2009 recordings at the RAN accelerometric station of Chieti Scalo and applied at the seismic bedrock. Physical phenomena responsible for site effects are discussed by comparing 1D and 2D site response analyses at selected points.

2 GEOLOGICAL SETTING

The historical center of Chieti is located on the top of a hill (330 m a.s.l.), in the Periadriatic sector of Central Apennines, consisting of Pleistocene clays to sands and conglomerates deposits of the Mutignano formation (FMT), carved by Pescara and Alento rivers. The courthouse area is located above landfill deposits rich in historical artifacts, up to 10 m thick, covering sub-horizontal sandy-conglomerate deposits, about 30 m thick, which in turn overlay pelitic-sandy (mostly grey clay) lithofacies of the FMT (Fig. 1a).

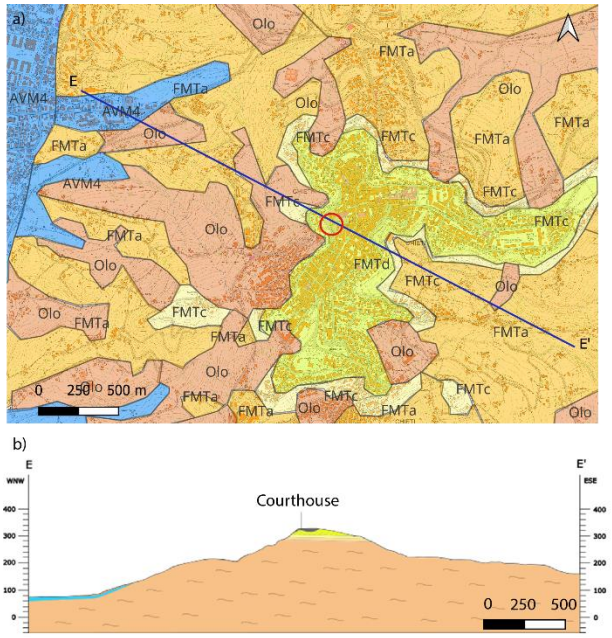

Figure 1. Geological map of Chieti (modified from CARG 361 Chieti https://www.isprambiente.gov.it/Media/carg/361_CHIETI/Foglio.html); FMT is Mutignano formation, when d is the sandy-conglomerate lithofacies, c is the sandy-pelitic lithofacies, and a is the pelitic-sandy lithofacies; the blue line depicted the EE' cross section; the red circle identifies the courthouse area (a). Cross section EE'; landfill deposits are represented only in the courthouse area and their position and thickness derived from available in-situ tests (b).

The geological cross section (Fig. 1b) shows a simplified version of the stratigraphic setting of Chieti hill. Landfill and Holocene slope deposits are only reported in the area of the Courthouse, due to the availability of data from boreholes, SDMT, DMT and SPT performing in previous studies. The seismic response is therefore analyzed in detail in the following only in this area.

3 SUBSOIL MODEL

The soil characterization for site response analyses was essentially based on the results of six seismic dilatometer (SDMT) tests, in virgin soil and in boreholes filled with sand, reaching a depth up to 50 m from ground level, carried out around the Courthouse (Amoroso et al., 2013). Average values for each lithotype were defined (Table 1); the Poisson ratio was assumed as 0.35 for all material with the exception of grey clay (0.43). Nonlinear normalized shear modulus (G/G_0) and damping (D) curves from literature were employed (Table 1). Cyclic simple shear tests were available for grey clays; however, given the high stiffness, a visco-elastic linear behaviour has been assumed for these materials. As matter of fact, the grey clays are characterised by shear wave velocity (V_S) values equal to 450-500 m/s in the upper part increasing with depth to 600 m/s as reported by down-hole (DH) tests available in the area of Chieti campus of the University of Chieti-Pescara (Italy) at the toe of the hill. No information is available on deep Vs profile in the FMTa. For this reason, the grey clays were characterized with an average value of 600 m/s and assumed as seismic bedrock in the deconvolution and direct site response analyses reported in the following.

Table 1. Reference subsoil model for Chieti hill with related mechanical parameters for each lithotype used in the analyses.

	Lithotype	γ (kN/m³)	Vs (m/s)	Nonlinear curves
1	Landfills (anthopogenic deposit)	17.1	260	Rollins et al. 1998 average curves
2	colluvium	18.7	400	Amoroso et al. 2015
3	Alluvial soils	18.5	300	Seed e Idriss 1970 upper bound
4	Silty sands	20.0	560	Seed e Idriss 1970 upper bound
5	Silty clay	20.6	700	Linear D=1%
6	Dense sands	20.6	900	Linear D=1%
7	FMTa (grey clays)	20.5	600	-

4 SEISMIC RESPONSE AT THE CHIETI COURTHOUSE

4.1 Definition of input motion

For the definition of the seismic input, reference was made to the L'Aquila earthquake recordings of April 6, 2009 earthquake at the CHT permanent station located at the Chieti campus of the University of Chieti-Pescara. The subsoil model at the station (Table 2) has been defined using existing borehole logs and DH tests in the area as well as multichannel analysis of surface waves (MASW) and single station noise measurements carried out at CHT in the framework of the present study.

Table 2. Subsoil model at CHT for deconvolution analyses (h: thickness of soil layers).

Lithotype	h (m)	γ (kN/m³)	Vs (m/s)	Nonlinear curves
cover	2	17.1	160	Rollins et al. 1998 avg.
Alluvial soils (sands and silts)	10	18.5	280	Seed e Idriss 1970 upper b.
	8	18.5	310	Seed e Idriss 1970 upper b.
Alluvial soils (gravels)	6	20.0	460	Rollins et al. 1998 avg
Grey clays	-	20.5	600	-

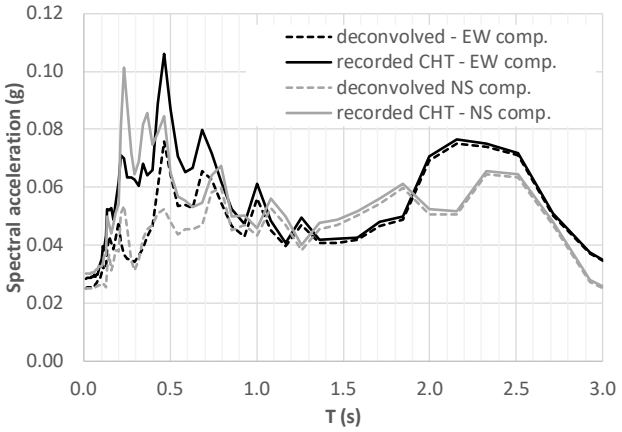

Figure 2. Recorded vs deconvoluted response spectra for April 6, 2009 earthquake.

Deconvolution analyses were therefore executed to derive the motion at seismic bedrock outcropping starting from the CHT recorded surface time history accelerations. Deconvolution analyses were executed with the 1D equivalent linear STRATA code (Kottke and Rathje, 2008) working in the frequency domain. It must be observed that the position of the real seismic bedrock (i.e. a material characterized by V_S equal or higher than 800 m/s) is unknown and the FMTa formation (mostly grey clays) at the bottom of the alluvial cover (V_S=600 m/s) were assumed as bedrock. Recorded and deconvolved response spectra are reported in Figure 2: as the amplification function is characterized by peaks at 2-4 Hz and 10-15 Hz, great reduction in spectral amplitude at outcropping bedrock is observed in the medium-to-low period range (i.e. below 0.5s).

4.2 2D seismic response analysis

Bidimensional site response analyses were carried out on the EE' cross-section (Fig. 1b) using the 2D finite element equivalent linear LSR2D code (https://www.stacec.com/). The computer code is extensively used in Italy especially for Seismic Microzonation purposes and it has been validated using other well-known 2D FEM codes like QUAD4M (Pagliaroli et al., 2020). The bedrock is constituted by the grey clays (V_S=600 m/s) and therefore the deconvolved motion has been assumed as input motion of the analyses. The physical and mechanical properties of the materials are reported in Table 1. Three control points were selected for output motions: A and B at eastern and western sides of the Courthouse, respectively and C at the location where maximum thickness of landfills is reached (Figure 3a). At these points, additional 1D STRATA analyses were also executed in order to assess the influence of morphological and topographic features on the ground motion through the 2D/1D comparison.

The comparison between 1D and 2D response is shown for node A in Figure 3; similar considerations can be made for the other nodes. The 2D analyses predicts higher spectral acceleration with respect the 1D model in the whole period range. The effects of the landfills is evident at low periods (0.1-0.2 s) where the coupling between stratigraphic and morphological effects leads to higher values in 2D analyses. At longer periods the response is essentially driven by 2D effects: in particular the amplification at 2-3s can be related to the 2D resonance of the upper part of the Chieti hill according to the model by Paolucci (2002). Other complex 2D effects take place at 0.4-0.6s.

The comparison of the 2D response in the three selected nodes (Figure 3) highlights the role of the landfills: nodes C, characterized by the higher fills thickness (around 12m) is characterized by major spectral accelerations exceeding 0.1 g in 0.15-0.25s range. Slightly higher amplitudes can be found at node B with respect to A in the same range showing ground motion variation in the Courthouse area. The spectral amplitude at 2-3s is the same in all the nodes thus confirming the 2D resonance of the hill as driving phenomena. The 2D effects at 0.4-0.6s (showing differences between A-B and C) are probably related

to topographic effects at the hill edge (A-B are closer to hill border than C) or to the buried morphology of the contact between landfill and the underlying sands.

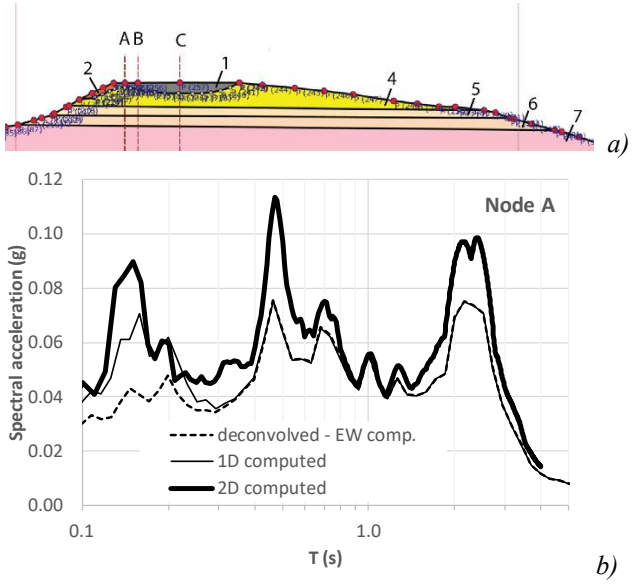

Figure 3. Stratigraphy of the courthouse area with the position of control points and lithotypes numbered as in Table 1 (a), 1D and 2D computed response spectra compared with input motion for EW component (b).

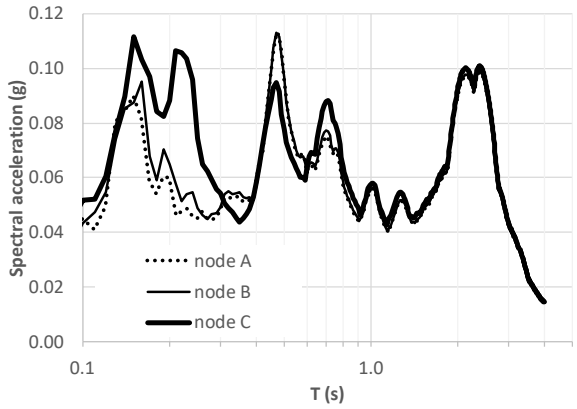

Figure 4. Response spectra computed with 2D analyses at node A-B-C for EW component.

5 CONCLUSIONS

The paper reports the results of the seismic response of Chieti hill during the April 6, 2009 earthquake which induced damage to the Courthouse historical building. The signal recorded by the CHT station at the toe of the hill was deconvoluted by means of 1D equivalent linear analyses to the outcropping of grey clays assumed as seismic bedrock of the area. *Ad hoc* MASW and single station microtremor tests were carried out for the geotechnical characterization of CHT site. The subsoil model of the Chieti hill has been reconstructed using several existing seismic dilatometer (SDMT) tests performed in the area of the Courthouse. The CHT deconvoluted signal was used as seismic input for 2D finite element modelling of the Chieti hill. The output results were processed in terms of acceleration response spectra with particular reference to the Court area where additional 1D modelling were executed, in order to highlight the 2D effects related to the buried and surficial morphology.

The comparison between 1D and 2D modelling highlighted amplification of ground motion related to stratigraphic effects of the landfill cover around 0.1s where spectral accelerations as high as 0.1g are reached. Additional 2D effects were found around 0.4-0.6s, including the fundamental period of the Courthouse, probably related to topographic effects at the hill edge and to the buried morphology. Finally, 2D resonance effects of the upper part of the hill is responsible for further amplification around 2-3 s.

The amplifications linked to the variations in thickness of landfills are relevant for the historical buildings of few floors located on the top of the Chieti hill. More efforts should be devoted to reconstruct the landfills distribution along the Chieti hill for a comprehensive seismic risk assessment of the building stock and cultural heritage of city centre.

REFERENCES

Amoroso S., Totani F., Totani G. (2013). Site characterization by seismic dilatometer (SDMT): the Justice Court of Chieti. *Proc. 18th Int. Conf. on Soil Mech. and Geotech. Eng., 2-6 Sept. 2013, Paris,* 1, 483-486, Les Presses des Ponts (eds).

Amoroso, S., Totani, F., Totani, G., Monaco, P. (2015). Local seismic response in the Southern part of the historic centre of L'Aquila. *Eng. Geol. for Society and Territory-Urban Geol., Sust. Planning and Landscape Exploitation*, Springer Int. Publ., 5(XVIII), 1097-1100, https://doi.org/10.1007/978-3-319-09048-1_208.

Kottke A. R., Rathje E. M. (2008). "Technical manual for Strata." Report No.: 2008/10. Pacific Earth. Engineering Research Center, Univ. of California, Berkeley.

Pagliaroli A., Pergalani F., Ciancimino A, Chiaradonna A., et al. (2020). Site response analyses for complex geological and morphological conditions: relevant case-histories from 3rd level seismic microzonation in Central Italy. *Bull. Earth. Eng.*, 18: 5741–5777, https://doi.org/10.1007/s10518-019-00610-7.

Paolucci, R. (2002). Amplification of earthquake ground motion by steep topographic irregularities. *Earth. Eng. Struct. Dynamics* 31, 1831-1853. https://doi.org/10.1002/eqe.192.

Rollins, K.M., Evans, M.D., Diehl, N.B., Daily III, W.D., (1998). Shear modulus and damping relationships for gravels. *J. Geotech. Geoenviron. Eng*, 124, 396–405.

Seed H, Idriss I. (1970). Soil moduli and damping factors for dynamic response analyses, *Report EERC 70-10. Earth. Eng. Research C.*, Univ. of California, Berkeley.

Proceedings of the XVIII ECSMGE 2024
GEOTECHNICAL ENGINEERING CHALLENGES
TO MEET CURRENT AND EMERGING NEEDS OF SOCIETY
© 2024 the Authors
ISBN 978-1-032-54816-6
DOI 10.1201/9781003431749-366
Open Access: www.taylorfrancis.com, CC BY-NC-ND 4.0 license

ECSMGE 24
XVIII EUROPEAN CONFERENCE ON SOIL MECHANICS AND GEOTECHNICAL ENGINEERING

EUROCODE 7 – Second generation - Interplay with Eurocode 8: Implications for ground investigation

EUROCODE 7 – Deuxième génération - Interaction avec l'Eurocode 8 Implications pour les investigations de terrain

G. Scarpelli*
Università Politecnica delle Marche, Ancona, Italy

L. Callisto
Sapienza Università di Roma, Roma, Italy

S. Foti
Politecnico di Torino, Torino, Italy

**g.scarpelli@univpm.it*

ABSTRACT: In the CEN/TC250 Programming Mandate M/515, the lack of compatibility between Eurocode 7 and Eurocode 8 was clearly addressed when directions for development of the new generation of EN 1997 and EN 1998 were outlined. In the present paper the most relevant modifications of the new Codes are illustrated outlining the inputs required by Eurocode 8, parts 1 and 5, for site categorisation and seismic geotechnical design, followed by the illustration of the new items introduced in Eurocode 7 to ensure that ground investigation and the resulting ground model properly consider seismicity between their objectives.

RÉSUMÉ: Dans le mandat de programmation M/515 du CEN/TC250, le manque de compatibilité entre l'Eurocode 7 et l'Eurocode 8 a été clairement abordé lorsque les orientations pour le développement de la nouvelle génération des EN 1997 et EN 1998 ont été définies. Dans le document, les modifications les plus pertinentes des nouveaux codes sont illustrées en présentant d'abord les entrées requises par l'Eurocode 8, parties 1 et 5, pour la catégorisation des sites et la conception géotechnique sismique, puis par l'examen des nouveaux éléments introduits dans l'Eurocode 7 pour garantir que l'investigation du sol et le modèle de sol qui en résulte prennent correctement en compte la sismicité entre leurs objectifs respectifs.

Keywords: Ground model; seismic geotechnical design; Eurocode 7; Eurocode 8; ground investigation.

1 INTRODUCTION

In the CEN/TC250 Programming Mandate M/515, the lack of compatibility between Eurocode 7 (EN 1997-1: 2004) and Eurocode 8 (EN 1998-5: 2004) was specifically addressed when directives for development of the new generation of EN 1997 and EN 1998 were given. To fulfil the Mandate, an Evolution Group 6 (EG6) was established by SC7 from which the following principles and line of actions were suggested: a) the design of a geotechnical structure is a unique process that needs to be accomplished by considering all possible boundary (e.g., loading) and environmental (e.g., seismicity) conditions since the very beginning of the design process; b) recommended design procedures must ensure a smooth transition between static and seismic design: transfer of seismic action effects to the ground should consider the possibility of permanent displacements of foundations and retaining structures and energy dissipation mechanisms in the ground; c) more emphasis is needed in both EN 1997 and EN 1998 for the assessment of seismic-dynamic properties of the ground: ground investigation covered in EN 1997-2 must include appropriate tests for seismic design (e.g.: geophysical methods for site investigation, cyclic and dynamic laboratory testing); d) verification of the seismic performance of a geotechnical structure should be possible with both approaches adopted in EN 1997, that is, Material factor approach (MFA) and Resistance factor approach (RFA).

Limiting to some relevant aspects only, the purpose of the paper is to illustrate and discuss from the specific perspective of Eurocode 7 how the Mandate

requirements have been implemented and the practical consequences for geotechnical design within the new generation of Eurocodes.

2 THE CONTRIBUTE OF EUROCODE 7 TO SEISMIC DESIGN

Reading through Part 1 and Part 5 of FprEN 1998, it is clear that prEN1997-2023, hereafter indicated as EN 1997 for simplicity, has been conceived considering also the geotechnical inputs for seismic design. Most relevant information is in fact included among the objectives of the Ground Model, that is a tool conceived to represent all basic properties of a site, specifically those not dependent from the programmed construction. The content of the Ground Model includes, but is not limited to, the following items:

- Bedrock & structural geology
- Geology & geomorphology
- Seismicity
- Hydrogeological conditions
- Geotechnical conditions

The Ground Model should be developed from the very beginning of design and progressively developed and updated with information from ground investigation (desk studies; field and laboratory investigations; information obtained with monitoring).

In FprEN 1998-1-1:2024, hereafter indicated simply as EN 1998-1, site conditions must be assessed before any quantitative evaluation of the seismic action expected at the site. With this aim, knowledge of the site geology and seismicity from regional seismic risk maps is needed; potentially active faults or other causes of permanent ground deformation and settlements, such as the presence of unstable slopes affecting the area or of potentially liquefiable soil deposits under the considered seismic action, should be identified. According to the above list, all these items are in fact the specific ingredients of the Ground Model to be progressively addressed from the beginning of the design process (JRC 2024).

In EN 1998-1, site conditions are discussed in Clause 5 for the evaluation of the seismic action. In this clause a site categorisation is proposed for simplified assessment of stratigraphic amplification. Categories are preferentially established on the basis of the profile of the shear wave velocity v_s in the ground and of the depth of the conventional seismic bedrock H_{800} (i.e., the depth at which v_s is larger than 800 m/s). According to EN 1998-1, the site may fall in one of six different categories, ranging between A and F, as described in Table 1, where $v_{s,H}$ is the equivalent shear wave velocity computed over the depth H_{800}.

Table 1. Site categorisation based on bedrock depth H_{800} and the equivalent shear wave velocity value $v_{s,H}$. (reproduced from FprEN 1998-1-1:2024).

	Ground class	**Stiff**	**Medium stiffness**	**Soft**
Depth class	$v_{s,H}$ range / H_{800} range	400 m/s ≤ $v_{s,H}$ < 800 m/s	250 m/s ≤ $v_{s,H}$ < 400 m/s	150 m/s ≤ $v_{s,H}$ < 250 m/s
very shallow	$H_{800} \leq 5$m	A	A	E
shallow	5m < $H_{800} \leq$ 30m	B	E	E
intermediate	30m < $H_{800} \leq$ 100m	B	C	D
deep	$H_{800} \geq 100$m	B	F	F

When the full set of information is not available, the normative Annex B of EN 1998-1 gives a simplified procedure to assign the site category. Such procedure relies upon a combination of qualitative and quantitative parameters, the former describing the predominant soil type and the latter its consistency, through an estimate of its stiffness range. Two more options are given by EN 1998-1 when information for site classification is incomplete: when direct measurements of v_s are not available, it is possible to estimate the v_s profile from well-established empirical correlations between v_s and geotechnical parameters or field test results; when the bedrock depth H_{800} is not known the soil category may be assigned from the equivalent value of the shear wave velocity $v_{s,H}$ and the fundamental frequency of the soil deposit f_0. Finally, the identification of the bedrock may also be obtained from geological, geophysical, or geotechnical

information, including microzonation maps. Whatever the procedure to characterise the ground is, standard or simplified, a field investigation is always needed to quantify ground properties. Such investigation shall include the identification of the soil constituting the deposit and some intrusive in situ testing (e.g. static or dynamic penetration tests, vane and pressuremeter tests or laboratory testing). With the 2nd generation of Eurocodes the geotechnical designer must keep well in mind that geotechnical seismic design needs to be supported with data collected with the ground investigation and that such data must be included in the Ground Model. This is not the case for the present version of Eurocodes, where the ground investigation for the seismic design is not explicitly included in the ground investigation for geotechnical design, resulting in a very weak link between EN 1998-5:2004 and EN 1997-2:2007 for the evaluation of ground properties.

A clear separation between the two Eurocodes can also be found in the approaches for verification of limit states. Significant steps have then been taken to implement compatibility between static and seismic geotechnical design. According to FprEN 1998-5:2024, hereafter shorted as EN 1998-5, both the Material Factor Approach (MFA) and the Resistance Factor Approach (RFA) may be used to verify that the design resistance R_d is greater or equal to the design value of the effects of actions E_d. This is not the case for the present version of EN 1998-5, that allows only verifications with MFA. Moreover, a very close link between EN 1998-5 and EN 1997-2 (2nd generation) emerges from Clause 6 of the seismic Code on ground properties. According to 6.1(2), derived and representative ground properties are explicitly considered for seismic design and their values are those indicated by the Ground Model and the Geotechnical design model respectively. Note that in the present version of EN 1998-5, a distinction between derived and characteristic values of ground properties was not considered, and design values did not appear explicitly in the code. On the contrary, with the 2nd generation of EN 1998-5, many requirements on the ground investigation are given. Among these: suggestion for measurement of the v_s profile with geophysical methods or alternatively the use of empirical correlations with standard penetration and/or static cone penetration tests. Finally, specific reference to cyclic and dynamic laboratory tests is made for a direct derivation of geotechnical properties, such as strain dependent stiffness and damping ratio. In turn, many clauses of its parts 1 and 2 provide indications on how implement the Ground model considering specific inputs for seismic design.

Criteria to design the ground investigation are given in EN 1997-2. In the preliminary investigation seismic hazard has to be addressed and determined. Moreover, within the scopes of the design investigation, seismic properties of ground are explicitly indicated in Clause 3. Criteria given for the planning of investigations in Clause 5.4.1 (4) prescribe that the extent of investigation shall cover the depth for calculation of the seismic ground response as specified in EN 1998-1 Clause 5 and EN 1998-5 Clause 6. A note to the same clause states that the Zone of Influence under cyclic, dynamic and seismic actions can be different from the one under static loading; consequently, the extent and the objectives of ground investigations must be revised accordingly. Although never actually stated in the Code, the above criteria must be reflected by the Ground Model whose extent should match the Zone of Influence that has been identified for the project and that must fully cover the volume of investigation.

The determination of ground properties for cyclic, dynamic and seismic design is addressed by EN 1997-2 Clause 10. Ground investigations should provide relevant information on:

- stress-strain response to cyclic actions, including small strain stiffness,
- energy dissipation properties,
- development of excess pore water pressures under cyclic actions,
- shear strength under cyclic action,
- post cyclic behaviour in terms of post-cyclic shear strength,
- dissipation of cyclic-induced pore water pressure, and other associated deformations,
- cyclic undrained shear strength for liquefaction assessment (see EN 1998-5).

The direct determination of the shear and compressional wave velocities is addressed by Table 10.2 of EN 1997-2 with a comprehensive list of geophysical tests followed by recommendations on their selection. Consistently with the cases considered by EN 1998-1 a list of tests to be used for indirect determination of the shear wave velocity profile is also given, with indication of the appropriate test standard to follow and of the requirements for interpretation of results. Particularly relevant to implement the seismic site categorisation of EN 1998-1 is the subclause 10.7, addressing the determination of the position of the bedrock and of the fundamental frequency f_0 of the soil deposits. Depth of the seismic bedrock may be obtained from geophysical tests or by indirect methods

if accompanied by direct inspection of samples retrieved from the bedrock layer. The fundamental frequency of soil deposits may be estimated from records of ambient vibrations at the ground surface transformed in the horizontal-to-vertical spectral ratio (HVSR). Laboratory tests for measuring response to cyclic and dynamic actions are listed in Table 10.1 of Clause 10, reproduced below as Table 2, with indications of the strain level for which each testing method is appropriate. A specific subclause considers laboratory testing to obtain information on the variation of the secant shear modulus and damping ratio against shear strain. These data are particularly relevant for numerical modelling of geotechnical structures subjected to seismic loading. When results from laboratory testing are not available, EN 1997-2 presents in Annex G methods to obtain seismic properties indirectly from empirical correlations with soil physical properties or with results of field testing.

Table 2. Laboratory tests for measuring response to cyclic and dynamic actions. (reproduced from prEN 1997-2).

	Laboratory test (and associated test standards)					
Test	**Cyclic torsional shear**	**Cyclic direct simple shear**	**Cyclic triaxial**	**Resonant column**	**Bender elements**	**Cyclic triaxial for rock**
Standard	See Table B.8					
Strain level						
Very small (< 10^{-5})	(full)	-	-	full	one	(full)
Small (10^{-5} -10^{-2})	full	full	(full)	(full)	-	full
Medium (10^{-2} -10^{-1})	-	(full)	full	-	-	-

- = not applicable; 'one' = one conventional value; 'full' = full curve; () = partially applicable

3 CONCLUSIVE REMARKS

The 2nd generation of Eurocode 7 has been conceived with the formalization of a new concept, that is the Ground Model defined as a site-specific collection of data about geometry and properties of the ground and groundwater, based on results from field investigation and other available data. This definition implies that also the seismic properties of the ground must be included in the Ground Model, and this has important consequences on the design of Ground Investigation and on Reporting. EN 1998-Parts 1 and 5 and EN 1997 Parts 1 and 2 have been considerably influenced by the assumptions that the Ground Investigation is a comprehensive activity, programmed to fulfil all the needs for geotechnical design including those motivated by seismic actions. The Ground Model is the tool to share among all the actors involved in design a comprehensive representation of the site. It contains all the features to ensure safety and serviceability for any possible design situations, including the seismic one. A specific Guideline on the implementation of the Ground Model will be made available by TC250/SC7, together with similar guidelines on the most innovative aspects of the 2nd generation of Eurocode 7.

REFERENCES

EN 1997-1: 2004 *Eurocode 7: Geotechnical design- Part 1: General rules TC250/SC7.*

EN 1997-2: 2007 *Eurocode 7: Geotechnical design-Part 2: Ground investigation and testing TC250/SC7.*

EN 1998-5: 2004 *Eurocode 8 – Design of structures for earthquake resistance. Part 5: Foundations, retaining structure and geotechnical aspects. TC250/SC8.*

FprEN 1998-1-1: 2024 *Eurocode 8 – Design of structures for earthquake resistance. Part 1-1: General rules and seismic action. TC250/SC8 N 1283.*

FprEN 1998-5: 2024 *Eurocode 8 – Design of structures for earthquake resistance. Part 5: Geotechnical aspects, foundations, retaining and underground structures*. TC250/SC8 N1284.

prEN 1997-1: 2023 *Eurocode 7: Geotechnical design- Part 1: General rules. TC250/*SC7 Doc. N1707.

prEN 1997-2: 2023 *Eurocode 7: Geotechnical design- Part 2: Ground properties*. TC250/SC7 Doc. N 1710.

JRC (2024). *Assembling the Ground model and the derived values*. Guidelines for the application of the 2nd Generation of Eurocode 7 – Geotechnical design. Joint Research Council (JRC) of the European Commission.

Proceedings of the XVIII ECSMGE 2024
GEOTECHNICAL ENGINEERING CHALLENGES
TO MEET CURRENT AND EMERGING NEEDS OF SOCIETY
© 2024 the Authors
ISBN 978-1-032-54816-6
DOI 10.1201/9781003431749-367
Open Access: www.taylorfrancis.com, CC BY-NC-ND 4.0 license

ECSMGE 24
XVIII EUROPEAN CONFERENCE ON SOIL MECHANICS AND GEOTECHNICAL ENGINEERING

Influence of pore fluid composition on shear strength of reconstituted normally consolidated kaolinite

Influence de la composition du fluide interstitiel sur la résistance au cisaillement de la kaolinite reconstituée et normalement consolidée

M. Schröder*, J. Grabe
Hamburg University of Technology, Hamburg, Germany
**Maximilian.schroeder.gbt@tuhh.de*

ABSTRACT: Kaolinite is a prominent proxy material in geotechnical engineering that is regularly used in small- and large-scale geotechnical modelling and testing. The material is usually mixed with demineralised water and reconstituted subsequently. This contribution investigates the influence of pore fluid composition on the angle of shearing resistance of very pure kaolinite through CIU triaxial tests. Potassium, sodium and calcium chloride are tested in different concentrations. The results show that adding salt increases the shearing resistance angle. However, other influential factors like pH, valence and atomic radius also play significant roles. Future investigations will expand towards illite and a broader range of studied salt concentrations.

RÉSUMÉ: La kaolinite est un matériau de substitution important dans l'ingénierie géotechnique, régulièrement utilisé dans la modélisation et les essais géotechniques à petite et grande échelle. Le matériau est généralement mélangé à de l'eau déminéralisée et reconstitué par la suite. Cette contribution étudie l'influence de la composition du fluide interstitiel sur l'angle de frottement de la kaolinite très pure au moyen d'essais triaxiaux CIU. Les chlorures de potassium, de sodium et de calcium sont testés à différentes concentrations. Les résultats montrent que l'ajout de sel augmente l'angle de frottement. Cependant, d'autres facteurs influents tels que le pH, la valence et le rayon atomique jouent également un rôle significatif. Les recherches futures s'étendront à l'illite et à une gamme plus large de concentrations de sel étudiées.

Keywords: Clay; shear strength; salt; kaolinite.

1 INTRODUCTION

Using reconstituted proxy materials for fine-grained soils is common in geotechnical engineering, the most prominent material being kaolin. Applications reach from triaxial testing for constitutive model development and application (Wichtmann and Triantafyllidis, 2018; Dao et al., 2023) to centrifuge modelling (Gaudin et al., 2011). In most cases, the industrial dry clay powder is mixed with demineralised or de-ionized water to prepare a slurry, which is consolidated afterwards.

This paper investigates the influence of the pore water composition on the shear strength of kaolinite as representative of the 1:1 clay mineral. For this purpose, slurries are mixed with different salt concentrations and types. A total of five CIU triaxial tests were performed. The results from tests with salt are compared to the use of demineralised water, representing the established approach from the literature.

2 FINDINGS FROM THE LITERATURE

Lambe (1958) elaborates that shear strength is reduced if

- salt concentration is lowered,
- pH increases or
- the valency of the compound (salt type) is lowered (e.g. from Ca^{++} to Na^{+}).

All the above-stated phenomena expand the double layer of the clay particles and reduce their attraction.

Warkentin and Yong (1962) explain that the shear strength of kaolinite strongly depends on the fabric and identify three different structure types with decreasing associated strength. They attribute the highest shear strength to an edge-to-face flocculated structure, which Lambe (1958) calls non-salt flocculation. This structure is created at low pH (Osipov, 1975). The strength is further reduced if the clay is dispersed or deflocculated (higher pH). The lowest shear strength is attributed to face-to-face flocculation. Lambe (1958) names this salt flocculation. It occurs at high salt concentrations when the diffuse double layer reduces,

and the repulsive forces of the negatively charged faces are reduced.

According to Warkentin and Yong (1962), the shear strength depends on the amount of contact per unit volume and the strength of the interparticle forces of each contact. This means that a flocculated fabric can lead to either high or low shear strength depending on the strength of the interparticle forces present.

3 MATERIALS

3.1 Pore fluids

A total of five different pore fluids, which are labelled according to Table 1, are studied. Pore fluid 1 represents demineralised water. The pore fluids 2 and 3 are a 0.01 molar calcium chloride ($CaCl_2$) and a one molar potassium chloride (KCl) solution as used in the GLOSOLAN-SOP-06 standard for soil pH determination (Global Soil Laboratory Network, 2021). The study then expanded towards using sodium chloride (NaCl) and calcium chloride solution at the same concentration in grams per litre at high salt content to provoke a strong influence of salt type. Table 2 shows the determined conductivity and pH values of the used fluids.

Table 1. Studied pore fluids – composition.

Salt type	Concentration [g/l]	Concentration [M]
demineralised	-	-
$CaCl_2$	1.11	0.01
KCl	74.55	1.00
NaCl	74.55	1.28
$CaCl_2$	74.55	0.67

Table 2. Studied pore fluids – conductivity and pH.

Pore fluid	Conductivity [mS]	pH [-]
demineralised	≈ 0	6.9
0.01M $CaCl_2$	2.35	8.0
1M KCl	108.4	7.5
1.28 M NaCl	109.4	6.7
0.67 M $CaCl_2$	103.6	10.1

3.2 Clay

3.2.1 General properties

An industrially available clay powder is studied in this work. The material is similar to the one in Martinez and Stutz (2019). The mineralogical composition of the materials and selected properties are given in Tables 3 and 4. The particle size distribution of the material is depicted in Figure 1.

Table 3. Studied kaolinite–selected properties.

Property	Value
Specific surface [m²/g]	14.8
D_{50}-value [µm]	0.7
Particle specific gravity [g/cm³]	2.675

Table 4. Studied clay – Mineralogical composition determined by high-quality XRD analysis.

Mineral	Mass per cent [%]
Quartz	1.1
Illite	3.2
Kaolinite	95.7
Clay (total)	98.9

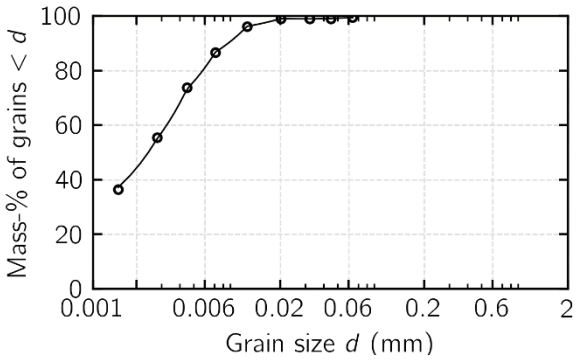

Figure 1. Particle size distribution of studied clay.

3.2.2 Atterberg limits and plasticity

Liquid limits, as determined by the Casagrande method, and plastic limits and indices are shown in Table 5. The results show the values determined from three tests. Dry powder and fluid were mixed at a mass ratio 1:2, left for four days to equilibrate and tested from wet to dry state, meaning that the slurry is dried further throughout the test.

Sodium chloride in such a high concentration affects kaolinite powder in such a way that the validity of classic Atterberg testing procedures should be questioned. The material does not behave like soil when remoulded. Most likely, this is due to the large atomic radius of sodium chloride. This reduces particle contact.

Table 5. Atterberg limits.

Pore fluid	Liquid limit [%]	Plastic limit [%]	Plasticity index [%]
demineralised	56.7	31.7	25.0
0.01M $CaCl_2$	59.1	34.5	24.5
1 M KCl	59.6	35.9	23.7
1.28 M NaCl	41.9	32.0	9.9
0.67 M $CaCl_2$	51.3	28.0	23.3

4 TESTING

4.1 Sample preparation

The dry industrial clay powder is pre-mixed with the solutions under atmospheric conditions, while the dry powder is mixed into the total liquid, not vice-versa. In the second stage, the pre-mixed slurry is homogenised by vacuum mixing for one hour. Finally, the slurry is carefully poured into consolidation columns and initially consolidated by applying a pressure of 300 kPa. The water content of the slurries is different for each pore fluid chosen, assuring good mixability while maintaining a high content of solids. All slurries are mixed at a minimum of 1.5 times the liquid limit but differ from the ratio used to determine Atterberg limits. All three samples for one test are cut out of the same batch using metal cylinders. Final consolidation takes place in the triaxial device.

4.2 Testing procedure

Tests are performed on normally consolidated samples with dimensions of 36 mm diameter and a sample height of 90 mm. The initial void ratios of the specimens are given in Table 6. The shearing velocity is set to 0.02 mm/min at 18 degrees Celsius. The back pressure is set to 400 kPa. Tests are performed with 400, 600 and 800 kPa effective confining pressure.

Table 6. Initial void ratios before consolidation (-) of the triaxial specimens.

Pore fluid	Sample 1 (400 kPa)	Sample 2 (600 kPa)	Sample 3 (800 kPa)
demineralised	1.429	1.465	1.471
0.01M $CaCl_2$	1.471	1.487	1.461
1 M KCl	1.822	1.790	1.796
1.28 M NaCl	1.365	1.334	1.370
0.67 M $CaCl_2$	1.391	1.385	1.423

4.3 Results

The slope of the Mohr-Coulomb failure envelope and the axis intercept are given below in Table 7. Regression analyses were performed in the t-s stress field, with the maximum stress ratio being set as the failure criterion. Membrane and filter paper corrections were not performed. Figure 2 shows the stress paths in the t-s field for the samples using demineralised water exemplarily. As expected, the samples behave normally consolidated.

Table 7. M-C failure envelope parameters for kaolinite.

Pure fluid	The slope of the curve φ [°]	Axis intercept c [kPa]
demineralised	20.16	23.81
0.01M $CaCl_2$	25.12	0.00
1 M KCl	32.23	0.00
1.28 M NaCl	24.15	1.78
0.67 M $CaCl_2$	23.24	1.09

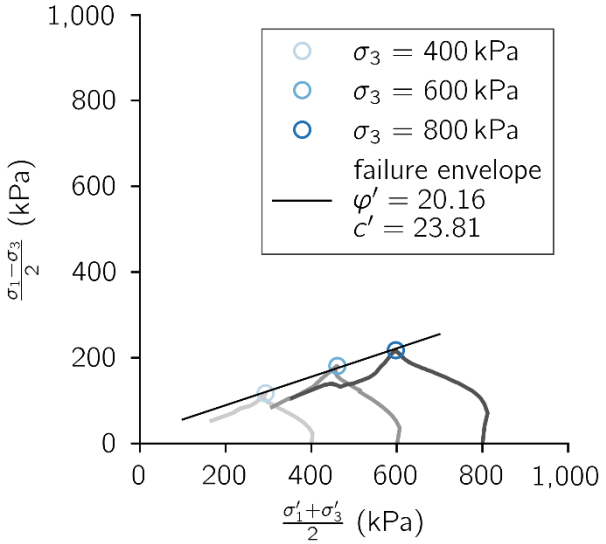

Figure 2. The stress paths of the samples made from kaolinite and demineralised water.

Figure 3 depicts the relationship between the angle of shearing resistance and plasticity index as taken from Table 5. A trend of declining angle of shearing resistance with increasing plasticity index (Lambe and Whitman, 1969) is not visible. Potassium and sodium chloride yield remarkable results. As mentioned before, kaolinite mixed with sodium chloride solution yields unusual results. The substantial increase in the angle of shearing resistance for potassium chloride is remarkable as the plasticity index is unaffected.

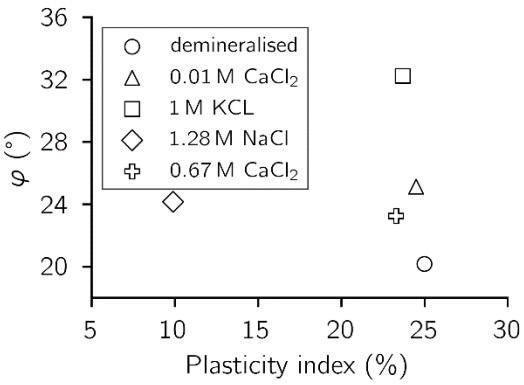

Figure 3. The determined angle of shearing resistance plotted over the plasticity index.

The determined angle of shearing resistance is plotted over pH in Figure 4. The trend for pH dependency is not clear. Generally, adding salt (increasing conductivity) to the pore fluid increases the angle of shearing resistance. A very high concentration of calcium chloride leads to a similar angle of shearing resistance compared to a low concentration. Adding about one gram per litre of calcium chloride strongly increases the angle of shearing resistance and pH. A high sodium chloride concentration increases the shearing resistance angle with a slight pH decrease. In contrast, a high potassium chloride concentration yields the highest angle of shearing resistance increase only with a moderate increase in pH.

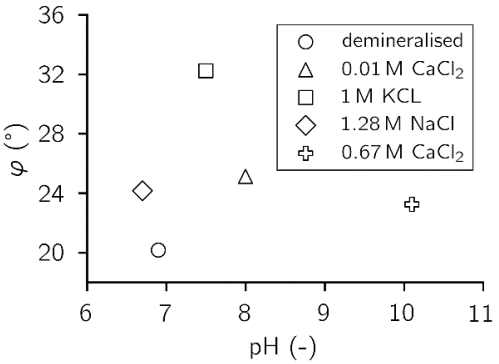

Figure 4. The determined angle of shearing resistances plotted over the pH value.

5 DISCUSSION

The angle of shearing resistance increases when salt is added to the pore fluid compared to demineralised water. This holds for each salt type and concentration presented in this study. Salt cancels out the potential repulsion forces between particles. It decreases the thickness of the diffuse double layer. However, the salt type and the concentration greatly influence the behaviour. The pH value, although significantly changed compared to demineralised water, does not seem to influence the angle of shearing resistance as much. The significant gain of shear strength with potassium chloride might be attributed to the small valence radius of K^+ ions that strongly bond the out-orientated tetrahedral oxygens of kaolinite particles.

6 CONCLUSIONS

The results show that the factors influencing the angle of shearing resistance and fabric in kaolinite are complex and interacting. Applying general textbook concepts proves to be complicated. Analysis of conductivity or salt concentration alone does not allow the prediction of the angle of shearing resistance development. pH, valence and atomic radius of salt types need to be considered. The study will be expanded towards lower concentrations of all three salt types and illite as representative of the 2:1 clay mineral group. It will be combined with sedimentation testing to identify fabric types.

ACKNOWLEDGEMENTS

The authors acknowledge Julia Patterson's support in conducting the tests and Mercedes Molina Gamez's valuable input. This work is funded by the Deutsche Forschungsgemeinschaft (DFG, German Research Foundation) – project number 51685914. This support is gratefully acknowledged.

REFERENCES

Dao, D. A., Alkateeb, D. and Schröder, M. (2023) Discrepancies between element tests and large-scale LDFE simulations: A case study on anchor kinematics during installation in clay. *Comput. Geotech*., 163, p. 105698, https://doi.org/10.1016/j.compgeo.2023.105698.

Gaudin, C., Bienen, B. and Cassidy, M. J. (2011) Investigation of the potential of bottom water jetting to ease spudcan extraction in soft clay. *Géotechnqiue*, 61(12), pp. 1043–1054, http://dx.doi.org/10.1680/geot.8.P.152.

Global Soil Laboratory Network GLOSOLAN (2021) Standard operating procedure for soil pH determination - GLOSOLAN-SOP-06.

Lambe, T.W. (1958) The structure of compacted clay. *ASCE J Soil Mech Found Div* 84(SM2), pp 1654–1 to 34, https://doi.org/10.1061/JSFEAQ.0000114.

Lambe, T. W. and Whitman, R. V. (1969) *Soil mechanics*, John Wiley and Sons.

Martinez, A. and Stutz, H. H. (2019) Rate effects on the interface shear behaviour of normally and overconsolidated clay, *Géotechnique,* 69, pp. 801–815, https://doi.org/10.1680/jgeot.17.P.311.

Osipov, V. I. (1975) Structural bonds and the properties of clays, *Bull. Int. Assoc. Eng. Geol.*, 12, pp. 13–28, https://doi.org/10.1007/BF02635423.

Schofield, R. K. and Samson, H. R. (1955) Flocculation of kaolinite due to the attraction of oppositely charged crystal faces. *Discussions of the Faraday Society*, 18, pp. 135–145, https://doi.org/10.1039/DF9541800135.

Warkentin, B. P. and Yong, R. N. (1962) Shear strength of montmorillonite and kaolinite related to interparticle forces. *Proc. 9th Nation. Conf. Clays Clay Miner*. Pergamon, pp. 210-218, https://doi.org/10.1016/B978-1-4831-9842-2.50014-6.

Wichtmann, T. and Triantafyllidis, T. (2018) Monotonic and cyclic tests on Kaolin - a database for the development, calibration and verification of constitutive models for cohesive soils with focus to cyclic loading. *Acta Geotechnica,* 13(5), pp. 1103-1128, https://doi.org/10.1007/s11440-017-0588-3.

Proceedings of the XVIII ECSMGE 2024
GEOTECHNICAL ENGINEERING CHALLENGES
TO MEET CURRENT AND EMERGING NEEDS OF SOCIETY
© 2024 the Authors
ISBN 978-1-032-54816-6
DOI 10.1201/9781003431749-368
Open Access: www.taylorfrancis.com, CC BY-NC-ND 4.0 license

ECSMGE 24
XVIII EUROPEAN CONFERENCE ON SOIL MECHANICS AND GEOTECHNICAL ENGINEERING

Groundwater statistics in the second-generation Eurocode 7

Statistiques des eaux souterraines dans l'Eurocode 7 de deuxième génération

T. Schweckendiek*
Deltares & Delft University of Technology, Delft, Netherlands

J. Estaire
CEDEX, Madrid, Spain

A.J. Bond
Geocentrix, Banstead, United Kingdom

**Timo.Schweckendiek@deltares.nl*

ABSTRACT: The second-generation Eurocodes, in particular EN 1990 and EN 1997, will rely more heavily on reliability and probability approaches for design (and verification) of geotechnical structures and for treating available data. The determination of groundwater levels will be based on concepts like annual probability of exceedance or fraction of time exceeded. When groundwater time series are available, the required groundwater levels can be determined using statistical analysis. In this paper we illustrate assessing the various groundwater levels values using extreme value statistics for real life data sets, highlighting pitfalls and providing practical recommendations for geotechnical practitioners. To that end, we address the selection of probability distributions, processing of the data to obtain annual extreme values and sanity checks of the results.

RÉSUMÉ: Les Eurocodes de deuxième génération, en particulier les EN 1990 et EN 1997, s'appuieront davantage sur des approches de fiabilité et de probabilité pour la conception (et l'évaluation) des structures géotechniques et également lors du traitement des données disponibles. L'évaluation des niveaux des eaux souterraines sera basée sur des concepts tels que la probabilité annuelle de dépassement ou la fraction de temps dépassée. Lorsque des séries chronologiques sur les eaux souterraines sont disponibles, les niveaux d'eau souterraines requis peuvent être déterminés à l'aide d'une analyse statistique. Dans cet article, nous illustrons l'évaluation des différentes valeurs des niveaux d'eau souterraine à l'aide de statistiques de valeurs extrêmes pour des ensembles de données réelles, en soulignant les pièges et en fournissant des recommandations pratiques aux praticiens géotechniques. À cette fin, nous abordons la sélection des distributions de probabilité, le traitement des données pour obtenir des valeurs extrêmes annuelles et les contrôles de cohérence des résultats.

Keywords: Groundwater; statistics; uncertainty; extreme values; design values.

1 INTRODUCTION

1.1 Second generation Eurocodes for geotechnical design

The second-generation Eurocodes will be published during the period 2023 to 2027 and will fully replace the current codes by 2028, when the first-generation Eurocodes are withdrawn. In the 2nd-Gen Eurocodes, the design of geotechnical structures is spread across four standards: EN 1990 for the *basis* of geotechnical design and three parts of EN 1997 for specific aspects of geotechnical design.

The scope of the 2nd-Gen EN 1990 (published in 2023) has been extended to include geotechnics (as reflected in its revised title *Basis of structural and geotechnical design*), which necessitated generalization of the core principles of EN 1990, particularly with respect to the verification of ultimate limit states (Bond et al., 2019).

The 2nd-Gen EN 1997 has been split into three parts, with general principles and rules in *Eurocode 7 – Geotechnical design* – Part 1: *General rules*; provisions for determining ground properties from ground investigation in Part 2: *Ground properties*; and specific rules for design and verification of common geotechnical structures in Part 3: *Geotechnical structures*.

1.2 Objectives and outline

According to a survey after the introduction of the first-generation Eurocodes, one of the main improvements that geotechnical engineers wanted to see in the 2nd-Gen Eurocode 7 was improved guidance on selection of water pressures (Bond, 2011). This has

been addressed both in the 2nd-Gen EN 1997-1 and in EN 1990:2023.

The objective of this paper is to show how to determine various groundwater level values using a real data set.

The concepts related to groundwater in the 2nd-Gen Eurocodes are explained before presentation of the example. Data is fitted with different distribution functions to obtain the various groundwater levels that are required for geotechnical design.

2 WATER ACTION VALUES

2.1 Classification of water actions

In the same way as other actions are handled, the characterization of water actions in EN 1990:2023 depends on whether they are classified as permanent, variable, or accidental.

When the variation in magnitude of the water action is small or monotonic throughout the design service life, it should be classified as permanent. Its representative value (denoted $F_{w,rep}$ or $G_{w,rep}$) is then given by one of three possible values:

- a single characteristic value G_{wk} equal to the mean value of G_w (= $G_{wk,mean}$)
- either the upper or lower characteristic value, $G_{wk,sup}$ or $G_{wk,inf}$, whichever is more onerous
- a nominal value $G_{w,nom}$

These choices are illustrated in the top part of Figure 1. A nominal value is often used in geotechnical design when there is sparse information about groundwater levels (and hence pressures). This paper, however, concentrates on the case where there is sufficient data available to determine characteristic values of water levels and pressures.

Alternatively, when the variation in magnitude of the water action is neither negligible nor monotonic, it should be classified as a variable action whose representative value $F_{w,rep}$ is made up of two components:

- a permanent component $G_{w,rep}$ taken as the mean value of G_w ($G_{wk,mean}$), i.e. the first option above
- a variable component $Q_{w,rep}$ that represents the variation in water action from the mean

These choices are illustrated in the middle part of Figure 1. The magnitude of the variable component $Q_{w,rep}$ depends on which combination of actions is appropriate for the design situation being considered and can be any of the alternatives given in Table 1.

Finally, when the water action is of significant magnitude and typically of short duration but unlikely to occur during the design service life, it should be classified as an accidental action whose representative value $F_{w,rep}$ (denoted $A_{w,wep}$) is as specified in bottom part of Table 1.

Table 1. Specification of water actions according to EN 1990:2023.

Variable or accidental water action	**Symbol**	**Probability of exceedance**
Characteristic	Q_{wk}	2% per annum (return period 50 years)
Combination	$Q_{w,comb}$	10% per annum (return period 10 years)
Frequent	$Q_{w,freq}$	Fraction of time exceeded = 1%
Quasi-permanent	$Q_{w,qper}$	Fraction of time exceeded = 50%
Accidental	$A_{w,rep}$	0.1% per annum (return period 1000 years)

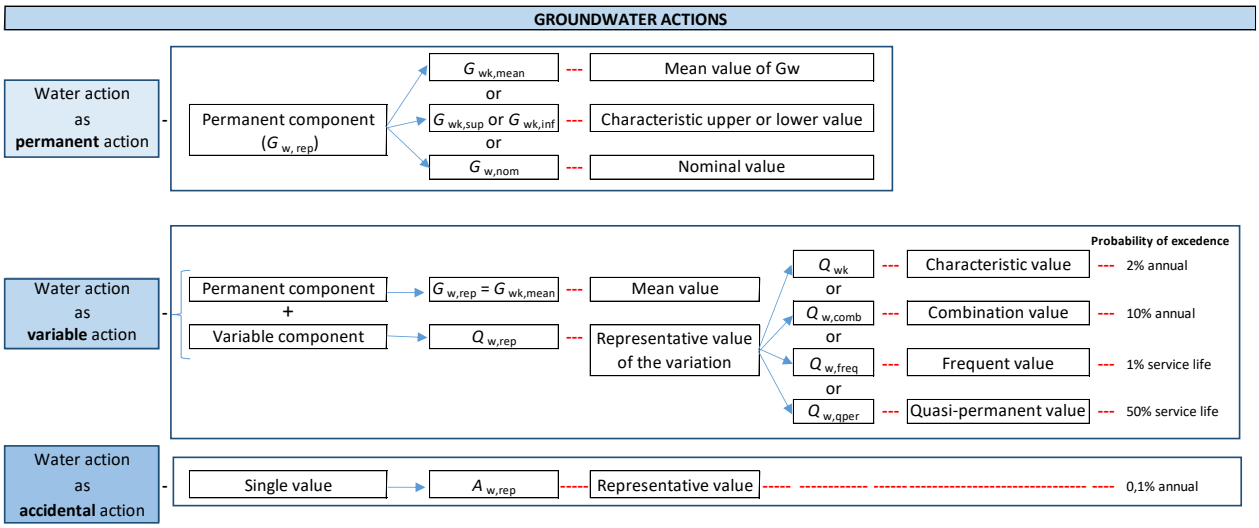

Figure 1. Determination of the representative value of water actions.

2.2 Statistical analysis

For basic theory, we refer the reader to standard textbooks on the topic; here we provide pointers to the approaches relevant to the determination of water action values.

For the quasi-permanent and frequent values, we simply assess the 50% quantile (median) and the 1% quantile of the entire data set (time series in Figure 2), respectively. This determination requires the data to be equally spaced in time, otherwise the data points have to be weighted according to the time period they represent.

The combination, characteristic and accidental values are defined with annual probabilities of exceedance. To obtain these values, the most straightforward option is to determine a probability distribution for the annual maxima (or minima), and then assess the respective quantiles according to Table 1. Since we deal with maxima or minima, the most common extreme value distributions to be considered for this task are:

- Generalized Extreme Value (GEV)
- Weibull
- Gumbel (e.g. Gumbel, 2013)

An alternative to analysing annual maximum or minimum values directly, which we illustrate in the example below, is the 'peaks-over-threshold' method (Lechner et al., 1993).

3 EXAMPLE

To illustrate the application of extreme value statistics for the various values of groundwater action as described above, we analyse a real-life data set and discuss the findings, possibilities and pitfalls.

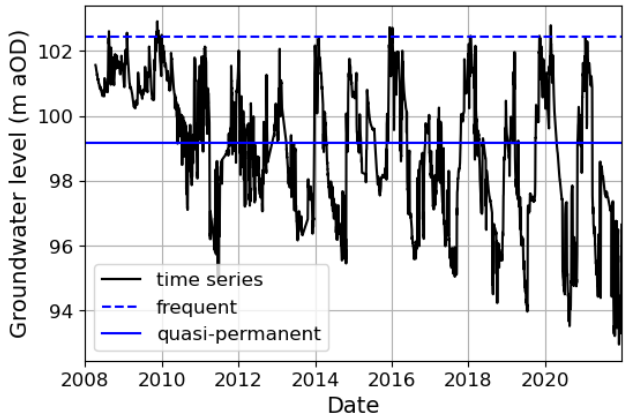

Figure 2. Groundwater level time series including quasi-permanent and frequent values.

3.1 Data set

The data set (from Dunshaughlin in Ireland) contains daily readings of groundwater levels between April 2008 and December 2021, so almost 14 years of data. Figure 2 also shows the quasi-permanent and frequent values, which were obtained from the data as explained in 2.2.

For our particular geotechnical design example, we are looking for exceedance of high groundwater levels. For simplicity in this example, we assume that low groundwater levels do not cause a limit state to be exceeded. We will use the annual maxima to assess the extreme value statistics. The data set exhibits an apparent downward trend in the low water levels, which we ignore here because the high groundwater levels, particularly the annual maxima, do not show such a trend.

3.2 Fitting extreme value distributions

Fitting the distributions mentioned in 2.2 using the maximum likelihood approach leads to the visual fit compared to the empirical cumulative distribution function (ECDF) in Figure 3. Visual comparison does not give a conclusive answer as to which distribution fits the data best, even though the Weibull distribution approximates the right tail (high values) best, as highlighted in Figure 3.

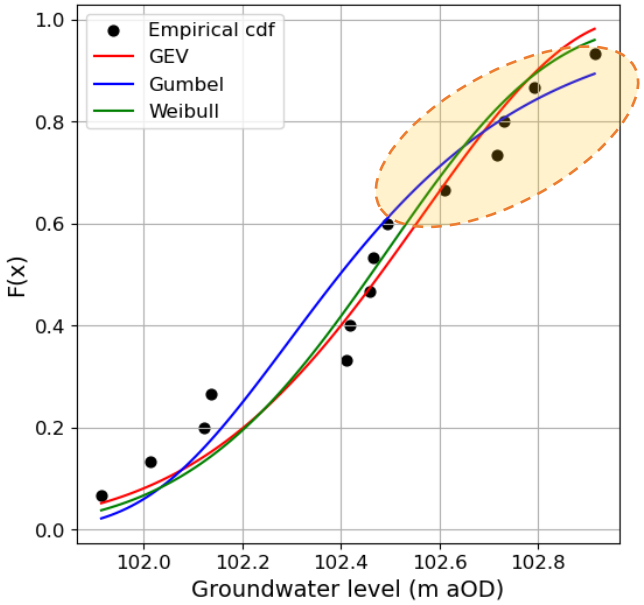

Figure 3. Extreme value distributions compared to Empirical Cumulative Distribution Function (ECDF).

Using the fitted extreme value distributions and the other definitions of water action values discussed in 2.2, the results are presented visually in Figure 4 and numerically in Table 2.

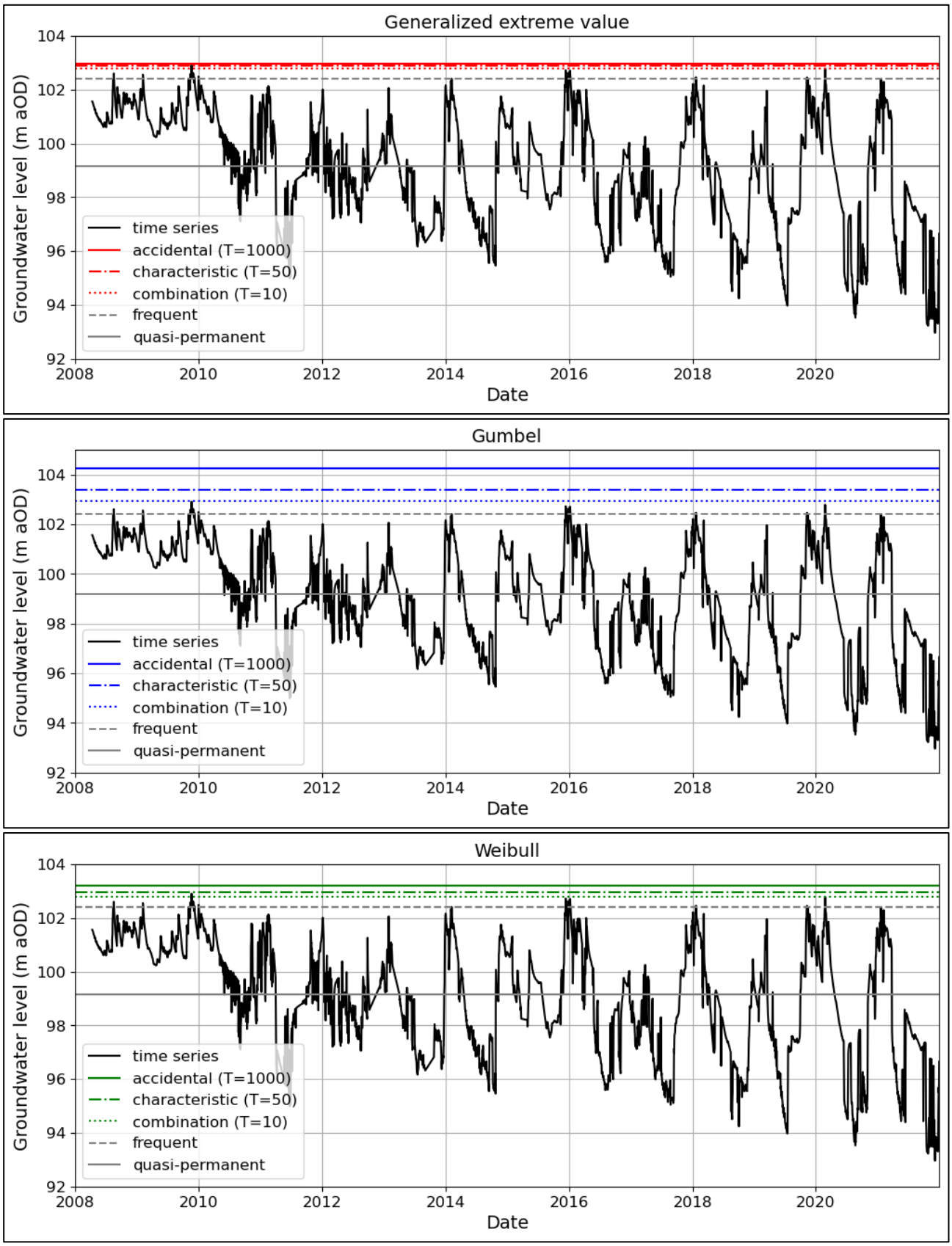

Figure 3. Comparison of extreme value distributions fitted to annual maxima of the time series (top: GEV; middle: Gumbel; bottom: Weibull).

Table 2. Groundwater levels, according to EN 1990 definitions, per distribution fit (in m aOD).

Value	Data set	Gumbel	GEV	Weibull
Characteristic	Annual maxima	103.40	102.91	102.98
Combination		102.93	102.80	102.80
Frequent	Time series	102.43 (independent)		
Quasi-permanent		99.18 (independent)		
Accidental	Annual maxima	104.26	102.98	103.20

3.3 Discussion

To begin with, we observe that the time series exhibits a considerable seasonal variation of roughly 7 to 8 m, while the variation in the extremes (maxima) falls within a relatively small bandwidth of approximately 1 m.

Furthermore, we observe that the quasi-permanent and frequent values are equal and independent of the choice of distribution (by definition), while the characteristic, combination and accidental values differ. Below we discuss observations and sanity checks of the fits to make the most appropriate choice.

Firstly, the combination values from the different distributions are practically identical, so we do not need to select a preferred distribution. For the characteristic and accidental values, we see bigger differences (around 0,5 m as maximum) between the distributions.

The GEV produces very similar values for the combination, characteristic and accidental cases, which is not credible. Therefore, we make a visual check by inspecting the probability density and cumulative distribution functions (PDF and CDF), as depicted in Figure 4.

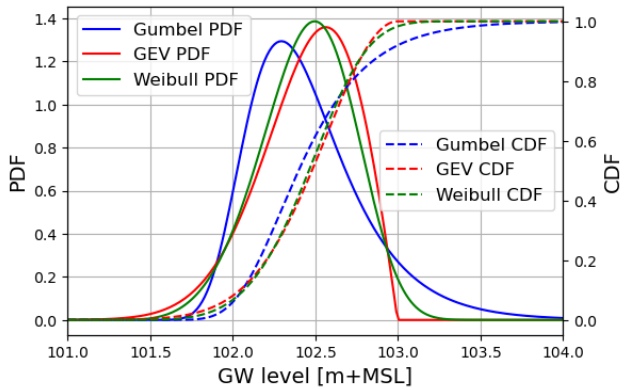

Figure 4. Extreme value distributions (PDF and CDF) fitted to the annual maxima using maximum likelihood.

We immediately observe that fitting the GEV distribution has actually led to a distribution of minima with a fat tail to the left. The sharp bend in the right tail, resulting in a right tail with zero thickness, is the reasonfor the little to no difference between the combination, characteristic and accidental values. Hence, the GEV is not suited to this case. The Gumbel distribution has the fattest right tail, while the Weibull distribution has a less fat right tail. As observed earlier from Figure 3, these latter distributions give a reasonable match to the data.

The Gumbel distribution produces values far higher than the observed range, with the highest value observed in 14 years still somewhat below the combination value (return period: 10 years).

The Weibull distribution exhibits clear separation of the combination, characteristic and accidental values. The combination value is exceeded exactly once in 14 years, while the maximum observed is still somewhat below the characteristic value.

Additionally, we may consider goodness-of-fit measures like chi-square or Kolmogorov-Smirnov tests. However, with such small data sets of 14 annual maxima, these have limited value and instead we prefer to decide on the distribution to use based on visual inspection. The conservative choice in this case is the Gumbel distribution with the associated values in Table 2, while choosing the Weibull distribution leads to more favourable but equally defendable values considering the information that is available. Of course, if more information (for example regarding a physical upper limit to the data) was available, this should be taken into account in the decision.

A final remark on the use of annual maxima is that maxima may stem from the same ‘event’, depending on the year limit used. Also, the peak-over-threshold method is prone to multiple peaks in the same event and not necessarily a remedy for this issue. The issue can be solved mostly, though, by choosing the year limit in summer, if high values are attained in autumn/winter.

4 CONCLUSIONS

In the 2nd-Generation Eurocodes (specifically EN 1990:2023), characteristic values of water actions are defined in terms of probability and frequency, requring statistical analysis. The alternative is to assess nominal values using judgment and experience.

Statistical analysis is rather straightforward and requires just a couple of lines of code (e.g. using SciPy in Python or R). Of course, reasonable data sets of sufficient length in time need to be available for statistical analysis to be beneficial.

As demonstrated in the example, there is no unique solution and judgment is also required for assumptions and choices in the statistical analysis, such as the type of (extreme value) probability distribution. Sometimes

also outliers have to be removed. At the same time, we have shown that reasonable choices can be made based on relatively simple sanity checks and visual inspection of the results. In that sense, the current exercise is no different to other experience-based assumptions in geotechnical engineering.

We recommend providing further guidance to practitioners for assessing water action values, also covering issues not addressed in this paper, such as dealing with very short time series of measurements or scaling extreme value distributions to different reference periods.

REFERENCES

Bond, A. (2011). *Future development of Eurocode 7*, BGA Symposium – Eurocode 7 Today and Tomorrow, Cambridge, UK.

Bond, A., Formichi, P., Spehl, P. and van Seters, A.J. (2019). *Tomorrow's geotechnical toolbox: EN 1990:202x*. Basis of structural and geotechnical design. XVII European Conference on Soil Mechanics and Geotechnical Engineering, Reykjavik (Iceland).

EN 1990:2023, *Eurocode – Basis of structural and geotechnical design*, CEN.

FprEN 1997-1:2024, *Eurocode 7 – Geotechnical design – Part 1: General rules*, CEN.

FprEN 1997-2:2024, *Eurocode 7 – Geotechnical design – Part 2: Ground properties*, CEN.

FprEN 1997-3:2024, *Eurocode 7 – Geotechnical design – Part 3: Geotechnical structures*, CEN.

Gumbel, E.J. (2013). *Statistics of extremes*. Echo Point Books & Media, July 2013.

Lechner J.A., Simiu E. and Heckert N.A. (1993). *Assessment of 'peaks over threshold' methods for estimating extreme value distribution tails*. Structural Safety 12 (4), 305-314.

Proceedings of the XVIII ECSMGE 2024
GEOTECHNICAL ENGINEERING CHALLENGES
TO MEET CURRENT AND EMERGING NEEDS OF SOCIETY
© 2024 the Authors
ISBN 978-1-032-54816-6
DOI 10.1201/9781003431749-369
Open Access: www.taylorfrancis.com, CC BY-NC-ND 4.0 license

ECSMGE 24
XVIII EUROPEAN CONFERENCE ON SOIL MECHANICS AND GEOTECHNICAL ENGINEERING

Analysis of the soil-structure interaction of a high-rise building near sensitive infrastructures

Analyse de l'interaction sol-structure d'un immeuble de grande hauteur à proximité d'infrastructures sensibles

M. Seip*, M. Hassan
Katzenbach GmbH, Germany

S. Leppla
Frankfurt University of Applied Sciences, Germany

A. Norkus
Vilnius Gediminas Technical University, Lithuania

**seip@katzenbach-ingenieure.de*

ABSTRACT: As a consequence of the growing population in urban areas even high-rise buildings have to be planned near existing sensitive infrastructures. In the east of Frankfurt am Main, Germany, a new high-rise building is planned. This new building is located directly between the river Main and the eastern inner harbour. The high-rise building will have a height of about 75 m and will be founded on a Combined Pile-Raft Foundation (CPRF) in the tertiary, soft marl. The new structure will be constructed next to important, sensitive traffic infrastructure. The foundation of the new high-rise building adjoins directly existing historic quay structures, which are more than 100 years old. For analysis of the stability and the serviceability of the heavily eccentric loaded foundation of the new high-rise building and the existing structures and for the investigation of the soil-structure interaction complex three-dimensional, non-linear numerical simulations have been carried out. The paper introduces into a very complex construction project in which the realistic consideration of the soil-structure interaction is very important for the serviceability of the foundation of the planned high-rise building as well as for the surrounding infrastructure.

RÉSUMÉ: En raison de la croissance démographique dans les zones urbaines, même les immeubles de grande hauteur doivent être planifiés à proximité des infrastructures sensibles existantes. À l'est de Francfort-sur-le-Main, en Allemagne, un nouveau bâtiment de grande hauteur est prévu. Ce nouveau bâtiment est situé directement entre la rivière Main et l'arrière-port est. Le bâtiment de grande hauteur aura une hauteur d'environ 75 m et sera fondé sur une fondation combinée sur pieux et radeaux (CPRF) dans la marne tertiaire molle. La nouvelle structure sera construite à côté d'infrastructures de circulation importantes et sensibles. Les fondations du nouveau bâtiment de grande hauteur jouxtent directement les structures de quai historiques existantes, vieilles de plus de 100 ans. Pour l'analyse de la stabilité et de l'aptitude au service des fondations chargées fortement excentriquement du nouveau bâtiment de grande hauteur et des structures existantes et pour l'étude de l'interaction sol-structure, des simulations numériques complexe tridimensionnelles et non linéaires ont été réalisées. L'article introduit un projet de construction très complexe dans lequel la prise en compte réaliste de l'interaction sol-structure est très importante pour la fonctionnalité des fondations du bâtiment de grande hauteur prévu ainsi que pour l'infrastructure environnante.

Keywords: Numerical analysis; deep foundation; CPRF; high-rise building; soil-structure interaction.

1 INTRODUCTION

A new high-rise building is planned in the east of Frankfurt am Main, Germany. The new building is located directly between the river Main and the eastern harbour. At the moment a filling covers the construction site, shown on Figure 1. The high-rise building will be a 75 m high hotel with 22 floors (Fig. 2). The hotel will be constructed directly by the roundabout intersection. Under the roundabout intersection two levels will be constructed for building equipment and appliances, for the entrance and for parking. The vehicle access will be facilitated under the southern bridge along the river Main by a ramp.

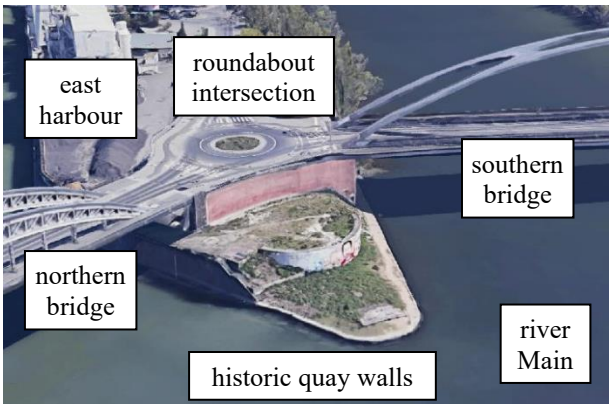

Figure 1. Construction site (google earth).


Figure 2. Visualisation of the planned high-rise building (B&L Group, Hamburg, Germany).

The high-rise building will be founded on a Combined Pile-Raft Foundation (CPRF). The 2 m thick foundation raft has a near to triangular shape and an area of 815 m². The load of the superstructure will be transferred into the CPRF through walls and columns also through a large single column at the tip of the triangular raft. The loads on the foundation raft are given in Table 1. The total load of the high-rise building including the foundation raft is estimated to be about $F_{tot,k} = G_{tot,k} + Q_{tot,k} = 507$ MN. The load has a non-symmetric distribution and is viewed as eccentric.

The foundation of the two levels under the roundabout intersection is a raft founded on micro piles. The micro piles are necessary to resist the uplifting at high water levels of the river Main. According to the regulations the whole project is classified into the Geotechnical Category GC 3, which is the category of the most complex construction projects (CEN 2004).

Table 1. Loads on the foundation raft.

Structural element	Type of load (characteristic)	Load magnitude
Walls and columns	Dead load	325 MN
	Live load	60 MN
Highly loaded single column	Dead load	65 MN
	Live load	15 MN

On the construction site and in the direct neighbourhood the following structures exist:

- Roundabout intersection (centre of Fig. 1)
- Historic quay walls
- Southern abutment of the northern bridge (left in Fig. 1)
- Northern abutment of the southern bridge (right in Fig. 1)

The roundabout intersection is founded on a classic pile foundation. The space under the roundabout intersection is partly filled. This filling has to be removed for the construction of the two levels which will be used for the high-rise building also in order to place the micro piles. The structure of the roundabout intersection includes abutments of the northern and the southern bridge.

The construction site is surrounded by quay walls. The quay walls consist of unreinforced concrete walls and of sheet pile walls. The concrete walls are more than 100 years old.

The southern abutment of the northern bridge is a huge block of concrete. The northern abutment of the southern bridge was founded on classic pile foundation. Both abutments are integrated into the structure of the roundabout intersection.

2 SUBSOIL CONDITIONS

Mainly by two core drillings the subsoil was investigated with the following results:

- artificial filling (0.7 m to 16 m thick)
- quaternary alluvial clay
- quaternary sand and gravel } 0.6 m to 3.1 m thick
- tertiary marl (minimum 80 m thick)

In addition to the core drillings a comprehensive programme of in-situ tests and laboratory tests has been carried out to detect the soil mechanical parameters. Several environmental laboratory tests on soil samples were carried out to classify the effort for disposal this excavation material.

The groundwater level on the construction site is equal to that of the river Main. At high water levels the construction site would be partly submerged under water.

3 FOUNDATION OF HIGH-RISE BUILDING

The foundation of the high-rise building is planned as a CPRF. A CPRF is a hybrid deep foundation system which combines the bearing capacity of a foundation raft and load transferring of the piles or barrettes. The CPRF is a technical and economical optimized

foundation system. The CPRF can be used for the foundation of classic high-rise buildings as well as for engineering constructions like bridges and towers. For the CPRF, the same technical regulations as for classic deep foundations can be applied. To complete the design and safety concept the international Combined Pile-Raft Foundation Guideline has to be considered (ISSMGE 2013). Due to the interaction between the foundation elements and the subsoil CPRFs have a very complex bearing and deformation behaviour. Hence CPRFs have to be classified into the Geotechnical Category GC3 according to EC 7 (CEN 2004). The advantages of a CPRF compared to a conventional spread foundation and to a classic pile foundation are the reduction of:

- settlements and differential settlements
- the bending moments of the foundation raft
- pile materials (30 % to 50 %)

and the increasing of the bearing capacity of spread foundations. More explanations about CPRF and several examples from engineering practice are given in Katzenbach et al. (2016).

The comprehensive numerical analysis using the Finite-Element-Method (FEM) led to the optimized geometry of the CPRF with a thickness of 2 m for the raft and 34 piles with a diameter of 1.5 m and length of 40 m and 45 m. Figure 3 shows the FE-model of the CPRF.

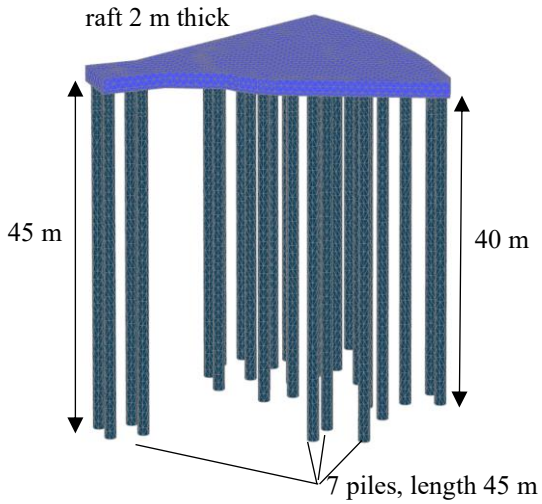

Figure 3. FE-model of the CPRF.

4 NUMERICAL MODEL OF THE PROJECT

The 3-dimensional FE-model (cutout) of the project is shown in Figure 4. The complete model consists of about 772,000 tetrahedral 10-node elements with about 1,170,000 nodes. The modelled subsoil has a base area of 200 m x 200 m and a depth of 105 m. For executing the numerical analysis, the FE-software PLAXIS 3D was used. Figure 5 shows all single structures in the whole construction site.

All construction phases on the project area which have taken place over the years are simulated in a sequence of single steps:

- initial situation
- construction of the quay walls
- construction of the abutment of the northern bridge
- construction of the piles of the roundabout intersection
- construction of the superstructure of the roundabout intersection
- construction of the abutment of the southern bridge
- removal of the filling on the construction site and under the roundabout intersection
- construction of the bored piles of the CPRF and of the micro piles below the roundabout intersection
- construction of the foundation raft of the CPRF and of the roundabout intersection
- hardening of the foundation rafts
- activation of dead loads and traffic loads of the superstructures

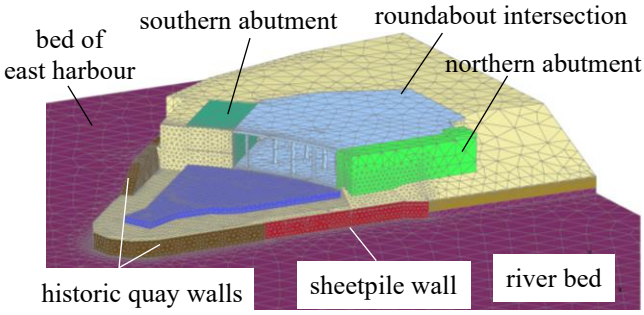

Figure 4. FE-model of the project (cutout).

These phases take into considerations the changes of stresses in the subsoil during all previous unloading and reloading of soil and stress cycles. It leads to a more realistic approach and estimation for the computed deformations as a result of constructing the new hotel building.

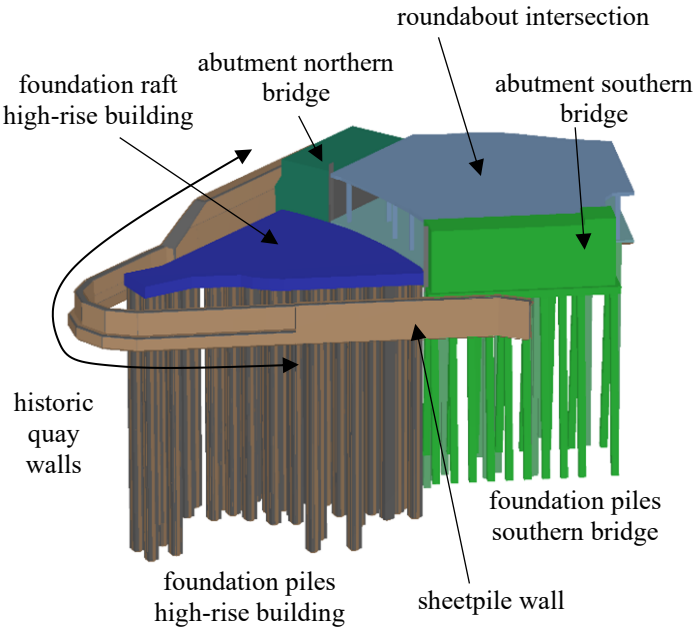

Figure 5. Structural model.

Different constitutive material laws for the different material behaviour of the soil and the structures were implemented. For the material behaviour of the artificial fillings a linear elastic-ideal plastic constitutive material law was used including the failure criterion of Mohr-Coulomb (MC). For this constitutive material law the relation between the Young´s modulus E and the stiffness E_s is defined by the Poisson ratio ν. In PLAXIS the modulus of stiffness E_s is named as E_{oed} according to the oedometer tests.

For the material behavior of the other soil layers the elasto-plastic constitutive material law "Hardening-Soil" (HS) was used. With this constitutive modelling the deformation behavior is described by a non-linear, hyperbolic, stress-dependent function, which enables the definition of different stiffness values depending on the stresses. Furthermore, effects of hardening after shear strain can be defined. The soil mechanical parameters used in the numerical simulation are shown in the Tables 2 and 3.

For the material behavior of the construction elements consisting of concrete respectively reinforced concrete (piles, rafts, walls etc.) and the sheet pile wall consisting of steel a linear elastic constitutive material law was used. In this constitutive material for the concrete resp. rein-forced concrete the Young´s modulus is E = 30.000 MN/m² and the Poisson ratio is υ = 0.2. For the steel the Young´s modulus is E = 210.000 MN/m² and the Poisson ration is υ = 0.3.

Table 2. Soil mechanical parameters.

Parameter	Symbol	Unit
Weight of saturated soil	γ_{sat}	kN/m³
Weight of moist soil	γ_{unsat}	kN/m³
Friction angle	φ'	°
Cohesion	c'	kN/m²
Dilatancy angle	Ψ	°
Young´s modulus / secant stiffness from triaxial test	E / $E_{50,ref}$	MN/m²
Modulus of stiffness / tangent stiffness of first loading from oedometer test	$E_{oed,ref}$	MN/m²
Tangent stiffness of unloading and reloading	$E_{ur,ref}$	MN/m²
Poisson ratio / Poisson ratio for unloading and reloading	ν / ν_{ur}	--
Earth pressure coefficient at rest	K_0	--
Ratio of failure stress	R_f	--

Table 3. Values of soil mechanical parameters.

	MC	HS		
	Filling	**Quaternary alluvial clay**	**Quaternary sand and gravel**	**Tertiary marl**
γ_{sat}	19	19	19.5	19
γ_{unsat}	19	19	19.5	19
φ'	20	25	35	22.5
c'	5	5	0	20
Ψ	0	0	5	0
E / $E_{50,ref}$	3	4	70	60
$E_{oed,ref}$	4	4	70	60
$E_{ur,ref}$		8	140	120
ν / ν_{ur}	0.3	0.3	0.3	0.25
K_0	0.5	0.5774	0.4264	0.6173
R_f	--	0.9	0.9	0.9

5 SPRING STIFFNESS AND SUBGRADE REACTION MODULUS OF THE HIGH-RISE BUILDING

For the structural analysis and dimensioning of the superstructure of the high-rise building the spring stiffness of the piles and the distribution of the subgrade reaction modulus of the raft are to be estimated and calculated. For the determination of the stiffnesses and the subgrade reaction modulus a FE-calculation was carried out with the sum of the full characteristic dead load $G_{tot,k}$ and the full characteristic traffic load $Q_{tot,k}$. The spring stiffness of the piles is defined by the relation of the load on the piles to the settlements of the pile head. The subgrade reaction modulus is defined by the relation of the stresses under the raft to the settlements of the raft. The calculated

settlements of the foundation are shown in Figure 6. The resulting spring stiffnesses and the subgrade reaction modulus for the calculation of the superstructure are shown in Figure 7.

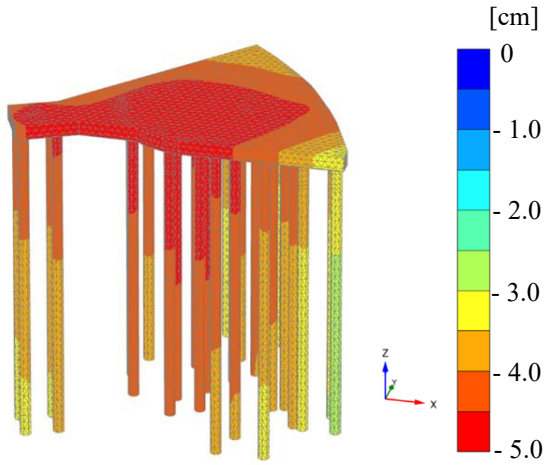

Figure 6. Calculated settlements of the CPRF for ($F_{tot,k} = G_{tot,k} + Q_{tot,k}$).

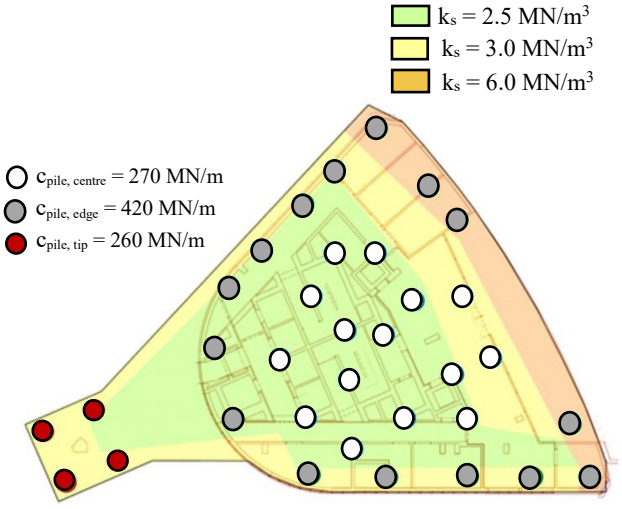

Figure 7. Spring stiffness and subgrade reaction modulus for calculation of the superstructure.

6 BEARING BEHAVIOUR OF THE CPRF

The bearing behaviour of the CPRF can be specified by the CPRF coefficient α_{CPRF}. The coefficient declares the relation between the resistance of the piles ($R_{pile,k}$=450 MN) and the total resistance ($R_{tot,k} = F_{tot,k}$) of the whole CPRF (507 MN), as shown in Equation (1). The CPRF coefficient of $\alpha_{CPRF} = 0$ means that the whole load $F_{tot,k}$ is carried by the foundation raft. A CPRF coefficient of $\alpha_{CPRF} = 1.0$ means that the whole load $F_{tot,k}$ is carried by the foundation piles as a classic pile foundation.

$$\alpha_{CPRF} = \frac{\sum R_{pile,k,i}(s)}{R_{tot,k}(s)} = \frac{450\ MN}{507\ MN} = 0.89 \qquad (1)$$

7 DISPLACEMENTS OF EXISTING STRUCTURES

For the investigation of the displacements of the existing structures as a result of the construction of the new high-rise building further FE-simulations were carried out. To estimate realistic displacements the simulations considered the full characteristic dead load $G_{tot,k}$ and 33 % of the characteristic traffic load $Q_{tot,k}$. As a so-called settlement active load F_{sett} the calculated settlements of the whole project area shown in Figure 8.

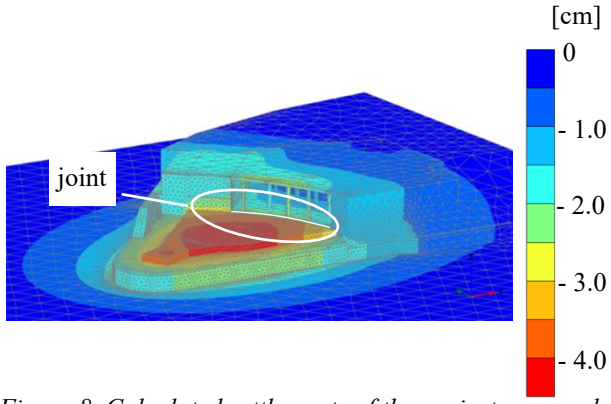

Figure 8. Calculated settlements of the project area and adjacent buildings for [$F_{sett} = G_{tot,k} + (1/3 \cdot Q_{tot,k})$].

The predicted settlements of the high-rise build-ing are estimated to be 2.5 cm and 4.5 cm. The predicted settlements of the existing bridge abutments and the structure of the roundabout intersection are between 0 cm and 2.5 cm, which in this case will not lead to any damage to these structures. The construction detail of the joint between the new high-rise building and the sublevels in the roundabout intersection (see Fig. 8) is very important for the serviceability of the new structure. The calculation forecasts differential settlements of about 0.5 cm and 2.0 cm. For these differential settlements the joint has to be designed to guarantee a watertight and plane passage.

The existing historic quay walls are very sensitive structures. The FE-simulation shows that the hori-zontal displacements in x-direction (Fig. 9 top) and in y-direction (Fig. 9 bottom) will be between 0 cm and ±0.5 cm. This will not lead to any major or considerable damage for these structures.

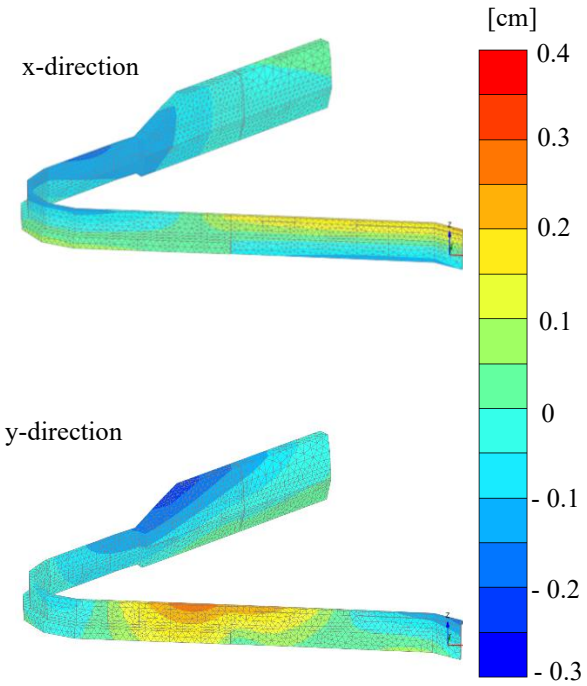

Figure 9. Calculated horizontal displacements of the quay walls for [$F_{sett} = G_{tot,k} + (1/3 \cdot Q_{tot,k})$].

Regarding the settlements of the historic quay walls the prediction is between 1 cm and 3 cm as shown in Figure 10. For the evaluation of the stability and the serviceability the criterion of maximum angular rotation ψ will be applied. For the prevention of any fissures in any structure the criterion is $\psi \leq 1/500$ (GGS 1993). The predicted maximum angular rotation of the historic quay walls is $\psi = 1/1{,}000$. Hence there will be no danger of damage for the historic walls.

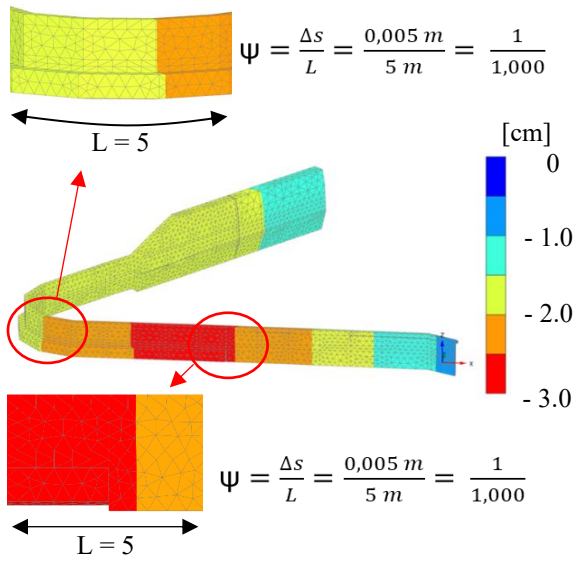

Figure 10. Calculated settlements of quay walls for [$F_{sett} = G_{tot,k} + (1/3 \cdot Q_{tot,k})$].

8 CONCLUSIONS

For analysis of the stability and the serviceability of the heavily eccentric loaded foundation of the new high-rise building and the existing structures and for the investigation of the soil-structure interaction complex three-dimensional, non-linear numerical simulations are very important. These numerical simulations have to take into account all geometric and material specific boundary conditions, including the history of the construction of the whole area.

The numerical simulations delivered the spring stiffness and the subgrade reaction modulus, which are needed for the analysis and the design of the superstructure.

The hybrid foundation system CPRF transfers the building load into the subsoil by the piles and by the raft. This leads to an optimized construction with a minimized impact on the environment.

Regarding the horizontal and vertical displacements of the existing structures due to the new high-rise building the numerical simulations show, that there will be no considerable risk.

REFERENCES

CEN European Committee of Standardization 2004. *EN 1997-1:2004 - Eurocode 7: Geotechnical design - Part 1: General Rules*.

GGS German Geotechnical Society 1993. *Empfehlungen "Verformungen des Baugrunds bei baulichen Anlagen": EVB*. Ernst & Sohn, Berlin, Germany.

ISSMGE International Society of Soil Mechanics and Geotechnical Engineering. 2013. *Combined Pile-Raft Foundation Guideline*. R. Katzenbach, D. Choudhury (ed). Darmstadt, Germany.

Katzenbach, R., Leppla, S., Choudhury, D. 2016. *Foundation systems for high-rise structures*. CRC Press Taylor & Francis Group, New York, USA.

Proceedings of the XVIII ECSMGE 2024
GEOTECHNICAL ENGINEERING CHALLENGES
TO MEET CURRENT AND EMERGING NEEDS OF SOCIETY
© 2024 the Authors
ISBN 978-1-032-54816-6
DOI 10.1201/9781003431749-370
Open Access: www.taylorfrancis.com, CC BY-NC-ND 4.0 license

ECSMGE 24
XVIII EUROPEAN CONFERENCE ON SOIL MECHANICS AND GEOTECHNICAL ENGINEERING

Performance of state parameter for undrained shear behaviour

Performance du paramètre d'état pour le comportement en cisaillement non drainé

S.U.U.S. Shah*
Zentrum Geotechnik, Technical University of Munich, Munich, Germany

A. Ahmad
AECOM, Virginia, U.S.A

**uzair.shah@tum.de*

ABSTRACT: In literature, the concept of state parameter, which is a difference between the current void ratio and the steady-state void ratio at the current stress level, is presented to be a useful state index for the comparison of shear behaviour under drained conditions. This is due to the nature of state parameter to simultaneously take into account the effects from void ratio and pressure as both control the volume change potential and hence, the shear behaviour. However, the analysis on undrained shear behaviour of some laboratory-standard sands shows that relationships between the state parameter and stress ratio at initial peak strength (which mobilizes upon the onset of strength reduction or softening leading to liquefaction) are influenced by the level of consolidation pressure. For some samples, at the same state parameter, the increase in consolidation pressure showed the increase in stress ratio mobilized at the instability state which means that the effect of densification (cause of dilative potential) overpowers the effect of pressure increase (cause of contractive potential). Whereas, other samples showed the decrease in stress ratio mobilized at the instability state with the increase in consolidation pressure against the same state parameter. This represents bias in the behavioural comparisons just on the basis of initial states which is also influenced by the curved geometry of the steady state line on e-log(p') plane. These equivocal effects on the basis of state parameter also hinder the applicability of such correlations in judging the influence of material properties on the instability state.

RÉSUMÉ: Dans la littérature, le concept de paramètre d'état, qui est une différence entre le rapport de vide actuel et le rapport de vide à l'état d'équilibre au niveau de contrainte actuel, est présenté comme un indice d'état utile pour la comparaison du comportement de cisaillement dans des conditions drainées. Ceci est dû à la nature du paramètre d'état qui prend simultanément en compte les effets du taux de vide et de la pression, car tous deux contrôlent le potentiel de changement de volume et, par conséquent, le comportement en cisaillement. Cependant, l'analyse du comportement en cisaillement non drainé de certains sables standard de laboratoire montre que les relations entre le paramètre d'état et le rapport de contrainte à la résistance maximale initiale (qui se mobilise au début de la réduction de la résistance ou de l'adoucissement conduisant à la liquéfaction) sont influencées par le niveau de la pression de consolidation. Pour certains échantillons au même paramètre d'état, l'augmentation de la pression de consolidation a montré l'augmentation du rapport de contrainte mobilisé à l'état d'instabilité, ce qui signifie que l'effet de la densification (cause du potentiel de dilatation) l'emporte sur l'effet de l'augmentation de la pression (cause du potentiel de contraction). En revanche, d'autres échantillons ont montré une diminution du ratio de contrainte mobilisé à l'état d'instabilité avec l'augmentation de la pression de consolidation par rapport au même paramètre d'état. Cela représente un biais dans les comparaisons comportementales sur la base des états initiaux, qui est également influencé par la géométrie incurvée de la ligne d'état stable sur le plan e-log(p'). Ces effets équivoques sur la base du paramètre d'état entravent également l'applicabilité de ces corrélations pour juger de l'influence des propriétés des matériaux sur l'état d'instabilité.

Keywords: State parameter; shear behaviour; liquefaction; steady state; instability state.

1 INTRODUCTION

Liquefaction is a significant reduction or loss of strength in saturated, loose and cohesionless sands upon the undrained shearing. Literature shows abundant laboratory tests on the loose sand samples undergoing high strength reduction followed by large strains. This loss of strength is induced by the increase of porewater pressure, and consequently, the reduction in effective stresses due to the contractive potential of loose samples. The liquefaction of granular soils,

particularly sands, has been systematically studied within the framework of steady state (or interchangeably, the critical state), which is defined as the ultimate state at which a mass of particles deforms with constant stress and constant volume (Poulos, 1981). In addition to the steady state (SS), the quasi-steady state (or QSS) which is a state of local minimum resistance mobilized during the undrained shearing has also been reported (Been et al., 1991; Ishihara, 1993; Yamamuro and Lade, 1998). Occurrence of QSS follows the mobilization of instability (IS) state which marks the local or initial peak in strength at which softening or even collapse of a loose grain skeleton triggers. The instability state is instantaneous in its occurrence, whereas, the QSS is a transitional state of temporary standstill in strength which persists during a certain range of strains (depending upon the sample state) and is followed by re-hardening towards the SS. The typical undrained behavior of sand sample showing the instability state and quasi-steady state is schematically presented in Figure 1(a). Used stress invariants are $q = \sigma'_{zz} - \sigma'_{xx}$ and $p' = (\sigma'_{zz} + 2\sigma'_{xx})/3$. Where, σ'_{zz} and σ'_{xx} are the vertical and radial normal stresses, which are also the major and minor principal stresses, respectively. $\sigma'_{xx} = \sigma'_{yy}$ due to the considered axisymmetry. Initial state parameter, $\Psi_{o(ss)}$, is the difference between void ratio (e) and e on the SS line at p'_c. As the contractive samples shows overshooting of state path across the steady state line towards the QSS on $e - p'$ plane, the reference state for instability state and post-instability softening should be the QSS at which the contractive potential exhausts (Figure 1-b). Therefore, $\Psi_{o(qss)}$ as the difference between void ratio and $e_{(qss)}$ corresponding to p'_c can also be examined. Moreover, the laboratory tests show that the initial states plotting underneath the SS line also show the instability and softening. Hence, the binary classification of shear behaviour on the basis of initial state with reference to the SS line in order to separate contractive/liquefiable states from the dilative/safe states can be misleading. Stress ratio mobilized at the instability state is lower than that mobilized at the quasi-steady state and steady state and shows high state dependencies as compared to that at the latter two states (Ishihara, 1993; Yamamuro and Lade, 1998; Murthy et al., 2007). Strength reduction following the instability state can lead to catastrophic failure in loose deposits, which suggests to consider it as a yield state. However, It is challenging to understand the influence of state on the stress ratio at instability from the literature due to high scatter in the correlations (Olson and Stark, 2003; Murthy et al, 2007; Rabbi, 2019) which hinders their field applicability.

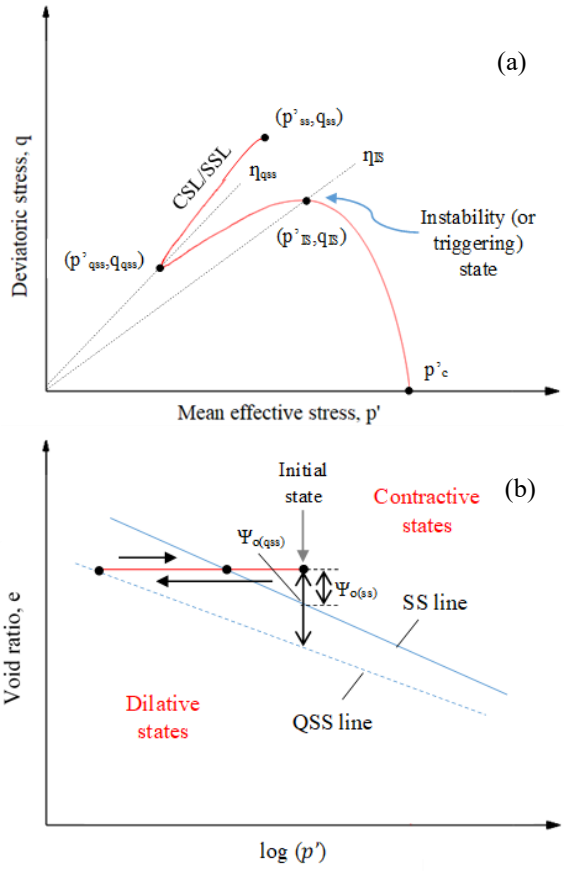

Figure 1. Schematic undrained behaviour showing temporary liquefaction or Quasi-steady state (a) effective stress path; (b) state path and loci on e-p' plane.

2 ANALYSIS ON LABORATORY TESTS

Analysis of the undrained triaxial test data from the literature was involved in order to understand the dependencies of strength behavior on state and material properties. Table 1 summarizes some index properties of sands for which the test behavior will be analyzed and discussed.

Table 1. Index properties of analysed sands.

Sand	D_{50} (mm)	C_u	Grain shape
Toyoura sand (TS)[1]	0.22	1.4	Angular
Fujian sand (FS)[1]	0.4	1.53	Angular to sub-rounded
Ottawa sand (OS)[2]	0.4	1.43	Rounded
TS finer[3]	0.17	1.7	Sub-angular

Sources: [1] from Yang and Wei (2012), [2] from Murthy et al. 2007 & [3] from Verdugo (1992)

Approximated steady state lines (SSLs) from the triaxial tests conducted on these materials are shown in Figure 2. Comparison of the two gradations of Toyoura sand shows the steady state lines of both to be parallel but translating downwards with the widening of gradation. A comparison can also be drawn between the steady state behavior of Fujian sand (FS) and Ottawa sand (OS) on the basis of their equal mean grain diameter (D_{50}). The steady state line of FS plots above the OS which can be attributed to its more angular grains despite the relatively wider gradation. A comparison can also be drawn between the Ottawa and Toyoura sand on the basis of their same C_u. The relatively upwards plotting of steady state line for TS can be due to its finer gradation (or smaller D_{50}) which can be linked with the corresponding higher settlement void ratios but owing to it angular grains, the steady state line of Toyoura sand is also relatively steeper.

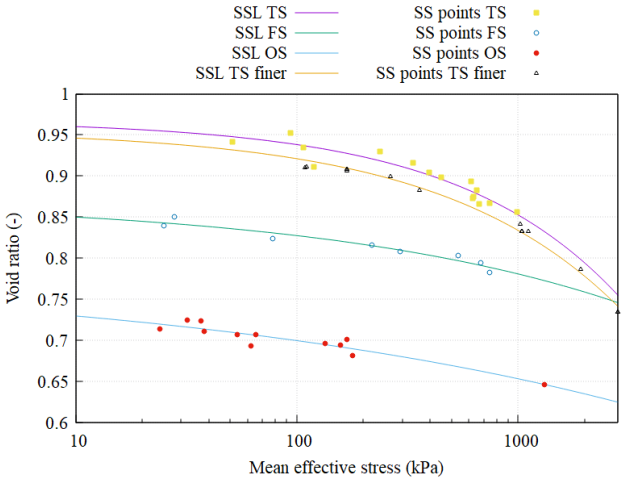

Figure 2. Steady state lines for analysed sands.

For behavioral comparison of instability stress ratio against the initial state parameter with reference from the SSL ($\Psi_{o(ss)}$), and QSSL ($\Psi_{o(qss)}$) are provided in Figure 3. Generally, the q_{IS}/p'_{IS} increases with the decrease in Ψ_o, which shows the proximity of sample state with the SSL. As the influence of consolidation pressure is present despite the normalized q_{IS}/p'_{IS} ratio (because the values of p'_{IS} hold the influence of p'_c), the bifurcation is performed here with respect to the p'_c. The analyzed tests on Fujian and Toyoura sand opted either the $p'_c = 100\ kPa$ or $p'_c = 500\ kPa$ which helped to understand the mechanics influenced only by the change in void ratio. The q_{IS}/p'_{IS} ratio is increasing with the increase in void ratio due to the decreasing availability of pore spaces for sand grains to rearrange into and showing higher grain interlocking and geometrical interference. The $q_{IS}/p'_{IS} - \Psi_o$ relations are fitted with straight lines.

For the case of finer TS, a higher scatter can be seen which is due to a wide range of consolidation pressures in this category, i.e. 1 MPa $\leq p'_c \leq$ 3 MP. For Toyoura, Fujian and Ottawa sands, the $q_{IS}/p'_{IS} - \Psi_o$ relation moves slightly downwards with the increase in p'_c. This shows that for samples at the same $\Psi_{o(ss)}$ or $\Psi_{o(qss)}$, effects from the increase in consolidation pressure (favoring contractive potential) overpower the densification (or reduction in the void ratio favoring dilative potential). Whereas, In the case of finer Toyoura sand, the $q_{IS}/p'_{IS} - \Psi_o$ relation for the higher p'_c values plots above the one for the lower consolidation pressure. At the same $\Psi_{o(ss)}$, gradual strengthening of the samples of finer TS with the increase in p'_c is seen from the test results by Verdugo (1992). This ratcheting in the $q_{IS}/p'_{IS} - \Psi_o$ relations due to the increase in p'_c limits their utilization.

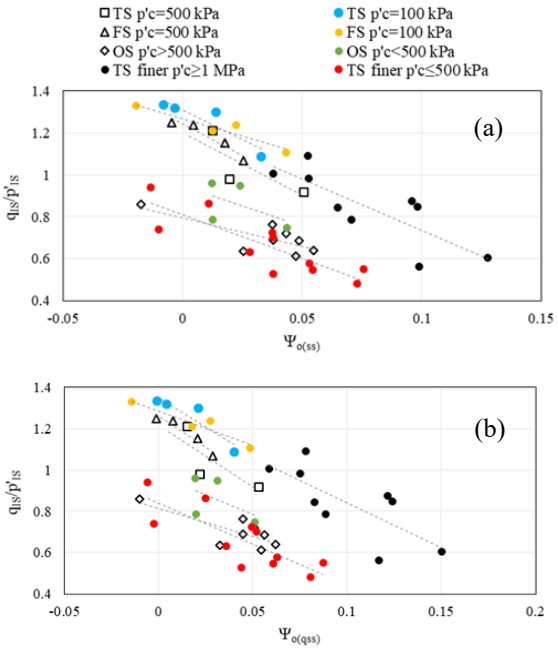

Figure 3. Instability stress ratio against initial state parameter with reference to (a) Steady state; (b) Quasi-steady state.

The instability or the post-peak softening mechanisms is present around $\Psi_{o(ss)} \leq 0$. This means that the samples with initial states lying under the approximated steady state line also showed the instability (or post-peak strength) behavior. To compare between the TS and TS finer, the TS finer has relatively wider composition with relatively less angular grains. The lower Cu, higher D50 and relatively angular grain shape of the TS suggest the higher interlocking in its sample. Therefore, the $q_{IS}/p'_{IS} - \Psi_o$ relation for the TS is plotting above than that of the finer TS. Behavior of FS and OS is

compared together due to their equal D_{50} but different particle shapes (OS being relatively more round grained) even though the gradation of the FS is relatively wider. Resultantly, the $q_{IS}/p'_{IS} - \Psi_{o(ss)}$ relations for the angular FS are plotting above that from the OS. These inferences on the basis of material properties are limited as the relations are simultaneous influenced by the consolidation pressure. Due to the diminishing of the contractive volumetric strain potential (or $\delta p' < 0$) coincides with the quasi-steady state which terminates the post-instability softening. With this expectation, relations between q_{IS}/p'_{IS} and $\Psi_{o(qss)}$ were presented but they also shows the similar dependencies.

3 CONCLUSIONS

Mobilization of the instability state triggers strength reduction which is expected to cause catastrophic failure in loose deposits. In the literature, it was attempted to draw relationships between the stress ratio at instability and the state parameter but the practical utilization of such relationships demands to study their unreasonably large scatters and dependencies. Stress ratio at instability cannot be defined as a function of state parameter due to its other state dependencies. The increase in consolidation pressure causes reverse effects (i.e. either strengthening or weakening) on such relations for different sands. Moreover, simultaneous and resembling effects from consolidation pressure and material properties make it challenging to judge their isolated influences on relationships between the instability stress ratio and state parameter which is schematically shown in **Error! Reference source not found.**. Practical utilization of instability state as yield condition demands to address the bias caused by initial state and points towards examining the performance of other state indices as well.

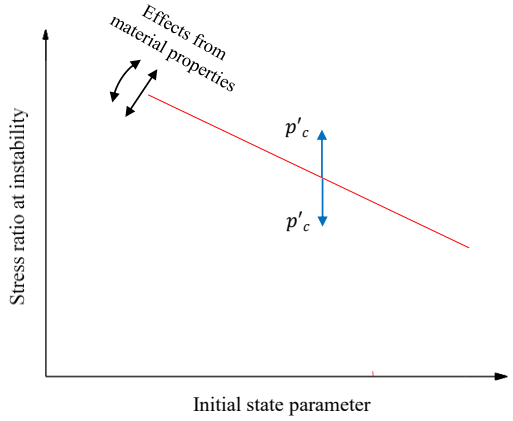

Figure 4. Schematic influences of p'_c on relations between the stress ratio at instability and initial state parameter.

REFERENCES

Been, K., M.G. Jefferies and J. Hachey. (1991). The critical state of sands. *Geotechnique*. 41(3):365–381. https://doi.org/10.1680/geot.1991.41.3.365.

Ishihara, K. (1993). Liquefaction and flow failure during earthquakes. *Geotechnique*. 43(3):351–451. https://doi.org/10.1680/geot.1993.43.3.351.

Murthy, T.G., D. Loukidis, J.A.H. Carraro, M. Prezzi and R. Salgado. (2007). Undrained monotonic response of clean and silty sands. *Géotechnique*. 57(3):273–288. https://doi.org/10.1680/geot.2007.57.3.273.

Olson, S. M., and Stark, T. D. (2003). Use of laboratory data to confirm yield and liquefied strength ratio concepts. *Canadian Geotechnical Journal*, 40(6), 1164-1184. https://doi.org/10.1139/t03-058.

Poulos, S. J. (1981). The steady state of deformation. *Journal of the Geotechnical Engineering Division*, 107(5), 553-562.

Rabbi, A. T. M. Z., Rahman, M. M., & Cameron, D. A. (2019). The relation between the state indices and the characteristic features of undrained behaviour of silty sand. *Soils and Foundations*, 59(4), 801-813. https://doi.org/10.1016/j.sandf.2019.05.001

Verdugo, R. (1992). *Characterization of sandy soil behaviour under large deformation*, Doctoral dissertation/thesis, University of Tokyo. https://dl.ndl.go.jp/pid/3095266/1/1.

Yamamuro, J.A. and P.V. Lade. (1998). Steady-state concepts and static liquefaction of silty sands. *J. of geotechnical and geoenvironmental engineering*. 124(9):868–877. https://doi.org/10.1061/(ASCE)1090-0241(1998)124:9(86.

Yang, J. and Wei, L.M. (2012). Collapse of loose sand with the addition of fines: the role of particle shape. *Géotechnique*, 62(12), pp.1111-1125. https://doi.org/10.1680/geot.11.P.062.

Proceedings of the XVIII ECSMGE 2024
GEOTECHNICAL ENGINEERING CHALLENGES
TO MEET CURRENT AND EMERGING NEEDS OF SOCIETY
© 2024 the Authors
ISBN 978-1-032-54816-6
DOI 10.1201/9781003431749-371
Open Access: www.taylorfrancis.com, CC BY-NC-ND 4.0 license

ECSMGE 24
XVIII EUROPEAN CONFERENCE ON SOIL MECHANICS AND GEOTECHNICAL ENGINEERING

Seismic bearing capacity of shallow foundations on soil reinforced by rigid inclusions

Capacité portante sismique des fondations sur sol renforcé par inclusions rigides

Y. Shen*
IMSIA (UMR 9219), CNRS, EDF, CEA, ENSTA Paris, Institut Polytechnique de Paris, Palaiseau, France / TERRASOL (SETEC Group), Paris, France

J. Pérez-Herreros, F. Cuira, S. Burlon
TERRASOL (SETEC Group), Paris, France

J-F. Semblat
IMSIA (UMR 9219), CNRS, EDF, CEA, ENSTA Paris, Institut Polytechnique de Paris, Palaiseau, France

**yuxiang.shen@setec.com*

ABSTRACT: The kinematic exterior approach, in the framework of the yield design theory, is widely utilised for assessing foundation bearing capacity. This study aims at extending this approach to shallow foundations on reinforced soil by rigid inclusions. The interaction diagram in the (V, H, M) space is obtained by combining the interaction curves derived from different failure mechanisms. The resisting forces provided by the rigid inclusions are evaluated using a multicriterion approach and are considered at the intersection of the inclusions with the failure surface. Furthermore, the soil inertia due to the horizontal seismic excitation is also considered in the analysis. The results reveal that the bearing capacity under seismic load is unaffected in the zone of interest for foundations with a sufficient safety factor under static loading.

RÉSUMÉ: L'approche cinématique par l'extérieur, dans le cadre de la théorie de calcul à la rupture, est largement utilisée pour évaluer la capacité portante des fondations. Cette étude vise à étendre cette approche aux fondations renforcées par inclusions rigides. Pour ce faire, le diagramme d'interaction dans l'espace (H, V, M) est obtenu en combinant les diagrammes d'interaction issus de différents mécanismes de rupture. L'effet de renforcement apporté par les inclusions rigides est pris en compte au moyen des forces résistantes développées à l'intersection de l'inclusion avec la surface de rupture, et sont évaluées à l'aide d'un multicritère. De plus, cette étude prend en compte les effets d'inertie du. Les résultats révèlent que la capacité portante sous charge sismique n'est pas impactée dans la zone d'intérêt pour les fondations présentant un facteur de sécurité suffisant sous charge statique.

Keywords: Yield design; bearing capacity; rigid inclusion-reinforced foundation; ASIRI+.

1 INTRODUCTION

The reinforcement technique using rigid inclusions (RI), represents an alternative foundation solution that offers significant technical and economic advantages in comparison to conventional pile foundations. This technique has been used successfully in numerous projects involving complicated geotechnical contexts.

This foundation concept consists of a shallow foundation on a reinforced soil with vertical rigid elements, known as rigid inclusions, which reduce the foundation settlement while enhancing its vertical bearing capacity. There is no direct connection between the shallow foundation and the RIs. Instead, a gravel layer is introduced as a load transfer platform (LTP) as depicted in Figure 1.

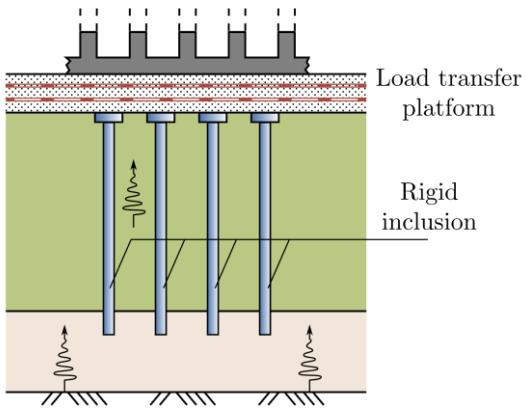

Figure 1. Shallow foundation on soil reinforced by rigid inclusions under seismic loading.

Recent studies have focussed on the dynamic response of such foundations (Shen et al., 2022a, b,

2023). However, the question of the bearing capacity under static and seismic loading has not yet been studied in detail and no practical methodology is available. Consequently, this study focuses on addressing the seismic bearing capacity problem of RI-reinforced foundations using the kinematic exterior approach.

2 KINEMATIC EXTERIOR APPROACH

2.1 Theoretical framework

Within the context of the yield design theory, the kinematic exterior approach operates as an upper-bound analysis method. This approach involves evaluating a kinematically admissible virtual velocity field $\underline{\hat{U}}$ and verifying whether the virtual power of external loads applied to the system, denoted as P_e, is less than or equal to the maximum resisting power of the soil, denoted as P_{rm}.

An upper-bound K encompasses the space delineated by:

$$K \subset \{P_{rm}(\underline{\hat{U}}) \geq P_e(\underline{\hat{U}})\} \quad (1)$$

The maximum resisting power P_{rm} is equal to:

$$P_{rm}(\underline{U}) = \int_\Omega \pi\left(\underline{\hat{d}}\right) d\Omega + \int_\Sigma \pi(\llbracket \underline{\hat{U}} \rrbracket)\, d\Sigma \quad (2)$$

where $\pi(.)$ represents the density of virtual power due to the strain rate $\underline{\hat{d}}$ within the volume Ω and to the virtual velocity $\llbracket \underline{\hat{U}} \rrbracket$ at the velocity discontinuity surface Σ. These quantities are derived from the strength criteria. The explicit formulation of the function $\pi(.)$ for various criteria, applicable to both continuous materials and interfaces, can be found in the work of Salençon (1983, 2002).

The virtual power of all external forces P_e applied to the system encompasses the power of the loads exerted on the foundation, in terms of forces and moments, as well as the body forces originating from soil inertia.

In the case of a foundation reinforced by RIs, the formulation of P_e remains unchanged when compared to the case without reinforcement. Nonetheless, the contribution of reinforcement by RIs, represented by P_{RIs}, should be added into the resisting power part, as outlined in:

$$K \subset \{P_{rm}(\underline{\hat{U}}) + P_{RIs}(\underline{\hat{U}}) \geq P_e(\underline{\hat{U}})\} \quad (3)$$

2.2 Application to the study of geotechnical structures

The kinematic exterior approach has been employed in previous work to investigate the bearing capacity of strip foundations resting on homogeneous cohesive and cohesionless soils subjected to static and seismic loads (Salençon and Pecker, 1995a, 1995b; Paolucci and Pecker, 1997; Soubra, 1999).

It can be also found that the kinematic exterior approach has already been used to study the stability problem of reinforced geotechnical structures, such as nailed slopes.

De Buhan et al. (1992) investigated the stability of nailed slopes using the kinematic exterior approach. The study comprised kinematic mechanisms based on triangular blocks and logarithmic spiral failure surfaces. Several slope stability softwares, including TALREN (Terrasol, 2023), PROSPER (De Sauvage and Rajot, 2018), and STARS (Antoine, 1990), also employ failure surfaces in the form of logarithmic spirals. The contribution of nail reinforcements is introduced by employing a multicriterion approach based on various failure modes associated with the nails.

Very few applications of the kinematic exterior approach to study RI-reinforced foundations have been conducted so far. This is partly due to the inherent complexity introduced by the presence of the three distinct components: the soft soil, the granular LTP, and the RIs, which makes it difficult to determine kinematically admissible virtual velocity fields $\underline{\hat{U}}$.

Pecker et al. (1998) evaluated the seismic bearing capacity of a shallow foundation on cohesive soil reinforced by RIs, using the kinematic exterior approach. The findings were compared with the results of five centrifuge tests carried out for the Rio-Antirrio bridge project. Figure 2 presents a kinematic mechanism considered in that study, which closely resembles the failure mechanism observed in the centrifuge tests.

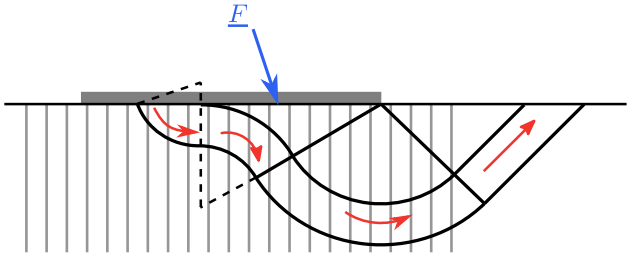

Figure 2. Virtual velocity field considered in the bearing capacity estimation of the Rio-Antirrio bridge foundation.

In this mechanism, the contribution of the RIs was considered by the intrinsic material resistance and their skin friction. Additionally, a failure criterion

representing the slide failure between the LTP and the foundation was introduced and superimposed onto the results obtained through the kinematic exterior approach.

3 BEARING CAPACITY OF A STRIP FOOTING ON REINFORCED SOIL

3.1 Description of the problem

This study focuses on the seismic bearing capacity of a strip foundation on reinforced soil by RIs. A strip foundation of width B is placed on a half-space consisting of a LTP of thickness h_{LTP} and purely cohesionless behaviour (friction angle φ), over a cohesive soft soil layer with a cohesion c and no tensile strength. The soft soil layer is reinforced with RIs, as illustrated in Figure 3.

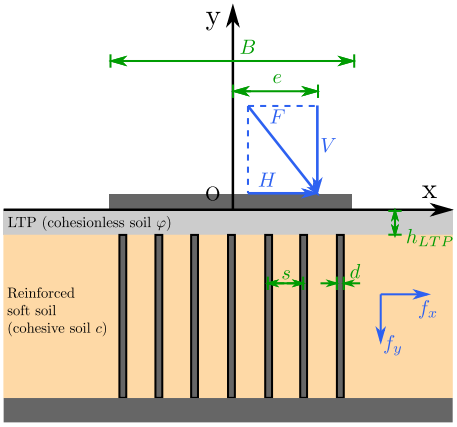

Figure 3. Studied configuration: strip foundation on reinforced soil by Ris.

The RI rows are modelled by embedded beams. They are assumed to be regularly spaced under the foundation with a spacing s and are embedded in the compact soil layer.

The force transmitted to the footing is denoted as $\underline{F}$, and the moment $\underline{M}$ is calculated by multiplying the vertical force by the eccentricity e.

Additionally, the soil inertia effects are considered through body forces due to seismic and gravity loading, denoted as $f_x = \rho a_x$ and $f_y = \rho(g \pm a_y)$, respectively. The horizontal

3.2 Simplified sub-systems

The presence of reinforcements and the LTP layer in RI-reinforced foundations introduces additional complexity to the failure mechanisms when compared to non-reinforced configurations. To address this, three simplified sub-systems (or cases), illustrated in Figure 5, are proposed, corresponding to the different potential failure mechanisms are investigated:

- Case I: This sub-system considers a homogeneous frictional soil, where the failure mechanism is primarily concentrated in the LTP, resulting in a failure depth lower than h_{LTP};
- Case II: This sub-system deals with the potential sliding and uplift at the interface between the LTP and the reinforced soft soil;
- Case III: Involves a homogeneous cohesive soil reinforced by RIs. The failure mechanism depth in this case exceeds h_{LTP} and intersects the RIs, that contribute thus to the resistance. It should be noted that the contribution of the soil and the RIs are calculated separately, as depicted in Figure 6.

The upper-bound solutions for the three cases are denoted $K^{up,I}$, $K^{up,II}$, and $K^{up,III}$. They are combined to determine the stability domain K^{up} of a foundation reinforced by RIs, as described in :

$$K^{up} = K^{up,I} \cap K^{up,II} \cap K^{up,III} \quad (4)$$

3.3 Failure analysis of a rigid inclusion

The RIs are considered by accounting for their action at the intersection with the failure surface. The RI is divided into two parts by the intersection: interior part with a length L_{int} and exterior part with length L_{ext}, as depicted in Figure 4 (a). The forces at this intersection are decomposed into an axial force T_n, a shear force T_c, and a bending moment M_c, as shown in Figure 4 (b). Their maximum value are limited by several criteria:

- Material intrinsic strength;
- Vertical interaction resistance;
- Lateral interaction resistance: plastification of the soil;
- Lateral interaction resistance: plastification of the RI.

3.3.1 Material intrinsic strength resistance

The combination of T_n, T_c, and M_c that occurs at the intersection of the RIs with the velocity discontinuity surface can be represented by:

$$\left(\frac{T_n}{R_n}\right)^2 + \left(\frac{T_c}{R_c}\right)^2 + \left|\frac{M_c}{R_m}\right| - 1 \leq 0 \quad (5)$$

where R_n, R_c, and R_m are the axial, shear, and flexural capacities of a rigid inclusion related to the material intrinsic strength and the inclusion's section. In the case with the presence of the steel reinforcement in the concrete inclusions, the reinforcement should be considered.

3.3.2 Axial soil-inclusion interaction resistance

The maximum axial force T_{nl} that a RI of diameter d can provide is also governed by parameters such as the skin friction, the forces at the head and the tip of the RI, and the internal "pullout" failure mechanism. This can be described by:

$$T_{nl} = min\,(F_0 + q_s L_{int}\pi d, F_L + q_s L_{ext}\pi d) \quad (6)$$

where F_0 represents the maximum force controlled by a Prandtl failure mechanism in the LTP, F_L represents the maximum force at the inclusion tip, which is typically of significant magnitude. Additionally, q_s denotes the characteristic value of the inclusion shaft friction.

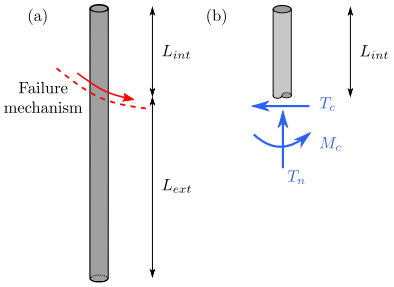

Figure 4. Scheme of a RI intersected by a failure mechanism: (a) interior length L_{int} and exterior length L_{ext} and (b) RI forces at the intersection.

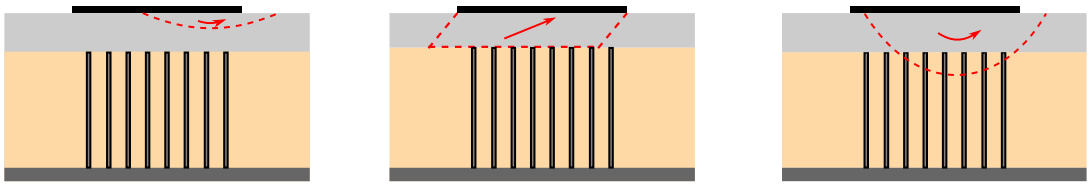

Figure 5. Simplified sub-systems for a foundation reinforced by Ris.

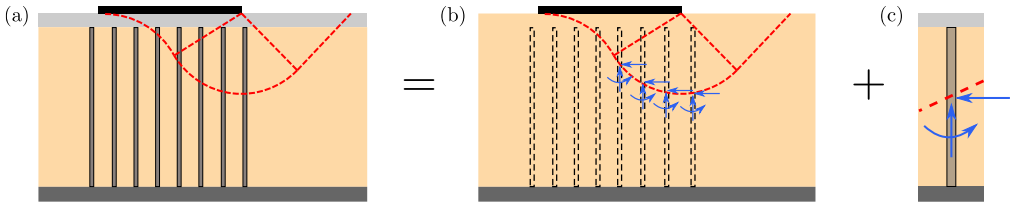

Figure 6. Detailed description for Case III: (a) multi-block failure mechanism, (b) simplified configuration, and (c) forces at the intersection of RI with failure interaction.

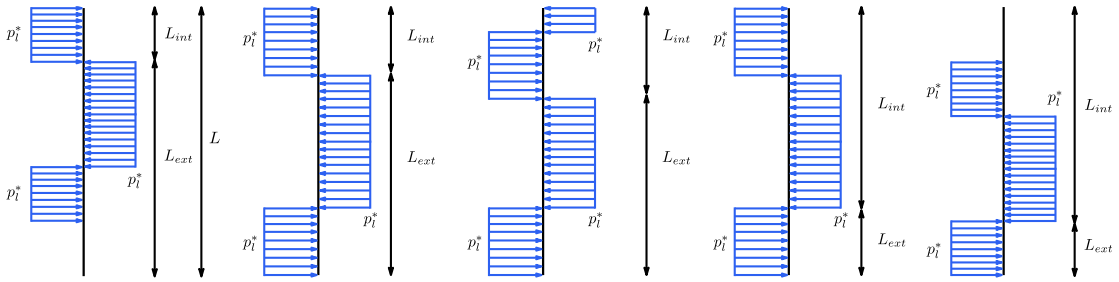

(a) $L_{int} < L/4$ (b) $L_{int} = L/4$ (c) $L/4 < L_{int} < 3L/4$ (d) $L_{int} = 3L/4$ (e) $L_{int} > 3L/4$

Figure 7. Distribution of lateral pressure for limit equilibrium model.

3.3.3 Lateral soil-inclusion interaction resistance

This criterion corresponds to the mobilised resistance due to lateral soil-inclusion interaction. The pressure within the interior length L_{int} or the exterior length L_{ext} of the RI is restricted by the limit pressure p_l^* in the soil.

The lateral interaction of the RI is analysed through a limit equilibrium model, as depicted in Figure 7. Several lateral pressure distributions for various lengths L_{int} and L_{ext} are considered.

The corresponding shear force T_{cl1} and bending moment M_{cl} at the intersection and the maximum bending moment M_{max} within the RI generated by the lateral pressure can be expressed with respect to the ratio L_{int}/L, as shown in Figure 8.

3.3.4 Formulation of the RI multicriterion

The combination of the four criteria in the T_n-T_c plane defines a useful stability domain, known as the RI multicriterion and illustrated in Figure 9. This domain

establishes the limits on the potential resisting forces provided by the RIs.

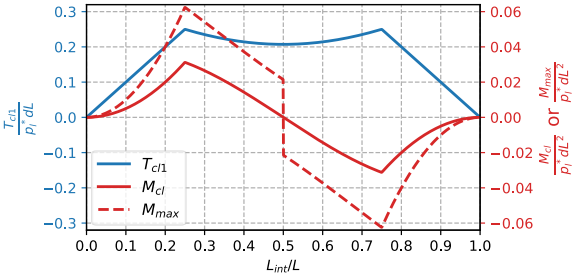

Figure 8. Evaluation of T_{cl1}, M_{cl}, and M_{max} due to soil-inclusion lateral interaction for different values of the ratio L_{int}/L.

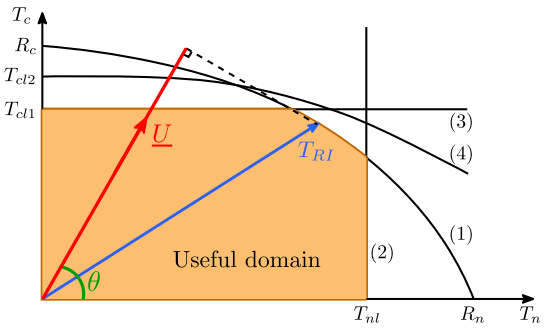

Figure 9. RI multicriterion in the T_n-T_c plane.

When failure occurs, the resisting forces developed by the RI must lie on the boundary of this useful domain, and its position is determined by the principle of maximum work. This principle indicates that the forces on the boundary are chosen in a way that maximises the resisting power provided by rigid inclusions within a given failure mechanism. Once the virtual velocity at the intersection of the inclusion with the failure surface is specified, the virtual power of the inclusion can be calculated.

3.4 Practical application

A typical foundation configuration is considered. It consists of a 10 m wide strip foundation, resting on a 0.5 m thick LTP layer with a friction angle of 38°. The soft soil is considered as cohesive, characterised by an undrained shear strength c of 25 kPa, a q_s = 25 kPa and p_l^* = 200 kPa. The soft soil is reinforced by rows of RI with a diameter of 0.4 m and a length of 10 m. The axis-to-axis spacing is 1.5 m, resulting in a coverage area ratio of 5.6 %. The head of the RI corresponds to the base of the LTP.

The bearing capacity of the foundation is studied using the approach presented in the previous sections. The interaction diagram is normalised by the product of the cohesion c and the width of the foundation B, as depicted in Figure 10.

For small vertical forces, the V-H interaction diagram is predominantly controlled by Case I (blue curve), corresponding to failure within the LTP layer. As the vertical force increases, a sliding mechanism between the LTP and the soft soil becomes apparent (green curve). Finally, for greater vertical forces, the interaction diagram is primarily controlled by Case III (red curve), which represents a failure mechanism in the reinforced soil.

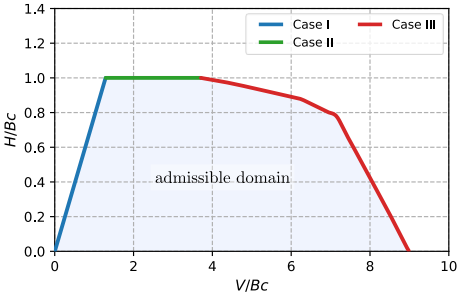

Figure 10. Bearing capacity of a strip foundation on reinforced soil by RI in the normalised V-H plane.

4 SOIL INERTIA EFFECT ON THE BEARING CAPACITY

4.1 Interaction diagram under various soil inertia values

The adverse impact of soil inertia forces on the bearing capacity of non-reinforced foundations can be significant, particularly for foundations designed with a low safety factor under a vertical centred load. This impact for RI-reinforced foundations is studied in this section.

The V-H interaction curves for several acceleration values in the soil ranging from 0 to 0.4 g are displayed in Figure 11.

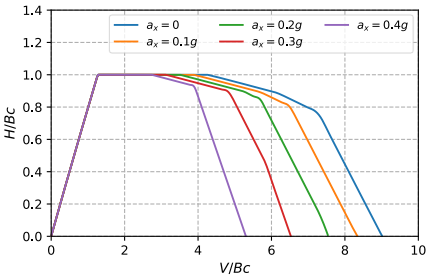

Figure 11. Normalised V-H interaction curves for different ground accelerations.

It is observed that the shape of the V-H interaction curves is not affected by soil inertia effects, and only the amplitude of their right-hand side (Case III), which is controlled by the failure mechanism traversing the reinforced soil, is influenced by the soil inertia.

4.2 Bearing capacity under different soil inertia values

The bearing capacity, denoted V_{max}, represents the maximum vertical centred force that a foundation can carry. Figure 12 explores the bearing capacity values with different soil inertia values due to the horizontal seismic excitation. The soil inertia values are represented by the dimensionless soil inertia forces $\bar{F} = \rho a_x B/c$. Comparing the non-reinforced configuration (orange curve) to the reinforced configurations (blue curves for different coverage area ratios α), it can be observed that the rigid inclusion improvement enhances the foundation bearing capacity V_{max} to withstand the soil inertia.

For example, at a dimensionless soil inertia force of $\bar{F} = 2$, corresponding to a situation with $a_x = 0.33$ g, $\rho = 1.8\ t/m^3$, $B = 10\ m$, and $c = 25\ kPa$, the non-reinforced foundation exhibits a 50 % reduction in its bearing capacity due to soil inertia effect. In contrast, the reinforced configuration with the same soil inertia still retains approximately 80 % of its bearing capacity.

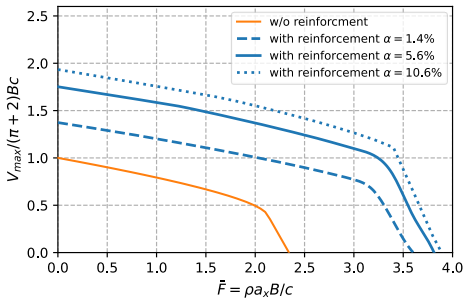

Figure 12. Evolution of the bearing capacity V_{max} of the foundation with respect to different soil inertia values.

5 CONCLUSIONS

This work extends the application of the kinematic exterior approach to rigid inclusion-reinforced foundations. To accurately estimate the contribution of the inclusions to the resistance of the system.

The bearing capacity under the soil inertia is studied for reinforced configurations with different coverage area ratios, revealing that the bearing capacity consistently increases as the coverage area ratio does. The interaction diagrams reveal that the bearing capacity under seismic load is unaffected in the zone of interest for foundations with a sufficient safety factor under static loading.

ACKNOWLEDGEMENTS

The authors are grateful for the financial support provided by Terrasol company. This research has received funding from the French National Research (ANR) project ASIRI_plus SDS reference No. ANR-19-CE22-0015-01.

REFERENCES

Anthoine, A. (1987). Stabilité d'une fouille renforcée par clouage. In: *Proc. 4th French-Polish Coll. appl. Soil Mech.*, Grenoble, France, pp. 129-154.

De Buhan, P., Dormieux, L. and Salençon, J. (1992). An interactive computer software for the yield design of reinforced soil structures. In *Coll. Informatique et Géotechnique,* Paris, France, pp. 181-188.

De Sauvage, J. and Rajot, J. P. (2018). Clouage des sols: conditions de long terme et amélioration du dimensionnement conventionnel. In *9emes JNGG.* Champs sur Marne, France

Paolucci, R. and Pecker, A. (1997). Seismic bearing capacity of shallow strip foundations on dry soils. *Soils Found.*, 37(3), pp. 95-105. https://doi.org/10.3208/sandf.37.3_95

Pecker, A., Harikiopoulos, H., de Buhan, P., Dormieux, L., Morand, P. (1998). Comportement sismique d'une fondation sur sol renforcé par inclusions rigides, Paris, France. Compte rendu pour MRES.

Salençon, J. (1983). *Calcul à la rupture et analyse limite*, Presses de l'École Nationale des Ponts et Chaussées, Paris, France.

Salençon, J. (2002). *De l'élasto-plasticité au calcul à la rupture*. Editions Ecole Polytechnique, Paris, France.

Salençon, J. and Pecker, A. (1995a). Ultimate bearing capacity of shallow foundations under inclined and eccentric loads. Part I: purely cohesive soil. *European journal of mechanics series a solids*, 14, pp. 349-349.

Salençon, J. and Pecker, A. (1995b). Ultimate bearing capacity of shallow foundations under inclined and eccentric loads. Part II: purely cohesive soil without tensile strength. *European journal of mechanics series a solids*, 14, pp. 377–96.

Shen, Y., Pérez-Herreros, J., Cuira, F., Semblat, J. F. and Burlon, S. (2022a). Interaction inertielle sol-structure d'un massif renforcé par inclusions rigides. In *11èmes JNGG*, Lyon, France.

Shen, Y., Pérez-Herreros, J., Cuira, F., Semblat, J. F. and Burlon, S. (2022b). Interaction cinématique sol-structure d'un massif renforcé par inclusions rigides sous séisme. In *11èmes JNGG*, Lyon, France.

Shen, Y., Pérez-Herreros, J., Cuira, F., Semblat, J. F. and Burlon, S. (2023). Evaluation des efforts d'origine inertielle dans les inclusions rigides. In *11ème Colloque National de l'AFPS*, Guadeloupe, France.

Soubra, A. H. (1999). Upper-bound solutions for bearing capacity of foundations. *J. Geotech. Geoenvironmental Eng.*, 125(1), pp. 59-68. https://doi.org/10.1061/(ASCE)1090-0241(1999)125:1(59)

Terrasol (2023) TALREN (v6): Advanced slope stability analysis with or without reinforcements, [Computer software].

Proceedings of the XVIII ECSMGE 2024
GEOTECHNICAL ENGINEERING CHALLENGES
TO MEET CURRENT AND EMERGING NEEDS OF SOCIETY
© 2024 the Authors
ISBN 978-1-032-54816-6
DOI 10.1201/9781003431749-372
Open Access: www.taylorfrancis.com, CC BY-NC-ND 4.0 license

ECSMGE 24
XVIII EUROPEAN CONFERENCE ON SOIL MECHANICS AND GEOTECHNICAL ENGINEERING

Influence of spatial variability of strength on bearing capacity for unsaturated soil

Influence de la variabilité spatiale de la résistance sur la capacité portante des sols non saturés

B.J. Shwan*
Water Resources Engineering Department, College of Engineering, Salahaddin University, Erbil, Iraq
**bestun.shwan@su.edu.krd*

ABSTRACT: Soil, even within a homogeneous layer, exhibits spatial variation in cohesion. Additionally, experimental tests have confirmed that spatial variability in cohesion can occur from changes in soil fabric under unsaturated conditions. Its significant effects on slope stability have been studied comprehensively, but limited to bearing capacity problems. This paper addresses, therefore, an analytical approach that utilises limit state analysis to investigate the influence of spatial variability in cohesion on the bearing capacity of a rigid surface strip footing. The analytical study considered various scenarios, accounting for different suction profiles that addressed the spatial variability in cohesion beneath and alongside the footing. The numerical results demonstrated a 18.5% increase in the ultimate bearing capacity, attributed to the effects of spatial variability in cohesion (changes in soil fabric). Inspection of the obtained failure mechanisms for the modelled scenarios revealed deeper and wider failure patterns when a higher multiplier/increase was applied to a greater cohesion value.

RÉSUMÉ: Le sol, même au sein d'une couche homogène, présente une variation spatiale de cohésion. De plus, des tests expérimentaux ont confirmé qu'une variabilité spatiale de la cohésion peut résulter de modifications du tissu du sol dans des conditions non saturées. Ses effets significatifs sur la stabilité des pentes ont été étudiés de manière approfondie, mais limités aux problèmes de capacité portante. Cet article aborde donc une approche analytique qui utilise l'analyse à l'état limite pour étudier l'influence de la variabilité spatiale de la cohésion sur la capacité portante d'une semelle filante à surface rigide. L'étude analytique a examiné divers scénarios, tenant compte de différents profils de succion qui traitaient de la variabilité spatiale de la cohésion sous et le long de la semelle. Les résultats numériques ont démontré une augmentation de 18,5% de la capacité portante ultime, attribuée aux effets de variabilité spatiale de la cohésion (changements dans la structure du sol). L'inspection des mécanismes de défaillance obtenus pour les scénarios modélisés a révélé des schémas de défaillance plus profonds et plus larges lorsqu'un multiplicateur/augmentation plus élevé était appliqué à une valeur de cohésion plus élevée.

Keywords: Soil fabrics; spatial variability; unsaturated soil; numerical analysis; bearing capacity.

1 INTRODUCTION

Soil, even within a homogeneous layer, exhibits spatial variation in strength. Additionally, spatial variability can arise from changes in soil fabrics under unsaturated conditions or due to the drying and wetting phenomenon. Understanding the characteristics of spatial variability is essential for assessing the reliability of geotechnical engineering problems. Researchers have studied the spatial variability in soils, emphasizing its significance in introducing uncertainties within the field of geotechnical engineering (see Tan et al., 2020).

Cho (2010) conducted a numerical study, extended the traditional limit equilibrium method of slices for the purpose of analysing the probabilistic stability of slopes, into the variations in soil strength parameters and their associated uncertainties. The results showed that the proposed method adequately addressed the causes of failure that arise from differences in soil characteristics. Jiang et al. (2018) used conditional random fields to analyse slope reliability and modelled the spatial variation in undrained shear strength of soil for a slope stability problem. The method successfully incorporated the data, from site investigation to model the differences, in soil properties using conditional random fields.

The preceding studies have indicated a significant effect of spatial variability on slope stability, but their focus was restricted to addressing bearing capacity problems. Changes in soil fabric can significantly affect shear strength (cohesion) (see Toll and Ong, 2003, Shwan and Smith, 2015 and Shwan, 2015). This paper addresses the effects of spatial variability (referring to variations in cohesion resulting from fabric changes due to suction) on the bearing capacity

of a rigid surface footing under different suction profiles, using an upper-bound theorem approach.

2 PROBLEM GEOMETRY AND MATERIALS

The schematic diagram of a rigid surface strip footing (1 m width) is depicted in Figure 1a with the obtained failure mechanics, not restricted to the boundaries. While, Figure 1b shows the soil water retention curve (SWRC) for a simulated soil, plotted using an SWRC equation proposed by Shwan and Smith (2014):

$$S_r = e^{-\kappa(s-AEV)} \quad (1)$$

where S_r is the degree of saturation, κ is a fitting parameter (kPa^{-1}) accounts for soil types (see Shwan, 2023a, 2023b, and 2023c), s is the suction (kPa) and AEV is the air entry suction. Equation 1 was validated against experimental data and fitted to the Fredlund and Xing (1994) model, (see Shwan, 2015, and 2017).

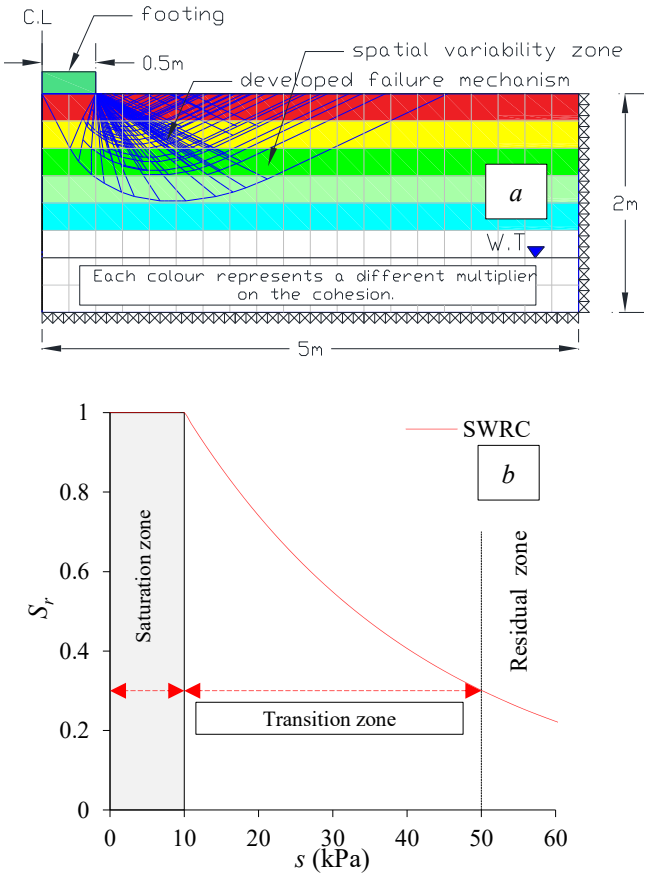

Figure 1. (a) Schematic diagram of the modelled footing, and (b) Simulated Soil-Water Retention Curve (SWRC).

The modelled suction range, applied by changing the water table level, ranged from 0 to 60 kPa.

The required parameters for the analysis were κ = 0.03 kPa^{-1} and AEV = 10 kPa, obtained through the SWRC in Figure 1b. The angle of shearing resistance (ϕ) and cohesion (c) values of 40° and 5 kPa, respectively, were used. In addition, dry, unsaturated and saturated unit weights were 14, 16 and 18 kN/m^3, respectively.

3 MODELLING SPATIAL VARABILITY

Soils exhibit different increases in effective stress under unsaturated conditions, (Bishop and Blight, 1963) attributed to different suction levels and soil structure, enhancing soil fabrics. Spatial variability in strength was, therefore, modelled in the UNSAT-DLO approach, a robust upper bound theorem approach modified by the author to account for the effects of unsaturated conditions on strength, using various scenarios. Spatial variability was attained by applying different multipliers (**M**) to cohesion (**M**× c), attributed to fabric changes, in each grid beneath the footing using different cases, see Figure 1a.

The suggested cases were categorised into two groups: Category 1 (C1), Figure 2, and Category 2 (C2), Figure 3. The case where cohesion exhibits no spatial variability (no changes in soil fabric, such as in fully dry and saturated conditions) was also simulated for comparison. Each category comprised three scenarios: SCE1, SCE2, and SCE3. Each colour in Figures 2 and 3 represents a spatial variability zone in cohesion where a different **M** value was utilised (i.e. **M**× c). The values of **M** used in the analysis are depicted in the legends of Figures 2 and 3, located in the last column of the colored grid. For the soil (grid) beneath the footing, a higher **M** value was applied, attributed to a higher applied suction which caused a higher enhancement in cohesion. As the soil was closer to the water table level (resulting in a lower suction value), a smaller **M** value was utilised. In C2, higher **M** values were applied compared to C1, as shown in Figure 3. SEC3 in Figure 3c represented the case in which the increase in cohesion due to suction was doubled (c = 10 kPa) with **M** = 2. As stated above, the fully saturated and fully dry cases (**M**=1, indicating no changes in soil fabric) were also considered, represented by the white colour in Figures 2 and 3.

4 NUMERICAL RESULTS

The failure mechanisms results obtained for C1 and C2 are shown in Figures 2 and 3, respectively. The case with no spatial variability (**M**=1), denoted as NS in the figure's legend, was superimposed with the modelled categories, denoted as SP. In Figure 2 (C1), similar

failure mechanisms were observed for both NS and SP cases, with the SP case exhibiting a higher ultimate bearing capacity ($\mathbf{Q_{ult}}$), discussed later. However, Figure 3 (C2) depicted wider and deeper failure mechanisms for cases with **M**=2 compared to C1. Clearly, the higher c value and **M**, the wider and deeper failure mechanism was obtained, see Figure 3c. The implications of the obtained failure mechanisms are significant, as strength mobilisation is a possible scenario attributed to changes in fabric,therefore, spatial variability in cohesion.

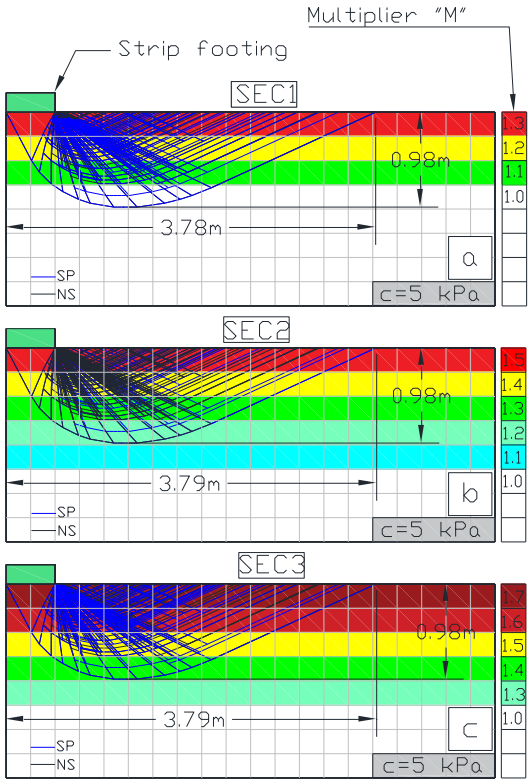

*Figure 2. Results of failure mechanisms for various scenarios with different values of **M** applied to cohesion in category 1 for (a) SEC1, (b) SEC2, and (c) SEC3.*

Figure 4 a and b shows the numerical results of the modelled scenarios previously presented in Figures 2 and 3. The x and y axes represent normalised suction and utlimate bearing capacity, respectively.

It is evident that the effect of unsaturated condition was significant compared to both the fully saturated condition (s=0 kPa) and dry case (plotted as a horizontal dashed line). For example, a 3.8-fold increase in normalised $\mathbf{Q_{ult}}$ was obtained at s/AEV = 4 for the NS case when compared with s = 0 kPa (S_r =1). Experimental studies in the literature have reported significantly higher increases in $\mathbf{Q_{ult}}$ (Mohamed and Vanapalli, (2006) (≈ 6 fold) and Shwan and Smith (2014) (≈ 10 fold). The ultimate bearing capacity was seen then to decrease, attributed to desaturation-induced strength reduction.

On the other hand, the effect of spatial variability in cohesion on the normalized $\mathbf{Q_{ult}}$ was significant. A 2.1% increase in $\mathbf{Q_{ult}}$ was obtained when comparing the C1-SEC1 with the NS cases (Figure 4a), even though almost identical failure mechanisms were obtained in Figure 2a as stated previously.

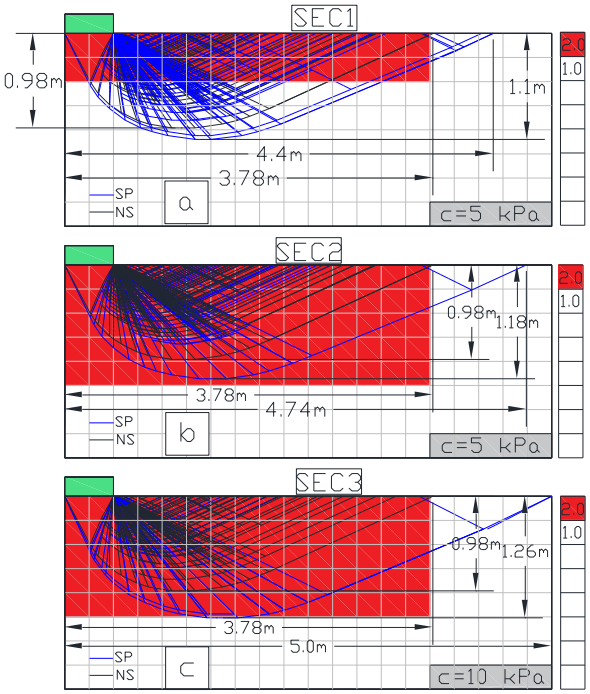

*Figure 3. Results of failure mechanisms for various scenarios with different values of **M** applied to cohesion in category 2 for (a) SEC1, (b) SEC2, and (c) SEC3.*

Figures 4a and b also exhibit other percentage increases in $\mathbf{Q_{ult}}$, when comparing SP cases with their respective NS cases. The case C2-SEC3 exhibited the highest increase in $\mathbf{Q_{ult}}$ (Figure 4b) as higher c=10 kPa and **M** =2 were used. The value **M**=2 represented the scenario where c increased by a factor of 2 due to suction effects. Experimentally, a 4.1-fold increase in c for unsaturated samples, attributed to fabric changes, was reported (Reis et al., 2011).

5 CONCLUSIONS

Even within a homogeneous deposit, soils may exhibit spatial variation in cohesion. This paper addressed a numerical study into the effects of spatial variability in cohesion for a simulated soil, attributed to fabric changes, on the ultimate bearing capacity ($\mathbf{Q_{ult}}$) for a rigid surface strip footing using an upper bound theorem, UNSAT-DLO approach. The approach, considers the effect of suction on strength, was utilised to model two different categories. Each category comprised three different scenarios. The scenarios accounted for spatial variability by applying different

multipliers (**M**) to cohesion (**M**×*c*), representing various improvements in soil fabric resulting from the application of different suction levels.

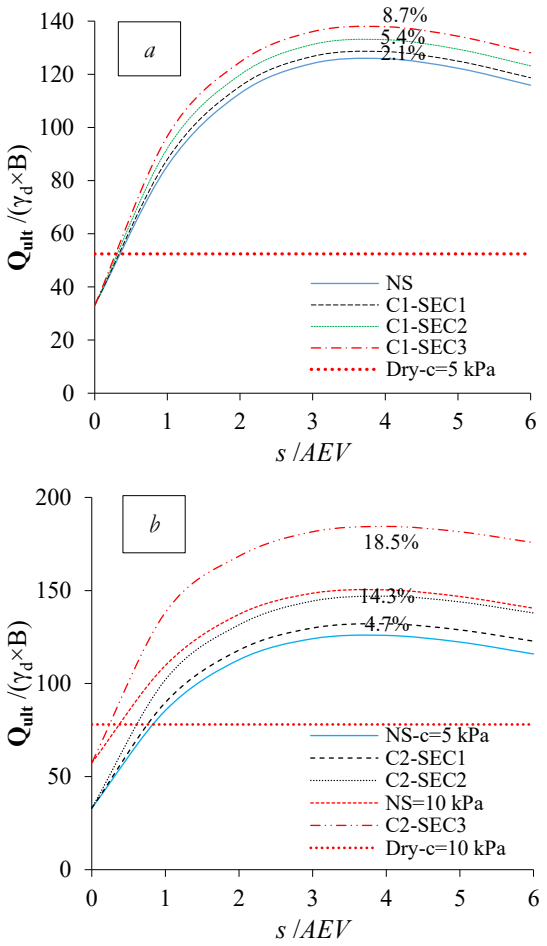

Figure 4. Normalised ***Q****ult versus normalised suction for various scenarios of the Category (a) C1 and (b) C2.*

The numerical results demonstrated a significant effect of spatial variability in cohesion on **Q**ult. Up to 8.7% and 18.5% increase in **Q**ult were obtained for various applied **M** values. Finally, different failure mechanism patterns were observed in the modelled scenarios. A wider and deeper failure mechanism was obtained when a higher **M** value was applied to a higher cohesion value case.

REFERENCES

Bishop, A. W., & Blight, G. E. (1963). Some aspects of effective stress in saturated and partly saturated soils. *Géotechnique,* 13(3), 177-197. https://doi.org/10.1680/geot.1963.13.3.177.

Cho, S. (2010). Probabilistic assessment of slope stability that considers the spatial variability of soil properties. *Journal of geotechnical and geoenvironmental engineering,* 136(7), 975-984. https://doi.org/10.1061/(ASCE)GT.1943-5606.0000309.

Fredlund, D.G. and Xing, A. (1994). Equations for the soil-water characteristic curve. *Canadian geotechnical journal,* 31(4), 521-532. https://doi.org/10.1139/t94-061.

Jiang, S.H., Huang, J., Huang, F., Yang, J., Yao, C. and Zhou, C.B. (2018). Modelling of spatial variability of soil undrained shear strength by conditional random fields for slope reliability analysis. *Applied Mathematical Modelling,* 63(374-389). https://doi.org/10.1016/j.apm.2018.06.030.

Mohamed, F. M. O. and Vanapalli, S. K. (2006). Laboratory investigations for the measurement of the bearing capacity of an unsaturated coarse-grained soil. *Proceedings of the 59th Canadian Geotechnical Conference, Vancouver.* 219-226.

Reis, R.M., de Azevedo, R.F., Botelho, B.S. and Vilar, O.M. (2011). Performance of a cubical triaxial apparatus for testing saturated and unsaturated soils. *Geotechnical Testing Journal,* 34(3). https://doi.org/10.1520/GTJ103256.

Shwan, B. J., and Smith, C. C. (2014). Application of limit analysis in unsaturated soils: numerical and experimental study of bearing capacity. *In Unsaturated Soils: Research & Applications*, CRC Press, 1757-1762. https://doi.org/10.1201/b17034-257.

Shwan, B. J., and Smith, C. C. (2015). Investigation of the shear strength of unsaturated sand using a modified direct shear apparatus. Edinburgh, *ICE Publishing*, 3353-3357. https://doi:10.1680/ecsmge.60678.

Shwan, B. (2023b). Effect of Hydro-Mechanical Hysteresis on Active Earth Pressure for Unsaturated Soils. *8th International Conference on Unsaturated Soils*. https://doi.org/10.1051/e3sconf/202338202006.

Shwan, B. J. (2015). *Experimental and numerical study of the shear strength of unsaturated sand,* Doctoral dissertation, University of Sheffield, Sheffield, UK.

Shwan, B. J. (2017). The effect of soil water retention curve hysteresis on the strength of unsaturated soils. *Journal of Duhok University,* 285-292. https://doi.org/10.26682/sjuod.2017.20.1.26.

Shwan, B. J. (2023a). Hydro-Mechanical Hysteresis Effect-Induced Bearing Capacity Variations for Unsaturated Sand. *International Journal of Geomechanics,* 23(7), 04023106. https://doi.org/10.1061/IJGNAI.GMENG-8255.

Shwan, B. J. (2023c). Microstructural interpretation of effective stress equations for unsaturated sands. *International Journal of Geo-Engineering,* 14(1), p. 4. https://doi.org/10.1186/s40703-022-00181-8.

Tan, X., Li, P., Shen, M., Hu, M., Hou, X. and Ma, H. (2020). Evaluation of the spatial variability characteristics of the unsaturated clay in Hefei, China. *Soils and Foundations,* 60(2), 454-465. https://doi.org/10.1016/j.sandf.2020.03.010.

Toll, D. G., and Ong, B. H. (2003). Critical-state parameters for an unsaturated residual sandy clay. *Géotechnique,* 53(1), 93-103. https://doi.org/10.1680/geot.2003.53.1.93.

Proceedings of the XVIII ECSMGE 2024
GEOTECHNICAL ENGINEERING CHALLENGES
TO MEET CURRENT AND EMERGING NEEDS OF SOCIETY
© 2024 the Authors
ISBN 978-1-032-54816-6
DOI 10.1201/9781003431749-373
Open Access: www.taylorfrancis.com, CC BY-NC-ND 4.0 license

ECSMGE 24
XVIII EUROPEAN CONFERENCE ON SOIL MECHANICS AND GEOTECHNICAL ENGINEERING

Prediction of load transfer curves in pile groups executed in profiles of granular soils from field test measurements

Prédiction des courbes de transfert de charge dans des groupes de pieux exécutés dans des profils de sols granulaires à partir de mesures d'essais sur le terrain

D.F. Silva*, A.S. Moura
Federal University of Ceará, Ceará, Brazil
**dantonfranca@alu.ufc.br*

ABSTRACT: Load transfer methods are relevant tools for predicting the load-settlement curve in single piles and pile groups. Several experimental studies use instrumentation data to evaluate the load transfer mechanism from the pile to the foundation soil. For pile groups, the load transfer t-z and q-z curves can be approximated to hyperbolic functions for each individual pile, adding the effect of interaction between piles through analytical formulations. Through the collection of data from 13 instrumented grouped piles (driven and bored) executed in granular soils and subjected to static loading tests, this study made predictions of the parameters that describe the hyperbolic t-z and q-z curves from correlations with field test measurements, standard penetration test (SPT) and cone penetration test (CPT), pile geometry, and initial geostatic stresses. The present research found that the parameters that describe the initial stiffness of the t-z and q-z curves have no correlation with field test measurements, unlike the parameters that describe the ultimate resistances. Therefore, in terms of load-settlement curve, the proposals were validated for a group of non-instrumented piles. The validation showed convergence of the load-settlement curve mainly for lower loads. Finally, predictions made from CPT test measurements showed more convergence to the experimental curve.

RÉSUMÉ: Les méthodes de transfert de charge sont des outils pertinents pour prédire la courbe de charge- déplacement des pieux simples et des groupes de pieux. Plusieurs études expérimentales utilisent des données d'instrumentation pour évaluer le mécanisme de transfert de charge du pieu au sol de fondation. Pour les groupes de pieux, les courbes de transfert de charge t-z et q-z peuvent être approximées par des fonctions hyperboliques pour chaque pieu individuel, en ajoutant l'effet de l'interaction entre les pieux au moyen de formulations analytiques. En recueillant des données sur 13 pieux de groupe instrumentés (enfoncés et excavés) enfoncés dans des sols granulaires et soumis à des essais de charge statique, cette étude a fait des prédictions sur les paramètres décrivant les courbes hyperboliques t-z et q-z sur la base de corrélations avec les mesures provenant d'essais sur le terrain, d'essais de percussion (SPT) et d'essais de pénétration par cône (CPT), de la géométrie des pieux et des contraintes géostatiques initiales. Cette recherche a montré que les paramètres décrivant la rigidité initiale des courbes t-z et q-z ne sont pas en corrélation avec les mesures des essais sur le terrain, contrairement aux paramètres décrivant les résistances dernières. Ainsi, les propositions ont été validées en termes de courbe charge-choc pour un groupe de pieux non instrumentés. La validation a montré une convergence de la courbe charge- déplacement, en particulier pour les charges les plus faibles. Enfin, les prédictions basées sur les mesures des essais CPT étaient plus conformes à la courbe expérimentale.

Keywords: Load transfer curves; pile group; load-settlement curve; hyperbolic functions.

1 INTRODUCTION

Load transfer methods are methodologies used to predict the distribution of the load applied to the pile into the soil. This is achieved by discretizing the pile into segments supported by nonlinear springs. The behavior of the nonlinear springs is defined based on load transfer curves, also known as t-z and q-z curves. These t-z and q-z curves are associated with the mobilization of lateral friction and end-bearing resistance, respectively, in relation to the corresponding displacement.

In this context, for grouped piles, various authors such as Gomes Filho and Moura (2021), Pan *et al.* (2017), and Zhang *et al.* (2016) propose that the t-z and q-z curves can be defined using a hyperbolic function that describes the behavior of an individual pile, as described by Fleming (1992), adding the group effect through analytical formulations, while considering the interaction between each pair of adjacent piles.

More recently, Silva and Moura (2023) proposed that the t-z and q-z curves in pile groups can be represented by hyperbolic functions. Silva and Moura (2023) also obtained the values of parameters *a* and *b* for hyperbolic t-z and q-z curves from the collected experimental studies. These parameters are associated with initial stiffness and maximum mobilized resistance, respectively, as shown in Figure 1 for the t-z curve.

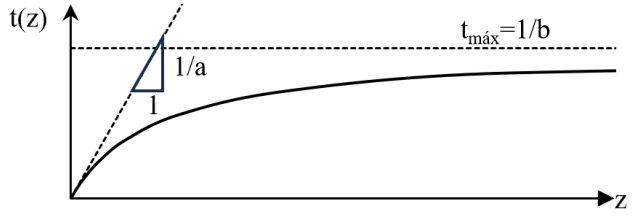

Figure 1. Hyperbolic function parameters: (a) t-z curve; (b) normalized t-z curve.

In this context, the objective of this study is to evaluate the possibility of predicting load-settlement curves in grouped piles and within granular soil profiles through correlations of hyperbolic t-z and q-z curve parameters with field test measurements. Specifically, the study focuses on measurements from cone penetration tests (CPT), including the tip resistance (q_c, in MPa) and the side friction resistance (f_s, in kPa), as well as measurements from the standard penetration test (SPT), which involves the penetration resistance index (N_{SPT}, in blow counts).

2 MATERIALS AND METHODS

Initially, the collected experimental studies were presented, as well as the characterization of the data collected about the geometry of the pile, the field tests conducted and the results of instrumented load tests.

Considering the adjustment and determination of parameters *a* and *b* for the hyperbolic t-z and q-z curves for each instrumented pile group, as well as the defined values of parameter M for pile groups as presented by Silva and Moura (2023), and the collection of field test measurements, N_{SPT}, q_c, and f_s, predictions were made for the parameters *a* and *b*. The parameter M can be defined as the initial stiffness of the load transfer curves normalized by the ultimate resistance (1/b) and pile diameter (D), and described by Equation 1. Consequently, predictions were made for the t-z and q-z curves, as well as load-settlement curves. These correlations were validated in terms of load-settlement curves for a group of non-instrumented piles.

$$M = \frac{1}{b}\frac{a}{D} \quad (1)$$

2.1 Collected field study locations

The research was developed based on the collection of field test results from instrumented, grouped piles subjected to static load tests (SLT) in granular soil profiles. To achieve this, five experimental studies were selected, totaling 10 instrumented pile groups, with 2 of them consisting of more than one instrumented pile in the group. Table 1 provides a description of the selected experimental study locations and the number of PCEs conducted.

Table 1. Locations of selected experimental studies.

Site (SLTs)	Area	Authors
1 (1)	Califórnia, USA	Briaud *et al.* (1989)
2 (3)	Ontário, Canadá	Abdlrahem and El Naggar (2020)
3 (1)	Kuwait City, Kuwait	Ismael (2001)
4 (3)	Gråbo, Suécia	Long (1993)
5 (2)	Lituânia	Norkus and Martinkus (2019)

2.2 Characterization of collected data

The characterization of the selected grouped piles from the experimental studies is presented in Table 2. The table provides identification of the used piles and their respective sites, the installation method (IM), pile diameter (D), embedded pile length (L), the maximum total load obtained in the pile group from the SLT, the quantity (N) of piles in the group, the spacing-to-diameter ratio (s/D) between the pile centers, and the maximum displacement values ($w_{máx}$).

Table 2. Characterization of selected instrumented piles.

Site	Pile Code	IM[a]	D (L) [mm]	LS[b]	Q_t [kN]	N (s/D)	$w_{máx}$ [mm]
1	1-2A	d	0.273	s	2,000	5 (3)	18.0
	1-2B		(9.15)				
	1-2C						
2	2-3A	b	0.172	r	1,975	4 (4.4)	8.8
	2-3B		(5.75)				
	2-4A		0.132		2,120	4 (2.6)	18.1
	2-5A		(5.75)		2,150	4 (4.4)	11.4
3	3-2A	b	0.10	s	1,177	5 (3)	21.0
			(2.25)				
4	4-4A	d	0.06	r	26.4	5 (4)	40.0
	4-5A		(2.1)		80.3	5 (6)	40.0
	4-6A				59.1	5 (8)	40.0
5	5-2A	d	0.219	s	640	4 (3)	25.0
	5-3A		(1.445)		700	4 (2)	22.5

[a] Installation method: driven (d) or bored (b);
[b] Loading speed of SLT: slow (s) or rapid (r).

In general, most of the instrumented grouped piles are driven, with diameters ranging from 0.10 to

0.273 m and lengths between 1.445 and 9.15 m. The groups consist of 4 or 5 piles and are spaced 2 to 8 times the pile diameter.

As for the load tests, the maximum load applied to the group varied from 26.4 to 2000 kN. The values of the maximum mobilized shaft resistance ($t_{máx}$) and end resistance ($q_{máx}$) ranged ranged from 6.1 to 278.4 kPa, and from 583 to 5115 kPa, respectively.

Regarding the field investigations conducted before the load tests, only the group related to site 3 lacks a CPT test, and sites 4 and 5 do not have associated SPT tests. The N_{SPT} values ranged from 17 to 40 blows, and the q_c and f_s values varied from 0.8 to 19.5 MPa and 10 to 174 kPa, respectively.

3 PREDICTION OF LOAD TRANSFER CURVES

To predict hyperbolic t-z and q-z curves in grouped piles subjected to axial compressive loads in sandy soil profiles, the parameters of the hyperbolic curve *a* and *b* obtained by Silva and Moura (2023) were used. For this purpose, it is defined that the parameters $a_{g,t}$ and $a_{g,q}$ correspond to the parameters *a* in grouped piles for the t-z and q-z curves, respectively. Similarly, the parameters $b_{g,t}$ and $b_{g,q}$ correspond to the parameters *b* of the hyperbolic curve for the t-z and q-z curves.

Thus, the aim is to make predictions for the parameters describing the hyperbolic t-z and q-z curves, $a_{g,t}$, $a_{g,q}$, $b_{g,t}$, and $b_{g,q}$. The correlations for the parameters *a* and *b* are carried out based on measurements from SPT and CPT tests, N_{SPT}, q_c, or f_s, as well as the pile diameter (D), initial geostatic stresses (σ'_{v0}), and the logarithm of the sum of relative distances between piles (ln $[\sum(r_{ij}/D)]$), where r_{ij} is the center-to-center distance between piles i and j.

Hence, correlations were established by combining one or more of these variables and adjusting their exponents to obtain curves that fit the experimental results of the instrumented piles. This was based on the coefficient of determination (R^2) of the fitting curve and the uniform distribution of experimental data points.

Figure 2 illustrates the correlation obtained for the parameter $a_{g,t}$. Equations 2 to 7 present the equations defining the correlations obtained for the parameters $a_{g,t}$, $a_{g,q}$, $b_{g,t}$, and $b_{g,q}$, with correlations for the latter two parameters derived from SPT and CPT test measurements separately: N_{SPT}, f_s e q_c. It is worth noting that the correlations for $a_{g,t}$ and $a_{g,q}$ did not converge with field test measurements and may be better described using other variables.

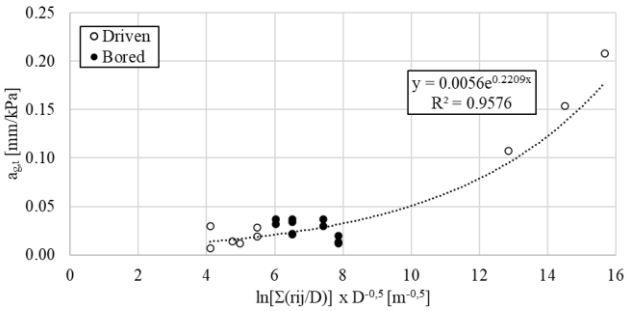

Figure 2. Correlation of the parameter $a_{g,t}$.

$$a_{g,t} = 0.0056 * e^{0,2209*\ln\left[\sum\left(\frac{r_{ij}}{D}\right)\right]*D^{-0.5}} \quad (2)$$

$$a_{g,q} = 0.0007 * e^{3.2725*\sigma'^{\,0.5}_{v0}*\ln^{-2}\left[\sum\left(\frac{r_{ij}}{D}\right)\right]*D} \quad (3)$$

$$b_{g,t} = 0.0015 * e^{0,3541*N_{SPT}^{-1}*\sigma'_{v0}} \quad (4)$$

$$b_{g,t} = 0.0014 * e^{7.0058*f_s^{-0.5}*\ln^{0.5}\left[\sum\left(\frac{r_{ij}}{D}\right)\right]} \quad (5)$$

$$b_{g,q} = 0.0014 * \left(N_{SPT}^{-0.5} * \ln\left[\sum\left(\frac{r_{ij}}{D}\right)\right] * D\right) + 2 * 10^{-5} \quad (6)$$

$$b_{g,q} = 9 * 10^{-5} * e^{0,8284*q_c^{-1}*\ln\left[\sum\left(\frac{r_{ij}}{D}\right)\right]} \quad (7)$$

In general, the fitted curves of the correlations showed high R^2, exceeding 0.93, except for the correlation of the parameter $a_{g,q}$ (R^2=0.89) and the parameter $b_{g,q}$ in relation to N_{SPT} (R^2=0.82).

It is worth noting that the method of installation of the piles did not influence the correlation results, as unique trends were observed in the correlations. Additionally, this study does not take into account the influence of various technologies for driven and bored pile installation.

To validate the correlations, the non-instrumented pile group from site 2, denominated as MPG1, was used. Two predictions were made (Figure 3), one based on N_{SPT} and the other based on f_s and q_c.

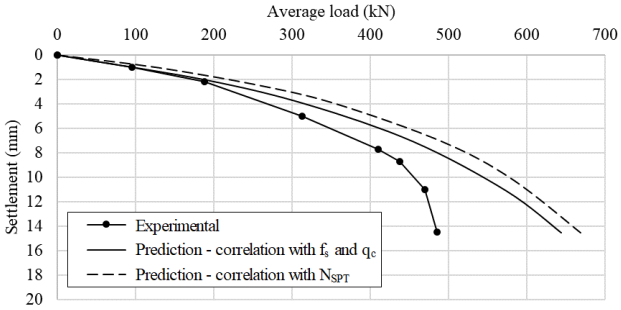

Figure 3. Comparison between the experimental and predicted load-settlement curves - MPG1 group.

From the figure, it can be observed that the predicted curves converged to the experimental curve, and the predictions based on correlations with f_s and q_c (CPT test) showed greater convergence compared to the curve obtained from correlations with N_{SPT}.

4 CONCLUSIONS

For the correlations of the parameters of the hyperbolic t-z and q-z curves in grouped piles, it was observed that both driven and bored piles showed a unique trend, allowing for predicting the parameter values from the same fitting curve.

Regarding the parameters $a_{g,t}$ and $a_{g,q}$, they are not correlated with field test measurements and converge when correlated with the diameter (D) of the pile, the spacing-to-diameter ratio of the pile (ln [$\Sigma(r_{ij}/D)$]), and the initial stress state ((σ'_{v0}), with R^2 equal to 0.96 and 0.89, respectively. It is noteworthy that this result was unexpected, considering that the formulations developed by Zhang *et al.* (2016) and Gomes Filho and Moura (2021) assume that the group effect is associated with the shear modulus (G) of the material under in situ conditions.

As for the parameters $b_{g,t}$ and $b_{g,q}$, they were estimated from field test measurements, showing convergence to the correlations with R^2 greater than 0.93, except in the correlation of the parameter $b_{g,q}$ from N_{SPT}. Furthermore, it can be observed that an increase in the value of field test measurements leads to a reduction in the parameter *b* and, consequently, an increase in mobilized resistance.

The validation in terms of load-settlement curves indicated adherence of the predicted curves to the experimental ones, especially through correlations with CPT measurements. Furthermore, it can be noticed that, for displacements up to 2 mm, the prediction through correlations with f_s and q_c surpasses the experimental curve. This suggests a greater convergence in the parameters describing the initial stiffness of the load transfer curves, $a_{g,t}$ and $a_{g,q}$.

ACKNOWLEDGEMENTS

The authors would like to thank the Department of Hydraulic and Environmental Engineering (DEHA) of the Federal University of Ceará (UFC) for supporting this research, and to the Brazilian Federal Agency for Postgraduate Education (CAPES) and the Brazilian National Council for Scientific and Technological Development (CNPq) for the financial support.

REFERENCES

Abdlrahem, M. A. and El Naggar, M. H. (2020) Axial performance of micropile groups in cohesionless soil from full-scale tests. *Canadian Geotechnical Journal*, 57(7):1006-1024. https://doi.org/10.1139/cgj-2018-0695.

Briaud J. L., Tucker L. M. and Ng E. (1989) Axially loaded 5 pile group and single pile in sand. *Proceedings of the 12th International Conference on Soil Mechanics and Foundation Engineering*, Rio de Janeiro, Brazil, 2:1121-1124.

Gomes Filho F. V. C. and Moura A. S. (2021) Proposal for considering the group effect in the prediction of settlements in pile groups through load transfer methods. *Soils and Rocks*, 44(2):e2021061320. https://doi.org/10.28927/SR.2021.061320.

Fleming, W. G. K. (1992). A new method for single pile settlement prediction and analysis. *Géotechnique*, 42(3):411–425. https://doi.org/10.1680/geot.1992.42.3.411.

Ismael N. F. (2001) Axial load tests on bored piles and pile groups in cemented sands. *Journal of Geotechnical and Geoenvironmental Engineering*, 127(9):766–773. https://doi.org/10.1061/(ASCE)1090-0241(2001)127:9(766).

Long P. D. (1993). *Footings with settlement-reducing piles in non-cohesive soil.* Linköping: Swedish Geotechnical Institute Report 43:45-93.

Norkus A. and Martinkus V. (2019) Experimental study on bearing resistance of short displacement pile groups in dense sands. *Journal of Civil Engineering and Management,* 25(6):551-558. https://doi.org/10.3846/jcem.2019.10403.

Pan D. D., Zhang Q. Q., Liu S. W. and Zhang S. M. (2017) Analysis on response prediction of a single pile and pile groups based on the Runge-Kutta method. *KSCE Journal of Civil Engineering*, 00(0):1-9. https://doi.org/10.1007/s12205-017-0578-x.

Silva D. F. and Moura A. S. (2023) Evaluation of fitting to hyperbolic functions of load transfer curves for piles in granular soil profiles. *International Journal of Geotechnical Engineering* 17(4):339-351. https://doi.org/10.1080/19386362.2023.2246254.

Zhang Q. Q., Liu S. W., Zhang S. M. and Wang K. (2016) Simplified non-linear approaches for response of a single pile and pile groups considering progressive deformation of pile-soil system. *Soils and Foundations*, 56(3):473-484. https://doi.org/10.1016/j.sandf.2016.04.013.

Proceedings of the XVIII ECSMGE 2024
GEOTECHNICAL ENGINEERING CHALLENGES
TO MEET CURRENT AND EMERGING NEEDS OF SOCIETY
© 2024 the Authors
ISBN 978-1-032-54816-6
DOI 10.1201/9781003431749-374
Open Access: www.taylorfrancis.com, CC BY-NC-ND 4.0 license

ECSMGE 24
XVIII EUROPEAN CONFERENCE ON SOIL MECHANICS AND GEOTECHNICAL ENGINEERING

Automated monitoring for effective implementation of observational method in an urban excavation in Lisbon, Portugal

Surveillance automatisée pour une mise en oeuvre efficace de la méthode observationnelle dans une excavation urbaine à Lisbonne, Portugal

A. Silva*
Measurand, São Paulo, Brazil

C. Levesque
Measurand, Fredericton, Canada

C. Martins, R. Tomásio
JET SJ, Lisboa, Portugal

**andre.silva@measurand.com*

ABSTRACT: Geotechnical and structural instrumentation and monitoring have developed significantly in recent years, with the emergence of new technologies, such as medium and long-range wireless transmission equipment, that allow faster and more efficient data collection and transmission. The article proposes the performance analysis of a retention wall structure defined for an urban excavation in Lisbon using an automated geotechnical monitoring plan. It discusses the benefits and potential improvements in implementing geotechnical monitoring solutions in national projects. The monitoring plan defined uses different instruments, including vibrating wire piezometers, MEMS load cells, Shapearray automated inclinometers and biaxial tiltmeters, which provide several daily readings available in a remote and online acquisition system. The objective is to ensure the best conditions of the solution's safety, efficiency, and cost, reducing the uncertainties inherent to geological-geotechnical conditions through the Observational Method.

RÉSUMÉ: L'instrumentation et la surveillance géotechniques et structurelles se sont considérablement développées au cours des dernières années, avec l'émergence de nouvelles technologies, telles que les équipements de transmission sans fil à moyenne et longue portée, qui permettent une collecte et une transmission plus rapides et plus efficaces des données. L'article propose l'analyse des performances d'une structure de mur de soutènement définie pour une excavation urbaine à Lisbonne à l'aide d'un plan de surveillance géotechnique automatisé et discute des avantages et des améliorations potentielles dans la mise en œuvre de solutions de surveillance géotechnique dans les projets nationaux. Le plan de surveillance défini utilise différents instruments, notamment des piézomètres à corde vibrante, des capteurs de pesage MEMS, des inclinomètres automatisés Shapearray et des inclinomètres biaxiaux, qui fournissent plusieurs relevés quotidiens disponibles dans un système d'acquisition à distance et en ligne. L'objectif est d'assurer les meilleures conditions de sécurité, d'efficacité et de coût de la solution, en réduisant les incertitudes inhérentes aux conditions géologiques et géotechniques grâce à la méthode d'observation.

Keywords: Geotechnical monitoring; instrumentation; observational method; inclinometers; piezometers.

1 PROJECT DESCRIPTION

The "Phoenix Building" project comprises the constructing a building with seven upper floors, one ground floor and three underground floors in a densely urbanized region of Lisbon, Portugal, with roads, railways and other buildings and infrastructures in its surroundings. The ground floor will be subdivided into three levels to connect with the surrounding streets. The earth retaining solution adopted consists of reinforced concrete diaphragm walls with a thickness of 50cm.

Prior to the start of construction, preliminary work was carried out, including removing soil and forming temporary slopes. The diaphragm walls were excavated mainly with a hydraulic grab, although in certain situations, vertical holes were drilled with a short auger and a Kelly rod.

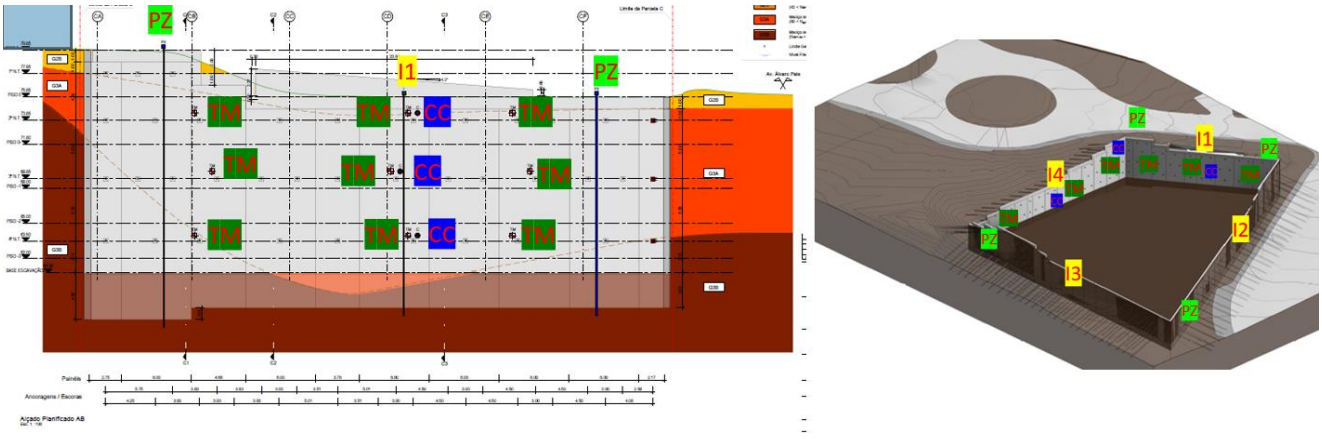

Figure 1. (Right)Instruments location in one of project cross-sections and (left)overview of a BIM 3D projection. I-inclinometer (ShapeArray); TM- Tiltmeter, CC-Load Cell, PZ-Piezometer.

During the provisional phase, the stability of the retaining wall was ensured through the application of prestressed anchors (2, 3 and 4 levels) and the installation of metal corner struts arranged at different levels.

In the final phase of construction, the integrity of the retaining wall was maintained by the structure of the building in relation to the pressures exerted by the ground and road loads. The support systems, including anchors and struts, will be decommissioned after the main structure is completed.

Summarizing, the "Phoenix Building" project encompasses the construction of a building in highly dense urban area with particular attention to retaining wall, excavation and interlocking, with the deactivation of the temporary systems after the completion of the main structure.

2 INSTRUMENTATION PLAN

The Instrumentation Plan aims to ensure safety and economy in the excavation and retaining wall of buried floors and to analyze the behaviour of structures and infrastructures during execution. The plan includes the measurement of horizontal displacements of the retaining wall, wall rotations, water level, load on the anchors and vertical displacements of the surrounding roads, using devices such as automated inclinometers (ShapeArrays), tiltmeters, piezometers, load cells and topographic marks. The plan was developed to analyze the main risks associated with executing stages.

The instruments were distributed across the four design elevations, as illustrated in the figure 1, where the instrumentation locations and 3D perspective are demonstrated. The load cells were placed in reference alignments, for which a calculation model was made, and these sections also have an inclinometer. On the other hand, 9 topographic marks were placed in total, 3 along the streets Sousa Lopes, 3 along Av. Álvaro Pais and 3 along the IP (Portugal Infrastructures) railway lines.

Table 1. Summary table of the instruments and monitored variables.

Quantities (un)	Instrument	Measured variables
4	Automated Inclinometers (ShapeArrays)	Horizontal displacements of the retaining wall
30	Tiltmeters	Retaining wall rotations
4	Vibrating wire Piezometers	Water level
16	Load Cells	Load on anchors
9	Topographic Prisms	Settlements of the surrounding structures

2.1 Collection Frequency

Given the characteristics of the project, it was recommended that the installed devices be read daily (every 6 hours) during the execution of excavation, retaining wall and superstructure work (and could be adjusted if necessary). The periodicity of reading of the topographic marks was monthly; these were the only non-automated instruments. The results were presented in online numerical tables and graphic plots and interpreted by the geotechnical consultant in collaboration with the site and supervision technicians.

2.2 Alarm Criteria

Based on the type and solution proposed for the containment executed, as well as the geology of the intervention site, it was possible to estimate the following criteria for the containment structure:

a) Alarm criterion: maximum displacements of 25mm in the horizontal direction and 10mm in the vertical direction.
b) Alarm criterion: maximum displacements of 35 mm in the horizontal direction and about 15 mm in the vertical direction.

2.3 Monitoring and Visualization System Automation

Automating geotechnical instrumentation using dataloggers and gateways is a technique increasingly used in construction and maintenance projects of geotechnical structures. This technique allows instrumentation data to be automatically collected by the data loggers and transmitted to a gateway, which sends the data to an online visualization platform.

The online platform (Level-GAM) for data visualization is a digital tool that allows the reading and interpretation of data collected by sensors installed in geotechnical structures in real-time. The platform can be accessed from anywhere, storing data in a secure and organized way, having been a valuable tool for long-term analysis of the behaviour of structures.

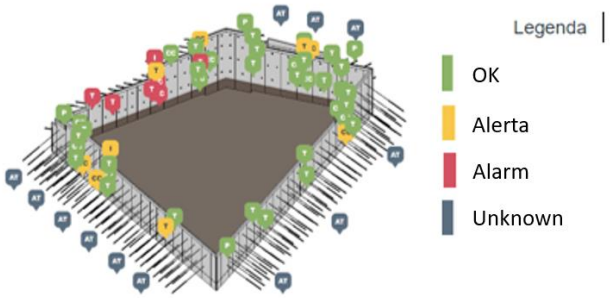

Figure 2. Level GAM online platform: Overview of the excavation, installed instruments and their status to date.

3 ANALYSIS AND INTERPRETATION

Subsequently, this paper will present and analyze the outcomes obtained from automated inclinometers strategically placed within the diaphragm walls. A comprehensive comparison will be drawn between the anticipated behaviour by numerical modelling and the actual observations made in the field.

These automated inclinometers played a pivotal role in the real-time monitoring of diaphragm wall stability, and they provided valuable correlations with other instrumentation systems such as load cells, tiltmeters, and piezometers.

The FEM models employed in this study utilize project-specific cross-sections as a reference. These models were instrumental in predicting the expected displacements within the structure. They consider geological and hydrogeological data, anchor characteristics (length, inclination, and load), and diaphragm wall parameters (thickness and sheet type). These models entail intricate mathematical calculations that factor in the geotechnical conditions of the site and the complex interactions with structural elements.

When conducting a comparative analysis between the numerical predictions and on-site results, several critical considerations must be taken into account. These include variations in geological and hydrogeological profiles, anchor quantity and load, and the distinct construction phases undertaken. It is essential to remember that numerical models are inherently predictive tools, and real-site conditions may deviate from these predictions. As such, monitoring remains an indispensable tool for substantiating these discrepancies and accurately assessing the actual field conditions

An integral facet of the analysis revolves around the pace at which excavation and anchor tensioning occurred. To shed further light on this aspect, the following figure will present the maximum cumulative displacements during the excavation phase, focusing on inclinometer I4, which exhibited the most substantial cumulative displacement.

Additionally, the figure 3 will depict the key milestones, including the testing dates of the closest anchors (N1, N2), the conclusion of the excavation phase in May 2022, a transitional period spanning from the completion of excavation to the initiation of the structural phase. Moreover, a specific emphasis will be placed on a notable period characterized by particularly intense rainfall between November and December 2022.

These temporal markers are crucial for a comprehensive understanding of the interplay between excavation and anchor tensioning and their influence on the behaviour of the diaphragm wall, especially in the context of external environmental factors such as heavy rainfall.

Table 2. Comparison table between expected and actual horizontal displacements.

ShapeArray	Estimated displacement (mm)	Actual displacement in May/2022 (mm)	Actual displacement in January/2023 (mm)	Alert Criterion (mm)	Alarm Criterion (mm)
I1	11,25	8,5	13,9	25,0	35,0
I2	11,25	5,4	8,5	25,0	35,0
I3	6,5	16,3	29,1	25,0	35,0
I4	6,5	15	38,5	25,0	35,0



Figure 3. Cumulative displacement plot with emphasis on the installation's stages of the anchors (N1, N2), end of excavation (F.E), period of heavy rains (Nov/Dec 22) and last reading made available (May/23), after reinforcement of the panel with complementary anchor.

4 DATA DISCUSSION

As depicted in Table 2, the behaviour of inclinometers I1 and I2 closely aligned with the predictions from the numerical models. These inclinometers also exhibited noticeable consistency between the excavation phases and the tensioning of anchors. Conversely, inclinometers I3 and I4 displayed deviations from the anticipated values generated by the numerical models, ultimately triggering alert and alarm criteria, respectively. It's worth noting that these inclinometers experienced a certain time lag between the excavation and tensioning phases, potentially attributable to their placement within a transitional zone spanning levels 2 and 3 of anchors. Particularly, inclinometer I3 exhibited the most pronounced deviation, possibly influenced by variations in the geological and geotechnical conditions.

Regarding the inclinometer behaviour, it's essential to mention that excavation reached its maximum depth in May 2022 and has since been halted. During this period, an unexpected upward trend in displacements was observed, deviating from the expected stabilization observed in I1 and I2. Moreover, this trend intensified notably between November and December.

In response to these deviations, especially with the attainment of alert and alarm criteria, on-site investigations were conducted to identify the root causes of the inconsistent behaviour in I3 and I4 compared to the initial expectations. It was determined that the malfunctioning of wedges within several anchors was the primary issue, preventing the proper locking of tensioned strands and, consequently, the stabilization of the walls. This issue was prevalent in various areas and was addressed at the end of December through corrective measures, including additional anchorages. Although the impact on inclinometers I3 and I4 was more pronounced, it resulted in the overall stabilization of the retaining wall behaviour, as illustrated in Figure 3. Notably, sections I3 and I4 were equipped with only two anchors levels, certainly limiting their capacity for redistribution.

Finally, the displacements acceleration between November and December was attributed to heavy rainfall during that period. It's important to highlight that the inclinometer instrument panels for I3 and I4 were installed on excavation slopes. The heavy rain, combined with the observed impermeability of the soil layers, likely led to increased loads from the back of the containment structure due to soil saturation on the slope. This, in turn, contributed to the observed displacements.

It's crucial to emphasize the Observation Method application benefits and also the remaining instrumentation, including tiltmeters and load cells, corroborated the observations made through the inclinometers. This underscores the significance of redundancy in instrumentation systems for validation and comprehensive structural behaviour monitoring.

5 CONCLUSIONS

The project's framework required the development of safe and cost-effective solutions that align with various constraints, including geological, geotechnical, and hydrogeological factors, as well as considerations for architectural preservation and the integrity of nearby structures and infrastructures.

In this context, the Instrumentation and Observation Plan played a crucial role in managing the performance of the retaining wall structure and adjacent infrastructures. It highlighted its essential role in an urban setting, reflecting the characteristics of the current project.

Moreover, the importance of employing an automated instrumentation system was emphasized. This system not only proved its value in detecting deviations from expected behavior during periods of reduced oversight but also showcased its ongoing usefulness in monitoring and evaluating the effectiveness of implemented corrective measures.

Proceedings of the XVIII ECSMGE 2024
GEOTECHNICAL ENGINEERING CHALLENGES
TO MEET CURRENT AND EMERGING NEEDS OF SOCIETY
© 2024 the Authors
ISBN 978-1-032-54816-6
DOI 10.1201/9781003431749-375
Open Access: www.taylorfrancis.com, CC BY-NC-ND 4.0 license

ECSMGE 24
XVIII EUROPEAN CONFERENCE ON SOIL MECHANICS AND GEOTECHNICAL ENGINEERING

Comparison of collapse loads obtained in 2D and 3D slope stability limit analysis

Comparaison des charges d'effondrement obtenues lors de l'analyse des limites de stabilité de pente 2D et 3D

W.T. Sołowski*, L.-A. Marchadour, L.A. Ikonen
Department of Civil Engineering, Aalto University, Espoo, Finland

**wojciech.solowski@aalto.fi*

ABSTRACT: The basis for the typical geotechnical designs of slopes and excavations are limit analysis calculations that assume 2D plane strain. The assumption is typically rather conservative, thus such design may require unnecessary additional construction material, as well as increase the construction time and environmental costs. In this paper, we present limit analyses of an embankment near a slope, typical for a temporary dead-end road in a mine or on a construction site. We modelled this problem in 2 and 3 dimensions, using Optum G2 and Optum G3 software, respectively. The results show that the 3D analysis provides collapse loads significantly higher than the 2D analysis. The shapes of the sliding surfaces also differ, as the 3D analysis allows us to determine the shape of the sliding surface in places where a 2D cross-section must be taken overly conservative. It, therefore, allows a better understanding of the mechanical behaviour of the studied structure. The collapse loads differ significantly between 2D and 3D analyses, potentially justifying the extra effort required for 3D calculations.

RÉSUMÉ: La base des conceptions géotechniques typiques des talus et des excavations repose sur des calculs d'analyse limite qui supposent une déformation plane 2D. L'hypothèse est généralement plutôt conservatrice, de sorte qu'une telle conception peut nécessiter des matériaux de construction supplémentaires inutiles, ainsi qu'augmenter le temps de construction et les coûts environnementaux. Dans cet article, nous présentons des analyses limites d'un remblai à proximité d'une pente, typique d'une impasse temporaire dans une mine ou sur un chantier de construction. Nous avons modélisé ce problème en 2 et 3 dimensions, en utilisant respectivement les logiciels Optum G2 et Optum G3. Les résultats montrent que l'analyse 3D fournit des charges d'effondrement nettement supérieures à l'analyse 2D. Les formes des surfaces de glissement diffèrent également, car l'analyse 3D nous permet de déterminer la forme de la surface de glissement aux endroits où une section 2D doit être prise de manière trop conservatrice. Cela permet donc de mieux comprendre le comportement mécanique de la structure étudiée. Les charges d'effondrement diffèrent considérablement entre les analyses 2D et 3D, justifiant potentiellement l'effort supplémentaire requis pour les calculs 3D.

Keywords: Limit analysis; 3D calculations; slope stability.

1 INTRODUCTION

Design of slopes in daily engineering practice typically uses 2D Limit Analysis or 2D Finite Element Method. Often, the Limit Analysis implementation is still one of the methods of slices, in which extra assumptions are necessary as, otherwise, the number of equations is insufficient to obtain the solution. The extra assumptions are typically conservative, yet in rare cases, they are not. This is because the method of slices ultimately calculates the upper limit load. The obtained value guarantees that the failure happens at the selected load, under assumptions taken. Yet, a not-analysed, different sliding surface with a lower bearing capacity may exist. In some cases, 3D analysis (still based on the method of slices that become prisms in 3D) may lead to a lower limit load (see e.g. Firincioglu and Ercanoglu, 2021), as the assumptions used for generating the extra equations for 3D analysis are slightly different. This should not be confused with an overall lack of safety when the method of slices is used. As shown in Krahn (2003), the collapse loads obtained from the Finite Element Method are often higher, as the extra assumptions used in the method of slices are typically conservative.

However, nowadays there are commercial software packages that allow for arbitrary accurate limit analysis, with no need for extra assumptions required for the method of slices, see for example Sloan (2011) and Krabbenhoft and Lyamin (2015). Such software gives upper and lower bounds for the

solution, hence the accuracy is governed by the limit analysis assumptions, created model, and the accuracy of the parameters used for the soil. The calculation error may be minimised to as low a value as deemed necessary by the designer. Alternatively, one can use Finite Element Analysis, where more advanced constitutive models for soil may be used, leading to a more accurate estimation of the collapse load. However, the numerical error is uncertain in such analysis as no upper and lower bound for the solution is given. Advanced Finite Element Method analyses are not considered in this paper, as the choice of extra parameters for the advanced constitutive model (e.g. related to softening of the material in line with the amount of shear strain) may lead to results that are far from the limit analysis results. On the other hand, results obtained with the Finite Element Method and Mohr-Coulomb model, under similar assumptions to those in limit analysis typically lead to collapse load in between the lower and upper bound computed with limit analysis. That is because the method giving the lower bound collapse load is similar to the Finite Element Method coupled with a special type of element.

In engineering practice, rarely the collapse load is computed in 3D. That may be due to the software package limitations or the extra effort to obtain the solution is considered not worth the savings. This paper shows that in some cases where the 2D cross-section must be taken as very conservative, the difference between 2D and 3D solutions can be very significant, potentially doubling the allowed load, and hence the use of 3D analysis for design may lead to substantial savings.

2 METHODS

Upper and lower bound limit analysis simulations were performed using Optum G2 and Optum G3 software. The problem studied represents a dead-end embankment placed next to a conical excavation, a situation often encountered in mines. We compute the upper and lower limit load based on a safely assumed 2D cross-section and then we perform the full 3D analysis.

The simulations assume undrained shearing, with soil described by a Tresca model, while the loads are transmitted to the ground through rigid plates. The choice of plates over layers of flexible pavement structure is made for simplicity. The plates are rigid as the limit analysis only handles rigid perfectly plastic materials.

The 2D and 3D geometry is given in Figure 1 and Figure 2, respectively. The total length of the domain in the horizontal direction is 78m. The embankment has a height of 2m and measures 36m at the bottom and 16m at the top, with the loaded plates taking the middle 8m. Below the embankment, there is a 1m deep dry crust soil layer. The hole has a 20m radius and a depth of 7m, reaching the end of the domain. The modelled depth of the soft clay layer below the dry crust is 18m. The 3D domain spreads additionally in the z direction for 40m, the diameter of the hole. The embankment slope spreads similarly 10m in the direction parallel to the embankment. All boundary conditions are standard, allowing for the movement of the material in the vertical direction at the sides and no movement at the bottom.

The embankment material is approximated with the Mohr-Coulomb model, with friction angle being 32 degrees and cohesion of 1 kPa, while its unit weight is 18 kN/m^3. The dry crust and soft clay layers are modelled as undrained Tresca materials. The dry crust layer has a constant undrained shear strength of 20 kPa and a unit weight of 18 kN/m^3. The clay layer has an undrained shear strength of 10 kPa, increasing by 1.7 kPa with each meter of depth and unit weight equal to 15 kN/m^3. The initial horizontal-to-vertical stress ratio K_0 in all the material is taken as 0.5. All the materials are assumed to have no tensile shear strength, with a vertical cut-off of the yield surfaces at zero mean effective stress. The forces are transmitted to the soil through rigid weightless plates.

3 RESULTS

The 2D analysis, made with approximately 50000 elements, resulted in collapse at the load between 30.5 kPa (lower bound) and 30.8 kPa (upper bound). Due to limitations in computer memory (32 GB), 3D analysis was also made with approximately 50000 elements and gave the failure load between 71 kPa (lower bound) and 79 kPa (upper bound), see Table 1 for a summary. The use of a larger number of elements would reduce the gap between the upper and lower bounds, though as the collapse load is guaranteed to be at least equal to the lower bound, the results show at least a 130% increase in the collapse load when 3D is taken into account. The shape of failure surfaces is given in Figure 3 for 2D calculations and in Figure 4 for the 3D case.

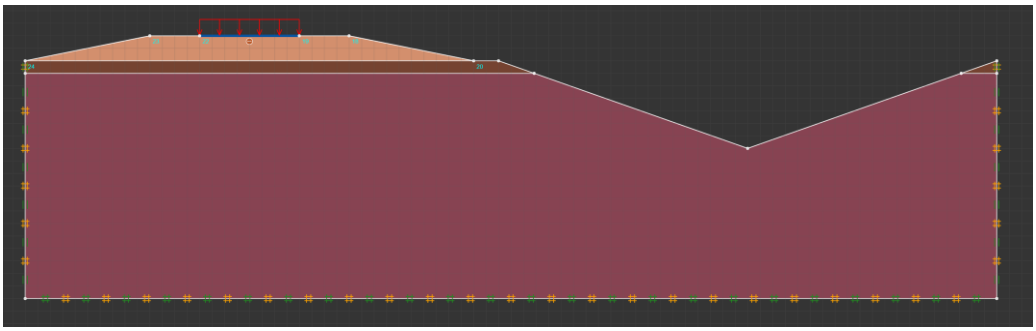

Figure 1. 2D geometry of the problem.

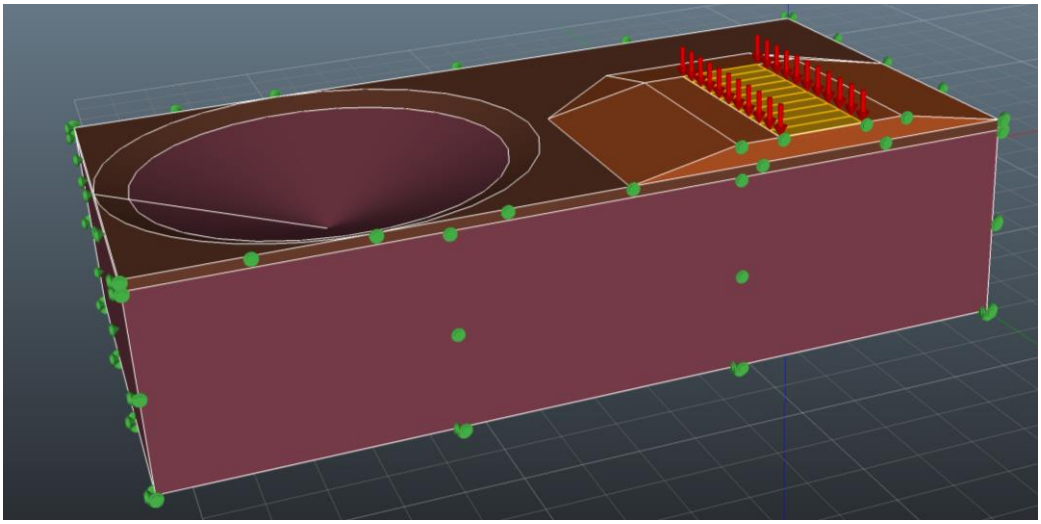

Figure 2. 3D geometry of the problem.

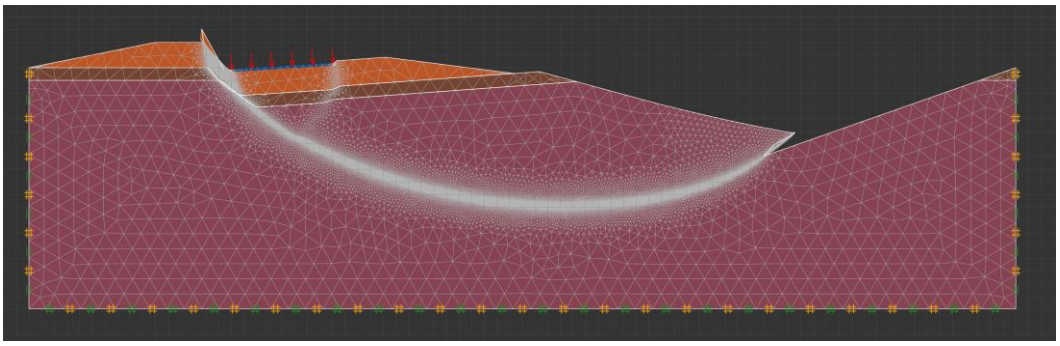

Figure 3. 2D failure surface.

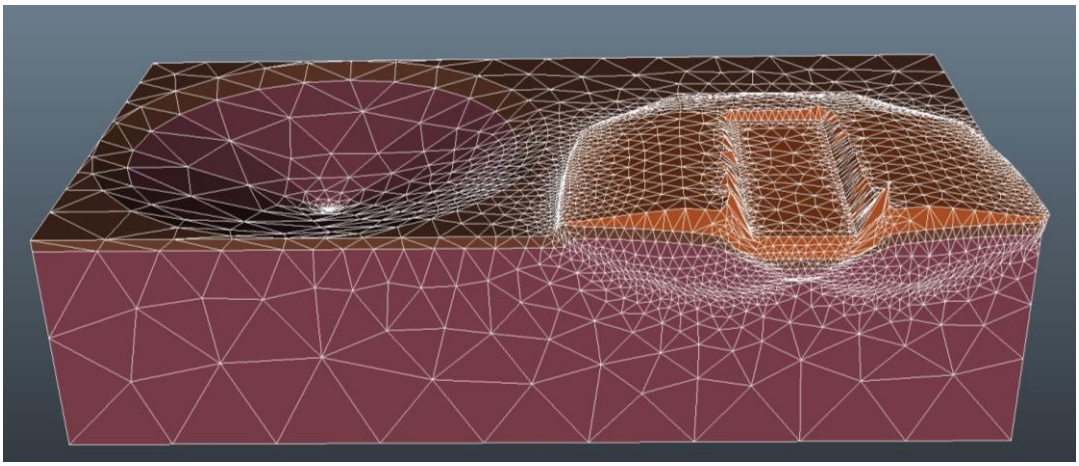

Figure 4. 3D failure surface.

Table 1. Obtained limit loads.

Analysis	Lower bound	Upper bound
2 Dimensional	30,5 kPa	30,8 kPa
3 Dimensional	71	79

4 DISCUSSION

The obtained results are very accurate for 2D analysis, with the difference between the lower and upper bound being around 1%. The difference grows to 10% in the case of 3D analysis. Nonetheless, as the lower bound load is guaranteed to be safe, the 3D analysis gives at least 2,3 times higher collapse load. This huge difference is due to a very conservative selection of the 2D cross-section, leading to different failure mechanisms in 2D and 3D, see Figures 3 and 4. This difference is large enough to have a real economic impact. Design based on 3D analyses can save money, materials and construction time.

However, 3D analysis requires a much larger amount of work as well as an investment in software and training. The 2D case can be easily computed in a day, a 3D case perhaps requires at least two or three days of work. The results indicate that the additional work can be justified by savings made. However, 3D design is something that can only be profitable for a company when the investors aim for lower cost of construction work, instead of lower cost of design and when the investors are willing to allow for additional time, likely required both for extra soil investigations, needed due to lower safety overall and longer design period.

Moreover, the 3D design, being unusual is relatively unexplored and the 3D analysis software is still under active development, unlike the relatively stagnant state of 2D analysis software. In 3D analyses, it is more difficult to check the results and be certain about the correctness of the defined problem. The accuracy of the results is lower unless much more time is spent on computation. Complex geometries are even more tricky, as it is very easy to make a mistake.

Finally, one has to sound a word of caution. The collapse load obtained with 3D limit analysis may be computationally correct but is still inaccurate due to the assumptions made. Limit analysis does not allow for altering of soil strength depending on the amount of shear strain. In reality, it is well established that the shear strength of clays and other fine materials depends on the amount of shear strain, with initial strain caused e.g. by settlements. In limit analysis, the rigid-perfectly plastic analysis will not capture such effects. Similarly, the approximation of the strength for dense granular materials, as well as variation of the strength in complex stress states, and effects of water flow and pore pressures may not be fully accounted for in such analyses. In short, limit analysis is still a relatively crude tool. For even more accuracy, one would need to perform 3D Finite Element analysis with a complex soil model that would capture those more advanced aspects of soil behaviour.

5 CONCLUSIONS

The paper shows that the 3D calculations may result in vastly different collapse loads when compared to the 2D calculations. In the analysed problem, the collapse load in the 3D case was at least 71 kPa, which is at least 2,3 times higher than the highest possible collapse load from 2D analysis (30,8 kPa).

This result indicates that we may have reserves in our 2D designs, and relying on 3D calculations can lead to a reduction in costs. Yet, both designers and construction companies are often aware of those reserves. Hidden high factors of safety are convenient in design, as they allow for design based on more uncertain soil parameters without worry. Similarly, construction companies are likely to slim down the designs on the construction site, especially when the work is temporary. Hence, the more accurate design methods resulting in an overall lower factor of safety would also require a change of practices both during design and construction. For a successful move to designs based on 3D analyses, designers would need much more accurately established soil properties. On the other hand, construction companies would need to construct the earth structures more carefully, likely instrumenting and monitoring the site more closely.

REFERENCES

Firincioglu, B.S. and Ercanoglu M. (2021) Insights and perspectives into the limit equilibrium method from 2D and 3D analyses. Engineering Geology 281, 105968, https://doi.org/10.1016/j.enggeo.2020.105968.

Krabbenhoft, K. and Lyamin, A. V. (2015) Strength reduction finite-element limit analysis. Géotechnique Letters 5, 250–253, http://dx.doi.org/10.1680/jgele.15.00110.

Krahn J., 2003. The 2001 R.M. Hardy lecture: the limits of limit equilibrium analyses. Can. Geotech. J., **40**(3), pp. 643-660. https://doi.org/10.1139/t03-024.

Sloan, S. W. (2011). Geotechnical stability analysis. Géotechnique 63, No. 7, 531–571, https://doi.org/10.1680/geot.12.RL.001.

Proceedings of the XVIII ECSMGE 2024
GEOTECHNICAL ENGINEERING CHALLENGES
TO MEET CURRENT AND EMERGING NEEDS OF SOCIETY
© 2024 the Authors
ISBN 978-1-032-54816-6
DOI 10.1201/9781003431749-376
Open Access: www.taylorfrancis.com, CC BY-NC-ND 4.0 license

ECSMGE 24
XVIII EUROPEAN CONFERENCE ON SOIL MECHANICS AND GEOTECHNICAL ENGINEERING

Optimal pavement design using the failure probability

Conception optimale de la chaussée à l'aide de la probabilité de défaillance

R. Varga, P. Jelušič*, T. Bračko, B. Macuh, B. Žlender
University of Maribor, Faculty of Civil Engineering, Transportation Engineering and Architecture, Maribor, Slovenia

*primoz.jelusic@um.si

ABSTRACT: In this paper, an optimal pavement design with and without geosynthetic reinforcement is discussed and evaluated. The probability of failure is calculated for these two optimal designs and the costs of the structures are compared. For this purpose, an analysis with three main steps was performed. The first step is to develop a deterministic model that includes a computational model of the response variables of interest for a given set of input parameters such as subgrade conditions and live load. In the second step, an uncertainty model was developed in which the California Bearing Ratio of the subgrade, the total number of axle load passes, and the depth of frost penetration were treated as random variables and their values were simulated using Monte Carlo simulation. In the final step, the response variables of the deterministic model were calculated according to the uncertain parameters defined in the uncertainty model. The results of the failure probability analysis allow us to evaluate important elements of the pavement structure that should be changed in order to reduce the probability of failure.

RÉSUMÉ: Dans cet article, une conception optimale de la chaussée avec et sans renforcement géosynthétique est discutée et évaluée. La probabilité de défaillance est calculée pour ces deux conceptions optimales afin de montrer la différence que fait le renforcement. Pour ce faire, une analyse en trois étapes principales a été réalisée. La première étape consiste à développer un modèle déterministe qui comprend un modèle de calcul des variables de réponse d'intérêt pour un ensemble donné de paramètres d'entrée tels que les conditions du sol et la charge réelle. Dans la deuxième étape, un modèle d'incertitude a été développé dans lequel le coefficient de portance californien du sol, le nombre total de passages de la charge à l'essieu et la profondeur de la pénétration du gel ont été traités comme des variables aléatoires et leurs valeurs ont été simulées à l'aide d'une simulation de Monte Carlo. Dans la dernière étape, les variables de réponse du modèle déterministe ont été calculées en fonction des paramètres incertains définis dans le modèle d'incertitude. Les résultats de l'analyse de la probabilité de défaillance nous permettent d'évaluer les éléments importants de la structure de la chaussée qui devraient être modifiés afin de réduire la probabilité de défaillance.

Keywords: Reliability based design; optimization; optimal pavement structure; geosynthetics.

1 INTRODUCTION

Efficient pavement design plays a critical role in the sustainable development and longevity of transportation infrastructure. As the world's population continues to grow and urbanization escalates, the demand for resilient and cost-effective pavements becomes increasingly urgent. In particular, the complexity of today's traffic volumes, environmental pressures and evolving material technologies require a paradigm shift towards the development of optimized pavements that can withstand a wide range of loads while minimizing environmental impact. In recent decades, great progress has been made in the field of pavement construction. These include several innovative methods and materials that promise longer life and lower maintenance costs. Several authors have been working on optimizing the pavement structure designs with and without the use of geosynthetics, with geosynthetics proving to be more favorable at lower CBR values of the subgrade (Jelušič, Varga, et al., 2023; Mamlouk et al., 2000; Nicholls, 1991; Santos & Ferreira, 2012). As mentioned before by new materials, researchers are also testing waste materials such as glass, car tire waste, lignin, and nylon bags to improve the California Bearing Ratio - CBR values of the unbound sub-base course and asphalt binder course (Abukhettala & Fall, 2021; Fatemi & Imaninasab, 2016; Huang et al., 2007; Jelušič, Gücek, et al., 2023; You et al., 2022). The studies all came to the same conclusion that using waste as a building material significantly reduces maintenance costs, construction costs, and reduces CO2 emissions. The studies also showed that asphalt is the main source of CO2 emissions during production, transportation, and installation in the structure. In second place are the unbound sub-base and the unbound base course, as the

use of waste material can reduce the thickness of the required layer. To further expand the optimization process and the use of materials, the reliability-based design approach should be considered as it takes a different perspective on the matter and can be critical to understanding the failure mechanisms. In contrast to its prevalent application in various geotechnical constructions, the utilization of reliability-based design optimization remains relatively limited in the context of pavement engineering. Nonetheless, several studies have underscored the significance of failure mechanisms derived from reliability-based design, emphasizing the pivotal role they play in offering critical insights and precise information regarding the operational lifespan of pavements. (Dilip et al., 2013; Jelušič & Žlender, 2022; Sanchez-Silva et al., 2005; Saride et al., 2019). By promoting a deeper understanding of the interplay between uncertain material properties, traffic loads, structural configurations, and environmental factors, this study will pave the way for the implementation of optimal pavement design based on reliability-based design and use of geosynthetics that can meet the diverse needs of modern transportation networks.

2 OPTIMIZATION MODEL

The deterministic optimization model (*PVT-OPT*) for the targeted pavement structure (see Figure 1) consists of several elements, including a comprehensive set of input data, an objective function (*COST*) that determines the properties of the pavement structure as determined by the geotechnical analysis and design constraints, and a set of variables is also included. In particular, the inclusion of the Monte Carlo simulation method in the reliability-based design serves to effectively account for and address the inherent uncertainties contained in these variables as we expand the deterministic model into an uncertainty model. To effectively use an evolutionary algorithm to perform the optimization the problem was translated into a mixed integer problem. Firstly, an optimal design based on the AASHTO and local technical specifications - TSC for roads (AASHTO, 1993; Nicholls, 1991; TSC 06.520:2009, 2009) was obtained and further evaluated using the expanded reliability-based design method. The probability of failure was calculated and determined for the proposed optimal designs. The expanded deterministic model was then also used to provide a graphical comparison between different soil conditions, ranging from $CBR_{subgrade}$ 1 % to $CBR_{subgrade}$ 8 % and effects of the geosynthetics and reliability on the price and longevity of the pavement structure. The parameters of interest are the thickness of asphalt surface course d_{as} (m), thickness of asphalt base course d_{ab} (m), thickness of unbound base course d_b (m) thickness of unbound sub-base course and pavement construction costs *COST* (€/m^2). Also, while optimizing using the reliability-based design the failure probability *Pf* (%). To obtain the optimal values for these parameters, six distinct conditions (see, Table 1) were established according to the AASHTO guides and local technical specifications (TSC).

2.1 Constrains in the optimization model

As already mentioned, Table 1 consists of the cost objective function and the necessary conditions for the optimization model (*PVT-OPT*). The cost objective function includes the individual costs (c_i - unit price) of the different soil and construction works for the construction of a pavement structure. The costs are listed in Table 2. The material properties (Young's modulus) per AASHTO are 320 MPa for granular base, 125 MPa for granular sub-base and depending on the CBR value the subgrade stiffness differs. The six conditions, based on the AASHTO and local TSC specifications, represent the basic design constraints. It should be noted that the denotation *mod* is used to describe the modified CBR value. For example, if the CBR value of the subgrade is on the lower side, unbound sub-base is used to increase this value for the safety and durability of the pavement structure.

Condition 1 states that the thickness index of the pavement structure (D_{total}) must be greater than the required thickness index of the structure (D_{req}). The equations consist of the equivalency factors a_i specified by the AASHTO and the thickness of the asphalt surface course d_{as}, the asphalt base course d_{ab} and the sub-base course d_b.

Condition 2 limits the required asphalt thickness to account for the number of vehicles (ESAL), as per TSC specifications ESAL is the only variable that determines the thickness of the asphalt course.

Condition 3 describes the required thickness of the unbound base course to ensure the load-bearing capacity of the pavement structure, as the quality and thickness is vital in providing a sufficient load bearing capacity when calculating the required thickness index of the pavement structure. The quality of the unbound base course is translated into the equivalent factor a_i as specified by AASHTO and TSC.

Condition 4 specifies the required total thickness of the pavement structure to combat the effect of frost penetration - h_{req}, which consists of h_m which is obtained based on the geographical location and is specified in the TSC and the factor f_{fr} that considers the soil conditions on the construction site based on laboratory tests.

Condition 5 specifies the minimum thickness of the unbound sub-base course to achieve a certain *CBR* value, also known as CBR_{mod}, which following TSC should be at least 15 %. This is done to artificially create better conditions for unbound base course, as the price of unbound sub-base course is cheaper and therefore ideal to increase the *CBR* value of the subgrade. The thickness required to obtain a given CBR_{mod} value is also reduced by the factor $\gamma_{geo,sb}$ when geosynthetic reinforcement is used. The value of the mentioned factor has been determined by laboratory and field tests and is considered to be 2.0 when geosynthetics are used.

Condition 6 sets minimum asphalt thickness requirements necessary for machine-based road construction.

Condition 7 is applied when designing based on probability of failure and considers all the above conditions. With the use of Monte Carlo simulation, 100,000 random numbers of the random variables reported in table 3 were created and the 100,000 random samples were than analyzed using condition 7 to estimate the failure probability of a pavement structure.

2.2 Results of the optimization model PVT-OPT

The evolutionary algorithm is used to optimize the design, effectively using the six previously mentioned conditions. Later the deterministic model is expanded with another condition, condition 7 (see Table 1) that includes the failure probability of the pavement structure. The previously obtained results were than analyzed and a probability of failure for a pavement structure with no reinforcement and with geosynthetic reinforcement was determined (see Table 3). The findings exhibit a mutual failure probability of 19.5 % of which 15.7 % is provided by the pavement thickness index (Condition 1) and 3.8 % is due to inadequate frost resistance thickness (Condition 4), as those are also the main conditions that are checked for failure. The input data for the reliability-based design analysis and optimization can be found in Table 4. Notably, it is imperative to highlight that pavement structure with no reinforcement is thicker for 29.5 % which also translates into a cost difference of 7.37 €/m^2 which for a standard road with a width of 7 m and a length of 1,000 m (the cost calculations therefore refer to 1 km of a given pavement) add to over 51.590 € in total costs (see, Table 3). Evidently, these observations show that a pavement structure with geosynthetic reinforcement is favorable in such conditions ($CBR_{subgrade}$ = 3.5 %, h_m = 80 m, f_{fr} = 0.7 and $N = 2.5 \cdot 10^6$). Further the study calculates the relationship between cost and failure probability of the pavement structure for different soil properties to showcase the usefulness of geosynthetic reinforcement in providing an economically and sustainable pavement design (see, Figure 2).

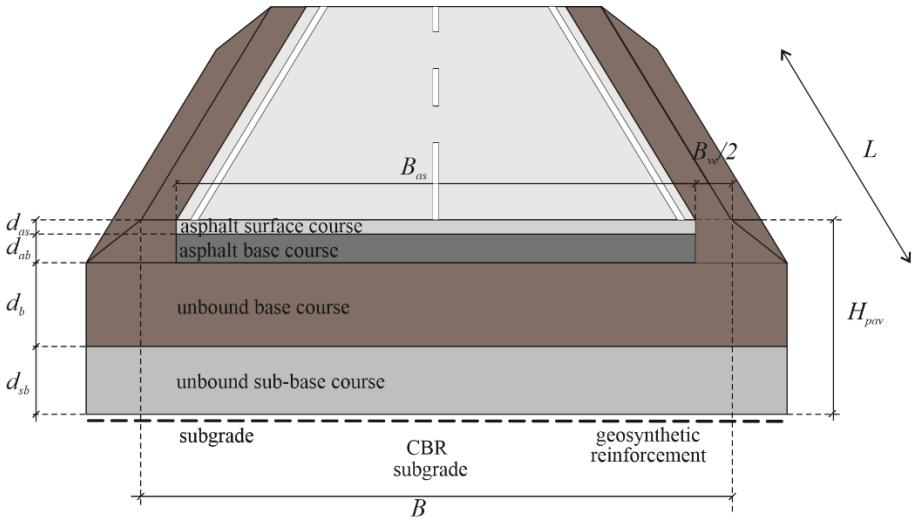

Figure 1. Cross section of the pavement design with the geometrical parameters shown.

Table 1. Optimization model PVT-OPT with all the required conditions.

Cost objective function for the PVT-OPT model	
$COST = C_{exc,re} + C_{gc} + C_{fill,b} + C_{as,subs} + C_{fill,sb} + C_{as} + C_{ab} + C_{geo}$	
$C_{exc,re} = c_{exc,re} \cdot h_{total} \cdot (B_{ve} + B_{as})$	$C_{gc} = c_{gc} \cdot (B_{ve} + B_{as})$
$C_{fill,b} = c_{fill,b} \cdot (B_{ve} + B_{as}) \cdot d_b$	$C_{as,subs} = c_{as,subs} \cdot B_{as}$
$C_{fill,sb} = c_{fill,sb} \cdot (B_{ve} + B_{as}) \cdot d_{sb}$	$C_{as} = c_{as} \cdot B_{as} \cdot d_{as}$
$C_{ab} = c_{ab} \cdot B_{as} \cdot d_{ab}$	$C_{geo} = c_{geo} \cdot (B_{ve} + B_{as})$
$C_{asb} = c_{asb} \cdot B_{as} \cdot d_{asb}$	
Condition 1	
$D_{total} \geq D_{req}$	
$D_{total} = d_{as} \cdot a_{i,as} + d_{ab} \cdot a_{i,ab} + d_b \cdot a_{i,b}$	$d_{b,CBR_{mod}} = ((c_1 - c_2 \cdot CBR) \cdot \ln(T_n) - c_3 + e^{(c_4 \cdot CBR) \cdot c_5})/\gamma_{geo,b}$ $note: \gamma_{geo,b} = 2$
$d_{asb,0} = a_1 \cdot {T_n}^{a_2}$	$d_{asb,0} = d_{as} + d_{ab}$ $note: d_{as} = 4\ cm$
$D_{req} = d_{asb,0} \cdot 0.38 + d_{b,CBR_{mod}} \cdot 0.14$	
Condition 2	
$d_{prov} \geq d_{asb,0}$	$d_{prov} = d_{as} + d_{ab}$
Condition 3	
$d_b \geq d_{b,req}$	$d_{b,req} = d_{b,CBR_{mod}}$
note: denotation *mod* stands for modified CBR value which is set to 15 %.	
Condition 4	
$h_{total} \geq h_{req}$	$h_{req} = h_m \cdot f_{fr}$
$h_{total} = d_{as} + d_{ab} + d_b + d_{sb}$	
Condition 5	
$d_{sb} \geq d_{sb,CBR_{mod}}$	$d_{sb,CBR_{mod}} = (b_1 \cdot (\frac{b_2 \cdot (CBR_{mod} - CBR)}{b_3 - CBR} + b_4))/\gamma_{geo,sb}$
Condition 6	
$d_{as} \geq d_{as,min}$	$d_{ab} \geq d_{ab,min}$
Condition 7	
$Pf = \frac{\sum_1^n A(n)}{n}$	
$If\ \frac{{D_{total}}^n}{{D_{req}}^n} \geq 1\ or\ \frac{{h_{total}}^n}{{h_{req}}^n} \geq 1\ ; than\ A\ (n) = 1; else\ \ A\ (n) = 0$	

Table 2. Unit price and material characteristics for pavement construction.

Symbol	**Meaning**	**Cost per unit**
$c_{exc,re}$	Ground excavation	9.0 €/m^3
c_{gc}	Ground compaction	2.5 €/m^2
$c_{as,subs}$	Asphalt substrate	1.5 €/m^2
c_{as}	Asphalt surface course	300.0 €/m^3
$c_{fill,b}$	Base-course fill	36.0 €/m^3
$c_{fill,sb}$	Sub-base fill	24.0 €/m^3
c_{ab}	Asphalt base course	200.0 €/m^3
c_{asb}	Single asphalt course	250.0 €/m^3
c_{geo}	Geosynthetic install.	4.5 €/m^2

Table 3. Optimal results obtained based on the deterministic model and the corresponding failure probability (Pf).

Type	d_{as} (m)	d_{ab} (m)	d_b (m)	d_{sb} (m)	COST (€/m^2)	*Pf* (%)
Reinforced:	4	12	27	31	67.42	19.5
Not reinforced:	4	12	27	62	74.06	19.5

Table 4. Prior knowledge of the random variables.

Random variables	Mean min.	Mean max.	CoV [%]	Standard deviation min.	Standard deviation max.
N (-)	$2 \cdot 10^6$	$2.5 \cdot 10^6$	2-10	$2 \cdot 10^5$	$5 \cdot 10^5$
CBR (%)	1/3/5	3/5/8	10-15	0.1/0.3/0.5	0.45/0.75/1.2
h_m	0.7	0.8	10-20	0.07	0.16

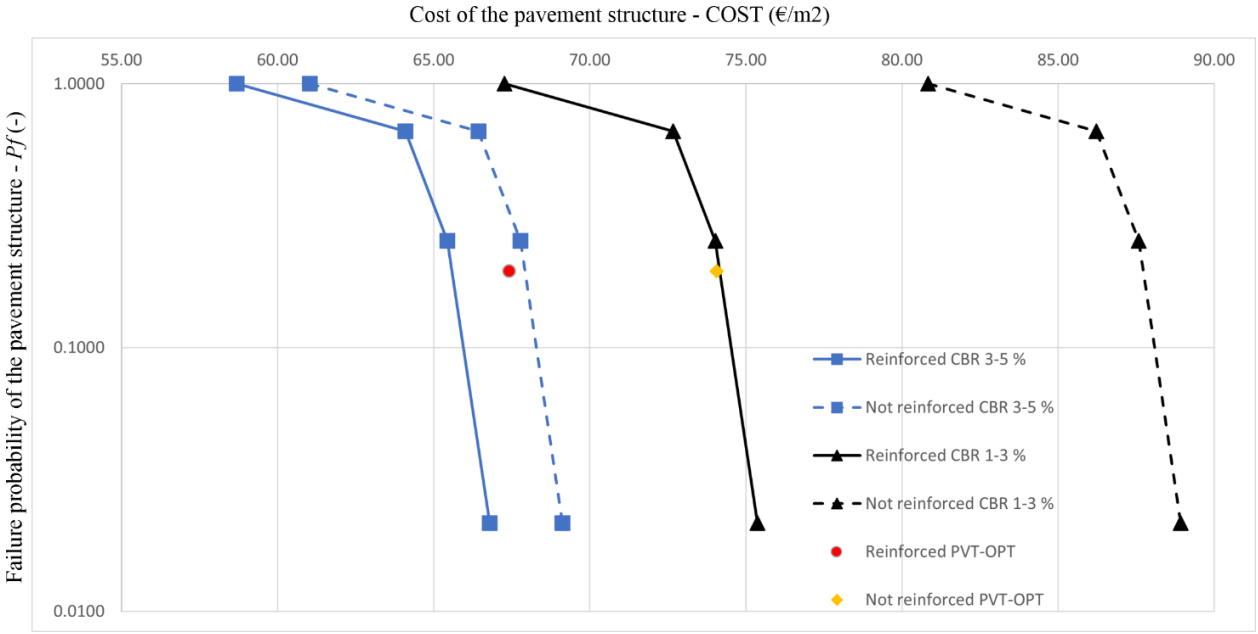

Figure 2. Relationship between COST and failure probability Pf for the optimal pavement designs.

3 CONCLUSIONS

The results of this study highlight the critical role of the thickness of the unbound base course in determining the longevity of an optimal pavement structure. Insufficient thickness of the unbound base course will result in its inability to withstand the combined effects of traffic loads and environmental stresses over a 20-year period with a probability of 15.7 %. In particular, the effects of frost depth on pavement structures with unbound sub-base courses are mitigated because these sub-base courses contribute an additional thickness to the overall structure. In addition, Figure 2 shows the correlation between the probability of failure and the cost of reinforced and unreinforced pavement structures and highlights the favorable performance of structures with geosynthetic reinforcement. Especially for soils with low modulus of elasticity and the resulting CBR values, the cost difference between traditional construction methods and those using geosynthetics is significant. Therefore, the use of geosynthetics is recommended to improve cost efficiency and environmental performance due to the reduced thickness required. Ultimately, this approach contributes to a lower probability of structural failure, highlighting its economic, environmental and performance benefits in pavement design and construction.

ACKNOWLEDGEMENTS

This research was founded by the Slovenian Research agency (ARIS, grant number P2-0268).

REFERENCES

AASHTO. (1993). AASHTO Guide for Design of Pavement Structures. In *American Association of State Highway and Transportation Officials*.

Abukhettala, M., & Fall, M. (2021). Geotechnical characterization of plastic waste materials in pavement subgrade applications. *Transportation Geotechnics*, *27*, 100472. https://doi.org/10.1016/J.TRGEO.2020.100472.

Dilip, D. M., Ravi, P., & Babu, G. L. S. (2013). System Reliability Analysis of Flexible Pavements. *Journal of Transportation Engineering*, *139*(10), 1001–1009. https://doi.org/10.1061/(ASCE)TE.1943-5436.0000578.

Fatemi, S., & Imaninasab, R. (2016). Performance evaluation of recycled asphalt mixtures by construction and demolition waste materials. *Construction and Building Materials*, *120*, 450–456. https://doi.org/10.1016/J.CONBUILDMAT.2016.05.117.

Huang, Y., Bird, R. N., & Heidrich, O. (2007). A review of the use of recycled solid waste materials in asphalt pavements. *Resources, Conservation and Recycling*, *52*(1), 58–73. https://doi.org/10.1016/J.RESCONREC.2007.02.002.

Jelušič, P., Gücek, S., Žlender, B., Gürer, C., Varga, R., Bračko, T., Taciroğlu, M. V., Korkmaz, B. E., Yarcı, Ş., & Macuh, B. (2023). Potential of Using Waste Materials in Flexible Pavement Structures Identified by Optimization Design Approach. *Sustainability*, *15*(17), 13141. https://doi.org/10.3390/su151713141.

Jelušič, P., Varga, R., & Žlender, B. (2023). Parametric analysis of the minimum cost design of flexible pavements. *Ain Shams Engineering Journal*, *14*(2), 101840. https://doi.org/10.1016/j.asej.2022.101840.

Jelušič, P., & Žlender, B. (2022). Pavement structure. In *Risk, Reliability and Sustainable Remediation in the Field of Civil and Environmental Engineering* (pp. 499–509). Elsevier. https://doi.org/10.1016/B978-0-323-85698-0.00005-8.

Mamlouk, M. S., Zaniewski, J. P., & He, W. (2000). Analysis and design optimization of flexible pavement. *Journal of Transportation Engineering*, *126*(2), 161–167. https://doi.org/10.1061/(ASCE)0733-947X(2000)126:2(161).

Nicholls, R. (1991). Optimization of AASHTO DNPS86 pavement design program. *Journal of Transportation Engineering*, *117*(2), 189–209. https://doi.org/10.1061/(ASCE)0733-947X(1991)117:2(189).

Sanchez-Silva, M., Arroyo, O., Junca, M., Caro, S., & Caicedo, B. (2005). Reliability based design optimization of asphalt pavements. *International Journal of Pavement Engineering*, *6*(4), 281–294. https://doi.org/10.1080/10298430500445506.

Santos, J., & Ferreira, A. (2012). Pavement Design Optimization Considering Costs and Preventive Interventions. *Journal of Transportation Engineering*, *138*(7), 911–923. https://doi.org/10.1061/(ASCE)TE.1943-5436.0000390.

Saride, S., Peddinti, P. R. T., & Basha, M. B. (2019). Reliability Perspective on Optimum Design of Flexible Pavements for Fatigue and Rutting Performance. *Journal of Transportation Engineering, Part B: Pavements*, *145*(2), 4019008. https://doi.org/10.1061/JPEODX.0000108.

TSC 06.520:2009. (2009). *Designing and dimensioning new asphalt pavement structures.*

You, L., Long, Z., You, Z., Ge, D., Yang, X., Xu, F., Hashemi, M., & Diab, A. (2022). Review of recycling waste plastics in asphalt paving materials. *Journal of Traffic and Transportation Engineering (English Edition)*, *9*(5), 742–764. https://doi.org/10.1016/J.JTTE.2022.07.002.

Proceedings of the XVIII ECSMGE 2024
GEOTECHNICAL ENGINEERING CHALLENGES
TO MEET CURRENT AND EMERGING NEEDS OF SOCIETY
© 2024 the Authors
ISBN 978-1-032-54816-6
DOI 10.1201/9781003431749-377
Open Access: www.taylorfrancis.com, CC BY-NC-ND 4.0 license

ECSMGE 24
XVIII EUROPEAN CONFERENCE ON SOIL MECHANICS AND GEOTECHNICAL ENGINEERING

Cathédrale de Beauvais: les accidents structurels des XIIIe et XVIe siècles eurent-ils une origine géotechnique? Partie 1: Contexte historique et naturel

Beauvais' cathedral: did the 13th and 16th centuries structural failures have a geotechnical cause? Part 1: Historical and natural context

J.D. Vernhes*
Institut Polytechnique UniLaSalle, Beauvais, France

P. Renault
BMI, Alfortville, France

Y. Zotna
Conservation régionale des monuments historiques, Amiens, France

**jean-david.vernhes@unilasalle.fr*

RÉSUMÉ: La cathédrale Saint-Pierre de Beauvais est la plus haute de voûte jamais construite au Moyen Age. Elle connut deux accidents structurels célèbres, dans le chœur en 1284 puis à la croisée du transept en 1573. En 2023 coexistent encore plusieurs types d'explications pour donner une origine à ces accidents, avec des causes structurelles, naturelles ou géotechniques. On montre que l'origine géotechnique n'est très vraisemblablement pas à retenir pour 1284. Elle peut être invoquée pour 1573, mais à titre secondaire. Le texte qui suit est la première partie de l'article.

ABSTRACT: Saint Peter's cathedral in Beauvais (France) has the highest vaults ever built during the Middle Ages. It was affected by two famous structural accidents, in the choir in 1284, and later at the transept crossing, in 1573. In 2023, there are still several explanations to account for what happened then, structural or natural causes, or geotechnical ones. We here show that nothing appears to justify a geotechnical origin in the 1284 collapse. It may be considered in 1573, nevertheless as a secondary cause. The following text is the first part of the article.

Keywords: Géotechnique et patrimoine; architecture gothique; fondations superficielles.

1 INTRODUCTION

La cathédrale Saint-Pierre de Beauvais (Figure 1) est la plus haute église gothique du monde. Elle marque l'apogée de ce style architectural qui a vu le jour en France dans les années 1140. Eugène Viollet-le-Duc, connu pour son œuvre de restauration de Notre-Dame de Paris au XIXe siècle, qualifia la cathédrale beauvaisienne de « Parthénon de l'architecture française » (Viollet-le-Duc, 1858-1868, T1, p. 71).

Cependant elle apparaît aujourd'hui comme un monument à la fois composite et inachevé. Cent soixante ans séparent la fin des travaux du chœur et le commencement du transept et sa nef gothique n'a jamais été construite (Murray, 2000). L'interruption des travaux comme leur inachèvement trouvent leur explication dans deux accidents structurels graves. Leur origine fait, encore à notre époque, l'objet de discussions qui incorporent parfois un mécanisme géotechnique (Renault, 2021).



Figure 1. Vue de la cathédrale Saint-Pierre de Beauvais depuis le sud-est, février 2014 (ph. J-D Vernhes).

La cathédrale de Beauvais a bénéficié depuis les années 1980 d'une surveillance car des fissures étaient apparues dans certaines voûtes.

L'objectif de cet article en deux parties n'est néanmoins pas de statuer sur son état actuel mais de tirer parti des données récemment collectées, à la faveur des diagnostics, pour étudier rétroactivement le rôle du système de fondations de l'édifice dans les deux accidents. Cette première partie de l'article porte sur les éléments de contexte utile à la compréhension du problème. Dans la deuxième partie de l'article (Vernhes et al., 2024b) sont exposés l'analyse géotechnique et une proposition de réponses argumentées aux questions posées. Les deux parties ainsi décrites forment un tout considéré comme indissociable.

2 DONNÉES GÉNÉRALES

2.1 Brève histoire des travaux

Dans cette partie, les sources suivantes sont exploitées pour les données générales : Viollet-le-Duc (1858-1868), Leblond (1926), Murray (2000), Bonnet-Laborderie (2006) et Meunier et Bonnet-Laborderie (2006).

2.1.1 Avant 1225: les premières cathédrales

Le centre épiscopal de Beauvais fut occupé dès le Haut Moyen Age par des églises cathédrales. Autour de l'An Mil celle qui existait fut reconstruite en style pré-roman, avec des pastoureaux calcaires (lutétiens) de remploi du rempart gallo-romain. Son transept (?) et son chœur furent agrandis au XIIe siècle mais disparurent par la suite.

En 1225, un incendie endommageait le chœur roman. L'évêque Milon de Nanteuil décida alors de le reconstruire en s'inspirant des plus grandes réalisations de son époque, dans le style *français* (gothique, alors *rayonnant*), tout en conservant provisoirement la nef et le transept romans pour le culte. L'ensemble des trois travées de la nef qui reste aujourd'hui est appelé Basse Œuvre (Figure 2).

2.1.2 1225-1340: nouveau chœur et accident

Les premiers travaux portèrent sur des éléments orientaux du transept, dont l'emprise au sol présentait un intérêt pour stabiliser au mieux l'extrémité ouest des futures parties hautes. La craie dure à silex (coniacienne à campanienne) de la carrière Saint-Pierre près de Frocourt et Bongenoult, à proximité de Beauvais, fut exploitée.

Le système de fondations utilisé n'est pas connu avec précision mais de grands terrassements préparatoires furent nécessaire pour atteindre le « niveau de bon sol » et y construire des puits à base élargie, pratique la plus courantes pour les constructions géantes du Moyen Age, selon Viollet-le-Duc. Le même affirme que les maîtres d'œuvre « (…) *ne manquaient jamais de relier entre eux tous les murs et massifs en fondation ; c'est-à-dire que, sous un édifice composé de murs et de piles isolées, par exemple, ils formaient un gril de maçonnerie sous le sol, afin de rendre toutes les parties des fondements solidaires.* » (op. cit., T5, p. 525).

Dans l'emprise des futurs chœur et partie est du transept, le remblai de comblement de l'excavation fut élevé environ deux mètres au-dessus du niveau de la rue au XIIIe siècle de telle sorte que leur dallage allait reposer sur un terre-plein.

Dans les années 1250, les deux premiers niveaux de construction étant achevés (grandes arcades et triforium), l'évêque Guillaume de Grès décida apparemment pour le troisième et dernier étage de l'édifice de sortir des proportions prévues originellement en ajoutant quelques mètres (de l'ordre de cinq) aux fenêtres hautes et donc aux voûtes. En 1272, le nouveau chœur put être occupé par le clergé, ce qui permit le lancement d'une phase préparatoire à la poursuite des travaux : sans doute le démantèlement du transept roman après fermeture et étaiement provisoire de l'ouest de la Haute Œuvre.

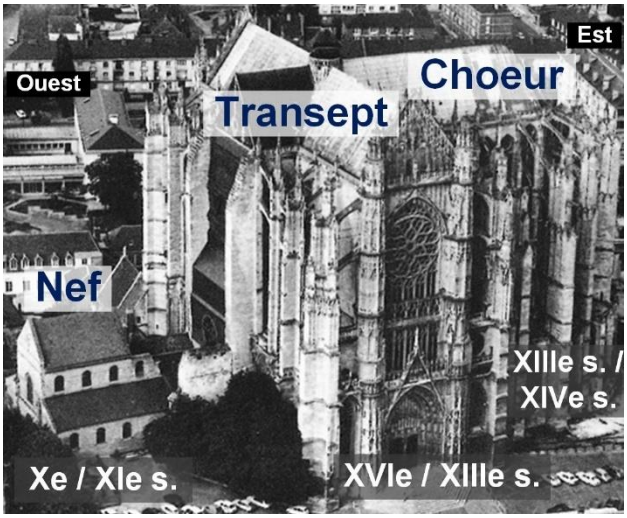

Figure 2. Vue aérienne de la cathédrale, fin des années 1970 (ph. : n. c. ; in : Bonnet-Laborderie, 2006), habillée.

Le 29 novembre 1284, durant cette nouvelle phase de chantier, des voûtains des travées droites du chœur, les plus vulnérables, s'effondrèrent (Figure 3), marquant pour tout l'Occident « *la dernière limite à laquelle la construction des grandes églises du XIIIe s. ait pu arriver* » (*op. cit.*, T1, p. 71). Le diagnostic nécessaire à la reprise des parties concernées et le chantier qui s'en suivi s'acheva en 1340. « *On mit donc plus de temps à réparer le chœur qu'à le construire* » (Murray, 2000).

2.1.3 1499-1605: nouveau transept et accident

1340 coïncide en France avec le début d'une période de crise militaire, sanitaire et économique qui eut pour effet d'interrompre presque totalement les grands chantiers en cours, ce qui advint à Beauvais.

L'embellie de la deuxième moitié du XVe siècle remit à l'ordre du jour, dès les années 1480, la poursuite des travaux par la construction des deux vaisseaux manquants du transept, dont le seul en place était resté mal étayé à l'ouest.

En septembre 1499, pendant 23 jours, furent réalisés des sondages derrière le chœur à la considérable profondeur de 10 toises (19 m) et un autre de 32 pieds (10 m) à l'emplacement du futur bras sud du transept ; les premiers pour s'assurer de la fermeté du terrain, le dernier pour obtenir des informations sur les fondations posées au XIIIe siècle (Meunier et Bonnet-Laborderie, 2006).

Le grand architecte Martin Chambiges fut chargé en 1500 de la délicate conception d'une « greffe » en style gothique *flamboyant*, compatible stylistiquement et mécaniquement avec le haut édifice en place, puis de la conduite des travaux pendant les 32 années qui suivirent, jusqu'à sa mort.

Pour les nouvelles fondations, dont les caractéristiques furent sans doute analogues aux précédentes, il choisit non la craie mais la pierre calcaire (lutétienne) des carrières de Mérard, Mouy et Mello, une trentaine de kilomètres à l'aval hydrographique de Beauvais. Le reste de l'œuvre fut réalisée avec les mêmes approvisionnements de craie qu'au XIIIe s. (*op. cit.,* 2006).

La construction du transept fut achevée après la mort de l'architecte, entre 1537 (bras nord) et 1550 (bras sud). C'est dans cette période que survint le projet de coiffer la croisée du transept d'une tour lanterne à trois niveaux surmontés d'une flèche (Figure 4a), et non d'une simple flèche en bois comme Chambiges avait dû le prévoir (*op. cit.*). La base du transept déjà construite était alors considérée comme capable d'en soutenir le poids, et l'ensemble devait tenir moyennant des modifications des parties hautes qui pouvaient encore être prises en compte.

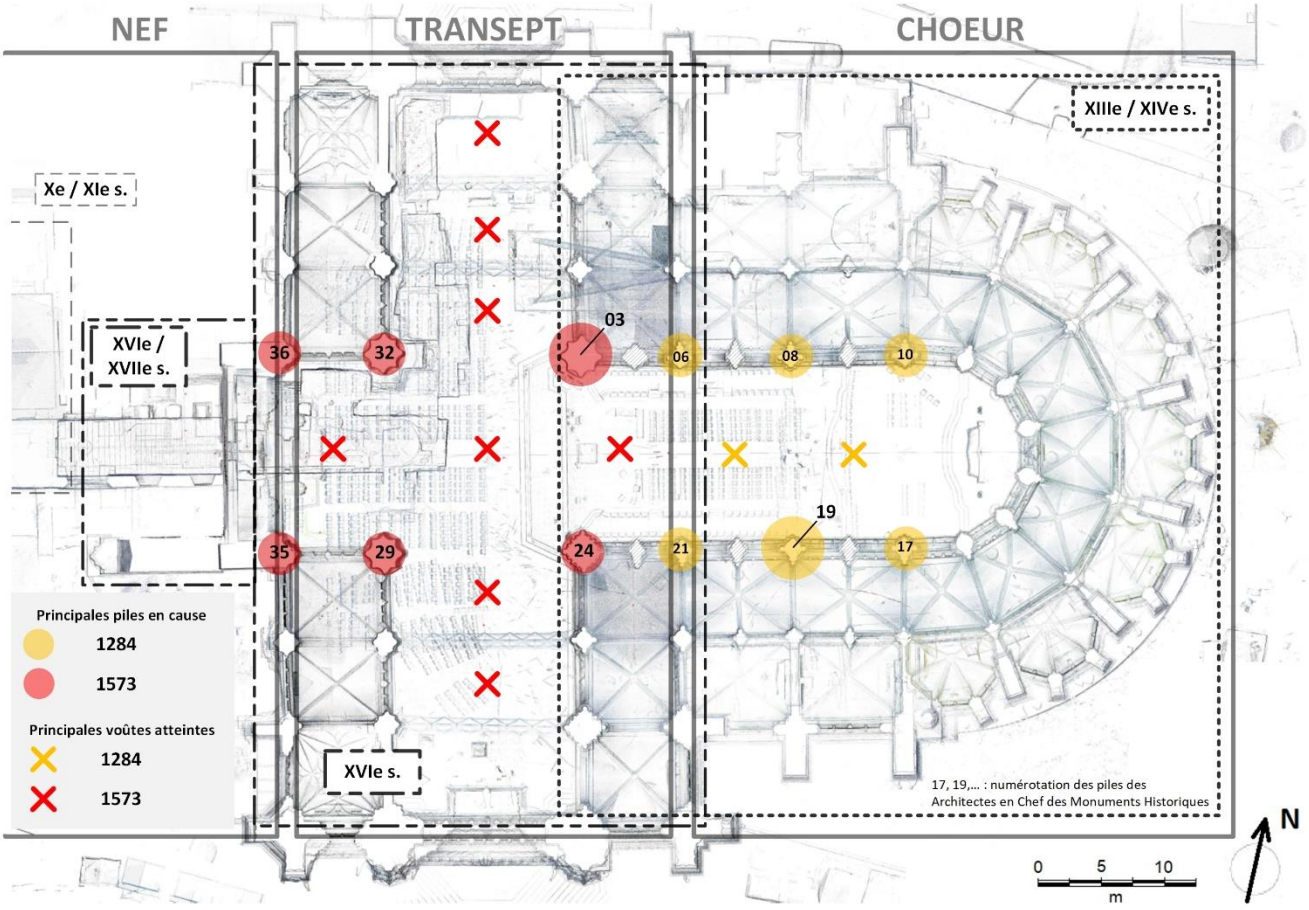

Figure 3. Localisation d'éléments liés aux accidents de 1284 et 1573 (fond de plan Lidar : Martin, 2021 ; habillé).

Ce nouveau projet, dont les pierres furent prélevées dans la carrière de calcaire lutétien de Saint-Leu-d'Esserent (à une quarantaine de kilomètres de Beauvais) dès 1558, et dont la réalisation s'étendit de 1563 à 1569, reporta la construction des deux premières travées centrales de la nef ainsi que le

démantèlement de nouvelles travées de la Basse Œuvre à 1572 (Lamboley, 1993, p. 1 ; Poncelet, 2002).

Après de nombreux signes avant-coureurs, un support de la tour lanterne s'effondra le jour de l'Ascension 1573, un 30 avril, le lendemain de chutes de fragments de pierre. C'est seulement le 16 août qui suivi que les trois supports restants cédèrent (op. cit., 1993), entraînant avec eux la lanterne, démolissant dans sa chute ou du fait de l'ébranlement toutes les voûtes des travées qui l'entouraient, y compris une du XIIIe siècle, ainsi que la pile n° 3 (Figure 3).

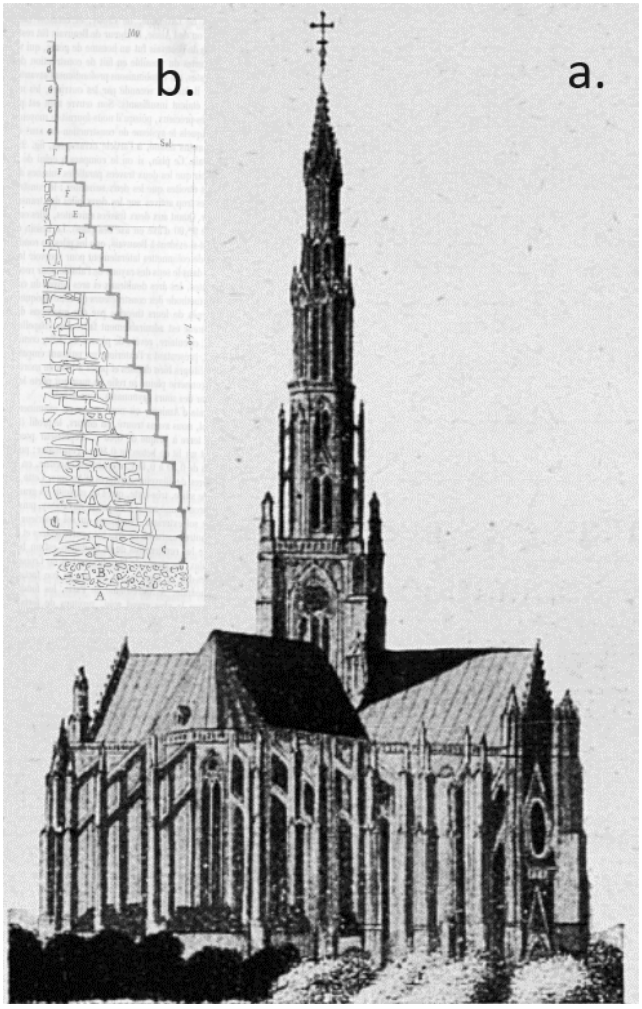

Figure 4. (a.) Vue cavalière de la cathédrale surmontée d'une tour de croisée avec flèche sommitale, en élévation de 1569 à 1573 (in Leblond, 1926, p. 27) ; (b.) En incrustation, coupe verticale d'un puits de fondation maçonné, observé par E.-E. Viollet-le-Duc à la cathédrale d'Amiens (op. cit., T4, p. 176).

Les travaux de réparation, restituant finalement le projet de Chambiges, un peu amoindri, s'étendirent jusqu'en 1605, sans qu'il ne reste assez de moyens pour construire la nef. Le contrebutement que la nef et les tours du massif occidental non construits auraient dû exercer sur le carré du transept pour en bloquer les poussées au vide, fut assuré de façon provisoire (jusqu'à nos jours) par des murs boutants, à l'emplacement des premières colonnes du vaisseau central de la nef (Figure 3, zone XVIe / XVIIe s.).

2.2 Géologie du centre historique de Beauvais

Située 60 km au nord de Paris, Beauvais est construite dans une vallée alluviale au socle crayeux. De ces deux données naturelles découleront un ensemble de caractéristiques géotechniques concernant la cathédrale Saint-Pierre.

2.2.1 Topographie et hydrographie

Le centre-ville historique de Beauvais, très plat, se situe à des altitudes situées dans la fourchette 65 à 70 m NGF (Nivellement Général de la France), avec 68/69 m NGF autour de la cathédrale.

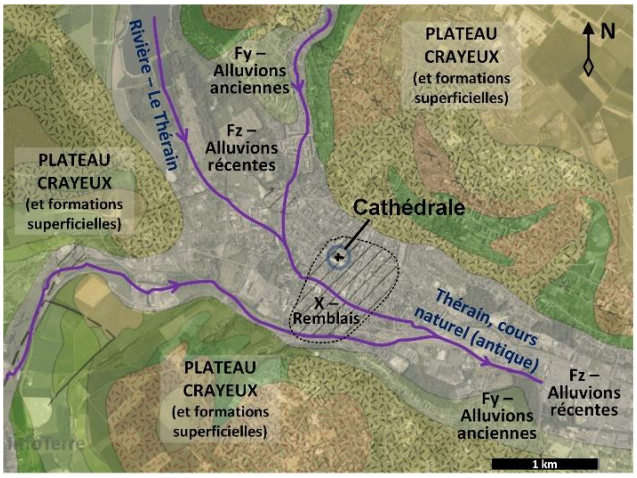

Figure 5. Extrait habillé de la carte géologique vecteur harmonisée (Blondeau et al., 1974), en transparence sur photo aérienne IGN, via Infoterre (BRGM, 2023).

Beauvais est située dans la vallée alluviale d'un affluent de l'Oise, le Thérain (Figure 5), très canalisé depuis l'Antiquité et dont le cours le moins artificiel passerait aujourd'hui au sud du centre-ville, en moyenne vers 63 m NGF.

2.2.2 Stratigraphie

L'altitude dans le quartier cathédrale devait être à peine à 65 m NGF avant les aménagements de l'époque gallo-romaine. La ville connut alors une surélévation artificielle par remblaiement de craie damée, le processus continuant avec l'accumulation de débris d'occupation urbaine au Moyen Age, des remblais anthropiques globalement notés X sur la carte géologique (Figure 5).

Au-dessous de ces remblais se trouvent les dépôts du Thérain en deux ensembles bien contrastés, Fz et Fy selon la terminologie du BRGM. Ce sont les alluvions récentes et anciennes, respectivement fines

(argile, limon et éventuellement tourbe), et grossières (sables et graviers de silex). Cette succession corrélant fortement âge et granularité s'explique par le dernier épisode d'eustatisme et ses conséquences en termes de régime hydraulique des rivières et donc de transportabilité des matériaux d'érosion, phénomène gouverné par le changement climatique entre pléistocène et holocène (Lebret *et al.*, 1991). Ces dépôts sont donc en principe relativement homogènes et leur interface assez franche.

Sous les alluvions se trouve la craie, roche tendre et gélive, datée du campanien. En fond de vallée, où est située la cathédrale, la craie a subi un rabotage de l'ordre de 50 m de hauteur, correspondant au dénivelé moyen avec le plateau picard. Ce processus, accentué par la gélifraction des âges glaciaires, a dégradé, dans ses premiers mètres supérieurs, la craie en place.

2.2.3 Hydrogéologie

Il existe deux nappes intéressant le fond de la vallée du Thérain à Beauvais, la nappe alluviale bien sûr, mais également celle de l'aquifère de la craie qui y trouve un exutoire continu.

Ces deux nappes sont en continuité hydraulique car les deux aquifères (craie à fissuration ouverte et alluvions anciennes) ne sont pas séparées par un niveau imperméable.

2.3 Reconnaissances *in situ*

Entre septembre 1499 et juin 2001, il ne semble pas qu'il y ait eu dans la cathédrale ou à ses abords immédiats de reconnaissances de sol, si ce n'est un sondage signalé par la BSS (BRGM, 2023), réalisé en 1967 « au pied d'un bénitier » dans le croisillon nord du transept, mais trop peu profond et surtout mal documenté pour être intéressant. Il faut cependant mentionner aussi deux bases de sismique réfraction réalisées par la Compagnie Générale de Géophysique en 1992, au nord et à l'est de la cathédrale, mais dont on a que les résultats interprétés (Lamboley, 1993).

En 2001 sont réalisés 4 sondages destructifs au pied de chaque pilier du carré du transept (BS Consultants, 2001), suivi en juin 2021 d'un sondage carotté dans le croisillon nord du transept également pour une reconnaissance de fondation de pile (Mazet et Marcie, 2021), sondages intéressants pour les questions soulevées dans cet article.

Pour étayer le modèle géotechnique global leur ont été adjointes les données de sondages localisés dans le centre-ville, cinq issus de la BSS (BRGM, 2023 ; ancienne nomenclature : 01024X0167PZ22, 01024X0093S, 01024X0111F, 01024X0124F.PAC, 01024X0095PIEU1) et une cinquantaine d'autres réalisés pour un projet immobilier (Arnassalon et Geisler, 2012).

2.3.1 Sols et eau, enseignements

Depuis la surface, l'ensemble des sondages consultés donnent des résultats convergents : la base des remblais est le plus souvent autour de 65 m NGF ; celle des alluvions modernes, variables en épaisseur, de 61 à 63 m NGF, altitudes qui sont également celle du toit des alluvions anciennes. Leur base est encore plus variable, de 55 à 59 m NGF, mais leur épaisseur ne semble jamais inférieure à trois mètres, typiquement quatre mètres sous la cathédrale.

La craie apparaît bien comme altérée dans les premiers mètres sous les alluvions anciennes, à tel point que ces dernières sont mécaniquement plus compétentes qu'elle. Vers 50 m NGF, la craie devient plus dure, c'est-à-dire à peu près 20 m sous le niveau de la cathédrale, profondeur atteinte par le sondage de 1499.

La compétence mécanique des horizons décrits est bien corrélée aux retours d'expérience : faible dans les remblais et alluvions modernes (q_c ou E_M typiques de 2 ou 3 MPa), quatre à sept fois plus élevée dans les alluvions anciennes mais seulement deux fois plus dans la craie altérée.

L'eau phréatique est une question plus délicate à traiter car son niveau moyen et ses variations actuelles peuvent difficilement être associés avec certitude à ceux de 1225 ou 1499. Mais, la nappe étant à la fois alimentée par une rivière régulée depuis l'époque gallo-romaine et bénéficiant d'un appoint constant d'approvisionnement par l'aquifère de la craie, on peut raisonnablement émettre l'hypothèse que les hauteurs piézométriques observées dans les dernières années présentent un intérêt rétroactif.



Figure 6. Photographie d'une caisse de carottes dans la zone de contact entre maçonnerie et sol support pour la pile n° 83 (Mazet et Marcie, 2021) habillée.

Il apparaît alors que le niveau d'eau dans le sol de la ville est assez stable au long de l'année, typiquement autour de 62/63 m NGF, avec un battement métrique. Cela veut dire que ce niveau est proche de l'interface entre les deux types d'alluvions, avec possible mise en

charge, modérée, des récentes, de perméabilité de l'ordre de grandeur de 10^{-6} m/s. Celle-ci contraste avec celle des alluvions anciennes et de la craie altérée, toutes deux proches de 10^{-4} m/s.

2.3.2 Fondations, enseignements

Les cinq sondages de reconnaissance de 2001 et 2021, concentrés sur le transept, ont trouvé des bases de fondation de piles à des cotes de 60,5 à 62,5 m NGF, bases reposant sur les alluvions anciennes (Figure 6), c'est-à-dire le « bon sol ».

Il est très vraisemblable que toutes les fondations de la Haute Œuvre (au XIIIe comme au XVIe siècle) ont été réalisées suivant le même principe. Ce qui reste beaucoup moins clair est la largeur d'empattement à leur base et leur caractère jointif à la base si l'empattement est important.

Taupin (1992) a considéré qu'elles étaient toutes liées à leur base, aboutissant à un cas de « radier général » du point de vue de la portance du terrain, suivant peut-être en cela (à défaut de les avoir vues) un exemple bibliographique issu des observations à la cathédrale d'Amiens, dans la même aire géographique que Beauvais et historiquement concordant (Figure 4b). Un fait est qu'avec un tel empattement, ces fondations sont très grandes à leur base, d'une largeur d'au moins cinq mètres, peut-être jusqu'à huit ou neuf.

Cela clôt la description des données nécessaires à l'analyse des accidents structurels de la cathédrale. Celle-ci se trouve dans la partie 2 du présent article.

RÉFÉRENCES

Arnassalon, V. et Geisler, J. (2012). Beauvais - Place du Jeu de Paume - Construction d'un centre commercial - Mission géotechnique de projet G2 - Dossier n°09P-0070-b01 - Note de synthèse géotechnique, bureau d'études FUGRO Geoconsulting SA, Nanterre, France, rapport 09P-0070-b01.v2.

Blondeau, A., Pomerol, B. et Pomerol, Ch. (1974). Carte géologique de la France à 1:50 000, n°102, Beauvais. Bureau de recherches géologiques et minières, Orléans, France.

Bonnet-Laborderie, Ph. (2006). La cathédrale Saint-Pierre de Beauvais. Tome I – Les premières cathédrales. GEMOB (éd.), Beauvais, France.

BRGM (2023). BSS : Banque de données du Sous-Sol [en ligne], accessible sur http://infoterre.brgm.fr/viewer/MainTileForward.do, dernière consultation le 23/10/2023.

BS Consultants Bureau d'études [auteur non précisé] (2001). Cathédrale de Beauvais, reconnaissance géotechnique, Courtabœuf, France, rapport R010551.

Lamboley Bureau d'études [auteur non précisé] (1993). Beauvais, cathédrale Saint-Pierre, diagnostic technique et pilotage des investigations, Lyon, France, rapport D724P02.

Leblond, V. (1926). La Cathédrale de Beauvais. Henri Laurens (éd.). Paris.

Lebret, P., Halbout, H., Clet, M., Huault, M.-F., Lautridou, J.-P., Lecolle, F., Levant, M., Van Vliet-Lanoë, B. (1991). Le quaternaire dans le Val-d'Oise. Centre de Géomorphologie du CNRS, Caen, France, pp. 237-239.

Martin, R. (2021). Beauvais, cathédrale Saint-Pierre, Restauration des toitures et des voûtes, dépose des étaiements, Dossier d'Avant-Projet Sommaire. Plans et élévations, élaboration Martin, R. (ACMH) ; données brutes Lidar : El Mustapha, M. (Université de Picardie).

Mazet, Th. et Marcie, C. (2021). Beauvais - Cathédrale Saint-Pierre - Rapport de mission géotechnique G5 - Pile n° 83, bureau d'études GEOLIA, Morangis, France, rapport G210527.

Meunier, F. et Bonnet-Laborderie, Ph. (2006). La cathédrale Saint-Pierre de Beauvais. Tome III – Le transept. GEMOB (éd.), Beauvais.

Murray, S. (2000). Le chœur gothique, In : La cathédrale Saint-Pierre de Beauvais, architecture, mobilier et trésor, AGIR-Pic. (asso. éd.), Amiens, France, pp. 14-19.

Poncelet, E. (2002). Beauvais - Cathédrale Saint-Pierre - Etude préalable concernant la résistance des sols au niveau de la croisée du transept [de l'Architecte en Chef des Monuments Historiques].

Renault, P. (2021). Beauvais - Cathédrale Saint-Pierre - Préconisations structurelles en vue de la dépose des étaiements et de la restauration des toitures hautes, bureau d'études BMI, Paris, France, rapport 21-058 ind. B.

Taupin, J.-L. (1992). Diagnostic technique [de l'Architecte en Chef des Monuments Historiques], 1ère phase.

Vernhes, J.-D., Renault, P. et Zotna, Y. (2024b). Cathédrale de Beauvais : les accidents structurels des XIIIe et XVIe siècles eurent-ils une origine géotechnique ? Partie 2 : accidents structurels et rôle de la géotechnique. Proceedings of the XVIII European Conference on Soil Mechanics and Geotechnical Engineering 2024. Lisbon, Portugal. ISBN 978-9935-9436-1-3

Viollet-le-Duc, E.-E. (1858-1868). Dictionnaire raisonné de l'architecture française du XIe au XVIe siècle. 10 tomes. B. Bance, Paris (T1 à T6), A. Morel, Paris (T7 à T10).

Proceedings of the XVIII ECSMGE 2024
GEOTECHNICAL ENGINEERING CHALLENGES
TO MEET CURRENT AND EMERGING NEEDS OF SOCIETY
© 2024 the Authors
ISBN 978-1-032-54816-6
DOI 10.1201/9781003431749-378
Open Access: www.taylorfrancis.com, CC BY-NC-ND 4.0 license

ECSMGE 24
XVIII EUROPEAN CONFERENCE ON SOIL MECHANICS AND GEOTECHNICAL ENGINEERING

Cathédrale de Beauvais: les accidents structurels des XIIIe et XVIe siècles eurent-ils une origine géotechnique? Partie 2: Accidents structurels et rôle de la géotechnique

Beauvais' cathedral: did the 13th and 16th centuries structural failures have a geotechnical cause? Part 2: Structural failures and role of geotechnics

J.D. Vernhes*
Institut Polytechnique UniLaSalle, Beauvais, France

P. Renault
BMI, Alfortville, France

Y. Zotna
Conservation régionale des monuments historiques, Amiens, France

**jean-david.vernhes@unilasalle.fr*

RÉSUMÉ: La cathédrale Saint-Pierre de Beauvais est la plus haute de voûte jamais construite au Moyen Age. Elle connut deux accidents structurels célèbres, dans le chœur en 1284 puis à la croisée du transept en 1573. En 2023 coexistent encore plusieurs types d'explications pour donner une origine à ces accidents, avec des causes structurelles, naturelles ou géotechniques. On montre que l'origine géotechnique n'est très vraisemblablement pas à retenir pour 1284. Elle peut être invoquée pour 1573, mais à titre secondaire. Le texte qui suit est la seconde partie de l'article.

ABSTRACT: Saint Peter's cathedral in Beauvais (France) has the highest vaults ever built during the Middle Ages. It was affected by two famous structural accidents, in the choir in 1284, and later at the transept crossing, in 1573. In 2023, there are still several explanations to account for what happened then, structural or natural causes, or geotechnical ones. We here show that nothing appears to justify a geotechnical origin in the 1284 collapse. It may be considered in 1573, nevertheless as a secondary cause. The following text is the second part of the article.

Keywords: Géotechnique et patrimoine; architecture gothique; fondations superficielles.

1 INTRODUCTION

Cet article est la deuxième partie d'un tout indissociable. Dans la première partie (Vernhes et al., 2024a), on trouvera tous les éléments de contexte nécessaires à l'argumentation utilisée dans les lignes qui suivent: éléments historiques, architecturaux, géologiques, hydrogéologiques et géotechniques. Nous conseillons donc au lecteur d'avoir lu le premier article avant d'aborder celui-ci.

2 ACCIDENT DE 1284

2.1 Cause d'après les sources

Il existe trois types d'interprétations pour expliquer l'effondrement partiel de voûtes du chœur en 1284, deux en partie haute de l'édifice, une en fondation.

Il s'agit pour la première de la rupture de colonnettes monolithes solidaires d'une maçonnerie appareillée dont les mortiers auraient progressivement tassé, provoquant la rupture d'arcs-boutants (Viollet-le-Duc, 1858-1868, T4, pp. 177-181; Heyman 1995). La deuxième invoque la mise en résonnance du système culée/arc-boutant au même endroit, et particulièrement au niveau de la pile dite n° 19 (Figure 1) causée par un vent en rafale (Lamboley, 1993, sur la base d'un rapport CEBTP de 1987; Murray, 2000).

La troisième suggère l'existence d'un tassement différentiel lent dans les fondations (Lamboley 1993, Heyman 1995), sans localisation précise du phénomène cependant. Pour justifier cela, Lamboley s'appuie sur des constats de fissurations dans les soubassements, mais qu'il est allé chercher au transept, où se trouve une fausse crypte, et non dans le chœur. Heyman considère, lui, que la durée de stabilité de 12 ans des parties hautes ainsi qu'une analyse structurelle

théorique exonèrent l'accident de 1284 d'une cause principalement structurelle; d'où il introduit l'idée d'une consolidation du sol en fondation dont la durée typique serait d'une douzaine d'année, celle-ci produisant l'accident.

2.2 Origine géotechnique en 1284?

Tout concours à penser que l'on consacra aux fondations de la cathédrale au XIIIe siècle les moyens nécessaires pour trouver « le bon sol », à une profondeur devenue considérable du fait de la surélévation de plusieurs mètres du niveau de la ville.

Des tassements de plusieurs centimètres pour des pressions estimées au sol de l'ordre de 5 bars (0,5 MPa) se produisirent en cours de travaux, possiblement différentiels, mais compensés par la lenteur des travaux, le suivi géométrique de l'œuvre et la souplesse de toute structure maçonnée. Une fois les travaux terminés en 1272, les tassements postérieurs restèrent sans doute limités car ni les alluvions anciennes, ni la craie altérée ne se présente comme susceptible de consolidation du fait de leur perméabilité élevée.

L'accident de 1284 est bien documenté comme s'étant produit dans les parties hautes des travées droites du chœur, structurellement les plus vulnérables par rapport au chevet ou à la travée centrale de transept déjà en place. Dès lors, l'hypothèse indémontrable d'un tassement différentiel de fluage venant à bout des systèmes culée-arc-boutant de ces seules travées droites, mais pas du reste de la Haute Œuvre, est sans grand intérêt.

Qui plus est, on remarquera aussi que les modifications structurelles de 1284 à 1340 n'ont pas inclus de reprises en sous-œuvre d'après l'analyse du bâti effectuée par Murray (2000), et au contraire, ont entraîné un alourdissement de la maçonnerie qui devait bien se reporter sur les fondations existantes, donc jugées dignes de confiance.

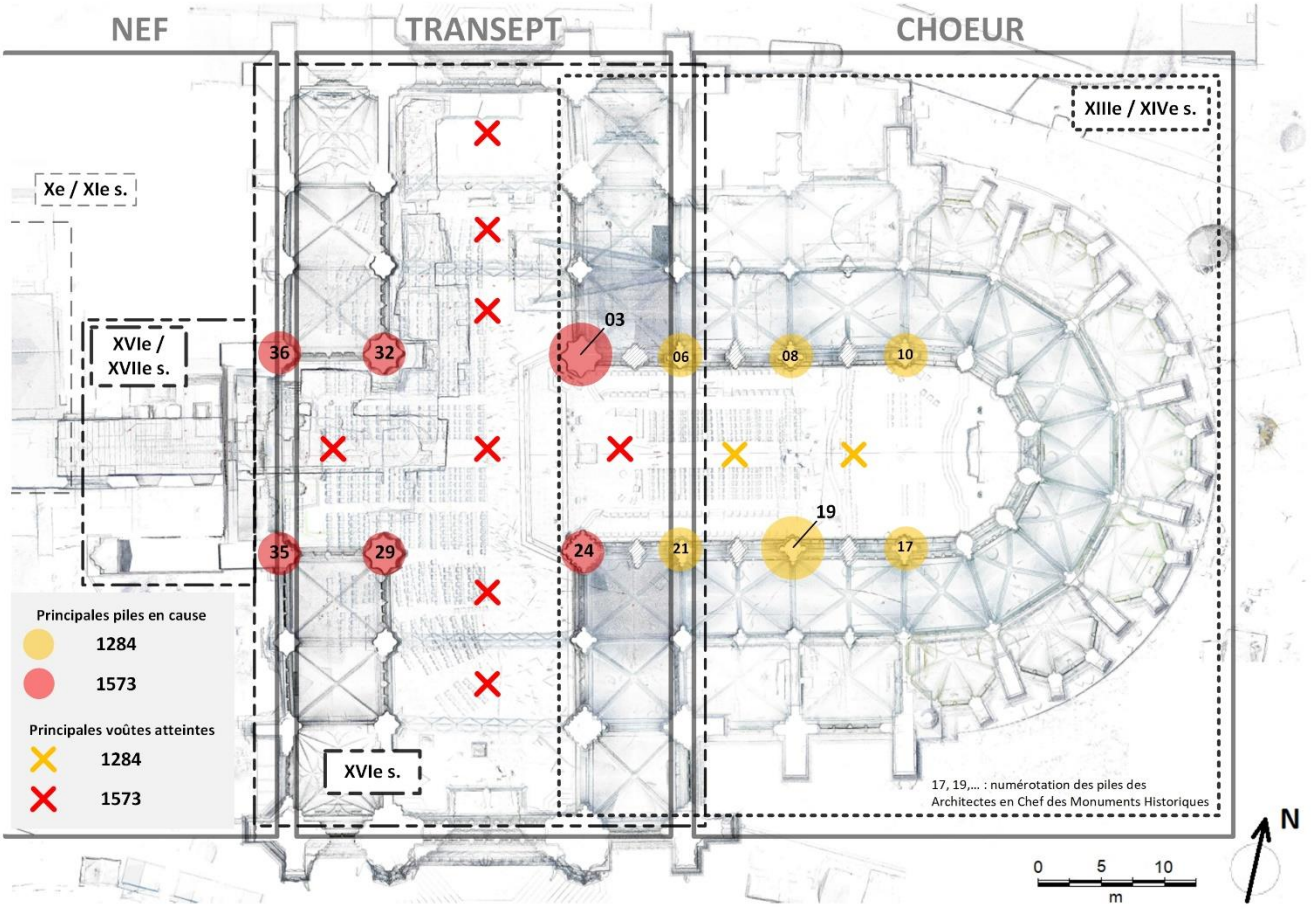

Figure 1. Localisation d'éléments liés aux accidents de 1284 et 1573 (fond de plan Lidar : Martin, 2021; habillé).

Du reste, l'explication la plus simple pour comprendre l'accident consiste à lire en creux les travaux qu'il entraîna : un raidissement généralisé des parties hautes atteintes. Elles s'étaient avérées trop souples, non pas en soi, mais en raison de la décision en cours de chantier de surélever de plusieurs mètres les voûtes de la cathédrale. Cette décision dû être prise au mépris des dimensions choisies pour les parties sous-jacentes, des proportions éprouvées, devenues inadaptées à contrer durablement le bras de levier

exercé par les nervures des voûtes quadripartites. Des déplacements somme toute très faibles mais permanents purent aboutir après quelques années à une perte de pression entre les claveaux des nervures des voûtes et ce qui s'en suivit.

Ainsi, nous ne souscrivons pas à l'hypothèse d'une origine géotechnique dans l'accident de 1284.

3 ACCIDENT DE 1573

3.1 Cause d'après les sources

La première cause de l'accident de 1573 évoquée dans les sources utilisées est celle d'un basculement de la tour-lanterne entraînée par un défaut de contrebutement à l'ouest, où la nouvelle nef n'était pas encore construite. La tour tout entière portait sur les quatre piliers élancés de la croisée du transept (Figure 1). La charge totale de la tour était de 10 000 tonnes environ, piliers porteurs compris. La charge en pied des piliers porteurs était alors environ trois fois plus importante qu'aujourd'hui. Aussi, cette absence de contrebutement entraînait une poussée au vide des niveaux voûtés et un lent déversement, tandis que la grande hauteur libre des piliers ainsi que le chargement colossal qu'elle subissaient pouvaient provoquer leur flambement.

Bien que la prise au vent de la tour lanterne et sa flèche soit non négligeable, les témoignages écrits des mois et même années précédant l'accident concordent à décrire un mécanisme de ruine lent et visible, donc indépendant du vent, assimilable par nature à une charge instantanée.

La cause première est donc une charge excessive, mais deux sources donnent explicitement un rôle aux fondations dans l'accident, Lamboley (1993) et Heyman (1995); le premier à travers l'insuffisance des fondations, se traduisant par des tassements différentiels prenant leur origine dans la craie molle rencontrée jusqu'à « 24 m de profondeur»; le deuxième évoquant un phénomène de poinçonnement des piliers du carré du transept, avec des tassements, de consolidation encore, de 20 à 30 centimètres d'amplitude, sans plus de détail sur le mécanisme et son lien avec les descriptions de l'époque.

3.2 Origine géotechnique en 1573?

Pour vérifier le rôle des fondations dans l'accident, on peut faire l'hypothèse que les déformées de la structure actuelle, héritées de l'accident et mesurables encore aujourd'hui, donnent la réponse. Or, certaines de ces mesures ont été faites en 1975, 1983 et 1985 et exploitées par l'Architecte en Chef des Monuments Historiques J.-L. Taupin en 1992 (Lamboley, 1993).

Compte-tenu de la souplesse de la structure, il aurait fallu des tassements différentiels pluri-décimétriques et postérieurs à 1569 pour provoquer le basculement évoqué, traduits par des variations de hauteurs des bases de piliers (36/32/03 et 35/29/24, Figure 1) qu'à ce jour aucune source n'atteste. En revanche, une rotation d'un pilier ou la rotation combinée de piliers dans l'axe ouest-est (Figure 2), même faibles, serait plus lourde de conséquences, d'une part parce que celle-ci entraînerait un excentrement des charges par rapport à l'axe de symétrie de leur support, avec possible divergence du phénomène, d'autre part parce que, comme en 1284, ces mouvements joueraient considérablement sur l'état mécanique des très hautes voûtes et nervures des trois tambours superposés, avec, à la première rupture, des conséquences en chaîne.

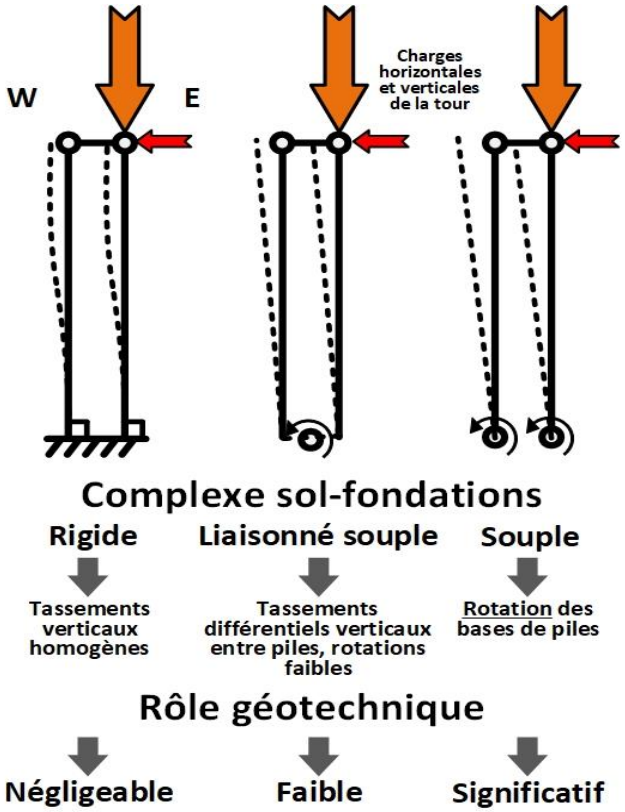

Figure 2. Situations mécaniques théoriques et simplifiées des piles de la travée centrale ouest du transept (voir localisation dans la Figure 3a, cadre en pointillés), soumises aux charges de la tour disparue.

Cela étant posé, la verticalité des bases de piliers attesterait de l'absence de rôle géotechnique dans l'accident de 1573, celui-ci se produisant par le fléchissement des piliers en section courante, singulièrement dans les parties les plus hautes.

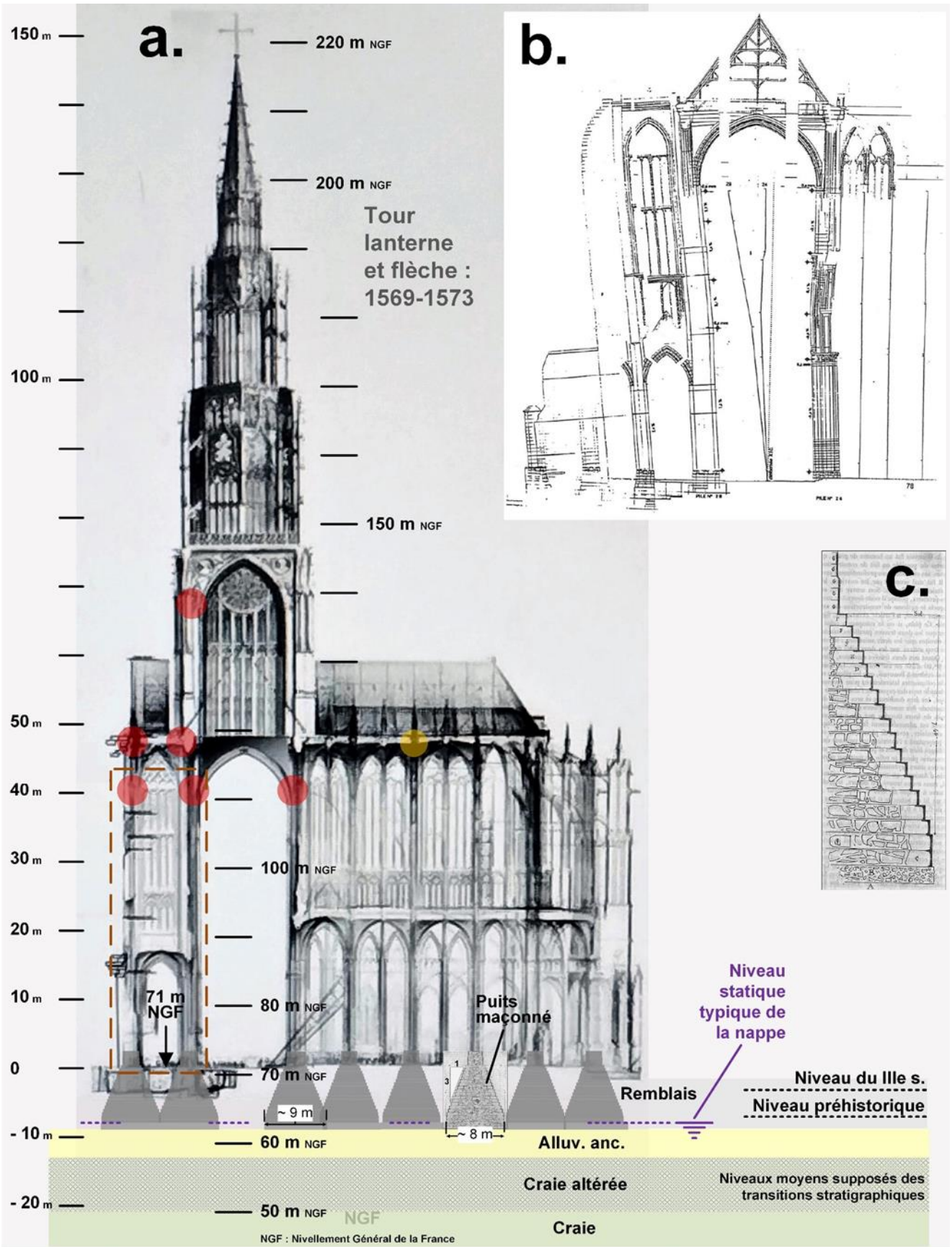

Figure 3. (a.) Coupe axiale ouest-est de la cathédrale avec évocation de sa tour lanterne et de ses fondations; habillée (fond Lidar : Martin, 2021; dessin de la tour : Woillez, E., v. 1838); (b.) Déformées restituées par Taupin, 1992, sur la hauteur des piles sud du carré du transept; (c.) coupe verticale d'un puits de fondation maçonné, observé par E.-E. Viollet-le-Duc à la cathédrale d'Amiens (op. cit., T4, p. 176).

L'extrait de la restitution avec exagération horizontale de Taupin en 1992 montre une combinaison des deux situations envisagées (Figure 3b), avec une rotation visible depuis la base des piliers occidentaux, amplifiée par des déformations des maçonneries elles-mêmes, notamment à la base du triforium. C'est jusqu'à 35 cm de déplacement à 40 m de hauteur qui ont été mesurés, soit une rotation de l'ordre de 1 %.

Nous avons vu précédemment que les fondations, certainement de grande largeur à la base (5 mètres et plus), reposent sur le « bon sol » des alluvions anciennes dont l'épaisseur est en moyenne moindre (4 mètres). Les contraintes diffusées concernent donc de façon significative la craie altérée sous-jacente, dont les quelques mégapascals de module de rigidité typique donnent à l'ensemble fondation / sol support un comportement suffisamment souple pour rendre compte des rotations à la base des piliers. En effet, un excentrement de charge et le développement d'une pression non uniforme sous la fondation entraînerait aisément quelques centimètres de tassement supplémentaires sur le côté plus chargé, ce qui se traduit bien par une rotation de l'ordre du pourcent.

Soulignons cependant avec insistance que les fondations de cette partie de la cathédrale et le sol sur lequel elles reposent ne sauraient être tenus pour responsable de l'accident de 1573. Elles en ont juste, possiblement, accéléré la survenue.

4 CONCLUSIONS

Nous pouvons donc conclure de cet inventaire d'informations disponibles que les accidents structurels de 1284 et 1573 à la cathédrale de Beauvais n'ont pas une origine géotechnique. Nous avons cependant montré que, au XVIe siècle, l'ensemble fondations / sols porteurs a potentiellement pris une part notable dans le « mécanisme de ruine », contrairement au cas du XIIIe siècle.

Aussi, ces conclusions permettent d'attirer l'attention sur le remarquable travail géotechnique réalisés par les maîtres-maçons des temps considérés, aussi bien dans la prise en compte du terrain, non exempt de risques, que des formidables descentes de charge qu'il allait subir pour de nombreux siècles.

REMERCIEMENTS

Que soit remercié Jean-François Madre, secrétaire de l'Association Beauvais Cathédrale et auteur en 2023 d'un opuscule sur les sculptures figuratives du chœur, qui a joué un rôle au point de départ de cet article. Merci également à Fabrice Reutenauer et François Haaz, du Service Archéologique municipal de Beauvais, pour leur communication de données altimétriques des niveaux archéologique et géologique au droit de l'exèdre à l'est de la cathédrale.

RÉFÉRENCES

Heyman, J. (1995). The stone skeleton. Structural engineering of masonery architecture. Cambridge University Press, Cambridge, England.

Lamboley Bureau d'études [auteur non précisé] (1993). Beauvais, cathédrale Saint-Pierre, diagnostic technique et pilotage des investigations, Lyon, France, rapport D724P02.

Martin, R. (2021). Beauvais, cathédrale Saint-Pierre, Restauration des toitures et des voûtes, dépose des étaiements, Dossier d'Avant-Projet Sommaire. Plans et élévations, élaboration Martin, R. (ACMH); données brutes Lidar : El Mustapha, M. (Université de Picardie).

Murray, S. (2000). Le chœur gothique, In : La cathédrale Saint-Pierre de Beauvais, architecture, mobilier et trésor, AGIR-Pic. (asso. éd.), Amiens, France, pp. 14-19.

Taupin, J.-L. (1992). Diagnostic technique [de l'Architecte en Chef des Monuments Historiques], 1ère phase.

Vernhes, J.-D., Renault, P. et Zotna, Y. (2024a). Cathédrale de Beauvais : les accidents structurels des XIIIe et XVIe siècles eurent-ils une origine géotechnique ? Partie 1 : contexte historique et naturel. Proceedings of the XVIII European Conference on Soil Mechanics and Geotechnical Engineering 2024. Lisbon, Portugal. ISBN 978-9935-9436-1-3.

Viollet-le-Duc, E.-E. (1858-1868). Dictionnaire raisonné de l'architecture française du XIe au XVIe siècle. 10 tomes. B. Bance, Paris (T1 à T6), A. Morel, Paris (T7 à T10).

Proceedings of the XVIII ECSMGE 2024
GEOTECHNICAL ENGINEERING CHALLENGES
TO MEET CURRENT AND EMERGING NEEDS OF SOCIETY
© 2024 the Authors
ISBN 978-1-032-54816-6
DOI 10.1201/9781003431749-379
Open Access: www.taylorfrancis.com, CC BY-NC-ND 4.0 license

ECSMGE 24
XVIII EUROPEAN CONFERENCE ON SOIL MECHANICS AND GEOTECHNICAL ENGINEERING

Interpretation of large diameter preliminary pile tests in Ampthill Clay, West Walton and Oxford Clay formations for Thame Valley viaduct

Interprétation des essais préliminaires de pieux de grand diamètre dans les formations Ampthill Clay, West Walton et Oxford Clay pour le Thame Valley viaduct

S. Vitorino*, H. Yeow
COWI UK Ltd, London, United Kingdom

**sergiovitorino@gmail.com*

ABSTRACT: Two instrumented preliminary test piles have been installed and tested in Aylesbury, UK, using Osterberg Cell bi-directional load test method, for the purpose of verifying the construction methodology and load performance of the bored piled foundations designed for the 880m long HS2 Thame Valley Viaduct. The local ground conditions comprise stiff clay and mudstone of Ampthill Clay, West Walton and Oxford Clay Formations which constitute part of the Ancholme Group. The significant length of the asset allowed a comprehensive ground investigation package of site and laboratory testing to be undertaken in developing a refined detailed design in accordance with the recommendations of Eurocode 7. The field test results of the two test piles have been interpreted and back-analysed using 3D finite element analyses undertaken to simulate the bi-directional loading of the Osterberg Cell testing method and compared against the ultimate pile capacity estimated during detailed design of the viaduct. Subsequent simulation of the pile loaded from pile head level using the calibrated finite element model provides the required load-settlement characteristic necessary to verify the performance of the pile under serviceability limit state.

RÉSUMÉ: Deux pieux d'essai préliminaires instrumentés ont été installés et testés à Aylesbury, au Royaume-Uni, en utilisant la méthode de test de charge bidirectionnelle Osterberg Cell, dans le but de vérifier la méthodologie de construction et les performances de charge des fondations sur pieux forés conçues pour le Thame Valley Viaduct, HS2, long de 880 mètres. Les conditions locales du sol sont constituées d'argile raide et de mudstone des formations d'argile Ampthill, West Walton et Oxford Clay, qui font partie du groupe Ancholme. La longueur significative de l'ouvrage a permis la réalisation d'un ensemble complet de tests sur site et en laboratoire pour développer une conception détaillée raffinée conforme aux recommandations de l'Eurocode 7. Les résultats des tests sur le terrain des deux pieux d'essai ont été interprétés et rétro-analysés à l'aide d'analyses par éléments finis en 3D réalisées pour simuler la charge bidirectionnelle de la méthode de test Osterberg Cell, et comparés à la capacité ultime des pieux estimée lors de la conception détaillée du viaduc. La simulation ultérieure du pieu chargé depuis le sommet du pieu à l'aide du modèle par éléments finis calibré fournit les caractéristiques de chargement-tassement nécessaires pour vérifier les performances du pieu dans l'état limite de service.

Keywords: Pile; trial; back-analysis; plaxis; Osterberg.

1 INTRODUCTION

Two preliminary test piles (PTP10A to PTP11) were installed and tested using bi-directional Osterberg Load Cell (O-cell) at the 880m long Thame Valley Viaduct, as part of the Aylesbury Area package of the High Speed 2 (HS2) project. The Arcadis, Setec, COWI Design Joint Venture (ASC) has been appointed by Eiffage, Kier, Ferrovial, and BAM Nuttall Joint Venture to provide detailed design services for the civil engineering assets within HS2. Bauer Keller joint venture (BKJV) were responsible for the installation of the piles while Fugro Loadtest was responsible for testing the piles.

Due to access and programme constraints, the test site was located approximately 200m north of the viaduct's proposed north abutment.

This paper presents the interpretation and back-analysis of the test data with the objective of verifying the performance of the pile under serviceability limit state.

2 THE SITE

2.1 Geological setting

Aylesbury Area is situated in the East Midlands Shelf which contains an Ancholme Group succession of clay and mudstone formation which were deposited in the Upper Jurassic period. The ground conditions at the test site are consistent with the ground conditions along the viaduct and comprise less than 1m of Head Deposits (HEAD) overlying Ampthill Clay (AMC), West Walton Formation (WWB) and Oxford Clay (OXC) to depth greater than 60m. AMC and WWB are generally described as stiff to very stiff Clays or calcareous Clays, with small localised pockets of siltstone and limestone, while OXC is generally described as extremely weak Mudstone.

2.2 Site investigation and soil parameters

The ground conditions at the test site have been characterised based on ground investigation works within a 200m radius, which includes 6No. CPTs, 11 No. boreholes 6 No. trial pits and respective in-situ and laboratory tests. The borehole descriptions at the test site and along the viaduct are not always consistent which could imply a very significant variation in the thicknesses of AMC and WWB, even in boreholes located adjacent to each other. This possibly highlights the difficulty in identifying the marker horizons that distinguish AMC, WWB and OXC, therefore resulting in very different stratigraphy being presented in adjacent boreholes. Despite the discrepancies noted above, the analysis of the Atterberg limits suggests a relatively flat stratigraphy throughout the northern section of the viaduct and the pile test site. Other markers such as calcareous siltstone, thinly interbedded limestone and limestone bands present in AMC and WWB formations also support an assumption of horizontal stratigraphy or otherwise a slight dip towards the south, which would be expected following the general trend of the geology in Aylesbury Area.

Figure 1 presents undrained shear strength and Atterberg limits versus elevation while considering the site GI data. Borehole ML065-CR532A has been drilled at the test site.

The undrained shear strength profile has been determined based on in-situ and laboratory tests.

- Where estimated from CPT, $c_u = \frac{q_c - \sigma_v}{N_{kt}}$ with N_{kt} assumed as 17.
- Where estimated from SPTs, $c_u = f_1 N_{60}$ as proposed in CIRIA R143 where $f_1 = 4.5$, based on plasticity index for most of the layers except WWB. For WWB f_1 has been taken as 6 for better fit with the triaxial test data.
- Where estimated from UCS, undrained shear strength was taken as $c_u = UCS/2$.

The design profile of the test pile has been developed based on the characteristic undrained shear strength profile shown as continuous black line in Figure 1.

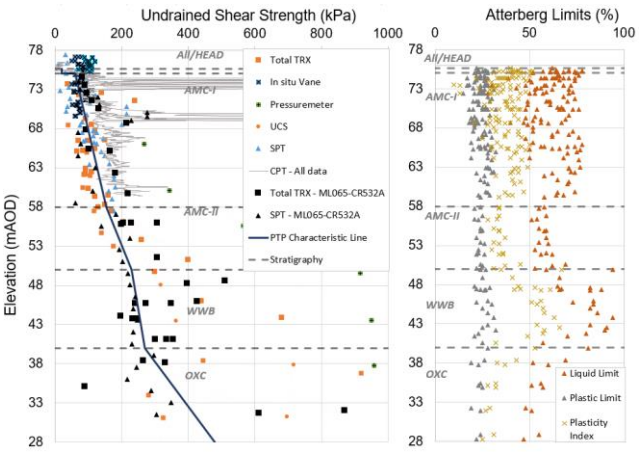

Figure 1. Undrained shear strength and Atterberg limits in the vicinity of the test site.

Table 1 summarises the stratigraphy and the key geotechnical parameters considered at the test site. AMC has been split into AMC I and AMC II to reflect a change in the plasticity index below 58mAOD, with a slight adjustment in the undrained shear strength profile. The equivalent undrained shear strength of the OXC has been determined using the UCS values from laboratory tests of an extremely weak mudstone.

Table 1. Stratigraphy and Geotechnical Parameters assumed at the test site.

Geolog. unit	Top of layer (mAOD)	Thickness (m)	c_u (kPa)	UCS (MPa)
HEAD	75.6	0.6	20	-
AMC I	75	17	60+5.5z	-
AMC II	58	8	154+9.6z	-
WWB	50	10	230+4z	-
OXC	40	Not proven	-	0.54+0.035z

3 VIADUCT AND PILE DESIGN

3.1 Description of the viaduct and the foundations

The viaduct carries HS2 over the Thame Valley flood plain, a relatively flat area of open fields surrounding the Thame River which runs approximately North East to South West across the proposed route.

Thame Valley Viaduct is a 36 span, 880m long continuous structure consisting of 4 No. 20m spans and 32 No. 25m spans. The piers are connected to 12x 2.5x1.8m deep pile caps which are in turn supported on a single row of three 1500mm diameter piles with a fixed pier providing longitudinal restraint. The fixed pier is connected to a 14x14x2m deep pile cap, supported by nine 1800mm diameter piles in a 3x3 layout. The abutments are supported on six 1500mm piles in a 3x2 layout. After completion of the test pile analysis, all the working piles have been constructed as typical cast in-situ bored piles in dry bores.

3.2 Pile Design

The unit shaft resistance in HEAD, AMC and WWB was estimated as $f_s = \alpha c_u$, where α is the empirical coefficient assumed as 0.5 and c_u is the undrained shear strength in Table 1. A limit to $f_s = \alpha c_u$ of 125kPa was applied to shaft resistance in clay. For the length of piles through OXC, the unit shaft resistance has been estimated as $f_s = 0.225\sqrt{UCS}$ (with UCS in MPa). A limit to f_s of 300kPa has been applied to the design.

The unit base resistance in the OXC has been estimated as $f_b = 4.5\,UCS$, where UCS is taken at the pile toe level. Table 2 presents the estimated ultimate resistance of the two test piles.

Table 2. Estimated Ultimate Resistance of the test piles.

Test Pile ID (diam.)	Pile length (m)	Shaft capacity (MN)	Base capacity (MN)	Total capacity (MN)
PTP10A (1.5m)	41.06	17.8	5.7	23.5
PTP11 (1.8m)	39.05	19.2	7.4	26.6

4 TEST PILES

4.1 Description of the tests

As shown in Figure 2, the instrumentation in the two piles included 4 pairs of extensometers and 9 sets of strain gauges. Loadtest provided measurement of the top plate, toe and pile head plus expansion of the o-cell.

The 1500mm test pile, PTP10A, was installed with length of 41.06m, incorporating the O-cell assembly at 36.1m below the pile head. The maximum sustained gross load applied to the pile was 10.75MN in each direction. At the maximum sustained load, the displacements above and below the O-cell assembly were 6.01 mm and 7.97 mm, respectively. At the next load increment with a gross applied load of 11.70 MN in each direction, the upper pile section above the O-cell was unable to sustain the applied load, see Figure 3.

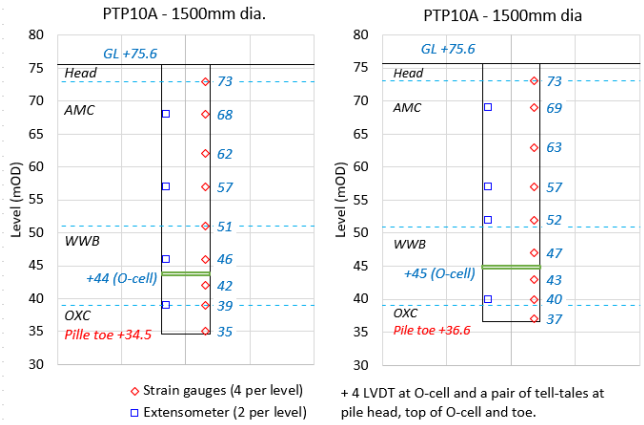

Figure 2. Schematic representation of the instrumentation in the two test piles.

The 1800mm test pile PTP11 was installed with length of 39.05m, incorporating the O-cell assembly at 30.5m below the pile head. The maximum sustained gross load applied to the pile was 13.32 MN in each direction. At this maximum sustained load, the displacements above and below the O-cell assembly were 4.97 mm and 10.13 mm, respectively. Again, the upper pile section was unable to sustain the applied load at the next load increment, see Figure 3.

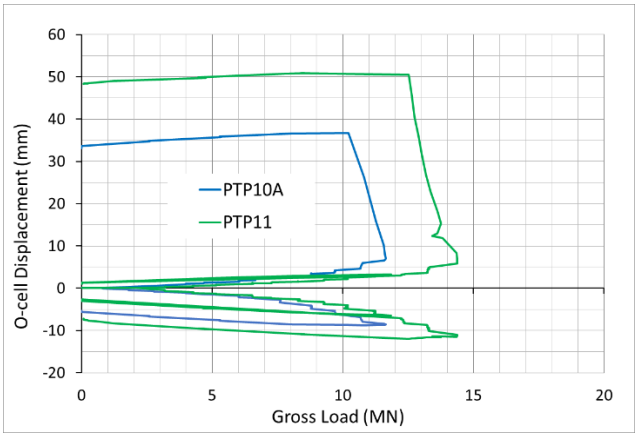

Figure 3. Upper and lower shaft movements.

4.2 Interpretation of the results

The unit shaft friction was estimated based on the interpreted results from strain gauges and this is summarised in Table 3. The strain gauges immediately above and below the O-cell have shown erroneous results and have been omitted from the interpretation on the basis that the close proximity to the O-cell may have led to spurious strain measurement as a result of high stress concentration or lower localised concrete

stiffness caused by anomalies when the concrete was tremied pass the O-cell assembly.

Table 3. Interpreted unit shaft friction.

Levels[(1)] (mAOD)	Strata	Unit shaft friction (kPa)	
		PTP10A	PTP11
75.6 - 73	HEAD	20	13
73 - 68.5	AMC	56	45
68 - 62.5		52	61
62 - 57		89	78
57 - 51.5		83	88
51 - 46	WWB	103	128
45 - 40		145	149
39 - 35	OXC	281	338

Notes: (1) Levels averaged between the two test piles.

The upward and downward movement has been analysed separately using the Cemset Analysis method (Fleming, 1992) to determine the behaviour of the pile above and below the O-cell. Table 4 presents the summary of input parameters for Cemset analysis that produce the best fit load-displacement profile to the measured test pile data. Given that both piles failed upwards, the base capacity has not been fully mobilised, therefore this base capacity has been estimated using the approach presented in Section 3.2 but slightly adjusted to fit the data for the downward movement curves of the two test piles. Figure 4 shows the equivalent top-loading curves for the two test piles determined by adding the upward and downward Cemset curves while corrected for the elastic shortening for a top loaded piles instead of bi-directional loading (according to method proposed by England, n.d.).

Table 4. Summary of input parameters for Cemset analysis above and below the O-cell.

Input Parameter	PTP10A		PTP11	
	Above O-cell	Below O-cell	Above O-cell	Below O-cell
Qs[(1)] (MN)	11.6	9.47	14.38	11.32
Ms (-)	0.0003	0.0004	0.0002	0.0006
Qb[(2)] (MN)	-	5.0	-	6.5
Eb[(3)] (MPa)	-	129	-	188
Lf (m)	31.6	9.46	30.54	9.46
Ke (-)	0.3	0.5	0.3	0.5
Ec (GPa)	40	40	40	40

Notes: (1) Ultimate shaft capacity; (2) Ultimate base capacity; (3) Soil modulus at base.

Table 5 shows the comparison of ultimate capacities between the design approach presented in Section 3.2 and those calculated from the Cemset analysis.

4.3 Comparison with viaduct design

Figure 5 shows a good agreement between the unit shaft friction estimated using the design profile and the values interpreted from the test pile data in most strata except the OXC where there is significant underprediction of the shaft resistance.

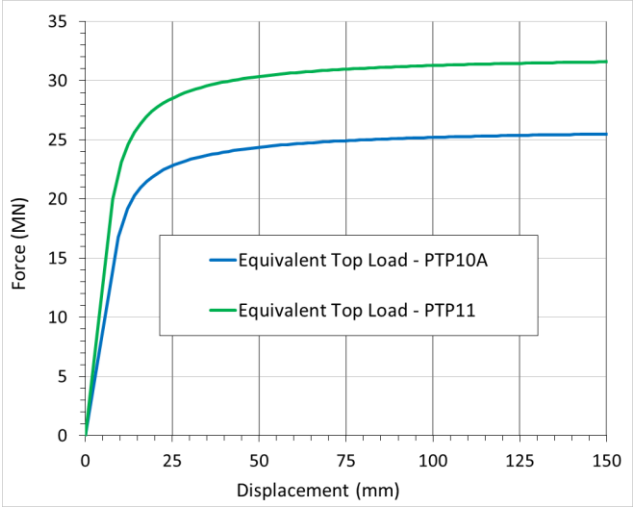

Figure 4. Equivalent top load displacement curves.

Table 5. Summary of estimated pile capacities.

Pile	Ultimate Capacity (MN)	
	Estimated in Section 3.2	Cemset Analysis
PTP10A	23.5 (Qs=17.8; Qb=5.7)	26 (Qs=21.0; Qb=5.0)
PTP11	26.6 (Qs=19.2; Qb=7.4)	32 (Qs= 25.5; Qb=6.5)

Notes: Qs=Ultimate shaft capacity; Qb=Ultimate base capacity;

Particularly throughout AMC-I, the estimation of unit shaft friction based on design profile is slightly lower than interpretation of the test data, as expected given the slightly cautious undrained shear strength profile for the site specific borehole data. There is no such trend for the AMC-II stratum except it is fair to assume the design values are in good agreement with the measured ones. The interpretation of the test data suggests constant unit skin friction between levels 52 and 62mAOD, which is unlikely to be a correct representation since gradual increase in soil strength is expected. In WWB, the estimation based on design profile is slightly lower than interpretation of the test data for the bottom half of this unit, because a limit to $f_s = \alpha c_u$ of 125kPa has been applied to shaft resistance in clay, otherwise a good agreement should be expected. It could be argued that such limit could be higher, for instance a limit to $f_s = \alpha c_u$ of 150kPa could be recommended, however the current limit is only conditioning the unit shaft friction over a short

length and therefore no significant conclusions should be drawn from this small contribution to the overall pile capacity. In OXC it becomes clear that the unit shaft friction based on design profile is being underestimated when compared with interpretation of test data. This is possibly due to the assumption of a conservative characteristic strength in the Mudstone layer that resulted from the wide scatter in the available GI data or a reflection of shaft roughness or overbreak in the OXC. While this is not demonstrated by Figure 5, it is also possible that the base capacity in OXC is being underestimated if the characteristic base parameters are conservative. However, noting that both piles only penetrated a short length into OXC and that more data should be considered to confidently infer any conclusions, it is considered prudent to keep the current approach in the viaduct pile design.

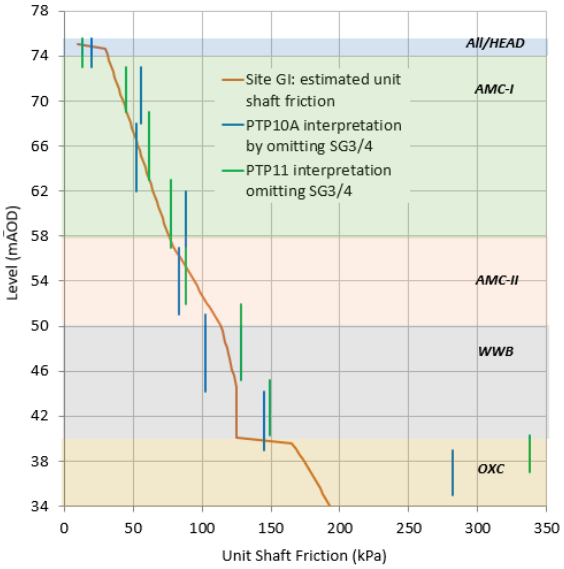

Figure 5. Comparison of unit shaft frictions determined by preliminary test piles and design.

4.4 Analysis using 3D finite element analysis

The preliminary test piles were back analysed using Plaxis 3D finite element (FE) program to mimic the measured performance of the test results under the bi-directional O-cell test before the introduction of load at pile head to derive the equivalent top loaded pile response. Although an axisymmetric 2D model would suffice the decision to adopt a full 3D model allows the assessment of lateral response of the pile be it as a single pile or as a pile group for the design of the viaduct foundations.

4.4.1 Methodology

In the FE model, the test pile was modelled by splitting the shaft into several sections to mimic the positions of the strain gauges installed to measure the load transfers during the test. Each of these shaft sections is then assigned a shear strength parameter to reflect the measured unit skin friction values, see Figure 6. Under the test load, the measure displacements of the O-cell's top and bottom plates, pile head and pile toe were compared and calibrated before the pile is loaded from the top.

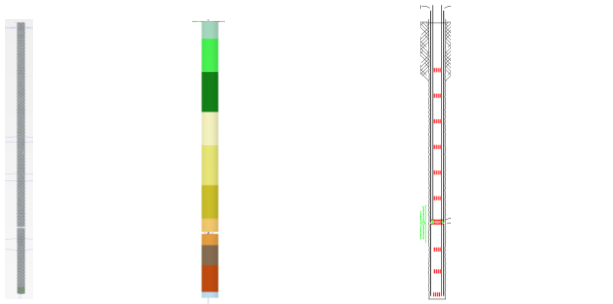

Figure 6. Pile shaft with different shear strength values.

It is worth noting that when assigning individual shear strength using interface element, Plaxis command codes were used to change the input shear strength parameters rapidly for multiple assessments to calibrate the load-displacement of the test pile. The use of automated Python script would speed up this calibration process but this is not used at this stage.

Apart from the shear strength parameters assigned to the test pile, soil properties of the ground and stiffness of the pile concrete are the other two variables which could affect the behaviour of the pile under the applied load. For the calibration undertaken, the following are the soil model and properties used in the FE model:

- concrete stiffness: 40-45 GPa;
- stiffness of the soils: E_u/c_u=500-750

Linear elastic perfectly plastic Mohr-Coulomb soil model has been used to represent the soils since parameters for more complex or advanced soil model are currently not available in this type of soils.

4.4.2 Test pile calibration

The process of calibration started with the first set of parameters based on the pile design approach indicated in Section 3.2 to derive the unit shaft friction of the pile. Due to the low unit shaft friction in the OXC, the lower section of the pile settled excessively beyond a test load of 8MN for PTP10A. Similar observation for PTP11 albeit with slightly higher applied O-cell load.

With the derived unit shaft resistance from the test piles, the load displacement profiles for both the test piles are shown in Figure 7.

When load is applied from pile head, the equivalent load-displacement profiles are shown in Figure 7.

When comparing this to the Cemset back-analysis, the difference in load-settlement performance of the piles at serviceability limit state is negligible although the ultimate capacity of the larger 1.8m diameter test pile is approximately 5% lower. This could be due to more pronounced pile base softening effects on the larger test pile.

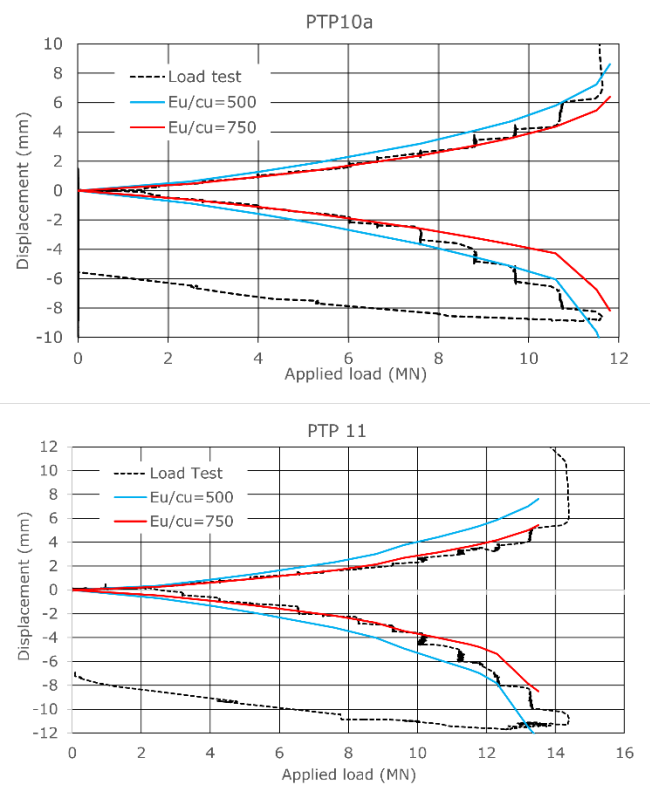

Figure 7. Load-displacement profiles for the two test piles back analysed using Plaxis 3D model.

5 CONCLUSIONS

The ultimate pile capacities estimated using the approach assumed by the designer outlined in Section 3.2 were calculated as 23.5 MN and 26.6 MN for test piles PTP10A and PTP11, respectively. In this approach the unit shaft resistance in HEAD, AMC and WWB was calculated as $f_s = \alpha c_u$, where α is the empirical coefficient assumed as 0.5 and c_u is the characteristic undrained shear strength profile determined based on site specific GI. A limit to $f_s = \alpha c_u$ of 125kPa has been applied to shaft resistance in clay, but this is only exceeded in the design over a short length. For the length of piles through OXC, the unit shaft resistance was assumed to be based on $f_s = 0.225\sqrt{UCS}$. Although a limit of f_s of 300kPa was applied to the design in OXC, this limit is not reached for a pile length of 41m. The unit base resistance has been estimated as $f_b = 4.5\ UCS$, where UCS is taken at the pile toe level.

When this approach is compared with the back-analysed unit shaft frictions from the test pile data, there was a good agreement in the clay layers but it underestimated in the Mudstone layers. It is possible that the assumption in the characteristic strength of the Mudstone layer is conservative. More GI data and pile test in these strata would be required to verify a more optimistic design approach in order to incorporate higher shaft resistance values.

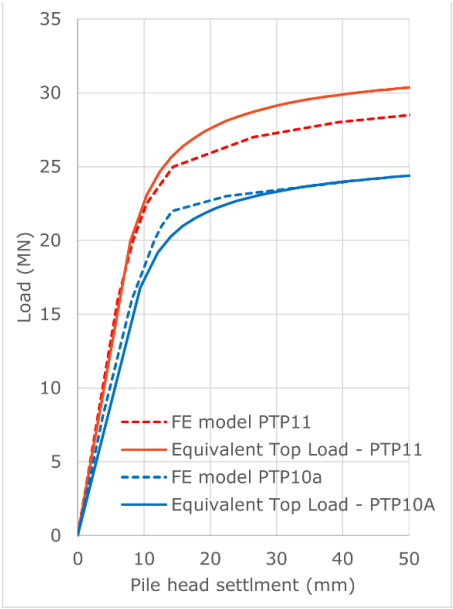

Figure 8. Load-displacement profiles for equivalent top loaded pile.

Due to the short length of pile in the OXC, where the most discrepancy in the shaft resistance value was found, the design approach presented for pile design in AMC/WWB/OXC is considered appropriate and slightly conservative for pile lengths between 39 and 41m. The two test piles are considered to verify the design approach and provide sufficient confidence to deliver the design of the 880m long Thame Valley Viaduct.

REFERENCES

W. G. K. Fleming. (1992). A new method for single pile settlement prediction and analysis. *Géotechnique*, Volume 42 Issue 3, September 1992, pp. 411-425.

C. R. I. Clayton, CIRIA143, The standard penetration test (SPT): methods and use (R143), 1995.

M. England, L. (n.d.). A Conservative Method of Analysis of test results from bi-directional static load tests. *Deep Foundations on Bored and Auger Piles – Van Impe & Van Impe (eds)*, 2009 Taylor & Francis Group, London, ISBN 978-0-415-47556-3.

Proceedings of the XVIII ECSMGE 2024
GEOTECHNICAL ENGINEERING CHALLENGES
TO MEET CURRENT AND EMERGING NEEDS OF SOCIETY
© 2024 the Authors
ISBN 978-1-032-54816-6
DOI 10.1201/9781003431749-380
Open Access: www.taylorfrancis.com, CC BY-NC-ND 4.0 license

ECSMGE 24
XVIII EUROPEAN CONFERENCE ON SOIL MECHANICS AND GEOTECHNICAL ENGINEERING

Surface roughness evolution of EPDM and its impact on the long-term sealant performance of gasketed joints of segmental shield tunnels

Évolution de la rugosité de surface de l'EPDM et son impact sur la performance à long terme des joints d'étanchéité des tunnels à bouclier segmentaire

J.C. Xie
Department of Geotechnical Engineering, College of Civil Engineering, Tongji University, Shanghai, China / Department of Civil and Environmental Engineering, Universitat Politècnica de Catalunya, Barcelona, Spain

X. Huang*
Department of Geotechnical Engineering, College of Civil Engineering, Tongji University, Shanghai, China / College of Civil Engineering & Architecture, Xinjiang University, Urumqi, China

**xhuang@tongji.edu.cn*

ABSTRACT: EPDM (Ethylene Propylene Diene Monomer) rubber gaskets were widely used as the waterproofing component at the joints of shield tunnels that are expected to serve for decades. However, the alterations in surface roughness of EPDM rubber gaskets due to ageing introduce an aspect that is not yet comprehensively understood in terms of its implications for sealant performance. In this study, a series of AFM (Atomic Force Microscope) tests were conducted on 6 groups of squared EPDM thin slices, each of which had been oxidatively aged to different levels before the tests. The analysis encompassed the determination of both the fractal dimension and the RMS (Root Mean Square)-slope of the surfaces. Supplementary tests utilizing Scanning Electron Microscopy (SEM) and Fourier Transform Infrared Spectroscopy (FTIR) were performed to elucidate the mechanisms governing surface roughening. The results show that the mean value of fractal dimension of EPDM specimens first decreased to 2.16 after 11.2-hour ageing and then increased to 2.42 after 39h-ageing. The evolution of RMS-slope exhibited similar tendencies, escalating from 0.55 to 1.16. Finally, a theoretical model to prognosticate the long-term waterproof capacity based on the percolation theory was proposed, which explicitly incorporated the impact of surface roughness. The outcomes underscore the considerable hydraulic deterioration resulting from surface roughening over a prolonged duration, ultimately leading to the complete loss of waterproof capacity in large opening scenarios.

RÉSUMÉ: Les joints en caoutchouc EPDM ont été largement utilisés comme composants d'étanchéité au niveau des joints des tunnels de protection qui sont censés fonctionner pendant des décennies. Toutefois, les modifications de la rugosité de la surface des joints en caoutchouc EPDM dues au vieillissement constituent un aspect qui n'est pas encore bien compris en termes d'implications pour les performances du mastic d'étanchéité. Dans cette étude, une série de tests AFM a été menée sur 6 groupes de tranches minces d'EPDM carrées, chacune ayant été vieillie par oxydation à différents niveaux avant les tests. L'analyse a porté sur la détermination de la dimension fractale et de la RMS-slope des surfaces. Des tests supplémentaires utilisant la SEM et la FTIR ont été réalisés pour élucider les mécanismes régissant la rugosité de la surface. Les résultats montrent que la valeur moyenne de la dimension fractale des échantillons d'EPDM a d'abord diminué à 2,16 après un vieillissement de 11,2 heures, puis a augmenté à 2,42 après un vieillissement de 39 heures. L'évolution de la pente RMS a montré des tendances similaires, passant de 0,55 à 1,16. Enfin, un modèle théorique a été proposé pour pronostiquer la capacité d'imperméabilisation à long terme sur la base de la théorie de la percolation, qui intègre explicitement l'impact de la rugosité de la surface. Les résultats soulignent la détérioration hydraulique considérable résultant de la rugosité de la surface sur une période prolongée, conduisant finalement à la perte totale de la capacité d'étanchéité dans les scénarios de grande ouverture.

Keywords: Shield tunnel; gasketed joint; sealant performance; EPDM; surface roughness.

1 INTRODUCTION

The hydraulic deterioration of gasketed joints causes leakage defects in shield tunnels in the long term (Xie et al., 2023b). Figure 1 depicts the progressive deterioration of the leakage defects, initially manifesting as wet stains, subsequently evolving into joint leakage indicative of substantial groundwater infiltration, and ultimately culminating in the water and soil gushing, signifying that the gasketed joints have lost all waterproof capacity. Hence, it is of great importance to elucidate the long-term sealant performance of gasketed joints (Shi et al., 2015).

Investigators have highlighted that the sealant performance of gasketed joints is a typical hydro-mechanical behaviour, prominently influenced by the assembly conditions of joints, i.e., the opening, offset, and rotation (Gong et al., 2018). Another main factor is the time-dependent behaviour of EPDM material, with stress relaxation constituting the predominant focus in prior investigations (Arnau et al., 2012; Shi et al., 2015; Zhang et al., 2020).

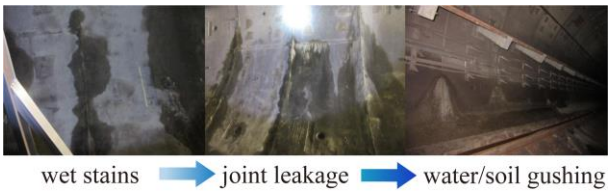

Figure 1. Leakage defects in shield tunnels.

However, the surface roughening of rubber surfaces, constituting another pivotal time-dependent attribute, has often been overlooked in analysing the sealant performance of gasketed joints. Physicians have underscored that the surface roughness has a significant effect on the sealant and seepage behaviours of the rubber seals (Persson, 2022; Persson and Yang, 2008). With an increase in surface roughness, the likelihood of leakage occurring at lower water pressures amplifies. Concurrently, the hydraulic aperture widens, consequently augmenting hydraulic conductivity. Thus, neglecting the phenomenon of surface roughening in gasketed joints may lead to an overestimation of waterproof capacity especially, in the long term.

In this paper, a comprehensive characterisation of the surface roughening phenomenon in EPDM was carried out through the utilisation of AFM tests. Additionally, SEM and FTIR tests were performed to elucidate the underlying mechanisms induced by the ageing process. Then, a refined theoretical model based on percolation theory was proposed to capture the influence of surface roughening on sealant performance. Finally, the model was applied in a specific engineering case, with its long-term waterproof capacity presented.

2 FRACTAL CHARACTERISTICS OF EPDM MATERIAL

2.1 Test methods

In the test, 6 groups of EPDM samples (see Figure 2(a)) were prepared, with dimensions measuring 6 mm × 6 mm × 2 mm. To enhance the generality of our findings, each set underwent three parallel tests. These groups were subsequently subjected to the thermo-oxidative ageing at a temperature of 150 ℃ for varying duration: 0 (unaged), 6.7, 11.2, 16.7, 22.3 and 39 h, as delineated in Figure 2(b) and tabulated in Table 1. Note that the upper side of the EPDM sample was scanned in the AFM test, as depicted in Figure 2(c). This approach ensured that the testing surface was in full contact with oxygen throughout the ageing process.

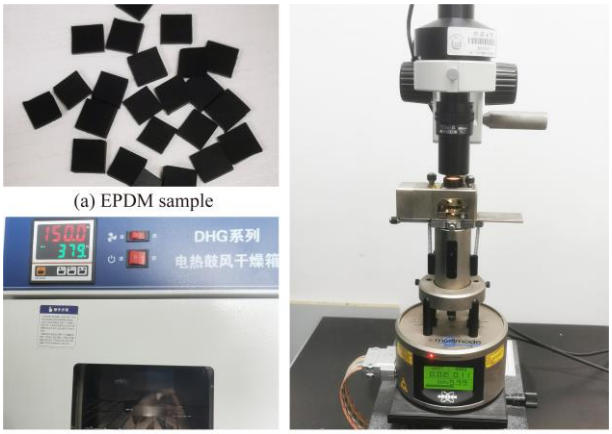

Figure 2. EPDM samples and test devices.

2.2 AFM results

Figure 3 depicts the surface topography of 6 groups, employing an observation scale of 5 μm × 5 μm. The outcomes indicate that the unaged EPDM surface (A1) exhibits a distinct degree of roughness, marked by the dense presence of clustered particles, as illustrated in Figure 3 (a). In the early stage of ageing process as shown in Figure 3 (b) and (c), the EPDM surfaces barely change in surface morphology, and with slightly smoother appearance compared with the unaged scenario in A3.

In the subsequent ageing periods, spanning from A4 to A6, a greater number of particles are observed to detach and accumulate on the EPDM surface over time, leading to the development of pronounced spikes. Importantly, these spikes formed through ageing are

notably sharper in comparison to those on the original surface, signifying a progressive increase in surface roughness. This qualitative evolution, as indicated by the test outcomes, is similar to that from Wang et al. (2020), suggesting that while the waterproof capacity might experience an initial enhancement within a short timeframe, it subsequently diminishes over prolonged duration, in alignment with the progression of roughness.

Table 1. Ageing times for each group.

group	A1	A2	A3	A4	A5	A6
Ageing time (h)	0	6.7	11.2	16.7	22.3	39

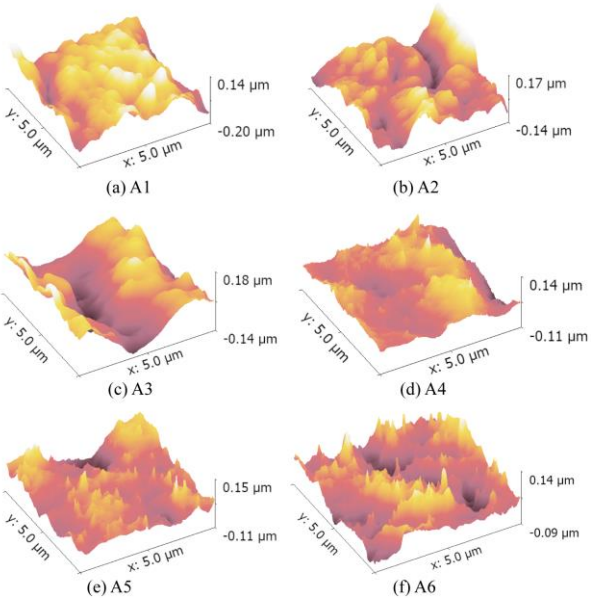

Figure 3. Surface roughness of different groups.

Figure 4 presents the evolution of fractal dimension D_f of the EPDM surface based on the obtained test data using the method of enclosing boxes. The D_f results in the same group exhibit certain disparities, attributed to the inherent discreteness of the surface topography. Nevertheless, the nonlinear variation of D_f with ageing time underscores the shift towards smoother surfaces initially, followed by a transition to increased roughness once the ageing duration surpasses 11.2 hours, corroborating observations in Figure 3. Specifically, the mean value of D_f firstly decreased from 2.27 to 2.16 after 11.2-hour ageing, subsequently ascending to 2.42 following 39-hour ageing.

RMS-slope ξ, another roughness-related parameter, can also be derived from the test data. Figure 5 presents the parallel results of RMS-slope, mirroring a comparable nonlinear ascending pattern as observed in the fractal dimension. Specifically, ξ experiences a slight reduction until the ageing duration reaches 11.2 h, after which it undergoes a significant escalation. When the ageing time approaches 39 h, the average value of ξ culminates at 1.16, notably surpassing that of 0.55 in the unaged scenario.

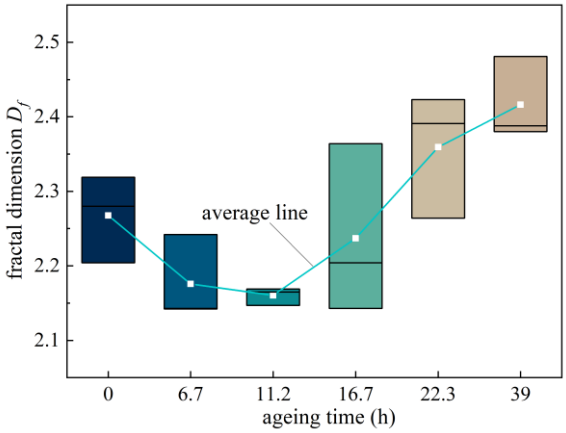

Figure 4. Fractal dimension of EPDM surface.

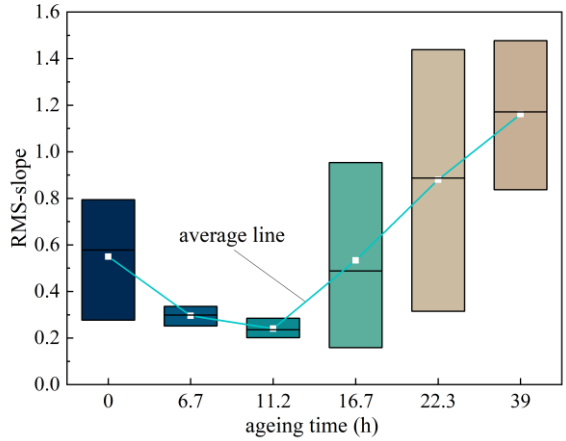

Figure 5. RMS-slope of EPDM surface.

2.3 SEM and FTIR results

To reveal the ageing mechanisms of EPDM surface, a series of SEM and FTIR tests were conducted. Figure 6 gives the surface roughness evolution over time observed through SEM scans, primarily capturing the degradation process prompted by elevated temperature. Evidently, an increased presence of particles becomes apparent, with a dense distribution observed on the EPDM surface. This observation aligns with the findings obtained from the AFM analysis, as illustrated in Figure 3.

Figure 7 graphically illustrates the alterations in chemical composition throughout the degradation process, revealing that ageing predominantly impacts components characterized by wave numbers proximate to 1500 cm^{-1}. This specific wave number range corresponds to the scissoring vibration of C-H bonds, with the intensity of its peak serving as an indicator of material degradation. Notably, the peak intensity of the

unaged sample is lower than that of the subsequent instances, offering insights into the chemical mechanisms driving the initial surface smoothing observed during the early stages of ageing in the AFM results.

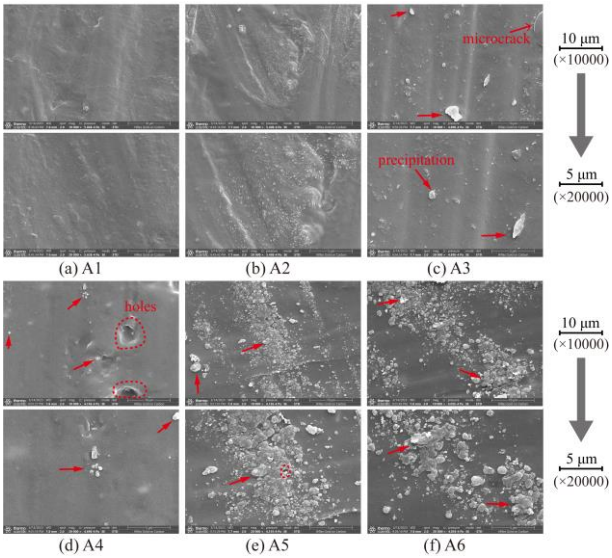

Figure 6. SEM results of EPDM surface of different ageing conditions from A1 to A6.

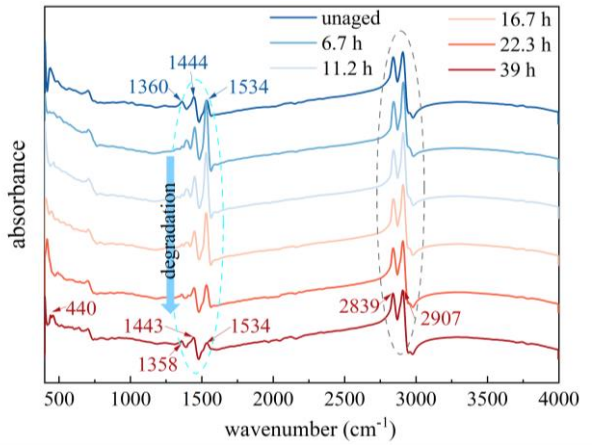

Figure 7. FTIR results of EPDM material of different ageing conditions from A1 to A6.

3 THEORETICAL MODEL OF SEALANT PERFORMANCE

Herein, a refined theoretical model aimed at assessing the sealant performance was introduced (Xie et al., 2023a). In the derivation, the percolation pressure (Persson, 2022) has been employed to elucidate the impact of surface roughness.

3.1 Percolation pressure

According to percolation theory, leakage from the contact area is prevented when the surface percolates at the highest magnification, i.e., the relative contact area $A(\zeta)/A_0$ exceeds 0.4 (Persson, 2022). Accordingly, we define the nominal pressure as percolation pressure P_{perc} when $A(\zeta)/A_0$ reaches 0.4 at a large wavenumber cut-off (Persson, 2022):

$$P_{perc} = \frac{\sqrt{2}}{2}\,\mathrm{erfinv}\left(\frac{A}{A_0}\right)E^*\xi \tag{1}$$

where E^* refers to the effective modulus of the rubber seals, and equals to $E_g/\left(2\times\left(1-v_g^2\right)\right)$ when the seal is composed of two pieces of gaskets in shield tunnel. v_g is the equivalent Poisson ratio of the gaskets, which varies with the compression strain.

3.2 Theoretical model implemented with percolation theory

The sealant performance of the gasketed joints is primarily influenced by the normal confining pressure P_c (Gong et al., 2019). This normal confining pressure undergoes augmentation when subjected to water pressurisation, a phenomenon recognised as the self-sealing effect (Shalabi et al., 2016), characterised by the slope k_0. Notably, the self-sealing effect becomes increasingly prominent, ultimately leading to the establishment of a critical leakage state when the confining pressure P_{c2} attains a value equivalent to the critical leakage water pressure P_{wc}

$$P_{wc} = \frac{1}{1-k_0}P_{c1} \tag{2}$$

where k_0 is the self-sealing coefficient and varies with compression strain ε, and P_{c1} refers to the initial confining pressure

$$P_{c1} = E_g\varepsilon \tag{3}$$

According to the previously mentioned percolation theory, the leakage transpires prior to the onset of the critical leakage state. By incorporating the influence of the percolation process, as symbolised by the percolation pressure P_{perc}, the final equation governing the critical water pressure (Xie et al., 2023a) can be derived as

$$P_{wc} = \frac{E_g\varepsilon - P_{perc}}{1-k_0} \tag{4}$$

Notably, Eq. (4) reflects the effect of surface roughness on waterproof capacity, that is, P_{wc} reduces as the EPDM surface gets rougher.

3.3 Model validation and long-term sealant performance prediction

Based on the proposed theoretical model, the long-term sealant performance of gasketed joints can be prognosticated. The test data from Gong et al. (2018) is used in the model validation. One representative engineering case, labelled as SC1, is subjected to analysis. First, the equivalent modulus of the gaskets E_g is derived based on the data of gasket-in-groove loading test, as given in Eq. (5):

$$E_g = 3 + 1.429 \times 10^{-6} \exp(36.81\varepsilon) \quad (5)$$

Significant nonlinearity of self-sealing effect is observed in these cases. Based on the test data (Gong et al., 2018), a correlation between the slope and compression strain (Xie et al., 2023a) was established. The results indicate that k_0 equal to $4.46\varepsilon^2$. The results of RMS-slope derived from the AFM test are used in calculating the percolation pressure. In the initial unaged condition, RMS-slope registers at 0.55, while following a 39-hour ageing period (full aged), this value increases to 1.16.

Figure 8 present the experimental and theoretical results of critical leakage pressure for case SC1. The results show that the theoretical results in unaged scenario align closely with the test data. When the opening is small, the theoretical estimations slightly exceed the experimental values. This discrepancy suggests an underestimation of the confining pressure within the theoretical model. One main reason for this is that the equivalent modulus is determined through the gasket-in-groove loading test, which does not account for lateral water pressurization. The modulus E_g is further enhanced under enormous water pressure.

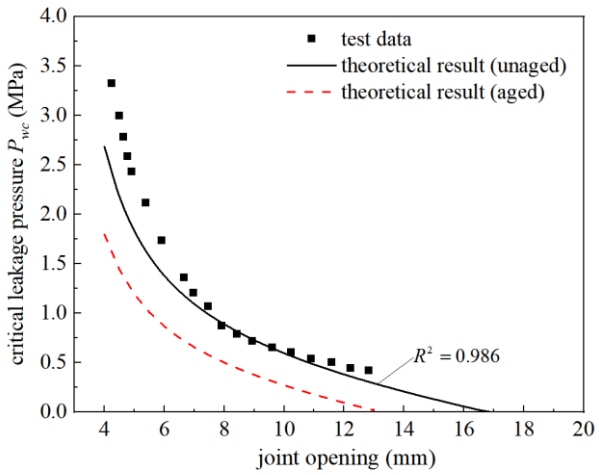

Figure 8. Critical leakage pressure for case SC1

The results of aged scenario represented in dashed lines indicate that the surface roughening has great effect of hydraulic deterioration. The critical leakage pressure experiences substantial decreases across all opening situations, causing the critical leakage pressure P_{wc} approaches 0 much earlier compared to the unaged scenario. The complete loss of waterproofing capacity occurs when the joint opening increases to 13 mm, primarily due to the escalating percolation pressure. In the unaged scenario, this critical opening value is approximately 17 mm.

According to the Arrhenius formula (Zhang et al., 2020), 39-h ageing time at 150°C corresponds to an 80-year service duration at room temperature (20°C). These findings underscore the substantial contribution of ageing-induced surface roughening in EPDM to the long-term hydraulic deterioration of gasketed joints.

4 CONCLUSIONS

The paper mainly focuses on the roughness evolution of EPDM surface induced by ageing, and its long-term implications on the sealant performance of gasketed joints. The results of AFM test reveal a distinctive pattern: the EPDM surface initially experiences a slightly smoothing effect during the early stages of ageing, followed by a progressive increase in roughness after approximately 39-hour ageing. This evolutionary trajectory is further corroborated by the outcomes derived from SEM and FTIR tests.

In response to these findings, a refined theoretical model is introduced to evaluate the long-term sealant performance of gasketed joints. The results underscore the substantial effect of surface roughening on the hydraulic deterioration. Specifically, the gasketed joints lose all waterproof capacity when opening is 17 and 13 mm, in the unaged and aged scenarios, respectively. These findings serve to underscore the critical significance of incorporating the concept of surface roughening in the evaluation of sealant performance of gasketed joints, which also aids in the design of waterproof in segmental tunnels by predicting the waterproof capacity affected by surface roughness and joint deformations.

ACKNOWLEDGEMENTS

This work was supported by the National Natural Science Foundation of China (52278407) and the Fundamental Research Funds for the Central Universities (22120210573). The first author also wants to thank the support from China Scholarship Council.

REFERENCES

Arnau, O., Molins, C., Blom, C. B. M. and Walraven, J. C. (2012) Longitudinal time-dependent response of segmental tunnel linings, *Tunnelling and Underground Space Technology*, 28(1), pp. 98-108, https://doi.org/10.1016/j.tust.2011.10.002.

Gong, C., Ding, W., Soga, K. and Mosalam, K. M. (2019) Failure mechanism of joint waterproofing in precast segmental tunnel linings, *Tunnelling and Underground Space Technology*, 84, pp. 334-352, https://doi.org/10.1016/j.tust.2018.11.003.

Gong, C., Ding, W., Soga, K., Mosalam, K. M. and Tuo, Y. F. (2018) Sealant behavior of gasketed segmental joints in shield tunnels: An experimental and numerical study, *Tunnelling and Underground Space Technology*, 77, pp. 127-141, https://doi.org/10.1016/j.tust.2018.03.029.

Persson, B. N. J. (2022) Fluid Leakage in Static Rubber Seals, *Tribology Letters*, 70(2), pp. 1-10, https://doi.org/10.1007/s11249-022-01573-8.

Persson, B. N. J. and Yang, C. (2008) Theory of the leak-rate of seals, *Journal of Physics Condensed Matter*, 20(31), pp. 1-11, https://doi.org/10.1088/0953-8984/20/31/315011.

Shalabi, F. I., Cording, E. J. and Paul, S. L. (2016) Sealant behavior of gasketed segmental tunnel lining – Conceptual model, *Geomechanik Und Tunnelbau*, 9(4), pp. 345-355, https://doi.org/10.1002/geot.201500030.

Shi, C., Cao, C., Lei, M., Peng, L. and Shen, J. (2015) Time-dependent performance and constitutive model of EPDM rubber gasket used for tunnel segment joints, *Tunnelling and Underground Space Technology*, 50, pp. 490-498, https://doi.org/10.1016/j.tust.2015.09.004.

Wang, Y., Yang, Y., Su, F. and Wang, L. (2020) Multiscale analytical method and its parametric study for lining joint leakage of shield tunnel, *Applied Sciences (Switzerland)*, 10(23), pp. 1-21, https://doi.org/10.3390/app10238528.

Xie, J., Huang, X. and Jin, G. (2023a) Analytical model for the sealant performance of tunnel gasketed joints based on multi-scale contact and percolation theories, *Underground Space*, 14, pp. 319-337, https://doi.org/10.1016/j.undsp.2023.08.004.

Xie, J., Huang, X., Zhang, Z. and Jin, G. (2023b) Cohesive zone model-based analyses of localized leakage of segmentally lined tunnels, *Frontiers of Structural and Civil Engineering*, 17, pp. 503-521, https://doi.org/10.1007/s11709-023-0927-4.

Zhang, Z., Zhang, J., Huang, X. and Zhuang, Q. (2020) Experimental study on prediction of long-term durability of sealing gasket of shield tunnel. *Journal of Zhejiang University (Engineering Science)*, 54(1), pp. 118-125, https://doi.org/10.3785/j.issn.1008-973X.2020.01.014.

Proceedings of the XVIII ECSMGE 2024
GEOTECHNICAL ENGINEERING CHALLENGES
TO MEET CURRENT AND EMERGING NEEDS OF SOCIETY
© 2024 the Authors
ISBN 978-1-032-54816-6
DOI 10.1201/9781003431749-381
Open Access: www.taylorfrancis.com, CC BY-NC-ND 4.0 license

ECSMGE 24
XVIII EUROPEAN CONFERENCE ON SOIL MECHANICS AND GEOTECHNICAL ENGINEERING

Prediction of the displacement field induced by the excavation of very shallow and large tunnels: A case study

Prédiction des déplacements induites par l'excavation de tunnels peu profonds et de grande taille: Une étude de cas

W. Yang*
School of Transportation, Southeast University, Nanjing, P. R. China; Department of Structural and Geotechnical Engineering, Sapienza University of Rome, Rome, Italy

D. Boldini
Department of Chemical Engineering Materials Environment, Sapienza University of Rome, Rome, Italy

D. Zhang
School of Transportation, Southeast University, Nanjing, P. R. China

**wenhui.yang@uniroma1.it*

ABSTRACT: Numerical simulation of mechanized tunnelling in urban areas, both in 2D and 3D conditions, is often carried out by simply applying a displacement pattern at the excavation boundary, especially when the objective of the analysis is the prediction of the displacements away from the tunnel. The principal assumption of this method is that the deformed tunnel shape is similar to the original shape, i.e. circular, while its centre is translated downward. This paper proposes to apply a different, more general, displacement pattern, based on further optimization of previous approaches, considering an elliptical contraction shape. Specifically, the upper and lower parts of the tunnel are allowed to contract assuming two independent elliptical shapes. The method is validated through three-dimensional finite element simulations, with special reference to the deformation pattern of a real case-history of a very shallow and large-diameter tunnel. The results show that: (1) the approach is applicable to shallow-buried and large-diameter tunnels; (2) the deformation pattern of very shallow and large-diameter tunnels is characterized by an elliptical shape in the upper portion of the section and by a circular one in the lower part; (3) the new approach can produce a more accurate prediction of the soil displacement field, if compared with the homothetic contraction of the tunnel section.

RÉSUMÉ: La simulation numérique du creusement mécanisé en milieu urbain, que ce soit dans des conditions en 2D ou 3D, est souvent réalisée en appliquant simplement un champ de déplacement à la limite de l'excavation, particulièrement lorsque l'accent est mis sur la prédiction des déplacements loin du tunnel. L'hypothèse principale de cette méthode est que la forme déformée du tunnel est similaire à la forme d'origine, c'est-à-dire circulaire, avec son centre déplacé vers le bas. Cet article propose un champ de déplacement plus général, fondé sur une optimisation approfondie des approches antérieures, en prenant en considération une forme de contraction elliptique. Notamment, les parties supérieure et inférieure du tunnel sont induites à se contracter selon deux formes elliptiques indépendantes. La méthode est validée par des simulations par éléments finis tridimensionnels, avec une référence particulière à un cas concret de tunnel très peu profond et de grand diamètre. Les résultats démontrent que: (1) l'approche est applicable aux tunnels peu profonds et de grand diamètre; (2) le motif de déformation des tunnels peu profonds et de grand diamètre est caractérisé par une forme elliptique dans la partie supérieure de la section et par une forme circulaire dans la partie inférieure; (3) par rapport à la contraction homothétique de la section du tunnel, la nouvelle approche peut prédire un champ de déplacement du sol plus précis.

Keywords: Tunnel excavation; displacement-controlled method; large and shallow tunnels; soil movements; HSsmall model.

1 INTRODUCTION

Tunnel excavation often results in significant ground displacements. Precise prediction of excavation-induced movements is crucial for ensuring tunnel construction safety with respect to pre-existing surface and subsurface structures located nearby (Mair, 2008). Excavation-induced ground movements can be predicted using various methods, including empirical approaches (Peck, 1969), quasi-analytical solutions (Loganathan and Poulos, 1998), or numerical simulations (Nguyen et al., 2021; Yang et al., 2023). When the focus is on ground displacements rather than

on lining design, the displacement-controlled method (DCM) can be employed for simulating tunnel excavation, without considering the presence of the lining (Boldini et al., 2018). Therefore, the setting of a reasonable excavation boundary contraction pattern is of utmost importance (Cheng et al., 2007). Furthermore, when combined with advanced soil constitutive models, such as the Hardening Soil model with small-strain stiffness (HSsmall), very satisfactory results can be obtained also for small values of volume loss (Benz, 2007; Fargnoli et al., 2015).

DCM can assume various displacement patterns. Sagaseta (1987) proposed an isotropic convergence pattern towards the centre of the tunnel boundary. However, especially for shallow tunnels and anisotropic in situ state of stress, the convergence along the tunnel boundary is not uniform, i.e. the displacement at the crown is obviously larger, while that at the invert arch is much smaller (Pinto and Whittle, 2006). Cheng et al. (2007) introduced a widely adopted Circular DCM that accounts for both circular contraction and vertical translation of the tunnel boundary, as shown in Figure 1. While numerous researchers have adopted these approaches and achieved satisfactory predictive results, their applications have been primarily focused on small-diameter or deep-buried tunnels, as for subway tunnels (Amorosi et al., 2014; Boldini et al., 2018). However, for shallow-buried large-diameter tunnels, for which the surrounding soil is characterized by more significant stress and stiffness variations, the accuracy of these displacement-controlled methods could be reduced.

In this study, a novel Bi-Elliptical DCM is introduced for the specific characteristics of shallow and large tunnels. To illustrate its effectiveness, this method is applied to an actual case-history and its performance is compared with the commonly used Circular DCM. Results show limitations of the Circular DCM in analysing the impacts of shallow and large tunnel excavation, while highlighting the advantages and potential applications of the Bi-Elliptical DCM model.

2 BI-ELLIPTICAL DISPLACEMENT-CONTROLLED METHOD

2.1 Limitations of existing DCM

The commonly used DCM currently have the following assumptions: 1) the convergence is not uniform; 2) the deformed tunnel shape is similar to the initial shape; 3) convergence point located between converged tunnel centre and invert (Cheng et al., 2007). Usually, this point is set as the invert, where no displacement occurs (Amorosi et al., 2014; Boldini et al., 2018).

The above displacement pattern is not necessarily realistic because the deformed tunnel shape may not necessarily be similar to the original excavation shape; in addition, due to the effect of unloading, the tunnel bottom may uplift, and its displacement should not be ignored. In practice, the excavation profile tends to be more elliptical in shape due to the non-linearity of the soil properties and the anisotropy of the in-situ state of stress (Loganathan and Poulos, 1998; Marshall et al., 2009).

2.2 Improved Bi-Elliptical DCM

A Bi-Elliptical DCM, which can also degrade to a Circular DCM when necessary, is proposed in the following. Figure 2 shows a schematic plot of the optimized bi-elliptical displacement pattern. There are three assumptions: 1) the deformed tunnel profile is divided into two separate ellipses, the upper and the lower ones, respectively above and below the tunnel axis, 2) the deformed profile is continuous at the two intersections, 3) the deformed tunnel profile is allowed for an overall vertical displacement.

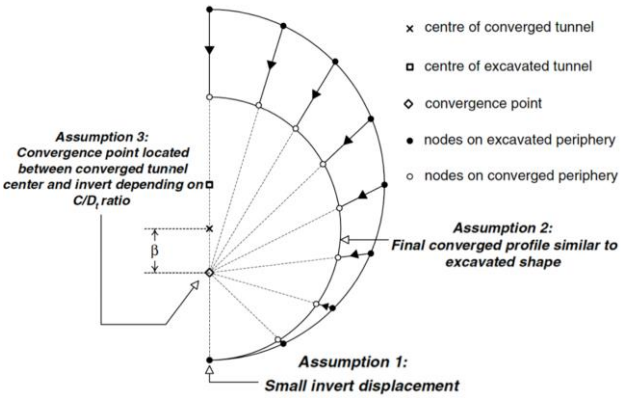

Figure 1. Commonly used Circular DCM (Cheng et al., 2007).

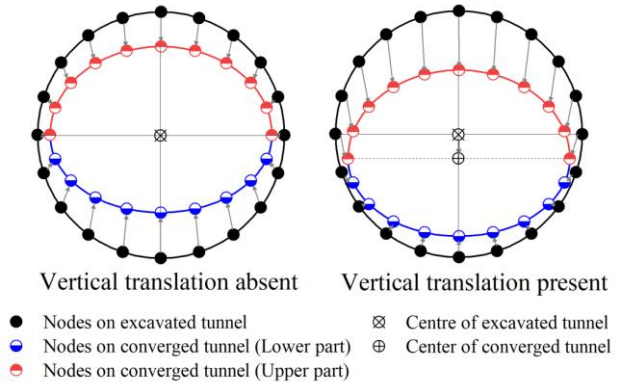

Figure 2. Schematic diagram of the optimized bi-elliptical displacement pattern.

3 NUMERICAL SIMULATION AND VERIFICATION OF BI-ELLIPTICAL DEFORMATION ASSUMPTION

3.1 Description of the reference case

The numerical model is set up on the basis of the very shallow and large Suzhou Tongjing road tunnel, characterized by a tunnel diameter (D) of 13.2 m, a lining thickness of 0.6 m, and an axis depth (H) of 16.7 m (Figure 3). The soil profile at the construction area is also shown in Figure 3. The soil is divided into 10 different layers, namely: 1- fill, 2- clay, 3- silty clay, 4- silt, 5- silty sand, 6- silty clay, 7- clay, 8- silty clay, 9- silty clay, and 10- silty clay. The TBM-EPB tunnel passes through layers 4- silt, 5- silty sand, 6- silty clay and 7- clay. The water table is at 1.5 m below the ground surface and the pore pressure distribution is hydrostatic. During simulation of tunnel excavation, soil layers 1, 4, and 5 are set as drained, while other soil layers are set as undrained.

3.2 Detail of the finite element model

In order to obtain a more accurate representation of the excavation boundary profile, a 3D step-by-step numerical tunnel excavation is implemented in Plaxis. This model incorporates detailed modelling of the TBM-EPB and the tunnel lining (Figure 4). Solid elements are used for the soil and the lining, while plate elements are employed to simulate the machine shield. The finite element discretization consists of over 132249 10-node tetrahedral elements. In the vicinity of the tunnel face, the mesh is refined to provide better approximation to handle significant stress and strain gradients in that region. Interaction surfaces are established between the tunnel lining and the soil, as well as between the shield machine and the soil (Figure 4). The face pressure and the grouting pressure of the shield, which follow a linear interpolation distribution with depth are set equal to the total horizontal stress and total vertical stress at those locations respectively.

The HSsmall constitutive law is adopted to get accurate numerical results. Table 1 shows the parameters of the HSsmall model: all the values are calibrated on laboratory and in-situ tests data (Yang, 2023). The elastic model is used for the lining and the shield (the values of parameters are listed in Table 2).

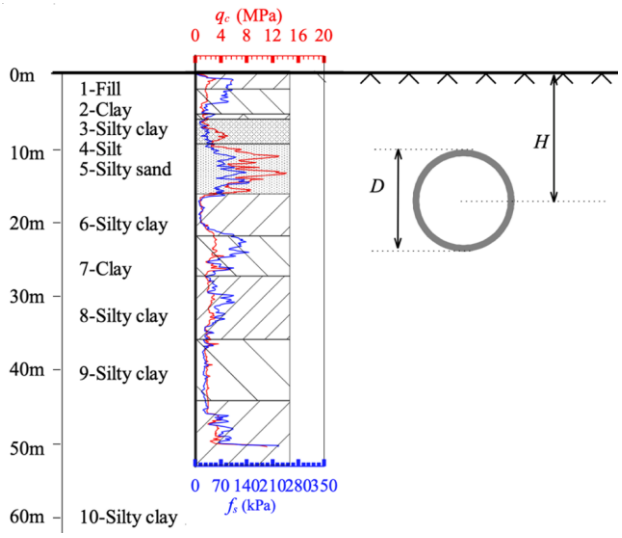

Figure 3. Geotechnical model at the Tongjing road tunnel site.

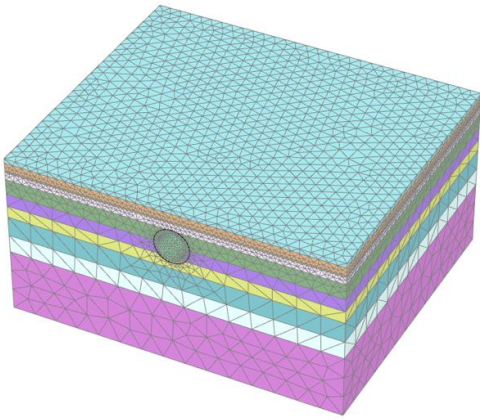

(a) Overall model

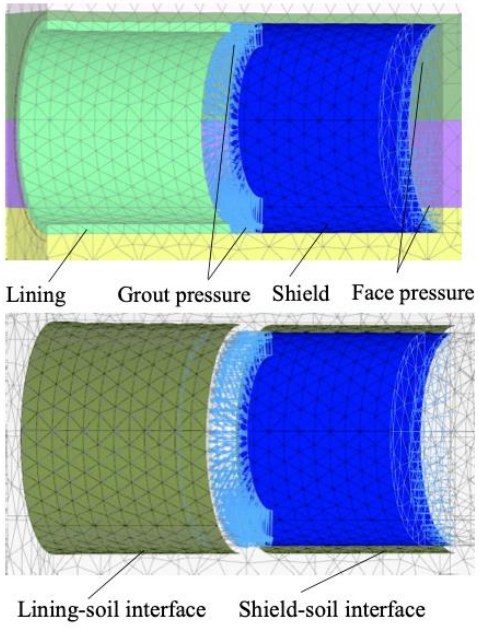

(b) Local details

Figure 4. Numerical model.

Table 1. Parameters of the HSsmall constitutive model.

Parameters	1-Fill	2-Clay	3-Silty clay	4-Silt	5-Silty sand	6-Silty clay	7-Clay	8-Silty clay	9-Silty clay	10-Silty clay
γ_{dry} (kN/m^3)	15.2	15.7	14.6	15.3	15.7	14.7	15.1	14.9	14.3	14.9
γ_{sat} (kN/m^3)	19.6	20.0	19.2	19.6	19.9	19.3	19.6	19.4	19.0	19.4
OCR	1	3.47	2.67	1	1	1.1	1.1	1.1	1.1	1.1
c' (kPa)	0	11.4	9.1	0	0	7.4	8.6	6.8	4.7	3.1
φ' (°)	30.1	24.8	26.6	33.95	35.6	27.4	27.6	27.1	27.9	29.1
ψ' (°)	10.0	8.3	8.9	11.3	11.9	9.1	9.2	9.0	9.3	9.7
m	0.6	0.8	0.75	0.5	0.45	0.7	0.8	0.8	0.75	0.75
ν_{ur}	0.25	0.2	0.2	0.25	0.25	0.2	0.2	0.2	0.2	0.2
G_0^{ref} (kPa)	96000	50000	55000	72000	102000	55000	95000	104000	85000	95000
E_{ur}^{ref}/E_0^{ref}	0.2	0.3	0.3	0.2	0.2	0.3	0.3	0.3	0.3	0.3
E_0^{ref}(kPa)	240000	120000	132000	180000	255000	132000	228000	249600	204000	228000
E_{ur}^{ref} (kPa)	48000	36000	39600	36000	51000	39600	68400	74880	61200	68400
E_{50}^{ref} (kPa)	16000	12000	13200	12000	17000	13200	22800	24960	20400	22800
E_{oed}^{ref} (kPa)	16000	12000	13200	12000	17000	13200	22800	24960	20400	22800
$\gamma_{0.7}$	1e-4	2.1e-4	2.1e-4	1e-4	1e-4	2.1e-4	2.1e-4	2.1e-4	2.1e-4	2.1e-4
p^{ref} (kPa)	100	100	100	100	100	100	100	100	100	100
K_0	0.50	0.98	0.86	0.44	0.42	0.56	0.56	0.57	0.56	0.54
K_0^{nc}	0.50	0.58	0.55	0.44	0.42	0.54	0.54	0.54	0.53	0.51
R_f	0.9	0.9	0.9	0.9	0.9	0.9	0.9	0.9	0.9	0.9
$\sigma_{tension}$	0	0	0	0	0	0	0	0	0	0
c_{inc} (kPa/m)	0	0	0	0	0	0	0	0	0	0

Table 2. Parameters of the shield and of the lining.

Material	ρ (Mg/m^3)	E (GPa)	ν
Shield	24.7	200	0.2
Lining	2.7	35	0.2

The construction process is modeled using a sequential excavation scheme (Fargnoli et al., 2015). Plaxis 3D provides a method to simulate tunnel volume loss by assigning a contraction rate (C_{ref}) to the tunnel boring machine shield, without pre-determining the final tunnel contraction pattern. This technique implements a contraction whose actual value depends on the stiffness of the surrounding clusters and objects. The equilibrium state is reached during the iterative calculation process, and the final deformation profile is related to the stiffness of the surrounding soils (Plaxis, 2020).

C_{ref} is set equal to 0.45% based on field surface settlement monitoring results. The corresponding surface volume loss, $V_{l,s}$, results to be 0.48% using a Gaussian distribution curve with a width parameter $K = 0.6$ (Figure 5). It can be observed that the numerical calculation results are in good agreement with the theoretical and monitoring results, indicating the reliability and accuracy of the numerical model used in this study.

Figure 6 illustrates the deformed shape and displacement of tunnel boundary, these latter being amplified by 100 times and normalized based on the tunnel radius. It is evident that for this large-diameter shallow-buried tunnel, the excavation boundary does not exhibit a circular or elliptical contraction. Instead, a distinct bi-elliptical contraction pattern is observed, which the upper part deforms into an ellipse, while the lower shrinks in a circular shape. This observation validates the assumptions of the proposed Bi-Elliptical DCM method.

4 APPLICATION AND COMPARISON OF THE BI-ELLIPTICAL DCM

To further validate the predictive accuracy of the newly proposed DCM for ground surface displacements, a series of numerical simulations are conducted using a single-step excavation method to simulate tunnel excavation without modelling the tunnel lining, as in Boldini et al. (2018). For the Bi-Elliptical DCM, displacements at the excavation boundary from Figure 6 are used as prescribed displacements. Additionally, predictions of ground settlement are made using Cheng's Circular DCM for comparison. β represents the overall tunnel translation magnitude, with $\beta = 0$ indicating no vertical translation, meaning the tunnel is contracting toward its center, and $\beta = 1$ signifying that the tunnel invert is translated to its initial position, i.e. that the tunnel is fixed at the bottom (Figure 1).

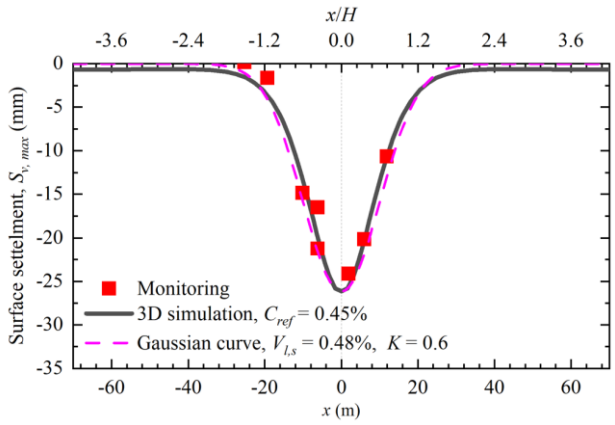

Figure 5. Comparison between numerical simulation results and field monitoring data.

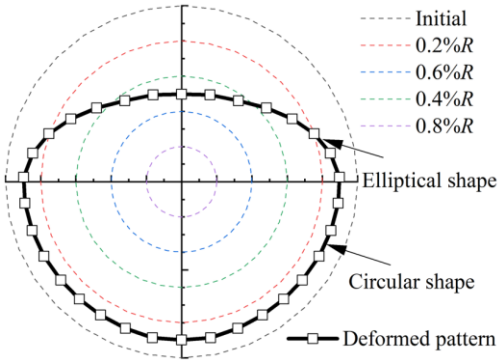

Figure 6. Final deformed tunnel profile for the reference case (Scale: 1:100).

Figure 7 presents the results of the Bi-Elliptical DCM and the Cheng's Circular DCM. For Bi-Elliptical DCM, the tunnel profile is controlled by the elliptical convergence parameters (n_1 and n_2), for the upper and lower parts, and the overall tunnel translation parameter (β). For the reference case, the values of n_1, n_2, and β were set equal to 0.9963, 1.0000, and 0.10, respectively. The Bi-Elliptical DCM, as emphasized before, successfully reproduces the ground settlement profile, showing an excellent agreement with measured data. In contrast, the Circular DCM predicts a wider settlement trough and typically underestimates the maximum ground displacement, especially for low values of β. Furthermore, even when β =1, the predictive profile is shallower than that obtained by the Bi-Elliptical DCM. This demonstrates the advantage of the Bi-Elliptical DCM in predicting ground surface displacements induced by shallow-buried large-diameter tunnel excavation.

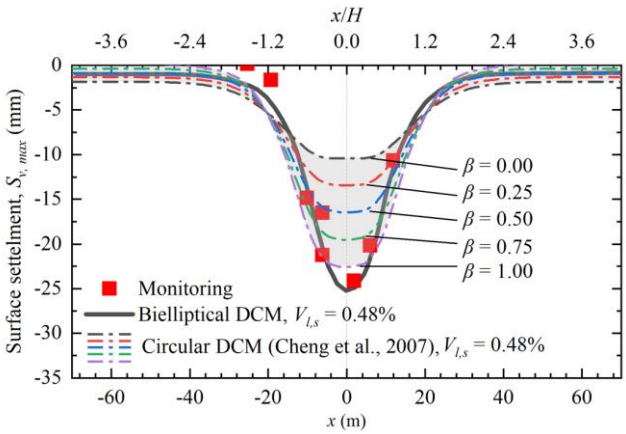

Figure 7. Comparison of the predicted surface settlement of Bi-Elliptical DCM and Circular DCM.

5 CONCLUSIONS

Based on the characteristics of shallow-buried large-diameter tunnels, this paper introduces the Bi-Elliptical deformation model for tunnel boundary. Using numerical simulations and a real case-history, this approach is validated and compared with the Circular DCM. Three key conclusions are obtained from this investigation:

(1) the excavation boundary of shallow-buried large-diameter tunnels exhibit distinct, independent contractions in the upper and lower parts, with the upper part forming an ellipse and the lower part contracting into a circle;

(2) the Circular DCM underestimates the maximum ground settlement and results in a wider settlement trough;

(3) the Bi-Elliptical DCM effectively reproduces the ground surface profile for a specific surface volume loss.

This research demonstrates the validity of the Bi-Elliptical deformation assumptions and its significant potential in accurately predicting ground surface displacements caused by the excavation of large-diameter shallow-buried tunnels.

ACKNOWLEDGEMENTS

The authors are grateful for the financial support provided by the China Scholarship Council (CSC, No.202006090343).

REFERENCES

Amorosi, A., Boldini, D., De Felice, G., Malena, M., & Sebastianelli, M. (2014). Tunnelling-induced deformation and damage on historical masonry

structures. *Géotechnique*, 64(2), 118-130. https://doi.org/10.1680/geot.13.p.032.

Benz, T. (2007). *Small-strain stiffness of soils and its numerical consequences*, Ph.D. Thesis. University of Stuttgart, Stuttgart, Germany.

Boldini, D., Losacco, N., Bertolin, S., & Amorosi, A. (2018). Finite element modelling of tunnelling-induced displacements on framed structures. *Tunnelling and underground space technology*, 80, 222-231. https://doi.org/10.1016/j.tust.2018.06.019.

Cheng, C. Y., Dasari, G. R., Chow, Y. K., & Leung, C. F. (2007). Finite element analysis of tunnel–soil–pile interaction using displacement controlled model. *Tunnelling and Underground Space Technology*, 22(4), 450-466. https://doi.org/10.1016/j.tust.2006.08.002.

Fargnoli, V., Boldini, D., & Amorosi, A. (2015). Twin tunnel excavation in coarse grained soils: Observations and numerical back-predictions under free field conditions and in presence of a surface structure. *Tunnelling and Underground Space Technology*, 49, 454-469. https://doi.org/10.1016/j.tust.2015.06.003.

Loganathan, N., & Poulos, H. G. (1998). Analytical prediction for tunneling-induced ground movements in clays. *Journal of Geotechnical and geoenvironmental engineering*, 124(9), 846-856. https://doi.org/10.1061/(asce)1090-0241(1998)124:9(846).

Mair, R. J. (2008). Tunnelling and geotechnics: new horizons. *Géotechnique*, 58(9), 695-736. https://doi.org/10.1680/geot.2008.58.9.695.

Marshall, A. M., Elkayam, I., & Klar, A. (2009). Ground behaviour above tunnels in sand-DEM simulations versus centrifuge test results. In *Euro: Tun 2009, Proceedings of the 2nd International Conference on Computational Methods in Tunnelling,* Bochum, Germany, pp. 9-11.

Nguyen, T. T., Do, N. A., Karasev, M. A., Kien, D. V., & Dias, D. (2021). Influence of tunnel shape on tunnel lining behaviour. *Proceedings of the institution of civil engineers-geotechnical engineering*, 174(4), 355-371. https://doi.org/10.1680/jgeen.20.00057.

Peck, B. B. (1969). Deep excavation and tunnelling in soft ground, State of the art volume. In *7th ICSMFE*, Mexico City, Mexico, Vol. 4, pp. 225-290.

Pinto, F., & Whittle, A. J. (2006). Discussion of "Elastic solution for tunneling-induced ground movements in clays" by KH Park. *International Journal of Geomechanics*, 6(1), 72-73. https://doi.org/10.1061/(asce)1532-3641(2006)6:1(72).

Plaxis, B. (2020). *Plaxis 3D - Tutorial Manual*. Connect Edition. V21.00, Delft, the Netherlands.

Sagaseta, C. (1987). Analysis of undrained soil deformation due to ground loss. *Geotechnique*, 37(3), 301-320. https://doi.org/10.1680/geot.1987.37.3.301.

Yang, W., Boldini, D., & Zhang, D. (2023). Some observations on numerical modelling of tunnelling-induced soil movements by a displacement-controlled technique. In *Proceedings 10th NUMGE 2023*, London, UK. https://doi.org/10.53243/NUMGE2023-310.

Yang, W. (2023). *Impact of a large-diameter shallow twin-tunnel excavation on adjacent high speed rail bridges and related protective measures*. Ph.D. Thesis, Sapienza University of Rome, Rome, Italy, and Southeast University, Nanjing, P. R. China.

Proceedings of the XVIII ECSMGE 2024
GEOTECHNICAL ENGINEERING CHALLENGES
TO MEET CURRENT AND EMERGING NEEDS OF SOCIETY
© 2024 the Authors
ISBN 978-1-032-54816-6
DOI 10.1201/9781003431749-382
Open Access: www.taylorfrancis.com, CC BY-NC-ND 4.0 license

ECSMGE 24
XVIII EUROPEAN CONFERENCE ON SOIL MECHANICS AND GEOTECHNICAL ENGINEERING

Evaluation of the induced axial force behaviour for bored tunnel construction adjacent to existing long piles

Évaluation du comportement de la force axiale induite pour la construction d'un tunnel ennuyé adjacent à des pieux longs existants

P. Yensri*, A. Faramarzi, N. Metje
School of Engineering, University of Birmingham, Edgbaston, Birmingham, United Kingdom
**pxy241@student.bham.ac.uk*

ABSTRACT: Population growth and increase in urbanisation contribute to an increased use of underground space. Consequently, new tunnel alignments are often situated near existing piled foundations. Thus, evaluating the induced forces and displacement in the piles caused by ground movements due to tunnelling must be considered. This study focused on assessing the maximum induced axial forces (*Max.N*) in long piles. A series of three-dimensional Finite Element Analyses were conducted. The model's validity was established by comparing it with data from a well-known literature. Parametric studies were performed, varying the tunnel depth (Z) and pile length (L_p) (lengths evaluated are 40 m, 50 m, and 59 m). The findings indicate that the behaviour of long piles in response to tunnelling exhibits two dominant characteristics. When tunnelling at a shallow depth ($Z/L_p < 0.5$), the *Max.N* in the piles remains relatively constant regardless of the pile length. However, for deep tunnel constructions ($Z/L_p > 0.5$), shorter piles are less affected compared to longer piles. These findings could benefit engineers when dealing with new pile construction plans or minimising potential impacts on existing piled foundations, as adjusted tunnel alignments could be considered.

RÉSUMÉ: La croissance de la population et l'urbanisation accrue contribuent à la demande d'utilisation de l'espace souterrain. Par conséquent, les nouveaux alignements de tunnels sont souvent inévitablement situés à proximité de fondations en pieux existantes. Selon cette situation, il est nécessaire de prendre en compte l'évaluation des forces induites et du déplacement dans les pieux causés par les mouvements du sol dus au creusement de tunnels. Cette étude s'est principalement concentrée sur l'évaluation des forces axiales maximales induites (Max.N) dans les pieux longs. Une série d'analyses par éléments finis tridimensionnels a été réalisée. La validité du modèle a été établie en le comparant avec la littérature bien connue. Des études paramétriques ont été réalisées, en faisant varier les profondeurs des tunnels (Z) et les longueurs des pieux (Lp) de 40 m, 50 m et 59 m. Les résultats indiquent que le comportement des pieux longs en réponse au creusement de tunnels présente deux caractéristiques dominantes. Lors du creusement à faible profondeur (Z/Lp < 0,5), le Max.N dans les pieux reste relativement constant quelle que soit la longueur du pieu. Cependant, pour un creusement profond (Z/Lp > 0,5), les pieux plus courts sont moins affectés par rapport aux pieux plus longs. Ces résultats pourraient être d'un bénéfice significatif pour les ingénieurs lorsqu'ils traitent de nouveaux plans de construction de pieux ou minimisent les impacts potentiels sur les fondations en pieux existantes, car des alignements de tunnels ajustés pourraient être envisagés.

Keywords: Tunnel; piled foundation; axial force; finite element analysis; parametric studies.

1 INTRODUCTION

The use of underground space has rapidly increased for several applications, such as transportation systems, water supply and drainage systems and cables, particularly in big cities, attributed to population growth and urbanisation and further development of infrastructure. Tunnelling is one of the most popular techniques to meet these demands, especially in congested urban areas. Often, new tunnel construction is aligned closely to existing structures supported by piled foundations, such as high-rise buildings and fly-over bridges. Hence, the potential impacts affecting these piles induced by tunnel construction activities should be considered.

Generally, tunnelling causes ground movements towards the tunnel in both vertical and horizontal directions (Basile, 2014). These ground movements can impact existing piled foundations and, at least two major aspects need to be carefully considered: (i) induced forces in the piles, including axial forces and bending moments; and (ii) tolerable structural movements (Basile, 2014).

To assess the interaction between piles and a new tunnel two configurations need to be considered: short piles and long piles (Loganathan, 1999). Several

research studies were conducted to understand the mechanisms of pile – tunnel interactions using various approaches, including full-scale experiments (Pang, 2006), physical and centrifuge model tests (Jacobsz et al., 2004; Marshall, 2009) as well as analytical and numerical analysis (Loganathan, 1999; Kitiyodom et al., 2005; Jongpradist et al., 2013). However, most of the studies focused on pile settlement and induced bending moments. The mechanism of induced axial force especially when focusing on the case of a long pile subjected to tunnelling is not well understood.

This paper presents the effect of tunnelling on a nearby long pile focusing on the maximum induced axial force (*Max.N*). A three-dimensional finite element analysis (3D-FEM) was adapted using the PLAXIS 3D software package. A parametric study has been conducted varying key parameters: pile lengths (L_p), clearance ($\times D$) and tunnel buried depths (Z). The model is validated using a well-documented historical case study. The effects of the relationship between L_p and Z on *Max.N* are presented and, recommendations on new piled foundation design are presented to minimise the potential impacts.

2 FINITE ELEMENT MODELLING AND VALIDATION

The model was validated using a historical case study reported by Pang (2006). Pier number 20, constructed as part of the Singapore's Mass Rapid Transit (MRT) North-East line project, was used as a prototype model.

The foundation details included a 2×2 square arrangement of four bored piles with a diameter of 1.2 m and a spacing of 3.6 m (centre to centre), with a length of 62 m below the ground surface. Various instrumentation, including inclinometers, settlement points, and strain gauges, were installed in the piled foundation to observe the potential effects of the piles' responses to the tunnel construction activities.

Two tunnels were sequentially constructed in this project at a depth of 21.0 m, named the Southbound (SB) and Northbound (NB) tunnels. The clearance between the outer tunnel lining and the pile group was 1.6 m, and 3.3 m for the SB and NB tunnel, respectively as presented in Figure 1. The volume losses, as reported by Pang (2006), were 1.38% and 1.67% for SB and NB tunnelling, respectively.

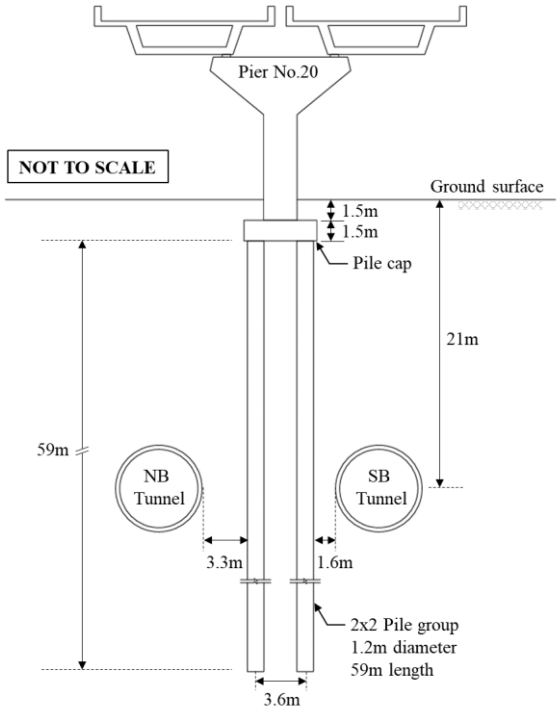

Figure 1. Pile – Tunnel configuration in MRT Singapore project (Modified from Pang, 2006).

2.1 Mesh and Boundary Conditions

Figure 2 presents the mesh and boundary conditions of the prototype model. The boundary of the modelled problem is 140 m long, with a 80 m width and a 75 m depth. The soils were modelled with 10-nodes tetrahedral elements. The tunnel lining and the pile cap were modelled with a plate element along with an interface element to consider the soil-structure interaction, while an embedded beam element was employed to model the bored piles.

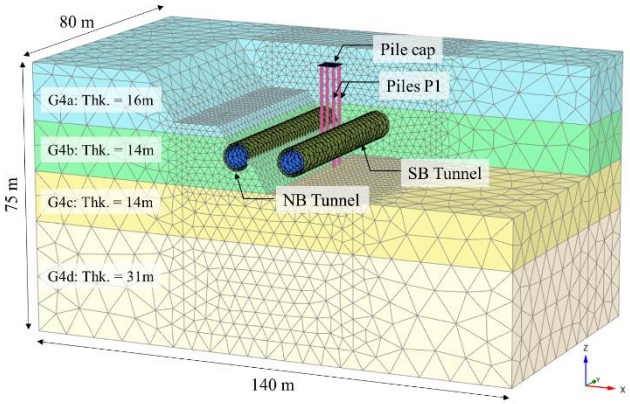

Figure 2. FE model validation mesh and boundary conditions.

2.2 Validation

Figure 3 illustrates the results of the analysis of pile P1 and the ground surface settlement induced by SB tunnelling, comparing them with the measured data as

well as other prediction methods: analytical method, boundary element and finite element analysis. The maximum difference between computed and the measured data for the pile's movements and the induced forces in the pile caused by SB tunnelling is 20%. This provides confidence that the FE model is suitable to use as a predictive model.

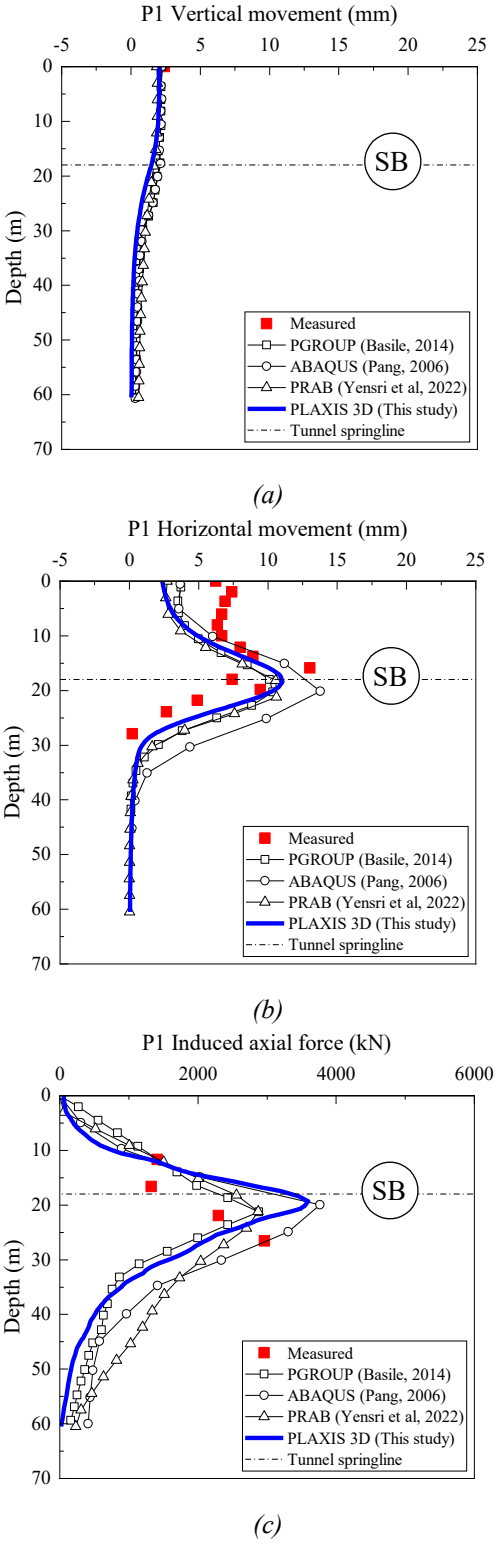

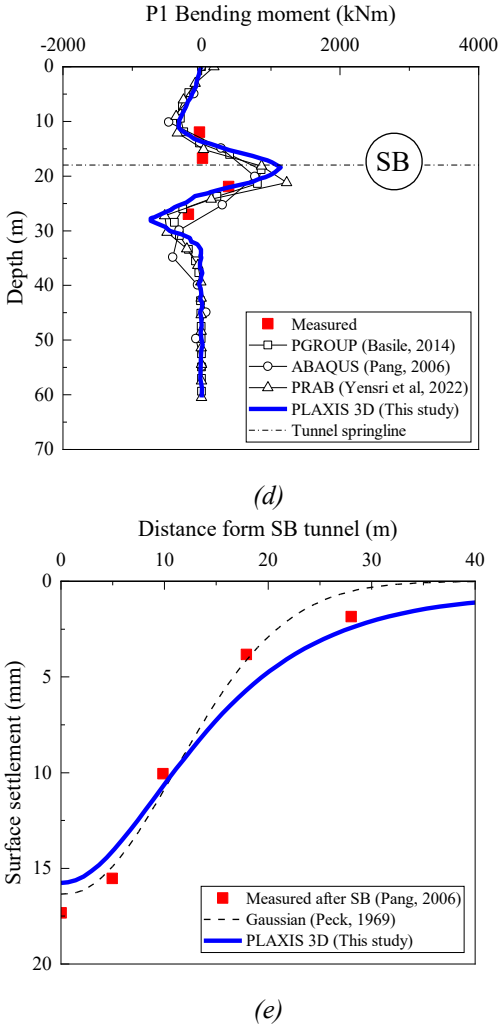

Figure 3. Pile P1 response to the construction of the SB tunnel after passing of the tunnel (a) Settlement (b) Horizontal movement (c) Induced axial force (d) Induced bending after SB (e) surface settlement.

3 PARAMETRIC STUDY

The effect of the pile – tunnel locations are observed through a parametric study using the validated FE model as a prototype model, with various key parameters:

- Pile lengths (L_p) are investigated at 40 m, 50 m and 59 m (same as the prototype)
- Clearance ($\times D_t$) is normalised with the tunnel diameter ($D_t = 6.3m$), and applied at $0.5D_t$, $1D_t$, $2D_t$ and $3D_t$.
- Tunnel buried depths (Z) are modelled at depths of 9.45m ($1.5D_t$), 22.05m ($3.5D_t$), 28.35 m ($4.5D_t$) and 40.95m ($6.5D_t$), representing Z1, Z2, Z3 and Z4, respectively.

Both the tunnel and pile maintain a constant diameter of 6.3 m and 1.2 m, respectively. In the simulation, a tunnel volume loss of 2.0% is used, incorporating face, shield and tail losses without

considering tunnel advancement. The surrounding soils are modelled using the Modified Cam Clay constitutive model, and the critical state parameters and strength properties of the materials are shown in Tables 1 and 2, respectively. The pile cap and tunnel lining are simulated using linear-elastic plate elements with material properties defined by flexural (EI) and axial stiffness (EA). The bored piles are modelled using the embedded beam element, which considers the actual properties and geometry of the pile as well as the geotechnical mechanisms, including skin friction and bearing capacity which can also be added to the model. The interface elements are automatically generated based on the strength of the layered soils. Further details can be found in PLAXIS 3D Scientific Manual (2023). Four different tunnel buried depths are investigated, and the normalisation of the tunnel depth against the pile length is presented in Table 3. The construction sequence begins with the construction of the piled foundation, followed by the tunnel construction.

Table 1. Critical state parameters (Pang, 2006).

Soil layer	κ	λ	e_{int}	M
G4a	0.018	0.113	1.8	1.113
G4b	0.023	0.104	1.9	1.2
G4c	0.007	0.07	2.0	1.2
G4d	0.007	0.07	2.0	1.2

Table 2. Strength parameters (Pang, 2006).

Soil layer	Cohesion (kPa)	Friction angle (°)
G4a	20	28
G4b	30	30
G4c	30	30
G4d	30	30

Table 3. Normalisation of tunnel depth to the pile length.

Tunnel depth	Z/L_p		
	L_p = 40m	L_p = 50m	L_p = 59m
Z1 (9.45m)	0.16	0.13	0.11
Z2 (22.05m)	0.48	0.38	0.32
Z3 (28.35m)	0.63	0.51	0.43
Z4 (40.95m)	0.95	0.76	0.64

4 RESULTS AND DISCUSSIONS

The *Max.N* values of pile P1 obtained from the analysis are discussed in this section. Based on these findings, the depth of the buried tunnels as well as the pile lengths significantly impact on the values of *Max.N* as investigated from each analysis case.

4.1 Maximum Induced Axial Force (*Max.N*)

Figure 4 illustrates the correlation between *Max.N* and the clearance of pile P1. The results show that the value of *Max.N* is notably influenced by the tunnel depth as well as the clearance. Regarding tunnel depths Z1 to Z3, the results indicate that the *Max.N* values are not significantly affected by the pile length. However, there is an exception, particularly for the case of L_p = 40 m at the depth Z3. At a clearance of $0.5D_t$, the *Max.N* is 4,306 kN, while for L_p = 50 m and 59 m, the values are 5,625 kN and 5,830 kN, respectively.

In the context of Z4, a notable difference appears in the behaviour of *Max.N* compared to the depths of Z1 to Z3. It can be observed that the increase in pile length contributed to an increase in the value of *Max.N*. For instance, at a clearance of $0.5D_t$, the *Max.N* values are 2,478 kN, 5,444 kN and 7,736 kN for L_p = 40 m, 50 m and 59 m, respectively.

Based on these findings, it can be concluded that for shallow tunnelling ($Z/L_p < 0.5$), the increase in pile length does not significantly impact the drag force subjected to the vertical ground movement along the pile shaft. In contrast, for deep tunnelling ($Z/L_p > 0.5$), changes in the toe level of the pile influence the developed drag force considerably.

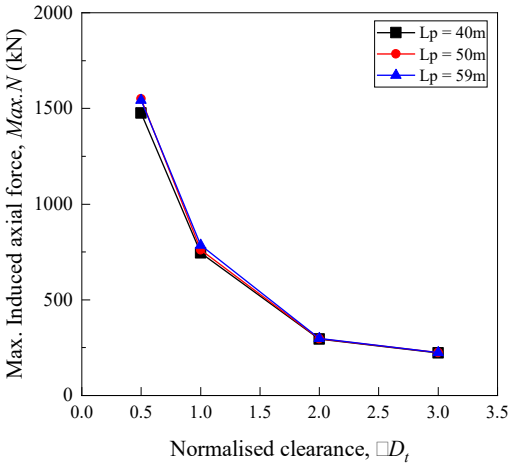

(a)

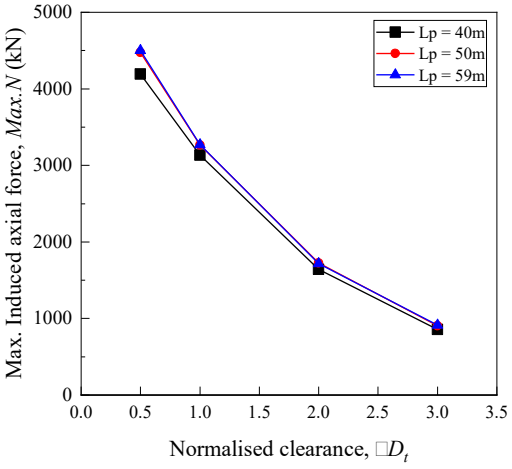

(b)

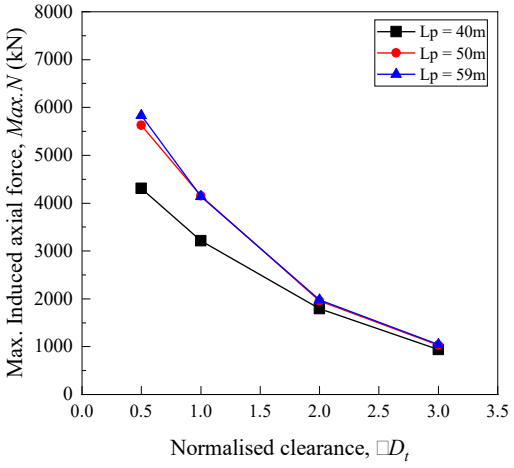

(c)

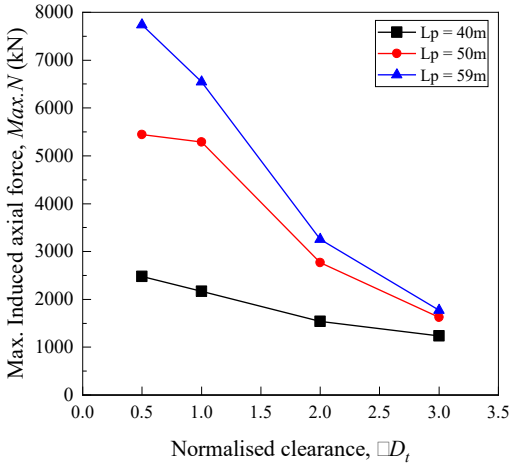

(d)

Figure 4. The maximum induced axial force in the pile against the normalised clearance at depths of (a) Z1, (b) Z2, (c) Z3 and (d) Z4.

4.2 Normalisation of *Max.N*

The normalisation of *Max.N* with respect to the applied working load for each pile length is discussed in this section. In order to assess the pile's structural and geotechnical capacity affected by tunnelling, this value can be utilised for evaluation purposes together with the load distribution along the pile length. The applied working loads adopted in this study are 7,500 kN, 11,000 kN and 12,500 kN for L_p = 40 m, 50 m and 59m, respectively. Figure 5 illustrates the analysed results, focusing on the *Max.N* for each tunnel buried depth.

Based on the results, it is indicated that, at depths of Z1 to Z3 where the value of Z/L_p ranges from 0 to 0.5, the shorter pile, in contrast to the longer pile, experiences a significantly higher induced axial force compared to their working load. For instance, at a depth of Z2 with a clearance of 0.5D_t, the normalised *Max.N* to working load ratios are 55.89%, 44.75% and 36.01% for Z/L_p = 0.47, 0.38 and 0.32, respectively, with L_p values of 40 m, 50 m and 59 m, respectively.

In the case of deep tunnelling, with values of Z/L_p approximately greater than 0.5, Max.N is reduced for the shorter pile compared to the longer pile, especially at small clearances (0.5D_t to 1D_t). For example, at a depth of Z4 with a clearance of 0.5D_t, the normalised *Max.N* values are 33.04%, 54.44% and 61.89% for the value of Z/L_p = 0.93, 0.75 and 0.64.

According to the results, it was demonstrated that the longest pile is advantageous in terms of minimising the impact from *Max.N* compared with the shorter pile, which could potentially affect a pile's structural capacity and stability during shallow tunnelling at depths ranging from Z/L_p = 0 to approximately 0.5. In contrast, for deep tunnelling configuration, i.e. Z/L_p > approximately 0.5, it suggests that the shortest pile play an important role in effectively decreasing *Max.N* compared to the longer piles.

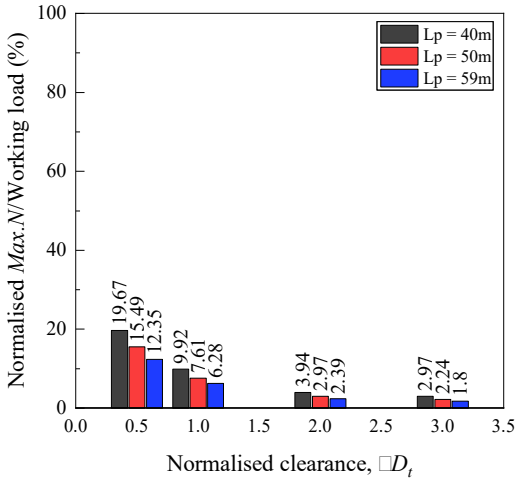

(a)

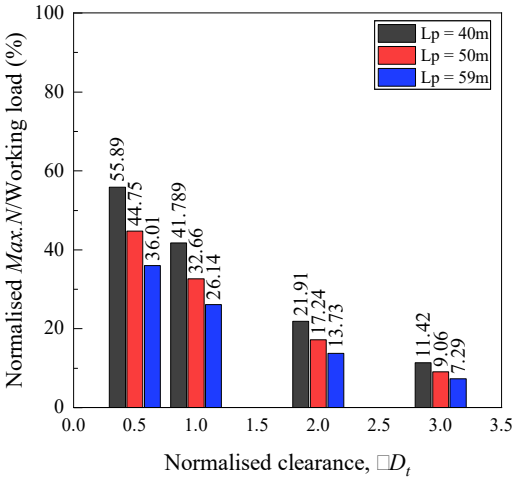

(b)

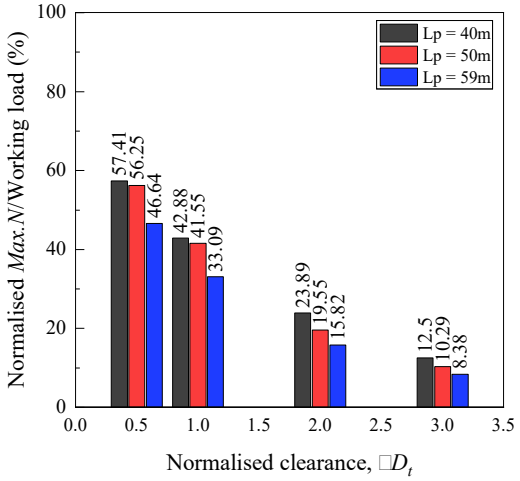

(c)

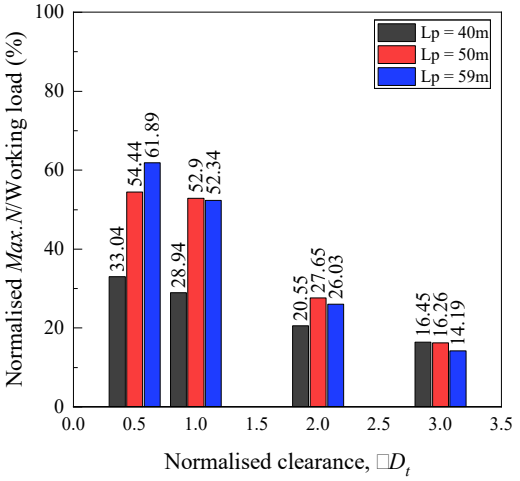

(d)

Figure 5. The comparison of normalised Max.N at depths of (a) Z1, (b) Z2, (c) Z3 and (d) Z4.

5 CONCLUSIONS

Based on the results obtained from the FE analysis, it is observed that the behaviour of the *Max.N* is significantly influenced by the tunnel buried depth relative to the pile length. Meanwhile, it can be deduced that the vertical change in tunnel alignment also contributes to the potential impact on the pile, particularly in terms of increasing axial force along the pile. The mechanisms are as follows:

- For shallow tunnelling ($Z/L_p < 0.5$), a longer pile is advantageous in terms of minimising the impact from the induced axial force, which could impact the stability of the pile (reduction of the factor of safety).
- In contrast, in the case of deep tunnelling ($Z/L_p > 0.5$), the longer pile appears disadvantageous compared to the shorter pile.

Recommendations can be made regarding minimising the *Max.N* in the new pile due to deep tunnel construction ($Z/L_p>0.5$) by adjusting the pile arrangement and decreasing the pile length. However, compromising on structural settlement, as well as pile stability must be taken into account in this case.

ACKNOWLEDGEMENTS

The authors are grateful for the support and funding provided by the National Buried Infrastructure Facility, School of Engineering, The University of Birmingham (grant reference number: EP/P013635/1).

REFERENCES

Basile, F. (2014). Effects of Tunnelling on Pile Foundations. *Soils and Foundations*, 54(3), pp. 280-295. https://doi.org/10.1016/j.sandf.2014.04.004.

Jacobsz, S.W., Standing, J.R., Mair, R.J., Hahiwara, T. and Suiyama, T. (2004). Centrifuge modeling of tunnelling near driven piles. *Soil and Foundations*, 44(1), pp. 49-56. https://doi.org/10.3208/sandf.44.49.

Jongpradist, P., Kaewsri, T., Sawatparnich, A., Suwansawat, S., Youwai, S., Kongkitkul, W. and Sunitsakul, J. (2013). Development of Tunneling Influence Zones for Adjacent Pile Foundations by Numerical Analysis. *Tunnelling and Underground Space Technology*, 34, pp. 96-109. https://doi.org/10.1016/j.tust.2012.11.005.

Kitiyodom, P., Matsumoto, T. and Kawaguchi, K. (2005). A Simplified Analysis Method for Piled Raft Foundations Subjected to Ground Movements induced by Tunnelling. *Int. J. Numer. Anal. Methods Geomech*, 29, pp. 1485-1507. https://doi.org/10.1002/nag.469.

Loganathan, N., (1999). *Effect of Tunnelling Adjacent to Pile Foundations*. Ph.D. Thesis, The University of Sydney.

Marshall, A.M., (2009). *Tunnelling in sand in its effect on pipelines and piles*. Ph.D. Thesis, University of Cambridge.

Pang, C.H. (2006). *The Effect of Tunnel Construction on Nearby Pile Foundations*. Ph.D. Thesis, National University of Singapore.

PLAXIS. (2023). *Scientific Manual 3D*. PLAXIS.

Yensri, P., Kitiyodom, P., Asanprakit, A., Duangsano, O., and Phienwej, N. (2022). Assessment of tunnelling on existing pile foundations in Bangkok MRT orange line. *ITA-AITES World Tunnel Congress 2022*, Copenhagen, Denmark, pp. 290–295.

Proceedings of the XVIII ECSMGE 2024
GEOTECHNICAL ENGINEERING CHALLENGES
TO MEET CURRENT AND EMERGING NEEDS OF SOCIETY
© 2024 the Authors
ISBN 978-1-032-54816-6
DOI 10.1201/9781003431749-383
Open Access: www.taylorfrancis.com, CC BY-NC-ND 4.0 license

ECSMGE 24
XVIII EUROPEAN CONFERENCE ON SOIL MECHANICS AND GEOTECHNICAL ENGINEERING

Application of numerical modelling in Next Generation of Eurocode 7

Application de la modélisation numérique dans la prochaine génération de l'Eurocode 7

H.C. Yeow*
COWI UK, London, UK

G. Katsigiannis
Ferrovial Construction UK, London, UK

**hoye@cowi.com*

ABSTRACT: The Next Generation (NG) of Eurocodes are currently being drafted and scheduled to be rolled out in later part of 2027. The existing code does not cover the use of numerical modelling in geotechnical design although its use for serviceability limit state assessment and even for ultimate limit state (ULS) design has gone on for many years. The draft document will provide some guidance on the use of numerical modelling for ULS design of geotechnical structures. Clause 8.2 in Part 1 of this new draft code covers the recommended procedure for the application of numerical modelling in ULS design of geotechnical structures. This paper describes the evolution of the use of numerical modelling in geotechnical design and the recommended procedure included in this new code. A comparison is also made on the consequences of this procedure on the existing design approaches currently implemented in the existing code.

RÉSUMÉ: La prochaine génération d'Eurocodes est en cours d'élaboration et devrait être déployée durant l'année 2027. Le code actuel ne couvre pas l'utilisation de la modélisation numérique dans la conception géotechnique, bien que son utilisation pour l'évaluation de l'état limite de service et même pour la conception de l'état limite ultime (ELU) se poursuivent depuis de nombreuses années. Le document en cours d'élaboration fournira des indications sur l'utilisation de la modélisation numérique pour la conception ULS des structures géotechniques. L'article 8.2 de la partie 1 de cette nouvelle version du code couvre la procédure recommandée pour l'application de la modélisation numérique dans la conception des structures géotechniques ULS. Cet article décrit l'évolution de l'utilisation de la modélisation numérique dans la conception géotechnique et la procédure recommandée pour être incluse dans ce nouveau code. Une comparaison est également faite sur les conséquences de cette procédure sur les approches de conception existantes actuellement mises en œuvre dans le courant code.

Keywords: Eurocode; numerical modelling; ultimate limit state.

1 INTRODUCTION

The Structural Eurocodes are the current European design standards for buildings and construction works covering a wide range of structural materials and fields of civil engineering. Eurocode 7 (EC7), which is the standard for geotechnical engineering design in Europe, introduces the concepts of limit state design and partial safety factors distinguishing between Serviceability Limit State (SLS) and Ultimate Limit State (ULS).

The development of advanced geotechnical software, together with the introduction of cutting edge and less expensive hardware has resulted in 2D and 3D advanced numerical methods such as Finite Element Method (FEM) being routinely used in the Geotechnical Engineering field. Moreover, the introduction of advanced constitutive models that allows for better simulation of the soil behaviour has resulted in the increasing use of advanced numerical methods in geotechnical engineering to predict deformations and verify against SLS.

Eurocode 7 allows the use of numerical methods for verification against ULS but gives no guidance to the designer in a number of important and practical issues regarding the implementation of the guidance. These issues have triggered an important debate in the geotechnical engineering community over the feasibility of routine use of FEM for ULS checks.

Various concerns were raised in the application of numerical methods in ULS geotechnical design in accordance with EC7 in late 1990s early 2000s, more specifically with the use of finite element modelling.

These include effects of initial stresses, effects of stress history, choice of soil model, when the partial factors are applied and significance of the failure of structural member (Bauduin *et al*. (2000, 2003), Katsigiannis (2017), Simpson and Yazdchi (2003), Yeow (2014, 2022)).

Despite these early concerns, application of numerical methods has been adopted widely by practitioners even with a lack of guidance in its use for ULS design under the existing EC7. The most commonly adopted approach is to undertake the analysis with characteristic ground parameters and subsequently apply partial factor to the structural forces or the *effects of actions*. As the UK adopt Design Approach 1 with the need to undertake two combinations of design assessments, Simpson and Yazdchi (2003), Katsigiannis et al. (2014, 2015) and Yeow (2014, 2015, 2018, 2019 and 2022) used the approach by taking modelling excursion to allow for ULS design with design material properties which allowed the stress state in the ground to be maintained at its characteristic value prior to the introduction of factored or design soil properties.

This paper outlines the approach currently drafted into the next generation (NG) of EC7 for the application of numerical methods in geotechnical design.

2 NUMERICAL MODELLING IN THE NECT GENERATION OF EC 7

The next generation of the Structural Eurocodes are currently being drafted and EC7 is near the stage of final votes in 2024 before finalisation of the documents likely during first half of 2025 for the preparation of nation annexes by individual countries by end of 2025. This paper focuses only on the numerical modelling aspects of the updated EC7 guidance and does not provide any details on other changes introduced to the revised standard.

In the revised standard, numerical models are defined as *calculation models involving numerical approximation to obtain solutions.* These include, but not limited to, finite element, finite difference boundary element, discrete-element and subgrade reaction methods. These models could be used for the verification of limit states including the failure modes and ground movements.

It is worth noting that when using numerical method, verification of specific mode of failure, e.g., sliding, overturning, bearing capacity etc, may not be possible as such approach would produce the most critical deformation and failure mode depending on the geotechnical structure being considered and the ground strength and stiffness of the model.

3 PROCEDURE OF NUMERICAL MODELLING IN THE NEXT GENERATION OF EC7

3.1 Procedure for numerical modelling

The guidance on the procedure for numerical modelling is given in Clause 8.2 of Part 1 of the revised standard. At the time of writing this paper, this clause stipulates that ULS verification of geotechnical structures should be based on the less favourable outcomes given by the:

- input factoring (of material properties):
  - factors on actions γ_F from Verification Case 3 (VC3) and;
  - factors on material γ_M from Set M2;
- output factoring (of the effects of actions):
  - factors on effects-of-actions γ_E from Verification Case 4 (VC4) and;
  - factors on material γ_M from Set M1.

The input factoring is also known as the Material Factor Approach (MFA) in the current code which is still in use in the revised code while the output factoring is the Effects Factor Approach (EFA) in the current code but is no longer used as a term in the next generation of EC7. Clause 8.2 also refers to Table 8.1 which details the above ULS verification procedure. The VC3 and VC4 can be found in Table A1.8 of the revised EN 1990 Eurocode and depending on the type of geotechnical structure, one or both of these verification cases will be recommended in the new code. These two tables are reproduced in Appendix A of this paper for information. It is worth noting that the details in these two tables are defined as National Determined Parameters (NDPs) under the new standard, hence each individual country should be able to make appropriate selection or changes in their National Annex accordingly.

3.2 Ultimate limit state modelling procedure

As discussed above, the next generation of EC7 requires that both input and output factoring combinations are checked when undertake ULS verifications using numerical methods in order to determine the least favourable outcomes to be used for design.

The most straight forward combination is the output factoring approach under VC4 whereby representative values of soil properties (M1) are used to analyse the geotechnical problem and the partial

factors are then applied to the output of the model or in this case the effects of actions.

The input factoring procedure under VC3 has two possible methods of applying the material factor M2. These two methods are discussed and compared in depth by Katsigiannis (2017).

In the first method, characteristic values of the parameters are used in the calculations, and at critical discreet stages, the user applies the material factor M2 for the ULS verifications. Such method is also known as the "modelling excursion" approach whereby partial factor M2 on soil properties is applied as and when necessary to invoke the design under VC3.

In the second (i.e. alternative) method, users apply the partial safety factors to the material parameters right from the start of the analysis and the calculations are carried out using the design values of the parameters.

Despite the apparent simplicity of the second method, the recommended method based on the updated standard is to only apply the material factor M2 to the soil properties at critical stages during the construction sequence. The main reason that this method is recommended, is mainly because users can verify against both SLS and ULS by carrying out their design using one numerical analysis model.

Figure 1 shows an example of the ULS design procedures for a retaining wall with multi-stage construction sequence.

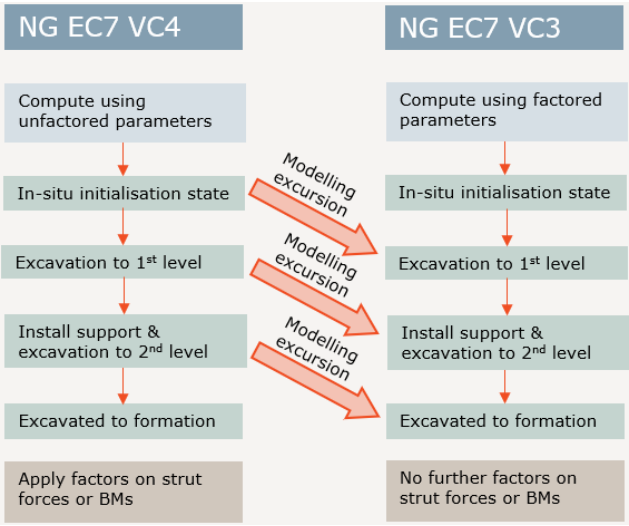

Figure 1. Procedures to undertake ULS verification as per next generation of EC7.

4 COMPARISON WITH CURRENT EC7 APPROACH

For the comparison with the design approaches under the existing EC7 when undertaking design verification using numerical methods, the partial factors published in Section A.3 of Annex A of BS EN1997-1 (2014) are used. No consideration is given of any variations implemented under the National Annex of individual countries.

4.1 Design Approach 1 (DA1)

In accordance with the DA1, ULS design verification of the design under the less favourable of the two combinations of partial factors in the following forms:

- Combination 1 (C1): A1 "+" M1 "+" R1
- Combination 2 (C2): A2 "+" M2 "+" R1

Under DA1 C1, the partial factors are applied to actions or the effects of actions with material factor set to unity, i.e., M1. This is the same with the output factoring (VC4 "+" M1) approach of the revised standard. For DA1 C2, the partial factors are applied to the material properties, i.e., M2, and this is the same with the input factoring (VC3 "+" M2) approach of the revised standard.

Except for pile design in the current standard, the resistance factor R1 is equal to 1.0 for the design of most geotechnical structures. Therefore, the geotechnical design undertaken using DA1 is consistent with the proposed procedures outlined in the revised next generation of EC7 and designers in countries which have adopted DA1 such as the UK, will see little impact on their current established practice when using numerical methods.

4.2 Design Approach 2 (DA2)

DA2 only requires one check based on the following combination:

- Combination: A1 "+" M1 "+" R2

This is similar to the output factoring (VC4 "+" M1) approach of the revised standard with the exception of the application of resistance factor R2 of greater than 1.0. The value of R2 ranges from 1.1 for sliding resistance and earth resistance for slope stability assessment to 1.4 for bearing capacity and earth resistance for retaining structure. However, when undertaking design assessment using numerical analysis, the introduction of a resistance factor to the model is not straight forward as these parameters are not input in the numerical calculations. Therefore, those who used numerical modelling resolve to applying a partial factor on the effects of actions similar to DA1 C1.

Under DA2 there is no verification by applying partial factor to the material properties, i.e., M2. Under conditions whereby input factoring (VC3 "+" M2) approach governs the design, such approach would be unsafe.

Some authors suggest the DA2* approach as an alternative to DA2 for numerical methods (Frank et al.,

2004). For retaining wall design, for example, DA2*, requires that the characteristic active earth pressures is used in the analysis while any variable surcharge is factored by $\gamma_G/\gamma_Q = 1.5/1.35 = 1.1$. The passive earth resistances need to be factored by the resistance factor γ_R and the load factor γ_G. The design values of the structural forces are obtained at the end of the analysis, after factoring the outputs by the load factor, γ_G. While the use of DA2* seems to be straightforward for simple methods of analysis such as Limit Equilibrium, factoring the passive earth resistance is not possible in advanced numerical analysis.

Based on the updated EC7 guidance, designers in countries which have adopted DA2 will have to carry out both input and output factoring approaches when using numerical methods, with the combination that gives the most adverse results being critical and governing the design.

4.3 Design Approach 3 (DA3)

DA3 only requires one check based on following combination:

- Combination: (A1* "or" A2†) "+" M2 "+" R3

* on structural actions

† on geotechnical actions

For DA3, the R3 resistance factor is equal to 1.0 hence for geotechnical actions the procedure is similar to input factoring (VC3 "+" M2) approach of the revised standard. For structural actions, however, applying both partial factors on both the actions (A1) and material properties (M2) would be more conservative than input factoring (VC3 "+" M2) approach. While currently under DA3 there is no need for verification with output factoring approach, according to the updated EC7 guidance, designers in countries which have adopted DA3 will have to carry out both input and output factoring approaches when using numerical methods.

5 CONCLUSIONS

The next generation of Eurocodes are currently being drafted to improve the guidance for designers both in the management of safety and risks in design and subsequent execution of construction works. The incorporation of more detailed and consistent guidance on numerical modelling in the revised EC7 will result in numerical methods to be more routinely used for ULS verifications while providing designers who have access to advanced design tools the ability to produce more economical and safer design. However, the use of such tools requires experience, fundamental understanding of the principles of soil mechanics and sound engineering judgement.

The revised EC7 is addressing one of the biggest challenges of the current standard by enabling further harmonization and ease-of-use. This is being achieved with the elimination of the different Design Approaches for numerical methods, effectively recommending all countries to follow the most critical case of the dual factoring approach. This approach seems to provide sufficient levels of safety, rigor and economy and reasonably consistent levels of reliability can be achieved for a wide range of construction problems This harmonization of practice among all countries adopting the Eurocodes definitely represents a major advance over the current version of the standard.

ACKNOWLEDGEMENTS

The authors would like to thank their colleagues from the International Society of Soil Mechanics and Geotechnical Engineering (ISSMGE) European Regional Technical Committee 10 (ERTC10) and the CEN/TC250/Subcommittee 7 for the valuable discussions on the topic.

REFERENCES

Bauduin, C, De Vos, M., Simpson, B. (2000) Some Considerations on the Use of Finite Element Methods in Ultimate Limit State Design, LSD 2000: International Workshop on Limit State Design in Geotechnical Engineering, Melbourne, Australia.

Bauduin, C., De Vos, M., Frank, R. (2003) ULS and SLS design of embedded walls according to Eurocode 7, Proc XIII ECSMGE, Prague, Vol 2 pp 41-46.

BS EN 1997-1:2004+A1:2013 (2014). Eurocode 7 – Geotechnical design, Part 1 – general rules, British Standards Institution, London.

Frank, R., Bauduin, C., Kavvadas, M., Krebs Ovesen, N., Orr, T., and Schuppener, B. (2004). Designers' guide to EN 1997-1: Eurocode 7: Geotechnical design – General rules. London: Thomas Telford.

Katsigiannis, G, (2017) Modern Geotechnical Codes of Practice and New Design Challenges Using Numerical Methods for Supported Excavations. Engineering Doctorate Thesis. Department of Civil, Environmental and Geomatic Engineering, University College London.

Katsigiannis, G, Ferreira, P and Fuentes, R (2014) Ultimate limit state design of retaining walls with numerical methods. Proceedings of the 8th European Conference on Numerical Methods in Geotechnical Engineering, NUMGE 2014, Delft, The Netherlands.

Katsigiannis, G, Schweiger, H.F., Simpson, B., Ferreira, P. and Fuentes, R. (2015). Eurocode 7 and new design challenges using numerical methods with different soil models. XVI European Conference on Soil Mechanics and Geotechnical Engineering, 13-17 Sep 2015, Edinburgh. ICE Publishing, pp. 4277-4282.

Simpson, B and Yazdchi, M (2003) Use of finite element methods in ultimate limit state design LSD2003: International workshop on Limit State Design in Geo Engineering practice, Cambridge, Massachusetts.

Yeow, H C. (2014) Ultimate limit state design using advanced BRICK model in finite element method, Proceedings of Geotechnical Engineering, ICE, UK.

Yeow, H C (2015) Ultimate limit state design of retaining wall using finite element method and advanced BRICK model, Proceedings of the XVI ECSMGE Geotechnical Engineering for Infrastructure and Development, UK.

Yeow, H C. (2018) Ultimate limit state design of retaining wall using finite element method and advanced soil models, Proceedings of the 9th European Conference on Numerical Methods in Geotechnical Engineering, NUMGE 2018, Porto, Portugal.

Yeow, H C (2019) "Ultimate limit state design using FEM and advanced soil model – a case history of a 30m deep excavation in London", Geo-Congress 2019, Philadelphia, Pennsylvania, USA.

Yeow, H C (2022), "Case histories of deep excavation and limit states design in accordance with Eurocode 7 using advanced soil model", ICSMGE 2021, Sydney, Australia.

Appendix A: Table A.1.8 (NG EN 1990 Eurocode) and Table 8.1 (NG EC7 Part 1)

Table A.1.8 (NDP). Partial factors on actions and effects for fundamental (persistent and transient) design situation.

Action or effect				Partial factors γ_F and γ_E for Verification Cases 1 to 4				
Type	Group	Symbol	Resulting effect	Structural resistance	Static equilibrium and uplift		Geotechnical design	
Verification case				VC1[a]	VC2(a)[b]	VC2(b)[b]	VC3[c]	VC4[d]
Formula				(8.4)	(8.4)	(8.4)	(8.4)	(8.5)
Permanent action (G_k)	All [f]	γ_G	unfavourable /destabilizing	$1{,}35k_F$	$1{,}35k_{Fdfdfdf}$	1,0	1,0	G_k is not factored
	Water	γ_{GW}		$1{,}2k_F$	$1{,}2k_F$	1,0	1,0	
	All [f]	$\gamma_{G,\,stb}$	stabilising [g]	not used	1,15 [e]	1,0		
	Water [l]	$\gamma_{GW,\,stb}$			1,0 [e]	1,0		
	All	$\gamma_{G,\,fav}$	favourable [h]	1,0	1,0	1,0	1,0	
Prestressing (P_k)		γ_P[k]		-	-	-	-	-
Variable ac Action (Q_k)	All [f]	γ_Q	unfavourable	$1{,}5k_F$	$1{,}5k_F$	$1{,}5k_F$	1.3	γ_Q/γ_G
	Water [l]	γ_{QW}		$1{,}35k_F$	$1{,}35k_F$	$1{,}35k_F$	1,15	1,0
	All	$\gamma_{Q,\,fav}$	favourable	0				
Effects of actions (E)		γ_E	unfavourable	effects are not factored				$1{,}35k_F$
		$\gamma_{E,\,fav}$	favourable					1.0
Notes *a to l* not included here								

Table 8.1 (NDP). Procedure for verification of ultimate limit state with numerical models.

			Factoring approach – see 8.2 (1)		
			EFA VC4 + M1	MFA VC3 + M2 (Recommended)	MFA VC3 + M2 (Alternative)
			See 8.2(2), (7) and (8)	See 8.2(2), (3) (4) and (6)	See 8.2(2), (5) and (6)
Construction Stage 1 (CS1)			Step 1 Representative Step	Step 1 Representative Step	Step 1 ---
	Input	Piezometric level or groundwater pressure	Representative Values		Not applicable Go directly to Step 2
		Ground properties	Representative Values		
		Structural element properties	Representative Values		
		External actions	Representative Values		
	Output	Movements	[1]		
		Structural forces	[1]		
			Step 2 ULS Verification Step	Step 2 ULS Verification Step	Step 2 ULS Verification Step
	Input	Piezometric level or groundwater pressure	Design level	Design level	Design level
		Ground properties	Design values by M1 combination	Partial factors M2	Design values by M2 combination
		Structural element properties	Representative values	Representative values	Representative values
		External actions	Design values by VC4 combination	Design values by VC3 combination	Design values by VC3 combination
	Output	Verification of ground failure	See 8.2(7) and 8.2(8)	ULS verified if equilibrium is attained in the ground with no failure of the structure	ULS verified if equilibrium is attained in the ground with no failure of the structure
		Verification of structural failure	Design value (E_d) obtained by applying γ_E to calculate results See 8.2(7) and (8)	Design value (E_d) obtained directly from calculate results See 8.2(6)	Design value (E_d) obtained directly from calculate results
CS2	Continue in the same way through any subsequent stage (CS2, CS3, etc.)				

[1] These output values can be used for SLS verifications

Proceedings of the XVIII ECSMGE 2024
GEOTECHNICAL ENGINEERING CHALLENGES
TO MEET CURRENT AND EMERGING NEEDS OF SOCIETY
© 2024 the Authors
ISBN 978-1-032-54816-6
DOI 10.1201/9781003431749-384
Open Access: www.taylorfrancis.com, CC BY-NC-ND 4.0 license

ECSMGE 24
XVIII EUROPEAN CONFERENCE ON SOIL MECHANICS AND GEOTECHNICAL ENGINEERING

Analysis of pore characteristics of natural structured clay applying the combination of SEM and MIP

Analyse des caractéristiques des pores de l'argile structurée naturelle en appliquant la combinaison de la SEM et de la MIP

X.W. Zhang
State Key Laboratory of Geomechanics and Geotechnical Engineering, Institute of Rock and Soil Mechanics, Chinese Academy of Sciences, Wuhan, China

G. Wang*
State Key Laboratory of Geomechanics and Geotechnical Engineering, Institute of Rock and Soil Mechanics, Chinese Academy of Sciences, Wuhan, China; University of Chinese Academy of Sciences, Beijing, China

X.Y. Liu
School of Civil and Hydraulic Engineering, Huazhong University of Science and Technology, Wuhan, China

**wanggang191@mails.ucas.edu.cn*

ABSTRACT: Pore characteristics have considerable effects on the physical properties and mechanical behavior of structured marine clay. However, the distribution characteristics and morphology of pores cannot be quantified by a single method, and a combination of methods with different measuring ranges is required. This paper focuses on a typical structured marine clay retrieved from Zhanjiang in China (referred to as ZJ clay). The methods of scanning electron microscopy (SEM) and mercury intrusion porosimetry (MIP) were used in combination to (i) analyze the microscopic characteristics of the pores in natural soil and (ii) establish the relationships between the microstructural characteristics and macro-mechanical behavior of the soil. The test results show that ZJ clay is characterized by a randomly oriented open-flocculated structure with cementation bonding, and the particles within ZJ clay are interconnected by edge-to-face or edge-to-edge contacts with high structural strength and stability. The results also show that the combination of SEM and MIP facilitates both qualitative and quantitative analysis of the complete pore size distribution characteristics of marine clay. The present study improves the understanding of the pore characteristics of marine clay from a microscopic perspective.

RÉSUMÉ: Les caractéristiques des pores ont des effets considérables sur les propriétés physiques et le comportement mécanique des argiles marines structurées. Cependant, les caractéristiques de distribution et la morphologie des pores ne peuvent pas être quantifiées par une seule méthode, et une combinaison de méthodes avec des gammes de mesure différentes est nécessaire. Cet article se concentre sur une argile marine structurée typique prélevée à Zhanjiang en Chine (appelée argile ZJ). Les méthodes de microscopie électronique à balayage (SEM) et de porosimétrie à intrusion de mercure (MIP) ont été utilisées en combinaison pour (i) analyser les caractéristiques microscopiques des pores dans le sol naturel et (ii) établir les relations entre les caractéristiques microstructurales et le comportement macro-mécanique du sol. Les résultats des essais montrent que l'argile ZJ se caractérise par une structure ouverte-floconneuse orientée aléatoirement avec une liaison de cimentation, et que les particules au sein de l'argile ZJ sont interconnectées par des contacts bord-à-face ou bord-à-bord avec une résistance et une stabilité structurelles élevées. Les résultats montrent également que la combinaison de la SEM et de la MIP facilite l'analyse qualitative et quantitative des caractéristiques complètes de distribution de la taille des pores de l'argile marine. La présente étude améliore la compréhension des caractéristiques des pores de l'argile marine d'un point de vue microscopique.

Keywords: Pore; clay; mercury intrusion porosimetry; scanning electron microscope; microstructure.

1 INTRODUCTION

Defined as the combination of soil fabric and interparticle bonding (Mitchell and Soga 2005), soil structure is acknowledged to be responsible for the mechanical responses of natural soil being distinct from those of remolded soil (Burland 1990). Among the most important indicators for the structure of soil are its pore characteristics, which were found to influence soil's geotechnical behavior, including its hydraulic conductivity, soil–water characteristics, and shear strength (Zhang et al. 2017). Specifically, natural soil derived from sedimentation or post-sedimentation is highly structured and has a different pore structure from that of remolded soil (Cotecchia and Chandler 2000), which lead to their distinct mechanical behaviors. Therefore, the different mechanical behavior of structured natural soil from that of the

remolded one is attributed mainly to their initial pore characteristics as well as the rearrangement and compression of pores during soil deformation. However, a valid method for characterizing and quantifying the pore structure (in particular, the intra- and inter-aggregate pores) of quaternary marine clay remains to be explored. In general, intra- and inter-aggregate pores are related to only the porosity of soil and have negligible influence on its mechanical behavior. However, although single intra-aggregate pores are relatively small, their total volume is relatively large; once the interparticle cementation bonding is destroyed, these pores released from the aggregation inevitably have significant influences on the soil's geotechnical behaviors, and so further studies are vitally important.

Various microscopy techniques have been adopted to investigate the pore characteristics of natural clay from a microscopic perspective including (i) Imaging techniques, e.g., scanning electron microscopy (SEM); (ii) Fluid-injection techniques, e.g., mercury intrusion porosimetry (MIP) (Zhang et al. 2017; Zhang et al. 2020). These techniques are applicable for different pore-size measurement ranges from microscopic to macroscopic, therefore combining them is an ideal way to fully realize their advantages for multiscale pore analysis, to sufficiently investigate the intra-aggregate pores within marine clay.

In this study, we combined SEM and MIP to investigate the pore evolution and the corresponding influencing factors of a typical marine structured clay, with the advantages and disadvantages of each method being quantified. This paper is organized as follows. First, the sampling details and testing methods are introduced concisely, then the basic soil characterizations of the studied clay are detailed. Next, the results of the different methods for testing the pore characteristics of the clay are presented; the pore characterization is evaluated quantitatively considering the measuring range of each method. Peculiar pores within the studied soil are also discussed, with the applicability of the combined analysis for characterizing the pores in marine clay being verified. The study improves our understanding of the structural characteristics of natural sedimentary soil and its corresponding geotechnical behavior.

2 MATERIALS AND METHODS

2.1 Soil materials

The undisturbed ZJ clay samples were retrieved at a foundation pit in Zhanjiang, China, by using thin-walled tube samplers from two depths at h_1 = 14.0–16.0 m and h_2 = 28.0–32.0 m, respectively. Some important index properties of the ZJ clay were summarized in Table 1. From this table, it can be found that ZJ clay comprises mainly clay components (over 70%), consistent with the high void ratio, high Atterberg limits, and low permeability of the soil. Besides, the specific surface area is also relatively high. Also, the studied clays from different depths have almost identical mineral compositions, including high content of illite, kaolinite, and quartz. Note that a content of 6% of iron-bearing minerals (pyrite and hematite) was also detected, which was proved to enhance the soil strength and stiffness by forming cementation in the soil structure (Zhang et al. 2017).

Both the natural and remolded samples were prepared (Zhang et al., 2020), with all samples being controlled with identical moisture content and dry density. Samples for strength tests were prepared as 50 mm in diameter and 100 mm in height, while those prepared for compression tests were prepared as 61.8 mm in diameter and 20 mm in height. Samples for SEM and MIP tests were dehydrated using vacuum freeze-drying to preserve the initial soil structure effectively (Mitchell and Soga 2005).

Table 1. Index properties of ZJ clay.

Index	Value	
	ZJ clay (h_1)	**ZJ clay (h_2)**
Void ratio e	1.43	1.30
Specific surface area (m^2/g)	138	125
Permeability coefficient K (10^{-8} cm/s)	7.33	2.65
Liquid limit w_L (%)	64.26	66.83
Plastic limit w_p (%)	32.25	29.57
Plasticity index I_p (%)	32.01	37.26
Clay fraction (%)	70.9	73.1

2.2 Test details

The compressibility and strength properties of the soil samples were measured through a standard oedometric compression test using incremental loading and unconfined compression strength (UCS) test following procedures from ASTM standards. Formal tests are performed on both natural and remolded samples after the saturation, which is realized by flooding the samples with distilled water under vacuum for 12 h.

Microstructural observations were performed on natural and remolded ZJ clay through SEM and MIP tests. An FEI-Quanta-250 SEM under multilevel magnifications (from × 800 to × 20000) was used to systematically investigate microstructural features from the primary morphologies to the contact modes among the soil particles. MIP tests were performed using a Quantachrome Pore Master 33 mercury

intrusion porosimeter. The results of MIP tests are presented as the cumulative pore volumes ($CV = \sum_i \Delta V_i$) and log-incremental pore volumes ($IV = -\Delta V_i/\Delta \log d_i$), where V_i is the measured total intruded pore volume corresponding to the diameter d_i. For convenience, the soil pores are classified based on the diameter d as macropores (d > 10 μm), mesopores (1 μm < d < 10 μm), micropores (0.1 μm < d < 1 μm), or nanopores (d < 0.1 μm) according to Brewer (1964).

3 COMPRESSION AND STRENGTH PROPERTIES

Fig. 1(a) shows the I_v–log σ'_v curve of ZJ clay (Burland 1990), with the intrinsic compression line (ICL) and the sedimentation compression line (SCL) proposed by Burland (1990) also being included. The yielding points of the compression curves of natural soils are located at the right side of the SCL, while the compression curves of the remolded clay are shifted to the left (approaching ICL) with no observable turning point, indicating the significant structural characteristics of natural clay. The gradual process of destruction of cementation bonding was reflected by that (i) after yielding, the I_v–log σ'_v curve approaches the ICL and (ii) when σ'_v = 3200 kPa, the compression curves tend to converge to the ICL.

The shear behaviors of ZJ clay obtained from the UC tests are shown in Fig. 1(b), from which the strain softening of the natural soil is evident with well-defined peaks, due to degraded cementation (Zhang et al. 2017). Natural ZJ clay has poor physical properties (w > 50% and e > 1.4) but relatively satisfactory mechanical properties (q_u = 175–190 kPa). However, the high strength of ZJ clay is decreased significantly by cementation degradation and fabric rearrangement, therefore it can be classified as a structured clay with high sensitivity.

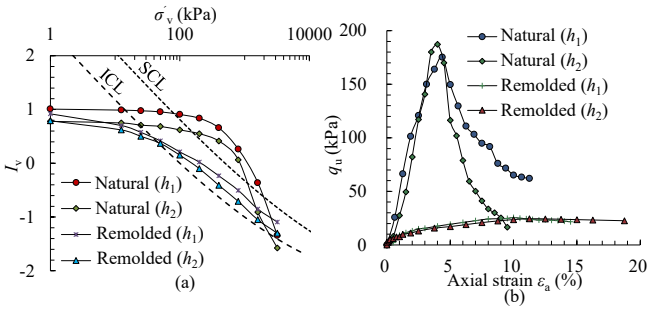

Figure 1. Results of (a) Compression tests and (b) strength tests of natural and remolded ZJ clay.

4 PORE CHARACTERISTICS OBTAINED USING SEM

Natural soil had an open-flocculated structure with interconnected soil aggregates [Figs. 2(a) and 2(b)]. Nonuniformly distributed pores in natural clay were not obviously connected, consistent with its low permeability, despite the high pore volume. The positively charged free iron oxides within natural clays distributed at the contacts between soil particles bind to the negatively charged soil particles to form larger soil aggregates with enhanced stability (Zhang et al., 2017), responsible for the high porosity and sensitivity of natural clay. The remolded soils [Figs. 2(e) and 2(f)] were mainly aggregates comprising irregular flaky clay plates with a more-dispersed and finer pattern. Macropores could be frequently observed in remolded soils due to remolding, which seldom appeared in the natural clay. Although the remolded soils had similar physical indices to the natural soil, their mechanical properties differed significantly from those of the natural soil because of the cementation degradation and particle rearrangement.

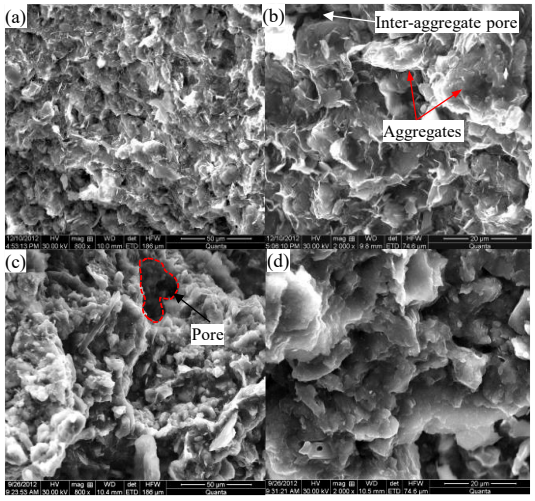

Figure 2. SEM images of soil samples. (a)−(b): natural soils; (c)−(d): remolded soils.

5 PORE CHARACTERISTICS OBTAINED USING MIP

For all natural and remolded samples, the intrusion–extrusion cycles show obvious hysteresis between the branches, indicating some intruded mercury remained in the pore system (Fig. 3). This hysteresis is attributed to the widely distributed ink-bottle type pores in ZJ clay. The nonuniformly distributed pores in the flocculated structures of the clay (Fig. 2) constitute the narrower throats and wider inner spaces of ink-bottle pores. Intrusion into the entire inner body occurs when the mercury is forced into the narrower pore neck;

during the extrusion, mercury withdraws in the opposite sequence, resulting in isolated mercury droplets in the inner pores. For remolded clay, less mercury was entrapped in the ink-bottle pores than that in natural clay, which reflects that (i) the ink-bottle effect is attenuated gradually by remolding and (ii) the occurrence of hysteresis is closely associated with the structural characteristics of the pores.

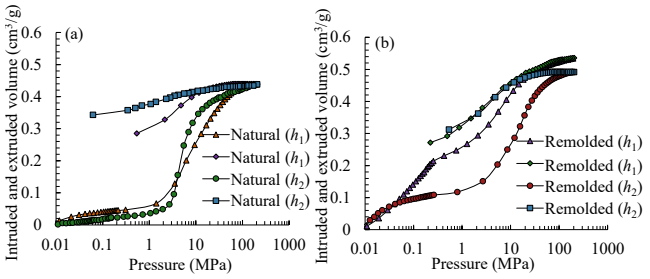

Figure 3. Mercury intrusion–extrusion curves of MIP tests on (a) natural clay and (b) remolded clay.

Fig. 4(a) shows that the cumulative pore volume (*CV*) distributions of the shallower and deeper ZJ clay were essentially identical. As shown in Fig. 4(b), the micropores within the ZJ clay dominated the total pore volume, followed by the nanopores, which is strongly associated with the single dominant peak of the pore size distribution (PSD) curve for the natural clay. Unlike the natural clay, a bimodal distribution of pore sizes occurred after remolding, with one peak at 0.1–1 μm and another at 1–10 μm. In particular, the total volume of micropores and nanopores decreased significantly, while the total volume of macropores and mesopores increased. The difference between the *CV* curves for the natural and remolded samples perhaps reflects the existence of tinier ($d < 0.01$ μm) intra-aggregate pores within the natural ZJ clay, which is consistent with the results from SEM analysis.

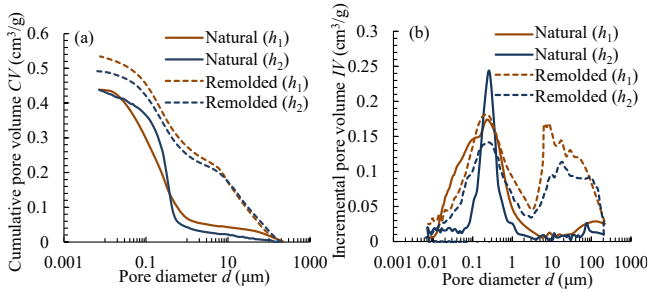

Figure 4. MIP test results of the studied soil: (a) cumulative pore volume; (b) pore size distribution.

Actually, these two adopted methods are characterized by different advantages and applicability for pore characteristics investigation. SEM is a direct observation of geometrical morphologies and sizes of soil pores and allowed qualitative analysis of the pore characteristics. On the contrary, MIP is for the quantitative evaluation of pore volume and the pore distribution. Therefore, combining SEM and MIP with distinct measuring ranges for obtaining the full-scale pore characteristics of marine clays with complete pore sizes ranging from nanopores to macropores.

6 CONCLUSIONS

The main conclusions are as follows:

(1) ZJ clay is a strongly cemented structured clay, and the strength of which is reduced significantly by cementation degradation and fabric rearrangement.

(2) By combining SEM and MIP techniques, the complete pore-size distribution of ZJ clay ranging from micropores to macropores was described well.

(3) ZJ clay is characterized by an open flocculated structure with interconnected domains; free iron oxides related to the cementation bonding bind to soil particles to form larger soil aggregates. These structural characteristics result in the high strength and sensitivity of ZJ clay.

(4) MIP test results verified the existence of ink-bottle pores in ZJ clay. After the degradation of interparticle cementation bonding, such pores released from the aggregations have significant influences on the mechanical properties of the soil.

ACKNOWLEDGEMENTS

The authors are grateful for the financial support provided by the National Natural Science Foundation of China (Nos. 42177148).

REFERENCES

Brewer, R. (1964). Fabric and Mineral Analysis of Soils. *Soil Science*, 100(1): 73.

Burland, J. B. (1990). On the compressibility and shear strength of natural clays. *Géotechnique*, 40(3): 329–378. https://doi.org/10.1680/geot.1990.40.3.329.

Cotecchia, F. and Chandler, R. J. (2000). A general framework for the mechanical behaviour of clays. *Géotechnique*, 50(4): 431–447. https://doi.org/10.1680/geot.2000.50.4.431.

Mitchell, J. K. and Soga, K. (2005). *Fundamentals of Soil Behavior*, 3rd ed. John Wiley & Sons.

Zhang, X. W., Kong, L. W., Yin, S., and Chen, C. (2017). Engineering geology of basaltic residual soil in Leiqiong, southern China. *Eng. Geol.*, 220: 196–207. http://dx.doi.org/10.1016/j.enggeo.2017.02.002.

Zhang, X. W., Liu, X. Y., Chen, C., Kong, L. W. and Wang, G. (2020). Engineering geology of residual soil derived from mudstone in Zimbabwe. *Eng. Geol.*, 277: 105785. https://doi.org/10.1016/j.enggeo.2020.105.

Proceedings of the XVIII ECSMGE 2024
GEOTECHNICAL ENGINEERING CHALLENGES
TO MEET CURRENT AND EMERGING NEEDS OF SOCIETY
© 2024 the Authors
ISBN 978-1-032-54816-6
DOI 10.1201/9781003431749-385
Open Access: www.taylorfrancis.com, CC BY-NC-ND 4.0 license

ECSMGE 24
XVIII EUROPEAN CONFERENCE ON SOIL MECHANICS AND GEOTECHNICAL ENGINEERING

Case study on interpretation of cone penetration tests in sandy soil layers

Étude de cas sur l'interprétation des essais de pénétration au cône dans les couches de sol sableux

Y. Zhang
Shandong Electric Power Engineering Consulting Institute Co. LTD, Jinan, China

X. Ma
College of Civil Engineering, Tongji University, Shanghai, China

C. Ji, X. Zhang
Shandong Electric Power Engineering Consulting Institute Co. LTD, Jinan, China

W. Li*, M Yang
College of Civil Engineering, Tongji University, Shanghai, China

**WeichaoLi@tongji.edu.cn*

ABSTRACT: Based on cone penetration tests (CPT) data, a number of soil's physical and mechanical parameters can be interpretated, like soil unit weight, etc. Even though various studies have been conducted and methods are proposed, uncertainties still exist and the applicability of each method needs be further clarified. A case study on the interpretation of CPT results is performed which based on the measured data from an offshore site close to Shandong Province, China. This paper focus on sandy soil layers and presents an assessment of CPT data interpretation methods for the derivation of sandy soil's unit weight, effective friction angle and relative density. It shows that Mayne's method proposed in 2016 provides better predictions of soil unit weight; Kulhawy's 1990 method performs well in predicting sandy soil's effective friction angle under low-stress conditions, while Robertson's 1983 method is more suitable for high-stress conditions; Schmertmann's model with Baldi's recommendation is better in predicting soil relative density.

RÉSUMÉ: Sur la base des données des essais de pénétration au cône (CPT), plusieurs paramètres physiques et mécaniques du sol peuvent être interprétés, tels que la masse volumique du sol, etc. Bien que diverses études aient été menées et des méthodes proposées, des incertitudes persistent et l'applicabilité de chaque méthode doit être clarifiée davantage. Une étude de cas sur l'interprétation des résultats du CPT est réalisée sur la base des données mesurées sur un site en mer près de la province du Shandong, en Chine. Cet article se concentre sur les couches de sol sableux et présente une évaluation des méthodes d'interprétation des données du CPT pour la détermination de la masse volumique du sol sableux, de l'angle de frottement effectif et de la densité relative. Les conclusions indiquent que la méthode R3 permet de mieux prédire la masse volumique du sol; FA2 performe bien dans la prédiction de l'angle de frottement effectif du sol dans des conditions de faible contrainte, tandis que FA1 est plus adaptée aux conditions de forte contrainte; DR2 montre une bonne capacité à prédire la densité relative du sol.

Keywords: Cone penetration test (CPT); unit weight; effective friction angle; relative density, sandy soil.

1 INTRODUCTION

Cone penetration tests (CPT) are widely used to characterize site conditions for its handiness, multifunctionality and automatization (Lunne *et al.* 1997), especially for offshore sites. During these tests, cone resistance, sleeve friction and pore water pressure (ASTM D5778) are commonly recorded during the probe's penetration (Mayne 2007). Based on these recorded data, a number of soil's physical and mechanical parameters can be interpretated, like soil behaviour type, soil unit weight, etc. Even though various studies have been conducted and methods are proposed (Robertson 2009), uncertainties still exist and the applicability of each method needs be further clarified. A case study on the interpretation of CPT results is performed which based on the measured data from an offshore site close to Shandong Province, China. In this site, series of in-situ cone penetration tests were conducted and soil samples were retrieved at various depth. From which, physical and mechanical

parameters were obtained from laboratory tests on these retrieved soil samples, as well as from the interpretation of CPT results. This paper focus on sandy soil layers and presents an assessment of CPT data interpretation methods for the derivation of sandy soil's unit weight, effective friction angle and relative density. Based on the comparison between values obtained by laboratory tests and those derived from CPT data according to various methods, the reliability and applicability of each method are clarified and the most suitable method for each soil parameter is recommended.

2 CURRENT METHODS

Based series of test data, several studies developed methods to derive soil's unit weight(γ), effective friction angle(ϕ'), as well as the relative density(D_r), which are commonly used. These methods are sumarized in Table 1.

Table 1. Summary of current models.

Parameter	Model	Tests	Model equation	Reference
Unit weight γ	R1	-	$\gamma/\gamma_w=0.27\log(R_f)+0.36\log\left(q_c/\sigma_{atm}\right)+1.236$ Where: R_f= friction ratio = $(f_s/q_t)100\%$, γ_w = unit weight of water in same units as γ, σ_{atm}= atmospheric pressure in same units as q_t.	(Robertson and Cabal 2010)
	R2	215	$\gamma=11.46+0.33\log(z)+3.1\log(f_s)+0.7\log(q_c)$ Where: z (m) = depth, f_s (kPa) = sleeve friction, q_c (kPa) = measured tip resistance.	(Mayne *et al.* 2010)
	R3	-	$\gamma/\gamma_w=\left[1.22+0.15\ln\left(100f_s/\sigma_{atm}\right)+0.01\right]$	(Mayne 2016)
Effective friction angle ϕ'	FA1	5	$\tan\phi'=\frac{1}{2.68}\left[0.29+\log\left(\frac{q_c}{\sigma_{v0}'}\right)\right]$	(Robertson and Campanella 1983)
	FA2	24	$\phi'=17.6+11\log(q_{t1})$ Where: q_{t1} = stress normalized tip resistance: $q_{t1}=(q_t/\sigma_{atm})\cdot(\sigma_{atm}/\sigma_{v0}')^{0.5}$	(Kulhawy and Mayne 1990)
Relative density D_r	DR	-	$D_r=\frac{100}{C_2}\cdot\ln\left(\frac{q_c}{C_0\cdot(\sigma_{v0}')^{C_1}}\right)$ Where: C_0 C_1 and C_2 are empirical coefficients parameters.	(Schmertmann 1978)

Model DR was used to interpret sandy soil's relative density from the CPT experimental data, and a total of 4 sets of model parameters (C_0, C_1 and C_2) were selected. These parameters were derived by analysing on sandy soils retrieved from different sites, and reproduced in Table 2.

Table 2. DR Model parameters.

Model	C_0	C_1	C_2	Reference
DR1	0.157	0.550	2.41	(Baldi and O'Neill 1995)
DR2	0.086	0.530	3.29	
DR3	0.140	0.550	2.90	(Jamiolkowski *et al.* 2003)
DR4	0.175	0.500	3.10	

3 CASE STUDY

3.1 General description

This offshore site is close to Shandong Province, belongs to the Yellow Sea of China. Water depth is about 32 m. Series of in-situ piezocone penetration tests were conducted and soil samples were retrieved at various depth. From which, physical and mechanical parameters were obtained from laboratory tests on these retrieved soil samples (GB/T 50123-2019、GB 50021-2001), as well as from the interpretation of CPT results. Figure 1 presents geotechnical stratigraphic log with USCS classification, the values of fines content and measured cone tip resistance, sleeve friction and porewater pressure on shoulder (u_2).

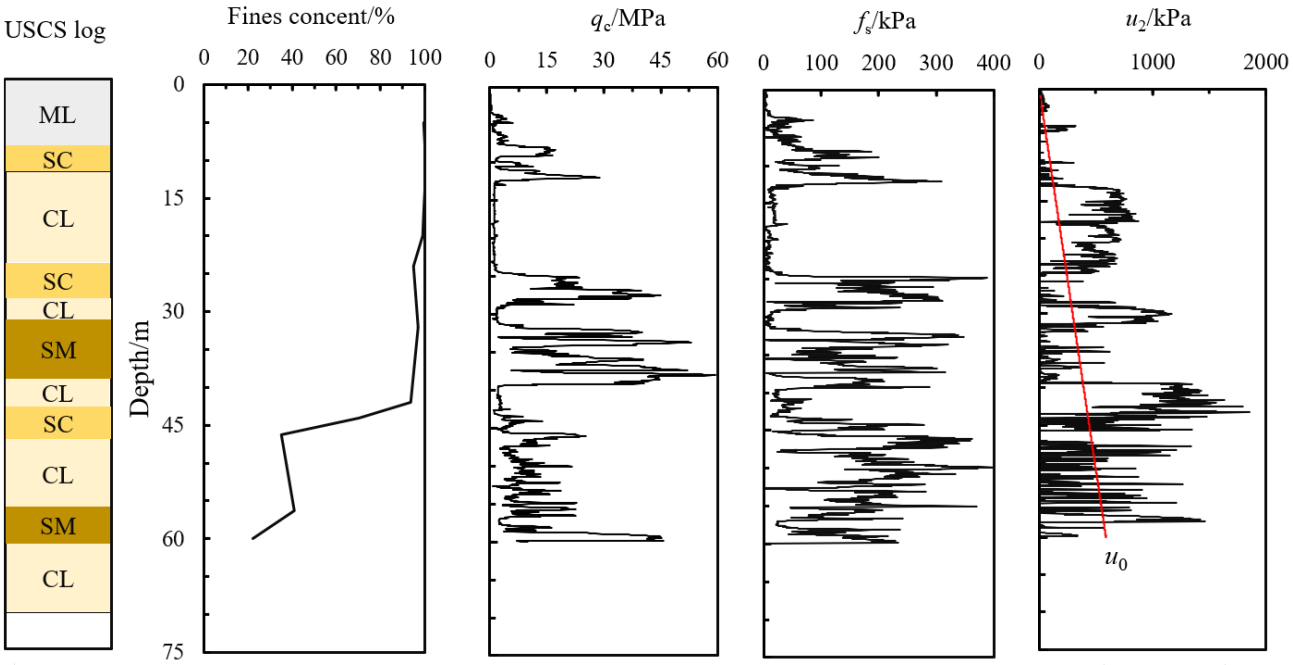

Figure 1. Geotechnical stratigraphic log with USCS classification, fines contents and the recorded CPT data.

3.2 Analysis and discussion

3.2.1 Soil unit weight

Figure 2 (a), (b) and (c) presents a comparison of soil unit weight between measured in lab and derived from CPT data with three methods (R1, R2 and R3) in Table 1. It can be seen that, in general, the relative errors of the three methods are within the range of ±15%, see Figure 2 (d), and they all overestimate the magnitude of soil unit weight, even though there is some underestimation at shallow depth. This overestimation may be caused by the soil disturbance, say stress release when being retrieved at depth below sea bed, which leads to an expansion of soil samples used in laboratory tests. Among these three methods, R3 agrees well with those values from laboratory tests, and R2 shows a poor estimation. Therefore, R3 is recommended to predict the unit weight.

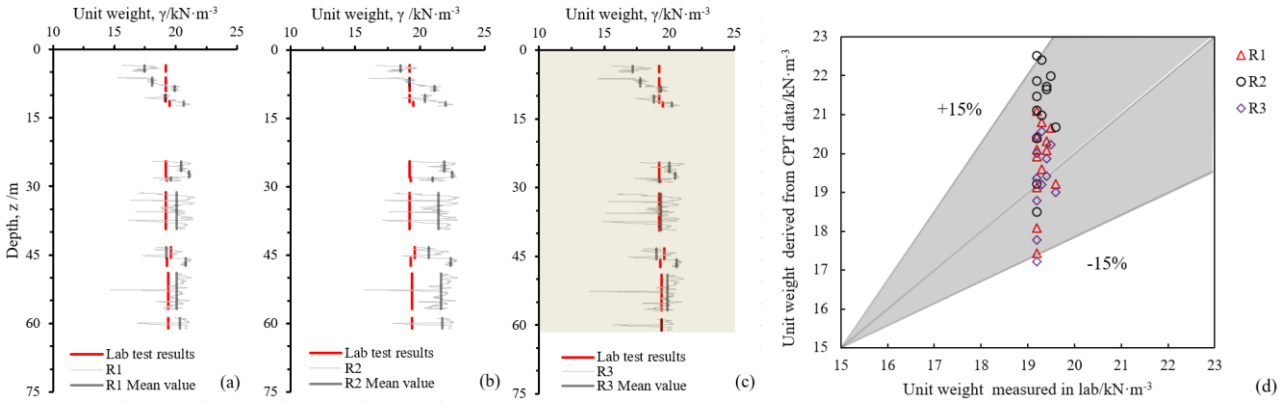

Figure 2. Comparison of soil unit weight between measured in lab and derived from CPT data.

3.2.2 Effective friction angle

Figure 3 (a) and (b) illustrates a comparison of effective friction angle between measured in lab and derived from CPT data with method FA1 and FA2 in Table 1, which shows that FA1 produces an overestimation and FA2 gives an underestimation. So mean values between those calculated with FA1 and FA2 for each layer are plotted in Figure 3 (c). It can be seen that the relative errors of the three methods are generally within the range of ±30%, see Figure 3 (d). In the shallow depth (less than 30m, and corresponding to a lower stress condition), FA2 provides a better prediction, while FA1 gives a very good prediction for the deep depth. The average of the two approaches brings the overall prediction closer to the laboratory test results but fails to produce a better prediction. So, FA2 can be employed at a lower stress condition, while FA1 should be better for higher stress condition.

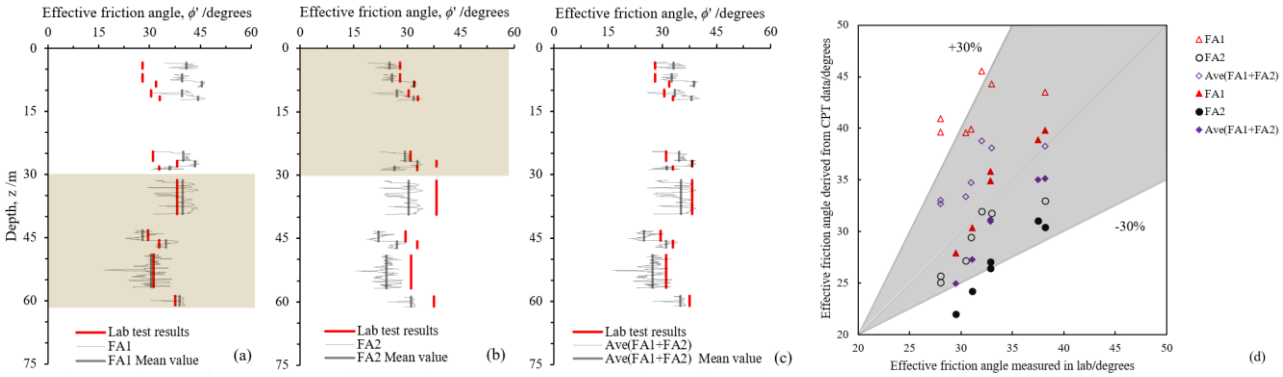

Figure 3. Comparison of soil effective friction angle between measured in lab and derived from CPT data.

3.2.3 Relative density

Figure 4 (a), (b), (c) and (d) shows a comparison of soil relative density between measured in lab and derived from CPT data with four methods (DR1, DR2, DR3 and DR4) in Table 2. It can be seen that, in general, the relative errors of the four methods are within the range of ±40%, see Figure 4 (d), and all these methods underestimate the magnitude of soil relative density, even though there is kind of extremely overestimation at shallow depth. Among these methods, DR2 clearly shows a better estimation, and is recommended to predict sandy soil's relative density.

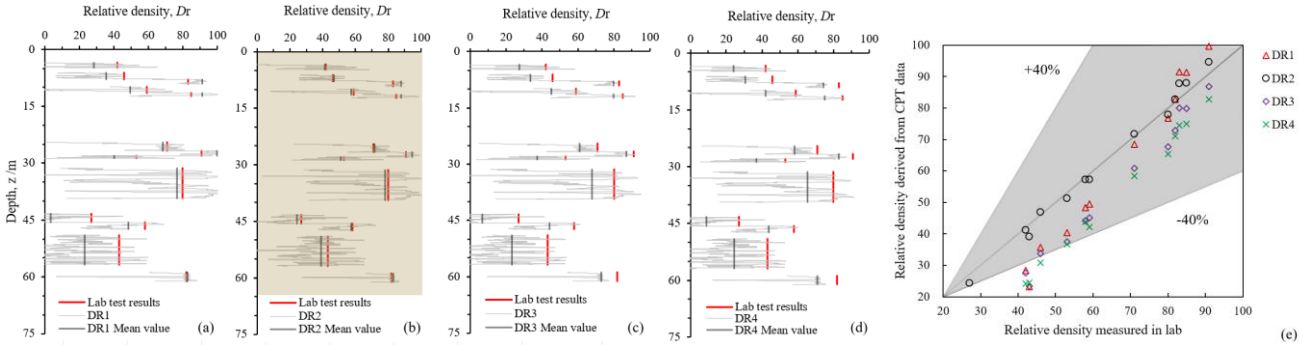

Figure 4. Comparison of soil relative density between measured in lab and derived from CPT data.

4 CONCLUSIONS

Based on a case study focusing on the offshore site in Yellow Sea of China, this paper presents an evaluation on current interpretation methods for CPT data recorded at sandy soil layers. By comparison of soil parameter values between tested in laboratory and interpretated from CPT data, main findings and recommendations are made for sandy soil layers:

Even though a lower estimation is shown in shallow depth, method R3 generally produces a relatively well estimation of soil unit weight. With regards to sandy soil's effective internal friction angle, FA2 produces a better prediction at shallow depth (i.e. lower stress condition) and FA1 suits for deep depth (i.e. higher stress condition). Compared with DR2, the other three methods show relatively poor estimations of sandy soils relative density, therefore DR2 is recommended. This study enables a further design optimization of monopiles used by offshore wind turbine constructed in this site.

ACKNOWLEDGEMENTS

The authors are grateful for the financial support provided by National Natural Science Foundation of China (41972275).

REFERENCES

ASTM D5778 - Standard Test Method for Electronic Friction Cone and Piezocone Penetration Testing of Soils.

Baldi, G., & O'Neill, D. A. (1995, October). Developments in penetration technology for geotechnical and environmental applications. In *International Symposium on Cone Penetration Testing* (pp. 19-33). CRC Press, Boca Raton, FL.

China Architecture & Building Press. (2009). GB 50021-2001: Code for Investigation of Geotechnical Engineering. Beijing, China: China Architecture & Building Press.

Jamiolkowski, M., Lo Presti, D. C. F., & Manassero, M. (2003). Evaluation of relative density and shear strength of sands from CPT and DMT. *In Soil behavior and soft ground construction* (pp. 201-238). https://doi.org/10.1061/40659(2003)7.

Kulhawy, F. H., & Mayne, P. W. (1990). Manual on estimating soil properties for foundation design (No. EPRI-EL-6800). *Electric Power Research Inst*., Palo Alto, CA (USA); Cornell Univ., Ithaca, NY (USA). Geotechnical Engineering Group.

Lunne, T., Powell, J. J., & Robertson, P. K. (2002). Cone penetration testing in geotechnical practice. CRC Press. https://doi.org/10.1201/9781482295047.

Mayne, P. W. (2016). Evaluating effective stress parameters and undrained shear strengths of soft-firm clays from CPT and DMT. Australian Geomechanics Journal, 51(4), 27-55.

Mayne, P. W., Peuchen, J., & Bouwmeester, D. (2010). Soil unit weight estimation from CPTs. sat, 227, 3.

Mayne, P. W. (2007). Cone penetration testing (Vol. 368). Transportation Research Board.

National Standardization Administration of China. (2019). GB/T 50123-2019: Test methods of geotechnical engineering. Beijing, China: China Planning Press.

Robertson, P. K. (2009). Interpretation of cone penetration tests—a unified approach. *Canadian geotechnical journal*, 46(11), 1337-1355. https://doi.org/10.1139/t09-065.

Robertson, P. K. and K. Cabal (2010). Estimating soil unit weight from CPT. *2nd International symposium on cone penetration testing*.

Robertson, P. K., & Campanella, R. G. (1983). Interpretation of cone penetration tests. Part I: Sand. *Canadian geotechnical journal*, 20(4), 718-733. https://doi.org/10.1139/t83-078.

Schmertmann, J. H. (1978). Guidelines for cone penetration test: performance and design (No. FHWA-TS-78-209). United States. Federal Highway Administration.

Proceedings of the XVIII ECSMGE 2024
GEOTECHNICAL ENGINEERING CHALLENGES
TO MEET CURRENT AND EMERGING NEEDS OF SOCIETY
© 2024 the Authors
ISBN 978-1-032-54816-6
DOI 10.1201/9781003431749-386
Open Access: www.taylorfrancis.com, CC BY-NC-ND 4.0 license

ECSMGE 24
XVIII EUROPEAN CONFERENCE ON SOIL MECHANICS AND GEOTECHNICAL ENGINEERING

Small- and full-scale test programme on uplift induced slope failure

Programme d'essais à petite et à grande échelle sur l'instabilité des pentes induite par le soulèvement de la couche imperméable

C. Zwanenburg*
Deltares, Delft, The Netherlands; TU Delft, Delft, The Netherlands

A.R. Koelewijn, B.J. van der Kolk, U. Förster, M. Post, H.T.J. de Bruijn
Deltares, Delft, The Netherlands

**cor.zwanenburg@deltares.nl*

ABSTRACT: Sub soil stratum in deltaic regions typically include a succession of permeable and non-permeable layers. Consequently, dikes built to protect delta areas, should be able to resist not only extreme surface water levels, but also an increase in hydraulic head in permeable layers. The rise in hydraulic head might result in uplift of the cover layer, inducing either backwards erosion piping or slope stability. A large research programme, including the combination of numerical analysis, centrifuge testing and field trials, is started to study the uplift phenomenon. Preliminary results show that uplift has a clear influence on dike stability. Horizontal compression of the cover, during uplift, might trigger slope failure. Large cracks in uplifted cover layer were not found in the field trials, although some local failure, resulting in sand boils, was observed. The test results provide valuable experimental data to further validate numerical tools and stability assessment procedures.

RÉSUMÉ: La stratification du sous-sol dans les régions deltaïques comprend généralement une succession de couches perméables et non perméables. Par conséquent, les digues construites pour protéger les zones deltaïques doivent pouvoir résister non seulement à des niveaux d'eau extrêmes, mais aussi à une augmentation des charges hydrauliques dans les couches perméables. L'augmentation de la charge hydraulique peut entraîner un soulèvement de la couche imperméable, induisant soit une érosion régressive, soit une instabilité des pentes par glissement rotationnel. Un programme de recherche, combinant des analyse numériques, expérimentations dans une centrifugeuse et expériences de terrain, a été lancé pour étudier le phénomène de soulèvement. Les résultats préliminaires montrent que le soulèvement exerce une influence évidente sur le glissement rotationnel des digues. La compression horizontale de la couche imperméable, pendant le soulèvement, semblerait déclencher le glissement rotationnel. Les expériences de terrain n'ont pas révélé de grandes fissures dans la couche imperméable une fois soulevée, bien que certaines ruptures locales, comme des bouillonnements, aient été observées. Les résultats expérimentaux fournissent des données précieuses pour valider davantage les outils numériques et les procédures d'évaluation du glissement rotationnel.

Keywords: Stability; experimental soil mechanics; uplift.

1 INTRODUCTION

Typically, hydraulic loads on water retaining constructions during design conditions not only include the free water acting on the dike body, but also changes in pore water pressures in sub soil layers. Figure 1 shows a classical case in which, due to a hydraulic connection between a sand layer and the free water, the hydraulic head increases until uplift of the non-permeable cover layer occurs, which reduces the slope stability. Moreover, due to uplift the cover layer might break, starting erosion of the sand layer: backward erosion piping.

In deltaic regions, subsoil stratification often contains a succession of permeable and non-permeable layers. As such, depending on design load conditions and dimensions of the dike, the typical deltaic subsoil is in principle susceptible to uplift.

Several studies have been conducted to show how the uplift phenomenon should be accounted for in stability assessment of dikes, Marsland & Cooling (1953), Marsland (1988), Van et al. (2005).

These studies assume that for uplift conditions the cover layer remains intact. Some guidelines on dike stability assessment (TAW, 2001) hypothesize that thin cover layers, < 4 m, will break and lose their

integrity during uplift. Consequently, in these guidelines, the cover layer is assumed to have no strength under uplift conditions.

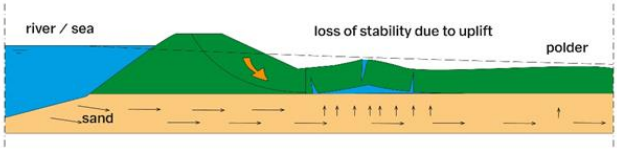

Figure 1. Sketch of slope instability due to breaking of the cover layer due to uplift.

Although local failure of the cover layer by cracks that result in sand boils and facilitate backward erosion piping, are regularly found (a.o. Bezuijen, 2017), field cases in which the cover layer completely loses its integrity, inducing slope failure, are not known to the authors.

Climate change and the corresponding sea level rise will result in a more frequent occurrence of the uplift mechanism. At the same time, the increase in urbanisation of deltaic areas will reduce the available space for dike reinforcement. Consequently, the uplift phenomenon needs to be properly understood to face future challenges in flood protection.

The study aims for generating experimental data and validate existing numerical tools for stability assessment of dikes. To maximise impact, the study includes numerical simulation, centrifuge testing and field trials. The centrifuge testing allows to study the impact of varying relevant parameters, like the thickness of the cover layer or cover layer properties under controlled and simplified conditions. A field trial includes all relevant uncertainties but is only related to the specific geometry and soil conditions at the test site. The combination of scale modelling and field trials allows for checking on possible scale or schematisation effects which might be incorporated in centrifuge modelling. Vice versa, scale modelling helps in generalising the results from the field trials.

2 NUMERICAL ANALYSIS

A numerical study employing advanced finite element analyses, Visschedijk (2020), showed 4 different potential failure mechanisms under uplift conditions, see Figure 2. In mechanism *a* uplift does not influence failure, resulting in a circular sliding plane. Mechanism *b* includes the uplifted zone and a passive failure plane. Mechanism *c* describes buckling of the cover layer, resulting in loss of integrity. Mechanism *d* shows horizontal compression of the cover layer followed by slope instability.

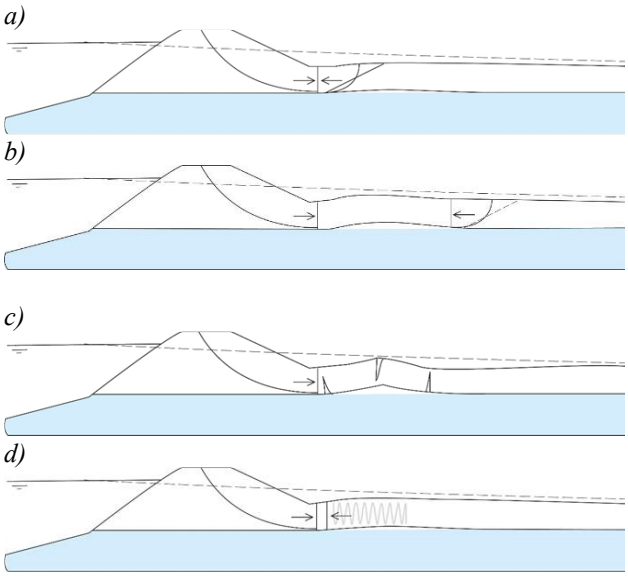

Figure 2. Sketch of the 4 different failure mechanisms observed in the numerical analysis, after Visschedijk (2020).

Mechanism *a* and *b* allow for stability assessment by Limit Equilibrium Methods, as shown by Van et al., (2005). For the few cases in which slope failure due to uplift was found in the field, no passive failure plane could be observed. This makes it difficult to distinguish between mechanisms *b* and *d* for field conditions.

The numerical analysis predicts mechanism *c* only for specific conditions, i.e. a thin cover layer < 2 m with large stiffness, Young's modulus > 3 MPa and high permeability in the sand layer to maintain the uplift pressure during deformation of the cover layer.

Mechanism *d* is dominated by the interaction between slope stability and horizontal compression of the cover layer. An unstable slope induces a horizontal compression on the cover layer, which increases when the cover layer is lifted. Further compression of the cover layer will induce displacements along the active part of the sliding plane. Depending on the material of which the dike is constructed, these deformations might start progressive failure, when locally the peak strength is exceeded.

The numerical analysis showed that mechanism *d* was the decisive mechanism for cover layer thicknesses up to 4 m. A numerical analysis, using PLAXIS 2D v22, was performed to get more understanding of this mechanism.

Figure 3 shows the horizontal displacements found at uplift of the cover layer. The geometry contains a dike with height 6 m, and slope 1(V): 2.5 (H). The cover layer thickness is 3 m and is followed by a 12 m thick sand layer. The Mohr-Coulomb model is used to model soil behaviour. Table 1 gives the relevant parameters. An interface, with the same strength

characteristics as the surrounding soil, was applied between the cover layer and sand layer to obtain a discrete shear plane. For this geometry, the maximum horizontal displacement is in the order of 0.17 m.

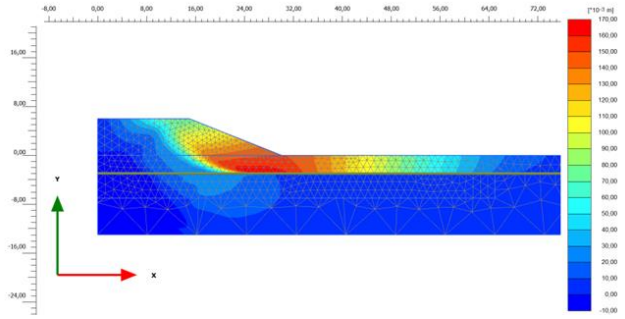

Figure 3. Horizontal displacements under uplift conditions.

Table 1. Soil properties for numerical simulations.

parameter	unit	dike	cover layer	sand
vol. weight, γ^*	[kN/m^3]	17	17	18
cohesion, c'	[kN/m^2]	18	18	0
friction angle, φ'	[°]	0	0	32
Young's modulus, *E*	[MN/m^2]	3	3	10
Poisson's ratio, ν	[-]	0.3	0.3	0.3

* equal for saturated and unsaturated conditions

3 CENTRIFUGE TESTS

A series of 13 centrifuge tests has been conducted. Details of the tests are presented by Cengiz et al. (2024). The tested model contains a sand layer, a clay cover layer and dike body build from sand. Uplift was activated at 80g after which the g-level was increased further to reach failure.

Figure 4 shows the horizontal displacements in the cover layer for a typical failure found in the test series. The horizontal displacements are assessed from the test results by Particle Image Velocimetry, PIV analysis. The observed mechanism complies well with the numerical results shown in Figure 3.

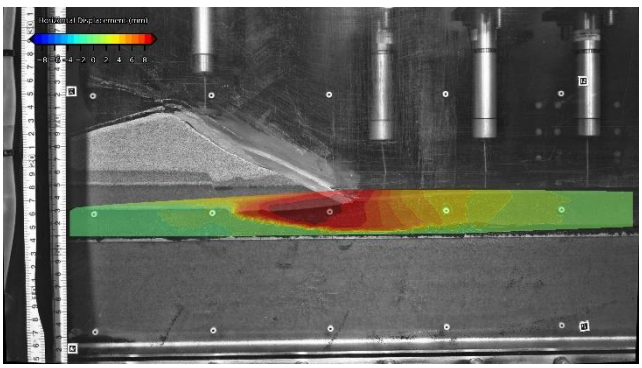

Figure 4. Horizontal displacements in cover layer at slope failure, green = 0 mm, red = 8 mm.

4 FIELD TRIAL

The field trial was conducted on a dike section along the River IJssel, near Kampen, the Netherlands. New flood protection works made this dike section redundant and as such available for testing.

The subsoil is divided into a cover layer containing a clay and peat layer followed by a sand deposit. To enhance instability additional measures were taken:

- The dike height was increased by 2.6m.
- At the toe, the soil was excavated by 1.25 m. total slope height was 7.75 m.
- 8 infiltration wells were placed to increase the hydraulic head in the sand layer.
- A drain was placed in the sand core to increase the phreatic level in the dike.
- Clay was added to the dike to prevent local slope instability.
- The slope was changed into 1(V): 2(H)
- A row of 10 containers, which could be filled remotely, was placed on top of the dike.

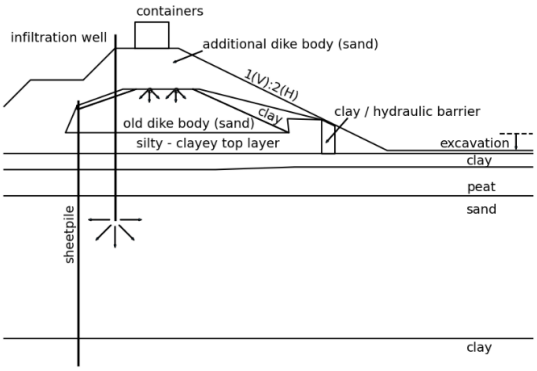

Figure 5. Test set-up, sketch of cross section.

Figure 5 shows the tested cross section. Prior to the main field trial, the uplift of the cover layer was tested in a separate but nearby field. This test showed that 1) the planned infiltration system could lift the cover layer, 2) that the uplift could be maintained for at least 3 days, after which the test was terminated and 3) hardly any leakage occurred despite the instrumentation that was placed in the cover layer or sand layer below.

The instrumentation of the main field trial was placed in three rows, containing 12 pore pressure transducers in the sand layer, 30 in the cover layer, 3 in top layer directly below the dike body, 7 open standpipes to measure the hydraulic head in the dike body, 15 inclinometers to measure horizontal displacements, 9 extensometer measuring vertical deformations at three different depths. Additionally, surface deformation was measured at 96 positions using a total station. Figure 6 presents an impression of the test set-up at the start of the main field trial.



Figure 6. Impression of the main field trial.

5 RESULTS

The test started on Monday 14 August 2023 at 9:00 by stepwise increasing the hydraulic head in the sand layer. Already in the first step the horizontal displacements directly responded to the hydraulic head increase.

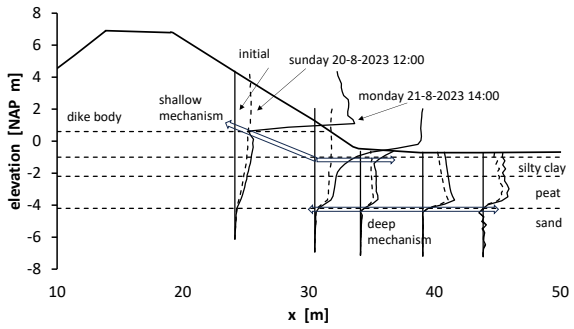

Figure 7. Horizontal displacements during the test.

Figure 7 shows the horizontal displacements measured during the test at the centre cross section. The horizontal displacement measurements at all but the left-most location clearly show a horizontal displacement at the interface of peat and sand. During the test the horizontal displacements developed uniformly over the cover layer thickness. This corresponds to mechanism *d* in Figure 2 and numerical analysis given by Figure 3. At these positions, the horizontal displacements are ranging between 0.05 to 0.10 m.

In the last stages of the test, starting on Sunday 20 August 2023, the last part of the sand core was filled, which caused a shallow failure plane to develop. The three instruments on the left side clearly indicate the position of the shallow sliding plane.

6 CONCLUSIONS

Uplift of a cover layer near the toe of a dike has impact on slope stability. This impact was studied by a combination of numerical analyses, centrifuge testing and a field trial. Analysis of the results is still ongoing. The experimental results clearly show the horizontal displacements which are induced at uplift of the cover layer. The observed displacement field corresponds to the numerical and experimental results, which clearly show that uplift results in horizontal compression of the cover layer.

In contrast to the centrifuge tests, the horizontal compression of the cover layer did not result in a deep failure in the field trial. Instead, the last stage in filling the sand core resulted in shallow failure.

Further analysis of the test results will lead to recommendations on stability assessment for dikes under uplift conditions.

ACKNOWLEDGEMENTS

The authors are grateful for the financial support provided by funding agency National Flood Protection Programme (HWBP) and water authority Drents Overijsselse Delta, WDOD.

REFERENCES

Bezuijen A. (2017). The influence of the leakage length on the initiation of backward erosion piping. *In: proceedings 25th meeting of the European Working Group on Internal Erosion,* Delft, The Netherlands.

Cengiz C., M. Cabrera, B. Wittekoek, M. Fransen, L. Wopereis , C. Zwanenburg (2024). Centrifuge tests on the uplift and deformation patterns of clay cover layers in deltas *in: proceeding ESCMGE24,* Lisbon (in progress).

Marsland A., Cooling L.F. (1953). Soil Mechanics Studies of Failures in the Sea Defence Banks of Essex and Kent *in: proceedings of the North Sea Floods Conference*, the institution of civil engineers.

Marsland A. (1988). Failure of Flood Banks Due to Under Seepage *in: proc. International conference on case histories in geotechnical engineering.21* https://scholarsmine.mst.edu/icchge/2icchge/2icchge-session3/21.

TAW (2001) Technisch Rapport Waterkerende grondconstructies, Technische adviescommissie voor de waterkeringen, publicatienummer P-DWW-2001-035, ISBN 90-369-3776-0: in Dutch.

Van, M., Koelewijn A.R., Barends F.B.J. (2005). Uplift Phenomenon: Model, Validation and Design. *International Journal of Geomechanics* (2):98-106 DOI: 10.1061/(ASCE)1532-3641(2005)5:2(98).

Visschedijk, M., van Hoven A., Zwanenburg C. (2020) POVM Opbarsten – Fase 2b. , rapport nr. 11204649-002; project report in Dutch.

D - Current and new construction methods
D - Méthodes de construction actuelles et nouvelles

Proceedings of the XVIII ECSMGE 2024
GEOTECHNICAL ENGINEERING CHALLENGES
TO MEET CURRENT AND EMERGING NEEDS OF SOCIETY
© 2024 the Authors
ISBN 978-1-032-54816-6
DOI 10.1201/9781003431749-387
Open Access: www.taylorfrancis.com, CC BY-NC-ND 4.0 license

ECSMGE 24
XVIII EUROPEAN CONFERENCE ON SOIL MECHANICS AND GEOTECHNICAL ENGINEERING

Improvement of local soils by adding marble powder

Amélioration des sols locaux par ajout de poudre de marbre

O. Aiche*, A. Medjnoun, R. Bahar
University of Sciences and Technology Houari Boumediene, Faculty of Civil Engineering, LEEGO, Algiers, Algeria

M. Khiatine
Yahia Farès University of Médéa, Faculty of Technology Department of Civil Engineering, Médéa, Algeria

*oaiche@usthb.dz

ABSTRACT: Soil compaction is a critical consideration in earthworks in arid areas because of a lack of water sources, low precipitation, and high evaporation rates. Water transportation is expensive and has a negative impact on the project's cost. The soil compaction with its natural moisture content is the alternative solution to achieve the earthworks projects in these areas. The present paper studies the feasibility of soil compaction at low water content using dune sand located in the Oued-Souf region of Algeria. A series of laboratory tests were conducted, including grain size distribution, standard and modified Proctor compaction tests, and California bearing ratio (CBR) tests. The used soil compacted at its natural moisture content, which is about 2%, with a progressive energy level in the first phases. The results show that increasing the energy level does not enhance the density or the California Bearing Ratio values. In the second phase of this paper, the grain size was corrected by the progressive addition of marble powder to the dune sand. The results of California bearing ratio (CBR) tests and density are significantly improved.

RÉSUMÉ: Le compactage des sols est un facteur critique dans les travaux de terrassement dans les zones arides en raison du manque de sources d'eau, des faibles précipitations et des taux d'évaporation élevés. Le transport d'eau est coûteux et a un impact négatif sur le coût du projet. Le compactage du sol avec sa teneur en eau naturelle est la solution alternative pour réaliser les projets de terrassement dans ces zones. Le présent article étudie la faisabilité du compactage des sols à faible teneur en eau d'un sable de dune localisé à la région d'Oued-Souf en Algérie. Une série d'essais en laboratoire ont été effectués, comportant l'analyse granulométrique, les essais de compactage Proctor normal et modifié et les essais de portance (CBR). Le sol utilisé est compacté à sa teneur en eau naturel, qui est d'environ 2%, avec un niveau d'énergie progressif dans la première phase. Les résultats montrent que la densité et portance du sol sont faible et l'augmentation de l'énergie de compactage est sans effet. Dans la deuxième phase, une correction de la granulométrie est effectuée par ajout progressive de poudre de marbre au sable de dune. Les résultats de la portance et de la compacité sont considérablement améliorés.

Keywords: Compaction energy; low water content; dune sand; marble powder.

1 INTRODUCTION

The development of Saharan regions requires the design of communication roadways, especially roads, to connect urban areas. The scarcity of materials and the arid climate have promoted engineers and researchers to look at various possible solutions to this challenge. One of these solutions is to reuse local materials, including dune sand, as a subgrade material in the engineering of Saharan pavements. The construction of pavements in deserted areas is challenged by the unavailability of water necessary for the compaction of materials. The scarcity of water makes compaction in these regions costly and difficult.

According to estimations, constructing 1 km of road in these areas could require up to 2,800 m3 of water, which could represent up to 20% of all construction costs. (Newill and O'Connell 2020). The Sahara covers about a third of the surface of Africa. Moreover, the dune sand covers about 30% of the Algerian Sahara, which represents around 80% of the surface of Algeria (Daheur, Goual et al. 2019). The use of dune sand for the construction of Saharan roads has great interest. Dry compaction is one of the most economical solutions for pavement structures For example, the experimental road embankment of a black silty clay of Sudan compacted at low moisture content has performed satisfactorily for one and a half years (Ellis 1980), and the road projects in Kenya constructed at low moisture content have performed equally well for two years (O'Connell 1987).Recently, many researchers have developed a lot of techniques and solutions to improve these materials at a reasonable cost, such as the effect of adding finer particles to the dune sand. The CBR value increased

with the increase in wastemarble powdercontent (Yorulmaz, Sivrikayaet al., 2021). 25% of marble dust has been considered to improve the CBR value of sandy soil. (Jain, Jha et al. 2020). The optimum moisture content (OMC) decreases as the percentage of marble powder increases; however, the values of the maximum dry density (MDD) increase as the percentage of marble powder increases to 6% (Rouaiguia, El Aal et al. 2020). The maximum dry density (MDD) increases with increasing ceramic waste and marble dust added to the soil. Moreover, the CBR values increase with the addition of ceramic waste and marble dust (Deboucha, Aissa Mamoune et al. 2020).

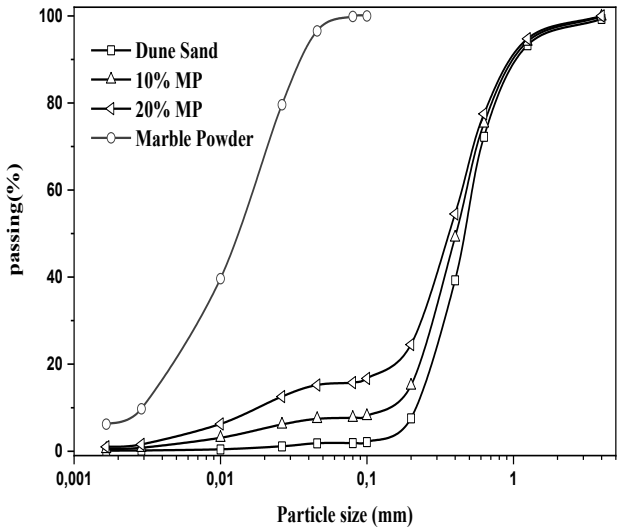

Figure 1. Particle size distribution of dune sand and Marble powder and mixture of dune sand with different adding of marble powder.

Table 1. Studied material formulations.

Designation	Dune sand (%)	Marble Powder (%)
DS100	100	0
DS90+MP10	90	10
DS80+MP20	80	20

2 MATERIALS AND METHODS

2.1 Dune sand of oued-souf

The dune sand (DS) is extracted from Oued-Souf city, located 640 km in the south-east of Algieria and characterized by a hot desert climate. This dune sand has a very high amount of sand (94%) and a low content of fine particles (2.5% silt and 0.5% clay). This dune sand is classified as fine sand (A-3) according to the American Association of State Highway and Transportation Organizations classification system (AASHTO) and poorly graded sand (SP) according to the Unified Soil Classification System (USCS).

2.2 Marble powder

The marble powder was obtained from the cutting and polishing of marble stones, and it was extracted from the FIL-FILA Quarry, which is about 25 km east of Skikda city, north-east of Algeria. The particle size distribution of the materials is presented in Figure 1.

2.3 Methods

The materials investigation is conducted by experimental tests, such as the sieve analyses and laser diffraction analysis (ASTM E3340-22), specific gravity (Gs), test by Gas Pycnometer (ASTM D5550-14)), sand equivalent test (ASTM D2419) and Methylene Blue Index (MVB)(ASTM C837) The particle size distribution of the materials is presented in Figure 1. Table 2 presents the principal properties of the materials. Standard and modified Proctor compaction testsis conducted according to the ASTM standard (ASTM D1557) in the aim to obtain the MDD and OMC. The same mould is used with a volume of 944 cm3 on each material. The California Bearing Ratio (CBR) tests are done in the CBR mould according to ASTM standard (ASTM D1893) to measuring the bearing capacity of the used soil at OMC.The dune sand is mixing with different proportions of marble powder which varying from 0, to 20% by weight. As seen in Table 1.

Table 2. Basic properties of dune sand.

Properties	Oued-Souf sand
Specific gravity	2.63
Gravel (%)	3
Sand (%)	94
Silt (%)	2.5
Clay (%)	0.5
Uniformity coefficient (Cu)	2.5
Coefficient of gradation (Cc)	0.9
MBV	0.07
Liquid Limit LL (%)	NP
IP	NP
ES	77

3 RESULTS AND DISCUSSION

3.1 Compaction caracteristique at the optimum

The result of compaction caracteristics as shown in figure 2, the Dune sand of Oued-souf under modified compaction effort, has a MDD value of 17.2 kN/m³, while under the normal compaction effort, is 16.9 kN/m³. For the modified compaction effort, the OMC is 7.6%, while for the normal compaction effort, it's 9%. The high sand content (94%) and lack of fines (3%) makes Oued-Souf soil less susceptible to compaction energy. This behaviour can be explained by the non reduce of voids between sand's particles because of its uniformed size, while compacting, as indicated by Cu and Cc coefficient, The CBR value under modified compaction test is 13%,wich is low value for the sub-grade construction.similar work has been seen in (Virgil Ping, Yang et al. 2002).

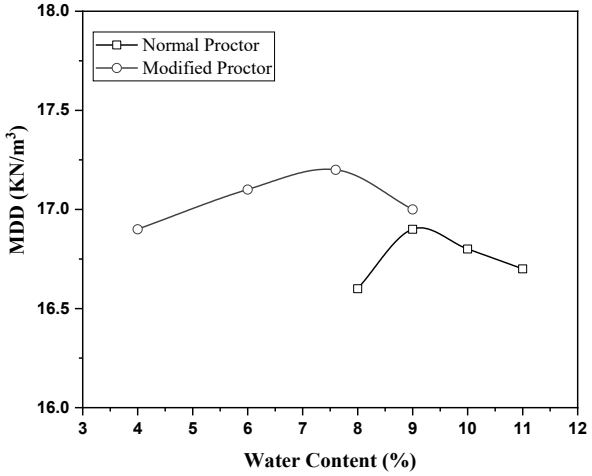

Figure 2. Normal and modified Proctor test curves.

3.2 Dune sand improvement by adding marble powder at low water content

3.2.1 Effect on grain size distributions

As shown in the figure 1, the progressive incorporation of marble powder (MP) modified the curve's shape; an upward movement was noticed of the grain size distribution curve for the treated soil. this shift is consequently due to the content of marble powder's role in displacing and reducing sand particles that leads to an increase of fine particles content in the mixture. the oued-souf material with no addition of marble powder has a poorly graded particle size distribution (cu = 2.25 and cc=1.05). the addition of 20% of marble powder changes the particle size distribution to to well graded, cu and cc rise respectively to 22.78 and 7.8, indicating that the particle size distribution has become less steep with a wide range of particle sizes.

3.2.2 Effect on compaction characteristics

The dune sand of Oued Souf under modified compaction effort at low water content (W=2%) reaching a maximum value of MDD, 20 KN/m^3 with the addition of 20% of marble powder (80DS + 20 MP) with an increase of 16%,as shown in Figure 3, this increase in MDD is related to the effect of finer particles that's helps the reduction fo voids in this dune sand, the peak of MDD at 20% of marble powder that's mean the powder occupied all the voids and reach the maximux density, similar behavior has been seen in (Omar, Zentar et al. 2022).

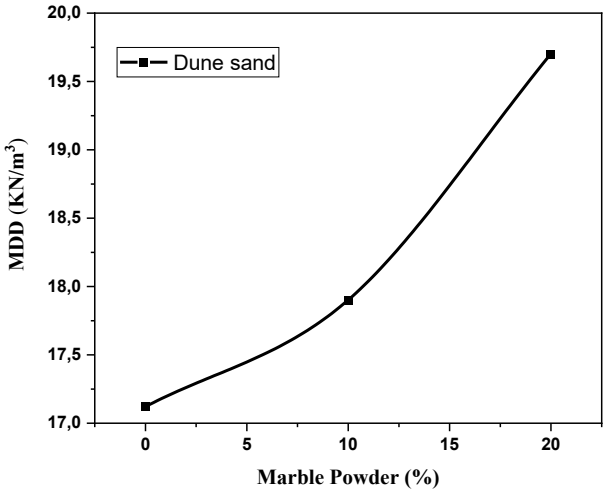

Figure 3. Effect of Marble Powder on the MDD of Dune sand.

3.2.3 Effect on the California Bearing Ratio (CBR) tests

The CBR values results for dune sand, with various content of marble powder is given by Figure.4. The CBR values increase from 10% to 37% Which is almost 4 times increase at the addition of 20% of marble powder, indicating that the material has reached its maximum compactness at this water content (W=2%).

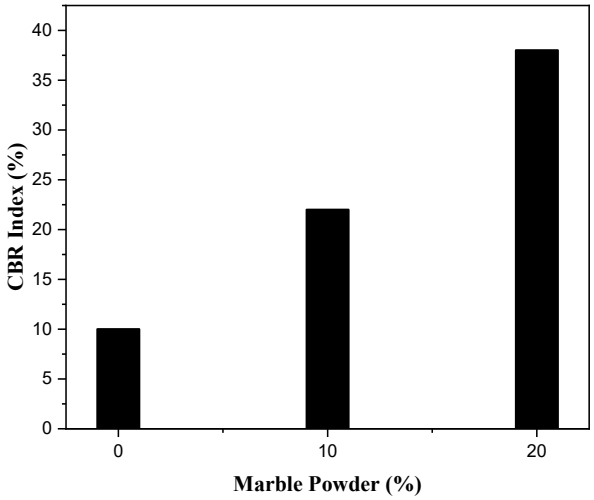

Figure 4. Effect of Marble Powder on on the CBR value of Dune sand.

4 CONCLUSION

The present experimental work on soil compaction at low water content involves mixing marble powder. The main results obtained are as follows. Increasing compaction energy has almost no effect on sand with uniform grain size as dune sand. The improvement of the density and bearing capacity of uniform grain size sand can be well achieved with the addition of insensitive water finer particles and mixing together. This solution helps to reduce the void ratio and increase the MDD. The compaction parameters as MDD and the CBR values have shown a considerable improvement with the addition of 20% of marble powder at low water content.

REFERENCES

Daheur, E. G., et al. (2019). "Effect of dune sand incorporation on the physical and mechanical behaviour of tuff:(experimental investigation)." 37: 1687-1701. https://doi.org/10.1007/s10706-018-0715-4.

Deboucha, S., et al. (2020). "Effects of ceramic waste, marble dust, and cement in pavement sub-base layer." 38(3):3331-3340. https://doi.org/10.1007/s10706-020-01211-x.

Jain, A. K., et al. (2020). "Improvement in subgrade soils with marble dust for highway construction: a comparative study." 50: 307-317. https://doi.org/10.1007/s40098-020-00423-5.

Newill, D. and M. O'Connell (2020). TRL research on road construction in arid areas. Engineering Characteristics of Arid Soils, CRC Press: 353-360. https://doi.org/10.1201/9781003077787-41.

O'CONNELL, M J et al, (1987). Soil compaction at low moisture contents in dry areas in Kenya. In: AKINMUSURU, J 0 et al (Eds). Soil Mechanics and Foundation Engineering. Ninth Regional Conference for Africa, Lagos, September 1987, Volume 1. Rotterdam: A A Balkema, 211-226.

Ellis, C. (1980). soil compaction at low moisture content. field trials in sudan. Proceedings of the Seventh Regional Conference for Africa, Accra, June 1980.

Omar, H. M., et al. (2022). "Co-valorization of Tuff and Sandy Residues in Roads Construction." 8(5): 1029-1045.https://doi.org/10.28991/CEJ-2022-08-05-013.

Rouaiguia, A., et al. (2020). "Enhancement of the geotechnical properties of soils using marble and lime powders, guelma city, Algeria." 38(5): 5649-5665. https://doi.org/10.1007/s10706-020-01368-5.

Virgil Ping, W., et al. (2002). "Laboratory simulation of field compaction characteristics on sandy soils." 1808(1): 84-95.https://doi.org/10.3141/1808-10.

Proceedings of the XVIII ECSMGE 2024
GEOTECHNICAL ENGINEERING CHALLENGES
TO MEET CURRENT AND EMERGING NEEDS OF SOCIETY
© 2024 the Authors
ISBN 978-1-032-54816-6
DOI 10.1201/9781003431749-388
Open Access: www.taylorfrancis.com, CC BY-NC-ND 4.0 license

ECSMGE 24
XVIII EUROPEAN CONFERENCE ON SOIL MECHANICS AND GEOTECHNICAL ENGINEERING

Design, construction and monitoring phases of a diaphragm wall shoring application near the Golden Horn

Phases de conception, de construction et de surveillance d'une application de soutènement en paroi moulée près de la Corne d'Or

Ö. Akçakal*, C. Acar, M.N. Velioğlu, O. Sevim

Zetaş Zemin Teknolojisi A.Ş., Istanbul, Türkiye

onder.akcakal@zetas.com.tr

ABSTRACT: One of the landmark buildings of Istanbul on the shores of the Golden Horn was damaged due to the large settlements occurred in the years after its construction. A comprehensive soil investigation study was held to determine the problem. The investigations revealed loose soil layers prone to settlement and also have liquefaction risk under earthquake loads. Remediation options were evaluated in the beginning of the construction. Demolishing of the existing structure and reconstruction of the new one with basement floors were recommended by the Consultant. A 9.5m excavation was planned for basement construction. It was decided to apply diaphragm wall supported with one row of strut and jet grouting on the toe. Due to the large excavation sizes and required long steel struts, king post barrettes were decided to be applied. Jet grout columns were applied with high efficiency monitor systems to obtain an improved layer and a thick bottom plug. Groundwater seepage was successfully minimized. Monitored displacements due to excavation were below the calculated ones. The project which was located in a very congested area with challenging soil conditions and construction difficulties was completed in a safe and timely manner.

RÉSUMÉ: Un des bâtiments emblématiques d'Istanbul, sur les rives de la Corne d'Or, a été endommagé en raison des vastes tassements survenus dans les années qui ont suivi sa construction. Une étude exhaustive du sol a été menée pour déterminer le problème. Les investigations ont révélé des couches de sol lâches susceptibles aux tassements et présentant également un risque de liquéfaction sous des charges sismiques. Des options de remédiation ont été évaluées dès le début de la construction. La démolition de la structure existante et la reconstruction d'une nouvelle avec des étages en sous-sol ont été recommandées par le consultant. Une excavation de 9,5 mètres a été prévue pour la construction du sous-sol. Il a été décidé d'installer un soutènement en paroi moulée supporté par un niveau de butons et du jet grouting en pied. En raison de la taille importante de l'excavation et des longs butons nécessaires, il a été décidé d'installer des supports intermédiaires via des barrettes avec des poteaux métalliques pré-fondés. Des colonnes jet grouting ont été appliquées avec des systèmes de surveillance à haute efficacité pour obtenir une couche améliorée et un bouchon épais au fond. Les infiltrations d'eau souterraine ont été efficacement minimisées. Les déplacements surveillés dus à l'excavation étaient inférieurs à ceux calculés. Le projet, situé dans une zone très congestionnée avec des conditions de sol difficiles et des difficultés de construction, a été achevé de manière sûre et opportune.

Keywords: Diaphragm wall; king-post barrettes; jet grout; monitoring.

1 INTRODUCTION

One of the remarkable buildings located alongside the Golden Horn was damaged due to large settlements. It was demolished and reconstructed with additional basement floors and this case study summarises the design, construction and monitoring phases of the diaphragm wall shoring applied to retain the basement excavation of this project.

Damaged building was constructed in the beginning of 70's and it was close to the Eminönü square which is a very congested side of Istanbul. There were some historical shops served for olive oil trade on this location before the building and large settlements were also detected under these ones (Toğrol et al., 1986). Therefore, some sand piles were implemented down to 25m before the construction of this building and shoreline was supported with fill (Peynircioğlu, 1976).

Large settlements were detected during its service life which threaten the structural stability of the building so it was decided to demolish and reconstruct it in the same place. To eliminate the settlement problem and increase the lateral stability it was decided to construct the building with two basement

floors standing on a block type thick soil improvement layer.

Within the soil investigation studies a total of 14 boreholes were applied with a maximum depth of 60 m. 10 of the boreholes were applied before the building demolition and 4 of them were after. SPT, PMT and MASW tests were conducted in the site. Site was close to the shoreline and groundwater table was encountered between 0.0m and 0.4m elevations. Soil profile and average SPT test results are given in Table 1 (Zemin Etüd ve Tasarım A.Ş., 2021).

Table 1. Soil Profile.

Average Depth	Layer
0 m / -38 m	Uncontrolled Fill Sand with Gavel and Clay. $(N_1)_{60ave}$=10
-38 m / -50 m	Clay $(N_1)_{60ave}$=15
under -50 m	Shale/Claystone

Distribution of the SPT $(N_1)_{60}$ values with the depth is given in the Figure 1.

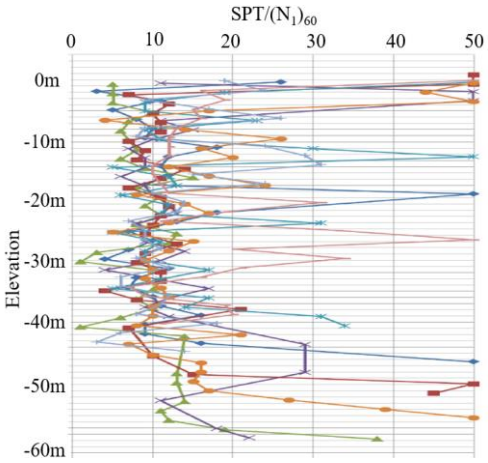

Figure 1. SPT $(N_1)_{60}$ distribution.

43 numbers of pressuremeter tests were conducted inside 4 numbers of the boreholes within the first 30 m depth. Menard Modulus E_M values were observed between approximately 1.5 and 47 MPa and net limit pressure P^*_{LM} values were between 0.1 and 1.9 MPa. Distributions of the E_M and P^*_{LM} values with the depth are given in the Figure 2.

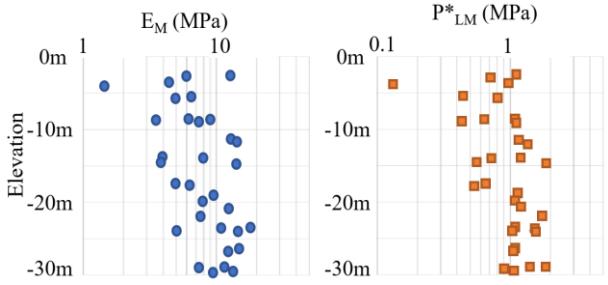

Figure 2. E_M and P^*_{LM} distributions.

MASW and PS logging tests were conducted within the geophysical survey. Besides, a ground penetration test was applied in the site to investigate the locations of the sand piles. Corrected Vs30 values were calculated between 190 and 330 m/s.

Plasticity index PI of the clay layer was calculated between 18 and 25, undrained cohesion value was 76 kPa. Unconfined compression values of the shale samples were observed between 14 and 40 MPa (Zemin Etüd ve Tasarım A.Ş., 2021).

Design parameters for shoring calculations were considered as in Table 2 based on the given soil investigation results. Fill layer was decided to split into 2 parts as above and below 20.0m. Elasticity modulus of the top uncontrolled fill layer was calculated as 20 MPa however it was considered as 6 MPa to be on the safe side due to high risks of debris and wood particles inside this layer.

Table 2. Considered Soil Properties.

Layer	Depth	γ kN/m³	Es MPa	c', kPa	φ',°
Fill	0-20m	18	6	1	30
Fill	20-38m	18	30	1	32
Clay	38-50m	18	8	7	25

2 DESIGN PHASE

After completion of the first phase of the boreholes, retrofitting and re-construction alternatives were discussed by the parties in the project. In overall stability analyses, structure had sufficient safety under static condition, but safety factor was calculated below the limits under the earthquake loads. Also, high liquefaction risk was pointed in the studies (Zemin Etüd ve Tasarım A.Ş., 2021).

After evaluating the gathered data re-constructing the structure after demolishing was determined as the best solution by the Employer and the Consultant.

Structure was planned to be constructed with 2 basements to remove some effective soil pressure under foundation. It was planned to be standing on a thick improved layer which will provide an efficient solution for settlements and lateral stability. A basement excavation with 9.5 m depth was required for construction as illustrated in the Figure 3.

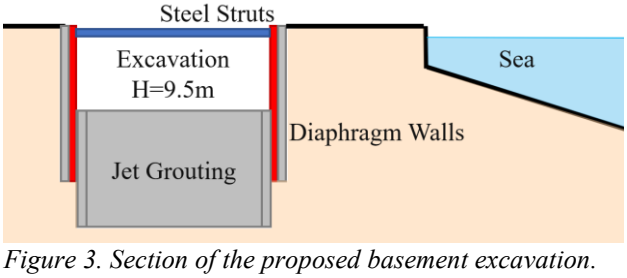

Figure 3. Section of the proposed basement excavation.

Site was at a very crowded and congested district of the city and close to many important infrastructure and historical places. Besides ground water table was close to surface. Due to these reasons shoring design became important in terms of waterproofness and displacements. Sheet pile, secant pile and diaphragm wall options were discussed in the design phase. The sheet pile option was eliminated because of the vibration risk under the existing historical structures. The diaphragm wall option was preferred instead of secant piles to provide better water tightness with reducing the number of joints between the vertical elements. Proposed thickness of the diaphragm wall was 800 mm with a depth of 17 m. Strutting was preferred instead of anchors due to the limited capacities which could be attained in the existing uncontrolled fill layer.

Jet grouting was selected as a ground improvement method which was the most suitable technique for the soil conditions. Jet grout columns were planned to be constructed with 1000 mm diameter in tangent pattern. In design UCS value of the jet grout columns was considered as 1.0 MPa due to the uncertain conditions of the fill layer. Elasticity modulus was considered as 300 times of the UCS value. Area replacement ratio between soil and jet grout columns was calculated as 0.79. Properties of the improved soil layer was calculated as the weighted average of the soil and jet grout columns.

Critical sections were modelled in Plaxis software as given in the Figure 4, displacements and section forces were calculated accordingly.

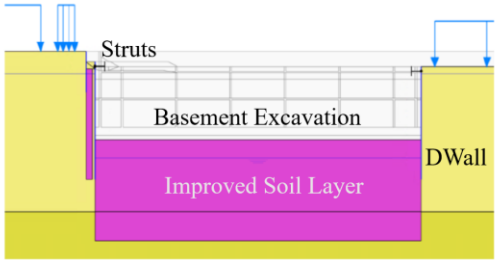

Figure 4. Plaxis Model of the Calculation Section.

Since the uncontrolled fill layer contains debris such as wood, plastic and bricks there were high risks in temporary stability of the excavated diaphragm wall shafts. Therefore, jet grout columns with 800 mm diameter were proposed under the guide walls adjacent to the diaphragm wall panel excavation. Diaphragm wall panel excavation could be done without any collapse.

Micropiles were implemented to support one part of the site which was 2.4 m higher than the rest. The shape of the basement was square with a side of 46 m as presented in the Figure 5.

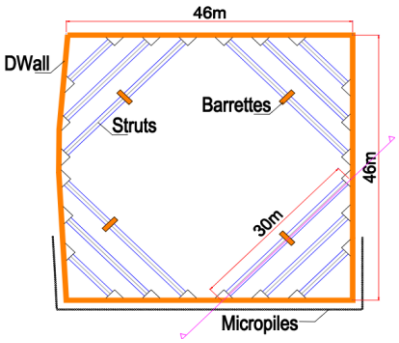

Figure 5. Layout of the Shoring System.

Four numbers of king-post barrettes were planned to be constructed to split the buckling length of struts for safety. Proposed shoring section was given in the Figure 6.

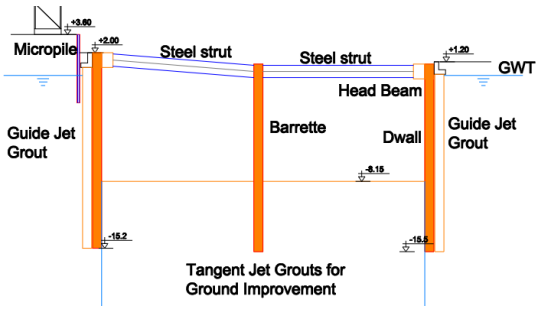

Figure 6. Section of the Shoring System.

Elevations were not equal everywhere in the site therefore different strut loads were calculated on the adjacent sides of the shoring. Due to these different strut loads, king-post barrettes needed to be checked in terms of lateral stability and cage design was prepared accordingly.

3 CONSTRUCTION PHASE

Application was started with jet grouting works. Trial jet grout columns were implemented to determine the application parameters. During these trials, with the permission of the Employer, large diameter jet grout columns were applied. Jet grout columns could be achieved up to 3.0 m in diameter with using high-efficient monitor and injection pump systems (Figure 7). A double fluid monitor was used with 6 mm diameter single nozzle, 400 bar pressure and 15 cm withdrawal rate.



Figure 7. Large Diameter (up to 3m) Jet Grouting Trial.

During the diaphragm wall excavation wood particles were encountered. To eliminate clogging in the plant these pieces were collected with a special sieve basket lowered inside the shaft during the operation (Figure 8).



Figure 8. Diaphragm Wall Construction.

Head beam was constructed with triangular parts to connect the struts perpendicular to reinforced concrete surface (Figure 9). Barrettes and these triangular parts cut and removed by the Employer parallel to the construction as planned in the early phases of the project.



Figure 9. Head Beam and Strut Installation.

This choice eased the precautions required for sliding safety of struts and provided a robust solution.

Diaphragm walls provided a watertight barrier and jet grout columns minimized groundwater seepage below the toe. Soil could be excaveted easily and transported under dry conditions. UCS values of the samples collected from jet grout columns were between 1.5 and 3.0 MPa. Additional excavations like lift pits could be done perpendicular and without any support with the help of high modulus and strength of the jet grout layer (Figure 10).



Figure 10. Excavation Phase.

4 MONITORING PHASE

Diaphragm walls were monitored with inclinometers during the excavation and lateral displacements were recorded approximately 10 mm which was calculated 25 mm during the design phase (Figure 11).

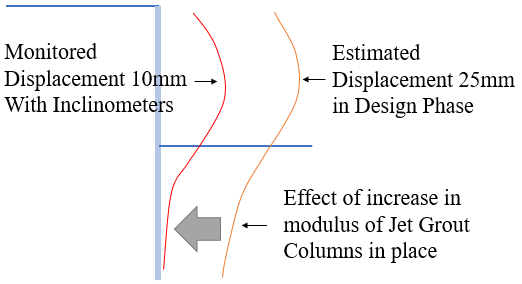

Figure 11. Calculated and Monitored Displacements.

UCS value of the jet grout columns was considered as 1 MPa with 400 kg/m^3 cement dosage and E/UCS ratio was considered as 300 to be on the safe side since there were debris and wood particles in the fill layer. Elasticity modulus of the jet grout layer was re-estimated by back calculation method with considering the encountered displacement 10 mm. Measured average UCS value was approximately 2 MPa and back calculation study pointed that 1200 MN/m^2 elasticity modulus could be considered for jet grout layer. E/UCS ratio is calculated approximately as 600 in this project for the fill layer.

5 CONCLUSION

Diaphragm wall shoring, steel strut and soil improvement with jet grouting techniques were successfully applied to support the basement excavation on the shores of the Golden Horn. Despite the challenging soil conditions and construction difficulties project completed in a safe and timely manner.

REFERENCES

Peynircioğlu, A.H., (1976), Haliç Sahillerinin Temel ve Stabilite Sorunları, *Proceedings of Conference on Stability Problems of Golden Horn*, Bosphorus University, pp. 391-401.

Toğrol, E., Güler, E., Özüdoğru, K., Ersoy, T., Aksoy, I. (1986), *Haliç'in Geoteknik Sorunları ve Çözüm Yolları*, Bosphorus University.

Zemin Etüd ve Tasarım A.Ş., (2021) *Veri ve Geoteknik Değerlendirme Raporları*, Istanbul.

Proceedings of the XVIII ECSMGE 2024
GEOTECHNICAL ENGINEERING CHALLENGES
TO MEET CURRENT AND EMERGING NEEDS OF SOCIETY
© 2024 the Authors
ISBN 978-1-032-54816-6
DOI 10.1201/9781003431749-389
Open Access: www.taylorfrancis.com, CC BY-NC-ND 4.0 license

ECSMGE 24
XVIII EUROPEAN CONFERENCE ON SOIL MECHANICS AND GEOTECHNICAL ENGINEERING

Physical, geometrical and chemical characterisation of incinerator bottom ash towards its use as recycled aggregate

Caractérisation physique, géométrique et chimique des mâchefers d'incinération en vue de leur utilisation comme granulet recyclé

F. Almeida, J.R. Carneiro*, M.L. Lopes
CONSTRUCT, Faculty of Engineering of University of Porto, Porto, Portugal
**rcarneir@fe.up.pt*

ABSTRACT: This work performs an extensive characterisation of incinerator bottom ash (IBA), analysing its physical, geometrical and chemical properties. Experiments included the determination of particle size distribution, flakiness and shape indexes, particle density and water absorption, the chemical analysis of the residue and also its leaching behaviour. The latter comprised, among others, the quantitative determination of different chemical species. The results obtained in the chemical analyses were compared with the limit values established in the European legislation for inert and non-hazardous waste classification. The outcomes of the investigation revealed that some properties of IBA were unsuitable for its use as recycled aggregate. To be a viable alternative to natural aggregates, IBA would need at least some preliminary treatment.

RÉSUMÉ: Ce travail réalise une caractérisation extensive des mâchefers d'incinération (IBA), en analysant leurs propriétés physiques, géométriques et chimiques. Les expériences ont inclus la détermination de la distribution granulométrique des particules, des coefficients d'aplatissement et de forme, de la masse volumique réelle et du coefficient d'absorption d'eau, de l'analyse chimique des résidus et également de leur comportement de lixiviation. Ce dernier comprenait, entre autres, la détermination quantitative de différentes espèces chimiques. Les résultats obtenus lors des analyses chimiques ont été comparés avec les valeurs limites établies dans la législation Européenne pour la classification des déchets inertes et non dangereux. Les résultats de l'enquête ont révélé que certaines propriétés des IBA n'étaient pas adaptées à son utilisation comme granulat recyclé. Pour constituer une alternative viable aux granulats naturels, les IBA nécessiterait au moins un traitement préliminaire.

Keywords: Incinerator bottom ash; chemical analysis; leaching behaviour; waste valorisation.

1 INTRODUCTION

The incineration process of municipal solid waste leads to the generation of large amounts of a residue known as incinerator bottom ash (IBA), which commonly ends up landfilled. The accomplishment of the targets included in the United Nations 2030 Agenda for Sustainable Development (UN, 2015) forces the development of solutions involving the valorisation of waste among the different industrial activities.

The use of IBA in the building and construction sector involves the implementation of an effective circular construction paradigm that depends on the will and joint work carried out by the government and construction professionals, including designers, entrepreneurs, manufacturers, contractors, engineers, architects and researchers (Almeida et al., 2022).

One core priority to assist designers in the decision-making process regarding the use of IBA as raw material is the understanding of its short and long term behaviour by assessing its mechanical, physical, geometrical and chemical properties.

IBA may be used in cementitious materials and as recycled aggregate in concrete or in road construction (Xuan et al., 2018). The latter application opens opportunities for IBA's valorisation in geotechnical engineering. Indeed, there is a wide range of potential geotechnical applications where IBA can be used as recycled aggregate, e.g., in backfill of trenches, in unbound layers of road pavements (base and subbase), in embankments of different transport infrastructures, or even in the subgrade of pedestrian and cycle paths. As can be understood, IBA might represent a significant source of raw materials, avoiding the excessive use of natural aggregates.

The aim of this work was to provide insights into several physical, geometrical and chemical properties of IBA considering its use as recycled aggregate in geotechnical engineering applications. To achieve such aim, an extensive experimental campaign was conducted.

2 EXPERIMENTAL DESCRIPTION

IBA was provided by a Portuguese incineration plant of municipal solid waste (Figure 1). Laboratory tests were conducted to obtain insights into its physical, geometrical and chemical properties. IBA was tested as received.



Figure 1. IBA.

The geometrical properties determined included particle size distribution, and flakiness and shape indexes. These properties were obtained according to EN 933-1 (CEN, 2012a), EN 933-3 (CEN, 2012b) and EN 933-4 (CEN, 2008), respectively. In addition, the coarse particles of IBA were classified based on the procedures defined in EN 933-11 (CEN, 2009). In this last test, a 20 kg sample of IBA with particles below 31.5 mm was passed through a 4 mm sieve. Then, around 4 kg of the particles larger than 4 mm (reduced sample) were classified as: R_u – unbound aggregate and natural stone; R_b – ceramics; R_g – glass; R_m – metals; or R_i – unidentifiable by-products of the incineration process. The results will be presented as the mass percentage of the constituents in the reduced sample.

Regarding physical properties, it was determined the particle density and water absorption (EN 1097-6 (CEN, 2022)) for two different particle size fractions: 0.063/4 mm and 4.0/31.5 mm.

The chemical characterisation of IBA included the determination of the parameters listed in the Council Decision 2003/33/EC (EU, 2003) both for the residue and its eluate. The eluate was obtained according to EN 12457-4 (CEN, 2002) at a liquid to solid ratio of 10 L/kg for the particle size fraction of IBA below 10 mm. The results obtained in the chemical analyses were compared with the limit values defined in the Council Decision 2003/33/EC (EU, 2003) for inert and non-hazardous waste.

3 RESULTS AND DISCUSSION

3.1 Physical and geometrical properties

The particle size distribution of IBA can be found in Figure 2. The maximum particle size (D_{max}) of IBA was 22.4 mm and the fines content (f) was 2.9 %. The values of C_U – coefficient of uniformity (20.57) and C_C – coefficient of curvature (1.88) indicate that IBA was a well graded aggregate having roughly 60% of its particles below 10 mm.

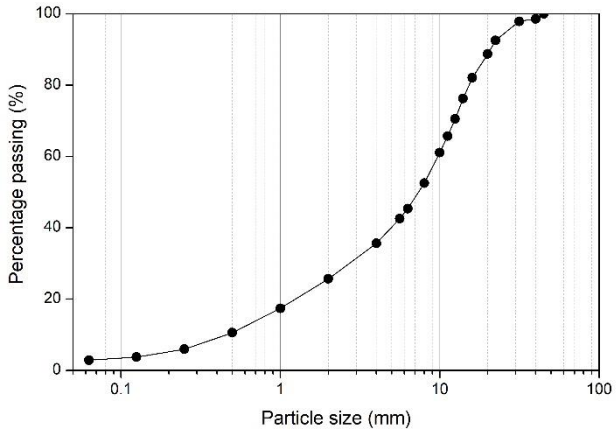

Figure 2. Particle size distribution of IBA.

The values obtained for the shape and flakiness indexes (Table 1) revealed that the coarse particles of IBA tended to be elongated and flaky. This is not a positive outcome considering, for instance, the use of IBA as filling material in road construction since that type of particles are more prone to fracturing when subjected to cyclic loads imposed by vehicle traffic.

Table 1. Shape and flakiness indexes of IBA.

Property	Result (%)
Shape index	40
Flakiness index	36

The main constituent of IBA was R_i, followed by R_g (Table 2). These two constituents accounted for 86.0% of the sample. The large amount of glass can be considered a drawback due to its brittle behaviour. This aspect can be associated with inadequate waste segregation conducted by households.

Table 2. Constituents of IBA.

Constituent	Percentage by mass (%)
R_u	2.1
R_b	9.4
R_g	37.4
R_m	2.5
R_i	48.5

The apparent (ρ_a), oven-dried (ρ_{rd}) and saturated (ρ_{ssd}) particle densities of the size fractions 0.063/4.0 mm and 4.0/31.5 mm, as well as the water absorption of IBA are shown in Table 3. The results showed that the size fraction 0.063/4.0 mm had lower densities (ρ_a, ρ_{rd} and ρ_{ssd}) and greater water absorption than the size fraction 4.0/31.5 mm. In addition, the densities of the size fraction 0.063/4.0 mm were below those normally found in natural aggregates. This feature, as well as the high water absorption, may configure a problem for using the lower size fraction of IBA as recycled aggregate in geotechnical engineering.

Table 3. Particle densities and water absorption of IBA.

Property	Size fraction	
	0.063/4.0	4.0/31.5
ρ_a (Mg/m^3)	2.28	2.40
ρ_{rd} (Mg/m^3)	1.69	2.12
ρ_{ssd} (Mg/m^3)	1.95	2.24
Water absorption (%)	15.2	5.5

3.2 Chemical analysis

The results obtained in the chemical analysis of IBA and its eluate are displayed in Tables 4 and 5. These tables also include the limit values defined in the Council Decision 2003/33/EC (EU, 2003) for inert (Criteria A) and non-hazardous (Criteria B) wastes, when applicable.

Table 4. Organic parameters of IBA (mg/kg).

Parameter	IBA	Criteria A
TOC	26000	30000
BTEX	5.5	6
PCBs	<0.021	1
Mineral oil	<20	500
PAHs	<0.16	100

Regarding the total content of organic parameters, IBA complied with all limit values to be classified as inert waste (Table 4), namely: TOC (total organic carbon), BTEX (benzene, toluene, ethylbenzene and xylenes), PCBs (polychlorinated biphenyls), mineral oil (C10 to C40), and PAHs (polycyclic aromatic hydrocarbons). The limit value of PAHs is set by each Member State and therefore the value indicated in Table 4 refers to the Portuguese legislation.

The results of the chemical analyses of the eluate (Table 5) showed that IBA complied with most of the requirements to be classified as inert waste. In total, five non-conformities were found: copper, chloride, sulphate, DOC (dissolved organic content) and TDS (total dissolved solids). When comparing with the criteria for non-hazardous waste, IBA complied with all limit values.

Table 5. Chemical analysis of the eluate (mg/kg).

Component	IBA	Criteria A	Criteria B
Arsenic	0.03	0.5	2
Barium	1.38	20	100
Cadmium	<0.04	0.04	1
Total chromium	<0.5	0.5	10
Copper	9.1	2	50
Mercury	<0.01	0.01	0.2
Molybdenum	0.28	0.5	10
Nickel	<0.3	0.4	10
Lead	<0.3	0.5	10
Antimony	<0.01	0.06	0.7
Selenium	0.01	0.1	0.5
Zinc	3.2	4	50
Chloride	4000	800	15000
Fluoride	<10	10	150
Sulphate	2200	1000	20000
Phenol index	0.3	1	—
DOC	580	500	800
TDS	15000	4000	60000

The copper and chloride contents were around 5 times higher than the limit values for classifying IBA as inert waste. Referring to the same classification, the excess in the sulphate content was smaller, being approximately twice the limit value. However, in this case, the Council Decision 2003/33/EC (EU, 2003) mentions that if the content of sulphate does not meet the 1000 mg/kg limit at a liquid to solid ratio of 10 L/kg, the residue can still be considered as complying if the value does not exceed 6000 mg/kg. Therefore, the excessive sulphate content in IBA ends up not being very relevant.

The excess in DOC was small, exceeding the limit value for classification as inert waste by 16.0%. The Council Decision 2003/33/EC (EU, 2003) also has a note for DOC, stating that if the waste does not meet the limit value for DOC at its own pH value (which was the case with IBA), it may be alternatively tested at a pH between 7.5 and 8.0. The test at this pH range was not carried out.

Finally, the TDS content exceeded by 3.75 times the limit value for classifying IBA as inert waste. The Council Decision 2003/33/EC (EU, 2003) does not provide any tolerance for TDS but mentions in a note that the value obtained for this parameter can be used alternatively to the values for sulphate and chloride. Therefore, considering that the sulphate and chloride contents were above the maximum allowable values, it is understandable that the TDS content exceeded its limit value. The previously mentioned note may also indicate that the analysis of TDS is not mandatory.

It should be noted that IBA is often pre-treated by natural weathering, which helps reducing its leaching potential (Bandarra et al., 2023). In the present work,

IBA was not submitted to any pre-treatment. Thus, the non-conformities with the acceptance criteria as inert waste could have been benefited if IBA had been subjected to weathering.

4 CONCLUSIONS

The results obtained in the physical, geometrical and chemical tests showed that most properties of IBA allow considering its use as recycled aggregate in geotechnical engineering applications. However, there were some non-conforming properties, which need to be improved. IBA pre-treatment operations are necessary.

The size fraction of IBA below 4 mm should be discarded due to its low densities and high water absorption. In addition, IBA will be benefited from the decrease of the glass content. Still, it should be noted that the high amount of glass may be a particularity of the sample studied in this work. IBA from other batches or generated in other incineration facilities may contain less glass.

IBA complied with the acceptance criteria defined in the European legislation for non-hazardous waste but failed some parameters declared for inert waste. Natural weathering of IBA, a common pre-treatment that was not adopted in this work, could be useful to improve the leaching behaviour, making this material more environmentally sustainable.

Finally, it will be important to carry out a more detailed analysis of the unidentifiable by-products of the incineration process (the main component of the coarse particles of IBA). Additional tests may include the determination of the elemental composition, the identification of mineral phases, the study of morphology, or the assessment of porosity.

ACKNOWLEDGEMENTS

This work was financially supported by: Base Funding – UIDB/04708/2020 with DOI 10.54499/UIDB/04708/2020 (https://doi.org/10.54499/UIDB/04708/2020) of the CONSTRUCT – Instituto de I&D em Estruturas e Construções – funded by national funds through the FCT/MCTES (PIDDAC). The authors wish to thank Lipor II (Maia, Portugal) for providing the incinerator bottom ash.

REFERENCES

Almeida, F., Vieira, C. S., Carneiro, J.R., Lopes, M. L. (2022). Drawing a Path towards Circular Construction: An Approach to Engage Stakeholders. *Sustainability*, 14(9): 5314. https://doi.org/doi.org/10.3390/su14095314.

Bandarra, B.S., Mesquita, G., Passos, H., Martins, R. C., Coelho, P. A. L. F., Pereira, J. L., Quina, M. J. (2023). An integrated characterisation of incineration bottom ashes towards sustainable application: Physicochemical, ecotoxicological, and mechanical properties, *Journal of Hazardous Materials*, 455(2023), 131649, https://doi.org/10.1016/j.jhazmat.2023.131649.

CEN (2002). EN 12457-4, Characterisation of waste – Leaching – Compliance test for leaching of granular waste materials and sludges – Part 4: One stage batch test at a liquid to solid ratio of 10 l/kg for materials with particle size below 10 mm (without or with size reduction), CEN, Brussels, Belgium.

CEN (2008). EN 933-4, Tests for geometrical properties of aggregates – Part 4: Determination of particle shape – Shape index, CEN, Brussels, Belgium.

CEN (2009). EN 933-11, Tests for geometrical properties of aggregates – Part 11: Classification test for the constituents of coarse recycled aggregate, CEN, Brussels, Belgium.

CEN (2012a). EN 933-1, Tests for geometrical properties of aggregates – Part 1: Determination of particle size distribution – Sieving method, CEN, Brussels, Belgium.

CEN (2012b). EN 933-3, Tests for geometrical properties of aggregates – Part 3: Determination of particle shape – Flakiness index, CEN, Brussels, Belgium.

CEN (2022). EN 1097-6, Tests for mechanical and physical properties of aggregates - Part 6: Determination of particle density and water absorption, CEN, Brussels, Belgium.

EU (2003). Council Decision 2003/33/EC establishing criteria and procedures for the acceptance of waste at landfills pursuant to Article 16 of and Annex II to Directive 1999/31/EC, Official Journal of the European Communities, L11/27, Brussels, Belgium.

UN (2015). Transforming our world: the 2030 Agenda for Sustainable Development – Resolution adopted by the General Assembly on 25 September 2015 (A/RES/70/1), United Nations, New York, United States of America.

Xuan, D., Tang, P., Poon, C. S. (2018). Limitations and quality upgrading techniques for utilization of MSW incineration bottom ash in engineering applications – A review. *Construction and Building Materials*, 190: 1091-1102. https://doi.org/10.1016/j.conbuildmat.2018.09.174.

Proceedings of the XVIII ECSMGE 2024
GEOTECHNICAL ENGINEERING CHALLENGES
TO MEET CURRENT AND EMERGING NEEDS OF SOCIETY
© 2024 the Authors
ISBN 978-1-032-54816-6
DOI 10.1201/9781003431749-390
Open Access: www.taylorfrancis.com, CC BY-NC-ND 4.0 license

ECSMGE 24
XVIII EUROPEAN CONFERENCE ON SOIL MECHANICS AND GEOTECHNICAL ENGINEERING

Design and execution of retaining-walls using the reinforced jet-grouting technique

Conception et réalisation de murs de soutènement par la technique du jet-grouting renforcé

J.L. Arcos*
Rodio Kronsa (Soletanche-Bachy Group), Madrid, Spain

X. Beal
Beal A.E.C., Escaldes-Engordany - Principat d'Andorra

R. Gil, J.M. Dimas, M. Segovia
Rodio Kronsa (Soletanche-Bachy Group), Madrid, Spain

**jlarcos@rodiokronsa.es*

ABSTRACT: This article presents a solution for the design and construction of reinforced jet-grouting structures. In particular, it discusses the application of reinforced jet-grouting for retaining walls in excavations for basement construction. The use of jet-grouting as a structural element with flexural work is not common, as this product is typically used almost exclusively under pure compression. Flexural forces require the reinforcement of this material with steel bars, and the use of a finite element model is presented as a possible design tool for this purpose. The work described was successfully completed using the concept of reinforced jet-grouting with corrugated steel bars. Additionally, the article outlines the specific procedure for performing jet-grouting in a complex colluvial geology with large, embedded rock blocks in a heterogeneous granular matrix, making it challenging to create ideal intersecting cylindrical jet-grouting columns.

RÉSUMÉ: Cet article présente une solution pour la conception et la réalisation de structures renforcées de jet-grouting. En particulier, l'étude de la solution de jet-grouting renforcé appliquée aux murs de soutènement des excavations pour la construction des sous-sols est commentée. La technique du jet-grouting en tant qu'élément de structure avec travail de flexion n'est pas courante puisque ce produit est généralement utilisé presque exclusivement en compression pure. Les efforts de flexion rendent nécessaire de renforcer ce matériau avec une armature en acier et l'utilisation d'un modèle d'éléments finis est présentée comme un outil de conception possible à cet effet. Les travaux commentés, menés à bien, ont été calculés et exécutés avec ce concept de jet-grouting renforcé de barres d'acier ondulées. De même, l'article présente la procédure particulière pour effectuer le jet-grouting dans une géologie colluviale complexe avec de grands blocs de roche encastrés dans une matrice granulaire hétérogène qui rendent difficile la réalisation de colonnes cylindriques idéales de jet-grouting se croisant.

Keywords: Jet-grouting; retaining walls.

1 GUIDELINES

This article introduces a specific procedure for the design and construction of retaining walls using the reinforced jet-grouting technique in areas with complex colluvial geology. To provide a practical example, the application of this method is illustrated through a project carried out in Andorra la Vella (Andorra). The project was designed by the architect Jordi Batlle Jordana, and the original calculations were performed by Beal AEC, S.L. using their own methods.

Jet-grouting technology enables the creation of cement-treated soil volumes with significantly improved strength and deformation properties compared to the original soil, while also achieving a substantial reduction in permeability. However, it is uncommon to use this technique for creating structural inclusions in the ground capable of withstanding flexural forces, such as retaining walls.

In the specific case we present, the choice of the structural type of retaining wall is influenced by two main factors:

- The ground consists of colluvial soil with large rock boulders (>1m) within a heterogeneous granular matrix.
- The water table is high, located above the excavation floor.

1.1 Containment geometry

The case that serves as our example involves an excavation for constructing multiple basement levels on a site with a sloping topographic surface, featuring an elevation difference of about 10 meters, ranging from 1028 to 1018. The site covers an area of approximately 8000 square meters, and the required excavation depth entails the construction of retaining walls, spanning heights from 7.50 to 16.50 meters. (See Figure 1 and Figure 2).

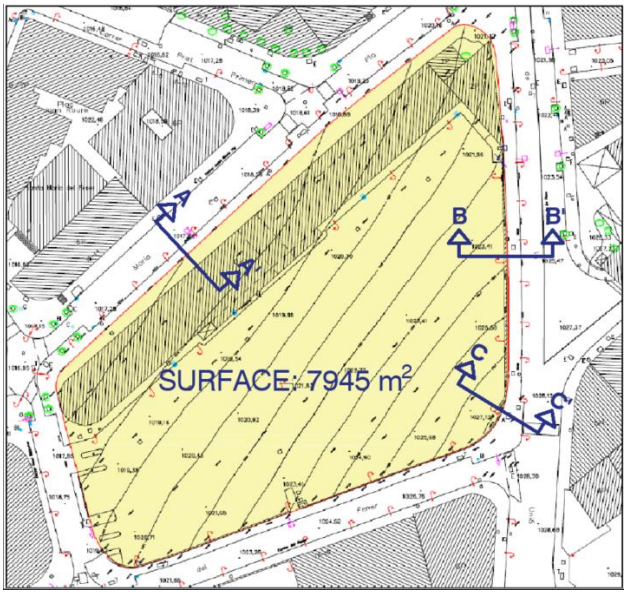

Figure 1. Perimeter of the excavation and location of the typical cross-sections.

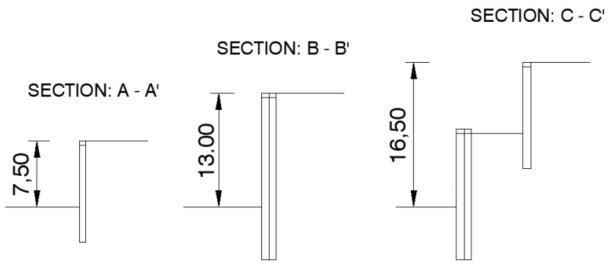

Figure 2. Typical cross-section, showing the highs of the contention in meters.

1.2 Ground characteristics

The ground to be excavated and retained consists of a thin anthropic layer followed by a thick, coarse fluvio-torrential alluvial layer with granite boulders of up to 1 meter in size, within a heterogeneous granular matrix of sand and gravel.

Distinct layers can be identified:

Geotechnical Layer 1: Surface Granular Material

- Density: 18 kN/m3
- Cohesion: 0,0 kN/m^2
- Friction Angle: 28º
- Deformation Modulus: 11 MPa

Geotechnical Layer 2: Fluvial-Torrential Granular Material (Figure 3)

- Density: 19,8 kN/m^3
- Cohesion: 5,0 kN/m^2
- Friction Angle: 30º
- Deformation Modulus: 44 MPa



Figure 3. Soil samples taken from Geotechnical Layer 2. Granite boulders wrapped in sandy clay matrix.

2 EXECUTION OF STRUCTURAL WALLS USING REINFORCED JET-GROUTING

The walls were constructed using secant soil columns treated with jet-grouting. Jet-grouting columns are created by mixing the soil with a slurry through drilling to the maximum depth of the column and blending it with cement slurry during the ascent, with rotation of the drilling rods. (See Figure 4).

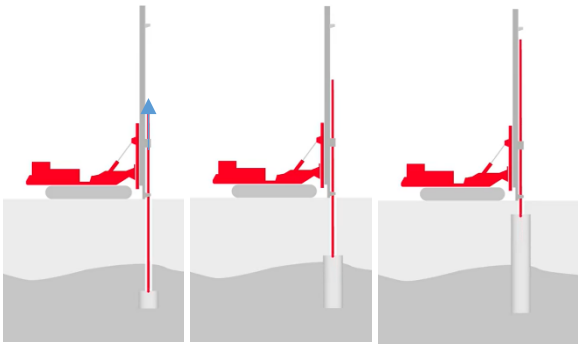

Figure 4. Execution of a jet-grouting column. From bottom to top, withdrawal with rotation while de cement slurry is injected.

Among the different variants of jet-grouting, the one commonly known as Type 1 jet-grouting was used, which employs a cement slurry as the cutting and mixing fluid (For further information on jet-grouting, you can refer to P. Croce 2014 book.).

However, executing a jet-grouting column in soil with large rock boulders, as is the case here, presents a

series of challenges that, until recently, seemed insurmountable:

2.1 Challenges in executing Jet-grouting columns in alluvial boulder deposits

- The initial drilling is generally performed with rotary drilling equipment, which is incapable of penetrating the rocky boulders that require rotary-percussive drilling. Rotary drilling is traditionally used for jet-grouting as it allows the injection of slurry through the drilling rods.
- Large boulders hinder the formation of a jet-grouting column with a cylindrical geometry since the "shadow effect" caused by any intercepted rock boulder screens the ideal axial symmetry of the jet. (See Figure 5)

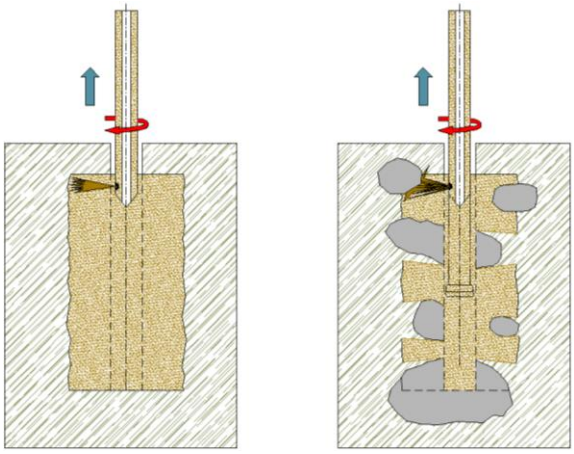

Figure 5. Comparison of Column Formation in Fine Granular Soil and Soil with Large Boulders.

2.2 Solution to the execution challenges of jet-grouting in rocky boulders

To address the previously mentioned problems, the following measures were taken:

a) A DHH pointed hammer was used at the bottom of the drilling to enable rotary-percussive drilling of the rocky boulders. In order to conduct the compressed air to the bottom hammer and, simultaneously, to conduct the cement slurry to the monitor at the bottom of the drilling rod, a Type 2 jet drilling rod with double concentric pipes was used. (See Figure 6).

Note: Commonly, the Type 2 jet drilling rod is a dual rod that allows the conduction of compressed air to a dual nozzle through which cement slurry is injected, enveloped in a concentric jet of air, reducing the dispersion of the jet and concentrating its energy in a smaller impact area.

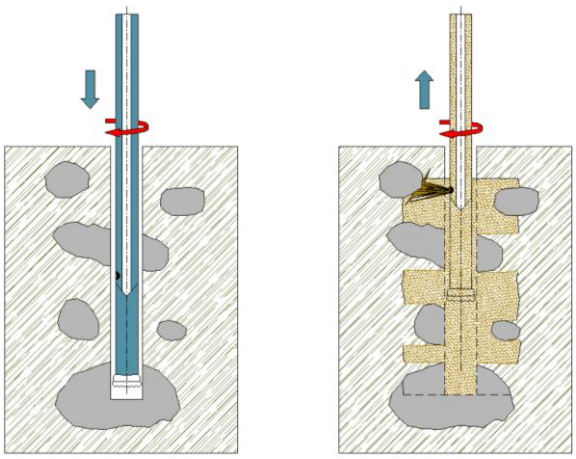

Figure 6. Drilling and injection phase. During drilling, the compressed air actions the hammer. During withdrwal, the cement grout jet erodes the soil and mixes with it.

b) The wall geometry is designed with two or three overlapping rows of jet-grouting columns, ensuring the continuity and impermeability of the wall despite the irregularities that may be caused by intercepted boulders. (See Figure 7).

Plan layout of jet-grouting columns: double or triple row of columns: (See Figure 7).

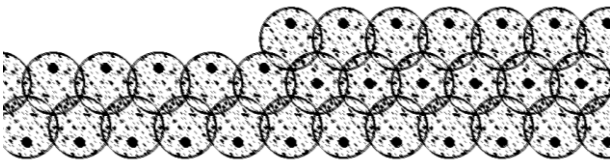

Figure 7. Layout of the jet-grouting columns in plan. The thickness of the wall is created by a double or triple row of intersecting columns.

3 ALTERNATIVE DESIGN METHODS FOR REINFORCED JET-GROUTING WALLS

The common approach for calculating or designing a jet-grouting wall is to model it as a plate element (or the cross section as a 1D beam) that interacts with the ground in terms of stress and deformation. It's also common to model the interaction between the wall and the ground using an elasto-plastic spring model.

When the jet-grouting wall is thick and unanchored, it can be considered as a gravity wall where the self-weight of the jet-grouted volume plays a crucial role in supporting the excavation. In cases where the jet-grouting wall is heavily reinforced, for example, with HEB-type beams and anchors, the stiffness of the wall is typically only considered with the metallic beams, disregarding the structural collaboration of the jet-grouting.

However, when the jet-grouting wall is designed as a two-dimensional, flexible, and anchored element, and its reinforcement is light, for example, with corrugated steel bars (rebars or threaded bars), various considerations arise when modeling this "composite retaining wall", particularly in terms of modeling the behavior of the jet-grouting material.

Since the thickness of the wall consists of a treated and resistant soil volume and steel reinforcement, similar to reinforced concrete, one could model the section as a two-dimensional element with the characteristics of a reinforced concrete plate. However, the configuration of jet-grouting walls consists of overlapping columns in one, two, or even three rows (see Figure 7). This makes the wall thickness significant in relation to the other two dimensions, and a 2D plate model raises certain doubts regarding its suitability.

For these cases of thick, lightly reinforced, anchored jet-grouting walls, we propose the possibility of using a finite element model with a specific representation of the jet-grouting wall thickness.

In the case study, we have created a model for different sections of the retaining wall with the grids shown in Figure 8.

This model offers the advantage of evaluating the influence of the jet-grouting wall thickness and its interactions with anchors and parallel walls.

World experience on the problem of reinforced jet-grouting working as a wall is presented as case studies for many authors, but references do not mention design method or simply reference to conventional D-Wall calculation or Soldier-pile calculation. For Finite Element design of this type of jet-grouting walls the authors could find the Thesis of David Tran Yohanes Armediaz: *On the Modelling of Jet Grouting for Deep Excavation Analysis*, Chalmers University of Technology, Gothenburg, Sweden 2021.

Regarding the modeling of jet-grouting material, there are also references that discuss how to parameterize a low-strength mass concrete using the parameters of a Mohr-Coulomb model (for reference, see: Plaxis Bulletin, Spring issue 2009, www.plaxis.nl).

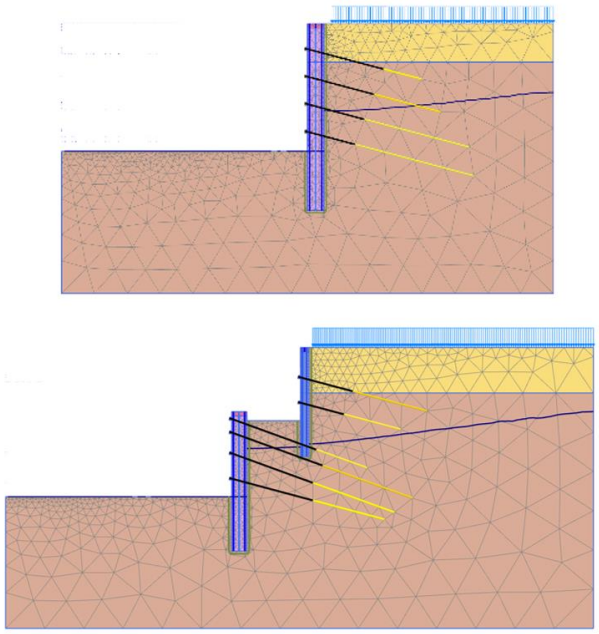

Figure 8. Finite element meshes used to model the jet-grouting walls in the case study.

Additionally, to account for the cracking of jet-grouting under tension, a conservative approach was taken by assuming zero tensile strength in the jet-grouting, instead of the usual approximate value of $f_{ctk}=10\%\cdot f_{ck}$, a value of $f_{ctk}=0$ was used. This consideration particularly affects the deformation of the wall since there is no tensile collaboration of the jet-grouting in the elastic phase before reaching plasticity.

Working in this manner and modeling the embedded steel bars in the jet-grouting as equivalent stiffness steel plate elements, it is possible to obtain the stresses generated in the jet-grouting and perform the corresponding design check (see Figure 9). The stresses in the reinforcing steel bars can also be obtained from this model based on the efforts in the plate elements that represent them.

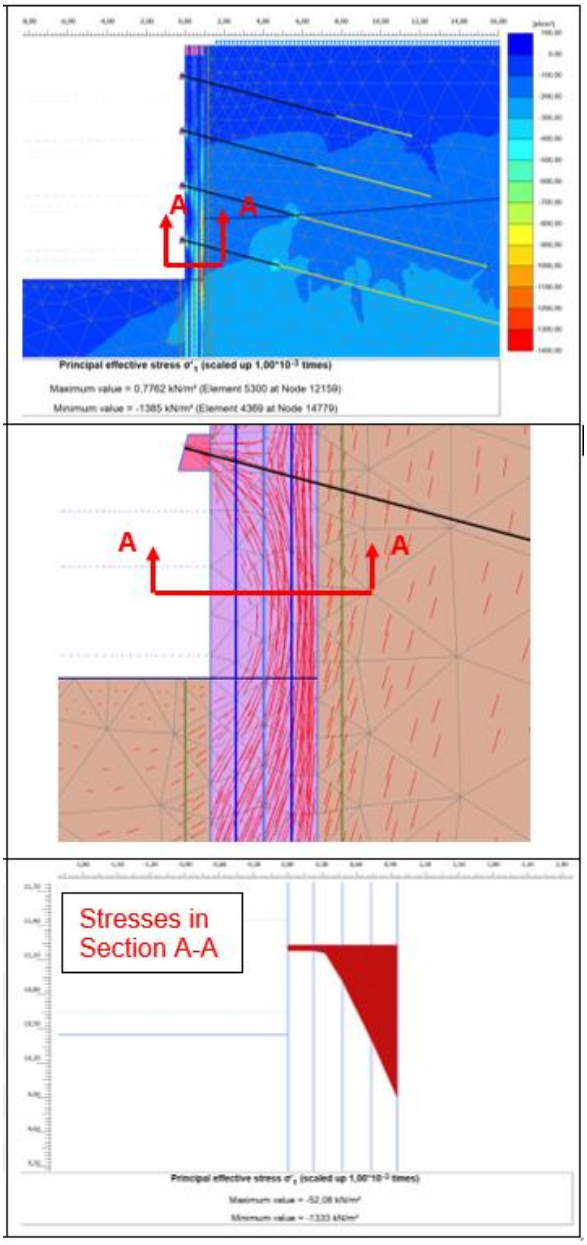

Figure 9. Estimation of the stresses generated in the body of the jet-grouting.

4 CONCLUSIONS

In the "El Fener" project in Andorra la Vella, a retaining wall has been successfully constructed using jet-grouting columns. The geotechnical complexity of the terrain required the development of jet-grouting execution systems that are compatible with the ability to drill throuh large granite boulders. To achieve this, the team has implemented rotary-percussive hammers at the tip of the drilling rods, under the jet-grouting nozzle holder.

The design of the wall, composed of 2 and 3 overlapping rows of overlapping jet-grouting columns, has ensured excellent structural performance as well as impermeability to the high-water table behind the wall.



Figure 10. Some photographs of the retaining wall after the excavation of the site.

The final result after excavation can be seen in the photographs in Figure 10.

The utilization of finite element models has made it easier to evaluate the stresses within the jet-grouting body and the embedded reinforcing steel. The finite element modeling has considered the behavior of the jet-grouting material according to an elasto-plastic Mohr-Coulomb type model, without tensile strength capacity.

Proceedings of the XVIII ECSMGE 2024
GEOTECHNICAL ENGINEERING CHALLENGES
TO MEET CURRENT AND EMERGING NEEDS OF SOCIETY
© 2024 the Authors
ISBN 978-1-032-54816-6
DOI 10.1201/9781003431749-391
Open Access: www.taylorfrancis.com, CC BY-NC-ND 4.0 license

ECSMGE 24
XVIII EUROPEAN CONFERENCE ON SOIL MECHANICS AND GEOTECHNICAL ENGINEERING

Pile driveability predictions of open ended tubular piles in sand using the Unified Method

Prédictions de la conduite des pieux tubulaires à extrémité ouverte dans le sable dense selon la méthode unifiée

K. Argyroulis*
SBE Engineering Consultants, Rotterdam, The Netherlands

J. Putteman
SBE Engineering Consultants, Sint-Niklaas, Belgium

K. Gavin
Civil Engineering and Geosciences, TU Delft, Delft, The Netherlands

A.A. Roubos
Civil Engineering and Geosciences, TU Delft, Delft, The Netherlands;
Port of Rotterdam Authority, Rotterdam, The Netherlands

**konstantinos.argyroulis@sbe-engineering.nl*

ABSTRACT: In this study, driving records of 18 open-ended steel tubular piles installed in dense sandy soil conditions at five sites in the Netherlands were utilized to evaluate models that are currently used in practice for predicting the static soil resistance during driving (SRD), as well as a recently developed method, known as the Unified Method. Since the Unified Method is a static axial capacity-CPT-based design method, slight modifications to the originally proposed formulas were examined to allow estimation of the SRD. This paper presents a modified format of the Unified Method and its performance is assessed by comparing predicted with measured hammer blow count profiles. It is eventually shown that the modified Unified Method leads to overall improved blow count predictions compared to current approaches.

RÉSUMÉ: Dans cette étude, les enregistrements de battage de 18 pieux tubulaires en acier à extrémité ouverte installés dans des conditions de sol sableux denses sur cinq sites aux Pays-Bas ont été utilisés pour évaluer les modèles actuellement utilisés dans la pratique pour prédire la résistance statique du sol pendant le battage (SRD), ainsi qu'une méthode récemment développée, connue sous le nom de méthode unifiée. Étant donné que la méthode unifiée est une méthode de conception basée sur la capacité axiale statique CPT, de légères modifications des formules initialement proposées ont été examinées pour permettre l'estimation du SRD. Cet article présente un format modifié de la méthode unifiée et ses performances sont testées en comparant les profils de nombre de coups de marteau prédits et mesurés. Il est finalement démontré que la méthode unifiée modifiée conduit à des prévisions globalement améliorées du nombre de coups par rapport aux approches actuelles.

Keywords: Pile driveability; SRD; Unified Method.

1 INTRODUCTION

The driving process is commonly assessed by utilizing commercially available pile driveability software that are based on 1-D wave equation analysis. These enable the modelling of the hammer – pile – soil system as a series of masses and springs and simulate the stress wave phenomena during the installation process.

The total soil resistance consists of both a static and a dynamic component and is usually represented by elasto-plastic springs with dashpots at the toe and around the pile shaft area. The static component, also referred to as SRD (static resistance during driving), represents the cumulative increase of shaft resistance with further pile penetration, and the toe resistance associated with each driving increment (Prendergast et al (2020)). The dynamic component is typically quantified by damping factors (Schneider et al (2010)) that depend on soil type and is expressed as function of the SRD.

This paper examines the applicability of the Unified Method (Lehane et al (2020)) in driveability predictions. The Unified Method is a CPT-based static axial capacity design method for driven piles in silica sand. This design approach is included in the 2022 edition of ISO-19901-4 replacing the four CPT methods (ICP-05, Fugro-05, NGI-05 and UWA-05).

Since SRD differs from pile axial capacity in terms of consolidation, stress equalization, and time effects (Schneider et al (2010), Byrne et al (2018), Prendergast et al (2020)) modifications are required to allow estimation of SRD. The modifications applied to the Unified Method are inspired by the ones proposed by Byrne et al (2018) and Prendergast et al (2020) that were successfully applied at very similar axial capacity design methods (ICP-05, UWA-05) for estimation of the SRD, leading to improved driveability predictions.

A common and practical way to assess the pile driving resistance using specific hammering equipment, is through the number of required hammer blows per 25 cm increment of penetration. Utilizing as input to the driveability model the impact hammer energy record of 18 open-ended tubular piles driven in mainly dense sand conditions at 5 sites in the Netherlands, an assessment of the modified Unified Method is made as well as a comparison with frequently used in practice SRD models in terms of predicted against measured hammer blows per 25cm.

2 MODIFIED UNIFIED METHOD

Analytical explanation of the Unified Method and of the formulas used to calculate the shaft and toe capacity can be found in Lehane et al (2020). The following sections provide the modifications that were applied to this method, which can also be found in detail in the Master Thesis by Argyroulis (2022). Section 2.3 provides the formulas of the modified Unified Method.

2.1 Modified shaft resistance

The Unified CPT-based Method was calibrated using the 'Unified database' (Lehane et al (2017)) comprising 71 static pile load tests in siliceous sand deposits with diameters between 300 and 800 mm. As explained in Lehane et al (2020), the shaft capacity of driven piles in sand increases with time over a period of about one year and the Unified Method was calibrated to estimate the shaft capacity at around 14 days after driving. Therefore, the shaft resistance during driving will be lower than the shaft capacity currently estimated by this approach.

Jardine et al (2006) interpretation of Intact Ageing Curves of piles installed in the Dunkirk (France) dense sand revealed that the shaft capacity 1 day after driving was approximately 70% of the shaft resistance estimated with the ICP-05 method (10-30 days after installation). Lehane et al (2017), included records from piles installed in dense sand at Blessington (Ireland) and Lavrik (Norway) and derived the following time factor (best fit line – (1)) that can be applied when using the pile capacity methods: API-00, ICP-05, UWA-05, Fugro-05 and NGI-05:

$$F_{time} = \frac{1}{exp(-0.1*t^{0.68})+0.45} + d_{offset} \qquad (1)$$

where t (days) after installation and d_{offset} (-) an offset value depending on the method used.

Setting the offset and time to zero a factor of about 0.7 is obtained. By using a time factor of 0.7, Byrne et al (2018) and Prendergast et al (2020) showed improved driveability predictions when using the ICP-05 and UWA-05 methods. Due to great similarity of the aforementioned CPT based design methods (API-00, ICP-05, UWA-05, Fugro-05 and NGI-05) with the Unified Method, 70% of the shaft capacity predicted with this method is considered to be a reasonable estimation of the shaft resistance mobilized during driving.

2.2 Modified toe resistance

The original toe resistance formulation cannot be directly used for pile driveability predictions since the base resistance estimated, is the one mobilized at pile tip displacements equal to 10% the pile diameter. In normal driving conditions though, the pile will only displace a few mm per hammer blow. Thus, for driveability analysis, it is required to define the maximum toe resistance that corresponds to the assumed quake value (displacement at yield). Signal matching analyses of dynamic driving data indicate quake values of about 2.5 mm for both the shaft and toe resistances.

Due to its simplicity the recommended by API (2000) tip load-displacement model (Table 1) was used in this case to derive an appropriate toe resistance mobilized during driving.

*Table 1. Pile tip-load-displacement (Q-z) curve (*API (2000)*).*

$\frac{w_b}{D}$	$\frac{q_b}{q_{b0.1}}$
0.002	0.25
0.013	0.5
0.042	0.75
0.073	0.9
0.1	1

where w_b represents the base displacement (mm), D is the pile diameter (mm), $qb_{0.1}$ is the mobilized toe resistance at 10% the pile tip displacement (kPa), and q_b (kPa) the mobilized toe resistance at w_b tip displacement. Utilizing the original formula of toe resistance of the Unified Method and a quake value of

2.5 mm, the mobilized q_b driving toe resistance can be determined.

Based on Table 1, equation (10) was developed to match the tabulated API base displacement response with the addition of an extra term used to account for residual loads (q_{res}) after a hammer blow. While Paik et al (2003) measured that residual stresses were in the range of 11-14% of the CPT qc value for 356 mm (diameter) open and closed-ended piles in dense sand, Byrne et al (2018) suggested values 1-10% of the qc in medium dense sands for large offshore steel open-ended monopiles. Clearly, there is an uncertainty on the residual loads, and thus a 10% of the $qb_{0.1}$ was used in the following case studies presented.

2.3 Formulas of modified Unified Method

Below the modified formulas of the Unified Method that can be used to estimate the SRD are presented.

Shaft resistance

$$Q_{shaft} = \pi * D * \int_0^L \tau f_{SRD} dz \quad (2)$$

$$\tau f_{SRD} = F_{time} * (\sigma'_{rc} + \Delta\sigma'_{rd}) * tan\delta_f \quad (3)$$

$$\sigma'_{rc} = \frac{q_c}{44} * A_{re}^{0.3} * \beta \quad (4)$$

$$\beta = \left[\max\left(1, \frac{h}{D}\right)\right]^{-0.4} \quad (5)$$

$$A_{re} = 1 - PLR * \left(\frac{D_i}{D}\right)^2 \quad (6)$$

$$PLR = \tanh\left[0.3 * \left(\frac{D_i}{D_{CPT}}\right)^{0.5}\right] \quad (7)$$

$$\Delta\sigma'_{rd} = \left(\frac{q_c}{10}\right) * \left(\frac{q_c}{\sigma'_v}\right)^{-0.33} * \left(\frac{D_{CPT}}{D}\right) \quad (8)$$

where:

τf_{SRD}	unit shaft resistance (kPa)
D	outer pile diameter (m)
D_i	inner pile diameter (m)
D_{CPT}	CPT cone diameter, 0.0357 m
F_{time}	time factor, 0.7 (-)
σ'_{rc}	radial effective stress (kPa)
β	fatigue factor (-)
h	distance of soil horizon from pile tip (m)
$\Delta\sigma'_{rd}$	increase in radial effective stress (kPa)
δ_f	constant volume friction angle, 29°
A_{re}	effective area ratio (-)
PLR	plug length ratio (-)

Toe resistance

$$Q_b = q_{b_{SRD}} * \pi * \frac{D^2}{4} \quad (9)$$

$$qb_{SRD} = 2.23 * \left(\frac{w_b}{D}\right)^{0.347} * q_{b0.1} + q_{res} \quad (10)$$

$$q_{b0.1} = (0.12 + 0.38 * A_{re}) * qc \quad (11)$$

$$q_{res} = 0.1 * q_{b0.1} \quad (12)$$

3 REMARKS ON MODIFIED UNIFIED METHOD

Some important notes regarding the modified and original Unified Method are summarized below.

With respect to the shaft resistance, the one calculated by equation (3) represents the shaft resistance developed at the external shaft area of the pile. Other SRD models, like the Alm & Hamre (2001) which is used for comparison in the case studies below, incorporate the internal shaft resistance to the external shaft formulation of open-ended piles, while the toe resistance is acting on the pile tip annular area. Contrary to these models, the Unified Method accounts for the internal shaft resistance (plug resistance) to the toe resistance formulation (equation (9)). In that sense it can be expected that for large offshore piles the (modified) Unified Method will predict lower (external) shaft resistance compared to the (external and internal) shaft resistance of Alm & Hamre (2001) model, while the opposite occurs for toe resistance since the modified Unified Method is applied at the gross pile base area, taking into account as well the (inner shaft resistance) plug resistance. This will eventually result in a similar estimation of SRD.

Furthermore, it should be noted that the shaft resistance of the (original) Unified Method considers variation of τf with the degree of soil displacement imparted during driving. This is quantified, as explained in Lehane et al (2020), with the effective area ratio A_{re} that represents the ratio of the soil volume displaced during installation to the pile total volume and the plug length ratio, PLR. Therefore, the original formulas are not only applicable to fully coring cases, but also to partially plugged piles ($PLR < 1$) or even to close ended piles ($A_{re} = 1$). Although the modified version is basically 70% (time factor) of the original shaft resistance, this paper evaluates only fully coring cases, while it would be interesting in the future to assess the performance of the modified Unified Method for closed-ended or partially plygged piles.

Finally, it is mentioned for the modified toe resistance that formula (10) allows the calculation of the maximum driving toe resistance for any quake value chosen (e.g., w_b based on specific project data), while the residual load used requires further research.

4 CASE STUDIES

The detailed analysis of the 18 open-ended piles can be found in (Argyroulis (2022)). In this section, the hammer blow count post-predictions of 5 open-ended piles from 5 locations (Port of Rotterdam, Eemshaven) in the Netherlands are presented (Figure 1, Figure 2, Figure 3). The modified Unified Method is denoted as UM (2020) SRD. It is stated that the piles of APM, RWG, SIF and HHTT terminals (Port of Rotterdam) were partially driven by a vibratory hammer (not examined in this paper), and later on the target depth was reached using hydraulic and diesel impact hammers. It is mentioned that the impact hammer energy was recorded during installation and was used as input into the driveability model, so that the outcome is mainly affected by the chosen SRD model. The results of the UM (2020) SRD are mainly compared to the most frequently used Alm & Hamre (2001) model, while for APM and RWG terminals, predictions were also made with the Stevens et al (1982) model. The AllWave-PDP driveability software was used for the purposes of this study.

5 CONCLUSIONS

Although this study is limited to pile diameters of 1.4 m (APM, RWG, SIF, HHTT terminals) and 0.76 m (EURIPIDES) it can be seen that the Unified Method, when slightly modified is capable of reproducing the hammer blows during installation. A way to assess the predictions made by the SRD models and the actual blow counts measured is through the Mean Absolute Percentage Error (MAPE) as a measure of average deviation between predicted and measured values. It was observed that the modified Unified Method has less deviation from the actual record of blows counts than the Alm & Hamre (2001) model in 13 out of 18 cases, whereas in 3 cases (out of 18) the modified Unified Method showed a slight over-under prediction, and in the remaining 2, both models showed the same deviation (Argyroulis (2022)). Despite that, the Alm & Hamre (2001) model is still very reliable model as can be seen in the figures below. The Stevens et al (1982) model, although it is a very practical and easy to use model, since it doesn't consider friction fatigue it tends to overpredict the number of blows (e.g., RWG terminal, Figure 1).

Further research is required to investigate the appropriate diameter range for which the modified Unified Method can be used, as well as variation in soil conditions (e.g., inclusions of soft clay layers).

Finally, the importance of collecting high quality driving records should be highlighted as the only way to improve the efforts made for more reliable driveability predictions, which may lead to minimization of installation risks and construction delays.

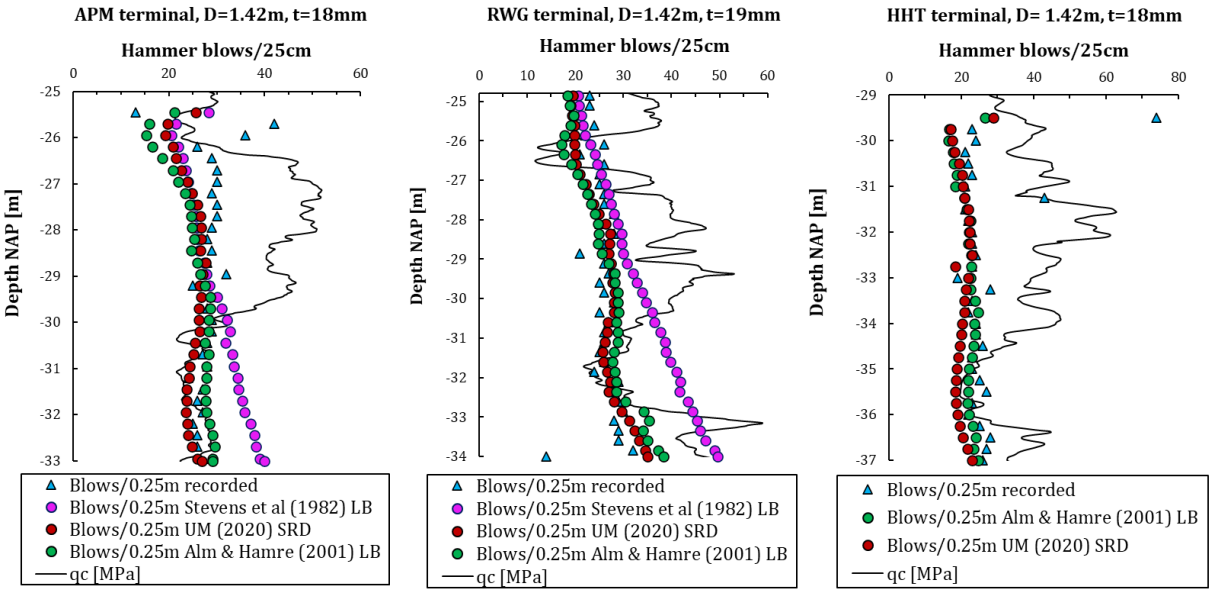

Figure 1. Post driveability predictions of hammer blow count profiles for terminals APM, RWG and HHTT at Maasvlakte, Rotterdam. Hydraulics hammers IHC S-200, IHC SC-200 and IHC S-280 were used.

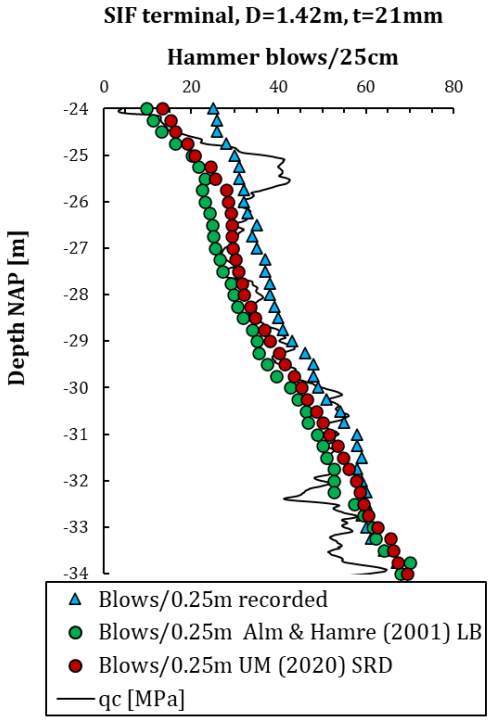

Figure 2. Post-predicted blow count profile for SIF terminal at Maasvlakte, Rotterdam. A Delmag D100-13 diesel hammer was used.

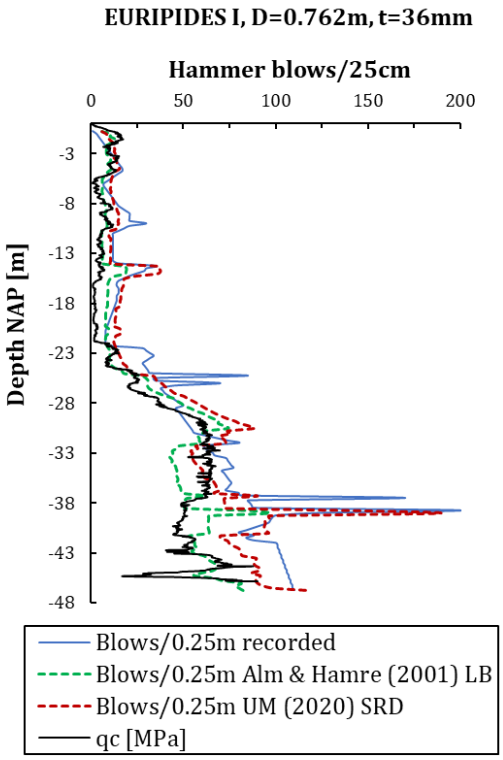

Figure 3. Post-predicted blow count profile for EURIPIDES project at Eemshaven. A IHC S-90 hydraulic hammer was used.

REFERENCES

Allnamics, AllWave-PDP, Driveability Software for Impact Driving, Available at: https://allnamics.com/en/portfolio-posts/allwave-pdp-driveability-software-for-impact-hammers/.

Alm, T., Hamre, L. (2001). Soil Model for Pile Driveability Predictions Based on CPT Interpretations. *Proceedings of the 15th International Conference on Soil Mechanics and Foundation Engineering,* Istanbul, Turkey, pp. 1297–1302.

API (2000). API RP2A-WSD, Recommended Practice for Planning, Designing, and Constructing Fixed Offshore Platforms–working Stress Design, American Petroleum Institute, Washington, DC.

Argyroulis, K. (2022). *Performance of steel open ended pile driveability prediction methods in dense sand*, Master Thesis, Delft University of Technology. Available at: http://resolver.tudelft.nl/uuid:bb85aefa-bd35-4c1d-90b3-1a5788d91050.

Byrne T., Gavin, K., Prendergast L.J., Cachim, P., Doherty P. and Pulukul S.C. (2018). Performance of CPT-based methods to assess monopile driveability in North Sea sands, *Ocean Engineering*, 166, pp.76-91, https://doi.org/10.1016/j.oceaneng.2018.08.010.

Jardine, R., Standing, J., Chow, F. (2006). Some observations of the effects of time on the capacity of piles driven in sand, *Geotechnique*, 56, pp.227–244, https://doi.org/10.1680/geot.2006.56.4.227.

Lehane, B.M., Lim, J.K., Carotenuto, P., Nadim, F., Lacasse, S., Jardine, R., van Dijk, B.F.J. (2017). Characteristics of Unified Databases for Driven piles, *Offshore Site Investigation Geotechnics 8th International Conference Proceedings*, London, UK, 1, pp.162-194, https://doi.org/10.3723/OSIG17.162.

Lehane, B., Liu, Z., Bittar, E., Nadim, F., Lacasse, S., Jardine, R. J., Carotenuto, P., Jeanjean, P., Rattley, M., Gavin, K., Haavik, J., & Morgan, N. (2020). A New 'Unified' CPT-Based Axial Pile Capacity Design Method for Driven Piles in Sand, In *Proceedings of the 4th International Symposium on Frontiers in Offshore Geotechnics*: *American Society of Civil Engineers*, pp.463-477.

Paik, K., Salgado, R., Lee, J., Kim, B. (2003). Behavior of open- and closed-ended piles driven into sands. *Journal of Geotechnical and Geoenvironmental Engineering*, 129, pp.296–306. https://doi.org/10.1061/(ASCE)1090-0241(2003)129:4(296).

Prendergast, L.J., Gandina, P., Gavin, K. (2020). Factors Influencing the Prediction of Pile Driveability Using CPT-Based Approaches, *Energies,* 13(12), [3128]. https://doi.org/10.3390/en13123128.

Schneider, J., Harmon, I. (2010). Analyzing drivability of open ended piles in very dense sands, *DFI Journal - The Journal of the Deep Foundations Institute*., 4(1), pp.32–4, https://doi.org/10.1179/dfi.2010.003.

Stevens, R., Wiltsie, E., Turton, T.(1982). Evaluating drivability for hard clay, very dense sand, and rock, *Offshore Technology Conference,* Houston, USA, https://doi.org/10.4043/4205-MS.

Proceedings of the XVIII ECSMGE 2024
GEOTECHNICAL ENGINEERING CHALLENGES
TO MEET CURRENT AND EMERGING NEEDS OF SOCIETY
© 2024 the Authors
ISBN 978-1-032-54816-6
DOI 10.1201/9781003431749-392
Open Access: www.taylorfrancis.com, CC BY-NC-ND 4.0 license

ECSMGE 24
XVIII EUROPEAN CONFERENCE ON SOIL MECHANICS AND GEOTECHNICAL ENGINEERING

Experimental study of geotextiles effects on bearing capacity of a non-lateritic tropical soil

Étude expérimentale de l'effet des géotextiles sur capacite portante d'um sol tropical non latéritique

M.G. Avelar*, P.C. Rodrigues
Instituto Federal do Espírito Santo, IFES, Nova Venécia (ES), Brazil

H.N. Pitanga
Universidade Federal de Juiz de Fora, UFJF, Juiz de Fora (MG), Brazil

**mavelar@ifes.edu.br*

ABSTRACT: This study presents the results of a series of California Bearing Ratio (CBR) index tests aimed at investigating reinforced soil samples with woven and non-woven geotextile inclusions positioned at H/2 and 1/4H from the top of the specimens, compacted at standard Proctor energies. The samples used in the research are derived from a residual soil of a typical soil profile in the state of Minas Gerais, Brazil, classified according to the Miniature, Compacted, Tropical (MCT) methodology as non-lateritic clayey (NG'). The main conclusions of the research were: i) the occurrence of reinforcement mechanisms in soils due to inclusions was not observed; ii) geotextiles positioned at H/2 from the top of the specimens exhibited higher CBR values; iii) the CBR test does not reflect the real conditions of soil-geosynthetic systems in the layers of a reinforced road.

RÉSUMÉ: Cette étude présente les résultats d'une série d'essais d'indice de portance Californie (CBR) visant à examiner des échantillons de sol renforcés avec des inclusions de géotextiles tissés et non tissés, positionnés à H/2 et 1/4H du sommet des éprouvettes, compactés aux énergies normales de Proctor. Les échantillons utilisés dans la recherche proviennent d'un sol résiduel d'un profil de sol typique de l'État de Minas Gerais, Brésil, classifié selon la méthodologie Moisture, Compacted, Tropical (MCT) comme argileux non latéritique (NG'). Les principales conclusions de la recherche étaient: i) on n'a pas observé l'occurrence de mécanismes de renforcement dans les sols en raison des inclusions; ii) les géotextiles positionnés à H/2 du sommet des éprouvettes ont montré des valeurs de CBR plus élevées; iii) l'essai CBR ne reflète pas les conditions réelles des systèmes sol-géosynthétiques dans les couches d'une route renforcée.

Keywords: Tropical soil; CBR; geotextile; non-lateritic soil; inclusions.

1 INTRODUCTION

1.1 General considerations

Geosynthetic effectiveness as roads reinforce is strictly related to several factors as subgrade quality, embankment layers composition and thickness, base and subbase, besides the applied load and materials interaction as discussed by Perkins (1999) and Ghosh and Medhav (1994). Support capacity plays as a crucial element for pavements construction and depends on soil features and its compression characteristics.

Santos et al. (1988) declared preference for granular materials as sands and graded crushed rocks due to their potential to increase the California Bearing Ratio (CBR) of the foundation soil.

However, project economic viability may be compromised depending on materials acquisitions and transportation costs, especially when importation is necessary as highlighted by Jotisankasa and Rurgchaisri (2018).

It is usual to use CBR for measurements of soil support capacity. Thus, geotextiles using in non-pavemented roads are recommended when CBR values of the foundation soil are less than 10% aimed to increase subgrade support capacity and to mitigate side effects of erosive processes and wear and tear from road traffic. However, geotextile using in asphaltic pavements news is less common, being economically justified for thick cover layers and/or chemically stabilized bases, where geotextile detain the development and propagation of cracks on the road. These specificities reinforce the importance of comprehensive understanding about choosing and applying geotextiles in road projects.

1.2 Mechanisms occurring while performing CBR tests in reinforced soil tests

Mechanisms involved in the application of CBR tests to reinforced soil samples are fundamental to determining the bearing capacity of these soils. The evaluation may be achieved through load tests in real scale (*in situ*), in laboratory (Nini, 2019), field CBR (Ghosh et al., 2014), CBR laboratory tests using conventional cylinder (Ashik, 2017) or modified (Gor et al., 2013), besides analytic studies or numerical analysis (Ouria and Mahmoudi, 2018). Despite limitations, conventional CBR analysis performed in laboratory, is the most used technique to value roads paved or not, establishing an analogy between the behavior of reinforcements in the test specimen and in the layers of a generic pavement (Mehrpazhouh et al., 2019).

Figure 1 illustrates the behavior of two tests specimen compacted under the piston load of the CBR press. In the absence of reinforce (Figure 1a), load concentration can be observed at the point of application, resulting in major vertical tension to the underbed. In contrast, under the reinforced condition (Figure 1b), it is possible to observe a more balanced distribution of loading to the subgrade as discussed by Giroud et al. (1985) e Love et al. (1987).

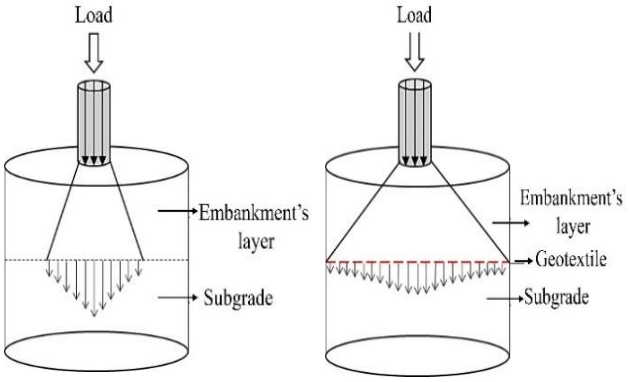

Figure 1. Stress distribution in soil layers within a CBR molded cylinder specimen.

The effects represented in Figure 1, involve in determining spread angle, denoted as β by adopting the trapezoidal model for the extension distribution in the embankment layer. This angle is more pronounced in reinforced structures compared to their unreinforced counterparts. Predictions about the behavior of reinforced soils based on β angle, are susceptible to mechanical properties changes affecting embarkment and underbed materials as discussed by Giroud et al. (1985) e Burd (2006). Burd (2006) observed that the magnitude of spread angle is greater to underbeds composed of soft soils compared to those underbeds composed of more rigid materials.

This research presents the results of CBR tests performed in order to investigate both the influence of different types of geotextiles and the insert position of this materials in the interaction among a tropical soil with non lateritic characteristics and the mentioned geotextiles.

2 MATERIALS AND METHODS

2.1 Materials

The material analyzed is a residual soil with transitioning characteristics among mature and juvenile. It composed by a significative percentage of clay being classified as silty sandy-clay. According to Transportation Research Board (TRB) and Unified Soil Classification System (USCS), is categorized as A-7-5(20) and MH, respectively. According to MCT (Miniature, Compacted, Tropical) methodology (Nogami and Villibor, 1981), it is classified as clay non-latelitic (NG'). In its mineralogy, primary (quartz and ilmenite) and secondary (kaolinite, goethite and hematite) coexist species coexist which reinforces its intermediate alteration feature.

To evaluation the bearing capacity parameters of the reinforced samples, two biaxial woven geotextiles made of polypropylene filaments were used, referenced in this study by the abbreviations T55 and T25, and a nonwoven needle-punched polyester geotextile represented by the abbreviation NT10. The main properties of these materials are presented in Table 1.

Table 1. Properties of geotextiles.

Properties		**T55**	**T25**	**NT10**
Nominal thickness (e), mm		0,93	0,66	1,99
Mass per unit area, g/m^2		244	117	210
Tensile strength, kN/m	longitudinal	55	25	10
	transverse	55	25	9
Deformation at nominal resistance, %	longitudinal	≤ 15	≤ 15	> 50
	transverse	≤ 15	≤ 15	> 50
Apparent opening of pores, O_{90}, mm**		0.20	0,25	0,13

2.2 Methods

In order to determine optimal compactation values (optimum moisture content – $W_{ót}$ and maximum dry apparent specific gravity - $\gamma d_{máx}$) from the studied soil at the standart Proctor correspondent energy, it was adopted procedures provided for the NBR 7182 (ABNT, 2016a).

Under the respective conditions of optimal soil compaction curves, the CBR tests were carried out, following the prescriptions of NBR 9895 (ABNT, 2016b), to obtain the California Bearing Ratio (CBR).

It was used four layers both without inclusions (Figure 2a) and reinforced samples, were compacted in four layers (for geotextile insertion) instead of five layers as NBR prescription, obviously remaining the same total compaction energy used in soils. For Proctor standard energy (560 kN.m/m^3) it was applied 15 coups per layer.

The geotextiles were cut to the diameter of the CBR cylinder (Figure 2) and inserted between compacted layers in two different configurations: after the second compacted layer (Figure 2b), that is, in the middle of the specimen (H/2), and after the third compacted layer (Figure 2c), located at ¼ of the top of the specimen (1/4H).

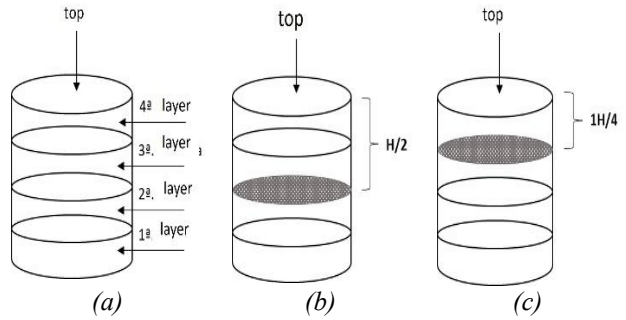

Figure 2. Positioning of the geotextile inside the specimen.

3 RESULTS AND DISCUSSIONS

Standard Proctor values of optimum moisture content ($w_{ót}$) and maximum dry apparent specific gravity were 33,82% e 12,82 kN/m^3, respectively.

Table 2 shows the results for compactation and CBR from the investigated sytems (soil and geotextiles), considering mean, standart deviation (SD) and coefficient of variation (CV).

The results of this research, suggest that geotextiles insertion did not increase CBR soil resistance, regardless of their type and position within the specimens. About reinforce position, changes in the geotextiles place directly affect the CBR values for the soil samples (ANOVA) being the H/2 position, the one in which the highest support capacity results were obtained between reinforced samples.

Figure 3 corresponds to the behavior of the reinforced samples in terms of stress spreading and its relationship with the location of the geotextiles within the specimen. Based on Love (1929) proposals it is estimated that, when the reinforcement material is positioned at half height of the test piece, the load applied by the piston reaches the geotextile in a proportion of approximately 19% (center of the loaded area) (Figure 3a), while, when located at ¼H, the vertical stresses spread with around 52% of the load request (center of the loaded area) (Figure 3b). It is also noted that, as the load approaches the edges of the geotextile, its intensity also decreases.

Table 2. Compactation and CBR results.

System	Geotextile position	Statistics	w (%)	g_d (kN/m^3)	CBR (%)
Soil	-	Média	33,03	12,79	6,33
		SD	0,23	0,10	0,34
		CV (%)	0,71	0,78	5,38
S – T55	H/2	Média	33,33	12,54	5,92
		SD	0,19	0,37	0,44
		CV (%)	0,56	2,93	7,44
	H/4	Média	33,18	12,58	5,71
		SD	0,16	0,20	0,44
		CV (%)	0,48	1,56	7,70
S – T25	H/2	Média	33,77	12,68	6,13
		SD	0,35	0,04	0,17
		CV (%)	1,03	0,30	2,72
	H/4	Média	33,52	12,66	5,20
		SD	0,21	0,24	0,25
		CV (%)	0,61	1,90	4,78
S – NT10	H/2	Média	33,27	12,73	6,03
		SD	0,24	0,14	0,46
		CV (%)	0,73	1,12	7,55
	H/4	Média	33,17	12,75	5,39
		SD	0,16	0,06	0,25
		CV (%)	0,47	0,48	4,56

Based on variance analysis (ANOVA) and on the Tukey test application, for all the soil-reinforce systems evaluated in this research, when the "type of reiforce" variable was not an influence factor, the incorporation of woven blankets was more effective in to increase the soil support capacity than the non-woven geotextile.

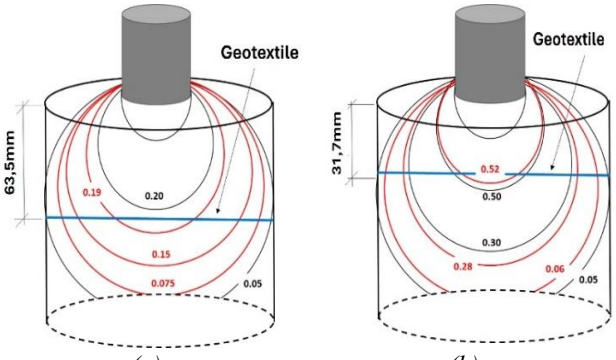

Figure 3. Stress spreading in the reinforced specimen.

The most important structural property of the geotextiles used as road reinforce is their rigidity. Gregory e Bang (1994) concluded that geotextiles fabrics impress a greater rigidity in the layers of a road compared to nonwoven geotextiles specially when underbed CBR is less than 11%.

4 CONCLUSIONS

The conclusions of this study highlight that the insertion of geotextiles, regardless of the type and position within the specimens, did not result in an CBR resistance increase of the soil.

Furthermore, results points that the soil-geotextile systems did not presents the expected support mechanisms, indicating that the CBR test may not be the most appropriate method to evaluate the support capacity of soils with inclusions.

The aforementioned situation can be explained based on Terzaghi (1943) proposition that if foundation pressures the ground, its pressure distributed over a region twice as large as the diameter of the foundation. Similarly, in the CBR test, where a 50 mm scope is used, the thickness distribution area is limited to the mold diameter of 150 mm. This suggests that the confinement of the standard CBR mold does not provide adequate space for the development of reinforcement mechanisms.

ACKNOWLEDGMENTS

Thanks to the Federal Institute of Education, Science, and Technology of Espírito Santo - Nova Venécia for sponsorship.

REFERENCES

ASSOCIAÇÃO BRASILEIRA DE NORMAS TÉCNICAS. *NBR 7182* (2016a), Solo – Ensaio de compactação. Rio de Janeiro: ABNT.

ASSOCIAÇÃO BRASILEIRA DE NORMAS TÉCNICAS. *NBR 9895* (2016b): Solos – Índice de suporte Califórnia. Rio de Janeiro: ABNT.

Ashik, M.M. (2017). Stabilization of soft subgrade soil with non-woven coir geotextiles. *International Journal of Emerging Trends in Science and Technology*, 4(5): 5200-5203. Available at: https://igmpublication.org/ijetst.in/index.php/ijetst/article/view/1109, accessed: 05/03/2024.

Burd, H.J. (2006). FE in geotechnical engineering. In: *Course on Computational Geotechnics*, Noordwijkerhout, Netherlands.

Ghosh, C., Madhav, M.R. (1994). Reinforced granular fill—soft soil system—membrane effect, *Geotextiles and Geomembranes*, 13(11): 743–759. https://doi.org/10.1016/0266-1144(94)90060-4.

Ghosh, B.; Ramesh, V.; Vibhuti, R.B. (2014) Improvement of soil characteristics using jute geo-textile, *International Journal of Science, Engineering and technology research*, 3 (7): 1983-1986. Avalable at:, acessed: 05/03/2024.

Giroud, J.P.; Ah-Line, C.; Bonaparte, R. (1985). *Design of unpaved roads and trafficked areas with geogrids*, Polymer Grid Reinforcement. Thomas Telford Limited, Thomas Telford, London, United Kingdom, pp. 116-127. Available at: http://worldcat.org/isbn/0727702270, acessed: 05/03/2024.

Gor, V.S., Thakur, L.S., Biyani, K.R. (2013). Study of typical characteristic of expansive subgrade with geotextiles and cushion materials, In: *Seventh International Conference on Case Histories in Geotechnical Engineering,* Chicago, USA, pp. 1-11. Available at: https://scholarsmine.mst.edu/cgi/viewcontent.cgi?article=3394&context=icchge, accessed: 05/03/2024.

Gregory, G.H., Bang, S. (1994). Design of flexible pavement subgrades with geosynthetics. In: *30th Symposium on Engineering Geology and Geotechnical Engineering*, Boise, Idaho, USA, pp 569-582.

Jotisankasa, A., Rurgchaisri, N. (2018). Shear strength of interfaces between unsaturated soils and composite geotextile with polyester yarn reinforcement, *Geotextiles and Geomembranes*, 3 (46): 338-353. https://doi.org/10.1016/j.geotexmem.2017.12.003.

Love, J.P; Burd, H.J.; Milligan, G.W.E.; Houlby, G. T. (1987). Analytical and model studies of reinforcement of a layer of granular fill on a soft clay subgrade, *Canada Geotechnical Journal*, 24 (4): 611–622. https://doi.org/10.1139/t87-075.

Love, A.E.H. (1929). *The stress produced in a semi-infinite solid by pressure on part of the boundary*, Philosophical Transactions of the Royal Society Serie A, 228, pp. 377-420. http://doi.org/10.1098/rsta.1929.0009.

Mehrpazhouh, A., Tafreshi, S.N.M., Mirzababaei, M. (2019). Impact of repeated loading on mechanical response of a reinforced sand, *Journal of Rock Mechanics and Geotechnical Engineering*, 11 (4): 804-814. doi:10.1016/j. jrmge.2018.12.013.

Nini, R. (2019). Effect of soaking period of clay on its California bearing ratio value, In: 4th *World Congress on Civil, Structural, and Environmental Engineering (CSEE'19*), Rome, Italy. doi:10.11159/icgre19.162.

Nogami, J. S.; Villibor, D. F. (1981). Uma nova classificação de solos para finalidades rodoviárias. In*: Brazilian Simposium of Tropical Soils in Engineering,* 1, pp. 30-41. Rio de Janeiro – RJ.

Ouria, A., Mahmoudi, A. (2018). Laboratory and numerical modeling of strip footing on geotextile-reinforced sand with cement-treated interface, *Geotextiles and Geomembranes*, 46(1):29-39. https://doi.org/10.1016/j.geotexmem.2017.09.003.

Perkins, S.W. (1999). Mechanical response of geosynthetic-reinforced flexible pavements, *Geosynthetics International*, 6(5): 347-382. https://doi.org/10.1680/gein.6.0157.

Santos, A.; Pastore, E.; Junior, F.; Cunha, M. (1988). *Estradas vicinais de terra: manual técnico para conservação e recuperação,* 2. ed., São Paulo: IPT.

Terzagui, k (1943). *Theoretical Soil Mechanics,* London: John Wiley and Sons, 510p.

Proceedings of the XVIII ECSMGE 2024
GEOTECHNICAL ENGINEERING CHALLENGES
TO MEET CURRENT AND EMERGING NEEDS OF SOCIETY
© 2024 the Authors
ISBN 978-1-032-54816-6
DOI 10.1201/9781003431749-393
Open Access: www.taylorfrancis.com, CC BY-NC-ND 4.0 license

ECSMGE 24
XVIII EUROPEAN CONFERENCE ON SOIL MECHANICS AND GEOTECHNICAL ENGINEERING

Enzymatically mediated precipitation of calcium phosphate compounds: a promising approach for sustainable soil enhancement

La précipitation enzymatique des composés de phosphate de calcium: Une approche prometteuse pour l'amélioration durable des sols

M. Avramenko*
Graduate School of Engineering, Hokkaido University, Sapporo, Japan

K. Nakashima, C. Takano, S. Kawasaki
Faculty of Engineering, Hokkaido University, Sapporo, Japan

**maksym.avramenko.ua@gmail.com*

ABSTRACT: Enzyme-induced soil enhancement through carbonate precipitation is a widely utilized technique, however it releases ammonium into the atmosphere during the hydrolysis reaction. This paper introduces a novel and environmentally friendly sustainable method called Enzyme Induced Calcium Phosphate Precipitation (EICPP) for soil improvement, which can address the ammonium emission problem. The EICPP method involves the application of enzymes to facilitate the hydrolysis reaction of urea, resulting in the precipitation of Calcium Phosphate Compounds (CPCs). To ensure sustainability, this method incorporates tuna fish bones, which are typically considered food waste from the industry, can be repurposed to provide valuable source of calcium and phosphorus. By utilizing this readily available and renewable resource, EICPP reduces waste generation and promotes circularity within the food industry, aligning with Sustainable Development Goals (SDGs). Various analyses, including Unconfined Compressive Strength (UCS), X-ray Powder Diffraction (XRD), Scanning Electron Microscopy (SEM), SEM with Energy Dispersive X-ray Spectroscopy (SEM-EDS) were conducted to assess the effectiveness of EICPP for binding samples and examine the characteristics and composition of the precipitates. Different calcium/urea ratios were examined to determine the optimal ratio for the best outcome. The results reveal the presence of brushite with needle-like crystals in the improved samples of Toyoura sand, demonstrating the successful implementation of EICPP for strengthening silicate soil. EICPP method offers a promising solution for soil enhancement while mitigating the ammonium emission problem associated with traditional techniques. By repurposing tuna fish bones, this approach demonstrates the potential for sustainable resource utilization and supports the achievement of SDGs.

RÉSUMÉ: L'amélioration des sols par la précipitation enzymatique de carbonate est une technique couramment utilisée, cependant elle libère de l'ammonium dans l´atmosphère pendant la réaction d´hydrolyse. Cette publication présente l'approche Enzyme Induced Calcium Phosphate Precipitation (EICPP), une méthode éco-innovante pour l´amélioration des sols, répondant au problème d´émission d´ammonium. La méthode EICPP résout le problème d'émission d'ammonium en facilitant la réaction d'hydrolyse de l'urée par des enzymes, conduisant à la précipitation de Composés de Phosphate de Calcium (CPC). Pour assurer sa durabilité, cette méthode inclut l´utilisation d´arêtes de thon, qui sont considérées comme des déchets alimentaires classiques de l'industrie, offrant une source précieuse de calcium et de phosphore. En utilisant cette ressource disponible et renouvelable, l'EICPP réduit la production de déchets et promeut la circularité dans l'industrie alimentaire, en adéquation avec les Objectifs de Développement Durable (ODD). Des analyses diverses utilisant les méthodes RCNC, DRX, MEB, et MEB-EDS ont été menées pour évaluer l'efficacité de l'EICPP à lier les échantillons et examiner les caractéristiques et la composition des précipités. Différents rapports calcium/urée ont été examinés afin de déterminer le rapport optimal pour l'obtention du meilleur résultat possible. Les résultats montrent la présence de brushite sous forme de cristaux en forme d´aiguille dans les échantillons améliorés de sable de Toyoura, démontrant le succès de l'EICPP pour renforcer les sols silicatés. La méthode EICPP offre une solution prometteuse pour l´amélioration des sols tout en atténuant les émissions d'ammonium liées aux techniques traditionnelles.

Keywords: Soil improvement; calcium phosphate compounds (CPCs); enzyme induced calcium phosphate precipitation (EICPP); brushite; tuna fish bones.

1 INTRODUCTION

Soil enhancement techniques play a crucial role in modern construction sector, ensuring the stability and possibility of using those soils for further construction works. Among most widely utilized ecofriendly methods for improving soil, the use of enzymes to induce carbonate precipitation in soil, namely Ureolytic Induced Calcite Precipitation (UICP), has proven effectiveness and sustainability (Saif et al., 2022; Fu et al., 2023). These techniques apply urease for precipitation of calcite which binds soil particles and improve properties of material. However, UICP comes with an environmental concern. The hydrolysis reaction in this process results in the release of ammonia into the atmosphere, and ammonium into ground environment contributing to ecosystem disruption. In response to this issue, a novel and environmentally friendly approach known as Enzyme Induced Calcium Phosphate Precipitation (EICPP) for soil improvement were introduced.

The EICPP method, similar to UICP, employing enzymes to facilitate the hydrolysis reaction of urea, leading to the precipitation of Calcium Phosphate Compounds (CPCs), unlike Calcite in UICP. CPCs are inorganic substances mainly composed of calcium, phosphorus, and oxygen. They are commonly found in living organisms, primarily in the form of bones and teeth. CPCs exhibit solubility in acids while being insoluble in alkaline environments and its precipitation requires lower pH of environment to be solidified, therefore less ammonia will be released into the atmosphere (Prajapati, 2014; Dorozhkin, 2016).

This study investigates the improvement of fine sand quality by applying EICPP, introducing new method by exploring its practical application and environmental impact. In addition to its effectiveness in improving soil, the EICPP in this study utilizes tuna bones, a resource commonly considered food waste in industry, turning it into valuable components for soil improvement. In this way, EICPP not only offers a sustainable and environmentally conscious alternative, but also actively promotes circularity in the food industry, which is aligned with the main SDGs.

During the experiments, pH values were monitored daily to better understand ammonia and ammonium pollution in the atmosphere and ground environment, aiming to demonstrate the eco-friendliness of this method. Moreover, UCS, SEM, SEM-EDS and XRD practices were used to investigate in more detail binding soil samples. To ensure efficiency, different calcium/urea ratios were applied to determine the most favourable conditions for achieving the desired results.

2 MATERIALS AND METHODS

2.1 Sand

The present study is based on commercially available sand supplied by Toyoura Keiseki Kogyo Co., Ltd. Japan. This sand was checked for particle size distribution and was classified as poorly graded sand (ASTM D2487-17, 2020).

2.2 Fish bone meal and chemical reagents

To successfully precipitate CPCs, it is necessary to obtain a supply of calcium (Ca) and phosphate (P) ions. In this research, Tuna fish bones sourced from a local fish company were selected for this purpose.

The process of extracting Ca and P ions from the fish bones involved several steps. First, the fish was cleaned, removing fillet and skin parts. Then, it underwent a treatment process that included crushing and the removal of organic matter using a 2% NaOH solution at a ratio of 1:3 (w/v), followed by boiling for 30 minutes. After this treatment, the fish bones were filtered and dried. Subsequently, the dried fish bones were ground into a powder and completely dissolved in a 1% HCl solution at a ratio of 1:2.4 (w/v). The dissolution process was carried out by stirring for 60 minutes at 1000 rpm and resulting dissolved filtrate was used as part of the treatment solution for the study.

Furthermore, acid urease and urea, both essential components for current research, were sourced from Nagase & Co., Ltd. and Wako Pure Chemical Industries, Ltd., respectively, based in Japan.

2.3 Solidification test

Six 30 ml syringes were filled with Toyoura sand, and each was injected with 10 ml of a treatment solution containing fish bone solution with a Ca^{2+} ion concentration of 10,000 ppm and pH 2.7-3.3. The treatment solution was prepared based on fish bone meal, 2g/l of acid urease, and urea, with varying Ca^{2+}/Urea concentration ratios in samples 1 to 6, specifically: 0.15, 0.25, 0.5, 1.0, 2.0, and the last sample without the addition of urea. Samples were placed in a 25°C incubator, and the injections were performed daily for 21 days. The samples were prepared with three replicates, and the reported results represent the average values.

Upon the completion of the treatment period, the sand samples were thoroughly rinsed with water, dried in an oven maintained at 60°C, and subsequently subjected to UCS testing. Additionally, the samples underwent SEM, SEM-EDS, and XRD analyses.

Figure 1 illustrates the syringe solidification test model.

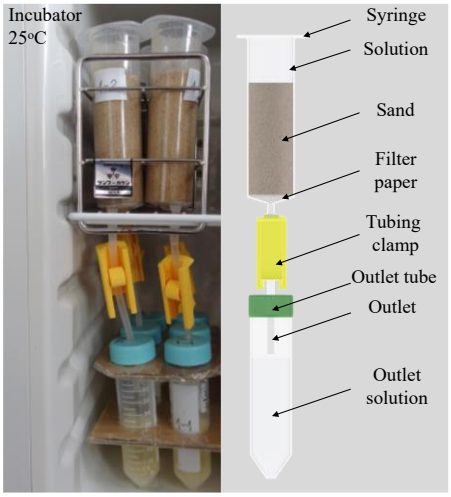

Figure 1. Visualisation of syringe solidification test model.

2.4 Measurements

The pH measurements were conducted using a pen-type pH meter, pH5S, manufactured by CEM Corporation in Tokyo, Japan. The UCS of the specimens was determined using a needle penetration test apparatus, SH-70, from Maruto Testing Machine Company in Tokyo, Japan. SEM and SEM-EDS analyses were performed using a JSM-IT200 Scanning Electron Microscope, manufactured by JEOL Ltd. in Tokyo, Japan. The microscope operated at an accelerating voltage of 15kV, and each sample was preliminarily coated with gold using a Sputter Coater DII-29010SCTR Smart Coater for 2 minutes. For the analysis of mineralogical composition, XRD was carried out using a MultiFlex X-ray diffractometer from Rigaku Corporation in Tokyo, Japan. The diffractometer utilized a Cu K-alpha source and operated at a scan rate of 6.5 degrees per minute, with a diffraction angle (2θ) ranging from 5 degrees to 70 degrees. The precipitation content was determined by calculating the percentage of dry weight loss after dissolving 1 g of the treated sample in 5 ml of 1% HCl solution.

3 RESULTS AND DISSCUSSION

3.1 Observation during treatment

Figure 2 shows treated samples after 21 days of EICPP with illustration of position of measuring UCS. Each sample solidified successfully, except for sample 6, without the addition of urea. The samples showed strong consolidation results with more precipitate on the top and less on the bottom. During treatment period samples 1 to 5 were showing pH in the range of pH 7-8.39. Sample 2 reached the highest pH 8.39 and sample 5 – lowest, 7.57.

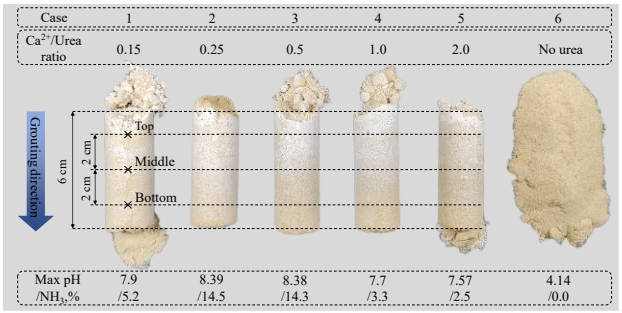

Figure 2. Illustration of the samples after treatment.

Based on the ammonium-ammonia conversion dependency (Prajapati, 2014), the maximum conversion rate to ammonia during the solidification of sample 2 and 5 was 14.5% and 2.5%, respectively. During conventional EICP pH increasing to the value pH 9 (Saif et al., 2022) resulting in converting 41.17% of ammonium into ammonia and uncontrollable pollution of atmosphere.

3.2 UCS and precipitation content

The mechanical properties were evaluated by conducting UCS tests, and the precipitation content was checked in experimental case samples. The results of these evaluations are shown in Figure 3.

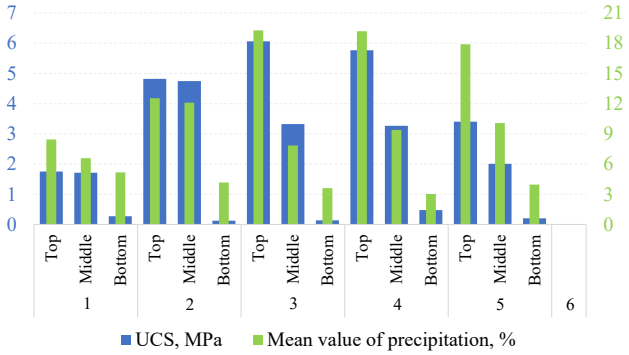

Figure 3. UCS results (blue bar, scale on the left) and precipitation content (green bar, scale on the right) of samples.

UCS results confirm the observations shown in Figure 2, indicating that a significant portion of the precipitation is concentrated in the upper and middle layers of the specimens, resulting in elevated values for both the UCS and the precipitation content. It is worth noting that specimen 3 showed the most remarkable results in terms of UCS and precipitation content, recording 6.05 and 19.27 % of CPCs precipitation in the top layer, respectively.

3.3 SEM and SEM-EDS

To further investigate the binding properties of the soil samples, SEM and SEM-EDS analysis were

performed and the results are shown in Figure 4. All samples showed inter-particle bonds, as well as a visible coating layer of sediment, except for sample 6 (without urea). SEM images were obtained from the middle of each sample, and SEM-EDS data showing sample 4.

In most cases, the needle-like crystals were observed approximately 100 nm in length. However, in case 5 a flower-shaped crystal was found. The SEM-EDS analysis showed the precipitates mainly covered the grains of sand and contained calcium and phosphorus, indicating the potential formation of CPCs.

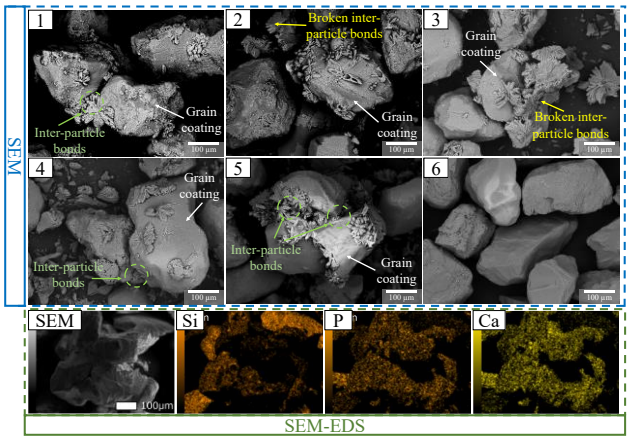

Figure 4. SEM images (blue rectangle) of samples 1 to 6 and SEM-EDS (green rectangle) results for sample 4.

3.4 XRD

The XRD results are shown in Figure 5, where clear peaks corresponding to brushite are observed in samples 2-5. In contrast, in case 1, there are only peaks associated with quartz and microcline, which are derived from sand, with no obvious brushite peaks.

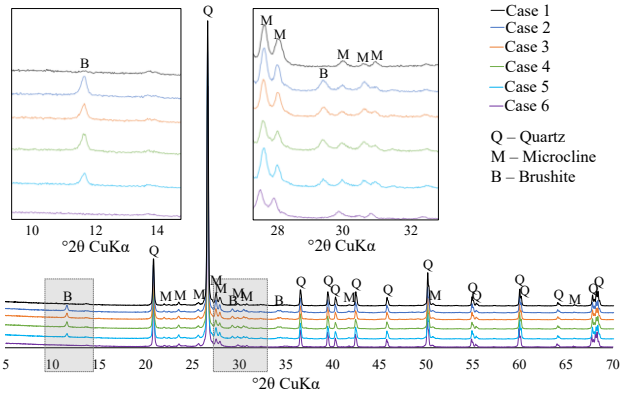

Figure 5. XRD analysis of samples 1 to 6.

Brushite, a member of the CPCs family, is known to precipitate easily in aqueous solutions in the pH range from 2 to 6. The formation of CPCs is strongly dependent on the pH and the Ca/P ratio in the medium. Taking into account the solubility characteristics of CPCs and their relationship with pH, brushite appears to be the most easily precipitated compound in the pH range mentioned above, which is confirmed by XRD analysis of the samples (Dorozhkin, 2016).

4 CONCLUSIONS

This study demonstrates the effectiveness and sustainability of EICPP for geotechnical applications involving fine sand. The improved sand exhibited strength, with UCS reaching 6 MPa, surpassing superior to conventional UICP while significantly reducing ammonia emissions to 3%.

Tuna fish bones, often discarded as food waste, proved to be an abundant source of calcium and phosphorus ions, addressing SDG challenges by repurposing these resources.

From a geotechnical point of view, it was determined that the most suitable calcium to urea ratios for soil improvement were 0.5 and 1.0 (samples 3 and 4). However, from an environmental point of view, maintaining a lower pH range is vital to ensure the method is environmentally friendly. The most optimal ratios were 1.0 and 2.0 (samples 4 and 5), which resulted in minimal ammonia emissions to the atmosphere - 3.3% and 2.5%.

REFERENCES

ASTM D2487-17 (2020). Standard Practice for Classification of Soils for Engineering Purposes (Unified Soil Classification System), West Conshohocken, PA: ASTM International. https://doi.org/10.1520/D2487-17.

Dorozhkin, S. V. (2016). Calcium orthophosphates ($CaPO_4$): occurrence and properties. *Progress in Biomaterials*, 5: 9-70. https://doi.org/10.1007/s40204-015-0045-z.

Fu, T. S., Saracho, A. C. and Haigh, S. K. (2023). Microbially induced carbonate precipitation (MICP) for soil strengthening: A comprehensive review. *Biogeotechnics*, 1(1): 100002. https://doi.org/10.1016/j.bgtech.2023.100002.

Prajapati, S. (2014). *Cation exchange for ammonia removal from wastewater,* Master of Science, Tampere University of technology. [online] Available at: https://core.ac.uk/download/pdf/196554889.pdf, accessed: 24/10/2023.

Saif, A. Cuccurullo, A. Gallipoli, D. Perlot, C. and Bruno, A.W. (2022). Advances in Enzyme Induced Carbonate Precipitation and Application to Soil Improvement: A Review. *Materials*, 15(3): 950. https://doi.org/10.3390/ma15030950.

Proceedings of the XVIII ECSMGE 2024
GEOTECHNICAL ENGINEERING CHALLENGES
TO MEET CURRENT AND EMERGING NEEDS OF SOCIETY
© 2024 the Authors
ISBN 978-1-032-54816-6
DOI 10.1201/9781003431749-394
Open Access: www.taylorfrancis.com, CC BY-NC-ND 4.0 license

ECSMGE 24
XVIII EUROPEAN CONFERENCE ON SOIL MECHANICS AND GEOTECHNICAL ENGINEERING

Activating decarbonisation in the piling supply chain

Activer la décarbonation dans la chaîne d'approvisionnement des pieux

C.A. Barker*
Arup, London, United Kingdom

J. Ly
Canary Wharf Group, London, United Kingdom

**chris.barker@arup.com*

ABSTRACT: Strategies to reduce embodied carbon for new developments have to date mostly been focused on the carbon emissions hierarchy of Build Nothing, Build Less, Build Clever and Build Efficiently from a developer/designer perspective. For some projects this approach can deliver significant reductions. However, for the many other projects, carbon reductions (if any) have been far more limited, and procurement processes have often not actively driven innovation for reduction of carbon. With a goal of reducing embodied carbon for all new developments at Canary Wharf, the role of carbon reduction within the piling supply chain was defined in the procurement approach. To actively decarbonise the piling contractor supply chain, direct engagement with piling contractors was done to measure and report embodied carbon consumption against a project target during construction. This paper shares the details of this carbon reduction supply chain engagement.

RÉSUMÉ: Jusqu'à présent, les stratégies visant à réduire le carbone incorporé pour les nouveaux développements se sont principalement concentrées sur la hiérarchie des émissions de carbone: Build Nothing, Build Less, Build Clever et Build Efficiently du point de vue du développeur/concepteur. Pour certains projets, cette approche peut entraîner des réductions significatives. Cependant, pour de nombreux autres projets, les réductions de carbone (le cas échéant) ont été bien plus limitées, et les processus d'approvisionnement n'ont souvent pas activement stimulé l'innovation en matière de réduction des émissions de carbone. Dans le but de réduire le carbone incorporé pour tous les nouveaux développements à Canary Wharf, le rôle de la réduction du carbone au sein de la chaîne d'approvisionnement des pieux a été défini dans l'approche d'approvisionnement. Pour décarboner activement la chaîne d'approvisionnement des entrepreneurs en battage, un engagement direct avec les entrepreneurs en battage a été réalisé pour mesurer et rapporter la consommation de carbone incorporé par rapport à un objectif du projet pendant la construction. Ce document partage les détails de cet engagement dans la chaîne d'approvisionnement en matière de réduction des émissions de carbone.

Keywords: Carbon; decarbonisation; sustainability; piles; construction.

1 INTRODUCTION

For many companies, supply chain-related emissions are their largest source of carbon emissions, and being outside their direct control, are the most challenging to reduce. Activating decarbonisation through supply chains is one of the most critical and effective pathways to reach net-zero (CDP, 2023).

However, with limited visibility and perceptions of limited influence on emission reduction measures, it can be challenging for many companies to bring the required change to their supply chain. Supplier engagement targets offer a way to influence decarbonization efforts within companies' supply chain when emissions data is challenging to track or unavailable.

Canary Wharf is forty hectares of land being progressively developed since the late 1980s on the site of the former West India Docks in East London, United Kingdom. It is the largest urban regeneration project in Europe containing commercial, retail and residential developments with many high-rise buildings and large basements.

In December 2020, Canary Wharf Group published its Net Zero Carbon Pathway, outlining its pathway for achieving net zero. A key aspect of the Pathway for new developments was supporting their supply chain in reducing carbon emissions and achieving their Science Based Targets.

This paper presents details of how the Pathway was implemented for the design, procurement and construction of new piled foundations for five new build projects.

2 DESIGN APPROACH

The five Canary Wharf projects presented in this paper are developments within a larger phased development. Foundation option selection process had determined piled foundations as the most suitable foundation solution. The subsequent carbon reduction approach during the design stages was one of reduction i.e. material selection and reducing material volumes. The principal ways this was achieved was through adopting lower partial factors in design permitted with preliminary and working pile load tests, which is further discussed in (Taggart and Barker, 2022) and by developing an efficient pile layout. This was achieved through maximising individual pile capacities within the capability of the piling industry while optimising the foundation layout through a geotechnical-structural iteration process to reduce the number of piles.

The scope of piling works was procured as contractor designed and for each of the five projects were:

Project A: comprised 500 No. 900mm and 1050mm diameter continuous flight auger (CFA) bearing piles with a typical pile length of 28m.

Project B: comprised 210 linear metres of 1200mm diameter hard-firm secant wall and 75 linear metres of 15m deep sheet pile wall and 7 No. 1500mm and 1800mm diameter rotary bearing piles with a typical length of 35m.

Project C: comprised 150 linear metres of anchored sheet piled dock wall and temporary cofferdam and capping beam with 26 No. 900mm diameter CFA anchor piles and 90 linear metres of 20m long 1200mm diameter hard-firm secant pile wall.

Project D: 300 No. 900mm diameter CFA bearing piles and 50 No. 900mm to 1800mm diameter marine piles.

Project E: comprised 120 No. 750mm CFA bearing piles typically 30m long, 80 No. 1050mm CFA bearing piles typically 32m long and 17 No. 1300mm rotary bearing piles with a typical length of 35m.

3 SUPPLY CHAIN ENGAGEMENT

With a goal of reducing embodied carbon in these new developments the role of embodied carbon was defined within the piling supply chain through the procurement process. Procurement, as shown in Figure 1, was historically on cost, quality and programme but for these projects embodied carbon was also now included.

To decarbonise the piling contractor supply chain, it was recognised that direct engagement with typically Tier 2 piling contractors was needed to calculate, measure and report embodied carbon consumption against a project target through the project delivery process, as shown in Figure 2.

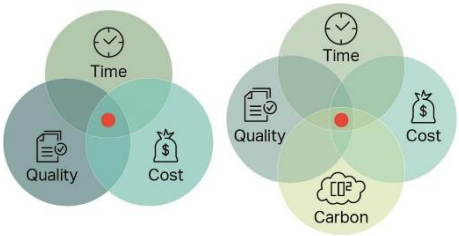

Figure 1. Historical and revised procurement values.

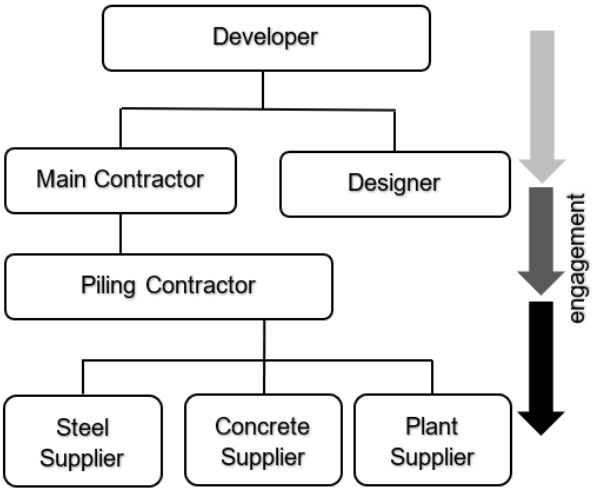

Figure 2. Supply chain engagement.

4 TENDER SPECIFICATION

To frame this approach new specification clauses were needed in the project piling specification. The two pages of new specification text (Barker, 2023) provide an aspirational embodied carbon target and requires all tendering piling contractors to use the free EFFC/DFI Carbon Calculator (EFFC and DFI, 2023) to estimate the embodied carbon in their tender design submissions. Concrete mix designs and any proposals for further embodied carbon reductions were also to be provided at tender. For the successful contractor, independently verified Environmental Product Declarations (EPD) were required for their construction materials and recalculating the estimated embodied carbon for their construction issue design was undertaken. Weekly reporting of embodied carbon consumption is provided by the contractor during construction. Also, at the end of construction, an as-built report is provided totalling the A1-A5 life cycle assessment modules (product and construction process stages) including waste emissions.

Table 1. Tender stage estimated embodied carbon (tCO2e).

	Project A	Project B	Project C	Project D	Project E
Target	*3000*	*2200*	*2600*	*4000*	*2160*
Contractor 1	2900	3300	3200	3300	2000
Contractor 2	3800	1300	-	3700	3800
Contractor 3	5800	1500	-	-	2400
Contractor 4	2500	-	-	-	2380
Contractor 5	-	-	-	-	2600

An EPD provides the independently verified carbon footprint of a product, e.g., concrete, diesel and steel reinforcement, in terms of Global Warming Potential (GWP) as measurable carbon dioxide equivalents (CO2e).

The calculation of embodied carbon consumption is easily undertaken during construction. Contractors are already routinely recording and reporting material volumes and resources. So, multiplying these quantities by a carbon factor is quite simple.

Table 1 presents the five separate contractor designed piling projects. The target embodied carbon was calculated and provided in the tender specification as an aspirational target assuming what a typical piling contractor was previously offering at tender. The remaining numbers are the calculated embodied carbon in contractor's tender returns. The piling industry's EFFC/DFI carbon calculator was specified as it was free, simple, easy to use and provided a common calculation method for all tenderers creating an equal tendering basis.

On the first project the range of estimates was quite large with a subsequent general trend of estimates reducing and the tender range narrowing.

5 CONSTRUCTION

Contractors were encouraged to engage with their suppliers to source low carbon materials and equipment. To drive beneficial changes in the supply chain, third party certified EPD carbon factors were preferred over published generic tables.

So as to not overburden construction administration, the weekly reporting format of carbon consumption during construction was decided by each contractor to best fit in with their established commercial monitoring processes. Typically, tables and plots were simply produced in Excel.

The principal areas of embodied carbon reduction are discussed below.

5.1 Concrete

Concrete is typically the most significant source of embodied carbon in piling. Typical piling tenders allow CEMIII/A with 40 - 50% GGBS (ground granulated blast furnace slag) cement replacement in piling concrete (210 kgCO2e/m^3). However, contractors can supply CEMIII/B piling concrete up to 70 - 80% GGBS cement replacement (163 kgCO2e/m^3). In unreinforced secant piles CEMIII/C can increase up to 95% GGBS cement replacement (49 kgCO2e/m^3).

While GGBS is an excellent supplementary cementitious material that helps displace clinker demand globally, it is a limited and constrained resource that is almost fully utilised globally. Therefore, whilst global supplies must continue to be fully utilised, locally increasing GGBS use at a project level is unlikely to decrease global emissions (Arnold *et al*, 2023).

Significant 52% carbon reduction shown in Table 2 were achieved in the secant wall on Project B, in part, through the use of high levels of GGBS in concrete mixes. This demonstrated the potential magnitude for carbon reductions in the future using new novel low carbon concrete mixes.

Tracking and reporting carbon consumption during CFA pile construction highlighted a +512 tCO2e increase over the target on Project A, the consequences, in part, of increased concrete wastage resulting from frequent concrete delivery delays.

5.2 Reinforcement cages

Suppliers of pile reinforcement source stock from steel mills both in the United Kingdom and the Europe Union and usually with high levels of recycled steel (>95%) which reduces carbon emissions. However, this may not always be the case, as on one project with two reinforcement suppliers their EPD showed significantly different values of 730 kgCO2e/t and 1100 kgCO2e/t steel. Adopting the circular economy principles in steel reuse is crucial.

5.3 Steel sheet piles

The introduction of an embodied carbon target in the Project C piling specification resulting in a tendering contractor to offer a 815 tCO2e saving by adopting 100% recycled steel sheet piles manufactured in an electric arc furnace (520 kgCO2e/tonne), for a cofferdam and new dock wall instead of more

Table 2. Measured as-built embodied carbon totals (tCO2e).

	Project A	Project B	Project C	Project D	Project E
Target	3000	2200	2600	4000	2160
Tender	2500	1300	3200	3300	2000
As-built	3512	1060	1400	tbc	tbc
Δ from target	+17%	-52%	-46%	tbc	tbc

typically procured steel sheet piles being source from blast furnace steel (2164 kgCO2e/tonne).

5.4 Fuel

A piling project at Canary Wharf (rigs, cranes, excavators, generators, pumps) can typically consume 80,000 to 150,000 litres of diesel (215 to 400 tCO2e).

Since 2012, Canary Wharf Group supply the estate and construction sites with certified renewable electricity being sourced from a mix of wind, thermal, solar and hydro. This enables the tendering process to engage contractors in transitioning piling plant and equipment from diesel fuel (2.68 kgCO2e/litre) to HVO biofuel (0.68 kgCO2e/litre) to renewable electricity (0 kgCO2e/kWh) or hydrogen.

5.5 Plant

Several of the projects have also achieved carbon reductions using electric crawler cranes, pumps and for site office power, HVO biofuel for plant as well as trialling electric piling plant. Contractors make significant capital investments in piling plant and the transition does benefit from active support in project procurement.

6 SUMMARY

Table 2 shows the five projects again but with the measured as-built embodied carbon total and difference from target. Projects D and E are still currently on site. The materials, fuel and plant carbon reductions achieved on Projects B and C illustrate what can be achieved from current 'normal' practice. The additional carbon consumed in Project A illustrates the significant additional carbon that can occur from concrete delivery delays.

7 CONCLUSIONS

Substantial embodied carbon reductions can be realised using currently available materials and methodologies and using the free the EFFC/DFI carbon calculator tool.

Activating decarbonisation in the piling supply chain can be readily achieved by specifying project embodied carbon targets for procurement followed by measuring and reporting embodied carbon consumption during construction. Such target setting is the step the industry now needs to take having identified baseline emissions and emission hotspots. Measuring and reporting data at a project level engages the whole supply chain: developer-consultant-contractor-suppliers and enables learning and continuous project improvements to be made by all parties.

Incorporating embodied carbon into the procurement and construction processes initiates a new level of engagement and learning for all parties. This is essential to drive change to enable the piling industry to capitalise on the coming opportunities in lower carbon materials and methodologies for a low carbon future.

REFERENCES

Arnold W. *et al* (2023). The efficient use of GGBS in reducing global emissions, Institution of Structural Engineers, United Kingdom.

Barker, C. A. (2023). UK Piling Spec Embodied Carbon Clauses, Available at: https://www.linkedin.com/feed/update/urn:li:activity:7109256270116728832/, accessed 23/10/2023.

BSI (2023). PAS 2080:2023 Carbon management in buildings and infrastructure, 2nd Edition, British Standards Institution, United Kingdom.

CDP (2023). *Scoping Out: Tracking Nature Across the Supply Chain - CDP Global Supply Chain Report 2022*, Carbon Disclosure Project Worldwide, London, United Kingdom.

EFFC (2022). EFFC Sustainability Guides for Foundation Contractors: Guide No. 1 Carbon Reduction, 1st Edition.

EFFC and DFI (2023) EFFC/DFI Carbon Calculator, Version 5, Available at: https://www.effc.org/how-we-operate/eco%e2%82%82-foundations/, accessed 23/10/2023.

Taggart J. and Barker C. (2022) Embodied carbon Assessment for a Multi-Phased Development Pile Testing Strategy. DFI-EFFC International Conference on Deep Foundations and Ground Improvement, Berlin, Germany.

Proceedings of the XVIII ECSMGE 2024
GEOTECHNICAL ENGINEERING CHALLENGES
TO MEET CURRENT AND EMERGING NEEDS OF SOCIETY
© 2024 the Authors
ISBN 978-1-032-54816-6
DOI 10.1201/9781003431749-395
Open Access: www.taylorfrancis.com, CC BY-NC-ND 4.0 license

ECSMGE 24
XVIII EUROPEAN CONFERENCE ON SOIL MECHANICS AND GEOTECHNICAL ENGINEERING

Use of the Brazilian test and frost sensitivity test for determining the aptitude for earthworks of difficult soils stabilized by special lime-based binder

Utilisation de l'essai Brésilien et de l'essai de sensibilité au gel pour déterminer l'aptitude à utiliser des sols difficiles traités par liant à base de chaux pour les terrassements

L. Batali*, G. Andrieş
Technical University of Civil Engineering Bucharest, Romania

C. Grégoire
Belgian Road Research Centre, Bruxelles, Belgium

**loretta.batali@utcb.ro*

ABSTRACT: Strength, durability and stability of earthworks during service depend on the quality of soils they are made of, the execution technology and maintenance. Often, earthworks have to be built using poor quality soils that needs improvement or stabilization by using binders. For establishing the modifications brought by binder mixing and the long-term characteristics of the improved materials, laboratory tests are used, many of them being adapted, as the resulting material is sometimes away of the untreated soil properties. Therefore, research is still conducted for determining the best way of testing the properties of improved soils, especially considering the extensive use nowadays of these techniques. The paper, which continues a series of articles published on the subject, will determine the degree of sensitivity to frost in comparison with the durability performances to freeze – thaw cycles. The research studied the performances during time of a clay treated by special lime – based binder (3 and 4 %) by analysing the mechanical and frost sensitivity behaviour. Sample to be tested where produced in laboratory using 2 compaction energies – normal and modified Proctor. The mechanical behaviour during the time was studied by determining the compression strength and the indirect tensile strength (Brazilian test), while the frost sensitivity was established based on the swelling coefficient and the consistency state of the soil after freezing.

RÉSUMÉ: La résistance, la durabilité et la stabilité des ouvrages de terrassement en service dépend de la qualité des sols mis en œuvre, de la technologie d'exécution et de l'entretien. Souvent les terrassements doivent être construits avec des sols de mauvaise qualité qui doivent être traités, généralement avec des liants. Pour déterminer les modifications apportées par le traitement et les caractéristiques à long terme obtenues on utilise des essais de laboratoire adaptés, puisque le matériau résultant est souvent loin du matériau initial. Des recherches sont encore menées pour déterminer la meilleure méthode d'essai pour les sols traités, spécialement si on prend en compte leurs utilisation intensive de nos jours. L'article, qui continue une série de papiers publiés sur ce sujet, étudie le degré de sensibilité au gel par comparaison avec la durabilité au gel – dégel. La recherche a porté sur les performances à long terme d'une argile traitée par un liant à base de chaux (3 et 4%) en analysant le comportement mécanique et la sensibilité au gel. Les éprouvettes ont été produites en laboratoire en utilisant 2 énergies de compactage – Proctor normal et modifié. Le comportement mécanique a été étudié en déterminant la résistance en compression et la résistance à la traction indirecte (essai Brésilien), alors que la sensibilité au gel a été établie sur la base du coefficient de gonflement et l'état de consistance du sol après le gel.

Keywords: Lime; stabilization; clay; laboratory tests.

1 INTRODUCTION

Strength, durability and stability of earthworks during service depend on the quality of soils they are made of, the execution technology and maintenance. Often, earthworks have to be built using poor quality soils, not meeting the technical requirements in terms of quality and bearing capacity, that needs improvement or stabilization by using binders.

The paper is dealing with the performances of clayey soils after improving by using a lime-based binder and their study in the laboratory. It is part of a series of papers of this subject, all developed in the framework of the PhD thesis of PhD student Gabriela

Andrieș. The first results have been published at the ECSMGE 2019 (Batali et al, 2019), showing the performances for 3 admixtures (3%, 3.5% and 4% of lime-based special hydraulic binder) of a fat clay, after modified Proctor compaction. This paper showed the results of laboratory and in situ tests in terms of physical and mechanical properties, after 3, 7, 14 and 28 days of curing and the results of durability tests (stability to water and freeze-thaw cycles). The obtained results emphasized the modifications that the binder produced on the clay, due to changes in the intimate structure of the soil. The study also allowed the assessment of various working procedures for some of the laboratory tests, according to European and Romanian standards. In 2021 was published a second paper at the 20ICSMGE (Batali & Andrieș, 2021) which approaches the study of the behavior during time of a test field for a road embankment, with the same fat clay as previously, stabilized with special lime-based hydraulic binder (3% and 4%). The paper studied mainly the influence of the compaction energy on the physical, mechanical and durability properties. Also, various curing times have been tested, up to 60 days. As well, a mineralogical analysis was performed to assess the modifications in the clay structure.

The present paper is analysing how the lime-based binder treatment of active clays used for the active area of road earthworks is improving the following:

- the sensitivity to freezing by assessing the freezing swelling coefficient and the consistency index after thawing;
- the freeze / thaw behaviour by assessing the indirect tensile test (the Brazilian test).

2 FUNDAMENTAL PRINCIPLES

Water content and temperature variations lead to modifications of earthworks bearing capacity, therefore influencing the strength and stability of the road structure. To prevent degradation of earthworks due to freeze / thaw cycles measures have to be taken, often these being based on soil treatment by mixing it with hydraulic binders. Lime or lime-based binders are modifying the intimate structure of the clay: change of the texture, loss of water and mass for some minerals and apparition of a new phase in the clay being previously reported (Batali & Andries, 2021), changes which are leading to an increased durability.

Especially for the soils used in the active zone of the earthworks it is required to determine the sensitivity to freeze/thaw and based on this to establish the corresponding measures to be taken.

There is no unique European practice for testing stabilised cohesive soils for freeze/thaw, EN 16907-4 referring to local practices. Our experimental program was, among others, aimed to test various procedures, standardized or not, inspired by procedures for stabilised aggregates and trying to simulate as much as possible the real behaviour in site conditions.

3 MATERIALS AND METHODS

3.1 Materials

The experimental plot for which the experimental program has been carried out is a road to be built on a ground composed of a fat, black clay, with 51% clay fraction (< 2 μ), 42% silt and 7 % sand, with 2% organic matter, very high free swell (120 %), very high plasticity (PI = 40 %) and also very high swelling pressure (190 kPa). It was therefore decided to stabilize the clay using mixing with a high lime-content hydraulic road binder, with a total amount of CaO+MgO higher than 60%, having also a cement content in order to increase the bearing capacity at short term. The complete description of the clay and the laboratory experimental program, including the compaction parameters for normal and modified Proctor compaction energies can be found in (Batali et al, 2019; Batali & Andrieș, 2021).

Two admixtures were studied for the present paper, meaning the clay mixed with 3% and 4 % special lime-based road binder, for which were determined the physical and mechanical characteristics, as well as the durability ones.

3.2 Methods

For the assessment of the sensitivity to freezing were used the freezing swelling coefficient and the consistency index after thawing. For the determination of these indices was used the procedure described in the Romanian standard STAS 1709/2 and 3-90 which specifically applies to road works. The freezing swelling coefficient, C_u is calculated as the percentage ratio between the additional height of the compacted sample after freezing (Δh) and the frost penetration depth in the sample (Z). The temperature at the upper surface of the sample should be -8° for 7 days, while the temperature is positive on the other end of the sample. The consistency index (I_c) after thawing is calculated using the water content of the soil in the frozen area of the sample. Based on the values of these 2 indices the soil can be classified as insensitive (C_u <2 and I_c >0.75), sensitive (2<C_u<8 and 0.5<I_c<0.75) or very sensitive (C_u>8 and I_c<0.5).

The indirect tensile strength, R_{it} has been assessed according to the Belgian Code CRR (2010) and Technical guide LCPC SETRA in France (2000). This

value allows to verify the freezing resistance of stabilised materials, being imposed to have a minimum R_{it} of 0.25 MPa for compacted samples at the age corresponding to freeze apparition.

4 EXPERIMENTAL RESULTS

4.1 Freeze sensitivity

The results obtained in terms of freezing swelling coefficient (C_u) are shown Figure 1 for untreated soil and the 2 studied admixtures (3% and 4% lime-based special binder), for samples compacted at 98% of the optimum standard and modified Proctor (noted PN and PM, respectively).

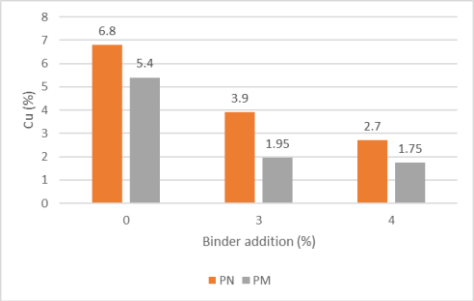

Figure 1. Freezing swelling coefficient vs binder addition.

For the analysed soil only samples compacted at modified Proctor had C_u values less than 2%, meaning insensitive to freezing. It can be seen that for modified Proctor compaction energy the C_u values are less than for standard Proctor, meaning that a stronger compaction brings less sensitivity to freezing. Also, the freezing swelling coefficient decreased by 42% for 3% addition and by 60% for 4% addition, compared to the untreated soil, for standard Proctor energy. In case of the modified Proctor energy, the reduction of C_u was of 64% for 3% addition and 74% for 4% addition. The decrease of the freezing swelling coefficient from 6.8% to 1.75% shows the attenuation of the clay activity when treated with lime-based binders, which reduces the swelling potential and increases the resistance to freeze/thaw.

In terms of consistency index after thaw, the results are shown Figure 2 and it can be observed that the values increased from 0.55 for the untreated clay to 0.66 and 0.71 for standard Proctor and from 0.62 % to 0.78% and 0.85 % for modified Proctor, for 3% and 4% binder addition, respectively. Also from this point of view the treated samples compacted at modified Proctor energy are insensitive to freezing, while all the others are classified as sensitive.

Although the treated samples compacted at standard Proctor energy are classified as being sensitive to freezing, in comparison with the untreated clay they are maintaining a high consistency after 7 days of freezing, increasing from 0.55 – 0.60 to more than 0.75 as the binder addition is increasing.

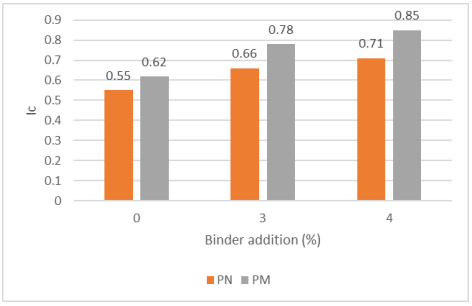

Figure 2. Consistency index after thawing vs binder addition.

The untreated samples exhibited destructuration and fissures after exposure to freezing (Figure 3a), while the treated samples remained compact, with no fissures (Figure 3b).

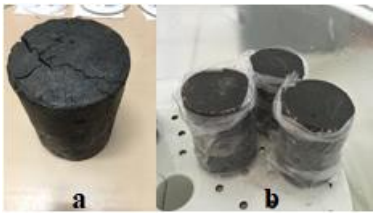

Figure 3. Samples after exposure to freezing.

4.2 Indirect tensile strength

The indirect tensile strength has been determined on samples of untreated clay (only for standard Proctor compaction) and treated clay with 3% and 4% lime-based binder addition, compacted at 98% of the optimum Proctor (standard and modified), at the optimum water content or at the optimum water content +2%. The test procedure was according to EN 13286-42, the samples being tested at 28 days of age, after being cured in the climatic chamber at 20°C and 95% humidity. All experimental values are shown Table 1.

Samples compacted at higher energy had indirect tensile strength values higher than 0.25 MPa, which is the criterion imposed in Belgium and France for freezing resistance. As well, it has been noted that increasing the compaction water content by 2% is not significantly influencing the results. In case of 4% addition and modified Proctor compaction energy there is a decrease from 0.32 MPa to 0.26 MPa, but in this case the value is satisfactory, remaining higher than 0.25 MPa. At least for this case it can be concluded that in-situ treatment with lime-base binders is ensuring the mechanical and durability properties, even when watered more than the optimum water content.

Table 1. Indirect tensile strength.

	Water content w (%)	Compaction degree Compaction energy	% binder	R_{it} 28 days (MPa)
Optimum	21.5	98% OPN	0	0.028
Proctor	23	98% OPN	3	0.13
water	24	98% OPN	4	0.2
content	19.2	98% OPM	3	0.27
(OPw)	20.2	98% OPM	4	0.32
Optimum	25	98% OPN	3	0.15
Proctor	26	98% OPN	4	0.21
water	21.2	98% OPM	3	0.25
content +			4	
2%	22.2	98% OPM		0.26

OPN – optimum standard Proctor, OPM – optimum modified Proctor.

The elasticity modulus and Poisson's coefficient were determined according to SR EN 13286-43 by using 4 LVDT transducers to measure the deformation of the horizontal diameter of the sample (0°) and the one of the diameter at 60° angle to the horizontal direction. The obtained curves have been analyzed to eliminate non-reliable values. After this selection still remained some values of Poisson's coefficient of 0.5 or even higher, which were not acceptable. The elasticity moduli were therefore corrected using ν = 0.25, value recommended by the Technical guidance LCPC SETRA (2000). All values, including the corrected ones are presented Table 2.

Table 2. Elasticity modulus and Poisson's coefficient.

	w %	Comp. degree Comp. energy	% add	E MPa	ν	E_{cor} MPa
OP	21.5	98% OPN	0	124	0.22	-
w	23	98% OPN	3	1523	0.22	1628
	24	98% OPN	4	2346	0.22	
	19.2	98% OPM	3	4504	0.56	2642
	20.2	98% OPM	4	6649	0.56	3558
OP	25	98% OPN	3	-	-	-
w	26	98% OPN	4	3640	0.47	2305
+	21.2	98% OPM	3	-	-	-
2%	22.2	98% OPM	4	6543	0.52	3720
	22.2	98% OPM	4	6616	0.52	3830
	22.2	98% OPM	4	5724	0.41	3710

5 CONCLUSIONS

The experimental study, continuing a series of tests already published, aimed at assessing other means for evaluating freeze/thaw durability of a fat clay treated with 3 or 4% lime-based road binder, meaning the freezing swelling coefficient, consistency index after thawing and indirect tensile strength. All these indices can be successfully used for assessing the durability.

The tests emphasized once more the influence not only of the binder addition and age, but also of the compaction energy, a higher energy offering better durability to freeze/thaw cycles.

ACKNOWLEDGEMENTS

The authors are grateful for the financial support provided by CARMEUSE HOLDING.

REFERENCES

Batali, L. and Andrieș, G. (2020). Experimental analysis of physical, mechanical and durability performances of a clay treated with special lime-based hydraulic binder. *Proceedings of the 20th International Conference on Soil Mechanics and Geotechnical Engineering,* Rahman and Jaksa (Eds), Vol. 2, pp. 2813-2814.

Batali, L., Andrieș, G. and Popa, H. (2019). Assessment of physico – mechanical and durability characteristics of difficult soils improved by mixing with special lime-based hydraulic binders. *Proceedings of the 17th European Conference on Soil Mechanics and Geotechnical Engineering*.

CRR (2010). *Code de bonne pratique pour le traitement des sols à la chaux et/ou aux liants hydrauliques*. Centre de recherches routières.

LCPC SETRA (2000). *Traitement des sols à la chaux et/ou aux liants hydrauliques. Application à la réalisation des remblais et des couches de forme*. LCPC SETRA

EN 13286-42 (2004). *Unbound and hydraulically bound mixtures - Part 42: Test method for the determination of the indirect tensile strength of hydraulically bound mixtures.*

STAS 1709/2 (1990). *Action of freeze – thaw for road works. Prevention and remediation of freeze/thaw degradations. Technical prescriptions.* (in Romanian)

STAS 1709/3 (1990). *Action of freeze – thaw for road works. Determination of freezing sensitivity for foundation grounds. Test method.* (in Romanian).

Proceedings of the XVIII ECSMGE 2024
GEOTECHNICAL ENGINEERING CHALLENGES
TO MEET CURRENT AND EMERGING NEEDS OF SOCIETY
© 2024 the Authors
ISBN 978-1-032-54816-6
DOI 10.1201/9781003431749-396
Open Access: www.taylorfrancis.com, CC BY-NC-ND 4.0 license

ECSMGE 24
XVIII EUROPEAN CONFERENCE ON SOIL MECHANICS AND GEOTECHNICAL ENGINEERING

The effect of the anisotropic state of stress on the normal force in a deep tunnel preliminary deformable lining

L'effet de l'état anisotrope de la contrainte sur la force normale dans un revêtement déformable préliminaire de tunnel profond

L. Batocchioni*, S. Miliziano, V. Rodrìguez González
La Sapienza University of Rome, Rome, Italy

**lorenzo.batocchioni@uniroma1.it*

ABSTRACT: When deep tunnels are excavated in poor ground, squeezing conditions occur and the design of supports must follow the yielding principle. To this aim, special elasto-plastic elements embedded in the temporary support can be employed. The presence of the elastic-plastic elements radically modifies the ground-lining interaction mechanisms making necessary the use of numerical analyses. Particularly relevant is the case of anisotropic geostatic state of stress. The paper reports and discusses, some results from 2D numerical ground-lining interaction of deformable temporary support with initial non-isotropic stress field. Results of the classic rigid support are also reported and compared.

RÉSUMÉ: Lorsque des tunnels profonds sont creusés dans un sol de mauvaise qualité, des conditions d'écrasement se produisent et la conception des supports doit suivre le principe de flexion. À cette fin, des éléments élasto-plastiques spéciaux incorporés dans le support temporaire peuvent être utilisés. La présence d'éléments élasto-plastiques modifie radicalement les mécanismes d'interaction entre le sol et le revêtement, ce qui rend nécessaire l'utilisation d'analyses numériques. Le cas d'un état de contrainte géostatique anisotrope est particulièrement pertinent. L'article rapporte et discute certains résultats de l'interaction numérique 2D entre le sol et le revêtement d'un support temporaire déformable avec un champ de contraintes initial non isotrope. Les résultats du support rigide classique sont également rapportés et comparés.

Keywords: Tunnelling; yielding principle; soil-lining interaction; squeezing conditions; anisotropic state of stress.

1 INTRODUCTION

When deep tunnels cross poor grounds the so-called squeezing conditions happens. This leads to huge risks for the construction project, higher construction times and costs. Furthermore, in conventional tunnelling, extremely high convergences and overload of rigid preliminary lining can be expected. The best way to face these difficulties is to design the preliminary support following the so-called yielding principle (Kovári, 1998): the support must be highly deformable, allowing the ground deformations and, by so doing, reducing the stress acting on the lining. There are various technological solutions to introduce local deformations into the preliminary lining (Wu et al., 2021; Moritz, 2011). This paper is focused on circumferential elastic-plastic elements (EPE). TH steel ribs, hiDCon, LSC, hiDSte and Wabe are the most commonly used ones in conventional tunnelling.

There is limited literature on numerical modelling for the design of yielding supports in deep tunnelling under squeezing conditions (Yang et al., 2022; Barla et al., 2011; Tian et al., 2018; Radončić, 2011). Indeed, the ground-lining interaction (GLI) with a yielding lining has not been widely studied leaving a notable gap on the comprehension of tunnels' behaviour with this kind of supports. Furthermore, there is a lack of study on the effect of geostatic anisotropic state of stress, which is usually faced in squeezing conditions, on the interaction mechanism.

The aim of our work is to fill this existing gap. Our research was firstly driven by the embedment of high deformable elements in the steel ribs (Batocchioni et al., 2023). Whereas this paper aims at understanding the mechanical behaviour of a temporary lining following the yielding principle, under an anisotropic state of stress. Considering that in deep tunnelling the horizontal and the vertical stress can be quite far from equal for the combined effect of gravity and tectonic.

The methodology is developed by following a numerical approach. In order to highlight how the anisotropy of initial geostatic stress field affects the GLI, the results obtained for both rigid and yielding lining, starting from isotropic and then anisotropic geostatic conditions, are presented and discussed.

2 NUMERICAL MODEL

2D numerical analyses, modelling a cross section of a circular tunnel supported by temporary lining, have been developed with the aim of studying the peculiarity of GLI under an anisotropic stress field. The methodology is in line with the one used by Batocchioni et al. (2023), but with a focus on the relationship between lining's normal force, *N*, and the EPE's closure as relaxation increases. Indeed, study the effects on *N* give a first clear picture on the GLI mechanism. The analyses were developed through the FDM code FLAC2D (Itasca, 2011). The model reproduces only one quarter of the tunnel thanks to the symmetries (Figure 1). The mesh is composed of 4876 elements. The boundary constraints are the ones depicted in the Figure 1. Several analyses were carried out: the lining with (yielding) and without (rigid) the EPE, with an isotropic ($k_0 = 1.0$) and anisotropic ($k_0 = 0.5$) state of stress while keeping the average in-situ stress constant. For symmetry reasons, by neglecting the gravity and studying $k_0 = 0.5$ condition is equivalent to study also $k_0 = 2$ condition.

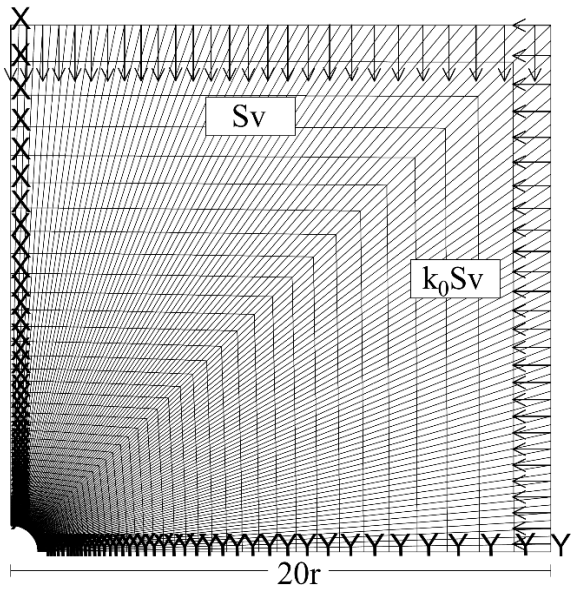

Figure 1. Numerical grid on FLAC 2D.

The mechanical behaviour of the ground has been modelled as isotropic elastic perfectly plastic with the parameters reported in Table 1. The severity of the conditions are quite high, in fact, the ratio between the uniaxial compressive strength and the mean in-situ stress is extremely low (≈ 0.06). Thus, leading to squeezing conditions (Ramoni and Anagnostou, 2010).

The excavation phase has been simulated with the well-known relaxation method, assuming the lining installation corresponds to a relaxation factor of 70%. The preliminary support has been modelled with one HEB240 steel rib per meter. For sake of simplicity, the presence of the shotcrete was neglected. The lining has been modelled with elastic perfectly plastic beam (yielding normal force of 2915 kN). Also the EPE has been simulated with the same beam elements, but with lower values of Young's modulus and yielding normal force. The EPE has been modeled as a generic yielding element, but akin to the hiDSte (the best solution to embed in the steel rib). Therefore the Young's modulus magnitude is the one obtained by compression in experimental analyses, whereas the yielding normal force has been set as half of the steel rib one. In the analyses, the EPE behave as a hinge, assuming a null value of the plastic moment of the beam. This is a reasonable simplification, because the capacity of withstanding bending moments of the EPE is quite small respect to the one of the steel rib. To simulate the controlled deformation of this kind of lining, a special FISH routine was written in FLAC. Thus making the EPE extremely rigid when they reach the 97% of its maximum deformation.

The lining is connected to the ground through an interface characterized by infinite compressive strength (elastic behaviour) and shear elastic-plastic behaviour with frictional Mohr-Coulomb criterion.

The accuracy of the numerical results is guaranteed by the high density and dimensions of the mesh (20 times the tunnel radius) and by the stringent convergence criterion set in the code (*sratio* equal to 10^{-5}). As well as by verifying the achievement of stationary conditions with the progress of calculation steps of the most relevant variables of the interaction problem.

Table 1. Parameters used in the numerical analyses.

	Ground	Steel Ribs	EPE	Interface
Friction angle (°)	30			20
Cohesion (kPa)	100			0
Normal and shear bond stiffness (MPa)				47e3
Average in-situ stress (MPa)	6.75			
Coefficient of earth pressure at rest, (-)	0.5, 1.0			
Young's Modulus (MPa)	1000	21e4	177	
Yielding Normal force (kN)		2915	1458	
Yielding Moment (kNm)		-	0	

3 RESULTS AND DISCUSSION

The Figure 2c reports the variation of *N* along the lining. As the relaxation increases, the *N* tends to incrase; the initial trend, higher at the sidewall, is a direct consequence of $k_0 < 1$ (arch effect). With further relaxation, the EPE start to close with progressively higher gradient (Figure 2b). As expected, initially the EPE at the sidewall ($\theta = 0° \; and \; 45°$) closes more than the rest. Thus, tending

to mitigate the strong *N* difference along the rigid lining (see Figure 2c dark-blue lines, rigid vs yielding at $\lambda = 0.8$). Continuing the relaxation, the closure gradient of the crown EPE ($\theta = 90°$) grows and at $\lambda = 0.98$ all the 3 EPE are close at the same level (around 80%). Whatching the *N* along the lining (Figure 2c, light green line), from this relaxation on until the first EPE reach the adimissible deformation, the trend is substantially the same with the istropic one (Figure 2c, black dotted line). This continue to emphasise the good benefit of the yielding lining on anisitropic mitigation. Indeed in these conditions, appear evident the effect of the EPE imposing the passage of the *N*-curve at their yielding value (1458 kN) and by so doing impeding the *N* value to rise more.

Whereas between the two EPE (in the rigid lining segment) the *N* rises because of the interface's shear strength, reaching the maximum value in the middle of the rigid segments (Radončić et al., 2009; Tian et al., 2018; Batocchioni et al., 2023).

The scenario changes when at $\lambda = 0.99$, the EPE in the crown is the first to reach the admissible deformation and finally at $\lambda = 0.995$ (Figure 2c, orange line) all the EPE are fully closed. In spite of such a small relaxation ($\Delta\lambda = 0.005$, Figure 2b), the effect on the *N*-curve is decisively clear: the interaction changes and inside all the lining with the close EPE (upper part of the tunnel) the *N* can rise. This difference of *N* (around 300kN) will remain constant until the end of relaxation considering that now on the lining behave as completely rigid (Figure 2c, red line). Therefore the final arrangement of the *N* is characterized by higher values at the crown. Unlike what was expected.

The explanation of these behaviours likely is in the different stress paths that experience the ground near the tunnel. Especially, looking at Figure 3, the first ground's element to reach the yielding (the only one before $\lambda = 0.7$, i.e. the installation of the lining) is the one at the sidewall; where the stress path induced by tynnelling tends to increase the mobilization of shear strength. The last to yield is the element in the crown (almost at the end of relaxation), where the deviatoric stress tends initially to reduce and after becoming isotropic, it tends to incrase, with an inversion of the principal stress direction. Thus, the plastic zone starts at the sidewall and then it extends to the upper part of the tunnel (Figure 2a).

In conclusion the effectiveness of the yielding lining can be highlighted by comparing the two dark-blue lines (Figure 2c, both thick and thin ones) representing the *N* on yielding and rigid lining (respectevely with and without the EPE) for the same level of relaxation ($\lambda = 0.8$). The *N* acting on the rigid

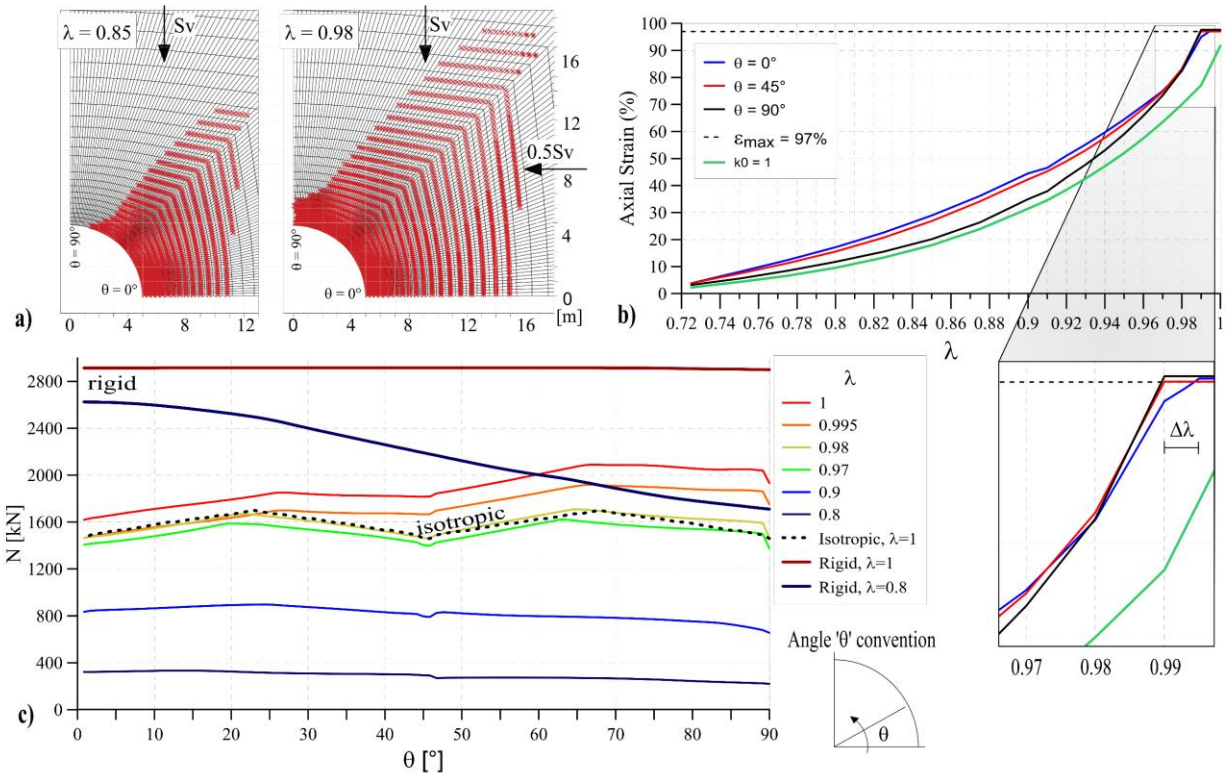

Figure 2. a) plastic zones around the tunnel with 2 different level of relaxation; b) EPE closure with the relaxation; c) normal force in the beam element along the tunnel (lining) with the relaxation.

lining are markedly higher than yielding one. Although less effectively than under isotropic stress field, the deformable lining is able to mitigate the effect of the anisotropic geostatic state of stress: the variation of *N* along the support is less pronunced respect to the rigid lining and the magnitude are rather lower.

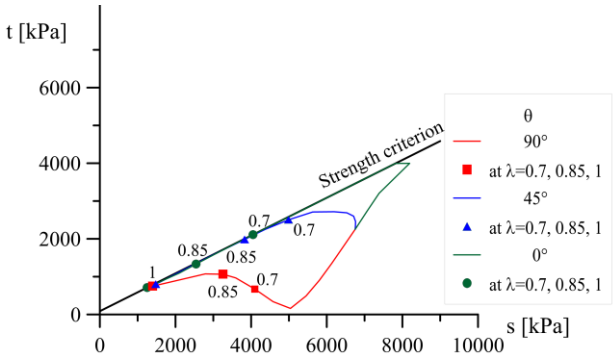

Figure 3. Stress path of different ground zone near the tunnel: green (θ=0°, sidewall), blue (θ=45°), red (θ=90°, crown) and black (strength criterion).

4 CONCLUSIONS

In the design of deep tunnel's preliminary lining squeezing conditions can be faced. In this case, a yielding lining must be conveniently employed. Moreover, due to the combined effect of gravity and tectonic, the initial stress state can be very far from isotropic.

In this paper, 2D numerical analyses have been developed with the aim of studying the interaction between temporary lining equipped with elasto-plastic elements and ground under geostatic anisotropic state of stress.

The main outcomes are the following:

- the study of the ground's plastic zones development is essential to understand the complex ground-lining interaction;
- if none of the elasto-plastic elements reach the admissible deformation, the yielding lining is able to minimize the effect of the anisotropic state of stress on the normal forces;
- if one or more elasto-plastic elements reach the admissible deformation, the most critic section turn out to be the one towards the maximum principal stress direction, differently from what happens with a rigid lining.

Regarding further development, in order to achieve a more complete picture of the ground-lining interaction of a yielding support under anisotropic state of stress, it will be necessary to consider the distribution and evolution of shear and bending moment, expected to be relevant.

REFERENCES

Barla, G., Bonini, M. and Semeraro, M. (2011). Analysis of the behaviour of a yield-control support system in squeezing rock. Tunnelling and Underground Space Technology, 26(1), 146-154. https://doi.org/10.1016/j.tust.2010.08.001.

Batocchioni, L., Gonzalez, V. and Miliziano, S., (2023). Soil-structure interaction of preliminary deformable lining for conventional tunnel in squeezing conditions using HiDSte elements, In: *2023 ISRM*, Salzburg, Austria, 135-140.

Itasca (2011). FLAC2D (Version 7.0). Available at: https://www.itascacg.com/software/flac2d.

Kovári, K. (1998). Tunnelling in squeezing rock. Tunnel 5/98.

Moritz, B. (2011). Yielding elements-requirements, overview and comparison. Geomechanics and Tunnelling.

Radončić, N., Schubert, W. and Moritz, B. (2009). Ductile support design. Geomechanics and Tunnelling, 2(5), 561-577. https://doi.org/10.1002/geot.200900054.

Radončić, N. (2011). Tunnel design and prediction of system behaviour in weak ground, PhD Thesis.

Ramoni, M. and Anagnostou, G. (2010). Thrust force requirements for TBMs in squeezing ground. Tunnelling and Underground Space Technology, 25(4), 433-455. https://doi.org/10.1016/j.tust.2010.02.008.

Tian, H. M., Chen, W. Z., Tan, X. J., Yang, D. S., Wu, G. J. and Yu, J. X. (2018). Numerical investigation of the influence of the yield stress of the yielding element on the behaviour of the shotcrete liner for yielding support. Tunnelling and Underground Space Technology, 73, 179-186. https://doi.org/10.1016/j.tust.2017.12.019.

Wu, K., Shao, Z., Qin, S., Wei, W. and Chu, Z, (2021). A critical review on the performance of yielding supports in squeezing tunnels. Tunnelling and Underground Space Technology, 115, 103815. https://doi.org/10.1016/j.tust.2021.103815.

Yang, K., Yan, Q., Shi, Z., Zhang, C. and Ma, S. (2022). Numerical Study on the Mechanical Behavior of Shotcrete Lining with Yielding Support in Large Deformation Tunnel. Rock Mechanics and Rock Engineering. https://doi.org/10.1007/s00603-022-03126-w.

Proceedings of the XVIII ECSMGE 2024
GEOTECHNICAL ENGINEERING CHALLENGES
TO MEET CURRENT AND EMERGING NEEDS OF SOCIETY
© 2024 the Authors
ISBN 978-1-032-54816-6
DOI 10.1201/9781003431749-397
Open Access: www.taylorfrancis.com, CC BY-NC-ND 4.0 license

ECSMGE 24
XVIII EUROPEAN CONFERENCE ON SOIL MECHANICS AND GEOTECHNICAL ENGINEERING

Lot 2: Lisbon Metro extension between Santos station and the terminal of Cais do Sodré station. Geological and geotechnical model and parameterisation

Lot 2: Extension du métro de Lisbonne entre la station Santos et la terminal de la station Cais do Sodré. Modèle géologique-géotechnique et paramétrage

J. Bento*, S. Ferreira, D. Teles Fortes, R. Pistone
COBA, Consultores Obras e Barragens, S.A., Lisboa, Portugal

N. Cruz, J. Cruz
Mota-Engil, Linda-a-Velha, Portugal

A. Tavares
Metro Santos Sodré ACE, Linda-a-Velha, Portugal

R. Pina
Metropolitano de Lisboa, Lisboa, Portugal

**j.bento@cobagroup.com*

ABSTRACT: Lot 2 of the Extension of the Yellow and Green Lines of the Lisbon Metro starts at the Santos Station and runs southwards across Av. D. Carlos I and Av. 24 de Julho up to the Cais do Sodré Station, connecting the Yellow Line to the Green Line. In this lot, several stages of prospection were carried out, resulting in an extensive set of field and laboratory works that enabled the preparation of the geological model and the geotechnical parameterisation of the lithological units considered in that model. In a length of only 665 m, several materials are crossed. In the survey campaign of the construction phase, among a wide range of works, 73 boreholes were driven for the geological-geotechnical, hydrogeological and geo-environmental components. Based on all information available from previous surveys and from historical and geological mapping, it was possible to draw up the geological model adopted in the Construction Design. Given the large number of results, statistical processing was used to limit and estimate the characteristic values of the parameters required in safety checks.

RÉSUMÉ: Le lot 2 de l'extension des lignes jaune et verte du métro de Lisbonne commence à la station Santos et se dirige vers le sud en traversant l'Avenue D. Carlos I et Avenue 24 de Julho jusqu'à la station Cais do Sodré, reliant la ligne jaune à la ligne verte. Dans ce lot, plusieurs étapes de prospection ont été réalisées, aboutissant à un vaste ensemble de travaux sur site et de laboratoire qui ont permis d'élaborer le modèle géologique et la paramétrisation géotechnique des unités prises en compte dans ce modèle. Sur une longueur de seulement 665 m, plusieurs matériaux sont traversés. Lors de la campagne d'étude de la phase de construction, parmi un large éventail de travaux, 73 forages ont été réalisés pour les composantes géologiques-géotechniques, hydrogéologiques et géo-environnementales. Sur la base de toutes les informations disponibles, provenant des études et campagnes précédentes et de la cartographie historique et géologique, il y a été possible d'élaborer le modèle géologique adopté dans les études d'exécution. Compte tenu de la grande quantité de résultats, il a été possible de limiter et d'estimer les valeurs caractéristiques des paramètres nécessaires pour les contrôles de sécurité à effectuer, grâce à l'aide de traitements statistiques.

Keywords: Lisbon; geologic model; geotechnical survey; geotechnical parametrisation.

1 INTRODUCTION

Lot 2 of the Extension of the Yellow and Green Lines of the Lisbon Metro begins at the Santos Station and extends for about 665 m until the Cais do Sodré Station. From a geomorphological and topographical perspective, the alignment is divided into two parts. The first part is located on the slope of the Madragoa neighbourhood, where the Santos Station is located, and the alignment mostly runs underground. It then transitions to the lower area along the riverfront, where it continues in a trench.

This lower area riverside evolution is presented in Figure 1.

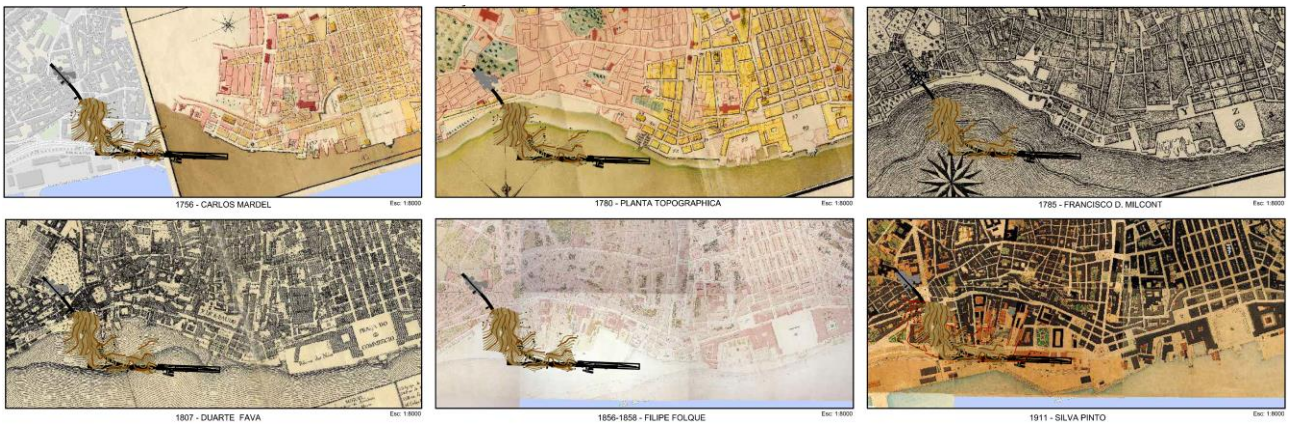

Figure 1. Maps dating from 1756 to 1911, showing the evolution of the riverside area of the Tagus River. The layout of the alignment shows that it lies partly on areas reclaimed from the river.

2 GEOLOGICAL MODEL

2.1 Geological and geotechnical zoning

In the initial part, the geological mapping is mainly composed of the Miocene unit of the Prazeres Clays (MPr), overlying materials from the Lisbon Volcanic Complex (CVL). In this area, in the upper part of the unit prevails basalt, often highly weathered and fractured and, in the lower part, tuffs and breccias. This complex overlies Cretaceous materials from the Bica Formation (mostly limestones). Approximately from Pk 1+575 onwards, the geology is dominated by the presence of alluvial soils underlying landfill deposits, as marked with lines in Figure 2. In this second part of the alignment, starting from the entrance into the Paleovalley (formed by a tributary of the Tagus and whose central zone broadly coincides with the designated Boavista landfill), it fits into an area with a flat surface morphology and the presence of alluvial deposits. In this zone, the geology is characterized, in the upper part, by the presence of landfill deposits – At, up to a depth of about 7.5 m (borehole SC22-Pz), beneath which prevail alluvial materials, predominantly sandy up to Pk 1+700, and predominantly clayey from there to the end of the trench section.

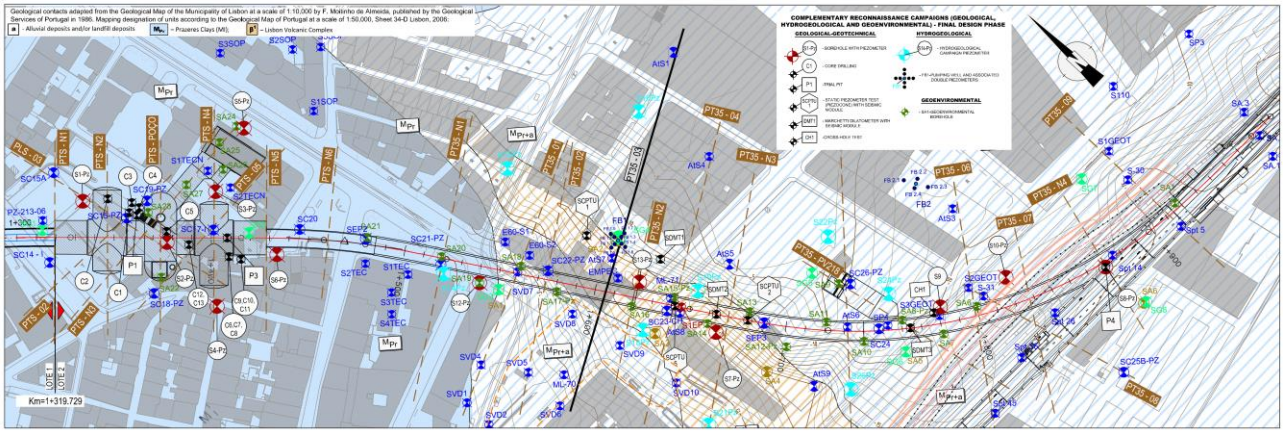

Figure 2. Geological map (adapted from geological mapping at a 1:10,000 scale). In blue, areas of the MPr-Prazeres Clays unit, and in brown, materials from the CVL-Lisbon Volcanic Complex ("line pattern" when under alluvial deposits). Contour lines indicate the topography of the substrate beneath the alluvial deposits in the paleovalley.

In the second section there is a noticeable rise of the Miocene substrate, reaching a maximum roughly between Pk 1+725 and 1+750, at the final of the paleovalley to the southwest. It is noteworthy that there is a prominence of the substrate in relation to the general base level trend toward the east throughout the alluvial/landfill area, with a positive differential of about 7 m. This substrate rise is attributed not only to the prominence of the former stream bank on the left side, but also because the alignment turns eastward here, running along the substrate. On the other hand, this local prominence of the substrate also marks, to some extent, the separation of alluvial deposits from the former stream (paleovalley) from those deposited

by the Tagus River. The overall structure of the Miocene monoclinal unit exhibits a general dip toward S-SE with strata dipping generally less than 15º, ranging from 5 to 10º, similar to the levels of the CVL. Despite the eventual faults in the second part of the alignment, it was decided not to represent them, as the model adopted allowed for the interpretation of the contacts between units without materializing disruptions caused by structural discontinuities. Another aspect worth noting in the model is its transversal variability, particularly around the paleovalley, as can be seen, for example, in the section at Pk 1+605, presented below in Figure 4

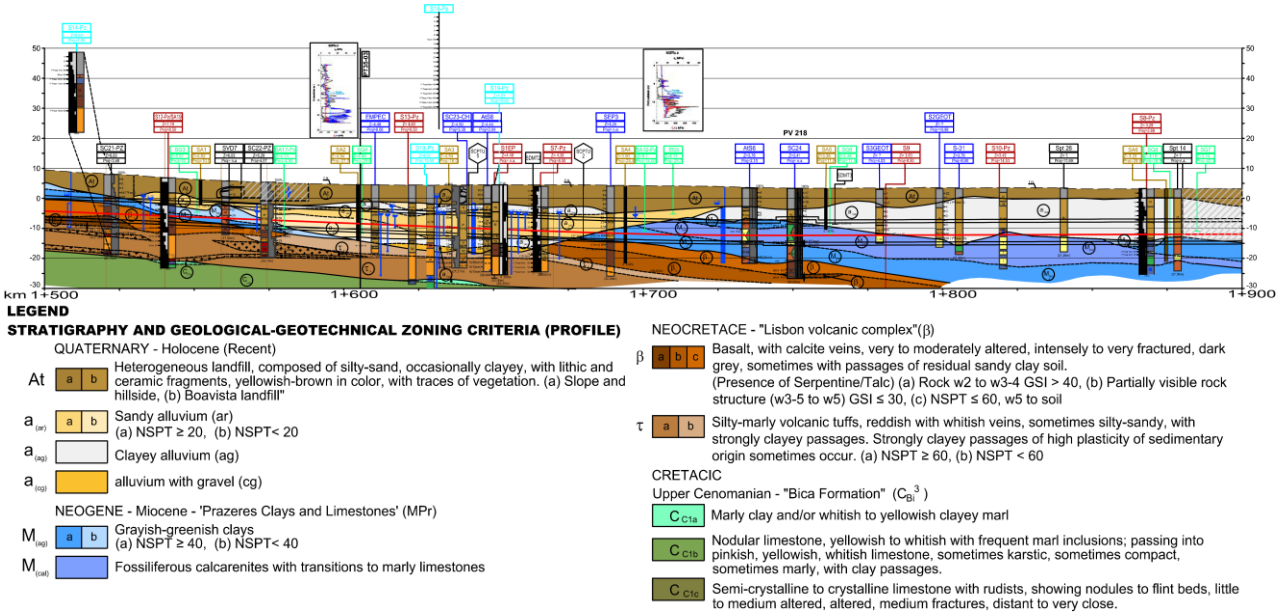

Figure 3. Geological model in the lower area, from pk 1+500 to pk 1+900. In the legend, stratigraphy and zoning criteria adopted in the geological and geotechnical model, in Bento et al. (2022).

The construction of the trench in the lower area, in an alignment that positions it as a barrier to the flow of groundwater along the paleovalley, also led to the need to carry out detailed hydrogeological studies. Taking into account the constraints arising not only by the trench to be built, but also by the basements and pumping systems of pre-existing buildings, these studies addressed the modelling of the current and post-construction conditions. These studies made it possible to design a solution for water to pass through the walls of the trench above the rail tunnel, achieved by drilling holes in the structure.

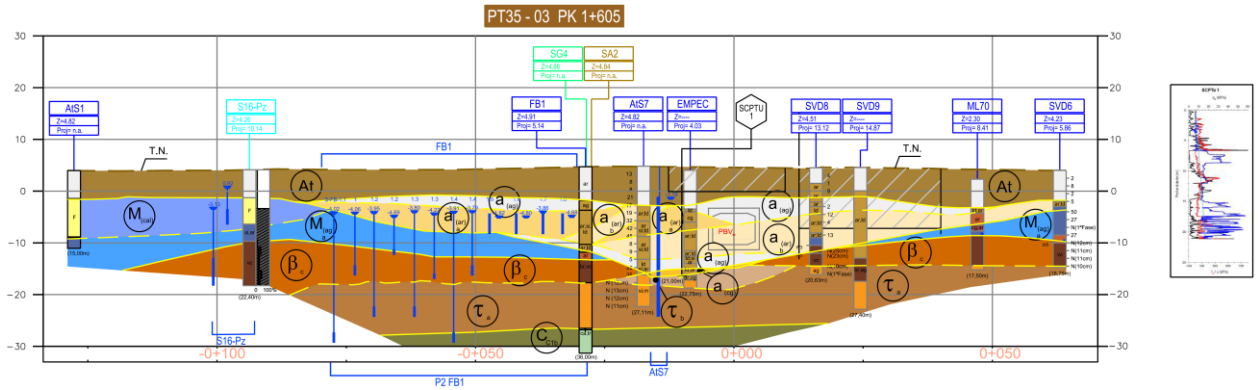

Figure 4. Profile PT35-03, geological model at pk 1+605, in the paleovalley area, in Bento et al. (2022). Particularly noteworthy are the piezometry results from borehole FB1 and the transversal variations of geologic strata. Profile PT35-05 location, at pk 1+600,5 signalled with black line in Figures 2 and 3.

The lithological units adopted in the geological model are part of the stratigraphic units, and different lithological units are considered depending on the type of soils found in each of the stratigraphic units. The

geologic model was primarily developed using geotechnical survey results, geological mapping, as well as ancient cartography, engravings and tile paintings. The geotechnical zoning adopted was based mostly on the analysis of the results of the geotechnical surveys carried out in the various ground investigation survey campaigns. All this data was weighed up against the type of works to be built. Regarding the geological units adopted, following the analysis of all the available data, it was decided to subdivide some of the lithological units in order to best tailor and optimise the solutions designed. This approach can be considered as geological and geotechnical zoning, primarily based on lithological criteria.

Thus, the zoning first identified a total of 6 distinct geologic units (Landfills, Alluvium, Miocene Complex, Volcanic Complex-Basalts, Volcanic Complex-Tuffs, and Cretaceous - Bica Limestones), as a result of which the different lithostratigraphic complexes crossed by the works were separated. In turn, some of these units were further first subdivided into lithological units and then in geotechnical zones, differentiating them according to their distinct mechanical properties.

In this context, in the alluvium geological unit, the sandy alluvial lithological unit was subdivided into $a(ar)_a$ and $a(ar)_b$, depending on whether the N_{SPT} value is greater or less than 20 blows, respectively.

The clayey Miocene unit was also subdivided into $M(ag)_a$ and $M(ag)_b$, depending on whether the N_{SPT} value is greater or less than 40 blows, respectively.

The basalts and tuffs of the CVL were also subdivided into β_a, β_b, and β_c, and τ_a and τ_b, respectively. The β_a basalts are low to moderately-highly weathered (W_2 to W_{3-4}) with GSI values > 40, the β_b basalts, while partially maintaining the rock structure, are moderately to highly weathered to decomposed (W_{3-4} to W_5) with GSI values < 25, and the β_c basalts consist of decomposed material (W_5) with N_{SPT} values $\leq$ 60 blows, commonly referred to as basaltic breccia in older campaign drillings. Tuffs τ_a and τ_b were subdivided based on N_{SPT} values equal to or less than 60 blows, respectively.

This process resulted in 17 geotechnical sub-zones, as presented in Figure 3.

2.2 Geotechnical survey

In addition to analysing and incorporating into the study the results obtained in 91 boreholes from previous campaigns, carried out both as part of previous phases of this project and other works in this densely populated area, a significant set of field and laboratory work was carried out as part of the studies. This included: 73 mechanical boreholes (17 geotechnical, 24 hydrogeological, and 32 geo-environmental); 13 core drillings; 3 inspection wells; 13 vane tests (FVT); 3 Marchetti dilatometric tests (DMT); 4 static penetration tests with seismic measurement (SCPTu); 39 Menard pressuremeter tests (PMT); 138 Lefranc permeability tests; 4 Lugeon permeability tests; collection of 30 undisturbed samples with a Shelby sampler for laboratory tests; Installation of 40 piezometers with a monitoring campaign; Laboratory tests for the physical and mechanical characterization of the soils, including particle size analyses, consistency limits, organic matter content, density of solid particles, volumetric weights, permeability tests, consolidation tests, and triaxial tests on soils; determination of bulk densities, unconfined compression tests, point load tests (PLT), and triaxial tests on rock; collection of water samples for laboratory analysis in environmental boreholes; pH, temperature, and electrical conductivity analyses in some piezometers; 4 pumping tests and 2 tide tests. The fieldwork is indicated on the plan in Figure 2.

3 GEOTECHNICAL PARAMETRISATION

3.1 Introduction

When possible, the estimation of the design geotechnical parameters for each geotechnical unit took into account the results of the work carried out in the various ground investigation campaigns available. When necessary, correlations established in the specialized literature were employed to convert the parameters obtained in the tests into design parameters.

The geotechnical field survey was parameterised using the following *in situ* tests: static cone penetration tests with seismic module (SCPTu's), Marchetti dilatometer tests with seismic module (SDMT's), Menard pressuremeter tests (PMT's), LNEC dilatometer tests (BHD's), Vane Tests (FVT) and permeability tests of the Lugeon and Lefranc types. Some results from laboratory soil tests were also used, namely uniaxial compression tests, determination of bulk density, and permeability determination obtained through triaxial tests. In addition, laboratory test results on rock samples were used, particularly uniaxial compression tests (UCS), point load tests (PLT), and determination of bulk density.

3.2 Methodology

Based on the mentioned tests, a statistical estimation of the possible characteristic values of the geotechnical parameters for the material of each considered unit was carried out.

Eurocode 7 recommends that "the characteristic value of a geotechnical parameter should be chosen to constitute a cautious estimate of the value that conditions the occurrence of the limit state under consideration." However, it is not specified what constitutes a "cautious estimate" of the value and how to calculate it.

As a contribution to the ongoing revision of EC7, Orr (2017), in Shen *et al* (2018), proposed the simplified equation (1), which was used as a preliminary calculation for the characteristic value of the geotechnical parameters:

$$X_k = X_{mean}\left(1 - 3aCOV/\sqrt{L_v}\right) \qquad (1)$$

After testing several approaches to determine the characteristic values, the project opted for equation (2), adapted from the simplified equation (1) proposed by Orr (2017):

$$X_k = X_{mean}\left(1 \pm 3aCOV/\sqrt{L_v}\right) \qquad (2)$$

where:

X_k –characteristic value of geotechnical parameter X;

X_{mean} –mean value of geotechnical parameter X;

a – factor responsible for the quality and extent of laboratory and field investigations. For high-quality and extensive investigations, a = 0.5; for average quality and extent of investigations, a = 0.75; and for values estimated from general experience or tabulated values, a = 1.

COV – coefficient of variation of geotechnical parameter X;

L_v –vertical dimension of the zone of influence.

The mentioned equation (2) was used, with a negative sign, whenever the number and consistency of tests allowed it, to calculate the characteristic values of the parameters undrained cohesion (c_u), effective friction angle (ø'), deformation modulus (E), and coefficient K_0, as these geotechnical parameters are more critical for the project the lower their values. On the other hand, for the unit weight (γ), saturated unit weight (γ_{sat}), and coefficient of permeability (k), which should be more critical for the project the higher their results, the equation was chosen with a positive sign.

The factor "*a*" and the coefficient of variation *COV* are important factors in these equations, as the first considers the quantity and quality of sampling, and the second, being a function of the standard deviation, reflects the dispersion of the data. For larger "*a*" and *COV* values, more cautious will the characteristic value obtained be.

A factor a = 0.5 was considered when the number of tests is greater than or equal to four, and a factor a = 0.75 when the number of tests is less than four.

The factor L_v is variable for each geotechnical unit, depending on the weighted thickness of the respective considered units, and also reflects the dispersion of the results. For a specific parameter with a certain range of results, the smaller the area in profile where this dispersion occurs, the lower the degree of confidence that these results provide. In other words, the lower the value of L_v, the more conservative the characteristic value obtained will be.

In the calculation of characteristic values, any results that significantly deviated from all others, i.e., those outside the overall pattern of a distribution (outliers), were excluded. For this purpose, the common method based on the interquartile range (IQR) was considered. This method involves identifying a result as an outlier if it is more than 1.5 times the IQR above the 3rd quartile (Q3) or more than 1.5 times the IQR below the 1st quartile (Q1)

It is important to note that, for almost all units, despite having few results to determine the characteristic value of some geotechnical parameters, which makes the estimate less valid from a statistical point of view, it was still decided to carry out this assessment, which serves as another element of careful analysis.

The data processing results for determining the characteristic value of undrained cohesion (cu) for the clayey alluvial unit a(ag) that occurs in the upper zone of the lower section of the alignment are presented in Figure 5. This unit is depicted in Figure 4 and is more extensively found in the alluvial deposits towards the end of the alignment.

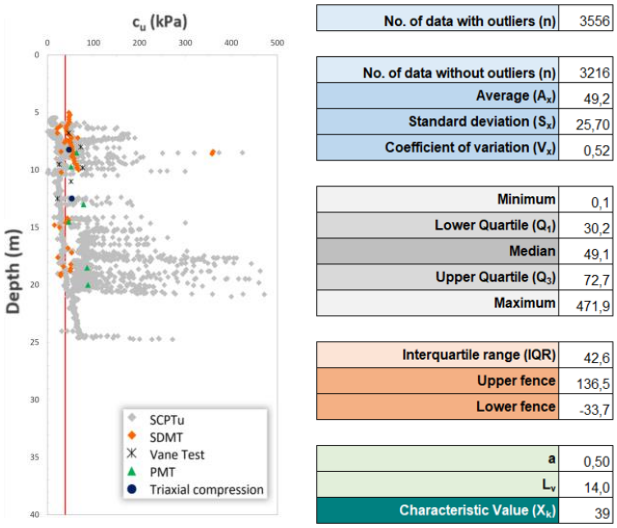

Figure 5. Alluvium a(ag) – Estimate of undrained cohesion (c_u).

For reference, the unit a(ag) is a clay, sometimes silty, with a characteristic value of N_{SPT} of 4 blows.

Table 1. Characteristic values for undrained cohesion (c_u) by test type in the clayey alluvium unit.

a(ag) unit	SDMT	SCPTu	PMT	Vane Test	Tri-axial
c_u (kPa)	41	39	62	40	47

The adopted characteristic value for c_u was 40 kPa. For this unit in particular, the need to consider different values in function of the depth, was also considered, being this variation obtained by the expression below the table in Figure 6.

Geotechnical Unit	γ (kN/m³)	γ_{sat} (kN/m³)	c_u (kPa)	E_u (MPa)	c' (kPa)	ø' (º)	E' (MPa)	K_0	k (m/s)	ν	σ (MPa) [rock]	E' (GPa) [rock]
At	18	20	---	---	0	29	5	0,5	10^{-5}	0,35	---	---
a(ag)	17	19	* (40)	20	0	28	4	0,5 - 0,7 ***	10^{-8}	0,46	---	---
$a(ar)_a$	19	21	---	---	0	37	78	0,5	10^{-4}	0,30	---	---
$a(ar)_b$	18	20	---	---	0	33	22	0,4	10^{-5}	0,32	---	---
a(cg)	20	22	---	---	0	35	75	0,5	10^{-6}	0,30	---	---
$M(ag)_a$	22	23	338	98	10	33	61	0,8 - 1,0 ***	10^{-8}	0,33	7	1
$M(ag)_b$	21	22	186	39	0	28	19	0,8 - 1,0 ***	10^{-8}	0,38	---	---
M(cal)	24	24	---	---	75	34	400	0,8 - 1,0 ***	10^{-5}	0,25	7	7
β_a	27	27	---	---	160	40	2000	0,7 - 1,0 ***	10^{-8}	0,25	30	16
β_b	25	25	---	---	60	38	500	0,5	10^{-6}	0,26	6	3
β_c	23	24	---	---	50	34	254	0,5	10^{-6}	0,28	---	---
τ_a	21	22	---	---	60	35	228	0,5 -1,0 ***	10^{-7}	0,27	5	0,5
τ_b	20	21	---	---	30	30	83	0,5	10^{-7}	0,3	---	---
Cc1a	23	24	---	---	50	32	60	0,5 - 1,0 ***	10^{-6}	0,23	4	1
Cc1b	24	24	---	---	100	38	400	0,5 - 1,0 ***	10^{-7}	0,21	9	3
Cc1c	25	25	---	---	300	40	3900	0,7 - 1,0 ***	10^{-6}	0,21	53	27

* c_u=2,157z+5,886 ***Advisable to perform sensitivity analysis

Figure 6. Table of design parameters adopted for geotechnical safety checks, in Bento at al. (2022)

3.3 Design geotechnical parameters adopted.

Following the methodology explained above, naturally adapted to each testing type, geological unit material, location in depth, test quantity and previous experiences, it was possible to establish the geotechnical parameters presented in the table in Figure 6.

4 CONCLUSIONS

The extent of the ground investigation campaign, which complements previous campaigns, made it possible to gather the data that led to the development of the geological model adopted. At the date of the publication, this model has proven to be accurate in the ongoing works. The method of adopting characteristic values eased the systematic treatment of data (of varied nature and quantity) necessary for defining the design geotechnical parameters used in the development and safety verification of the construction works. Based on these characteristic values, the final adoption of parameters was naturally guided by the engineering practice and expertise, which are crucial in the process. developments.

ACKNOWLEDGEMENTS

The authors express their sincere gratitude for the support extended by the Owner (Metropolitano de Lisboa EPE) and the Construction Consortium (Metro Santos Sodré ACE), by allowing the publication of this article.

REFERENCES

Shen, M. Koshenvisan, S.; Zhang, Y. Juang, H. Assessing Characteristic Value Selection Methods for Design with LRFD – A design robustness perspective. *Canadian Geotechnical Journal* (2018). DOI:10.1139/cgj-2018-0038

Bento, J.; Teles Fortes, D.; Ferreira, S.; Mateus, G.; Pistone, R. Extension of the yellow and green lines: Rato - Cais do Sodré - Lot 2. Metropolitano de Lisboa, E.P.E. Lot 2: Execution between Santos station and the end of Cais do Sodré station, from pk 1+319.729 to pk 1+984.273 *Final Design. Geology and Geotechnics. Volume I – Geological, Geotechnical, Hydrogeological and Geoenvironmental Study.* COBA, Lisbon (2022). *In Portuguese.*

Proceedings of the XVIII ECSMGE 2024
GEOTECHNICAL ENGINEERING CHALLENGES
TO MEET CURRENT AND EMERGING NEEDS OF SOCIETY
© 2024 the Authors
ISBN 978-1-032-54816-6
DOI 10.1201/9781003431749-398
Open Access: www.taylorfrancis.com, CC BY-NC-ND 4.0 license

ECSMGE 24
XVIII EUROPEAN CONFERENCE ON SOIL MECHANICS AND GEOTECHNICAL ENGINEERING

In situ and laboratory investigation of dynamic performance of a cement-stabilised Chalk trial embankment

Etude in situ et en laboratoire de la performance dynamique d'un remblais d'essai de craie stabilisé au ciment

O. Boumendjel-Game
ARCADIS, UK

M. Vowles
COWI, UK

M. Fleetwood, H. Saroglou*
Eiffage Keir Ferrovial BAM (EKFB) JV, UK

G. Katsigiannis
Ferrovial Construction, UK

**harry.Saroglou@ekfb.com*

ABSTRACT: Use of stabilised soils in the construction of high-speed rail embankments is a desirable engineering solution as more site-won soils may be used locally thus reducing the volume and mass haul of imported and site-won materials. In the south of contract area C23, significant volumes of weathered structureless chalk will become available due to the construction of cuttings. However, presently there is little data available in the public domain to characterise the dynamic performance of a cement-stabilised chalk for use as high-speed rail embankment fill material. This paper presents the results of a field trial comprising in situ and laboratory testing of a large embankment constructed from three different chalk-cement mixes. By controlling pulverisation, stabilisation, and compaction procedures during construction, the observed variability of material grading, air voids, and density are presented in relation to the natural variation of the chalk, moisture content, added cement content, and stiffness of the supporting foundation. E_{V2} modulus values are shown to meet HS2 performance requirements but are highly sensitive to cement curing time. On the other hand, the Rayleigh wave characteristics are found to exceed HS2 criteria and the assumed shear value velocity for engineered fill, providing the justification for an increased value to be recommended for optimisation and efficiency.

RÉSUMÉ: L'utilisation de sols stabilisés dans la construction de remblais ferroviaires à grande vitesse est une solution d'ingénierie souhaitable pour HS2, car davantage de sols gagnés sur site peuvent être utilisés localement, réduisant ainsi le volume et le transport en masse de matériaux importés et gagnés sur site. Dans le sud de la zone contractuelle C23, d'importants volumes de craie altérée sans structure deviendront disponibles en raison de la construction de déblais. Cependant, à l'heure actuelle, il existe peu de données disponibles dans le domaine public pour caractériser les performances dynamiques d'une craie stabilisée au ciment destinée à être utilisée comme matériau de remblai de chemin de fer à grande vitesse. Cet article présente les résultats d'un essai sur le terrain comprenant des essais in situ et en laboratoire d'un grand remblai construit à partir de trois mélanges crayeux-ciment différents. En contrôlant les procédures de pulvérisation, de stabilisation et de compactage pendant la construction, la variabilité observée du classement des matériaux, des vides d'air et de la densité est présentée en fonction de la variation naturelle de la craie, de la teneur en humidité, de la teneur en ciment ajouté et de la rigidité de la fondation porteuse. Il a été démontré que les valeurs de module E_{V2} répondent aux exigences de performance HS2 mais sont très sensibles au temps de durcissement du ciment. D'autre part, les caractéristiques de l'onde de Rayleigh dépassent les critères HS2 et la vitesse de la valeur de cisaillement supposée pour le remblai technique, ce qui justifie une augmentation de la valeur recommandée pour l'optimisation et l'efficacité.

Keywords: Chalk; material stabilisation; trial embankment; high speed rail; dynamic performance.

1 INTRODUCTION

1.1 Background

The High Speed Two (HS2) project is a High-Speed Railway Line currently under construction in the UK. Phase 1 of HS2 runs between London and Birmingham across the English Midlands

The scope of the C23 contract, which has been awarded to Eiffage, Kier, Ferrovial Bam Joint Venture (EKFB), includes 45 embankments and 30 cuttings supporting HS2 C23 mainline.

As per HS2 Technical Standard for Earthworks (TS-E) (HS2, 2019), the design of these mainline earthworks shall comply with challenging static and dynamic performance criteria, reflective of the high operational speed of the rail. Compliance needs to be verified during construction with testing. Both the Technical Standard for Earthworks (HS2, 2019) and HS2 Specification for Engineering Works 600 series – Earthworks (HS2, 2022), indicate that field trials are a prerequisite element of the design and construction control validation process.

For mainline embankments, large volumes of engineered fill are expected to be used as upper and lower embankment fill (UEF & LEF) and as foundation treatment, i.e. excavate & replace backfill. In this context and considering the complex logistics associated with this aspect of the scope, opportunities to maximise the use of the site won material generated during excavation for the formation of the mainline cuttings is continuously being sought.

As a result, the field trials scope has been extended to include assessment and validation of site won material performance for use as embankment fill and replacement fill for earthwork foundations.

1.2 Scope & objectives

The main objective of the Earthworks field trials was to demonstrate suitability of proposed unstabilised/stabilised soils for High-Speed Railway embankment fill, to provide earthworks control and verification to validate the performance of the earthworks during and following construction and to review suitable improvement options for re-use of any excavated materials for embankment fills.

This paper discusses the results of the embankment trial of Cement Stabilised Chalk which was performed at Great Missenden. The embankment was constructed using structureless Chalk (Class 3B1) stabilised using cement mix to produce a Class 9M1 fill material for use as UEF, LEF and foundation treatment. The trial's aim was to control, validate, and optimise the earthworks construction method to ensure that the Class 9M1 fill derived from the class 3B1 chalk could reasonably achieve the design requirements set out in the TS-E (HS2, 2019).

2 THE SITE

2.1 Trial location

The trial embankment site is located near Great Missenden, Buckinghamshire. The nearest mainline asset to the trial site is South Heath Cutting. The completed trial embankment is presented in Figure 1. The excavated fill was generally structureless Chalk. The trial site layout plan is shown in Figure 2.



Figure 1. Completed trial embankment.

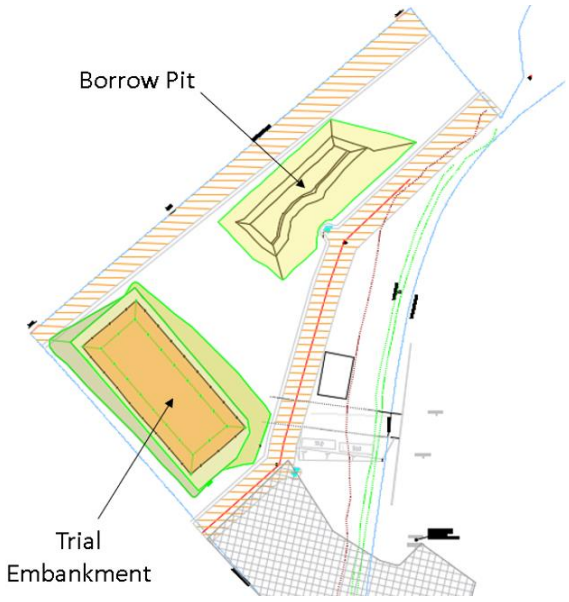

Figure 2. Trial Site Layout Plan and proposed testing locations.

2.2 Ground conditions

Based on the ground investigation at the borrow pit area, the site is characterised by structureless Chalk comprising 1m of grade Dm Chalk becoming grade Dc with depth (Figure 3). Localised zones of more structured Chalk (grades B & C) were also observed over the excavated depth.

Interpretation of available ground investigation data at the trial site indicated that the ground conditions below foundation platform level comprise grades Dm/Dc structureless Chalk over structured Chalk of Grades B/C. This is generally consistent with the ground conditions revealed at the borrow pit location.

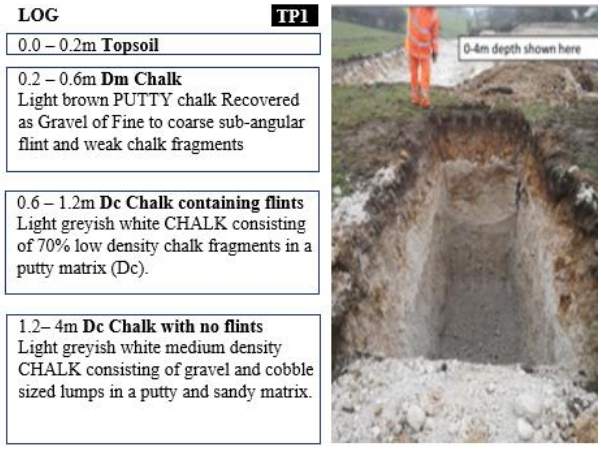

Figure 3. Photo of trial pit in the borrow pit area.

3 EMBANKMENT CONSTRUCTION

The Trial embankment was split into two areas (Area 1 and 2). Layers 1 to 3 of both Area 1 and 2 were constructed using Dm chalk mixed with 2% cement. Above layer 3, Area 1 and 2 were constructed with different binder contents, but both with Grade Dc white chalk. Area 1 used 2% cement for layers 4 to 8 and finished construction at layer 8. Area 2 used 3% cement for layers 4 to 8 and 4% cement for layers 9 to 13 and finished construction at layer 13. Individual layers were specified to achieve a compacted thickness of 250mm.

Due to variation in ground elevation, the trial location was levelled, using cut and fill within the hillside to form a basal foundation platform for the trial embankment. A 2% cement mix was used to stabilise the base.

Targeted in situ and laboratory testing were undertaken both during construction of the trial embankment and on completion to provide the necessary data for use in the assessment of the suitability of site won stabilised structureless Chalk Class 9M1 as HSR embankment fill.

4 PERFORMANCE REQUIREMENTS

4.1 Performance requirements for HSR fill

The performance requirements specified in the TS-E (HS2, 2019) are as follows:

4.1.1 Dynamic performance

The TS-E (HS2, 2019) (Table 4.2/1) specifies the performance criteria to be satisfied by the earthworks design and construction verification testing as a limiting Rayleigh wave velocity (V_R), measured at Formation Level:

$$V_R \geq 1.6 \times DS \quad (1)$$

where DS is the design speed, which for HS2 Contract C23 has been set at 360km/hr (100m/s).

This minimum V_R value is to be achieved over a frequency range of 10-50Hz.

In the beginning of the design, due to lack of information, a minimum V_S design value of 250m/s has been adopted for engineered fill forming embankments and earthwork foundation strata. This value is used for benchmarking the dynamic performance results from testing of the Class 9M1 material forming the trial embankment. The V_S design value has been revised to 300m/s at a later stage based on the evidence from field trials.

4.1.2 Static performance

TS-E specifies the minimum Deformation Modulus (E_{V2}) for Chalk when used as UEF to achieve static performance criteria:

$$(E_{V2}) \geq 45\text{MPa} \quad \text{(1m above LEF)} \quad (2)$$

$$(E_{V2}) \geq 60\text{MPa} \quad \text{(at surface of UEF)} \quad (3)$$

4.1.3 Layer thickness

The following requirements are set out in HS2 Specification, 600 series – Earthworks (2022):

- All fill materials - deposited in layers not exceeding 250mm uncompacted thickness.
- Cement stabilised materials - upper limit of 250mm may be increased depending on confirmation from field trials.

4.1.4 Testing and compaction requirements

Testing methods adopted for measuring in-situ dry density (DD) comprised: Nuclear Density Gauge (NDG), core cutter (CC), and sand replacement density (SRD). Only the NDG results were considered for assessing the material DD. The testing locations are shown in Figure 4.

Degree of compaction achieved is determined based on assessment of the DD as a proportion of maximum dry density (MDD), determined from a defined compaction test converted to a percentage. A similar method was adopted to measure the air voids (AV) in that the particle density (PD) determined from

the embankment trial was used together with the moisture content (MC) and DD readings to determine the AV.

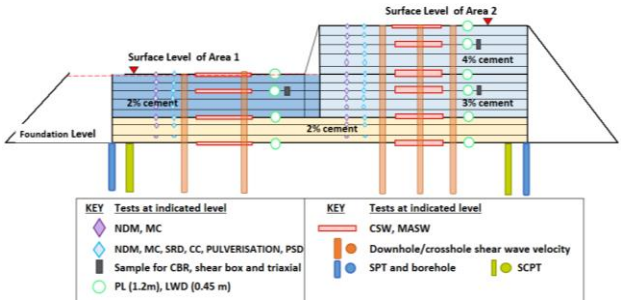

Figure 4. Testing locations and schedule for trial embankment.

Degree of compaction achieved is to be assessed against compaction data from either a standard (2.5kg) or modified (4kg) Proctor tests completed on sample of Chalk fill prior to construction. The Proctor test method used as a benchmark for the trial is determined based on the DD data obtained during compaction optimisation trials.

5 TESTING, RESULTS AND ANALYSIS

5.1 Design performance

5.1.1 Dynamic performance

Surface wave tests, comprising of Continuous Surface Wave (CSW) and Multi-channel Analysis of Surface Wave (MASW), were undertaken at foundation level and at different layers, as shown in Figure 4.

Additionally, Downhole and Crosshole seismic testing was conducted through the embankment fill and foundation strata to compare with the inverted values of Vs from MASW/CSW surveys.
The results are summarised in Table 1.

Table 1. Summary of Shear wave velocities obtained from Geophysical testing performed in Class M91 fill.

CSW (m/s)	MASW (m/s)	Downhole (m/s)	Crosshole (m/s)
400-500	500-600	400-600*	500-700

*Note - *Lower bound value is influenced by the averaging methodology considering the less stiff foundation material below the trial embankment.*

Surface wave geophysical methods are indirect ways of measuring Vshv, and therefore the VS derived from indirect methods (CSW and MASW) were benchmarked against direct methods (downhole and crosshole geophysics). Where surface wave geophysical methods were used, MASW results were considered superior in quality compared to CSW as lower variability was observed.

Benchmarking the testing results obtained from the four test types against the designed assumption of V-shv ≥ 250m/s showed mixed results throughout Areas 1 and 2 of the trial embankment. Nonetheless, all data obtained from all four test types demonstrated that the trial embankment formed of Class 9M1 fill with 2-4% cement contents exceeded the assumed Vshv value of 250m/s. A V_S of 570m/s was considered representative of 3% cement compared to 470m/s for 2% cement. A 2% cement content was considered sufficient to satisfy the dynamic requirement for the reuse of stabilised structureless Chalk Class 9M1 as embankment fill.

5.1.2 Static performance

To account for the depth of influence for a 600mm plate test (AFNOR, 2000), E_{V2} tests were performed within Layers 8 and 13. Also, to ensure that reliable and consistent results are obtained, only E_{V2} tests completed within 24hrs of compaction were assessed for each cement mix. The refined dataset, the results, the average value and percentage exceeding the Upper LEF and UEF requirements for Class 9M1 fill with 2%, 3% and 4% cement are presented in Table 2.

Table 2. Summary of E_{V2} testing results for different cement mix for Class 9M1 fill.

Fill Type	Range E_{V2} (MPa)	%Passing UEF Criteria (base)*	%Passing UEF Criteria (surface)
Class 9M1 (2% cement)	65-205	100%	100%
Class 9M1 (3% cement)	107-375	100%	100%
Class 9M1 (4% cement)	115-450	100%	100%

*Note - *: result represents tests at 1m above the top of the LEF.*

The testing results demonstrated that the static performance criteria for the use of Class 9M1 as UEF fill are met for all binder contents. Also, although E_{V2} values increased with higher cement contents, a 2% cement mix should be considered sufficient for the stabilised structureless Chalk to meet the static performance criteria when used as embankment fill.

5.2 Compaction assessment

5.2.1 Compaction optimisation

Compaction optimisation trials were performed to determine a suitable number of passes on layers 1, 2 and 3, with 9 No. NDG recordings taken after:

- 4, 6 and 8 passes on layer 1;
- 6, 8 and 10 passes on layer 2; and
- 8 and 10 passes on layer 3.

Variable MC were measured for each layer, ranging from 21% in layer 1 to about 22% in layer 2 and 25.5% in Layer 3. Therefore, compaction between layers could not be assessed collectively as MC skewed the degree of compaction and AV achieved. It was also noted that the material below 23% MC showed a reduced performance in AV, and therefore layers 1 and 2 were discounted from the compaction optimisation assessment.

From a review of the compaction optimisation trial results on Layer 3, presented as Figure 5, an increase in compaction was observed between 8 and 10 passes. Based on this, 10 passes using a 19t smooth drum roller traveling at <4kmph were adopted for the remaining duration of the trial.

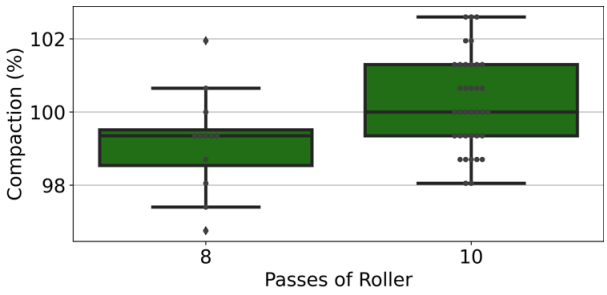

Figure 5. Trial Compaction Optimisation Results

5.2.2 Degree of Compaction and Air Voids

Based on the comparison between DD values achieved during compaction optimisation trials and laboratory Proctor tests, it was determined that the field dry density for the trial embankment compared closely to the standard (2.5kg) Proctor tests completed on 2% cement stabilised 9M1 material prior to construction. Therefore, compaction was benchmarked against MDD determined from standard Proctor tests.

Based on a comparative review of the Proctor tests, it was identified that Grade Dm chalk often produced a higher MDD than Dc Chalk by approximately 0.04Mg/m3. Based on the trial Proctor test data, MDD of 1.54Mg/m3 and 1.50Mg/m3 were determined for Dm and Dc Chalk, respectively, as Shown on Figure 6.

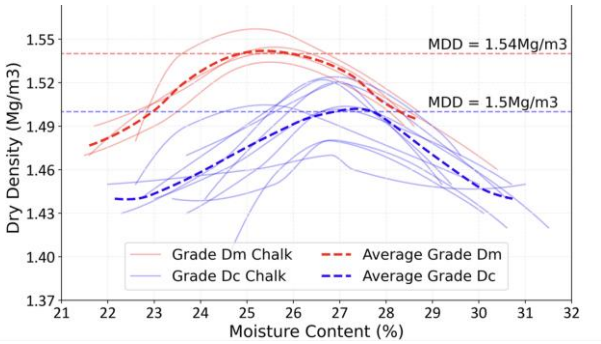

Figure 6. Trial Proctor Test Results

The degree of compaction of Dm and Dc chalk has been calculated against these respective MDD values. It is advised that compaction assessment for embankment fill during construction will need to be compared using locally determined MDD from asset specific Proctor tests for both Dm and Dc chalks used to produce Class 9M1 fill.

Optimum MC (OMC) was determined to be 25% for Grade Dm Chalk and 27% for Grade Dc Chalk. Based on average MC readings on each layer, 50% of the embankment layers (Layers 2,4,7 and 8) were dry.

Compaction data was screened to remove the following:

- Data points where cement content did not equate to 2%;
- Data points on layers where the number of passes of the roller did not equate to 10;
- Data points below an MC of 23% as the majority of this data did not achieve an AV<5%;
- Data points where NDG recordings were not recorded at 200mm depth.

When assessing the refined dataset for the trial embankment, 90% of the data exceeded a degree of compaction of 98.7% at the trial embankment, as shown on Figure 7.

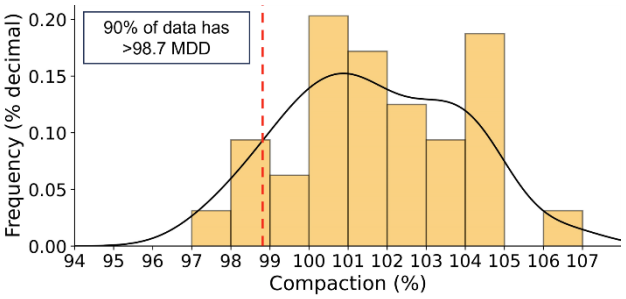

Figure 7. Histogram showing the distribution of degree of compaction for Class 9M1 fill.

The AV data from the revised dataset established showed that 90% of the data had an AV<6.1% as shown on Figure 8.

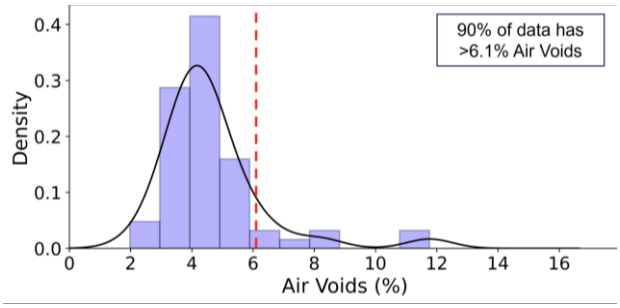

Figure 8. Histogram showing the distribution of air voids (AV) for Class 9M1 fill.

5.2.3 Pulverisation

Based on the trial data, the degree of pulverisation (DoP) ranged from 39% to 90% after the second pulverisation stage when cement was added. The three lowest values were considered outliers and, therefore, were excluded from the assessment. Based on the remaining dataset, a DoP of 60% was recommended after the second stage of pulverisation when adding cement.

5.3 Impact of layer thickness

The layer thickness during construction of the trial embankment ranged from 134-287mm, with six of the layers exceeding 250mm compacted thickness.

Compaction recordings were divided by the overall average compaction to normalise the data. From this, the average compaction of each layer was determined and plotted against the layer thickness.

The comparative review indicated that with increasing layer thickness, the normalised compaction tended to slightly decrease (albeit by less than 1% over a range of compacted layer thickness from 200-250mm). In light of the evidence from the trial, it is considered that layer thickness has a smaller impact on the degree of compaction compared to other variables (e.g. MC).

6 CONCLUSIONS

Based on the response of the structureless Chalk (Class 3B1) during trial embankment construction, pulverisation and testing, the following were identified as key requirements to ensure that the stabilised Chalk Class 9M1 fill meets the suitability criteria in terms the static and dynamic performance criteria:

- Class 3B1 Chalk should not be stockpiled due to drying effects reducing the materials ability to achieve the AV acceptability criteria (TRL, 1992).
- On classifying the chalk as either a grade Dm or grade Dc chalk, local Proctor testing should be undertaken to identify an appropriate compaction curve and MDD so that relative compaction can be assessed accurately for the asset specific embankment.
- The use of 2-4% cement during the trials have shown to not compromise static and dynamic performance requirements set in the TS-E. It is advised that the best percentage (by weight) of cement is 2%, as it has been shown to achieve the design performance criteria, whilst being the most sustainable percentage of cement to add.

The field trial results at Great Missenden have demonstrated that the site won structureless Chalk Class 3B1 can be improved to a Class 9M1, using controlled cement mix. They also demonstrated that the stabilised Chalk Class 9M1 met the static and dynamic performance criteria set by the TS-E (HS2, 2019) for use as HSR embankment fill subject to target construction requirements and trial compaction testing to determine an appropriate site specific maximum relative density.

Moreover, and based on a comparative review of results from various geophysical testing techniques, the dynamic performance in terms of Rayleigh wave velocity (V_R) was found to exceed the minimum assumed in design. An equivalent Vs design value of 300m/s is recommended for the Class 9M1 material.

ACKNOWLEDGEMENTS

The authors are grateful for the support of HS2 Ltd. in the preparation of this paper.

REFERENCES

AFNOR. (2000). Soils: Recognition and Testing, Part 1: Module under static load to the plate (E_{V2}). Document Number: NF P 94-117-1. *L'Association Française de Normalisation*.

Britpave. (2017). *Soil Improvement and Soil Stabilisation Definitive Industry Guidance, BP/62.*

CIRIA (2002). *Report C574: Engineering in chalk.*

High Speed 2 Ltd. (2019). *Technical Standard - Earthworks* (TS-E), Doc. HS2-HS2-GT-STD-000-000001 Rev P08.

HS2 Ltd. (2022). *Specification for Civil Engineering Works (SCEW), 600 Series – Earthworks,* Doc. HS2-HS2-CV-SPEC-000-010600.

TRL 151. (1992). Stabilized capping layers using either lime, or cement, or lime and cement. *Transport Research Laboratory.*

Proceedings of the XVIII ECSMGE 2024
GEOTECHNICAL ENGINEERING CHALLENGES
TO MEET CURRENT AND EMERGING NEEDS OF SOCIETY
© 2024 the Authors
ISBN 978-1-032-54816-6
DOI 10.1201/9781003431749-399
Open Access: www.taylorfrancis.com, CC BY-NC-ND 4.0 license

ECSMGE 24
XVIII EUROPEAN CONFERENCE ON SOIL MECHANICS AND GEOTECHNICAL ENGINEERING

Secant piles pit enclosure made with deep soil mixing columns and CFA piles

Parois en pieux sécants composée de colonnes DSM et de pieux CFA

A. Boureanu, D. Ciumeică, A. Măgureanu*
SBR Soletanche Bachy Fundații SRL, Bucharest, Romania

L. Sata
Technical University of Civil Engineering Bucharest Romania

magureanu@sbr.ro

ABSTRACT: This article presents an alternative solution for an excavation pit within a residential project in Târgu Mureș (Romania). Secant deep soil mixing columns in addition to CFA piles, proves to be a very effective, environmentally friendly (lower carbon footprint), cost and time saving solution, compared to traditional secant piles pit enclosure. Main challenge was to find an effective solution to build a proper dimensioned retaining wall considering not only the excavation depth, surrounding buildings, nearby streets and traffic but also restrained site dimensions. Given the non-cohesive soil layer, which is 2 metres thick, and due to the presence of ground water within, it was important just to seal this layer, to prevent water in-flow into the excavation pit. Deep soil mixing columns were 600 mm diameter and were done by the means of a special tool having three levels of mixing paddles. Calibration of grout flow, advancement speed and mixing rpms were very important for obtaining the proper BRN (blade rotation number) adapted to the soil conditions on the site. All criteria were monitored real-time using monitoring devices installed on the drilling rig and pumps. Design criteria, technology presentation and effective response of the solution are presented further.

RÉSUMÉ: Cet article présente une solution alternative pour une enceinte dans le cadre d'un projet résidentiel à Târgu Mureș (Roumanie). Par rapport à une enceinte traditionnelle, les colonnes DSM (deep soil mixing), en plus des pieux CFA, s'avèrent être une solution très efficace, favorable à l'environnement, économique et rapide. Le principal défi était de trouver une solution efficace pour construire un mur de soutènement aux dimensions appropriées, en tenant compte non seulement de la profondeur d'excavation, des bâtiments environnants, des rues avoisinantes et de la circulation, mais aussi des dimensions restreintes de la place. Compte tenu de la couche de sol non cohésive de 2 mètres d'épaisseur et en raison de la présence d'eau souterraine à l'intérieur, il était important de sceller cette couche pour empêcher l'eau de s'écouler dans l'enceinte. Les colonnes DSM avaient un diamètre de 600 mm et étaient réalisées par un outil spécial rotatif à axes verticaux à trois niveaux. L'étalonnage de l'écoulement du coulis, de la vitesse d'avancement et du régime de mélange était très important pour obtenir le BRN approprié aux conditions du sol sur le site. Tous les critères ont été surveillés en temps réel à l'aide de dispositifs de contrôle installés sur l'outil de forage et les pompes. Les critères de conception, la présentation de la technologie et efficacité de la solution sont présentés plus en détail.

Keywords: Excavation; pit enclosure; deep soil mixing; sealing.

1 INTRODUCTION

The proposed design had to give a technical and economical solution for the support of an excavation for a residential project, "DOX Apartments", located in Targu Mures city, Mures County, Romania.

Due to the limited space of approximately 780 sqm and the existing neighbouring buildings, the jobsite came with a lot of challenges regarding execution and design (Figure 1).

The scope of works was design and build of a pit enclosure, ensuring a 7,5 metres deep excavation in an urban environment.



Figure 1. Site layout.

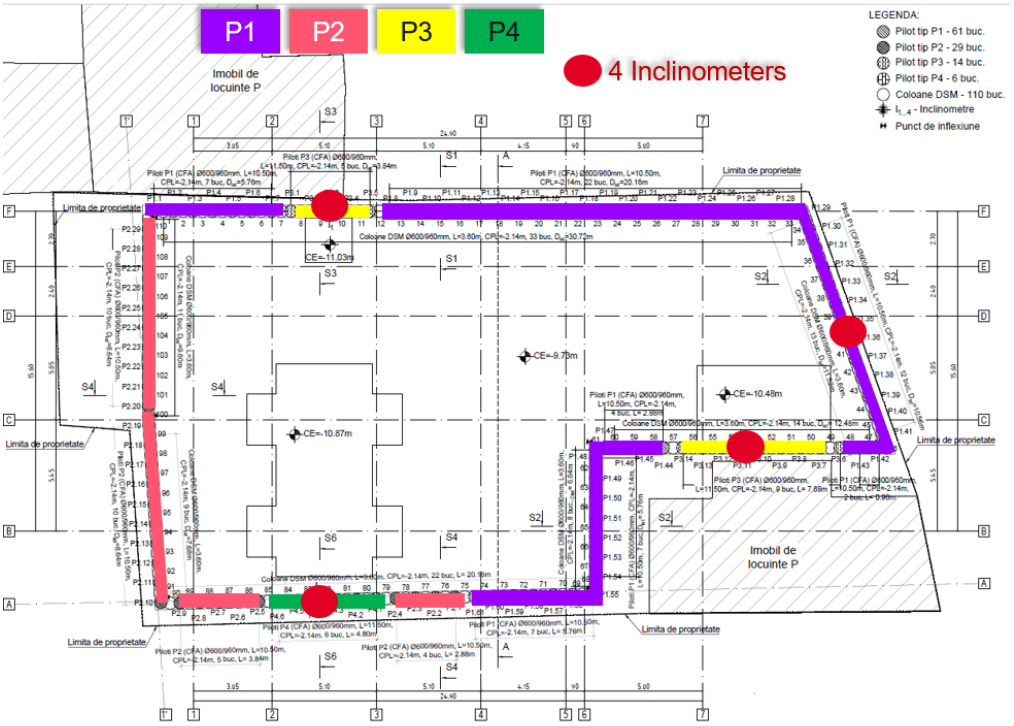

Figure 2. Pit enclosure layout.

2 SOLUTION

The soil stratigraphy encountered based on the geotechnical study was a succession of clayey sandy silt followed by a 2 metres thick non-cohesive layer, in which the water was embedded and finally a stiff marly clay.

The main solutions for properly ensuring the safe excavation until the designed level for the raft foundation consisted of making either a diaphragm wall or secant pile wall enclosure, supported by one strut level. But both diaphragm wall solution and secant piles were unable to achieve cost effectiveness, time schedule and CO2 carbon footprint as the hybrid solution presented further.

Due to the limitation of space and neighbouring buildings, the diaphragm wall solution was not feasible in this case, so the secant pile wall solution was further developed (Figure 2).

Taking into consideration the soil stratigraphy particularities in Targu Mures area, and the need to properly seal a relatively thin layer of non-cohesive soil of 2 metres, an alternative solution based on primary deep soil mixing (Colmix®) columns 600 mm and Secondary CFA 600 mm piles was proposed for this project (Figure 3).

With this solution, not only the execution schedule and the material quantities improved but also the environmental impact was lowered substantially, resulting in a much lower carbon footprint for the overall project.

Considering the purpose of the DSM columns, the most important characteristic of the treated soil was established to be the permeability and not the UCS strength, in order to properly seal the enclosure. The final mix was targeted to have low permeability (between 10^{-8} m/s and 10^{-9} m/s) and an average UCS of 1-2 MPa, to easily break through the mixed column with the CFA600 augers (secondary piles).

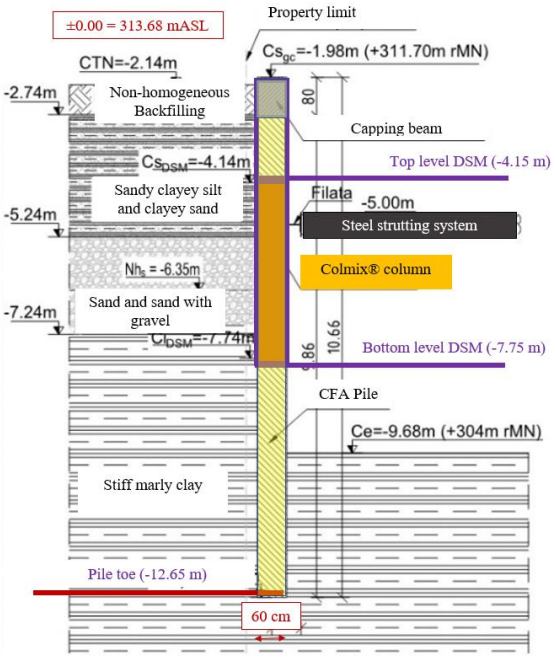

Figure 3. Characteristic section.

Bored piles give to the actual retaining wall bearing capacity, dimensioned in accordance with the loads, excavation depth and ground conditions.

Deep soil mixing columns were designed to be executed from natural ground level (-2.15 m) and embed 50 cm in the marly clay level (-7.75 m). Drilling length per one deep soil mixing column was 5.60 m with a diameter of 600 mm (Figure 4).



Figure 4. Construction site photo.

An important measure of the mixing energy imparted to the soil during deep soil mixing process is the blade rotation number (BRN), which requires a fine balance between thorough mixing and cost efficiency.

The targeted soil mixing index BRN was 360, with a permeability of 10^{-9} m/s (lower if possible) up to 10^{-8} m/s (maximum accepted to properly seal the non-cohesive layer).

Secondary piles, 600 mm diameter CFA, were done accordingly, between primary DSM columns, with specific drilling lengths as required by the design, resulting four different types of piles positioned depending on the distance to existing vicinities, on the difference of working platform levels or on locations of various sump pits.

Design approach and calculations were performed according to current regulations both Eurocode 7, (ASRO, 2004), corresponding national annex, ASRO (2007) and Romanian regulations regarding deep soil mixing and bored piles execution, ASRO (2005, 2015).

3 COLMIX® PROCESS

The Colmix® process is one of the deep soil mixing techniques and involves using a single or multiple tool to build soil mixing columns. Use of this tool requires to be attached to a capable piling rig (Figure 5).

Part of this solution is choosing the right tool and right machine for doing the process. In this case, it has been chosen a single tool having 3 levels of mixing paddles.

The tool is inserted into the ground, and it is being rotated, while the grout is injected into the soil. The tool is then raised, and the process is repeated until desired depth is reached.

The fact that this technique is relatively fast and efficient and is being also relatively environmentally friendly, made Colmix® the most suitable solution for this job. After setting up the suitable equipment, during design phase, according to site and ground conditions all construction parameters must be evaluated and selected.

Once the recipe of grout used for the mixing phase was designed, several preliminary drilling tests were performed, not only to validate proposed parameters but also to calibrate drilling speed, advancement and the quality of the mixing itself.

As required for reaching the desired blade rotation number (BRN) for local conditions, there have been established the volume of grout which needed to be incorporated by mixing, water cement ratio and, of course, the required quantity of cement.



Figure 5. Deep soil mixing tool.

After first preliminary drilling tests, it was concluded that, despite the fact that deep soil mixing was required only for 3,6 metres (from -4,15 down to -7,75 m), it was better to treat also the first two metres (from working platform level to -4,15 m), not necessarily for sealing purposes but to prevent nozzles from clogging and to reach the desired top level of actual DSM columns much more easily.

From that point down to designed bottom level of Colmix® columns, normal phase of treatment procedure – like rotation speed, tool advancement (vertical) speed and grout delivery - were followed.

Implementation of this deep soil mixing process is accompanied by real-time monitoring from a screen located in the cabin, allowing the operator to comply with the execution instructions and recording the main operating parameters during construction of each column.

An important issue is quality control which involves taking samples of the fresh soil-cement mixture to check the density of the mixture and eventually to get them tested for permeability and UCS values (Soletanche Bachy, 2013).

4 TEST RESULTS ON DSM SAMPLES

Core samples of the treated soil were collected from the spoil (the excavated material) created when the mixing tool was withdrawn from the ground after the mixing process was complete.

Laboratory testing was performed on three sets of samples, each set with three test cylinders from each DSM column, at 7, 14, and 28 days.

The tests included unconfined compressive strength (UCS) testing and permeability testing in consolidation cells.

On fresh samples collected on cylinders, permeability showed good values between 10^{-9} and 10^{-8} m/s (between targeted results) and UCS value at 28 days exceeded targeted value (2 MPa) with lower values at 14 days (about 1 MPa) and at 7 days (about 0,5 MPa).

Although UCS value exceeded the expected, primary DSM columns were easily drilled through by 600 mm CFA augers.

Core samples (Figure 6) were also tested from several columns and showed also good UCS values at an average of 1,8 MPa, with permeability values within the expected range.



Figure 6. Core samples from a DSM test column.

5 CONCLUSIONS

Deep soil mixing (DSM) columns are a proven and reliable ground improvement technique that offers several advantages over other solutions, including cost-effectiveness, sustainability, and efficiency.

The final solution for this project - combined retaining wall using deep soil mixing technique for the primary piles and CFA technology for secondary piles proved to be the perfect mix between tradition and innovation, resulting in a very successful project with an overall carbon footprint reduction of approximately 40 tons of equivalent CO2.

In other words, DSM columns are a versatile and sustainable ground improvement technique that can be used to achieve significant cost and environmental savings.

REFERENCES

SR EN 1536+A1:2015, *Execution of special geotechnical work - Bored piles, National Annex / "Execuţia lucrărilor geotehnice speciale. Piloţi foraţi".*

SR EN 1997-1:2004, *Eurocode 7: Geotechnical design - Part 1: General rules / "Eurocod 7: Proiectarea geotehnică. Partea 1: Reguli generale"*

SR EN 14679:2005, *Execution of special geotechnical works - Deep mixing / "Executia lucrărilor geotehnice speciale. Stabilizarea în adâncime a pământurilor prin malaxare".*

NP 120-2014, *Normative regulations for design and execution of deep excavations in urban areas / "Normativ privind cerinţele de proiectare şi execuţie a excavaţiilor adânci în zone urbane".*

NP 124-2010, *Normative regulations for geotechnical design of retaining structures / "Normativ privind proiectarea geotehnică a lucrărilor de susţinere".*

Soletanche Bachy (2013). *Rules & recommendations. Making and curing soil mixing samples.*

Proceedings of the XVIII ECSMGE 2024
GEOTECHNICAL ENGINEERING CHALLENGES
TO MEET CURRENT AND EMERGING NEEDS OF SOCIETY
© 2024 the Authors
ISBN 978-1-032-54816-6
DOI 10.1201/9781003431749-400
Open Access: www.taylorfrancis.com, CC BY-NC-ND 4.0 license

ECSMGE 24
XVIII EUROPEAN CONFERENCE ON SOIL MECHANICS AND GEOTECHNICAL ENGINEERING

Foundation solutions near Trancão river, in Lisbon

Solutions de fondations pour les travaux situés près de la rivière Trancão, à Lisbonne

I. Braz*; A. Pinto
JETsj Geotecnia Lda., Lisbon, Portugal

C. Simões
Oliveiras S.A., Lisbon, Portugal

T. Gomes
Geosol S.A., Lisbon, Portugal

C. Caxias
ANP Systems, Lisbon, Portugal

**ibraz@jetsj.com*

ABSTRACT: This paper describes the foundations solutions for the main stage for the World Youth Day in Lisbon 2023. The stage is located on an urban solid waste landfill that is sealed through a PEAD geomembrane, which made it impossible to use indirect foundations at an early phase. Underlying the deposits of municipal solid waste, emerges the alluvial formation composed of compressible soils, with weak mechanical characteristics, with variable thickness. In order to reduce the amplitude of differential displacements that could damage the structure, a preload landfill was carried out, in order to minimize the settlements that would occur at the time of the stage installation. During the time of permanence of the preload landfill, several reading campaigns of the instrumentation (topographic marks) were carried out in order to validate the initial assumptions. From the data collected from the instrumentation as well as from the tests carried out on site, the solution of the foundation for the stage was defined. The solution for the cover foundation was defined using ductile iron micropiles driven using the dry method, reinforced with self-drilling rod in the center, properly sealed in the miocene.

RÉSUMÉ: Cet article décrit les solutions de fondation pour la scène principale de la Journée Mondiale de la Jeunesse à Lisbonne en 2023. La scène est située sur une décharge urbaine scellée par une géomembrane PEAD, rendant impossible l'utilisation de fondations indirectes à une phase précoce. Sous les dépôts de déchets solides municipaux, émerge la formation alluviale composée de sols compressibles, aux caractéristiques mécaniques faibles, avec une épaisseur variable. Afin de réduire l'amplitude des déplacements différentiels susceptibles d'endommager la structure, un remblai de précontrainte a été réalisé pour minimiser les tassements qui se produiraient lors de l'installation de la scène. Pendant la période de permanence du remblai de précontrainte, plusieurs campagnes de lecture de l'instrumentation (repères topographiques) ont été menées afin de valider les hypothèses initiales. À partir des données collectées à partir de l'instrumentation ainsi que des tests réalisés sur place, la solution de fondation pour la scène a été définie. La solution pour la fondation de la couverture a été définie en utilisant des micropieux en fonte ductile en utilisant la méthode sèche, renforcés avec une tige autoperceuse au centre, correctement scellée dans le miocène.

Keywords: Micropiles; foundation solutions; preload landfill.

1 INTRODUCTION

For the World Youth Day event, a stage had to be set up in Parque Tejo, Lisbon. However, a challenge arose because the selected location was on a landfill of urban solid waste. Between this landfill and the competent Miocene substrate, there was a layer of sludgy materials with weak strength and high deformability characteristics. Consequently, a foundation solution had to be devised to meet the structural requirements of the installation. To address this, it was necessary to install a pre-loading embankment at the site where the stage would be supported by direct foundations. Part of the stage and its covering had to resort to indirect foundations due to an increase in the load.

To validate the solution, tests were conducted on self-drilling micropiles within the embankment.

Figure 1 shows the location of mentioned structure and their surroundings.



Figure 1. Location of the main stage.

2 MAIN CONSTRAINTS

2.1 Geological and geotechnical constraints

The target intervention area is located in a low and flat area on the right bank of the Tejo estuary.

The Main Stage will be founded on the Beirolas landfill, consisting of deposits of contaminated soils and urban waste, located on a heterogeneous landfill layer containing silty-clay materials mixed with sand and rubble of artificial origin. As the site approaches the river, the thickness of the 'artificial' landfill decreases until it disappears in the tidal zone. Beneath the artificial landfill layer, there is an alluvial formation composed of compressible silty mud soils, with highly variable thickness in the Beirolas landfill area. In the Stage area, the depth of silty mud soils increases from 2m to 25m towards the river, remaining nearly constant in the north-south direction. Underlying this layer of clayey mud, there is a Miocene formation consisting of sandstones, calcareous sandstones, and limestones, with variable presence of marly levels.

In Figure 2, we can see a schematic cross section of the main stage.

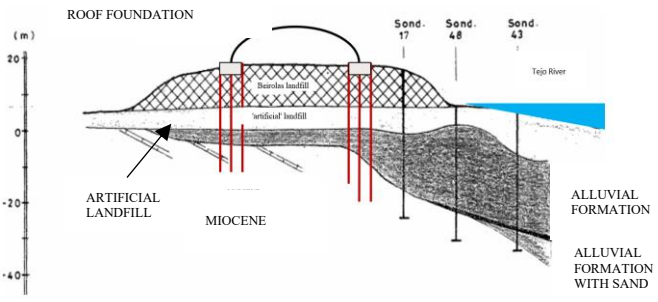

Figure 2. Cross section of the main stage. Roof foundations.

2.2 Constraints related to existing structures

To establish the foundation solutions for the stage, the initial concept was that indirect foundations were not viable due to the presence of the geomembrane protecting the landfill, making perforation impossible. Moreover, extracting the contaminated soil was not advisable. This premise applied to the entire intervention area, except for the rear zone of the stage – the southern zone – where indirect foundations were contemplated due to the magnitude of the loads to be transmitted to the foundation and the maximum permissible deformations.

2.3 Constraints related to the temporary nature of the structure

When establishing the foundation solutions for the stage, it was considered that the structure would be temporary and later dismantled. Consequently, a solution was selected for its ease of disassembly, allowing its components to be repurposed in the context of a future project.

3 ADOPTED SOLUTIONS

3.1 Pre-load embankment

The solution consisted of a pre-load embankment with a height of 3.20m in the Stage's implantation zone. The embankment was constructed with material with a bulk density of approximately 20kN/m3. The purpose of this pre-load embankment was to minimize settlements that would occur during the assembly and use of the Stage. The pre-load embankment remained in place for a period of 90 days, experiencing a maximum settlement of 25cm. To verify the design assumptions and anticipate settlements during the assembly of the stage, 16 settlement markers and 2 extensometers were installed during the pre-load phase. The outcomes for the marker A016 are illustrated in Figure 3. In Figure 4 we can see the location of all the settlement marks installed in the area of the pre-load embankment, with the identification of the marker A016.

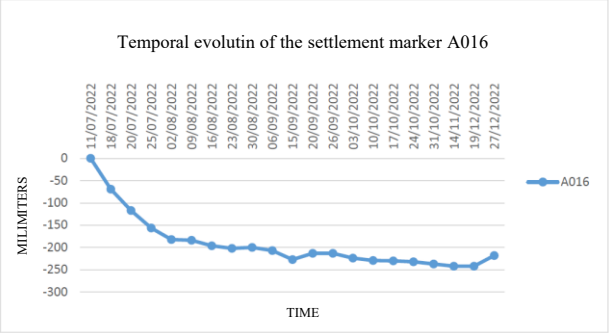

Figure 3. Time-Strain Graph. Instrumentation of the Pre-load Embankment Zone.

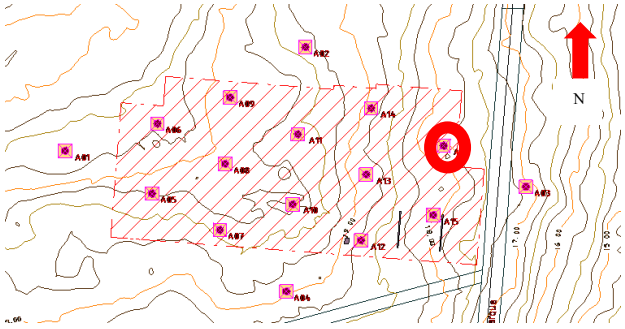

Figure 4. Location of the settlement marker A016.

3.2 Foundation

To maximize the uniformity of load transmission to the ground, the recommended solution involves the construction of a foundation slab consisting of precast hollow-core slabs with a minimum thickness of 30 cm. Due to the increased magnitude of loads in certain alignments and the irregular geometry of the foundation masses of the stage's roof, it was necessary to recommend an in-situ concrete foundation solution in these areas. Thus, the solution is divided into 4 different types:

- Current area: Solution with hollow-core slabs simply supported on precast peripheral beams with an L-shaped or rectangular section, depending on the existing level difference.
- Periphery of the stage roof foundation: Solution consisting of an in-situ concrete slab with a thickness of 30cm.
- Rear alignments – East and West zones: Solution consisting of an in-situ concrete slab with a thickness of 25cm.
- Rear alignments – central zone:

Foundation beam with a section of 1.65x1.20 m2 supported on ductile iron driven piles with a section of 170x7.5mm filled with C35/45 concrete and 3ø32mm bars inside. The foundation solution in this area was coordinated with the foundation solution of the stage roof, excluded from the scope of this article.

Figure 5 presents the 3D model of the entire foundation solution. Figure 6 and Figure 7 was taken during the construction phase and we can see the assembly of the hollow-core slabs. Figure 8 show the section of the ductile iron driven pile and the asse.

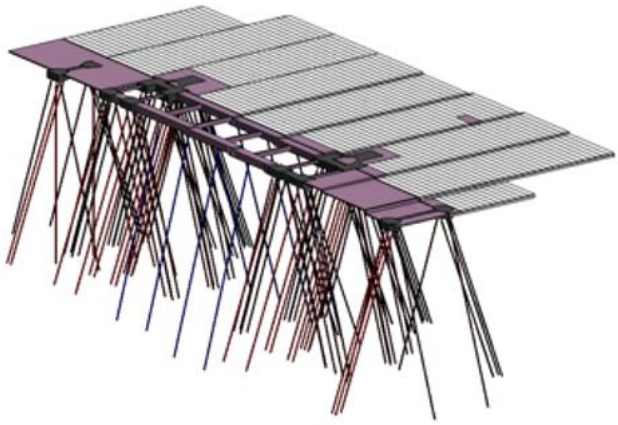

Figure 5. 3D view of the stage and roof foundations.



Figure 6. Precast hollow-core slabs.



Figure 7. Top view of the spread foundation of the stage already assembled.

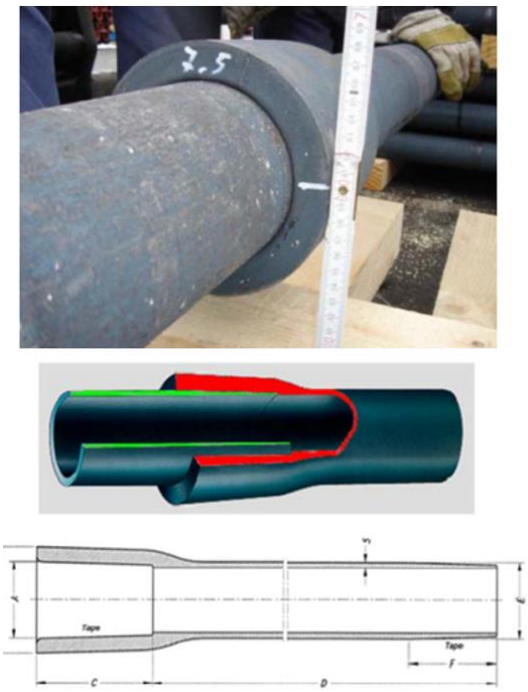

Figure 8. Ductile iron driven piles with a section of 170x7.5mm.

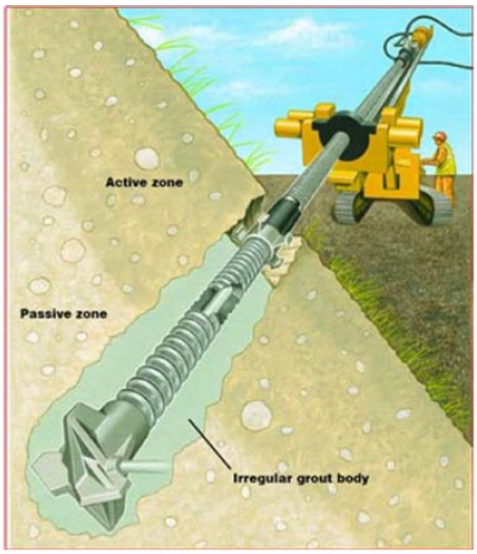

Figure 9. Self-drilling micropile system along the grout bonding legth. Solution for the stage roof foundation.

4 LOAD TESTS OF DRIVEN MICROPILES

Given the uncertainty associated with the behaviour of the micro piles executed in these materials, it was necessary to carry out load tests to validate the design assumptions. For this purpose, two full-scale load tests were conducted, one in compression and one in tension.

For both test micropiles, interior instrumentation was applied using strain gauges introduced with a ø16mm rod.

4.1 Tension load test

The reaction structure was materialized through a reinforced concrete mass, approximately 2.5m x 2.5m x 1m in size, as shown in Figure 9. The tested micropile had a length of 30.50m, reaching the Miocene substrate, and the self-drilling interior micropile had a length of 41.5m with an approximately 10m grout bonding length in the Miocene substrate (Bustamante and Doix, 1985). The planned test load was 850kN. The load test was conducted with four loading cycles up to the maximum load of 922kN. Additionally, a fifth loading cycle was performed up to 1598kN to test the load-bearing capacity of the sealing in the Miocene stratum. Even after reaching the load of 1598kN, no failure was observed.



Figure 10. Tension load test.

For the 922kN test load, a strong response was observed in all loading cycles, with a plastic deformation of approximately 13mm and a maximum deformation of 33mm. In the 5th loading cycle, a total deformation of about 59mm was observed, with a residual deformation of 20mm. A set of strain gauges was installed at depths of 2.5m, 10m, 20m, 26m, 30m, and 38.5m, particularly at the transition between the embankment and the alluvial stratum.

The consistency of results in the 4 loading cycles is noticeable, with pressure curves parallel to each other. It is clear that the top of the alluvial stratum is at an elevation of 20m, which is consistent with the results of the boreholes conducted on-site. It is observed that 50% of the load is transmitted to the embankment, and 30% of the grout bonding length was not engaged. However, due to the significant heterogeneity of the embankment material, it was considered that the sealing length should not be less than 10m (Bustamante and Doix, 1985), in order to accommodate the entire tensile load.

The main results of the conducted test are shown in Figure 10 and Figure 11.

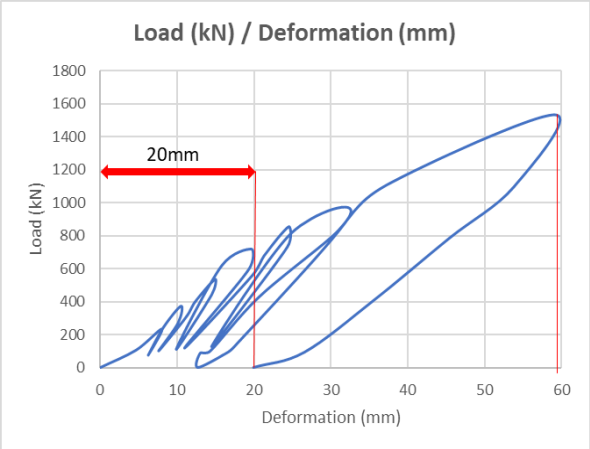

Figure 11. Load-displacement graph at the head. Tension load test.

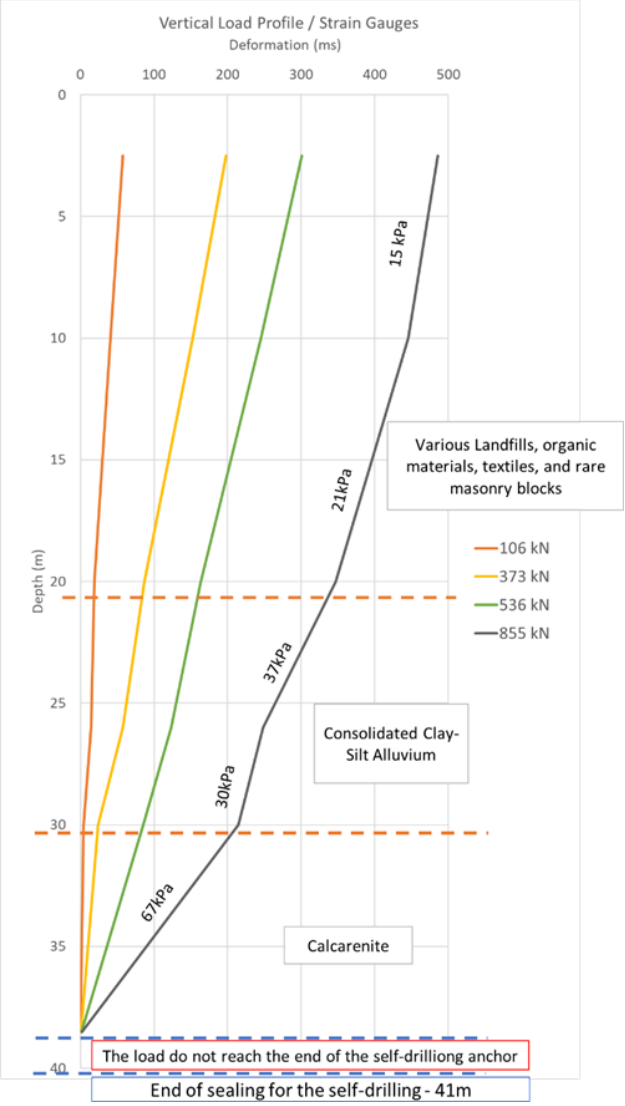

Figure 12. Strain gauges graph - Tension pre-test.

4.2 Compression load test

The reaction structure was constructed using a portal frame consisting of metal profiles supported on 4 micropiles similar to the micropile tested in tension. The structure is illustrated in Figure 13. The tested micropile had a length of 34.00m, reaching the Miocene substrate. The planned test load was 1820kN. Despite extreme care in aligning the jack with the axis of the micropile, instability of the micropile head mass was observed above a load of 1400kN with horizontal displacement of the mass to the west and north, as shown in Figure 14. Despite the rotation of the mass when the load exceeded approximately 1400kN, a continuous increase in load capacity of approximately 300kN was observed up to 1723kN.



Figure 13. Reaction structure for the compression load test.

The main results of the conducted test are shown in Figure 14 and Figure 15.

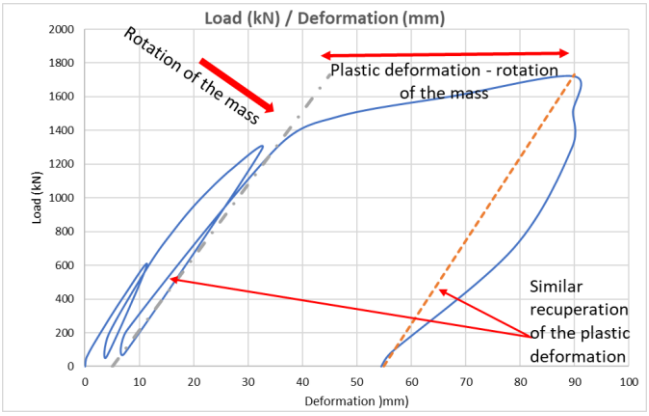

Figure 14. Load-displacement graph at the head. Compression load test.

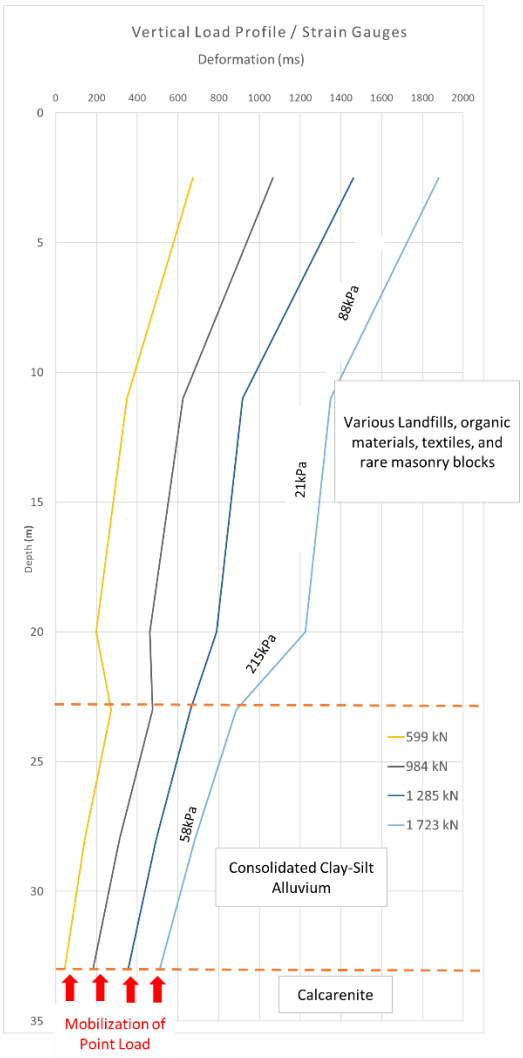

Figure 15. Strain gauges graph - Compression pre-test.

Figure 15 shows te measuring results of a set of strain gauges was installed at depths of 2.5m, 11m, 20m, 23m, 28m, and 33m, particularly at the transition between the embankment and the alluvial stratum. There is consistency in the results in the 4 loading cycles with pressure curves parallel to each other. It is clearly observable that the top of the alluvial stratum is at an elevation of 23m, which is consistent with information from boreholes conducted on-site. There was a significant load transmission capacity to the embankment with a firm response between 2.5m and 11m and a very good response between 20m and 23m depth. Between the depths of 11m and 20m, the load transmission to the embankment was negligible. The mobilized tip load is estimated to be around 600kN for a load on the order of 1700kN. It is estimated that the compressive capacity of the pile formed by the ductile iron outer micropile and the self-drilling inner bar is above 1800kN, with a plastic displacement of about 20mm and 40mm when subjected to a load of 1800kN.

5 CONCLUSIONS

The purpose of this article was to present the foundation solution for the main stage of the World Youth Day, highlighting the various constraints that influenced the choices and decisions made.

Based on the previously described constraints and on the results of the mentioned load tests, the adopted solution consists of a foundation slab made up of precast hollow-core slabs with a minimum thickness of 30 cm, which can be removed. In the heavily loaded alignments, the solution transitions from direct to indirect foundations using ductile iron driven micropiles, topped with foundation beams measuring 1.65x1.20m, connected by perpendicular beams with a section of 0.40x0.80m.

The possibility of removing the structures was taken into consideration, and whenever possible, solutions were adopted that would simplify demolition/dismantling, allowing the constituent parts of the structures to be potentially reused.

To validate the design assumptions of the foundation micropiles, two load tests were conducted at the stage location, one in compression and one in tension. The obtained results allowed for the early validation of the main design assumptions, ensuring the suitability of the solution to the local geological-geotechnical context.

The suitability of the solution to the implementation site was verified based on the results of the conducted tests and continuous monitoring of the construction work and the micropile driving results.

ACKNOWLEDGEMENTS

We thank the Project Owner for the permission to publish this article.

We also express our gratitude to the team that made the described work possible, particularly to the companies Oliveiras S.A and Geosol S.A, as well as to the company responsible for overseeing the project, Engexpor – Consultores de Engenharia S.A.

REFERENCES

Bustamante, M e Frank, R (1999). Current French Design Practice for Axially Loaded Piles. LCPC.

Proceedings of the XVIII ECSMGE 2024
GEOTECHNICAL ENGINEERING CHALLENGES
TO MEET CURRENT AND EMERGING NEEDS OF SOCIETY
© 2024 the Authors
ISBN 978-1-032-54816-6
DOI 10.1201/9781003431749-401
Open Access: www.taylorfrancis.com, CC BY-NC-ND 4.0 license

ECSMGE 24
XVIII EUROPEAN CONFERENCE ON SOIL MECHANICS AND GEOTECHNICAL ENGINEERING

Earth retaining solutions and facades underpinning, for the refurbishment an historic building, in Lisbon

Solutions de soutènement et de repris en sous-œuvre de façades, pour la rénovation d'un bâtiment historique, à Lisbonne

I. Braz*, A. Pinto
JETsj Geotecnia Lda., Lisbon, Portugal

D. Henriques, R. Santos
PPE – Planeamento e Projetos de Engenharia Lda., Lisbon, Portugal

**ibraz@jetsj.com*

ABSTRACT: This article presents the earth retaining, underpinning and facades retaining solutions as part of the refurbishments works of the 260 years old Pedrosas (CTT) Palace, in Lisbon. To allow the construction of new basements, under the original foundations of the masonry building, it was necessary to design earth retaining and facades underpinning compatible solutions.The earth retaining solution consists of a reinforced concrete wall, built using the King Post Wall technique, temporary braced by ground anchors and steel struts. The underpinning and the temporary structures of the foundation were carried out using tubular micropiles. The main design criteria are presented, as well as the main monitoring and survey results.

RÉSUMÉ: Cet article présente les solutions de soutènement du terrain, de reprise en sous-œuvre et de maintien des façades dans le cadre des travaux de rénovation du Palais Pedrosas (CTT), avec 260 ans, à Lisbonne. Pour permettre la construction de nouveaux sous-sols sous les fondations d'origine du bâtiment en maçonnerie, il a été nécessaire de concevoir des solutions compatibles de soutènement du terrain et de sous-bassement des façades. La solution de soutènement consiste en une paroi avec la technique de King Post Wall, en béton armé, temporairement stabilisé par des ancrages au sol et des tirants en acier. Les travaux de fondation, de reprise en sous-œuvre et des structures temporaires ont été réalisés à l'aide de micropieux tubulaires.Les principaux critères de conception sont présentés, ainsi que les principaux résultats de surveillance et d'étude.

Keywords: Earth retaining wall; underpinning; façade retaining.

1 INTRODUCTION

In the scope of the redevelopment of Palácio das Pedrosas (CTT), located on São José Street in Lisbon, it was necessary to carry out a project involving excavation and peripheral earth retaining with facade underpinning. According to the aerial view presented in Figure 1, it is possible to identify the approximate layout of the construction, as well as some of the most relevant boundaries and constraints. The referenced area has boundaries to the north with an existing building that needs to be preserved.

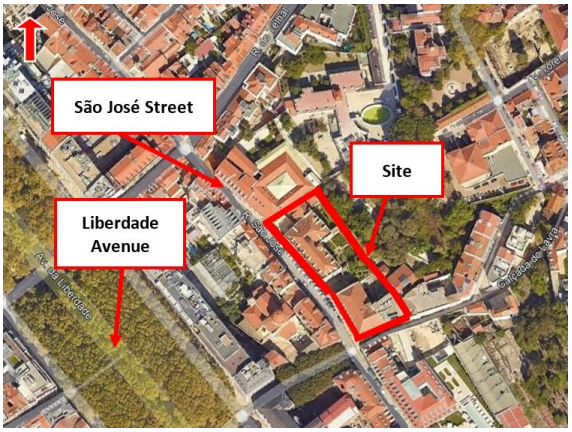

Figure 1. Site location.

The following figure shows the areas to be excavated beneath the existing structure.



Figure 2. Areas to be excavated under the existing structure.

As an old building, the solution to be adopted was conditioned by various factors, making this project quite challenging.

2 MAIN CONSTRAINTS

2.1 Constraints related to the building's boundaries

In this intervention, several underground floors will be executed, being adjacent to neighbouring buildings and roads. The proposed solutions must, therefore, be compatible with preserving the integrity of all structures and infrastructure located outside the perimeter of the construction site, ensuring their functionality conditions.

2.2 Constraints related to the need to preserve facades and structural walls.

Given the necessity to maintain the integrity of the majority of the main building facades, it is considered essential that the intervention be carried out in a way that minimizes its impact on their stability and appearance. Equally important was the adoption of construction solutions compatible with the use of equipment suitable for the available spaces and access, allowing the execution of the works while limiting the occurrence of vibrations and noise.

2.3 Geological and geotechnical constraints

According to the data collected during the geotechnical characterization campaign and considering the geology described in the geological map, the following lithological strata were identified on-site:

- Landfills: Detected in the superficial zone of all boreholes, with thickness ranging from approximately 0.20 to 0.50m. They are heterogeneous landfills with masonry fragments, primarily silty-clayey, and brownish.
- Prazeres Clays and Limestones: The Miocene levels are represented by alternating silty and clayey levels. The silty levels sometimes have transitions with fossil fragments and/or marly materials, with greenish to greyish tones. The more clayey levels often appear slightly micaceous and with darker tones. Generally, they exhibit plastic behaviour.

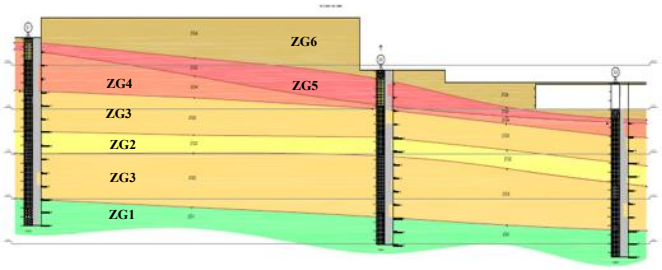

Figure 3. Soil profile.

Table 1. Geological and geotechnical parameters.

Geotechnical zone	N_{SPT}	Lithology	φ' (°)	C' (kPa)	γ' (kN/m3)	E' (MPa)
ZG6	-	Silt-sandy embankments with masonry fragments, all-in-one, concrete, and pavements	5 - 10	-	16 - 17	5 - 10
ZG5	2 - 9	Clayey silts and silty clays	10 - 15	5 - 15	17 - 18	10 - 15
ZG4	16 - 26 (16 - 18)*	Clayey silts and silty clays	15 - 20	15 - 20	18 - 19	20 - 25
ZG3	21 - 56 (21 - 42)*	Clayey silts and silty clays	20 - 25	20 - 30	19 - 20	30 - 40
ZG2	>60	Clayey silts and silty clays	25 - 30	40 - 60	20 - 21	50 - 60
ZG1	>60	Clayey silts, silty clays, calcareous marls/marly limestones	25 - 35	60 - 80	21 - 23	60 - 100

3 ADOPTED SOLUTIONS

The proposed solutions for the execution of facade underpinning and excavation with peripheral earth retaining are interconnected and are as follows:

- Excavation and peripheral earth retaining: to be carried out using the king post wall technology.
- Underpinning and earth retaining of preserved facades: to support the existing facades, it is proposed to install a steel structure for earth retaining and stabilization. The solution of the

facade containing structure is beyond the scope of this article.

The proposed solutions considered the necessary coordination between the two types of interventions described.

Concerning the structure of the peripheral earth retaining wall, considering the evaluation of the main constraints, it was proposed that, in general, the excavation of the underground floors be carried out under a peripheral earth retaining using the king post wall technology. The proposed construction technology for the 'king post wall' type earth retaining wall involves the phased execution, from top to bottom, of reinforced concrete panels supported by vertical micro-piles. These micro-piles, materialized by tubular profiles Ø88.9x9.0mm and Ø114.3x9.0mm with external joints, made of high-strength steel (fsyd > 560MPa), will also support the underpinning beams of the facade. These elements should be executed with the minimum possible distance from the facade and walls of neighbouring buildings, solidified through steel brackets.

The total length of the micro-piles will vary based on the elevation geometry, and the minimum of the sealing lengths (calculated by the Bustamante method) to be executed using the IRS system (repetitive and selective injection), employing a double plug and check valves, in competent soils with strength and deformability characteristics compatible with N_{SPT} greater than 35 blows and geologically stable concerning the excavation geometry.

This solution has the advantage of allowing the execution of the permanent wall during excavation. The number of temporary bracings (steel props and anchors), as well as excavation constraints, can be redefined during the construction phase based on the actual characteristics of the excavated soils and the results of the Instrumentation and Observation Plan.

In cases where underpinning the facade is necessary, a beam is required to have the capacity to transmit loads from the facades to the foundations, materialized by the micro-piles.

In the permanent phase, the structure of the slabs and foundation elements will be responsible for the stability of the earth retaining wall, and the temporary props will be removed after the completion of the said structure, and the anchors will be deactivated.

A 3D model is presented in Figure 4, where the existing facade elements to be preserved are represented in light blue, the underpinning beam to be executed in orange, and the earth retaining walls to be constructed for excavation work are shown in grey.

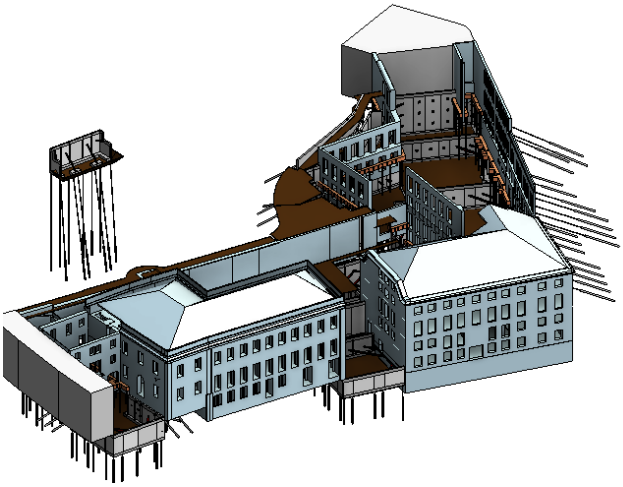

Figure 4. 3D view of solutions for excavation and peripheral earth retaining.

4 DESIGN

The finite element program Plaxis 2D was used for the design of the peripheral earth retaining walls to be executed using the king post wall technology.

Micro-piles and walls were modelled as "Plate" elements, sealing bulbs were modelled as "Embedded beam row" elements, and pre-stressing tendons were modelled as "Node-to-node-anchor" elements.

The forces are estimated considered the construction process, especially the excavation and construction phases of the peripheral earth retaining wall. Soil elements were modelled considering the previously presented geo mechanical properties and following the "Harding Soil" model.

Figure 5 shows the adopted model. This section corresponds to the maximum excavation height with the highest number of anchors in the whole retaining structure.

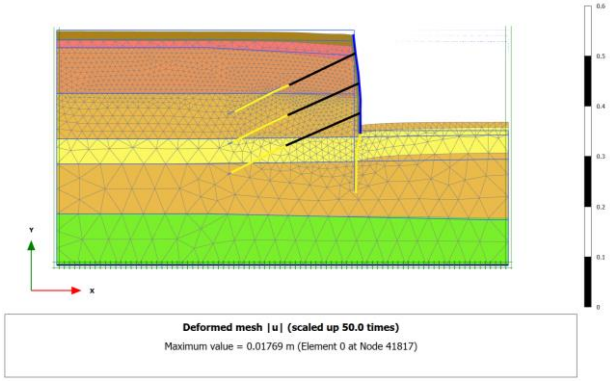

Figure 5. Total displacements – 1.7cm.

After the execution of the interior structure of the building, in the permanent phase, the bracing of the earth retaining is guaranteed by the structure of the underground floors. In the design of the peripheral

earth retaining, loads from the building structure were considered. For locations where the micro-pile is located outside the earth retaining wall, it was necessary to verify safety against buckling. In areas where the micro-pile is used simultaneously to support the peripheral earth retaining and for facade underpinning, the additional load from it was considered.

5 MONITORING AND SURVEY PLAN

As the construction is still in the early stages of demolition, the results of the monitoring and survey plan are not yet available. However, the proposed Monitoring and Survey Plan aims to ensure the safe and economical execution of demolition, excavation, and construction of earth retaining structures. It also involves the analysis of the behaviour of preserved facades and neighbouring structures and infrastructure during this construction phase. Thus, the proposed plan should allow the measurement, during excavation and construction of earth retaining structures and the underground floor, of the following parameters:

- Horizontal and vertical displacements of earth retaining structures.
- Horizontal and vertical displacements of neighbouring constructions.
- Measurement of tension/load at ground anchorages.
- Horizontal displacements in neighbouring structures and in the earth retaining.

The parameters described above will be measured using the following:

- Topographic targets for measuring parameters mentioned in a).
- Topographic targets for measuring parameters mentioned in b).
- Load cells in anchorages for measuring the parameter mentioned in c).
- Inclinometers for measuring the parameter mentioned in d).

6 FINAL REMARKS

The purpose of this article was to present the underpinning and peripheral earth retaining solutions adopted in a rehabilitation project to be carried out in the centre of Lisbon, in a densely urbanized area.

One can conclude that each work is unique, and even if the solution is conceptually the same, it should always be adjusted to the existing and exclusive constraints of each work itself. In this case, an attempt was made to define a solution that would better adapt to all mentioned constraints, from both technical and economic issues.

ACKNOWLEDGEMENTS

We thank the Project Owner for the permission to publish this article.

REFERENCES

Bustamante, M and Frank, R (1999). Current French Design Practice for Axially Loaded Piles. LCPC.

Bustamante, M. and Doix, B. (1985). Une méthode pour le calcul de tirants et des micropieux injectés. Bulletin de Liaison des Laboratoires des Ponts et Chaussées, Ministère de L'Équipement, du Logement, des Transports et de la Mer, Paris. nº140, pp.75-92.

Proceedings of the XVIII ECSMGE 2024
GEOTECHNICAL ENGINEERING CHALLENGES
TO MEET CURRENT AND EMERGING NEEDS OF SOCIETY
© 2024 the Authors
ISBN 978-1-032-54816-6
DOI 10.1201/9781003431749-402
Open Access: www.taylorfrancis.com, CC BY-NC-ND 4.0 license

ECSMGE 24
XVIII EUROPEAN CONFERENCE ON SOIL MECHANICS AND GEOTECHNICAL ENGINEERING

The use of foam glass for a lightweight fill and highway foundation on soft soil conditions

L'utilisation de verre mousse pour un remblai léger et une fondation d'autoroute sur des sols mous

J.W.R. Brouwer*, C.R. van Laerhoven
Geobest BV, Vianen, The Netherlands

**roel.brouwer@geobest.nl*

ABSTRACT: In soft soil conditions, the construction of embankments may cause significant subsidence during lifetime of the construction. The standard procedure to avoid large remaining settlements after project completion is pre-loading, often in combination with vertical drainage. However, this approach is time-consuming, costly, and has a considerable carbon footprint. For a highway in the province of Zeeland (The Netherlands), an alternative solution was found using foam glass as a lightweight fill material. The subsoil consists of highly compressible clay and peat layers with an average thickness of 8 m. Foam glass was also used to construct a stabilized foundation layer for support of the road construction. The stabilization consists of a mixture of foam glass, cement, in situ clay and the Geosta® additive. This innovative approach accelerates the building process and reduces the carbon footprint of the project considerably. Furthermore, the stabilized foam glass forms a foundation layer with considerable strength and stiffness, which may reduce the required asphalt thickness.

RÉSUMÉ: Dans des conditions de sol mou, la construction de remblais peut provoquer un affaissement important pendant la durée de vie de la construction. La procédure standard pour éviter les tassements importants après l'achèvement du projet est le préchargement, souvent associé à un drainage vertical. Cependant, cette approche prend du temps, est coûteuse et a une empreinte carbone considérable. Pour une autoroute dans la province de Zélande (Pays-Bas), une solution alternative a été trouvée en utilisant du verre mousse comme matériau de remplissage léger. Le sous-sol est constitué de couches d'argile et de tourbe hautement compressibles d'une épaisseur moyenne de 8 m. Du verre mousse a également été utilisé pour construire une couche de fondation stabilisée destinée à soutenir la construction de la route. La stabilisation est constituée d'un mélange de verre mousse, de ciment, d'argile in situ et de l'additif Geosta®. Cette approche innovante accélère le processus de construction et réduit considérablement l'empreinte carbone du projet. De plus, le verre mousse stabilisé forme une couche de base présentant une résistance et une rigidité considérables, ce qui peut réduire l'épaisseur d'asphalte requise.

Keywords: Stabilisation; Geosta®; foam glass; embankment; compressible.

1 PREAMBLE

The municipality of Borssele, located in the southern part of the Netherlands, intends to construct a new road around the village of Hoedekenskerke. This new road is required because of the increasing traffic in the centre of this village.

The new road will be built on an embankment on soft soil. The municipality, in collaboration with contractor Traas en Ovaa, sought to find an economical yet sustainable solution, where the carbon footprint is reduced using innovative solutions.

Traditionally, road construction in such areas would involve creating an embankment of sand, topped with an aggregate layer and asphalt. The soft soil conditions however would urge to pre-load the soil with sand or granular material. Preliminary assessments indicated that sand fills up to 8 meters high would be required to meet settlement requirements post-project completion. This approach would not only lead to significant delays but also result in a substantial carbon footprint, primarily due to the extensive need for sand transport. Additionally, concerns about traffic noise, vibrations, and pollution in the small village could potentially provoke considerable local protests. In response to these challenges, an alternative was found in the use of lightweight fill materials and a lightweight foundation layer but with a strength and stiffness larger than traditional foundation layers.

2 SOIL CONDITIONS

The geotechnical investigation for the proposed road construction in Borssele was comprehensive, involving Cone Penetration Tests (CPT), boreholes with undisturbed sampling, and an extensive laboratory testing program that included triaxial and oedometer tests. The CPTs were conducted using ISO 22476-1 Class 2 equipment. Figure 1 presents a typical CPT profile from the site, illustrating the subsurface stratigraphy. The results revealed soft, compressible soil layers extending to approximately 8 meters below ground level. These layers belong to the Holocene epoch and are primarily composed of normally consolidated clay, interspersed with organic material in some strata.

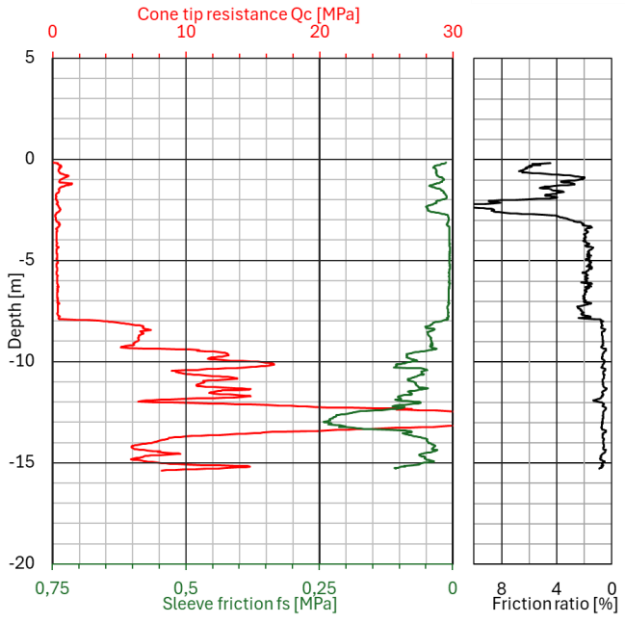

Figure 1. Typical CPT at project location.

3 DESIGN

3.1 The material foam glass

Foam glass is a porous glass foam material. It is made by heating a mixture of crushed or granulated glass and a blowing agent (chemical foaming agent) such as carbon or limestone. Near the melting point of the glass, the blowing agent releases a gas, producing a foaming effect in the glass. After cooling the mixture hardens into a rigid material with gas-filled closed-cell pores comprising a large portion of its volume. The grain shape of the material can be compared to natural sand.

Glass foam has a dry unit weight of 2 kN/m^3. The foam consists of closed cells, which prevents water attachment to the glass particles. In theory, the unit weight of the material in an embankment would remain at the original value. However, when placed below groundwater levels, some water intake may occur over the lifetime of the construction. This absorption can increase the unit weight of the material to approximately 7 kN/m^3. In this case study the foam glass was only used above groundwater levels, so this would not be a problem. As a safe approach, a unit weight of 4 kN/m^3 was adopted in the design of the embankment and the settlement calculations, which is still considerably lower than usually adopted sand as fill material (unit weight 18 kN/m^3 when compacted).

Foam glass is an environmentally safe material and causes no pollution when (in long term) used in embankments. The environmental aspects of the foam glass material are described in Rood and Klein (2014).

3.2 Embankment fill with foam glass

The practical experience with foam glass in the construction of embankments on compressible soils is described in Gold and Dietrich (2014).

The embankment for the new road utilizes foam glass as its primary fill material, capitalizing on its unique properties to address the challenges posed by the underlying soft soil. The key advantage of using foam glass in the embankment is its significantly lower unit weight compared to traditional fill materials, such as compacted sand or gravel. This reduced weight decreases the vertical stress exerted on the soft subsoil, minimizing the risk of excessive settlement and instability. Additionally, the closed-cell structure of foam glass offers excellent resistance to water absorption, maintaining its low weight and structural integrity even in varying environmental conditions.

In the construction of the embankment, careful attention was given to the layering and compaction of foam glass to ensure uniformity and optimal load distribution. The design also took into consideration the drainage and erosion control aspects, ensuring the longevity and durability of the embankment. By choosing foam glass, the project not only addresses the geotechnical challenges but also contributes to sustainability, as foam glass is often made from recycled materials.

3.3 Stabilised foundation layer

The foundation layer of the new road is a composite structure, stabilized with a mixture of foam glass, cement, in situ clay, and the Geosta® additive. This innovative approach creates a foundation layer with enhanced strength and stiffness, suitable for supporting the road structure while distributing loads evenly across the underlying soft soil.

The stabilization process involves thoroughly mixing the components, where the foam glass provides volume and reduces the overall weight, while cement

acts as the primary binding agent. The addition of Geosta® enhances the mixture's properties, improving flexibility and load-spreading behaviour, crucial for road foundations over soft soils. The use of in situ clay in the mix helps in achieving an eco-friendly solution by recycling existing materials and reducing the need for importing new fill materials.

The layer's design ensures it has sufficient bearing capacity to support the road and traffic loads without undergoing significant deformation or settlement. The stabilized foundation layer also contributes to a reduction in the required thickness of the overlying asphalt layer, leading to cost savings and a further reduction in the project's carbon footprint. This layer represents a fusion of traditional and modern construction techniques, resulting in a durable, resilient, and environmentally sensitive road foundation.

4 SOIL STABILISATION PRINCIPLE

4.1 Use of Geosta®

Geosta® is a mixture of inorganic salts, that in combination with hydraulic binders such as Portland cement or lime, is applied in soil stabilisation. By adding Geosta® to the cement a noticeable improvement of the soil stabilisation is realized (Omotosho, 2005), especially in flexibility and load spreading behaviour. Geosta® is a mixture of zeolites, oxides (aluminium, magnesium, and silicon oxide) or chlorides (magnesium, sodium, potassium and calcium chlorides). A regular formula is a mixture of 1.5 – 2.0 kg Geosta® with 100 kg cement per m^3 of soil.

Geosta® stabilised soil is applied as a hardstand foundation for several wind farms in the Netherlands (Brouwer and van der Veer, 2021).

4.2 Lime pre-treatment

In cases where the stabilization involves clayey soil, a pre-treatment with lime is often necessary. Clay particles tend to exhibit a delayed and often incomplete chemical reaction with cement and lime. Pre-treating the clay with lime leads to a more effectively stabilized product. This is attributed to the chemical interactions between lime and clay particles, as represented by the following reactions:

$$CaO + H_2O \rightarrow CA(OH)_2 \quad (1)$$

$$CA(OH)_2 + CO_2 \rightarrow CACO_3 + H_2O \quad (2)$$

where:

- CaO presents (quick) lime.
- H_2O is water.
- $Ca(OH)_2$ is hydrated lime.
- $CaCO_3$ is calcium carbonate.
- CO_2 is carbon dioxide.

This process leads to an upgrade of the clay material with considerably lower water content and a more granular-type behaviour.

5 TESTING

5.1 Laboratory

Prior to the design of the embankment and road foundation, samples were made in laboratory circumstances. Figure 2 shows 2 samples that were constructed. The mix consisted of clay, as found in the top layer at the project site, foam glass, cement and the Geosta® additive. The relation between the amount of foam glass and clay varied between 1:2 and 1:3.



Figure 2. Sample of stabilised foam glass.

The above mentioned samples were tested in the laboratory for compression strength. The results showed that the unconfined compression strength (UCS) varied between 1.9 and 2.1 N/mm^2. A clear distinction between the several used mixtures in terms of relation between foam glass and clay could not be made.

5.2 Test site

A test site was constructed by the contractor on a location close to the new road. Soil conditions at the test site were comparable to the final road location.

At the test site, a mixture was made (mixed in place) consisting of the locally available clay, Portland cement, Geosta® and foam glass. The ratio between clay and foam glass was initially set on 1:2. The mixture furthermore consisted of 150 kg Portland cement

and 1.5 kg Geosta® per m^3 soil/foam glass. The stabilised layer had a thickness of 400 mm and was constructed on top of the clayey subsoil.



Figure 3. Test site 1.

For the design of the road construction, the unconfined compression strength UCS and the static flexural stiffness $E_{stat,flex}$ was required. Plate load test according to DIN 18134 were carried out on the test site with a plate diameter of 300 mm to derive the static stiffness modulus. The results proved to be on the lower site. An average E_{v1} modulus of 85 MPa was derived, which is considered very low for a cement stabilised soil. This value was sufficient for the road deign design but insufficient to reduce the thickness of asphalt layers.

Additionally, cores were drilled to assess the strength of the layer in the laboratory. The drilled samples exhibited significantly lower unconfined compression strength (UCS) values, ranging between 0.4 N/mm² and 1.1 N/mm²

5.3 Comparison with literature and database

Numerous publications exist on the topic of the correlation between strength and stiffness of stabilised soils. A very large variation in correlations can be observed (Biswal et al, 2018).

The Geobest in-house database contains a large number of tests on Geosta® stabilised soil samples where UCS as well as flexural stiffness is determined in the laboratory. Based on these results, a correlation can be determined between both parameters. The results are graphically shown in Figure 4. A distinction was made between soil stabilisation with granular and cohesive materials.

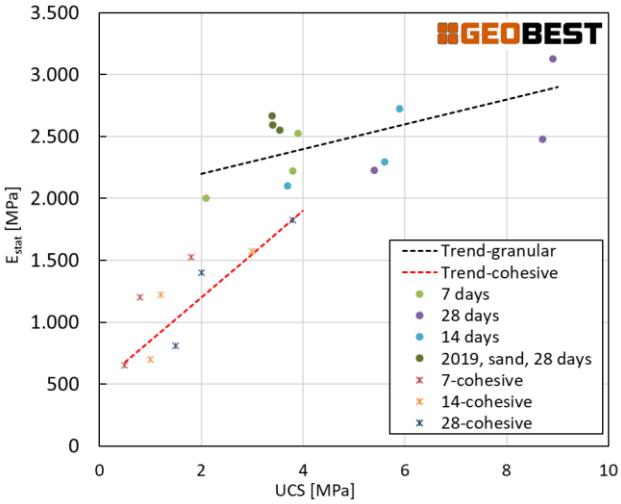

Figure 4. Static flexural E-modulus based on UCS tests.

Based on the correlation for cohesive soils, a stiffness of between 500 and approx 750 MPa could be expected. This is considerable higher than the above mentioned values form the plate load tests.

The large difference between the E_{v1} modulus determined in the field and the E-modulus in the correlation can be explained by a number of reasons:

- The modulus from the plate load test is a purely settlement related parameter and may be regarded as an short term oedometer stiffness rather than a flexural stiffness.
- The plate load test has an influence depth of 2D-3D, so in the worst case 900 mm. With a layer thickness of 400 mm, the compressible subsoil will influence the outcome significantly.
- The relationship from Figure 4 was derived under ideal laboratory conditions and therefore may not fully reflect the values that can be reached in practice.
- The execution of the test site was not ideal in terms of compaction, water saturation and particle size of the glass foam particles.

Based on these findings, it was decided that an additional test site was required and that further study on the flexural stiffness would be beneficial for the project.

6 CONCLUSIONS

This example demonstrates the potential of foam glass as a sustainable alternative for embankment construction in soft soil conditions.

The use of foam glass in a stabilised foundation layer is still an innovative and new solution. Additional research has to be performed towards the ideal mixing circumstances and the strength and stiffness parameters that can be obtained. The method is promising and may lead to a reduction of foundation and asphalt thickness, which is beneficial in terms of reduction of costs and carbon footprint.

At this moment the municipality of Borssele is in the process of decision making on this project. Construction of the road may take place in the second or third quarter of 2024. First step is to construct an additional test site, where the lessons learned from previous test sites are incorporated. The additional tests will lead to an upgraded design where all the benefits of this innovative method are included.

ACKNOWLEDGEMENTS

The authors would like to thank the contractor Traas en Ovaa BV and the municipality of Borssele for their cooperation for this paper.

REFERENCES

Biswal, D.R., Sahoo, U.C., Dash, S.R. (2018), Strength and Stiffness Studies of Cement Stabilized Granular Lateritic Soil, Springer International Publishing AG, http://doi.org/10.1007/978-3-319-61902-6_25.

Brouwer, J.W.R., van der Veer, M.D. (2021) Wind Farm Deil, Solid Foundation for Crane Setup Sites (In Dutch), *Land en Water* 4, April 2021.

Deutsches Institut für Normierung (2012), Subsoil - Tests and Testing Equipment – Plate Load Test (DIN 18134) (In German), Beuth Verlag, Berlin.

Gold, G and Ditrich, M. (2014), Use of Foam Glass Granulate as a Transition between a Settlement-Reduced Deep Foundation and a High Embankment Fill with High Residual Settlement Potential (In German), *In: Seminar Infrastruktur 2*.

Omotosho, O. (2005), Influence of Geosta Addition on cement-stabilised Chioco Mud of the niger Delta., in American Journal of Environmental Science 1 (1), pp 59-63.

Rood, J.N., Klein, B. (2014), Environmental Assessment of Foam Glass in Civil Engineering Works (In Dutch), HB Adviesbureau, Alkmaar, the Netherlands.

Proceedings of the XVIII ECSMGE 2024
GEOTECHNICAL ENGINEERING CHALLENGES
TO MEET CURRENT AND EMERGING NEEDS OF SOCIETY
© 2024 the Authors
ISBN 978-1-032-54816-6
DOI 10.1201/9781003431749-403
Open Access: www.taylorfrancis.com, CC BY-NC-ND 4.0 license

ECSMGE 24
XVIII EUROPEAN CONFERENCE ON SOIL MECHANICS AND GEOTECHNICAL ENGINEERING

Sensitivity analysis of load transfer curves in case of rigid inclusions

Analyse de sensibilité des courbes de transfert de charge dans le cas d'inclusions rigides

P. Burtin*
Menard, Chaponost, France

J. Racinais
Menard, Orsay, France

**pierre.burtin@menard-mail.com*

ABSTRACT: The soil reinforcement by rigid inclusions is usually a suitable solution in various projects such as shallow foundations, slab-on-grade, embankments, tanks, etc. In most cases, the settlement is a key point. The interactions between the rigid inclusion and the surrounding soil must therefore be well established, especially the behaviour laws along the shaft (skin friction) and at the tip (end-bearing). In France, the Frank and Zhao load transfer curves are often used to model those interactions. The input parameters are determined from the pressuremeter tests. Those tests are not always available, especially outside France. Some authors and standards have proposed other load transfer curves. This article summaries the main used interaction behaviour laws and presents sensitivity analysis, based on simulated load tests on isolated rigid inclusions and also based on regular design cases.

RÉSUMÉ: Le renforcement de sol par inclusions rigides est généralement une solution adaptée dans divers projets tels que fondations superficielles, dallages sur terre-plein, remblais, réservoirs, etc. Dans la plupart des cas, le tassement est un point clé. Les interactions entre l'inclusion rigide et le sol environnant doivent donc être bien estimées, notamment les lois de comportement en frottement latéral le long du fût et en pointe de colonne. En France, les courbes de transfert de charge proposées par Frank et Zhao sont souvent utilisées pour modéliser ces interactions. Les paramètres d'entrée sont déterminés à partir des essais pressiométriques. Ces sondages géotechniques ne sont pas toujours disponibles, notamment hors de France. Certains auteurs et normes ont proposé d'autres courbes de transfert de charge. Cet article résume les principales lois de comportement d'interaction utilisées et présente des analyses de sensibilité, basée sur des tests de chargement sur des inclusions rigides isolées mais aussi sur des cas de dimensionnement classique.

Keywords: Rigid inclusions; load transfer curves; skin friction; end-bearing; soil reinforcement.

1 INTRODUCTION

As a solution of soil reinforcement, rigid inclusions (RI) often serve as a valued engineered substitution to deep foundation techniques such as piles, and provide cost savings, shorter schedules, and high effectivity in difficult foundation conditions such as loose/soft fine-grained soils and organic soils (Magnan 1994, Briet & Plomteux 2010, Burtin & Racinais 2016, Sahyouni et al. 2021). The technique widely used today has experienced a great evolution in the number of projects carried out and the fields of application since the 1990s (Racinais et al. 2016). The fields of application cover all areas of construction: housing, industrial and commercial buildings, road embankments, railway embankments, storage tanks and finally onshore wind turbine (ASIRI 2013).

Rigid inclusions are an intermediate solution between shallow and deep foundations to reduce settlement and increase the bearing capacity and/or ensuring the stability (Figure 1). A load transfer platform (LTP) is generally placed or not in between the foundation and the rigid inclusion head, in both cases the important advantage is to be not linked to the structure.

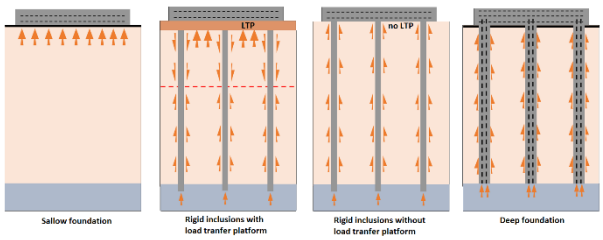

Figure 1. The various types of foundations.

The ground improvement by rigid inclusion consists in the transfer of a part of the load into the columns the other part going into the surrounding soft soil. The load transfer platform permits to share the load from the structure onto both elements at the level of column head. Then deeper, the contrast of the rigidity and loading generates a differential settlement and a load transfer from the soil to the columns is developed by negative skin friction along the shaft of the inclusion. At a certain elevation the settlement of the soil and the column is equal, that level is called "neutral plan". Below the column settles more than the soil, a load transfer from the column to the soil is generated by positive skin friction. At the toe of the rigid inclusion a load transfer occurs into the anchorage layer (end-bearing).

The interactions between the soil and the rigid inclusion are an important assumption and depend on the different load transfer especially along the shaft (skin friction) and at the tip (end-bearing). Several authors have proposed load transfer curves that are based on different approaches, return of experience such as static load test, etc.

During the design stage of a rigid inclusion project the designer should assume the above soil/inclusion interactions. The article proposes to present a part of the author propositions around the world in term of load transfer curves Then the settlement during a static load test on an isolated column will be predicted with the various approaches. In second part, the calculations of the slab-on-grade founded on the rigid inclusion will be presented and also with the different assumptions.

2 LOAD TRANSFER CURVES

The following list present various load transfer curves in term of load-displacement law. More details could be found in the respective referenced articles. In this section, the main information is shown and focus on analytical methods. Only the Frank & Zhao is based on the pressuremeter test.

2.1 Frank & Zhao / NF P 94-262 (2012)

In order to characterize the soil-structure interaction in a soil reinforced by columns, Frank & Zhao (1982) proposed two semi-empirical mobilization laws for skin friction at the interface of the column and for end-bearing at the toe of the column. This model is based on pressuremeter data.

The skin friction mobilization law is defined according to the relationship between the shear stress τ and the relative displacement $S_{(s-i)}$ between the rigid inclusion and the soil around the shaft of the column (Figure 2 left). This law depends directly on the limit value of skin friction q_s which could be correlated from the limit pressure p_l.

The end-bearing mobilization law is defined according to the relationship between the stress at the column toe q and the vertical displacement at the inclusion toe S_b in the anchor layer (Figure 2 right). This law depends directly on the limit value of the end-bearing resistance q_b, correlated from the limit pressure p_l.

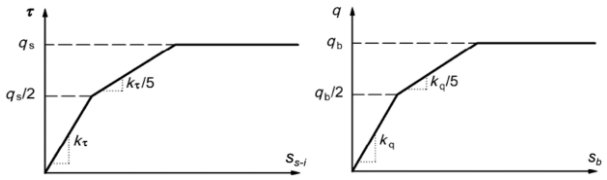

Figure 2. Semi-empirical mobilization law for skin friction (left) and for end-bearing (right) (NF P94-262).

The parameters of the slopes k_τ and k_q depend on the type of soil, the pressuremeter modulus E_m and the diameter of the isolated column B (Table 1).

Table 1. Parameters of the k_τ and k_q slopes of Frank & Zhao according to the type of soil.

Slope of the Trilines	Fine grained soil	Coarse grained soil
k_τ	$2\ E_m/B$	$0.8\ E_m/B$
k_q	$11\ E_m/B$	$4.8\ E_m/B$

2.2 American Petroleum Institute (2000)

The API recommendations in 2000 propose some load transfer curves about skin friction and end-bearing for clay and non-carbonate sand. The approach defines "point by point curves" such as one example below concerning the tip behaviour:

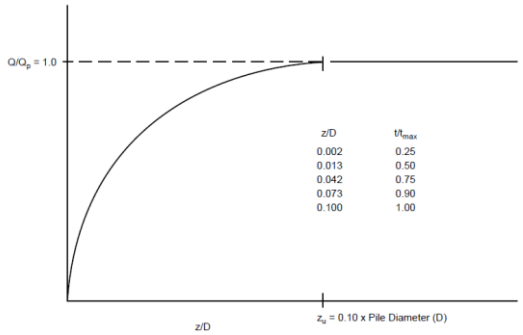

Figure 3. Pile tip load displacement curve (API 2000).

2.3 Bohn (2015)

According to the works, 2 mains load transfer curves were proposed: cubic root curves and hyperbolic curves. The 2 following figures present the laws.

		Mathematical expression	Curve shape
Cubic root curves	Shaft	$q_s = \min\left(\left(\frac{s_s}{s_{s,\lim}}\right)^{1/3} \cdot q_{s,ult}; q_{s,ult}\right)$	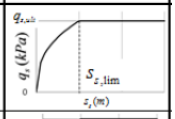
	Tip	$q_b = \min\left(\left(\frac{s_b}{s_{b,\lim}}\right)^{1/3} \cdot q_{b,ult}; q_{b,ult}\right)$	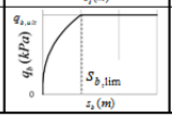

Figure 4. Proposed cubic root load transfer curves (Bohn).

		Mathematical expression	Curve shape
Hyperbolic curves	Shaft	$q_s = \frac{q_{s,ult} \cdot s_s}{M_s \cdot B + s_s}$	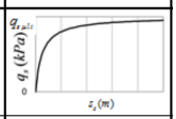
	Tip	$q_b = \frac{q_{b,ult} \cdot s_b}{M_b \cdot B + s_b}$	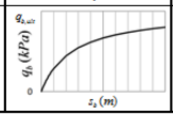

Figure 5. Proposed hyperbolic load transfer curves (Bohn).

The parameters $s_{s,lim}$, $s_{b,lim}$, M_s and M_b are defined either for mean or for conservative approach and fixed for all inclusion installations and ground types.

2.4 FHWA-IF-99-025 (1999)

Depending on the soil nature (cohesive or cohesionless soil), the shaft and the end-bearing load transfer curves are proposed. An example of the relationship is presented in the figure 6.

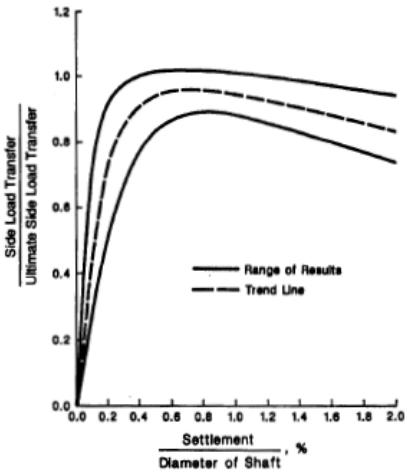

Figure 6. Normalized side load transfer for drilled shaft in cohesive soil. (FHWA-IF-99-025).

2.5 Fleming (1992)

This author proposed hyperbolic laws to estimate the load transfer soil/column interaction in both case shaft and end-bearing. Depending on the stiff or soft soil behavior some assumptions are defined. The young modulus of the anchorage layer is directly impacting the load-displacement equation.

2.6 Gwizdala & Krasinski (2016)

According to the analyses, root curves are defined with the following principle:

$$q = q_{bu} \cdot \left(\frac{z}{z_f}\right)^{\beta} \quad for\ z \le z_f \qquad (1)$$

$$q = q_{bu} \quad for\ z > z_f \qquad (2)$$

where:

- q: pile base resitance (kPa)
- q_{bu}: bearing capacity of the soil beneath pile base (kPa)
- z: pile head displacement (-)
- z_f: the displacement of the pile head, at with the soil bearing capacity under the pile base is mobilized (-)

The parameters β and z_f (and α and z_v about the skin friction) depend on the nature of the soil: cohesive or non-cohesive but also the methodology of the inclusion installation: driven, bored/CFA, vibro, etc.

2.7 Randolph & Wroth (1978)

Following to the method, the behavior of the shaft and the tip could be defined with:

- a linear part where the shear modulus of the soil has a direct impact.
- And then a limit equal to the maximum allowable skin friction and end-bearing resistance.

3 STATIC LOAD TEST

3.1 Presentation

The next section presents the impact of the load transfer curves when the static load test (SLT) on an isolated rigid inclusion is modelled. This test is a high-value quality control of the soil reinforcement technic. That consists in the loading, with generally a hydraulic jack below at reaction support, of the column head. The positive skin friction and the end-bearing of the inclusion is mobilized.

3.2 Sensitivity analysis

Considering all the above load transfer curves, the analysis assumes 3 different cases about soil profile

and soil parameters, inclusion installation type, diameter and length of the columns:

- Case 1: large and long rigid inclusion with soil displacement, anchored into a stiff layer.
- Case 2: RI with soil displacement, low end-bearing resistance in clayed condition.
- Case 3: RI with soil extraction in very soft soil above the gravel anchorage layer.

The following figures show the settlement predictions in function of the loading at inclusion top.

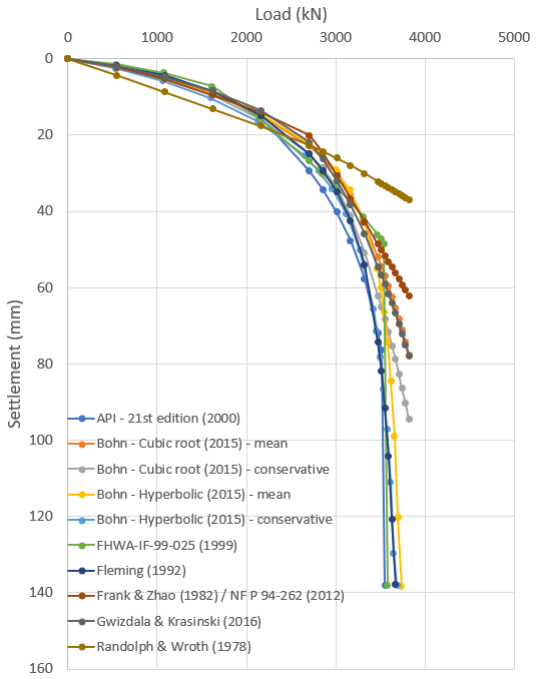

Figure 7. Settlement prediction for a static load test 1.

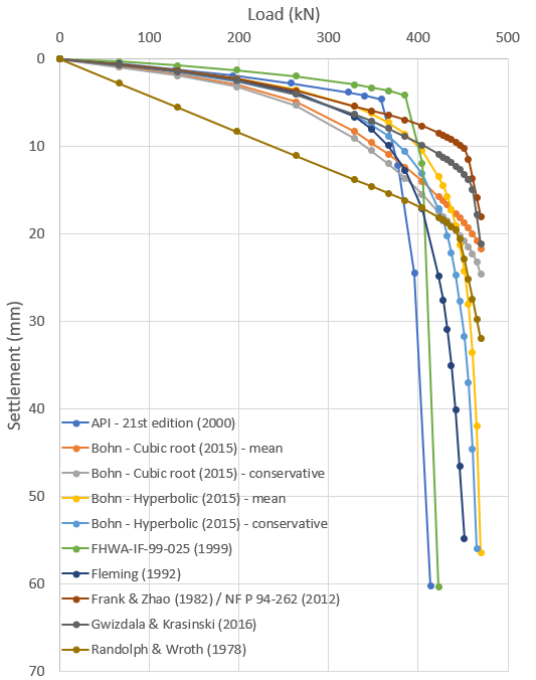

Figure 8. Settlement prediction for a static load test 2.

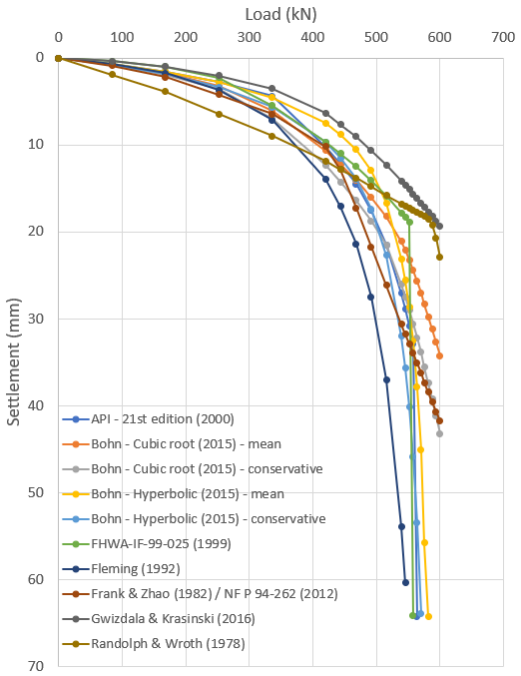

Figure 9. Settlement prediction for a static load test 3.

Closed the bearing capacity failure of the inclusion, the different methods present a large range of settlement predictions. However, at the creep load, the differences are limited. That is not obvious to define an author who over or under estimate the settlement prediction. Indeed depending on the percentage of the load, the curves intersect themselves and the final result at the RI head is a combination of different skin friction behavior of the multilayer and the end-bearing behavior.

4 UNIT CELL CALCULATION

4.1 Presentation

A design of a slab-on-grade over RI could consider the biphasic model which examines the interaction between the domain of inclusions and the complementary soil in a unit cell. That can be used to determine the distribution of forces and settlement profiles of the two domains (figure 11). The 2 domains are linked by load transfer curves.

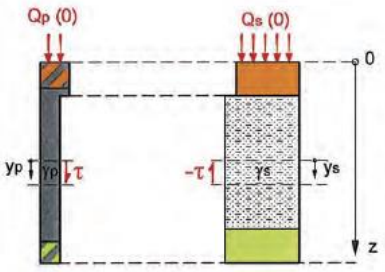

Figure 10. Biphasic model of the unit cell (ASIRI 2013).

4.2 Sensitivity analysis

Considering all the load transfer curves in section 2, the analysis assumes 3 different cases about soil profile and soil parameters, inclusion installation type, diameter and length of the columns:

- Case 1: large and long rigid inclusion with soil displacement, anchored into a stiff layer, with a high load in the slab.
- Case 2: RI with soil displacement, low end-bearing resistance in clayed condition and with no LTP between inclusion and slab.
- Case 3: RI with soil extraction into very soft soil over gravel anchorage layer.

The 2 following figures show the settlement (at the slab level, the punching into the LTP and the punching into the bearing layer) and loads into the RI (head, maximal, bottom) in function of different approaches for the case 1. The next table summaries the results in the 3 cases. The first line presents the average values of all the laws. The other lines show the variation in percent compared to the average. The cells should be read as "case 1" / "case 2" / "case 3".

The main design criteria for slab are typically the total settlement (in grey in figure 12 and 2nd column in table 2) and the maximal load into the RI (in grey in figure 13 and 6th column in table 2).

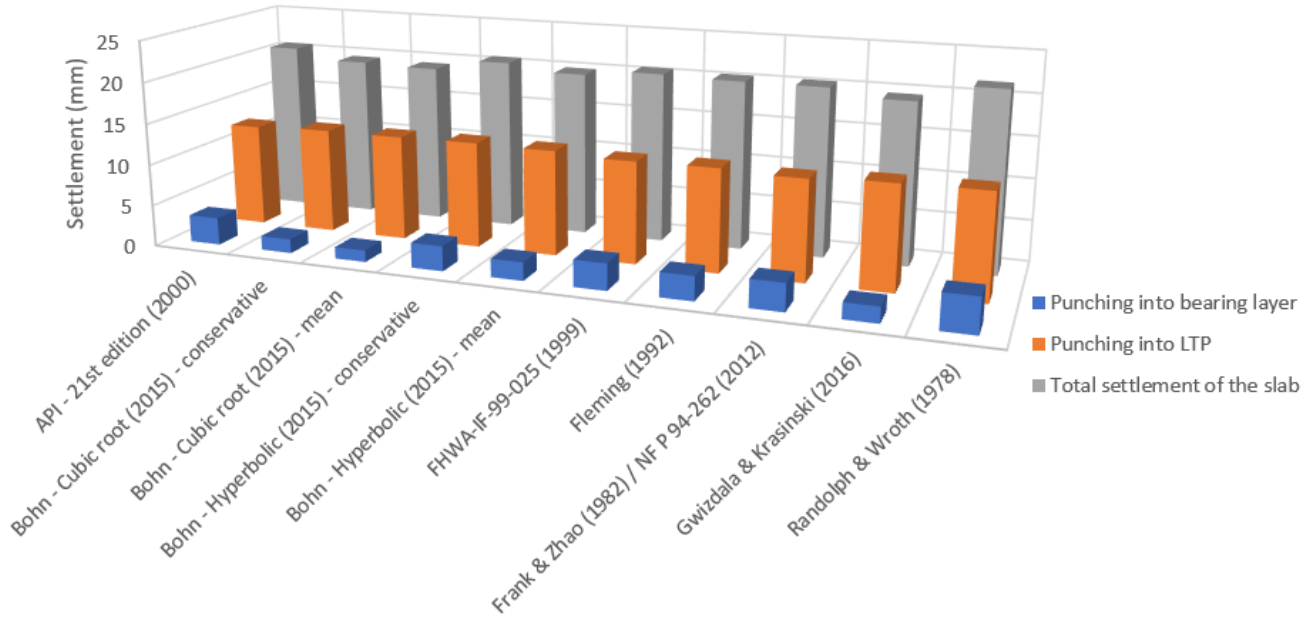

Figure 11. Settlement prediction for slab-on-grade loading - case 1.

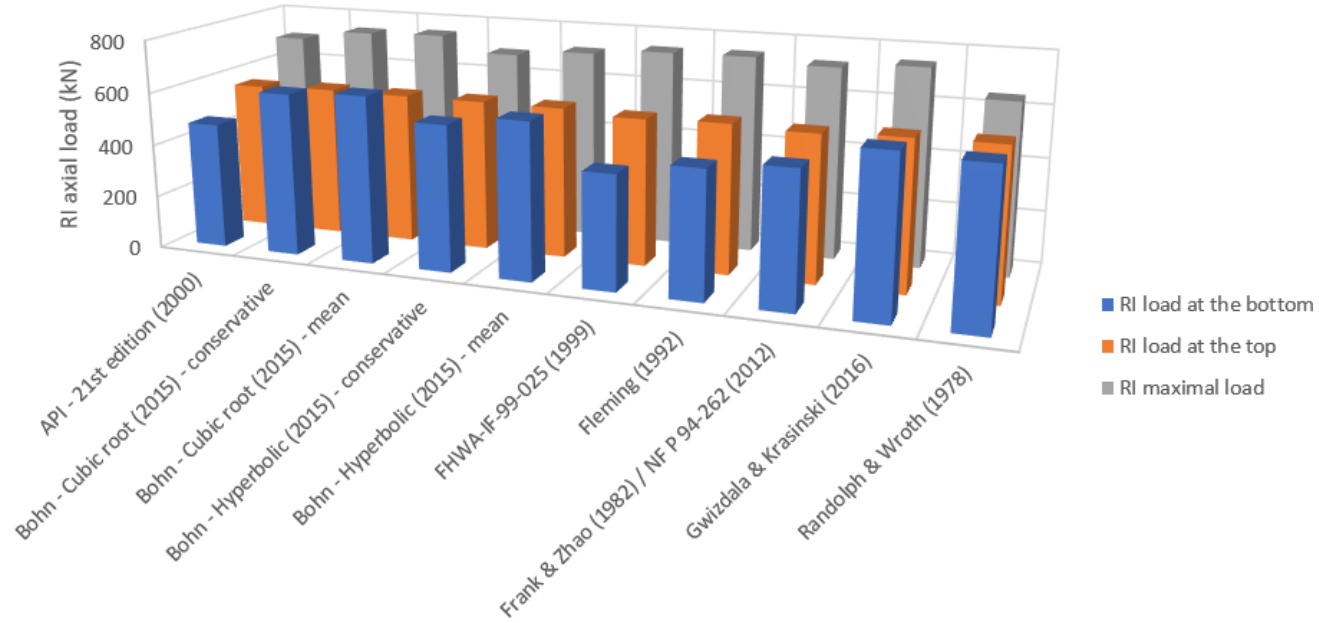

Figure 12. Load distribution into the inclusion for slab-on-grade loading - case 1.

Table 2. Summary of the results (settlement and load) about "case 1" / "case 2" / "case 3".

Load transfer curve	Settlement of the slab	Punching into LTP	Punching into bearing layer	RI load at top	RI load max	RI load at bottom
Average (in mm or kN)	***20/27/26 mm***	***12/0/23 mm***	***3/3/1 mm***	***562/93/41 kN***	***722/93/70 kN***	***541/28/48 kN***
API - 21st edition (2000)	**2/-2/1%**	-1/0/1%	19/-21/16%	0/0/0%	**-3/0/-2%**	-12/-12/-1%
Bohn - Cubic root (2015) – cons.	**-4/-1/0%**	2/0/3%	-38/-9/-77%	1/4/0%	**3/4/-2%**	14/14/21%
Bohn - Cubic root (2015) - mean	**-5/-2/-1%**	2/0/3%	-49/-15/-88%	1/7/0%	**4/7/-1%**	17/21/24%
Bohn - Hyperbolic (2015) – cons.	**2/-1/0%**	3/0/1%	9/-12/-7%	1/0/0%	**-4/0/-1%**	2/9/6%
Bohn - Hyperbolic (2015) - mean	**-2/-3/0%**	2/0/1%	-20/-27/-41%	1/0/0%	**0/0/1%**	9/23/12%
FHWA-IF-99-025 (1999)	**2/-5/1%**	-1/0/1%	16/-47/16%	-2/0/0%	**3/0/0%**	-21/1/-7%
Fleming (1992)	**1/2/0%**	-1/0/0%	5/20/-19%	0/0/0%	**3/0/0%**	-12/-60/-46%
Frank & Zhao / NF P 94-262	**1/-2/-1%**	-3/0/-4%	19/-18/62%	-2/0/0%	**1/0/3%**	-6/12/-15%
Gwizdala & Krasinski (2016)	**-4/-2/0%**	0/0/1%	-31/-15/-54%	0/5/-1%	**4/5/7%**	10/9/17%
Randolph & Wroth (1978)	**7/20/0%**	1/0/-4%	52/163/132%	1/-18/0%	**-10/-18/-7%**	7/-30/5%

The punching into the bearing layer presents important variations but that concerns a low value of displacement: 1 to 3mm. The law with the biggest gaps compared to the average is Randolph and Wroth. Indeed, a linear load transfer curve could be too simplified. About all the other, the variation is between -5 to +7% about the 2 mains criteria in bold text in the above table (settlement of the slab and maximal load into the RI).

5 CONCLUSIONS

When a rigid inclusions project is designed, the load transfer (stress/displacement) between the soil and the inclusions must be assumed. Various authors proposed load transfer curves depending in the nature and stiffness of the soil and the inclusions installation. This paper summarised a part of the different approaches and performed comparisons in typical cases of rigid inclusion applications.

The final design of rigid inclusions seems to be not significantly impacted by the different studied load transfer curves. However, the analysis is limited to 3 cases of static load test and 3 cases of slab-on-grade.

REFERENCES

API. (2000). Recommended practice 2A-WSD (RP 2A-WSD) Twenty-first edition, 2000.

ASIRI National Project. (2013). Recommendations for the design, construction and control of rigid inclusion ground improvements.

Bohn, C. (2015). Serviceability and safety in the design of rigid inclusions and combined pile-raft foundations. PhD thesis, University of Paris-East and Technical University of Dramstadt.

Burtin, P. and Racinais, J. (2016). Embankment on Soft Soil Reinforced by CMC Semi-Rigid Inclusions for the High-speed Railway SEA. Proc. 3rd Int. Conf. Transportation Geotechnics. https://doi.org/10.1016/j.proeng.2016.06.045.

Briet, S. and Plomteux, C. (2010). Integrated Ground Improvement Solution for Windmill Foundation Support in soft soils. Proc. 63rd Canadian Geotechnical Conference.

FHWA-IF-99-025. (1999). Drilled shafts construction procedures and design methods. US Department of transportation - Federal highway administration.

Fleming, W.G.K. (1992). A new method for single pile settlement prediction and analysis. Géotechnique 42 (3), 411-425. https://doi.org/10.1680/geot.1992.42.3.411.

Gwizdala, K. and Krasinski, A. (2016). Pile foundations, calculations following to Eurocode 7 and national experiences (Polish). Acta Sci. Pol. Architectura 15 (2), 3-22. https://www.architectura.actapol.net/pub/15_2_3.pdf.

Magnan, J.P. (1994). Methods to reduce the settlement of embankments on soft clay. ASCE, 1994.

NF P 94-262. (2012). Normes d'application nationale de l'Eurocode 7 - Fondations profondes.

Racinais, J., Thomas, B. and Ong, R. (2016). Twenty Years of CMC Successful Application. Proc. 19th Southeast Asian Geotechnical Conference, Kuala Lumpur, Mass.,5.

Racinais, J., Maucotel, F., Varaskin, S. and Hamidi, B. (2017). Beneficial Use of Pressuremeter Tests for Accurate Modelling by Finite Elements of a Rigid Inclusion Ground Improvement Solution. Proc. 19th Int. Conf. Soil Mechanics and Geotechnical Engineering, 2017, Seoul, Mass.,4.

Randolph, M.F. and Wroth C.P. (1978). Analysis of deformation of vertically loaded piles. Journal of the geotechnical engineering division 104 (2), 1465-1488. https://doi.org/10.1061/AJGEB6.0000729.

Sahyouni, A., Burtin, P., Racinais, J., Quandalle, B., Briancon, L. and Grange, S. (2021). Instrumentation and numerical modelling of a static load test carried out on rigid inclusion reinforcing an onshore wind turbine foundation. Proc. 20th International Conference on Soil Mechanics and Geotechnical Engineering, Sydney.

Proceedings of the XVIII ECSMGE 2024
GEOTECHNICAL ENGINEERING CHALLENGES
TO MEET CURRENT AND EMERGING NEEDS OF SOCIETY
© 2024 the Authors
ISBN 978-1-032-54816-6
DOI 10.1201/9781003431749-404
Open Access: www.taylorfrancis.com, CC BY-NC-ND 4.0 license

ECSMGE 24
XVIII EUROPEAN CONFERENCE ON SOIL MECHANICS AND GEOTECHNICAL ENGINEERING

Benefits of finite element method analysis to the design of the Saint Maur Créteil caverns metro station

Apports de la modélisation numérique pour le dimensionnement des cavernes de la gare de Saint Maur Créteil

M. Cahn*, N. Simon, N.H. Nguyen, S. Burlon
Terrasol Setec, Paris, France

E. Talut, J. Subervie
Eiffage, Romainville, France

**martin.cahn@setec.com*

ABSTRACT: The Saint Maur Créteil metro station of the Grand Paris Express is the deepest one in France. It consists of a central shaft and two underground caverns located on either side. The caverns are carried out using Sequential Excavation Method in chalk with high groundwater pore pressure. Due to the dense urban environment, the design of theses caverns has been addressed by complex finite element method analysis to assess ground surface settlements. The caverns geometries are almost as wide as they are long: this unsual geometry requires to be considered to assess the settlements in a relevant way. Comparisons between plane strain modelling using the principle of superposition and the Attewell's formula, 3D "One step" modelling and full 3D modelling were performed and consistent results were obtained. Other FEM calculations allowed to define the execution procedures to control the groundwater pore pressures dissipation and the hydraulic gradient reduction, with the aim to ensure the lateral abutment stability of the caverns. In these calculations focusing on stability assessment, chalk specific behaviour, intermediate between rock and soil, were accounted for using different constitutive laws.

RÉSUMÉ: La gare de Saint-Maur Créteil pour le métro du Grand Paris Express est la plus profonde de France. Elle est formée d'un puits central et de deux cavernes souterraines de part et d'autre. Les cavernes sont réalisées en méthode traditionnelle, dans la craie avec une forte pression d'eau. La présence en surface d'une zone urbaine dense a nécessité la validation des solutions constructives par le biais d'une importante étude aux éléments finis pour évaluer les tassements de surface. La géométrie atypique des cavernes, presque aussi larges que longues, a dû être prise en compte pour évaluer les tassements de manière pertinente. Des comparaisons entre un modèle en déformations planes utilisant le principe de superposition et la relation d'Attewell, un modèle 3D stationnaire et un modèle 3D complet ont été menées. Des résultats cohérents entre les différentes approches ont été obtenus. D'autres modèles ont permis de définir les dispositions constructives pour contrôler la dissipation de pressions interstitielles et la réduction de gradients hydrauliques, avec l'objectif d'assurer la stabilité des culées des cavernes. Dans ces calculs orientés stabilité, le comportement particulier de la craie, à la frontière entre roche et sol, a été pris en compte via l'utilisation de lois de comportement différentes.

Keywords: Cavern; Grand Paris; finite element modelling; chalk.

1 SAINT MAUR CRETEIL METRO STATION

Saint-Maur Créteil metro station is located southeast of Paris new metro line 15 and is part of the "Grand Paris Express". Initiated in 2017, the metro station should be finished by the end of 2025. The station is composed of:

- a central oblong-shaped shaft, 56 m long by 36.8 m wide and 58 m deep, sheltered by diaphragm walls with a thickness of 1.8 m.
- two underground caverns located on either side of the shaft, excavated using conventional methods, with a height of 13.6 m, a width of 21.3 m and a length of 30 m. 43 m of ground cover is found upon the vault (*cf.* Figure 1).

This new metro station is right underneath the existing surface RER-A train station: strong demands for limiting ground settlements were therefore needed, both in absolute and relative values.

This construction is carried out on behalf of the Société du Grand Paris by the joint venture of Eiffage and Razel-Bec. The project management is handled by Systra, and Terrasol is involved as an execution engineering firm for the design of underground caverns, the subject of this communication.

1.1 Geotechnical context

At South-east of Paris, project stratigraphy is typical of Paris Basin: Under the made ground, a first layer of coarse alluvium with a thickness of 10 m is found, followed by 3.5 m of fine sand covering a layer of 20 m of Ypresian Plastic Clay, softened in its upper part. This layer of Plastic Clay, overconsolidated and subjected to swelling, may exhibit weak mechanical properties, making it challenging to excavate underground sections using traditional methods. Underneath, a layer of 5 m of marl-limestone is encountered, covering the Campanian Chalk, partially altered in the upper part over approximately 5 m. The TBM and the caverns supporting the platforms, are entirely located in Campanian Chalk, which is a soft rock (σ_{ci}=6 MPa and GSI=57) with relatively low permeability (k=1.10^{-7} m/s).

Two water tables are encountered, the first in the alluvial deposits supported by Plastic Clays, and the second, slightly lower, in the chalk. For the design of the caverns, only the chalk water table is considered, corresponding to a pore water pressure of approximately 485 kPa at the invert of the caverns.

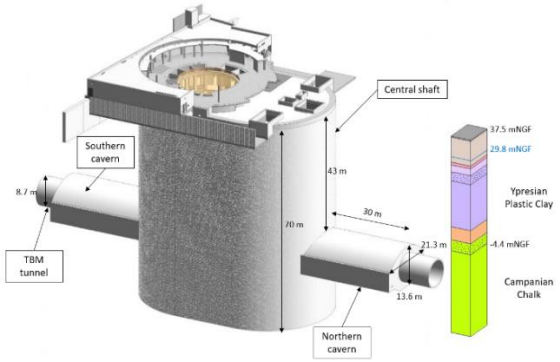

Figure 1. 3D View of the station and stratigraphy.

1.2 Execution procedures

The main tunnel was excavated using an Earth Pressure Balance Tunnel Boring Machine and has an internal section of 8.7 meters.

The excavation of the cavern is carried out with the Sequential Excavation Method aiming at minimize displacements by using rigid supports wherever possible as shown in Figure 2. At first the tunnel boring machine tunnel passes through the unexcavated shaft. Prior to the excavation of the caverns, a 5 m thick injection ring around the caverns is created from the segment lining tunnel through boreholes with Blow out Preventers. The tunnel is then backfilled with a self-compacting filling material "Regimix" (0). After that (1), superior abutments are excavated in parallel. Then (2), inferior abutments are bored. Abutments are then filled with concrete from bottom to top in two phases. Excavation of main gallery is then performed in two phases top-heading (3) and invert (5, each one followed by installation of definitive lining (4) (6). Let's note that each step of top-heading excavation was carried out in two steps: central part is excavated and supported before dealing with the lateral parts.

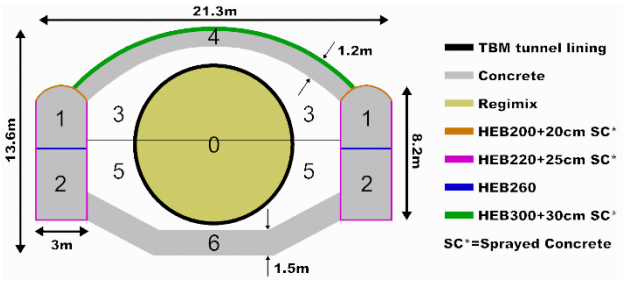

Figure 2. Sequential excavation of the cavern section.

The two underground caverns were excavated in parallel, and all the excavations were carried out continuously along their entire length. The start of the abutment galleries took place in May 2022 and Main gallery excavation began in late 2022, top-heading operations ended in early Spring 2023.

2 ASSESSING GROUND SETTLEMENTS

2.1 Results of geotechnical monitoring

To ensure that no critical damage is induced to buildings within the Geotechnical Zone of Influence (GZI), an extensive monitoring campaign has been performed. Various monitoring methods have been used: theodolites with reflector monitoring prisms, horizontal inclinometers above abutment galleries, oblique extensometers, from the surface to the caverns, electronic level indicators, piezometers, vibrating wire extensometers. As shown in Figure 1, most of the surface sensors have been placed near the RER-A station, since differential settlement could lead to important traffic disruptions.

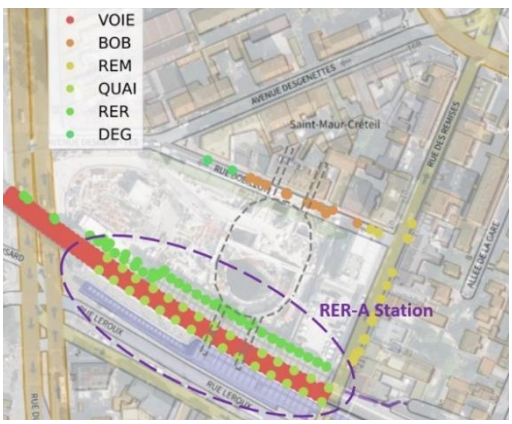

Figure 3. Optic sensors in the GZI.

Data from underground sensors were very unclear, with pikes corresponding to works at ground level near extensometer heads for instance. Chalk piezometer had problems during construction phase, and horizontal inclinometers provided values relatively close to what was expected, but with unexpected shape. Indeed, the maximum displacement is found at the final pass of the cavern, inconsistent with the distribution of surface settlements and every performed 3D FEM calculation (see Figure 9). Therefore, the authors chose to focus on data from surface settlement prisms shown in Figure 3. No clear tendency is visible on REM sensors: they are parallel to tunnel axis, but too far from it. Thus, five series of sensors were used:

- Rue Bobillot (BOB), from the angle with Rue des Remises to Avenue Desgenettes (included)
- Prisms beneath northern RER platform (Q01) and southern RER platform (Q02)
- Prisms along the wall common to RER and new metro station (RER) and Prisms on rail tracks, e.g southern rail of northern railway (V012).

If the first batch corresponds to a zone of residential buildings, with 2-3 floors, the others sensors are within the existing RER station, fixed on rigid structures (rails, concrete platforms, a wall 100m-long, …). The station itself is superficially founded, and long continuous walls give inertia to the structure, potentially perturbating the readings compared to a greenfield settlement trough.

To allow comparisons between measurements and results of numerical computations, Peck theory of gaussian settlement trough (Peck, 1969) has been used. Thus, if x denotes the transverse coordinate, the transversal settlement s is considered of Gaussian form:

$$s(x) = S_{max} \exp\left(-\frac{x^2}{2i^2}\right) \qquad (1)$$

with S_{max} the maximal settlement, and i the distance from tunnel axis to trough inflexion point. An algorithm has been used to get the two parameters' best fit, following a least squares procedure to assess errors. It also provides the covariance matrix, allowing the estimation of an elliptic joint confidence interval for each sector (Vugrin et al., 2007).

The procedure is illustrated with the case of Bobillot Street, and then applied to the four other series. First step corresponds to data cleaning: some sensors are reading irrelevant, chaotic data, while some others are missing months of data. Daily fluctuations are lessened using a moving average.

Data examination across the whole period reveals that if tunnelling boring machine passing through the unexcavated shaft induced quick oscillations of measures, it can't be accounted for any significant settlements.

The subsequent analysis is therefore limited to cavern excavation, divided in four phases: abutments excavation and filling with concrete, and then excavation of cavern upper part followed by permanent lining installation. Last phase of lower excavation isn't considered as no settlement was induced.

At the beginning of cavern excavation, all sensors registered a strong ascendant and unexplained displacement, independent of the ground injection. Over 19 sensors, 13 were kept after data cleaning. The white line on Figure 4 corresponds to tunnel face of the main gallery passing beneath Bobillot Street.

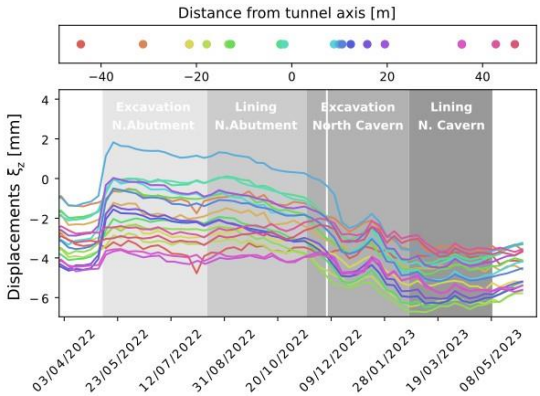

Figure 4. Time evolution of vertical displacements after data cleaning BOB (and rolling mean over 7 days).

Incremental ground displacements during abutment and main cavern operations along a transverse profile show Gaussian curve shape settlement trough (Figure 5). Let's note however that for abutment phase (May 2022 to Nov. 2022), best fit troughs are centred at fifteen meters from cavern axis, instead of the nine-meter distance expected from geometrical considerations.

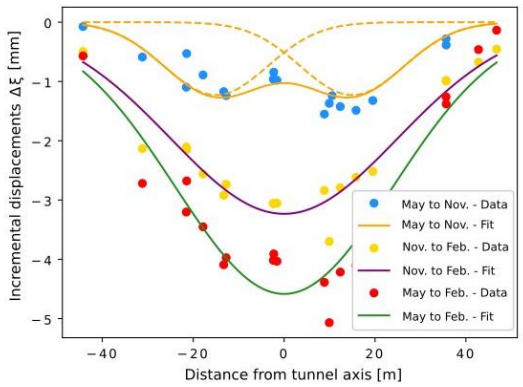

Figure 5. Incremental transverse trough along the Bobillot street for three periods: May-Nov 2022 (abutment construction), Nov-Feb 2023 (cavern excavation), Feb-May 2023 (cavern lining).

For other sensors, due to RER-A station rigidity, only final settlement through the whole period can be used. Procedure described earlier allows to get best fit parameters, and confidence ellipse at 90%, for each set of data (Figure 6).

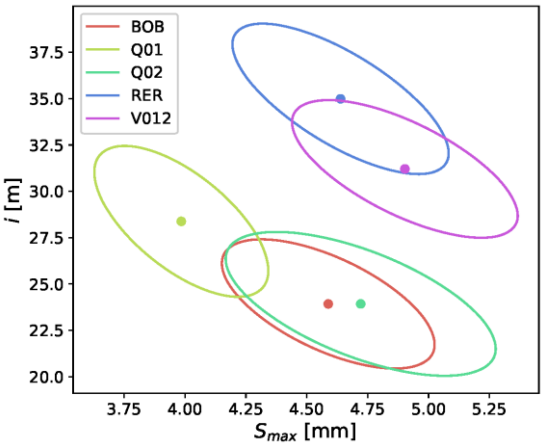

Figure 6. Elliptic joint confidence interval for each dataset.

According to Peck theory (Peck, 1969), greenfield trough width i defined earlier only depends on ground type. Therefore, its variability can be seen as a scale of the existing building stiffness: low stiffness for Bobillot Street to high stiffness for northern RER continuous wall. Maximum settlement also depends on distance from metro shaft and will be discussed later (cf.Figure 9).

2.2 Finite Element strategies

2.2.1 Integration from 2D calculation using Attewell's formula

When performing FEM numerical analysis, first step is 2D plane strain analysis. If deconfinement rate allows to consider excavation step's and distance to the tunnel face influence (Panet, 1995), the raw transversal trough obtained corresponds to an infinite tunnel excavation.

Attewell (1982) proposed a procedure to assess finite settlement trough considering that underground volume loss is punctual. This theory amounts to considering an incremental volume loss associated with each excavation step. After adapting Peck gaussian trough to radial coordinate in case of single point volume loss, a finite integration between points x_i and x_f leads to equation (2):

$$w(x,y) = \frac{V}{2\pi i^2}\int_{x_i}^{x_f} exp\left[\frac{-((x-x_0)^2+y^2)}{2i^2}\right]dx_0$$

where x is parallel to the tunnel centre line, y is normal to the tunnel centre line, i the trough width and $V = S_m\sqrt{2\pi}i$ the volume lost in surface trough per linear meter (linked to excavated volume by empirical relations). Therefore, after bidimensional computation, one only has to extract ground displacements and fit Peck parameters to predict the finite tridimensional surface trough.

However, finding the "right" deconfinement rate remains an issue. Theoretically, the convergence-confinement method (Panet, 1995) doesn't apply to sequential excavation since previous phases altered initial stress state (which in Campanian Chalk is supposed to be isotropic). In practice, the method is commonly applied using either a mean effective stress over the outline of tunnel section, or its value at face centre. Since tunnelling operations already decompressed part of the section, the deconfinement rate has been chosen with the mean effective stress. Deconfinement rate is thus calculated with an area-derived equivalent radius, and implicit method of (Nguyen-Minh & Guo, 1998) allows to consider lining stiffness influence over deconfinement at support installation.

2.2.2 Integration from 3D "one-step" computation

To avoid the issue of the choice of deconfinement rate while keeping calculation time reasonable, one can think of making use of the same notion of incremental loss in a 3D calculation, since excavation step is explicitly considered. Used since Corbetta (1990), the "one-step solution" consists in adding a finite number of incremental troughs corresponding to a single calculation: time integration is transformed into discrete space integration.

If this method allows to get quickly consistent results, without the intervention of deconfinement, the stationarity principle has strong limits. Indeed, it is impossible to consider any kind of aperiodicity regarding the loading (RER-A train station has finite dimensions) or the geometry (presence of the shaft).

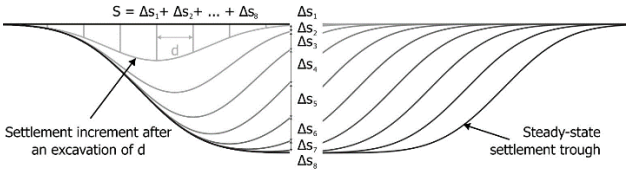

Figure 7. Principle of stationarity and "One-step" method.

2.2.3 3D complete computation

Finally, to grasp all the complexity of the problem, a full 3D study was performed. The shaft was explicitly modelled to account for the friction of the soil along its diaphragm walls, and surface loadings are located according to the position of RER-A station footings, as shown on Figure 8.

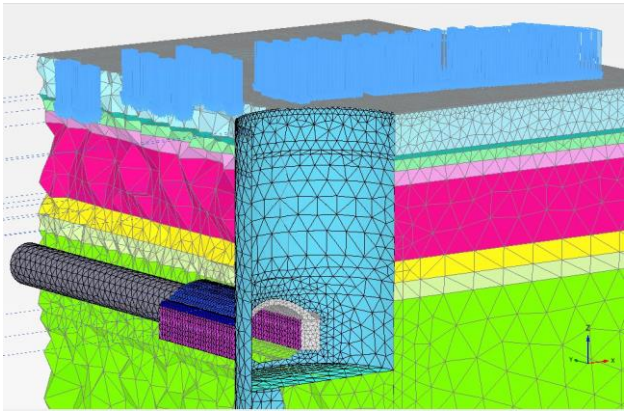

Figure 8. Plaxis 3D mesh.

A second model, considering only an average surface load, representative of the conditions encountered in the north, has also been produced. The results proved to be equivalent to the model representing the south, both in terms of maximum settlement and the location of the inflection point.

The simulation phasing of the underground sections closely follows, the sequence selected for the construction works, and two variants are tested: main gallery's permanent vault lining is installed either at the very end (a), or during excavation in (b), with five steps. During each excavation stage the effects of water flow are explicitly calculated considering a steady-state flow regime.

2.3 Conclusion on settlement estimation

The true behaviour is somewhere between (a) and (b): only vault lining steps 1 and 2 were completed before the whole excavation works was completed. Therefore, finding geotechnical monitoring results between 3D-Complete curves (a) and (b) appears to be satisfying.

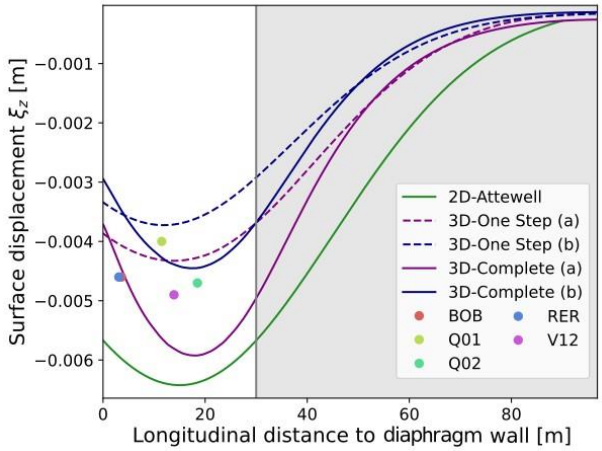

Figure 9. Longitudinal surface troughs.

Although all results seem to be in good agreement with the measurements, the "one step" 3D model tends to slightly underestimate settlements. This may be due the presence of the diaphragm walls of the shaft, the RER structures, and the excavation sequence, which does not comply the condition of stationarity on which the validity of the one-step method is based. On the contrary, Attewell's method seems to overestimate surface settlements. The cylindrical (instead of spherical) nature of the groundwaterflow leads to stronger tunnel convergence, which can probably be accounted for settlements' overestimation, along with hazardous deconfinement computation and limits to Attewell & Peck theories. However, it is interesting to note that integration from a simple 2D FEM computation gives settlements consistent with much more advanced 3D models.

Figure 10 allows to compare computed trough width to measured settlements. It appears that settlement troughs obtained from ground sensors, interpreted in terms of trough width with Peck, are well approached by full 3D calculation with support installation during excavation (scenario (b)).

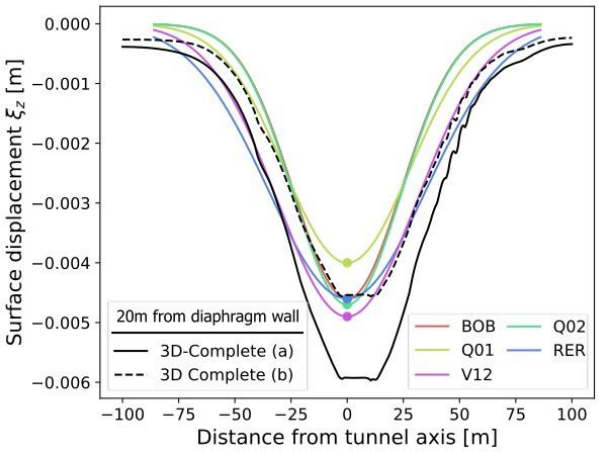

Figure 10. Comparison of monitored and computed transverse troughs.

3 ASSESSING STABILITY

The numerical models have also facilitated the choice of temporary construction arrangements. By installing a very rigid support, a significant part of the ground load moves to the structure and passes through the abutment galleries. Finite element deformations plane simulations have shown such result during the excavation of the Stross: instability due to punching of the abutment galleries could occur.

The low safety factors regarding the bearing capacity of the abutments resulted from a combination of various aspects: an eccentricity of the load acting upon the foundation, the presence of an adjacent "slope" to the structure, and water flow forces with very steep gradients (see Figure 11).

In a soft, low-permeability rock like Campanian Chalk, considering steady-state flow in models is likely pessimistic (homogeneous flows is considered in the matrix and not through potential fracture networks). Nevertheless, the consequences of the occurrence of the feared event were deemed unacceptable.

To adjust the construction arrangements to be implemented, two different hypotheses of constitutive laws were considered: an Hardening Soil Model with equivalent rock mass strength parameters defined in the contract, and a Hoek and Brown Model whose parameters were adjusted based on additional laboratory tests and survey of the abutment galleries face. Both types of constitutive laws have proven to be consistent, and additional construction measures adopted consisted of:

- Implementing, from the upper half-section, 5 rows of 3 sub-vertical passive drains per cavern.
- Creating an un-reinforced, 20 cm thick concrete protection slab during the Stross excavation progress.

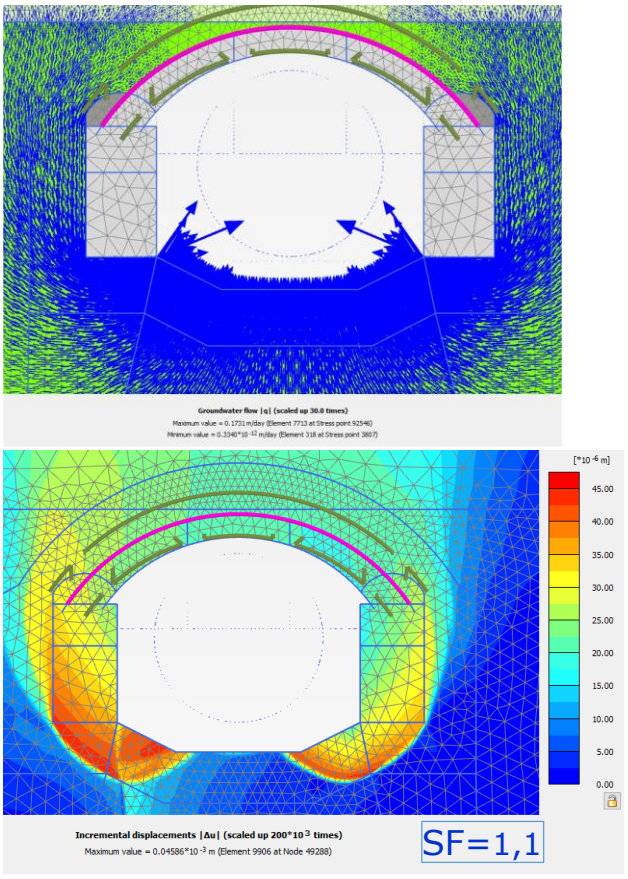

Figure 11. Ground water flow around the abutment galleries and highlighting the failure mechanism in a phase of c-φ reduction without additional measure.

These measures have thus ensured the confinement of the soil beneath the excavation bottom, reduced pore water pressures, increased the average effective stress, and consequently, the shear strength of the chalk.

As the natural permeability of Campanian chalk is low (k=1.10-7 m/s), the injection performed with bentonite/cement did not aim to further decrease its transmissivity but solely to ensure hydraulic homogeneity in the 5 m treated crown. The passive drains are used to control water inflows in this area, reduce flow forces, and prevent potential flushing phenomena.

Considering these additional construction measures, safety factors greater than 1.3 were consistently obtained.

4 CONCLUSIONS

The finite element simulations conducted during the execution phase of the Saint Maur Créteil station proved to be a valuable tool for designing the construction arrangements. The models, increasing in complexity, used to estimate surface settlements provided assurance to all stakeholders about controlling displacements below the specified thresholds. The models demonstrated good consistency with measurements. Regarding the evaluation of abutment stability during the Stross excavation phase, plane deformation models using different constitutive laws helped define additional construction measures that could be easily integrated into the chosen excavation process and were robust.

REFERENCES

Attewell, P.B., and Woodman, J.P. (1982), Predicting the dynamics of ground settlement and its derivitives caused by tunneling in soil, *Ground Engineering,* September 1982, pp.13-20.

Corbetta, F. (1990), *Nouvelles méthodes d'étude des tunnels profonds: calculs analytiques et numériques*, PhD thesis, École nationale supérieure des mines de Paris.

Duc Nguyen-Minh and Chifei Guo (1998). *A new approach to Convergence Confinement Method*. Advances in Rock Mechanics, World Scientific, pp.267-279. https://doi.org/10.1142/9789812839640_0025.

Panet, M. (1995*), Le calcul des tunnels par la méthode convergence-confinement*, Presses de l'École nationale des ponts et chaussées, Paris.

Peck, R.B. (1969), Deep excavations and tunneling in soft ground, In: *Proc 7th Int. Conf. SMFE, Mexico City*, pp.225-290.

Vugrin, K. W., L. P. Swiler, R. M. Roberts, N. J. Stucky-Mack, and Sullivan, S. P. (2007), Confidence region estimation techniques for nonlinear regression in groundwater flow: Three case studies, *Water Resour. Res.*, 43. https://doi.org/10.1029/2005WR004804.

Proceedings of the XVIII ECSMGE 2024
GEOTECHNICAL ENGINEERING CHALLENGES
TO MEET CURRENT AND EMERGING NEEDS OF SOCIETY
© 2024 the Authors
ISBN 978-1-032-54816-6
DOI 10.1201/9781003431749-405
Open Access: www.taylorfrancis.com, CC BY-NC-ND 4.0 license

ECSMGE 24
XVIII EUROPEAN CONFERENCE ON SOIL MECHANICS AND GEOTECHNICAL ENGINEERING

Fiber optic sensors in geotechnical works - a review

Capteurs à fibre optique dans les travaux géotechniques - une revue

P. Caldas
CISAS, Escola Superior de Tecnologia e Gestão, Instituto Politécnico de Viana do Castelo, Viana do Castelo, Portugal
INESC TEC - Institute of Systems and Computer Engineering, Technology and Science (Centre for Applied Photonics), Department of Physics and Astronomy, Faculty of Sciences, University of Porto, Porto, Portugal

M.L. Laranjo*
PROMETHEUS, Escola Superior de Tecnologia e Gestão, Instituto Politécnico de Viana do Castelo, Viana do Castelo, Portugal

**mlopes@estg.ipvc.pt*

ABSTRACT: Monitoring plays an important role in what geotechnical works and investigation are concerned. Either for assessing stiffness on laboratory tests, or for evaluating forces or displacements in the field, instrumentation is of crucial relevance for a wide range of situations. Instrumentation provides critical data for subsurface characterization, determination of soil properties, assessment of groundwater conditions, monitoring of geotechnical structures, validation of design assumptions and research works. Over the last years, a number of different types of mechanical, electrical and optical sensors have been developed for geotechnical monitoring field. Among these, optical fibre sensors feature several important advantages, such as: durability; stability and insensitivity to external disturbances; embedding capability and possibility of distributed sensing over large distances and multiplexing of point sensors that are especially useful for long-term health assessment in geotechnical monitoring. Over time, the range of geotechnical parameters that can be measured using fibre optic sensors has expanded. Optical Fibre sensors are now utilized for monitoring a variety of geotechnical parameters, including strain, deformation, displacement, temperature, pressure, and even pore water pressure. Optical fiber sensors can be applied in slope stability monitoring, landslide detection, tunnel monitoring, foundation monitoring, and offshore geotechnical investigations, among other applications. This paper presents a comprehensive review of applications of optical fibre sensor for geotechnical monitoring.

RÉSUMÉ: La surveillance joue un rôle important en ce qui concerne les travaux et investigations géotechniques. Que ce soit pour évaluer la rigidité lors d'essais en laboratoire, ou pour évaluer des forces ou des déplacements sur le terrain, l'instrumentation revêt une importance cruciale pour un large éventail de situations. L'instrumentation fournit des données critiques pour la caractérisation du sous-sol, la détermination des propriétés du sol, l'évaluation des conditions des eaux souterraines, la surveillance des structures géotechniques, la validation des hypothèses de conception et les travaux de recherche. Ces dernières années, un certain nombre de types différents de capteurs mécaniques, électriques et optiques ont été développés pour le domaine de la surveillance géotechnique. Parmi ceux-ci, les capteurs à fibre optique présentent plusieurs avantages importants, tels que la durabilité, la stabilité et l'insensibilité aux perturbations externes, la capacité d'intégration et la possibilité de détection distribuée sur de grandes distances et le multiplexage de capteurs ponctuels qui sont particulièrement utiles pour l'évaluation de la santé à long terme en géotechnique surveillance. Au fil du temps, la gamme de paramètres géotechniques pouvant être mesurés à l'aide de capteurs à fibre optique s'est élargie. Les capteurs à fibre optique sont désormais utilisés pour surveiller divers paramètres géotechniques, notamment la déformation, la déformation, le déplacement, la température, la pression et même la pression interstitielle de l'eau, appliqués à la surveillance de la stabilité des pentes, à la détection des glissements de terrain, à la surveillance des tunnels, à la surveillance des fondations et aux enquêtes géotechniques offshore, entre autres applications. Cet article présente un examen complet des applications des capteurs à fibre optique pour la surveillance géotechnique.

Keywords: Fiber optic sensor; geotechnics; distributed sensors; optic point sensors.

1 INTRODUCTION

Geotechnical engineering covers a wide range of applications amongst which pile foundations, soil movements, stabilization anchors, mining and more. Due to the harsh environment, sometimes hard accessibility and long working period of geotechnical structures, monitoring methods are necessary to avoid accidental infrastructure failure that can cause human and economic losses. Over the last years, a variety of

mechanical, electrical and optical sensors have been developed and used for geotechnical engineering. Among these, optical fibre sensors are offering new monitoring possibilities. Using the advantages of optical fibre such as durability, lightweight, high sensitivity, stability and insensitivity to external disturbances associated with embedding capability (into soil or structure) and possibility of distributed sensing over large distances and multiplexing of several point sensors, it's possible to create a range of optical fiber sensors that can simultaneously monitor several parameters, such as strain, temperature, and deformation of the geotechnical structure (Soga et al. 2019, Wu et al. 2020, Singh et al. 2023).

The optical fibre sensors use changes in light parameters such as light intensity, phase, polarization state, wavelength, or frequency by the external parameters to monitor geotechnical structures.
This paper proposes a review of working principles and the application of optical fiber sensing technologies in geotechnical engineering.

2 WORKING PRINCIPLES OF OPTICAL FIBER SENSORS FOR GEOTECHNICS

The typical configuration of optical fiber sensor in represented in Figure 1. Light from a optical source is injected into the fiber system. After crossing coupler or a circulator is guided to sensing region. Depending on the sensing approach it is possible to detect the transmited or reflected spectrum.

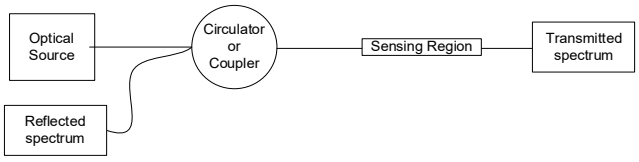

Figure 1.Generic configuration of optical fiber sensor.

The development of optical fiber sensors for geotechnics uses two approaches based in sensors head distribution, working principles and field of application (Ma et al. 2023):

(i) point sensor based in Fiber Bragg Grating (FBG), long period grating (LPG) or interferometric sensor configuration where the measurand was carried out in a specific point (Singh et al. 2023).

(ii) distributed sensors able to measure the parameters across the entire length of fiber based in Raman, Brillouin or Rayleigh scattering light (Bado and Casas 2021, Mohamad et al. 2023)

The FBG sensor is a well-established fiber optic-based point sensor. In this method, a tiny portion of the fibre core is subjected a periodical modulation of the refractive index by a powerful UV light (Hill et al. 2008). When broadband light with several wavelength passes through the fiber, the FBG reflected back one wavelength, called Bragg wavelength, while the remainder wavelengths pass through fiber (Figure 2). The Bragg wavelength is dependent on thermal changes or physical elongation of the sensors, and the Bragg wavelength shifts when subjected to an external parameter like temperature or strain. Measuring this change, allows to obtain the external parameter.

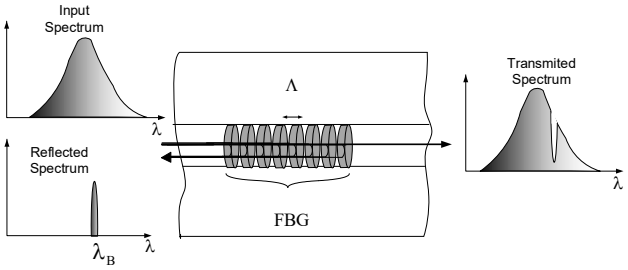

Figure 2. Fiber Bragg Grating.

The LPG is similar to the FBG but the modulation period is higher than FBG and couples some wavelength to the fiber cladding. The LPG couples a fraction of light to a specific cladding mode, whereas the remaining light keeps propagating in the fiber core. In this case, the transmissions spectrum presents some missing wavelengths that change the position when the LPG region is subjected to external parameters. The LPG can be fabricated using several techniques like UV light, using a CO_2 laser or the electric-arc technique (Rego et al. 2021).

The final point sensor is the in fiber interferometric sensor. In this case, the light from an optical source is divided into two beams: one beam is signal light and the other beam is reference light. Interference occurs when they meet. The interference spectrum changes by influence of external factors (Caldas and Rego 2021).

Distributed Sensors use the backscattered light of the optical fibre to feedback the performance of the optical fibre. When a light travels through an optical fibre, it interacts with the constituent atoms and molecules, and the light is deviated from a straight trajectory due to its non-uniformity. This deviation creates back scattering that brings a very small portion of the beam to go back to the source (Soga and Luo 2018).

The detected backscattered light power returned at various points along the length of the fiber contains information about external changes (strain or temperature change) along of fiber, which changes the characteristics of the back scattered beam (Figure 3). The distributed sensors use these changes in the recovered beam to quantify strain, temperature or vibration occurring along the standard optical fibre cable.

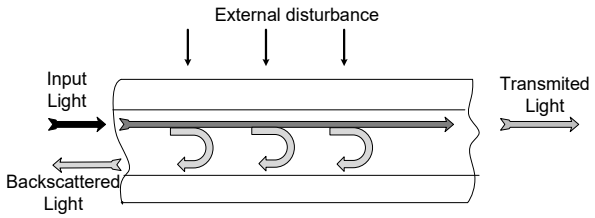

Figure 3. Backscattered light in distributed sensors.

In fact, the distributed system transforms an optical fiber cable into an array of virtual sensing devices when attached to a geotechnical structure or embedding, allow to monitor the changes of ambient parameters of the monitored object.

Using the point sensor or distributed sensors several applications has been developed in the last years. The next section presents the last applications of optical fiber sensor in Geotchnical engeneering.

3 APPLICATIONS

The optical fiber sensors are extensively used in various fields and given its small size, which allows it to be placed on the surface or embedded structures. In this section we focus in applications for geotechnical engineering based in point sensors and distributed optical fiber sensors.

One application of optical fibre sensors is the monitorization of health conditions of bridges (concrete, cables and suspenders) where the optical fiber sensors is an alternative for continuous real−time monitoring for identification, damage detection, safety condition assessment, and structural performance prediction (Costa and Figueiras 2012, He et al. 2013). In the case of crack detection in concrete, it is hard to monitor due to the complexity of the materials (Bao et al. 2010), but some solutions to determine the crack location and width evolution over time using distributed optical fiber sensors present accuracy equivalent to traditional electrical foil gauges (Berrocal et al. 2021).

The temperature and humidity changes of concrete are other important parameters for monitoring the structural health and providing information for maintenance, rehabilitation, repairing, upgradation or rebuilding of structures. Some optical fiber sensors using point detection based in FBG or interferometer configurations are proposed and the results are similar to the electronic sensors (Farhan et al. 2023).

Optical fiber sensors have also other applications for structural monitoring like tunnels, pipelines or wind turbine towers. Tunnels are complex: encompassing longer and wider tunnels, excavations through increasingly difficult ground conditions under densely populated zones or in seismic areas. Solutions using point or distributed sensors have been successfully applied in tunnels, to measure the displacement of a tunnel lining, monitoring its stability during the backfilling and traffic-operating periods or surrounding geotechnical and hydrological conditions (Gue et al. 2015).

Pipelines are one important and economic way to transport water, oil, natural gases and telecommunication cables across extensive distances. Maintenance and, in particular, health conditions of pipelines after earthquakes, or if pipelines are located in complex and hazardous environments, is important. The optical fiber sensors present an important advantage for pipeline leakage detection, corrosion or deformation along the time (Bang et al. 2012, Glisic and Yao 2012, Ye et al. 2013, Zhu et al. 2022).

Wind turbines are one of the most used renewable sources of power. The wind turbine structures are subject to several forces, dynamic or static, and vibrations. In the last years, the optical fiber sensors were performed for monitoring, in real time or not, the load/maximum strain and the load/maximum displacement profiles of wind structure or wind turbine blade bending and torsional loads (Z. H. Zhang et al. 2020).

Regarding the applications in geotechnical engineering, optical fiber sensor are applied in pile foundations, soil movements (landslides and soil subsidence), stabilization anchors, mining and more.
In pile foundations, the strain distribution of the pile under different scour effect, using point detection (Sang et al. 2020) based in FBG or distributed detection (Zhaohui Zhang et al. 2022) is possible using an optical fiber sensor pile strain profile.

Other applications include monitoring soil movements that are crucial for the prevention and control of disasters. For examples, in soil nails where the results using optical fiber sensors show that the rainfall infiltration and rise in groundwater pressures will lead to mobilization of tensile forces in soil nails. The obtained results demonstrate the capacity of optical fibre to measure strain of the soil nail under active and passive loading modes (Guo et al. 2019).

Optical fibre sensors also demonstrate great potential for dam health monitoring, especially fully distributed optical sensing technologies that are widely used for monitoring the deformation, stress, and leakage of dams (Zhou et al. 2019).

4 CONCLUSIONS

This paper reviews the application status of optical fiber sensors in geotechnical health monitoring with an emphasis on working principles, the detection

parameters and applications in geotechnical engineering. The results and recents papers published show that optical fibre sensors technologies are attracting more and more attention due to their excellent performance in this area.

REFERENCES

Bado, M. F. and J. R. Casas (2021). "A Review of Recent Distributed Optical Fiber Sensors Applications for Civil Engineering Structural Health Monitoring." Sensors **21**(5). https://doi.org/10.3390/s21051818.

Bang, H.-J., et al. (2012). "Measurement of strain and bending deflection of a wind turbine tower using arrayed FBG sensors." International Journal of Precision Engineering and Manufacturing **13**(12): 2121-2126. https://doi.org/10.1007/s12541-012-0281-2.

Bao, T., et al. (2010). "A fiber optic sensor for detecting and monitoring cracks in concrete structures." Science China Technological Sciences **53**(11): 3045-3050. https://doi.org/10.1007/s11431-010-4111-4.

Berrocal, C. G., et al. (2021). "Crack monitoring in reinforced concrete beams by distributed optical fiber sensors." Structure and Infrastructure Engineering **17**(1): 124-139. https://doi.org/10.1080/15732479.2020.1731558.Caldas, P. and G. Rego (2021). "Optical Fiber Interferometers Based on Arc-Induced Long Period Gratings at INESC TEC." Sensors **21**(21): 7400. https://doi.org/10.3390/s21217400.

Costa, B. J. A. and J. A. Figueiras (2012). "Fiber optic based monitoring system applied to a centenary metallic arch bridge: Design and installation." Engineering Structures **44**: 271-280. https://doi.org/10.1016/j.engstruct.2012.06.005.

Farhan, K. Z., et al. (2023). "Temperature and humidity sensor technology for concrete health assessment: a review." Innovative Infrastructure Solutions **8**(10). https://doi.org/10.1007/s41062-023-01255-x.

Glisic, B. and Y. Yao (2012). "Fiber optic method for health assessment of pipelines subjected to earthquake-induced ground movement." Structural Health Monitoring **11**. https://doi.org/10.1177/1475921712455683.

Gue, C. Y., et al. (2015). "The monitoring of an existing cast iron tunnel with distributed fibre optic sensing (DFOS)." Journal of Civil Structural Health Monitoring **5**(5): 573-586. https://doi.org/10.1007/s13349-015-0109-8.

Guo, X., et al. (2019). "Testing Mechanical Properties of Rock Bolt under Different Supports Using Fiber Bragg Grating Technology." Sensors **19**(19): 4098. https://doi.org/10.3390/s19194098.

He, J., et al. (2013). "Optic fiber sensor-based smart bridge cable with functionality of self-sensing." Mechanical Systems and Signal Processing **35**(1): 84-94. https://doi.org/10.1016/j.ymssp.2012.08.022.

Hill, K. O., et al. (2008). "Photosensitivity in optical fiber waveguides: Application to reflection filter fabrication." Applied Physics Letters **32**(10): 647-649. https://doi.org/10.1063/1.89881.

Ma, J., et al. (2023). "A review of previous studies on the applications of fiber optic sensing technologies in geotechnical monitoring." Rock Mechanics Bulletin **2**(1): 100021. https://doi.org/10.1016/j.rockmb.2022.100021.

Mohamad, H., et al. (2023). "Distributed fibre optic inclinometer with cloud-based monitoring system." Engineering Science and Technology-an International Journal-Jestech **41**. https://doi.org/10.1016/j.jestch.2023.101406.

Rego, G., et al. (2021). "Arc-Induced Long-Period Fiber Gratings at INESC TEC. Part I: Fabrication, Characterization and Mechanisms of Formation." Sensors **21**(14): 4914. https://doi.org/10.3390/s21144914.

Sang, S., et al. (2020). "Experimental Research Based on the Optical Fiber Sensing Technology for a Jacked PHC Pipe Pile Penetration Process." Advances in Civil Engineering, **2020**:1-8. https://doi.org/10.1155/2020/8873308.

Singh, M. J., et al. (2023). "Applications of fibre Bragg grating sensors for monitoring geotechnical structures: A comprehensive review." Measurement **218**. https://doi.org/10.1016/j.measurement.2023.113171.

Soga, K., et al. (2019). "Advances in Geotechnical Sensors and Monitoring." Geotechnical Fundamentals for Addressing New World Challenges. N. Lu and J. K. Mitchell. Cham, Springer International Publishing**:** 29-65. https://doi.org/10.1007/978-3-030-06249-1_2.

Soga, K. and L. Luo (2018). "Distributed fiber optics sensors for civil engineering infrastructure sensing." Journal of Structural Integrity and Maintenance **3**(1): 1-21. https://doi.org/10.1080/24705314.2018.1426138.

Wu, T., et al. (2020). "Recent Progress of Fiber-Optic Sensors for the Structural Health Monitoring of Civil Infrastructure." Sensors **20**(16): 4517. https://doi.org/10.3390/s20164517.

Ye, X. W., et al. (2013). "Safety Monitoring of Railway Tunnel Construction Using FBG Sensing Technology." Advances in Structural Engineering **16**(8): 1401-1409. https://doi.org/10.1260/1369-4332.16.8.1401.

Zhang, Z., et al. (2022). "Analysis of horizontal bearing capacity of offshore pile foundation based on DPP-BOTDA." Journal of Civil Structural Health Monitoring **12**(4): 747-756. https://doi.org/10.1007/s13349-021-00506-8.

Zhang, Z. H., et al. (2020). "Horizontal Loading Performance of Offshore Wind Turbine Pile Foundation Based on DPP-BOTDA." Applied Sciences-Basel **10**(2). https://doi.org/10.3390/app10020492.

Zhou, H., et al. (2019). "Temperature Field Reconstruction of Concrete Dams based on Distributed Optical Fiber Monitoring Data." KSCE Journal of Civil Engineering **23**(5): 1911-1922. https://doi.org/10.1007/s12205-019-0787-6.

Zhu, H.-H., et al. (2022). "Distributed Acoustic Sensing for Monitoring Linear Infrastructures: Current Status and Trends." Sensors **22**(19): 7550. https://doi.org/10.3390/s22197550.

Proceedings of the XVIII ECSMGE 2024
GEOTECHNICAL ENGINEERING CHALLENGES
TO MEET CURRENT AND EMERGING NEEDS OF SOCIETY
© 2024 the Authors
ISBN 978-1-032-54816-6
DOI 10.1201/9781003431749-406
Open Access: www.taylorfrancis.com, CC BY-NC-ND 4.0 license

ECSMGE 24
XVIII EUROPEAN CONFERENCE ON SOIL MECHANICS AND GEOTECHNICAL ENGINEERING

Biocementation treatment of a Portuguese motorway slope to prevent ravine formation

Traitement par biocimentation d'un talus d'une autoroute portugaise pour éviter l'érosion par ravinement

R. Cardoso*, M. Oliveira
CERIS/IST Universidade de Lisboa, Lisbon, Portugal

M. Cruz, I. Gonzalez
Brisa Gestão de Infraestruturas, Lisbon, Portugal

A.T. Rodrigues, B. Anjos
Rodio Portugal, Lisbon, Portugal

L. Sapin, A. Esnault-Fillet
Soletanche-Bachy, Paris, France

**rafaela.cardoso@tecnico.ulisboa.pt*

ABSTRACT: Biocementation is an environmentally sustainable technique for soil improvement, in which the precipitation of calcium carbonate is promoted by using biological agents such as bacteria or enzymes. The precipitated calcium carbonate, or biocement, is responsible for soils strength and stiffness increment due to the bonds created between the particles, and for reducing the permeability caused by pore clogging. The shallow treatment of sandy soils to increase resistance to the formation of ravines is a new application. This treatment was carried out in a real case to avoid ravines caused by rain and is being monitored over time as part of an ongoing project of Instituto Superior Técnico funded by FCT (ref. PTDC/ECI-EGC/1086/2021). This case-study is an excavation slope in sandy soil on the A13 Motorway managed by Brisa. The treatment was carried out by Rodio Portugal, from the Soletanche-Bachy group, who provided the technology to inject into the soil the treatment fluids with bacteria. The first monitoring data are presented, consisting in the amounts of calcium carbonate measured right after treatment and after the first heavy rains, with encouraging results.

RÉSUMÉ: La biocimentation est une technique écologiquement durable d'amélioration des sols, dans laquelle la précipitation du carbonate de calcium est favorisée par l'utilisation d'agents biologiques tels que des bactéries ou des enzymes. Le carbonate de calcium précipité, ou biociment, est responsable de l'augmentation de la résistance et de la rigidité des sols en raison des liaisons créées entre les particules, et de la réduction de la perméabilité causée par le colmatage des pores. Le traitement superficiel des sols sableux pour augmenter la résistance à l'érosion par ravinement est une nouvelle application. Ce traitement a été réalisé dans un cas réel pour éviter les ravins causés par la pluie et est surveillé au fil du temps dans le cadre d'un projet en cours de l'Instituto Superior Técnico financé par FCT (réf. PTDC/ECI-EGC/1086 /2021). Cette étude de cas est une pente d'excavation en sol sableux sur l'autoroute A13 gérée par Brisa. Le traitement a été réalisé par Rodio Portugal, du groupe Soletanche-Bachy, qui a fourni la technologie pour injecter dans le sol les fluides de traitement contenant des bactéries. Les premières données de suivi sont présentées, constituées des quantités de carbonate de calcium mesurées juste après le traitement et après les premières fortes pluies, avec des résultats encourageants.

Keywords: Biocementation; excavation slope; ravines; monitoring; calcium carbonate.

1 INTRODUCTION

Biocementation is an environmentally sustainable technique for soil improvement, in which the precipitation of calcium carbonate is promoted by using biological agents such as bacteria or enzymes. The precipitated calcium carbonate, or biocement, is responsible for soils strength and stiffness increment due to the bonds created between the particles, and for reducing the permeability caused by pore clogging.

Non-pathogenic urease-producing bacteria are used for the treatment. The urease enzyme from the bacteria catalyses the hydrolysis of urea (Eq. 1), and calcium carbonate (biocement) precipitates in the presence of a source of calcium (Eq. 2):

$$CO(NH_2)_2 + 2H_2O \rightarrow 2NH_4^+ + CO_3^{2-} \quad (1)$$

$$Ca^{2+} + CO_3^{2-} \rightarrow CaCO_3 \quad (2)$$

This treatment is used in many geotechnical applications, for example to increase load bearing capacity of foundations, provide soil resistance to erosion and against liquefaction, and to reduce the collapse potential of soils (see for example Al Qabany *et al.* 2012). The shallow treatment of sandy soils to increase resistance to the formation of ravines is a recent application tested in small-scale laboratory tests (Fernandez and Cardoso, 2022), and was applied in a real slope in Portugal to investigate the durability of the treatment, in the scope of the ongoing project of Instituto Superior Técnico funded by the Portuguese Foundation for Science and Technology (ref. PTDC/ECI-EGC/1086/2021). This case-study is an excavation slope of the A13 Motorway, managed by Brisa. The treatment was carried out by Rodio Portugal, from the Soletanche-Bachy group, who provided the bacteria. The treatment applied in the slope and the first monitoring data are presented in this paper.

2 CASE STUDY

2.1 Overview

The slope treated (Figure 1) is located at A13 Motorway near Benavente, 40 km from Lisbon, Portugal. It was selected to meet the following criteria: excavated in a sandy geological foundation, maximum 6 m in height, slope smaller than 30º, no accentuated signs of ravine, and be accessible from the top.

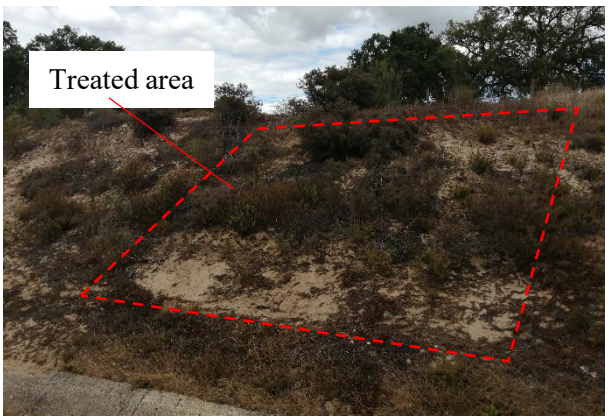

Figure 1. Slope before the treatment and treated area.

The soil of the treated area classifies as a well graded sand (SW) with 2% non-plastic fines and no gravel. The average dry unit weight is 15.5 kN/m^3 and the permeability measured was 2.4x10^{-4} m/s.

2.2 Bacteria and feeding solutions

Bacteria *Sporoscarcina Pasteurii* in lyophilized form were used, supplied by Soletanche-Bachy. They were mixed with tap water. The feeding solution was prepared also with tap water, using equal concentrations of urea and calcium chloride (0.5 M each).

2.3 Treatment

The area treated was the upper part of the slope (around 6 m × 6 m, see Figure 1), being left an untreated horizontal stripe (1 m width) in the bottom, which would receive the treatment fluids that would not be infiltrated in the treated area.

The treated area was divided into two vertical stripes to test two different methodologies: injection and irrigation was applied in the right side, and irrigation was applied in left side (Figure 2). The irrigation would treat only a surface layer, with a thickness expected to be between 0.08 and 0.10m. The injection was done using pipes (5 columns and 12 rows) placed at a depth of 0.5 m. The treatment protocol followed was identical for both methods. It was designed to reach the minimum percentage of calcium carbonate of 4%. The treatment was applied in September 2022 by Rodio Portugal and had the duration of 5 days.

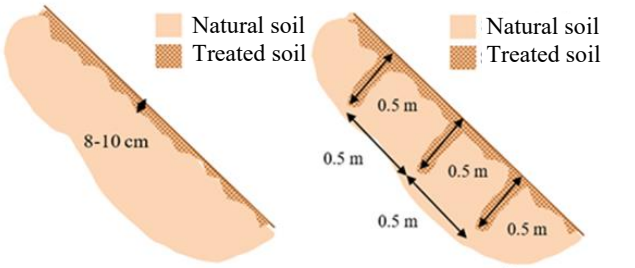

Figure 2. Treatment methods adopted for the two vertical strips of the slope.

The construction site was organized in the first day, being the slope surface levelled and the injection pipes installed (Figure 3). A plastic membrane was placed in the bottom to collect the effluent fluids during the treatment and from the final washing.

The treatment was applied in the following three days, with two applications in each day. It consisted in adding the bacteria solution to the soil followed, one hour later, by the addition of the feeding solution. These fluids were pumped from the mixer where they were prepared (Figure 3) into the injection pipes with valves. The injections were applied in the 5 pipes of each row, starting in the top of the slope, and were controlled pipe by pipe.




Figure 3. Installation of the injection pipes (left) and mixer used to prepare the bacteria and feeding fluids (right).

In the last day, the slope was washed with water through injection and irrigation and the plastic membrane at the bottom was removed.

2.4 Monitoring

The monitoring campaigns took place on average every two months, from September 2022 to July 2023, knowing that the treated slope will be observed for at least two years. A 5x5 grid, with dimensions 5.5 m x 5.5 m, was created to define the positions to extract small soil samples for measuring the percentage of calcium carbonate in the laboratory (Figure 4). These samples were extracted to 3 cm depth.

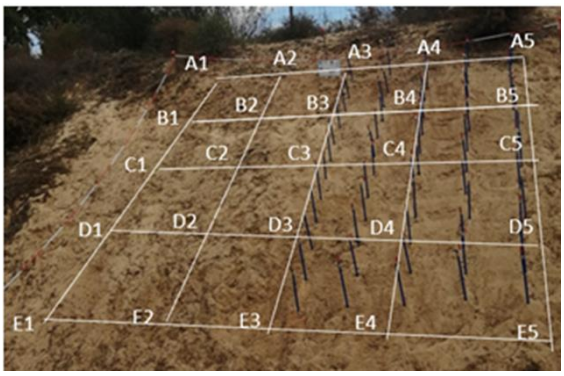

Figure 4. Grid defined for sampling during monitoring.

The percentage of calcium carbonate ($\%CaCO_3$) is given by Eq. 3., where m_{before} is the initial weight of the dried samples, and m_{after} is the weight of the same samples dried after being washed with hydrochloric acid (0.5 M):

$$\%CaCO_3 = \frac{m_{after} - m_{before}}{m_{before}} \quad (3)$$

3 CALCIUM CARBONATE DISTRIBUTION

The percentage of calcium carbonate measured in the samples collected allowed plotting the calcium carbonate distribution maps presented in Figure 5 using the Surfer® program (Golden Software, 2023).

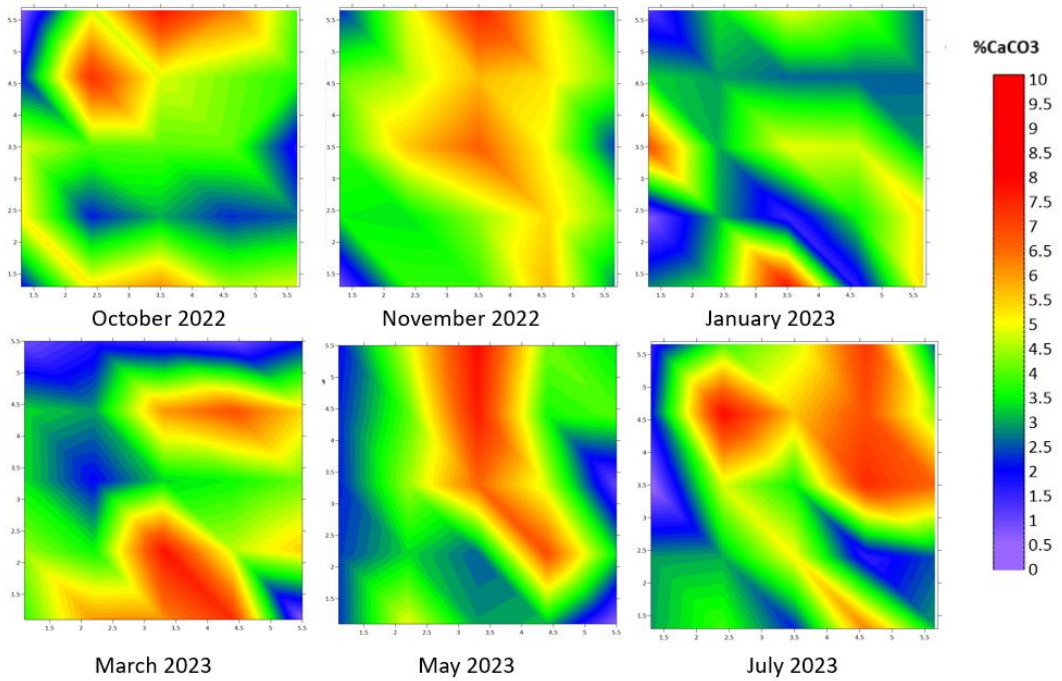

Figure 5. Distribution maps of the percentage of calcium carbonate in the treated area.

It can be seen that the treatment was heterogeneous and the $\%CaCO_3$ varied after successive sampling along time in each position. Some calcium carbonate was accumulated in the central zone, mostly at the top, where the treatment was applied by irrigation and injection. The temporal oscillations might be explained by some surface erosion caused by rain events. The $\%CaCO_3$ was not investigated in depth to avoid destroying the slope during the first year after the treatment.

The ravines formed in the treated slope surface were mainly caused by the treatment fluids and rain occurring during the treatment (see Figure 3) and they remained stable once they were formed. This can be seen in the photographs taken in October 2022 and in July 2023 (Figure 6). The ravines in the bottom are in the untreated horizontal strip. It can also be seen that vegetation is starting to appear in the top of the slope.



Figure 6. Photographs of the slope showing stable ravines in the treated area and the growth of a bush.

In general, the percentages of calcium carbonate measured were larger than the predicted value of 4%, as it can be seen in Figure 7, presenting its evolution along the horizontal alignment C in the middle of the treated area. The fact that the values are stable for the observed period suggests that the treatment is durable. Due to the dispersion of the results (Figs. 5 and 7) there is no obvious distinction between the zones where the two different treatment methodologies were used.

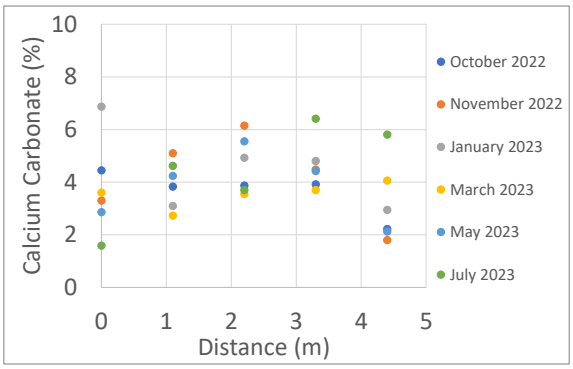

Figure 7. Values measured in horizontal alignment C.

Finally the presence of hard aggregates with high $\%CaCO_3$ is another evidence of the heterogenity.

4 CONCLUSIONS

The photographs of the slope surface during the monitoring period confirm the presence of ravines caused by water. This extreme form of surface erosion started during the treatment, appearing to become stable along the monitoring time. The values of the percentage of calcium carbonate measured in the different zones of the treated area presented some oscillation along the monitoring time, which was explained by some erosion caused by rain. Nevertheless, they were larger than the target value of 4% and remained stable, which indicates that the amount of biocement is stable, and therefore the treatment is being durable. The slope will be under observation for a longer period to understand better the durability of the treatment.

The results are inconclusive in what it concerns if the treatment by injection and irrigation can be more effective than just by irrigation. The ongoing investigation of the distribution of calcium carbonate in depth is fundamental to better evaluate each methodology.

Finally, the growth of a small bush in the top of the slope suggests that vegetation can grow in the presence of the biocement. This will also be confirmed with further observation of the slope.

ACKNOWLEDGEMENT

The authors are grateful for the financial support provided by funding agency FCT I.P. through project CALCITE (ref. PTDC/ECI-EGC/1086/2021).

REFERENCES

Al Qabany, A., Soga, K. and Santamarina, C. (2012). Factors affecting efficiency of microbially induced calcite precipitation. *J. Geotech Geoenv Engineering*, 138, pp. 992-1001. https://doi.org/10.1061/(ASCE)GT.1943-5606.000066.

Fernandez, R. and Cardoso, R. (2022). Study of biocementation treatment to prevent erosion by concentrated water flow in a small-scale sand slope. *Transportation Geotechnics*, 37, 100873. https://doi.org/10.1016/j.trgeo.2022.100873.

Golden Software (2023) *Software Surfer*, online https://www.goldensoftware.com/products/surfer/.

Proceedings of the XVIII ECSMGE 2024
GEOTECHNICAL ENGINEERING CHALLENGES
TO MEET CURRENT AND EMERGING NEEDS OF SOCIETY
© 2024 the Authors
ISBN 978-1-032-54816-6
DOI 10.1201/9781003431749-407
Open Access: www.taylorfrancis.com, CC BY-NC-ND 4.0 license

ECSMGE 24
XVIII EUROPEAN CONFERENCE ON SOIL MECHANICS AND GEOTECHNICAL ENGINEERING

Load-penetration response of a site-won soil reinforced with natural fibres. Application for unpaved roads

Réponse charge-pénétration d'un sol local renforcé avec des fibres naturelles. Application pour des routes non pavées

D.M. Carlos, J. Macedo, M. Pinho-Lopes*
RISCO/Department of Civil Engineering/University of Aveiro, Aveiro, Portugal
**mlopes@ua.pt*

ABSTRACT: Unpaved roads are fundamental infrastructure worldwide. Forest roads provide access to forest areas to enable exploring the forest value chain products and access for firefighting. Usually, unpaved roads are formed using a superficial layer of unsealed gravel or aggregate, and often local soils or a mix of both materials. Reinforcements can be used to improve the mechanical properties of soil and aggregate, which enable reducing the quantities of good quality materials required for construction of these roads and delay the occurrence of defects leading to maintenance operations. Commonly, geosynthetics are used. However, alternative solutions can be defined, namely by applying locally available products. Resourcing natural reinforcements locally available can contribute to increasing the sustainability and decreasing the carbon footprint of the solutions adopted. Although natural materials tend to biodegrade, in areas such as forests where they are readily available, they can be a valid alternative. This study analysed the behaviour of a site-won fine soil reinforced with natural fibres from the forest value chain (pine needles), to assess the possibility of their use on unpaved forest roads. CBR tests were carried out to assess the load-penetration response of the soil and the soil-pine needles composite material. These tests and their interpretation have limitations, but they provide information commonly adopted in design methods for unpaved roads. The tests results allowed to conclude that the force-penetration response and CBR of the soil was improved by including pine needles; the greatest gain was observed for soil reinforced with 1% fibres, in mass.

RÉSUMÉ: Les routes non revêtues sont cruciales à l'échelle mondiale. Elles servent notamment les routes forestières permettant l'accès aux zones boisées pour explorer les produits de la chaîne de valeur forestière et prévenir les incendies. Généralement, sont composées d'une couche superficielle de gravier ou de granulats non scellés, souvent associés à des sols locaux. Les renforts améliorent les propriétés mécaniques du sol, réduisant le besoin de matériaux de qualité supérieure et retardant les défauts nécessitant des opérations d'entretien. Malgré l'utilisation courante des géosynthétiques, des alternatives locales, comme les renforts naturels, accroissent la durabilité et réduisent l'empreinte carbone. Les matériaux naturels, bien que sujets à la biodégradation, restent une alternative viable, notamment dans des zones comme les forêts, où ils sont facilement accessibles. Cette étude a analysé le comportement d'un sol fin obtenu sur site et renforcé par des fibres naturelles de la chaîne de valeur forestière (aiguilles de pin), afin d'évaluer la possibilité de les utiliser sur des routes forestières non revêtues. Des essais CBR ont été réalisés pour évaluer la réponse charge-pénétration du sol et du matériau composite sol-aiguilles de pin. Bien que ces essais aient des limites, ils fournissent des informations communément adoptées dans les méthodes de conception des routes non revêtues. Les résultats des essais ont permis de conclure que la réponse force-pénétration et le CBR du sol ont été améliorés par l'inclusion d'aiguilles de pin; le gain le plus important a été observé pour le sol renforcé avec 1% de fibres, en masse.

Keywords: Biodegradable reinforcement; unpaved roads; CBR tests; sustainability; percentage of incorporation.

1 INTRODUCTION

Unpaved forest roads are essential infrastructure worldwide, contributing to the economic, social, and cultural development of rural and forest areas, providing access to explore forest products. They have lower construction costs than paved roads and are an important part of the road network in many countries. They also play an important role in safeguarding and defending the forest against fires by ensuring access for preventive works, surveillance, or firefighting.

Usually, unpaved forest roads have low traffic volumes but are subject to high loads from heavy timber transport vehicles and forestry equipment. These roads are formed using a superficial layer of unsealed gravel or aggregate, and often local soils or a mix of the two types of material, placed above the foundation soil (roadbed). When subjected to traffic loads, the performance of these roads is influenced by

the quality of the construction materials used. Low-quality materials (e.g., materials with large quantities of fine particles) can decrease the resistance of the pavement, leading to deformations (in wet conditions) and dust (in dry conditions) (Pinard and Hongve, 2020). Repeated loads can cause the accumulation of plastic deformation and ruts, due to the reduction in aggregate layer thickness and owing to the deformation of the foundation (Dawson, 2001). Using good-quality natural materials (soils and aggregates often unavailable at the road site) has high extraction and transport costs and environmental impacts.

Alternative solutions can be used, for example applying locally available products or reinforcements to improve the mechanical properties of soils and aggregates. The main purpose is to reduce the quantities of good quality materials and to delay the occurrence of defects and the necessary maintenance operations. Pinho-Lopes (2022) and Magalhães et al. (2022) evaluated the use of industrial by-products and waste to improve the behaviour of soils for road applications. By-products from the forestry value chain (bottom and fly ashes) were used with the same purpose by Nienov et al. (2023) and Cepriá et al. (2021). Reinforcement with geosynthetics is a very popular solution to extend the useful life of these roads (Bräu and Vogt (2018), Al-Qadi et al. (2011)).

This work analyses the behaviour of a site-won soil reinforced with natural fibres (pine needles) from the forest value chain, to assess their use in unpaved forest roads. Although natural reinforcement materials may biodegrade, they can be a valid alternative in areas where they are readily available. To assess the load-penetration response of the fibre-reinforced soil composite, California Bearing Ratio (CBR) tests were carried out, analysing the influence of the percentage of fibres incorporated into the soil.

2 METHODOLOGY

2.1 Experimental programme

This paper includes results of CBR tests, carried out on a fine soil reinforced with pine needle fibres. The response of the soil, unreinforced and with fibre reinforcement, tested under the same conditions, was compared. The reinforced specimens analysed had different needles percentages of incorporation (NPI): 0% (unreinforced), 0.5%, 1.0%, 1.5%, 2.0% and 3.0%, in mass. Three specimens were tested per condition.

2.2 Materials

The fine soil used was collected from a salt pan wall in the Aveiro lagoon, Portugal, and characterised using laboratory tests. According to USCS, Unified soil classification system (ASTM D2487, 2011), the soil is ML - sandy silt. Additional characteristics of the soil: percentage of fine particles (<0.074 mm) 65.7%; average grain size (D_{50}) 0.023 mm; liquid limit (w_L) 35%; plastic limit (w_P) 25%; plasticity index (I_P) 10%; apparent unit weight (γ) 18.3 kN/m^3. The compaction characteristics of the soil, obtained from modified Proctor tests (ASTM D1557, 2012) are: maximum dry density (γ_{dmax}) 18.09 kN/m^3 and optimum water content (w_{opt}) 13.9%. Figure 1 illustrates the grain size distribution of the soil.

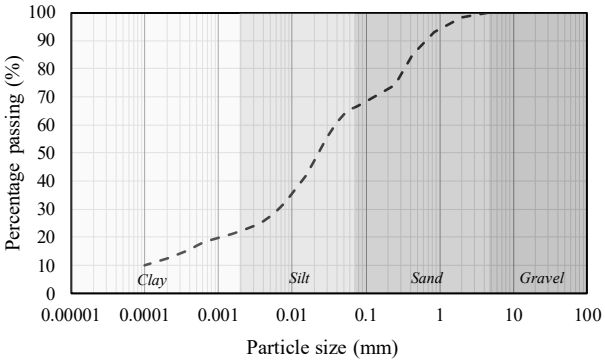

Figure 1. Grain size distribution of the soil studied (USCS, Unified soil classification system, soil fractions).

The pine needles were collected from a stone pine (botanical name *Pinus pinea*), also from the region of Aveiro, Portugal. Their geometric properties, namely length and width, were quantified using a 15 g sample. The pine needles ranged in length from 60 to 180 mm (mean value 117 mm and 42.4 mm standard deviation) and in width from 0.62 to 1.11 mm (mean value 0.87 mm and 0.15 mm standard deviation). The pine needles had a mean aspect ratio (length to width) of 134. The normalised length, L_N, and width, D_N, of the pine needles relatively to the average particle size of the soil (D_{50}) was 5087 and 38, respectively. The biochemical and mechanical properties of the fibres were not assessed. According to Dinesh et al. (2023), red pine needles contain 52-60% cellulose, 20% hemicellulose, 13-15% lignin and 5% of other extractives and have a maximum tensile strength between 35.8 and 36.94 MPa.

2.3 CBR tests

CBR tests were carried out following the procedure outlined in LNEC E198 (1967), which differs to ASTM D1883 (2007) on the imposed axial displacement rate only (1.00 instead of 1.27 mm/min).

Prior to the tests, the soil was dried, then its water content was adjusted to the required value (w_{opt}=13.9%). The soil was left to rest during 24 hours

under controlled conditions (temperature 20 ºC, relative humidity 65%); according to ASTM D1557 (2012), for ML soils this period should be longer than 16 hours. For the reinforced specimens, dry pine needles were added and mixed with the soil after the procedure referred, i.e., immediately before preparing the test specimens. The fibres were mixed with the soil in 5 portions, one per layer of the specimen.

A metal mould was used to produce cylindrical specimens (diameter 152 mm; height 125 mm). Each specimen was created by compacting 5 layers (25 mm high each) of soil or a mix of soil with needles with 25 blows of a rammer (4.54 kg; drop height 457 mm). Then, the specimens were soaked for 96 hours in an immersion tank filled with water. The swelling was registered; for specimens with NPI up to 1.0%, it stabilised after 96 hours; for specimens with NPI >1%, the soaking process was terminated after 96 hours (even if the swelling had not finished).

CBR tests were performed at an axial displacement rate of 1 mm/min., using a 50 mm diameter piston and a constant surcharge (by three annular plates, 24.52 N each) at the upper surface of the specimen.

3 RESULTS AND DISCUSSION

3.1 Summary of results

The force-penetration response for three specimens per condition (Figure 2) and the CBR of the specimens were defined. Herein the CBR was obtained from Equation 1, as the ratio of the force measured during the test for a value of penetration of 2.5 mm ($F_{2.5}$) to the corresponding force for a standard material ($F_{2.5S}$):

$$CBR = \frac{F_{2.5}}{F_{2.5S}} \times 100 \qquad (1)$$

The CBR values reported include mean values for 3 specimens prepared and tested under similar conditions (Table 1) and the corresponding 95% confidence intervals. Table 1 also includes the improvement ratio (IR) obtained for different values of NPI studied. The IR is the ratio between the CBR of reinforced specimens to that of the unreinforced soil.

Figure 3 illustrates changes in the soil density (ρ), water content, and swelling of the specimens after the compaction of the soil inside the mould (unsoaked), and after soaking (soaked). These parameters, which influence the behaviour of the composite material, depend on the incorporation rate NPI.

Reinforced specimens (Figure 4) exhibited agglomeration of fibres (overlapping in certain areas of a specimen) and fibres bent near the edge of the mould (for fibres longer than the mould diameter).

Table 1. CBR and improvement ratio (IR) for different NPI.

NPI (%)	CBR (%)				IR (-)
	Specimen				
	1	2	3	Mean value	
0	3.0	4.7	3.1	3.6 (±1.1)	-
0.5	6.0	5.4	3.4	4.9 (±1.6)	1.36
1.0	9.2	6.6	6.3	7.4 (±1.8)	2.06
1.5	6.5	7.6	5.3	6.5 (±1.4)	1.81
2.0	4.8	5.1	4.9	4.9 (±0.2)	1.36
3.0	4.5	3.7	3.9	4.0 (±0.5)	1.11

(95% confidence intervals in brackets)

3.2 Discussion

An important scatter of responses was observed (Figure 2, Table 1), without and with reinforcement. The force-penetration response varied, depending on the NPI considered, particularly for smaller values of penetration. Globally, the inclusion of pine needles led to a stiffer response for all values of NPI. A NPI of 1.0% and 1.5% led to responses much stiffer than that of the unreinforced soil; overall, the best response corresponds to NPI=1.0%. For NPI of 2.0% and 3.0%, the fibre benefit was less evident; relative to the average response, the fibres are detrimental for penetration up to ~0.6 mm (NPI=2.0%) and ~1.5 mm (NPI=3.0%); for larger values of penetration the addition of fibres was always beneficial.

The CBR increased with the pine needle reinforcement, for all NPI considered: 12% (NPI=3.0%) to 105% (NPI=1.0%). The specimens incorporating 1.0% of pine needles showed the best force-penetration response and CBR, with IR~2. For NPI >1.0%, the improvement in behaviour was less pronounced and eventually declined (IR between 1.1 and 1.8). Again, this suggests that the optimal NPI for this soil was 1.0%.

The improved response of the reinforced specimens can be ascribed to the redistribution of stresses and strains induced by the inclusion of fibres, through interaction mechanisms. The fibres have an effective effect on the soil when they are mobilised, i.e., subject to external forces and deform.

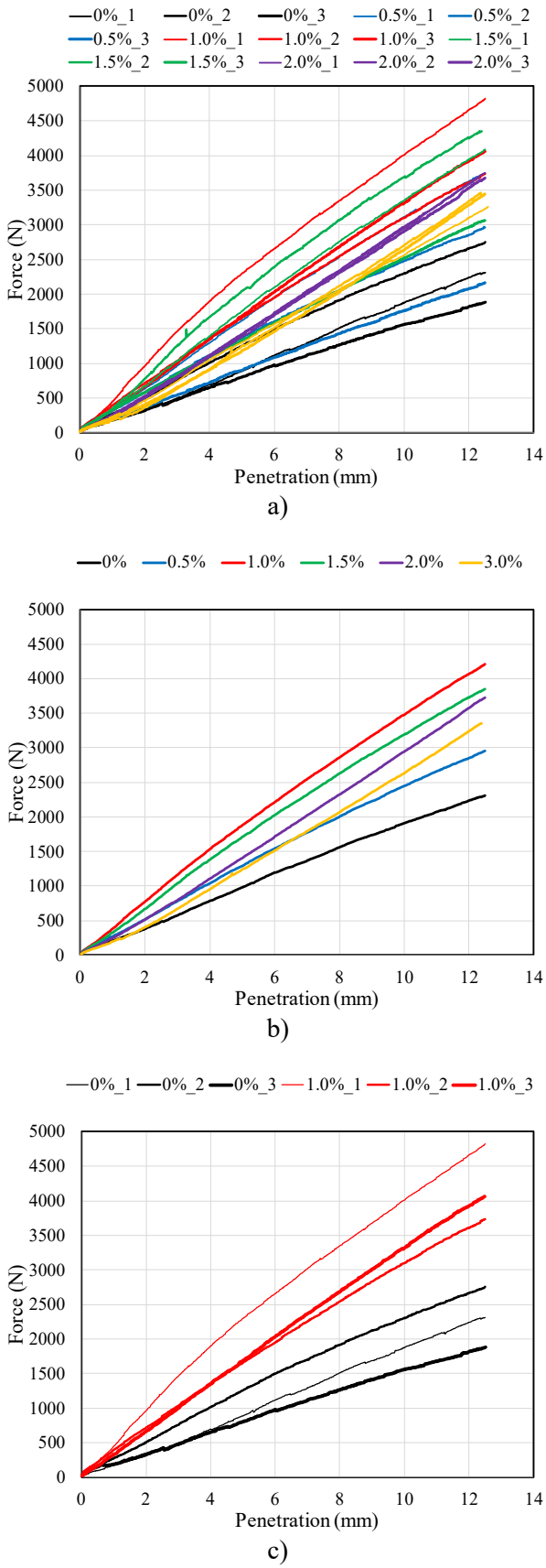

Figure 2. Force-penetration response for different percentages of incorporation (NPI): a) all specimens tested (3 specimens per condition); b) average for 3 specimens tested per NPI; c) optimal response (NPI=1%) and unreinforced specimens (NPI=0%), all specimens.

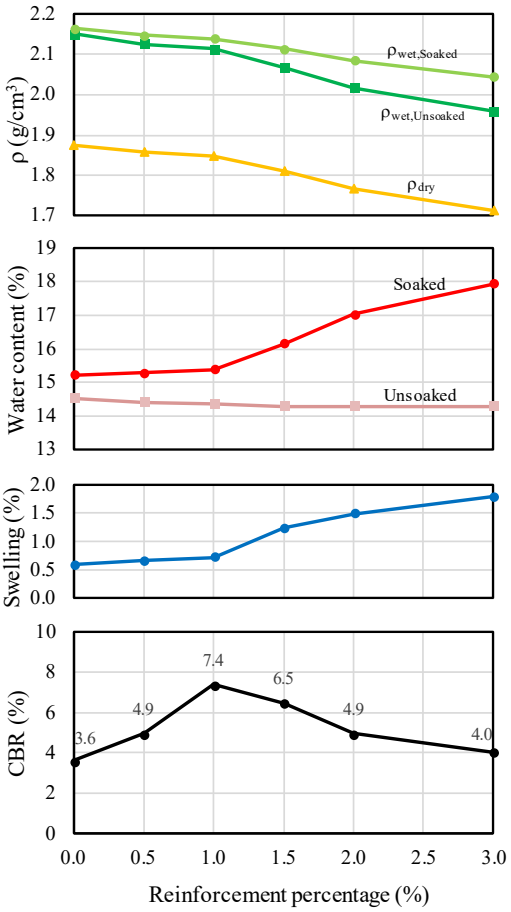

Figure 3. Influence of the pine needles percentage of incorporation, NPI, on the density (ρ), moisture content, swelling, and CBR (mean values for 3 specimens).



a) b)

Figure 4. Specimen of soil reinforced with pine needles: a) inside view (specimen cut along its height); b) outside view.

The soil skeleton was affected by the inclusion of fibres and, consequently, the distribution of stresses and strains inside the soil. The inclusion of fibres decreased the density of the specimens (Figure 3), especially above the optimum NPI (1.0%). This occurred because the fibres tend to restrict the soil grain packing, creating larger voids in their vicinity. The length of the pine needles used, in their natural state, (117 mm) was close to the diameter of the mould

(152 mm). This made the process of mixing the fibres into the soil difficult, resulting in heterogeneous orientation and spatial distribution of the fibres in the specimen (Figure 4). Therefore, the voids near the fibres tended to increase with larger percentage of incorporation of the fibres (NPI), and the amount of soil in the specimens reduced. In addition, the density dropped, because part of the specimen was occupied by fibres, less dense than the soil. The compaction process was also made more difficult due to the elastic behaviour of the fibres and due the voids created next to the fibres, which absorbed the impact forces generated by the rammer. Thus, among other causes, the decrease in the specimen density may have contributed to deteriorating the response of the material and lowering the CBR for larger NPI values.

The structure of the soil and of the soil-pine needles composite material was also modified during the soaking process because both materials (soil and fibres) absorbed water and underwent volumetric expansion (swelling). The inclusion of fibres increased the swelling and water absorption, mainly for NPI larger than 1.0%, illustrated by the variation of swelling and water content (Figure 3). The greater expansibility of the needles (hydrophilic material with high absorbent capacity) compared to the expansibility of the soil created preferential paths for water to flow through the soil, leading to an increase in the water content of the specimens. The increase in voids near the fibres also contributed to increasing the water flow into the specimens, raising the water content. Consequently, the increased water content led to a worse force-penetration response and reduced the CBR of the soil. This effect was particularly important for specimens with NPI larger than 1.0%.

The specimens exhibited agglomeration of fibres (overlapping in certain areas of a specimen) and some fibres were bent near the edge of the mould (Figure 4). This is related to the length of some fibres (longer than the mould diameter) and the compaction process. The resulting heterogeneity of the composite material was more important for higher NPI values. Many fibres were overlapping and could not be mobilised effectively during loading. Observation of the specimens after the tests showed that some fibres were bended or broken into smaller pieces. The reduced contacts between soil particles and fibres observed for higher values of NPI decreased the effectiveness of the mobilisation of the fibres.

In addition, the water incorporated into the specimens during the soaking process makes the interaction mechanisms at the interface between the materials less effective, since the water decreases the effective stresses, reducing frictional shear stresses and inducing sliding and ruptures at the interface.

The 95% confidence intervals for the mean value of CBR (Table 1) were rather high, showing some variability in the tests results. This may be caused by heterogeneity of the materials studied (soil, needles and composite material). Such heterogeneity is an intrinsic characteristic of soils, since they are natural materials. In this work, each specimen was prepared with new soil, so the soil in each specimen is a slightly different. The needles are also heterogeneous (section 2.2). Additional factors influence the heterogeneity of the reinforced soil specimens, such as the specimen preparation process. The specimens were prepared with soil reinforced with randomly distributed fibres, which suggests a certain degree of heterogeneity in the structure of the reinforced soil. The pine needles were used in one piece; many were longer (60 to 180 mm length) than the specimens (152 mm diameter and 125 mm height). The large volume filled with fibres (particularly for higher NPI) also made it difficult to mix the fibres with the soil, greatly increasing the heterogeneity of the specimens' structure.

The CBR test setup also does not guarantee that the reinforcement mechanisms mobilised during the test are realistic, since the tests are small-scale compared to real structures. The boundary conditions in the test can restrain the effect of the reinforcements. These limitations were mentioned before in several works about the force-penetration response of soils reinforced with several types of materials (geosynthetics, fibres).

4 CONCLUSIONS

The study analysed the behaviour of a site-won fine soil reinforced with natural fibres from the forest value chain (pine needles), to assess the possibility of their use on unpaved forest roads. CBR tests were carried out to assess the load-penetration response of the soil and of the soil-pine needles composite material. The results of the tests carried out allowed to conclude that:

- The force-penetration response and CBR of the soil improved with the inclusion of pine needles.
- Soil specimens with 1.0% of pine needles (in mass) led to an optimal response (force-penetration and CBR value).
- Percentages of incorporation larger than 1.0%, did not result in further improvement. The fibres affected the packing of the soil particles, as well as the swelling of the composite material.
- Due to water absorption capacity of the natural fibres, larger percentages of incorporation of fibres decreased the density and increased the water content and swelling of the specimens.

The effectiveness of the interface between both materials may also have been reduced.

- These parameters are linked, making it difficult, if not impossible, to reach a conclusion on which parameter has the most influence on the behaviour of the pine needle reinforcement.

Thus, further investigations should include the analysis of that the effect of fibres geometry (considering needles with different length), the effect of soaking process (comparing the behaviour of unsoaked and soaked specimens), and the effect of specimens' dimensions (using larger mould).

ACKNOWLEDGEMENTS

This study was funded by the PRR - Recovery and Resilience Plan and by the NextGenerationEU funds at Universidade de Aveiro, through the scope of the Agenda for Business Innovation "Transform - Transformação digital do setor florestal para uma economia resiliente e hipocarbónica" (Project no.34 with the application C644865735-00000007). This work was financially supported by FCT ("Fundação para a Ciência e a Tecnologia"- Portugal) through the project UIDB/04450/2020 (RISCO).



REFERENCES

ASTM D1557 (2012e1). Standard Test Methods for Laboratory Compaction Characteristics of Soil Using Modified Effort (56,000 ft-lbf/ft^3 (2,700 kN-m/m^3)). ASTM International, West Conshohocken, PA, USA.

ASTM D1883 (2007e2). Standard Test Method for CBR (California Bearing Ratio) of Laboratory-Compacted Soils. ASTM International, West Conshohocken, PA, USA.

ASTM D2487 (2011). Standard Practice for Classification of Soils for Engineering Purposes (Unified Soil Classification System). ASTM International, West Conshohocken, PA, USA.

Al-Qadi, I. L., Dessouky, S., Tutumluer, E. and Kwon, J. (2011). Geogrid mechanism in low-volume flexible pavements: accelerated testing of full-scale heavily instrumented pavement sections. *International Journal of Pavement Engineering*, 12(02): 121-135, https://doi.org/10.1080/10298436.2010.535534

Bräu, G. and Vogt, S. (2018). Field and laboratory tests on the bearing behaviour of unpaved roads reinforced by different geosynthetics. *Geotechnical Engineering Journal of the SEAGS & AGSSEA*, 49(4): 115-123.

Cepriá, J. J., Orejana, R., Miró, R., Martínez, A., Barra, M., Aponte, D. and Baloochi, H. (2021). Waste paper ash as an alternative binder to improve the bearing capacity of road subgrades. *Proceedings of the Eleventh International Conference on the Bearing Capacity of Roads, Railways and Airfields,* I. Hoff, H. Mork and R. G. Saba (eds.), CRC Press, Vol. 1, pp. 172-181, http://doi.org/10.1201/9781003222880-17.

Dawson, A. R. (2001). Engineering the forestry road pavement. In m Annual Symp. on Forestry engineering. Group of the Institute of Agricultural Engineers. Available online at www.nottingham.ac.uk/~evzard/me/ardrefs. (pp. 1-15).

Dinesh, Kumar, B. and Kim, J. (2023). Mechanical and dynamic mechanical behavior of the lignocellulosic pine needle fiber-reinforced SEBS composites. *Polymers*, 15(5): 1225, http://doi.org/10.3390/polym15051225.

Hoare, D. J. (1979). Laboratory study of granular soils reinforced with randomly oriented discrete fibers. *Proceedings of International conference of soil reinforcement*, Paris, France, Vol. 1, pp. 47-52.

LNEC E198 (1967). Determinação do CBR. Especificação LNEC, Lisboa, Portugal (in Portuguese)

Magalhães, A. J., Gomes, G. J. C. and Pires, P. J. M. (2022). Toward improved performance of unpaved roads: laboratory tests and field investigation of a soil-byproduct base layer. *Road Materials and Pavement Design*, 23(1): 184-198, http://doi.org/10.1080/14680629.2020.1809503.

Nienov, F. A., Júnior, G. R., Zampieri, L. Q., Luvizão, G., Lorenzatto, D., Michelon, W. and Viancelli, A. (2023). Soil geotechnical improvement by using waste from the paper industry. *Proceedings of the Indian National Science Academy*, Springer, Vol. 89(1), pp. 228-234, http://doi.org/10.1007/s43538-023-00155-z.

Pinard, M. and Hongve, J. (2020). Pavement Design of Low Volume Roads using the DCP-DN Method. London: ReCAP for UK aid. https://www.gov.uk/research-for-development-outputs/pavement-design-of-low-volume-roads-usingthe-dcp-dn-method-manual#link

Pinho-Lopes, M. (2022). Sand reinforced with recycled cotton textiles from waste blue-jeans: stress–strain response. *International Journal of Geosynthetics and Ground Engineering*, 8(5): 59. https://doi.org/10.1007/s40891-022-00404-z.

Proceedings of the XVIII ECSMGE 2024
GEOTECHNICAL ENGINEERING CHALLENGES
TO MEET CURRENT AND EMERGING NEEDS OF SOCIETY
© 2024 the Authors
ISBN 978-1-032-54816-6
DOI 10.1201/9781003431749-408
Open Access: www.taylorfrancis.com, CC BY-NC-ND 4.0 license

ECSMGE 24
XVIII EUROPEAN CONFERENCE ON SOIL MECHANICS AND GEOTECHNICAL ENGINEERING

Assessment of stiffness parameters of stone columns

Évaluation des paramètres de rigidité des colonnes ballastées

E. Carvajal Díaz*
Keller SWE, Madrid, Spain

P. Ruiz-Terán
Ferrovial Construcción, Madrid, Spain

J. Castro, M. Miranda
Universidad de Cantabria, Santander, Spain

**enmanuel.carvajal@keller.com*

ABSTRACT: This paper presents theoretical formulations for determining stiffness parameters of stone columns that can be evaluated from the results of load tests, such as: Young's moduli, confined moduli (oedometric), triaxial moduli and moduli of subgrade reaction. Theoretical examples and real load test measurements are presented, where different stiffness parameters of stone columns are compared, and recommendations are provided for proper characterization of these stiffness parameters, aimed to facilitate their use in numerical calculations with advanced constitutive models, as well as for simplified analytical calculations. As conclusions, based on these theoretical assessments and the experience, it is indicated that regardless of the installation method, the moduli of stone columns should be evaluated under triaxial conditions and adopting values from 20 to 100 MPa, approximately. Moduli higher than 120 MPa may imply risky overestimations.

RÉSUMÉ: Cet article présente des formulations théoriques pour déterminer les paramètres de rigidité des colonnes ballastées qui peuvent être évalués à partir des résultats d'essais de charge, tels que: les modules de Young, les modules confinés (œdométriques), les modules triaxiaux et les modules de réaction du sol de fondation. Des exemples théoriques et des mesures d'essais de charge réelles sont présentés, où différents paramètres de rigidité des colonnes ballastées sont comparés, et des recommandations sont fournies pour une caractérisation appropriée de ces paramètres de rigidité, visant à faciliter leur utilisation dans les calculs numériques avec des modèles constitutifs avancés, ainsi que pour des calculs analytiques. En conclusion, sur la base de ces évaluations théoriques et de l'expérience, il est indiqué que quelle que soit la méthode d'installation, les modules des colonnes ballastées doivent être évalués dans des conditions triaxiales et en adoptant des valeurs de 20 à 100 MPa environ. Des modules supérieurs à 120 MPa peuvent impliquer des surestimations risquées.

Keywords: Stone columns; triaxial modulus; load tests; settlements.

1 INTRODUCTION

Stone columns installed by deep vibrators have been used successfully in numerous of projects since the 1960s to reinforce soft or loose soil with high compressibility, speed up the consolidation process, decrease settlement, increase bearing capacity, and mitigate soil liquefaction. This deep vibro technique has a specific European Standard (EN 14731:2005, Ground treatment by deep vibration).

The so-called bottom-feed method consists of gravel insertion into the ground through a system of tubes attached to a vibrator coupled at the bottom. The whole rod is introduced into the ground aided by lateral displacement, vibration, vertical pull-down force and compressed air. Once the required depth is reached, the tubes stabilize the cavity and allow the gravel feeding. The general motions of deep vibrator compact the gravel by successive lowering and uplifting moves until the column is finished (Figure 1a). Other methodologies and equipment are also available, like the Rammed Aggregate Piers (RAP) firstly appeared during the 1990s. Figure 1b describes this method, which consists of extraction drilling and gravel feeding from the working platform. The compaction is only carried out vertically, through tamping by impact produced by a plate in contact with the gravel. The stability of the drilled cavity is highly important to implement this method, especially when the water table or very soft soil are found.

Attempts are usually made to evaluate the stiffness of stone columns by means of relatively quick plate load tests, where the induced settlements produced by the load increments are measured. Based on such results, the first approach to evaluate the column stiffness is the modulus of subgrade reaction (k_{col}),

defined as the ratio of the applied stresses to the measured settlements. Nevertheless, the determination of column moduli (stress - strain relationship) is a more complex procedure, strongly affected by the boundary conditions and loading procedure.

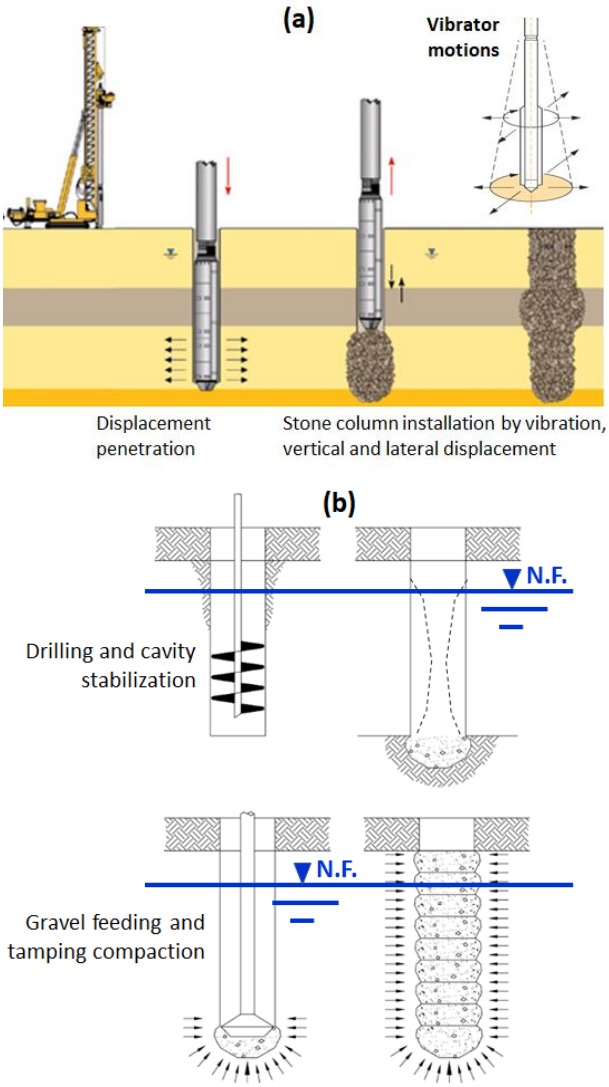

Figure 1. Methods: (a) vibro stone columns by bottom-feed; (b) Rammed Aggregate Pier with top-feed.

2 STIFFNESS EVALUATION

A range of moduli between 170 and 300 MPa is sometimes erroneously assumed for the stone columns. This assumption attributes abnormally high values for the moduli of stone columns, which is not in accordance with the actual values reported in the literature and practitioners' experience.

To properly assess the modulus of the stone columns, loading and boundary conditions must be correctly assumed. It is highly recommended to take reference values of moduli from the literature or conduct triaxial laboratory tests.

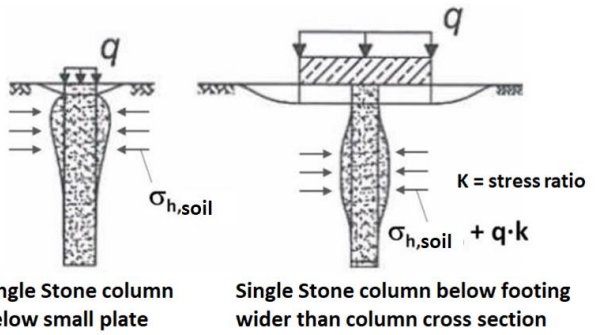

Figure 2. The triaxial conditions of stone columns below foundations and plate load tests.

Indeed, triaxial conditions correspond to the most representative state that stone columns undergo to support the foundation loading. Figure 2 shows the compression triaxial state usually produced in stone columns and surrounding soil under a foundation structure (similar to laboratory triaxial tests). Stone columns mainly deform through lateral bulging when subjected to compressive loading in triaxial conditions and are supported by the horizontal confining stress exerted by the surrounding soil. This behaviour has been demonstrated and extensively described by several researchers (Priebe, 1976; Priebe, 1995; Barksdale and Bachus, 1983; Goughnour and Bayuk, 1979; Wehr, 2004; Kirsch and Kirsch, 2010; Greenwood and Kirsch, 1983; Hu, 1995; Castro and Sagaseta, 2009).

The most common range of moduli values of stone columns in triaxial conditions varies from 20 to 100 MPa, approximately, according to many researchers who carried out comprehensive analyses by laboratory testing, field measurements, and numerical modelling (Han and Ye, 2001; Balaam and Booker, 1981; Castro, 2017; Bachus and Barksdale, 1983; Kirsch and Kirsch, 2010). The lowest moduli are obtained in the softest soils which offer the lowest confining stresses. It is worth mentioning that instead of the stone column stiffness, its friction angle and its diameter (i.e. the area replacement ratio) are the parameters with the largest impact on the improvement achieved with the treatment (Herle et al., 2007; Priebe, 1995).

Regarding the friction angle of stone columns, it is particularly interesting the investigation carried out by Duncan et al. (2007) about the same kind of material used for the stone columns (sizes 10–40 mm, approx.), which shows that moderately dense to very dense gravel may have a ϕ_{col} of approximately 55º for a very reduced level of lateral confining stress, of approximately 28 kPa (possibly in layers located at a depth of between 1.5 and 2.5 m); however, the same gravel with the same level of relative density experiences a significant decrease of ϕ_{col} to values between 40º and 47º, when the pressure is greater than

approximately 80 kPa (i.e., at depths of more than 4.5 to 7.0 m, approx.).

Figure 3 shows the degradation law of ϕ_{col} with the confining pressure, in accordance with the study by Duncan et al. (2007). It is particularly important to assess the risks that may arise if the design ϕ_{col} value is erroneously interpreted regarding the level of confining pressure to which they would be subjected, which not only depends on the initial stress state of the soil, but also on the stress state to which the soil and columns will be subjected due to the application of foundation loading.

Although the modulus in triaxial conditions (E_{TX}) is the most representative and widely used module to characterize stone columns, the subgrade reaction modulus, defined as the ratio between the vertical pressure applied on the foundation and the resulting settlement ($k_{col} = \Delta\sigma/s$), with density units (kN/m^3, t/m^3), is also usually considered.

Thus, based on the vertical pressures ($\Delta\sigma$) and the resulting settlement (s), it is possible to determine the subgrade reaction modulus of the columns (k_{col}) and the soil (k_s) by means of loading tests using small plates (0.30 to 1.0 m). For that reason, and because it is an affordable kind of test regarding execution times and costs, the execution of these plate loading tests is considered as an attempt to assess the stiffness of stone columns, or more precisely, of the soil-column system.

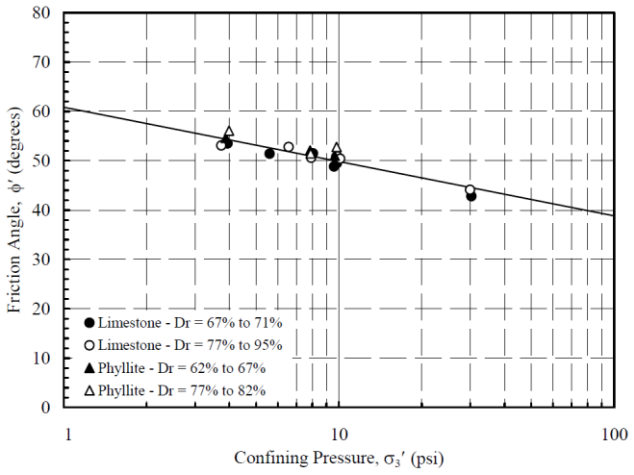

Figure 3. Duncan et al. (2007) investigation on internal friction angles on coarse aggregate type AASHTO #57.

However, these tests involve a number of limitations that complicate the proper assessment of column stiffness, such as: (i) small load plate tests only reach small depths (0.6 to 1.5 m); (ii) plate diameters usually only cover the column diameter, which limits the analysis of the real columns behaviour below the foundations which have greater area than the columns, Figure 2; (iii) plate tests are performed by fast loading and unloading procedures to complete the test in a few hours (e.g. NLT-357/98 or ASTM D-1143 Standards), therefore, the results mainly correspond to undrained conditions, which do not properly reproduce the elastic-plastic strains that govern the behaviour of stone columns and surrounding soil in the long-term; (iv) appropriate calculation procedures must be implemented to convert the measured reaction modulus (k_{col}) into the triaxial modulus (E_{TX}), as described in following sections.

Based on loading tests with a similar diameter to that of the stone columns, several researchers have compiled the "k_{col}" values, proposing empirical correlations between "k_{col}" and SPT blow-count, without the need of performing load plate tests. Figure 4 shows the correlation proposed by Sehn and Blackburn (2008), with recommended reaction modulus values for stone columns, considering both granular and cohesive soils around the columns.

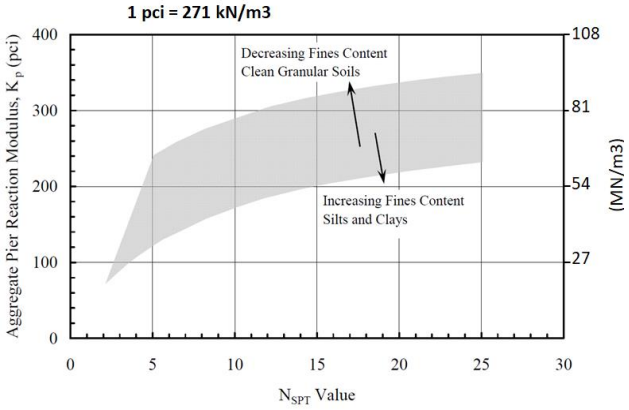

Figure 4. Correlation proposed by Sehn and Blackburn (2008) to estimate the reaction modulus for stone columns.

2.1 Stiffness formulation of stone columns

From the elasticity theory, a very simplified approach to estimate the settlement for a given soil element could be considered through Eq. (1):

$$S = \frac{\sigma_v}{E} . L \qquad (1)$$

where S is the settlement, E is the Young modulus of the column, L is the length of the considered element and σ_v is the axial stress applied.

Using the definition of reaction modulus (k_{col}) of a given soil element according to Eq. (2), it can be obtained a relationship between E and k_{col}:

$$k_{col} = \frac{\sigma_v}{S} = \frac{\sigma_v}{\frac{\sigma_v}{E} \cdot L} = \frac{E}{L} \; ; \; E = k_{col} \cdot L \qquad (2)$$

Then, under the simplified assumption that the induced stress during a field loading test has maximum value at the top of the element L, and reaches zero

stress at the bottom of the element, it can be considered that the average induced stress in the element is half of the applied stress at the top ($\sigma_{v,average} = \sigma_v / 2$). Thus, replacing σ_v by $\sigma_{v,average}$ in Eq. (2) the Eq. (3) can be obtained which represents a simplified relationship between the Young modulus (E) and the reaction modulus to evaluate the results from plate loading tests.

$$E = \frac{k_{col} \cdot L}{2} \quad (3)$$

More precisely, Boussinesq presented the closed-form solution to determine the settlement (S) under a rigid circular plate subjected to uniform load on an elastic and isotropic semi-space, as shown in Eq. (4).

$$S = \sigma_v \cdot R \cdot \frac{(1-\nu^2)}{E} \cdot I_a \quad (4)$$

where:
R: foundation radius
I_a: influence factor (in this case: $I_a = \pi / 2$)
σ_v: vertical stress
E: Young modulus ($E = \sigma_v / \varepsilon_v$; for $\sigma_h = 0$)
ν: Poisson's ratio ($\nu = \varepsilon_h / \varepsilon_v$)

From equation (4) the reaction modulus (k_{col}) can be determined as described in Eq. (5):

$$k_{col} = \frac{\sigma_v}{S} = \frac{E}{(1-\nu^2)} \cdot \left(\frac{2}{\pi}\right) \cdot \left(\frac{1}{R}\right) \quad (5)$$

Eq. (6) shows the relationship between Young's modulus (E) and the reaction modulus (k_{col}):

$$E = k_{col} \cdot (1-\nu^2) \cdot R \cdot \left(\frac{\pi}{2}\right) \quad (6)$$

Finally, looking back to the relationship between the oedometric and Young moduli (E_{oed} / E) based on Poisson's ratio (ν), depicted in Eq. (7), it is interesting to estimate the oedometric modulus both based on the simplified modulus (8) and based on the modulus derived from the Boussinesq's solution for rigid circular plate (9).

$$E_{oed} = E \cdot \left[\frac{1-\nu}{(1-2\nu)(1+\nu)}\right] \quad (7)$$

$$E_{oed} = \frac{k_{col} \cdot L}{2} \cdot \left[\frac{1-\nu}{(1-2\nu)(1+\nu)}\right] \quad (8)$$

$$E_{oed} = k_{col} \cdot R \cdot \left(\frac{\pi}{2}\right) \left[\frac{(1-\nu)(1-\upsilon^2)}{(1-2\nu)(1+\nu)}\right] \quad (9)$$

The relationships between k_{col}, E_{oed} and E from the Boussinesq's solution (Equations 6 and 9) include the implicit consideration of the influence depth of the foundation load, which may correspond to the plate load tests on stone columns in triaxial conditions and subjected to the confining stress of the surrounding soil. This implies a remarkable advantage over equations obtained from the simplified approach, because it allows the estimation of the moduli without the need of assigning arbitrary values to the original length of the soil element that needs to be studied (L), as is required with equations (3) and (8). Figure 5 shows the depth affected by the loads according to the Boussinesq's solution for homogeneous semi-space (one layer) and also shows the solution of Poulos and Davis (1974) for a bilayer model.

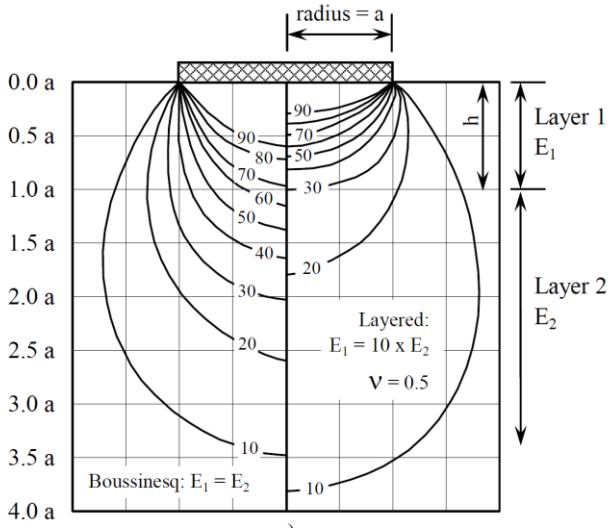

Figure 5. Influence depth of loaded rigid circular plate: (left) Boussinesq solution for homogeneous soil model; (right) Poulos and Davis (1974) for a bilayer model.

2.2 Example of moduli estimation

An example of moduli estimate for stone columns is shown, considering the following input data:

- Bearing plate diameter of 60 cm.
- Poisson's ratio of $\nu = 0.45$ for compacted gravel (Priebe, 1995).
- Reaction modulus, $k_{col} = 55$ MN/m^3. According to Figure 4, it could match a soil with SPT = 3–5; k_{col} could also be obtained from a plate load test on a column with 230 kN load (820 kN/m^2) and resulting settlement of 1,5 cm (820 kN/m2 /0.015 m) ≈ 55 MN/m^3.

Table 1 summarizes the results when using equations related to E_{oed}, E and k_{col}, from Boussinesq's solution. The results show a triaxial or Young modulus of 21 MPa and oedometric modulus of 78 MPa. These values are far from the aforementioned range of 170–300 MPa, showing that regardless of the execution

method, such values exceed the real stiffness of stone columns.

Table 1. Example moduli estimation of stone column.

Parameters	Bousinnesq (Equations 6 and 9)	Plain strain (Equations 3 and 8)
Influence depth, L	1.05 m	6.25 m
E_{oed}	78 MPa	652 MPa
E	21 MPa	172 MPa

Table 1 also shows the results for the simplified approach, considering an influence depth of L = 6.25 m, which is necessary to obtain a modulus of the stone column of approximately E = 170 MPa.

This depth would be 20.8 times the radius of the foundation. In order to achieve E = 300 MPa it would be necessary to increase the influence depth to L = 11 m, which would be 37 times the radius of the plate.

2.3 Load tests on stone columns

Stuedlein and Holtz (2008) performed an extensive study regarding the results of several load tests on small groups of stone columns (footings with 3 to 7 columns) and isolated columns with plate diameter of 76 cm.

Figures 6 and 7 show part of the results of this study, where very similar behaviour is observed in the columns performed with both methods (vibro bottom-feed and rammed aggregate piers).

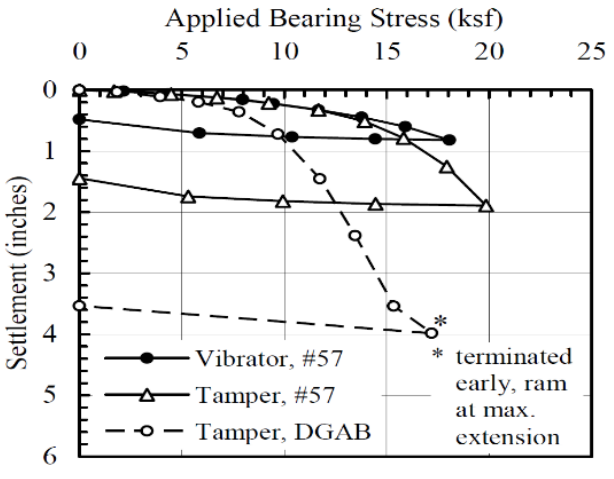

a) 30-inch-diameter plate load tests

Figure 6. Plate Footing load tests on rammed aggregate piers (Tamper #57 and Tamper DGAB) and by bottom-feed deep vibrators (Vibrator #57), (Stuedlein and Holtz, 2008).

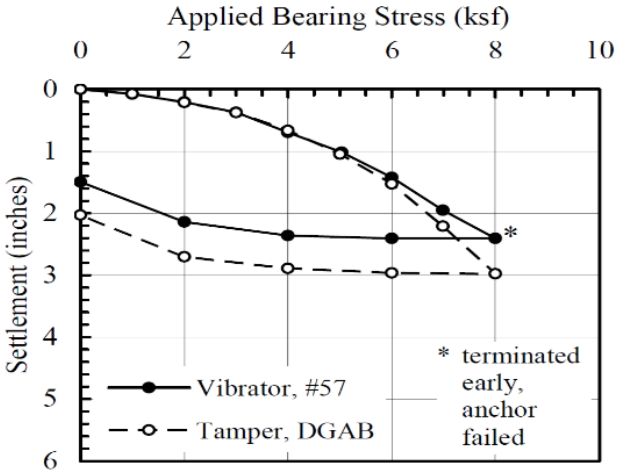

b) 9 ft x 9 ft footing load tests

Figure 7. Footing load tests on rammed aggregate piers (Tamper #57 and Tamper DGAB) and by bottom-feed deep vibrators (Vibrator #57), (Stuedlein and Holtz, 2008).

This similarity shows that the columns moduli are approximately the same for both execution methods, at least in the upper part of the columns, which can be assessed by plate load tests.

The dashed line in Figure 6 corresponds to a specific plate load test over one rammed aggregate pier, where relevant higher settlements is noticed. Further details of this specific load test can be found in Stuedlein and Holtz (2008).

3 CONCLUSIONS

Stone columns by deep vibrators, which are introduced into the ground by displacement and bottom-feed of gravel, have been successfully implemented for more than 60 years worldwide. This method has automatic control systems for execution parameters and one specific European Standard (EN 14731:2005).

Other procedures were developed around the 1990s, which include rammed aggregate piers as an alternative method, performed with extraction drilling, top-feed of gravel from working platform and compaction by vertical ramming.

The stone column moduli must be assessed under triaxial conditions. According to the experience and reported cases in literature the most common values of triaxial moduli vary from 20 to 100 MPa, the lowest moduli are obtained in the softest soils which offer lowest confining stresses. The consideration of column triaxial moduli higher than 120 MPa could imply a design overestimation regarding the reduction of settlement. Plate loading tests on isolated columns and small groups of columns show very similar behaviour in stone columns performed by both

methods. Tests on isolated columns with small plate diameters (30–60 cm) only allow assessments up to a depth of 1–1.5 m, so they do not represent the real behaviour of the entire column.

The Boussinesq's closed-form solution to determine the settlement (S) under a uniform loaded rigid circular plate on an elastic and isotropic semi-space can be considered for analytically interpretation of plate load tests, so that can be estimated the triaxial modulus of stone columns as a function of the measured reaction modulus during the test.

It is worth mentioning that instead of the stiffness, the friction angle and the diameter of stone columns present higher impact to maximize the improvement effects.

For adequate estimation of the friction angle of stone columns, it is essential to take into consideration the degradation law of ϕ_{col} with the confining pressure. This is particularly important to assess the risks that may arise if the design ϕ_{col} value is erroneously interpreted regarding the level of lateral confining pressure to which they would be subjected, which not only depends on the initial stress state of the soil, but also on the stress state to which the soil and columns will be subjected due to the application of foundation loading.

REFERENCES

Balaam N. P. and Booker J. R. (1981). Analysis of rigid rafts supported by granular piles. *Int. J. Num. Anal. Meth. Geomech.* 5: 379-403. https://doi.org/10.1002/nag.1610050405.

Barksdale, R. D. and Bachus, R. C. (1983). Design and Construction of Stone Columns. Federal Highway Administration, Washington DC, Final Report SCEGIT-83–104, 1983.

Castro, J. and Sagaseta, C. (2009). Consolidation around stone columns. Influence of column deformation. *Int. J. Num. Anal. Meth. Geomech.* 33 (7), 851-877. https://doi.org/10.1002/nag.745.

Castro, J. (2017). Modelling Stone Columns. *Materials* 10: 782. https://doi.org/10.3390/ma10070782.

Duncan, J. M., Brandon, T., Jian, W., Smith, G., Park, Y., Griffith, T., Corton, J., Ryan, E. (2007). Densities and Friction Angles of Granular Materials with Standard Gradations 21b and #57. Center for Geotechnical Practice and Research, Virginia Tech, Report No. 45, August, 2007.

EN-14731 (2005). Execution of special geotechnical works – Ground treatment by deep vibration. European Standard.

Goughnour, R. R. and Bayuk, A. A. (1979). Analysis of stone column–soil matrix interaction under vertical load. C.R. Coll. Int. Reinforcement des Sols. Paris.

Greenwood, D. A. and Kirsch, K. (1983). Specialist ground treatment by vibratory and dynamic methods, Advances in Piling and Ground Treatment for Foundations, London.

Han, J. and Ye, S. L. (2001). Simplified method of consolidation rate of stone column reinforced foundation. *J. Geotech. Geoenviron. Eng. ASCE* 127: 597–603. https://doi.org/10.1061/(ASCE)1090-0241(2001)127:7(597).

Hu, W. (1995). *Physical modelling of group behaviour of stone column foundations*. PhD Thesis. Univ. of Glasgow.

Herle I., Wehr J. and Arnold M. (2007). Influence of pressure level and relative density on friction angle of gravel in vibrated stone columns. Pfahl Symp. TU Braunschweig, 84.

Kirsch K. and Kirsch, F. (2010). *Ground Improvement by Deep Vibratory Methods*. Spon Press.

Priebe, H. J. (1976). Estimating settlements in a gravel column consolidated soil. Die Bautechnik 53(5): 160–162 (in German).

Priebe, H. J. (1995). Design of vibro replacement. *Ground Eng.* 28(10): 31-31.

Poulos, H. G. and Davis, E. H. (1974). *Elastic Solutions for Soil and Rock Mechanics*. John Wiley and Sons, New York.

Sehn, A. L. and Blackburn, J. T. (2008). Predicting Performance of Aggregate Piers. 23rd Central Pennsylvania Geotechnical Conference, ASCE, May 28-30, 2008; Hershey, PA.

Stuedlein, A. W. and Holtz, R. D. (2008). Statistical Analyses of Aggregate Pier Load Tests. Proc. 2nd U.S.-Japan Workshop on Ground Improvement, Geotechnical Earth-quake Engineering and Soil Dynamics IV, ASCE, Sacramento, CA.

Wehr, J. (2004). Stone columns – single columns and group behaviour. 5th Int. Conf. Ground Improvement Technologies, Kuala Lumpur, 329-340.

Proceedings of the XVIII ECSMGE 2024
GEOTECHNICAL ENGINEERING CHALLENGES
TO MEET CURRENT AND EMERGING NEEDS OF SOCIETY
© 2024 the Authors
ISBN 978-1-032-54816-6
DOI 10.1201/9781003431749-409
Open Access: www.taylorfrancis.com, CC BY-NC-ND 4.0 license

ECSMGE 24
XVIII EUROPEAN CONFERENCE ON SOIL MECHANICS AND GEOTECHNICAL ENGINEERING

A case study of offshore stone columns by the novel S-Alpha Dive system: San Ignacio bridge in Bilbao

Une étude de cas de colonnes de pierre offshore grâce au nouveau système S-Alpha Dive: pont de San Ignacio à Bilbao

E. Carvajal Díaz*
Keller SWE, Madrid, Spain

P. Ruiz-Terán
Ferrovial Construcción, Madrid, Spain

**enmanuel.carvajal@keller.com*

ABSTRACT: A case history is presented to describe the application of the "S-Alpha hydraulic Dive" system for the installation of stone columns offshore. This system comprises equipment able to be dived in the sea up to a maximum water depth of approximately 25 m, allowing to reduce the effective weight of the whole system and thus allowing the execution of deeper treatments of stone columns with dry bottom-feed method until approximately 70 m depth. It is described the soil improvement to support the foundation of one abutment for the San Ignacio bridge built over the Bilbao estuary in Spain. As conclusions, the satisfactory application of the "S-Alpha hydraulic Dive" system for the installation of stone columns offshore in very soft soils is highlighted, as well as the capacity of the improved soil to consolidate and increase the shear strength required to carry out this type of marine works.

RÉSUMÉ: Un cas historique est présenté pour décrire l'application du système "S-Alpha Hydraulic Dive" pour l'installation de colonnes ballastées en mer. Ce système comprend des équipements capables d'être plongés dans la mer jusqu'à une profondeur maximale d'environ 25 m, permettant de réduire le poids effectif de l'ensemble du système et permettant ainsi l'exécution de traitements plus profonds de colonnes ballastées avec méthode d'alimentation par le fond sec jusqu'à environ 70 m de profondeur. Il est décrit l'amélioration du sol pour soutenir la fondation d'une culée du pont de San Ignacio construit sur l'estuaire de Bilbao en Espagne. En conclusion, on souligne l'application satisfaisante du système "S-Alpha Hydraulic Dive" pour l'installation de colonnes ballastées offshore dans des sols très meubles, ainsi que la capacité du sol amélioré à consolider et à augmenter la résistance au cisaillement nécessaire pour réaliser ce type de travaux maritimes.

Keywords: Stone columns; deep vibrators; offshore; S-Alpha system; soft silts.

1 INTRODUCTION

Stone columns installed by deep vibrators represent a well-known ground improvement method with long history of development since 1960s (Kirsch and Kirsch, 2010). Recently significant advances regarding the installation of stone columns have been developed. This work attempts to address several of those improvements, essentially corresponding to the execution of stone columns for offshore sites considering that the literature about this kind of technology is still limited compared with the literature about the conventional execution of stone columns onshore (Carvajal and Mora-Rey, 2014).

Furthermore, the typical soil conditions to be improved in maritime works, which usually need large improvement depths and columns installation in very soft layers below seabed suppose an additional challenge for the execution technologies. Thus, the development of equipment able to assure the treatment objectives and proper quality control is of great interest. Particularly, the implementation of some relevant developments related to the execution and control systems of maritime works by stone columns are presented for the construction of abutment structures which support the San Ignacio bridge over the Nervion river in Bilbao, Spain.

2 STONE COLUMNS OFFSHORE

Before describing the advances for the installation of offshore stone columns, it is important to tackle some of the conventional methods. The oldest method consists of placing a bed of gravel on the seabed, thereafter, the gravel is crossed by means of deep

vibrators coupled to their whole system of rods (vibrator, extension tube, couplings), so that the gravel could fall into the cavity generated when the vibrator is lowering with the depth.



(a) (b)

Figure 1. Conventional system of stone column execution offshore: (a) gravel bed method on the seabed, (b) method of mechanically gravel feeding.

The deep vibrators in this system are aided by a water jet which enable their capacity to penetrate the different layers. Figure 1 shows a sketch of this methodology.

One of the most used methods, and which represented an important advance at the time, consists of "feeding gravel mechanically" or using the Hopper Method. In this case, the use of two barges is usually necessary; one for the crane with the vibrator hanging from an auxiliary crane, and the second with the gravel collection and an extendable arm excavator that feeds the hopper on top of the vibrator.

This system includes a double compartment chamber between the hopper and the vibrator where a mixture of compressed air and gravel is used to transport the gravel to the tip of the vibrator. The gravel is then compacted in the usual way by raising and lowering the vibrator. This method is illustrated in Figure 1b. The most recent technological development of special equipment for stone columns has allowed the treatment of very deep soft soils, both in marine and onshore works.

Figure 2a shows an execution system that represents a new generation of development. This is the so-called "alpha hydraulic system", consisting of a circuit to propel the gravel by pumping to a discharge chamber connected to the feeder tube through which the gravel flows until its final discharge into the ground through the lower part of the vibrator.

Figure 2b shows the "mechanical alpha system", where the gravel is deposited by a loader directly into the hopper. After filling the hopper with gravel, it is raised by wire rods until the top of the feeding tube, from where it is poured until it outflows by the bottom of the vibrator. In both alpha systems (hydraulic and mechanical), the whole rod composed by the hopper, feeding tube and vibrator is usually coupled to the arm of a crane (crane boom), to enable the execution of treatments at very deep depths up to app. 60 m.

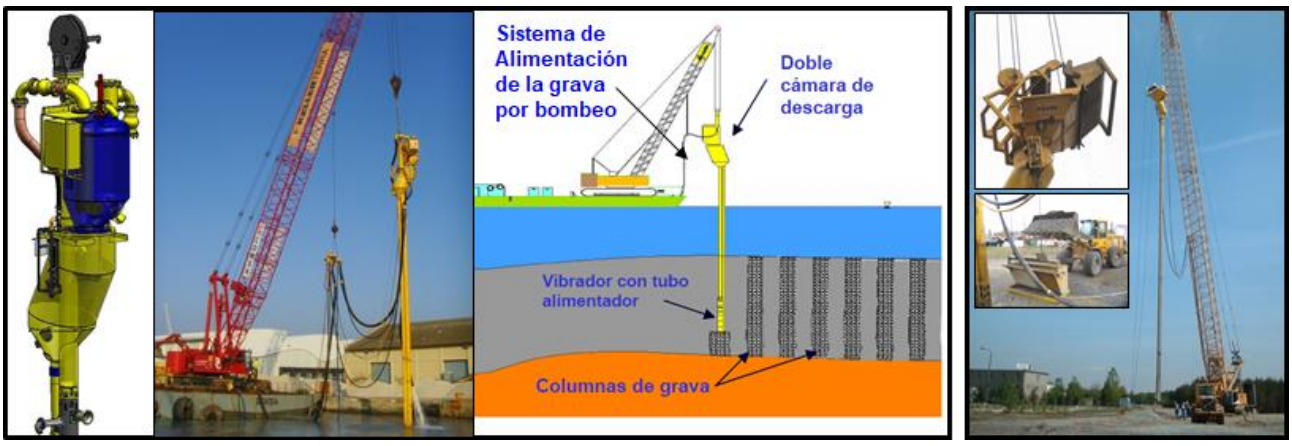

(a) (b)

Figure 2. S-Alpha systems for installation of stone columns: (a) hydraulic, (b) mechanical.

3 NEW SYSTEM S-ALPHA DIVE

As a part of the continued development of the new generation of equipment for offshore stone column, significant improvements have been made to the Alpha hydraulic system. Figure 3 shows the new "S-Alpha hydraulic Dive" system, which consists of an equipment capable of diving in the sea to a maximum depth of approximately 25 m, allowing the effective weight of the entire system to be reduced and thus facilitate the execution of deeper treatments of stone columns with bottom-feed procedure, up to approximately 70 m deep. This method significantly improves the execution conditions of the entire system, making possible a very similar procedure as the well-known bottom-feed and dry system of stone column usually performed in onshore conditions. The possibility of submerging the system also facilitates the optimization of the capacity required by the cranes and increases the production rates. One of the most important aspects of the "Hydraulic S-Alpha Dive" system consists of obtaining a compact integration of all the components of the gravel feeding and diving system to the vibrator.

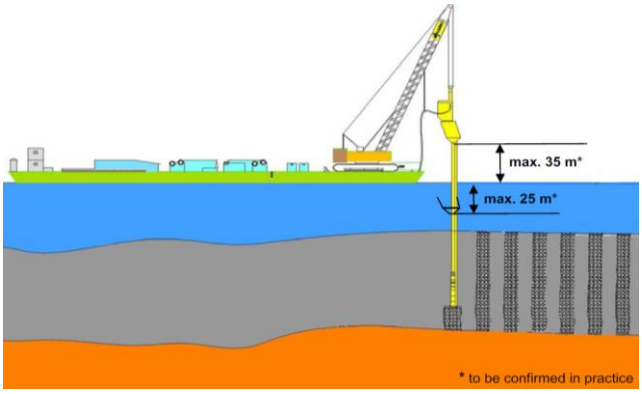

Figure 3. New system S-Alpha dive.

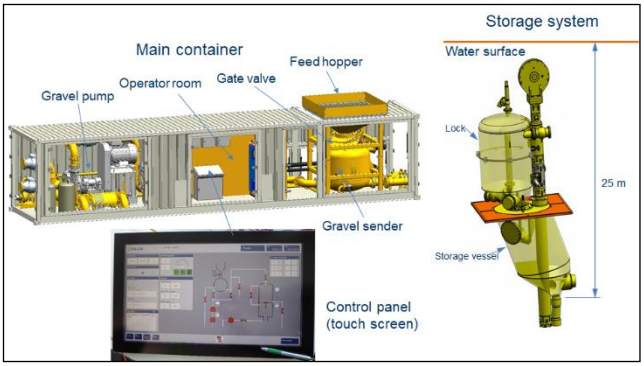

Figure 4. Components of S-Alpha dive system.

As can be seen in Figure 4, in a single type of container structure with approximately 12 m in length, where are deployed the gravel delivery pumps, the hopper for accumulation and dosing of the volumes of gravel supplied to the vibrator, as well as a control room where the panels are located that show the most important parameters of the power system. Additionally, another smaller container is considered where compressors, auxiliary pumps and a generator are placed.

As this new system can reduce the space and weight of all the necessary infrastructure, it also allows the system to require small barges or pontoons.

As a part of the execution procedure of this new system, it is necessary to use an auxiliary crane to transport the gravel from its general stockpile site to the hopper located in the main container. In some cases, for nearshore treatments, both the storage and auxiliary crane can be located on the land side, and when the treatments are located offshore, the storage must be located either on the main barge or on an auxiliary barge.

4 CASE HISTORY: SAN IGNACIO BRIDGE

Figure 5 shows a plan view and typical section of a treatment using offshore gravel columns, for the foundation of an abutment corresponding to the San Ignacio bridge, to be built on the Bilbao estuary (Spain). Basically, the stone columns installed with the system "S-Alpha hydraulic Dive" are aimed to consolidate and reinforce the soft silty soils with low-plasticity, which are located until maximum depths of 8 to 15 m below the seabed and represent an important risk of instability and non-allowable long-term settlements for both the abutment foundation and the adjacent embankments. These soft silts have undrained shear strengths in the order of 10 to 50 kPa, which pose a significant challenge to achieve the installation of the stone columns and meet the design objectives. In this case the crane, the main container and the barge used to carry out the works occupied an area of approximately 470 m2.

Figures 6 shows photographs of the work environment, where can be seen the auxiliary crane located next to the gravel storage, on the land side, and one front view of the S-Alpha dive system.

It is important to highlight that with this new system a more continuous feed of the gravel is achieved than that obtained by the conventional methods, due to the continuous drive system located in the main container, which is located a few meters from the main crane that supports the system of tubes connected to the vibrator. Figure 7a shows a typical log of the execution parameters of offshore stone columns using conventional systems. In this case, the vibrator penetrates to the desired depth, and then in

successive phases it incorporates gravel and compacts it, for which it must spend some time when finishing each stage of gravel compaction, to install the amount of gravel corresponding to each column segment.

Figure 7b shows this procedure using the new "S-Alpha Dive" system. The penetration phase of the equipment into the ground is similar, but in the phase of gravel feeding and its compaction with the vibrator, a continuous process is followed. These improvements represent a significant increase in the production rate, and therefore reductions in execution times. In both cases, the execution parameters are recorded continuously and automatically from the monitoring systems. Likewise, in both cases a GPS positioning system is used.

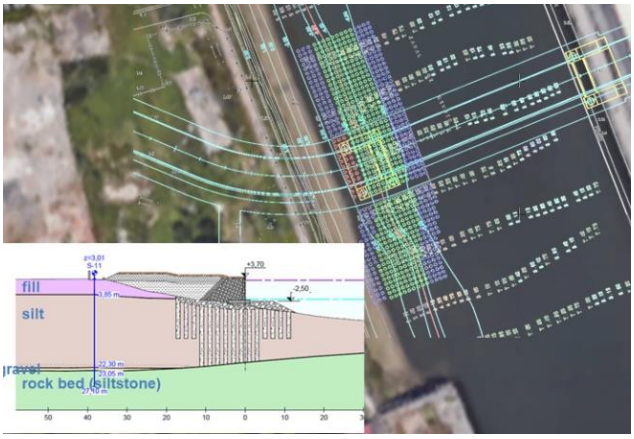

Figure 5. Treatment overview. San Ignacio bridge.



Figure 6. S-Alpha system at San Ignacio bridge site.

5 CONCLUSIONS

The satisfactory application of the "S-Alpha hydraulic Dive" system for the installation of stone columns offshore in very soft silts is highlighted, as well as the capacity of the improved soil to consolidate and increase the shear strength and reduce the soil compressibility required to carry out this type of marine works to build the west abutment of San Ignacio Bridge in Bilbao. Moreover, the new S-Alpha dive system comprises a number of operations easier, safer, faster and more effective than the older offshore methods, including: handling, assembly-disassembly of equipment, production rate, improvement depth, smaller barges and smaller cranes.

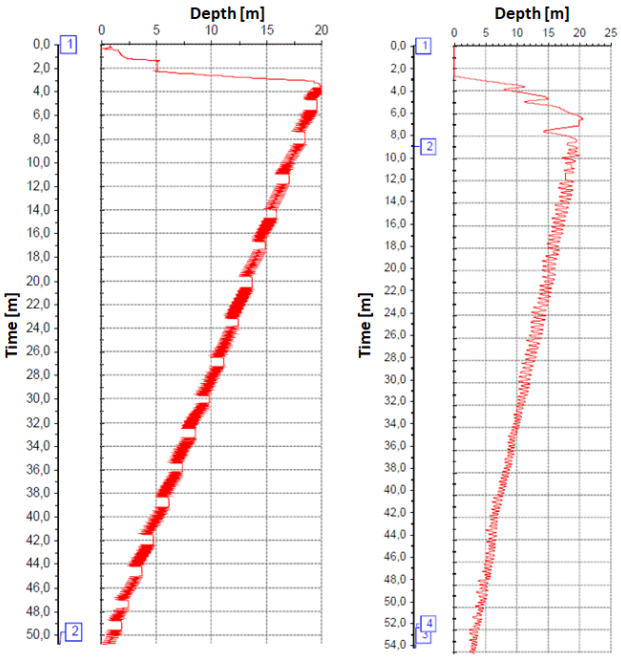

(a) *(b)*

Figure 7. Logs of execution parameters: (a) discontinue bottom-feed method, (b) new continue bottom-feed system.

ACKNOWLEDGEMENTS

The authors greatly appreciate the kind contribution of the company Ferrovial Construcción for enable most of the data about the project of San Ignacio bridge.

REFERENCES

Carvajal, E., Vukotić G., Castro J. and Wehr W. (2013). Comparison between theoretical procedures and field test results for the evaluation of installation effects of vibro-stone columns. Proc. Int. Conf. on Installation Effects in Geotechnical Engineering. Rotterdam. GEO-INSTALL.

Carvajal, E. and Mora-Rey, C. (2014). Stone columns by vibro-replacement: technology development, design and case histories. XXVII Reunión Nacional de Ingeniería Geotécnica. México.

Kirsch, K. and Kirsch, F. (2010). Ground Improvement by Deep Vibratory Methods. S. P.

Proceedings of the XVIII ECSMGE 2024
GEOTECHNICAL ENGINEERING CHALLENGES
TO MEET CURRENT AND EMERGING NEEDS OF SOCIETY
© 2024 the Authors
ISBN 978-1-032-54816-6
DOI 10.1201/9781003431749-410
Open Access: www.taylorfrancis.com, CC BY-NC-ND 4.0 license

ECSMGE 24
XVIII EUROPEAN CONFERENCE ON SOIL MECHANICS AND GEOTECHNICAL ENGINEERING

Numerical analyses of the optimum length of stone columns and their encasements

Analyses numériques de la longueur optimale des colonnes ballastées et de leurs enveloppes géotextiles

J. Castro*, M. Miranda, A. Márquez
Universidad de Cantabria, Santander, Spain

J. Fernández-Ruiz
Universidad da Coruña, A Coruña, Spain

S. Melentijevic
Universidad Complutense de Madrid, Madrid, Spain

**castrogj@unican.es*

ABSTRACT: Stone columns are vertical inclusions in soft soils formed by gravel. In very soft soils, they may be wrapped typically with a geotextile to increase its lateral capacity. In the latter case, they are usually named encased stone columns. Their critical or optimum length may be defined as the one where further lengthening of the column provides a negligible improvement and it is therefore not cost-effective to build columns longer than it. Besides, for encased stone columns, the optimum length of the encasement is also relevant. In previous finite element analyses, the authors have studied the column and encasement critical length considering a uniform soft soil layer with a linear elastic perfectly plastic behaviour for simplicity. For those cases, the optimum column length is around 1.5-2.0 times the footing diameter for encased stone columns, and slightly lower for ordinary stone columns, namely around 1.5. These critical lengths should be related to the loaded area and not to the column diameter. Here, the authors extend those previous analyses using a constitutive model that considers a stress-dependent soil stiffness, namely the Hardening Soil model. The results are very similar, but columns are slightly more effective when considering stress-dependent stiffness and the optimum column length is slightly lower. Finally, the critical length of the encasement is found to be slightly lower than the critical column length.

RÉSUMÉ: Les colonnes ballastées sont des inclusions verticales dans les sols mous, composées de gravier. Dans les sols très mous, elles peuvent être enveloppées dans un géotextile pour augmenter leur capacité latérale. Dans ce dernier cas, elles sont généralement appelées colonnes ballastées enveloppées. Leur longueur critique ou optimale peut être définie comme celle où un allongement supplémentaire de la colonne apporte une amélioration négligeable, donc il n'est pas rentable de les construire plus longues. En plus, pour les colonnes ballastées enveloppées, la longueur optimale du géotextile est également importante. Dans les analyses précédentes, les auteurs, pour simplifier, ont étudié la longueur critique de la colonne et du géotextile en considérant, une couche de sol uniforme avec un comportement élastique parfaitement plastique. Dans ces cas, la longueur optimale de la colonne est d'environ 1.5-2.0 fois le diamètre de la semelle pour les colonnes ballastées enveloppées, et légèrement inférieure pour les colonnes ballastées classiques, à savoir environ 1,5. Ces longueurs critiques devraient être liées à la surface chargée et non au diamètre de la colonne. Ici, les auteurs étendent ces analyses précédentes en utilisant un modèle de comportement du sol qui prend en compte leur rigidité en fonction des contraintes, le modèle Hardening Soil. Les résultats sont très similaires, mais les colonnes sont légèrement plus efficaces lorsque l'on considère une rigidité dépendante de la contrainte, et la longueur optimale est légèrement inférieure. Enfin, la longueur critique du géotextile est légèrement inférieure à la longueur critique de la colonne.

Keywords: Finite element analyses, encased stone columns, critical length, settlement.

1 INTRODUCTION

Ground improvement using stone columns, also known as granular piles or aggregate piers, is a widely spread technique to improve soft soils for foundation of embankments or structures (e.g. Barkdale and Bachus 1983; Kirsch and Kirsch 2010). In very soft soils, stone columns may suffer of lack of lateral confinement ($c_u \leq 5 - 15\ kPa$) (e.g., Wehr, 2006). In those cases, stone columns are usually encased with geotextiles or other geosynthetics (e.g., Alexiew and Raithel, 2015; Almeida et al., 2019)

Ordinary or encased stone columns (OSC or ESC) may reach a rigid substratum (end-bearing columns) or may be embeded just on a soft soil layer (floating columns). For the latter case, the length of the columns is an important design parameter to be chosen. In some cases, it may be more cost-effective to add additional columns than increase the length of the columns. In this way, the concept of the optimum or critical length of stone columns appear. For columns longer than the optimum length, the improvement achieved with stone columns does not notably change or increase. Although the load transfer mechanisms are different from piles, the concept of optmimum or critical length is equivalent (e.g., Fleming et al., 2009). The authors have also applied this concept to dynamic problems (Fernández-Ruiz et al., 2021).

Some existing proposals for the column critical length include those by Hughes and Withers (1974), McKelvey (2002) and Black et al. (2011), amongst others. The authors (Castro et al., 2019; Miranda et al., 2021) have analysed them and have shown that the column critical length should be expressed in terms of the footing width or diameter (B, D) because the column length to diameter ratio, L/d_c (slenderness of the column), has a minor influence (second order effect) on the ground improvement achieved with stone columns.

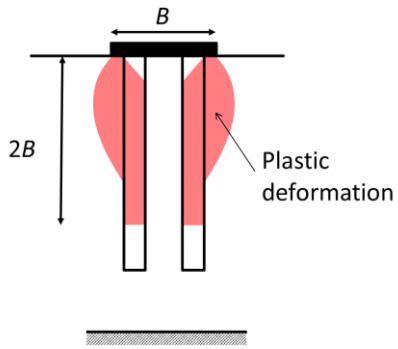

Figure 1. Justification of critical column length in a homogeneous soil layer.

Muir Wood et al. (2000) pointed out the importance of the deformation mechanism beneath the footing. Castro (2017) conceptually showed that the critical column length for bearing capacity depends on the failure mechanism and the critical column length for settlement reduction is related to the extension of the pressure bulb beneath the footing. Since the critical length is larger for settlement reduction, this is the one that is normally used. The pressure bulb is a useful concept, but it is strictly only valid for an elastic behaviour, which is not usually the case for an efficient design of OSC or ESC. The authors (Castro et al., 2019; Miranda et al., 2021) have shown that the critical column length is related to the extension of plastic deformation in the soil and column (Figure 1).

The concept of optimum column length is useful only for footings or small groups of columns because for large loaded areas (e.g., embankments), the critical length is larger than the soft soil layer thickness and then, there is no critical length in practise (e.g., Yoo, 2010).

Here, the authors extend their previous work on column critical length (Castro et al., 2019; Miranda et al., 2021), which considered a simple linear elastic perfectly plastic model ("Mohr-Coulomb", M-C) to reproduce the soil and column behaviour, to cases where a more advanced constitutive model is used to reproduce the soil behaviour, namely the Hardening Soil Model (HSM) (Schanz et al., 1999).

2 NUMERICAL MODEL

The finite element code Plaxis 2D 2023 (Brinkgreve et al., 2023) was used to represent a simplified 2D axisymmetric model of only one centred column beneath a rigid circular footing (Figure 2). This is the same 2D simplified model used in previous analyses by the authors (Castro et al., 2019; Miranda et al., 2021) and provides similar values of the footing settlement than those of a full 3D model of a group of columns with the same area replacement ratio and the same encasement stiffness to column diameter ratio (J_g/d_c). The area replacement ratio (a_r) is the ratio between the area of the columns and the loaded area.

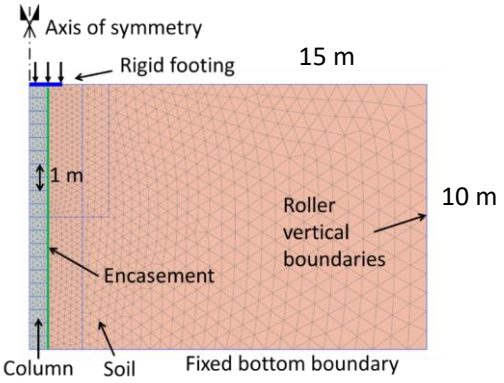

Figure 2. Numerical model and finite element mesh.

As a starting point, the same reference case as in previous analyses was used. The footing diameter, D, was 2.5 m and the column diameter (d_c=1.37 m) was chosen to give an area replacement ratio of a_r=30%. The soil profile was simplified to only one homogeneous soil layer, with a thickness of H=10 m (Fig. 2). The rigid footing was assumed as perfectly rough and modelled as a very stiff plate (EA = 10^{10} kN/m and EI = 10^{12} kN m^2/m) that

produces uniform settlements. Drained conditions were assumed for all the process, i.e. no excess pore pressures were generated. Geostatic initial stresses were generated using the effective soil unit weight (γ') and the coefficient of lateral earth pressure at rest, K_0=0.6. For simplicity, the ground water level was assumed to be at the ground surface and an effective unit weight of γ'=10 kN/m^3 for soil and column was directly considered without modelling pore water pressures. The applied pressure on the footing, p_{app}, was 100 kPa.

The column length was varied from L =10 m (end-bearing column, L/H=1) to L=0 m (no column) in steps of 0.5 m (Figure 2). The critical column length was identified from the variation of the settlement reduction factor with the column length. The settlement reduction factor (β) is the ratio between the settlement with columns and the settlement without columns (s_z/s_{z0}). Some mesh sensitivity (of around 3%) was observed between different cases, but the same mesh was used to identify each critical column length, i.e. for each case with different column lengths.

Table 1. Column and soil parameters using M-C.

Material	E (MPa)	ν (-)	c (kPa)	ϕ (º)	ψ (º)
Soil	2	0.33	5	25	0
Column	30	0.33	0.1	45	10

In previous analyses (Castro et al., 2019; Miranda et al., 2021), the soil and column were modelled using the M-C model (Table 1). Here, the column constitutive model and parameters were kept, but the soil is modelled using the HSM to be able to reproduce, for example, its stress-dependant stiffness. A reasonable common set of parameters that gives a similar settlement as in previous calculations was adjusted (Table 2). The reference pressure for the stiffnesses values is p_{ref}=100 kPa. Since stone columns are commonly employed in clays, the stress-dependant stiffness parameter was chosen equal to m=1 (oedometric behaviour).

Table 2. Soil parameters using HSM.

E_{50}^{ref} (MPa)	E_{oed}^{ref} (MPa)	E_{ur}^{ref} (MPa)	ν_{ur} (-)	c (kPa)	ϕ (º)	ψ (º)
8.7	8.7	26.1	0.2	5	25	0

3 NUMERICAL RESULTS

3.1 Influence of soil constitutive model

The results of the non-encased case for different a_r values are summarized in Figure 3. The value of a_r was varied by varying the column diameter. The settlements without column for the MC and HSM are the same and equal to 121 mm because the HSM stiffness parameters (Table 2) were calibrated to provide the same settlement. With column, the settlement reduction factor is slightly lower for the HSM than for the MC model because columns are more effective in a soil which stiffness increases with depth, than for a uniform stiffness, even more for short columns and large area replacement ratios.

The column optimum length is approximately indicated around 1.5D because the settlement reduction beyond that depth is negligible. A detailed analysis indicates that the column optimum length slightly decreases for larger values of a_r and for the HSM.

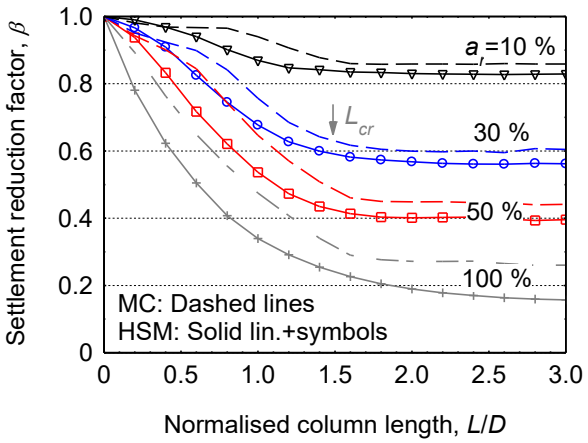

Figure 3. Settlement reduction factor for different column lengths, area replacement ratios and soil constitutive models.

3.2 Encasement critical length

Here, the numerical results considering an encasement with a circumferential stiffness of 0.5, 2 or 5 MN/ml are presented. A null Poisson's ratio is assumed for the geosynthetic encasement (ν_g=0) because it is assumed to have two major directions (radial and longitudinal), which behave independently.

Just as there may exist a column optimum length, there may exist an encasement optimum length. To systematically analyze them, both the column and the encasement lengths were varied (please, refer to Miranda et al., 2021 for details).

Table 3. Values of optimum column and encasement length for different area replacement ratios and geotextile encasement stiffnesses.

J (MN/ml)	a_r=10%	a_r=30%	a_r=50%
0.5	1.7D / 1.4D	1.6D / 1.3D	1.5D / 1.1D
2	1.8D / 1.5D	1.7D / 1.3D	1.6D / 1.1D
5	2.0D / 1.7D	1.8D / 1.3D	1.6D / 1.2D

The optimum column and encasement lengths for different a_r and J values are summarized in Table 3. It may be observed that the optimum encasement length slightly increases with higher geotextile stiffnesses, as the applied load is transmitted deeper. On the other hand, the critical encasement length reduces with the increment of a_r. Both trends are similar to the ones of the optimum column length (Table 3), but the values of the optimum encasement length are slightly lower. Therefore, from these numerical analyses, the optimum encasement length is slightly lower than the critical column length. Leaving the column tip without encasement could also contribute to create an enlarge column tip (Dash and Bora, 2013), whose effect has not been considered in the presented numerical simulations. On the other hand, leaving the column tip without encasement has disadvantages for the column construction process and consequently, it is not generally cost-effective. Thus, encasing the full column length is usually the best option. When partial encasement could be calculated as beneficial (e.g. Murugesan and Rajagopal, 2006), it will be more economical in most cases to reduce the whole column length and keep the full encasement of the column.

4 CONCLUSIONS

Previous analyses by the authors of the optimum column length are here extended using a constitutive model that considers a stress-dependent soil stiffness, namely the Hardening Soil model. The results show that the optimum column length for the analyzed cases (without encasement) is around 1.5 times the footing diameter (loaded area). Besides, the column optimum length slightly decreases for larger values of a_r and for the HSM when compared with the cases using the MC model. Finally, the critical length of the encasement is found to be slightly lower than the critical column length.

REFERENCES

Alexiew, D. and Raithel, M. (2015). Geotextile-Encased Columns: Case Studies over Twenty Years. In *Embankments with Special Reference to Consolidation and Other Physical Methods*, Indraratna, Chu and Rujikiatkamjorn (eds.), pp. 451-477. Butterworth-Heinemann.

Almeida, M., Riccio, M., Hosseinpour, I. and Alexiew, D. (2019). *Geosynthetic Encased Stone Columns for Soft Soil Improvement*. CRC Press, Leiden.

Barksdale, R. T. and Bachus, R. C. (1983). *Design and construction of stone columns*. Report FHWA/RD-83/026. Nat Tech Information Service, Springfield.

Black, J. A., Sivakumar, V. and Bell, A. 2011. The settlement performance of stone column foundations. *Géotechnique* 61(11): 909-922. https://doi.org/10.1680/geot.9.P.014.

Brinkgreve, R. B. J., Kumarswamy, S. et al. (2023). Manuals of Plaxis 2023. Bentley Systems.

Castro, J., Miranda, M., Da Costa, A., Cañizal, J. and Sagaseta, C. (2019). Critical length of stone columns. *Proceedings of the XVII ECSMGE-2019*. 1-7 September 2019, Reykjavik, Iceland.

Dash, S. K. and Bora, M. C. (2013). Influence of geosynthetic encasement on the performance of stone columns floating in soft clay. *Canadian Geotechnical Journal* 50, 754-765. https://doi.org/10.1139/cgj-2012-0437.

Fernández-Ruiz, J., Miranda, M., Castro, J. and Medina Rodríguez L. (2021). Improvement of the critical speed in high-speed ballasted railway tracks with stone columns: A numerical study on critical length. *Transportation Geotechnics* 30, 100628. https://doi.org/10.1016/j.trgeo.2021.100628.

Fleming, K., Weltman, A., Randolph, M. and Elson, K. (2009). *Piling engineering*. 3rd Edition. Taylor and Francis, Oxon.

Hughes, J. M. O. and Withers, N. J. (1974). Reinforcing of soft cohesive soils with stone columns. *Ground Engineering* 7 (3), 42-49.

Kirsch, K. and Kirsch, F. (2010). *Ground improvement by deep vibratory methods*. Spon press, London.

McKelvey, D. (2002). *The performance of vibro stone column reinforced foundations in deep soft ground*. PhD thesis, Queen's University of Belfast.

Miranda, M., Fernández-Ruiz, J. and Castro, J. (2021). Critical length of encased stone columns. *Geotextiles and Geomembranes* 49 (5), 1312-1323. https://doi.org/10.1016/j.geotexmem.2021.05.003.

Murugesan, S. and Rajagopal, K. (2006). Geosynthetic-encased stone columns: Numerical evaluation. *Geotextiles and Geomembranes* 24 (6), 349–358. https://doi.org/10.1016/j.geotexmem.2006.05.001.

Muir Wood, D., Hu, W. and Nash, D.F.T. (2000). Group effects in stone column foundations: model tests. *Géotechnique* 50, 689-698. https://doi.org/10.1680/geot.2000.50.6.689.

Schanz, T., Vermeer, P. A. and Bonnier, P. G. (1999). The hardening-soil model: Formulation and verification. In *Beyond 2000 in Computational Geotechnics*, R. B. J. Brinkgreve (ed), pp. 281-290. Balkema, Rotterdam.

Wehr, J. 2006. The undrained cohesion of the soil as criterion for the column installation with a depth vibrator. *Proc. Int. Symp. Vibrat. Pile Driv. Deep Soil Vibrat.* Compact. TRANSVIB, Paris, 157-162.

Yoo, C. (2010). Performance of Geosynthetic-Encased Stone Columns in Embankment Construction: Numerical Investigation. *Journal of Geotechnical and Geoenvironmental Eng., ASCE* 136(8), 36-45. https://doi.org/10.1061/(ASCE)GT.1943-5606.0000316.

Proceedings of the XVIII ECSMGE 2024
GEOTECHNICAL ENGINEERING CHALLENGES
TO MEET CURRENT AND EMERGING NEEDS OF SOCIETY
© 2024 the Authors
ISBN 978-1-032-54816-6
DOI 10.1201/9781003431749-411
Open Access: www.taylorfrancis.com, CC BY-NC-ND 4.0 license

ECSMGE 24
XVIII EUROPEAN CONFERENCE ON SOIL MECHANICS AND GEOTECHNICAL ENGINEERING

End bearing of large diameter piles in sand during driving

Résistance de pointe des pieux de grand diamètre lors du battage dans le sable

D. Cathie*
Cathie Group, Brussels, Belgium

S. Raymackers, T. Vergote, G. Haine
DEME Offshore, Zwijndrecht, Belgium

J. Saraiva, A. Burgraeve
Cathie Group, Brussels, Belgium

**david.cathie@cathiegroup.com*

ABSTRACT: Current methods for calibrating the end bearing component of soil resistance to driving (q_u) in sand are based on factoring or capping the cone tip resistance (q_c). Results of a detailed back analysis of driving behaviour of large diameter piles in sand using a large database of pile driving data from several windfarm sites are presented. Self-weight penetration (SWP) records are assessed indicating q_u/q_c~0.5. Signal matching for piles in the PAGE JIP indicated unit end bearing <0.2q_c. Back analysis of three large windfarm sites revealed q_u in the range 0.13-0.25q_c with the lower value being more reliable. Differences between SWP and dynamic end bearing are explained in terms of drained and undrained soil resistance. The undrained resistance is much lower than the drained resistance because the operational undrained shear strength is affected by the effective stresses around the pile tip during dynamic penetration which in turn are governed by hydraulic fracture and cavitation.

RÉSUMÉ: Les méthodes actuelles de calibration de la composante en pointe de la résistance du sol au battage (q_u) dans les sables sont basées sur un facteur de réduction ou le plafonnement de la résistance à la pointe du cône (q_c). Les résultats d'une analyse à postériori détaillée du comportement de battage de pieux de grand diamètre dans le sable à l'aide d'une vaste base de données de battage de pieux provenant de plusieurs parcs éoliens sont présentés. Les mesures de pénétration sous poids propre (SWP) sont évaluées et indiquent q_u/q_c~0,5. L'analyse par calage de signaux sur les pieux effectués dans le cadre du PAGE JIP a indiqué une résistance unitaire de pointe <0,2q_c. L'analyse à postériori de trois grands parcs éoliens a révélé que q_u se situait entre 0,13 et 0,25q_c, la valeur la plus faible étant la plus fiable. Les différences entre le SWP et la résistance en pointe dynamique s'expliquent en termes de résistance du sol drainée et non drainée. La résistance non drainée est beaucoup plus faible que la résistance drainée parce que la résistance opérationnelle au cisaillement non drainé est fonction des contraintes effectives autour de la pointe du pieu pendant la pénétration dynamique qui, elles-mêmes, sont régies par la fracture hydraulique et la cavitation.

Keywords: Pile; driveability; end bearing; cone resistance; undrained.

1 INTRODUCTION

Current pile driveability methods do not always provide good predictions for large diameter monopiles and various authors and groups are addressing this problem (Stergiou et al, 2023, Yenigul et al, 2023; Jones et al, 2020; Vergote et al, 2022; Cathie et al, 2020). The two components of the Soil Resistance during Driving (SRD) are shaft friction and annulus end bearing. The end bearing component is the subject of this paper. Starting with static end bearing assessed from self-weight penetration, the study investigates the end bearing using a detailed back analysis of driving data over the full range of penetration depths and correlation to the cone penetration resistance, q_c.

Three major monopile installation projects are considered in this paper with a total of 190 locations. Pile diameters were 6.7 – 7.8m OD and pile tip wall thickness 56 – 85mm. All sites were in the North Sea in predominantly fine to medium sand, although some locations contain layers of dense silt and clay (which do not dominate the SRD but are useful to indicate rapid changes in end bearing).

An independent approach to assessing unit end bearing is also reported using signal matching of dynamic pile monitoring measurements.

2 END BEARING ASSESSMENT

2.1 Previous work

Methods of assessing the annulus end bearing resistance during driving of offshore tubular piles (q_u) in sand are widely based on the cone tip resistance (q_c) using a ratio q_u/q_c. Alm and Hamre (2001) proposed q_u = 0.15 q_c* where q_c* is $(q_c/\sigma'_{v0})^{0.2}$, which lead to approximately q_u/q_c of 0.35-0.55, while Maynard et al (2019) found q_u/q_c=0.1. Schneider and Harmon (2020) studied three well documented cases and found q_u/q_c =0.35-0.45. Jones et al (2020) adopted q_u/q_c =0.6 for all soils.

Others have assessed end bearing driving resistance by adapting the static end bearing capacity (Byrne et al, 2012; Lehane et al, 2022). Lehane et al consider the mobilisation distance for end bearing and select q_u=0.4q_c in their adaptation of the Unified method. How the raw cone resistance profile is smoothed is important for most methods, for example by considering ±1.5D* (where D* is the equivalent diameter) above and below the pile tip (Lehane et al, 2022).

Independent back analysis of a large quantity of driving data by Stergiou et al (2023) led to a correlation: $q_u = (0.15 + 0.35A_r)q_c$. For the monopiles used in the present study, the area ratio, A_r is in range 0.03-0.04 leading to q_u/q_c~0.16.

Cathie et al (2020) in a detailed signal matching study for a large diameter monopile (7.8m OD) imbedded in a very dense sand layer (qc > 100MPa) at 30m depth, in a water depth of 30m, revealed a unit end bearing in the range 6 – 7.5MPa. Using a q_c limit of 50MPa indicated q_u/q_c of 0.12 - 0.15 which was considered to be constrained by cavitation of the pore water during dynamic penetration.

Based on strain measurements during penetration, White (2002) showed that for drained penetration in sand significant grain crushing and particle breakage occurs just below the pile tip in a "nose cone" with zones of vertical compression/horizontal extension, horizontal compression/vertical extension and dilation. Rapid loading tests of piles in sand in a centrifuge by Hölscher et al. (2012) confirm the different zones of contraction and dilation as measured by the excess pore pressure response either positive or negative (suction). The pore pressure response was also dependent on the partial dissipation which occurs during the rapid loading test.

When using CPT data for driveability studies, the pile embedment depth into a stronger layer and the effects of a weaker layer below influence the correlation between q_c and q_u. In dense sand, a "critical depth" to achieve "quasi-stationary" penetration resistance is between 10 – 20 times the governing dimension – either the cone diameter, or the pile diameter for closed or plugged piles (Puech and Foray, 2002). For unplugged piles, the pile wall thickness at the tip may be considered the relevant dimension, which is the case for all piles considered in this paper. Thus, pile penetrations into stronger layers require 1.0-1.5m to develop full quasi-static resistance.

Whether the pile tip response is drained or undrained may be a key consideration for assessing end bearing. The normalised velocity $v.d/c_v$ where v is the pile velocity, d the pile wall thickness, and c_v the coefficient of consolidation of the sand), may be used: when $v.d/c_v$<0.1 drained conditions may be assumed whereas for $v.d/c_v$>30 undrained conditions apply (White et al, 2018). Considering a pile wall thickness of 75mm and a rate of penetration of 2m/s (rise time of about 5ms, penetration 0.01m), c_v limits for drained and undrained conditions are >1.5 or <0.005 m^2/sec, respectively. Many dense fine to medium sands will fall between these limits (partially drained) while dense fine silty/clayey sands may well respond undrained. This may explain the uncertainty which currently exists on the appropriate end bearing resistance.

Accumulation of excess pore water pressure may develop around the shaft in fine sands due to partial drainage under typical blow rates of 30-100 blows/minute. However, this is less likely around the pile annulus despite the highly variable strain field with areas of contraction and dilation (White, 2002). Nevertheless, particle breakage will occur due to the very high stresses associated with driving in dense sand which cause contraction and average pore pressure increases and lower operational undrained shear strength.

Finally, the need to consider the spatial variability of the cone resistance in the vertical direction has led to the various methods developed to smooth the cone resistance for pile resistance calculations (see Lehane et al, 2022). However, the spatial variation of the cone resistance around the perimeter of a large monopile will also be significant. A discussion on spatial variability is outside the scope of this paper and may be considered a scale effect of using the CPT cone resistance as an indicator of end bearing resistance.

2.2 Penetration rates

During initial pile installation (pile stabbing), the pile penetration velocity is a similar order of magnitude to the penetration rate of a standard cone penetration test (0.02m/s) and the normalised penetration rate lies in the drained region for sand. Therefore, this self-weight penetration (SWP) resistance is considered a static,

drained resistance. Back analysis of the SWP of piles during stabbing provides a reliable benchmark (drained) resistance for performing back analysis during driving.

During pile driving, the average penetration rate is approximately 0.01m/s during normal driving (25 blows/0.25m) and 0.001m/s during hard driving (125 blows/0.25m) depending on the blow rate indicating drained end bearing response during multiple blows even if the single blow response is partially drained or undrained.

In current SRD assessment methods (Alm & Hamre, 2001; Maynard et al, 2019, Stergiou et al, 2023) the (drained) cone resistance (q_c) is used to estimate the (potentially undrained) pile annulus resistance. This has led to applying limiting values to the measured q_c to avoid overestimating the unit end bearing (Cathie et al, 2020).

3 END BEARING RESISTANCE DURING SELF-WEIGHT PENETRATION

The measured SWP under either pile weight or pile plus hammer weight provides a direct measure under essentially static conditions of the soil resistance. At low penetrations in sand, the soil resistance is dominated by end bearing. By reducing the pile and hammer weight by the estimated shaft resistance, the unit end bearing (q_u) can be evaluated with some confidence.

In this study, the SWP for pile and hammer together has been used since all the studied projects involved scour protection and not all piles punched through the scour protection under their own weight. The additional overburden pressure caused by the scour protection increases the effective stresses in the soil and thus the soil resistance. An overburden correction was applied to the raw CPT data (collected in the absence of scour protection) considering the additional stress increment using elastic theory and the effect of this increase on cone tip resistance using the correlations of Krogh et al (2022). As noted above, the cone resistance was smoothed over a 1m interval (+-0.5m from the depth considered).

The shaft resistance to be deducted from the overall pile plus hammer weight to give the end bearing component was obtained using the Alm and Hamre (2001) method after demonstrating in a preliminary study that the SWP was well predicted.

Figure 1 shows the measured SWP plotted against the calculated unit end bearing, normalized by the cone tip resistance (q_u/q_c) at the pile tip depth. q_u/q_c appears to reduce slightly with depth but is generally within the range 0.4 – 0.6.

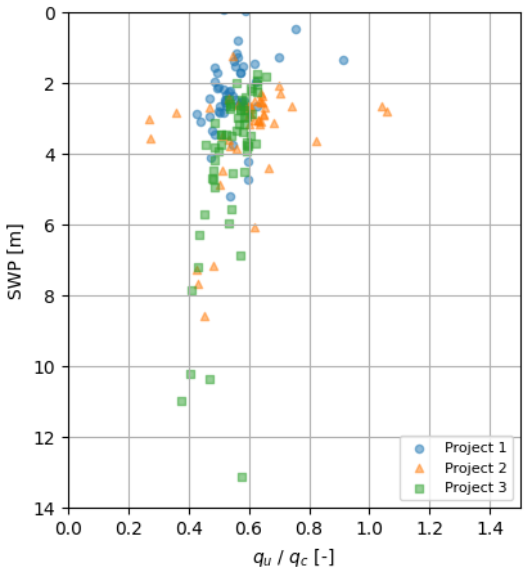

Figure 1. Normalised unit end bearing from self-weight penetration results.

Considering the pile tip wall thickness (t) for the projects in this study, the quasi-static end bearing resistance should be achieved after a penetration of about 1.6m (20*t). Since almost all points exceed this criterion, a correction for shallow penetration is not necessary and therefore the depth dependency is not due to shallow penetration into a layer.

The depth dependency in q_u/q_c appears to be related to the vertical effective stress and the depth dependency disappears when using the Alm and Hamre (2001) formulation for the unit end bearing: $q_u = s_1\, q_c\, (q_c/p_0')^{0.2}$ where p_0' is the effective overburden pressure.

A best fit value s_1=0.15 was derived from this data set which confirms the original formulation of Alm and Hamre is quite appropriate for SWP assessment of large diameter piles although the simpler use of q_u/q_c~0.5 is also satisfactory.

4 END BEARING RESISTANCE DURING DRIVING

4.1 Unit end bearing from signal matching

Since no pile monitoring data was available for the monopile driving for the 3 test sites, the end bearing from the PAGE JIP have been used to provide an independent indicator and backdrop for this study. The PAGE JIP (Cathie et al, 2023) analysed 25 high quality dynamic pile load tests at End of Drive (EoD) and during Restrike by signal matching for piles with diameters between 1.3 - 3.4m. The signal matching process yields the shaft resistance and end bearing at

the time of driving. Although signal matching is not as reliable as static measurements or SWP data to assess end bearing, it still provides a realistic estimate of the end bearing resistance for large diameter piles during driving and is the best data available at the present time. End bearing derived from signal matching includes not only the annulus resistance but a component of the shaft resistance very close to the pile toe which cannot be resolved in the wave equation model. In the data presented below, no attempt has been made to correct for the shaft resistance component and therefore the results should be considered a high estimate of the annulus end bearing.

From the PAGE dataset, the unit end bearing is plotted as a function of the cone tip resistance in Figure 2. Cone tip resistance in this figure is the average q_c over +-1.5D from pile tip. The best fit q_u/q_c is 0.20 for the signal matching results.

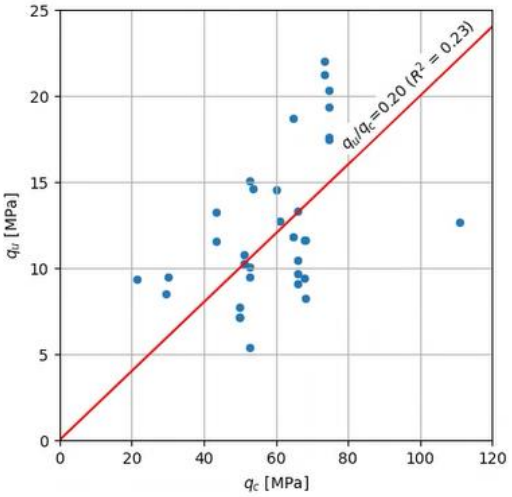

Figure 2. Unit end bearing from signal matching.

4.2 End bearing resistance from back-calculated SRD

Performing a back analysis using a wave equation solution of the three study projects using measured blowcounts, hammer energy and taking account of energy losses due to submergence (Vantomme et al, 2019) leads to a continuous back figured SRD v depth. In the back analysis, a fixed set of quake and damping factors was adopted (quake: 2.5mm, damping shaft and toe: 0.5s/m) to give consistency of SRD with that found from signal matching in sands.

Using the continuous SRD v depth plots, the change in SRD when transitioning from a stronger to a markedly weaker layer may be used to approximately assess the annulus end bearing change (Figure 3). While the shaft resistance is cumulative and only changes relatively gradually with depth, the end bearing resistance reduces rapidly as it penetrates a stronger or weaker soil. The reduction in SRD (ΔQ) is primarily due to a change in end bearing (although a small component of this change is due to the incremental increase in shaft resistance due to the additional penetration and the decrease due to friction fatigue). This can be compared to the reduction in cone resistance (Δq_c) at the layer change, which can be used to develop the approximate relation between Δq_u / Δq_c where $\Delta q_u = \Delta Q/A$ and A is the pile annulus area.

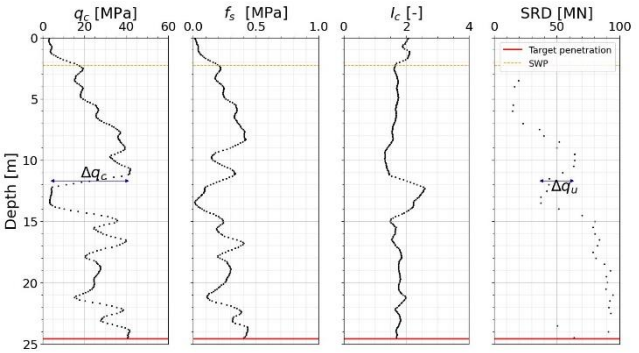

Figure 3. Example of back analysis results and selection of Δq_c and Δq_u.

A manual approach selecting clearly defined cases, and an automatic approach were undertaken. For the manual approach, the main criteria adopted for selecting the locations and depth windows included a) a well-defined change in q_c (typically at least 20MPa), and a sufficiently deep layer of weaker material that the annulus end bearing during driving would reach a quasi-static value (taken as 2m). An example is shown in Figure 3.

There is some subjectivity in the selection of data points in the manual procedure. To exclude any bias, the whole dataset was analysed numerically comparing $\Delta q_u/\Delta q_c$ over a 2m window (selected to obtain a significant change in q_c and q_u, but not too large to be unduly affected by the change in shaft resistance. For the same reason, the dataset was filtered on the soil behaviour index, selecting only cases for Ic>2.4 at the bottom of the window, and Δq_c<-10MPa. The two sets of results are shown on Figure 4 and the histograms on Figure 5.

The manual approach on a much smaller dataset took account of depth mismatches between changes in q_c and q_u, indicates a median $\Delta q_u/\Delta q_c$=0.25, i.e. q_u=0.25q_c. Quite a large scatter of Δq_u may be seen including some locations where there is very little change in SRD despite cone resistance changes in excess of 30MPa.

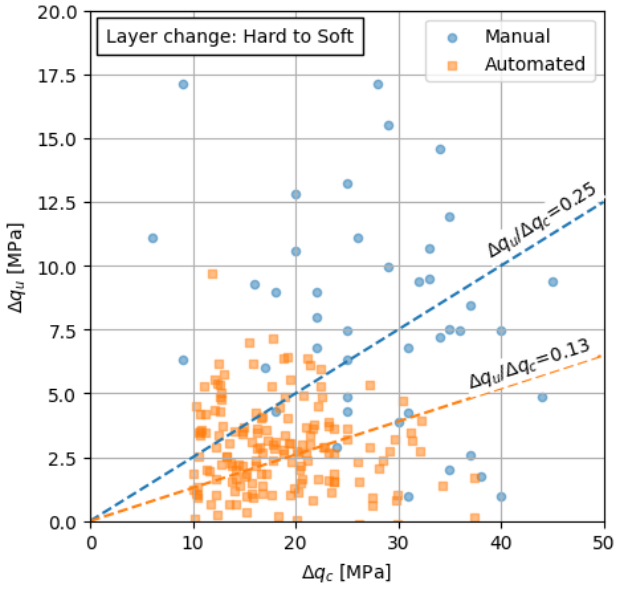

Figure 4. Change in cone resistance and end bearing for reducing q_c (absolute values plotted)

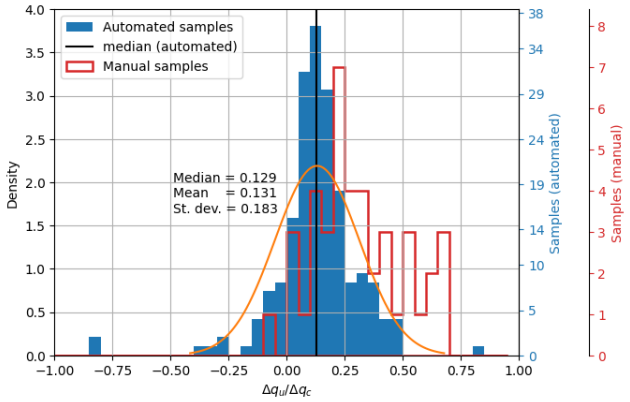

Figure 5. Change is cone resistance and end bearing for reducing q_c (sand into silt/clay) using 2m window applied to full dataset

The automated approach did not account for a depth mismatch between CPT and SRD data but overall, a clearer trend is found compared to the manual method with q_u= 0.13q_c being the best fit. Both approaches assume that the CPT data is representative for the entire pile diameter.

5 DISCUSSION

Based on the static resistance during SWP, the q_u/q_c ratio found for the sand profiles in this study approaches 0.4 below 10m penetration. From signal matching the ratio is less than 0.2, while from back analysis we have 0.13 - 0.25, with the lower 0.13 corresponding to the better data set. The difference between static and dynamic penetration are believed to be due to the different mechanisms occurring during drained static penetration (pile during SWP and CPT) and undrained or partially drained dynamic penetration (pile). In soft clays, House et al (2001) demonstrated a factor of 3.4 difference between drained and undrained penetration resistance while recently Carotenuto et al (2022) have shown by variable rate penetration testing in silts a ratio between cone resistance in drained and undrained conditions respectively of 3.0. Both studies are for contractive soils. In contrast, White et al (2018), in considering free-fall penetrometers, suggests higher undrained resistance for all but very loose sands due to dilation-induced suction pressures based on theoretical considerations.

Applying the White et al undrained strength model for a silica sand with relative density of 90% leads to a mean effective stress at failure of 7.2MPa, an undrained shear strength of 4.7MPa, and q_u of 35MPa. This is not consistent with the results of this study.

The White et al model does not take account of pore water cavitation during driving as discussed by Cathie et al (2020). If the cavitation limits are respected, at 30m penetration and 30m water depth, the mean effective stress at failure is limited to 0.99MPa, the undrained shear strength 0.63MPa and q_u 4.8MPa which is well aligned with the back analysis results.

Lower undrained end bearing during driving in sand may also result from extremely high instantaneous hydraulic gradients around the pile tip. Carotenuto et al (2022) indicated pressure differences between the cone tip and shaft that exceeded u/σ'_{v0} of 3 at a penetration rate of 0.1m/s and could exceed 4-5 during a blow (2m/s). This would translate to upward hydraulic gradients far greater than needed for hydraulic fracturing of the soil and temporary relief of the effective stresses around the pile tip area as the pressure wave in the pore water propagates outwards from below the pile tip. Such pore pressure gradients can also be inferred from the high volumetric strain rate gradients around a pile tip observed by White (2002) during drained penetration.

6 CONCLUSIONS

Based on the methods and data used in this study for large diameter piles in sand, the annulus end bearing observed during self-weight penetration (SWP) was between q_u/q_c = 0.4-0.6. During driving, the ratio was much lower due to undrained (or partially drained) conditions with the data pointing to q_u/q_c<0.2 by signal matching and q_u/q_c~0.13 (for the most reliable results) from global back analysis of the driving logs.

Differences between the drained SWP results and the driving back analysis results are due to the undrained or partially drained conditions operating

during a single blow, and the shear strength dependence on a) pore pressure cavitation, and b) hydraulic fracture in dynamic conditions near the pile toe.

Further work is required to evaluate these effects and to test theoretical concepts on databases such as the one used in this paper.

REFERENCES

Alm, T., Hamre, L., (2001). Soil model for pile driveability predictions based on CPT interpretations. Int. Conf. on Soil Mechanics and Geotechnical Engineering. pp. 1297–1302.

Byrne, T., Gavin, K., Prendergast,L.J. Cachim. P, Doherty, P, Pulukul, S.C (2018). Performance of CPT-based methods to assess monopile driveability in North Sea sands, Ocean Engineering, Vol.166, pp 76-91. https://doi.org/10.1016/j.oceaneng.2018.08.010.

Carotenuto. P et al (2023) Study of partial drainage effects in a natural silty deposit using variable rate CPTU testing, Proc. 9th Int. SUT Offshore Site Investigation and Geotechnics Conf, London.

Cathie, D. Jaeck, C. Ozsu, E. and Raymackers, S (2020) Insights into the driveability of large diameter piles, Int. Symp. Frontiers in Offshore Geotechnics, Austin, Texas.

Cathie, D. Jardine, R, Silvano, R. Kontoe, S. and Schroeder, F. (2023). Axial capacity ageing trends of large diameter tubular piles driven in sand, Soils and Foundations, Vol. 53, 6, https://doi.org/10.1016/j.sandf.2023.101401.

House, A. R., Randolph, M., & Watson, P. (2001). In-situ assessment of shear strength and consolidation characteristics of soft sediments. In C. Aubeny, & J-L. Briaud (Eds.), Proc. OTRC 2001 Int. Conf., Houston, USA, pp. 52-63. Offshore Technology Research Centre.

Hölscher, P., van Tol, A.F., Huy, N.Q., 2012. Rapid pile load tests in the geotechnical centrifuge. 9th Int. Conf. on Testing and Design Methods for Deep Foundations 52, 1102–1117.

Jones, L. Rattley, M. and Mancea, S (2020) A CPT-based soil resistance to driving (SRD) method for offshore pile driveability analysis, Proc. Piling 2020 Conf., ICE Publishing, pp 207-216.

Krogh, L. Quinteros, S. Engin, H.K. and Lunne, T (2022) Revisiting interpretation of relative density from shallow depth CPTs in sand, Can. Geotech. J. 59: 808–826, https://dx.doi.org/10.1139/cgj-2021-0200.

Lehane, B. Igoe, D. Gavin, K. Bittar, E. (2022) Application of the Unified CPT method to assess the driving resistance of pipe piles in sand. 11th Int Stress Wave Conf., Rotterdam.

Maynard, A.W., Hamre, L., Butterworth, D., Davison, F., 2019. Improved pile installation predictions for monopiles. 10th Int. Conf. on Stress Wave Theory and Testing Methods for Deep Foundations. ASTM Int.pp.426–449, http://dx.doi.org/10.1520/STP161120170164.

Puech, A., Foray, P., 2002. Refined Model for Interpreting Shallow Penetration CPTs in Sands. Presented at the Offshore Technology Conference, Houston, Texas.

Schneider, J.A., Harmon, I.A., 2010. Analyzing drivability of open-ended piles in very dense sands. J. Deep Found. Inst. 4, 32–44.

Stergiou, T. Perikleous, G. and Meissl, S. (2023). MonoDrive: A novel SRD methodology for offshore wind monopile foundations developed based on an extensive driveability database, Proc. 9th Int. SUT Offshore Site Investigation and Geotechnics Conf, London.

Vergote, T and Raymackers, S (2022). Building a framework for probabilistic assessment accounting for soil, spatial, operational and model uncertainty, applied to pile driveability, Ocean Engineering, Vol.266, part 5.

Vantomme, F. Versteele, H. and Cathie, D (2019) Driving energy losses for constant diameter and tapered submerged monopiles, Applied Ocean Research, 82, pp337-345.

White, D.J., 2002. An investigation into the behaviour of pressed-in piles, PhD Thesis, University of Cambridge.

White, D.J., O'Loughlin, C.D., Stark, N and Chow, S.H. Free fall penetrometer tests in sand: Determining the equivalent static resistance, Cone Penetration Testing 2018, pp695-701.

Yenigul, N. Yan, Y. Braakenburg, L.C.H. and Thumann, V.M. (2023) Evaluation of pile driveability predictions in sand, Proc. 9th Int. SUT Offshore Site Investigation and Geotechnics Conf, London.

Proceedings of the XVIII ECSMGE 2024
GEOTECHNICAL ENGINEERING CHALLENGES
TO MEET CURRENT AND EMERGING NEEDS OF SOCIETY
© 2024 the Authors
ISBN 978-1-032-54816-6
DOI 10.1201/9781003431749-412
Open Access: www.taylorfrancis.com, CC BY-NC-ND 4.0 license

ECSMGE 24
XVIII EUROPEAN CONFERENCE ON SOIL MECHANICS AND GEOTECHNICAL ENGINEERING

Degradation mechanisms of the hydro-mechanical behaviour of a lime-treated clay exposed to wetting and drying cycles

Mécanismes de dégradation relatifs à l'altération du comportement hydromécanique d'une argile traitée soumise à des cycles hydriques

N. Chabrat*
LEMTA (UMR 7563) CNRS, Université de Lorraine, Nancy, France

G. Russo, E. Vitale
DiSTAR, University of Naples Federico II, Naples, Italy

O. Cuisinier, F. Masrouri
**Nicolas.Chabrat@univ-lorraine.fr*

ABSTRACT: The present experimental study is focused on analysing the degradation processes of the mechanical performances of a lime-stabilised expansive clay exposed to wetting/drying cycles of various amplitude. Fully cured specimens were exposed to several wetting and drying cycles with suction-controlled techniques, and the maximum suction applied during the cycles ranged from 0.30 MPa to 95 MPa. This study highlighted that the main deterioration mechanism of lime-treated expansive soils exposed to cyclic wetting and drying is connected to micro-structural changes whose intensity were controlled by the amplitude of the cycles. The improved understanding of these mechanisms, as provided by this work, has the potential to more effectively forecast the conditions that could promote durability of lime-stabilised expansive soil.

RÉSUMÉ: L'objectif de cet article est d'évaluer les processus d'altérations relatifs à l'exposition d'une argile traitée à des cycles de séchage et d'humidification. Des éprouvettes traitées à la chaux ont été exposées à des cycles hydriques d'amplitudes allant de 0,30 MPa à 95 MPa. L'étude a permis de montrer que le mécanisme principal de dégradation du comportement mécanique des éprouvettes était la formation de fissure dont l'intensité était contrôlée par l'amplitude de succion appliquée. Ainsi, l'altération observée est principalement mécanique et résulte d'un endommagement des liaisons cimentaires, ce qui permet d'expliquer le rôle primordial de l'amplitude des cycles hydriques sur le comportement à long terme des sols argileux traités.

Keywords: Soil stabilization; durability; wetting and drying cycles; expansive soils; compressibility; microstructure.

1 INTRODUCTION

The alteration of mechanical performances over the service life of treated soils when exposed to seasonal wetting and drying cycles is one of the major concerns of the improvement technique. Indeed, several studies showed that wetting and drying cycles can alter the beneficial effects of treatments on soil performances (e.g., Khattab et al., 2007). Various methodologies have been employed to simulate the wetting and drying cycles during laboratory experiments. The major importance of the experimental protocol to impose the wetting and drying cycles has been highlighted by some authors. Stoltz et al. (2014) studied the impact of the amplitude of wetting and drying cycles on the mechanical behaviour of an expansive clay treated with lime, evidencing a progressive increase of swelling associated to strength reduction for increasing suction levels. They employed osmotic suction-controlled techniques to impose different wetting and drying amplitudes to the specimens. The results evidenced a progressive increase of the swelling properties associated to a loss of strength with higher suctions applied upon drying. Therefore, a key factor in the degradation of the mechanical performance of lime-stabilised soils exposed to wetting and drying cycles is the amplitude of the wetting and cycles. Nevertheless, only very few studies investigated the role of the amplitude of the cycles.

In addition, the degradation mechanisms associated to wetting and drying cycles are still poorly understood. Indeed, most of the available studies on the impact of wetting and drying cycles are based on results obtained at the macroscopic scale, without deciphering the different microstructural processes occurring during cycles. Thus, the mechanisms responsible for the degradation of lime-stabilised soils exposed to wetting and drying cycles still need to be

identified. Tang et al. (2011) provided some evidences that the bonding induced by lime-treatment could be altered by successive wetting and drying, with a significant modification of the microstructure along the cycles. There is thus a limited knowledge on the mechanisms involved in the alteration processes triggered by the exposure to successive wetting and drying cycles, and the relative importance of each process.

In this context, a laboratory study has been performed to understand the link between wetting and drying amplitude, micro-scale changes in fabric and the modification of the mechanical behaviour of a lime-treated expansive soil exposed to wetting and drying cycles. Lime-stabilised specimens were exposed to successive wetting and drying cycles of different amplitudes. The hydromechanical behaviour of the expansive soil was then determined using oedometer tests. The microstructure was also evaluated to identify the alteration mechanisms involved. In this paper, the characteristics of the lime-stabilised expansive soil specimens employed in this study are first provided. The experimental techniques are then successively exposed. The effect of the number of cycles and their amplitudes on the mechanical behaviour of the lime-stabilised soil and on the microstructure are then discussed. This work provides new understandings of environmental-driven alteration of lime-stabilised expansive soils that is discussed in the last section.

2 MATERIAL AND METHODS

2.1 Tested soil

The soil employed in this study was a clayey soil classified as CH according to the Unified Soil Classification System, mainly composed of clay minerals such as illite, muscovite, and montmorillonite, along with the presence of quartz and feldspars. The geotechnical characteristics of this soil can be found in Table 1. The shrinkage potential of the untreated soil, initially prepared at optimum moisture content, equal to 14.1 %, while the addition of 1% quicklime reduced the shrinkage potential to 0.1% (Stoltz et al., 2012).

Treated specimens were retrieved from the internal part of an experimental embankment built in 2010 with this expansive soil treated with 4 % quicklime by vertical coring. The embankment was thoroughly studied by Chabrat et al. (2023), who showed that the internal part of the structure was not affected by significant alterations due to environmental-driven processes.

Table 1. Geotechnical properties of the studied soil.

Parameters	Values
Passing sieve 80 μm (%)	90
Clay size content (<2 μm) (%)	70
Specific gravity Gs (-)	2.675
Liquid limit (%)	71
Plastic limit (%)	29
Plasticity index (%)	42

2.2 Experimental techniques

To prepare the specimens from the cores, a dicing saw equipped with a diamond wire was employed. Water was used to avoid heating of the sample during the cutting process. The specimens were subsequently carefully trimmed to a diameter of 70±0.1 mm and a height of 12 ± 2 mm. Two specimens were exposed to the same combination of suction amplitude and number of cycles. One of the specimens was used to determine the compressibility of the material while the other was employed for the microstructural analysis. The different experimental techniques employed are successively introduced in this section.

2.2.1 Drying-wetting experimental procedures

One of the main goals of the study was to assess the impact of the range of suction applied during wetting and drying tests on the behaviour of the treated specimens. For this purpose, two different methods were chosen to apply different ranges of suctions. The first method employed osmotic suction-controlled oedometers. The cycles were applied between saturation (s = 0 MPa) and suction values ranging from 0.30 MPa to 8.00 MPa were applied to the specimens following the protocol developed by Stoltz et al. (2014). The second method employed climatic chamber to control the relative humidity of the soil. This method, also derived from the one developed by Stoltz et al. (2014), was chosen to simulate high-amplitude cycles, with H_R = 50% corresponding to s = 95 MPa and H_R = 80% corresponding to s = 30 MPa. During the cycles, the dimensions of the specimens were monitored to evaluate their swelling and shrinkage potential along the cycles.

2.2.2 Tests procedures

Following the drying and wetting cycles, some specimens were subjected to oedometer testing under saturated conditions. These tests involved saturating the specimens and loading them by increment. For microstructural analysis, cubes with approximate dimensions of 10±2 mm were cut from a sample after

the cycles. The samples were dried using the freezing/drying method. The specimens were first immersed in liquid nitrogen at a temperature of -196°C. They were then placed in a vacuum chamber to undergo water sublimation. Observations with Scanning Electron Microscopy (SEM) were performed using the Hitachi SU5000 microscope. Prior to observations, a gold coating was applied to the sample on a fresh fracture surface. SEM images were taken at different magnifications of x1000 and x5000.

3 RESULTS

The axial deformation during the cycles was first analysed (Figure 1). After 2 wetting and drying cycles, the extent of variation in swelling and shrinkage behaviour appeared closely related to the maximum suction imposed during the cycles, ranging from less than 1% during drying at 0.30 MPa of suction up to 8 % when drying at a suction level of 95 MPa (Figure 1). The initial drying phase upon all the ranges of suction applied consistently led to irreversible shrinkage. Subsequently, during the wetting stage following the first drying, limited swelling occurred, resulting in irreversible shrinkage strains by the end of the first cycle.

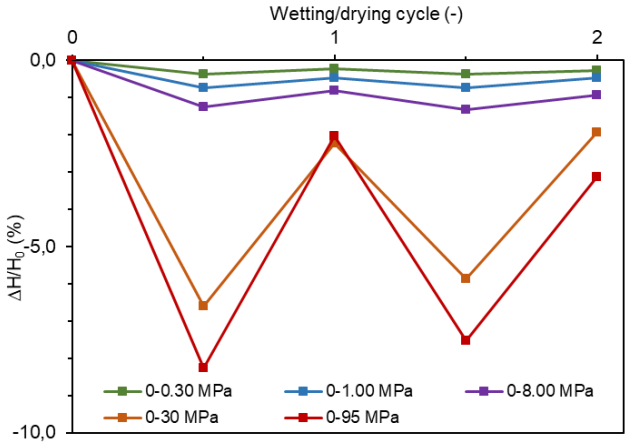

Figure 1. Volumetric variations obtained during 2 wetting and drying cycles.

Following the imposition of the suction cycles, the specimens were subjected to loading tests to determine their compressibility, and thus assess the impact of treatment (Figure 2). The compression curves obtained were compared to the one of the treated sample unexposed to wetting and drying periods (corresponding to N=0). The difference between the hydromechanical behaviour of the untreated and the treated soil suggests that the addition of lime effectively improved the mechanical performances of the soil. The compressibility of the specimens collected *in situ* was similar to the compressibility of specimens prepared in the laboratory. The impact of the cycles on the mechanical behaviour can be assessed by analysing the compressibility curves (Figure 2). After the first two cycles, it can be seen that the higher the suction applied during the drying phase, the larger the degradation of the mechanical behaviour. Up to an applied suction of 8.00 MPa, the compressibility is still significantly impacted by the lime treatment, as the yield stress of the soil was higher than 900 kPa. Beyond 8.00 MPa, the effect of lime stabilisation vanished, with values of yield stress lower than 100 kPa.

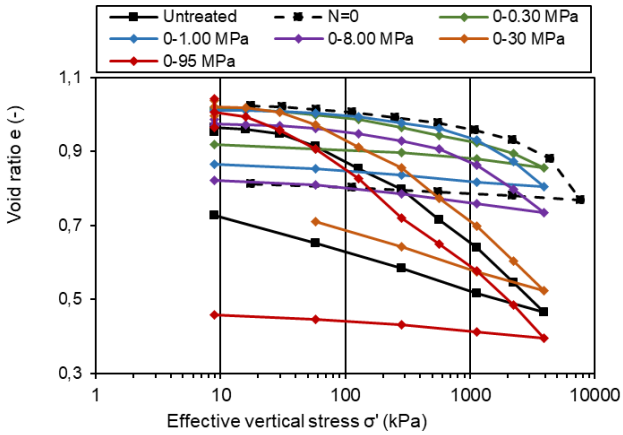

Figure 2. Compression curve of lime-treated specimens exposed to 2 wetting and drying cycles with different ranges of suctions.

Thus, for all amplitudes of wetting and drying periods, the first cycle induced plastic shrinkage deformation while only elastic deformation was generated during the subsequent cycles (Figure 1). The yield stress and the stress sensitivity were plotted as a function of the moisture content variation applied during the cycles (Figure 3). Extent of degradation was rather limited when the cycles were performed between 0.30 MPa and full saturation while the most significant mechanical degradation was observed when the applied suction during the cycles was larger than 8.00 MPa.

The microstructure was observed with SEM for the stabilized material unexposed to wetting and drying periods (Figure 4a), and then to specimens experimenting different ranges of suction applied (Figure 4b, c, d, e and f). The clayey particles observed on the unaltered specimen appear to be grouped together in aggregates bounded by macropores of about 1 µm wide, with a length higher than 10 µm. A coating on the surface of the particles was also observed that can be attributed to the precipitation of hydrated gel (i.e. C-S-H gel) as a result of the development of pozzolanic reactions (e.g., Vitale et al., 2020).

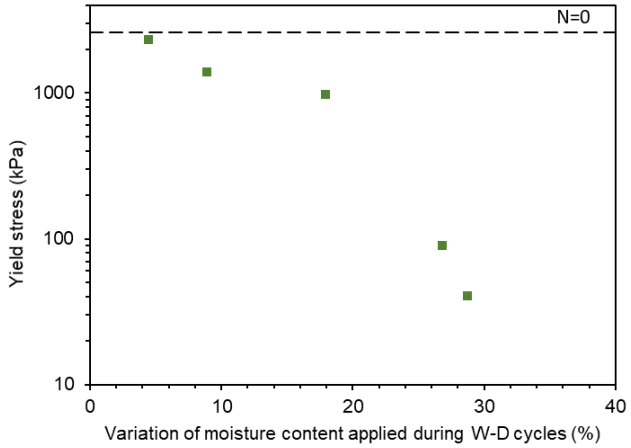

Figure 3. Effect of suction-controlled wetting and drying cycles on the yield stress of the quicklime-treated materials.

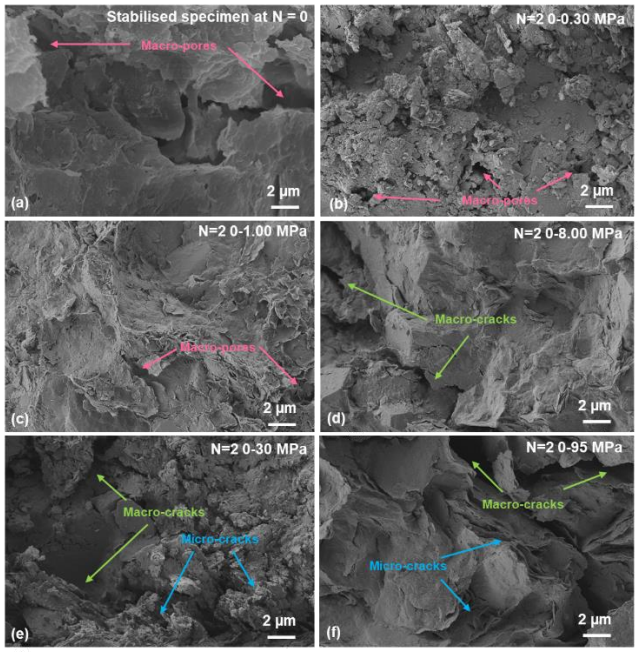

Figure 4. SEM pictures from specimens exposed to 2 wetting and drying cycles with different ranges of suctions.

Observations made on specimens exposed to a suction of 0.30 MPa (Figure 4b) showed low differences with the observations made on the unaltered treated soil (Figure 4a). The coating of the clayey particles is still visible and no significant evolution of the structure of the material could be observed. Specimens exposed to a suction of 1.00 MPa during the drying phase exhibited some longitudinal macro-cracks with a width of about 1 µm (Figure 4c). At the micro scale, the fabric of the specimens appeared to be massive and similar to the stabilised specimen unexposed to wetting and drying conditions. The newly formed macro-pores were even more present at an applied suction of 8.00 MPa, while the C-S-H gels were still visible on soil aggregates (Figure 4d). At 30 MPa and 95 MPa, macro-cracks could also be observed (Figure 4e and f). It was however possible to identify individual clay particles separated by pores smaller than 1 µm. Thus, a significant degradation of the microstructure was evidenced with the formation of macropores after the cycles when the maximum suction applied during the cycle was higher than 1 MPa. Beyond an applied suction of 8.00 MPa the cycles induced an additional alteration of the microstructure that led to the individualization of clay particles.

4 DISCUSSION

The purpose of this section is to explore the relationship between the modification of the microstructure, the amplitude of the wetting and drying cycles and the degradation of the compressibility. When the applied suction during wetting and drying periods was 0.30 MPa, the mechanical degradation of the material was very limited (Figure 2 and Figure 3), and the fabric of the soil seemed unaltered by the cycles. The height variation of the specimens occuring during wetting and drying cycles was also limited to 1% (Figure 1). When the maximum suction during the cycles was comprised between 1.00 and 8.00 MPa, newly formed macro-cracks were observed (Figure 4c and d). For suctions higher than 8.00 MPa, a complete change of the structure of the soil was evidenced, as both micro-cracks and macro-cracks were visible (Figure 4e and f). This rearrangement of the microstructure was associated to a complete degradation of the compressibility of the material.

The formation of cracks has been recognized as a key factor to explain the degradation of naturally cemented soft rocks containing clay exposed to wetting and drying cycles. Indeed, wetting-drying cycles can cause cyclic expansion and contraction of the clay minerals, and this repeatedly act on soil microstructure, resulting in fatigue damage, leading to a mechanical degradation of the material (e.g., Liu et al., 2020). The amount of cracks is likely related to the shrinkage experienced by the specimens during the cycles. Therefore, these observations demonstrate that a key damage mechanism could be associated to the formation of cracks during the cycles, indicating a degradation of the bonds between the soil particles associated to the pozzolanic reactions induced by the lime addition.

5 CONCLUSION

The main objective of this study was to analyse the impact of the wetting and drying cycles amplitude on

the behaviour of lime-stabilised samples, and to understand the associated degradation mechanisms. Fully cured specimens were exposed to several wetting and drying cycles. The amplitude of the cycles was controlled using suction-controlled techniques, and the maximum suction applied during the cycles ranged from 0.30 MPa to 95 MPa. The height variation was monitored during the cycles, and the compressibility of the soil was determined through oedometer tests. Structural modifications at the micro-scale were evaluated through scanning electron microscopy.

The study demonstrated that the compression behaviour of the treated material could be significantly altered by wetting and drying periods. The alteration of the material was mainly explained by the formation of cracks upon drying. The number and intensity of the newly formed cracks in the stabilised material were promoted by the increase of the maximum suction applied. The improved understanding of these mechanisms, as provided by this work, has the potential to more effectively forecast the conditions that could promote durability of lime-stabilised expansive soil.

ACKNOWLEDGEMENTS

The study presented in this paper is a part of the first author's PhD thesis that has been funded by Ginger CEBTP. The authors gratefully thank Dr. Michel Khatib from Ginger CEBTP for their valuable support and fruitful discussions. Dr. Abner Colella, Dr. Claudia Di Benedetto and Dr. Roberto De Gennaro are gratefully acknowledged for their valuable support in conducting microstructural investigations.

The project has received funding from the European Union's Horizon 2020 research and innovation program under the Marie Skłodowska-Curie grant agreement No 778120.

REFERENCES

Chabrat, N., Cuisinier, O., Masrouri, F. (2023). In Situ Alteration of the Hydro-Mechanical Behaviour of a Compacted Stabilised Expansive Soil. Geotechnics 3, 921–936. https://doi.org/10.3390/geotechnics3030049.

Khattab, S.A., Al-Mukhtar, M., Fleureau, J.-M. (2007). Long-Term Stability Characteristics of a Lime-Treated Plastic Soil. Journal of Materials in Civil Engineering 19, 358–366. https://doi.org/10.1061/(ASCE)0899-1561(2007)19:4(358).

Liu, S.-Y., Cai, G.-H., Cao, J.-J., Wang, F. (2020). Influence of soil type on strength and microstructure of carbonated reactive magnesia-treated soil. European Journal of Environmental and Civil Engineering 24, 248–266. https://doi.org/10.1080/19648189.2017.1378925.

Stoltz, G., Cuisinier, O., Masrouri, F. (2014). Weathering of a lime-treated clayey soil by drying and wetting cycles. Engineering Geology 181, 281–289. https://doi.org/10.1016/j.enggeo.2014.08.013.

Stoltz, G., Cuisinier, O., Masrouri, F. (2012). Multi-scale analysis of the swelling and shrinkage of a lime-treated expansive clayey soil. Applied Clay Science 61, 44–51. https://doi.org/10.1016/j.clay.2012.04.001.

Tang, A. m., Vu, M. n., Cui, Y.-J. (2011). Effects of the maximum soil aggregates size and cyclic wetting–drying on the stiffness of a lime-treated clayey soil. Géotechnique 61, 421–429. https://doi.org/10.1680/geot.SIP11.005.

Vitale, E., Deneele, D., Russo, G. (2020). Microstructural Investigations on Plasticity of Lime-Treated Soils. Minerals 10, 386. https://doi.org/10.3390/min10050386.

Proceedings of the XVIII ECSMGE 2024
GEOTECHNICAL ENGINEERING CHALLENGES
TO MEET CURRENT AND EMERGING NEEDS OF SOCIETY
© 2024 the Authors
ISBN 978-1-032-54816-6
DOI 10.1201/9781003431749-413
Open Access: www.taylorfrancis.com, CC BY-NC-ND 4.0 license

ECSMGE 24
XVIII EUROPEAN CONFERENCE ON SOIL MECHANICS AND GEOTECHNICAL ENGINEERING

Deformation characteristics of existing three-line tunnels with connected aisle induced by three-line mechanized tunnels under-crossing

Caractéristiques de déformation des tunnels à trois lignes existants avec allée connectée induites par le passage sous les tunnels mécanisés à trois lignes

J.Q. Chang*, D.M. Zhang, H.W. Huang
Tongji University, Shanghai, China

M. Thewes
Ruhr University Bochum, Bochum, Germany

**1910278@tongji.edu.cn*

ABSTRACT: Deformation characteristics of exiting tunnel induced by tunnel under-crossing is crucial for the safety of existing tunnel. A combination of manual low-frequency monitoring and wireless sensing high-frequency monitoring was used for an under-crossing case. The case is existing three-line tunnels under-crossed by new three-line mechanized tunnels and there is a connected aisle between two existing tunnels. The monitoring measured settlement and deformation of existing tunnels. Settlement monitoring results show that the settlement of existing tunnel during under-crossing experienced 2 stages: (i) heave, (ii) subsidence. The settlement profiles of the existing tunnels induced by the second tunnel under-crossing were found to be asymmetric with respect to the second tunnel line and the location of maximum settlement point deviated toward the center of the first under-crossing tunnel and the second under-crossing tunnel. For the third tunnel under-crossing, the situation is similar but the offset is not as much. Besides, the connected aisle also caused a longitudinal asymmetric distribution of deformation. Rotational deformation monitoring results show that the deformation of existing tunnel is more complex. When the cutter of tunnel boring machine (TBM) is right below the existing tunnel, the existing tunnel heaved during TBM advancing and subsided during TBM halting. When the shield tail is 0.4D in front and behind the existing tunnel in horizontal direction where D is the diameter of TBM, the existing tunnel heaved at most of time while subsided if the grouting volume is insufficient.

RÉSUMÉ: Les caractéristiques de déformation de la sortie du tunnel induites par le passage sous le tunnel sont cruciales pour la sécurité des tunnels existants. Une combinaison de surveillance manuelle à basse fréquence et de surveillance à haute fréquence par détection sans fil a été utilisée pour un cas de passage souterrain. Il s'agit de tunnels existants à trois lignes traversés par de nouveaux tunnels mécanisés à trois lignes et d'une allée connectée entre deux tunnels existants. Le contrôle a mesuré le tassement et la déformation des tunnels existants. Les résultats du contrôle du tassement montrent que le tassement du tunnel existant pendant la traversée a connu deux étapes : (i) le soulèvement, (ii) l'affaissement. Les profils de tassement des tunnels existants induits par la traversée du deuxième tunnel se sont révélés asymétriques par rapport à la ligne du deuxième tunnel et l'emplacement du point de tassement maximal s'est écarté vers le centre du premier tunnel traversant et du deuxième tunnel traversant. Pour le troisième tunnel, la situation est similaire, mais le décalage n'est pas aussi important. En outre, l'allée connectée a également provoqué une distribution longitudinale asymétrique de la déformation. Les résultats du contrôle de la déformation rotationnelle montrent que la déformation du tunnel existant est plus complexe. Lorsque la fraise du tunnelier se trouve juste en dessous du tunnel existant, ce dernier se soulève lors de l'avancement du tunnelier et s'affaisse lors de l'arrêt du tunnelier. Lorsque la queue du bouclier se trouve à 0,4D devant et derrière le tunnel existant dans la direction horizontale, D étant le diamètre du tunnelier, le tunnel existant s'est soulevé la plupart du temps et s'est affaissé si le volume d'injection est insuffisant.

Keywords: Wireless sensing; shield tunneling; under-crossing.

1 INTRODUCTION

With the development of underground space, more and more tunnels are constructed in city area. The construction of new tunnel will affect the surrounding environments, like existing tunnels, pipelines, buildings. For the case of under-crossing existing tunnels, it is important to ensure both the serviceability of the existing tunnel and the safety of the new tunnel

(Fang et al., 2015). The earth balanced pressure shield (EPBS) machine under-crossing existing tunnels at close distance causes considerable deformation and devastating additional stress, especially in water-rich sand or silt stratum (Chen et al., 2018).

Many methods have been applied to study the effects of adjacent tunneling on existing structures, including empirical or semiempirical methods (Peck, 1969; Lai et al., 2017; Chen et al., 2018), physical model experiments (Byun et al., 2006;), numerical methods(Do et al., 2014; Avgerinos et al., 2017; Li et al., 2022), analytical methods (Liu et al., 2022), and field observations (Fang et al., 2022; Li and Yuan, 2012). Field observation provides the monitored data for all other methods. The models, assumptions need the field observation to be validated. Thus, field observation is the basis for other methods and is the most direct and reliable method.

The studies about tunnel-induced ground settlement have focused on complex crossing situations, such as new twin-line tunnel under-crossing existing single line (Lai et al., 2020), new twin-line tunnel under-crossing existing twin-line (Chen et al., 2018). In this paper, a more complicated crossing situation, new three-line tunnels under-crossing existing three-line tunnels, is studied by field monitor method to investigate the deformation characteristic of the existing three-line tunnels.

Traditional field method applied total station, level and other manual equipment for settlement measurement. These manual methods are time-consuming and less frequent. The monitoring results are often more difficult to reflect the deformation pattern of the existing tunnel during the under-cross process, i.e., deformation of the existing tunnel due to each construction cycle of the shield machine during under-crossing is difficult to be monitored. Thus, in this research, a new monitoring method, wireless sensing network (WSN) is combined with manual level for settlement measurement in the existing tunnels.

2 SITE MONITORING INFORMATION

The project is a new three-line tunnels under-crossing existing three-line tunnels in China. The relative positions between the tunnels are shown in Figure 1. Tunnel 1#, 2#, 3# are existing tunnels, Tunnel 4#, 5#, 6# are new constructing tunnels. The horizontal distance between Tunnel 1# and Tunnel 2# is 8.3 m. The horizontal distance between Tunnel 2# and Tunnel 3# is 10.3 m. The distance between Tunnel 4# and Tunnel 6# is 4.0 m. The distance between Tunnel 5# and Tunnel 6# is 4.0 m. The new constructing tunnels cross silty clay and clayey silt. The stratum between the existing tunnel and the new constructing tunnel is clayey silt. The properties of the stratum can be found in Table 1. The overburden of existing tunnel is around 22.0 m for Tunnel 1#, 2# and 19.65 m for Tunnel 3#. The vertical distance between the existing tunnels and new constructing tunnels is 3.6 m. The outer diameter of the tunnels is 6.6 m, the thickness of the tunnel lining is 0.35 m and the width of segmental ring is 1.5m.

The direction of construction progress is from north to south. Tunnel 1# is the first tunnel to be under-crossed. Tunnel 2# is the second tunnel to be under-crossed. Tunnel 3# is the third tunnel to be under-crossed. Tunnel 4# is the first to be constructed, then Tunnel 5# begin construction, and Tunnel 6# is the last to be constructed. After Tunnel 4# under-crosses Tunnel 3#, Tunnel 5# begins to under-cross Tunnel 1#. After Tunnel 5# under-crosses Tunnel 3#, Tunnel 6# begins to under-cross Tunnel 1#.

The monitored sections are shown in Figure 2. There are 35 settlement monitoring cross-sections in Tunnel 1#, 35 settlement monitoring cross-sections in Tunnel 2# and 43 settlement monitoring cross-sections in Tunnel 3#. The distance between two adjacent cross-sections of settlement monitoring is 2 m. WSN nodes are installed on the segmental ring of Tunnel 2# and the Ring No. are 478, 479 and 481, which are right above the Tunnel 6#. The installation of WSN nodes is shown in Figure 3 (a). Four tilt WSN nodes are installed on the segmental lining with the angle of 45° and 120° from vertical direction. The WSN nodes are installed in the position to reduce the effect of the deformation of segments (). The accuracy of manual level is 0.002mm, the accuracy of the tilt nodes is 0.01°. The monitoring frequency of manual level is 1~1/15 days^{-1} and that of WSN nodes is 1/3~1/10 minutes^{-1}. The WSN nodes on site is shown in Figure 3(b).

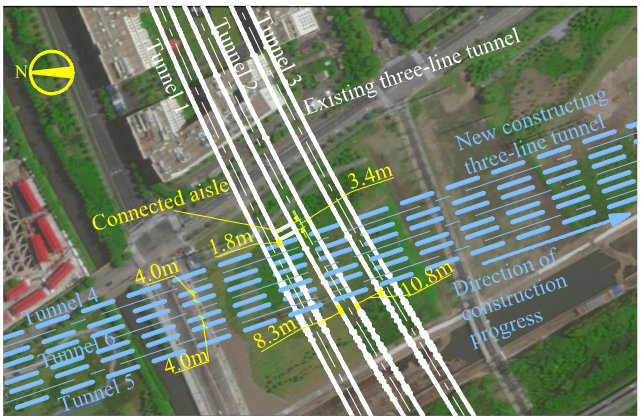

(a)

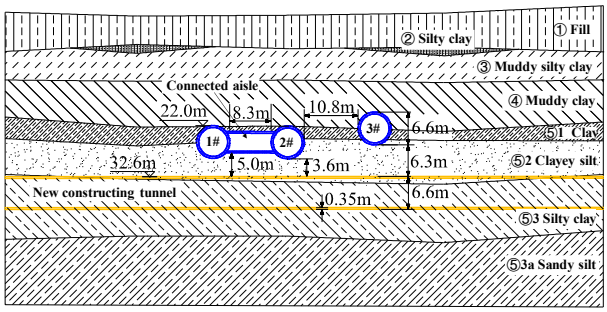

(b)

Figure 1. Site information: (a) relative position between newly constructed tunnels and existing tunnel; (b) ground profiles.

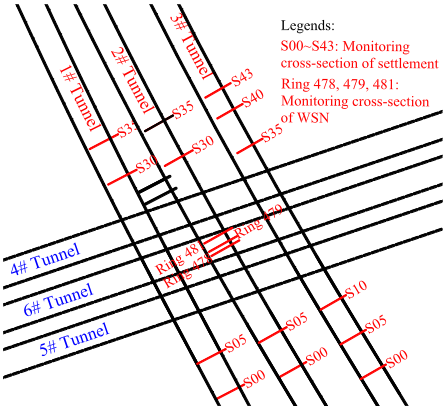

Figure 2. Monitored sections of existing tunnels.

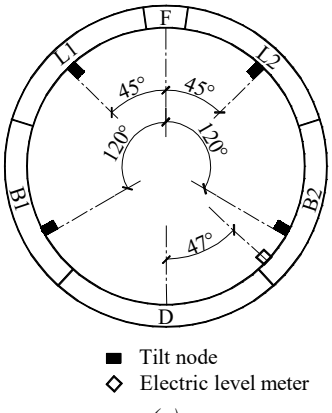

(a)

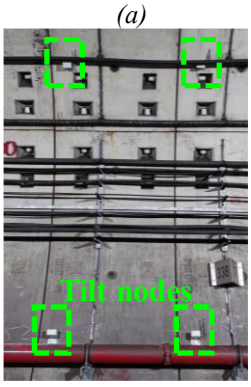

(b)

Figure 3. WSN monitoring: (a) installation diagram; (b) WSN nodes on site.

3 MONITORED DATA OF MANUAL LEVEL

The three typical relative position between tunnel boring machine (TBM) of new constructed tunnel and existing tunnel are shown in Figure 4. For position 1, the cutterhead of TBM is just about to enter directly below the existing tunnel. For position 2, the TBM has just passed directly below the existing tunnel. For position 3, the TBM is already 30 m away from the existing tunnel in horizontal direction. The monitored data from manual level at the three positions is shown in Figure 5 and the dashed line represents the center of the newly constructed tunnel. In Figure 5 (a), the existing tunnel is Tunnel 1# and the new constructed tunnel is Tunnel 4#, i.e., M equals to 1 and N equals to 4. For others: (b) M=1, N=5; (c) M=1, N=6; (d) M=2, N=4; (e) M=2, N=5; (f) M=2, N=6; (g) M=3, N=4; (h) M=3, N=5; (i) M=3, N=6.

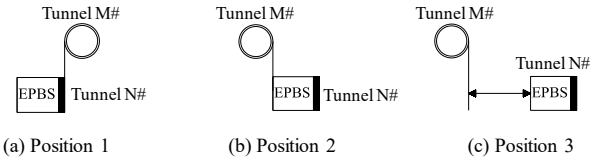

Figure 4. Three typical relative position between TBM of new constructed tunnel and existing tunnel.

At position 1, the existing tunnels heave. At position 2, the existing tunnels continue to heave and the troughs of settlement appear. At position 3, the settlement troughs of the existing tunnels have formed. During all nine under-crossing process the exsiting tunnels showed a deformation pattern of heave followed by settlement, although the final shape of the settlemnet troughs is different. The settlement troughs are “V” shape when the existing tunnels under-crossed by the first tunnel, “W” shape when under-crossed by the second tunnel, and “V” shape when under-crossed by the third tunnel.

The change of settlement over time is shown in Figure 6. S18 in Tunnel 1#, S18 in Tunnel 2# and S21 in Tunnel 3# are the sections directly above the newly constructed Tunnel 6#. The ranges between two adjacent straight lines in Figure 6 represent the under-crossing process of Tunnel 4#, 5#, 6#. During the under-crossing process, the existing tunnels heave firstly and then settle. However, the frequency of manual level monitoring is too low to display the deformation details of existing tunnels during under-crossing process. Thus, WSN is applied with a high monitoring frequency (Chang, et al., 2022).

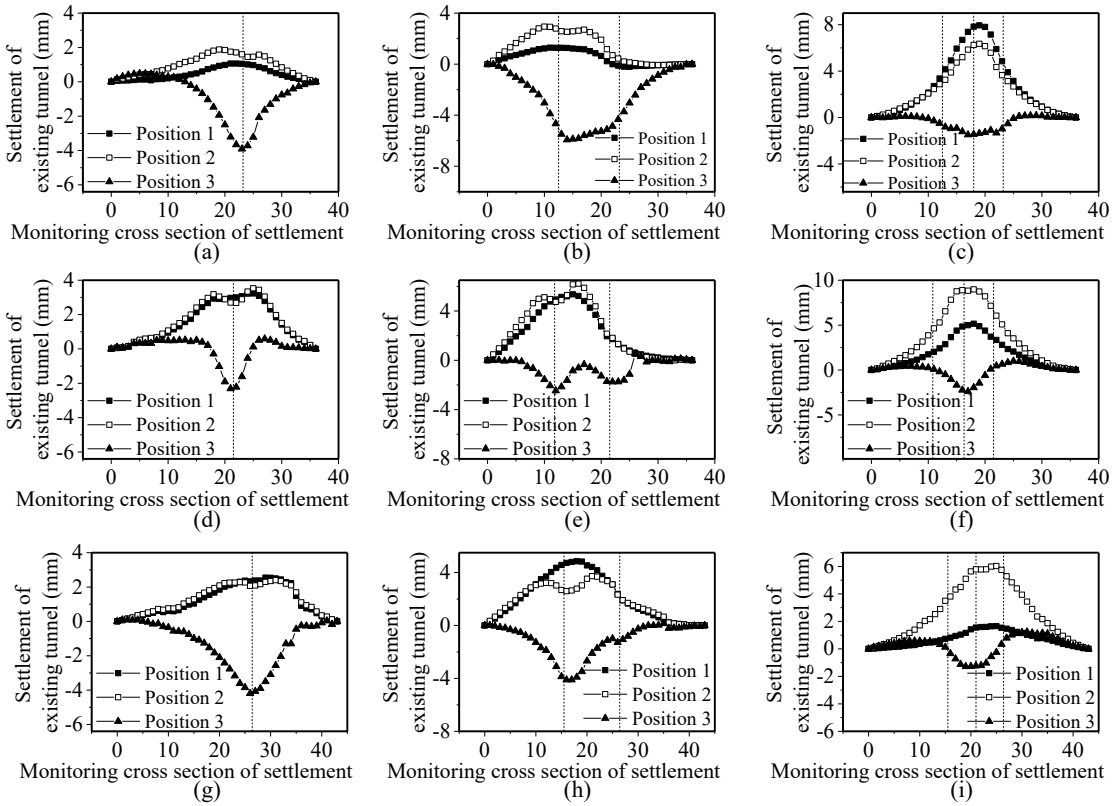

Figure 5. Monitored data from manual level.

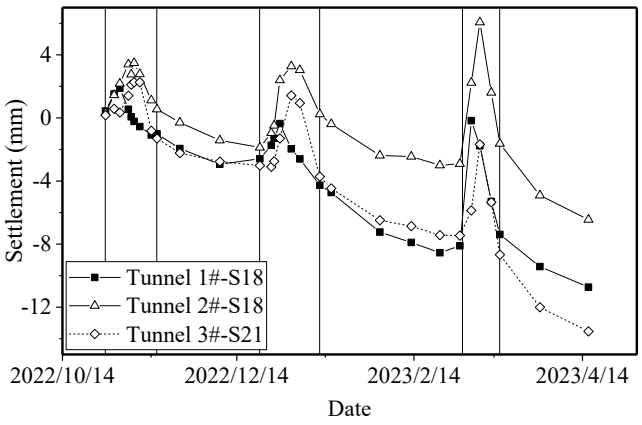

Figure 6. Data of manual level over time.

4 MONITORED DATA OF WSN

The monitored data of WSN is shown in Figure 7. There are 3 monitored sections, i.e., Ring 478, Ring 479 and Ring 481. In each section there are 4 WSN nodes. The monitored sections are in Tunnel 2# and are located directly above the newly constructed Tunnel 6#. According to the previous research (Wang et al., 2020), the convergence of horizontal diameter of segmental lining can be calculated by the data from WSN as:

$$\Delta D = L \cdot (\Delta\theta_1 - \Delta\theta_2) \cdot cos\ \alpha \qquad (1)$$

where L is the distance from point A to point B in Figure 3 (a); A is at the joint between segment B1 and segment D; B is at the horizontal side of segmental ring; $\Delta\theta_1$ is the tilt change of WSN node DR; $\Delta\theta_2$ is the tilt change of WSN node DL; α is the angle between vector AB and vertical direction as shown in Figure 3 (a). Using equation (1), the convergence of horizontal diameter of segmental lining can be calculated as shown in Figure 8. The increase in convergence value represents a decrease in diameter, i.e., a vertical ovalization deformation. The decrease in convergence value represents an increase in diameter, i.e., a horizontal ovalization deformation. The changing trend of diameter convergence is similar with the data from manual level. Comparing Figure 6 and Figure 8, horizontal ovalization and heave occur simultaneously, while vertical ovalization and settlement occur simultaneously. Using the least squares method, the relationship between convergence and settlement can be got as:

$$y = -2.68x + 2.40 \qquad (2)$$

where y is the settlement monitored by manual level and x is the convergence calculated by data from WSN on Ring 479. The results of the fitting are shown in Figure 9.

Thus, the deformation of existing tunnels including the diameter convergence and settlement with high

monitoring frequency can be obtained by WSN monitoring. The monitored results during the under-crossing process of Tunnel 6# is shown in Figure 10. The data is from UR node on Ring 479 of Tunnel 2#. The increase of data represents vertical ovalization and settlement of existing Tunnel 2# while the decrease of data represents horizontal ovalization and heave of existing Tunnel 2#. The gray boxes represent the advance process of TBM, while the other parts represent the halt process of TBM. During advance process, the data decreases so the existing Tunnel 2# shows horizontal ovalization and heave deformation because of the soil pressure on face and grouting pressure. The deformation of the existing tunnel induced by the under-crossing process is divided into 3 stages here:

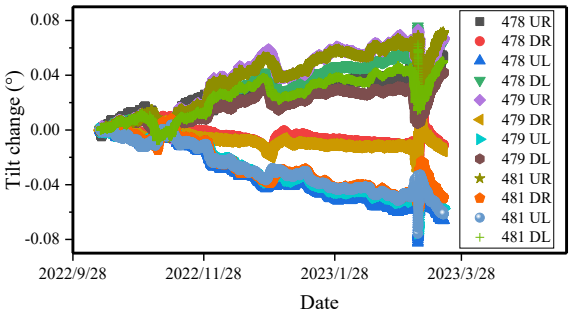

Figure 7. Monitored data of WSN.

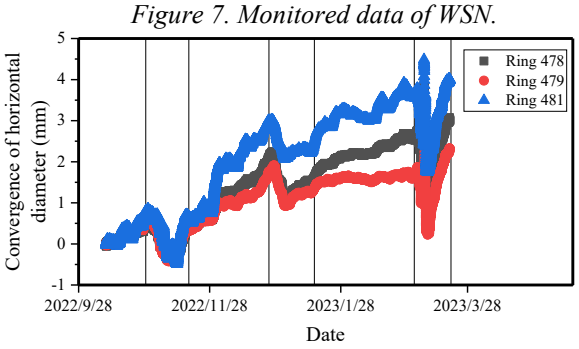

Figure 8. Convergence of horizontal diameter of segmental lining.

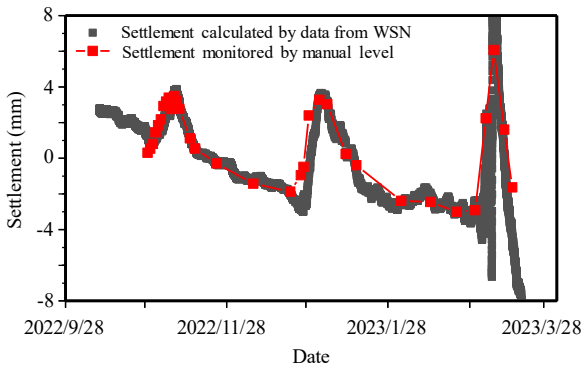

Figure 9. Settlement calculated by convergence of horizontal diameter and monitored by manual level.

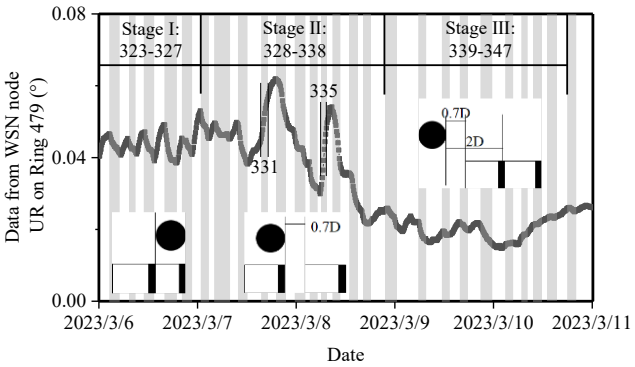

Figure 10. Deformation of existing tunnel monitored by WSN.

Stage I: During the construction of Ring 323 to Ring 327 of Tunnel 6#. At this stage, the cutterhead of TBM of Tunnel 6# is right below the existing Tunnel 2#. When TBM advances, the negative soil pressure on face causes the increase of pore water pressure in the stratum between Tunnel 2# and Tunnel 6#. As shown in Figure 1, the stratum between them is clayey silt and its permeability coefficient is relatively high compared with clay. Thus, in this stage, the heave and horizontal ovalization induced by TBM advance will disappear when the TBM halts because the excess pore water pressure decreases quickly.

Stage II: During the construction of Ring 328 to Ring 338 of Tunnel 6#. At this stage, the shield tail is no further than 0.7D from the existing Tunnel 2# in horizontal direction where D is the diameter of TBM. When shield advance, the grout is injected into the soil through the shield tail. The heave and horizontal ovalization of existing Tunnel 2# are mainly caused by the injection of grouting. Thus, the recovery of deformation during TBM halts is small at this stage. It should be noted that during the construction process of Ring 331 and Ring 335 of Tunnel 6#, the grouting volume is significantly insufficient, thus leading to significant settlement in the existing Tunnel 2#.

Stage III: During the construction of Ring 339 to Ring 347 of Tunnel 6#. At this stage, the shield tail is from 0.7D to 2D from the existing Tunnel 2# in horizontal direction. At this stage, the heave and horizontal ovalization caused by grouting decreases and the existing Tunnel 2# begins to settle again.

5 CONCLUSION

A complicated under-crossing construction case: newly constructed three-line tunnels under-crossing existing three-line tunnels is studied in this research. Manual level monitoring is combined with WSN monitoring. The results show that the connected aisle will decrease the heave of the first tunnel being under-

crossed and increase the heave of the second tunnel being under-crossed. The shape of settlement troughs after the first under-crossing are “V” shape, the shape of settlement troughs after the second under-crossing are “W” shape and the shape of settlement troughs after the third under-crossing are “V” shape. Because the third newly constructed tunnel is in middle of the first and second tunnel. The settlement can be calculated by the WSN monitoring data. The WSN data show that there are three stages of deformation of existing tunnels during under-crossing. In the first stage when the cutterhead is directly below the existing tunnels, the existing tunnels show heave and horizontal ovalization deformation during TBM advances because of the soil pressure on face. But when TBM halts, the heave and horizontal ovalization recover. In the second stage when the TBM tail is no further than 0.7D from the existing tunnels in horizontal direction, the existing tunnels show heave and horizontal ovalization deformation during TBM advances because of tail grouting. And when TBM halts, the heave and horizontal ovalization do not recover. In the third stage when the TBM tail is from 0.7D to 2D from the existing tunnels in horizontal direction, the influence of tail grouting decreases gradually and the existing tunnels begin to settle.

REFERENCES

Avgerinos, V., Potts, D.M. and Standing, J.R. (2017). Numerical investigation of the effects of tunnelling on existing tunnels. Geotechnique 67, 808-822. https://doi.org/10.1680/jgeot.SiP17.P.103.

Byun, G.W., Kim, D.G. and Lee, S.D. (2006). Behavior of the ground in rectangularly crossed area due to tunnel excavation under the existing tunnel. Tunn. Undergr. Space Technol. 21 (3–4). https://doi.org/10.1016/j.tust.2005.12.178.

Chang, J.Q., Huang, H.W., Zhang, D.M., Wu, H.M. and Yan, J.Y. (2022). Transverse deformational behaviors of segmental lining during shield tunneling: A case study. Structural Control & Health Monitoring 29. https://doi.org/10.1002/stc.3097.

Chen, R. P., Lin, X. T., Kang, X., Zhong, Z. Q., Liu, Y., Zhang, P. and Wu, H. N. (2018). Deformation and stress characteristics of existing twin tunnels induced by close-distance EPBS under-crossing. Tunnelling and Underground Space Technology, 82, 468–481. https://doi.org/10.1016/j.tust.2018.08.059.

Fang, Q., Zhang, D.L., Li, Q.Q. and Wong, L.N.Y. (2015). Effects of twin tunnels construction beneath existing shield-driven twin tunnels. Tunn. Undergr. Space Technol. 45, 128–137. https://doi.org/10.1016/j.tust.2014.10.001.

Peck, R.B. (1969). Deep excavation and Tunneling in Soft Ground State of the Art Report. In: Proc, 7th Int. Conf. on soil Mechanics and Foundation Engineering, Mexico city, pp. 225–290. https://doi.org/10.1061/(ASCE)0733-9410(1996)122:11(886).

Lai, H.P., Zhao, X., Kang, Z. and Chen, R. (2017). A new method for predicting ground settlement caused by twin-tunneling under-crossing an existing tunnel. Environmental Earth Sciences 76. https://doi.org/10.1061/(ASCE)0733-9410(1996)122:11(886).

Lai, H.P., Zheng, H.W., Chen, R., Kang, Z. and Liu, Y. (2020). Settlement behaviors of existing tunnel caused by obliquely under-crossing shield tunneling in close proximity with small intersection angle. Tunn. Undergr. Space Technol. 97. https://doi.org/10.1016/j.tust.2019.103258.

Liu, X., Fang, Q., Jiang, A.N. and Li, J.Y. (2022). Deformation analysis of existing tunnels with shearing and bending stiffness reduction at movement joints. Tunn. Undergr. Space Technol. 123. https://doi.org/10.1016/j.tust.2022.104408.

Wang F., Shi J.K., Huang H.W., Zhang D.M. and Liu D. (2020). A horizontal convergence monitoring method based on wireless tilt sensors for shield tunnels with straight joints. Structure and Infrastructure Engineering. 2020; 17(9): 1-16. https://doi.org/10.1080/15732479.2020.1801767.

Proceedings of the XVIII ECSMGE 2024
GEOTECHNICAL ENGINEERING CHALLENGES
TO MEET CURRENT AND EMERGING NEEDS OF SOCIETY
© 2024 the Authors
ISBN 978-1-032-54816-6
DOI 10.1201/9781003431749-414
Open Access: www.taylorfrancis.com, CC BY-NC-ND 4.0 license

ECSMGE 24
XVIII EUROPEAN CONFERENCE ON SOIL MECHANICS AND GEOTECHNICAL ENGINEERING

Fluid rheology and its implications for flow and cuttings transport in horizontal directional drilling (HDD) bores

Rhéologie des fluides et ses implications pour l'écoulement et le transport des déblais dans les forages de forage dirigé horizontal (FDH)

S.P.C. Che*, C.O. Menkiti
Geotechnical Consulting Group, London, UK

S.A. Jefferis
Environmental Geotechnics Ltd, Oxford, UK

s.che@gcg.co.uk

ABSTRACT: Common misconceptions about the appropriate fluid properties for horizontal directional drilling (HDD) often lead to inefficient hole cleaning strategies increasing the risk of hydrofractures, ground heave and mud loss, with significant cost and programme implications. This paper explores the fundamentals of flow behaviour in HDD showing that in-bore flow rates and hence fluid shear strain rates are so low that the traditional Bingham fluid model based on 300 and 600 rpm data from a Fann-type direct indicating viscometer is not valid. An example involving HDD bores for cable landfall of an offshore windfarm is discussed to illustrate the practical consequences of the cuttings transport processes. Analysis of rare annular pressure monitoring data has provided valuable insights into the cuttings behaviour in the bore. The importance of fluid property and pressure monitoring, and having a coherent hole cleaning strategy are highlighted. The paper concludes with recommendations to minimise the risks of hydrofracture and bore blockage.

RÉSUMÉ: Les idées fausses courantes concernant les caractéristiques fluides appropriées pour le forage dirigé horizontal (FDH) entraînent souvent des approches inefficaces de nettoyage du trou, augmentant ainsi le risque de fractures hydrauliques, de soulèvement du sol et de perte de boue, avec des conséquences significatives en termes de coûts et d'implications sur le programme. Cet article explore les principes fondamentaux du comportement de l'écoulement en FDH. L'article montre que le taux d'écoulement dans le forage et par conséquent les taux de cisaillement du fluide sont si faibles que le modèle traditionnel de fluide de Bingham basé sur des données à 300 et 600 tr/min provenant d'un viscosimètre direct de type Fann n'est pas acceptable. Un exemple impliquant les forages FDH pour les câbles sous-marins d'un parc éolien offshore est présenté afin d'illustrer les implications concrètes des processus de transport des déblais. L'analyse de données de surveillance de la pression annulaire, bien que peu fréquentes, ont livré des précieuses observations sur le comportement des déblais à l'intérieur du forage. L'importance des caractéristiques du fluide, la surveillance de la pression et avoir une stratégie de nettoyage du trou cohérente sont soulignées. L'article se termine en offrant des recommandations visant à réduire les risques de fractures hydrauliques et d'obstruction du forage.

Keywords: Horizontal directional drilling (HDD); drilling fluid; rheology; cuttings transport; hydrofracture.

1 INTRODUCTION

Horizontal directional drilling (HDD) was initially developed in the 1970s and is now widely used. Global challenges to mitigate climate change impacts through increased reliance on renewable energy and improved infrastructure resilience have increased the attractiveness of HDD technology. The technique is now capable of installing pipelines of up to 1.5 m diameter and up to 5.2 km length (Yan et al., 2019; Underground Construction, 2018). HDD is ideally suited to crossings beneath natural and man-made obstacles and offers substantial cost, safety and environmental benefits, as compared to alternative methods of pipeline and cable installation. However, despite the now wide use of HDD, there remain concerns regarding project risk in certain situations.

Key to HDD success is good management of the drilling fluid (often referred to as the mud), and the avoidance of excessive mud loss. Fundamental risks in HDD drilling arise from pressure build-up in-bore leading to hydrofracturing of the ground, heave of the overburden and mud loss – either to formation, subsurface infrastructure or up to the surface.

Table 1. Summary examples of mud use and shear rates in Europe in clayey ground. For shear rates using Bingham and Herschel-Bulkley models, parameters in Figure 2 have been assumed. P = pilot bore, R = fully reamed bore.

Category	Bore diameter (P & R)/ drill rod diameter (m)	Min/ max flow velocities in annulus (m/s)	Nominal Newtonian Shear rate range (s^{-1})	H-B shear rate range (s^{-1})	Bingham shear rate range (s^{-1})
Energy landfall HDD (efficient mud recycling ~1km+)	P:0.356 - 0.476; R:0.610 - 0.635/ 0.168	P:0.106/ 0.357; R:0.062/ 0.154	P:4.1 - 22.8; R:1.7 - 4.2	P:8.6 - 43.9; R:3.7 - 8.7	P:48.7 - 120.6; R:30.5 - 48.9
Long urban crossings (basic recycling ~500m+)	P:0.203 - 0.254; R:0.508 - 0.661/ 0.089	P:0.057/ 0.096; R:0.022/ 0.071	P:4.1 - 10.1; R:0.64 - 5.2	P:8.6 - 20.1; R:1.5 - 10.6	P:48.6 - 77.7; R:18.7 - 54.5
Short urban crossings (no mud reuse, ~200m)	P:0.153; R:0.457 - 0.559/ 0.089	P:0.105/ 0.262; R:0.007/ 0.016	P:19.8 - 49.5; R:0.17 - 0.52	P:38.3 - 92.9; R:0.45 - 1.2	P:111.6 - 185.6; R:9.5 - 16.8

In addition to ground heave, these problems can lead to slow progress rates, high mud consumption and risk of equipment damage or loss. Once hydrofracture has been initiated, fracture re-opening is easy and achievable in-bore pressures become limited, thereby constraining the available operational pressure range.

Poor cuttings transport can trigger bore blockage, generate hydrofracture and crystallise the above risks. At mud flow rates used in practice, hydrofractures can propagate significant distances in the ground before bore blockage is identified and mitigated.

These operational challenges are most severe for landfall HDD bores such as that shown in Figure 1 where drilling starts at a clifftop and descends to punchout in the sea. In-bore pressures before punchout are elevated by the hydrostatic head of the drilling fluid from the clifftop entry pit.

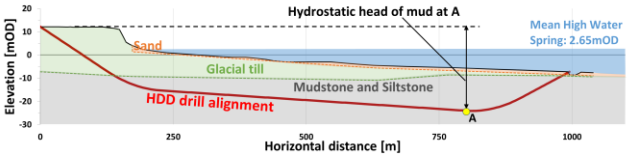

Figure 1. Example HDD vertical alignment for cable landfall (note expanded vertical scale, typical inclination of the entry section is about 9°).

2 THE DRILLING FLUID

For an HDD fluid key issues include: (a) carriage of the cuttings from the cutter head in the bore to the drill pit at the surface, (b) minimising the pressure required for cuttings carriage so as to minimise the risk of hydraulic fracture, and (c) limiting fluid loss from the bore. This discussion will focus on modelling the rheology and pumping pressure which are necessary precursors to the consideration of cuttings transport.

Typically in the UK the drilling fluid used for HDD works will be a bentonite-based slurry with an array of additives available including thinners, viscosifiers, agents to improve cuttings carriage, fluid loss control agents and fibrous materials to seal voids and fractures. Polymer fluids without bentonite have yet to achieve the prominence in UK HDD which they have achieved for piling world-wide.

Both bentonite slurries and polymer fluids are non-Newtonian fluids as indeed will be any fluid laden with soil cuttings. For these fluids, shear stress will be a non-linear function of the applied shear rate as can be seen from the data points in Figure 2 which are the average of many sets of shear stress - shear rate data for a bentonite-based fluid from an HDD bore. It can be seen that the data are strongly non-linear at low shear rates. Therefore when modelling non-Newtonian fluid behaviour it is essential to consider the operational shear rate.

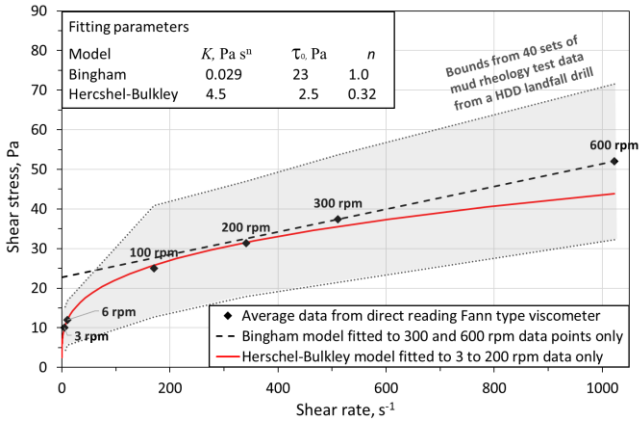

Figure 2. Shear stress - Shear rate data for a bentonite based slurry used in landfall HDD. Data obtained with a direct indicating viscometer of the Fann-type.

For a Newtonian fluid flowing with average velocity v in an annulus of external diameter d_o, and inner diameter d_i the shear rate at the wall $\dot{\gamma}$ is:

$$\dot{\gamma} = 12v/(d_o - d_i) \qquad (1)$$

For a circular pipe the same formula applies except that the number 12 is replaced by 8 and $(d_o - d_i)$ by the pipe diameter. For non-Newtonian fluids modelled wall shear rates will be higher than the nominal

Newtonian wall shear rate by a factor which will depend on the rheological model used, the selected model parameters, the flow rate, and the bore diameter (see for example, shear rates in Table 1). By way of an example of the significance of Equation 1, if the flow rate in an HDD bore is 1600 litre/min and the bore and drill pipe diameters are 0.356 and 0.168 m (14 and 6.625 in) then the nominal Newtonian shear rate will be 22 s^{-1} which will drop to 2.3 s^{-1} if the bore is reamed to 0.635 m (25 in).

Now the typical six-speed Fann-type viscometer used for assessing drilling fluids has a shear rate range of 5.1 to 1022 s^{-1} (3 to 600 rpm). Thus for HDD operations the in-bore shear rate is likely to be towards the lower end or below the range of shear rates that can be obtained with this type of viscometer (see Table 1 for typical examples and Figure 2). The best that can be done is to interpolate/extrapolate the low shear rate data (which themselves can be rather unsteady because of the low readings).

Two models have been used to fit the data in Figure 2, the Bingham and Herschel-Bulkley models. Both can be represented by the equation:

$$Shear\ stress = K\dot{\gamma}^n + \tau_0 \qquad (2)$$

where n is the power law index, K the consistency coefficient (Pa s^n) and τ_0 the yield stress (Pa). For the Bingham model $n = 1$.

It can be seen that the Bingham model based on the 300 and 600 rpm readings (511 and 1022 s^{-1}) gives entirely erroneous results at low shear rates. It predicts that there should be no flow below a shear stress of 23 Pa (y-axis intercept) whereas the measured data show flow at lower shear stresses. Despite this the Bingham model based on the 300 and 600 rpm data is the most widely used in the industry (Yan et al. 2020, Caenn et al. 2017, Lam et al. 2015). Indeed some Fann-type viscometers have only two speeds, 300 and 600 rpm. Whilst of no value for HDD flow modelling, the 300 and 600 rpm data can be useful for quality control as typical values are widely reported.

For all fluid modelling it is essential to adopt a model appropriate to the shear rates. For HDD this must be a model which can fit the low shear rate data, for example, the Heschel-Bulkley model (Chhabra and Richardson, 1999) and to use a viscometer capable of providing data at the relevant shear rates.

2.1 Pressure drop during drilling

Typically the drill rods may lie at the base of the bore but for order of magnitude pressure assessments it is convenient to assume that the bore is an annulus with central drill rods. Based on this assumption, Figure 3 has been developed to show the required pumping pressure per metre of bore for two bore diameters as a function of flow rate using the model parameters shown in Figure 2.

From Figure 3 it can be seen that for the Bingham model based on the 300 and 600 rpm data, flow rate has little effect on the pressure drop which is dominated by the inappropriately high modelled yield stress. The Herschel-Bulkley model fitted to the 200 to 3 rpm data gives greater sensitivity to the flow rate as the data fitting results in a lower yield stress but a much higher relative consistency coefficient.

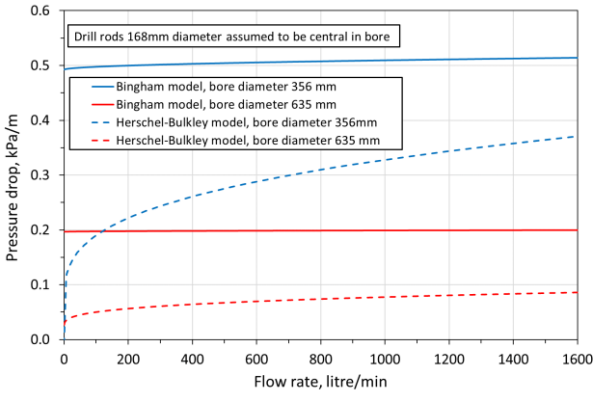

Figure 3. Modelled Pressure drop-Flow rate plots using Bingham and Herschel Bulkley Models.

However, a striking feature of both models is that the predicted pressures are low, much lower than those observed in the field with the clear implication that bores are not being effectively cleaned by the fluid flow and/or that the fluid discharged from the bore is not representative of the fluid in other parts of the bore. Indeed by way of comparison, the predicted pressures are much lower than the hydrostatic pressure which will be at least 10 kPa per metre vertical distance from cutter head to discharge pit.

2.2 Carriage of cuttings

Experience with slurry tunnelling machines suggests that a minimum velocity of about 3 m/s is necessary to carry the spoil in the pipeline from the cutter head. In HDD bores velocities are unlikely to reach 1 m/s (see Table 1). HDD cutter heads therefore must be designed and operated so as to cut the soil into pieces small enough to be carried by the fluid flow, sizes which can be expected to be of the order of 1 mm or less. This brings with it substantial demands with respect to soil-slurry separation. However, it must be recognised that in HDD, cuttings have to settle only the short distance across the bore to become part of a bed load which may be kneaded into a paste by the drill pipe and which may adhere to the pipe and/or walls of the bore so tending to block the bore. Good cuttings carriage will be

particularly important during reaming as the enlarged bore diameter will result in lower annular velocities potentially coupled with high solids loadings.

3 CUTTINGS LOAD FROM STATIC PRESSURE MEASUREMENTS

3.1 Background

Multiple HDD bores, each 1 km long, were drilled at a site off the UK east coast to enable the cable landfall of an offshore windfarm. The geology of the site comprises marine sand and glacial till overlying a mudstone bedrock. A bentonite-based drilling fluid with the average rheology shown in Figure 2 was used.

The initial phase of the HDD work was to form a pilot bore. The typical downhole assembly (DHA) used for pilot drilling is shown in Figure 4. It consists of a drill bit, a mud motor, and a gyro, behind which drill pipes are attached. The gyro measures the inclination and azimuth to determine the position of the drill downhole. The gyro unit also provides real-time measurements of fluid pressure both inside the drill pipe and in the annulus behind the mud motor. The annular pressure, which is reflective of conditions of the bore downhole, forms a focus of this paper.

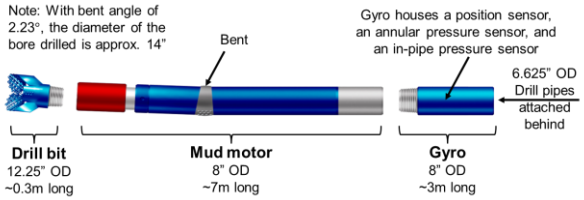

Figure 4. Schematic configuration of a pilot downhole assembly (DHA).

As discussed in earlier sections, hydrofractures and hole cleaning issues are key challenges in HDD. Current practice to mitigate hydrofracture risks involves careful monitoring and control of drilling parameters, particularly the dynamic annular pressure while drilling. On the other hand, the static annular pressure, which is the pressure of the mud plus cuttings suspended in the mud when there is no flow in the annulus, is rarely discussed or monitored. This paper sets out a novel and unique approach for tracking the cuttings content along the HDD bore, using the static annular pressure measured by the gyro.

3.2 Methodology

Following typical HDD site practice, after each pipe is drilled, the mud pump is turned off, the drill string is disconnected from the drill rig along with the internal electrical cable that transmits the signal from the gyro to the control cabin, a further pipe is inserted, cable reconnected, mud pump restarted and drilling resumed.

During pipe connections, opportunity was taken to capture the static annular pressure downhole after the mud pump was turned off, but before the disconnection of the signal cable. Such readings are rarely recorded in practice, although not difficult to obtain.

With the mud pump turned off, the annular pressure in the annulus should equilibrate to hydrostatic conditions. Hydrostatic pressure of fluid in the bore is calculated based on the density of mud returns exiting the bore at surface, and the depth change from the bore entry point to the annular sensor position, reflecting the current bore location. The density of mud returns measured at surface ranges from 1.01 to 1.2 kg/L. This range forms an envelope of hydrostatic pressures within which the static annular pressure measurements are expected to fall.

3.3 Results and findings

Figure 5 shows an example of the static annular pressures recorded during pilot drilling of a HDD bore in virgin ground. The measurements were compared to the expected range of hydrostatic pressures calculated based on the density of mud returns.

The static annular pressures are generally higher than hydrostatic from the first bend of the drill alignment where the bore path becomes flatter (at ~215 m from entry). This could be attributable to suspended cuttings not being effectively carried out to the surface, resulting in a higher in-bore mud density than that measured at surface. Cuttings will be held-up in the bore as they will tend to settle back so that their net velocity is less than that of the mud during their ascent to surface along the inclined section of the bore. However, as the excess pressures are more apparent in the horizontal section than the inclined, it seems that a more significant mechanism is the formation of blockages in the bore, which choke the flow and trap pressure within the bore. The trapped in-bore pressures take time to dissipate from the drilling conditions to hydrostatic.

In either case, the measurements indicate that cuttings were being held up and/or the bore blocked, which highlights the need for improved hole cleaning by optimising cutter head design, and/or mechanical hole cleaning coupled with attention to mud rheology. Not surprisingly, the highest concentration of trapped cuttings appears to coincide with the lowest point of the alignment before the ascent (~820 m from entry).

During the works, as drilling progressed to Pipe 53 (~510 m from entry), the front part of DHA (including

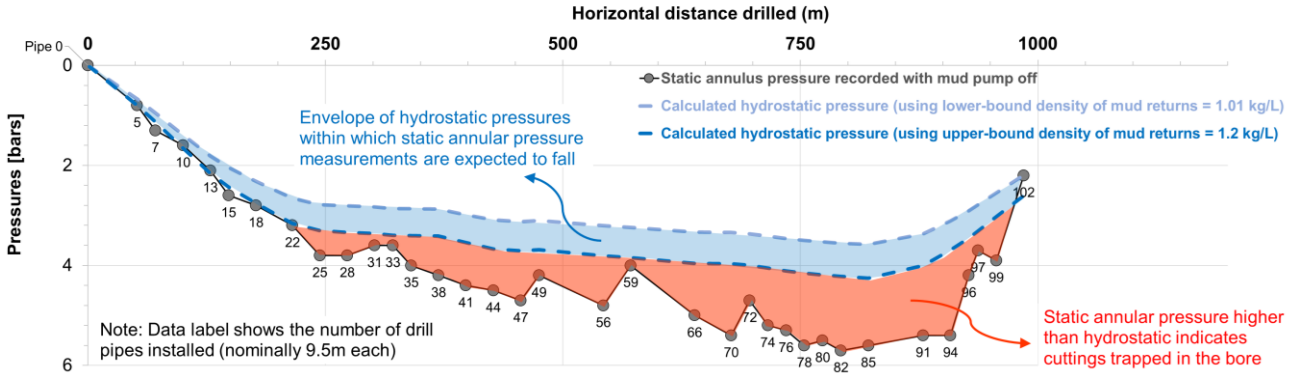

Figure 5. Comparison of static annular pressures with calculated hydrostatic pressures.

the drill bit and the mud motor) sheared off from the system and was lost downhole. A fishing operation was performed using a 11.25" diameter overshot housing a grappler. The lost tool was successfully retrieved and was tripped out to the surface. This tripping out was essentially also a mechanical hole cleaning. Cuttings in the form of large clay "sausages" were observed being tripped out (Figure 6). This confirmed that cuttings were trapped within the bore, as indicated by the high static annular pressures measured, which would not have been cleaned had the tripping out not been performed. Static annular pressures were also recorded for another HDD bore, and these findings were repeated, with high annular pressures indicating the presence of trapped cuttings. It is proposed that the monitoring of static annular pressures should be employed regularly as a simple and insightful means to inform the bore cleanliness, increase the confidence of hole cleaning performance and improve quality control.

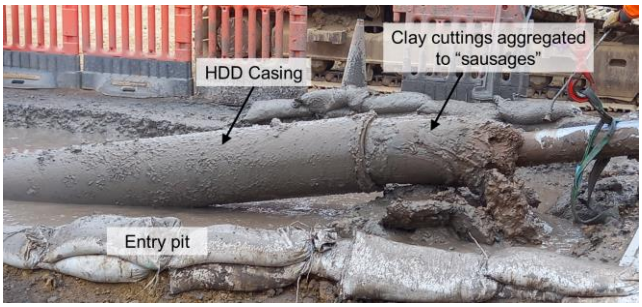

Figure 6. Photo of large "clay sausages" tripped out.

4 DISCUSSION AND CONCLUSIONS

The key issue from this brief analysis of HDD flow behaviour is that it is fundamental to: (i) consider the relevant shear rate for the process under consideration, (ii) use a fluid model appropriate to the shear rate and (iii) use a viscometer with which relevant data can be obtained. A Bingham fluid model based on the 300 and 600 rpm readings (shear rates of 511 and 1022 s^{-1}) on a direct indicating Fann-type viscometer will not be appropriate for HDD processes, as these shear rates are too high and the results will be dominated by the high modelled yield stress.

The Hershel-Bulkley model can better fit the data for bentonite slurries at the low shear rates of HDD processes and indeed the shear rates for all civil engineering applications of support fluids.

However, for HDD, both models show much lower pressures than are typically observed in the field demonstrating that pressures are controlled by constrictions/ blockages in the bore or zones of stiffer mud (sausages) and this needs to be addressed.

When designing fluids and additives for HDD it is essential to consider the low shear rate rheology and to be prepared to ignore 300 and 600 rpm data.

Static annular pressure measurements, which are rarely recorded in practice, were shown in this paper to provide valuable insights into the bore cleanliness. Static readings higher than hydrostatic indicate the presence of trapped cuttings in the bore, demonstrating that improved hole cleaning is required, either by optimising cutter head configuration and drill mud rheology, and/or mechanical hole cleaning. As these readings are not difficult to acquire, it is recommended that they are measured and monitored more regularly.

Experience has shown that HDD hydrofracture and heave risk may be of most significance in urban applications, where movement-sensitive infrastructure is crossed. Planning, pricing and constructing of such crossings requires careful consideration of drilling-induced ground movements, including both settlement and heave risks. Mitigation of ground movement risks hinge on good hole cleaning and mud management strategies, as discussed in this paper.

A hazard associated with hydrofracturing, which is well recognised in oil drilling but poorly appreciated in the HDD field, is "ballooning" ground or "well breathing" (e.g. Baldino et al., 2019). This is a phenomenon where drilling-induced ground hydro-fracturing, as well as engagement and opening of pre-

existing natural discontinuities, results in large mud loss to the formation during drilling with circulation. However, when drilling stops, large fluid flowback from the ground to the surface occurs. As no flow is expected when circulation pumps are off, this is often perceived as an unexpected occurrence. Flowback in ballooning ground is due to a network of fractures which are inflated during drilling, and are subsequently deflated by geostatic stresses at pumps-off when the in-bore fluid pressures fall. Ballooning may occur in grounds where an extensive fracture network is induced/ exists in which drilling fluid can be stored, but which is insufficiently extensive and open to drain the fluid away permanently. HDD project experience in the UK indicates that in ballooning ground, daily mud losses can reach 300 m^3/ day, of which about 25 - 85% can be recovered as daily flowback. In addition to other issues, this requires that sufficient mud storage capacity is available.

5 RECOMMENDATIONS

At HDD planning and design stage, ground investigations (GIs) should be carried out to provide detailed information on the fabric of the soil and rock formations to be transversed, and obtain information on hydrofracture and clogging risks. GIs should include borehole logs with detailed descriptions, accurate logging of pre-existing discontinuities and, where possible, judiciously designed in-situ hydrofracture tests outside the HDD alignment.

When developing HDD muds and other civil engineering support fluids, their rheology should be studied using equipment with sufficient precision at the relevant shear rates.

During HDD works, the actual shear rates should be considered, these will be lower than the standard shear rates historically adopted from the oil industry and applied to HDD.

During HDD drilling, downhole static annular pressures should be measured, monitored and analysed regularly to inform bore cleaniness and hole cleaning strategy.

To optimise the chances of project success, a good mud management strategy should be considered which is cognisant of the actual hole cleaning capability of the mud at the flow rates employed. Supplementary hole cleaning processes (such as periodic cleaning trip-outs) are helpful, but if overused in some geological settings there are risks of damage to or deviation from the already drilled bore.

Vigilant and documented monitoring of the mud returns is important for mitigating hydrofracture risk and should be embraced by the whole site team as an important quality control tool.

In some ground conditions, excessive hydro-fracturing, possibly coupled with opening of pre-existing natural discontinuities, can lead to ballooning ground with both large fluid losses and large flowbacks. This hazard is not well known in the HDD industry and is highlighted here.

ACKNOWLEDGEMENTS

The project experience reflected in this paper comes from a large number of projects, each of which has only been possible due to the work of a large group of people too numerous to list individually. The authors are grateful to all. Special thanks go to Andy Barwise and Phil Cowlishaw of RWE and Amandine Brosse and Jerry Love of GCG.

REFERENCES

Baldino, S., Miska, S. Z, Ozbayoglu, E. M. and Zhang, J. (2019). Borehole-breathing/ kick discriminator; diagnostic tool and potential resource for in-situ formation characterization. *SPE Drilling & Completion*, 34(03): 248–267. https://doi.org/10.2118/195689-PA.

Caenn, R., Darley, H.C.H. and Gray, G.R. (2017). The rheology of drilling fluids, In: *Composition and properties of drilling and completion fluids*, 7th ed., Gulf Professional Publishing, Cambridge, USA.

Chhabra, R.P. and Richardson, J.F. (1999). Flow in pipes and conduits of non-circular cross-sections, In: *Non-Newtonian flow in the process industries*, Butterworth-Heinemann, Oxford, England, pp 73-161.

Lam. C., Martin, P. J. and Jefferis, S. A. (2015). Rheological properties of PHPA polymer support fluids. *ASCE Journal of Materials in Civil Engineering*, Vol. 27, No. 11.

Underground Construction (2018). "2018 Large directional drilling rig census", November 2018, No. 73, Vol. 11. Available at: [https://undergroundinfrastructure.com/magazine/2018/november-2018-no-73-vol-11], accessed: 29/9/2023.

Yan, X., Ariaratnam, S.T. and Ma, B. (2019). World record 5.2 km HDD twin crossings of the Hong Kong Harbor. *Pipelines 2019*, ASCE. https://doi.org/10.1061/9780784482490.075.

Yan, X., Lan, H., Moore, I.D. and Ma, B. (2020). Flow properties of fresh mud (drilling fluid) used in horizontal directional drilling, *ASCE Journal of pipeline engineering systems*, ISSN 1949-1190.

Proceedings of the XVIII ECSMGE 2024
GEOTECHNICAL ENGINEERING CHALLENGES
TO MEET CURRENT AND EMERGING NEEDS OF SOCIETY
© 2024 the Authors
ISBN 978-1-032-54816-6
DOI 10.1201/9781003431749-415
Open Access: www.taylorfrancis.com, CC BY-NC-ND 4.0 license

ECSMGE 24
XVIII EUROPEAN CONFERENCE ON SOIL MECHANICS AND GEOTECHNICAL ENGINEERING

Enhancing soil-cement mixture's performance with GGBS

Améliorer les performances du mélange sol-ciment avec GGBS

S. Choudhary, K. Meena, M. Kumar, L. Borana*
Indian Institute of Technology Indore, India

**lalitborana@iiti.ac.in*

ABSTRACT: A soil-cement composite, comprising a thoroughly blended mix of soil, cement, and water, has played a crucial role in the construction of various civil infrastructures like bridge foundations, tunnels, highway embankments, foundations for port and harbour structures, and many more. Though efficient, traditional high-cement formulations pose severe environmental concerns, leading to the exploration of alternative materials that can bring sustainability to construction practices. This study focuses on utilizing "Ground-Granulated Blast-Furnace Slag" (GGBS) to explore its impact on the engineering characteristics of soil-cement mixtures. In this investigation, clay soil is blended with 20% of OPC and varying proportions of GGBS (20%, 30%, and 40% by weight of cement) as a replacement for OPC. The composite mixture is subjected to several Unconfined Compressive Strength (UCS) tests to assess the undrained shear strength of soil-cement-GGBS mixtures at distinct curing intervals (7, 14, and 28 days). Field emission scanning electron microscopy (FE-SEM) is also employed to examine the microstructure of the soil-cement composite, revealing the arrangement of particles, pore structures, and the distribution of cementitious materials. The results show that the composition having clay soil and 20% cement, replaced with 20% GGBS, yields maximum strength among all tested compositions with a significant increase of 24% compared to the conventional soil-cement mixture of clay soil and 20% cement only.

RÉSUMÉ: Un composite sol-ciment, comprenant un mélange soigneusement mélangé de terre, de ciment et d'eau, a joué un rôle crucial dans la construction de diverses infrastructures civiles telles que les fondations de ponts, les tunnels, les remblais d'autoroutes, les fondations de structures portuaires et bien d'autres. Bien qu'efficaces, les formulations traditionnelles à haute teneur en ciment posent de graves problèmes environnementaux, ce qui conduit à l'exploration de matériaux alternatifs susceptibles d'apporter de la durabilité aux pratiques de construction. Cette étude se concentre sur l'utilisation du « laitier de haut fourneau granulé moulu » (GGBS) pour explorer son impact sur les caractéristiques techniques des mélanges sol-ciment. Dans cette étude, un sol argileux est mélangé avec 20% d'OPC et des proportions variables de GGBS (20%, 30% et 40% en poids de ciment) en remplacement de l'OPC. Le mélange composite est soumis à plusieurs tests de résistance à la compression sans confinement (UCS) pour évaluer la résistance au cisaillement non drainé des mélanges sol-ciment-GGBS à des intervalles de durcissement distincts (7, 14 et 28 jours). La microscopie électronique à balayage par émission de champ (FE-SEM) est également utilisée pour examiner la microstructure du composite sol-ciment, révélant la disposition des particules, les structures des pores et la répartition des matériaux cimentaires. Les résultats montrent que la composition contenant un sol argileux et 20% de ciment, remplacée par 20% de GGBS, donne une résistance maximale parmi toutes les compositions testées avec une augmentation significative de 24% par rapport au mélange sol-ciment conventionnel composé d'un sol argileux et de 20% de ciment uniquement.

Keywords: Soil-cement; ground-granulated blast-furnace slag (GGBS); unconfined compressive strength (UCS); scanning electron microscopy (SEM).

1 INTRODUCTION

There has been a significant advancement in using soil-cement mixtures in geotechnical engineering. Dry or wet cement is combined with clayey soils to create a durable composite material called soil-cement mixture, which has several advantages over traditional building materials like cement concrete. The soil-cement mixture is considered a cost-effective remedy for soil stabilization in construction projects due to the economic benefit of utilizing locally accessible materials and minimizing dependency on costly imported materials mix (Solihu 2020; Choudhary et al. 2023). Ordinary Portland Cement (OPC) is the key component in soil-cement mixtures that serves as a fundamental binder, and it is readily used as a chemical additive in soil stabilization due to its several advantages like easy availability, low cost, durable end products, resistance towards acid and chemical attacks and many more. However, the extensive use of OPC leads to negative environmental consequences, primarily due to the high energy consumption during production and significant carbon dioxide emissions (Gupta and Chaudhary 2020). To mitigate this negative environmental impact, several researchers

attempted to find appropriate substitutes and cement alternatives that can provide appreciable strength. Out of all the conventional supplementary cementitious materials (SCM), Ground-Granulated Blast-Furnace Slag (GGBS) is considered one of the best cement substitutes. When added in a certain proportion, GGBS enhances the strength and endurance of the cement hydration products. GGBS is a by-product obtained from the blast furnaces used in the iron and steel manufacturing, exhibiting inherent pozzolanic properties. The addition of GGBS enhances the physical and mechanical characteristics of soil-cement mixtures by reacting with calcium hydroxide (lime), produced during the early stages of cement hydration, forming additional cementitious compounds like Calcium Silicate Hydrate (C-S-H) gel, Calcium Alumino-Ferrite (CAF), and Calcium Hydroxide (CH) which reduces the void spaces in the soil-cement matrix. Recently, some studies have shown the possible utilization of industrial waste-based SCMs to improve the engineering properties of clay soils (Åhnberg et al. 2003; Horpibulsuk et al. 2012; Singh et al. 2021). However, very few researchers have studied the utilization of SCMs to replace a part of lime and cement in soil stabilization. D.D. Higgins et al. (1998) conducted several laboratory tests such as UCS, CBR, swelling index, and many more on GGBS mixed lime-clay mixtures to analyze the changes in the engineering characteristics of clay soil. The results obtained revealed that the addition of GGBS considerably increased the clay soil's compressive strength. Arulrajah et al. (2018) studied how industrial waste by-products like fly ash (F) and slags (S) can enhance soft soil treatment using deep soil mixing methods. The study conducted laboratory experiments on test samples with varying water content levels (0.75, 1.0, and 1.25). The results showed appreciable improvement in the strength and stiffness of soft clay soils with an optimal binder content of 20% and an ideal mix of 5% F class and 15% S class fly ash. Du et al. (2017) conducted a comparative study on lightweight cement-treated soil with lightweight geopolymer-treated soils by performing several tests like UCS, mercury intrusion porosimetry (MIP), hydraulic conductivity, SEM images, and thermogravimetric analysis (TGA). They found that lightweight geopolymer-treated soils improved the permeability and strength properties and provided better engineering performances than lightweight cement-treated soils.

This study explores the strength gain characteristics by blending clay soil with 20% cement (by weight of dry soil) and varying proportions of GGBS (20%, 30%, and 40% by weight of cement) by conducting UCS tests. SEM was employed to observe the microstructure of the soil-cement composite, revealing the arrangement of particles, pore structures, and the distribution of cementitious materials.

2 MATERIALS AND METHODOLOGY

The clay soil used in this study is sourced from a test pit at the IIT Indore campus, located in Madhya Pradesh (India). The raw clay soil is sieved through a 2 mm Indian Standard (IS) sieve, dried in a hot air oven for 24 hours, and kept in an air-tight container. OPC and GGBS were obtained through collaboration with industrial partners. Using the Unified Soil Classification System (USCS), as adopted from ASTM D-2487-98, the soil is categorized as highly expansive clay soil. The grain size distribution curve (GSD) is illustrated in Figure 1. The basic properties of the clay soil are listed in Table 1.

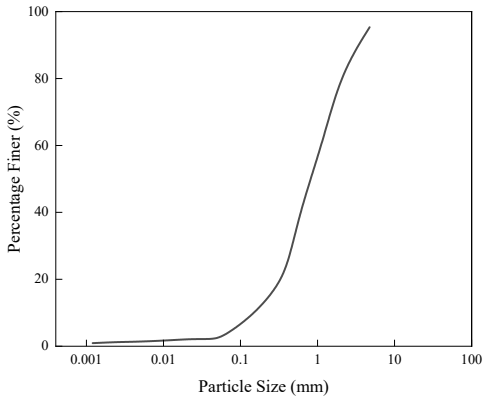

Figure 1. Grain size distribution (GSD) curve of clay soil.

Table 1. Basic properties of clay soil.

Property	Value
Natural water content (%)	15.38
Specific gravity	2.71
Liquid limit (%)	81.05
Plastic limit (%)	36.44
Optimum moisture content (%)	29
Maximum dry unit weight (kN/m^3)	1.425
Shrinkage limit (%)	11.20
USCS soil classification	CH

In this study, prepared raw clay soil was added with 20% of cement (specific gravity G_s = 3.10) and appropriate water content to obtain slurry-type consistency. The major constituents, including clay soil, cement, GGBS, and water, were thoroughly mixed with the help of a mechanical mixer.

Sixteen samples of soil-cement-GGBS compositions were prepared using high polymer

density molds (HPDM) with an internal diameter of 44 mm and a height of 98 mm. The soil was mixed with a cement content of 20%, and cement was subsequently substituted with 0%, 20%, 30%, and 40% by weight of dry cement. To preserve the consistency in the mixtures and provide adequate hydration, the amount of water added was 1.5 times the liquid limit of the soil (Choudhary et al. 2023). Each mixture was then carefully poured into the molds, and the sample was air-free with the help of a mechanical stirrer. The freshly molded mixtures were left for 24 hours at room temperature to achieve appreciable strength. After 24 hours of sample preparation, the samples were removed from the molds and placed in a curing tank, where they underwent a continuous curing procedure in a submerged condition. Afterward, a series of UCS tests were conducted to evaluate the mixture's undrained shear strength and unconfined compressive strength at 7-days, 14-days and 28-days of curing. Following the completion of UCS testing, SEM imaging was also utilized on the tested samples to provide insights into microstructural details.

3 RESULTS AND DISCUSSION

3.1 Unconfined compressive strength

The UCS test, conducted following ASTM D7012-23, was employed to evaluate the undrained shear strength and unconfined compressive strength of soil-cement-GGBS mixtures. A compression load at the strain rate of 1.25 mm per minute was applied to the specimens during the UCS test. The test includes samples with varying mixture combinations and curing times. The test results demonstrated increased compressive strength of all mixes correspondingly with longer curing times. An optimum content of 20% of cement has often been considered in previous studies, which showed significant strength and stability in the soil-cement mixture (Pham et al. 2021; Solihu 2020). Figure 2 (a), (b), and (c) show that the strength gain variation of samples with varying constituents increases for varying curing times of 7-days, 14-days, and 28-days, respectively. Moreover, it has been experimentally determined that specimens subjected to a 28-day curing period exhibit maximum compressive strength gain among all the compositions.

A soil mixture with 20% cement and 20% GGBS blend shows maximum values of 0.41925 N/mm^2 and 0.2096 N/mm^2 for undrained shear strength and unconfined compressive strength, respectively. The strength of the specified composition is 24% higher in comparison to that of the traditional soil-cement mixture with 20% cement content. The obtained results greatly emphasize the importance of GGBS in improving the strength qualities of combinations while encouraging the use of sustainable materials.

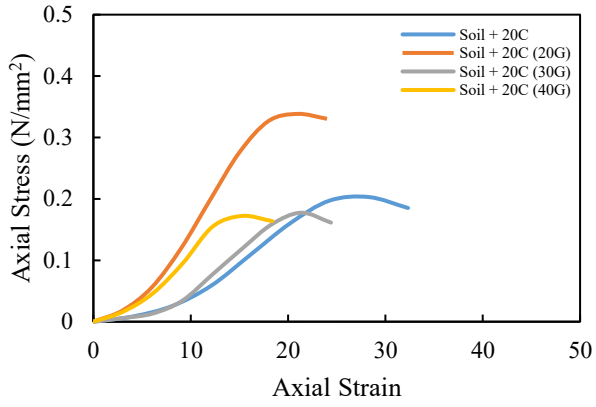

(a)

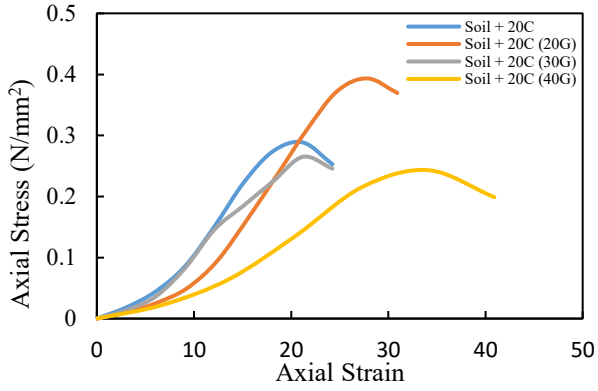

(b)

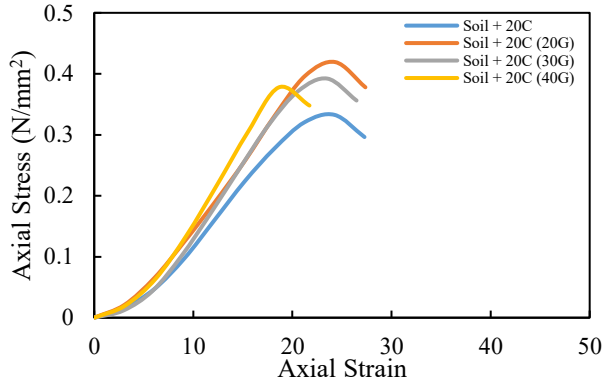

(c)

Figure 2. Stress-Strain curve of soil-cement-GGBS mixture with varying GGBS percentage for a curing period of (a) 7-days, (b) 14-days, and (c) 28-days.

3.2 Scanning electron microscopy

In this work, FE-SEM was conducted using FE-SEM Supra 55 (Carl Zeiss, Germany) with a magnification of 500X on a sample of GGBS blended soil-cement mixture having 20% cement with 20% GGBS as replacement of cement cured for 28 days as illustrated in Figure 3. The SEM image confirms bond formation and development of hydration products such as

calcium aluminate hydrates (CAH), calcium silicate hydrates gel (C-S-H gel), and Ettringite. Hydration production is confirmed by the creation and dispersion of these products, which helped develop the strength of composites. The angular shape of the GGBS particles also helps in better interlocking and strength development. The SEM images provide crucial insights into the interfacial connection of GGBS and soil-cement particles.

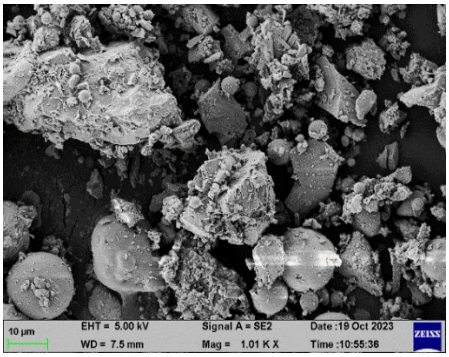

Figure 3. SEM image of Clay Soil + 20% cement + GGBS (20% of cement) at 28-days of curing.

4 CONCLUSIONS

The current study illustrates the strength properties of soil-cement-GGBS mixture with varying compositions for different curing times. The conclusions drawn from the results are as follows.

- It exhibits a strong reaction with calcium hydroxide ($Ca(OH)_2$), a by-product of cement hydration, leading to the formation of additional cementitious compounds., reducing the cavities and improving the overall strength and durability of the soil-cement mixture.
- The mixture of clay soil with 20% cement and 20% GGBS blend cured for 28 days shows a significant increase in the values of undrained shear strength and unconfined compressive strength of 0.41925 N/mm^2 and 0.2096 N/mm^2 respectively, as compared to other compositions. This composition exhibits a 24% increase in strength compared to the conventional soil-cement mixture with 20% cement content.

It is worth mentioning that this experimental study emphasizes mainly the strength development of clay soil mixed with 20% cement, and the cement proportion is replaced with GGBS at varying ratios. However, there are more areas in which further investigation is required to improve the current understanding of various parameters, such as optimization of mix ratios, the effect of curing conditions, long-term performance, time-dependent stress-strain behaviour, field scale validation, and many more.

REFERENCES

Åhnberg, H., S.-E. Johansson, H. Pihl, and T. Carlsson. 2003. "Stabilising effects of different binders in some Swedish soils." *Proc. Inst. Civ. Eng. - Gr. Improv.*, 7 (1): 9–23. https://doi.org/10.1680/grim.2003.7.1.9.

Arulrajah, A., M. Yaghoubi, M. M. Disfani, S. Horpibulsuk, M. W. Bo, and M. Leong. 2018. "Evaluation of fly ash- and slag-based geopolymers for the improvement of a soft marine clay by deep soil mixing." *Soils Found.*, 58 (6): 1358–1370. Japanese Geotechnical Society. https://doi.org/10.1016/j.sandf.2018.07.005.

ASTM D7012-23, 2023. Standard Test Methods for Compressive Strength and Elastic Moduli of Intact Rock Core Specimens under Varying States of Stress and Temperatures ASTM International, West Conshohocken, PA, USA (2023).

ASTM D-2487-98 Standard practice for classification of soils for engineering purposes. American Society for Testing and Materials, USA.

Choudhary, S., M. J. Singh, and L. Borana. 2023. "Time-dependent settlement behaviour of clayey soil treated with deep cement mixed column." *Smart Geotech. Smart Soc.*, 752–757. https://doi.org/10.1201/9781003299127-100.

D.D. Higgins, J. M. K. and S. W. n.d. "Soil Stabilization using Lime-Activated Ground Granulated Blast Furnace Slag." *ACI Symp. Publ.*, 178. https://doi.org/10.14359/6023.

Du, Y.-J., B.-W. Yu, K. Liu, N.-J. Jiang, and M. D. Liu. 2017. "Physical, Hydraulic, and Mechanical Properties of Clayey Soil Stabilized by Lightweight Alkali-Activated Slag Geopolymer." *J. Mater. Civ. Eng.*, 29 (2): 1–10. https://doi.org/10.1061/(asce)mt.1943-5533.0001743.

Gupta, S., and S. Chaudhary. 2020. "State of the art review on Supplementary Cementitious Materials in India – I: An overview of legal perspective, governing organizations, and development patterns." *J. Clean. Prod.*, 261: 121203. Elsevier Ltd. https://doi.org/10.1016/j.jclepro.2020.121203.

Horpibulsuk, S., W. Phojan, A. Suddeepong, A. Chinkulkijniwat, and M. D. Liu. 2012. "Strength development in blended cement admixed saline clay." *Appl. Clay Sci.*, 55: 44–52. Elsevier B.V. https://doi.org/10.1016/j.clay.2011.10.003.

Pham, T. A., J. Koseki, and D. Dias. 2021. "Optimum material ratio for improving the performance of cement-mixed soils." *Transp. Geotech.*, 28 (May): 13–15. https://doi.org/10.1016/j.trgeo.2021.100544.

Singh, M. J., L. Borana, F. Weiqiang, and D. S. Xu. 2021. "Long-term swelling characteristics of montmorillonite clay with and without fly ash: Wetting-drying cycle influence in 1d oedometer condition." *J. Test. Eval.*, 51 (1). ASTM International. https://doi.org/10.1520/JTE20210248.

Solihu, H. 2020. "Cement Soil Stabilization as an Improvement Technique for Rail Track Subgrade, and Highway Subbase and Base Courses: A Review." *J. Civ. Environ. Eng.*, 10 (3). https://doi.org/10.37421/jcde.2020.10.344.

Proceedings of the XVIII ECSMGE 2024
GEOTECHNICAL ENGINEERING CHALLENGES
TO MEET CURRENT AND EMERGING NEEDS OF SOCIETY
© 2024 the Authors
ISBN 978-1-032-54816-6
DOI 10.1201/9781003431749-416
Open Access: www.taylorfrancis.com, CC BY-NC-ND 4.0 license

ECSMGE 24
XVIII EUROPEAN CONFERENCE ON SOIL MECHANICS AND GEOTECHNICAL ENGINEERING

Consolidating existing road structures using self-drilling bars

Consolidation des structures routières existantes à l'aide de barres autoperceuses

I.A. Ciocaniu*, A.C. Onescu, S. Manea
Technical University of Civil Engineering of Bucharest, Bucharest, Romania

P. Uta
GEOSOND SA, Bucharest, Romania

**ionut.ciocaniu@geosond.com*

ABSTRACT: The article presents design methods and execution technologies for consolidating geotechnical structures and roads in mountains areas of Romania, considering the specific conditions for each site. The design process took into consideration the difficult site conditions respectively , the working space - the consolidation and drainage works must be strictly performed within the road area (approximately 9m wide) and the execution phases – the works must be executed in such a way that traffic can proceed safely. The paper will present several situations encountered in different locations in Romania, with their respective geotechnical and hydrogeological characteristics and the specific technical solutions chosen at the design stage and implemented throughout the execution. Detailed solutions will be offered for the drainage system and the surface and underground water, as well as for the restoration of existing structures. The degradation over time of the road-associated structures is a widespread problem and it is influenced, among others, by geotechnical conditions and water action. Such deterioration compromises traffic safety leading to partial failure with impact to the usual traffic and even to complete failure. The pressing need for safety usually demands an emergency intervention plan, with technical solutions that can be quickly executed in the event of a major hazard. With this innovative approach, roads can be made safer and more resilient against future deterioration caused by changing geotechnical conditions or other environmental factors.

RÉSUMÉ: L'article présente des méthodes de conception et des technologies d'exécution pour consolider les structures géotechniques et les routes dans les zones montagneuses de Roumanie, en tenant compte des conditions spécifiques de chaque site. Le project a pris en considération les conditions difficiles du site, respectivement l'espace de travail - les travaux de consolidation et de drainage doivent être strictement effectués dans la zone routière (environ 9 m de largeur) et les phases d'exécution - les travaux doivent être exécutés de manière à ce que la circulation puisse se dérouler en toute sécurité. Le document présentera plusieurs situations rencontrées dans différents endroits de Roumanie, avec leurs caractéristiques géotechniques et hydrogéologiques respectives et les solutions techniques spécifiques choisies lors de la phase de conception et mises en œuvre tout au long de l'exécution. Des solutions détaillées seront proposées pour le système de drainage et l'eau de surface et souterraine, ainsi que pour la restauration des structures existantes. La dégradation au fil du temps des structures associées aux routes est un problème répandu et elle est influencée, entre autres, par les conditions géotechniques et l'action de l'eau. Une telle détérioration compromet la sécurité routière, entraînant une défaillance partielle avec un impact sur la circulation habituelle et même une défaillance complète. Le besoin urgent de sécurité exige généralement un plan d'intervention d'urgence, avec des solutions techniques qui peuvent être rapidement exécutées en cas de danger majeur. Avec cette approche innovante, les routes peuvent être rendues plus sûres et plus résistantes à la dégradation future causée par les changements des conditions géotechniques ou d'autres facteurs environnementaux.

Keywords: Self-drilling bars; micropile; anchors; consolidating structures.

1 INTRODUCTION

Recent changes in construction work sector and the creation of special, modern equipment have allowed the development of new solutions for applied geotechnics.

One of these relatively recent technologies is the self-drilling bars, used as soil anchors and also as micropiles for deep foundation works, which is successfully applied in Romania in projects for consolidation and foundation works for road construction, slope protection structures and landslide stabilization etc., in difficult soil and space conditions.

Consolidating existing road structures is a crucial aspect of infrastructure development, especially in mountainous regions. The challenging terrain and specific geological conditions in these areas require specialized design methods and execution technologies to ensure the stability and longevity of

the road structures. One approach to consolidating road structures in mountainous regions is using self-drilling bars. These self-drilling bars provide a cost-effective and efficient solution for reinforcing the geotechnical structures and stabilizing the road foundations. Consolidation significantly influences soil strength and the stability of structures. Accurate prediction of consolidation and settlement is essential for the construction, design, and safety of engineering projects in mountainous regions. Over the past ten years, many road construction projects in Romania encountered difficulties that heightened the vulnerability to landslides.

In every situation, it was needed to use small but strong equipment that could change according to work conditions.

2 CONSOLIDATION WORKS FOR EXISTING RETAINING WALLS IN THE MOUNTAIN AREA

The high traffic in the city of Brasov, situated in a mountain area in the center of Romania, led to the accentuated degradation of some structures and traffic restriction in the area.

The existing structures were made of raw stone and cyclopean concrete, with a poor strength plain concrete foundation. The walls dimensions were variable as follows: widths between 0.60 m and 3.00 m at the base of the wall, lengths between 40.00 m and 80.00 m and heights varying from 0.90 m up to 10.00 m.

A visual inspection of the retaining walls was performed prior to the consolidation works design which revealed existing degradations such as cracks, displacements, settlements, that endangered the stability and resistance of these structures, the degradations being mostly still an active process. Some of the retaining walls had drainage systems, but due to the degradation of the roadway water infiltration took place and led to the collapse of one part of the walls and road, and also affected some houses downstream. These situations with degraded structures and signs of loss of stability have led to the restriction or even stop of road traffic, requiring immediate interventions to ensure stability of the area. The lithology in the site consisted of conglomerate layers that represent the bedrock, and on top of the bedrock, the soil was formed by soft reddish-brown, yellowish-brown clayey silt or silty clay representing the Quaternary age alteration blanket and contains fragments of rocks in variable percentages.

Consolidation works (Figure 1) consisted of micropiles executed by drilling vertically into the body of the structure, with two stage injection, which were connected at the top by a reinforced concrete beam. In addition, the walls were supported by inclined micropiles executed on two levels, respectively at the top and center of each wall height, with 45º inclination and lengths of 12.00 – 15.00 m. Furthermore, the consolidation works involved the restoration of the drainage system, where existing, or otherwise, execution of a new drainage system.

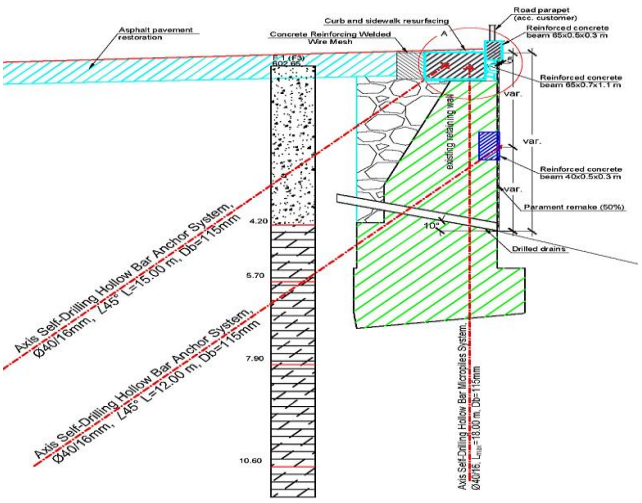

Figure 1. Characteristic section - designed solution for consolidation of the retaining wall.

The works were executed in well-defined steps as the consolidation of the retaining walls had to be done under traffic, on narrow streets and without changing the specific architectural aspect of the area (Figure 2). The geotechnical design of the structures rehabilitation was carried out in accordance with the requirements of European and Romanian standards.



Figure 2. Picture from the site during execution.

The structure was modeled in 2D design software, using both the limit equilibrium method and the reaction coefficient method, and verifications were

performed at the ultimate limit states: structural (STR) and geotechnical (GEO), considering normal and seismic design situations.

The geotechnical design was verified for the following ultimate limit states:

- internal failure or excessive deformation of the structural elements, in which the material strength contributes significantly to ensuring the resistance (STR);
- failure or excessive deformation of the soil, in which the foundation soil parameters contribute significantly to ensuring the resistance and global stability (GEO);

The main consolidation elements were the self-drilling bars. Their sizing was done preliminarily with the formula (1) below, then by automatic calculation the influence of these as a group effect on consolidation and displacement reduction was verified.

$$L = \frac{T_w * F_s}{\pi * D * T_{ult}} + l \qquad (1)$$

where T_w is the design force (kN); F_s is the safety factor equal to 2, dimensionless; D is the design diameter of the anchor/micropile (m); T_{ult} is the lateral friction resistance of the injected micropile (kPa); l is the free length (m).

The equilibrium conditions were verified in the first step, through which the dimensions and geometry of the micropiles were determinate to ensure the stability of the system under the action of the soil pressures and other external loads. Then, in the second step, the structural design, the necessary sectional strength characteristics were established for the new system to be able to safely take all the loads and stresses (bending moments, shear and axial forces).

3 CONSOLIDATION WORKS FOR LANDSLIDES ON A NATIONAL ROAD

On a national road in Romania, in the mountain area, with high traffic accentuated degradation and instabilities were discovered with fast evolution accentuated by the rainy condition. Thus, from day to day, the degree of damage was greater, which endangers road traffic without taking urgent rehabilitation measures (Figure 3).



Figure 3. Photo of the affected road area

The geotechnical investigation, including inclinometer measurements (Figure 4), showed a first layer of soft sandy clay and loose sand to a depth of approx. 6.00 m over a layer of consolidated marl clay. Groundwater was intercepted at depths between 0.40-4.10 m, sometimes having a under presure character, due to clay intercalations in the first layer that locally block groundwater flow and generate springs locally.

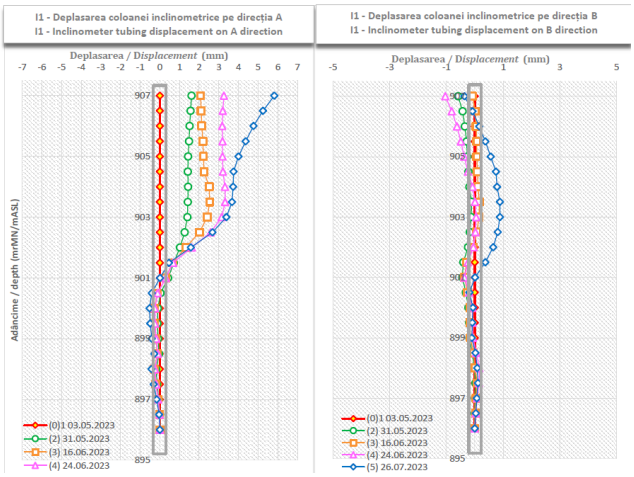

Figure 4. Inclinometer measurement that show the evolution of displacement at different time intervals

Following the stability analyzes performed, it resulted that the soil is stable in dynamic and static conditions only when the soil layer is not saturated.

Thus, through the project, works were foreseen to ensure the controlled flow of surface water and groundwater, the consolidation of soft ground and ensuring the general and local stability of the site.

The engaging was the condition that the consolidation and drainage works must be strictly performed within the road area (approximately 9m wide) and the execution phases – the works must be executed in such a way that traffic can proceed safely.

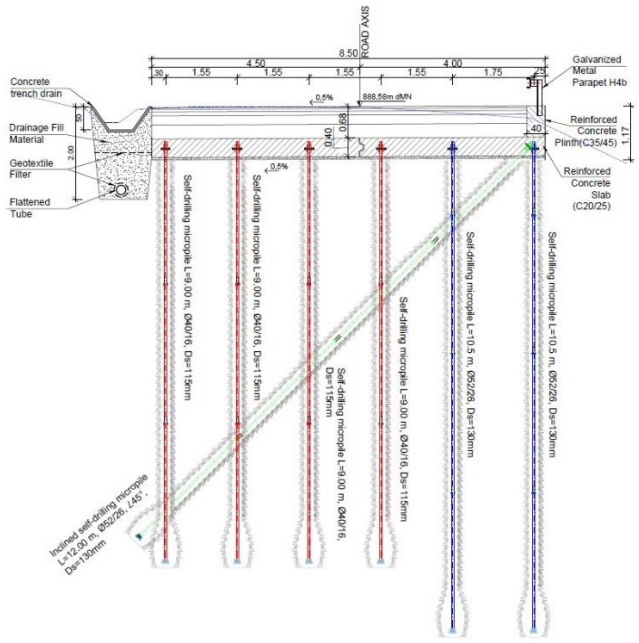

Figure 5. Section with the designed solution

In this case it was designed a complex solution with self-drilling micropiles, vertical and inclined, that ensures the soil improvement where difficult soil conditions were encountered and load transfer to the deeper layers and also the stability of the area (Figure 5).

The advantage of this solution is that it is based on a fast and efficient execution technology because the self-drilling bars allow dynamic grouting during drilling. In addition to significantly reducing execution time, it also allows efficient injection of soil near the micropiles.

The execution of the proposed works will eliminate the need to occupy surfaces outside the road and through the proposed execution solution, does not require closing traffic, because the equipment involved in the implementation of the works has small size an weight and the time required for execution is very reduced, reducing the inconvenience caused by single-wire traffic.

For groundwater drainage, an infiltration water collection system was provided consisting of a perforated rifled tube, wrapped in a geotextile filter, mounted at about 2.00m depth and drainage filling, on the route of the concrete channel projected on the left side of the road, in the direction of increasing mileage.

4 CONCLUSIONS

According to the specific conditions of the site, it is important to choose the consolidation solution for both structural damage of structure and soil degradation that appears due to the actions of natural or anthropic factors, it is very important to be minimally invasive and highly effective. Dynamic grouting during drilling process offers the advantage of improving the near soil by injection, also the execution can be performed with modern small dimensions equipment. The use of self-drilling bars for consolidation and foundation works it is a modern and efficient solution that which can be applied in cases.

The possibility of execution of both inclined and vertical self-drilling bars can ensure the soil improvement and also the stability of the area.

The solution was successfully applied in many projects in Romania associated with drainage works.

ACKNOWLEDGEMENTS

This paper was developed from the projects designed and executed by the company Geosond SA, Bucharest, Romania.

REFERENCES

Ciocaniu, I.A., Uta, P., Ene, I., Duta, O., Manea, S., Ciortan, R., and Vasilache, E. 2021. Strengthening existing structures using self-drilling bars. Proceedings of the XIVth National Conference on Geotechnics and Foundations, Bucharest, Romania, 541-548.

Ciocaniu, I.A., Uta, P., Duta, O., Manea, S., Ciortan, R., and Vasilache, E. 2021. Improvement of deep foundation ground. Proceedings of the XIVth National Conference on Geotechnics and Foundations, Bucharest, Romania, 409-416.

Ciocaniu, I.A., Pascalau, R., and Duta, O., 2020. Ground injection works. Construction Magazine, Bucharest, Romania, 22-23.

Uta, P., Ciocaniu, I.A., Iustin, E. 2020. Strengthening existing structures using self-drilling bars. Construction Magazine, Bucharest, Romania, 48-49.

SR EN 12715:2002. Execution of special works – Grouting.

SR EN 14199:2015. Execution of special works – Micropiles.

Proceedings of the XVIII ECSMGE 2024
GEOTECHNICAL ENGINEERING CHALLENGES
TO MEET CURRENT AND EMERGING NEEDS OF SOCIETY
© 2024 the Authors
ISBN 978-1-032-54816-6
DOI 10.1201/9781003431749-417
Open Access: www.taylorfrancis.com, CC BY-NC-ND 4.0 license

ECSMGE 24
XVIII EUROPEAN CONFERENCE
ON SOIL MECHANICS AND
GEOTECHNICAL ENGINEERING

Geotechnical works for an underground electric power station, in Bucharest

Travaux de fondations spéciales pour une centrale électrique souterraine, à Bucarest

D. Ciumeică*, A-E. Popa
SBR Soletanche Bachy Fundații SRL, Bucharest, Romania

L. Sata, S. Manea
Technical University of Civil Engineering, Bucharest, Romania

**ciumeica@sbr.ro*

ABSTRACT: This article presents design phases, special foundation works, and technology used for construction of an electrical power station, with two basements, in a crowded area of the city. The surface of the underground structure is 700 sqm. Both effective design solution and technology standards cope with challenging demands such as neighbour buildings, high traffic area and restrained site area. As for environmental concerns, this project used low carbon concrete, which significantly reduced carbon footprint of the entire construction. Pit enclosure consisted of CFA piles and one row of horizontal steel struts. Further challenges such as limited water in-flow, due to electrical equipment installed inside the basements were coped by infrastructure design and execution, as well. To assure safe excavation works at the depths of -10 meters and -11.50 locally and then to build the reinforced concrete raft and infrastructure, retaining wall piles was required. Based on site characteristics, soil conditions (silty clay and ground water level at approx. -7,50 m, distanced CFA piles of 60 cm and 40 cm diameter were built. Considering the architectural and structural configuration proposed, the building's foundation system consists of a general raft. Infrastructure consists of columns, beams, walls made of reinforced concrete and slabs. The perimeter structural walls of basements are 25-30cm thick with additional waterproofing requirements applied. Optimised solution proved to be effective for both civil and geotechnical works, delivering the project on time.

RÉSUMÉ: Cet article présente les phases de conception, les travaux de fondation spéciales et la technologie utilisée pour la construction d'une centrale électrique avec deux sous-sols, dans un quartier surpeuplé de la ville. La surface de la structure souterraine est de 700 m². La solution de conception efficace et les normes technologiques répondent aux exigences difficiles telles que les bâtiments voisins, la zone à fort trafic et la zone de site restreinte. En ce qui concerne les préoccupations environnementales, ce projet a utilisé du béton bas carbone ce qui a considérablement réduit l'empreinte carbone de toute la construction. L'enceinte se compose de pieux CFA et d'une rangée d'entretoises horizontales en acier. D'autres défis tels que le débit d'eau limité, en raison de l'équipement électrique installé à l'intérieur des sous-sols, ont également été relevés par la conception et l'exécution de l'infrastructure. Des pieux de mur de soutènement ont été nécessaires afin d'assurer la sécurité des travaux d'excavation à des profondeurs de -10 mètres et -11,50 localement, puis pour construire la base et l'infrastructure en béton armé. Etant donné les caractéristiques du site et les conditions du sol (argile limoneuse et niveau des eaux souterraines à env. -7,50 m), des pieux CFA de 60 cm et de 40 cm de diamètre ont été construits. Compte tenu de la configuration architecturale et structurelle proposée, le système de fondation du bâtiment se compose d'un radier général. L'infrastructure se compose de poteaux, de poutres, de murs et de dalles en béton armé. Les murs structurels de périmètre des sous-sols ont une épaisseur de 25-30 cm et des exigences d'étanchéité supplémentaires sont appliquées. La solution optimisée s'est avérée efficace pour les travaux civils et géotechniques, livrant le projet à temps.

Keywords: Excavation; pit enclosure; urban; electric station.

1 INTRODUCTION

Being built on a crowded area of the city of Bucharest, the new electrical power station which is designed for electrical power supply to the new Promenada Mall extension, needed the right solution to cope with the local ground conditions, multiple requirements by the electrical system supplier and with restrained site area.

The location is in northern side of the city and quite a restrained space was handed over, a working space

which required proper coordination, right technology to be chosen and a tight time schedule to fit in.

The project required design and build solution for a safe deep excavation, in an urban area, for two basements with an excavation depth from 9.72 metres to 11.52 metres, locally.

Being a deep excavation surrounded by adjacent structures, close enough to current project property limits, it was particularly important to follow up a rigorous and sensitive monitoring programme.

2 PROJECT HIGHLIGHTS

2.1 Vicinities

Total surface of the construction site is just 1000 sqm and it has several neighbour buildings such as an office building on North-West with 1 basement and 7 stories height, at the South with another office building with 4 basements and 10 stories. At East it is one of the busiest avenues (Barbu Văcărescu) especially on rush hours (Figure 1).



Figure 1. Pit enclosure vicinities.

2.2 Ground conditions

Prior ground investigation, through its two 35 meters long boreholes, revealed relatively homogenous ground lithology, but with various widths and compressibility characteristics for each layer (Table 1).

The ground is mainly characterized by alternance of cohesive with non-cohesive layers, the ground water being found within the second layer at approximately 7 meters below natural ground level.

2.3 Service state requirements

The structure by its purpose – as an electrical power supply station – needed to bear the active pressure, overloads caused by neighbour buildings and to limit as much as possible any ground water infiltrations which might occur during the electrical power station service state.

Therefore, besides usual design approaches for these kind of structures, special attention was paid to the waterproofing solution of the infrastructure.

Table 1. Ground conditions.

Layer	Level	Width	Description
I	GL … -1,20 m	0,90 m … 1,00 m	Brown clayey sand, gravel and waste construction materials
II	-1,20 m … -15,00 m	14,00 m	Clay / silty clay / sandy grey clay, firm to stiff
III	-15,00 m … -19,40 m	4,50 m	Clayey sand / compact silty greyish sand
IV	-19,40 m … -29,50 m	10,00 m	Clay / sandy grey clay, stiff
V	-29,50 m … -32,80 m	3,50 m	Clayey sand / grey sand, compact
VI	-32,80 m … -35,00 m	2,00 m	Grey clay, stiff

2.4 Retaining structure solution

Because of the constrained site space required for the works, the chosen solution was a contiguous pile wall supported by one level of steel struts and locally, an additional level where the excavation level was the deepest.

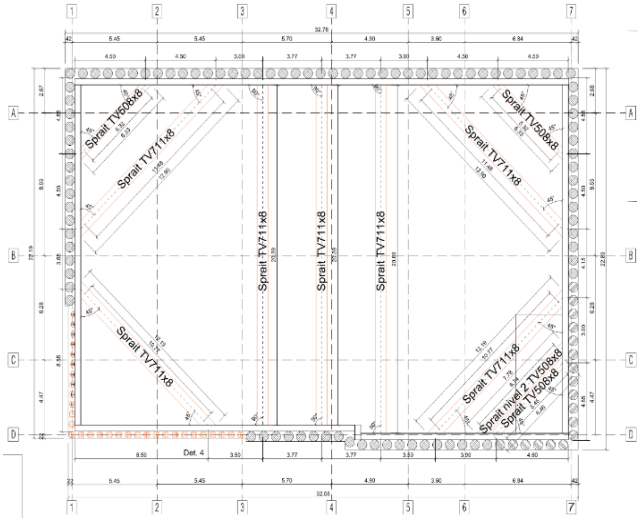

Figure 2. Contiguous pile wall and steel struts layout.

For the temporary retaining wall (Figure 2), there can be distinguished three different sections characterized by different supporting solution.

The first one, contiguous pile wall with one level of steel struts supporting system. (Figure 3 – left).

For a single area where the excavation was deepened with about 2 meters, for the sump pits, an additional steel strutting level was installed (Figure 3 – middle).

For both characteristic sections of the pit enclosure, 60 cm diameters CFA piles with a spacing of 80 cm, were designed.

The section of the pile wall near the existing neighbour building's diaphragm wall – part of the 4 ground floors office building, was dimensioned accordingly, 40 cm diameter CFA piles with a spacing of 60 cm (Figure 3 – right).

The entire pile wall is solidarized by a reinforced concrete capping beam.

The building's foundation system consists of a general raft. Reinforced concrete columns, beams, walls and slabs are part of building's infrastructure. The perimeter structural walls of basements are 25 -30 cm thick with additional waterproofing elements applied.

3 EXECUTION STAGES

Regarding execution sequence, prior to retaining wall execution, a safe, stable, and solid enough working platform was prepared at approximately -1.00 m level. To limit deviations of the piles and to ensure a proper drilling position, guide walls were cast in place. Piles were then made using CFA technology, following the guiding walls perimeter, changing the auger type from 600 mm to 400 mm diameter in the vicinity of the neighbour building's existing diaphragm wall.

After the piles concrete has reached the specified strength, piles were trimmed down to the designed level and the interior guide wall was demolished to make the formwork, install the rebar and pour the concrete in the capping beam.

The operational team proceeded then with a general excavation down to -4.00 m, to install the main steel strutting system at -3.00 m.

After all the elements were safely put in place, confronting also monitoring results in sequent stages, final excavation has been performed and secondary strutting system was installed on the corner side, where the excavation level went almost 2 meters deeper. After finishing the pit enclosure, waterproofing works and power station's infrastructure (reinforced concrete raft, vertical and horizontal structural elements) were done.

Monitoring works were confirming the results obtained by the design, ensuring a smooth continuation of the works in highly safe conditions.

4 DESIGN

Retaining walls dimensions were established considering the limitation of deformations, as well as for technological reasons, aiming to obtain a quasi-impermeable pit enclosure, by assuring the embedment in the lower layers of clay with low permeability.

Design was made using the Eurocode's DA1, Combination 1, DA1 Combination 2, complying also with Romanian regulations.

Design situations followed up different approaches, such as the regular design situation, accidental situation considering an additional excavation and the calculation in the hypothesis of seismic action, according to SR EN 1998-5:2004 (ASRO, 2004).

To obtain the efforts in the retaining wall, the support system was modelled using two-dimensional numerical calculation, in a plane stress and plane strain.

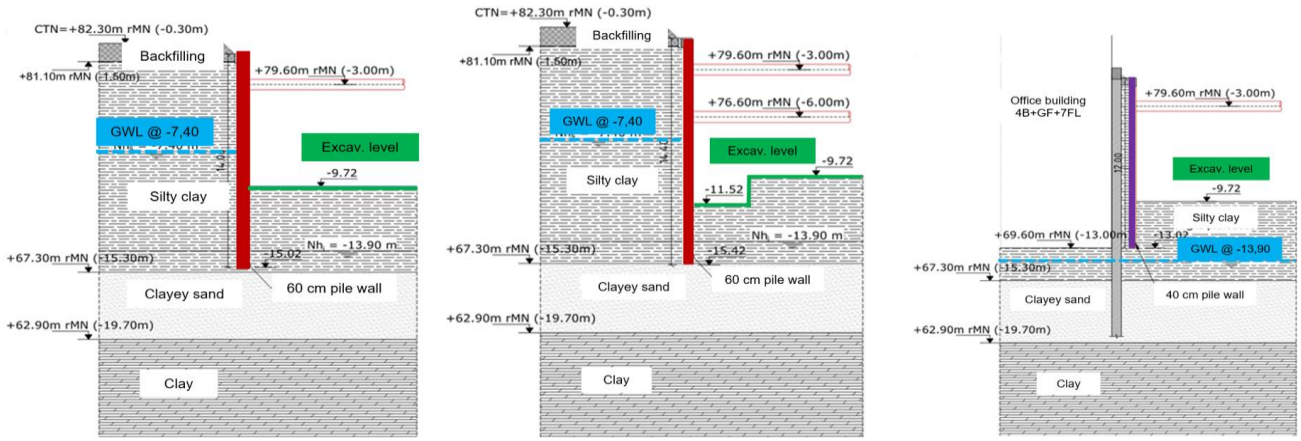

Figure 3. left: characteristic section 1, middle: characteristic section 2, right: characteristic section 3

The calculation is based on the finite element method, through Plaxis 2D software.

Maximum horizontal displacement of the retaining wall, calculated, towards inside pit area, was 25 millimetres (Figure 4).

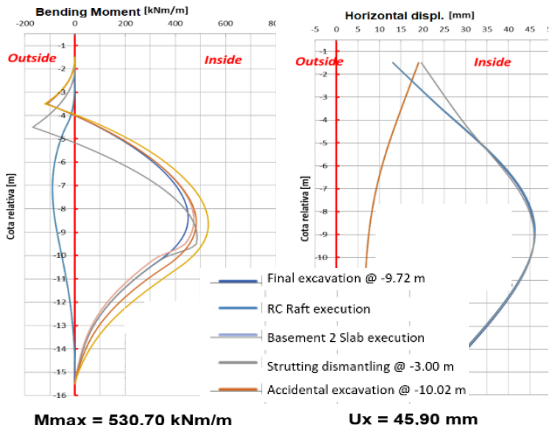

Figure 4. Contiguous pile wall and steel struts layout.

5 MONITORING

To conduct proper monitoring works both for the new infrastructure works and for the neighbour existing buildings, there were installed two inclinometers and used new and existing settlement monitoring marks on both two buildings.

Monitoring works were conducted according to a specific programme which followed each key step of new infrastructure construction.

Measurements were compared to displacement values obtained within design phase to confirm the design assumptions, and, if it is the case to take corrective actions as quick as possible.

Monitoring reports revealed a maximum horizontal displacement of the retaining wall of about 10 mm, less than the one provided by design and vertical displacement of neighbour buildings within required parameters (Figure 5).



Figure 5. Inclinometer measurements and working stage.

6 CONCLUSIONS

This project was a particularly challenging one, not necessarily due to the technology used for the infrastructure works, but since the works required a deep excavation in a congested urban area, in a particularly narrow working space and being surrounded by buildings that must not be affected in any way with the newly power station execution works. In this way, it is once again noted the importance of preparing and conducting monitoring works, both for newly built structure and for vicinities also (Figure 6).

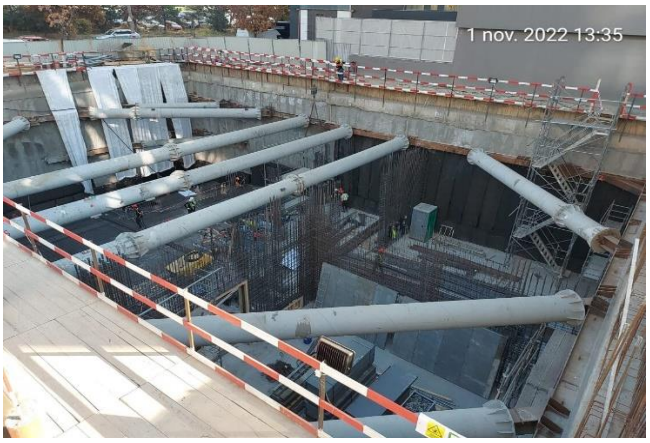

Figure 6. Site photo during infrastructure works.

REFERENCES

SR EN 1536+A1:2015. *Execution of special geotechnical work - Bored piles / "Execuția lucrărilor geotehnice speciale. Piloți forați".*

SR EN 1997-1:2004, Eurocode 7. *Geotechnical design - General rules / "Eurocod 7: Proiectarea geotehnică. Partea 1: Reguli generale".*

SR EN 1997-1:2004/NB:2007, Eurocode 7. *Geotechnical design - General rules. National Annex / Eurocod 7: Proiectarea geotehnică. Partea 1: Reguli generale. Anexa Națională,*

SR EN 1998-5:2004/NA:2007, Eurocode 8. *Design of structures for earthquake resistance Part 5: Foundations, retaining structures and geotechnical aspects. National Annex / "Eurocod 8: Proiectarea structurilor pentru rezistența la cutremur. Partea 5: Fundații, structuri de susținere și aspecte geotehnice. Anexa națională".*

NP 120-2014. *Normative regulations for design and execution of deep excavations in urban areas / "Normativ privind cerințele de proiectare și execuție a excavațiilor adânci în zone urbane".*

NP 124-2010. *Normative regulations for geotechnical design of retaining structures / "Normativ privind proiectarea geotehnică a lucrărilor de susținere".*

Proceedings of the XVIII ECSMGE 2024
GEOTECHNICAL ENGINEERING CHALLENGES
TO MEET CURRENT AND EMERGING NEEDS OF SOCIETY
© 2024 the Authors
ISBN 978-1-032-54816-6
DOI 10.1201/9781003431749-418
Open Access: www.taylorfrancis.com, CC BY-NC-ND 4.0 license

ECSMGE 24
XVIII EUROPEAN CONFERENCE ON SOIL MECHANICS AND GEOTECHNICAL ENGINEERING

Compressibility transition between a marine onshore clay to artificial carbonate silt soil behaviour

Transition de compressibilité entre le comportement d'un sol argileux marin onshore et le comportement d'un sol limoneux carboné artificiel

A. Conrado-Palafox*, T. Newson, A. Ahmed
Geotechnical Research Centre, Department of Civil and Environmental Engineering, University of Western Ontario, London, Ontario, Canada

*aconrado@uwo.ca

ABSTRACT: Wind turbines are rapidly moving to offshore environments to lessen onshore land use, reduce visual impact, and take advantage of higher and more constant wind speeds. A clear example is the Gulf of Mexico and its surroundings, which have a high potential for offshore wind farms. The most attractive offshore areas have shallow water depths, such as Florida, the Yucatan shelf, and the Bahamas, which are characterized by crushable carbonate sediments. Since it is expensive to obtain *in situ* carbonate sediment samples, the creation of an artificial simulant consisting of calcite particles and clay soil was used for this research. Compressibility tests were carried out to identify the compression responses of several clay – calcite and silicate silt mixes were used to provide an initial screening of suitable materials. The results show an improvement in the void index with addition of silica and calcite particles to the reconstituted clay, and although both forms of silt particles decreased the compression index; the calcite mixtures with higher than 85% of calcite particles reached and exceeded the C_v of the reconstituted clay. Moreover, the calcite particles decreased the liquid limit to a lesser extent than the silicate mixtures.

RÉSUMÉ: Les éoliennes se déplacent rapidement vers les environnements offshore pour réduire l'utilisation des terres terrestres, réduire l'impact visuel et tirer parti de vitesses de vent plus élevées et plus constantes. Un exemple clair est celui du golfe du Mexique et de ses environs, qui présentent un fort potentiel pour les parcs éoliens offshore. Les zones offshore les plus attrayantes ont des eaux peu profondes, comme la Floride, le plateau du Yucatan et les Bahamas, caractérisées par des sédiments carbonatés écrasables. Comme il est coûteux d'obtenir des échantillons de sédiments carbonatés in situ, la création d'un simulant artificiel composé de particules de calcite et de sol argileux a été utilisée pour cette recherche. Des tests de compressibilité ont été effectués pour identifier les réponses à la compression de plusieurs mélanges d'argile – calcite et limon silicaté afin de fournir un premier criblage de matériaux appropriés. Les résultats montrent une amélioration de l'indice de vide avec l'ajout de particules de silice et de calcite à l'argile reconstituée, et bien que les deux formes de particules de limon diminuent l'indice de compression ; les mélanges de calcite avec plus de 85 % de particules de calcite atteignaient et dépassaient le Cv de l'argile reconstituée. De plus, les particules de calcite diminuent la limite de liquidité dans une moindre mesure que les mélanges de silicates.

Keywords: Compressibility; carbonate silt; artificial offshore marine sediments.

1 INTRODUCTION

This study focuses on the geotechnical properties of soils in the near offshore carbonate areas of the Gulf of Mexico and Caribbean, more specifically on the Yucatan Shelf, Florida Shelf, Bahamian Platform and Gulf of Batabano in Cuba. These areas are of great interest because they are adjacent to existing offshore oil industry areas, such as the Campeche Bay or the continental shelf of Texas, and they have reasonable wind capacity factors (~40%) making them potentially viable for future offshore wind farms. The capacity factor is determined based on raw wind data obtained from the ERA-5 and MERRA-2 wind climate estimations and standard wind turbine power curves, enabling estimates of the energy production. It should be noted that the average capacity factor currently achieved offshore in Europe was 45% in 2018 (Hernández Galvez et al. 2022).

These offshore areas are characterized by either extensive shallow water depths with low wave energy, e.g. Florida Bay, Bahamian Platform and the Gulf of Batabano (because of their protected shelf lagoon singularities), or high energy wave environments with open, deeply submerged shelves, e.g. the West Florida Shelf and Yucatan Shelf (Logan et al. 1969).

The carbonate sediments in the Gulf of Mexico are generally formed from coral reefs, sands and mud

materials, whose composition depend on wave energy and carbonate precipitation. The sediments are found to transit from sand and lime sands to lime muds, with increasing mud composition (clay size particles), for greater water depth and lower wave energies (Logan et al. 1969; Purdy 1963; Ginsburg 1956; Hoskins 1964).

There are four main particle size distribution (PSD) types in the carbonate areas of the Gulf of Mexico (See Figure 1). These are: 1) sand material with less than 12% silt and <5% clay particles; this is characterized by skeletal carbonate materials, such as mollusk grains or non-skeletal grapestone particles (shown with brown lines); 2) silty sand sediments with around 20% silt particles and <10% clay size particles, with the skeletal portions coming from coral algae particles, angular molluscan fragments and foraminifera, and the oölitic portion from non-skeletal particles (shown with red lines); 3) lime muds with 50% silt material with less than 20% clay size particles (shown with green lines); 4) carbonate mud sediments formed with clay size particles around 50% and less than 25% sand particles (shown with yellow lines). The carbonate silt and mud sediments are mostly non-skeletal silt grains, such as faecal pellets, peloids and ooids, while clay size grains are often aragonite precipitated particles and some terrigeneous clays close to Campeche bay, the Texas shelf and southeast Cuba, (Logan et al. 1969; Purdy 1963; Ginsburg 1956; Hoskins 1964).

As can be seen in Figure 1, although these materials are generally all carbonate in nature, there is a significant range of particle size distributions along the Gulf of Mexico, e.g. carbonate muds (4) can be found on the Yucatan Shelf with Campeche Calcilitutie, as well as in Florida and Bahamas, with Cudjoe Keys and South Bright, respectively. Whilst silty sands (2) are in Progreso, Yucatan, Florida Bay and the Bahamas.

Most geotechnical investigations for carbonate soils have been carried out with sand or silty sands (e.g. Coop 1990; Wang et al. 2020) to determine the crushability influences of these weak particles, leaving a gap in the literature with very few carbonate silts and mud samples being investigated and particularly those of the Gulf of Mexico. This paper describes a study of the variations in compression behaviour observed and other basic geotechnical properties of an artificial offshore sediment made from a high sensitivity terrigenous clay with additions of crushable carbonate silt particles. These carbonate silt-clay mixtures are also compared with similar silicate silt-clay mixtures to determine any behavioural differences due to the calcite minerals. Thus, this paper investigates the transition behaviour between lime mud or Marquesa Lagoon sediments to the Cudjoe keys or South Bright carbonate mud sediments, as shown in Figure 1.

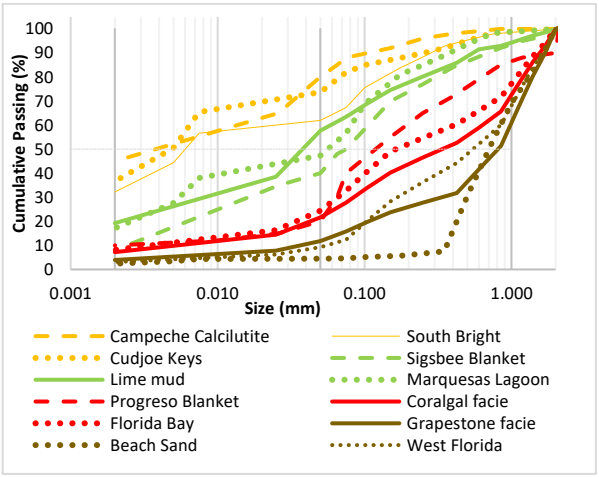

Figure 1. PSD of carbonate sediments in the Gulf of Mexico.

2 MATERIALS AND METHODS

Since it is expensive to obtain offshore marine *in situ* sediments and because carbonate minerals have high sensitivity values from 2 to 50 leading to significant disturbance during sampling, some researchers have attempted to better understand calcareous and carbonate soils based on artificial soils (e.g. Chen et al. 2013; Liu et al. 2016). In this paper, the same approach has been taken as a first step to creating realistic simulants for artificial offshore carbonate clayey-silt materials and provides a good screening tool to assess the most promising materials.

The clay material used to make the soil mixtures is an onshore clay from Eastern Canada (Ottawa), which was selected as a reference material due to its glaciolacustrine sediment characteristics (Nader 2014); comparable in relation to its sedimentation processes to some marine sediments. This high plasticity clay (CH) has a liquid limit of 55%, plastic limit of 26% and a plastic index of 29%.

2.1 Calcite and silicate mixtures

Artificial calcite particles were created in a chemistry laboratory at Western University based on Na_2CO_3 and $CaCl_2$ adjusting the pH to 10 with HCl, to produce a uniformly graded carbonate silt material. SEM images of these particles show them to have hexagonal and rhombohedral shapes, a tendency to aggregate and a crushability index Br of 0.54 (Conrado-Palafox et al. 2023). The silicate silt is a commercial Sil-Co-Sil-106 sub-angular ground quartz (Schmidt 2015).

Both types of silt particle were mixed with the Ottawa clay soil at different percentages: 25%, 50%, 75%, 87.5% and 93.5%, to obtain the resulting compressibility and other basic geotechnical behaviour of the clay. Figure 2 shows that the pure artificial calcite particle size distribution (PSD) has a

generally uniform grading, while the silicate silt material has a more well-graded curve (Table 1 shows d_{50} values), with 25% of the particles smaller than 0.002mm. The Ottawa clay soil has 70% of its particles smaller than 0.002mm.

The carbonate silt mixtures show better graded curves for 25% and 50%, while the curve with 75% calcite lies closer to the uniform distribution; the corresponding d_{50} and uniformity coefficients (C_u) are shown in Table 1. This is important because the particle sized distribution in the sample plays a significant role in the compressibility behaviour.

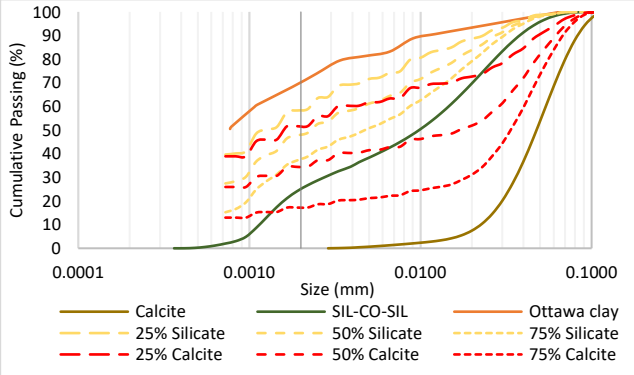

Figure 2. PSD of silicate silt, calcite, and Ottawa clay mixes.

Table 1. PSD characteristic parameters.

Soil sample	Silt (%)	d_{50} (mm)	C_u
Reconstituted clay	0	0.0080	
Silicate	25	0.0015	2.65
Silicate	50	0.0022	5.18
Silicate	75	0.0050	10.48
Silicate	100	0.0100	
Calcite	25	0.0018	5.18
Calcite	50	0.0180	36.14
Calcite	75	0.0340	48.19
Calcite	100	0.0500	

2.2 1-D oedometer test

Oedometer tests were carried out with reconstituted samples formed at 1.5 times their liquid limit, to determine the compressibility variations (void ratio vs stress) due to the calcite and silicate admixtures. To visualize any potential bonding and structure behaviour of our mixes, the intrinsic compression line (ICL) and sedimentation compression line (SCL) after Burland (1990) was determined using the void index (I_v) approach with the following equations (1 – 3) and compared to the void index relationships of the different mixtures;

$$I_v = \frac{e - e_{100}}{C_c*} \quad (1)$$

$$e_{100} = 0.109 + 0.679e_L - 0.089e_L^2 + 0.016e_L^3 \quad (2)$$

$$C_c* = 0.256e_L - 0.04 = e_{100} - e_{1000} \quad (3)$$

where e_L is the void ratio at the liquid limit and e_{100}, e_{1000} are the void ratio at 100 kPa and 1,000 kPa.

3 RESULTS

3.1 Compression behaviour

The initial void ratios (e_0) and void ratios at 25 kPa (e_{25}) for the intact clay and reconstituted clay are e_0 = 2.07, 1.39 and e_{25} = 2.04, 1.27 respectively. The silicate mixtures presented initial void ratios from 1.46 to 0.76, decreasing with higher silicate % and their e_{25} range are from 1.25 to 0.67; while e_0 of the calcite mixtures are 2.03 to 1.18 and e_{25} are 1.87 to 1.01.

Figure 3 (a) shows the 1-D oedometer compression curves of the calcite-clay mixtures, while 3 (b) shows the results of silicate-clay mixtures. The void ratio (e) was normalized by the void ratio at 25 kPa (e_{25}). Two distinct behaviours are seen, with calcite compressibility curves moving upwards (increasing e/e_{25}) with increasing silt %, while the silicate mixes went downwards (reducing e/e_{25}), in comparison to the reconstituted Ottawa clay material reference.

The compressibility indices (C_c) of the silicate materials show a reduction with silicate percentage increases, while the C_c values for the calcite mixes keep increasing until 93.5%, where it actually exceeds the reconstituted clay value. On the other hand, the swelling index decreased with both the addition of the silicate and calcite minerals; the silicate mixes reduce their C_s with higher percentages of silicate, while the calcite mixes presented lower C_s values with lower calcite percentages (see Table 1).

Figure 4 shows compressibility index (C_c) with liquid limit (LL). As expected, LL decreases with silicate or calcite addition. However, the silicate reduced the LL more than the calcite. It can be seen in Figure 4 that LL of the calcite mixes range from 35-42%. Intact samples from Mexico and other offshore regions show higher LL, thereby increasing their compressibility indices. This is likely to due to the minerology and chemistry of the offshore materials.

Figure 5 shows the ICL and SCL developed by Burland (1990) obtained with a meta-study of natural clay results. According to Cotecchia and Chandler (2000) the sensitivity can also be determined with the SCL and ICL curves. Therefore, the SCL obtained by Burland (1990) with intact clay samples shows a sensitivity of approximately S_t=5 in respect to its ICL. The undisturbed Ottawa clay is far above the SCL

meaning that the clay tested has a sensitivity higher than 5 at lower stresses. At a vertical effective stress (σ'_v) above 500 kPa, the line converges on the SCL, while for reconstituted Ottawa clay void index (I_v) lies between the SCL and ICL lines, showing the influence of structure on the intact clay compression behaviour.

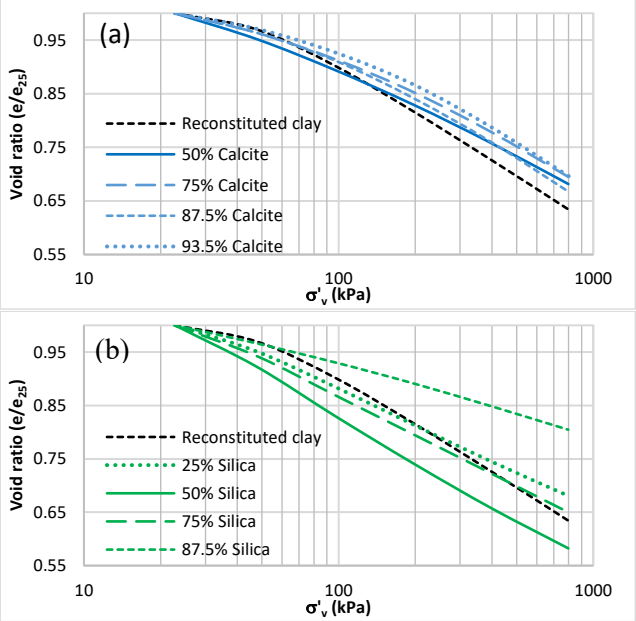

Figure 3. Normalized compression curves of calcite (a) and silicate (b) mixes with Ottawa clay.

Table 2. Compression index (C_c) and swell index (C_s).

Soil sample	Cc	Cs
Reconstituted clay	0.348	0.036
25% Silicate	0.263	0.027
50% Silicate	0.251	0.016
75 % Silicate	0.146	0.011
87.5% Silicate	0.091	0.010
50% Calcite	0.222	0.016
75% Calcite	0.269	0.018
87.5% Calcite	0.325	0.024
93.5% Calcite	0.455	0.026

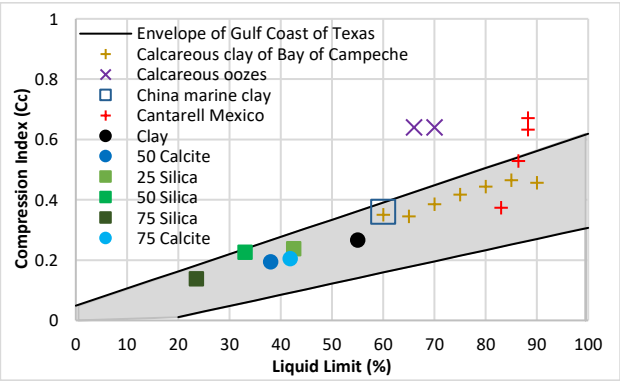

Figure 4. Compression index with limit liquid.

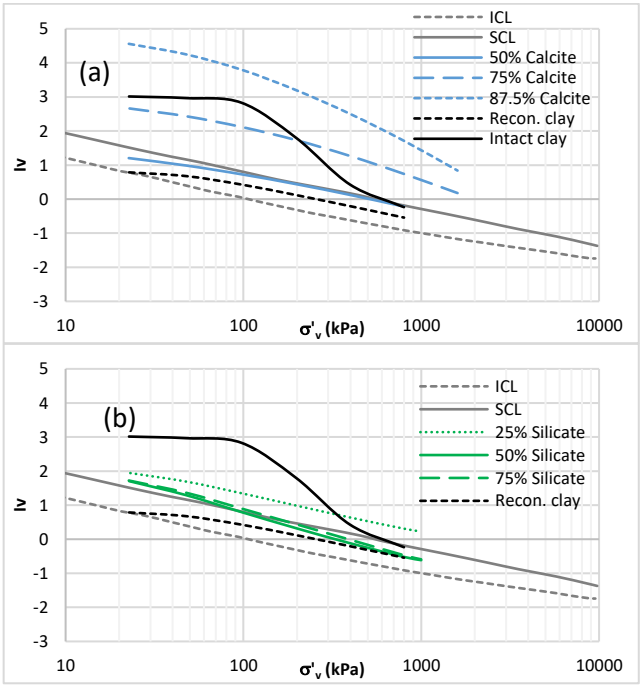

Figure 5. Void indices (I_v) of clay and calcite (a) and silicate (b) mixes.

The calcite mixture curves have increased void index values with calcite % increases, lying well above the reconstituted clay curve. At higher calcite contents (>75%), the calcite curves reach the undisturbed clay curve and eventually exceed it. In contrast, the silicate mixtures with less than <75% present similar curves laying around or beneath Burland's SCL, reproducing the similar behaviour to the very low % calcite mixes.

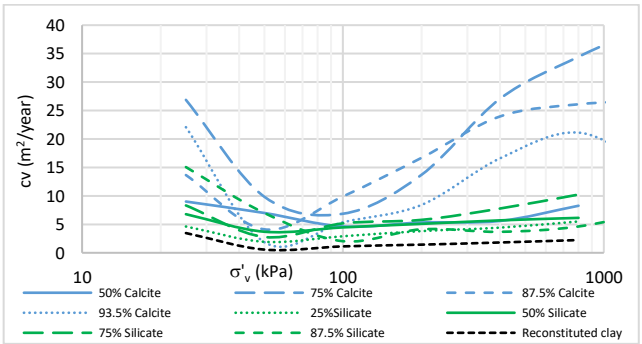

Figure 6. Coefficient of consolidation (C_v) with stress.

The values of coefficient of consolidation (C_v) are shown in Figure 6 and show lower values for silicate mixtures compared to the calcite. The 50% calcite mixture presents the lowest C_v in comparison with the other mixtures. The highest C_v values are the calcite mixtures greater than 75%, although at 50 kPa the values are about the same as the silicate or 50% calcite.

4 CONCLUSIONS

This study shows the changes in basic geotechnical behaviour of a high plasticity terrigenous clay due to the addition of precipitated calcite particles and manufactured silicate particles. Firstly, the addition of 50%, 75% of silicate and 50% calcite shows PSDs similar to the upper limits found in the Gulf of Mexico marine sediments. Adding more calcite particles (75% and 87.5%) provides PSD curves similar to the Coral facies or Progresso Blanket curves. The clay – silicate mixes are less compressible than the clay – calcite mixes, and sediments with more than 85% of calcite particles present compressibilities and void ratios higher than a structured intact high plasticity clay. Moreover, the calcite particles do not reduce the clay plasticity as much as silicate particles, and the calcite addition increases the coefficient of consolidation more than the silicate material. Although not tested in the study, it is expected changes in the shear strength and sensitivity of the silicate and calcite mixes will occur, based on the ICL and SCL curves of the clays. Further testing using more sophisticated stress-strain approaches will be used to further validate the obtained materials.

ACKNOWLEDGEMENTS

The authors acknowledge the scholarship provided by the CONAHCYT (Consejo Nacional de Humanidades Ciencias y Tecnologías).

REFERENCES

Burland, J. B. (1990). "On the Compressibility and Shear Strength of Natural Clays." Geotechnique 40 (3):329–78. http://doi.org/10.1680/geot.1990.40.3.329.

Chen, Ch., Fang J., Luo, A. and Shao, Sh. (2013). "Study of Artificial Structural Loess under the True Triaxial Tests." Advanced Materials Research 671–674:343–48. http://doi.org/10.4028/www.scientific.net/AMR.671-674.343.

Conrado-Palafox, A, Newson, T. and Ahmed, A. (2023). "The Effect of Artificial Carbonate Silt Particles on the Compressibility and Crushing of Calcareous Clay." In GeoSaskatoon, Bridging Infraestructue & Resources. Saskatoon.

Coop, M. R. (1990). "The Mechanics of Uncemented Carbonate Sands." Geotechnique 40 (4): 607–26. https://doi.org/10.1680/geot.1990.40.4.607.

Cotecchia, F., and Chandler, R. J. (2000). "A General Framework for the Mechanical Behaviour of Clays." Geotechnique 50 (4): 431–47. https://doi.org/10.1680/geot.2000.50.4.431.

Ginsburg, R. N. (1956). "Environmental Relationships of Grain Size and Constituent Particles in Some South Florida Carbonate Sediments." AAPG Bulletin 40 (10): 2384–2427. https://doi.org/10.1306/5CEAE598-16BB-11D7-8645000102C1865D.

Hernández-Galvez, G., Chuck, D., Sarracino, O., Lastres, O., Dorrego, J., Trujillo, A., Saldaña, R., Pampillón, L., Perea-Moreno, A. and Hernandez-Escobedo, Q. (2022). "Harnessing Offshore Wind Energy along the Mexican Coastline in the Gulf of Mexico—An Exploratory Study Including Sustainability Criteria." Sustainability 14 (10): 5877. https://doi.org/10.3390/su14105877.

Hoskins, C. W. (1964). "Molluscan Biofacies in Calcareous Sediments, Gulf of Batabano, Cuba." Bulletin of the American Association of Petroleum Geologists 48 (10): 1680–1704. https://doi.org/10.1306/BC743DAD-16BE-11D7-8645000102C1865D.

Liu, E., Chen, Sh., Lai, Y., Wei W. and Fu, Zh. (2016). "Particle Breakage of Artificially Crushable Materials Subject to Drained Cyclic Triaxial Loading." Soil Dynamics and Earthquake Engineering 89: 262–68. https://doi.org/10.1016/j.soildyn.2016.08.008.

Logan, B., Bass, M., Cebulski, D. and McBirney, A. (1969). Carbonate Sediments and Reefs, Yucatan Shelf, Mexico and Other Papers on Florida and British Honduras and Tectonic Relations of Nothern Central America and the Western Caribbean - The Bonacca Expedition. American Association of Petroleum Geologists. https://doi.org/10.1306/M11366.

Nader, A. (2014). "Engineering Characteristics of Sensitive Marine Clays-Examples of Clays in Eastern Canada." University of Ottawa.

Purdy, E. G. (1963). "Recent Calcium Carbonate Facies of the Great Bahama Bank. 2. Sedimentary Facies." The Journal of Geology 71 (4): 472–97. https://doi.org/10.1086/626920.

Schmidt, C. (2015). "Static and Dynamic Response of Silty Toyoura Sand with PVA Fibre and Cement Additives." Western University of Ontario. london: Electronic Thesis and Dissertation Repository 2841.

Wang, G., Wang, Zh., Ye, Q. and Wei, X. (2020). "Particle Breakage and Deformation Behavior of Carbonate Sand under Drained and Undrained Triaxial Compression." International Journal of Geomechanics 20 (3): 04020012. https://doi.org/10.1061/(ASCE)GM.1943-5622.0001601.

Proceedings of the XVIII ECSMGE 2024
GEOTECHNICAL ENGINEERING CHALLENGES
TO MEET CURRENT AND EMERGING NEEDS OF SOCIETY
© 2024 the Authors
ISBN 978-1-032-54816-6
DOI 10.1201/9781003431749-419
Open Access: www.taylorfrancis.com, CC BY-NC-ND 4.0 license

ECSMGE 24
XVIII EUROPEAN CONFERENCE ON SOIL MECHANICS AND GEOTECHNICAL ENGINEERING

Development and laboratory testing of a low-cost wireless in-place inclinometer prototype

Développement et tests en laboratoire d'un prototype d'inclinomètre sans fil à faible coût

R. Correia dos Santos*, J. Marcelino
Laboratório Nacional de Engenharia Civil, Lisboa, Portugal

**ricardos@lnec.pt*

ABSTRACT: This paper introduces a low-cost in-place inclinometer tailored for geotechnical engineering applications, specifically designed for monitoring lateral (transverse) deformations in embankments, retaining walls or natural slopes. The developed system utilizes Micro-Electro-Mechanical System (MEMS) accelerometers, which are pivotal in tilt measurement, offering precise and compact solutions for monitoring inclinations in geotechnical applications. The hardware configuration involves connecting multiple accelerometer sensors in series, interfacing them with small low-cost microcontrollers. These sensors communicate data wirelessly to a central master node. The master node further transmits the collected data to the web infrastructure. The software architecture of the system is developed to achieve real-time data processing and analysis. This integration enables efficient storage, retrieval, and visualization of the displacement data, empowering geotechnical engineers with accurate, timely, and actionable insights. Laboratory testing and validation of this inclinometer system demonstrates that it may be useful in providing general information for slope stability assessments, excavation safety, and foundation integrity evaluations. The MEMS accelerometer used is quite low-cost, with a mere 10-bit output resolution, and, thus, may not meet the requirements for high-risk projects. Plans are underway to explore alternative MEMS that offer enhanced precision and accuracy for tilt measurement while still maintaining affordability.

RÉSUMÉ: Cet article présente un système d'inclinomètre à faible coût conçu sur mesure pour les applications de génie géotechnique, spécifiquement élaboré pour surveiller les déformations latérales (transversales) dans les remblais, les murs de soutènement ou les pentes naturelles. Le système développé utilise des accéléromètres à système micro-électromécanique (MEMS), cruciaux pour la mesure de l'inclinaison, offrant des solutions précises et compactes pour la surveillance des inclinaisons dans les applications géotechniques. La configuration matérielle implique la connexion en série de plusieurs capteurs d'accéléromètre, en les interférant avec de petits microcontrôleurs économiques. Ces capteurs transmettent sans fil les données à un nœud central maître. Ce nœud maître transmet ensuite les données collectées à l'infrastructure Web. L'architecture logicielle du système est conçue pour permettre un traitement et une analyse des données en temps réel. Cette intégration permet un stockage, une récupération et une visualisation efficaces des données de déplacement, fournissant aux ingénieurs géotechniciens des informations précises, opportunes et exploitables. Les tests de laboratoire et la validation de ce système d'inclinomètre démontrent qu'il peut être utile pour fournir des données cruciales pour les évaluations de la stabilité des pentes, la sécurité des excavations et l'intégrité des fondations. Le capteur MEMS utilisé est assez économique, avec une résolution de sortie de seulement 10 bits, et pourrait ne pas répondre aux exigences des projets hautement significatifs et à haut risque. Des plans sont en cours pour explorer des capteurs alternatifs offrant une précision et une précision accrues pour la mesure de l'inclinaison tout en maintenant un coût abordable.

Keywords: Fixed-in-place inclinometer; low-cost; MEMS acceleration sensors; ground movement; embankments.

1 INTRODUCTION

Inclinometer monitoring is a geotechnical technique used to measure and track the changes in inclination of a natural slope, retaining wall, or embankment, over time. This method typically involves the use of a metal or plastic pipe (casing) with inner grooves in two orthogonal directions that is installed into a borehole drilled within the ground being monitored (Dunnicliff, 1982; Stevens and Zehrbach, 2000). By regularly measuring the inclinations of that casing at specific depths, engineers and geotechnical experts can determine the lateral deformations in two directions and assess the stability of slopes, tunnels, excavations, dams, and other geotechnical structures (Ding et al., 2000; Stark and Choi, 2008; Uhlemann et al., 2016).

Inclinometer monitoring provides valuable data on ground movements, enabling also early detection of potential issues and allowing for timely remedial

actions to prevent accidents or damage to structures (Stark and Choi, 2008).

The most used instrument type, the transversing inclinometer probe, which uses a servo-accelerometer sensor, was introduced to the industry in the late 60s (Green and Mikkelsen, 2008). Servo accelerometers measure acceleration based on force balance and inertial principles, and are known for their high precision, robustness, durability, and ability to withstand harsh environments. The casing's shape is established through consecutive manual measurements, usually placing the transversing probe at 50 cm intervals, which is the typical distance between the wheels that guide the probe along the casing grooves. These measurements yield a profile of the casing in two orthogonal directions. Machan and Bennett (2008) presents a detailed description of the procedures involved in the measurement and data collection using the transversing inclinometer probe.

One notable drawback of servo accelerometers used in such probes is their relatively high cost. Other limitations, which can cause measurement errors if not properly accounted for, include sensitivity to temperature changes and limited frequency response (high frequency readings may result in feedback loop that can introduce phase lag). These limitations make servo accelerometers less suitable and prohibitive for applications that require the use of a fixed In-Place Inclinometer (IPI) solution, or automatic acquisition and remote access of high-frequency reads.

IPI involve the installation of multiple sensors at discrete depths along the tube casing and are useful when frequent monitoring of ground movement is essential or when site accessibility is limited (Uhlemann et al., 2016). This approach saves valuable time and labour that would otherwise be spent on manual measurements using the transversing inclinometer probe. Additionally, it enables the seamless collection of regular data through the utilization of automated data acquisition equipment, providing valuable information on the ground deformation vector and rate of movement.

Micro Electro-mechanical Systems (MEMS) accelerometers have gained prominence in the last decade (Li et al., 2014), supplanting the traditional servo accelerometer, and finding a growing application in IPI.

The principle of MEMS accelerometers relies on detecting changes, for example, in capacitance, piezoelectricity, or thermal conductivity caused by accelerative forces (Niu et al., 2018). When the accelerometer undergoes acceleration, these microstructures move, leading to a change in capacitance or other quantifiable properties. This change is then converted into an electrical signal, which can be analysed and used to ascertain the acceleration applied to the sensor.

Ground movements are typically deemed quasi-static. Thus, by measuring the components of the gravitational acceleration vector along a three axis MEMS accelerometer, mathematical algorithms can be applied to ascertain the sensor's orientation relative to Earth's gravitational field.

The rapid advancements in MEMS technology as led to significant reductions in sensor cost, size, and energy consumption of inclinometer solutions. At present, some companies, including, SISGEO.com, GEOSENSE.co.uk, SIGNALQUEST.com, MEASURAND.com and SOILINSTRUMENTS.com, have their own commercially available IPI solutions.

Those solutions use a series of accelerometers housed within rigid bodies that are somewhat interconnected by flexible joints enabling relative tilt movement between each sensor. Each available solution features its joint mechanism and rigid body design. Some are specifically designed for insertion into traditional grooved casings, whereas others offer greater versatility, allowing placement inside unguided casings. The IPI from MEASUREMENT don’t require any centring of the rigid bodies within the casing, relying on the casing’s wall for the support of the flexible joints. Full information about the MEMS accelerometers used in commercial solutions is not disclosed by the companies. Recently, Freddi *et al.* (2023) presented laboratory testing of prototypes and preproduction samples of a lightweight IPI solution, using carbon fibre rods for the rigid body.

These solutions can result in relatively expensive IPI systems, specially, for use cases where many inclinometers, with a high sensor count, are necessary. Often, to reduce costs, only a minimal number of sensors are placed, or they are installed far apart from each other (Allasia et al., 2020). Also, all of them transmit data from sensors through wires, using a serial wired communication protocol (e.g., RS485 or SDI-12).

A prototype of a low-cost IPI system, designed for budget-constrained scenarios, is presented. A notable aspect of the developed system is the wireless transmission of data from each sensor to a master node. This minimizes the need for extensive wiring and connections and results in cost savings.

While there is an inherent acceptance of reduced tilt precision and accuracy in comparison with available expensive commercial solutions, the system's design should be tailored to maintain its utility and reliability across typical geotechnical monitoring applications.

2 MATERIALS AND METHODS

The IPI prototype comprises four sensor nodes and a master node. Each sensor node wirelessly transmits angle data obtained from its accelerometer to the master node. The master node forwards this data to a web-based timeseries database at predetermined time intervals.

2.1 Hardware components

Sensor nodes comprise an accelerometer board (HW-86C) and a microcontroller (ESP8266 D1 mini R2), both readily available at affordable prices (< 3 euros per unit). A custom-designed PCB board manages power distribution and ensures seamless communication between the microcontroller and the accelerometer with no wiring. Figure 1(a) shows the main components of each sensor node.

The sensor board employs the consumer-grade ADXL345, a triple-axis MEMS accelerometer with 10-bit digital output, providing a wide measurement range and low power consumption. Table 1 shows an estimate of the main source of error and the corresponding tilt errors. After compensation of some errors, through calibration, the ideal performance corresponds to a tilt error of 0.1º. Despite being 10 to 100 times less accurate than servo-accelerometers, this error level, if achieved, could be adequate for some less demanding cases.

Table 1. ADXL345 error source estimate (Analog Devices).

Sensor parameter	Performance	Condition/Note	Tilt Error
Noise density	290 *u*g/√Hz	Bandwidth at 6.25 Hz	0.05º
Bias drift	-	10 days	0.057º
Initial offset	35 mg	No compensation	2º
		With compensation	0º
Total error	No compensation	Bandwidth at 6.25 Hz	2.1º
	With compensation	Bandwidth at 6.25 Hz	0.1º

The electronic components of each sensor node are enclosed within a stainless-steel pipe (probe) with about 30 mm outer diameter and 10 mm length. Node sensors are powered by an 5V parallel circuit source. Each one operates at around 50 mA when active and can peak at a maximum of 300 mA (during 1 to 5 milliseconds) wireless transmission. Wireless transmission occurs in a staggered manner, one sensor at a time, with intervals of about 100 miliseconds, to prevent current overload.

The connection between each sensor probe is established using multi-layer ½ inch (PVC?) pipes and compression pipe fittings typicaly used in fluid applications. Figure 1(b) shows the prototype setup prior assembly with the four node sensors. A flexible joint is omitted, because laboratory testing is conducted using an apparatus with a rigid casing (Figure 1(c)). The goal is to eliminate potential errors arising from joint movements, focusing exclusively on assessing the accuracy and precision of sensor‘s angle measurements. To ensure a precise fit and centering in the rigid casing, 3D printed PLA elements are affixed at the extremities of each probe.



Figure 1. (a) sensor node components; (b) inclinometer prototype setup; (c) calibration rigid casing used in tests.

2.2 Software of nodes and acquisition system

Each sensor node's microcontroller is programmed in C++ using Arduino IDE to: (i) retrieve gravitational forces (g_x and g_y) from the accelerometer via the I2C protocol, (ii) compute the corresponding angles (a_x and a_y), (iii) employ a low-pass filter for enhanced accuracy, and (iv) wirelessly transmit this data to the master node. Each ESP device has a unique MAC address which is used to identification purposes. The transmission occurs at regular intervals controlled by a user variable. In the laboratory tests, data was transmitted every 10 s. Wireless transmission is achieved using the ESP-NOW protocol. ESP-NOW enables direct, fast, and low-power communication among multiple ESP microcontrollers over long distances (up to 400 m) without the need for a router.

The master node acts as an acquisition system and an internet gateway, being composed by two ESP8266 microcontrollers. The first microcontroller receives

data wirelessly from the node sensors, stores the readings in an array, and sends the aggregated sensor data in JSON format over Serial at regular intervals (30 seconds interval has been set in lab tests). Its code also features a timeout mechanism to ensure data transmission, even if not all sensors have provided readings within a specified time frame. The second microcontroller establishes a secure Wi-Fi connection, receives incoming JSON data from the Serial port (containing measurements from all sensors), and forwards it to a remote broker using the MQTT (Message Queuing Telemetry Transport) protocol. This microcontroller operates as an MQTT client, publishing data to a specific topic (with a name defined by an inclinometer code).

A free MQTT broker has been established using HiveMQ's cloud service (hivemq.com), which controls and aggregates all messages published.

A local server with Telegraf, InfluxDb and Grafana docker containers was established. Telegraf systematically gathers data from MQTT topics. This data is seamlessly relayed to an InfluxDB timeseries database, wherein a timestamp is attributed to each message, forming a robust backend infrastructure. Finally, the visual representation of the acquired data is facilitated through integration with a Grafana dashboard viewer, enhancing the overall monitoring and visualization capabilities of the system.

2.3 Setup of laboratory testing

The inclinometer prototype underwent testing utilizing an apparatus equipped with a top-mounted pivot, enabling a rigid casing to rotate within a range of +/- 20º along a vertical plane. Each sensor probe was manually aligned to ensure that the accelerometer's X and Y axes corresponded with the orthogonal grooves on the casing. A portable tiltmeter (servo accelerometer from Slope Indicator with a tilt error of approximately 0.011º) was positioned on a tilt plate installed perpendicular to the casing. All readings from the sensor probes and tiltmeter were zeroed with respect to the vertical position of the casing to eliminate any potential zero-g bias offset errors.

The angles computed from the sensor probes were then compared with those recorded by the tiltmeter. The prototype was placed into the casing with two different orientations to assess the angles of rotation along the sensor's X and Y axes (a_x and a_y). Readings from the sensor and tiltmeter were taken at regular intervals of about 0.5º within a range of about ±15º, under an ambient temperature of 18ºC.

3 RESULTS AND DISCUSSION

Figure 2 shows the results obtained when the X-axis of the accelerometers is aligned with the casing tilt motion. Results for the other prototype orientations are omitted due to space limitations, as they align closely with the findings presented here.

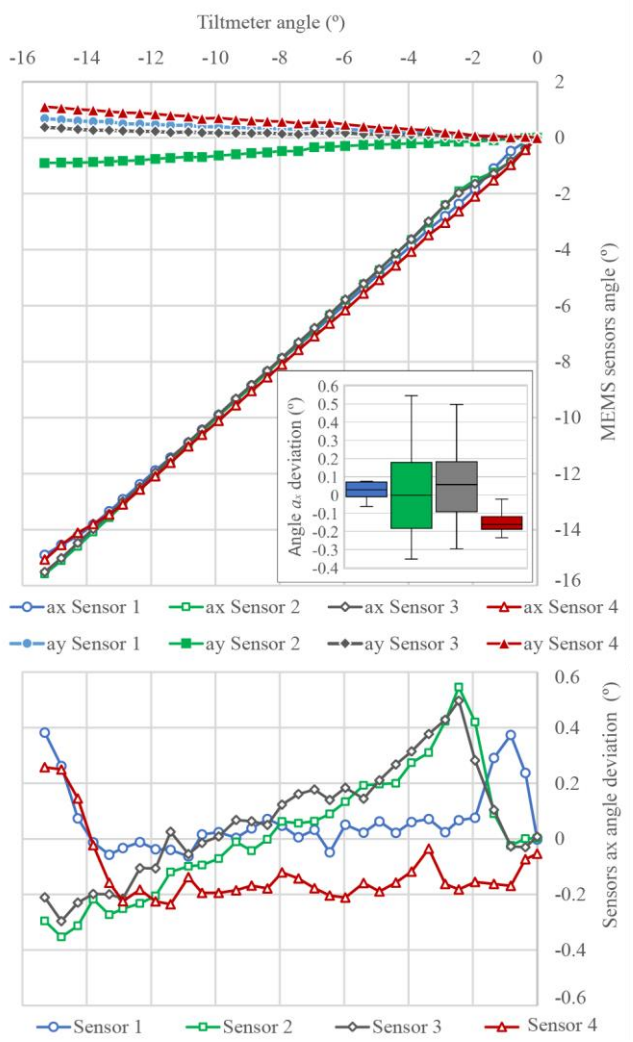

Figure 2. Results from the inclinometer prototype, with the X-axis sensors aligned to the casing rotation (-15º to 0º).

The top plot displays the relative angles resulting from each sensor probe (a_x and a_y) against the relative angles computed from the uniaxial tiltmeter. The bottom plot depicts the deviation of a_x relative angles from sensors in relation to those provided by the tiltmeter. The points of these plots derived from an average of not less than ten measurements for each sensor at every casing tilt position. The boxplot shows the interquartile range between the first and third quartiles, and the median of the deviation angles a_x of the sensors in relation to the tiltmeter for the entire range of rotation tested.

The results shown in Figure 2 allow for the following main findings:

- Average a_x angle deviations of sensors are within ±0.2º for the most of the tested range; Higher deviations, up to 0.5º, are observed in Sensor 1 within the tilt range [0.5º; 1.5º], and in Sensors 2 and 3 in [2º; 4º]; All sensors exhibit increasing a_x deviations for tilt angles greater than 14º but remain below 0.4º.
- All sensors show non-null relative a_y angles, demonstrating an almost linear relationship with the casing tilt angles; At a tilt angle of 15º, the sensor's a_y deviations range between ±1º; This suggests a misalignment of the accelerometers' actual axes, wherein the casing's tilt motion induces an undesired roll movement of the sensors (a_y).

Median values of a_x deviations for the entire tested range are 0.028º, -0.0006º, 0.057º and -0.163º for sensors 1, 2, 3 and 4, respectively; Sensors 1 and 4 show narrow interquartile range for the a_x deviations (less than 0.06º), when compared with sensors 2 and 3 (up to 0.35º).

As anticipated, owing to the extremely low-cost of the tested accelerometers, which are based on the consumer-grade ADXL345, the angle deviations are considerably higher when compared to force balanced sensors used in the transversing inclinometer probes.

Observed errors exceed the advertised total error of 0.1º for this sensor. This discrepancy may arise from certain limitations in the way angles are compared within the testing apparatus and misalignment due to the zero-g offset of sensors in relation to the casing orientation. The uniaxial tiltmeter used as reference also exhibits some error, with an expanded uncertainty of 0.011º/º (e.g., an error of 0.055º for a 5º tilt). Future enhancements to the testing apparatus and the calibration of sensor probes, ensuring their precise alignment within the casing tube, are required to yield reduced errors.

Results also suggest that precision and accuracy of the ADXL345 vary among different batches of the sensor. This variation is likely attributed to microstructural imperfections, resulting from the sensor's manufacturing process or other factors. It is also noted that errors due to temperature drift have not been addressed (the datasheet indicates a variation of 0.02º/ºC).

MEMS accelerometers of greater sensitivity, accuracy, and precision than the ADXL345 are available. For instance, the ADXL355 is promoted with a total angle error that is about 20 times lower, but it also comes with a 20-fold increase in cost, and a larger chip form factor. In ongoing developments, alternative MEMS featuring newer technologies and manufacturing processes will be assessed, all of which incur only a slight additional cost compared to the ADXL345.

4 CONCLUSIONS

This paper presents a prototype for a low-cost in-place inclinometer system, integrating MEMS accelerometers, and wirelessly transmitting its data to a master node acting as an acquisition system and a gateway to the internet.

Laboratory test results suggest that an in-place inclinometer based on this prototype may offer a general understanding of ground movements in low-risk scenarios, where total errors of about 0,4º are acceptable. Compared to pricier existing IPI systems, this specific equipment offers a cost-effective alternative. Its use is however not advised in high-risk works where extreme precise inclinometer monitoring is critical.

Investigations are ongoing to incorporate the optimal commercial MEMS accelerometer from other manufacturers in the developed prototype, with a focus on achieving the best price-to-quality ratio.

Compared to pricier existing IPI systems, this specific equipment offers a cost-effective alternative.

REFERENCES

Allasia, P., Godone, D., Giordan, D., Guenzi, D., and Lollino, G. (2020). Advances on Measuring Deep-Seated Ground Deformations Using Robotized Inclinometer System. *Sensors*, *20*(13), 3769. https://doi.org/10.3390/s20133769.

Ding, X., Ren, D., Montgomery, B., and Swindells, C. (2000). Automatic Monitoring of Slope Deformations Using Geotechnical Instruments. *Journal of Surveying Engineering*, *126*(2), 57–68. https://doi.org/10.1061/(ASCE)0733-9453(2000)126:2(57).

Dunnicliff, J. (1982). *Geotechnical Instrumentation for Monitoring Field Performance. National Cooperative Highway Research Program. Synthesis of Highway practice, nº. 89*.

Freddi, F., Mingazzi, L., Pozzi, E., and Aresi, N. (2023). Laboratory Assessment of an In-Place Inclinometer Chain for Structural and Geotechnical Monitoring. *Sensors*, *23*(20), 8379. https://doi.org/10.3390/s23208379.

Green, G. E., and Mikkelsen, P. E. (2008). *Deformation Measurements with Inclinometers. Transportation Research Record, n. 1169*.

Li, C., Fernandes-Steeger, T. M., Link, J. A., May, M., and Azzam, R. (2014). Use of MEMS accelerometers/inclinometers as a geotechnical monitoring method for ground subsidence. *Acta Geodynamica et Geomaterialia*, 337–349. https://doi.org/10.13168/AGG.2014.0015.

Machan, G., and Bennett, V. G. (2008). *Use of Inclinometers for Geotechnical Instrumentation on Transportation Projects. State of the Practice. Transportation Research Circular, nº. E-C129*.

Niu, W., Fang, L., Xu, L., Li, X., Huo, R., Guo, D., and Qi, Z. (2018). Summary of Research Status and Application of MEMS Accelerometers. *Journal of Computer and Communications*, *06*(12), 215–221. https://doi.org/10.4236/jcc.2018.612021.

Stark, T. D., and Choi, H. (2008). Slope inclinometers for landslides. *Landslides*, *5*, 339–350.

Stevens, W. R., and Zehrbach, B. E. (2000). Inclinometer Data Analysis for Remediated Landslides. *Geotechnical Measurements*, 126–137. https://doi.org/10.1061/40518(294)10.

Uhlemann, S., Smith, A., Chambers, J., Dixon, N., Dijkstra, T., Haslam, E., Meldrum, P., Merritt, A., Gunn, D., and Mackay, J. (2016). Assessment of ground-based monitoring techniques applied to landslide investigations. *Geomorphology*, *253*, 438–451. https://doi.org/10.1016/j.geomorph.2015.10.027.

Proceedings of the XVIII ECSMGE 2024
GEOTECHNICAL ENGINEERING CHALLENGES
TO MEET CURRENT AND EMERGING NEEDS OF SOCIETY
© 2024 the Authors
ISBN 978-1-032-54816-6
DOI 10.1201/9781003431749-420
Open Access: www.taylorfrancis.com, CC BY-NC-ND 4.0 license

ECSMGE 24
XVIII EUROPEAN CONFERENCE ON SOIL MECHANICS AND GEOTECHNICAL ENGINEERING

Earth retaining structures in the form of diaphragm walls and their application in *Liberdade* underground station

Structures de soutènement de terres de type paroi moullée et son application á la station du métro de la *Liberdade*

C.H. da Costa, A.T. Rodrigues, M. Fernandes*
Rodio Portugal, Alenquer, Portugal

J.L. Arcos
Rodio Kronsa, Madrid, Spain

**marcelo.fernandes@rodio.pt*

ABSTRACT: The continuous development of urban areas has had implications in how the planning and management of the cities is performed. In that regard, it comes up the need to take advantage of underground spaces, as well as to repurpose the built heritage. In this article, a study is intended to be conducted covering the urban and geotechnical limitations that lead to the decision of adopting earth retaining structures, specifically diaphragm walls, along with their structural analysis. This research also aims to display practical cases of civil works where the assessments of the technical support team during the execution phase will be approached. The studies realized are mainly based in the information gathered through instrumentation and monitoring, along with the geological and geotechnical surveys realized locally. The case presented reveals to be characteristic of a familiar reality in the daily work of an enterprise dedicated to the field of geotechnical engineering, where sometimes the unpredictability of the ground can lead to modifications in design during the construction works. The need to solve singular and imponderable situations, using convenient and effective alternatives of execution, contributes to an endless development of the geotechnical knowledge and the evolution of the technique.

RÉSUMÉ: La croissance continué des zones urbaines a entraîné des graves conséquences sur la planification et la gestion du territoire des villes. En ce sens, il est nécessaire profiter des espaces souterrains et de réutiliser le patrimoine bâti. L'ingénierie civil, en particulier la géotechnie, a joué un rôle clé dans le développement de technologies qui répondent aux défis structurels, géologiques et géotechniques et aux contraintes d'excavation en milieu urbain. Avec cet article, nous avons l'intention de présenté une étude sur les contraintes géotechniques et urbaines qui conduisent à la décision d'adopter des structures de soutènement des terres, du type paroi moullée, ainsi que son analyse structurelle. Cette analyse se reflète également dans la présentation d'un cas pratique d'un ouvrage de cette nature, où seront abordées les études de suivi technique réalisées pendant la phase d'exécution des travaux, résultant d'incidents ayant entraîné une modification de la conception et des procédures constructives. Les études ont été principalement basées sur des recherches géologiques et géotechniques réalisées localement. Le cas présenté caractérise une réalité familière au travail quotidien d'une entreprise dédiée à la Géotechnie, où l'imprévisibilité du comportement des terrains conduit parfois à l'analyse et à la modification du projet au cours des travaux. La nécessité de résoudre des situations singulières et impondérables avec des alternatives d'exécution rapides et efficaces conduit à une connaissance géotechnique continue et au développement de la technique.

Keywords: Earth retaining structures; diaphragm walls; civil works; geotechnical characterization; instrumentation.

1 INTRODUCTION

For the construction of diaphragm walls (Soletanche Bachy, 2011) there are essentially two kinds of excavating tools, grabs composed by mechanical cables (Figure 1) or hydraulic systems, and the Hydrofraise (Figure 2). The former is implemented for drilling and excavation of loose soils with low resistance, even though it can be suitable for higher resistances by implementing pre-drilling techniques with the aid of some other tools, like a chopping bit.

On the other hand, the Hydrofraise allows for excavation of ground with higher resistances, without the need of pre-drilling tools. The system is composed by two counter-rotating drums on horizontal axes fitted with cutting teeth. It allows for the penetration of the ground, as well as for its extraction, using reverse circulation of the drilling fluid.

The drilling system of the Hydrofraise, due to its reliance on more complex procedures and more robust and powerful equipment, has been rarely used in Portugal. For this reason, the article is dedicated to a

project currently underway at the time of submission in the city of Porto, whose drilling and excavation processes uses the mentioned technique for retaining walls.



Figure 1. Grabs for diaphragm wall.



Figure 2. Hidrofraise.

2 CASE STUDY

2.1 Location

The mentioned project is in the city of Porto (Figure 3), and it will be incorporated as part of the of the subway network, enabling to close the loop of several lines in the metropolitan area in a circular manner. The purpose of this project is to enhance the sustainability of mobility and relief the center of the city from congestion.



Figure 3. Project location, in Praça da Liberdade, at the end of Av. dos Aliados and extending up to São Bento Station and Largo dos Lóios.

2.2 Project

The retaining structure is a diaphragm wall ranging between 11,5 and 23 meters of depth, for an excavation height between 9 and 20 meters The shoring system consists in the execution of slabs from the final structure using a Top-Down procedure.

2.3 Geological and geotechnical characterization

The project is situated in a geological context characterized by granitic rock with varying degrees of weathering (Figures 4 to 7).

The available geotechnical data before the beginning of the works (Metro do Porto, 2019a), allowed for the identification of a granitic rock material with variable weathering across the soil profile. The overall geotechnical cross-section of the metro line allowed for the identification of the lowering of the weathered rock in the valley where the construction of the future Estação Liberdade – São Bento is expected.

According to the geotechnical profiles available (Figure 8), the drilling equipment would reach the geotechnical zones between G2-G7, being G5-G7 soil materials, G2-G4 rock type materials from low to high weathering. The technical design report of the project, based on the information presented previously, didn´t identify the presence of an intersection with geotechnical zone G1. Moreover, even though G2 was indeed identified, it was only present in the deeper layers of soil or as an isolated granite block.



Figure 4. General layout of the subway line and the geotechnical surveys, adapted from Metro do Porto 2019a.

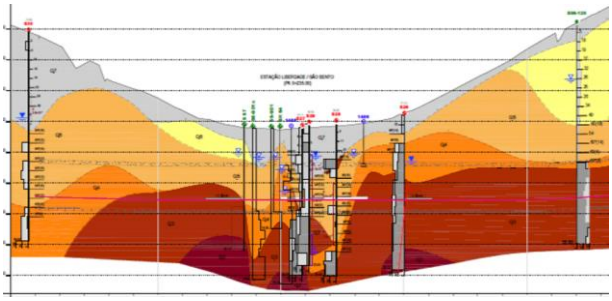

Figure 5. Geotechnical Profiles of the Construction Site (layout I of III), adapted from Metro do Porto 2019b.

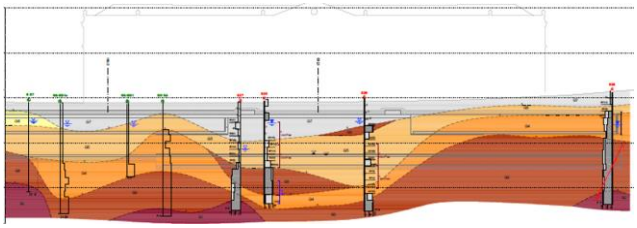

Figure 6. Geotechnical Profiles of the Construction Site (layout II of III), adapted from Metro do Porto 2019b.

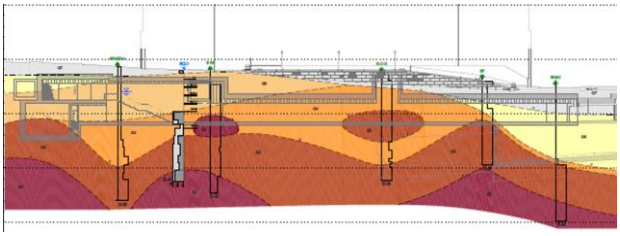

Figure 7. Geotechnical Profiles of the Construction Site (layout III of III, adapted from Metro do Porto 2019b.

ZONAMENTO GEOTÉCNICO	LITOLOGIA	GRAU DE ALTERAÇÃO		GRAU DE FRATURAÇÃO	CONDIÇÕES DAS DESCONTINUIDADES	N_{SPT}	GSI
G1	γ	W1	Granito são	F1-F2	d1-d2	na	65-85
G2	γ	W2	Granito pouco alterado	F2-F3	d2-d3	na	45-65
G3	γ	W3	Granito medianamente alterado	F3-F4	d3-d4	na	30-45
G4	γ	W4	Granito muito alterado	F4-F5	d4-d5	na	15-30
G5	γ	W5	Granito decomposto	na	-	>50	-
G6	γ	W6	Solos residuais graníticos	na	-	<50	-
G7	Aterro/ Aluviões	na		na	-	Variável	-

Figure 8. Summary of Geotechnical Characterization (Metro do Porto, 2019a).

3 WORKS EXECUTION AND CONSTRUCTION PROCEDURE

Given all the constraints and limitations inherent in a project of this scale and in an urban environment, the execution procedure led to the use of a Compact Hydrofraise. This equipment, being smaller in size than the typical Hydrofraise, made excavation work possible and allowed other activities related to the project to occur simultaneously, without hindering the normal progress of the work.

The construction sequence (Figure 9) considered the execution of primary and secondary panels with cutting back into the concrete of the previously executed panel ("bite"). Figure 10 illustrates some general photos of the construction works.

4 CHALLENGES & SOLUTIONS

4.1 Observations during works

An interesting detail of the excavation with the Hydrofraise is the need to control the verticality of the drilling (Rodio Portugal, 2022), which can be corrected thanks to the devices incorporated in the equipment, enabling the recovery of possible deviations in real time.

However, due to the celerity and localized nature of the deviations, it is not possible to avoid them when the root is the stiffness of the ground. In these cases, it is only possible to rectify them by re-drilling to regain the desired position. For this reason, specific characteristics of the drilled ground can result in an increase of difficulty when correcting deviations, like the ones identified during the works by Rodio. Figure 12 illustrates some important elements to consider while working with a Hydrofraise.

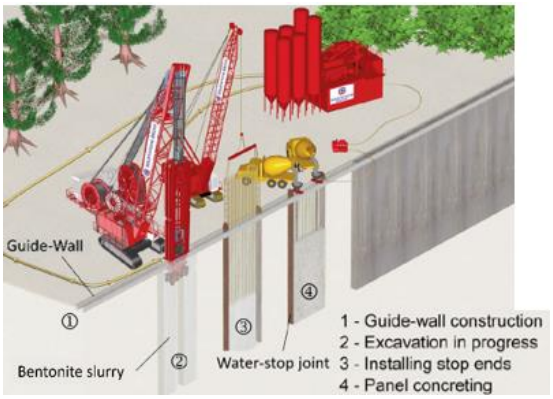

Figure 9. Representation of the Execution Process (Soletanche Bachy, 2011).

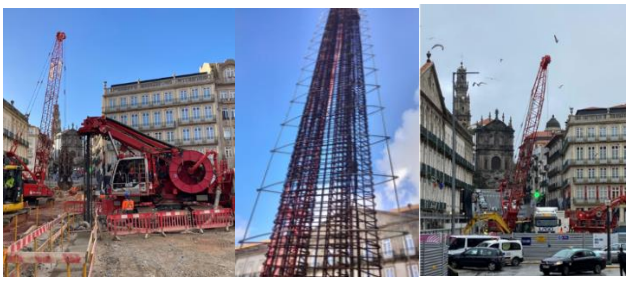

Figure 10. General Photos of the Construction Site.

During the hydrofraise drilling, in the area of *Largo dos Lóios* and *Praça da Liberdade,* abnormally high rock resistance was observed compared to what would be expected for that location and working depths. The increased hardness of the granitic rock caused not only slight deviations in the panels but also a decreasing of the expected drilling yields.

However, the uniaxial compressive strength (UCS) tests conducted on samples collected from the site's boreholes showed values below 45 MPa in all samples

located at depths higher than the base of the Diaphragm Wall. These resistances were consistent with the estimated yields for excavation during the project's study phase.

4.2 Followed approaches

To understand the reason behind the difference between the expected yields and the actual drilling performance during the works, multiple additional boreholes were executed, and samples were collected for laboratory tests, along with supplementary geotechnical studies.

The reports from these supplementary studies (ENGGEO, 2023), provide geological and geotechnical information for 20 boreholes, including sample extraction, analysis, and uniaxial compression tests. A total of 59 uniaxial compressive strength (UCS) tests were conducted in these campaigns.

An analysis was conducted on the uniaxial compression tests performed before and during the construction. From this analysis, the representation of the obtained total strength values resulted in a Strength vs. Depth graph, illustrated in Figure 11.

The results presented in the graph reveal the occurrence of slightly weathered granitic rock with high resistance at much shallower depths than what could be inferred from the project's prior information.

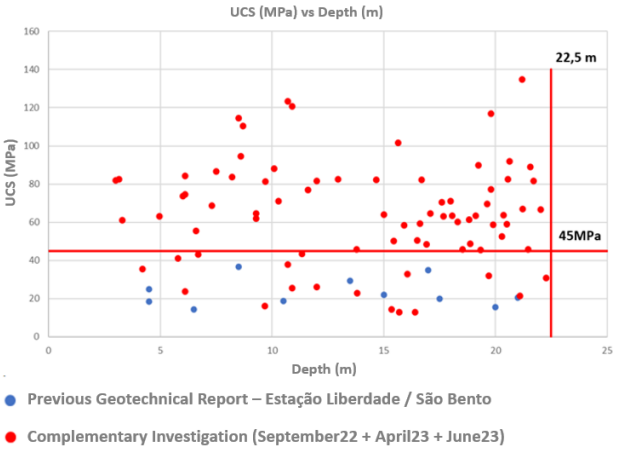

Figure 11. Strength vs Depth representation of the initial and complementary surveys.

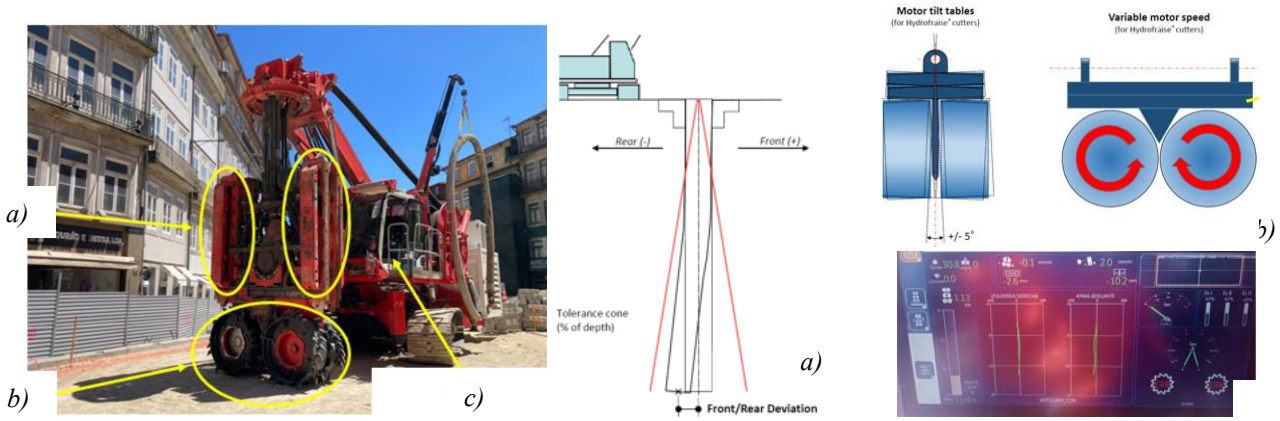

Figure 12. Details of the Hydrofraise: vertical control (a), counter-rotating drums (b) and monitoring system (c).

5 CONCLUSIONS

Being Hydrofraise a less common technique in the execution of diaphragm walls, it is estimated that the case studied is the second application in Portugal. Given the geological and geotechnical constrains, as well as the limited space and location, it has proven to be an important contribution to a better understanding of these type of geotechnical solutions.

Regarding the resistances of the intersected rock, in general, and up to the present date, the project's base information significantly differs from reality. It can be observed that, initially, in any part of the initial geotechnical information, soils with resistances below 45 MPa were predicted. However, after conducting additional geotechnical boreholes, an extraordinarily high percentage of samples with resistances exceeding 45 MPa (78%) was observed.

As for remaining challenges, the project was proactively executed, looking to improve the performance of the panels day by day and to solve the incidences and issues that have been occurring, as stated in this article, leading to an elevated prior preparation of the works so they could be developed as efficiently as possible.

ACKNOWLEDGEMENTS

The aknowledgements extend to the construction owner Metropolitano do Porto, to the general contractor and client of Rodio, Ferrovial-ACA conglomerate, and to the ENGGEO company, author of the complementary geotechnical survey study.

REFERENCES

Soletanche Bachy (2011). Technical Guide Vol. I, pp. 19-23. Rueil-Malmaison, France.

Metro do Porto (2019a). Geotechnical Report "Projeto de Execução". Vol 6. Code: P-PR-LI-8000-GG-MD-SCN-000001-04. Porto, Portugal.

Metro do Porto (2019b). Technical Report "Projeto de Execução". Vol 5.2. Code: P-PR-LI-8001-ET-MD-SCN-001001-03. Porto, Portugal.

Rodio Portugal (2022). Execution Procedure "Execução de Paredes Moldadas com recurso a Hidrofresa". Code: C-IN-LI-8000-GE-PR-FAG-000050-01. Alenquer, Portugal.

ENGGEO (2023). Geotechnical Surveys from September 14th 2022, April 4th 2023 and May 10th 2023. Procedure nº230010. Porto, Portugal.

Proceedings of the XVIII ECSMGE 2024
GEOTECHNICAL ENGINEERING CHALLENGES
TO MEET CURRENT AND EMERGING NEEDS OF SOCIETY
© 2024 the Authors
ISBN 978-1-032-54816-6
DOI 10.1201/9781003431749-421
Open Access: www.taylorfrancis.com, CC BY-NC-ND 4.0 license

ECSMGE 24
XVIII EUROPEAN CONFERENCE ON SOIL MECHANICS AND GEOTECHNICAL ENGINEERING

Shear wave velocity and permeability evolution of MICP-treated carbonate bearing sand

Vitesse des ondes de cisaillement et évolution de la perméabilité des sables carbonatés traités au MICP

G. Das*, S. Joshi, M. Judge, F. McDermott, M. Long, S. Donohue
University College Dublin, Dublin, Ireland

**geetanjali.das@ucd.ie*

ABSTRACT: Microbially induced calcite precipitation (MICP), a promising method developed for soil stabilization, demonstrates potential as an eco-friendly approach capable of significantly improving the geotechnical properties of soil. However, research indicating the evolution of permeability requires further investigation to substantiate the effectiveness of MICP treatment in enhancing permeability. In this aspect, this study investigates the evolution of shear wave velocity (V_s) and permeability (k) in MICP-treated carbonate bearing sands. Compacted specimens were subjected to MICP-treatment using 5ml/min and 10ml/min injection flow velocities. Injection velocities of 5ml/min produced heterogeneous $CaCO_3$ precipitation across the sample, with maximum precipitation near the injection point after 6 cementation cycles. This led to clogging near the injection point, resulting in a decrease in k by an order of magnitude and a constant V_s, showing a maximum value of 554.2m/s. On the other hand, specimen subjected to a 10ml/min injection velocity showed a relative homogeneous $CaCO_3$ distribution throughout. This resulted in a consistent permeability and V_s continued to increase beyond 6 cementation cycles and reached a constant value of 950m/s after 13 cementation cycles. Thus, injection flow velocity is an important variable to be considered when investigating permeability modifications in MICP treated soils.

RÉSUMÉ: La précipitation de calcite induite par voie microbienne (MICP), une méthode prometteuse développée pour la stabilisation des sols, démontre son potentiel en tant qu'approche respectueuse de l'environnement capable d'améliorer de manière significative les propriétés géotechniques des sols. Cependant, la recherche indiquant l'évolution de la perméabilité nécessite une étude plus approfondie pour prouver l'efficacité du traitement MICP dans l'amélioration de la perméabilité. Dans cette optique, cette étude examine l'évolution de la vitesse des ondes de cisaillement (V_s) et de la perméabilité (k) dans des sables carbonatés traités au MICP. Des échantillons compactés ont été soumis à un traitement MICP en utilisant des vitesses d'injection de 5ml/min et 10ml/min. Des vitesses d'injection de 5ml/min ont produit une précipitation hétérogène de $CaCO_3$ dans l'échantillon, avec une précipitation maximale près du point d'injection après 6 cycles de cimentation. Cela a conduit à un colmatage près du point d'injection, entraînant une diminution de k d'un ordre de grandeur et une V_s constante, montrant une valeur maximale de 554,2m/s. D'autre part, l'échantillon soumis à une vitesse d'injection de 10ml/min a montré une distribution relativement homogène du $CaCO_3$ dans l'ensemble de l'échantillon. Cela a entraîné une perméabilité constante et V_s a continué à augmenter au-delà de 6 cycles de cimentation et a atteint une valeur constante de 950m/s après 13 cycles de cimentation. Ainsi, la vitesse d'injection est une variable importante à prendre en compte lors de l'étude des modifications de perméabilité dans les sols traités au MICP.

Keywords: MICP-treated sand; flow velocity; shear wave velocity; permeability; calcium carbonate precipitation.

1 INTRODUCTION

MICP is a biocementation method in which microbial activity drives the precipitation of calcium carbonate at within and/or around soil particle to improve engineering properties (Fu et al., 2023; Tang et al., 2020).

Several laboratory studies have shown the efficacy of MICP treatment in improving the strength, stiffness, and bearing capacity of soils (Lui et al., 2021; Fu et al, 2023). However, studies investigating the impact of MICP-treatment on the soil permeability have demonstrated a range of effects (Jian and Soga, 2017; Martinez et al., 2013; Sharma et al., 2021; Whiffin et al., 2007). For example, Sharma et al. (2021) documented the permeability evolution in MICP treated sands after 6, 12, and 18 days of treatment. They reported a maximum decrease of 91% in the coefficient of permeability (k) after 18 days in MICP-treated sand compared with an untreated specimen. This reduction in 'k' was attributed to the decrease in porosity resulting from calcium-carbonate ($CaCO_3$) precipitation. Similarly, Martinez et al. (2013) reported a decrease in 'k' of up to two orders in

magnitude with an increase in shear wave velocity (V_s) of about 1000 m/s in MICP treated Ottawa 50-70 sands. On the other hand, Whiffin et al. (2007) reported that the 'k' value of MICP-treated sand remained almost unchanged, though a significant development in the soil's strength and stiffness occurred. Likewise, Jiang and Soga (2017) reported a limited impact of cementation on the reduction of 'k' in MICP-treated sand-gravel mixture. The impact of MICP-treatment on 'k' has been attributed to several factors. Zamani and Montoya (2016) showed that the reduction in 'k' with increase in cementation level is governed by soil grain size. Other studies reported that the concentration of cementation solutions has a significant impact on the reduction of 'k' (Harkes et al., 2010; Tang et al., 2020). These uncertainties motivated the present study to investigate further the impact of selected MICP-treatment parameters on the permeability evolution of sands.

This study aims to investigate the 'V_s' and 'k' evolution in MICP-treated carbonate-bearing sands subjected to different flow rates of solution injections. The first part of the study presents the 'V_s' and 'k' monitored throughout the MICP-treatment process and in the second part, the variability in $CaCO_3$ precipitation throughout the specimens were measured to provide an interpretative framework for the observed results.

2 MATERIALS AND METHODOLOGY

2.1 Soil and solutions properties

Fine sand, sampled from Blessington quarry, Ireland, with a fine content (< 0.063mm) of 35% and initial carbonate content of 20% was used. Four types of chemical solutions were prepared. To mimic the field's groundwater, artificial groundwater (AGW) was prepared for preparation and saturation of the specimens. Yeast (Y), Biostimulation (BS), and Cementation (CM) solutions were prepared for the MICP-treatment. Further details of these solutions are presented in Table 1.

2.2 Sample preparation

Air-dried sands were placed in soil columns of 5cm diameter, and 10cm height. The placement was made in three layers, with each layer tamped 15 times to reach the minimum void ratio of 0.53. Specimens were then fully saturated by pumping 1 pore volume flow (PVF) of AGW into the specimen from beneath.

Table 1. Chemical solutions.

Solutions	Composition and concentrations
AGW	Potassium Nitrate: 0.04mM; Magnesium sulphate: 0.45 mM; Calcium chloride: 1.75 mM; Sodium Nitrate: 0.04 mM; Sodium Bicarbonate: 1.10mM; Potassium Bicarbonate: 0.06mM
Y	Yeast extract: 0.2g/L; Sodium acetate trihydrate: 42.5mM
BS	Yeast extract: 0.2g/L; Sodium acetate trihydrate: 42.5mM; Urea: 350mM; Ammonium chloride: 100mM
CM	Yeast extract: 0.2g/L; Sodium acetate trihydrate: 42.5mM; Urea: 350mM; Ammonium chloride: 12.5mM; Calcium chloride: 250mM

2.3 MICP-treatment and shear wave velocity measurement

Saturated specimens were subjected to MICP treatment through biostimulation. This initially involves the injection of Y solution to enhance the growth of native ureolytic bacteria present in the soil. Then, 4 cycles of BS solutions (BS1-BS4) were injected to allow the bacteria to induce ureolytic reactions, thus producing carbonates. This was then followed by cementation cycles using cementation solutions to allow the precipitation of $CaCO_3$ (Tang et al., 2020). Throughout the cementation cycles, V_s was measured to monitor the stiffness evolution of the soil using bender elements, as per ASTM D8295-19 (2019). The cementation cycles continued until a constant V_s was reached to ensure that no further precipitation of $CaCO_3$ were possible.

2.4 Permeability measurement

All chemical solutions were injected through the inlet present at the base of the soil columns. Effluents were collected from the outlet located at the top of the column. The chemical solutions were injected at two different flow rates, i.e., at 5ml/min and 10ml/min using a pump. A constant hydraulic gradient is maintained throughout the injection between the pump and the injection point. The coefficient of permeability is calculated using Darcy's equation. In the following sections, specimens subjected to MICP treatment processes involving injection of solutions at 5ml/min and 10ml/min are represented as SP1, and SP2, respectively. Thus, SP1 is the specimens subjected to relatively slower MICP treatment than SP2.

2.5 Calcium-carbonate measurement

At the end of cementation cycles for SP1 and SP2, specimens were sampled from top, middle, and bottom

parts of the samples to check the spatial distribution of calcite precipitation. Calcite was measured as per ASTM D4373-02 (2017).

3 RESULTS AND DISCUSSIONS

Figure 1 presents the V_s evolution throughout the cementation cycles in specimens SP1 and SP2. SP1 reached a V_s of 554.2m/s after the 6 cementation cycles. With further injection of cementation solutions, V_s showed no change. This indicates that no further $CaCO_3$ precipitations can occur, as the increase in V_s is reported to be directly related to the $CaCO_3$ precipitations (Lui et al., 2021). Thus, the injection was stopped after the 8th cementation cycle. By contrast, the V_s value obtained after 6 cementation cycles in SP2 was slightly lower and reached the same value as SP1 after the 8 cementation cycles. This V_s increased further with further injection of cementation solutions and reached about 950m/s after 13 cementation cycles. This value remained constant with further injection of cementation solutions up to 15 cementation cycles.

Figure 2 presents the permeability evolution in specimens SP1 and SP2. The initial value of 'k' in specimen SP1 is lower than specimen SP2. This is attributed to the difference in flow velocity maintained in specimens SP1 and SP2, since the rate of discharge of solution is directly proportional to 'k' at a given hydraulic gradient as per Darcy's law. Further, with incremental cementation cycles in SP1, the magnitude of 'k' reduced by an order of magnitude, which corresponds to the constant value of V_s reached after 6 to 8 cementation cycle (Figure 1). However, for specimen SP2, where the cementation cycles continued up to 15 cementation cycles, the magnitude of 'k' remained in between 6.8×10^{-6} to 5.7×10^{-6} m/s, thus, showing no significant change.

Table 2 presents the percentage increment in $CaCO_3$ measured in the specimens sampled from the three layers of SP1 and SP2, at the end of 8 and 15 cementation cycles, respectively. The percentage increment is represented with respect to the untreated sand. At the end of cementation cycle, the weight % $CaCO_3$ was 6% higher in the bottom sampled specimen of SP1, near the injection point compared to the top and middle sampled specimens. Such heterogeneity in $CaCO_3$ distribution has been a concern in several MICP studies (Fu et al., 2023; Tang et al., 2020). However, in specimen SP2, the distribution of $CaCO_3$ is relatively homogeneous irrespective of position in the column (Table 2). Such differences in $CaCO_3$ distribution between specimens SP1 and SP2 highlight the fact that the low flow velocity (5ml/min) in SP1 caused maximum deposition of $CaCO_3$ near to the injection point. This caused clogging, which was confirmed after observing white thick precipitation between the porous stone and the specimen near the injection point. This probably restricted the flow of calcium ions to the middle and top region of SP1 beyond 6 cementation cycle. This phenomenon results in a decrease of permeability (Figure 2) and restricted further increase in V_s with further injection of cementation solutions (Figure 1).

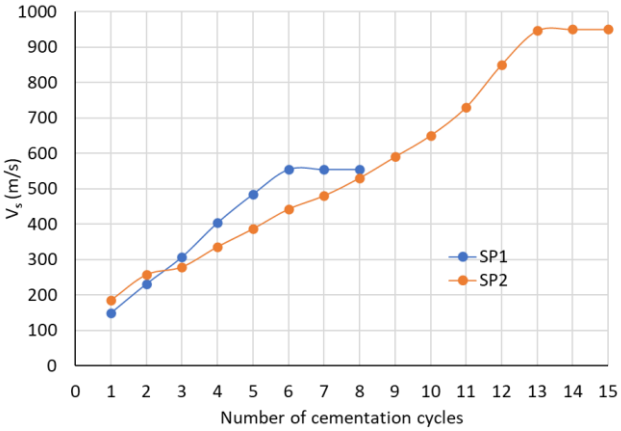

Figure 1. Shear wave velocity evolution in SP1 and SP2.

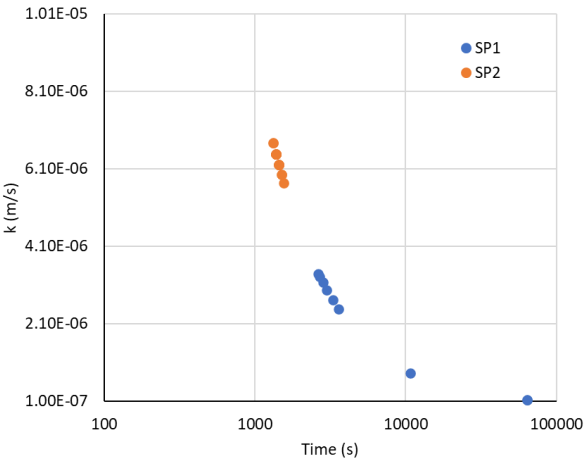

Figure 2. Permeability measured in SP1 and SP2.

A higher flow velocity of 10ml/min in SP2 enabled uniform calcium dispersal throughout the sample uniformly beyond the 6th cementation cycles, resulting in a more homogeneous $CaCO_3$ distribution (Table 2). This phenomenon increases the V_s beyond the 6th cementation cycles (Figure 1). A homogeneity in $CaCO_3$ distribution prevented clogging near the injection point. This led to no significant change in the permeability (Figure 2), unlike SP1.

Table 2. $CaCO_3$ percentage in SP1 and SP2.

Specimens	$CaCO_3$ (%)		
	Top	Middel	Bottom
SP1	10	10	16
SP2	12	12	13

4 CONCLUSIONS

The study investigated the shear wave velocity and permeability evolution in a MICP-treated carbonate bearing sand column subjected to different flow velocities. The main conclusions are:

1) A greater flow velocity (10ml/min) produced a more homogeneous $CaCO_3$ distribution throughout the MICP-treated specimen. compared with that subjected to 5ml/min flow velocity.
2) Deposition of $CaCO_3$ near the injection point in specimen subjected to low flow velocity MICP treatments, led to clogging of specimens. This restricted the uniform flow of calcium ions throughout the specimen, thus, restricting further increase in shear wave velocity. For the same type of compacted specimens, specimen subjected to 10ml/min flow velocity showed a increase in shear wave velocity up to 13 cementation cycles, while that subjected to a 5ml/min flow velocity did not show an increase in shear wave velocity after the 6th cementation cycles.
3) Clogging of the specimen near the injection point led to a decrease in permeability. The k value decreased by an order of magnitude in the specimen subjected to flow velocity of 5ml/min, whereas it remain unchanged in the corresponding specimen subjected to a flow rate of 10ml/min.

This study highlights that flow velocity is an important parameter that needs to be considered which investigating the stiffness and permeability evolution in MICP treated sand columns.

ACKNOWLEDGMENTS

This work was funded by Science Foundation Ireland (SFI), Grant Number 19/US-C2C/3606, under the US–Ireland Centre to Centre Programme. The authors acknowledge the contribution of Dr. Christine Spencer in designing the initial prototype of the column test apparatus used in this study.

REFERENCES

ASTM D8295–19. (2019). Standard Test Method for Determination of Shear Wave Velocity and Initial Shear Modulus in Soil Specimens Using Bender Elements. ASTM International, West Conshohocken. https://doi.org/10.1520/D8295-19.

ASTM D4373-02. (2017). Standard Test Method for Rapid Determination of Carbonate Content of Soils. ASTM International, West Conshohocken.

Fu, T., Saracho, A. C., Haigh, S. K. (2023). Microbially induced carbonate precipitation (MICP) for soil strengthening: a comprehensive review, *Biogeotechnics*, 1(1), 100002. https://doi.org/10.1016/j.bgtech.2023.100002.

Harkes, M. P., Van Paassen, L. A., Booster, J. L., Whiffin, V. S., van Loosdrecht, M. C. (2010). Fixation and distribution of bacterial activity in sand to induce carbonate precipitation for ground reinforcement, *Ecological Engineering*, 36(2), 112-117. https://doi.org/10.1016/j.ecoleng.2009.01.004.

Jiang, N. J. & Soga, K. (2017). The applicability of microbially induced calcite precipitation (MICP) for internal erosion control in gravel–sand mixtures, *Géotechnique*, 67(1), 42-55. https://doi.org/10.1680/jgeot.15.P.182.

Liu, J., Li, G., Li, X. A. (2021). Geotechnical engineering properties of soils solidified by microbially induced CaCO3 precipitation (MICP). *Advances in Civil Engineering*, 2021, 1-21. https://doi.org/10.1155/2021/6683930.

Martinez, B. C., DeJong, J. T., Ginn, T. R., Montoya, B. M., Barkouki, T. H., Hunt, C., Major, D. (2013). Experimental optimization of microbial-induced carbonate precipitation for soil improvement, *Journal of Geotechnical and Geoenvironmental Engineering*, 139(4), 587-598. https://doi.org/10.1061/(ASCE)GT.1943-5606.0000787.

Sharma, M., Satyam, N., Reddy, K. R. (2021). Hybrid bacteria mediated cemented sand: Microcharacterization, permeability, strength, shear wave velocity, stress-strain, and durability, *International Journal of Damage Mechanics*, 30(4), 618-645. https://doi.org/10.1177/1056789521991196.

Tang, C. S., Yin, L. Y., Jiang, N. J., Zhu, C., Zeng, H., Li, H., Shi, B. (2020). Factors affecting the performance of microbial-induced carbonate precipitation (MICP) treated soil: a review, *Environmental Earth Sciences*, 79, 1-23. https://doi.org/10.1007/s12665-020-8840-9.

Whiffin, V. S., Van Paassen, L. A., Harkes, M. P. (2007). Microbial carbonate precipitation as a soil improvement technique, *Geomicrobiology Journal*, 24(5), 417-423. https://doi.org/10.1080/01490450701436505.

Zamani, A., Montoya, B. M. (2016). Permeability reduction due to microbial induced calcite precipitation in sand, In: *Geo-Chicago 2016*, Chicago, Illinois, USA, pp. 94-103. https://doi.org/10.1061/9780784480120.011.

Proceedings of the XVIII ECSMGE 2024
GEOTECHNICAL ENGINEERING CHALLENGES
TO MEET CURRENT AND EMERGING NEEDS OF SOCIETY
© 2024 the Authors
ISBN 978-1-032-54816-6
DOI 10.1201/9781003431749-422
Open Access: www.taylorfrancis.com, CC BY-NC-ND 4.0 license

ECSMGE 24
XVIII EUROPEAN CONFERENCE ON SOIL MECHANICS AND GEOTECHNICAL ENGINEERING

The practice of testing ground nails

La pratique des essais de clous

M. de Carvalho
National Laboratory for Civil Engineering (LNEC), Lisbon, Portugal
**marc@lnec.pt*

ABSTRACT: The soil nailing construction technique is often used to stabilise a ground mass by installing reinforcing elements (nails). The European Standard EN 14490:2010 defines general principles for execution, supervision, testing and monitoring of soil nailing. This paper presents tests results obtained in several ground nails executed in recent geotechnical works. These tests were carried out in sacrificial nails, before and during the works. As shown in this paper, the execution of the nails, the test system and test procedures affect their results quality. Thus, a critical analysis of the tests results is performed to assess the behaviour of the ground nails, framed by EN 14490:2010, in accordance with the design and contract specifications.

RÉSUMÉ: Le clouage est une technique de construction utilisée pour améliorer la stabilité d'un massif du terrain par la mise en place d'éléments de renforcement (clous). La norme européenne EN 14490:2010 établit les principes généraux pour la construction, les essais, le suivi et les contrôles d'exécution des ouvrages avec clouages. Cet article présente les résultats d'essais obtenus sur des clous exécutés lors de travaux géotechniques récents. Ces tests ont été réalisés sur des clous sacrificiels, avant et pendant la construction. Comme s'expose dans cet article, l'exécution des clous, le système de test et les procédures des essais affectent la qualité des résultats obtenus. Ainsi, une analyse critique des résultats des essais est réalisée afin d'évaluer le comportement des clous, encadrée par la norme EN 14490:2010, conformément aux spécifications du projet et du contrat.

Keywords: Nail; load test; proof load; sacrificial nail.

1 INTRODUCTION

Ground nails mobilise frictional forces along their entire length, which contributes to improve the ground stability if the stability conditions are adverse.

The stability is achieved by inserting reinforcing nail elements into the ground. To validate the ground nail resistance, to assess their behaviour or design considerations, nail load tests shall be carried out.

The test procedures and locations of a nail test shall be validated. Previously, the tests program shall be defined, all the elements presented, evaluated, and confirmed. The contractors equipment and their calibration certificates shall be evaluated and identified for each test.

This paper presents the results of sacrificial nail tests, obtained in recent geotechnical works.

The sacrifitial nails were instaled in the same way as the production nails, only to establish the pullout capacity, and do not forming a part of the ground nail structure.

Based on the collected data, recorded in the tests sheets, this paper presents tests results analysis in accordance to EN 14490:2010 specifications. Conclusive synthesis and recommendations are presented.

2 GROUND NAIL LOAD TESTS

The EN 14490:2010 recognizes two distinct types of static load tests: i) in sacrificial nails; and ii) in production nails. Testing requirements are stated in EN 14490:2010.

Normally, a sacrificial nail test involves loading the test nail to failure, or to the characteristic value of the resistance anticipated in the design.

It is essential that the test nail be axially loaded. The facing system or the load test reaction system cannot influence the test results.

Static load testing can be used for a variety of purposes, including to verify the nail ultimate bond resistance, used in the design, and to demonstrate the satisfactory nail performance.

3 EQUIPMENTS AND PROCEDURES

3.1 Layout of the nail test system

In the nail load tests presented in this paper, the load was measured directly, with a load cell, and indirectly, with a calibrated pressure gauge monitoring the pressure of the hydraulic stressing jack (Figure 1).



Figure 1. General view of a ground nail load test layout.

To control the bar and wall movements, the displacement monitoring system was installed in an independent support. The jack extension was also monitored.

The equipment has been previously calibrated.

3.2 Tests programs and procedures

The test programmes were designed in accordance with EN 14490:2010 requirements, considering two cycles, with the first cycle up to the load of $0.5P_p$ and the second up to the proof load, P_p.

The sacrificial nail test intends to verify the ultimate pullout resistance and creep characteristics of the nail. Concluded the load test program, when the bond length had not reached the failure, it was recommended a second load test phase to evaluate the nail load capacity (according EN 14490:2010, C.3.3.3). The second program test phase presented in this paper, was defined considering the tensile capacity of the nail bar, which consists in a single steel bar with 25 mm of diameter. In the geotechical works presented, the nails bond length varies between 2 m and 8 m.

The presented ground nailing work was done in 71 granitic slopes stabilization works with various weathering levels and joint patterns (Figure 2). These works had technical assistance from the paper author.



Figure 2. Examples of slope stabilisation in granitic rock masses that have different weathering levels and joint patterns.

4 TESTS RESULTS

45 sacrificial test nails have been done but, in this paper, only five examples of test results are presented, represented by diagrams of the displacement evolution with applied load. The results are presented for two different monitoring systems: (i) load cell and bar displacement (Cell-Bar); (ii) load pressure gauge and stressing jack displacement (pressure gauge-jack extension). These diagrams also present the evolution of elastic and plastic displacements with load of the reinforcing element (δ_e; δ_p), the datum load (P_a) and the proof load (P_p). Figure 3 to Figure 7 represent the results of the in-situ sheets data tests of the contractors' reports.

The theoretical value of the elastic displacement of the bar (δ_{et}) is obtained by:

$$\delta_{et} = \frac{\Delta P L_{lt}}{E A_t} \quad (1)$$

considering E=200 (kN/mm^2); the nail steel cross section A_t= 490.87 (mm^2); the total de-bonded length $L_{lt}=L_l+L_e$ (mm); and the theoretical value of the difference between the proof load (P_p) and the datum load (P_0), as in the program test ($\Delta P=P_p-P_0$).

5 REQUIREMENTS

It is necessary to ensure that the nail has the pullout capacity to support the P_p and comply with the standard EN 14490:2010 criteria, namely:

a) In a sacrificial nail test the creep rate (k_s) must be less than 2 mm at P_p unless the design defines a lower value.
b) In a load test, the extension measured in the nail head, at P_p, is not less than the expected elastic extension (δ_{et}) for the nail de-bonded length.

The quality of the data field registrations, a correct equipment installation and an adequate test program are primordial to achieve the test goal.

6 RESULTS ANALYSIS

6.1 Monitoring with redundancy

Monitoring with redundancy is not a standard requirement of the EN 14490:2010. However, the redundancy of recording loads and displacements data results in important benefits, namely the possibility to

clarify doubts and confirm aspects associated with the nail behavior, if necessary.

Figure 3 and Figure 4 present the values obtained in the same test for two diffent systems. One of the systems consists of monitored the values by the load cell and the bar displacements gauge. The other system is composed by the pressure gauge pump and by the extension jack, to monitor the load and displacement, respectively.

The data obtained with both systems shows a diferent mechanical behaviour (Figure 3), namely a diferent elastic behaviour in each cicle. However, in Figure 4 the behaviour diferences are smaller.

Other advantage of the redundancy, is the possibility to conclude the test if a device has problems during the test.

6.2 Creep rate (k_s)

The creep rate, k_s (mm), is defined as (eq. 2):

$$k_s = \frac{d_2 - d_1}{log_{10}(t_2/t_1)} \quad (2)$$

where d_1 and d_2 are the measured displacements (mm) at time 1 and 2 (minutes), respectively.

The value obtained for k_s, in the successful nail tests, was smaller than 0.5 mm, So, the creep rate respects the statements of EN 14490:2010.

6.3 Mechanical behaviour

The results obtained on the nail nº4 indicate an adequate mechanical response (Figure 3a) and Figure 4), satisfying the design and standard EN 14490:2010 requirements.

In the test nail nº3b and 4.1 (Figure 5a, and Figure 6a, respectively) the bond failure was reached. In these cases, the nails do not have lateral resistant capacity to support P_p. So, the test does not meet the conditions to be considered valid, the procedures of the nail construction shall be reviewed and / or the design reanalysed.

The nail nº3b reached the failure in the beginning of the 1st cycle (Figure 5a), and also presents a high deformability from the datum load, P_a, which indicates that the nail has: (i) execution deficiencies; or (ii) the bond length may be insufficient; or (iii) the ground, eventually, does not have the design resistance characteristics estimated for that location.

However, in the case of the nail nº 4.1 (Figure 6a), given the value reached, the failure could have occurred in the sealed area or in the nail steel bar.

At the beginning of the nail nº8 test (Figure 5b) signs of test execution deficiencies were shown. These anomalies could be related, amongst other possibilities, to the equipment assembly, with the displacement's measurement, for instance due to movements of the fixed reference, or the occurrence of gaps or friction, which were not eliminated before the beginning of the test. These deficiencies outcomes in difficulties that do not allow the reliable determination of displacements and, consequently, the determination of the corresponding value of k_s, and / or the evaluation of the nail mechanical behaviour, namely the accurate value of the permanent and elastic displacements, for example, for the test nail nº8 (Figure 7a) those displacements do not comply the EN 14490:2010 requirements.

The results obtained in the nail test 4.2 (Figure 6b), show a pronounced hysteresis, particularly in the 2nd cycle. This hysteresis may be related with the prestressed system or with the nail mechanical behaviour, as it only has 2 m of bond length. However, it appears to have the capacity to withstand the proof load and the test results (Figure 7b) fulfil the EN 14490:2010 requirements.

Deficiencies are often observed in nail tests. In these cases, the tests do not exhibit quality, have unsuccessful results and they do not meet the requirements to consider the ground nail work valid.

In this context, it should be noted that the test quality depends on the previous preparation of the operational procedure for carrying out the nailing works and their tests, the previous equipment calibration, and their approval, as well as on the workers quality, equipment installation control, data registration quality, amongst other aspects.

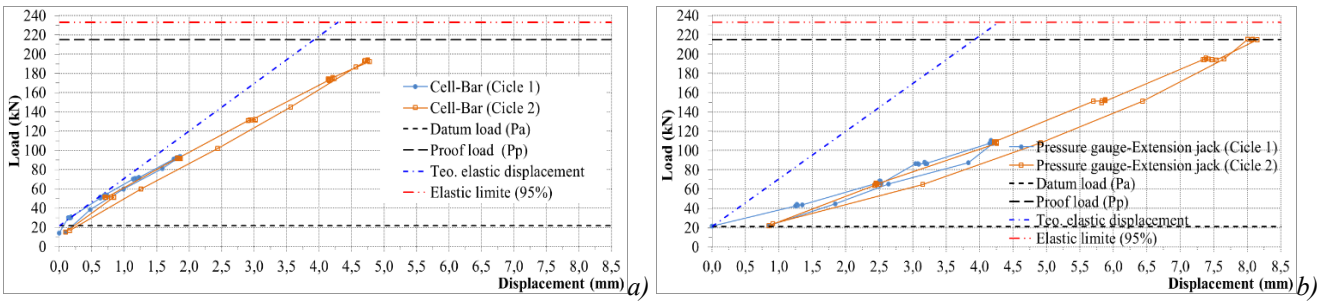

Figure 3. Nail nº4. Evolution of the displacements with load: a) cell-bar; and b) pressure gauge-jack extension.

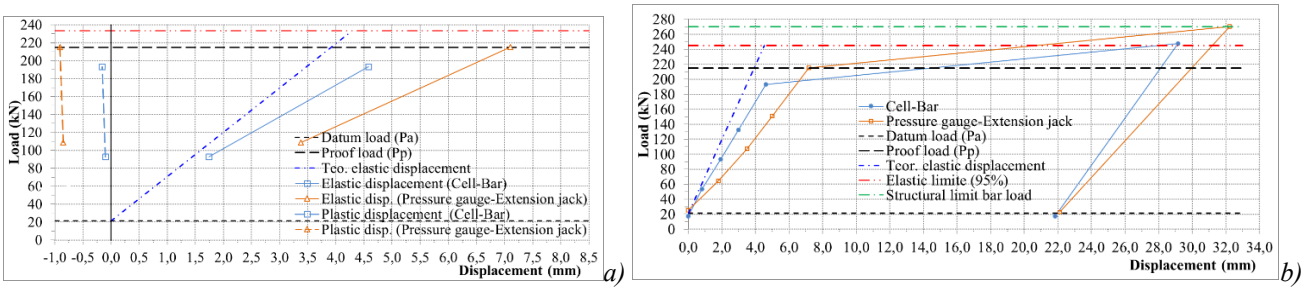

Figure 4. Nail n°4. Results obtained in both monitoring systems. Evolution of the plastic and elastic displacements with load (a), and evolution of the total displacement with load, in the 2d test phase (b).

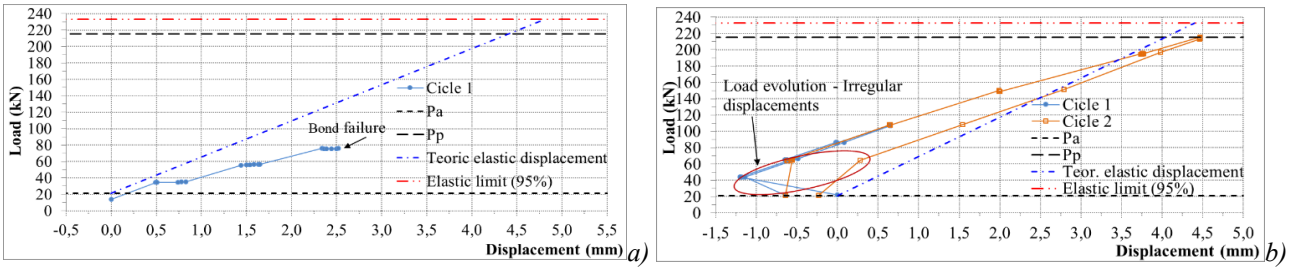

Figure 5. Evolution of the displacements with load, of the nails n° 3b (a) and n° 8 (b).

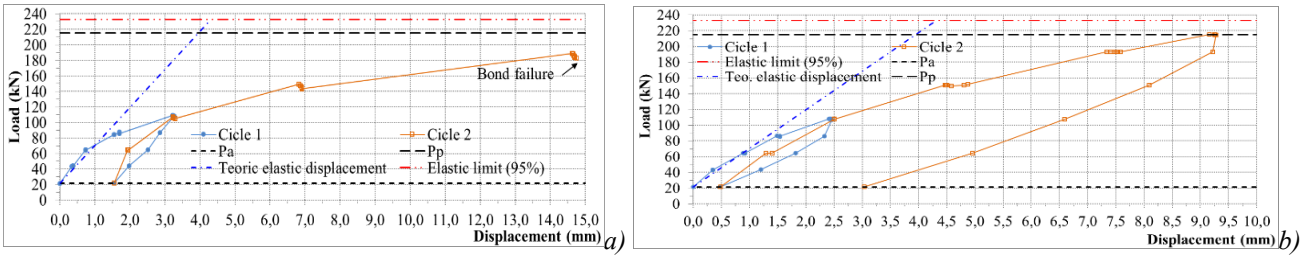

Figure 6. Evolution of the displacements with load, of the nails n° 4.1 (a) and n° 4.2 (b).

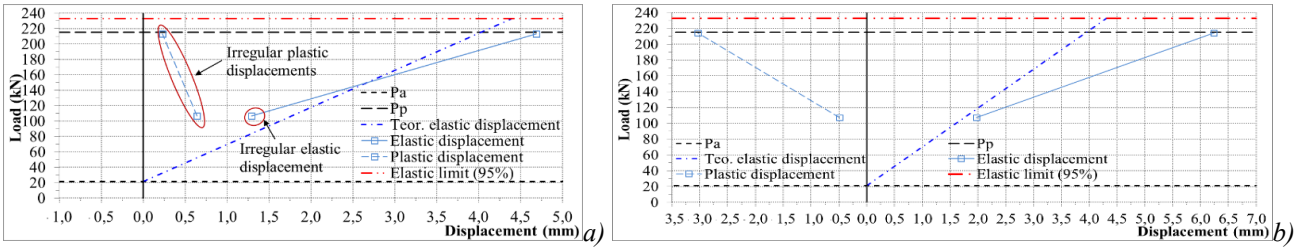

Figure 7. Evolution of the plastic and elastic displacements with load of the nails n° 8 (a) and n° 4.2 (b).

7 CONCLUSIONS

Some tests results do not comply the EN 14490:2010 criterions, either due to the occurrence of permanent displacements manifestly greater than the elastic ones, or by because of the abnormally reduced values of elastic displacement and, also, because there are tests where negative permanent displacements were recorded. These cases may be related to anomalous circumstances, nail failure, tests lack quality, which present inconsistent data, such as displacement reduction as the load increases, among other events. To allow to understand the nail behaviour, the tests quality should be warranted.

The creep values (k_s), like expected for granites, was low so, regarding the creep behaviour, they are not constraints in the geotechnical areas where tests results comply the EN 14490:2010 requirements.

In each ground conditions, the sacrificial nail test intend to allow to: i) validate the construction method; ii) ensure that the required nail design capacity is guaranteed; and iii) ensure that the nails mechanical behaviour is adequate. The production nail test allows to demonstrate that the nails installation methods and the ground conditions encountered result in satisfactory nails behaviours, at the proof load.

It is clearly relevant the necessity of doing tests in ground nailing works, either in soil or rock.

REFERENCES

EN 14490:2010 (2010). European Committee for Standardization. Execution of special geotechnical works - Soil nailing. CEN, Brussels.

Proceedings of the XVIII ECSMGE 2024
GEOTECHNICAL ENGINEERING CHALLENGES
TO MEET CURRENT AND EMERGING NEEDS OF SOCIETY
© 2024 the Authors
ISBN 978-1-032-54816-6
DOI 10.1201/9781003431749-423
Open Access: www.taylorfrancis.com, CC BY-NC-ND 4.0 license

ECSMGE 24
XVIII EUROPEAN CONFERENCE ON SOIL MECHANICS AND GEOTECHNICAL ENGINEERING

Studying impact of reclamation technique on vibrocompaction performance

Analyse de l'impact du vibrocompactage selon la technique de remblaiement d'un terre-plein gagné sur la mer

A. Debaize*, T. Pille, K. Dedecker
JAN DE NUL GROUP, Aalst, Belgium

**antoine.debaize@jandenul.com*

ABSTRACT: The process of creating new lands from seas or riverbeds is an efficient and pragmatic approach responding to an increasingly growing global demand for commercial exchanges. The material is dredged and reclaimed via dumping, rainbowing or pumping ashore. In almost all cases, the newly reclaimed site can be enhanced using soil improvement (such as Rapid Impact Compaction, Dynamic Compaction or Vibrocompaction) and consolidation techniques (such as Prefabricated Vertical Drains with a preloading surcharge). In this paper, vibrocompaction data in a reclaimed silica-based clean sand, with 12% fines maximum, and less than 2% of 2µm clay particles, has been analysed for a jobsite located in South America. On this project, unexpected difficulties were encountered. Correlating the needle's amperage with 150 pre and post-CPTs (Cone Penetration Tests), the descending and ascending phases of vibrologs have been split and studied independently. The influence of grid size and the number of passes has been investigated. The resulting in-depth data analysis identifies clear differences in soil improvement performances depending on the reclamation technique. The article also includes an analysis of the ageing effect after a 100-days resting period by means of CPTs.

RÉSUMÉ: Le processus de création de nouvelles terres à partir des mers ou des lits de rivières est une approche efficace et pragmatique répondant à une demande mondiale croissante en matière d'échanges commerciaux. Le matériau est dragué et déposé par déversement, par largage en arc-en-ciel ou par pompage. Dans presque tous les cas, le site nouvellement crée et gagné sur la mer peut être amélioré en utilisant des techniques d'amélioration du sol (telles que le Compactage par Impact Rapide, le Compactage Dynamique ou le Vibrocompactage) et des techniques de consolidation (telles que les Drains Verticaux Préfabriqués avec surcharge). Dans cet article, le vibrocompactage d'un sable à base de silice, avec 12% de fines au maximum et moins de 2% de particules d'argile (2µm) est analysé pour un chantier situé en Amérique du Sud. Là-bas, nous avons fait face à de nombreuses difficultés. En corrélant l'ampérage de l'aiguille vibrante avec 150 pre & post CPTs, les phases descendantes et ascendantes des enregistrements de paramètres ont été séparées et étudiées indépendamment. L'influence du maillage et du nombre de passes a été étudiée. L'analyse de données qui en résulte met en évidence des différences claires dans les performances d'amélioration du sol, fonction de la technique de remblaiement du sable. L'article inclut également une analyse de l'effet du temps après une période de repos de 100 jours par mesures de pénétrations statiques (CPTs).

Keywords: Reclamation technique; vibrocompaction; data mining; grid size; ageing effect.

1 INTRODUCTION

The study project is located in South America where 1,080 points were vibrocompacted. To verify the actual improvement of the ground, 150 pre- and post-CPTs were conducted. After analysis, the upper part of the sand reacted perfectly to compaction, while the lower part showed only slight improvement.

This article focusses on the used reclamation techniques (rainbowing and dumping) and compares how they influence vibrocompaction performances. Usual state-of-art parameters (such as the spacing grid, the number of passes and the ageing effect) are also studied using a statistical analysis.

2 METHODOLOGY

The study considered the following key aspects:

Needle Amperage Analysis: The descending and ascending phases of vibrologs were studied independently to correlate needle amperage with soil improvement. This analysis aimed to identify trends in amperage changes during the vibrocompaction process.

Influence of Grid size: Different grid sizes were used during the vibrocompaction process. The study examined how grid size influenced the rate of soil improvement.

Number of Passes: In some cases, a two-pass approach was utilized during vibrocompaction. The research investigated the impact of the number of passes on soil improvement.

Ageing effect: An essential aspect of the study involved analyzing the soil's response to vibrocompaction after a 100-day resting period. CPTs were conducted to assess changes in soil strength over time.

3 DREDGING AND RECLAMATION SEQUENCES

- **Step 1:** Depending on the area of the quay, the *in-situ* clay is removed using a Cutter Section Dredger (CSD) down to depths of -26.50mCD to -31.00mCD,
- **Step 2:** Sand is dredged from a borrow area by a Trailing Suction Hopper Dredger (TSHD),
- **Step 3:** The dredged sand is dumped by opening bottom doors up to -10.00mCD to -14.50mCD,
- **Step 4:** The sand is reclaimed using rainbowing up to target level,
- **Step 5:** Vibrocompaction works are performed up to -26.50mCD to -31.00mCD, depending on the area.

4 AMPERAGE

During vibrocompaction works, the needle vibrates during the entire process. The production is split into three main parts: a descending phase, an ascending phase and a stationary phase. The descending phase is done in one continuous movement while ascending and stationary phases are alternating.

Thus, the descending phase represents the soil behaviour before compaction.

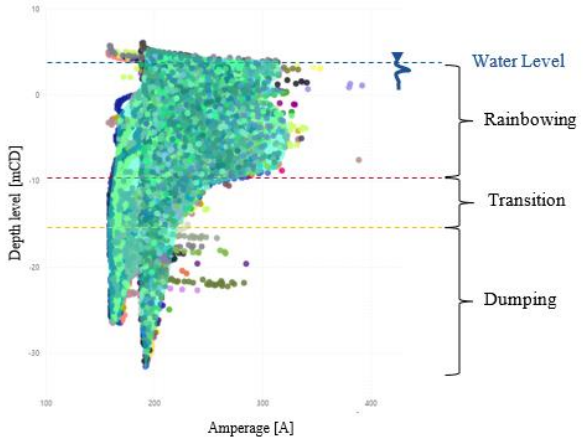

Figure 1. Descending phase compared to the reclamation technique.

As shown in Figure 1, the recorded amperage in the rainbowed sand varies significantly, ranging from 190A to 330A, whereas the amperage in dumped sand falls in the range of 190A to 230A.

This difference comes from the placement method and disposal circumstances: under water, a rainbowed sand is naturally more compacted than a dumped sand.

5 POST SOIL IMPROVEMENT ANALYSIS

5.1 Grid patterns

On site, several grid sizes were tested, including among others: a triangular grid pattern in 4.40x4.40 m² (1 and 2 passes), and a rectangular pattern in 5.00x5.00 m² (2 passes).

Comparing both patterns requires a unified geometric model. A converted axisymmetric model centred on each vibrocompaction point is applied, as defined below:

$$R = \sqrt{\frac{Area\ of\ the\ grid}{\pi}} \quad (1)$$

where R (m) is the radius of influence, depending on the Area of the grid (m²).

Table 1. Radius of influence for each grid.

Grid pattern	Radius [m]
Triangular 4.40x4.40 m² - 1 pass	2.096
Triangular 4.40x4.40 m² - 2 passes	1.632
Rectangular 5.00x5.00 m² - 2 passes	1.994

5.2 Influence of grid on the improvement degree

For each grid, we compared the average of pre-CPTs with the average post-CPTs (after vibrocompaction) after 30 days of resting period.

5.2.1 Triangular grid pattern (4.40x4.40 m² - 1 pass)

As Figure 2 illustrates, pre-CPTs show a homogeneous q_c profile apart from the first 4 m, where the ground was compacted and levelled with excavators and graders.

CPTs after vibrocompaction (also called post-CPTs) show a q_c value which is 82% higher on average. We also notice that the improvement is higher in rainbowed sand when compared to dumped sand.

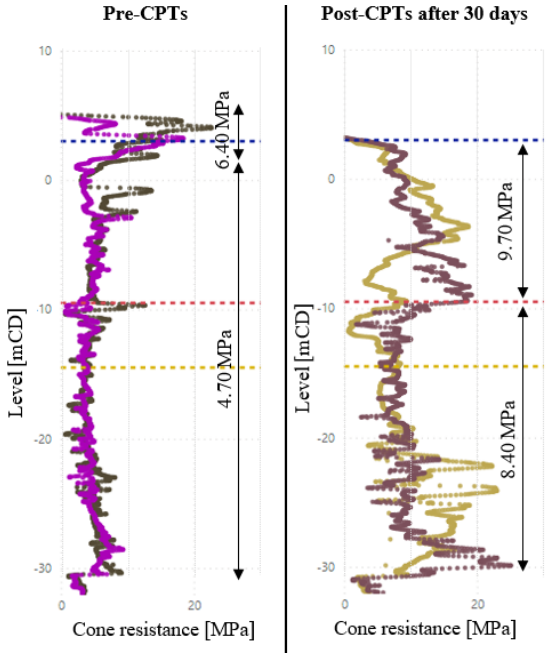

Figure 2. Triangular grid - 1 pass - R=2.096m - Pre&Post-CPTs comparison.

5.2.2 Triangular grid pattern (4.40x4.40 m² - 2 passes)

Based on pre-CPTs introduced in Figure 3, we can't see a clear difference between dumped and rainbowed sand. Over the first 3 to 4 m, the sand is more compacted.

Vibrocompaction improved the entire average profile by 108% in a homogeneous way. The hard top layer is no longer visible. There is also a clear difference between improved rainbowed sand and improved dumped sand.

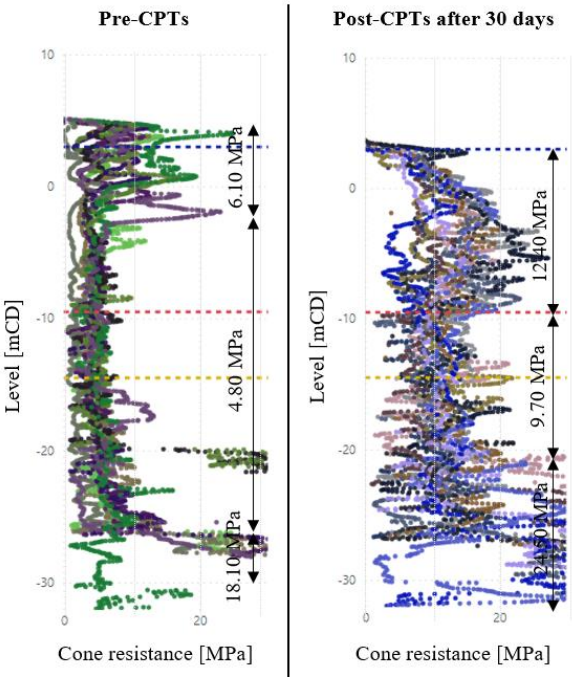

Figure 3. Triangular grid - 2 passes - R=1.632m - Pre&Post-CPTs comparison.

5.2.3 Rectangular grid pattern (5.00x5.00 m² - 2 passes)

Looking at pre-CPTs (Figure 4), we can see again the hard top layer.

The vibrocompacted soil presents a global improvement of 81% on average. Cone resistance in a vibrocompacted rainbowed sand is almost two times higher than a vibocompacted dumped sand.

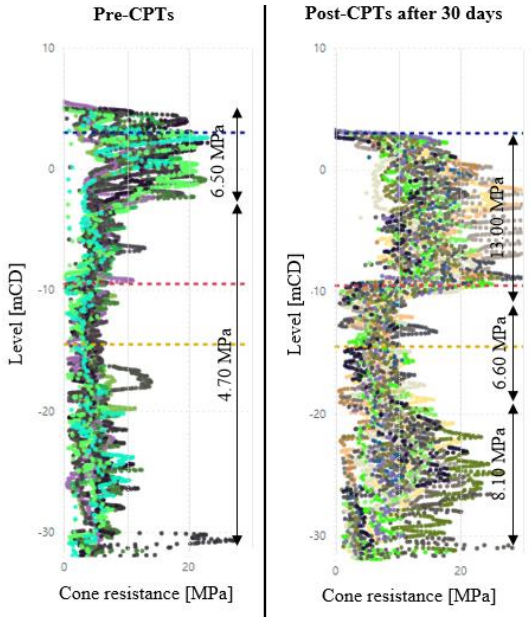

Figure 4. Rectangular grid - R=1.994m - Pre&Post-CPTs comparison.

5.2.4 Comparison of vibrocompaction performances

- (A), (B), (C): The global improvement is directly linked to the radius of influence. Thus, the narrower the spacing between each point, the better the improvement will be. The improvement is higher in a rainbowed sand as compared to a dumped sand.
- (A) & (B): The improvement increases with a second pass by 26%.
- (A) & (C): The radius of influence is near-identical, and as a result, the global improvement as well. Using either two passes or an equivalent one-pass shows equivalent result.

Table 2. Performances measured for each grid.

Reference	Grid pattern	Radius [m]	Global improvement (30 days)
(A)	Triangular 1 pass	2.096	82%
(B)	Triangular 2 passes	1.632	108%
(C)	Rectangular 2 passes	1.994	81%

6 AGEING EFFECT

CPTs performed too soon after the completion of compaction show pessimistic results due to pore water pressure, the rearrangement of particles and the possible presence of temporarily trapped release air. When CPTs are repeated after a resting period, an improvement is observed. This is called the ageing effect.

Thus, 150 CPTs where performed from 0 to 195 days after the first point compacted.

We studied the ageing effect over two approaches: by comparing grid patterns, and by comparing the improvement above, and below -10.00mCD (corresponding to the interface between rainbowing and dumping).

6.1 Influence of the grid

As illustrated on Figure 5, the improvement degree is higher with a triangular grid (the smallest radius of influence), reaching 114%.

In both rectangular and triangular grids, at least 60% of improvement is observed four days after the completion of the first pass. Then, tests performed the same day as the second pass show an effective loss of 10 to 20% in improvement.

After the second pass, the rectangular grid zone improves by an additional 30% and the triangular grid zone by 55%.

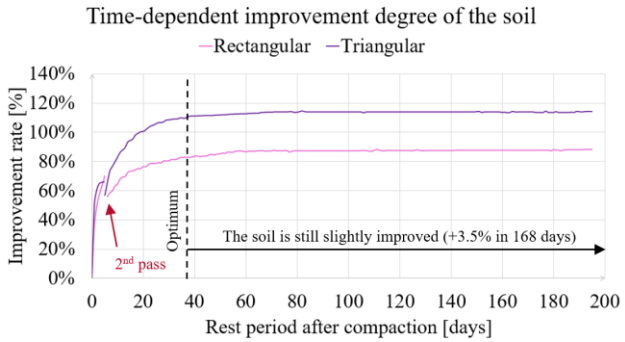

Figure 5. Time-dependent improvement rate of the soil - Rectangular & Triangular grids.

Based on these results, the optimum ageing time seems to be reached between 25 to 30 days after the second pass. Beyond this point, the soil will carry on its improvement over time but the delta between rectangular and triangular grid remains constant.

6.2 Influence of the reclamation technique

As previously shown, the measured amperage differs whether we are in rainbowed or dumped sand. In order to determine if the post-compaction results are different, we have separated the results at the -10.00mCD threshold.

Thus, above -10.00mCD refers to the rainbowed sand, while below -10.00mCD corresponds to the dumped sand. The transition zone is included in the dumping cycle, but does not influence the results.

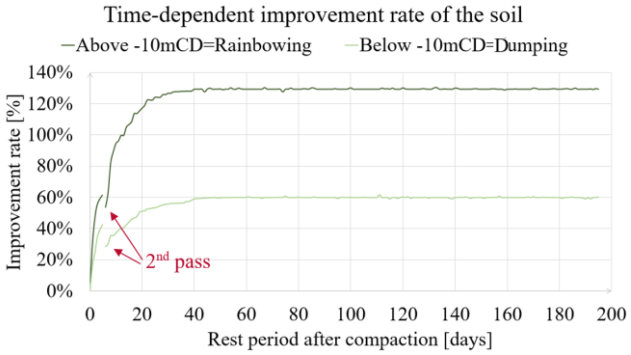

Figure 6. Time-dependent improvement rate of the soil - Above & below -10.00mCD.

Figure 6 clearly shows that the improvement rate is 70% higher in the rainbowed vibrocompacted sand as compared to the dumped vibrocompacted sand.

This difference likely arises from the dumped sand capturing sedimentation layers, which are then mixed together by vibrocompaction, resulting in a lower but consistent effectiveness of the compaction.

This phenomenon depends on the length of the dumping cycle and the presence of sediments in the water.

7 CONCLUSION

While the upper layer reacted as expected, unusual results were observed in the lower part of the fill. For the first time, we encountered difficulties in compacting the dumped layer. After analyzing the various effects discussed in this article, we believe this is likely due to fines in the sand matrix captured during each dumped load, resulting in a mixed soil layer with a high fines content.

To address these issues, a two-pass triangular approach yielded the best results. The amperage seems to be the best parameter to analyze the first soil response. Thence, a dumped soil presents lower post improvement values than a rainbowed sand. On this project, a second pass of compaction, or an equivalent narrow first pass appears to be the most efficient solution to improve the dumped soil.

Finally, depending on soil's properties, q_c values are improved by 60%, 4 days after the 1st pass. The ageing effect can improve the *in-situ* soil by an additional 25% after at least 30 resting days.

Proceedings of the XVIII ECSMGE 2024
GEOTECHNICAL ENGINEERING CHALLENGES
TO MEET CURRENT AND EMERGING NEEDS OF SOCIETY
© 2024 the Authors
ISBN 978-1-032-54816-6
DOI 10.1201/9781003431749-424
Open Access: www.taylorfrancis.com, CC BY-NC-ND 4.0 license

ECSMGE 24
XVIII EUROPEAN CONFERENCE ON SOIL MECHANICS AND GEOTECHNICAL ENGINEERING

Site tests on retaining systems and uplift anchors of Nordhavnstunnel in Denmark

Essais d'un système de soutènement et d'ancrages de soulevement pour le Nordhavnstunnel au Danemark

B. Demir*
Cowi (Former Niras), Copenhagen, Denmark

C. Bauduin, M. Palaiologou
NV BESIX SA, Brussels, Belgium

J.D. Christensen
MT Højgaard Danmark, Copenhagen, Denmark

S. Yding, S.K. Tomac
Niras, Copenhagen, Denmark

**bedr@cowi.com*

ABSTRACT: The Nordhavnstunnel, located in the Nordhavn region of Copenhagen, Denmark, extends the existing Nordhavnsvejtunnel over 1,4 km, passing below the Svanemøllehavn and in the Nordhavn area. It is designed as a rectangular reinforced concrete cut and cover tunnel constructed between anchored retaining walls. A successful design and construction in the challenging location and ground conditions require a series of preliminary sheet pile driveability tests and anchor investigation tests. This paper presents a comprehensive summary of the test results, offering valuable insights and recommendations. Furthermore, it delves into the implications of these findings on the updated design of the tunnel's retaining system and uplift anchors. The conclusions drawn from this study provide crucial insights pertinent to the Nordhavnstunnel but also offer valuable lessons for future projects in Copenhagen encountering similar geotechnical conditions.

RÉSUMÉ: Le Nordhavnstunnel, situé dans la région de Nordhavn à Copenhague, au Danemark, s'étend sur plus de 1,4 km depuis le tunnel existant de Nordhavnsvejtunnel jusqu'à la mer, passant sous le Svanemøllehavn et la zone de Nordhavn. Il est conçu comme un tunnel rectangulaire en béton armé construit entre des murs de soutènement. La conception et la construction à cet emplacement et dans ces conditions géotechniques difficiles nécessite une série de tests préliminaires de faisabilité d'enfoncement de palplanches et d'ancrages. Cet article présente un résumé des résultats des essais, offrant des informations précieuses et des recommandations. De plus, il explore les implications de ces résultats sur la conception mise à jour du système de soutènement du tunnel et des ancres de soulèvement. Les conclusions tirées de cette étude fournissent des informations cruciales qui ne sont pas seulement pertinentes pour le Nordhavnstunnel, mais offrent également des leçons précieuses pour les projets futurs à Copenhague rencontrant des conditions géotechniques similaires.

Keywords: Road tunnel; retaining wall; uplift anchor; limestone; investigation test.

1 INTRODUCTION

The new Nordhavnstunnel extends the existing Norhavnvejtunnel to the east in the Nordhavn region of the Copenhagen, Denmark. The project owner is Danish Road Directorate (Vejdirektoratet) and design and build contract is awarded to Besix & MT Højgaard joint venture with design support from Niras (all permanent works), Jacobs UK (M&E design) and Besix Engineering Department (all temporary works).

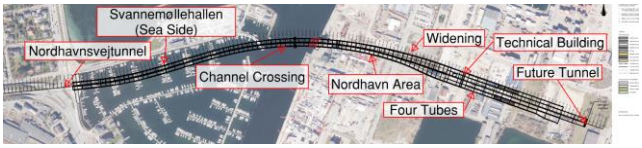

Figure 1. Plan view of the Nordhavnstunnel.

The tunnel is 1.4 km long. It is connected at its west end to the existing Nordhavnsvejtunnel. A 800 m long part of the tunnel passes under the existing harbour of Svanemøllen and crosses the access channel to the Nordhavn quays. After construction, the harbour and

the access channel will be reinstated. The channel must maintain a width of 40 m all along the construction period. East of the channel crossing, the tunnel continues under the Nordhavn Area, which is intended to be further developed in a nearby future. The Nordhavnstunnel will be extended by a future Eastern tunnel that will connect the Nordhavn area to the Copenhagen airport.

The section in the Svanemøllehavn and channel crossing is a two-tube rectangular section of constant width. East of the harbour and the channel crossing, in the Nordhavn area, the tunnel widens to consist of four tubes: the two outer tubes will act as a ramp for Nordhavn area, and middle two tubes will be kept as blind tunnel for connection to Eastern Ring Road.

The clearance height between the bottom and slab is 6.65 m, allowing for a 4.65 m high traffic clearance profile, 1 m high mechanical and electrical installations profile above traffic and a pavement and ballast concrete layer of about 1m. The width of the tunnel tubes starts from 9 m and increases up to 19 m at the widening section.

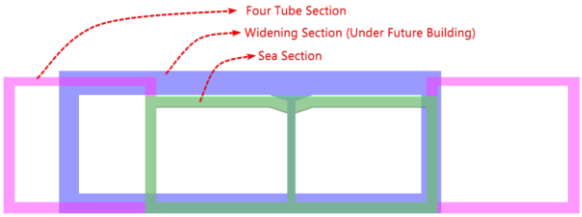

Figure 2. Various Cross-section used in Nordhavnstunnel.

The project includes the design and construction of two large pumping stations along the tunnel as well as a main technical building located on top of the tunnel in the Nordhavn area, as well as various road infrastructure and upgrades of existing tunnel structures and buildings.

The geotechnical conditions at the project location consist of following (simplified) layering (from bottom to top):

- Copenhagen Limestone at starting at level -12 to -16 m DVR 90. The limestone is highly indurated in its upper meters, low fractured except at the east end of the project due to the presence of the Svanemolle fault zone.
- Greensand, thickness 2 to 3 m. The Greensand is not found in the Nordhavn area.
- Glacial till, of quite variable thickness 4 to 8 m over the project location. The glacial till can be described as a clayey silt to silty clay.
- Interbedded layers of melt sand in the glacial till at Nordhavn
- The top 2 to 4 m at Nordhavn consist of man-made sandy and very heterogeneous fill

The values of the geotechnical parameters are shown in the Table 1 and Table 2.

Table 1. GIR Parameters (simplified mean value - ½ std dev).

Soil type	γ_b kN/m³	S_u kPa	φ'_{pl} °	c kPa	E_{50} MPa	E_{ur} MPa	σ'_{pc} kPa
Existing fill -sand	20	-	32	0	25	75	0
Existing fill -clay	20	65	29	5	15	45	0
Clay till	22	400	33	35	30	90	>1000
Glacial Sand	20		37	0	30	85	>1000
Greensand	21	500	32	50	65	200	>1000

Table 2. Limestone properties (Hoek-Brown properties transformed into equivalent Mohr Coulomb properties).

Soil type	γb kN/m³	UCS MPa	GSI	m i	D	φ'_{pl} °	c kPa	E_{50} MPa
Limestone (passive)	22	15	65	7	0	45	100 (450)	1200
Limestone (vertical)	22	30	70	7	0	55	900	1200

** Limestone properties for vertical capacity were upgraded based on preliminary vertical bearing capacity estimations through dynamic testing (see discussion in 4.3).*

The limestone has a separate, potentially artesian, hydrological regime compared to the above layers.

The tunnel is secured against uplift by means of post tensioned bar anchors fixed in the limestone. 50 cm toe is used throughout the tunnel to increase the uplift resistance.

The tunnel is constructed by the cut and cover method, from a hydraulic fill forming a temporary working platform in the Svanemøllen harbour, and from the existing ground in the Nordhavn area. The tender documentation provided "for information" by the Road Directorate to the tenderers proposed a secant pile wall retaining system with multiple anchor levels. The depth of the secant pile wall was determined by the geotechnical and hydrological design to reduce the water discharge by dewatering. The proposal of secant pile wall was in-line with the retaining system that had been used for the Nordhavnsvejtunnel. The Contractor decided to adopt a sheet pile retaining wall system in combination with grouting to create a water cut off. This solution was considered to bring in significant productivity and potentially sustainability related benefits to the project. An indicative cross section of the excavation pit and the retaining wall system in the marine area is illustrated in Figure 3.

Risks related to driveability of the sheet piles through the clay till/greensand and in the limestone were identified and from the early design stages different scenarios with various penetration depths in the limestone were assessed. Early driveability testing

was placed in the planning, to allow early risk mitigation and design improvement.

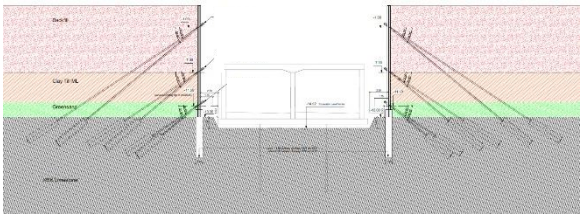

Figure 3. Temporary works cross-section in the marine area, illustrating the excavation pit: sheet pile wall with multiple anchor levels, grout injection, berm support of sheet pile.

This paper presents the results of the investigation tests of uplift anchors and sheet piles performed at the initial phase of the project. To optimize the design, a set of uplift anchor investigation tests, anchors with bond length in the clay till, and sheet pile driveability tests have been carried out. Additional test data and project information are also shared to document the various know-hows obtained during the early phases of the project.

2 UPLIFT ANCHORS

2.1 Design against uplift

Uplift checks of the tunnel have been performed as per the Client's Requirements and DS EN 1997. The requirements are summarized below for completeness.

Load combinations for UPL in Danish annex have been separated into two to consider the additional risks related to frictional resistance. If frictional resistance and tensile elements such as anchors are used, Table A.4-1 should be used: 0.9 x Favourable - 1.1 x K_{fi} x Unfavourable. If only self-weight is used to resist against uplift, the factors are lowered due to reduced uncertainty: 1.0 x Favourable - 1.05 x K_{fi} x Unfavourable (Water). Since a very conservative friction between concrete and backfill is included in all cases, only Table A.4-1 is used in Nordhavnstunnel. Therefore, the overall safety factor against uplift can be calculated as 1.35, considering K_{fi}=1.1 as per the Client's Requirements.

Additional requirements by Client includes future excavations in certain areas, artesian pressures that create additional water pressure from the bottom of tunnel, requirement of post-tensioning the anchors.

The typical failure mode of the anchors (see figure 4) has been checked throughout the design process.

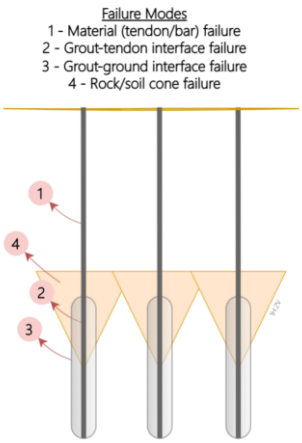

Figure 4. Anchor failure modes.

Following criteria are considered for the definition of anchor lengths:

- All bond lengths should be embedded in the limestone with minimum of 1 m from the top of the limestone.
- Free length = Minimum 4 m

Since the anchors are embedded in the limestone, main design criteria become the material failure (failure mode 1). To be able to increase the anchor spacings, S670/800 MPa bar anchors are considered in the design. As per the DS EN 1997-1, material capacity is $R_{t;d} = A_{anchor} \cdot \min\{k_1 \cdot f_{pk}; k_2 \cdot f_{p0.1k}\}$. In this equation, k_1=0.8 and k_2=0.95. The steel bar should be able to carry the proof load. The proof load is determined as the 1.43 x design load. Therefore, the capacity $R_{t;d}$ is reduced by 1.43 to reach the design capacity. Due to conservative requirement on the $R_{t;d}$, the limitation as per the EN 1993-5 does not govern – as the requirement to check for proof load is only for $R_{t;d}$. With these assumptions, Ø50, Ø57.5 and Ø63.5 S670/800 anchors result in $R_{t,d}$ of 874 kN, 1156 kN and 1410 kN, respectively.

2.2 Investigation tests uplift anchors in limestone

The typical bond strength (referring to failure mode 3) assumption for Copenhagen limestone has been increasing over the years from 650 kPa to 900 kPa – the latter value is being used widely in the latest projects.

Considering that the number of anchors in Nordhavnstunnel is more than 700, even a slight increase in the capacity optimizes the project significantly. More importantly, ensuring that the problems during the construction and testing phase is critical, also considering that 10% of the anchors will be suitability tested, and acceptance test load is increased to same level with suitability test load, i.e. 1.43 x design load.

Uplift anchor tests have been carried out in two different locations on the land-side of the project. In total, 8 anchors were tested. The anchor data are summarized below:

Bond length = 3 and 5 m

Top of anchor – top of limestone = 1 m and 2 m

Strand anchor to reach the capacities.

Proof load: 3350 kN – corresponds to 2090 kPa adhesion for 3 m bond length.

Test Method 1 is used in Denmark. The interpretation method for anchor failure in Denmark is the creep rate method. The methodology is described in DS/EN ISO 22477-5:2018. The creep rate is the rate of increase in deformation under constant load with logarithm of elapsed time. As per the DS EN 1997-1, creep rate limits are 2 mm/log(min) for acceptance and suitability tests and 5 mm/log(min) for investigation tests. Based on this methodology, the success vs. failure will be implemented as shown below:

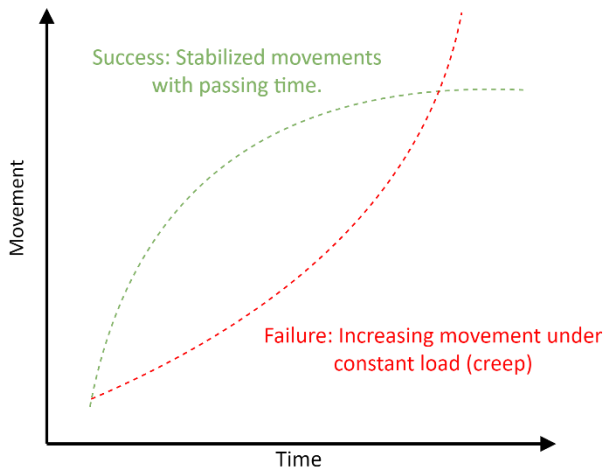

Figure 5. Success vs. failure of anchor test.

The data has processed in a way that all durations starting from t=1 min are checked for maximum creep rate, i.e. b/w 1-3 min, 1-5 min, 1-10 min, 1-15 min, 1-30 min, 1-45 min, 1-60 min. Although ISO recommends using the last stabilized portion of the curve, most critical creep rate has been found from test results conservatively.

The test results have shown that all the creep values were significantly below the 5 mm level for failure. To make sure the results are correct, all individual measurement points are used separately to calculate the creep rate. The results are summarized for adhesion (kPa) – which is the applied load per surface area of the bond.

The highest creep rate observed in the tests were 2.13 mm/log(min) – and not at the highest adhesion. The highest creep is observed for an anchor with 861 kPa loading.

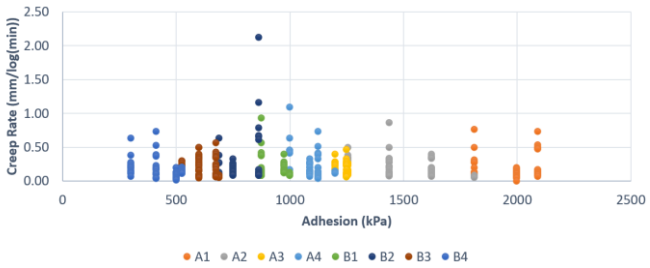

Figure 6. Creep rate vs. adhesion.

The highest anchor loads (in terms of adhesion) are shown in table 1. For a load (friction) of 2091 kPa, the creep rate is less than 1 mm/log(min). Therefore, the failure has not been reached even at the maximum adhesion of 2091 kPa.

Table 3. Creep rates at highest proof loads.

Name	Region	Load (kPa)	Duration (min)	Bond Length (m)	Friction (kPa)	Creep Rate (mm/log(min))
A1-3350-3	A1	3350	3	3	2091	0.73
A1-3350-20	A1	3350	20	3	2091	0.53
A1-3350-15	A1	3350	15	3	2091	0.51
A1-3350-30	A1	3350	30	3	2091	0.49
A1-3350-5	A1	3350	5	3	2091	0.48
A1-3350-10	A1	3350	10	3	2091	0.47
A2-3350-3	A2	3350	3	3	2091	0.17
B2-3350-3	B2	3350	3	3	2091	0.17
B1-3350-30	B1	3350	30	3	2091	0.14
B2-3350-30	B2	3350	30	3	2091	0.14
B1-3350-20	B1	3350	20	3	2091	0.13
B2-3350-20	B2	3350	20	3	2091	0.13
B2-3350-15	B2	3350	15	3	2091	0.13

2.3 Comparison with literature

Several papers in the literature (Kristensen et. al., 2000, Roesen & Trankier, 2021, Lyse, 2022) discuss bond of anchors in the Copenhagen limestone. The maximum tested adhesion was reported by Lyse (2022) as high as 2060 kPa. None of the studies have reported failure in the Copenhagen limestone. Therefore, it can be concluded that the Nordhavnstunnel test results increased the number of tests above 2000 kPa, reaching a new limit.

2.4 Design decisions for uplift anchors in the limestone

To reduce the risk to an acceptable level, an adhesion of 1200 kPa has been selected. Using a common drilling diameter of 150 mm. this resulted in 3.6 m bond length for 63.5 mm diameter anchor to sustain the design uplift load of 1410 kN.

3 ANCHORS IN THE GLACIAL TILL

A series of anchor investigation tests with the anchor grout body in the clay till was set up during the design phase.

16 inclined investigation tests were performed on inclined anchors at two specified test sites adjacent to the tunnel location on land (Nordhavn area). These anchors were all made to investigate the anchors' suitability for the glacial clay till. The test anchors were inclined by 35 degrees to the horizontal plane, drilled in OD Ø170 mm dimension using a Ø152 mm casing, and each was installed with 12 No. of 0,62" Y1860 strands. The test proof load was 1600 kN. 12 anchors with bond length 6,9 and 12m were installed with primary injection during installation and using 6 to 7 bar grout pressure when extracting the casing around the tendon bond length. 4 anchors with 9m bond length were post grouted using two reinjection tubes.

Anchors with no post grouting could take a load between 720 and 960kN, without reaching failure, however a creep rate of 2 mm per time decade was reached even at the lower end of the mentioned loading range.

Post grouted anchors could undertake test loading up to 1440 kN for a 9 m bond length (displacement criterion $\Delta s=s_b-s_a<0.5$mm was exceeded at the last step of 1600kN or creep rate of 2mm per time decade was reached).

The investigation tests confirmed that anchors in the clay till with post grouting have a resistance of approximately 265kPa (the corresponding adhesion factor α would be equal to 0.65 assuming S_u=400kPa and adhesion=α x c_u). This resistance, however, was not sufficient for the current project demands.

As the sheet pile wall design requires proof load tests ranging up to 1600 to 1800 kN, it was decided not to go forward with the anchors bond in the clay till, but to adopt a grout body in the limestone.

4 TEMPORARY WORKS - RETAINING STRUCTURE

4.1 Design summary

The construction sequence in the Svanemøllehavn foresees a hydraulically installed working platform from which the sheet piles and vertical anchors are installed passing through the fill, clay till, greensand to the limestone. In the Nordhavn area, retaining walls and vertical anchors are to be driven from the existing ground level. Grouting is to be performed to extend the water cut-off role of the sheet piles into the limestone over 2 to 9 m depth. Dewatering (with re-injection) is installed to allow staged dry excavation and installation of the grout anchors at one to three levels depending on the depth of the building pit. The retaining height reaches up to 15 m in the deepest parts. (see Figure 3). In the Svannemolen area, the bottom slab of the tunnel is up to two meters below the limestone top. As the sheet piles do not reach the depth of the bottom slab in these areas, a berm will be left below the toe of the sheet pile to reach full excavation depth.

An extended driveability campaign at 5 locations with different hammers and modifications (e.g. driving shoe at the toe of the sheet pile, pre-trenching/relaxation of the soil) was performed. Heavy duty U-sections with flange thickness around 20 mm, were selected from the beginning and used on all test piling locations. Testing was done, using panel driving of three double piles at each testing location, to simulate the piling process for the production sheet piles, that are properly interlocked. These sheet piles were considered more likely to be driven through the hard underground thanks to their shape and stiffness.

4.2 Sheet pile driveability tests

A variety of hammers were used for the sheet pile driveability tests, including a 9-ton free fall hydraulic hammer along with hydraulic accelerated hammer types IHC S-120 and S-150, both representing equivalent drop weights of 12 ton and 15 ton, respectively. The result of the driveability tests was that the free fall 9 ton hammer proved to be adequate for sheet pile driving to the limestone, as well as the IHC hammers.

Potential benefits from pretrenching/loosening the soil of upper layer were not observed. A driving shoe was found to have benefits (stress reduction during driving) but given the sheet pile section selected (the sheet pile section could also be installed without a driving shoe), a driving shoe was not deemed necessary.

Through the campaign it was proven possible to drive the U-shaped sheet piles smoothly through the glacial till and greensand layers to the top of limestone. However, penetration in the limestone could not be demonstrated. Some sheet piles were extracted at the end of campaign to witness toe damage. Sheet piles in general demonstrated acceptable minor or no damage. However, there were cases where sheet pile toe got damaged to force sheet piles into limestone (Figure 7).

As multiple inclined anchors are necessary for the support of the wall, it is easily understood that the vertical load on the sheet pile is high and vertical bearing capacity is thus critical. The initial design has been adapted to sheet piles stopping with refusal to the top of limestone. The end bearing capacity will have to be confirmed by dynamic testing: PDA-measurements and CAPWAP-analysis and by the introduction of a reliable set criterion when installing

the sheet piles. Preliminary dynamic testing allowed for an estimation of an unfactored toe bearing resistance of 4514kN/m (or factored as per DS EN 1997-1 approximately 2257kN).

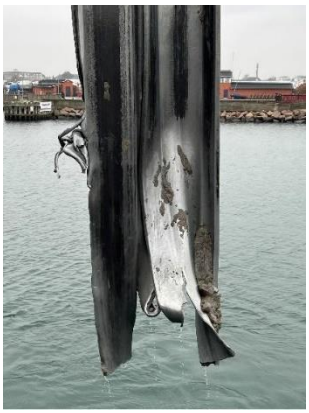

Figure 7. Damaged sheet pile toe as retrieved.

4.3 Limestone berm support at pile toe level

Where excavation extends deeper than the toe of the sheet piles, a berm at the sheet pile toe is provided to ensure sufficient end bearing capacity. This design includes a purpose specific assessment of the effective limestone strength accounting for its anisotropy in the given the loading conditions.

By including anisotropy of the limestone, in combination with the nature and circumstances of the load from the retaining wall onto the limestone berm, two different sets of equivalent strength properties can be attributed to the limestone due to the different failure mechanisms. Thus, one set of strength parameters was used for the vertical capacity and berm stability, and a specific set of values was used for the determination of horizontal passive resistance in the earth pressure calculations.

The design strategy furthermore foresees site assessment of the limestone conditions and properties based on face logging results at the centre of the excavation before excavation towards the sheet piles is continued. Rock bolts are foreseen as mitigation measure in case of unfavourable geological and geotechnical conditions (e.g. unfavourable fissuring).

5 CONCLUSIONS

Uplift anchor investigation tests, inclined anchors investigation tests in the clay till and sheet pile driveability tests have been carried out to validate and optimize the design of the Nordhavnstunnel.

Uplift anchor tests reached confirmed adhesion as high as 2091 kPa and the anchors did even not come close to failure. Therefore, traditional 650-900 kPa values should not be used anymore, and higher values should be adapted in Copenhagen. Nordhavnstunnel design adopts 1200 kPa – while higher values are open to explore. Preliminary anchor testing allowed a refinement of the anchor grout body length, contributing to financial optimisations.

The benefits of post grouting of anchors in the clay till could be demonstrated. An increase of capacity by minimum 60% was reported, with post grouted anchors of 9m grout body in the clay till demonstrating a capacity around 1440kN.

U-shape heavy duty (20mm web thickness) sheet piles were found to be able to be smoothly driven in the clay till and greensand layers of Copenhagen, but no penetration in the limestone could be demonstrated.

Placing the driveability campaign early in the project allowed for an in-time design refinement and risk mitigation and enabled the adoption of a sheet pile solution instead of a traditional secant pile wall. The very good collaboration between design and execution team, the contractor and the client allowed preliminary investigation tests, taking calculated risks/opportunities, and led to an improved productivity and potentially sustainability related performance during design and execution.

6 ACKNOWLEDGEMENT

The authors would like to express their gratitude to VejDirektoratet for their support during the project and for their approval of the paper.

REFERENCES

DS/EN 1997-1 DK NA (2021) National Annex to Eurocode 7: Geotechnical Design – Part 1: General rules.

DS/EN ISO 22477-5:2018 Geotechnical investigation and testing – Testing of geotechnical structures – Part 5: Testing of grouted anchor.

Kristensen, P. S., Madsen, J. And Nymand, J. (2000) Christiansbro, kontor. Permanente jordankre i København Kalk (Copenhagen, NGM 2000).

Lyse, C. (2022) Performance of a tension element installed in the Copenhagen Limestone. In *ITA-AITES World Tunnel Congress 2022* and 48th General Assembly Bella Center, Copenhagen 2-8 September 2022.

Roesen, B. S., & Trankjær, H. (2021). Permanent uplift anchors in Copenhagen limestone. In IOP Conference Series: Earth and Environmental Science. IOP Publishing.

Proceedings of the XVIII ECSMGE 2024
GEOTECHNICAL ENGINEERING CHALLENGES
TO MEET CURRENT AND EMERGING NEEDS OF SOCIETY
© 2024 the Authors
ISBN 978-1-032-54816-6
DOI 10.1201/9781003431749-425
Open Access: www.taylorfrancis.com, CC BY-NC-ND 4.0 license

ECSMGE 24
XVIII EUROPEAN CONFERENCE ON SOIL MECHANICS AND GEOTECHNICAL ENGINEERING

Acceleration of embankment construction on soft soils of Salamanga using wick drains and counterweight fills

Accélération de la construction de remblais sur sols mous de Salamanga à l'aide de drains verticaux et des remblais de contrepoids

H. Dete*, C. Quadros
TÉCNICA – Engenheiros Consultores Ltd., Maputo, Mozambique
**hans.brigido@gmail.com*

ABSTRACT: The construction of embankments on soft soils is an inevitable solution in the case of roads crossing thick clayey alluvial deposits. In such cases, consolidation acceleration techniques can be adopted, in order to prevent excessive settlements to occur as a result of the stress increase induced by the embankment or causing it to fail due to insufficient shear strength of the foundation. This paper evaluates technical solutions for accelerating the construction of embankments on soft soils using wick drains and counterweight fills. This solution was implemented on the construction of a 9.6 m high embankment between the years 2016 and 2017, along the Maputo River floodplain, in Salamanga District. The construction was preceded by an extensive geotechnical investigation, including in situ and laboratory tests, which identified the existence of a 39 m thick deposit of soils that were not only highly compressible and of low permeability, but also had a low shear strength, reason why counterweight fills were adopted to prevent failure of the embankment during the staged construction. Because of the uncertainties involved in the characterization of soft soils, related to the sedimentation process, and spatial variation of their properties, and in predicting their behavior when loaded, an instrumentation and monitoring plan of the construction was implemented, whose results were used to calibrate the geotechnical model. From the collected data, it was concluded that the designed solution performed satisfactorily and the project assumptions regarding the allowable residual settlements and stability of the embankment were met before laying the pavement.

RÉSUMÉ: La construction de remblais sur sols mous est une solution incontournable dans le cas de routes traversant des alluvions argileuses épais. Dans ces cas, des techniques d'accélération de la consolidation peuvent être adoptées, afin d'éviter que l'augmentation des contraintes induite par le remblai ne produise des tassements excessifs ou ne provoque pas sa rupture en raison d'une résistance au cisaillement insuffisante de la fondation. Cet article évalue des solutions techniques pour accélérer la construction de remblais sur sols mous à l'aide de drains verticaux préfabriqués et des remblais de contrepoids. Cette solution a été mise en œuvre pour la construction d'un remblai de 9,6 m de hauteur entre 2016 et 2017, le long de la plaine inondable du fleuve Maputo, dans la région de Salamanga. La construction a été précédée d'une vaste investigation géotechnique, y compris des essais in situ et en laboratoire, qui a identifié l'existence d'un dépôt de 39 m d'épaisseur de sols qui étaient non seulement hautement compressible et de faible perméabilité, mais avaient également une faible capacité portante, raison pour laquelle des bermes à contrepoids ont été adoptées pour éviter la rupture du remblai lors de sa construction par étapes. En raison des incertitudes liées à la caractérisation des sols mous, à cause de leur nature sédimentaire et à la variation spatiale de leurs propriétés, et à la prédiction de leur comportement en charge, un plan d'instrumentation et de surveillance de la construction a été établi, dont les résultats ont été utilisés pour calibrer le modèle géotechnique, à partir duquel il a été conclu que les hypothèses du projet concernant les tassements résiduels admissibles et la stabilité du remblai étaient respectées avant la construction de la chaussée.

Keywords: Acceleration of embankment construction; soft soils; wick drains; counterweight fills.

1 INTRODUCTION

Among several factors, the design of a highway is constrained by the topography, geology and hydrology of the site.

Indeed, in the cases where a road layout crosses a river valley, it is frequent to build embankments adjacent to the bridge abutments to avoid overtopping of the roadway during extreme floods.

In such cases, the viability of such construction must be very well analysed, for the river valleys are generally composed of saturated alluvial soils, of low bearing capacity and high compressibility, requiring the use of non-conventional construction methods to prevent excessive settlements of the infrastructure during the service phase.

According to Almeida & Marques (2010), the choice of the most adequate method depends on the

geotechnical characteristics of the deposit, use of the area, including the neighbourhood, as well as construction deadlines and costs involved.

Therefore, this paper presents the use of wick drains with surcharge loading and counterweight fills (berms) as an alternative method for the construction of embankments on soft soils.

2 TECHNIQUES TO ACCELERATE THE CONSTRUCTION OF EMBANKMENTS ON SOFT SOILS

2.1 Wick drains with surcharge loading

The construction of road embankments on deep soft soil deposits is usually done by preloading the ground through an additional depth of fill, during a period long enough to allow most of the consolidation settlements to occur before laying the pavement.

Due to the low permeability of soft soils, the consolidation period might be too long (Terzaghi et al., 1996), thus not complying with the construction deadlines.

In such cases, the preloading is combined with wick drains (Figure 1), which are installed relatively close to each other to reduce the drainage distance up to 1 to 2 meters, therefore accelerating the consolidation (Espinoza et al., 2020).

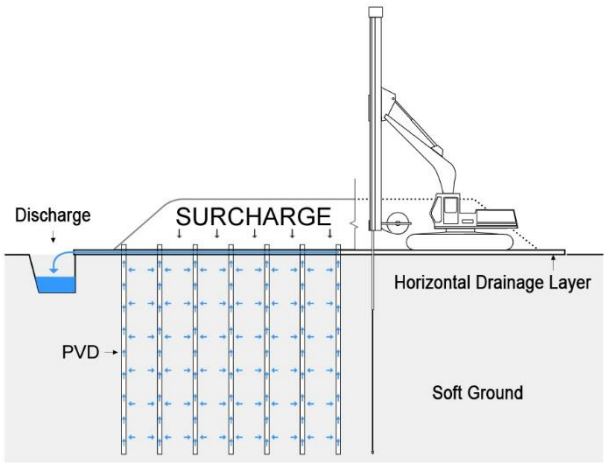

Figure 1. Preloading embankment combined with wick drains. (Source: Prefabricated Vertical Drains, 2017).

2.2 Counterweight fills

Despite the fact that the construction of embankments on soft foundation must account for excessive settlements, it is also necessary to ensure that the embankment height will not cause failure of the foundation due to its low undrained strength.

According to (Jakobson, 1948), if the required embankment height does not comply with the foundation shear strength, counterweight fills (loading berms) can be adopted to decrease the shear stress along the critical failure surface (Figure 2).

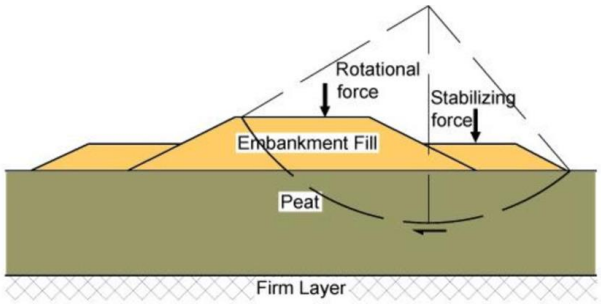

Figure 2. Effect of counterweight embankment on the stability of the embankment. (Muhammad, 2018).

3 CASE STUDY

3.1 Project description

The new Maputo – Ponta do Ouro road crosses an alluvial floodplain within the Salamanga District, near the Maputo River.

Since the ground level was +3.0 m and the design flood level was +8.054 m, it was necessary to build an embankment to enable the safe vehicle circulation during extreme floods.

After an extensive geotechnical survey along the road alignment, it was observed that the foundation mainly comprised fat clay with sand (CH) along 3.6 km up to a maximum of 39 m deep, as illustrated on Table 1A and Table 1B (CRBC, 2018).

Table 1A. Soil profile characterization.

Layer (depth, m)	**Soil**	***c* (kPa)**	**ϕ (°)**	**γ (kN/m³)**	**e_0 (-)**
1 (0.0 – 3.8)	CH	12	14	14.6	2.298 3.412
2 (3.8 – 9.3)	SC	12	13.4	14.5	3.412 2.487 2.547
3 (9.3 – 18.6)	CH	12	14	14.2	2.607 2.619 2.619

Table 1B. Soil profile characterization (cont.).

Layer (depth, m)	**Soil**	***c* (kPa)**	**ϕ (°)**	**γ (kN/m³)**	**e_0 (-)**
4 (18.6 – 33.6)	CH	17	22.4	16.1	0.722 2.165 1.852 1.645
5 (33.6 – 39.0)	CH	17.9	17.8	18.3	0.948 0.946 0.949

As per the geotechnical investigation results, the foundation soil has a very low shear strength and is highly compressible (compressibility index between 0.973 and 1.864), requiring special construction methods prior to the final loading.

In this context, the engineering design adopted a solution based on the consolidation process, which consisted of installing wick drains (prefabricated vertical drains). Additionally, counterweight fills (loading berms) were adopted to increase the factor of safety against the slope failure, during the staged construction.

A general scheme of the adopted engineering solution is presented on Figure 3.

For this study, a road section with 379 m of length was considered. On this section, the design height of the embankment was 6.7 m, the top width was 11.5 m and 1:1.5 slopes. The counterweight fills were 3 m high and 15 m of width on both sides of the main embankment.

The wick drains were installed up to 30 m deep, under a triangular pattern.

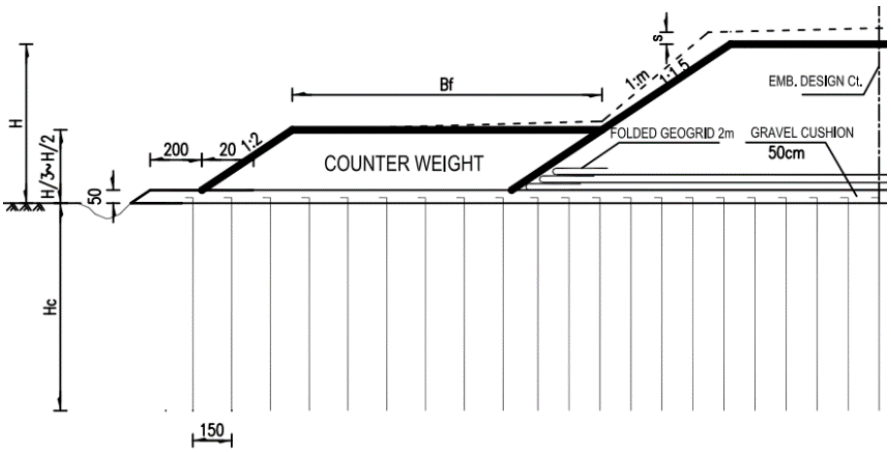

Figure 3. General scheme of the adopted engineering solution (all the dimensions are in centimetres).

3.2 Settlement prediction and design criteria

Settlements were predicted using the horizontal consolidation coefficient (c_h) determined by the Asaoka's observational method, as per the settlements measured until 5.3 m height of the embankment (Figure 4). Further calculations indicated that the consolidation settlements with respect to the design embankment is 2.6 m.

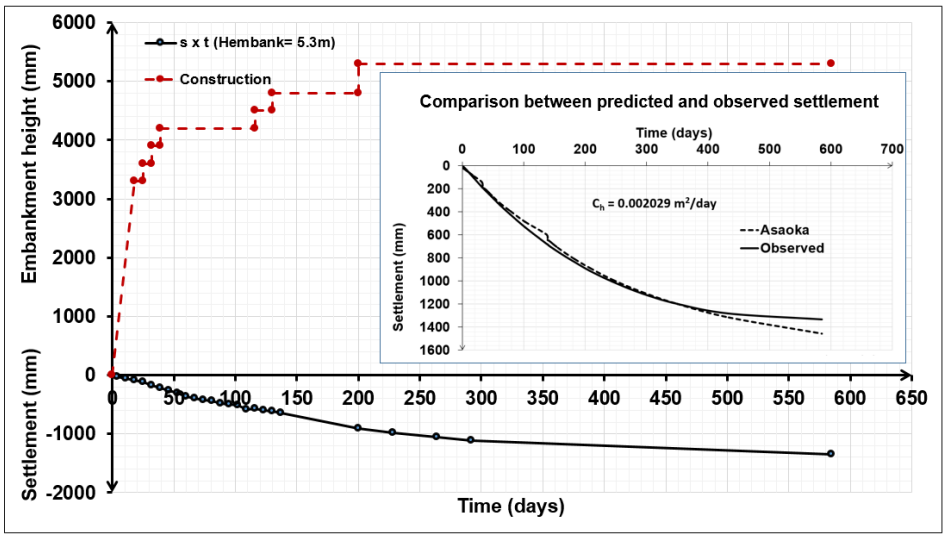

Figure 4. Observed and predicted settlement of the embankment during construction.

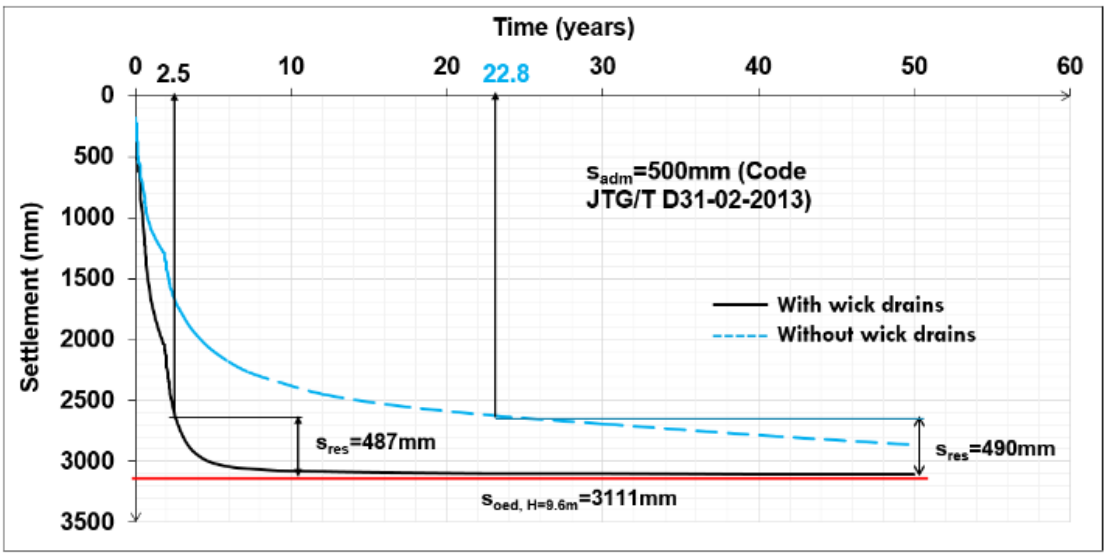

Figure 5. Settlement vs. time curve of the foundation with and without wick drains.

In order to comply with the design height of the embankment and thus, of the road elevation, an additional surcharge fill of 2.9 m was prescribed for the construction stage. Therefore, the total height of the fill was 9.6 m, which would cause a total consolidation settlement of 3.1m (Figure 5).

The construction took 26 months and, according to JTG/T D-31-02-2013, the residual settlement should not exceed 500 mm on the transition section between the embankment and the box culverts (piled foundation with almost no settlement).

Moreover, it was expected that the consolidation process would end 4 years after the construction, reason why maintenance measures such as refilling the pavement on critical sections were prescribed in order to provide good driving conditions.

4 CONCLUSIONS

This paper presented the engineering solution adopted to accelerate the construction of the road embankment accross the Maputo River floodplain, in Salamanga District.

From the study, it is concluded that the installation of wick drains led to a significant acceleration of the consolidation process, keeping the residual settlements within the pavement allowable settlement. In fact, the settlement-time curve presented on Figure 5 shows that without this technique, that process would last for almost 22 years, what is clearly unfeasible.

Finally, it is important to note that the success of the described solution relies not only on the extensive geotechnical investigation, but also on the evaluation of the settlement measurements acquired during the construction monitoring.

5 REFERENCES

Almeida, M. de S. S., & Marques, M. E. S. (2010). *Aterros sobre Solos Moles - projecto e desempenho*. Oficina de Textos.

CRBC. (2018). *Republic of Mozambique South Maputo Link Roads Project AS-built drawing* (Vol. 1).

Espinoza, D., Li, C., De Melo, L., & Gupta, R. (2020). Application of Hybrid Drained-Undrained Model for Analyzing the Stability of Reinforced Soil Structures Over Soft Foundations with Prefabricated Vertical Drains. *ISSMGE International Journal of Geoengineering Case Histories*, *5*(3), 138–151. https://doi.org/10.4417/IJGCH-05-03-01.

Jakobson, B. (1948). The design of embankments on soft clays. *Geotechnique*, *1*(2), 80–90. https://doi.org/10.1680/geot.1948.1.2.80.

JTG/T D-31-02-2013. (2013). *Technical Guidelines for Design and Construction of Embankment on Soft Ground*. China Communications Press.

Muhammad, N. (2018). *The effect of temperature and kaolin mixture on plasticity characteristics and shear strength behaviour of natural soil* (Issue July). Malaysia Pahang.

Prefabricated Vertical Drains. (2017). https://greencosmos.com.sg/prefabricated-vertical-drains-pvd/prefabricated-vertical-drains.

Terzaghi, K., Peck, R. B., & Mesri, G. (1996). *Soil Mechanics in Engineering Practice* (3rd ed.). Wiley-Interscience.

Proceedings of the XVIII ECSMGE 2024
GEOTECHNICAL ENGINEERING CHALLENGES
TO MEET CURRENT AND EMERGING NEEDS OF SOCIETY
© 2024 the Authors
ISBN 978-1-032-54816-6
DOI 10.1201/9781003431749-426
Open Access: www.taylorfrancis.com, CC BY-NC-ND 4.0 license

ECSMGE 24
XVIII EUROPEAN CONFERENCE ON SOIL MECHANICS AND GEOTECHNICAL ENGINEERING

The sustainable future of vertical drains

L'avenir durable des drains verticaux

J.W. Dijkstra*
Cofra B.V., Amsterdam, The Netherlands

R. Bodamer
Geotechnics, Amsterdam, The Netherlands

**Jeroen.Dijkstra@cofra.com*

ABSTRACT: Vertical drains are a common technique for accelerating consolidation in soft compressible material and improving soil strength for a variety of applications, such as embankment construction for infrastructure. They also help reduce the residual settlements of green- and brownfield developments and mitigate liquefaction risks. The sustainable future of vertical drains for ground improvement is a rapidly developing area of research. The objective of this paper is to explore the current trends in the use of sustainable vertical drain systems, with a focus on environmentally friendly materials, innovative construction processes, and potential design implications. Biodegradable or recycled materials have started to replace the traditional synthetic materials. Additionally, construction processes are being refined to reduce waste and minimize the ecological footprint. The use of sustainable vertical drain systems benefits the environment while also having potential design implications, requiring different approaches to soil improvement in some cases. In summary, the sustainable future of vertical drains for ground improvement requires a holistic approach to design, construction, and materials selection. The continued development of innovative and sustainable solutions will ensure that vertical drains remain a valuable tool for geotechnical engineers. This paper provides an overview of the latest trends, innovations, and potential design implications for sustainable vertical drain systems.

RÉSUMÉ: Les drains verticaux sont une technique courante pour accélérer la consolidation des matériaux souples et compressibles et améliorer la résistance du sol pour diverses applications, telles que la construction de remblais pour les infrastructures. Ils contribuent également à réduire les tassements résiduels des développements en milieu urbain et rural et à atténuer les risques de liquéfaction. L'avenir durable des drains verticaux pour l'amélioration des sols est un domaine de recherche en plein essor. L'objectif de cet article est d'explorer les tendances actuelles dans l'utilisation de systèmes durables de drains verticaux, en mettant l'accent sur les matériaux respectueux de l'environnement, les processus de construction novateurs et les implications potentielles en matière de conception. Les matériaux biodégradables ou recyclés commencent à remplacer les matériaux synthétiques traditionnels. De plus, les processus de construction sont affinés afin de réduire les déchets et de minimiser l'empreinte écologique. L'utilisation de systèmes durables de drains verticaux bénéficie à l'environnement tout en ayant des implications potentielles en matière de conception, ce qui nécessite parfois d'adopter des approches différentes pour l'amélioration des sols. En résumé, l'avenir durable des drains verticaux pour l'amélioration des sols nécessite une approche holistique de la conception, de la construction et de la sélection des matériaux. Le développement continu de solutions novatrices et durables garantira que les drains verticaux restent un outil précieux pour les ingénieurs géotechniciens. Cet article offre un aperçu des dernières tendances, innovations et implications potentielles en matière de conception des systèmes durables de drains verticaux.

Keywords: Vertical drains; sustainability; ground improvement; consolidation.

1 INTRODUCTION

Vertical drains are extensively used in the consolidation of low permeable and weak soils, such as clay and peat deposits. The drains offer several advantages, including reduced construction time, improved control of residual settlements, and accelerated soil strength development. Typically composed of an oil-based plastic core surrounded by an oil-based PP or PET geotextile sleeve or sheet, vertical drains, also known as prefabricated vertical drains (PVD), band drains, or wick drains, have been widely implemented in many projects all over the world. Every year, hundreds of millions of meters of drainage material are installed to remain in the ground.

While the discussion on environmental impact of plastics has mainly focused on consumer goods, it has started to reach the civil engineering sector as well. Manufacturers in the field of geosynthetics are feeling the urge to provide green alternatives and promote sustainability. The establishment of the European

Association of geosynthetic product manufacturers (AEGM) exemplifies their collective effort to promote the use and their sustainable practices on a European scale.

Vertical drain manufacturers are also actively seeking new materials that reduce the overall environmental impact, such as the carbon footprint and material usage, motivated by the impending introduction of CO_2 taxes and the growing popularity of environmental impact assessment tools in certain countries.

To provide a comprehensive understanding of the current state of vertical drain technology, this paper aims to address the evolving environmental awareness and provide an overview of the currently available sustainable alternatives.

2 THE USE OF VERTICAL DRAINS

The vertical drain plays a crucial role in facilitating the short consolidation period during the construction of embankments, typically within a year. These drains are designed to expedite the process of soil consolidation, while ensuring stability and durability of the embankments. However, once the intended functional period is complete, the vertical drains remain embedded in the soil beneath the groundwater level.

Unlike other plastic products that contribute to environmental pollution, vertical drains have minimal impact in terms of microplastic pollution. They rarely come into contact with the environment, as they are situated beneath the pavements or structures. Their exposure to the environment occurs only during soil excavation. Additionally, a significant portion of the drains extracted during excavation are reused in other construction projects or required to be removed, further minimizing waste.

From a technical and environmental standpoint, vertical drains are considered to be safe and sustainable. Therefore, when civil engineers are questioned about the future of vertical drains, concerns about their impact on the environment are often non-existent. This is however slowly changing.

3 ENVIRONMENTAL AWARENESS

Despite the relatively low environmental impact and functional application, there is a growing awareness among civil engineers about the potential environmental consequences and potential consequences for future generations. In the Netherlands, a shift is ongoing towards the use of environmentally friendly alternatives, which has prompted ongoing research into the use of biobased and compostable/degradable materials as substitutes for the current materials used.

The research is particularly focusing on materials compatible with common PVD extrusion devices in relation to the specific characteristics that a PVD needs to possess. The material should be strong enough to withstand ground pressures, flexible enough to accommodate settlement and the installation processes, and have a low creep component to ensure long-term discharge and performance.

Finding biodegradable materials that meet all of these criteria has been challenging. After years of testing, at least three types of PVDs made from (partly) biobased plastics have now entered the market that meet the aforementioned characteristics. Several successful projects have already been executed in the Netherlands. These drains, based on biobased plastics, will be called biodrains in the remainder of the paper.

In addition to these recent developments with biodrains, there is another type of natural drain, the fiber drain, that has been available for over 30 years but has not gained widespread popularity due to the higher costs and lower discharge properties compared to the regular PVD. This drain is manufactured using jute and coconut materials, making it 100% biobased. The production mainly takes place in South East Asia and India, and while this drain has been used in projects across Asia, it has yet to be adopted on other continents except through research programs (Nguyen 2020).

The following chapters will separately discuss both types of drain: The biodrain and the fiber drain.

4 BIODRAINS

Drains made of biobased plastics are now available from various PVD manufacturers. These drains are degradable under industrial conditions, typically at temperatures of around 60 degrees Celsius. However, claims that these drains are fully compostable can be misleading, as they are often left underwater after construction, not exposed to UV radiation, and subject to low oxygen and low temperatures. In such conditions, the drain will retain its form, similar to other plant materials found in organic soils. Some degradation, especially strength (Borelbach et al 2023) may occur due to bacteria, but it can generally be assumed that the drains will remain in the ground for the required service life.

Biodrains, due to the use of the same extrusion production process as regular PVDs, have a similar look, feel, and functionality. All biobased PolyLactic Acid (PLA) drain types contain various additives in addition to the PLA base. These additives, which can

be oil-based or of different natural origins, are necessary to improve extrusion characteristics, provide sufficient strength during installation, and meet compression, flexibility, and creep requirements to ensure adequate discharge capacity over the drains' lifespan. However, the additives and properties of PLA are not as optimized for PVD production compared to other polymers. Consequently, the current versions of biodrains are often thicker and heavier than regular oil-based drain types.

As a result of their increased weight and changed material properties with a higher stiffness and lower creep, biodrains tend to over-perform in terms of discharge capacity. In some cases, they can provide 300% to 400% higher discharge compared to regular PVD types, depending on testing pressures and increasing with a greater confining pressure due to the material properties. Refer to Table 1 for testing results of one of the biodrain types available in the market.

Table 1. Measured discharge capacity in the laboratory of Geotechnics in Amsterdam under 120kPa loading and 0.1 gradient after 28 days.

Drain type	Discharge capacity [ml/s]
MD7407	75
Corrugated biodrain	220
Fiber drain	8

5 NATURAL PREFABRICATED VERTICAL DRAIN OR FIBER DRAINS

Natural vertical drains, which were initially patented by NUS and researched by Professor Chew in Singapore, are currently manufactured in India, Bangladesh, and Indonesia. These drains typically consist of two materials: coconut ropes/coir encased by jute filters. Unlike regular drain types, natural fiber drains do not have free flow channels but rely on the natural fibers, or the space between the coirs to facilitate water drainage. As a result, the discharge capacities of these drains are generally lower compared to conventional PVD or biodrains (refer to Table 1).

Several researchers have published studies on the use of fiber drains, including Lee et al. (1994), Venkatappa Rao et al. (2000), Kim and Cho (2008), Lekha and Kavitha (2006), Vinod and Minu (2010), and Artidteang et al. (2015). Nguyen (2018) summarized the development of multiple drain types over the years, ranging from round drains to drains with 4 to 16 coir strands to a coconut coir mat wrapped in a jute filter. Despite the research conducted, all fiber drain types have achieved more or less similar discharge capacities, with no significant improvement over time. Reported values range between 5 and 15ml/s, depending on the confining pressure. This aligns with the measurements presented in Table 1. Researchers are still trying to find the best way to draw clear conclusions on the most optimal type for the market due to the complex mix of parameters influencing the success, such as drain costs in relation to manufacturing efficiency, confusion regarding the best material and structure options, natural variations in material, and uncertainty about biodegradation over time (Nguyen, 2018).

Field observations have shown rapid degradation of jute drains in some cases (Kim 2008), while other instances demonstrate no significant biodegradation during soil consolidation. This was confirmed by a field trial conducted in Australia and described by Nguyen et al in 2020. Despite the large differences in discharge capacity and concern on the biodegradability, the fiber drain performed remarkably well compared to the regular drain type, with similar settlement rates during the process of consolidation.

When a PVD type with a very low discharge manages to achieve similar settlement rates and results compared to an already well-optimized regular PVD, it raises two possibilities. Either the discharge capacity of the regular PVD type used in the test is very low, making it behave similarly to the fiber drain, where discharge is not highly affected by kinking, or the discharge capacity of regular PVD types is highly over dimensioned. To gain a better understanding and further optimize PVD types or explore drains made of natural materials, additional trial fields and a deeper understanding of PVD behaviour in relation to the consolidation process are required. An additional test is therefore currently being performed by the authors in the Netherlands where different biobased drain concepts are tested on their performance in a large field test.

6 THE CO2 TAXED FUTURE IN EUROPE

As CO_2 emissions will be taxed in the future in the European Union, it is also essential to evaluate the CO_2 balance of the PVD. The European Union is planning to tax emissions with rates mentioned as high as 125 euros per ton of CO_2. Similarly, the municipality of Amsterdam is considering to price the CO_2 contribution as high as 418 euros per ton in their tenders.

Regular PVDs have a CO_2 footprint of approximately 0.15 to 0.2 kg per meter of drain. This translates to a CO_2 tax of 2.5 cents for the European tax rate of 125 euros per ton of CO_2 and 8.4 cents according to the Amsterdam calculation model. These

numbers provide additional insight into the cost differences that may arise between regular drains and alternative options, such as biodrains, when CO_2 costs will be incorporated into tender processes.

The tested biodrain type demonstrated a reduction of over 35% in CO_2 footprint. This reduction is valued at 3 cents. It also means that when CO_2 costs are incorporated, the biodrain can only be 3 cents more expensive in the Amsterdam model to arrive at the same cost price. When it is more expensive, the regular drain with CO_2 costs included will be cheaper.

Fiber drains, on the other hand, exhibit a negative CO_2 footprint due to the storage of CO_2 in the plant-based material. These drains can be valued at and may become easily 10 cents or more expensive when CO_2 costs are included.

Therefore, it is crucial for future projects to consider the CO_2 costs and emissions associated with different drain options as part of their overall sustainability assessment and decision-making processes. By incorporating these factors, companies can make more informed decisions and contribute to a greener and more environmentally responsible construction industry.

It is up to manufacturers, however, to find ways to make the biobased solutions also financially attractive and to expand their research.

7 CONCLUSION

In order to meet the needs of the present without compromising the ability of future generations to meet their own needs, clients and the market must make informed choices regarding the available drain options. Suppliers and installers have already taken steps to offer clients a range of PVD types, from traditional polymeric PVDs to alternatives such as fiber drains. At the same time, they are actively working towards reducing the current price gap, making their environmentally friendly products more affordable. The adoption of different drain types will vary from country to country, depending on environmental awareness and regulations such as the CO2 tax being implemented in Europe.

By considering the CO2 footprint, material usage, and the overall environmental impact of different drain options, the construction industry can contribute to a sustainable future. Making responsible choices in drain selection will not only help mitigate climate change but also align with the growing demand for environmentally friendly construction practices.

The sustainable future of vertical drains relies on finding a product with the lowest CO_2 footprint and material usage, while maintaining a competitive price compared to conventional drains. Further research is therefore necessary to gain a better understanding of the discharge capacity of fiber drains in relation to current standards. For the biodrains it is key to reduce on the material usage and find ways to arrive at similar discharge capacities within the boundaries set in this paper. This will ensure that biodrains and fiber drains can become a mature green alternatives that eliminates the use of plastic in conventional PVD types.

REFERENCES

Artidteang, S., Bergado, D.T., Chaiyaput, S. and Tanchaisawat, T. (2015). Embankment reinforced with limited life geotextiles on soft clay. *Proceedings of the Institution of Civil Engineers - Ground Improvement*, 168(2): pp. 130-143. DOI: 10.1680/grim.13.00014.

Borelbach, P.; Kopitzky, R.; Dahringer, J.; Gutmann, P. Degradation Behavior of Biodegradable Man-Made Fibers in Natural Soil and in Compost. *Polymers* 2023, 15, 2959. DOI: 10.3390/polym15132959.

Kim, J.H. and Cho, N. (2008). Pilot scale field test for natural fiber drain. *Proceedings of the 4th Asian Regional Conference on Geosynthetics*. pp. 409-414. DOI: 10.1007/978-3-540-69313-0_78.

Lee, S.L., Karunaratne, G.P., Ramaswamy, S.D., Aziz, M.A. and Das Gupta, N.C. (1994). Natural geosynthetic drain for soil improvement. *Geotextiles and Geomembranes*, 13(6–7): pp. 457-474. DOI: 10.1016/0266-1144(94)90008-6.

Lekha, K.R. and Kavitha, V. (2006). Coir geotextile reinforced clay dykes for drainage of low-lying areas. *Geotextiles and Geomembranes*, 24(1): pp. 38-51. DOI: 10.1016/j.geotexmem.2005.05.001.

Nguyen T.T. (2018) On the use of biodegradable natural fibre drains to stabilise soft soil – experimental and theoretical studies PhD, Available at: https://ro.uow.edu.au/theses1/214.

Nguyen, T. Trung., Indraratna, B. & Baral, P. (2020). Biodegradable prefabricated vertical drains: from laboratory to field studies. *Geotechnical Engineering*, 51 (2), 39-46. RIS ID 143928.

Venkatappa Rao, G., Sampath Kumar, J.P. and Banerjee, P.K. (2000). Characterization of a braided strip drain with coir and jute yarns. *Geotextiles and Geomembranes*, 18(6): pp. 367-384. DOI: 10.1016/S0266-1144(00)00006-6.

Vinod, P. and Minu, M. (2010). Use of coir geotextiles in unpaved road construction. *Geosynthetics International*, 17(4): pp. 220-227. DOI: 10.1680/gein.2010.17.4.220.

Proceedings of the XVIII ECSMGE 2024
GEOTECHNICAL ENGINEERING CHALLENGES
TO MEET CURRENT AND EMERGING NEEDS OF SOCIETY
© 2024 the Authors
ISBN 978-1-032-54816-6
DOI 10.1201/9781003431749-427
Open Access: www.taylorfrancis.com, CC BY-NC-ND 4.0 license

ECSMGE 24
XVIII EUROPEAN CONFERENCE ON SOIL MECHANICS AND GEOTECHNICAL ENGINEERING

Giant shear box tests on recycled 6F5 for tracked plant platforms

Tests de boîte de cisaillement géante sur 6F5 recyclé pour plates-formes d'usines sur chenilles

S. Divall*, M.C.R. Davies, S.E. Stallebrass
City, University of London, London, UK

J. Mahony, S. Quintavalle, J. Bowen-Bravery, T. Johnson-Watts, R. Mulligan
Skanska, Costain, STRABAG S1 & S2 Joint Venture, London, UK

**sam.divall@city.ac.uk*

ABSTRACT: The use of recycled 6F5 aggregate is widely seen as a necessary option in civil engineering projects to meet carbon offset targets. This material is used for a range of applications such as load distribution platforms, capping layers, sub-bases and general backfill. It can consist of fresh aggregate or recycled components and its engineering characteristics can, therefore, vary widely. Independent of the application, it is important to characterise accurately the material properties of the aggregate in order to guarantee safe, economical solutions. The angle of friction is often the main parameter required for geotechnical design and usually obtained by direct shear tests. However, when using standard laboratory equipment there is an upper limit to the size of particle that can be tested, rendering such apparatus inappropriate for obtaining the shear parameters of 6F5 aggregate, which has a specified size fraction of 0-125 mm. The paper describes the design of a series of giant shear box tests, with a shear plane area 2.25 m^2, on recycled 6F5 together with details of the testing procedure and the results of these full-scale tests.

RÉSUMÉ: L'utilisation de granulats 6F5 recyclés est largement considérée comme une option nécessaire dans les projets de génie civil pour atteindre les objectifs de compensation carbone. Ce matériau est utilisé pour une gamme d'applications telles que les plates-formes de répartition des charges, les couches de forme, les sous-couches et le remblai général. Il peut être constitué de granulats frais ou de composants recyclés et ses caractéristiques techniques peuvent donc varier considérablement. Quelle que soit l'application, il est important de caractériser avec précision les propriétés mécaniques du granulat afin de garantir des solutions sûres et économiques. L'angle de frottement est souvent le principal paramètre requis pour la conception géotechnique et est généralement obtenu par des essais de cisaillement direct. Cependant, lors de l'utilisation d'un équipement de laboratoire standard, il existe une limite supérieure à la taille des particules qui peuvent être testées, ce qui rend un tel appareil inapproprié pour obtenir les paramètres de cisaillement de l'agrégat 6F5, qui a une fraction granulométrique spécifiée de 0 à 125 mm. L'article décrit la conception d'une série d'essais en boîte de cisaillement géante, avec une surface de plan de cisaillement de 2,25 m^2, sur du 6F5 recyclé, ainsi que des détails sur la procédure d'essai et les résultats de ces essais à grande échelle.

Keywords: Piling platforms; full-scale testing; carbon reduction.

1 INTRODUCTION

During large infrastructure projects, such as the rail infrastructure project HS2 (one of the largest and most complex infrastructure projects ever undertaken in the UK), to facilitate the construction of the permanent works contractors must utilise temporary civil engineering structures (e.g. load distribution platforms, capping layers, sub-bases and general backfill). In the UK, the material widely used to create these structures is "recycled 6F5 aggregate". 6F5 is defined as any recycled aggregate made up of crushed hardcore materials including crushed concrete. In general, this crushed material ranges in size from 0 to 125 mm (BSI, 2018). The description accompanying material of this strength is "specified well-graded material laid and fully compacted to DoT Specification and protected below with geotextile". A characteristic angle of friction, φ', is required for determining the thickness of these tracked plant platforms. The recognised range that the industry usually assume is generally between 30°-45° degrees. BRE 470 (2004) recommends a maximum value of 45° for "strong" (rock compressive strength, q_c > 50 MPa) particle strength materials. An alternative industry practice guide, TWf (2019), states that values of φ' > 45° can

only be used if suitably high quality controls for design, inspection and maintenance are in place. However, this can only be achieved if it is possible to obtain reliable values of the shear strength of the fill.

The inherent issues of both variability and particle size associated with 6F5 aggregate present significant challenges in measuring its characteristic shear strength parameters. It is not possible to obtain these parameters using standard apparatus because the particle size is too great. Even commercially available "large" direct shear boxes, which have plan dimensions of 300 mm x 300 mm, are too small to meet box diameter to particle size ratios recommended in both ASTM Standards (D3080, 2011) and BSI (1990). The heterogeneity of 6F5 aggregate results in it not being possible to use the technique of testing samples of the material in which the grading curve has been scaled down to allow testing in standard apparatus (Tanghetti, 2021). Therefore, to obtain reliable values of the shear strength parameters of 6F5 aggregate it is necessary to test the material in suitably large – non-standard –shear apparatus.

This led to a collaboration between SCS Railways (Skanska, Costain, STRABAG S1 & S2 Joint Venture) – one of the joint venture organisations constructing HS2 - and City, University of London to develop a reliable method to measure the characteristic shear strength parameters of 6F5 aggregate. This study was based on testing 6F5 aggregate obtained from a number of HS2 sites in a series of direct shear tests using the Giant Shear Box facility developed at City, University of London, Tanghetti *et al.* (2019, 2021).

2 TEST DETAILS

2.1 Giant Shear Box facility

The City, University of London Giant Shear Box facility (Figure 1) has been described in Tanghetti *et al*. (2019 and 2021). A series of comparative tests reported by Tanghetti (2021) provided confidence in the use of the large shear box for testing large (≤ 100 mm) particle size materials at higher values of normal stress, which are consistent with the range of stresses typically encountered in engineering practice. The facility comprises of a large split box (internal dimensions 1.5 m x 1.5 m x 1 m) constructed from 254x254x132 UC steel sections. The upper half of the box is prevented from moving horizontally during shear by a reaction frame, while the bottom half is free to move horizontally in order to shear the sample. To minimise friction between the top and bottom of the box during shearing, Acetal sheets are fixed to the lower and upper flanges of the top- and bottom-halves of the box, respectively. Prior to testing standard machine grease is applied to these sheets to provide additional lubrication.

The system to facilitate the movement of the bottom half consists of three I-beams, which are firmly attached to a strong floor in the laboratory and have the role of providing runways in which machine skates can slide. This arrangement retains the bottom half of the shear box laterally to ensure horizontal movement occurs in the direction of shear only.

The shear force is applied to the sample through four 500 kN hydraulic jacks (maintained in position by a reaction frame), which push the bottom section of the box in a horizontal direction creating a horizontal shear plane. The normal load is applied by a single 5 MN hydraulic jack fixed to a beam that is bolted to the reaction frame. The vertical stress is applied to the sample via a platen comprising a stiffened 30mm thick plate designed to minimise deflections even at the maximum applied stress.

During testing potentiometers measured vertical displacement in four positions on the loading platen and the horizontal displacement in two positions on the bottom half of the box. Two load cells mounted between the inside of the reaction frame and the top half of the box measured the horizontal force applied to the shear plane during shear and resisted by the stationary top-half of the box. In addition, an in-line pressure transducer also recorded the hydraulic pressure required to move the bottom-half of the box by the hydraulic jacks. All measurements were recorded on a bespoke LABVIEW data logger.

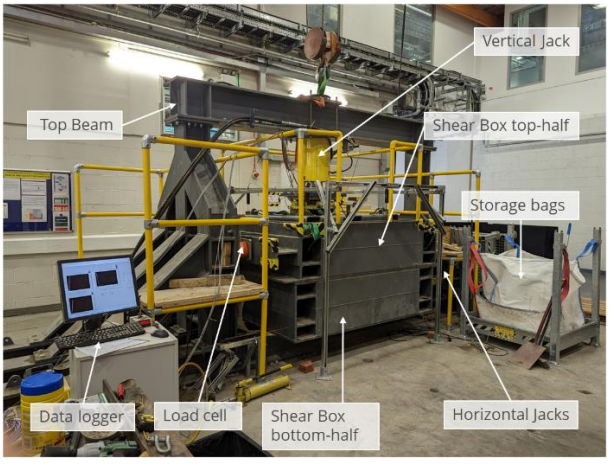

Figure 1. View of Giant shear box facility.

2.2 Material

The recycled 6F5 aggregate reported in this paper was described as "medium level control". This description referred to both the particle size distribution and the constituent materials in the aggregate. The distribution by weight of the constituent parts of this aggregate

together with the particle size distribution are presented in Figures 2(a) and 2(b), respectively. This data was obtained by sampling, conducted by SCS Railways, directly from the construction site prior to the material being bagged for transporting to City, University of London for testing.

The specified limits for the grading of the material are plotted in Figure 2(b) together with the grading curve for the material sampled for testing. From this it can be seen that the "medium control" material is within the contractually agreed limits for recycled 6F5. However, there is still considerable variation within these limits. The constituents of the batches of 6F5 from which material was taken for shear testing, presented in Figure 2(b), indicate that the aggregate consisted of 45-55% "concrete or concrete products" and roughly 25% "clay masonry units" but only 20% "unbound aggregates". In Figure 2(a) the constituents given are; R_c - "Concrete, concrete products & concrete masonry", R_u - "Unbound aggregate, natural stone & Hydraulically bound aggregates", R_b - "Clay masonry units (i.e. bricks & tiles), calcium silicate masonry units & aerated non-floating concrete, calcium silicate", R_a - "Bituminous Material", R_g - glass, X - "Other: Cohesive (i.e. clay & soil), gypsum plaster, miscellaneous - metals (ferrous & non-ferrous), non-floating wood" and FL - "Floating Particles - given as the percentage remaining".

2.3 Sample preparation

Material was delivered to City, University of London in five 1 m^3 capacity full drop flap discharge bulk bags. Each bag was filled with approximately 800 kg of material but was weighed prior to being placed in the shear box to obtain the exact mass of the sample.

Samples were prepared by compacting the 6F5 aggregate in the box in layers after having first removed any aggregate over 125 mm or metal rebar components. To ensure each layer was uniform it was compacted using a small wacker-plate that was passed over the material layer for 2 minutes. The sample was formed of five compacted layers with an average thickness of approximately 200 mm. Because of the size of the box, the first two layers were first prepared in the bottom half before the top half was put in position. Once the box was fully assembled the three further layers could be prepared. In this way, one of the layers spanned the interface between the two halves of the box.

Following the compaction of each layer its thickness was determined. The sum of the thicknesses together with the sum of the mass of each layer allow calculation of the voids ratio and density of the complete specimen to be determined. Once the fifth material layer had been prepared the loading platen was lifted into place and the vertical loading system assembled.

2.4 Testing

Following compaction of the samples and completion of the assembly of the apparatus. All samples were first loaded to a vertical stress of 500 kPa (at this stress level the force applied to the top cap was 1125 kN). This gave all samples the same pre-consolidation stress and therefore similar stress histories. Six samples were included in this series of tests. Three were sheared following the application of the peak vertical stress of 500 kPa and the other three following unloading to a vertical stress of either 200, 300 or 400 kPa.

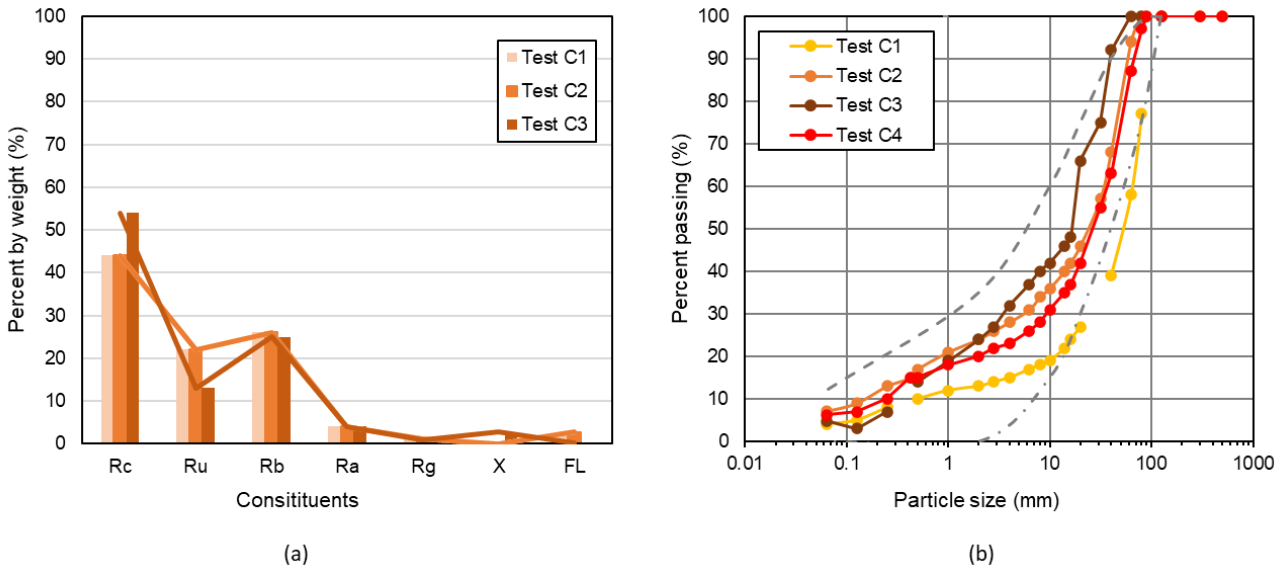

Figure 2. Recycled 6F5 (a) Constituents report and (b) Particle Size Distribution plot with acceptance limits.

Shearing commenced once all displacements following compression or unloading, as appropriate, had reached a plateau. The shear force was applied by increasing the pressure to the horizontal jacks at a constant rate causing the bottom-half of the Giant Shear Box to move. The test was stopped once both the horizontal potentiometers measured displacements greater than $\Delta h = 300$ mm (for a typical sample height $z = 1000$ mm this corresponded to a shear strain, γs, of $\Delta h/z = 30\%$). In most cases this allowed significant post peak shear strength behaviour of the samples to be observed

3 RESULTS

3.1 Application of vertical stress

Figure 3 shows the average settlement for one of the six samples, obtained from the measurements of the four vertical potentiometers, when the sample was subjected to an increased normal stress via the vertical jack. The loading was increased in a number of steps with settlement allowed to stabilise before the next increment of loading was applied. As indicated above, all six tests were pre-loaded to 500 kPa.

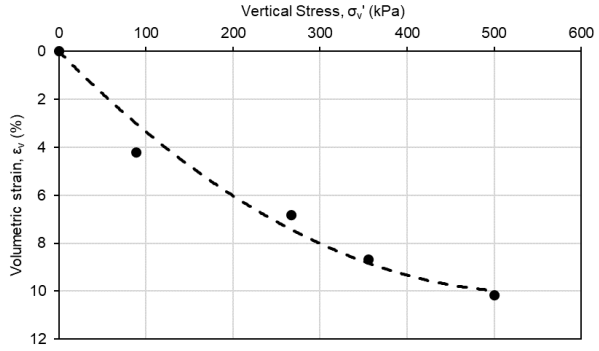

Figure 3. Sample behaviour during compression.

3.2 Shearing

In direct shear box tests the area of the shear plane decreases with displacement and, consequently, although the normal force acting on the top cap of the specimen remains constant, the stress acting on the shear plane will increase. Similarly, in the analysis of the result of direct shear tests the variation of the area of the shear plane with displacement is accounted for in the calculation of shear stress. Therefore, to quantify the relationships during shear between shear stress and shear strain, γ_s, or volumetric strain, ε_v, values of shear stress, τ, should be normalised by the vertical stress, σ', at the same displacement.

Figure 4 shows the results of a shear test conducted at an initial vertical stress (i.e. before shearing commenced) of 200 kPa having been initially compress to and unloaded from 500 kPa. As would be expected from a soil that has been compressed to a significantly higher value of stress than its *in-situ* state, this sample displays a "dense" (or "dry of critical") response to shearing. This is manifest by dilation and a distinct peak value of normalised shear stress. Post peak the rate of dilation decreases and at the end of the test both the normalised shear stress and the volume of the specimen were approaching a steady state. At this stage the Giant Shear Box had reached the end of travel and so it was not possible to achieve critical state.

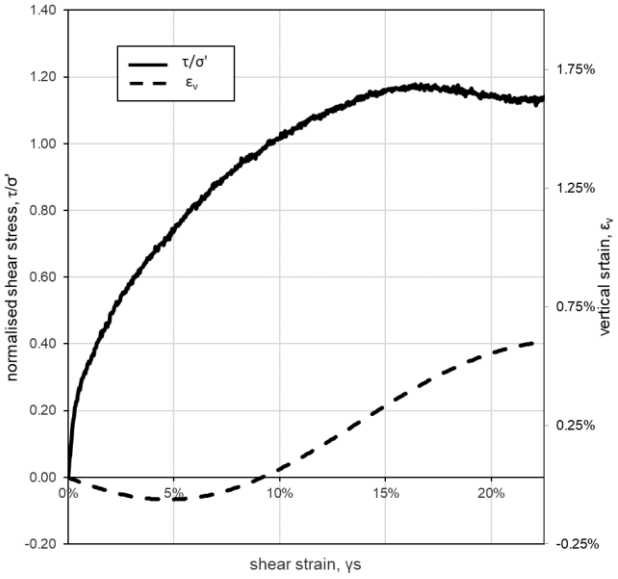

Figure 4. Sample behaviour during shearing.

3.3 Determination angle of friction, φ'

The peak shear stress and vertical effective stress for each of the six tests are plotted in Figure 5 from which it is possible to calculate the angle of friction for the 6F5 aggregate material. A line of best fit has been drawn (passing through the origin) and this yields an angle of friction of $\varphi' = 47.6°$. The coefficient of determination, R^2, of this line is 0.9923. Given the scale and variability of the material over the six tests this is considered to be a very good fit to the Coulomb friction model. This is demonstrated further by a confidence interval of $\varphi_{90}' = 47.6° \pm 2.1°$ at the 90% confidence level, which is also plotted in Figure 5.

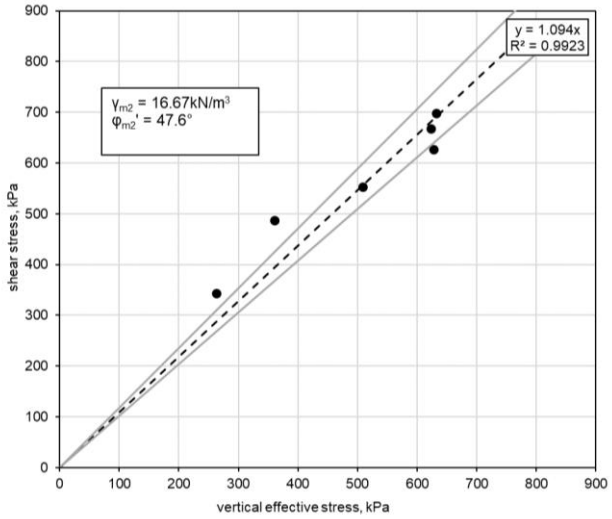

Figure 5. Peak angle of friction from six Giant Shear Box tests.

4 CONCLUSIONS

In geotechnical design it is important to characterise accurately the material properties of any aggregate to guarantee safe, economical solutions. In this paper a series of Giant Shear Box tests were carried out at City, University of London with SCS Railways to ascertain the characteristic angle of friction, φ', of recycled 6F5 aggregates.

Six tests were conducted at a range of vertical stresses on the recycled 6F5 aggregate taken from some HS2 construction sites. Each test used approximately 3.5 tonnes of material and showed a very consistent set of results.

The results indicate the characteristic angle of friction, φ', was found to be 47.6° and with a confidence interval of $\varphi_{90}' = 47.6° \pm 2.1°$ at the 90% confidence level. Although the quality of the material was considered to be a "medium" level of control (i.e. test results reviewed by designer together with regular inspection and maintenance, as specified in TWf, 2019), the material showed a higher value than the 45° generally accepted as the maximum value specified in current guidance. This angle of friction, φ', if adopted during the design phase, has the potential to reduce the tracked plant platform thickness and potentially have a saving in terms of material, cost and carbon.

ACKNOWLEDGEMENTS

The authors are grateful for the financial support provided by HS2 Innovation Execution Plan and SCS Railways (Skanska, Costain, STRABAG S1 & S2 Joint Venture).

REFERENCES

ASTM D3080/D3080M (2011). Standard Test Method for Direct Shear Test of Soils Under Consolidated Drained Conditions. ASTM International. West Conshohocken, PA, USA.

BRE (2004). Working platforms for tracked plant. BR 470.

BSI (1990). BS EN 1377-7:1990 - Methods of test for soils for civil engineering purposes - Shear strength tests (total stress), British Standards Institution.

BSI (2018). BS EN 13285:2018 - Unbound mixtures. Specifications, British Standards Institution.

Tanghetti, G. (2021). Stability of Working Platforms for Tracked Plant. Doctoral Thesis, City, University of London.

Tanghetti, G., Davies, M. C. R. and Goodey, R. J. (2021). Comparison of small- and full-scale shear box tests on large particle size aggregate, In: *Proceedings of the 20th International Conference on Soil Mechanics and Geotechnical Engineering, Sydney 2021*, Sydney, Australia, pp. 75-80.

Tanghetti, G., Goodey, R. J., Divall, S., McNamara, A. M. and McKinley, B. (2019). Design and development of a large shear box for testing working platform material, In: *Proceedings of the XVII ECSMGE-2019*, Reykjavik, Iceland, pp. 1-7.

TWf (2019). TWf2019:2 Working Platforms - Design of granular working platforms for construction plant: A guide to good practice. Temporary Works Forum, c/o Institution of Civil Engineers, One Great George Street, London, SW1P 3AA, England.

Proceedings of the XVIII ECSMGE 2024
GEOTECHNICAL ENGINEERING CHALLENGES
TO MEET CURRENT AND EMERGING NEEDS OF SOCIETY
© 2024 the Authors
ISBN 978-1-032-54816-6
DOI 10.1201/9781003431749-428
Open Access: www.taylorfrancis.com, CC BY-NC-ND 4.0 license

ECSMGE 24
XVIII EUROPEAN CONFERENCE ON SOIL MECHANICS AND GEOTECHNICAL ENGINEERING

Forensic evaluation of gabion walls

Évaluation forensique des murs de gabions

M. Duffy-Turner
Coffey Geotechnics, Manchester, United Kingdom

M.G. Winter*
Winter Associates, Kirknewton, Scotland, United Kingdom

I.M. Nettleton
Coffey Geotechnics, Manchester, United Kingdom

P. Liew
National Highways, Birmingham, United Kingdom

**mwinter@winterassociates.co.uk*

ABSTRACT: The effective design, specification and construction of geotechnical assets or Special Geotechnical Measures (SGMs) is critical to the efficient operation of the National Highways Strategic Road Network (SRN) in England. Given the required performance of the SRN in terms of resilience, reliability, redundancy and recovery it is essential that SGMs are themselves reliable in terms of performance and life; resilient to external conditions such as earthworks deterioration and extraordinary conditions (e.g. climate change). Around 100 different types of SGMs are used on the SRN and the early installations of some SGMs are approaching the end of their design life and the design, specification and application of many of these techniques is based on limited studies. A series of forensic examinations of gabion walls in various settings on the SRN was undertaken and the results used to develop advice on the design, construction, inspection, maintenance and decommissioning of such structures and to make a series of recommendations on their future use. Principle amongst these is that the evidence suggests that when properly designed, specified, constructed and maintained, including an appropriate inspection regime, Gabion Walls can meet the required design life of such SGMs.

RÉSUMÉ: La conception, la spécification et la construction efficaces d'actifs géotechniques ou de mesures géotechniques spéciales (SGM) sont essentielles au fonctionnement efficace du réseau routier stratégique national (SRN) en Angleterre. Compte tenu des performances requises du SRN en termes de résilience, de fiabilité, de redondance et de récupération, il est essentiel que les SGM soient eux-mêmes fiables en termes de performances et de durée de vie; résistant aux conditions externes telles que la détérioration des terrassements et les conditions extraordinaires (par exemple, le changement climatique). Environ 100 types différents de SGM sont utilisés sur le SRN et les premières installations de certains SGM approchent de la fin de leur durée de vie et la conception, la spécification et l'application de bon nombre de ces techniques sont basées sur des études limitées. Une série d'examens médico-légaux des murs de gabions dans divers contextes sur le SRN a été entreprise et les résultats ont été utilisés pour élaborer des conseils sur la conception, la construction, l'inspection, l'entretien et le démantèlement de ces structures et pour formuler une série de recommandations sur leur utilisation future. Le principe parmi ceux-ci est qu'il n'y a aucune preuve convaincante que lorsqu'ils sont correctement conçus, spécifiés, construits et entretenus, y compris un régime d'inspection approprié, les murs de gabions ne peuvent pas respecter la durée de vie requise de ces SGM.

Keywords: Geotechnical; asset; retaining; wall; gabion.

1 INTRODUCTION

This paper provides a brief summary of a study that investigated gabion walls. Typically, Gabion Walls are used on the Strategic Road Network (SRN) as relatively low height (generally less than 5m high) retaining walls at the toe of embankments, often to reduce land take. They are often, but not always, adopted during the construction phase to deal with unforeseen site constraints as they arise. This can lead to rapid decision-making and an apparent lack of design and/or construction control and supervision.

This work forms part of a wider study (Duffy-Turner et al., 2022a) of the performance of geotechnical asset types, known as Special Geotechnical Measures (SGMs), including gabion walls (Duffy-Turner et al., 2022b), block walls (Winter et al., 2022), counterfort drains (Nettleton et al, 2022) and soil nails (Duffy-Turner et al., 2022c).

An account is given of issues identified from gabion wall inspections on the SRN along with issues for their design, construction, inspection, maintenance and recommendations for their future use.

2 ISSUES IDENTIFIED

Two types of gabion baskets were observed on the network: woven gabions and welded mesh gabions. Welded mesh gabions were more prevalent with nine out of 13 identified during the inspections. A wide variety of issues were identified with both types of gabion walls, and these included but were not restricted to the issues that follow.

A wide range of stone fill materials was observed, ranging from a granite, that clearly conformed to the requirements of the Manual of Contract Documents for Highway Works (MCHW), to a shale (argillaceous) that did not and was showing significant signs of deterioration. Other seemingly unsuitable fill materials observed included chalk and waste-derived concrete, asphalt and brick.

The fill used in the gabion baskets pictured in Figure 1 is also oversized compared to the allowable limit in the MCHW. This undoubtedly contributed to the overall unsatisfactory condition of the baskets which were observed to be barely containing the fill due to distortion and breakage of both the wire and the fastenings. The embankment slope retained by the gabion wall was observed to be moving which may be, in part, attributed to loss of support from the gabion below.



Figure 1. Oversize concrete fill leading to large voids within the gabion baskets. The oversize fill also means that the gabions have been unable to be properly sealed along the top, instead they are secured at pinch points where the fill allows (A42).

Other than where carefully placed, the use of oversized stone was associated with significant voids; voids were also associated with undersized material that could be readily removed from the baskets.

One issue that was observed for welded mesh baskets, but is relevant to both types, is that large voids can be created if filling of the baskets is not undertaken with great care. This can lead to movement of the fill within the basket during the service life putting undue strain on the mesh and the system used to join the panels of the baskets.

Significant corrosion was observed in a series of baskets that were placed in a marine environment. The damage was significant and in places the loss of fill exceeded 80% rendering the SGM ineffective in fulfilling its support function (Figure 2). While gabions can be used in marine environments care is required, especially in active tidal areas which can be challenging for all SGMs, and this indicates the importance of the correct specification selection for gabions and the materials they are formed from.



Figure 2. Gabions used within a marine environment leading to significant corrosion and loss of fill. (A27/M3 Junction).

Both galvanised and plastic-coated corrosion protection were observed and both good and bad instances were observed of each. The poor examples showed damage (possibly caused during transport, construction or in service) to the galvanised and plastic corrosion protection and on some of the welded baskets this could be peeled off using the observer's fingers without difficulty (Figure 3). Corrosion or damage to the corrosion protection was not observed on any of the woven baskets, albeit that the majority of the baskets inspected were of welded mesh. Clearly the loss of corrosion protection, is something of a problem in terms of durability and resilience with both the level of protection offered and the expected life of the wire reduced.

Significant apparent vandalism was also observed at two separate locations; vandalism was observed where the mesh appeared to have been cut and this had led to loss of fill and corrosion of the wire. Similarly, vehicle overrun appeared to be the cause of the damage

to another gabion wall (Figure 4) which was located in a layby alongside a dual carriageway.



Figure 3. Coating peeling away from the mesh on a welded gabion basket (A453).



Figure 4. Vehicle overrun appears to be the primary cause of the significant damage to low height Gabion Wall at this location (A453).

Notwithstanding the issues outlined above, gabion walls can be a resilient form of structure and can be beneficial in terms of the accommodation of movements without reaching either their serviceability or ultimate limit states. In the majority of cases, even where issues were observed, the overall gabion walls were performing as intended and this is one of the strengths of such SGMs.

3 DESIGN

The most comprehensive source of design guidance for gravity retaining walls (UK) is the British Standard BS 8002 the Code of Practice for earth retaining structures (BSI, 2015). When it comes to specifications the guidance is clear, with several sources of information for mesh products and geotextiles being available.

Design of gabions needs to take into account a number of different elements and these include layout of the baskets, type of gabion required (i.e. woven or welded), details of the wire and corrosion protection, type and size of fill and how it should be placed, the use of filter geotextiles and the environmental setting.

4 CONSTRUCTION

Some construction guidance is available for Gabion Walls in the British (BSI, 2015) and MCHW; however, this is not particularly comprehensive as it typically refers to the manufacturer's installation instructions. The manufacturer's instructions tend to be detailed and further guidance is readily available from them if required. The majority of manufacturers will also provide on-site advice.

Gabion units should be constructed to maintain tightness of mesh and, if woven, should be laced securely with wire. During construction, internal tie wires (bracing) should be inserted, and units tensioned in accordance with the manufacturer's instructions; failure to do can result in deformed gabions.

The rock fill placed in a gabion basket is integral to the durability of the wall and filling must be undertaken with care so as not to damage the baskets and the associated corrosion protection and also to ensure that the fill is placed such as there are no significant voids and that materials cannot escape or be removed from the exposed mesh face(s): e.g. baskets have been observed with incorrectly secured panel joins and significant voids.

Adequate and competent personnel for construction and supervision are essential for what is often an artisanal form of construction.

5 MAINTENANCE AND INSPECTION

Inspection and maintenance (and demolition) of the structure or SGM should be considered throughout the design, specification and construction process and plans should be prepared and incorporated into handover documentation.

Visual assessments will, in almost all cases, be the most likely mode of inspection and will require the application of sound engineering judgement. Gabion Walls shall be assessed qualitatively; however, it is noted that quantitative judgements are difficult since conditions will vary greatly with the quality of fill used, type of basket, age, subsoil conditions, drainage, geometry, weathering factors and local expectations. Things to inspect should include, but not be limited to, condition of the baskets and stitching or clips, type of corrosion protection and its condition, type and condition of the fill including weathering details, signs of bulging, leaning or spilling, existing loads and the condition of the retained slope, presence of vegetation

and environmental stresses such as vehicle impacts or surface water.

6 CONCLUSIONS AND RECOMMENDATIONS

Based on the walls inspected, which ranged from eight to 46 years old, the evidence suggests that when properly designed, specified, constructed and maintained, including an appropriate inspection regime, Gabion Walls can meet the required design life (120 years) of such SGMs. This is especially so when manufactured gabions are used in accordance with the manufacturer's recommendations.

Advice in standards and other related documents for Gabion Walls is well defined in some areas (such as specification) and limited in others (such as construction), which rely heavily on the manufacturer's own guidance. Through the course of this work a number of key issues have been identified and these are set out as recommendations below:

Recommendation 1: The most appropriate Gabion Wall type (woven or welded mesh) is selected for its application.

Recommendation 2: That the use of a filter/separator behind the wall should be required in all cases unless specific conditions allow for its omission.

Recommendation 3: That modifying gabion baskets on site shall be reserved for only those instances in which recognised manufacturers cannot produce a prefabricated suitable solution. Any modifications should be done in accordance with manufacturer's instructions and will require agreeing as part of the technical approvals process.

Recommendation 4: As part of the technical approval process, it should be ensured that a Gabion Wall solution is the most appropriate for the environment. This includes careful consideration before designing Gabion Walls within marine and especially tidal environments; adjacent to public footpaths where vandalism is a possibility; and low-height gabions placed in location where vehicle over-run is likely.

Recommendation 5: Gabion fill which does not meet the requirements of the MCHW should not be used on site unless there is a specific aesthetic requirement. Any deviations, including materials potentially susceptible to weathering, should be discussed in advance and agreed as part of the approvals process.

Recommendation 6: Issues identified during the site inspections highlighted that double corrosion protection was not always used and that the wire may be thinner than required; therefore, it is apparent that further enforcement of the specification is required by the Works Examiner.

Recommendation 7: Contractor self-certification of SGMs is not recommended. Observations on the SRN and of the wider UK infrastructure portfolio have found the self- certification process to be suboptimal.

Recommendation 8: Any inspections for the acceptance of constructed Gabion Walls should be undertaken prior to the site becoming fully operational and while items are visible and remedial measures can be readily implemented; and it is recommended that provision for early inspection should be built into the contract.

ACKNOWLEDGEMENTS

This work was undertaken through the National Highways Designated Fund scheme in support of the Geotechnical Resilience and the Geotechnical Climate Change Adaptation Programmes.

REFERENCES

British Standards Institution. 2015. BS 8002: Code of practice for earth retaining structures. British Standards Institution, London.

Duffy-Turner, M, Winter, M G, Nettleton, I M and Butler, G. (2022a). Forensic examination of Critical Special Geotechnical Measures. PPR 1032. TRL, Wokingham.

Duffy-Turner, M, Winter, M G and Nettleton, I M. (2022b). Forensic examination of Critical Special Geotechnical Measures: Gabion Wall Information Note. PPR 1036. TRL, Wokingham.

Duffy-Turner, M, Nettleton, I M, Winter, M G and Webber, I. (2022c). Forensic examination of Critical Special Geotechnical Measures: Soil Nail Information Note. PPR 1033. TRL, Wokingham.

Manual of Contract Documents for Highway Works.
MCHW 1: Specification for Highway Works.
MCHW 2: Note for Guidance on the Specification for Highway Works. (Accessed February 2022).
https://www.standardsforhighways.co.uk/mchw.

Nettleton, I M, Winter, M G and Duffy-Turner, M. (2022). Forensic examination of Critical Special Geotechnical Measures: Counterfort Drain Information Note. PPR 1034. TRL, Wokingham.

Winter, M G, Duffy-Turner, M. and Nettleton, I M. (2022). Forensic examination of Critical Special Geotechnical Measures: Gravity Block Wall Information Note. PPR 1035. TRL, Wokingham.

Proceedings of the XVIII ECSMGE 2024
GEOTECHNICAL ENGINEERING CHALLENGES
TO MEET CURRENT AND EMERGING NEEDS OF SOCIETY
© 2024 the Authors
ISBN 978-1-032-54816-6
DOI 10.1201/9781003431749-429
Open Access: www.taylorfrancis.com, CC BY-NC-ND 4.0 license

ECSMGE 24
XVIII EUROPEAN CONFERENCE ON SOIL MECHANICS AND GEOTECHNICAL ENGINEERING

Numerical modelling of suction bucket foundations subjected to axial loading

Modélisation numérique de fondations à godets aspirants soumises à un chargement axial

E. Eleftheriou*
National Technical University of Athens, Athens, Greece

D.M.G. Taborda
Imperial College London, London, United Kingdom

**eug.eleftheriou@gmail.com*

ABSTRACT: In multi-caissons foundations, the overturning moments are crucial for the design. The foundation resists to those moments through compression and tension. The tensile capacity of the upwind caisson should be considered in the design. To investigate this tensile behavior, numerical analyses are performed in PLAXIS 2D using a constitutive model which combines a Mohr-Coulomb failure criterion with the concept of state-parameter for sands. Initially, the tensile capacity of the suction bucket in fully drained and undrained conditions is investigated. The suction bucket is pulled out by applying small displacements, until its ultimate capacity is reached. Different values of densities are examined to monitor their effect on the ultimate capacity of the foundation. A parametric coupled consolidation analysis is then performed to study the impact of the permeability of the soil and of the pull-out rate. It is observed that the fully drained and undrained conditions constitute, respectively, the lower and upper boundaries of the ultimate tensile capacity of the foundation. The higher densities lead to higher tensile capacities. With faster loading rates and lower permeabilities, the response of the suction bucket approaches the undrained capacity, as suction is developed beneath the bucket.

RÉSUMÉ: En ce qui concerne les fondations à caissons multiples, les moments de renversement sont cruciaux pour la conception. La fondation résiste à ces moments par la compression et la tension. Cette capacité de traction du caisson en amont doit être prise en compte. Pour étudier ce comportement de traction, des analyses numériques sont effectuées dans PLAXIS 2D, en utilisant un modèle constitutif qui combine un critère de défaillance de Mohr-Coulomb avec le concept d'état-paramètre pour le sable. Premièrement, la capacité de traction du caisson dans des conditions entièrement drainées et non drainées est étudiée. Le caisson est retiré en appliquant de petits déplacements, jusqu'à ce que sa capacité ultime soit atteinte. Différentes valeurs de densités sont examinées pour surveiller leur effet sur la capacité ultime de la fondation. Une analyse paramétrique de consolidation couplée est ensuite réalisée pour étudier l'impact de la perméabilité du sol et du taux d'arrachement. Il est observé que les conditions entièrement drainées et non drainées constituent, respectivement, les limites inférieure et supérieure de la capacité de traction ultime de la fondation. Les densités plus élevées conduisent à des capacités de traction plus élevées. Avec des taux de chargement plus rapides et des perméabilités plus faibles, la réponse du caisson se rapproche de la capacité non drainée, étant donné qu'une aspiration se développe sous le godet.

Keywords: Suction bucket; suction caisson; offshore wind turbine, axial loading; tensile.

1 INTRODUCTION

Climate change constitutes one of the most challenging problems that our world has to deal with. Most of the countries have set the ambitious target of a net zero carbon footprint by 2050, in order to contribute to sustainability and to environmental protection. This target leads more and more to the use of renewable sources of energy as a replacement to fossil fuels. Offshore wind energy has gained in popularity during the last decades. The most common type of offshore foundation is a monopile, particularly for relatively shallow waters. Alternatively, a suction caisson, which is essentially an upturned bucket, can be used as part of the foundation system for offshore wind generators. In effect, in deeper waters, where the loads are higher and the turbines are larger, multiple caisson foundations can be used in tripod or tetrapod structures which include, respectively, three or four caissons. For offshore wind generators, the most important loads are the horizontal forces from waves, currents and wind and the overturning moments that these loads apply to the foundation. The latter are resisted by developing tension and compression forces

on the upwind and downwind legs of the structure (Byrne et al., 2002). In this paper the tensile behaviour of the upwind bucket is investigated by conducting parametric numerical analysis in PLAXIS 2D.

2 NUMERICAL MODEL

2.1 Geometry of the problem and ground conditions

The dimensions of the foundation were chosen so as to depict a realistic structure. The diameter (D) of the caisson is 8 m, while the length (L) of the skirt is equal to 4 m (L/D = 0.5). The thickness of the lid (t_{lid}) is 0.2 m and that of the skirt (t_{skirt}) is chosen as 0.05m. The skirt's thickness to diameter t_{skirt}/D ratio is, therefore, 0.625%. Due to the geometry and loading characteristics of the problem, axisymmetric numerical models were used in PLAXIS 2D.

The region modelled extends 44m (5.5D) from the axis of symmetry, while the bottom boundary of the domain is located at a distance of 40 m (10L) below the tip of the skirt. Such dimensions were observed to eliminate any boundary effects. The soil domain was discretised using 15-noded triangular elements, whereas the bucket was simulated using plate elements. The soil-structure interaction was modelled using interface elements, where the normal and shear stiffness values were adopted as $K_N = K_S = 10^6\ kN/m^3$. A Mohr-Coulomb failure criterion was employed to describe the strength of the interface, with an angle of shearing resistance matching that of the soil at Critical State, i.e. $\phi_{interface} = \phi_{CS} = 32°$ (see section 2.2).

A single layer of Dunkirk sand (see Zdravkovic et al. (2020) for additional information on this material) with the groundwater table at the surface (to correctly modelled the effective stress) was considered. The coefficient of earth pressure at rest, K_0, was assumed to be 0.47 ($= 1 - \sin\ \phi_{CS}$).

2.2 Materials and constitutive modelling

The soil was simulated using the IC MAGE M02 model (Taborda et al., 2021), implemented as a PLAXIS User-Defined Soil Model. This model combines a non-associated Mohr-Coulomb failure criterion with the state-parameter framework proposed by Been and Jefferies (1985). Thus, the strength and dilatancy of the material are direct functions of the state parameter, defined as $\psi = e - e_{CS}$ where e_{CS} denotes the void ratio at Critical State for the current mean effective stress level. According to this model, for denser-than-critical samples, i.e. $\psi < 0$, the peak strength of the material is larger than that at Critical State, with the material exhibiting plastic dilatancy. As the sample approaches Critical State, $\psi \to 0$, the available strength reduces to that at Critical State (quantified simply by ϕ_{CS}) and the dilation decreases to 0. Full details on the formulation of this model are given in Taborda et al. (2022). Within the elastic region, soil behaviour is defined by a hypoelastic model, according to which the shear modulus depends on void ratio, mean effective stress and deviatoric strain (Equation 1).

The selected constitutive model was calibrated for Dunkirk sand and validated by successfully reproducing the field tests on large diameter monopiles performed as part of the PISA project. The full set of parameters is listed in Table 1. The suction bucket's material is steel, with a unit weight of γ_{steel} = 78.5 kN/m^3, Young's modulus of E_{steel} = 200 GPa and a Poisson's ratio of ν = 0.3. It is assumed that it behaves elastically.

$$G_{max} = G_0 \frac{1.0}{0.3+0.7 \cdot e^2} \left(\frac{p'}{p'_{ref}}\right)^{0.5} \qquad (1)$$

Table 1. IC MAGE M02 parameters for Dunkirk sand.

Parameter	Value	Parameter	Value
Plastic behaviour		*Elastic behaviour*	
$e_{CS,ref}$	0.91	G_{ref}	88.6 MPa
λ	1.05	m_G	0.5
ξ	0.19	ν	0.17
ϕ_{CS}	32°	a	4E-04
k_1	1.5	b	1.40
k_2	-0.2	R_G	0.10
l_1	4.3	p'_{ref}	101.3 kPa
l_2	0.2		

2.3 Loading and type of analysis

The suction bucket is pulled upwards by applying a prescribed displacement at the centre of the lid until the maximum capacity is reached.

At first, fully drained and undrained elastoplastic analyses were performed to characterise the response of the suction bucket under these two limiting conditions. Different values of relative density (D_R = 60%, 75% and 90%) were also examined to assess the effect of the density on the tensile capacity of the foundation. Following that, a set of coupled consolidation analyses were performed. These analyses were performed for D_R = 75% and different values of permeability (k = 10^{-3}, 10^{-4}, 10^{-5} and 10^{-6} m/s), which were combined with various pull–out rates, in order to assess how close each combination of parameters was to drained and undrained conditions.

3 RESULTS

3.1 Drained and undrained conditions

The capacity curves for both drained and undrained conditions are depicted in Figure 1. As expected, the capacity in the undrained cases (dashed lines) is higher than that in the drained cases (solid lines) because in the latter the basic resistance of the suction bucket to the upward moving derives solely from the side friction developed inside and outside the skirt (Houlsby, Kelly & Byrne, 2005). As a result, the full capacity mobilises at very small displacements, with the lid of the suction bucket quickly losing contact with the foundation soil. Conversely, in undrained conditions, the resistance of the suction bucket to the upward movement is controlled by the suction within the soil that develops due to the tensile loading, which in this case was limited to a maximum negative pressure of 100 kPa. Therefore, the full separation between the bucket and the soil requires considerably larger displacements than those observed for the drained analysis, with a much higher capacity being mobilised. Clearly, the effect of the relative density of the soil is almost unnoticeable when the strength of the interface is assumed to be independent of the characteristics of the surrounding soil. This is in agreement with the fact the tensile axial capacity is controlled predominantly by the strength of the interface. Additional analysis, where the value of $\phi_{interface}$ was adjusted to reflect the changes in peak strength resulting from increases in relative density, showed a considerable spread in tensile capacity (Figure 2). These are described in Eleftheriou (2021) but are not reported herein for brevity.

3.2 Coupled consolidation analysis

3.2.1 Effect of pull-out rates

Fully coupled consolidation analyses were also conducted as part of this study, which required the definition of hydraulic boundary conditions. These consisted of considering the axis of symmetry as 'closed', thus preventing flow through it, whereas the top of the soil mass was assumed to remain at constant head, implying that water could flow across it as needed. Assuming a relative density of 75% and a relatively low value of soil permeability ($k = 10^{-6}\ m/s$), 6 different coupled consolidation analyses were performed. In each analysis, the maximum vertical displacement applied was 20 mm, with the duration per loading phase controlling the pull-out rate in mm/s, which varied between 0.000012 mm/s (or 1 day/mm) and 0.14 mm/s (or 0.00008 days/mm).

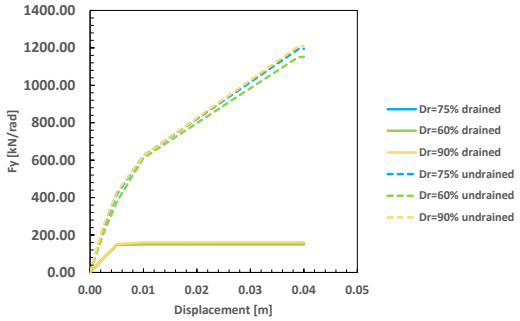

Figure 1. Comparison of capacity of drained and undrained conditions for different values of density.

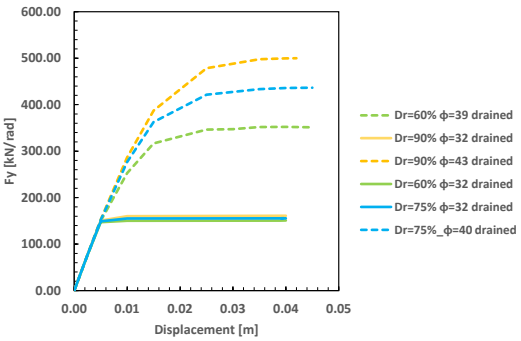

Figure 2. Capacity curves of the buckets for different values of density and different values of angle of shearing resistance at the interface – drained conditions.

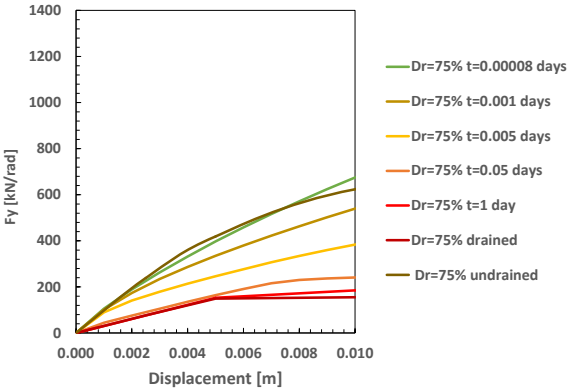

Figure 3. Tensile capacity of the suction bucket for different pull-out rates and a permeability of 10^{-6} m/s.

As shown in Figure 3, when the bucket was pulled out at the fastest rate (green line), the modelled response was similar to that of the fully undrained analysis. As the rate of loading decreases, the behaviour of the foundation approaches that observed for drained conditions (dark red line). Clearly, the tensile capacity increases as loading rate increases, while a higher displacement is needed in order for the tensile capacity to be fully mobilised.

3.2.2 Effect of permeability

Clearly, the transition from drained to undrained is not solely a function of the loading rate, with the permeability having a crucial role. For two distinct

pull-out rates (0.002 mm/s or 0.005 days/mm, and 0.14 mm/s or 0.00008 days/mm) different values of permeability were examined, covering the range typically observed for sand deposits: 10^{-6} m/s, 10^{-5} m/s and 10^{-4} m/s.

The obtained results are shown in Figure 4 (slow pull-out rate) and Figure 5 (fast pull-out rate). It is interesting to note the combined effects of the permeability and loading rate: for the larger pull-out rate, a permeability of 10^{-6} m/s was sufficiently low to guarantee undrained conditions. However, for the lower pull-out rate, this value of permeability leads to a response between those observed in the drained and undrained analyses. Similar patterns can be observed for the other values of permeability.

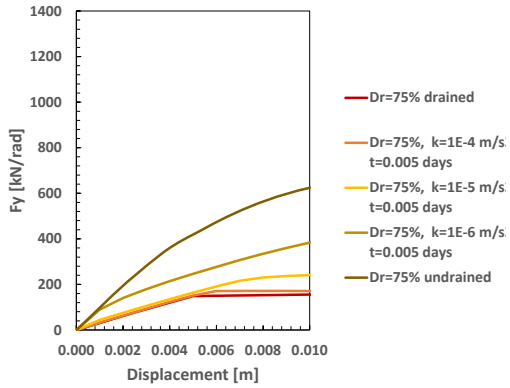

Figure 4. Tensile capacity of the suction bucket for different values of permeability (loading rate = 0.002 mm/s).

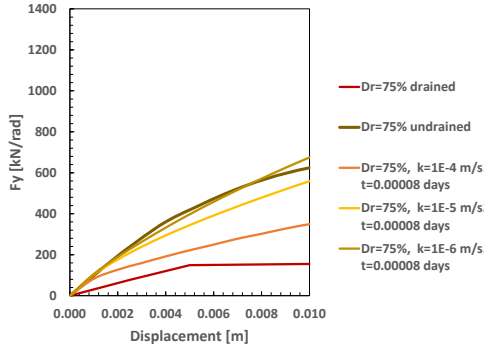

Figure 5. Tensile capacity of the suction bucket for different values of permeability (loading rate = 0.14 mm/s).

4 CONCLUSIONS

The objective of this paper was to determine the role of density, loading rate and permeability in the tensile capacity of a suction bucket, founded on a dense sand (Dunkirk sand). The obtained results show that the tensile axial behaviour of the suction bucket is primarily controlled by the characteristics of the interface. As a result, the density of the soil has negligible effect on the modelled response unless the changes in soil strength are reflected on that of the interface. As expected, the simulated behaviour is highly affected by the drainage conditions, with the undrained response being characterised by considerably higher capacity. Therefore, the balance between pull-out rate and permeability needs to be considered carefully as the two control the ability to prevent the build-up of negative pore water pressures below the lid. Both low pull-out rates and high permeability provide opportunity for water to flow around into the area beneath the lid, leading to conditions closer to those in drained analyses.

REFERENCES

Been, K., Jefferies, M. G. (1985) A state parameter for sands, *Géotechnique*, 35(2), pp. 99-112. http://doi.org/10.1680/geot.1985.35.2.99.

Byrne, B., Houlsby, G., Martin, C., Fish, P. (2002) Suction caisson foundations for offshore wind turbines, *Wind Engineering,* 26(3), pp. 145–155. http://doi.org/10.1260/030952402762056063.

Eleftheriou, E. (2021) Numerical modelling of suction bucket foundations subjected to axial loading. MSc thesis, Imperial College London, London.

Houlsby, G. T., Kelly, R. B., Byrne, B. W. (2005) The tensile capacity of suction caissons in sand under rapid loading, In: *Frontiers in Offshore Geotechnics, ISFOG 2005 - Proceedings of the 1st International Symposium on Frontiers in Offshore Geotechnics,* Perth, Australia, pp. 405–410.

Houlsby, G. T., Kelly, R. B., Huxtable, J., Byrne, B. W. (2006) Field trials of suction caissons in sand for offshore wind turbine foundations, *Géotechnique*, 56(1), pp. 3–10. http://doi.org/10.1680/geot.2006.56.1.3

Kelly, R. B., Houlsby, G. T., Byrne, B. W. (2006) Transient vertical loading of model suction caissons in a pressure chamber, *Géotechnique*, 56(10), pp. 665–675. http://doi.org/10.1680/geot.2006.56.10.665.

Taborda, D. M. G. , Kontoe, S. , Tsiampousi, A. (2021) IC MAGE Model 02 – simple state-parameter dependent model with isotropic small strain stiffness (Version 2.0). Zenodo. http://doi.org/10.5281/zenodo.5018863.

Taborda, D. M. G., Pedro, A. M. G., Pirrone, A. I. (2022) A state parameter-dependent constitutive model for sands based on the Mohr-Coulomb failure criterion, *Computers and Geotechnics*, 148, 104811. http://doi.org/10.1016/j.compgeo.2022.104811.

Zdravkovic, L., Jardine, R. J., Taborda, D. M. G., Abadias, D., Burd, H. J., Byrne, B. W., Gavin, K. G., Houlsby, G. T., Igoe, D. J. P., Liu, T., Martin, C. M., McAdam, R. A., Muir Wood, A., Potts, D. M., Skov Gretlund, J., Ushev, E. (2020) Ground characterisation for PISA pile testing and analysis, *Géotechnique*, 70(11), pp. 945–960. http://doi.org/10.1680/jgeot.18.PISA.001.

Proceedings of the XVIII ECSMGE 2024
GEOTECHNICAL ENGINEERING CHALLENGES
TO MEET CURRENT AND EMERGING NEEDS OF SOCIETY
© 2024 the Authors
ISBN 978-1-032-54816-6
DOI 10.1201/9781003431749-430
Open Access: www.taylorfrancis.com, CC BY-NC-ND 4.0 license

ECSMGE 24
XVIII EUROPEAN CONFERENCE ON SOIL MECHANICS AND GEOTECHNICAL ENGINEERING

Discrete element modelling of centrifuge experiments on pile jacking

Modélisation par éléments discrets des expériences de centrifugation sur le fonçage de pieux

A. Ezzeddine*, B. Cazacliu, P. Richard, R. Artoni
Univ Gustave Eiffel, MAST-GPEM, Bouguenais, France

L. Thorel
Univ Gustave Eiffel, GERS-CG, Bouguenais, France

**alice.ezzeddine@univ-eiffel.fr*

ABSTRACT: The cyclic behavior of pile foundations is studied using the Discrete Element Method (DEM) through simulated centrifuge experiments. The centrifugal acceleration enables reproducing real-scale problems on reduced models, while DEM provides access to microscopic information on the particles-structure interactions. First, a discrete model based on spherical particles involving elasticity, friction and rolling resistance is calibrated against monotonic, drained triaxial tests to reproduce the behavior of Fontainebleau NE34 sand. Then, the cyclic response of the material is evaluated by means of cyclic triaxial tests. Finally, the model is applied to a quasi 2D simplification (semi-infinite plate with periodic boundary conditions) of the behavior of a pile foundation. After an investigation of the effect of sample size and boundary conditions, the study tests different pile jacking techniques, monotonic and cyclic strokes, exploring their impact on the total of the shaft and tip resistance of the pile. The importance of installation velocity is investigated for each technique. The geometry of future experiments in the geotechnical centrifuge is presented in this work and used as a basis for the numerical simulations. In conclusion, this research provides important information about the impact of different modes of installation on pile foundation behavior.

RÉSUMÉ: Le comportement cyclique des fondations sur pieux est étudié à l'aide de la méthode des éléments discrets (DEM) au moyen d'expériences simulées en centrifugeuse. L'accélération centrifuge permet de reproduire des problèmes à échelle réelle sur des modèles réduits, tandis que le DEM donne accès à des informations microscopiques sur les interactions particules-structure. Dans un premier temps, un modèle discret basé sur des particules sphériques impliquant élasticité, frottement et résistance au roulement est calibré sur des essais triaxiaux drainés monotones pour reproduire le comportement du sable de Fontainebleau NE34. Ensuite, la réponse cyclique du matériau est évaluée au moyen d'essais triaxiaux cycliques. Enfin, le modèle est appliqué à une simplification quasi 2D (plaque semi-infinie avec conditions aux limites périodiques) du comportement d'une fondation sur pieux. Après une étude de l'effet de la taille de l'échantillon et des conditions aux limites, l'étude teste différents types de techniques de fonçage de pieux, à coups monotones et cycliques, en explorant leur impact sur la résistance totale du fût et de la pointe du pieu. L'importance de la vitesse d'installation est étudiée pour chaque technique La géométrie des futures essais dans la centrifugeuse géotechnique est présentée dans ce travail et sert de base aux simulations numériques. En conclusion, cette recherche fournit des informations importantes sur l'impact des différents modes d'installation sur le comportement des pieux.

Keywords: DEM simulations; pile jacking; fontainebleau sand NE34; centrifuge modelling.

1 INTRODUCTION

Wind turbines play a significant role in the generation of renewable energy and have several important advantages. However, it is essential to recognize the challenges that arise throughout the implementation process. One technique that is often used for the installation of such structures is pile jacking. Applying quasi-static stress cycles to jack the pile in the ground is one method of installation. Studies on different techniques for pile jacking using centrifuge model testing are previously done by El Haffar et al. (2017); Blanc et al. (2019). Interesting results revealed a significant difference between piles installed at 1g and at 100g. Three times higher resistance in compression

was recorded for piles jacked at 100g. Differences were also seen between piles jacked monotonically and those jacked cyclically (by a series of strokes). The tip capacity in compression decreased, while the pull-out capacity showed a clear tendency to increase with the increasing number of installation strokes.

Numerous studies have explored the effects of cyclic loading using discrete element method (DEM) (Cundall and Strack, 1979) simulations such as the work by Jiang et al. (2019); Zorzi et al. (2017), that studied the behavior of model sands during a cyclic triaxial loading path. Other studies have demonstrated the ability of DEM to model soil-structure interactions (Ciantia et al., 2019; Arroyo et al., 2011). Moreover, Zhang and Wang (2015) used DEM to simulate monotonic pile jacking at increased acceleration to simulate and compare with experiments in the geotechnical centrifuge.

The capability and constraints of DEM for simulating soil structure problems need to be fully explored through further research. For this purpose, this work studies the effect of sample and particle size as well as the installation speed on the response of a quasi-two-dimensionally simplified pile foundation installed under centrifugal acceleration, with monotonic and cyclic strokes. The geometry of experiments from the geotechnical centrifuge are shown as a basis for the numerical simulations that will later be used for similar experiments aiming to confirm the validity of the DEM model.

2 EXPERIMENTAL SETUP

The experimental setup of the centrifuge model, which is used as a reference for the simulations, is detailed in Figure 1. The setup comprises a container of dimensions 800x450x200mm with one transparent side made of plexiglass enabling the visual observation of the soil during installation followed by PIV analysis. To allow this observation around the pile as well as the comparison with the numerical model, a wall is taken as a quasi 2D pile of width 16mm, depth of 224mm and thickness of 200mm. Dry Fontainebleau NE34 sand is deposited in the container by air pluviation, aiming to achieve a relative density (D_r) of 68% up to a depth of 400mm. The material properties of NE34 are documented in Andria-Ntoanina et al. (2010).

During the tests, a centrifugal acceleration of 25 times gravity is applied. The model wall is installed at a velocity of 0.1 mm/s. Both the wall and the soil are instrumented with sensors to measure the total stress exerted within the system during the tests.

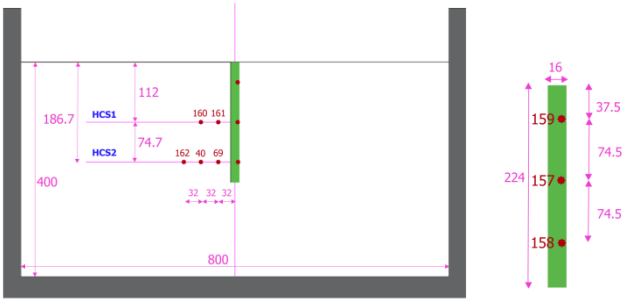

Figure 1. Experimental setup showing the model wall and the positions of total stress sensors in the sand and on the wall shaft.

3 DEM MODEL

A quasi 2D model pile is installed in a material that is calibrated to reproduce the behavior of NE34 using YADE, an open-source software developed by Kozicki and Donze (2009). The numerical model used is a classical linear contact law with Mohr-Coulomb plasticity surface and a moment that resists rolling to account for real particle shape when using spheres. The model description and calibration process are found in Ezzeddine et al. (2023), while the parameters used are presented in Table 1.

Table 1. Calibrated parameters of the contact model.

E (MPa)	α	φ (°)	α_r	η_r	Density (kg/m^3)
500	0.3	24	0.1	0.4	2650

The sample is generated with periodic boundary conditions on the horizontal directions and a rigid wall serving as a boundary at the bottom of the sample depth while keeping a free surface at the top. To enhance computational efficiency, the particle size distribution of NE34 is multiplied by a scaling factor denoted as "F". Particles are initially generated within a confined box and left to settle under the influence of gravity. Once they settle and the forces stabilize, a sample of dimensions L, w, and h is prepared as shown in Figure 2. In order to be able to obtain samples with different values of initial porosity, the inter-particle friction angle φ set in YADE is decreased during the preparation process to obtain denser samples.

4 PILE JACKING SIMULATIONS

In order to establish sample boundaries that effectively mitigate any finite size effects, a systematic investigation is done, examining the influence of sample dimensions and particle size.

Samples with varying L and F are generated at a constant $\varphi = 10°$ during preparation. φ is then changed

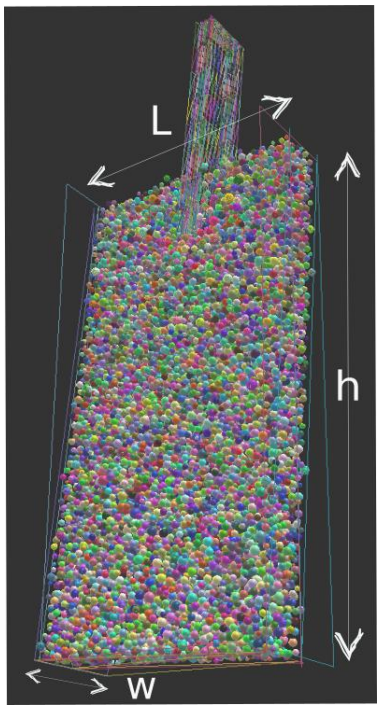

Figure 2. Numerical sample dimensions and boundaries.

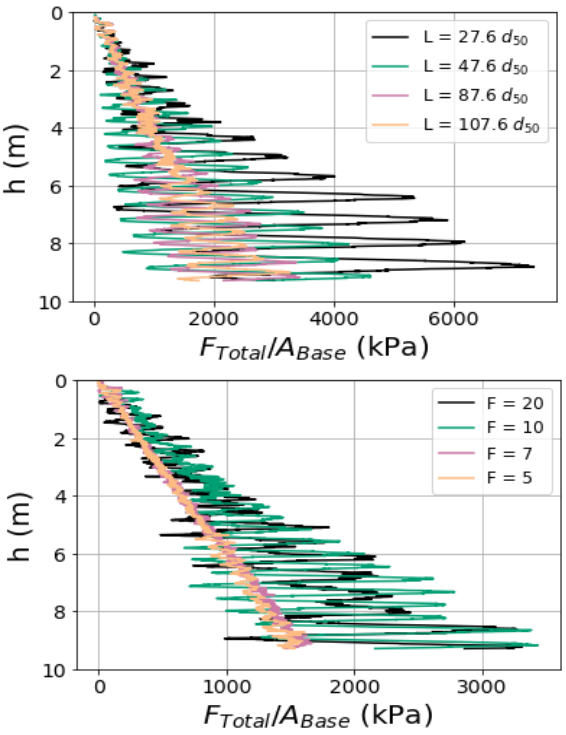

Figure 3. Total normalized force on the wall with depth for varying a) normalized length L/d_{50} b) factor F.

to its calibrated value in Table 1. The resultant average porosity of the sample is maintained at 0.44. The model wall has a width of 16mm, depth 100mm and is infinite on the periodic direction w whose value is taken as the width of the sample $10d_{50}$. To select an appropriate value for w two values, $10d_{50}$ and $20d_{50}$, are initially examined and found to give close results. It is then installed at a velocity v_p such that the ratio of inertial forces to confining forces is $I < 10^{-2}$ for quasi-static conditions (Janda and Ooi, 2016), under an acceleration of 100g, effectively simulating conditions similar to those in a centrifuge experiment. Results are compared in terms of total (tip and shaft) unit resistance to assess the influence of each variable. The results are presented in prototype scale. The total force is normalized by the area of the tip to obtain the unit resistance.

4.1 Effect of dimension L

Four values of L are compared: L/d_{50} = 27.6, 47.6, 87.6, 107.6, where F = 10 and d_{50} = 2.1mm. The results are shown in Figure 3, where it is evident that in the sample with the smallest dimension L, the distance between the walls within the periodic sample is insufficient to avoid their interaction, leading to noticeable fluctuations in the results. As L increases, these fluctuations diminish. Furthermore, it can be observed that the effect of L on pile resistance is more pronounced at greater depths, owing to the fact that the zone of influence of the pile extends with increasing depth. The test with L/d_{50} = 87.6 seems to avoid any significant boundary effects while maintaining a reasonable computational time Let's denote this value of L as «L_1» in further analysis.

4.2 Effect of F

Additional tests are done keeping L_1 and varying F = 5, 7, 10, 20 to investigate the influence of particle size on the pile's response. Strong fluctuations are seen for F = 10, 20. With the decrease of F from 10 to 7, a variation of the pile to grain size ratio shows a clear influence on the behavior. When further decreasing F to 5, no effect is seen.

4.3 Effect of v_p: monotonic and cyclic strokes

The sample with L_1 and F = 7 constituting of 249254 spheres is selected as the reference configuration for the subsequent tests. Three values of jacking velocity (v_p = 0.1, 0.5, 1 m/s) are compared for two cases: monotonic installation and by strokes of 10 mm (1 m prototype scale). The effect of the velocity in the monotonic case is only noticeable at the starting point. It is clearly more crucial for the installation by strokes, where the high fluctuations seen for v_p = 1 m/s, particularly at higher depths decrease but stay visible at v_p = 0.5 m/s, and diminish at v_p = 0.1 m/s. This suggests that, in cyclic jacking, conditions that are more restrictive may be imposed on the criterion for choosing the velocity than in monotonic loading, since jacking by subsequent strokes can induce important force fluctuations.

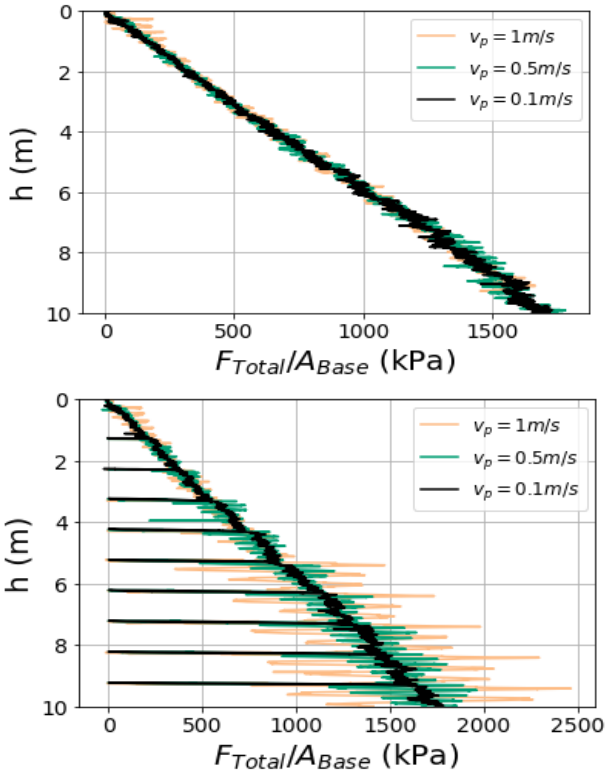

Figure 4. Effect of velocity on the total normalized force on the wall with depth for a) monotonic b) cyclic case.

5 CONCLUSIONS

In this study, the installation of pile foundations is investigated through simulated DEM centrifuge experiments. A simplified 2D representation of a pile is modelled and the effect of model and particle size on the behavior of the quasi 2D model during installation are explored. After deciding on the suitable model dimensions, the effect of jacking velocity on the pile's resistance is checked for the monotonic and cyclic jacking techniques. This work aims to explore the effect of various parameters on DEM's ability to simulate complex geotechnical soil-structure interactions. In the very next future, numerical simulations of the jacking and pullout of the model pile, with the parameters identified in this work, will be performed and compared to the corresponding centrifuge model tests.

ACKNOWLEDGEMENTS

The authors would like to thank the high-performance computing centre of Pays de la Loire (CCIPL) and the European project GEOLAB for their valuable support during the course of this research. The acknowledgments are further extended to Gustave Eiffel University and the Region Pays de la Loire for their financial support through thesis grants.

REFERENCES

Andria-Ntoanina, I., Canou, J., and Dupla, J.-C. (2010). Caractérisation mécanique du sable de Fontainebleau NE34 l'appareil triaxial sous cisaillement monotone, Laboratoire Navier, Paris, France, Rapport projet SOLCYP. 21p.

Arroyo, M., Butlanska, J., Gens, A., Calvetti, F., and Jamiolkowski, M. (2011). Cone penetration tests in a virtual calibration chamber, *Géotechnique*, 61(6), 525–531. https://doi.org/10.1680/geot.9.P.067.

Blanc, M., El Haffar, I., and Thorel, L. (2019). Centrifuge modelling of the impact of the installation method on the lateral response of the pile, In: *ECSMGE 2019, 17th European Conference on Soil Mechanics and Geotechnical Engineering*, Reykjavik, Iceland, 8-p. https://dx.doi.org/10.32075/17ECSMGE-2019-0256.

Ciantia, M., O'Sullivan, C., and Jardine, R. J. (2019). Pile penetration in crushable soils: Insights from micromechanical modelling, In: *ECSMGE 2019, 17th European Conference on Soil Mechanics and Geotechnical Engineering*, Reykjavik, Iceland, 298-317. https://doi.org/10.32075/17ECSMGE-2019-1111.

Cundall, P. A., and Strack, O. D. (1979) A discrete numerical model for granular assemblies, *Géotechnique*, 29(1): 47–65. https://doi.org/10.1680/geot.1979.29.1.47.

El Haffar, I., Blanc, M., and Thorel, L. (2017). Impact of pile installation method on the axial capacity in sand, *Géotechnique Letters*, 7(3), 260–265. https://doi.org/10.1680/jgele.17.00036.

Ezzeddine, A., Cazacliu, B., Richard, P., Thorel, L., and Artoni, R. (2023). Discrete numerical analysis of cyclic loading on a model sand, In: *NUMGE 2023, 10th European Conference on Numerical Methods in Geotechnical Engineering*. London, UK. https://doi.org/10.53243/NUMGE2023-218.

Janda, A. and Ooi, J., (2016). DEM modeling of cone penetration and unconfined compression in cohesive solids, *Powder Technology*, 293, 60–8. https://doi.org/10.1016/j.powtec.2015.05.034.

Jiang, M., Zhang, A., and Li, T. (2019). Distinct element analysis of the microstructure evolution in granular soils under cyclic loading, *Granular Matter*, 21, 1–16. https://doi.org/10.1007/s10035-019-0892-8.

Kozicki, J., and Donze, F. V. (2009) YADE-OPEN DEM: An open-source software using a discrete element method to simulate granular material, *Engineering Computations*, 26(7), 786-805. https://doi.org/10.1108/02644400910985170.

Zhang, Z., and Wang, Y.-H. (2015). Three-dimensional dem simulations of monotonic jacking in sand, *Granular Matter*, 17, 359–376. http://dx.doi.org/10.1007%2Fs10035-015-0562-4.

Zorzi, G., Kirsch, F., Gabrieli, F., and Rackwitz, F. (2017). Long-term cyclic triaxial tests with DEM simulations, In *PARTICLES V: proceedings of the V International Conference on Particle-Based Methods: fundamentals and applications*, Barcelona, Spain, 273–2.

Proceedings of the XVIII ECSMGE 2024
GEOTECHNICAL ENGINEERING CHALLENGES
TO MEET CURRENT AND EMERGING NEEDS OF SOCIETY
© 2024 the Authors
ISBN 978-1-032-54816-6
DOI 10.1201/9781003431749-431
Open Access: www.taylorfrancis.com, CC BY-NC-ND 4.0 license

ECSMGE 24
XVIII EUROPEAN CONFERENCE ON SOIL MECHANICS AND GEOTECHNICAL ENGINEERING

Mechanical behavior of Ypresian plastic clays

Comportement mécanique des argiles plastiques de l'Yprésien

S. Fanelli*, L. Makki, E. Bourgeois, F. Szymkiewicz, P. Reiffsteck
Université Gustave Eiffel, Champs-sur-Marne, France

**sonia.fanelli@univ-eiffel.fr*

ABSTRACT: Ypresian plastic clays are formations with a complex behavior, particularly due to their anisotropy and their swelling properties, which can make it difficult to interpret the results observed during laboratory or in situ tests campaigns. It is therefore sometimes necessary to use different methods to better understand their mechanical behavior. This communication presents the results of tests carried out in laboratories as part of several projects in the Paris region on Ypresian Clay formation. The soils studied come from deep core drillings taken between 20 and 70 m deep during various geotechnical investigation campaigns. The tests include both static and dynamic tests, making it possible to observe the mechanical behavior evolution of the material according to the stress path used. The different results were achieved using the cyclic triaxial, the resonant column, the shear wave propagation measurements from the Bender Elements, the stress paths and K_0 measurements at the triaxial. An analysis of the decrease in the shear modulus is then carried out, which will feed a rheological model and calibrate it according to the confining pressure.

RÉSUMÉ: Les argiles plastiques de l'Yprésien sont des formations au comportement complexe du fait, notamment, de leur anisotropie et de leur caractère gonflant qui peuvent rendre difficile l'interprétation des résultats obtenus lors de campagnes d'essais en laboratoire ou in situ. Il est donc parfois nécessaire d'avoir recours à différentes méthodes pour mieux comprendre leur comportement mécanique. Cette communication présente les résultats d'essais réalisés en laboratoire dans le cadre de plusieurs projets de la région parisienne sur les formations de l'Yprésien argileux. Les sols étudiés sont issus de sondages carottés profonds prélevés entre 20 et 70 m de profondeur lors de différentes campagnes de reconnaissance géotechnique. Les essais regroupent à la fois des essais statiques et dynamiques qui permettent d'observer le comportement mécanique du matériau en fonction de la sollicitation utilisée. Les différents types d'essais ont été réalisés à partir du triaxial cyclique, de la colonne résonante, des mesures de propagation des ondes de cisaillement aux Bender Elements, des chemins de contraintes et des mesures de K_0 au triaxial. Une analyse de la diminution du module de cisaillement est ensuite réalisée, ce qui permettra d'alimenter un modèle rhéologique et de le calibrer en fonction de la pression de confinement.

Keywords: Ypresian clay; shear modulus; laboratory tests.

1 INTRODUCTION

In urban environnements, modern practices of building construction or large structures can lead to new problems of interaction between soils and structures, particularly when using more fragile materials that can tolerate less strains.

The structures are mainly designed from methods incorporating mechanical characteristics defined by a single type of test and therefore only one mode of loading. However, depending on the actual stress path in the soil, the stiffness observed during the tests may not be realistic. Indeed, depending on the soils properties, the type of structure and its location, applied loads can be different and induce different mechanical responses. In order to identify the most representative test for in situ stresses, it is necessary to compare different methods for evaluating the mechanical parameters of materials. The improvement of the design of the structures through a better evaluation of the response of the soils to low-intensity loads is therefore an important issue.

Since several years, a database of tests carried out on Ypresian plastic clays, concerning Grand Paris Express worksites and other construction projects in the Parisian region, has been collected.

After a brief presentation of the geological context and the location of the sites studied, this communication will present the results of tests that have provided an overall view of the mechanical behavior of these plastic clays. These tests include controlled deformation and stress path triaxial tests, tests to define the earth pressure coefficient at rest K_0, resonant column tests, cyclic triaxial tests and wave propagation velocity measurements with Bender

Elements. We carried out nine monotonic triaxial tests under drained conditions (three specimens each) and 27 under undrained conditions, 15 cyclic undrained tests, 15 resonant column tests, 12 bender element tests, 23 triaxial tests following a specific stress path (drained and undrained), and five tests under K_0 condition.

The results which are presented in the following paragraphs will enable us to define a modulus degradation curve and different mechanical parameters. Then these parameters will be implemented in a finite elements numerical model which will be able to reliably represent the mechanical behavior of the soil nearby a structure.

2 GEOLOGICAL CONTEXT

Plastic clays are part of an impermeable geological formation of fluvio-lacustrine origin identified at the base of the Ypresian (Lower Eocene), called the Sparnacian, which also includes the upper sands, false glaises and Auteuil sands (Filliat et al., 1981).

This formation is framed by Campanian flint chalk (Upper Cretaceous) and Lutetian coarse limestone (Middle Eocene). The plastic clays or "argiles bariolées" are very compact and composed of clays sometimes marbled with various colors ranging from red to gray, bluish, black or yellowish (figure 1). They vary in thickness from 8 to 12 m depending on their location.



Figure 1. Plastic clay samples (Paris15e).

Their main characteristics are their high plasticity (plasticity index over 50) and their sensitivity to water, which gives them a swelling behavior that requires certain precautions to be taken, particularly when sampling them and carrying out experimental studies in the laboratory.

3 LOCATION OF STUDY SITES

The sites studied are part of the Grand Paris Express project, which involves the construction of several metro lines and stations in the Paris region (figure 2). The plastic clays that are the subject of this article are located on line 15 west at La Défense and line 14 south at Paris 13e.

Two other sites are also being studied, related to other construction projects in Paris 15e and Paris 12e.

Soil samples were taken at depths ranging from 20 m to 70 m, depending on location.

4 EXPERIMENTAL ANALYSIS

Various tests were carried out in the laboratory: the drained monotonic triaxial, the cyclic undrained triaxial, the resonant column, measurement of shear wave propagation velocity at the Bender Elements, stress paths in drained and undrained conditions and measurements of the earth pressure coefficient at rest K_0 at the triaxial.

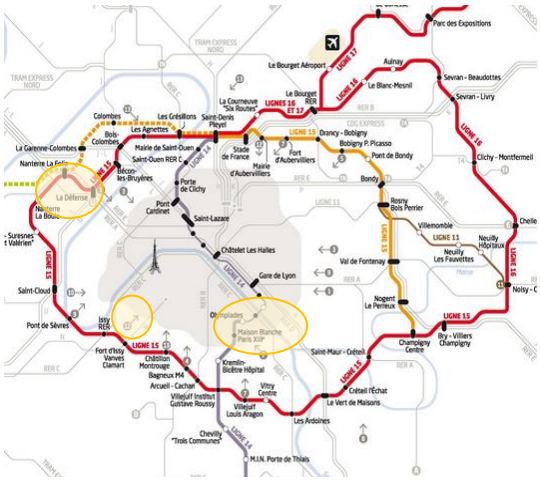

Figure 2. Location of sites studied in Paris region (source www.societedugrandparis.fr).

4.1 Consolidation and swelling of specimens

Assembly, saturation, measurement of Skempton B coefficient and consolidation were carried out in the same way for all specimens except those in the K_0 test, where a cell pressure corresponding to the vertical stress in place was applied with taps closed, in order to limit swelling due to water absorption before the saturation phase. A value of 800 kPa of back pressure was applied.

Consolidation phases were stopped once constant back volume had been achieved. Consolidation times varied from several hours to several days. Tests were then carried out with confining pressures ranging from 200 to 920 kPa, depending on the depth of the samples.

4.2 Triaxial drained and undrained tests

Drained consolidated tests were used to obtain mechanical parameters such as long term cohesion, angle of internal friction and Poisson's ratio with the variation in specimen volume. The results give an

average of 20 kPa for effective cohesion, 15° for the effective internal friction angle, and 0.45 for Poisson's ratio.

4.3 Cyclic triaxial tests

Cyclic tests were carried out with force control and global strain measurement. A loading program was established with 9 loading phases ranging from 2 to 500 kPa, each consisting of 5 cycles starting from a minimum effective axial stress equal to the consolidation stress plus 10 kPa. Some results are shown in figure 3.

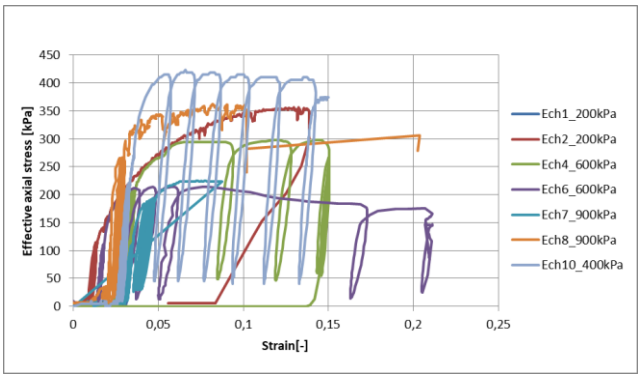

Figure 3. Example of cyclic tests at different confinement.

4.4 Resonant column tests

Resonant column tests were carried out at various confining pressures ranging from 200 to 920 kPa. Shear modulus results were obtained at strain values between 10^{-3} and 10^{-6}. A shear modulus degradation curve was established from the various tests (figure 4).

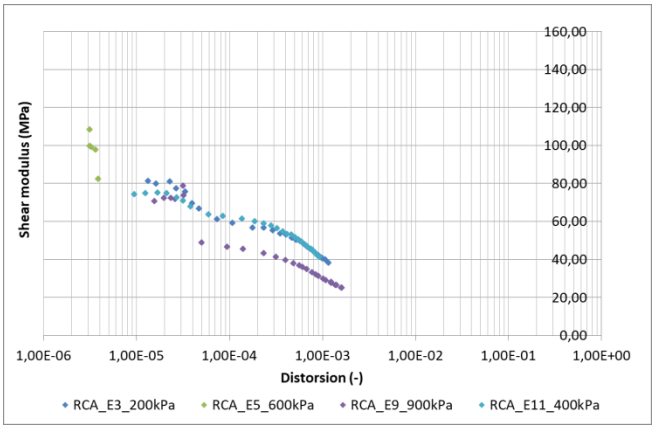

Figure 4. Shear modulus degradation curve for four samples.

4.5 Shear wave propagation tests

Shear wave propagation tests were carried out using a set of Bender Elements at confining pressures ranging from 0 to 900 kPa. Measurements at 0 kPa correspond to the stage before saturation just after installation in the cell. The figure 5 shows an example of a wave propagation test result.

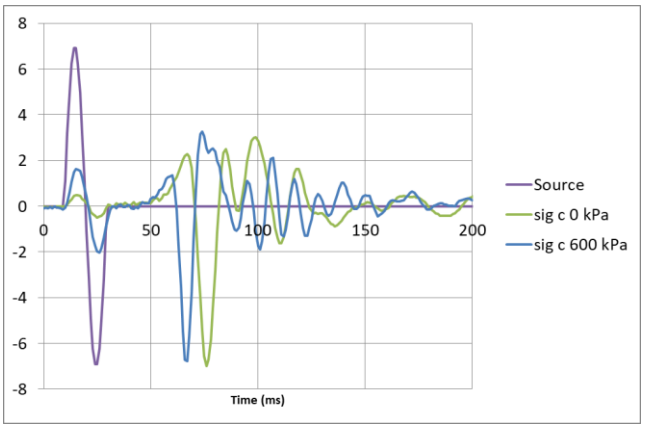

Figure 5. A specimen test results with the Bender Elements.

4.6 Stress paths

Specimens were tested along deviatoric paths according to mean stress p and deviator q in drained and undrained conditions. Two types of path were used for stress path testing. The first one describe the path tests in line with simulations and the life of the structure. The different stages are defined below:

1: geostatic stress state
2: existing loads (loading)
3: unloading/reloading cycle
4: simulation of earthworks (excavation)
5: end of project stresses
6: creep (long term condition)

The second type of stress path test has the same four stages as the first type but the deconfinement is realized until failure.

The curves shown in figure 6 represent the degradation curves of secant modulus observed during these tests.

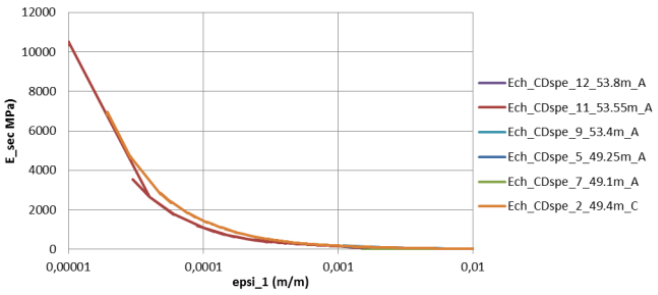

Figure 6. Secant modulus degradation curve for different stress path tests.

4.7 K_0 tests

The earth pressure coefficient at rest K_0 has been extrapolated directly from laboratory tests by imposing a condition of no radial displacement of the specimen. The cell pressure is increased and the axial force is controlled to limit diameter variation.

The figure 7 shows four tests. The K_0 value is close to 1 for three specimens. Another specimen, for which swelling was observed at saturation, shows a higher K_0 value, which then decreases to 1 as it approaches in-place stress.

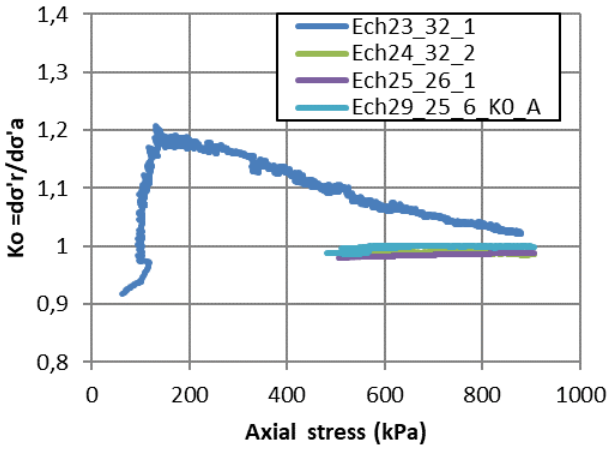

Figure 7. Results of four K_0 tests.

5 RESULTS SYNTHESIS

The different laboratory tests carried out eneabled us to obtain a degradation of the shear modulus, normalized with the G_0 modulus at very low strains, as a function of distortion for each site studied.

The figure 8 shows results of Bender Elements, resonant column and cyclic triaxial tests carried out for the site located in Paris 15^e. It shows a marked decrease in shear modulus for strains of between 0.001% and 0.1%.

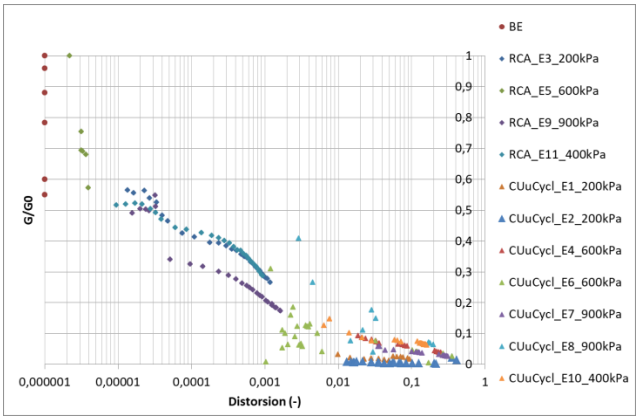

Figure 8. Shear modulus degradation curve on the site Paris 15^e.

The modulus degradation curve will be used to feed a rheological model and calibrate it as a function of confining pressure.

6 CONCLUSION

The tests presented here are used to determine the parameters of a model specifically developed to improve the representation of displacements in finite element simulations of the behavior of specific structures in the Grand Paris station projects, in particular vertical displacements around the structures. At present, it is difficult to know which models are really suitable for modeling structures. The simplest models sometimes provide vertical ground displacements that do not necessarily reflect ground movements observed in reality. It is therefore important to be able to propose a model that aims to take better account of ground behavior on unloading stress paths. The parameters obtained from these tests will then be used to feed a rheological model and calibrate it as a function of confining pressure.

REFERENCES

Abbiss C.P. (1981) Shear wave measurements of the elasticity of the ground, Géotechnique, 31, 91-104. https://doi.org/10.1680/geot.1981.31.1.91.

ASTM D3999 Standard Test Methods for the Determination of the Modulus and Damping Properties of Soils Using the Cyclic Triaxial Apparatus, ASTM International, West Conshohocken, PA, 2011.

Filliat G., Duvauchelle, C., Diffre, P., Marvy, J., Vachat, J., 1981 La pratique des sols et fondations, Editions du moniteur, ISBN: 2-86282-162-4 (in French).

Jovicic V., Coop M.R., Simic M. (1996) Objective criteria for determining Gmax from bender elements Géotechnique, 46 (2), 357-362. https://doi.org/10.1680/geot.1996.46.2.357.

Viggiani G., Atkinson J.H (1995): 'Interpretation of Bender Element Tests, Géotechnique, 45 (1), 149-154. https://doi.org/10.1680/geot.1995.45.1.149.

Proceedings of the XVIII ECSMGE 2024
GEOTECHNICAL ENGINEERING CHALLENGES
TO MEET CURRENT AND EMERGING NEEDS OF SOCIETY
© 2024 the Authors
ISBN 978-1-032-54816-6
DOI 10.1201/9781003431749-432
Open Access: www.taylorfrancis.com, CC BY-NC-ND 4.0 license

ECSMGE 24
XVIII EUROPEAN CONFERENCE ON SOIL MECHANICS AND GEOTECHNICAL ENGINEERING

Lisbon new circular Metro underground line: Centenary buildings underpinning

Nouvelle ligne circulaire du métro de Lisbonne: Reprise en sous-œuvre des bâtiments centenaires

C. Fartaria*, A. Henriques, C. Martins, A. Pinto, R. Tomásio
JETsj, Geotecnia, Lisbon, Portugal

cfartaria@jetsj.com

ABSTRACT: The new Lisbon metro line will cross a densely urbanized part of the city, connecting Rato station located at one of the hills of the city and Cais do Sodré station at the Tagus River right bank. Thus, the underground excavation intersects a wide range of materials, from rock mass to soft soils. The new Santos Station will be located partially beneath XIX century buildings with a cover depth of about 15 m, being these structures highly sensitive to differential settlements given its masonry and timber composition with multiple structural pathologies. Given the building conditions, its heterogeneous soil foundation and the level of surface settlements induced by NATM excavation, an underpinning solution was needed aiming to mitigate the buildings potential damages. Hence, high length micropiles, concrete reinforced beams and walls were executed from the building ground floor aiming to transfer buildings loads to the soils located underneath the tunnel excavation. This paper presents an overall description of the adopted solutions, how they were implemented and the buildings' behaviour during the underground works.

RÉSUMÉ: La nouvelle ligne de métro de Lisbonne traversera une partie densément urbanisée de la cité, reliant la gare de Rato, située sur l'une des collines de la cité, et la gare de Cais do Sodré, sur le Tage fleuve. Ainsi, l'excavation souterraine recoupe une large gamme de matériaux, de la masse rocheuse aux sols meubles. La nouvelle station de Santos sera située en partie sous des bâtiments du XIXe siècle avec une profondeur de couverture d'environ 15 m, ces structures étant très sensibles aux tassements différentiels compte tenu de sa maçonnerie et du bois avec de multiples pathologies structurelles. Compte tenu des conditions du bâtiment, de l'hétérogénéité de la fondation du sol et du niveau de tassement de surface induit par l'excavation NATM, une solution de reprise en sous-œuvre était nécessaire afin d'atténuer les dommages potentiels du bâtiment. Par conséquent, des micropieux de grande longueur, des poutres et des murs renforcés en béton ont été exécutés à partir du rez-de-chaussée du bâtiment dans le but de transférer les charges des bâtiments vers les sols situés sous l'excavation du tunnel. Cet article présente une description globale des solutions retenues, de la manière dont elles ont été mises en œuvre et du comportement des bâtiments lors des travaux souterrains.

Keywords: Metro; underpinning; centenary buildings; excavation.

1 INTRODUCTION

The new Lisbon circular metro line will include a new Station in Santos that will be partially located beneath some XIX century buildings with a cover depth of about 15 m, being these structures highly sensitive to differential settlements given its masonry and timber composition while presenting already multiple structural pathologies.

The underground excavation of this tunnel, using the technology known as New Austrian Tunnelling Method, was analysed with numerical models and surface settlements were estimated considering the geological scenario previously accessed. This information was used to evaluate the building vulnerability to those settlements also considering their structural condition and it was concluded the deficient structural conditions of those structures to support the estimated settlements without major damage. Given this scenario, a buildings underpinning solution was proposed mitigating the impact of the underground excavations on those centenary buildings.

2 AFFECTED BUILDINGS

Considering the vulnerability analysis conducted, two buildings with masonry walls and timber floors were classified with a moderated potential damage induced by the underground excavation. Those XIX century buildings have 3 and 5 upper floors and had a superficial foundation (see Figure 1).



Figure 1. Centenary buildings located above de tunnel.

The buildings are located on a hillside on the area where a monastery collapsed due to a strong magnitude earthquake that took place in 1755. Therefore, is it possible that the superficial foundation is located on top of debris fills which worsen its foundation conditions and can justify the differential settlements that were already visible.

Considering this scenario and the settlements estimation from the underground excavation numerical analysis, using Burland's (1997) classification it was concluded that those building, without reinforcement, would potentially suffer moderate to severe damage.

3 MAIN CONSTRAINS

3.1 Geological-geotechnical constrains

The geological investigation campaign included the execution of multiple boreholes that allowed the characterization of the soil units underneath the buildings (see Figure 2). It was possible to confirm that its superficial foundation was on top a 10m thickness Anthropocene fill layer. Bellow that layer, Miocene and Lisbon Vulcanic Complex materials were found showing satisfactory resistance and deformation characteristics.

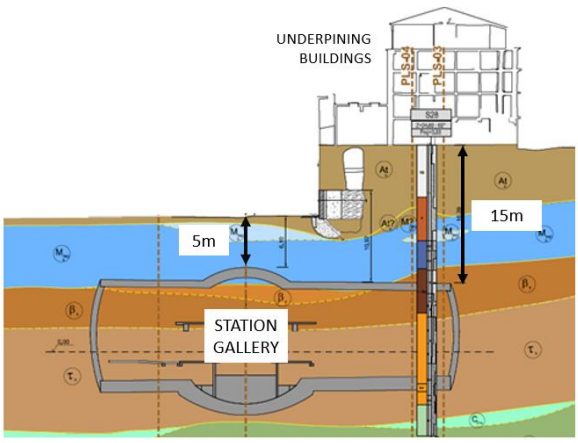

Figure 2. Geological scenario.

3.2 Constructive technologies constrains

The reinforcement solutions must respect the local constraints regarding the accessibility of equipment. Considering the need to work inside the buildings, the solutions must be compatible with equipment that can operate with a minimal ceiling height of about 2,5m.

3.3 Underground works constrains

Underground works consider the excavation using the NATM method which include the use of reinforcement elements such as umbrella soil nails and geodrains that go beyond the tunnel section. The position of those elements must be considered on the underpinning solution to avoid intersection of those elements.

4 UNDERPINNING SOLUTION

To materialize the solution of buildings underpinning, it was proposed the execution of the following elements at the ground floor level:

- Reinforced concrete beams grid, connected to the masonry walls with prestressed threaded bars to promote an effective load transfer do micropiles (see Figure 3) [concrete beams 60cmx80cm | ϕ32mm GEWI bars];

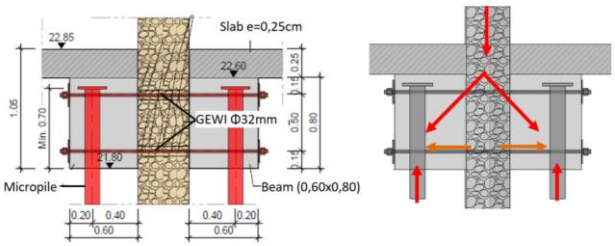

Figure 3. Underpinning solution – Load transfer beams.

- Reinforced concrete lining walls connected to the masonry peripheral walls with stell bolts to promote an effective load transfer [30cm thickness wall];
- Reinforced concrete slab on beam grid for materialization of the ground floor, overall rigidification of the solution and control of torsional forces in the beams [25cm thickness slab];
- Application of sprayable reinforcement mortars reinforced with carbon fibre meshes on internal masonry walls for their confinement and structural reinforcement [S&P ARMO-mesh | S&P ARMO-crete w] (see Figure 4);



Figure 4. S&P ARMO system application.

- Micropiles, vertical and sub-vertical, executed in the alignments of the walls and connected to the beams grid. Its 6m bond length materialized with repetitive selective injection (IRS) is placed outside the excavation influence area, in materials from the Lisbon Volcanic Complex geological unit (see Figure 5) [N80 tube 127x9mm].

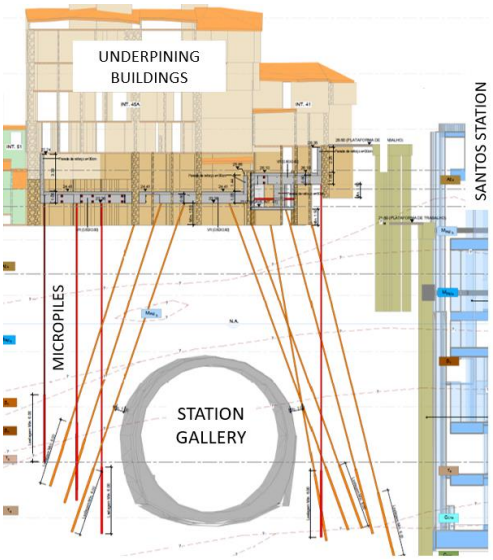

Figure 5. Underpinning solution - Cross section.

The underpinning solution was design to transfer the totality of the buildings load to Lisbon Volcanic Complex competent materials through micropiles with lengths from 20m to 25m, totalling about 4000m of micropiles tubes. That load transfer will occur when the underground works induces a settlement at build foundation level so it is expected that the load transfer can occur gradually with the tunnel excavation progress.

5 SOLUTION DESIGN

The underpinning concrete beam grid was designed using structural models within the SAP2000 software. The grid joint support was placed on micropiles location considering its inclination and using a spring to simulate the axial stiffness of the micropile free length. Those models made it possible to estimate beams structural forces as well as its elastic deformation (see Figure 6).

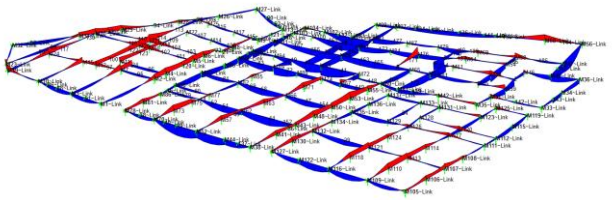

Figure 6. Beams grid SAP2000 analysis – Bending moments.

Considering the joint support springs on the structural model, the maximum design axial load on each micropile was estimated, allowing the safety validation of those steel elements. Since the micropiles free length is placed on influence excavation area it was necessary to account for second order effects so a 20mm as the maximum eccentricity a micropile can be subjected and therefore its design accounted for axial-bending moment verification. A numerical model considering NATM excavation phasing allowed the confirmation of displacements on micropiles to be less than 20mm (see Figure 7).

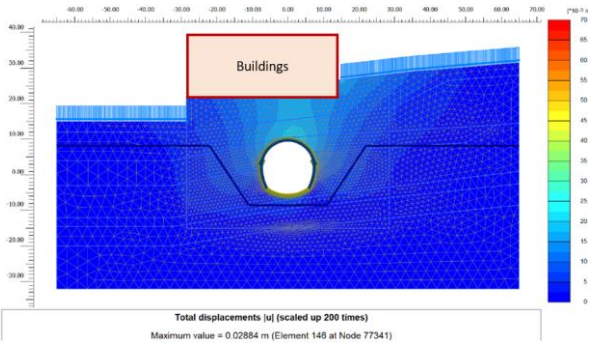

Figure 7. Plaxis 2D – Total displacements.

6 MONITORING AND SURVEY PLAN

Given the highly complexity of the present solution as well as the geotechnical substantial risk scenario a reinforced monitoring plan was implemented. Regardless of the underground excavation typical monitoring plans, at surface inside and outside the underpinning buildings multiple devices were installed such as inclinometers, topographic targets, tiltmeters, crack meters and liquid level sensors. Automated total stations (ATS) were used to access data daily aiming the access of in real-time building behaviour while the underground excavation is implemented and allowing for risk mitigation measures promptly if needed (see Figure 8).

The monitoring and survey plan the establishment of threshold values included for each monitoring

device. The numerical analyses results were used to determine reference values for measured parameters that were used to set warning and alarm values, considering warning alarms thresholds as 80% and 120% of the reference values, respectively. Thus, the reach of warning limit means the approximation of the estimated behaviour and alarm means it was surpassed by 30% and therefore the works must stop, and reinforcement measures must be taken.

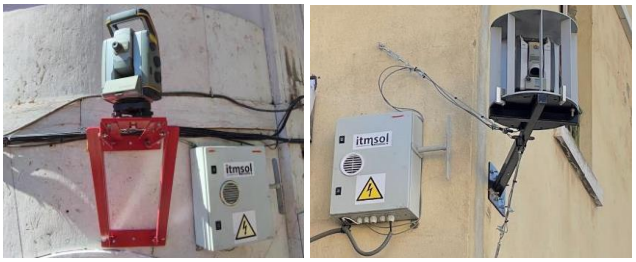

Figure 8. Automated total stations.

Up to this date, the monitoring survey plan has been implemented with daily measures and the buildings behaviour during the underpinning works and later with underground excavation has been proven as expected, with low settlements reaching a maximum of 3mm (see Figure 9).

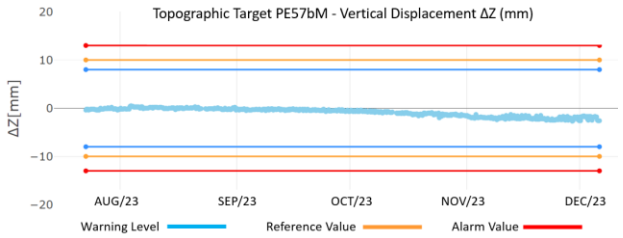

Figure 9. Topographic target - Vertical displacement.

Since the underpinning buildings are located on a hill the mass movements of the soil were also a concern since the station and tunnel underground excavations are taking place at the hill bottom. Thus, inclinometers with 35m long were installed behind those buildings to access deep horizontal soil movements that cloud indicate any global stability issue (see Figure 10).

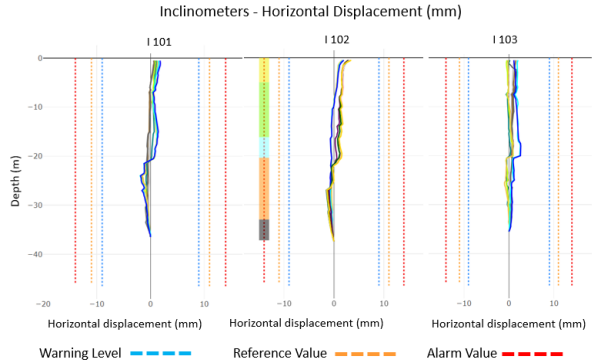

Figure 10. Inclinometers - Horizontal displacement over.

7 CONCLUSIONS

Underground excavations can lead to surface settlements that can impact the structural safety of buildings, particularly centenary buildings were multiply pathologies can already be observed. The use of numerical models for settlement estimation combined with Burland's method to access a buildings potential damage is crucial to determine the necessity of additional reinforcement measures. For extreme scenarios, such as the one presented, an underpinning solution can be most suitable way to maintain the building integrity despite this type of solution often as multiple constrains regarding equipment access and operation (see Figure 11). An adequate monitorization plan is essential to confirm an effective load transfer to the underpinning system while the underground excavation take place.

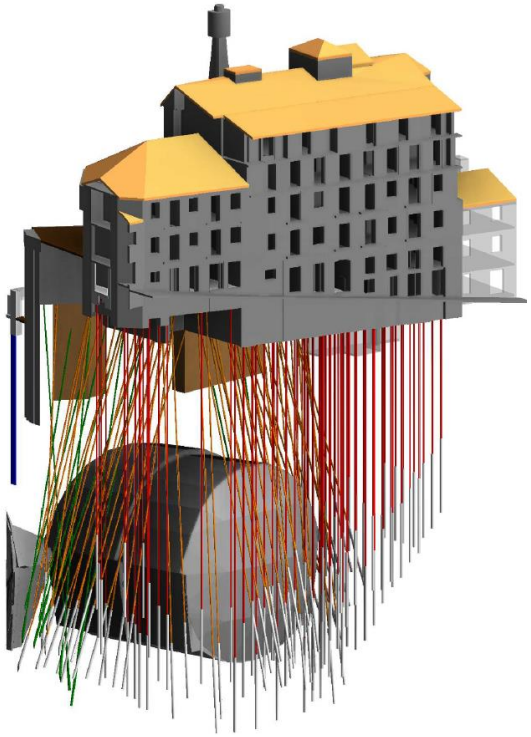

Figure 11. Buildings underpinning view.

ACKNOWLEDGEMENTS

The authors are grateful to the Metropolitano de Lisboa for permission to present this paper.

REFERENCES

Burland, J.B. (1997). Assessment of risk of damage to buildings due to tunnelling and excavation. *Earthquake Geotechnical Engineering*, Balkema, pp. 1189-1201.

Proceedings of the XVIII ECSMGE 2024
GEOTECHNICAL ENGINEERING CHALLENGES
TO MEET CURRENT AND EMERGING NEEDS OF SOCIETY
© 2024 the Authors
ISBN 978-1-032-54816-6
DOI 10.1201/9781003431749-433
Open Access: www.taylorfrancis.com, CC BY-NC-ND 4.0 license

ECSMGE 24
XVIII EUROPEAN CONFERENCE ON SOIL MECHANICS AND GEOTECHNICAL ENGINEERING

Execution and quality control applied on the construction of soil-cement embankments

Exécution et contrôle qualité appliqués à la construction de remblais sol-ciment

E. Fernandes*, P. Antunes, J.P. Simões, J. Ramalho
Geovia, S.A., Lisbon, Portugal

B. Monteiro
Infraestruturas de Portugal, Almada, Portugal

**emfernandes@geovia.pt*

ABSTRACT: The use of cement in the treatment and stabilization of soils *in situ*, using high-power equipment, allows the optimization of the existing natural resources from the sites, resulting in less expensive suitable technical solutions. Given the performance of these new technologies, it becomes necessary to have innovative methods for quality control of built-up layers in addition to the traditional laboratory tests, which are performed on site laboratories, in order to ensure the binomial deadline-quality of the construction in effective terms. This paper presents both the solution adopted in the design phase and the methodology applied in the Quality Control during the construction of large embankments (with a maximum height of approximately 70 m) on the stretches of the motorway A4 that access to the Marão tunnel, in the North of Portugal. This solution made it possible to incorporate an important volume of materials obtained from the excavation works of the line and the tunnel, and to optimize surface occupation, due to the fact of being possible to adopt steeper slopes with the cement treatment of the embankment. The solution adopted in the construction of these embankments is deemed sustainable since it maximises the usage of local resources (excavation volumes) and is better integrated in the natural landscape.

RÉSUMÉ: L'utilisation du ciment dans le traitement et la stabilisation des sols in situ, à l'aide d'équipements de forte puissance, permet d'optimiser les ressources naturelles existantes des sites, aboutissant à des solutions techniques adaptées à des conditions financières avantageuses. Compte tenu des performances de ces nouvelles technologies, il devient nécessaire de disposer de méthodes innovantes de contrôle qualité des couches bâties en plus des essais traditionnels en laboratoire, qui sont effectués dans les laboratoires de chantier, afin d'assurer le binôme délai-qualité de la construction en termes efficaces. Cette communication présentera la solution adoptée dans la conception et la méthodologie utilisée dans la perspective du contrôle de qualité pour la mise en œuvre de grands remblais, d'une hauteur maximale d'environ 70 m, sur les tronçons de l'autoroute A4 qui accède au tunnel du Marão, au Nord du Portugal. L'adoption de cette solution a permis d'incorporer un volume important de matériaux provenant des excavations de la ligne et du tunnel, en maintenant une occupation raisonnable du terrain grâce à la possibilité d'adopter de fortes pentes dans le remblai, constituant ainsi une solution durable compte tenu de la rentabilité des ressources locales et intégrées dans le paysage.

Keywords: Embankments; soil-cement; road works; soil stabilization.

1 INTRODUCTION

In this article it is presented the solution adopted in the design and construction of the large embankments (with a maximum height of approximately 70 m) located in the stretches of the A4 motorway that approach the Marão tunnel, in the North of Portugal.

This solution, based on the use of cement in the treatment and stabilization of the embankments, was developed for the construction of the embankments that approach the East and West portals of the Marão Tunnel. It was applied in 4 places, having been designated as walls M14, M24, M40A and M41. The solution consisted in executing reinforced backslopes with soil-cement (with a cement rate of approximately 4%) with a slope of a 1:1 (V:H) and benches at every 15 m in height. The maximum heigh obtained for these embankments was 69 m.

The adoption of this solution made it possible to incorporate an important volume of materials obtained from the excavation works of the line and the tunnel while allowing a lower surface occupation due to being possible to adopt steeper slopes in the embankment face. The maximisation of the reusage of local resources (excavated volumes) and the better

integration in the natural landscape makes it a sustainable solution.

Figure 1 shows a photograph with an overview of the M24 reinforced embankment after the completion of the works, highlighting its good landscape integration.



Figure 1. General view of the M24 embankment, reinforced with soil-cement.

This case study also intends to present a synthesis of the methodology used in the perspective of Quality Control, which was defined in the design phase and implemented during the construction stage.

2 GEOLOGICAL SETTING

The A4 motorway is mainly located in eruptive terrains of a granitic nature and metamorphic terrains that are essentially schist. The first occurs from between the beginning of the motorway up to about km 12, where the embankments concerned on this paper are located. Metamorphic terrains are predominant in the remaining motorway length. Both eruptive and metamorphic terrains can provide sub-rocky embankment materials (soils rich in rock fragments/blocks), suitable for the construction of embankments.

The granites are interwoven by multiple joint families and posess thick layers of residual soils which are derived from a deep weathering of the rock.

From a geotechnical point of view, and according to the nomenclature of the International Society for Rock Mechanics (ISRM), schists are moderately weathered (W3), and intensely fractured (F4-5).

3 DESIGN SOLUTION

The design solution was developed for the construction of the embankments that approach the East and West portals of the Marão Tunnel. The solution was applied in 4 sites, designated as walls M14, M24, M40A and M41. In general, the solution included the execution of embankments with 1:1 (V:H) slopes, presenting along its development 1 to 5 embankment slopes separated by 3 m wide benches and at every 15 m of heigth. For slope stabilization, a mixture of soil-cement with a cement rate of approximately 4% was employed.

Figure 2 shows a typical section of the solution adopted.

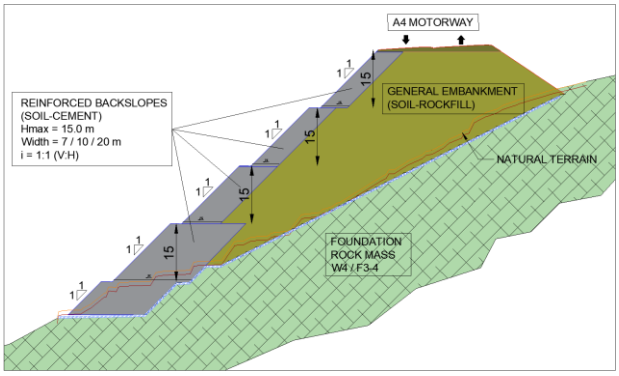

Figure 2. Typical section of the solution.

Table 1 shows the main characteristics of each of the embankments considered in the present case study.

Table 1. General characteristics of the executed soil-cement embankments.

General Characteristics	Embankment			
	M14	**M24**	**M40**	**M41A**
Length (m)	558	413	304	336
Max. height (m)	69	55	24	52
Nº of benches	4	3	0	2
Max. Side slope width (m)	20	16	7	10
Soil-cement volume (m3)	175.000	125.000	30.000	85.000
Embankment volume (m3)	510.000	175.000	20.000	210.000

Regarding the embankment foundation, a 1m deep over-excavation of the natural terrain was required in order to obtain good support conditions (W4 rock or better) throughout the embankment area.

It was considered the need to reinforce the backslope foundation whenever, after over-excavation, W4 and F3-4 rock mass (or better) was not detected. This reinforcement consists of over-excavation of about 2 m in the width of the backslope and later filling with cyclopean concrete and / or a concrete slab with two vertical nailing alignments.

4 CONSTRUCTIVE ASPECTS

4.1 Materials

The characteristics of the embankment materials, mainly soil-rockfill mixtures derived from schists and granites, should comply with the requirements of the Design's Technical Specifications. Additionally it was defined that the values presented in Table 2 must be achieved after the compaction of treated and untreated embankments.

Table 2. General characteristics of soil-cement embankments.

Parameters	Embankment	
	Soil-rockfill	Soil-cement
Friction angle (º)	36	38
Specific weight (kN/m^3)	20 – 22	20 – 22
Cohesion (kPa)	5	200
Passing the #200 sieve (ASTM) (%)	< 25	< 25
Max. Diameter (m)	0.25	0.25
Uniaxial compressive strength (MPa)	N/A	1.0 (7d) 2.0 (28d)
Diametral compressive strength (MPa)	N/A	0.25 (28d)
Deformation modulus (MPa)	N/A	2000 (28d)

The control of these parameters was carried out during the quality control process defined for the construction phase, using laboratory and *in situ* tests.

5 QUALITY CONTROL

Special attention was given to the definition of the quality control for the execution of embankments right from the design phase (with a large emphasis on the reinforced zones). Thus, the 2 main phases to ensure proper execution of the design solution were identified in the Design phase:

- Study Phase;
- Construction Phase.

The studies, methodologies and tests to be carried out in order to guarantee the strength parameters that guarantee the stability and safety of the structure were defined in the Design phase.

5.1 Study phase

During the study phase, in order to define the mixture of cement soil to be applied on site, as well as its application technique, the following methodology was adopted (*Figure 3*).

5.1.1 Mixing study

Before commencing work, a laboratory study was carried out to formulate the mixture to be applied *in situ*.

This study, which should contain at least 3 different cement dosages, presented:

- Grain size distribution curve of the material resulting from the action of the "recycler";
- Cement content and its characteristics;
- Water content, which should be optimized in order to ensure maximum mechanical resistance;
- Results of the modified Proctor test on the "soil (aggregate) / cement" mixture;
- Proctor density corresponding to the water content of the installation;
- Results of strength tests on moulded test specimens with a degree of compaction of 98%, referring to the modified Proctor test;
- Simple and diametral compression tests at 7 and 28 days (or 90 days for CEM II);
- Workability period.

The study of the mixture was carried out, considering specimens composed by schist and granitic materials, with 3 different dosages of cement. The different mixtures were then subjected to simple and diametral compression tests at 7, 28 and 90 days, in order to assess whether the values obtained were in line with the design reference values.

The results showed that, in general, the use of materials of a schist-grade nature, made it possible to meet the established requirements, even for a 3% cement dosage.

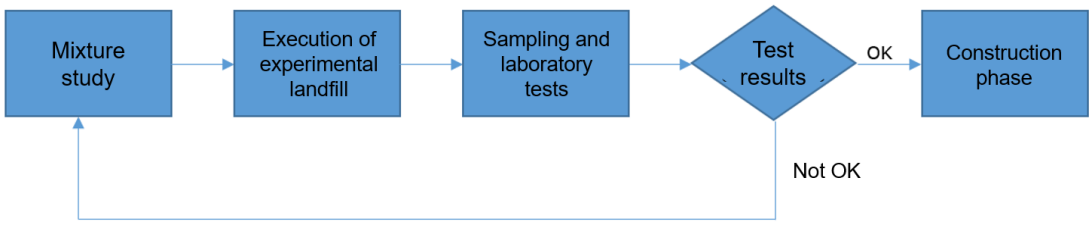

Figure 3. Methodology to be applied in the Study Phase to define the mixture.

In contrast, with the use of materials of a granitic nature, the minimum strength values defined were only achieved with a minimum cement dosage of 4%.

5.1.2 Experimental embankment

After the study of the mixture, the phase of experimental embankment construction began, which allowed the design and study assumptions to be confirmed. It was particularly important to evaluate the obtained strength for the percentage of cement added and its temporal evolution, particularly in the early days.

The results obtained in samples from the experimental embankment tests confirmed the values obtained in the study of the mixture.

It was defined that the soil-cement mixture should contain a minimum cement rate of 4%, in order to obtain the desired resistance parameters, namely when the reinforced embankment is being carried out using materials of a granitic nature.

5.2 Construction phase

5.2.1 In situ and laboratory tests

After the study and definition of the soil-cement mixture to be used, the construction of the reinforced embankments begins according to the assumptions defined during the study phase.

During the construction phase, the quality control carried out was based on the comparison between laboratory tests and on-site tests, when possible.

Thus, in addition to the tests that are usually caried out in order to ensure that the embankment is properly built, the following tests were carried out to validate the design parameters:

- Uniaxial compressive strength – Obtained by testing samples in a hydraulic press, in laboratory;
- Diametral compressive strength - Obtained by testing samples in a hydraulic press, in laboratory;
- Deformation modulus – Evaluated *in situ* with a portable impact deflectometer - PRIMA 100.

It is important to mention that, during the construction phase, it was essential to adjust the time necessary for carrying out the tests and obtaining the respective results to the production needs and on-site efficiency.

In order to solve this issue, it was defined that the laboratory tests to be carried out, namely for the evaluation of simple and diametral compressive strength, would be performed at young ages (≤ 7 days). Then, through the calibration obtained during the study phase, it was possible to carry out the projection of the results for the most advanced ages (28 and 90 days).

5.2.2 Monitoring

In addition to the Quality Control works, the monitoring with geotechnical instrumentation (topographic marks / targets and inclinometers) allowed to evaluate in real time the response of the embankment, by controlling its deformations at the surface and in depth.

Throughout the construction work, and after its completion, the instrumentation showed a good behaviour of the embankments.

6 CONCLUSIONS

The solution developed for the stabilization of the M14, M24, M40 and M41A embankments, located in the stretches of the A4 motorway that approach the east and west portals of the Marão tunnel, allowed to incorporate an important volume of materials obtained from the excavation works. The use of reinforced backslopes in soil-cement allowed steeper slopes, which reduced surface occupation.

The combination of these two important initial premises resulted in the development of this innovative technique, allowing the execution of large embankments, both in height and in length. Thus, it was possible to make the best use of local resources and achieve a better landscape integration, resulting in an economically and environmentally sustainable solution.

The quality control of the construction works was, in our understanding, the main condition for the success of the Project's execution. The proposed methodologies guaranteed not only the quality of execution and consequent stability of the embankment but also the fulfillment of the established deadlines, especially since it is an innovative solution and, therefore, on which there was little experience and knowledge.

ACKNOWLEDGEMENTS

The authors would like to thank Eng. Carlos Matos, from Somague, Eng. Miguel Gião and Eng. Mário Lopes, from Opway, and Eng. Marco Aguiar from Ferrovial Agroman, for exchanging opinions on the execution of these embankments. The authors also thank Infraestruturas de Portugal (IP) for the authorization to present this article.

Proceedings of the XVIII ECSMGE 2024
GEOTECHNICAL ENGINEERING CHALLENGES
TO MEET CURRENT AND EMERGING NEEDS OF SOCIETY
© 2024 the Authors
ISBN 978-1-032-54816-6
DOI 10.1201/9781003431749-434
Open Access: www.taylorfrancis.com, CC BY-NC-ND 4.0 license

ECSMGE 24
XVIII EUROPEAN CONFERENCE ON SOIL MECHANICS AND GEOTECHNICAL ENGINEERING

Solutions of excavations and peripherical earth retaining walls in dense urban area

Solutions d'excavations et de murs de soutènement périphériques en zone urbaine dense

L. Fernandes*, R. Justiniano
JETsj – Geotecnia, Lda., Lisbon, Portugal

**lfernandes@jetsj.com*

ABSTRACT: This paper describes the main design and execution criteria for peripheral earth retaining solutions required to construct a multi-family residential building on Avenida Conde Valbom in Lisbon. The building covers approximately 200m², encompassing three underground and seven elevated floors. The excavation area is bordered by a 10-floor building with one underground level to the north and an 8-floor building with five underground stories to the south. Geological findings indicate a groundwater level of around 4 meters. Soil investigations reveal clayey fill materials, rocky fragments, and other elements atop dark gray clays, followed by Miocene formations named "argilas e cálcarios dos prazeres" and "Formação de Benfica" from the Eocene-Oligocene era. For excavation and containment, the proposed method involves utilizing the "king post wall" technique horizontally supported by a slab strip. This approach includes phased construction of vertically reinforced concrete panels, supported by micro-piles. The slab strip provides load-bearing support and incorporates HEB140 double shorings where necessary. This solution permits a thinner wall (0.30m) and simultaneous execution during excavation. To ensure stability against soil pressures during excavation, concrete pouring of panels directly into the ground is planned, with support from the slab strip and metallic shorings at existing floor levels. Monitoring and survey plan aims to execute excavation and containment structures safely and economically while assessing the behavior of neighbouring structures during construction. It addresses identified constraints and quantifies risks associated with the construction phase.

RÉSUMÉ: Le document décrit les principaux critères de conception et d'exécution des solutions périphériques de retenue des terres nécessaires à la construction d'un immeuble résidentiel multifamilial sur l'Avenida Conde Valbom à Lisbonne, couvrant une superficie d'environ 200m² comprenant trois étages souterrains et sept étages surélevés. La zone de fouille est délimitée par un bâtiment de 10 étages avec un sous-sol au nord et un bâtiment de 8 étages avec cinq sous-sols au sud. Les résultats géologiques indiquent un niveau d'eau souterraine d'environ 4 mètres, tandis que les investigations du sol révèlent des matériaux de remplissage argileux, des fragments rocheux et d'autres éléments sur des argiles gris foncé, suivis par des formations du Miocène appelées "argilas e cálcarios dos prazeres" et "Formação de Benfica" de l'ère de l'Éocène-Oligocène. Pour l'excavation et le support, l'approche proposée implique l'utilisation de la méthode "king post wall" soutenue horizontalement par une bande de dalle. Cette méthode comprend une construction par phases de panneaux en béton armé verticalement soutenus par des micro-pieux. La bande de dalle assure le support de charge et intègre des étais doubles HEB140 là où nécessaire. Cette solution permet un mur plus mince (0,30m) et une exécution simultanée pendant l'excavation. Pour assurer la stabilité contre les pressions du sol pendant l'excavation, la coulée de béton des panneaux directement dans le sol est prévue, avec le soutien de la bande de dalle et des étais métalliques aux niveaux de sol existants. Le plan d'instrumentation et d'observation vise à exécuter les structures d'excavation et de retenue en toute sécurité et de manière économique, tout en évaluant le comportement des structures environnantes pendant la construction. Il aborde les contraintes identifiées et quantifie les risques associés à la phase de construction.

Keywords: Earth retaining wall; slab strip; king post wall; monitoring and survey plan.

1 INTRODUCTION

The present article describes the solutions adopted for the excavation and peripheral soil containment, necessary for the construction of the 3 underground floors of a multi-family residential building located on Avenida Conde Valbom nº21-25, in Lisbon. In Figure 1, the location of the construction site is presented, highlighting the following boundaries for the excavation area:

- Conde Valbom Avenue side: The terrain is approximately at the level of floor 0.
- Northern side: Existing building with 10 floors and 1 basement floor.

- Southern side: Existing building with 8 elevated floors and 5 basement floors.
- Rear side: Boundary with the existing backyard.



Figure 1. Aerial view of the intervention site (images taken from Google Earth).

The building to be constructed has a footprint area of approximately 200 square meters, comprising three underground floors and 7 elevated floors plus a rooftop.

2 MAIN CONSTRAINTS

2.1 Neighbourhood conditions

The excavation and peripheral containment solutions must be compatible with preserving the proper functionality of all structures and infrastructures located near the excavation area. The Figure 2 illustrates the plan view of the neighbourhood main constrains.

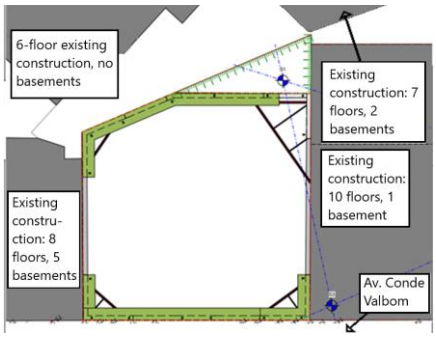

Figure 2. Plan view of the neighbourhood constrains.

2.2 Geological and geotechnical conditions

The geological-geotechnical survey encompassed three boreholes for SPT tests and sample collection. Reported groundwater levels approximate 4 meters. Survey results reveal primarily brown clayey fill materials to a depth of about 3.0 meters. Subsequently, Miocene formations display whitish-gray silts, and lower layers exhibit clayey and silty sands, attributed to the Eocene-Oligocene.

The findings categorized three geotechnical zones: ZG1 (NSPT 7-15) for recent cover deposits, ZG2 (NSPT 18-45) for uncompressed in situ masses, and ZG3 (NSPT 45-60) representing the more robust "Formação de Benfica".

3 EXCAVATION AND PERIPHERAL EARTH RETAINING SOLUTIONS

In the design of the adopted peripheral earth retaining solutions, the objective was to maintain crucial principles such as: (a) Manage soil deformation and safeguard neighbouring structures and infrastructures against excavation-related impacts; (b) Minimize disruptions to adjacent structures and infrastructures as much as possible.

Considering the existence of various conditioning factors, the excavation and peripheral containment were executed using the "king post wall" technology, coupled with the installation of a slab strip as illustrated on Figure 3.

The construction approach for the "king post wall" type containment wall involves a phased assembly, from top to bottom, of reinforced concrete panels supported by vertical micro-piles. The profiles are inserted into holes and sealed along the sealing bulb length using the IGU injection system in competent terrain. The slab strip integrates a section of the final slab to bear soil loads, while double shorings are deployed in areas where the slab strip isn't possible to execute. Provided the assumptions hold, panels will be directly concreted into the ground to stabilize the containment wall against soil pressures during excavation, supported by the slab strip and metallic shorings at existing floor levels (0, -1, and -2). The following figures represents the plan view of the -1, -2 and -3 floor. To minimize soil decompression, strict adherence to the proposed construction phasing is important, notably ensuring a 24-hour maximum gap between excavation and concreting. In the definitive phase, floor slabs at levels 0, -1, and -2 will themselves ensure the containment wall's stability, transitioning temporary props to permanent upon completing the mentioned structure.

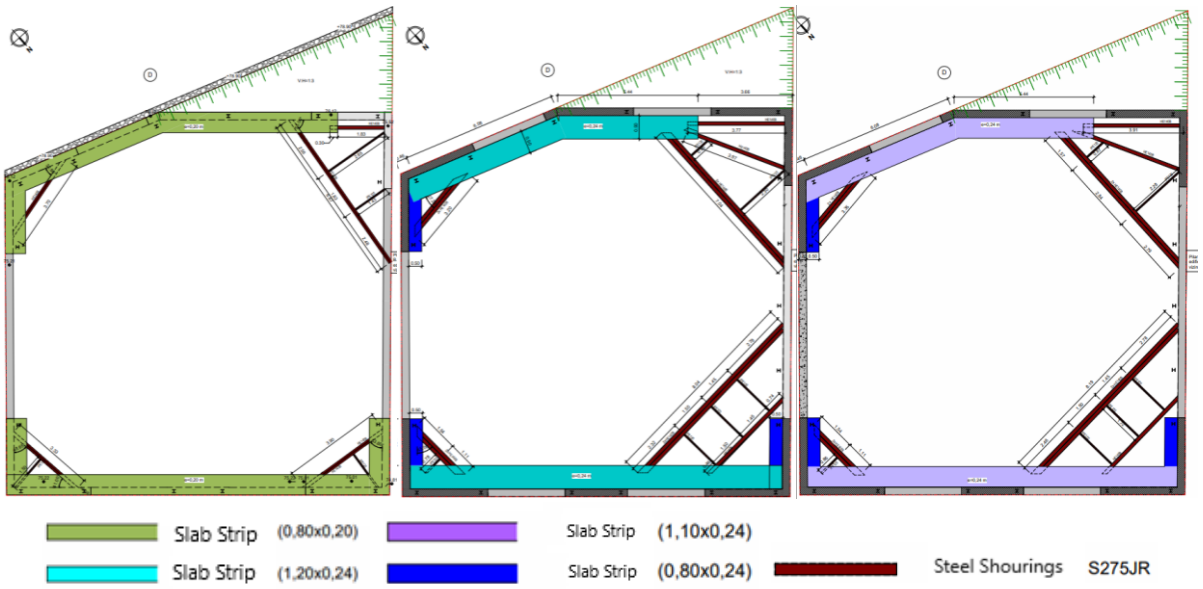

Figure 3. Design plan view of the peripheral earth retaining solution at levels 0, -1 and -2.

4 GEOTECHNICAL AND STRUCTURAL DESIGN

The evaluation of the proposed methods for the peripheral earth retaining solutions in terms of forces and deformations encompassed a comprehensive analysis across construction phases. This assessment utilized dedicated finite element program PLAXIS 2D, purpose-built for this specific task. A constitutive model was developed to mimic the behaviour of "Hardening Soil," considering nonlinear constitutive relationships and variations in soil stiffness under differing stress states. These outlined parameters from Table 1 were then implemented in PLAXIS 2D to accurately model the behaviour of the soils.

Table 1. Geotechnical soil parameters.

Soil Type	ZG_3	ZG_2	ZG_1
N_{SPT}	7-15	18-45	45-60
Υ [kN/m^3]	18	18	20
Φ [°]	27	30	38
E_{50}^{ref} [MPa]	10	40	90
E_{ur}^{ref} [MPa]	30	120	270

ZG_1 – *Loosely compact clay fill*; ZG_2 – *moderately compact silt soil and clayey sandy soil;* ZG_3– *compact clayey sand soil.*

In these models, the "king post wall" and the vertical micropile were represented using "plate" elements exhibiting elastic behavior. Meanwhile, the slab strip and the steel struts were simulated as "anchors." The behaviour of the peripheral retaining structure underwent analysis, evaluating design aspects such as containment structure forces, deformations, stress conditions, and soil stability. Figure 4 showcase specific displacement results derived from these developed models.

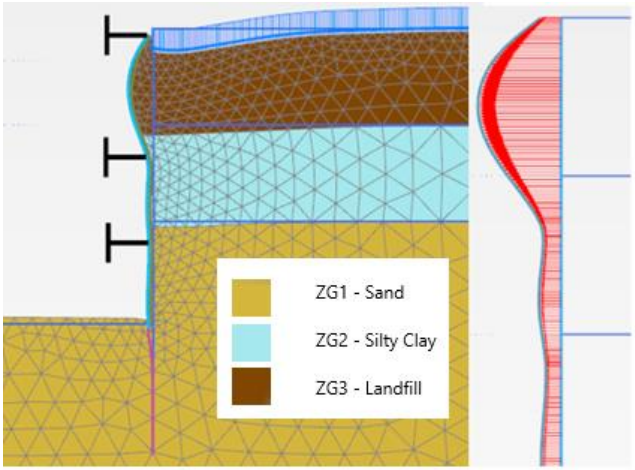

u	*16,34 mm*	u_x	*15,82 mm*

Figure 4. Expected maximum total displacements (u) and maximum horizontal displacements (ux).

5 MONITORING AND SURVEY PLAN

Based on the complex framework of the site, a Monitoring and Survey Plan (MSP) was established to ensure safety and optimal functionality during excavation and the construction of geotechnical structures, as well as for neighbouring structures and infrastructures. Within this plan, the following instruments were installed: (a) 20 topographic targets positioned along the earth retaining solution and placed along neighbouring infrastructure; (b) 1 inclinometer placed behind the peripheral containment wall.

Alert and alarm criteria were established for all instruments and monitored structures based on the conducted modelling. Overall, the readings consistently remained below the defined alert and alarm criteria outlined in the project. Figure 5 and Figure 7 illustrates the schematic locations of the instrumentation devices along with some of the most noteworthy results.

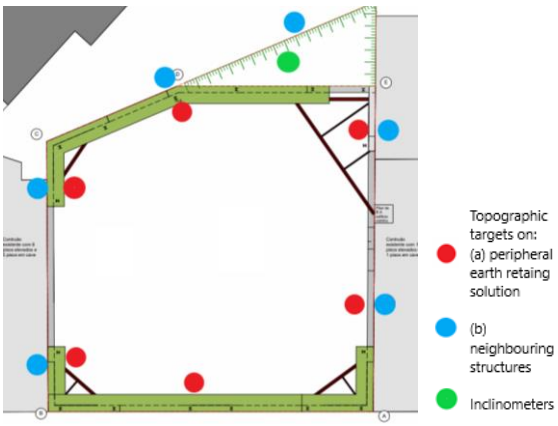

Figure 5. Instrumentation and monitoring plan.

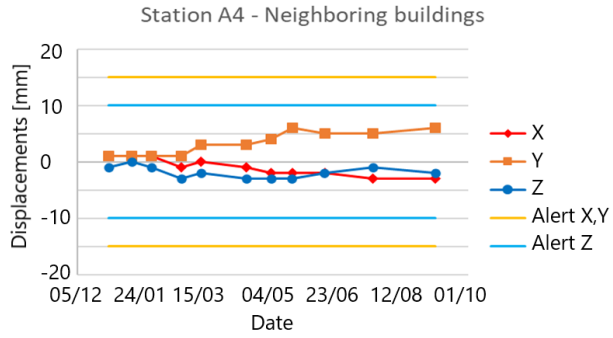

Figure 6. Maximum displacements on neighbouring structure (station A4).

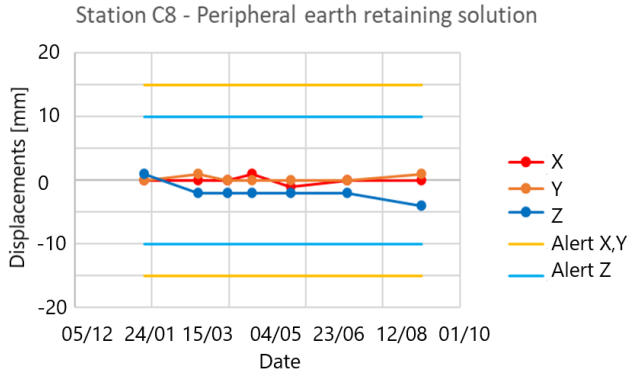

Figure 7. Maximum displacements on peripheral earth retaining solution (station C8).

In general, maximum displacements of about 6mm were recorded for neighbouring structures, and approximately 3mm for the peripheral containment solution, values well below the alert and alarm criteria set at the beginning of the excavation, which were 15mm and 30mm, respectively. As for vertical displacements, a maximum value of around 4mm was registered, equally well below the alert and alarm criteria of 10mm and 20mm, respectively. The apparent discrepancy between estimated and observed deformations can be attributed to several factors, notably the geomechanical attributes of the soils involved. Specifically, the Miocenic formations exhibit superior characteristics compared to those initially considered in the design calculations.

6 CONCLUSIONS

In the scope of this article, it was possible to demonstrate the technical efficiency of king post wall braced by various structural elements such as struts, and slab stripes. The peripheral earth retaining solution presented actual displacements lower than those estimated in project and displayed a highly stable behaviour during the excavation works. Additionally, the use of slab bands not only overcame the encountered limitations due to the excavation´s site proximity to the technical gallery and the future underground parking lot, but also incorporated elements of the final structure, enhancing the economic efficiency of the solutions. One of the most daunting hurdles encountered throughout the project was the limited space available for the construction site. Situated within a densely urbanized environment, the work site posed significant challenges, primarily due to its restricted area. This spatial constraint significantly impacted various aspects of the construction process, from material storage to site infrastructure and the removal of excavated soil.

ACKNOWLEDGEMENTS

The authors are grateful for SOSIDIS -Atividades Hoteleiras, Lda. for granting permission to publish this article, as well as to the Ecociaf for their execution of excavation and earth retaining solution works.

Proceedings of the XVIII ECSMGE 2024
GEOTECHNICAL ENGINEERING CHALLENGES
TO MEET CURRENT AND EMERGING NEEDS OF SOCIETY
© 2024 the Authors
ISBN 978-1-032-54816-6
DOI 10.1201/9781003431749-435
Open Access: www.taylorfrancis.com, CC BY-NC-ND 4.0 license

ECSMGE 24
XVIII EUROPEAN CONFERENCE ON SOIL MECHANICS AND GEOTECHNICAL ENGINEERING

Effects of soil improvement on the axial load capacity of drilled displacement piles – a CPT based case history analysis

Effets de l'amélioration du sol sur la capacité de charge axiale des pieux forés à déplacement – une analyse historique de cas basée sur le CPT

G. Figueroa Palacios, A. Lemnitzer*
University of California Irvine, Irvine, United States
**alemnitz@uci.edu*

ABSTRACT: Pile installation is known to affect the surrounding soil, its mechanical properties, and consequently its performance under any type of loading. Data from 11 construction sites, where Cone Penetration Tests (CPT) were performed before (CPT_{PRE}) and after (CPT_{POST}) pile construction, was used to analyze the change in soil resistance surrounding the Drilled Displacement Piles (DDP). Six of the 11 project sites included static axial load tests, allowing for a comparison between axial pile load predictions using CPT_{PRE} data, load test results during field testing, and analytical capacities obtained through CPT_{POST} data. This paper will first present a comparison of post-installation soil improvement observed at all 11 sites. The improvement ratio was defined as the CPT tip resistance post-installation ($q_{c.post}$) divided by the pre-installation resistance ($q_{c.pre}$). Hereafter, the axial load capacity is analytically estimated using soil resistance parameters before and after the pile construction. Results do not differ considerably when using CPT parameters for stratified soil profiles but showed notable analytical improvement (by a factor of 1.4) for cohesionless soils. However, when comparing analytical estimates using CPT-post data to in-situ failure loads observed from axial load tests, the use of post-installation CPT-based soil parameters for design was deemed premature. While field improvement is evident, its benefit is not correctly reflected in the predicted pile performance, primarily attributed to the uncertainty of capacity predictions for these specialty type of foundations. For cohesive sites, the analytical pile capacity estimated with the CPT_{POST} and the axial load test data did not show a consistent trend.

RÉSUMÉ: L'installation de pieux est connue pour affecter le sol environnant, ses propriétés mécaniques et, par conséquent, ses performances sous tout type de chargement. Les données de 11 chantiers de construction, où des tests de pénétration du cône (CPT) ont été effectués avant (CPT_{PRE}) et après (CPT_{POST}) la construction des pieux, ont été utilisées pour analyser le changement dans la résistance du sol entourant les pieux forés à déplacement (DDP). Six des 11 sites du projet comprenaient des tests de charge axiale statique, permettant une comparaison entre les prévisions de charge axiale des pieux à l'aide des données CPT_{PRE}, les résultats des tests de charge lors des essais sur le terrain et les capacités analytiques obtenues grâce aux données CPT_{POST}. Cet article présentera d'abord une comparaison de l'amélioration du sol après l'installation observée sur les 11 sites. Le taux d'amélioration a été défini comme la résistance de la pointe CPT après l'installation ($q_{c.post)}$ divisée par la résistance avant l'installation ($q_{c.pre}$). Ci-après, la capacité de charge axiale est estimée analytiquement en utilisant les paramètres de résistance du sol avant et après la construction du pieu. Les résultats ne diffèrent pas considérablement lors de l'utilisation des paramètres CPT pour les profils de sols stratifiés, mais ont montré une amélioration analytique notable (d'un facteur 1,4) pour les sols sans cohésion. Cependant, lors de la comparaison des estimations analytiques utilisant les données CPT-post aux charges de rupture in situ observées lors des essais de charge axiale, l'utilisation de paramètres de sol basés sur le CPT après l'installation pour la conception a été jugée prématurée. Bien que l'amélioration sur le terrain soit évidente, ses avantages ne sont pas correctement reflétés dans les performances prévues des pieux, principalement attribuées à l'incertitude des prévisions de capacité pour ces types spéciaux de fondations. Pour les sites cohérents, la capacité analytique des pieux estimée avec le CPT_{POST} et les données des tests de charge axiale n'ont pas montré de tendance cohérente.

Keywords: Displacement piles; axial load test, CPT; soil improvement; pile installation.

1 INTRODUCTION

Drilled Displacement piles (DDPs) are unique in their ability to displace and compact soil around the pile during installation, with the potential to improve the pile's load-bearing capacity. Numerous elements, including soil type and its mechanical characteristics,

the construction tool, the configuration of the displacement body, as well as the arrangement and geometry of the piles, collectively influence the extent of soil enhancement and the load-bearing capacity of the piles.

Researchers have observed cohesionless soils to experience a considerable improvement of soil resistance after pile installation; an inverse relationship between the level of improvement and the initial resistance was found by Siegel *et al.* (2007). Meng *et al.* (2015) studied the installation of DDPs in cohesive soils by measuring the lateral soil displacement and the pore water pressure dissipation, both were found to be highly dependent on time. Maximum displacements were observed after pile concreting, and a reduction of around 50% of the deformations was measured after 15 days.

Semi-empirical methods for estimating axial load capacities of DDPs have been formulated through case history data accompanied by finite element models. CPT-based methods include Brettmann and NeSmith (2000; 2005) and Bustamante and Gianeselli (1993;1998). Basu and Prezzi (2009) developed an axial pile capacity method grounded in lateral earth pressure concepts, and Park et al., (2013) predict axial load capacities through the t-z spring method. All the above-mentioned methods utilize soil properties prior to the pile installation without accounting the soil change due to the pile construction. Consequently, these methods frequently yield conservative predictions of pile capacity and pile design.

The complexity of the DDP installation techniques and its influence on the axial pile capacity was further evidenced by Moshfeghi and Eslami (2018), who studied the reliability of CPT- based predictions for axially loaded DDPs. Moshfeghi and Eslami found the accuracy of the predicted pile capacity to be dependent on the drilling tool; for instance, the capacity of Atlas piles was best predicted by the Brettmann and NeSmith (2005) method. The study also showed that for some CPT direct methods, the axial load capacity results are highly conservative for clayey soils. Figueroa *et al*. (2021) evaluated the predicted accuracy of CPT and SPT based direct methods in estimating axial pile load capacity for DDPs in sand-like, clay-like, and mixed soil sites. Results showed that among all CPT-based methods used to predict axial pile capacities, the closest agreement between measured and analytically predicted failure load in sands was obtained with Brettmann and NeSmith (2000; 2005). The closes agreement in mixed soils was obtained using Bustamante and Gianeselli (1993;1998), and clayey soils were best predicted using Eslami and Fellenius (1997).

This paper aims to present the change in soil properties following pile installation and its influence on the pile bearing capacity. DDP's CPT-based analytical capacity was obtained with CPT_{PRE} and CPT_{POST} data to be later compared with the experimental results of static axial load tests.

2 DDP CASE HISTORIES

The project data is summarized in Table 1 showing the site location, Ground Water Table (*GWT*) depth, and soil categorization (SC)- i.e., (1) homogeneous cohesionless soil profiles, (2) homogeneous cohesive soil profiles, and (3) stratified soil profiles. The pile diameter (*D*), pile length (*L*), and DDP pattern and spacing (*S*), expressed in terms of pile diameter *D* (if applicable) are also listed. Furthermore, Table 1 provides the number of CPT_{PRE} and CPT_{POST} at each site along with the distance between CPT_{POST} and DDP in terms of the pile diameter (*D*). A total of 53 CPTs (15 CPT_{PRE} and 38 CPT_{POST}) were analyzed. The sites consisted of either homogeneous cohesionless or cohesive sites, or mixed soils with strongly stratified sand, silt, and clay layers. The number of days between pile construction and CPT_{POST} testing is also detailed. The number of Static Axial Load Tests (ALT), compression (C) or Tension (T) are listed for every project site. The nominal shaft diameter varies from 40.6 cm to 45.7 cm (16 to 18 in). The embedment length of the piles ranged from 6 m to 15 m (19.7 ft to 50 ft). Figure 1 shows a representative project site CPT tip resistance (q_c) for each site category.

As detailed in Table 1, among the 11 project sites, 6 of them included axial load tests. The in-situ axial load that triggered plunging behavior (high deformation with a low increase of the load) was either obtained directly from the load test ($Q_{f.in\text{-}situ}$) or estimated using Van der Veen's Criteria, 1953 when the plunging behavior was not reached experimentally ($Q_{f.int}$).

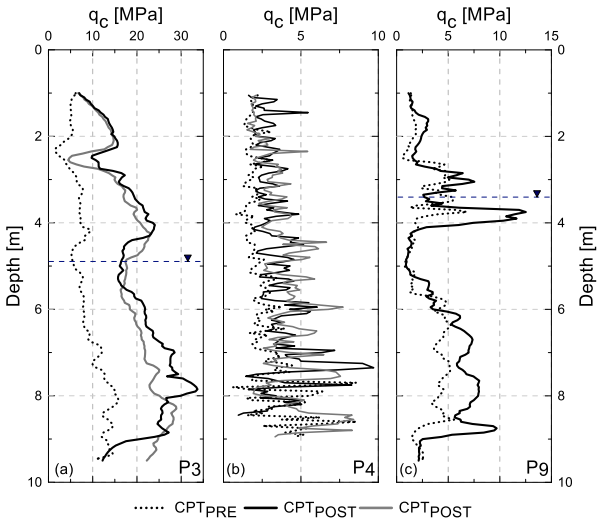

Figure 1. CPT tip resistance (q_c) before and after pile installation for (a) cohesionless, (b) cohesive, and (c) stratified soil profiles.

In addition to identifying the pile failure loads, the axial load that triggers a settlement equal or higher than 10% of D ($Q_{\Delta=10\%D}$) was also determined (whenever pile settlements reached that level of deformation). The maximum load ($Q_{max.test}$) and corresponding settlement (Δ_{max}) were also collected for further analysis.

Table 1. Overall information of each project site and tested piles.

Location		SC	GWT Depth (m)	D (m)	L (m)	Arrangement - Spacing	# PRE-CPT	# POST-CPT	Distance pile-CPTpost	# Days	ALT
P1	Tampa, FL	1	4	0.45	7.6	Square - 4D	1	3	1-2D	1	1T-1C
P2	Myrtle Beach, SC	1	0.8	0.40	8	Square - 6.8D	2	10	1-5D	7	-
P3	Orlando, FL	1	4.9	0.40	12	Square - 3.5D Triangle 3.0D	1	2	1.7-2.5D	7	-
P4	San Francisco, CA	2	-	0.45	10.2	Square - 2.7D	1	2	1D	10	1C
P5	Los Angeles, CA	2	-	0.40	12	Square - 3D	1	2	1.5-2.1D	11	1C
P6	Los Angeles, CA	3	1.8	0.40	10.3	Triangle - 7.5D	1	1	3.8D	6	1C
P7	San Jose, CA	3	-	0.40	7.2	Square - 7.5D	1	2	2.5-3.8D	2	2C
P8	San Francisco, CA	3	5	0.45	6.4	Single	1	2	1-1.7D	27	1C
P9	Milipitas, CA	3	3.5	0.40	9.5	Square - 3D	1	2	1.5-2.1D	7	
P10	Redwood, CA	3	1.8	0.45	7.6	Triangle - 3D	1	2	1.5D	6	1C
P11	Sacramento, CA	3	4	0.45	14.5	Square - 3D	4	10	1-4D	10	-

3 DATA ANALYSIS

3.1 CPT_{PRE} and CPT_{POST} data analysis

An initial assessment of raw CPT measurements, i.e., tip resistance (q_c) and side friction (f_s), showed that for homogeneous soil profiles the improvement in q_c and f_s can be easily noticed and the improvement of both resistances are closely associated. For stratified soil profiles, the change in CPT measurements was observed to be smaller and cannot be easily quantified by visual inspection, unless a substantially large uniform layer is present, as exemplarily depicted in Figure 1(c) from 6 m to 8 m depth.

The CPT tip resistance improvement ratio was calculated as $q_{c.post}/q_{cpre}$ and plotted against the tip resistance prior to pile installation (q_{cpre}) for all site categories. Figure 2 shows the improvement ratio vs, q_{cpre}. Results suggest an inverse relationship between achievable improvement and soil resistance prior to pile installation.

Figure 2(a) suggests nearly immediate improvement for homogeneous soil profiles with mostly clean sands and sand-like soil types. Homogeneous cohesive soil layers, as shown in Figure 2(b), have the time-dependent capability to enhance their resistance due to a low initial soil resistance. The data points in Figure 2(b) showing an improvement ratio higher than 5 come from CPT_{POST}s executed 11 days after pile installation. For stratified sites, the change in the CPT tip resistance was not visually quantifiable. Nearly $q_{c.post} \cong q_{cpre}$ or a reduction of the q_{cpre} ($q_{c.post}/q_{cpre}<1$) can be observed. Improvable layers (e.g., sand layers within a stratified profile) only showed visible improvement when a sufficient layer thickness (> 0.7 m) was available. The beneficial effects of soil homogeneity on the achievable

improvement can also be observed in Figure 1(c) from 6 to 9m depth.

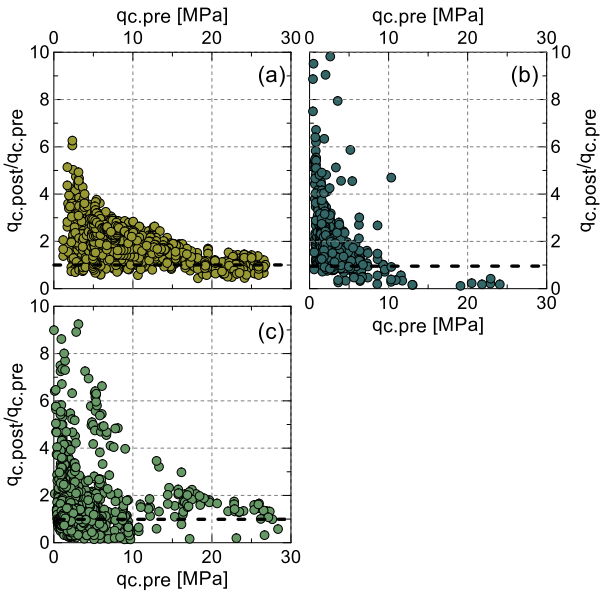

Figure 2. CPT tip resistance ($q_{c.pre}$) vs. $q_{c.post}/q_{cpre}$ for (a) cohesionless, (b) cohesive, and (c) stratified soil profiles.

Further analysis showed that the level of soil resistance improvement is contingent upon several other parameters, including the pile arrangement, separation between the piles (S) and the location where the improvement is being assessed; consequently, it cannot be predicted solely based on the initial soil resistance. A more detailed analysis by the authors with recommendations to predict the expected soil improvement following DDP installation is currently in review (see Figueroa *et al*. 2024).

3.2 Comparison of axial load capacities estimated with CPT_{PRE} and CPT_{POST} data

An improvement in soil behavior surrounding the DDP as observed in the case studies listed beforehand could suggest a potential increase in axial pile load capacity as benefit of the unique installation technique. The CPT data obtained before and after pile construction was utilized to predict the axial load capacity of the DDP. Brettmann and NeSmith (2000; 2005), Eslami and Fellenius (1997), and Bustamante and Gianeselli's (1993;1998) analytical CPT methods were employed for cohesionless, cohesive, and stratified soil profiles, respectively. Since Bustamante and Gianeselli (1993; 1998) estimate the load corresponding to the settlement of 10%D, Eslami and Fellenius (1997) method was employed for stratified soil sites where the $Q_{max.test}$ corresponding settlement is lesser than 10%D. This theoretical exercise helped visualize how installation effects, i.e., the change in raw soil resistance data, could translate into potential changes of overall pile capacity.

The bar chart of Figure 3 separates the axial pile resistance into the analytically estimated toe resistance (Q_{toe}, Figure 3(a)), side friction (Q_{side}, Figure 3(b)), and the total, ultimate load (Q_u, Figure 3(c)) based on before and after soil data. Except for P4, all sites maintain or improve their analytical tip resistance and indicate similar or higher toe capacity. Similar observations can be made for the cumulative shaft resistance shown in Figure 3(b). Except for P7, which is mostly composed of silt-like and clay-like soils, all piles maintained or increased their side friction due to the installation technique. The CPT_{POST} for P7 was performed 2 days after the pile construction, hence potential improvements are likely not captured.

For homogeneous cohesionless sites, the total pile axial load capacity analytically increased by a factor of 1.3 to 1.7 when using CPT_{POST} vs. CPT_{PRE} data. Almost all mixed soil type projects (P7, P8, P9, P10 and P11) showed ratios of post vs. pre ultimate pile capacities near 1.0, deeming its improvement benefit negligible.

More importantly, is the comparison of analytically predicted axial load capacities with experimentally observed failure loads. The in-situ axial load that triggered plunging behavior ($Q_{f.in\text{-}situ}$), the interpreted failure load ($Q_{f.int}$), the axial load that triggers a settlement equal or higher than 10% of the pile diameter ($Q_{\Delta=10\%D}$) and the maximum load during the test ($Q_{max.test}$) are also presented in Figure 3 to assess the pile behavior more completely. Projects P2, P3, P9, and P11 do not have axial load test data, therefore the comparison between the analytical capacity and experimental failure load was not possible for these sites. When the red and blue dashed lines are next to each other, the axial load test reached plunging failure and the failure load equals the max applied load accordingly. This was the case for P6, P8, and P10.

Results presented in Figure 3(c), suggest the data and methods to be assessed more closely, making it difficult to draw general conclusions given the limited availability of data. Projects P4 and P8 show very good agreement between the in-situ pile load failure, and the capacity analytically estimated with the CPT_{POST} data. Both projects were analyzed using Eslami and Fellenius method. The analytical predictions for P1(Δ_{max}=2.0 cm) and P6 (Δ_{max}=2.4 cm) notably overestimate the actual pile load capacity. P1 consists of clean sand and sand-like materials, and the use of CPT_{POST} data overestimates the expected pile capacity. Project P6, a highly mixed site, analyzed with Eslami and Fellenius shows similar trends, the analytically estimated capacity (using both, CPT_{PRE} and CPT_{POST}) being unconservative. Given the broad spectrum of

comparative results, a generalized conclusion is nearly impossible and warrants the plea for future testing or sharing of existing results that encompass a wide range of axial load tests in various soil types with before-after testing.

4 LIMITATIONS OF THIS STUDY

Factors affecting a 1:1 comparison of CPT_{PRE} and CPT_{POST} measurements include the non-horizontality of the soil layers that can produce a wrong comparison between the pre and post measurements. The "thin-layer effect" in comparing CPT data arises from the load cell of the testing instrument sensing the next soil layer before reaching its depth, thereby impacting soil resistance measurements, especially in highly stratified soils.

Simultaneously, the analytical methods are limited by their empirical derivation. While the Brettmann and NeSmith (2000; 2005) method was developed for DDP, the DDPs consisted of Augered Pressure-injected Drilled Displacement Piles (APID). Likewise, Bustamante and Gianeselli (1993; 1998) method was developed based on Franki-Atlas, De Waal, Omega, and Spire DDP. The difference between the installation tool may alter the level of soil displacement and therefore the pile behavior.

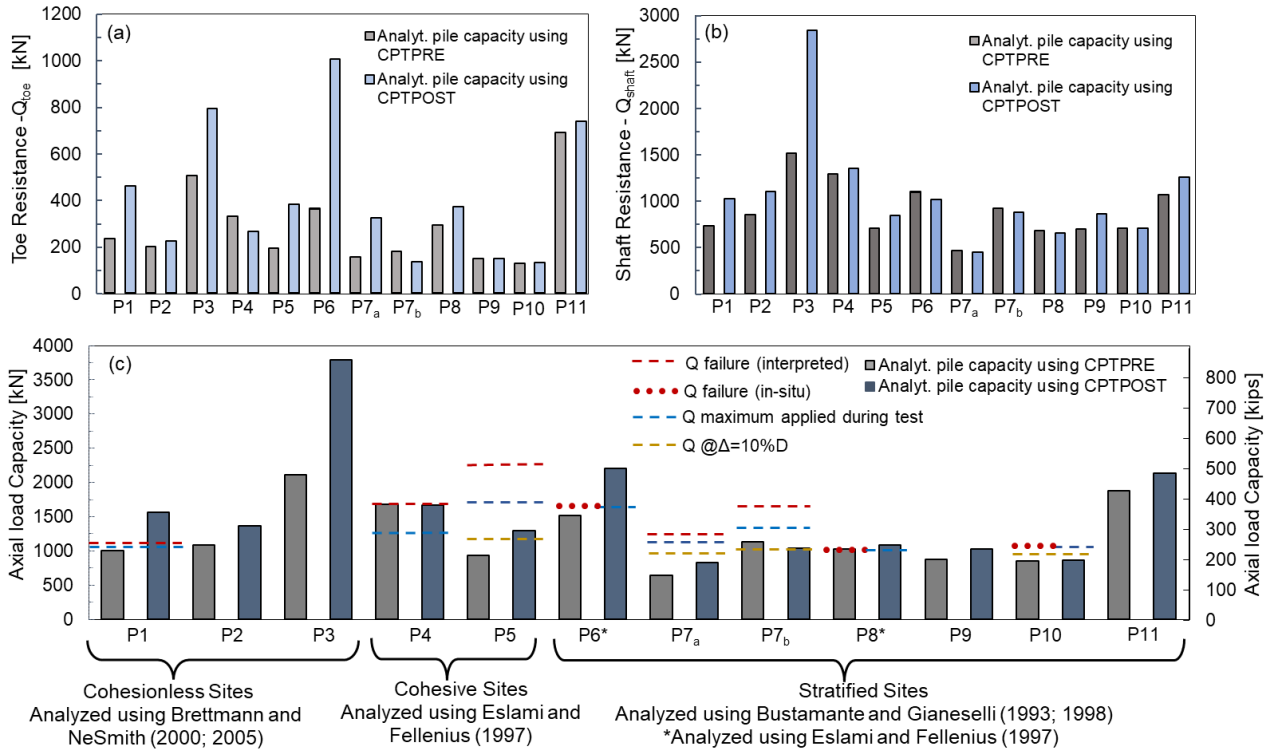

Figure 3. Analysis of the axial load capacity of the DDP using the CPT_{PRE} and CPT_{POST} data. (a) Analytical Q_{toe} capacity, (b) Analytical Q_{shaft} capacity, (c) Total capacity Q_u showed in bars, $Q_{failure}$, $Q_{max.test}$, and $Q_{\Delta=10\%D}$ showed with dashed lines.

5 CONCLUSIONS

An initial assessment of raw CPT data showed clear (and nearly immediate) improvement for soil profiles with homogeneous clean sands and sand-like soil types. Cohesive soils were found to improve recognizably when the soil profiles consisted of thick and homogeneous layers. The number of days between the DDP construction and CPT_{POST} execution suggested a strongly time-dependent improvement for cohesive soils. For stratified or cohesive soil profiles, with no thick homogeneous soil layer, the change in the CPT tip and side friction was not visually quantifiable, and in some cases lower resistances were measured.

For all site categories, the CPT-based soil resistance ratio ($q_{c.post}/q_{c.pre}$) was found to be dependent on the initial soil resistance, and follows an inverse relationship, i.e., the lower the initial resistance (q_{cpre}), the higher the achievable improvement. For cohesive soils with low initial tip resistances, q_{cpre}, improvement ratios of up to 6 times the initial resistance were observed, when continuous, thick homogeneous soil layers were present.

Available axial load test results were compared to analytical predictions. Best agreement between

analytically predicted pile capacity obtained with the CPT_{POST} data and in-situ failure loads was achieved for primarily homogeneous soil profiles. For projects with the pile toe resting in a strong sand layer, the analytical methods appear to overestimate the in-situ pile capacity of the elements, while for projects with thin sand layers between clayey soils, the analytical pile capacity underestimated the axial load pile capacity in the field.

While important trends could be identified with the data sets available to the authors, the need for future field testing became critically apparent. Particularly well-designed field programs that include spatial, time, and geometric aspects of DDPs as well as more diversified field instrumentation is recommended to gain additional insight into the soil improvement due to the installation technique and pile load-behavior. Similarly, the assessment of short term vs. long term improvement aspects of the installation technique remains unexplored to date.

ACKNOWLEDGEMENTS

This work was supported primarily through the National Science Foundation, Grant CMMI 1752303, and supported in part by the DFI ACIP Technical Committee Project Fund. We extend our sincere appreciation to the following professionals for their support on this project and their generous willingness to share data: Sam Warren (Farrell Design-Build, Inc.), Morgan NeSmith (Berkel and Company), Peter Faust (Malcolm Drilling), and Derek Deutscher† (formerly Condon Johnson).

REFERENCES

Basu, P., & Prezzi M. (2009). *Design and Applications of Drilled Displacement (Screw) Piles*. Publication FHWA/IN/JTRP-2009/28. Joint Transportation Research Program, Indiana Department of Transportation and Purdue University. doi.org/10.5703/1288284314278

Brettmann, T., & NeSmith W. (2005). *Advances in auger pressure grouted piles: design, construction, and testing*. Advances in Designing and Testing Deep Foundations. Austin, Texas, United States, ASCE, 262–274. doi:10.1061/40772(170)5

Bustamante, M., & Gianeselli, L. (1993). Design of auger displacement piles from in-situ tests. Deep Foundations on Bored and Auger Piles, BAP II, Balkema: Rotterdam, 21–34.

Bustamante, M., & Gianeselli., L. (1998). *Installation parameters and capacity of screwed piles*. Deep Foundations on Bored and Auger Piles, BAP III, Balkema: Rotterdam, 95–108.

Eslami, A., & Fellenius, B. H. (1997). Pile capacity by direct CPT and CPTU methods applied to 102 case histories. *Canadian Geotechnical Journal*, Vol. 34, 886–904. DOI: 34(6) 886–904

Figueroa, G., Marinucci, A., & Lemnitzer, A. (2022), Axial Load Capacity Predictions of Drilled Displacement Piles With SPT- and CPT-based Direct Methods. *DFI Journal - The Journal of the Deep Foundations Institute*, 16(2). 10.37308/DFIJnl.20220512.262.

Meng Z., Chen J., Zhang L., Wang J., and Yao J. (2015). Field Tests to Investigate the Installation Effects of Drilled Displacement Piles with Screw-Shaped Shaft in Clay. *Journal of Geotechnical and Geoenvironmental Eng.– ASCE*. 141. DOI: 10.1061/(ASCE)GT.1943-5606.0001371.

Moshfeghi, S., & Eslami, A. (2018). *Failure analysis of CPT-based direct methods for axial capacity of driven piles in sand.* Georisk: Assessment and Management of Risk for Engineered Systems and Geohazards. 13, 1-19. DOI: 10.1080/17499518.2018.1478105

Park S., Roberts L., Misra A. (2012) Design Methodology for Axially Loaded Auger Cast-in-Place and Drilled Displacement Piles. *Journal of Geotechnical and Geoenvironmental Engineering*. 138(12), 1431-1441. DOI:10.1061/(ASCE)GT. 1943-5606.0000727.

Siegel, T. C., NeSmith W. M., & Cargill, P. E. (2007). *Ground Improvement resulting from Installation of Drilled Displacement Piles.* Deep Foundation Institute 32nd Annual Conference, Colorado Springs.

Van der Veen, C. (1953). *The bearing capacity of a pile proceedings.* 3rd International Conference on Soil Mechanics and Foundation Engineering, 2, 84-90.

Proceedings of the XVIII ECSMGE 2024
GEOTECHNICAL ENGINEERING CHALLENGES
TO MEET CURRENT AND EMERGING NEEDS OF SOCIETY
© 2024 the Authors
ISBN 978-1-032-54816-6
DOI 10.1201/9781003431749-436
Open Access: www.taylorfrancis.com, CC BY-NC-ND 4.0 license

ECSMGE 24
XVIII EUROPEAN CONFERENCE ON SOIL MECHANICS AND GEOTECHNICAL ENGINEERING

Use of a natural inorganic binder to improve the mechanical properties of mining tailings

Utilisation d'un liant inorganique naturel pour améliorer les propriétés mécaniques des résidus miniers

M.M.M. Fontes*, M.D. de O. Corrêa, A.M. Santos, A.B.S.P. de Paiva, G.M. de D. Vieira
Fonntes Geotécnica, Belo Horizonte, Brazil

**michel@fonntesgeotecnica.com*

ABSTRACT: In order to reduce the environmental impact generated in the manufacture of products and applications in civil construction and geotechnical works, there is an increasing search for alternative materials to conventional ones, such as cement, which can reduce emissions of harmful gases into the atmosphere, such as CO_2, and energy consumption in their production. With this in mind, this study proposes the use of a natural inorganic binder, which has the function of absorbing CO_2, in the stabilization of iron ore tailings in order to improve their mechanical properties. To this end, a dosage test was carried out to define the best levels of the product in the tailings, using simple compressive strength tests. The tests evaluated the application of 3%, 4% and 5% of the binder in relation to the dry mass of tailings and showed that the three dosages showed significant gains in terms of peak strength and deformations when compared to the virgin sample of tailings, with 3% of the product already showing significant results. Therefore, the use of the product proved promising in the stabilization of tailings, helping to improve both the mechanical characteristics, which are important in geotechnical works projects, and to reduce the environmental impacts of these processes.

RÉSUMÉ: Afin de réduire les impacts environnementaux générés par la fabrication de produits et d'applications dans la construction civile et les travaux géotechniques, on recherche de plus en plus des matériaux alternatifs aux matériaux conventionnels, tels que le ciment, qui peuvent réduire les émissions de gaz nocifs dans l'atmosphère, tels que le CO_2, et la consommation d'énergie lors de leur production. Dans cette optique, cette étude propose l'utilisation d'un liant inorganique naturel, qui absorbe le CO_2, pour stabiliser les résidus de minerai de fer afin d'améliorer leurs propriétés mécaniques. À cette fin, un test de dosage a été réalisé pour définir les meilleurs niveaux de produit dans les résidus, en utilisant des tests simples de résistance à la compression. Les essais ont évalué l'application de 3 %, 4 % et 5 % du liant par rapport à la masse sèche des résidus et ont montré que les trois dosages présentaient des gains significatifs en termes de résistance maximale et de déformations par rapport à l'échantillon vierge de résidus, 3 % du produit montrant déjà des résultats significatifs. Par conséquent, l'utilisation du produit s'est avérée prometteuse pour la stabilisation des résidus, en contribuant à améliorer les caractéristiques mécaniques, qui sont importantes dans les projets de travaux géotechniques, et à réduire les impacts environnementaux de ces processus.

Keywords: Mining tailings; natural inorganic binder; stabilization.

1 INTRODUCTION

The mining sector, which is extremely important for the Brazilian economy, accounting for around 4% of the country's GDP (ANM, 2023), faces the constant challenge of reconciling its significant growth with the pressing need to reduce the environmental impacts associated with traditional tailings disposal practices. Faced with this reality, the dry stacking technique has emerged as a promising alternative to dam structures, as it proposes the deposition of tailings in the best compaction conditions for stacking, thus reducing instabilities in these structures and risks of liquefaction. However, even this technique is prone to instability and ruptures, especially during heavy rainfall events. For this reason, it is often necessary to stabilize the tailings to improve their mechanical characteristics and optimize the processes, the most common currently being the use of Portland cement. The biggest problems associated with cement are its high energy demand in production and high emissions of harmful gases into the atmosphere (CARVALHO et al., 2016), which is why there is an increasing search for ecological and effective alternatives in the stabilization processes of mining tailings for piling.

This study proposes an innovative approach in the search for sustainable practices in the geotechnics of mining tailings, using an inorganic cementing agent HPA PLUS to replace traditional cement. This agent

seeks to promote the chemical stabilization of iron ore tailings, aiming not only to improve the mechanical properties of these materials, but also to reduce the environmental impacts associated with cement production.

2 MATERIALS AND METHODS

The study included the physical and mechanical characterization of iron ore tailings from a mining company in the Iron Quadrangle in Minas Gerais, as well as the tailings mixtures with the addition of the HPA Plus product. For physical characterization, tests were carried out on the grain size, specific mass of the grains, Atterberg limits and compaction of the tailings.

For mechanical characterization, the unconfined compressive strength test was carried out on both the pure tailings samples and the mixtures with the addition of 3%, 4% and 5% HPA Plus. These levels were used to obtain the optimum dosage and all the tests were carried out in duplicate to improve the reliability of the results.

2.1 Iron ore tailings

The iron ore tailings used in this research come from a mine in Minas Gerais, Brazil. Figure 1 shows an image of the material.

The tailings sample collected went through the mining processes until the final dewatering stage, when it had the consistency of pulp and 22.93% moisture.



Figure 1. Iron Ore Tailings used in this research.

2.2 Cementing agent - HPA plus

HPA Plus is part of a range of new products offered by Fonntes Geotécnica for different geotechnical solutions. It acts as a cementitious agent when added in appropriate dosages to the tailings matrix, where the material is chemically stabilized through alkaline activation processes, improving its mechanical properties. Figure 2 below shows the material used in the research.



Figure 2. HPA Plus.

HPA Plus is made up of a mixture of oxides of silicon, aluminum, magnesium, among other elements, and for this reason it acts as a cementing agent in the mixture, because the ions present in its formulation are attracted to those of the tailings, there is cation exchange, and so the whole alkaline activation process takes place, such as agglomeration between the particles, hydration and pozzolanic reactions arising from the hydration stage of the mixture, forming C-S-H and C-A-H gels, which make the structure of the material more cohesive, obtaining a more rigid material that is less susceptible to shrinkage and expansion (WILKINSON et al. , 2010).

The oxides present in HPA Plus can trap CO_2 through a process called carbon mineralization or CO_2 mineralization. The oxide reacts with atmospheric CO_2, transforming it into a stable carbonate that is harmless to the environment.

Table 1 below shows some of the product's characteristics.

Table 1. Characteristics of HPA Plus.

Charactheristics	Correspondents
Color	White
Format	Powder
Odor	Odorless
Bulk Density	0.3 g/cm³
Solubility	Practically insoluble in water
pH	10,3 (20°C)

2.3 Methodology

In order to properly assess the effect of the cementing agent on the matrix, characterization and mechanical tests were carried out on the pure tailings and the mixture of tailings with the addition of HPA at dosages of 3%, 4% and 5%.

The laboratory tests were carried out in accordance with the specific norms and standards in force in Brazil. In summary, the samples were prepared and the tests carried out in accordance with the criteria recommended by the Brazilian Association of Technical Standards (ABNT).

3 RESULTS

3.1 Characterization of the tailings sample

The particle size curve obtained for the tailings is shown in Figure 3. It shows 16.1% clay, 75.1% silt, 8.4% sand and 0.5% gravel. The tailings were therefore classified as clayey silt with little sand.

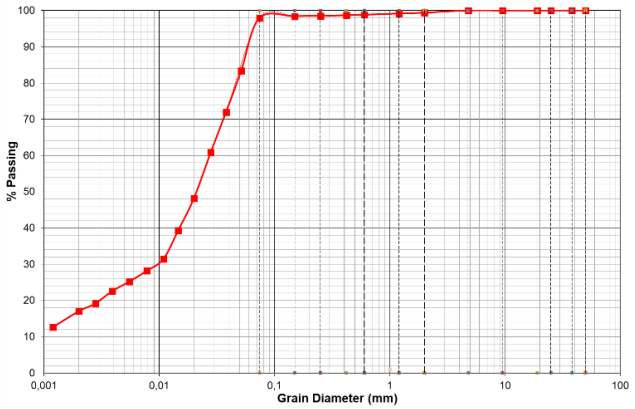

Figure 3. Iron ore tailings granulometry.

The specific mass of the grains obtained was 3.34 g/cm³. With regard to consistency limits, a liquidity limit (LL) of 22% and plasticity limit (LP) of 18% were obtained for the tailings sample.According to the Plasticity Index (PI) of 4, the material was classified as slightly plastic.

Papini et al. (2018) evaluated an iron ore tailing belonging to the same mine as this study and obtained results of 2.98 g/cm³ specific mass of the grains. X-ray diffraction analysis showed the presence of quartz, hematite, magnetite, goethite, kaolinite and gibbsite, the latter three being finer minerals, which corresponds to the fine fraction seen in the grain size results. In this study, chemical analyses were also carried out, showing a composition of 13.79% iron, 67.57% silica, 1.20% alumina, 0.22% manganese and 0.03% phosphorus in the global tailing's samples.

3.2 Normal Proctor

The compaction test was carried out on the virgin tailings, and the results obtained were 14.9% optimum humidity and 2.069 maximum dry specific mass. Figure 4 shows the compaction curve obtained.

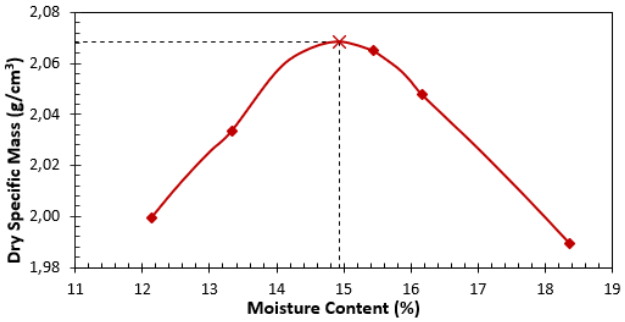

Figure 4. Iron ore tailings compaction curve.

3.3 Unconfined compressive strength

Figure 5 shows the graph with the results of the unconfined compressive strength (Axial Stress versus Axial Deformation) of the virgin samples and those treated with the addition of 3%, 4% and 5% HPA.

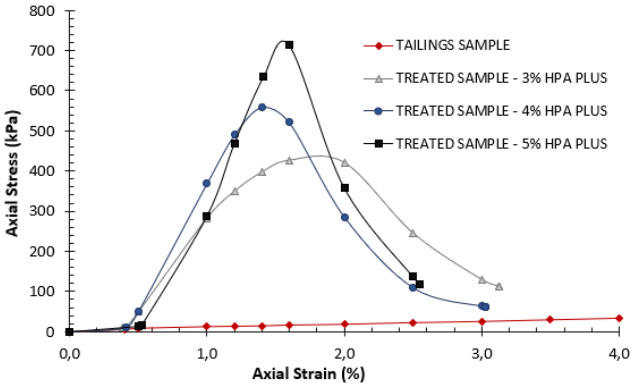

Figure 5. Unconfined compressive strength test results.

Table 2 shows the results of the tests carried out with HPA Plus. It should be noted that the results are an average of the duplicates carried out.

Table 2. Unconfined compressive strength test results.

SAMPLES	Umidity (%)	Compressive Strength (kPa)	Strain (%)
Tailings Sample	22.30	44.90	5.00
Treated Sample – 3% HPA Plus	16.70	466.83	1.60
Treated Sample – 4% HPA Plus	16.85	537.86	1.50
Treated Sample – 5% HPA Plus	16.80	676.00	1.80

The results presented show that the dosage of HPA Plus was directly proportional to the increase in Simple Compression Resistance, however, with the addition of 3% of the product, there was already a significant increase in simple compression resistance, which led to this content being defined as the optimum for the product. Regarding the deformation of the

samples, there was a significant reduction when the product was added, which indicates that HPA Plus gives the tailings rigidity, which was expected due to its properties as a cementitious agent.

4 CONCLUSIONS

In summary, the results of this study show that the addition of the inorganic cementing agent HPA Plus to iron ore tailings substantially increased simple compressive strength and reduced axial deformation, indicating a significant improvement in the material's geotechnical properties. The potential for expressive gains with doses as low as 3% highlights the effectiveness of HPA The environmental relevance of the study is emphasized by the favorable comparison with conventional cement, suggesting that HPA Plus not only improves mechanical properties, but also represents a more sustainable alternative, contributing to the reduction of CO_2 emissions associated with the stabilization of iron ore tailings in the mining industry.

ACKNOWLEDGEMENTS

To Fonntes Geotécnica for their full support of the research and the use of the HPA Plus product and to the clients for providing the iron ore tailings samples.

REFERENCES

ABNT, Brazilian Association of Technical Standards (2012). NBR 16097: *Determination of moisture content - Expedited test methods.*

ABNT, Brazilian Association of Technical Standards (2016). NBR 6457: *Soil samples - Preparation for compaction and characterization tests.*

ABNT, Brazilian Association of Technical Standards (2016). NBR 6459: *Soil - Determination of liquidity limit.*

ABNT, Brazilian Association of Technical Standards (2016). NBR 7180: *Soil - Determination of plasticity limit.*

ABNT, Brazilian Association of Technical Standards (2016). NBR 6458: *Grains of pebble retained on the 4.8 mm sieve - Determination of specific mass, apparent specific mass and water absorption.*

ABNT, Brazilian Association of Technical Standards (2018). NBR 7181: *Soil - Particle size analysis.*

ABNT, Brazilian Association of Technical Standards (2020). NBR 7182: *Soil - Compaction test.*

ABNT, Brazilian Association of Technical Standards (2022). NBR 12770: *Soil - Determination of Unconfined Compressive Strength of Cohesive Soil.*

Carvalho, P. S. L; Mesquita, P. P. D. and Melo, L. (2016). *Cement: Sector Panoramas and Climate Change*. BNDES Research Department, 7p.

National Mining Agency - ANM (2023). *There is no sustainable mining without a strong ANM*. Available at: [https://www.gov.br/anm/pt-br/nao-ha-mineracao-sustentavel-sem-a-anm-forte-destaca-mauro-sousa], accessed: 29/11/2023.

Papini, R. M.; Furtado, V. M.; Paiva, F. L. P.; Tameirão, D. R. and Gomes, A. C. F.(2018). *A statistical approach to the magnetic separation of iron ore tailings*. XIV Argentinean Mineral Processing Conference, 10p.

Wilkinson, A.; Haque, A. and Kodikara, J. (2010). *Stabilization of clayey soils with industrial by-products: part a.* Proceedings of the Institution of Civil Engineers: Ground Improvement, 163(3), 149 - 163. https://doi.org/10.1680/grim.2010.163.3.149.

Proceedings of the XVIII ECSMGE 2024
GEOTECHNICAL ENGINEERING CHALLENGES
TO MEET CURRENT AND EMERGING NEEDS OF SOCIETY
© 2024 the Authors
ISBN 978-1-032-54816-6
DOI 10.1201/9781003431749-437
Open Access: www.taylorfrancis.com, CC BY-NC-ND 4.0 license

ECSMGE 24
XVIII EUROPEAN CONFERENCE ON SOIL MECHANICS AND GEOTECHNICAL ENGINEERING

The influence of partial saturation on the engineering properties of a metakaolin-improved sand

L'influence de la saturation partielle sur les propriétés techniques d'un sable amélioré au métakaolin

A. Fraccica
Istituto Superiore per la Protezione e la Ricerca Ambientale, Rome, Italy

E. Romero*, M. Arroyo
Universitat Politècnica de Catalunya UPC, CIMNE, Barcelona, Spain

G. Spagnoli
Sweco, Essen, Germany

**enrique.romero-morales@upc.edu*

ABSTRACT: Ground improvement by injection of sustainable binders and geopolymers is generating much interest. The use of these products in foundations, landslides, excavations, retaining structures and tunnel applications is being progressively considered in geotechnical standards. This fact would require consideration of material evolution under mechanical or environmental action, including changes in the hydraulic state of the ground. An extensive laboratory investigation was conducted on sand specimens treated with a metakaolin-based geopolymer to evaluate the effect of different saturation conditions on the main properties required for ultimate and serviceability limit states for ground improvement works. Curing the treated samples under partially saturated conditions dramatically affected the stiffness characteristics at low strains, the shear strength under unconfined and axisymmetric conditions, and the response to cyclic loading. In any case, the geopolymer satisfactorily avoided liquefaction initiation within the number of cycles investigated. A decrease in water permeability was observed as a function of the degree of filling of the voids with the binder and an increase in retention capacity and air-entry value compared to the untreated material. Mercury intrusion porosimetry and micro-CT provided microstructural insight into these phenomenological observations.

RÉSUMÉ: L'amélioration des sols par injection de liants durables et de géopolymères suscite un grand intérêt. L'utilisation de ces produits dans les fondations, les glissements de terrain, les excavations, les structures de soutènement et les tunnels est progressivement prise en compte dans les normes géotechniques. Cela nécessiterait de prendre en compte l'évolution des matériaux sous l'action mécanique ou environnementale, y compris les changements dans l'état hydraulique du sol. Une étude approfondie en laboratoire a été menée sur des échantillons de sable traités avec un géopolymère à base de métakaolin afin d'évaluer l'effet de différentes conditions de saturation sur les principales propriétés requises pour les états limites ultimes et de service pour les travaux d'amélioration du sol. Le durcissement des échantillons traités dans des conditions partiellement saturées a considérablement affecté les caractéristiques de rigidité à faibles déformations, la résistance au cisaillement dans des conditions non confinées et axisymétriques, ainsi que la réponse aux chargements cycliques. Dans tous les cas, le géopolymère a évité de manière satisfaisante l'initiation de la liquéfaction dans le nombre de cycles étudiés. Une diminution de la perméabilité à l'eau a été observée en fonction du degré de remplissage des vides par le liant et une augmentation de la capacité de rétention et de la valeur d'entrée d'air par rapport au matériau non traité. La porosimétrie par intrusion de mercure et la micro-CT ont fourni un aperçu microstructural de ces observations phénoménologiques.

Keywords: Sand improvement; metakaolin; partial saturation; geotechnical properties.

1 INTRODUCTION

Ground improvement aims to increase the mechanical properties of soils and rocks while decreasing permeability in engineering applications.

The traditional Ordinary Portland Cement (OPC) is used for ground improvement. However, other materials, known as non-conventional binders, are used as an alternative to OPC for ground improvement purposes, such as colloidal silica, resins, micro-fine cement, and geopolymers (e.g., Anagnostopoulos and Sapidis, 2017; Salvatore et al., 2020; Spagnoli et al., 2022; Fraccica et al., 2022).

It is critical to analyse the hydro-mechanical behaviour of non-conventional binders that could be used as an alternative to OPC in sustainable

engineering practices. When exposed to acid solutions, geopolymer materials outperform OPC (e.g., Bakharev, 2005).

This work has focused on Soil Deep Mixing (SDM)-adaptable binder (metakaolin-based geopolymer - MK). To the authors' knowledge, no commercial applications of MK-based binders for ground improvement are known. Most laboratory studies on geopolymer-treated soils focus on volcanic ash, fly ash, or ground blast-furnace slag (e.g. Verdolotti et al., 2008; Rios et al., 2017). Metakaolin-based geopolymers have received little attention for soil treatment and have typically been used with other geopolymers or OPC (e.g. Kolovos et al., 2013). Furthermore, in many laboratory investigations, soil and geopolymer precursor powders are combined dry before the activator is applied, and the samples are compacted (e.g. Zhang et al., 2013). However, this does not reflect how SDM is often performed in situ because already-activated slurries are combined with wet soils and no compaction is performed (Yaghoubi et al., 2018). Consoli et al. (2011) and Spagnoli et al. (2022) have demonstrated that the soil structure obtained after compaction (final porosity and amount of binder) has a significant impact on the strength and stiffness of the treated material.

Finally, few studies have been conducted to investigate the combined impact of extreme dry curing conditions and lengthy curing times on soil binder performance (e.g. Rios et al., 2017).

The current paper focuses on the permeability, static and cyclic strength of sandy soils treated with a metakaolin-based geopolymer after curing in dry and wet conditions at a relative humidity RH = 50% and 100%, respectively.

2 MATERIALS AND METHODS

The base material used in this study is a medium quartz sand (Holcim 0.2–0.6 mm), while the binder is an alkali-activated metakaolin. The metakaolin is activated with a water solution of potassium silicate. Potassium silicate solution, water and metakaolin are mixed in equal masses, leading to a geopolymer with a fluid/metakaolin mass ratio of 2:1 and a mass ratio between dry metakaolin and dry sand of 5.2% and 13% for initial slurry volumetric void filling F_{MK} values of 40% and 100%, respectively. Specimens were prepared by pouring the pure sand or the sand+geopolymer mixture into moulds. Specimens for Unconfined Compression (UC) tests are 70 mm in diameter and 164 mm in height. In contrast, those for cyclic and monotonic triaxial undrained compressions (CTX, STX) are 38 mm in diameter and 96 mm in height. After an initial 3-day common stage in the casting mould (at 20°C and RH = 50%), some specimens were cured at 20°C in dry conditions and some in wet conditions, at a relative humidity RH = 50% and 100%, respectively. The last condition was achieved by submerging the samples in water after three days of curing. The following nomenclature identifies the specimens: S, sand; MK, geopolymer; SMK, geopolymer+sand. The F_{MK} achieved is indicated between parenthesis; the curing condition is indicated by a letter (W: water immersion, D: curing at 50% RH) and a number indicating the curing time in days. For example, SMK(100)D7 indicates sand+geopolymer, with a F_{MK} = 100%, dry-cured for 7 days. D or W is not indicated for specimens at 3 days curing as they were submitted to a common preparation stage.

3 HYDRO-MECHANICAL TESTS

3.1 Microstructural observations

Treated soil's microstructure was investigated using mercury intrusion porosimetry (MIP), X-ray tomography, Field Emission Scanning Electron Microscopy (FESEM) and paraffin tests (Spagnoli et al., 2022; Fraccica et al., 2022). An increase in macro-pores was observed in the dry-cured specimens by MIP, resulting from micro-cracks formation in the geopolymer and detachment at the grain/geopolymer contact (FESEM). X-ray and paraffin tests revealed a decrease in dry density with dry curing (void ratio $e \approx 0.42$ after three days and $e \approx 0.47$ after 100 days).

3.2 Hydro-mechanical properties

After evaluating the bar wave velocity v_b in dry- and wet-cured samples through an ultrasonic pulse velocity tester (Proceq Pundit Lab Lab+, see Spagnoli et al., 2022), the small-strain Young's modulus was calculated as follows:

$$E_0 = \rho(t_c) v_b^2 \quad (1)$$

where $\rho(t_c)$ is the bulk density at a given curing time. At similar curing times, lower stiffness values were observed on dry-cured samples than on wet-cured ones (Table 1).

UC tests were conducted at a 0.5%/min axial deformation rate on specimens with a height/diameter ratio between 2 and 2.5. Lower Unconfined Compression Strengths (UCS) were observed in dry-cured samples, with a slight decreasing trend with curing time (Table 1).

Isotropically consolidated undrained triaxial compression (TXCIU) tests were performed under monotonic and cyclic conditions. After saturation, the water permeability was evaluated under steady-state conditions by imposing a back pressure of 200 kPa at the bottom and 10 kPa at the top cap. The treatment progressively contributed to decreased soil water permeability as the F_{MK} and the curing time increased due to void clogging and the solidification of geopolymers (Figure 1).

Table 1. Mechanical properties of treated sand under dry and wet curing.

Specimen	E_0 (GPa)	UCS (MPa)
SMK(100)3	-	1.44
SMK(100)3	-	2.07
SMK(100)D7	0.59	1.18
SMK(100)W7	3.44	2.05
SMK(100)D28	0.71	1.10
SMK(100)W28	5.40	1.51

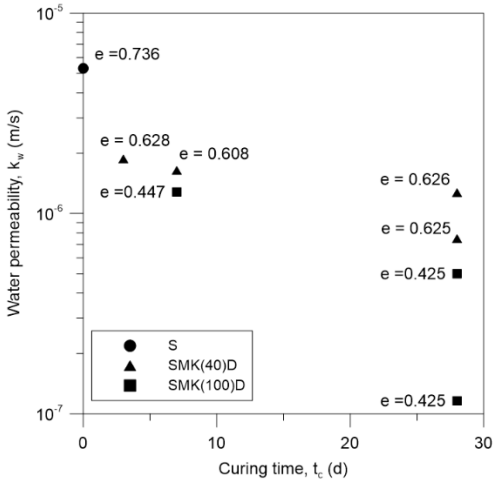

Figure 1. Water permeability of geopolymer-treated sand at different curing times. Void ratio as labels.

Consolidation was induced under isotropic stresses p'_0 = 200 and 600 kPa. The shearing phase was carried out with a back-pressure of 500 kPa under stress-controlled conditions (47 kPa/min). Increasing F_{MK} resulted in more dilatant, stiffer and stronger specimens (Fraccica et al., 2022). Similar to what was observed for UC tests, samples with longer dry curing periods presented slightly lower shear strength starting from similar isotropic consolidation pressures (Figure 2). The different treatments of F_{MK} increased soil cohesion with no changes in the friction angle.

Cyclic undrained triaxial compressions (CTXCU) were performed; consolidation was carried out under K_0 = 0.5 until reaching σ'_1 = 250 kPa. Cyclic shearing was imposed through 600 cycles (1 Hz) at a cyclic stress ratio CSR = 0.25 and a back pressure of 400 kPa (Fraccica et al., 2022). The untreated sand underwent large strains (i.e. higher than 5%) after the first ten cycles with a fast increase in r_u (Figure 3) and liquefaction. The treatment reduced strains (i.e. lower than 0.07%), cyclic stiffness degradation and excess pore pressures.

Small treated soil subsamples (~300 mm^3) were extracted from dry-cured specimens to evaluate their water retention properties. A dew-point psychrometer measured total suction while gravimetric water content was assessed by oven drying at 105°C. Results from MIP tests were converted into Soil Water Retention Curves (SWRC) through the procedure explained by Romero (1999). The main drying curve of the treated sand was evaluated starting after 28 days of dry curing (Figure 4).

The soil's air-entry value rose after the treatment. The soil's ability to retain water decreased with greater total suctions, as seen by a sharp decline in the degree of saturation S_r.

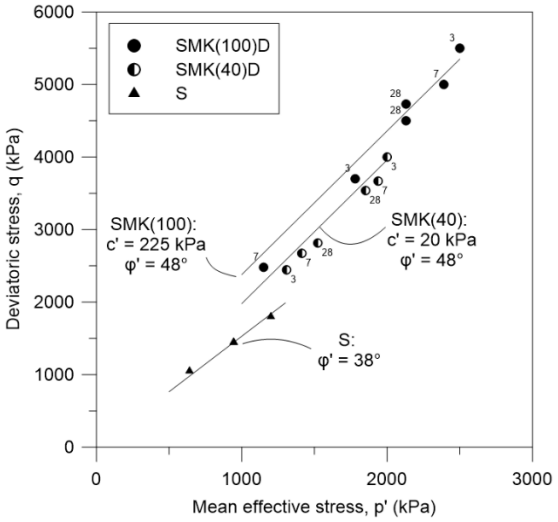

Figure 2. Shear strength envelopes for untreated and treated sand. Curing days as labels.

4 DISCUSSION AND CONCLUSIONS

Dry curing impacted the microstructure and hydro-mechanical behaviour of the metakaolin-treated sand.

Compared to wet-cured samples, microcracks and grain-binder detachments led to a decrease in stiffness and strength over time and an increase in the void ratio. Unlike untreated conditions, void clogging, filling ratio, and binder solidification helped reduce permeability and boost shear strength.

The treated soil's higher stiffness contributed to lower strains and excess pore pressures in the CTXCU, avoiding liquefaction. The almost saturated material showed a very high air-entry value due to the higher void filling with fine clayey material; this behaviour

was likely caused by the microstructural changes previously noted. The S_r value then sharply decayed. Therefore, when assessing the effects of such a ground improvement technology on geotechnical parameters in partially or saturated soils, consideration should be given to slurry void filling, curing duration, and *RH* conditions.

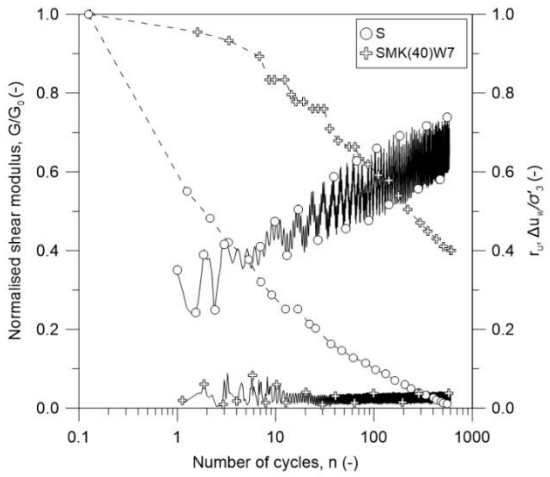

Figure 3. Cyclic stiffness degradation (dotted lines) and normalised excess pore pressure (continuous lines).

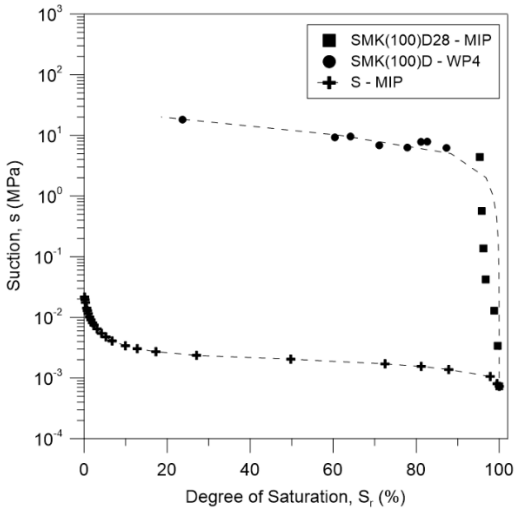

Figure 4. SWRC of treated and untreated sand.

REFERENCES

Anagnostopoulos, C. A. and Sapidis, G. (2017). Mechanical behaviour of epoxy resin-grouted sand under monotonic or cyclic loading. *Géotechnique Letters*, 7(4): 298-303. https://doi.org/10.1680/jgele.17.00063.

Bakharev, T. (2004). Resistance of geopolymer materials to acid attack. *Cement and Concrete Research*, 35(4): 658-670. https://doi.org/10.1016/j.cemconres.2004.06.005.

Consoli, N. C., Cruz, R. C., and Floss, M. F. (2011). Variables controlling strength of artificially cemented sand: influence of curing time. *Journal of Materials in Civil Engineering*, 23(5): 692-696. https://doi.org/10.1061/(ASCE)MT.1943-5533.0000205.

Fraccica, A., Spagnoli, G., Romero E., Arroyo, M., and Gómez, R. (2022). Exploring the mechanical response of low-carbon soil improvement mixtures. *Canadian Geotechnical Journal*, 59(5): 726-742. https://doi.org/10.1139/cgj-2021-0087.

Kolovos, K.G., Asteris, P.G., Cotsovos, D.M., Badogiannis E., and Tsivilis, S. (2013). Mechanical properties of soilcrete mixtures modified with metakaolin. *Construction and Building Materials*, 47: 1026–1036. https://doi.org/10.1016/j.conbuildmat.2013.06.008

Rios, S., Ramos, C., Viana Da Fonseca, A., Cruz, N., and Rodrigues, C. (2017). Mechanical and durability properties of a soil stabilised with an alkali-activated cement. *European Journal of Environmental and Civil Engineering*, 23(2): 245-267. https://doi.org/10.1080/19648189.2016.1275987.

Romero, E. (1999). *Characterisation and thermo-hydro-mechanical behaviour of unsaturated Boom clay: an experimental study*. PhD thesis. Universitat Politècnica de Catalunya (Spain).

Salvatore, E., Modoni, G., Mascolo, M.C., Grassi, D. and Spagnoli, G. (2020). Experimental evidences on the effectiveness and applicability of colloidal nanosilica grouting for liquefaction mitigation. *Journal of Geotechnical and Geoenvironmental Engineering*, 146(10):04020108. https://doi.org/10.1061/(ASCE)GT.1943-5606.0002346.

Spagnoli, G., Romero E., Fraccica, A., Arroyo, M., and Gómez, R. (2022). The effect of curing conditions on the hydro-mechanical properties of a metakaolin-based soilcrete. *Géotechnique*, 72 (5): 455–469. https://doi.org/10.1680/jgeot.20.P.259.

Verdolotti, L., Iannace, S., Lavorgna, M. and Lamanna R (2008). Geopolymerization reaction to consolidate incoherent pozzolanic soil. *Journal of Materials Science*, 43: 865–873. https://doi.org/10.1007/s10853-007-2201-x.

Yaghoubi, M., Arulrajah, A., Disfani, M.M., Horpibulsuk, S., Bo, M.W. and Darmawan, S. (2018). Effects of industrial by-product based geopolymers on the strength development of a soft soil. *Soils and Foundations*, 58: 716-728. https://doi.org/10.1016/j.sandf.2018.03.005.

Zhang, M., Guo, H., El-Korchi, T., Zhang, G., and Tao, M. (2013) Experimental feasibility study of geopolymer as the next-generation soil stabiliser. *Construction and Building Materials*, 47: 1468–1478. https://doi.org/10.1016/j.conbuildmat.2013.06.017.

Proceedings of the XVIII ECSMGE 2024
GEOTECHNICAL ENGINEERING CHALLENGES
TO MEET CURRENT AND EMERGING NEEDS OF SOCIETY
© 2024 the Authors
ISBN 978-1-032-54816-6
DOI 10.1201/9781003431749-438
Open Access: www.taylorfrancis.com, CC BY-NC-ND 4.0 license

ECSMGE 24
XVIII EUROPEAN CONFERENCE
ON SOIL MECHANICS AND
GEOTECHNICAL ENGINEERING

Muck identification and anomaly detection in earth pressure balance shield based on multi-task deep learning

Identification des déblais et détection des anomalies dans le bouclier à pression de terre basée sur l'apprentissage profond multi-tâches

L. Fu*, D.M. Zhang, H.W. Huang
Department of Geotechnical Engineering, Tongji University, Shanghai, China

A.G. Cohn
School of Computing, University of Leeds, Leeds, UK

Z.Q. Liu
Department of Natural Hazards, Norwegian Geotechnical Institute, Oslo, Norway

**2110011@tongji.edu.cn*

ABSTRACT: A lack of understanding of geological conditions and improper muck disposal often leads to serious accidents, such as ground settlement or machine damage, during shield tunneling. The image data of muck on the conveyor belt reflects the general soil type of the excavated strata and the discharge condition, providing abundant and valuable information for EPB shield construction decisions. This paper aims to use a multi-task deep learning method to establish an image recognition model that can track the type and location of the muck and estimate whether the muck is discharged smoothly at the same time. The first task is an object detection task and the second is an image classification task. A convolutional neural network for a multi-task learning setting has been designed, and then used to build a multi-task muck recognition model using a specially constructed labeled muck dataset. The mAP for the muck identification task reaches 92.72%, and the accuracy for the anomaly detection task reaches 96.26%. The model is applied to Metro Line 14 in Shanghai, and the results show that the model performs well on both target tasks, meeting the real-time requirements at 45 frames per second.

RÉSUMÉ: Le manque de compréhension géologique et une élimination inadéquate des déblais peuvent entraîner des accidents graves, tels que l'affaissement du sol ou des dommages aux machines lors du creusement de tunnels avec un bouclier. Les images du tapis roulant reflètent le type de sol et la condition de décharge, offrant des informations cruciales pour les décisions de construction. Cet article utilise une méthode d'apprentissage profond multi-tâches pour créer un modèle de reconnaissance d'image suivant le type et l'emplacement des déblais, estimant simultanément la décharge correcte. La première tâche est la détection d'objets, la seconde est la classification. Un réseau neuronal convolutionnel est conçu pour un environnement d'apprentissage multi-tâches, utilisé pour construire un modèle de reconnaissance de déblais avec une APM de 92,72% pour l'identification des déblais et une précision de 96,26% pour la détection d'anomalies. Appliqué à la ligne 14 du métro de Shanghai, le modèle répond aux exigences en temps réel à 45 images par seconde, montrant une performance exceptionnelle sur les deux tâches.

Keywords: Muck identification; anomaly detection; multi-task deep learning; earth pressure balance shield.

1 INTRODUCTION

The shield method, with its safe, efficient, and labor-saving nature, is widely adopted in urban tunneling projects. Understanding the soil condition and discharging the muck smoothly play an essential role in reducing the disturbance to the environment and ensuring construction safety. Information about the soil type at the excavated face facilitates the adjustment of current construction decisions. When operating an earth pressure balance (EPB) shield machine, the muck produced by the machine and discharged by the screw and belt conveyor reflects the general soil type of the strata being excavated. Valuable information such as the soil condition ahead of the cutters and the muck discharge condition can all be obtained through the images of the muck on the conveyor belt. However, the number of experienced drivers is far from the needs of hundreds of shield tunneling projects. Furthermore, the manual vision-based inspection of the muck is comparatively subjective, uncertain, time-consuming, and labor-intensive. Nowadays, with the rapid development of artificial intelligence, especially deep learning (DL), automatic extraction of muck information

using computer vision presents an opportunity to automate the investigation of muck conditions.

DL has been applied to learn from muck images of tunnel boring machines (TBM) to estimate the size and shape of rock chips (Zhou et al., 2021) and grade the rock fragments in TBM construction (Yang et al., 2021). For soil muck generated by an EPB shield, which is more challenging than rock muck, Zhang et al. (2023) have tried to identify soil types based on muck images and achieved good results. Nevertheless, previous models can only extract a single aspect of information from muck images, while there is a lot of construction information that technicians care about in the muck images. If multiple similar tasks can be completed in one model, that should be very beneficial for the practical deployment and application on site. In this study, the authors aim to establish a multi-task deep learning-based model that can not only identify muck types but also simultaneously estimate whether the muck is discharged smoothly only using the site closed circuit television data. The method presented in this paper can be used to further develop more feature-rich visual recognition models of muck.

2 METHODOLOGY

2.1 Multitask learning

Multitask learning (MTL) is an inductive transfer mechanism whose principal goal is to improve generalization performance (Caruana, 1997). MTL can leverage the domain-specific information contained in all the related tasks. Useful information learned from any task will be shared across all tasks by training them in parallel using a shared representation.

MTL can not only help to train a model for completing multiple tasks simultaneously, but also there may be an useful improvement of generalization in the model resulting from the use of MTL. Moreover, training a single model for all the tasks using MTL can considerably enhance computational efficiency and conserve computational resources compared with training models for each task separately.

2.2 Network architecture

Owing to the exceptional performance of deep learning on image data processing, this study develops a convolutional neural network to train a multi-task recognition model for muck images.

The convolutional neural network architecture constructed in this study is shown in Figure 1. The network is composed of three parts, backbone, classifier, and detector. The backbone of Darknet53 (Redmon et al., 2018) is the shared layers which are responsible for extracting common useful features for both tasks. The classifier and detector are the task-specific layers for the two tasks. These layers are designed to further select and integrate features based on the characteristics of different tasks, achieving better performance on each task. The classification task is much easier than the object detection task. So the classifier consists of only a few simple layers, used for extracting global features, while the detector is the detection head of YOLOv3 (Redmon et al., 2018), which is excellent in the speed and accuracy of detecting objects of varied sizes and aspect ratios.

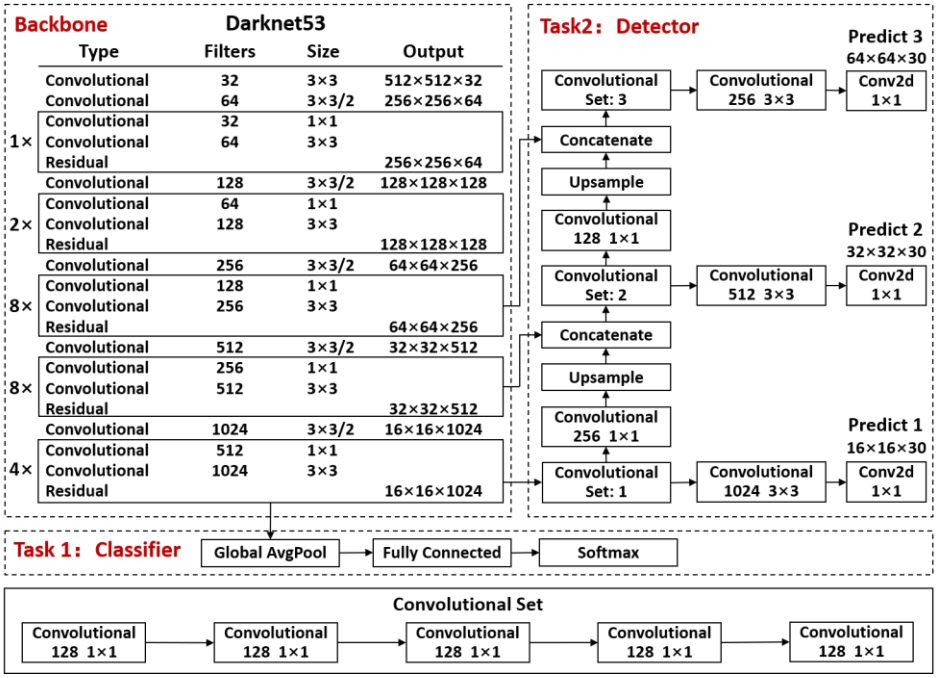

Figure 1. Architecture of the muck recognition network.

2.3 Evaluation metrics

Mean average precision (mAP) is used to evaluate the performance of the model on the muck-type identification task. Average precision (AP) is the averaged precision across all values of recall between 0 and 1, and it can be obtained by calculating the area under the precision–recall curve (i.e., *P*-*R* curve; Everingham et al., 2010) as shown in Equation 1:

$$AP = \int_0^1 P(R)dR \quad (1)$$

The average value of the APs over all categories is the mAP of the model as shown in Equation 2:

$$mAP = \frac{\sum_{n=1}^{C} AP(n)}{C} \quad (2)$$

where C is the number of categories, P and R are precision and recall respectively, and $P(R)$ represents the *P*-*R* curve.

Accuracy is used to evaluate the performance of the model on the task of determining whether the muck is discharged normally. Accuracy calculates the proportion of images correctly classified by the model out of the total number of images. The formula for accuracy is shown in Equation 3:

$$Accuracy = \frac{TP+TN}{TP+TN+FP+FN} \quad (3)$$

TP is the correct prediction count for positive samples, TN is the correct prediction count for negative samples, FN is the count of positive samples incorrectly predicted, and FP is the count of negative samples incorrectly predicted.

Frames per second (FPS) is frequently used to evaluate the inference speed of a model. In general, a model can achieve real-time detection when FPS reaches 30 (Ma et al., 2020).

3 DATASET

3.1 Data collection and preprocessing

Above the shield machine's conveyor belt, a surveillance camera monitors muck discharge. Video footage from this camera serves as the primary data for our muck dataset. In this study, muck image data is collected from three tunnel intervals excavated by the EPB shield machine of Metro Line 14 in Shanghai.

Surveillance video, being low in information density, requires preprocessing. Initially, stable excavation stages in valid videos are identified, and muck images are extracted at regular intervals. Muck images exhibiting significant changes in morphology and construction scenes are selected while pixelated and redundant images resulting from video lag are eliminated.

3.2 Dataset establishment

Following preliminary data processing, 2080 high-quality muck images were obtained from collected videos. Among these, 1200 images depict normal muck discharge, while the remaining 880 showcase abnormal discharge. The collected muck images from Shanghai encompass five types: soft clay, normal clay, hard clay, silty sand, and mixed soil. The 1200 images of normal muck discharge equally represent each muck type at 240 images per type, while the abnormal discharge images specifically focus on soft clay.

Each image in the dataset is assigned corresponding labels for the two tasks. For the object detection task identifying muck types, LabelImg (Tzutalin, 2015) was used for manual annotation, stored in Pascal VOC format with XML files. For the image classification task determining normal muck discharge, the 1200 normal discharge and 880 abnormal discharge images are segregated into folders labeled "normal" and "abnormal," respectively.

4 IMPLEMENTATION AND RESULTS

4.1 Model development

All the experiments were executed on a workstation with an Intel Core i7-10700K CPU, an NVIDIA GeForce RTX 3080 with 16GB memory, and a Ubuntu 20.04 operating system. The neural network was constructed using Python 3.7 and PyTorch 1.7.0.

Hyperparameter settings: Original images were resized to 512 × 512 pixels for network input, with a batch size of 8. Stochastic gradient descent optimized the network parameters over 120 epochs. The initial learning rate was 0.001, linearly decreasing to 0.0001 with each epoch. Momentum and weight decay were set at 0.9 and 0.0005, respectively.

4.2 Model evaluation

The model was evaluated on the testing set. The performance of the model on the muck detection task is presented in Table 1. The detector has quite high accuracies on all five classes of muck, and the model achieves 92.72% mAP on the VOC metric (IOU = 0.5). The AP of soft clay is the highest, followed by normal clay and mixed soil, and finally hard clay and silty sand. The larger number of images for the soft

clay type may be one of the reasons for its optimal performance. Besides, soft clay is the type most easily recognized even by the naked eye, so it might be the same for the model. The morphological and texture characteristics of silty sand and hard clay will change with the application of soil conditioners, so the values of the evaluation indexes of these two categories are relatively low.

Table 1. The AP values for each muck type.

	Soft Clay	Normal Clay	Hard Clay	Silty Sand	Mixed Soil
AP	94.83%	93.43%	91.10%	90.17%	94.08%

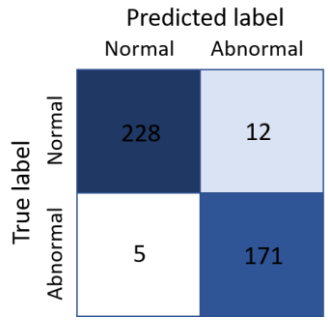

Figure 2. Confusion Matrix.

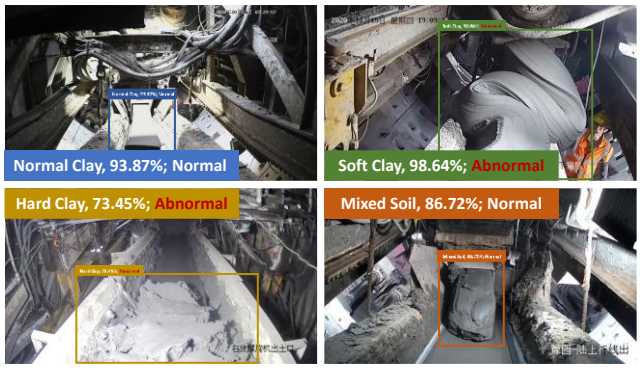

Figure 3. Muck recognition results.

The model achieves a 96.26% accuracy in anomaly detection. Figure 2 displays the confusion matrix for the binary classification task. It reveals that most misclassifications involve normal muck discharge cases mistakenly identified as abnormal, reflecting a conservative judgment less likely to impact tunneling safety. Figure 3 shows the detection and classification results of the model with four muck images. The model performs well on both tasks. The muck type is well-identified and the location of the muck is predicted accurately. The situation of muck discharge is also correctly discriminated, and abnormal muck discharge is highlighted in red. The model can process 45 frames of muck images per second, which can meet the real-time requirements.

5 CONCLUSION

This study developed a multitask-deep-learning-based model that can simultaneously accomplish two muck image recognition tasks in real time. The model can identify the muck type and locate the muck position precisely, reaching 92.72% in mAP. In the image classification task to determine whether the muck is discharged smoothly, the model achieves an accuracy of 96.26%. The model has the potential to increase the safety and steady tunneling rate of shield projects. The method used in this paper to build a multi-task muck recognition model could also be extended to build other models enabling the automation of different muck recognition tasks.

ACKNOWLEDGEMENTS

We gratefully acknowledge the financial support of the National Natural Science Foundation of China (grant No.52022070), Shanghai Science and Technology Committee Program (No.20dz1202200).

REFERENCES

Caruana, R. (1997). Multitask Learning. *Machine Learning*, 28(1), 41–75. https://doi.org/10.1023/a:1007379606734.

Everingham, M., Van Gool, L., Williams, C. K. I., Winn, J., and Zisserman, A. (2009). The Pascal Visual Object Classes (VOC) Challenge. *International Journal of Computer Vision*, 88(2), 303–338. https://doi.org/10.1007/s11263-009-0275-4.

Ma, H., Liu, Y., Ren, Y. and Yu, J. (2020). Detection of collapsed buildings in post-earthquake remote sensing images based on the improved YOLOv3. *Remote Sensing*, 12(1), 44. https://doi.org/10.3390/rs12010044.

Redmon, J., and Farhadi, A. (2018). YOLOv3: An incremental improvement. *arXiv preprint arXiv:1804.02767*.

Tzutalin. LabelImg. Git code (2015). https://github.com/tzutalin/labelImg.

Yang, Z., He, B., Liu, Y., Wang, D. and Zhu, G. (2021). Classification of rock fragments produced by tunnel boring machine using convolutional neural networks. *Autom. in Constr.*, 125, 103612. https://doi.org/10.1016/j.autcon.2021.103612.

Zhang, D., Fu, L., Huang, H., Wu, H. and Li, G. (2023). Deep learning-based automatic detection of muck types for earth pressure balance shield tunneling in soft ground. *Computer-Aided Civil and Infrastructure Engineering*, 38(7), 940-955. https://doi.org/10.1111/mice.12914.

Zhou, X., Gong, Q., Liu, Y. and Yin, L. (2021). Automatic segmentation of TBM muck images via a deep-learning approach to estimate the size and shape of rock chips. *Autom. in Constr.*, 126, 103685. https://doi.org/10.1016/j.autcon.2021.103685.

Proceedings of the XVIII ECSMGE 2024
GEOTECHNICAL ENGINEERING CHALLENGES
TO MEET CURRENT AND EMERGING NEEDS OF SOCIETY
© 2024 the Authors
ISBN 978-1-032-54816-6
DOI 10.1201/9781003431749-439
Open Access: www.taylorfrancis.com, CC BY-NC-ND 4.0 license

ECSMGE 24
XVIII EUROPEAN CONFERENCE
ON SOIL MECHANICS AND
GEOTECHNICAL ENGINEERING

Reconstitution of samples for the study of mechanical behaviour of sulphide-rich soils

Reconstitution des échantillons pour l'étude du comportement mécanique des sols riches en sulfures

N. Garcia*, P. Gunnvard, Q. Jia, J. Laue
Luleå University of Technology, Luleå, Sweden

**nelson.garcia@ltu.se*

ABSTRACT: Sulphide-rich soil, a prevalent soft alluvial type along the Baltic Sea coast, is characterised by its sulfur content, low strength, high compressibility and significant organic components. Common practice involves replacing this soil with more resilient subgrade materials; however, excavated sulphur-rich soil necessitates to be treated as environmentally hazardous, due to its oxidation potential, leading to increased construction expenses. If instead, sulphide-rich soil is going to be used as subgrade, it becomes crucial to define its cyclic mechanical properties. This requires representative samples, which may not always be available through conventional undisturbed sampling methods. In this paper, the slurry deposition method was adopted to generate reconstituted samples of sulphide-rich soil for static triaxial testing. The method provided consistent samples and captured the characteristics of the natural soil. The triaxial results are the first step towards the understanding and definition of the cyclic behaviour of sulphide-rich soil.

RÉSUMÉ: Les sols riches en sulfures, un type alluvial mou prévalent le long de la côte de la mer Baltique, se caractérisent par leur teneur en soufre, leur faible résistance, leur grande compressibilité et leur teneur significative en matières organiques. La pratique courante consiste à remplacer ce sol par des matériaux de sous-fond plus résilients. Cependant, le sol riche en soufre excavé doit être traité comme dangereux pour l'environnement en raison de son oxydation, ce qui entraîne des coûts de construction accrus. Si, au contraire, le sol riche en sulfures doit être utilisé comme sous-fond, il devient essentiel de définir ses propriétés mécaniques cycliques. Cela nécessite des échantillons représentatifs, qui ne sont pas toujours disponibles par le biais de méthodes d'échantillonnage classiques non perturbées. Dans cet article, la méthode de dépôt de boue a été adoptée pour générer des échantillons reconstitués de sol riche en sulfures en vue d'essais triaxiaux statiques. Cette méthode a fourni des échantillons cohérents et a capturé les caractéristiques du sol naturel. Les résultats triaxiaux constituent la première étape vers la compréhension et la définition du comportement cyclique du sol riche en sulfures.

Keywords: Slurry deposition; sulphide-rich soil; triaxial testing.

1 INTRODUCTION

The construction of roads and railways in regions characterised by sulphide-rich soil deposits, particularly prevalent along the Baltic coastal areas of Sweden and Finland, presents a pressing geotechnical challenge. This unique fine-grained soil is known for its soft properties and high natural void ratio, with voids containing high amounts of water, organic matter, and sulphides, resulting from its anaerobic sedimentation during the last glaciation in tranquil brackish estuaries (Pousette et al., 2008). The soft nature of sulphide-rich soil, defined by low undrained strength and high compressibility and viscosity (e.g. Yu, 1993; Westerberg et al., 2005), implies significant obstacles to geotechnical structures leading to a common practise of excavating and replacing this soil. In addition, the sulphide-rich sediment produces acidic leachate when oxidised. Hence, excavated sulphide-rich soil is treated as environmental hazardous waste, increasing project costs and transportation emissions.

Recent advancements in soil stabilization and reinforcement techniques offer potential solutions for utilising sulphide-rich soil as a subgrade material. The subgrade of a road or railway embankment may not require a high bearing capacity, but it is subjected to high-cycle loads, characterised by large numbers of cycles with small amplitudes. Accurate predictions of deformation and pore pressure development are needed to ensure the long-term performance of the transportation network. However, the cyclic behaviour of sulphide-rich soil, with its unique properties, is not well studied.

Representative samples are needed to define the behaviour of a soil by laboratory testing. The softness of sulphide-rich soil prevents, in most cases,

undisturbed sampling. Making conventional sampling techniques, such as piston sampling, impractical or potentially disruptive. Disturbed samples can be reconstituted into representative samples instead. The slurry deposition method was initially devised for the reconstitution of sandy soils with fines. The method can also be applied to reconstitute silts and clays (Liu et al., 2017). However, its applicability on the reconstitution of organic fine-grained soils, such as sulphide-rich soil, needs to be investigated.

The aim of the research project is to investigate the cyclic behaviour of sulphide-rich soil and provide valuable insights for the design and construction of roads and railways in regions abundant with this distinctive soil type. Prior to cyclic triaxial testing, it is necessary to conduct static triaxial testing to obtain basic strength parameters of the soil and establish optimal test conditions. This paper covers the application and suitability of the slurry deposition method for the static triaxial testing of reconstituted samples of sulphide-rich soil.

2 SAMPLE RECONSTITUTION

The reconstitution of samples is a common practise in laboratory investigations of silts. Various techniques have been proposed for this purpose, such as moist tamping methods, water or air pluviation, and slurry deposition (Ladd, 1978; Kuerbis and Vaid, 1988; Carraro and Prezzi, 2008). Evaluations of the merits and drawbacks of these different reconstitution techniques can be found in Bradshaw and Baxter (2007) and Reid et al. (2022). When dealing with sulphide-rich soil, some challenges arise: the inability to dry the soil due to cementation and potential oxidation, the need for homogeneous reconstitution to the desired conditions, and disturbances by preparing the sample directly within the triaxial cell. The most fitting of the considered techniques, meeting all stipulated criteria, is the slurry deposition method. As the name suggests, the method involves consolidating the sample to the desired conditions starting from a slurry.

2.1 Soil Characteristics

The soil used for this study is a clayey silt, sourced from a landfill of freshly excavated soil from the Northern coastal area of Sweden. An overview of the basic parameters of the soil can be found in Table 1.

Table 1. Basic Soil Properties.

Property	
Clay Content	10 %
Silt Content	60 %
Sand Content	30 %
Organic Content	4 %
Specific Gravity	2.76
Water Content	40 %
Liquid Limit	33 %

2.2 Sample Preparation

The following equation by Liu (2017) is used to determine the amount of slurry needed for one sample,

$$m_{slurry} = (\pi \cdot h \cdot r^2) \cdot \rho_{dry} \cdot (1 + \omega_{slurry}) \quad (1)$$

where m_{slurry} corresponds to the mass of slurry to be poured, h is the height of the final sample, r denotes the radius of the final sample, ρ_{dry} corresponds to the target dry density, and ω_{slurry} is the water content of the slurry. Figure 1 shows the procedure followed for the sample reconstitution:

a) Assembly of the latex membrane, split mould, and bottom filter onto the triaxial base plate. Talc powder is applied to the mould exterior to prevent adhesion of the membrane.
b) Three strips of filter paper are placed inside the membrane to quicken the slurry consolidation.
c) A rubber support is fixed to the upper section of the split mould with two clamps.
d) An extension tube is inserted into the rubber support and fastened using the two clamps.
e, f) A funnel with an elongated nozzle is used to pour the predetermined m_{slurry}. As the slurry is gradually poured, the funnel is slowly raised with the nozzle end following the slurry surface.
g) A top filter and plug are positioned at the uppermost section of the extension tube. The consolidation process is initiated with a surcharge load atop the plug and vacuum pressure at the base. Both the surcharge and vacuum are maintained at pressures lower than the minimum confining pressure applied during the triaxial test. Water is added at the top to ensure that the sample remains fully saturated.
h, i) When the defined sample height h is reach, the surcharge load and vacuum pressure are removed, and the rubber support and clamps are detached. The soil sample is then cut at the top of the split mould. The part of the sample remaining in the extension tube is used to determine water content and soil density.
j) The prepared sample is mounted onto the triaxial apparatus following the standard procedure.

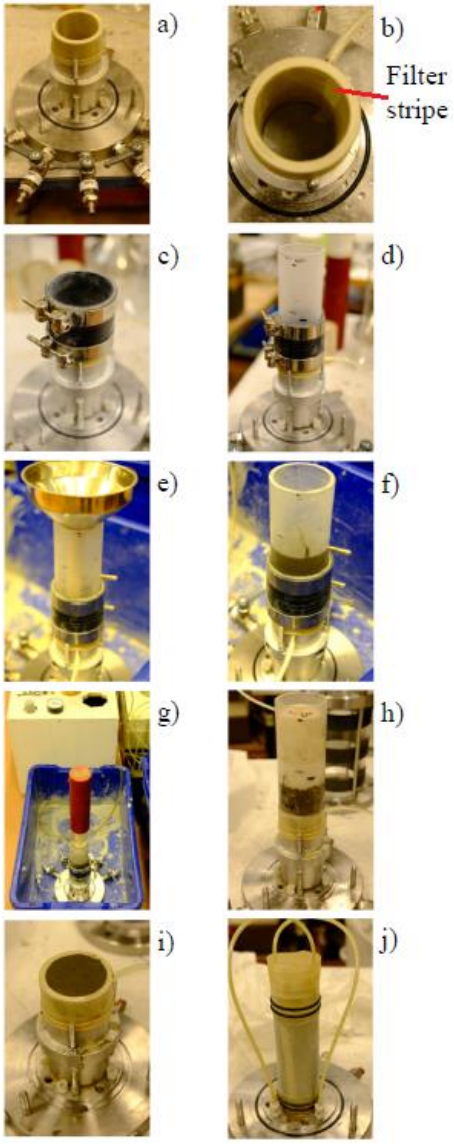

Figure 1. Steps for reconstitution of a sample by slurry deposition.

3 RESULTS

The presented results serve as an initial assessment to validate the suitability of the slurry deposition method for sulphide-rich soil. Four consolidated drained triaxial tests were carried out on reconstituted samples, with confining pressures of 30, 60, 100 and 200 kPa, respectively. The density, water content and void ratio of the four samples are shown in Figure 2. The samples exhibit a satisfactory level of homogeneity. The range of results from the reconstituted samples is in fact narrower than the relatively broad range in results obtained from testing undisturbed samples of this soil type.

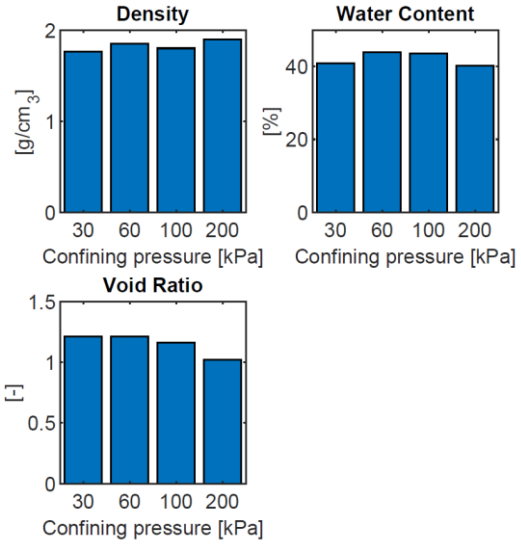

Figure 2. Measured density, water content and void ratio from the reconstituted samples for triaxial testing.

The triaxial test results are plotted in Figure 3 and 4. As the confining pressure increases, the samples exhibit failure at higher deviatoric loads, accompanied by a more distinct peak strength (Figure Figure 3a). Moreover, it is noteworthy that the failure of these samples takes place at high strains, undergoing significant consolidation while shearing, denoted by the large volumetric strains (Figure 3b), which is common for undisturbed samples (Yu, 1993). An indication of comparable behaviour between samples is the assymptotic tendency of the volumetric strains at failure around the same value (Lade, 2016). Also, the critical points utilized in deriving the critical state line (Figure 4) align well.

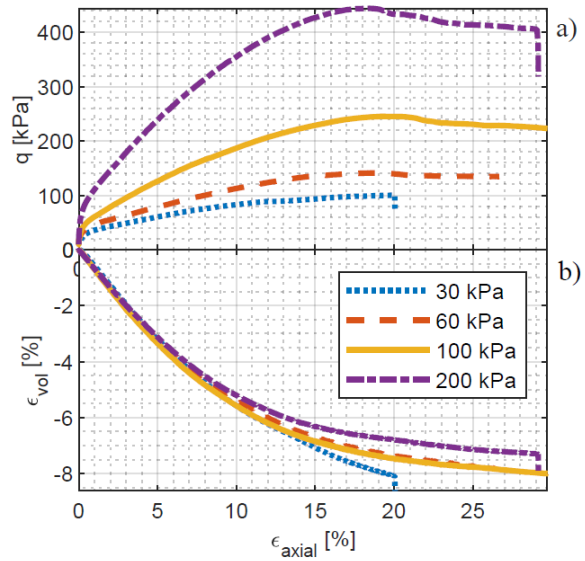

Figure 3. Results from the static triaxial tests: a) axial strain ϵ_{axial} vs deviatoric stress q, and b) axial strain ϵ_{axial} vs volumetric strain ϵ_{vol}.

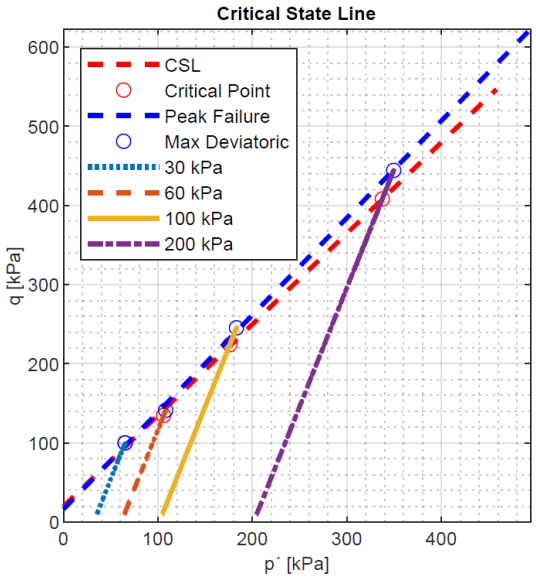

Figure 4. Derived critical state line (CSL) and peak failure line on the plane of deviatoric stress (q) and mean effective stress (p′).

4 CONCLUSION

The slurry deposition method was evaluated for generating reconstituted samples of sulphide-rich soil. Index property tests and consolidated drained triaxial tests were performed on reconstituted samples. The results show that the slurry deposition method not only yielded samples with remarkable homogeneity, both within and across multiple samples, but also provided the flexibility to influence sample density, allowing for a closer match to in-situ conditions. Triaxial testing of the reconstituted samples displayed the main typical characteristics of undisturbed samples, i.e. failure at large deformations and significant volumetric strain change. However, it is essential to acknowledge that the natural soil exhibits an array of anisotropies that cannot be replicated using this method.

Sulphide-rich soils are frequently observed to be overconsolidated, particularly in the uppermost strata of the deposit. Samples obtained through the slurry deposition method and isotropically consolidated in the triaxial are normally consolidated, as shown by the contractant behaviour of the tested samples. This condition does not pose a significant concern, as the targeted overconsolidation ratio can be reached by adding a second consolidation step in the triaxial test.

Based on the results of this paper, the slurry deposition method is a valuable tool for the reconstitution of sulphide-rich soil samples in geotechnical studies. To have a final verdict about the method, reconstituted sulphide-rich soil samples will be compared with undisturbed samples of the same source material.

ACKNOWLEDGEMENTS

The authors are grateful for the financial support provided by funding agency Branschsamverkan i grunden (BIG). The project presented in this article is supported by the Swedish Transport Administration.

REFERENCES

Anantanasakul, P. and Kaliakin, V. N. (2012). Stress-strain and strength characteristics of silt-clay transition soils, *Journal of Geotechnical and Geoenvironmental Engineering*, 138(10), pp. 1257–1265. https://doi.org/10.1061/(ASCE)GT.1943-5606.0000692.

Bradshaw, A. S. and Baxter, C. D. P. (2007). Sample preparation of silts for liquegaction testing, *Geotechnical Testing Journal*, 30(4), pp. 324–332. ASTM International https://doi.org/10.1520/GTJ10364J.

Carraro, J. A. H. and Prezzi, M. (2008). A new slurry-based method of preparation of specimens of sand containing fines, *Geotechnical Testing Journal*, 31(1), pp. 1–11. https://doi.org/10.1520/GTJ100207.

Kuerbis, R. and Vaid, Y. P. (1988). Sand sample preparation-the slurry deposition method, *Soils and Foundations*, 28(4), pp. 107–118. https://doi.org/10.3208/sandf1972.28.4_107.

Ladd, R. S. (1978). Preparing test specimens using undercompaction, *Geotechnical testing journal*, Vol. 1, pp. 16–23. http://doi.org/10.1520/GTJ10364J.

Lade, P. V. (2016). *Triaxial testing of soils*, 1st ed., Wiley Blackwell, Chichester, United Kingdom. https://doi.org/10.1002/9781119106616.

Liu, W., Tang, X. and Yang, Q. (2017). A slurry consolidation method for reconstitution of triaxial specimens, *KSCE Journal of Civil Engineering*, 21(1), pp. 150–159. https://doi.org/10.1007/s12205-016-0199-9.

Pousette, K., Eriksson, L. and Knutsson, S. (2008). Acidification properties of sulphide soil: a classification system based on leaching tests, In: *Proceedings of the 15th Nordic Geotechnical Meeting (NGM 2008)*, Sandefjord, Norway, pp. 415–422.

Reid, D., Fanni, R. and Fourie, A. (2022). Slurry deposition preparation method for tailings characterisation: history, debates, techniques and benefits, In: *Proceedings of the 8th International Conference on Tailings Management (Tailings 2022)*, Online conference.

Westerberg, B., Albing, D. and Larsson, R. (2005). Research on strength and deformation properties of Swedish fine-grained sulphide soils, In: *Proceedings of the 16th international Conference on Soil Mechanics and Geotechnical Engineering*, 2(1), pp. 623–626. https://doi.org/10.3233/978-1-61499-656-9-623.

Yu, Y. (1993). *Testing and modelling of silty and sulphide-rich soils*, PhD thesis, Luleå University of Technology, ISSN 0348-8373, 121 [print].

Proceedings of the XVIII ECSMGE 2024
GEOTECHNICAL ENGINEERING CHALLENGES
TO MEET CURRENT AND EMERGING NEEDS OF SOCIETY
© 2024 the Authors
ISBN 978-1-032-54816-6
DOI 10.1201/9781003431749-440
Open Access: www.taylorfrancis.com, CC BY-NC-ND 4.0 license

ECSMGE 24
XVIII EUROPEAN CONFERENCE ON SOIL MECHANICS AND GEOTECHNICAL ENGINEERING

A case study on energy-based evaluation of deep vibro compaction method

Une étude de cas sur l'évaluation basée sur l'énergie de la méthode de compactage par vibration profonde

A. Gokalp*, A. Dinc, S. Adatepe, R. Düzceer
Kasktas A.S., Istanbul, Turkey

**alp.gokalp@kasktas.com.tr*

ABSTRACT: This case history describes a well-documented and recently completed project in the Caribbean consisting of densification of hydraulic fills by vibro compaction method. The results of compaction are discussed based on energy criteria. The project site covers approximately 13,500 m^2 with an average depth of 9.5 m are densified to a minimum relative density of 65% against liquefaction. Soil classification for initial state of the hydraulic fills is investigated based on CPTU tests. Before the commencement of the works, vibro compaction parameter tests were carried out in 3 different test areas. The physical properties of the hydraulic fill and the details of the densification applications are presented. A comprehensive quality control program was pursued in the project. The successful execution of works illustrates the effectiveness of the selected method. In this study, the total amount of compaction energy transferred per unit volume of loose hydraulic fill, corresponding increase in cone resistance (Δq_c), the grid spacing, the vibro compaction production time are presented for each type of soil and results are presented.

RÉSUMÉ: Cette étude de cas décrit un projet bien documenté et récemment achevé dans les Caraïbes, qui consiste à densifier des remblais hydrauliques par la méthode du vibrocompactage. Les résultats du compactage sont discutés sur la base de critères énergétiques. Le site du projet couvre une superficie d'environ 13,500 m^2 et le sol y est densifié jusqu'à une profondeur moyenne de 9.5 m et une densité relative minimale de 65% contre la liquéfaction. La classification du sol pour l'état initial des remblais hydrauliques est étudiée sur la base des résultats de l'essai de pénétration au piézocône (Piezocone Penetration Test CPTu). Avant le début des travaux, des essais sur les paramètres de vibrocompactage ont été effectués dans 3 différentes zones d'essai. Les propriétés physiques des remblais hydrauliques et les détails des travaux de densification sont présentés. Un programme compréhensif de contrôle de la qualité a été mis en place dans le cadre du projet. L'exécution satisfaisante des travaux illustre l'efficacité de la méthode choisie. Dans cette étude, la quantité totale d'énergie de compactage transférée par unité de volume de remblai hydraulique meuble, l'augmentation correspondante de la résistance du cône, (Δq_c), l'espacement des grilles, le temps de production du vibrocompactage sont présentés pour chaque type de sol et les résultats pertinents sont indiqués.

Keywords: Hydraulic fill; compaction energy; vibro compaction; liquefaction; cone Penetration Test (CPT).

1 INTRODUCTION

The proposed port in the Caribbean has been under operation since 1929. Due to the development of the maritime transport methods and port facilities in the recent years, a development plan was implemented for future port layout design to meet traffic demand through 2020.

The project involves the redevelopment of the existing port. The project will enhance the passenger experience and provide additional business opportunities for the local population. The project will also include the construction of a new terminal building; the creation of an event and entertainment area; investments in retail facilities; and the design and construction of new food and beverage facilities. The project consists of expansion of the existing cruise pier, combi-wall driving works on existing wharf, construction of two new marinas for tour boats, dredging, densification of dredged hydraulic fill by vibro compaction method, expanding the port area by reclaiming and renovating & refurbishing of existing piers, arrival building, museum, signature restaurant, amphitheatre, 3 pier buildings, canopies, town square, market place, landscape works and all relevant construction, mechanical, electrical and architectural activities.

With the completion of all construction activities, the renovated port is expected to welcome over 4 million passengers annually. The location and general layout of the project site are shown in Figure 1.

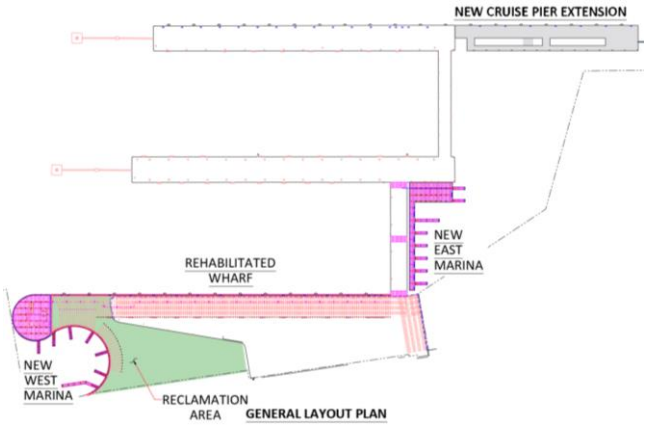

Figure 1. General layout of project site.

2 SUBSOIL CONDITION AND DREDGING WORKS

A total of five boreholes were carried out within the scope of preliminary soil investigations in the project area. Among these boreholes, B-5 and B-7 were carried out on the land side, and B-4, B-6, and B-9 boreholes were carried out on the sea side. Samples from soil and rock layers were taken by the Standard Penetration Test (SPT) and NQ rock coring. Borehole layout plan given in Figure 2.



Figure 2. Borehole layout plan.

The idealized soil profile of the proposed project site and BIM model of seabed are shown in Figure 3. For onshore boreholes, the groundwater elevations are typically the same as the sea level in the adjacent port area.

The project consists of a construction of a 250-meter-long pier extension to the east of the northernmost existing cruise ship pier and the reclamation of the quay area at the south end of the port, between the pier structure and the coastline, by filling with hydraulic fill sand. A new combi-wall consisting of steel pipe piles and sheet piles was constructed in front of the existing combi-wall system to renovate the existing system. Behind the combi-wall, dredged loose granular hydraulic fill material covering an area of approximately 13,500 m^2 with an average depth of 9.5 m was placed. Then the hydraulic fill was compacted by vibroflotation method to achieve a minimum relative density of 65%.

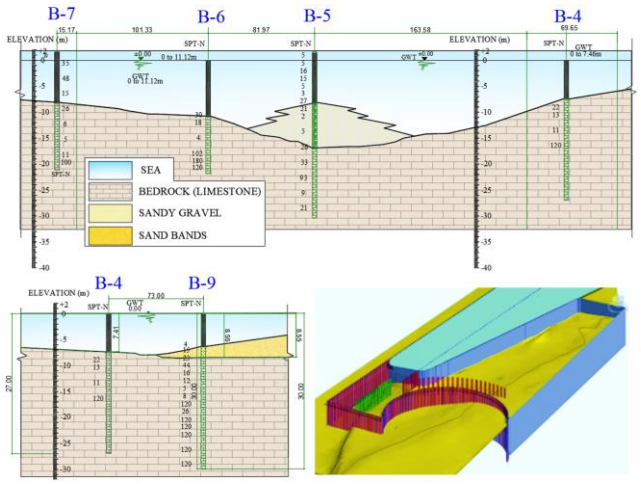

Figure 3. Idealized soil profile and BIM model of seabed.

In total, approximately 127,530 m^3 of loose granular fill material was dredged from the seabed and transported to the reclamation area by pipelines. Double rows of silt curtains are installed on the outside of the combi-wall to reduce and limit turbidity.

2.1 Evaluation of Fill Material Quality

Two methods were used to evaluate the quality of fill material. In the first evaluation method, with the help of the relation developed by Brown (1977), the suitability of the fill material for vibro compaction method was determined according to the soil grain size:

$$SN = 1.7\sqrt{\frac{3}{D_{50}{}^2} + \frac{1}{D_{20}{}^2} + \frac{1}{D_{10}{}^2}} \qquad (1)$$

where D50 is the diameter of the grain through which 50% of the soil passes, D20: It is the diameter of the grain through which 20% of the soil passes. D10: It is the diameter of the grain through which 10% of the soil passes. The suitability numbers method is an accepted and widely used method used to decide on the improvement of the fill material by the vibro compaction method. It is stated that vibro compaction is suitable for fill materials where the suitability numbers are in the range of 1 to 30.

The preliminary evaluation of the samples taken from the hydraulic fill from the project site area shows that suitability of the hydraulic fill is good to excellent. The results of the sieve analysis and suitability numbers (SN) performed on 13 samples taken from the filling area are summarized in Figure 5.

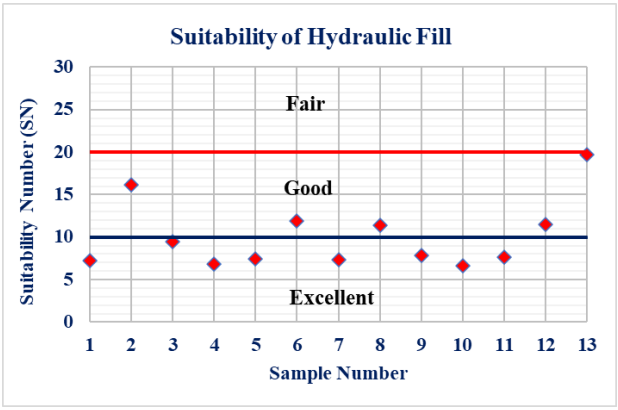

Figure 4. Suitability number of hydraulic fills.

In the second method, the results of the two pre-CPT tests performed in the center of the reclamation area were evaluated for compactability of the hydraulic fill by using the method proposed by Massarsch (1991). The results show that the hydraulic fill is marginally compactible to compactible as shown in the Figure 5.

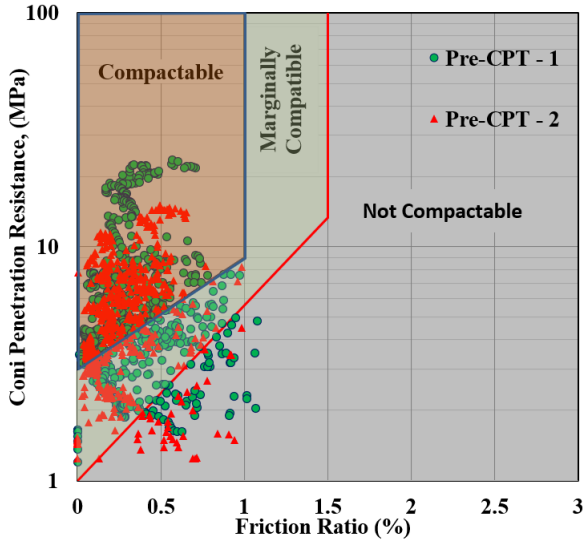

Figure 5. Compatibility assessment of hydraulic fill.

3 FULL-SCALE FIELD TESTS

To verify the installation parameters of vibro compaction works, preliminary tests were performed at a designated test area before the commencement of the works. In the test area, different grids of vibro compaction were tested with an equilateral triangular grid of 3.25x3.25m, 3.50x3.50m and 3.75x3.75m. These grid configurations were chosen to assess the performance of the vibro compaction method under different grid spacing. Before the tests, pre-CPT (Cone Penetration Test) were performed at the center of the test area for evaluating the initial state of the hydraulic fill.

Post CPT tests were performed ten days after the completion of the vibro compaction application. The layout plan for full scale preliminary tests is shown in Figure 6.

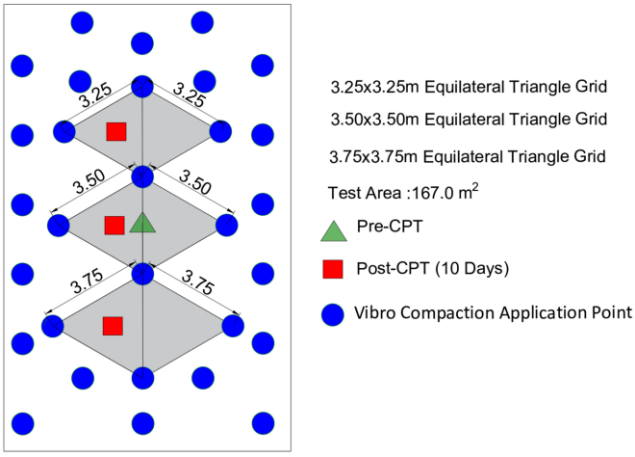

Figure 6. Layout plan for full scale preliminary tests.

Since the hydraulic fill is marginally compactible a double pass application method was introduced and tested. The double pass method consists of two passes over the same location by using vibroflot as shown in Figure 7. This approach is commonly employed to achieve a higher degree of compaction compared with single pass method.

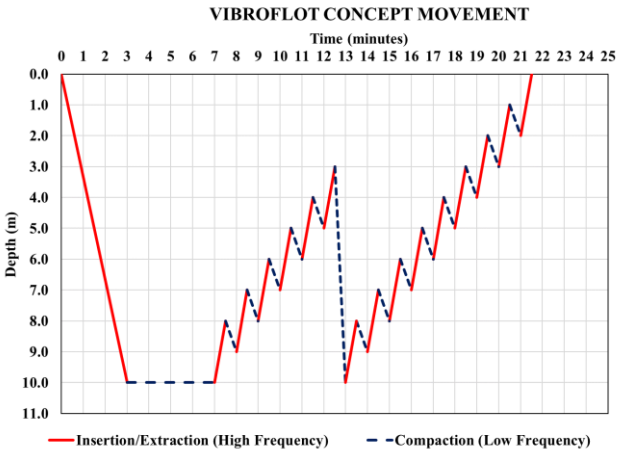

Figure 7. Vibro compaction with double pass method.

CPTs performed before and after the densification by vibroflotation method and the energy applied to the soil in the vicinity of CPT test location (TA-7) are shown in Figure 8.

In order to measure and evaluate the effectiveness of vibro compaction application, production parameters were recorded with the help of a full-time electronic data collection unit. Using the obtained data, compaction energy was calculated precisely along the depth. The correlation developed by Baldi et al. (1986) was used to convert the targeted relative density value

into the equivalent cone end resistance with overburden pressure correction.

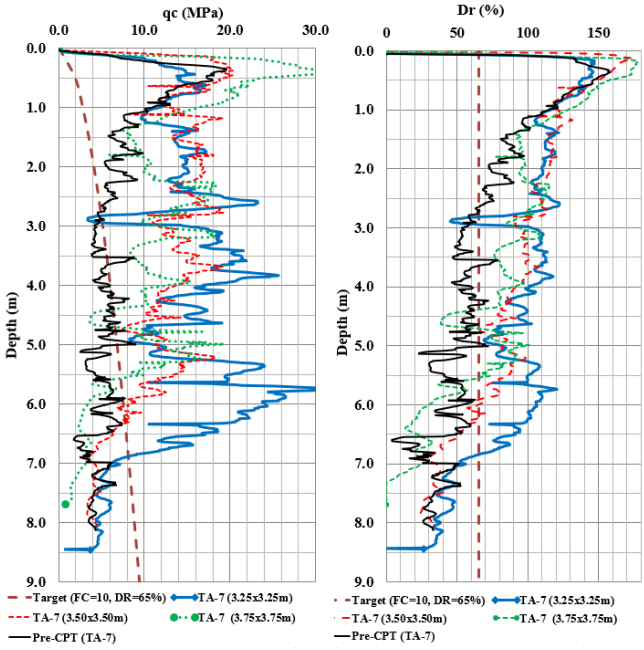

Figure 8. Cone penetration test results of TA-7.

Vibro compaction application with double passes and CPTs were performed using different grid spacing. According to the post-CPT results, all applications using the double pass method fulfils the target cone tip resistance and average relative density criteria (65%), and an average increase in cone tip resistance was obtained between 65% and 124%. The results of the full-scale field experiment using different grid spacings are summarized in Table 1.

Table 1. Full-scale field tests results.

Grid Spacing (m)	Avg. Depth (m)	Average Compaction Energy (kJ/m^3)	Δqc (Mpa)	Δqc (%)
3.25	8.80	2201.85	7.67	**124%**
3.50	8.50	1843.09	5.67	**91%**
3.75	8.00	1737.38	4.01	**65%**

In vibro compaction works, an optimization is required for production parameters in order to optimize production time and grid spacing. After determining the targeted improvement rate, the compaction energy that needs to be transferred to the fill material can be calculated with the help of the relationship given below. Since compaction energy is calculated using vibro compaction application parameters, this relationship can be used to evaluate whether the parameters are chosen correctly. As a result of the preliminary tests carried out in three different areas within the proposed site, a 93.8% linear correlation was obtained between the increase in cone tip resistance (Δqc) and compaction energy. The relationship between compaction energy and increase in cone tip resistance (Δqc) is given in Figure 9 and equation 2.

$$\Delta qc = 0.0073xE_c - 8.27 \qquad (2)$$

where Δqc is the increase in tip resistance (Mpa) and Ec is the vibro compaction energy (kJ/m^3).

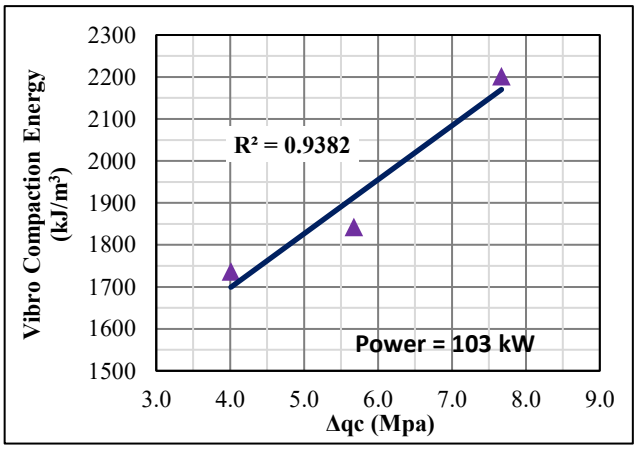

Figure 9. Relationship between vibro compaction energy and Δqc.

3.1 Evaluation of time-dependent improvement rate

An additional in-situ preliminary field test was conducted in Test Area-4 to evaulate time-dependent improvement behaviour after completion of vibro compaction works. The general layout plan of the test area is shown in Figure 10.

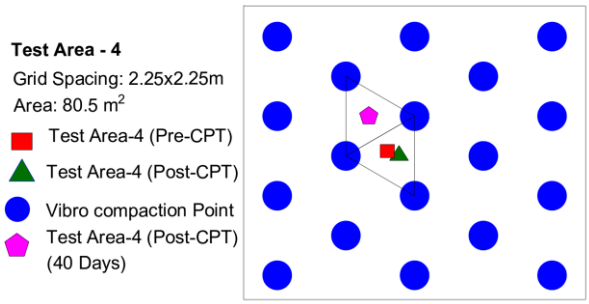

Figure 10. Layout of test area-4.

The time dependent behaviour is shown in Figure 11 by comparing pre-CPT, 2-day, 10-day, and 40-day Post-CPT cone tip resistance with depth.

According to the 40-day post Cone Penetration Test (CPT) results, in vibro compaction applications using a high-pressure water jet, the water jet initially increases the pore water pressure in the soil. After the completion of the compaction process, the pore water

pressure starts to decrease over time, and soil particles come closer together. As the excess pore water pressure in the soil diminishes over time, the cone tip resistance is observed to increase gradually because the soil particles transit to a denser arrangement pattern. The rate and magnitude of time-dependent improvement varies depending on various factors, such as the soil permeability, coefficient and drainage conditions.

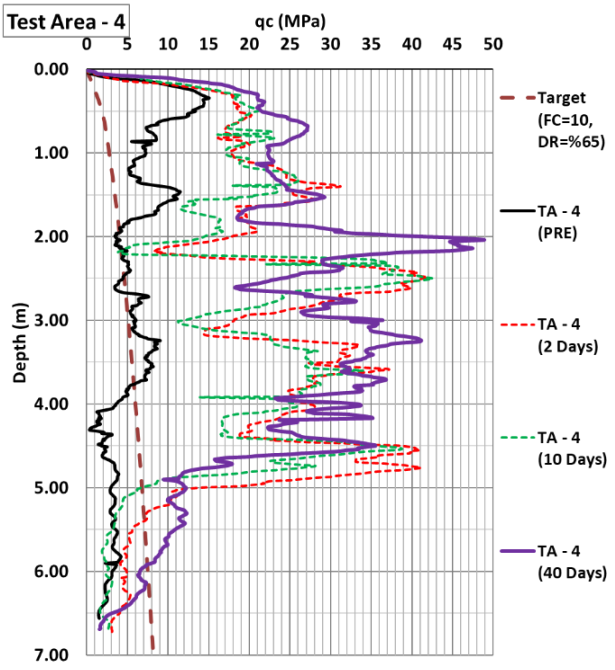

Figure 11. Cone penetration test results of TA-4.

It was determined that there was an increase in average cone tip resistance along the depth in the Cone Penetration Test conducted 40 days after the vibro compaction application. Thus, results support and confirm other studies conducted in this context in the literature.

4 CONCLUSION

This study emphasized the importance of selecting correct relationship between improvement rate and energy consumption per unit soil volume in vibro compaction applications. This would enhance the efficiency of quality control and design processes, while also offering advantages in terms of cost, quality control and work schedule in large-scale soil improvement projects.

Within the scope of this study, the initial engineering properties of the filling material acquired by dredging from the seabed and placed hydraulically in the reclamation area, the details of the seabed dredging application, the details of the vibro compaction application, the details of the full-scale field experiment carried out from the reclamation area, and the results obtained are explained.

In the double-pass vibro compaction application, in which three different grid spacings are realized with equilateral triangle grid spacing, it has been observed that the cone tip resistance decreases with the increase in the grid spacing.

The study investigated the correlation between the energy applied during vibro compaction, the resulting CPT tip resistance values, and the actual improvement rate of the soil. This analysis aimed to assess the effectiveness of the vibro compaction method in achieving the desired improvement rate in soil engineering properties.

The correct handling of the relationship between the improvement rate and the energy consumed per unit soil volume in vibro compaction applications is believed to enhance the efficiency of the quality control and design processes. By optimizing this relationship, it is possible to achieve desired improvements in soil properties.

The results obtained from the study are expected to significantly contribute to the design and quality control processes in large-scale soil improvement projects. These findings likely provide insights into the relationship between energy consumption, improvement rates, and soil performance, allowing for more efficient and effective planning and execution of vibro compaction projects.

Overall, the study emphasizes the importance of proper handling of energy consumption and improvement rates in vibro compaction applications. By ensuring the correct balance and understanding of this relationship, advantages can be gained in terms of cost-effectiveness, quality control, and adherence to work schedules in large-scale soil improvement projects.

REFERENCES

Baldi, G., Bellotti, R., Ghionna, V., Jamiolkowski, M., Pasqualini, E. (1986). Interpretation of CPT's and CPTU's. 2nd Part: drained penetration. In: Proceedings 4th International Geotechnical Seminar, Singapore, pp. 143e156.

Brown, R. E. (1977). Vibroflotation compaction of cohesionless soils. ASCE J Geotech Eng Div, 103(12).

Gokalp, A. (2006). Energy-based evaluation of vibration compaction. Pollack Periodica.

Massarsch, K. R. (1991). Deep Soil Compaction Using Vibratory Probes. In Deep Foundation Improvements: Design, Construction, and Testing. ASTM International.

Proceedings of the XVIII ECSMGE 2024
GEOTECHNICAL ENGINEERING CHALLENGES
TO MEET CURRENT AND EMERGING NEEDS OF SOCIETY
© 2024 the Authors
ISBN 978-1-032-54816-6
DOI 10.1201/9781003431749-441
Open Access: www.taylorfrancis.com, CC BY-NC-ND 4.0 license

ECSMGE 24
XVIII EUROPEAN CONFERENCE ON SOIL MECHANICS AND GEOTECHNICAL ENGINEERING

Performance evaluation of CDC compaction for warehouses: a case study of European projects

Évaluation des performances de CDC compaction pour les entrepôts: une étude de cas des projets européens

C. Guglielmelli*, J.W. Dijkstra
Cofra B.V., Amsterdam, The Netherlands
**claudio.guglielmelli@boskalis.com*

ABSTRACT: In recent years, Cofra Dynamic Compaction (CDC), a heavy Rapid Impact Compaction (RIC) technique, has been increasingly used worldwide to compact granular subsoils prior to the construction of, for example, warehouses, reclamations, hotels, wind turbines, and infrastructures. This paper provides an overview of the test results and final work methods with a focus on the compaction design for two projects. The discussed case studies include a touristic complex project located in Portugal and a terminal project in the Netherlands. Each project required, due to their own particularities, a specific work method and monitoring of the compaction activities. In all cases, the improvement of the subsoil conditions beneath the surface and foundation elements was necessary to ensure either sufficient bearing capacity while reducing total and differential settlement of shallow foundations and floor slabs or to ensure homogenization of the areas for future use. Ad hoc detailed designs were prepared to ensure that different structural elements were treated individually to meet the project requirements. Compaction efforts were constantly monitored using a GPS-based crane monitoring system to assess the effectiveness of the compaction method and adapt compaction energy where necessary. The observational method used during the compaction operations proved to be a valuable tool to optimize production but also to improve the result of the compaction works. Verification of the compaction effort was achieved by means of pre- and post-compaction CPTs, and the requirements were checked in accordance with Eurocode 7.

RÉSUMÉ: Au cours des dernières années, la technique de Cofra Dynamic Compaction (CDC), une technique lourde de Rapid Impact Compaction (RIC), a été de plus en plus utilisée dans le monde entier pour compacter les sols granulaires avant la construction, par exemple, d'entrepôts, de réclamations, d'hôtels, d'éoliennes et d'infrastructures. Cet article présente un aperçu des résultats des tests et des méthodes de travail finales, en mettant l'accent sur la conception du compactage pour deux projets. Les études de cas discutées concernent un projet de complexe touristique et un projet de terminal situés aux Portugal et au Pays-Bas. Chaque projet nécessitait, en raison de leurs particularités propres, une méthode de travail spécifique et un suivi du compactage. Dans tous les cas, l'amélioration des conditions du sous-sol sous les éléments de surface et de fondation était nécessaire pour garantir soit une capacité portante suffisante tout en réduisant les tassements total et différentiel des fondations peu profondes et des dalles de sol, soit pour assurer l'homogénéisation des zones en vue d'une utilisation future. Des conceptions détaillées ad hoc ont été préparées pour garantir que différents éléments structuraux soient traités individuellement afin de répondre aux exigences du projet. Les efforts de compactage étaient constamment surveillés à l'aide d'un système de suivi de grue basé sur le GPS pour évaluer l'efficacité de la méthode de compactage et adapter l'énergie de compactage si nécessaire. La méthode d'observation utilisée pendant les opérations de compactage s'est avérée être un outil précieux pour optimiser la production, mais aussi pour améliorer le résultat des travaux de compactage. La vérification de l'effort de compactage a été réalisée à l'aide de CPTs (essais de pénétration statique) avant et après le compactage, et les exigences ont été vérifiées conformément à l'Eurocode 7.

Keywords: Rapid impact compaction, RIC; cofra dynamic compaction, CDC; warehouse; granular soil; densification; cone penetration test, CPT; GPS-based crane monitoring system.

1 INTRODUCTION

As part of the design of warehouses and infrastructure projects on loose granular soils, the method of deep compaction is often overlooked in favour of deep foundations or ground improvement techniques such as stone columns and rigid inclusions.

However, the alternative approach using Heavy Rapid Impact Compaction (RIC) has proven to be highly effective and cost-efficient compared to commonly chosen solutions. Compaction with RIC ensures that the compacted materials easily meet the necessary support requirements for the loads imposed by the superstructure.

Cofra Dynamic Compaction (CDC), a heavy Rapid Impact Compaction technique, is often employed to effectively densify the uppermost soil layers, typically 6 to 10 meters deep, depending on the local soil conditions. Within the compaction process, the drop weight (9-ton to 20-ton), drop height (from 0.2 m to 1.5 m), grid spacing, and effort (number of blows given at a frequency of 0.7-1.2 Hz) are optimized to allow for the application of various tailored work sequences to meet the specific requirements of different foundation elements.

The high production and efficiency of the technique can be attributed to the constant contact between the foot (with a diameter ranging from 1.5 m to 2.6 m) and the ground surface, which transfers kinetic energy into compression and shear waves. The shear waves, combined with the dense compaction grid used during the operations, ensure uniform and highly effective compaction.

The process is schematically illustrated in Figure 1.

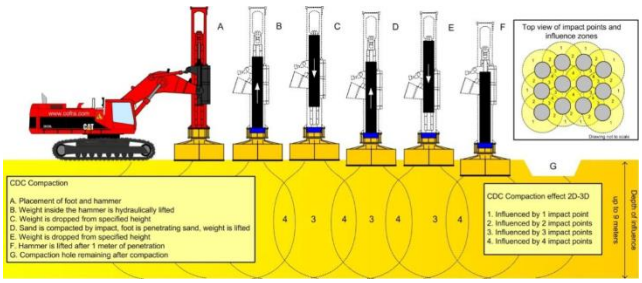

Figure 1. Illustration of the CDC work method and overlap of influence zones.

During compaction operations, several parameters are logged and displayed alongside the AutoCAD design drawing on the operator's screen. Compaction is stopped once the anticipated number of blows, maximum vertical displacement of the foot, or target settlement per blow is reached. To ensure the compaction process is both homogeneous and effective, real-time measurements of the field performance are sent back to the operator's screen and to the geotechnical engineer by uploading these into the data cloud. This enables adjustments to be made during the compaction process, such as change in foot size, grid spacing, drop height, and number of blows. Additionally, updated drawings can be immediately transferred back to the machine. Such an approach results in an optimal work process and outcomes.

This paper provides two case studies out of numerous projects executed worldwide. The examples were chosen to highlight the effect on relatively small-scale application areas where the observational method used during compaction played an important role to the projects' success. Moreover, case study 1 was selected to describe the use of RIC with challenging soil conditions, being the material to be compacted rounded dune sand.

2 CASE STUDY 1: ALDEAMENTO COLOMEIAS I PROJECT, TRÓIA, PORTUGAL

The Aldeamento Colmeias I project is located in the dune area on the Tróia Peninsula, in Portugal (Figure 2). The dune sand underneath several future buildings (logistics, restaurant, spa, hotel, luxury villas and reception facilities) required compaction over a thickness of 6 m to 7.5 m. This was needed in order to use shallow foundations with different sizes and loading configurations. The total surface area to be compacted was around 31,000 m^2.



Figure 2. Overview of the project scope (Aldeamento Colmeias I, Tróia) with an indication of the compaction points in light blue.

The compaction design focused on achieving the required bearing capacity with a minimal settlement for the different prefabricated footing configurations of the various buildings. With the main aim to reach the required depth of influence and sufficient densification, a design was prepared to perform RIC compaction using a 16-ton hammer (Figure 3) with 1.2 m drop height and a range of compaction efforts to consistently meet the requirements.



Figure 3. CDC equipment deployed on the project.

During the field trials, four combinations of compaction energy were tested, and based on their performance, two configurations were selected for the project. These two configurations were deployed on the basis of the pre-compaction CPTs, as well as the required bearing capacity and settlement behaviour following the treatment.

2.1 Results

After a single pass of CDC hammer, the functional requirements were successfully met at all tested locations up to a depth of 7.5 m. The result of the homogeneous compaction is shown in Figure 4, which illustrates the pre- and post-compaction CPT cone resistances (qc) of the trial area. During the trial, two passes were executed. To investigate its effect, CPTs were carried out on and in-between the compaction locations to show the lateral difference. Figure 4 clearly indicates that the second pass resulted in an increased qc over a greater depth of influence. Moreover, the qc values measured within one compaction location and between four compaction locations showed minimal variation, suggesting a satisfactory overlap of the compaction influence zones. This effect was also shown in Vink et al. (2016).

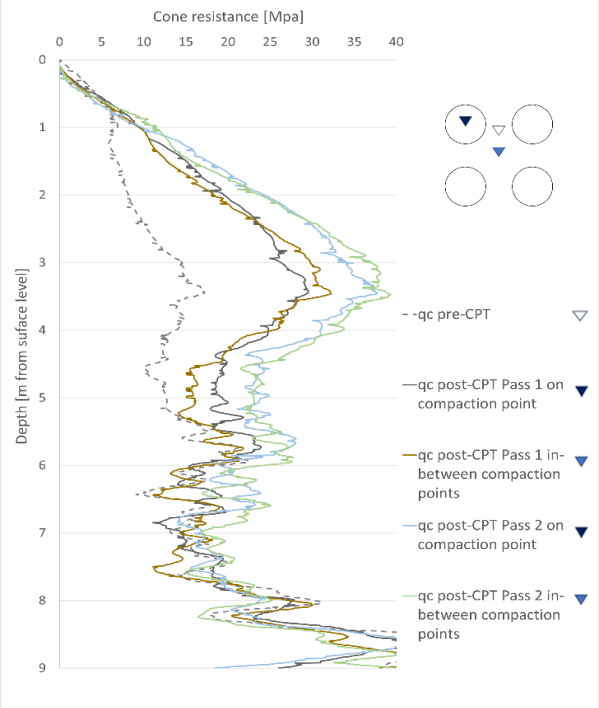

Figure 4. Cone resistance before compaction (pre-CPT), cone resistance after first pass compaction (post-CPT Pass 1) and cone resistance after second pass compaction (post-CPT Pass 2).

The effect of CDC compaction in terms of settlement is shown in Table 1. This is calculated using the Schmertmann's method (Schmertmann, 1978) for square footings, in line with Eurocode 7 (BS EN 1997-1, 2004).

Table 1. Part of the compliance check based on CPTs using Schmertmann's method from Eurocode 7.

Project area	Bearing capacity [kPa]	Settlement before CDC [mm]	Settlement after CDC [mm]
Logistic1	200	8.9	1.1
Colmeia 7	200	10.4	1.2
Colmeia 31	200	8.2	1.3
Colmeia 69	200	9.9	1.3
SPA	200	12.6	1.2
Hotel	200	6.3	1.2

3 CASE STUDY 2: TERMINAL AREA, MOERDIJK, THE NETHERLANDS

The following case study is a compaction project for a brownfield development of a new terminal located in Moerdijk, southeast of Rotterdam, The Netherlands. The project required compaction of the subsoil within loosely backfilled zones right underneath a number of demolished warehouses. The main purpose of the ground improvement (over a maximum depth of maximum 3 m) was to obtain a homogeneously densified sand fill with the surrounding existing soil, to accommodate for the heavy loads that the future terminal will need to support. The total surface area to be compacted was around 37,000 m^2.



Figure 5. CDC equipment deployed on the project.

3.1 Stop criterion: settlement per blow

For this project, a specific work method was developed to carry out RIC with a 9-ton hammer (Figure 5) and reduced drop height of only 0.9 m, using a settlement per blow stop criterion. The compaction process was monitored using the advanced GPS-based crane monitoring system, which measures the settlement of the compaction foot for each blow. During the field trial, a fixed grid was tested on both the backfilled area and the existing soil, with a baseline of 40 blows. The collected settlement data was analysed to establish a

correlation between qc and settlement per blow. As a result, a specific settlement per blow target was chosen for the project. This was generally reached after the first few blows in the non-excavated area and at the end of the compaction sequence in the backfilled area. This target settlement was implemented in real-time during the operations, and the measurements were visible to the operator of the rig, facilitating and optimizing the compaction process.

The outcome of the homogeneous compaction achieved in this project can be observed in Figure 6 and Figure 7. Whilst Figure 8 displays the number of blows given at each compaction point to reach the target settlement per blow.

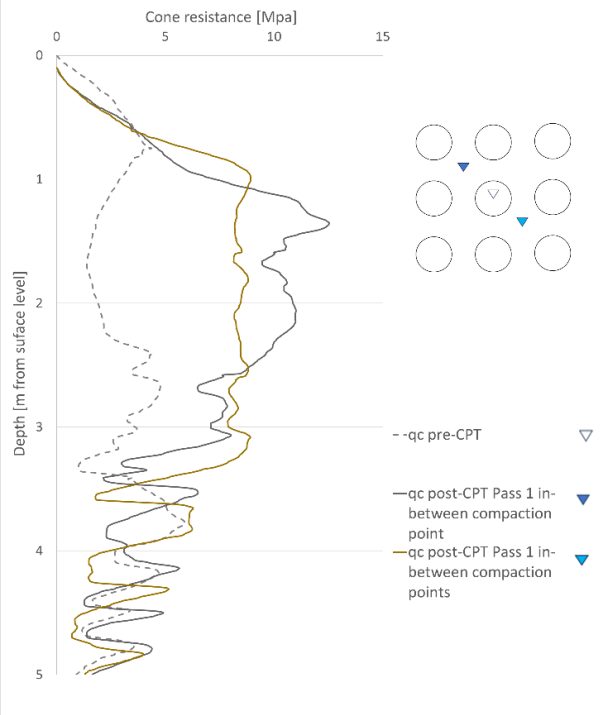

Figure 6. Cone resistance before compaction (pre-CPT) and cone resistance after first pass compaction (post-CPT Pass 1) using the settlement per blow stop criterion.

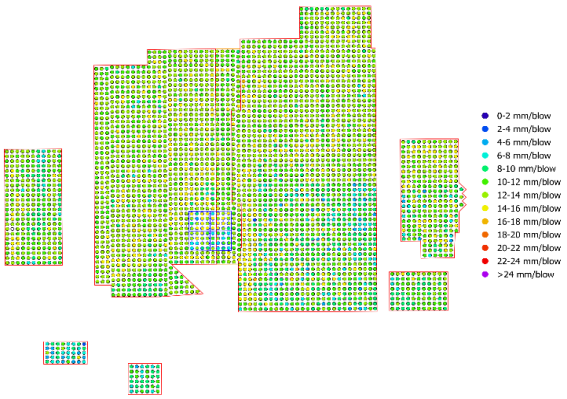

Figure 7. As-built settlement per blow after CDC compaction.

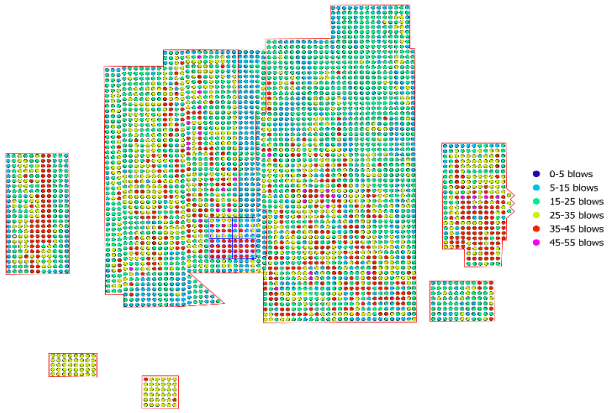

Figure 8. As-built number of blows from CDC compaction.

4 CONCLUSION

This article highlights the effectiveness of project-specific RIC design methods through two project examples. These methods enabled the treatment of loose granular subsoils up to a depth of 7.5 meters in compliance with the project requirements, leading to cheaper soil improvement solutions, as less compaction energy was used during the execution.

Over the past decade, numerous projects worldwide have been executed using this observational method, thanks to the development of a tailored ad hoc design that addresses the specific needs of each project. This approach relies on a GPS-based crane monitoring system and fully automated processing of real-time data. The evaluation of the field performance during the implementation of the Cofra Dynamic Compaction technique has consistently demonstrated its high effectiveness not only in mitigating the risks of liquefaction, differential settlement, and ensuring sufficient bearing capacity for prefabricated footings of varying sizes, but also in optimising the production and the quality of the compaction works.

REFERENCES

BS EN 1997-1. (2004). Eurocode 7: Geotechnical design - Part 1: General rules. Doi: 10.1680/dgte7.31548.bm01

Schmertmann, J.H., Hartman, J.P. and Brown, P.R. (1978). Improved strain influence factor diagrams. *Journal of Geotechnical and Geo-environmental Engineering*, 104(GT8), 1131-1135. Doi: 10.1061/AJGEB6.0000683.

Vink, J.W., Dijkstra J.W. (2016). CDC Compaction at Berth 9 Quay Extension Felixstowe, UK. International Conference on Transportation Geotechnics (ICTG 2016). Doi: 10.1016/j.proeng.2016.06.173.

Proceedings of the XVIII ECSMGE 2024
GEOTECHNICAL ENGINEERING CHALLENGES
TO MEET CURRENT AND EMERGING NEEDS OF SOCIETY
© 2024 the Authors
ISBN 978-1-032-54816-6
DOI 10.1201/9781003431749-442
Open Access: www.taylorfrancis.com, CC BY-NC-ND 4.0 license

ECSMGE 24
XVIII EUROPEAN CONFERENCE ON SOIL MECHANICS AND GEOTECHNICAL ENGINEERING

Artificial Ground Freezing for underground excavation: a coupled modelling approach supporting tunnelling design

Congélation artificielle du sol pour l'excavation souterraine: une approche de modélisation couplée soutenant la conception de tunnels

G. Guida*, F. Casini
Università degli Studi di Roma Tor Vergata, Rome, Italy

A. Restaini, A. Celot
Webuild Group S.p.A – Milan, Italy

**giulia.guida@uniroma2.it*

ABSTRACT: This study develops a numerical thermo-hydraulic model to simulate the Artificial Ground Freezing (AGF) intervention as a ground improvement. Frozen soil is modelled based on the partially saturated framework, considering a three-phase material composed of solid grains with liquid water and ice filling the voids. A physically based criterion is proposed to estimate the freezing temperature at which the soil attains the impermeable conditions and thus is completely frozen. According to this criterion, coarse-grained soils freeze around a temperature of -1°C, and fined-grained soils freeze progressively for lower temperatures, down to -9°C. The modelling approach is applied to the AGF case study of the Isarco River Underpass in the Brenner Base Tunnels project. The incoherent and heterogeneous coarse-grained soils under a water seepage regime that characterise the site, within the few-meters thin covering separating the tunnel from the riverbed, make using the AGF necessary to furnish the proper safety conditions for the excavation works. The accessible geotechnical investigation surveys and the monitored soil temperature data aimed to validate the proposed numerical model. The model predictions regarding temperatures reveal a strong dependence of the freezing process on the soil's hydraulic and thermal properties and the seepage flow regime. An optimised freezing temperature aims to improve the process of artificial freezing by reducing the time of freezing activation and designing an efficient configuration of probes, maintaining equal levels of safety against the waterproofing of the excavation area.

RÉSUMÉ: Cette étude développe un modèle thermohydraulique numérique pour simuler l'intervention Artificial Ground Freezing (AGF) en tant qu'amélioration du sol. Le sol gelé est modélisé sur la base du cadre partiellement saturé, en considérant un matériau triphasé composé de grains solides avec de l'eau liquide et de la glace remplissant les vides. Un critère physique est proposé pour estimer la température de congélation à laquelle le sol atteint les conditions imperméables et est donc complètement gelé. Selon ce critère, les sols à gros grains gèlent autour d'une température de -1 °C et les sols à grains fins gèlent progressivement pour des températures plus basses, jusqu'à -9 °C. L'approche de modélisation est appliquée à l'étude de cas AGF du passage inférieur de la rivière Isarco dans le projet de tunnels de base du Brenner. Les sols incohérents et hétérogènes à gros grains sous un régime d'infiltration d'eau qui caractérisent le site, à l'intérieur de la mince couche séparant le tunnel du lit de la rivière, rendent l'utilisation de l'AGF nécessaire pour fournir les conditions de sécurité appropriées pour les travaux d'excavation. Les enquêtes géotechniques accessibles et les données de température du sol surveillées visaient à valider le modèle numérique proposé. Les prédictions du modèle concernant les températures révèlent une forte dépendance du processus de congélation sur les propriétés hydrauliques et thermiques du sol et le régime d'écoulement d'infiltration. Une température de congélation optimisée vise à optimiser le processus de congélation artificielle en réduisant le temps d'activation de la congélation et en concevant une configuration efficace des sondes, en maintenant des niveaux de sécurité égaux contre l'étanchéité de la zone d'excavation.

Keywords: Frozen soils; excavations; numerical modelling; unsaturated soils.

1 INTRODUCTION

Artificial ground freezing (AGF) is a temporary excavation support technique adopted in various engineering applications (*e.g.*, Harris, 1995; Viggiani & Casini, 2015). Its basic principle is to reduce soil temperature below 0°C by circulating cooled fluid through freezing pipes installed in the ground around the future excavation section, creating a close and stable waterproof shell. The AGF design should be performed by thermal and structural analyses (Chang & Lacy, 2008). The thermal analysis will provide shape and temperature profiles of the frozen body. The

structural analysis will use the resulting frozen ground structure to evaluate whether it is stable during the excavation. Modelling the freezing process is challenging since it has a strongly coupled thermo-hydro-mechanical nature that should include phase changes. This article proposes a new method to optimise the thermal analysis design of AGF based on the theoretical framework of unsaturated soils extended to frozen conditions (Casini *et al*., 2023). This novel approach was applied to the case study of AGF intervention adopted for the Isarco River underpass tunnels within the Brenner Base Tunnel*s* project, performing numerical simulations with a coupled *thermo*-hydraulic model implemented in a finite element code.

2 THE METHOD

During the AGF operation, the soil temperatures must be continuously recorded to check the thickness and tightness of the frozen shell. The soil can be considered frozen when the temperature falls below a target value, conservatively assumed to be T^*= - 10°C, regardless of the soil type. However, the volume of liquid water that changes phase into ice depends highly on the temperature applied, the type of soil, and its hydraulic properties.

Figure 1 reports literature experimental data from Williams (1964) relating the temperature *vs* the degree of liquid water saturation (Soil Freezing Curve) for sand, silt and clay, interpolated by Clausius-Clapeyron joined with the van Genuchten laws (Casini, 2021; Nishimura *et al*., 2009):

$$S_{ew} = \left\{ 1 + \left[\frac{-\left(1-\frac{\rho_i}{\rho_w}\right)P_w - \rho_i L \ln\left(\frac{T}{273.15}\right)}{P} \right]^{\frac{1}{1-m}} \right\}^{m} \qquad (1)$$

where S_{ew}=(S_w-S_{res})/(1-S_{res}) is the effective degree of liquid water saturation, ρ_i e ρ_w are the density of ice and water, respectively, P_w is the pore water pressure, L is the latent heat of water fusion, and P and m are the parameters of the van Genuchten retention curve. According to the Soil Freezing Curve, frozen conditions are achieved when the liquid phase is discontinuous, and the effective degree of liquid water saturation is close to the residual values: S_{ew}≈0.05÷0.10. It occurs for different temperatures depending on soil type, generally greater as grain size increases. In Figure 1, the soil frozen condition corresponds to a temperature range of: -0.6 to -2.0°C, for sand; -1.3 to -2.6°C for silt; -5.9 to -10.5°C for clay. Thus, based on the water retention properties of the soil, the target freezing temperature can be estimated as T_{sand}*=-1°C, T_{silt}*=- 2°C and T_{clay}*=-9°C, respectively.

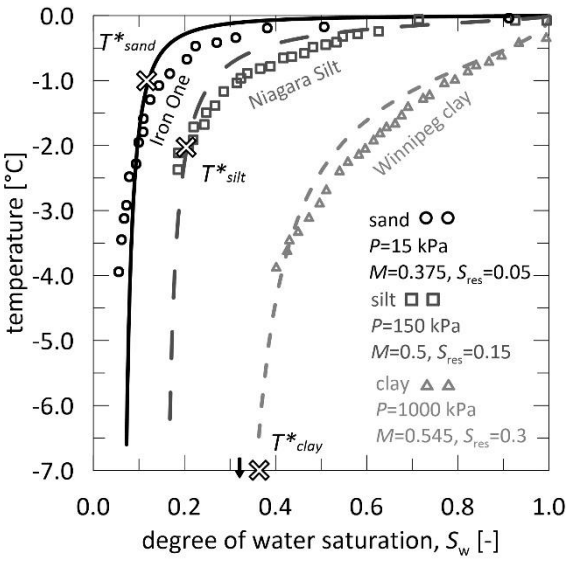

Figure 1. Relation between the degree of liquid water saturation and the temperature. Experimental data after Williams (1964).

3 THE CASE STUDY

AGF is typically adopted in contexts such as excavations in heterogeneous soils below the water table, characterised by issues related to instability and significant seepage flows. The case study under examination is the Isarco River underpass tunnel, whose critical conditions due to the low coverage (about 5 m) and the need to excavate through loose, coarse-grained soils below the water table made AGF the unique safe intervention possible. The area is located 1 km north of Fortezza in the Isarco Valley (Bolzano), at an elevation of about 750-850 m above sea level. A plan view of the underground structures is shown in Figure 2(a): four shafts, named POBDN, POBDS, POBPN, and POBPS, were constructed to allow the excavation of the four underpass tunnels of about 50-55 m in length. This work simulates the freezing operations in the first tunnel to be completed, highlighted in red in Figure 2(a) between the POBPN and POBPS shafts. The reference excavation cross-section is 12 m distant (S12m in Fig.2a) from the POBPN shaft. The AGF was carried out by driving the freezing pipes around the excavation section parallel to the development of the tunnel, as shown in Figure 2(b). Freezing was activated with liquid nitrogen, entering at about - 196°C (open circuit) and maintained using brine (calcium chloride) at approximately -35°C, which recirculates through a refrigeration plant. The excavation operations start when the frozen body becomes 1 m thick. Optic fibres

installed in 42 thermometric rods parallel to the tunnel development monitored every 25 cm the temperature of the soil and the growth of the frozen body.

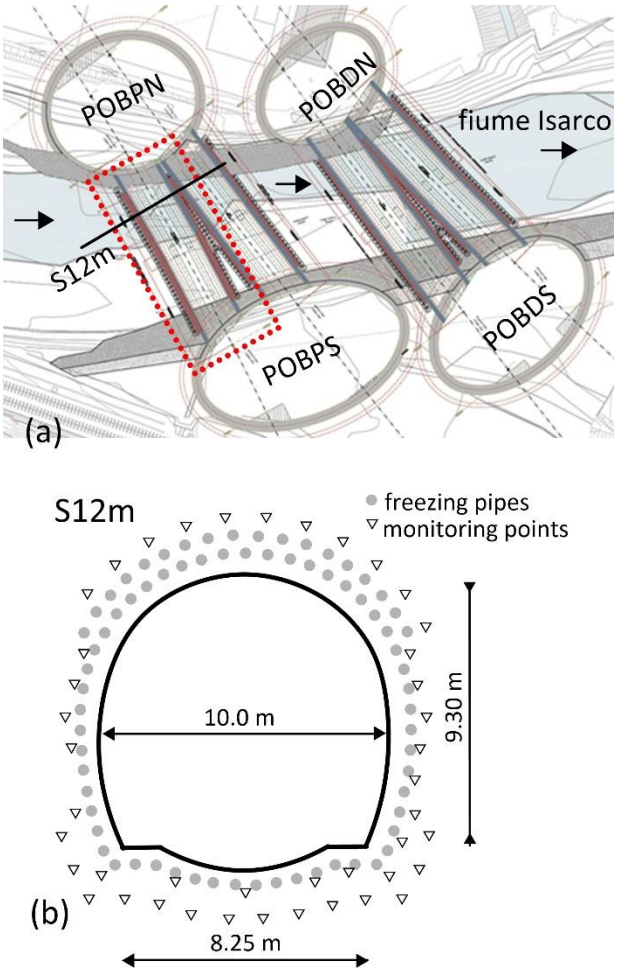

Figure 2. (a) Plan view of the underground structures; (b) enlarged view of the tunnel cross-section under examination specifying the position of the freezing pipes and the monitoring points.

Figure 3(a) shows the evolution over time of the temperatures in the monitoring points M1 and M2 arranged at two different points of the tunnel cross-section (Fig. 3b). The lowest temperatures were recorded at the end of the activation phase (~day 9), which are approximate -10°C and -28°C, in M2 and M1, respectively. In the following maintenance phase with brine, the monitored temperatures increase and reach a thermal equilibrium around day 12. The differences between trends can be attributed to the relative distance between the freezing pipes and the thermocouples, the seepage effect, and the soil heterogeneity.

4 NUMERICAL SIMULATIONS

The AGF process was numerically reproduced using a coupled thermo-hydraulic model capable of accounting for the phase change from liquid water to ice induced by temperature below 0°C, Soil Freezing Curve, and seepage. For details of the implementation and parameters adopted, see Casini *et al*. (2023). Figure 3(a) compares the model predictions and monitoring data at the two monitoring points, M1 and M2. The simulations were conducted considering uncertainty about the position of the freezing probes of ± 10 cm in the horizontal and vertical directions due to possible deviations of the perforations. The envelope of model predictions qualitatively reflects the monitoring data trends in the liquid nitrogen activation and brine phases. However, the model predictions overestimate the monitoring data, especially in the activation phase (up to day 9). The discrepancy is possibly due to the faster achievement of the subzero temperature at the freezing pipes boundary conditions. Figure 3(b) shows the contour lines of temperatures evaluated at the end of the liquid nitrogen activation phase (9th day). The formation of a closed, frozen wall with temperature values below -10°C is observed around the entire tunnel excavation area. The imposed seepage regime from left to right (0.7 m water gradient in 60 m) determines the non-symmetry of the contour lines. Figure 4 reports the evolution with time of the equivalent thickness th_{eq} of the frozen wall, quantitatively evaluated from the images of the numerical temperature contours considering as target value T*=-10°C and T_{sand}*=-1°C. The curves have the same monotonous increasing trend with time. The proposed method allows an optimised design of the frozen wall thickness and the duration of the nitrogen activation phase, while maintaining the same level of safety against waterproofing (see Casini *et al.,* 2023).

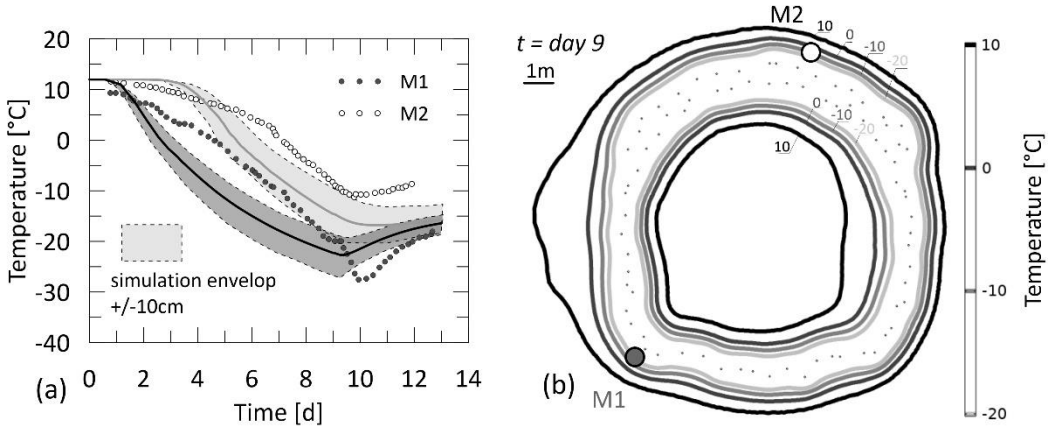

Figure 3. (a) comparisons of temperature evolution over time at measurement points M1 and M2; (b) Contour plots of temperatures obtained from simulations on day 9 between monitoring data and model predictions.

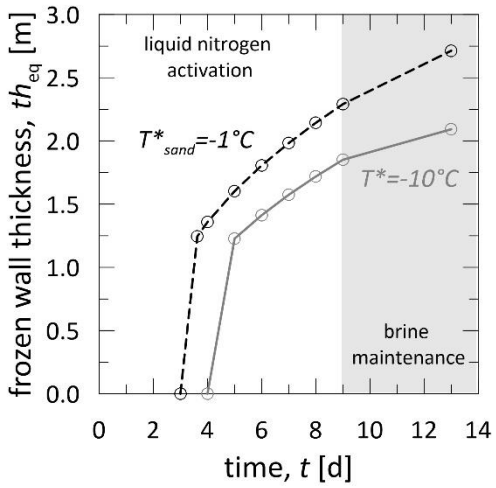

Figure 4. Equivalent frozen wall thickness evolution with time adopting two different target temperatures T.*

5 CONCLUSIONS

This work proposed a new design criterion to optimise the design and monitoring of the artificial ground freezing intervention. It consists of defining the target temperature value to identify the frozen state of the soil based on the Soil Freezing Curve. The new approach is then applied to the artificial ground freezing case study of the Isarco River underpass tunnel, showing a potential reduction of the activation phase duration without compromising safety against waterproofing.

ACKNOWLEDGEMENTS

Dr Giulia Guida obtained Regione Lazio's financial support through her position as a fixed-term researcher (POR-FSE 2014/20 Contributions for the permanence of excellence in the academic world, No. 65629/2020). We would like to thank the WEBUILD SPA Company and its technicians for the contribution offered in the drafting of this article and for the opportunity given to us to visit the construction site during the various phases of artificial ground freezing and Marco Carosi for his collaboration during his master thesis work.

REFERENCES

Casini, F. (2021). Multiphase soil mechanics for landscape protection: from testing to modelling. *Rivista Italiana di Geotecnica*, 55(2), 5-34. https://doi.org/10.19199/2021.2.0557-1405.005.

Casini, F., Guida, G., Restaini, A. and Celot, A. (2023). Water Retention Curve–Based Design Method for the Artificial Ground Freezing: The Isarco River Underpass Tunnels within the Brenner Base Tunnel Project. *Journal of Geotechnical and Geoenvironmental Engineering*, 149(3). https://doi.org/10.1061/JGGEFK.GTENG-10723.

Chang D.K. and Lacy H.S. (2008). Artificial Ground Freezing in Geotechnical Engineering. *Proceedings of the 6th International Conference on Case Histories in Geotechnical Engineering*, Arlington, VA, August 11-16, 2008.

Harris J.S. (1995). *Ground Freezing in practice*, Thomas Telford Services Ltd, Thomas Telford House, 1 Heron Quay. London.

Nishimura, S., Gens, A., Olivella, S., and Jardine, R. J. (2009). THM-coupled finite element analysis of frozen soil: formulation and application. *Géotechnique*, 59(3): 159-171. https://doi.org/10.1680/geot.2009.59.3.159.

Viggiani, G.M.B. and Casini, F. L. (2015). Artificial Ground Freezing: from applications and case studies to fundamental research. In *Geotechnical Engineering for Infrastructure and Development*, pp. 65–92. http://doi:10.1680/ecsmge.60678.

Williams, P. J. (1964). Unfrozen water content of frozen soils and soil moisture suction. *Géotechnique*, 14(3), 231-246. https://doi.org/10.1680/geot.1964.14.3.231.

Proceedings of the XVIII ECSMGE 2024
GEOTECHNICAL ENGINEERING CHALLENGES
TO MEET CURRENT AND EMERGING NEEDS OF SOCIETY
© 2024 the Authors
ISBN 978-1-032-54816-6
DOI 10.1201/9781003431749-443
Open Access: www.taylorfrancis.com, CC BY-NC-ND 4.0 license

ECSMGE 24
XVIII EUROPEAN CONFERENCE ON SOIL MECHANICS AND GEOTECHNICAL ENGINEERING

Innovative and sustainable geosynthetic solutions in the field of bridge abutment construction

Solutions géosynthétiques innovantes et durables dans le domaine de la construction de culées de ponts

H. Hangen*, O. Detert
HUESKER Synthetic GmbH, Gescher, Germany

**Hangen@HUESKER.de*

ABSTRACT: The constant increase in traffic volume and the dilapidated condition of many existing infrastructure requires constant maintenance, modernisation, and reconstruction. Bridge structures play a particularly important role in this context. The use of geosynthetics can help to overcome this challenge in a more cost-effective and sustainable way compared to established technologies. Geosynthetic-reinforced soil structures can be used, for example, to relief the foundation or the abutment structure from earth-pressure. In many cases it can even be used to form the abutment as such. In any case these solutions impress with their simplicity in construction, robustness, and their quick implementation. This is demonstrated by means of completed projects.

RÉSUMÉ: L'augmentation continue du volume du trafic et l'état de délabrement de nombreuses ouvrages d'infrastructure existants nécessitent un entretien, une modernisation et une reconstruction constants. Les ponts jouent un rôle particulièrement important dans ce contexte. L'utilisation de géosynthétiques peut aider à relever ce défi d'une manière plus rentable et plus durable que les technologies traditionnelles. Les structures de sol renforcées par des géosynthétiques peuvent être utilisées, par exemple, pour soulager la fondation ou la structure de la culée de la pression du sol. Dans de nombreux cas, elles peuvent même être utilisées pour former la culée en tant que telle. Dans tous les cas, ces solutions séduisent par leur simplicité de construction, leur robustesse et leur rapidité de mise en œuvre. Des projets réalisés le démontrent.

Keywords: Bridge abutment; geogrid reinforced soil; sustainability; earth pressure relief; geosynthetic encased columns.

1 INTRODUCTION

1.1 Geosynthetic reinforced retaining structures

Due to their ecological and economic advantages over traditional construction materials the use of geosynthetic reinforcement products is common practice today. Geosynthetic-reinforced retaining structures (GRS) occupy a special position here and represent one of the oldest and most common application of geosynthetics. A comprehensive overview about the beginnings of GRS can be found, for example, in (Allen et al., 2002); a systematic survey and evaluation of the structural behaviour of representative GRS can be found, for example, in (Crouse and Wu, 1996). Bathurst (Bathurst, 2014) provides an overview of the current state of the art and current developments in design concepts and modelling. Overall, GRS can be characterized by the following main advantages over conventional construction methods:

1. ductile load-bearing behaviour enables reduced requirements for subsoil and backfill materials
2. fast and therefore cost-effective construction or disposal (for temporary structures) using conventional earthworks equipment
3. low global warming potential (GWP)
4. wide range of architectural design options.

1.2 Geosynthetic reinforced bridge abutments

Many investigations and reference projects have shown that GRS structures can also withstand extremely high loads without failing or exhibiting excessive deformations. This was demonstrated very impressively, for example, in real-scale load tests at the Landesgewerbeanstalt Nürnberg (LGA) (Alexiew, 2007) and (Alexiew and Detert, 2008) or (Bräu and Bauer, 2001). Figures 1 and 2 show the test arrangement as well as the horizontal and vertical deformations of the 4.5 m high GRS for vertical loading with a 1.0 m wide and 3.0 m long concrete beam. The horizontal deformation which was measured for a vertical stresses of 200 to 250 kN/m²,

reached a value of about 4 mm. The corresponding settlement was approx. 6 mm. The structure started to show signs of imminent failure only when the load was increased to about 500 kN/m² following two unloading and reloading cycles with only marginal elastic deformation. Clear failure, however, could not be achieved even under the maximum applicable load of 650 kN/m². Such behaviour is described also from other researchers such as or (Bräu and Bauer, 2001). The maximum bearing capacity is even given as up to 1200 kN/m².

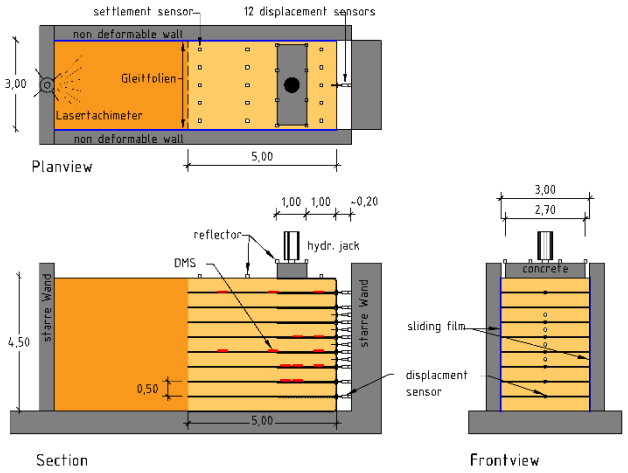

Figure 1. Testing arrangement at LGA-Nuremberg (Hangen and Jaramillo, 2016, translated from German).

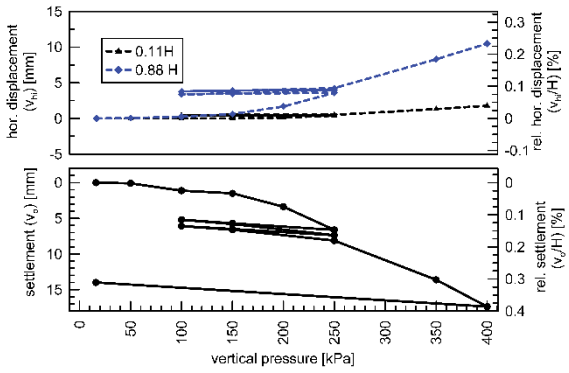

Figure 2. Monitoring of horizontal and vertical deformations for increasing vertical stress (Hangen and Jaramillo, 2016, translated from German).

Based on this experience it is reasonable to use GRS even for the construction of highly loaded bridge abutments and several reference structures show that this is feasible. However, in many countries GRS-bridge abutments have only rarely been used to date.

2 TYPICAL APPLICATIONS OF GRS-BRIDGE ABUTMENTS

2.1 GRS for wing walls and raised abutments

As shown in Figure 3 GRS can be used focusing several differing objectives. The simplest application of GRS bridge abutments is the formation of raised abutments and wing walls (Figure 3 upper left). In this application, dead weight of the bridge and traffic loads are usually transferred conventionally via piles into stable ground. This option is appropriate in case of very high abutments loads or bridges with continuous girders and if the subsoil conditions are extremely unfavourable.

Beside cost savings for GRS compared to reinforced concrete (RCC) it is basically construction time and logistics which makes GRS attractive in this case. Drilling rigs could be acting from the top of the GRS when all abutment and backfilling of the ramp have been finished. Access and construction would not interfere with traffic at the base of structure in this case. This can be a huge advantage in case reconstruction needs to be done in tight spaces. Furthermore, this construction sequence would allow to reduce or exclude negative skin friction and horizontal earth-pressure acting on the foundation piles.

2.2 GRS to relief earth-pressure

Another possible application of GRS is the formation of so-called earth pressure absorbers, ref. Figure 3 upper right. In this case, the GRS is used to absorb the horizontal earth pressure of the abutment backfill. Depending on the bridge designer's structural concept, this can be done over the entire height of the abutment or only in the upper area of the structure. This can be temporary, to secure certain construction stages or permanent. In most cases GRS is designed to eliminate the entire earth pressure acting on a neighbouring structure. Theoretically, however, it would be possible to design for a reduced earth pressure only. In practice, unfortunately, there is not yet a method available as to reliably quantify the stress-reduction.

The construction of an earth pressure relief opens possibilities for significant changes or optimization in the structural design of the bridge structures, particular regarding torsional loading and bending. This is of particular interest wherever crossings are skewed. Earth-pressure relief with GRS can also be combined to optimise the design of integral bridges, eliminating complex bearings and transition structures but reducing maintenance costs in particular. The advantages of GRS for the construction of integral bridges, have been reported by (Pötzl and Naumann,

2005). One of the largest reference structures using this construction method in Germany is the so-called taxiway bridges at Frankfurt Airport (Steiger et al., 2012).

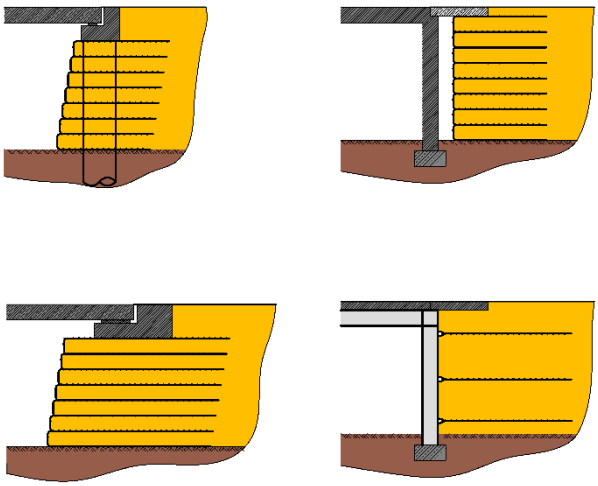

Figure 3. Configuration of GRS in bridge abutments (Hangen and Jaramillo, 2016).

2.3 GRS directly supporting the superstructure

The design of a bridge abutment, in which GRS is used to transfer the entire structural loads (ref. Figure 3 lower left), offers by far the greatest opportunities for optimization and benefit in sustainability. However, as the external forces acting on the structure increase, so do the requirements for the design and input parameters such as reinforcement products and fill-material. Increased attention also needs to be given for the quality of execution. In addition to the verification of the ultimate limit state (ULS), proof of the serviceability limit state (SLS) needs to be addressed more in detail. Latter is still challenging from an academic point of view since adequate analytical models allowing for a realistic estimation of the deformation behaviour of GRS are still lacking. Therefore, finite element modelling (FEM) is recommended to enable a safe prediction of the SLS. When using FEM however, one needs to consider that most deformations of a GRS are generated during the construction. Proper modelling should therefore address especially those deformations which are generated under service loads. Deformations encountered during construction usually could be balanced before the structure goes into operation.



Figure 4. Preloading of bridge abutment at Motorway A 74, Venlo, Netherlands (HUESKER).

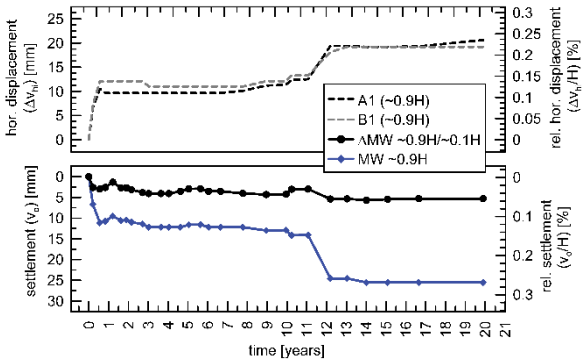

Figure 5. Average settlement and horizontal displacement at monitoring points A1 and B1 (~0,9 x H), Motorway A 74, Venlo, Netherlands (Hangen and Jaramillo, 2016 and Duijnen van, 2012).

Figures 4 and 5 show a GRS-bridge abutment under the motorway A74 close to Venlo in the Netherlands. In this project a preloading with concrete blocks was applied for about two weeks as to induce deformation of the GRS and the subsoil prior to the installation of the bridge superstructure. Total vertical deformation generated during this short preloading time was about 10 mm. After removal of the preloading the settlement increased to 15 mm due to consolidation of the subsoil.

Additional settlement of about 10 mm was monitored when the bridge deck was installed. The differential vertical displacement between the crest and the base of the GRS (ΔMW in Figure 5), however, did not exceed the initial value of about 5 mm, indicating that most deformation of the structure can be allocated to deformations of the subsoil. This observation matches perfectly with the findings of the real scale test at LGA, Figures 1 and 2: once the GRS is "sufficiently activated" additional loading will result in marginal deformation only. Settlement of the subsoil of course needs to be considered carefully and ground improvement may be required prior to the erection of the GRS. Differential settlement, however, is not critical if the superstructure would be resting on

a GRS. Abutment and embankment would be deforming at the same amount and rate. This is in contrast with typical designs, where the bridge is built on piles, the approach embankment however, built without any ground improvement.

Consequently, if properly designed and constructed, it is obvious that GRS is not only strong enough to resist the loading of a bridge superstructure but also stiff enough to fulfil the requirements of the serviceability limit state (SLS).

Further details about the design, materials and monitoring of the project in Venlo are presented in (Duijnen van et al., 2012).

2.4 GRS as anchor element for conventional retaining structure

Geosynthetic reinforcement can be used to anchor conventional retaining structures like sheet pile walls or soldier pile walls. This technology requires special care with regard to its design and installation and hence only been used in a few cases. It will not be discussed here, but interesting information about a small-scale experiment and FE-modelling of an geogrid anchored sheet pile wall has been published from Wittekoek et al. (2022).

3 LATERAL EARTH PRESSURE RELIEF USING GEOSYNTHETIC ENCASED COLUMNS (GEC)

Advantages of earth pressure relief using GRS have already been discussed in section 2.2. The application of geotextile encased sand columns (GEC), however, is another possibility to optimise the design of bridge foundations. This concept can be used to reduce horizontal pressure acting on foundation piles: vertical load generated by the backfill material of the abutment is mainly transferred by GECs down to a competent foundation level. Therefore, the embankment load is generating only marginal horizontal pressures. GECs are non-cohesive soil columns encased by a seamless, tubular geosynthetic reinforcement sleeve. GECs are typically uniformly arranged in a triangular pattern and the axial spacing varies between 1.7 m and 2.4 m. The diameter typically ranges between 600…800 mm. The remarkable reduction of lateral loads on bridge piles using CFP has been demonstrated in successfully executed projects (Alexiew et Thompson, 2016).

Figure 6 shows the typical section of the abutment of a single-span bridge of a motorway in the north of Germany (span w = 23 m) and its approach embankment. The abutment is built on in-situ-concrete piles with a diameter of D ~ 0.50 m and a pile inclination of 4:1.

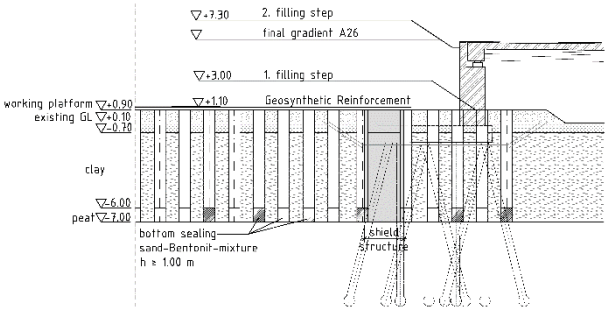

Figure 6. Typical longitudinal section of a piled bridge abutment with GEC-foundation and in-situ soil replacement as shield-structure (Hortmann et. al., 2019).

Due to logistic reasons the bridge foundation, however, had to be built prior to the approach embankment. As the concrete piles had not been designed to withstand lateral loads which would be generated by the embankment filling, a shield structure incorporating GEC was erected in the initial construction phase. The shield structure is a local soil replacement built like a secant wall and has a width of b = 3.5 m. This replacement zone, is entirely encircled by GECs and covered with horizontal reinforcement, ref. Figure 7.

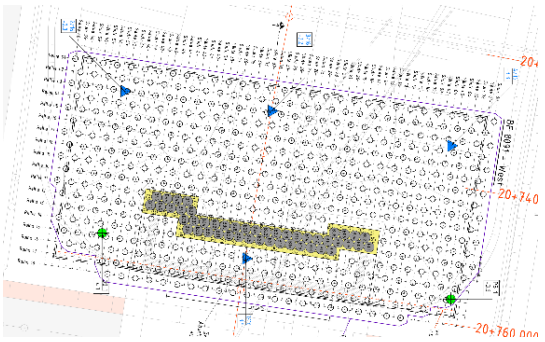

Figure 7. Site plan of GEC columns and shield structure, Bridge BW 8091-West, (Hortmann et. al., 2019).

Design verification of the shielding structure was carried out using a simplified approach as described in EA-Pfähle (2007): consideration of lateral stresses can be omitted if the estimation of the overall slope stability results in a utilization factor $\mu \leq 0.75$, where μ is defined as the degree of utilization ($\mu = 1/FOS$) acc. to DIN 1054 (2021) and DIN 4084 (2021). The improving effect of the GECs was taken into account using the concept of an equivalent cohesion. Thus, the GECs are transformed into discrete soil layers with enhanced shear strength parameters estimated in accordance with Raithel (1999). Additionally, a horizontal basal reinforcement is considered in the calculation.

In other projects it could be demonstrated that a "conventional ground improvement" using GEC was sufficient to fulfil the $\mu \leq 0.75$ requirement. In those

cases, the in-situ soil replacement (shield) structure was not required and consequently not installed on-site.

4 SUSTAINABILITY OF GRS BRIDGE ABUTMENTS

The environmental benefits of using geosynthetics have already been demonstrated in various studies such as EAGM (2011) or WRAP (2010). A reduction of up to 85..90 % cumulative greenhouse gas emissions could be demonstrated depending on the application and the particular design situation. More recent studies have focused on the environmental of bridge construction. Görtz and Pham (2023) have analysed that the bridge abutments contribute significantly to the overall impact of a bridge construction, where the impact of construction materials showed to be most relevant. Figure 8 shows an exemplary comparison of the CO_2 emissions for the construction of a conventional abutment and a corresponding GRS structure (with and without the use of lime-cement stabilizers) for an abutment height of 4.8 m: the reduction in CO_2 emissions is maximum for small bridges and strongly depending on the fill-material that is used. The use of lime-cement stabilizers has a remarkable negative impact. Hence, hydraulic binders should only be used to enable construction with (local) fill-material of marginal quality (if this leads to positive result of the LCA) or in limited amount if technically unavoidable e.g. to increase the stiffness of the GRS. If lime-cement stabilizers are used one should not forget to prove that the reinforcement material is durable in high alkaline conditions. Otherwise, the durability of the structure would be endangered. Recent research (Detert and Koroliuk, 2018) has shown that products from polyethylene terephthalate (PET), for example, would not fulfil this requirement due to the strong impact of external hydrolysis. Reinforcement from polyvinyl alcohol (PVA), however, is durable even in high-alkaline conditions and would provide a proven alternative in such case.

An additional benefit of GRS which has not been considered in the studies of Görtz is the effect of construction speed. GRS can immediately be loaded once they are erected, deshuttering times as would be required for in-situ reinforced concrete are not required.

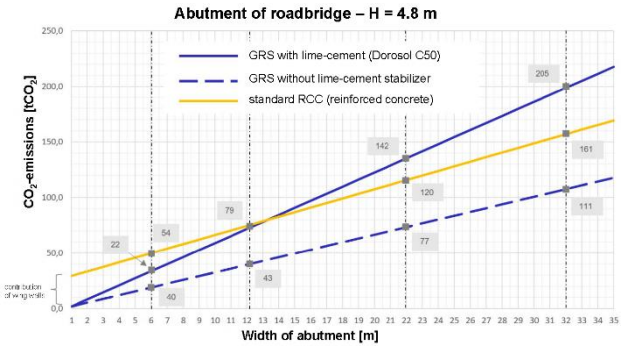

Figure 8. Estimation of CO_2-emission for the construction of a bridge abutment, comparison of different construction techniques (Görtz and Pham., 2023).

Combining modular bridge systems and GRS can therefore contribute to significantly decrease construction time of a bridge and all related impact from traffic-jams or total closures of traffic connections (roads and railroads).

5 CONCLUSIONS

Practical experience as well as academic knowledge about geosynthetic reinforced soil retaining structures (GRS) has significantly increased over the last decades. Overall, the performance of GRS which have carefully been designed and properly erected has shown to be good. More recently even highly loaded bridge abutments have been built with GRS. Using GRS in bridge construction can contribute to limit the impact of differential settlement between abutment and backfill, to reduce horizontal stresses and additional loads generated by negative skin friction in foundation piles or to cut off completely horizontal stresses in form of an earth pressure relief. Various reference projects have shown that GRS is even able to fully replace structural reinforced concrete in the abutment.

Comparative LCA has shown that the quantity of CO_2 emitted for the abutment construction can be reduced significantly using GRS. Additional benefits can be observed as GRS can be erected much faster than in-situ reinforced concrete. A combination of modular bridge systems and GRS would generate the biggest advantage in that regard.

Despite of the advantages of GRS its application is still limited in many countries. The mindset of designers as well as limitations prescribed by design codes and local regulations would be the reason for that. However, continued development and enthusiasm in the construction industry as well as updates of international standards such as EC7 (Eurocode 7) or specific local regulations will help to overcome this problem.

REFERENCES

Allen, T.M., Bathurst, R.J. und Berg, R.R. (2002). Global level of safety and performance of geosynthetic walls: An historical perspective, *Geosynthetics International* 9 (5-6): 395-450, https://doi.org/10.1680/gein.9.0224.

Alexiew, D. (2007). Load tests on a 1:1 model of a geogrid-reinforced bridge abutment, In: *Tagungsband des 14. Darmstädter Geotechnik-Kolloquiums*, Mitteilungen des Institutes und der Versuchsanstalt für Geotchnik der Technischen Universität Darmstadt, Heft Nr. 76, 205-218. (In German).

Alexiew, D., Detert, O. (2008). Analytical and Numerical Analyses of a Real Scaled Geogrid Reinforced Bridge Abutment Loading Test, In: *Proceedings of the 4th European Geosynthetics Conference*, Edinburgh, UK, Vol. 4, pp. 7-10.

Alexiew D., Thomson G. (2016). Geotextile encased columns (GEC) relief lateral pressure on rigid pile groups In: *Proceedings of „Geotechnics for Sustainable Infrastructure Development – Geotec*, Hanoi, ISBN 978-604-82-0013-8.

Bathurst, R.J. (2014). Challenges and recent progress in the analysis, design and modelling of geosynthetic reinforced soil walls. In: *Proceedings of the 10th International Conference on Geosynthetics-Giroud Lecture*, Berlin, Germany, p.38. Paper 235. ISBN 978-3-9813953-9-6.

Bräu, G., Bauer, A. (2001). Versuche im Boden mit gering dehnbaren Geogittern. In: *Tagungsband der 7. Informations- und Vortragstagung über „Kunststoffe in der Geotechnik“ (KGEO) Sonderheft der Zeitschrift Geotechik der DGGT*, München, Germany. (In German).

Crouse, P.E.; Wu, J.T.H. (1996). Long-Term Field Performance of Geosynthetic-Reinforced Soil Retaining Walls, Center for Mechanically Stabilized Backfill Research University of Colorado, Denver, USA, Report No. CDOT-DTD-97-12.

Detert, O., Koroliuk, S. (2018). Acceleration of chemical degradation of polyester reinforcement products under mechanical stress in high alkaline conditions. In: *Proceedings of 11th International Conference on Geosynthetics (11ICG)*, Seoul, South Korea, pp. 986-989, ISBN: 978-1-7138-0608-0.

DIN 1054 (2021). Subsoil – Verification of the safety of earthworks and foundations – Supplementary rules to DIN EN 1997-1, Normenausschuss Bauwesen (NaBau) im DIN, Germany.

DIN 4084 (2021). Soil – Calculation of embankment failure and overall stability of retaining structures, Normenausschuss Bauwesen (NaBau) im DIN, Germany.

Duijnen van, P.G., Linthof, T., Brok, C.A.J.M., Eekelen van, S.J.M. (2012). Measuring deformations of a 10 m high geosynthetic reinforced earth retaining wall. In: *Proceedings of the 5th European Geosynthetics Conference*, Valencia, Spain, Vol. 5, pp. 157-161.

EA Pfähle (2007). Recommendation of the Piling working group – EA Pfähle, German Geotechnical Society, e.V., Working Group 2.1, Kassel, Germany.

Eurocode 7 (2013). Geotechnical design - Part 1: General rules; German version EN 1997-1:2004 + AC:2009 + A1:2013, Beuth, Berlin, Germany.

Görtz, S., Pham, T. K. D. (2023) CO2-Bilanzierung und Optimierung von Brückenbauwerken. Schlussbericht Forschungsvorhaben der EKSH, Gesellschaft für Energie und Klimaschutz Schleswig-Holstein GmbH, Kiel, Germany. Available at: https://www.eksh.org/fileadmin/redakteure/downloads/foerderung/Abschlussberichte_HWT/8_12_52_Abschlussbericht_HWT_CO2-Bilanzierung-Br%C3%BCckenbauwerke_FHKiel.pdf, accessed 17/03/2024.

Hangen H., Jaramillo J. (2016). Langzeitverhalten von geokunststoffbewehrten Stützkonstruktionen - zukünftig eine Standardbauweise auch für Brückenwiderlager?, In: *Proceedings of 26.th Dresdner Brückenbausymposium*, Dresden, Germany, pp 177-191. (In German).

Hortmann, M. T., Taetz, S., Blume, K. H., & Raithel, M. (2019). Bridge approach embankments on holocene peat improved with Geosynthetic Encased Columns (GEC) in Northern Germany, In: *Proceedings of the 16th Asian Regional Conference on Soil Mechanics and Geotechnical Engineering*, Taipei, Taiwan.

Pötzl, M., Naumann, F. (2005). Fugenlose Betonbrücken mit flexiblen Widerlagern, *Beton- und Stahlbetonbau*, 100. Jahrgang, Heft 8, S. 675 – 685, https://doi.org/10.1002/best.200590184 (In German).

Raithel, M. (1999). *Zum Tragverhalten von geokunststoffummantelten Sandsäulen*, PhD thesis, Kassel: Universität GH Kassel - Fachgebiet Geotechnik, Kassel, Germany. ISBN 3881229914

Steiger, H.; Zeißler, T.; Bernhard, M.; Meyer, H. (2012). Integrale Großbrücken mit flexiblen Widerlagern. In: *Beton- und Stahlbetonbau*, Heft 3, S. 175–182, (In German).

Stolz P., Frischknecht R. (2011). Summary - Comparative Life Cycle Assessment of Geosynthetics versus Conventional Construction Materials. European Association of Geosynthetic product Manufacturers (EAGM), Uster, Switzerland. Available at: https://www.eagm.eu/_files/ugd/e700f9_ba39a8ff53e94568a5667bf458f7fd8d.pdf, accessed: 17/03/2024.

Wittekoek, B., Van Eekelen, S. J. M., Terwindt, J., Korff, M., Van Duijnen, P. G., Detert, O., Bezuijen, A. (2022). Geogrid-anchored sheet pile walls; a small-scale experimental and numerical study. *Geosynthetics International*, 30(6), 561-583, https://doi.org/10.1680/jgein.22.00501.

WRAP (2010). Sustainable geosystems in civil engineering applications, Banbury, UK, Geosystems Report MRF116-001. Available at: http://www.geosynthetica.com/Uploads/WRAP_GeosystemsGuidance_Feb2010.pdf, accessed: 17/03/2024.

Proceedings of the XVIII ECSMGE 2024
GEOTECHNICAL ENGINEERING CHALLENGES
TO MEET CURRENT AND EMERGING NEEDS OF SOCIETY
© 2024 the Authors
ISBN 978-1-032-54816-6
DOI 10.1201/9781003431749-444
Open Access: www.taylorfrancis.com, CC BY-NC-ND 4.0 license

ECSMGE 24
XVIII EUROPEAN CONFERENCE ON SOIL MECHANICS AND GEOTECHNICAL ENGINEERING

Consequences of geometrical imperfections for deep dry mixing columns in a deep excavation pit

Conséquences des imperfections géométriques pour les colonnes de mélange sèches et profondes dans une fouille profonde

M.K. Haugen*
Norwegian Geotechnical Institute, Trondheim, Norway

M.Kahlström, P.A. Mortensen
Norwegian Geotechnical Institute, Oslo, Norway

K.M. Kjærstad, Y. Pan
Løvlien Georåd, Oslo, Norway. NTNU, Trondheim, Norway

**martin.keiseras.haugen@ngi.no*

ABSTRACT: Few studies have analysed the deep excavation retaining wall system response when passive-sided panels of load-bearing deep dry mixing columns are installed with geometrical imperfections. This study applies parametric 3D modelling to generate DDM panel geometries with random geometric imperfections for individual columns drawn from a probability distribution. Simulations are performed with FEA to investigate the retaining wall response from imperfect panels. Comparisons are made to both idealized rectangular panels and panels consisting of octagonal columns without imperfections. Four column imperfections are considered - XY offset, azimuth, length and inclination. Results indicate that geometric panel imperfections contribute to overall greater horizontal displacement, shear force, bending moment and strut forces in the retaining wall system. This study considered 101 simulations with imperfect panels. Although the number of simulations performed in this study is modest, initial results indicate that the moving average of the response is converging as the simulation count is increased.

RÉSUMÉ: Peu d'études ont analysé la réponse d'un mur de soutènement dans une excavation profonde lorsque des panneaux de contreforts en colonnes traitées à la chaux à sec contiennent des imperfections géométriques. Dans cette étude, une modélisation paramétrique 3D est utilisée afin de générer des panneaux DDM avec des imperfections géométriques aléatoires pour des colonnes individuelles tirées d'une distribution de probabilité. Des simulations numériques sont effectuées pour étudier la réponse du mur de soutènement à partir de panneaux imparfaits. Des comparaisons sont faites avec des panneaux rectangulaires idéalisés et des panneaux constitués de colonnes octogonales sans imperfections. Quatre imperfections de colonne sont prises en compte: décalage XY, azimut, longueur et inclinaison. Les résultats indiquent que les imperfections géométriques des panneaux contribuent à un déplacement horizontal, une force de cisaillement, un moment de flexion et des forces d'appui globalement plus importants dans le système de mur de soutènement. Cette étude a considéré 101 simulations avec des panneaux imparfaits. Bien que le nombre de simulations effectuées dans cette étude soit modeste, les premiers résultats indiquent que la moyenne glissante de la réponse converge à mesure que le nombre de simulations augmente.

Keywords: Deep mixing panels; parametric modelling; geometric imperfections; installation error.

1 INTRODUCTION

Ground improvement with deep dry mixing columns is often used in geotechnical engineering to reduce deformation of retaining walls, and to enhance the stability and safety in a deep excavation pit. Column installation is complicated, and several imperfections could evolve during the installation (Larsson, 2005, Pan et al., 2019). Imperfections may introduce non-stabilized soil to occur within the DDM-panels lowering the panel capacity to resist and transfer loads. Installation errors include XY offset, azimuth, length deviation and inclination, depicted in Figure 1.

During engineering design, deep mixing panels are often simplified as an idealized panel geometry (rectangular) in plain strain, neglecting the potential for imperfections.

In this study, DDM installation data from a construction project is used to simulate probability

distributions for the actual offset and length deviation imperfections.

The main purpose of the study is to investigate if and how installation errors for DDM columns affect the retaining wall system response considering deformation, bending moment and shear force in the retaining wall, in addition to strut and beam forces, when the DDM panels act as load-bearing stiffeners on the passive side.

A parametric script is developed to generate the DDM panel geometry, with or without imperfections. The DDM panels are then imported into the FEA software, in this case Plaxis, with the excavation pit. Calculations with defined phases are performed, and the simulations are then compared.

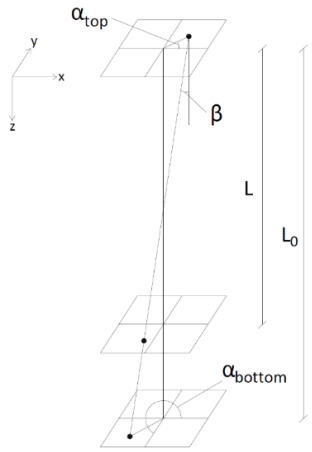

Figure 1. Illustration of main installation errors. XY offset at top, azimuth top and bottom (α), inclination (β) and deviation between design and installed length (L_0-L).

2 CASE STUDY

The case study use data from a cut-and-cover tunnel in Drammen, Norway. The excavation pit consists of sheet pile walls and two strut levels with DDM-panels in one part of the excavation pit. The geometry is shown in Figure 2.

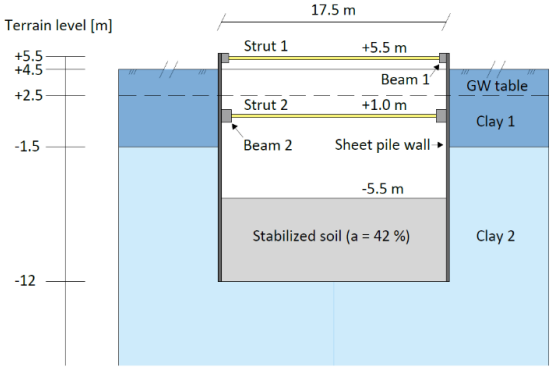

Figure 2. Plain-strain view of the case study excavation pit. The figure illustrates the situation after the final excavation phase.

The DDM panels have two rows of columns with a column diameter of 800 mm and a column overlap of 20 % of the diameter. The spacing between each panel is 3.05 m and strut spacing is 5.00 m.

3 PROBABILITY DISTRIBUTIONS OF GEOMETRIC IMPERFECTIONS

During the case study project, GPS coordinates and total length for the columns were recorded. Azimuth top, offset and length deviation are calculated from these measurements. The data package consisted of 3365 columns in total, and there was generated a boxplot with outliers. The outliers were excluded from the final data package.

3.1 Offset

The recorded offset has been adapted with a Weibull distribution, illustrated by Figure 3, along with generated random variables from the same Weibull distribution.

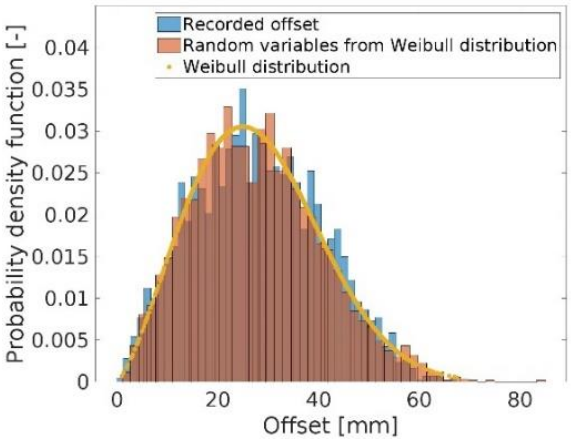

Figure 3. Recorded offset, and random offset variables from Weibull distribution fit in a probability density function.

3.2 Azimuth

The calculated azimuth angle is simplified to be uniformly distributed based on recorded XY offset.

3.3 Length deviation

A Cauchy distribution has been adapted to the recorded length deviation to generate random variables. The average value has been assigned as the location factor, and a scaling factor γ of 4.5 has been utilized. A similar plot as Figure 3 have been made.

3.4 Inclination

Inclination for the DDM columns is not measured during installation. In this study, the inclination is

assumed to follow a uniformly distributed function with maximum inclination of 1.15 degrees, which is based on the inclination demand from Eggen et al. (2012) considering installation data from Norway.

The inclinations reported by Eramo et.al. (2011) and Croce & Modoni (2007) were reviewed but not considered in this study. By including these one may get different outcome which could be interesting for future work.

4 PARAMETRIC MODELLING

Parametric 3D modelling is utilized in this study to generate the DDM columns geometries. The columns are generated as octagonal columns to reduce the number of mesh elements, and therefore decreasing the computing capacity and computing time.

Chosen parameters versus original parameters are illustrated in Figure 4. The chosen geometry parameters are different from the original parameters to ensure that the degree of coverage is approximately the same for both situations.

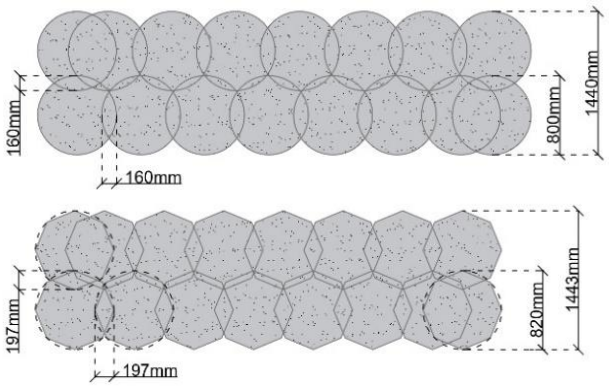

Figure 4. DDM column geometry in case study versus chosen DDM column geometry for this study.

5 FEM-MODEL

The FEM model in Plaxis 3D is a symmetric model of the excavation pit, as depicted in Figure 5 during calculation after the last excavation phase. A refined mesh is applied around the excavation pit. As illustrated, there is only one DDM panel modelled, this to reduce the computing time by reducing the number of mesh elements. The extent of the model in y-direction is set to 3.05 m, and the DDM panel is in the centre. An equivalent axial-stiffness is applied for the two struts. Total stress analysis is considered.

The deformation in y-direction is set to zero, equalling a plain strain situation. The boundary conditions are fixed at the bottom, while no deformation in x-direction is allowed along the symmetric line.

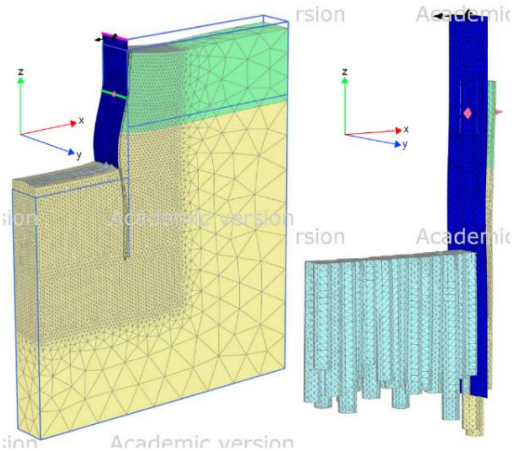

Figure 5. FEM model shown during calculation after the last excavation phase. Deformations are scaled up to the left. The surrounding unstabilized soil is hidden to the right.

6 RESULTS AND DISCUSSION

101 simulations with random imperfections were calculated using Plaxis 3D. Strut forces, shear force, bending moment and horizontal displacement of the retaining wall, along with safety factor F were inspected as the result parameters. Figure 6 shows the resulting maximum bending moment for the retaining wall after the final excavation stage. The result for a situation with octagonal columns without imperfections, along with an idealized, rectangular panel are also shown. Similar graphs are made for the other result parameters.

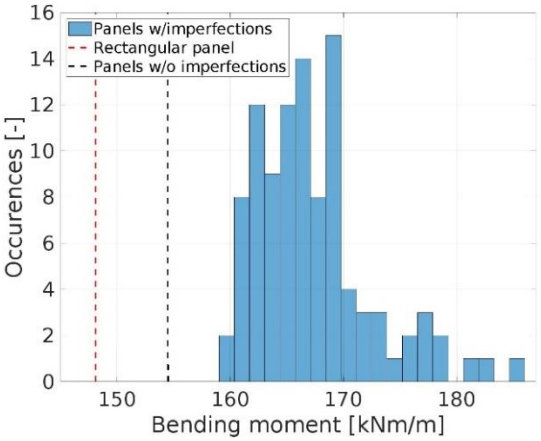

Figure 6. Maximum bending moment for the retaining wall after the last excavation phase.

Table 1 presents results for shear force, bending moment and horizontal displacement for the retaining wall, with average values for imperfect panels. The results expose that installation deviations will generally increase both loads and displacement for the retaining wall, due to occurrence of non-stabilized soil in between the DDM-panels.

Table 1. Results from the simulations with shear force, bending moment and horizontal displacement for the retaining wall.

Model type	Shear force [kN/m]	Bending moment [kNm/m]	Displac-ement [mm]
Rectangular panel	175.2	148.1	92.4
Panel w/o imperfections	198.7	154.5	95.8
Panels w/imperfections	217.9	167.4	105.4

Because of limited simulation capacity, a plot in Figure 7 depicts the continuous floating average and moving average to gauge result reliability. It can be observed that the floating average, moving average and percentile values of the resultant bending moment each have notable similarity between 80 simulations and 100 simulations, indicating a convergence of results.

When considering total horizontal stresses in the DDM panels, the results expose greater stresses in the imperfected panels versus the panels without imperfections, as shown in Figure 8.

The presented results manifest that geometric imperfections in DDM panels will decrease the panels characteristics as load-bearing stiffeners on the passive side in an excavation pit.

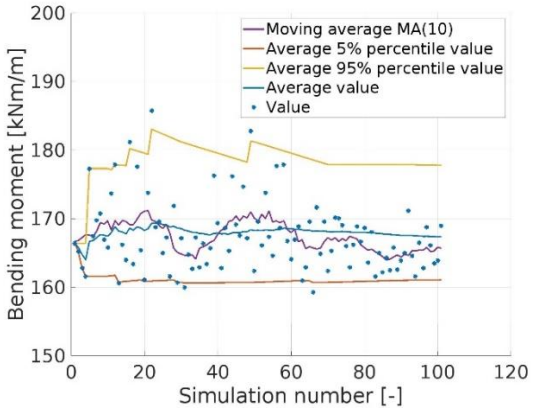

Figure 7. Continuous floating average and moving average for the bending moment.

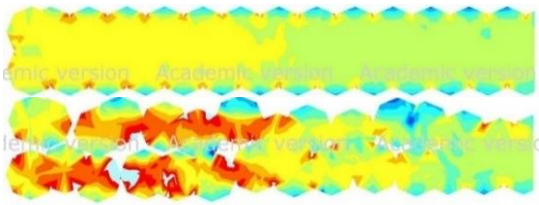

Figure 8. Total horizontal stresses in x-direction in DDM panel without imperfections and with imperfections. Increasing compression stresses from blue to red. The sheet pile wall is located to the right.

7 CONCLUSION

Simulations using 101 different DDM panel geometries drawn from probability distributions show that geometric imperfections decrease the panels characteristics to resist and transfer earth pressure. Geometric imperfections for DDM panels should be accounted for during geotechnical design to avoid unwanted displacement and possible system failure.

Initial results with 101 simulations show that the continuous average and moving average appear to converge.

Future work should focus on the following: (1) increase the number of calculations, (2) include more case studies, (3) investigate more retaining wall system parameters, e.g. excavation depth and (4) modify material parameters for soil and DDM panels.

ACKNOWLEDGEMENTS

The authors are grateful for the support provided by the Norwegian Geotechnical Institute and NTNU.

REFERENCES

Croce, P., Modoni, G. (2007). Design of jet-grouting cut-offs, In: *Proceedings of the Institution of Civil Engineers Ground Improvement (11(1),* Cassino, Italy. https://doi.org/10.1680/grim.2007.11.1.11.

Larsson, S. (2005). State of practice report – Execution, monitoring and quality control, Royal Institute of Technology, Stockholm, Sweden.

Pan, Y., Liu, Y., Chen, E.J. (2019). Probabilistic investigation on defective jet-grouted cut-off wall with random geometric imperfections, *Geotechnique,* 69 (5), pp. 420-433. https://doi.org/10.1680/jgeot.17.P.254.

Eggen, A., Jensen, T.G., Karlsrud, K., Gjelsvik, V. (2012). Veiledning for grunnforsterkning med kalksementpeler, *Guidance on ground improvement with lime cement columns*, (in Norwegian). Norwegian geotechnical society.

Eramo, N., Modoni, G., Arroyo, M. (2011). Design control and monitoring of a jet grouted excavation bottom plug, In: *7th International Symposium on Geotechnical Aspects of Underground Construction in Soft Ground*, Rome, Italy. https://doi.org/10.1061/(ASCE)GT.1943.

Proceedings of the XVIII ECSMGE 2024
GEOTECHNICAL ENGINEERING CHALLENGES
TO MEET CURRENT AND EMERGING NEEDS OF SOCIETY
© 2024 the Authors
ISBN 978-1-032-54816-6
DOI 10.1201/9781003431749-445
Open Access: www.taylorfrancis.com, CC BY-NC-ND 4.0 license

ECSMGE 24
XVIII EUROPEAN CONFERENCE ON SOIL MECHANICS AND GEOTECHNICAL ENGINEERING

Deep excavation solutions for the construction of a logistic park in Loures (Lisbon)

Solutions de excavation profonde pour la construction d'un parc logistique à Loures (Lisbonne)

A. Henriques*, R. Tomásio
JET_{SJ} Geotecnia Lda, Lisbon, Portugal

F. Ramalho
NORTON Edifícios Industriais, Lisbon, Portugal

J. Dias
Triaxial – Engenharia Geotécnica, Lisbon, Portugal

**ahenriques@jetsj.com*

ABSTRACT: This paper aims to describe the deep excavation solutions adopted for the construction of a logistics park with an implantation area of approximately 107 000 m^2, located in the municipality of Loures in Lisbon. The use of this site for the construction of a large-scale building with demanding future performance criteria proved to be extremely challenging, particularly because the original place had previously been used as a limestone quarry and subsequently as a landfill for various materials associated with the construction of the nearest main road network. Given the existing constraints, particularly the desired implantation area, the geological-geotechnical study and the neighboring conditions, a deep excavation solution was defined for a maximum height of 20 m, consisting of a bored pile wall with 800 mm diameter and with shotcrete between the piles, braced by permanent anchors and complemented with a concrete Berlin-type wall solution in areas where the limestone rock, with low degrees of alteration and fracturing, emerged above the excavation bottom. In addition to the adopted design criteria, the proposed instrumentation and monitoring plan for the retaining solution and neighboring infrastructure are also presented.

RÉSUMÉ: Cet article vise à décrire les solutions de excavation profonde adoptées pour la construction d'un parc logistique d'une superficie d'environ 107 000 m^2, situé dans la municipalité de Loures à Lisbonne. L'utilisation de ce site pour la construction d'un bâtiment à grande échelle répondant à des critères de performance futurs exigeants s'est avérée extrêmement difficile, en particulier parce que l'endroit d'origine avait été précédemment utilisé comme carrière de calcaire, puis comme décharge pour divers matériaux associés à la construction du réseau routier principal le plus proche. Compte tenu des contraintes existantes, en particulier de la superficie d'implantation souhaitée, de l'étude géologique-géotechnique et des conditions environnantes, une solution de excavation profonde a été définie pour une hauteur maximale de 20 m, comprenant un mur de pieux forés de 600 mm de diamètre avec du béton projeté entre les pieux, renforcé par des ancres permanentes et complété par des solutions de mur "Berlin" dans les zones où la roche calcaire, avec des degrés d'altération et de fracturation faibles, émergeait au-dessus du fond de excavation. En plus des critères de conception adoptés, le plan d'instrumentation et de surveillance proposé pour la solution de soutènement et les infrastructures avoisinantes sont également présentés.

Keywords: Deep excavation; bored pile wall; concrete Berlin-type wall.

1 INTRODUCTION

The deep excavation solutions presented in the present article are located in the municipality of Loures (Figure 1) and were developed and designed to enable the construction of a logistic park with an approximately 55,000 m^2 footprint.



Figure 1. Site identification (Google Earth image).

The use of this site for the implementation of a large-scale building with demanding future performance criteria proved to be extremely challenging due to the fact that the original land had previously been used as a limestone quarry and subsequently as a dumping for various materials. These two situations determined, during excavation, the occurrence of very abrupt geological transitions and completely distinct geotechnical behaviors over very short distances.

After an extensive geological-geotechnical characterization, substantiated by various prospecting campaigns, the best deep excavation and earth support solutions were adapted for both excavation and embankment areas; the latter, however, are not covered in the present article.

For the excavation areas located in the southern elevation, adjacent to the national road EN250, a bored pile wall was adopted, with a maximum height of 20 m, permanently anchored and complemented with a concrete Berlin-type wall in areas where the limestone mass, with low degrees of alteration and fracturing, emerged above the excavation bottom.

On the other side, for the embankment areas, on the western, northern and eastern elevations, considering the existing levels, available space, and the need to ensure the maximum possible storage capacity for surplus soils from the embankment platform, a gabion wall and a reinforced earth wall with facing panels of precast reinforced concrete were constructed.

2 MAIN EXISTING CONDITIONS

2.1 Geological-geotechnical conditions

Four prospecting campaigns were conducted in the area of the logistics park from 2019 to 2021, that involved the execution of around fifty hollow stem auger borings, accompanied by dynamic penetration tests of the SPT type at every 1.5 m, reaching depths of 34 m, twenty-four exploratory pits, using an excavator, with depths ranging from 0.70 to 4.90 m and ten seismic refraction profiles.

The borings from the second and fourth phases were considered particularly representative for the design of the bored pile wall solution due to their location, almost coinciding with the boundary perimeter of the existing quarry. The analysis of these campaigns confirmed the variability of encountered terrains and abrupt geological variations (Figure 2).

During the excavation process, it was also observed that within a few meters, there was a transition from a rocky mass near the surface to a rocky mass below the excavation bottom (Figure 3).

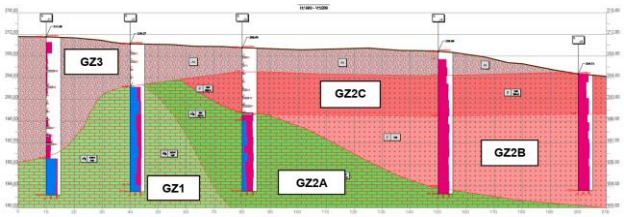

Figure 2. Geotechnical interpretative profile along the alignment of the bored pile wall.



Figure 3. View of abrupt transitions between landfill zones and vertical faces of the limestone quarry.

The analysis of the geological-geotechnical campaign allowed the individualization of the 5 geotechnical zones identified below:

GZ3 - Corresponds to landfill deposits;

GZ2C – Soils corresponding to volcanic breccias and decomposed volcano-sedimentary formations from the Lisbon Volcanic Complex;

GZ2B – Soils corresponding to volcanic breccias and decomposed volcano-sedimentary formations from the Lisbon Volcanic Complex;

GZ2A - Massif corresponding to basalts, volcanic breccias, and decomposed volcano-sedimentary formations or rock ranging from highly altered to moderately altered from the Lisbon Volcanic Complex;

GZ1 - Massif corresponding to whitish crystalline limestones to grayish marly limestones ranging from little to moderately altered.

2.2 Pre-existing conditions

The intervention area is located, in part, over former limestone quarries that were subsequently used as a landfill. In this context, there was a high level of uncertainty about the composition of the fill materials but also about the configuration/inclination of the cut slopes, which were created during the quarrying activities.

2.3 Topographic constrains

The land used for the construction of the logistics park had a slope towards the north, with the area adjacent to national road EN250 being the highest and the area adjacent to a watercourse on the opposite elevation

having lower elevations. To achieve a level platform, as previously mentioned, it was necessary to develop a retaining structure through excavation along the northern elevation and part of the western elevation (Figure 4). Additionally, gabion retaining walls and reinforced earth walls were designed on the southern elevation, part of the western elevation, and part of the eastern elevation. As mentioned above, this article will exclusively address the deep excavation solutions in the northern and western elevations.

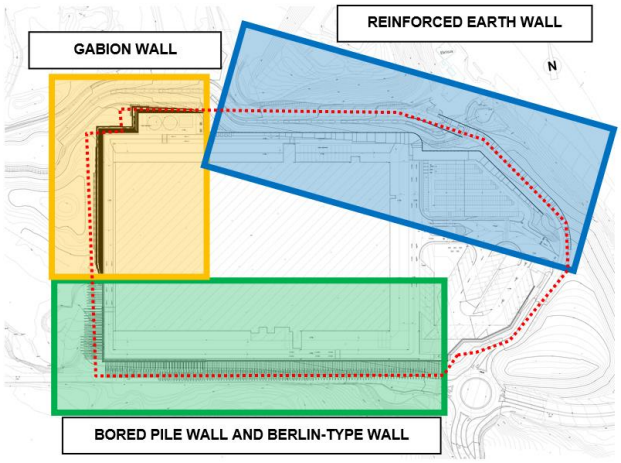

Figure 4. Identification of the retaining and embankment solutions and lot boundary (highlighted in red).

3 PROPOSED SOLUTIONS

3.1 Bored pile wall

Based on the existing constraints, particularly topographical, geological-geotechnical, neighboring occupancy, and the need for rapid execution, it was adopted a bored pile wall, with a 800 mm diameter and spaced at a center-to-center distance of 1.5 m (Figure 5). This arrangement enabled an excavation of about 20 m in maximum height.

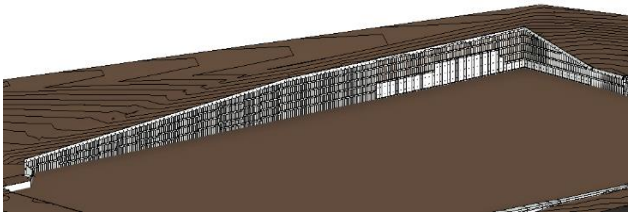

Figure 5. 3D perspective oof the bored pile wall solution.

Given the geological conditions of the site and the length of the piles, they were entirely executed using a telescopic Kelly bar, occasionally with temporary casing at the borehole entrance. When encountering larger blocks or to ensure anchoring in the rock mass, a tricone bit, rock auger, and coring tool were used.

To enhance efficiency in excavation, the wall was braced using 2 to 5 levels of permanent anchors with planar spacings of 3.0 m, aiming to provide temporary and definitive horizontal balance of the containment against ground impulses, both in static and seismic conditions.

To ensure a more even distribution of forces on the wall and prevent excessive load concentration, reinforced concrete distribution beams were implemented and properly anchored to the piles (Figure 6).

The anchors were installed at different inclinations to the horizontal (between 15º and 30º) and with variable free lengths (between 9 m and 17 m), with a minimum sealing length of 8 m (Bustamante and Doix., 1985) and a maximum long-term traction of 900 kN.

Considering the permanent nature of the anchors, the provisions of NP EN 1537 were followed regarding the characteristics of the tendons, injection grout, anchor head protection components, and anti-corrosion protection.

The exposed soil between piles was protected with a sprayed concrete coating applied in two layers and reinforced with metal fibers. The area was properly drained using geodrains between piles.



Figure 6. Excavation works near the bored pile wall.

3.2 Concrete Berlin-type retaining wall

As indicated in the geological-geotechnical study, an intersection of the piles with slightly altered limestone occurred near the corner of the wall. In this area, the pile wall was underpinned using micro-piles. The remaining excavation was carried out with advances under a concrete Berlin-type retaining wall with rock bolts (Figure 7).

In this type of solution, the retaining wall is constructed in levels, from top to bottom. Each level is created by constructing reinforced concrete panels (first the primary panels and then the secondary ones), supported by spaced micro-piles, on average 3 m apart. These micro-piles are installed before the start of

excavation work and function to support the vertical loads to which the retaining wall is subjected. The panels, with a theoretical minimum thickness of 30 cm, are cast against the open vertical face of the limestone mass and connected at the top through a reinforced concrete beam with pre-stressed anchors. This beam simultaneously ensures the underpinning of the base of the bored pile wall and the partial transfer of vertical loads to the micro-piles.

Regarding the horizontal bracing of this wall, the execution of high-strength steel tie rods with a diameter of 32 mm was anticipated.



Figure 7. Excavation works near the concrete berlin-type retaining wall.

4 DESIGN METHODS

To analyze the behavior of the retaining wall solutions with respect to forces and deformations, finite element models were employed using the PLAXIS 2D software.

The analyses conducted generally involved studying various cross-sections deemed representative of the diverse geometries along the lengths of each of the construction solutions used.

The geomechanical behavior of soils was simulated using Hardening-Soil constitutive models, while for more rocky materials, their behavior was simulated using elasto-plastic Mohr-Coulomb constitutive models, and thus, without hardening.

Structural elements, such as the bored pile wall, concrete Berlin-type retaining wall, and anchors, were modeled based on their elastic properties. The modeling limited their maximum strength to ultimate limit states, allowing for the assessment of the maximum global safety factor.

5 MONITORING PLAN

The implemented monitoring plan aimed to ensure the safe and cost-effective execution of activities related to excavation process and during the lifespan of the logistics park. Additionally, it involved analyzing the surrounding behavior during this phase of construction, leading to adaptations based on the obtained results.

Installed devices allowed for the measurement of the following parameters on a weekly basis:

- Horizontal and vertical displacements of the retaining structures using topographic targets;
- Horizontal displacements of the soil behind the retaining solutions using inclinometers;
- Measurement of tension load in the anchors using load cells.

As of the current date, no significant deviations from the project estimates have been recorded based on the available readings. The maximum horizontal movements on the targets and inclinometers are approximately 15 mm, associated with a maximum excavation height of about 15 m and anchor load increments of less than 10%.

6 CONCLUSIONS

Considering the positive outcomes of the established instrumentation and observation plan, along with the accomplishments during the excavation works, it is concluded that the alternative solutions developed in the context of the design and construction process carried out in collaboration between the designer (JET_{SJ}) and the contractor (Norton EI), have proven to be extremely versatile and well-suited to local constraints.

ACKNOWLEDGEMENTS

The authors express their gratitude to the Client (LIDL) for granting permission for the drafting and publication of this article. It is also important to emphasize that the implemented solutions were the result of a team effort developed in collaboration with the contractor (Norton EI), subcontractors (Ancorpor, MaccaferriI, VSL, among others), and supervision (Duplano).

REFERENCES

Bustamante, M.; Doix, B. (1985). Une méthode pour le calcul de tirants et des micropieux in-jectés. Bulletin de Liaison des Laboratoires des Ponts et Chaussées, Ministère de L'Équipe-ment, du Logement, des Transports et de la Mer, Paris. 140, 75-92.

CT156 LNEC (2016). NP EN 1537 – Execution of special geotechnical works. Groud anchors. In portuguese.

Proceedings of the XVIII ECSMGE 2024
GEOTECHNICAL ENGINEERING CHALLENGES
TO MEET CURRENT AND EMERGING NEEDS OF SOCIETY
© 2024 the Authors
ISBN 978-1-032-54816-6
DOI 10.1201/9781003431749-446
Open Access: www.taylorfrancis.com, CC BY-NC-ND 4.0 license

ECSMGE 24
XVIII EUROPEAN CONFERENCE ON SOIL MECHANICS AND GEOTECHNICAL ENGINEERING

Management of the dynamic performance of earthworks for High-Speed Rail

Gestion de la performance dynamique des travaux de terrassement grandes lignes pour Train a Grande Vitesse

A. Hope
Engineering Geology Ltd, NZ

O. Boumendjel-Game
Arcadis, London, UK

H. Wood
WSP, Guildford, UK

H. Saroglou*, G. Katsigiannis
Ferrovial Construction, London, UK

S. Butler, J. Dudfield
HS2 Ltd, Birmingham, UK

**harry.saroglou@ekfb.com*

ABSTRACT: The interaction of a high-speed train with the track system, and the response of the supporting ground can result in amplification of quasi-static track deflections as the train speed approaches a critical velocity. Numerous factors govern the development of this phenomenon, but of particular importance is the propagation of surface waves (Rayleigh waves) in the supporting ground. To avoid dynamic amplification, criteria for the design of earthwork structures are commonly specified as a minimum Rayleigh wave velocity as a function of train speed. Whilst this geo-dynamic phenomenon is recognised within the industry, there are no well-established guidelines or standards for assessing and mitigating this risk. This paper presents the approach used for contract C23 on Phase 1 of the HS2 project to assess and manage this risk, including the design of foundation treatment to improve the dynamic response of the earthwork structure.

RÉSUMÉ: L'interaction d'un train à grande vitesse avec le réseau de voies ferrées et la réponse du sol d'appui peuvent entraîner une amplification des déformations quasi statiques de la voie lorsque la vitesse du train s'approche d'une vitesse critique. De nombreux facteurs régissent le développement de ce phénomène, mais la propagation des ondes de surface (ondes de Rayleigh) dans le sol de support revêt une importance particulière. Pour éviter l'amplification dynamique, les critères de conception des ouvrages de terrassement sont généralement spécifiés comme une vitesse minimale de l'onde de Rayleigh en fonction de la vitesse du train. Bien que ce phénomène géodynamique soit reconnu au sein de l'industrie, il n'existe pas de lignes directrices ou de normes bien établies pour évaluer et atténuer ce risque. Cet article présente l'approche utilisée pour le contrat C23 de la phase 1 du projet HS2 afin d'évaluer et de gérer ce risque, y compris la conception du traitement des fondations afin d'améliorer la réponse dynamique de la structure de terrassement.

Keywords: High-speed rail; critical velocity effects; geo-dynamic performance; Rayleigh waves.

1 INTRODUCTION

1.1 Background

The HS2 project is a High-Speed railway line currently under construction in the UK. Phase 1 of HS2 runs between London and Birmingham and this paper focuses on an 80 km long open route section between Wendover in Buckinghamshire and Southam in Warwickshire (Contract C23).

High Speed 2 Ltd are the delivery authority for the project with Eiffage, Kier, Ferrovial Bam Joint Venture (EKFB) the appointed Contractor for C23 supported by an Arcadis, Setec, COWI Joint Venture (ASC) providing design services for the main civil engineering assets.

This section of the route will be constructed using track slab with a design speed of 360 km/hr which is significantly higher than traditional railways. At higher train speeds, there are additional engineering

issues to consider, of particular importance is a form of resonance between the train and the supporting track-bed, termed Critical Velocity Effect, which is heavily influenced by the dynamic response of the underlying earthworks. Critical velocity effects have been recorded at various rail sites around the world (Woldringh et al 1999), with the phenomenon being linked to the proximity of the train speed to the site critical velocity (Madshus et al 2000).

There are no well-established design basis, guidelines and/or standards for assessing and mitigating the risks in routine design. This paper describes a simplified design approach developed for the design of HS2 earthworks to meet the dynamic performance criteria defined in HS2 Technical Standards for Earthworks (TS-E) (HS2, 2019a). The approach provides a robust and repeatable methodology for carrying out the design of earthworks and managing the associated uncertainty and risk.

The HS2 earthworks dynamic performance criteria were established based on precedent from past projects and the back analysis of problematic sections of existing track on other railways. The approach adopted by the TS-E does not establish wave amplitudes or particle velocities for the dynamic performance serviceability limit state of the track bed, but rather sets a minimum dynamic stiffness requirement for the earthwork, based on the design speed of the train, with the objective of ensuring that resonance is avoided.

1.2 Critical Velocity Effects

As a train travels over the ground, it creates a downward, deflection of the track bed due to the load of the wheels and bogies. In doing so, it generates surface waves that propagate through the track bed and supporting ground. At low train speeds, the surface waves travel faster than the train. As the train speed increases towards the speed of the propogating wave a critical velocity is reached at which resonance can occur, resulting in the dynamic amplification of the deflections.

The wave sources that are applicable for design of the earthwork structures are based on where there is likely to be significant variations in the magnitude of repetitive load applications. This is limited to the vertical load applied through the bogies and individual wheel axles of the train. (Arup, 2017). Each bogie and wheel axle act as a moving load that creates a downward deflection of the track along the railway line (Arup, 2017 & HS2, 2019b). As such, the loading at any given point is applied over a very short period (instantaneous) and at a frequency that is dependent upon the train speed.

The design of the earthwork structure needs to consider how the waves propagate longitudinally within the track bed-earthworks system and continue to interact with the moving train. It has been shown that the site critical velocity is governed by the minimum phase velocity of the fundamental Rayleigh wave mode of the foundation and embankment profile at the site (Madshus et al, 2000).

According to studies on the soil structure interaction between slab track and supporting earthwork (Arup, 2017), there are two wave velocities that may affect the overall performance of a track-earthworks systems:

- Track slab ‘Winkler Beam’ bending wave speed; and
- Rayleigh wave velocity of the earthworks structure.

One conclusion of the study is that the bending stiffness of the track slab does not affect the critical Rayleigh wave velocity of the earthworks but may reduce the displacements with stiffer track bed elements. This enables the stiffness requirement of the earthworks structure to be decoupled and designed for separately to the rail system (i.e. track bed) once the overall system performance and earthworks design criteria have been established.

Figure 1 summarises the terminology that defines and groups the track bed and earthworks components. This paper covers the earthwork structure and foundation located below the Protection Layer.

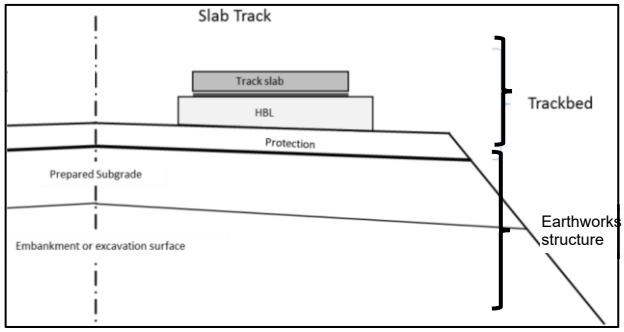

Figure 1. Schematic section illustrating track-earthworks system terminologies (adapted from HS2, 2019a).

2 FUNDAMENTALS OF RAYLEIGH WAVE PROPOGATION

The theoretical Rayleigh wave velocity for an elastic half space can be estimated using Poisson‘s ratio (ν), Youngs Modulus (E) and density (ρ), as the governing parameters:

$$V_R = \left(\frac{0.87 + 1.12\nu}{1+\nu}\right)\sqrt{\frac{E}{2\rho(1+\nu)}} \quad (1)$$

The waves are characterised by an anti-clockwise particle motion relative to the direction of travel as shown in Figure 2 below.

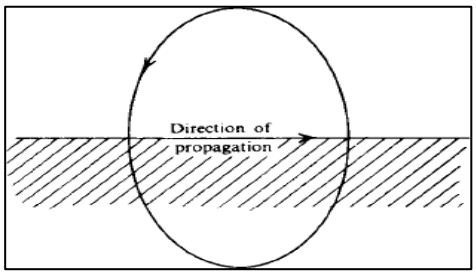

Figure 2. Particle motion on the surface during the passage of Rayleigh wave in an elastic homogenous half space (from Richard et al., 1970).

The frequency or wavelength affects the depth of influence beneath the surface. Lower frequencies with a longer wavelength excite particles to a deeper depth. This geometrical zone of influence normalised to wavelength is illustrated in Figure 3 below.

Reflecting on this zone of influence, a common ground profile with increasing stiffness with depth will have a higher Rayleigh wave velocity at lower wave frequencies (longer wavelength) and lower wave velocities at high frequencies.

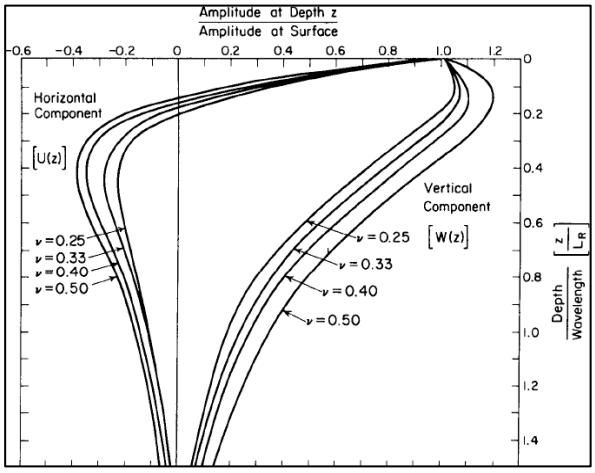

Figure 3. Amplitude ratio vs dimensionless depth for Rayleigh waves in a homogenous half space (from Richard et al., 1970).

This type of profile is known as normally dispersive. A profile that has decreasing stiffness with depth is known as inversely dispersive and will result in lower Rayleigh wave velocities for lower wave frequencies. This concept is graphically presented in Figure 4 below.

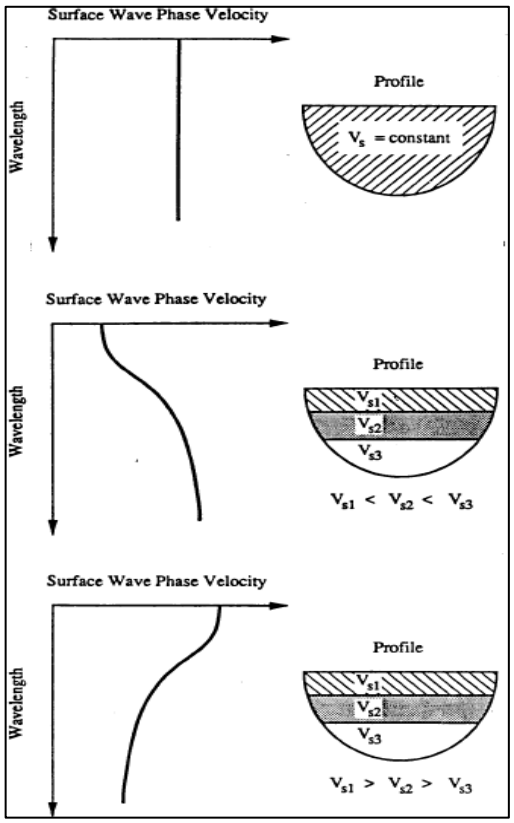

Figure 4. Example of non-dispersive (homogenous half space), normally dispersive and inversely dispersive profile (from Rix, 1988).

Surface waves will decay as the distance from the source increases. This decay is partly caused by the geometrical attenuation as the wave front spreads. This phenomenon is illustrated in Figure 5.

There is also hysteretic damping within the soil that dissipates energy due to straining of the soil, referred to as material damping. While geometric and material damping rapidly attenuates the wave energy, they do not affect the fundamental Rayleigh wave velocity of the system and the potential for amplification to occur.

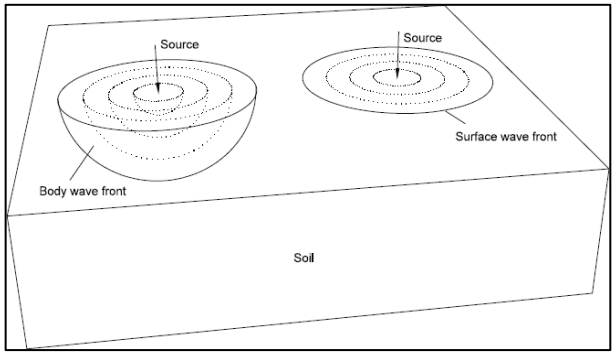

Figure 5. Geometrical attenuation of vibrations.

3 DYNAMIC PERFORMANCE CRITERIA AND REQUIREMENTS

The TS-E (HS2, 2019a) defines the earthworks dynamic stiffness as the *"transient stiffness of the earthwork at any defined level in response to dynamic loading"*. The same TS-E (Table 4.2/1) specifies the performance criteria to be satisfied by the earthworks design and construction verification testing as a limiting Rayleigh wave velocity (V_R), measured at Formation Level:

$$V_R \geq 1.6 \times DS \quad (2)$$

where DS is the design speed which for HS2 Contract C23 has been set at 360 km/hr (100 m/s). The standard requires that the dynamic performance is demonstrated by design and validated by construction verification testing. This has been achieved through verification by calculation in design, supported by the undertaking of demonstration field trials, and by end product testing of the completed earthworks.

4 DYNAMIC PERFORMANCE DESIGN APPROACH

4.1 Risk assessment method

Initially, a qualitative screening was used to determine sections of subgrade of potentially low stiffness that were at risk of requiring foundation treatment to achieve the specified minimum Rayleigh wave velocity criteria. A risk rating process was followed to focus risk mitigation activities at the different stages of the design and construction.

The first step was to identify areas along the route where the in-situ ground may have low stiffness. The risk levels were derived from assessment of predicted shear wave velocity profiles based on the geological model and published data. The risk categories applied in the early stages of design development are summarised in Table 1. The shear wave velocity for individual layers within a layered deposit is more familiar to design engineers and is a useful indicator of the expected Rayleigh wave response. This was therefore used as part of the screening exercise. Based on the initial mapping, various areas along the route were categorised as being at high risk of requiring foundation treatment to achieve the HS2 dynamic performance criteria, notably:

- Shallow/at grade embankments and shallow cuttings;
- Faulted zones and dissolution features (soft infill/voids);
- Transitions between cuttings and embankments.

Table 1. Risk Categories relative to HS2 Rayleigh Wave Performance criteria and equivalent shear wave velocity.

Parameter	Low Risk (1)	Medium Risk (1)	High Risk
Rayleigh Wave Velocity V_R (m/s)	>200	160<V_R<200 and where there are local heterogeneities (<50m)	<160
Shear Wave Velocity V_S (m/s)	>210	170<V_S≤210 and where there are local heterogeneities (<50m)	<170

(1) – For V_R, the boundary between Medium and Low Risk is defined as (1.6×DS)×1.25

In the initial categorisation of risks and development of the scheme design, a partial factor of 1.25 was adopted to reflect uncertainty in the ground investigation data that was available and the potential effectivness of proposed mitigation measures. In addition, field trials were initiated to better define the dynamic properties of the proposed fill material and investigate the improvement in dynamic response achieved by the proposed foundationt treatment methods.

4.2 Design methodology

The HS2 project involved developing a Scheme Design followed by a Detailed Design for the earthworks. At each stage, the risk assessment was updated based on the latest information. Two methods for predicting the dynamic performance of the completed earthworks by calculation were developed, starting from the simplest form:

- Direct comparison of shear wave velocity profiles for each layer in the earth structure to ensure that all layers are greater than 1.7 x the design speed using a simplified relationship between shear wave velocity and Rayleigh wave velocity (Richart et al 1970)
- Forward modelling, 1D analysis method to establish the anticipated performance of the entire layered Earth Structure.

To forward predict the performance of the earthwork using a 1D analysis method, a weighted average velocity forward modelling approach has been used to estimate the Rayleigh wave dispersion curve for a layered deposit (Leong *et al*., 2012 & 2013). The method enables the rapid assessment of multi-layered systems, including; in situ strata and the engineered earthwork structure, and provides the resulting estimated Rayleigh Wave velocity (V_R) dispersion curve at formation level. The modelling requires the Shear wave velocity (V_S) and the Poisson's ratio (ν) of each layer for the ground profile representing an

earthwork asset. The analysis can be rerun to establish the depth of treatment needed to improve the stiffness of the layered system to ensure that the dynamic performance criteria are achieved.

This method allows individual, low stiffness layers to be assessed as being acceptable due to the compensating response of stiffer layers within the profile. The 1D analysis method was used to develop standard look up charts for the design of foundation treatment which were used as an intermediate step in the design process. The design process followed for the design of the earthworks is given in Figure 6.

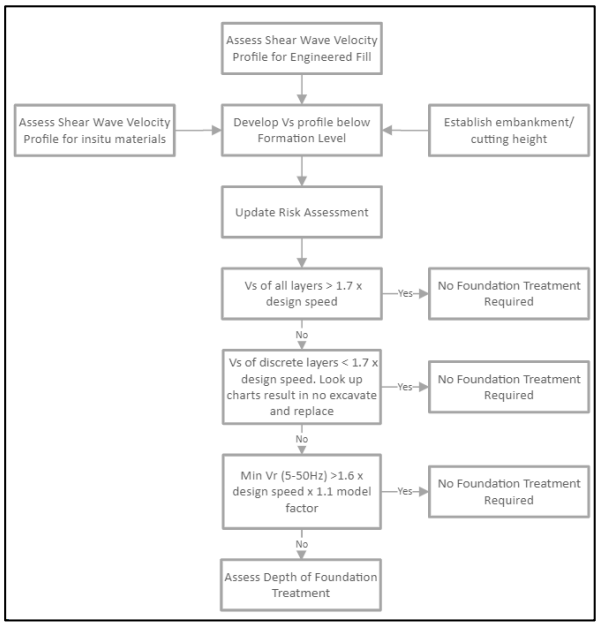

Figure 6. Design process for dynamic performance risk assessment and foundation treatment design.

For engineered fill forming the earthworks, the Shear wave velocity (V_S) was conservatively assumed as 250 m/s through Scheme Design with the same shear wave velocity value being assigned to the foundation replacement fill. This value was investigated as part of Detailed Design field trials which subsequently allowed an increase in the design value to 300 m/s to reflect increased confidence in the performance of the specified fill materials to be placed within the high-speed rail earthworks.

4.3 Foundation Treatment Design

4.3.1 Treatment options

The foundation treatment options focussed on achieving a homogenous improvement in the foundation to the high-speed rail earthworks. This was necessary due to the need to verify the minimum Rayleigh wave velocity of the completed earthwork using in-situ testing of end-product performance. Solutions that consist of locally stiffened elements such as rigid inclusions would not enable these construction stage verifications to be readily completed. The excavate and replace solution using a combination of imported engineered and stabilised site won fill was selected as the preferred solution. This in effect, modifies the 1D layered model by replacing a low velocity layer with a higher velocity layer to provide an increase in the overall dynamic performance of the earthwork.

The performance of the layered soil system was verified by a series of field trials carried out on earthworks constructed with replacement fill material to confirm the overall Rayleigh wave velocity as detailed in Section 5.

4.3.2 Target design criteria and construction verification testing

Following the results of the earthworks field trials the additional safety factor of 1.25 applied in Scheme Design was subsequently removed, but a model factor of 1.1 was adopted in the 1D analysis to recognise the uncertainty inherent in the forward modelling method and its relationship to field measurements.

To reflect the discrete extent of ground investigations and the variable nature of the natural materials, additional construction risk management controls are specified in the design to ensure that the completed earthworks meet the end product testing requirements. To account for potential variability of each fill material type demonstration areas are required during the works for each unique source of fill, construction team (workmanship), and/or unique subgrade strata.

Measurement of compacted fill density and E_{V2} stiffness will be used for earthworks quality control to ensure the engineered fill achieves the minimum shear wave velocity required to improve the overall Rayleigh Wave performance. Surface geophysical testing in advance of foundation treatment will also be used to manage potential variability in natural ground conditions for higher risk areas.

Ultimately, the completed earthwork structure is required to be verified using an end product test in accordance with the Technical Standard. Continuous Surface Wave (CSW) geophysical testing is proposed to be utilised at final earthworks formation level for this field verification. This is following the sucessful demonstration during the Detailed Design field trials and calbration during cosntruction stage demonstration areas for each fill type.

5 DETAILED DESIGN FIELD TRIALS

Six earthworks field trials have been undertaken on site to date to assess the static and dynamic performance of different fill types as well as their suitability for use in earthworks' construction including as replacement fill for foundation treatment. Material types used in the trials comprised granular fill (imported and site won), stabilised glacial tills, and both stabilised and unstabilised Chalk. Embankments up to 3.6m high were constructed and tested before construction, during fill placement and after construction to validate key design assumptions.

For the dynamic performance, geophysical testing was performed at various stages during construction and after completion of the earthworks. The results obtained demonstrated the improved dynamic performance of the earthwork due to increased stiffness of the replacement fill adopted for foundation treatment.

In addition to the improvement with increasing depth of replacement fill material, the results also validated the suitability of the 1D weighted velocity forward modelling method and Figure 7 shows a comparative example of Rayleigh wave velocity dispersion curves predicted from the 1D analysis and those obtained from the field specific trial for that tested location. A good agreement between the two sets is observed.

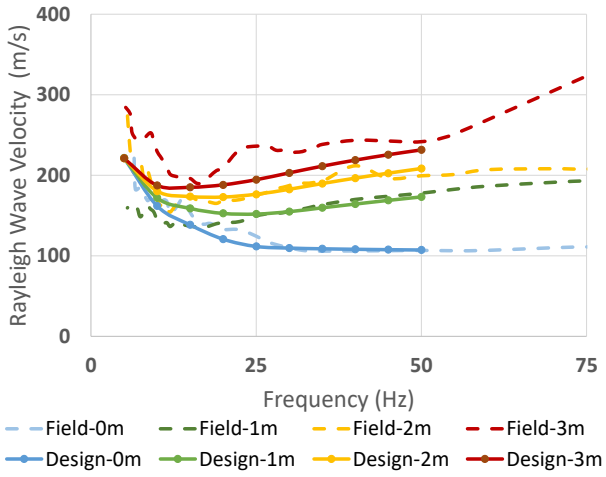

Figure 7. Typical Example of comparative Rayleigh Wave velocities dispersion curves obtained from the design forward analytical tool and from field trials.

6 CONCLUSIONS

The risk management-based design approach adopted for assessing the dynamic performance of the earthwork structures, and the design of foundations treatment has been found to be reliable in demonstrating compliance with dynamic performance criteria and requirements specified for the HS2 earthworks structures.

The use of a relatively simple, 1D wave propagation forward modelling method has enabled a more efficient design to be developed that considers the improvements obtained from stiffer layers of earthworks constructed over less stiff in-situ foundation materials.

ACKNOWLEDGEMENTS

The Authors acknowledge the support of the Integrated Project Team (IPT) and the corresponding design, construction, and assurance teams from ASC, EKFB and HS2. Input from HS2 Expert Panel members William Powrie and Nick O'Riordan and HS2 Head of Geotechnics Nick Sartain to a HS2 specific dynamic performance workshop in December 2021 is specifically recognised.

REFERENCES

Arup, (2017). *Track-Earthworks Interaction. Ref No*. C861-ARP-GT-REP-000-000026 Rev P01, March 2017.

High Speed 2 Ltd. (HS2) (2019a). *Technical Standard - Earthworks* (TS-E), Doc. HS2-HS2-GT-STD-000-000001 Rev P08.

HS2 (2019b*). Technical Standards - Train load models for civil engineering design*, Doc. No. HS2-HS2-CV-SPE-000-010600 Rev P05.

Leong, E. C., and Aung, A. M. W. (2013). Global Inversion of Surface Wave Dispersion Curves Based on Improved Weighted Average Velocity Method. *Journal of Geotechnical and Geoenvironmental Engineering*, 139(12). https://doi.org/(ASCE)GT.

Leong, E. C., and Aung, A. M. W. (2012). Weighted average velocity forward modeling of Rayleigh surface waves. *Soil. Dyn. Earthquake Eng.,* Vol. 43, 218–228. https://doi.org/j.soildyn.

Madshus, C. and Kaynia, AM (2000) High speed railway lines on soft ground: dynamic behaviour at critical train speed, *Journal of Sound and Vibration*, 231(3), 689-701. https://doi.org/jsvi.

Richart et al. (1970). *Vibration of soils and foundations. New Jersey*, Prentice-Hall, p. 414.

Woldringh, R., New, B. (1999): 'Embankment design for high speed trains on soft soils' Twelfth European Conference on Soil Mechanics and Geotechnical Engineering, Balkema, Amsterdam.

Proceedings of the XVIII ECSMGE 2024
GEOTECHNICAL ENGINEERING CHALLENGES
TO MEET CURRENT AND EMERGING NEEDS OF SOCIETY
© 2024 the Authors
ISBN 978-1-032-54816-6
DOI 10.1201/9781003431749-447
Open Access: www.taylorfrancis.com, CC BY-NC-ND 4.0 license

ECSMGE 24
XVIII EUROPEAN CONFERENCE ON SOIL MECHANICS AND GEOTECHNICAL ENGINEERING

Enhanced ductility and energy absorption of coal wash-rubber crumb mixtures for track substructure

Amélioration de la ductilité et de l'absorption d'énergie des mélanges de lavage au charbon et de mie de caoutchouc pour la sous-structure de la voie

H. Hunt, B. Indraratna*, Y. Qi
University of Technology Sydney, Sydney, Australia
**Buddhima.Indraratna@uts.edu.au*

ABSTRACT: Particularly within developed countries, landfill and stockpile volumes of industrial waste materials are reaching alarming levels. Two examples of these wastes are coal wash (CW), a by-product of the coal washing process; and scrap rubber tyres, which can be shredded to produce granulated rubber crumbs (RC). Moreover, high-quality natural aggregates are growing in scarcity, leading to increased procurement difficulties and associated costs. Consequently, reusing CW and RC in large-scale civil engineering applications is both a financially and environmentally attractive alternative to traditional granular materials. This study evaluates the ductility and strain energy density of CW-RC mixtures, at varying RC contents and compacted at the same void ratio, under static triaxial shearing. Expectedly, including rubber enhances the ductility and energy absorption of these waste mixtures. Improving these characteristics makes CW-RC mixtures a promising energy-absorbing alternative to traditional track substructure design as rail loads are expected to increase in the future. Additionally, this study proposes an empirical model for strain energy density as a function of RC content and shear strength.

RÉSUMÉ: En particulier dans les pays développés, les volumes d'enfouissement et de stockage de déchets industriels atteignent des niveaux alarmants. Deux exemples de ces déchets sont le charbon de lavage (CW), un sous-produit du processus de lavage du charbon; et les pneus en caoutchouc usagés, qui peuvent être déchiquetés pour produire des miettes de caoutchouc granulé (RC). De plus, les granulats naturels de haute qualité se font de plus en plus rares, ce qui entraîne une augmentation des difficultés d'approvisionnement et des coûts associés. Par conséquent, la réutilisation de CW et RC dans des applications de génie civil à grande échelle est une alternative financièrement et écologiquement attrayante aux matériaux granulaires traditionnels. Cette étude évalue la ductilité et la densité d'énergie de déformation des mélanges CW-RC, à différentes teneurs en RC et compactés au même taux de vide, sous cisaillement triaxial statique. Comme on pouvait s'y attendre, l'inclusion de caoutchouc améliore la ductilité et l'absorption d'énergie de ces mélanges de déchets. L'amélioration de ces caractéristiques fait des mélanges CW-RC une alternative prometteuse d'absorption d'énergie à la conception traditionnelle des sous-structures de voie, car les charges sur les rails devraient augmenter à l'avenir. De plus, cette étude propose un modèle empirique pour la densité d'énergie de déformation en fonction de la teneur en RC et de la résistance au cisaillement.

Keywords: Coal wash; rubber crumbs; ductility; energy absorbing capacity.

1 INTRODUCTION

Coal wash (CW) is a coarse-grained by-product derived from the coal washing process, with annual productions exceeding a hundred million tonnes in Australia alone (Leventhal and De Ambrosis, 1985). Prior research has been undertaken into the application of this waste material as an alternative to traditional granular geomaterials (e.g. Rujikiatkamjorn et al., 2013), although its high susceptibility to particle breakage limits is viability for use in dynamic loading environments (Qi et al., 2018).

Moreover, Australia's annual production of waste rubber tyres is expected to reach 488,000 tonnes in the year 2024-25, with about 30% being disposed on site, stockpiled, illegally dumped, or sent to landfill (O'Farrell, 2019). This can create environments that attract harmful wildlife, as well as increase the risk of fires and the release of toxic gases. Reusing waste tyres for geotechnical applications has been standardised by ASTM (2012), although less than 10% are currently used (Tasalloti et al. 2021). Rubber is an attractive material due to its low weight, high ductility, and high energy absorbing capacity, although it has a low shear strength. For important structures like railways where failure can be catastrophic, prolonged ductile failure is preferred to brittle behaviour. Rubber has been previously shown to improve the ductility of sand (Sheikh et al., 2013) and other waste material

mixtures (Indraratna et al., 2018). It has also been reported to improve energy absorption and particle breakage characteristics (Indraratna et al., 2018). Therefore, adding granulated rubber crumbs (RC), produced by shredding rubber tyres, may improve the ductility and reduce CW breakage, rendering the mixture suitable for use as an energy absorbing track substructure layer. However, it should be noted that European countries have recently proposed to tighten controls on, and possibly cease, the use of rubber due to the potential release of microplastics into the environment as a result of the recovery and recycling process (Coopland and Winter 2021).

Using the consolidated drained static triaxial tests conducted by Indraratna et al. (2019), this study aims to investigate how RC content influences the ductility and strain energy absorption of a compacted CW-RC mixture. These mixtures were blended at RC:CW ratios of 0%, 5%, 10%, and 15% based on weight. To simulate the typically low confinement conditions for subballast, these tests were conducted at effective confining pressures (σ_3') of 10, 25, 50, and 75 kPa. Additionally, to align with Australian Rail Track Corporation (ARTC, 2010) compaction requirements for a capping layer, the test specimens were all compacted at the same initial void ratio of about 0.3 using a modified energy level. The particle size distributions (PSD) of each mixture are portrayed in Figure 1, while Indraratna et al. (2019) should be referred to for further detail on specimen preparation and testing methodology.

2 DUCTILITY

The stress-strain response of the CW-RC mixtures with varying RC content at $\sigma_3' = 25$ kPa is shown in Figure 2. Understandably, increasing the RC content

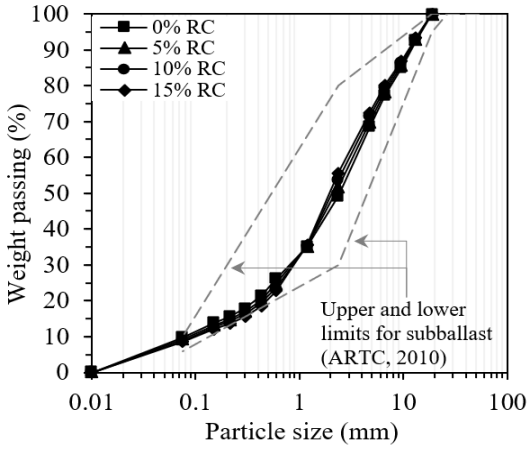

Figure 1. PSD of CW-RC mixtures with varying rubber content (modified after Hunt et al., 2023).

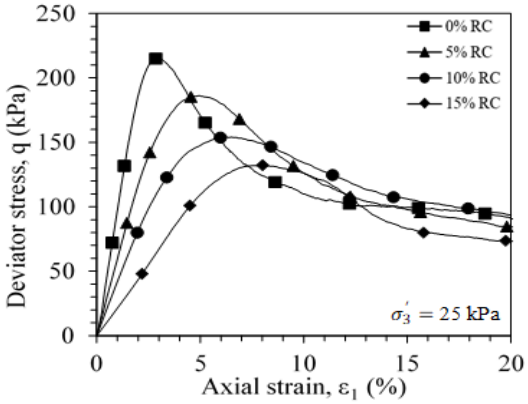

Figure 2. Stress-strain response of CW-RC mixtures under $\sigma_3' = 25$ kPa (modified after Hunt et al., 2023).

corresponds to a reduction in the peak deviatoric stress (q_{peak}) due to the inferior shear strength of rubber in comparison to the CW particles. As RC content increases, the curvature around q_{peak} is broadened as the post-peak state of the mixture transitions from being predominately brittle to more ductile, which can be attributed to the increasing rubber-to-rubber particle contacts and interactions within the soil skeleton (Sheikh et al., 2013; Qi et al., 2018). Although a larger settlement is experienced, this increase in ductility translates to a substructure material that is capable of sustaining larger post-peak loads, thus lowering the risk of catastrophic train derailments due to failure. The CW-RC mixture ductility can be quantified by calculating its brittleness index (I_B), as proposed by Consoli et al. (1998) and defined by Equation (1):

$$I_B = \frac{q_{peak}}{q_{residual}} - 1 \qquad (1)$$

where $q_{residual}$ is the residual deviatoric stress, and a lower brittleness index equates to a higher ductility. Figure 3 presents the variation in brittleness index of the CW-RC mixtures at different RC contents and

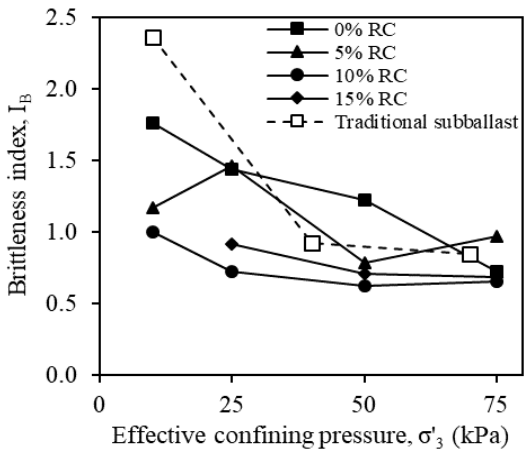

Figure 3. I_B values of CW-RC mixtures compared to traditional subballast (modified after Hunt et al., 2023).

confining pressures. Generally, I_B decreases as σ_3' increases, although this does fluctuate for the 5% RC mixture. Compared to traditional subballast material, all four mixtures have a greater ductility at the lower confining pressures ($\sigma_3' \leq 25$ kPa), while those comprised of ≥10% RC maintained a lower I_B for the entire set of confining pressures tested. These results indicate ductility is maximised for the mixture with 10% RC since this content yielded the smallest I_B for each confining pressure, after which brittleness increased as the reduction in particle breakage becomes less significant at higher RC contents.

3 STRAIN ENERGY ABSORPTION

3.1 Strain energy density

The strain energy absorption can be quantified by calculating the area enveloped by the shear stress-strain curve up to the point of failure (Equation (2) and Figure 4), which is termed strain energy density (E):

$$E = \int_0^{\gamma_f} \tau d\gamma \qquad (2)$$

where τ_f is the shear strength, γ is the shear strain, and γ_f is the shear strain at failure. The results in Figure 4 emphasises how influential even a small amount of RC is on improving the energy absorption of the CW-RC mixture. Without rubber, CW has a much lower energy absorbing capacity compared to traditional subballast and a steel furnace slag-coal wash (SFS-CW) mixture tested by Qi et al. (2018). However, at 5% RC, the mixture is superior at the lower confining pressures ($\sigma_3' \leq 25$ kPa) in terms of energy absorption, although further improvement is less significant with larger RC proportions. These low confining pressures are typical for Australian railways and therefore selecting a preferred RC content (e.g. 5% or 15%) to enhance the CW-RC mixture's strain energy absorption under lighter axle loads makes little difference. Although, at the higher confining pressures, they do not perform as well, where only the 15% RC mixture is more energy absorbing at $\sigma_3' = 50$ kPa. This can be attributed to the increased particle breakage of CW at higher confinement reported by Indraratna et al. (2019). Therefore, in terms of strain energy absorption, these CW-RC mixtures are more suitable for use within lower confining pressure ranges when compared with traditional subballast.

3.2 Strain energy density relationship

Referring to Figure 5, the strain energy density of the mixtures can be represented as a function of the shear strength and rubber content by Equations (3a,b):

$$E = \psi \tau_f \qquad (3a)$$

$$\psi = a_1 X_{RC} + a_2 \qquad (3b)$$

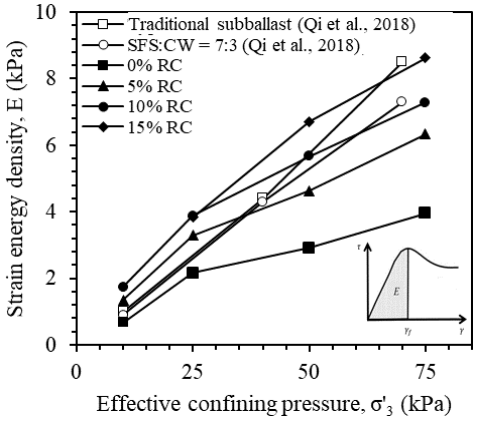

Figure 4. E values of CW-RC mixtures compared with subballast and SFS-CW (modified after Hunt et al., 2023).

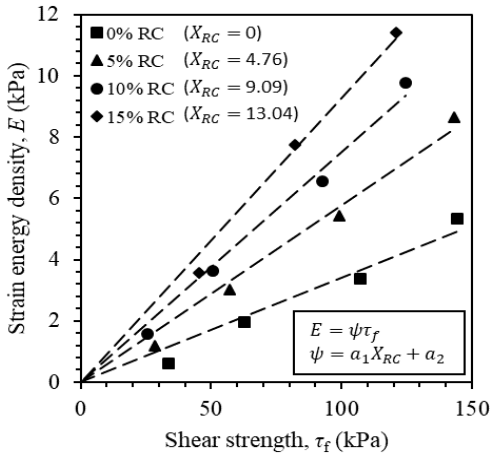

Figure 5. Increase in E with respect to shear strength of CW-RC mixtures (modified after Hunt et al., 2023).

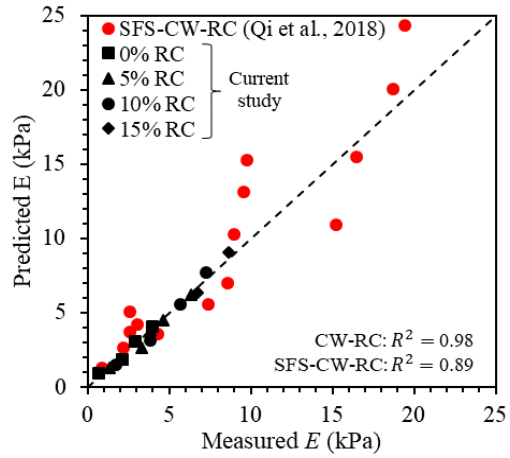

Figure 6. Predicted vs. measured E for CW-RC and SFS-CW-RC mixtures (modified after Hunt et al., 2023).

where ψ is an empirical parameter accounting for the shape of the stress-strain curve as a function of RC content, a_1 and a_2 are calibration parameters ($a_1 = 0.0036$, $a_2 = 0.0282$), and X_{RC} is the RC percentage relative to the total mixture. For further detail on these equations, see Hunt et al. (2023). The strain energy density of the CW-RC mixtures is approximated well with an R^2 value of 0.98 (Figure 6). Extending this to SFS-CW-RC mixtures (0–30% RC) tested by Qi et al. (2018), the model still performs well with an R^2 value of 0.89, although the authors recommend recalibrating the parameters a_1 and a_2 for different mixtures.

4 CONCLUSIONS

The ductility and strain energy absorption of coal wash when blended with rubber crumbs subjected to triaxial shearing was investigated in this study. Expectedly, adding rubber to coal wash significantly enhances its ductility and strain energy absorbing capabilities, particularly when 10% RC is added where ductility is at a maximum. An empirical relationship to estimate the strain energy density based on shear strength and rubber content was also proposed in this study. The model performed well on both the experimental and validation data, although the empirical constants should be recalibrated for different mixtures. When compared to typical subballast material and confining pressures, the CW-RC mixture with 10% RC is more ductile and energy-absorbing, making it suitable for use as an energy absorbing track substructure layer.

ACKNOWLEDGEMENTS

The authors would like to acknowledge the financial support provided by the Australian Research Council Linkage Project (ARC-LP200200915). The financial and technical assistance provided by various industry partners over the years, including the Australasian Centre for Rail Innovation (ACRI), RMS and Sydney Trains, c/o Transport for NSW, SMEC, Bestech, Bentley Institute, Douglas Partners, ASMS, South 32, Ecoflex Australia, Bridgestone, and Tyre Crumbs Australia) is also gratefully acknowledged. Lastly, the first author would like to acknowledge the University of Wollongong and supervision of the co-authors at the Centre for Geomechanics and Railway Engineering.

REFERENCES

American Society for Tests and Materials, standard practice for use of scrap tires in civil engineering applications. ASTM D6270-08 (R2012), West Conshohocken.

Consoli, N. C., Prietto, P. D. M., and Ulbrich, L. A. (1998) Influence of fiber and cement addition on behavior of sandy soil, *Journal of Geotechnical and Geoenvironmental Engineering*, 124(12), pp. 1211–1214. https://doi.org/10.1061/(ASCE)1090-0241(1998)124:12(1211).

Coopland, P. and Winter, M. G. (2021) The Use of Waste-derived Materials in Road Construction, Winter Associates Limited and Coopland Consultancy Limited, Scotland.

O'Farrell, K. (2019) Tyre flows and recycling analysis. Project report (Final report), Envisage Works, Melbourne, Australia. Available at [https://www.agriculture.gov.au/sites/default/files/documents/tyre-flows-recycling-analysis.pdf].

Hunt, H., Indraratna, B., and Qi, Y. (2023) Ductility and energy absorbing behaviour of coal wash – rubber crumb mixtures, *International Journal of Rail Transportation*, 11(4), pp. 508–528. https://doi.org/10.1080/23248378.2022.2095539.

Indraratna, B., Qi, Y., and Heitor, A. (2018) Evaluating the properties of mixtures of steel furnace slag, coal wash, and rubber crumbs used as subballast, *Journal of Materials in Civil Engineering*, 30(1), pp. 04017251. https://doi.org/10.1061/(ASCE)MT.1943-5533.0002108.

Indraratna, B., Rujikiatkamjorn, C., Tawk, M., and Heitor, A. (2019) Compaction, degradation and deformation characteristics of an energy absorbing matrix, *Transportation Geotechnics*, 19, pp. 74–83. https://doi.org/10.1016/j.trgeo.2019.02.002.

Leventhal, A. and De Ambrosis, L. (1985) Waste disposal in coal mining – a geotechnical analysis, *Engineering Geology*, 22(1), pp. 83–96. https://doi.org/10.1016/0013-7952(85)90040-7.

Qi, Y., Indraratna, B., Heitor, A., and Vinod, J. S. (2018) The Influence of Rubber Crumbs on the Energy Absorbing Property of Waste Mixtures, In: *Proceedings of the International Symposium on Geotechnics of Transportation Infrastructure (ISGTI 2018)*, Delhi, India, pp. 455–460.

Rujikiatkamjorn, C., Indraratna, B., and Chiaro, G. (2013) Compaction of coal wash to optimise its utilisation as water-front reclamation fill, *Geomechanics and Geoengineering*, 8(1), pp. 36–45. https://doi.org/10.1080/17486025.2012.727475.

Sheikh, M. N., Mashiri, M. S., Vinod, J. S., and Tsang, H.-H. (2013) Shear and compressibility behavior of sand-tire crumb mixtures, *Journal of Materials in Civil Engineering*, 25(10), pp. 1366–1374. https://doi.org/10.1061/(ASCE)MT.1943-5533.0000696.

Tasalloti, A., Chiaro, G., Murali, A., and Banasiak, L. (2021) Physical and mechanical properties of granulated rubber mixed with granular soils – A literature review, *Sustainability*, 13, pp. 4309. https://doi.org/10.3390/su13084309.

Proceedings of the XVIII ECSMGE 2024
GEOTECHNICAL ENGINEERING CHALLENGES
TO MEET CURRENT AND EMERGING NEEDS OF SOCIETY
© 2024 the Authors
ISBN 978-1-032-54816-6
DOI 10.1201/9781003431749-448
Open Access: www.taylorfrancis.com, CC BY-NC-ND 4.0 license

ECSMGE 24
XVIII EUROPEAN CONFERENCE ON SOIL MECHANICS AND GEOTECHNICAL ENGINEERING

Exploring the use of fine surplus silica sand in low CO_2 emission earth construction

Exploration de l'utilisation de sable de silice excédentaire fin dans la construction terrestre à faible émission de CO_2

A. Iravanian*, A. Wayu, H. Gustavsson, L. Korkiala-Tanttu
Aalto University, Espoo, Finland

anoosheh.iravanian@aalto.fi

ABSTRACT: The usage of industries' by-products and recycled materials in construction has become crucial for a sustainable future, as it reduces waste, has economic benefits, and helps to preserve natural resources while lowering CO_2 emissions. This research explored the possibility of utilizing fine silica sand, a by-product of quarrying, as a construction material aligned with circular economy strategies. Investigating various by-products alongside surplus fine silica sand from Nilsiä district, Finland, the study aimed to identify optimal recipes for stabilized silica sand blocks. The main focus was on experimentally assessing the technical properties of these blocks and evaluating the suitability of silica sand for sustainable rammed earth construction techniques. The filler and aggregates used were silica sand as well as quarry fines, while the binders included bio-based fly ash, bottom ash, green liquor dreg, lime kiln dust and cement. The material's index properties were measured, and the binders were tested for the flexural and compressive strength. Selected binders, exhibiting strength properties, were incorporated with sand and quarry fines to prepare cylindrical blocks, subsequently subjected to uniaxial compression tests. The comparison of 28 days cured compressive strength of different recipes revealed that samples containing bio-based fly ash with ratios of 1:5 and 1:6 binder to aggregate demonstrated superior results, with the best recipe containing a 50%-50% ratio of quarry fines to sand and a binder to aggregate ratio of 1:6, containing fly ash sourced from paper and pulp industry.

RÉSUMÉ: L'utilisation des sous-produits industriels et des matériaux recyclés dans la construction est devenue cruciale pour un avenir durable, car elle réduit les déchets, offre des avantages économiques et aide à préserver les ressources naturelles tout en réduisant les émissions de CO2. Cette recherche a exploré la possibilité d'utiliser du sable de silice fine, un sous-produit de l'exploitation de carrières, comme matériau de construction aligné sur les stratégies d'économie circulaire. En étudiant divers sous-produits aux côtés du surplus de sable de silice fine du district de Nilsiä, en Finlande, l'étude visait à identifier des recettes optimales pour des blocs de sable de silice stabilisés. L'accent principal a été mis sur l'évaluation expérimentale des propriétés techniques de ces blocs et sur l'évaluation de la pertinence du sable de silice pour les techniques de construction en terre battue durables. Les charges et agrégats utilisés étaient du sable de silice ainsi que des résidus de carrière, tandis que les liants comprenaient des cendres volantes biologiques, des cendres de fond, des résidus de liqueur verte, de la poussière de four à chaux et du ciment. Les propriétés index du matériau ont été mesurées et les liants ont été testés pour leur résistance à la flexion et à la compression. Des liants sélectionnés, présentant des propriétés de résistance, ont été incorporés avec du sable et des résidus de carrière pour préparer des blocs cylindriques, ensuite soumis à des tests de compression uniaxiale. La comparaison de la résistance à la compression des différentes recettes durant une période de 28 jours de durcissement a révélé que les échantillons contenant des cendres volantes biologiques avec des ratios de liant à agrégat de 1:5 et 1:6 ont montré des résultats supérieurs, avec la meilleure recette contenant un ratio de 50%-50% de résidus de carrière à du sable et un ratio de liant à agrégat de 1:6, contenant des cendres volantes provenant de l'industrie du papier et de la pâte.

Keywords: Sustainable construction; low CO_2 binders; circular economy; silica sand; quarry fine.

1 INTRODUCTION

Within the last decade, due to the increased environmental and economic benefit, re-use of recycled glass as the source material in glass and China production is adapted in many European countries. Due to this, the demand for fine-grained (< 1 mm) silica sand has decreased, and it is resulted in a problem in mass balance and surplus of the material on many quartzite quarry sites. Additionally, transporting large quantities of this material to regions with higher demand is deemed unsustainable.

In addition, with the rise of awareness about circular economy, it is essential to acquire by-

products from mining, forestry, and energy industries in a manner that is consistent with the trend.

This study tries to evaluate the usage possibility of fine sand together with other secondary materials in non-load-bearing structure construction. This may provide a sustainable solution for the surplus of the material, assist with the waste management, and foster a more environmentally responsible approach to building practices.

One of the methods of construction that employs the use of secondary materials is rammed earth technology. In this method of construction, a damp material composed of soil, sand, silt or clay is rammed into a formwork. After the material has achieved the desired height the formwork is removed revealing a monolithic wall structure. In modern construction, besides the artistic reasons, the primary objective of utilizing rammed earth is to enhance its strength properties to meet the standards' requirements. To achieve this, stabilized rammed earth compositions typically integrate a small proportion of cement, typically ranging from 5% to 10% (Avila et al., 2022). In the stabilized rammed earth technique, the binder interacts with the available water, initiating a hydraulic binding process that contributes to the structural cohesion of the material (Jaquin, 2012). Numerous studies on the rammed earth technique highlight the influence of water content on the final strength of the structure. Unconfined compressive strength (UCS) achieved through the rammed earth technique typically span from 0,5 to 4 MPa, while the stabilized rammed earth technique can attain strengths exceeding 10 MPa after 7 days of curing. The strength ranges can vary depending on the type of aggregates and binders and the amount of water used. Nevertheless, the process of hydration and strength gain is gradual in these types of structures, therefore, the immediately post-construction strength measurements may not provide a realistic result (Jaquin et al., 2009; Walker et al., 2005).

In an experimental study, Holopainen (2022) investigated the possibility of using the recycled materials generated in Helsinki metropolitan area in rammed earth technology by constructing a testing-scale wall. In their work they studied the compressive strength of blocks made of different recipes of fly ash, crushed concrete, slag, and excavated desulphurization products with small amounts of cement. The compressive strength of his laboratory samples varied between 0,43-11,85 MPa, and it was concluded that the variation of the test results was an indicator of the susceptibility of the method to errors in the construction work. The main factors affecting the final results were named as: thoroughness of material mixing, initial moisture content of the mixture, and the compaction method.

Limited research exists on the properties of quarry fines in relation to rammed earth technology. However, Zhang et al. (2019) investigated the mechanical properties of stabilized quarry fines to be used in base and subbase layers in pavement construction. The quarry fines size ranging 0 to 4 mm were stabilized with cement, Ecolan Infra 80 (composed of coal ash, wood biomass, lime, and 20% cement) and fly ash from 100 % coal combustion residuals. Their cement stabilized samples showed acceptable performance for base layer applications when compacted to at least 93% of its maximum dry density.

The use of clean, fine quarried silica sand, characterized by angular-shaped grains, in conjunction with recycled material has not yet been explored in existing literature. However, the use of foundry sand, primarily consisting of uniformly sized, round-grained silica sand, has been studied in a few previous works. Zhang et al. (2021) have studied the use of stabilized waste foundry sand, (WFS) for applications in pavement structures. After monitoring the strength and durability properties of the proposed mixtures, they concluded that stabilized waste foundry sand (WFS) in combination with crushed rock exhibits promising potential for utilization in pavement structural layers. Malathy et al., (2022) tried to address the depletion of natural aggregates, by investigating the use of industrial silica sand as a substitute for natural fine aggregates in concrete. In their study it was concluded that all silica sand samples perform lower strength when compared to reference river sand and manufactured sand, and that the workability of concrete substituted with silica sand is superior to the concrete samples containing river sand.

In the current research, the silica sand from Nilsiä district of Finland was tested together with quarry fines as the main frame of the mixtures for the testing program. The by-products of a close-by forestry (paper and pulp) industry, namely bio-based fly ash, bottom ash, lime kiln dust and green liquor dreg together with by-products of a local energy company, namely: bio-based fly ash and bottom ash, was used as possible binders together with small amounts of cement as activator, to prepare samples. The aim of the research is to explore the potential application of different low carbon embedded recipes within the construction industry, in alignment with circular economy principles, as well as to determine the suitable ratios for the silica sand-containing mixtures adapted for different construction needs including non-load-bearing structures and noise barrier walls.

2 MATERIALS AND METHODS

The sand sample used in the study was a uniform poorly graded silica sand obtained from SIBELCO company's quarrying operation in Nilsiä located in Northern Savonia region of Finland. The fine fraction of silica sand (0.1 to 0.6 mm) is of less demand in the industry and is recently considered as a side stream product in quartzite quarrying activities.

As the coarser portion of the mixtures, quarry fines were used. The quarry fines (QF) are secondary product of the rock crushing process, characterized by a high fine grain size content. The quarry fines used in this study had a grain size distribution of 0 to 8 mm and the geological composition of the source rock was identified as Quartz syenite.

The material used for main frame of the mixtures, sand and QF, was dried for 24 hours at at the oven of 110 ± 5 °C. Subsequently, quartering was performed to prepare the samples for their index properties testing. Specific gravity and sieve analysis tests were performed according to SFS-EN ISO 17892-3 and SFS-EN 933-1, respectively. The maximum dry density (MDD) and optimum moisture content (OMC) of the material were then determined according to SFS-EN 13286-2 standard by using modified Proctor test. The Index properties of the material can be found in Table 1.

Table 1. Index properties.

Property	Silica sand	Quarry fine
Specific gravity	2,65	2,72
Percent fine <0,063 mm, (%)	0,1	6,15
C_u	2,5	0,9
D_{50}, (mm)	0.6	0,9
OMC, (%)	10	10,5
MDD, (g/cm^3)	1,57	2,15

To explore potential sustainable binder materials, an initial investigation was undertaken to identify locally sourced by-products. The aim was to minimize the requirement for long-distance transportation, thereby lowering CO_2 emissions. Stora Enso Oy, a provider in the renewable bio-products industry operating within the same region, supplied this work with five types of by-products: bio-based fly ash (1), two variants of bottom ash (1 & 2), lime kiln dust (LKD), and green liquor dreg. Additionally, Savon Voima, a local energy company, provided two of their own by-products: bio-based fly ash (2) and bottom ash (3). To assess the binding properties of these products in the presence of an activator, the flexural and compressive strengths of the hardened mortars, were tested after curing for 28 days, following the European standard SFS-EN 196-1:2016. Following the methodology outlined by Holopainen (2022), the proportion of activating agent, CEM I, was set up at 20%, while the remaining 80% was allocated to various binders. The test results of the strength properties of activator added binders are provided in table 2. The green liquor dreg did not exhibit any hardening properties, attributable to its high initial water content. Consequently, it was excluded from the designed recipes.

Table 2. Strength of activated binders.

Specimen	Flexural strength (MPa)	Compressive strength (MPa)
Fly ash 1 + CEM I	2,5	7,5
Bottom ash 1 + CEM I	1,5	4,5
Lime kiln dust + CEM I	0,4	0,9
Fly ash 2 + CEM I	1,6	5,8
Bottom ash 2 + CEM I	4,4	23,1
Green liquor dreg+ CEM I	NA	NA
Bottom ash 3 + CEM I	3,2	10,1

3 RESULTS AND DISCUSSIONS

The initial combination utilized in this study, referred to as Recipe-1, contain 75% quarry fines and 25% silica sand serving as the frame material together with binders. The binders were added at ratios of 1:5 and 1:6 binder to aggregate, respectively, to develop potential working recipes.

For evaluating the compressive strength following a 7-day curing period, a total of twelve specimens were prepared using an intensive compactor tester (ICT) machine. As shown in Figure 1, the stabilized mixture containing Fly ash 1, from Stora Enso, showed the highest recorded strength of 6,85 MPa. This fly ash was collected from a bed boiler that has a 150 MW thermal output and operates at an efficiency of 88%, with the annual production output of 5000 metric tons fly ash. Wood-based fuels such as bark, wood chips, forest chips and wood residue classes A and B, which are obtained from the factory and external sawmills are used as the main fuel type for this boiler. In addition, peat and sewage treatment plant sludge can be burned and coal is used as back-up fuel. The elevated chloride content present in this fly ash could be attributed to its higher strength, as chlorides are recognized accelerators of compressive strength in mortars and concrete. Fly ash 1, in particular, contains chloride, different oxides, and sulphate ions. The presence of chloride ions within the hydrated cement pore water stimulates the activator's hydration, thereby enhancing the strength

gain (Galan and Glasser, 2015). Similarly, at a ratio of 1:5, the mixture containing fly ash 2 exhibited promising results, likely due to the same mechanism. Conversely, to the fly ash bearing samples, the remaining four binders exhibited less favourable outcome for the 1:5 and 1:6 binder-aggregate ratios. Consequently, a higher binder content was deemed necessary for these recipes, prompting an adjustment to binder-aggregate ratio to 1:3.

The percentage increase in strength, comparing the 1:5 to 1:3 ratios of binder to aggregates, were 25%, 77%, 132%, and 4% for samples containing bottom ash 1, lime kiln dust, bottom ash 2, and bottom ash 3, respectively as visible in Figure 1.

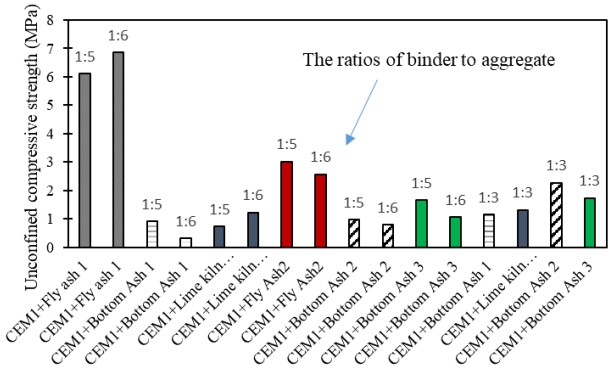

Figure 1. Unconfined compressive strength of 7-day.

Based on the revised recipes, the four best-performing binders exhibiting strengths were selected along with their corresponding ratios. Three specimens were prepared for each recipe to undergo testing for 28-day cured compressive strength. On the other hand, in order to maximize the utilization of the fine side stream sand, Recipe-2 was introduced, which involved a reduction in the amount of quarry fines by 25%, while maintaining the same ratios of binders. Following changing the ratio of quarry fines to sands to 50-50% the 7 days strength of samples were measured, and the comparison of result can be seen in figure 2. It is evident that the impact of this change varies across different recipes. For samples containing lime kiln dust, the frame material ratio change led to a notable 65% enhancement in strength compared to Recipe-1. However, in the remaining samples, it resulted in a strength reduction ranging from 26% to 117%.

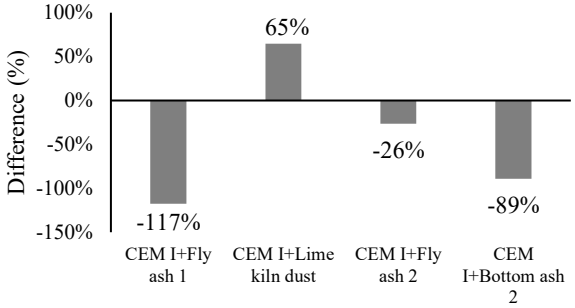

Figure 2. Comparison of 7-day strength difference from 75-25% (recipe 1) to 50-50% quarry fine-sand (recipe 2).

Among the recipes yielding better results in Recipe-2, those containing fly ash 1 and lime kiln dust (LKD) demonstrated strengths of 3.15 MPa and 3.17 MPa, respectively. These two samples were selected for comparison of their 28-day compressive strengths. Table 3 displays the results for both 7-day and 28-day compressive strengths of the selected samples of Recipe-1 and Recipe-2. These samples were prepared by ramming technique in five layers with a 4 kg hammer dropped 20 times from 0.45meter height. It can be observed that all samples, except those containing lime kiln dust, demonstrated strength gain with the extension of curing time.

Previously, it has been noted that incorporating lime kiln dust (LKD) into ash-bearing concrete mixtures and mortars leads to an increase in their water demand (Dvorkin and Zhitkovsky, 2023). This phenomenon suggests that LKD retains a higher water absorption capacity compared to CEM I, potentially attributed to its porous and larger particle size (Latif et al., 2015). In stabilized samples prepared using the rammed earth technique, compaction occurs at a relatively low water content. Consequently, the rapid absorption of available water by LKD can impede the hydration process of the remaining calcite (both from the activator and binder) in the mixture. This can lead to a cessation or even reversal of the strength gain process.

Table 3. Compressive strength of the final recipes.>

Quarry fine to sand ratio	Binder	Binder to aggregate	7 days strength (Mpa)	28 days strength (Mpa)
75%-25%	CEM I+Fly ash 1	1:6	3,15	4,83
75%-25%	CEM I+Fly ash 2	1:5	2,39	4,89
75%-25%	CEM I +Bottom ash 2	1:3	1,2	3,17
75%-25%	CEM I+Lime kiln dust	1:3	3,73	3,67
50%-50%	CEM I+Fly ash 1	1:6	3,15	6,61
50%-50%	CEM I+Lime kiln dust	1:3	3,73	2,56

4 CONCLUSIONS

The suitability of utilizing by-products of fine silica sand and quarry fines as construction materials was evaluated through a comparative study, with a particular focus on the compressive strength properties. Six different types of low CO_2 binders were employed to produce stabilized mixtures. Two ratios of 25% to 75 % and 50% to 50% of quarry fines to sand were kept as the base for frame material, while the proposed binders were added at 1:6, 1:5 and 1:3 ratios of binder to aggregate. Overall, samples containing bio-based fly ash in different mixtures and recipes demonstrated superior results, with the best recipe containing 50%-50% quarry fines to sand ratio, containing the bio-based fly ash from paper and pulp industry. It can be concluded that the higher concentration of fine silica sand particles in the mixture resulted in a wider range of gradation distribution of material within the standard upper and lower limits of aggregates. This, in turn, leads to a tighter packing of materials, particularly when combined with quarry sand and fly ash. Consequently, the reduction in void space within the material contributes to an increase in compressive strength. Additionally, it was observed that the effect of curing time on lime kiln dust containing samples was slightly detrimental. Further research is still required to assess the durability of utilized recipes over the long term and to enhance their strength properties.

ACKNOWLEDGEMENTS

The authors are grateful for the financial support provided by SIBELCO NORDIC mineral company. We thank Stora Enso and Savon Voima for providing the by-products, as well as Kiertomaa Oy for providing the quarry fines. All the experiments were done at the Aalto university laboratories.

REFERENCES

Ávila, F., Puertas, E. and Gallego, R. (2021) Characterization of the mechanical and physical properties of unstabilized rammed earth: A review. *Construction and Building materials*. 270. https://doi.org/10.1016/j.conbuildmat.2020.121435.

Dvorkin, L., and Zhitkovsky, V. (2023). Cement–ash concrete with the addition of lime kiln dust. *Frontiers in Materials,* Vol. 10, 1196407. https://doi.org/10.3389/fmats.2023.1196407.

Galan, I. and Glasser, F. P. (2015). Chloride in cement. *Advances in Cement Research*, 27(2), 63-97. https://doi.org/10.1680/adcr.13.00067.

Holopainen, K. (2022). *Uusiomateriaaleista sullotun maan tekniikalla valmistettu meluseinäkoerakenne.* Master's thesis. Aalto University. Available at: https://aaltodoc.aalto.fi/items/6a660e3e-8e1c-41e8-9ea4-c2832303ff81.

Jaquin, P. (2012). *History of earth building techniques*. In Modern Earth Buildings. Woodhead Publishing. pp. 307-323.

Jaquin, P., Augarde, C., Gallipoli, D. and Toll, D.G. (2009). The strength of unstabilised rammed earth materials. *Géotechnique.* 59 (5) 487-490. https://doi.org/10.1680/geot.2007.00129.

Latif, M. A., Naganathan, S., Razak, H. A., and Mustapha, K. N. (2015). Performance of lime kiln dust as cementitious material. In: *Procedia Engineering*, 125, 780-787. https://doi.org/10.1016/j.proeng.2015.11.135.

Malathy, R., Rajagopal Sentilkumar, S., Das, B., Chung, I.-M., Kim, S.-H., and Prabakaran, M. (2022). Use of Industrial Silica Sand as a Fine Aggregate in. *Buildings*. 12(8), 1273.

SFS-EN ISO 17892-3:en. (2015). Geotechnical investigation and testing. Laboratory testing of soil. Part 3: Determination of particle density. Helsinki: Finnish standards association. 19 p.

SFS-EN 933-1:en. (2012). Tests for geometrical properties of aggregates. Part 1: Determination of particle size distribution. Sieving method. Helsinki: Finnish standards association. 19 p.

SFS-EN 13286-2:en. (2011). Unbound and hydraulically bound mixtures. Part 2: Test methods for laboratory reference density and water content. Proctor compaction. Helsinki: Finnish standards association. 30 p.

SFS-EN 196-1:2016:en. (2016). Methods of testing cement. Part 1: Determination of strength. Helsinki: Finnish standards association. 33 p.

Walker, P., Keable, R., Marton, J. and Maniatidis, V. (2005). Rammed Earth – Design and construction guidelines. IHS BRE Press. 156 p.

Zhang, Y., Korkiala-Tanttu, L. and Borén, M. (2019). Assessment for Sustainable Use of Quarry Fines as Pave-ment Construction Materials: Part II-Stabilization and Characterization of Quarry Fine Materials. *Materials.* 12 (15) 2450. https://doi.org/10.3390/ma12152450.

Zhang, Y., Sappinen, T., Korkiala-Tanttu, L., Vilenius, M. and Juuti, E. (2021). Investigations into stabilized waste foundry sand for applications in pavement structures, *Resources, Conservation and Recycling*, 170, 105585, https://doi.org/10.1016/j.resconrec.2021.105585.

Proceedings of the XVIII ECSMGE 2024
GEOTECHNICAL ENGINEERING CHALLENGES
TO MEET CURRENT AND EMERGING NEEDS OF SOCIETY
© 2024 the Authors
ISBN 978-1-032-54816-6
DOI 10.1201/9781003431749-449
Open Access: www.taylorfrancis.com, CC BY-NC-ND 4.0 license

ECSMGE 24
XVIII EUROPEAN CONFERENCE ON SOIL MECHANICS AND GEOTECHNICAL ENGINEERING

Framework for evaluating scour risk and optimising scour mitigation

Cadre d'évaluation du risque d'affouillement et d'optimisation de son atténuation

J. Irvine*, I. Torres, M. Divilly
Cathie, Newcastle, UK

**Jamie.Irvine@cathiegroup.com*

ABSTRACT: Scour poses a significant risk to seabed foundations. Common practice is to design scour protection to ensure protection against extreme metocean events such as 50-year storms. This may have been acceptable for oil and gas projects but, with the increasing size of offshore wind projects, this could result in excessive costs associated with the transportation and installation of scour protection. This paper aims to provide a framework to evaluate the main factors influencing scour risk such as; soil conditions including surface soils and the depth to potentially scour resistant soils, the metocean conditions which could result in scour, the potential rate of scour, as well as understanding the potential consequences of scour on foundation performance. This understanding will allow the specification of appropriate scour mitigation.

RÉSUMÉ: L'affouillement se produisant autour des structures sous-marines peut engendrer un risque important pour la stabilité des fondations. La pratique courante consiste à concevoir une protection contre l'affouillement visant à assurer une protection contre les évènements météo-océaniques extrêmes tels que les tempêtes de période de retour 50 ans. Cette approche était acceptable pour les projets pétroliers et gaziers. Mais, du fait de la taille croissante des projets de développement éoliens offshore, implémenter cette même approche pourrait engendrer des coûts excessifs associés au transport et à l'installation de protection anti-affouillement. Cet article vise à fournir un cadre pour évaluer les principaux facteurs influençant le risque d'affouillement, tels que: les conditions du sol, y compris les sols de surface et la profondeur des sols potentiellement résistants à l'affouillement, les conditions météo-océaniques qui pourraient générer l'affouillement, le taux potentiel d'avancement d'affouillement avec le temps, ainsi qu'une compréhension des conséquences potentielles de cet affouillement sur les performances des fondations. Une telle compréhension permettra de définir des mesures d'atténuation appropriées.

Keywords: Offshore foundations; scour protection; scour risk; scour mitigation.

1 INTRODUCTION

The installation of structures such as offshore wind turbine foundations is likely to cause a local increase in seabed stresses due to wave and current motions. This increase can result in local erosion of seabed soils around the structure. This process is generally known as scour whereas widespread sediment mobility away from structures is known as 'global sediment mobility'.

Scour can result in reduced foundation capacity and/or a 'softer' foundation response, potentially resulting in natural frequency or fatigue issues. The risk of scour is usually mitigated by using rock berms placed around the foundations to 'shield' the seabed, however, alternatives such as filter units and fronded mattresses can also be used.

Scour assessment and subsequent scour protection design usually consider extreme metocean events such as 50-year storms and assume any significant scour is unacceptable. This may have been acceptable for oil and gas projects but, with the increasing size of offshore wind projects, this could result in excessive costs associated with the transportation and installation of scour protection around hundreds of offshore structures.

The aim of this paper is to propose a framework to better understand the risk of scour and potential consequences, to then determine the most appropriate scour mitigation measures. It should be noted that global seabed mobility is not considered as part of this paper.

2 SCOUR PRINCIPLES

Scour processes are commonly triggered as a result of the presence of a structure which disturbs pre-existing

flow patterns, increasing the fluid velocity / current speed as it flows around the structure. At the seawater-seabed interface, this increased velocity is translated into a bed shear stress. This can subsequently lead to higher local erosion occurring around a foundation structure, reducing with distance from the structure.

The evolution of the scour mainly depends on several parameters such as soil characteristics, the prevailing metocean conditions, and structure geometry, as discussed below.

2.1 Soil characteristics for scour resistance

The characteristics of the shallow seabed soils can significantly influence scour potential. For example, in cohesionless soils: smaller, lighter soil particles are more prone to scour than larger heavy particles. Effective soil cohesion also increases soil scour resistance.

As a minimum, the following soil parameters are required:

- Sediment specific gravity (density of soil grains);
- Sediment size (particle size distribution);
- Cohesion.

Other factors such as grain shape or clay plasticity may also be a factor but are considered less critical.

2.2 Metocean parameters for scour propagation

The prevalent metocean conditions, such as tidal current and waves, can have a significant influence on scour potential. The collection of site-specific metocean data is considered an invaluable asset to aid in the development of the risk-based approach for initial categorising of the site. The following parameters are required as a minimum:

- Maximum current velocity and direction at seabed level (or just above);
- Metocean parameters for anticipated design conditions i.e., 1 year storm, 5-year storm, etc would also add significant value.
- Wave parameters including wave direction, maximum wave height and period.
- Low-water and high-water levels.

Metocean criteria and input for design should be contemplated as part of a site specific metocean assessment. In order to select realistic conditions for a 50-year event, consideration should be given to the realities of climate change. What were previously considered extreme events may become more frequent and therefore expectations of what constitutes an extreme event should be updated as part of the metocean assessment.

2.3 Structure size

The classical representation of flow modification around a vertical pile is shown in Figure 1. Local scour is often induced by the generation of the horseshoe vortex (rotation of the incoming flow), vortex shedding (generation of lee-wake vortex behind the pile) and the contraction of the streamlines around the structure (Sumer and Fredsoe, 2002).

The larger the structure, the larger the flow disturbance.

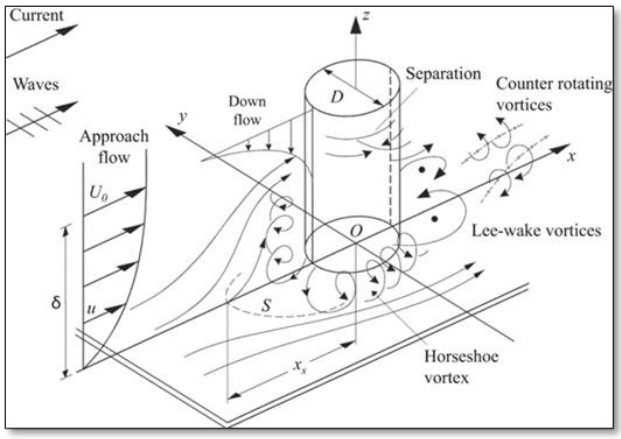

Figure 1. Flow around a vertical pile – extract Sumer and Fredsoe (2002).

3 SCOUR RISK ASSESSMENT PROCESS

The risk of scour should be considered throughout the development cycle to ensure sufficient information is collected and evaluated to allow for informed decisions without unnecessary or abortive work. The following process is hence recommended:

1. Initial site characterisation (basic soil and metocean parameters);
2. Initial scour risk evaluation and sensitivity analysis;
3. Detailed site characterisation;
4. Detailed scour assessment;
5. Evaluation of scour consequences;
6. Cost benefit analysis of scour mitigation options / measures.

4 INITIAL SITE CHARACTERISATION

At early project stages, limited information is likely to be available. Therefore, there should be a detailed desk study including a review of all public domain information and likely conditions across the planned development area including water depth, anticipated seabed sediments, potential bedforms, shallow geology and indicative metocean parameters.

Ideally, the desk study information should also provide an initial qualitative scour risk assessment. Identification of seabed features such as sand waves, megaripples, etc. are meaningful indicators that scour should be considered a risk. Whilst a relatively flat featureless seabed with high strength clay or rock at seabed would be considered lower risk.

Even if the available data are not of sufficient resolution to identify potential bedform features, the indication of water depth and metocean parameters should also be somewhat informative.

The outcome of the initial risk assessment should inform the scope of future survey campaigns. For example; a geophysical survey undertaken in order to accurately identify bedforms, potentially with multiple phases to monitor bedform migration speed. The planned surveys should be scoped to provide the information required for the scour analysis.

Key outputs:

- Qualitative risk assessment across site;
- Input into future survey scopes.

5 INITIAL RISK EVALUATION

Once site specific data are available in the form of seabed soils and metocean data, then initial numerical analysis can be undertaken to better understand scour potential. At this stage, a relatively simple numerical analysis is likely to offer reasonable understanding of the risk.

5.1 Metocean seabed stresses

The seabed stresses developed by the current are dependent upon the current velocity, water density and the turbulent flow regime. Specific formulation can be used to estimate current induced seabed stresses.

5.2 Shields stability method

Shields (1936) proposed a detailed, rational approach to the problem of hydrodynamic stability by defining the erosion limit in terms of the particle Reynolds number (a dimensionless parameter detailing the ratio of inertial to viscous forces) and the critical Shields parameter (normalised critical seabed stresses). Shields‘ theory can then be extended to the combined action of currents and waves.

It is noted that based on the randomness of the packing of the particles at the seabed, McEwan and Heald (2001) observed that, for a given bed stress or shear velocity, some particles are more vulnerable to erosion than others. The physical significance of this phenomenon was better described by Sato (1966), who studied erosion under wave action. Sato defined two levels of seabed mobility, called “surface layer movement” and “completely active movement”, respectively. Surface layer movement corresponds to the state where the first layer of particles of the seabed moves in the direction of the wave propagation. Completely active movement corresponds to such movement of bed material as to produce a notable variation in the seabed profile and Sato classifies “completely active” behaviour as more than 8% of sediment by volume.

5.3 Initial risk evaluation outputs

The initial risk assessment shall assess the conditions across the planned site for a number of potential metocean conditions to better understand scour risk.

The site could be split into zones of similar seabed sediments and water depth (and metocean conditions) and then an assessment undertaken to understand scour risk for the different conditions. For example:

- Zone A (deep water, high strength clays) – low risk;
- Zone B (medium water and coarse sands) – potential surface movement (medium risk);
- Zone C (shallow water, fine sands) – potential for ‘completely active’ movement (high risk).

6 DETAILED SITE CHARACTERISATION

The initial scour risk assessment should provide an indication of scour risk across the potential development area. The planned surveys including sediment sampling and potentially in-situ testing should be tailored based on these results. The site characterisation should aim to identify the main soil units anticipated across the development area, map the lateral and vertical distribution of these units, and provide sufficient information to allow scour potential to be accurately determined for each of the soil units.

In zones where a high risk of scouring is indicated, it may be necessary to plan additional tests potentially including benthic flume testing.

6.1 Sediment sampling

Representative seabed sediment core samples should be collected from across the site. The planned campaigns should obtain sediment samples of the main shallow soil units anticipated across the development area.

These soils can be targeted based on the scour risk assessment previously undertaken. Engineering judgement should be applied in order to obtain and preserve as many intact samples as necessary, particularly in higher risk zones to potentially perform

erosion tests as discussed in section 6.1.2. Additionally, it is important to perform sufficient index testing of the surface sediments in order to properly characterise the soils.

Samples shall generally be obtained using vibro-cores or boxcores (and potentially even boreholes) in order to obtain a better understanding of the most surficial soils and allow for a number of subsamples for testing (and for example, to verify cohesion).

6.1.1 Onshore laboratory testing - classification

As outlined above, soil characteristics which have the largest effect on scour occurrence and severity are:

- Soil type. Clay soils are most resistant to scouring whereas sands are often prone to scour.
- Particle size and specific gravity. Larger heavier soils tend to be more scour resistant.
- Cohesion. Experience indicates that sands which possess some levels of cohesion are far more scour resistant than those without.

As part of the geotechnical testing campaigns, it is vital to identify the main soil units present across the development area, and characterise each unit with sufficient index and other laboratory tests such as:

- Particle density (specific gravity);
- Particle size distribution (PSDs) for d50 and fines content;
- Shear box testing for cohesion.

6.1.2 Onshore laboratory testing – erosion

The initial numerical assessment detailed in section 5 is considered a useful indicator, but physical erosion testing should be considered to validate and/or optimise these results, particularly in high-risk areas.

Erosion testing generally comprises placing a soil sample in a flume and increasing the flow speed to investigate the sediment erosion with current speed.

It is important to use test conditions that are representative of the site and preferably based on measured metocean data.

The soil samples should undergo detailed assessment prior to onshore flume testing to ensure that they are representative of the anticipated soil units to the base of the potential scour depth.

The flow speeds should be carefully specified to represent anticipated field conditions and provide an accurate indication of the flow velocity to initiate erosion.

The main aim of erosion testing is to identify:

- Flow velocity at which mobility begins;
- Erosion rate at various current speeds.

Examples of results from indicative soils including sand, silt and clay are shown in Figure 2 below. These results indicate clays are generally highly resistant to scour with limited erosion even at significant current speeds (>1m/s), sands can erode at relatively low current speeds and even relatively limited cohesion can provide significant additional resistance against scour.

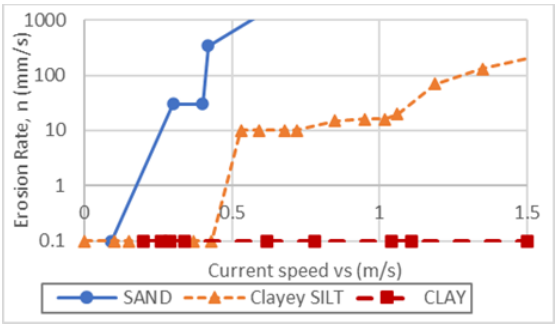

Figure 2. Erosion test results example.

It should be noted that testing a reasonable sample size can provide indications of the bulk behaviour of the soils. For example, there may be preferential erosion of smaller particles which leaves a layer of coarse sediments, shells and gravel at surface which is more resistant to scour. If this occurs, then it is recommended to carefully observe the test to understand the potential for sediment winnowing and the point at which the 'shield' layer becomes unstable. Consideration could also be given to testing the 'shield' layer at reduced velocities to better understand the benefits of this shielding.

Key outputs:

- Current velocity to initiate scour for each soil unit;
- Scour rate for each soil unit;
- Understand potential for formation of 'shield' layers and the potential benefits.

6.1.3 In-situ benthic flume testing

The Seaflume (KC Denmark, 2023) is a device which can provide an understanding of the in-situ erodibility of seabed sediments, particularly sands, fine gravels, and silts.

In-situ testing like this should be considered in zones which are high risk as it can provide a rapid insight to the reality and severity of erosion at an expected "worst-case" location. However, it should be noted that seabed flume testing is likely to incur additional offshore time and costs, and should be carefully planned as part of the survey campaigns.

Key outputs:

- Current velocity to initiate scour at representative locations;
- Scour rate for representative locations at anticipated flow velocities.

6.1.4 Near-bed flow monitoring

Collection of flow data (current speed and direction) very close to the seabed (within 2m) and through the water column at relatively small vertical intervals (0.25 m or 0.5 m maximum) is recommended. This requires specific instrumentation; it aims to provide valuable site-specific data on those flows which are most relevant to scour assessment and within the scour protection zones.

A current measuring system within a configuration which permits very near-bed flow measurement, detailed water column resolution and which preferably can also measure waves is suggested. Data should be collected for a period which includes more quiescent tidally dominated conditions (e.g., summertime) and more energetic wave dominated conditions.

7 SCOUR PROPAGATION ANALYSIS

In order to undertake a detailed evaluation of the risk of scour to the installation, it is necessary to undertake detailed modelling, utilising the results of site-specific testing and site specific metocean data and their analyses.

7.1 Sub-structure influence

The presence of the substructure is likely to result in acceleration and/or disturbance of the flow which would increase the seabed stresses. The magnitude of the stress increase could be determined using Computational Flow Dynamics (CFD) and/or scale model testing.

Key output:

- Relevant flow acceleration factors for the structures.

7.2 Numerical model

Numerical model using the time domain metocean data, scour test results, and sub-structure flow modification to estimate scour propagation with time can be valuable to understand anticipated scour depth and propagation timescales for various events i.e., 1-year, 5-year and 50-year storms.

The numerical study should also consider the potential for ‘natural’ backfill with time after the significant design events.

8 SCOUR CONSEQUENCES

The consequences of scour can vary significantly depending upon the substructure and foundation types as outlined below:

- Monopiles – Significant scour could result in a reduced lateral capacity and a shift in the natural frequency which may have implications for the structure fatigue life;
- Jacket pin-piles - The axial capacity of jacket piles is generally the design driver. Scour may not have a significant influence on the design capacity, however, stiffnesses and frequency response should be checked;
- Suction caissons -The axial capacity of suction caissons is usually the design driver for jacket structures. Scour could result in a significant reduction in design capacity;
- Gravity Base Structures - GBS structures rely on full base contact. Scour could result in uneven settlement and/or foundation ‘rocking’. Therefore, any scour risk is likely to be unacceptable.

The sensitivity of the structure type to scour should be carefully considered. It should also be noted that the overall foundation ‘stiffness’ can change with time; i.e., thixotropy effects increasing stiffness of piles / caissons. Cyclic loading potentially ‘softening’ stiffness after a significant storm.

Sensitivity checks could be undertaken to determine allowable stiffnesses and associated scour depths in conjunction with other considerations such as thixotropy. This could be used to develop an understanding of ‘acceptable’ scour depth and timescales as well as understanding timescales for remediation, for instance:

- 2.5m scour during 5-year storm – acceptable;
- 4.5m scour due to 50-year storm – soft response increases fatigue – must be remediated within 3 months.

9 SCOUR MITIGATION OPTIONS

9.1 Scour allowance design and observation

The main suggestion of the proposed framework is to understand storm risk and incorporate a suitable scour allowance into the scour protection design. This option would require regular monitoring of the scour evolution and resultant effects on the foundation dynamic response.

Highly specified monitoring of the offshore environment is recommended as the usual means of de-risking the engineering work into the future and for

providing the project development team with a suitable level of reassurance that an accurate understanding of marine conditions as they relate to recent scour issues is available (as far as it can be in practice).

Implementation of some form of monitoring is considered to be crucial to de-risking the issues related to scour and to improving asset integrity over the timeframes of an offshore windfarm (typically 25-30 years).

9.2 Full scour protection (Rock Berm)

Rock berms are one of the most common scour protection solutions. The thickness and lateral extent of the rock berm, and resultant required rock volume, will depend on multiple factors including the berm design approach, water depth, metocean input, ground conditions, and stone gradings, amongst others.

The rock berms are generally designed to be stable under 50-year design conditions. Additionally, the rock berms are usually surveyed regularly to ensure they remain stable. Measurement errors and tolerances must also be considered. Monitoring and inspection are generally undertaken every six months for the first 2 years, covering the seabed level, local scour at the unprotected areas around the foundations, and the condition of the scour protection at each location, using appropriate methods.

The cost of rock berms and post construction survey is usually significant. However, rock berms are considered highly effective as long as they are properly designed to account for design metocean events, winnowing, and edge scour.

9.3 Alternatives (anti-scour frond mattresses)

The market offers other alternative and proven solutions for preventing scour that could potentially be economically advantageous. An example of this is the anti-scour frond mattress constructed of aerated polyethylene fronds that when installed on the seabed will naturally float to resemble natural seaweed. As the sediments are transported through the frond mattresses with the current, the soils amass onto the mattress forming a natural fibre reinforced sand bank protecting the area of interest.

Installation methods for this type of solution may include; weight ballast bags attached around the perimeter mattresses, the use of frond mattresses pre-fitted to a concrete mattress offering instant scour protection and easier installation in a high subsea current environment, or the use of divers with anchors driven into the seabed.

The cost of fronded mats is lower than rock berms; however, they may be less effective, resulting in higher residual risk.

10 CONCLUSIONS

The paper provides a framework to understand and make an informed decision on the optimal risk mitigate strategy for scour.

REFERENCES

DNVGL-ST-0126. Support structures for wind turbines. 2021.

KC Denmark, 2023, (https://www.kc-denmark.dk/products/other-products/sea-flume.aspx).

Lin C., Han J., Bennett C. & Parsons R.L., "Analysis of laterally loaded piles in soft clay considering scour-hole dimensions". Ocean Eng 2016; 111:461–70. DOI:10.1016/j.oceaneng.2015.11.029.

Lin Y. & Lin C., "Effects of scour-hole dimensions on lateral behaviour of piles in sands". Comput Geotech 2019; 111:30–41. DOI:10.1016/j.compgeo.2019.02.028.

McEwan I. & Heald J., "Discrete Particle Modelling of Entrainment from Flat Uniformly Sized Sediment Beds", Journal of Hydraulic Engineering, ASCE, 127 (7), pp. 588-597, July 2001. DOI:10.1061/(ASCE)0733-9429(2001)127:7(588).

Sato, S., "Coastal Sediment", Summer Seminar on Hydraulic Engineering, Japan Soc. Civil Engineers, pp. 19.1-19.29. 1966.

Schaaff E., Grenz C., Pinazo C. & Lansard B., "Field and laboratory measurements of sediment erodibility: A comparison". Journal of Sea Research 55(1):30-42, January 2006. DOI:10.1016/j.seares.2005.09.004

Shields, A., "Application of Similarity Principles and Turbulence Research to Bed-Load Movement. California Institute of Technology", Mitt. Preuss. Versuchsanst. Wasser. Schiffsbau, 26, pp. 1-26. 1936. (in German).

Sumer, B.M. & Fredsøe J., "The mechanics of scour in the marine environment", Advanced series on ocean engineering: River Edge, N.J, 2002. DOI:10.1142/4942.

Proceedings of the XVIII ECSMGE 2024
GEOTECHNICAL ENGINEERING CHALLENGES
TO MEET CURRENT AND EMERGING NEEDS OF SOCIETY
© 2024 the Authors
ISBN 978-1-032-54816-6
DOI 10.1201/9781003431749-450
Open Access: www.taylorfrancis.com, CC BY-NC-ND 4.0 license

ECSMGE 24
XVIII EUROPEAN CONFERENCE ON SOIL MECHANICS AND GEOTECHNICAL ENGINEERING

Field tests on vertical and horizontal resistance of steel sheet piles installed by the Press-in with Auger

Essais sur le terrain de résistance verticale et horizontale des palplanches en acier installées par Enfonçage avec Tarière

Y. Ishihara*, K. Okada, M. Eguchi, A. Mori, T. Miyanohara
GIKEN LTD., Kochi, Japan

**ishihara@giken.com*

ABSTRACT: The steel sheet piles, which have long been used for temporary retaining structures, are recently being applied to non-temporary structures such as coastal levees, railway bridge foundations and others. However, the number of load tests on the sheet piles conducted so far is limited, and their design methods seem to have room for sophistication. In addition, the installation methods have some influence on their performance. This paper focuses on the installation method of the "Press-in with Auger" (PA) which can be applied to hard ground conditions with SPT *N* being greater than 50. In PA, a sheet pile is penetrated into the ground together with an auger device, and then the auger device alone is extracted while the soil is refilled. In this research, the full-scale installation tests and the static load tests were conducted at two filed testing sites having different ground conditions, to investigate the vertical and horizontal resistance of PA sheet piles. The results showed that the vertical and horizontal capacity were dependent on the refilling condition. Tin addition, the axial jacking force in the termination was suggested to correlate with the vertical and horizontal capacity, reflecting the inhomogeneity of the ground.

RÉSUMÉ: Les palplanches en acier, qui ont longtemps été utilisées pour des structures de retenue temporaires, sont récemment appliquées à des structures non temporaires telles que les digues côtières, les fondations de ponts ferroviaires et autres. Cependant, le nombre d'essais de charge sur les palplanches effectués jusqu'à présent est limité, et leurs méthodes de conception semblent pouvoir être perfectionnées. En outre, les méthodes d'installation ont une certaine influence sur leurs performances. Cet article se concentre sur la méthode d'installation de "l'enfoncement à la tarière" (PA) qui peut être appliquée à des sols durs dont le SPT N est supérieur à 50. Dans la méthode PA, une palplanche est enfoncée dans le sol en même temps qu'une tarière, puis la tarière seule est extraite tandis que le sol est rechargé. Dans le cadre de cette étude, des essais d'installation en grandeur réelle et des essais de charge statique ont été menés sur deux sites d'essai déposés présentant des conditions de sol différentes, afin d'étudier la résistance verticale et horizontale des palplanches PA. Les résultats ont montré que la capacité verticale et horizontale dépendait des conditions de remplissage. En outre, il a été suggéré que la force de poussée axiale dans la terminaison était en corrélation avec la capacité verticale et horizontale, reflétant l'inhomogénéité du sol.

Keywords: Static vertical load test; static horizontal load test; steel sheet pile; Press-in with Auger.

1 INTRODUCTION

The steel sheet piles have long been used for the construction of temporary retaining structures. In recent years, they are increasingly applied to non-temporary structures such as coastal levees (Ishihara et al., 2020), railway bridge foundations (Kasahara et al., 2018), architectural buildings (GIKEN, 2016; Kondo et al., 2023) and so on. For the reliable use of the sheet piles for the non-temporary structures, the performance of the sheet piles has to be adequately considered in design.

The performance of the sheet pile is influenced by its installation method. The press-in method (IPA, 2016) is a static pile installation method and has been preferred in the construction in dense cities or with difficult conditions. One of the four branch installation techniques in the press-in method is the "Press-in with Auger" (PA), which is applicable to hard grounds with the SPT *N* values being greater than 50. In PA, the auger device (Figure 1) is attached to the sheet pile in its narrow side. The sheet pile and the auger device are penetrated into the ground together while the soil around the auger head is temporarily lifted up to the ground surface. After the termination of the penetration, the auger device alone is extracted while the lifted soil or other material is refilled.

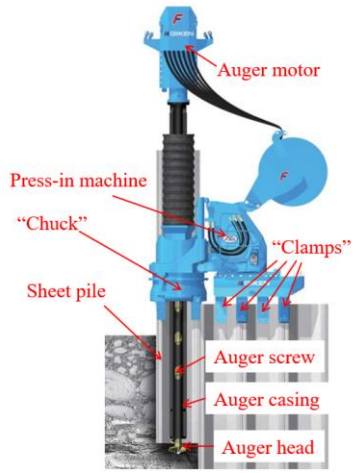

Figure 1. Example of auger device used in PA.

The installation process of PA, especially the conditions of termination and refilling, will be influential to the performance of the sheet pile. However, there has been no load test databases on the PA piles so far. This paper investigates into the vertical and horizontal resistance of the PA sheet piles, by conducting field tests. In addition, the test results will be compared with the design calculation results.

2 METHODS OF FIELD TESTS

Two sets of field tests, J2001 test series in a soft cohesive ground (Figure 2a) and J2101 test series in a dense non-cohesive ground (Figure 2b), were conducted. The test used sheet piles with the width of 600 mm (SP-IIIw). The test layout is shown in Figure 3. The test conditions and the press-in conditions are summarized in Tables 1 & 2, where v_d, v_u and v_r are the downward, upward and peripheral velocity of the sheet pile or the auger head, Q'_{UL} and T'_{UL} are the upper limits for the axial jacking force and rotational torque, and f_a is the flowrate of the air injected in the auger head.

2.1 J2001 test series

The test procedures were as follows. (1) The reaction sheet piles were installed by PA. (2) The installation test was conducted, where the test pile was installed by SP or PA down to the depth of 6.45 m. (3) The vertical static load test was conducted on each test pile. (4) The horizontal static load test was conducted on each test pile that previously experienced the vertical load test.

In the installation test, the press-in machine (F201) grasped the reaction sheet piles at its Clamps and installed the test pile. The interlocks of the test pile and the reaction sheet pile were not connected with each other. The jacking force (Q') and the penetration depth

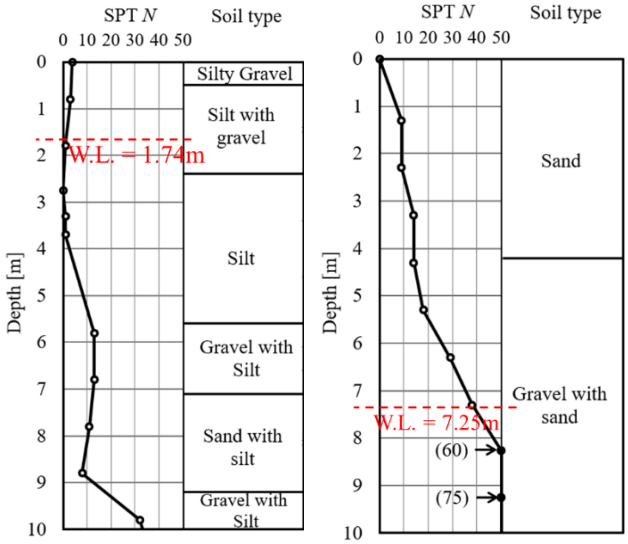

(a) J2001 test series *(b) J2101 test series*

Figure 2. Site profiles.

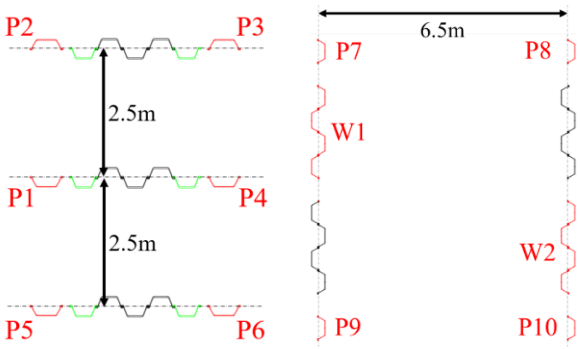

(a) J2001 test series *(b) J2101 test series*

Figure 3. Test layout (black: reaction piles, green: dummy piles without embedment).

were obtained by the measurement system equipped in the press-in machine. The sheet pile was installed monotonically or with the displacement-controlled "surging" (repeated penetration and extraction) when the jacking force (Q') or torque (T') was smaller than Q'_{UL} or T'_{UL}, and was installed with the load-controlled surging when Q' or T' exceeded Q'_{UL} or T'_{UL}.

In the termination condition [A] for the SP sheet pile, the sheet pile was installed by l_T with the upper-limit (Q'_{UL}) being removed, at the velocity of smaller than 10 mm/s. In the termination condition [B] (in Figure 4) for the PA sheet piles using the normal auger head, (1) when the penetration depth of the auger became $z_T - l_T$ (where z_T is the final penetration depth), the auger device was extracted to above the sheet pile base, (2) the sheet pile and the auger device were installed together while the auger was rotated, until the penetration depth of the sheet pile became $z_T - l_T$, (3) the sheet pile and the auger device were installed together to z_T without the auger being rotated. In the termination condition [C], (1) when the penetration

depth of the auger became $z_T - l_T$, the auger device was extracted so that the penetration depth of the auger became shallower than that of the sheet pile, (2) the sheet pile and the auger device were installed together to z_T, without the auger being rotated.

It should be noted that the actual termination condition in P6 was irregular. A greater value of l_T was adopted, expecting a greater pile capacity. In the procedure (3), when the penetration depth of the sheet pile became z_T – 0.07 m, the further installation became difficult because Q' reached Q'_{UL}. To cope with this, the auger device was extracted by 0.07 m before completing the procedure.

Table 1. Test conditions. (a) J2001 test series

Test No.	Installation technique	Type of auger head	Termination condition	Refilling condition
J2001-P1	PA	540 mm (expandable)	C	C
J2001-P2	PA	400 mm	B	C
J2001-P3	PA	400 mm	B	A
J2001-P4	SP*	–	A	–
J2001-P5	PA	400 mm	B	B
J2001-P6	PA	400 mm	B	A

*SP: Standard Press-in (press-in without installation assistance)

(b) J2101 test series

Test No.	Refilling condition	Loading direction
J2101-W1	C	–
J2101-W2	A	–
J2101-P7	C	Towards narrow side
J2101-P8	C	Towards wide side
J2101-P9	A	Towards narrow side
J2101-P10	A	Towards wide side

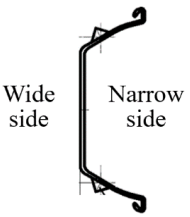

Common conditions: installation technique (PA), type of auger head (400mm), termination condition (B).

Table 2. Press-in conditions. (a) J2001 test series

Test No.	Penetration						Termination			Refilling				
	v_d	v_u	v_r	Q'_{UL}	T'_{UL}	f_a	l_T	l_{pa1}	l_{pa2}	z_{a1}	z_{s1}	l_{a1}	l_{a2}	Q'_{a1}
		mm/s		kN	kNm	m³/min.		mm		m		mm		kN
J2001-P1	25	38	961	200	20	1.2	50	380	120	2.0	-	-	-	-
J2001-P2	25	19	712	200	20	1.1	50	240	260	2.0	-	-	-	-
J2001-P3	25	38	461	200	20	1.2	50	240	260	2.5	0.4	50	50	-
J2001-P4	200	166	-	300	-	-	50	-	-	-	-	-	-	-
J2001-P5	25	38	461	200	20	1.2	50	240	260	4.5	-	-	-	300
J2001-P6	25	38	461	200	20	1.8	400	240	260	4.5	0.5	50	50	-

(b) J2101 test series

Test No.	Penetration						Termination			Refilling				
	v_d	v_u	v_r	Q'_{UL}	T'_{UL}	f_a	l_T	l_{pa1}	l_{pa2}	z_{a1}	z_{s1}	l_{a1}	l_{a2}	Q'_{a1}
		mm/s		kN	kNm	m³/min.		mm		m		mm		kN
J2101-W1	25	38	712	300	350	0	50	250	250	2.0	-	-	-	-
J2101-W2	25	38	712	300	350	0	50	250	250	2.2 1.6 2.5 2.6	0.5 0.5 0.4 0.4	50	50	-
J2101-P7	25	38	712	300	350	0	50	250	250	2.0	-	-	-	-
J2101-P8	25	38	712	300	350	0	50	250	250	2.0	-	-	-	-
J2101-P9	25	38	712	300	350	0	50	250	250	2.0	0.5	50	50	-
J2101-P10	25	38	712	300	350	0	50	250	250	2.5	0.4	50	50	-

In the refilling condition [A] (in Figure 5), (1) the temporarily lifted soil was returned by the reverse rotation and compacted by the repeated extraction (500 mm) and penetration (250 mm), until the penetration depth of the auger became z_{a1}, (2) the auger device was extracted completely, and newly prepared sands (mean diameter D_{50} = 1.37 mm, uniformity coefficient U_c = 1.78, fine fraction content F_c = 0.4 %) were filled into

the void up to the depth of z_{s1}, (3) the filled sands were compacted by the penetration of the auger by l_{a1}, (4) additional sands were filled into the void up to the ground surface, (5) the filled sands were again compacted by the penetration of the auger by l_{a2}, (6) additional sands were filled into the void up to the ground

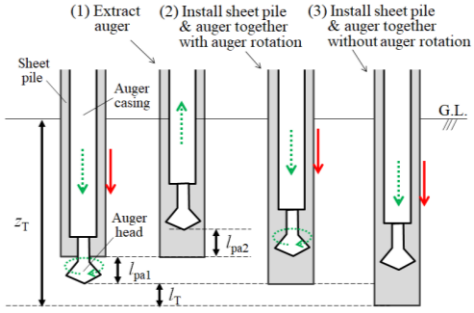

Figure 4. Termination condition (B).

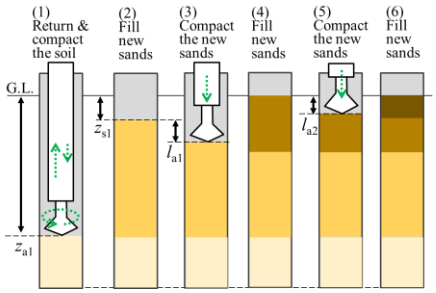

Figure 5. Refilling condition (A).

surface. In the refilling condition [B], the procedures of (4) and (5) in [A] were omitted, and the compaction in the procedure (3) in [A] was conducted in a load-controlled manner until Q' reached Q'_{a1}. In the refilling condition [C], (1) the temporarily lifted soil was returned by the reverse rotation, until the penetration depth of the auger head became z_{a1}, (2) the auger device was extracted completely, and the remaining of the temporarily lifted soil was returned manually into the void.

The static vertical load test was conducted, basically based on the JGS Standard (JGS 1811-2002) (JGS, 2002). The elapsed time from the end of installation to the start of the vertical load test (t_{VLT}) was 14 days or longer. The press-in machine (F201) was used for securing the reaction force from the reaction sheet piles. The head load (Q) was applied by a hydraulic jack which was sandwiched between the steel plate placed on the pile head and the steel jig grasped by the Chuck of the press-in machine, as shown in Figure 6, and was measured by a load cell placed on the pile head. The pile head displacement was obtained by displacement transducers. The loading condition was one-cycle continuous loading.

The static horizontal load test was conducted, basically based on the JGS Standard (JGS 1831-2010) (JGS, 2010). The elapsed time from the end of installation to the start of the horizontal load test (t_{HLT}) was 16 days or longer. The horizontal load (P) was applied to two test piles at the same time, by connecting the two test piles by a steel chain and shortening the steel chain gradually, and was measured by a load cell. The loading height was 0.2 m above the ground surface. The loading direction was towards the narrow side of the sheet pile. The horizontal displacement was measured by displacement transducers. The loading condition was one-cycle continuous loading.

2.2 J2101 test series

The test procedures were as follows. (1) Reaction sheet piles were installed by PA. (2) The installation test was conducted, to form the single PA sheet pile or the PA sheet pile wall down to the depth of 6.5 m. (3) The horizontal static load test was conducted.

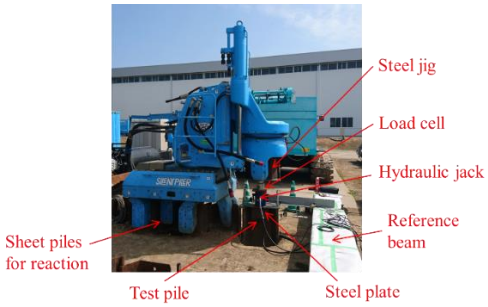

Figure 6. Situation of static vertical load test in J2001.

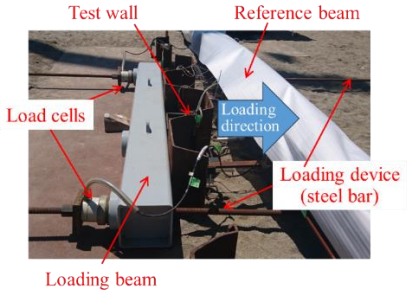

Figure 7. Situation of static horizontal load test in J2101 test series.

The installation test was conducted in the same way as in J2001 test series. The termination condition was [B], and the refiling condition was either [A] or [C].

The static horizontal load test was conducted, basically based on the JGS Standard (JGS 1831-2010). t_{HLT} was 16 days or longer. As shown in Figure 7, a beam was placed behind each sheet pile or sheet pile wall, and a pair of the beams were connected with steel bars. The horizontal load (P) was applied by shortening the steel bars using a hydraulic jack. The

loading height was 0.2 m above the ground surface. Load cells were used to measure *P*. The horizontal displacement was measured by displacement transducers. The loading condition was one-cycle continuous loading.

3 RESULTS AND DISCUSSIONS

3.1 Vertical capacity in soft cohesive ground

Figure 8 shows the load displacement curves obtained in the static vertical load tests in J2001 test series, as well as the lines representing the results of design calculation based on JARA (1999). The resistance was higher in the tests with complex refilling condition (P3, P6) than in the tests with simple refilling condition (P1, P2). The resistance of PA sheet piles in the weakest cases (P1, P2) were about half of that of the SP sheet pile (P4). This ratio is consistent with the description in JARA (1999).

The greater value in P3 than in P4 and the smaller value in P5 than in P1 or P2 are believed to be due to the ground condition. The site is sandwiched with a hill in the side of P3 and a river in the side of P5, and the soil layers may be tilting towards the direction from P3 to P5. The soil layer beneath the sheet pile base may have been harder in P3 and weaker in P5.

If the vertical capacity is defined as the head load recorded at the pile head displacement of 0.1 $D_{o,eff}$, where $D_{o,eff}$ represents the outer diameter of the equivalent tubular pile having the same sectional area as the sheet pile (= 36 mm for SP-IIIw), the measured vertical capacity of the single PA sheet pile was comparable with or greater than that estimated based on JARA (1999).

3.2 Horizontal capacity

Figure 9 shows the results of the load tests and the design calculation in J2001 test series (in the soft cohesive ground). The horizontal resistance was found to vary in accordance with the complexity of the refilling condition, being the greatest in P3 and P6 and the smallest in P1 and P2. It was also influenced by the type of the auger head (expandable or normal). It ranged from 40 % to 85 % of that of the SP sheet pile.

Figure 10 shows the results of the load tests and the design calculation in J2101 test series (in the dense non-cohesive ground). As for the single PA sheet pile, the horizontal resistance was 1.5 times or 2 times larger in the tests with complex refilling condition (P9, P10), and was larger in the tests with the loading direction being towards the wide side of the sheet pile (P7, P9). The effect of the loading direction was smaller in the tests with complex refilling condition.

As for the PA sheet pile wall in J2101 test series, the horizontal resistance was 1.25 times larger in the test with complex refilling condition. The smaller effect of the refilling condition in the sheet pile wall than in the single sheet pile is thought to be partly because the refilled sands in the installation of one sheet pile was disturbed in the PA installation of the next sheet pile.

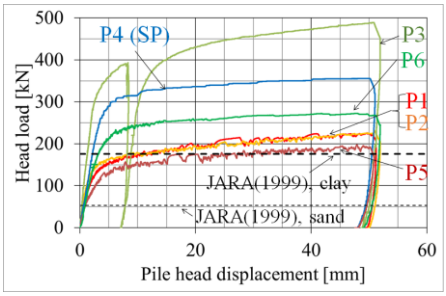

Figure 8. Results of vertical load tests in J2001.

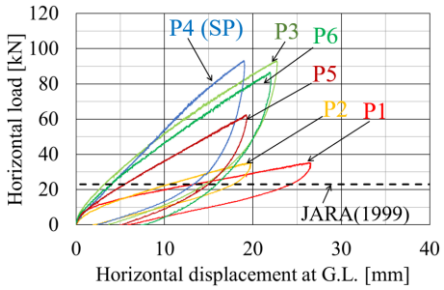

Figure 9. Results of horizontal load tests in J2001.

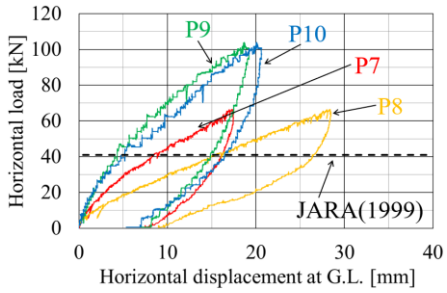

(a) Single PA sheet pile

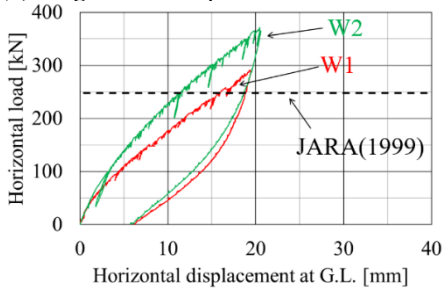

(b) PA sheet pile wall

Figure 10. Results of horizontal load tests in J2101.

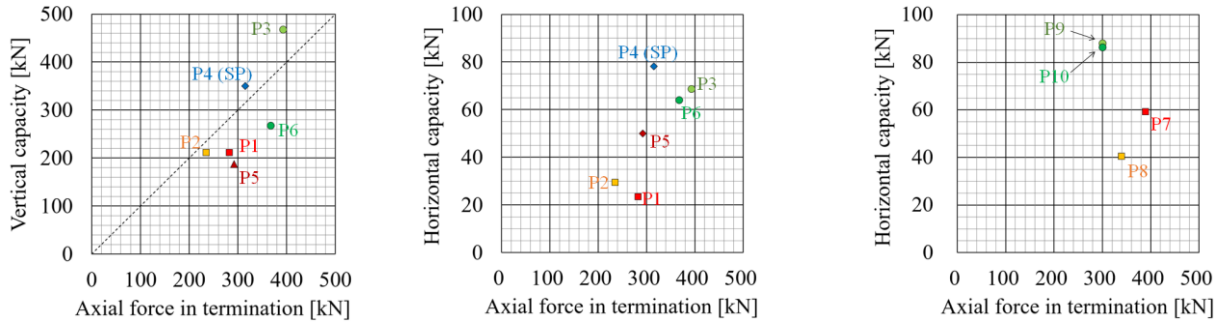

(a) Vertical capacity in J2001 *(b) Horizontal capacity in J2001* *(c) Horizontal capacity in J2101*

Figure 11. Effect of maximum axial jacking force in termination on pile capacity.

In JARA (2012), the allowable horizontal displacement for the foundation of a highway bridge is taken as 15 mm at the ground surface. If the horizontal capacity is taken as the horizontal load recorded at this displacement, it was comparable with or greater than the design calculation results based on JARA (1999).

3.3 Effect of axial jacking force in termination

Figure 11 shows the correlation between the maximum axial jacking force recorded in the termination (Q_T) and the vertical or horizontal capacity. In J2001, both the vertical and horizontal capacity showed a positive correlation with Q_T. On the other hand, the correlation between the horizontal capacity and Q_T was very weak.

From these facts, the following are hypothesized. If the ground is homogeneous, the horizontal capacity is little influenced by Q_T and depends more on the refilling condition. If the ground is not homogeneous, the vertical and the horizontal capacity depend both on Q_T and the refilling condition.

4 CONCLUSIONS

By conducting the field tests and the design calculation based on JARA (1999) on the sheet piles installed by the Press-in with Auger (PA), the following findings were obtained. (1) The vertical and horizontal capacity of the single PA sheet pile in the soft cohesive ground were dependent on the refilling condition, and were comparable with or greater than the design calculation results. (2) The horizontal resistance of the single PA sheet pile in the non-cohesive ground was influenced by the refilling condition and the loading direction, and was comparable with or greater than the design calculation results. The effect of loading direction was smaller for the sheet piles with more complex refilling condition. (3) The horizontal resistance of the PA sheet pile wall in the non-cohesive ground was influenced by the refilling condition, and was comparable with or greater than the design calculation results. The effect of refilling condition was smaller on the sheet pile walls than on the single sheet piles, presumably because the refilled sands were disturbed in the installation of the next sheet pile. (4) The axial force in termination was influential on the vertical and the horizontal capacity in the soft cohesive ground. This was thought to be reflecting the ground inhomogeneity.

REFERENCES

GIKEN. (2016). Load Bearing Steel Intensive Basement - Press-in Method and Thorough Inspection Technique, Case Study, 28p.

International Press-in Association (IPA). (2016). *Press-in Retaining Structures: a Handbook*, First edition 2016, 520p.

Ishihara, Y., Yasuoka, H. and Shintaku, S. (2020). Application of Press-in Method to coastal levees in Kochi Coast as countermeasures against liquefaction. *Geotechnical Engineering Journal of the SEAGS & AGSSEA*, 10p.

The Japanese Geotechnical Society (JGS). (2002). Method for static axial compressive load test of single piles. *Standards of Japanese Geotechnical Society for Vertical Load Tests of Piles*, pp. 49-53.

The Japanese Geotechnical Society (JGS). (2010). *Method for Lateral Load Test of Piles*, 63p.

Japan Road Association (JARA). (1999). *Road Earthwork – Temporary Structure Engineering Guidelines*, 378p.

Japan Road Association (JARA). (2012). *Specifications for Highway Bridges, Part 4 Substructures*, p. 270.

Kasahara, K., Sanagawa, T., Nishioka, H., Sasaoka, R. and Nakata, Y. (2018). Seismic reinforcement for foundation utilizing sheet piles and soil improvement. *Proceedings of the First International Conference on Press-in Engineering 2018, Kochi*, pp. 555-562.

Kondo, Y., Sato, K., Nishimori, Y., Nakagawa, D. (2023). Giken Research Building: challenge for structure using sheet piles (part 2). *Steel Technology*, pp. 34-43. (in Japanese).

Proceedings of the XVIII ECSMGE 2024
GEOTECHNICAL ENGINEERING CHALLENGES
TO MEET CURRENT AND EMERGING NEEDS OF SOCIETY
© 2024 the Authors
ISBN 978-1-032-54816-6
DOI 10.1201/9781003431749-451
Open Access: www.taylorfrancis.com, CC BY-NC-ND 4.0 license

ECSMGE 24
XVIII EUROPEAN CONFERENCE ON SOIL MECHANICS AND GEOTECHNICAL ENGINEERING

Case history of installation and static vertical load testing on piles executed by the rotary cutting press-in in Amsterdam

Étude de cas d'installation et d'essai de chargement verticale statique sur des pieux installés par enfonçage à coupe rotative à Amsterdam

Y. Ishihara*, K. Okada, Y. Toda, Y. Kitano
GIKEN LTD., Kochi, Japan

**ishihara@giken.com*

ABSTRACT: The press-in method is a piling method using a hydraulic jacking force to install a prefabricated pile. Its applicability in hard ground has been enhanced by the relatively recent development of its branch techniques such as the press-in with auger and the rotary cutting press-in (RCP). In RCP, a tubular pile equipped with several cutting teeth on its base is pushed and rotated, so that even concrete or rock can be penetrated through by the pile. The RCP piles are usually used for retaining walls, but are also used for structures where their axial stiffness and capacity are of concern. In this paper, three sets of subsurface information (CPT cone resistance), the piling data of the RCP and the static vertical load test results on the RCP piles with an outer diameter of 508 mm are reported, which were obtained in preparation for the project of updating the quay walls in the World Heritage-listed Canal Ring Area of Amsterdam. In addition, the cone resistance and the vertical capacity are estimated from the piling data obtained during the RCP, and are compared with the results of the CPT and of the load tests.

RÉSUMÉ: La méthode d'enfoncement est une méthode de battage utilisant une force de vérinage hydraulique pour installer un pieu préfabriqué. Son applicabilité aux sols durs a été améliorée par le développement relativement récent de ses techniques dérivées, telles que l'enfoncement à l'aide d'une vis sans fin et l'enfoncement par découpe rotative (RCP). Dans le RCP, un pieu tubulaire équipé de plusieurs dents de coupe à sa base est poussé et tourné, de sorte que même les bétons ou les rochers peuvent être pénétrés par le pieu. Les pieux RCP sont généralement utilisés pour les murs de soutènement, mais également pour les structures dont la rigidité et la capacité axiale sont importantes. Dans cet article, trois ensembles d'informations sur la subsurface (résistance du cône CPT), les données sur les pieux en RCP et les résultats des essais de charge verticale statique sur les pieux RCP avec un diamètre extérieur de 508 mm sont rapportés, qui ont été obtenus en préparation du projet de mise à jour des murs de quai dans la zone de la ceinture du canal d'Amsterdam classée au patrimoine mondial. En outre, la résistance du cône et la capacité verticale sont estimées à partir des données sur les pieux obtenues en RCP, et sont comparées aux résultats du CPT et des essais de charge.

Keywords: Steel tubular pile; rotary cutting press-in; static vertical load test; piling data.

1 INTRODUCTION

The press-in method is one of the static piling methods to install a prefabricated pile using a hydraulic jacking force (IPA, 2016; Bolton et al., 2021). Based on its principle to achieve a reaction force from previously installed piles, it saves temporary works and is applicable to the piling projects with severe restrictions of space and headroom. It has also been applicable to hard ground conditions since the development of its branch installation techniques such as the press-in with auger and the rotary cutting press-in (RCP). In RCP, a tubular pile equipped with several cutting teeth on its base is pushed and rotated, so that the hard ground or materials including concretes or rocks can be penetrated though. The RCP piles are usually used for cantilever type retaining walls, but are also used for structures where their axial stiffness and capacity are of concern. However, since RCP is a relatively new installation technique, its design methods have not been well established. To improve the situation, accumulation of piling data and of vertical load test results in different soil conditions are essential.

On the other hand, in the press-in method, piling data such as the jacking force, torque and penetration depth are obtained for every single pile. Methods to utilize the piling data for autonomous operation of the press-in machine, for the estimation of subsurface information (Ishihara & Kusakabe, 2021) and for the estimation of the pile capacity (Ishihara, 2023) have been developed. To put these methods into practice reliably, further validation is necessary.

Based on these backgrounds, this paper reports three sets of subsurface information (obtained by Cone Penetration Testing, CPT), the piling data of the RCP and the static vertical load test results on the RCP piles, which were obtained in preparation for the project of updating the quay walls in the World Heritage-listed Canal Ring Area of Amsterdam, as shown in Figure 1. In addition, the cone resistance and the vertical capacity are estimated from the piling data obtained during the RCP, and are compared with the results of the CPT and of the load tests.

2 PILE INSTALLATION AND STATIC LOAD TESTS

2.1 Test methods

The cone resistance (q_c) obtained by the CPT and the soil type estimated from the CPT results are shown in Figure 2, where the reference level was taken as the NAP (Normal Amsterdam Peil). The shallow layers consist of relatively soft clays and sands, while the deeper layers dominantly contain sands with q_c being around 20 MPa.

The test conditions and the test layout are shown in Table 1 and Figure 3, respectively. A total of three tests were conducted. In each test, three reaction piles were installed in advance to the installation of the test pile. The embedment length of the reaction piles was in between 1/2 and 1/3 of that of the test pile.



Figure 1. Project of updating the quay walls in the World Heritage-listed Canal Ring Area of Amsterdam.

The specification of the test pile is shown in Figure 4. It was a steel tubular pile with an outer diameter of 508 mm and a thickness of 22.2 mm. It was equipped with a base ring having 8 cutting teeth, and the outer diameter and the thickness of the base ring were 518 mm and 32 mm, respectively. It was also equipped with 2 small-diameter pipes to allow water injection in the pile base. It was instrumented with 2 optical fibers to measure the axial strains at 14 sections.

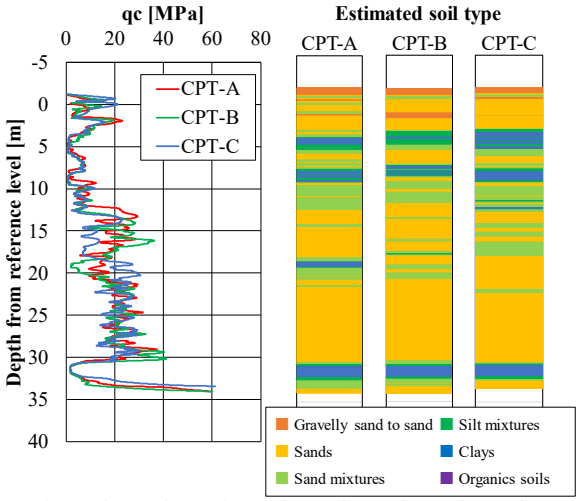

Figure 2. Site profile (CPT q_c and estimated soil type).

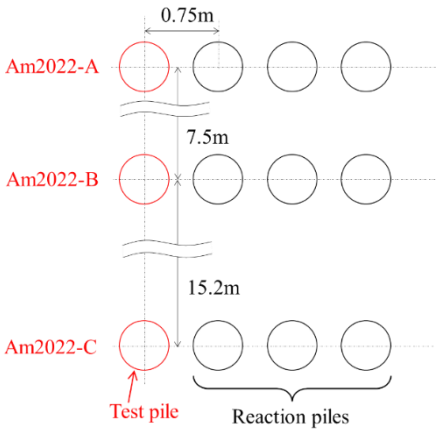

Figure 3. Test layout.

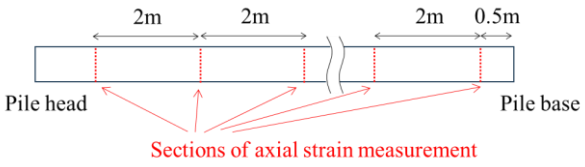

(a) Side view

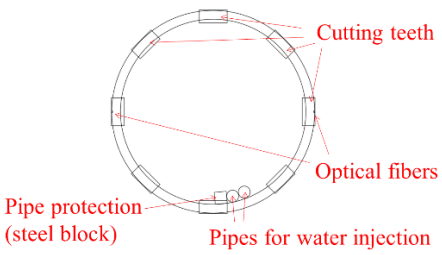

(b) Plan view

Figure 4. Structure of test piles.

Table. 1. Specification of piles and press-in conditions.

Test No. (Am2022-) CPT No.	A CPT-A	B CPT-B	C CPT-C
Outer diameter of pile [mm]	508	508	508
Thickness of pile [mm]	22.2	22.2	22.2
Outer diameter of base ring [mm]	518	518	518
Thickness of base ring [mm]	32	32	32
Number of cutting teeth	8	8	8
Embedment depth [m]	26.5	26.5	26.5
Flow rate of water [l/min.]	80	80	80
Downward displacement [mm]	250	250	250
Upward displacement [mm]	79	79	70
Downward velocity [mm/s]	22, 33	33	22, 33
Upward velocity [mm/s]	41	41	41
Rotational velocity [rpm]	15, 23	20, 23	15, 23
Upper limit of jacking force [kN]	200	200	200
Upper limit of torque [kNm]	130	130	130
Curing period [day]	72	70	67

The test procedures were as follows; (1) the reaction piles were installed by the vibro-hammering method, (2) the test pile was installed by the RCP and (3) the static load test was conducted on the test pile. The elapsed time from the end of installation to the start of load test (curing period, t_{LT}) was about 70 days.

The test pile was installed by the RCP using the press-in machine GRV0611e, as shown in Figure 5, while gaining the reaction force from the three reaction piles. The press-in conditions are summarized in Table 2. The installation was conducted using the semi-automatic operation system. The jacking force (Q'), torque (T') and the penetration depth were obtained by an automatic measurement system equipped in the press-in machine. In the end of installation, the inner soil column length (h_{sc}) was obtained by manually measuring the distance from the pile head to the surface of the inner soil column using a tape measure. When the penetration depth reached one D_o above the final depth, the flowrate of water injection in the pile base was minimized to around 10 *l*/min. At the end of installation, the test pile was axially loaded without rotation and water injection, with the jacking force (Q'_T) of 600 kN. Exceptionally in Am2022-A, after the axial loading, the test pile was installed by 50 mm, by the RCP with water injection by 40 mm and by the RCP without water injection by 10 mm.

The static axial load test was conducted based on the guideline of the Class A1 test in NPR 7201+A1. The reaction force was secured by using weights. The load and displacement at the pile head were measured by a load cell and displacement transducers. The readings of the optical fibers were offset to be zero just before the start of the load test. The residual load acting on the pile at the start of the load test, which will result from the installation of the pile, is unknown. As shown in Figure 6, the load was increased in a multi-cycle way, and was maintained for 30 minutes or longer in each cycle. If the displacement rate under the maintained load was higher than 0.1 mm per 20 minutes, the constant load stage was increased up to 4 hours.

2.2 Test results

Figure 7 shows the variation of Q', T' and h_{sc} with depth during installation. Both Q' and T' were small at shallow de pth and increased in deeper sandy layers, with Q' reaching its upper limit in several depth ranges. As a result, the pile was installed with load-controlled surging in these depth ranges. According to the plot of h_{sc} obtained in the end of installation in each test, the value of h_{sc} was about one-third of the penetration depth. This indicates that the installation process was "partially plugged" on average. In Am2022-C, T' became too large when the penetration depth was about one D_o above the pile base, and the pile was largely extracted (by around 3 m) and installed again.

Table 2. Press-in conditions in the end of installation.

	Am2022-A	Am2022-B	Am2022-C
Last 1 D_o	Water injection was minimized to 10 *l*/min.	Water injection was minimized to 10 *l*/min.	Water injection was minimized to 10 *l*/min.
Axial loading at the end of installation	Started at 50 mm above the planned final depth. Axial load of 600 kN was applied for 1 min. without water injection. Pile head displacement was zero. After this, pile was installed by RCP to the planned final depth by 40 mm with water injection and 10 mm without water injection.	Started at the planned final depth. Axial load of 600 kN was applied for 5 min. without water injection. The maximum and the residual pile head displacement were 5 mm and 2 mm respectively.	Started at the planned final depth. Axial load of 600 kN was applied for 5 min. without water injection. The maximum and the residual pile head displacement were 20 mm and 13 mm respectively.

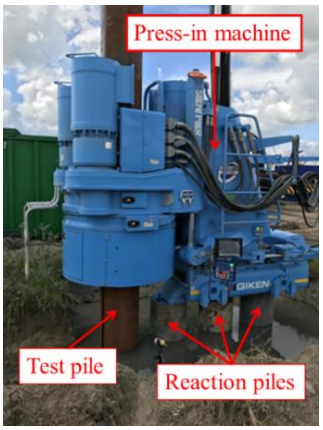

Figure 5. Installation of test pile.

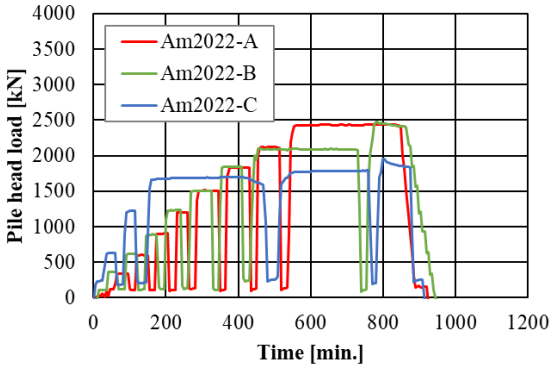

Figure 6. Loading record in static vertical load tests.

Figure 8 shows the variation of Q'_T with time, which was recorded during the axial loading at the end of installation. Q'_T was maintained at 600 kN intermittently with time, by setting Q'_{UL} to be 600 kN and applying a downward motion to the pile repeatedly. The duration of loading was shorter in Am2022-A. The pile head displacement recorded during this loading and unloading is summarized in Table 2.

The load-displacement curves obtained in the static load tests are shown in Figure 9. If the yielding load (Q_y) is taken as the "first-limit-resistance" in the JGS Standard (JGS 1811-2002), the Q_y values in the three tests are determined as shown in Table 3. The same table shows the ultimate capacity at the pile head, base and shaft (Q_f, Q_{bf} and Q_{sf}) as well, which were defined as the values recorded when the pile head displacement reached 0.1 D_o. The values of Q_y and Q_f were similar in each test. This trend was different from the four load test results conducted in Japan (JSCE, 2021) where Q_y / Q_f was around 0.45.

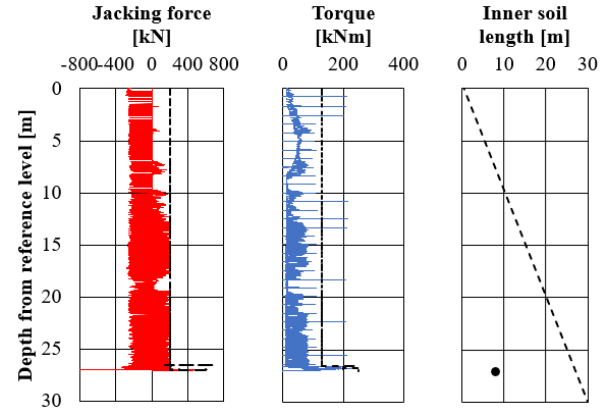

(a) Am2022-A

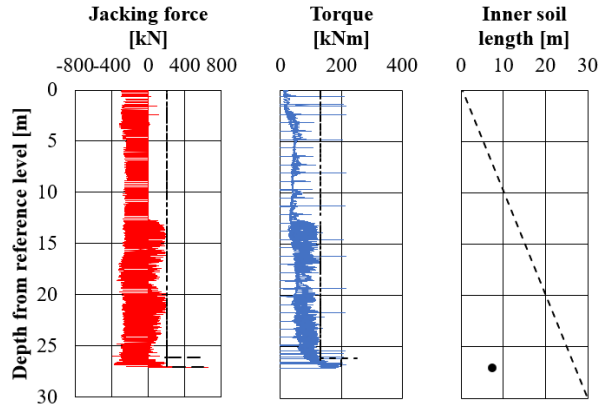

(b) Am2022-B

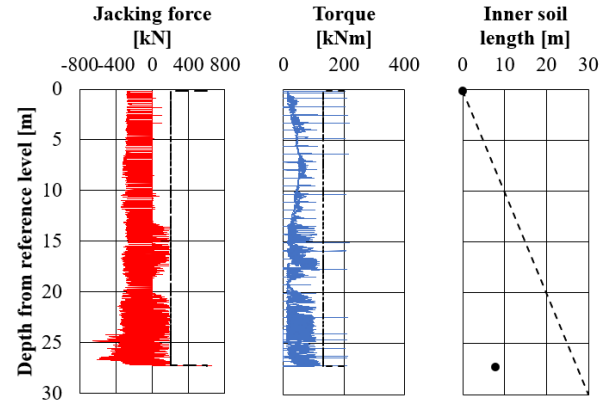

(c) Am2022-C

Figure 7. Piling data obtained in RCP installation.

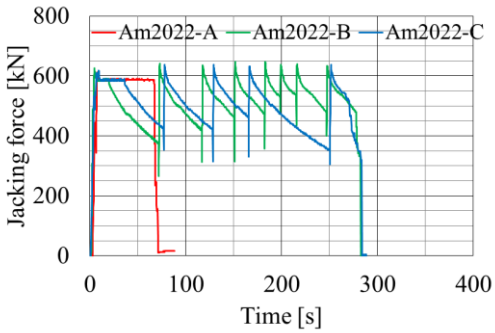

Figure 8. Record of axial loading at the end of installation.

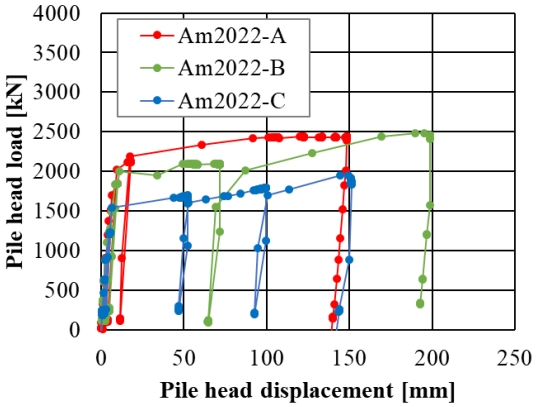

Figure 9. Load-displacement curves obtained in static vertical load test.

Table 3. Results of static vertical load tests (unit: kN).

Test No.	Am2022 -A	Am2022 -B	Am2022 -C
Total resistance at yield	2155	2033	1538
Total capacity	2214	2080	1592
Base capacity	662	508	427
Shaft capacity	1552	1572	1165

3 VERIFICATION OF CONE RESISTANCE AND VERTICAL CAPACITY ESTIMATED FROM PILING DATA

3.1 Methods of estimation

The estimation methods were basically based on those proposed by Ishihara (2023). They are composed of the following four steps.

The first step is to decompose the head load (Q) and the head torque (T) during the installation into the base and shaft components (Q_b, Q_s, T_b and T_s). To avoid the instrumentation on the pile, four equations are introduced: the base stress (q_b) is used to link Q_b and T_b, and the frictional stress on the pile shaft is assumed to be shared by Q_s and T_s in proportion to the ratio of vertical to rotational velocity.

The second step is to use the estimated Q_b and T_b for calculating the Specific Energy (SE, the energy required for installing something into the ground by a unit volume) consumed in the pile base. The effect of surging (repetitive downward and upward motion of the pile) is incorporated by taking into account the energy consumed in all the downward motions.

The third step is to convert the calculated SE into the subsurface information (CPT q_t or SPT N). For this, the SE in the RCP, in the CPT and in the SPT are assumed to linearly correlate with each other. More precisely, the knowledge that the SE in rock drilling and the unconfined compressive strength of the rock are linearly correlated (Hughes, 1972; Li & Itakura, 2012) is assumed to apply to the penetration of any material into the ground. In other words, the SE in the RCP, in the CPT and in the SPT are assumed to linearly correlate with the strength of the ground.

The fourth step is to input the estimated subsurface information into the bearing capacity formulae. The formula for the base capacity is derived from the CPT-based UWA-05 method. A parameter representing the plugging condition (IFR) is calculated by considering the estimated base stress during the installation. On the other hand, the formula for the shaft capacity is based on the SPT-based method, with the parameter being adjusted using the load test databases on RCP piles in Japan.

The above methods were applied to the piling data obtained in the installation tests. As for Am2022-C, the data recorded in the depth range where the large extraction was conducted (from 24 m to 27 m) was only partially used: the data prior to the extraction was omitted.

3.2 Comparison between the test results and estimated results

Figure 10 shows the comparison of the cone resistance obtained by the CPT and that estimated from the piling data. As a whole, the estimated values were comparable with or smaller than the measured values. The best agreement was found in Am2022-A. The underestimating tendency in Am2022-B might suggest that the ground around the position of this test was relatively soft. The underestimation in the depth range from 24 m to 27 m in Am2022-C was mainly due to the large extraction in this depth range. The time and resistance required for the installation after the large extraction were smaller than those required in the corresponding depth range in the other two tests.

Figure 11 shows the comparison of the total vertical capacity measured in the load tests and that estimated from the piling data. Generally, the estimated values were comparable with or greater than the measured values. This trend is different from the one using the datasets (piling data and load test data) obtained in Japan, where the estimated values were comparable with or smaller than the measured values (Ishihara, 2023).

To mitigate the extent of overestimation, the upper limit for the unit shaft resistance ($q_{sf,UL}$) was introduced. In Figure 11, the hollow and the solid dots correspond to the estimation with $q_{sf,UL}$ being 90 kPa and 50 kPa, respectively. If $q_{sf,UL}$ was taken as 90 kPa, which roughly corresponds to the values adopted in Ishihara (2023), the extent of overestimation was significant in two of the three tests (31% and 37%).

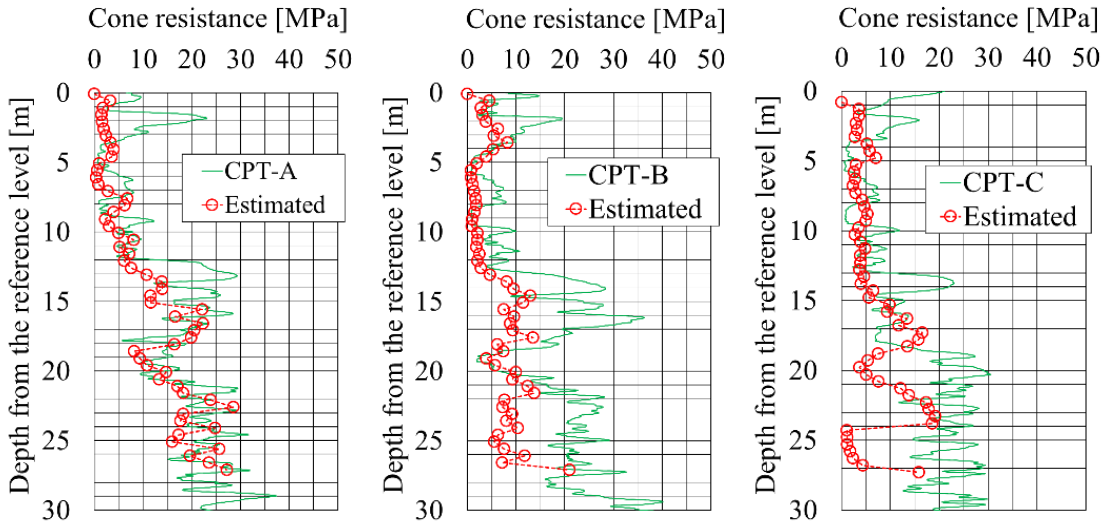

(a) Am2022-A *(b) Am2022-B* *(c) Am2022-C*

Figure 10. Comparison of cone resistance obtained by CPT and that estimated from piling data.

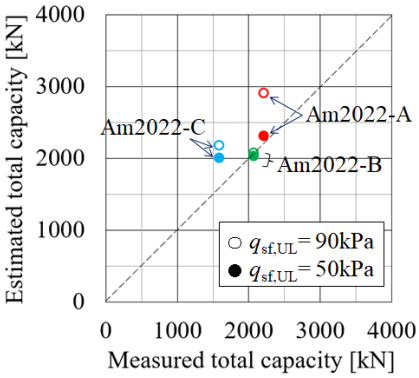

Figure 11. Comparison of pile capacity obtained by load test and that estimated from piling data.

If $q_{sf,UL}$ was reduced to 50 kPa, which corresponds to the recommended value in JSCE (2021), the overestimating trend was seen only in one test, by 25%.

4 CONCLUSIONS

Three sets of CPT cone resistance (q_c), the piling data and the static vertical load test results on the RCP piles, which were obtained in preparation for the actual project in Amsterdam, were reported. The obtained piling data were then processed to estimate the cone resistance and the pile capacity, and the estimation results were compared with the measured values. As a result, the estimated q_c was comparable with or smaller than the measured values, while the estimated capacity was comparable with or larger than the measured values. Further study is necessary to work out the causes for these inconsistent trends.

ACKNOWLEDGEMENTS

The authors appreciate the members of G-Kracht for the information of the three static load tests.

REFERENCES

Bolton, M. D., Kitamura, A., Kusakabe, O. and Terashi, M. (2021). *New Horizon in Piling: Development and Application of Press-in Piling*, CRC Press, 170p.

Hughes, H. M. (1972). Some aspects of rock machining. *International Journal of Rock Mechanics & Mining Sciences*, 9, 205-211. https://doi.org/10.1016/0148-9062(72)90023-X.

International Press-in Association (IPA). (2016). *Press-in Retaining Structures: a Handbook*, First edition 2016, 520p.

Ishihara, Y. and Kusakabe, O. (2021). State of the art report on the use of press-in piling data for estimating subsurface information. *Proceedings of the Second International Conference on Press-in Engineering 2021, Kochi*, pp. 42-66.

Ishihara, Y. (2023). *Use of Press-in Piling Data for Estimating Subsurface Information and Pile Performance*. Doctoral Thesis, University of Tokyo, 421p.

Japan Society for Civil Engineers (JSCE). (2021). *Technical Evaluation for the Design and Construction Method for Rotary Press-in Piling Method (Gyropress Method)*, Certificate No. 25.

Li, Z. and Itakura, K. (2012). An analytical drilling model of drag bits for evaluation of rock strength. *Soils and Foundations*, Vol. 52(2), pp. 206-227.

Proceedings of the XVIII ECSMGE 2024
GEOTECHNICAL ENGINEERING CHALLENGES
TO MEET CURRENT AND EMERGING NEEDS OF SOCIETY
© 2024 the Authors
ISBN 978-1-032-54816-6
DOI 10.1201/9781003431749-452
Open Access: www.taylorfrancis.com, CC BY-NC-ND 4.0 license

ECSMGE 24
XVIII EUROPEAN CONFERENCE ON SOIL MECHANICS AND GEOTECHNICAL ENGINEERING

Construction method and methodology for the optimization of panels overlap in cut-off walls in Santa Maria Dam, Sinaloa

Méthode de construction et méthologie pour l'optimisation du chevauchement des paaneaux dans les murs de refen du barrage de Santa Maria, Sinaloa

E. Jiménez Ontiveros*, F.J. Blanco Blanco, V.H. Olivera Luis
TECNOSUELO S.A. de C.V. Mexico City, Mexico

**eloy_ontiveros@yahoo.es*

ABSTRACT: The Santa Maria Dam on the Baluarte River is a concrete face rockfill dam with a total height of 152 m from the rock stratum, located 32 m depth. Cofferdams will be constructed upstream and downstream. At the foundation of the upstream cofferdam, a cut-off wall has been constructed. Alluvial soils with rocky blocks generate difficulties on the verticality control of the cut-off walls. A combination of construction methods and instrumentation of the excavation avoids deviations of the bentonite cement diaphragm wall. A pre-excavation and fill with fine sand prevent deviations and improves the production yields in the construction of the diaphragm wall. A methodology for the optimization of panel overlap is defined based on the instrumentation of the panel verticality, during excavation works. The adoption of a conservative overlap is usual if there isn't a detailed analysis of the site conditions. By the overlap optimization, it is improved the efficiency of the project, saving time and resources. The excavation of the adjacent primary panels and their deviations are independent events, their analysis allows defining a statistical distribution and the confidence interval for the overlap value.

RÉSUMÉ: Le barrage de Santa Maria sur la rivière Baluarte est un barrage en enrochement avec un parament en béton, avec une hauteur totale de rideau de 152 m à partir de la strate rocheuse, située à 32 m de profondeur. Des batardeaux seront construits en amont et en aval. Un mur de séparation a été construit à la base du batardeau en amont. Les sols alluviaux avec des blocs rocheux génèrent des difficultés sur le contrôle de la verticalité des murs de séparation. Une combinaison de méthodes de construction et d'instrumentation de l'excavation permet d'éviter les déviations de la paroi moulée en ciment bentonite. Une pré-excavation et un remplissage avec du sable fin évitent les déviations et améliorent les rendements de production dans la construction de la paroi moulée. Une méthodologie pour l'optimisation du chevauchement des panneaux est définie sur la base de l'instrumentation de la verticalité des panneaux, pendant les travaux d'excavation. L'adoption d'un chevauchement conservateur est habituelle en l'absence d'une analyse détaillée des conditions du site. L'optimisation du chevauchement permet d'améliorer l'efficacité du projet et d'économiser du temps et des ressources. L'excavation des panneaux primaires adjacents et leurs déviations sont des événements indépendants, leur analyse permet de définir une distribution statistique et un intervalle de confiance pour la valeur du chevauchement.

Keywords: Construction; optimization; monitoring; statistical analysis.

1 SANTA MARIA DAM COFFERDANS

The Santa María dam is part of the Baluarte-Presidio System, in Sinaloa, Mexico, and regulates the Baluarte River and its tributaries through the construction of a dam. The materials on which the Santa Maria dam is located consist of a rocky substrate of extrusive andesitic and intrusive rocks of the dioritic porphyry type. Quaternary alluvium is located on the bedrock, corresponding to the current deposits of the Baluarte river. The thickness of alluvium is about 33 m below the riverbed.



Figure 1. Diaphragm wall excavation with hydraulic grabs (Baya TEC Systems) on mobil crane Liebherr.

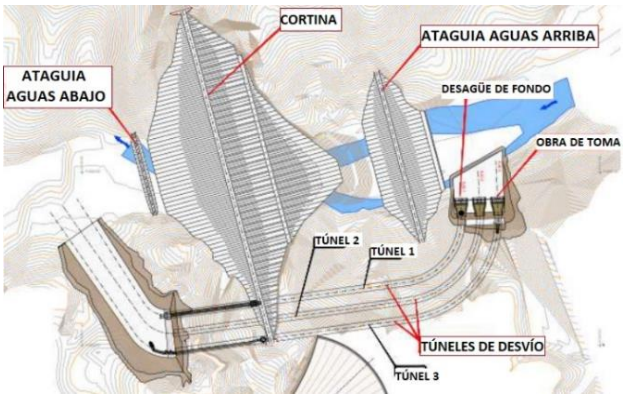

Figure 2. Layout Santa Maria Dam project.

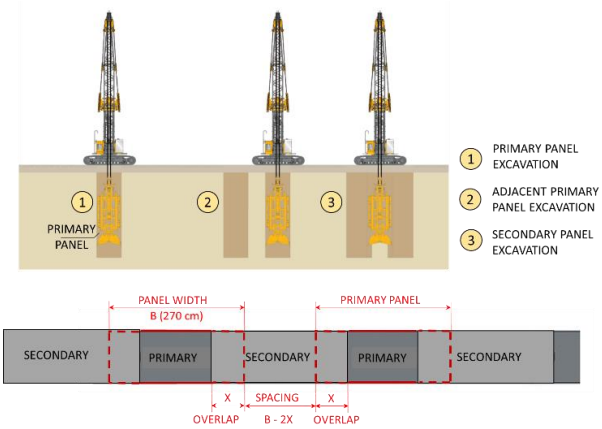

Figure 3. Diagram of primary and secondary panels.

The upstream cofferdam is a homogeneous embankment dam made of rockfill. The waterproofing above the riverbed level is made with a geomembrane layed on the upstream slope, achored on a lower plinth. The waterproofing below the level of the riverbed is made with a bentonite-cement cut-off wall, which crosses the alluvium until it reaches the underlying rock. The downstream cofferdam is placed on a regularization platform on the riverbed.

The purpose of this paper is to expose the construction procedure and present a methodology that allows us to define the optimum overlap between panels based on the control and statistical analysis of verticality deviations during excavation, in order to ensure the continuity of the cut-off wall.

1.1 Diaphragm wall construction procedure

First, the primary panels (PP) are executed with a spacing between them equivalent to the width of the grab minus an overlapping margin to ensure that there are no gaps between panels. In the space between each two primary panels, the secondary panels (PS) are executed. The trajectory of the secondary panels is guided by the inclination trend that was generated during the primary panel excavation process. The deviation in the construction of the primary panels depends on the equipment used, the material excavated and the operator's expertise.

The type of alluvial deposit has a key influence on the verticality of the excavations, since the presence of very coarse materials in the riverbed can force a deviation tendency, by causing greater opposition to the excavation in one of the directions. This is why the greatest deviations occur in the vicinity of the bedrock, where there is a greater presence of blocks.

The following factors have been incorporated in the construction procedure in order to control the deviations:

- Pre-drill. A pre-excavation in the alluvium deposit and fill with fine sand improves the production yields in the construction of the diaphragm wall, and prevent deviations.
- Equipment. Hydraulic grab Baya (TEC System) with semi kelly, and automatic half turn and verticality control.
- Geotechnical monitoring with Jean Lutz instrumentation system, with real time recording of depth, deviation in the vertical plane (parallel to the axis of the wall), deviation in the vertical plane (perpendicular to the axis of the wall), and deviation due to the rotation.

This construction procedure with monitoring instrumentation system, hydraulica grabs with semi kelly has been used in projects such as the Misicuni Dam (Tecnosuelo, 2018), or the cut-off wall in Xochimilco (Jimenez, 2023).

1.2 Recording deviations on the cut-off wall

Once the deviation data were obtained from the primary panels, they were classified into left deviation, data with a negative sign, and right deviation, with a positive sign. The following aspects are observed:

- Most of the data obtained are in values less than 4 cm and in percentage values less than 0.30%.
- Diaphragm wall deviation is cumulative with depth, for the definition of the overlap it will be necessary to make the analysis for the maximum expected depth.
- There are a limited number of panels with high deviation values, which increase in the final depth of each panel, due to the presence of blocks or bedrock.

2 STATISTICAL ANALYSIS OF DEVIATIONS IN PRIMARY PANELS

Probability theory is used in modelling the behaviour of a variable if a sufficient set of measurements is available. Quantitative evaluation of soil variability

modelling requires the use of descriptive and inferential statistical techniques, as well as probabilistic modelling to process the data from the measurements made.

The stages leading to the probabilistic modelling of a random variable are shown schematically in Figure 4. Descriptive analysis includes the calculation of the sample moments of the recorded measurements, mainly mean and variance and the skewness and kurtosis coefficients, as well as the inspection of data and histograms. The inferential analysis includes the selection of the distribution function, estimation of its parameters and the goodness-of-fit test to the source data. The result is the obtaining of a probability model for the analysed variable, which, in this case study, will allow us to evaluate the probability of occurrence of a certain deviation in the verticality of the primary panels and from these results establish an overlap value, with a sufficient level of confidence that no discontinuities are generated on the diaphragm wall.

Table 1. Sample descriptive parameters.

Diaphragm wall Deviation (%)	
Mean	0,055%
Median	0,035%
Mode	0,000%
Variance	0,188%
Kurtosis coefficient	1,131183368
Skewness coefficient	0,195754426
Range	1,209%
Maximum (right deviation)	0,67%
Minimum (left deviation)	-0,54%
Data	7124

For the selection of statistical distributions, the concept of "entropy maximization" is usually adopted, which states that the least biased model that encodes the available information is the one that maximizes entropy while remaining consistent (Uzielli et al. 2007). From the physical sense of the measurements and the expected values, the most appropriate distribution can be chosen, as shown in Table 2. From this analysis the distribution that maximizes entropy and, therefore, would best fit the data is the normal probability distribution.

A normal distribution has been adopted with mean values 0.0553% and standard deviation 0.188%. To check the goodness of fit, the quantile-quantile diagram was obtained, with similar conclusions. It is observed that the central part of the diagram fits very accurately to the normality hypothesis, and that in the tails of the distribution there are some slight mismatches, influenced by the outliers. Considering the inherent heterogeneity of an alluvial stratum, the goodness of fit is acceptable.

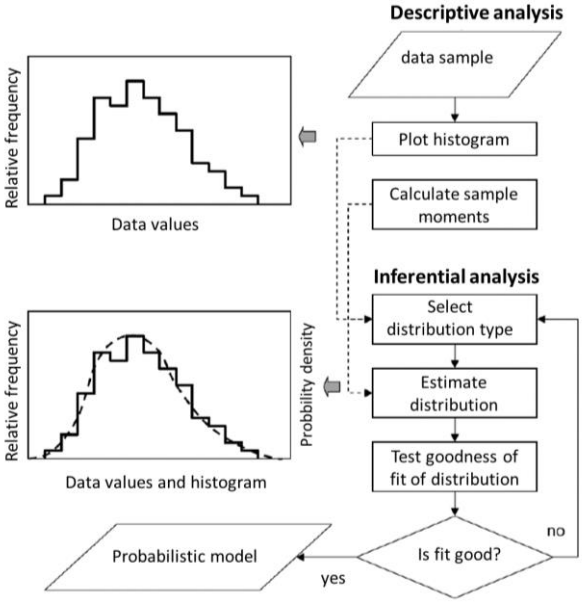

Figure 4. Integrated descriptive and inferential analysis for probabilistic modelling of a random variable (Uzielli 2006).

Table 2. Maximum-entropy criteria and constraints for the selection of a probability distribution (Uzielli et al. 2007).

Mean	*Variance*	*Negative values*	*Upper / lower bounds*	*Maximun entropy distribution*
Unknown	Unknown	Acceptable	Known	***Uniform***
Known	Known	Acceptable	Unknown	***Normal***
Known	Known	Unacceptable	Unknown	***Lognormal***
Known	Known	Acceptable	Known	***Type- I Beta***

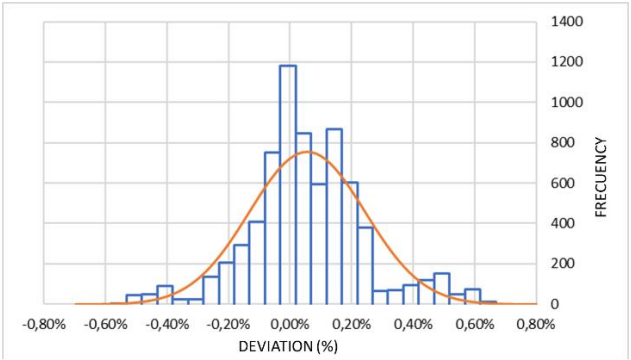

Figure 5. Normal probability distribution fit to histogram of diaphragm wall deviations data.

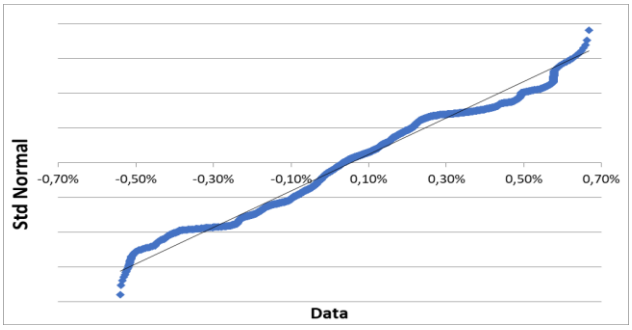

Figure 6. Goodness-of-fit in quantile-quantile plot.

3 OVERLAP BETWEEN PRIMARY AND SECONDARY PANELS. PROBABILITY OF DEVIATION

From the probability model obtained, it is possible to obtain the probability of the occurrence of a right or left deflection greater than that allowed by the overlap.

The probability that the deviation of subsequent primary panels is in opposite directions is governed by the criterion of dependent probability which establishes that, for any independent number of events, the probability that these events occur simultaneously is the product of the individual events occurring.

The probability that the overlap is less than a given value is obtained by calculating the simultaneous probability of the different combinations of deflections that produce the indicated overlap. It has been estimated for different values of overlapping (table 3).

Table 3. Combination of left and right deviations that maximize the probability of exceeding the overlap.

Overlap (cm)	Σ Overlap (cm)	Deviation. Rigth/ Left. (cm)	Dev. Rigth Probability (%)	Dev. Left Probab. (%)	Deviation > Overlap Probability (%)
40,00	80,00	(40.0,-40.0)	0,0000056%	1.9E-7%	1.1E-14%
30,00	60,00	(30.0,-30.0)	0,0047%	0,00035%	1.6E-8%
20,00	40,00	(22.0,-18.0)	0,27%	0,24%	0,000654%
15,00	30,00	(17,5,-12.5)	1,56%	2,05%	0,032%
12,50	25,00	(15.0,-10.0)	3,55%	4,51%	0,16%
10,00	20,00	(12,5, -7.5)	7,28%	8,95%	0,65%
7,50	15,00	(10.0, -5.0)	13,46%	16,02%	2,16%
5,00	10,00	(7.0, -3.0)	24,65%	23,76%	5,86%
2,50	5,00	(5.0, 0.0)	34,29%	38,43%	13,18%

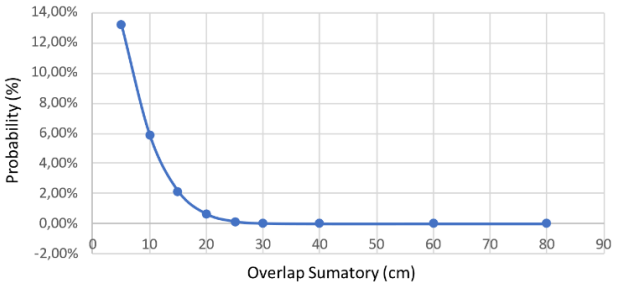

Figure 7. Probability that the deviation exceeds the overlap.

4 CONCLUSIONS

The impermeabilization of the upstream and downstream cofferdams of the Santa María Dam, in Sinaloa, has been achieved below the level of the riverbed through the execution of a bentonite - cement diaphragm wall. The instrumentation of the excavation process and the use of equipment with hydraulic grabs makes it possible to control the risks of vertical deviation and its correction during excavation by measuring the deviations in real time.

This makes it possible to establish a methodology to optimize the separation between primary panels by reducing overlapping. In the cofferdams of the Santa Maria dam, this optimization allowed a primary panel spacing of 2.30 m, with grabs of 2.70 m excavation width, compared to the 1.90 m that were initially considered, achieving a saving of 20%. The required volume of slurry is reduced, waste is reduced and execution timeschedule is improved.

As a relevant conclusion, the use of semi-guided and instrumented excavation equipment provides important economic and time advantages compared to other types of equipment in which the excavation process is not controlled, with more uncertainties. Introducing imaginative measures such as pre-drilling and backfilling with fine sand in a first stage, ensures verticality and continuity of the cut-off wall in difficult soils.

An overlap of 20 cm on each side of the panel has been considered, with a confidence margin of 99.9993% that the deviations in the verticality do not cause defects. The process has a control greater than 4.5 σ, where only every 152,833 measurements could find a point with out-of-range values.

ACKNOWLEDGEMENTS

Acknowledgements to the firms ICA and CONAGUA for involving us in the "Presa Santa María" project.

To Antonio Blanco Amador, General Director of Tecnosuelo, on the 50th anniversary of the company. 50 years in which he has shared his experience and knowledge for the benefit of Mexico. To the Tecnosuelo team, in Mexico City and Huamantla.

REFERENCES

Comisión Nacional del Agua (2021, 2022). *Baluarte project. Santa Maria Dam advances*. Mexico.

Jiménez, R. (2022). *Introducción a la fiabilidad de las obras geotécnicas*. Proceedings of the XI National Symposium of Geotechnical Engineering. Mieres (Asturias). Spain. Vol. 1, pp 85-108.

Jiménez, E., Blanco, F.J., Arévalo, J.D. (2023) *Cut-off wall and refoundations after 2017 earthquake in abrupt variation zone, Xochimilco, Mexico City.* Proceedings of the Geo-Congress 2023. ASCE. Los Ángeles. USA.

Olivera, V.H., Blanco, F.J. (2022) *Informe de Optimización de traslape de páneles de pantalla flexoimpermeable. Proyecto presa Santa María, en el Rosario, Sinaloa, México* Requitec, Grupo Tecnosuelo.

Tecnosuelo (2018) tecnosuelo.com.mx/tecnosuelo/presas.

Uzielly, M., Lacasse, S., Nadim F., Phoon, K.K. (2006) *Soil variability analysis for geotechnical practice*. Proceedings of the 2nd International Workshop on Characterisation and Engineering Properties of Natural Soils. Singapore. 1653-1752.

Proceedings of the XVIII ECSMGE 2024
GEOTECHNICAL ENGINEERING CHALLENGES
TO MEET CURRENT AND EMERGING NEEDS OF SOCIETY
© 2024 the Authors
ISBN 978-1-032-54816-6
DOI 10.1201/9781003431749-453
Open Access: www.taylorfrancis.com, CC BY-NC-ND 4.0 license

ECSMGE 24
XVIII EUROPEAN CONFERENCE ON SOIL MECHANICS AND GEOTECHNICAL ENGINEERING

Soil improvement methods in the Mediterranean railway corridor, Pulpí – Vera stretch, Almería

Méthodes d'amélioration des sols dans le corridor ferroviaire Méditerraéen tronçon Pulpí – Vera, Almería

E. Jiménez Ontiveros*, L.M. de la Rosa Domínguez
UTE Ofiteco Urci, Almería, Spain

D. Martínez Sánchez
Ineco, Almería, Spain

J. Lavado Rodríguez
UTE Ferrovial Acciona, Almería, Spain

**eloy_ontiveros@yahoo.es*

ABSTRACT: The project involves the construction of the railbed for a section of high-speed line, in the Pulpí – Vera stretch with 25.7 km, in the Murcia – Almería section. It is part of the Mediterranean railway corridor and will improve the connectivity of Almería. A variable geology is observed with a predominance of Miocene and Pleistocene materials. The lithology is composed of Miocene marls with gypsum lenses and a cover of alteration soils and fills. The railway runs through areas with a significant thickness of soft soils in the embankments R-15, R-17, R-21 and R-33 (glacis deposits with sandy silts, valley deposits with clayey silts) and a zone with anthropic landfill from agricultural activities in the embankment R-14. From this background, high deformability and low strength of soils are mitigated by a wide range of soil improvement techniques. Rigid inclusions are installed with objective to support concrete structures and culverts to prevent structural damages due to excessive settlements. Transitions with non-treated areas are solved by increasing the inclusions spacing, by a soil improvement with surcharge and wick drains or by combining the inclusions with stone columns to match the settlements between the embankment and the treated area (R-14).

RÉSUMÉ: Le projet porte sur la construction de la voie ferrée d'un tronçon de la ligne à grande vitesse, sur le tronçon Pulpí - Vera, d'une longueur de 25,7 km, dans la section Murcie - Almería. Il fait partie du corridor ferroviaire méditerranéen et améliorera la connectivité d'Almería. On observe une géologie variable avec une prédominance de matériaux du Miocène et du Pléistocène. La lithologie est composée de marnes du Miocène avec des lentilles de gypse et une couverture de sols d'altération et de remblais. La voie ferrée traverse des zones présentant une épaisseur importante de sols meubles dans les remblais R-15, R-17, R-21 et R-33 (dépôts de glacis avec des limons sableux, dépôts de vallée avec des limons argileux) et une zone de décharge anthropique dans le remblai R-14. La grande déformabilité et la faible résistance des sols sont atténuées par un large éventail de techniques d'amélioration des sols. Des inclusions rigides sont installées dans les structures en béton et les ponceaux pour prévenir les dommages structurels dus à des tassements excessifs. Les transitions avec les zones non traitées sont résolues en augmentant l'espacement des inclusions, en améliorant le sol avec une surcharge et des drains à mèche ou en combinant les inclusions avec des colonnes de pierre pour faire correspondre les tassements entre le remblai et la zone traitée (R-14).

Keywords: Soil improvement techniques; stone columns; rigid inclusions; staged construction.

1 SOIL IMPROVEMENT METHODS IN THE MEDITERRANEAN CORRIDOR

The Pulpi Vera stretch of the Mediterranean corridor runs over a variable geology with a predominance of Miocene and Pleistocene materials, covered by colluvial and alluvial alteration soils or anthropic fillings from agricultural activities. These alteration soils and uncontrolled fills constitute a variable thickness of soft soils exceeding 10 m in the case studies, which would cause settlement between 50 and 80 cm, as well as stability problems, which are not compatible in times and magnitude with the structures and embankments of the project.

1.1 Initial project limitations

A problem of the initial project is the execution of embankments with underpasses or large drainage

structures above soft soils. The initial approach of the project was the treatment of soft soils with some techniques that accelerate the consolidation times or make it compatible with the construction schedule. This approach had the disadvantage of not taking into account the lower allowable deformability of the concrete structures compared to the embankments.

The project's initial solution was to carry out the improvement to consolidate initially the embankment and, once the settlements were reached, excavate the areas where the concrete structures are located, and excecute them in a second stage. (Adif, 2018) This construction system has the following disadvantages:

- Cost: use of temporary embankments and subsequent removal for construction of concrete structures.
- Time: Execution by stages and increasing of construction times.
- Necessity of temporary drainage culverts, although with a lower return period than the definitive elements.

1.2 Soil improvement solutions

Use of rigid inclusion that makes deformations compatible with allowable settlements of concrete structures. This solution is combined with other consolidation and treatment techniques in enbankments.

The project includes the following solutions:

- Stone columns and rigid inclusions below the underpass 509+900, at the embankment R-14
- Rigid inclusions below concrete structures and surcharge and wick drains in transitions, at the embankments R-17, R-21.
- Rigid inclusions with a gradation in the spacing of inclusions at embankments R-22 and R-33.
- Soil improvement with surcharge and wick drains, embankment staged construction, R-15.

2 SOIL IMPROVEMENT WITH RIGID INCLUSIONS AND STONE COLUMNS

The treatment area in the R-14 embankment is located between the km 509+825 and km 509+960, with the presence of the 509+900 underpass (Figures 1 and 2). The embankment runs over a lithology with a thickness of soft soils exceeding 10 m in some areas.

The geology is composed by the M_m formation of Miocen marls with a lithology of clayey silts and marls with intercalations of sandstones, siltstones and gypsum lenses. Above M_m unit are the Qg unit of glacis deposits of silt and fine sands with scattered gravels, and the Rv unit of uncontrolled fills (Table 1).



Figure 1. Improvement treatment with stone columns and rigid inclusions at the embankment R-14.

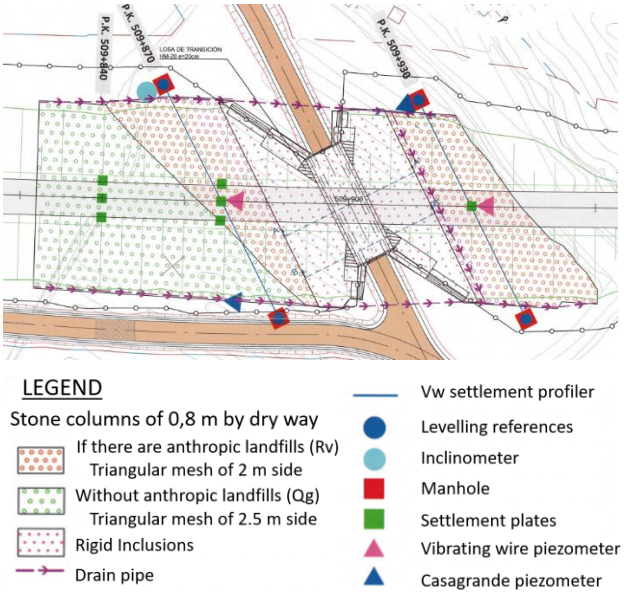

Figure 2. Layout of soil improvement treatment and geotechnical monitoring at the embankment R-14.

Table 1. Geotechnical parameters at Embankment R-14.

Unit	Depth (m)	γ_{ap} (t/m^3)	c (t/m^2)	Φ (º)
Rv	0,00 - 6,00	1,80	1,0	12
Qg	6,00 - 12,00	1,90	8,2	13
Mm	> 12,00	2,00	2,0	28
Embankment		2,00	1,0	30

The untreated solution presents stability problems, with safety coefficients lower than 1.5 and 1.1 required in static and seismic situations. Bishop method has been used in stability analysis. Settlements of up to 0.80 m are obtained, which would occur in more than 10 months, with a consolidation degree of 90% in 5 months, which is considered unacceptable. Results has been obtained with a stress method basis in Boussinesq and Westergaard theory with the software Settle 3D.

2.1 Stone columns improvement

Soil improvement is proposed with a treatment using stone columns of 0.80 m diameter and 6 m long, executed by dry method, with pre-drilling. The improvement is considered by substitution and improvement of the drainage, without densification. The treatment with stone columns has been executed with a 2 x 2 m triangular mesh in the area of anthropic fills, between Km 509+863 and Km 509+941, and with a 2.5 x 2.5 m mesh in the area without fills. A 0.5 m thick layer of granular material is placed above the columns. (Hernández, 2020) (Martínez, 2022)

With the 2 x 2 m spacing in the backfill area, and a 10.04 m embankment height, settlement is reduced to 48.8 cm, reaching more than 90% of the total settlement a month after completion. In the area without landfills, with a 2.5 x 2.5 m spacing, and a 9m height, the expected settlement is 47.5 m. Stone columns has been calculated with Priebe method, obtaining a settlement ratio of 0.55. (Adif, 2018)

The geotechnical monitoring plan includes control sections with settlement plates, control lines with vibrating wire settlement profiler, vibrating wire piezometer, inclinometer and Casagrande piezometer. Geotechnical monitoring will be a key factor in the evaluation of the achievement of the improvement objectives. (Hernández, 2020)

2.2 Rigid inclusions

The initial project considered a soil improvement using stone columns, however settlements under the structure exceeded the admissible values (5 cm for concrete structures). The solution under the structure of the underpass was a soil improvement through rigid inclusions (Figure 3). The spacing between inclusions has been designed to achieve a transition of stiffness with the improvement with stone columns. One of the problems to avoid with this type of soil improvement is an abrupt change in soil stiffness that can lead to differences in settlement between the area treated with stone columns and rigid inclusions. It is relevant to mention the time effects, since settlements with stone columns are usually produced during construction and rigid inclusion need some time for consolidation.

The treatment below the concrete frame of the 509+900 underpass is a 2 x 2 m mesh of inclusions of 36 cm diameter and 12 m depth, with 20 MPa concrete. According to the geotechnical survey, the stratigraphic profile is as follows, the columns will be embedded 3 meters in the Mm unit. The estimated maximum settlement was 4.54 cm, obtained with a FEM model with Plaxis 2D (Figure 4). For an adequate transition, the rigid inclusions will be extended outside the structure with a gradation in the treatment.



Figure 3. Rigid inclusions construction.

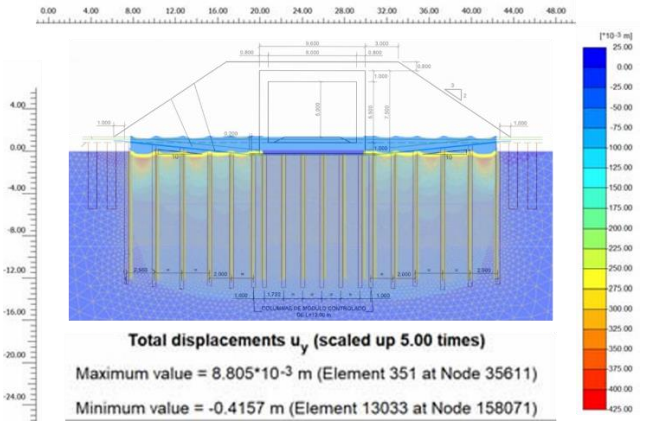

Figure 4. Geotechnical model with Plaxis 2D and section of the treatment with rigid inclusions (Hernández, 2020).

The distribution outside in transitions is defined as 1 row of columns at 1 meter from the frame columns and 2 additional rows separated by 2 meters, always keeping the transverse spacing at 2 meters. The gap between the transition zone of the wing walls and the frame will be filled with a inclusions grid of 2.5x2.0 meters. (Hernández, 2020) (Martínez, 2020)

A FEM model with Plaxis 2D shows a maximum settlement of 14.8 cm between the frame and the first row outside the structure, 30.7 cm between the second and third rows (separated by 2 meters) and 37.8 cm between the rows with 2.5 m spacing and 42.5 cm in the contact with stone columns. (Hernández, 2020)

3 SOIL IMPROVEMENT WITH RIGID INCLUSIONS, SURCHARGE AND WICK DRAINS

Soil improvement has been carried out combining rigid inclusions and embankment staged construction, with wick drains in embankments R-17 and R-21.

The case study in the R-21 embankment runs through km 515+521 to 515+740, with the 515+600 and 515+700 drainage structures with a section 8 x 5.5 m. The lithology of this area consists of uncontrolled anthropic fills (Rv), with a thickness of 3 m. (Figure 5)



Figure 5. Soil improvement with rigid inclusions below concrete structures and surcharge and wick drains in R-21 embankment and in Burjulu bridge abutments location.

The Qfv unit is formed by alluvial deposits of valley bottom, with a thickness of up to 13 m, consisting of silty clays and muddy clayey silts. The Miocene materials (Unit Mm) are found as substratum, formed by clayey marly silts and loams.

The maximum settlements obtained without improvement are estimated at 49.4 cm for more than one year, being unacceptable. The stability of the untreated solution is below the admissible safety coefficients. (Adif, 2018)

A solution of rigid inclusions is adopted in the area of the concrete structures, with 6 rows of columns of 36 cm diameter, 2 m spacing and 14 m length for the 515+60 frame and 12 m for the 515+70 frame. The treatment is extended outside the structure with another 6 rows with increased spacing to achieve a transition of deformations and stiffnesses with the area improved with preloading. Expected settlement with the treatment varies between 4.58 cm under the structure, gradually increasing up to 40.4 cm, with an increment of spacing until 2.5x2 m. (Hernández, 2020) (Villegas, 2021)

Soil improvement with preloading and wick drains, arranged in 2 m triangular mesh, with a length between 6 and 11 m depending on the area (Figure 6). The improvement technique was the embankment staged construction with an initial stage of 6.5 m for 3 months and other stage between 1 and 4 months up to 11.23 m.

4 RIGID INCLUSIONS COMBINED WITH REMOTION OF SOFT SOILS

A solution with rigid inclusions combined in the adjacent areas with replacement of soft soils in a thickness of about 1 - 1.5 m, and embankment staged construction at the locations R-33, R-22 and R-21 between km 515+740 and 516+480. (Martínez, 2022)



Figure 6. Wick drains installation in R-21 embankment.

5 CONCLUSIONS

The initial project proposed soil improvement through consolidation processes, with subsequent removal of the embankment at the location of drainage structures or underpasses. The advantage of the proposed methods is the combination of different soil improvement techniques to make the allowable deformations between concrete structures and embankments compatible. Rigid inclusions have been used in combination with other techniques, in conjunction with wick drains, stone columns, soft soil removal or embankment staged construction.

ACKNOWLEDGEMENTS

To the geologist team on site, Susana Montiel and Luis María de la Rosa (co-author). To the Ofiteco – Urci technical team. To Acciona – Ferrovial technical team. To Juan Carlos Hernández, from Geotécnica del Sur.

REFERENCES

ADIF (2018). Construction Project Platform Construction of the Murcia - Almeria railway mediterranean corridor. Pulpí – Vera. Getinsa Euroestudios. TPF Ingeniería.

Hernández Garvayo, J. C. (2020). Technical Reports nº 05, 09, 11, 12, 17, 31, 34, 35 and 36. Soil improvement in embankments R-14, R-15, R-17, R-21, R-22 and R-33. Geotécnica del Sur, Granada

Hernández Garvayo, J. C. (2020). Technical Report nº 27. Geotechnical monitoring plan. Geotécnica del Sur, Granada

Martínez Sánchez, D. (2022). Modified Construction Project No. 1 of the Platform Construction Project of the Murcia - Almeria High Speed Mediterranean Corridor. Section Pulpi - Vera.

Villegas Barranco, I. (2020). Report GEO.NT.016 and 22. revision technical notes NT 05, and NT-22. UTE Ofiteco – Urci.

Proceedings of the XVIII ECSMGE 2024
GEOTECHNICAL ENGINEERING CHALLENGES
TO MEET CURRENT AND EMERGING NEEDS OF SOCIETY
© 2024 the Authors
ISBN 978-1-032-54816-6
DOI 10.1201/9781003431749-454
Open Access: www.taylorfrancis.com, CC BY-NC-ND 4.0 license

ECSMGE 24
XVIII EUROPEAN CONFERENCE ON SOIL MECHANICS AND GEOTECHNICAL ENGINEERING

Solution of excavation and peripheral earth retaining walls near sensitive structures – O'Living Development, Lisbon

Solutions d'excavation et murs de soutènement périphériques à proximité des structures sensibles – Développement O'Living, Lisbonne

R. Justiniano*
JETsj Geotecnia, Lisbon, Portugal

A. Pinto
JETsj Geotecnia, Lisbon, Portugal

**rjustiniano@jetsj.com*

ABSTRACT: This paper refers to the excavation and retaining wall solutions for a residential development located in Lisbon, where part of the basement structure is located 4m above the Lisbon Metro (ML) tunnel crest. The constraints related to the execution of peripheral earth retaining walls are discussed, using the technology of Munich Walls, Berlin Walls, and Mixed Walls, duly adapted to the existing constraints. Finally, the results of the Monitoring and Survey Plan are pointed out, confirming its importance as risk management tool in a work of high geotechnical complexity and located very close to very sensitive structures, as it was ML tunnel.

RÉSUMÉ: Cet article fait référence aux solutions d'excavation et de mur de soutènement pour un développement résidentiel situé à Lisbonne, où une partie de la structure du sous-sol est située à 4 m au-dessus de la crête du tunnel du métro de Lisbonne (ML). Les contraintes liées à l'exécution des murs de soutènement périphériques sont discutées, en utilisant la technologie des murs de Munich, des murs de Berlin et des murs mixtes, dûment adaptée aux contraintes existantes. Enfin, les résultats du plan de surveillance et d'arpentage sont soulignés, confirmant son importance en tant qu'outil de gestion des risques dans un ouvrage de grande complexité géotechnique et situé très près d'ouvrages très sensibles, comme il s'agissait d'un tunnel ML.

Keywords: Munich walls, Berlin walls, mixed walls, deep excavations.

1 INTRODUCTION

This paper describes the excavation and peripheral retaining walls solutions, designed and executed in a residential development, in Lisbon, whose excavation bottom level was about 4m from the vault of the Lisbon Metro (ML) tunnel, corresponding to the section of the Red Line, located between the stations of Moscavide and Encarnação, executed using NATM technology. The work studied includes two buildings (Plot 1 and Plot 2), with Plot 1 consisting of 8 upper floors and 2 underground basements and Plot 2 consisting of 8 upper floors and 3 buried basements. Figure 1 shows an aerial view of the location of the site.

This article aims to address in more detail the solutions of Mixed Berlin (peripheric wall where the upper side is as munich walls (concrete) and lower side is as Berlin walls (timber lagging), with soldiers piles connecting both type of wall), and Suspended Munich walls (supported by adjacent peripheric walls), conditioned by the proximity of sensitive structures, such as the ML gallery.



Figure 1. Site Plan and ML path.

There was a need to resort to studies of non-conventional solutions considering the regulations and standards of the ML, which does not allow the execution of structural and foundation elements within 3m of the ML.

2 CONSTRAINTS

Given the location of the ML tunnel, about 4m below the entire North peripheral retaining wall of Plot 1, it was not possible to execute the traditional Munich Walls (as Figure 2). Likewise, in Plot 2, in an extension of about 20m, it was not possible to execute piles or micropiles, due to the need to respect the precautionary distance of 3m to the ML tunnel.

According to ML documents (Metropolitano de Lisboa 2010a), in addition to the need to respect the precautionary distance of 3m, during the excavation and peripheral containment works, the following criteria of maximum deformation were also imposed, to be proven by the instrumentation:

- The structure of the ML tunnel could not suffer displacements greater than 7 mm vertically and/or horizontally;
- On the ML rails, it was not possible to verify a variation of relative displacement, between sections of 8m distance, greater than 3mm.

These rules are applied to any excavation that takes place within 25m of the ML tunnel, which was the case (Metropolitano de Lisboa 2010b).

3 CONCEPTUAL SOLUTIONS

3.1 PLOT 1

The conceptual solution for Plot 1 North area was with the execution of a Mixed Berlin Wall (Figure 2 and 3). In this solution, a Munich wall was executed in the top area of the retaining wall and a Berlin wall was executed in the bottom area, because the space between the mixed berlin walls and the definitive wall of the building was to be fille (as Figure 3).

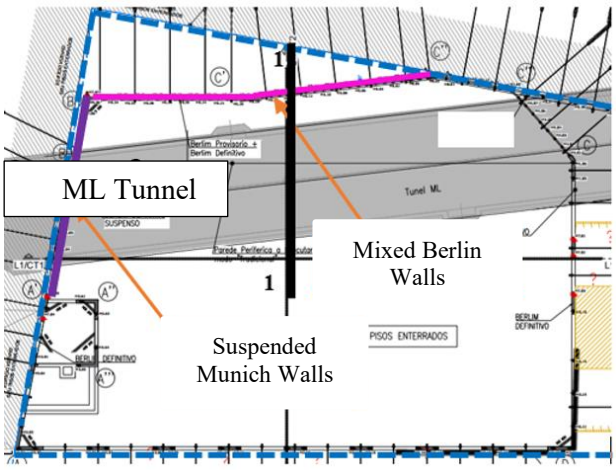

Figure 2. Plot 1 – Conceptual solution.

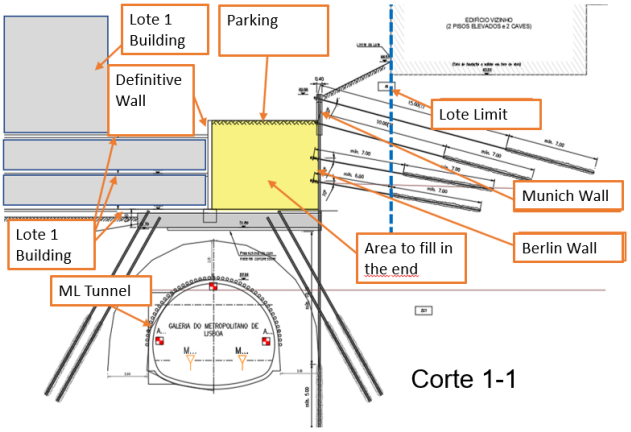

Figure 3. Plot 1 – section 1.

3.2 PLOT 2

The conceptual solution for Plot 2 North area was with the execution of a Suspended Munich Wall (Figures 4 and 5). In this solution, the micropiles in the suspended Munich wall are in tension, to transmit the vertical load from the wall to the top beam (with 2m height). Due to the suspended load, reinforcement of the micropiles in the end of Munich wall is required, to hold all vertical load from the suspended Munich wall.

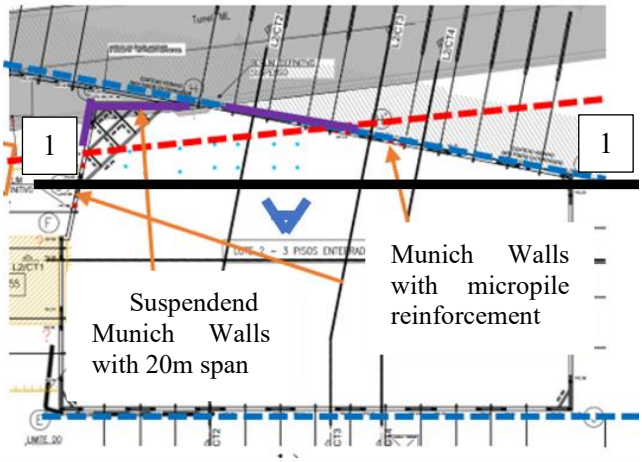

Figure 4. Plot 2 – Conceptual solution.

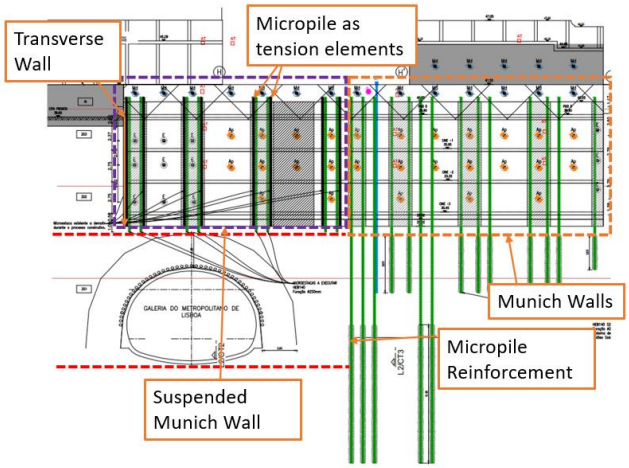

Figure 5. Plot 2 – section 1.

4 EXECUTION

4.1 PLOT 1

Figures 6 and 7 show the site at completion of the excavation. Figure 7 shows the beginning of execution of the permanent wall of the building and the space (min 3m) to the Mixed Berlin Wall.



Figure 6. Plot 1 – Mixed Berlin Wall.



Figure 7. Plot 1 – Suspended Munich Walls.

4.2 PLOT 2

Figure 8 show the suspended Munich wall solution at bottom excavation. To reduce vertical load, 3 levels of props were adopted.

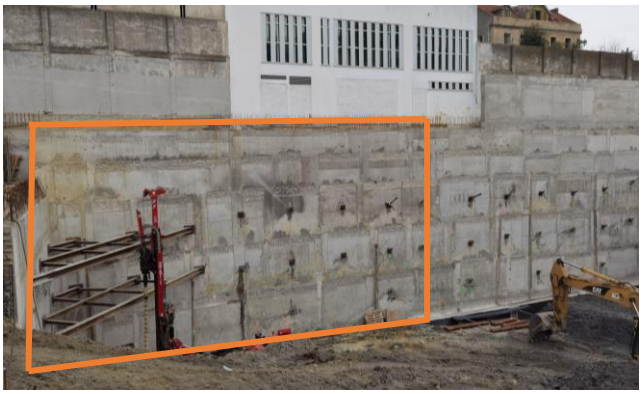

Figure 8. Plot 2 – Suspended Munich Walls.

5 MONITORING AND SURVEY PLAN

The instrumentation adopted in situ, consisted of a wide range of devices, as the following:

- Topographic targets in the peripheral retaining structures, placed during their execution;
- Topographic targets in the surrounding structures, installed before the start of excavation work;
- Piezometers, installed to control the position of the water table;
- Inclinometers, installed to control the evolution of horizontal displacements of the ground;
- Load cells, used to evaluate loads on temporary anchors;

Topographic targets and topographic marks installed inside the ML gallery to control the relative (convergences) and absolute deformations of the vault and rails, respectively. Figures 9 to 13 show the results.

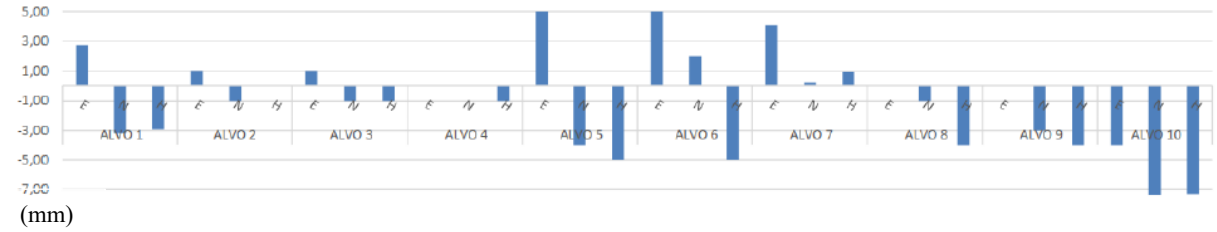

Figure 9. Surrounding Structures settlements (mm).

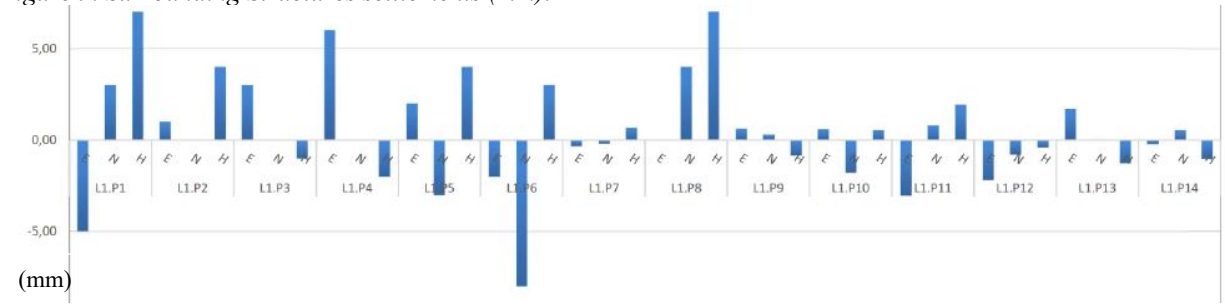

Figure 10. Plot 1 Peripheric wall settlements (mm).

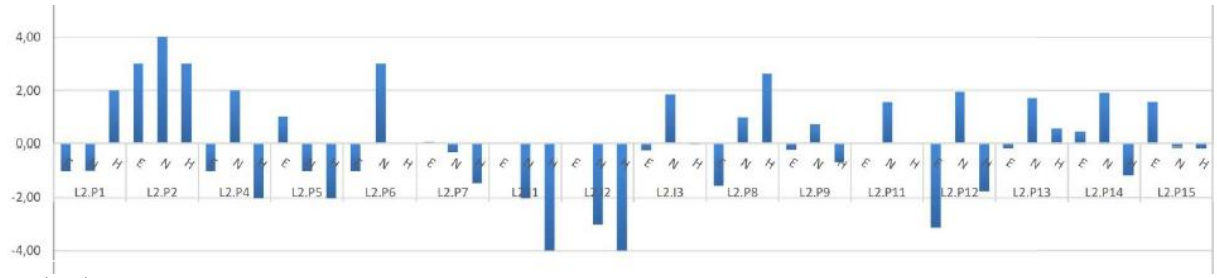

(mm)

Figure 11. Plot 2 Peripheric wall settlements (mm).

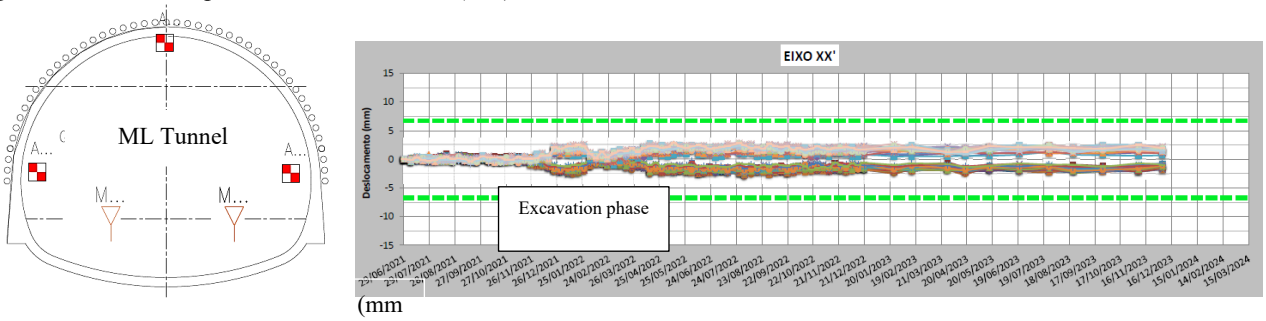

(mm

Figure 12 - ML Tunnel – Topographic longitudinal settlements of the vault (mm).

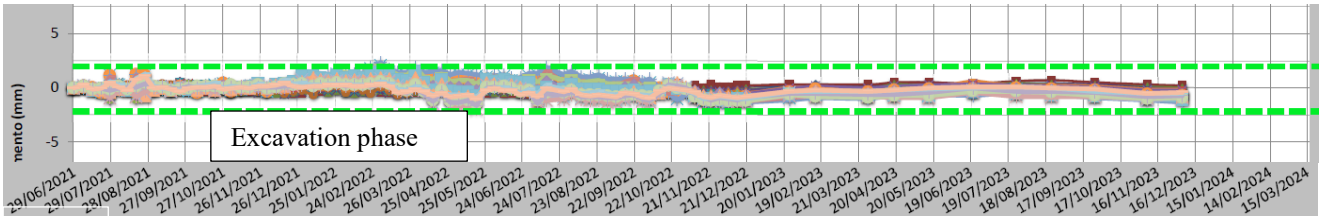

(mm)

Figure 13. ML Tunnel – Rails vertical settlements (mm).

Settlement result of the peripheric retaining wall suggest good correlation with the model considered in the design. Settlement result of surrounding structures were compatible with the profile of those structures. ML tunnel settlement was lower than max acceptable value. Rails settlements were at the max acceptable value (3mm) during excavation phase.

6 CONCLUSIONS

This article highlights the main solutions of peripheric earth retaining walls in a sensitive geotechnical area, due the vicinity of the ML Tunnel. Risk management, soil behaviour with good correlation with design models and assessment of good behavior of the structures were only possible with the execution of a Monitoring and Survey Plan.

ACKNOWLEDGEMENTS

The authors are grateful for the Mexto S.A., Developer, for the permission to present this paper as well Cofrasilvas Group (Main Contractor) and Geosol FG (geotechnical contractor), for the collaboration and trust placed in JETsj.

REFERENCES

Metropolitano de Lisboa (2010a). Interferência de Terceiros em Estruturas ML em Exploração – Procedimentos – Inspeção Técnica às Estruturas de Metropolitano de Lisboa, ML EPE, Lisboa, Portugal. (in portuguese)

Metropolitano de Lisboa (2010b). Interferência de Terceiros em Estruturas ML em Exploração – Procedimentos – Projeto e Monitorização das Estruturas de Metropolitano de Lisboa, ML EPE, Lisboa, Portugal. (in portuguese)

Proceedings of the XVIII ECSMGE 2024
GEOTECHNICAL ENGINEERING CHALLENGES
TO MEET CURRENT AND EMERGING NEEDS OF SOCIETY
© 2024 the Authors
ISBN 978-1-032-54816-6
DOI 10.1201/9781003431749-455
Open Access: www.taylorfrancis.com, CC BY-NC-ND 4.0 license

ECSMGE 24
XVIII EUROPEAN CONFERENCE ON SOIL MECHANICS AND GEOTECHNICAL ENGINEERING

Deep and complex excavation in an urban environment in Miraflores, Oeiras

Excavation profondes et complexes en milieu urbain à Miraflores, Oeiras

R. Justiniano*, A. Pinto

JETsj Geotecnia, Lisbon, Portugal

**rjustiniano@jetsj.com*

ABSTRACT: This paper addresses the design and building solutions for the peripheral earth retaining structures, required for the construction of a development, which is a building complex of two building each 14 storeys high. The excavation footprint has approximately 6000 m2 with the deepest excavation depth of 9 m. The majority of the excavation intersected on heterogenous landfills, resting on top of Lisbon's Vulcanic Complex. The site is located in Miraflores, near Monsanto Forest Park. Surrounding the site there are public roads and other building constructions taking place. To minimize settlements around the excavation a secant pile wall was built, and braced either by a concrete strip slab or temporary ground anchors, the north elevation has an open filed, which was used to create a slope, to access to the final excavation level allowing an easy way to remove the soil.

RÉSUMÉ: Cet article traite des solutions de conception et de construction pour les structures périphériques de soutènement en terre, nécessaires à la construction d'un lotissement, qui est un complexe immobilier de deux bâtiments de 14 étages chacun. L'empreinte d'excavation est d'environ 6000 m2 avec une profondeur d'excavation maximale de 9 m. La majorité des fouilles ont été recoupées sur des décharges hétérogènes, reposant sur le complexe vulcanique de Lisbonne. Le site est situé à Miraflores, près du parc forestier de Monsanto, autour du site, il y a des routes publiques et d'autres constructions en cours. Pour minimiser les tassements autour de l'excavation, un mur de pieux sécants a été construit et contreventé soit par une dalle de béton ou des ancrages au sol temporaires, l'élévation nord a un dépôt ouvert, qui a été utilisé pour créer une pente, pour accéder au niveau d'excavation final permettant un moyen facile d'enlever le sol.

Keywords: Munich walls; Berlin walls; mixed walls; deep excavations.

1 INTRODUCTION

This paper addresses the peripheral earth retaining walls solution for the construction of a private condominium with two buildings of 14 storeys high on a plot with over 6000m^2, and three levels below ground, with a maximum excavation over 9 m.
The main constraints of earthwork were the tight deadline to execute the excavation work, the geological and geotechnical environment, and the proximity to nearby constructions. Figure 1 presents the locations of the constructions site.



Figure 1. Site Plan plus ML path.

This article aims to address in more detail the solutions of peripheric retaining walls taking account than in west side is not possible to execute provisory anchors and that 60 000 m3 needed to be excavated in less than 6 months.

2 MAIN CONSTRAINTS

From the site geological and geotechnical investigation, it was possible to confirm that the site was located on the Lisbon's Vulcanic Complex, covered by a heterogeneous landfill deposit layer. In Figure 2 is presented the geological chart of Portugal, 34-D Lisbon.

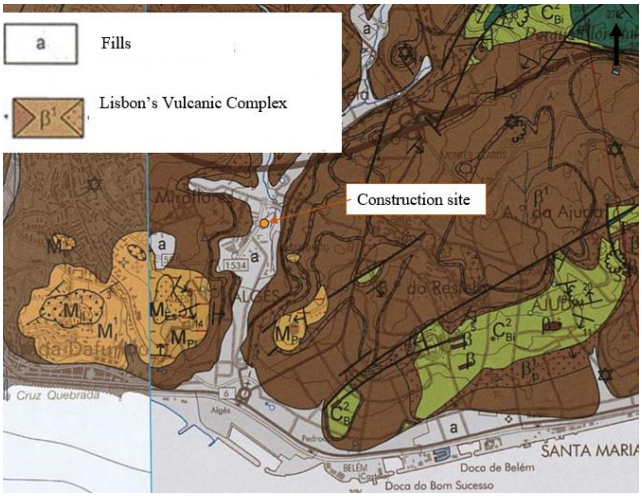

Figure 2. Geological Chart of Portugal.

The laboratory testing on the basalt rock mass shows a high modulus of elasticity and compressive resistance, in line with historical results in excavations in the area.

The existence of two PT (Transformation Post) constraints the solution, as electric cables with median tension were active in the area with no possible deactivation.

At last, the main constraint was the time schedule for the execution of the peripheric retaining walls and the excavation, in less than 6 months.

3 CONCEPTUAL SOLUTIONS

The conceptual solution for the excavation was developed considering time restrictions, space limitation and the type of geotechnical field. The design solution was an overlapped pile wall consisting on 500mm diameter piles spaced 400mm. The primary piles consist of unreinforced piles, which reach the basalt rock mass. As for the secondary piles, which are reinforced, they have an embedment length of 2,5 m on the rock mass underneath the maximum excavation depth, ranging from 7 to 12 m. Figure 3 and 4 show pile wall section.

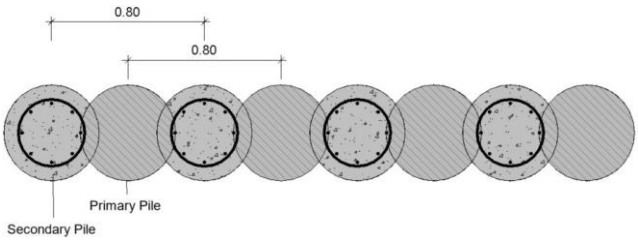

Figure 3. Overlap pile wall.



Figure 4. Overlap pile wall preparation in situ with marks.

The overlapped pile wall was horizontally supported by two types of solution. In South, North and East side, provisory anchor levels were considered with pretension. Figure 5 shows the section solution.

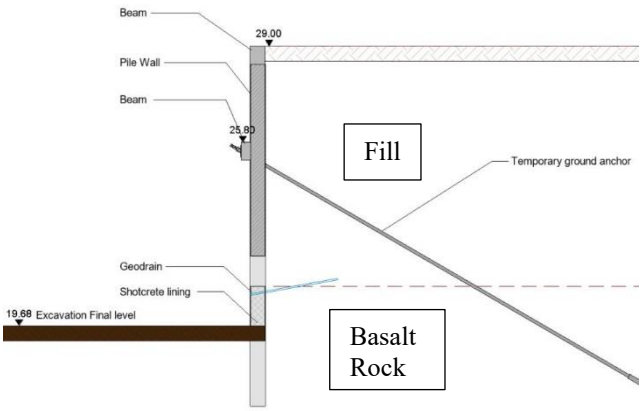

Figure 5. Section solution for North, South and East side.

On the West side, provisory anchors were not possible due to the proximity to adjacent lot excavation.

Due to time restrictions, the solution for horizontal support was slab bed solution. In this solution, the slab is partially executed before the full excavation. The pile wall has enough stiffness to allow 3m excavation with no support, followed by the execution of the slab bed that is fixed in the extremities by the pile wall showed in Figure 5 and or by sub vertical micropile elements, as Figure 6.

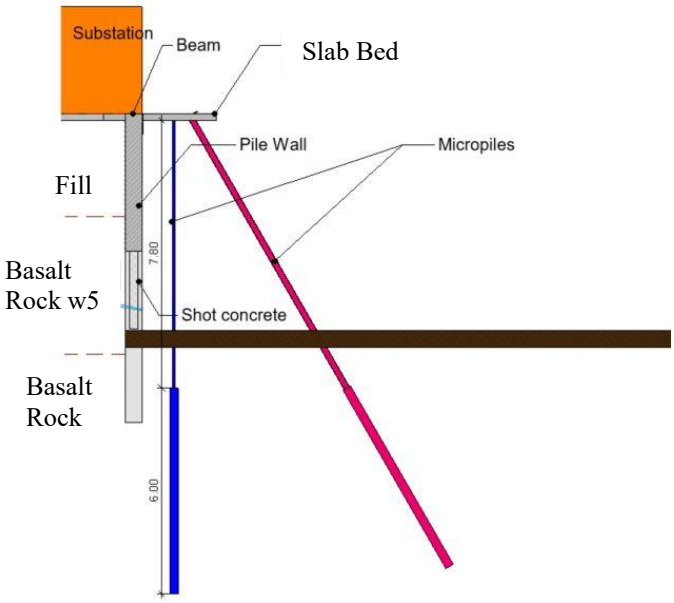

Figure 6. Section solution for West side.

Due to length of the slab bed, vertical support was needed to control the deformation of the slab bed in excavation phase.

Taking in consideration the overall force in the slab bed in excavation phase, additional reinforcement bars were considered, in addition to the reinforcement bars predicted in the stability project. Figure 7 show BIM model for the excavation.

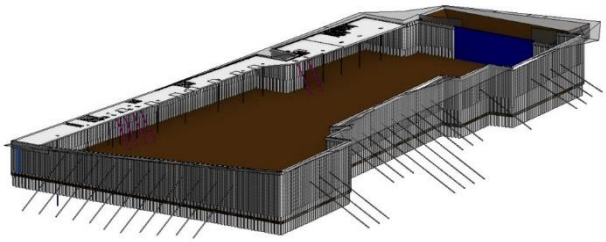

Figure 7. BIM model.

The design of the peripheric retaining wall was developed with Plaxis 2D models and Autodesk Robot models for the strip slab (figure 8 and 9).

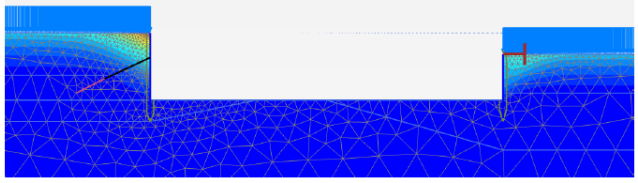

Figure 8. Plaxis 2D model.

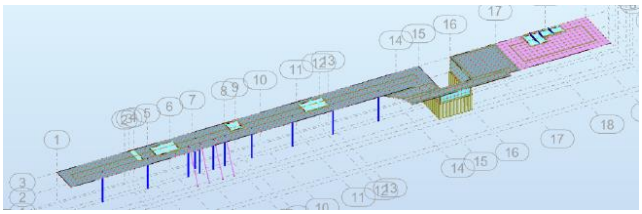

Figure 9. Autodesk Robot Model.

Due to the complexity of the geotechnical field, it was executed a survey and observation plan in situ, to confirm the design criteria and evaluate the behaviour of peripherical retaining wall structure.

4 EXECUTION

The solution of pile wall allows the execution of the peripheric retaining wall with multiple site fronts, with 5 pile machines at the same time.

Intended to support the high intensity work of 5 pile machines, 2 auto concrete mixers were in site to support the piles machines.



Figure 10. East Side with 2 pile machines.

Figures 11, 12, 13 and 14 show the retaining pile wall solution at bottom excavation or during excavation.



Figure 11. West Side solution with slab bed.



Figure 12. East Side solution with provisory anchors.



Figure 13. South Side solution with provisory anchors. (definitive structure already in place).



Figure 14. West Side (Left) and East Side (Right) solution at bottom excavation. (definitive structure already in place).

5 MONITORING AND SURVEY PLAN

The instrumentation adopted in situ consisted of a wide range of devices, of which the following stand out:

- Topographic targets in the peripheral retaining structures, placed during their execution.
- Topographic targets in the surrounding tower cranes, installed before the start of excavation work.
- Piezometers, installed to control the position of the water table.
- Inclinometers, installed to control the evolution of horizontal displacements of the terrain at depth;
- Load cells, used to evaluate loads on temporary anchors;

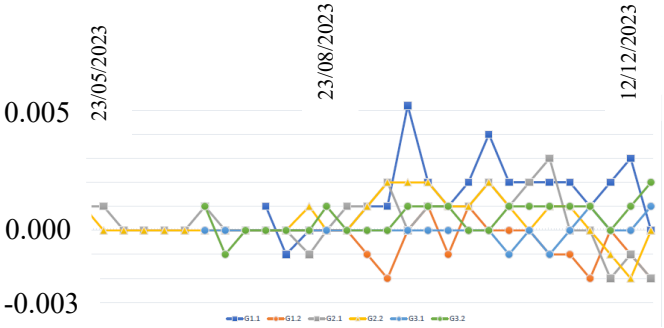

Figure 15. Towers Cranes vertical deformation (m).

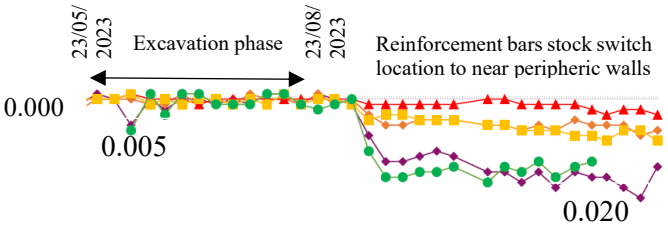

Figure 16. Horizontal deformation pile wall (m).

The survey and observation plan confirmed the design criteria of the project. Nevertheless, during the construction of the structure from the bottom of the excavation, the reinforcement bars stock switch to a very close area near the peripheric retaining wall, which results in a significant horizontal deformation, yet, under accepted values.

6 CONCLUSIONS

This article highlights the mains solutions of peripheric earth retaining walls with time constrains and nearby excavations constrains. Risk management, conceptual confirmation, assessment of good behaviour of the structures were only possible with the execution of a Monitoring and Survey Plan.

ACKNOWLEDGEMENTS

The authors are grateful to Norfin, for permission to present this paper as well as to Alves Ribeiro Group, Main Contractor, for the collaboration and trust placed in JETsj.

Proceedings of the XVIII ECSMGE 2024
GEOTECHNICAL ENGINEERING CHALLENGES
TO MEET CURRENT AND EMERGING NEEDS OF SOCIETY
© 2024 the Authors
ISBN 978-1-032-54816-6
DOI 10.1201/9781003431749-456
Open Access: www.taylorfrancis.com, CC BY-NC-ND 4.0 license

ECSMGE 24
XVIII EUROPEAN CONFERENCE ON SOIL MECHANICS AND GEOTECHNICAL ENGINEERING

Performance investigation of a newly proposed drainable pipe fitting

Enquête sur les performances d'un nouveau raccord proposé de tuyau d'évacuation

K. Kawai*, K. Nakashima
Kindai University, Higashi-Osaka, Japan

K. Maeda, S. Fukatsu
Okabe Co., Tokyo, Japan

**kkawai@civileng.kindai.ac.jp*

ABSTRACT: We propose a versatile drainage system that incorporates drainage inlets for pipe fittings that can connect to standard steel and PVC pipes. In existing drainage pipe systems, soil entering from small openings clogs the drainage path and is a cause for concern. With the proposed pipe fittings, however, it is possible to freely design the drainage inlet shape, position and inflow path, thereby reducing the amount of soil entering the drainage route. In this study, drainage performance and sediment control capabilities of the newly proposed drainable pipe fittings were investigated through laboratory and full-scale model experiments. Consequently, it was found that the drainable pipe fittings ultimately possessed equivalent drainage performance to conventional drainage pipes with better control of sediment discharge. Further inlet shape improvements can provide effective drainage systems for geotechnical engineering sites.

RÉSUMÉ: Nous proposons un système d'écoulement polyvalent qui intègre des entrées d'évacuation grâce à un raccord de tuyauterie pouvant se connecter à des tuyaux standard en acier ou en PVC. Dans les systèmes de canalisations d'écoulement existants, la terre pénètre par de petites ouvertures et bouche l'entrée des conduites d'écoulement et constitue un problème. Néanmoins, avec le raccord de tuyauterie proposé, il est possible d'établir librement la forme, l'emplacement et l'afflux des ouvertures d'écoulement, réduisant ainsi la quantité de terre entrant dans les voies d'écoulement. Dans cette étude, les performances des écoulements et les capacités de contrôle des sédiments du nouveau raccord de tuyauterie a écoulement proposé ont été étudiées en laboratoire et sur modèles à grande échelle. Par conséquent, il a été constaté que les raccords de tuyau d'écoulement possèdent finalement des performances d'écoulement équivalentes à celles des tuyaux d'écoulement conventionnels et peuvent mieux contrôler l'écoulement des dépôts de sédiments. D'autres améliorations de la forme peuvent fournir un système d'écoulement efficace pour les sites d'ingénierie géotechnique.

Keywords: Drainage system; underground pipe; permeability test.

1 INTRODUCTION

Limited methods exist for draining excessive water from natural slopes or existing earth structures. Drainage pipe systems, which drive a perforated steel pipe into ground with high phreatic surfaces offers not only the advantage of requiring a relatively small construction space and small workforce, but also the ability to increase the rigidity of the penetration area owing to a nailing effect (Saito et al., 1968). However, challenges arise when soil material intrudes into the pipe and clogs the drainage holes, leading to a rapid decline in drainage efficiency. Additionally, the loosening of the ground along the drainage route due to the induction of soil also causes concern. In this study, a new pipe fitting is proposed with a drainage function and mechanism to reduce soil leakage into the drainage route by directing the flow against gravity. Here, the performance of the newly developed pipe fitting was investigated through laboratory and full-scale model tests.

2 DRAINABLE PIPE FITTING

The pipe fitting proposed in this study is designed to have drainage functionality at the joint connecting the prefabricated PVC or steel pipes. This drainable pipe fitting, as shown in Figure 1, features a bulge on the side that serves as the drainage inlet. Generally, drainage pipes are installed with a 5-degree upward slope. The drainable fitting is used with the drainage

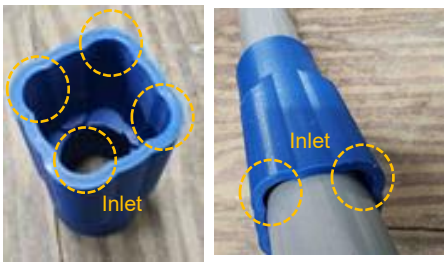

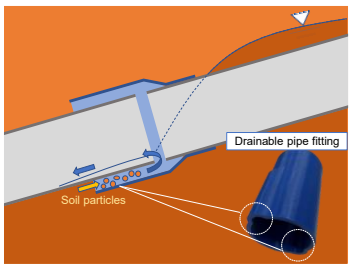

(a) Photos of drainable pipe fitting (b) Drainage mechanism

Figure 1. Overview of the newly proposed drainable pipe fitting.

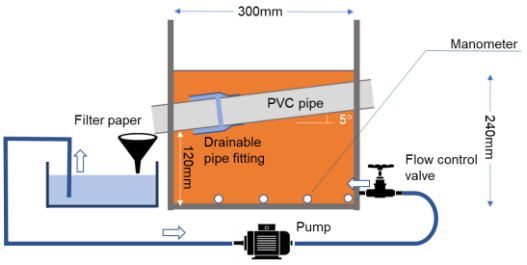

Figure 2. Laboratory model test.

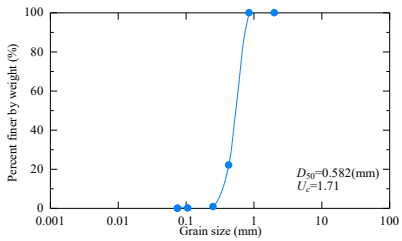

Figure 3. Particle size distribution.

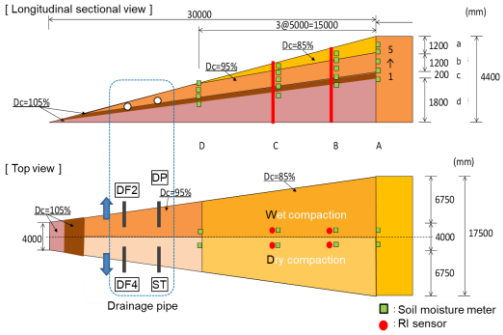

Figure 4. Overview of full-scale model.



Figure 5. Alignment of drainage pipe.

inlets at the lower slope position, as illustrated in Figure 1. This configuration allows groundwater to flow upward through the drainage inlet into the drainage route and then to drain from the end of the non-perforated pipe. As a result, less soil particles are expected to enter the drainage route, because they would have to defy gravity to flow upward. Furthermore, the use of prefabricated pipes garners the advantage of applying existing drilling and pipe installation methods without modification. Incorporating multiple fittings increases the number of drainage inlets, and as drainage positions are specified, it is also possible to strategically lower the phreatic surface using this system.

3 EXPERIMENTAL PROCEDURES

3.1 Laboratory model test

Figure 2 illustrates an overview of the model test. The model box has internal dimensions of 300mm width, 300mm height, and 200mm depth, allowing the installation of the drainage pipe at a 5-degree upward angle from the central part of one side of the model box with a water inlet at the lower part of the upstream side. Drainage from the outlet of the pipe was collected in an attached tank through filter paper and recirculated by a pump. During the test, volumes of drainage water and soil were measured periodically. To simulate materials prone to enter the drainage path, silica sand No. 5 ($G_s = 2.67$) was used. Figure 3 shows the particle size distribution of the soil test material. Through maximum and minimum density tests, a maximum void ratio of 1.050 and a minimum void ratio of 0.708 were obtained. When making the soil model, dry samples were compacted in 10 layers to a height of 240mm to achieve a void ratio of 0.70 (as determined from a separately conducted permeability test ($k = 3.4 \times 10^{-3}$ m/sec). To prevent drainage during the experiment, the soil model was first saturated up to lower part of the drainage pipe. Then, the flow control valve was adjusted to establish a constant hydraulic gradient while monitoring the manometers at the inflow section to confirm a steady state. The water level was raised every 1cm until soil leakage became significant and the drainage pipe was completely clogged.

3.2 Full-scale model test

The performance of the proposed drainage systems was investigated on a full-scale embankment model (Figure 4) constructed at Kobe Airport. The drainage systems tested consist of four types, as shown in Figures 5 and described as follows: DF4 and DF2 are the drainable fittings proposed in this study, with 4 and 2 drainage inlets, respectively; ST is a steel drainable fitting that incorporates drainage functionality into existing anchor rods, maintaining the same shape with two drainage inlets; and DP is a perforated PVC pipe installed for comparison purposes. All the drainage systems were inserted at an upward angle of 5-degrees from the slope surface to a depth of 2 meters. Drainable fittings were connected to pipes at every 50 cm, including at the tip (DF4, DF2, ST). ST, a self-

drilling type of pipe made of rust-resistant steel, had high rigidity and allowed for being driven into position using impact. Placements for DP, DF2, and DF4 were pre-augured before insertion to ensure that the auger holes had stable walls. The pipes were then inserted and installed. Drainage from the drainage pipes was collected in acrylic containers, and the drainage water and soil were measured periodically. Additionally, during the measurement period, the drainage process was recorded with a time-lapse camera, and days with drainage were recorded.

4 EXPERIMENTAL RESULTS AND DISCUSSIONS

First, we discuss the results of the laboratory model tests. Before testing the drainage fittings, model tests were conducted using PVC pipe with small hole perforations and an inner diameter of 31mm. Soil entered from the upper holes of the perforated pipe regardless of the drainage process for the soil sample. To compare the drainable pipe fitting systems, all the holes on the upper surface of the perforated pipe without the drainable pipe fittings and those upstream of the drainable pipe fitting were sealed with waterproof tape. Figure 6 shows the results of the perforated pipe model test. During the test, due to sensitivity issues with the manometers, hydraulic gradient was calculated by dividing the difference between the water level in the inflow section manometer and the height of the lowermost hole by the horizontal distance. As the hydraulic gradient increased, the drainage volume also increased linearly. In the case of the perforated pipe, there was a constant amount of soil leakage even at low hydraulic gradients; however, a significant amount of soil leakage was observed once the hydraulic gradient exceeded 0.2.

Next, we conducted experiments using a drainable pipe fitting. The experimental results are shown in Figure 7. Although it is difficult to directly compare the absolute values of the hydraulic gradient, the trend of increasing drainage volume with increasing hydraulic gradient is the same. At low hydraulic gradients, soil leakage was not observed; however, once soil began to leak, it increased exponentially, and clogging due to soil leakage made it impossible to continue the experiment above a hydraulic gradient of 0.2. The drainable pipe fittings had a drainage design with a 5-degree upward angle at the inflow section, which resulted in a greater flow velocity than gravity acting on soil particles. This design could not sufficiently prevent soil from leaking.

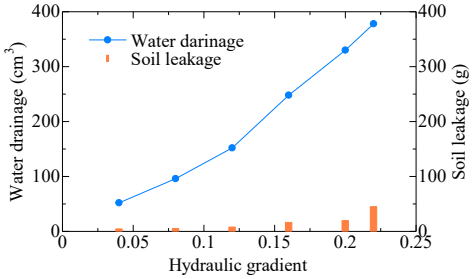

Figure 6. Test results for perforated pipe.

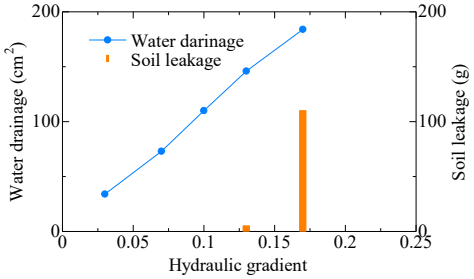

Figure 7. Test results for drainable pipe fitting.

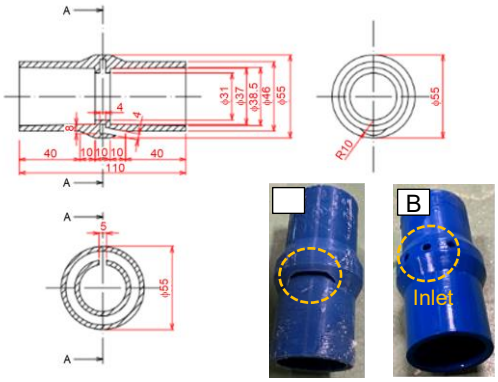

(a) Shape and photos

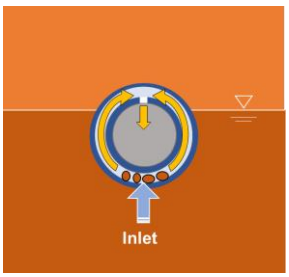

(b) Drainage mechanism

Figure 8. Modified drainable pipe fiting.

Therefore, as shown in Figure 8, we improved the fitting design. The modified drainable pipe fitting utilized an inlet at the bottom of the drainage pipe and a drainage route confluence point at a higher position inside the drainage pipe, creating a structure with greater height differences. We prepared two different inlet shapes, denoted as A and B. Figure 9 shows the test results using the modified drainable pipe fittings. There was no significant difference in the results between fittings A and B. The results showed that the inlet shape had little impact on the drainage and sediment control functions on the same internal structure. Compared to before the improvement, soil

leakage was reduced; however, once the hydraulic gradient exceeded a certain threshold, soil leakage became excessive, making it difficult to continue the experiment. As mentioned earlier, direct comparison of the absolute values of the hydraulic gradient was not appropriate, so we compared the drainage components based on the relationship between drainage volume and soil leakage, as shown in Figure 10. In the case of the perforated pipe, soil leakage was observable even at low drainage volumes, whereas the proposed drainable pipe fittings hardly had any soil leakage. Nevertheless, it was evident that significant soil leakage occurred once the drainage volume exceeded a certain threshold, which appeared to be strongly dependent on the rate of water level rise.

Drainage and soil leakage in the full-scale embankment test were measured over six separate periods. Figure 11 shows the precipitation during each measurement period. There was little to no substantial rain between autumn and winter, while precipitation increased significantly from early spring to the rainy season, resulting in variations during the measurement period. Figures 12 and 13 show the measured drainage and soil leakage, respectively. It is difficult to compare the type of drainage pipe since the installation locations and soil conditions were different. However, it is evident that there is not a significant difference in drainage volume between perforated pipes and drainable pipe fittings. This suggests that drainable pipe fittings provide a comparable drainage performance to perforated pipes. On the other hand, soil leakage was rarely observed during periods of low precipitation and was most pronounced with perforated pipes. Observation from time-lapse cameras revealed that drainage occurred only on days with substantial rainfall exceeding 30mm. Tensiometers indicated that the conditions for perched water to accumulate in this embankment occurred with daily rainfall of around 25mm. Below this threshold, water dissipated through surface runoff or evaporation without generating perched water, indicating that the drainage system is effective during times when free water, such as perched water, is generated.

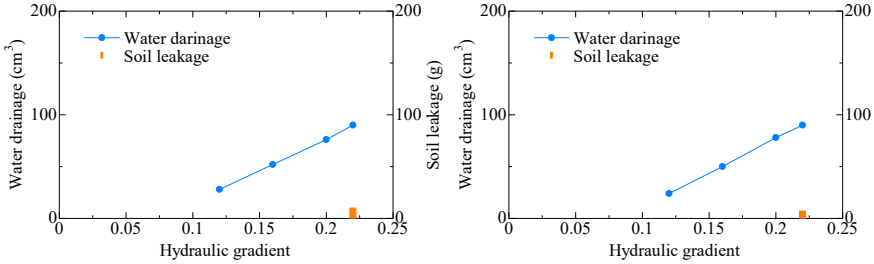

(a) Shape A *(b) Shape B*

Figure 9. Test results for modified perforated pipe.

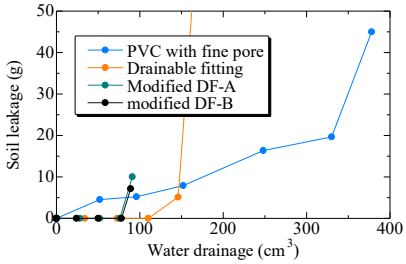

Figure 10. Relationship between water drainage and soil leakage.

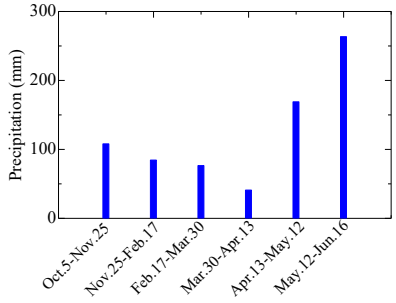

Figure 11. Precipitation during measurement period.

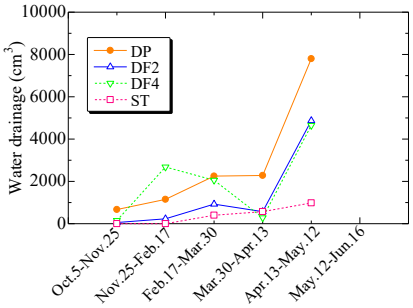

Figure 12. Drainage volume during measurement period.

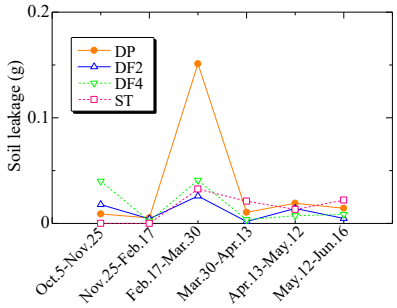

Figure 13. Soil leakage during measurement period.

5 CONCLUSIONS

In this study, we conducted model experiments to investigate the drainage function and soil leakage control function of drainable pipe fittings with a new drainage mechanism. As a result, we found that the new drainable pipe has sufficient drainage capacity and offers soil leakage control under low hydraulic gradients.

REFERENCES

Saito, M., Uesawa, H., Menjo, S. and Yasuda, Y. (1968) Effect of drainage for stability of embankment slopes by perforated pipes on the New Tokaido Line, *Railway Technical Research Report*, 631, pp.1-18 (in Japanese).

Proceedings of the XVIII ECSMGE 2024
GEOTECHNICAL ENGINEERING CHALLENGES
TO MEET CURRENT AND EMERGING NEEDS OF SOCIETY
© 2024 the Authors
ISBN 978-1-032-54816-6
DOI 10.1201/9781003431749-457
Open Access: www.taylorfrancis.com, CC BY-NC-ND 4.0 license

ECSMGE 24
XVIII EUROPEAN CONFERENCE ON SOIL MECHANICS AND GEOTECHNICAL ENGINEERING

Use of CO_2-induced siderite and dolomite with nanoclay for soil improvement

Utilisation de sidérite et dolomite induites par l' injection de CO_2 avec de la nanoargile pour l'amélioration de sols

H.A. Keykha, M. Mavroulidou*
Department of Civil and Building Services Engineering, BEA, London South Bank University, London, UK
H. Mohamadzadeh Romiani
Department of Civil Engineering, Buein Zahra Technical University, Buein Zahra, Qazvin, Iran
**mavroum@lsbu.ac.uk*

ABSTRACT: We studied the precipitation of carbonate minerals used as cements for ground improvement. The carbonate minerals were prepared by combining divalent ions (Mg^{2+}, Ca^{2+}, and Fe^{2+}) with carbonate ions (CO_3^{2-}) induced by microbial activity. Scanning electron microscopy (SEM) and X-Ray Diffraction (XRD) analyses observed the shapes and sizes of the minerals and attested the formation of dolomite ($CaMg(CO_3)_2$) and siderite ($FeCO_3$). Consolidated drained triaxial tests (CD) were performed on treated specimens of silica sand with the CO_2-induced siderite and dolomite cements with and without the addition of nanoclay. Specimens treated with siderite had higher strengths than dolomite-treated specimens. The addition of nanoclay further increased the shear strength of the specimens and reduced their brittleness. Moreover, it was found that the shearing resistance of fully saturated specimens was not considerably reduced compared to that of dry specimens, as it only decreased by 5–15% compared to that of dry specimens.

RÉSUMÉ: Nous étudions la précipitation de carbonates que nous utilisons comme ciments pour l'amélioration de sols. Les minéraux carbonatés ont été préparés en combinant des ions divalents (Mg^{2+}, Ca^{2+}, et Fe^{2+}) avec des ions carbonate (CO_3^{2-}) formés à partir de l'activité métabolique microbienne. La forme et la taille des minéraux ont été observées par analyses microscopiques (microscope électronique à balayage). L' analyse minéralogique des minéraux (par diffraction des rayons X) a confirmé la formation de dolomite ($CaMg(CO_3)_2$) et de sidérite ($FeCO_3$). Ces minéraux ont ensuite été utilisés pour l'amélioration des propriétés d'un sol granulaire. Des essais triaxiaux consolidés drainés (CD) ont été effectués sur des échantillons de sable siliceux traités par la sidérite et dolomite ainsi produites, avec ou sans nanoargile. Les échantillons traités à la sidérite avaient une résistance au cisaillement plus élevée que ceux traités à la dolomite. L'ajout de nanoargile a augmenté la résistance des échantillons au cisaillement ainsi que leur ductilité. De plus, la résistance des échantillons saturés n'était pas considérablement inférieure à celle des échantillons secs, n'ayant diminué que de 5 à 15% par rapport à celle des échantillons secs.

Keywords: MICP; siderite; dolomite; soil improvement.

1 INTRODUCTION

Sustainable precipitation of carbonate minerals has the potential to offer environmentally friendly ways of improving soils of poor engineering characteristics preventing soil erosion, slope instability, or low bearing capacity. Microbially-induced carbonate precipitation (MICP) has emerged as one such potentially more sustainable process, as it uses natural mechanisms to induce mineral precipitation in the soil pore space leading to soil cementation (Keykha et al., 2017, 2019; Wang et al. 2021, Romiani et al. 2023).

The precipitation of minerals by microbial activity, which may be extracellular precipitation, is known as biologically induced mineralization. In various types of living organisms, the extracellular mineralization-related carbonate precipitation is a well-known phenomenon (Lowenstam, 1989). By altering the surrounding environmental conditions and acting as nucleation sites, bacteria can promote mineral precipitation in microenvironments in some challenging natural conditions in terms of pH and temperature (Sánchez-Román et al. 2011).

MICP works have mostly studied $CaCO_3$ precipitation biotechnology using ureolytic bacteria to hydrolyse urea to carbonate by producing urease enzyme release as shown in equations 1-2 (Ivanov & Chu, 2008; Tang et al. 2020):

$$CO(NH_2)_2+2H_2O \xrightarrow{urease\ enzyme} CO_3^{2-} + 2NH_4^+ \quad (1)$$

$$CaCl_{2\,(aq)} + CO_3^{2-}{}_{(aq)} \rightarrow CaCO_3\,(s) \quad (2)$$

MICP can produce different polymorphs of $CaCO_3$ such as aragonite, calcite, and vaterite, as well as $CaCO_3$ monohydrate, $CaCO_3$ hexahydrate, and amorphous $CaCO_3$ (Mortensen et al. 2011).

This study aims to evaluate the use of various types of precipitated carbonate minerals other than only $CaCO_3$ to improve mechanical properties of soils. The minerals were obtained using carbonate ions (CO_3^{2-}) produced by the metabolic action of microbes as an *ex situ* process, to overcome complications of bacteria activity and survival in different soil environments. The carbonate minerals thus produced were then combined with nanoclay additive, to further enhance the mechanical properties of the treated soil.

2 MATERIAL AND METHODS

2.1 Bacteria type strain and culture media

The present study used urease-producing bacteria *Sporosarcina pasteurii* (PTCC 1645), grown in NH_4-YE, a medium made up of 800 mL of Tris-buffer 0.13 mol/L (pH = 9.0), 20.0 g of yeast extract, 10.0 g of $(NH_4)_2SO_4$, and 100 ml of distilled water. Before autoclaving, the pH of the growth medium solution was measured to be adjusted in 9.0. After that, the components were individually autoclaved (at 121 °C for 15 min) before being cooled and combined in an Erlenmeyer flask. Bacteria were cultivated at pH=9.0, which was the optimal pH for *S. pasteurii* growth. The bacteria were transferred to the medium broth in an incubator (30 °C) and shaken aerobically for 3 days at 200 rpm. A previously established optical density of 1.6 at 600 nm (about 108 cells/mL), was obtained. The bacteria were recovered from an overnight culture by centrifugation at 8000 g for 10 min. Next, 100 mL of urea (1M) was mixed with 100 mL of the bacteria culture to produce a free carbonate ion solution. The carbonate ions thus produced were combined with Fe^{2+}, Mg^{2+}, or Ca^{2+} ions (using $FeSO_4$, $MgCl_2$, and $CaCl_2$ solutions respectively) to induce $FeCO_3$, $CaCO_3$ and $CaMg(CO_3)_2$ mineral precipitation according to equations 3-4:

$$FeSO_{4\,(aq)} + CO_3^{2-}{}_{(aq)} \rightarrow FeCO_3\,(s) \quad (3)$$

$$CaCl_2/MgCl_{2\,(aq)} + CO_3^{2-}{}_{(aq)} \rightarrow CaMg(CO_3)_2(s) \quad (4)$$

The characteristics of the reagents used are listed in Table 1.

Table 1. Chemical reagents used.

Reagents	Molarity	Cation:Carbonate Ratios
$FeSO_4{\cdot}7H_2O$	1M	Fe^{2+}: CO_3^{2-} 1:1
$CaCl_2$/ $MgCl_2$	1M	Mg^{2+}/Ca^{2+}: CO_3^{2-} 1:1

2.2 SEM and XRD Analysis

Selected carbonate samples were analysed using various techniques including scanning electron microscopy (SEM) and X-ray diffraction analysis (XRD). SEM was used to examine the size, shape, and arrangement of mineral crystals. To ensure good conductivity, the dry powder specimens were coated with gold before SEM testing. During these tests, we applied accelerating voltages between 2 and 10 kV. Additionally, XRD was employed at 30 kV and a 30 mA current to identify the mineral type.

2.3 Soil treatment and triaxial testing

The soil used in this study was clean silica sand of a particle size distribution shown in Figure 1, a uniformity coefficient of 2.74, a specific gravity of 2.65, and maximum and minimum void ratios of 0.90 and 0.57, respectively.

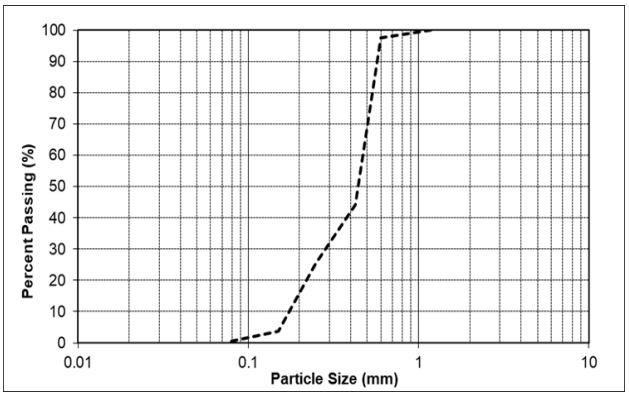

Figure 1. Particle size distribution of silica sand.

To conduct triaxial tests, cylindrical specimens of 10cm length and 5cm diameter were prepared by combining sand with a 15% content of carbonate minerals (specifically, $FeCO_3$ and $CaMg(CO_3)_2$) in accordance with ASTM D2166 standards. In some specimens 2% nanoclay was also introduced into the carbonate mixture. The specimen preparation procedure is presented in Table 2. After allowing the specimens to cure for 7 days, consolidated drained triaxial tests (CD) were performed on the treated samples following ASTM D7181 guidelines with a triaxial cell pressure of 100 kPa. All experiments

were carried out in triplicate under both dry and fully saturated conditions respectively.

Table 2. Properties of sample preparation.

Sample NO.	Carbonate mineral (15%)	Nano -clay (%)	W (%)	γ (g/cm^3)
D15	Dolomite	0	10	1.98
D15+nano2	Dolomite	2	10	2
S15	Siderite	0	10	1.98
S15+nano2	Siderite	2	10	2

3 RESULTS AND DISCUSSION

3.1 Carbonate mineral production

Figure 2 shows the formed carbonate minerals. $FeCO_3$ particles exhibit a polycrystalline, spherical shape with sizes ranging from 0.5-2 µm (Figure 2 (a)). Conversely, Ca-$Mg(CO_3)_2$ crystals have a botryoidal shape, with sizes ranging from 5-16 µm (Figure 2(b)). The XRD analysis confirms the presence of $FeCO_3$ as siderite and $CaMg(CO_3)_2$ as dolomite (Figure 3).

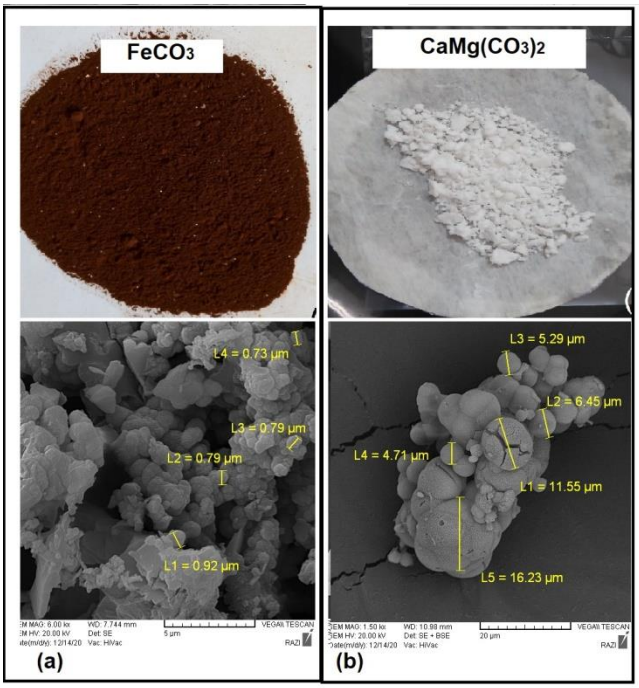

Figure 2. Macro and microstructure of carbonates.

3.2 Triaxial Compressive Strength (CD)

Figure 4 presents the stress-strain behaviour of samples treated with carbonates in a triaxial test conducted under dry conditions (CD). As illustrated, the samples treated with siderite exhibited greater strength compared to those treated with dolomite. Furthermore, samples treated with a combination of carbonate minerals and nanoclay displayed even higher strength when compared to the other treatments, with the highest strength recorded at 525 kPa observed in the sample treated with siderite and nanoclay. Additionally, the specimens treated with siderite and nanoclay were more ductile than specimens treated solely with siderite.

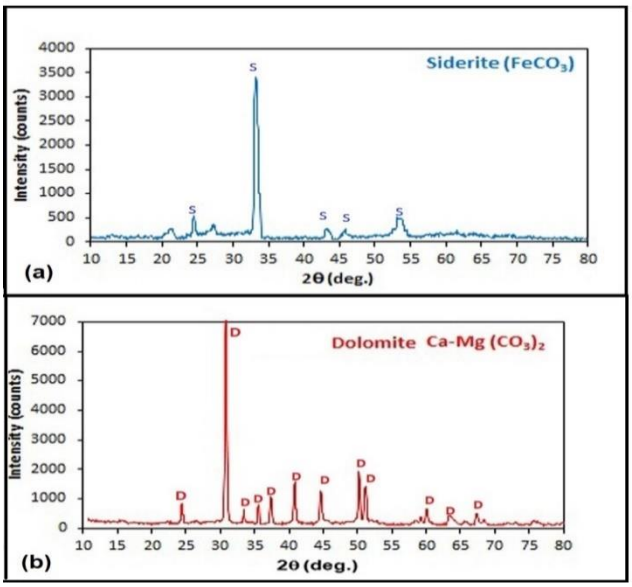

Figure 3. XRD analysis of carbonate minerals (a) Siderite, and (b) Dolomite.

The results of the triaxial test conducted under saturated conditions closely resembled those obtained under dry conditions (Figure 5). Strengths de-creased by 5% to 15% for all saturated specimens, compared to those of dry specimens; the highest strength recorded under saturated conditions was approximately 464 kPa, in the specimens treated with siderite and nanoclay. The secant modulus E_{50} of specimens decreased with the addition of nanoclay (Figure 6).

4 CONCLUSION

In this study, microbially induced carbonate precipitation was used to generate free carbonate ions (CO_3^{2-}). Different carbonate minerals were formed by introducing Fe^{2+}, Mg^{2+}, and Ca^{2+} ions into CO_3^{2-} solutions, resulting in the precipitation of siderite ($FeCO_3$) and dolomite ($CaMg(CO_3)_2$). Scanning electron microscopy (SEM) analysis revealed that siderite had a polycrystalline, spherical morphology ranging from 0.5 to 2 µm, while dolomite displayed a botryoidal shape ranging from 5 to 16 µm.

Consolidated drained triaxial tests (CD) were conducted on treated silica sand samples with siderite and dolomite carbonate cements (15%) as well as

nanoclay (2%), under both dry and saturated conditions. The findings indicated that specimens treated with siderite had higher strengths compared to those treated with dolomite in both dry and saturated conditions. The addition of nanoclay resulted in further strength increase, with the highest recorded strength at 525 kPa observed in specimens treated with siderite and nanoclay. Nanoclay-treated samples had a reduced brittleness and can be advantageous for soil improvement.

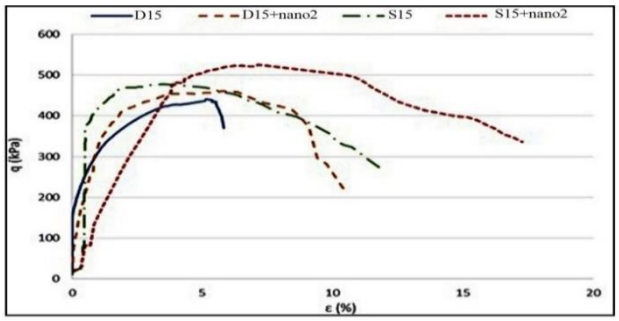

Figure 4. Stress-strain curves of dry specimens treated with 15% siderite, 15% dolomite and 2% nanoclay.

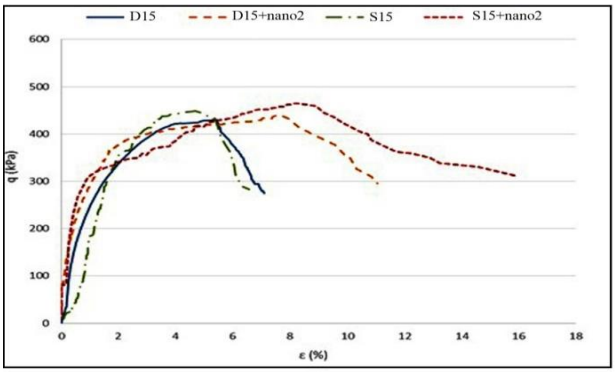

Figure 5. Stress-strain curves of saturated specimens treated with 15% siderite, 15% dolomite & 2% nanoclay.

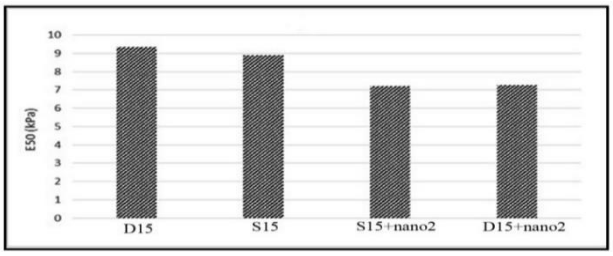

Figure 6. E_{50} variation for treated samples.

ACKNOWLEDGEMENTS

The research on this topic carried out by Dr Keykha at London South Bank University is linked to the UKRI-funded MSCA-PF project COSMIC (Grant EP/Y029607/1).

REFERENCES

American Society for Testing and Materials (Filadelfia, Pennsylvania). (2016). ASTM D2166/D2166M-16: Standard Test Method for Unconfined Compressive Strength of Cohesive Soil. ASTM.

American Society for Testing and Materials (2011). ASTM D7181. Standard test method for conso-lidated drained triaxial compression test for soils. ASTM International, West Conshohocken, Pa.

Ivanov, V.and Chu, J. (2008) Applications of microorganisms to geotechnical engineering for bioclogging and biocementation of soil in situ. *Rev. Environ. Sci. Biotechnol.*, 7, pp. 139–153. https://doi.org/10.1007/s11157-007-9126-3.

Keykha, H.A., Asadi, A. and Zareian, M. (2017). Environmental factors affecting the compressive strength of microbiologically induced calcite precipitation-treated soil. *Geomicrobiol. J*, 34(10), pp. 889 – 894.https://doi.org/10.1080/01490451.2017.1291772.

Keykha, H.A., Asadi, A., Huat, B.B. and Kawasaki, S. (2019). Microbial induced calcite precipitation by Sporosarcina pasteurii and Sporosarcina aqui-marina. *Environmental Geotechnics*, 6(8), pp. 562–566. https://doi.org/10.1680/jenge.16.00009.

Mortensen, B.M., Haber, M.J., DeJong, J.T., et al (2011). Effects of environmental factors on microbial induced calcium carbonate precipi-tation. *J. Appl. Microbiol.*, 111(2), pp. 338–349. DOI: 10.1111/j.1365-2672.2011.05065.x.

Lowenstam, H.A. and Weiner, S. (1989). *On Biomineralization*; Oxford University Press: New York, NY, USA.

Romiani, H.M., Keykha, H.A.,Talebi, M., et al (2023). Green soil improvement: Using carbon dioxide to enhance the behaviour of clay. *Ground Improve-ment.* 176(5), pp. 301–309. https://doi.org/10.1680/jgrim.20.00073.

Sánchez-Román, M., Romanek, C.S., Fernández-Remolar, D.C., et al (2011). Aerobic biomineraliza-tion of Mg-rich carbonates: Implications for natural environments. *Chem. Geol.*, 281(3-4), pp.143–150. https://doi.org/10.1016/j.chemgeo.2010.11.020.

Tang, C.S., Yin, L.Y., Jiang, N.J., et al (2020). Fac-tors affecting the performance of microbial-induced carbonate precipitation (MICP) treated soil: A review. *Environ. Earth Sci.*, 79:94. https://doi.org/10.1007/s12665-020-8840-9.

Wang, Z., Zhang, N., Jin, Y., et al (2021). Applica-tion of microbially induced calcium carbonate precipitation (MICP) in sand embankments for scouring/erosion control. *Mar. Georesources Geotechnol.*, 39(12), pp. 1459–1471. https://doi.org/10.1080/1064119X.2020.1850949.

Proceedings of the XVIII ECSMGE 2024
GEOTECHNICAL ENGINEERING CHALLENGES
TO MEET CURRENT AND EMERGING NEEDS OF SOCIETY
© 2024 the Authors
ISBN 978-1-032-54816-6
DOI 10.1201/9781003431749-458
Open Access: www.taylorfrancis.com, CC BY-NC-ND 4.0 license

ECSMGE 24
XVIII EUROPEAN CONFERENCE ON SOIL MECHANICS AND GEOTECHNICAL ENGINEERING

Staged construction of surcharged embankments over peat for a national road in Co. Donegal, Ireland

Construction etagé pour des remblais surchargés sur des sols tourbe pour un route national à Donegal en Irlande

P. Kissane*, F.J. Buggy, G. Ward
ROD Consulting Engineers, Dublin, Ireland

B.A. McCabe, F. Fattahi Masrour
University of Galway, Galway, Ireland

F. Towey
Donegal County Council, Donegal, Ireland

**paul.kissane@rod.ie*

ABSTRACT: The paper describes innovative geotechnical methods to implement staged construction of surcharged embankments up to 5.5 m high on very soft blanket peat soils in north west Ireland. Shear wave velocities, CPT ball tests and direct simple shear tests were used to assess the undrained strength of the peat. Intermediate hold periods and consolidation benefits were exploited to optimise the filling schedule. Changes to instrumentation, basal reinforcement, anchorage detailing and filling rates were implemented to assure stability. Detailed interpretation of settlement and pore pressure responses during loading and unloading at instrument clusters is presented, including back-calculated field coefficients of consolidation and observed deformation ratios.

RÉSUMÉ: L'article décrit des méthodes géotechniques innovantes pour mettre en œuvre la construction par étapes de remblais surchargés jusqu'à 5,5 m de haut sur des sols tourbeux très mous dans le nord-ouest de l'Irlande. Les vitesses des ondes de cisaillement, les essais à la bille CPT et les essais de cisaillement simple direct ont été utilisés pour évaluer la résistance non drainée de la tourbe. Les périodes de détention intermédiaires et les avantages de la consolidation ont été exploités pour optimiser le calendrier de remplissage. Des modifications apportées à l'instrumentation, au renforcement basal, aux détails d'ancrage et aux taux de remplissage ont été mises en œuvre pour garantir la stabilité. Une interprétation détaillée des réponses au tassement et à la pression interstitielle pendant le chargement et le déchargement au niveau des groupes d'instruments est présentée, y compris les coefficients de consolidation sur le terrain rétro-calculés et les taux de déformation observés.

Keywords: Peat soils; observational approach; multistage construction; surcharge.

1 INTRODUCTION

The N56 national road forms the major transportation corridor along the remote, north-west coast of Co. Donegal, Ireland. Route upgrades require maintenance of existing 'lifeline' traffic and provision of new alignments. Much of the route is underlain by Atlantic Blanket Bog peat and shallow Caledonian Granite bedrock. The paper describes works on a 4.1 km two-lane road located just north of Glenties, the southern half of which falls within the Owenea River Freshwater Pearl Mussel catchment. Concerns about potential impacts of mass excavation of peat on this protected aquatic species led to a solution involving crushed rock fill and surcharge (Figure 1).



Figure 1. Looking south towards Glenties: temporary diversion on left and main embankment at surcharge level.

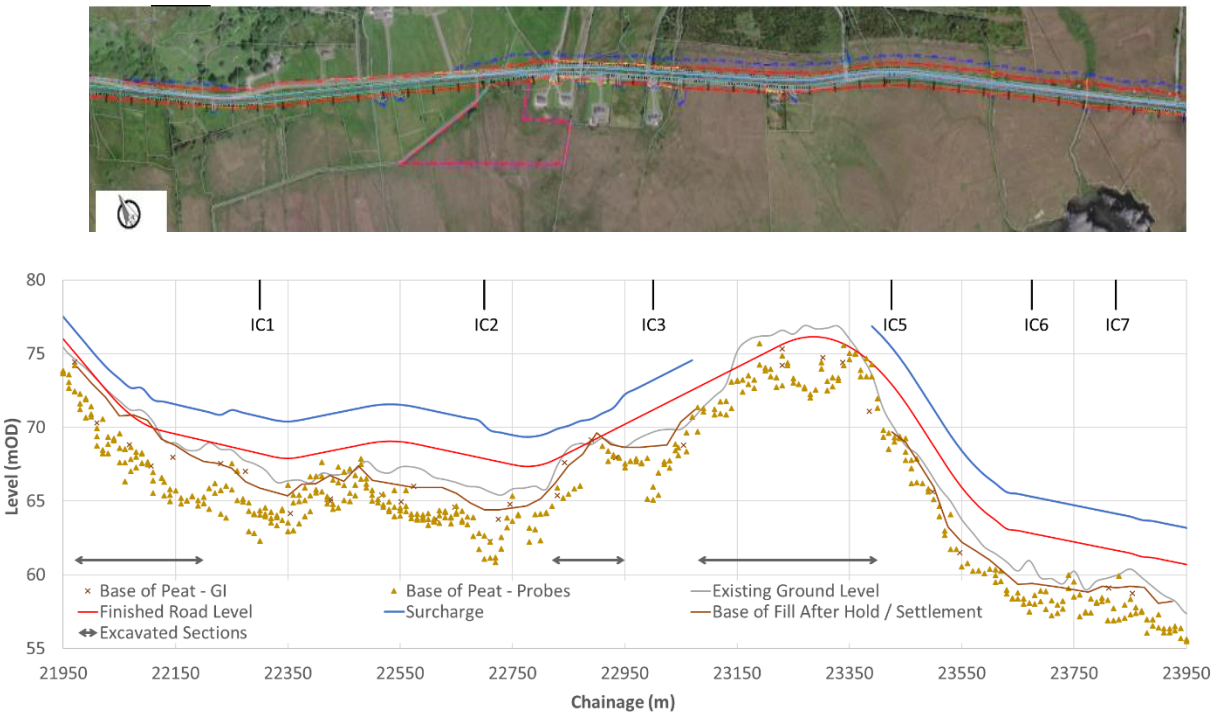

Figure 2. Aerial map of alignment and profile of peat and fill levels (surcharge and final settlements).

A 1.25 km long section was constructed directly onto extremely low-strength soils, using geosynthetic basal reinforcement, multi-stage construction and 1.5–2.5 m high temporary surcharge (Figure 2), informed by extensive instrumentation. The full surcharge height was achieved in all of this section with the exception of Chainage 23080 to 23400.

Construction commenced in early 2021, diverting traffic onto a 1.5 km single-lane temporary road (Figure 1), with supplemental investigations and refinements to the proposals prior to multi-stage embankment construction. Just under 50% of the surcharge material brought to site was used efficiently after completion of the hold period, filling excavations where peat removal was necessary (where at-grade or in cutting into peat). Geosynthetic reinforcement of the pavement foundations was also provided to mitigate differential creep movements. The completed works were opened to traffic in late 2022.

2 INVESTIGATING PEAT PROPERTIES

2.1 Peat probing

The construction contract required confirmation of peat thicknesses at 10 m intervals upon possession of the site. The contractor, Wills Bros. Ltd., provided the peat probes, noting depths in the range 0.3 m to 5.2 m, as shown in Figure 2. This probing provided more useful information in several areas than previous investigations, which were confined to locations close to the existing road embankments, typically 1.0 m in height above surrounding peat and prone to long-term deformation. Upwelling of pore pressures from the base of some probes was also observed, which was consistent with high ground water levels and low (hand) shear vane strengths at these locations.

2.2 Temporary road hand vane data

Construction of the temporary road (Figure 1) provided an opportunity to review some design assumptions from the perspective of risk avoidance, as disastrous peat slides had been initiated elsewhere in the county in the months prior to commencement.

Hand vane tests performed at shallow depths of 0.3 m to 0.6 m gave undrained strengths (c_u) typically in the range 5–50 kPa along the subgrade of the temporary road prior to its construction. Failure by extrusion at the edges of the temporary road was observed in the softest deposits, coincident with saturated conditions due to a shallow rock profile. It is likely that the filling rate was greater for the temporary road than for the mainline, with approximately 1.0m placed directly onto 30 kN grade geogrids.

2.3 Peat moisture contents and humification

Peat moisture contents (w) range from 600-1500% across the site, averaging ≈1000%. The degree of humification, according to the Von Post (1922) classification, generally increases with depth from H3 to H6/H7. Most of the peat incorporates fine and

coarse fibres, with a significant timber content observed at the northern end of the site.

2.4 Shear wave velocities & direct simple shear laboratory testing

In-situ shear wave velocities (V_s) in the range 14-40 m/s were measured at critical locations on site. An innovation on this project was the use of V_s profiles to infer c_u values, using the following established correlation: $c_u = 55.8(V_s/w)^{0.683}$ (Trafford and Long 2020). This confirmed extremely low strengths of the order of 4-6 kPa. These values fall slightly below Direct Simple Shear (DSS) test results conducted at normal stresses of between 6 and 7 kPa. Peat samples used for the DSS tests were retrieved from block samples at 0.6m depth. Both sets of strength data are shown in Figure 3.

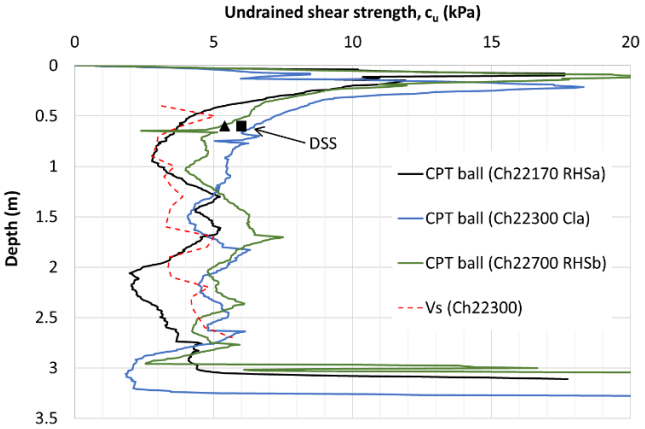

Figure 3. Undrained shear strengths derived from DSS tests, CPT ball tests and shear wave velocities.

2.5 CPTu / ball cone penetration testing

In-situ cone penetration testing (using a lightweight rig, Figure 4) was undertaken with standard piezocone and ball-cone apparatuses suited to lower strength organic peat soils at critical locations between the temporary road and the previous N56. Profiles of c_u values inferred from the CPT ball data (adopting $N_{t\,ball}$ = 15) are also shown in Figure 3 and are in keeping with those derived from shear wave velocities and DSS data.

2.6 Laboratory oedometer testing

A total of six maintained load oedometer tests were performed on 80 mm diameter, 19 mm high peat specimens obtained from serrated edge, thin-walled tubes. Sample depths ranged from 0.5 m to 2.4 m and natural moisture contents from 520% to 1136%. Load stages, each 24 h in duration, were 2.5, 5, 7.5, 10, 20, 40, 80, 120 and 80 kPa. The unloading generated an effective surcharge overload ratio (also known as Adjusted Amount of Surcharge or AAOS; Ladd 1971) of (120-80)/80, i.e. 50%, for the final stage. Two tests showed evidence of a yield pressure in the peat of between 5 and 10 kPa. Coefficients of consolidation c_v typically varied between 2 and 5 m^2/yr at initial load stages, reducing to 0.2 to 0.6 m^2/yr above 40 kPa. These values are at the lower end of those reported by Long & Boylan (2013) for Irish peats.



Figure 4. Lightweight CPT rig using ball-cone apparatus.

An extended (7-month duration) oedometer test with a maximum load of 100 kPa and AAOS of 69% was carried out on a block sample with natural moisture content 1030%. At maximum load, the normally consolidated creep strain rate was C_{sec}=0.017 with corresponding C_α=0.26 (assuming specific gravity G_s=1.5; initial void ratio e_0=15.5). This value is consistent with values quoted by Long & Boylan (2013). After reloading, a much-reduced secondary creep coefficient C_{sec}=0.001 was observed. However, this improvement was short-lived; the normally consolidated creep rate was re-established after a period of 2 months. This post-surcharge creep strain behaviour was also observed in research on Norwegian peats (Keary, 2020).

3 CONSTRUCTION DETAILING & INSTRUMENTATION

3.1 Stability analysis and design changes

Originally, a 200 kN geogrid was envisaged across the embankment base without any anchorage detail at the toes and a second 400kN layer to be wrapped back fully over and overlapping in the middle of the

embankment as part of the next fill stage. Given the lower than anticipated peat strengths, refinements were made by swapping the order of the geosynthetics and providing an anchorage length in Class 6I/6J fill on the basal layer. Side-slopes were reduced from 1:1 (vertical:horizontal) to 1:2, compromising the original goal of maximising the surcharge treatment on the underlying peat for a more stable arrangement. The embankment cross section at IC1 is shown in Figure 5.

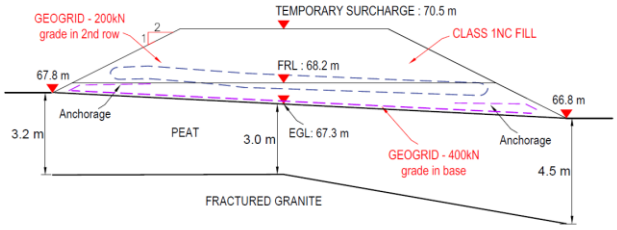

Figure 5. Embankment cross section at IC1, showing levels and geosynthethic reinforcement.

3.2 Detailed instrumentation clusters

Six instrument clusters (IC1, IC2, IC3, IC5, IC6, IC7), were incorporated along the surcharged embankment (locations shown in Figure 2), each comprising:

(i) a single settlement plate, installed at or close to the centre of the embankment cross section and at the original peat surface,
(ii) a single vibrating wire piezometer, installed at or close to the centre of the embankment cross section, intended for mid-depth within the peat,
(iii) a sub-surface profile gauge (SSPG) spanning transversely underneath the embankment, immediately beneath the original peat surface,
(iv) a pair of inclinometers, located within 1 m on either side of the embankment toes.

The purpose of these clusters was to inform the timing of surcharge release and monitor embankment stability throughout construction, in areas of weakest peat (as observed in geophysics, CPTu ball cone and probing) and considering local maxima in peat depths and fill heights. Regular instruments including settlement plates and Toe Survey Monuments (TSM) were placed at intervals of 25 m to 50 m along the alignment for continuity of measurement between IC locations. Additional peat testing and sampling was undertaken at these instrument cluster locations.

3.3 Staged filling & consolidation

Embankment filling stages above peat soils were limited in the contract specification to 0.5 m following a 2-week minimum hold period, equating to a maximum filling rate of 0.25 m/week. In practice, this global filling rate was never exceeded by the contractor, who achieved the maximum temporary surcharge height within 90 to 215 days, with average fill rates from 0.1 to 0.2 m/week. A target of 90% consolidation was specified by the designers for the final surcharge load stage with a minimum hold duration of 90 days at maximum height. Values of AAOS varied from ≈23% to ≈77% from across the six ICs, partly due to local alignment issues and avoiding variability in surcharge heights.

4 ANALYSIS OF MONITORING DATA

4.1 Practicalities for observational control

Processing of twice-weekly instrument readings assisted in directing the contractor away from areas with higher deformation ratios or pore pressures in order to control filling in areas of highest risk. This did not result in delays to the contract overall, due to ease of access across the site enabled by the proximity of the new alignment to both the existing alignment and the temporary road.

4.2 Settlements and consolidation

An example of the vertical settlement response (from the SP and central SSPG measurements) to eight stages of embankment loading at IC1 is presented in Figure 6, at which the peat thickness was ≈3 m. The embankment loading is presented as a total stress increase, corrected for submergence, as the lower portion of the embankment settled beneath the groundwater table (≈0.6 m deep at this location). The early stress increments (Stages 1–3) involved an initially fast becoming slower settlement rate, with a steadier rate from Stage 4 onwards. This is probably due to the cumulative effects of consolidation carried over from previous increments, while also reflecting the dramatic reduction in the coefficient of consolidation (c_v) characteristic of peat at higher effective stress levels (e.g. Carlsten, 1988). There is broad agreement between the SP and (central) SSPG settlements at IC1, with primary consolidation strains of ≈46% and ≈41% respectively at the time of surcharge release.

The corresponding degree of consolidation (U_v) at this time, estimated by applying the Asaoka (1978) method to the settlement plate data, was 96–100% at all ICs. An overall c_v was computed for the entire construction process, assuming that the full embankment height was attained instantaneously at the midpoint of the staged loading period. Double drainage was assumed based on ground investigation data, and a reducing peat layer thickness as a result of settlement was modelled. The values of c_v ranged

between 2 to 8.5 m^2/yr across all ICs, corresponding to effective stress ranges from 38 to 97 kPa.

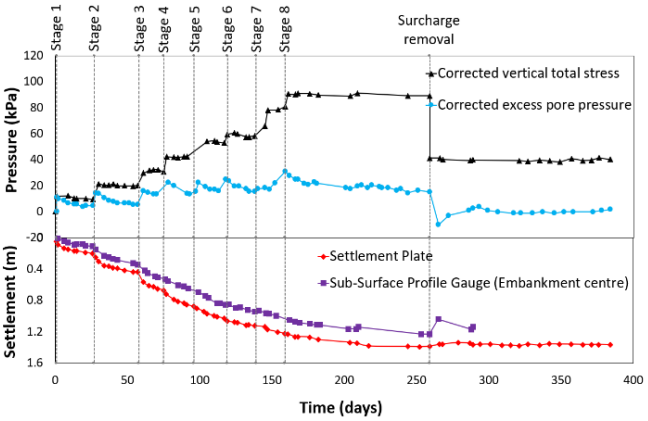

Figure 6. Excess pore pressure and settlement response to embankment loading at IC1.

Values of the compression index (C_c) were back-figured from the SP data, using settlements from Stage 3 onwards, at which stage the yield stress will have been exceeded. The average water at each IC location was used to calculate e_0. C_c was typically found to fall in the range 4 to 15.8, broadly in keeping with values for other Irish peats (Long and Boylan 2013).

4.3 Pore pressures

The large strains in Figure 6 also had implications for the pore pressure interpretation, with the piezometric datum changing as a consequence of piezometer settlement. For example, at IC1, it was assumed that the piezometer settled by 42% of the surface settlement, given (i) its initial depth of ≈1.75 m within the peat, (ii) that the stress increase within the central peat imposed by the embankment decayed little over the peat depth, and (iii) the uniformity of the peat itself, evidenced from water contents and shear wave velocity profiles. Excess pore pressures, corrected on this basis, are also shown in Figure 6. Temporary negative excess pore pressures were measured for a period of ≈3 weeks after surcharge removal, in tandem with minor swelling, before reverting to ≈0 kPa.

The increments in corrected total stress and excess pore pressure at the start of each of the stages were examined; the sums of each over the entire eight stages were found to be approximately equal (when allowance was made for the time lag between filling and the first piezometer reading). Therefore, the maximum excess pore pressure corresponding to instantaneous embankment construction was assumed to be equal to the corrected total stress reached by Stage 8. U_v values were corrected to relate to the mean of the entire peat layer, rather than at just the piezometer level; these ranged from 64–88% across all ICs with corresponding values of c_v ranging from 0.5–2.1 m^2/yr, lower in general than the Asaoka-derived values and requiring more assumptions. Possible reasons for discrepancies between c_v values derived from laboratory, pore pressures and settlements will be explored in a later publication.

4.4 Deformation and stability

The concomitant interrogation of inclinometer and SSPG data at the IC locations on this scheme was considered a novel means of monitoring embankment stability on peat. The ratio of the lateral deformation at the toe of the embankment on both sides of the mainline (ΔY), inferred from the inclinometer pair to the maximum settlement of the embankment (ΔS) at any time deduced from the SSPGs was computed. For single-stage embankments constructed on deep, soft mineral soils, a global trend of $\Delta Y/\Delta S < 0.3$ is considered acceptable (Jardine, 2002), but it is recognised that this might vary for shallow peat soils. In Figure 7, it can be seen that the deformation ratio history falls within this limit for IC1. The 'jagged' nature of the ratio observed in the early load stages may be because the lateral position at which the maximum SSPG settlement occurred varied.

Considering the broader dataset, the range of lateral movements per 0.5 m incremental loading stage were in the range of 50-70 mm on average, but extrema of the order of 100-200 mm were observed on the first and second fill stages. Higher ΔY/ΔS ratios arose where instruments were sited close to the previous load alignment (pre-compressed ground), in which case low central SSPG readings were compared with modest lateral displacements in softer ground along the margins. This was unrepresentative of the material behaviour overall.

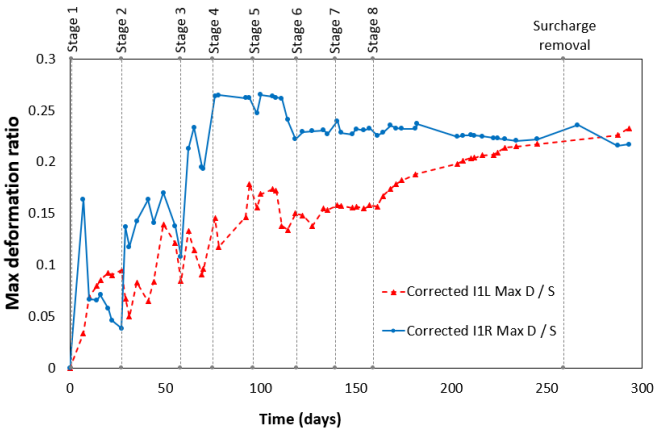

Figure 7. Maximum deformation ratio for IC1.

4.5 Lessons learned on monitoring equipment and informing stage/surcharge releases

Continuous pore pressure monitoring would have been preferable to capture more reliable baseline pore pressures and for greater resolution on the response to each fill increment. A companion extensometer would have been useful to establish the exact position of each piezometer as consolidation of the peat progressed.

Movement trends in TSMs and settlement plates were effective in informing the range of deformations along the embankments in addition to the detailed ICs. The TSM readings were more useful for detecting lateral movements in the early stages, predominantly because of the closer spacings (25 m) and size of dataset. The settlement plates were reliable but did not give as good a picture of overall deformations across each section and tended to be influenced by previous road embankment/field accesses in some locations. Hence the collective view afforded by concentrated (IC) and longitudinal (TSM/SP) data was vital.

Also, when fill becomes buoyant upon settling below the water table, there is effectively a very modest unloading phase during each intermediate hold if sufficient time is allowed. Observations of slight recovery in lateral movements close to release points were noted. These helped to signal a suitable point to recommence filling, if also confirmed using the other instruments, particularly the piezometers. This behaviour requires further research.

Consolidation targets were difficult to validate at two ICs; excess pore pressures upon surcharge release were ≈10 kPa higher than baseline levels. This topic will be explored in a future publication.

5 CONCLUSIONS & FUTURE RESEARCH

Innovative investigation techniques and sampling methods were utilised to establish extremely low peat strengths and refine the proposed embankment design configurations to be implemented at the N56 site. Building embankments up to 5.5 m high on very soft peat up to 5 m deep was challenging but was successfully executed without failures, primarily due to adoption of slow, controlled filling rates, geosynthetic basal reinforcement and substantial specialised ground information and instrumentation monitoring.

A total duration of 8–10 months was required to perform the earthworks related to embankment plus surcharge construction, hold and removal. This is approximately 6–8 months longer than standard excavate and replace methods in peat of similar depths. Some further optimization of geosynthetic reinforcement and construction filling rates could potentially reduce costs and construction durations by 1–2 months. It should be noted that the surcharge strategy boasts significantly better carbon credentials than an excavate-and-replace approach.

Analysis of settlement data interpreted by the Asaoka (1978) method showed that consolidation was achieved generally between 80 and 100 days. These field rates of consolidation are significantly faster than implied by laboratory oedometer tests.

In a novel research project led by the University of Galway, long term settlements are being monitoring at the N56 site with a view to quantifying by how much (and for how long) the surcharging process reduces the secondary settlement rate in the peat.

ACKNOWLEDGEMENTS

The authors are grateful for permission/support from Roughan & O'Donovan, Wills Bros Limited, Donegal County Council and Transport Infrastructure Ireland to publish this paper using project information. The views expressed are the authors' personal opinions.

REFERENCES

Asaoka, A. (1978) Observational procedure of settlement prediction. *Soils and Fndtns*, 18, 4, 87-101. https://doi.org/10.3208/sandf1972.18.4_87.

Carlsten, P. (1988) The use of preloading when building roads on peat, *Proceedings of the 2nd Baltic Conference on Soil Mechanics and Foundation Engineering*, 135-142.

Jardine, R.J. (2002) Stability and instability: soft clay embankment foundations and offshore continental slopes. *International Symposium on Coastal Geotechnical Engineering in Practice*, 99-118.

Keary, N. (2020). *Response of peat to surcharge loading*, MEng thesis, University College Dublin.

Ladd, C.C. (1971) Settlement analysis for cohesive soils. *MIT Research Report R71-2*. Soil Publication Series 272.

Long, M. & Boylan, N. (2013). Predictions of settlements in peat soils, *Quarterly Journal of Engrg. Geology and Hydrogeology*, 46, 303-322 https://doi.org/10.1144/qjegh2011-063.

Trafford, A. and Long, M. (2020). Relationship between shear-wave velocity and undrained shear strength of peat, *ASCE Journal of Geotechnical and Geoenvironmental Engineering*, 04020057-1. 10.1061/%28ASCE%29GT.1943-5606.0002298.

von Post, L. (1922) Sveriges geologiska undersoknings torvinventering och nagre av dess hittils vunna resultat, Sr. Mosskulturfor, 1, 1-2

Proceedings of the XVIII ECSMGE 2024
GEOTECHNICAL ENGINEERING CHALLENGES
TO MEET CURRENT AND EMERGING NEEDS OF SOCIETY
© 2024 the Authors
ISBN 978-1-032-54816-6
DOI 10.1201/9781003431749-459
Open Access: www.taylorfrancis.com, CC BY-NC-ND 4.0 license

ECSMGE 24
XVIII EUROPEAN CONFERENCE ON SOIL MECHANICS AND GEOTECHNICAL ENGINEERING

New concept of drilling auger for displacement pile installation

Nouveau concept de tarière pour la mis en œuvre de pieux déplacés

A. Krasiński*
Gdansk University of Technology, Gdansk, Poland
**adam.krasinski@pg.edu.pl*

ABSTRACT: In 2020, a new version of the screw displacement auger for pile installation in soil was developed and patented in Poland. It was named DPDT (Displacement Pile Drilling Tool). The general aim of its development was to reduce the soil resistances to the auger during screwing into the ground while maintaning a good load-bearing capacity for the screw displacement piles. The "DPDT-Auger" prototype was tested as a scaled-down model in the laboratory as well as in full-scale in the field. Its efficiency was compared with an ordinary SDP auger in two ways: by assessing soil resistances during screwing into the ground and by assessing the bearing capacity of completed piles. This paper presents the field tests and their results. Over 80 piles were tested in six test sites. Among them, 24 piles were instrumented and subjected to static load tests. The test results were generally positive and showed that the DPDT auger generates less torque than the SDP auger but requires more rotations and a slightly longer pile installation time. When it comes to the bearing capacity of the compression load, both DPDT and SDP piles showed similar characteristics.

RÉSUMÉ: En 2020, une nouvelle version de la tarière à vis pour l'installation de pieux dans le sol a été développée et brevetée en Pologne. Il a été nommé DPDT (Displacement Pile Drilling Tool). L'objectif général de son développement était de réduire les résistances du sol à la tarière lors du vissage dans le sol tout en conservant une bonne capacité portante aux pieux vissés. Le prototype "DPDT-Auger" a été testé en modèle réduit en laboratoire ainsi qu'en vraie grandeur sur le terrain. Son efficacité a été comparée à celle d'une tarière SDP ordinaire de deux manières: en évaluant les résistances du sol lors du vissage dans le sol et en évaluant la capacité portante des pieux terminés. Cet article présente les tests sur le terrain et leurs résultats. Plus de 80 pieux ont été testés sur six sites d'essai. Parmi eux, 24 pieux ont été instrumentés et soumis à des essais de chargement statique. Les résultats des tests ont été globalement positifs et ont montré que la tarière DPDT génère moins de couple que la tarière SDP mais nécessite plus de rotations et un temps d'installation des pieux légèrement plus long. En ce qui concerne la capacité portante de la charge de compression, les pieux DPDT et SDP présentent des caractéristiques similaires.

Keywords: Screw displacement pile; pile drilling tool; pile installation; bearing capacity of pile.

1 INTRODUCTION

Screw displacement piles and columns are currently one of the most popular technologies for piling and subsoils improvement. They are characterized by several technical and economic advantages, such as: quick construction, no excavation, no shocks and noise, and relatively good load-bearing capacity and stiffness in the ground (Bottiau, 2006; Basu & Prezzi, 2009). However, the disadvantage of this technology is the high resistance during the screwing of pile augers (drills, tools), especially in non-cohesive soils. These resistances require the use of piling machines (drilling rigs) with high rotational power and make it difficult to pass through dense intermediate layers and to create longer piles in the bearing layers.

The high screwing resistance was primarily the reason for the development of various varieties and shapes of displacement drills (SDP, "Omega", FDP, CMC, "DeWaal", APGD and others). Also, the author of this article, who has been dealing with the subject of screw displacement piles at the Gdansk University of Technology for years (habilitation thesis - Krasiński, 2013), has developed his own prototype version of the DPDT (Displacement Pile Drilling Tool) pile auger. It was patented in Poland (Krasiński, 2020, patent No PL 235442 B1). The scheme of the DPDT auger is shown in Figure 1.

In the DPDT auger, the disc helix, which is in the lower part of the typical SDP or CMC augers, has been replaced with a less prominent bar helix (round or square). The main reason for this was to reduce the torque M_T value when screwing the augur into the soil

and to reduce or eliminate the loosening of non-cohesive soil around the pile base. A side effect of the change is the slightly conical shape of the pile base which, however, according to research (Krasiński et al., 2022a,b), does not significantly reduce soil resistance under the pile base. An additional advantage of the DPDT drill is its simple design, which reduces the costs of its production and regeneration.

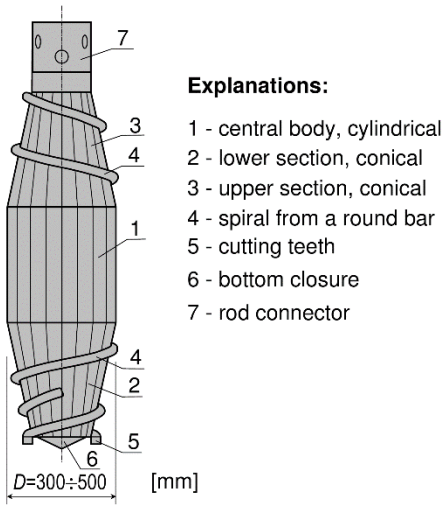

Figure 1. Scheme of new DPDT pile auger (Krasiński, 2020).

2 RESEARCH PROJECT

The development of the DPDT auger became an inspiration to launch the 2019-2022 "DPDT-Auger" research project by the consortium of Gdansk University of Technology and the Polish geotechnical contracting company Budokop Geotechnika Sp. z o. o. (Consortium Leader).

The research project examined the effectiveness of the DPDT auger by comparing it with other drills, first in the laboratory and then in situ in full-scale. Model-scale studies gave generally positive results as described, e.g., in Krasiński et al. (2022b).

The results of the entire research project, which, in addition to comparative research, also included several other issues regarding the execution, calculation and design of screw displacement piles and columns, were included in the Report (Krasiński et al. 2022a) and briefly characterized in the works of Krasiński et al. (2022b, 2023) and Krasiński (2023).

In a field study of the research project, a prototype DPDT auger was tested against an SDP auger. Figure 2 presents photographs of the tested drill bits, which also shows a modified version of the new DPDT-S auger, with the central cylindrical section (soil displacement body) shortened by half. Field tests were carried out on prepared experimental plots, where drill and pile tests were combined with in-situ and laboratory tests of the subsoil.



Figure 2. View of pile augers to be tested.

3 FIELD INVESTIGATIONS OF AUGERS AND PILES

As part of the research project, 6 field experimental plots were organized in several places in northern Poland. A total of over 80 screw displacement piles were made and tested by consortium member - Budokop Geotechnika. The given number included 24 research piles, and the rest were anchor piles for test loading stands. The geotechnical structure of the subsoil in the plots was determined using boreholes, CPTU and DMT soundings, and laboratory tests of soil samples. During the field study, first the augers from Figure 2 were tested for resistance and parameters of their drilling into the ground during the installation of research and anchor piles. Then, in each plot, static load tests were performed on 4 test piles, instrumented by a chain of vibrating wire extensometers.

4 TEST RESULTS

The complete results of field tests of the augers and piles are included in the Report (Krasiński et al., 2022a). This article presents only sample results regarding auger screwing resistance and pile settlement characteristics (Q-s) from load tests. All the results are characterized only qualitatively. A detailed quantitative and statistical analysis of the discussed results has been omitted in this article due to space limitations.

4.1 Test results of auger screw-in resistances

The resistance of the augers when screwing into the ground was defined by three basic parameters: torque M_T, specific number of rotations per unit of penetration

n_R and total time of pile hole drilling t_D. Other parameters were omitted as less important derivatives of the three above parameters (Krasiński, 2014). The SDP, DPDT and DPDT-S augers are compared in terms of M_T, n_R and t_D in Figure 3, 5, 7 and 9. They concern three selected research plots (No. II, IIIab and IV). In order to connect screwing resistances with the soil conditions, the auger resistance graphs appear alongside geotechnical profiles and q_c cone resistance charts from CPTu soundings. The research plots were specially selected due to their non-cohesive soils in load-bearing layers.

The aim of the pile tests and measurements was to determine the load-bearing capacity and Q-s characteristics of the piles, divided into the shaft (Q_s) resistances and the base (Q_b) resistances in the lower load-bearing soil layers. Comparative charts from static tests of piles in selected experimental plots No. II, III and IV are presented in Figure 4, 6 and 8. Both these results and those from the remaining experimental plots showed that piles made with the tested DPDT and DPDT-S augers and SDP auger are characterized by similar parameters of interaction with the soil (bearing capacity and Q-s characteristics for compression loads).

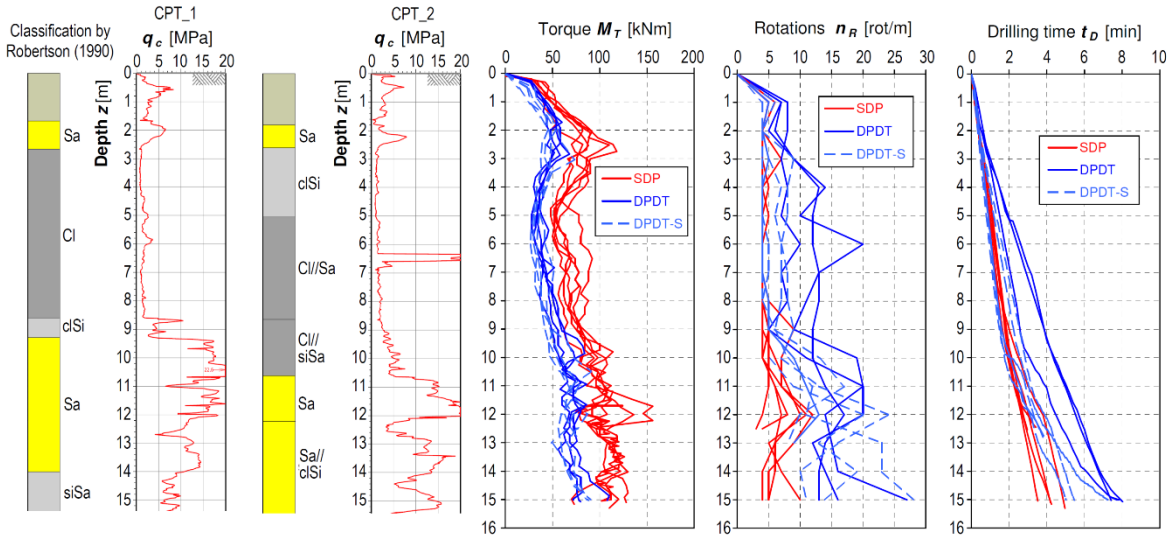

Figure 3. Drilling resistances of pile augers with CPTu diagrams on the experimental plot No. II.

The presented results confirmed observations previously made in the model studies described in Krasiński et al. (2022), and should generally be assessed positively. As expected, the prototype DPDT and DPDT-S augers generated lower values of M_T torques than the SDP auger. However, it was obtained at the expense of a larger number of rotations n_R and a longer pile hole drilling time t_D. The quantitative differences between individual plots are not the same and depend on the geotechnical structure of the subsoil. However, the general patterns in these differences were consistent or similar in all cases.

4.2 Pile load test results

Static pile load tests (SPLT) in field plots were carried out with additional instrumentation of pile shafts using a chain of vibrating wire extensometers Geokon - model 1300 (A9) (Geokon, 2023).

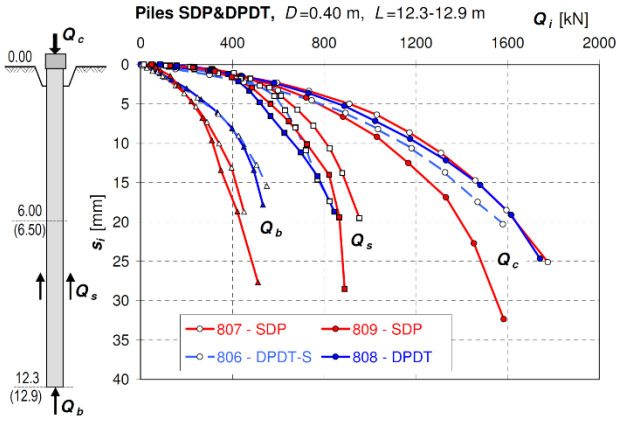

Figure 4. SPLT results of piles on the field experimental plot No. II.

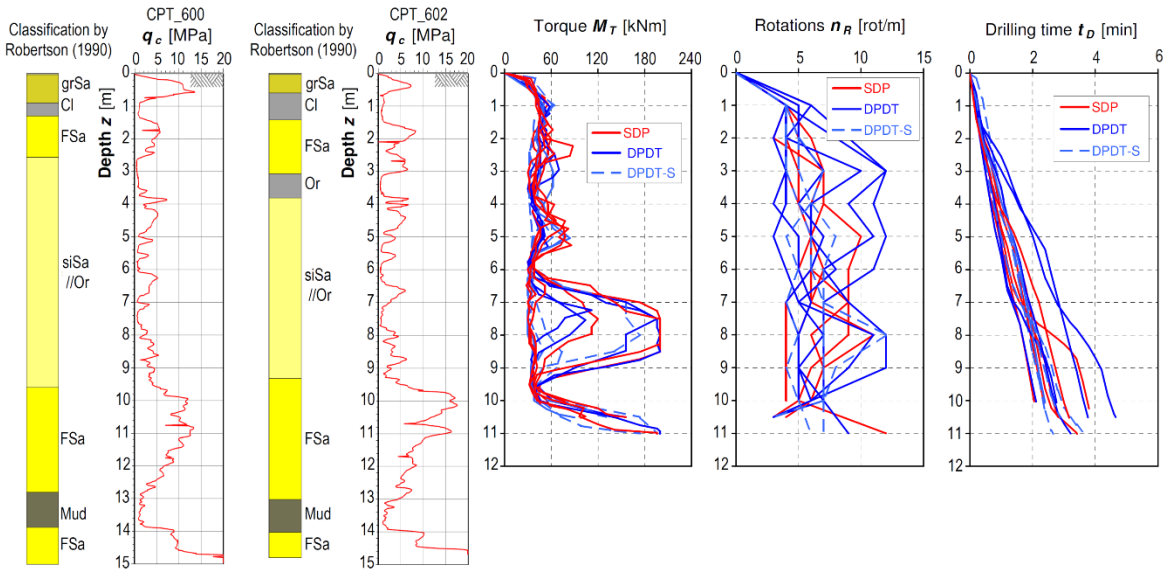

Figure 5. Drilling resistances of pile augers with CPTu diagrams on the field experimental plot No. IIIa.

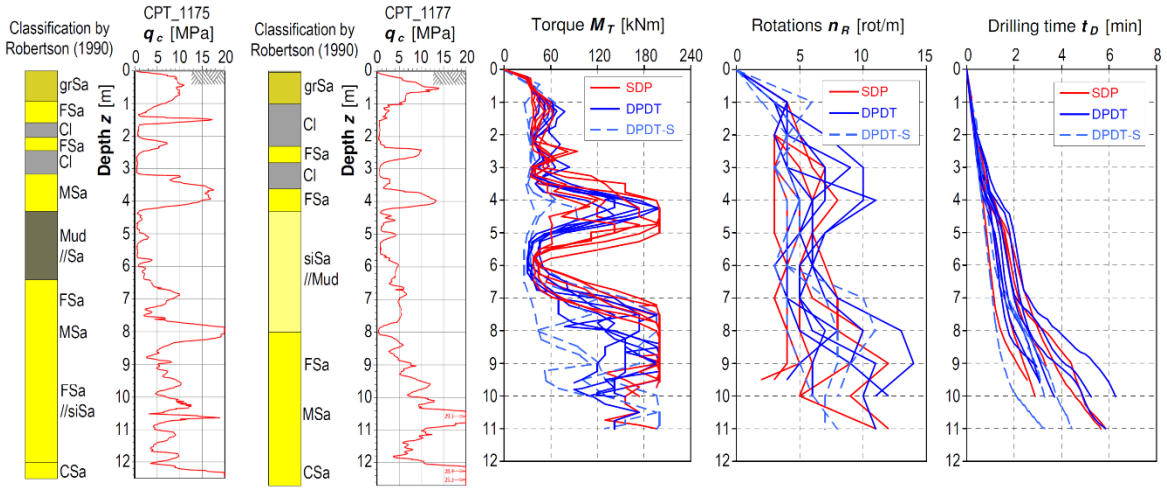

Figure 6. Drilling resistances of pile augers with CPTu diagrams on the field experimental plot No. IIIb.

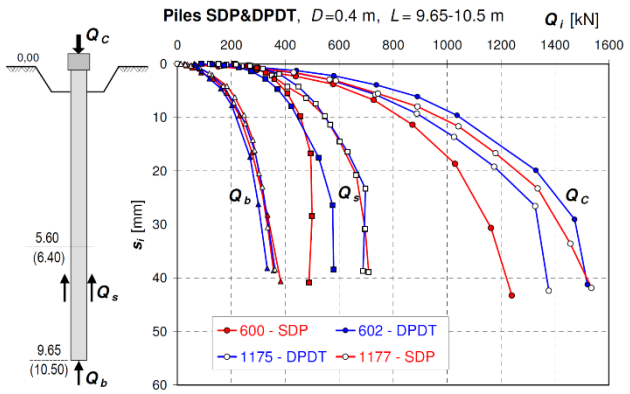

Figure 7. SPLT results of piles on the field experimental plot No. III.

To sum up, the performance of the prototype DPDT and DPDT-S drill bits should once again be positively assessed, mainly due to the fact that they generate a lower M_T torque value than the SDP drill bit. This advantage is crucial and outweighs the disadvantage of increased n_R and t_D parameter values. A lower value of M_T makes it possible to achieve greater auger penetration depths, and thus create longer piles with greater load-bearing capacities. It also provides a greater guarantee of successfully overcoming stronger interlayers in the subsoil and creating piles of desired lengths. At the same time, the shapes of the DPDT and DPDT-S drill bits do not deteriorate the load-bearing capacity or *Q-s* characteristics of the thus constructed piles.

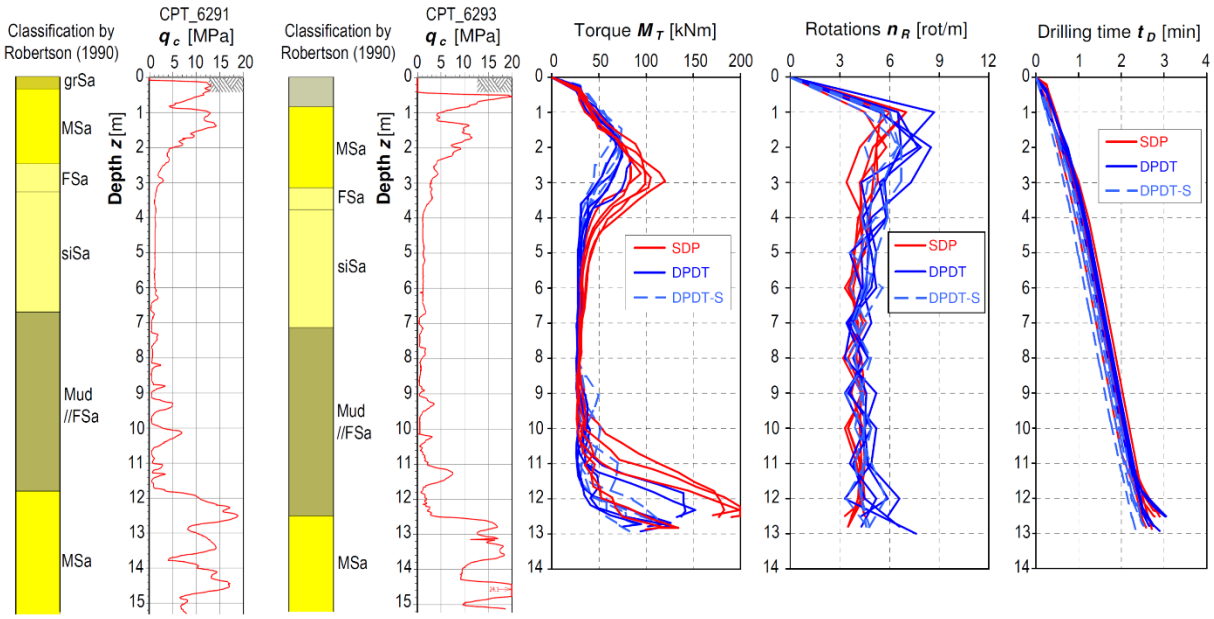

Figure 8. Drilling resistances of pile augers with CPTu diagrams on the experimental plot No. IV.

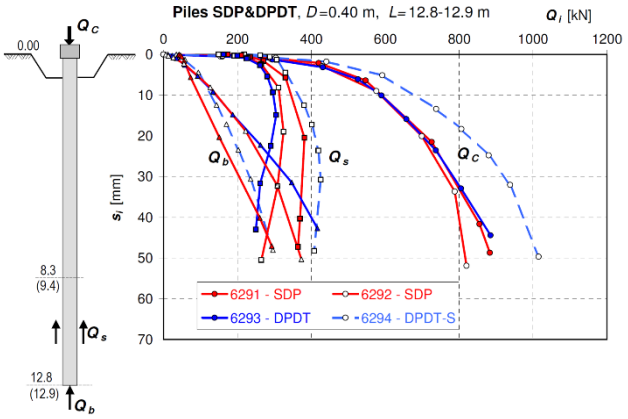

Figure 9. SPLT results of piles on the experimental plot No. IV.

5 CONCLUSIONS

i) Comparative analyses showed that the DPDT and DPDT-S auger indeed required lower torque M_T values but a higher number of rotations per depth unit n_R and longer drilling time t_D in comparison with the SDP auger. The middle section of the DPDT-S auger is shortened by half in relation to the DPDT auger. Thanks to this, the value of the torque M_T is additionally reduced. The overall balance of screwing resistance should be considered favorable for the DPDT and DPDT-S augers, because the generation of a lower torque value allows for the achievement of greater drilling depths and pile lengths, and more effectively overcomes stronger soil layers.

ii) Piles made with SDP and DPDT (DPDT-S) augers are characterized by very similar interaction with subsoils of various geotechnical configurations. Statistically, the load-bearing capacity and stiffness of both types of piles are similar.

iii) In practice, the use of DPDT and DPDT-S drills may be of technical and economic benefit without any significant risk of lowering the quality and load-bearing capacity of the piles in comparison to those made by traditional augers, e.g. SDP. On the contrary, piles and columns made with DPDT drills can achieve more favorable shaft shapes with smaller deformations, neckings and soil inclusions, which are observed when using classic drills with disc helix spirals. They are also more advantageous when making piles in contaminated soils and landfill areas.

ACKNOWLEDGEMENTS

The described test and analyses results of augers and piles were obtained from research works conducted in the "DPDT Auger" research project, financially supported by the Polish National Centre for Research and Development (project No. POIR 4.1.4. 0124/18, “Development of a method and tools for the installation of screw displacement columns/piles in various ground conditions in Poland, together with the preparation of a methodology for the design and acceptance of works”). The project was carried out by the consortium of Gdansk University of Technology and the Polish geotechnical company Budokop Geotechnika Sp. z o.o.

REFERENCES

Basu, P. and Prezzi, M. (2009). Design and Applications of Drilled Displacement (Screw) Piles. *Publication*

FHWA/IN/JTRP-2009/28. Joint Transportation Research Program, Indiana Department of Transportation and Purdue University, West Lafayette, Indiana. https://doi.org/10.5703/1288284314278.

Bottiau, M. (2006): Recent evolutions in deep foundation technologies. *Proceedings of the DFI/EFFC 10th Int. Conf. On Piling and Deep Foundations*, Amsterdam.

Geokon (2023). GEOKON®, Geotechnical + Sructural Instrumentation. Retrievable extensometer, Model 1300 (A9). https://www.geokon.com/1300, accessed: 20/09/2023.

Krasiński, A. (2013). Pale przemieszczeniowe wkręcane. Współpraca z niespoistym podłożem gruntowym (Screw displacement piles. Bearing capacity and work in non-cohesive soils) (in Polish). (*Habilitation thesis*, Gdansk University of Technology), *Monografie* Nr 134, Wydawnictwo Politechniki Gdańskiej, Gdańsk, Poland, p. 250.

Krasiński, A. (2014). The analysis of soil resistance during screw displacement pile installation. *Studia Geotechnica et Mechanica*, Vol. XXXVI (3), 49-56. https://doi.org/10.2478/sgem-2014-0026.

Krasiński, A. (2020). Świder do wykonywania pali przemieszczeniowych wkręcanych. Opis patentowy Nr PL 235442 B1. (Drill for screw displacement piles execusion. Patent description No. PL 235442 B1) (In Polish). Patent Office of the Republic of Poland, Warsaw, Poland.

Krasiński, A., Więcławski, P., Kusio, T., Wiszniewski, M., Tisler, W. (2022a). *Raport końcowy z projektu badawczego "DPDT-Auger"*, nr POIR.04.01.04-00-0124/18 "Opracowanie metody i narzędzi do wykonywania kolumn/pali przemieszczeniowych wkręcanych w różnorodnych warunkach gruntowych na obszarze Polski wraz z przygotowaniem metodyki do projektowania i odbioru robót". (*Final report from research project "DPDT-Auger"*, No. POIR.04.01.04-00-0124/18 "Development of a method and tools for the installation of screw displacement columns/piles in various ground conditions in Poland, together with the preparation of a methodology for the design and acceptance of works") (Unpublished data). Opracowanie tekstowe. Gdansk University of Technology, Gdansk, Poland.

Krasiński, A., Więcławski, P., Wiszniewski, M., Kusio, T. (2022b). Model tests of cast-in-place piles formed by using different types of auger. *Proc. of the 20th Int. Conf. on Soil Mechanics and Geotechnical Engineering,* Australian Geomechanics Society, Sydney, Australia, pp. 1227-1232.

Krasiński, A., Więcławski, P., Kusio, T., Wiszniewski, M., Tisler, W. (2023). Results of the "DPDT-Auger" research project on screw displacement piles, *Architecture, Civil Engineering, Environment* (*ACEE*, (3)), 89-99. https://dx.doi.org/10.2478/ACEE-2023-0036.

Krasiński, A. (2023). Estimation of Screw Displacement Pile-Bearing Capacity Based on Drilling Resistances, *Studia Geotechnica et Mechanica*, (Forthcoming). https://doi.org/10.2478/sgem-2023-0014.

Robertson, P. K. (1990). Soil classification using the cone penetration test. *Canadian Geotechnical Journal*, 27(1): 151-158. https://doi.org/10.1139/t90-014.

Proceedings of the XVIII ECSMGE 2024
GEOTECHNICAL ENGINEERING CHALLENGES
TO MEET CURRENT AND EMERGING NEEDS OF SOCIETY
© 2024 the Authors
ISBN 978-1-032-54816-6
DOI 10.1201/9781003431749-460
Open Access: www.taylorfrancis.com, CC BY-NC-ND 4.0 license

ECSMGE 24
XVIII EUROPEAN CONFERENCE ON SOIL MECHANICS AND GEOTECHNICAL ENGINEERING

Comparative trials of geosynthetic materials in the base of road pavement on the section of the Central Ring Road in the Moscow Region

Essais comparatifs de matériaux géosynthétiques dans la base du revêtement routier sur le tronçon du Périphérique Central de la région de Moscou

A. Kuznetsova*
Soterra Engineering/Moscow, Russia
**Anna.kuznetsova@soterra.ru*

ABSTRACT: During the period from 2016 to 2019, a complex comparative trial was conducted by "Russian Highways" State Company on the Central Ring Road in Moscow region. Under extremely high traffic volume of 10161 vehicles per day, 22 trial section, with various geosynthetic materials below the aggregate base layer were constructed and monitored in order to demonstrate the improvement in pavement performance. This paper describes a series of static plate loading and falling weight deflectometer tests together with rut depth measurement. On the basis field tests and monitoring, polypropylene geogrids appeared to be the most effective materials for aggregate layers stabilisation. The greatest effect from the use of polypropylene geogrids was achieved by reducing the rut depth. As a result, there is an increase in the residual life of pavement, which for polypropylene geogrids ranges from 22 to 105%, depending on the manufacturer.

RÉSUMÉ: Entre 2016 et 2019, un essai comparatif complexe a été mené par la société d'État « Autoroutes russes » sur le périphérique central de la région de Moscou. Sous un volume de trafic extrêmement élevé de 10161 véhicules par jour, 22 sections d'essai avec divers matériaux géosynthétiques sous la couche de base de granulats ont été construites et surveillées afin de démontrer l'amélioration des performances de la chaussée. Cet article décrit une série d'essais de chargement statique de plaques et de déflectomètre à poids tombant ainsi que la mesure de la profondeur de l'ornière. Sur la base des tests terrain et du suivi, les géogrilles de confinement en polypropylène sont apparues comme les matériaux les plus efficaces pour la stabilisation des couches de granulats. Le plus grand effet de l'utilisation de géogrilles en polypropylène a été obtenu en réduisant la profondeur de l'ornière. Il en résulte une augmentation de la durée de vie résiduelle du revêtement qui, pour les géogrilles en polypropylène, varie de 22 à 105 %, selon le fabricant.

Keywords: Geosynthetic materials; pavement optimization; stabilization.

1 INTRODUCTION

The current trend towards increasing axle loads and driving speeds on highways has clearly identified the problem of rapid wear of road pavement materials. The use of geosynthetic materials in the asphalt and base layers can increase the strength and stiffness of the structure, improving its service life. In 2008 Russian Federal Highway Agency approved a manual for flexible pavements with reinforced aggregate layers design. Original concept and design method for mechanically stabilized granular layers was developed in Saint Petersburg Military Engineering-Technical University (VITU) on the basis of laboratory and field tests in 1999-2002. The effect of aggregate modulus increasing using geogrid is presented by enhancement factors, incorporated into traditional pavement design procedure. Enhancement factors are calculated depending on the thicknesses and modules of the structural layers, the diameter of the wheel footprint and the brand of geogrid. Only polypropylene punched and drawn (P&D) geogrids were tested by VITU and therefore included into the design manual.

Later, in 2015, a national standard GOST R 56338 “Geosynthetic materials for reinforcing the lower layers of road pavement bases” was issued approving the minimum tensile strength required as 30kN/m.

Since then, pavement optimisation via geogrid installation has become widely spread. At the same time, construction industry explored various types of geosynthetic materials with reinforcing/stabilising functions, like hexagonal, welded and glued geogrids, woven geotextiles and geocells. The mechanism of their interaction with aggregate and the effect they produce differs significantly. Haliburton et al. identified a few mechanisms of enhancement, the main

ones being lateral restrain and tensioned membrane. The first is realized due to the interlock of crushed stone particles in the rigid cells of the geogrid, and the second due to frictional contact with subsequent tension of the geosynthetic material.

State Company "Russian Highways" (an operator for toll roads in Russia) decided to run comparative research on this subject and validate the performance of different geosynthetic materials on the federal level.

2 TEST SITE

A perfect opportunity arose during the construction of a temporary bypass for the section of Central Ring Road in Moscow region in 2016. Expected traffic volume of 10161 vehicles with 22% heavies per day provided an accelerated testing with about 4 million ESALs in a two-year period. Typical road cross-section is shown on the Figure 1.

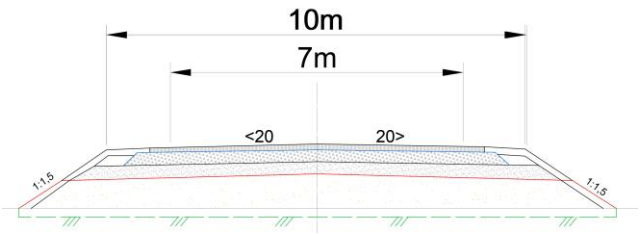

Figure 1. Road cross-section.

2.1 Pavement structure and geosynthetic materials

Pavement structure is shown, Figure 2. It consisted of two asphalt concrete layers (AC), aggregate mix type C-4 with maximum particle size of 80 mm and medium sized sand. Geosynthetic materials were placed between base and sand layers.

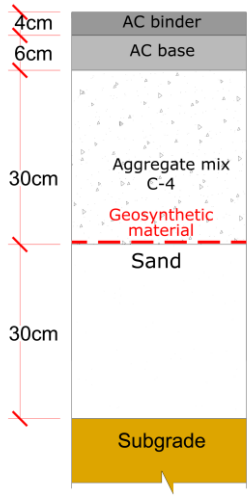

Figure 2. Pavement section.

Along 720m of test section 22 types of geosynthetic materials together with control site with no reinforcement were installed. Each reinforced section was 20m long. The following material were presented:

- 6 types of 40kN/m punched and drawn (P&D) polypropylene (PP) biaxial geogrids;
- 2 types of hexagonal (TX) geogrid 17 and 20kN/m;
- 4 woven geotextiles from 40 to 100kN/m;
- 6 types of woven polyester (PE) geogrids/composites 50kN/m;
- 2 types of basalt geogrid;
- 2 types of geocells.

The full list of geosynthetic materials is presented in the Table 1.

Table 1. List of geosynthetic materials.

Section	Description	Acronym
1	PP P&D 40kN	PPBXGG1
2	PP P&D 40kN	PPBXGG2
3	PE 50kN	PEGG1
4	PE 50kN	PEGG2
5	PP geotextile 80kN	PPGT1
6	Control	Control
7	PP geotextile 50kN	PPGT2
8	PP geotextile 40kN	PPGT3
9	PE 50kN	PEGG3
10	PE composite 50kN	PEGC1
11	PP P&D 40kN	PPBXGG3
12	PE geotextile 100kN	PEGT1
13	PP P&D 40kN	PPBXGG4
14	PP P&D Hexagonal 20kN	PPTXGG1
15	PP P&D Hexagonal 17kN	PPTXGG2
16	Geocell	GCell1
17	PE 50kN	PEGG4
18	PP P&D 40kN	PPBXGG5
19	Basalt 50kN	BGG1
20	PE 50kN	PEGG5
21	Geocell	GCell2
22	Basalt 40kN	BGG2
23	PP P&D 40kN	PPBXGG6

Materials on site are shown, Figures 3-5.



Figure 3. Geocell.



Figure 4. Geocomposite.



Figure 5. Hexagonal P&D geogrid.

Geosynthetic materials samples were taken in order to perform quality control tests on tensile strength and strain at maximum load in accordance to GOST R 55030 (equivalent to ISO 10319).

2.2 Testing

Static plate loading tests were carried out in accordance with standard STO AUTODOR 10.3-2014 (close equivalent to DIN 18134, plate diameter 300mm, maximum pressure 0.5MPa). Under this standard, E_{v1} and E_{v2} modulus are measured together with "resilient modulus", obtained from the recovered resilient part of settlement during the uploading stage. The ratio of E_{v2} to E_{v1} characterizes the quality of the layer compaction and should be less than 2.5.

First series of static plate tests was conducted on the sand subbase layer surface. Average resilient modulus appeared to be 75.15MPa and was lower than designed 108MPa value.

The second series of plate tests was conducted on the surface or aggregate base. Results for modulus are shown in the section 3.

For the further analysis, the effect of geosynthetic materials on the total resilient modulus on the surface of the asphalt concrete layers had to be evaluated. These tests were carried out with the falling weight deflectometer (FWD). The tests had been being carried out during two years, twice a year in mid-August and the third ten days of April. Typical results are shown in Section 3.

After two years in-service a rut depth measurement was performed using a mobile road diagnostic laboratory equipped with a system based on planar lasers and video cameras as shown on the Figure 6.



Figure 6. Mobile road laboratory.

At that moment, the site had passed about 4 million ESALs.

3 TEST RESULTS

3.1 Static plate tests and FWD

Test results for resilient modulus on the base surface, E_{v2} to E_{v1} ratio, and results for asphalt are shown on the Table 2. Control section modulus on the base level was 114MPa.

Table 2. Plate test results.

N	Material	Base surf. MPa	Comp. indicator	Asphalt surf. MPa
1	PPBXGG1	134	2.24	288
2	PPBXGG2	139.5	2.26	301
3	PEGG1	119.5	2.74	322
4	PEGG2	115	3.65	315
5	PPGT1	150	1.74	293
6	PPGT2	124	2.70	249
7	PPGT3	132	2.56	266
8	PEGG3	161	3.48	261
9	PEGC1	128.5	1.25	243
10	PPBXGG3	117.6	4.37	305
11	PEGT1	131.5	2.50	244
12	PPBXGG4	137	1.28	310
13	PPTXGG1	136.7	1.27	323
14	PPTXGG2	131.5	1.13	316
15	GCell1	112	2.27	288
16	PEGG4	126.5	1.04	250
17	PPBXGG5	169	1.02	265
18	BGG1	139	3.72	295
19	PEGG5	154.5	1.16	282
20	GCell2	152	1.22	149
21	BGG2	175	1.07	273
22	PPBXGG6	131	3.05	283

Due to the compatitive ethics material names were hidden from the participants. In gerenal, all section with geosynthetics had shown higher resilient modulus (up to 1.5 times higher) compared to the control before asphalt layers installation.

The average resilient modulus on the base surfest for 8 sections with punched and drawn (P&D) polypropylene (PP) geogrids appeared to be the highest one, followed by polyester geogrids and textiles. Modulus over geocell sections was not consistent, but on average the lowest one.

3.2 Falling weight deflectometer tests

Typical results of summer measurements (2019) are shown, Figure 7.

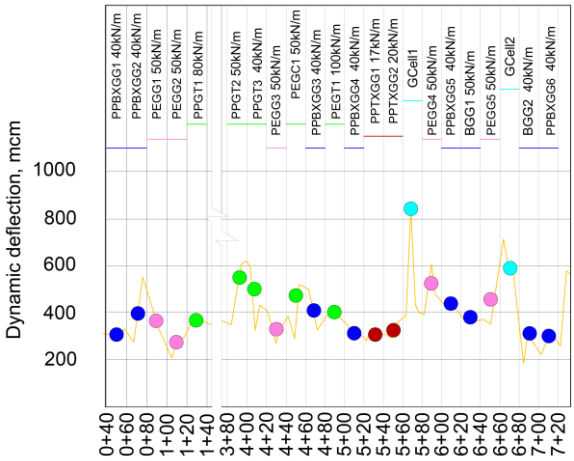

Figure 7. Typical results of FWD measurements.

In general, it was obresved that geocell materials had shown the lowest modulus, followed by geotextiles. Almost all geogrids performed better with polipropylen punched and drawn leading.

3.3 Rut depth control

Control section showed the rut depth of 17mm. Measurements for other sections are shown on the Figure 8.

The majority of sections with geosynthetic materials accumulated less rut depth that control section. This fact is related to the better base layer performance and its resistance to the structural deformation when reinforced or stabilised.

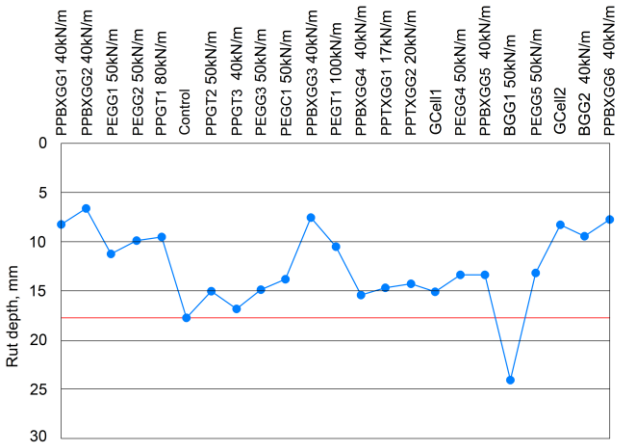

Figure 8. Rut depth measurements.

The best results had been observed along sections with punched and drawn (P&D) polypropylene (PP) biaxial geogrids.

Woven geotextiles with strength approximately equal to that of geogrids showed lower modulus values on the base and asphalt concrete, as well as deeper ruts. 80 and 100 kN geotextiles showed a high modulus at the base level, but after two years of service the modulus at the asphalt concrete surface was lower than in areas with geogrids

4 CONCLUSIONS

Whitin the described research, the most effective materials for reinforcing/stabilising discrete layers are polypropylene geogrids. The greatest effect from the use of polypropylene geogrids is achieved by reducing the rut depth. As a result, there is an increase in the residual life of road pavement, ranging from 22 to 105% depending on the manufacturer. Modulus measurements for the best performing group of geogrids are presented on the Figure 9.

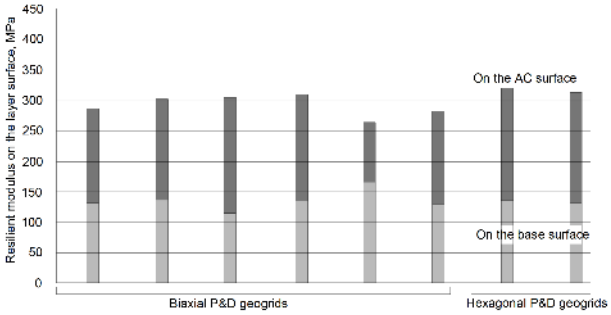

Figure 9. Resilient modulus on the top of AC and base layers.

Hexagonal geogrids having two times lower tensile strength comparing to biaxial one had shown sufficient efficiency and were included into national standard GOST R 56338 in 2023.

Geotextiles and woven geogrids, operating on the principle of a tensioned membrane, on average showed lower modules on the base surface and after two years of service, the deflection of asphalt concrete above them was greater.

Rigid geogrids, operating on the principle of limiting the lateral movement of aggregate particles, ensured high performance during construction and subsequently maintained the rigidity of the base and the entire structure as a whole.

At the moment, "Russian Highways" State Company promotes stiff stabilising geogrid installation as competitive alternative to cement or bitumen treatment.

ACKNOWLEDGEMENTS

The author is grateful to the "Russian Highways" State Company and Road Research Centre of the Siberian Automobile and Road Construction Academy.

REFERENCES

FSUE Informavtodor (2008) ODM 218.5-002-2008 Guidelines for the use of polymer geogrids for pavement aggregate base layers reinforcement, Moscow.

Haliburton, T.A., Lawmaster, I.D. and McGuffey, V.C. (1981) Use of Engineering Fabrics in Transportation Related Applications, FHWA DTFH61-80-C-Q0094, USA.

Kuliznikov A. M. et al. (2019) Report about research work/ Results of work at the site “Highway A-107 “Moscow Small Ring” between the Kyiv and Minsk highways, near the village of Kobyakovo and the village NII Radio with falling weight deflectometer (FWD) and georadars, RosDorNII, Moscow, Russia.

Levashov G. M. (2019) Report about research work (revised). Analysis of the monitoring results of experimental polygon for geosynthetic materials built as part of the construction of temporary highways of the fifth launch complex of the Central Ring Road (A-113), DIC SibADI, Omsk, Russia.

Rosstandart (2015) GOST R 56338 Automobile roads of general use. Geosynthetic for reinforcement of lower base layers of road pavement. Specifications, Standardinform, Moscow.

Rosstandart (2012) GOST R 55030 Public roads and highways. Geosynthetic for road construction. Test method for tensile strength, Standardinform, Moscow.

Proceedings of the XVIII ECSMGE 2024
GEOTECHNICAL ENGINEERING CHALLENGES
TO MEET CURRENT AND EMERGING NEEDS OF SOCIETY
© 2024 the Authors
ISBN 978-1-032-54816-6
DOI 10.1201/9781003431749-461
Open Access: www.taylorfrancis.com, CC BY-NC-ND 4.0 license

ECSMGE 24
XVIII EUROPEAN CONFERENCE ON SOIL MECHANICS AND GEOTECHNICAL ENGINEERING

Degradation of expanded clay strength after creep tests

Dégradation de la résistance de l'argile expansée après des essais de fluage

C.B. Laskowski*
Universidad Politécnica de Madrid, Madrid, Spain/ Universidad Nacional de la Patagonia San Juan Bosco, Comodoro Rivadavia, Argentina

J. Estaire
Laboratorio de Geotecnia (CEDEX), Madrid, Spain

E. Roces
Universidad Politécnica de Madrid, Madrid, Spain

**belen.laskowski@gmail.com*

ABSTRACT: After subjecting a material to a constant load maintained over time (creep), it is expected that internal crack growth will occur, resulting in a degradation (decrease) of its strength. This paper analyses the strength of single expanded clay grains after being subjected to constant loads for a period of 40 days. These tests, which, from now on, will be, referred to as creep tests, were performed using three different load magnitudes. To determine whether there is a degradation of the grain strength or not, the results are compared with those obtained in grains tested in simple compression without performing a creep test previously. Expanded clays are a lightweight expanded ceramic aggregate also known as LECA, obtained from heating clay soils in two phases (drying and expanding phases) to high temperatures (above 800ºC and 1100ºC, respectively) in a rotary kiln. The expanded clay obtained is characterized for presenting a very porous and low-density core, and a densely vitrified outer shell, notably more resistant.

RÉSUMÉ: Après avoir soumis un matériau à une charge constante maintenue dans le temps (fluage), on s'attend à ce que des fissures internes se développent, entraînant une dégradation (diminution) de sa résistance. Cet article analyse la résistance de grains d'argile expansée après avoir été soumis à des charges constantes pendant une période de 40 jours. Ces essais, qui seront dorénavant appelés essais de fluage, ont été réalisés en utilisant trois magnitudes de charge différentes. Pour déterminer s'il y a ou non dégradation de la résistance des grains, les résultats sont comparés à ceux obtenus avec des grains testés en compression simple sans essai de fluage préalable. Les argiles expansées sont des agrégats céramiques, également connus sous le nom de LECA, obtenus en chauffant des sols argileux en deux phases (séchage et expansion) à des températures élevées (supérieures à 800ºC et 1100ºC , respectivement) dans un four rotatif. L'argile expansée obtenue se caractérise par un noyau très poreux et de faible densité, et une enveloppe extérieure densément vitrifiée, notablement plus résistante.

Keywords: LECA; strength degradation; creep; breakage.

1 INTRODUCTION

Lightweight expanded clay aggregate (LECA) is an artificial ceramic aggregate that has numerous uses in construction, such as the manufacture of lightweight concrete, lightweight geotechnical backfill on structures, fills over compressible soils, and the manufacture of concrete for the construction of new buildings (Prisco, 2007).

LECA grains have a rather spherical shape and a size that usually varies between 10 and 20 mm, although there are other commercial diameters (Figure 1).

The LECA strength, as for other ceramic materials, presents values with certain variation that can be adjusted by means of a statistical Weibull function. This type of distributions were used for simple compressive strength of different ceramic materials, (Roces-Alonso et al., 2021, Anaya et al., 2022) and for other breakage modes (Lei et al., 2020, Lei et al., 2021).



Figure 1. Intact lightwight expanded clay grains.

Considering that the breakage of a grain is associated with the presence of defects in its interior,

it is more likely that a larger volume element will have more and larger defects, so it is common that the strength of the different grains decreases with increasing element size. Thus, it is reasonable to introduce the grain volume, in the Weibull strength distributions of the grain (McDowell et al., 2013).

When a material is subjected to previous stresses or aggressive atmospheres, its strength characteristics degrade significantly. Numerous examples of this phenomenon can be found in literature, for different materials and after different situations, such as: freeze–thaw cycles for rock (Jia et al., 2015), granite (Tan et al., 2011) or concrete (Qu et al., 2023), freeze–thaw and fatigue for marble (Song et al., 2021), sandstone in carbon dioxine atmosphere (Laskowski et al., 2023) or after fatigue for various materials, such as composites (Philippidis et al., 2007) or sandstone (Chu et al., 2022).

In this article, the degradation of the compressive strength of LECA grains after being subjected to a 40-day creep test is analyzed.

2 MATERIAL AND METHODS

2.1 Materials

The expanded clay used for the tests was manufactured by LECA at its plant in Avelar (Portugal). The main components of the expanded clay are silicon oxide (SiO_2) and aluminium oxide (Al_2O_3), which account for more than 75% of the total grain composition (Roces, Muñiz-Menéndez et al. 2021)

The grains tested had an average diameter (obtained as the mean of three perpendicular diameters measured with callipers) between 14 and 18 mm, as it can be seen in Fig 1.

Each of the grains consisted of a vitrified outer shell and a porous core that gives it its characteristic lightness. The specific dry weight of the grains tested is 5.7 kN/m^3.

2.2 Methods

For the performance of this research, 340 individual grains of expanded clay were tested (121 grains tested under creep loads and 219 tested applying instantaneous loads), according to the following procedure:

- Determination of the weight of each of the grains using a balance with an accuracy of 0.001 g.
- Measurement three of perpendicular diameters (the largest, the smallest and a third perpendicular to the two previous ones) using a calliper of precision 1/50 mm. Grains with an average diameter of less than 14 mm or more than 18 mm were discarded.
- Mechanical test on the grains. These tests were of two types:
  - Simple compression breakage, using a Point Load type equipment, according to ASTM D5731-16 standard. The maximum breaking load of the grain is recorded.
  - To perform the creep tests, each grain was mounted on an oedometer-type equipment. This equipment allows a load to be applied by means of weights and maintained over time. In this paper, the testing period chosen was 40 days. The grains that survived this test were further subjected to a uniaxial compressive stress, to determine their residual strength, performing a Point Load Test.

A scheme of these tests is shown in Figure 2. All these tests were carried out at the Laboratorio de Geotecnia-CEDEX in Madrid (Spain).

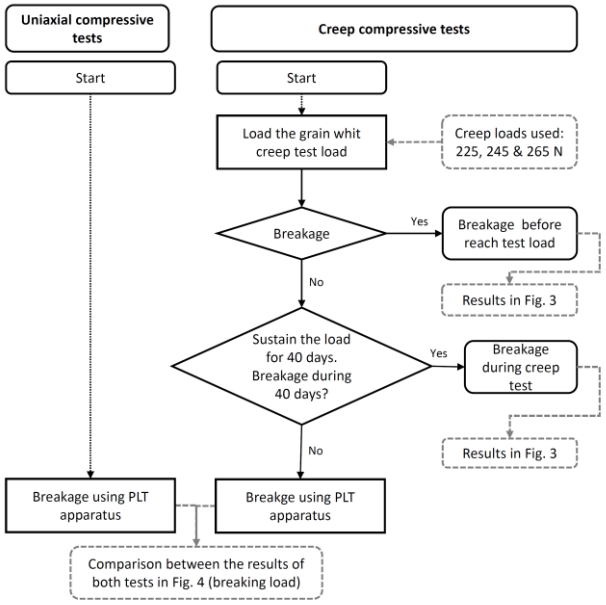

Figure 2. Flowchart of the work carried out.

The stress in a grain subjected to uniaxial compression can be estimated from the following Equation:

$$\sigma = \alpha \cdot \frac{F}{d^2} \quad (1)$$

Being σ the grain stress, F the force applied to the grain, d the grain diameter (calculated as the arithmetic mean of the three measured diameters) and α a constant. In this study, a value of $\alpha = 1$ will be used as recommended by (McDowell et al., 2000).

3 RESULTS

In Figure 3, the results obtained from performing creep tests over 121 LECA grains are presented. In this plot, the breakage time of each of the grains tested is shown in terms of its average diameter and the constant load to which it was subjected during the 40-day testing period. Those grains that broke before reaching the creep load are indicated as BB. Grains that did not break during the entire duration of the test are indicated as NB. These last were furtherly tested under an instantaneous uniaxial compressive stress, being these results plotted in Figure 4. Finally, the grains that broke during the 40-day period are represented between BB and NB.

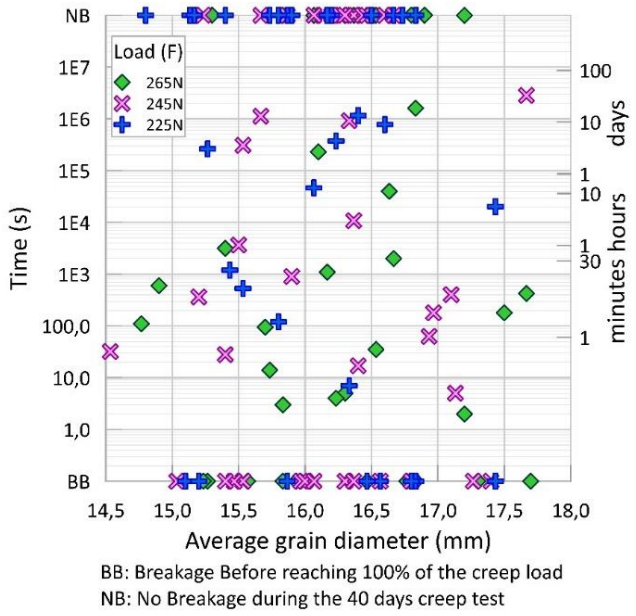

Figure 3. Time required for the breakage of creep-tested grains, depending on their diameter and the load tested.

Since the value of the breaking stress obtained according to Eq. 1 for LECA grains is not a deterministic function, but a stochastic value, in order to estimate the influence of the creep loads and time on the breaking stress of the grains, distribution functions must be compared. For this purpose, the strengths obtained are sorted and, depending on the number of tests available, the cumulative distribution function (CFD) is performed.

Figure 4 shows the comparison between grains previously creep tested (depending on the creep load used) and the tests carried out on grains without previous creep test.

In order to be able to make this comparison, the following aspects must be taken into account: the weakest grains of those tested at creep have already broken before reaching the creep load (BB in Fig 3) or have broken during the creep test for a time of less than 40 days (Figure 3 shows the grains that have broken during creep). Therefore, it seems logical to shift the CFD of the failure stress of these grains by a value equal to the percentage of grains broken during the creep test. This percentage is determined by summing up both the grains that failed while the creep load was being applied, as well as the ones that failed during the 40-day proposed application period of the constant testing load. Bearing this in mind, as it is indicated in Figure 4, the CFD curve corresponding to the grains tested under an instantaneous uniaxial compressive load after being subjected to a 225 N constant load during 40 days was shifted 57%, while the curves representing the grains that resisted 245 N and 265 N creep loads were shifted 70% and 74%, respectively. In Figure 4, both the CFD curves corresponding to the grains previously tested under constant loads and the ones only tested under an instantaneous uniaxial compressive stress are plotted.

In order to minimize the influence of grain size on grain strength, the results were taken for similar mean diameter values. The mean values for each of the series are shown in Figure 4.

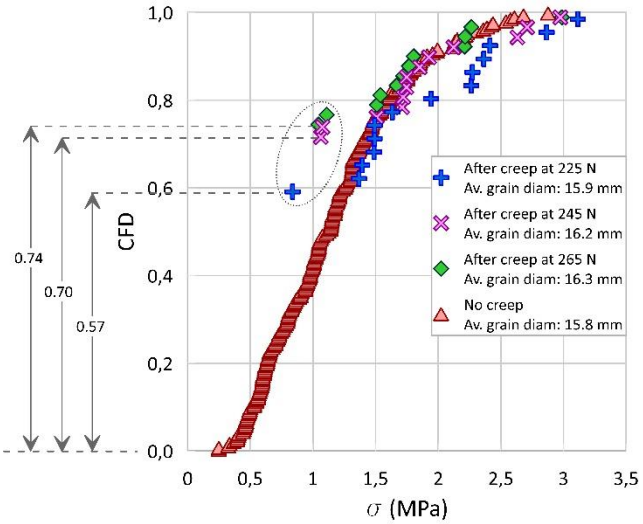

Figure 4. Comparison of breakage stresses of broken grains after creep tests of grains without previous creep test.

Figure 4 shows that there is a great coincidence between the results obtained from performing a point load test on grains previously and not previously tested under creep loads. It can also be seen that the coincidence is not exact, as there are 5 grains from the previously creep-tested group, that don't seem to have the same behavior. These LECA grains, marked in the graph with an ellipse, have a residual strength of approximately 0.5 MPa lower than the expected one. This value is determined by comparing the strength values of the CFD curves obtained for each of the previously creep-tested grains and the CFD curve obtained for the not previously tested grains.

4 CONCLUSIONS

An experimental study was carried out on the failure of expanded clay grains at room temperature, under simple compression, both under sustained and instantaneous loads. The study includes the results obtained from testing 340 grains (121 grains subjected to creep loads and 219 tested under instantaneous loads).

For grains that did not fail after a 40-day period of load application during creep tests and were tested under uniaxial instantaneous compression loading, there was no significant variation between the remaining strength and the original strength. Only in 5 grains marked with an ellipse in Figure 4. a lower strength than that obtained for grains without prior creep test is observed. This decrease in strength could be due to internal crack growth during creep or to statistical variation in the results.

REFERENCES

Anaya, R., Martínez, J.M., Hernández, M.F., Herrea, M.S. and Rendtorff, N.M. (2022). Individual diametral compression behavior of a ceramic proppant. Ceramics International, 48(21), pp. 32357-32365. https://doi.org/10.1016/j.ceramint.2022.07.179.

Chu, Z., Wu, Z., Wang, Z., Weng, L., Liu, Q. and Fan, L. (2022). Micro-mechanism of brittle creep in saturated sandstone and its mechanical behavior after creep damage. International Journal of Rock Mechanics and Mining Sciences, 149, pp. 104994. https://doi.org/10.1016/j.ijrmms.2021.104994.

Jia, H., Xiang, W. and Krautblatter, M. (2015). Quantifying rock fatigue and decreasing compressive and tensile strength after repeated freeze-thaw cycles. Permafrost and Periglacial Processes, 26(4), pp. 368-377. https://doi.org/10.1002/ppp.1857.

Laskowski, C., Manzanal, D., Muñiz-Menéndez, M., Orlandi, S. and Allard, J. (2023). Carbon dioxide impact on the mechanical properties of a sandstone from San Jorge Gulf Basin (Argentina). 15th International ISRM Congress & 72nd Geomechanics Colloquium. Challenges in rock mechanics & rock engineering. Austrian Society for Geomechanics, pp. 2176-2181.

Lei, W., Yu, Z., Zhang, P. and Qian, G. (2021). Standardized Weibull statistics of ceramic strength. Ceramics International, 47(4), pp. 4972-4993. https://doi.org/10.1016/j.ceramint.2020.05.024.

Lei, W., Zhang, P., Yu, Z. and Qian, G. (2020). Statistics of ceramic strength: Use ordinary Weibull distribution function or Weibull statistical fracture theory? Ceramics International, 46(13), pp. 20751-20768. https://doi.org/10.1016/j.ceramint.2020.05.024.

Mcdowell, G.R. and Amon, A. (2000). The application of Weibull statistics to the fracture of soil particles. Soils and foundations, 40(5), pp. 133-141. https://doi.org/10.3208/sandf.40.5_133.

Mcdowell, G.R. and De Bono, J.P. (2013). On the micro mechanics of one-dimensional normal compression. Géotechnique, 63(11), pp. 895-908. https://doi.org/10.1680/geot.12.P.041.

Philippidis, T.P. and Passipoularidis, V.A. (2007). Residual strength after fatigue in composites: Theory vs. experiment. International Journal of Fatigue, 29(12), pp. 2104-2116. https://doi.org/10.1016/j.ijfatigue.2007.01.019.

Prisco, C.D. (2007). Applicazioni geotecniche e caratterizzazione meccanica dell'argilla espansa Leca. Bregnano (Co), Italia: Leca.

Qu, G., Zheng, M., Wang, X., Zhu, R., Su, Y. and Chang, G. (2023). A freeze–thaw damage evolution equation and a residual strength prediction model for porous concrete based on the Weibull distribution function. Journal of Materials in Civil Engineering, 35(5), pp. 04023074. https://doi.org/10.1061/(ASCE)MT.1943-5533.0004745.

Roces, E., Muñiz-Menéndez, M., González-Galindo, J. and Estaire, J. (2021). Lightweight expanded clay aggregate properties based on laboratory testing. Construction and Building Materials, 313, pp. 125486. https://doi.org/10.1016/j.conbuildmat.2021.125486.

Roces-Alonso, E.A., González-Galindo, J. and Estaire, J. (2021). Experimental study on grain failure of lightweight expanded clay aggregate under uniaxial and biaxial load conditions. Powder Technology, 383, pp. 542-553. https://doi.org/10.1016/j.powtec.2021.01.052.

Song, Z., Wang, Y., Konietzky, H. and Cai, X. (2021). Mechanical behavior of marble exposed to freeze-thaw-fatigue loading. International Journal of Rock Mechanics and Mining Sciences, 138, pp. 104648. https://doi.org/10.1016/j.ijrmms.2021.104648.

Tan, X., Chen, W., Yang, J. and Cao, J. (2011). Laboratory investigations on the mechanical properties degradation of granite under freeze–thaw cycles. Cold Regions Science and Technology, 68(3), pp. 130-138. https://doi.org/10.1016/j.coldregions.2011.05.007.

Proceedings of the XVIII ECSMGE 2024
GEOTECHNICAL ENGINEERING CHALLENGES
TO MEET CURRENT AND EMERGING NEEDS OF SOCIETY
© 2024 the Authors
ISBN 978-1-032-54816-6
DOI 10.1201/9781003431749-462
Open Access: www.taylorfrancis.com, CC BY-NC-ND 4.0 license

ECSMGE 24
XVIII EUROPEAN CONFERENCE ON SOIL MECHANICS AND GEOTECHNICAL ENGINEERING

On the ground settlements observed during execution of jet grouting columns in urban area adjacent to a historic building

Tassements au sol observés lors de l'exécution de colonnes de jet grouting en zone urbaine adjacente à un bâtiment historique

J. Logar*, B. Pulko, J. Smolar, K. Oštir
University of Ljubljana, Ljubljana, Slovenia

**janko.logar@fgg.uni-lj.si*

ABSTRACT: During the execution of jet grouting columns for the stability of deep excavation of the construction pit for new residential building, the adjacent historical building settled for 15 to 35 mm causing cracks in its masonry walls. The historical building is 132 m long and 18 m wide having shallow foundation 2 m below ground surface. The cracks of the building during the execution of JG columns were noticed up to 90 m away from the construction activities. In the paper, we present the tentative explanation of the reasons for the observed behaviour and the activities that brought us to the conclusions. The ground profile consists of three characteristic soil layers resting on a weak bedrock. The foundation layer for the historic building is a very dense clean alluvium gravel with a thickness of 10 m. Next 10 m consist of saturated very loose to loose silty gravel with sand. Following some hints from the literature, we believe that the drilling and jet-grouting procedures affected the loose structure of the layer between 10 and 20 m depth resulting in far reaching settlements of entire upper stiff gravel layer and structures resting on it.

RÉSUMÉ: Lors de l'exécution des colonnes de jet grouting pour la stabilité de l'excavation profonde de la fosse de construction d'un nouveau bâtiment résidentiel, le bâtiment historique adjacent s'est affaissé de 15 à 35 mm, provoquant des fissures dans ses murs en maçonnerie. Le bâtiment historique mesure 132 m de long et 18 m de large et possède des fondations peu profondes à 2 m sous la surface du sol. Les fissures du bâtiment lors de l'exécution des colonnes JG ont été constatées jusqu'à 90 m des travaux de construction. Dans cet article, nous présentons une explication provisoire des raisons du comportement observé et des activités qui nous ont amenés aux conclusions. Le profil du sol est constitué de trois couches caractéristiques reposant sur un substrat rocheux fragile. La couche de fondation du bâtiment historique est un gravier alluvionnaire propre et très dense d'une épaisseur de 10 m. Les 10 m suivants sont constitués de gravier limoneux saturé, très meuble à meuble, avec du sable. Suite à quelques indications tirées de la littérature, nous pensons que les procédures de forage et de jet grouting ont affecté la structure lâche de la couche entre 10 et 20 m de profondeur, entraînant des tassements étendus de toute la couche supérieure de gravier rigide et des structures reposant sur elle.

Keywords: Jet grouting; settlements; deep excavation.

1 INTRODUCTION

The stability of 13.2 m deep construction pit was provided by total 127 jet grouting (JG) columns, subsequently anchored by pre-stressed ground anchors in three levels. 25 m deep JG columns 2 m in diameter at 1.8 m spacing were used in order to reach impervious bedrock and make the construction pit watertight.

After one month of execution, 85 JG columns were installed. The last 5 JG columns were made in the immediate vicinity of adjacent historic building. The subsequent inspection of this building showed that cracks occurred not only in the vicinity of construction works but up to 90 m away from the location of executed JG columns. The historic building is 132.3 m long, 18.4 m wide and 19 m high having 3 storeys and the attic.

Geodetic measurements showed that the maximum settlement of the historic building from the beginning of the works were 31 mm at the most exposed SE corner of the building. 30 m farther away, the settlement of the building was still 15 mm.

Before the complete stop of the installation of JG columns, additional 21 columns were made at minimum distance of 15 m from the historic building. These JG columns caused additional 5 mm of settlements of the SE corner of the building.

At this stage, investigations started in order to understand the ground behaviour during installation of JG columns, to assess the state of the historic building, to design the rehabilitation measures for it and to adjust the procedure for installation of final 20 JG columns.

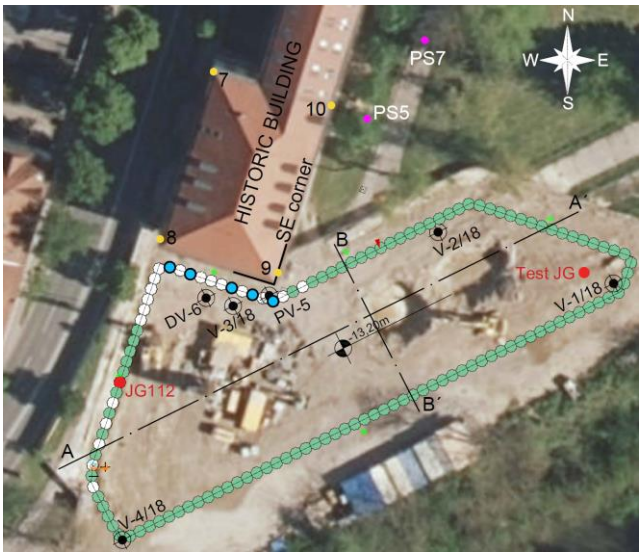

Figure 1. Layout of the construction pit and adjacent historical building, location of boreholes (black), benchmark points (yellow), test JG columns (red) and persistent scatterers (magenta). Ground profile along section A-A' is shown in Figure 2.

2 GROUND CONDITIONS

Four boreholes were made in the design phase. The geotechnical cross-section A-A' is presented in Figure 2. Below 1-2 m thick fill layer, a layer of very dense sandy gravel appears down to the depths between 9 to 13 m. Between this stiff gravely layer and the weak bedrock at a depth of 24 m, proluvial loose gravels with 15 to 25 % of fines were found. A significant difference in stiffness was observed with depth. The upper dense sandy gravel and the lower loose silty gravel were characterized by elastic moduli of 95 MPa and 5 MPa, respectively.

Groundwater level is generally 14 m below the ground surface but can rise up to 10 m below the ground surface.

From Figure 2 one can observe that the loose ground layers vanish at the western side of the construction pit.

3 CONSTRUCTION

3.1 Jet grouting columns

JG columns of 2 m diameter at a spacing of 1.8 m were made using two phase technology with 7 mm nozzle, grout pressure of 420 bar with flow rate 525 l/min and air pressure of 8 bar. Other parameters varied according to the soil profile and are given in Table 1.

Table 1. JG execution parameters.

Depth (m)	w/c ratio	Lift (cm/min)	Rotations/ minute
0.0 – 9.5	1.0	50	9
9.5 – 14.8	1.0	40	8
14.8 – 24.0	1.4	36	6
> 24.0	1.4	30	10

3.2 Monitoring

Observation of settlements/heave of historic building and nearby road had been foreseen during construction works. Zero reading of all benchmark points was made before the works started. However, further readings were not made until cracks were observed in the historic building 1 month after the start of construction work. At that time, 2 mm to 31 mm settlements were recorded on the adjacent building.

Detailed inspection of the historic building showed that cracks extended up to 90 m away from the construction activities.

3.3 Temporary suspension of construction

Due to the observed harmful influences of the execution of JG columns on the historic building next to the construction site, construction activities were temporarily suspended.

Structural engineers were employed to inspect and reinforce the historic building and geotechnical experts were asked to find the reasons for the observed ground response and give guidance for the execution of remaining 20 JG columns.

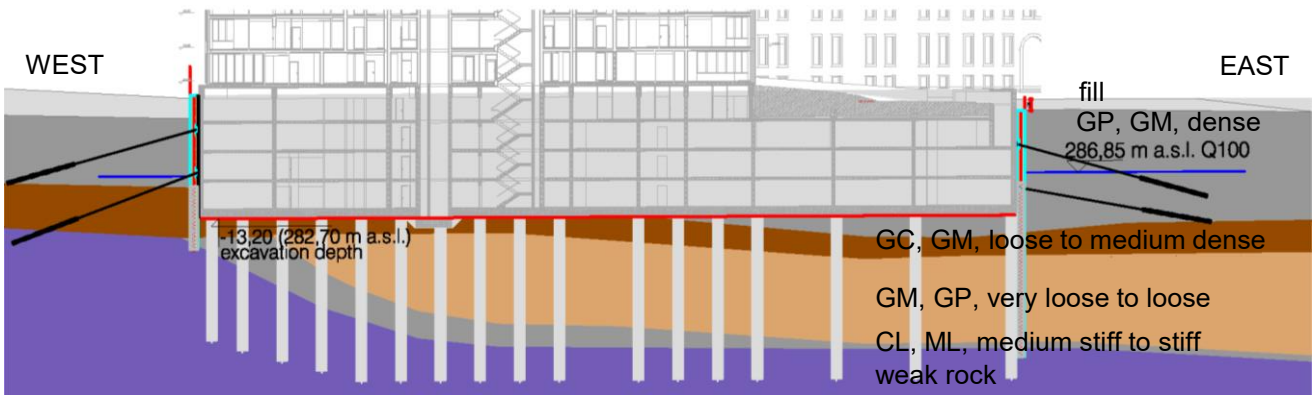

Figure 2. Cross section

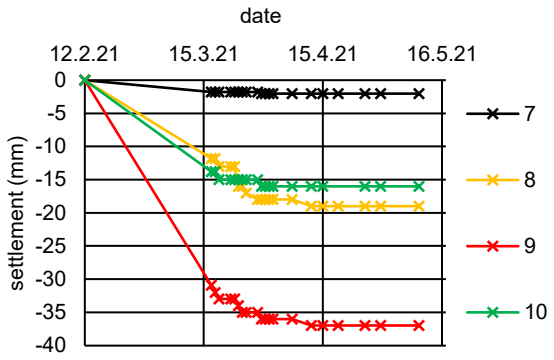

Figure 3. Settlements of the historic building measured at benchmark points.

4 ADDITIONAL INVESTIGATIONS

Initially, it was believed that the damage of the existing building was due to the execution of the last 5 JG columns exactly on the day when cracks were noticed by the users of the historic building (5 JG columns coloured in blue at the southern side of the historic building in Figure 1).

Although this explanation seemed reasonable, it could not explain the appearance of cracks of the building up to 90 m away from its southern wall. Alternative assumption was made that the settlements of the building occurred gradually throughout the execution of all JG columns. In order to test this assumption, satellite radar interferometry (InSAR) was used for displacement observation in the absence of geodetic measurements of installed benchmarks. Furthermore, additional boreholes were drilled (PV-5 and DV-6), two test JG columns were made ("Test JG" and "JG 112") and FEM analyses were performed.

4.1 Satellite InSAR

We have performed Persistent Scatterer Interferometric Synthetic Aperture Radar (PS InSAR) processing on Sentinel-1 satellite radar images. Sentinel-1 acquires an image every 6 days; in total, 41 images from September 2020 to May 2021 were used. PS InSAR is a technique used to estimate local ground deformation with millimetric accuracy. It focuses on the phase-stable scatterers and identifies pixels in which a single persistent scatterer (PS) represents the dominant backscattering signal in a series of interferograms. In built areas, permanent scatterers can be detected on man-made structures (roofs, fences, roads, etc.); many PS were detected within the construction period in the area.

Several PS were found on the historic building and enabled the interpretation of displacements during the entire construction period. The absolute accuracy of interpreted individual displacements (in the period of 6 days) is 2 to 3 mm, while relative accuracy is ~1 mm/year (for the time series). Figure 4 presents the movements of two scatterers, PS5 and PS7, located close to the SE corner of the historic building (see Figure 1). It can be clearly observed that movements started immediately after the start of the execution of JG columns and continued at a nearly constant rate throughout the grouting works.

4.2 Literature review

From the reported case histories on the influence of execution of JG columns on ground movements it can be learned that heave is more often a problem than ground settlements. Nevertheless, few papers report settlements during the execution of JG columns (Eramo et al, 2011; Guan and Yang, 2019) without giving any explanations for such ground behaviour.

Byle (2017) reports that loose gravels with high percentage of fines are prone to inner instability and represent challenging conditions for drilling and grouting operations in terms of ground movements.

4.3 Execution of test JG columns

Two JG columns were made with continuous measurements of settlements at 2, 4, 6, 8 and 10 m distance from the JG column centre (Figure 5). Test JG columns are marked as "Test JG" and "JG 112" in Figure 1.

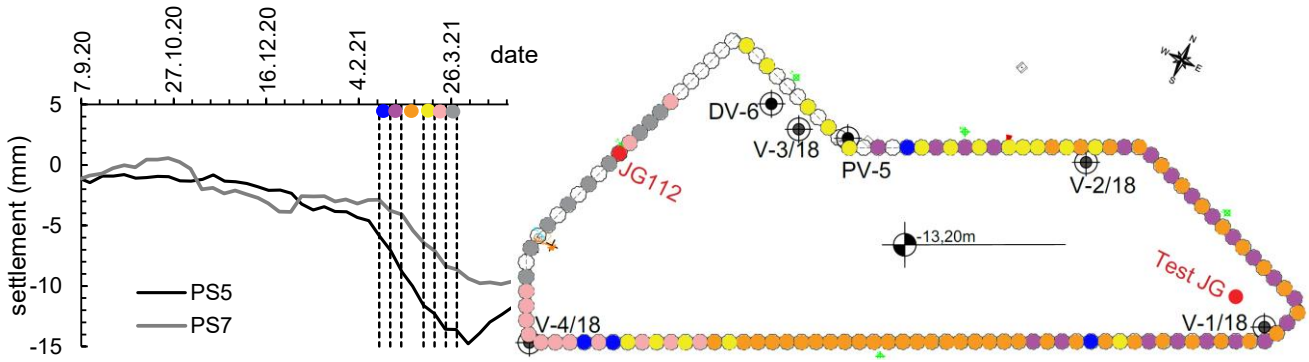

Figure 4. Left: Ground settlements from InSAR data for PS 5 and PS 7 (locations are shown in Figure 1); Right: Time sequence of execution of JG columns is shown by respective colours shown on left graph.

During the execution of "Test JG", from 0.6 mm to 0.4 mm settlements were observed at 2 m and 10 m distance respectively. Surprisingly, 0.6 mm settlement was observed also at the SE corner of the historic building, which is located 40 m away from the "Test JG".

The execution of "JG 112" which is located within the JG wall had much less effect on its surroundings. Maximum settlement at 2 m distance was 0.2 mm, at 4 m 0.1 mm and no settlements were measured at larger distances including benchmarks on historic building. This is partly due to the fact that it is located between two adjacent already executed and hardened JG columns and partly to the fact that the layer of loose silty gravel is thinner at this location.



Figure 5. Settlement monitoring during execution of TestJG.

4.4 Numerical analyses

Based on the suggestion by Byle (2017), volume reduction of loose ground may occur during drilling and grouting operations. Hence, a simple 2D FEM analysis was performed along the section B-B' (see Figure 1) of the construction pit. Measured difference in stiffness of two dominating soil layers was considered. Volume change within JG body was imposed on the model (i) along the entire height of the JG column, (ii) only in the upper layer and (iii) only in the loose lower layer.

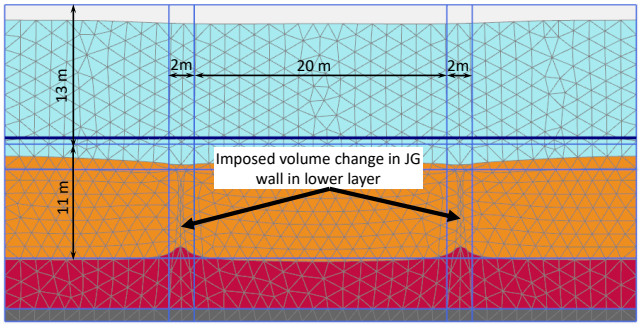

Figure 6. Displacements from 2D FEM analysis considering volume change within JG column body in lower layer.

The first two models resulted in surface settlements concentrated in the vicinity of JG column walls. Only the third model gave the behaviour, similar to the observations on site (Figure 6) where settlements extended far beyond the extent of the construction pit.

5 CONCLUSIONS

Based on the analyses of all the collected data, we have concluded that the most likely cause of the deformation of the ground and the adjacent historic building is a lower layer of very loose to loose silty gravel with sand. Drilling and grouting procedures cause the change in loose structure of the soil, which leads to a volume reduction of this soil layer in the vicinity of each individual JG column and consequently settlements of the ground surface. Due to the presence of stiff 10 m thick upper layer of clean gravel above the layer of loose silty to clayey gravel, the deformations are detected even at very large distances from the executed JG columns. That is why the ground outside the construction pit gradually settled during the entire period of construction of JG columns. Cracking of the historic building was therefore not only the consequence of the execution of the 5 JG columns next to the southern wall of the historic building.

The installation of remaining 19 JG columns started 2 months after the first damage on historic building had been observed. These works had hardly any effect on the nearby structure. The reasons for this are (i) a large number of JG columns had been already in place for over 2 months and represented a significant reinforcement of the soil, (ii) only one JG column per day was executed near the historic building with reduced w/c ratio of the grout and (iii) the observation during execution of test JG column "JG 112" showed that by a proper order of execution, most of the remaining JG columns can be executed in-between previously executed JG columns thus reducing ground settlements.

REFERENCES

Byle, M. (2017). Drilling and Grouting Challenges in Broadly Graded Soils. *Grouting*, doi: https://doi.org/10.1061/9780784480793.021.

Eramo, N., Modoni, G., Arroyo, M. (2011). Design control and monitoring of a jet grouted excavation bottom plug. *7th International Symposium on »Geotechnical Aspects of Underground Construction in Soft Ground«*, Rome, Italy, pp. 611-618.

Guan, C. and Yang, Y. (2019). Field Study on the Waterstop of the Rodin Jet Pile Method in a Water-Rich Sandy Gravel Stratum, Appl. Sci., 9(8), 1709, doi: https://doi.org/10.3390/app9081709.

Proceedings of the XVIII ECSMGE 2024
GEOTECHNICAL ENGINEERING CHALLENGES
TO MEET CURRENT AND EMERGING NEEDS OF SOCIETY
© 2024 the Authors
ISBN 978-1-032-54816-6
DOI 10.1201/9781003431749-463
Open Access: www.taylorfrancis.com, CC BY-NC-ND 4.0 license

ECSMGE 24
XVIII EUROPEAN CONFERENCE ON SOIL MECHANICS AND GEOTECHNICAL ENGINEERING

Precision measurements constrain the implementation of more accurate testing in earthworks quality assurance

Les mesures de précision limitent la mise en œuvre de tests plus précis dans l'assurance qualité des travaux de terrassement

B.G. Look*
AGTRE, Brisbane, Australia
**lookburt@agtre.au*

ABSTRACT: Density was selected as the key Quality control (QC) parameter as its high precision was recognized in the early days. Precision in QC was chosen in favour of more relevant but difficult to measure parameters at the time. Precision is not the same as accuracy. As dry density ratio (DDR) index is now fully embedded in QC, one may mistakenly think that the factors measured are the key factors. DDR was intended to be just part of the decision-making process of quality and verification of the design requirements. On projects which use end product specifications, a DDR value then becomes THE de facto decision on pass / fail. This simplifies the site decision in having assessment metronomically stated. Because traditionally industry did not or cannot measure something should not diminish its importance. Several in-situ devices have been available for the past two decades and various research has shown the benefits. Data was acquired as part of field trials over multiple "live" projects. Conventional QC testing was supplemented with other field strength and modulus tests. Correlating to established DDR tests is blind to the influences of other factors influencing strength and modulus. Such tests measure a combination of underlying material, material quality, moisture content and density. A 95% DDR does not have a singular strength or modulus value as measured with one-to-one correlated testing as this is governed by material type.

RÉSUMÉ: La densité a été choisie comme paramètre clé du contrôle de la qualité (CQ), car sa haute précision a été reconnue dès les premiers jours. La précision en CQ a été choisie au profit de paramètres plus pertinents mais difficiles à mesurer à l'époque. La précision n'est pas la même chose que l'exactitude. Comme l'indice de rapport de densité sèche (DDR) est maintenant entièrement intégré dans le contrôle qualité, on peut penser à tort que les facteurs mesurés sont les facteurs clés. Le DDR devait n'être qu'une partie du processus décisionnel de qualité et de vérification de la conception. Sur les projets qui utilisent des spécifications de produit final, une valeur DDR devient alors LA décision de facto sur la réussite / l'échec. Cela simplifie la décision du site en ayant l'évaluation métronomiquement énoncée. Le fait que, traditionnellement, l'industrie ne mesurait pas ou ne pouvait pas mesurer quelque chose ne devrait pas en diminuer l'importance. Plusieurs dispositifs in situ ont été disponibles au cours des deux dernières décennies et diverses recherches ont montré les avantages. Les données ont été acquises dans le cadre d'essais sur le terrain dans le cadre de plusieurs projets « en direct ». Les essais de contrôle qualité conventionnels ont été complétés par d'autres essais d'intensité de champ et de module. La corrélation avec les tests DDR établis est aveugle à l'influence d'autres facteurs influençant la résistance et le module. Ces tests mesurent une combinaison du matériau sous-jacent, de la qualité du matériau, de la teneur en humidité et de la densité. Un DDR à 95% n'a pas de valeur de résistance ou de module unique, telle que mesurée par des tests corrélés un à un, car elle est régie par le type de matériau.

Keywords: Dry density ratio; precision; accuracy; quality control; earthworks; Modulus; CBR.

1 INTRODUCTION

The aim of compaction is to reduce the air voids, and with many associated gains such as strength, reduction of permeability, reduced settlement, etc. The use of maximum dry density (MDD), optimum moisture content (OMC), dry density ratio (DDR) and California Bearing Ratio (CBR) originated from studies completed in the 1930s and standardised by the 1960s. The DDR compares the field dry density to the laboratory MDD.

The standard density test has revolutionized construction testing, enabling engineers to assess and control soil compaction in a consistent manner. DDR has been used successfully as density tests are very precise. Precision is not the same as accuracy, which is closeness to a "true" value, while precision is the closeness of the measurement to each other.

Look (2018) showed that DDR is very precise but is not very accurate. Conversely, the plate load is (PLT) is accurate, but not very precise. Such findings

were also apparent when adopting DDR as the defacto standard as a quality QC measurement. The decision on pass / fail can then be simply applied to the site decision making process in having your daily assessment activities metronomically stated. This may create a false confidence in the design and construction process when precision is not the same as accuracy.

Engineers assume a direct relation between density and strength or modulus (i.e., the greater the density achieved, the higher the strength or modulus of the compacted material). However, the peak CBR does not necessarily occur at the MDD. Seed and Chan (1959) had shown the peak strength is lower at the MDD due to the lower moisture content even when the density is lower (Figure 1 from Leroueil and Hight, 2013).

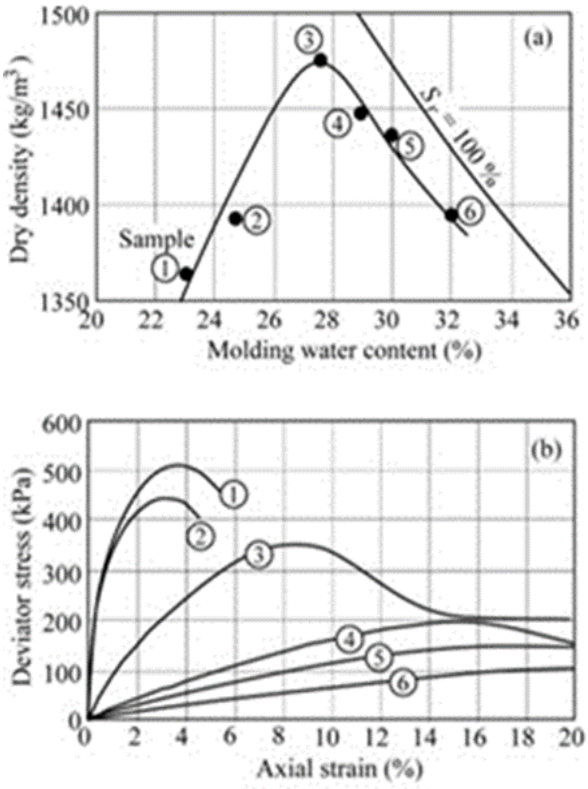

Figure 1. (a) Influence of moulding water content on the dry density and (b) stress-strain relationships.

Several in-situ devices have been available to industry for the past two decades with many benefits being constrained by correlations to DDR. Nazarian and Correia (2009) show the field modulus is highly dependent on the moisture content (Figure 2). Drying or wetting after compaction can significantly influence the modulus result. A minor change in moisture content results in 6% change in density, but 300% change in modulus. Most of these modulus values still satisfy a 95% MDD criteria – but at a different moisture content.

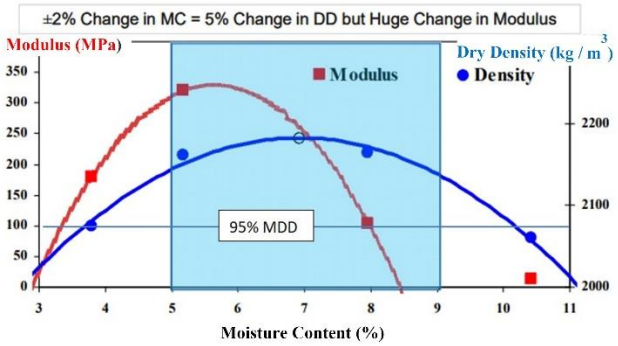

Figure 2. Impact of moisture on density and modulus.

2 HISTORICAL DDR AND CBR IN QC

2.1 Past decisions with present considerations

Figure 3 shows a retrospective decision process using a force field analysis to arrive at accepting DDR in QC testing. This approach is used as a decision-making tool. It compares the forces that are either driving the movement toward a decision or goal (helping forces) as compared to the factors blocking the movement towards that goal or decision (hindering forces).

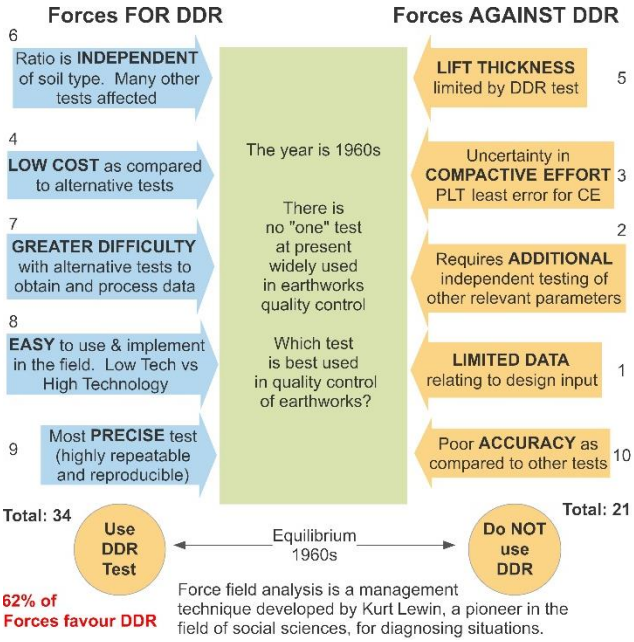

Figure 3. Force field analysis decision to use DDR as the main QC parameter in the 1960s. 10 is most desirable.

Adopting DDR as the main QC parameter far outweighs the negative considerations. High precision, ease of use, and greater difficult of technology of the tine outweigh negative considerations of accuracy. Thus, using DDR was logical choice in the 1960s based on the technology of the time.

Figure 4 uses the similar considerations in the decision to use DDR as the main QC parameter in the

2020s but updated for current technology. The decision is now weighted against using DDR given current technology in current times.

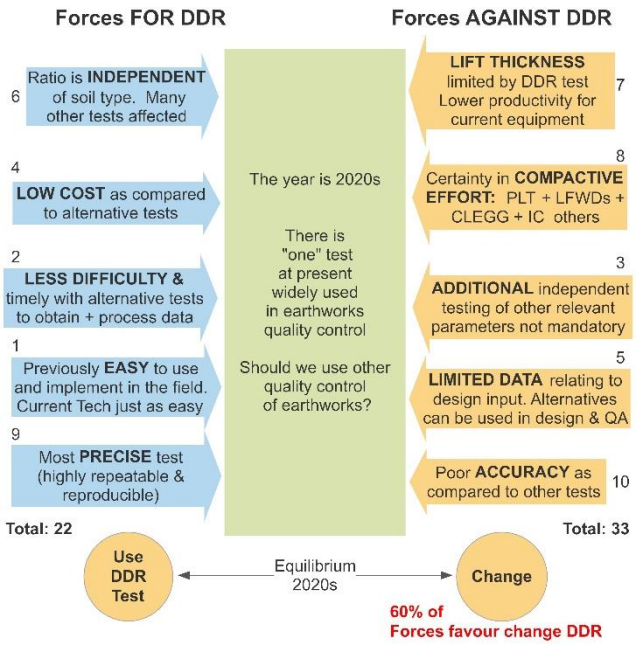

Figure 4. Force field analysis decision to NOT use DDR in the 2020s using similar considerations as the 1960s.

2.2 Historical testing and compaction history

The CBR test was developed to assess the load-bearing capacity of soils. In modern times it is used to correlate with resilient modulus.

A heavier compaction roller can achieve greater compaction energy and soil density. Early machines prior to 1900 were 6 tons but increased to 10 to 12 tons by the time the compaction test in the 1930s, and 15–20 tons in the 1940s by the time the modified compaction test was introduced.

During the early standardisation of tests (1950s) the development of smooth drum vibratory compaction rollers further improved compaction efficiency, with machine around 20-25 tons. By the 1990s, advances in engineering and construction materials allowed for larger compaction rollers with typical weights of 30-35 tons. High-frequency vibratory compaction rollers from 2000, and sophisticated control systems has led to larger and heavier models weighing over 40 tons.

Vehicles weights also changed over the years. However, it is truck axle loads that governs road performance. The average truck axle load was around 2.5t in the 1920s and increased to approximately 8.5t by the 1980s with technological in truck design.

3 COMPARSION OF TESTS

3.1 Early days to assess benefits of tests

In the symposium on compaction of earthworks and granular bases, Selig and Truesdale (1967) examined various testing devices for various factors affecting compaction. They found density has a low variability compared to other tests. Thus, precision took preference over the more useful but wider variability of other measurements of the time.

3.2 Current tests and benefits

A survey of engineers ranking what attributes are desirable in a test equipment showed that accuracy is the preferred attribute (Look, 2018). The ranking order for the 8 attributes of a test equipment was:

1. Accuracy; 2. Precision
3. Time to conduct test / Ease of use
4. Time to process results / Ease to process & report
5. Amount of data obtained / Cost of equipment

Field trials were used to benchmark the various alternative equipment and compared with traditional DDR measurements for various sites (Table 1).

Table 1. COV for various tests considered over 5 sites.

Test	**Coefficient of Variation (%)**		
	Median	Low	High
Density Ratio	2.0	1.8	2.9
Geogauge	26.5	19.1	34.5
Prima LFWD	33.5	15.0	35.7
CBR	40	17.0	58
Zorn LFWD	34.1	21.6	51
Clegg	36.0	26.0	54
PANDA			
(50 – 100mm)	53	34	74
(150 – 200mm)	50	48	92
DCP			
(50 – 100mm)	38.0	28	97
(150 – 200mm)	53	34	74
Plate Load Test	77	14	142

The lot coefficient of variation (COV = standard deviation / mean) at each site was used to judge the precision, and the DDR test is the standout leader (COV < 3.0%), with the Plate Load test (PLT), the most variable as compared to other tests.

However, precision is the 2nd preference attribute as compared to accuracy. Accuracy was assessed in terms of how well the results compared with each other for similar order of the high to the low values for the various test sites. The PLT was the most accurate, but is the least precise test (Look, 2018).

4 DISCUSSION

Density has historically satisfied a 1 parameter need in QC assessment. Other quality parameters are assessed independently. A 95% DDR does not have a singular strength or modulus value – although this is an implicit assumption (Table 2). This is not rock fill testing as all materials conform to "soil" after compaction.

Table 2. Modulus and strength at 95% DDR (Look, 2021).

Fill Material Origin	PLT E_{V2} (MPa)	In situ angle of friction φ (°)	
		Smooth	Padfoot
Sandstone	70	45	45
Interbedded Siltstone/Sandstone	40	41	39
Basalt	65	39	43

When field supervisors ask for a correlation of modulus to provide a linkage with DDR as the de facto standard, a poor correlation often results. This is due to different zones of influence, modulus being affected by several factors (not just DDR), and the DDR having a normal probability density function (PDF) and other tests having a non-normal PDF. Look (2021) show a methodology to avoid such correction inconsistencies

LFWD results (Figure 5) show that both Type I and Type II errors are occurring when DDR is compared with LFWD data. A Type I error is the incorrect rejection of a true null hypothesis. Type II error is the failure to reject a false null hypothesis. A direct paired correlation had 20% "errors" in its assessment.

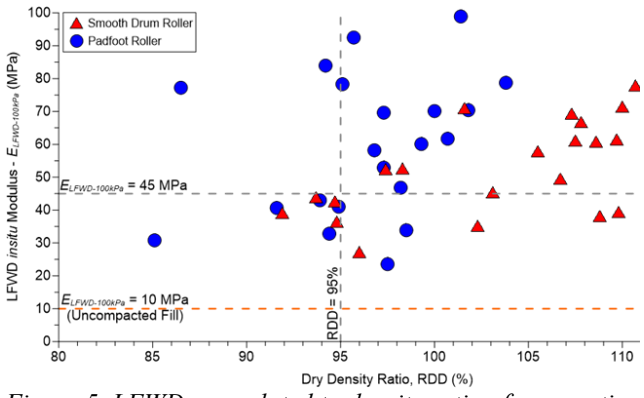

Figure 5. LFWDs correlated to density ratio of compaction for sandstone material.

Riad et al. (2023) review various testing equipment in compaction QC in the U.S. Curently, 93.5% of state agencies use density specifications rather than modulus based compaction controls. Similarly, in Australia, modulus based compaction levels are curently the exception. A requirement on parallel testing with DDR leads to additional cost and time.

5 CONCLUSIONS

Modern pavement designs are based on modulus and strength values. When such measurements are correlated to QC density testing, a poor correlation often results as this is a multivariate relationship.

Traditional QC testing density has focused on its key benefit of precision and simplicity without appreciating the poor accuracy associated with this measurement. The decision is between the past comforts and success of using density measurements vs the technical benefits of modern testing equipment. The early benefits of using DDR now seem to impede what should be possible given current technologies.

REFERENCES

Leroueil, S. and Hight, D.W. (2013). Compacted soils: From physics to hydraulic and mechanical behaviour. *Proceedings of the 1st Pan American Conference on unsaturated soils*, Colombia, 41-45. http://doi.org/10.1201/b14393-6 (doi.org).

Look, B.G. (2018). Compaction QA Limitations: Benefits of alternative testing methods, AGS *Victoria Symposium on Geotechnics and Transport Infrastructure*.

Look, B.G. (2021). An earthworks quality assurance methodology which avoids unreliable correlations. *4th International Conference on Transportation Geotechnics*, Chicago, USA. In: Tutumluer, E., Nazarian, S., Al-Qadi, I., Qamhia, I.I. (eds) *Advances in Transportation Geotechnics IV. Lecture Notes in Civil Engineering*, 166. 179 – 192, Springer. http://doi.org/10.1007/978-3-030-77238-3_14 (doi.org).

Nazarian, S. and Correia, A. (2009). Mechanistic-based field evaluation of pavement foundation. *Geostrata*, May/June, 32-36.

Riad, B. Zhang Z., Liu J and Wang Y. (2023). Compaction Quality Assurance Specifications of Unbound Materials. *Journal of Transportation Engineering Part B: Pavements, Vol. 149, No. 1, ASCE.* https://doi.org/10.1061/JPEODX.0000403.

Seed, H.B. and Chan, C.K. (1959). Structure and strength characteristics of compacted clays. *Journal of the Soil Mechanics and Foundations Division (ASCE),* 85, SM5, 87-128. https://doi.org/10.1061/JSFEAQ.0000229.

Selig E T, and Truesdale W B (1967). Properties of Field Compacted Soils. *Highway Research Record*, Issue 177, National Research Council, 77 – 97.

Proceedings of the XVIII ECSMGE 2024
GEOTECHNICAL ENGINEERING CHALLENGES
TO MEET CURRENT AND EMERGING NEEDS OF SOCIETY
© 2024 the Authors
ISBN 978-1-032-54816-6
DOI 10.1201/9781003431749-464
Open Access: www.taylorfrancis.com, CC BY-NC-ND 4.0 license

ECSMGE 24
XVIII EUROPEAN CONFERENCE ON SOIL MECHANICS AND GEOTECHNICAL ENGINEERING

Ground improvement solutions at the plot 14 of the Northern Lisbon logistic platform

Solutions d'amélioration du sol sur le lot 14 de la Plateforme Logistique du Nord de Lisbonne

M. Lopes*, A. Pinto
JETsj Geotecnia Lda, Lisbon, Portugal

A.L. Gonçalves
Terratest, Lisbon, Portugal

J. Moreno
JM Ingeniería Geológica, Madrid, Spain

**mlopes@jetsj.com*

ABSTRACT: The present work addresses the ground improvement solutions adopted for the soft soils as foundation of the future industrial warehouse, to be built at the plot 14 of the Northern Lisbon Logistic Platform, at Castanheira do Ribatejo, Vila Franca de Xira, Portugal, comprising an area of 49 813 m^2. A description of the existing conditions is made, particularly of the geological-geotechnical scenario, highlighting the existence of an alluvial layer, with clayed soft soils, with low characteristics of strength and stiffness as well as very low average permeability. The solution adopted consists in the execution of preload embankments associated with (i) stone columns, executed at the area of the warehouse indoor pavements, and (ii) vertical prefabricated geodrains, at the area of the outdoor pavements, in the places designed for car parking and circulation of light and heavy vehicles. This article describes the criteria and methods used at the design of the preload fills, seeking to reduce the hydrodynamic consolidation schedule. The Monitoring and Survey Plan and respective results are also presented.

RÉSUMÉ: Le présent travail traite des solutions d'amélioration du sol adoptées pour les sols meubles comme fondation du futur entrepôt industriel qui sera construit sur le lot 14 de la plate-forme logistique du nord de Lisbonne, à Castanheira do Ribatejo, Vila Franca de Xira, Portugal et qui comprend une superficie de 49 813 m^2. Une description des conditions existantes est faite, en particulier du scénario géologique-géotechnique mettant en évidence l'existence d'une couche alluviale et de sols meubles et argileux, aux faibles caractéristiques de résistance et de rigidité, ainsi qu'une très faible perméabilité moyenne. La solution adoptée consiste à l'exécution de remblais de pré chargement associés à (i) des colonnes ballastées exécutées dans la zone d'entrepôt des trottoirs intérieurs et (ii) des geodrains préfabriqués verticaux au niveau des trottoirs extérieurs aux endroits prévus pour le stationnement et la circulation des véhicules légers et lourds. Cet article décrit les critères et méthodes utilisés lors de la conception des remblais de pré chargement cherchant à réduire le temps de consolidation hydrodynamique. Le plan d'observation et de surveillance et les résultats respectifs sont également présentés.

Keywords: Ground improvement; soft soils; preloading embankments.

1 INTRODUCTION

The Northern Lisbon Logistic Platform (NLLP) is located at Vila Franca de Xira, Portugal, in an area of approximately 1 000 000 m^2. This platform was built with the intend of creating an interconnection point for international, national, and regional logistical flows within the Lisbon and Tagus Valley region.

On plot 14 of the stated platform, the construction of a new industrial building is expected, with an area of approximately 32 968 m^2. In the aerial view in Figure 1, it is possible to identify the target area for intervention, as well as the limits of the NLLP.

2 GEOLOGICAL AND GEOTECHNICAL CONDITIONS

The area is located on the right bank of the Tagus River, dominated by the alluvial soils of the Lower Tagus, ancient deposits of river terraces and, in depth, by soils dating from the Miocene.



Figure 1. Aerial view of the construction site (image taken from Google Earth).

According to the information obtained during the geotechnical investigations, it is confirmed that the local geological-geotechnical scenario is characterized, superficially, by a layer of landfills, developing to a depth variable between 1.1 m and 3.4 m. According to the available sampling, it is a heterogeneous layer made up of silts with calcareous gravel.

Immediately below the layer of landfills, to a maximum depth of 20,0 m, there are alluvial deposits, essentially made up of soft silts and very soft high plasticity clays, with a high content of organic matter and shell fragments.

Underlying the alluvial layer, colluvial formations can be identified, composed of sandy clays of medium consistency with rounded heterometric gravel of an essentially quartzite nature.

The position of the water table is dependent on the water level in the Tagus River, being influenced not only by seasonal variations, but also by the daily tidal cycles felt in the estuary. During the prospecting geotechnical works, the presence of the water table was detected at a depth varying between 1.3 m and 3.4 m, generally occurring at the level of the interface between the natural terrain and the overlying landfills.

3 GROUND IMPROVENT SOLUTIONS

Given the presence of soft clayey soils, with low strength and stiffness, as well as reduced support capacity, and considering the extended period available for the execution of the works, it was decided to implement ground improvement solutions with the aim of increasing the geomechanical characteristics of the foundation soils, thus providing favourable conditions to obtaining total and differentials settlements compatible with the good performance of the pavements during the service lifetime of the new industrial building.

In this context, a consolidation ground improvement solution was adopted using preload embankments.

To accelerate the process of hydrodynamic consolidation of the compressible materials (soft clayey soils), the introduction of drainage elements was considered, namely, stone columns, at the area of the warehouse indoor pavements, and prefabricated vertical drains (PVD), at the area of the outdoor pavements, in the places designed for car parking and circulation of light and heavy vehicles. It should be noted that the stone columns were installed in a previous work in 2010, while the PVD were installed more recently in 2022.

Considering the magnitude of the predicted service load in the indoor and outdoor pavements (50 kN/m^2 and 20 kN/m^2, respectively), it was proposed to build 8.0 m and 4.0 m high embankments, with slopes H=1.5; V=1.0.

The stone columns were arranged in a square array with 3.0 m centre-to-centre spacing. The PVD were installed in a triangular arrangement with 1.2 m spacing. Both these elements were executed up to an estimated average depth of 20.0 m, in relation to the work platform elevation.

In Figure 2 the typical cross section of the consolidation ground improvement solution is presented.

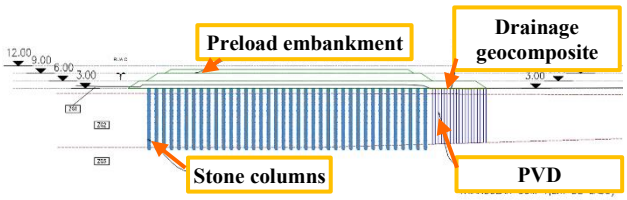

Figure 2. Typical cross section of the consolidation ground improvement solution (not to scale).

Given the presence of a surface layer of landfills, the execution of the PVD required pre-drilling works (Figure 3).



Figure 3. Installation of the prefabricated vertical drains.

After the installation of the PVD, and prior to the execution of the pre-load embankments, a drainage geocomposite responsible for directing the inflowing water to the vertical geodrains was applied (Figure 4).



Figure 4. Aerial photograph of the drainage geocomposite installation.

Figure 5 shows an aerial photograph of the preload embankments.



Figure 5. Aerial photograph of the preload embankments.

4 DESIGN

4.1 Settlements

The total settlement of the compressible soil as a result of the increase in vertical stresses can be calculated by adding the portions corresponding to (i) the immediate settlement, produced during construction in undrained conditions, therefore without volume variation; (ii) primary settlement, resulting from the expulsion of water due to the dissipation of excess pore pressure, during the development of the primary consolidation process; (iii) and secondary settlement, corresponding to the continuation of soil deformation after conclusion of primary consolidation, corresponding to secondary consolidation or creep.

For the problem under study, immediate and primary consolidation settlements were considered.

The value of immediate settlement was estimated, adopting, for the foundation soil, an isotropic linear elastic behaviour at constant volume and carefully choosing the deformability modulus in undrained conditions.

The methodology for calculating settlements by primary consolidation included the application of Terzaghi's theory of one-dimensional consolidation, associated with a two-dimensional distribution of loads transmitted to the ground.

For this purpose, the settlement by primary consolidation was estimated based on the parameters obtained in the oedometer laboratory tests, discretizing the compressible stratum into layers, and estimating the total settlement considering the variation in effective stresses in depth.

The stress increments for the stated calculation and, as such, for definition of the height of the preload embankments, were determined, considering the self-weight of the embankments (temporary and permanent), the self-weight of the pavement slab and the different service loads. It should be noted that in this estimate second-order effects associated with the expected settlement of landfills were considered.

The estimate of the duration of the primary consolidation process involved calculating the estimated vertical and horizontal consolidation times and subsequently the total value resulting from these two mechanisms.

Having knowledge of the total settlement value associated with a given embankment height, as well as the law that governs its evolution over time, it was possible to estimate the settlement evolution curves over time shown in Figure 6.

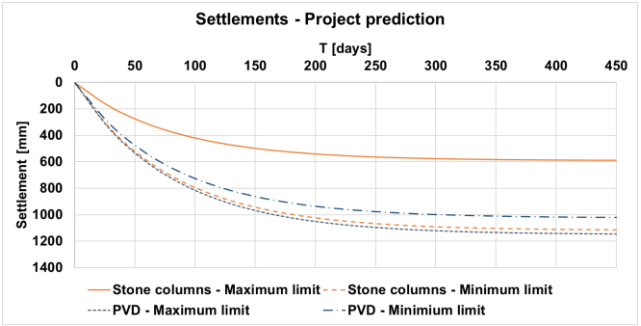

Figure 6. Primary consolidation settlements prediction at design stage.

4.2 Slope stability

As part of the verification of the global stability of the pre-load embankment slopes and the bearing capacity of the foundation, including the quantification of safety factors, an automatic calculation program designed for this purpose was used: SLIDE (V6.0) which allows carrying out analyses in a limit equilibrium regime. This software made it possible to carry out a stability analysis, using circular failure surfaces based on the Bishop-Simplified Method. Two-dimensional finite element analysis was also carried out in parallel using the PLAXIS 2D software.

5 MONITORING AND SURVEY PLAN

To guarantee the carrying out, in safe conditions, of the ground improvement works, mainly the stability of the embankments/foundation and the evolution of settlements/degree of consolidation, a Monitoring and Survey Plan was employed.

In this context, it was considered essential to monitor the following quantities:

a) Water levels installed on the ground, through the installation of 72 vibrating wire piezometers, arranged in a total of 18 locations, at 4 different depths.

b) Horizontal movements of the ground measured using 6 inclinometers, arranged on the periphery of the embankments.

c) Surface settlements of the natural terrain and embankments/platforms, through the measurement of topographic marks supported on 52 settlement plates.

Figures 7 and 8 show, respectively, the vertical displacements measured in the settlement plates, recorded until March 9, 2023, in the area where the stone columns and PVD were built.

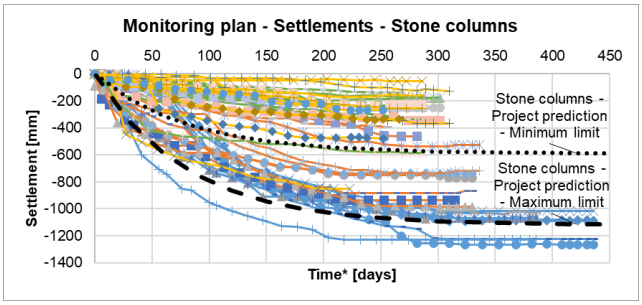

Figure 7. Observed settlements – stone columns.

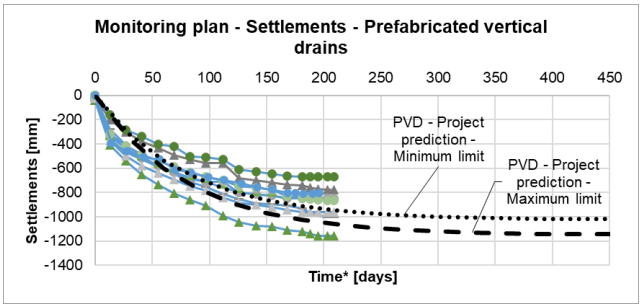

Figure 8. Observed settlements – prefabricated vertical drains.

Regarding measurements of water levels and horizontal displacements, it is important to note that the late installation of piezometers and inclinometers did not allow for a complete record of these quantities to be obtained from the beginning of the construction of the pre-load embankments. Nevertheless, the evolution recorded is in accordance with the project prediction, particularly regarding the reduction, over time, of pore water pressures tending towards values that are close to the hydrostatic distribution. Regarding the recording of horizontal displacements, the mobilization of displacements of greater magnitude was observed at the depths corresponding to the existence of the soft clayey stratum, with a higher rate of evolution during the construction period, which stabilized after the end of the construction of the embankments.

6 FINAL REMARKS

The framework of the work described, including the available time, determined the need to develop innovative ground improvement solutions aiming to provide favourable conditions for the future employment of economic foundation solutions, compatible with the structure serviceability, not only on plot 14, but also on adjacent plots, taking profit of both soil behaviour knowledge (from monitoring results) and existent preloading embankment.

In this context, it should be noted that the adopted solutions make it possible to mitigate, during the life of the future industrial structure, high magnitude settlements, resulting from the primary consolidation process, developed at the level of soft clayey alluvial layers.

The importance of the Monitoring and Survey Plan in managing the behaviour of the work is highlighted, allowing the interpretation of the observed settlements and the establishment, with greater accuracy, of the time necessary to obtain the specified degree of consolidation. As such, it is an indispensable tool in a geotechnical work, with the characteristics of this one.

It is noted that the magnitude of settlements estimated at the project stage, in general, was in line with the values measured on site. The exception to this statement were the settlements recorded in the NW area of the plot, where the stone columns were installed, and where settlements of a magnitude considerably lower than the values recorded and estimated for the SE area were observed. This difference is attributed to the effect of the prolonged presence of previously constructed pre-load embankments, as well as the effect of reinforcing the ground provided by the stone columns.

ACKNOWLEDGEMENTS

The authors would like to thank the site owner for the permission to present this paper. It is also worth highlighting the fact that the earthworks were carried out by the company “Iranzo Excavaciones” and the work related to the execution of the geodrains by the company “Terratest”.

Proceedings of the XVIII ECSMGE 2024
GEOTECHNICAL ENGINEERING CHALLENGES
TO MEET CURRENT AND EMERGING NEEDS OF SOCIETY
© 2024 the Authors
ISBN 978-1-032-54816-6
DOI 10.1201/9781003431749-465
Open Access: www.taylorfrancis.com, CC BY-NC-ND 4.0 license

ECSMGE 24
XVIII EUROPEAN CONFERENCE ON SOIL MECHANICS AND GEOTECHNICAL ENGINEERING

The foundations of the Rhine bridge Hard-Fussach (Austria)

Les fondations du pont Hard – Fussach sur le Rhin (Autriche)

F. Lopez*, E. Steinlechner
Tiroler Rohre GmbH, Hall in Tirol, Austria

**freddy.lopez@trm.at*

ABSTRACT: Due to the high damage potential that a possible flood event has for the densely populated areas along the 26 km-long International Stream of the alpine Rhine, the discharge capacity needs to be expanded from the current 3100 m³/s (100-year flood) to 4300 m³/s (300-year flood), in line with the requirements of the Swiss-Austrian project RHESI Flood Control for the Rhine Valley. In this context, a new Rhine Bridge connecting the Austrian towns of Hard and Fussach was designed to replace the old structure, which is no longer able to ensure the primary framework conditions for neither flood protection nor the increasing volume of traffic. The extremely unfavourable subsoil conditions, consisting of shallow, very soft to soft plastic lacustrine clay deposits, required a deep foundation solution for the substructure (abutments and piers). Due to the high flood risk, the construction of the substructure could only be carried out during a period of low water discharge (winter), resulting in a very tight construction schedule (winter half-year 2020/2021). For the deep foundation of the substructure, several options were evaluated. Finally, a solution consisting of pile grillages, executed with ductile cast-iron driven piles (320 mm of diameter), was adopted for the project. The fast, safe and simple execution of the piles allowed for the successful erection of the substructure within the limited available time frame. The completion of this construction stage was critical for the further phases. After a construction time of only 28 months, the Rhine Bridge Hard- Fussach was officially opened for traffic on November 18, 2022. The following technical paper presents an overview of the adopted deep foundation solution, covering the design and execution of the piled foundation.

RÉSUMÉ: En raison du potentiel élevé de dommages qu'une éventuelle inondation pourrait avoir pour les zones densément peuplées situées le long du cours d'eau international du Rhin alpin, long de 26 km, la capacité d'écoulement du cours d'eau d'une valeur actuelle de 3100 m³/s (crue centennale) doit être augmentée à 4300 m3/s (crue tricentennale), conformément aux exigences du projet austro-suisse RHESI de protection contre les crues dans la vallée du Rhin. Dans ce contexte, un nouveau pont sur le Rhin reliant les villes autrichiennes de Hard et Fussach a été conçu pour remplacer l'ancien ouvrage qui ne répondait plus aux exigences modernes des infrastructures vis-à-vis de la protection contre les crues et de l'augmentation du trafic. Les conditions géotechniques extrêmement médiocres du sol, constitué de dépôts alluvionnaires d'argile lacustre plastique, molle à très molle, ont nécessité une solution de fondations profondes pour les appuis (culées et piles de pont). En raison du risque élevé d'inondation, la construction des appuis n'a pu être réalisée que pendant une période de faible débit d'eau (hiver), ce qui a entraîné un calendrier des travaux très serré (semestre hivernal 2020/2021). Pour les fondations profondes des appuis, plusieurs options ont été évaluées. Finalement, une solution constituée d'un maillage de pieux, réalisés avec des pieux battus enrobés en fonte ductile (diamètre 320 mm), a été retenue pour le projet. La mise en œuvre rapide, sûre et simple des pieux a permis avec succès l'élévation des appuis dans les délais limités disponibles. L'achèvement de cette étape de construction était crucial pour les phases suivantes. Après une durée de construction de seulement 28 mois, le pont sur le Rhin reliant Hard à Fussach a été officiellement ouvert à la circulation le 18 novembre 2022. Cet article technique présente une description de la solution de fondations profondes adoptée, couvrant la conception et la mise en œuvre des fondations sur pieux.

Keywords: Bridge foundation; ductile cast-iron piles; sustainability.

1 FLOOD CONTROL OF THE ALPINE RHINE

The alpine Rhine is the section between Reichenau in the Swiss Canton of Graubünden and the confluence with Lake Constance. The Swiss-Austrian flood control project RHESI aims to protect the habitat of about 300'000 people living in the valley along the "international stream" of the alpine Rhein, where the river flows today towards Lake Constance, in a canal-type bed with fortified embankments (Figure 1a).

With the implementation of the RHESI project, the middle channel of the Rhine will be significantly widened and the foreland consequently reduced, creating more space for the river (Figure 1b), with the correspondent increment of the current discharge capacity of 3100 m³/s (100-year flood) to 4300 m³/s (300-year flood).



Figure 1. Current (a) and future (b) layout of the alpine Rhine (mod. after Int. Rheinregulierung, 2022).

2 THE RHINE BRIDGE HARD-FUSSACH

The existing 255m-long Rhine Bridge connecting the Austrian towns of Hard and Fussach is the last Rhine crossing before reaching the Lake of Constance. It was built in 1971 and its substructure is founded on wooden piles. The bridge is no longer able to ensure the primary requirements for flood protection acc. to the RHESI project. In addition, the standard cross-section of the supporting structure no longer meets today's traffic engineering requirements and therefore the bridge needed to be replaced by a new structure.

The new Rhine Bridge Hard-Fussach, a state-of-the-art steel composite bridge with a separated cable (rope) construction (Figure 2), was designed to meet the new requirements for flood protection as well as to satisfy the increasing volume of traffic.

With a self-weight of approx. 12000 metric tons, the new bridge has three new piers, two of which support the pylons that carry the cable structure. The new structure (4-span girder) has a total length of 255.60 m and a width of approx. 24 m, ensuring enough space for two traffic lanes (one in each direction), one exclusive bus lane, a sidewalk and a bicycle path.



Figure 2. New and old Rhine Bridge Hard-Fussach in November 2022 (ORF, 2022).

3 THE FOUNDATIONS OF THE NEW RHINE BRIDGE HARD-FUSSACH

3.1 Subsoil conditions

The subsoil conditions in the project area are characterized by the presence of loose to medium dense floodplain sands with rather favourable mechanical properties, underlain by highly compressible cohesive soils (silts and clays with high organic content), fine to medium grained silty sands with moderate load-bearing capacity and very soft to soft lacustrine clay deposits (alluvium) with unfavourable geotechnical properties (Figure 3).

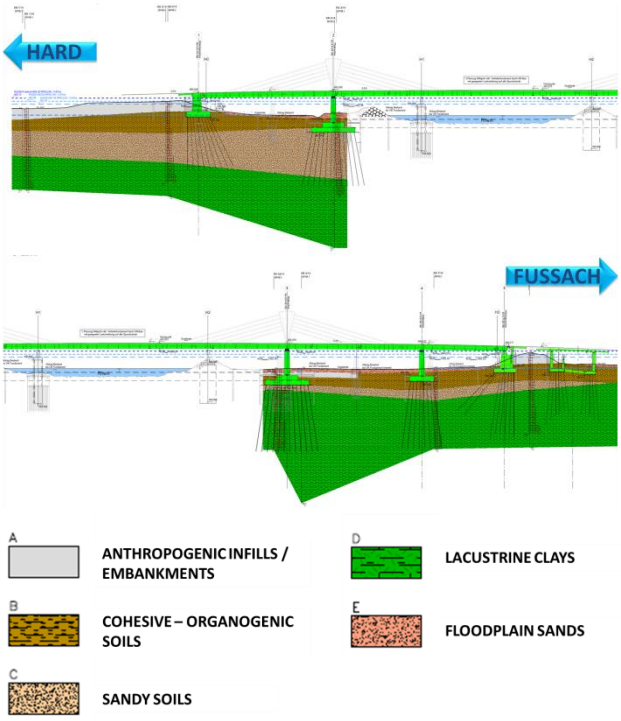

Figure 3. Subsoil profile along the new Rhine Bridge Hard-Fussach (mod. after BGG Consult, 2016).

The geotechnical properties of the identified soil units are summarized in Table 1.

3.2 Deep foundations

On account of the aforementioned unfavourable subsoil conditions, a shallow foundation was not feasible and a deep foundation solution for the substructure (abutments and piers) was unavoidable, nevertheless, due to the presence of high compressible lacustrine clays, encountered up to the investigation depth of 50 m below natural ground level, a classical solution based on end-bearing piles (i.e. cast-in-place bored piles or drilled shafts) with reasonable lengths was unsuitable for the foundation of the substructure. As an alternative to end-bearing piles, downwards fanned out pile grillages (a combination of vertical and racked floating piles) were proposed to support the substructure (Figure 4) with the goal to obtain the largest possible foundation area to achieve an optimum load distribution in order to maintain the deformations (settlements) within acceptable ranges.

Table 1. Geotechnical parameters of the soil units (after BGG Consult, 2016).

Layer	Description	Thicknes (m)	φ' (°)	c' (kN/m²)	γ/ γ' (kN/m³)	UCS (kN/m²)	E_s (MN/m²)
E	Floodplain sands, loose to medium dense	1.2 – 2.0	30	-	18 / 10	-	-
B	Cohesive/organogenic soils, very soft to soft	2.0 – 10.0	17 - 22	5 - 10	15 / 16	15 – 55	0.8 – 3.6
C	Silty sands, fine to medium grained, loose to medium dense	2.0 – 12.0	32 - 35	5 - 9	21 / 11	8 - 27	8.0 – 17.0
D	Lacustrine clays, very soft to soft	undefined	25 - 30	1 - 15	19 / 9	1 - 44	2.8 – 11.0

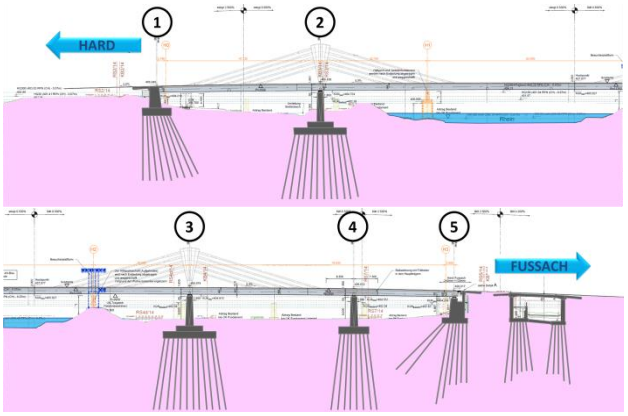

Figure 4. Longitudinal view of the pile grillages (mod. after Schimetta Consult, 2020).

3.3 Adopted piling system

An extensive analysis of different piling systems was conducted for the project. The most suitable and cost-effective solution was provided by ductile iron piles (DIP), due to the flexibility and large adaptability of the equipment, as well as the high installation speed.

DIP are low vibration, driven, full-displacement piles, installed using a medium-sized excavator and a hydraulic breaker hammer with a modified shank that seats into the pile socket (bell) for driving, using the hammer's percussive energy. The hydraulic hammers typically range from 1200 kg to 2500 kg and operate at frequencies between 250 and 500 blows per minute, delivering much higher frequency than traditional high-impact, low-frequency driven piling systems (Lopez and Steinlechner, 2023). The hammer size (energy) is matched with the size of the pile and the subgrade driving conditions to develop the most efficient installation while not overstressing the pile material (Plaskett et al., 2022).

DIP are used to transfer loads from the superstructure into the lower soil layers and/or to limit deformations and have the flexibility to be installed to transfer the loads developing skin friction and/or end-bearing capacity (Lopez and Steinlechner, 2023). A central reinforcing bar can be inserted in the wet concrete if required for tension or additional compression capacity. For the project, frictional (grouted) DIP were adopted (Figure 5) and their execution is schematically presented in Figure 6.



Figure 5. Frictional (grouted) ductile iron piles.

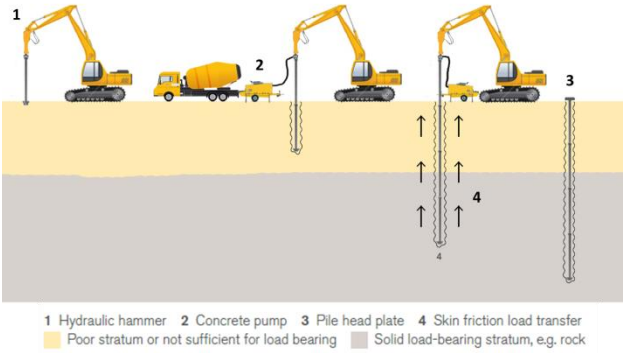

Figure 6. Execution of frictional (grouted) ductile iron piles (Lopez and Steinlechner, 2023).

3.4 Design

The relevant parameters for the estimation of the load-displacement behaviour of the piles were obtained from the results of a load test, carried out on a test pile group, comprised of 4 grouted DIP (25 m long), connected by a rigid pile cap.

The results of the load test are presented in Figure 7.

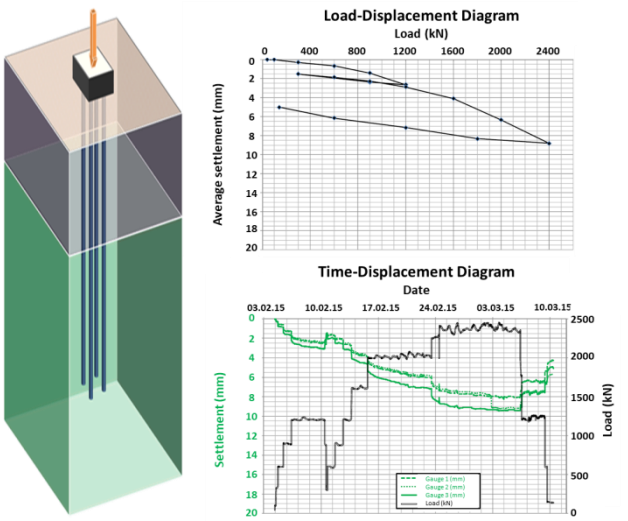

Figure 7. Load test results (mod. after BGG Consult, 2016).

An average group settlement of about 25 mm was limited for the verification of the serviceability limit state (SLS). For the aforementioned settlement, an allowable service load of about 1200 kN (300 kN per pile) could be derived. For the ultimate limit state (ULS), a characteristic external load-bearing capacity of 750 kN (both in compression and in tension) for a single 25 m-long pile could be defined. The results of the load test and the available local experience were also used to predict the time dependent load-displacement behaviour of the piles, based on their interaction with the local lacustrine clays.

The lacustrine clays showed a slight creep behaviour in the load transfer area, where almost 80% of the registered settlement for each load stage occurred over a time period between 2 and 3 days after applying the load increments.

Taking into account the above mentioned considerations, the required pile reinforcement could be defined for the project. A summary of the pile reinforcement is presented in Table 2. The racked piles were designed to counter act the large horizontal forces acting on the piers and abutments. Taking into consideration the provisions and requirements for the corrosion protection (BMK, 2020), the permanent piles were designed for a service life of 100 years.

3.5 Execution

Due to the high flood risk, the construction of the substructure could only be carried out during a period of low water discharge (winter), resulting in a very tight construction schedule (winter half-year 2020/2021).

The piling works for the bridge were carried out between late September 2020 and early March 2021. Figure 8 presents some pictures of the installation:



Figure 8. Execution of the piling works.

Table 2. Pile requirements (after Schimetta Consult, 2020).

Substructure	Pile type	Amount of piles	Length (m)	Diameter (m)	Inclination[1)] (°)	Design load (ULS)	
						Compression (kN)	Tension (kN)
Abutment (Axis 1)	TRM 170 | 9.0	21 vertical 168 racked	20 20	0.32	0.0 3.2 – 26.1	550 550	350 170 - 550
Pier (Axis 2)	TRM 170 | 9.0	0 vertical 264 racked	- 20	0.32	0.0 1.0 – 11.7	- 550	- 0
Pier (Axis 3)	TRM 170 | 9.0	0 vertical 264 racked	- 25	0.32	0.0 0.8 – 9.4	- 550	- 550
Pier (Axis 4)	TRM 170 | 9.0	0 vertical 128 racked	- 25	0.32	0.0 1.4 – 9.6	- 550	- 550
Abutment (Axis 5)	TRM 170 | 9.0	24 vertical 168 racked	18 18 - 25	0.32	0.0 1.8 – 45.0	550 550	350 0 - 290

[1)] Measured from the vertical

The use of adequate equipment (hydraulic manipulator) offered the required flexibility and precision for the execution of piles with different inclinations (Table 2), enabling to carry out interventions in areas with restricted space (i.e. excavation pits), causing only small affection to the surrounding work environment.

With the completion of the last pier on the Hard side at the beginning of April 2021 and final re-cultivation works in the Rhine floodplains, the construction of the substructure (abutments and piers) was successfully completed as planned at the end of April 2021. With this critical construction phase (substructure) finalized, the further construction works covering the longitudinal shifting of the steel box girders, the concrete carriageway slab, the stiffening of the supporting form of a harp-shaped span with the pylons and tensioning cables, the construction of the edge beams, the installation of the bridge railing and the paving works were completed in November 2022 (Baumanagement, 2022).

4 SUMMARY AND FINAL REMARKS

The new Rhine Bridge Hard-Fussach, a state-of-the-art steel composite bridge with a separated rope construction, was designed to meet the new requirements for flood protection as well as to satisfy the increasing volume of traffic. With an estimated investment of 70 million €, the construction of the new bridge began on June 29, 2020 and was entirely opened to traffic just 28 months later, on November 25, 2022.

The extremely unfavourable subsoil conditions (shallow, very soft to soft plastic lacustrine clay deposits) required a deep foundation solution for the substructure (abutments and piers). The proposed solution consisting of frictional (grouted) ductile iron piles (DIP) was proven to be the most suitable and cost-effective for the project, due to the flexibility, large adaptability and installation speed.

A very professional work preparation together with a high level of commitment of all the people involved in the project made possible to complete the project on time and to the required quality standards, overcoming additional challenges such as the construction in the hazardous area of the alpine Rhine under unfavourable weather conditions and the supply difficulties associated with the corona pandemic.

ACKNOWLEDGEMENTS

The authors are grateful for the invaluable support and contributions provided by Michael Egger (Department of Road Construction Management of the Federal State of Vorarlberg, Austria), Martin Lenzi (BGG Consult, Austria), Carina Kirchmair, Bernhard Schrötter and Neville Wood (Tiroler Rohre GmbH, Austria) and Guido Maier and his team (Winsauer Bau GmbH, Austria).

REFERENCES

Baumanagement (2022). The construction of the Rhine Bridge Hard-Fussach, available at: www.youtube.com/watch?v=G-Zp5e9xDm0, accessed: 10/10/2023.

BGG Consult (2016), Geotechnisches Gutachten, Geotechnical report (in German), Hohenems, Austria, Rep. GU-2016-018.

Bundesministerium für Klimaschutz, Umwelt, Energie, Mobilität, Innovation und Technologie, BMK (2020), Österreichische Bauzulassung GZ:2020-0.094.414 (in German), Vienna, Austria,

Internationale Rheinregulierung (2022), available at: www.rhesi.org/planungsstand/hochwasserschutz, accessed: 30/09/2023.

Lopez, F. and Steinlechner, E. (2023). A new approach for the calculation of the external load-bearing capacity of ductile iron piles. In: *Proceedings of the 18th Portuguese National Congress of Geotechnical Engineering*, Évora, Portugal.

Österreichischer Rundfunk, ORF (2022). Neue Rheinbrücke ist nun befahrbar, New Rhine bridge is open to traffic (in German), available at: www.vorarlberg.orf.at/stories/3182766/ accessed: 12/10/2023.

Plaskett, B., Johnson, K. and Caskey, M. (2022). Solving variable bedrock challenges with ductile iron piles. In: *Proceedings of the 47th Annual Conference on Deep Foundations*, National Harbor (Maryland), USA.

Schimetta Consult (2020). Ausführungsprojekt Rheinbrücke Hard – Fussach, Detailed design and execution drawings (in German), Innsbruck, Austria, Rep. BR-2015-027.

Proceedings of the XVIII ECSMGE 2024
GEOTECHNICAL ENGINEERING CHALLENGES
TO MEET CURRENT AND EMERGING NEEDS OF SOCIETY
© 2024 the Authors
ISBN 978-1-032-54816-6
DOI 10.1201/9781003431749-466
Open Access: www.taylorfrancis.com, CC BY-NC-ND 4.0 license

ECSMGE 24
XVIII EUROPEAN CONFERENCE ON SOIL MECHANICS AND GEOTECHNICAL ENGINEERING

Role of tunnel ground loss on the mitigating effect of pile-wall barriers

Rôle de la perte de volume au tunnel sur l'effet atténuant des murs à pieux

N. Losacco*
Politecnico di Bari, Bari, Italia
**nunzio.losacco@poliba.it*

ABSTRACT: Pile wall barriers are an effective mitigation measure to protect heritage or infrastructure from tunnelling-induced ground movements. This paper presents the results of parametric finite element analyses aimed at studying the effect of tunnel volume loss on the efficiency of end-bearing pile wall barriers, accounting for shearing at the soil-pile interface. The considered scenario is the field trial of a pile wall barrier installed at an experimental site during the construction of the Line C of Rome underground railway. Results indicate that, at small volume loss, the excavation induced movements can propagate across the barrier. Contrarily, at larger applied tunnel volume loss, shearing at the pile interface, enhanced due to the barrier embedment in the stiff bottom layer, results in the progressive formation of a slip plane that prevents the transmission of soil displacements behind the wall, thus acting as a smooth continuous diaphragm wall. The transition from perfect compatibility to slipping between the soil and the barrier affects the propagation of the ground loss, and hence surface settlements, on both sides of the wall.

RÉSUMÉ: Les barrières à parois de pieux constituent une mesure d'atténuation efficace pour protéger le patrimoine bâti, ou les infrastructures, du mouvements de sol induits par la construction des tunnels. Cet article présente les résultats d'analyses paramétriques par éléments finis visant à étudier l'effet de la perte de volume au tunnel sur l'efficacité des barrières de pieux portantes aux extrémités, en tenant compte du cisaillement à l'interface sol-pieu. Le scénario considéré est l'essai sur le terrain d'une barrière à murs de pieux installée sur un site expérimental lors de la construction de la ligne C du métro de Rome. Les résultats indiquent que, avec une faible perte de volume, les mouvements induits par l'excavation peuvent se propager à travers la barrière. Au contraire, lorsque la perte de volume du tunnel est plus importante, le cisaillement à l'interface des pieux, accru en raison de l'encastrement de la barrière dans la couche inférieure rigide, entraîne la formation progressive d'un plan de glissement qui empêche la transmission des déplacements du sol derrière le mur, agissant ainsi comme une paroi moulée continue lisse. Le passage d'une compatibilité parfaite au glissement entre le sol et la barrière affecte la propagation des pertes de terrain, et donc des tassements de surface, de part et d'autre du mur.

Keywords: Tunnelling; ground movements mitigation; pile wall barrier; numerical analyses.

1 INTRODUCTION

The construction of tunnels can affect existing building heritage and infrastructures in urban areas. Numerous case studies (e.g. Bai et al., 2014) have shown that embedded bored pile walls are an effective protective measure to minimise ground movements induced by tunnelling. Furthermore, the installation of pile wall barriers induces less soil disturbance with respect to continuous diaphragm walls, whose construction, instead, may cause displacements as large as those induced by tunnelling (L'Amante et al., 2012).

The mechanical behaviour of diaphragm walls for various geometries and wall-soil interface roughness has been extensively characterised by means of centrifuge experiments and numerical analyses (Bilotta 2008; Rampello et al., 2019; Song et al., 2023). Results of those studies show that a smooth diaphragm deeper than the tunnel invert represents a slip plane causing a strong discontinuity in the displacement field induced by tunnel excavation, such that no soil ground loss is transferred to the rear of the wall. A rough interface, instead, results in non-negligible settlements behind the wall. Recent research on the efficiency of protective barriers consisting of bored piles focused on relatively low volume losses (Ledesma and Alonso, 2017; Masini and Rampello, 2021; Franza et al. 2021) with numerical results somewhat indicating that the pile wall efficiency might increase with tunnel ground loss (Bilotta and Russo 2011).

This paper presents the results of FE parametric analyses of a tunnel interacting with a pile-wall barrier, focusing on the role of volume loss on the

efficiency of the barrier in mitigating ground movements. The problem geometry and the employed geotechnical model (soil stratigraphy, mechanical properties, groundwater conditions), as well as the 3D reference numerical solution for model validation, obtained with a detailed simulation of the physical processes occurring around the TBM, are the same already published for the class-A predictions of the excavation of the Metro C running tunnels through the AMA site in Rome (Losacco et al. 2019; Losacco and Viggiani, 2020).

2 CASE STUDY

The geotechnical model of the field trial used for the parametric study presented in this paper was thoroughly discussed in Losacco et al. (2019) and Losacco and Viggiani (2020). The barrier is approximately 43 m long and is composed of 48 bored piles with length L_p = 34.5 m, diameter d_p = 0.6 m, spacing $s_p = 1.5\ d_p$.

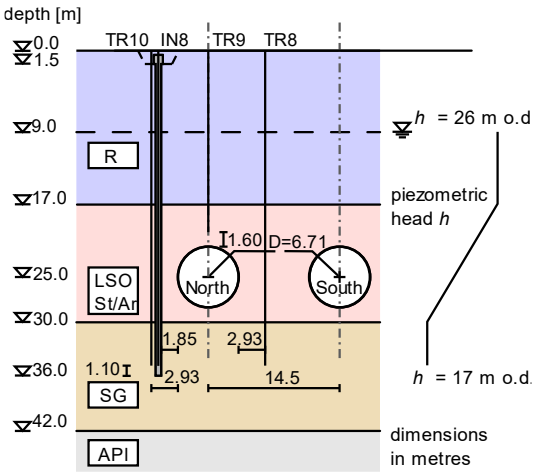

Figure 1. Geotechnical model and problem layout.

The monitoring cross-section, at midspan of the barrier, is drawn in Figure 1, also showing the soil stratigraphy and piezometric head distribution. Soil strata, starting from the ground surface, are:

- R: 17 m thick madeground layer, made of gravelly sand in pyroclastic matrix;
- LSO – St/Ar: 13 m thick recent or Pleistocene alluvial silty sands, sandy silts and silty clays;
- SG: 12 m thick Plio-Pleistocene Paleotevere fluvial deposits consisting of sand and gravel;
- APl: very thick Pliocene stiff silty clays "Argille Vaticane", the impervious bedrock of the whole city.

The groundwater table is found at 9 m depth b.g.l. in the R layer. The inferred piezometric head distribution shown in Figure 1 implies downward seepage in the LSO layer.

The base of the piles is embedded into the stiff, coarse-grained SG layer, hence beneficially influencing the performance of the barrier in minimising tunnel-induced settlements. Twin tunnels with diameter D = 6.7 m are excavated at z_0 = 25 m axis depth in the LSO-St/Ar layer, with s = 14.5 m spacing between their axes. The study presented here only considers excavation of the first tunnel (North Tunnel), that is carried out at quite a short distance from the barrier (1.85 m springline to pile shaft).

3 NUMERICAL MODEL

The parametric analyses were carried out using the FEA software Abaqus. The calculations were performed in terms of effective stress and assuming drained conditions; this is a reasonable assumption given the relatively large permeability obtained from field tests for the fine-grained soil layer (LSO – St/Ar), and the results of hydromechanically coupled class A analyses of the same site (Losacco and Viggiani, 2020) due to the relatively low advance rate of the excavation (average 8.5 m/day). The FE mesh employed for the analyses is shown in Figure 2.

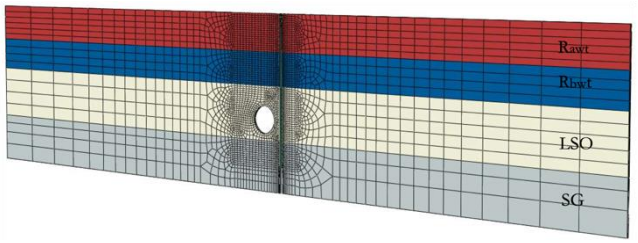

Figure 2. FE mesh.

Two hypoplastic constitutive models were chosen to simulate the mechanical behaviour of the R and the LSO layers: the von Wolffersdorff (1996) model for coarse-grained materials for the former and a critical-state based model for clays (Mašín, 2005) for the latter. The values of the material constants are provided in Losacco and Viggiani (2020). A simple linear elastic-perfectly plastic material model was employed for the deep SG layer. The top of the Apl layer represents the base of the numerical model.

The barrier was modelled with solid elements as a separate body from the soil, assuming linear elastic behaviour, with elasticity coefficients and unit weight of concrete. A no-penetration/no-tension behaviour was employed for the contact between the barrier and the soil in the normal direction, whereas a Coulomb frictional law was adopted in the tangential direction, assuming a rough interface (i.e. $\delta = \varphi'$), with φ' the effective soil friction angle and δ the friction angle at the pile-wall interface.

Assuming an infinitely long barrier and the tunnel excavation carried out simultaneously throughout its length (i.e. neglecting the excavation advance), an $s_p/2$ long domain only was modelled, containing half pile, resulting in a quasi-2D simulation. Standard mechanical constraints were prescribed at the sides of the mesh and hydraulic boundary conditions were applied to reproduce the piezometric head distribution depicted in Figure 1. After an initial stage of geostatic equilibrium, the barrier was activated. Then, tunnel excavation was simulated by applying a homothetic contraction of the tunnel boundary, focused on the tunnel axis (Boldini et al., 2016; Masini and Rampello, 2021). This simulation technique was chosen as the results exhibited the best agreement with those obtained through the detailed 3D simulation of the mechanised excavation process in the same site. The minimum tunnel radius after homothetic contraction (i.e. the tunnel volume loss $V_{L,T}$) was calibrated separately for the analysis with the barrier and for the greenfield case, by matching the reference 3D solutions.

4 RESULTS

In this study, the adopted 2D simulation technique is aimed at performing parametric analyses to assess the effect of tunnel volume loss on the settlement field behind a barrier of end-bearing piles, which would be unfeasible using the detailed—computationally expensive—3D simulation method. Hence, the simplified technique is validated with respect to the predictions provided by the detailed simulation, taken as a reference solution here, rather than to field measurements.

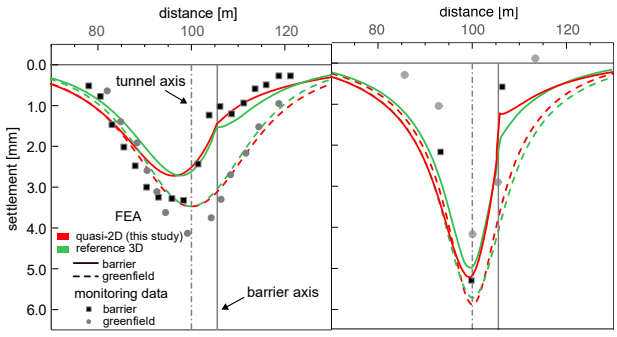

Figure 3. Settlements in greenfield and with the barrier: at ground surface (left) and at 17 m b.g.l. (right).

In this respect, Figure 3 shows the comparison between the surface settlements predicted with the adopted approach, the reference 3D solution, and monitoring data, obtained through precise levelling. Field measurements were carried out , both for the greenfield and the barrier monitoring section. The same comparison is shown at 17 m b.g.l. (1.2 D above tunnel axis), where field data are obtained from Trivecs measurements. The results of the 2D analyses, calibrated as explained in the previous section, show a good agreement with the reference solution, somewhat improving the quality of the predictions behind the barrier and at depth.

Hence, the proposed simulation technique is employed to carry out parametric analyses varying the tunnel ground loss from 1.7% (value used in Figure 3) to 4.5%. Figure 4 shows the predicted settlement troughs in greenfield conditions and when the barrier is present, at the ground surface and at 17 m depth. The embedded end-bearing barrier is seen to significantly reduce soil settlements and volume loss, both behind and in front of the barrier, for all values of imposed tunnel volume loss. Clearly the most significant reduction occurs right behind the wall. More interestingly, the settlements behind the barrier seem to achieve a limit value, as negligible settlement increase occurs for $V_{L,T} > 3.0\%$, in particular at depth. This confirms the efficiency increase of the barrier with $V_{L,T}$, as already suggested by Bilotta and Russo (2011). Conversely, the relative reduction of maximum settlement w_{max} with respect to the greenfield case diminishes with increasing $V_{L,T}$.

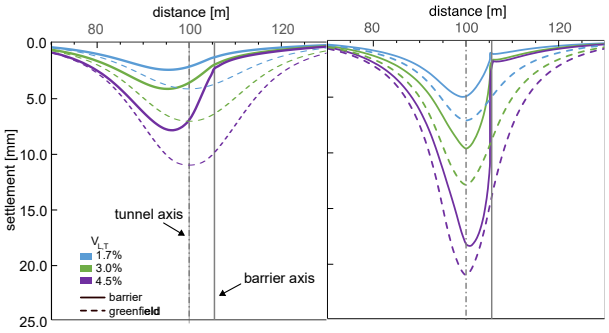

Figure 4. Predicted settlements in greenfield and with the barrier: at ground surface (left) and 17 m b.g.l (right).

To explain the observed behaviour, Figure 5 displays the sliding occurring along the vertical of the pile shaft facing the tunnel, and the mobilised tangential stress at the same location, compared to the maximum available shear strength of the interface. Positive sliding and shear stress imply downward movement of the soil with respect to the wall. The plots show that little sliding occurs along the pile for $V_{L,T} = 1.7$ % and $V_{L,T} = 3\%$, both above and below the tunnel, with different sign, whereas no sliding occurs right at tunnel depth, where soil movements are predominantly horizontal. The maximum sliding takes place in the LSO – ST/Ar layer, due to the significant compliance of the soil. For the same $V_{L,T}$, sliding is not observed on the top 1/3 – 1/4 of the pile,

as the downward tangential stresses have not reached the limit value. Conversely, above tunnel crown depth, for the largest $V_{L,T}$ = 4.5% the shear strength at the soil-pile interface is fully mobilised up to the pile head, resulting in large sliding.

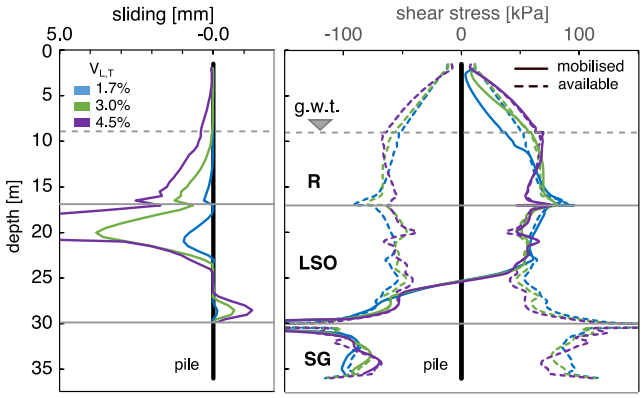

Figure 5. Interface behaviour along the pile shaft vertical facing the tunnel: sliding (left) and shear stress (right).

5 CONCLUSIONS

The results presented in this paper highlighted the relative influence of the volume loss applied at the tunnel boundary on the performance of an embedded barrier of end-bearing bored piles. The analyses have been performed with reference to a specific representative case study. The proposed quasi-2D simulation technique, if properly calibrated, can reproduce correctly the predictions provided by quite more complex 3D simulations.

The parametric analyses show that the efficiency of an end-bearing pile wall barrier increases significantly with increasing prescribed tunnel volume loss. This is due to sliding at the pile-soil interface facing the tunnel, occurring when, for large $V_{L,T}$, the shear strength along the pile shaft is fully mobilised. Shearing causes the soil behind the pile wall to disconnect from the soil ahead of the barrier, so that no further settlements are generated for increasing volume loss, as the incremental response of the barrier approaches that of a smooth diaphragm.

REFERENCES

Bai, Y., Yang, Z., and Jiang, Z. (2014). Key protection techniques adopted and analysis of influence on adjacent buildings due to the Bund Tunnel construction. *Tunnelling and Underground Space Technology*, 41(1): 24–34. https://doi.org/10.1016/j.tust.2013.11.005

Bilotta, E. (2008). Use of diaphragm walls to mitigate ground movements induced by tunnelling. *Géotechnique*, 58(2): 143–155. https://doi.org/10.1680/geot.2008.58.2.143

Bilotta, E., and Russo, G. (2011). Use of a line of piles to prevent damages induced by tunnel excavation. *Journal of Geotechnical and Geoenvironmental Engineering*, 137(3): 254–262. https://doi.org/10.1061/(ASCE)GT.1943-5606.0000426

Boldini, D., Losacco, N., Bertolin, S., and Amorosi, A. (2016). Modelling of Reinforced Concrete Framed Structures Interacting with a Shallow Tunnel. *Procedia Engineering*, 158: 176-181. https://doi.org/10.1016/j.proeng.2016.08.425

Franza, A., Losacco, N., Ledesma, A., Viggiani, G.M.B., and Jimenez, R. (2021). Protecting surface and buried structures from tunnelling using pile walls: a prediction model. *Canadian Geotechnical Journal*, 58(10): 1590–1602. https://doi.org/10.1139/cgj-2020-0476

L'Amante, D., Flora, A., Russo, G., and Viggiani, C. (2012). Displacements induced by the installation of diaphragm panels. *Acta Geotechnica*, 7(3): 203-218. https://doi.org/10.1007/s11440-012-0164-9

Ledesma, A., and Alonso, E.E. (2017). Protecting sensitive constructions from tunnelling: the case of World Heritage buildings in Barcelona. *Géotechnique*, 67(10): 914–925. https://doi.org/10.1680/jgeot.SiP17.P.155

Losacco, N., Romani, E., Viggiani, G. M. B., and Di Mucci, G. (2019). Embedded barriers as a mitigation measure for tunnelling induced settlements: A field trial for the Line C in Rome. *Proceedings of the WTC 2019*. https://doi.org/10.1201/9780429424441-618

Losacco, N, and Viggiani, G. M. B. (2020). Mechanised Tunnel Excavation Through an Instrumented Site in Rome: Class A Predictions and Monitoring Data. *Lecture Notes in Civil Engineering*, 40: 245-254. https://doi.org/ 10.1007/978-3-030-21359-6_26

Mašín, D. (2005). A hypoplastic constitutive model for clays. *International Joural of Numerical and Analytical Methods in Geomechanics* 29: 311–336. https://doi.org/10.1002/nag.416

Masini, L. and Rampello, S. (2021). Predicted and observed behaviour of pre-installed barriers for the mitigation of tunnelling effects. *Tunnelling and Underground Space Technology*, 118: 104200. https://doi.org/10.1016/j.tust.2021.104200

Rampello, S., Fantera, L., and Masini, L. (2019). Efficiency of embedded barriers to mitigate tunnelling effects. *Tunnelling and Underground Space Technology*, 89: 109–124. https:// 10.1016/j.tust.2019.03.027

Song, G., Xu, J., and Marshall, A. M. (2023). Numerical study on the effect of protective wall depth in reducing structure deformations caused by tunnelling. *Computers and Geotechnics*, 158: 105374. https://doi.org/10.1016/j.compgeo.2023.105374

von Wolffersdorff, P.-A. (1996). A hypoplastic relation for granular materials with a pre-defined limit state surface. *Mechanics of Cohesive-Frictional Materials*, 1: 251–271. https:// 10.1002/(SICI)1099-1484(199607)1:3<251::AID-CFM13>3.0.CO;2-3

Proceedings of the XVIII ECSMGE 2024
GEOTECHNICAL ENGINEERING CHALLENGES
TO MEET CURRENT AND EMERGING NEEDS OF SOCIETY
© 2024 the Authors
ISBN 978-1-032-54816-6
DOI 10.1201/9781003431749-467
Open Access: www.taylorfrancis.com, CC BY-NC-ND 4.0 license

ECSMGE 24
XVIII EUROPEAN CONFERENCE ON SOIL MECHANICS AND GEOTECHNICAL ENGINEERING

Sand-rubber mixtures as vibration dampening foundation materials: scaled physical model studies

Mélanges de sable et de caoutchouc comme matériaux de fondation amortissant les vibrations: études sur modèles physiques à l'échelle

B.R. Madhusudhan*
A'Sharqiyah University, Ibra, Oman
**madhusudhan.ramu@asu.edu.om*

ABSTRACT: The accumulation of scrap rubber tires is a serious environmental issue. Rubber is a good damping material. In view of these, it is prudent to use rubber along with soil for engineering applications in general and possibly as foundation materials in particular. In this regard, some past studies have discretely evaluated the physical and mechanical properties of soil-rubber mixtures. However, there is a lack of comprehensive experimental studies highlighting the significance of the use of sand-rubber mixtures as vibration dampening foundation materials. The present study deals with the instrumented laboratory scaled physical models subjected to a series of impact hammer tests. Different base conditions for the physical models consisting of fixed base, and structure founded on sand-rubber mixture layer in a tank filled with sand are considered. The impact force and the acceleration responses of the structure are recorded using an HBM made amplifier with the data acquisition system. The damping ratio values are estimated from the frequency response function plots of the measured signals. The results of the present study show that the sand-rubber mixtures possess an adequate potential for their application as vibration dampening foundation materials for low-rise buildings.

RÉSUMÉ: L'accumulation de pneus usés en caoutchouc constitue un grave problème environnemental. Le caoutchouc est un bon matériau amortisseur. Compte tenu de cela, il est prudent d'utiliser le caoutchouc avec la terre pour des applications techniques en général et éventuellement comme matériaux de fondation en particulier. À cet égard, certaines études antérieures ont évalué discrètement les propriétés physiques et mécaniques des mélanges sol-caoutchouc. Cependant, il manque des études expérimentales complètes mettant en évidence l'importance de l'utilisation de mélanges sable-caoutchouc comme matériaux de fondation amortisseurs de vibrations. La présente étude porte sur des modèles physiques instrumentés à l'échelle d'un laboratoire soumis à une série d'essais au marteau. Différentes conditions de base pour les modèles physiques constitués d'une base fixe et d'une structure fondée sur une couche de mélange sable-caoutchouc dans un réservoir rempli de sable sont prises en compte. La force d'impact et les réponses d'accélération de la structure sont enregistrées à l'aide d'un amplificateur fabriqué par HBM avec le système d'acquisition de données. Les valeurs du rapport d'amortissement sont estimées à partir des tracés de fonction de réponse en fréquence des signaux mesurés. Les résultats de la présente étude montrent que les mélanges sable-caoutchouc possèdent un potentiel adéquat pour leur application comme matériaux de fondation amortisseurs de vibrations pour les bâtiments de faible hauteur.

Keywords: Sand rubber mixtures; damping; foundation; scaled physical models.

1 INTRODUCTION

The accumulation of scrap rubber tires is an environmental issue which requires immediate attention. The accumulation of rubber causes serious environmental imbalances. It is known as 'black pollutant' (Xiong and Li, 2013). In the past, few studies have been conducted on scrap rubber tire-sand mixtures (Madhusudhan et al., 2017, 2020, 2021). These laboratory studies investigated the properties of scrap rubber tire-sand mixtures under various testing conditions, such as monotonic and cyclic triaxial, cyclic simple shear tests, etc. These studies show the favourable response required for their applications as seismic base isolation materials of buildings. Few recent numerical studies (Boominathan et al, 2019) also investigate the same and concur on the merits of using these mixtures for a similar purpose. Hence, the potential of sand rubber mixtures needs to be further investigated for the stated application. This paper presents the experimental results related to the evaluation of the damping response of scaled physical models founded on scrap rubber tire-sand mixtures by carrying out 1g model tests. The present study further strengthens the benefits of using scrap rubber tire-sand mixtures as vibration dampening foundation materials for buildings.

2 MATERIALS USED FOR TESTING

The sand used for testing was locally available sand (Figure 1) used for the building construction. The rubber tire shreds (devoid of embedded steel wires) were obtained by shredding the tires in a tire shredding machine. The fine size rubber particles of desired size (less than 2mm) were obtained by (Figure 1). The grain size distribution of sand and rubber materials are shown in Figure 2. Table 1 presents the properties of sand and rubber tire shreds.

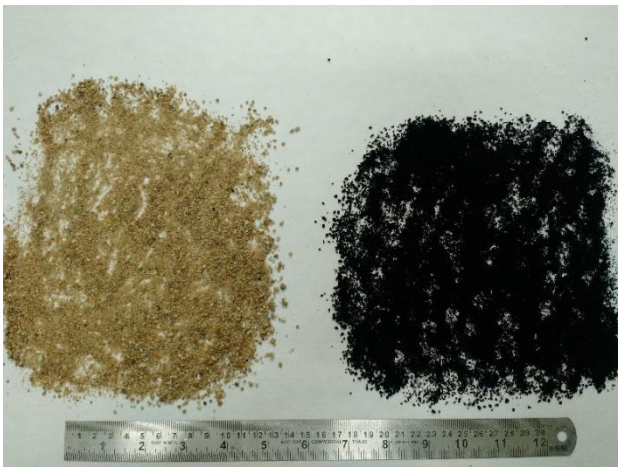

Figure 1. Materials used - sand and rubber tire shreds.

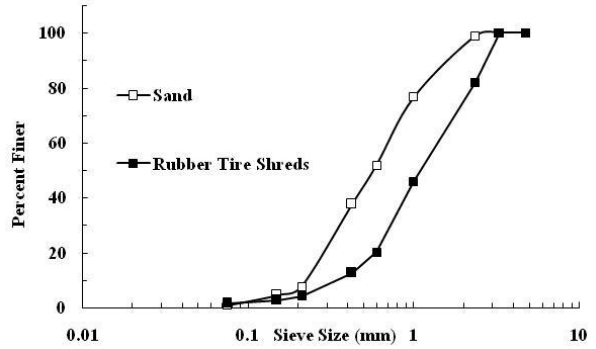

Figure 2. Grain size distribution of materials used.

Table 1. Properties of the materials used for testing.

Item	G_s	D_{10} (mm)	C_u	C_c	γ_{dmax} (kN/ m^3)	γ_{dmin} (kN/ m^3)
Sand	2.68	0.22	3.18	0.8	17.6	15.3
Rubber	1.14	0.35	3.57	1.12	5.2	2.8

3 EXPERIMENTAL SETUP, PROCEDURE AND ANALYSIS

The prototype structure considered has a plan area of 6 sq.m and consists of ground floor + up to 2 storeys (each storey 3m height). The steel model was made of square steel rods (beam size 10mm, column size 12mm) with each storey height 30cm. The footing size of the model was 10cm x 10cm x 1cm. The scaling laws as proposed by Iai (1989) were adopted.

Foundation conditions consisted of 4 cases as shown in Table 2. Rigid connections were made between model footings and heavy steel sections in the fixed base case (Figure 3a). Other base conditions had the model structure founded on pure sand, 10% sand-rubber tire mixture (gravimetric) and pure rubber. In latter cases, the model was setup within a 1.5m diameter and 0.85m height steel tank internally covered with EPS strips. These strips were provided to prevent reflection of the vibrations from the boundaries. The procedure reported in Madhusudhan et al. (2017, 2020) was adopted to create a sand bed inside the tank. The dense sand bed was made in various layers with each layer given an adequate number of tamping.

Careful placement of the model structure footing was ensured in the foundation block to maintain the desired footing depth from the sand surface level. The test setup is shown in Figure 3(b).



(a) *(b)*

Figure 3. Test setup (a) Scaled model with fixed base (b) Scaled model structure placed on sand-rubber mixture.

The impact was applied to the model structure using a PCB Piezotronics made impact hammer (086D20 model, 22.2kN capacity). The response of the structure was measured using PCB Piezotronics made accelerometers (393B04 model, cylindrical shape, dia 25mm, height 31mm, screw mounted). These sensors were attached to the model at various locations (floor levels, footing, and tank boundary). The hammer and the sensors were connected to the HBM made digital carrier frequency amplifier system. Notations *A1*, *A2*, and *A3* were used for the sensors mounted on the ground, first-floor, and second-floor beam levels respectively.

The impact locations were at storey beam levels (middle of the beam). The resulting acceleration time

histories were recorded by the mounted sensors. They were further converted to the frequency domain using Fast Fourier Transforms (*FTT*). Further, the Frequency Response Function (*FRF*) is the ratio of the output response of the system and the input excitation given to the system. Both the output and input signals in the frequency domain i.e., the Fourier amplitudes were used to obtain the *FRF* plot as a complex spectrum of the system. Figure 4 shows the typical frequency response of a hammer impact, the corresponding acceleration response of the structure, and the resulting *FRF* magnitude plot calculated using the *FFT*s of hammer input and the acceleration response.

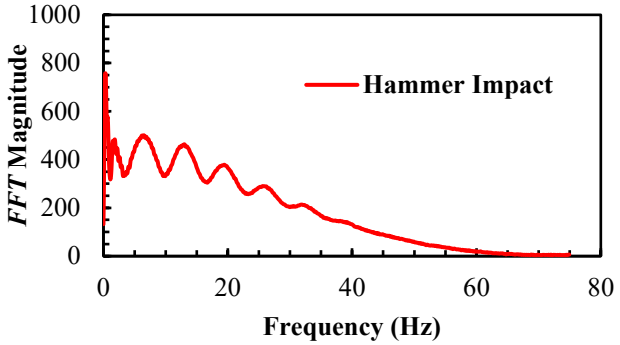

(a) FFT of hammer impact

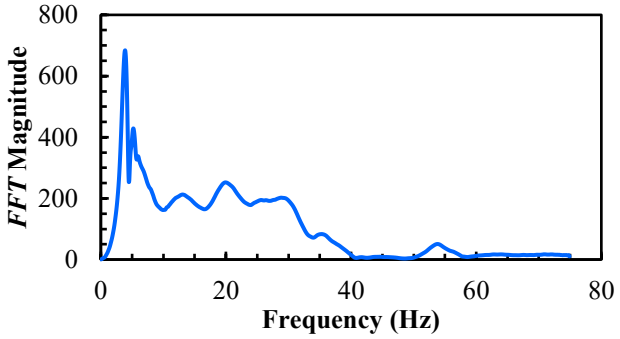

(b) FFT of an accelerometer signal

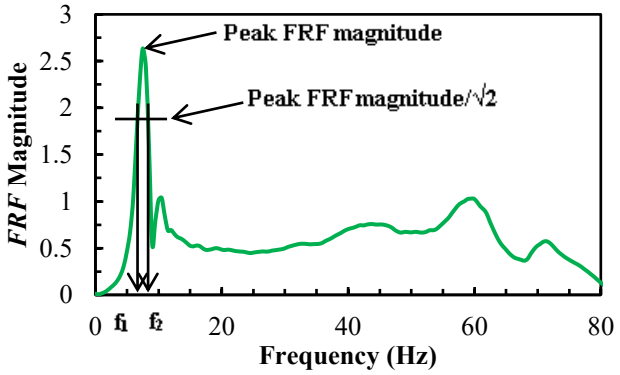

(c) FRF magnitude plot

Figure 4. Estimation of the damping ratio from the FRF magnitude plot using half-power bandwidth method.

The damping ratios were estimated from the FRF plots using the Half-Power Bandwidth method (Chopra, 2023) as given by Equation 1.

$$D = \frac{f_2 - f_1}{2 * f_n} \quad (1)$$

where f_1 and f_2 are the frequencies corresponding to the peak *FRF* magnitude/√2, and, f_n is the fundamental frequency of the system. The frequency corresponding to the peak of the *FRF* magnitude plot represents the fundamental frequency of the system

4 RESULTS AND DISCUSSION

Tables 2 to 4 present the damping ratio of the structure with different floors and hammer impact locations. (Note: Ground Floor is abbreviated as *GF*).

Table 2. Damping ratio of GF structure (GF hammer hit location).

Base condition	Load factor	Damping Ratio (%)	
		At *A1*	At *A4*
Fixed Base	*NL*	4.6	-
	1	4.5	-
	1.5	-	-
Pure Sand	*NL*	21.0	23.1
	1	11	-
	1.5	-	-
10% Mixture	*NL*	18.9	21.0
	1	16.1	-
	1.5	-	-
Pure Rubber	*NL*	11.5	10.6
	1	12.6	11.6
	1.5	14.4	13.3

Table 3. Damping ratio of GF+1 structure (GF hammer hit location).

Base condition	Load factor	Damping Ratio (%)		
		At *A1*	At *A2*	At *A4*
Fixed Base	*NL*	-	-	-
	1	10.5	11.1	-
	1.5	16.3	14.3	-
Pure Sand	*NL*	7.3	10.4	8.6
	1	7.6	8.6	5.7
	1.5	-	-	-
10% Mixture	*NL*	13.9	13.6	10.8
	1	11.6	11.6	13.3
	1.5	5	12.3	14.3
Pure Rubber	*NL*	11.8	11.8	10
	1	15.7	-	16.7
	1.5	31.2	18.7	20

Table 4. Damping ratio of GF+2 structure (GF hammer hit location).

Base condition	Load Factor	Damping Ratio (%)			
		At *A1*	At *A2*	At *A3*	At *A4*
Fixed Base	NL	13.2	11.0	9.3	-
	1	8.2	16.7	11.3	-
	1.5	8.9	20.0	10.2	-
Pure Sand	NL	-	11.4	-	-
	1	18.2	-	-	-
	1.5	-	18.5	17.0	-
10% Mixture	NL	14.6	12.5	12.8	-
	1	17.8	14.3	14.3	13.5
	1.5	15.0	11.6	10.8	-
Pure Rubber	NL	16.5	15.8	-	12.0
	1	22.5	21.0	7.83	23.7
	1.5	12.5	16.2	14.6	36.7

At the outset, the damping ratio was found to be lowest for the structure whose base was fixed. This is because the displacements developed upon impact were the least in the case of a structure with a fixed base. This is in line with the known fact that at low strains, the damping ratio is minimal.

When the base condition of the structure was changed from fixed to pure sand, an increase in the damping ratio was observed. Further, for the structure with sand-rubber tire shred mixture foundation (10% mix), the damping ratio remained more or less the same as observed in the case of pure sand. However, in many cases, the damping values of the system were observed to increase. Interestingly, for the structures on the pure rubber tire shred block, the overall damping ratio was found to be comparatively less than that of the cases where the structure was founded on pure sand and the 10% sand rubber tire shred mixture. This observation is also supported by the experimental results from the laboratory element tests where the pure rubber tire shreds were found to show the least damping ratio in comparison with the damping ratio observed for pure sand and the 10% sand-rubber tire shred mixture (Madhusudhan et al., 2017, 2019, 2020).

5 CONCLUSION

The dynamic responses of scaled physical models were studied using impact hammer testing. The base conditions of the foundation and the loading on the models were varied. The results are higlighted in terms of the damping ratios.

The damping evaluated for the case of a model structure founded on a 10% sand-rubber mixture foundation block is higher than the cases where other materials are used in the foundation.

The present experimental study shows that the 10% sand-rubber mixture can be a promising material. The results of the present study show that this mixture has a potential to act as a vibration dampening foundation material for low-rise buildings. However, future research is essential for more rigorous analysis under more realistic conditions.

ACKNOWLEDGEMENTS

The conference support and encouragement offered by A'Sharqiyah University, Sultanate of Oman is sincerely acknowledged. The author grateful acknowledges the support of Indian Institute of Technology Madras. The suggestions offered by Dr. A. Boominathan and Dr. Subhadeep Banerjee of IIT Madras are sincerely acknowledged.

REFERENCES

Boominathan, A., Banerjee, S., Dhanya, J. S. (2019) Geo-Base Isolation with geogrid reinforcement for buildings, In: Geotechnics Fundamentals and Applications in Construction, 1st Ed., CRC Press, London, UK, pp. 86-92, http://dx.doi.org/10.1201/9780429058882-18.

Chopra, A. K. (2023). *Dynamics of structures*, 6th Ed., Pearson, London, UK.

Iai, S. (1989) Similitude for shaking table tests on soil-structure-fluid model in 1 g gravitational field, *Soils and Foundations*, 29(1): 105–118. https://doi.org/10.3208/sandf1972.29.105.

Madhusudhan, B. R., Boominathan, A., Banerjee, S. (2017) Static and large-strain dynamic properties of sand-rubber tire shred mixtures, *Journal of Materials in Civil Engineering*, 29(10), https://doi.org/10.1061/(ASCE)MT.1943-5533.0002016.

Madhusudhan, B. R., Boominathan, A., Banerjee, S. (2019) Factors affecting strength and stiffness of dry sand-rubber tire shred mixtures, *Geotechnical and Geological Engineering*, 37, https://doi.org/10.1007/s10706-018-00792-y.

Madhusudhan, B. R., Boominathan, A., Banerjee, S. (2020) Cyclic simple shear response of sand-rubber tire chip mixtures, *International Journal of Geomechanics*, 20(9), https://doi.org/10.1061/(ASCE)GM.1943-5622.0001761.

Madhusudhan, B. R., Boominathan, A., Banerjee, S. (2021). Dynamic pore pressure responses of sand–rubber tire shred mixtures from cyclic simple shear and cyclic triaxial tests, In: *Soil Dynamics*, 1st Ed., Springer, Singapore, pp. 23-34. https://doi.org/10.1007/978-981-33-4001-5_3.

Xiong, W., Li, Y. (2013) Seismic isolation using granulated tire-soil mixtures for less developed regions: experimental validation, *Earthquake Engineering and Structural Dynamics*, 42(14): 2187-2193, https://doi.org/10.1002/eqe.2315.

Proceedings of the XVIII ECSMGE 2024
GEOTECHNICAL ENGINEERING CHALLENGES
TO MEET CURRENT AND EMERGING NEEDS OF SOCIETY
© 2024 the Authors
ISBN 978-1-032-54816-6
DOI 10.1201/9781003431749-468
Open Access: www.taylorfrancis.com, CC BY-NC-ND 4.0 license

ECSMGE 24
XVIII EUROPEAN CONFERENCE ON SOIL MECHANICS AND GEOTECHNICAL ENGINEERING

Performance assessment of a combined foundation system of end-bearing and floating piles in a challenging soil profile

Évaluation des performances d'un système de fondation combiné de pieux porteurs et de pieux flottants dans un profil de sol complexe

A. Magdy*, M. Shahien, M. El Sawwaf, A. Nasr
Faculty of Engineering, Tanta University, Tanta, Egypt
**Alaa.magdy@f-eng.tanta.edu.eg*

ABSTRACT: This study evaluates the performance of a combined foundation system of end-bearing and floating piles in a challenging soil profile consisting of a sand layer of thickness of 12 m overlying a substantial deposit of soft to medium stiff clay in Egypt Nile Delta deposits. The objective is to assess the effectiveness of this foundation system in providing stability highlighting the load-sharing ratios. This system offers a time-efficient alternative to conventional soil improvement techniques such as wick drains or vacuum consolidation. These methods often require considerable time and may have limited effectiveness on deep clay soil, especially beyond a depth of 10 - 15 meters below ground level, hence the challenge arises. By incorporating piles of varying lengths, this system provides a rapid solution for achieving the desired stress distribution by capitalizing on the high end-bearing capacity in sand and the skin friction provided by long piles in clay. 3D numerical simulations were conducted to assess the performance of three systems, using only end-bearing piles, only friction piles, and the combined foundation system. The insights gained assured that this system has a superior performance on decreasing settlement and benefiting from all factors, piles end bearing in sand, high friction from piles rested in clay, and bearing capacity of soil beneath the raft.

RÉSUMÉ: Cette étude évalue les performances d'un système de fondation combiné de pieux en bout et flottants dans un profil de sol difficile, composé d'une couche de sable d'une épaisseur de 12 m recouvrant un dépôt substantiel d'argile molle à moyennement raide dans les dépôts du delta du Nil en Égypte. L'objectif est d'évaluer l'efficacité de ce système de fondation dans la fourniture de stabilité, en mettant en évidence les ratios de partage de charge. Ce système offre une alternative efficace en termes de temps aux techniques conventionnelles d'amélioration des sols telles que les drains de mèche ou la consolidation sous vide. Ces méthodes nécessitent souvent un temps considérable et peuvent avoir une efficacité limitée sur les sols argileux profonds, en particulier au-delà d'une profondeur de 10 à 15 mètres sous le niveau du sol, d'où le défi. En incorporant des pieux de longueurs variables, ce système fournit une solution rapide pour atteindre la distribution de contraintes souhaitée en capitalisant sur la capacité portante élevée en bout dans le sable et la friction de la peau fournie par les pieux longs dans l'argile. Des simulations numériques 3D ont été réalisées pour évaluer les performances de trois systèmes, en utilisant uniquement des pieux en bout, uniquement des pieux de friction et le système de fondation combiné. Les informations obtenues ont confirmé que ce système offre des performances supérieures en termes de réduction des tassements et bénéficie de tous les facteurs, la capacité portante des pieux en bout dans le sable, la friction élevée des pieux reposant dans l'argile et la capacité portante du sol sous la dalle.

Keywords: Piled raft foundations; challenging soil profile; numerical simulations; load-sharing ratios; floating piles.

1 INTRODUCTION

The utilization of piled rafts (PRs) for the construction of high-rise buildings and offshore structures has proven to be an effective and cost-efficient solution for controlling total and differential settlements and increasing bearing capacities. Traditional design approaches often adopt the assumption that all structural loads are supported by piles, neglecting the significant load-sharing potential of soil beneath the raft, depending on the pile group concept. However, remarkable research, e.g., by Cooke (1986) has emphasized that about 30% of the total load can be effectively supported by the soil. Furthermore, Katzenbach, et al. (1998) pointed out the importance of taking the soil-structure interactions between raft, soil, and piles while designing a PR. Hence, the design approaches for PRs, which consider this load-sharing effect, are more rational and economical. Over the past decades, researchers have studied the behavior of PRs using various techniques for different soil types. Experimental studies have been conducted to understand the PRs behavior in sandy soils, for instance, by Elwakil

and Azzam (2016) and in saturated clay such as Hoang et al. (2024), and Hoang and Matsumoto (2020). Numerical methods have been employed to investigate PR behavior in stiff clay, e.g., Mali and Singh (2018). It is worth noting that the suitability of PRs can differ depending on geological soil profiles. Poulos (2001) pointed out that in situations with end-bearing piles and a layer of loose sand or soft clay near the foundation surface, PRs may not be the best choice because of the limited contribution of the soil after losing contact due to several factors. Reul and Randolph (2003) analyzed PRs in over-consolidated clay. Furthermore, the application of PRs extends to various soil types, as evidenced by studies in Frankfurt stiff clay (Sommer, et al. 1985) and Berlin Sand (El-Mossallamy, et al. 2006). Researchers have explored the behavior of PRs in soft clay as well, such as studies conducted by El Sawwaf et al. (2022a, 2022b) who proved the applicability of PRs in soft clay, under reasonable stress, emphasizing the ability of soil to carry a substantial portion of the load conditional on the shaft resistance of the piles.

1.1 Research objectives and methodology

In areas of the Egypt Nile Delta with a soil profile featuring a sand layer overlying soft to medium stiff clay, traditional ground improvement techniques like vertical drains and vacuum consolidation may not be effective due to the limited efficacy of the upper fill on the clay and the time required for these methods. Therefore, this study proposes a piled raft (PR) solution. End-bearing piles, where all tips are in sand, may not be optimal due to limited friction from short lengths and the decreased end bearing because of soft layers beneath while using long piles, where all tips are in soft to medium stiff clay, sacrifices end-bearing. To address these challenges, numerical simulations will be conducted to evaluate three scenarios: Short piles with all tips in sand (end-bearing piles), long piles with all tips in clay (friction piles), and mixed configurations combining end-bearing and friction piles. Through these simulations, the research aims to provide insights into cost-effective foundation solutions for structures in challenging soil profiles like those found in the Egypt Nile Delta.

2 SOIL PROFILE DESCRIPTION

This study was carried out on an actual soil profile situated within the Nile Delta deposits of Egypt. The soil profile consists of a 12-meter layer of medium to dense sand, which is underlain by an extensive 48-meter layer of soft to medium stiff clay. Beneath this clay layer, a further layer of dense sand extends to the end of the boreholes. The groundwater level is situated at a depth of approximately 3.0 meters below the ground level. The site investigation was conducted by Hamza Associates, a reputable organization in Egypt, with expertise in geotechnical studies.

3 FINITE ELEMENT MODELING

The foundation was subjected to a uniform load (q) of 150 kPa (the raft own weight and additional stress). The constitutive model, mesh, boundary conditions and piles and raft modelling are presented in the following subsections.

3.1 Constitutive model

In this study, the Hardening Soil (HS) model was adopted for all soils, as the (HS) model can simulate the behavior of both stiff and soft clays (Schanz, 1998). In addition, Brinkgreve et al. (2010) reported that the HS model covers the behavior of a wide range of sands. A distinctive attribute of the HS model is its ability to account for stress path and their consequent impact on soil behavior. It considers three stiffnesses, the secant stiffness (E_{50}^{ref}), Oedometer loading stiffness, (E_{oed}^{ref}), and unloading/reloading stiffness, (E_{ur}^{ref}). Furthermore, this model considers the stress-dependency of stiffness.

3.2 Finite element mesh and boundary conditions

The parametric investigation was executed on a quarter-section of the PR, chosen for its symmetry. The lateral limits of the soil domain were restricted to prevent horizontal translation while permitting vertical soil displacement. The horizontal boundary was 4 times of raft width from the raft edge. The vertical soil boundary was set to exceed three times the width of the raft below the equivalent raft depth, as per the equivalent raft concept proposed by Tomlinson (2001) for the case with the longest piles. The model employed a medium-mesh size, although a finer mesh was utilized within the active zone.

3.3 Modelling of raft and piles

The raft was modeled using a 10-node tetrahedral element, while the piles were modeled as 3-noded embedded beam elements with fixed head conditions. The study also considered the interaction between the soil and the structural elements, incorporating an interface strength value of 0.7 for the concrete-soil interface, Elwakil and Azzam (2016). Bored piles were utilized

in the study, with layer-dependent pile friction activated. The end-bearing value of the piles was not limited, allowing it to be obtained from the program solution.

3.4 Construction stages

The analysis included 5 stages, shown in Figure 1, the initial stage, excavation up to the depth of 2.0m, pile installation, raft construction, and loading. The excavation was carried out with appropriate slopes to prevent side falling. The displacement was set to be zero after the pile installation stage, where the raft settlement was the summation of the raft construction and loading stages. Tables (1-3) show the input parameters.

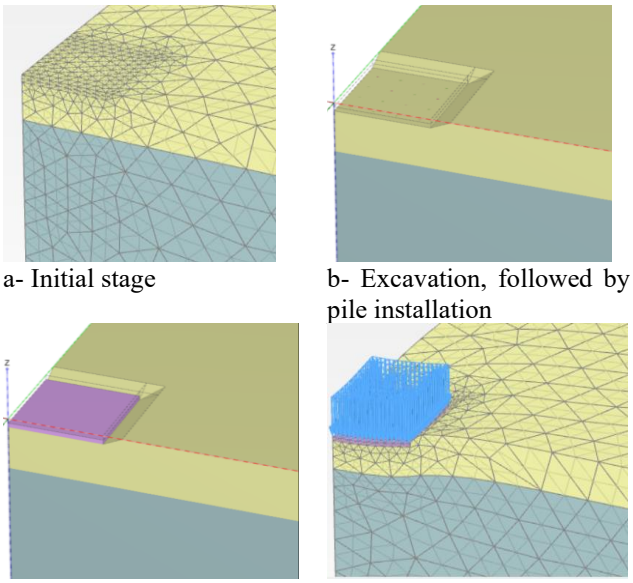

a- Initial stage b- Excavation, followed by pile installation

c- Raft construction stage d- Loading stage

Figure 1. Stages of construction.

Table 1. Parameters of soft to medium clay layer.

Parameter	Soft to medium stiff clay
Elevation, below ground level (m)	12 – 60
Drainage type	Undrained (A)
Saturated unit weight (kN/$\mathbf{m^3}$)	17.50
$\mathbf{E_{50}^{ref}}$ (MPa)	8
$\mathbf{E_{oed}^{ref}}$ (MPa)	8
$\mathbf{E_{ur}^{ref}}$ (MPa)	24
Reference pressure, Pref (kPa)	100
Drained cohesion intercept, c' (kPa)	1
Drained friction angle, ϕ' (°)	26

Table 2. Parameters of sand layers.

Parameter	Upper Sand	Lower Sand
Elevation (m)	0 – 12	60 – 80
Drainage type	Drained	Drained
Unit weight (kN/$\mathbf{m^3}$)	18.0	19.0
$\mathbf{E_{50}^{ref}}$ (MPa)	45	60
$\mathbf{E_{oed}^{ref}}$ (MPa)	45	60
$\mathbf{E_{ur}^{ref}}$ (MPa)	135	180
Drained friction angle, ϕ' (°)	36	38
Dilatancy angle, Ψ' (°)	6	8

Table 3. Parameters of raft and piles.

Parameter	Raft	Pile
Model	Linear elastic	-
Unit weight (kN/$\mathbf{m^3}$)	25	24
Elastic modulus, E (MPa)	2.2×10^4	2.0×10^4

3.5 Parametric study

The vertical settlement and load sharing ratio (LSR), load carried by piles, were obtained for all cases where the raft was (40 × 40 × 1) m, and pile number (n), pile diameter (d), and pile spacing (s) were 64, 0.80 m, 6d, respectively. To study the effect of increasing pile length for the case of end-bearing piles, simulations were carried out on a PR with piles of 5, 6, 7, 8, and 9m. These lengths were changed to 20, 25, 30, and 35m in case of friction piles. Appropriate lengths of end-bearing piles, and friction piles would be selected to create the combined foundation system of end-bearing and friction piles. Figure 2 presents the different configurations studied of the combined foundation system.

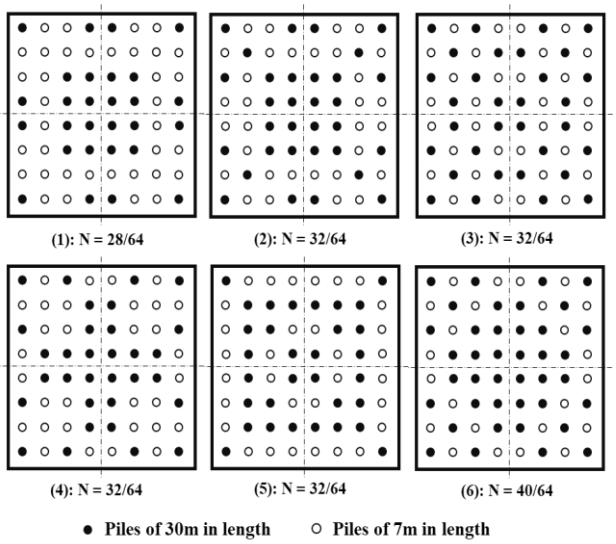

Figure 2. Different configurations of the combined foundation system of end-bearing and friction piles.

4 RESULTS AND DISCUSSIONS

A detailed analysis of findings, organized into three distinct categories is presented as follows:

1- using only end-bearing piles, 2- using only friction piles, and 3- using the combined foundation of end-bearing and friction piles.

4.1 Using only end bearing piles

As depicted in Figure 3, the various lengths of end-bearing piles consistently exhibited similar behavior even with increasing pile length. This may be explained as the longer pile length could affect the soft to medium stiff clay layer, as it brought the pile tips closer to this layer, resulting in higher load transmission through the end bearing. Regarding load sharing, it was observed that the total pile loads exhibited a gradual increase as the pile length increased up to 7.0 meters, (see Figure 4). Beyond this point, the rate of increase became limited. This can be attributed to the following: given that the skin friction of the piles increased marginally, the primary factor influencing load sharing was the end bearing; it was determined that pile lengths exceeding 7.0 meters were impacted by the presence of a weaker layer, soft to medium clay, as the depth beneath the pile tips was insufficient to achieve a higher end bearing capacity.

4.2 Using only friction piles

The primary aim was to evaluate how floating piles could effectively mitigate settlement in such a challenging soil profile. As illustrated in Figure 5, there was a notable reduction in vertical settlement as the length of the floating piles increased. This superior performance of floating piles compared to end-bearing piles could be the result of the substantial lengths, which provided a greater capacity for generating frictional resistance against movement. Additionally, under the same applied stress, the pressure bulb resulting in the case of long piles (friction piles) had a greater depth compared to that resulting in the case of short piles (end-bearing piles), (see Figure 6). Therefore, the settlement was smaller, as the stress was distributed over a larger volume of soil, causing less compression of soil particles. Regarding load sharing, Figure 7 illustrates the relationship between pile length and load sharing ratio. It was observed that the total pile loads exhibited a gradual increase with increasing pile length because of increasing pile friction. This increase was expected with increasing lengths; however, it can be linked to the increased vertical stress resulting from the own weight and external loads, leading to heightened horizontal stresses and consequently, an enhancement in frictional resistance.

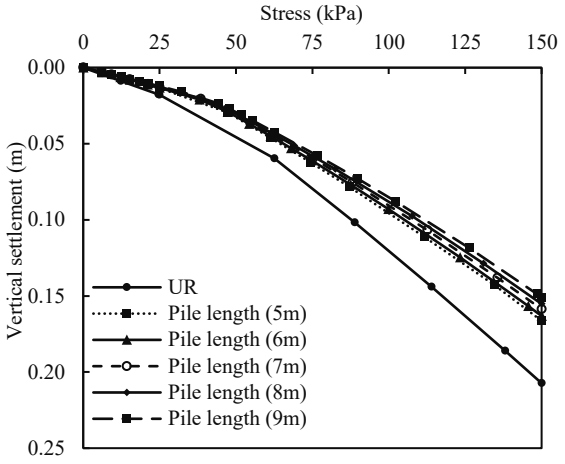

Figure 3. Relationship between stress and vertical settlement for UR and PR with all tips in sand.

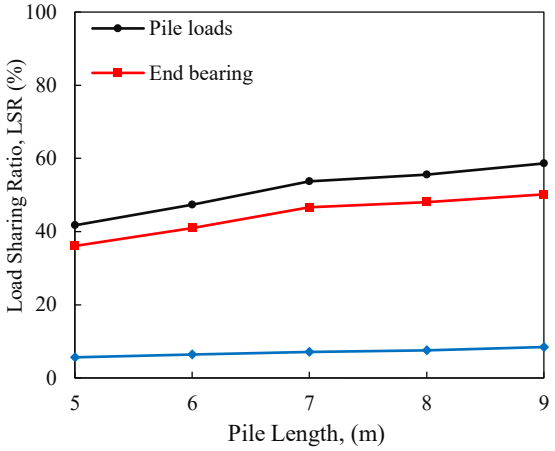

Figure 4. Relationship between pile length and load sharing ratio (LSR) for piled rafts with all tips in sand.

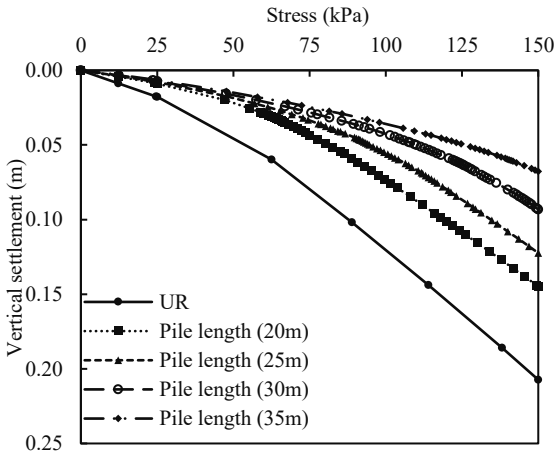

Figure 5. Relationship between stress and vertical settlement for UR and PR with all tips in clay.

4.3 Using a combined system of end bearing and friction piles

For this system, the lengths of 7.0m, and 30m were chosen for end-bearing piles, and friction piles,

respectively. The length of 7.0 m for end-bearing piles was proven to be the most appropriate one, whereas the length of 30m for friction piles was chosen from an economic perspective. The relation between the applied stress and vertical settlement for the different configurations is presented in Figure 8. Mainly, the combined foundation system could achieve a decrease in the vertical settlement more than the chosen case from cases of end-bearing piles only. However, this system couldn't achieve the same decrease in settlement of the case of only friction piles, it may be adoptable based on the project criteria and requirements. The decrease in settlement was a result of benefiting from the frictional resistance of long piles and high-end bearing from short piles. Moreover, this system expanded the pressure bulb more than in all cases of end-bearing piles only (not presented due to space limitations), so the settlement of individual particles was reduced. To go deeper among the mixed systems, system 3 exhibited comparatively lower efficiency due to the random configuration of long piles, particularly away from the raft center. Conversely, system 6 was the most efficient choice, due to the higher number of piles. The performance of this system in decreasing settlement was nearly 90% of the friction piles system with 40 long piles and 24 short piles. The economic benefit was not using 552 m of concrete (around 278 m^3 of concrete). Therefore, employing this system can be a safe and economical solution. For the mixed systems 1, 2, 4, and 5, their stress-settlement behavior displayed similarities. This superiority of system 1 even with less number of piles was attributed to its strategically concentrated pile positioning around the center of the raft, coinciding with the location of maximum vertical settlement. For the load sharing, Table 4 shows that the piles carried around half of the total load in all cases, which was around 30% carried by frictional resistance. This assured the importance of growing friction in deeper soil that was influenced by the increase in horizontal stresses.

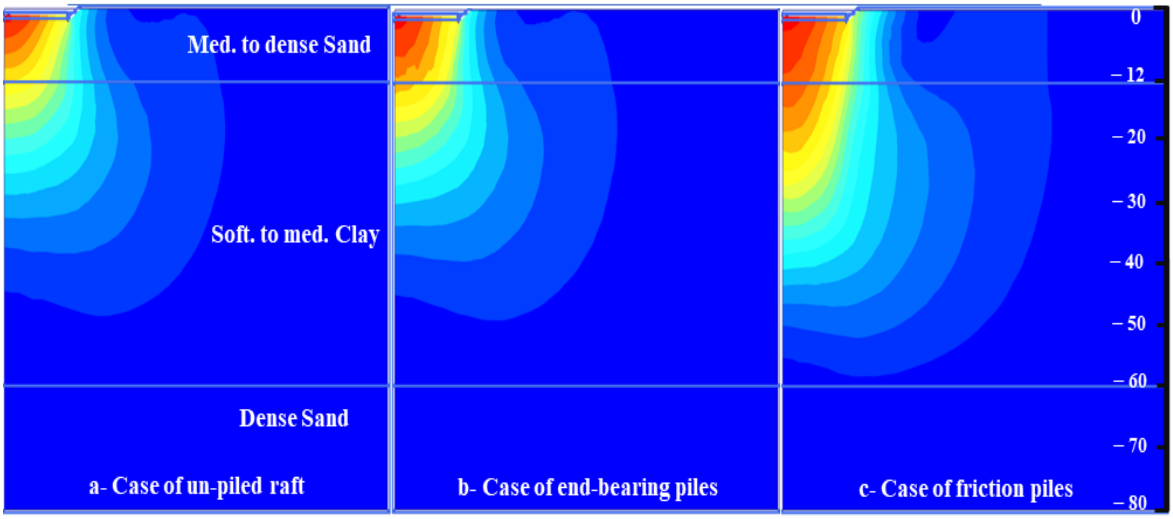

Figure 6. Stress distribution for different cases (a- un-piled raft; b- case of end-bearing piles; case of friction piles).

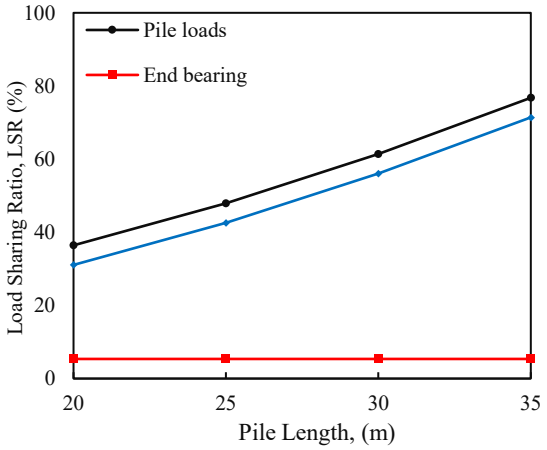

Figure 7. Relationship between pile length and load sharing ratio (LSR) for piled rafts with all tips in clay.

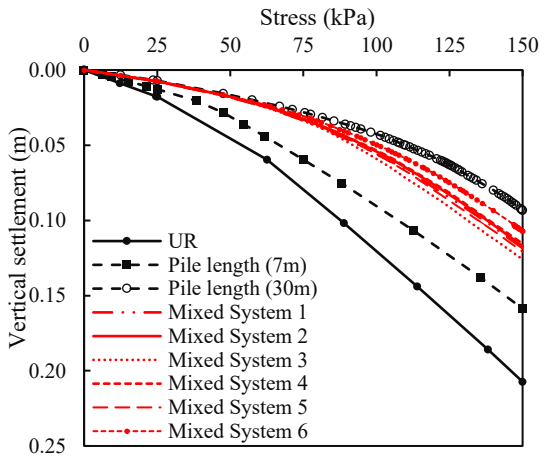

Figure 8. Relationship between stress and vertical settlement for UR, PR, and the combined foundation systems.

Table 4. Load sharing ratios as a ratio of total applied load.

	Pile loads (%)	End bearing (%)	Skin Friction (%)
1	51.79	23.31	28.48
2	52.44	20.08	32.37
3	50.64	21.72	28.92
4	52.10	20.05	32.05
5	52.37	20.46	31.92
6	53.33	14.97	38.35

5 CONCLUSIONS

Due to the potential for unacceptable settlements resulting from the utilization of un-piled rafts, this research compares three solutions of piled rafts: those with all pile tips in sand, those with all pile tips in clay, and a mixed system with some pile tips in sand and some in clay. Based on the study, the following remarks can be drawn:

- Friction piles were highly effective in decreasing settlement in such a challenging soil profile due to increased frictional resistance and bigger pressure bulbs.
- The combined system reduced settlement remarkably compared to using end-bearing piles alone. The system of higher pile numbers was the most efficient choice, offering nearly 90% of the friction piles system benefits while being economically advantageous.

REFERENCES

Brinkgreve, R. B. J., Engin, E., & Engin, H. K. (2010). Validation of empirical formulas to derive model parameters for sands. Numerical methods in geotechnical engineering, 1, 137-142. https://doi.org/10.1201/b10551-25.

Cooke, R.W. (1986) Piled Raft Foundations on Stiff Clays: A Contribution to Design Philosophy. Geotechnique, 36, 169-203. http://dx.doi.org/10.1680/geot.1986.36.2.169.

El-Mossallamy, Y., Lutz, B., Richter, T. (2006). Innovative application of piled raft 419 foundation to optimize the design of high-rise buildings and bridge foundations. Proc. 420 10th Int. Conference on Piling and Deep Foundations, 31 May-2 June, Amsterdam.

El Sawwaf, M., Shahien, M., Nasr, A., & Magdy, A. (2022). The applicability and load-sharing behavior of piled rafts in soft clay: experimental study. Innovative Infrastructure Solutions, 7(6), 362. https://doi.org/10.1007/s41062-022-00959-w.

Elsawwaf, M., Shahien, M., Nasr, A., & Magdy, A. (2022). The behavior of piled rafts in soft clay: Numerical investigation. Journal of the Mechanical Behavior of Materials, 31(1), 426-434. https://doi.org/10.1515/jmbm-2022-0050.

Elwakil, A. Z., & Azzam, W. R. (2016). Experimental and numerical study of piled raft system. Alexandria Engineering Journal, 55(1), 547-560. https://doi.org/10.1016/j.aej.2015.10.001.

Hoang, L. T., Xiong, X., & Matsumoto, T. (2024). Effect of pile arrangement on long-term settlement and load distribution in piled raft foundation models supported by jacked-in piles in saturated clay. Soils and Foundations, 64(2), 101426. https://doi.org/10.1016/j.sandf.2024.101426.

Hoang, L. T., & Matsumoto, T. (2020). Long-term behavior of piled raft foundation models supported by jacked-in piles on saturated clay. Soils and Foundations, 60(1), 198-217. https://doi.org/10.1016/j.sandf.2020.02.005.

Katzenbach, R., Arslan, U., Moormann, C., & Reul, O. J. D. G. (1998). Piled raft foundation: interaction between piles and raft. Darmstadt Geotechnics, 4(2), 279-296.

Mali S, Singh B (2018) Behavior of large piled-raft foundation on clay soil. Ocean Eng 149:205–216.

Poulos, H. G. (2001). Piled raft foundations: design and applications. Geotechnique, 51(2), 95-113. https://doi.org/10.1680/geot.2001.51.2.95.

Reul, O., and Randolph, M. F. (2003). "Piled rafts in overconsolidated clay—Comparison of in-situ measurements and numerical analyses." Geotechnique, 53(3), 301–315.

Sommer, H., Wittmann, P., and Ripper, P., (1985). Piled raft foundation of a tall building in Frankfurt clay. In International conference on soil mechanics and foundation engineering. 11 (pp. 2253-2257).

Tomlinson, M. J., & Boorman, R. (2001). Foundation design and construction. Pearson education.

Proceedings of the XVIII ECSMGE 2024
GEOTECHNICAL ENGINEERING CHALLENGES
TO MEET CURRENT AND EMERGING NEEDS OF SOCIETY
© 2024 the Authors
ISBN 978-1-032-54816-6
DOI 10.1201/9781003431749-469
Open Access: www.taylorfrancis.com, CC BY-NC-ND 4.0 license

ECSMGE 24
XVIII EUROPEAN CONFERENCE ON SOIL MECHANICS AND GEOTECHNICAL ENGINEERING

Study of the behaviour of treated load transfer platform on rigid inclusions

Etude du comportement des plateformes en sol traité sur inclusions rigides

J. Mannah*
Arcadis ESG/INSA Lyon, Lyon, France

C. Chalak, H. Farhat
Arcadis ESG, France

L. Briançon, S. Grange
INSA Lyon, Lyon, France

K. Varain
Cerema, Rouen, France

D. Dias
Université Grenoble Alpes, Grenoble, France

T. Lenoir
Université Gustave Eiffel, Paris, France

**julien.mannah@arcadis.com*

ABSTRACT: Rigid inclusion is a ground improvement method that has been significantly developed in recent years. Granular load transfer platforms (LTP) are commonly used in this technique leading to an increase in the use of natural resources. In this context, soil treatment can be considered as an alternative solution to use the in-situ soil, improve its characteristics, and limit the pressure on the granular material resources. As part of the national ASIRI+ project, two full-scale tests have been carried out to test the efficiency of treated LTP. An experimental program has been conducted to fully characterize the soil and find the best treatment for the LTP with consideration for the environmental and the economic effects. Then, both tests have been carried out in an 8m x 8m pit with 16 rigid inclusions of 30cm diameter and 1m height. Settlement and stress sensors were installed to monitor the mechanism of load transfer within the platform. Numerical simulation tests have also been performed to better understand the behaviour of the treated LTP.

RÉSUMÉ: Le renforcement du sol par inclusions rigides est une méthode d'amélioration du sol qui a été développée de manière significative ces dernières années. Les plateformes de transfert de charge (PTC) granulaires sont couramment utilisées dans cette technique, ce qui entraîne une augmentation de l'utilisation des ressources naturelles. Dans ce contexte, le traitement du sol peut être considéré comme une solution alternative pour utiliser le sol in situ, améliorer ses caractéristiques et limiter la pression sur les ressources granulaires. Dans le cadre du PN ASIRI+, deux essais en vraie grandeur ont été programmés pour tester l'efficacité des PTC traitées. Un programme expérimental a été mené pour caractériser le sol et trouver le meilleur traitement en tenant compte des effets environnementaux et économiques. Les essais ont été réalisés dans une fosse expérimentale de 8m x 8m avec 16 inclusions rigides de 30cm de diamètre et de 1m de hauteur. Des capteurs de tassement et de contrainte ont été installés pour observer les mécanismes de transfert de charge. Des modélisations numériques ont également été réalisées pour mieux comprendre le comportement de la PTC traitée.

Keywords: Soil treatment; rigid inclusions, load transfer platform, full-scale test.

1 INTRODUCTION

Rigid inclusion is a soil reinforcement technique that has been widely spread during the last 50 years (Briancon *et al.*, 2020). It consists of installing rigid columns known as rigid inclusions (RI) in soft soils and a load-transfer platform (LTP) that transfers the loads applied on the surface to the RI through the arching effects. The difference of settlement between the RI and the soft soil creates negative friction along the RI leading to a better load transfer. The field of application for this technique has been widely extended given its many advantages: rapid implementation, increase of the bearing capacity and the soil resistance and decrease of the settlements of the surface structure (ASIRI, 2012).

Granular LTP formed of sand or gravel are quite common in this technique (Girout *et al.*, 2013) leading to an increase in the exploitation of natural resources, hence the need to find an alternative solution to use the in-situ soil, improve its characteristics and limit the pressure on granular material resources has led to consider treated LTP. This article presents a full-scale experiment to test the efficiency of treated LTP on rigid inclusions.

2 EXPERIMENTAL STUDY

An experimental campaign was held to characterize the soil used for the LTP and find the best treatment with regards to the economic and the environmental effects. Mechanical soil tests were conducted to determine the efficiency of the treatment.

2.1 Soil treatment

The soil used for the treated LTP is silt, extracted from Dieppe in the north of France of type F1 (low plasticity silt) according to the new French guide for earthworks, embankments, and subgrades (GTR, 2023). It has a water content between 17 and 23%.

Three different formulas were adopted for the test:

- SLC: soil + 1% lime + 4% cement
- SLCO: soil + 1% lime + 4% COmpaxem
- SA: soil + 5% Argiliant+

The 1st treatment "SLC" and the percentages of lime and cement were chosen based on the state of art, the French technical guide for soil treatment (GTS, 2000), and for the fact that it is widely used for treating working platforms on construction sites. It has a workability time of 1 hour. The lime is supplied by the Lhoist group (quicklime CL90-Q), and the cement is CEM II 32.5.

The 2nd and the 3rd treatments "SLCO" and "SA" were considered to take into effect the environmental effects. Argiliant+ and COmpaxem are binders that comply with the French norm NF P15-108 and are perfectly suited to soil treatment, with a workability time of 1h30 and 6h respectively. They are composed of different metakaolin/cement ratios. Table 1 shows the different studied formulations.

Table 1. Treatment formulations

Treatment	Lime (%)	Cement (%)	Metakaolin
SLC	1	4	-
SLCO	1	2.4	1.6
SA	1	1.5	2.5

2.2 Mechanical properties

Mechanical soil tests were conducted at different curing periods by laboratory standardized tests according to the French norms to explore the effect of the treatment on the mechanical resistance. Samples were prepared and kept for curing with reference to the French norms.

The shear strength was determined by triaxial tests. The natural soil has a friction angle of 29° and a cohesion of 34 kPa. The friction angle does not vary with treatment and remains around 29°. The treated soils show an increase in cohesion. The results are presented in figure 1 with SLC presenting the best long-term cohesion at 550 kPa.

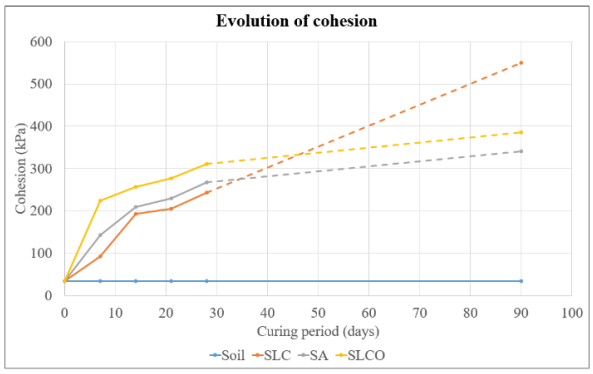

Figure 1. Evolution of cohesion.

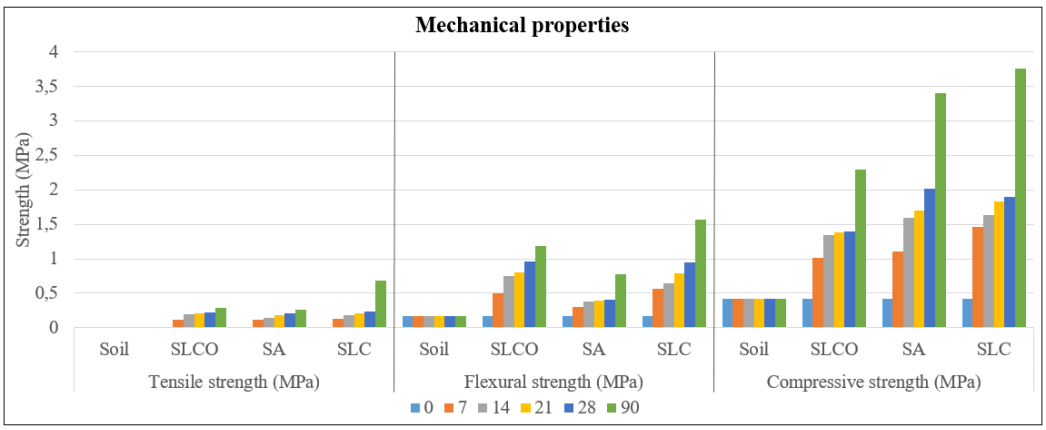

Figure 2. Mechanical properties of treated soil.

The evolution of other mechanical properties is presented in figure 2 through tensile, flexural, and compressive strengths with SLC presenting the best results compared to SLCO and SA.

2.3 Experimental study

The full-scale test in Cerema's experimental pit is representative of the real-life case of a soil reinforced with rigid inclusions. This 64 m^2 pit features 16 rigid inclusions of 30 cm diameter and 1 m height, set in a 2 m square mesh (Figure 3).



Figure 3. Experimental pit – Cerema.

The system, designed to test the effectiveness of treated LTP, consists of several layers of soil, a treated LTP and different types of loading.

A first layer of 2.5 cm thick of wooden grating is installed, followed by a 10 cm layer of biocofra (honeycomb cardboard planks). Biocofra is very rigid when dry but biodegrades uniformly throughout its thickness in the presence of water, hence the need for the grating layer to facilitate water supply.

Dissolving the biocofra will be used only if necessary to achieve failure of the treated LTP, as this may help us to better understand the failure mechanism and behaviour of the treated platform.

A third 40 cm layer of Deltagom (tire aggregate) is installed. Due to its compressibility, this material can help us to obtain a representative settlement of what happens in the real case. Above the Deltagom, a 37.5 cm layer of sand is installed to reach the level of the heads of the rigid inclusions (Height = 1m).

Compaction of the sand is possible on the Deltagom and the combination of these 2 soil layers represents the soft soil found in the real case of a site reinforced with rigid inclusions.

For the load transfer platform, the “SLC” treatment was chosen, based on the mechanical strength tests and for being widely used for treating working platform on construction sites. The soil cannot be treated directly in the pit, as there is a risk of consuming all the Deltagom settlement and damaging the sensors on the heads of the RI. Therefore, the soil was prepared aside, homogenized, treated with lime, and followed by cement one hour later. This procedure reduces the water content of the soil, facilitates particle flocculation, and brings the soil to an optimal state, ideal for effective cement treatment.

After cement treatment, the mixture is transported to the pit by tractors and the LTP is installed in 2 layers of 20 cm to ensure good compaction of the mix and good soil density.

Finally, a 1.5 m embankment is placed on top of the treated platform. The LTP is loaded after 14 days of compaction. This curing time has been chosen to ensure that the platform reaches the required mechanical strength to withstand the different loadings. The embankment was kept for 1 month to monitor the load transfer mechanisms, then, surcharges were added and left for 14 days before the final phase: dissolving the biocofra.

Figure 4 shows a cross-section of the entire experimental setup. Instrumentation is carried out using stress and settlement sensors installed in the different layers of the setup to monitor the load transfer mechanisms, measure the soil settlement, and test the efficiency of the treated platform.

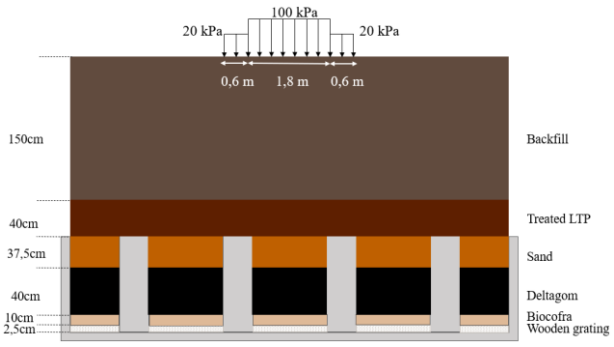

Figure 4. Cross section of the experimental setup.

3 RESULTS

In order to understand the load transfer mechanisms and the behaviour of the treated platform, the evolution of stresses and settlements was studied as well as the LTP’s behaviour and the failure mechanisms.

3.1 Stress evolution

Stress sensors were installed within the differents layers of the setup presented in figure 4. Instrumentation was performed on the central mesh to eliminate the edge effects. Figure 5 presents the stress at the base and the head of the RI as well as the soil (sand) during the different phases of construction.

Based on the stress evolution we noticed:

- The good functioning of the system where a load transfer towards the rigid inclusions in relation to the soil was observed.
- A proper load transfer where the stress is higher at the base than it is at the heads due to the negative friction along the entire length of the RI.
- The load transfer is immediate for the treated platform. When the embankment is placed the stress goes up directly to 742 kPa at the head of the RI. During the 1 month's wait, it increases only by 9.9% (816 kPa) indicating that the load transfer started the minute the embankment was placed for the treated LTP. This was not the case for the granular LTP where the same test was carried out by (Terqueux *et al.*, 2022) using the same experimental setup and instrumentation. The results for the granular LTP showed that load transfer mechanisms were more gradual and during the 1 month's wait, the stress increased by 79.4% at the head of the RI.

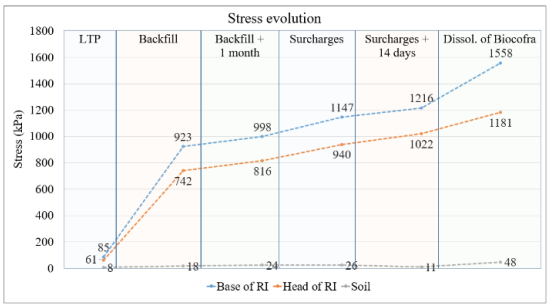

Figure 5. Stress evolution.

3.2 Settlement evolution

Same as for the stress sensors, settlement sensors were installed on the different layers to monitor the settlement of the system (Figure 6).

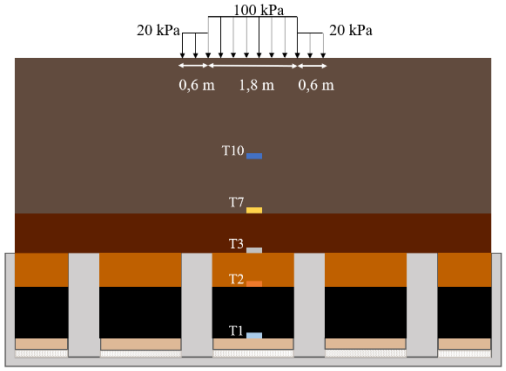

Figure 6. Settlement sensors.

Based on the settlement evolution presented in Figure 7, we noticed:

- The experimental protocol has been validated in terms of the dissolution of the biocofra that is very rigid when dry (0 cm of settlement during all the stages of loading) but biodegrades uniformly throughout its thickness in the presence of water (9.2 cm of settlement was observed for the sensor T1 placed on the biocofra once it was dissolved).
- The settlement was evolving in a homogeneous way across the different layers of soil, indicating that a punching shear was taking place at the RI. After the dissolution of the biocofra, the final settlement was around 20 cm.

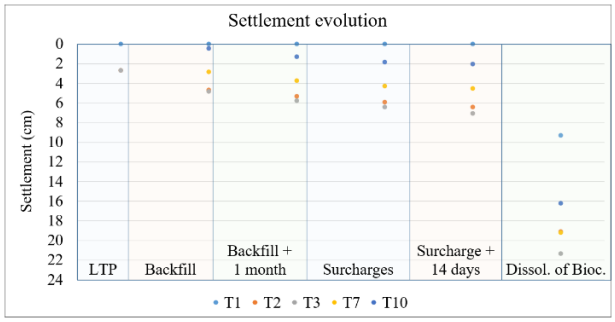

Figure 7. Settlement evolution.

3.3 LTP behaviour

To study the behaviour of the treated platform, the stress measured on the LTP is presented in function of the settlement in Figure 8.

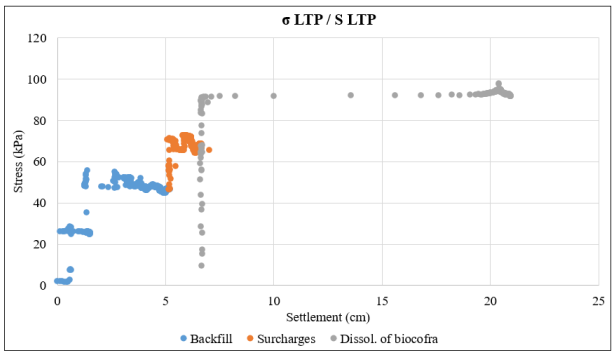

Figure 8. LTP behaviour.

We can clearly see that when the embankment was laid, the stress increases on the treated platform and then, during the 1 month's wait, it is the settlement that increases for a constant stress. This indicates that a punching shear is taking place at the LTP, and the platform is behaving like a slab that settles uniformly and homogeneously. This phenomenon was repeated when the loads were added and during the dissolution of the biocofra. However, we noticed that when the biocofra was dissolved, the stress drops suddenly to 0 due to the rupture within the treated platform, before going back up due to the fact that the embankment and the loads are now resting entirely on the LTP. After the failure of the LTP, we have a total settlement of 20 cm.

3.4 Failure mechanisms

Based on the stress and the settlement evolutions and the behaviour of the treated LTP, we concluded that the failure of the platform was caused by a punching shear that took place at the RI, with a total settlement of 20 cm.

Figure 9 shows the initial and the final state of the LTP. There was a 10 cm crush at the heads of the RI, with the surrounding soil settling by 20 cm as already measured.

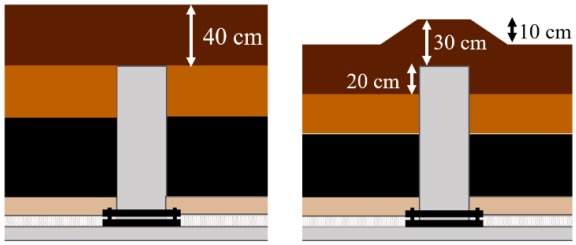

Figure 9. Initial and final state of the treated LTP.

The failure mechanisms were visually validated after disassembling the setup. The punching shear and the settlement are presented in the figure 10 below.

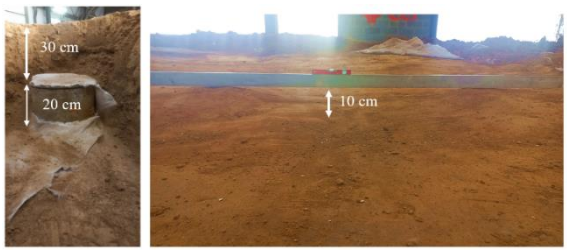

Figure 10. Failure of the platform.

4 CONCLUSIONS

As part of the national ASIRI+ project, a study of the behaviour of treated load transfer platform has been planned. This study aims to improve the understanding of load transfer mechanisms in treated platforms. A full-scale test was carried out to test the efficiency of treated LTP and the following conclusions were formed:

- Treated LTP was properly installed and controlled during the test.
- Experimental protocol was validated (good functioning of sensors, load transfer, dissolution of biocofra …)
- Load transfer was immediate for the treated LTP.
- Treated platform behaved like a slab.
- Punching shear failure has occurred in the treated platform.

Numerical modelling is underway to better understand the load transfer mechanisms in the treated LTP. A second test will also be carried out with some modifications:

- A 10cm treated working platform will be added under the LTP to homogenize the compaction and reduce the punching shear effects.
- A gammadensimeter will be used to control the density of the treated platform throughout the test.

ACKNOWLEDGMENTS

This work was carried out as part of the national ASIRI+ project. The authors would like to thank all the members of this project for their support.

REFERENCES

ASIRI (2012), Recommandations pour le dimensionnement, l'exécution et le contrôle de l'amélioration des sols de fondation par inclusions rigides, Presses des ponts, Paris.

Briancon, L., Simon, B. and Thorel, L. (2020), "Le projet ASIRI+: Amélioration et Renforcement des Sols par Inclusions RIgides", JNGG2020, p. 8, doi: https://hal.archives-ouvertes.fr/hal-03200347.

Girout, R., Blanc, M. and Thorel, L. (2013), "Apport des géosynthétiques dans le renforcement par inclusions rigides des sols compressibles", p. 11, doi: https://www.researchgate.net/publication/275654918.

GTR. (2023), Guide Des Terrassements, Des Remblais et Des Couches de Forme, GTR.

GTS. (2000), Guide Technique Traitement Des Sols à La Chaux et/Ou Aux Liants Hydrauliques - Application En Remblais et Couches de Forme – SETRA / LCPC, 2000.

Terqueux, C., Briancon, L., Delmas, P., Jacqueline, D., Racinais, J., Pantet, A. and Gotteland, P. (2022), "Renforcement d'un sol compressible par inclusions rigides: étude des transferts de charge au sein de la plateforme granulaire renforcée par des géosynthétiques", JNGG2022, doi: https://hal.archives-ouvertes.fr/hal-03720103.

Proceedings of the XVIII ECSMGE 2024
GEOTECHNICAL ENGINEERING CHALLENGES
TO MEET CURRENT AND EMERGING NEEDS OF SOCIETY
© 2024 the Authors
ISBN 978-1-032-54816-6
DOI 10.1201/9781003431749-470
Open Access: www.taylorfrancis.com, CC BY-NC-ND 4.0 license

ECSMGE 24
XVIII EUROPEAN CONFERENCE ON SOIL MECHANICS AND GEOTECHNICAL ENGINEERING

Comparison of the effects of different additives on the improvement of physical and mechanical properties of clayey soil

Comparaison des effets de différents additifs sur l'amélioration des propriétés physiques et mécaniques des sols argileux

N. Marinković*, E. Zlatanović, Z. Bonić, N. Romić, D. Cvetković, B. Stanković
Faculty of Civil Engineering and Architecture, University of Niš, Serbia

nemanja.marinkovic@gaf.ni.ac.rs

ABSTRACT: Bearing in mind that fine-grained clayey soils are the most sensitive to changes in moisture content, the paper presents the results of testing the effects of chemical stabilisation of clayey soils by considering a variety of chemical additives. In addition to the previously known chemical stabilisers, such as calcium carbonate and magnesium carbonate, less frequently used materials such as sodium silicate and potassium hydroxide were also considered. For each of the considered chemical stabilisers mixing was performed with three different percentages of a share of a stabiliser in the mixture with clay, in order to determine the optimal amount of a stabiliser in the mixture. Furthermore, with an aim to evaluate the durability and permanence of the effect of clay stabilisation, which is of crucial importance in geotechnical engineering, changes in the physical and mechanical properties of the treated clay were also determined in four different time intervals after the chemical treatment. Based on the results of this research, it can be concluded that different chemical stabilisers have different effects on the physical and mechanical properties of clayey soil, such as Atterberg limits and uniaxial compressive strength. The general conclusion is that the physical and mechanical properties of clayey soil can be significantly improved by applying chemical stabilisers, which opens up the possibility of applying the technique of chemical soil stabilisation in solving numerous geotechnical problems.

RÉSUMÉ: Considérant que les sols argileux fins sont les plus sensibles aux changements de teneur en eau, l'article présente les résultats des essais sur les effets de la stabilisation chimique des sols argileux en considérant divers additifs chimiques. En plus des stabilisateurs chimiques déjà connus, tels que le carbonate de calcium et le carbonate de magnésium, des matériaux moins fréquemment utilisés ont également été pris en compte, tels que le silicate de sodium et l'hydroxyde de potassium. Pour chacun des stabilisateurs chimiques considérés, le mélange a été réalisé avec trois pourcentages différents de la part du stabilisateur dans le mélange avec l'argile, afin de déterminer la quantité optimale de stabilisateur dans le mélange. De plus, dans le but d'évaluer la durabilité et la permanence de l'effet de la stabilisation de l'argile, ce qui est d'une importance cruciale en génie géotechnique, les changements dans les propriétés physiques et mécaniques de l'argile traitée ont également été déterminés à quatre intervalles de temps différents après le traitement chimique. Sur la base des résultats de cette recherche, on peut conclure que différents stabilisateurs chimiques ont des effets différents sur les propriétés physiques et mécaniques du sol argileux, tels que les limites d'Atterberg et la résistance à la compression uniaxiale. La conclusion générale est que les propriétés physiques et mécaniques du sol argileux peuvent être significativement améliorées en appliquant des stabilisateurs chimiques, ce qui ouvre la possibilité d'appliquer la technique de stabilisation chimique des sols pour résoudre de nombreux problèmes géotechniques.

Keywords: Chemical stabilisation; clayey soil; additives; uniaxial compressive strength; Atterberg limits.

1 INTRODUCTION

Clayey soils are a challenge in the construction industry due to their characteristics, caused by the mineral composition of clay and its water content, which make them prone to cracking or swelling. They are characterised by low bearing capacity, high compressibility, and high sensitivity to moisture content. Due to these facts, these soils in their natural state are not suitable for direct application in construction projects. In such cases, it is necessary to apply soil stabilisation and improvement procedures in order to meet the minimum requirements regarding the bearing capacity and quality of the soil. In an effort to make clayey soils more suitable for construction purposes, a number of techniques have been developed and numerous materials (stabilisers, reagents, additives) have been used for their

stabilisation. One of the most common techniques is chemical soil stabilisation, which is in the focus of this research.

Chemical soil stabilisation is an engineering technique that has evolved throughout history to enable the construction of safe and durable structures on a variety of soil types. The development of this technique dates back thousands of years, from early attempts to use materials such as lime and ash to improve soil characteristics. The ancient Greeks and Romans used lime to stabilise the soil, which was the forerunner of contemporary methods (Han, 2015).

Nowadays, researchers and engineers continue to improve methods of chemical soil stabilisation. Advanced research in the field of analysis and testing enables a more precise approach to soil stabilisation problems. In addition, environmental-friendly additives and materials are being examined in order to reduce the impact on the environment. Chemical stabilisation is an approach that seeks to improve the engineering and physical properties of weak soil by adding soil stabilisers or other binding additives. The effect of an additive can vary depending on the type of soil to which it is applied. Chemical treatment is predominantly used to improve the properties of fine-grained clayey soils, since these types of soils are highly susceptible to high water content (Marinkovic et al., 2021).

Soil stabilisers can be categorised into two groups. The first group includes materials that are commonly used in construction industry, such as cement, lime, fly ash, and bituminous products. In practice, in over 80% of cases, these materials are most often used for soil stabilisation (Onyelowe and Okafor, 2012). These additives have a long history of application and they are proven to be effective in improving soil properties. The second group includes chemical reagents that do not have a commercial use in geotechnics, and studies on their effects on the soil properties are current all over the world. These stabilisers provide flexibility and customisation, allowing engineers to adjust their approach to specific project needs and local soil characteristics. The application of new chemical stabilisers has opened up new possibilities for solving the challenges posed by clayey soils, offering more sustainable and cost-effective solutions for construction industry projects.

Reactions between the stabiliser and the clay occur through two distinct processes: the process of rapid ion exchange reactions, known as soil modification, and the process of slower pozzolanic reactions, known as soil stabilisation or hardening (Maaitah, 2012).

In the present research, in addition to the previously known chemical stabilisers, such as lime (calcium carbonate) and magnesium carbonate, less commonly used materials such as sodium silicate and potassium hydroxide were also considered. Soil modification was evaluated by monitoring changes in Atterberg limits and uniaxial compressive strength (UCS) during chemical stabilisation. With an aim of determining the optimal amount of a chemical stabiliser in the mixture, for each of the considered stabilisers clay samples were treated with 3%, 5%, and 7% of a share of a stabiliser in the mixture with clay (in relation to the dry weight of the soil sample). After the chemical treatment, for each of the considered stabilisers samples were tested at time intervals of 3, 7, 14, and 28 days.

2 MATERIALS AND METHODS

Clayey soil from the Crvena Reka borrow pit, along the route of the E-80 Niš–Dimitrovgrad Highway in the south-eastern part of the Republic of Serbia, was used for the tests. During the construction of the Highway, a landslide was triggered at this location. The designed remediation measures included a support structure in the form of a curtain of piles. Samples of clayey soil for the laboratory tests were taken during the construction of bored piles, from the depth at which the sliding surface was registered.

2.1 Properties of soil

The basic characteristics of the natural soil material are shown in Table 1.

In order to evaluate the effects of chemical stabilisation of the clayey soil by considering a variety of additives, changes in Atterberg limits (Liquid Limit - LL and Plastic Limit - PL) and the associated Plasticity Index - PI, as well as uniaxial compressive strength (UCS), were monitored. The tests were carried out in the Laboratory for Geotechnics at the Faculty of Civil Engineering and Architecture of University of Niš (Serbia).

2.2 Properties of additives

One of the most widely used materials for soil stabilisation is *lime (calcium carbonate) - $Ca(OH)_2$*. This naturally occurring mineral, often found in the form of limestone, has been used for decades in various construction industry projects. Lime is a versatile and cost-effective solution, primarily due to its neutralising effect on soil acidity. When added to acidic soils, lime reacts with the acidic compounds, increasing the soil pH value and improving its engineering properties.

Table 1. Properties of the clayey soil used in the research.

Property	Symbol (unit)	Value
Particle Density	Gs (1)	2.705
Liquid Limit	LL (%)	49
Plastic Limit	PL (%)	23
Plasticity Index	PI (%)	26
Grain Size Distribution	Gravel (%)	1.2
	Sand (%)	4.9
	Silt (%)	40.6
	Clay (%)	53.3
Coefficient of Uniformity	Cu (1)	8.0
Coefficient of Curvature	Cc (1)	2.0
Soil Classification	USCS Symbol	CI
Maximum Dry Density	MDD (g/cm^3)	1.903
Optimum Moisture Content	OMC (%)	18.5
Uniaxial Compressive Strength	UCS (kPa)	2.05

This stabiliser also stimulates the flocculation of soil particles, thus reducing the soil swelling potential and enhancing the soil shear strength. According to Bell (1996), all types of clay minerals react with lime. In addition, the most suitable for stabilisation with lime is clayey soil of medium to high plasticity, where PI > 15%.

While lime remains a standard choice for soil stabilisation, several less common materials have demonstrated soil stabilising potential in specific applications.

Magnesium carbonate ($MgCO_3$) represents a viable option for improving the physical and mechanical soil properties, particularly for soils with a high clay or silt content. This additive has been shown to be effective in increasing the cohesion, reducing the plasticity, and enhancing the load-bearing capacity of the treated soil (Yi et al., 2013).

Sodium silicate (Na_2SiO_3), also known as *water glass*, has been used for soil stabilisation in specific conditions. It contributes to reducing the permeability and improving the cohesion of fine-grained soils. Sodium silicate forms chemical bonds with soil particles, reducing their susceptibility to moisture-induced expansion and contraction. A research of Pakir et al. (2015) indicated the successful application of this additive for improving the properties of marine clay.

Potassium hydroxide (KOH) is a highly alkaline substance that can be utilised for soil stabilisation in certain conditions. It is particularly effective for improving the bearing capacity and compactness of clayey soils. The addition of potassium hydroxide initiates reactions that enhance the soil strength and reduce its sensitivity to changes in moisture content.

2.3 Methods

The *uniaxial compressive strength (UCS*) *test* was applied to all specimens according to the standard SRPS EN 13286-41:2022 (ISS, 2022). Each sample had been compressed until peak load was achieved, where the applied load was recorded by a data acquisition system. The UCS test was used to determine the compressive strength of soil in natural conditions and chemically treated soil for each of the four considered stabilisers. The result represents the average value of three tested samples.

The *testing of Atterberg limits* was performed according to the standard SRPS EN ISO 14688-2:2018 (ISS, 2018). The samples were dried, crushed, and sieved through a 425 μm sieve and mixed with different reagent contents to determine the effect of each on the change in values of LL, PL, and PI.

3 RESULTS AND DISCUSSION

The aforementioned tests were performed on clayey soil samples, taking into account different amounts of each of the considered stabilisers (3%, 5%, and 7%), as well as different curing periods, specifically at 3, 7, 14, and 28 days after the chemical treatment.

3.1 Uniaxial Compressive Strength (UCS)

Figure 1 provides an overview of the UCS test results of the treated soil, for each of the used chemical stabilisers: lime, magnesium carbonate, sodium silicate, and potassium hydroxide. Each result represents the mean value of three tested samples for each of the used stabilisers, for each of the considered contents of stabilisers, and for each of the considered time intervals after the chemical treatment.

In general, it is evident that each stabiliser has a beneficial effect on the UCS of the treated soil. It can be observed that the UCS values increased significantly over time as the soil was treated with lime and magnesium carbonate. On the other hand, there was a slight improvement of the UCS values when the soil was treated with sodium silicate and potassium hydroxide.

The highest values of UCS after the treatment were obtained in samples treated with ***lime***. The improvement of UCS with regard to these samples is clearly noticeable with the increase in the percentage of a share of a stabiliser in the mixture with clay. The results showed a particularly significant improvement when the lime content was increased from 3% to 5%, whereas an increase to 7% gave approximately the same results as for the 5% lime content. Regardless of the amount of the added reagent, it was clearly

observed that a remarkable improvement occurred over time. For example, after a curing period of 3 days, the UCS value increased from 2.05 kPa (for natural clay) to 4.35 kPa after the clay treatment with the addition of 3% lime, whereas with the addition of 7% lime an increase to 6.22 kPa was registered. After 28 days, an increase to 8.96 kPa and 11.78 kPa was detected for the addition of 3% and 7% lime, respectively.

The addition of ***magnesium carbonate*** gave similar results as for the lime when the content was 5% and 7%, but only in the first 14 days. After 28 days, however, samples with the addition of magnesium carbonate resulted in approximately 30% lower UCS values when compared to the lime. When the magnesium carbonate content was of 3%, a significant difference was noticed already after 7 days in comparison with the case of lime. Furthermore, as it was the case with the addition of lime, a higher increase in UCS values was observed when the content of magnesium carbonate was increased from 3% to 5%, compared to the increasing the content from 5% to 7%. Thus, after 3 days, the value of UCS was 4.04 kPa with the stabiliser content of 3%, 5.21 kPa with the content of 5%, and 5.91 kPa with the content of 7%. After 28 days, the value of UCS with the addition 3% of the stabiliser was 4.55 kPa, 7.44 kPa with the addition of 5%, whereas the value of UCS with the addition of 7% was 8.03 kPa.

The measured UCS values with the addition of sodium silicate and potassium hydroxide were significantly lower than the values obtained with the addition of lime and magnesium carbonate; however, their application certainly resulted in an increase in soil uniaxial compressive strength.

The maximum UCS value with added ***sodium silicate*** was 3.79 kPa at 5% content after 28 days. The results also indicated that with the addition of 5% sodium silicate slightly higher values of UCS were obtained than with the addition of 7% in the corresponding time intervals.

The samples treated with ***potassium hydroxide*** resulted with the maximum UCS value of 4.83 kPa at 7% content after 14 days. It can also be observed that similar UCS values were obtained after 14 days and after 28 days, regardless of the percentage of added reagent. In contrast to the three previously mentioned stabilisers, a trend of steady increase in UCS values with increasing content of potassium hydroxide was observed for all the considered time intervals. Therefore, further research could focus on the effects of using a higher percentage of potassium hydroxide to determine the optimal reagent content in the clay mixture.

The observed soil strength enhancement during the curing process can be attributed to the formation of a gel-like material with highly binding properties. This material is being formed as a result of the interaction between the soil and the stabilising reagent.

Furthermore, extended duration of curing plays a vital role in enhancing the rate of reaction among the soil particles and the stabiliser. This is primarily due to the amplified positive charge within the mixture, which leads to the repulsion of soil particles and facilitates more effective stabilisation (Latifi et al., 2013).

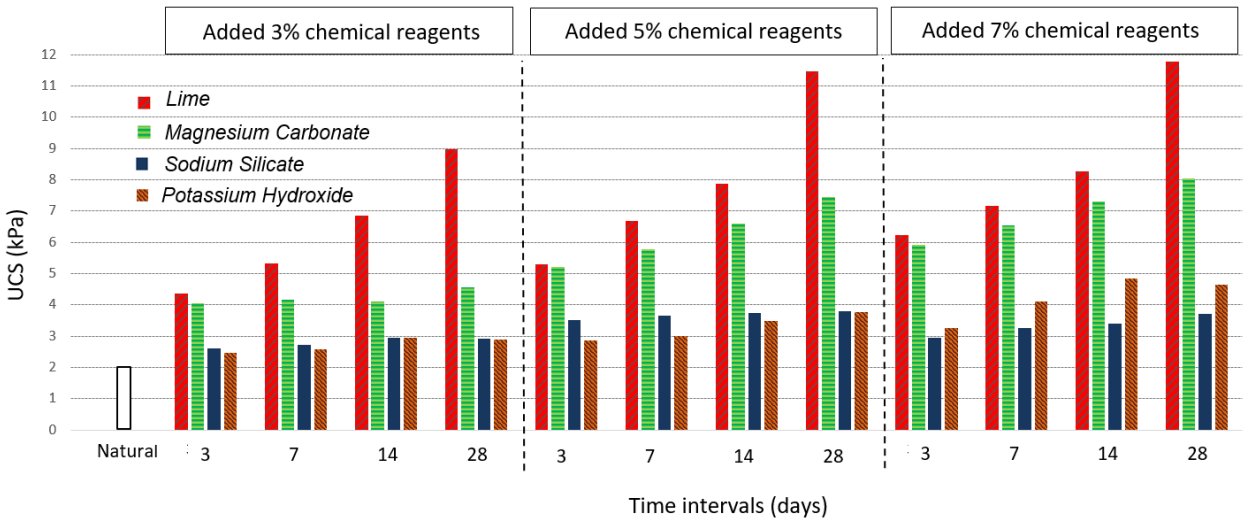

Figure 1. Change in the UCS values of the clayey soil after the chemical stabilisation with different additives.

3.2 Atterberg limits

Table 2 shows the obtained values of consistency limits for clayey soil mixtures with three different percentages of share and at four time intervals after the treatment for each of the four considered stabilisers. For the sake of comparison, it should be noted that the measured values of LL, PL, and PI of the untreated clay (soil in natural conditions) were 49%, 23%, and 26%, respectively (Table 1).

For all the considered stabilisers, the ***LL value*** did not change significantly, either with increasing stabiliser content or over time. Three days after the chemical treatment, a more pronounced increase in LL values was detected only in the samples with the addition of sodium silicate. After 7 days, all tested samples had similar LL values and this trend was also observed in testing after 14 days and 28 days. The highest increase was registered for the case of the addition of 5% magnesium carbonate after 28 days, when the registered LL value was of 54%.

A change in ***PL*** and ***PI values*** was observed in the case of all tested samples over time. A trend of increasing PL values and decreasing PI values over time may be considered positive, since there are no major changes in LL values as stated previously. Such changes indicate the possibility that clay can remain in a semi-solid state of consistency even with a higher water content. The greatest change in PL and PI values occurred after 28 days. The maximum value of PL after 28 days was 37% and was determined for the soil sample with the addition of 5% sodium silicate. The same sample also had the lowest PI value of 12%. All other samples had PI value after 28 days in the range of 17% to 20%, which indicates that the results did not significantly differ from each other regardless of the type of chemical stabiliser.

4 CONCLUSIONS

In this research, a clayey soil of unfavourable physical and mechanical properties in its natural state was examined in laboratory before and after chemical stabilisation, considering a variety of stabilisers, different percentages of stabilisers in the mixture with clay, as well as different time intervals after stabilisation.

The results presented in this paper confirmed that the improvement of soil properties can be successfully achieved by applying lime, magnesium carbonate, sodium silicate, and potassium hydroxide as stabilisers of clayey materials. All the considered stabilisers added to the natural clayey material contributed to a significant increase in the load-bearing capacity of the clay and thus enabled its application for various practical construction purposes.

Modification of the values of Atterberg limits and UCS were tested. From the aspect of these two parameters, the addition of all the considered stabilisers resulted in a significant improvement of the soil properties. The most important findings are:

- It has been proven that lime and magnesium carbonate are the most effective stabilisers, in particular from the aspect of increasing the UCS values of the treated clayey soil.
- After a period of 14 days, the UCS values obtained with regard to both reagents are quite similar, whereas after 28 days, the addition of lime contributes to a significantly better soil improvement.
- Considering both stabilisers, the increase of UCS values is more pronounced with the content increase from 3% to 5% than the increase from 5% to 7%, which indicates that the optimal content in terms of these stabilisers could be considered around 7%.

Table 2. Change in the consistency limits of the clayey soil after the chemical stabilisation with different additives.

Sample	After 3 days			After 7 days			After 14 days			After 28 days		
	LL	PL	PI	LL	PL	PI	LL	PL	PI	LL	PL	PI
	(%)											
Soil + 3% lime	49	25	24	51	28	23	51	31	20	51	34	17
Soil + 5% lime	50	26	24	49	28	21	50	33	17	52	34	18
Soil + 7% lime	50	29	21	52	29	23	52	37	15	53	36	17
Soil + 3% mag. carb.	49	24	25	50	29	21	50	29	21	50	33	17
Soil + 5% mag. carb.	49	25	24	52	30	22	51	32	19	54	34	20
Soil + 7% mag. carb.	48	25	23	51	29	22	52	35	17	52	35	17
Soil + 3% sod. silic.	52	25	27	50	30	20	49	31	18	51	34	17
Soil + 5% sod. silic.	51	28	23	50	32	18	52	36	16	49	37	12
Soil + 7% sod. silic.	53	27	26	53	34	19	51	33	18	53	36	17
Soil + 3% pot. hydrox.	49	24	25	48	28	20	51	30	21	52	32	20
Soil + 5% pot. hydrox.	50	26	24	48	27	21	51	33	18	52	33	19
Soil + 7% pot. hydrox.	51	24	27	51	29	22	50	32	18	51	34	17

- Sodium silicate and potassium hydroxide have a smaller effect on soil strength in comparison with lime and magnesium carbonate; however, they certainly contribute to the improvement in relation to the natural soil properties.
- With the addition of 5% sodium silicate slightly higher UCS values were obtained than with the addition of 7% in the corresponding time intervals. This indicates that the optimal content considering this stabiliser is 5%.
- With the addition of potassium hydroxide, the maximum UCS values were reached after 14 days for all the considered stabiliser contents.
- A trend of constant increase in UCS values with increasing content of potassium hydroxide was observed for all the considered time intervals. Therefore, further research could focus on the effects of using a higher percentage of potassium hydroxide, in order to determine the optimal reagent content in the clay mixture.
- Significant improvement of LL values compared to a natural soil was not achieved with any of the considered stabilising materials, either with increasing stabiliser content or over time.
- On the other hand, each of the considered stabilisers resulted in an increase in PL value, in particular over time, which ultimately contributed to a decrease in PI values over time. Such changes indicate the ability of clay to remain in a semi-solid state of consistency even with a higher water content.

In addition to the significant improvement of soil material properties, lime is also the most cost-effective stabiliser. In comparison with sodium silicate and potassium hydroxide, the cost of using lime as chemical stabiliser is several times lower, whereas compared to magnesium carbonate it is even several tens of times lower.

It should be noted that the results presented in this paper refer to local soil materials. Therefore, there is a necessity for more comprehensive further research, which will include soil samples from a wider area, as a larger number of tests on a greater variety of clayey soil materials will give more reliable results. In addition, in order to meet the requirements of a specific project, site-specific soil testing with the selected stabiliser should be a mandatory part. Current practice shows that in most cases 3% stabiliser content would be quite sufficient; however, a large number of studies in this area, including the one presented, indicate that the optimal amount of additives still depends both on the stabiliser itself and on the composition of the particular type of soil.

ACKNOWLEDGEMENTS

The authors gratefully acknowledge the support of the Science Fund of the Republic of Serbia in the scope of the scientific–research project “A New Concept in Improvement of Geotechnical Properties of Ground – Chemical Electrokinetic Treatment of Soils (ElectroSoil)”, Grant No. 7742530.

REFERENCES

Bell, F. G. (1996). Lime stabilization of clay minerals and soils, *Engineering Geology*, 42(4), pp. 223-237. http://doi.org/10.1016/0013-7952(96)00028-2.

Han, J. (2015). *Principles and practice of ground improvement,* John Wiley & Sons, Hoboken, New Jersey, USA.

ISS - Institute for Standardization of Serbia (2022). SRPS EN 13286-41:2022 Unbound and hydraulically bound mixtures - Part 41: Test method for the determination of the compressive strength of hydraulically bound mixtures, Belgrade.

ISS - Institute for Standardization of Serbia (2018). SRPS EN ISO 14688-2:2018 Geotechnical investigation and testing - Identification and classification of soil - Part 2: Principles for a classification, Belgrade.

Latifi, N., Eisazadeh, A., Marto, A. (2013). Strength behavior and microstructural characteristics of tropical laterite soil treated with sodium silicate-based liquid stabilizer, *Environmental Earth Sciences*, 72(1), pp. 91-98, http://doi.org/10.1007/s12665-013-2939-1.

Maaitah, O. N. (2012). Soil stabilization by chemical agent, *Geotechnical and Geological Engineering*, 30(6), pp. 1345-1356, http://doi.org/10.1007/s10706-012-9549-7.

Marinkovic, N., Jovanovski, M., Zlatanovic, E., Bonic, Z., Davidovic, N. (2021). Chemical stabilization of soil using lime as a chemical reagent, *Scientific Journal of Civil Engineering*, 10(1), pp. 37-43, http://doi.org/10.55302/SJCE21102037m.

Onyelowe K. C., Okafor, F. O. (2012). A comparative review of soil modification methods, *ARPN Journal of Earth Sciences*, 1(2), pp. 36-42.

Pakir, F., Marto, A., Mohd Yunus, N. Z., Ahmad Tajudin, S. A., Tan, C. S. (2015). Effect of sodium silicate as liquid based stabilizer on shear strength of marine clay, *Jurnal Teknologi*, 76(2), pp. 45-50, http://doi.org/10.11113/jt.v76.5432.

Yi, Y., Liska, M., Unluer, C., Al-Tabbaa, A. (2013). Carbonating magnesia for soil stabilization, *Canadian Geotechnical Journal*, 50(8), pp. 899-905, http://doi.org/10.1139/cgj-2012-0364.

Proceedings of the XVIII ECSMGE 2024
GEOTECHNICAL ENGINEERING CHALLENGES
TO MEET CURRENT AND EMERGING NEEDS OF SOCIETY
© 2024 the Authors
ISBN 978-1-032-54816-6
DOI 10.1201/9781003431749-471
Open Access: www.taylorfrancis.com, CC BY-NC-ND 4.0 license

ECSMGE 24
XVIII EUROPEAN CONFERENCE ON SOIL MECHANICS AND GEOTECHNICAL ENGINEERING

Lisbon new circular metro line: interconnection section between new line and existing terminus

Nouvelle ligne circulaire du métro de Lisbonne: section d'interconnexion entre la nouvelle ligne et le terminus existant

P. Marques*, C. Martins, C. Fartaria, R. Tomásio, A. Pinto
JETsj, Geotecnia, Lisbon, Portugal

**pmarques@jetsj.com*

ABSTRACT: The new Lisbon metro line will cross a densely urbanized part of the city, connecting Rato station located at one of the hills of the city and Cais do Sodré station at Tagus River right bank. The interconnection between the new line and the existing terminus is located close to the Tagus River bank where the landfill and clayed soft soils rasting over the Miocene bedrock have more than 20m thickness. Given this geotechnical scenario and the constrains related to the densely urbanized area, the cut and cover excavation solutions have been designed to minimize the surrounding ground perturbance and surface settlements. Diaphragm walls braced by steel struts were used to hold a 20m depth excavation. The connection was materialized by the existing wall demolition and the simultaneous construction of a new structural system inside the terminus structure. This intervention included the construction of new reinforced concrete beams and columns with a meticulous construction phasing aligned with the demolition works using as well temporary support systems. The complexity of those works was increased by the constrains inside the terminus where the impact on Metro circulation should be minimized. This paper presents an overall description of the adopted solutions, how they were implemented as well as the monitoring plan that allowed the risk management of those complex works.

RÉSUMÉ: La nouvelle ligne de métro de Lisbonne traversera une partie densément urbanisée de la ville, reliant la station Rato située sur l'une des collines de la ville et la station Cais do Sodré sur la rive droite du Tage. L'interconnexion entre la nouvelle ligne et le terminus existant est située à proximité de la rive du Tage, où la décharge et les sols meubles argileux reposant sur le substratum rocheux du Miocène ont une épaisseur de plus de 20 mètres. Compte tenu de ce scénario géotechnique et des contraintes liées à la zone densément urbanisée, les solutions d'excavation en tranchée couverte ont été conçues pour minimiser les perturbations du sol environnant et les tassements de surface. Des parois diaphragmes contreventées par des étais en acier ont été utilisées pour maintenir une excavation de 20 m de profondeur. La connexion a été matérialisée par la démolition du mur existant et la construction simultanée d'un nouveau système structurel à l'intérieur de la structure du terminus. Cette intervention comprenait la construction de nouvelles poutres et colonnes en béton armé avec un phasage de construction méticuleux aligné sur les travaux de démolition en utilisant également des systèmes de support temporaires. La complexité de ces travaux a été accrue par les contraintes à l'intérieur du terminus où l'impact sur la circulation du métro devait être minimisé. Cet article présente une description générale des solutions adoptées, la manière dont elles ont été mises en œuvre ainsi que le plan de surveillance qui a permis la gestion des risques de ces travaux complexes.

Keywords: Metro; terminus; diaphragm walls; deep excavation.

1 INTRODUCTION

The new Lisbon circular metro line will cross a densely urbanized part of the city, connecting Rato Station, located at one of the hills of the city, and Cais do Sodré Station at the Tagus River right bank. Where the construction of the tunnel section is closer to the river a Cut&Cover method is used.

In the Cais Sodré area, the new metro line intersects the terminus of the existing metro line, and this is one of the points of intersection between the existing and new construction of the new Lisbon metro circular line. This type of connection, associated with geological and geotechnical constraints, existing infrastructures, a dense urban environment, the need for demolition and new construction, required the construction of a diaphragm wall, reinforced concrete framing structure, metal elements, micropile foundations and the use of hydraulic jacks and specific monitoring.

2 AFFECTED BUILDINGS

In the area intercepted by the connection of the new metro line to the existing terminus, the intervention essentially intersects one of Lisbon's busiest streets, Avenida 24 de Julho. Road and rail traffic will be affected, forcing the temporary and phased diversion of these infrastructures (see Figure 1).

Inevitably, this intervention, as already mentioned, intersects the structure at the terminus of the existing metro line. The structure of the existing terminus appeared to be in good condition, and parts of it could continue to be used in the new structural solution.

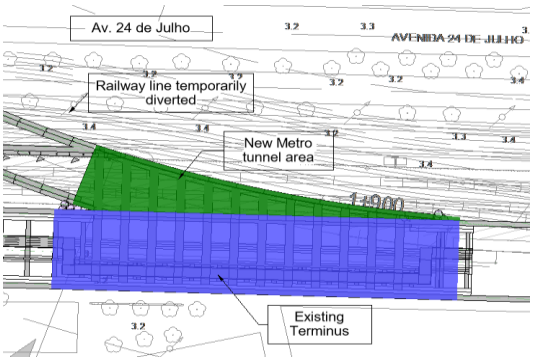

Figure 1. Plan: Layout of the new tunnel and the existing terminus.

3 MAIN CONSTRAINS

3.1 Geological and geotechnical constrains

The geological investigation campaign included the execution of multiple boreholes that allowed the characterization of the ground units along the extension of the Cut&Cover trench on which the intervention is based (see Figure 2). As the line progressed approaching the Tagus River, based on prospecting and geotechnical and geological surveys, it was possible to confirm a progressive increase in the thickness of the materials of recent genesis (landfill and alluvium - essentially sandy type), reaching a thickness of around 17.0m, in parallel with the decrease of the Miocene layer depth overlying the units of the Lisbon Volcanic Complex.

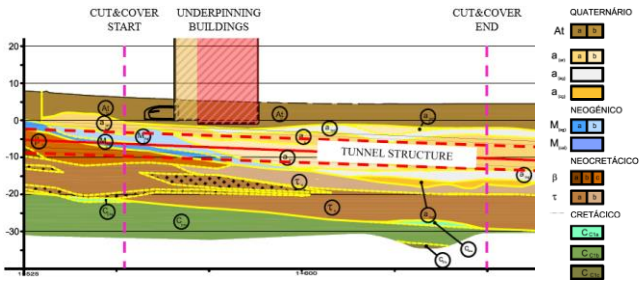

Figure 2. Longitudinal geological section.

It is also worth mentioning that, given the proximity of the Tagus River, the groundwater level was considered to be 1,0m below the surface.

3.2 Constructive technologies constrains

The solutions had to respect the local constraints regarding the accessibility of equipment and material, guarantee the partial operational continuity of the terminus throughout the intervention as well as its opening hours and the deadline for completion of the construction work. It should also be mentioned that the intervention ensured that the embankment over the existing terminus cover slab remained in place throughout the intervention, so as not to further restrict transport infrastructure in the area. Considering the need to work inside the existing terminus, the solutions had to be compatible with equipment and material that could initially be transported in an opening with a width of 2.0m and solutions that could be carried out in a short period of time.

3.3 Demolitions and load transfer procedure

The solution had to guarantee the safe partial demolition of elements of the existing terminus, while preserving the existing conditions above the terminus' roof slab. In this way, it was necessary to implement reinforcement solutions that would allow the demolition of one of the side walls of the terminus, duly reconciled with the other constraints described. Since the embankment over the roof slab of the existing structure and its partial functioning were preserved, to minimize the occurrence of pathologies on the roof and surface, due to differential settlements, the solutions and construction phases had to be compatible with a procedure of controlled load transfer from the existing structural solution to the new structural solution, which was carried out using hydraulic jacks accompanied by monitoring equipment to interpret the behaviour of the systems.

4 SOLUTION DESCRIPTION

The solution adopted consists of executing a diaphragm wall to carry out the excavation in the Cut&Cover trench, provisionally restrained by horizontal metal struts. This excavation solution allowed the demolition work to begin and equipment and materials to enter through the side wall of the existing terminus. Inside the terminus for the demolition phase, porticoed structures made of metal elements were defined, using hydraulic jacks and prestressed bars for provisional stability.

For the final phase of the terminus structure, the work generally consisted of building a new porticoed reinforced concrete structure. Locally, metal columns were used to support the concrete beams and the existing foundations were reinforced with micro-piles. The Figure 3 shows the Cut&Cover excavation solution adopted.

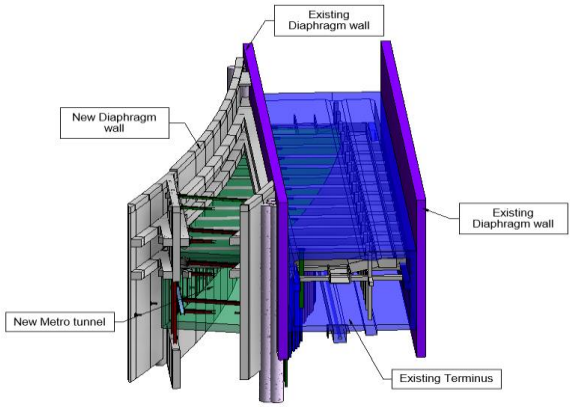

Figure 3. 3D View: Cut&Cover excavation and final structure of the terminus.

4.1 Cut&Cover excavation solution

The Cut&Cover solution was generally composed of an 800mm thick diaphragm wall that was horizontally braced by distribution beams and metal struts, materialised by HEB 400 to 600 profiles. It should also be noted that in this connection area, the existing diaphragm wall was used as a containment for excavation. This existing diaphragm wall had been used 25 years ago to build the structure of the terminus (see Figure 4).

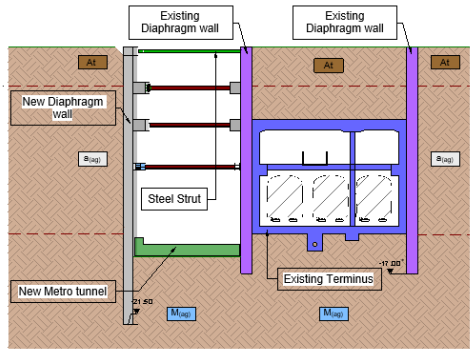

Figure 4. Section: Cut&Cover excavation solution.

4.2 Demolitions and load transfer procedure

For the demolition phase, it was initially decided to make an opening in the side wall of the existing terminus to bring in the equipment and materials needed to carry out the temporary reinforcement. Initially, the connection between the side wall of the existing terminus and the existing diaphragm wall was guaranteed by means of prestressed bars, and then a metal portal with hydraulic jacks at the top was installed along the entire length of the north side wall of the terminus to be demolished (see Figure 5).

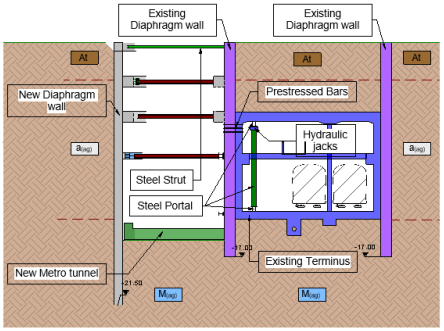

Figure 5. Section: Cut&Cover excavation, demolitions, and load transfer procedure solution.

After some secondary demolition, the existing diaphragm wall and the north side wall of the existing termination were demolished in 4.0 metre strips (see Figure 6).

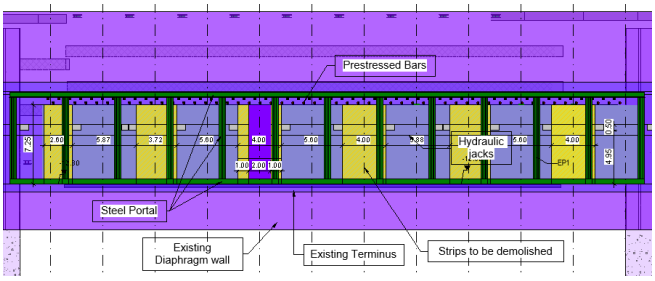

Figure 6. Elevated: Cut&Cover excavation, demolitions, and load transfer procedure solution.

The metal portal was materialised by HEB 500 vertical profiles and two HEB 500 horizontal beams.

Hydraulic jacks were used to ensure a smoother transfer of loads between the existing structure and the new structural solution.

4.3 Final structural solution for terminus

The final structural solution for the terminus consisted of making foundation micropiles on top of the existing floor slab to accommodate the localised load increase of the new solution. A wall beam (VPA) was built over these micropiles to distribute the loads from the new reinforced concrete columns (PB) (see Figure 7 and Figure 8).

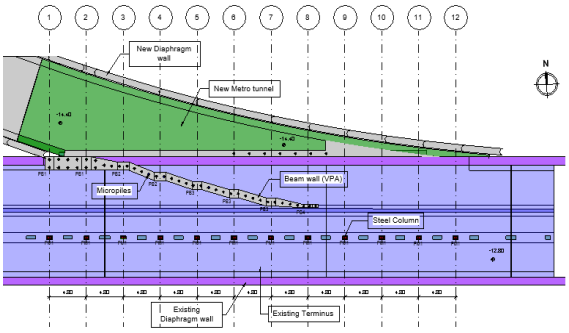

Figure 7. Plan: Foundation of the final solution to the terminus.

Beams (VB1) were built on top of the new columns, running between the south side wall of the existing terminus and the new north side wall of the new line's tunnel. Once the entire new structure was built, demolition of the remaining existing north side wall was completed along the length of the connection between the structures, in order to guarantee the track areas and widths defined in the project.

The structural system described has the capacity to replace the demolished north side wall of the terminus, leaving it with the capacity to support the roof slab and guarantee the correct connection between the new tunnel structure and the existing structure (see Figure 7 and Figure 8).

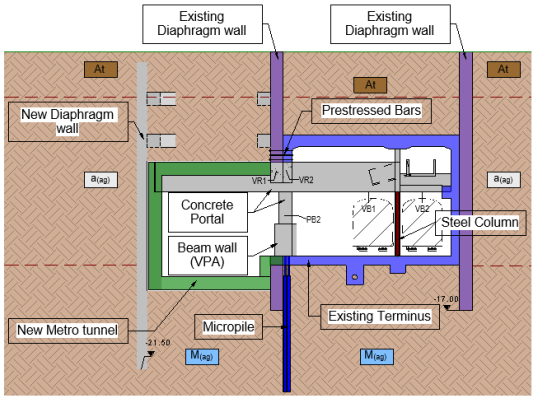

Figure 8. Section: final structural solution for terminus.

5 SOLUTION DESIGN

The temporary diaphragm wall containment was dimensioned using a two-dimensional model in *Plaxis 2D* software. In this model, the diaphragm wall elements were modelled with plates, and the metal struts by anchor elements.

The final structure of the terminus was designed using a three-dimensional model in SAP2000 software. All the walls and slabs were modelled using shell elements, and the beams and columns were modelled using frames. The structural model was vertically braced using compression springs to simulate the foundation soil of the floor slab, and horizontal compression springs to simulate the resistance of the ground (see Figure 9).

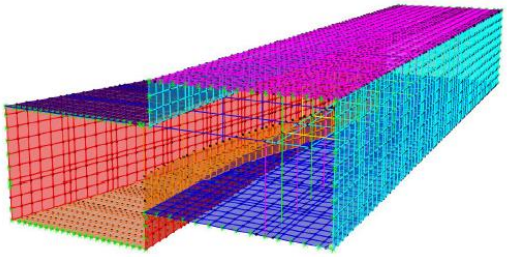

Figure 9. 3D View: Structural model developed in SAP 2000.

This model made it possible to estimate the design forces in the new and existing structural elements.

The model also made it possible to estimate the deformations in the various structural elements of the terminus, considering the new structural solution.

6 MONITORING PLAN

For monitoring the Cut&Cover excavation, traditional elements such as topographic targets, inclinometers and piezometers were used.

In addition to the instruments used in the Cut&Cover excavation, a monitoring plan was installed using liquid level sensors and strain gauges to measure the settlement behaviour of the existing terminus cover slab during the demolition phase.

The monitoring plan establishes alert and alarm values for the limits of each device. With the aim of guaranteeing safety and compliance with the values estimated in the project.

7 FINAL REMARKS

The definition and implementation of a new metro line in a densely urbanised area, on recent soil, with a high water level, with a circular shape and using the structures of the existing metro, leads to areas of connection between new and existing structures, requiring demolition and construction work. For scenarios such as the one presented in this work, based on experience in this type of construction work with these geological-geotechnical conditions and the other constraints mentioned, the solution for carrying out the excavation using a diaphragm wall restrained by metal struts seemed to be the most appropriate for maintaining the integrity of the existing structures and infrastructures. The remaining solution adopted for connecting the new structure to the existing one also

proved to be adequate, guaranteeing all the regulatory safety criteria.

An adequate monitoring and survey plan was essential to confirm the suitability of the solution during excavation work, and also to manage the transfer of loads between the new structural system and the new structural system. the shoring system during excavation work.

ACKNOWLEDGEMENTS

The authors are grateful to the Metropolitano de Lisboa for permission to present this paper.

Proceedings of the XVIII ECSMGE 2024
GEOTECHNICAL ENGINEERING CHALLENGES
TO MEET CURRENT AND EMERGING NEEDS OF SOCIETY
© 2024 the Authors
ISBN 978-1-032-54816-6
DOI 10.1201/9781003431749-472
Open Access: www.taylorfrancis.com, CC BY-NC-ND 4.0 license

ECSMGE 24
XVIII EUROPEAN CONFERENCE ON SOIL MECHANICS AND GEOTECHNICAL ENGINEERING

Application of Machine Learning algorithms to drilling data for deep foundations and soil treatments

Application d'algorithmes d'apprentissage automatique aux données de forage pour les fondations profondes et les traitements de sol

E. Martínez García*
Menard España/Departamento de Ingeniería Civil: Construcción, E.T.S de Ingenieros de Caminos, Canales y Puertos, Universidad Politécnica de Madrid, Madrid, Spain

M. García Alberti
Departamento de Ingeniería Civil: Construcción, E.T.S de Ingenieros de Caminos, Canales y Puertos, Universidad Politécnica de Madrid, Madrid, Spain

A.A. Arcos Álvarez
Departamento de Ingeniería y Morfología del Terreno, E.T.S de Ingenieros de Caminos, Canales y Puertos, Universidad Politécnica de Madrid, Spain

emartinez@menard.es

ABSTRACT: Modern machinery for executing deep foundations and soil treatments is equipped with sensors that allow the measurement of execution parameters such as torque, thrust, and speed (Measurement While Drilling, MWD). These parameters are related to soil characteristics and, by using machine learning (ML) algorithms, it is possible to translate them into a penetrometric soil profile. Therefore, each perforation can provide analogous information of that obtained from a penetrometer. However, in order to apply these algorithms in the specific case of pile drilling and soil treatment, several factors must be considered in both ML techniques and specific to geotechnics. These factors include the presence of anomalous values in the data, the distance between the penetrometers and the drilling points or the selection of the most appropriate algorithms, among others. This paper proposes a specific methodology that outlines the various steps required in order to apply ML algorithms to drilling data for deep foundations and ground treatments.

RÉSUMÉ: Les machines modernes pour l'exécution de fondations profondes et de traitements du sol sont équipées de capteurs qui permettent de mesurer les paramètres d'exécution tels que le couple, la poussée et la vitesse (Measurement While Drilling, MWD). Ces paramètres sont liés aux caractéristiques du sol et, en utilisant des algorithmes d'apprentissage automatique (ML), il est possible de les traduire en un profil penétrométrique du sol. Ainsi, chaque perforation peut fournir une information équivalente à celle d'un pénétromètre. Cependant, afin d'appliquer ces algorithmes dans le cas particulier du forage de pieux et du traitement des sols, plusieurs facteurs doivent être considérés à la fois généraux à ML et spécifiques à la géotechnique. Ces facteurs incluent la présence de valeurs anormales dans les données, la distance entre les pénétromètres et les points de forage, les algorithmes les plus appropriés, entre autres. Cet article propose une méthodologie spécifique qui décrit les différentes étapes nécessaires pour appliquer les algorithmes ML aux données de forage pour les fondations profondes et les traitements de sol.

Keywords: Machine learning; measurement while drilling; penetrometer; rigid inclusions.

1 INTRODUCTION

Machine Learning (ML) can be defined as the extraction of information from large data sets by using mathematical algorithms applied by computers. One of the advantages of this approach is its ability to reveal hidden relationships between variables that are difficult to observe otherwise.

Geotechnical engineering is a field characterized by complex and often empirical relationships between variables, making it an ideal domain for the application of ML. Consequently, ML has gained increasing attention in recent years, leading to the establishment of a dedicated Technical Committee, TC309, by the International Society for Soil Mechanics and Geotechnical Engineering (ISSMGE, 2022).

There are numerous applications of ML in geoscience, including soil and rock classification, soil stratification, settlement analysis, bearing capacity

estimation, slope stability assessment, dam monitoring, and more (Liu and Lacasse, 2022).

The objective of this paper is to show how to apply ML to correlate drilling data from deep foundations and soil treatments with the values of penetrometers.

2 PENETROMETERS

The penetrometer is a soil investigation technique that measures the resistance to perforation by using a standardized cone. There are two main types of penetrometers: static and dynamic (CEN, 2008; ISO/TC 182 Geotechnics, 2012). An example of the output of a penetrometer can be seen in Figure 1.

One advantage of penetrometers is their ability to provide continuous information along their length. As a result, they are well-suited for correlation with drilling parameters.

3 MEASUREMENT WHILE DRILLING

Measurement While Drilling (MWD) refers to the continuous collection of data during the drilling process. Modern geotechnical machinery and equipment are equipped with ample instrumentation that enables the measurement of various drilling parameters, including drilling speed, rotary torque, rotary speed, and applied crowd.

These parameters should be correlated with the characteristics of the soil being traversed, and several authors have developed compound parameters to establish these relationships (Laudanski et al, 2012). There is a standard specific to MWD (CEN, 2016) that primarily focuses on boreholes but can also be applied to geotechnical equipment.

Instead of relying on compound parameters, an alternative approach is to utilize ML to correlate the drilling feedback at a certain depth with the previous penetrometer value at the same level.

4 DATA FORMAT

The information obtained from penetrometers and drilling can be provided in various formats or, in some cases, without any specific format. Therefore, to effectively utilize ML, it is recommended to standardize all the information into a consistent format.

For geotechnical data, a suitable option is to employ the AGS format (Association of Geotechnical & Geoenvironmental Specialists, 2023a). This format can be easily converted and utilized with a dedicated library (Association of Geotechnical & Geoenvironmental Specialists, 2023b).

5 DATA PREPROCESSING

Data preparation and cleaning are crucial steps when using ML algorithms, which include handling missing values. Additionally, it is essential to detect outliers, as this is a common task in all ML problems. However, the criteria for identifying outliers can vary depending on the specific case.

5.1 Penetrometers outlier detection

An approach to identify outliers could be the distance from the mean value. But this is not possible due to the difference in nature of soil layers. A value of 15 blows could be an outlier at depth 4 m, but no at a depth of 10 m (Figure 1).

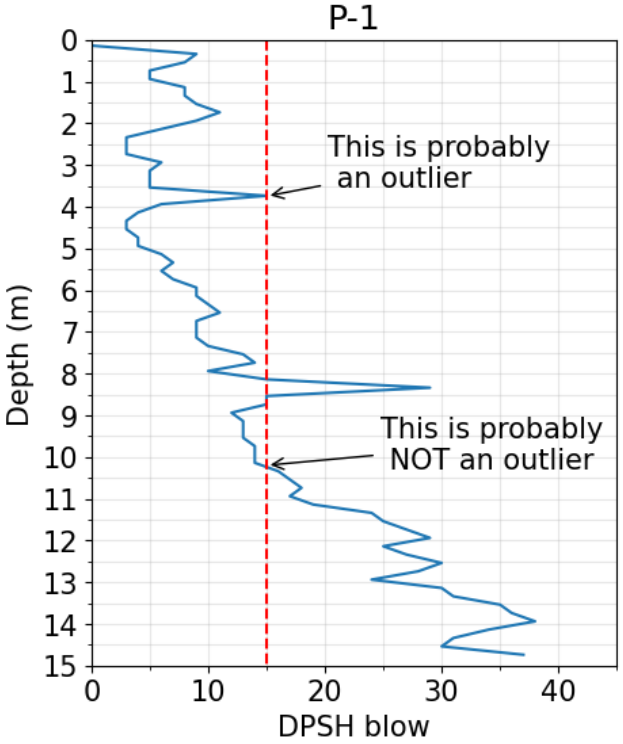

Figure 1. Example of a DPSH penetrometer output.

To assess this issue, a moving average of the penetrometer can be used, with a window that depends on the desired level of smoothness. It is very difficult to know if a strange value in the penetrometers is an outlier (i.e. the presence of some gravels) or a true soil condition. Using a moving average allow to keep the value while softening the profile.

5.2 Drilling data outlier detection

In the case of the drilling data, the detection of outlier becomes more complicated as is a multivariate

problem. A high value of one parameter can be normal or not depending on the values of the other parameters.

For this problem, a specific outlier detection, such as isolation forest (Liu et al, 2008), can be used. Isolation forest classifies outliers by how difficult the sample is to isolate, with easier to isolate meaning more probability to be an outlier.

5.3 Data labelling

To correlate the drilling data to the penetrometric profile, a value of it should be assigned to each sample of the data. This could seem easy enough: assign the value from the closer penetrometer as the proper level.

But the closer penetrometer could be quite far. In fact, these correlations are interesting because the geotechnical data are usually scarce. In Figure 2, inclusions 1 and 2 are closer to the penetrometer P1. At inclusion 1 there is a small error, but at inclusion 2 the error is much greater due to distance and changes in the soil.

To address this problem, Bunieski (2022) proposed two different methods. The variability method establishes a maximum distance where the error is considered acceptable. The continuous method uses the mean value of close penetrometers but establishing and information level depending on distance. Points with low information are discarded. Both methods consider how the soil profile changes in the available penetrometers.

6 CHOOSE ML ALGORITHM

The selection of the algorithm to be used is very case dependent. Some of them need some preprocessing of the data for being used (for example a normalization of the values). Others can avoid preprocessing but would benefit from previously applied algorithms. On top on that, the hyperparameters that control the process should be tuned for each problem, greatly affecting the performance.

As can be seen, finding the most adequate approach is no easy task.

One possible solution is to use an auto-ML library, such as TPOT (Olson et al., 2016), which will suggest the best possible pipelines after a series of iterations.

A disadvantage for this approach is that it can be very computationally demanding and time consuming, depending on the data. The number of iterations can be limited, but that will decrease the possibility of reaching the best pipeline.

7 PROPOSED PIPELINE

The proposed pipeline for the use of ML with MWD data is as follows:

- Transform the available information to a consistent data format.
- Data preprocessing.
  - Outlier detection
  - Data labelling (special care to distance)
- Auto-ML and selection of algorithms.
- Evaluation of the obtained results (correlation coefficient, root of mean squared error, etc.)
- Auto-ML and selection of algorithms.
- Evaluation of obtained results (correlation coefficient, root of mean squared error, etc.)

Figure 3 shows the scheme of this process.

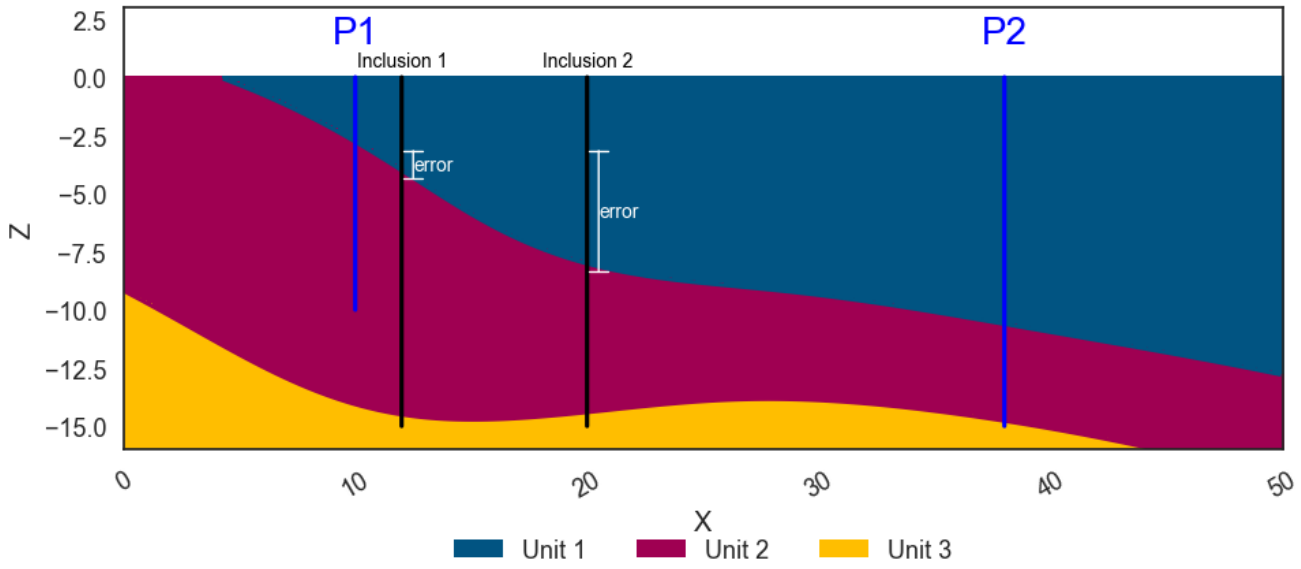

Figure 2. Soil cross section. Error introduced by distance between inclusion and penetrometer.

8 CONCLUSIONS

This paper has highlighted the specific challenges associated with using ML for MWD data, particularly emphasizing the significance of considering the distance between the perforation and penetrometer, as well as the detection of outliers. It is evident that expert knowledge plays a critical role in addressing ML problems, especially in the geotechnical field where it is difficult to account for every variable that may affect the process. But, with the proper pipeline, ML is a very interesting tool to extract information from perforations.

ACKNOWLEDGEMENTS

The authors gratefully acknowledge Menard Spain for supplying the data used in this study.

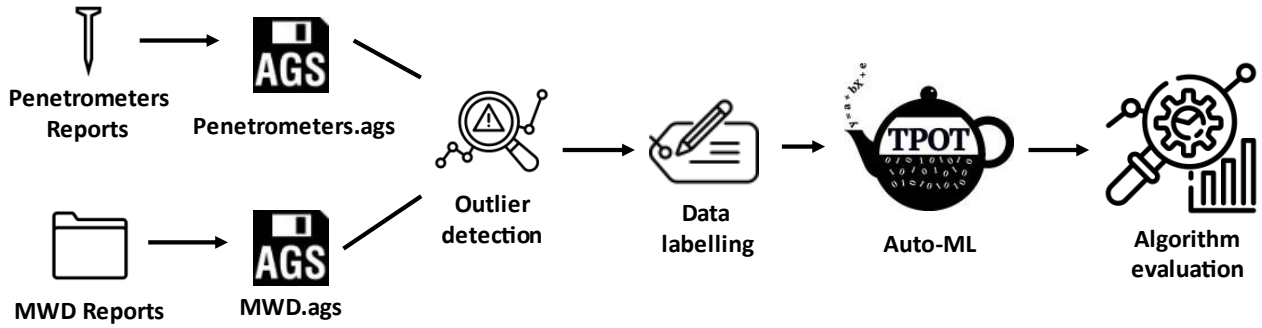

Figure 3. Proposed pipeline.

REFERENCES

Association of Geotechnical & Geoenvironmental Specialists (2023a) *AGS Data Format*. Available at: https://www.ags.org.uk/data-format/.

Association of Geotechnical & Geoenvironmental Specialists (2023b) *AGS Python Library*. Available at: https://gitlab.com/ags-data-format-wg/ags-python-library.

Bunieski, S. (2022) 'Practical methodologies to apply machine learning algorithms to ground improvement data', in.

CEN (2008) 'UNE-EN ISO 22476-2. Investigación y ensayos geotécnicos. Ensayos de campo. Parte 2: Ensayo de penetración dinámica'. AENOR.

CEN (2016) 'UNE-EN ISO 22476-15. Investigación y ensayos geotécnicos. Ensayos de campo. Parte 15: Registro de parámetros de perforación'. AENOR.

ISO/TC 182 Geotechnics (2012) 'Geotechnical investigation and testing. Field testing. Part 1: Electrical cone and piezocone penetration test (ISO 22476-1:2012)'.

ISSMGE (2022) *Reference List for Machine Learning and its Applications in Geotechnical Engineering*. Available at: https://www.issmge.org/news/reference-list-for-machine-learning-and-its-applications-in-geotechnical-engineering-part-i-need-to-know-knowledge0 (Accessed: 25 June 2022).

Laudanski, G., Reiffsteck, J.-L. and Benoît, J. (2012) 'Experimental study of drilling parameters using a test embankment', in. *Geotechnical and Geophysical Site Characterization 4*.

Liu, F.T., Ting, K.M. and Zhou, Z.-H. (2008) 'Isolation Forest', in *2008 Eighth IEEE International Conference on Data Mining. 2008 Eighth IEEE International Conference on Data Mining (ICDM)*, Pisa, Italy: IEEE, pp. 413–422. Available at: https://doi.org/10.1109/ICDM.2008.17.

Liu, Z. and Lacasse, S. (2022) 'Machine learning in geotechnical engineering: Opportunities and applications', in M. Rahman and Jaksa Mark (eds) *Proceedings of the 20th ICSMGE-State of the Art and Invited Lectures*. Sydney, Australia: Australian Geomechanics Society, pp. 543–558.

Olson, R.S. *et al.* (2016) 'Evaluation of a Tree-based Pipeline Optimization Tool for Automating Data Science', in *Proceedings of the Genetic and Evolutionary Computation Conference 2016. GECCO '16: Genetic and Evolutionary Computation Conference*, Denver Colorado USA: ACM, pp. 485–492. Available at: https://doi.org/10.1145/2908812.2908918.

Proceedings of the XVIII ECSMGE 2024
GEOTECHNICAL ENGINEERING CHALLENGES
TO MEET CURRENT AND EMERGING NEEDS OF SOCIETY
© 2024 the Authors
ISBN 978-1-032-54816-6
DOI 10.1201/9781003431749-473
Open Access: www.taylorfrancis.com, CC BY-NC-ND 4.0 license

ECSMGE 24
XVIII EUROPEAN CONFERENCE ON SOIL MECHANICS AND GEOTECHNICAL ENGINEERING

Lisbon new circular Metro line: Buildings underpinning

Nouvelle ligne circulaire du métro de Lisbonne: Reprise en sous-œuvre des bâtiments

C. Martins*, C. Fartaria, R. Tomásio, A. Pinto
JETsj, Geotecnia, Lisbon, Portugal

cmartins@jetsj.com

ABSTRACT: The new Lisbon circular metro line will crosses a densely urbanized part of the city, connecting Rato Station located at one of the hills of the city and Cais do Sodré Station, at the Tagus River right bank. The underground excavation intersects a wide range of materials, from rock mass to soft soils. Where the construction of the tunnel section is closer to the river, with about 10 m of cover, a Cut&Cover method is used. In this metro the tunnel intersected a pile foundation of two reinforced concrete buildings with 9 upper floors and 1 basement, determining the need to underpin the structures and change permanently its foundation system. The geotechnical and geological conditions present in this metro, associated to highly limited access and working conditions, led to the execution of the retaining walls using jet-grouting technology. Those elements were also used as the building deep foundations, which consists of a reinforced concrete slab (length=50m, width=13m and thicknesses=1.4m and 1.8m), being also responsible for the structure underpinning. In this complex process is defined a controlled load transfer between the structure and the new slab, which was executed using hydraulic jacks, limiting the building differential settlements thought gradual jacks opening and according with monitoring. This paper presents an overall description of the solutions, how they were implemented and the buildings' behaviour during the underground works.

RÉSUMÉ: La nouvelle ligne de métro circulaire de Lisbonne traversera une zone densément urbanisée de la ville, reliant la Station Rato, située sur l'une des collines de la ville, et la Station Cais do Sodré, sur la rive droite du Tage. L'excavation souterraine couvre une large gamme de matériaux, depuis les masses rocheuses jusqu'aux sols meubles. Lorsque la construction du tronçon de tunnel est plus proche de la rivière, avec une profondeur de couverture d'environ 10 m, la méthode de tranchée couverte est utilisée. Dans cette section, la ligne a traversé une fondation sur pieux de deux bâtiments en béton armé de 9 étages supérieurs, ce qui a déterminé la nécessité de soutenir la structure et de modifier de manière permanente son système de fondation. Les conditions géotechniques et géologiques présentes dans ce section, associées à des conditions d'accès et de travail très limitées, ont conduit à la matérialisation de murs de soutènement grâce à la technologie du jet-grouting. Ces éléments ont également servi de nouveau fondations profondes des bâtiments, constitué d'une dalle en béton armé (longueur = 50 m, largeur = 13 m et épaisseurs = 1,4 m et 1,8 m), qui est également chargée de soutenir la structure. Dans ce solution complexe, un transfert de charge contrôlé est défini entre la structure et la nouvelle dalle, qui a été réalisé à l'aide de vérins hydrauliques, limitant les tassements différentiels du bâtiment grâce à l'ouverture progressive des vérins et au contrôle concomitant. Cet article présente une description générale des solutions, de la manière dont elles ont été mises en œuvre et du comportement des bâtiments lors des travaux souterrains.

Keywords: Metro; underpinning; reinforced concrete building; jet-grouting; excavation cut&cover.

1 INTRODUCTION

The new Lisbon circular metro line will cross a densely urbanized part of the city, connecting Rato Station, located at one of the hills of the city, and Cais do Sodré Station at the Tagus River right bank.

Where the construction of the tunnel section is closer to the river a Cut&Cover method is used. In this section the line path intersected a pile foundation of reinforced concrete buildings with 9 upper floors and 1 basement, determining the need to underpin these structures.

The geotechnical and geological conditions in this section, associated to highly limited access and working conditions, led to the execution of retaining walls using jet-grouting technology. Those elements were also used as deep foundations of an reinforced concrete slab with 1.4m and 1.8m tick, built for the structure underpinning.

In this complex process was defined a controlled load transfer between the structure and the new slab, which was executed using hydraulic jacks and specific monitoring to control the buildings differential settlements.

2 AFFECTED BUILDINGS

The metro line tunnel intersets buildings nº 42 and nº 44 at Avenida D. Carlos I. Both buildings were built in the XX century, presenting a reinforced concrete structure and pile foundations. The buildings have 9 elevated floors and 1 basement (see Figure 1).



Figure 1. Reinforced concrete buildings above de tunnel.

Building nº42 was recently subject to rehabilitation works for conversion into residential use. As a result of the changes needed, was designed a reinforcement of both the structure and foundations, the latter with micropiles. Building nº44, on the other hand, is in its original conditions, used for offices, and showing a good state of conservation. In Figure 2 is presented the buildings plan superimposed with the tunnel structure layout, showing the need to underpin several columns over intervention area.

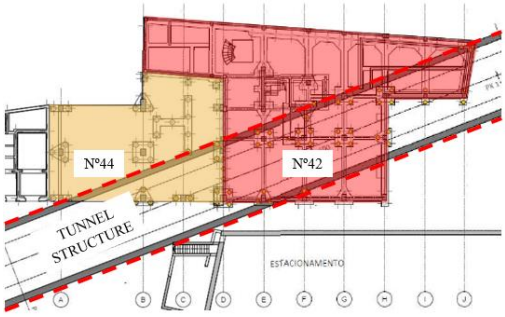

Figure 2. Buildings plan view and tunnel structure projection.

3 MAIN CONSTRAINS

3.1 Geological and geotechnical constrains

The geological investigation campaign included the execution of multiple boreholes that allowed the characterization of the ground units along the extension of the Cut&Cover trench over which the buildings to be underpinned are located (see Figure 3). It was possible to confirm that in the increasing direction of the mileage of the trench, there is a progressive increase in the thickness of recent materials (landfill and alluvium - essentially sandy type) in parallel with the decrease of the Miocene layer depth overlying the units of the Lisbon Volcanic Complex.

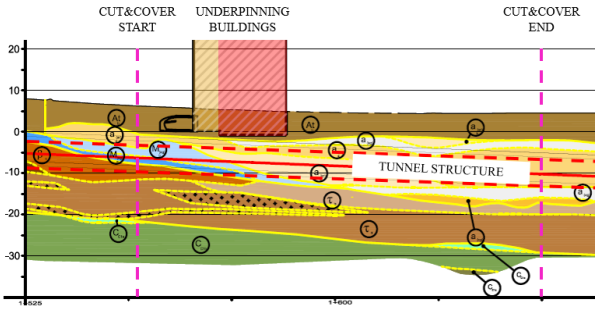

Figure 3. Geological and geotechnical scenario.

3.2 Constructive technologies constrains

The solutions had to respect the local constraints regarding the accessibility of equipment. Considering the need to work inside the building's basements, the solutions had to be compatible with equipment that can operate with a minimal ceiling height of about 3,0m.

3.3 Load transfer procedure

To minimize the occurrence of pathologies in the underpinning buildings, due to differential settlements, the solutions and construction phases had to be compatible with a procedure of controlled load transfer from the buildings to the new foundation system, which was carried out using hydraulic jacks accompanied by monitoring equipment to interpret the behaviour of the buildings and new foundation system.

4 SOLUTION DESCRIPTION

The solution consists of an underpinning system of the buildings columns and pile caps located above the tunnel alignment, which will allow the deactivation of the existing piles and the maintenance of the building's structure functionality and, simultaneously the construction and operation of the new metro tunnel.

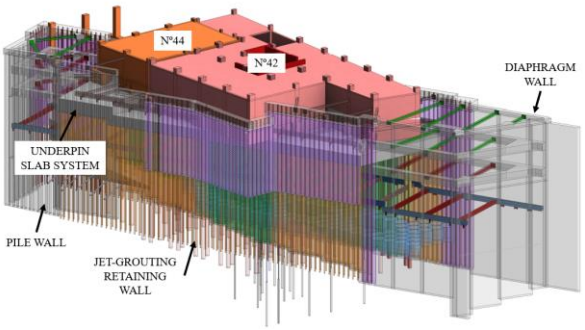

Figure 4. 3D view: Cut&Cover excavation and underpinning solution.

Once the underpinning system had been placed, which is composed of a reinforced concrete slab laterally supported by a double jet-grouting columns curtain wall, the excavation works done inside this curtain and below of the underpinned slab.

4.1 Cut&Cover excavation solution

Since the underpinning solution is connected with the Cut&Cover solution, a brief description is given of, although this is not the focus of this paper.

The Cut&Cover solution was generally composed of a double jet-grouting columns retaining wall with 1000mm diameter columns, spaced 700mm apart, and reinforced with tubular steel profiles, which have a dual function as a foundation of the underpinned slab, as well as retaining the soil and water to allow the excavation required to build the tunnel. In addition to this, and to reach the underpinned slab level, it was executed a third row of jet-grouting columns, also reinforced with steel profiles (Figure 5).

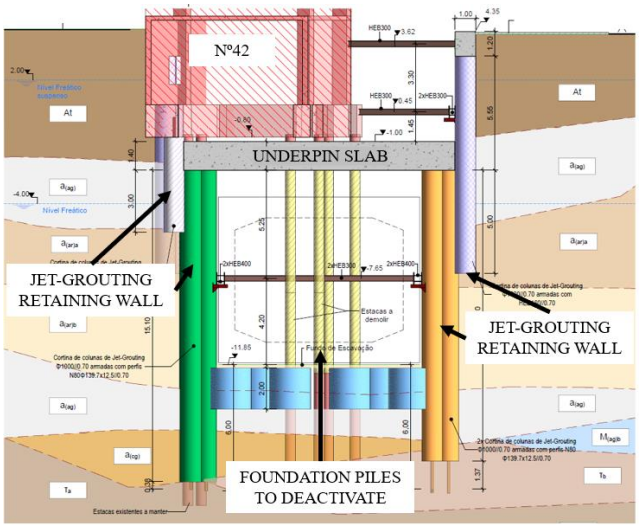

Figure 5. Section: Cut&Cover excavation and underpinning solution.

Finally, the retaining walls were temporary propped each other using four levels of steel struts, 5m apart, resting over steel and reinforced concrete distribution beams. However, in the underpinning area, reinforced concrete slab was used as the third strut level.

4.2 Underpinning solution

The underpinning solution consists of a reinforced concrete slab, not prestressed, supported indirectly on jet-grouting columns, reinforced with steel profiles in order to increase their ductility and stiffness, placed outside the tunnel. The underpinned slab was positioned below the existing pile caps and above the tunnel alignment, with geometry of approximately 50,0m by 13,0m and a variable thickness between 1.40m and 1.80m (see Figure 6).

Taken together, these elements make it possible to change the foundation system of the buildings, transferring the loads from the structural columns to the slab which, basically by cylindrical bending, transmits them to the two rows of jet-grouting columns, which finally transmit the reactions to the competent ground layers located below the bottom slab of the tunnel.

This solution makes it possible to deactivate the piles foundation of the buildings existing over the tunnel area, as well as to proceed with the excavation works to build the new tunnel.

4.3 Load transfer procedure

Hydraulic jacks were used in order to ensure a smoother transfer of loads between the buildings columns and the underpinned reinforced concrete slab, and thus allow for greater control of the settlements occurring in this process. Hydraulic jacks positioned between the underpinned slab and the pile caps, will be responsible for relieving the loads of the foundation piles, using the reaction provided by the slab.

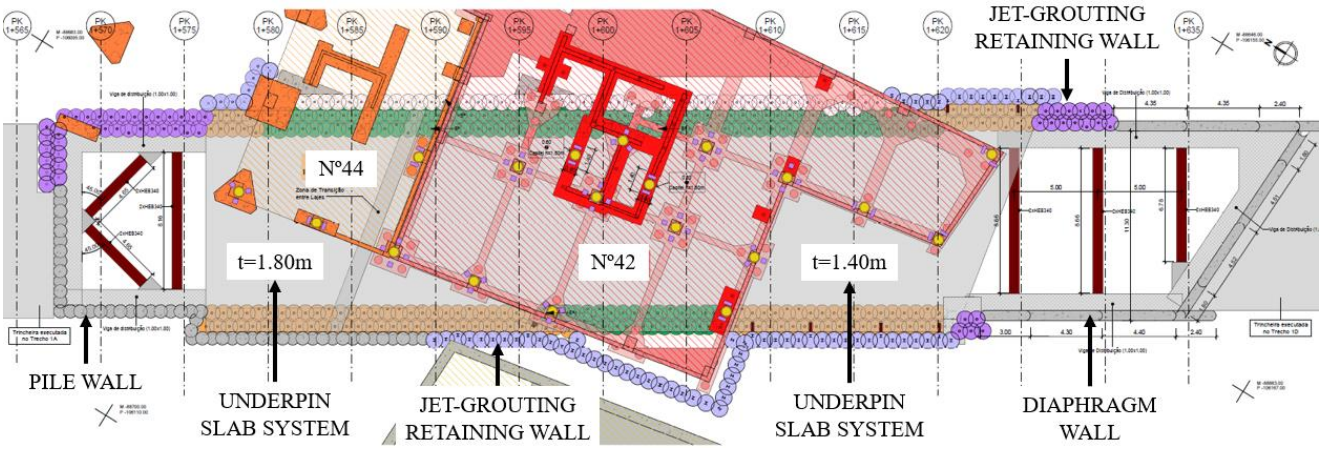

Figure 6. Plan view: Cut&Cover excavation and underpinning solution.

The phases related to the load transfer are summarized below and illustrated in Figure 7:

1. Installation of the instrumentation system at the columns;
2. Excavation to the bottom level of the slab;
3. Sheathing of the piles followed by slab construction and hydraulic jacks installation;
4. Excavation under the slab, followed by hydraulic jacks activation and subsequent existing piles demolition, managed by monitoring data analysis.

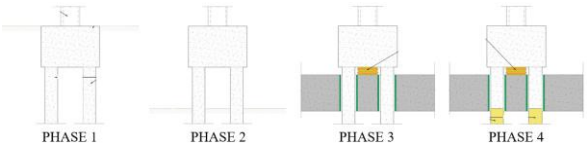

Figure 7. Underpinning solution – Load transfer beams.

5 SOLUTION DESIGN

The underpinning concrete slab was designed using structural models within the *SAP2000* software.

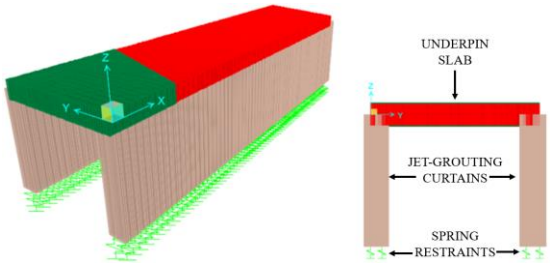

Figure 8. SAP2000 analysis model for underpin slab.

The underpinned slab, as well as the supporting jet-grouting columns, were modelled using shell type elements, and in the case of the latter, these were supported on springs type restraint. This model made it possible to estimate slab structural efforts (see, for example, bending moments in Figure 9) as well as its elastic deformation (see Figure 10).

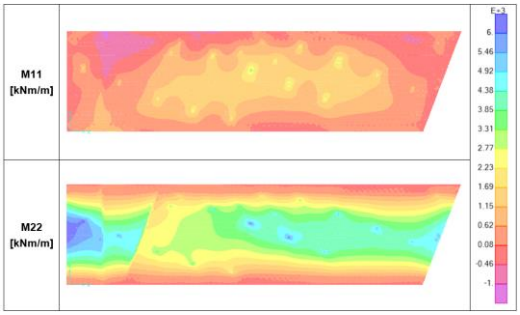

Figure 9. SAP2000 – Underpin slab bending moments.

Considering the support springs on the structural model, was estimated the maximum design axial load on each jet-grouting column, allowing, in parallel analysis with the geotechnical model for Cut&Cover solution, the safety validation of those elements.

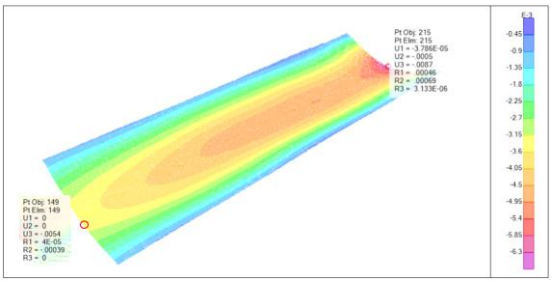

Figure 10. SAP2000 – Underpin slab displacements.

6 MONITORING PLAN

Complementarity, fort the Cut&Cover excavation, a monitoring plan using liquid level sensors and strain gages was installed to measure the settlement behaviour of the slab and columns, as well as the interaction between them (see Figure 11).

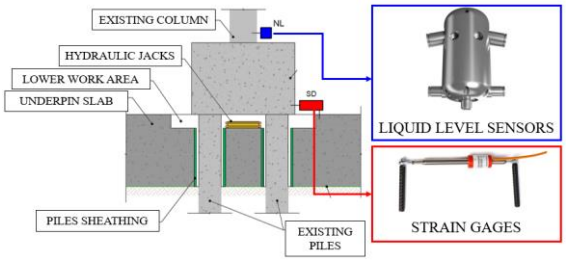

Figure 11. Monitoring devices: liquid level sensors and strain gages

The monitoring plan establishes threshold values for each device. The numerical analyses results were used to determine reference values for measured parameters that were used to set warning values, for 80% of the reference values, and alarm ones, for 120%.

7 FINAL REMARKS

The definition and implementation of a new metro line in a densely urbanized area may lead to interference with existing structures. For scenarios such as the one presented in this paper, an underpinning solution was the most appropriate way to maintain the integrity of the existing structures, although this type of solution often presents multiple restrictions regarding equipment access and operation.

An adequate monitoring and survey plan is essential to manage the load transfer to the underpinning system during the excavation works.

ACKNOWLEDGEMENTS

The authors are grateful to the Metropolitano de Lisboa for permission to present this paper.

Proceedings of the XVIII ECSMGE 2024
GEOTECHNICAL ENGINEERING CHALLENGES
TO MEET CURRENT AND EMERGING NEEDS OF SOCIETY
© 2024 the Authors
ISBN 978-1-032-54816-6
DOI 10.1201/9781003431749-474
Open Access: www.taylorfrancis.com, CC BY-NC-ND 4.0 license

ECSMGE 24
XVIII EUROPEAN CONFERENCE ON SOIL MECHANICS AND GEOTECHNICAL ENGINEERING

Effect of the binder content in a soft stabilized soil unreinforced and reinforced subjected to cyclic loading – energy evaluation

Effet de la teneur en liant dans un sol stabilisé mou non renforcé et renforcé soumis à une charge cyclique - évaluation énergétique

L.A. Martins*, A.A.S. Correia, P.J. Venda Oliveira, L.J. Lemos
University of Coimbra, Coimbra, Portugal

**uc2020142548@student.uc.pt*

ABSTRACT: When a soil is subjected to cyclic loading, there are changes in the behaviour of the material that need to be characterized for a safe design. To this end, a series of unconfined compressive strength (UCS) tests were performed, with and without the application of cyclic loading, to study the effect of the binder content on the behaviour of a soft soil stabilized under cyclic loading, unreinforced and reinforced with polypropylene fibres. The results were analysed in terms of the evolution of plastic deformation, and of the elastic and plastic energy. It was observed that plastic energy prevails in the first cycles but decreases with the increase in the number of loading cycles, and the increase of the binder content is associated with the decrease of the initial plastic energy. The accumulated plastic deformation occurring during the cyclic loading induces a strain hardening effect that is responsible for the increase in the undrained resilient modulus. The addition of polypropylene fibres prevents the development of some cementitious bonds and promotes an increase in the plastic deformation energy, leading to an increase in the accumulated plastic strains and to a reduction in the undrained resilient modulus during the cyclic loading stage.

RÉSUMÉ: Lorsqu'un sol est soumis à une charge cyclique, il y a des changements dans le comportement du matériau qui doivent être caractérisés pour une conception sûre. À cette fin, une série d'essais de résistance à la compression non confinée (UCS) a été réalisée, avec et sans application d'une charge cyclique, pour étudier l'effet de la teneur en liant sur le comportement d'un sol mou stabilisé sous charge cyclique, non renforcé et renforcé avec des fibres de polypropylène. Les résultats ont été analysés en termes d'évolution de la déformation plastique et de l'énergie élastique et plastique. Il a été observé que l'énergie plastique prédomine dans les premiers cycles mais diminue avec l'augmentation du nombre de cycles de chargement, et l'augmentation de la teneur en liant est associée à la diminution de l'énergie plastique initiale. La déformation plastique accumulée pendant le chargement cyclique induit un effet d'écrouissage qui est responsable de l'augmentation du module de résilience non drainé. L'ajout de fibres de polypropylène empêche le développement de certaines liaisons cimentaires et favorise une augmentation de l'énergie de déformation plastique, ce qui entraîne une augmentation des déformations plastiques accumulées et une réduction du module de résilience non drainé pendant la phase de chargement cyclique.

Keywords: Stabilized soil; reinforced soil; cyclic loading; energy.

1 INTRODUCTION

One of the techniques that has been applied to improve the geomechanically behaviour of soils is chemical stabilization, in which the natural soil is mixed in situ with chemical stabilizers such as Portland cement (Horpibulsuk et al. 2003; Lemos et al. 2021; Venda Oliveira et al. 2013). However, the composite material is in general characterized by brittle behaviour and poor tensile strength. In this context, the inclusion of randomly distributed fibres to the stabilized soil promotes the increase in the tensile strength as well as increases the ductility (Consoli et al. 2009; Correia et al. 2015; Tang et al. 2007).

When a cycling loading is applied to a fibre-reinforced stabilized soil there are changes in the material's behaviour that need to be characterized. So far, the knowledge acquired about such behaviour is still limited and sometimes inconsistent. Dall'Aqua et al. (2010); Venda Oliveira et al. (2017) presented an increase in the plastic deformations induced by cyclic loading, with the most significance during the first loading cycles. Instead, Chauhan et al. (2008)

observed an increase in the plastic deformations for a high number of loading cycles.

The application of the energy concept in geotechnical studies has focus on elucidating the behaviour of cohesionless soils subjected to dynamic loads in which the deformation of a material under cycling loading corresponds to the dissipation of energy (Lenart 2008; Sas et al. 2017). In cases of cyclic loading, stress-strain hysteresis loops provide a means to analyse the plastic energy, equivalent to the area enclosed by the hysteresis loop. Simultaneously, the elastic energy is determined by the area beneath the unloading curve (Sas et al. 2017). The energy concept has been applied to a limited number of fibre-reinforced stabilized soils subjected to cyclic loading. Narani et al. (2021) observed that the plastic energy is higher in initial cycles but decreases rapidly with the increase in the number of cycles and increases with cement content. Additionally, the addition of fibres induces a reduction in plastic energy, due to the absorption of deformation by the fibres, resulting in less energy transfer to the soil matrix.

Despite the existing research, the impact of the number of the loading cycle on the behaviour of a fibre-reinforced stabilized soft soil has not been adequately explored. So, this study aims to improve the knowledge regarding the cyclic loading behaviour of fibre-reinforced stabilized soft soil.

2 MATERIALS AND PROCEDURES

2.1 Characteristics of the materials

It was used a soft soil from Coimbra, Portugal. The geotechnical characterization revealed a grain size composition of 77% of silt, 12% of clay and 11% of sand, a liquid limit of 72%, a plastic limit of 45%, organic matter content of 9.5%, and a natural moisture content of 81%. The soil was classified as a high plasticity organic silt (OH) (ASTM-D2487, 1998) and presents a pH of 4.6 (Martins et al. 2023).

The binder chosen was Portland cement Type I 42.5 R (EN-197-1, 2000) characterized by a high composition of calcium oxide (CaO) 63% and silica oxide (SiO_2) 19%. It was used a binder content of 12, 21, 30 and 39% (dry weight ratio of binder to soil).

In the case of reinforced samples, polypropylene fibres were used as reinforcing elements. The fibres have a length of 12 mm and a diameter of 32 µm. The content of fibres added to the chemically stabilized soil was 1.2% (weight ratio of dry fibre to dry soil).

2.2 Experimental procedures

The samples used for this research were prepared based on the laboratory procedure described in Correia (2011); EuroSoilStab (2002); Martins et al. (2023): (i) the soil, in its natural water content, the cement and the fibres were mixed in a mechanical mixer at a speed of 142 rpm for four minutes; (ii) the paste was introduced into PVC moulds (37 mm diameter, 85 mm high) and compacted in three layers each (tapping the moulds against a wooden table twenty times by hand); (iii) the samples were cured under water in a room with temperature and humidity control (20±2°C and 95±5%, respectively) for 28 days; (iv) at the end of the curing period, the samples were removed from the moulds and the surfaces were cut to obtain 76 mm high samples.

A monotonic UCS test was carried out to define the mechanical characteristics under monotonic loading conditions, with a constant axial strain rate of 1% min (BSI-1377-7 (1990). The UCS cyclic loading tests were carried out for a deviatoric stress level of 50%; an amplitude of ±10% of the maximum unconfined compressive strength (defined in the monotonic UCS test), a frequency of 0.5 Hz and during 5,000 loading cycles.

3 RESULTS

3.1 Plastic deformation

The evolution of the accumulated plastic axial strain with the numbers of loading cycles is shown in Figure 1 for the different binder content in both unreinforced and fibre-reinforced stabilized soil.

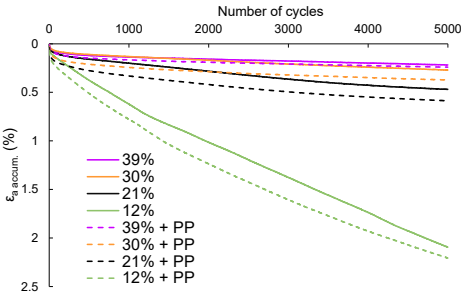

Figure 1. Evolution of the accumulated plastic axial strain with the number of loading cycles.

The analysis of the results reveals that the samples with binder content between 21 and 39% show a rapid increase in axial strain within the first 100 loading cycles, followed by a gradual, asymptotic approach to a constant value over subsequent cycles. Distinct behaviour is noted for samples stabilized with the lowest binder quantity, 12%, exhibiting a continuous

increase in accumulated permanent axial strain during all the cyclic stage. It is possible to observe a decreasing of accumulated plastic axial strain as the binder quantity increases. This trend aligns with the understanding that a higher binder quantity promotes the formation of cementitious bounds, resulting in a stronger and stiffer stabilized matrix, as seen in previous studies (Kaniraj and Havanagi 2001).

Furthermore, the results suggest that the addition of fibres may reduce the development of certain cementitious bonds within the stabilized matrix, leading to a composite material with lower strength and stiffness. Consequently, fibre-reinforced stabilized material experiences higher plastic axial strains during cyclic loading. The reduction of the impact of the fibre addition as the binder content increases is attributed to the constant amount of fibres added across all fibre-reinforced stabilized samples, resulting in a decrease in relative fibre importance.

3.2 Plastic and Elastic Energy

The plastic energy corresponds to the area enclosed by the hysteresis loop, while the elastic energy is calculated as the area beneath the unloading curve (Martins et al. 2023; Narani et al. 2021; Ostadan et al. 1996). These calculi were carried out utilizing the trapezoidal rule integration method in Matlab software, employing an in-house algorithm. The results are illustrated in Figures 2 and 3.

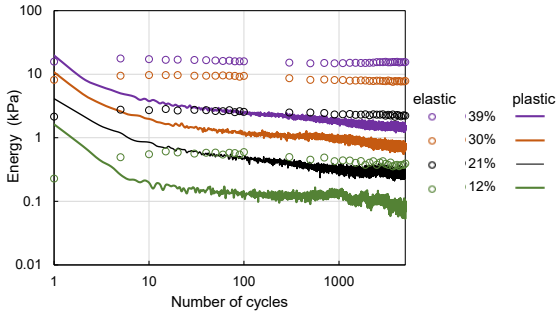

Figure 2. Evolution of plastic and elastic energy with the number of loading cycles – without fibres.

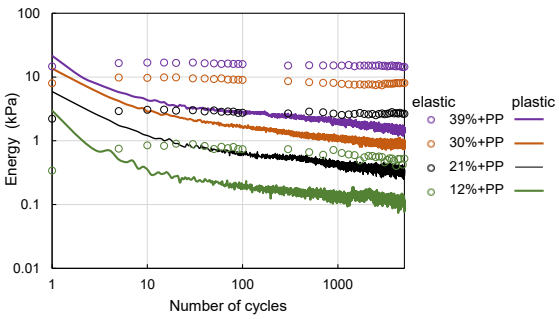

Figure 3. Evolution of plastic and elastic energy with the number of loading cycles – with fibres.

For both unreinforced and fibre-reinforced stabilized materials, the initial cycles reveal a dominance of plastic energy, which gradually reduce as the number of loading cycles increases. In contrary, elastic energy exhibits a progressive increase, particularly evident in the first 10 cycles. During the early loading cycles, the external cyclic load primarily dissipates energy as plastic, with some residual energy absorbed elastically by the composite material. However, this dynamic shifts rapidly as cycles progress, leading to a quasi-steady hysteretic response of the stabilized material, as observed from Figures 2 and 3.

Analysing the addition of fibres, it is possible to observe that the introduction of fibres amplifies the plastic energy and diminishes the elastic energy. This behaviour seems to be induced by the combined effects of the polypropylene fibres' high compressibility (Narani et al. 2020) and the presence of fibers potentially impeding the development of specific cementitious bonds.

For both unreinforced and fibre-reinforced stabilized materials, there is a noticeable transition of energy from plastic to elastic, particularly pronounced in the initial cycles.

4 CONCLUSIONS

The outcomes from the unconfined compressive strength tests conducted on both unreinforced and fibre-reinforced stabilized samples subjected to a cyclic loading stage. lead to the following conclusions:

i) The accumulated plastic axial strain decreases with the increase in binder content, attributed to a larger amount of cementitious bonds leading to a stronger and stiffer stabilized matrix.

ii) In the initial loading cycles, most of the energy applied by the external cyclic load is dissipated as plastic energy, with the remaining energy absorbed elastically by the composite material. This trend changes with the increase in the number of cycles. After a limited number of cycles (10 to 100). The results suggest the predominant dissipation mechanism involves the breakage of cementitious bonds, inducing plastic deformations in the solid skeleton, particularly intensified with lower binder content.

iii) The addition of fibres amplifies plastic energy, especially noticeable in the initial cycles. These results are coherent with a high accumulation of plastic axial strains in the first steps of cycling loading.

ACKNOWLEDGEMENTS

The authors would like thanks to CIMPOR and Biu International for supplying the binders and the fibres, and to the institutions that financially supported the research: individual research grant 2021.05748.BD, project research grant FCT (POCI-01-0145-FEDER-028382) and ACIV. This work was partly financed by FCT/MCTES through national funds (PIDDAC) under the R&D Units CIEPQPF (UIDB/00102/2020), ISISE (UIDB/04029/2020), and ARISE (LA/P/0112/2020).

REFERENCES

BSI-1377-7, (1990). Methods of test for soils for civil engineering purposes. Shear strength tests (total stress) (British Standards Institution, London, UK)

Chauhan, M.S., Mittal, S., and Mohanty, B., 2008. Performance evaluation of silty sand subgrade reinforced with fly ash and fibre in *Geotextiles and Geomembranes,* 26 (5), 429-35.https://doi.org/10.1016/j.geotexmem.2008.02.001

Consoli, N.C., Vendruscolo, M.A., Fonini, A., and Rosa, F.D., 2009. Fiber reinforcement effects on sand considering a wide cementation range in *Geotextiles and Geomembranes,* 27 (3), 196-203.https://doi.org/10.1016/j.geotexmem.2008.11.005

Correia, A.A.S., 2011. Applicability of deep mixing technique to the soft soil of Baixo Mondego, PhD Thesis (Univ. of Coimbra, Coimbra, Portugal).

Correia, A.A.S., Venda Oliveira, P.J., and Custódio, D.G., 2015. Effect of polypropylene fibres on the compressive and tensile strength of a soft soil, artificially stabilised with binders in *Geotextiles and Geomembranes,* 43 (2), 97-106.10.1016/j.geotexmem.2014.11.008

Dall'Aqua, G.P., Ghataora, G.S., and Ling, U., 2010. Behaviour of fibre-reinforced and stabilized clayey soils subjected to cyclic loading in *Studia Geotechnica et Mechanica,* 32, 3-16

EuroSoilStab, (2002). Development of design and construction methods to stabilise soft organic soils: Design guide soft soil stabilisation (Industrial and Materials Technologies Programme (Brite-EuRam III), European Commission, p. 94.)

Horpibulsuk, S., Miura, N., and Nagaraj, T.S., 2003. Assessment of strength development in cement-admixed high water content clays with Abrams' law as a basis in *Géotechnique,* 53 (4), 439-44.10.1680/geot.2003.53.4.439

Kaniraj, S.R. and Havanagi, V.G., 2001. Behavior of Cement-Stabilized Fiber-Reinforced Fly Ash-Soil Mixtures in *Journal of Geotechnical and Geoenvironmental Engineering,* 127 (7), 574-84.doi:10.1061/(ASCE)1090-0241(2001)127:7(574)

Lemos, L.J.L., Correia, A A S, and Venda Oliveira, P.J., 2021. Behavior of chemically stabilized soils reinforced with fibers under monotonic and cyclic loading in *Geotecnia Journal - Special Issue Commemorating the 50th Anniversary,* 152, 509-29.https://doi.org/10.14195/2184-8394_152_16

Lenart, S., 2008. The Use of Dissipated Energy at Modeling of Cyclic Loaded Saturated Soils in Takumi Miura and Yuuki Ikeda (ed.), *Earthquake Engineering: New Research* (New York Nova Science Publishers, Inc., New York), 29

Martins, L.A., Correia, A.A.S., Venda Oliveira, P.J., and Lemos, L.J.L., 2023. Effect of the number of loading cycles on the behavior of a stabilized fiber reinforced soft soil – energy evaluation in *Journal of Materials in Civil Engineering* https://doi.org/10.1061/JMCEE7.MTENG-15231

Narani, S.S., Abbaspour, M., Hosseini, S.M.M.M., and Nejad, F.M., 2020. Long-term dynamic behavior of a sandy subgrade reinforced by Waste Tire Textile Fibers (WTTFs) in *Transportation Geotechnics,* 24, 100375.https://doi.org/10.1016/j.trgeo.2020.100375

Narani, S.S., Zare, P., Abbaspour, M., Fahimifar, A., Siddiqua, S., and Mir Mohammad Hosseini, S.M., 2021. Evaluation of fiber-reinforced and cement-stabilized rammed-earth composite under cyclic loading in *Construction and Building Materials,* 296, 123746.https://doi.org/10.1016/j.conbuildmat.2021.123746

Ostadan, F., Deng, N., and Arango, I., 1996. *Energy-based Method for Liquefaction Potential Evaluation. Phase 1, Feasibility Study* (National Institute of Standards and Technology, Building and Fire Research …)

Sas, W., Głuchowski, A., Bursa, B., and Szymański, A., 2017. Energy-based analysis of permanent strain behaviour of cohesive soil under cyclic loading in *Acta Geophysica,* 65 (2), 331-44.10.1007/s11600-017-0028-7

Tang, C., Shi, B., Gao, W., Chen, F., and Cai, Y., 2007. Strength and mechanical behavior of short polypropylene fiber reinforced and cement stabilized clayey soil in *Geotextiles and Geomembranes,* 25 (3), 194-202.https://doi.org/10.1016/j.geotexmem.2006.11.002

Venda Oliveira, P.J., Correia, A.A.S., and Garcia, M.R., 2013. Effect of Stress Level and Binder Composition on Secondary Compression of an Artificially Stabilized Soil in *Journal of Geotechnical and Geoenvironmental Engineering,* 139 (5), 810-20.doi:10.1061/(ASCE)GT.1943-5606.0000762

Venda Oliveira, P.J., Correia, A.A.S., Teles, J.M.N.P.C., and Pedro, A.M.G., 2017. Effect of cyclic loading on the behaviour of a chemically stabilised soft soil reinforced with steel fibres in *Soil Dynamics and Earthquake Engineering,* 92, 122-25.10.1016/j.soildyn.2016.10.006

Proceedings of the XVIII ECSMGE 2024
GEOTECHNICAL ENGINEERING CHALLENGES
TO MEET CURRENT AND EMERGING NEEDS OF SOCIETY
© 2024 the Authors
ISBN 978-1-032-54816-6
DOI 10.1201/9781003431749-475
Open Access: www.taylorfrancis.com, CC BY-NC-ND 4.0 license

ECSMGE 24
XVIII EUROPEAN CONFERENCE ON SOIL MECHANICS AND GEOTECHNICAL ENGINEERING

Underpinning and strengthening of an existing port infrastructure to allow 8m depth dredging for the installation of a high-capacity vessel synchrolift

Soutènement et renforcement d'une infrastructure portuaire existante pour un dragage à une profondeur de 8 mètres pour l'installation d'un synchrolift pour navires de haute capacité

P. Matias Ramos*, L. Esteves
Teixeira Duarte EC, Oeiras, Portugal

**pmr@teixeiraduarte.com*

ABSTRACT: This article describes the structural and geotechnical solutions devised to the underpinning and reinforcement of an existing gravity-type block retaining wall quay. These enhancements were essential to allow an 8-meter seabed dredging, extending from -10.00ZH to -18.00ZH, to enable the installation and operation of a high-capacity vessel *synchrolift*, in a region characterized by high seismic activity. In addition to the extensive dredging, the project included the construction of high-capacity complementary strengthening structures, designed to work in perfect interaction with both the soil and the existing quay infrastructure, ensuring their capacity to support the significant load increase resulting from the lifting, onshore transfer, and dry-docking operation of vessels weighing up to 9000 tonnes on reinforced concrete platform slabs, supported on bored cast-in-situ foundation piles. Focusing on the design principles, the seismic design methodologies and the sensitivity analysis procedures towards safety factor maximisation, this article spotlights key local constraints and their influence on the cost-benefit analysis process that ultimately dictated the adopted technical solutions. The article also addresses a summary of the construction sequence, highlighting the critical role of a meticulous project timeline planning. The knowledge acquired from past experience and a thorough analysis of all process variables, from conception and design to construction, proved to be indispensable to successfully achieve an unconventional underpinning and strengthening solution in a complex geotechnical environment, by means of technical systems that permitted a substantial dredging under the foundation level of an existing infrastructure, significantly enhancing its resistance in compliance with current regulations.

RÉSUMÉ: Article décrivant les solutions structurelles/géotechniques développées pour le renforcement et le soutènement d'un quai existant, afin de permettre le dragage du fond marin jusqu'à une profondeur de 8 mètres, du niveau -10,00ZH au niveau -18,00ZH, pour l'installation d'un *synchrolift* d'haute capacité dans une région à haute sismicité. En plus du dragage significatif, cette intervention a imposé la construction de structures de renforcement complémentaires, conçues pour fonctionner en parfaite interaction et interconnexion avec le sol et avec l'infrastructure du quai existante, afin de permettre une augmentation massive de charge résultant de l'élévation, transfert à terre et du stationnement (à sec) de navires jusqu'à 9000 tonnes de déplacement sur des dalles de plateforme en béton armé, construites sur des pieux de fondation. L'article se concentre sur les approches de conception, les méthodologies de calcul sismique adoptées et les procédures d'analyse de sensibilité, réalisées pour maximiser les coefficients de sécurité, en soulignant les principales contraintes existantes et leurs effets sur le processus d'analyse coût-bénéfice qui a déterminé les solutions techniques adoptées. Il résume également la séquence de construction et l'importance d'une planification minutieuse lors de la conception du processus chronologique. L'expérience et l'analyse méticuleuse de toutes les variables du processus, de la conception à la construction, sont éléments essentiels pour mettre en œuvre une solution de soutènement/renforcement non conventionnelle dans un environnement géotechnique complexe, en adoptant des systèmes qui ont permis un dragage considérable sous le niveau de fondation d'une infrastructure existante, lui conférant une résistance significative, en conformité avec la réglementation en vigueur.

Keywords: Dredging; underpinning; strengthening.

1 GUIDELINES

The naval base of the Project described in this article houses a naval repair sector occupying approximately 16 hectares within its premises (Figure 1). To support the maintenance and repair of the operating vessels, the base was equipped with a lifting platform capable of handling ships up to 3000 tons, enabling their transitions between the sea and the port platform.



Figure 1. Naval Base location.

As time passed, the detection of deformations in the quay wall structures and signs of corrosion in the steel and electromechanical elements of the lifting platform prompted the responsible entities to initiate an international tender for the development and implementation of a rehabilitation and reinforcement solution.

The objective was to facilitate the installation of a new synchrolift with a 9000-ton capacity, aligning with the size and capacity demands of the existing operational vessels. In general terms, the requirements expressed in the tender specifications determined:

- The design of onshore and offshore reaction structures, to support a vessel lifting platform measuring 25m x 145m and a 9000-ton capacity.
- Reinforcement of the current quay walls, enabling the dredging procedures ranging from 3 to 8m in depth within the new berthing quay and the new lifting platform zones.
- Development of a 145m length transference zone, for ship transfer operations between the lifting platform and five parking areas for the construction, repair, and maintenance of vessels, with lengths ranging from 100 to 150m.
- Design of a 623m length circulation path for two overhead cranes with lifting capacity of 40 tons, at a 50m distance.
- Construction of support and control buildings, along with extensive network grid systems and operational equipment.

These requirements resulted in the occupational layout shown in Figure 2.

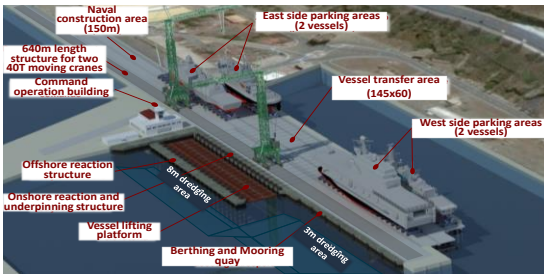

Figure 2. 3D image of the conceived intervention layout.

2 EVALUATION OF EXISTING SOIL AND INFRASTRUCTURES

Figure 3 shows the stability design assessment of the existing quay walls, which have their base at the seabed level (-10.00ZH). This assessment implied an extensive geotechnical survey involving multiple activities which included 25 boreholes along with various characterization procedures and laboratory tests. The data collected was summarized in geotechnical reports, which provided the basis for the interpretation and assignment of geomechanical parameters used in subsequent calculations.

- C2 - Heterogeneous port backfills: Ø'=25º; c'=5kN/m2; γ=19kN/m3;
- C3A - Clay with sand intercalations ($15<N_{SPT}<30$): Ø'=25º; c'=3kN/m2; γ=20kN/m3;
- C3B - Silty clays ($30 < N_{SPT} < 60$): Ø'=25º; c'=50kN/m2; γ = 20kN/m3;
- C4 - Compact marls ($N_{SPT} >60$): Ø'=30º; c'=50kN/m2; γ = 20kN/m3.

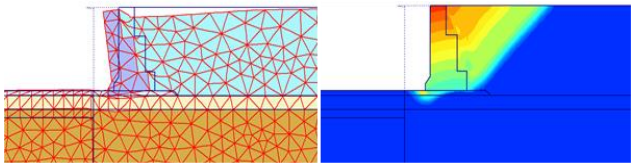

Figure 3. Numerical simulation of the existing quay structures (SF ≅ 1.1 => very low).

3 PROJECT DESIGN

The assessment of the existing quay confirmed the complexity of the tender demands. In addition to rehabilitating, retrofitting and strengthening a highly sensitive infrastructure, to comply with current regulation standards, this project involved the reinforcement of the port's backfill and of the pre-existing quay to cope with the substantial load increase resulting from the vessel suspension, transfer and parking operations.

Furthermore, the ship's draft specifications, the thickness of the new lifting platform and the characteristics of the new transfer system (including supporting trestles and bogies) dictated the necessity to deepen the seabed by 8 meters. This operation extended from -10.00ZH to -18.00ZH, requiring the underpinning of the existing quay walls.

Even though the singularities of the *synchrolift* operations impose a wide range of load actions whose description is beyond the scope of this article, Figure 4 provides a visual representation of the maximum loads managed by all 38 suspension winches (19

onshore and 19 offshore) during the new vessel lifting operations.

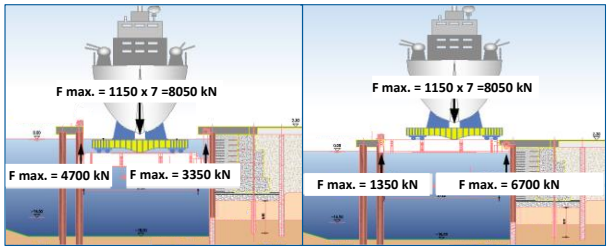

Figure 4. Maximum loads on onshore / offshore structures.

Alongside the load increment due to vessel lifting and transfer procedures, the solution needed to address the substantial ≈21meter earth pressure differential arising from the differential between the level of the elevation of the new port platform (+3.20ZH) and the post-dredging seabed level (-18.00ZH).

Furthermore, it's essential to emphasize the significance of seismic activity, a decisive factor in the design for Ultimate Limit States. Considering all the specified criteria and following extensive research, evaluating numerous technical solutions and construction scenarios, the outcomes led to the implementation of an integrated structural approach, where the new transfer and parking areas shall function as integral load-bearing components, in conjunction with the existing quay walls and their innovative underpinning solution.

The designed underpinning structure consists of a retaining wall curtain formed by Φ1200mm cast-in-place bored piles with a 1.35m spacing, acting with the complementary stabilizing resistance of the existing quay walls and by a plain concrete fill placed in the 6m gap between these two structures.

The massive loadings resulting from ship transfer and parking led to the use of a transfer system carried out by bogies, circulating on rail tracks positioned over a grid of reinforced concrete beams (2.0mx1.8m). Along with the reinforced concrete platform slabs, this grid of high-capacity beams forms a horizontal diaphragm element which is supported by Φ1500mm bored piles, reaching depths compatible with suitable penetration into the marl substrate, occurring from a depth of 16m. This diaphragm allows for the joint mobilization of the passive soil earth pressure along the pile foundation shafts that, functioning together with the underpinning structure, proved to be capable to counteract the ≅21m active earth pressures actions resulting from dredging procedures.

The joint interaction between existing and strengthening structures imposes a suitable interconnection between all interface areas, capable of ensuring their monolithic behaviour. This interconnection proved to be essential for the overall solution stability, where the bond between structural elements was achieved by suitable dowel steel bars, attached to the existing quay walls through epoxy resins and to the new reinforced concrete structural elements by means of embedded anchoring lengths.

Over the existing quay, the impossibility of large diameter deep foundation drilling across the existing concrete structures led to the adoption of micropiles, suitably spaced according with their resistance and the applied load values. These micropiles (N80-Ø177.8×15mm) were grouted into the marl substrate through a repetitive and selective injection system.

The described solution is generically shown in Figure 5, by the schematic illustration of the lifting platform suspension operations over the offshore and onshore reaction structures, allowing the vessel ascent that precedes its transfer to the parking areas.

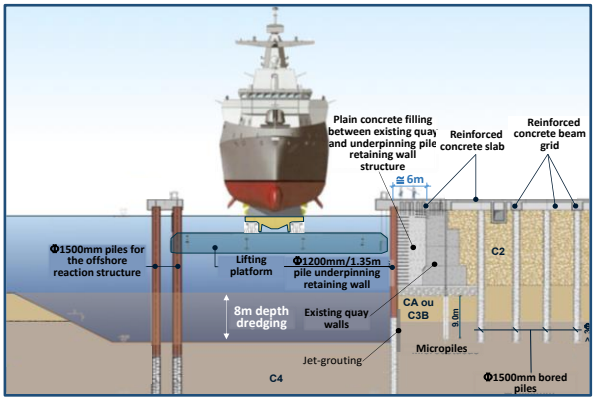

Figure 5. Typical section cut of the described solution.

The design of the adopted solution was performed with 2D and 3D nonlinear numerical simulations, using different software and conducting sensitivity analyses by judicious comparison of the obtained results. The 2D models were developed using the software PLAXIS, where the soil is simulated through finite elements governed by Mohr-Coulomb failure criteria, and the remaining elements (micropiles, quay walls, backfill, piles, beams, and slabs) through linear/elastic behaviour elements. In these models, it was possible to simulate the construction phasing and determine the combined design stresses, forces, deformations, and safety factors for each intervention stage (Figure 6).

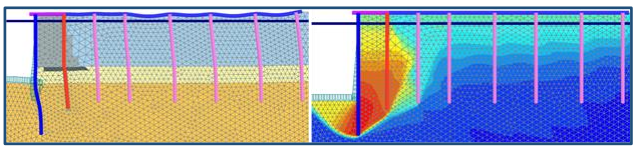

Figure 6. Calculation deformations ($\delta_{max\ horiz.}$=1.7cm) and failure surfaces of the adopted solution (SF ≈ 2.6).

As sown in Figure 7, the 3D design models, using SAP2000, simulated the soil/structure interaction through nonlinear spring elements, with stiffness corresponding to the soil's Winkler modulus and plastic behaviour corresponding to the value of the passive earth pressure in depth. The steel, plain concrete and reinforced concrete elements were simulated by linear/elastic finite elements.

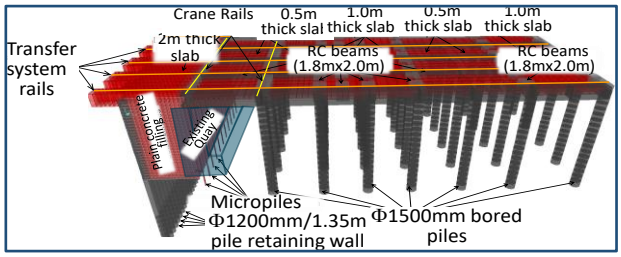

Figure 7. 3D model for the transfer zone structural body.

With the developed numerical calculation models, properly adapted to the characteristics/particularities of the various structures and intervention areas, it was possible to determine the maximum values of forces, stresses and displacements for all Ultimate Limit State and Service Limit State combinations, by numerical simulation of all structural elements and interconnections considering all construction phases.

In addition to the global numerical simulations, the calculations also involved numerous additional lower scale models, performed to address more specific situations. Figure 8 presents two images of one of these supplementary models.

In this case, the calculations were performed to simulate the solution's stability immediately after the dredging procedures. In this construction phase it was mandatory to have the micropiles for existing quay foundation strengthening, the pile retaining wall curtain and the plain concrete stabilization filling fully concluded. However, the connection to the platform slab, that establishes the stabilization diaphragm of the solution in its final stage, was yet to be completed, which imposed additional verifications.

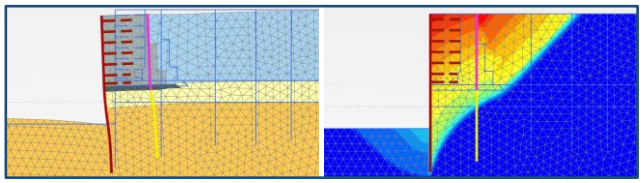

Figure 8. Evaluation of temporary dredging effects.

4 CONSTRUCTION METHODS AND PHASES ADOPTED

The underpinning of the existing quay walls, whose main operations are represented in Figure 9, began with the execution of micropiles foundation strengthening elements, followed by sequential vibro-driving of a curtain of permanent steel casing tubes, with an internal diameter of Φ1200mm and a thickness of 12mm, ensuring a 6m distance between its axis and the existing quay wall elements. With lengths of approximately 16m (5m driven into the ground => casing toe approximately at -15.00ZH), these steel casing elements were positioned with a 1.35m spacing between axes, establishing a retaining wall curtain parallel to the existing quay, covering the entire length of the dredging area.

The "hook" connection that assembles these casing tubes, establishing a continuous joint element, allowed for subsequent underwater concrete placing between the curtain and the existing quay, preventing material leakage into the sea.

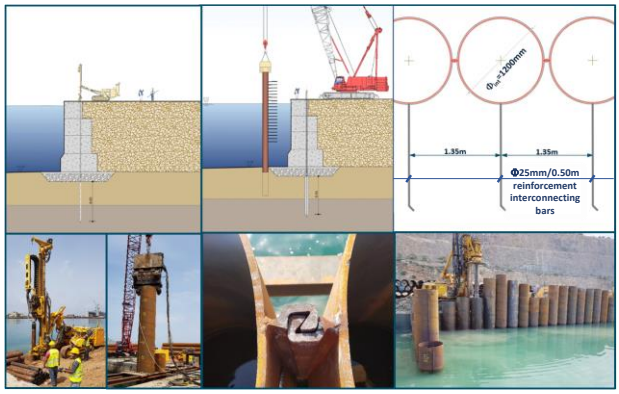

Figure 9. Schemes and images of micro-pile execution and steel casing driving.

The drilling, reinforcement positioning and concrete pouring operations for the execution of the underpinning curtain piles, presented in the schemes and images of Figure 10, were carried out with machinery operating from the port backfill, through the steel casing, using drilling equipment attached to powerful cranes or a suspended fly-drill equipment, reaching depths compatible with the -26.00ZH level.

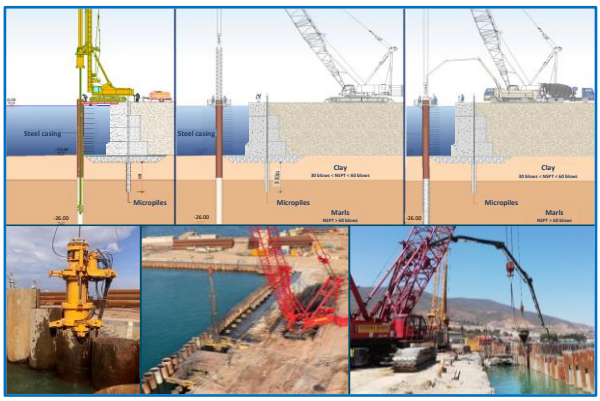

Figure 10. Schemes and images of the construction operations of the bored piles of the underpinning curtain.

Following the defined phasing sequence, the construction works proceeded with the filling of the gap between the underpinning pile curtain and the existing quay walls through submerged pouring of plain concrete, followed by the execution of jet-grouting columns that filled the 15cm gap between adjacent piles, located below the base of the tubes (and their connecting elements), exposed after dredging procedures of the seabed (from -10.00ZH to -18.00ZH).

These operations were executed along with the installation of interconnection dowel bars, which were sealed with epoxy resins or incorporated into the new structural elements, designed to ensure a monolithic behaviour between the piles, the existing quay, the plain concrete filling, and the reinforced concrete structural slab/beam grid (Figure 11).

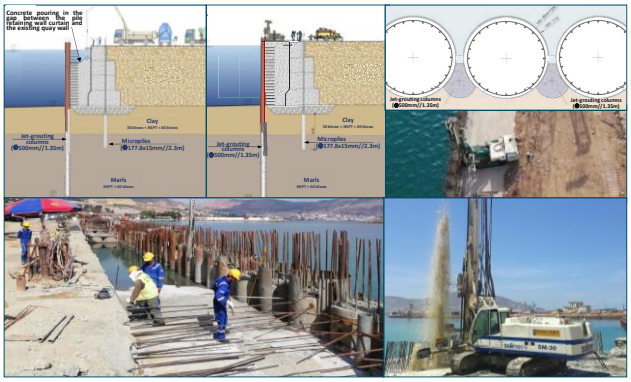

Figure 11. Concrete pouring in the gap between the pile retaining wall curtain and the existing quay wall and execution of the jet-grouting columns.

Following the previously described design established phasing procedures, the conclusion of the primary underpinning reinforcement curtain, including the plain concrete filling, allowed to begin the dredging operations (Figure 12), to deepen the seabed in 8m, achieving the required clearance for the Project vessel draft, including the height of the synchrolift system's platform structure and the ship supporting berth beams (trestles).



Figure 12. Dredging reaching maximum depths of 8.0m, up to the -18.00 ZH level.

These dredging operations involved the removal of marl material from the C3A, C3B, and C4 geotechnical layers, occurring under approximately 1.0m of sedimentary material.

The construction of the 411 foundation piles (72 Ø1200mm and 339 Ø1500mm) for the reinforced concrete beam foundation for the crane runway and the ship transfer/parking platforms was executed simultaneously with the previously described quay underpinning and foundation strengthening operations.

As illustrated in the schematic drawings and images of Figure 13, these structural elements are located on the port backfill areas. Ensuring a minimal penetration of 3Ø into the marl formations, the piles have variable lengths between 21m and 25m, and were designed to support vertical loads and to provide a supplementary horizontal stability solution through the mobilization of passive earth pressure along their shafts.



Figure 13. Execution of foundation piles for the ship transfer and parking platform.

The conclusion of all dredging operations allowed the beginning of the construction of the offshore reaction structure, located approximately 28m from the alignment of the quay's underpinning pile curtain.

This structure consists of a reinforced concrete 1.6m thickness slab, placed over 42 bored Φ1500mm piles, executed by drilling through steel casing previously introduced into the ground (Figure 14).

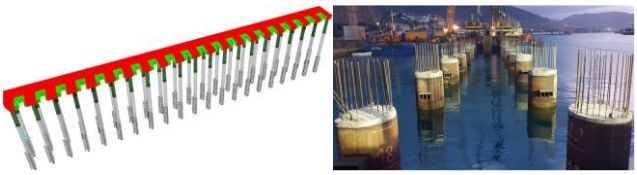

Figure 14. Design model and pile execution of the offshore structure, using floating platforms.

The vibro-driving of the permanent casing, the drilling, reinforcement placement, and concrete pouring for the execution of the offshore piles followed similar procedures to those described earlier, with the particularity of being carried out by equipment operating on floating platforms.

5 CONCLUSIONS

The imposition of new exploitation requirements on old maritime structures generally implies the execution of complex and expensive structural interventions. In this context, the execution of reinforcement and underpinning interventions requires the adoption of multidisciplinary solutions and suitable construction methodologies, capable of overcoming existing constraints and achieving the structural behaviour required by the new operating conditions.

Whenever the geomechanical characteristics of the soils don't allow element driving, such as sheet piles, until the required depths for underpinning structures, the option for bored cast-in-place piles may be advantageous. This methodology, which uses drilling with soil extraction, overcomes many of the constraints imposed by driving limitations, enabling the achievement of the design depths through the use of suitable drilling tools.

The extreme constraints of this intervention required the design of an integrated solution where the overall equilibrium is achieved throughout the joint functioning of both existing and reinforcing structural elements. It's imperative to highlight that this global integrated system required a thorough analysis of all material rheological properties, evaluating the structural behaviour of both existing and strengthening elements, considering the geomechanical characteristics of the soil and of the structural interaction between all components. This option, which proved to be crucial in the success achieved in this complex Project, is shown in Figures 15 and 16.



Figure 15. Project site after conclusion of the control building and installation of the synchrolift.

The combined structural behaviour between the underpinning pile curtain, the existing quay walls, the plain concrete filling, jet grouting columns, micropiles, and foundation piles, all interconnected by a top diaphragm consisting of reinforced concrete beams and slabs, made it possible to obtain a resistance capacity compatible with a significant load increase and a significant dredging, enabling the Project vessel lifting and transfer operations, such as shown in Figure 16, meeting the current regulation requirements and achieving significant safety factors.



Figure 16. Approach, lifting, and transfer of 8500 tons vessel.

Proceedings of the XVIII ECSMGE 2024
GEOTECHNICAL ENGINEERING CHALLENGES
TO MEET CURRENT AND EMERGING NEEDS OF SOCIETY
© 2024 the Authors
ISBN 978-1-032-54816-6
DOI 10.1201/9781003431749-476
Open Access: www.taylorfrancis.com, CC BY-NC-ND 4.0 license

ECSMGE 24
XVIII EUROPEAN CONFERENCE ON SOIL MECHANICS AND GEOTECHNICAL ENGINEERING

Effects of sheet pile driving on soil density within soil exchange drillings

Effets du battage de palplanches sur la densité du sol dans les forages d'échange de sol

U.Matthiesen*, M.Pohl
Federal Waterways Engineering and Research Institute, Hamburg, Germany
**ulf.matthiesen@baw.de*

ABSTRACT: For the overhaul of a major port construction soil exchange drillings using large diameter cased boreholes were carried out along the wall alignment to support the installation process of the subsequent pile driving. In order to minimise the environmental impact, the exchange drillings were backfilled using the excavated drilling material. If the material was deemed unsuitable, sand from an offshore depot was used instead. During the pile driving several of the king piles sank up to 9 m into the ground with minimal application of driving energy. An extensive investigation was launched to identify the cause of these failures. Different fill materials as well as backfilling methods of the exchange drillings were investigated using before and after cone penetration tests (CPT). In order to assess the structural integrity of the driven king piles, CPTs were carried along the wall alignment, adjacent to and within the double beam piles. This paper presents the findings of the above-mentioned investigation focussing on the installation effects of the pile driving on the soil density within the exchange drillings. The CPT results suggest a sufficient compaction of the fill material due to the pile driving process even in areas where the piles initially sank into the ground.

RÉSUMÉ: Dans le cadre de la remise en état d'une construction portuaire majeure, des forages d'échange de sol ont été réalisés à l'aide de trous tubés de grand diamètre le long de l'alignement du mur afin de soutenir le processus d'installation du battage de pieux ultérieur. Afin de minimiser l'impact sur l'environnement, les forages d'échange ont été remblayés à l'aide des matériaux excavés. Si le matériau n'était pas approprié, du sable provenant d'un dépôt offshore a été utilisé à la place. Pendant le battage des pieux, plusieurs des pieux centraux se sont enfoncés jusqu'à 9 m dans le sol avec une application minimale de l'énergie de battage. Une enquête approfondie a été lancée pour identifier la cause de ces défaillances. Différents matériaux de remplissage ainsi que des méthodes de remblayage des forages d'échange ont été étudiés à l'aide d'essais de pénétration au cône (CPT) avant et après. Afin d'évaluer l'intégrité structurelle des pieux battus, des CPT ont été effectués le long de l'alignement du mur, à côté et à l'intérieur des pieux à double poutre. Cet article présente les résultats de l'étude susmentionnée, en mettant l'accent sur les effets de l'enfoncement des pieux sur la densité du sol dans les forages d'échange. Les résultats du CPT suggèrent un compactage suffisant du matériau de remblai dû au processus de battage des pieux, même dans les zones où les pieux se sont initialement enfoncés dans le sol.

Keywords: Soil exchange drillings; soil structure interaction; combined sheet pile wall; installation effects.

1 INTRODUCTION

The overhaul of a major tidal port construction in Germany entails a new, approximately 2.2 km long and 15 m high, quay wall in front of the existing wall at a distance of 5 m. The new combined sheet pile wall consists of over 30 m long double beam HZM 1080 king piles as structural supports, and AZ sheet piles as intermediate infill elements. The wall is tied back using pressure grouted steel displacement piles (Figure 1).

Due to the predominating very dense sands, locally occurring soft marine clay as well as debris from WW2 bombings, soil exchange drillings using large diameter cased boreholes were carried out along the wall alignment to support the installation process of the pile driving. The exchange drillings were backfilled using, if suitable, the excavated drilling material as well as sand from a nearby depot. During installation, several king piles sank over several metres (up to 9 m) into the ground with minimal application of driving energy.

The works were stopped in order to investigate the cause of this phenomenon. This paper contains a description of the investigations carried out as well as an assessment of the installation effects of the pile driving on the surrounding soil and the possible causes of the observed sinking of the piles.

2 GROUND CONDITIONS

The local geology is composed of superficial quaternary soils, consisting of soft cohesive soils and sand. Onshore, along the quay wall, the upper layer consists of made ground underlain by soft marine clay followed by medium dense to dense sands. The upper layer of the harbour basin consists of mud of up to 5 m thickness underlain mostly by sand and in parts by marine clay or silty sands (Figure 1).

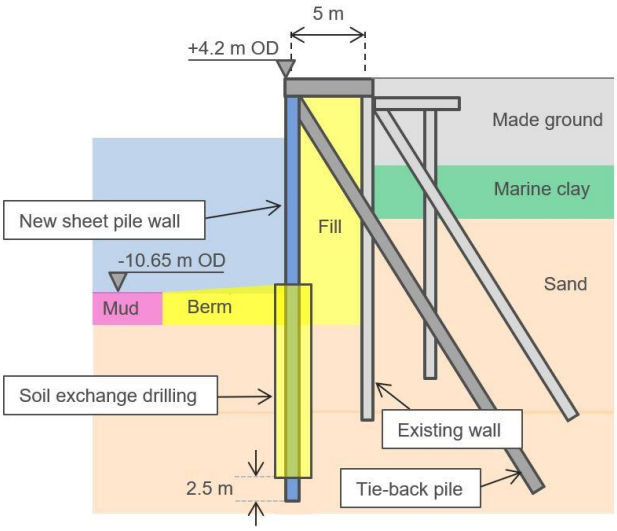

Figure 1. Cross section of the old and new quay wall including ground conditions.

3 CONSTRUCTION & ANOMALIES

3.1 Construction sequence

The first step of construction was to remove the fluid mud layer in front of the existing wall and replace it with a sand berm in order to stabilize the structurally inadequate quay wall and to avoid settlement of the future backfill. This was achieved by dredging the material using water injection while simultaneously backfilling with sand (Matthiesen et al., 2015). Prior to the driving of the new combined sheet pile wall, the soil exchange drillings using large diameter cased boreholes were carried out along the wall alignment. The installation of the wall was followed by the driving and connecting of the tie-back piles. Finally, the space between old and existing wall was incrementally backfilled and the new platform was constructed.

3.2 Soil exchange drillings and sheet pile driving

The soil exchange drillings were carried out from a jack-up barge along the alignment of the new sheet pile wall using large diameter cased boreholes. The soil was extracted using the Kelly drilling method. The boreholes were drilled to a depth of 2.5 m above the bottom of the king piles (Figure 1) to ensure sufficient toe resistance of the piles. After completion of the borehole the excavated material was reinstalled as backfill material. Before its reuse the soil was checked for obstacles and its suitability as filling soil. If necessary it was replaced by sand from a nearby offshore depot. Figure 2 shows an example of the alignment and the sequence of the soil exchange drillings.

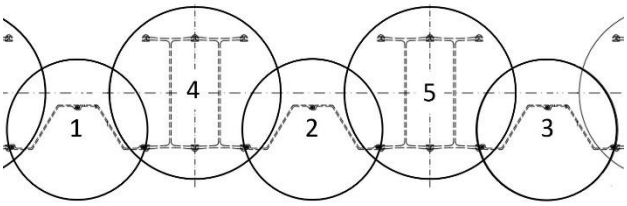

Figure 2. Soil exchange drillings - alignment and construction sequence.

In order to ensure that the king piles were installed within the specified tolerance, the piles were fixed into position within a pile-driving template using welded bracket guides as well as leader rig guidance (Figure 3). The piles were installed using the large driving sequence (back-step method) which ensured that the pile toe encountered soil uniformly on its total circumference and not just on one side.

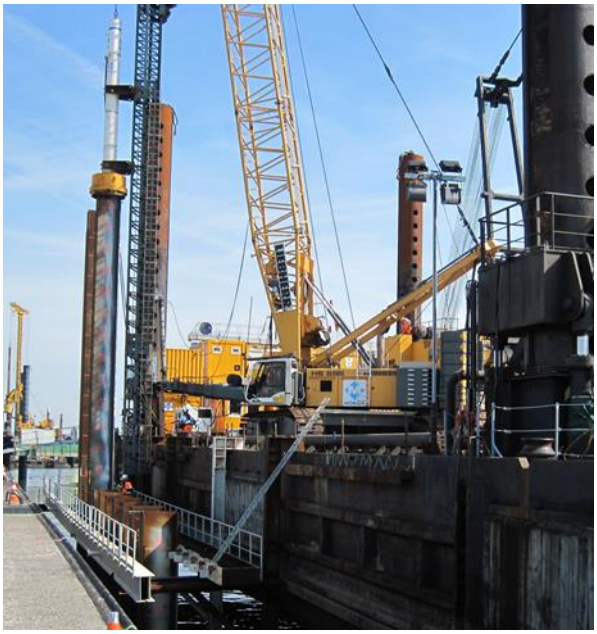

Figure 3. Installation of the king piles.

3.3 Anomalies

In the course of the works, a large number of the soil exchange drillings required a considerable additional amount of backfilling material of up to twice the

arithmetic volume of the borehole (Matthiesen & Pohl 2021).

During the subsequent pile installation, several king piles sank over several metres (up to 9 m) into the ground with minimal application of driving energy. This occurred in the upper metres of the piles and affected 16 of the 53 king piles installed until the works were stopped in order to investigate the cause.

4 INVESTIGATION

In order to identify the cause of the aforementioned sinking of the piles as well as the additional filling material required an extensive investigation was launched. Different fill materials as well as backfilling methods of the exchange drillings were investigated using before and after cone penetration tests (CPT). The findings of these investigations are presented in (Matthiesen and Pohl, 2021).

In order to assess the structural integrity of the driven king piles, CPTs were carried out along the wall alignment, adjacent to and between two neighbouring king piles. The position of the CPTs is shown as an example in Figure 4. The CPTs were used to determine the relative density D_r of the sand surrounding the piles as well as for the detection of potential embedded cohesive layers within the fill. As a baseline reading additional CPTs were carried out in the adjacent natural ground at a distance of 5 m to the piles, which showed no effect of the pile driving.

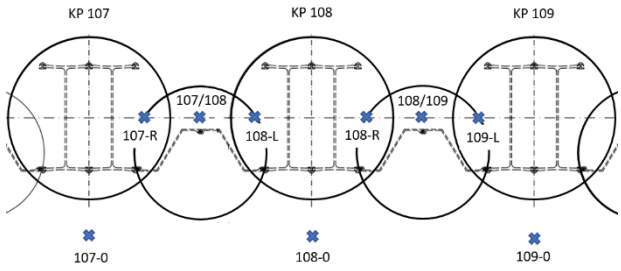

Figure 4. Locations of CPTs at king pile locations KP 107 / 108 / 109.

It was noticeable that the phenomenon of the sinking of the piles occurred in groups of consecutive king piles. The CPTs were therefore carried out at several locations of 3 king piles each. The selected locations included both well driven piles, showing a steadily increasing driving energy with depth, and locations where the sinking of the piles occurred.

5 ANALYSIS

For the purpose of this evaluation, two representative pile groups are compared below. These are king piles 81-83, showing a normal or good driving progress with depth and king piles 107-109, which sank over several meters into the ground during driving. To this end, the soil conditions and the pile driving data are being analysed.

Table 1 gives a summary of the driving data of the aforementioned piles, showing the number of blows and total energy required for the driving of the piles. On average, the number of blows and total driving energy is twice as high for the first pile group, the biggest difference being between king piles 81 and 107 showing a factor of 4.6 in the number of blows and a factor of 6 in the required total driving energy.

Table 1. Summary of pile driving data.

King Pile	No. of blows	Total Energy [kN]
81	2441	203.910
82	1771	133.770
83	2103	176.513
107	528	34.096
108	1438	112.330
109	1187	98.724

Additionally, Figure 5 depicts the driving progress with depth for each of these piles. While the first pile group (KP 81-83) shows a steady increase in the number of blows with depth due to a compaction of the fill material as a result of the driving and an increase in skin friction, the second pile group clearly shows the aforementioned sinking of the piles into the ground within the first 9 m with minimal application of driving energy.

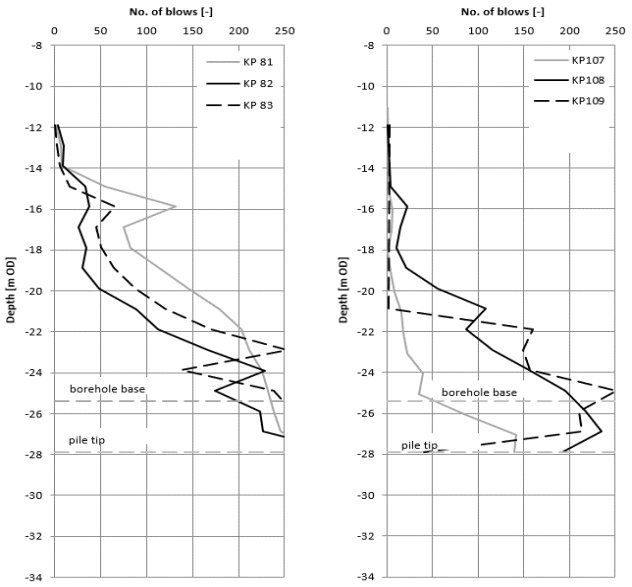

Figure 5. Number of blows with depth for king piles 81/82/83 (left) and 107/108/109 (right).

The relative density D_r within the exchange drillings prior to driving for these pile locations is unknown. Investigations have shown, however, that

the execution of the exchange drillings result in a decrease in cone resistance q_c of up to 76 % irrespective of the fill material used (Matthiesen and Pohl, 2021). Therefore, a loose to very loose relative density D_r can be assumed within the exchange drillings prior toe driving.

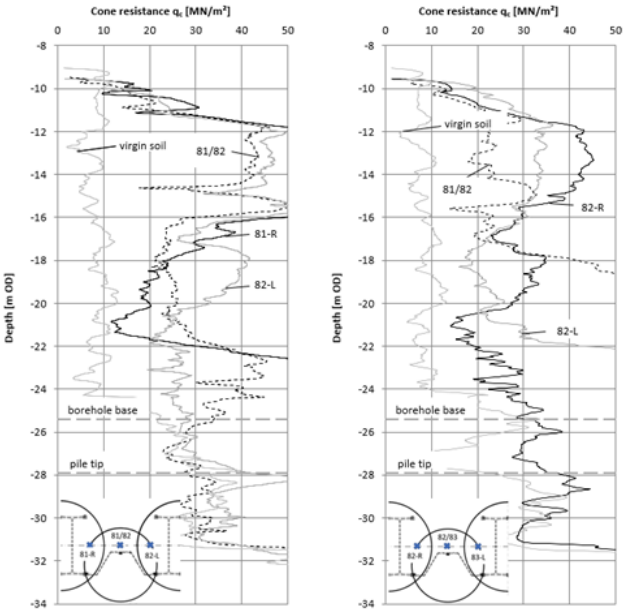

Figure 6. Cone resistance q_c between king piles KP 81/82 and KP 82/83.

Figures 6 and 7 show the cone resistance q_c of the CPTs carried out within the fill material of the exchange drillings for the respective pile groups. The first pile group (Figure 6) shows an average q_c of 33.6 MPa within the exchange drillings, corresponding to a dense to very dense relative density D_r after pile driving. The CPT results show a significantly higher cone resistance than the virgin (natural) soil outwith the borehole over the entire length of the pile. The CPTs in between the piles (CPTs 81/82, 82/83) also depict a similar – in some places higher - increase in soil strength than the ones directly adjacent to the piles showing that pile driving also leads to significant compaction in the neighbouring exchange drillings.

The CPTs carried out within the area of the second pile group (Figure 7) show, in parts, lower cone resistances q_c, especially in the upper parts of the pile (i.e. CPT 107-R, 107/108, 108-L). This was to be expected as this is the area where the sinking of the piles occurred. However, the cone resistances q_c are still consistently higher than those of the virgin (natural) soil, which formed the basis of the structural design. Some CPTs within this pile group also show cone resistances q_c similar to the previously discussed group. The average cone resistance q_c in this pile group is 25.1 MPa, also confirming a dense to very dense relative density D_r.

Surprisingly, no significant increase in cone resistance q_c can be observed between the base of the exchange drilling and the pile toe in either of the pile groups. In fact, the cone resistances q_c are of similar magnitude than the virgin soil conditions suggesting no or little compaction of the soil in this area.

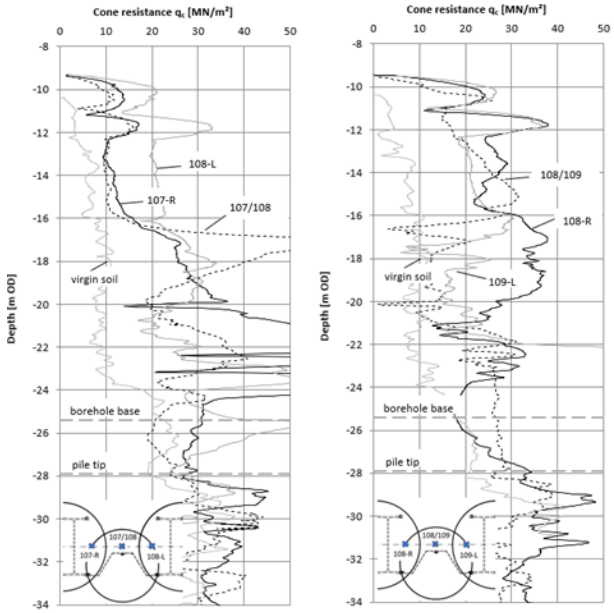

Figure 7. Cone resistance q_c between king piles KP 107/108 and KP 108/109.

6 CONCLUSIONS

Although some piles sank into the ground over several metres at the start of the pile driving due to the very loose soil conditions within the exchange drilling, the CPTs suggest a sufficient compaction of the fill material due to the pile driving process, when compared to the natural ground conditions, which formed the basis of the original structural design. The driving energy which is transferred into the surrounding soil leads to a compaction not only of the fill material within the exchange drilling but also the neighbouring regions, leading to soil densities higher than the natural ground before drilling, therefore confirming the validity of the original structural design.

REFERENCES

Matthiesen, U., Eickmeyer D. and Pohl M. (2015). Geotechnical challenges of overhauling the naval port Wilhelmshaven. *Proc. XVI ECSMGE*, Edinburgh, UK. https://doi.org/10.1680/ecsmge.60678.

Matthiesen, U. and Pohl, M. (2021). Installation effects of soil exchange drillings on sheet pile driving. *Proc. of 20th ICSMGE*, Sydney, Australia, pp 2991-2994. ISBN 978-0-9946261-4-1.

Proceedings of the XVIII ECSMGE 2024
GEOTECHNICAL ENGINEERING CHALLENGES
TO MEET CURRENT AND EMERGING NEEDS OF SOCIETY
© 2024 the Authors
ISBN 978-1-032-54816-6
DOI 10.1201/9781003431749-477
Open Access: www.taylorfrancis.com, CC BY-NC-ND 4.0 license

ECSMGE 24
XVIII EUROPEAN CONFERENCE ON SOIL MECHANICS AND GEOTECHNICAL ENGINEERING

Use of xanthan gum produced by a bacteria to reduce the soil permeability

Utilisation de la gomme xanthane produite par une bactérie pour réduire la perméabilité du sol

A. Mendonça*, P.J. Venda Oliveira, P. Morais, A.P. Chung
University of Coimbra, Coimbra, Portugal

**amaandamendonca@hotmail.com*

ABSTRACT: The construction of Civil Engineering structures on some soils requires their stabilization. Portland cement as a stabilizing agent presents many environmental concerns, so it is fundamental to find sustainable alternatives for soil stabilization in the construction field. Thus, this work analyzes the ability of the xanthan gum-like biopolymer, produced by the Stenotrophomonas maltophilia strain Faro439 (LabXG), to reduce the permeability of a sandy soil. In addition, the effectiveness of this LabXG is compared with the use of a commercial xanthan gum (XG) and Portland cement for different hydraulic gradients and curing times. The results of permeability tests show that the treatment with any type of XG can be used to replace cement in the short term (cure time of less than 14 days), although a higher level of effectiveness is obtained with the use of commercial XG due to its higher level of purity. SEM images show that treating the soil with LabXG creates a mesh of fibers that bind the soil particles together, while commercial XG fills the voids with a homogeneous paste.

RÉSUMÉ: La construction d'ouvrages du génie civil sur certains sols nécessite leur stabilisation. Le ciment Portland en tant qu'agent stabilisant présente de nombreux problèmes environnementaux, il est donc fondamental de trouver des alternatives durables pour la stabilisation des sols dans le domaine de la construction. Ainsi, ce travail analyse la capacité du biopolymère de type gomme xanthane, produit per la souche Faro439 de Stenotrophomonas maltophilia (LabXG), à réduire la perméabilité d'un sol sablonneux. En outre, l'efficacité de ce LabXG est comparée à l'utilisation d'une gomme xanthane commerciale (XG) et du ciment Portland pour différents gradients hydrauliques et temps de durcissement. Les résultats des tests de perméabilité montrent que le traitement avec n'importe quel type de XG peut être utilisé pour remplacer le ciment à court terme (temps de cure de moins de 14 jours), bien qu'un niveau d'efficacité plus élevé soit obtenu avec l'utilisation de XG commerciale en raison de son niveau de pureté plus élevé. Les images MEB montrent que le traitement du sol avec le LabXG crée un maillage de fibres qui lient les particules du sol entre elles, tandis que le XG commercial remplit les vides avec une pâte homogène.

Keywords: Biopolymer; soil stabilisation; xanthan gum; sandy soil.

1 GUIDELINES

The rising demand for urban infrastructure requires construction on challenging soil types. Traditional enhancement of these soils has predominantly involved the use of conventional cement. However, environmental concerns have catalyzed the exploration of biomaterial alternatives. Xanthan gum (XG) has emerged as a promising candidate for soil stabilization, inducing significant reduction in permeability and improvement in mechanical properties, particularly in sandy soils (Ayeldeen et al., 2017). However, the environmental footprint of industrial-scale production of commercial XG remains a significant concern. This study proposes the use of xanthan gum derived from a specific bacterial strain (LabXG) as a sustainable alternative. The primary aim is to evaluate the effectiveness of LabXG with commercial XG and traditional cement to soil stabilization, with a specific focus on the coefficient of permeability in sandy soil. The research also explores the impact of other parameters, including curing time (7 and 28 days), hydraulic gradient, XG content and content of cement. The characterization of treated soil involves the use of scanning electron microscopy (SEM) along with energy dispersive X-ray (EDX) analysis to examine the microstructure and chemical composition of soil samples treated with LabXG and commercial XG.

1.1 Soil characterization

The particle size distribution and the main characteristics of the soil used are shown in Table 1. It is a non-organic, non-plastic silty sand, composed of

72.7% sand and 27.3% silt, classified as SM (ASTM D2487, 2017). The soil compaction characteristics achieved using the standard Proctor test (ASTM D698, 2012) show an optimum water content (w_{opt}) of 14.3% and a maximum dry weight (γ_{dmax}) of 16.2 kN/m^3. The pH value of the untreated soil is approximately 7.1.

Table 1. Main characteristics of the soil.

Properties	Values
Particle size distribution	
Sand (%)	72.7
Silt (%)	27.3
Clay (%)	0
Specific density, G	2.66 g/m^3
Consistency limits	NP(**)
Proctor test [ASTM D698]:	
Maximum dry weight, $_{dmax}$	16.2 kN/m^3
Optimum water content, w_{opt} (%)	14.3
Organic matter content, OM (%)	0.19
pH	7.1

1.2 Production of Xanthan Gum-based biopolymer compound

The production of the biopolymer compound involves a systematic process, as outlined by Ayeldeen et al. (2017): (i) Cultivation of Stenotrophomonas maltophilia strain Faro439 on R2A agar plates for 3 days at 25 °C; (ii) Inoculation of cultured cells into xanthan medium in a batch system, followed by a 24-hour incubation on a shaker at 150 rpm. The resultant cells are employed as inoculum in a subsequent batch system with xanthan medium, incubated for 3 days on a shaker at 150 rpm, and then subjected to centrifugation to recover the biomass containing the biopolymer; (iii) Draining the biomass for 24 hours to eliminate excess water, followed by a 24-hour freeze-drying process to obtain a powdered form for convenient mixing with soil.

The use of this xanthan-enriched compost is justified by its uncomplicated production process, which skips purification phases, solvents or equipment that may pose ecological consequences. With a pH of 7.1, the production of xanthan gum is considered environmentally friendly compared to commercial XG. Its cost-effectiveness, together with its ecological attributes compared to other biopolymers and its proven ability to reduce soil permeability, further enhance its attractiveness as a sustainable solution.

1.3 Commercial Xanthan gum

Commercial XG is available in powder form and is produced by the bacterium *Xanthomonas campestris* through the fermentation of glucose/sucrose. It is a heteropolysaccharide made up of glucose, mannose and glucuronic acid units. It is a non-toxic hydrophilic colloid with pseudoplastic rheological properties (Chang et al., 2019) and is stable over a wide range of temperatures (10ºC-80ºC) and pH values (1-13).

1.4 Portland cement

Part of the mixtures in this research (Table 2) were chemically stabilised with Portland cement type I 42.5 R, which is made up of 45% particles of less than 45 mm. The cement is mainly composed of calcium oxide (CaO = 63%), which induces a spontaneous reaction with water, i.e. hydraulic properties.

1.5 Test procedure

The permeability tests utilized samples prepared in six distinct configurations: natural soil, a blend of soil with the biopolymer compound xanthan gum-based produced by bacteria (Lab XG) at 0.33%, a mixture of soil with commercial biopolymer xanthan gum at concentrations of 0.33% and 0.16%, and a mixture of soil with cement at concentrations of 0.33% and 1.0%. Each mixture type underwent testing across various hydraulic gradients (6.9, 8.2, 9.4, and 10.6) and two distinct curing times (7 and 28 days). The comprehensive test program details are presented in Table 2. While all samples were uniformly prepared, the permeability tests were conducted three times for each condition to ensure the quality and reproducibility of the obtained results.

2 RESULTS AND DISCUSSION

The Figures 1 and 2 show the permeability coefficients obtained experimentally for different mixtures and hydraulic gradients, considering the different curing times. The natural soil serves as a reference to evaluate the impact of each material on the permeability coefficient of the treated soil; the chemically stabilised samples with cement were included to compare the effectiveness of two types of xanthan gum (commercial and produced by bacteria) with the use of cement in reducing soil permeability.

The detailed analysis reveals a significant dispersion in the results, attributed to the heterogeneity of the natural soil and the challenges in producing homogeneous samples with low xanthan gum content. Remarkably, an increase in the commercial xanthan

gum content from 0.16% to 0.33% results in a substantial reduction in the dispersion of the results.

Table 2. Programme of tests.

Materials added			Hydraulic gradient (m/m)	Curing time (days)
Lab XG (%)	Commercial XG (%)	Cement (%)		
--	--	--	6.9 8.2 9.4 10.6	--
--	0.16	--	6.9 8.2 9.4 10.6	7 / 28
--	0.33	--	6.9 8.2 9.4 10.6	7 / 28
0.33	--	--	6.9 8.2 9.4 10.6	7 / 28
--	--	0.33	6.9 8.2 9.4 10.6	7 / 28
..	--	1.0	6.9 8.2 9.4 10.6	7 / 28

2.1 Effect of the hydraulic gradient

Most results indicate a slight decrease in the permeability coefficient with an increase in hydraulic gradient, especially for soil treated with 0.16% commercial XG. Some exceptions were noted, such as in the mixture of soil with Lab XG during a 14-day curing time. Although this trend is not in line with most of the results showed by Cabalar et al. (2017) for a hydraulic gradient range of 5 to 100, in some cases, increasing the hydraulic gradient from 5 to 10 (similar to the range considered in this study) also results in a decrease in soil permeability. This trend contrasts with previous studies and can be attributed to the specific methodology of measuring water flow. The results suggest that an increase in hydraulic gradient raises effective vertical stress (flow from top to bottom), reducing soil void ratio, and consequently, permeability. Samples with a high degree of stabilization, especially with 0.33% commercial XG and cement, exhibited lower sensitivity to variations in hydraulic gradient due to the stronger solid skeleton promoted by stabilization.

2.2 Effect of the curing time

Independent of the XG production process, a substantial decrease in soil permeability is observed in the first 3 days of curing, followed by a gradual decline until reaching a minimum coefficient at 14 days of curing. Although this indicates that the hydrogel's hydration occurs mainly in the short term (< 3 days), there is also evidence of continuous hydration during the initial 14 days. After this period, there is a slight increase in soil permeability, attributed to the potential biodegradation of XG and/or dehydration of the hydrogel. These factors increase the pore spaces in the soil, facilitating the flow of water and resulting in an increase in the permeability coefficient.

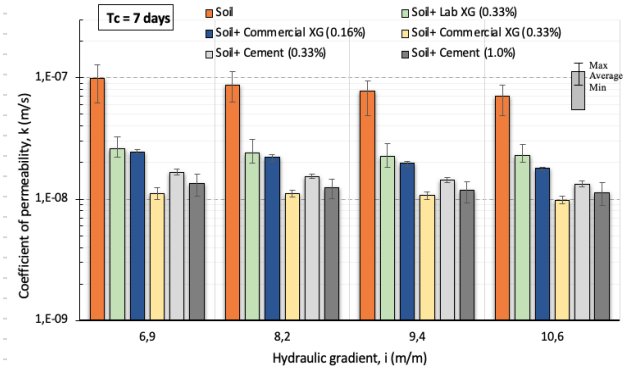

Figure 1. Permeability coefficient of natural and stabilised soil at 7-day curing time (Mendonça et al., 2021).

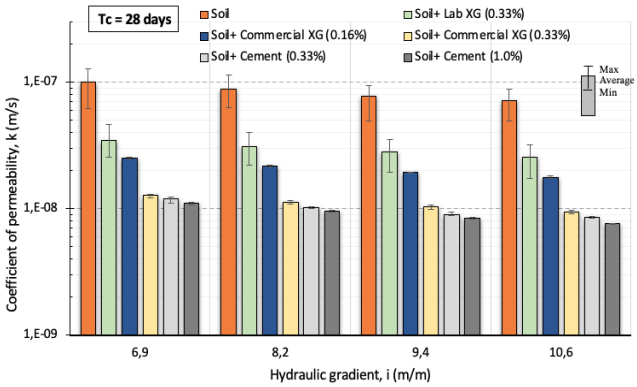

Figure 2. Permeability coefficient of natural and stabilised soil at 28-day curing time (Mendonça et al., 2021).

The literature (Venda et al., 2019) supports the observed short-term decrease in permeability. As expected, cement-stabilised specimens show a reduction in permeability over time due to pozzolanic reactions.

2.3 Analysis of the structures formed in the biopolymer-soil mixture

The Figures 3 and 4 illustrate the SEM images of soil treated with Lab XG and commercial XG. Lab XG creates fibre-like structures connecting soil particles, reducing voids, and decreasing permeability. In contrast, commercial XG forms a homogeneous paste, likely due to hydrogel hydration, resulting in reduced permeability. Both effects are compared to the natural soil and the distinct structure types correspond to

variations in their effectiveness. Lab XG's open structure is linked to higher permeability, while commercial XG's homogeneous paste restricts water flow.

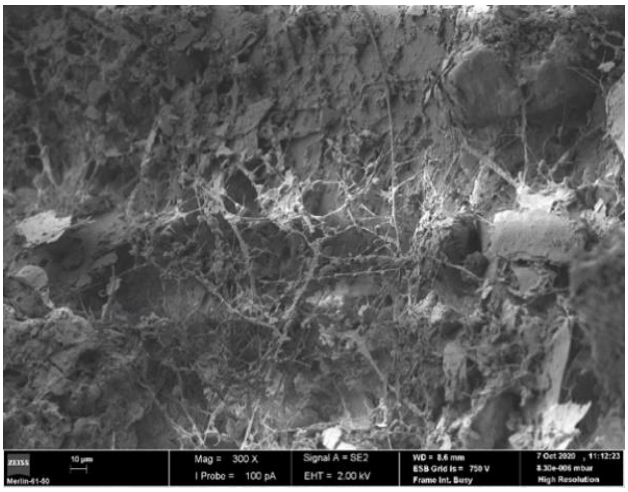

Figure 3. SEM image of the stabilized soil with Lab XG (Mendonça et al., 2021).

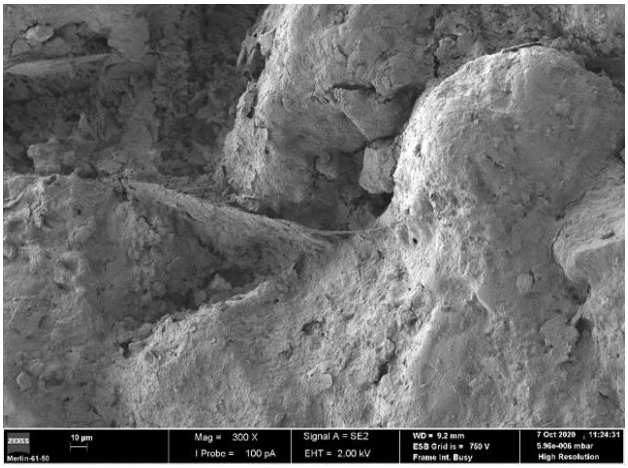

Figure 4. SEM image of the stabilized soil with Commercial XG (Mendonça et al., 2021).

3 CONCLUSIONS

This study compares the effectiveness of xanthan gum obtained directly from the *S. maltophilia Faro439* strain (LabXG) with commercial xanthan gum (XG) and Portland cement in reducing the permeability coefficient of a sandy soil. Both types of XG significantly reduced the permeability coefficient compared to untreated soil, with commercial XG been more effective. The use of 0.33% commercial XG was more effective than 1% of cement, suggesting its potential temporary replacement. Increasing the hydraulic gradient resulted in a slight reduction in permeability. The microstructure of the treated soil modified, with LabXG associated with a fibre-like network and commercial XG with a homogeneous paste. LabXG emerges as an interesting alternative, but future studies are needed to ensure its safety, as S. maltophilia falls under BSL-2 without specific regulations for environmental release.

ACKNOWLEDGEMENTS

The authors would like to express their sincere gratitude to the institutions that financially supported the research: individual research grant FCT 2021. 07819.BD, project research grant FCT (POCI-01-0145-FEDER-028382) and ACIV. This work was partly financed by FCT/MCTES through national funds (PIDDAC) under the R&D Units ISISE (UIDB/04029/2020) and ARISE (LA/P/0112/2020).

REFERENCES

Ayeldeen, M., Negm, A., El-Sawwaf, M. and Kitazume, M. (2017). Enhancing mechanical behaviors of collapsible soil using two biopolymers. *J. Rock mech. Geotech. Eng.*, 9: 329–339. https://doi.org/10.1016/j.jrmge.2016.11.007.

ASTM (2012). *Standard Test Methods for Laboratory Compaction Characteristics of Soil Using Standard Effort (12.400 ft-lbf/ft³ (600 kN-m/m³)*. D698-12e2 American Society for Testing and Materials, USA.

ASTM (2017). *Standard Practice for Classification of Soils for Engineering Purposes (Unified Soil Classification System)*. D2487-17e1. American Society for Testing and Materials, USA.

Cabalar, A.F., Wiszniewski, M. and Skutnik, Z. (2017). Effects of Xanthan Gum Biopolymer on the Permeability, Odometer, Unconfined Compressive and Triaxial Shear Behavior of a Sand. *Soil Mechanics and Foundation Engineering*, 54: 356–361. https://10.1007/s11204-017-9481-1.

Chang, I., Kwon, Y.-M., Im, J. and Cho, G.-C. (2019). Soil consistency and interparticle characteristics of Xanthan gum biopolymer–containing soils with pore-fluid variation. *Can. Geotech. J.*, 56: 1206–1213. https://doi.org/10.1139/cgj-2018-0254.

Mendonça, A., Morais, P.V., Pires, A.C., Chung, A.P. and Venda Oliveira, P.J. (2021). Reducing Soil Permeability Using Bacteria-Produced Biopolymer. Appl. Sci., 11: 7278. https://doi.org/10.3390/app11167278.

Venda Oliveira, P.J. and Neves, J.P.G. (2019). Effect of Organic Matter Content on Enzymatic Biocementation Process Applied to Coarse-Grained Soils. *Journal of Materials in Civil Engineering*, 31(7): 5533.0002774. https://doi.org/10.1061/(ASCE)MT.1943.

Proceedings of the XVIII ECSMGE 2024
GEOTECHNICAL ENGINEERING CHALLENGES
TO MEET CURRENT AND EMERGING NEEDS OF SOCIETY
© 2024 the Authors
ISBN 978-1-032-54816-6
DOI 10.1201/9781003431749-478
Open Access: www.taylorfrancis.com, CC BY-NC-ND 4.0 license

ECSMGE 24
XVIII EUROPEAN CONFERENCE ON SOIL MECHANICS AND GEOTECHNICAL ENGINEERING

Experimental study on strength and deformation properties of treated clay soils under triaxial and oedometric conditions

Étude experimentale de la résistance et de la déformabilité de deux sols argileux traités au ciment sous triaxiale et œdométrique conditions

J. Milosevic
Keller Grundbau Ges.mbH, Vienna, Austria

S. Zivaljevic*
University of Montenegro, Podgorica, Montenegro

T. Santana
Universidade NOVA de Lisboa, Lisbon, Portugal

**slobodanzivaljevic1979@gmail.com*

ABSTRACT: This paper presents an experimental study to evaluate the influence of adding 5% of cement, by dry mass of soil, on the strength and deformability of two different clays. Oedometer tests were performed on specimens of two different clayey soils, low plasticity Portugal clay and high plasticity Pljevlja clay, compacted according to standard Proctor test. Adding cement to the specimens resulted in reduction of instantaneous and time-dependent deformations under oedometric conditions. The increase in the preconsolidation stress, as determined by the oedometer test, along with the foregoing, indicates that adding cement has the similar effect as to pre-consolidate the clay. Conventional triaxial compression tests (CU) were performed on specimens of Portugal clay. The results of these tests showed that, with added cement, the compressive strength and secant Young's modulus E50 increases. Results of the CU tests indicated also that, once the cement is added, the soil behaviour changes from plastic to brittle plastic along with the pore pressure dropping during the shear stage.

RÉSUMÉ: Cet article présente une étude expérimentale pour évaluer l'influence de l'addition de 5% de ciment, par poids sec de sol, sur la résistance et la déformabilité de deux argiles différentes. Des éssais œdométriques ont été effectués sur des échantillons des deux sols argileux différents, l'argile du Portugal à faible plasticité et l'argile de Pljevlja à haute plasticité, compactés avec le même poids volumique sec déterminé par les éssais Proctor. L'ajout de ciment aux échantillons a entraîné une réduction des déformations instantanées et dépendantes du temps dans des conditions œdométriques. L'augmentation de la contrainte de préconsolidation, telle que déterminée par le test œdométrique, ainsi que ce qui précède, indique que l'ajout de ciment a le même effet que la pré-consolidation de l'argile. Des essais de compression triaxiale (CU) conventionnels ont été réalisés sur des échantillons d'argile du Portugal. Les résultats de ces éssais ont montré qu'avec l'ajout de ciment, la résistance à la compression et le module d'Young sécant E50 augmentent. Les résultats des tests CU ont également indiqué qu'une fois le ciment ajouté, le comportement du sol passe de plastique à plastique cassant et la pression interstitielle diminnue pendant l'étape de cisaillement.

Keywords: Cement-stabilized soil; clay soil; triaxial compression test; oedometer.

1 INTRODUCTION

Numerous reviews of soil stabilization using cement (Jawad, 2023) emphasize the efficiency of this old soil improvement method. Most of the researchers are focused on the strength parameters of the cemented soil, with fewer researchers oriented to the deformation properties (Rios et al, 2019). Moreover, in the field of improved soil strength, the unconfined compressive strength (UCS) has received much attention in comparison to the triaxial shear behaviour of cement improved soil (Azneb et al, 2021;Rios et al, 2019), due to the simplicity of determining this parameter. This paper presents an experimental study to evaluate the influence of the amount of cement on the strength and deformability of two different clayey soils.

2 EXPERIMENTAL INVESTIGATION

For the purpose of testing the characteristics of the cement-stabilized clay soil, the laboratory testing was

performed including oedometer tests and conventional triaxial compression tests.

2.1 Materials

A sample of a clay soil was obtained along the local road in the place Capuchos of the Almada County, south of Lisbon, Portugal (Miocene "Xabregas blue clays"), hereinafter referred to as the Portugal clay. The samples of the Miocene lacustrine clay, referred as the Pljevlja clay were collected from the construction site of the transformer station 400/220/110Kv Pljevlja 2, K.O. Ilino Brdo Municipality of Pljevlja in Montenegro (Figure 1). The basic physical properties of these two soils are summarized in Table 1. X-ray diffraction (XRD) was performed on Portugal clay. According to XRD, Portugal clay is mainly composed of quartz (52.9%), albite (18.3%), muscovite (10.8%), microcline (10.3%), calcite (3.0%), donbasite (3.2%).



Figure 1. Sampling locations of of the tested clays.

Table 1. Tested soil physical properties.

Soil	Portugal clay	Pljevlja clay
Unit weight (kN/m^3)	19.5	20.7
Liquid limit (%)	39	62
Plasticity limit (%)	25	24
Plasticity index (%)	14	38
D_{50} (mm)	0.20	0.0035
Unified Soil Classification	CL	CH
Optimal moisture content OMC (%)	13.5	-

The cement used for the purposes of this work was PC 35M (V-L) 32,5R, which represents a Portland-composite cement containing 64-79% clinker and 21-35% mixed silica fume and fly ash and lime. The water used was from public water system (potable water).

2.2 Specimen preparation and test procedure

Conventional triaxial tests were performed at the geotechnical laboratory of the Department of Civil Engineering, NOVA University of Lisbon. The testing involved the consolidated undrained triaxial tests (CU) on specimens of Portugal clay compacted at energy level of the standard Proctor's. Six specimens were tested, out of which three cemented-soil specimens with 5% of added cement. Oedometric tests were performed at the geotechnical laboratory of the Faculty of Civil Engineering, University of Montenegro in Podgorica. One non-cemented and one cemented specimens (5% of added cement) per each clay type were tested. A review of the specimens properties before testing is given in Table 2.

Table 2. Review specimen's properties before testing.

Soil	Test	w(%)	γ_d (kN/m^3)
Portugal clay	Triaxial	12.6	18.7
	Oedometer	13.5	16.1
Pljevlja clay	Oedometer	13.5	16.5

2.2.1 Oedometer test

Cement in quantity of 5% of the total dry weight was added to the clay, after which water was added. For specimens of both clays, a water content of 13.5% was achieved. The specimens for the oedometer test were compacted in oedometer cell by a 2.5 kg hammer dropped from the height of 30.5 cm, with 6 blows per one layer. This way, the compaction energy of 572 kJ/m^3, similar to the one specified by Standard Proctor test (624 kJ/m^3), was achieved. Immediately upon preparation, the non-cemented specimen was placed in the oedometer cell and then subjected to testing. Two cemented-soil specimens were cured for 7 days. The initial load applied was 100 kPa, with each subsequent load increment doubling the previous value, i.e. 200, 400 and 800 kPa respectively. Each loading step lasted for 24 hours and exceptionally for 48 hours.

2.2.2 Triaxial compression test

Cement in quantity of 5% of the total dry weight was added to clay that was in a relatively loose condition with the moisture content varying around 0.79%.

Upon achieving the moisture content, on dry side of optimal, of 12.6% (OMC – 0.9%), the specimens were compacted. The two-part cylindrical mould was used. Specimen diameter was D = 70 mm and the specimen height was H = 140 mm. The soil was compacted in four layers of 3.5 cm in thickness, using the 2.5 kg hammer dropped from the height of 30.5 cm.

This way, the equivalent compaction energy of 566 kJ/m^3 was achieved. The specimens were kept in plastic bags for 8 days to preserve moisture content of the specimen to the highest extent possible. Triaxial automated system (GDS Instruments) was used for the purposes of conducting CU test. The test was performed in three phases - saturation, consolidation and shear under undrained conditions with pore pressure readings. The specimen was sheared at rate of 0.05 mm/min.

3 RESULTS AND DISCUSSION

3.1 Oedometer test

Comparative diagrams of the total settlement to time and vertical load σ_z to vertical strain ε_z for the two clay specimens are shown in Figure 2 and Figure 3, respectively. Adding cement to soil specimens results in reduction of vertical settlement and vertical strains ε_z in vertical load σ_z range from 100 to 800 kPa, for specimens cured for 7 days.

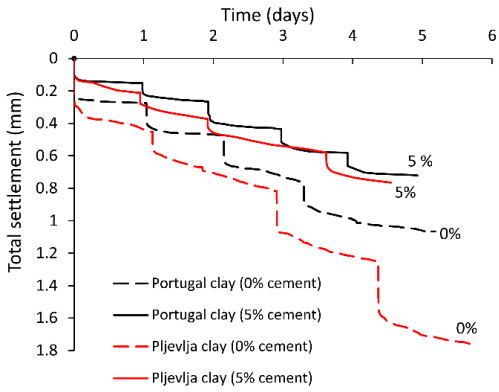

Figure 2. Comparative diagram of total settlement in relation to time for the clay specimens.

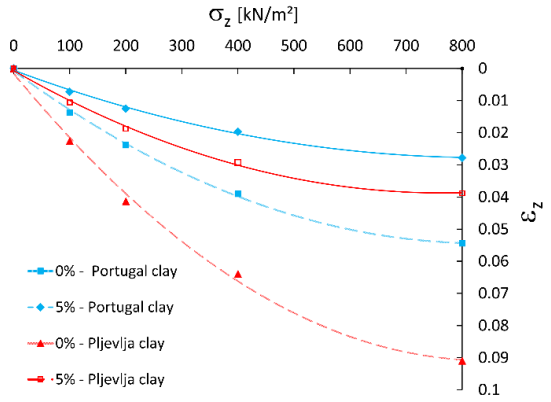

Figure 3. Comparative σz–εz diagram for the two clays.

Adding of cement affects the reduction in the instantaneous and time-dependent deformations (primary consolidation and/or creep), i.e. increases in the oedometric modulus E_{oed}. Calculated values of E_{oed} for cemented specimens are from 2.1 to 2.8 times higher compared to untreated specimens. The increase in the E_{oed}, can be partly attributed to the hardening, i.e. hydration of cement over the course of time.

The pre-consolidation stress can be defined by means of the Casagrande's method (1936), provided that the values of void ratio are known. For the cement-treated specimen of Portugal clay with the 5% added cement, the pre-consolidation stress p‘ is approximately 300 kPa, which is by 2.3 times higher than the p‘ for the same clay without added cement (p‘=130 kPa). The obtained result is compliant with the conclusion reached by Tugba (2015), indicating that the pre-consolidation stress changes with adding of cement, meaning, that increases with the percentage of cement.

3.2 Triaxial test

Figure 4 presents the deviator stress relation with axial strain of the non-cemented and cement-treated clay specimens of Portugal clay. The diagram indicates that for each value of the consolidation pressure of 100, 200 and 400 kPa, the maximum deviator stress of the cement-treated specimens is approximately 1.5 times higher than the deviator stress of the non-cemented specimens. It is also characteristic that at all levels of the all-around stress of 100, 200 and 400 kPa the cement-treated specimens underwent brittle failure at relatively low values of axial strain of about 5-7%. The non-cemented specimens underwent ductile failure, while in case of the cement-treated specimens a failure plane (shear bands) can be easily observed (Figure 4).

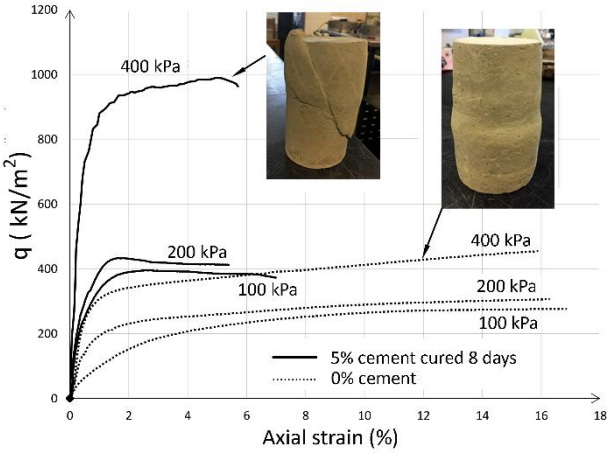

Figure 4. Diagram of ratio between the axial strain and deviator stress.

The effective stress paths for all specimens are illustrated in Figure 5. Reducing pore pressures during shearing of the non-cemented clay specimens (negative pore pressures for σ_c’=100 kPa) suggests

that the tested Portugal clay has the properties of the overconsolidated clay.

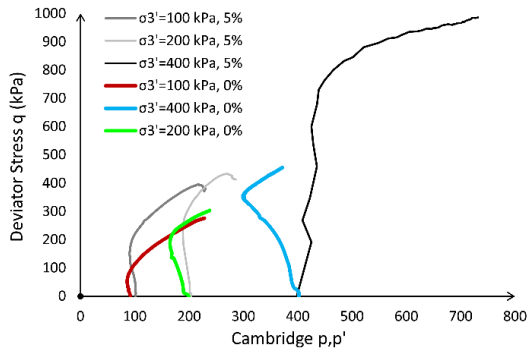

Figure 5. Effective stress paths for all specimens.

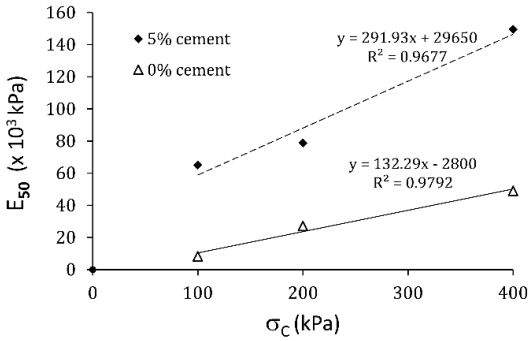

Figure 6. Diagram of the Young's modulus of elasticity E_{50} and lateral stress σ'c.

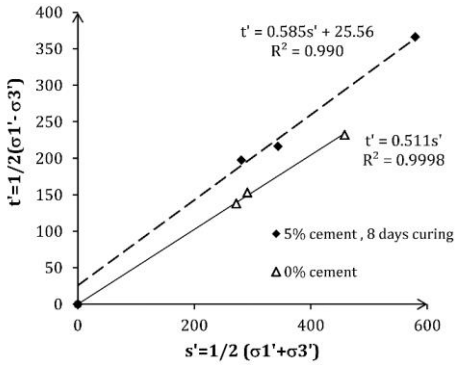

Figure 7. Mohr-Coulomb failure envelope for effective stresses for cement-treated and non-cemented specimen.

Secant elastic moduli of clay E_{50} have been obtained as a value of ratio of 50% of total deviator stress to the corresponding axial strain. E_{50} of the cement-treated specimens 3 to 7 times higher compared to the results of the non-cemented specimens under a lateral stress range from 100 to 400 kPa (Figure 6). Figure 7 shows Mohr-Coulomb failure envelopes for the cement-treated and non-cemented test specimens. It can be observed from the diagram, that for the non-cemented specimen the effective cohesion c' is 0 kPa as expected, and the angle of internal friction ø' is 30.7°. These values for the cement-treated specimen are cohesion c'=25.5 kPa and ø'=35.8°. Observed cohesion intercept indicates existence of true cohesion which results from chemical bonds between particles.

4 CONCLUSIONS

According to the results of oedometer test, adding of cement by 5% affects the reduction in the deformations of both clay specimens. Calculated values of E_{oed} for cemented specimens are from 2.1 to 2.8 times higher compared to untreated specimens. Results of CU triaxial tests on specimens of Portugal clay indicate an increase in value of the cohesion from zero value to 25.5 kPa, angle of internal friction from 30.7° to 35.8° and elastic moduli E_{50} by 3 to 7 times, compared to relevant values of parameters of nontreated soil. For Portugal clay, the increase in the preconsolidation stress by 2.3 times compared to the non-cemented clay and transition from ductile to brittle failure mode indicates that adding cement has the similar effect as the overconsolidation of the clay. Bearing in mind the limited scope of experimental testing, the verification of the above conclusions is foreseen through the directions of further research that may include other percentages of cement and longer times of curing, conducting similar tests at higher compaction energy (Modified Proctor test) conducting in-situ tests on the selected trial location of the cement-stabilized soil.

REFERENCES

Azneb, A.S., Banerjee, S., Robinson, R.G. (2021). Shear Strength of Cement-Treated Marine Clay under Triaxial and Plane Strain Conditions, In: *Proc. Inst. Civ. Eng. Ground Improv Vol.174*, pp.143–156. DOI:10.1680/jgrim.18.00090.

Casagrande, A. (1936). The Determination of the Pre-Consolidation Load and Its Practical Significance, In: *Proceedings of the 1st International Conference on Soil Mechanics*, Harvard, Vol. 3.

Jawad,I.T.,Taha,M.R.,(2023) Portland Cement Treated Soil: Evaluation and Conflict Results, *Civil Engineering and Architecture*, 11(2), pp.560-568. DOI:10.13189/cea.2023.110203.

Tugba, E., (2015) Influence of Cement Treatment on Unconfined Compressive Strength and Compressibility of Lean Clay with Medium Plasticity, *Arabian Journal for Science and Engineering*,40(3),pp.763—772. DOI:10.1007/s13369-015-1579-z.

Rios, S. et al. (2019) Mechanical and durability properties of a soil stabilised with an alkali-activated cement, *European Journal of Environmental and Civil Engineering*, 23(2), pp.245–267. DOI: 10.1080/19648189.2016.1275987.

Proceedings of the XVIII ECSMGE 2024
GEOTECHNICAL ENGINEERING CHALLENGES
TO MEET CURRENT AND EMERGING NEEDS OF SOCIETY
© 2024 the Authors
ISBN 978-1-032-54816-6
DOI 10.1201/9781003431749-479
Open Access: www.taylorfrancis.com, CC BY-NC-ND 4.0 license

ECSMGE 24
XVIII EUROPEAN CONFERENCE ON SOIL MECHANICS AND GEOTECHNICAL ENGINEERING

Assessment of the bearing capacity of bored piles with Expander Body technology using pressuremeter test-based methods

Évaluation de la capacité portante des pieux forés avec la technologie Expander Body à l'aide de méthodes basées sur des tests pressiométriques

F.F. Monteiro*, A.S. Oliveira
Unichristus, Fortaleza, Brazil

R.P. Cunha
University of Brasília, Brasília, Brazil

M.F.P. Aguiar
Federal Institute of Education, Science and Technology of Ceará, Fortaleza, Brazil

C.M. Silva
EMBRE, Brasília, Brazil

P.J.R. Albuquerque
State University of Campinas, Campinas, Brazil

**fernando.monteiro@unichristus.edu.br*

ABSTRACT: This study aimed to evaluate the accuracy of various semi-empirical methods for estimating the bearing capacity of bored piles with the innovative Expander Body technology in lateritic soils. The study analyzed the precision and accuracy of different methods based on PMT tests using the Ranking Distance Index (RD). Results showed that methods based on PMT tests were adequate for estimating the load capacity of piles equipped with the Expander Body technology in lateritic soils.

RÉSUMÉ: Cette étude visait à évaluer la précision de diverses méthodes semi-empiriques pour estimer la capacité portante des pieux forés avec la technologie innovante Expander Body dans les sols latéritiques. L'étude a analysé la précision et l'exactitude de différentes méthodes basées sur des tests PMT utilisant le Ranking Distance Index (RD). Les résultats ont montré que les méthodes basées sur les essais PMT étaient adéquates pour estimer la capacité de charge des pieux équipés de la technologie Expander Body dans les sols latéritiques.

Keywords: Expander body; pile load test; pile bearing capacity; pressuremeter; bored piles.

1 INTRODUCTION

The development in the civil construction sector results in increasingly complex buildings, necessitating progressively greater loads in foundations. In order to meet this demand, techniques are developed and refined to enable such constructions. A notable example is the Expander Body (EB) technology, a device installed at the tip of the pile, providing an increase in its bearing capacity. As indicated by Terceros Herrera and Terceros Arce (2016), this technique was conceived in the 1980s by the Swedish engineer Bo Skoberg and subsequently perfected in Bolivia, aiming to enhance the installation process and monitor the soil adjacent to the pile base (Fellenius and Terceros Herrera, 2014; Terceros Herrera and Massarsch, 2014; Fellenius et al. 2018).

The selection of an appropriate foundation type requires carrying out tests to obtain preliminary information into the characteristics of the soil under investigation, with an emphasis on its resistance. These tests include the pressuremeter tests (PMT) and many other in-situ testing procedures.

To estimate the bearing capacity of the pile-soil system, many semi-empirical approaches are used, including those proposed by Ménard (1963), Baguelin *et al*. (1978), and NFP 94-262 (2012). However, the results of these approaches are frequently variable. As a result, it is up to the practitioner to select the best

method for calculating the load-bearing capability of the evaluated pile-soil system. Compared to data obtained through pile load testing, acceptability criteria such as the Ranking Distance Index (RD) improve decision-making regarding the most accurate methodology. Orr and Cherubini (2003) proposed the use of a statistical index (RD - Ranking Distance), which assesses both accuracy through the mean and precision through the standard deviation of the ratio Q_p/Q_m (predicted/measured values) of any quantities, as described in the following equation:

$$RD = \sqrt{\left\{1 - \left[\mu\left(\frac{Q_p}{Q_m}\right)\right]\right\}^2 + \left[s\left(\frac{Q_p}{Q_m}\right)\right]^2} \qquad (1)$$

Where $\mu(Q_p/Q_m)$ and $s(Q_p/Q_m)$ represent the mean and standard deviation of the values (Q_p/Q_m), respectively. The optimum point occurs when $(Q_p/Q_m) = 1$ and $s = 0$.

Based on PMT test results from the Federal District of Brazil, this study assesses the accuracy and precision of three methods used to estimate the load-bearing capacity of mechanically bored piles equipped with Expander Body (EB) technology. The precision of the pile bearing capacity estimation methods is evaluated by comparing them to the results from pile load tests conducted on mechanically bored piles equipped with EB at the University of Brasilia's experimental field of foundations and in-situ tests.

2 EXPANDER BODY

The Expander Body System (EB) is a 0.12 m wide (initial diameter) by 1 to 2 m long bent steel tube that is inflated (expanded) during the first pressure-grouting stage and discharged over a grouting tube inside the rebar, as depicted in Figure 1. Distinct EB models enable expansion to a diameter of 400 to 800 mm. During the EB expansion process, grout pressure and volume are continuously recorded. The EB bottom tip rises as a result of the lateral expansion of the EB, which causes the EB tube length to shorten by approximately 0.1 m. As a result of this expansion, the soil beneath the EB decompresses, which is compensated by a second grouting stage of the soil at the pile tip (Figure 2).

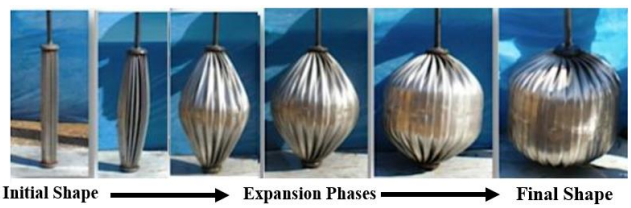

Figure 1. Expander Body expansion in-air.

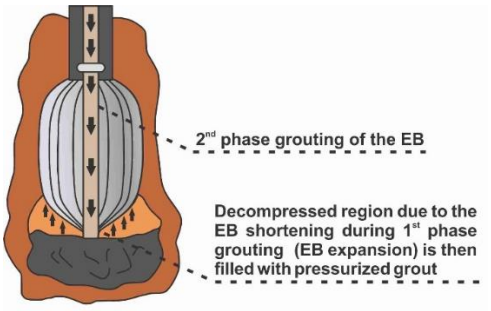

Figure 2. Post-grouting stage after Expander Body expansion.

Bored cast-in-situ piles can be constructed using a variety of techniques. Although each approach has some variation, the overall concept is the same. Drilling mud with permanent or temporary casing are typically combined with a rotary or percussive approach for pile drilling. Drilling ceases as soon as the design depth is achieved. Concrete is subsequently poured into the borehole after the reinforcement cage has been installed. Bored cast-in-situ piles that have EB technology installed use a similar installation process. The installation process of a bored cast-in-situ pile equipped with an EB system is shown in Figure 3.

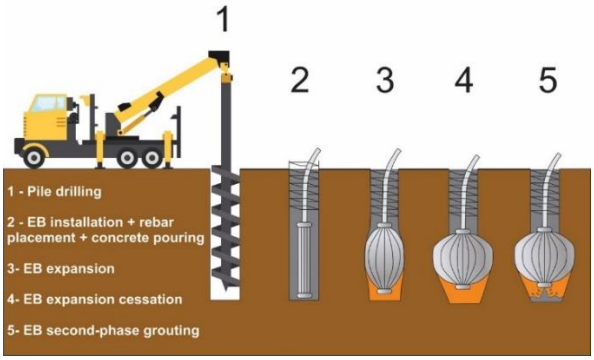

Figure 3. Bored cast-in-situ piles equipped with EB system installation technique.

The installation procedure of bored piles equipped with EB technology can be divided into five steps (Figure 3). Initially, pile drilling is carried out. Secondly, the EB is placed at design depth along with the reinforcement bar, and then, concrete is poured into the borehole. The next step consists of an initial grouting phase, delivered through a hollow schedule tube (EB expansion). After EB expansion ceases, the second-phase grouting step is carried out so that the decompressed region (pile tip) is filled with pressurized grout. Both injection pressure and volume are continuously monitored using a mortar pump and pressure gauge. This equipment not only provides adequate monitoring of the EB expansion but also provides pressure *versus* volume charts. The Expander Body effective diameter (D_{EB}) is determined from calibration curves for each EB model.

3 CASE STUDY

The Federal District is enclosed on the south by the 16°03' parallel and on the north by the 15°30' parallel, with a total area of 5814 km^2. The research location of the UnB geotechnical group has already been thoroughly explored and described in the literature (Cunha, 2011). This research location used various piling techniques, and the piles were horizontally and vertically loaded. Furthermore, several laboratory and in-situ tests have been conducted at this location. Block samples were collected and transferred to the laboratory, where triaxial, direct shear, oedometer, and routine characterization tests were performed. In the upper portion of this region, the soil strata change between clay, silt, and silty sand.

Two bored cast-in-situ piles equipped with EB technology with 8.8 and 10 m length were excavated with a rotating auger at the University of Brasilia experimental site, displayed in Figure 4. More details regarding the pile's geometric characteristics are shown in Table 1.

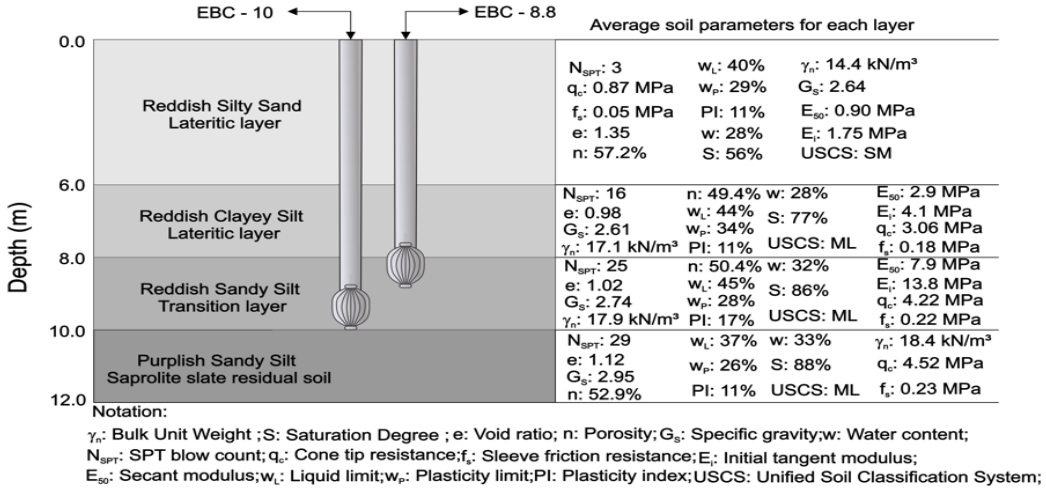

Figure 4. Typical soil profile at the UnB research site.

Figure 5 depicts the pressuremeter curves acquired during PMT tests in the experimental field. It is possible to determine relevant parameters such as limit pressure (p_L) and the coefficient of earth pressure at rest (K_0) from pressuremeter curves to use methods for assessing load-bearing capacity based on pressuremeter tests. The value obtained at a depth of 1 m was discarded due to issues with the test measurement. An increase in effective pressure with depth and a significant development in effective pressure in the saprolitic horizon are noticed.

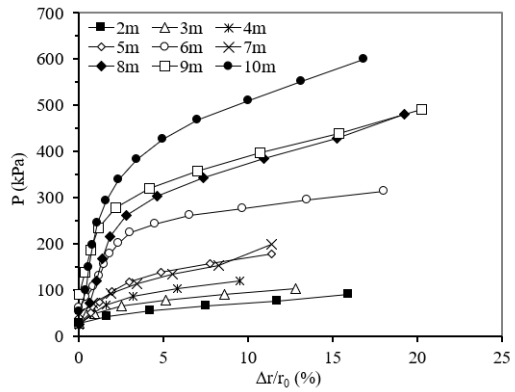

Figure 5. Pressuremeter test (PMT) curves.

A reaction beam, reaction piles, hydraulic jack, loading platform, and calibrated load cell were used to apply load. The spacing between reaction piles was at least three pile diameters. Mechanically bored, cast-in-place piles with the EB System were subjected to compression (Figure 6). The Brazilian Standard ABNT NBR 12131 (2006) specifies four pile load test conditions: slow maintained load, rapid maintained load, combined load, and cyclic load test.

All piles in this study were submitted to slow-maintained load tests, as shown in Table 1.

Table 1. Pile geometric characteristics, load type and velocity.

Test Pile	D (m)	D_{EB} (m)	Load condition	Load increment (kN)
EBC - 8.8	0.30	0.6	Slow maintained	100
EBC - 10	0.30	0.6	Slow maintained	120

The load increments were conducted in ten corresponding load stages, each representing 20% of the working load of the piles analyzed in the study. In the load tests performed, it was observed that the

displacement of the piles varied between 52.21 and 66.51 mm, reaching settlements close to the limit of the deflectometer (70 mm), thus noting displacements exceeding 10% of the diameter of the pile shaft. In this work, semi-empirical methods for predicting the load bearing capacity based on the limit pressure (p_L) measurements from the PMT test conducted in Brazil were studied. The methods used were Ménard (1963), Baguelin *et al*. (1978), and NFP 94-262 (2012).

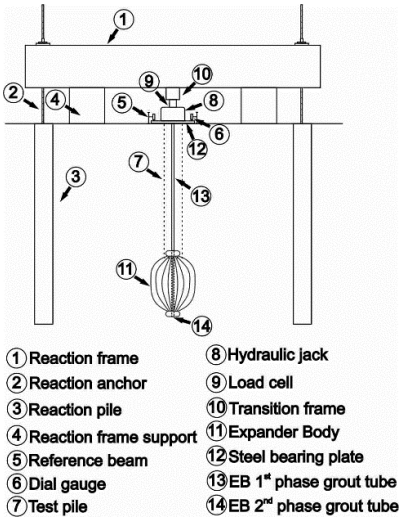

Figure 6. End view of compression pile load test set-up.

4 RESULTS

The load-displacement curves for the analyzed piles are presented in Figure 6. The pile with a length of 10 m, equipped with EB technology, sustained a load of up to 1200 kN, while the pile with a length of 8.8 m, also equipped with EB technology, reached a maximum load of approximately 1000 kN. Based on the displacement levels observed in the load tests, the conventional failure load of each pile can be determined using the 10% criterion of the pile shaft diameter. This criterion, widely adopted in European countries in accordance with Eurocode 7 (ECS, 2004) recommendations, results in interpreted conventional failure loads of 1140 and 823 kN for the bored piles equipped with the EB system, respectively.

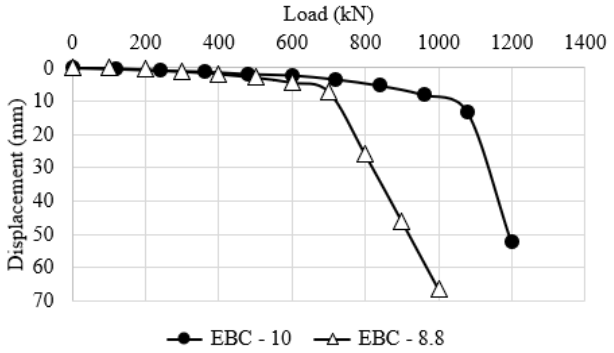

Figure 7. Load-displacement curves of analyzed piles.

Figures 8 and 9 present ratios between predicted and measured load capacities (Q_p/Q_m). Comparing the load capacity estimates from semi-empirical methods with the failure load interpreted from the conventionally determined load for a settlement equivalent to 10% of the pile diameter, it is observed that the methods proposed by Ménard (1963) and NFP 94-262 (2012) showed ratio values (Q_p/Q_m) below the range of ±20% for both piles equipped with the EB technology. While the Baguelin *et al*. (1978) method overestimates the reference values obtained from the interpretation of the pile load test results.

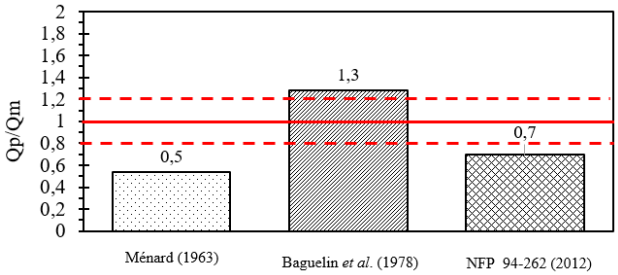

Figure 8. The ratio between predicted and measured load capacities for the EBC – 8.8 pile.

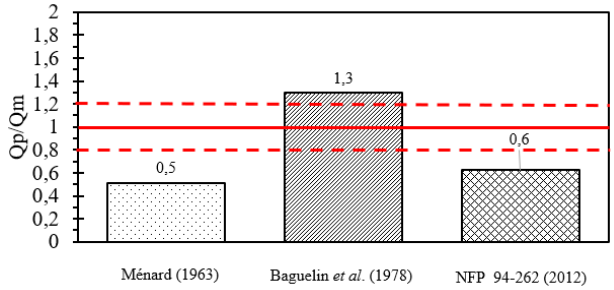

Figure 9. The ratio between predicted and measured load capacities for the EBC – 10 pile.

The semi-empirical methods for bearing capacity, based on pressuremeter tests, often use charts or tables to determine the tip resistance and side friction of piles. These methods require input parameters such as the limit pressure measured during the test, soil type, pile installation process, pile slenderness ratio (L/D),

and a load capacity factor (K_p) according to the soil type. The determination of the pile tip load capacity unit requires the use of the load capacity factor (K_p), while the unit side friction resistance is intrinsically linked to the values of the effective limit pressure of the soil layers through which the pile is installed. The determination of the effective limit pressure of the soil layers is influenced by various factors, including soil type, soil density, stress history, degree of saturation, anisotropy, variation of horizontal stress (directly related to the determination of K_0 values), and test depth. The pressuremeter tests in pre-drilled holes (MPM) carried out at the UnB Experimental Field presented effective limit pressure values between 77 and 466 kPa. According to the results obtained from the pre-drilled hole pressuremeter tests (MPM), using curve-fitting techniques, it was found that the K_0 values for the porous clay of Brasília varied between 0.34 and 0.72 along the depth, with an average value of 0.5. The K_p values range from 1.2 to 9.2 for different pile installation methods in the Baguelin *et al*. (1978) method. In the estimate presented in Figures 8 and 9, a load capacity factor (K_p) equivalent to 7.5 was adopted, explaining the likely overestimation of the load capacity of the piles equipped with EB. On the other hand, for other methodologies, the estimates are conservative due to the use of lower load capacity factor (K_p) values (between 1.2 and 2.1).

Table 2 presents the average values and standard deviations for the ratios between predicted and measured load capacity values (Q_p/Q_m) of the analyzed piles in this study. From these values, the Ranking Distance Index (RD) is determined. Low RD values represent an estimation method with high accuracy and precision. As RD values increase, this statistical index characterizes the estimation methodology as less accurate and less precise.

Table 2. Statistical analysis of the Q_p/Q_m ratios for the evaluated methods.

Method	Average (Q_p/Q_m)	Standard deviation (Q_p/Q_m)	RD
Ménard (1963)	0.50	0.0	0.50
Baguelin et al. (1978)	1.30	0.0	0.29
NFP 94-262 (2012)	0.30	0.1	0.35

Among the load capacity estimation methodologies based on PMT tests analyzed in this study, it is observed that the Baguelin et al. (1978) method presents the lowest RD value, making it the most accurate and precise methodology despite the estimated values being overestimated. On the other hand, the method proposed by Ménard (1963) shows the highest RD value, making it the least accurate and precise technique in relation to the data analyzed in this study. However, it was verified that using a load capacity factor (K_p) of magnitude 4 for the three methods results in Q_p/Q_m ratios between 0.8 and 1.0. This suggests, preliminarily, that the bearing capacity estimation using semi-empirical methodologies based on PMT test results for bored piles equipped with Expander Body technology in lateritic soils is satisfactory at the design level.

5 CONCLUSIONS

This work emphasized results obtained from load tests on mechanically bored piles equipped with the Expander Body technology, conducted at the Geotechnical Experimental Field of the University of Brasília. The analyzed foundations were axially loaded under compression, producing load-displacement curves that were interpreted to assess the precision and accuracy of load capacity prediction methodologies for bored piles equipped with the Expander Body system in the tropical soil of the Federal District, based on PMT test results.

Experimental data acquired from load tests and load capacity estimates using the methodologies of Ménard (1963), Baguelin et al. (1978), and NFP 94- 262 (2012) were compared for bored piles equipped with the EB technology, and these were presented and discussed. Although the results are confined to the conditions of the analyses, based on a limited dataset, they allow for preliminary generalizations of the overall behavior. Furthermore, they highlight the fact that the phenomena involved in such processes are considerably complex. In this regard, this research provided a better understanding of some characteristics involved in the loading mechanisms of single piles equipped with EB technology in lateritic soils. It should be noted, however, that some analyses were formulated as hypotheses to explain the results and need further research for a more informed appreciation in the future. Therefore, based on the observed trends in the data and analyses, some general conclusions can be drawn:

- The Baguelin *et al*. (1978) method shows the lowest RD value, making it the most accurate and precise methodology analyzed in this study;
- The method proposed by Ménard (1963) indicates the highest RD value, making it the least accurate and precise method in relation to the data analyzed in this study;

- Based on the experimental results and bearing capacity calculations, it is observed that the bearing capacity estimates, using methodologies reliant on PMT tests and considering a bearing capacity factor (K_p) of magnitude 4, prove to be suitable tools for estimating the load capacity of bored piles equipped with the Expander Body technology in lateritic soils.

It should be emphasized that the described conclusions need to be considered of limited scope and applicability. However, these results, along with the experience gained during the research, can be of great interest to foundation researchers and designers in this region and beyond.

ACKNOWLEDGEMENTS

This research was conducted with the participation of the Foundation and Field Testing Research Group (GPFees) from the Graduate Program in Geotechnics at the University of Brasília and the Special Foundations and Geotechnics Research Group (GPFEG) from the Undergraduate Program in Civil Engineering at Unichristus. The authors would like to express gratitude for the field assistance provided by the engineering company EMBRE and for the scholarship granted for this first author during his Ph.D.(GM/GD-140423/2017-6) by the governmental sponsorship organization CNPq (National Council for Scientific and Technological Development).

REFERENCES

ABNT NBR (2006). Piles – Static load test – Test method NBR – 12131, ABNT, Rio de Janeiro (in Portuguese).

Baguelin, F., Jézéquel, J. F., Shields, D. H. (1978). *The pressuremeter and foundation engineering.* Trans Tech Publications.

Cunha, R. P. C. (2011). Acquired knowledge on the behavior of deep foundations vertically and horizontally loaded in the soil of Brasília. *Soils and Rocks*, 34(3): 177-194. https://doi.org/ 10.28927/SR.343177.

European Committee for Standardization (2004). Eurocode 7 – Geotechnical Design – Part 1: General rules, ECS, Brussels.

Fellenius, B. H., Terceros, M. H. (2014). Response to load for four different bored piles. *Proceedings of International Conference on Piling and Deep Foundations*, Stockholm, Vol. 1, pp. 99-120.

Fellenius, B. H., Massarsch, K. R., Terceros Herrera, M. A., Terceros Arce, M. (2018). A study of the augmenting effect of equipping piles with an Expander Body. *Proceedings of International Conference on Deep Foundations and Ground Improvement: Urbanization and Infrastructure Development Future Challenges*, Rome, Vol. 1, pp. 114-123.

Ménard, L. (1963). Calcul de la force portante des fondations sur la base des resultats des essais pressiometriques. *Sols Soils*, 5(2): 9-24.

NFP (2012). Justification des ouvrages géotechniques - Normes d'application nationale de l'Eurocode 7 - Fondations profondes NF P 94-262, NFP, Paris (in French).

Orr, T.L. e Cherubini, C. (2003). Use of the Ranking Distance as an Index for Assessing the Accuracy and Precision of Equations for the Bearing Capacity of Piles and At-Rest Earth Pressure Coefficient. *Canadian Geotechnical Journal*, 40(6): 1200-1207.https://doi.org/10.1139/t03-063.

Terceros, H. M., Massarsch, K. M. (2014). The use of the expander body with cast in-situ piles in sandy soils. *Proceedings of International Conference on Piling and Deep Foundations*, Stockholm, Vol. 1, pp. 347-358.

Terceros Herrera, M.A., Terceros Arce, M. (2016). Recent advances in the expander body technology. *Proceedings of 18th Brazilian Conference on Soil Mechanics and Geotechnical Engineering*, Belo Horizonte, Vol. 1, pp. 31-38.

Proceedings of the XVIII ECSMGE 2024
GEOTECHNICAL ENGINEERING CHALLENGES
TO MEET CURRENT AND EMERGING NEEDS OF SOCIETY
© 2024 the Authors
ISBN 978-1-032-54816-6
DOI 10.1201/9781003431749-480
Open Access: www.taylorfrancis.com, CC BY-NC-ND 4.0 license

ECSMGE 24
XVIII EUROPEAN CONFERENCE ON SOIL MECHANICS AND GEOTECHNICAL ENGINEERING

Influence of temperature on strut loads in braced excavations

Influence de la température sur les charges des butons dans les excavations contreventées

P.-A. Mortensen*, T. Sandane
Norwegian Geotechnical Institute (NGI), Oslo, Norway

*per.anders.mortensen@ngi.no

ABSTRACT: For deep excavations a significant portion of the total load on steel struts originates from temperature variations. Ignoring the temperature induced load can lead to failure of the support system as the temperature induced load has been recorded as high as 65 % of the total load. The paper presents measurements of strut temperature load variations from 4 different deep strutted excavations in central Norway. The site conditions vary between the projects, from soft, normally consolidated quick clays to stiff, overconsolidated clays, and glacial moraine deposits. A total of 29 instrumented struts have been evaluated. The measured strut load and air temperature variations are analysed and used to define the degree of end restraint for each of the instrumented struts. Measured temperature loading is compared with estimates based on empirical relations proposed in the literature and with finite element analysis. The difference in soil conditions, excavation depth and number of strut levels are further used to evaluate the differences in the measured and estimated results.

RÉSUMÉ: Dans le cas des fondations profondes, une part significative de la charge totale sur les entretoises en acier provient des variations de températures. Ne pas prendre en compte la charge induite par la température peut mener à la rupture du système de support étant donné que des charges induites pouvant atteindre 65% de la charge totale ont été enregistrées. Cet article présente des mesures de charges induites par la température sur des entretoise profondes installées sur 4 excavations profondes différentes dans le centre de la Norvège. Les conditions de terrain sur chaque site sont différentes, allant d'argiles molles sensibles normalement consolidées à des argiles raides surconsolidées ou des dépôts morainiques (dépôts glaciaires). Au total, 29 entretoises instrumentées ont été évaluées. La charge mesurée et les variations de températures sont analysées et utilisées pour définir le degré d'encastrement de chaque entretoise instrumentée. Les charges induites par la température mesurées sont comparées aux estimations basées sur des relations empiriques proposées dans la littérature et sur des analyses par éléments finis. Les différences entre le type de sols, la profondeur d'excavation et le nombre de niveaux d'entretoise sont ensuite utilisés pour évaluer les différences entre résultats mesurés et estimés.

Keywords: Deep excavation; strut loads; retaining wall; temperature effects; load cells.

1 INTRODUCTION

When designing deep excavations, the estimation of forces acting on the retaining structure and bracing is of the outmost importance. There is a wide range of methods proposed in the literature for estimating the strut loads. Most common in design is apparent earth pressure (AEP) diagrams and numerical models such as finite element method (FEM) analysis. The AEP envelopes are derived from measurements of actual maximum strut loads (Peck, 1969). This means that the AEP diagrams implicitly include some effect of temperature on strut load (Twine and Roscoe, 1999; Hashash et al., 2003). 29 instrumented struts from four case studies in Norway are presented in this paper showing that the temperature induced strut load can become as high as 65% of the total load. If numerical models are used in the design process, additional temperature load must therefore be properly included in the final design load (Blackburn et al., 2005). Two of the cases presented, UDK02 and Wergelandstunnelen, are railway projects located in Drammen and Eidsvoll respectively. At UDK02 the ground conditions are normally consolidated quick clay of decreasing thickness over moraine. At Wergelandstunnelen the soils are dominated by low sensitive, stiff overconsolidated silty clays. The Havnelageret highway tunnel excavation in Oslo was performed in a refilled harbour basin. The top mases consisted of sand, gravel and brick remains, above a soft normally consolidated silty clay (Johansen and Woldsengen, 2014). Schweigaardsgate 33 was a commercial development project in Oslo where a ten-storey building with two basements was constructed. The ground conditions were about 4 m of fill material over clayey silt and sand, over soft normally consolidated clay.

2 MEASURED STRUT LOADS

Boone and Crawford (2000) plotted incremental changes in load against incremental changes in temperature with a best-fit line through the origin with slope m. The coefficient m, named thermal load coefficient, assumes a linear-elastic response in the soil and retaining wall system. Hashash et al. (2003) show with numerical analysis that thermal load coefficient is stage-dependent, meaning that it varies with the excavation depth and number of struts installed. Blackburn et al. (2005) suggested that the thermal load coefficient should be calculated for expansion and contraction separately and the study finds that the coefficient is larger for expansion. This would however suggest that the temperature fluctuations give rise to a steady increase in load for each temperature fluctuation, and this is not observed in the data presented here in this study. The method of analysing the data proposed by Boone and Crawford (2000) is therefore implemented, with the results of Hashash et al. (2003) in mind. For each load cell, a period during which little or no construction work took place is identified. The measured strut force is plotted against measured air temperature, and the thermal load coefficient is estimated as shown in Figure 1.Twine and Roscoe (1999) defines the degree of end restraint as the ratio between the occurring temperature load (P_T) over the theoretically induced temperature load in a fully restrained strut in which no expansion occurs, given by:

$$DR = \frac{\mathrm{P}_T}{\alpha_S E_S A_S \Delta T} = \frac{m}{\alpha_S E_S A_S} \qquad (1)$$

where DR is the degree of end restraint, α_S is the coefficient of thermal expansion of the steel, E_S is the elastic modulus of the steel and A_S is the cross sectional area of the strut. Table 1 summarizes the excavation geometry, site conditions and resulting measurements.

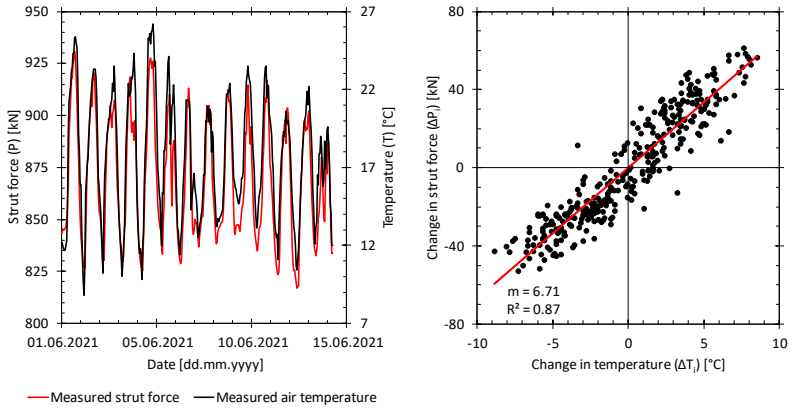

Figure 1. Example plots of measured strut force and air temperature and the determination of the thermal load coefficient (m).

3 ESTIMATED STRUT LOADS

Four methods of estimating DR have been employed. The first method, referred to as E1, was proposed by Chapman et al. (1972) and is based on a combination of the equations of deformation of an elastic half-space under a uniform rectangular foundation and the equation of thermal expansion of the strut. The second method, referred to as E2 was proposed by Boone and Crawford (2000) and is also based on Boussinesq solution, but for a smaller foundation given by the horizontal strut spacing (c/c) and the vertical equidistant (s) from subject strut to the strut above and below. The third method, referred to as E3, was proposed by Wu et al. (2019) and is an approximation utilizing Mindlin solution i.e. beam-on-elastic-foundation (BEF). The fourth and final method, referred to as E4, is based on FEM analysis using Plaxis 2D and the model established in the design of each case. The temperature loading from the FEM analysis is determined using the method proposed by NGF (2019), in which the strut is replaced by point loads with the same magnitude as the calculated load. The point loads are increased according to the assumed temperature load and the displacements are evaluated. This is repeated until the applied temperature load and resulting displacements matches a specific degree of end restraint. The estimated DR is shown in Table 1 for each case. The in-situ soil stiffness is the undrained soil stiffness achieved by triaxial testing or plate loading tests. When results are lacking, empirical relationships, such as Duncan and Buchignani (1976) have been employed. The residual standard deviation of E1, E2, E3 and E4 is 14.9%, 12.4%, 27.8% and 13.2%, and the measured value is on average 2.9, 0.78, 0.41 and 1.6 times the estimate, respectively.

Table 1. Summary of site conditions, construction details, measured and estimated degree of end restraint (DR).

Project	Strut no. & level	Strut area [cm²]	Strut length [m]	Strut spacing (s x c/c) [m]	Depth of strut level [m]	Depth of excavation [m]	EI supp. wall [MNm²/m]	EI waling [MNm²]	Soil Stiffness [MPa]	DR mea.	DR E1	DR E2	DR E3	DR E4
UDK02	1-1	156	17	5.2 x 5.0	0.3	11	188	168	22	17 %	7.3 %	26 %	37 %	5.7 %
	2-1	156	14	2.8 x 5.0	0.3	12	188	90.7	22	8.8 %	7.2 %	11 %	56 %	7.0 %
	2-2	195	14	6.3 x 5.0	5.6	12	188	225	40	31 %	10 %	31 %	40 %	18 %
	3-1	235	13	3.2 x 5.0	2.0	13	2035	1640	25	32 %	5.5 %	9.1 %	23 %	5.9 %
	3-2	274	13	8.8 x 5.0	6.3	13	2035	1640	45	41 %	8.1 %	29 %	29 %	17 %
Wergelandstunnelen	1-2	235	11	4.2 x 5.0	5.0	16	242	814	56	7.0 %	5.9 %	22 %	37 %	19 %
	1-3	274	11	8.7 x 5.0	9.2	16	242	1155	73	16 %	6.5 %	35 %	37 %	11 %
	2-2	235	11	4.2 x 5.0	4.9	16	242	814	56	7.7 %	5.9 %	22 %	37 %	19 %
	2-3	274	11	8.7 x 5.0	9.2	16	242	1155	73	16 %	6.5 %	35 %	37 %	11 %
	3-1	100	11	2.7 x 4.5	0.9	20	242	90.7	38	13 %	7.0 %	20 %	89 %	14 %
	3-2	235	11	4.2 x 4.5	5.4	20	242	814	58	18 %	4.6 %	24 %	34 %	16 %
	3-3	356	11	7.2 x 4.5	9.3	20	242	1369	75	24 %	4.0 %	27 %	34 %	5.6 %
	3-4	356	11	8.8 x 4.5	14	20	242	1824	89	17 %	4.6 %	32 %	34 %	5.6 %
	4-1	100	11	2.8 x 4.5	1.0	20	242	90.7	38	12 %	7.0 %	20 %	91 %	14 %
	4-2	235	11	4.2 x 4.5	5.5	20	242	814	59	12 %	4.7 %	24 %	35 %	13 %
	4-3	356	11	4.1 x 4.5	9.4	20	242	1369	75	11 %	4.0 %	21 %	31 %	4.2 %
	4-4	356	11	8.8 x 4.5	14	20	242	1824	89	18 %	4.7 %	33 %	34 %	5.6 %
Havnelageret	1-1	156	16	6.0 x 4.0	1.0	12	508	315	12	17 %	3.2 %	14 %	29 %	5.7 %
	1-3	188	16	2.8 x 4.0	7.0	12	508	429	13	12 %	1.4 %	6.2 %	10 %	3.9 %
	2-1	156	16	2.5 x 4.0	0.9	9.4	508	189	12	14 %	3.3 %	5.8 %	29 %	1.9 %
	2-2	220	16	3.8 x 4.0	4.9	11	508	676	22	11 %	3.6 %	14 %	20 %	5.0 %
	2-3	220	16	4.8 x 4.0	8.4	11	508	676	13	14 %	2.2 %	11 %	11 %	5.9 %
	3-1	156	14	5.5 x 4.0	0.5	11	508	189	8.4	19 %	2.6 %	9.2 %	28 %	4.8 %
	3-2	220	14	3.8 x 4.0	4.5	11	508	676	21	7.2 %	3.1 %	13 %	19 %	2.5 %
	3-3	220	14	4.8 x 4.0	8.0	11	508	676	13	5.5 %	1.9 %	9.3 %	9.3 %	5.9 %
Schwei-gaardsgate 33	1-1	195	32	1.8 x 5.0	0.5	7.7	125	225	9.3	18 %	5.9 %	4.4 %	31 %	0.9 %
	1-2	235	32	3.6 x 5.0	3.5	7.7	125	542	11	37 %	5.6 %	11 %	15 %	11 %
	2-1	235	33	1.8 x 5.0	0.5	7.7	125	225	9.3	19 %	5.1 %	3.8 %	27 %	0.3 %
	2-2	274	33	3.6 x 5.0	3.5	7.7	125	542	11	17 %	4.9 %	10 %	13 %	5.1 %

Based on the given dataset E2 and E4, yields the best estimate. E2 and E3 overestimates, while E1 and E4 underestimates the temperature loading on average. Chapman et al. (1972) and Boone and Crawford (2000) both commented that the soil stiffness needed to achieve the measured DR seems to be systematically higher for E1 and lower for E2. As done by Boone and Crawford (2000), the soil stiffness is back-calculated and a linear best fit is proposed. The linear fit, shown in Figure 2, relates the measured in-situ soil stiffness with the stiffness which should be used in the empirical relationship to achieve the best possible DR estimation. Using the proposed best fit line in E2 lowers the standard deviation from 12.4% to 9.1%.

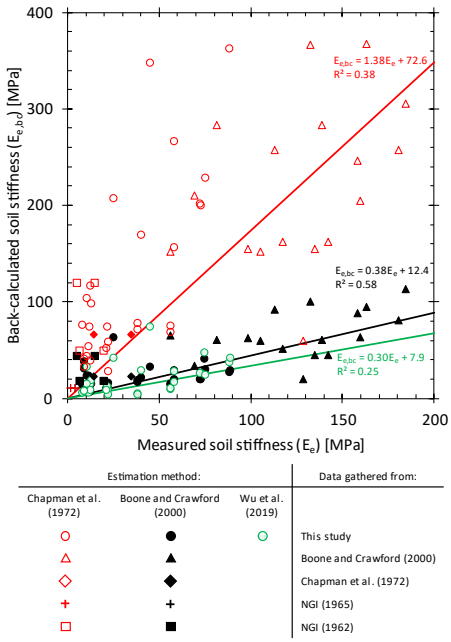

Figure 2. Back-calculated soil stiffness as a function of the measured soil stiffness.

Looking at the outliers we see that strut 3-1 and 3-2 of UDK02 are underestimated by all methods. These measurements are the only ones performed on a secant pile wall, and we see that the stiffness of the wall is much larger than for the other cases. Twine and Roscoe (1999) found that both wall and soil stiffness correlated with DF. However, none of the empirical methods include wall stiffness. The measurements from Schweigaardsgate 33 are also underestimated by all methods except E3. The strut length is the main deviation compared to the other cases, suggesting that longer struts lead to greater risk of underestimating the temperature load.

4 CONCLUSIONS

Estimating the temperature loading with the method proposed by Boone and Crawford (2000) gives the best fit to the case studies presented. This fit is further improved by using an empirical relationship between the measured soil stiffness and the stiffness utilized in the calculation. FEM gives just slightly higher residual standard deviation. However, FEM underestimates the temperature load on average, which could imply that the soil stiffness in the calculations is on average too low. The temperature load is underestimated when the supporting wall is very stiff, and in the case with long struts.

REFERENCES

Blackburn, J.T., Finno, R.J., and Sylvester, K. (2005). Observed bracing responses at the Ford Design Center excavation. *Proc., 16th Int. Conf. on Soil Mech. and Geotech. Eng.,* Osaka, Japan, pp. 1443-1446. https://doi.org/djdnk9.

Boone, S.J. and Crawford, A.M. (2000). Braced excavations: Temperature, elastic modulus, and strut loads, *J. Geotech. Geoenviron. Eng.,* 126(10), pp. 870-881. https://doi.org/bb5whg.

Duncan, J.M. and Buchignani, A. (1976). *An engineering manual for settlement studies,* University of California, Berkley, USA.

Chapman, K.R., Cording, E.J. and Schnabel, H. (1972). Performance of a braced excavation in granular and cohesive soils. *Proc., Spec. Conf. on Perf. of Earth and Earth Supported Struct.*, New York, USA, pp. 271-293.

Hashash, Y.M.A., Marulanda, C., Kershaw, K.A., Cording, E.J., Druss, D.L., Bobrow, D.J. and Das, P.K. (2003). Temperature correction and strut loads in central artery excavations. *J. Geotech. Geoenviron. Eng.,* 129(6), pp. 495-505. https://doi.org/cvtzxn.

NGF (2019). *Byggegropsveiledningen, Excavation Guidance (in Norwegian)*, 1st ed., Norwegian Geotechnical Society. Oslo, Norway.

Peck, R.B. (1969). Deep excavations and tunnelling in soft ground. *Proc., 7th Int. Conf. on Soil Mech. and Foundation Eng.,* Mexico City, Mexico, pp. 225-290.

Johansen, T. and Woldsengen, V. (2014). Experiences from deep excavations. E18 between the Festning tunnel and Ekeberg tunnel. Havnelageret contract. SVV, Oslo, Norway, Rep. Nr. 326.

Twine, D. and Roscoe, H. (1999). Temporary propping of deep excavations – guidance on design. CIRIA, London, UK, Rep. Nr. C517.

Wu, M., Du, C., Geng, X., Liu X., Tangdai, X. and Yang K. (2019). A new empirical approach to estimate temperature effects on strut loads in braced excavation. *J. Tunnelling and Undergournd Space Technology,* 94(Article 103115). https://doi.org/10.1016/j.tust.2019.103115.

Proceedings of the XVIII ECSMGE 2024
GEOTECHNICAL ENGINEERING CHALLENGES
TO MEET CURRENT AND EMERGING NEEDS OF SOCIETY
© 2024 the Authors
ISBN 978-1-032-54816-6
DOI 10.1201/9781003431749-481
Open Access: www.taylorfrancis.com, CC BY-NC-ND 4.0 license

ECSMGE 24
XVIII EUROPEAN CONFERENCE ON SOIL MECHANICS AND GEOTECHNICAL ENGINEERING

Development of a pioneering foundation system for a 225 000 m^3 LNG storage tank in Canada by using driven closed-ended steel piles non-connected to the concrete slab (rigid inclusions)

Optimisation du système de fondation d'un réservoir GNL de 225 000 m^3 au Canada avec l'utilisation de pieux battus en acier à pointe fermée déconnectés de la dalle en béton (inclusions rigides)

J. Munoz-Castelblanco*, N. Lafreme, Z. Gilbert, P. Moine, L. Boutillon
Vinci Construction Grands Projets, Nanterre, France

jose.munoz-castelblanco@vinci-construction.com

ABSTRACT: This paper presents the optimisation of the foundation system of a LNG storage tank of 225 000 m^3 volume, built in Kitimat, Canada. Site geology consists of a 160 m thick alluvial deposit, composed by alternating layers of clayey silts and gravelly sands. Surficial deposits are prone to liquefaction due to their low density and the high seismic activity in the area. To mitigate this risk, the design was optimised to a system of rigid inclusions, instead of the initial system proposed in the FEED, consisting of a piled foundation with a system of stone columns. This system was innovative in the LNG industry as it was the first time it was used for a LNG tank of such dimensions.
The robustness of the design has been confirmed by the performance of: CPTs after pile installation, confirming the increase of soil density; static and dynamic pile tests, validating the pile bearing capacity; and, monitoring of tank settlement, verifying that settlements are within the criteria defined in the project specifications.

RÉSUMÉ: Cet article présente l'optimisation du système de fondation d'un réservoir de Gaz Naturel Liquéfié (GNL) de 225 000 m^3, construit à Kitimat, Canada. Le site est caractérisé par un dépôt alluvial de 160 m d'épaisseur, composé par une alternance de limons argileux et sables graveleux. Les sols de surface sont potentiellement liquéfiables à cause de leur faible densité et du niveau de sismicité fort. Afin de réduire ce risque, la fondation a été optimisée avec un système d'inclusions rigides, au lieu de la conception FEED initiale, composé par une fondation sur pieux accompagnée par de colonnes ballastées. Ce système est novateur dans l'industrie du GNL car il est utilisé pour la première fois dans un réservoir GNL de ces dimensions.
Le système a été confirmé par différents types d'essais: des CPTs après l'installation des pieux qui ont confirmé la densification du sol; des essais de chargement statique et dynamique des pieux qui ont validé leur capacité portante; et, le suivi des tassements qui a prouvé que la fondation est dans les critères de tassement exigés par les spécifications du projet.

Keywords: Liquefied Natural Gas (LNG); foundation; rigid inclusions; design.

1 INTRODUCTION

Particular attention should be given to the foundation design of large diameter LNG tanks. The choice of foundation is governed by the natural heterogeneity of the soils, seismic hazard, nature of soils and behaviour, among other natural risks. The cost and feasibility of a LNG project is thus impacted by the soil condition.

This paper presents the optimization of the foundation system for a LNG tank located within the LNG Canada Site, close to Kitimat in British Columbia, Canada. The project includes the design and construction of an onshore 225 000 m^3 LNG tank; Figure 1 shows a generalized cross section of the tank, which is approximately 100 m diameter.

A risk of liquefaction has been detected in the area, which is driven by the following site conditions: the site soils are mostly sandy, the groundwater table is close to the ground surface, and the area is of high seismicity. A soil improvement method using driven closed-ended steel piles as rigid inclusions under the tank slab, was chosen to mitigate the risk of liquefaction. The system allows also to keep the settlement and differential settlement of the tank within the criteria and to improve the ground bearing capacity.

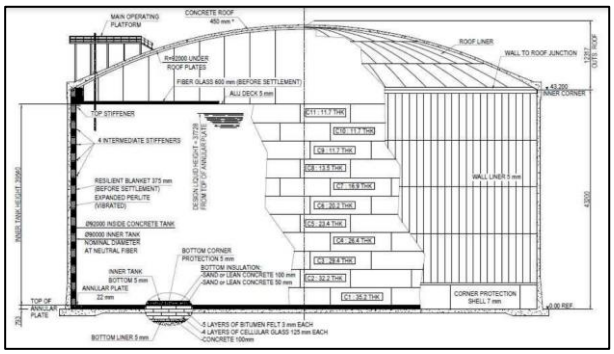

Figure 1. Cross section of the LNG tank.

The parties in the project are: The Owner, LNG Canada Development Inc. (LNGC, Shell); the Company, JGC Fluor BC LNG JV (JFJV); the Contractor, Entrepose Contracting Vinci Construction Grands Projets JV (EVJV); and, the Professional Engineer, Advisian (Worley).

2 CONTEXT

2.1 Geology, stratigraphy, geotechnical parameters

The whole plant area is located in the floodplain of Kitimat River, composed by a deposit of more than 120 m of interbedded and highly variable alluvial/deltaic Holocene sediments, overlying late Pleistocene marine clays. Bedrock is deeper than 260 m.

These sediments consist of predominantly fine sand and non-plastic to low plasticity silts. A gravellier layer is often encountered at depths ranging between 5 m and 10 m, and some gravel lenses can be found at greater depths. Cobbles and boulders are known to be present within some layers including the noted gravelly layer. Apart from this gravelly layer, which appears stronger that the surrounding sandy and silty layers, the average strength of the soils is low but slightly increases with depth. The silty layers are noticeably weaker than the sandy layers.

Deltaic progradation of the Kitimat River in the period since the last ice age has resulted in deposition of interbedded fine and coarse sediments that are relatively steeply dipping towards the south. The high horizontal variability of the sediments is worth to notice as boreholes closely spaced may show very different soil conditions at equivalent depths.

Based on geotechnical data, the soil layers encountered are presented, from top to bottom, in Table 1. The geotechnical parameters, presented in Table 2 and Table 3, have been defined from CPT data and some boreholes with sample extraction.

Table 1. Soil stratigraphy.

Unit	Description
S0	Very silty loose SAND with some layers of firm silt, 3 m to 6 m thick.
S1	Medium dense SAND and GRAVEL, 4 m to 32 m thick, with large lenses of firm sandy SILT within (LC1).
C1	Very sandy, very low plasticity, very stiff to hard SILT, 4 m to 18 m thick.
S2	Very silty and very gravelly medium dense to dense SAND and GRAVEL, 13 m to 26 m thick.
C2	Sandy, low plasticity, very stiff to hard SILT, 6 m to 15 m thick.
SC	Silty SAND composed by a mix of dense to very dense SAND and hard, low plasticity, SILT, approximately 60 m to 66 m thick.
C3	Predominantly hard, low plasticity to medium plasticity LEAN CLAY, with minor interbedded layers of silty sand and silt. The bottom of this layer has not been encountered and extends to more than 160 m depth.

Table 2. HSM soil stiffness values.

Unit	$E_{50,ref}$ (MPa)			M		
	LB	BE	UB	LB	BE	UB
S0	8.1.	13.5	27.0	0.5	0.5	0.5
S1	20.3	37.8	13.5	0.8	0.5	0.5
LC1	8.1	13.5	20.3	0.6	0.6	0.8
C1	10.8	20.3	31.1	0.6	0.8	1.0
S2	13.5	23.0	43.2	0.8	0.6	0.5
C2	5.0	13.5	40.5	0.7	0.6	0.5
SC	10.8	21.6	47.3	1.0	0.9	0.7
C3	4.7	7.4	14.9	1.0	1.0	0.8

Table 3. Shear strength parameters.

Unit	S0	S1	LC1	C1	S2	C2	SC	C3
γ (kN/m^3)	18	19	18	19	19	20	20	20
ϕ' (°)	30	34	28	28	34	28	32	28

Three levels of soil stiffness have been estimated for settlement calculations and liquefaction analyses: best estimate (BE), upper bound (UB) and lower bound (LB).

Hardening Soil Model (HSM) parameters, calibrated from soil data, were used for calculations. The pressure of reference (P_{ref}) is equal to 100 kPa. The oedometers modulus ($E_{oed,ref}$) is taken equal to the modulus at 50% of axial deformation (E_{50}). Unloading-reloading modulus (E_{ur}) is equal to three times E_{50}. Apparent cohesion was taken equal to 0 for all layers.

2.2 Seismic hazard

In order to evaluate the site soil potential to liquefaction, a Probabilistic Seismic Hazard Analysis (PSHA) has been performed to define the design motions and the cyclic shear stress for the two return periods required in the specifications: 475 years and 2 475 years, corresponding to the Operational Basis Earthquake (OBE) and the Safe Shutdown Earthquake (SSE) respectively. Most of the seismic events used to define the design motions have a magnitude (Mw) of 7.5.

The minimum factors of security against liquefaction required in the design phase, as per Standards, are 1.25 for OBE and 1.00 for SSE.

2.3 Codes and standards

The design and construction of the tank is governed by a list of Standards and Codes as defined in the project specifications. The order in which they are applied in the project is as follows, among other documents applicable:

Project Specifications (JFJV, 2016 & 2018);
DEP specifications (Shell, 2014);
American Standards (ACI 376-11, CFEM);
British Standards;
European Standards;
French ASIRI guidelines (IREX, 2012).

In case of any discrepancy between the recommendations given by the Standards, the instruction from the Owner is to apply the most conservative one. This point was source of discussion concerning the Factor of Safety (FoS) for the axial pile bearing capacity.

The other subject of debate was the design of the rigid inclusions system, considering that the design of this technique is defined by the French ASIRI guidelines (IREX, 2012), while neither the project specifications nor the Canadian codes include such recommendations.

A discussion on this is presented in section 5.

3 CHARACTERISTICS OF THE FOUNDATION SYSTEM

3.1 FEED Foundation system

The foundation system proposed by the Company at FEED design stage includes about 1800 stone columns up to 40m depth to mitigate the risk of liquefaction, and 500 driven open steel piles of 1m diameter and 40 to 45m length, connected to the slab, to control settlement and to ensure the bearing capacity.

This system has been optimised by the Contractor as presented below.

3.2 Foundation system for optimized design

The foundation system of the LNG tank is composed by a reinforced concrete raft of variable thickness (Figure 2), and ground improvement consisting of 1937 driven closed-ended driven steel rigid inclusions and a granular load transfer platform (Mattress).

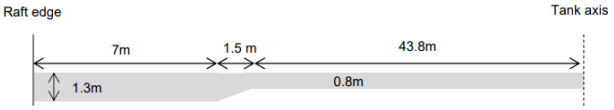

Figure 2. Cross section of the slab.

3.3 Foundation properties

The rigid inclusions used have the following characteristics: 1937 driven closed-ended steel tubes with diameter of 610mm, length of 18.5 m and thickness of 12.7 mm; top plate with diameter of 810 mm and thickness of 38 mm; and, steel conical shoe with diameter of 610 mm.

The inclusion mesh or spacing depends on the bearing layer at the inclusion toe level, and on the concentration of loads in the edge of the raft due to the weight of the tank wall. The tank area has been divided in four zones with different spacing (Figure 3). The toe of inclusions (20 m depth) is on silty soils in the North area and on sandy soils in the South area. Site sands are denser than silts, thus, spacing is bigger at the South area.

The load transfer platform located between the raft and the head of the rigid inclusions have the following properties: bulk unit weight (γ) of 20 kN/m^3; apparent cohesion (c') of 0 kPa, internal friction angle (ϕ') of 38°, and deformation modulus of compacted material (E) of 80 MPa.

In addition, the mattress material is complying with the following requirements: maximum particle size 100 mm; minimum 97% passing 75 mm sieve; 0 to 8% passing 63 µm sieve; D60/D10 minimum 7.5; and, maximum Los Angeles coefficient = 40.

3.4 Design loads

The static load cases are represented in Figure 4 for the main phases of the project: End of construction, Hydrotest (i.e. maximum pressure), and Operation (full tank condition).

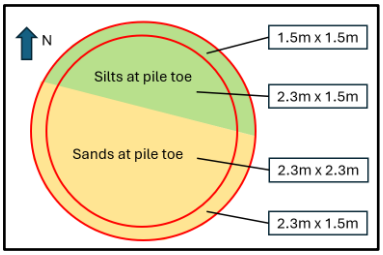

Figure 3. Inclusions' spacing.

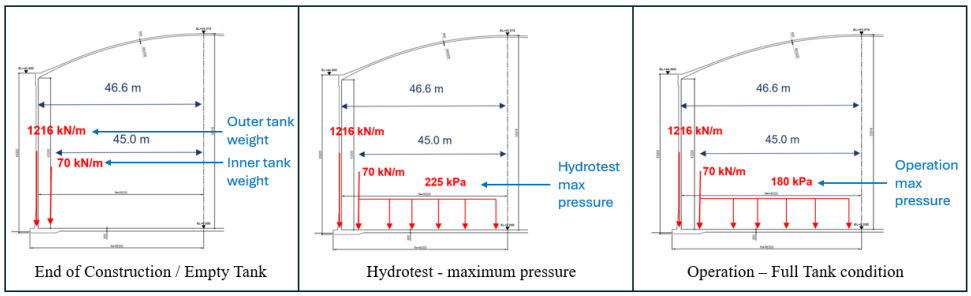

Figure 4. Load cases at the main phases of the project.

4 FIELD MEASUREMENTS TO VALIDATE THE DESIGN

4.1 CPTs after installation

The driving of closed-ended piles into the soil increases the global stiffness of the soil and helps to mitigate the liquefaction potential. While driving, the rigid inclusions displace the soil laterally, generating an increase of the density of the soil between the inclusions.

Several CPT tests have been performed to prove the effectiveness of the optimised foundation system. Figure 5 shows the characteristic values of cone tip resistance (q_c) for three situations: initial value before foundation works, estimated value of improved q_c in the design, and measured value after the installation of inclusions. The values are given for the three soil layers traversed by the inclusions.

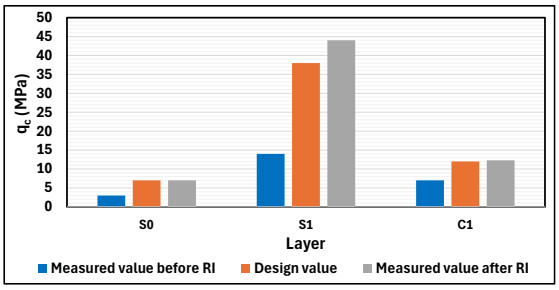

Figure 5. Characteristic values of q_c.

Figure 6 shows the profiles of factor of safety (FoS) against liquefaction for one measurement point under the higher seismic level, SSE. The potential of liquefaction is analysed from CPT data, using the methodology proposed by Boulanger & Idriss (2014). The analyses are done for the conditions before and after soil improvement.

The results show a clear improvement at the first 20 m soil layers; the densification is significant and even greater than what was expected. These measurements prove the effectiveness of the rigid inclusions system to mitigate the risk of liquefaction.

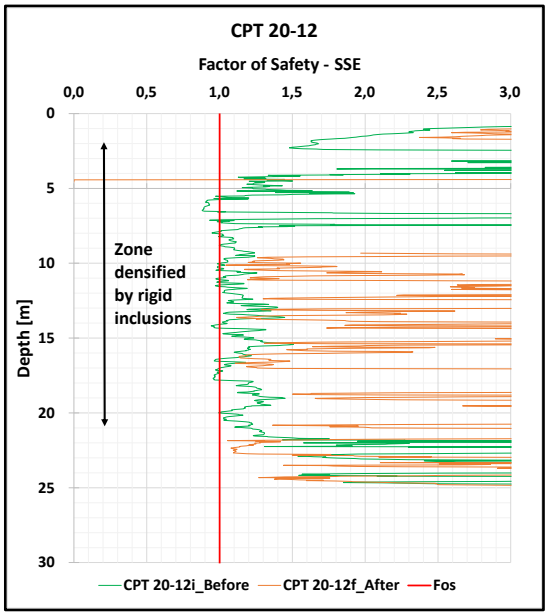

Figure 6. FoS liquefaction – CPT 20-12 – SSE.

4.2 Static and dynamic pile load tests

Figure 7 and Figure 8 present the values of pile bearing capacity for the North zone and the South zone, respectively. This division was done considering the pile toes are in different soil conditions.

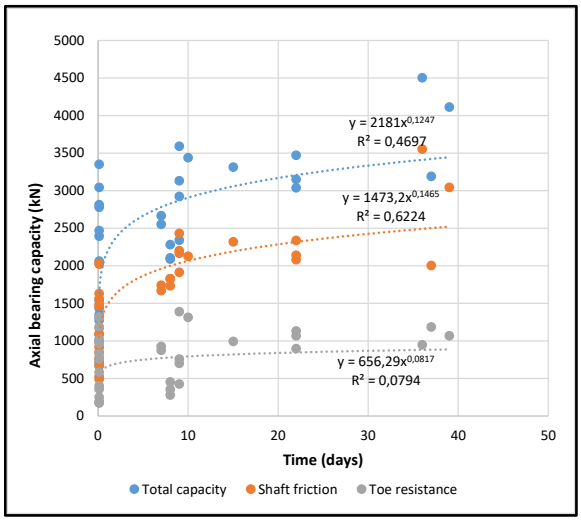

Figure 7. Pile capacity measured with PDA – North zone.

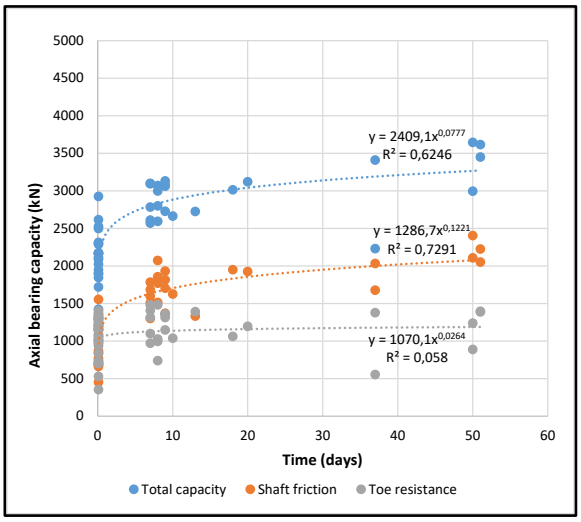

Figure 8. Pile capacity measured with PDA – South zone.

The bearing capacity is estimated from PDA (Pile Driving Analyzer) tests. 80 PDA tests have been performed on 40 piles across the tank area. Half of them were done at the End of Initial Driving (EOID), and the other half at the Beginning of Restrike (BOR) few days after EOID. For the EOID, the tests were performed by recording the driving data at the last 4 or 5 blows of the initial driving during pile installation.

The expected total capacity in the design is between 2387 kN (centre) and 2413 kN (outer ring) in the North zone, and, between 3653 kN (centre) and 3734 kN (outer ring) in the South zone. These values were estimated in the design considering the CPT data before improvement and the recommendations from the Canadian Foundation Engineering Manual (2006).

The data in Figure 7 and Figure 8 show an increase of pile bearing capacity with time. The comparison between the measured values with PDA and the expected values in the design shows: the expected bearing capacity is reached 7 or 10 days after driving in the North zone; and, the measured bearing capacity is lower than the expected in the South area at the time of measurement. Using the regression equation shown in the figures, the design expected capacity would be reached in about 250 days.

Further verifications of the bearing capacity of the tank were done using the measured values. The analyses show the bearing capacity is ensured with factors of safety in accordance with the Standards.

In addition, one static control load test has been performed on a working pile of the foundation. The test was performed one month after the pile installation. The results show the application of the maximum test load of 2065 kN (i.e. 1.5 times the maximum service load as per the design) generates a maximum settlement of about 8 mm, which is close to 1% of pile diameter and lower than the failure criteria displacement, set at 22mm.

4.3 Settlement monitoring

Tank settlements are measured by two systems: 1) topographical monitoring of survey markers at the tank periphery (Figure 9, left); and, 2) two chains of inclinometer sensors fixed along two horizontal tubes, placed perpendicularly each other across the slab (Figure 9, right).

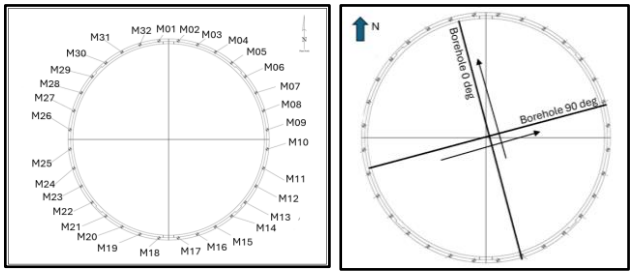

Figure 9. Survey markers and inclinometer pipes

The settlement model, developed using Plaxis 2D axisymmetric, has been updated with the real construction dates (Table 4). Due to the silty nature of the in-situ soils, a consolidation phase between each phase has been included in the calculation. Geotechnical parameters have been used as defined in the design.

Table 4. Construction dates.

Milestone	Start	Finish	Duration (days)
Raft construction	Jul. 20	Nov 20	129
Wall construction	Oct. 20	Jul. 21	287
Roof construction	Aug. 21	Nov. 21	76
Modules top side	Sep. 22	Dec. 22	78
Inner tank	Mar. 22	Feb. 23	361
Hydrotest	May 23	Jun. 23	32

Figure 10 and *Figure 11* show the vertical displacements at the center and the edge of the raft, respectively (purple triangles). The estimated values of vertical displacements are presented for each phase, based on the settlement model developed in the design, which considers the bounds of soil stiffness (Table 2).

The measured settlements follow the theoretical design settlements and are between the Upper Bound and Best Estimate curves. This fact implies that the design is validated. The measured values also follow the general trend of settlement with time, as predicted in the model, which confirms the hypothesis taken in terms of consolidation parameters.

The analysis also shows the measured settlement follow the project criteria in terms of the slope of the slab (1/300), general tilt (1/500), and perimetral settlement (1/500).

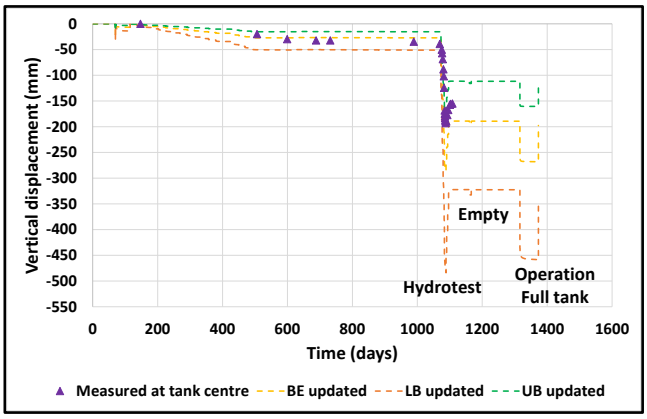

Figure 10. Settlement curves at the center of the tank.

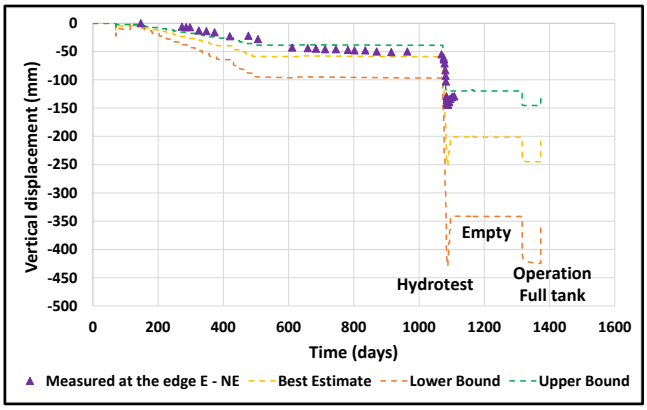

Figure 11. Settlement curves at the edge of the tank.

5 COMPLIANCE TO STANDARDS

In the tender design, the Contractor applied the recommendations from the Canadian Foundation Engineering Manual (2006), in which a global FoS of 2.0 for the axial pile bearing capacity is recommended.

However, the American Standard, ACI 376-11 (2013), requires a FoS of 3.0 for operation and OBE and 2.5 for SSE. This point has been solved by adding a larger top plate, 0.81 m in diameter instead of 0.61 m in the initial design, which helped to reach the required FoS.

6 CONCLUSIONS

The analysis and data presented in this paper show the effectiveness of the closed-ended driven steel piles, working as rigid inclusions, used as foundation system for a large diameter LNG tank. The solution allows to improve the bearing capacity, to mitigate the risk of liquefaction and to control the differential settlement. The last one is the main criteria to guarantee the integrity of the structure during the life cycle of the project.

Compared with the foundation system proposed in the FEED, the system designed and constructed by the Contractor helped to save in quantities and to reduce the time of construction of the slab, as piles and slab are not connected.

In other hand, the verifications performed during the design together with the control tests performed during construction helped to give confidence to the parties of the project on the solution, and thus, it is an open door to propose it for future projects.

ACKNOWLEDGEMENTS

The authors are grateful for the support of the parties in the project: the Owner, LNG Canada Development Inc. (LNGC, Shell); the Company, JGC - Fluor BC LNG JV (JFJV); and the Contractor, Entrepose Contracting - Vinci Construction Grands Projets JV (EVJV). Special thanks to Darren Beaumont from Advisian for his invaluable advice and support during the design of the tank foundations.

REFERENCES

American Concrete Institute, ACI. (2013). ACI 376-11 Code Requirements for Design and Construction of Concrete Structures for the Containment of Refrigerated Liquefied Gases and Commentary, 149p.

Boulanger R.W. and Idriss I.M. (2014). CPT and SPT based liquefaction triggering procedures. Report No. UCD/CGM-14/01. Center for Geotechnical Modelling, University of California, Davis.

Canadian Geotechnical Society. (2006). Canadian Foundation Engineering Manual, 4th Edition, 488p.

IREX. (2012). ASIRI National Project. Recommendations for the design, construction and control of rigid inclusion ground improvements. 383p.

JFJV. (2016). L001-00000-CG-7880-1001. Technical specification for geotechnical and foundation engineering including site investigation. 23p.

JFJV. (2018). L001-03100-CX-7739-1801. Specification for Full Containment Refrigerated LNG Storage Tank. 133pShell. (2014). DEP 34.51.01.32-Gen. DEP Specification. Full Containment Refrigerated LNG Tanks. 104p.

Proceedings of the XVIII ECSMGE 2024
GEOTECHNICAL ENGINEERING CHALLENGES
TO MEET CURRENT AND EMERGING NEEDS OF SOCIETY
© 2024 the Authors
ISBN 978-1-032-54816-6
DOI 10.1201/9781003431749-482
Open Access: www.taylorfrancis.com, CC BY-NC-ND 4.0 license

ECSMGE 24
XVIII EUROPEAN CONFERENCE ON SOIL MECHANICS AND GEOTECHNICAL ENGINEERING

Soil biocementation using the carbonic anhydrase metabolic pathway

Biocimentation des sols par la voie métabolique de l'anhydrase carbonique

W. Mwandira, M. Mavroulidou*, M.J. Gunn
London South Bank University, London, UK

D. Purchase
Middlesex University, London, UK

**mavroum@lsbu.ac.uk*

ABSTRACT: Biocementation, i.e., the soil cementation using cements produced biomimetically, has recently been introduced as a method of ground improvement, which is potentially more eco-friendly than conventional ground improvement methods. To date, the vast majority of researchers have used the urea hydrolysis metabolic pathway to biocement soils. We present instead work focusing on a less researched and potentially more interesting pathway, the carbonic anhydrase route, which produces biocement while sequestering CO_2. In this paper we present experimental results of bioprecipitate analysis and biocementation using CA producing bacteria; indicative results using the same bacteria though the ureolytic pathway are also shown; their modelling is then discussed instructed by studies on the ureolytic pathway. The results of this study based on bioprecipitate characterisation prove the precipitation of calcium carbonate using the CA pathway. The biocementation by biostimulation of the soil using the CA pathway was also proven, based on the unconfined compressive strengths of the treated soil ranging 0.5-1 MPa depending on cementing solution molarity vs the zero unconfined compressive strength of the untreated soil.

RÉSUMÉ: La biocimentation, c.a.d. la production de ciments biomimétiques, a été récemment introduite comme une méthode d' amélioration du terrain potentiellement plus éco-respectueuse que les techniques d' amélioration du terrain conventionnelles. Jusqu' à présent la plupart des chercheurs ont adopté la voie métabolique par uréolyse pour biocimenter les sols. En revanche, notre étude a pour objectif d' examiner une voie métabolique mois étudiée mais potentiellement plus intéressante, à savoir la voie métabolique de l'anhydrase carbonique, qui permet à la fois la biocimentation du sol ainsi que la séquestration du CO_2. Cette communication présente des résultats expérimentaux portant sur l' étude des minéraux bioprécipités et la résistance à la compression non confinée, confirmant la biocimentation du sol traité. Des résultats indicatifs obtenus par la voie métabolique par uréolyse (utilisant les souches isolées) sont aussi présentés. Nous traitons enfin du sujet de la modélisation de ce processus en puisant dans les exemples de la modélisation de la biocimentation par la voie uréolytique.

Keywords: Biostimulation; carbonic anhydrase; biocementation.

1 INTRODUCTION

To meet the objectives of net-zero carbon transition and environmental sustainability, geotechnical engineering practices must change radically. Whilst ground improvement will become increasingly important towards sustainable industry practices, ground improvement methods are still machinery-heavy and energy-intensive and often rely on Portland cement or lime to improve the ground; thus, they involve considerable GHG emissions for their production (Mavroulidou et al, 2022). Biomimetic cements, i.e., biocements, produced by the metabolic action of non-pathogenic microorganisms, have recently emerged as potentially more environmentally-friendly alternatives. Recent Life Cycle Assessment (LCA) research however, which considered different metabolic pathways to obtain biocements, questioned the actual sustainability of most processes and pathways (Porter et al, 2021). Porter et al's results showed that different metabolic pathways used for biocementation may have considerably varying and potentially negative environmental impact (especially considering the extent of industrial scale projects). These may be linked to the by-products of the particular metabolic pathway and also the purity of the input chemicals. However, they pointed out that the biotic metabolic pathway of interconversion between CO_2 and the bicarbonate ion HCO_3^- mediated by heterotrophic carbonic-anhydrase (CA) producing bacteria, would be the most environmentally friendly

and sustainable metabolic biocementation pathway. This pathway has the potential of consuming CO_2 (e.g. captured, industrial CO_2), while biocementing the soil, thus offering a dual way of addressing net zero carbon targets within the ground improvement industry. In this process CA utilises gaseous CO_2 to form hydrated aqueous CO_2 (aq) (Eq. 1), which reacts with water to form H_2CO_3 (Eq. 2). Once the H_2CO_3 is formed it ionises in water to generate H^+ and HCO_3^- (Eq. 2); under alkaline conditions, the HCO_3^- further ionises to form CO_3^{2-} and H_2O (Eq. 3). To form a biomineral, metal ion (e.g., Ca^{2+}, Mg^{2+} or Fe^{2+}) precipitates are formed from the reaction. For example, Ca^{2+} with CO_3^{2-} (Eq. 5) forms calcium carbonate. This reaction can occur either with CA-producing bacteria or purified CA enzyme (E) serving as nucleation sites.

$$CO_2\,(g) \leftrightarrow CO_2\,(aq) \quad (1)$$

$$CO_2\,(aq) + E.ZnH_2O \leftrightarrow H_2CO_3 \quad (2)$$

$$H_2CO_3 \leftrightarrow H^+ + E.ZnHCO_3^- \quad (3)$$

$$E.ZnHCO_3^- + E.ZnOH^- \leftrightarrow CO_3^{2-} + E.ZnH_2O \quad (4)$$

$$Ca^{2+} + CO_3^{2-} \leftrightarrow CaCO_3(s) \downarrow \quad (5)$$

Recent work of our team, funded by the European Commission (project *NOBILIS*, 101025184), has focused on the study of biocementation using the CA metabolic pathway (Mwandira et al 2023a-d). The study involved isolation and screening of CA-producing bacteria from a railway embankment foundation fine-grained soil in East Anglia. Bacteria with high CA activity were applied to biocement the native soil. Some salient results of the laboratory study are shown in this paper. This is followed by a discussion on the modelling of the processes, which is the next task of our ongoing work. Although CA metabolic pathway was the main focus of this study, results based on the ureolytic pathway using the same isolated strains are also shown indicatively, as this is a pathway used in most other biocementation research.

2 MATERIALS AND METHODS

The soils studied came from two trial pits accompanying the corresponding window samples from two boreholes (labelled BH01 and BH02 respectively in Table 1) from a site in East Anglia, UK. They came from depths of 0.6-2.9m. They were sandy clay or silty sandy clay soils except for soil sample BH01_0.6-1.1m, which was clayey sandy silt.

CA-producing bacteria were isolated from the accompanying window samples. Namely, 1 g of soil was placed in 10 mL of sterile deionised water and homogenised using a vortex mixer. The soil suspension was serially diluted to 10^{-4} using sterile deionised water; 0.1 mL of the dilution was plated on CM0003 Nutrient agar (Oxoid) consisting of 1g/L meat extract, 2g/L yeast extract, 5g/L peptone, 5.0g/L sodium chloride and 15 g/L agar); 3 mM p-Nitrophenyl acetate (p-NPA), was used as an indicator for CA-positive-producing bacteria. Bacteria colonies with CA-producing ability gave an intense yellow colouration as a result of the hydrolysis of p-NPA into paranitrophenol (pNP). The plates were placed in an incubator for 3 days at 30 °C, At the end of the incubation period the soil yielded 41 CA-producing bacteria with different morphologies. A preliminary microorganism identification was performed using matrix-assisted laser desorption/ionization time-of-flight/time-of flight tandem mass spectrometry (MALDI-TOF/TOF MS) proteomic-based biotyping approach, using a Bruker Daltonics MALDI Biotyper (Mwandira et al, 2023a).

Table 1. Basic physicochemical characteristics of site soils.

ID	LL %	PL %	PI %	W %	pH	Organ. cont. %
BH01_ 0.6-1.1m	-	-	-	32.4 %	7.9	7.8%
BH01_ 1.2-2.2m	63	33	30	47.6 %	7.7	3.9%
BH02_ 0.6-1.1m	35	22	13	34.4 %	7.8	5.5%
BH02_ 1.2-2.2m	39	23	16	36.1 %	7.8	5.8%
BH02_ 2.2-2.9m	40	26	15	34.3 %	7.7	4.0%

The CA enzyme activity was determined colorimetrically as follows: the activity of p-nitrophenyl acetate hydrolysis was determined at room temperature in a reaction mixture (1.35 ml) containing freshly prepared 3 mM p-nitrophenyl acetate in phosphate buffer (0.13M and pH 7.2). The reaction was allowed to proceed for 5 minutes, and the change to A348 per min recorded. Then the CA activity was characterised by the amount of p-nitrophenol produced per unit of time, and enzyme activity expressed as shown in Eq 6.

$$\text{A activity}\left(\frac{\text{U}}{\text{mL}}\right) = \frac{(\Delta A_{348}T - \Delta A_{348}B)\times 1000}{5\times V} \quad (6)$$

where $\Delta A_{348}B$ is the initial uncatalysed reaction (Blank) at a wavelength of 348 nm; $\Delta A_{348}T$ is the final reading of absorbance; 1 U (μmol/min) is the

amount of the enzyme that catalyses the conversion of 1 micromole of substrate per minute; and V is the volume of bacterial suspension added to the cell.

The urease activity of the isolated strains was also determined using the electrical conductivity (EC) method. It was expressed in mM of urea hydrolysed per minute, calculated as shown in Eq. 7, where EC_1 and EC_5 are respectively EC measured at 1 and 5 min.

$$\text{Urease activity}\left(\text{mM}\frac{\text{Urea}}{\text{min}}\right) = \frac{EC_1 - EC_5}{5} 10 \cdot 11 \quad (7)$$

Bioprecipitate analyses were conducted using precultured bacteria in peptone agar p-NPA and B4 (0.4% yeast extract,0.5% dextrose, 0.25% calcium acetate, 1.4% agar) agar media respectively for CA and ureolytic bacteria) at a concentration of 9×10^8 cells/L (i.e., suspension of OD_{600} of 0.5 -MacFarland Standard). This cell concentration was diluted in the applied bioaugmentation solutions ($Ca(CH_3COO)_2$ and $NaHCO_3$ and $CaCl_2$ and $CO(NH_2)_2$ respectively for the CA and ureolytic pathways). The mixtures were incubated for 6 hours at 37°C with shaking (160 rpm) and then further centrifuged (15,000 rpm for 5 minutes) to collect the bioprecipitates, which were then characterised.

To induce biocementation, biostimulation was used. The treatments used are shown in Table 2. This study refers to the treatment of the clayey sandy silt soil BH01_0.6-1.1 (see Table 1), which was just about coarse enough to allow treatment by injection. Soil layers which were more fine-grained were treated electrokinetically (see Mwandira et al, 2023a). The biostimulation process was conducted as in Mwandira et al 2023(a), according to optimised conditions. Biostimulation media were injected first; then after 3 days (i.e., the optimal growth time of the isolated bacteria, see Mwandira et al, 2023a,d), the optimised cementation reagent solutions respectively for CA and UA pathways (see Table 2) were injected.

Table 2. Biostimulation treatments.

ID	Biostimulation	Cementation
CA pathway		
Yeast Extract	10 g/L	-
Sodium Bicarbonate	100 mM	0.25M/0.5M
Zinc Sulphate	1 µM	-
Calcium Acetate	-	0.25M/0.5M
Ureolytic pathway		
Yeast Extract	20 g/L	-
Urea	330mM	-
Urea	-	1M
Calcium Chloride	-	1M

3. RESULTS

Maldi-TOF results on the 41 CA-producing strains that returned matches of secure or probable genus identification were identified as of the *Bacillus* genus. Indicative results of bioprecipitate study on selected CA-producing strains which also showed ureolytic activity are presented in Figure 1.

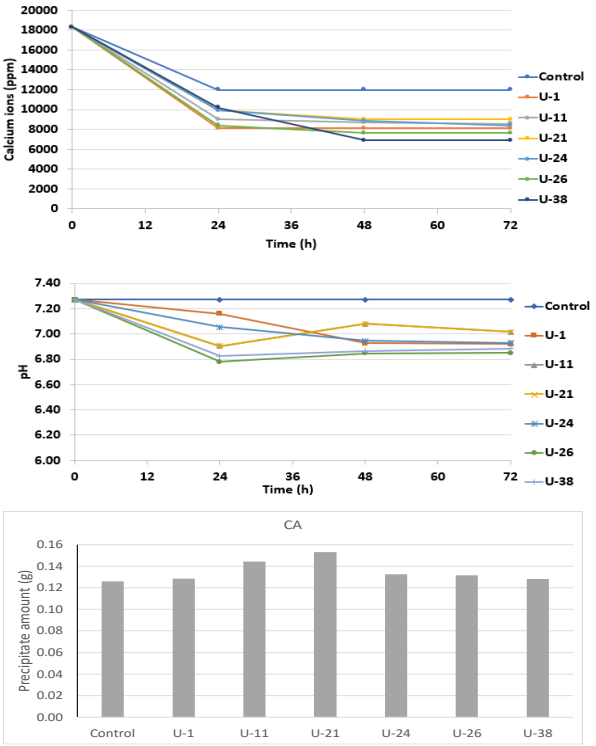

(a)

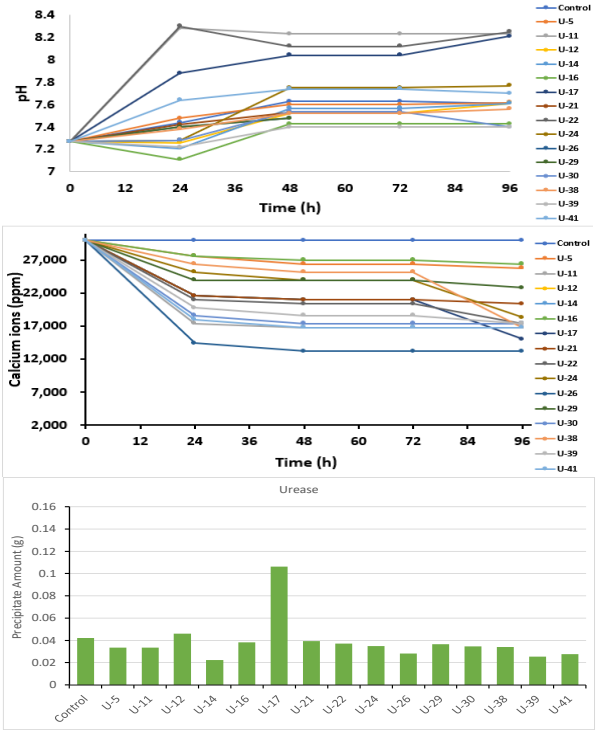

(b)

Figure 1. Bioprecipitates (a) CA route; (b) ureolytic route.

Figure 2 shows indicative SEM-EDS results of bioprecipitates obtained from the CA and ureolytic pathways. Carbonate minerals were confirmed, in most cases showing the typical calcite morphologies but rounder vaterite crystals were also detected depending on cementing solution molarity (not shown, for brevity). Figure 3 shows indicative photos of biocemented samples (after biostimulation) using the CA pathway, against untreated soil samples (control) and Figure 4 their unconfined compression strengths. The biocement can be clearly seen on the surface of biostimulated samples, concurring with the unconfined strength increase of the treated samples. Note that the ureolytic results were produced using a higher cementing solution molarity and this could be a factor leading to their higher strength increase.

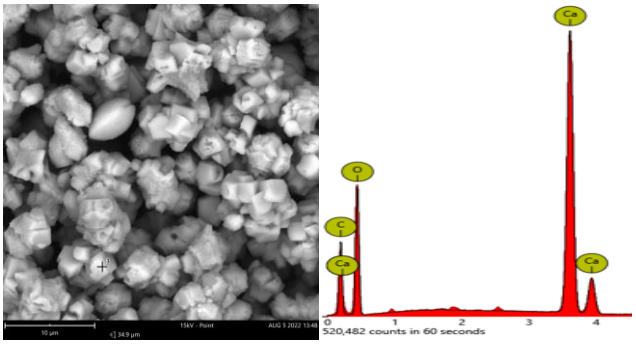

(a)

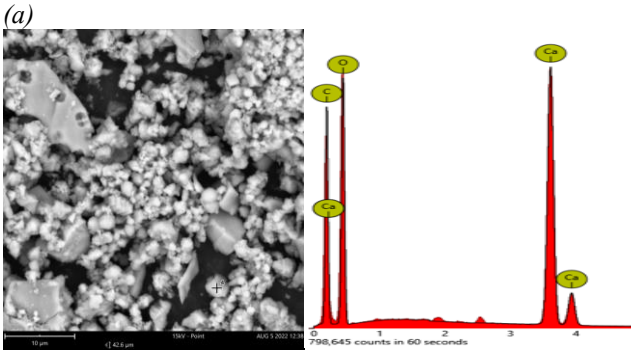

(b)

Figure 2. SEM-EDS (a) CA route; (b) ureolytic route.



(a) *(b)*

Figure 3. Soil samples (a)control; (b)biostimulated (CA).

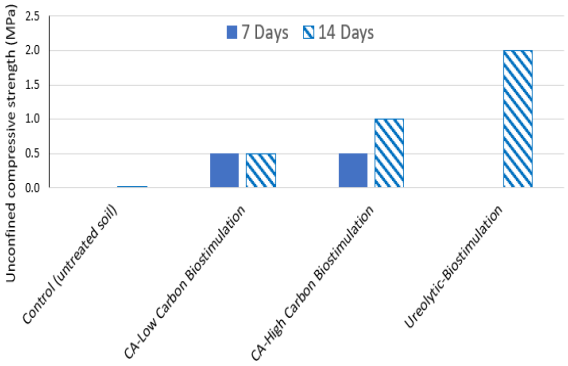

Figure 4. Unconfined compression test results.

4. MODELLING

Biocementation modelling comes under the general heading of reactive transport, whose origins go back to the 1980s with concerns about various environmental issues generally involving the flow and/or removal of contaminating chemicals in the ground (e.g. Lichtner et al., 1996). Traditionally three coupled processes are modelled: advection, dispersion, and chemical reactions taking place between solutes in the groundwater. Applying mass continuity, we obtain the basic differential equation for 1D advection-dispersion:

$$D^* \frac{\partial^2 c}{\partial x^2} - v_x \frac{\partial c}{\partial x} = \frac{\partial c}{\partial t} \qquad (8)$$

where v_x is the Darcy velocity in x direction, t is time

Generalisation of (8) to 3-D is straightforward and solutions are normally obtained numerically. In the general case there will be several different solutes (say N with different initial distributions of concentration) and this will lead to all these concentrations varying with time. The problem of solving a set of equations for a single set of concentrations which vary with time and space has been transformed by multiplying the number of equations to be solved by N. The final part of the picture is that these different solutes may react together (possibly forming new chemical substances) in a process which continues with time until overall chemical equilibrium is achieved. Techniques for the computer-based modelling of simultaneous chemical reactions have been in use since the 1990s and are now well established (Bethke, 2022). The most basic approach of coupling chemical reactions with the transport processes is to carry out the chemical reaction calculations following each transport time step (known as the Sequential non-iterative approach or SNIA -it is important here to consider the relative time rates between the chemical and transport processes to determine the appropriate approach). There are some additional processes which are significant in modelling biocementation as bacteria play an important role in biocementation by producing

enzymes which catalyse up important chemical reactions in the precipitation of calcite; the bacterial growth and enzyme activity needs therefore to be included in the modelling. Bacteria are commonly modelled as chemical species, where the bacterium in suspension is considered irreversibly attached to solid surfaces in the soil profile and independent of velocity and bacteria growth. Biofilm creation (coating the soil particles help promote sites for the calcite to precipitate) has been discussed and modelled for ureolytic bacteria (e.g. Faesli et al, 2023). The rate of the forward reaction (r_e) of CO_2 hydration catalysed by generic carbonic anhydrase may be described e.g. according to the Michaelis–Menten model. The reaction mechanism of CA has been extensively studied in other scientific fields or applications but we found no work so far modelling CA biocementation. Kinetics of the recombinant CA from bacteria have been reported in some CO_2 sequestration studies (e.g., Russo et al, 2016) and can be instructive. The final step for CA biocementation would be the precipitation of $CaCO_3$ as an immobile mass. This can be incorporated in the CA-pathway models in a similar way as in existing ureolytic models (e.g., Cunningham et al., 2019; Martinez et al., 2014; van Wijngaarden et al., 2011).

5. CONCLUSIONS

The work has focused on the little researched CA biocementation pathway, studying the biocemntation potential of bacteria isolated from soil under a railway embankment. The results proved the formation of calcium carbonate precipitates with calcite morphology, following the CA pathway, and the biocementation potential of these strains, corroborated by the increase in the unconfined compressive strength of the soil. Future work is addressing the modelling of the CA biocementation process, for which no information has been found in the literature. However existing studies on biocementation via the ureolytic pathway can be instructive, whereas further laboratory testing can serve in providing modelling parameters.

ACKNOWLEDGEMENTS

The research was funded by the European Commission (project NOBILIS, 101025184).

REFERENCES

Bethke, C. M. (2022) *Geochemical and Biogeochemical Reaction Modeling*, 3rd ed., Cambridge University Press.

Cunningham, A. B. Class H., Ebigbo A., Gerlach R., Phillips A. J., and Hommel J.,(2019) Field-scale modeling of microbially induced calcite precipitation *Comput. Geosci.*, 23(2):399–414. https://doi.org/10.1007/s10596-018-9797-6.

Faeli Z., Montoya B.M., Gabr M.A (2023) Elucidating factors governing MICP biogeochemical processes at macro-scale: A reactive transport model development, *Comput. Geotech.*, 160: 105514 https://doi.org/10.1016/j.compgeo.2023.105514.

Lichtner, P. C., Steefel, C. I. & Oelkers, E. H. (eds.) (1996) Reactive Transport in Porous Media, Volume 34 of *Reviews in a Mineralogy, the Mine-ralogical Society of America*, Washington, USA.

Martinez B. C., DeJong J. T., and Ginn T. R., (2014) Bio-geochemical reactive transport modeling of microbial induced calcite precipitation to predict the treatment of sand in one-dimensional flow, *Comput. Geotech.*, 58:1–13. https://doi.org/10.1016/j.compgeo.2014.01.013.

Mavroulidou M, Gray C, Gunn MJ, Pantoja-Muñoz L. (2022) A Study of Innovative Alkali-Activated Binders for Soil Stabilisation in the Context of Engineering Sustainability and Circular Economy. *Circular Economy and Sustainability*, 2: 1627–1651 https://doi.org/10.1007/s43615-021-00112-2.

Mwandira W., Mavroulidou M, Satheesh A, Gunn MJ, Gray C., Purchase D., Garelick J. (2023a) An electrokinetic-biocementation study for clay stabilisation using carbonic anhydrase-producing bacteria *Environmental Science and Pollution Research*, 30: 104916–104931 https://doi.org/10.1007/s11356-023-29817-7.

Mwandira W, Purchase D, Mavroulidou M, Gunn MJ (2023b) Synthesis and Utilisation of Hybrid Metal-Carbonic Anhydrase Enzyme Carrier System for Soil Biocementation, *Applied Sciences* 13 (17): 9494 https://doi.org/10.3390/app13179494.

Mwandira W., Mavroulidou M, Gunn MJ, Purchase D., Garelick H., Garelick J. (2023c) Concurrent Carbon Capture and Biocementation through the Carbonic Anhydrase (CA) Activity of Microorganisms -a Review and Outlook *Environmental Processes*, 10(4):56 https://doi.org/10.1007/s40710-023-00667-2.

Mwandira W., Mavroulidou M, Gunn MJ, Gray, C, Garelick J., Purchase D., (2023d) Biocementation mediated by native carbonic anhydrase-producing microbes. In. *Proceedings of the 10th Int. Conf. on Environmental Management, Engineering, Plan-ning & Economics Skiathos Island, Greece*, June 5-9, 2023 237-246, ISBN: 978-618-5710-25-5.

Porter, H.; Mukherjee, A.; Tuladhar, R.; Dhami, N.K. (2021) Life Cycle Assessment of Biocement: An Emerging Sustainable Solution? *Sustainability*, 13: 13878. https://doi.org/10.3390/su132413878.

Russo ME, Bareschino P, Olivieri G et al (2016) Modeling of slurry staged bubble column for biomimetic CO_2 capture. *International journal of greenhouse gas control* 47:200-209. doi: 10.1016/j.ijggc.2016.01.045.

van Wijngaarden W. K., Vermolen F. J., van Meurs G. A. M., and Vuik C., (2011) Modelling Biogrout: A New Ground Improvement Method Based on Microbial-Induced Carbonate Precipitation, *Transp. Porous Media*, 87(2): 397–420. https://doi.org/10.1007/s11242-010-9691-8.

Proceedings of the XVIII ECSMGE 2024
GEOTECHNICAL ENGINEERING CHALLENGES
TO MEET CURRENT AND EMERGING NEEDS OF SOCIETY
© 2024 the Authors
ISBN 978-1-032-54816-6
DOI 10.1201/9781003431749-483
Open Access: www.taylorfrancis.com, CC BY-NC-ND 4.0 license

ECSMGE 24
XVIII EUROPEAN CONFERENCE ON SOIL MECHANICS AND GEOTECHNICAL ENGINEERING

Brief report on the construction of the Liberdade/São Bento Station of circular line G (Pink Line) of the Porto Metro

Bref rapport sur la construction de la station Liberdade/São Bento de la ligne circulaire G (Ligne Rose) du métro de Porto

V. Nascimento
Plengil – Soluções de Engenharia e Gestão, Porto, Portugal

S. Mateus
TPF– Consultores de Engenharia e Arquitetura, S.A, Porto, Portugal

I. Coelho*
Metro do Porto, S.A., Porto, Portugal

**ines.coelho@metrodoporto.pt*

ABSTRACT: Liberdade/São Bento station (L/SBS) is one of the four stations that are part of the new circular line, also known as "Line G" or "Pink Line". This new project will increment 3 km's to Oporto light rail system and will connect the existing stations of São Bento and Casa da Música. Once it is located in the heart of Oporto city centre, it was important to ensure the minimum impact at the surface and traffic disruption, which why Liberdade/São Bento station is being built using a mix of cut-and-cover and top-down construction methodologies. The station is formed by its main body, which develops longitudinally to the axis of the railway, and by its surface accesses, which develops perpendicularly to the railway axis at both ends and in the central area of the station body. Due to its location and dimension, the construction process has revealed himself as extremely challenging, once it combines the complexity of building in an high urban area, extremely affected by various services (water supply, wastewater network, rainwater, gas, electricity and all telecommunication services), but also historical (proximity to several monuments and the appearance of new archaeological monuments during excavations), along with the geological-geotechnical conditions considered in the design of excavations, retaining support and foundations (structural support and protection of buildings; high levels of groundwater; groundwater contamination). This paper aims to describe the main constraints that are being faced during the execution and explain how are they being managed and overcome.

RÉSUMÉ: La station Liberdade/São Bento (L/SBS) est l'une des quatre stations qui font partie de la nouvelle ligne circulaire, également connue sous le nom de "Ligne G" ou "Ligne rose". Ce nouveau projet ajoutera 3 km au système de métro léger de Porto et reliera les stations existantes de São Bento et Casa da Música. Une fois située au cœur du centre-ville de Porto, il était important de minimiser l'impact sur la surface et les perturbations du trafic. C'est pourquoi la station Liberdade/São Bento a été construite en utilisant un mélange de méthodologies de construction en tranchée couverte et de construction de haut en bas. La gare est formée par son corps principal, qui se développe longitudinalement à l'axe du chemin de fer, et par ses accès de surface, qui se développent perpendiculairement à l'axe du chemin de fer aux deux extrémités et dans la zone centrale du corps de la gare. En raison de son emplacement et de sa dimension, le processus de construction s'est révélé extrêmement difficile, une fois qu'il combine la complexité de la construction dans une zone urbaine élevée, extrêmement affectée par divers services (approvisionnement en eau, réseau d'eaux usées, eaux pluviales, gaz, électricité et tous les services de télécommunication), mais aussi historique (proximité de plusieurs monuments et apparition de nouveaux monuments archéologiques pendant les fouilles), ainsi que les conditions géologiques-géotechniques prises en compte dans la conception des fouilles, des confinements et des fondations (soutien structurel et protection des bâtiments; niveaux élevés des eaux souterraines; contamination des eaux souterraines). Ce document vise à décrire les principales contraintes rencontrées au cours de l'exécution et à expliquer comment elles sont gérées et surmontées.

Keywords: Metro; construction; cut-and-cover, top-down, granite.

1 INTRODUCTION / GENERAL FRAMEWORK OF THE WORK

Liberdade/São Bento station (L/SBS) integrates the new circular line (aka Line G, or Pink Line) of Metro do Porto light rail system, which will increment 3km's to the current network. It is located in a consolidated urban area of Oporto city centre, and it will connect the existing station of São Bento and Casa da Música.

Considered as a Unesco World Heritage area, the implementation of this new station demanded a careful and thorough study of the spatial, structural and planning constraints.



Figure 1. Plant insertion of Liberdade/S. Bento Station (L/SBS).

In order to enable the construction in such a narrow space (Figure 1) and ensure the safety of all the building and historical heritage on the surroundings, it was necessary for the design team to study and conceive new approaches and solutions, once the standard solutions (foundation piles, e.g.) were not possible to implement.

The density of utilities and services affected (namely wastewater, water supply, electricity, etc.) and the crossing of an ancient underground rainwater galleries (Rio da Vila), demanded a complex coordination between the several specialities projects, in order to achieve a feasible and integrated solution.

2 URBAN CONSTRAINTS

By way of background, it is important to highlight the existence of a combination of determining factors that led to an atypical metro station, especially in geometric and functional terms. These are summarised below: the small width of the urban roads for the insertion of a current metro station; intense road and pedestrian traffic on the surface as well as the presence of buildings next to the work, some of which are of heritage and historical importance; the convergence in "Praça da Liberdade" of a system of rain galleries (called Rio de Vila (RV)) that runs southwards towards the Douro river, which constitutes a barrier that is very difficult to overcome; the crossing of "Praça da Liberdade" through the tunnel of metro line C, heading north towards Aliados; the need for an underground pedestrian link between line C and the Circular line, connecting the new station to São Bento metro station.

Due to the above mentioned, a complex and dynamic coordination between design teams was needed, in order to ensure the feasibility of the technical solutions adopted.

3 THE STRUCTURAL SOLUTIONS ADOPTED

Due to the constraints presented, the L/SBS is being built, mostly, using the so-called top-down method, with peripheral retaining support in Diaphragm Walls (DW). Due to the proximity of the buildings and the need to drill through a relatively competent rock mas without percussion, an hydromill trench cutter was used, with specific dimension limitations.

This structural solution aims to ensure: structural continuity between the roof slab and the peripheral containment (first phase of the structure), labelled connections between diaphragm walls and the remaining station slabs (Mezzanine and Back Slab).

In order to simplify the work and enhance its durability, standard structural solutions were favoured, avoiding complex connections, mainly resulting from: intermediate vertical elements to be built in the first phase (top-down method), the support of the roof on walls to be built in the second phase (open excavation).

It should be noted, however, that it was necessary to use the support of the roof slab in an intermediate DW alignment in the body of the station, otherwise, considering the spans presented, it was necessary to increase significantly the thickness of the roof slab, what would have been unaffordable, because of the land cover intended.

Mainly due to the factors described and the need to minimize the traffic disruption, the construction had to be adapted to the several varied moments of diversions transition, with the execution of the station's structural elements being subdivided into 11 Phases (Figure 2).



Figure 2. Division of the Station for the execution of the structural elements.

The areas highlighted in red were executed entirely from the bottom up; the green area represents the top-down construction method.

4 GEOLOGICAL, GEOMORPHOLOGICAL AND TECTONIC SETTING

The route of the project is located in the Central Iberian Zone, where there is a characteristic granite massif with complex geotechnical conditions, marked by the tectonic framework of the granite massif and the hydrothermal and meteoric alteration that followed its installation (Santos et al, 2019).

According to Santos (2019), from a tectonic point of view, the influence of the Hercynian orogeny and the proximity of the Porto-Albergaria-a-Velha-Coimbra-Tomar Shear Belt, with a NNW-SSE orientation, which passes through the Foz do Douro and Nevogilde areas, stand out.

The granite massif of Porto is generally sandy and kaolinised, heterogeneous and geotechnically complex where granite soils and rock levels occur without a pattern. This is largely due to the proximity of an intense deformation zone which favoured a large fracture network and deep fluid circulation (hydrothermal alteration) which was intensified by meteoric alteration conditioned by the climate, surface water infiltration conditions and the relief in general.

From a geomorphological point of view, the route is located in a flattened region slightly inclined towards the sea, where low areas are followed by hills with flattened tops, intersecting the valleys of the tributary watercourses of the River Douro.

The L/SBS is built on several watercourses, which are currently channelled / diverted and substantially earthed, the main one being the RV, which means that the working levels reach minima close to 10m.

4.1 Geological-Geotechnical Zoning (GGZ)

In order to carry out the geological-geotechnical reconnaissance and elaborate the GGZ (Figure 3) of the massif, all the existing elements relevant to the project presented here were collected and analysed, two geotechnical prospecting campaigns were carried out and all the available data was subsequently analysed and systematised. Two prospecting campaigns were carried out with 48 geotechnical rotary boreholes, accompanied by the systematic execution of SPT tests and the complete collection of rock mass, with the installation of 24 open tube piezometers, 41 Lugeon tests and 43 Lefranc tests, plus 37 simple compressive strength tests.

The boreholes reached depths varying between 23.0 and 46.5 metres.

In order to determine the aggressiveness of the groundwater to the concrete, 8 samples were taken from boreholes along the route and chemical analyses of the groundwater were carried out to obtain pH values, sulphate content, aggressive carbon dioxide, nitrogen and magnesium.

51 samples were also selected to be subjected to tests to determine density, porosity and resistance to uniaxial compression with determination of the modulus of deformability.

GEOTECHNICAL ZONING	LITHOLOGY	WEATHERING GRADE		FRACTURATION GRADE	JOINTING CONDITIONS	N_{SPT}	GSI
G1	γ	W1	FRESH GRANITIC	F1-F2	d1-d2	NA	65-85
G2	γ	W2	SLIGHTLY WEATHERED GRANITE	F2-F3	d2-d3	NA	45-65
G3	γ	W3	MODERATELY WEATHERED GRANITE	F3-F4	d3-d4	NA	30-45
G4	γ	W4	HIGHLY WEATHERED GRANITE	F4-F5	d4-d5	NA	15-30
G5	γ	W5	COMPLETELY WEATHERED GRANITE	NA	-	>50	-
G6	γ	W6	RESIDUAL SOIL GRANITE	NA	-	<50	-
G7	EMBANKMENT /ALLUVIUM	NOT APPLICABLE (NA)		NA	-	VARIABLE	-

Figure 3. Geotechnical zoning adopted and its reference parameters (adapted from Santos, 2019).

The GGZ of the L/SBS was defined on the basis of information from 5 geotechnical boreholes, with depths between 21 and 25m, complemented by information available from the 1st phase of the construction of the Metro do Porto when the line was built to the existing ESB (Santos, 2019).

Through GGZ, the station mostly intersects G7 and G5, to a lesser extent G4, and occasionally G3. Unit G7 is made up of embankments and alluvium that cover the underlying granite formation, reaching depths of between 2 and 9 metres (Figure 4).

Unit G5 is made up of very compact granitic soils (NSPT>60 strokes), with occasional rocky cores and is located between 2 and 19m deep, exceeding the

station's implantation level in the central zone (Santos, 2019).

According to Santos (2019), in the central area of the station, the rock mass only occurs below the station's base level (G4 and occasionally G3). To the east and west, the G4 and G3 massifs are already found between the top and base of the station. Circumscribed G3 rock cores can, however, be intercepted above the station's base level.

The G3 rock unit occurs at depth, with some continuity from 8-24m deep, and the G2 unit is punctual and not very continuous, usually between 18 and 25m.

According to Santos (2019), the high oxidation of the granite massif's fractures, some filled with organic soils, and the interception of a passage of monogranular rolled sands within the decomposed massif (G5), indicate the presence of an uncompressed granite massif, with open fractures and high underground percolation.

The water table is close to 5 metres deep (Santos, 2019).

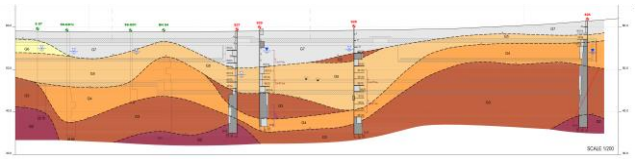

Figure 4. Longitudinal Geological-Geotechnical Profile of the L/SBS (excerpt from Drawing with code P-PR-LI-8000-GG-DS-SCN-000002-00), for legend of the GGZ see Figure 3.

5 CONCLUSIONS

Liberty/São Bento station represents a great example of the importance of exploring the underground space in urbanized cities. However, it also teaches us the importance of the existence of updated registrations and records for the underground services and utilities, which can compromise, severely, the construction process.

Location revelead itself as one of the major factors for the selection of the construction method, design and construction premisses: due to the proximity to residential, commercial and historical buildings, it was necessary to implement a solution which allowed to preserve the integrity of the built heritage, but also minimize the impact on the surface near the residents and population. Despite the careful and thorough coordination of the design teams for the several specialities during the design process, several question marks remained during the entire excavation, thus the importance of an high engagement of all the stakeholders involved (namely design teams, owner, constructor and municipality), such as a risk and expectation management.

An effective communication and engagement of the several competent authorities, are crutial to ensure the city dynamic, communication and disclosure of information near the population.

ACKNOWLEDGEMENTS

The authors are grateful for Metro do Porto allowing to publish data from the project presented here.

REFERENCES

Santos, L., Aguiar. A., Azevedo, A. (2019) Linha Circular Troço Liberdade/S. Bento – Boavista/Casa da Música - Projeto de Execução – Volume 6 – Geologia e Geotecnia – Memória Descritiva, Report n.º: P-PR-LI-8000-GG-MD-SCN-000001-04, Metro do Porto, SENER, CJC e NSEEngineering, Portugal.

Azevedo, A., (2020) Linha Circular Troço Liberdade/S. Bento – Boavista/Casa da Música - Projeto de Execução – Volume 00 – Enquadramento Geral. Código: P-PR-LI-8000-GE-MD-SCN-000001-03, Metro do Porto, SENER, CJC e NSEEngineering, Portugal.

Pina Jr, N., Mazzella. I., Azevedo, A. (2019) Linha Circular Troço Liberdade/S. Bento – Boavista/Casa da Música - Projeto de Execução – Volume 5 – Tomo 5.2 – Obras de Contenção – Especificações Técnicas, Código: P-PR-LI-8000-ET-ET-SCN-000001-02, Metro do Porto, SENER, CJC e NSEEngineering, Portugal.

Proceedings of the XVIII ECSMGE 2024
GEOTECHNICAL ENGINEERING CHALLENGES
TO MEET CURRENT AND EMERGING NEEDS OF SOCIETY
© 2024 the Authors
ISBN 978-1-032-54816-6
DOI 10.1201/9781003431749-484
Open Access: www.taylorfrancis.com, CC BY-NC-ND 4.0 license

ECSMGE 24
XVIII EUROPEAN CONFERENCE ON SOIL MECHANICS AND GEOTECHNICAL ENGINEERING

Finite element analyses of slurry trench stability and deformations – back-calculation of field tests in soft clay

Analyses par éléments finis de la stabilité et des déformations des tranchées à coulis - Rétro-calcul des tests de terrain en argile molle

E. Nilsen*, K. Karlsrud, E.J. Lande
NGI, Oslo, Norway

**eirik.nilsen@ngi.no*

ABSTRACT: The slurry trench method has, since the early 1970s, been used in Norwegian soft clays to construct diaphragm walls to support deep excavations. The technique involves excavation of a deep trench stabilized by a fluid/slurry that exerts a pressure on the trench walls. When the method was used for construction of diaphragm walls for a subway and railway tunnel through central Oslo in the 1970s there was little experience with the method in soft clays. Therefore, a field test program with several test trenches was initiated which included monitoring of ground settlements, pore pressures, and horizontal deformations at depth. The present study analyses results from two slurry trenches at Vaterland, one of size 1×5 m and the other of size 1×1.8 m. These trenches were deliberately brought to failure by drawdown of the supporting slurry. Finite element analysis (FEA) is used to back-calculate the observed behaviour with respect to safety and deformations. The NGI-ADP model is used for the clay at the test site. The results are compared with the observed behaviour and the factor of safety calculated using a simplified analytical approach proposed earlier. The analyses show that the NGI-ADP model can predict failure with satisfying accuracy, and that effect of the trench shape on the stability is well captured.

RÉSUMÉ: La méthode des tranchées à coulis est utilisée depuis le début des années 1970 dans les argiles molles norvégiennes pour construire des parois moulées destinées à soutenir des excavations profondes. La technique consiste à creuser une tranchée profonde qui est stabilisé par un fluide/boue, en exerçant une pression sur les parois de la tranchée. Lorsque cette méthode a été utilisée dans les années 1970 pour la construction de parois moulées pour un tunnel de métro et de chemin de fer traversant le centre d'Oslo, il y avait peu d'expérience dans son utilisation avec les argiles molles. Un programme de tests sur le terrain impliquant plusieurs tranchées d'essai a donc été lancé. Le programme comprenait des mesures de tassement, des pressions interstitielles et des déformations. La présente étude analyse les résultats de deux tranchées à coulis à Vaterland, l'une de dimension 1×5 m et l'autre de dimension 1×1,8 m. Ces tranchées ont été délibérément poussées jusqu'à la rupture en abaissant le niveau du coulis de support. L'analyse par éléments finis (FEA) permet de rétro-calculer le comportement observé relatif à la sécurité et les déformations. Le modèle NGI-ADP est utilisé pour l'argile sur le site de test. Les résultats sont comparés au comportement observé, et le facteur de sécurité est calculé à l'aide d'une approche analytique simplifiée proposée précédemment. Les analyses montrent que le modèle NGI-ADP peut prédire la rupture, et que l'effet de la forme de la tranchée sur la stabilité est bien capturé.

Keywords: Slurry trench; stability; FEA.

1 INTRODUCTION

The slurry trench method for constructing, for example, diaphragm walls is a technique that has been used in Norwegian soft clays in the past and is seeing an increased relevancy today. The technique involves excavation of a deep trench that is stabilized with a suitable fluid, called slurry.

In Norway, the slurry trench method was used during the construction of the *Fellestunnelen* rail- and subway tunnel in central Oslo in the 1970s, involving construction of diaphragm walls to depths up to 28 m. At the time there was little experience with this method in soft clays typical to Norway.

Therefore, test sites were established at three locations in central Oslo. The tests included trenches of different sizes with extensive instrumentation and monitoring. The collected data include ground surface settlements, pore pressures, trench wall deformations, and horizontal deformations measured by inclinometers, collected from slurry trenches in Kongens gate, Vaterland (DiBiagio *et al.*, 2020), and Studenterlunden (DiBiagio and Myrvoll, 1972). Schäfer and Triantafyllidis (2004) and Grandas-Tavera and Triantafyllidis (2012) have previously analysed slurry trenches at the Studenterlunden test site using a visco-hypoplastic constitutive model.

In this study, the data collected at the Vaterland test site is revisited. The site includes two trenches, one 1×5 m and the other 1×1.8 m. Finite element analyses (FEA) is used to back-calculate the observed behaviour using the NGI-ADP constitutive model. The aim to investigate the ability of the NGI-ADP model to predict the safety and deformations of slurry trenches through 3D modelling of the field tests.

2 BACKGROUND

2.1 Soil conditions

The terrain at the Vaterland test site is approximately level and situated at elevation +2 m above sea level. The bedrock surface forms a gulley (Figure 1). The trenches are situated roughly at its centre, where the depth to bedrock is 18–22 m. In the northwest and southeast directions, the depth to bedrock decreases.

The soil consists of a 1–2 m thick layer of fill material over a deposit of normally consolidated marine clay. The top part of the clay has been weathered to form a dry crust extending to a depth of 2–4 m. Underneath, is a soft marine clay with liquid limit of 40–45 %, plastic limit of about 25 %, and water content of 35–40 %. The ground water table is located at a depth of about 1 m.

The undrained shear strength (c_u) of the clay is estimated based on vane tests and triaxial tests on piston samples from the site, and CPTUs from a nearby location (Figure 2). For the vane tests, the correction factor proposed by Aas (1986) is used to estimate the average field c_u. The active shear strength c_{uA} is obtained using a ratio of direct to active strength calculated as proposed by Karlsrud and Hernandez-Martinez (2013). The CPTUs were interpreted using the correlations presented by Karlsrud et al., (2005). An overall assessment of both the N_{kt} correlation and the $N_{\Delta u}$ correlation for six different CPTUs is the basis for the interpreted profile in Figure 2.

The final input profile for the FEA is determined by an overall assessment of the different data, considering the likely effect of sample disturbance on the anisotropically consolidated undrained compression test (CAUC) results (Karlsrud and Hernandez-Martinez, 2013).

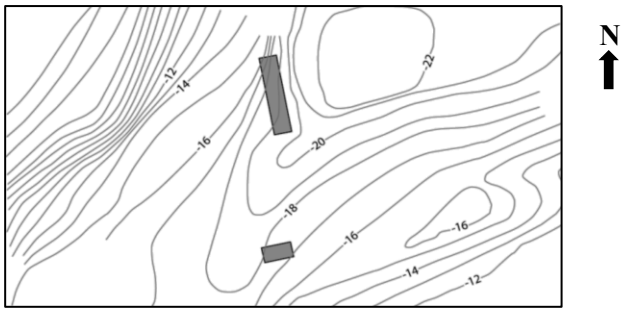

Figure 1. Map of bedrock elevation at the slurry trench test site and the location of the two trenches (shaded).

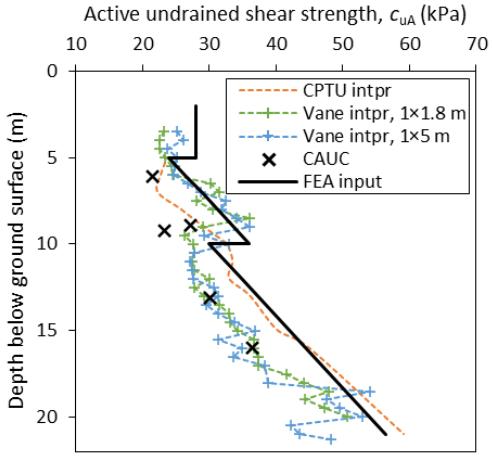

Figure 2. Active undrained shear strength vs. depth.

2.2 Instrumentation and test timeline

The trenches were instrumented and monitored with hydraulic deformation gauges, settlement anchors inclinometers, and pore pressure. The instrumentation layout is described by DiBiagio et al., (2020).

Excavation started February 26, 1970, by excavation of the 1.8 m trench. Then, the 5 m trench was excavated, followed by a series of tests involving replacement and drawdown of the stabilising fluids (Table 1). The slurry had an average specific gravity of 1.17, while the oil had a specific gravity of 0.85. Failure was initiated in the 1.8 m trench during drawdown to 8.3 m depth, while failure of the 5 m trench was initiated by drawdown to 4.7 m. Drawdown was performed at a rate of 1 m every 30 min.

Table 1. Timeline for the slurry trench test at Vaterland, reflected in the FEA calculation phases.

Phase	Date
Excavation of 1.8 m trench with slurry	26 Feb.
Excavation of 5 m trench with slurry	2 March
Replacement with water in 1.8 m trench	4 March
Lowering of water to 4.3 m in 1.8 m trench	5 March
Refilling of water in 1.8 m trench	5 March
Lowering of water to 8.3 m in 1.8 m trench	6 March
Refilling of water in 1.8 m trench	6 March
Replacement with slurry in 1.8 m trench	9 March
Replacement with water in 5 m trench	9 March
Replacement with oil in 5 m trench	11 March
Replacement with water in 5 m trench	14 March
Lowering of water to 4.7 m in 5 m trench	19 March

3 FEA MODEL

A 3D FEA model was established to analyse the slurry trench tests. The soil was divided into five layers. Down to a depth of 1.5 m is a layer of fill material. Then comes a layer of dry crust above clay which is divided into three sublayers. The geometry of the model is shown in Figure 3.

The model has normal constraints on vertical boundaries and the bottom boundary is fully fixed. The top surface is free, while distributed loads are applied on the inside surfaces of the trenches representing the pressure from the stabilising fluids. The calculation phases reflects the timeline s in Table 1. «

3.1 Soil parameters

3.1.1 Clay

Undrained behaviour is assumed for the clay, using the NGI-ADP material model Grimstad et al. (2012). The input parameters are based on the field and laboratory tests and are summarized in Table 2.

3.1.2 Fill material and dry crust

For the fill material and dry crust, the HS-small model (Benz, 2007) is used. The material properties are summarised in Table 3, and are mostly typical values.

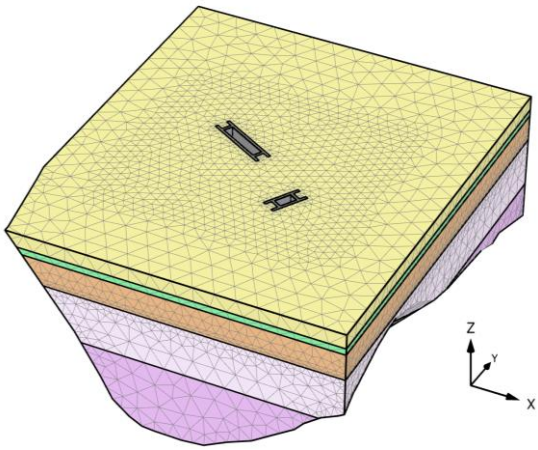

Figure 3. 3D perspective view of the FEA geometry.

Table 2. NGI-ADP material properties for the clay in the FEA model.

Parameter	Value
Unit weight, γ (kN/m^3)	18.5
Relative unloading modulus, $G_{\mathrm{ur}}/c_{\mathrm{uA}}$ (-)	700
Failure strain in compression, $\gamma_{\mathrm{f}}^{\mathrm{C}}$ (%)	0.8
Failure strain in extension, $\gamma_{\mathrm{f}}^{\mathrm{E}}$ (%)	6
Failure strain in direct shear, $\gamma_{\mathrm{f}}^{\mathrm{DSS}}$ (%)	3
Active shear strength, c_{uA} (kPa)	Fig. 2
Relative passive strength, $c_{\mathrm{uP}}/c_{\mathrm{uA}}$ (-)	0.35
Initial mobilization, τ_0/c_{uA} (-)	0.5
Relative DSS strength, $c_{\mathrm{uD}}/c_{\mathrm{uA}}$ (-)	0.67

Table 3. HS-small material properties for the fill material and the dry crust in the FEA model.

Parameter	Fill / dry crust
Unit weight, γ (kN/m^3)	20 / 17
Reference Young's modulus, E_{50}^{ref} (kPa)	3.0×10^4
Reference oedometer modulus, $E_{\mathrm{oed}}^{\mathrm{ref}}$ (kPa)	3.0×10^4
Reference unloading modulus, $E_{\mathrm{ur}}^{\mathrm{ref}}$ (kPa)	9.0×10^4
Poisson ratio for unloading, ν_{ur} (-)	0.20
Power, m (-)	0.50
Reference shear strain, $\gamma_{0.7}$ (-)	1.0×10^{-4}
Small strain shear modulus, G_0^{ref} (kPa)	1.0×10^5
Cohesion, c'_{ref} (kPa)	0
Friction angle, φ' (°)	32
Dilation angle, ψ (°)	0
Over-consolidation ratio, OCR (-)	1.0
Failure ratio, R_{f} (-)	0.90
Normal consolidation stress ratio, K_0^{NC} (-)	0.47

4 RESULTS

The FEA results show reasonable agreement with the observed/measured behaviour. As an example, Figure 4 compares the calculated reduction in trench width for the 1.8 m trench during drawdown to 4.3 m depth to the measured values. The agreement is generally good, particularly along the upper part. The difference seen at large depths can be due to inaccuracy in the geometry of the bedrock surface in the FEA and the effect the bedrock has on the stresses, and/or the shear strength being underestimated at large depths.

Furthermore, the FEA showed that the displacement in the 1.8 m trench increased rapidly when drawdown was continued to 8.3 m, reaching values of decimetres. The maximum displacement during this phase occurs at a depth of 8.5–9 m, that is, just below the top level of the water in the trench (Figure 5). Similarly, large, displacements were calculated for the 5 m trench during drawdown to 4.7 m depth. Consequently, these two drawdown phases can be considered close to failure. This is in line with the observed behaviour of both trenches.

Using the simplified analytical approach described by Aas (1976) the following factors of safety can be calculated for the two drawdown phases described above (DiBiagio *et al.*, 2020):

- Drawdown in 1.8 m trench to 8.3 m: 0.99
- Drawdown in 5 m trench to 4.7 m: 0.70

It is, thus, seen that the FEA using the NGI-ADP model is in line with the analytical method for the 1.8 m trench as both indicate failure for drawdown to 8.3 m. For the 5 m trench the analytical method results in a factor of safety of 0.7. Actually, a factor of safety of less than 1 is obtained for a drawdown of only 1 m.

This indicates that the analytical method underestimates the safety for this trench size as the field observations (and the FEA) shows that the 5 m trench is stable at this drawdown. The analytical method, thus, seems to underestimate the geometric effects for trenches with larger width to depth ratios.

5 CONCLUSIONS

The FEA using the NGI-ADP model can predict displacements with reasonable accuracy as well as accurately capture safety with respect to failure of the slurry trenches. The simplified analytical approach presented by Aas (1976) agrees well with the FEA and the measurements for the 1.8 m trench but seems to underestimate the safety for the 5 m trench.

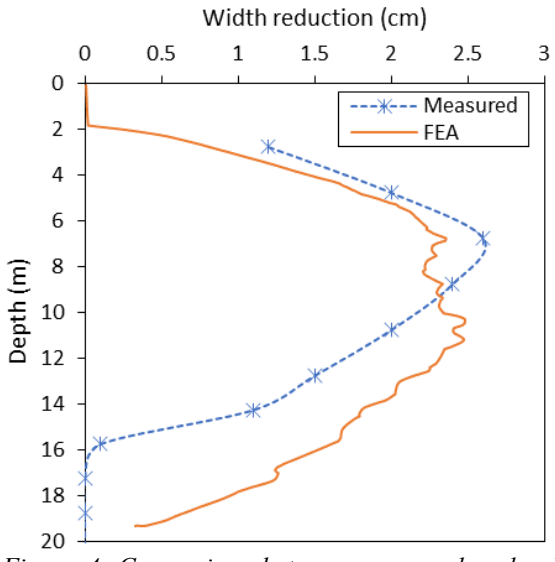

Figure 4. Comparison between measured and calculated trench width reduction during drawdown to 4.3 m in the 1.8 m trench.

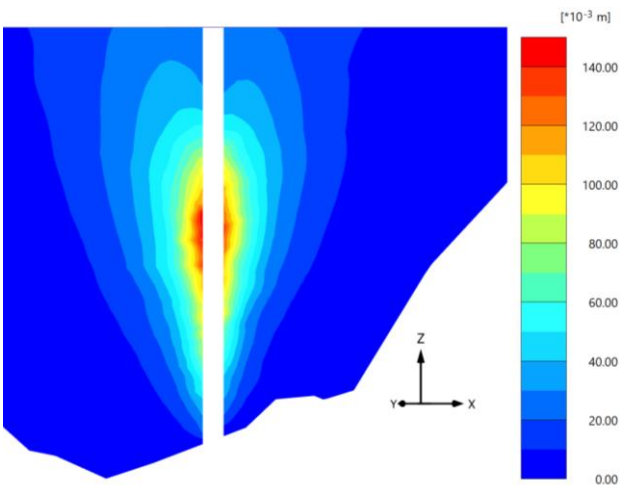

Figure 5. Contours of total displacement calculated in a cross section perpendicular to the 1.8 m trench after drawdown to 8.3 m depth.

ACKNOWLEDGEMENTS

The authors are grateful for the financial support provided by the Research Council of Norway through the public basic funding for research institutes.

REFERENCES

Aas, G. (1976) Stability of Slurry Trench Excavations in Soft Clay, In: Norwegian Geotechnical Institute Publication 111, NGI, Oslo, Norway, pp. 1–7.

Aas, G. (1986) In situ investigation techniques and interpretation for offshore practice. Recommended interpretation of vane tests. Final report, NGI, Oslo, Norway.

Benz, T. (2007) Small-Strain Stiffness of Soils and its Numerical Consequences, Doctoral dissertation. Universität Stuttgart. Available at: https://d-nb.info/984776931/04, accessed: 27/10/23

DiBiagio, E. et al. (2020) Deliberate Failure of Slurry Trench Excavations in Soft Clay, Geotechnical Engineering, 51(4), pp. 209–223. Available at: https://www.researchgate.net/publication/352166347_Deliberate_Failure_of_Slurry_Trench_Excavations_in_Soft_Clay, accessed: 27/10/23.

DiBiagio, E. and Myrvoll, F. (1972) Full Scale Field Tests with a Slurry Trench Excavation in Soft . Clay, In: Proceedings of the 5th European Conference on Soil Mechanics and Foundation Engineering, Madrid, Spain, pp. 461–471.

Grandas-Tavera, C.E. and Triantafyllidis, T. (2012) Simulation of a corner slurry trench failure in clay, Computers and Geotechnics, 45, pp. 107–117. https://doi.org/10.1016/j.compgeo.2012.05.007.

Grimstad, G., Andresen, L. and Jostad, H.P. (2012) NGI-ADP: Anisotropic shear strength model for clay, International Journal for Numerical and Analytical Methods in Geomechanics, 36(4), pp. 483–497. https://doi.org/10.1002/nag.1016.

Karlsrud, K. et al. (2005) CPTU correlations for clays, In: Proceedings of the 16th International Conference on Soil Mechanics and Geotechnical Engineering, Osaka, Japan, pp. 693–702. https://doi.org/10.3233/978-1-61499-656-9-693.

Karlsrud, K. and Hernandez-Martinez, F.G. (2013) Strength and deformation properties of Norwegian clays from laboratory tests on high-quality block samples, Canadian Geotechnical Journal, 50(12), https://doi.org/10.1139/cgj-2013-0298

Schäfer, R. and Triantafyllidis, T. (2004) Modelling of earth and water pressure development during diaphragm wall construction in soft clay, International Journal for Numerical and Analytical Methods in Geomechanics, 28(13), pp. 1305–1326. https://doi.org/10.1002/nag.388.

Proceedings of the XVIII ECSMGE 2024
GEOTECHNICAL ENGINEERING CHALLENGES
TO MEET CURRENT AND EMERGING NEEDS OF SOCIETY
© 2024 the Authors
ISBN 978-1-032-54816-6
DOI 10.1201/9781003431749-485
Open Access: www.taylorfrancis.com, CC BY-NC-ND 4.0 license

ECSMGE 24
XVIII EUROPEAN CONFERENCE ON SOIL MECHANICS AND GEOTECHNICAL ENGINEERING

The role of nano-materials and nanotechnology as a high-tech technology in geotechnical engineering

Le rôle des nano-matériaux et de la nanotéchnologie comme une téchnologie avancée en géotechnique

H. Niroumand*
Buein Zahra Technical University (IKIU-BZ), Qazvin, Iran

L. Balachowski
Gdansk University of Technology, Gdansk, Poland

**niroumand.mrud@gmail.com*

ABSTRACT: In the field of soil mechanics, various initiatives have been launched recently to use Nano- Materials (NM) to enhance the characteristics of soils. Numerous studies have been done using various methods to determine how micro- and nano- particles affect the geotechnical characteristics of soils. Most of the research done over the last ten years is reviewed in this research paper. According to the new classification, clay particles vary between 0.1 and 2 mm, while NM specimens contain particles in the range from 1 to 100nm. All findings suggested that adding Nano-Particles (NP) as a Nano Soil-Improvement (NSI) technique to soil improved its mechanical and physical characteristics, the type, quality, and quantity of NM applied, as well as the properties of the native soil, all influence this enhancement natural soil properties. In this paper, a new categorization was introduced to investigate the important effects of NP and NM on soil properties as a Nano Ground-Improvement (NGI) method.

RÉSUMÉ: Des initiatives nouvelles dans le domaine de la mécanique des sols sont récemment introduites en ce qui concerne l'usage des nanomatériaux (NM) pour l'amélioration des sols. De nombreuses études sont effectuées pour déterminer l'influence des micro et nano-particules sur les caractéristiques des matériaux géotechniques. La majorité des études réalisées dans la décennie écoulée est analysée dans cette publication. Selon une classification nouvelle,la dimension des particules d'argile varie entre 0.1 et 2µm, tandis que NM contiennent éléments entre 1 et 100nm. Toutes les trouvailles suggérent que l'addition des nano-particules (NP) comme nano-technique d'amélioration des sols (NSI) revise leurs caractéristiques mécaniques et physiques. Une sorte, qualité et quantité de NM appliqués ainsi que les propriétés du sol naturel influencent l'état d'amélioration du sol concerné. Dans cet article, une classification nouvelle est introduite pour étudier les effets majeures de NP et NM sur les paramètres géotechniques par la méthode de nano-amélioration des sols (NGI).

Keywords: Nano-materials (NM), nano-particles (NP), nano soil-improvement (NSI), nano ground-improvement (NGI).

1 NANOTECHNOLOGY AND GEOTECHNICAL ENGINEERING

Nanotechnology is related to the nano-scale of materials. Most of the materials and minerals are in the micro-scale, although various materials have nano-scale components in their natural conditions. Existing knowledge is based on micro-scale analysis in geotechnical engineering. A few researchers and scientists have started various tests on the nano-scale of minerals and soils in geotechnical engineering. The performance of the nano-scale of soils and minerals in soil mechanics and rock mechanics is very important because nanotechnology in geotechnical engineering is a cutting-edge knowledge and high-tech technology. According to existing soil classifications, gravel, sand, clay and silt are included in soil mechanics, but a new term of nanosoil is needed. Nanosoil has a size range between 1-100 nm. According to new results, the nano-scale of soils improved various properties of different types of soils (Niroumand et al., 2023). Geotechnical engineering focuses on the behavior and performance of different soils, while nanotechnology focuses on the nano-scale of materials and their behaviors and feedbacks. Using nanotechnology in geotechnical engineering has two objectives:

First, nanotechnology can explore new knowledge about the structure of soils at the nano-scale rather than the existing knowledge at the micro-scale. A complete introduction and knowledge of the nano-scale of soils can develop new theories for advanced soil mechanics and foundation engineering.

Secondly, using the nano-scale of soils and additives can investigate soil behaviors and improve existing soils. The role of the nano-scale of additives in soil mechanics is related to soil stabilization as a technique of soil improvement.

A lot of soils have various problems worldwide. The role of the nano-scale of additives as soil stabilizers can change the role of micro-scale additives in current and ongoing projects. Existing knowledge for micro-scale additives in soil improvement has learned various lessons in geotechnical engineering, such as additive properties, soil type, additive percentages, water amount, improvement methods, etc., that are related to ground improvement methods in different projects. The nano-scale of materials is similar to the micro-scale of additives because existing factors are applicable for ground improvement in geotechnical engineering.

2 EXISTING KNOWLEDGE OF NANOTECHNOLOGY IN GEOTECHNICAL ENGINEERING

In this part, a few existing achievements on two objectives of nanotechnology in geotechnology are described, although various researchers have evaluated the performance of nano additives in various soils. Only selected experiences of authors are presented for this manuscript.

a) Niroumand et al. (2013) investigated the performance of nano-scale clay as an additive and soil stabilizer in bricks. Earth is a basic material in heritage, historic buildings and earth buildings in earth architecture style. Traditional bricks have been used in many countries, especially in the Middle East and Arabic countries. According to traditional methods, various additives such as Sarooj, straw, lime, cement, egg, and etc. were used as additives and stabilizers in bricks.

In this study, the authors used different percentages of nano-scale additives in earth bricks in a soil laboratory. Nano kaolinite was selected as a type of nano clay in this study. According to their results, the compressive strength of treated bricks with nano-scale additives was 4.8 times higher than untreated bricks at 14 days curing time. The best percentage of nano additives was 5% compared to untreated bricks. They mentioned that Nano-Bricks (NB) can be used as modern bricks rather than existing bricks as Micro-Bricks (MB) in various applications and projects as shown in Fig. 1. They used powder technique for brick improvement. (Niroumand et al., 2013)



Figure 1. Micro- and Nano- Earth Bricks (Niroumand et al., 2013).

b) Khaksar et al. (2023) produced a new spray for protecting and restoring historic adobe walls and buildings. They used nano-scale montmorillonite in their research. According to the results of various tests, such as scanning electron microscopy, atomic force microscopy, porosity tests, water capillary absorption, and compressive strength, they showed that the use of a 1% nanomontmorillonite clay solution exhibited the best results, filling cavities and reducing pores on the adobe surface, increasing compressive strength, and reducing water absorption and hydraulic conductivity. The study concludes that this innovative method using nanomontmorillonite clay can help address the challenges of historic adobe walls, such as erosion, cracking, and surface damage.

This research contributes to the growing field of nanotechnology applications in architecture and civil engineering, particularly in soil stabilization and improving the properties of building materials. It introduced new concepts of "Nano-Heritage", "Nano-Spray for Historic Buildings and Earth Houses", and "Nano Spray-Improvement" as shown in Fig. 2. (Khaksar et al., 2023)



Figure 2. Nano-Spray for Historic Buildings and Earth Houses (Khaksar et al., 2023).

c) Zyenali et al. (2023) investigated the role of micro- and nano-scale fly ash as a green material in geotechnical engineering. They used fly ash because it was an eco-friendly material and a waste additive that

can be used as a recycled material in the building industry. They evaluated the role of these additives at micro- and nano-scale in various soil mechanics tests. They used scanning electron microscopy (SEM), X-ray fluorescence (XRF), and X-ray powder diffraction (XRD) to evaluate the soil and additive structures at micro- and nano-scale. They also investigated various percentages of micro- and nano-fly ash in cohesive soils to explore the soil mechanic behavior of micro- and nano-scale additives in soil stabilization.

Nano Soil-Stabilization (NSS) is a new theory for improving soil in Nano Soil-Improvement (NSI) or Nano Ground-Improvement (NGI). The results showed that adding 7% of nano-fly ash to the soil improved its unconfined compression strength by 8.2 times and its triaxial strength by 8 times. The researchers concluded that nano-fly ash significantly improved the strength and stiffness of the soil-fly ash mixture by filling the pores and bonding the soil particles. They reported a cutting-edge knowledge for the performance of Nano-Additives (NA) in earth building technology that can be used to build new houses with high performance in the future. They used suspension technique for soil improvement as shown in Fig. 3. (Zyenali et al., 2023)

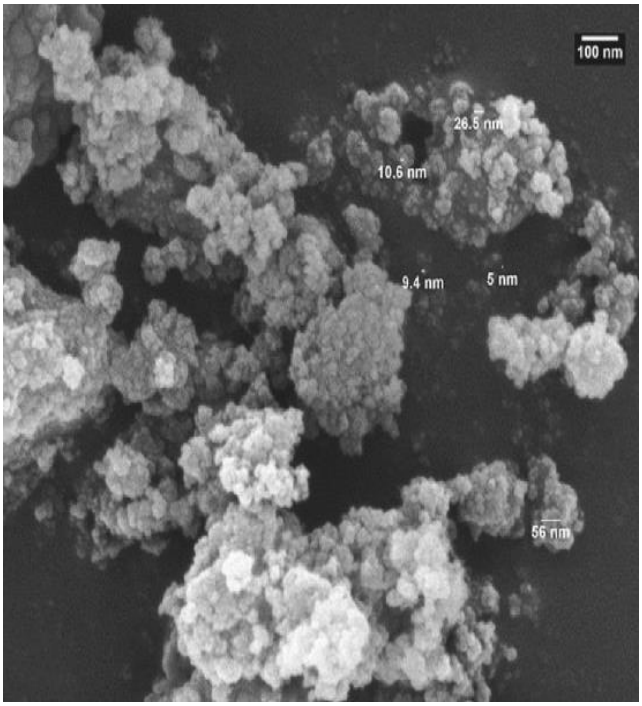

Figure 3. Nano – Fly ash (Zeynali et al., 2023).

d) Niroumand et al. (2023) described the role of micro- and nano-scale cement in geotechnical engineering. They selected a natural field soil site as untreated soil for soil stabilization objectives. They tried various percentages of micro- and nano-scale cement in soil stabilization as a soil improvement technique as shown in Fig. 4. They found that an optimum percentage of nano-cement was 7%, which increased the unconfined compressive strength by up to 29 times and reduced the strain at rupture by 74% compared to untreated soil. According to their results, they found a significant improvement of nano-scale cement on the strength and stiffness of the untreated soil-cement mixture. They used suspension method for soil improvement.



Figure 4. Micro- and Nano- Cement and NSI (Niroumand et al., 2023).

e) Cheraghalikhani et al. (2023) investigated the performance of micro- and nano-scale bentonite in geotechnical engineering. They used suspension technique for improving the cohesive soil properties. By using different percentages of micro- and nano-scale bentonite, they achieved good performance on the physical and mechanical properties in soil mechanics as shown in Fig. 5. They used SEM, XRD and XRF to control the properties, shape and size of soil and additive at micro- and nano-scale analysis. According to this investigation on clayed sand soil, at one day of curing time, the addition of 1% micro-bentonite increased the secant modulus to 2500 kg/cm^2, while 1% nano-bentonite increased it to 3000 kg/cm^2. The researchers emphasized the performance of suspension method rather than powder technique in micro- and nano-scale additives because suspension had a good performance in uniformity and soil mixing for various specimens and samples in soil mechanics laboratory.

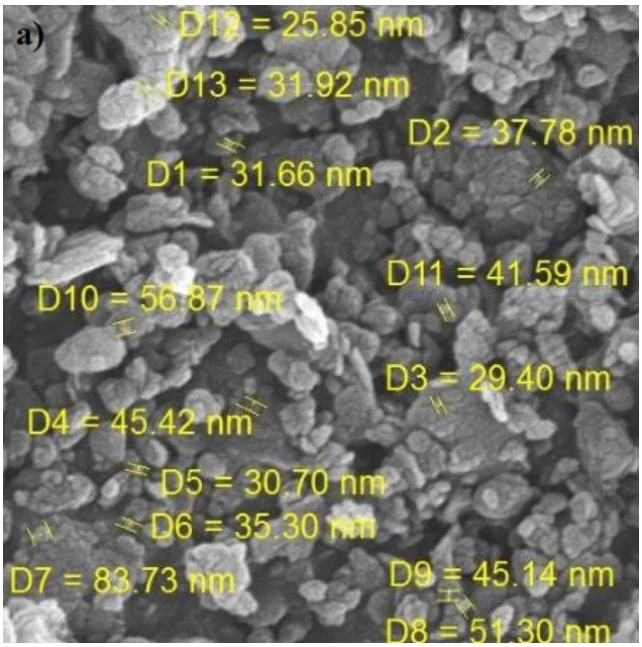

Figure 5. Nano-Bentonite and NSI (Cheraghalikhani et al., 2023).

3 THE FUTURE OF NANOTECHNOLOGY IN GEOTECHNICAL ENGINEERING

According to existing knowledge and results, the future of nanotechnology in geotechnical engineering, soil mechanics and rock mechanics looks promising. Existing knowledge proves the role of nano-scale soils as a good achievement for developing new techniques in the future of geotechnical engineering projects worldwide. The performance of nanotechnology started in soil stabilization and soil improvement, but it can be developed to various types of Nano-Foundations (NF), Nano-Additives (NA), Nano- Piles (NP), Nano Sheet-Piles (NSP), Nano-Geosynthetics (NG), NSI and subsidence as Nano-Subsidence, NSI and sinkhole as Nano-Sinkhole, and etc. The use of nano-scale materials has proven a good performance of the durability and soil properties in existing research. A new classification needs to be developed in soil classification; in other words, Nano-Soil (NS) needs to be added to existing soil classifications. These new terms emphasize new theories and techniques in soil mechanics and rock mechanics. It means a new way has opened in geotechnical engineering that requires various research and collaboration for modern types of materials in geotechnical engineering to improve the existing level of geotechnical engineering.

ACKNOWLEDGEMENTS

The authors acknowledge the financing of the Polish National Agency for Academic Exchange.

REFERENCES

Niroumand, N., Zain, M.F.M., Naghavi Alhosseini, S. (2013), The Influence of Nano-clays on Compressive Strength of Earth Bricks as Sustainable Materials, *Procedia - Social and Behavioral Sciences*, 89, Pages 862-865, https://doi.org/10.1016/j.sbspro.2013.08.945.

Niroumand, H., Balachowski, L. & Parviz, R. (2023), Nano soil improvement technique using cement. *Sci Rep*., 13, 10724 (2023). https://doi.org/10.1038/s41598-023-37918-z.

Cheraghalikhani, M., Niroumand, H., and Balachowski, L. (2023). Micro- and nano- bentonite to improve the strength of clayey sand as a nano soil-improvement technique. *Sci Rep*., 13, 10913. https://doi.org/10.1038/s41598-023-37936-X.

Zeynali, Y., Niroumand, H., Ziaie Moayed, R. (2023). Stabilizing cohesive soils with Micro- and Nano- fly ash as Eco-friendly Materials: An experimental study, *Construction and Building Materials*, Elsevier, 399, 132490. https://doi.org/10.1016/j.conbuildmat.2023.132490.

Khaksar, M., Niroumand, H., Afsharpour, M., and Balachowski, L. (2023). Spray-Based Method for Protecting and Restoring Historic Adobe Walls Using Nanomontmorillonite Clay. *ACS Omega*, 12, 11373–11380, https://doi.org/10.1021/acsomega.3c00124.

Proceedings of the XVIII ECSMGE 2024
GEOTECHNICAL ENGINEERING CHALLENGES
TO MEET CURRENT AND EMERGING NEEDS OF SOCIETY
© 2024 the Authors
ISBN 978-1-032-54816-6
DOI 10.1201/9781003431749-486
Open Access: www.taylorfrancis.com, CC BY-NC-ND 4.0 license

ECSMGE 24
XVIII EUROPEAN CONFERENCE ON SOIL MECHANICS AND GEOTECHNICAL ENGINEERING

Investigations of material discharge caused by groundwater flow during the installation of bored piles

Investigations sur le déversement de matériaux causé par l'écoulement des eaux souterraines lors de l'installation de pieux forés

H. Nissen*
Federal Waterways Engineering and Research Institute, Karlsruhe, Germany

C. Fierenkothen
Ingenieurgesellschaft für Spezialtiefbau mbH, Wuppertal, Germany

E. Dornecker
Federal Waterways Engineering and Research Institute, Karlsruhe, Germany

M. Herten
University of Wuppertal, Wuppertal, Germany

**hanna.nissen@baw.de*

ABSTRACT: Bored piles are often installed below the groundwater level. During installation, it has to be ensured that groundwater flow does not lead to a reduction of the pile integrity from pouring until the concrete has stiffened. The European Standard EN 1536, the German Recommendations on Piling "EA-Pfähle" (2013) and international guidelines refer to possible problems resulting from groundwater flow. However, no information is given as to which groundwater flow velocity is critical in which ground. In order to be able to estimate the risk of cement particle removal or redistribution, model piles were installed with the tremie method at the University of Wuppertal in a joint research project. These piles were exposed to several water flow velocities during installation. The created flow velocities were substantially higher than the groundwater flow velocities which occur in field. In a first series of tests, the focus was on test piles made of tremie concrete which were placed in sandy soils. In a second series of tests, a variation of concrete mix design and surrounding soil was performed to obtain a more general statement. In summary, it could be shown that no critical flow velocity could be reached which lead to a "washing-out effect" of cement on the pile surface within the scope of both series of tests.

RÉSUMÉ: Les pieux forés sont souvent installés sous le niveau de la nappe. Lors de l'exécution, il faut s'assurer que l'écoulement des eaux souterraines ne remette pas en cause l'intégrité du pieu, à partir du bétonnage et jusqu' à la prise du béton. La norme européenne EN 1536, les recommandations allemandes sur les pieux "EA-Pfähle" (2013) et les recommandations internationales font référence aux problèmes possibles résultant de l'écoulement des eaux souterraines. Cependant, aucune information n'est donnée quant à la vitesse d'écoulement de la nappe phréatique qui est critique dans chaque terrain. Afin de pouvoir estimer le risque d'arrachement ou de redistribution des particules de ciment, des pieux tests bétonnés au tube plongeur ont été installés à l'université de Wuppertal, dans le cadre d'un projet de recherche partenariale. Ces pieux ont été exposés à plusieurs vitesses d'écoulement de l'eau pendant leur exécution. Les vitesses d'écoulement imposées étaient considérablement plus élevées que les vitesses d'écoulement des eaux souterraines observées in situ. Dans une première série de tests, l'accent a été mis sur les pieux d'essai bétonnés au tube plongeur, qui ont été réalisés dans des sols sableux. Dans une deuxième série de tests, des compositions du béton a été étudiée, dans des sols également différents, pour obtenir une analyse plus générale. En conclusion, il a pu être montré qu'aucune vitesse d'écoulement critique pouvant entraîner un "effet de lavage" du ciment à la surface du pieu lors des deux séries de tests n'a pu être atteinte.

Keywords: Bored piles; groundwater flow.

1 INTRODUCTION

Bored piles (EN 1536) are used in a variety of applications and often extend below the groundwater table. Below the groundwater table, they are produced by using the tremie method with temporary casing or with support fluid (e.g. EFFC/DFI Concrete Task Group, 2018). In international standards and recommendations, it is pointed out that high groundwater flow velocities can lead to erosion of particles from the fresh concrete. As a result, the

cement particles may be redistributed or removed from the freshly concreted pile.

The European Standard covering bored piles EN 1536:2010 points out that special attention must be paid to groundwater flow. Accordingly, groundwater flow can lead to a "washing-out" effect and reliable protection is advised, e.g., by permanent casing or lining. Related guidance can be found in other international standards and recommendations as:

- Finland: "Instructions for drilled Piling - Design and Execution Guide" (FINNRA, 2003)
- Germany: Recommendations on Piling "EA-Pfähle" (2013)
- United States of America: "Drilled Shafts: Construction Procedures and Design Methods" (Brown et al., 2018)
- Europe: Displacement piles (EN 12699: 2015).

There is consensus in all standards and recommendations that there is a potential risk of discharge of cement particles by groundwater flow. However, there are no limits given for a critical flow rate, neither could scientific studies be found which address this subject.

In 2012, laboratory tests were carried out on jet columns with cement paste at the University of Wuppertal (Department of Geotechnical Engineering). It could be shown that high groundwater flow can lead to a removal of cement paste which changes the shape and size of jet columns (Drzewiecki, 2012). However, the results cannot be transferred one-to-one to concrete piles, so further tests were carried out.

2 IMPLEMENTATION OF THE EXPERIMENTAL STUDY

2.1 Experimental set up

A test set up was designed at the University of Wuppertal for a systematic investigation of the influence of groundwater flow on bored piles (Fierenkothen et al., 2020). This set up enables the investigation of different groundwater flow velocities and different methods for the execution of bored piles such as borehole support by casing or by support fluid. The dimensions of the test set up are shown in Figure 1.

A temporary casing with an external diameter of 219.1 mm was used for the construction of the model piles. For technical reasons, it was necessary to install the casing first. Afterwards, the sand was placed under water in layers and compacted. For the construction of model piles with excavation supported by support fluid, the suspension was first placed under the protection of the temporary casing. Before concreting, the casing was pulled except for a small part that remained as lead-in tube and the borehole was left under fluid support for 30 min.

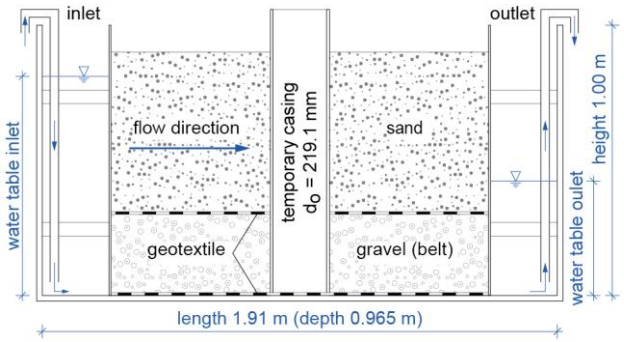

Figure 1. Test set up for the test with gravel belt, before concrete placement.

A pump circuit ensured a continuous flow through the experimental box. Inlet, outlet and flow direction are shown in Figure 1. For an evaluation of potential cement erosion at the pile cubature due to flow, the cured piles were recovered, visually inspected, and measured.

2.2 Experimental boundary conditions

Flow velocity, soils and concrete mixtures were varied in two series of tests. In the first series of tests, the filter velocity and the support of the borehole wall were investigated in particular. Two different sands were used as surrounding ground. The second series of tests focussed on the influence of the concrete mixture and a more coarse-grained soil as surrounding soil. The test stand allows for medium gravel as an upper limit. An overview of all tests and selected boundary conditions is given in Table 1.

Narrowly graded soils were investigated as surrounding ground, as these have a high permeability. In addition, they have a lower filter stability towards cement paste than wide-graded soils. For the second test series with gravel as surrounding soil, the challenge was to create a flow velocity as high as possible in the experimental box. This was achieved by arranging a gravel belt.

The grain size distributions of the three soils tested are shown in Figure 2. The estimation of the permeability coefficients was carried out according to Darcy and Beyer & Schweiger.

Table 1. Matrix of the physical model experiments.

soil		**concrete / suspension mix design**				**support**	**filter velocity v_f**
type	k_f	max. grain size	distribution	fly ash	plasticiser		in m/day
sand1	$k_{f,1}$	(cement paste)	-	yes	-	TL	100
		8 mm	B8	yes	p1	SF	120
			B8	yes	p1	TL	15 / 115 / 150
		16 mm	B16	yes	p1	TL	145
sand2	$k_{f,2}$	(cement paste)	-	yes	-	SF/TL	280/290
		2 mm	-	no	-	TL	435
		8 mm	B8	yes	p1	SF	380
			B8	yes	p1	TL	65 / 350 / 700
		16 mm	B16	yes	p1	TL	670
			A16	yes	p1	TL	280 / 295
gravel (belt)	$k_{f,3}$	2 mm	-	no	-	TL	1310 / 1540
		8mm	B8	yes	p1	TL	>> 846
			B8	no	p1 / p2	TL	1445 / 1320
			C8	no	p1	TL	1355
		16 mm	B16	yes	p1	TL	1365
			B16	no	p1/p2	TL	1330 / 1335
		32 mm	A32	no	p1	TL	1380
			B32	yes	p1	TL	1285
			B32	no	p1 / p2	TL	1575 / 1350

Explanation of abbreviations:
- $k_{f,1}$, $k_{f,2}$, $k_{f,3}$: permeability coefficients of the soils tested;
- distribution: grain size distribution as standardised in the German National Annex DIN 1045-2 to EN 206-1;
- p1, p2: different types of superplasticiser used for the concrete mixture;
- SF: support fluid;
- TL: temporary casing.

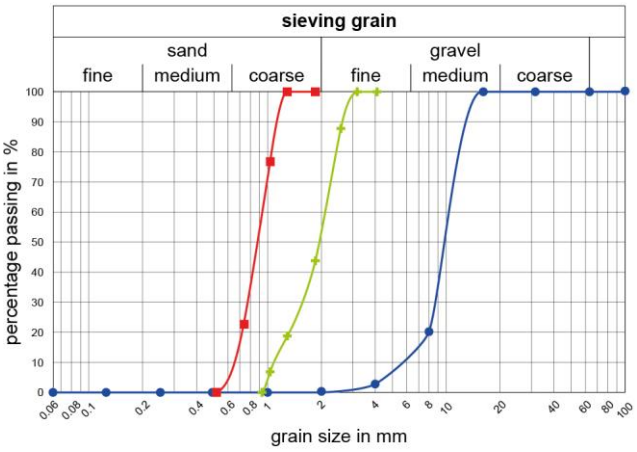

Figure 2. Grain size distribution of the surrounding soils. red = sand1, green = sand2 and blue = gravel (belt).

This results in the following permeability coefficients for the investigated soils:

- sand1: $k_{f,1} \sim 4 \cdot 10^{-3}$ m/s
- sand2: $k_{f,2} \sim 1 \cdot 10^{-2}$ m/s
- gravel: $k_{f,3} \sim 4 \cdot 10^{-1}$ m/s.

Different filter velocities were investigated. The filter velocity (v_f) is calculated as the ratio of the flow rate to the cross-sectional area of the groundwater flow at the location of the model pile. Depending on the soil and the flow velocity, different phreatic lines occur between inflow and outflow. As a result, only the lower part of the piles are exposed to groundwater flow (Figure 3 and Figure 4).

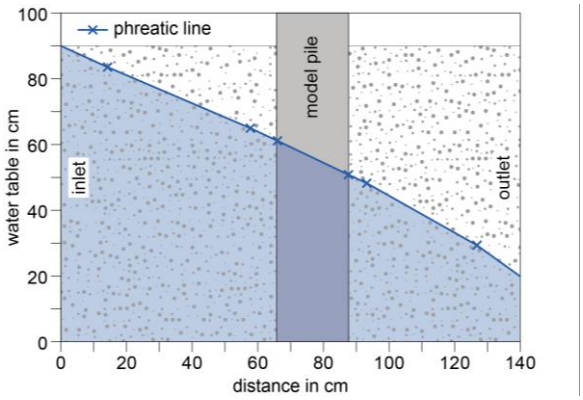

Figure 3. Exemplary phreatic line of the sands with representation of the level measurement points for sand1 with v_f = 120 m/d, according to Fierenkothen et al., 2022.

The mix design for the concrete consists of water, cement (CEM III/B 42,5), fly ash, aggregate and superplasticiser. In order to exclude the possibility of a different result when using a particle size distribution with a drop-out grain size or other admixtures, the

grain size distribution and the admixtures were also varied in the concrete mixture.

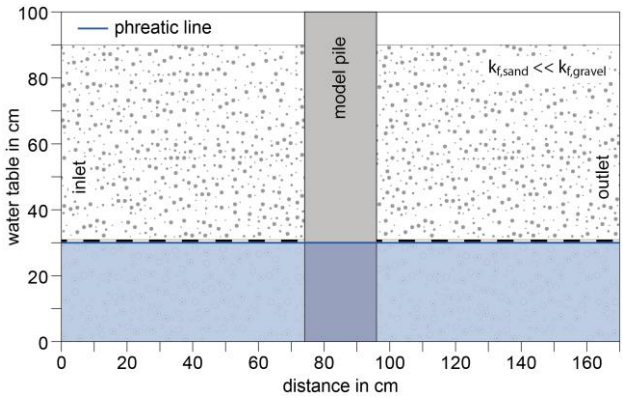

Figure 4. Exemplary phreatic line for the gravel belt.

Fly ash and superplasticizer have a strong influence on the consistency and stability of fresh concrete. Since the mode of action of the superplasticizer depends on the type of superplasticizer, a second type was used for the investigation. Superplasticiser p1 is based on a polycarboxylate ether and superplasticiser p2 is based on melamine/naphthalene sulphonate. In order to investigate the influence of fly ash, mix designs with and without fly ash were examined.

In addition, model piles were made using cement paste and mortar.

3 RESULTS

3.1 Bored pile excavation supported by casing

The cast in situ concrete model piles with temporary casing in both sand and gravel showed no visible anomalies in the contour after uncovering (Figure 5). Likewise, no visual anomalies could be observed on the cured and excavated model piles after pile installation in gravel (belt), regardless of the concrete mix.

For all cast-in-place concrete model piles with temporary casing, no critical flow velocity could be achieved which lead to anomalies. It was not possible to determine significant differences in pile diameter in and across the flow direction. Even though the flow velocities examined were often significantly higher than those occurring in practice (Table 1).

In contrast the model piles made of pure cement paste (in sand1 and sand2), clearly showed redistribution of the cement particles (Figure 6). The redistributions were significantly greater in the model pile with the higher flow velocity in sand2.

The cement particles have deposited as a plume in the shadow area of the model piles. The investigations showed that the strength of the deposits decreased with increasing distance from the pile.



a) *b)* *c)*

Figure 5. Contour of cast in situ model piles with temporary casing and max. grain size 8 mm: a) sand1: v_f = 115 m/d; b) sand2: v_f = 700 m/d (Fierenkothen et al., 2020); c) gravel (belt): v_f = 1445 m/d.



Figure 6. Exposed cement/sand plume of the model pile from cement suspension in sand2: v_f = 290 m/day (Fierenkothen et al., 2020).

3.2 Bored pile excavation supported by fluid

While a redistribution of cement particles was observed on the model piles made of cement paste with excavation supported by casing, in contrast, with support fluid (bentonite slurry), no discharge of the cement particle could be detected (Figure 7c).

Similarly, no visible discharge of cement particles was detected on the model piles made of concrete in sand with support fluid. During production, the support fluid was able to penetrate approx. 5 cm into the soil – except for the area of the lead-in tube at the pile head (Figure 8). A filter cake was formed due to penetration of the support fluid into the soil. No visual removal or displacement of penetratet support fluid resulting from groundwater flow could be detected.



a) b) c)

Figure 7. Contour of model piles constructed under support fluid: a) sand1: concrete with max. grain size 8 mm, v_f = 120 m/d; b) sand2: concrete with max. grain size 8 mm, v_f = 380 m/d; c) sand2: cement paste, v_f = 280 m/d (Fierenkothen et al., 2022).



a) b)

Figure 8. Penetration of the support fluid into the soil for sand2: cement paste, v_f = 280 m/d (Fierenkothen et al., 2022).

The model piles could be produced without anomalies in the contour due to the protection of the filter cake of the support fluid. It has been shown that the filter cake forms a protective layer against the discharge of cement particle.

All tests with the gravel belt with concrete as pile material and temporary casing showed no visual discharge of cement particles of the concrete. Therefore, concreting under support fluid was not further investigated.

4 CONCLUSIONS AND FUTURE PERSPECTIVES

During the investigations which were carried out in this study, no visible discharge of cement particles could be detected for the cast in situ concrete piles with excavation supported by casing or by support fluid. The investigated flow velocities were significantly higher than those generally observed in nature.

During the tests with cement paste (supported by casing), cement particles were redistributed into the surrounding soil. The production under support fluid prevented discharge. The filter cake of the suspension support forms a protective layer against an influence from groundwater flow.

The restrictions from standards and recommendations could not be confirmed for cast in situ concrete piles in sand and medium gravel. The contours of the piles did not show any changes. Additional investigations of the hardened concrete properties of the model piles are planned. In particular, it should be investigated whether there has been a change in the structure and strength of concrete in the edge area of the piles.

REFERENCES

Brown, D. A., Turner, J. P., Castelli, R. J. and Loehr, E. J. (2018). Drilled Shafts: Construction Procedures and Design Methods, National Highway Institute U.S., Washington D.C., United States of Amerika, Rep. FHWA NHI-18-024.

Deutsche Gesellschaft für Geotechnik e.V. (2013). Recommendations on Piling (EA-Pfähle), 2nd ed., WILEY Ernst & Sohn, Berlin, Germany. DOI:10.1002/9783433604113.

Drzewiecki, M. (2012). *Mögliche Auswirkungen von strömendem Wasser auf Form und Größe von Düsenstrahlsäulen,* Diploma Thesis, University of Wuppertal. [unpublished].

EFFC/DFI Concrete Task Group (2018). Guide to Tremie Concrete for Deep Foundations, Second Edition, European Federation of Foundations Contractors & Deep Foundations Institute.

EN 12699:2015: Execution of special geotechnical works. Displacement piles, European Committee for Standardization, Brussels, Belgium.

EN 1536:2010. Execution of special geotechnical work - Bored piles, European Committee for Standardization, Brussels, Belgium.

Fierenkothen, C., Grebien, F., Pulsfort, M. and Herten, M. (2020). Einfluss von strömendem Grundwasser auf die Frischbeton-Integrität von Ortbetonpfählen, In: *Geotechnik und Wasser – RuhrGeo Tag 2020*, Essen, Germany, pp. 119–139.

Fierenkothen, C., Pulsfort, M. and Herten, M. (2022). Untersuchungen zur Frischbeton-Integrität bei der Herstellung von Ortbetonbohrpfählen im strömenden Grundwasser, In: *37. Baugrundtagung*, Wiesbaden, Germany, pp. 161–169.

FINNRA - Finnish Road Administration (2003). Instructions for drilled piling. Design and execution guide, Guidelines for design and implementation, Helsinki, Finland.

Proceedings of the XVIII ECSMGE 2024
GEOTECHNICAL ENGINEERING CHALLENGES
TO MEET CURRENT AND EMERGING NEEDS OF SOCIETY
© 2024 the Authors
ISBN 978-1-032-54816-6
DOI 10.1201/9781003431749-487
Open Access: www.taylorfrancis.com, CC BY-NC-ND 4.0 license

ECSMGE 24
XVIII EUROPEAN CONFERENCE ON SOIL MECHANICS AND GEOTECHNICAL ENGINEERING

Industrial warehouse retaining walls and pavements strengthening at Quinta do Adarse, Alverca, Portugal

Renforcement des murs de soutènement et des chaussées d'un entrepôt industriel à Quinta do Adarse, Alverca, Portugal

T.M.L. Paludeto*, M. Lopes, A. Pinto
JETsj Geotecnia, Lisbon, Portugal

**tpaludeto@jetsj.com*

ABSTRACT: The aim of this article is to present the solutions for the main retaining walls and pavement strengthening, adopted in an industrial warehouse at Quinta do Adarse, in the proximities of the Tagus River right bank, at Alverca, Portugal. The existent cantilever reinforced concrete wall with 300m of length and 6m of maximum height, was strengthened with a cap distribution beam due to excessive deformation. The cap distribution beam was supported by inclined steel struts and founded on micropiles. At the warehouse pavements, some differential settlements were detected around the stiffer structural foundations, mainly due to the water inflow at the pavement earth fill foundation, which required a strengthening solution. Therefore, injections were used to avoid the replacement of the pavement and minimize the impacts on the warehouse's normal operation.

RÉSUMÉ: Le but du présent article est de présenter les solutions pour les principaux murs de soutènement et le renforcement de la chaussée, adoptées dans un entrepôt industriel à Quinta do Adarse, à proximité de la rive droite du Tage, à Alverca, Portugal. Le béton armé en porte-à-faux existant, qui est un mur de 300 m de longueur et 6 m de hauteur maximale, a été renforcé avec une poutre de répartition de couverture en raison d'une déformation excessive. La poutre de distribution du chapeau était soutenue par des entretoises en acier inclinées et fondée sur des micropieux. Au niveau des revêtements de l'entrepôt, certains tassements différentiels ont été mobilisés autour des fondations structurelles plus rigides, principalement en raison de l'afflux d'eau au niveau des fondations en terre de la chaussée, ce qui a nécessité une solution de renforcement. Par conséquent, des injections ont été utilisées pour éviter le remplacement du revêtement et minimiser les impacts sur le fonctionnement normal de l'entrepôt.

Keywords: Strengthening; wall; micropiles; pavement; injection.

1 INTRODUCTION

The aim of the present work is to present the adapted solutions for strengthening the retaining walls and pavements of an operating industrial warehouse, by using micropiles, cap distribution beams, and ground consolidation with polyurethane resin injection.

The reinforcement and strengthening of retaining walls and pavements at operating industrial warehouses require solutions with minimum impact on the normal operation.

Strengthening solutions with micropiles have advantages due to their diversity and execution possibilities for small spaces with difficult access, or sensitive to noise and vibrations, as well as soils with the presence of boulders, rock, concrete, and voids. The micropiles are also distinguished by the fact that they can be carried out on slopes (Barbosa, 2019).

To strengthen the pavements, a non-invasive technique may be required, with the physical-mechanical characteristics of the injected material remaining unchanged over time, so the solution of injecting expansive resin to treat the pavement foundation ground allows for a safe and practical intervention (Favaretti et al., 2014).

2 THE INDUSTRIAL WAREHOUSE

The site is a warehouse with an area of 20,250 m^2 (270 m x 75 m), built in the 1990's at Quinta do Adarse, Alverca, Portugal (Figure 1). The retaining wall is a reinforced concrete cantilever structure with 6 m of height extending over 320 m of length. The wall was designed to support the difference of approximately 4 m, existing between the lot where the warehouse is located and the adjacent areas.

The pavements with 5.0 m x 5.0 m panels were built with 0.10 m concrete industrial ground floor reinforced with steel mesh AR 30. The pavements

were founded on a 0.20 m thick layer of crushed stone or aggregates fill, separated from the underlying ground, most likely pre-existing landfills by a geotextile blanket. As it was an operating industrial warehouse under operation (Figure 2a), the stresses on the pavement are related to the weight of the materials stored on shelves (Figure 2b) as well as to the traffic of loading and transport equipment (forklifts).



Figure 1. Aerial view of the site (Google Earth).



Figure 2. a) External view of the warehouse and b) Internal view of the materials stored on shelves.

3 GEOLOGICAL AND GEOTHECNICAL PROFILE

The site under study is located, from a geological point of view, over an alluvium (a) and river terrace deposits (Qf), from the Quaternary, associated with the Tagus River basin, according to Sheet 34 B - Loures of the Geological Chart of Portugal at scale 1/50.000. It is constituted of clays, silty clays, sands, and silty sands with pebbles and sometimes conglomerates with limestone elements. These formations are based on Miocene layers of sands, sandstones, mudstones, and limestones from the Tortonian (MT).

The solutions proposed are based on the results of the tests carried out in the geological-geotechnical study, and in the values presented in the reference bibliography for alluvial soft silty-clay in Portugal (Esteves, 2014).

4 PATHOLOGIES

4.1 Retaining wall pathologies

There are occasional and localized phenomena of instability in the walls leading to cracks and excessive deformation (Figure 3).

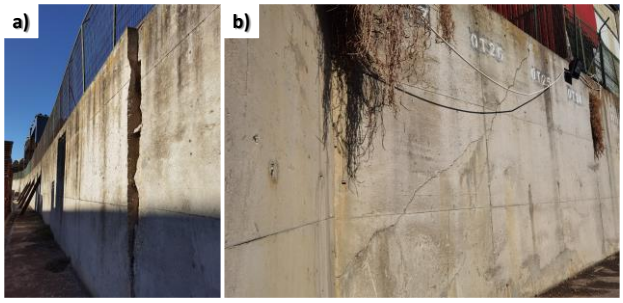

Figure 3. Pathologies at the retaining wall: a) excessive deformations b) cracks.

It should be noted the presence of four silos on the upper level, whose foundation solution was unknown. These structures may have increased ground pressure on the retaining walls. It can also be seen that, in some cases, the walls have already been reinforced in the past, with steel bracing solutions (Figure 4a) and nails or using tie rods (Figure 4b), which failed to stabilize the wall.

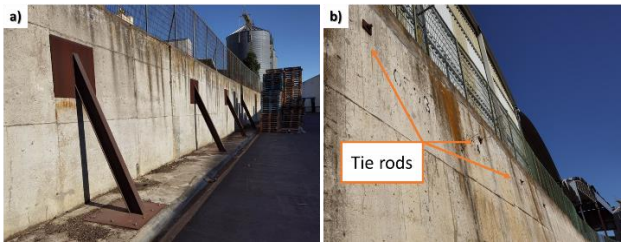

Figure 4. a) Steel bracing b) nailing or tie rods on the retaining wall.

4.2 Pavements pathologies

The loads to which the warehouse pavements are submitted are due to the weight of the materials stored on the shelves as well as the loads associated with the passage of loading and transport equipment (forklifts). It was seen that the pathologies worsened in the southern part of the warehouse indicating an increase in the pavements loads (Figure 5).

The pathologies, which required the adapted strengthening solutions, were identified in the pavements, facades, unloading dock, and stairs.

Close to the facades and columns, the presence of cracks in the concrete pavement was observed, as well as evidence of differential settlements between the pavement and the remaining structural elements (Figure 5a-b). On the walls of the east and west

facades, which were built of prefabricated concrete slabs, horizontal cracks were also observed (Figure 5c).

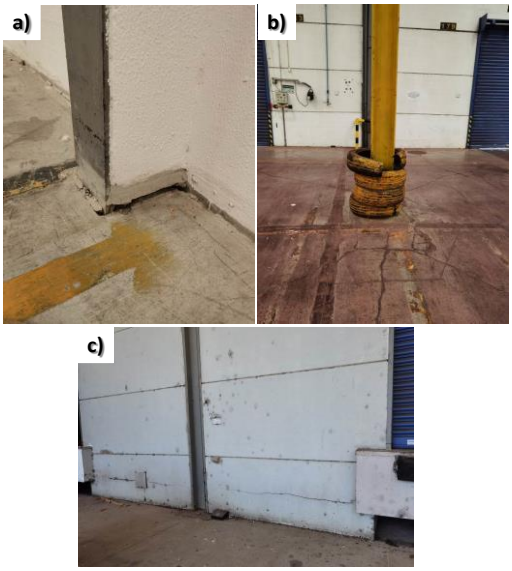

Figure 5. Main pathologies. a) differential settlements between the pavement and the facade, b) degradation of the pavement around a pile cap, c) cracking in the east side of the warehouse.

5 COMPRESSION STRENGTH TESTS ON CONCRETE

To find out the compressive strength of the existing wall concrete, six drillholes were made along the length of the wall, located at a height of 2.0 m perpendicular to the wall face. The collected specimens had a diameter of 82 mm and a length between 37.5 cm and 41.5 cm.

In general, the specimens were homogeneous, with a good distribution of limestone aggregate, but with some voids. These voids may indicate a lack of vibration during pouring.



Figure 6. Uniaxial compression-strength testing – UCS.

Uniaxial compression strength (UCS) tests were carried out on five of the collected specimens (Figure 6) to measure the mechanical resistance of the existing concrete wall. The uniaxial compression strength of the samples ranged between 16.56 MPa and 28.30 MPa.

6 STRENGTHENING SOLUTIONS

6.1 Retaining wall strengthening

The proposed solution includes the construction of a bracing element with the aim of increasing the wall resistance to horizontal pressure. This element consists of a 0.45 x 0.70 m distribution beam at the wall's mid-height, which is designed to transfer the horizontal forces to inclined micropiles, with tubular section of Ø88.9 x 12.0 mm and Ø88.9 x 9.5 mm, spaced 4.50 m, in the direction of the wall's development. The micropiles had a variable length of between 14 m and 15 m, thus guaranteeing minimum sealing lengths of 8 m and 9 m in the ground layer (natural ground with a NSPT of more than 20 blows).

To accommodate the increased vertical load caused by the axial force on the inclined micropiles, capping and distribution beams, were also built. Vertical micropiles were installed, also spaced 4.50 m. The vertical micropiles had an estimated variable length of between 11 m and 13 m, thus guaranteeing minimum sealing lengths of 6 m and 8 m in the stiffer ground layer.

The boreholes for placing the micropiles were at least Ø220 mm, and the tubes were subjected to filling and sealing injection. The injection was carried out using an appropriate system – I.R.S. (Repetitive and Selective Injection), using non-return valves and a double plug, for the length corresponding to the sealing bulb.

As the beam is supported directly on the micropiles, part of the steel tube was exposed permanently. Therefore, the micropiles were properly protected against corrosion, with a sacrificial thickness, compatible with the conditions of the environment and the life of the structure. Figure 7 shows the typical cross-section of the proposed solution.

Sub-horizontal geodrains with a diameter of Ø50 mm, creped and wrapped in 300 gr/m^2 geotextile, with a length of 3 m, were also installed, to relieve hydrostatic pressures. In addition, cracks in the existing wall were filled with non-shrinking mortar. To prevent the reoccurrence of pathologies, AISI316 stainless steel staples were also installed, spaced 0.40 m, whenever the cracks were larger than 10 mm.

Compression tests were performed in the concrete to evaluate the state of degradation of the wall. The structure was initially modelled using the GEO5

software to represent the current situation of the existing reinforced concrete wall, which only resists the static conditions, with a unitary safety factor. Subsequently, a second model was developed also considering the actions correspondent to earth pressures and surcharger to estimate the respective efforts and, therefore, to calculate the reinforcement structure in accordance with current regulations.

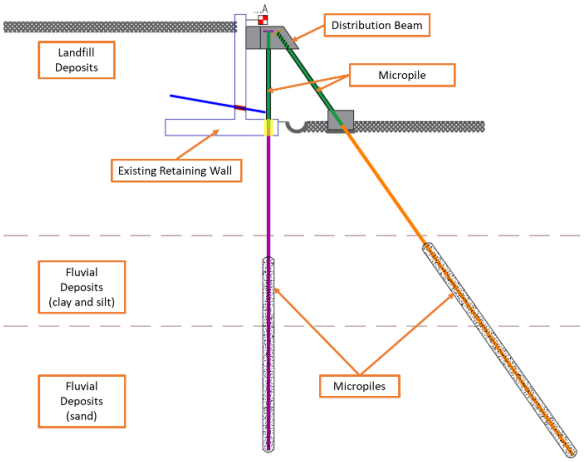

Figure 7. Cross section of the wall reinforcement solution

6.2 Pavement strengthening

The locations where internal erosion of the soil underlying the pavement was suspected a ground consolidation solution using the Uretek - Floor Lift type resin, or equivalent, was chosen. The resin has a density of 45 kg/m^3 (minimum) and expansion capacity up to 30 times its initial volume in free expansion.

This technique makes it possible to increase the compactness of the ground immediately below the pavement, without excavations, vibrations, or mechanical forces, thus minimizing the risk associated with possible damage to existing structures. The injections were made through small diameter holes, thus avoiding the need to build a new pavement structure (Uretek Floor Lift, 2023). In addition, this technology allowed to restore the pavement's planimetry and re-establish its contact with the ground (Figure 8).

In this context, the adapted solution consisted of drilling small diameter holes, arranged in a square grid of 1.20 x 1.20 m. Injection tubes were installed in these holes, approximately 6 and 12 mm in diameter. Through these tubes, a polyurethane resin was injected between the base of the industrial floor and up to approximately 1.0 m depth. In the first injection phase, the polyurethane resin, which is in liquid form, penetrates the voids in the soil and subsequently expands, sealing the surrounding soil, forming a rigid foam that increases the ground compactness. The injection process is monitored by reading equipment based on laser technology, indicating the increase in the soil's load-bearing capacity and the recovery of the differential settlements.

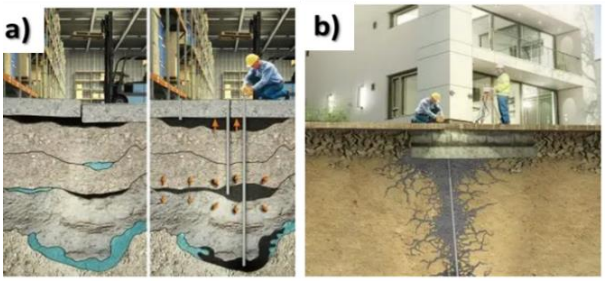

Figure 8. Injection system - Uretek Floor Lift (https://www.uretek.pt).

7 FINAL REMARKS

The aim of the present work was to present the designed solutions for strengthening main retaining walls and warehouse pavements. The strengthening solutions were defined considering the constraints, the severity of the detected pathologies and economic viability, with the aim of improving and guaranteeing the continued safe use of the warehouse area.

In the case of the retaining walls, the solution was associated to the construction of a bracing element for the existing support structure, which is a 0.45x0.70m distribution beam at the wall's mid-height, designed to transfer the horizontal forces to inclined micropiles. For the pavement, a ground consolidation solution of the Uretek - Floor Lift type was used, followed by drilling of holes in a square grid where polyurethane resin was injected.

REFERENCES

Barbosa, Y. (2019). *Microestaca Injetada Instrumentada: Avaliação do Comportamento sob Prova de Carga Estática e Ensaio de Carregamento Dinâmico*, M.Sc. thesis, State University of Campinas (in Portuguese).

Esteves, E. (2014). *Aluviões Silto-Argilosos Moles de Portugal Parametrização para Dimensionamento de Estruturas Geotécnicas*, Ph.D. thesis, University of Porto (in Portuguese).

Favaretti, M.; Germanino, G.; Pasquetto A. and Vinco G. (2004). Obras de consolidación de suelos de cimentación de un campanario con inyecciones de resina de elevada presión de expansión, In: *XXII Congreso Nacional De Geotécnica, Proceedings*, Palermo, Italy (in Spanish).

Uretek Floor Lift (2023). Uretek Floor Lift – Injeções Resina Expansiva sob Pavimentos, available at: https://www.uretek.pt/, accessed: 07/12/2023 (in Portuguese).

Proceedings of the XVIII ECSMGE 2024
GEOTECHNICAL ENGINEERING CHALLENGES
TO MEET CURRENT AND EMERGING NEEDS OF SOCIETY
© 2024 the Authors
ISBN 978-1-032-54816-6
DOI 10.1201/9781003431749-488
Open Access: www.taylorfrancis.com, CC BY-NC-ND 4.0 license

ECSMGE 24
XVIII EUROPEAN CONFERENCE ON SOIL MECHANICS AND GEOTECHNICAL ENGINEERING

Application of Cutter Soil Mixing technology in retaining walls

Application de la technique Cutter Soil Mixing dans les structures de soutènement

A. Peixoto*, P. Gomes
Artur Peixoto Lda., Braga, Portugal

**artur.peixoto@apgeotecnia.pt*

ABSTRACT: This article describes the Cutter Soil Mixing (CSM) technology as a solution for constructing peripheral retaining walls, presenting its characteristics, advantages over other technologies used in retaining walls, and how to design a retaining wall solution with CSM panels, which can be adapted to braced, anchored or top-down excavations. At the end, three case studies are listed, two braced retaining walls, one of which is prestressed, and one supported by slab bands, where the use of this technology proved to be important for the solution of excavation in an urban environment.

RÉSUMÉ: Cet article décrit la technique du Cutter Soil Mixing (CSM) comme une solution de construction de murs de soutènement périphériques, en présentant ses caractéristiques, ses avantages par rapport aux autres techniques utilisées dans les murs de soutènement, et la conception d'un mur de soutènement avec des panneaux CSM, qui peut être adapté à des excavations étayées, ancrées ou de haut en bas. Pour finir, trois études de cas sont indiquées, deux murs de soutènement contreventés, dont un précontraint, et un soutenus par des bandes de dalles, où l'utilisation de cette technologie s'est avérée importante pour la solution de l'excavation dans un environnement urbain.

Keywords: Urban excavations; deep excavations; Cutter Soil Mixing; CSM, retaining walls.

1 INTRODUCTION

The continued concentration of the world's population in large centres is forcing the construction of large habitable areas on an ever-smaller surface area. This is leading both to an increase in the height of buildings and the utilisation of the subsoil.

Due to the limited space and confinement of the available areas, excavations have to be made with a vertical face, requiring retaining walls near buildings or other structures that must be preserved.

Taking into account the growing public concern about environmental issues, it has become necessary to look for solutions that minimise the environmental impact of buildings, whether during exploration or construction. Over time, innovative and versatile techniques have been developed that allow local soils to be used as a construction material by mixing them in situ with stabilising compounds.

This article presents the Cutter Soil Mixing (CSM) technology as a solution for the construction of vertical, impermeable retaining walls capable of reaching great depths of known geometry, using soil as the construction material.

From a list of successful projects, it can be said that CSM technology is an interesting solution both technically and economically, and has been applied in various projects all over the world. This article lists three projects where this technology has been used to build vertical retaining walls in urban environments.

2 DESCRIPTION OF CSM TECHNOLOGY

Cutter Soil Mixing technology derives from Deep Soil Mixing (DSM) technology, combining its concepts with some of the principles of diaphragm walls, such as the use of hydromill and the geometry of the panels, as shown in Figure 1. A cutting tool for making CSM panels consists of two sets of cutting wheels that rotate around horizontal axes to produce soil-cement panels with a rectangular cross-section, unlike the DSM technology, which uses cutting tools that rotate around vertical axes to produce soil-cement columns (Stoetzer et al., 2006).

The cutting tool is attached to the bottom of a kelly bar, in a crawler crane fitted with a vertical tower.

The process of making a CSM panel comprises essentially two phases, the cutting phase and the extraction and mixing phase.



Figure 1. CSM equipment with rotation around horizontal axes and view of a CSM panel.

The cutting phase takes place during the descending movement of the tool to the required depth. As the cutting tool advances in depth, the hydraulic binder (usually cement grout) is added. The speed of the cutting tool and the volume of hydraulic binder added must be adjusted by the operator to optimise the use of energy and create a mass of homogeneous material that allows the tool to be lowered and raised easily. In difficult geological conditions or for CSM panels at great depths, it may be necessary to use bentonite during the cutting phase, with the cement grout being added to the panel only during the extraction and mixing phase (Peixoto et al., 2012a).

Once the desired depth has been reached, the kelly bar begins to rise by reversing the rotation of the cutting wheels and continuing to inject cement grout at low pressure. Figure 2 shows the execution process described.

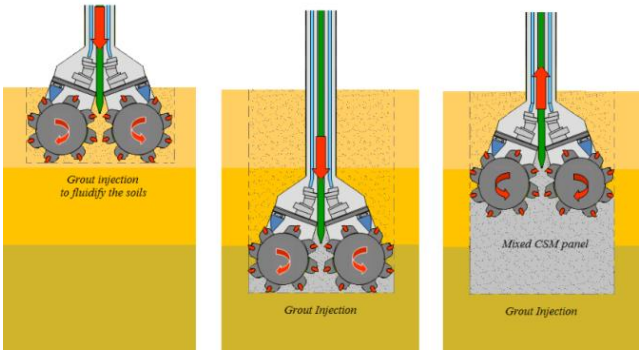

Figure 2. Illustration of the main phases of the execution of a CSM panel.

One of the particularities of this technology is that it allows the soil to be incorporated in situ into the retaining structure itself, with the retaining walls being executed sequentially by primary and secondary panels with a project-defined overlap length between them to obtain a continuous CSM wall. The fact that this technology allows soil to be used as a construction material, avoiding large volumes of material going to waste, is an advantage from an environmental and economic point of view compared to traditional technologies such as pile walls or diaphragm walls. A second advantage that should be emphasised is the knowledge of the exact geometry of panels in depth, since the equipment allows real time monitoring of the cutting tool's deviations during its advance in depth, making it possible to correct its positioning at any time. The process of mixing the hydraulic binder with the disintegrated soil can be influenced by various factors. In order to obtain CSM panels with the right characteristics, ensuring the homogeneity and reproducibility of the characteristics of the resulting material, it is essential to effectively control the execution parameters such as the speed of the cutting tool, the volume of grout added at depth, deviations of the cutting tool, among others (Bringiotti et al., 2009). Other advantage of this technology is that it can be applied to all types of soil, although the effectiveness of the application is not the same on all types of soil. Generally, the best results are obtained in sandy soils, as lower strengths are obtained in clay and silty soils for the same quantity of cement.

As illustrated in Figure 3, the use of soil-cement panels with a rectangular cross-section made using CSM technology for retaining walls has advantages when compared to the use of soil-cement columns made using DSM methods that use cutting tools that rotate around vertical axes (Fiorotto et al., 2005), and the following main advantages can be highlighted:

- reduction in the volume of soil treated to obtain the same effective treatment section and the consequent reduction in costs associated with this;
- reduction in the number of wall joints;
- the possibility of using different types of reinforcing elements for the panels, whose positioning in the panel itself can also be optimised.

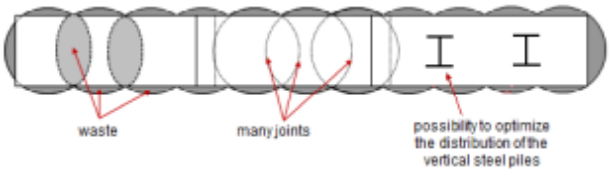

Figure 3. Comparison of the rectangular geometry of the CSM panels with the columns of the DSM methods.

3 RETAINING WALL SOLUTION

The most widely used peripheral retaining wall solution using Cutter Soil Mixing technology is the construction of a continuous wall of successive panels

2.4 metres wide and a constant thickness of 55 to 80 cm, depending on the project.

In order to ensure a continuous wall, panels are executed sequentially between primary and secondary panels, with an overlap length of 0.20 metres between them to ensure a good connection between adjacent panels in depth, as shown in Figure 4 (Peixoto et al., 2012b).

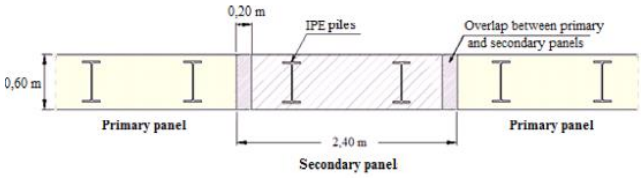

Figure 4. Primary and secondary panels of the CSM retaining wall.

The panels are made long enough to ensure the structural stability of the bottom and minimise the inflow of water into the excavation area.

Panels usually need to be reinforced to resist bending stresses. The most common method is to place steel sections inside the panel immediately after it has been made. The preference for IPE sections is due to the better flexural modulus to weight ratio. Placing the sections inside the CSM panels also protects them from possible buckling phenomena due to the confinement provided, and also minimises corrosion phenomena caused by the aggressiveness of the surrounding terrain.

The steel sections can be joined together with a reinforced concrete beam at the top of the wall.

The horizontal stability of the retaining wall is achieved in a similar way to the other types of peripheral retaining walls, such as horizontal bracing between elevations or for the excavation bed, temporary or permanent ground anchoring, or even through permanent slabs in top-down solutions. Due to the low shear resistance of CSM panels, horizontal forces must be redistributed to the anchors or struts through distribution beams.

The distribution beams or slabs that will resist the horizontal forces are supported on the retaining wall by steel sections, as shown in Figure 5.

In the case of permanent peripheral retaining walls, it is usual the construction of a reinforced concrete wall against the CSM panels. This wall can be built from the top down as the excavation progresses or from the bottom up when the structure is built. It is common to build this covering wall with a thickness between 0.15 and 0.20 m.



Figure 5. Photo of the HEA sections for connecting the slab at "Largo do Ambiente".

The Figure 6 shows a typical cross-section of a peripheral retaining wall executed with CSM panels and provisionally braced.

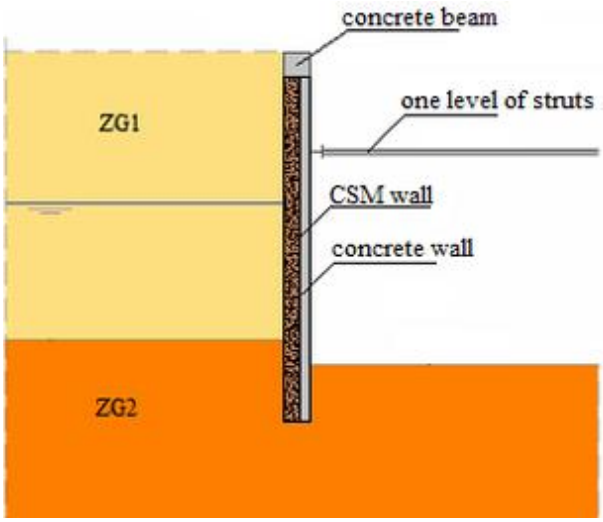

Figure 6. Cross-section of the retaining wall of the "Villa Paradisio" project.

4 DESIGN METHODOLOGY

In order to analyse the retaining wall, one or more calculation sections are defined that together represent the entire retaining structure.

The behaviour of each representative section is studied using analytical methods, such as free-earth support" or "fixed-earth support", or using automatic calculation programmes, such as PLAXIS® or PHASE2®.

All the elements of the retaining wall are designed in accordance with the legal standards, namely the Eurocodes in the European Union and Norway.

The vertical steel sections are designed to resist all the forces acting on the wall, disregarding the resistance of the soil-cement mixture, except for the seismic action in which the resistance is taken into account.

The soil-cement mixture, when in service, must have a sufficient compressive resistance to transmit the pressures to which it is subjected to the vertical steel sections. The transmission of these pressures is verified through the arc effect, as shown in Figure 7.

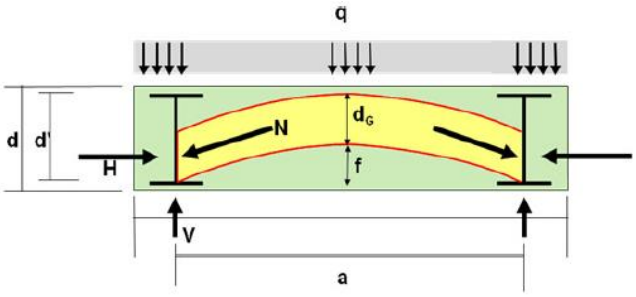

Figure 7. Distribution of horizontal stress in the cross-section of the retaining wall.

Horizontal support elements, such as anchors or struts, are designed in the same way as for other retaining wall construction techniques.

In the case of excavations below the water table, the hydraulic stability of the bottom of the excavation must also be verified, namely hydraulic uplift and internal erosion (piping), and the estimation of the volume of water that will flow into the excavation for designing the pumping system.

5 QUALITY CONTROL

The variability of the resistance and deformability parameters of the soil-cement resulting from the application of CSM technology is directly related to the degree of homogeneity of the mixture and it is influenced by various factors such as the type of soil involved, the presence of water, the distribution of the binder in the disintegrated soil mass, the presence of air as a component, the chemical reactions that take place during the mixing process, among others. For these reasons, it is necessary to take special care and carry out effective monitoring, both during execution and afterwards when evaluating the quality of the mixture according to the design requirements.

One of the main advantages of CSM technology over other alternative techniques, apart from the economic and environmental aspects (the use of in situ soil as a construction material), is the possibility of real-time control of the execution parameters by the equipment operator (Larsson, 2005). The operator has an instrument panel, as shown in Figure 8, that allows him to monitor and correct, in real time, parameters such as the advance speed of the cutting wheels, the amount of binder added, the density of the fluids involved (water-cement ratio) and the verticality of the panel, among others.



Figure 8. Cutter control panel.

In addition to the control made by the operator during the execution of CSM panels, the control is also achieved through laboratory tests combined with field tests on panels constructed for this purpose, which allow the execution parameters to be calibrated. Once the execution parameters have been calibrated, the construction of the CSM panels of the retaining wall can begin, from which samples are also taken for laboratory tests.

During excavation, monitoring is done following the Observation and Instrumentation Plan, which may include the placement of topographic targets on the retaining wall and neighbouring buildings, marks on the pavements, inclinometers, strain gauges installed in the struts and load cells in the soil anchors.

6 CASE STUDIES

6.1 Initial considerations

Cutter Soil Mixing technology is already being applied to retaining walls all over the world. This chapter presents two projects realised in the south of France and one in Luanda, Angola.

6.2 "Villa Paradisio" project

One of case studies is an excavation in Cannes for the construction of four underground floors of the "Villa Paradisio" building. The excavation site has a floor area of around 840 m^2, with an average excavation depth of 12 m, and directly faces neighbouring buildings and streets.

Despite the fact that the excavation is 12 metres deep in an urban context with the water table at about half the height of the excavation, the presence of the fractured dolomitic bedrock detected above the maximum excavation depth provided good support for the lower part of the retaining wall, allowing a solution

that included only one level of horizontal metal struts. This solution, in addition to containing the excavation with a vertical face, had a second objective of limiting the inflow of water into the excavation area (Peixoto et al., 2012c).

In this context, a retaining wall solution was proposed and designed consisting of a continuous wall of soil-cement panels with a rectangular cross-section with a thickness of 0.55 metres, up to an average depth of 15 metres, in order to guarantee a minimum length of 3 metres below the bottom of the excavation, reinforced with two IPE 450 beams in each CSM panel. A horizontal support level was defined for the approximately 12 m of total excavation height, materialised by tubular metal struts associated with metal distribution beams built along the perimeter of the site, as shown in Figure 9.

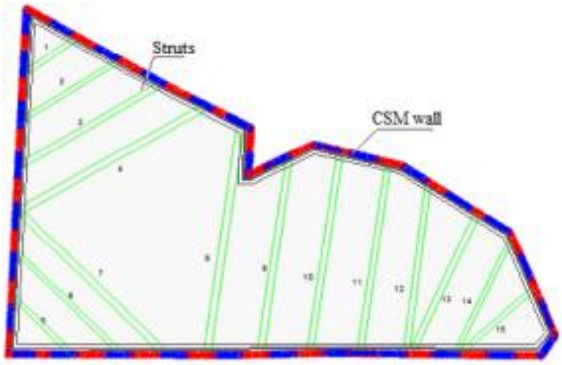

Figure 9. Plan representation of the retaining wall solution adopted for the "Villa Paradisio" project.

6.3 "May Flower" building

The "May Flower" building, located in Antibes, France, consists of eight elevated floors and four underground floors over an area of 317 m^2 and is bordered by streets and buildings.

The main challenge encountered in this project consisted of excavating to an average depth of 11 m in a densely constructed area, in the presence of soils with very variable mechanical characteristics, generally with low resistance values and high deformability to depths below the excavation base, and in the presence of a water table close to the surface (Gomes et al., 2016).

The solution proposed and designed consisted of a continuous wall of CSM panels, temporarily supported by four levels of metal bracing, with the lower three levels prestressed.

Limiting the inflow of water into the excavation was one of the project's concerns. To this end, a minimum embedment length of 6 metres was set from the bottom of the excavation and the panels were built to an average length of 17 metres.



Figure 10. Photo of the "May Flower" construction site before the application of the second level of bracing.

6.4 "Largo do Ambiente" underground parking

The "Largo do Ambiente" is an underground car park built in the city of Luanda, Angola. With capacity for 525 cars, it has two to five underground levels, corresponding to a variable excavation height between 8.0 and 17.4 metres. The excavation site directly faces existing buildings and streets and has a rectangular layout with an area of approximately 4,735 m^2.



Figure 11. Photo of the execution of the fifth and final slab band at "Largo do Ambiente".

The retaining wall was executed through soil-cement panels by the application of Cutter Soil Mixing (CSM) technology, reinforced with vertical steel piles. Taking in account the constrains related to the urban surrounding, including the proximity of buildings and streets, two to five levels of reinforced concrete slab bands were implemented, creating a rigid support system of the four elevations. The slab bands were incorporated on the final structure of the building and with this solution the execution of ground-anchors with big lengths that would lead to the occupation of the neighbour underground was dispensed. Furthermore, this solution brought some economic benefits, especially due to the incorporation of elements used in the final structure at the preliminary

stage of the work. The main objectives of the retaining wall were allowing the vertical excavation assuring simultaneously the stability of nearby structures and infrastructures, and also reduce the inflow of water into the interior of the excavation during the construction (Peixoto et al., 2016).

7 CONCLUSIONS

The application of CSM technology in retaining walls allows, with different geological and hydrogeological scenarios, to carry out excavations to the desired heights without compromising the stability of neighbouring structures.

With regard to the advantages of applying CSM technology compared to traditional techniques, should be emphasised the possibility of knowing the exact geometry of the soil-cement panels and the deviations that occur in depth, as well as the versatility of the equipment used. In these cases, the advantages were particularly important since, on the one hand, the knowledge of the exact geometry of the panels and the deviations in depth made it possible to achieve an effective connection between panels and a reduction in the inflow of water into the excavation area and, on the other hand, the versatility of the equipment made it possible to pass through the different materials that form the subsoil.

ACKNOWLEDGEMENTS

The authors would like to thank Geo-Rumo, Tecnologia de Fundações, S.A. for the photos provided and for authorising the inclusion of their work in this article.

REFERENCES

Bringiotti, M., Dossi, M., Nicastro D. (2009). Miscelazione profonda dei terreni: metodi classici e tecnologie innovative – CSM by BAUER. *Geofluid* 2009.

Fiorotto, R., Schöpf, M. and Stötzer, E. (2005). Cutter Soil Mixing (CSM) An innovation in Soil mixing for creating Cut-off and Retaining walls. In: *16th International Conference on soil mechanics and geotechnical engineering*, Osaka, Japan, Vol. 3, pp. 1185-1188. https://doi.org/10.3233/978-1-61499-656-9-1185.

Gomes, P., Peixoto, A. e Borges, R. (2016). Estrutura de contenção periférica executada com a tecnologia de cutter soil mixing no edifício "May Flower" em Antibes – França. Solution of earth retaining structure using cutter soil mixing technology at the "May Flower" in Antibes – France. In: *15º Congresso Nacional de Geotecnia*, Porto, Portugal (in portuguese).

Larsson, S. (2005). State of Practice Report – Execution, Monitoring, and Quality Control. In: *International Conference on Deep Mixing. Best Practice and Recent Advances*. Deep Mixing ´05, Stockholm, Sweden, Vol. 2, pp. 732-785.

Peixoto, A., Sousa, E. e Gomes, P. (2012a). Permanent Excavation Support in Urban Area using Cutter Soil Mixing technology at Cannes, France. In: *ISSMGE TC 211: International Symposium & Short Courses. Recent Research, Advances & Execution Aspects of Ground Improvement Works*, Brussels, Belgium, Vol. III, pp. 233-242.

Peixoto, A., Sousa, E. e Gomes, P. (2012b). Solution of earth retaining structure using Cutter Soil Mixing technology: "Parking Saint Nicolas" Project at Cannes, France. In: *ISSMGE TC 211: International Symposium & Short Courses. Recent Research, Advances & Execution Aspects of Ground Improvement Works*, Brussels, Belgium, Vol. III, pp. 251-260.

Peixoto, A., Sousa, E. e Gomes, P. (2012c). Earth Retaining Structure using Cutter Soil Mixing technology for the "Villa Paradisio" Project at Cannes, France. In: *ISSMGE TC 211: International Symposium & Short Courses. Recent Research, Advances & Execution Aspects of Ground Improvement Works*, Brussels, Belgium, Vol. III, pp. 223-232.

Peixoto, A., Gomes, P. e Baptista, M. (2016). Estrutura de contenção periférica executada com a tecnologia de cutter soil mixing no "Parque de Estacionamento do Largo do Ambiente" em Luanda – Angola. Solution of earth retaining structure using cutter soil mixing technology at the "Largo do Ambiente underground parking" in Luanda – Angola. In: 15*º Congresso Nacional de Geotecnia*, Porto, Portugal (in portuguese).

Stoetzer, E., Brunner, W., R., Gerressen, F.W. and Schoepf, M. (2006). CSM Cutter Soil Mixing – A New Technique for the Construction of Subterranean Walls Initial Experiences Gained on Completed Projects. In: P*roceedings DFI/EFFC 10th International Conference on Piling and Deep Foundations*, Amsterdam.

Proceedings of the XVIII ECSMGE 2024
GEOTECHNICAL ENGINEERING CHALLENGES
TO MEET CURRENT AND EMERGING NEEDS OF SOCIETY
© 2024 the Authors
ISBN 978-1-032-54816-6
DOI 10.1201/9781003431749-489
Open Access: www.taylorfrancis.com, CC BY-NC-ND 4.0 license

ECSMGE 24
XVIII EUROPEAN CONFERENCE ON SOIL MECHANICS AND GEOTECHNICAL ENGINEERING

The description of underground works evolution in Hospital Santo António station (Porto Metro)

Description de l'évolution des travaux souterrains de la station Hospital Santo António (Métro de Porto)

A. Pereira*, T. Azeredo, A. Carvalheira
CJC Engenharia e Projetos, S. Paulo, Brasil

I. Coelho
Metro do Porto, Porto, Portugal

**antonyy.pereira@gmail.com*

ABSTRACT: Currently, the particular context of each underground work leads to the choice of different constructive methodologies in view of the wide variety of existing options and in this sense the article will focus on the description of underground works evolution, in an urban environment, on Porto Metro, specifically the Hospital Santo António station. Hospital Santo António station is part of the future circular line, section Liberdade / S. Bento - Boavista / Casa da Música, and its location is conditioned by: proximity to a road tunnel (Túnel de Ceuta); by an underground water line (Rio Frio); the need to preserve tree species in the existing garden (Jardim do Carregal) and to minimize disturbances to adjacent buildings and traffic during construction. These constraints led to a unique geometric solution and constructive methodology, consisting basically of two large-section tunnels (approximately 200 m^2), which intersect obliquely, two large-diameter shafts with an approximate area of 400 m^2 (for access, ventilation and emergency exit) and two inclined tunnels to arrive at distribution floor for access to the dock platform. The methodology adopted in the tunnels is the NATM "New Austrian Tunneling Method", while in the large diameter shafts the vertical sequential excavation method was chosen. These methodologies are an excavation procedure with minimal support, which depends on the geomechanical and hydrogeological properties of the terrain, because it considers that the tunnel surrounding terrain contributes to its own support.

RÉSUMÉ: Actuellement, le contexte particulier de chaque ouvrage souterrain conduit au choix de différentes méthodologies constructives compte tenu de la grande variété d'options existantes et, en ce sens, l'article se concentrera sur la description de l'évolution des travaux souterrains, en milieu urbain, dans le Métro de Porto, plus précisément la station Hospital Santo António. La station Hospital Santo António fait partie de la future ligne circulaire, section Liberdade / S. Bento - Boavista / Casa da Música, et son emplacement est conditionné par: la proximité d'un tunnel routier (Túnel de Ceuta); par une conduite d'eau souterraine (Rio Frio); la nécessité de préserver les espèces d'arbres dans le jardin existant (Jardim do Carregal) et de minimiser les perturbations des immeubles adjacents et de la circulation pendant la construction. Ces contraintes ont conduit à une solution géométrique et une méthodologie constructive uniques, constituées essentiellement de deux tunnels de grande section (environ 200 m^2), qui se croisent obliquement, de deux puits de grand diamètre et d'une superficie approximative de 400 m^2 (pour l'accès, la ventilation et la sortie de secours) et deux tunnels inclinés pour arriver au plancher de distribution pour accéder à la plateforme du quai. La méthodologie adoptée dans les tunnels est la méthode NATM "New Austrian Tunneling Method", tandis que dans les puits de grand diamètre, la méthode d'excavation séquentielle verticale a été choisie. Ces méthodologies sont une procédure d'excavation avec un soutènement minimal, qui dépend des propriétés géomécaniques et hydrogéologiques du terrain, car elle considère que le tunnel entourant le terrain contribue à son propre soutènement.

Keywords: Underground infrastructure; urban environment; large diameter shafts; tunneling; Porto Metro.

1 INTRODUCTION

The "Santo António Hospital's" station, which is currently under construction, belongs to the Porto Metro circular line project, also known as Pink Line. The circular line extends through the central axis of the city of Porto, with a length of approximately 3.1 kilometers, and it foresees the construction of four new stations: Liberdade/S.Bento, Hospital de Santo António, Galiza and Boavista/Casa da Musica (Sener/CJC/NSE, 2020).

The Hospital Santo António (HSA) station is located in the Carregal garden, in the center of Porto and in the vicinity of the hospital with the same name, and its construction is influenced by several

constraints (Figure 1). One of them is the Ceuta tunnel (road tunnel), which crosses over the tunnel of the future circular line, immediately before the station, requiring a special care during the station's implementation. Furthermore, once the construction takes place in one of the most emblematic and ancient gardens in the city, there's a need to preserve, as much as possible, the tree species in the Carregal garden and minimize the disturbances on the surrounding environment and traffic during the construction phase, to ensure the easy access to the hospital. These factors had a significant impact on the decision to locate accesses and shafts, on the surface, as well as on the construction solution and method (Pereira, 2023).

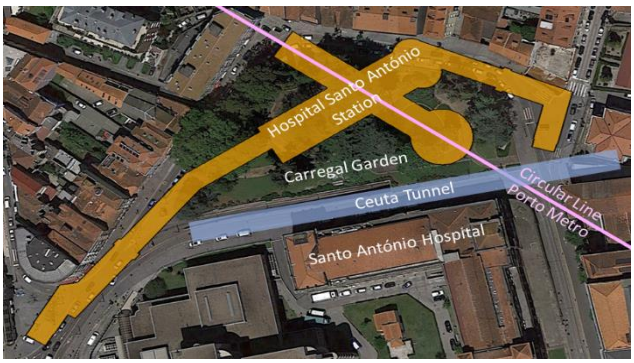

Figure 1. View of the Hospital Santo António station location.

2 CONSTRUCTION SOLUTION

The execution project, (Sener/CJC/NSE, 2019a), of the Hospital de Santo António station consists in the interconnection of two galleries with an angle of 66 degrees and a minimum cover of 11 meters.

The first gallery, named *Caverna Cais* (CC), extends for approximately 61 meters, covering an excavated area of approximately 172 m². In its cross section, the CC has a width of 18 meters and reaches a maximum excavation height of 12 meters. At the southeast end of the CC is the emergency exit shaft (EES). The EES has a circular configuration, with an average excavation diameter of around 24 meters (corresponding to an area of approximately 450 m²) and reaching a depth of approximately 27 meters.

The second gallery, named *Caverna Mezanino* (CM), extends approximately 62 meters, occupying an excavated area of around 260 m². In its cross section, the CM has a maximum excavation width of 20 meters and reaches a maximum excavation height of 17 meters. At the northeast end of the CM is the elevator shaft (ES). The ES has an elliptical shape, with an average excavation width of around 23 meters on the major axis and 18 meters on the minor axis (which corresponds to an approximate area of 325 m²) and has a depth of around 27.5 meters.

From the ES, there will be a connection with the surface through the construction of the east access tunnel (EAT). This tunnel will be approximately 25 meters long and its cross section will be variable. Initially, in the shaft-surface direction, the excavation section will be larger, covering around 130 m², with a height of 10.5 meters and a width of 15 meters. At the end of the tunnel, the excavation section will decrease to approximately 57 m², with a height of 8.3 meters and a width of 8.5 meters.

From the southwest end of the CM, a connection with the surface will be established through the construction of the western access tunnel (WAT). With an approximate length of 70 meters, this tunnel will feature a single excavation section, with an area of approximately 57 m², a height of 8.3 meters and a width of 8.5 meters and it will connect to the open ditch at its end. A three-dimensional modelling is presented in Figure 2.

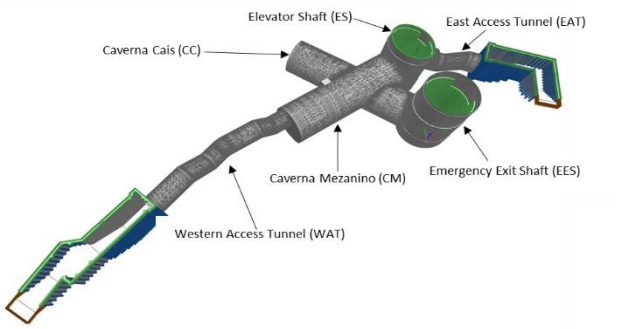

Figure 2. Three-dimensional modeling of the Hospital Santo António station (Pereira, 2023).

2.1 Construction methodology

The Hospital Santo António station will adopt three different methodologies: the underground station, composed of CM, CC, EAT and WAT, which will be carried out according to the NATM methodology; the connection of the east and west accesses to the surface, which will be executed through an open ditch and the two attack shafts to the station will be executed using a vertical sequential methodology (Sener/CJC/NSE, 2019a).

2.2 Geological-geotechnical background

The city of Porto is closely linked to its impressive granite massif. This massif stands out in the outcrops along the coastline and on the city's cliffs. However, the geotechnical conditions are complex due to the tectonic setting of the granite massif and the hydrothermal changes and weathering that occurred after its formation.

This granite massif, called *Granito do Porto*, has two micas, with a predominance of muscovite, and has a medium grain, sometimes coarse. Fine-grained aplite-pegmatite transitions are also common.

The geology in the region, of the future circular line of the Porto Metro, is characterized by the granite massif covered by landfills and, frequently, by alluvial soils (Sener/CJC/NSE, 2019b).

The geological-geotechnical characterization of the region where the HSA station is located (Figure 3), defines that the upper lands, made up of landfills and alluvium whose development follows the morphology of the paleo valley represents, as a whole, the filling of the Rio Frio valley and are part of the geotechnical unit G7 which reaches 10 to 12 meters deep. The landfills are sandy and heterogeneous, including granite blocks, organic levels and debris remains. The lower alluvial soils are essentially made up of silty-clayey sands and sandy-clayey silts, brown or dark grey (Sener/CJC/NSE, 2019b).

The G6 and G5 units follow the G7 unit in depth. These geotechnical zones consist of very compact granite alteration soils and decomposed granite, respectively, characterized by a sub-horizontal development, with corrugated boundaries, which reaches a depth of 21 to 24 meters. In some areas of the station, the decomposed granite massif (G5) transitions to highly altered granite massifs (G4). The G3 geotechnical zone occurs below the G5 unit, occasionally appearing in the form of loosely continuous blocks within the G5 unit. The granite massif of unit G3 is classified as moderately altered, with closely spaced and moderately spaced, oxidized and open fractures. In the center of the station, the G3 granite massif quickly evolves into G2, characterized as little altered. Locally, there are intersections of sub-vertical fracture alignments, mainly without filling, which represent preferential zones of percolation and water storage in the rock mass. Before excavations began, the average water level was approximately 7 meters deep from the surface (Sener/CJC/NSE, 2019b).

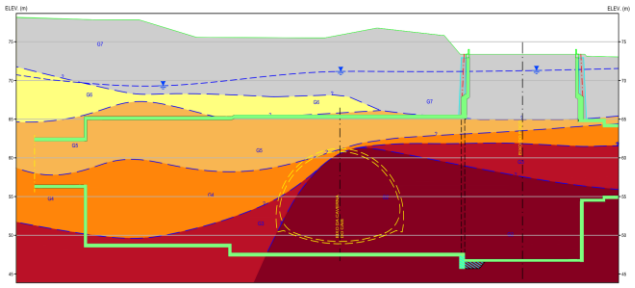

Figure 3. Geological-geotechnical longitudinal profile of the Hospital Santo António station.

3 EXECUTIVE SEQUENCE

Before the beginning of the excavation works, preparatory works were meticulously carried out in March 2021. These preparations were essential to enable the construction of the station and included the following tasks: alteration of local road traffic routes; execution of infrastructure diversion, including the diversion of the Rio Frio; carrying out an archaeological survey campaign and installation of the geotechnical instrumentation system in the massif and adjacent structures.

After the preparatory work are completed, the construction of the HSA station began. At this point, it is important to highlight that the construction process took place in a progressive and structured way. A concise summary of the activities that have been carried out up to the beginning of October 2023 will be now presented, as following.

The works on the HSA station began with the construction of the EES. Considering the presence of G7 surface terrain, it was necessary to implement a perimeter treatment into the massif surrounding the two attack shafts, which consisted in vertical drying jet-grouting columns with 0.8 meter in diameter. Once the jet-grouting columns were completed, the excavation works for the shafts started. The excavation works and application of the primary lining was carried out dividing the shaft into levels, with 1 meter high and panels 6 meters long, up to 27 meters deep, according to the execution project. From a depth of 9 meters, geodrains were installed to relieve hydrostatic pressure in the temporary lining, without causing a sharp lowering of the water level. The primary lining around the main tunnel and CC were reinforced to allow the excavation works to begin on both structures, dismissing the execution of the definitive lining of the shaft at this stage.

Subsequently, the works on the CC proceeded, interspersed with the advancement of the main tunnel, using the NATM methodology and divided into two phases: top heading divided into side-drift and enlargement and undercut. After advancing 6 meters, a stoppage wall was created. This front is on hold until the CM definitive lining work is completed.

When the execution of the EES was 15 meters deep, the ES excavation work began, following the same sequential methodology for executing the EES. The ES excavation was temporarily halted at a depth of 17 meters, which is the depth coinciding with the height of the CM top heading, EAT and WAT invert. After the completion of the excavation work on the top heading and the first undercut of the CM, the excavation of the ES will be resumed.

The CM excavation is expected to be carried out in a sectional manner: in a top heading (divided into side-drift and enlargement), first and second undercut, respecting the NATM methodology (Figure 4).

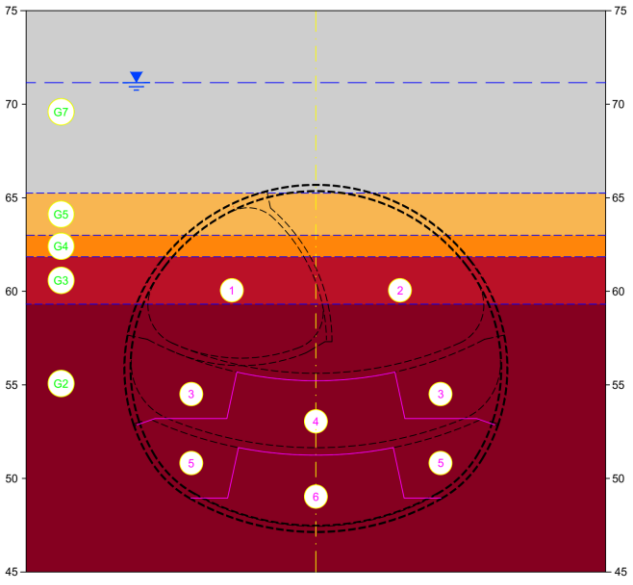

Figure 4. Executive phasing of Caverna Mezanino.

The excavation works, from the ES, began with the contour and front treatments of the CM and EAT portal. After the excavation of the CM side-drift was able to proceed. The enlargement of the CM's top heading began as soon as the side-drift was in the middle of the CM. After completion of the CM top heading, the stop wall and treatments of the WAT portal were carried out. The first undercut will begin once all the works for the WAT are concluded, from this work front.

While the CM was excavated, the excavation of the EAT also began, following the NATM construction sequence, up to approximately 12 meters in advance. Regarding WAT, underground excavation works advanced by around 12 meters. On the date of completion of this article, the EAT and WAT excavation fronts were being stopped, waiting the progress of the works being held from the surface, for the completion of the EAT and WAT excavation work.

At the same time and in order to guarantee the success of the project, a team of geologists and geotechnical engineers were designated to monitor the development of the works, on a daily basis. This group of professionals played a fundamental role in carrying out detailed cartography of the excavation fronts, carefully documenting the geological, geotechnical and hydrogeological characteristics found.

A geotechnical instrumentation plan was also implemented, during all the progress. This plan is based on a flexible project philosophy, providing a systematic control of the works and ensuring the project's assumptions. It also allows to adapt and adjust the project, if necessary, to ensure the compliance with deadlines and eases the management in case of geological-geotechnical and urban context unforeseen events, without underestimating safety.

4 CONCLUSIONS

The construction of the Santo António Hospital station, as part of the Porto Metro circular line, faced a series of constraints that required a careful designed constructive solution. This solution, with a bold and avant-garde approach, has proven to be suitable, even in an urban environment.

As the works approaches to the completion, it will be relevant to consider producing a scientific article addressing the geological complexities faced during construction, the performance of support structures over time and the impacts on the massif and structures adjacent. This will allow a critical assessment of what was predicted in the execution project compared to what was found during the construction phase.

ACKNOWLEDGEMENTS

The authors express their gratitude to Metro do Porto for the authorization granted to use elements of the project and photographs of the work in the presentation of this article.

REFERENCES

Pereira, J.A. (2023). *Metodologia de execução de poços de grande diâmetro em ambiente urbano. Methodology for executing large diameter shafts in urban environment*. Master thesis, Instituto Superior de Engenharia do Porto, Portugal (in Portuguese).

Sener/CJC/NSE (2019a). Memória descritiva da estação Hospital Santo António da linha circular do Metro do Porto. Descriptive memory of the Hospital Santo António station on the Porto Metro circular line. Report No. P-PR-LI-8003-TU-MD-SCN-001001-02. Porto, Portugal (in Portuguese).

Sener/CJC/NSE (2019b). Memória descritiva da geologia e geotecnia do projeto de execução da linha circular do Metro do Porto. Descriptive memory of the geology and geotechnics of the project for the execution of the Porto Metro circular line. Report No. P-PR-LI-8000-GG-MD-SCN-00001-04. Porto, Portugal (in Portuguese).

Sener/CJC/NSE (2020). Enquadramento geral do projeto de execução da linha circular do Metro do Porto. General framework of the Porto Metro circular line execution project. Report No. P-PR-LI-8000-GE-MD-SCN-000001-03. Porto, Portugal (in Portuguese).

Proceedings of the XVIII ECSMGE 2024
GEOTECHNICAL ENGINEERING CHALLENGES
TO MEET CURRENT AND EMERGING NEEDS OF SOCIETY
© 2024 the Authors
ISBN 978-1-032-54816-6
DOI 10.1201/9781003431749-490
Open Access: www.taylorfrancis.com, CC BY-NC-ND 4.0 license

ECSMGE 24
XVIII EUROPEAN CONFERENCE ON SOIL MECHANICS AND GEOTECHNICAL ENGINEERING

Influence of curing under stress on the geotechnical behavior of a treated silty soil

Influence sur le comportement mécanique d'une pression appliquée pendant la cure d'un limon traité

L. Pigeot
GeM, Ecole Centrale de Nantes, Nantes, France / GeoCoD, Cerema, Aix-en-Provence, France

L. Pigeot, N. Dufour*, A. Soive, H. Calissano, L. Batilliot
GeoCoD, Cerema, Aix-en-Provence, France

F. Dermenonville
Egis Structures et environnement, Seyssins, France

A. Loukili
GeM, Ecole Centrale de Nantes, Nantes, France

**Nathalie.dufour@cerema.fr*

ABSTRACT: Improving the soil in place by adding lime, hydraulic binder and increasing compaction is widely used to carry out geotechnical works. Laboratory test campaigns are conducted to validate the treatment and its consistency with the expected mechanical properties. They allow on the one hand to follow the mechanical evolution due to hydration of the cement phases and on the other hand to observe the soil response under various stresses. The standards for treated soils recommend carrying out tests on specimens which have undergone curing conditions in airtight packaging, at a temperature of 20°C and atmospheric pressure. However, if these normalized conditions represent the conditions of a low height embankment, when the structure is of great height it is interesting to take into account the pressure to which the material is subjected during its curing. The study focused on comparing the evolution of the mechanical properties of silt treated with lime and hydraulic binder then compacted, when it was subjected to a normalized cure or a confined cure of 500 kPa. In order to monitor the mechanical gain of the confined specimen regularly and without modifying its curing conditions, a resonant column apparatus (RCA) in torsion mode was used. With this device carrying out measurements of the shear modulus in very small deformations, the curing and testing phases could be coupled, the tests not being destructive. The curing stress brings the expected properties more quickly and confers superior properties of around 15% in the long term.

RÉSUMÉ: L'amélioration des sols en place par ajout de chaux, liant hydraulique et compactage est largement employée pour réaliser des ouvrages géotechniques. Des campagnes d'essais en laboratoire sont conduites afin de valider le traitement et sa cohérence avec les propriétés mécaniques attendues. Elles permettent de suivre l'évolution mécanique liée à l'hydratation des phases cimentaires et d'observer la réponse du sol sous diverses sollicitations. Les normes sur les sols traités préconisent de conduire les essais sur des éprouvettes ayant subi des conditions de cure dans un emballage hermétique, à température constante de 20°C et à pression atmosphérique. Cependant, si ces conditions normalisées représentent bien les conditions d'un remblai de faible hauteur, pour un ouvrage de grande hauteur, il est intéressant de prendre en compte la pression à laquelle le matériau est soumis. L'étude s'est portée sur la comparaison de l'évolution des propriétés mécaniques d'un limon traité à la chaux et au liant hydraulique puis compacté, soumis à une cure normalisée ou une cure confinée de 500 kPa. Afin de suivre le gain mécanique de l'éprouvette confinée de manière régulière et sans modifier ses conditions de cure, une colonne résonnante en mode torsion a été utilisée. Avec cet appareil réalisant des mesures du module de cisaillement en très petites déformations, les phases de cure et d'essais ont pu être couplées, les essais n'étant pas destructifs. La pression pendant la cure apporte plus rapidement les propriétés attendues et confère sur le long terme des propriétés supérieures d'environ 15%.

Keywords: Stabilized soil; lime and binder treatment; resonant column apparatus; curing stress conditions; shear modulus.

1 INTRODUCTION

The use of stabilized soils in geotechnical infrastructure works is widespread today because it provides ecological and economic gain. This reduces CO^2 emissions linked to the transport of excavated and backfilled material, and minimises the use of non-renewable materials from quarries. In order to predict

the reaction of the soil to the treatment and the mechanical gain that could be provided over time, experimental campaigns in the laboratory are carried out. Overall, laboratory experimental conditions tend to represent *in situ* conditions as closely as possible (state of stress, saturation and draining condition, compaction etc.). In the case of improved soils, the mechanical properties of these materials vary according to the curing time, as they are a function of the hydration reactions of lime and binder's cementitious phases. This is because the hydrated phases form shells around the soil that has flocculated after the lime has been added (Cabane, 2004). To ensure these reactions, the standards recommend curing conditions in laboratory for treated specimens: stored hermetically at a temperature of 20°C and at atmospheric pressure (LCPC/SETRA, 2000). These test conditions generally make it possible to well simulate the *in situ* soil conditions in low-rise structures. However, previous authors have noted that notable differences in terms of mechanical properties were measured between specimens of materials cemented in the laboratory and specimens cored when the soil was taken at great depth (Consoli et al., 2000). This phenomenon is studied in the field of Cement Paste Backfill (CPB) (Zhao et al., 2021) or cemented sands (Basas et al., 2020) but currently little for treated fine soils (Åhnberg, 2006).

The objective of this article was to highlight the mechanical property differences for a stabilized silty soil with two curing conditions: one curing at atmospheric pressure and the other with isotropic curing stresses (500 kPa) applied throughout the curing time (up to 70 days). For this purpose, it was necessary to measure the evolution of the mechanical properties of the confined specimen without modifying its curing conditions. A resonant column apparatus (RCA) in torsion mode was therefore used in the study. It allowed the measurement of the shear modulus G as a function of the distortion in very small deformation (between $10e^{-7}$ and $10e^{-4}$) (Lang et al., 2020). Furthermore, this test being non-destructive, it was possible to carry out all measurements on the same sample kept confined throughout its treatment. The results of these tests were compared to tests carried out on specimens which had had a standardized cure and a specimen of untreated silty soil.

2 MATERIALS AND METHODS

2.1 Materials

The material used was a low plasticity silty soil that comes from northern France. In the 0.2 mm sieve, 80% of the granulometry corresponds to silts. The X-ray diffraction (XRD) analysis indicated a composition of quartz, carbonate phases (calcite and dolomite), silicates (muscovite, microcline and clinochlore) feldspaths (albite), clay minerals (kaolinite) and hematite. To this soil with poor geotechnical properties was first added 1% lime. This lime is made up of approximately 90% quicklime (CaO). Then 5% of a hydraulic binder was added. This binder has a claimed composition of approximately 35% Portland cement clinker and 65% blast furnace slag (similar to a CEM III/A).

2.2 Specimen preparation

The freshly treated soil was then placed in a single layer in a mould for static compaction. The force was applied on both sides of the cylinder until 96% of optimal density and w = OMC+1% (Optimum Moisture Content). displayed by the proctor curve was reached (Figure 1). This curve indicates that the maximum dry density measured (ρ_d = 1.75 Mg/m^3) corresponds to an OMC = 17.5% The saturation ratio (Sr [%]) lines on the figure correspond to 100%, 90% and 80% pore water saturation.

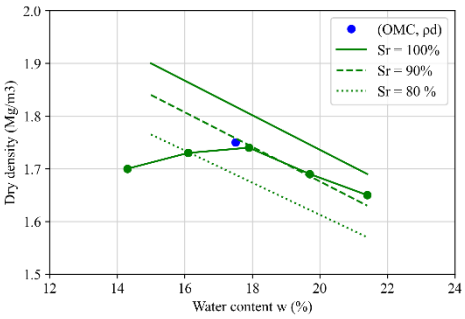

Figure 1. Proctors curve and saturation lines (Sr).

A compaction curve was plotted for each compacted specimen. The curves with e, the void index, as a function of sigma, the axial stress [kPa] in Figure 2 illustrate the homogeneity of the specimens produced. The average void index of the 10 specimens was e = 0.58, the minimum 0.55 and maximum 0.59. The standard deviation of these measurements is 0.014. To be able to compare mechanical results tests, the initial void index of the specimens must be equal.

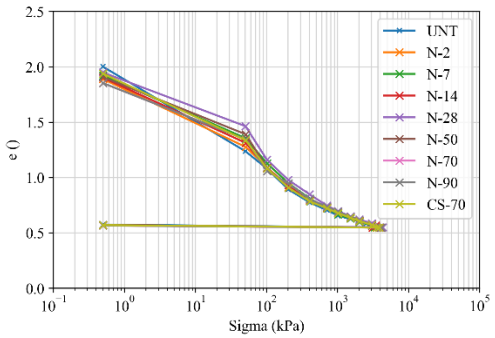

Figure 2. Compaction curves.

2.3 Curing and testing conditions

The characteristics of the 9 tested specimens are listed in. The untreated specimen (UNT) did not require any curing time and was tested immediately after being compacted with an isotropic confining pressure of 500 kPa. Normalized specimens (N-2, N-7, N-14, N-28, N-50, N-70 and N-90) were hermetically protected and placed in an air-conditioned room at 20°C without being subjected to curing stresses. Those were maintained in this condition for a define curing time and a different specimen was used for each curing time test. In contrast, to study the specimen subjected to curing stress, the soil specimen was not packed but directly placed in the RCA cell with an isotropic curing stress (CS) of 500 kPa for 70 days (CS-70). At the beginning of this curing time, one test per day was done, with one test per week conducted at its end. All the present tests were conducted on unsaturated specimens with drain open to the air, at testing pressure of 500 kPa.

Table 1. Curing and testing conditions.

Specimen	Curing time (days)	Curing stress (kPa)	Testing pressure (kPa)	Gmax modulus (MPa)
UNT	untreated		500	175
N-2	2	0	500	512
N-7	7	0	500	571
N-14	14	0	500	632
N-28	28	0	500	860
N-50	50	0	500	966
N-70	70	0	500	1069
N-90	90	0	500	1127
CS-70	70	500	500	1267

*UNT: untreated **N: normalized curing conditions ***CS: curing stress conditions

2.4 Resonant column apparatus tests

The evolution of the shear modulus as a function of distortion is obtained by torsion tests in the RCA. In this apparatus, the specimens are held fixed at the base and torsionally excited at the top. For each step of imposed amplitude, the resonance frequency corresponding to the maximum measured amplitude is determined. The tests were performed starting at the lowest amplitudes (0.005 V) up to the highest (1 V) with about 25 measurement points. At each point, the resonance frequency f_n [Hz] of the material can be used to calculate an angular frequency ω_n [rad·s^{-1}] (1). The resonance frequency is the lowest frequency at which the torsion is 90° out of phase with the rotational displacement. From the angular frequency it is possible to calculate the shear wave velocity V_S, which is used to calculate the shear modulus G [MPa] (1).

$$\omega_n = 2\pi f_n \qquad V_s = \frac{\omega_n L}{\beta} \qquad G = \rho V_s^2 \quad (1)$$

Where L [m] is the length of the specimen and β depends on the apparatus specificities and the specimen geometry. ρ is the specimen density [g.cm^3]. The maximum amplitude A_{max} [V] corresponding to the resonance frequency provides the distortion ϒ (2):

$$\Upsilon = \frac{4{,}596.A_{max}.D}{f_n.L} \quad (2)$$

The G modulus measured at the smaller amplitudes (0.005 V) and distortions is called Gmax.

3 RESULTS

As detailed above, torsional RCA tests provide shear modulus decrease curves as a function of distortion. The test results are presented for each curing condition (standardised then confined) and compared with an untreated and compacted silty specimen. A total of 38 tests were carried out.

3.1 G modulus as function of distortion

The results of tests carried out on specimens under normalized curing conditions are shown in Figure 3 in which each curve corresponds to a specimen. The results of the tests on the curing stress specimen (CS-70) are shown in Figure 4. During 70 days of curing, each of the 30 tests was carried out at a curing time specified in the legend (e.g. CS-70-2 d; for a test at 2 days curing time). In these two figures, the blue curve (▼) corresponds to the untreated silty specimen which has a Gmax of 175 MPa at a shear deformation of 5e^6. By comparison, the specimens of treated soil are located on much smaller deformations.

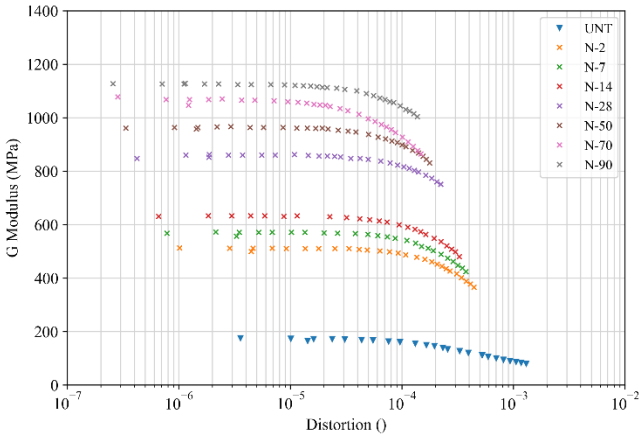

Figure 3. G modulus as function of distortion for normalized curing conditions.

The mechanical evolution within the specimen as a function of curing time is visible at several levels: the evolution of the shape of the curves, the increase in Gmax as a function of time, and the shift of the curve towards smaller deformations. In these figures, it is remarkable that the greatest mechanical gain takes place in the first 2 days of curing time.

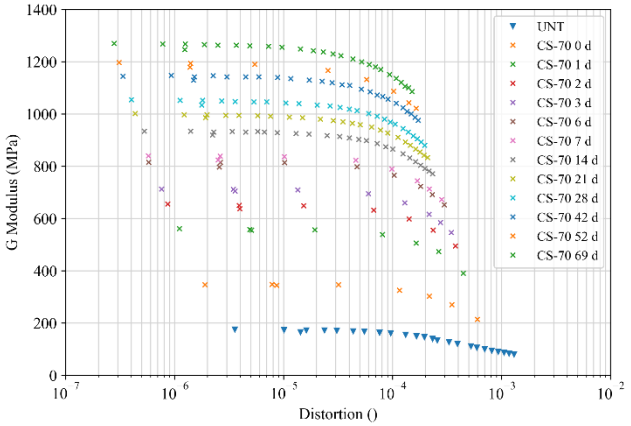

Figure 4. G modulus as function of distortion for curing stress conditions.

3.2 Kinetics comparison

The Figure 5 shows the Gmax as a function of time for the 35 tests performed. It highlights two different hydration kinetics. The first one corresponds to the specimen cured with a curing stress (CS-70) and second one corresponds to specimens cured without stress and tested at different curing times with the RCA (N, green curve). Therefore, the specimen CS-70, after 42 days with a curing stress of 500 kPa (CS-70-42 d on Figure 4), reaches the Gmax as the specimen N-90 curing without stress (CS-70-41 d, Gmax = 1137 MPa; N-90, Gmax = 1127 MPa).

A difference of approximately 200 MPa between the Gmax of the two curing conditions is measured from 14 days and up to 90 days.

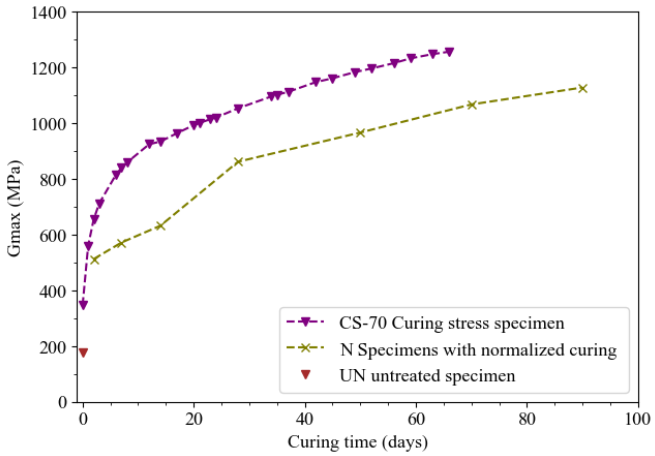

Figure 5. Gmax as function of time.

4 CONCLUSIONS

This experimental campaign showed that there was indeed a difference between the evolution of the shear modulus measured for the confined and unconfined soil specimen during its curing time. It also highlighted the fact that the resonant column is a good tool for studying soils treated in the laboratory (allowing small deformation and non-destructive measurements). Further work is underway to investigate the microstructure and chemical composition inherent to these mechanical tests.

ACKNOWLEDGEMENTS

The PhD project is funded by EGIS STRUCTURES ET ENVIRONNEMENT and Centrale Nantes. We also wish to thank the Seine Nord Europe Canal Company.

REFERENCES

Åhnberg, H. (2006). Strength of stabilised soils : A laboratory study on clays and organic soils stabilised with different types of binder. Department of Construction Sciences, Lund University.

Basas, V. G., Pantazopoulos, I. A., & Atmatzidis, D. K. (2020). Torsional and flexural resonant column testing of grouted sands. Soil Dynamics and Earthquake Engineering, 139, 106360.

Cabane, N. (2004). Sols traités à la chaux et aux liants hydrauliques : Contribution à l'identification et à l'analyse des éléments perturbateurs de la stabilisation. Université Jean Monnet - Saint-Etienne.

Consoli, N. C., Rotta, G. V., & Prietto, P. D. M. (2000). Influence of curing under stress on the triaxial response of cemented soils. Géotechnique, 50(1), 99-105.

Lang, L., Li, F., & Chen, B. (2020). Small-strain dynamic properties of silty clay stabilized by cement and fly ash. Construction and Building Materials, 237, 117646.

LCPC/SETRA. (2000). Traitement des sols à la chaux et/ou aux liants hydrauliques. Application à la réalisation des remblais et des couches de forme. Guide de Traitement des sols (GTS) (Réf. D9924). LCPC.

Zhao, Y., Taheri, A., Karakus, M., Deng, A., & Guo, L. (2021). The Effect of Curing under Applied Stress on the Mechanical Performance of Cement Paste Backfill. Minerals, 11(10), 1107.

Proceedings of the XVIII ECSMGE 2024
GEOTECHNICAL ENGINEERING CHALLENGES
TO MEET CURRENT AND EMERGING NEEDS OF SOCIETY
© 2024 the Authors
ISBN 978-1-032-54816-6
DOI 10.1201/9781003431749-491
Open Access: www.taylorfrancis.com, CC BY-NC-ND 4.0 license

ECSMGE 24
XVIII EUROPEAN CONFERENCE ON SOIL MECHANICS AND GEOTECHNICAL ENGINEERING

Ground improvement and special foundations at North Lisbon Logistic Platform, plot 1, Portugal

Solutions d'amélioration du sol et fondations spéciales sur la Plateforme Logistique au Nord de Lisbonne, parcelle 1, Portugal

A. Pinto, M. Lopes*, P. Marques
JETsj Geotecnia Lda, Lisbon, Portugal

A.L. Gonçalves
Terratest, Lisbon, Portugal

A. Perez, J. Moreno
Terratest, Madrid, Spain

J. Moreno
JM Ingeniería Geológica, Madrid, Spain

mlopes@jetsj.com

ABSTRACT: The North Lisbon Logistic Platform is located over soft soils at Tagus river right bank. At the Plot 1 an industrial warehouse with about 100.000 m^2 was built. For the warehouse foundations the following solutions were adopted: i) structural elements: reinforced concrete driven piles; ii) indoor pavements: load transfer platform, granular fill reinforced with geosynthetics, over rigid inclusions, geoconcrete columns (GCC) with under reamed base and capped by stone columns; iii) outdoor pavements: load transfer platform, granular fill reinforced with geosynthetics, over stone columns. The main design and execution criteria are presented, as well as the main results of both site monitoring and full-scale load tests.

RÉSUMÉ: La plateforme logistique du nord de Lisbonne est située sur des sols meubles sur la rive droite du Tage. Sur la parcelle 1, un entrepôt industriel d'environ 100.000 m^2 a été construit. Pour les fondations de l'entrepôt, les solutions suivantes ont été adoptées: i) éléments structurels: pieux battus en béton préfabriqué; ii) revêtements intérieurs: plateforme de transfert de charge, remblai granulaire renforcé de géosynthétiques, sur inclusions rigides, colonnes en géobéton (GCC) avec base sous alésage et coiffées par des colonnes ballastées; iii) revêtements extérieurs: plateforme de transfert de charge, remblai granulaire renforcé de géosynthétiques, sur colonnes ballastées. Les principaux critères de conception et d'exécution sont présentés, ainsi que les principaux résultats du suivi du chantier et des essais de charge en vraie grandeur.

Keywords: Driven piles, rigid inclusions, stone columns; load transfer platform; soft soils

1 INTRODUCTION

The North Lisbon Logistic Platform (NLLP) is located in Castanheira do Ribatejo, Portugal. This platform was built with the intend of creating an interconnection point for international, national and regional logistical flows within the Lisbon and Tagus Valley region. An example of recent construction in NLLP is presented in Lopes et al (2023) .

On plot 1 of the NLLP a new industrial building with an area of approximately 100.000 m^2 was built. In the aerial view in Figure 1, it is possible to identify its location.

The target area of intervention is located on the right bank of the Tagus River, that, from a geological-geotechnical point of view, is dominated by the alluvial terrain of the lower Tagus, characterized by the presence of soft soils with reduced bearing capacity. In the particular area where the new structure is located, the alluvium reaches considerable depths, of the order of 12.0 to 18.0 m, posing serious challenges to the construction of any structure in that location.



Figure 1. Aerial view of the construction site (image taken from Google Earth).

2 GEOLOGICAL AND GEOTECHNICAL CONDITIONS

The site under study fits, from a geomorphological point of view, in the middle of the alluvial plain of the Tagus river, close to the right bank of this main watercourse.

Local geological conditions therefore indicate alluvial formations, of Holocene age, deposited over a sedimentary substrate, called terrace deposits, attributed to the Plio-Pleistocene.

According to the information obtained during the geotechnical investigations, it appears that the local geological-geotechnical scenario is characterized by a layer of surface deposits, developing to a depth variable between 2.0 m and 3.0 m. According to the available sampling, it is a heterogeneous layer made up of a mixture of very soft to medium consistency clays, silts and sands ($0<N_{SPT}<8$). It is considered likely that these materials present an overconsolidated state, as a result of fluctuations in the water table.

Immediately below the layer of surface deposits, to a maximum depth of 12.0 to 18.0 m, there are alluvial soils, essentially made up of (i) very loose to loose sandy-silty horizons detected with thicknesses varying between 1.5 and 6.0 m ($0<N_{SPT}<8$); and (ii) very soft to soft silty clays with thicknesses varying between 6,0 and 11.0 m ($0<N_{SPT}<4$).

Underlying the alluvial layer, there are deposits of Plio-Pleistocene terraces, characterized by the interspersed occurrence of clay, sand and of gravel horizons, all with significant lateral continuity.

As depth advances, an increase in the resistant behaviour exhibited by this formation is observed, as shown by the generally increase of N_{SPT} values in depth, with the lowest values, generally varying between 14 and 30 blows, coming from the top of the formation, showing the occurrence of a more weathered surface zone, with behaviour of moderately dense to dense materials and generally hard to very hard consistency. An exception is made for some specific levels where the SPT tests indicate soft to medium consistency soils among the most compact materials.

The position of the water table is dependent on the water level in the Tagus river, being influenced not only by seasonal variations, but also by the daily tidal cycles felt in the estuary. During the prospecting geotechnical works, the presence of the water table was detected at a depth varying between 1.68 m and 2.12 m.

3 SOLUTIONS

Given the existence of highly compressible cohesive soils, the presence of geological and geotechnical conditions that are globally unfavourable to the accommodation of high and/or persistent loads is evident, with the risk of accentuated and evolving deformable behaviour over time. Consequently, there is a concern about mitigating immediate and deferred deformations, in accordance with the structure serviceability requirements. In this context, the following solutions were adopted:

a) Pile foundations for the warehouse resistant structure;
b) Ground improvement solutions of the foundation soil of interior and exterior pavements using (i) rigid inclusions, using the GEOPIER® GCC system, with a bi-module gravel and concrete cap and (ii) stone columns, using the GRAVA IMPACT® system.

3.1 Pile foundations

The proposed deep foundation solution consists of prefabricated reinforced concrete driven piles, of the TERRA® type, capable of accommodating compression, tension, flexural-compression, flexural-tension and shear loads.

T-350 piles (350x350mm) with a minimum length of 25.0 m were considered, with a seismically reinforced section in the first 12.0 m to be considered from the base of the pile cap. In Figure 2 a photograph of the prefabricated reinforced concrete driven piles on the construction site is presented.



Figure 2. Driven piles.

The stated piles are capped by reinforced concrete pile caps of 1, 2, 3, 4, 5, 6 and 7 piles that, whenever submitted to bending moments that are not possible to accommodate by the binary of forces achieved by axial stresses developed on the vertical piles, are interconnected by a grid of foundation beams, also in reinforced concrete.

Along the peripheral alignment, a solution using sub-verticals piles (10º from the vertical) was also defined. These will have the function of accommodating the vertical and horizontal forces coming from the earth retaining walls on the periphery of the building.

In addition to what was mentioned above, the piles must also be responsible for dissipating the shear coming from the pillars and walls, as well as ensuring the accommodation of the bending stresses developed in depth due to the action of the shear forces.

In Figure 3 a view of the 3D geometric model of the structure's foundation solution is presented.

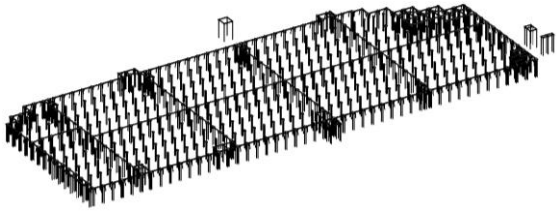

Figure 3. 3D geometric model of the structure's foundation solution (not to scale).

3.2 Ground improvement

Considering the geotechnical conditions described, aiming to reduce total and differential settlements, it was decided to implement, for the indoor pavement as well as the exterior loading/unloading docks pavement area where heavy vehicles will be parked, a ground improvement solution comprising the execution of rigid inclusions, using the Geo-Concrete Columns (GCC®) of the GEOPIER system, with under reamed base, under a load transfer platform, consisting of layers of granular fill reinforced with geosynthetics

The aforementioned rigid inclusions are arranged in different square arrays depending on the magnitude of the expected service live load. In Figure 4 and Table 1, a schematic plan is presented, with the location, spacing and magnitude of the different service live loads considered.

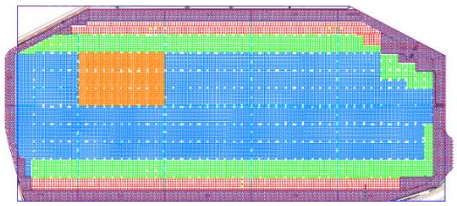

Figure 4. Schematic plan with the ground improvement solutions (not to scale).

Table 1. Live loads and ground improvement techniques considered for the pavement's foundation soil.

Zoning	Live load	System	Spacing
1	75 kN/m^2	GCC Rigid inclusions	2,30 m
2	50 kN/m^2		2,60 m
3	32 kN/m^2		3,10 m
4	20 kN/m^2		3,25 m
5	20 kN/m^2	IMPACT Stone columns	2,50 m

Prior to the installation of the rigid inclusions, in order to reach the levels foreseen for the pavements, an embankment with an average thickness of approximately 2.0 m was built. In this context, to minimize the excavation works, it was decided to execute pre-drilling works and install a stone column cap on top of the concrete columns.

For the exterior pavements, in the area intended for car traffic, likewise aiming to minimize total and differential settlements, a ground improvement solution using stone columns, using the GRAVA IMPACT® system was adopted. The stone columns are arranged in a triangular mesh spaced 1.2 m, under a load transfer platform, consisting of layers of granular fill reinforced with geosynthetics.

In Figure 5 a photograph of the load transfer platform is presented.



Figure 5. Load transfer platform.

4 DESIGN

4.1 Pile foundations

The foundations as well as the building's structure were modelled using the SAP2000 finite element software, in which the various structural elements were represented with their true dimensions and stiffness. In Figure 6 the 3D foundation model is presented.

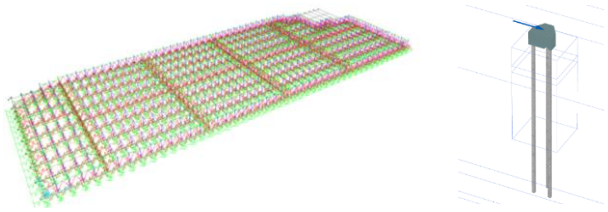

a) *b)*

Figure 6. a) Foundation's structure 3D SAP2000 finite element model. b) Pile Plaxis 3D finite element model.

For a more realistic analysis of the forces and displacements to which the structure and its foundations will be subjected, spring elements with vertical, horizontal and flexural stiffness of the various types of pile cap and prefabricated piles in each vertical structural element (columns and façades) were considered. The vertical and flexural spring stiffness were estimated based on the vertical static load tests carried out. The Plaxis 3D finite element software was

used to determine the horizontal stiffness of the piles, as well as to quantify the axial stresses due to the effect of negative skin friction and bending moment distribution along the piles.

4.2 Ground improvement

The study of the ground improvement solutions was based on an initial calibration phase through stress-strain analyses, namely, two-dimensional finite element analysis, in axisymmetry condition, using the Plaxis 2D software, simulating two of the static vertical load tests carried out on site.

In a second phase, the project ground improvement solutions were modelled, also through two- and three-dimensional finite element analysis using the Plaxis 2D and Plaxis 3D software respectively.

With this analysis the stresses, strains and displacements in the rigid inclusions, stone columns and geosynthetics were estimated. The settlements on the pavements were also calculated and compared with the floor's serviceability requirements. In Figure 7 some of the 2D and 3D calculation models are presented.

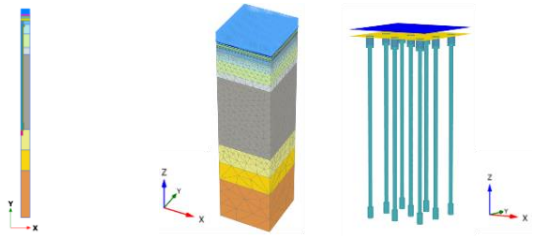

a) *b)*

Figure 7. Ground improvement finite element calculation models a) Plaxis 2D, axisymmetry conditions. b) Plaxis 3D.

5 MONITORING AND FULL-SCALE LOAD TESTS

Prior to the execution of the work, a set of static and dynamic load tests on vertical prefabricated driven piles were carried out. The aforementioned tests allowed the analysis of the behaviour of the piles with regard to force-settlement curves, being therefore fundamental elements in the design stage.

As part of the quality and execution control of the stone columns, as well as the GCC rigid inclusions, a set of static vertical load tests were also carried out, considering loads higher than the expected service load.

Additionally, in order to evaluate the performance of the ground improvement solution in the medium and long term, a full-scale test was carried out, through the construction of an experimental landfill over four GCC rigid inclusions lasting approximately 5 months, up to 200% of the service load. The results, presented in Figure 8, confirmed that the expected settlement was inferior to the considered admissible value. In Figure 9, it is possible to view the full scale and static vertical load tests.

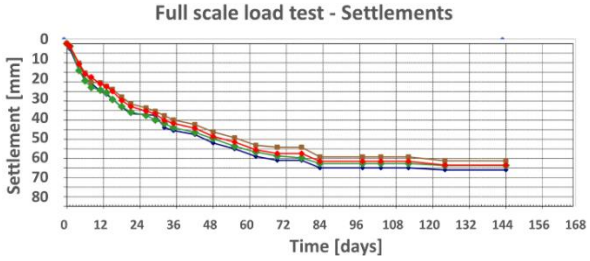

Figure 8. Full scale load test – Settlement evolution over time.



a) *b)*

Figure 9. a) Full scale load test. b) Static vertical load test.

6 FINAL REMARKS

The framework of the work described determined the need to develop economic foundation solutions compatible with the structure serviceability.

In this context, it should be noted that the adopted ground improvement solutions allow for the reduction, in the foundation structural elements, of the design seismic horizontal forces originating from the expected high magnitude pavements live loads.

It also made it possible to reduce shear stresses and bending moments at the floor slab, thus allowing for considerable savings in the reinforced concrete pavement structure.

ACKNOWLEDGEMENTS

The authors would like to thank the site owner and GSE for authorizing the presentation of this paper. It is also worth highlighting the fact that the pile and ground improvement works were carried out by the company "Terratest".

REFERENCES

Lopes, M.; Pinto, A.; and Gonçalves, A.L. (2023). Soil Improvement Solutions executed in lot 14 of the Northern Lisbon Logistic Platform, In: *Proceeding of the XVIII Portuguese Geothecnical Conference*, Évora, Portugal, pp. 443-452 (in Portuguese).

Proceedings of the XVIII ECSMGE 2024
GEOTECHNICAL ENGINEERING CHALLENGES
TO MEET CURRENT AND EMERGING NEEDS OF SOCIETY
© 2024 the Authors
ISBN 978-1-032-54816-6
DOI 10.1201/9781003431749-492
Open Access: www.taylorfrancis.com, CC BY-NC-ND 4.0 license

ECSMGE 24
XVIII EUROPEAN CONFERENCE ON SOIL MECHANICS AND GEOTECHNICAL ENGINEERING

Special foundations at the cycle-pedestrian bridge over the Trancão river, Portugal

Fondations spéciales du pont cyclable-piéton sur la rivière Trancão, Portugal

A. Pinto*
JETsj, Geotecnia, Lisbon, Portugal

A. Rodrigues, P. Santos
RODIO, Lisbon, Portugal

C. Caxias
ANP Systems GmbH, Lisbon, Portugal

**apinto@jetsj.com*

ABSTRACT: This paper describes the special foundations solutions adopted at the cycle-pedestrian bridge built over the Trancão River, connecting Lisbon to Loures. The bridge structure is a laminated wood deck, supported by steel cables, with a 65m central main span. Considering the very low resistance and high deformability of the superficial alluvial layers, it was necessary to design a deep foundation solution, resting at the Miocene bedrock. Reflecting the local geological scenario, as well as the restraints related with the use of heavy equipment at the riverbanks, the foundation solution consists of micropiles, vertical and inclined, executed using the self-drilling methodology, associated with the execution of 500mm diameter mini jet grouting columns, ranging from about 30 to 20m. The main quality control / quality assurance (QC/QA) results, including two full scale tension load tests, are presented.

RÉSUMÉ: Cet article décrit les solutions de fondations spéciales adoptées pour le pont cyclable-piéton construit sur la rivière Trancão, reliant Lisbonne à Loures. La structure du pont est un tablier en bois lamellé collé, soutenu par des câbles en acier, avec une travée centrale de 65 m. Compte tenu de la très faible résistance et de la déformabilité élevée des couches alluviales superficielles, il était nécessaire de concevoir une solution de fondation profonde, reposant sur le substratum rocheux du Miocène. Compte tenu du scénario géologique local, en plus des contraintes liées à l'utilisation d'équipements lourds sur les berges, la solution de fondation consiste en des micropieux, verticaux et inclinés, exécutés selon la méthodologie de auto forage, associés à l'exécution de mini colonnes de jet grouting de 500 mm de diamètre, allant de 30 à 20 m. Les principaux résultats du contrôle de la qualité e du contrôle de l'exécution (CQ/QA), bien aussi que deux tests de charge de traction à grande échelle, sont présentés.

Keywords: Jet grouting; micropiles.

1 INTRODUCTION

The new cycle and pedestrian bridge over the Trancão river was built before the World Youth Day 2023 (WYD), with the main objective to connect the paths already existent at both banks of the Trancão river (Loures at North and Lisbon at South).

With this purpose, a three span (28m+65m+28m, 121m overall length) cable stayed bridge, with laminated wood deck, steel towers and cables, resting over reinforced concrete columns and abutments, was built. At Loures and Lisbon sides, respectively, access ramps with 82m and 70m were built, the last one parallel to the Trancão river (Figures 1 and 2).



Figure 1. Bridge location (Google maps, without a scale).

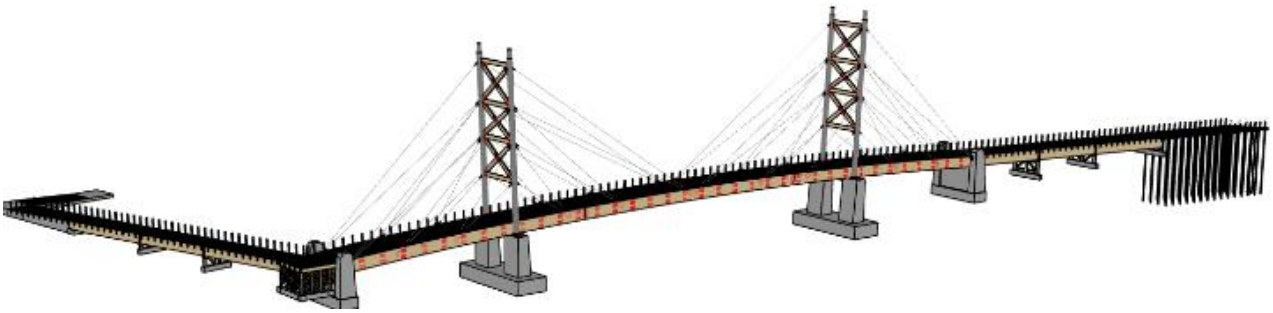

Figure 2. Bridge 3D view (JETsj project).

2 GEOLOGICAL CONSTRAINS

The geological investigation campaign included the execution of four boreholes and allowed the confirmation of the ground geotechnical zones (ZG). It was possible to confirm, from the surface, the existence of 2.5m heterogeneous landfills (ZG1), resting over very soft alluvial (Tagus River basin) materials with overall thickness ranging from 14 to 22m, with N_{SPT} blows not bigger than 2 and undrained shear strength (Su) not bigger than 20kPa (ZG2).

Under that layer, the Miocene loose sandy soils (ZG3) over the sandstone bedrock (ZG4) were found, the last one with very good resistance and deformation characteristics (Figure 3).

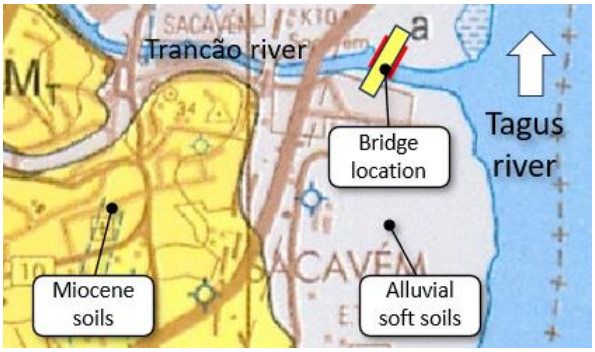

Figure 3. Geological scenario plan with bridge location (Portugal geological map, without a scale).

3 FOUNDATIONS SOLUTION

Considering the geological and geotechnical restraints, the compression and tension loads to be transmitted by the bridge to the ground, as well the restraints related with the use of heavy equipment at the riverbanks soft soils, the foundation solution consisted on micropiles ANP ϕH1600-76mm, ϕH0950-51mm and ϕH0550-38mm hollow steel bars with sacrificial grouting bits, vertical and inclined, executed using the upper – bottom self-drilling methodology, associated with the execution of 500mm diameter mini jet grouting columns at the ZG1, ZG2 and ZG3 geotechnical zones, ranging from about 30 to 20m (Figure 4).

Maximum jet grouting pressure was 200bar, compatible with the micropiles coupler's resistance. Due to the Atlantic Ocean proximity, leading to water chlorides, for durability reasons, pozzolanic cement with a consumption ratio of 160kg/m^3 was used.

The jet grouting columns had three main functions: i) increase the micropiles stiffness mainly against buckling; ii) increase the micropiles protection against corrosion; iii) reduce the micropiles overall length at the Miocene bedrock, particularly when the columns intersected the Miocene loose sands, at the South riverbank.



Figure 4. View of the micropiles hollow bars and bits.

The micropiles were capped by reinforced concrete caps, supporting the bridge columns and abutments. The loads were transmitted to the Miocene layer mainly by shaft resistance: i) at the South riverbank, starting at the loose sandy materials taking advantage of the 500mm jet grouting columns shaft resistance (qs); ii) at the North riverbank, at the Miocene bedrock, where the maximum diameter was only 250mm (Figure 5).

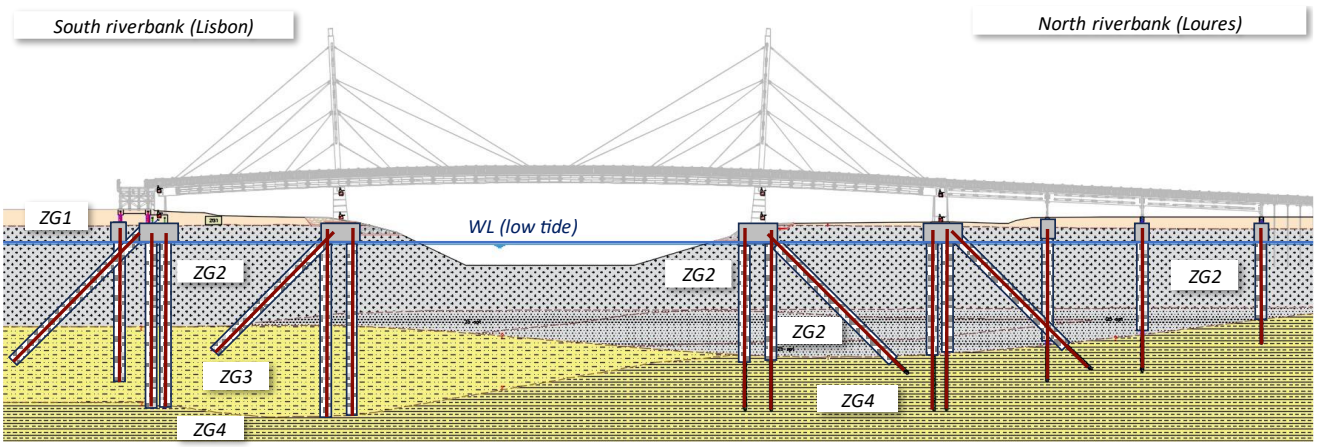

Figure 5. Bridge elevation with geotechnical zones (JETsj project, without a scale).

4 QUALITY CONTROL AND QUALITY ASSURANCE

4.1 Trial columns

Before the execution of the full-scale load tests, several jet grouting trial columns, with different cement consumption, were performed to check both the columns geometry and resistance at the very soft resistance alluvium layer (ZG2).

The columns resistance was evaluated trough unconfined compression strength (UCS) tests, performed trough cores collected from the columns at 28 days. At UCS tests both the columns unconfined compression resistance and Young's modulus were checked and compared with the design requests at 28 days: 3MPa and 1GPa, respectively (Figure 6).



Figure 6. Trial column view.

4.2 Tension full scale load tests

To confirm the design main assumptions, mainly the micropiles and jet grouting shaft resistance (qs), two suitability tension full scale load tests were performed, one in each riverbank, close from the bridge central columns.

The reaction structure was a reinforced concrete cap (2x2x1m^3) supported by four inclined self-drilling micropiles. The central tested micropile was reinforced with one ϕ35mm Gewi Plus S670/800 bar, protected by a smooth sheath at the landfill (ZG1) and alluvium (ZG2) layers, ensuring the unbonding length. A hollow plunged jack was used to apply a maximum load of 500kN to the micropile through the ϕ35mm bar (Figure 7). The maximum applied load was 1.67 times bigger than the maximum tension service load, approximately 350kN (Figures 8 and 9).



Figure 7. Full scale tension test: reaction structure view.

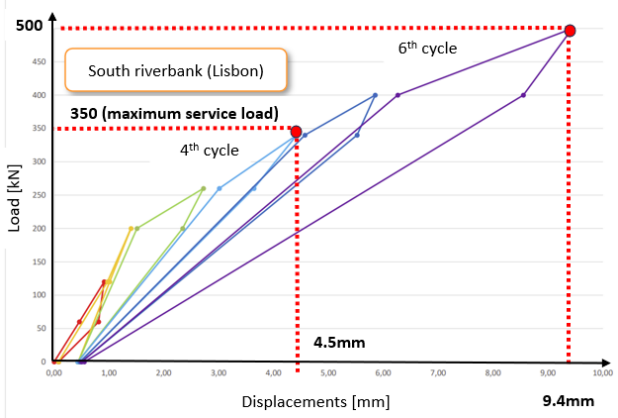

Figure 8. Load vs head displacements (South riverbank).

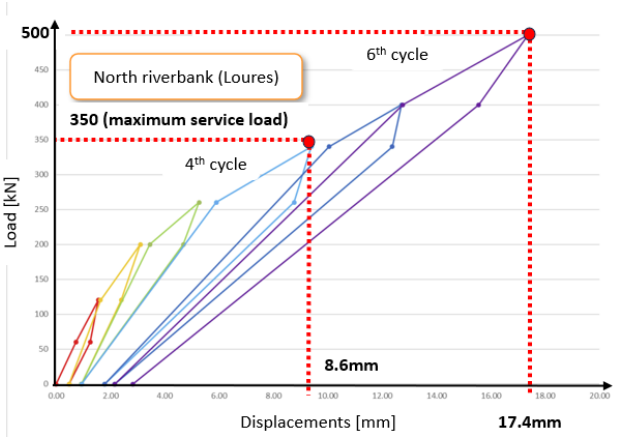

Figure 9. Load vs head displacements (North riverbank).

After 6 load and unload cycles the maximum displacements were 9.4mm and 17.4mm at, respectively, the South and North riverbank load tests. The plastic displacements were, respectively, 0.5mm and 2.5mm. The explanation for those differences could be related with the micropiles stiffness, as on the South riverbank the loaded micropile full length was inside a jet grouting column at the Miocene loose sandy soils (ZG3, with qs not lesser than 25kPa) and the alluvium (ZG2) thickness is lower (Figure 5).

Despite the tension loads at the micropiles are mainly due to wind and seismic loads, on both load tests the creep coefficient, for a minimum permanent load time of 30 minutes, was lesser than 1mm. The obtained results allow to confirm the suitability of the design and execution parameters.

4.3 Execution parameters recorder

All the jet grouting execution parameters were automaticallty recorded using a computer device and compared with the ones established based on the trial columns and suitability full scale load tests results.

5 DESIGN

The bridge foundations were designed using PLAXIS 2D, FEM stress-strain software. The shaft resistance values were initially estimated using reliable proposals (Bustamante, 2002) for jet grouting. The model was adjusted by back analysis after the full-scale load tests. According to the bridge monitoring, using prisms and topographic readings, since its opening to cycling and pedestrian traffic (Figure 10), the deck displacements have been in accordance with the estimated ones at the design stage.



Figure 10. Bridge view just before the YWD, August 2023 with the deck being reinforced for the pope's car crossing.

6 FINAL REMARKS

The presented case study allowed to confirm the advantages of foundation solutions using mini jet grouting columns combined with self-drilling micropiles in complex geological and geotechnical scenarios. As main advantages, compared with conventional solutions, can be pointed out: light, small and versatile equipment, minimum ground extraction, schedule prediction, and overall costs.

ACKNOWLEDGEMENTS

The authors are grateful to EMEL and Lisbon Municipality for the permission to present this paper.

REFERENCES

Bustamante, M (2002). Bearing capacity and integraty control of jet grouting columns. *Séminar Franco Tunisien: Pathologie des sols e des fondations*, Hammamet. Tunisia (in French).

Proceedings of the XVIII ECSMGE 2024
GEOTECHNICAL ENGINEERING CHALLENGES
TO MEET CURRENT AND EMERGING NEEDS OF SOCIETY
© 2024 the Authors
ISBN 978-1-032-54816-6
DOI 10.1201/9781003431749-493
Open Access: www.taylorfrancis.com, CC BY-NC-ND 4.0 license

ECSMGE 24
XVIII EUROPEAN CONFERENCE ON SOIL MECHANICS AND GEOTECHNICAL ENGINEERING

Stabilization of the access platform to an electrical substation: diagnosis, design and site works follow-up

Stabilisation de la plate-forme d'acces a un poste de transformation électrique: diagnostic, conception et suivi des travaux

G. Pisco*, N, Nogueira, S. Pinto
Tetraplano - Engenharia, Lisbon, Portugal

A. Carvalheira
REN - Rede Elétrica Nacional, Maia, Portugal

**gpisco@tetraplano.pt*

ABSTRACT: This article presents the design and execution guidelines of the Carvoeira, Portugal, electrical facility road embankment stabilization. The embankment is 15 m high and has a history of pathologies since construction. In 2011, the embankment collapsed. Despite the implementation of stabilization and reinforcement measures, carried out in 2012, in the last few years, the embankment has showed signs of a continuous and evolutive process that could lead to a new collapse. The failure patterns are discussed based on the initial project data, the history, and main constraints, especially concerning geological, geotechnical and hydrogeologic conditions. The impact of the existing infrastructures and the need to maintain the electrical facility operational are discussed as well. In 2020, a new rockfill solution is presented, highlighting the design process, the criteria to select the rock materials and the strength and drainage capacity of the solution. The main points of the execution phase and some unforeseen events and respective solutions are presented.

RÉSUMÉ: Cet article présente les directives de conception et d'exécution de la stabilisation du remblai d'accès à la sous-station électrique de Carvoeira, Portugal. Le remblai, avec 15 m de hauteur, présente diverses pathologies d'instabilité, depuis sa construction. En 2011, l'accès s'est effondré. Malgré les mesures correctives adoptées en 2012, l'accès a continué à présenter des signes d'un processus continu et évolutif qui pourrait conduire à un nouvel glissement. L'instabilité a été analysée sur la base des données initiales du projet, l'historique et les principales contraintes, en particulier les conditions géologiques, géotechniques et hydrogéologiques. L'impact des infrastructures existantes et la nécessité de maintenir l'installation électrique opérationnelle ont été également discutés. En 2020, une nouvelle solution constituée par un remblai en enrochement a été développée. La conception de la nouvelle solution est présentée, ainsi que les critères de sélection des matériaux rocheux, l'importance de la résistance et la capacité de drainage de la solution étudiée. Les principales étapes de la phase d'exécution et quelques événements imprévus, ainsi que leurs solutions respectives, sont également présentés.

Keywords: Embankment; collapse; rockfill; stabilization.

1 INTRODUCTION

The access to the Carvoeira substation is made through a 550 m road, of which 130 m are constructed in an embankment with a maximum height of 15 m. All the infrastructure is in a natural hillside with slight unfavorable inclination. The embankment slopes had a 1V:1,5H and one middle bench. Since its construction in 2008, the platform has shown several pathologies resulting in the collapse of the fill in 2011. Different stabilization measures were considered. A gabion wall and a group of rockfill drains at the base of the embankment were executed to achieve a higher level of safety and improve the drainage capacity. Part of the fill was excavated and replaced by material with better properties. Part of the foundation material was excavated, too. The slopes geometry has been changed accordingly.

Despite all the corrective measures, through the years, several pathologies have been registered and the instrumentation shows a movement tendency.

The different phases of the study will be presented from the geotechnical survey to the execution.

2 SITE CONSTRAINTS

2.1 Geology and hydrogeology

The substation is in a natural hillside of Jurassic materials characterized by intercalations of clays, claystones, sandstones and limes. Due to the

deposition process and the proximity of a water course, the material layers thickness has important variations resulting in different foundation horizons. In some areas colluvial and deposit materials were identified, even after the embankment construction.

To characterize all the existing materials, four geotechnical campaigns were conducted in the area, as represented in Figure 1. The first in 2011, in orange, before the construction works, the second, in red, after the collapse and the last two, in 2019, in blue, and 2020, in green, in the context of the new project. Based on the obtained results a geotechnical zoning was defined:

- GZ 1 – Heterogeneous clayed fill.
- GZ 2 – Decompressed Jurassic clays.
- GZ 3 – Jurassic clays intercalated with marls and limestones.

A geotechnical profile is represented in Figure 1.

The water level was measured at 2,4 to 6 m depth, and at the toe at 7 to 7,5 m depth. This data indicates the presence of water inside the embankment and the percolation of water between GZ3 and GZ2.

2.2 Existing infrastructure

Apart from geological and geotechnical, the existing substation and the related infrastructure (water supply and electrical distribution wires and poles) were the main constraint to the stability and execution of the future works. All the electricity distribution facilities were kept operational in their original locations, which was considered in every stage of the project in different ways. The water supply and sewage system contributed to the existing pathologies and were moved to guarantee its operation and the conservation of the future platform.

3 DIAGNOSE AND RETROANALYSIS

The analysis of the existing situation was based on different types of information, like the results of instrumentation and geotechnical campaigns, reports of inspection and diagnose of external entities (Cardoso, 2020), parts of previous projects and site observation.

The presence of several cracks and abatements of the pavements showed the development of a new rupture mechanism. To confirm this situation inclinometers and piezometers were installed. The results show the formation of slip surface in depth approximately at the GZ2. The piezometers show a stabilized level of water at the base of the GZ3, both at the base and top of the embankment.

Based on this evidence, it was concluded that the collapse of the embankment was caused by the combination of several situations:

- The presence of high plastic clays at the base of the embankment.
- The material used in the construction of the embankment had a high percentage of fine materials resulting in inappropriate characteristics in terms of granulometry, strength and permeability.
- It was observed a relation between the piezometer's levels and the increase in horizontal movements. The presence of water at fill and the low permeability of its materials were considered key aspects that contributed to the collapses.

To confirm this evidence and to establish a coherent scenario with the *in-situ* situation, a set of retroanalysis models were created using the finite element analysis program Plaxis 2D.

To obtain the unitary factor of safety, the "phi-c reduction" method was used. In this the soil parameters are reduced until the slip surface with lower FS is formed. The soil behavior was simulated with the Hardening-Soil model (Brinkgreve et al. 2017), an elastic-plastic model with a multi-surface yield criterion that simulates the increasing of soil stiffness with deformation. In Figure 2 are represent both the retroanalysis slip surfaces of the initial configuration of the embankments and of the geometry before the project.

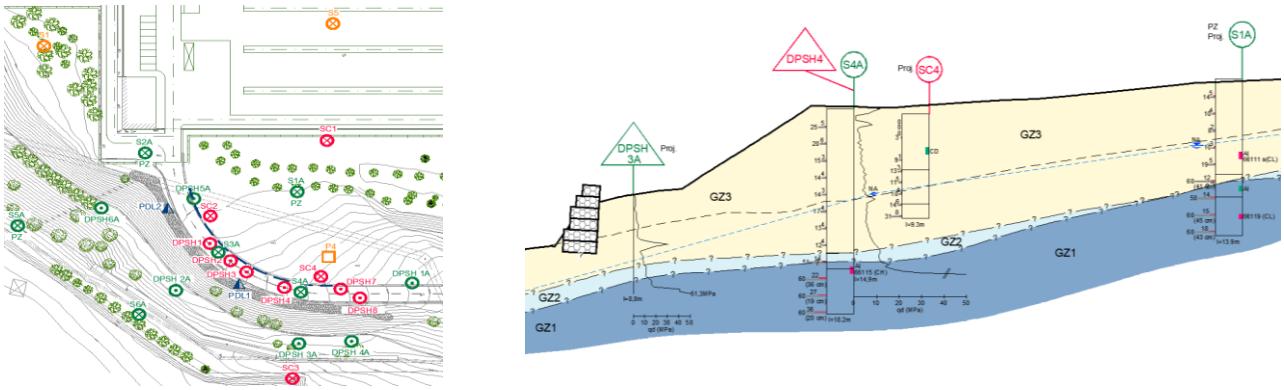

S_i – Borehole with SPT test; $DPSH_i$ - Dynamic probe super heavy *test; PDL_i – Light Dynamic Penetrometer; PZ_i - Piezometer; P_i – Pit*

Figure 1. Geotechnical survey and general geotechnical profile.

In *Table 1* are represented the obtained parameters.

Table 1. Retronanlysis resulting soil parameters.

Geotechnical Zones	γ (kN/m³)	ϕ' (°)	c' (kPa)	E (MPa)
GZ 3	18	26	5	8
GZ 2	20	32	15	30
GZ 1	20	33	30	50

γ - Volumetric weight, ϕ' – Angle of internal friction, c' – cohesion, E – Young modulus

4 PROPOSED SOLUTION

Several solutions for the stabilization of the embankment were studied. The developed and implemented solution involved the excavation and complete removal of the fill materials corresponding to GZ3, which had a strong clay component and inappropriate geotechnical characteristics.

Subsequently, the embankment was constructed using rockfill material. The excavation of the layers belonging to GZ2 and the superficial zone of GZ1 was also considered. To ensure proper connection of the rockfill to the foundation ground, a keyed excavation was planned, ensuring greater stability of the materials in this area. To ensure a better granulometric transition and filter conditions, a layer of gravel 10/30 mm was placed between the natural ground and the rockfill.

The compaction of the rockfill materials prescribed pretended to concentrate the deformation in the early stages of the works and guarantee the adequate resistant characteristics of the materials. To accomplish this, for each layer, the particles with large diameter are placed first decreasing the diameter with the height of the layer. Large quantities of water are used to promote the breakage of the rock material and adequate interlocking of the different blocks.

The thickness of the layers and the compaction processes implemented were determined based on experimental embankments. The materials were characterized following Ferreira et al. (1995) and Rocha (2013). This analysis also considered the characteristics of the existing rockfill in nearby quarries and the desired performance requirements. The rockfill prescribed characteristics are resumed in Table 2 and Table 3.

To achieve the desired drainage capacity, the configuration of the excavation base was conceived in such a way that all the waters are guided to two drainage trenches, 1 m width and 2 m height, with 300 mm PVC tubes wrapped in gravel. These elements were positioned at the transition between the fill material and the natural soil and at the lowest point of the embankment. Minimum inclinations of 0,5% were considered and, at the discharge points, dissipation structures were created.

Several complementary works, like the access reconstruction (pavement, signage, and safety equipments) and the redefinition of the water supply system were included in this project.

In terms of design, a model based on the retroanalysis conclusions was used. The safety of the different phases of excavation and fill were checked, considering the position of the expected water level. For the final geometry, the stability was verified considering the seismic action according to the pseudo-static method of Part 5 of Eurocode 8.

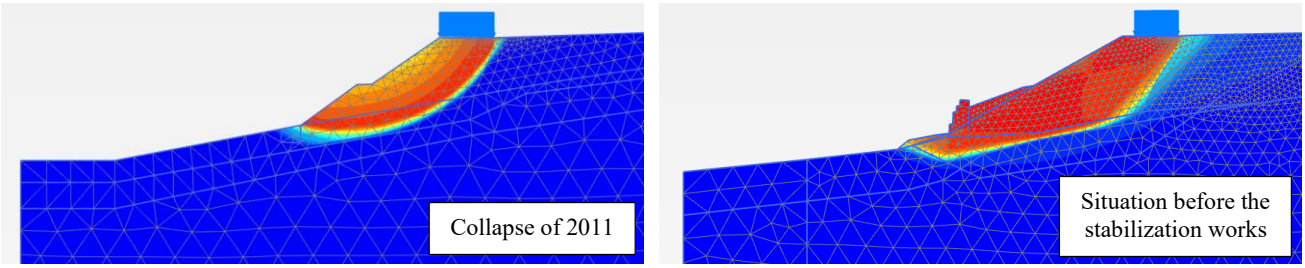

Figure 2. Retroanalysis of the two embankment configurations.

Table 2. Rockfill geomechanical parameters.

γ (kN/m³)	ϕ' (°)	E (MPa)	UC	% #200 (ASTM)	% D>50 mm	Los Angeles	Dmáx
22	≥ 43 °	≥ 60	> 10	< 12 %	>60 %	≤ 45 %	> 2/3 of layer thickness after compaction

γ - Volumetric weight, ϕ' – Angle of internal friction, E – Young modulus, UC – Uniformity Coefficient, D – Particle diameter

Table 3. Rockfill grain size distribution.

Dimensions	D_5	D_{15}	D_{50}	D_{85}	D_{100}
Minimum(mm)	-	4	40	200	300
Maximum (mm)	6	15	150	500	600

5 CONSTRUCTION PHASE

The construction phase started in December of 2020, a very rainy month, which was an additional challenge for the works. Considering the presence of clay materials in the existing fills and natural soils, a close monitorization of the excavation works was implemented. This measure was essential to anticipate and correct some local instabilities observed in the weaker materials. In Figure 3 to Figure 5 are represented the different work phases, from excavation to compaction. In Figure 6 is represented a view of the area after the works.



Figure 3. View of the slope and protective measure.



Figure 4. View of the final excavation stage.



Figure 5. Embankment construction and compaction.

6 CONCLUSIONS

The history of instabilities, the characteristics of the embankment and especially the geological complexity of the site, determined the need for an in-depth study to address the current situation.

The rockfill solution ensures the strength and drainage characteristics necessary to guarantee the appropriate safety levels. In this type of geotechnical structure, the design, control and testing of execution methodologies are key aspects to guarantee the expected behavior of the embankment.

Finally, it should be noticed the importance of a proper instrumentation and observation plan, to control the behavior of materials, continuously validate the project assumptions, and to ensure the safe execution of the works.



Figure 6. View of the area after the works conclusion.

ACKNOWLEDGEMENTS

The authors express their gratitude to the project sponsor, REN - Rede Elétrica Nacional, S.A., for granting permission for the drafting and publication of this article.

REFERENCES

Brinkgreve, R.B.J., Kumarswamy, S. Swolfs, W.M. (2017) Plaxis – Material Models Manual 2017, Delft, Netherlands.

Cardoso, R. (2020). Stability assessment of slopes in the vicinity of the Carvoeira substation (in Portuguese), Torres Vedras, Lisbon, Portugal.

Ferreira, M. Q., Pinto, A.V., Rodrigues, J. D., Monteiro, B. P. B. (1995) Characterization of rock materials for rockfill works (in Portuguese). In: 5º Portuguese National Geotechnical Congress, Coimbra, Portugal.

Rocha, M. (2013). Rock Mechanics (in Portuguese), 1th ed, LNEC, Lisbon, Portugal.

Proceedings of the XVIII ECSMGE 2024
GEOTECHNICAL ENGINEERING CHALLENGES
TO MEET CURRENT AND EMERGING NEEDS OF SOCIETY
© 2024 the Authors
ISBN 978-1-032-54816-6
DOI 10.1201/9781003431749-494
Open Access: www.taylorfrancis.com, CC BY-NC-ND 4.0 license

ECSMGE 24
XVIII EUROPEAN CONFERENCE ON SOIL MECHANICS AND GEOTECHNICAL ENGINEERING

Consideration of the variable contact geometry between the drum and the soil surface in vibratory roller compaction

Prise en compte de la géométrie de contact variable entre le cylindre et la surface du sol lors du compactage par rouleau vibrant

J. Pistrol*, M. Hager, D. Adam
TU Wien, Institute of Geotechnics, Vienna, Austria

F. Kopf
FCP - Fritsch, Chiari & Partner ZT GmbH, Vienna, Austria

**johannes.pistrol@tuwien.ac.at*

ABSTRACT: The paper presents a comparatively simple mechanical model, which describes the dynamic interaction between the drum of a vibratory roller and the underlying soil during compaction. The main non-linearities of the dynamic system are the continuously varying contact conditions and geometry between the drum and the subgrade as well as the curved drum geometry. As the drum penetrates the soil during the loading phase, the contact area between the two contact partners increases, which in turn affects the resulting soil reaction force and influences the motion behaviour of the drum at the same time. Moreover, a periodic loss of contact between drum and soil during the unloading phase may occur, and the two subsystems move separately and independently from each other for a short period of time. The model introduced in the paper allows for a consideration of the challenging contact conditions and the variable drum contact geometry. Moreover, it enables the consideration of varying soil resistance as a result of the changing contact conditions. The model is tested on the example of a typical vibratory roller and the results are compared to a simulation with a constant contact geometry between drum and soil. The presented findings allow for a more accurate consideration of the actual contact conditions between the drum of a vibratory roller and the soil and are considered valuable for the further development of measurement values of Intelligent Compaction.

RÉSUMÉ: Cet article présente un modèle mécanique relativement simple, qui décrit l'interaction dynamique entre le tambour d'un rouleau vibrant et le sol sous-jacent pendant le compactage. Les principales non-linéarités du système dynamique sont les conditions de contact et la géométrie continuellement variables entre le cylindre et le sol de fondation, ainsi que la géométrie incurvée du cylindre. Au fur et à mesure que le cylindre pénètre dans le sol pendant la phase de chargement, la surface de contact entre les deux partenaires augmente, ce qui affecte la force de réaction du sol et le comportement de mouvement du cylindre. En outre, une perte de contact périodique entre le tambour et le sol pendant la phase de déchargement peut se produire, et les deux sous-systèmes se déplacent séparément et indépendamment l'un de l'autre pendant une courte période. Le modèle présenté dans cet article permet de prendre en compte les conditions de contact difficiles et la géométrie variable du contact entre le tambour et le sol. En outre, il permet de prendre en compte la résistance variable du sol résultant de l'évolution des conditions de contact. Le modèle est testé sur l'exemple d'un rouleau vibrant typique et les résultats sont comparés à une simulation avec une géométrie de contact constante entre le tambour et le sol. Les résultats présentés permettent une prise en compte plus précise des conditions de contact réelles entre le tambour d'un rouleau vibrant et le sol et sont considérés comme précieux pour le développement ultérieur des valeurs de mesure du compactage intelligent.

Keywords: Roller compaction; soil dynamics; intelligent compaction; non-destructive testing.

1 INTRODUCTION

This paper presents a comparatively simple semi-analytical vibratory roller-soil simulation model to describe the interaction system, characterized by its challenging contact conditions. Previous models consider, if at all, only a constant geometry of the contact area between drum and soil (Adam, 1996). However, the width of the contact area increases during the loading phase, making the drum contact width a variable parameter. The presented model can account for this variability of the drum contact width in the loading phase of vibratory roller compaction. The model is part of an ongoing research project to develop a novel Intelligent compaction meter value (ICMV) for roller compaction (Pistrol et al., 2023).

2 MECHANICAL MODEL

2.1 Modelling of the roller subsystem

The cylindrically curved drum of the roller is excited at a specific frequency f by an unbalance, which is mounted on a drive shaft in the axis of the drum. The resulting vibration of the drum yields a predominantly vertically directed loading of the soil.

The drum is connected to the frame of the roller using rubber buffers. If the rubber buffers and the frame are suitably designed, the frame and drum can be regarded as largely decoupled. Therefore, the influence of the frame on the motion behaviour of the drum is limited to its dead weight ($m_f g$) and the roller subsystem is reduced to a single degree of freedom with the position coordinate z_1 (see Figure 1).

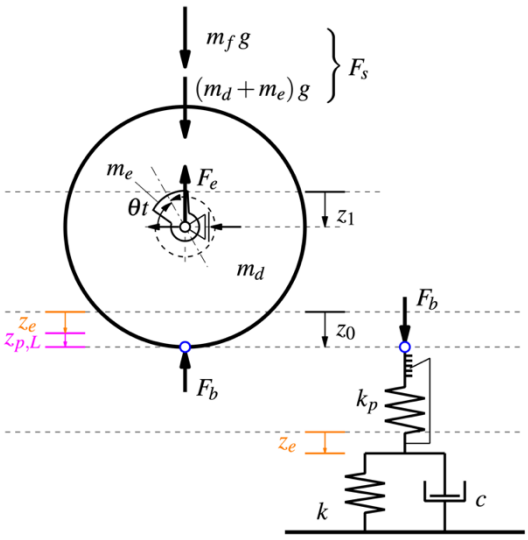

Figure 1. Free-body diagram of the simplified simulation model at time t during the first load cycle.

The application of the principle of linear momentum yields the equation of motion for the roller subsystem by means of the resulting soil contact force F_b which comprises the inertia force F_a, the static load F_s, and the excitation force F_e:

$$F_b = -F_a + F_s - F_e = -(m_d + m_e)\ddot{z}_1 + (m_d + m_e + m_f)g - m_e e\theta^2 \sin(\theta t) \quad (1)$$

where m_d and m_e are the masses of the drum and the eccentric, e is the eccentricity of the unbalance and θ is the angular frequency of the excitation.

2.2 Modelling of the soil subsystem

The soil subsystem is modelled as a Kelvin-Voigt element, which is extended by an additional spring connected in series (see Figure 1). The calculation of the spring stiffness k and the dashpot coefficient c is based on considerations by Wolf (1994). Therefore, the approximately rectangular contact area between drum and soil with half side lengths a and b is converted into a circle with an equivalent radius, which represents the top surface of a downward unlimited truncated cone. The parameters are defined as (Wolf, 1994):

$$k = \frac{Gb}{1-\nu}\left[3.1\left(\frac{a}{b}\right)^{0.75} + 1.6\right] \quad (2)$$

$$c = \kappa 4\sqrt{2\rho G \frac{1-\nu}{1-2\nu}}ab \ldots \text{(adapted)} \quad (3)$$

where G, ρ, and ν are the shear modulus, density, and Poisson's ratio of the soil, and κ is a factor for increased damping to account for spatial effects. The Kelvin-Voigt model is only able to capture the elastic soil behaviour in the far-field of dynamic compaction. Therefore, an additional elastic spring with stiffness k_p is introduced. The spring deforms proportionally during loading but remains locked otherwise (during unloading and separation) and, therefore, simulates the plastic behaviour in the near-field. The stiffness k_p is estimated by the introduction of a dimensionless condition factor ε that describes the ratio of elastic to elasto-plastic deformations and provides a relationship between k_p and k (Adam, 1996):

$$\varepsilon = \frac{z_e}{z_e + z_p - z_{p,p}} = \frac{k_p}{k_p + k} \Leftrightarrow k_p = \frac{\varepsilon k}{1-\varepsilon} \quad (4)$$

where z_e and z_p are the absolute elastic and plastic deformations of the soil, and $z_{p,p}$ is a compensation variable to account for the periodic increase in vertical displacements under cyclic loading. In this paper, a condition factor of $\varepsilon = 0.85$ is defined to simulate the "partial uplift" mode of operation.

2.3 Coupling of roller and soil subsystem

The coupling and separation of the two subsystems is characterized by three operating phases – loading, unloading, and separation – which may occur during each period of excitation.

2.3.1 Loading phase

The soil with its position coordinate z_0 follows the movement of the drum during the loading phase ($z_0 = z_1$) and the soil contact force F_b, as well as its gradient have a positive sign. The spring k_p is active during loading and, therefore, elastic (z_e) and relative plastic ($z_{p,L}$) deformations occur. The sum $z_e + z_{p,L}$ is the basis for the calculation of the variable drum contact width (see section 2.4).

The soil contact force for the roller subsystem is given in Equation (1). For the soil subsystem, F_b comprises the forces in the elastic spring (F_k) and the viscous dashpot (F_c):

$$F_b = F_k + F_c = kz_e + c\dot{z}_e \quad (5)$$

Roller and soil subsystem are coupled by the spring with stiffness k_p:

$$F_b = \left[(z_0 - z_e) - z_{p,p}\right]k_p + F_{p,p} = z_{p,L}k_p + F_{p,p} \quad (6)$$

The variable $z_{p,L}$ compensates the periodic increase in plastic deformations due to cyclic loading and allows for the calculation of the relative plastic deformations during each load cycle. Therefore, $z_{p,p}$ describes the cumulative pre-deformation of spring k_p, which increases by $z_{p,L}$ at each transition from loading to unloading. If the drum does not lose its contact after the unloading phase, a residual preload $F_{p,p}$ of the spring k_p must be taken into account.

The loading phase ends when the soil contact force stops increasing and its gradient is less or equal to zero. The loading phase is always followed by an unloading phase.

2.3.2 Unloading phase

During the unloading phase, the soil continues to follow the movement of the drum ($z_0 = z_1$), and Equations (1) and (5) remain applicable for the calculation of the soil contact force. F_b is still positive, while its gradient is negative ($\dot{F}_b \leq 0$). The spring with stiffness k_p is locked ($k_p = \infty$) and therefore only elastic deformations occur.

The unloading phase ends, if the soil contact force starts to increase again without a full unloading and another loading phase begins. In this case, the residual preloading of the spring k_p is taken into account by the variable $F_{p,p}$.

The unloading phase also ends if the soil contact force becomes zero. The separation phase begins since the soil cannot bear tensile forces and the two subsystems move independently from each other.

2.3.3 Separation phase

Drum and soil move separately and independently of each other and the soil contact force in Equations (1) and (5) is zero. The soil creeps back towards its initial position during the separation phase. The preload $F_{p,p}$ of the spring k_p is set to zero in case of separation.

The separation phase is always followed by a loading phase.

2.4 Variable drum contact width

The contact area between the two subsystems decisively determines the dynamic interaction between drum and soil. Due to the cylindrically curved drum geometry, the contact area is a variable quantity during the loading phase. The drum increasingly penetrates the soil, and the contact width between the subsystems steadily increases, while the length of the load area remains largely constant and equals the length of the drum ($2a$).

In contrast to previous research (Adam, 1996), the presented model enables the consideration of the variable contact width $2b$ during the loading phase. The instantaneous drum contact width is determined using the circular arc segment shown in Figure 2, which is defined by the sagitta Δz and the circular chord s.

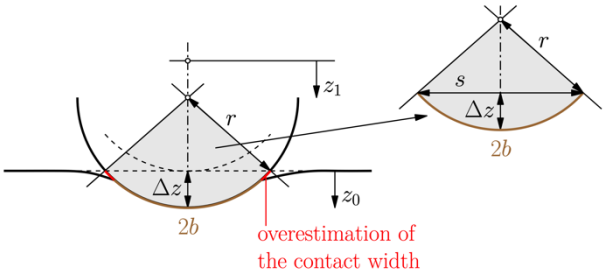

Figure 2. Calculation of the variable drum contact width.

With the known drum radius r and the elasto-plastic deformations $\Delta z = z_e + z_{p,L}$, the circular chord s and the circular arc length $2b$ can be calculated according to Equations (7) and (8).

$$s = 2\sqrt{2r\Delta z - \Delta z^2} \quad (7)$$

$$2b = 2r\,arcsin\left(\frac{s}{2r}\right) \quad (8)$$

During the unloading phase, $2b$ is assumed to be constant and corresponds to the value at the end of the loading phase since only elastic deformations occur.

The variable drum contact width results in a variable spring stiffness k and dashpot coefficient c during the loading phase. The definition of k_p by means of a condition factor ε according to Equation (4) also makes k_p a variable quantity.

3 CALCULATIONS AND RESULTS

Selected results from simulations with the presented mechanical roller-soil model are presented for a HAMM H13i single-drum roller. The roller and soil parameters of the simulations are given in Table 1. The soil parameters were selected to ensure the "partial

uplift" mode of operation. Ninety revolutions of the eccentric mass were simulated (duration = 3 s), to guarantee a steady state of the simulation.

Table 1. Roller and soil parameters of the simulation.

Parameter	Value
Radius of the drum r	0.752 m
Length of the drum $2a$	2.14 m
Eccentricity e	23.21 mm
Mass of the frame m_f	3323.0 kg
Mass of the drum m_d	3722.5 kg
Mass of the eccentric m_e	69.47 kg
Excitation frequency f	30 Hz
Shear modulus G	50 MN/m^2
Poisson's ratio ν	0.3
Density ρ	1800 kg/m^3
Damping factor κ	4
Condition factor ε	0.85

Figure 3 shows the calculated soil contact force F_b (black) and its components for four periods of excitation. For the roller subsystem, the contact force is calculated from the inertia force F_a of the vibrating mass shifted upwards by the static axle load F_s (blue) and reduced by the excitation force F_e (green). If the blue and green lines coincide, the soil contact force does not contribute to the inertia force (Equation 1), drum and soil are separated, and the soil contact force becomes zero. The soil contact force shows a recurring pattern for each unbalance revolution, amplitudes and contact times are identical, which means that the roller operates in the "partial uplift" mode.

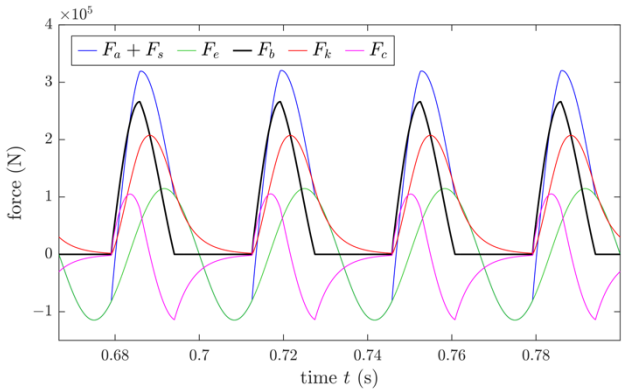

Figure 3. Soil contact force F_b and its components for the roller and soil subsystem over four periods of excitation.

The soil contact force F_b can also be calculated for the soil subsystem as sum of the elastic spring force F_k and the force F_c in the dashpot. It becomes zero in the separation phase since the spring and damping forces have the same magnitude.

The force-displacement diagram in Figure 4 shows the relation between the soil contact force F_b (black) and the corrected relative vibration displacement of the drum z_1. The curved force-displacement line of the spring force F_k (red) results from the nonlinearities of the compaction process: the variable drum contact area and plastic deformations during the loading phase. The change in contact conditions due to the separation phase results in a pronounced kink in the development of the damping force F_c (magenta).

Additional simulations were performed, considering a constant contact width, only. The results are shown in orange ($2b = 6$ cm) and cyan ($2b = 12$ cm) colour in Figure 4.

A comparison of the force-displacement diagrams with and without variability of the contact width shows that only the described model extension leads to results that are close to reality and comparable with measured data (Adam, 1996).

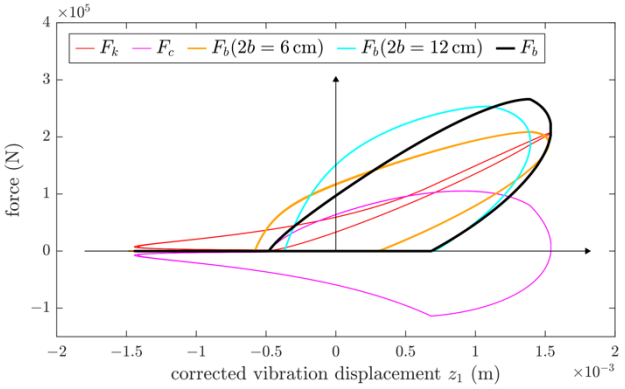

Figure 4. Force-displacement diagrams for a variable and two constant contact widths in comparison.

4 CONCLUSIONS

The presented semi-analytical model allows to consider the vertical drum motion of a vibratory roller, while considering the variable drum contact width during the loading phase. The theoretical force-displacement diagram in Figure 4 provides the basis for the development of a novel Intelligent Compaction Meter Value (ICMV) for vibratory roller compaction.

REFERENCES

Adam, D. (1996). *Continuous Compaction Control (CCC) with vibrating rollers*, PhD thesis, TU Wien.

Pistrol, J., Hager, M., Kopf, F., Adam D. (2023). Consideration of the variable contact geometry in roller compaction. *Infrastructures*, 2023 (8): 110. https://doi.org/10.3390/infrastructures8070110

Wolf, J. P. (1994). *Foundation vibration analysis using simple physical models*, 4th ed., PTR Prentice Hall, Upper Saddle River, NJ, USA.

Proceedings of the XVIII ECSMGE 2024
GEOTECHNICAL ENGINEERING CHALLENGES
TO MEET CURRENT AND EMERGING NEEDS OF SOCIETY
© 2024 the Authors
ISBN 978-1-032-54816-6
DOI 10.1201/9781003431749-495
Open Access: www.taylorfrancis.com, CC BY-NC-ND 4.0 license

ECSMGE 24
XVIII EUROPEAN CONFERENCE ON SOIL MECHANICS AND GEOTECHNICAL ENGINEERING

Circular diaphragm wall for a deep shaft

Parois moulée circulaire pour un puits profond

C. Radu*
Concept Structure SRL, Bucharest, Romania

D. Ciumeică, A. Boureanu, L. Sata
SBR Soletanche Bachy Fundații SRL, Bucharest, Romania

**cristian.radu@c-st.ro*

ABSTRACT: This article presents a case study regarding a circular retaining structure adopted for a technological shaft constructed within an aluminium processing plant in Mediești Aurit, Satu Mare County, Romania. Works were carried out in 2023 in order to accommodate a monolithic reinforced concrete structure with dimensions of 6.3m x 3.95 m, with the bottom slab level of -11.07m (from the reference elevation level, ±0.00m), and a piston with a diameter of approx. 1 m, laid at -18.30m. Geotechnical investigation indicates cohesive and semi-cohesive soils to a depth of 6.4 m, followed by a layer of gravel with sand and boulder to the depth of about. 39.4 m. The groundwater level is located at -6.4m with respect to natural ground level. A self-supporting circular diaphragm wall shaft was the adopted solution, which has been modelled by means of finite element method (FEM) in the two critical stages: Excavation down to -14.7m, taking into account the existence of water and water exhausting down to -11.30m, after high permeability soils in the bottom of the diaphragm wall have been replaced with low permeability layers of soil. The diaphragm wall shaft was executed from the working platform (constructed at level -2.70 m) down to -17.8 m, creating an internal diameter of 8.0 m, inside which, soil was excavated down to -14.70m (under water) and a concrete plug was poured with a thickness of about 3 m (replacing the excavated soil), to ensure up-lift resistance during temporary stage.

RÉSUMÉ: Cet article présente une étude de cas sur une enceinte circulaire pour un puits technologique dans une usine de transformation de l'aluminium à Mediești Aurit, située dans la région de Satu Mare, Roumanie. Les travaux ont été exécutés en 2023. L'objectif des travaux consistait de l'étude et l'exécution d'un puits circulaire afin d'accueillir une structure monolithique en béton armé de dimensions 6,3m x 3,95 m, avec le niveau de fondation de -11.07m (à partir de l'élévation de référence, ±0.00m) au niveau du sol, et un piston d'un diamètre d'environ 1 m, avec le niveau inférieur de -18.30m. Les conditions géotechniques montrent des sols cohésifs et semi-cohésifs jusqu'à une profondeur de 6,4 m, suivis d'une couche de gravier avec du sable et des rochers jusqu'à une profondeur d'environ 39,4 m. Le niveau de la nappe phréatique se trouve au niveau -6,4 m. La solution proposé a été un puits circulaire de paroi moulée autoportant qui a été numérisé par la méthode de l'élément fini (MEF) dans les deux étapes critiques: excavation jusqu'à -14,7 m, en tenant compte de l'existence d'eau et le stage après l'évacuation de l'eau, après le débouchage du béton. Le puits de la paroi moulée a été réalisé depuis la plateforme de travail (niveau -2,70 m) jusqu'à -17,8 m, avec un diamètre intérieur de 8,0 m, à l'intérieur duquel le terrain a été excavé jusqu'à -14,70 m (sous l'eau) et un bouchon en béton a été coulé sur une épaisseur d'environ 3 m pour assurer la résistance au soulèvement lors de l'étape temporaire.

Keywords: Circular shaft; deep excavation; diaphragm wall; uplift.

1 INTRODUCTION

The project's scope of works consisted in the design and execution of a deep excavation undergone inside a circular shaft in order to ensure conditions for the bottom up construction of an interior structure, part of the vertical casting machine objective, a technological facility serving the future investment (Figure 1).

In order to facilitate an efficient productivity for the Client and the Contractor, the project required a solution regarding the rapid construction of the future underground equipment (part of the expansion of the Aluminium extruded profiles factory), while minimizing the influence on the facility's technological flow and logistics.

The site is located in Mediești Aurit, a city in the county of Satu Mare, situated in the north-western region of Romania, close to the Hungarian border.

The aim of the special foundations works was to obtain an efficient structural system in terms of correlation with the future structure and equipment, by adopting a solution optimally adapted to the particularities of the project that will ensure the work flow is enhanced for carrying out the construction works.

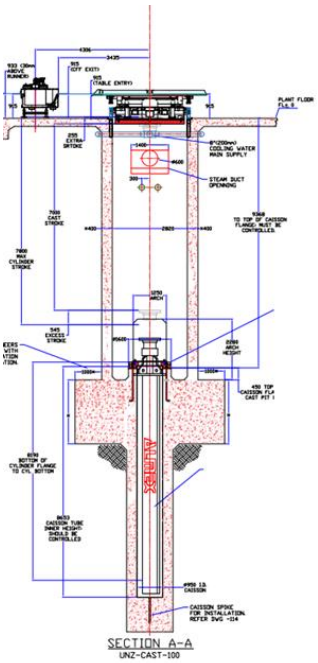

Figure 1. Technical concept – Vertical casting machine.

Due to its underground positioning, the casting shaft dimensions and adjacent operating equipment which are designed to function inside a reinforced concrete infrastructure, the foundation level was designed at a depth of 11,3 meters with respect to natural ground level.

2 GEOTECHNICAL CONDITIONS

The on-site geotechnical report is based on several boreholes, with a maximum depth of 50 meters, determined by in-situ tests and electrometric investigations.

The general site lithology indicates thick layers of sand and gravel (down to over -40.0 meters),

- ±0.00 m ... -1.00 m – organic fillings;
- -1.00 m ... -5.20 m – stiff clay;
- -5.20 m ... -6.40 m – sandy clay;
- -6.40 m ... -40.00 m – sand and gravel;

The theoretical water level indicated by the geotechnical report is set at -6.50 meters.

The sand and gravel layer contains minor percentages of fine particles, 10-20% clay & silt, thus, in order to reach the designed depth, in common projects, the high permeability of the stratum would generate the need to adopt a difficult dewatering system that would interfere with the factory's water supply.

The local design norms related to geotechnical documentations offer maximum score in terms of the theoretical solution to be adopted regarding the dewatering necessary for constructing the reinforced concrete under an approximate water table of 6.0m.

3 CIRCULAR DEEP SHAFT SOLUTION

3.1 General information

In order to construct the aforementioned structure laid at -11.30m, considering the project's particularities, the adopted solution consists in a circular shaft of 8 meters diameter, constructed as diaphragm wall (slurry wall) reinforced concrete panels which will ensure construction and installation of the interior vertical casting machine's structure in conditions of maximum safety and efficiency.

Following dedicated calculations, the diaphragm wall thickness has been set at 60 cm and the specific polygonal shape generated by the panelling layout was executed aided by shaped guiding walls (Figure 2).



Figure 2. Isometric view of circular shaft and casting shaft geometry.

In the design process, multiple excavation support solutions have been regarded (ground anchors, horizontal or inclined temporary struts, top-down excavation method, etc.).

Calculations were performed with design approaches according to current regulations such as Eurocode 7 with corresponding national annexes, or local Romanian regulations, NP 120 (2014) and NP 124 (2010).

In order to achieve a retaining system which can provide excavation protection, as well as an increased productivity of execution, by implementing the circular shaft solution, for which earth and water pressure loads are transferred as compression by means of arch effect of in the concrete mass, resulting in a self-supporting diaphragm wall, no internal or external bracing is required.

The length of the designed diaphragm wall panels is 15 meters, embedded in sand and gravel ground layers.

Due to the presence of large packs of sand and gravel, in terms of financial efficiency, embedment in a lower clay layer has not been feasible, thus generating the necessity of adopting a soil improvement method for isolating the base of the diaphragm wall below excavation level in order to limit dewatering works that could generate multiple exploitation risks.

The adopted soil improvement solution consists in substituting permeable layers of soil with hydraulic concrete on a certain length under the designed foundation level.

The resulting concrete layer is designed with a thickness of approximately 3 meters.

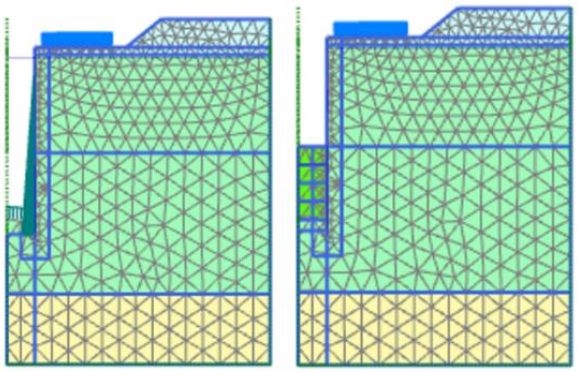

Figure 3. Finite Element Model of circular shaft (axisymmetric model).

The axisymmetric model is used in cases where circular structures are modelled, with uniform sections and loads distributed around the central rotation axis. The basic premise for this model is the identical configuration in any radial direction regarding soil lithology and loads (Figure 3).

3.2 Design particularities

Due to the particularities of the project and to the fact that the diaphragm wall is not embedded in a clay level, FEM modelling of the circular shaft has been performed for critical stages such as excavation down to -14.7 meters, with no water evacuation, as well as water evacuation down to -11.70 meters, after the execution and hardening of the concrete soil improvement.

To establish the geometry of the soil improvement, thus leading to the thickness of the newly poured hydraulic concrete layer, dimensioning has been performed for several structural internal verifications that were required for internal stability of the pit, both for temporary and permanent phases.

The most important verification for uplift checks consists in validating the thickness of the concrete layer so it withstands the under pressure generated by the difference between the exterior water table and the interior water table resulted after water exhaustion takes place.

The inferior level of the VCM (vertical casting machine) structure is situated at -18.00 meters under the natural terrain level and is laid on a reinforced concrete raft laid at a level of approximately -11.10 meters with respect to natural ground level (Figure 4).

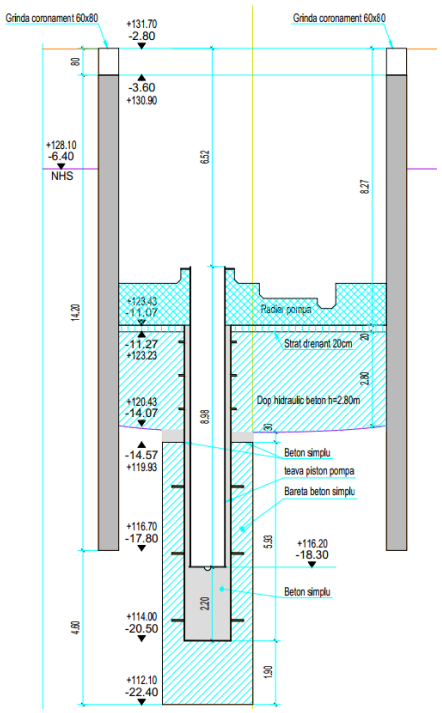

Figure 4. Shaft's cross section with concrete plug.

The casting shaft's piston is designed to slide inside a technological steel pipe with a section of 1400x10 mm, from -11.10 meters level, down to approximately -18.00 meters.

In order to accommodate the future pipe and to ensure verticality is obtained, a supporting barrette, has been constructed inside the shaft, as support of the casting shaft's pipe, and as a supplementary support for the casting shaft against water under pressure due to uplift.

4 MONITORING OF THE RETAINING STRUCTURE

Lateral pressure generated by the soil massif acting on the exterior surface of the diaphragm wall is transferred by arching effect in the concrete structure as hoop forces.

The diaphragm wall's thickness is dependent on the diameter of each circular cell with a direct impact on the arching effect of the lateral loads.

A higher diameter of the circular cell generates an amplified soil pressure, caused by the decreasing arching effect.

Monitoring of the circular shaft was obtained by means of strain gauges, installed on steel rebar cages (Figure 5).

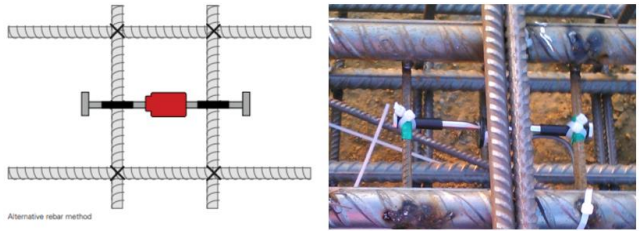

Figure 5. Concrete strain gauge installation.

Values resulted from monitoring indicate variation of stresses that are situated below dimensioning value (maximum 5 MPa measured value with respect to 10.2 MPa corresponding to the designed value).

Other factors that have to be considered in the design process are related to non-uniform loads that may appear from various equipment and logistics at ground level as well as excavation sequencing, or discontinuity in soil layers and their relevant parameters (Figure 6).



Figure 6. Excavation inside the shaft.

5 CONCLUSION

This particular project combines previously acquired information and return of experience in similar projects that allowed the proposal for a much more effective solution, with reduced quantities (approximately up to 35% less materials) and a performant execution time management.

The reduction of the materials' quantities also resulted in a reduction of the CO2eq emissions of 45%.

Using the right materials and minimising as much as possible the distances for their supply, proved to be particularly effective in reducing the project's carbon footprint (Figure 7).

The monitoring performed during the execution process provided valuable information for future developments of similar projects, both in heavy or light industry for factories and other special facilities, as well as other private applications or research & development purposes.

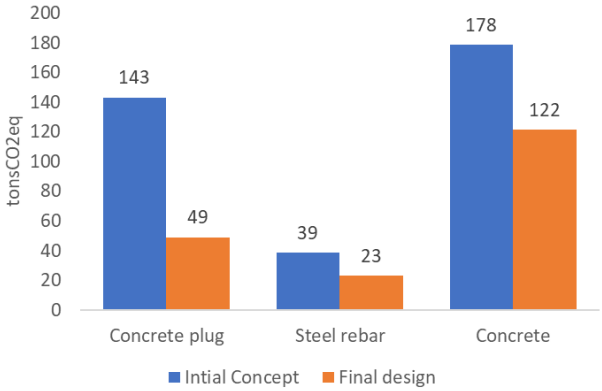

Figure 7. Comparison of materials' CO2eq emissions between initial concept and final design.

In conlusion, using right technology, considering a circular design of the shaft taking into account arching effect in the concrete structure, using proper reduced CO2 emissions materials, prove to be a proper solution of small technological shafts.

REFERENCES

SR EN 1997-1:2004, *Eurocode 7: Geotechnical design - Part 1: General rules* / "*Eurocod 7: Proiectarea geotehnică. Partea 1: Reguli generale*".

SR EN 1997-1:2004/NB:2007, *Eurocode 7: Geotechnical design - Part 1: General rules. National Annex* / *"Eurocod 7: Proiectarea geotehnică. Partea 1:Reguli generale. Anexa Națională"*.

SR EN 1538+A1:2015, Execution of special geotechnical works. Diaphragm walls / "*Execuția lucrărilor geotehnice speciale. Pereți mulați*".

NP 120-2014, *Normative regulations for design and execution of deep excavations in urban areas* / "*Normativ privind cerinţele de proiectare şi execuţie a excavaţiilor adânci în zone urbane*".

NP 124-2010, Normative regulations for geotechnical design of retaining structures / "*Normativ privind proiectarea geotehnică a lucrărilor de susţinere*".

EFFC DFI (2023). *Project Carbon Calculator.*

Soletanche Bachy France, *A permanent circular diaphragm wall with unreinforced concrete for the Grand Paris Express.*

Proceedings of the XVIII ECSMGE 2024
GEOTECHNICAL ENGINEERING CHALLENGES
TO MEET CURRENT AND EMERGING NEEDS OF SOCIETY
© 2024 the Authors
ISBN 978-1-032-54816-6
DOI 10.1201/9781003431749-496
Open Access: www.taylorfrancis.com, CC BY-NC-ND 4.0 license

ECSMGE 24
XVIII EUROPEAN CONFERENCE ON SOIL MECHANICS AND GEOTECHNICAL ENGINEERING

Deep foundation system of the Promenada Mall extension in Bucharest, Romania

Système de fondations profondes de l'extension du centre commercial Promenada à Bucarest, Roumanie

C. Radu*, C. Năstase, T. Matei, P. Danilov, I. Buzilă, M. Popa, O. Chițu, R. Geanguș
Concept Structure, Bucharest, Romania

**cristian.radu@c-st.ro*

ABSTRACT: The paper describes the designed deep foundation system of a future multi-storey commercial center laid at -23.0m below natural ground level with considerations on the particularities of the superstructure's configuration being addressed. A particular aspect within the paper consists in the presentation of the analyses performed for various stages of construction with respect to soil-structure interaction thus resulting in an iterative design methodology. The necessary parameters to be considered in order to validate and optimize the initially tendered design are determined on a dedicated testing procedure carried out by means of Osterberg cells that have been performed within the initial phases of the project. A full assessment has been obtained by processing data from the Osterberg cell testing, allowing advanced numerical modelling of the soil-structure interaction and resulting in an optimal layout of the foundation elements. The paper presents essential results obtained from numerical analyses and performed in situ testing resulting in a full simulation of the final soil-structure interaction fundaments.

RÉSUMÉ: L'article décrit le système de fondations profondes conçu pour un futur centre commercial à plusieurs étages posé à -23,0 m sous le niveau du sol naturel en prenant en compte les particularités de la configuration de la superstructure. Un aspect particulier de l'article consiste en la présentation des analyses effectuées pour les différentes étapes de la construction en ce qui concerne l'interaction sol-structure, aboutissant ainsi à une méthodologie de conception itérative. Les paramètres nécessaires à prendre en compte pour valider et optimiser la conception initialement proposée sont déterminés sur la procédure de test de barrette réalisée au moyen de cellules Osterberg qui a été réalisée dans les phases initiales du projet. Une évaluation complète a été obtenue en traitant les données des tests de la cellule Osterberg, permettant une modélisation numérique avancée de l'interaction sol-structure et aboutissant à une disposition optimale des éléments de fondation. L'article présente les résultats essentiels obtenus à partir d'analyses numériques et d'essais in situ effectués aboutissant à une simulation complète des fondements finaux de l'interaction sol-structure.

Keywords: Deep foundation; load testing; barrettes; soil-structure interaction; finite element.

1 INTRODUCTION

The New Promenada Mall extension project represents an undergoing commercial development in Bucharest, Romania, comprising roughly 100 000 sqm of parking infrastructure constructed beneath ground level, and approximately 120 000 sqm of superstructure representing an investment that will consist in a cinema, shopping area, offices and entertainment facilities for one of the city's most active business hubs.

In terms of geotechnical aspects, due to its size and complex architectural conformation (Figure 1), the future development represents an important challenge on the local engineering market.

The site layout is a land lot of roughly 12 500 sqm and the designed depth of the future 7 storey basement is generally 23.0m beneath natural ground level.



Figure 1. General render of the future Mall extension.

The paper aims to describe the main aspects of the deep foundation design and study, with focus on the technical methodology and challenges encountered.

2 GEOTECHNICAL CONDITIONS

The site is located in an area where several investments were carried out over the last decade and valuable geotechnical information was available for the site and neighbouring locations, as well as information gathered from site monitoring. The geotechnical report indicates an uniform alternation of soil layers, as following, with respect to the working platform level set up at an inferior level (considered -7.00m);

- -7.00m ... -17.30m – clayey silt;
- -17.30m ... -21.30m – sand and gravel;
- -21.30m ... -29.30m – stiff silty clay;
- -29.30 m ... -31.60 m – sand and gravel;
- -31.60 m ... -37.20 m – clay;
- -37.20 m ... -43.20 m – sand and gravel;
- -43.20 m ... -54.90 m – clay with concretions;
- -54.90 m ... -60.00 m – fine sand.

The raft is laid at approximately -23.00m with respect to natural ground level.

Parameters provided by the geotechnical report are determined based on 7 (seven) boreholes drilled down to depths of 70.0m (circa 50.0m beneath final excavation level).

Following the design methodology adopted in similar documented soil-structure interaction response, the adopted material parameters are derived from soil investigations and correspond to the Mohr Coulomb, Hardening Soil and Hardening Soil with Small Strain stiffness constitutive models. Several sensibility analyses were performed in order to assess the influence of the uncertainties in the soil profile (Tschuchnigg, 2011) for a preliminary setup of design hypotheses.

3 FOUNDATION SYSTEM

The superstructure presents several geometry changes both in height as well as in layout distribution. As a result, the building is divided into several modules with 2 main cores (approximately 250 sqm per each core) and 2 secondary cores (approximately 120 sqm per each core) and a general distribution of columns in the basement levels of 8.0x8.0m that bear loads from superstructure columns which span over a 16.0x16.0m distribution and support loading from asymmetrical conditions.

One main advantage for the general layout of columns (with dimensions of 80x80cm up to 140x140cm) is the high unitary capacities (large section and high strength concrete allowing up to 55 MN loads), allowing an equal distribution of columns in the underground levels and allowing foundation elements to be embedded in the construction's technological staging, by efficiently adopting the "top down" excavation method and including temporary metallic profiles into the final concrete columns as part of the final superstructure.

Furthermore, the architectural configuration allows that the high point loads generated from the superstructure to be directly transferred to deep foundation elements (piles or barrettes constructed under bentonite slurry).

Several levels of loads in RC columns for the different designed stages of construction have been studied, both for temporary and final loading sequences and have been considered for the numerical models that were developed (Figure 2).

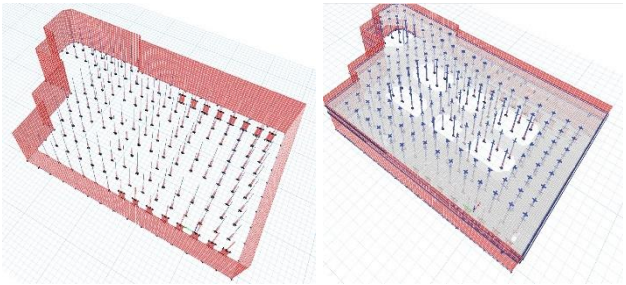

Figure 2. Distribution of pile loads based on staged construction sequence.

Variable loads were considered in the design of the temporary phase when the excavation's retaining system (top-down system) imposed several technological limitations, requiring a rigorous study. Examples of eccentric loading scenarios are represented by the crane positioning next to the excavation pit, technological shafts and openings, positioning of concrete trucks or other temporary deposits for materials.

4 ANALYSIS OF SOIL-STRUCTURE INTERACTION

4.1 Instrumented barrette loading

Due to the fact that excavation is undergone at minimum 23.0m below ground level under a top-down construction sequence, the proper and practical solution to achieve the high testing load values necessary for validating the design was considered by means of the Osterberg cell procedure.

Preliminary load tests were performed on two 2800x800mm barrettes (TB01 and TB02), that were each set up with single level 2x330mm hydraulic cells in order to properly estimate skin friction and end bearing capacity values.



Figure 3. Installation of O-cells in instrumented barrettes.

The Osterberg cell load tests were conducted in 17 nominally equal increments in order to reach their initially considered hydraulic capacity of 15.40 MN, after which increment size was increased to 150% of the previous increments until loading reached a maximum of 9.32 MN applied to the barrette above and below the O-cells, thus completing the test at 18.64 MN.

The instrumented barrettes (Figure 3) constructed for testing purposes were completed under bentonite slurry with an excavated depth of 58.50 metres and a concreted length of approximately 41.00 metres. The adopted lengths were designed in order to ensure both sections (top segment and bottom segment) can generate sufficient friction and results could produce the proper information in order to optimize the foundation system.

Skin friction was evaluated on six (6) layers of four sister bar vibrating wire strain gauges installed on different levels that were fixed on the reinforcement cages. The adopted positions were considered relevant for the determination of the required information.

4.2 Numerical modelling

Preliminary design of the foundation system was based on assumptions on parameters that were considered with the aid of prescriptions provided by the local norm regarding pile design (Romanian Design Norm NP 123:2010).

The results of the O-Cell testing allowed for full stage construction analyses to be carried out by means of finite element method, as well as calibration of results to be implemented in the aforementioned soil-structure interaction study.

The assessment of the soil structure interaction phenomena required the use of several numerical models, as well as advanced constitutive models (Zehentner et al., 2012), in order to process and back analyse the significant volume of available information.

In terms of results, by taking into account the shape of the foundation (broadly consisting in a vast area of symmetry due to the architectural configuration), an initially adopted approach was to model the foundation subjected to vertical forces by means of an axisymmetric model (Pereira et al., 2017), as well as tri dimensional models for local areas which were of interest in terms of the superstructure's response (loads and settlements), such as core areas and areas with extreme localized loads where high capacity RC columns were distributed next to low capacity ones, thus resulting in differential settlements, or areas for which uplift pressure effects imposed the infrastructure's dimensions.

Reduced size numerical models (Figure 4) enable parametric analyses to be performed for interpreting the variation in geometry or soil stiffness, also considering that the results are not significantly influenced by the nonsymmetric outer part of the structure.

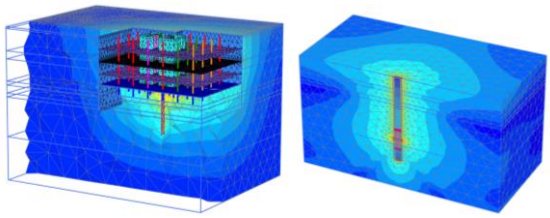

Figure 4. Strain development in calibration models for preliminary dimensioning of foundation elements.

The calculations developed for the final proposed layout of the deep foundation elements generated an extended full tri dimensional model, enabling a refined review for the dimensioning of all elements in the infrastructure.

The superstructure's architectural complexity involves several shifts in the superstructure's height; thus, foundation loads vary in a wide range of values for forces between 6000 kN/point of compression, to over 8000 kN/point of tension.

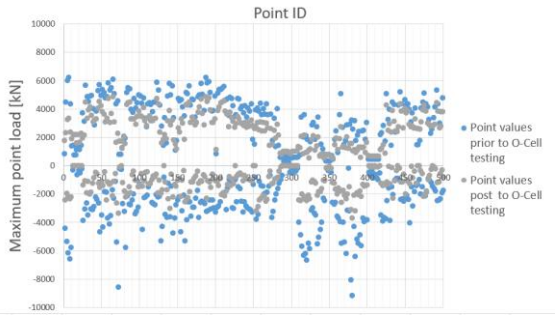

Figure 5. Point load distribution of forces in foundation elements as per numerical model simulation and calibration.

Individual deep foundation elements are defined by several points, associated with loads plotted in Figure 5. The sum of the point values per each element generates the final dimension of the deep foundation geometry and depth, resulting in the final distribution of the foundation system consisting in bored piles with

a diameter of 100cm up to 140cm and barrettes with dimensions of 80x280cm.

Maximum compression loads for the foundation elements have reached up to 15 MN in some positions for seismic loading and 10 MN for temporary loading in the execution stage from the top-down sequence mostly generated by the construction process (equipment and materials).

The infrastructure is constructed inside an excavation pit consisting of perimetral diaphragm walls. Due to the depth of the excavation and the presence of the inferior under pressure aquifer, special attention was necessary for complementary checks regarding the final design stages, such as uplift in the exploitation phase.

The final difference in water quota and effects due to buoyancy have been evaluated, loads of up to 180 kPa being generated at raft level as forces are significant with regard to the underground structure's configuration.

Following on site testing and calibration of numerical models, different stiffness values were computed for several loading scenarios and an optimized version of the foundation system was implemented in the project as shown in Figure 6.

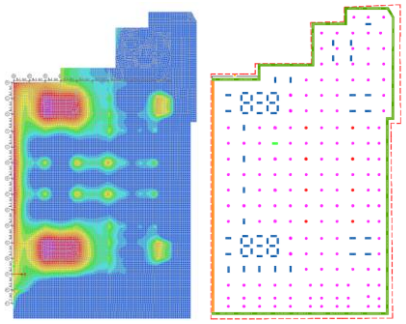

Figure 6. Distribution of soil pressure diagrams and resulting foundation elements.

Although the designed foundation level is considered at a depth where the superstructure's loads will transmit similar pressures to the ones of the excavated soil massif, the designed foundation system's stiffness is adjusted to ensure a proper compatibility both for reduction of maximum settlements and for limiting differential settlements between areas subjected to different loading conditions, due to the project's configuration.

The foundation system has been dimensioned for the ultimate limit states with respect to the provisions of Design Approach 1 from EN 1997-1:2004.

In order to properly assess the structural response, load-settlement diagrams for compressive and tensile loads were derived based on the determined soil parameters and settlement predictions have been verified by comparison to the construction's design limitations. Results of iterations for soil structure interaction indicate that the initially adopted parameters considered for the dimensioning generated a fairly conservative preliminary design if the processed data is limited to regular geotechnical investigations and references from local norms.

5 CONCLUSIONS

The paper has presented a deep foundation system and its study on soil-structure interaction was undergone in order to correctly address the design of an advanced geotechnical engineering project.

A number of analyses and interpretations of data have been performed for designing the deep foundation system. Finite element analyses and in situ testing were carried out for supporting the structural design, as several calculations and iterations were carried out in order to properly adapt and adjust the foundation system and infrastructure of a large-scale project (Figure 7).

The final design generated significant saving compared to the preliminary stages as back analysed data generated relevant results and in-situ testing proved utmost importance, particular emphasis being required for the soil structure iterative design process in order to validate and improve the considered design assumptions.



Figure 7. Aerial view of the construction site during execution of the deep foundation elements.

REFERENCES

Pereira, G., Lam, P. and Jeanmaire, T., Deep foundation systems of ultra high-rise buildings: the Entisar tower in Dubai, *Proceedings 19th International Conference on Soil Mechanics and Geotechnical Engineering,* Seoul, South Korea, 2017

Tschuchnigg, F., Optimization of a deep foundation with diaphragm wall panels employing 3D FE analysis, *Proceedings 21. European Young Geotechnical Engineers Conference (EYGEC),* Rotterdam, The Netherlands, 2011

Zehentner, H., Tschuchnigg, F. & Schweiger, H.F., Die Baugrube des Sky Tower in Bukarest*, Proc. of 26th Christian Veder Kolloquium,* Graz, 147-162, 2011.

Proceedings of the XVIII ECSMGE 2024
GEOTECHNICAL ENGINEERING CHALLENGES
TO MEET CURRENT AND EMERGING NEEDS OF SOCIETY
© 2024 the Authors
ISBN 978-1-032-54816-6
DOI 10.1201/9781003431749-497
Open Access: www.taylorfrancis.com, CC BY-NC-ND 4.0 license

ECSMGE 24
XVIII EUROPEAN CONFERENCE ON SOIL MECHANICS AND GEOTECHNICAL ENGINEERING

Analysis and re-sloping for slope stabilization in São José neighbourhood, João Pessoa, Paraíba, Brazil - case study

Analyse et re-profilage pour la stabilisation des pentes dans le quartier de São José, João Pessoa, Paraíba, Brésil - étude de cas

A.V.F.S. Ramos*, G.K.S. Simões, F.L. Soares
Federal University of Paraíba, João Pessoa, Brazil

**arthur_vinicios_@hotmail.com*

ABSTRACT: The disorderly occupation of slopes and hillside by socioeconomically vulnerable populations has caused changes in vegetation and topography in these areas, which can accelerate the occurrence of mass movements, resulting in material and human losses. Although there are available technologies and slope stability solutions, they are often inaccessible to communities in high-risk areas due to high costs and lack of investment from public authorities. This study was conducted in the São José neighbourhood, located in João Pessoa, Paraíba, Brazil. The soil involved belongs to the Barreiras Formation and has been analysed geologically and geotechnically. Currently, a section of the slope experiences active seasonal mass movement, aggravated during periods of high rainfall. The objective is the slope stability analyses under natural conditions and perform a back analysis for the triggering of the mass movement. As a proposed stabilization measure, the analyses results show the necessity and feasibility to adopt slope flattening, along with surface drainage works and the application of vegetative protection using Vetiver grass as a stabilizing action to guarantee the safety of the residents in the region.

RÉSUMÉ: L'occupation désordonnée des pentes et des collines par des populations socialement vulnérables a provoqué des modifications dans la végétation et la topographie de ces domaines, ce qui peut accélérer la survenue de mouvements de masse, entraînant des pertes matérielles et humaines. Bien que des technologies et des solutions de stabilité de pentes soient disponibles, elles sont souvent inaccessibles aux communautés situées dans des zones à haut risque en raison de leur coût élevé et du absence d'investissement des autorités publiques. Cette étude a été ramenée dans le quartier de São José, situé à João Pessoa, Paraíba, au Brésil. Le sol concerné appartient à la Formation de Barreiras et a été analysé sur le plan géologique et géotechnique. Actuellement, une section de la pente subit un mouvement de masse saisonnier actif, aggravé pendant les périodes de fortes précipitations. L'objectif est d'analyser la stabilité de la pente dans des conditions naturelles et d'effectuer une analyse rétrospective pour déterminer les causes du mouvement de masse. Comme mesure de stabilisation proposée, les résultats indiquent la nécessité et la faisabilité d'adopter un aplanissement de la pente, accompagné de travaux de drainage en surface et de la mise en place d'une protection végétative à l'aide de l'herbe de Vetiver en tant qu'action de stabilisation pour garantir la sécurité des habitants de la région.

Keywords: Back analysis; mass movement; slope stability; re-sloping; risk areas.

1 INTRODUCTION

This study proposes slope reinforcement as a low-cost stability solution in risk areas in João Pessoa, the capital of the Paraíba state, Brazil.

The uncontrolled urban expansion of major towns in recent decades has led socioeconomically vulnerable populations to seek residence in hillside areas. Therefore, this work aims to address the issue of the lack of accessible and effective solutions for slope stabilization in risk areas within the city of João Pessoa. The research is justified by the significance of developing low-cost solutions in the field of civil engineering.

Most risk areas are in underprivileged communities that lack the financial resources to afford complex and costly solutions. Furthermore, the adoption of low-cost solutions can significantly reduce the risk of accidents caused by mass movements, saving lives, and preserving public and private property (Alheiros *et al.*, 2003; Ministério das Cidades, 2006).

In this context, the present study analyses the slope stability and proposes a low-cost and secure solution for the high-risk area in the study region.

2 THEORETICAL FOUNDATION

2.1 Triggering agents

2.1.1 Rainfall

According to Highland and Bobrowsky (2008), mass movements primarily occur during periods of cumulative rainfall, presenting a risk to the population living in landslide-prone areas. According to Lima (2002) *apud* Ramos *et al*. (2022), there is a correlation between cumulative rainfall and landslides, as rainfall is classified as one of the main triggering factors, leading to increased soil saturation and erosion at the top, body, and foot of slopes, reducing cohesion and the angle of friction, resulting in a drastic reduction in soil resistance.

2.1.2 Geomorphological and morphological factors

Geomorphological factors are related to the properties of the soil type in which the process takes place. In this context, the terrains will be prone to the influence of certain landslide or erosion phenomena, according to their lithological properties, texture, structure, and pre-consolidation (Simões, 2023).

Morphological factors are related to the shape in which the slope presents itself, that is, the susceptibility to landslide occurrence, which, according to Alheiros et al. (2003), is related to how high and extensive the slope is and its characteristics, such as low sinuosity, concave profile, and high slope.

2.1.3 Anthropogenic actions

Anthropogenic factors are strongly related to the composition of risk, as they correspond to human activities and how the population interacts with the environment in which they live. According to Oliveira (2021), this interaction occurs in various ways, such as excavation and filling for housing, leakage in supply and drainage pipelines, the discharge of wastewater and/or sewage, the construction of septic tanks, irregular disposal of garbage and/or debris, as well as changes in vegetation, all of which are susceptibility factors. In addition, the population density is considered a vulnerability factor.

2.2 Climate characteristics in João Pessoa

The climate of the municipality of João Pessoa, Paraíba - Brazil, is characterized by its location at low latitudes and its proximity to the Atlantic Ocean. According to the National Institute of Meteorology-INMET (2023), the region climate is characterized by an average annual precipitation of 1837 mm and an approximate annual average temperature of 26.9°C, with the rainiest period occurring from April to July, as shown in Figure 1.

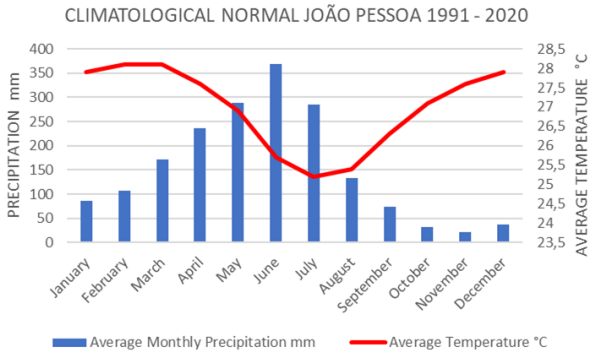

Figure 1. Climatological Normal João Pessoa 1991 - 2020.

2.3 Characterization of the soil

Some soils of João Pessoa-PB were characterized by Nascimento (2008) *apud* Soares (2011), confirming the predominance of Red-Yellow Argisols in the Coastal Plateaus of the Barreiras Formation. According to Barbosa (2015) *apud* Bezerra (2017), the majority of João Pessoa's territory is situated on the Barreiras Formation, covering approximately 67% of the municipality's total area.

2.4 Landslide risk areas in the city

The city of João Pessoa experienced significant urban growth starting in the 1960s, following the pattern observed in many other cities in Brazil. However, this growth occurred without proper urban planning, leading to the occupation of hillsides and river valleys by low-income residents and, consequently, an increase in population density in risk areas.

Currently, according to the Municipal Coordination of Protection and Civil Defense of João Pessoa, as evidenced by Ramos *et al*. (2022), the city of João Pessoa has 27 areas located in mass landslide risk zones.

2.5 Neighbourhood data

The neighbourhood began with the occupation of land along the banks of the Jaguaribe River by families from the former Beira-Rio community, with predominantly substandard residential characteristics. The neighbourhood reflects the land parceling and occupancy typical of spontaneous settlements (Filipeia, 2023).

According to data from the last Demographic Census conducted by the Brazilian Institute of Geography and Statistics-IBGE (2010), the neighbourhood covers a territorial area of approximately 34,98 hectares and is home to a population of 7.078 residents. It is characterized by

social inequality, with the river and slope acting as physical barriers that separate it from more affluent neighbourhoods.

Over the years, there have been eight occurrences of mass movements in the neighbourhood recorded between 2000 and 2016, as reported by Silva (2018). The frequent landslides in the area could be attributed to factors such as the extremely steep slope profile, with some sections having inclinations exceeding 45 degrees, as well as the presence of large trees at the top of the hillside and constructions at the toe of the slope. These factors contribute to an increased vulnerability to mass movements.

2.6 Re-sloping

Re-sloping can be directed towards a specific slope angle or aimed at altering the entire profile of the slope. These are interventions designed to stabilize the slope by reshaping its form through cuts in the uppermost part, with the goal of regularizing the surface and, as much as possible, artificially restoring the topography of the barrier, thereby enhancing soil stability. This solution is often combined with compacted fills to act as stabilizing loads at the toe of the slopes.

Alheiros *et al*. (2003) provides some important analysis characteristics. For cut sections, cuts with a height of less than five meters can be continuous, while cuts with heights exceeding five meters should be terraced in steps through berms or benches.

Each soil or sediment variety, when subject to denudation, defines its equilibrium profile, which stabilizes when vegetation becomes established. Cuts disrupt this equilibrium, thus enhancing erosive processes and mass movements. According to Alheiros *et al*. (2003), these changes can be offset by reshaping, ensuring that fill slopes do not exceed a ratio of 1:2 (vertical:horizontal), cut slopes maintain a ratio of 1:1,5 (vertical:horizontal), constructing berms whenever possible at the toe of the fill, restoring surface cover, and implementing drainage at the cut-off drain, berm drain and toe drain the slope.

2.7 Vegetative protection

One of the most important mechanical properties of vegetation in soil is its roots, due to their tensile strength in contrast to the soil's resistance to compressive forces. Therefore, the combined action of the soil and roots results in reinforced soil (Baets *et al.,* 2008 *apud* Júnior, 2019). However, according to Simões (2023), it is advisable to avoid planting large trees on the top or along the slope, since, due to the action of gravity combined with strong winds, it causes tensions in the soil due to the lever effect, which can disaggregate the soil, triggering mass landslides or tree toppling.

3 METHODOLOGY

3.1 Studied slope

The study was conducted in the São José neighbourhood, through field visits and a bibliographic survey of the area's landslide history. Subsequently, in collaboration with Federal University of Paraíba, the mass landslide risk map for the São José neighbourhood was generated, as shown in Figure 2.



Figure 2. Landslide risk map of São José.

Next, the Z3 zone (purple), classified as high risk of mass movement, was selected for the study. The studied area exhibits a well-defined soil crack, indicating a soil rupture zone due to a seasonal mass movement process that began in 2015 and intensified further in 2021 up to the present day. The crack is approximately 13,20 m in length and 3,50 m from the top of the hillside, as shown in Figure 3.



Figure 3. Crack at the top of the slope.

Through field visits and photogrammetric survey using a drone, the local features were obtained, described as: natural hillside with concave terrain and average inclinations of 45 degrees, the presence of tree

vegetation on the slope surface, and banana trees at the toe of the slope.

3.2 Characterization studies

3.2.1 Laboratory tests

The tests were conducted in the Geotechnical Laboratory of the Department of Civil Engineering at the Federal University of Paraíba, following all applicable technical standards from the Brazilian Association of Technical Standards (ABNT). The laboratory tests were conducted:

- Soil - Grain size analysis;
- Specific gravity of solids;
- Determination of Atterberg limits:
  - Liquid limit;
  - Plastic limit;
- Compaction test;
- Direct shear test.

3.2.2 Soil classification using correlations with SPT sounding parameters

A nearby borehole on the slope was used to establish a correlation between the Standard Penetration Test (SPT) and soil classification based on the methods proposed by Godoy (1972) and Teixeira (1996) *apud* Neto (2018). This correlation was utilized to determine cohesion, friction angle, and natural unit weight values through the number of blows in the test.

3.2.3 Instrumentation

The landslide area was instrumented with crackmeters using 2 mm thick glass plates measuring 52 mm x 40 mm to monitor the displacement of cracks. In total, four glass plates were strategically placed. Figure 4 shows two of the glass plates used in the instrumentation.



Figure 4. Crack instrumentation.

4 RESULTS

4.1 Results of the characterization studies

Table 1 presents the data used in the slope stability study. The parameters of friction angle, cohesion, and specific weight were determined through back analysis for layers 1 and 2. Thus, the back analysis was conducted based on the data obtained from laboratory tests, in which the friction angle, cohesion, and specific weight varied between the natural and saturated soil states to obtain the parameters at the slope failure moment (FS≈1,00). For layers 3, 4, 5, and 6, the parameter values were obtained through correlation with the samples borehole data.

Table 1. Adopted parameters of angle of friction, cohesion, and specific weight.

Layer	Friction angle (°)	Cohesion (kPa)	Specific weight (kN/m³)
1 natural	25°	7,19	16
1 back analysed	22°	5	18
2 natural	25°	7,19	16
2 back analysed	22°	6	18
3	31°	10	20
4	35°	10	20
5	35°	20	20
6		(rock)	

4.2 Slope modelling

Using georeferencing, the cross-sectional profile of the slope was plotted, with the slope having an approximate elevation of 13,79 meters and a distance of 20 meters from the dwellings, displaying a concave profile, as shown in Figure 5.

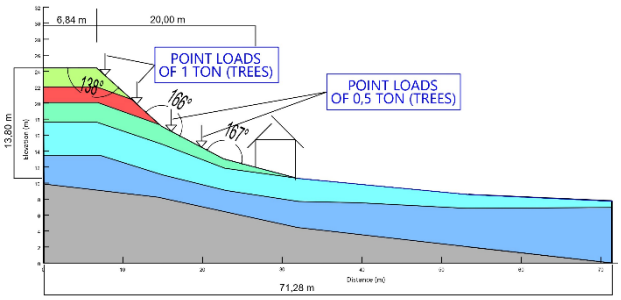

Figure 5. Profile of the relief of the studied slope.

During the field visits, the presence of large and medium-sized trees along the slope was observed, and their loads were modeled pointwise on the slope face in the GeoStudio software.

4.3 Results of back analysis

In the back analysis, the objective was to determine the safety factor (FS) for the natural conditions of the slope during rainy seasons, which triggered the crack growth. For this purpose, the analysis was conducted using GeoStudio 2022.1 software through a student license, with the SLOPE/W module. Based on the soil

data, the hillside was modeled and analysed, considering two scenarios: saturated soil for the back analysed condition and the other scenario for the natural soil condition. In this way, the safety factor was calculated for scenario 1 and scenario 2, through three analysis methods: Bishop, Fellenius, and Janbu, with the purpose of obtaining a thorough analysis in the region. The results are expressed in Table 2.

Table 2. Results of the slope analysis.

Method	FS - back analysis	FS - Natural Soil
Bishop	1,035	1,203
Fellenius	1,007	1,268
Janbu	0,986	1,186
Average	1,009	1,219

It is evident that, in all the analyses conducted, that the safety factor (FS) found is less than the minimum value of 1,4 recommended by NBR 11682 (ABNT, 2009). The low Safety Factor found can explains the slow movement of the slope that has been occurring in the region since 2015, characterizing a seasonal process of mass movement during periods of heavy precipitation and accumulated rainfall. This leads to soil saturation and, consequently, an increase in density, a decrease in the angle of friction, and a decrease in apparent cohesion, which can become virtually negligible.

4.4 Stabilization proposal

For the study slope, a stabilizing action is necessary to ensure the safety of the residents in the area. The soil in the region exhibits well-graded particle sizes, with a significant percentage of sand, providing good cohesion and friction angle results for the natural and submerged scenarios. These results are considered suitable for use in the stabilization of the slope.

Considering the favorable soil characteristics and the fact that the slope has sufficient space at the top and toe, along with a favorable height, it supports the feasibility of stabilizing the slope through the process of re-sloping, using the excavated soil itself as fill material. This solution allows for a more cost-effective construction.

In the project, the original slope was divided into two distinct slopes, separated by a 2-meter-wide berm. The profiles of the new slopes were reshaped to smooth the inclinations, adopting a 30-degree slope, with a width-to-height ratio of 2:1,15, as shown in Figure 6.

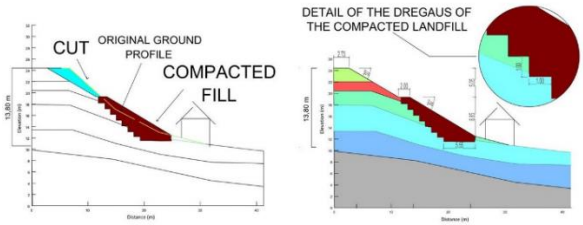

Figure 6. Re-sloping profile.

For the study, the parameters of the compacted fill from the sample taken from the slope were adopted and input into SLOPE/W (2022). Stability analysis was conducted in two scenarios: scenario 1, representing the conditions identified in the back analysis, and scenario 2, representing the natural soil conditions. This allowed the calculation of the safety factor using the analysis methods: Bishop, Fellenius, and Janbu, as shown in Table 3.

Table 3. Results of slope stabilization analysis.

Method	FS – Scenario 1	FS – Scenario 2
Bishop	1,46	1,80
Fellenius	1,62	1,77
Janbu	1,40	1,68
Average	1,49	1,75

The analysis results indicate that in all the scenarios considered, the Safety Factor (FS) found is higher than the minimum value recommended by NBR 11682 (ABNT, 2009) of 1,4. Therefore, it can be stated that the proposed re-sloping project complies with the criteria established by the standard.

To complement the stabilization through re-sloping, the implementation of vegetative cover and a surface drainage system was proposed. In this study, the use of Vetiver grass as a vegetative cover was chosen due to its rapid growth, especially in the Northeastern coastal region, as documented by Júnior (2019). Additionally, the design of the surface drainage system followed the recommendations of Institute of Technological Research-IPT (1991) with the aim of collecting and directing surface runoff water and part of the internal percolation water from the slope, as shown in Figure 7.

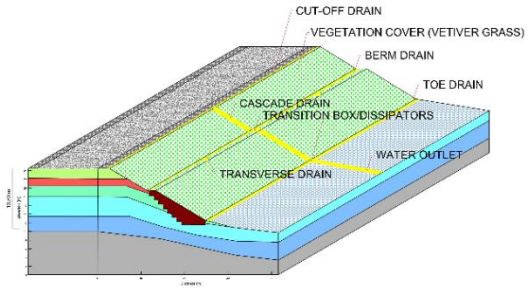

Figure 7. Isometric perspective view of the re-sloping project.

5 CONCLUSION

The results obtained indicate that the São José neighbourhood, located in João Pessoa, Paraíba, Brazil, is predominantly composed of substandard housing and individuals with low income per capita. This is further exacerbated by frequent landslides due to the following characteristics: extremely steep slopes, tree vegetation on the slope's crest, and constructions at the base of the slope. The soil in the region belongs to the Barreiras Formation, displaying well-graded particle sizes, a high percentage of sand, low plasticity, and satisfactory cohesion and friction angle.

The studied slope features an actively behaving crack, which moves seasonally during periods of high accumulated rainfall. Therefore, it is recommended to stabilize the slope through the re-sloping process, considering its technical and economic feasibility, complemented by vegetative cover and a surface drainage system. Consequently, this stabilization project should be promptly executed by the responsible authorities to prevent a disaster from occurring at the site.

REFERENCES

Alheiros, M, M.; *et al*. (2003). *Occupation Manual of the Hills of the Metropolitan Region of Recife,* FIDEM, Recife-PE, Brazil. ISBN 85-88632-04-7, (in Portuguese).

NBR 11682/2009 – Slope Stability. ABNT, Rio de Janeiro, Brazil, 33 p. ISBN 978-85-07-01702-8 (in Portuguese).

Filipeia (2023). *Municipal Atlas of João Pessoa,* online, Available at: https://filipeia.joaopessoa.pb.gov.br/, accessed: 30/March/2023, (in Portuguese).

Highland, L.M., and Bobrowsky, Peter. (2008). *The landslide handbook – A guide to understanding landslides,* USGS. Circular 1325, 129p. Reston, Virginia, U.S.A.

IBGE (2023). *Brazilian Institute of Geography and Statistics,* João Pessoa-PB, Brazil, (in Portuguese).

INMET (2023). National Institute of Meteorology, João Pessoa-PB, Brazil, (in Portuguese).

IPT (1991). *T Highway Slopes: guidance for diagnosis and solutions to their problems,* São Paulo, Brazil, (in Portuguese).

Lima, A. F. (2002). *Geomechanical behavior and stability analysis of a slope from the Barreiras Formation in the urban area of the city of Recife,* Master dissertation, UFPE, Recife-PE, Brazil, (in Portuguese).

Ministério das Cidades (2006). *Prevention of Landslide Risks on Slopes: Guide for the Elaboration of Municipal Policies*, Ler Comunicação, Brasília, Brazil, (in Portuguese).

Neto, M. V. S. (2018). *Containment Solution for a Landslide in the City of Serra Redonda – PB*, Undergraduate degree, UFPB, João Pessoa-PB, Brazil, (in Portuguese).

Ramos, A. V. F; Simões, G. K. S; Soares, F. L. (2022). Risk Mapping and Environmental Education in the Roger neighborhood in the city of João Pessoa, In: *VIII Conferência Brasileira sobre Estabilidade de Encostas*, Pernambuco, Brazil, V.3, pp. 237-244, (in Portuguese).

Silva, N. T. (2018). *The Rains in the Municipality of João Pessoa: Impacts, Risks, and Socio-environmental Vulnerability, Master dissertation,* UFPB, João Pessoa-PB, Brazil (in Portuguese).

Simões, G. K. S. (2023). *Landslide Risk Management in the City of João Pessoa-PB*. Undergraduate degree, Universidade Federal da Paraíba, João Pessoa-PB, Brazil, (in Portuguese).

GeoSudio (2022). Slope/W for slope stability analysis (2022.1), computer program. Available at: https://www.geoslope.com/, accessed: 15/ August /2023).

Bezerra, J. M. B. (2018) *Characterization of the Barreiras Formation in the City of João Pessoa Based on SPT Borings and Geotechnical Study of a Slope with High Risk of Landsliding*, Master dissertation, Universidade Federal de Pernambuco, Recife, Brazil, (in Portuguese).

Júnior, F. É. B. (2019) *Utilization of vetiver grass as a bioengineering solution for erosion control in Mata Redonda,* Undergraduate degree, UFPB, João Pessoa-PB, Brazil, (in Portuguese).

Soares, W. C. (2018) *Geological-Geotechnical Database Based on Percussion Borings and Use of GIS: Spatial Analysis of Water Table Depth and NSPT for Foundation Works in João Pessoa - PB*. PhD thesis, University of São Paulo, São Carlos, Brazil, (in Portuguese).

Proceedings of the XVIII ECSMGE 2024
GEOTECHNICAL ENGINEERING CHALLENGES
TO MEET CURRENT AND EMERGING NEEDS OF SOCIETY
© 2024 the Authors
ISBN 978-1-032-54816-6
DOI 10.1201/9781003431749-498
Open Access: www.taylorfrancis.com, CC BY-NC-ND 4.0 license

ECSMGE 24
XVIII EUROPEAN CONFERENCE ON SOIL MECHANICS AND GEOTECHNICAL ENGINEERING

Numerical modelling of shafts – comparison between SBE and EBS construction methods

Modélisation numérique des puits – comparaison entre les méthodes de construction SBE et EBS

L.M. Repsold*
COBA Group, Lisbon, Portugal

A.M.G. Pedro
University of Coimbra, ISISE, ARISE, Department of Civil Engineering, Coimbra, Portugal

J. Almeida e Sousa
University of Coimbra, Department of Civil Engineering, Coimbra, Portugal

**lucasrepsold@gmail.com*

ABSTRACT: The use of underground space in urban environment has increased considerably in recent years due to the construction of tunnels and underground stations. Shafts appear as one of the main structures associated with these works because they permit direct access to the underground. Generally, the shaft construction methods can be divided into two main categories: SBE – where the support is placed before excavation; and EBS – where the excavation is performed before the application of a support. Having as reference the case of the Shaft WA2, built as part of the Dublin Port Tunnel project, and excavated using the SBE method, this paper investigates the advantages and limitations of each construction method by performing a numerical study. After the calibration of the model based on the results of the instrumentation, the shaft excavation is alternately simulated using the EBS method. The comparison of the achieved results shows that although both methods have merits, the construction using the EBS method was probably the most adequate solution given the soil conditions at the site. In this particular case, the use of the EBS method would permit to employ a thinner support while keeping the deformations of the ground induced by the excavation at very small values.

RÉSUMÉ: L'utilisation de l'espace souterrain en milieu urbain a considérablement augmenté ces dernières années en raison de la construction de tunnels et de stations souterraines. Les puits apparaissent comme l'un des principaux ouvrages associés à ces ouvrages car ils permettent un accès direct au sous-sol. Généralement, les méthodes de construction de puits peuvent être divisées en deux catégories principales: SBE – où le support est placé avant l'excavation; et EBS – où l'excavation est réalisée avant l'application d'un support. Ayant comme référence le cas du puits WA2, construit dans le cadre du projet de tunnel du port de Dublin et creusé selon la méthode SBE, cet article étudie les avantages et les limites de chaque méthode de construction en réalisant une étude numérique. Après l'étalonnage du modèle sur la base des résultats de l'instrumentation, l'excavation du puits est simulée en alternance à l'aide de la méthode EBS. La comparaison des résultats obtenus montre que, même si les deux méthodes présentent des avantages, la construction selon la méthode EBS était probablement la solution la plus adéquate compte tenu des conditions du sol du site. Dans ce cas particulier, l'utilisation de la méthode EBS permettrait d'employer un support plus fin tout en gardant les déformations du sol induites par l'excavation à des valeurs très faibles.

Keywords: Shaft excavation; numerical modelling; construction method.

1 INTRODUCTION

The use of underground urban space has increased considerably due to the construction of tunnels and underground stations. In this context, shafts appeared as one of the main structures associated with this type of works because they permit direct access to the underground. Shaft excavation methods can be classified in two main groups: SBE (Support Before Excavation) – where the support, such as diaphragm walls, is installed prior to the excavation; and EBS (Excavation Before Support) – where the excavation is performed and only after the support, such as shotcrete, is installed. The analysis of case studies (Faustin et al., 2018) shows that, depending on the design requirements and site conditions one technique may be more applicable than the other. However, in some cases, it is not clear which one would be the most appropriate and there are few well-documented cases in the bibliography that discuss the impact of adopting a certain constructive method on the behaviour of

shafts. Having as reference the case of the Shaft WA2, built as part of the Dublin port tunnel project, this paper aims to evaluate through numerical analysis the advantages and limitations of adopting the abovementioned construction methods.

2 SHAFT WA2

The shaft WA2 was built in 2001 and served as a launching platform for the twin tunnel excavation of the Dublin Port Tunnel (DPT). The circular shaft with an internal diameter of 56.6 m has a depth of around 29.0 m and it was built following the SBE method, with the support being materialised by a 1.5 m-thick diaphragm wall. The depth of the wall varied slightly, but it was approximately 32.5 m, coinciding with the top of the bearing stratum, a Limestone layer. Beside the capping beam, a ring concrete beam with a section of 2.5x2.5 m^2 at the depth of 13 m was also executed. A 1 m-thick concrete base slab was built once the excavation reached its bottom. Figure 1 shows a photograph of shaft WA2 at the time of its completion where all the supporting structures can be seen.

Ground conditions at the site comprised the well-known Dublin boulder clays overlying a limestone layer. A complete description of the Dublin boulder clays can be found in Long & Menkiti (2007). At the site of shaft WA2, the Dublin Clays stratigraphy was composed of 2 m of the Upper Brown (UBrBC) layer, followed by the Upper Black (UBkBC) layer, which had a thickness of around 12 m. The third layer was the Lower Brown (LBrBC) layer, with a thickness of 11 m and, finally, the Lower Black (LBkBC) layer with 7.5 m thick was found. The stratigraphy and the shaft dimensions and support can be seen in Figure 2.

The performance of the shaft excavation was monitored by 9 inclinometers, which were installed inside the diaphragm wall panels.

3 MODELLING PROCEDURES

3.1 Dimensions and mesh

In order to simulate the shaft excavation, the finite element program RS2 was employed. All analyses were performed considering an axisymmetric model and a total stress condition given the nature of the materials simulated. Figure 3 presents the model adopted in the SBE analysis. A width of 200 m and a depth of 100 m were considered so that all stresses and deformations fields would not be influenced by the presence of the boundaries.



Figure 1. Shaft WA2 (Looby and Long, 2007).

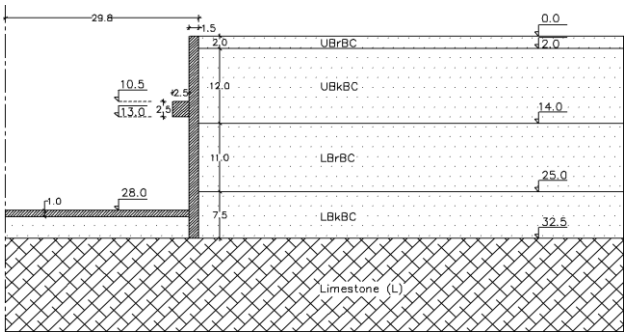

Figure 2. Stratigraphy and geometry of WA2 shaft.

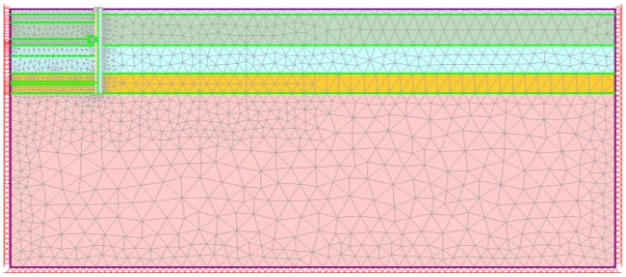

Figure 3. Mesh employed in the SBE numerical model.

The shaft dimensions, its support and ground profile were simulated accordingly with Figure 2. The mesh is constituted by isoparametric triangular finite elements with 6 nodal points and has a total of 1961 elements, with a refinement in the shaft vicinity. Boundary conditions were assumed as standard for axisymmetric conditions: free at surface, only vertical displacements allowed in the vertical boundaries and all movements restrained at the base of the model. Elastic interface elements were considered between the soil and the diaphragm wall so that relative movements could occur. The diaphragm wall was considered to be elastic while for the soil layers a linear elastic-perfectly plastic constitutive model with a Tresca failure criterium was adopted.

3.2 Construction sequence

The definition of the construction sequence followed the description presented by Cabarkapa et al. (2003), so that the obtained results could be compared against the inclinometer data. A total of 6 stages were considered in the SBE shaft excavation: 1) initial stress state, considering geostatic conditions and a K_0 profile; 2) installation of the diaphragm wall as

wished-in-place; 3) excavation up to a depth of 13m; 4) installation of the ring beam; 5) final excavation of the shaft to a depth of 29m; and 6) construction of the base slab.

3.3 Calibration of the numerical model

A class A prediction of the shaft performance was presented by Cabarkapa et al. (2003), where a coupled-consolidation analysis to simulate the short-term behaviour of the excavation was employed. The final horizontal displacements obtained by Cabarkapa et al. (2003) are presented in Figure 4. Superimposed in the figure are also the results of the inclinometers (and its envelope) to facilitate the comparison. The results show that both the trend and magnitude of the displacements are not correctly captured by the analyses, with the authors claiming that the parameters adopted for the materials at the design stage were very conservative and also justifying that the poor connection between the diaphragm panels permitted a cantilever deflection in the upper part of the shaft, which is not possible to simulate in the numerical model.

Having as reference the inclinometer data and also the extensive geotechnical characterisation on the Dublin boulder clays performed by Long & Menkiti (2007) and Long et al. (2013) a back analysis study was performed in order to calibrate appropriately the mechanical parameters of the Dublin boulder clay layers. The obtained final horizontal displacements are also presented in Figure 4, where it is possible to observe that, although the displacements near the surface are smaller than those measured at site, overall, a reasonable agreement, well within the inclinometer's envelope, is obtained. As mentioned previously it should be noted that with an axisymmetric model it is not possible to simulate the poor connection of the panels and therefore to improve the adjustment near the ground surface.

The parameters adopted as reference for the Dublin boulder clay layers in the analyses are presented in Table 1. For the structural elements (diaphragm wall, ring beam and base slab) a linear

Table 1. Soil parameters adopted in the analysis.

Material	γ (kN/m³)	S_u (kPa)	E_u (MPa)	ν	K_0
UBrBC	21	60	60	0.49	1.5
UBkBC	22.5	225	450	0.49	1.5
LBrBC	22	375	750	0.49	1.35
LBkBC	22.5	375	750	0.49	1.2
L	26	500	1000	0.3	1.0

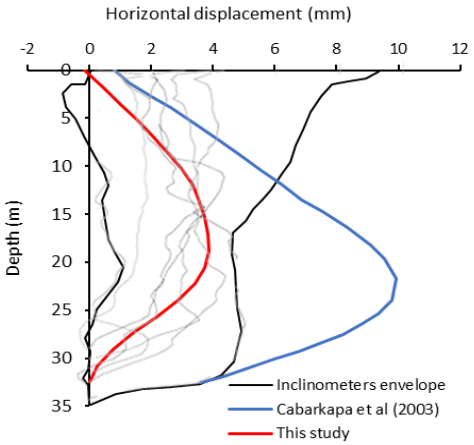

Figure 4. Calibration of the numerical model having as reference the inclinometer data.

elastic behaviour, characterised by a Young's modulus of 25 GPa, Poisson's ratio of 0.15 and unit weight of 25 kN/m³, was adopted. For the interface elements, an elastic model was assumed with normal and shear stiffness of 1×105 kPa/m and 1×104 kPa/m, respectively.

4 EBS SHAFT EXCAVATION

The EBS shaft excavation followed the typical principles of a sequential excavation. An excavation step of 2 m was adopted, which resulted in a total of 15 excavation stages until a depth of 29 m was reached (the last stage was only 1 m deep). Support for the excavation was provided by a shotcrete layer with a thickness of 0.5 m. For ease of comparison the parameters of the shotcrete were considered as equal as those of the diaphragm wall. In total, 31 stages were simulated in the EBS model. After the initial stress state, the first 2 m excavation step was performed followed by the installation of the shotcrete. These 2 stages were then repeated continuously until the bottom of the excavation was reached and the base slab installed.

5 COMPARISON OF THE RESULTS

The comparison between the main results obtained for the final stage of the excavation of the SBE and EBS models is presented in Figure 5. Although the horizontal displacements (a) obtained with the EBS model show a similar trend to the displacements obtained from the SBE, they are considerably higher as a consequence of the soil decompression which is inherent to the unsupported excavation performed. Is also interesting to verify that, had the excavation been performed without support (blue line) the horizontal

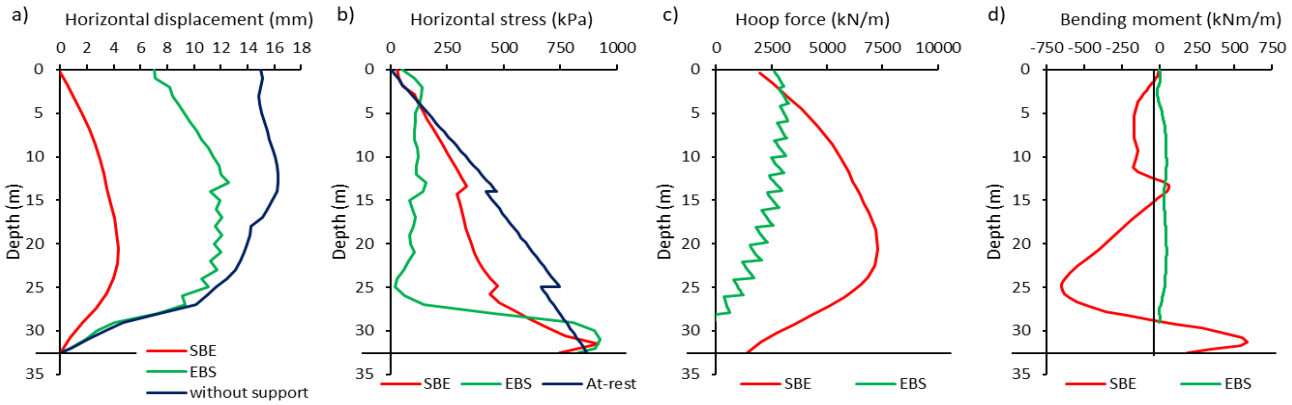

Figure 5. Comparison between the SBE and EBS methods: a) horizontal displacement; b) horizontal stress; c) hoop force; d) bending moment.

displacements would have been only slightly larger than those observed in the EBS model, implying that the ground strength is very high. Nevertheless, given that the overall movements do not surpass 16mm they can be considered very small. The results of the horizontal stress (b) are in agreement with the horizontal movements with the EBS model showing a much smaller final stress as consequence of the soil decompression. In the SBE a much smaller soil decompression is observed with the horizontal stress values being much closer to those adopted in the initial stress state. The structural forces in the diaphragm / shotcrete wall show that with SBE methodology much higher forces, both hoop (c) and bending moments (d) are to be expected. Those come as consequence of small reduction of horizontal stresses that are allowed due to the installation of the diaphragm wall before the beginning of the excavation.

6 CONCLUSIONS

Having as reference the case of the WA2 shaft in Dublin the following conclusions can be drawn:

- A SBE construction reduces considerably the decompression of the ground during the excavation process, which results in very small deformations. As a result, this method is ideal to minimize the impact of shaft excavation on nearby infrastructure. However, since the soil decompression is not allowed, the forces in the support, both hoop and bending moments, are expected to be very high and demand a robust support;
- The almost exact opposite was observed in the EBS model, where the excavation without support allowed for a maximum soil decompression, which resulted in higher horizontal movements but much smaller horizontal stresses and structural forces;
- Based on the achieved results for the case of WA2 shaft, the application of the EBS method would be feasible and highly competitive, as it would allow to considerably reduce the volume of materials used and the execution time, without significantly increasing the ground deformations or compromising the shaft stability.

  It should be noted that these conclusions relate to the specific case of the WA2 shaft and should not be directly generalised to other projects where the geotechnical conditions would be different.

REFERENCES

Cabarkapa, Z., Milligan, G. W. E., Menkiti, C. O., Murphy, J. & Potts, D. M. (2003) Design and performance of a large diameter shaft in Dublin Boulder Clay. In *Proceedings of the BGA International Conference on Foundations: Innovations, observations, design and practice, Dundee, UK.* Newson, T. (ed.), Thomas Telford, London, UK, pp. 175-185.

Faustin, N. E., Elshafie, M. Z. E. B. & Mair, R. J. (2018) Case studies of circular shaft construction in London. *Proceedings of the Institution of Civil Engineers-Geotechnical Engineering*, 171 (5), pp. 391-404. https://doi.org/10.1680/jgeen.17.00166.

Long, M. & Menkiti, C. O. (2007) Geotechnical properties of Dublin boulder clay. *Geotechnique*, 57 (7), pp. 595-611. https://doi.org/10.1680/geot.2007.57.7.595.

Long, M., Quigley, P. & O'Connor, P. (2013) Undrained shear strength and stiffness of lrish glacial till from shear wave velocity. *Ground Engineering*, pp. 26-27.

Looby, M. & Long, M. (2007) Deep excavations in Dublin recent developments. *Meeting of the Geotechnical Society of Ireland at Engineers Ireland, 11 December 2007, Engineers Ireland, Dublin*. pp. 1-15.

Proceedings of the XVIII ECSMGE 2024
GEOTECHNICAL ENGINEERING CHALLENGES
TO MEET CURRENT AND EMERGING NEEDS OF SOCIETY
© 2024 the Authors
ISBN 978-1-032-54816-6
DOI 10.1201/9781003431749-499
Open Access: www.taylorfrancis.com, CC BY-NC-ND 4.0 license

ECSMGE 24
XVIII EUROPEAN CONFERENCE ON SOIL MECHANICS AND GEOTECHNICAL ENGINEERING

Cost effective & sustainable solutions for embankments on soft soils - performance review of geocells in embankment

Solutions rentables et durables pour les remblais sur sols meubles - évaluation des performances des géocellules dans les remblais

K.A. Ria Zamara*
Tensar International Ltd, Blackburn, United Kingdom

J. Kawalec
Silesian University of Technology, Gliwice, Poland

M. Wayne
Tensar International Corp., Alpharetta, USA

**Kasia.Zamara@cmc.com*

ABSTRACT: Geosynthetic solutions offer sustainable alternatives, delivering long-lasting, stable embankment foundations that are easier and faster to build compared to traditional methods, reducing not only construction time and costs but also contribute to carbon footprint savings. This publication describes cellular foundation mattresses technology called Stratum that consists of 1m high bespoke geocell structure, as described in BS 8006-1: 2010. This solution has been utilised on infrastructure projects such rail and highways, acting as embankments foundations. This paper presents a case study of a highway embankment built in 1990s and is supplemented by recently obtained information on the performance of a road embankment after 30 years from its installation. This example proves the long tracked record of 1m high, bespoke geocell mattresses economical advantage over the alternative traditional solutions. 1m high geocells offer reduction of excavation volumes of unsuitable soils that typically would be replaced with engineered fill, or remove the need for piling works, delivering solutions without compromising on performance.

RÉSUMÉ: Les solutions géosynthétiques offrent des alternatives durables, fournissant des fondations de remblai durables et stables, plus faciles et plus rapides à construire par rapport aux méthodes traditionnelles, réduisant non seulement le temps et les coûts de construction, mais contribuant également à la réduction de l'empreinte carbone. Cette publication décrit la technologie de matelas de fondation cellulaire appelée Stratum qui consiste en une structure géocellulaire sur mesure de 1 m de haut, comme décrit dans la norme BS 8006-1: 2010. Cette solution a été utilisée sur des projets d'infrastructure tels que les chemins de fer et les autoroutes, agissant comme fondations de remblais. Cet article présente une étude de cas d'un remblai routier construit dans les années 1990 et est complété par des informations récemment obtenues sur la performance d'un remblai routier 30 ans après son installation. Cet exemple prouve l'avantage économique des matelas géocellulaires sur mesure de 1 m de haut par rapport aux solutions traditionnelles alternatives. Les géocellules de 1 m de haut permettent de réduire les volumes d'excavation de sols inappropriés qui seraient généralement remplacés par des remblais techniques, ou suppriment le besoin de travaux sur pilotis, offrant ainsi des solutions sans compromettre les performances.

Keywords: Geomattress; embankments; soft soils; monitoring instrumentation.

1 INTRODUCTION

Embankments are a key feature of many infrastructure projects such highways, railways or flood defence schemes. It is vital that these structures are built on firm and stable foundations ensuring minimal maintenance required over their service life. This can be challenging when dealing with weak, variable and saturated subgrade soils. Traditional solution for construction of foundation embankments, involve digging and replacing soft deposits with engineered fill, piling an embankment or to utilising other deep ground improvement methods such as, e.g.: vibro concrete, stone columns, dynamic compaction, deep ground mixing, load transfer platforms etc. These approaches are technically valid, but they are also expensive, time consuming, heavy on carbon footprint and often involve extensive temporary works.

A 1m high, bespoke geocell foundation mattresses, as defined by BS 8006-1 (2010) constructed using uniaxial geogrids (Figure 1), offers a cost-effective solution alternative to the traditional methods.

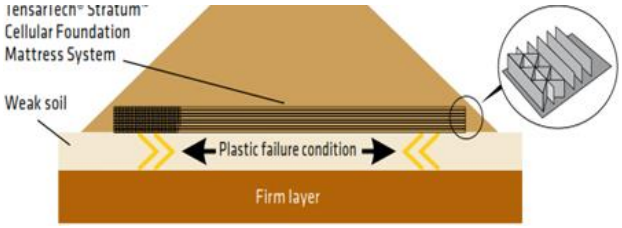

Figure 1. Typical section through embankment constructed on Cellular Foundation Mattress System.

To the Authors's knowledge the technology is still relatively uncommon and underutilised. Kuznietzowa and Doulala-Rigby (2015) and Pyne (1993) present cost comparison between this and alternative technologies that is based on site efficiencies and production costs. This shows already considerable advantage of geosynthetic solution over the alternative methods. However, these do not consider additional savings due to programme time reductions or more importantly carbon footprint reductions that geosynthetic solutions offer (Rimoldi et al. 2021).

Geocell mattress technology involves construction of a three dimensional, typically 1m high, honeycombed structure on site using uniaxial geogrids that form interlocking cells (Figure 1). These get filled with suitable aggregate and form foundation of the embankment (or are used for temporary working platforms construction).

Embankments built on geocell mattresses are characterized by an even distribution of typically heterogeneous settlements (e.g. Pyne 1993, Jenner et al. 2008, Lees et al. 2020). The mattress built into the base of an embankment creates a stiffened platform, which allows an application of higher loads directly on the mattress, and the stresses transmitted by the mattress are distributed over a larger area, reducing unit stresses acting directly on the base. BS 8006-1: 2010 presents an analytical method of calculating the bearing capacity of embankments reinforced with geocell mattresses on cohesive soils.

The method presented in BS 8006-1 (2010) and described in more detail in Jenner et al (1988) is based on the conditions of plastic deformation of the substrate under a wide embankment. The bearing capacity resulting from the slip line analysis should be compared with the additional stresses resulting from the installation of the embankment and its weight in order to estimate the safety factor and check if the equilibrium condition is met.

It should be noted that this method does not apply to geosynthetics of smaller dimensions (so-called geocells 0.15 m to 0.3 m high). The method applies to geomattresses that reach at least 0.5 m in height, but more typically 1 m or 1.2 m height. The method allows to estimate bearing capacity of the mattress, as well as to select the appropriate type of a uniaxial geogrid from which the mattress will be constructed.

Whilst utilisation of cellular foundation mattresses on projects globally is not widespread, there exists a lot of evidence of their performance, in a variety of applications, e.g.: embankments (Jenner et al. 2008), temporary working platforms (Lees et al. 2020) and shallow foundations for steel structure - warehouse (Duffin and Jenner 2000).

2 CASE STUDY: DARTFORD HIGHWAY EMBANKMENT 1992 (UK)

The current records of the project are scarce, however, the site of Dartford Highway Embankment was monitored and information about the historical project details were reported by Payne (1993). In addition, Payne (1993) described the design and construction stages of the embankment built at Dartford, UK, in 1992 (East London).

To summarise, the embankment was built using geocell mattresses technology. In addition, prefabricated vertical drains at 1.5 m intervals (in a triangular grid) were used to accelerate the process of consolidation under the embankment. The embankment was 4.3 m high, the width in the crest was 27 m to accommodate the total of 4 lanes (2 in each direction). The length of the section of the embankment on the weak subsoil was 350 m. The site geology was dominated by alluvial deposits of the Thames River, which flows in the immediate vicinity of the embankment. This also resulted in a high level of groundwater table in the subsoil. The layer of plastic clay was 10 m deep with subsurface interlayer of peat (Figure 2). The subsoil was characterized by an undrained shear strength Su value of 10 kPa, although in some areas this was considered an overestimated assumption and the actual value of Su was in the range 4.5 – 8 kPa (Pyne 1993).

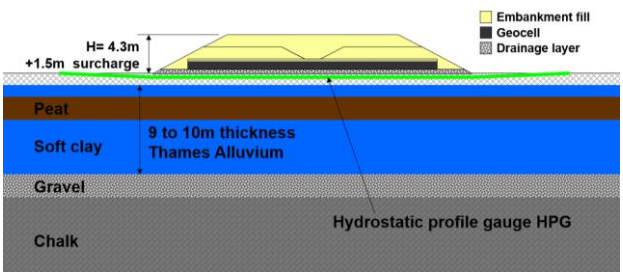

Figure 2. Geological setting of the Dartford road embankment (source Jenner et al. 2008).

The designed solution for this project took advantage of the rigid bespoke 1m high geocell foundation mattresses ensuring even load distribution

over weak soils in the sub-base. All four lanes of the roadway were constructed on one mattress.

Embankment deformation was monitored at the level between the mattress and the subsoil. The profile of vertical displacement (Figure 3) showed a very even settlement across the embankment with a mattress providing load distribution and control necessary to achieve the required bearing capacity and stability of the embankment. Figure 3 shows the values of settlement during construction and embankment overload. Settlement over time is clearly visible, with a very even deformation over the entire width of the base of the embankment and very limited differential settlement across the embankment. This is an essential feature considering long term use of the efficient, economical and durable structure. The monitoring confirms the assumptions of the cellular mattress technology, which refer to the creation of a semi rigid foundation structure at the base of the embankment that allows uniform settlements at the base of the embankment.

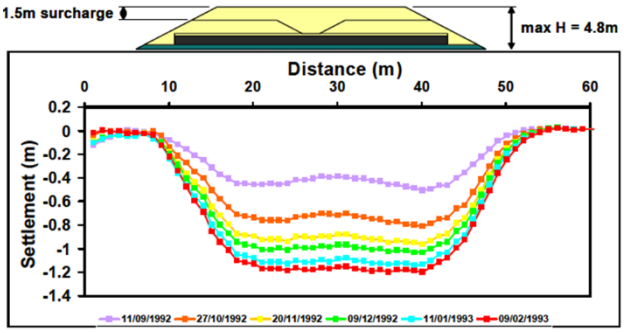

Figure 3. Settlements records under the embankment with time (source Jenner et al. 2008).

3 CURRENT STATE OF THE EMBANKMENT

Up to date quantitative data on the embankment performance are not available, however, the authors of this paper investigated the qualitative in-service performance of the embankment during a recent site visit. The authors interviewed the local road maintenance contractor who has been engaged with resurfacing works on the relevant section of the road by the local County Council. The following remarks and statements were collected from the contractor:

- There has been no major works undertaken on the embankment after its installation,
- The only works undertaken on the section, were the scheduled cyclic resurfacing maintenance works,
- Major resurfacing works took place in late 2000s, there was no need for major restorations to the structure of the embankment,
- No works related to kerbs alignments were needed, as all of them were in place with no noticeable horizontal or vertical displacements,
- No works related to manholes and drains relating to embankment settlement took place.

Moreover, during the site visit by the authors, the examination of the road and photo records (Figure 4 & 5) were collected, as a part of the evidence to support the Contractor's statement. Whilst no quantitative data is available to assess scientifically the performance of the embankment 30 years after its installation, the above statements are satisfying and the site visit with the surface examination confirmed long term performance of geocell mattresses under highway embankments from the user and owner perspective. It is evident that the majority of the settlements of the embankment occurred during the first months after the installation (Figure 3). Following that the embankment remained stable with not recorded differential settlements or stability problems that would cause issues to the asset owner or maintenance contractor.



Figure 4. Current photos of the embankment showing high water table – water ponds in close vicinity of the embankment (on Thames River side).



Figure 5. Current photo of the embankment: Pavement and footpath photo showing smooth, even surface.

The mechanism of the reduction of subsidence (with vs without cellular foundation mattresses), however, is not yet sufficiently well understood to be able to accurately estimate the reduction of subsidence at the design stage. Typically, settlements should be monitored during the project implementation by installing measuring instruments that verify the results and assumptions of the project. Recent publication of a project back analysis using numerical modelling approaches, advance the understanding and predictions made for serviceability limit state where settlements and differential settlements reductions of the cellular mattresses solution can be quantitatively estimated (Lees et al 2020).

4 CONCLUSIONS

Cellular foundation mattresses comprise a cost-effective and carbon footprint saving alternative to more traditional ground improvement technologies. Dartford embankment shows an example where after 30 years from embankment installation on extremely soft grounds, no issues with the solution was recorded. The technology is versatile it can offer the asset owner or contractor multiple benefits:

- Provides significant carbon reductions compared with any other ground deep improvement methods
- Can be installed on most types of weak or heterogeneous soils (as well as in municipal landfills, i.e. Duffin and Jenner (2000),
- Eliminates or limits the need for excavation, as it is a trenchless solution, performed directly on the existing ground. This allows the work to be carried out without damaging the natural structure of the substrate,
- Requires a short time of execution and implementation - proper arrangement of geogrids and filling the cells is not a time-consuming task, an additional advantage is the fact that geocell mattresses are part of the embankment. The construction of the cellular foundation mattresses is therefore a phase in the construction of the embankment, which reduces the time needed to build the entire embankment,
- Does not require specialised workforce - installation of geocells is very simple, there is no need to use special construction machines. Typical earthmoving construction machines are sufficient to properly install a geocells in the ground,
- Can be installed in conjunction with prefabricated vertical drains accelerating the consolidation of the substrate.

Cellular foundation mattresses reduce uneven settlement as well as contribute to the reduction of total settlement. More research and construction of structures with long term monitoring will be beneficial to advance the knowledge on the mechanisms of the cellular foundation mattresses performance.

REFERENCES

BSI (2010). BS8006-1: 2010, Code of practice for strengthened/reinforced soils and other fills. British Standard Institution.

Duffin, J.P. & Jenner, C. (2000). Elstow waste transfer station: The application of a geocell for building foundations on a landfill site. *Proceedings of EuroGeo Conference 2000*.

Jenner CG, Bush DI, Basset RH. (1988). The use of slip line fields to assess the improvement in bearing capacity of soft ground given by a cellular foundation mattress installed at the base of an embankment. *Proceedings of International Geotechnical Symposium on Theory and Practice of Earth Reinforcement*, Fukoka, Japan 5-7 October 1988.

Jenner, C.G., Turnic, L., Baslik, R. (2008). Use of Cellural Geocell Mattresses As Embankment Foundations. Foundations: *Proceedings of the Second BGA International Conference on Foundations, ICOF2008*.

Kuznetsova, A & Doulala-Rigby C. (2015). C. The construction of a 12m high embankment over weak soils in St Petersburg, Russia, utilizing the use of a cellular foundation mattress system. *The News of EEEGM*, 96, 13-16.

Lees, A., Dobie, M., Bhawanin, M. (2020). Back-analysis of the Vung Tau full-scale trial using FEA simulation of geogrid stabilization and the geocell mattress. *Geotechnics for Sustainable Infrastructure Development*. Lecture Notes in Civil Engineering 62, January 2020.

Payne, I.R. (1993). Building a Dartford road embankment on jelly. *Highways and Transportation*, December 1993.

Rimoldi, P., Shamrock, J., Kawalec, J., Touze, M., (2021). *Sustainable Use of Geosynthetics in Dykes*. Sustainability 13(8):4445.

Proceedings of the XVIII ECSMGE 2024
GEOTECHNICAL ENGINEERING CHALLENGES
TO MEET CURRENT AND EMERGING NEEDS OF SOCIETY
© 2024 the Authors
ISBN 978-1-032-54816-6
DOI 10.1201/9781003431749-500
Open Access: www.taylorfrancis.com, CC BY-NC-ND 4.0 license

ECSMGE 24
XVIII EUROPEAN CONFERENCE ON SOIL MECHANICS AND GEOTECHNICAL ENGINEERING

Geotechnical challenges of excavating the deepest metro station in Lisbon - Estrela station

Défis géotechniques pour creuser la station de métro la plus profonde de Lisbonne - station Estrela

V. Ribeiro*, J.E. Simões, J.C. Andrade
CJC Engenharia e Projetos Ltda, Brazil

N. Vaz, P. Araújo, O. Marques
Zagope Construção e Engenharia SA, Portugal

**vasco.ribeiro@cjceng.com.br*

ABSTRACT: As part of the future circular line of the Lisbon Metro System, Estrela Station stands out for being the deepest in the network, with a depth of around 60m. Excavated using the NATM methodology from a shaft with quadrangular and circular sections in Miocene and Cretaceous limestone, it posed challenges inherent to this type of work due to its section size, geological singularities or the need to increase productivity. Production was optimized with the excavation of a pilot tunnel from the T33 track tunnel in order to have another front for debris extraction and also serving for geological reconnaissance. Intercepted rock faults, recognized or not in the previous design phases, were addressed in order to mitigate excessive deformations or even potential instabilities. The presence of the second unit of the "Caneças Formation" in the lower section of the station chamber, of a more marl-clayey nature and potentially more deformable, led to the adoption of complementary support solutions foreseen in the project, as well as specific reinforcements.

RÉSUMÉ: Faisant partie de la future ligne circulaire du métro de Lisbonne, la station Estrela se distingue pour être la plus profonde du réseau, avec une profondeur d'environ 60 mètres. Creusée selon la méthodologie NATM à partir d'un puits à sections quadrangulaires et circulaires dans des calcaires du Miocène et du Crétacé, elle posait des défis inhérents à ce type de travaux en raison de la taille de ses sections, des singularités géologiques ou de la nécessité d'augmenter la productivité. La production a été optimisée avec le creusement d'un tunnel pilote à partir du tunnel ferroviaire T33 afin de disposer d'un autre front d'extraction des débris, partialisant la demi-tronçon et servant également à la reconnaissance géologique. Les failles interceptées dans le massif, reconnues ou non lors des phases de conception précédentes, ont été considérées afin d'atténuer les déformations excessives voire les instabilités potentielles. La présence de la deuxième unité de la « Formation Caneças » dans la partie inférieure de la chambre de la station, de nature plus marne-argileuse et potentiellement plus déformable, a conduit à l'adoption de solutions complémentaires prévues dans le projet, ainsi que de solutions de renforcement spécifiques.

Keywords: NATM; shaft; underground station; deepest Lisbon metro station.

1 INTRODUCTION

The newest Lisbon Metro expansion unites the existing Rato and Cais do Sodré stations from the yellow and green lines, respectively, forming a close ring line. This paper refers to Lot 1 with an extension of 1320m, which includes, the Estrela Station, the T33 and T34 double track tunnels (figure 1). Due to the surface level and the track slope limits, the station had to be located approximately 60 meters below surface, which presented some challenges.

The circular section shaft and the station as whole were excavated and monitored using the principles of NATM.

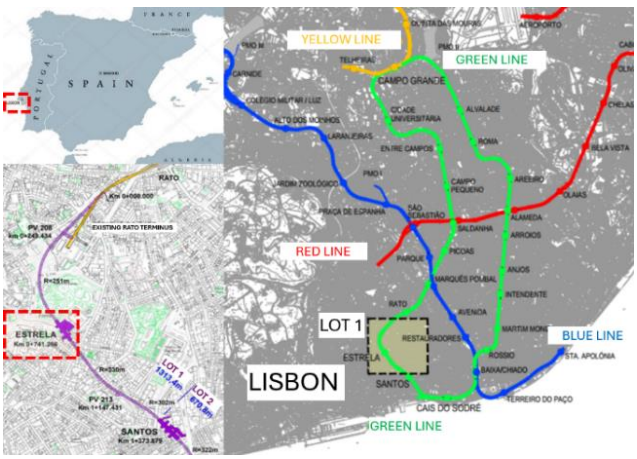

Figure 1. Estrela Station location map.

2 GEOLOGICAL AND GEOTECHNICAL FEATURES OF THE SITE

In the Estrela station area, the geology and geotechnical parameters were previously well known, complemented by a specific survey and in situ and laboratory tests during design phase. Three units were identified with different lithologies and geotechnical parameters (2021a) as shown in figure 2:

-Landfills, with little expression;

-Miocene of Lisbon, namely clays and calcarenites;

-Upper Cretaceous formations having very varied deformability and resistances. Caneças Formation, the lowermost, is characterized by limestones, marls and clays, thus with a wide range in compressive strength and deformability. This formation was intersected at the shaft base and at the northernmost station section. The circular shaft and the station gallery were built within the 40m thick Bica Formation, made of crystalline limestones with high strength and low deformability. All these formations have a 15º tilt to southeast.

Underground water was almost absent and restricted to a level in the Miocene and to sporadic vertical infiltrations in the cretaceous limestones.

Symbology	Formation	Depth (m)	Lithology
Landfill		0-2.0	Landfill, dark brown silty clay with lithic and ceramic fragments
M_{ag}	Prazeres Fm.	2.0-3.4	Brown to grey silty-marly clay, with hardened shell layers.
M_{cal}		3.4-13.0	White to yellowish marly limestone, with levels of calcarenites, somewhat vacuolar.
C_{c1b}	Bica Fm.	13.0-18.2	Yellowish nodular limestone with marls.
C_{c1c}		18.2-25.4	Whitish and very fractured and weathered limestone.
C_{c1c}		25.4-40.0	Yellowish crystalline limestone, very weathered, fractured and slightly karstified.
C_{c1d}		40.0-52.1	Whitish to yellowish compact limestone with veins, weathered and fractured.
C_{c2a}	Caneças Fm.	52.1-60.2	Weathered and fractured marly limestone, with dark gray clay.
C_{c2b}		52.1-68.3	Weathered and fractured marly limestone, with dark gray clay.

Figure 2. Geological-geotechnical profile (M- Miocene; C – Cretaceous).

3 DESIGN FEATURES

The preliminary design defined the need to install the station shaft in a restricted space, limited by buildings and without occupying public roads (figure 3).

Its first level has a square section with dimensions of ~32x32m^2, and containment walls made up of 57 piles with 800mm diameter. On the sides facing the existing buildings, 126 micro piles with 280mm diameter were used, reinforced with HEA160 steel beams. Depending on the height of the containment, between two and four anchoring levels were installed, with variable lengths and net working loads between 365 and 635kN. Their lower section is inbeded in the limestones and locked by a reinforced concrete transition slab to the top of the circular shaft.

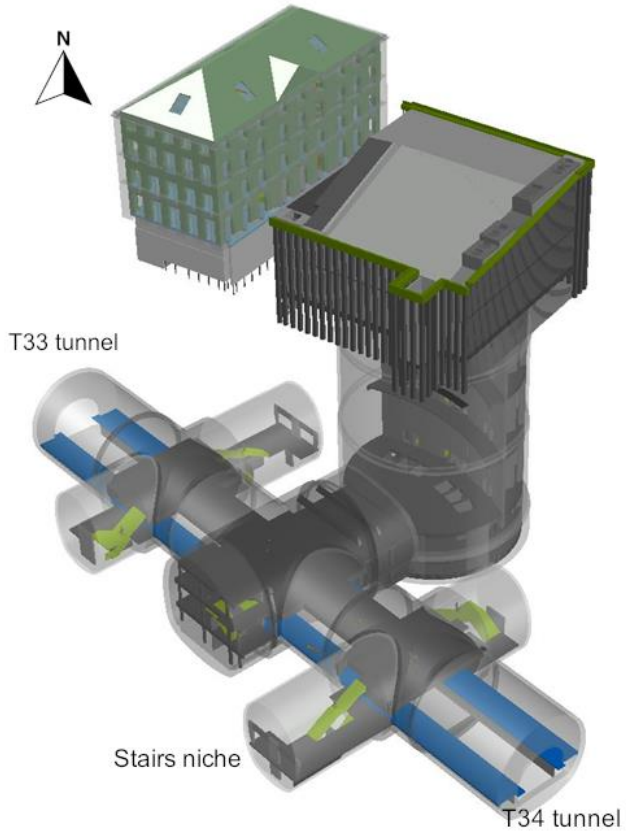

Figure 3. Estrela Station 3D model.

With a diameter of ~30 meters and a stepped and progressivelly larger section in depth, the primary lining of the circular section shaft is 0.20m to 0.30m thick, consisting of shotcrete and double wire mesh. This was complemented by a mesh of 4.0m long Swellex PM12 rockbolts and occasional 2.0m long geodrains. The advance depth was initially 0.90m, increasing to 2.10m, divided into eight segments, or panels, of the perimeter.



Figure 4. Transition between the square and circular section shafts.

A transversal gallery connects the circular shaft to the station main gallery which is 104m long, 15m high and 16m wide with a total section varying between 220 and 223m2. Four transversal niches accommodate stairs and elevators.


Figure 5. Upper piled wall with temporary ground anchors.

The presence of too closed existing buildings in two sides of the shaft required the use of micro piles with 260mm diameter reinforced with HEB160 steel beams instead of typical 800mm piles. The transition to the circular section shaft was made with a transition concrete slab as illustrated in the following figures.


Figure 6. Piled retaining wall and the transition slab to the circular section shaft.


Figure 7. Micro pile retaining wall and beginning of excavation of circular section shaft.

4 SPECIAL OCCURENCES

As the shaft excavation rate was slower than expected, due to limestone with high compressive strength, and as the T33 double track tunnel reached the station face early on, it was studied a smaller section pilot tunnel (figure 8) to attack the station top head section from the double track tunnel. Thus, a considerable volume of rock could be retrieved earlier, leading to an output increase, but also there was the opportunity to make extra geologic mapping since a major fault was a possibility inside the northern station section, as foreseen in the project.



Figure 8. Pilot tunnel section against the station top heading section.

In the south section, an unexpected fault (figure 9), with a *terra rossa* infill, promoted some instability leading to adoption of local reinforcement with extra rockbolts, mesh and shotcrete to smooth the gap. In the falt zone, the transversal niches were also reinforced with longer and less spaced forepoles.



Figure 9. Fault materialized by the reddish-brown clay.

In the station northern section, not only a fault was considered to occur, but also the lower part of the Caneças Formation, with fine bedded grey marls and clays. As the fault was not confirmed during the pilot tunnel survey - it occurred in the final meters of the T33 tunnel- the primary lining that consisted of 0.30m thick lattice girders, shotcrete and, in the bench section, of 6m long Swellex PM16 rockbolts, was maintained.

The Caneças Formation, although dry, were found at the invert level to the middle of the station, and in the bottom of the shaft. This led the designer to request the increase in the reinforcements at the interface with the limestones. These consisted of two lines of 12m long, 25mm diameter steel bars grouted in a 78mm diameter bore with a 30º downward attitude.



Figure 10. Lattice girders extensions at bench height, were the limestone-clay transition is clearly visible.



Figure 11. Southern station section showing in the middle the double track tunnel and side niches for the stairs and elevators.

5 CONCLUSIONS

The executed project was delivered according to expectations, without major issues. We should note that in this kind of underground works underneath urban areas, there are always some uncertainties concerning the rock mass quality, geologic fault occurrences or underground water behaviour, mainly in long tunnels where survey is, sometimes, very spaced with major gaps in between. The few unexpected conditions were addressed by the designer, the designer representative on site and the contractor to successfully adapt the project.

ACKNOWLEDGEMENTS

We would like to acknowledge the Metropolitano de Lisboa, E.P.E and, in particular, to Mr. Rui Pina.

REFERENCES

CJC Engenharia e Projetos, Ltda (2021a). Estudo Geológico e Geotécnico, Projeto de execução da empreitada de projeto e construção dos toscos no âmbito da concretização do plano de expansão do Metropolitano de Lisboa prolongamento das linhas amarela e verde (Rato-Cais do sodré) lote 1: Execução dos toscos entre o término da Estação Rato e a Estação Santos, do pk 0+000 ao pk 1+319,729, Geological and Geotechnical Report, as part of the implementation of the expansion plan for the Lisbon Metro, extension of the Yellow and Green lines (Rato-Cais do Sodré) lot 1: Execution of the civil works between the end of the Rato Station and Santos Station from km 0+000 to km 1+319,729, São Paulo, Brasil (in Portuguese).

CJC Engenharia e Projetos, Ltda (2021b). Projeto de execução da empreitada de projeto e construção dos toscos no âmbito da concretização do plano de expansão do Metropolitano de Lisboa prolongamento das linhas amarela e verde (Rato-Cais do Sodré) lote 1: Execução dos toscos entre o término da Estação Rato e a Estação Santos, do pk 0+000 ao pk 1+319,729. Design and built construction contract for the civil works as part of the implementation of the expansion plan for the Lisbon Metro, extending the Yellow and Green lines (Rato-Cais do Sodré) lot 1: Execution of the civil works between the end of the Rato Station and Santos Station, from km 0+000 to km 1+319,729, São Paulo, Brazil(in Portuguese).

Proceedings of the XVIII ECSMGE 2024
GEOTECHNICAL ENGINEERING CHALLENGES
TO MEET CURRENT AND EMERGING NEEDS OF SOCIETY
© 2024 the Authors
ISBN 978-1-032-54816-6
DOI 10.1201/9781003431749-501
Open Access: www.taylorfrancis.com, CC BY-NC-ND 4.0 license

ECSMGE 24
XVIII EUROPEAN CONFERENCE ON SOIL MECHANICS AND GEOTECHNICAL ENGINEERING

From design to the construction – the case of the track tunnels T33 and T34 between Rato and Santos of the future circular line of Lisbon metro

Du projet à la construction – le cas des tunnels T33 et T34 entre Rato et Santos de la future ligne circulaire du métro de Lisbonne

V. Ribeiro*, J.C. Andrade, J. Simões
CJC Engenharia e Projetos Ltda, São Paulo, Brazil

O. Marques, P. Araújo, N. Vaz
Zagope Construção e Engenharia SA

**vasco.ribeiro@cjceng.com.br*

ABSTRACT: The extension of the Yellow Line of the Lisbon Metro between Rato and Santos Stations, to be integrated into the future circular line, included the creation of the 60m deep Estrela Station, a ventilation shaft and two new track tunnels executed with the NATM methodology. The construction solutions foreseen in the design phase, the monitoring and Special Technical Assistance to the construction, the analysis of the instrumentation and the additional measures adopted in the execution of about 1300m of tunnel in Cretaceous calcareous rocks, with a maximum cover of 50m, are addressed. The waterproofing works, the secondary lining execution in the terminus track tunnel which had the unique feature of having a variable section, the excavation of marls and clays from the Caneças Formation and the final stretch of the T34 tunnel partially excavated in tuffs and basalts of the Lisbon's Volcanic Complex are highlighted.

RÉSUMÉ: L'extension de la Ligne Jaune du métro de Lisbonne entre les stations Rato et Santos, à intégrer dans la future ligne circulaire, a prévu la création de la station Estrela de 60 m de profondeur, un puits de ventilation et 2 nouveaux tunnels de voie exécutés avec la méthodologie NATM. Les solutions constructives prévues dans la phase de projet, le suivi et l'Assistance Technique Spéciale à la construction, l'analyse de l'instrumentation et les mesures complémentaires adoptées dans l'exécution d'environ 1300 m de tunnel dans le massif calcaire du Crétacé, avec une couverture maximale de 50 m, sont adressées. Sont soulignés les travaux d'étanchéité, l'exécution du revêtement secondaire du tunnel de la voie terminus avec section d'élargissement, l'excavation des marnes et argiles de la Formation de Caneças et le tronçon final du tunnel T34 partiellement creusé dans tufs et basaltes du Complexe Volcanique de Lisbonne.

Keywords: NATM; rock excavation; monitoring; technical assistance.

1 INTRODUCTION

Sections T33 and T34 of the Lisbon Metro are double-track tunnels, included in the Design and Construction Contract for the Lisbon Metro Expansion Plan – Extension of the Yellow and Green Lines (Rato – Cais do Sodré), more specifically in Lot 1 – Execution of civil works between the end of Rato Station and Santos Station, from km 0+000 to km 1+319,729.

This extension aims to better serve the southern area of Lisbon's metropolitan network and extends in a N-S corridor, connecting Marquês de Pombal and the riverside area of Lisbon at Cais do Sodré, starting at the Rato Terminus on the Yellow Line (Figure 1). When completed, this expansion will form the Circular Line connecting the Green to Yellow line.

This connection solution between the two lines – Yellow and Green – will improve mobility in the central area of the city of Lisbon.

2 GEOLOGY

From top to bottom, the following formations occur (CJC 2021a):

- Landfills - Silty clay, sometimes with blocks, resulting from intense human activity;
- Miocene of Lisbon, namely clays and calcarenites;
- Lisbon Volcanic Complex - Formation of a volcano-sedimentary nature, not always

present, consisting of basalt flows with alternating deposition of clayey volcanic tuffs;

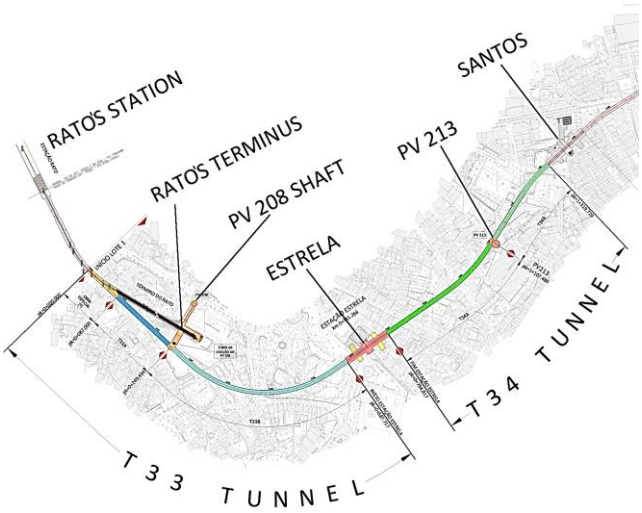

Figure 1. Lisbon Metro Lot 1 extension.

- Upper Cretaceous Bica Formation, with crystalline limestones, sometimes karsified, very permeable and generally dry. Caneças Formation, the lowermost unit, consists of limestones, marls and clay (figure 2).

In the T33 double track tunnel, groundwater was limited to vertical infiltrations in cretaceous limestones settling at first impermeable layers. In the T34 final hundred meters, the water table was found at level 1.20 m with high productivity occurring in a very karsified layer.



Figure 2. Lowermost Caneças formation with limestones, marls and fine layers of clays at the T33 tunnel.

3 DESIGN FEATURES

The design has foreseen several lining sections for the double track tunnels, T33 and T34, to be used according to the materials to be excavated. The cross sections have areas from 61.46 to 64.70 m^2, with a height of 7.50-8.70 m and a width of approximately 10 m (figure below). The construction phasing was designed for sequential excavation following the NATM principles, with variable advance length from 1 to 3.60 m and excavation in full section or top heading and invert.

The primary lining system was dependent on the Rock Mass Ratio (RMR). Consisted of sections R1 (RMR>56) and R2 (55>RMR>40), with a shotcrete thickness of 0.10m and 0.15m respectively. Both were reinforced with wire mesh and 4m long Swellex PM12 rockbolts. For section M, foreseen for the main tunnel junctions with the primary galleries and shafts or when RMR<40 (figure 3), shotcrete reinforced with steel lattice girders and 4m long Swellex PM12 rockbolts at foot level were used. Section S was specific for soils, basically a M section but with an invert arc without rockbolts.

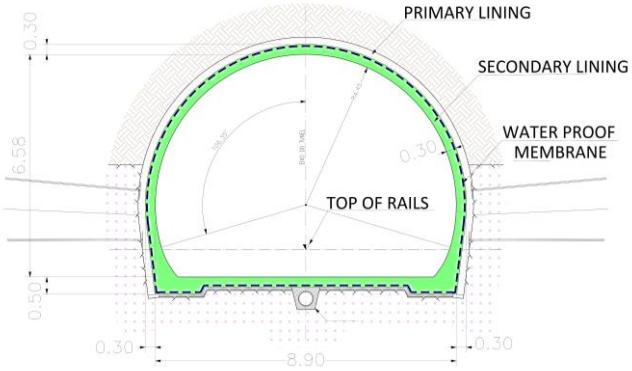

Figure 3. Primary and secondary lining for section M (CJC,2021b).

In the specific case of Tunnel T34, between Estrela and Santos, the section E used under the library building, was reinforced with an inside wire mesh and shotcrete, to minimize deformation near the foundation piles (figures 4).

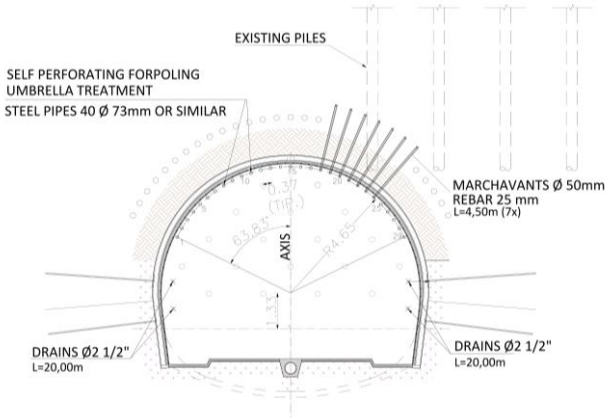

Figure 4. Section E used under the library (CJC,2021b).

Locally, as shown in figure 4 and 5, in substitution of the forepoling, 4,5m long, 25mm diameter rebars were used as *marchavants*.

The forepoling umbrella treatments, specified for the whole T34 tunnel (sections M, E and S) due to its RMR<40, were carried out with injected 10m long Schedule 40 tube with a diameter of 73mm introduced into 100mm holes spaced 37cm apart.

The front face treatments were carried out with 10m long 20mm diameter fiberglass bars introduced into 50mm diameter holes filled with cement grout, in a 1.00x1.00m mesh. Groundwater control was carried out using temporary short geodrains, designed to relieve hydrostatic pressure in the primary lining without lowering the water table very far. This water control system is suitable for rock masses with medium to low permeability, such as the case studied.

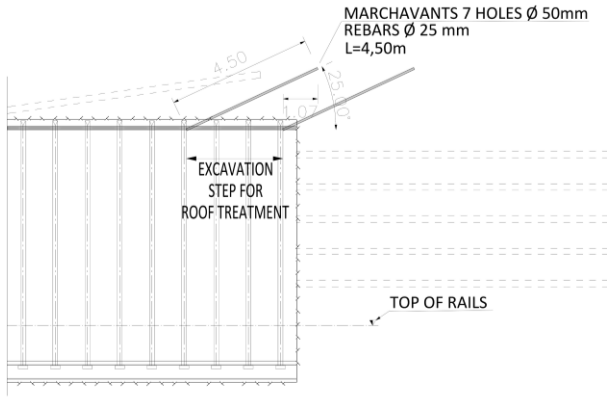

Figure 5. Special section E treatment in longitudinal view (CJC,2021b).

The tunnel is waterproofed by a 2mm PVC sheet membrane, protected by a 500g/m² geotextile around its entire contour making it completely watertight. The definitive or secondary lining is cast in situ with a 10m long formwork and reinforced with steel bars.

4 THE T34 TUNNEL SPECIAL CASE

The last section between the ventilation shaft PV213 and the Santos Station underneath the university campus, featured an increasingly thinner overburden with some geotechnical singularities:

- Crossing under the library building, with pile foundation, was the object of a particular reinforced section, as stated before;
- The final hundred meters were partially executed in the Cretaceous limestones with volcanic clayed tufts and breccia at top, sometimes with irregular karsified contact surface (figure 6);
- The inverted tunnel arc reached the level -5m, with the water table at 1.20m as previously stated, creating a potentially hazardous scenario if the limestones proved to be very karsified. Fortunately, the karsified layer was not intersected and the water flow was much lower than the worst scenario considered (figure 7);
- Initially, the T34 tunnel would connect in to the Santos Station body, but due to changes in construction schedules, this was not possible. A transition zone with new forepoling with fiberglass, face reinforcement and temporary drainage(figures 8 and 9).



Figure 6. Limestones and volcanic breccia with large blocks and irregular contact.



Figure 7. TunnelT34 final section after primary lining was completed.



Figure 8. Waterproof lining.



Figure 9. Secondary lining at the Santos Station face.

5 EXCAVATION METHODS

Since the geology was constituted mostly by sedimentary rocks, mechanical methods were primarily used. These included hydraulic hammers and roadheaders couple to Liebherr 944 excavators.

At some point, in the tunnel T34, between the Estrela Station and the ventilation shaft PV213, the limestone got so hard, with the uniaxial compression strength over 80MPa, that production turned very uneconomical. A drill and blast alternative were envisaged, studied and approved to increase production while minimizing impacts at surface, either in the buildings or people. Vibration velocities and frequencies were kept bellow the standard´s recommended values.

6 MONITORING AND OBSERVATION

In accordance with the principles of NATM, an instrumentation, monitoring and observation plan was implemented, based on the risk assessment and numerical models carried out.

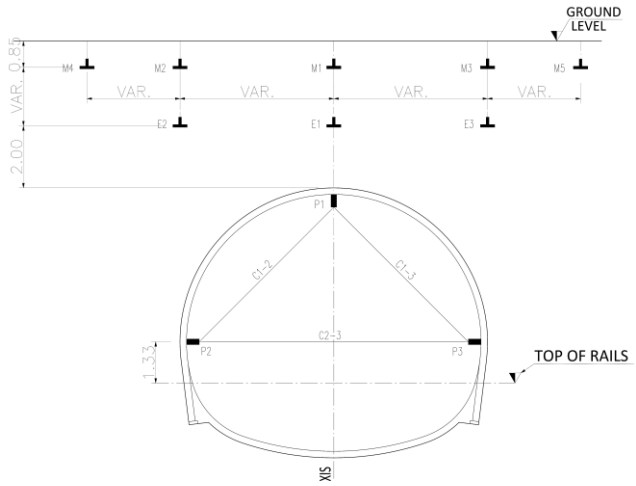

Figure 10. Monitoring section with both internal and external devices. (CJC,2021b).

Instruments such as inclinometers, piezometers, tiltmeters and seismographers were used, the latter to measure vibrations associated with heavy hydraulic hammers operation and rock blast. The tunnel sections, as shown in figure 10, included surface settlement pins (M), extensometers (E), convergence pins (P) and were widely used to monitor the lining performance.

The monitoring data was provided in a daily basis and checked against the design expected values.

7 CONCLUSIONS

The project was executed according to expectations, without major issues. We should note that in this kind of underground works underneath urban areas, there are always some uncertainties concerning the rock mass quality, geologic fault occurrences or underground water behaviour, mainly in long tunnels where survey is, sometimes, very spaced and with major gaps in between. The few unexpected conditions were addressed by the designer, the designer representative on site and the contractor.

The tunnel support solution used under the library was quite successful, with reported reduced displacements and of the order of magnitude of the predicted. Another example was the use of explosives in an urban area without major impact.

ACKNOWLEDGEMENTS

We would like to acknowledge the Metropolitano de Lisboa, E.P.E and, in particular, to Mr. Rui Pina.

REFERENCES

CJC Engenharia e Projetos, Ltda (2021a). Estudo Geológico e Geotécnico, Projeto de execução da empreitada de projeto e construção dos toscos no âmbito da concretização do plano de expansão do Metropolitano de Lisboa prolongamento das linhas amarela e verde (Rato-Cais do Sodré) lote 1: Execução dos toscos entre o término da Estação Rato e a Estação Santos, do pk 0+000 ao pk 1+319,729, Geological and Geotechnical Report, as part of the implementation of the expansion plan for the Lisbon Metro, extension of the Yellow and Green lines (Rato-Cais do Sodré) lot 1: Execution of the civil works between the end of the Rato Station and Santos Station from km 0+000 to km 1+319,729, São Paulo, Brasil (in Portuguese).

CJC Engenharia e Projetos, Ltda (2021b). Projeto de execução da empreitada de projeto e construção dos toscos no âmbito da concretização do plano de expansão do Metropolitano de Lisboa prolongamento das linhas amarela e verde (Rato-Cais do sodré) lote 1: Execução dos toscos entre o término da Estação Rato e a Estação Santos, do pk 0+000 ao pk 1+319,729. Design and built construction contract for the civil works as part of the implementation of the expansion plan for the Lisbon Metro, extending the Yellow and Green lines (Rato-Cais do Sodré) lot 1: Execution of the civil works between the end of the Rato Station and Santos Station, from km 0+000 to km 1+319,729, São Paulo, Brazil(in Portuguese).

Proceedings of the XVIII ECSMGE 2024
GEOTECHNICAL ENGINEERING CHALLENGES
TO MEET CURRENT AND EMERGING NEEDS OF SOCIETY
© 2024 the Authors
ISBN 978-1-032-54816-6
DOI 10.1201/9781003431749-502
Open Access: www.taylorfrancis.com, CC BY-NC-ND 4.0 license

ECSMGE 24
XVIII EUROPEAN CONFERENCE ON SOIL MECHANICS AND GEOTECHNICAL ENGINEERING

Erosion testing on sloped ground treated with enzyme-induced carbonate precipitation

Essais d'érosion sur un terrain en pente traité avec une précipitation de carbonate induite par une enzyme

L. Rivera, P. Bandini*
New Mexico State University, Las Cruces, New Mexico, United States of America
*paola@nmsu.edu

ABSTRACT: Enzyme-induced carbonate precipitation (EICP) is a novel biogeotechnical soil improvement technique in which calcium carbonate is precipitated abiotically from the hydrolysis of urea catalysed by plant-derived urease enzyme. The EICP technique and solution application methods are in development to control soil erosion induced by rainfall. The paper presents the results of preliminary erosion tests on two EICP-treated and untreated soil plots on the slope of an earthen dam. The mobilised soil volume during simulated rainfall in the treated plot was approximately eight times smaller than in the untreated plot. Raking the soil surface prior to treatment helped reduce the solution runoff and increase solution percolation. Applying the treatment solution with two-step percolation prevented early precipitation and equipment clogging.

RÉSUMÉ: La précipitation de carbonate induite par une enzyme (EICP) est une nouvelle technique biogéotechnique d'amélioration des sols dans laquelle le carbonate de calcium est précipité de manière abiotique à partir de l'hydrolyse de l'urée catalysée par l'enzyme uréase d'origine végétale. La technique EICP et les méthodes d'application de solutions sont en cours de développement pour contrôler l'érosion des sols induite par les précipitations. L'article présente les résultats d'essais préliminaires d'érosion sur deux parcelles de sol traitées et non traitées avec l'EICP sur la pente d'un barrage en terre. Le volume de sol mobilisé lors de pluies simulées dans la parcelle traitée était environ huit fois plus petit que dans la parcelle non traitée. Le ratissage de la surface du sol avant le traitement a permis de réduire le ruissellement de la solution et d'augmenter percolation de la solution. L'application de la solution de traitement avec percolation en deux étapes a permis d'éviter la précipitation précoce et le colmatage des équipements.

Keywords: Soil improvement; erosion; biogeotechnics; cementation; calcium carbonate.

1 INTRODUCTION

Enzyme-induced carbonate precipitation (EICP) is an abiotic biogeotechnical method that precipitates calcium carbonate via hydrolysis of urea between soil particles to form a lightly cemented soil mass or crust. EICP differs from microbially-induced calcite precipitation (MICP) in that the hydrolysis of urea is catalysed by plant-derived free urease enzyme instead of microbially produced urease, thus no microorganisms are involved in the EICP treatment. The net reaction is:

$$CO(NH_2)_2 + 2H_2O + CaCl_2 \xrightarrow{Urease} CaCO_3 + 2NH_4Cl \quad (1)$$

where aqueous solutions of urea and calcium chloride react to precipitate calcium carbonate. The most desirable precipitate is calcite because it is the most stable and least soluble of the calcium carbonate polymorphic forms. Ammonium chloride is a bioproduct of the reaction and should be considered depending on the concentration, use, and site characteristics. Engineering applications of the EICP technique are in development for fugitive dust mitigation (Hamdan and Kavazanjian, 2016), water erosion (Ossai et al., 2020; Ossai, 2021), and foundation support with biocemented soil columns (Martin et al., 2020). The treatment solution can be applied to the soil by percolation, spraying, injection, or soil mixing.

Using the EICP technique to create a cemented crust in sand has the potential to be an alternative to current practices for controlling soil erosion caused by rainfall and runoff in civil engineering infrastructure. EICP treatment can improve the strength and other properties of sand. The level of cementation of the treated soil depends on several factors, such as the soil gradation and mineralogy, particle packing, number of treatments, and composition and concentration of the treatment solution (e.g., Almajed et al., 2018; Ossai 2021). Jack bean (*Canavalia ensiformis*), soybean

(*Glycine max*), sword bean (*Canavalia gladiata*), and watermelon seeds have been used as sources of urease for EICP because of their high concentrations of the enzyme. Crude extract of urease can be produced from jack beans with a simple method at a considerably lower cost than the refined, laboratory-grade urease (Khodadadi Tirkolaei et al., 2020).

This paper presents the results of erosion tests on two EICP-treated and untreated soil plots on the slope of an earthen dam. The volumes of mobilised soil particles during the simulated rainfall in the EICP-treated and untreated plots are compared.

2 METHODS AND MATERIALS

2.1 EICP treatment solution and urease

The EICP treatment solution was prepared with 1 mol of urea, 0.67 mol of calcium chloride dihydrate, 4 g of non-fat powder milk, and 20 ml of crude urease extract (all amounts per litre of tap water). The crude extract of urease was prepared by crushing unhusked jack beans in water with a food blender for at least two minutes, until the solution had uniform, smooth consistency. Prior to crushing, the beans were soaked in water for about 24 hours. The liquid was extracted from the bean paste using a juicer. To produce approximately 110 ml of crude extract of urease, 63 g of unhusked beans and 200 ml of water were used. Adding non-fat powder milk increases the precipitate at interparticle contacts rather than on the particle surface (e.g., Martin et al., 2021).

2.2 Test site and soil

The test plots were on the East (upstream) slope of the embankment of Tortugas Site 2 Dam, located in Doña Ana County, New Mexico, USA. It is a dry flood control earthen dam, built in 1962 and modified in 1967 and 1993. The site was selected because the area is closed to public access and has slopes with sandy soil amenable to EICP treatment. The slope angle was about 45°. The soil was silty sand (SM) according to the Unified Soil Classification System and had 24.0% particles finer than 75 μm (No. 200 sieve), determined by washing. The coefficients of uniformity and curvature were 8.9 and 1.9, respectively. The maximum and minimum void ratios were 0.90 and 0.49, respectively. The specific gravity of the solids was 2.69. The in situ dry unit weight was 17.4 kN/m^3.

2.3 Block specimens

Prior to treating field plots, block specimens were prepared in triplicates for each condition and treated with the ECIP solution in the laboratory to confirm that the soil from the test site was amenable to EICP cementation and to select an appropriate solution application method and the number of treatment cycles for this native soil. In a previous study, Ossai (2021) found that EICP cementation of some New Mexico native sands increased when the soil was washed or rinsed prior to EICP treatment. Thus, some specimens were prepared with soil that was previously rinsed with tap water and oven dried.

The block specimens had the shape of a square prism. The internal length, width, and height of the moulds were 102, 102, and 51 mm, respectively. The dry unit weight of the soil specimens ranged from 15.3 and 16.1 kN/m^3. A first series of block specimens of rinsed sand were treated with either percolation, two-step percolation, or modified mix-compact methods (Ossai, 2021) and cured at room temperature (20-23°C) for ten days. Based on the results of the first test series, a second series of block specimens of unrinsed sand was prepared with the two-step percolation method. The percolation method consisted of slowly pouring the solution on the soil surface using a large syringe (without a needle). The two-step percolation method divided the EICP solution in two parts, first pouring slowly on the soil the crude extract urease and non-fat powdered milk solution (step 1), followed by percolating the calcium chloride and urea solution (step 2). For the modified mix-compact method, the EICP solution was mixed with the dry soil in a bowl using a spatula for approximately one minute. The soil was transferred to the mould and compacted to the target density with a small tamper. Subsequent treatment cycles applied the solution by percolation.

The specimens received three or five applications of EICP solution. The total volumes of EICP solution applied in the first and second treatment cycles were equal to 100 and 40% of the estimated pore space (Ossai, 2021). In subsequent treatment cycles, the solution volume was 30% of the pore space. Larger solution volume was needed in the first treatment because the soil was dry. After curing, the specimens were removed from the moulds and submerged in water several times to remove the uncemented or loose particles and determine the percent cemented mass.

2.4 Field plot treatment and erosion tests

Preliminary field treatment application trials were conducted. Two 1.2 m by 1.2 m plots (also called trial plots) were treated with EICP solution to test the feasibility of the application method and equipment on a slope in the field. In one of these trial plots, half of the surface was raked to create small horizontal channels (parallel to the dam crest) and the other half

of the plot surface was unraked (each area was 0.6 m wide) to compare crust formation with these two conditions. Two 2.4 m by 2.4 m plots (also called erosion test plots) were used for the erosion tests. One plot was treated with EICP, and the other plot was left untreated. The surface of both plots was raked.

The EICP treatment was applied with 15-liter backpack chemical sprayers with the spout set at the largest opening. The solution components were measured in the laboratory and mixed on site shortly before application. All the plots received five treatments with the two-step percolation method. The treatment cycles were spaced three days. Grass and gravel-size particles on the soil surface were removed.

The simulated rainfall was applied with a calibrated portable rainfall simulator (Figure 1). The rainfall intensity and duration were 96 mm/h and 30 min; the average raindrop speed was 2.52 m/s; and the average droplet size over the plot area was 0.85 mm. Soil particle mobilization due to raindrops and surface water erosion was assessed before and after the erosion tests using a Trimble SX10 Scanning Total Station. This equipment measured three-dimensional differences in elevation of the soil plots and attributed these differences to either cut or fill as a result of surface erosion. The mobilised soil volume after the simulated rainfall was estimated as the difference between the fill and cut volumes. The erosion tests were conducted when the wind speed was minimal and below the threshold that could affect the rainfall characteristics. After the erosion tests, the crust thickness, cementation strength, and precipitated calcium carbonate content (CCC) were assessed. The relative strength of the crust was appraised with a portable Mecmesin shotcrete penetrometer. The CCC precipitated was determined with acid digestion, as described by Ossai (2021), for two cemented soil samples from nine locations on the treated plot (total of 18 samples). The net CCC values reported were calculated as the difference between the acid digestion results for the cemented soil and the untreated soil.

3 RESULTS AND DISCUSSION

3.1 Results of block specimens

Table 1 shows the average values of the cemented mass as a percentage of the total soil mass prior to treatment for each test condition of the block specimens. In the first series of rinsed soil, two-step percolation produced the greatest percentage of cemented mass. There was either a small reduction or minor improvement in the average percentage of cemented mass of rinsed soil when increasing the treatment cycles from three to five (from 52.5% to 50.5% for percolation and from 75.4% to 78.3% for two-step percolation for three and five treatments, respectively). The results for the mix-compact method were not included in Table 1 because the cementation was negligible. This method was not considered in the rest of the testing program. The reason for the lack of cementation with the mix-compact method could not be confirmed but interaction of the treatment solution with the surface of the mixing bowl was suspected. When preparing block specimens with percolation (in one step), the syringe tip often clogged because the carbonate precipitation began before the EICP solution was poured on the soil. Unless the application equipment for the field tests could prevent the mixing of the solution components prior to being applied on the soil surface, the percolation method was expected to cause clogging of the spout. On the other hand, the two-step perolation avoided the challenges of early carbonate precipitation. In additon, soil rinsing prior to EICP treatment was not feasible when treating large soil volumes. Thus, the focus of the second specimen series was on two-step percolation with unrinsed soil.

The series of block specimens of unrinsed soil prepared with the two-step percolation method resulted in less cementation (in terms of percentage of cemented mass) compared with the rinsed soil specimens. For unrinsed soil, five treatment cycles produced much greater cemented mass (on average 40.2%) than three treatment cycles (on average 11.3%) using the two-step percolation method. Despite lesser cemented mass in unrinsed soil, five cycles provided sufficient cementation to form a crust in the field plots.

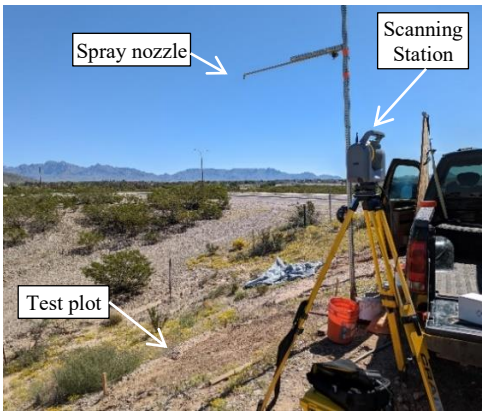

Figure 1. Erosion test plot, rainfall simulator (stand and spray nozzle), and Trimble SX10 Scanning Total Station.

Table 1. Cemented mass (%) for block specimens.

Soil pretreatment	Treatment method	Treatment cycles	
		3	5
Rinsed	Percolation	52.5	50.5
Rinsed	Two-step percolation	75.4	78.3
Unrinsed	Two-step percolation	11.3	40.2

3.2 Results of field plots

When the treatment was applied to the unraked plot surface, excessive downward runoff of the solution and pooling at the bottom of the plots were observed.

Horizontal raking before EICP treatment created small surface channels or grooves that helped retain the solution on the soil surface to allow percolation. In the trial plots, the average penetration resistance of the crust of the raked and unraked portions was 41.5 N and 26.3 N, respectively. Raking the soil surface prior to treatment increased the uniformity of crust strength and the average penetration resistance.

The average crust thickness of the EICP-treated erosion test plot was 12.5 mm (after the erosion test), which was considerably less than the target thickness of 50 mm. The net CCC of the soil after five treatments varied throughout the plot, ranging from nearly 0 to 7.4%, with an average and standard deviation of 2.4% and 2.1%, respectively. When the results were averaged based on sample location, the net CCC values in the upper third, middle, and lower third of the plot were 2.6, 2.0, and 2.8%, respectively.

Table 2 shows the cut and fill volumes and net mobilised soil volume after the erosion tests in the treated and untreated plots. The bottom 100 mm of the erosion test plots were not considered because it was the location of most accumulation of eroded soil particles, so the plot area considered for the results in Table 2 was 5.52 m^2. The volume of mobilised soil in the EICP-treated plot was about 8.3 times less than that in the untreated plot. These results show promise of EICP treatment to reduce erosion in sloped sandy soil.

Table 2. Mobilised soil in plots during erosion tests.

	Untreated	EICP-treated
Cut volume (m^3)	0.01699	0.00453
Fill volume (m^3)	0.00283	0.00283
Mobilised soil (m^3)	0.01416	0.00170

4 CONCLUSIONS

The two-step percolation method showed feasibility for creating an EICP crust in a native soil in the field, avoiding early precipitation and equipment clogging issues. Despite having the viscosity similar to water, the EICP solution drained downwards excessively when applied on a 45° slope, which is a concern to be addressed in future testing. Surface raking prior to treatment helped reduce considerably the solution runoff and obtain more uniform cementation throughout the plot. The relatively high fines content of the soil also affected the EICP reaction, leading to a thinner crust than wanted. Stronger, thicker crust is expected in sand with lower or no fines content.

ACKNOWLEDGEMENTS

This material is based upon work primarily supported by the National Science Foundation (NSF) under Award EEC-1449501. Any opinions, findings and conclusions, or recommendations expressed are those of the authors, and do not necessarily reflect those of the NSF. Construction Survey Technologies (CSTi) provided in-kind staff and equipment for soil scanning.

REFERENCES

Almajed, A., Khodadadi Tirkolaei, H., and Kavazanjian Jr., E. (2018). Baseline Investigation on Enzyme-Induced Calcium Carbonate Precipitation. *Jornal of Geotechnical and Geoenvironmental Engineering*, 144(11). https:// doi.org/10.1061/(ASCE)GT.1943-5606.0001973.

Hamdan, N., and Kavazanjian, E. (2016). Enzyme-induced carbonate mineral precipitation for fugitive dust control. *Géotechnique*, 66(7): 546-555. https://doi.org/10.1680/jgeot.15.P.168.

Khodadadi Tirkolaei, H., Javadi, N., Krishnan, V., Hamdan, N., and Kavazanjian Jr., E. (2020). Crude urease extract for biocementation. *Journal of Materials in Civil Engineering*, 32(12). https:// doi.org/10.1061/(ASCE)MT.1943-5533.0003466.

Martin, K.K., Khodadadi, T.H., and Kavazanjian, E. (2020). Enzyme-induced carbonate precipitation: Scale-up of bio-cemented soil columns. In *Geo-Congress 2020: Biogeotechnics (GSP 320)*, E. Kavazanjian Jr., J.P. Hambleton, R. Makhnenko, and A.S. Budge (eds.), pp. 96-103. Reston, VA: American Society of Civil Engineers (ASCE). https://doi.org/10.1061/9780784482834.

Martin, K., Khodadadi Tirkolaei, H., and Kavazanjian, E. (2021). Enhancing the strength of granular material with a modified enzyme-induced carbonate precipitation (EICP) treatment solution. *Construction and Building Materials*, 271 (121529). https://doi.org/10.1016/j.conbuildmat. 2020.121529.

Ossai, R. (2021). *Application Methods for Erosion Control of Sand in Sloping Ground.* Ph.D. Dissertation, New Mexico State University, Las Cruces, NM, USA.

Ossai, R., Rivera, L., and Bandini, P. (2020). Experimental study to determine an EICP application method feasible for field treatment for soil erosion control. In *Geo-Congress 2020: Biogeotechnics (GSP 320)*, E. Kavazanjian Jr., J.P. Hambleton, R. Makhnenko, and A.S. Budge (eds.), pp. 96-103. Reston, VA: ASCE. https://doi.org/10.1061/9780784482834.

Proceedings of the XVIII ECSMGE 2024
GEOTECHNICAL ENGINEERING CHALLENGES
TO MEET CURRENT AND EMERGING NEEDS OF SOCIETY
© 2024 the Authors
ISBN 978-1-032-54816-6
DOI 10.1201/9781003431749-503
Open Access: www.taylorfrancis.com, CC BY-NC-ND 4.0 license

ECSMGE 24
XVIII EUROPEAN CONFERENCE
ON SOIL MECHANICS AND
GEOTECHNICAL ENGINEERING

Ground improvement between stone columns: a performance study on various soil types using in-situ testing

Amélioration du sol entre des colonnes ballastées: une étude de performance sur divers types de sols en utilisant des tests in situ

L. Roldan*, M. Sottile, A.O. Sfriso
SRK Consulting, Buenos Aires, Argentina

J. Rola
SRK Consulting, West Perth, Australia

**lroldan@srk.com.ar*

ABSTRACT: This study investigates the effectiveness of ground improvement between stone columns in various soil types, including coarse and fine tailings, clay with organic traces, and overconsolidated fine grained soils. A series of trial pads were constructed to evaluate the performance of stone columns with different replacements ratios. CPTu tests were conducted outside the improved area and between the stone columns, and variations were analysed to understand the improvement achieved in each soil type, in terms of soil behaviour type, state parameter, peak and residual strength. The findings of this research demonstrate the viability of stone columns as an effective ground improvement technique across some of the coarser soil units and provides insights into their impact on finer materials.

RÉSUMÉ: Cette étude examine l'efficacité de l'amélioration du sol entre des colonnes ballastées dans différents types de sol, y compris les résidus grossiers et fins, l'argile contenant des traces organiques et les sols fins surconsolidés. Une série de plateformes d'essai ont été construites pour évaluer les performances des colonnes en pierre avec différents taux de remplacement. Des tests CPTu ont été réalisés à l'extérieur de la zone améliorée et entre les colonnes en pierre, et les variations ont été analysées pour comprendre l'amélioration obtenue dans chaque type de sol, en termes de comportement du sol, de paramètre d'état, de résistance maximale et résiduelle. Les résultats de cette recherche démontrent la viabilité des colonnes en pierre en tant que technique d'amélioration du sol efficace pour certaines unités de sol plus grossières et fournissent des informations sur leur impact sur les matériaux plus fins.

Keywords: Ground improvement; stone columns; tailings; in-situ testing; CPT.

1 INTRODUCTION

Stone columns (SC) are widely used to mitigate the risk of liquefaction of loose non-plastic soils with fines. Vertical inclusions made of clean crushed rock are installed in a grid pattern using a vibro-replacement method, expecting that these columns will increase the density of the surrounding soil, contribute to the average shear strength of the ground, and provide drainage for the dissipation of pore pressure. This technique has been used successfully to reinforce the foundation of several dams, e.g. Salmon Lake Dam (Luehring et. al., 2001); Mormon Island Auxiliary Dam (Nickell, 1994) and Steel Creek Dam (Keller, 1987).

This study presents the procedure used to characterize and quantify the effectiveness of SC to improve the foundation of a downstream-raised tailings dam, which comprises tailings, clay with organic traces, and overconsolidated fine soils of alluvial origin. Two trial pads were constructed near the toe of the dam; SC were installed with five different replacement ratios (RR), ranging from 14.5% to 35.8%; Cone Penetration Tests (CPTu) were conducted outside the improved area and in between SC (Figure 1). Frequency analyses were performed on the data to assess the ground improvement between SC in terms of peak and residual undrained shear strength and state parameter.

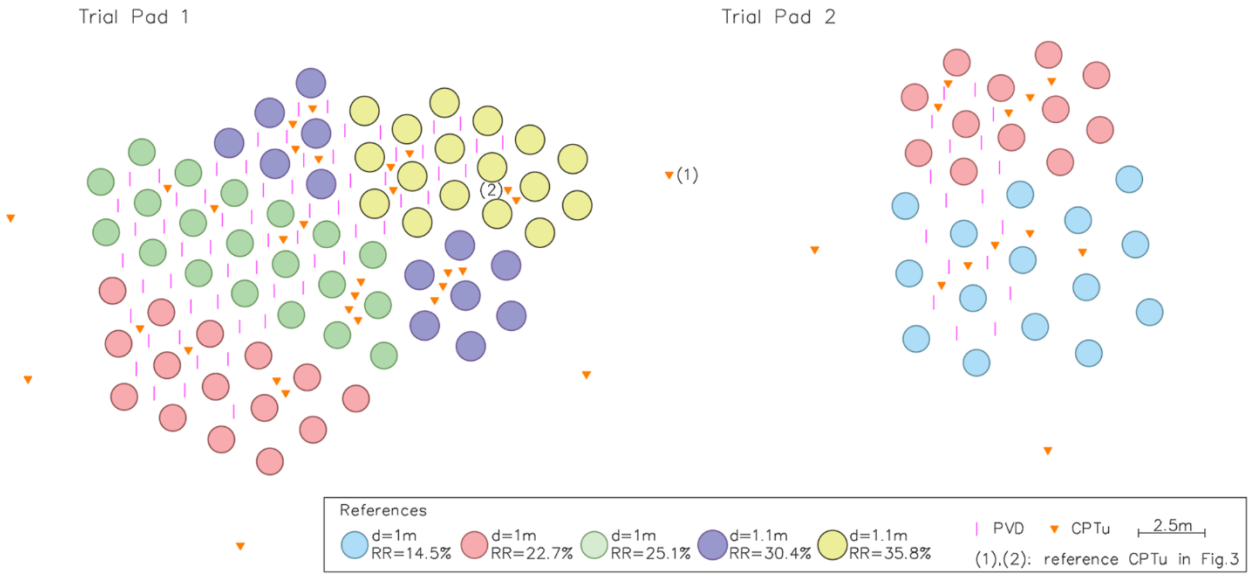

Figure 1. Trial pads: pattern of stone columns (SC), prefabricated vertical drains (PVD) and CPTu test locations.

2 GROUND MODEL

The dam is founded atop of historically deposited fine and coarse tailings within a broad valley. The natural foundation is formed by fine-grained alluviums, roughly split in an upper, soft unit and a lower overconsolidated unit. The upper alluvium contains layers of coarse, free-draining material interbedded with silts and clays. No surface clearing was undertaken prior to the historic tailing's deposition, leaving a very soft clay layer with organic underlying the impoundment area.

Although slightly irregular in thickness, the stratigraphy of the trial pad area can be summarized as: topsoil, tailings, organic clay, upper alluvium and lower alluvium (Table 1). This stratigraphy is rather uniform throughout the site, as confirmed by more than 200 CPTu soundings and 35 boreholes.

Table 1. Foundation stratigraphy.

Layer	Thickness (m)
Topsoil	0.5 – 1.0
Tailings	3.5 – 4.0
Organic clay	0.5 – 1.0
Upper Alluvium	5.0-15.0
Lower Alluvium	> 15.0

The coarse and fine tailings were placed together, with the coarse frequently encountered in the upper tailings layer and the fine in the lower tailings layer. Classification data is presented in Table 2 and Figure 2. The phreatic level is approximately 3.15 m below ground level at the trial pads. A largely hydrostatic pore pressure field was measured throughout the site.

Table 2. Classification test results.

Layer	γ (kN/m³)	LL (%)	PL (%)
Tailings	16.5	Non plastic	
Organic clay	17.0	23-51	13-25
Upper Alluvium	19.0	18-65	11-44

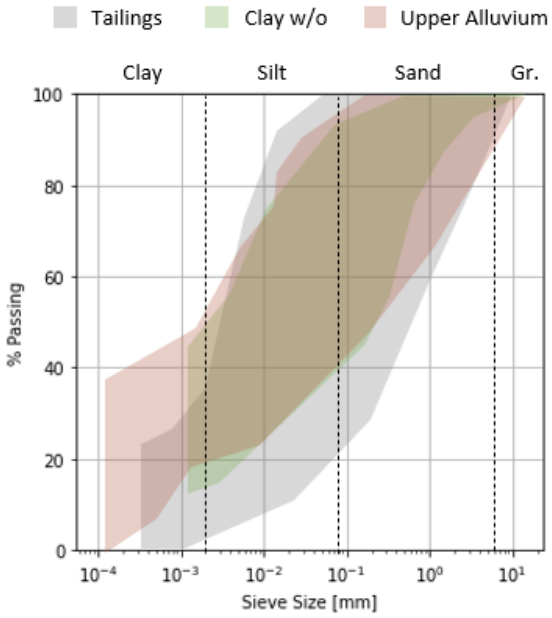

Figure 2. PSD distributions of the main geotechnical units.

3 TRIAL PADS

For the construction of the two trial pads, the topsoil layer was removed, and a working platform, 0.8 m thick, was built on top of the exposed tailings surface. SC were installed with five different RRs: 14.5%, 22.7% and 25.1% (1 m diameter SCs); and 30.4% and 35.8% (1.1 m diameter SCs).

Prefabricated vertical drains (PVD) were installed in some regions prior to installing SCs, to study their effectiveness as a draining path for excess pore pressures generated during the installation of the SCs. Figure 1 shows the location of the different SC configurations and PVDs.

4 CONE PENETRATION TESTS

4.1 Location

CPTu was the main test method employed for the foundation characterization. Figure 1 shows the location of each sounding, both in the unimproved areas and between SCs. The location of each test was selected to cover improved areas with different RR, with and without PVDs.

4.2 Change indicators

The Soil Behaviour Type (SBTn) employing Robertson (2016) formulas, the state parameter (ψ) employing the Plewes method (1992), the peak undrained shear strength ratio, using Mayne and Peuchen (2022) method and the residual undrained shear strength ratio, using Robertson (2022) correlations were employed as change indicators due to ground improvement. Also, the normalized friction ratio (f_s/σ'_{v0}) was employed as a lower bound estimate for the residual undrained shear strength ratio. Materials are considered potentially liquefiable when ψ>-0.06. An example of unimproved vs improved ground is shown in Figure 3. The relevant correlations characterizing the strength and behaviour of each foundation were processed using frequency analysis and are presented in Section 5.

5 IMPROVEMENT CHARACTERIZATION

5.1 Scope of the interpretation effort

This section aims to quantify the strength improvement of materials between SCs. The improved soil strength is later used as an input to compute equivalent strength parameters (SC + improved soil) to perform stability analyses.

The analyses only consider data below the water table since typical CPTu correlations don't account for partially saturated soil conditions. Therefore, the platform, topsoil, and the upper portion of the tailings are not included in the analyses. Additionally, only data for depths shallower than 12 m, the SC length, is presented; therefore, the lower alluvium and the bottom of the upper alluvium are also neglected in the analyses.

5.2 Soil Behaviour Type

Figure 4 presents the Soil Behaviour Type (SBTn, Robertson 2016) for areas outside and inside the ground improvement zone on both trial pads. It is observed that the installation of SCs in their various arrangements and RR consistently reduce the frequency of data points indicating contractive behaviour in the coarser materials, but do not change fine materials: i) in the tailings, a reduction from 36% to 16%; ii) in the organic clay, a slight increase from 65% to 69%; iii) in the coarse upper alluvium, a reduction from 30% to 15%; and iv) in the fine upper alluvium, an increase from 56% to 67%. The improved areas consistently show fewer data points within the CCS (claylike-contractive-sensitive) region.

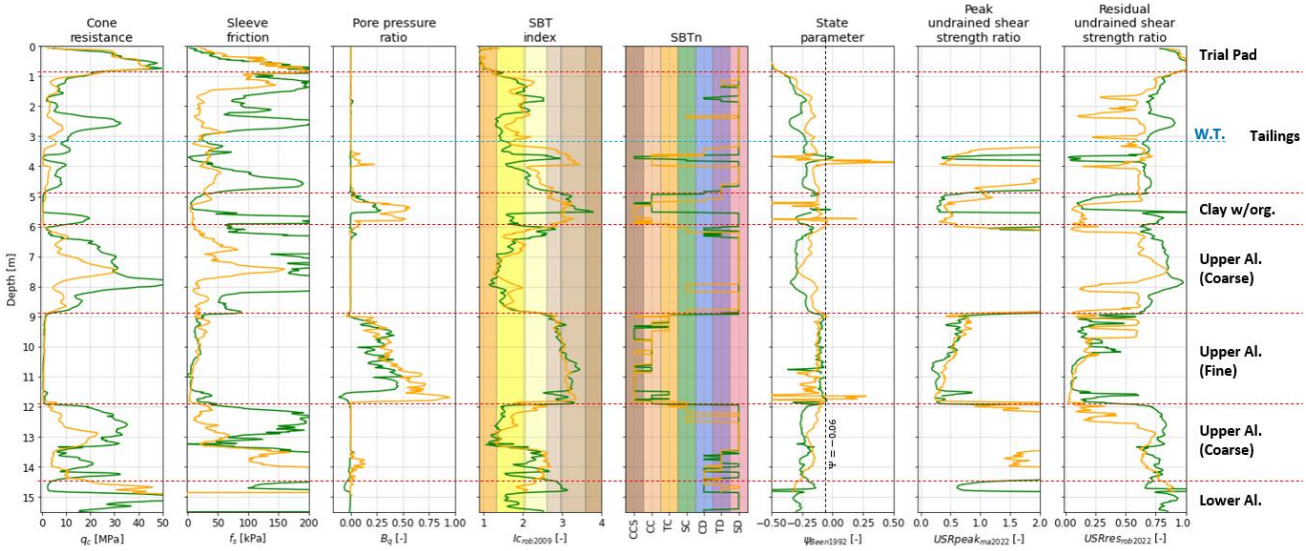

Figure 3. Example of the CPTu interpretation for an unimproved (yellow – 1) and improved region (green -2).

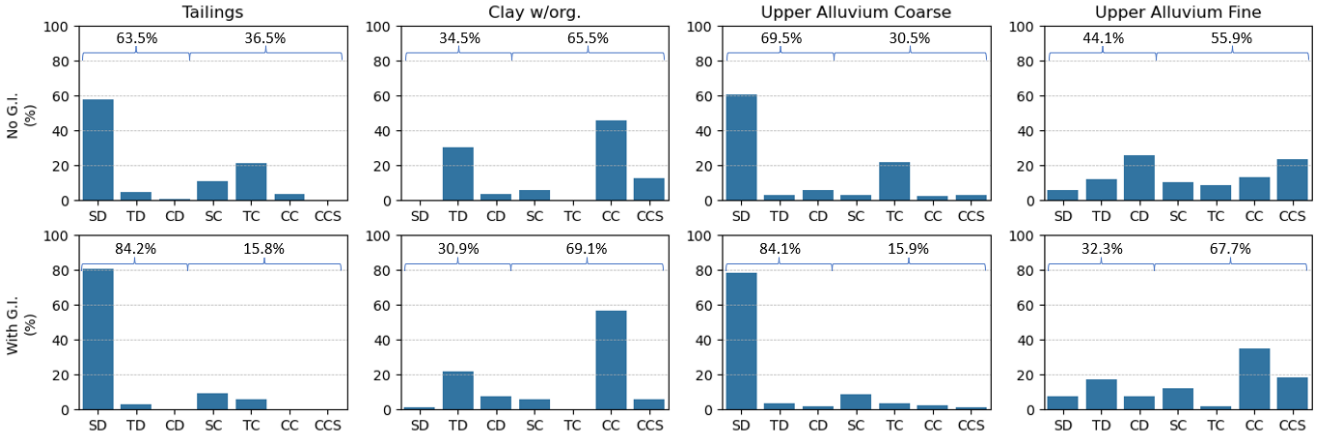

Figure 4. SBTn distribution in each layer, with and without ground improvement.

5.3 State parameter

As expected, densification of coarse tailings and upper alluvium produce a noticeable reduction in their state parameters for all RR (Figure 5). At a confidence level of 70%, state parameter goes from -0.15 to -0.20 in the tailings, from -0.11 to -0.09 in the organic clay, from -0.13 to -0.18 in the coarse upper alluvium and from -0.11 to -0.08 in the fine upper alluvium. Even for the finer materials, the state parameter falls in the dilative behaviour zone. The shift is the state parameter is consistent with the shift in the SBTn: coarser materials display a decrease in contractiveness while finer materials display an increase.

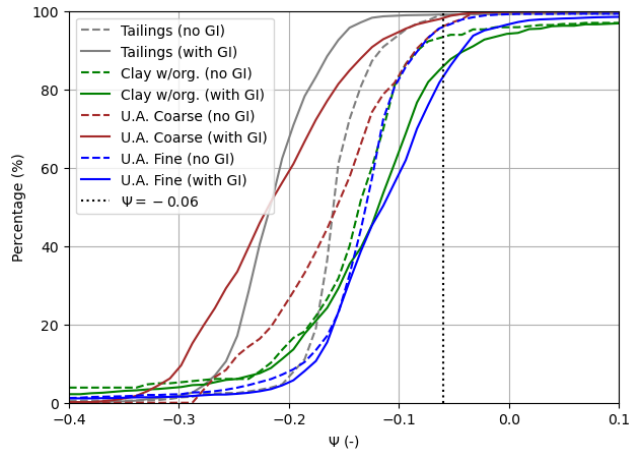

Figure 5. State parameter cumulative density function.

5.4 Peak Undrained Shear Strength

Figure 6 shows the cumulative histogram for the computed peak undrained shear strength ratios; only values smaller than 0.6 are shown, as higher values would be capped by the materials drained shear strength.

Finer layers (clay and fine upper alluvium), show a decrease in peak USR, likely due to a remoulding effect produced by the installation of the SC. Coarser layers (tailings and coarse upper alluvium) showing very high USR, denoting the likely effect of partial drainage during CPTu penetration.

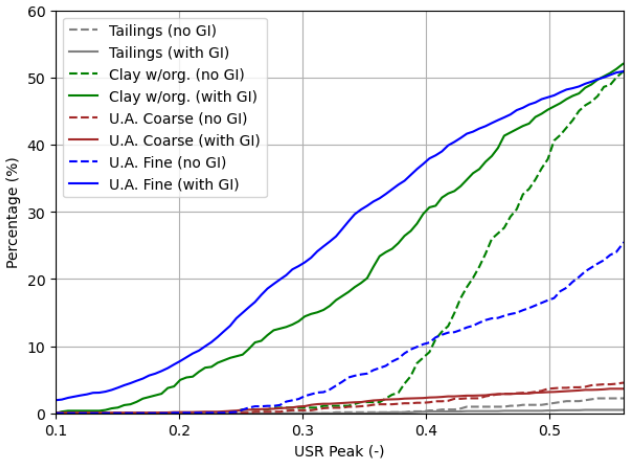

Figure 6. Peak USR cumulative density function.

5.5 Residual Undrained Shear Strength

Figure 7 shows the improvement in residual strength. Note that in coarse materials there is a significant amount of data with USR < 0.3 in unimproved ground but, after the SC installation, more than 90% of the data displays USR > 0.60, suggesting that drained shear strength would cap the adopted USR.

Fine upper alluvium shows a similar trend, slightly increasing its USR in the full range of pre-improvement USR. However, improvement in the organic clay was only evident for USR values less than 0.3. Although the mean USR remained largely unchanged, the SC installation seems to reinforce the weakest zones while potentially remoulding the stronger segments. This is an overall improvement in behaviour, as the design USR at the adopted confidence level in improved.

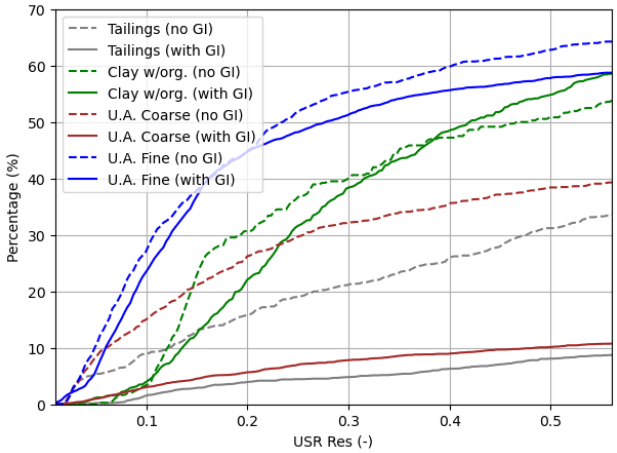

Figure 7. Residual USR cumulative density function.

Figure 8 shows the normalized sleeve friction. As expected, the curves are similar to those of Figure 7, in particular for finer materials as the definition of residual USR is the same.

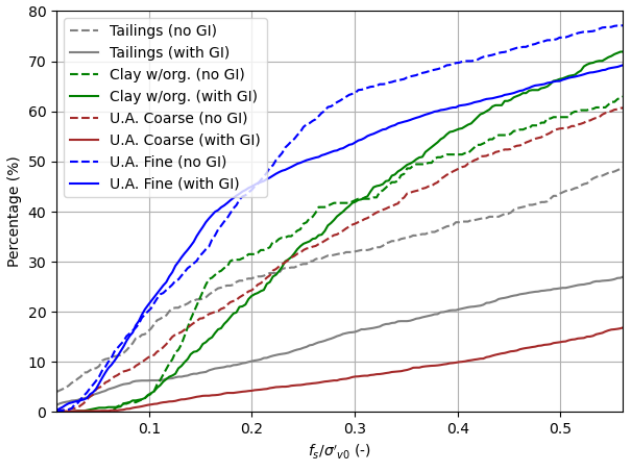

Figure 8. Normalized sleeve friction cumulative density function.

5.6 Replacement ratio and prefabricated vertical drains effect

No correlation was found between the RR and the degree of improvement. As an example, Figure 9 shows the cumulative density function of residual USR in the fine upper alluvium for all the RR employed. It can be observed that the highest strength is achieved at a RR = 25.1%, which is on the lower end of the range. This is not surprising for fine compact soils that might undergo destructuration and remoulding during SC installation. The average design strength, which includes both the post-improvement USR and the shear strength of the SCs, does increase with the RR.

It was also not possible to identify an effect of using PVDs, as shown in Figure 10. This could be due to the tailings being rather coarse, and therefore the effect of improved drainage negligible.

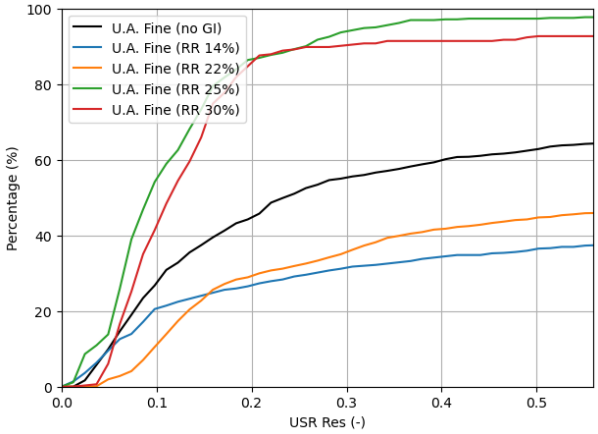

Figure 9. Residual USR cumulative density function for different RR in the fine upper alluvium.

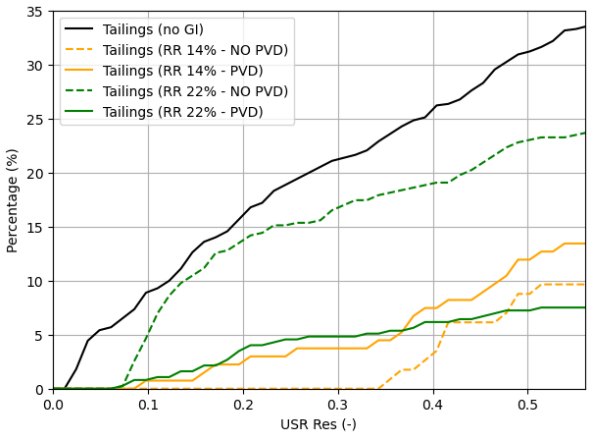

Figure 10. Residual USR distribution with and without PVD in tailings.

6 CONCLUSIONS

In this study, CPTu testing was employed to assess the improvement of soft soils at the foundation of a tailings dam, using SC. Two trial pads and a range of RR were employed. The analysis was performed in terms of state parameter, peak and residual undrained shear strength ratio, using state-of-the-practice correlations.

Significant improvement was observed in the coarse materials, whereas the finer soils, including fine tailings, exhibited negligible improvement and, in some cases, a reduction in strengths. It is interesting to note that the residual undrained shear strength of finer materials did improve in the weaker lenses and pockets, a result which allows for an increase in the design USR at the confidence level selected for the analyses.

No correlation could be established between the SC RR and the degree of ground improvement. The average design strength, which includes both the post-improvement USR and the shear strength of the SCs, does increase with the RR.

REFERENCES

Keller, T. O., Castro, G. O. and Rogers, J. H. (1987). Steel Creek Dam foundation densification, In: *Proceedings of the Symposium on Soil Improvement – A Ten Year Update*, ASCE Geotechnical Special Publication, Vol. 12, Atlantic City, USA.

Luehring, R., Snorteland, N., Stevens, M. and Mejia, L. (2001). Liquefaction mitigation of a silty dam foundation using vibro-stone columns and drainage wicks: a case history at Salmon Lake Dam, In: *Proceedings of 21st USSD Annual Meeting*, Denver, USA.

Mayne, P. W. and Peuchen, J. (2022). Undrained shear strength of clays from piezocone tests: a database approach, In: *Proceedings of the 5th Intl. Symposium of Cone Penetration Testing*, Bologna, Italy, Paper ID 1107: 546-551.

Nickell, J. S, Allen, M. G and Ledbetter, R. H. (1994). Seismic remediation for liquefiable gravels: Mormon Island auxiliary dam and others in Northern California, In: *Proceedings of the International Workshop on Remedial Treatment of Liquefiable Soils*, Tsukuba Science City, Japan.

Plewes, H. D., Davies, M. P. and Jefferies, M. G. (1992). CPT based screening procedure for evaluating liquefaction susceptibility, In: *Proceedings of the 45th Canadian Geotechnical Conference*, Toronto Ontario, Canada, pp. 41-49.

Robertson, P. K. (2009). Performance based earthquake design using the CPT, In: *Proceedings of the international conference on performance-based design in earthquake geotechnical engineering*, Tokyo, Japan.

Robertson, P. K. (2016) CPT-based Soil Behaviour Type (SBT) Classification System – an update, *Canadian Geotechnical Journal*, 53(12), pp. 1910-1927, https://doi.org/10.1139/cgj-2016-0044.

Robertson, P. K. and Cabal K. (2022). *Guide to Cone Penetration Testing*, 7th ed., Gregg Drilling LLC, Signal Hill, USA.

Proceedings of the XVIII ECSMGE 2024
GEOTECHNICAL ENGINEERING CHALLENGES
TO MEET CURRENT AND EMERGING NEEDS OF SOCIETY
© 2024 the Authors
ISBN 978-1-032-54816-6
DOI 10.1201/9781003431749-504
Open Access: www.taylorfrancis.com, CC BY-NC-ND 4.0 license

ECSMGE 24
XVIII EUROPEAN CONFERENCE ON SOIL MECHANICS AND GEOTECHNICAL ENGINEERING

Rough pile stereolithography for centrifuge modelling

Stéréolithographie pour la modélisation en centrifugeuse de pieux rugueux

G. Sabaliauskaite
Department of Civil Engineering, City, University of London, UK

S. Divall*, A.M. McNamara, S.E. Stallebrass, R.N. Taylor
Department of Civil Engineering, City, University of London, UK

**sam.divall@city.ac.uk*

ABSTRACT: The capacity of bored cast in situ concrete piles in clay is typically governed by shaft resistance, which is usually achieved through skin friction. Skin friction is dependent on the proportion of the soil strength that is mobilised by the pile – and can vary depending on the roughness of the pile. Valuable insights into the behaviour of piles under loading can be obtained through physical model testing at reduced scale in a geotechnical centrifuge if the soil pile interface can be modelled appropriately. Therefore, it is important to consider how the surface of a pile should be modelled to achieve a comparable roughness between the model and the prototype pile. In this paper, a method for designing a pile with a specified roughness using stereolithography, also known as 3D printing, is described. The normalised roughness of the model pile is determined based on the likely failure mechanism of the pile and the mean soil particle size. The rough surface profile is then designed using 3D modelling software with the calculated arithmetic average surface roughness. Data are presented from preliminary centrifuge model tests on piles with different surface roughness.

RÉSUMÉ: La capacité des pieux en béton coulés forés dans de l'argile est généralement déterminée par la résistance à la traction, qui est généralement obtenue par friction latérale. La friction latérale dépend de la proportion de la résistance du sol mobilisée par le pieu, et peut varier en fonction de la rugosité du pieu. Des informations précieuses sur le comportement de ces pieux sous charge peuvent être obtenues grâce à des essais de modélisation physique à échelle réduite dans une centrifugeuse géotechnique si l'interface sol-pieu peut être modélisée de manière appropriée. Par conséquent, il est important de réfléchir à la manière dont la rugosité d'un pieu doit être modélisée pour obtenir une rugosité comparable entre le modèle et le pieu prototype. Dans cet article, une méthode de conception d'un pieu avec une rugosité spécifiée à l'aide de la stéréolithographie, également connue sous le nom d'impression 3D, est décrite. La rugosité normalisée du pieu modèle est déterminée en fonction du mécanisme de défaillance probable du pieu et de la taille moyenne des particules du sol. Le profil de surface rugueux est ensuite conçu à l'aide d'un logiciel de modélisation 3D avec la rugosité moyenne arithmétique calculée. Des données seront présentées à partir d'essais préliminaires de modélisation en centrifugeuse sur des pieux ayant différentes rugosités de surface.

Keywords: Centrifuge modelling; stereolithography; pile roughness; skin friction.

1 BACKGROUND

The ultimate capacity of a pile typically depends on the pile end bearing capacity and the friction between the pile shaft and the soil in which the pile is installed. The installation method and soil type have an effect on the proportion of base capacity and shaft friction generated by a pile (Mandolini *et al.*, 2005; Panchal *et al.*, 2019). The end bearing capacity of bored, cast in situ piles in clay is usually mobilised at a vertical pile displacement of about 30% of the pile diameter (Budhu, 2010), which is beyond the typical magnitude of the working load of a pile foundation. However, the shaft resistance in these conditions is mobilised at much smaller vertical displacements.

2 INTRODUCTION

As most of the capacity of a bored, cast in situ pile at working load is typically generated via pile shaft resistance, the interface between the soil and pile is an important aspect when conducting pile load tests. Previous studies assessing the effect of surface roughness on clay-interface shear behaviour observed greater mobilisation of shear in tests with rougher surfaces than those with smoother surfaces (Martinez & Stutz, 2019). Taha & Fall (2014) found that increasing the surface roughness also increased interface strength.

Hammoud & Boumekik (2006) and Feligha *et al.* (2016) observed three modes of interface shearing which depend on the roughness parameter *R* (the

relative roughness of a surface). The relative roughness is defined as the centre line average value of roughness divided by the mean particle diameter, D_{50}, of the soil particles with which it interacts. The three proposed modes are: full sliding at the interface (when $R < 0.3$), shear failure within the soil (when $R > 1$), and both sliding and shear failure within the soil occurring simultaneously (when $0.3 < R < 1$).

Lemos & Vaughan, (2000) found that for a very smooth interface, the interface shear resistance is lower than the soil-on-soil residual strength, although it is unlikely that such surfaces would occur in practice.

In geotechnical centrifuge testing, pile foundations are typically modelled as steel (Ebeido *et al.*, 2018; Netietd *et al.*, 2023), or aluminium (Haffar *et al.*, 2017) tubes. Some authors have also utilised cast resin (Lalicata *et al.*, 2023) and mortar (Ganiyu *et al.*, 2018). The use of steel and aluminium tubes is commonly used as they are inexpensive and relatively quick to machine. However, unless a roughness is applied to the profile, these model piles would essentially present a smooth surface during testing – thus reducing the interface shear resistance between the pile and the soil. In addition, when conducting a series of centrifuge pile tests, this applied roughness to the model pile is not repeatable throughout the test series.

Some researchers, in order to make steel or aluminium model piles more representative of prototypes, have added rough profiles to the model pile surface by either machining a roughness on the pile surface (O'Hara & Martinez, 2022) or by gluing sand particles, or sandblasting the outside of model piles (Ouzzine *et al.*, 2023). Although these methods provide the required roughness for testing piles in sand, it is extremely difficult to replicate the exact roughness profile on all piles used in a series of centrifuge tests.

Using cast resin and mortar also has drawbacks for geotechnical centrifuge testing. Although cast mortar piles have been effective in reproducing the behaviour of prototype piles, their implementation has been relatively time consuming due to the curing time necessary in the mould before testing (Ganiyu *et al.,* 2018). A proposed solution to overcome these time constraints has been to use fast cast resin. However, drawbacks were noted as the curing process of the resin in the clay model appears to affect the soil-pile interface properties owing to possible chemical bonding between the clay and the resin (Lalicata *et al.,* 2023).

The aim of this paper is to establish a quick and reliable method of producing representative and repeatable model piles for centrifuge testing with the aid of stereolithography. The relative roughness of five 3D printed blocks with different surface roughness has been determined and compared to that of a cast concrete block.

3 MEASURING ROUGHNESS

The relative roughness, R, value can be calculated from the measured centre line average, CLA, roughness value, R_a, for a sample. R_a is measured by defining a centre line for a surface profile (Figure 1) where the area between the peaks of the surface and the centre line are equal to the area between the troughs of the surface and the centre line.

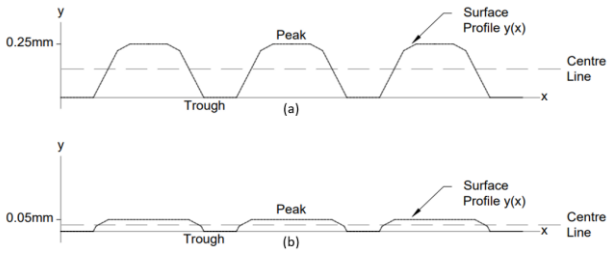

Figure 1. Schematic diagrams of surface profiles with offset distances of (a) 0.25mm, (b) 0.05mm.

R_a is then calculated as the mean value of the vertical deviation from the centre line of the surface profile using

$$R_a = CLA = \frac{1}{L}\int_0^L |y(x)|dx \qquad (1)$$

With L being the profile sampling length. In order to define the roughness value in terms of the scale of the soil grains at the interface, R_a is expressed in terms of the average diameter, D_{50}, of the soil grains, giving R:

$$R = \frac{R_a}{D_{50}} \qquad (2)$$

For the purpose of this paper, the piles are assumed to be in contact with Speswhite kaolin clay, which is commonly used in centrifuge model tests in clay. Thus, the average diameter of the soil grains is assumed to have a maximum value of 2.00µm.

4 ROUGHNESS SAMPLES

Five rough gauge blocks were drawn using the 3D modelling software SolidWorks. Each block was modelled with an inclusion in which a standard

polyhedron pattern with varying offset distances was applied. The offset distances ranged between 0.05 to 0.25mm at 0.05mm intervals. Figure 2 shows two rendered roughness gauge blocks which were then 3D printed using a micro carbon fibre filled nylon filament, known as Markforged Onyx, and their roughness measured using a Mitutoyo Surftest SJ-210 surface roughness measurement instrument.

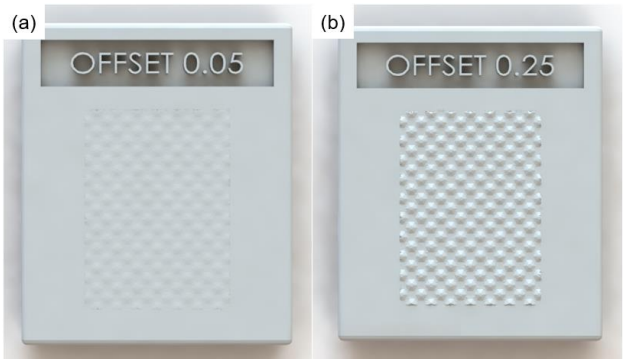

Figure 2. 3D modelled roughness gauge blocks with an offset distance of (a) 0.05mm, and (b) 0.25mm.

The roughness parameters of the rough gauge blocks were compared to the roughness of a 100x100x100mm concrete block, with a cement to sand to aggregate ratio of 1:2:3, in order to see which offset distance would be the most appropriate to employ when applied to the model piles in geotechnical centrifuge testing. The roughness of the concrete block was measured using the same instrumentation, taking an average roughness value. In addition, the roughness parameters of a resin pile, as used in a study by Gorasia & McNamara (2016), a pile coated in sand, and a smooth aluminium pile (Figure 3) were also measured, in order to investigate which mode of interface shearing would likely take place between the model piles and clay during a geotechnical centrifuge test.

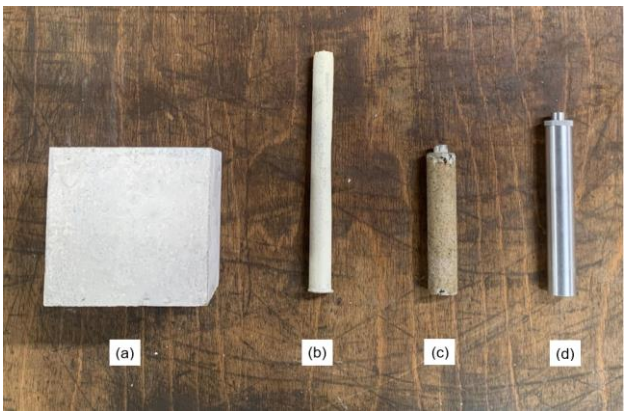

Figure 3. Samples used for roughness parameter comparison (a) concrete block (b) resin cast pile (c) sand coated pile (d) smooth aluminium pile.

5 RESULTS AND DISCUSSION

The centre line average and relative roughness of the four sample elements (concrete block, resin pile, sand coated pile, and aluminium pile), in addition to the five rough gauge blocks are presented in Table 1. The surface roughness measuring instrument was calibrated to an accuracy of 0.13% against a machined roughness gauge with a roughness of 3μm, to ensure the readings were correct.

All five roughness gauge blocks were found to have a relative roughness greater than 1. This means that applying any offset distance equal to or greater than 0.05mm onto a model pile would lead to an interface shear resistance equal to that of soil-on-soil shear resistance. However, comparing the values of relative roughness on the gauge blocks to that of the concrete block, it is evident that an offset of 0.25mm provides the most comparable surface profile for concrete pile modelling.

It can be observed that the relative roughness of the resin pile would also provide an interface shear resistance equal to the soil-on-soil shear resistance. However, as noted above, due to the curing process of the resin, the soil-pile interface is affected.

The smooth aluminium pile was found to have the lowest surface roughness, with the relative roughness smaller than 1.00. Therefore, when testing this pile in clay, the interface shear resistance would be lower than that of soil-on-soil shear resistance, and marginally greater than 0.30, leading to a combination of sliding and soil-on-soil shear at the interface during testing. Although the smooth aluminium pile surface can provide ease for repeatable testing, the low roughness renders the pile unrepresentative of the prototype.

The surface profile of the sand coated pile presented difficulties for measuring its roughness as the values were beyond the measurable range. However, it can easily be assumed that this pile would have a relative roughness greater than 1, providing an interface shear resistance between the pile and a clay soil sample to be that of soil-on-soil shear resistance. Nonetheless, it is difficult to replicate the exact surface finish with this method for a series of piles as the pile is simply coated in an adhesive and submerged in, or covered with sand. Hence, each pile is likely to possess a random distribution of sand particles. In addition, when testing these piles at elevated ***g***-levels in clay, there is a risk of the adhesive separating from the pile, thus changing the interface between the pile and the clay.

Table 1. Surface roughness parameters of sample elements and roughness gauge blocks.

Roughness parameter	Samples					Roughness gauge block texture offset distance (mm)				
	Calibration sample	Concrete block	Resin pile	Sand coated pile	Aluminium pile	0.05	0.10	0.15	0.20	0.25
R_a (μm)	3.00	12.06	3.37	N/A	0.63	4.90	7.88	8.79	10.56	11.98
$R_{(avg)}$	1.5	6.03	1.69	N/A	0.32	2.45	3.94	4.40	5.28	5.99

6 CONCLUSIONS

The surface roughness of five roughness gauge blocks was measured, quantified and these values compared to that of the surface roughness of a 100x100x100mm concrete block, with a cement to sand to aggregate ratio of 1:2:3.

The roughness profiles of three different piles were also measured and their potential modes of interface shearing analysed.

It was found that although the roughness gauge block offset texture does not have an effect on the mode of interface shear, comparing the relative roughness value with that of the concrete block, it can be seen that applying an offset distance of 0.25mm to a model pile would make it most representative to that of a prototype.

REFERENCES

Budhu, M., 2010. *Soil mechanics and foundations*. John Wiley and Sons.

Ebeido, A., Elgamal, A. and Zayed, M., 2018. Pile response during liquefaction-induced lateral spreading: 1-g shake table tests with different ground inclination. In *Physical Modelling in Geotechnics, Volume 2* (pp. 1335-1339). CRC Press.

El Haffar, I., Blanc, M. and Thorel, L., 2017. Impact of pile installation method on the axial capacity in sand. *Géotechnique Letters*, *7*(3), pp.260-265. https://doi.org/10.1680/jgele.17.00036.

Feligha, M., Hammoud, F., Belachia, M. and Nouaouria, M.S., 2016. Experimental investigation of frictional behavior between cohesive soils and solid materials using direct shear apparatus. *Geotechnical and Geological Engineering*, *34*, pp.567-578.

Ganiyu, A.A., Rashid, A.S.A., Osman, M.H. and Ajagbe, W.O., 2018. Model tests on soil displacement effects for differently shaped piles. In *Physical Modelling in Geotechnics, Volume 2* (pp. 1353-1358). CRC Press.

Gorasia, R.J. and McNamara, A., 2016. High-capacity ribbed pile foundations. *Proceedings of the Institution of Civil Engineers-Geotechnical Engineering*, *169*(3), pp.264-275. https://doi.org/10.1680/jgeen.15.00073.

Hammoud, F. and Boumekik, A., 2006. Experimental study of the behaviour of interfacial shearing between cohesive soils and solid materials at large displacement.

Lalicata, L.M., Ritchie, E., Stallebrass, S.E. and McNamara, A., 2023. Novel experimental technique to model impression piles in centrifuge testing. *International Journal of Physical Modelling in Geotechnics*, pp.1-14. https://doi.org/10.1680/jphmg.22.00065.

Lemos, L. J. L. & Vaughan, P. R., 2000. Clay–interface shear resistance. *Géotechnique* 50, No 1, 55–64. https://doi.org/10.1680/geot.2000.50.1.55.

Mandolini, A., Russo, G. and Viggiani, C., 2005, September. Pile foundations: Experimental investigations, analysis and design. In *Proceedings of the international conference on soil mechanics and geotechnical engineering* (Vol. 16, No. 1, p. 177). AA Balkema Publishers.

Martinez, A. and Stutz, H.H., 2019. Rate effects on the interface shear behaviour of normally and overconsolidated clay. *Géotechnique*, *69*(9), pp.801-815. https://doi.org/10.1680/jgeot.17.P.311.

Nietiedt, J.A., Randolph, M.F., Gaudin, C. and Doherty, J.P., 2023. Centrifuge model tests investigating initiation and propagation of pile tip damage during driving. *Journal of Geotechnical and Geoenvironmental Engineering*, *149*(5), p.04023024.

O'Hara, K.B. and Martinez, A., Shaft and Base Capacity of Snakeskin-Inspired Piles from Centrifuge Pile Tests. In *Geo-Congress 2022* (pp. 170-180).

Ouzzine, B., de Sauvage, J., Madabhushi, G., Viggiani, G. and Reiffsteck, P., 2023. Centrifuge modelling of an energy pile group with ground water flow. *International Journal of Physical Modelling in Geotechnics*, pp.1-25. https://doi.org/10.1680/jphmg.22.00041.

Panchal, J.P., McNamara, A.M., Halai, H. and Divall, S., 2019, September. Centrifuge modelling to determine the influence of pile stiffness on pile capacity. In *Proceedings of the XVII European Conference on Soil Mechanics and Geotechnical Engineering*. International Society for Soil Mechanics and Geotechnical Engineering.

Proceedings of the XVIII ECSMGE 2024
GEOTECHNICAL ENGINEERING CHALLENGES
TO MEET CURRENT AND EMERGING NEEDS OF SOCIETY
© 2024 the Authors
ISBN 978-1-032-54816-6
DOI 10.1201/9781003431749-505
Open Access: www.taylorfrancis.com, CC BY-NC-ND 4.0 license

ECSMGE 24
XVIII EUROPEAN CONFERENCE ON SOIL MECHANICS AND GEOTECHNICAL ENGINEERING

Performance of segmental driven geothermal energy piles subjected to impact and bending loads

Performance d'un pieu géothermique à entraînement segmentaire soumis à des charges d'impact et de flexion

H. Sadeghi, R.M. Singh*
Norwegian University of Science and Technology, Trondheim, Norway
**rao.m.singh@ntnu.no*

ABSTRACT: Geothermal energy pile foundations can extract and store geothermal energy as a renewable, sustainable, and affordable solution for heating and cooling buildings, besides providing structural support. The majority of energy piles are cast-in-place concrete piles that require drilling which is expensive and time-consuming. Another competitive option is driven energy piles made from precast concrete segments, that are cast in a concrete factory in large quantities and of high quality, then transported and installed on a construction site using innovative steel joints presented in this paper. Apart from providing structural integrity, these steel joints can provide leak-proof couplings for fluid circulation pipes inside sidewall channels, which are shielded using a steel cover plate riveted to the joint. Precast-driven pile foundations can be manufactured from high-strength concrete quadratic segments with 27 cm or 35 cm width, which are assembled via steel joints. There can be one U-loop in 270-mm piles or two U-loops in 350-mm piles. Steel pins connect the joints, and easy couplings connect the pipes quickly. The steel joints presented in this paper provide the opportunity to utilize segmental precast concrete pile foundations as energy piles. Field-scale impact tests and laboratory bending tests were carried out to ensure the piles were not affected by installation and service dynamic forces due to the incorporation of new joints. It was found that the segmental driven energy piles could easily take a minimum of 1000 blows without structural or leakage failure and also demonstrated a satisfactory bending stiffness.

RÉSUMÉ: Les fondations sur pieux d'énergie géothermique représentent une solution renouvelable, durable et abordable pour le chauffage et le refroidissement des bâtiments, tout en assurant un support structurel. La plupart des pieux énergétiques actuels sont en béton coulé sur place, nécessitant des forages coûteux et chronophages. Une alternative plus efficace réside dans l'utilisation de pieux énergétiques battus préfabriqués, composés de segments de béton de haute qualité, fabriqués en grande quantité en usine, puis transportés et installés sur site à l'aide d'innovants joints en acier présentés dans cet article. Outre leur rôle dans le maintien de l'intégrité structurelle, ces joints en acier assurent l'étanchéité des canaux latéraux destinés à accueillir les tuyaux de circulation de fluide. Protégés par des plaques de recouvrement en acier rivetées aux joints, ces canaux garantissent un fonctionnement optimal. Les fondations sur pieux battus préfabriqués peuvent être conçues à partir de segments de béton de 27 cm ou 35 cm de largeur, assemblés grâce à des joints en acier, avec une boucle en U pour les pieux de 270 mm ou deux boucles en U pour les pieux de 350 mm. Des broches en acier relient les joints, tandis que des raccords facilitent la connexion rapide des tuyaux. Les joints en acier présentés ici ouvrent la voie à l'utilisation de fondations segmentaires sur pieux en béton préfabriqué comme solution énergétique. Des essais sur le terrain et en laboratoire ont démontré la capacité de ces pieux énergétiques à supporter plus de 1000 impacts sans défaillance structurelle ni fuite.

Keywords: Precast concrete driven piles; geothermal energy piles; segmental piles; steel joint.

1 INTRODUCTION

Geothermal energy pile foundations can be used as a sustainable heating and cooling energy source for buildings (Hashemi et al., 2023). Based on the method of construction, energy piles can be categorized into two groups of cast-in-place and precast energy piles (Sadeghi & Singh, 2023c). Cast-in-place concrete energy piles dominated the market of energy piles, mainly due to some existing unresolved issues with precast concrete energy piles. The main limitation of precast concrete driven energy piles is that they are manufactured in segments of 12 m so that they can be transported to the installation site. In order to install these piles up to the competent bedrock level, several segments must be connected using steel joints. The main challenge about these steel joints is to couple the heat transfer loops between the segments, which was solved previously using a novel type of joint (Sadeghi & Singh, 2023a). Precast concrete driven energy piles have a higher quality, as they are manufactured in a concrete factory. Additionally, they require no

drilling, so they are more cost-effective, and their payback time is shorter compared to cast-in-place piles, and borehole heat exchangers (Sadeghi et al., 2022). Driven energy piles can also be used for storing thermal energy on a seasonal scale for buildings (Sadeghi et al., 2024).

In this study, the impact and bending performance of two sizes of concrete segmental driven energy piles, which are made of two segments connected by a novel steel joint are presented. The piles demonstrated a promising performance, which proves that they can be used in construction projects as a CE-certified product and with minimum risk.

2 DRIVEN ENERGY PILE JOINT

To connect precast concrete driven energy piles, a novel joint was previously designed and patented at the Norwegian University of Science and Technology (NTNU), known as driven energy pile (DEP) joints (Sadeghi & Singh, 2023d). DEP joints were developed in two sizes of 270 mm and 350 mm, which have two and four side wall channels, respectively, as shown in Figure 1.

DEP joints have two male and female dowels which are connected by strong steel pins, which are inserted into the joint from the pin ports on the side walls as shown in Figure 1. The heat transfer pipes are coupled inside the two sidewall channels, using commercially available fusion welding pipe couplings and the channels are subsequently covered using a shielding plate to protect the pipes from severe frictions in the ground.

Casting pile segments using the DEP joint is very simple and similar to the normal precast concrete piles. The only difference is that heat transfer pipes should be installed in the steel rebar cage before pouring the concrete into the formwork. The method of manufacturing the piles using driven energy pile joints was explained elsewhere (Sadeghi & Singh, 2023b).

Before using DEP joints in the construction industry, they must be tested according to the BS EN 12794 standard (Precast Concrete Products - Foundation Piles BS EN 12794:2005, 2005) to ensure their impact and bending performance. For this purpose, a total of six piles, which included three 270-mm and three 350-mm piles, were tested.

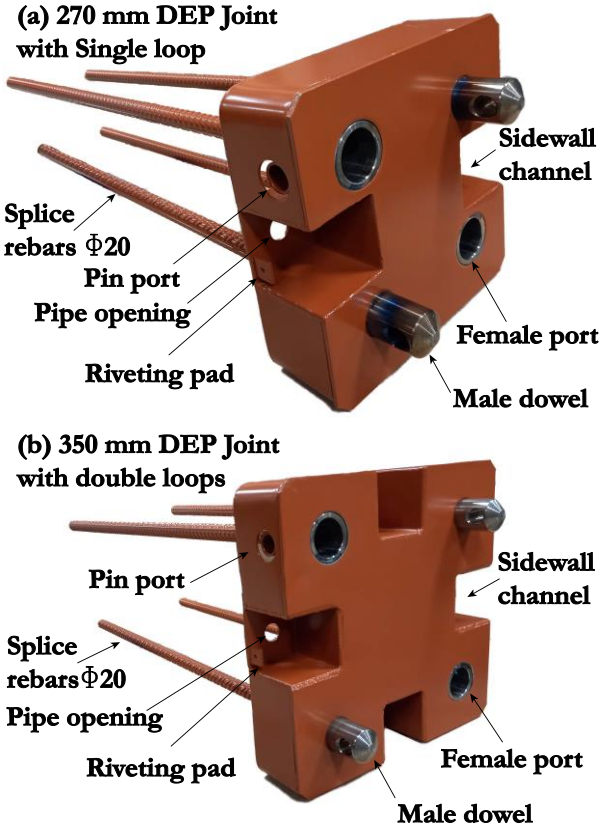

Figure 1. Details of DEP joint components, (a) 270-mm joint; (b) 350 mm joint (Sadeghi & Singh, 2024).

3 IMPACT TEST

According to the BS EN 12794 standard, the impact test consisted of applying 1000 impacts imposing a minimum of 28 MPa of compressive stress. Three piles were tested in each size (350 mm and 270 mm), which were composed of two segments that were 3 meters long. The pile segments had to stand vertically over a stiff bedrock or a flat steel plate in such a way that after applying the 1000 impacts, the joint remained above the ground. The pile segments were assembled, heat exchange pipes were coupled at the joint, and then the pile was taken inside a rigid steel box. The steel box could maintain the pile in place during the impact tests, without any penetration into the ground.

The stress level was monitored using pile driving analyzer (PDA) sensors that were installed below the joint as shown in Figure 1 (a). The number of the blows was counted both using a PDA device and also using the pile driving rig as shown in Figure 1 (b). After every 500 blows, the structure of the pile and the joints were visually inspected, and no cracks were observed. Additionally, the top and bottom segments were well-aligned (no inclination larger than 1:150). The impact test results are summarized in Table 1. The piles P4, P5, and P6 were 270 mm and piles P12, P9, P8 were 350 mm.

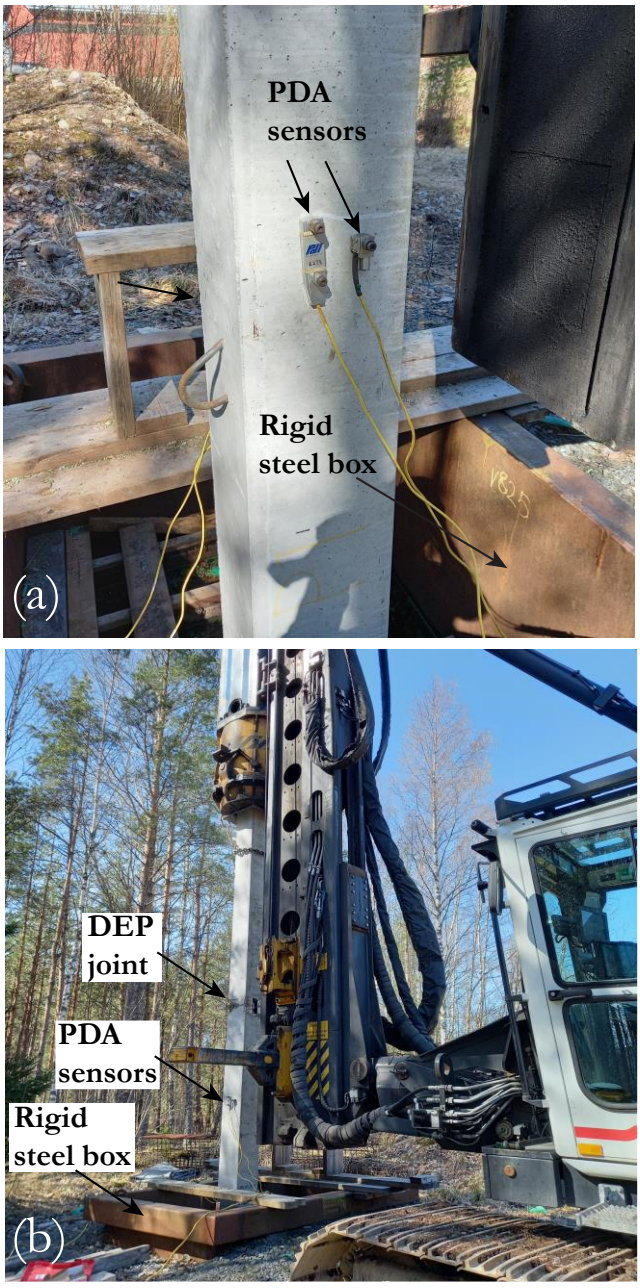

Figure 2. Impact test setup (Sadeghi & Singh, 2024).

Table 1. Measured stress levels and settlements during impact and blow tests.

Test piles	Average CSX [MPa]	Average CSI [MPa]	Blows	Settlement for 500/1000 blows [mm]
P6	32.1	39.2	≥ 1000	8 / 9
P5	29.9	40.0	≥ 1000	5 / 7
P4	30.5	42.6	≥ 1000	6 / 8
P12	29.3	32.9	≥ 1000	6 / 9
P9	28.8	30.7	≥ 1000	6 / 8
P8	29.5	35.3	≥ 1000	8 / 9

4 BENDING TESTS

After finishing the impact tests, the same piles were cut from both ends, so that their slenderness (width/length ratio) was between 11 and 12, and then they were sent to the structural laboratory for bending tests. Before doing the bending tests, the gap between the joints was measured due to its weight, and the weakest direction of the pile was chosen for the bending test. The setup for the measurement of the initial gap of the joint due to the self-weight of the pile is shown in Figure 3 and the results are summarised in Table 2.



Figure 3. Setup for the measurement of the initial gap of the joint due to the self-weight of the pile.

Table 2. Measured pile deflection values due to self-weight.

Test piles	Deflection due to own weight, Δy [mm] Side 1	Side 2	Side 3	Side 4	Opening Angle [°]
P6	0.27	0.27	0.27	0.27	0.020
P5	0.18	0.24	0.19	0.24	0.018
P4	0.23	0.36	0.23	0.37	0.028
P12	0.29	0.29	0.28	0.29	0.018
P9	0.37	0.31	0.35	0.32	0.022
P8	0.27	0.3	0.27	0.3	0.018

In the bending tests, two point-loads were applied to the piles at a distance of 1/3 of the total length of the piles from the supports. Three displacement sensors were used to measure the vertical displacement and also the changes in the gap between the two segments at the interface of the joints. The bending test setup is shown in Figure 4. The bending test results are summarized in Table 3. The yielding load and the maximum bending load were calculated using moment deformation curves for each pile.

The piles were loaded until the flexural failure occurred. As the flexural failure happened in the concrete structure of the piles after the calculated bending was reached, all of the piles passed the bending tests. Figure 5 shows the flexural failure, which happened in the concrete and the joints remained undamaged.

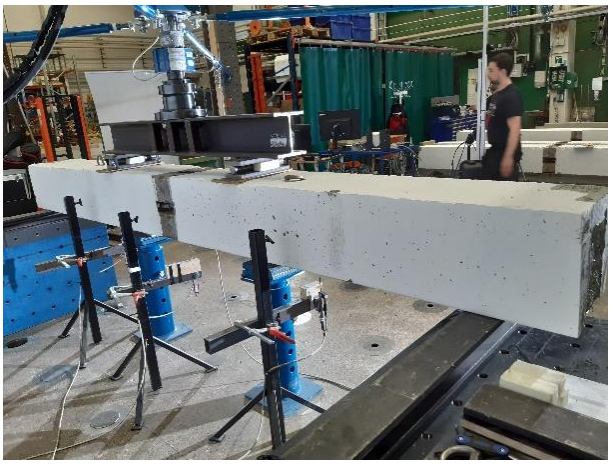

Figure 4. Bending test setup.

Table 3. Bending capacity results for the test piles.

Test piles	Max. external load [kN]	Max. moment [kN.m]	Yielding moment [kN.m]	Calculated Max. moment [kN.m]
P6	136	69.9	64	70
P5	140	71.1	65	70
P4	137	70.5	65	70
P12	180	109.8	96	103
P9	180	109.7	96	103
P8	180	109.8	97	103



Figure 5. Flexural failure outside the steel joint.

5 CONCLUSIONS

Large-scale impact and bending structural tests were performed on an innovative segmental precast concrete driven energy pile, which is composed of two segments connected using a steel joint.

The results of this study show that segmental driven energy piles have promising structural performance, similar to normal pile foundations. Driven energy piles can be considered as an option for future energy piling projects.

ACKNOWLEDGEMENTS

The authors are grateful for the financial support provided by the Research Council of Norway (project number: 332839). The authors are also grateful for the technical support from Leimet Oy, Finland for the production of the steel joints, and Sandnes and Jærbetong AS, Norway for manufacturing the concrete piles.

REFERENCES

Hashemi, A., Sutman, M., Medero, G. M. (2023). A review on the thermo-hydro-mechanical response of soil–structure interface for energy geostructures applications. *Geomechanics for Energy and the Environment*, *33*, 100439. https://doi.org/10.1016/j.gete.2023.100439.

Precast Concrete Products - Foundation Piles BS EN 12794:2005, 3 European Standard (2005).

Sadeghi, H., Ijaz, A., Singh, R. M. (2022). Current status of heat pumps in Norway and analysis of their performance and payback time. *Sustainable Energy Technologies and Assessments*. https://doi.org/10.1016/j.seta.2022.102829.

Sadeghi, H., Jalali, R., Singh, R. M. (2024). A review of borehole thermal energy storage and its integration into district heating systems. *Renewable and Sustainable Energy Reviews*. https://doi.org/10.1016/j.rser.2023.114236.

Sadeghi, H., Singh, R. M. (2023a). An innovative steel joint for driven geothermal energy piles. *12th Annual Conference on Deep Foundation Technologies for Infrastructure Development in India*.

Sadeghi, H., Singh, R. M. (2023b). Casting and installation of segmental precast quadratic concrete driven geothermal energy piles. *Symposium on Energy Geotechnics 2023*, 1–2.

Sadeghi, H., & Singh, R. M. (2023c). Driven precast concrete geothermal energy piles: current state of knowledge. *Building and Environment*, *228*(109790). https://doi.org/10.1016/j.buildenv.2022.109790.

Sadeghi, H., Singh, R. M. (2023d). *Joints for pre-cast driven piles* (WO2023084125A1). WIPO. https://patentscope.wipo.int/search/en/detail.jsf?docId=WO2020094923&_cid=P11-LI76OG-56648-1.

Sadeghi, H., Singh, R. M. (2024). A novel joint for driven concrete geothermal energy pile foundations. *Engineering Structures*, *301*(117270). https://doi.org/10.1016/j.engstruct.2023.117270.

Proceedings of the XVIII ECSMGE 2024
GEOTECHNICAL ENGINEERING CHALLENGES
TO MEET CURRENT AND EMERGING NEEDS OF SOCIETY
© 2024 the Authors
ISBN 978-1-032-54816-6
DOI 10.1201/9781003431749-506
Open Access: www.taylorfrancis.com, CC BY-NC-ND 4.0 license

ECSMGE 24
XVIII EUROPEAN CONFERENCE ON SOIL MECHANICS AND GEOTECHNICAL ENGINEERING

Influence of soil constitutive models on settlement prediction of urban tunnelling

Influence des modèles constitutifs du sol sur la prévision du tassement des tunnels urbains

B. Salehi*, B.S. Muntau
Universität Innsbruck, Innsbruck, Austria

**Bahram.Salehi@student.uibk.ac.at*

ABSTRACT: The validity of material models is a major field of research in soil mechanics. Different constitutive models have distinct stress-strain behavior, which can affect the results of the predicted deformation, failure mechanism, and load-bearing capacity of a geotechnical structure. In this regard, in this contribution, the application of three constitutive models in a Finite Element Analysis (FEA) of a well-documented case study is presented. This case study - Arash-Esfandiar tunnel - is a particular under-passing tunnel in the north of Tehran, Iran, starting from Modares highway and running to Niayesh highway. The tunnel project has a total length of 1532 m and was constructed with shallow overburden. The results indicate the necessity of using axial and bending elements as tunnel support measures at the same time. According to the large span of the tunnel and the geotechnical conditions, a combination of 4 different support elements was propose which includes, nails, micropiles, fore poling and, lattice girder. Various monitoring stations, including settlement points and geodetic points, have been installed as part of this project, providing extensive records of subsidence and tunnel deformation. The main goal of the numerical simulations is to investigate the influence of the material models on the results of accumulated subsidence for the stage construction method. The analysis outputs have been validated on available monitoring results of this actual tunnelling project. The results show a significant better performance of the hardening soil model when simulating the tunnel construction effects on the deformations of the excavation area and comparing them with the measurements results.

RÉSUMÉ: La validité des modèles de matériaux est un domaine de recherche majeur en mécanique des sols. Différents modèles constitutifs ont un comportement contrainte-déformation distinct, qui peut affecter les résultats de la déformation prévue, du mécanisme de rupture et de la capacité portante d'une structure géotechnique. À cet égard, dans cette contribution, l'application de trois modèles constitutifs dans une analyse par éléments finis (FEA) d'une étude de cas bien documentée est présentée. Cette étude de cas - tunnel Arash-Esfandiar - est un tunnel souterrain particulier dans le nord de Téhéran-Iran, partant de l'autoroute Modares et allant jusqu'à l'autoroute Niayesh. Le projet de tunnel a une longueur totale de 1532 m et a été construit dans un déblais peu profound peu profond. Les résultats indiquent la nécessité d'utiliser simultanément des éléments axiaux et de flexion comme mesures de soutènement du tunnel. Compte tenu de la grande portée du tunnel et des conditions géotechniques, une combinaison de 4 éléments de soutènement différents a été proposée : clou, micropieu, avant-pieu et poutre en treillis. Diverses stations de surveillance, y compris des points de règlement et des points géodésiques, ont été installées dans le cadre de ce projet, fournissant des enregistrements détaillés de l'affaissement de surface et de la déformation du tunnel. L'étude de l'influence des modèles de matériaux sur les résultats d'affaissement cumulé pour la méthode de construction d'étage est l'objectif principal des simulations numériques. Les résultats de l'analyse ont été validés sur les résultats de surveillance disponibles de ce projet de tunnel réel. Les résultats montrent une performance significativement meilleure du modèle de sol durcissant lors de la simulation des effets de la construction du tunnel sur les déformations de la zone d'excavation et en les comparants aux résultats des mesures.

Keywords: Tunnel; constitutive soil models; FEM, instrumentation.

1 INTRODUCTION

Any major cities worldwide require underground transportation systems, especially those grappling with issues related to population density and traffic congestion. The construction of tunnels and underground spaces may potentially impact the ground, leading to ground movement and settlement. These effects can be critical enough to disrupt the functionality of nearby structures. Consequently, one of the foremost concerns in tunnel construction revolves around ensuring the safety of the construction process itself, as well as safeguarding nearby structures, particularly in urban areas.

Geotechnical engineering is an evolving field focused on enhancing the precision of numerical analysis tools employed in simulating the interaction between soil and structures under complex load conditions. A critical aspect of this improvement is the development and validation of constitutive models that accurately represent the soil behavior. This paper endeavors to tackle the challenges associated with the selection of appropriate soil models for conducting realistic design analyses. In this regard, a specific case study has been chosen to examine the application of three different constitutive models (including: mohr-coulomb, hardening soil and hardening soil model with small strain) within a Finite Element Analysis (FEA) framework and to corroborate the findings with the data obtained from on-site monitoring.

2 SOIL CONSTITUTIVE MODELS

Material constitutive models range from simple elastic perfectly plastic models (Drucker and Prager, 1952 and Mohr-Coulomb, by Jaeger and Cook, 2009) to models using critical state concepts models using multi-yield surfaces (Prevost, 1977), and double hardening models (Lade, 1977), to name a few.

In this research Mohr-Coulomb model (MC) is chosen from the available models due to its simplicity and widespread use in practical applications. Numerical modelling of the tunnelling with MC has proven inaccurate due to the lack of ability to properly simulate the phenomenon of unloading and the lack of distinction between the hardships of initial loading and unloading/reloading (Schanz et al, 1999). To overcome that disadvantage the Hardening Soil model (HS) selected as second model. HS is an advanced elastoplastic constitutive model that is used for simulating both stiff and soft soil behaviors (Schanz et al, 1999). HS also relates stiffness parameters to the stress-level and simulates the development of plastic strains under compressive loading. HS can distinguish between loading and unloading path.

The third model used is the hardening soil model with small strain stiffness (HSS). This model is an extension of HS considering increased stiffness for small strains (Benz, 2007). At low strain levels, most soils exhibit a higher stiffness, and this stiffness varies non-linearly with strain.

3 CASE STUDY

In this research, an underground tunnel located in the northern region of Tehran, the capital of Iran, will be examined. This tunnel, known as the Arash-Esfandiar-Niayesh Tunnel, is situated within the third district of Tehran Municipality. It is constructed to facilitate east-to-west connectivity in this locality, connecting East Arash Street with the starting point of Niayesh Highway. (Figure.1). The current study is modified after Salehi et al (2023).

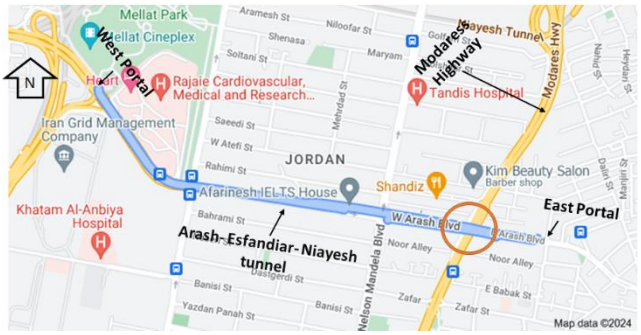

Figure 1. Plan of Arash- Esfandiar tunnel.

This project is constructed by New Austrian Tunneling Method (NATM). NATM was introduced in Austria during 1957-1965 by Rabcewicz. The idea of this method is to allow a certain amount of deformation in the surrounding rock or soil to reduce the stresses acting on the final support of the tunnel, (FHWA, 2009).

3.1 Soil Condition

The geological and geotechnical characteristics of the different soil types were established through laboratory assessments conducted on numerous samples obtained from seven boreholes and four test pits. For this study, we focused on four boreholes, each with a depth of 50 meters, and one test pit with a depth of 19 meters, all located within the project area. There was no sign of water table level up to the end of borehole (50m). After conducting laboratory tests and on-site investigations, the soil types were classified cemented granular and as follows: medium dense silty gravel up to 3.5 m depth, very dense silty sandy gravel and dense clay sand (located beneath the gravel layer). (found at depths of -3.5 to -50 meters),

Table 1 presents an overview of the key geotechnical parameters essential for our research and based on each constitutive soil model. Shear strength parameters are extracted from in situ shear, direct shear and triaxial tests. Stiffness parameters are extracted from pressuremeter test and plate load test is carried out to investigate the ratio of loading and unloading. Instead of using the Young's modulus as a stiffness parameter, alternative stiffness parameters were used (Eoed and G) and the young's modulus calculated automatically. Oedometer modulus (Eoed) is obtained for 90 kPa stress level to account to the tunnel depth at the top of the excavation.

Table 1. Geotechnical parameters.

First layer (0 to -3.5)	Second layer (-3.5 to -50) m
$\varphi = 30^\circ$	$\varphi = 37^\circ$
$c = 9.8$ kN/m^2	$c = 24$ kN/m^2
$\gamma = 17$ kN/m^3	$\gamma = 18$ kN/m^3
HS and HSS specified parameters	
$\nu_{ur} = 0.2$	$\nu_{ur} = 0.2$
$E_{ref\,(50)} = 4.0$ e04 kN/m^2	$E_{ref\,(50)} = 7.0$ e04 kN/m^2
$E_{ref\,(oed)} = 4.0$ e04 kN/m^2	$E_{ref\,(oed)} = 7.0$ e04 kN/m^2
$E_{ur(HS)} = 12.0$ e04 kN/m^2	$E_{ur(HS)} = 21.0$ e04 kN/m^2
m= 0.5	m= 0.5
$G_{0\,(ref)} = 5.856$ e04 kN/m^2	$G_{0\,(ref)} = 11.7$e 04 kN/m^2
$\gamma = 0.1$ %	$\gamma = 0.1$ %
M – C specified parameters	
$\nu = 0.2$	$\nu = 0.2$
$E_{oed} = 4.0$ e04 kN/m^2	$E_{oed} = 7.0$ e04 kN/m^2
G = 1.15 e04 kN/m^2	G= 2.625 e05 kN/m^2

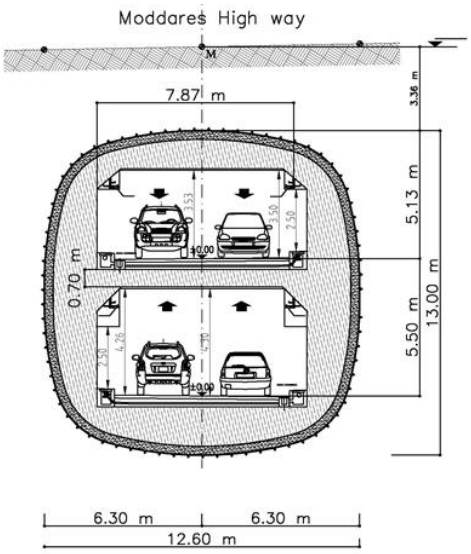

Figure 2. Modares two-level tunnel section

3.2 Tunnel Geometry

On one hand, there was a need to establish multiple entry points to access the project site from West Arash Street and Esfandiar. On the other hand, project constraints made it necessary to employ various geometric configurations during construction. To address the requirement for a two-way traffic option beneath Modares Highway, despite limited available space, the decision was made to implement a two-level tunnel. Thus, the Modares two-level tunnel became a component of the Arash-Esfandiar-Niayesh tunnel project. The tunnel section measures 12.2 meters in width and 13 meters in height, as shown in Figure 2. Given the shallow depth of the tunnel and its passage beneath major urban arteries close to tall buildings, the New Austrian Tunneling Method (NATM) was chosen as the construction method for this project.

3.3 FEM Model

The tunnel structure and the surrounding soil have been simultaneously simulated using the PLAXIS 2D finite element program. The construction stages and the continuous implementation of tunnel excavation were incorporated into the model to align with the actual construction process. To represent the various layers of the ground, 15-node triangular elements were employed, as shown in Figure 3. To comprehensively assess the extent impacted by the construction of underground structures, a model with a width of 80 meters and a height of 40 meters was created, which is 10 times the tunnel's diameter in width and 3 times in height. The tunnel's overburden within the investigated sections is a minimum of 4 meters, which has been considered in the geometric definition of the model. In this paper, the stress reduction or relaxation method is utilized to simplify the model and simulate the 3D problem. The relaxion factor are estimated based on previous research concerning this project (Golshani et al., 2018),) according to a 3D model and the Vlachopoulos and Diederich (2009) methods. The relaxation factors (RF) for each excavation phase are as follows: 35% in Top (Stage I to III), 20% in Bench (Stage IV to IX) and 15% in Invert (Stage X to XII).

3.4 Support System

Within the New Austrian Tunneling Method (NATM), various elements are employed to provide both temporary and permanent support for tunnels. Shotcrete is a commonly utilized material for temporary support during tunnel excavation. This choice is primarily made because no other support method can effectively bond the ground surface, preventing it from deteriorating or loosening in the same manner that shotcrete does.

A rock bolt or nail serves as a supporting element to enhance the stability of rock excavations, often employed in tunnels or rock cuts. Its primary function is to shift the load from the less stable outer areas to the more solid and robust interior of the rock mass. Rock bolts function by essentially "knitting" together the rock mass, preventing it from moving significantly and potentially coming apart piece by piece, which could lead to instability or failure.

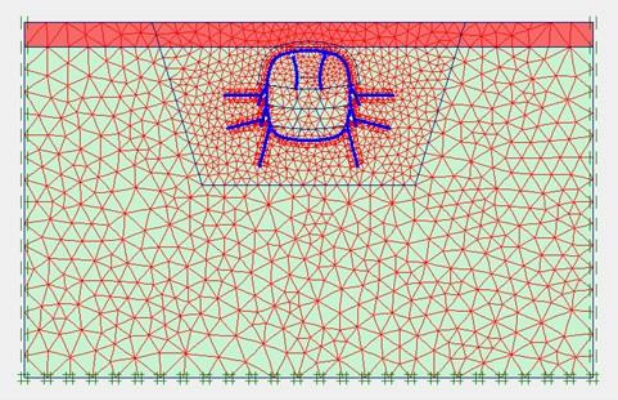

Figure 3. Meshing plot of Modares two level tunnel

One way to mitigate ground movements caused by tunneling is to employ in-tunnel support methods, such as the forepoling umbrella system. This system consists of steel pipes that offer structural support to the soil surrounding and above the tunnel excavation. Forepoling arches are specific tunnel heading reinforcements utilized to bolster the unsupported section of the tunnel heading during the excavation of tunnels in soft ground or loose soil conditions. In the current research according to the large span of the tunnel and the geotechnical conditions, a combination of 4 different support elements was proposed. A classification of the suggested support system and their combination is provided in Table 2.

In the two-level section, known as the Modares Tunnel, the primary walls will receive support through a combination of 35 cm thick shotcrete and lattice girder truss metal structures. In cases where additional support is needed, forepoling elements will be incorporated alongside micropiles and nails.

Additionally, the temporary walls will be reinforced with 25 cm thick shotcrete and lattice structures. In the numerical model, the shotcrete support is simulated with parameters corresponding to 7-day and 28-day settings, including Elastic Modulus values of 18.7+06 kPa and 23.4+06 kPa, respectively. The loading in this section is primarily static and results from the overburden of the tunnel. Additionally, the model takes into account the load imposed by the traffic on Modares Highway, which amounts to 20 KN/m per meter.

The initial lining of the tunnel was constructed with thicknesses of 35 cm and 25 cm, using shotcrete of class C25 and lattice girder steel bars of type III. In the modeling process, the lining structure was represented using plate elements, and a linear elastic behavior was assigned to the reinforced shotcrete material. Once stable initial conditions were established, and traffic-related loads were activated, simulations of the excavation and stage stabilizations is proceeded. It should be mentioned that the term "top" refers to stages 1 to 3 of excavation, "bench" refers to stages 4 to 9 and "invert" refers to stages 10 to 12, presented in Figure. 4.

Table 2. Classification of the examined support systems in Modares two-level tunnel.

Support system	Class
Lattice+shotcrete	A
Lattice+shotcrete+forepoling	B-I
Lattice+shotcrete+micropile	B-II
Lattice+shotcrete+nail	B-III
Lattice+shotcrete+forepoling+nail	B-IV
Lattice+shotcrete+forepoling+micropile	C-I
Lattice+shotcrete+nail+micropile	C-II
Lattice+shotcrete+forepoling+nail+ micropile	D

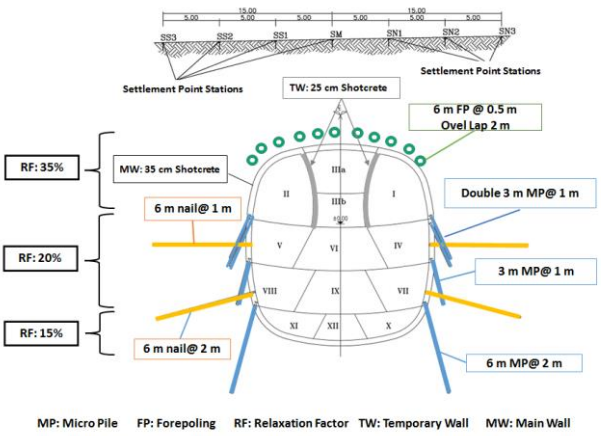

Figure 4. Excavation stages, initial support (Class D), and settlement points on Modares two-level tunnel.

3.5 Instrumentation

In the Arash-Esfandiar-Niayesh tunnel project, several measurement techniques were employed to monitor ground settlements and validate the numerical model across different profiles. In the two-level section of the project, a settlement measurement system was implemented to capture surface deformations, denoted as Settlement South (SS), Settlement Middle (SM), and Settlement North (SN). The layout of the instrumentation plan is depicted in Figure 4. It's important to note that the internal deformation is measured using optical reflectors, but since this research does not encompass internal convergence, it won't be discussed in this paper.

4 RESULTS

After solving the model, it was determined that using only shotcrete and lattice for temporary support would lead to develop a shear zone during the second bench excavation and tunnel will collapse. Consequently, to ensure a stable excavation process, 76 mm pipes with a 5 mm thickness were introduced for forepoling. However, despite the inclusion of forepoling in the model, structural instability resurfaced in tunnel excavation section VIII. To reduce the stresses from the initial support (shotcrete and lattice), additional axial elements were introduced. In this scenario, self-drilling nails with a 32 mm diameter (86 mm drilling diameter) and spaced 1 meter apart were chosen and implemented at two different heights.

Furthermore, the potential use of micropile elements was investigated as a meansof managing the vertical displacements. The calculations for the characteristics of micropiles resembled those of self-drilling nails. However, when micropiles were employed in isolation, the model once again exhibited instability during excavation in section X. As a result, the subsequent step involved investigating the combined use of forepoling and nails.

Given the project's sensitivity and its passage beneath a major urban traffic road, a decision was made to reinforce the tunnel using a class D support system. By combining axial and bending support structures, such as forepoling and nails, not only can displacement be minimized, but tunnel stability can also be ensured.

The overall pattern of recorded displacements aligns with the outcomes derived from the Finite Element calculations. The HS model oversestimates the displacements. In contrast, the MC and HSS models consistently produce results that underestimate the observed displacements. On the other hand, the absolute maximum settlement values align with the result of the numerical analysis. For example, when the temporary wall was removed, a measured settlement of 1 cm corresponded to the numerical results. It should be noted that in nearly all stages, there is a significant and immediate increase in settlements (a change in slope) in the FEM analysis results earlier than what's observed in the monitoring data. The results of the Finite Element Method (FEM) analysis indicate total vertical displacements of 2.7 cm, 2.1 cm, and 1.4 cm for the Hardening Soil, Small Strain Hardening Soil, and Mohr-Coulomb soil models, respectively.

In contrast, according to the settlement point records, the maximum vertical displacements at the ground surface were observed to be 2.6 cm as shown in Figure 5.

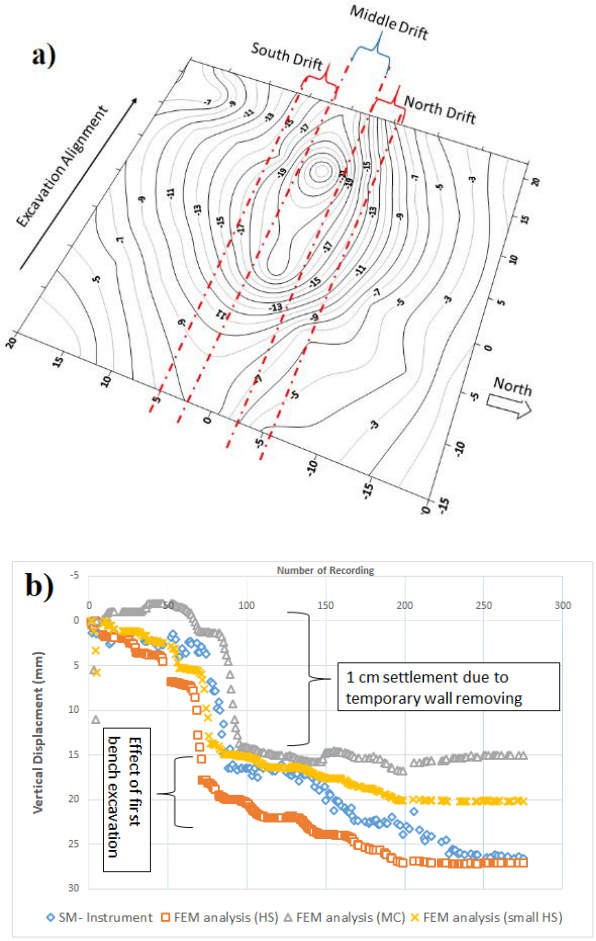

Figure 5. Surface Settlement: a) Normalized recording charts, b) Comparison of onsite measurements and FEM results in SM station (above the tunnel axis).

In Figure 5b, The horizontal axis is the number of instrument recordings (can be interpreted as time) in the construction site which is synchronized by the excavation and FEM model construction stages. The cumulative sum of settlements is selected to illustrate the progressive subsidence attributed to the excavation stages.

5 CONCLUSIONS

The findings from both the analysis and field data highlight the substantial influence of the tunnel's geometric shape on its stability and the distribution of stress. Prior to commencing operations, various options for stabilization methods were thoroughly reviewed and subjected to numerical modeling. The results obtained underscore the inadequacy of conventional support systems for shallow tunnels with an ovoid section. In such cases, relying solely on shotcrete and lattice girder elements, even in combination with forepoling, proves insufficient to ensure both structural and geotechnical stability of the

tunnel. This limitation is primarily attributed to the significant height of the tunnel section and the high bending moment experienced by the beam elements. In addition to employing micropiles and forepoling to control surface settlement, the use of nails at two levels becomes imperative to alleviate stresses on the shotcrete and lattice and ensure the structural stability of the tunnel.

The results from the numerical model indicate that the incorporation of forepoling elements results in arching around the structure, leading to a decrease in surface settlements as well as a reduction in bending moments and shear forces. The minimum settlement achieved with the selected support system (type D) amounts to 2.7 cm at the surface.

The settlement monitoring records indicate a maximum vertical displacement of 2.7 cm at both the surface and within the tunnel. The absolute value of the final settlement in the numerical analysis method (based on the HS model) aligns with the measured data. However, there are some differences in the trends of the two diagrams (as shown in Fig. 5 (b)). In the on-site measurements, the slope in settlement curve becomes zero after the temporary lattice girders are removed, and despite the excavation of the first bench, the displacements exhibit a constant trend. In contrast, numerical model still show increase in displacements. This could be attributed to the application of relaxation factors during the excavation of the first bench. In practice, no increase in displacement was observed until the excavation of the middle part of the first bench (excavation section VI, Figure 4). This trend is also evident in the second bench excavation but with less impact. Furthermore, the final stage of excavation (invert) had minimal effect on surface displacements.

However, in complex situations with quasi-rectangular geometric sections, complicated support systems and high side walls, 3D modelling is required for accurate assessment. If the 2D method is used, simplification requires a more specific approach. In particular, the relaxation factor should be calibrated based on each soil constitutive model. This topic is an ongoing research in our team and results will be presented at the upcoming events.

REFERENCES

Benz, T. (2007). *Small-Strain Stiffness of Soils and its Numerical Consequences*. PhD thesis. Geotechnical Institute – University of Stuttgart. Available at: [https://www.igs.uni-stuttgart.de/dokumente/Mitteilungen/55_Benz.pdf], accessed: 22/10/2022.

Drucker, D.C. and Prager, W. (1952). Soil mechanics and plastic analysis or limit design, *Quarterly of Applied Mathematics,* 10 (2), pp.157-175. https://doi.org/[10.1090/qam/48291].

FHWA (2009). Technical manual for design and construction of road tunnels civil elements., Department of transportation federal highway administration, Washington, D.C, USA, Rep. -NHI-09-010.

Golshani, A., Varnusfaderani M. and Majidian S (2018). Comparing Field Displacement History with Numerical Results to Estimate Geotechnical Parameters: Case Study of Arash-Esfandiar-Niayesh under Passing Tunnel, 2.5 Traffic Lane Tunnel, Tehran, Iran. *International Journal of Geotechnical and Geological Engineering*, 12(9):180-195. https://doi.org/[10.5281/zenodo.1474509].

Jaeger, J.C., Neville GW.C. and Robert Z. (2009). *Fundamentals of rock mechanics*. John Wiley & Sons, New York, USA. https://doi.org/[10.1017/CBO9780511735349].

Lade, P. V. (1977). Elasto-plastic stress-strain theory for cohesionless soil with curved yield surfaces, *International Journal of Solids and Structures*, 13(11), pp.1019-1035, https://doi.org/[10.1016/0020-7683(77)90073-7].

Prevost, J. H. (1977). Mathematical modeling of monotonic and cyclic undrained clay behavior, *International Journal of Numerical and Analytical Methods in Geomechanics*, 1(2), pp.195-216. https://doi.org/[10.1002/nag.1610010206].

Salehi, B., Golshani, A., Rostami, J. and Munatu, B.S. (2023). Simulation of Complex Support Systems for Large Span Tunnels: Investigation on Support Interferences and Effects of Constitutive Models*, KSCE Journal of Civil Engineering,* (submitted).

Schanz, T., Vermeer, PA. and Bonnier, PG. (1999). The Hardening Soil model: Formulation and Verification. In: *Beyond 2000 in Computational Geotechnics*, Rotterdam, Holland, pp. 281-296.

Vlachopoulos, N. and Diederichs, M. (2009). Improved Longitudinal Displacement Profiles for Convergence Confinement Analysis of Deep Tunnel. *Rock Mechanics and Rock Engineering*. 42. 131-146. https://doi.org/[10.1007/s00603-009-0176-4].

Proceedings of the XVIII ECSMGE 2024
GEOTECHNICAL ENGINEERING CHALLENGES
TO MEET CURRENT AND EMERGING NEEDS OF SOCIETY
© 2024 the Authors
ISBN 978-1-032-54816-6
DOI 10.1201/9781003431749-507
Open Access: www.taylorfrancis.com, CC BY-NC-ND 4.0 license

ECSMGE 24
XVIII EUROPEAN CONFERENCE ON SOIL MECHANICS AND GEOTECHNICAL ENGINEERING

Pressure cell results for a ballasted railway track section tested in the CEDEX Track Box

Résultats de la cellule de pression pour un tronçon de voie ferrée testé dans la boîte à outils CEDEX Track Box

M. Santana*, S. Merino, J. Estaire
Laboratorio de Geotecnia/CEDEX/Madrid, Spain

**Maria.S.Ruiz@cedex.es*

ABSTRACT: CEDEX Track Box (CTB) is a 21 m long, 5 m wide and 4 m deep facility whose main objective is to test, at 1:1 scale, complete railway track sections of conventional and high-speed lines for passenger and freight trains, at speeds up to 420km/h. Its special characteristics allow the testing of different railway sections, types of trains, passing by velocities and materials in advance of their use in the real railway. In this work, we present the results obtained from pressure cells located at several depths inside the railway track section, after testing two different types of trains at eight different passing-by speeds (from 50 to 400 km/h). The railway train section tested in this work has the same requirements as the Spanish ballasted high-speed track sections. These tests show the distributions of pressures underneath the superstructure and how they are affected by the different loads of each type of train and the several passing-by speeds.

RÉSUMÉ: Le CEDEX Track Box (CTB) est une installation de 21 m de long, 5 m de large et 4 m de profondeur dont l'objectif principal est de tester, à l'échelle 1:1, des tronçons complets de voies ferrées de lignes conventionnelles et à grande vitesse pour les trains de passagers et de marchandises, à des vitesses allant jusqu'à 420km/h. Ses caractéristiques particulières permettent de tester différents tronçons ferroviaires, types de trains, vitesses de passage et matériaux avant leur utilisation dans le réseau ferroviaire réel. Dans ce travail, nous présentons les résultats obtenus à partir de cellules de pression situées à plusieurs profondeurs à l'intérieur de la section de voie ferrée et après avoir testé 2 types de trains différents à 8 vitesses de passage différentes (de 50 à 400 km/h). La section de voie ferrée testée dans ce travail répond aux mêmes exigences que les sections de voies à grande vitesse ballastées espagnoles. Ces essais montrent la répartition des pressions sous la superstructure et la manière dont elles sont affectées par les différentes charges de chaque type de train et les différentes vitesses de passage.

Keywords: Railway track section; pressure cells; train velocities.

1 INTRODUCTION

Mobility policies in the European Union are encouraging the use of rail transport to promote more sustainable mobility. Considering the lower environmental impact of railway transportation mode compared to other modes of mass transportation (road, air, maritime), the European Green Deal aims to shift to rail transport to reduce CO_2 emissions.

Spain has an important network of high-speed lines, with more than 3,400 km. The vast majority of the railway sections of these lines are built with a ballast layer instead of slab track. In recent years, comparative studies of the pros and cons of one construction system versus the other have pointed to the need for greater maintenance on the sections built with ballast (Charoenwong et al. 2023).

Ballast maintenance operations consist mainly of tamping the layer or replacing the material when track movement levels are excessive. Since one of the main functions of the ballast layer is the absorption of loads transmitted by the train, it is interesting to study how these loads are transmitted to the lower layers of the section and what factors may be involved.

One of the tasks carried out by Laboratorio de Geotecnia - CEDEX is the auscultation of railway sections. This auscultation on real tracks is the perfect complement to the tests carried out at the CEDEX Track Box (CTB) facility.

2 CEDEX TRACK BOX

CEDEX Track Box (CTB) is a 21 m long, 5 m wide and 4 m deep facility whose main objective is to test, at 1:1 scale, complete railway track sections of conventional and high-speed lines for passenger and freight trains, at speeds up to 420 km/h. Figure 1 shows

a general view of the testing facility and the hydraulic actuators that apply the loads to simulate the railway traffic (Estaire et al., 2018).



Figure 1. General view of the CEDEX Track Box and the hydraulic actuators.

Its principal advantage is the possibility of performing fatigue tests in a fast way as in 10 working days, the effect of a train passing-by during a year in a real section can be modelled.

The reproduction of the effect of the approaching, passing-by and departing of a train in a test cross-section, as it occurs in a real track section, is performed by application of loads, unphased as a function of the train velocity which is being simulated, produced by three pairs of hydraulic actuators (each of them can apply a maximum load of 250 kN at a frequency of 50 Hz), placed on each rail and 1.5 m longitudinally separated.

The railway track response, in terms of displacements, velocities accelerations and pressures, is collected from LVDTs, geophones, accelerometers and pressure cells installed both inside the embankment and the bed layers of the track. The railway superstructure response is recorded with mechanical displacement transducers, laser sensors, geophones and accelerometers installed on the different track components (rail, sleeper and railpad).

CTB has been used to research different matters, such as the measurement of track vertical stiffness under different track conditions and the determination of track lateral stability. More detailed information is described at Estaire et al. (2018).

In this work, the tests carried out on the installation were used to determine the vertical pressure in the different layers of the railway section, produced by different types of trains and passing speeds.

3 TESTS DESCRIPTION

3.1 Introduction. General aspects

This work is part of a larger study of ballast degradation as a function of the type of trains and speeds modelled in the tests. The results shown were obtained from the analysis of static and dynamic tests and focused on measurements obtained with pressure cells placed inside the layers of a ballasted track model built in CTB.

The load applied by the trains is transmitted from the rail to the sleepers and the layers constituting the railway section. One of the ballast layer main functions is to absorb these loads. The placement of pressure cells at the different transitions between layers will make it possible to analyse how loads are transmitted from the rail to the embankment and whether the speed of the train passing through has any effect on those pressures.

3.2 Static load tests

The static load is applied by two hydraulic actuators (one in each rail) installed in the central cross-section of the model under study: a typical ballasted rail track.

The static tests, whose aim is to determine the track stiffness, consisted of three loading-unloading cycles in which a maximum load of 95 kN (per actuator) was reached, applied step by step, simulating the effect of a passenger train. The duration of each static test was around 50 minutes. This test is inspired by ADIF technical specification ET 03.360.570.0. Figure 2 shows the three load cycles of each static test.

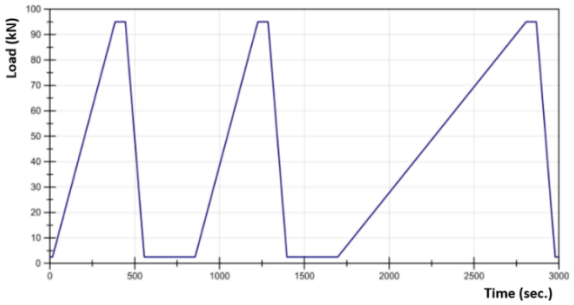

Figure 2. Sequence of load-unload cycles applied in the static tests.

3.3 Dynamic load tests

Dynamic load tests allow the modelling of the passing-by of trains at different speeds. For this purpose, the three pairs of hydraulic actuators (Figure 1) are synchronised in such a way as to reproduce the effect of the approach, passing-by and departure of the train in the central section of the model for any kind of train running up to 420 km/h.

3.4 Description of trains

The following table shows the most relevant characteristic of the trains modelled in the CTB: train type, number of axles and their total weight. Of the types of trains operating on the Spanish network, the following two trains were chosen because of their different axle configuration: bogies (Siemens S103) and isolated wheels (Talgo S112).

Table 1. Main characteristics of trains used in the study.

Train	Number of axles	Total Weight (t)
Talgo S112	21	357.0
Siemens S103	32	463.3

3.5 Passing-by train speeds

For each of the trains described above, dynamic tests were carried out at 50, 100, 150, 200, 250, 300, 350 and 400 km/h. Therefore, a total of 16 tests were performed.

It can be highlighted that the two greater speeds (350 and 400 km/h) are above the current nominal speeds (300 km/h) at high-speed train lines, although 350 km/h is usually used for the approval tests.

3.6 Instrumentation

The railway track section is profusely instrumented. In this work, only the results obtained with pressure cells are analysed. Figure 3 shows the location of pressure cells in the central section of the test and Figure 4 a detail of these cells placed at the sleeper bottom.

Rectangular and circular pressure cells of 25x15 cm and 17 cm diameter were used respectively. The measuring range of these cells varies according to the interface analysed: 0-1 MPa at sleeper-ballast, 0-0.5 MPa at ballast-subballast, 0-1 MPaat subballast-form layer and 0-0.2 MPa at form layer-embankment interfaces. Cell pressures are located under the rails to measure the stress peak since it is known that the contact surface and the stress distribution beneath the sleeper are not uniform.

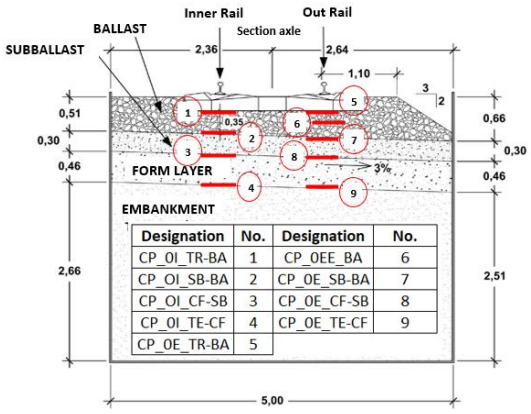

Figure 3. Load configuration for each train at CTB.



Figure 4. Pressure cell placed under the sleeper.

4 RESULTS OBTAINED

4.1 Results in the different layer interfaces

Figure 5 shows the variation of pressure with depth, measured by pressure cells, during the third cycle of static tests. The vertical stress distribution due to a rectangular load according to Fadum's theory is also shown.

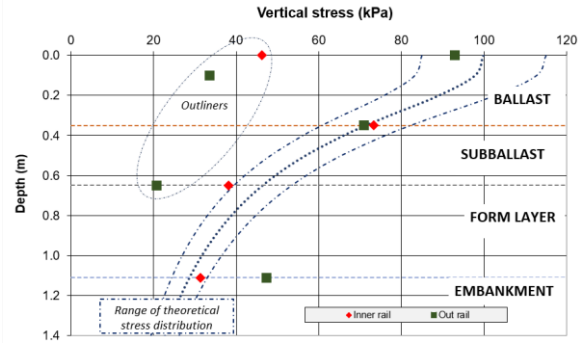

Figure 5. Pressure values measured by a pressure cell and theoretical stress distribution.

The measured values globally follow Fadum's theory which shows the stress distribution inside the track bed layers. This implies that in the subballast top surface, the stress is reduced to 70% of the stress transmitted by the sleeper while in the form layer and the embankment below, the vertical stress is around 30-40% of the initial stress.

On the other hand, three of the nine measures can be considered as outliners, two of them being relative to the ballast layer. This is due to the great size of the ballast particles which provokes that the stress in the ballast layer is transmitted through contact points whose loads are difficult to capture by the measuring surface of the pressure cells. This difficulty in obtaining accurate pressure measurements with this type of instrumentation is one of the main aspects to be highlighted as a result of the present work.

4.2 Results obtained with train speed variation

This section shows the measurements obtained with the pressure cells placed under the inner rail in the dynamic tests for different train speeds. Figure 6 shows the maximum pressure values, relative to the values obtained at 50 km/h, for the two trains modelled, as a function of the train speed. The graphs also include the dynamic amplification factor DAF $[DAF = \frac{1}{\sqrt{1-\left(v/v_{crit}\right)^2}}]$ for a critical velocity (v_{crit}) of

- 600 km/h, a typical value of a high-speed line, to model the platform layers, and
- 430 and 450 km/h, to model the ballast layer.

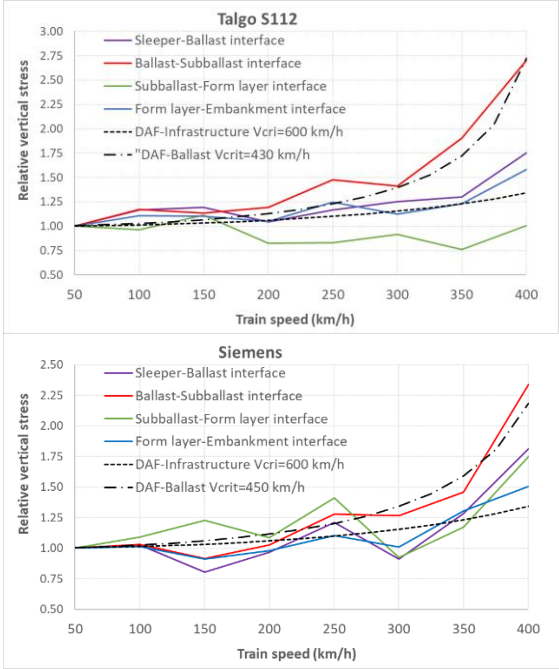

Figure 6. Relative pressure cell measurements placed under the inner rail and Dynamic Amplification Factor.

These graphs show that the vertical stresses are fluctuant due to the problems derived from this kind of measurements, although an increasing trend can be seen, similar to the one shown by DAF. An increase of around 20%, relative to the static value, when the speed is 300 km/h is seen. However, two aspects show a significant increase, out of the general trend: the measurements done in the ballast-subballast interface (plotted with red lines) and the ones obtained in the tests performed at 400 km/h.

Finally, Figure 7 and Figure 8 show the vertical stress measured in the ballast-subballast interface during the tests in which trains were modelled running at 50 and 300 km/h. The stresses measured follow quite well the loads imposed by the train axle.

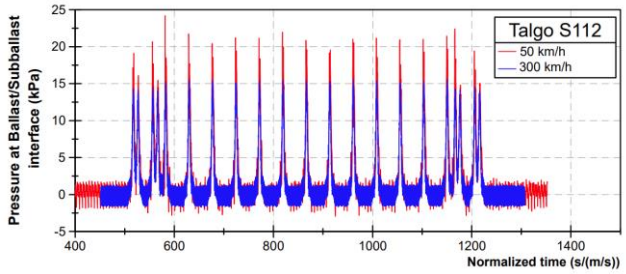

Figure 7. Vertical stress measured during the modelling of Talgo S112 train at 50 and 300 km/h

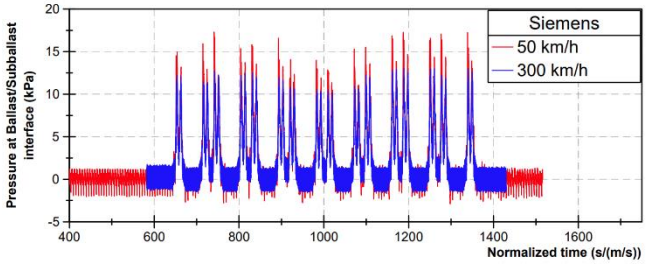

Figure 8. Vertical stress measured during the modelling of Siemens train at 50 and 300 km/h

5 CONCLUSIONS

The CTB allows modelling and measuring the response of a railway track section under laboratory conditions. This work shows the results obtained on pressure cells placed at different depths of the section, which were tested with the passage of two types of trains at different speeds.

The results show that the measurements obtained with this instrumentation are a bit erratic, on many occasions, due to the difficulty of measuring normal pressures in a granular medium by a flat surface where several contact points are produced. The fact that the pressure, in the different interfaces present in railway sections, transmitted by the trains, follows Fadum's law of load distribution under a rectangular load was verified. The increase of the vertical stress with the speed of the trains and the fact that, during the pass-by of trains at different speeds, the normal pressure varies according to the loads imposed by the train axles were also observed.

REFERENCES

ADIF (2005). Especificación Técnica ET 03.360.570.0. Placas elásticas de asiento para sujeción VM. Ensayo de rigidez vertical secante 20 / 95 kN. ADIF. 1ª edición, diciembre de 2005.

C. Charoenwong, D.P. Connolly, A. Colaço, P. Alves Costa, P.K. Woodward, A. Romero, P. Galvín, (2023). Railway slab vs ballasted track: A comparison of track geometry degradation. *Construction and Building Materials*, (378), 131121,ISSN 0950-0618.

Estaire J., Cuéllar V., Pardo F. and Santana M. (2018). Testing railway tracks at 1:1 scale at CEDEX Track Box. *360.Rev.alta velocidad*, 5 junio, pp.191-217.

Proceedings of the XVIII ECSMGE 2024
GEOTECHNICAL ENGINEERING CHALLENGES
TO MEET CURRENT AND EMERGING NEEDS OF SOCIETY
© 2024 the Authors
ISBN 978-1-032-54816-6
DOI 10.1201/9781003431749-508
Open Access: www.taylorfrancis.com, CC BY-NC-ND 4.0 license

ECSMGE 24
XVIII EUROPEAN CONFERENCE ON SOIL MECHANICS AND GEOTECHNICAL ENGINEERING

Foundation piles and submerged wall of berths 6, 7 and 8 at the Port of Maputo

Pieux de fondation et mur immergé des quais 6, 7 et 8 du Port de Maputo

J. Santos*, L. Tomás
Mota-Engil Engenharia e Construção, S.A., Lisbon, Portugal
**joao.p.santos@mota-engil.pt*

ABSTRACT: The Maputo Port Development Company decided in June 2018 to proceed with the rehabilitation of berths 6, 7, and 8 of the Port of Maputo, with 630 meters long, which involved the demolition of the existing quay, to build new quay infrastructures ready to service depths of -16,0 m (CD). The existing berths with construction dates between 1913 (Berth 6) and 1951 (Berth 8) were extremely damaged and partially destroyed, and the future quay consisting of a combiwall of ∅2032 x 22 mm piles and double AZ28-700 intermediate sheet piles, required the execution by maritime means, with significant disturbance in the port operations. Based on the experience developed over the years in maritime works, Mota-Engil proposed an alternative solution to the Employer's design, consisting of a pile supported concrete deck and a submerged combiwall to retain the existing slope to be dredged, which minimized the mobilization of human and material resources using a more simplified and systematized approach of construction processes. This communication addresses the construction aspects, namely the cantitravel method adopted for the execution of the piles in maritime environment and the driving of the combiwall to be installed under water.

RÉSUMÉ: La Maputo Port Development Company a décidé en juin 2018 d'avancer dans la réhabilitation des postes d'amarrage 6, 7 et 8 du port de Maputo, d'une longueur de 630 mètres, qui a impliqué la démolition du quai existant, pour construire de nouvelles infrastructures de quai prêtes à fonctionner profondeurs de -16,0 m (CD). Les postes d'amarrage existants dont les dates de construction sont comprises entre 1913 (poste 6) et 1951 (poste 8) ont été extrêmement endommagés et partiellement détruits, et le futur quai constitué d'un mur combiné de pieux ∅2032 x 22 mm et de doubles palplanches intermédiaires AZ28-700, a nécessité l'exécution par voie maritime, avec des perturbations importantes dans les opérations portuaires. S'appuyant sur l'expérience développée au fil des années dans les travaux maritimes, Mota-Engil a proposé une solution alternative à la conception de l'Employeur, composée d'un tablier en béton soutenu par pieux et d'un mur combiné immergé pour retenir la pente existante à draguer, ce qui minimisait la mobilisation des humains. et les ressources matérielles en utilisant une approche plus simplifiée et systématique des processus de construction. Cette communication aborde les aspects constructifs, à savoir la méthode cantitravel adoptée pour l'exécution des pieux en milieu maritime et le battage du combiwall à installer sous l'eau.

Keywords: Combiwall; cantitravel; piling works; underwater combiwall; water jetting.

1 INTRODUCTION

The Maputo Port Development Company (MPDC) is a private Mozambican company, which resulted from the partnership between the Caminhos de Ferro de Moçambique, CFM, and a joint venture mainly constituted by Grindrod and DP World, one of the main maritime operators of the world.

Within the scope of development and optimization of the entire concession area, MPDC has made several investments to modernize the Port of Maputo in the last 10 years, including the deepening of the access channel, the increase of capacity of the several terminals, and the rehabilitation of the old berths, including the contract for rehabilitation of berths 6, 7 and 8 of the Port of Maputo.

2 CHARACTERIZATION OF THE EXISTING STRUCTURE

The existing platforms were all constructed in a similar way with rows of quadrangular piers along the quays at typical intervals between 3.1 and 3.6 m, which extended between 14 and 52 meters landwards beneath the quay surfaces and warehouses. The quay structures were closed at the back by a concrete retaining wall (Figure 1).

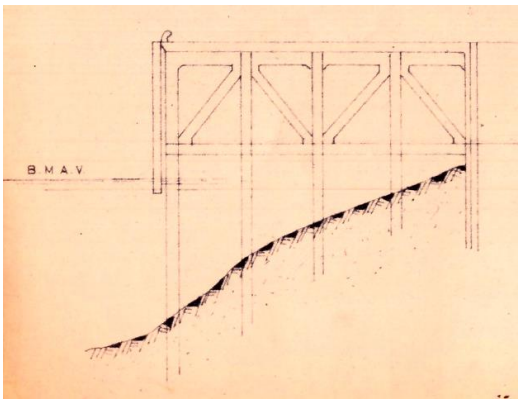

Figure 1. Cross section of the existing structure of berth 6.

The Maputo Port Investigation (NIRAS 2000) reported that the piles, lower beams and the lower part of the vertical elements below mean sea level were generally in good condition, with the concrete layer on the reinforcement remaining intact. However, the vertical elements and diagonal bracings were generally in poor condition, with severe deterioration above the high tide level, between +3.5 and +4.5 m (CD), with several cracks and exposed reinforcement. (Figure 2 and Figure 3).

The condition of the edge beam was also poor, with missing or loose concrete, probably due to ship impacts, and at Pier 8, the deck slab had collapsed.



Figure 2. View underneath the old quays.



Figure 3. Reinforced concrete columns and bracings.

3 GEOTECHNICAL INVESTIGATION

The Geotechnical Investigation report (Aucamp 2014) describes "the regional geology of the area is composed of recent clayey and sandy alluvial material, covering the Ponta Vermelha Formation (from 2 million years (Ma) to 5 Ma) which is composed of silty sand that becomes yellowish red sandstone with depth". The synthesis of geotechnical parameters is presented on Table 1.

4 STRUCTURAL SOLUTION

The alternative project executed was an open berth with a reinforced concrete beam slab supported by reinforced concrete piles ∅1000 mm, in a 7.2 m x 6.0 m mesh and built at the intervals between the existing piles, without having the need to extract the old piles and only to demolish the current deck slab, as presented in Figure 4.

The concrete piles were encased in steel pipes and had typical embedment between 5 m and 20 m at "Ponta Vermelha" geological layer with SPT – N > 60 (up to -28.5 m CD). To validate the embedding depth of the piles in the competent ground, were carried out three Bi-directional load tests using Osterberg cells. From the results obtained in the strain gauges placed along the entire length of the piles, it was possible to measure with greater accuracy the lateral friction in each layer of soil and the tip resistance of the pile.

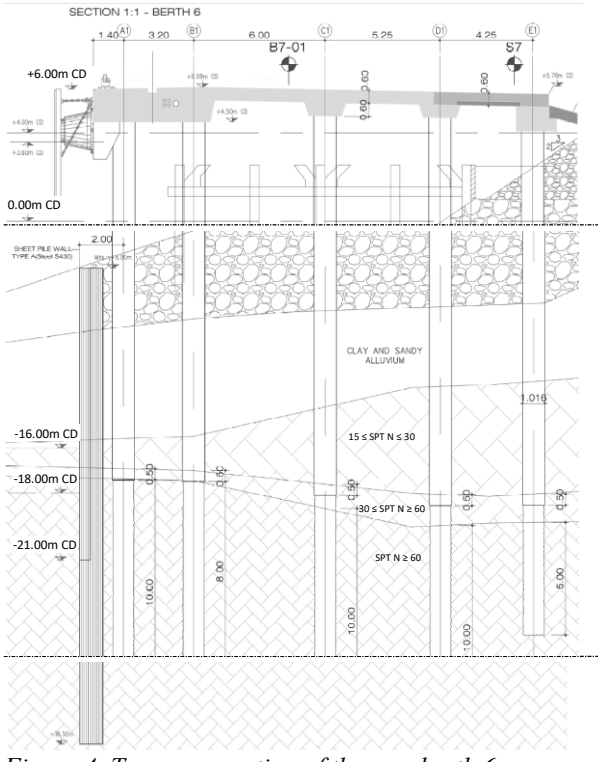

Figure 4. Top cross section of the new berth 6.

Table 1. Synthesis of geotechnical parameters.

Geological layer	Material description	Dry density (kN/m³)	Static Young's modulus (MPa)	Φ (º)
Alluvium	Very loose/ very soft sediment	15	< 1 – 7	< 32
Ponta Vermelha SPT – N < 30	Loose to medium dense zones	14 – 16	5 – 20	< 32
Ponta Vermelha SPT – N > 60	Dense to very dense	14 – 16	50 – 100	28 – 41

These tests allowed a significant reduction in the embedment length of the piles in the Ponta Vermelha layer, by less than 40%.

To increase the depth of the berth to -16.0 m (CD), a self-supporting submerged combiwall was installed, with a variable cantilever between 6 and 10 m, to guarantee the stability of the existing embankment, which would later be dredged.

The type of sheet piles applied varied according to the inclination of the existing natural ground, being the largest in berth 6 (area with a steeper slope and greater height) and decreasing towards berth 7. For the most unfavourable situation, the principal elements were 2xHZ1180M weighing 23.5 t and 28.5 m long, that were driven up to -36.5 m (CD), with 18.5 m driven into very dense soil, of the "Ponta Vermelha" layer SPT – N > 60. This solution was designed for a design life of 100 years and allows future dredging of the service area to -18.0 m (CD).

5 CONSTRUCTIVE ASPECTS

To complete the project, 871 units of reinforced concrete piles were executed, totalling 30,678 ml, and to hold the submerged slopes, 3,050 t of steel profiles and 8,430 ml, were applied over an extension of 544 m long.

The specificity and complexity of the project was fundamentally due to the current condition of the existing deck and the difficulty of the works taking place in a live terminal, with the consequent need to find solutions that could reduce maritime and road traffic, and thus minimize interference in the port's operations.

5.1 Execution of reinforced concrete foundation piles

For the construction stage of the piling works, the cantitravel methodology was adopted, which allows the work to progress independently of maritime conditions, avoiding the mobilization of both floating equipment and heavy equipment for driving piles, which were not available in the region, and without stepping in water also means less impact on the environment and port traffic. The sliding platform worked in two ways: laid on the recently new deck, executed in longitudinal bands using a deck sliding formwork; and supported by the recently executed piles, as shown on Figure 5.

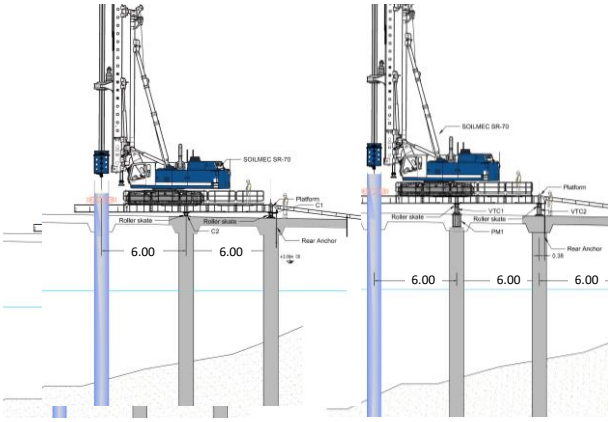

Figure 5. Sliding cantitravel for execution of piles.

The steel pipes were driven up to the SPT layer – N > 60 using a vibrofonceur, and then cleaned on the inside using a Kelly bar, without the need of any methodology to stabilize the drilled hole, given the ability to self-support for a period.

5.2 Execution of the submerged combiwall

The installation of the combiwall proved to be a very complex activity due to the geological environment that is very unfavourable for driving (granular soils with SPT – N > 60), the considerable penetration lengths in very dense soils, the size of the wall, and also the fact that it is submerged, and it is not possible to see the actual work on the surface.

With this scenario, auxiliary techniques had to be used to facilitate the installation, given that the energy developed by the hammers was not enough to fully drive the profiles, with refusal occurring before accomplishing the project levels. On the other hand, for smaller profiles, there was a tendency for the profile to be destroyed at its head, firstly by the energy of the vibrohammer and then of the impact hammer.



Figure 6. Water jetting and impact hammer activities.

To be able to drive the profiles up to the final project levels, pre-drilling was used before installing the principal elements, and water jetting with a similar method to jet grouting (JET 2 system), as per Figure 6, with the injection of air and water at high pressure to break the cohesion of the soil in the extent where the profiles were installed.

The water jet loosens the soil, reducing the resistance to penetration of the pile tip during driving. Under some soil conditions, water flowing along the pile acts as a lubricant and can also reduce surface friction. The jetting allowed sheet piles to be successfully driven into the dense ground.

The pressure applied was 260 bars (3 nozzles) during drilling until the end of the driving level, and 380 Bar (2 nozzles) during cut and upward movement, as illustrated in Figure 7.

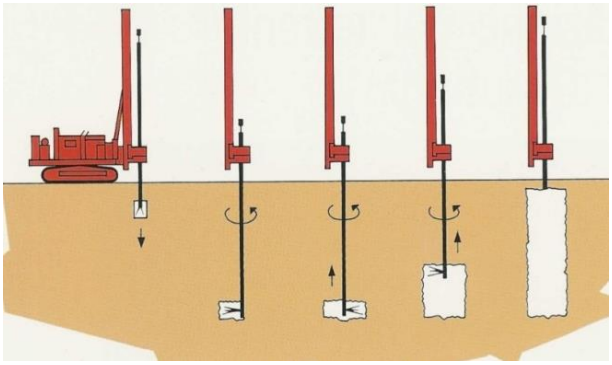

Figure 7. Sequence of the water jetting works.

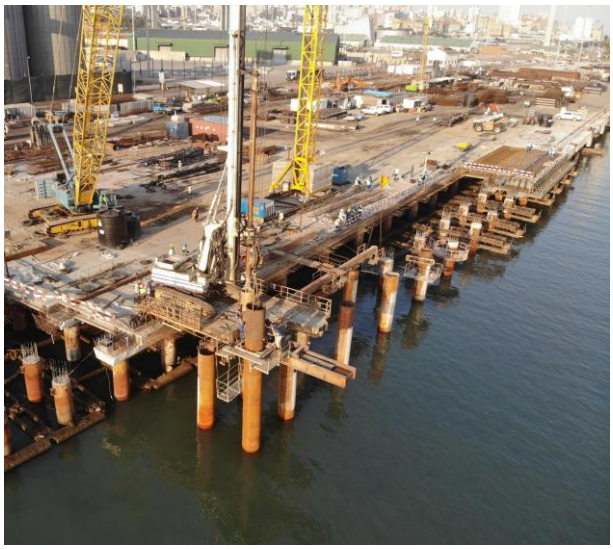

Figure 8. Execution of piles with cantitravel.

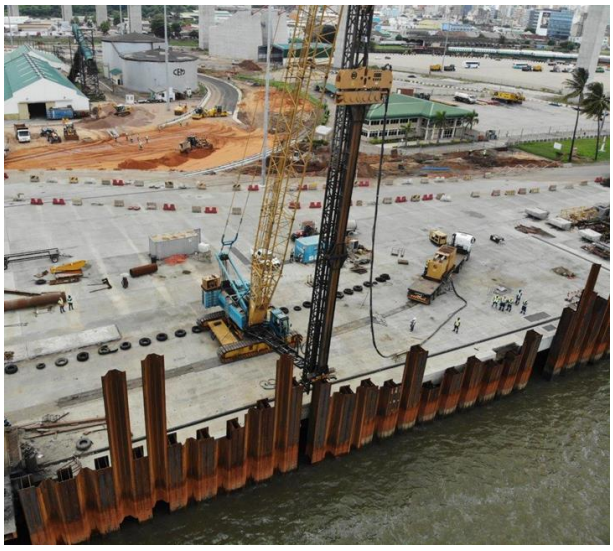

Figure 9. Execution of the submerged combiwall.

Given the very limited space available for driving the profiles, 18 m followers were attached to the driving equipment, an APE300-6 vibrating hammer and a D100-13 impact hammer, that allowed the driving to be done next to the new quay edge and underwater.

REFERENCES

NIRAS (2000). Maputo Port Investigation, NIRAS Portconsult A/S, Alleroed, Denmark

Aucamp, P (2014). Geotechnical Investigation for Maputo Port, SRK Consulting & WML Coast, Johannesburg, South Africa

Proceedings of the XVIII ECSMGE 2024
GEOTECHNICAL ENGINEERING CHALLENGES
TO MEET CURRENT AND EMERGING NEEDS OF SOCIETY
© 2024 the Authors
ISBN 978-1-032-54816-6
DOI 10.1201/9781003431749-509
Open Access: www.taylorfrancis.com, CC BY-NC-ND 4.0 license

ECSMGE 24
XVIII EUROPEAN CONFERENCE ON SOIL MECHANICS AND GEOTECHNICAL ENGINEERING

The threaded displacement piling system technical and economical efficiency leading to sustainable foundations solutions

L'efficacité technique et économique du système de pieux vissés conduisant à des solutions de fondations durables

L. Sata*, S. Manea
Technical University of Civil Engineering, Bucharest, Romania
**sata@sbr.ro*

ABSTRACT: The search of the economic and sustainable alternatives to lower the costs and to reduce the carbon footprint of the foundations by the diversification of the piling technologies is a continuous task for the special foundation industry. Even though the displacement piles usually have increased bearing capacities compared with the bored piles, their execution is associated with vibration, dynamic and phonic pollution of the local environment. One of the recent economical deep foundation solutions is the threaded displacement piling system, the "screw" concept. The pile identified by two diameters (core / threads) is successfully applied in the range 330/500 to 530/700mm not only in Great Britain, France, but also in Central – East Europe in Romania, Poland, Hungary, recent successes being registered as well in South Africa. The technique is fully covered in Europe by the standard EN 12699:2015 adopted in Romania as SR EN 12699:2015. The paper present by means of more than 250 simple and instrumented loading tests the technological details, the constructional principles and the choosing of dimensions, the application possibilities, the design approaches according to Eurocode 7 as well as to the Romanian Pile design norm NP123, and finally the ecological impact analysis and sustainability evaluation of the Screwsol threaded displacement piling system.

RÉSUMÉ: La recherche d'alternatives économiques et durables pour diminuer les coûts et réduire l'empreinte carbone des fondations par la diversification des technologies de pieux est une tâche continue pour l'industrie des fondations spéciales. Même si les pieux à refoulement latéral du sol ont généralement des capacités portantes accrues par rapport aux pieux forés, leur exécution est associée à des vibrations, à une pollution dynamique et phonique de l'environnement local. L'une des solutions économiques récentes pour les fondations profondes est le système de pieux vissés, le concept de « vis ». Le pieu identifié par deux diamètres (noyau/filetage) est appliqué avec succès dans la gamme 330/500 entre 530/700mm non seulement en Grande-Bretagne, en France, mais aussi en Europe Centrale et de l'Est en Roumanie, en Pologne, en Hongrie, des succès récents étant également enregistrés en Afrique du Sud. La technique est entièrement couverte en Europe par la norme EN 12699:2015 adoptée en Roumanie sous le nom de SR EN 12699:2015. A l'aide de plus de 250 tests de chargement simples et instrumentés, l'article présente les détails technologiques, les principes de construction et le choix des dimensions, les possibilités d'application, les approches de conception selon l'Eurocode 7 ainsi que selon la norme roumaine NP123, et enfin l'analyse d'impact environnementale et l'évaluation de la durabilité du système de pieux vissés Screwsol.

Keywords: Displacement piles; screw piles; design approach; sustainability.

1 INTRODUCTION

One of the recent optimal soil displacement drilling solutions is given by the rotary displacement piling system, the Screwsol concept, defined as follows:

Pile in which the pile or pile tube comprises a limited number of helices at its toe, and which is installed under the combined action of a torque and a vertical thrust. By the screwing-in and/or by the screwing-out, the ground is essentially laterally displaced, and no soil is removed. The technology is covered by the standard ASRO SR EN 12699:2004.

The article presents a list of simple and instrumented loading tests for several load types; technological details, design approaches; constructional principles and the choosing of dimensions; application possibilities; the ecological impact analysis and evaluation of the Screwsol rotary displacement piling system (Sata, 2005, Kaltenbacher et al., 2008).

The pile identified by two diameters (core / threads) is applied in the range 330/500 to 530/700mm (Figure 1) (Sata and Manea, 2012).

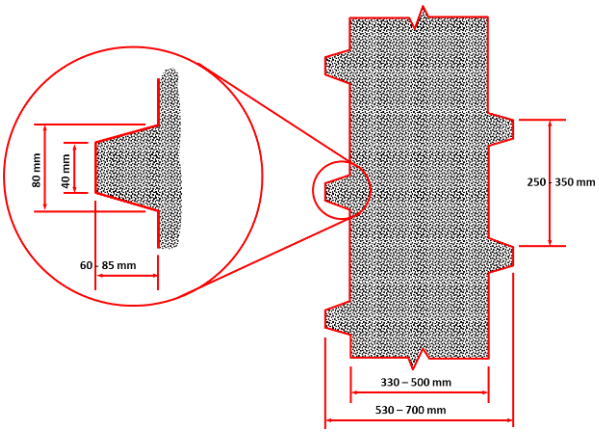

Figure 1. Screwsol pile longitudinal section and thread details.

2 ALIZEU WIND FARM TEST / 2013

The test pile was a Screwsol pile with a diameter of d=330/500 mm (meaning 330 mm cylinder diameter and 500 mm external diameter) and a toe depth of H = 20.95 m from ground level (actual pile length of L = 20.60 m), reinforced on its entire length, to provide support for the strain gages and to protect the pile head from local crushing at high loads. Four reaction piles were used for the load test, executed with the same technology.

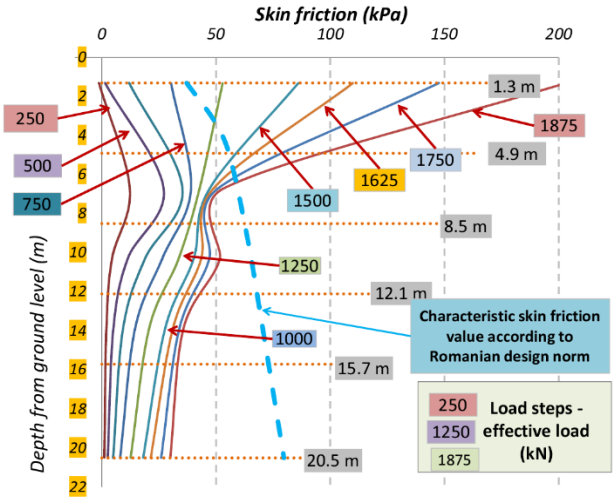

Figure 2. Skin friction diagram.

The static load test was carried out in equal steps of 125 kN, until failure. Application of a load increment was conditioned by stabilization of settlements for the previous step. Additionally, the pile was equipped with 17 extensometers and during the load test the deformation of the concrete was monitored with a frequency of 1 reading / minute.

Pile failure occurred at the 16th load step (2000 kN), most likely by crushing of the pile head due to eccentrical application of the load. This observation is supported by the load-settlement diagrams of the four individual sensors that measured the settlement of the pile, located at the four corners of the pile.

Strain gauge measurements were processed in several steps to determine the detailed pile behaviour, and to confirm or contradict the preliminary conclusions based on the classical load test results.

In case of the Screwsol pile, the most important uncertainty is the choice of the cross-sectional area A (which automatically influences the lateral surface considered in the calculation of skin friction – Figure 2). Also, the displacement of the soil needs to be taken into consideration when computing pile forces and skin frictions. A third uncertainty is the elastic modulus of the combined concrete-steel pile, which can be safely evaluated for design purposes.

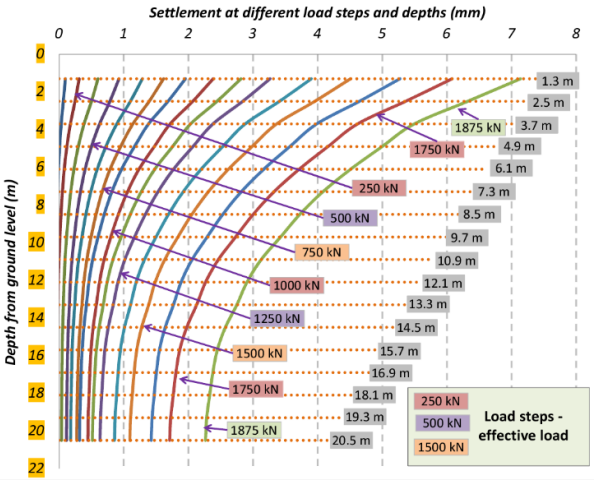

Figure 3. Settlement diagrams.

The results presented (Figure 3) consistently reveal the pile's tendency to consume most of the loads in the upper half of its length. In case of efficiently designed non-displacement piles it is expected that most of the loads are transferred through the lower part of the shaft (skin friction) and by tip resistance. Skin frictions in the upper few meters reach values of 200 kPa and more, compared to a maximum of 80 kPa given by the design norm.

However, in this case there are factors that suggest a different behaviour. Due to the presence of the threads, combined with the displacement of the soil, larger shear stresses may develop in the upper part of the shaft. Equally importantly, the soil is homogenous, even at the pile toe level, while in most design scenarios the soil layers towards the pile toe are significantly stiffer.

3 LIDL LOGISTIC CENTER CRAIOVA / 2021

The CPT-based design of the foundations was performed according to EC7:

$$R_{c;k} = \left(R_{b;k} + R_{s;k}\right) = \frac{R_{b;cal} + R_{s;cal}}{\xi} = \frac{R_{c;cal}}{\xi} = \text{Min}\left\{\frac{\left(R_{c;cal}\right)_{med}}{\xi_3}; \frac{\left(R_{c;cal}\right)_{min}}{\xi_4}\right\} \quad (1)$$

Based on the calculations few of the determined pile lengths were the following:

D330/500 – 950kN – L=16.05m

D330/500 – 1100kN – L=17.25m

D430/600 – 1450kN – L=16.55m

Five preliminary, instrumented load tests were executed on area A2. The instrumentation consists of strain gauges and base plates. The strain gauges were placed on the reinforcement cage at a vertical spacing of 1.5 m, with 3 gauges per each level being installed to achieve more precise results (Figure 4) and to confer redundancy in case some gauges would be damaged during pile installation. The base plates were installed on the bottom of the reinforcement cages, practically at pile toe level.

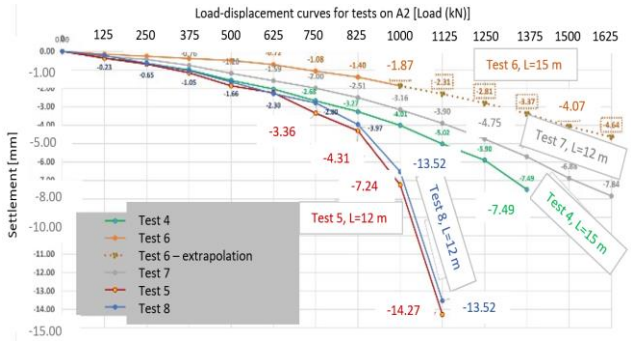

Figure 4. Load-settlement curves for all tests (5 piles).

It is noted that all 5 test piles exhibited a load-displacement pattern which is characteristic for friction piles, represented by a considerable quasi-elastic domain until 875 kN to 1625 kN, which represents 17.5% up to 32.5% of the representative diameter, considered as 50 mm, given that most of the load (and practically all service load) is carried by the shaft. These values are also very close or even exceed the structural capacity of the pile, which can be approximated as Aint x fc,d = 0.085 m2 x 16.7 MPa = 1425 kN.

However, it is noted that all other tests exhibited an extremely favourable pile behaviour. In case of two tests (test 4 and 7) the cracking of the pile head occurred after 1375 to 1625 kN, which are sufficiently large values of ultimate capacity to allow for an efficient pile design after division with partial safety factors. In case of test 6, for which pile head cracking occurred after 1000 kN, an extrapolation was performed, given the large pile length and the extremely small pile displacements (<2 mm) up to this point, to avoid unnecessary overdesign.

The distribution of the skin friction and toe resistance is presented in Figure 5, using a first approach in which the skin friction was calculated while the toe resistance was determined by subtracting the total skin friction from the load step applied during testing.

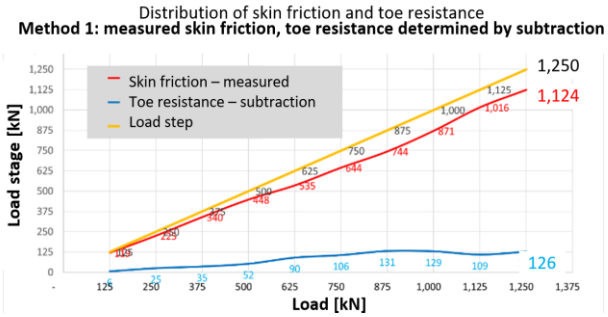

Figure 5. Distribution of skin friction and toe resistance – method 1, test 4.

The diagram shows that the pile shaft carries the largest part of the loads, approximately 90% and practically constant during the load steps.

4 DESIGN OF SCREWSOL PILES

4.1 Design based on CPT results (SR EN 1997-2: Annex D, D.7)

The maximum base resistance can be derived as:

$$p_{max;base} = 0{,}5\ \alpha_p\ \beta\ s\left(\frac{q_{c;I;mean} + q_{c;II;mean}}{2} + q_{c;III;mean}\right) \quad (2)$$

The maximum shaft resistance can be derived as:

$$p_{max;shaft;z} = \alpha_s \times q_{c;z;a} \quad (3)$$

Based on more than 250 load test evaluations, values proposed for α_p and α_s are presented in Table 1.

Table 1. Proposed values for α_p and α_s.

Soil type	q_c	α_p	α_s
non cohesive	for min values as per EC7	0.9 - 1.0	0.004 - 0.007
	for medium values	0.6 - 0.7	
cohesive	for min values as per EC7	0.8	0.020 - 0.028
	for medium values	0.5	

4.2 Design according to NP123:2022

$$R_{c,d} = \frac{A_b \cdot q_{b,k}}{\gamma_{b,2}} + \frac{U \sum(q_{s,k_i} \cdot l_i)}{\gamma_{s,2}} - G \qquad (4)$$

where $q_{b,k}$ is the base resistance and $q_{s,ki}$ the shaft resistance.

For the shaft resistance a correlation factor, k_x, is introduced with the values:

1.0 – cohesive soils

0.4 - 0.6 – non cohesive soils

The safety coefficients related to the shaft and base resistance of the Screwsol threaded piles:

$\gamma_{s,i,2}$ = 1.9 (cohesive) / 1.2 (non-cohesive)

$\gamma_{n,k}$ = 1.2 (cohesive / non-cohesive)

5 ANALYSIS AND EVALUATION OF THE CO2 FOOTPRINT OF SCREWSOL

The use of materials (concrete, steel) is responsible for approximately 95% of total CO2 emissions generated by construction activity.

For the example, it was considered a project with 500 piles with a length of 10.0 m, in two versions: executed with CFA technology and diameter of 600mm, respectively Screwsol technology and diameter 430/600, their bearing capacities being considered to be similar.

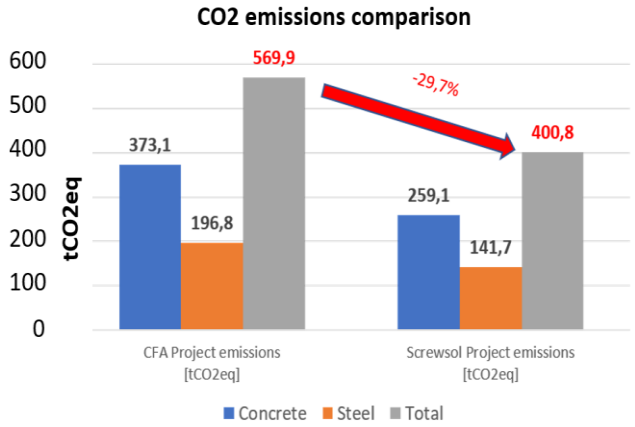

Figure 6. CO2 emissions for CFA and Screwsol.

The solution with CFA technology and a diameter of 600mm is responsible for a carbon footprint approximately 30% higher than the Screwsol piles of diameter 430/600.

6 CONCLUSIONS

The applicability of Screwsol has been successfully proven both in non-cohesive soils, but also in medium stiff and plastic clay conditions. The execution length of the piles is limited by the characteristics of the in situ soil and the refusal criteria of the soil – drilling torq combination.

The maximum efficiency of the piles is obtained for non-cohesive soil conditionsterrain – fine and medium – in loose or medium density. In the case of cohesive soils, the efficiency is high plastic clays. Due to the fact that the dynamic effects produced during execution are reduced through the execution technology, they can also be used to treat soils with liquefaction potential. The presence and level of the groundwater has neither negative influence to the execution technology nor to the efficiency of the piles.

REFERENCES

ASRO. SR EN 12699:2015, Execution of special geotechnical works - Displacement piles (in Romanian: Execuția lucrărilor geotehnice speciale. Piloți de îndesare).

ASRO. SR EN 1997-2:2007, Eurocode 7: Geotechnical design - Part 2: Ground investigation and testing (in Romanian: Eurocod 7: Proiectarea geotehnică. Partea 2: Investigarea și încercarea terenului).

Kaltenbacher, T., Sata, L. and Deli, Á. (2008). The applications of the Screwsol soil displacement piling solution, *Közúti és Mélyépítési Szemle*, Budapest, Hungary. (in Hungarian: (A Screwsol talajkiszorításos cölöpözés alkalmazásának lehetőségei).

NP 123-2022, *Regulations on the geotechnical design of pile foundations (in Romanian: Normativ privind proiectarea geotehnică a fundațiilor pe piloți).*

Sata, L. and Manea S. (2012). Screwsol – threaded displacement pile, *Revista Construcţiilor*, ISSN 1841-1290, Bucharest, Romania. (in Romanian: (Screwsol – Pilot de îndesare înşurubat).

Sata, L. (2005). Small and large diameter soil displacement Screwsol piles in the deep foundation practice, *Proceedings of the 10th Geotechnical Conference (V4)*, Ráckeve, Hungary.

Proceedings of the XVIII ECSMGE 2024
GEOTECHNICAL ENGINEERING CHALLENGES
TO MEET CURRENT AND EMERGING NEEDS OF SOCIETY
© 2024 the Authors
ISBN 978-1-032-54816-6
DOI 10.1201/9781003431749-510
Open Access: www.taylorfrancis.com, CC BY-NC-ND 4.0 license

ECSMGE 24
XVIII EUROPEAN CONFERENCE ON SOIL MECHANICS AND GEOTECHNICAL ENGINEERING

Large-scale test on basal steel-reinforced piled embankments

Essai à grande échelle sur les remblais basaux en pieux renforcés par de l'acier

M. Schneider*
Technical University of Darmstadt, Institute of Geotechnics, Germany

M. Hell, P. Pandrea
Keller Holding, Germany

B. Wittekoek, S.J.M. van Eekelen
Deltares, Netherlands

M. Topolnicki
Keller Polska, Poland

K. Makowska, R. Sieńko
SHM System, Poland

H. Zachert
Technical University of Darmstadt, Institute of Geotechnics, Germany

**marc.schneider1@tu-darmstadt.de*

ABSTRACT: This paper presents a novel large-scale test setup at TU Darmstadt to investigate the behaviour of basal reinforced piled embankments. The study focuses on the impact of welded steel mesh reinforcement. The study addresses key questions related to soil arching, deformations, strain distribution in the embankment and the steel mesh grid. The large-scale test setup, 25 m^2, at a 1:1.6 scale, includes 16 piles, a dry medium coarse river sand fill, a steel mesh reinforcement and a two-step system to model the soft soil compaction. State-of-the-art Distributed Fibre Optic Sensing (DFOS) technology enabled precise monitoring of soil and reinforcement strain and 3D deformation. Results indicate that the reinforcement stiffness minimally affects soil arching, matching the Concentric Arches (CA) model (van Eekelen et al., 2013, 2015) that was developed for geosynthetic reinforced piled embankments (GRPS). The deformation pattern and strain distribution in the steel differ from GRPS, illustrating the need for a specific load-deflection model. The measured critical height matches the prediction of Topolnicki and Kłosiński et al. (2022). The study contributes to understanding the complex interaction between steel reinforcement and soft soil in piled embankments, guiding future design considerations.

RÉSUMÉ: Cet article présente un nouveau dispositif d'essai à grande échelle à l'Université Technique de Darmstadt pour étudier le comportement des remblais sur pieux renforcés par une nappe de treillis soudés. L'étude se concentre sur l'impact de l'armature en treillis soudé sur les mécanismes de transferts de charge. L'étude aborde des questions clés liées à l'effet d'arche du sol, aux tassements et à la distribution des déformations dans le remblai et dans le treillis soudé. L'installation d'essai à grande échelle, 25 m^2, à l'échelle 1:1,6, comprend 16 pieux, un remblai de sable fluviatile moyennement grossier sec, un renforcement en treillis soudé et un système double pour modéliser le tassement du sol meuble. La technologie de pointe de la détection par fibre optique répartie (DFOS) a permis un contrôle précis du tassement du sol et du treillis soudé ainsi qu'une visualisation de la déformation en 3D. Les résultats indiquent que la rigidité du renforcement affecte peu la formation d'arches dans le sol, ce qui correspond au modèle d'arches concentriques (van Eekelen et al., 2013, 2015) qui a été développé pour les remblais sur pieux renforcés par des géosynthétiques (GRPS). La déformation et la distribution des contraintes dans l'acier sont différentes de ceux du GRPS, illustrant la nécessité d'un modèle charge-déformation spécifique. La hauteur critique de remblai mesurée correspond à la prédiction de Topolnicki et Kłosiński et al. (2022). L'étude contribue à la compréhension de l'interaction complexe entre le treillis soudé et le sol mou dans les remblais sur pieux, guidant les considérations de dimensionnement futurs.

Keywords: Piled embankments; steel basal reinforcement; large-scale physical modelling; distributed fibre optic sensing.

1 INTRODUCTION

Reinforced piled embankments with a geosynthetic reinforcement (GR) are commonly built in soft soil areas (van Eekelen and Han, 2020). Replacing GR for steel reinforcement (SR) is particularly appealing to reduce deformations caused by high embankments (Topolnicki et al., 2019).

This paper presents a large-scale test setup, nearly in full scale, 1:1.6, constructed at TU Darmstadt to allow investigation of piled embankments with basal reinforcement made of steel or geosynthetics. The test setup is part of a broader research initiative called PEBSTER (Piled Embankments with Basal Steel Reinforcement), including small-scale tests (van Eekelen et al., 2024) to investigate the following:

1. Does the soil arching in a piled embankment differ if SR is used instead of GR?
2. Are deformations different with SR instead of GR?
3. What is the influence of flexible vs. rigid piles?
4. Do the answers to these questions depend on the scale of model tests?
5. Can the current design methods for piled embankments using GR be applied for SR or do they require a modification?

2 LOAD DISTRIBUTION

Soil arching develops when soil between piles deforms more than the piles, resulting in a non-uniform load distribution. A significant portion of the vertical load (labelled as 'A' in Figure 1) is directly transferred to the piles. The residual load, 'B+C' in Figure 1, is supported by the subsurface between the piles.

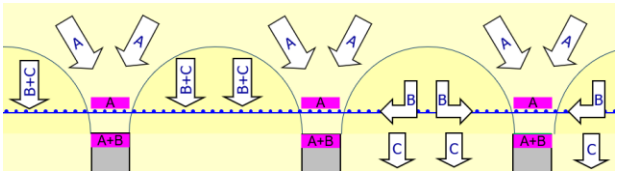

Figure 1. Load distribution in a PS embankment.

Several design guidelines and standards, such as BS8006 (2010), EBGEO (2011), ASIRI (2013), CUR226 (2016), and Topolnicki and Kłosiński et al. (2022), provide equations to divide the total vertical load into A and B+C. These guidelines then offer methods for calculating the strain in the reinforcement from the acting load B+C, considering the load-deflection behaviour of the reinforcement.

Many researchers have investigated the influence of geometry and material properties on soil arching. Van Eekelen et al. (2012) showed that the soil arching quickly develops, even when the deflection of the GR is minimal. In line with this finding, they showed that the GR tensile stiffness has a limited impact on soil arching, while the shear properties of the fill (internal friction angle) play a significant role. These conclusions were valid for GR. An important question of the PESBTER project is, whether the high axial and bending stiffness of the SR affects the soil arching in the fill.

3 LARGE-SCALE TEST SETUP

Figure 2 depicts the test setup designed to model piled embankments with a steel basal reinforcement. The model embankment represents a prototype embankment of 4.7 m height above the pile head.

This test setup was constructed within a part of the geotechnical test pit at the Institute of Geotechnics of TU Darmstadt. It occupies a base area of 5 by 5 m and has a total height of 5.5 m. The test setup includes 16 piles passing through the layer of soft soil model.
The embankment fill was modelled using dry medium coarse river sand ('Darmstadt Sand'). The soil model was installed by means of air pluviation achieving a mean density of 1.735 g/cm³, equivalent to 92 % relative density, and $\varphi'_{cv} = 34.8^{o}$.

The choice of a model embankment height of H = 2.9 m was determined by geometric scaling, in line with typical dimensions found in real piled embankments. This decision also took into consideration to safely surpass the critical height estimate of 1.52 m according to Topolnicki and Kłosiński et al. (2022), where the critical height represents the minimum vertical distance above the pile heads to reach a plane of uniform settlement above and between the supports. Concentrating soil pressure, strain and deformation measurements in the range between piles and critical height allows a thorough analysis of soil arching behaviour in the embankment.

3.1 Piles

The 16 piles are modelled using hollow S235 steel tubes with an outer diameters d = 244.5 mm and a wall thickness of t = 6.3 mm.

To better recreate the surface roughness found in concrete piles, the very smooth surface of the steel tubes was altered. The pile skin in contact with the sand layer above the soft soil model was covered with epoxy resin and poured sand. The pile skin below was not modified but kept smooth.

Previous experiments usually neglected pile settlements by using rigid supports. Natural load-bearing layers are stiff, but usually not rigid. To investigate the effect of flexible supports on the soil arching and load distribution behaviour the pile bases were equipped with springs with a stiffness of 5 MN/m (Figure 2). The LVDT transducer in the centre measures pile settlement and allows to derive the pile base force using spring calibration.

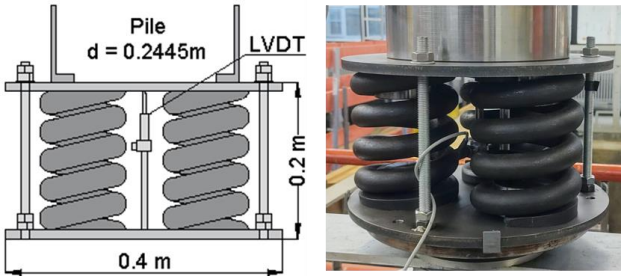

Figure 2. Three springs below each pile base, modelling a system with flexible supports.

Vertical loads acting on pile heads and pile settlements at the pile base were measured on 10 out of 16 piles to capture the behaviour of centre, edge and corner piles (Figure 2). Specially constructed pile heads, accommodating a standard load cell, allowed to measure the resulting vertical pile load directly.

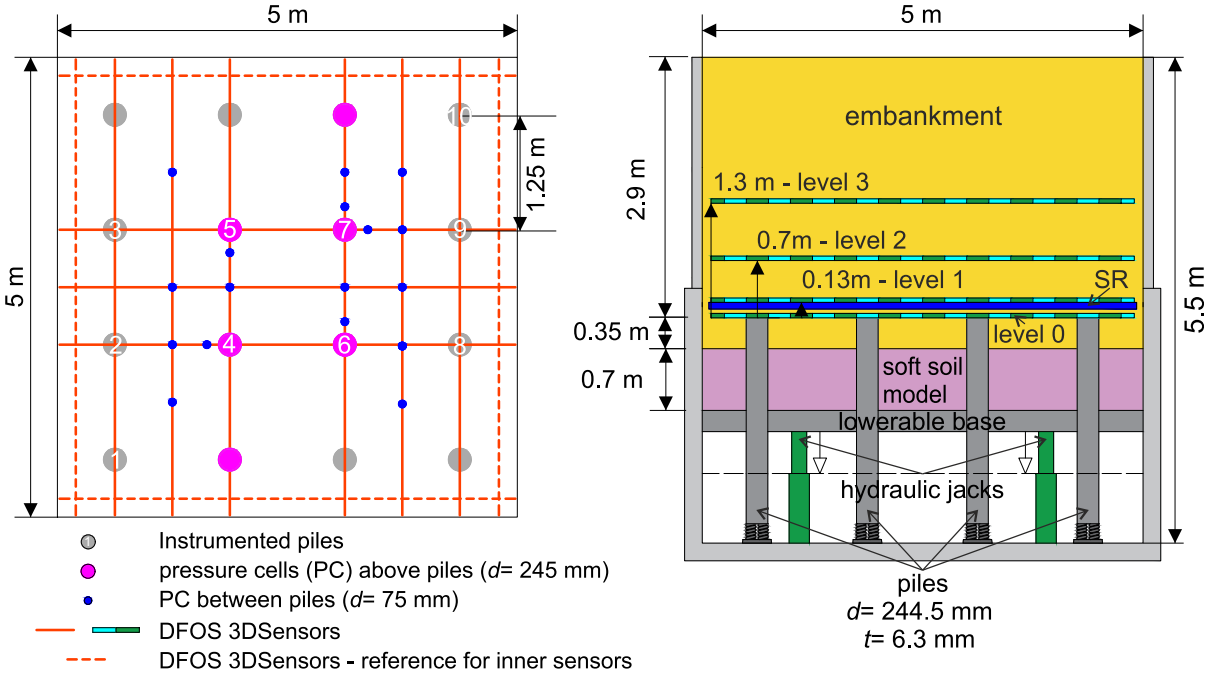

Figure 3. Large-scale test setup for basal reinforced piled embankments.

3.2 Soft soil model

The soft soil below the embankment was modelled using crumb rubber with grains of 1.5 to 5 mm in diameter. The rubber layer thickness was 0.7 m, with an average density of 0.48 g/cm³. To investigate the one-dimensional compressibility of the rubber, a special oedometer test was carried out using a specimen 285 mm in diameter and 50 mm in height and with a comparable initial density. The data presented in Figure 4 illustrate that crumb rubber tends to creep after each loading step.

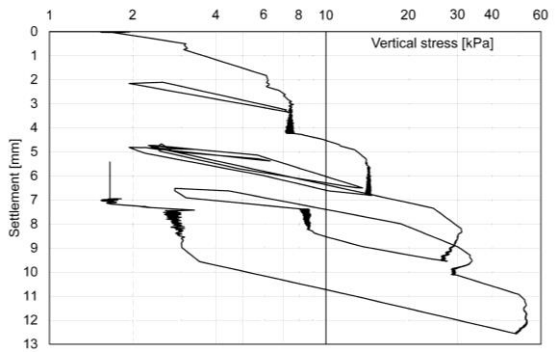

Figure 4. Large oedometer test of crumb rubber.

Also, after unloading steps there is a noticeable rebound of deformation under a stable load. Further analyses of the crumb rubber behaviour will therefore be required.

Due to consolidation and creep of soft soils, the subsoil reaction C can disappear over time. To model this situation, the rubber layer was placed on a stiff base supported by four hydraulic jacks. At the end of the test, the base plate was lowered incrementally 220 mm in total, creating a partial void below the steel mesh.

3.3 Steel mesh reinforcement

The basal steel mesh reinforcement consists of 8 mm ribbed bars (S235 steel), welded with a c/c spacing of 100×100 mm. The resulting tensile and bending stiffnesses of the mesh are EA = 105558 kN/m and EI = 0.2577 kN·m²/m, respectively.

In practice, steel meshes are produced in sheets and are connected on site using overlapping across and steel hooks along the embankment. The model arrangement consists of three sheets S1 to S3 (Figure 5). Sheet S1, with a size of 2.5×5 m, is connected with hooks to two smaller meshes S2 and S3, while S2 and S3 are connected by overlapping. In total, 49 hooks were used, and 16 of them were equipped with strain gauges to measure strain and study the interactions between the separate sheets.

3.4 Instrumentation

The development of soil arching begins near the pile heads when the soil in between piles starts to settle more than the piles themselves. To study this, the majority of the sensors were placed close to the pile heads and above or surrounding the piles. In total, 52 carefully selected sensors were used to measure forces, pressures and displacements in the system to allow an insight into the load distribution pattern as well as total loads at the system boundaries. Table 1 lists the mentioned sensors.

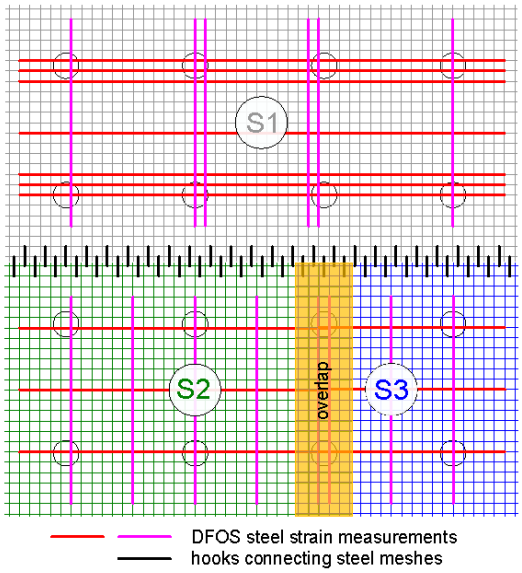

Figure 5. The arrangement of steel sheets S1, S2 and S3 in the test setup, and the location of the overlap and hooks.

Table 1. Measurement equipment for loads, pressures and vertical displacements.

Sensor Type	Quantity	Location [level]
Force	10	Pile head [0]
Pressure	6	Above pile locations [1]
Pressure	18	Distributed on SR between piles [0, 1]
Total load	4	Below model base frame
Displacement	10	Pile base
Displacement	4	Model base frame

Table 2. Measurement equipment for soil and reinforcement strains and displacements.

Sensor Type	Quantity	Location [level]
Strain in steel bars	8	DFOS steel strain, glued to the bars [1]
DFOS EpsilonSensor	2	DFOS soil strain [1]
DFOS 3DSensor	40	All levels [0-4]
Reference displ. DFOS	16	Outer test setup walls

Table 2 gives an overview of the sensors used to capture strains and deformation in the system, either by conventional strain gauges or by distributed fibre optical sensors (DFOS) from the Nerve-Sensor family.

In total, 40 DFOS 3DSensors were used to capture soil and steel deformation at four different levels (Figure 2). Each 3DSensor consists of four strain fibres that measure strains along the sensors' length and allow calculation of deformations in three directions. However, the results shown in this paper solely consider vertical displacements due to the mainly vertical nature of deformation of the system.

The 3DSensors were installed in a grid to measure deformations and strains above and between the piles. Figure 2 (left) shows the DFOS grid at level 1. The DFOS sensors at level 2 were identical, while levels 0 and 3 had a reduced number of sensors.

Furthermore, eight optic fibres were glued to the steel mesh to capture steel strains, and two DFOS EpsilonSensors were installed to measure soil strains.

The level 1 DFOS 3DSensors were placed directly on the SR, effectively measuring the deflection of the steel bars. Levels 2 and 3 were located at chosen elevations to study soil deformations inside the embankment in the middle and close to the upper boundary of the expected soil arching.

4 RESULTS

4.1 Load distribution

Figure 6 compares the measured load part that was transferred to the piles via soil arching (load part A) during embankment construction with values calculated using established analytical models, developed for geosynthetic reinforcement. They do not consider reinforcement bending stiffness as an input parameter. Nevertheless, the measured values match the calculations reasonably well.

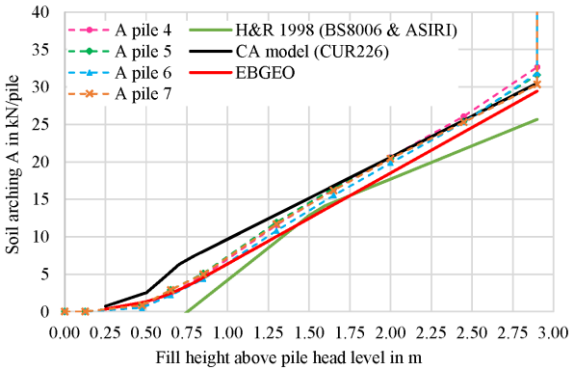

Figure 6. Load part A measured in the test and calculated with analytical models during embankment construction.

This analysis together with the findings of van Eekelen et al., 2024 supports the statement that the reinforcement stiffness does not have a significant impact on the load distribution pattern in the system (arching). Since the test only displays one combination of reinforcement stiffness and soil friction angle, further investigations are needed to experimentally confirm this conclusion.

4.2 Observed deformation pattern

Figure 7 a shows the measured vertical deformations at level 1, just above the steel. The graph includes two perpendicular directions over the whole model width, at the moment the full embankment height had just been achieved (test stage T2). In all unit cells, the deformation pattern is rather similar, validating the expected model performance and confirming the high quality of the applied monitoring system. Each of the following plots in Figure 7 shows data solely for the unit cell comprising the four inner piles.

Figures 7 b and 7 d show the absolute vertical deformation of the steel mesh at level 1 and levels 2 and 3, respectively, observed during three stages of the test, including the lowering of the model base frame (T3). To facilitate a direct and consistent comparison of these measurements, obtained at different locations and levels, the data have been normalized with respect to 'base lines'. These base lines connect the peaks in the deformed steel grid, above the (relatively rigid) piles. The measured deformations were normalised with respect to these base lines, and the normalised results are plotted in Figures 7 c and 7 e. They illustrate a more or less symmetrical deformation pattern at all levels and increasing deformation during successive stages of the test. Soil arching is caused by the differential deformation of the steel mesh above and between piles (Figure 7 c). Differential deflections of the steel bars running through the centre between the piles start to develop already during early embankment construction with average field centre deflections of 15.6 mm for 1.05 m high embankment. With progressing embankment height and the subsequent reduction of subsoil support, the differential deflections increase significantly, up to 32.4 mm in-between piles.

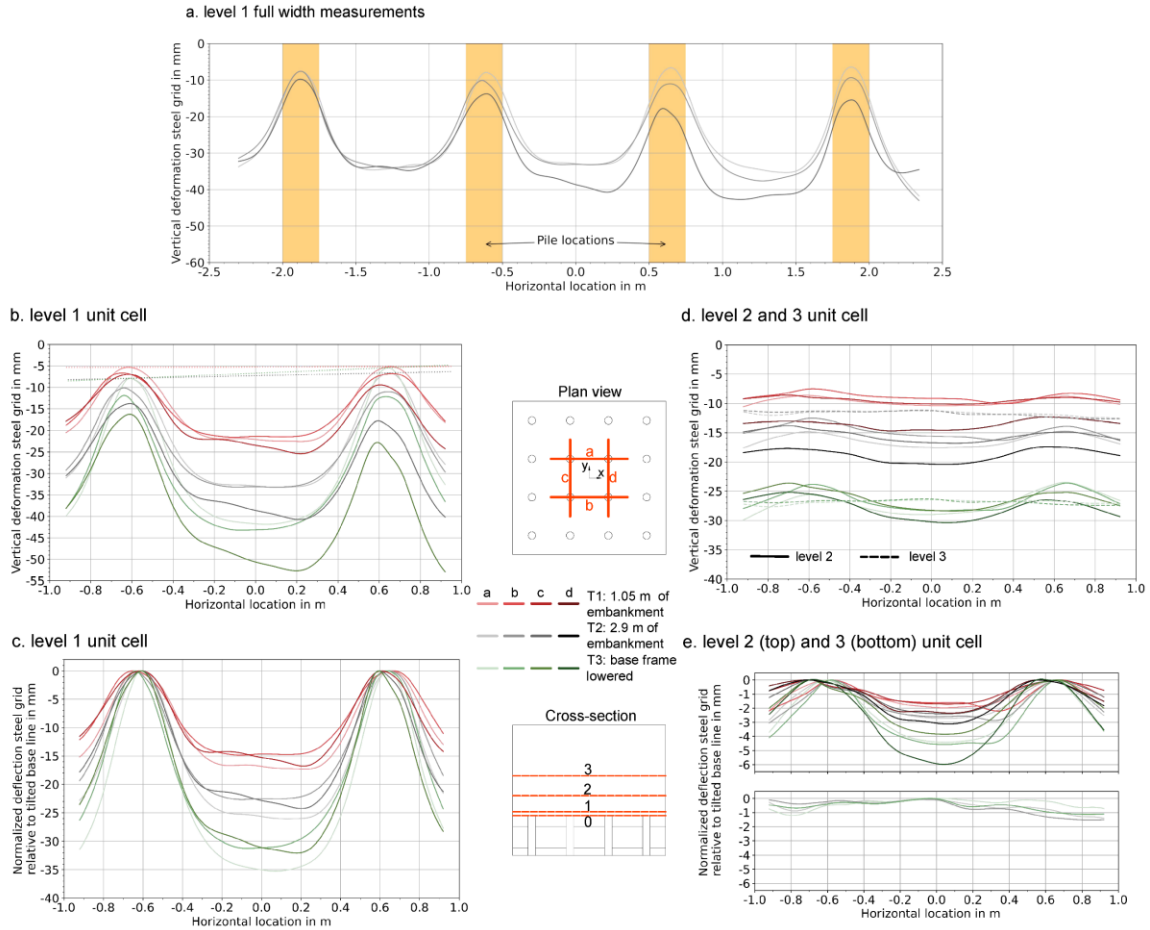

Figure 7. Measured vertical displacements of the steel mesh during and after embankment construction and after the removal of the subsoil support. a. full width, unaltered measurements above piles at stage T2. B. and d. Measured deflections of levels 1, 2 and 3 at stages T1, T2 and T3, along lines a, b, c, d and tilted base lines (b for level 1, and d for levels 2 and 3). c. and e. as b and d, but presented relative to the tilted base lines.

When comparing deformations in levels 2 and 3 (Figures 7 d and 7 e), a significant decrease of absolute and differential settlement is visible, indicating that the plane of equal settlement (critical embankment height) is located slightly above level 3, which is in line with the prediction of Topolnicki and Kłosiński et al. (2022).

5 CONCLUSIONS

This paper presents a large-scale model test on steel-reinforced piled embankments. This is part of a larger research, that also includes a series of small-scale tests and numerical analyses. Based on the test results presented in this paper, we draw the following preliminary conclusions.

- The reinforcement tensile and bending stiffness do not significantly affect the soil arching. This is supported by the test data of the stiff SR matching analytical calculations for load A for GR and the observations made by van Eekelen et al. (2024).
- Three main European design methods for GRPS embankments closely align with the measured soil arching, with the CA model exhibiting the best match.
- The high spatial resolution of DFOS sensors allows a unique look into the soil model and a thorough comparison of measured deformations and strains with calculated values.
- The steel reinforcement shows significant differential deflection and steel strain in the bars that bridge adjacent piles. This is in line with the deformation pattern observed in geosynthetic-reinforced piled embankments.
- The strain distributions in steel reinforcement differ from geosynthetic reinforcement. The main calculation models for geosynthetics assume zero reinforcement strain above the piles, assuming that the geosynthetic is clamped between soil and pile cap. The steel reinforcement in this test shows strains both in between and above the piles.

ACKNOWLEDGEMENTS

The authors are grateful for the funding received from the European Union's Horizon 2020 research and innovation program under Grant Agreement No. 101006512 for the transnational GEOLAB project PEBSTER, the TKI-PPS funding of the Dutch Ministry of Economic Affairs and the financial and practical support of Keller.

REFERENCES

ASIRI (2013). Recommendations for the design, construction and control of rigid inclusions ground improvements (French version is of 2012).

BS8006-1 (2010). Code of practice for strengthened/reinforced soils and other fills. British Standards Institution, UK.

CUR226 (2016). See Van Eekelen & Brugman (2016).

EBGEO (2011). Recommendations for Design and Analysis for Earth Structures using Geosynthetic Reinforcements (German version is of 2010).

Hewlett, W.J. and Randolph, M.F. (1988). Analysis of piled embankments. Ground Engineering, 21(3): 12-18.

Topolnicki, M., Sołtys, G., Brzozowski, T., 2019. Performance and modelling of road embankment supported on rigid inclusions and a transfer platform with steel geogrid, Proc. of the XVII ECSMGE-2019, Geotechnical Engineering foundation of the future, Reykjavik. DOI: 10.32075/17ECSMGE-2019-0811.

Topolnicki, M., Kłosiński, B. (eds.) et al., 2022. Recommendations for Ground Improvement with Rigid Inclusions - Design, Execution and Control (in Polish). PWN SA. ISBN 978-83-01-22578-0.

van Eekelen, S.J.M., Nancey, A., Bezuijen, A. (2012). Influence of fill material and type of geosynthetic reinforcement in a piled embankment, model experiments. In: Proc. Eur. Geosynthetic Congress., Valencia, Spain, Vol 5, 167-171.

van Eekelen, S.J.M., Bezuijen, A. van Tol, A.F., (2013). An analytical model for arching in piled embankments. Geotextiles and Geomembranes 39: 78-102. DOI: https://doi.org/10.1016/j.geotexmem.2013.07.005.

Van Eekelen, S.J.M., Bezuijen, A., van Tol, A.F., (2015). Validation of analytical models for the design of basal reinforced piled embankments. Geotextiles and Geomembranes Volume 43, Issue 1, 56 – 81. DOI: https://doi.org/10.1016/j.geotexmem.2014.10.002.

van Eekelen, S.J.M. & Brugman, M.H.A., Eds. (2016). Design Guideline Basal Reinforced Piled Embankments (CUR226). CRC press, Delft, Netherlands.

van Eekelen, S.J.M. and Han, J. (2020). Geosynthetic-reinforced pile-supported embankments: state of the art. Geosynthetics International 27 (2) 112-141. DOI: https://doi.org/10.1680/jgein.20.00005.

van Eekelen, S.J.M, Schneider, M., Hell, M., Wittekoek, B., Makowska, K., Zdanowicz, K., Pandrea, P., Sieńko, R., Schauber, P., Topolnicki, M., Zachert, H., (2024). 3D small-scale tests on steel-reinforced piled embankments. In: Proc. ECSMGE 24, Lisbon, Portugal.

Proceedings of the XVIII ECSMGE 2024
GEOTECHNICAL ENGINEERING CHALLENGES
TO MEET CURRENT AND EMERGING NEEDS OF SOCIETY
© 2024 the Authors
ISBN 978-1-032-54816-6
DOI 10.1201/9781003431749-511
Open Access: www.taylorfrancis.com, CC BY-NC-ND 4.0 license

ECSMGE 24
XVIII EUROPEAN CONFERENCE ON SOIL MECHANICS AND GEOTECHNICAL ENGINEERING

The pile inspector, a new quality tool to read pile base enlargement of bored piles

L'inspecteur de pieux, un nouvel appareil de contrôle pour mesurer l'élargissement à la base de pieux foré

N. Schneider
GuD Geotechnik und Dynamik Consult GmbH, Berlin, Germany

O. Stahlhut*, P. Lenz
BBI Geo- und Umwelttechnik Ingenieur-Gesellschaft mbH, Hamburg, Germany

**O.Stahlhut@b-b-i.de*

ABSTRACT: The pile inspector allows to measure the geometrical enlargement of pile bases during the construction phase. Either connected to the kelly bar or attached to the service crane, the pile inspector is lowered into the drilled hole and measures the geometrical profile at the pile base, using 4 prestressed arms. Once the pile inspector is lifted out of the drilled hole, the installed reader transfers the gained data to the computer of the site engineer. The installed visualisation programme allows to visualise the results within a short period of time and displays the shape of the base of enlarged pile and the profile of the pile shaft.

RÉSUMÉ: L'inspecteur de pieux permet de mesurer l'élargissement géométrique des bases de pieux pendant la phase de construction. Connecté à la tige kelly ou à la grue de service, l'inspecteur de pieux est descendu dans le forage et mesure le profil géométrique de la base du pieu à l'aide de 4 bras précontraints. Une fois que l'inspecteur de pieux est sorti du forage, le lecteur intégré transfère les données acquises à l'ordinateur de l'ingénieur sur site. Le programme de visualisation installé permet de visualiser les résultats en peu de temps et affiche la forme à la base et le profil du pieu.

Keywords: Bored pile; base enlargement; increased load capacity; shaft profile; pile inspector.

1 INTRODUCTION

Pile base enlargement allows to increase the design load for bored piles. Areas of application for base enlarged piles are the transfer of high individual and surface construction loads into the ground.

The enlarged bored pile contact area enables an adjustment to the actual pile load and can therefore enable a significantly more favourable pile layout considering the internal pile load capacity. It may therefore be possible to replace a group of piles with a base enlargement and thus save pile concrete. The increased pile contact area also leads to reduced pile shaft diameters at lower drilling depths.

The technical developments in recent years like post-grouting or deep soil mixing have pushed pile base enlargement into the background. Another reason why the design of a bored pile with base enlargement is not often used is the increased additional effort involved in checking the actual geometry of the enlarged pile base.

With the help of the new construction of the pile inspector, the geometry of the base expansion can now be measured and evaluated during the production of the bored pile.

2 GEOTECHNICAL REQUIREMENTS

According to EA-Pfähle 2012 [Chapter 2.2.1.6], base enlargement can only be created in sufficiently stable soil. In unstable soils or if the expansion area is below the groundwater level, the base expansion must be secured with the help of a bentonite or cement suspension.

The geometry is limited and depends on the stability of the ground conditions. For non-cohesive soils or cohesive soils, limit values for the ratio of foot height to foot projection are set in accordance with EA-Pfähle [Chapter 5.5]. The ratio values are:

- In cohesive soils 2:1;
- In non-cohesive soils 3:1.

The extent of expansion is determined based on the soil encountered and the boundary criteria according to the static requirements.

The pile design postulates a complete filling of flawless concrete into the enlarged pile base.

2.1 Construction of the pile base enlargement

The type of bored pile depends on the existing soil and the groundwater conditions. Various drilling methods can therefore be used to produce the borehole. These include kelly bar drilling, auger drilling, displacement drilling, either with water or bentonite slurry support.

Depending on the encountered soil conditions, the borehole must be supported with casings or with partial casings. After completing the drill hole, the reaming tool is connected to the kelly bar. (see Figure 1).



Figure 1. Pile base cutter in operation.

After reaching the designed depth, the cutting arms of the pile toe cutter are extended by pressing vertically with the kelly bar. The removed drilling material is collected in the drilling bucket. In EA-Pfähle 2012 [Chapter 2.2.1.6] the geometry of the pile base produced is described as a truncated cone with a dome-shaped base and a lower cylindrical extension.

2.2 Evidence of pile base enlargement

There are several technical options available for verifying the enlargement of the pile base, which are usually carried out in combination.

Verification methods when producing the pile base expansion are:

- Climb measurement control The contact angle of the measuring arms, which are evenly distributed at a 90-degree angle across the cross section, is measured (see Figure 3). The arms are preloaded via springs and are released by a predetermined signal.
- Ultra-sonic profile reading
- Geotechnical confirmation
- Depth adjustment
- Concrete volume balancing

After the construction of the pile, the following methods are possible:

- Temperature distribution along the pile axis
- Pile load tests

When comparing the concrete volume in relation to the rise of concrete level, a first conclusion of the geometry of the pile base can be drawn, however no remediations or corrections are possible. The actual shape of the pile is unknown until the pile has been concreted.

A new approach to verify the geometry of the pile base is provided by the pile inspector which can verify the generated geometry of the pile base via the hydrostatic pressure recording and the angle measurement of the measuring arms. The following chapter goes into more detail about the manufacturing process and the use of the pile inspector.

3 PILE INSPECTOR

The pile inspector is a newly developed measuring concept that mechanically records the borehole wall and records its depth. The pile inspector is comparable to a drilling tool. After reaching the final depth, it is coupled to the kelly bar of the rotary drilling rig via the kelly box and lowered to the embedment horizon (see Figure 2).

The measurement data is saved in the pile inspector. The measuring run takes place from bottom to top. Both the cased and uncased part of the hole as well as a possible foot extension can be accommodated. The measurement accuracy is so precise that the transition from the uncased to the cased bore can be recorded. There is no coupling of the pile inspector with the data acquisition of the rotary drilling rig. The depth measurement required for later evaluation takes place in the pile inspector, which registers the depth using hydrostatic pressure sensors.

After the end of the measuring cycle, the pile inspector is pulled out of the borehole and the data transfer from the built-in measuring box to the project engineer's notebook takes place immediately using bluetooth technology.

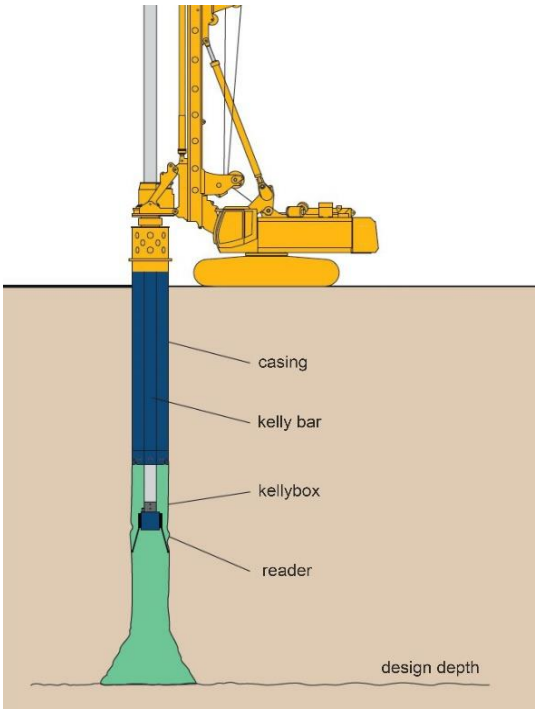

Figure 2. Use of the pile inspector.

In practical terms, this means that the pile inspector is placed at the bottom and remains there for a period of approximately 2 minutes. The associated constant pressure triggers the pre-stressed joints and the arms are pressed against the wall (see Figure 3) with spring force. The joints are electrically connected to the data logger and are transferred to the central unit. The angle that the arms make to the wall is the relevant measurement that is recorded to capture the distance to the wall of the hole. The angle detection is linked to the self-sufficient depth measurement, so that the measured angle is always depth-related. Contact with the wall occurs via rollers, runners or contact strips.

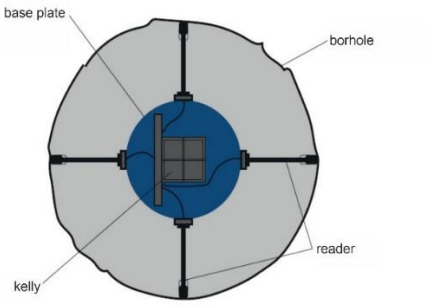

Figure 3. Arrangement of the measuring arms.

After the pile has been expanded by the pile base cutter, the pile inspector is lowered into the depth and the arms are triggered to unfold. The lowering of the pile inspector is not necessarily linked to the kelly bar of a rotary drilling rig, but can also be done using a service crane. With the exception of the upward pulling force, no forces have to act for the measuring process. What is important is the change in angle that has formed in the transition area between the expansion and the shaft profile.

This means that the essential parameter for the pile base expansion can be measured. In fact, the pile inspector records three pile sections, namely the opening angle of the pile base expansion, the contour of the uncased pile shaft and the cased part. The transition to the cased part will be discretely measurable.

The specific dimensions for the pile inspector have been implemented in steel construction drawings (see Figure 4). The control connection to the drilling rig is made via the kelly box. The data logger with the battery unit to power the sensors is located centrally. A total of 4 arms can be connected. The length of the arms can be adjusted on site. The main frame of the pile inspector is a steel structure. The attachments are aluminum components. The entire construction is transported on a carrier pallet. The energy is supplied by batteries that are charged before use. The duration of the energy charge allows operation of 8 hours. The construction has been designed for drilling operations using appropriate spacers and protective profiles.

The geometric details of the pile inspector and the measuring distances can be found in Figure 4 below. The construction is designed so that the pile inspector fits into a casing with a diameter of 900 mm. With a maximum arm length of approx. 115 cm, an expansion of up to 218 cm can be recorded. The support structure below is designed so that sedimentation residues can be driven through. This mechanical form of scanning offers the advantage that the measurement recording is independent of the slurry properties and the measurement can therefore be carried out either before desanding or after desanding.

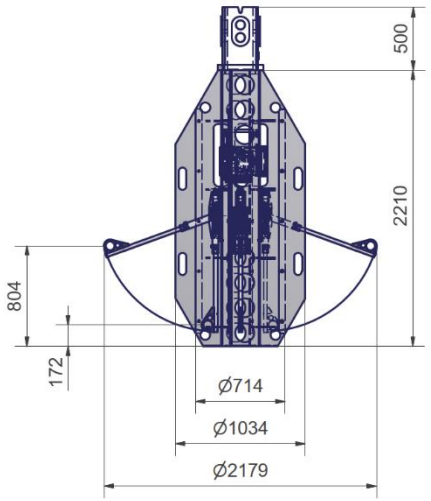

Figure 4. Technical dimensions of the pile inspector.

3.1 Data transmission and visualization of the measurement data

The measurement data is recorded in the pile inspector and stored in the data logger. The construction site name, pile number, index of the measurement trip and the target depth of the drilling can be entered in advance. The measuring journey takes place from bottom to top.

The time, depth and angle of the measuring arms are recorded as measured variables. The measuring depth is recorded by a hydrostatic sensor that records the hydrostatic suspension pressure. This continuous measurement data recording is coupled to the angles of the arms at predetermined time intervals, which allows to determine the distance to the wall. This continuous data recording creates a continuous profile of the pile wall.

The start of data recording is set so that when the hydrostatic pressure stays constant for a defined period, the arms are unlocked and come into contact with the wall as a result of the pre-stressed arms. The measurement accuracy is very high. When the pile inspector is lifted out of the borehole, the data is transferred to the project engineer's notebook in already prepared graphics so that the relevant dimensions of the borehole contour can be read, right after the reading cycle. The measured distances are displayed individually for each arm. This graphical preparation of the measurement trip immediately afterwards allows a short-term decision to be made as to whether the trip needs to be repeated.

4 GEOLOGY AND GROUNDWATER

Figure 5 shows the results of the site investigation and the possible position of the bored pile with the base expansion. The position of the pile is designed in relation to the geological profile and the pile length is determined based on this profile. It can also be seen from the drilling results that the pile base lays below the groundwater level and therefore stabilization with a supporting fluid is necessary during production.

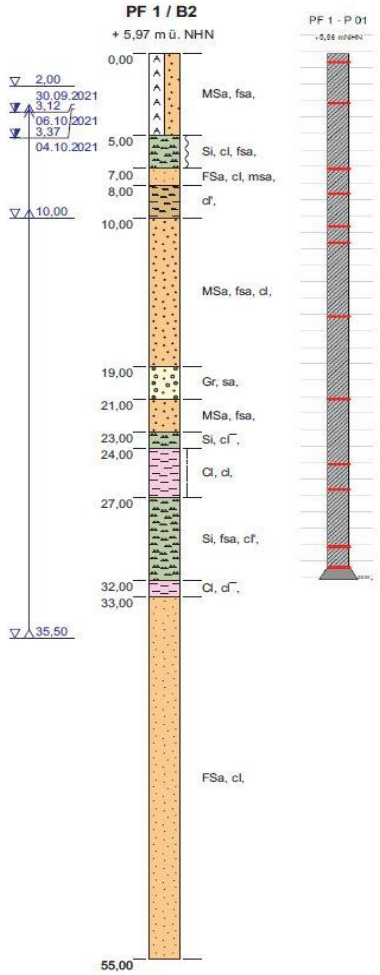

Figure 5. Idealized drilling including position of the bored pile with base expansion.

5 CONSTRUCTION PROCESS

The following chapter introduces the construction process for cutting the pile base expansion. Once the designed borehole depth has been reached, the drilling tool is changed and the pile base cutter is mounted on the kelly bar of the drill rig. On the planned depth of the pile, the cutting blades extend via the vertical force of the kelly and thus create the rotationally symmetrical pile base. Following the expansion, the pile cutter is removed from the borehole again. A detailed manufacturing sequence is shown in Figure 6 and 7.

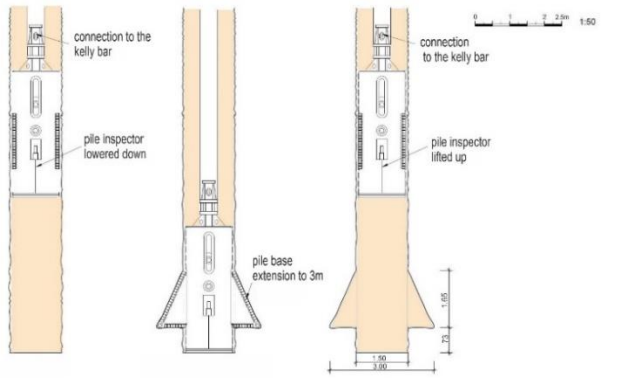

Figure 6. Expanding the pile base.

After the expansion has been completed, the pile inspector will be connected to the drilling rig's kelly bar or a service crane and guided into the borehole. After reaching the target position, the measuring arms of the pile inspector fold out and record the geometry of the pile base that has actually been produced (see Figure 7).

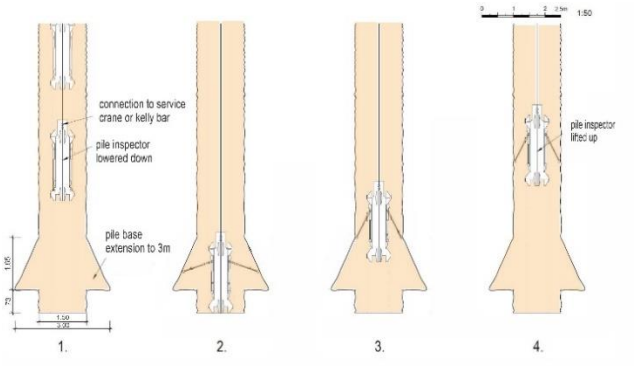

Figure 7. Measuring the pile base with the pile inspector.

Due to the high measurement accuracy, deviations in the geometry can be identified during the installation process and corrected before the reinforcement cage is installed. It may be necessary to repeat the cutting and measuring process.

6 SITE APPLICATION

The field application offered the possibility to check the pile inspector in two operational ways, the kelly bar mounted (see Figure 8) and the crane mounted operation (Figure 9). Since the drilling rig is essential for the overall progress on site, the crane application proved to provide significant time advantages. Once the final depth is reached and the pile base cut, the rig moves to the next drilling location, while the profile of the base expansion is scaled by the pile inspector.



Figure 8. Kelly mounted pile inspector.

7 INTERPRETATION OF THE READINGS

The readings are taken at pre-determined depth and show the distance to the casing and to the cut profile at the pile base. A hydrostatic pressure meter in the pile inspector is calibrated on the actual drilling depth and allows to define reading levels at constant distances. The addition of opposite reading arms confirms the internal diameter of the casing.

At the level where the casing ends, an increase in pile diameter is recorded. All four arms prove this changeover at the same depth. The soil at this transition zone has been flushed out during the piling works with the drilling bucket.

The enlargement in the pile base area reaches over the pile shaft diameter and shows an uniform inclination of the cutting profile in all directions. This profile angle in combination with the construction drawings of the cutting tool enables a confirmation of the cutting width.



Figure 9. Service crane mounted pile inspector.

8 ALTERNATIVE VERIFICATION METHODS FOR THE CONTOUR VERIFICATION OF BORED PILES

8.1 Thermal evidence

Alternatively, the base expansion of a concrete pile can be demonstrated by thermal measurements during hydration.

The sensors are most expediently mounted on the longitudinal reinforcement of the bored piles and read during the setting process. The distribution of the setting heat during the hydration time is recorded and evaluated across both the cross section and the pile length.

An even distribution is evidence of a planned enclosure of the sensors, lower temperatures indicate constrictions, cracks or imperfection of the concrete enclosure.

Obviously, the temperature development in the area of the foot expansion will be significantly higher than the normal range along the pile shaft.

8.2 Ultrasound measurements

The geometry of the wall can also be recorded using ultrasound measurements.

The sensor is positioned over the borehole before the pile is concreted and the ultrasonic transmitter is lowered into the borehole. The measurement results are visualized simultaneously with the measurement.

The ultra-waves run through the suspension and the running time is measured. The diameter can be derived indirectly from this. The purity of the suspension has a decisive influence on the speed of sound transmission.

9 CONCLUSIONS

The results of a pile base reading are displayed in Figure 10.

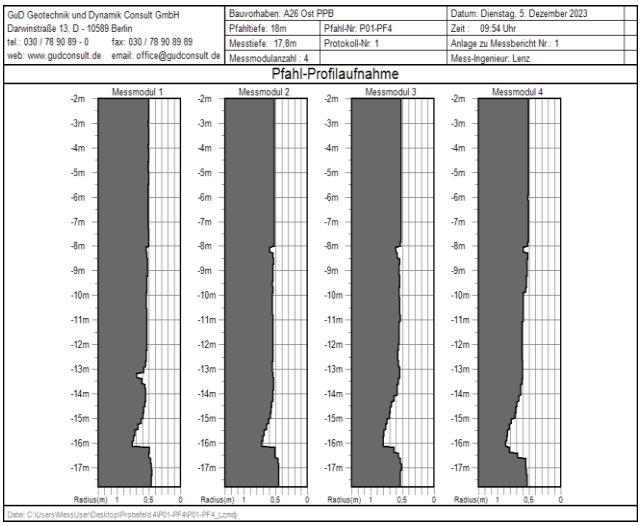

Figure 10. Visualisation of reading results.

The presented pile inspector is a tailored form of evidence for the quality assurance of bored piles. This allows the geometry of pile base expansions and the borehole walls of the piles to be verified.

The kelly-adaptable measuring device allows it to be used effectively before concreting the pile, without significantly intervening in the construction processes. If necessary, the pile inspector can also be operated by a service crane.

The mechanical measuring principle enables high measuring accuracy. By linking the measurement data of the depth and angle of the measuring arms, the results can already be processed in the pile inspector and are available to the project engineer immediately after the measurement trip.

By using the pile inspector, the quality of the base expansion of bored piles can be assured. The associated higher utilization of the load-bearing capacity with reduced material use in the pile shaft and the simultaneous increase in tensile and compressive loads can sustainably improve the economic viability and sustainability of pile foundations.

REFERENCES

DGGT (2013). Recommendations on Piling. Ernst und Sohn.

Proceedings of the XVIII ECSMGE 2024
GEOTECHNICAL ENGINEERING CHALLENGES
TO MEET CURRENT AND EMERGING NEEDS OF SOCIETY
© 2024 the Authors
ISBN 978-1-032-54816-6
DOI 10.1201/9781003431749-512
Open Access: www.taylorfrancis.com, CC BY-NC-ND 4.0 license

ECSMGE 24
XVIII EUROPEAN CONFERENCE ON SOIL MECHANICS AND GEOTECHNICAL ENGINEERING

Highrise building NION with a combined pile-barrette-raft foundation

Immeuble de grand hauteur NION avec fondation mixte radier-pieux-barettes

M. Seip*, S. Fischer, R. Katzenbach
Ingenieursozietät Professor Dr.-Ing. Katzenbach GmbH, Darmstadt, Germany

**seip@katzenbach-ingenieure.de*

ABSTRACT: For the NION project, a highrise building with roughly 100 m height in Frankfurt am Main, Germany, a 4-story basement is planned directly next to a railroad embankment, in the settlement active Frankfurt soils. A diaphragm wall up to 1.2 m thickness is planned as retaining wall with the cut-and-cover method, which will also be the permanent outer basement wall of the final building. Due to the necessity of watertightness, great attention had to be paid to a compatible settlement between foundation slab and diaphragm wall during the design. Due to the near-edge column positions of the high-rise building and the partial load transfer of the high-rise loads into the diaphragm wall, the compatibility of the deformations of the individual diaphragm wall elements had to be investigated numerically. The foundation of the highrise building is planned to be a combined pile-barrette-raft foundation. A variation of the well-known and often used combined pile raft foundation (CPRF) in Frankfurt am Main.

RÉSUMÉ: Un immeuble der grande hauteur d'environ 100 m est prévu à Francfort-sur-le-Main dans le cadre du projet NION. Le site se trouve directement à coté d'un remblai des chemin de fer. Le bâtiment est projeté avec 4 étages du sous-sol et sera fondé dans les sol actifs de Francfort. Le mur de soutènement de la fouille est prévu avec une paroi moulée d'une épaisseur de 1,2 m qui sera également le mur extérieur permanent des sous-sols du bâtiment final. Pour assurer l'étanchéité, une grande attention a été nécessaire à la compatibilité des tassements entre le radier et la paroi moulée dans la phase de conception.Donc, la compatibilité des déformations des différents panneaux de la paroi moulée a dû être étudiée numériquement respectant la position proche des colonnes de l'immeuble de grande hauteur et le transfert partiel des charges du bâtiment dans la paroi moulée. En raison des charges élévées de terre et de pression d'eau, la fouille est planifiée avec une construction de haut en bas.La fondation du bâtiment est prévue avec une composition du radier, des pieux et des barettes. Il s'agit d'une variation des la fondation mixte radier-pieux (CPRF en anglais) bien connue et réalisée souvent à Francfort-sur-le-Main.

Keywords: combined pile-barrette-raft foundation, highrise building, settlement active soils, cut-and-cover, diaphragm wall

1 BUILDING AND LOCATION

The highrise building NION is planned with 26 upper storeys and a 4-storey basement as an office tower (Figure 1).

The site is located in the city centre of Frankfurt am Main, Germany, directly on a railway embank-ment opposite the exhibition centre (Figure 2). The high-rise building is accompanied by a 7-storey base building with one underground garage. Figure 3 shows a cross section through the building NION.



Figure 1. Rendering of the NION highrise building.

The approx. 17,5 m deep excavation pit will be executed as a watertight cut-and-cover construction with a diaphragm wall, which will also be the permanent outer wall of the basement. Due to this planning the foundation slab as even the ceilings are

connected to the retaining wall in order to avoid differential settlements. The excavation base is located around 13.5 m below the groundwater level.

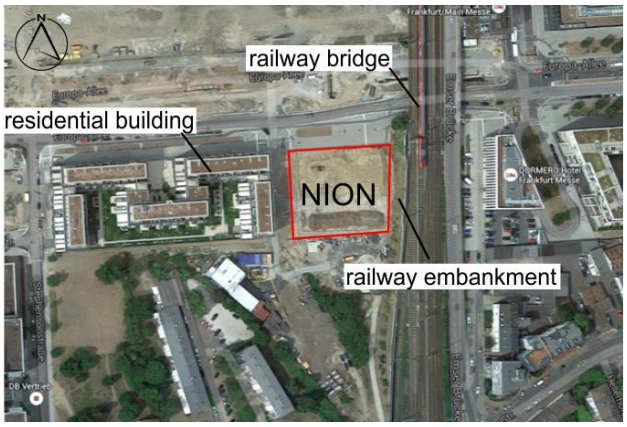

Figure 2. location of the NION highrise building.

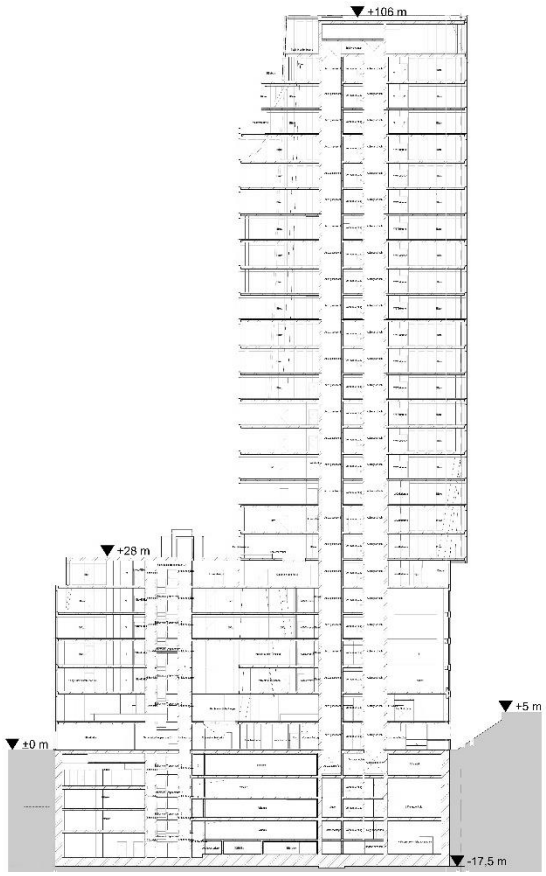

Figure 3. Cross section through the NION highrise building.

2 SOIL AND GROUNDWATER

Due to the 4-storey basement, deep soil investigations up to a depth of 100 m were carried out.

Based on exploration drillings and the soil investigations from adjacent sites the following soil model has been elaborated:

- Layer I : filling
- Layer IIa : quaternary clay
- Layer IIb : quaternary sand and gravel
- Layer III : tertiary sand/gravel/silt
- Layer IV : tertiary “Frankfurt Clay”

Figure 4 shows a simplified cross section through the subsoil of Frankfurt am Main in west (left) to east (right) direction.

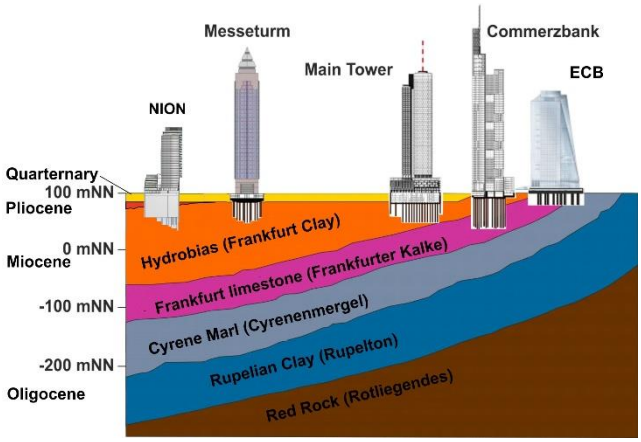

Figure 4. Cross section through the subsoil of Frankfurt am Main (west to east).

The settlement of the building is decisively influenced by the settlement behaviour of the Frankfurt clay. The Frankfurt Clay essentially consists of settlement active clay. In detail the Frankfurt Clay appears as an alternating sequence of clay, limestone banks, hydrobien sand layers and dolomite banks. Figure 5 shows a drill core from the site in a depth of 32 m to 36 m.



Figure 5. Drill core in a depth of 32 m to 36 m.

Regarding this drill core, in a depth of 34.15 m a limestone bank of approx. 0.5 m thickness begins. This limestone banks (and the dolomite banks, too) are fissured and strongly aquiferous.

The groundwater circulates in different (mostly three) partly interconnected groundwater levels in the project area. The free groundwater level is in the quaternary sand and gravel, approx. 4 m below ground elevation.

3 EXCAVATION PIT

The excavation is carried out under the protection of a 1.2 m thick and up to 46 m long diaphragm wall.

The diaphragm wall is planned as a retaining wall with the cut-and-cover method and will also be the permanent outer basement wall of the final building and part of the foundation.

Figure 6 shows a cross section through the basement of the building. The ceilings aren‘t continuous in east-west direction. This so-called split-level construction method means that the ceilings have to transfer horizontal loads into the lateral diaphragm walls.

Due to the high loads, among others caused from the groundwater, the retaining wall is planned with different depths as a dissolved diaphragm wall. One diaphragm wall element is made of three stitches, whereby one stitch (the one in the middle) is shorter than the surrounding ones to create a so called hydraulic window and reduce the water pressure onto the retaining wall. Figure 7 shows the formation of the hydraulic windows.

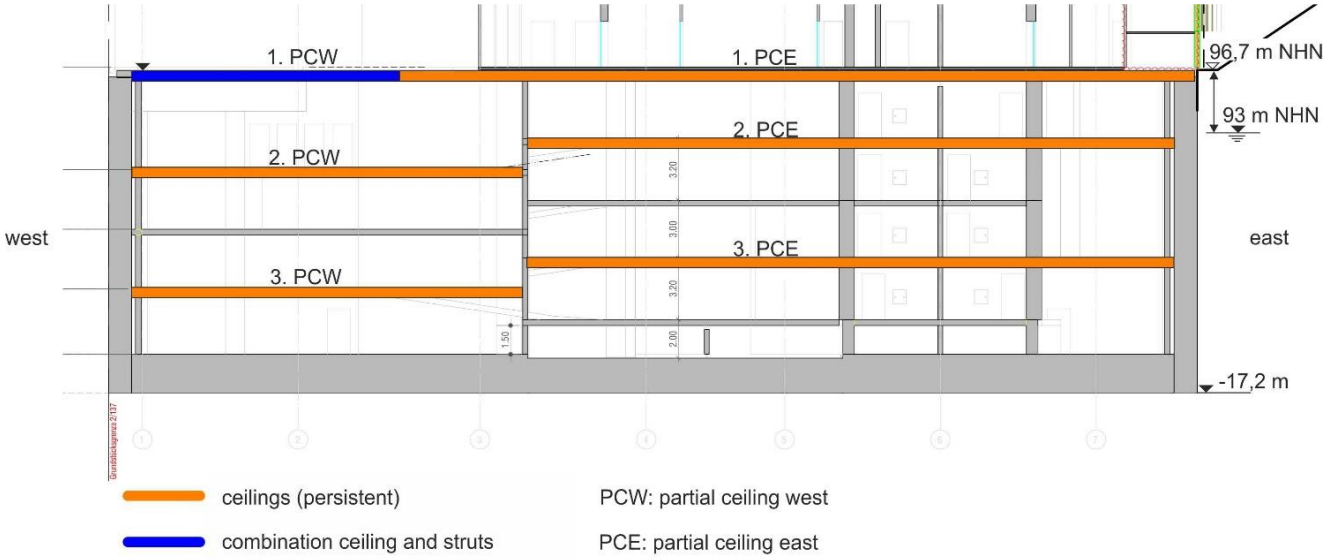

Figure 6. Cross section through the basement of the building.

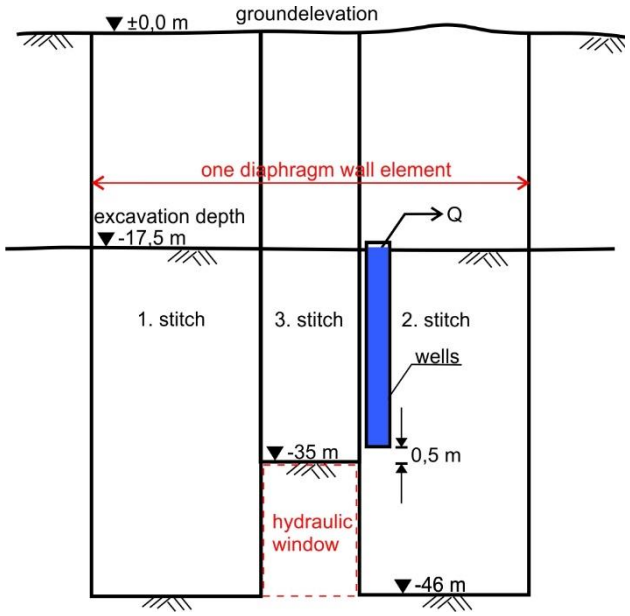

Figure 7. Formation of the hydraulic windows.

Wells are installed to keep the excavation pit dry and to establish safety against hydraulic failure (limestone and dolomite banks), whereby the impermeable Frankfurt Clay is used as a sealing base. Due to the previous usage of the area as a railway freight station these wells have to be shorter than the watertight diaphragm wall in order to avoid the mobilisation of existing contaminations of the groundwater. For this reason the hydraulic windows starts 0.5 m below the lower edge of the wells (Figure 7).

4 DEEP FOUNDATION

The Foundation of the NION consists of a foundation slab with varying thickness (1.3 m and 1.8 m, see Figure), 39 piles with length up to 40 m which will also be used through the construction state for founding the supports of the ceilings, the retaining wall and six diaphragm baretts with lengths up to 44 m (Figure 8).

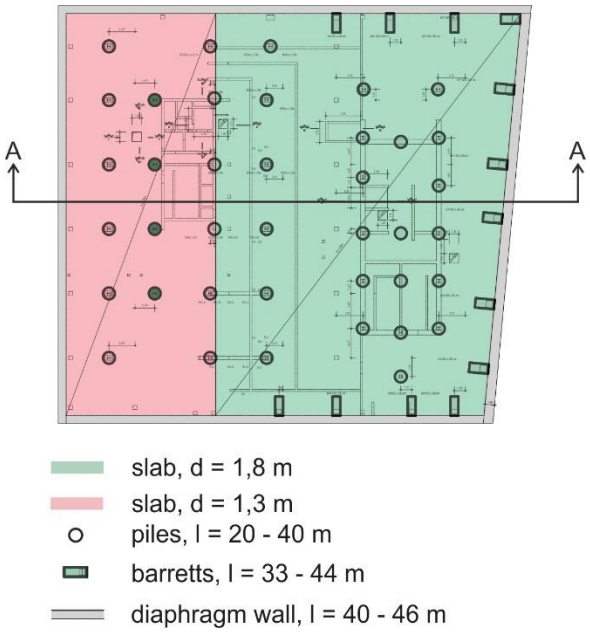

Figure 8. Foundation of the NION.

An overview on the design of piled rafts and its behavior, especially in Frankfurt am Main, is given in Reul (2000). For the prediction of the settlements and especially to proof the acceptable differential settlement between retaining wall (persistent basement wall) and foundation slab, various three dimensional numerical calculations were executed. For consideration the general interaction between the different parts of the foundation, scientific works like Randolph (1994), Katzenbach et al. (1998) etc. were taken into account. For the special conditions in Frankfurt the scientific work of Moormann (2002) were taken into account, too. Figure 9 shows the dimensions of the numerical model.

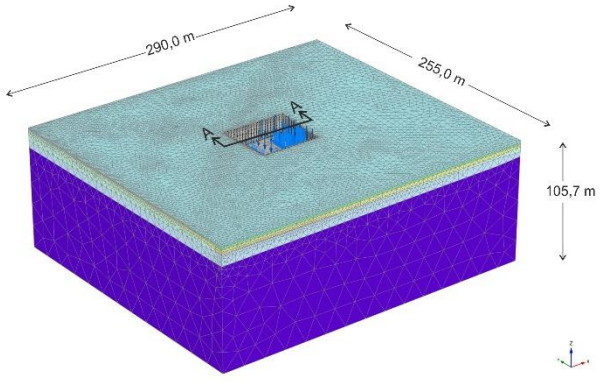

Figure 9. Dimension of the numerical model for the prediction of the settlements.

Figure 10 shows the cross section A-A from Figures 8 and 9 with the soil stratification used in the numerical calculations.

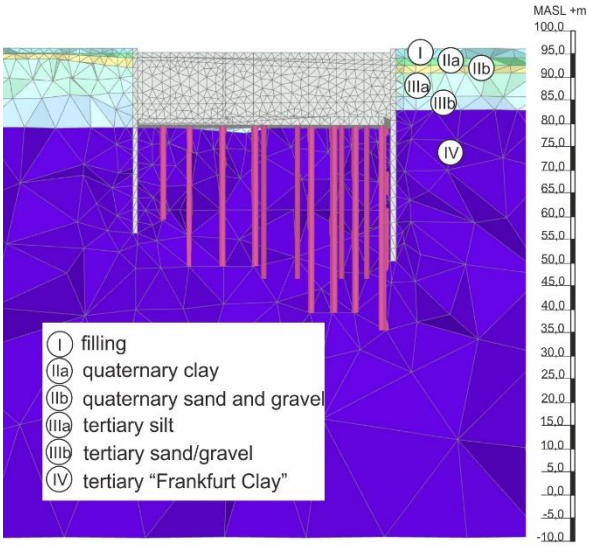

Figure 10. Cross section A-A with soil stratification.

In order to be able to make a statement about the differential deformations of the diaphragm wall elements and thus about the watertightness of the joints, the diaphragm wall had to be modelled in its individual elements. Modelling was done with interface elements between the single diaphragm wall elements and also the foundation slab (Figure 11).

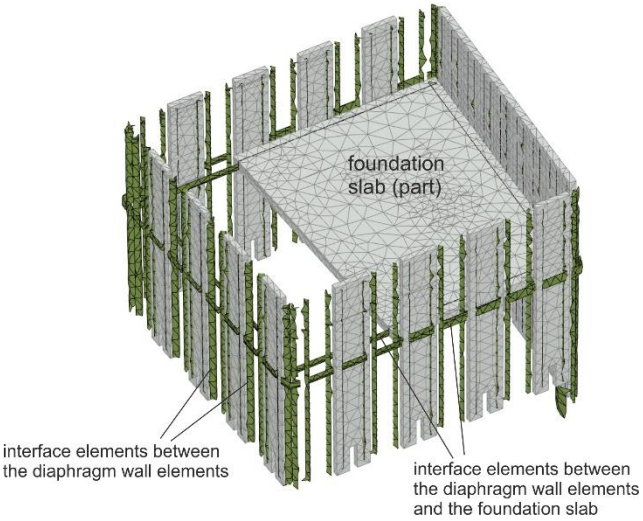

Figure 11. Modelling of the connection between diaphragm wall and foundation slab.

Due to the very robust foundation, no incompatible displacements were calculated either in the area of the joints between the foundation slab and diaphragm wall or in the area of the joints between the individual diaphragm wall elements.

Table 1 shows the loads of the high-rise building NION, where $G_{tot,k}$ are the characteristic dead loads and $Q_{tot,k}$ are the characteristic life loads.

Table 1. loads of the high-rise building NION.

$G_{tot,k}$	920 MN
$Q_{tot,k}$	180 MN
$P_{tot,k} \triangleq R_{tot,k}$	1.100 MN

The bearing behaviour of a CPRF (see Katzenbach and Deepanker 2013) can be specified by the so called CPRF coefficient α_{CPRF}. The coefficient gives the ratio between the resistance of the piles ($\Sigma R_{pile,k,i}$ = 980 MN, including also the resistance of the barretts and the diaphragm wall) and the total resistance of the whole CPRF ($R_{tot,k}$ = 1.100 MN). If the CPRF coefficient becomes 0, the foundation works as a raft-foundation. If the CPRF coefficient becomes 1, the foundation works as a pile-foundation.

$$\alpha_{CPRF} = \frac{\sum R_{pile,k,i}(s)}{R_{tot,k}(s)} = 0{,}89 \qquad (1)$$

Figure 12 shows the prediction of the settlements for the NION building (load case P_{sett}, Eq. 2) which is calculated smaller than 4 cm and also compatible torsions for the foundation slab. A_{mid} is the buoyancy force at mean groundwater level.

$$P_{sett} = G_{tot,k} + \frac{Q_{tot,k}}{3} - A_{mid} \qquad (2)$$

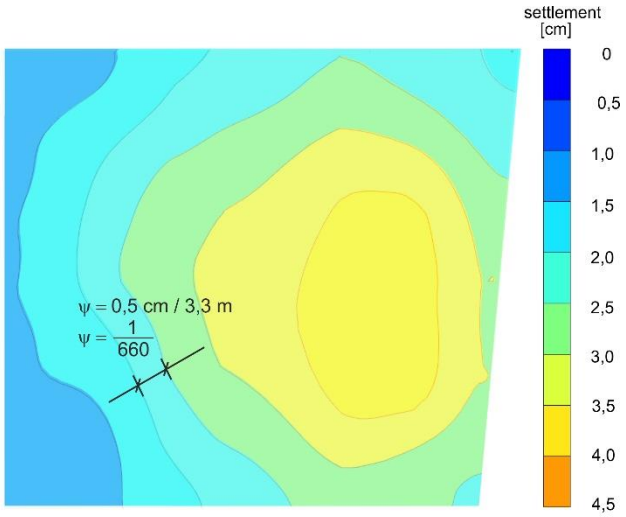

Figure 12. Prediction of the settlements for P_{sett}

5 CONCLUSIONS

For a new highrise building – NION – in Frankfurt, the retaining wall for the 4-storey basement should be used as persistent outer wall for the basement. Due to the high water pressure on the diaphragm wall and very high supporting loads next to the retaining wall, the client was concerned about the watertightness of the later exterior wall.

By means of complex numerical calculations, the deformations between the individual diaphragm wall elements and also between the diaphragm wall and the foundation slab could be predicted. In the numerical simulation, the foundation elements could be adjusted in that way that the differential displacements at the joints were reduced to a level which is suitible for the joint sealings.

REFERENCES

Katzenbach R. and Deepanker C. (2013). ISSMGE Combined Pile-Raft Foundation Guideline.

Katzenbach, R., Arslan, U., Moormann, C. and Reul, O. (1998). Piled raft foundation – Interaction between piles and raft. Proc. Int. Conf. on Soil-Structure Interaction in Urban Civil Eng., Darmstadt Geotechnics 4(2), pp 279-296.

Moormann, C. (2002). Load-bearing and deformation behaviour of deep excavations in cohesive soils taking into account soil-structure and soil-groundwater interaction. („In german“)Mitteilungen des Instituts und der Versuchsanstalt für Geotechnik, Technische Universität Darmstadt, Heft 59.

Randolph, M. F. (1994). Design Methods for pile groups and piles rafts Proceedings 13th ICSNFE, New Dehli, Vol. 5, pp 61-82, Rotterdam: Balkema.

Reul, O. (2000). In-situ measurements and numerical studies on the load-bearing behaviour of the combined pile-raft foundation („In german“) Mitteilungen des Institutes und der Versuchsanstalt für Geotechnik der Technischen Universität Darmstadt, Heft 53.

Proceedings of the XVIII ECSMGE 2024
GEOTECHNICAL ENGINEERING CHALLENGES
TO MEET CURRENT AND EMERGING NEEDS OF SOCIETY
© 2024 the Authors
ISBN 978-1-032-54816-6
DOI 10.1201/9781003431749-513
Open Access: www.taylorfrancis.com, CC BY-NC-ND 4.0 license

ECSMGE 24
XVIII EUROPEAN CONFERENCE ON SOIL MECHANICS AND GEOTECHNICAL ENGINEERING

Deep excavation solutions in an urban environment - Distrikt residential project, Lisbon

Solutions d´excavation profonde en milieu urbain – Projet résidentiel Distrikt, Lisbonne

J. Silva*, I. Braz, A. Pinto
JETsj – Geotecnia, Lda., Lisbon, Portugal

** jsilva@jetsj.com*

ABSTRACT: This paper describes the main design and execution criteria adopted for the peripheral earth retaining solutions, required for the construction of three underground floors for the Distrikt Residential Buildings, located in the south of Parque das Nações, in Lisbon. The excavation, with 11 m of maximum depth, mainly intersected landfill layers and Lisbon Miocene soils (Areolas do Cabo Ruivo e Areolas do Braço de Prata). The excavation site is confined by several underground infrastructures, which are mostly inside a technical gallery, close to the excavation pit boundaries. It is also noteworthy the proximity to two buildings with several basements, as well as the possibility that the excavation can coexist with the construction of an underground car park, under Rua Mário Botas. To minimize the ground disturbance, as well as the deformations of the mentioned structures, a reinforced concrete bored pile wall with 600mm diameter was defined, braced in general by steel props and temporary ground anchors. In the elevations where the neighbourhood conditions didn't allow the execution of ground anchors, the retaining wall was braced by concrete slab's strips, which were connected to pile buttresses and supported by HEB200 micropiles. The main results of the monitoring plan are drawn and presented, including the analyses and comparison with the estimated values from the design phase.

RÉSUMÉ: Cet article décrit les principaux critères de conception et d'exécution adoptés pour les solutions de retenue périphérique du sol nécessaires à la construction de trois étages souterrains pour les bâtiments résidentiels Distrikt, situés au sud du Parque das Nações, à Lisbonne. L'excavation, d'une profondeur maximale de 11 mètres, a principalement traversé des couches de remblai et des sols miocènes de Lisbonne (Areolas do Cabo Ruivo et Areolas do Braço de Prata). Le site d'excavation est confiné par plusieurs infrastructures souterraines, principalement à l'intérieur d'une galerie technique, à proximité des limites de la fosse d'excavation. Il est également à noter la proximité de deux bâtiments avec plusieurs sous-sols, ainsi que la possibilité que l'excavation puisse coexister avec la construction d'un parking souterrain, sous la rue Mário Botas. Pour minimiser la perturbation du sol, ainsi que les déformations des structures mentionnées, un mur de palplanches en béton armé de 600 mm de diamètre a été défini, renforcé en général par des étais en acier et des ancrages temporaires. Aux endroits où les conditions du quartier ne permettaient pas l'exécution d'ancrages au sol, le mur de soutènement était renforcé par des bandes de dalle en béton, reliées à des contreforts de pieux et supportées par des micropieux HEB200. Les principaux résultats du plan de surveillance sont présentés, y compris les analyses et la comparaison avec les valeurs estimées de la phase de conception.

Keywords: Earth retaining walls; pile walls; slab bands; buttress; temporary ground anchors.

1 INTRODUCTION

The present article describes the solutions adopted for the excavation and peripheral soil containment, necessary for the construction of 3 underground floors of the Distrikt enterprise. The enterprise is located in the southern area of Parque das Nações.

The project envisages the construction of 4 towers with 13 elevated floors and 3 common underground floors, which occupy the total area of the plot and are expected to be used for car parking and technical areas. Figure 1 displays an aerial perspective of the intervention site.



Figure 1. Virtual view of the future residential building´s.

Previous research, such as Carvalho & Pinto, 2019; Tomásio & Pinto, 2019 and Pinto et al., 2017, have developed similar earth-retaining solutions for deep excavations in urban environments, as it will be presented in the following chapters.

2 MAIN CONSTRAINTS

2.1 Geological and geotechnical conditions

To characterize the geotechnical behaviour, associated with the soils present at site, a prospecting campaign was conducted involving the execution of 16 mechanical boreholes accompanied by Standard Penetration Tests (SPT) and the collection of samples for macroscopic classification. Additionally, 5 hydraulic piezometers were installed in some of the boreholes. According to the results obtained, the geological structure of the site is characterized by the presence of Miocene substrates corresponding to Areolas do Cabo Ruivo (M_{CR}) and Areolas do Braço de Prata (M_{BP}), overlaid by modern anthropogenic materials, Landfill Deposits (At), with a thickness ranging from 1.5 m to 7.9 m. The Miocene formations are mainly composed of fine silty sands with carbonate nodules or fossil remains. This units have a considerable thickness, reaching the end of the boreholes. Bio-calcarenite levels (pebble beds) with variable thicknesses ranging from 0.1 m to 2.0 m were also identified.

In the sample collection, it was identified the contamination of the uppermost layers of fossiliferous limestone (pebble beds), revealing the presence of hydrocarbons in 6 of the boreholes conducted, all located on the north of the plot.

In terms of hydrogeology, the Miocene layers function as a multilayer system, consisting of alternating permeable layers (sands, sandstones, and some limestones) with other semi-permeable layers, such as clays and siltstones. Therefore, the higher the percentage of fines (silt and clay), the lower the permeability. On the other hand, bio-calcarenite layers are often highly permeable due to their high porosity and can constitute more productive layers.

2.2 Neighbourhood conditions

The excavation site, bordered by roads, infrastructures, and buried networks, is notably close to the Parque das Nações technical gallery, where diverse service infrastructures are established. The integrity and operability of these infrastructures must be maintained during construction work, thus influenced the design of peripheral earth retainment solutions.

During the project´s development, excavation works could potentially occur simultaneously with the construction of the underground levels of the parking lot to be developed immediately adjacent to the plot. In this context, and for this elevation, it had to be defined interior bracing solutions that did not require occupying neighbouring plots. In the following figure it is possible to observe the main boundaries of the excavation site.

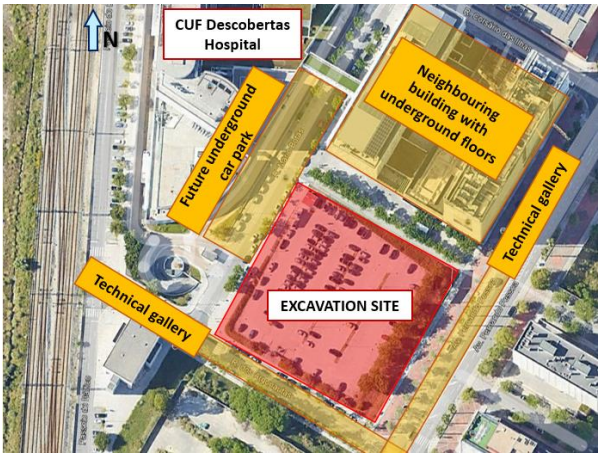

Figure 2. Main boundaries of the excavation site.

3 EXCAVATION AND PERIPHRAL EARTH RETAINING SOLUTIONS

In the design of the adopted peripheral earth retaining solutions, the following fundamental principles were sought to be respected, beyond the necessary horizontal retainment of the excavated grounds:

- Control soil deformations and surrounding structures and infrastructures to the excavation, allowing the adaptation to possible geological and geotechnical singularities;
- Ensure minimal interference with all adjacent structures and infrastructures.

Considering the existence of several conditioning factors, a reinforced concrete bored pile wall with 600 mm diameter piles and spaced 1.20 m, was defined. The bored pile walls were constructed using a telescopic Kelly bar technology, with temporary casing employed only at the top of the terrain to penetrate through the fill layers, when necessary.

During the excavation phase, the exposed soil between bored pile walls was generally protected with sprayed concrete with a minimum thickness of 8 cm, reinforced with metallic fibers, applied in two layers and properly drained through drainage pipes. These devices were served to collect and conduct water to the building's drainage system through vertical drainage pipes installed at the back of the wall and between the bored piles. In the regions where there was a higher probability of increasing locally the permeability

and/or contamination of the soil, it was constructed a permanent reinforced concrete wall with 25 cm thickness, properly integrated to the bored pile walls.

The reinforced concrete bored pile wall was braced, in general, by multiple levels of steel props and pre-stressed ground anchors, to ensure the horizontal balance of the provisional earth retaining structures.

To ensure a better distribution of the forces along the curtain wall, as well as to prevent the excessive concentration of loads, the temporary ground anchors and steel props were connected to distribution concrete beams and crown beams. In the definitive phase, the stability of the curtain wall is provided by concrete slab strips, which will integrate the definitive concrete slabs of the underground floors, and the temporary ground anchors and steel props are deactivated after the completion of the definitive structure.

In elevations where the presence of neighbouring infrastructures or structures constrained the execution of ground anchors, a bracing system was defined, consisting in reinforced concrete slab bands, which function has horizontal beams (with the section of the future underground floors). The slab bands offer high stiffness to the earth retaining wall, resisting and transmitting the impulses acting on the curtain wall directly to the buttresses, which were also formed by bored piles. Considering the excavation depth, bracings were implemented at levels -1 and -2, with the initial excavation section carried out under a curtain wall that will be functioning as a cantilever. The design of the structural elements considered not only the necessary strength and stiffness to ensure safety and proper functionality but also the construction process associated with both the excavation and the execution of the underground floors. Figure 3 and 4 shows 2 plan views of the peripheral earth retaining structures and the respective shoring elements at each underground floor level.

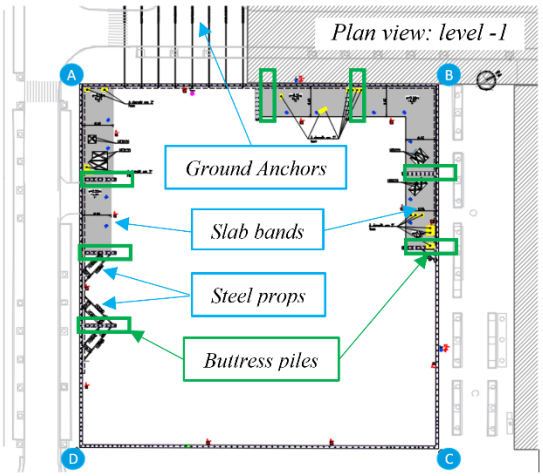

Figure 3. Design plan view of the peripheral earth retaining solution at level -1.

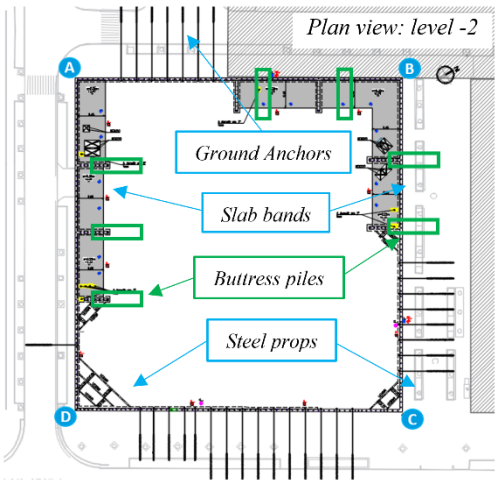

Figure 4. Design plan view of the peripheral earth retaining solution at level -2.

The ground anchors comprised 6 and 7 strands, each with a diameter of 0.6 inches, spaced at intervals of 3.60 m. A tensile load ranging from 600 kN to 800 kN was applied to these anchors, which varied in both length and inclination. The anchors inclination was specifically determined to prevent potential intersections with existing infrastructures and structures. Additionally, these inclinations facilitated the execution of the primary grout in geologically stable soil concerning the excavation´s geometry (Figure 5). The bond lengths were accomplished using the IRS system, incorporating double obturators and non-return valves, with a minimum hole diameter of 200 mm.



Figure 5. Bored pile wall shored by temporary ground anchors.

The configuration of the slab sections was defined with the aim of minimizing interference with the construction of the pillars and other structural elements within the ground floors. The slab bands exhibited an average width and thickness of 6.50 m and 25 cm, respectively. During the excavation phase, the slab

bands were supported on the retaining walls and on HEB200 profiles, spaced approximately 6.50 m apart (Figure 6). These profiles were bonded for a length of 2.0 m within sections of Ø600 mm piles, reaching a depth of 4.0 m below the excavation´s bottom. The execution of the slab strips took place during the excavation phase, involving concreting against the ground over a layer of levelling concrete and plastic film.



Figure 6. Concrete slab strips supported by HEB200 micropiles and buttresses.

To ensure the bored pile wall essential´s drainage conditions, sub-horizontal drainage pipes were installed between the curtain´s piles, measuring 4 m in length and 50 mm in diameter. These pipes were made from high density polyethylene (HDPE), covered in a geotextile with a density of 150 g/m^2. It´s primary function was to facilitate internal drainage within the massif, thereby averting potential hydrostatic impulses resulting from rainwater infiltration. To guarantee the gravitational flow of collected water, these drainage elements were positioned with an upward slope of 10º from the horizontal and with a horizontal spacing of 3.60 m.

The water collected by drainage pipes was directed into the peripheral rain gutter, which ran parallel to the retaining wall. Below the excavation bottom level, there was no interference with the hydrogeological system, as the piles, being discrete and spaced elements, did not form a barrier to the water flow.

4 GEOTECHNICAL AND STRUCTURAL DESIGN

The assessment of the presented peripheral earth retaining solutions in terms of forces and deformations was conducted for all major construction phases using finite element programs such as PLAXIS 2D and 3D, specifically designed for this purpose. A constitutive model was developed to simulate the soil behaviour characteristics of a "Hardening Soil", considering a nonlinear constitutive relationship and variations in the soil's stiffness under applied stress states. The parameters outlined in Table 1 were applied in PLAXIS to model the soils.

Table 1. Geotechnical soil parameters.

Soil Type	ZG_{1A}	ZG_{1B}	ZG_{2A}	ZG_{2B}	ZG_{2C}
N_{SPT}	<10	10-30	10-30	30-60	60
Υ [kN/m^3]	18	19	19	20	21
Φ' [º]	27	31	32	33	36
E_{50}^{ref} [MPa]	8	20	40	50	200
E_{ur}^{ref} [MPa]	24	60	120	150	600
m [-]	0,5	0,5	1	1	1
R_f [-]	0,9	0,9	0,9	0,9	0,9

Soil Type: ZG_{1A} – Loosely compact sandy-clay fill; ZG_{1B} – moderately compact sandy-clay fill; ZG_{2A}– moderately compact sandy-silt soil; ZG_{2B} – compact sandy-silt soil; ZG_{2C} – very compact sandy-silt soil.

Soil Parameters: Υ – Volumetric weight; Φ' – effective friction angle; E_{50}^{ref} – elastic modulus corresponding to 50% of the ultimate tensile stress defined for a reference pressure (p_{ref} = 100kPa); E_{ur}^{ref} - elastic modulus for unloading/reloading at a stress level equal to the reference pressure (p_{ref} = 100kPa); m – power that controls the stress dependency of the elastic modulus; R_f – failure ratio.

The study of the reinforced concrete bored pile wall sections braced by slab bands, steel struts or temporary ground anchors was conducted through the development of a Plaxis 2D model. In contrast, due to the distance of the buttresses and the interaction of the slab bands with these elements, an analysis of this solution was performed using a Plaxis 3D model.

In the developed models, the curtain wall´s, slab bands and buttresses were represented using "plate" elements with elastic behaviour, while the ground anchors were modelled as "node-to-node anchor" elements, with the respective bond lengths modelled using "embedded beam row" elements.

The behaviour of the peripheral retainment structure was analysed for the main excavation phases, assessing crucial design parameters such as forces of the containment structures, deformations, stress states and stability of the soils to be contained. Figures 7 and 8 present the deformed mesh of the developed models.

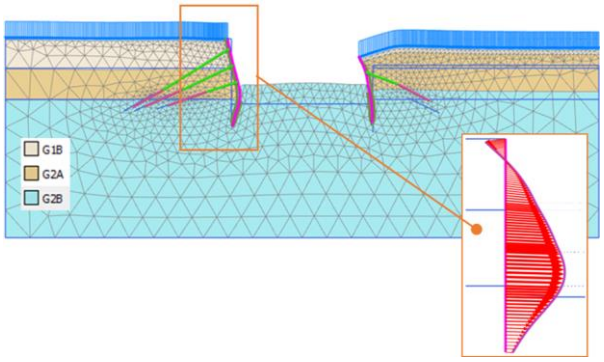

Figure 7. Deformed mesh of the excavation's base level phase - Curtain wall braced by temporary pre-stressed ground anchors model.

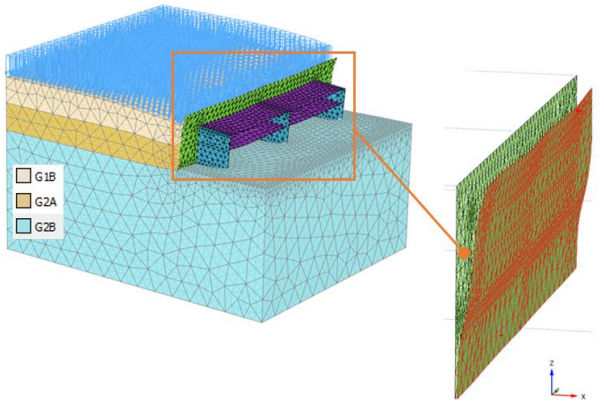

Figure 8. Deformed mesh of the excavation's base level phase - Curtain wall braced by slab bands and buttresses model.

The maximum horizontal displacement estimated for the curtain wall supported by temporary ground anchors was 9 mm, and with slab bands and buttresses, it measured 56 mm. The results obtained were as expected, considering that the model composed of passive elements (slab bands and buttresses) exhibits greater flexibility and can accomodate larger deformations in the surrounding ground and curtain wall compared to the model incorporating active elements (temporary pre-stressed ground anchors).

Throughout the construction phase, deformations were observed to be less pronounced than those projected during the design phase, as it will be presented in the following section.

5 MONITORING AND SURVEY PLAN

Based on the complex framework of the site, a Monitoring and Survey Plan (MSP) was established with the aim of ensuring safety conditions and optimal functionality during the excavation and the execution of the geotechnical structures, as well as neighbouring structures and infrastructures. In this context, the following instruments were installed:

- 27 topographic targets distributed along the bored pile walls and edges of the slab bands to measure horizontal and vertical displacements;
- 4 load cells to measure the load of the temporary ground anchors;
- 2 inclinometers positioned behind the peripheral containment walls, to measure ground horizontal displacements;
- 2 piezometers to measure underground water pressure;
- 1 seismograph for vibration control during the excavation of areas with higher resistance.

Based on the conducted modelling, alert and alarm criteria was established for all instruments and monitored structures. Overall, readings consistently remained below the alert and alarm criteria defined in the project. In Figure 9, the schematic location of the instrumentation devices and some of the most notable results are presented.

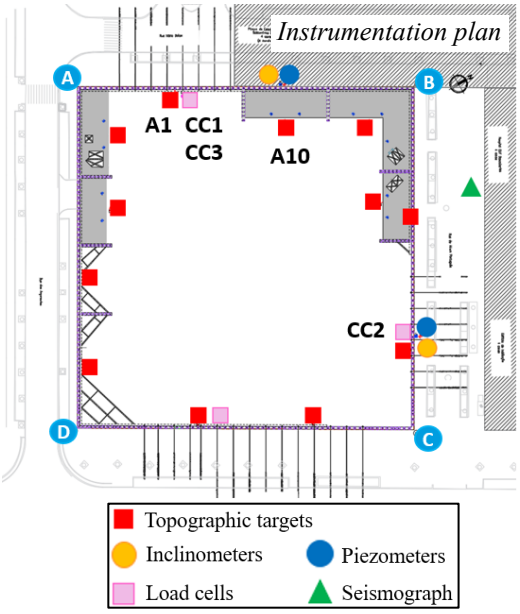

Figure 9. Instrumentation and monitoring plan.

As observed in the examples below, deformation values consistently remained below the alert criteria outlined in the project (yellow line in the graph), as shown in Figure 10. Regarding the monitoring of load cells, a minor adjustment to the initial load applied to the anchor tendons was noted, facilitated by a hydraulic jack. Subsequently, the load values remained nearly constant throughout the construction process (between June 2022 and January 2023), confirming the satisfactory performance of the project (Figure 11).

These conclusions are applicable to the remaining data instruments. However, in December 2022, a notable increase in water levels was observed due to heavy rainfall. In response, additional drainage pipes

and temporary water collection zones were established to address this issue.

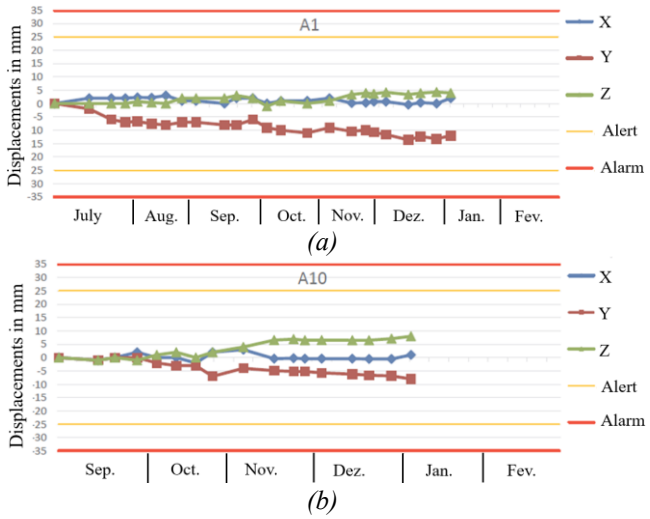

Figure 10. Displacement results on station A1(a) and A10(b).

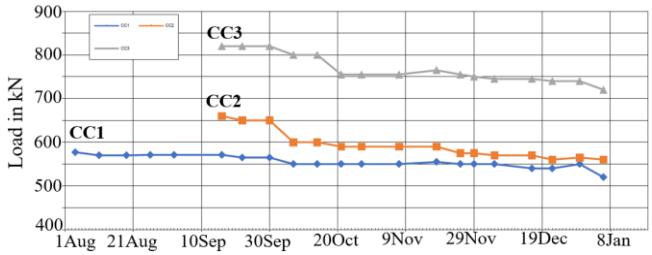

Figure 11. Load cell evolution of the ground anchors CC1, CC2 and CC3.

Considering the above, as of the present date with the conclusion of excavation and peripheral containment works, the instrumentation results serve to validate the suitability of the implemented solutions and the geomechanical parameters meticulously considered in the modelling. This paves the way for prospective optimization of similar geological and geotechnical solutions in the future.

6 CONCLUSIONS

In the scope of this article, it was possible to demonstrate the technical efficiency of reinforced concrete bored piles braced by various structural elements such as struts, temporary ground anchors and slab bands. The peripheral earth retaining solution presented displacements lower than those estimated in project and displayed a highly stable behaviour during the excavation works. Additionally, the use of slab bands not only overcame the encountered limitations due to the excavation´s site proximity to the technical gallery and the future underground parking lot, but also incorporated elements of the final structure, enhancing the economic efficiency of the solutions.

However, there were some on-site challenges that led to adjustments to the initial project solutions. The main challenge arose from an increased water flow into the excavation, given the intense rainfall experienced in December 2022 towards the end of the excavation works. To address this unforeseen circumstance and to ensure the integrity of the sprayed concrete between the piles, in response to the rising water flow into the excavation area, the number of drainage pipes was increased, and temporary water collection zones were established. In the definitive phase, the water collected by the pipes will be directed to the building's general drainage system.

ACKNOWLEDGEMENTS

The authors express their gratitude to Kronos, the Project Owner, for granting permission to publish this article, as well as to Casais and Ancorpor for their execution of excavation and earth retaining solution works, and finally to the project´s supervision, overseen by FICOPE.

REFERENCES

Carvalho, C. e Pinto, A. (2019). AR53 – Ground Improvement and Earth Retaining Solutions in Lisbon Downtown. *17th European Conference on Soil Mechanics and Geotechnical Engineering*. Reykjavik, Iceland. Discussion Section D3-6 (Preservation of Historic Sites). ISBN 978-9935-9436-1-3.

Tomásio, R. e Pinto, A. (2019). Retaining Wall Solutions for Underground Extension of Hospital da Luz in Lisbon – Portugal. *17th European Conference on Soil Mechanics and Geotechnical Engineering*. Reykjavik, Iceland. Discussion Section D5-5 (Soil Structure). ISBN 978-9935-9436-1-3.

Pinto, A.; Fartaria, C.; Pita, X. e Tomásio, R. (2017). FPM41 high rise building in central Lisbon: innovative solutions for a deep and complex excavation. *19th International Conference on Soil Mechanics and Geotechnical Engineering*. Seoul, Korea. pp 2029 – 2032, TC 207 (Soil Structure). ISBN 978-89-952197-5-1.

Proceedings of the XVIII ECSMGE 2024
GEOTECHNICAL ENGINEERING CHALLENGES
TO MEET CURRENT AND EMERGING NEEDS OF SOCIETY
© 2024 the Authors
ISBN 978-1-032-54816-6
DOI 10.1201/9781003431749-514
Open Access: www.taylorfrancis.com, CC BY-NC-ND 4.0 license

ECSMGE 24
XVIII EUROPEAN CONFERENCE ON SOIL MECHANICS AND GEOTECHNICAL ENGINEERING

Excavation, earth retaining solutions and facades underpinning of a historic building in Estoril, Portugal

Excavation, solutions de soutènement des terres et reprise en sous-œuvre des façades d´un bâtiment historique à Estoril, Portugal

J. Silva*, C. Martins, A. Pinto
JETsj – Geotecnia, Lda., Lisbon, Portugal
**jsilva@jetsj.com*

ABSTRACT: This paper aims to present the solutions for excavation, peripheral earth retaining walls and centenary facades underpinning of a future residential building, located in Estoril, Cascais, Portugal. Firstly, to preserve the building´s facades, a temporary structural system was installed, allowing the facades bracing, ensured by the execution of horizontal steel distribution beams and vertical steel frames, founded on vertical micropiles. Secondly, the facades were underpinned through the execution of two twin underpinning beams, connected by pre-stressed bars, founded also on vertical micropiles. For the execution of the underground floors, it was necessary to excavate a maximum of 9 m under the original building´s foundations, using the king post walls earth retaining technique braced horizontally by steel props, ensuring the compatibility of the underpinning and the retaining facades solutions. Lastly, the monitoring and observation of the peripheral retaining structure and facades is also pointed out, encompassing detailed analyses and comparisons with the initially estimated values from the design phase.

RÉSUMÉ: Cet article vise à présenter les solutions pour l'excavation, les murs de soutènement périphériques et la reprise en sous-œuvre des façades centenaires d'un futur immeuble résidentiel situé à Estoril, Cascais, Portugal. Tout d'abord, pour préserver les façades du bâtiment, un système structurel temporaire a été installé, permettant le contreventement des façades assuré par la réalisation de poutres de distribution horizontales en acier et de cadres verticaux en acier, fondés sur des micropieux verticaux. Deuxièmement, les façades ont été soutenues par l'exécution de deux poutres de soutènement jumelles, reliées par des barres précontraintes, également fondées sur des micropieux verticaux. Pour l'exécution des étages souterrains, il a été nécessaire d'excaver jusqu'à une profondeur maximale de 9 m sous les fondations originales du bâtiment, en utilisant la technique de soutènement des murs à paroi berlinoise, contreventée horizontalement par des étais en acier, assurant la compatibilité entre le soutènement et les solutions de soutènement des façades. Enfin, la surveillance et l'observation de la structure de soutènement périphérique et des façades sont également soulignées, englobant des analyses détaillées et des comparaisons avec les valeurs initialement estimées lors de la phase de conception.

Keywords: Earth retaining structures; king post walls; underpinning; facades; micropiles.

1 INTRODUCTION

The present article outlines the solutions adopted for the retention and underpinning of an existing old facade, as well as for the excavation and peripheral earth retaining structure, enabling the construction of an underground parking lot for a future residential building.

Within the intervened plot, there was a vacant building whose main facades were, for the most part, preserved. The exterior walls were composed by ordinary stone masonry, with a thickness of 0.80 m, decreasing in height. Generally, the facades exhibited a considerable state of degradation, particularly on the southern facade, with the possible risk of partially collapsing. Figure 1 presents an aerial perspective of the intervention site before the construction work´s.



Figure 1. Aerial view of the intervention site, in its current state.

The new building will be situated on Avenue Senhora Monte da Saúde, covering an approximate ground area of 670 m^2. It will comprise a parking lot, a ground floor, three elevated floors and a slopping roof. The intervention area, within which the building is situated, encompasses around 1446 m^2. Figure 2 depicts a virtual view of the future residential building.



Figure 2. Virtual view of the future residential building.

2 MAIN CONSTRAINTS

2.1 Geological and geotechnical conditions

To characterize the geotechnical behaviour, associated with the soils present at the site, a prospecting campaign was conducted involving the execution of two mechanical boreholes accompanied by Standard Penetration Tests (SPT) and the collection of samples for macroscopic classification. Additionally, one hydraulic piezometer was installed in one of the boreholes.

According to the results obtained, the geological structure of the site is characterized, superficially, by the presence of Landfill Deposits (At) mainly composed of rocky blocks and clayey sands with an average thickness of 1.0 m. Notably, no standard penetration test was conducted on these modern anthropogenic materials. Subsequently, underlying these fill deposits, Cretaceous formations (C^1_{Ba} e C^1_A) are manifested at this location by three geotechnical horizons. The conducted borehole surveys unveiled the presence of clays and sandy clays (ZG_{2A} - C^1_{Ba}), with variable thickness ranging between 7,50 m and 10,50 m and N_{SPT} values ranging from 15 to 41 blows. Addtionally, fine clayey sands to sandy clays (ZG_{2B} - C^1_{Ba}) were encountered at depths varying from 7,5 m and 12,0 m, with N_{SPT} values spanning from 23 to 46 blows. Lastly, a lower stratum was characterized by moderately to highly altered and fractured limestones (ZG_{2C}-C^1_A), interspersed with fine-grained sandstones, in which Rock Quality Designation (RQD) values ranged from 32% to 49%. This unit was identified at the dephs of 10.0 m and 11.8 m.

In terms of hydrogeology, there is no water level at the excavation site according to the conducted survey, which should not interfere with the local hydrogeological regime.

2.2 Neighbourhood conditions

The excavation site is situated in an urbanized area, bounded by Avenue Senhora Monte da Saúde to the West, and several other neighbouring constructions. To the North, the plot is bordered by two residential buildings with two and three elevated floors, respectively, and both without underground basements. To the South, it is delineated by the backyard and annex of a neighbouring plot. To the East, it is surrounded by a one-story church, also without underground basements.

Additionally, it is worth noting the presence of party walls along the lot boundaries and the proximity of an existing wall, located inside the lot, to the proposed king post wall solution at the rear of the façade to be preserved. In Figure 3 it is possible to observe the main boundaries of the excavation site.



Figure 3. Main boundaries of the excavation site.

3 ADOPTED SOLUTIONS

3.1 Facades retention and underpinning

Given the facades high deterioration level, particularly on the southern side, and the need to demolish/dismantle a portion of it, it was decided that, prior to the facades retention work, an extensive treatment to the existing cracks should be undertaken through the injection of grouts based on hydraulic lime. Subsequently, steel angle profiles were installed at the corners of the facades to be preserved, and three levels of tensioned 26 mm galvanized tie rods were

installed to ensure the maximization of safety during the facades retention works (Figure 4).



Figure 4. Prior facade retention works, involving the installation of steel angles and steel tie rods per floor.

The facade retention structure was composed by steel distribution beams, which had the primary objective of equalizing horizontal loads on the wall and directing it towards 8 bracing frames, particularly loads induced by wind action. These distribution beams were constituted by HEB 180 and UPN 260 steel profiles, while the bracing frames were constructed using steel trusses comprised by HEB 240 vertical columns, HEB 200 horizontal beams and LNP 150x150x10 diagonal steel angles.

In order to provide an appropriate foundation with adequate stiffness and strength for the bracing frames of the retention structure, considering tensile and shear forces to which the structure might be subjected, reinforced concrete massif´s were executed, indirectly founded on micropiles. The micropiles were executed using N80 Ø139.7x10mm profiles with external connections between sections and sealed through the Repeated and Selective Injection system (IRS), in competent and geologically stable ground, with N_{SPT} > 60 blows.

To underpin the facades, a system composed by two rows of micropiles was designed, connected by two underpinning beams (one on the exterior and another on the interior of the existing walls), joined by prestressed Gewi type bars. In Figure 5 , the defined facades retention and underpinning solution can be observed.



Figure 5. Facades retention and underpinning solution.

Additionally, given the high deterioration level of the facades, there was the need to reinforce the stone masonry walls by executing a reinforcement wall with a thickness of 8 cm. This wall consisted of a reinforcement mesh and shotcrete, executed from the interior and securely anchored to the existing facades (Figure 6). Upon completion of the facades retention and underpinning works, excavation and peripheral containment activities were initiated.



Figure 6. Strengthening of stone masonry walls with a reinforced concrete layer.

3.2 Excavation and peripheral earth retaining structures

The excavation and peripheral earth retaining structures were executed following the King Post Wall technology, with careful consideration given to compatibility with the facades retention and underpinning works. This solution involved a phased construction, from top to bottom, of reinforced concrete panels. The process commenced with the execution of the primary panels, followed by the secondary, and ultimately, the tertiary panels.

The panels were horizontally braced by provisional elements such as steel props, tie rods and temporary pre-stressed ground anchors, and vertically supported by micropiles. The bracing elements were composed by HEB 180 and HEB 220 steel profiles, braced by HEB 120 profiles with S275 JR steel grade. In convex corners, resistance to impulses was ensured by pre-stressed Gewi tie rods.

The executed ground anchors comprised 4 strands, each with a diameter of 1.5 cm, and with a tensile load of 450 kN. The bonded lengths were accomplished using the IRS system, incorporating double obturators and non-return valves, with a minimum hole diameter of 200 mm and minimum length of 4.0 m. To prevent potential intersections with existing infrastructures and structures, as well as to allow proper sealing in competent and geologically stable soil, these anchors were inclined at 30.0º and 35.0º horizontally.

Vertical micropiles were designed to support the vertical loads imposed on the peripheral earth retaining structure, particularly by the self-weight and by the vertical component of the ground anchors. These elements were executed using N80 Ø139.7x10.0 mm tubular profiles with external joints, made of high-strength steel (f_{syd} > 560MPa), placed inside a 200 mm hole diameter and bonded for a length of 6.0 m, using the IRS system. The micropiles were connected at the top by capping beams and were generally embedded in the king post walls, which had a thickness of 0.30 m.

In Figure 7, the excavation and peripheral earth retaining solution are depicted.

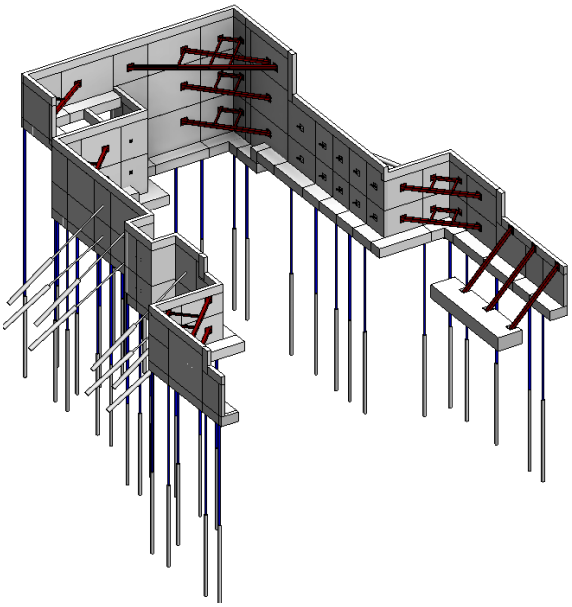

Figure 7. Excavation and peripheral earth retaining solution (BIM model in software Revit).

4 GEOTECHNICAL AND STRUCTURAL DESIGN

4.1 Facades retention and underpinning

The behaviour of the facades retention structure was analysed in terms of forces, reactions and deformations using finite element models created in the Autodesk Robot Structural Analysis Professional 2022 software (Figure 8). This allowed the simulation of the wind effects, the most critical factor to this case. The facades bracing system was modelled in the program using "steel members" type elements with their respective mechanical properties. The micropiles were depicted as fixed supports.

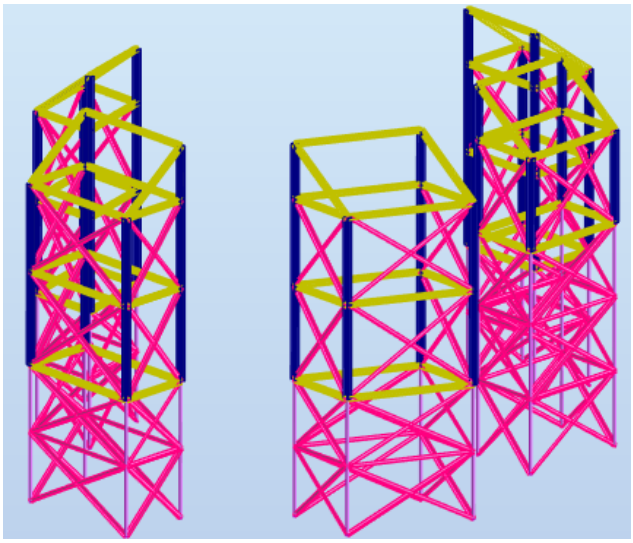

Figure 8. Facades retention structural model, developed in Robot software.

4.2 Excavation and peripheral earth retaining structures

The assessment of the presented peripheral earth retaining solution in terms of forces and deformations was conducted for all major construction phases using a finite element program, PLAXIS 2D. A constitutive model was developed to simulate the soil behaviour characteristics of a "Hardening Soil", considering a nonlinear constitutive relationship and variations in the soil's stiffness under applied stress states. In the context of soil geomechanical parameterization, the reference values obtained from the geological-geotechnical study were incorporated in PLAXIS software, to simulate the soils behaviour, as detailed in Table 1.

Table 1. Geotechnical soil parameters.

Soil Type	ZG_1	ZG_{2A}	ZG_{2B}	ZG_{2C}
N_{SPT}	-	15-41	23-46	> 60
Υ [kN/m^3]	19	20	20	21
Φ [º]	25	-	35	35
c_u/c' [KPa]	-	90	1	5
E_{50}^{ref} [MPa]	7,5	30	50	180
E_{ur}^{ref} [MPa]	22,5	90	150	540
m [-]	0,5	0,7	0,9	1

Soil Type: ZG_1 – *Loosely compact sandy-clay fill*; ZG_{2A}– *clay and sandy clay soil;* ZG_{2B} – *fine clayey sand to sandy clay soil;* ZG_{2C} – *fractured limestones interspersed with fine-grained sandstones.*

Soil Parameters: Υ – *Volumetric weight;* Φ' – *effective friction angle;* E_{50}^{ref} – *elastic modulus corresponding to 50% of the ultimate tensile stress defined for a reference pressure* (p_{ref} = *100kPa);* E_{ur}^{ref} *- elastic modulus for unloading/reloading at a stress level equal to the reference pressure* (p_{ref} = *100kPa); m – power that controls the stress dependency of the elastic modulus.*

In the developed models, the king post walls and micropiles were modelled using "plate" elements with elastic behaviour. However, the zones corresponding to the free length and the bond lengths of the micropiles were modelled using "embedded beam row" elements. The temporary ground anchors were modelled using "node-to-node anchor" elements and their respective bond lengths were modelled using "embedded beam row" elements. The steel props were modelled using "anchors", with the equivalent stiffness to the defined bracing system.

The behaviour of the peripheral retainment structure was analysed for the main excavation phases, assessing crucial design parameters such as forces of the containment structures, deformations, stress states and stability of the soils to be contained. The bonded lengths of the micropiles and temporary ground anchors were determined according to the methodology proposed by Bustamante and Doix (1985). Figure 9 and Figure 10 present the deformed mesh of the developed PLAXIS models.

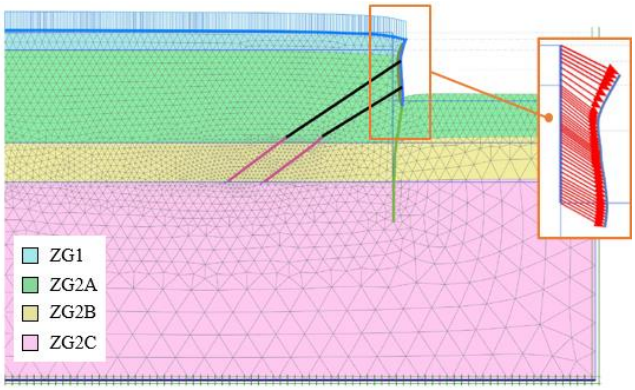

Figure 9. Deformed mesh of the excavation´s base level phase - King post walls braced by pre-stressed ground anchors.

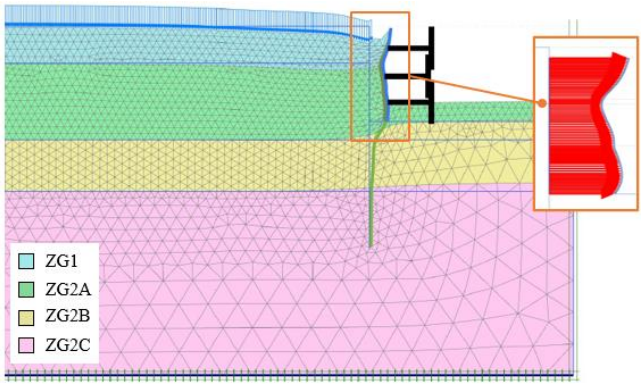

Figure 10. Deformed mesh of the excavation´s base level - King post walls braced by steel props.

The maximum horizontal displacement estimated for the king post wall supported by two levels of pre-stressed ground anchors was 10,90 mm, for a total excavation height of 5,90 m (L/540), meeting the ELS requirements.

For the scenario in which the earth retaining structure is braced by three levels of steel props, for a total excavation height of 8,20 m, the maximum horizontal displacement estimated was 9,40 mm (L/870), meeting the ELS requirements.

5 MONITORING AND SURVEY PLAN

The established Monitoring and Survey Plan (MSP) on site had as its main objective to ensure the safe execution of the demolition, retention and underpinning works of the facades, as well as the peripheral earth retaining structure of the underground floors. Additionally, it aimed to analyse the behavior of neighboring structures and infrastructures during the construction works.

In the initial phase, for the control of displacements, rotations and measurement of masonry wall crack openings during the demolition and reinforcement of existing structures, an automated monitoring system was implemented for a 2-month construction period.

The entire field data reading and acquisition system were fully automated, with readings taken every 1 hour. Sensors were installed for data acquisition and transmission to a wireless web platform. Figure 11 illustrates the application of the web monitoring system for this specific construction project.

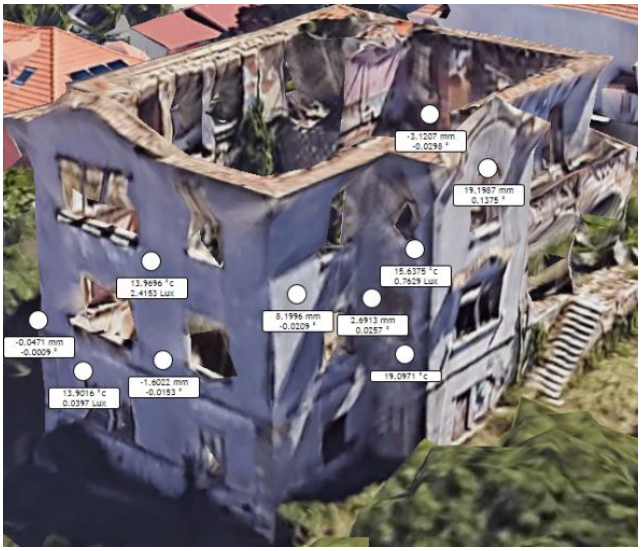

Figure 11. Aerial view of the intervention site (Google Earths image) – Web Monitoring System

The implementation of this automated monitoring system not only enabled a more accurate and systematic control of the behaviour of all critical structures, but also streamlined the adjustment of construction methodologies during the execution of the new structures, potentially resulting in enhanced productivity.

The implemented MSP on the existing facades included the following fully automated sensors/instruments:

- 12 triaxial tiltmeters for measuring rotations and displacements of the preserved facades and neighboring structures and infrastructures;
- 4 vibrating wire crackmeters (strain gauges) for measuring crack openings;
- 40 manually read crackmeters for measuring crack openings;
- 2 Gateways, which correspond to the data collection and network data transmission system via 3G;
- 2 solar panels for energy supply to the Gateway.

In the second phase, for excavation and peripheral earth retaining construction works, the following instruments were installed, for a 6-month construction period:

- 14 triaxial tiltmeters placed on the king post walls, to measure rotations and displacements;
- 4 electric load cells, to measure the pre-stressed loads applied to the temporary ground anchors;
- 1 inclinometer positioned behind the peripheral earth retaining walls, to measure horizontal and vertical displacements of the retaining walls;
- 1 piezometer to measure underground water pressure.

Based on the conducted modelling, alert and alarm criteria was established for all instruments and monitored structures.

6 CONCLUSIONS

In the scope of this article, it is expected to demonstrate the technical efficiency of the facades retention and underpinning solution as well as the king post walls solution, braced by various structural elements, such as struts and temporary ground anchors. Furthermore, it is expected that the peripheral earth retaining solution present´s actual displacements lower than those estimated in design and display a highly stable behaviour during the excavation works currently underway.

ACKNOWLEDGEMENTS

The authors express their gratitude to PRET INVESTIMENTOS, the Project Owner, for granting permission to publish this article. The described works were performed by ENGCON (general contractor) and GEOSOL (geotechnical works contractor).

REFERENCES

Bustamante M., Doix B. (1985). *Une méthode pour le calcul des tirants et des micropieux injectés*. Bull. liaison Labo. P. & Ch. 140, nov.-déc., pp.75-91, 1985.1996, pp.543-550, Balkema/Rotterdam/Brookfield (in French).

Proceedings of the XVIII ECSMGE 2024
GEOTECHNICAL ENGINEERING CHALLENGES
TO MEET CURRENT AND EMERGING NEEDS OF SOCIETY
© 2024 the Authors
ISBN 978-1-032-54816-6
DOI 10.1201/9781003431749-515
Open Access: www.taylorfrancis.com, CC BY-NC-ND 4.0 license

ECSMGE 24
XVIII EUROPEAN CONFERENCE ON SOIL MECHANICS AND GEOTECHNICAL ENGINEERING

Behavior of geocell reinforced sandy soils under static load

Comportement des sols sableux renforcés par géocellules sous charge statique

M.C. Simsek, N. Huvaj*
Middle East Technical University, Ankara, Turkey
**nejan@metu.edu.tr*

ABSTRACT: Geocell is a three-dimensional cellular geosynthetic product to provide all-around confinement by the interaction of infill soil, cell walls and cell geometry. This study comprises of laboratory model tests of geocell-reinforced sandy soil with different dimensions of geocells to evaluate the amount of the contributions of the geocells with regards to height of the cell, width of the cell and loading location. In addition, the load is applied at the center of the cell and at the intersection of polymer boundaries of geocells. Tests are conducted in a tank with dimensions of 1 m width, 1 m length and various heights depending on geocell height, where static loading is applied via a steel plate on the sand surface. The results are presented in terms of pressure-settlement plots. It is observed that for a predetermined settlement value, presence of the geocells increased the bearing capacity of the footing by 38% to 73% compared to unreinforced cases and reduced the settlements under a given pressure. Bearing capacity increased with increasing geocell height independently from geocell width. Decreasing of geocell width increased the bearing capacity of the footing independently from geocell height.

RÉSUMÉ: Geocell est un produit géosynthétique cellulaire tridimensionnel destiné à assurer un confinement complet grâce à l'interaction du sol de remplissage, des parois cellulaires et de la géométrie cellulaire. Cette étude comprend des tests sur modèle de laboratoire de sol sableux renforcé de géocellules avec différentes dimensions de géocellules pour évaluer la quantité de contributions des géocellules en ce qui concerne la hauteur de la cellule, la largeur de la cellule et l'emplacement de chargement. De plus, la charge est appliquée au centre de la cellule et à l'intersection des limites polymères des géocellules. Les tests sont effectués dans un réservoir de dimensions 1 m de largeur, 1 m de longueur et différentes hauteurs en fonction de la hauteur de la géocellule, où une charge statique est appliquée via une plaque d'acier sur la surface du sable. Les résultats sont présentés sous forme de tracés de pression et de tassement. On observe que pour une valeur de tassement prédéterminée, la présence des géocellules augmente la capacité portante de la semelle de 38% à 73% par rapport aux cas non renforcés et réduit les tassements sous une pression donnée. La capacité portante augmente avec l'augmentation de la hauteur des géocellules, indépendamment de la largeur des géocellules. La diminution de la largeur des géocellules a augmenté la capacité portante de la semelle indépendamment de la hauteur des géocellules.

Keywords: Geocell; sand; bearing capacity; settlement.

1 INTRODUCTION

Geocell is a three-dimensional cellular geosynthetic product providing all-around confinement by the interaction of infill soil, cell walls and cell geometry, reducing the lateral movement of soil and forming a stiffened mattress to distribute applied loads to a wider area (Han et al., 2008). They have been successfully used worldwide to construct retaining walls, slopes and to reinforce road bases (Han et. al., 2008). They are effective in increasing the bearing capacity of the roads, while enabling faster application with easy deployment and transportation.

Behavior of geocell reinforced soil can be affected by many factors such as height, width, thickness and material of geocell, as well as type and density of basement and infill soils. Geocell width and height are two major factors that influence the geocell performance. Effects of these factors on the load carrying capacity and settlement performance of geocell-reinforced soils have been investigated (Shin et al., 2017; Gurbuz and Mertol, 2012; Latha et. al, 2006). However, most of the model experimental studies used only one cell and there is a need for studies with multiple geocells to better represent overall behaviour in the field. Furthermore, the size of geocells that are used widely in the market have not been used in most of the previous studies, which developed the need to investigate this topic. Additional study is needed to investigate the effect of loading location (in the middle of the cell or at the intersection of polymer cell boundaries) on the behaviour of the geocell-reinforced soils.

The objectives of this study are (i) investigation of the amount of improvement in the case of using different heights of geocells and different geocell openings, (ii) the effects of geocell width on the behaviour of the bearing capacity, (iii) investigation of the significance of loading location by applying the load at the center and also intersection of the boundaries of the geocell. For this aim, 13 static plate load tests were conducted. Contributions of the geocell usage on the bearing capacity performance of the footing were compared with tests on unreinforced soil.

2 TEST SETUP AND MATERIALS

The test box used in the experiments has base dimensions of 100 cm × 100 cm and 60 cm height. It comprises of ten aluminium box segments, each having 10 cm height (Figure 1, 2). Static loading is applied on the ground surface via a 26-cm-diameter, 2.5-cm-height rigid steel plate using pneumatic loading system. In order to examine the load-displacement characteristics of geocell reinforced and unreinforced sandy soil under static load, settlement of the loading plate as well as the force on the plate are measured by using two dial gauges and a load cell connected to a data logger, respectively.

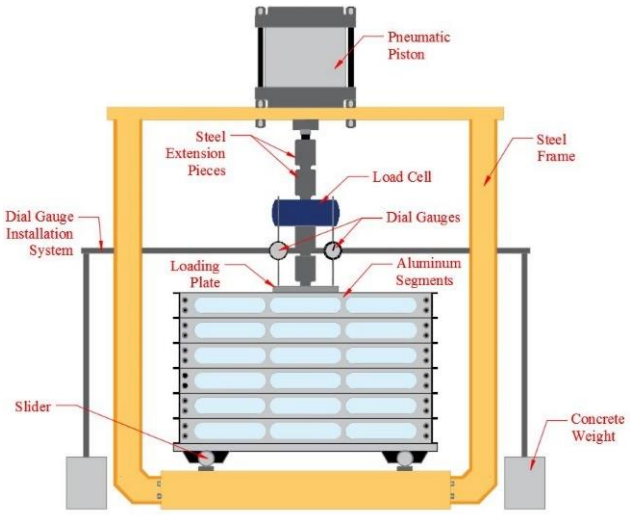

Figure 1. Schematic view of the front view of test set up.

2.1 Materials

Fine Sand from Türkiye is used as base soil and infill soil of geocells. The soil consists of quartz, feldspar and rock fragments having sub-angular to angular particle shape. Properties of the sand are given in Table 1, where all tests are carried out two or three times and average values are also presented in Table 1.

Two different HDPE type, perforated and ultrasonically welded geocells are used: Geocell 40 with 25 × 30 cm openings and 1.1 mm material thickness, and Geocell 60 with 35 × 40 cm openings and 1.3 mm sheet thickness (Figure 3). Each geocell had three different cell height versions: 10, 15 and 20 cm.



Figure 2. View of testing tank showing 6 aluminum segments, 10 cm high.

Table 1. Soil used in this study.

Property/Parameter	Value
Gravel content (%>4.75 mm)	0
D_{50} (mm)	0.37
D_{10} (mm)	0.16
Fines content (%<0.074 mm)	1.36
USCS name	SP
Max. dry density, ρ_{dmax} (g/ml)*	1.765
Min.-max. void ratio range, e_{min}-e_{max}*	0.505-0.89

* ASTM D7382-08, ASTM D4254-14

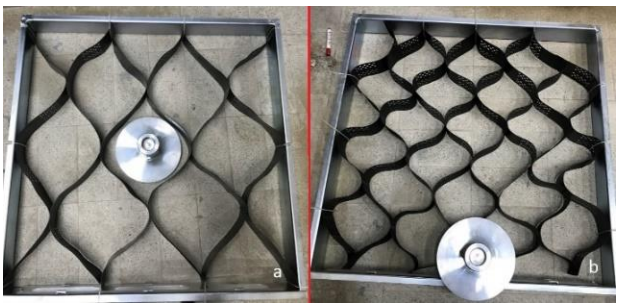

Figure 3. 26-cm diameter loading plate and (a) Geocell 60 (showing loading applied at the center/inside of a geocell), (b) Geocell 40.

2.2 Sample preparation

Dry air pluviation via a sand raining system is used to fill the tank with sand (Figure 4). Based on trial sand raining tests using different sieves; sieve hole diameter of 2.8 mm and 15 mm center-to-center distance between holes are used.

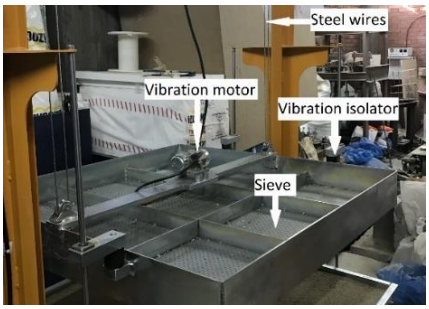

Figure 4. Dry air pluviation (sand raining) system.

Trial relative density tests are performed to investigate the effect of sand raining elevation on the variance of the relative density (Figure 5). Considering the geocell heights (10, 15, 20 cm), the sand raining elevations vary from 5 cm to 25 cm at any level of testing tank. For a 10-cm-high segment of the box, relative density values of the sand are found as 61%, 62% and 64% when sand raining height was 5, 15 and 35 cm, respectively. Increase in sand raining elevation slightly increases the relative density. When sand raining height was kept constant at 5 cm, the relative density was 62% and 67% at the uppermost and lowermost segment of the tank, respectively, in a test having total of 55 cm sand height. Relative density differences between the center, edge and corner at the same elevation (Figure 5) are less than 2%. It shows that an acceptable uniform sand raining was carried out at the any location of the tank. In all tests, sand raining height is 5 cm and relative density is between 61% and 67%.

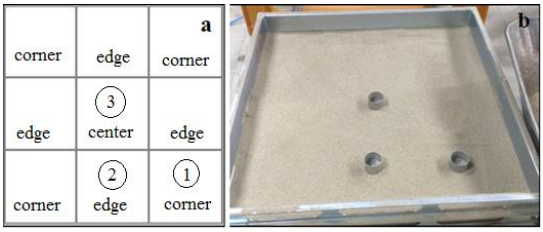

Figure 5. Air pluviation (sand raining) trial tests.

Sample preparation starts by filling the first (bottom) 10-cm-high segment of testing tank with sand by using sand raining system (sand raining height 5 cm). Adding new 10-cm-high segment and repositioning of the sieve continued till the setup reached to the desired height. With the difference of unreinforced tests, geocell is placed in the pre-determined levels in geocell reinforced tests. In all geocell reinforced tests, 30 cm height (3 segments of testing tank) of sand base layer and 5 cm height of sand cover above the geocell are kept constant. Only the height of geocells is changed between these sand layers and hence final height of sands are obtained as 45 cm, 50 cm and 55 cm for geocells that have 10 cm, 15 cm and 20 cm heights, respectively.

Geocells are tied with plastic clamps to the edge of the 10-cm-high segment of the tank to keep the cells open and also stressed during the sand raining process (Figure 6). After sand filling is completed, these clamps are cut and thus, getting additional strength of geocells are prevented. Filled testing tank is then moved under the loading system, and placed under the piston, a steel loading plate (diameter 26 cm, thickness 2.5 cm) is placed at the center of the tank on the ground surface (Figure 2).



Figure 6. Placement of geocell tied segments to sand filled testing tank (clamps are cut after tank filling is completed).

3 RESULTS

The results of 13 model static plate load experiments are summarized in Table 2 and in Figure 7.

Table 2. Summary of static plate load tests

Test No.	Total Sand Height (cm)	Geocell Width (cm)	Geocell Height (cm)	Loading Location*	Pressure at 5.2 cm** settlement (kPa)
1	45	No Geocell		-	430
2	50	No Geocell		-	457
3	55	No Geocell		-	480
4	45	35 x 40	10	center*	603
5	45	35 x 40	10	intersection	585
6	50	35 x 40	15	center	655
7	50	35 x 40	15	intersection	665
8 #	55	35 x 40	20	center	753
9	55	35 x 40	20	intersection	825
10	45	25 x 30	10	center	620
11	50	25 x 30	15	center	730
12	55	25 x 30	20	center	830
13 #	55	35 x 40	20	center	736

* loading is applied at ground surface, at the center (inside) of one cell, or at the intersection of the geocell polymer boundaries

** 5.2 cm is selected as the 20% of plate diameter of 26 cm.

Test No. 13 is a repeated test of Test No. 8; difference between results is 2.3%, which is considered sufficient repeatability.

A clear failure is observed in unreinforced (no geocell) tests (Test no 1, 2, 3) unlike geocell-reinforced ones (Figure 7). 430 kPa, 457 kPa and 480 kPa pressure values obtained under the loading plate at the 5.2 cm settlement indicate a

small/acceptable variation. Geocell reinforced test results are compared with corresponding unreinforced ones and amount of improvement is calculated as percentage (%). For a predetermined settlement value, the presence of the geocells increased bearing capacity of the footing by 38% to 73% compared to unreinforced cases (Table 2).

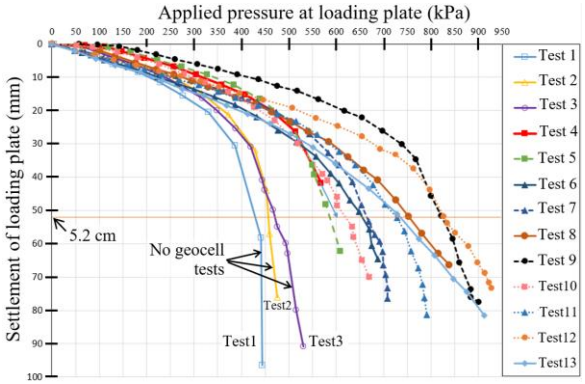

Figure 7. Results of 13 tests

Effect of loading location (tests 4, 5, 6, 7, 8, 9): Loading at the center of the cell and at the intersection of polymer boundaries of cells are applied to sand reinforced by Geocell having 35 cm x 40 cm opening, since the other geocell could not be used in these tests because the loading plate (26 cm diameter) is bigger than the geocell opening area (25 cm x 30 cm) and the plate could not be located at the center of the cell. For 10 cm, 15 cm and 20 cm geocell heights, -3.1%, 1.5% and 9.6% more load carrying capacities are obtained when loading plate placed at the intersection of the polymer boundaries rather than geocell center. As height of geocell increases, geocell starts to act as a load carrying beam, and this effect increases the load carrying capacity until settlement of plate reaches to 55.2 cm. Loading on the intersection of geocell polymer boundaries (as compared to the center) showed higher improvement in the case of using geocells with bigger heights. Loading location did not effect the ultimate bearing capacity more than 10%; geocell shows almost homogenous behavior regardless of loading location.

Effect of the geocell height and width: For a given geocell widh (25 × 30 cm), as height of geocell increases from 10 cm to 20 cm, a higher bearing capacity is obtained (620 kPa to 830 kPa). Independently from geocell width, increase in geocell height increases the load carrying capacity of the footing at the same settlement value. Additionally, for bigger geocell opening, percentage of improvement increases when geocell height increases. In other words, in the case of using 15 cm height geocell instead of 10 cm, improvement percentage increases from 38.14% to 44.42%. In a similar manner, using of 20 cm height geocell instead of 15 cm, improvement percentage increases from 44.42% to 63.54%. Independently from geocell height, decrease in geocell width, increases the load carrying capacity.

4 CONCLUSIONS

Major conclusions are summarized below:

1) Geocell reinforcement in any sizes contributed to bearing capacity of the footing corresponding to settlement value of 20% of diameter of it, compared to unreinforced ones. Geocells increased the bearing capacity of the footing by 38% to 73% compared to unreinforced cases.

2) A clear failure is observed in unreinforced tests however, it is not observed in geocell reinforced tests, in the other words, geocell reinforced sand showed a more ductile behavior.

3) Bearing capacity increased with increasing geocell height independently from geocell width.

4) Decreasing of geocell width increased the bearing capacity independently from geocell height.

5) Importance of the location of the loading plate is investigated. In any case, less than 10% difference on the bearing capacity of the footing at 52 mm displacement is observed, i.e. geocell shows almost homogenous behavior regardless of loading location relative to geocell structure.

It should be noted that only one type of loading plate, one type of geocell with different heights and widths and one type of sand were used in this study; the results obtained may be different than those of full-scale tests in field and also using of different materials.

REFERENCES

Gurbuz, A. & Mertol, H.C. (2012). Interaction between assembled 3D honeycomb cells produced from high density polyethylene and a cohesionless soil. Journal of Reinforced Plastics & Composites, 31(12), pp.828–836. https://doi.org/10.1177/0731684412447529.

Han, J., Yang, X., Leshchinsky, D., & Parsons, R. (2008). Behavior of geocell-reinforced sand under a vertical load. Transportation Research Record: Journal of the Transportation Research Board 2045, pp. 95-101. https://doi.org/10.3141/2045-11.

Latha, G. M., Rajagopal, K., & Krishnaswamy, N. R. (2006). Experimental and Theoretical Investigations on Geocell-Supported Embankments. International Journal of Geomechanics, 6(1), pp. 30-35. https://doi.org/10.1061/(ASCE)1532-3641(2006)6:1(30).

Shin, E. C., Kang, H. H., & Park, J. J. (2017). Reinforcement efficiency of bearing capacity with geocell shape and filling materials. KSCE Journal of Civil Eng., 21(5), pp. 1648-1656. https://doi.org/10.1007/s12205-016-1649-0.

Proceedings of the XVIII ECSMGE 2024
GEOTECHNICAL ENGINEERING CHALLENGES
TO MEET CURRENT AND EMERGING NEEDS OF SOCIETY
© 2024 the Authors
ISBN 978-1-032-54816-6
DOI 10.1201/9781003431749-516
Open Access: www.taylorfrancis.com, CC BY-NC-ND 4.0 license

ECSMGE 24
XVIII EUROPEAN CONFERENCE ON SOIL MECHANICS AND GEOTECHNICAL ENGINEERING

Evaluating the effects of a deep excavation on monumental buildings: MarmorKirken station in Copenhagen

Évaluation des effets d'une excavation profonde sur des bâtiments monumentaux: gare MarmorKirken à Copenhague

F.M. Soccodato*, G. Tropeano
University of Cagliari, Italy

**soccodato@unica.it*

ABSTRACT: This paper describes the Building Risk Assessment (BRA) process implemented during the design and construction of MarmorKirken metro station in Copenhagen. Being the box station very near the monumental church, the evaluation of the effects induced by the excavation on the church was a key issue of the design. Surveys, structural and geotechnical investigations were carried out to setup reliable structural and geotechnical numerical models on which BRA, at the design stage, was based. During construction works, design predictions were systematically compared with monitoring measures, allowing to update the BRA. According to BRA results, no significant effects of construction works on the church was observed.

RÉSUMÉ: Cet article décrit le processus d'Evaluation des Risques liés aux Bâtiments (BRA) mis en œuvre lors de la conception et de la construction de la station de métro MarmorKirken à Copenhague. Le box étant très proche de l'église monumentale, l'évaluation des effets induits par les fouilles sur l'église a été un enjeu clé de la conception. Des études, des investigations structurelles et géotechniques ont été réalisées pour établir des modèles numériques structurels et géotechniques fiables sur lesquels BRA, au stade de la conception, s'est basé. Lors des travaux de construction, les prévisions de conception ont été systématiquement comparées aux mesures de suivi, permettant ainsi de mettre à jour le BRA. Selon les résultats du BRA, aucun effet significatif des travaux de construction sur l'église n'a été observé.

Keywords: Deep excavations; soil-structure interaction; numerical analyses.

1 INTRODUCTION

Deep excavations and tunnelling in the urban environment require a careful evaluation of the effects of works on existing structures. Very often, the building risk assessment (hereinafter referred to by the acronym BRA) process plays a major role in design, especially when monumental structures are involved.

In this case, at a given design stage, numerical analyses with different levels of complexity are carried out, geotechnical and structural aspects of the problem needing to be properly addressed (Rampello et al., 2012; Burghignoli et al., 2013; Pascariello et al., 2023). Expected building damage may be then evaluated by looking at stress and strain fields or patterns in the structure.

During construction stages, monitoring data are of primary importance to assess numerical predictions and, when needed, to update the BRA.

This paper describes some features of the BRA process carried out for the construction of MarmorKirken metro station in Copenhagen.

2 MARMORKIRKEN STATION

Marmorkirken station box is about 35 m in depth; diaphragm walls have a length of 40 m. The retaining walls are located only 3 m away from the foundations of the church (Figure 1). A full top-down construction technique was adopted to minimise excavation induced settlements of the church.

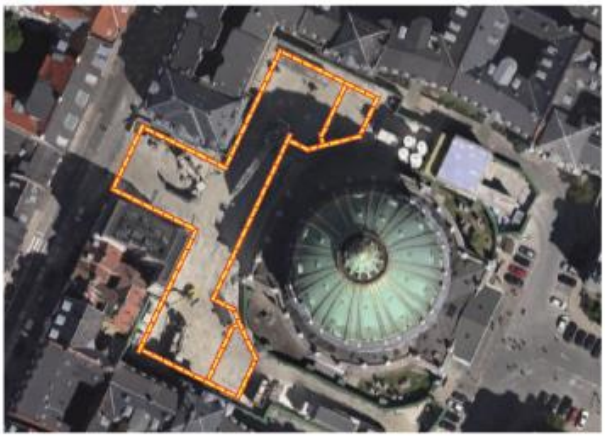

Figure 1. View of MarmorKirken area.

3 BRA PROCESS

The BRA process carried out consisted of different stages, starting from the acquisition of relevant data used for the setup of numerical models. BRA was based on the evaluation of predicted stresses and strain field changes due to construction activities. The interpretation of monitoring measurements allowed for checking and updating the BRA during construction works.

3.1 Survey and testing

It is worth noting that reliable structural and geotechnical numerical models should be based on reliable structural and geotechnical investigations, the first of them being rather difficult to be obtained for monumental buildings, often due to conservative issues. For MarmorKirken, the following activities were addressed:1) historical research (drawings and texts); 2) a laser scanner survey to define geometry; 3) endoscopy and lab testing on cored samples (marble); 4) flat jack and sonic tests on walls (masonry);
Before the construction activities, no significant crack patterns were observed in the structure.

The geotechnical investigation (boreholes, piezometers, seismic tests and samples tested in the laboratory) allowed for a reliable geotechnical characterization of the foundation soil. Boreholes and excavation pits enabled to identify materials and depth of the ring foundation of the Church.

3.2 Structural and geotechnical model

The church may be broadly divided in four main parts: foundation level (rock blocks), entrance level (marble blocks, for both inner and outer structure), drum and dome (masonry). The ring foundation has a thickness of about 3 m, with an inner and outer diameter of about 25 and 50 m, respectively. The dome has a diameter equal to 31 m, ant it reaches a height of about 46 m.

About 50000 finite elements were used to define the structural model of church (Figure 2). Both masonry and marble were modelled using a linear, isotropic elastic model due to the expected small strain levels. The estimated total load acting at foundation level was about 300 MN.

Figure 6 shows soil profile and geometry of the excavation in front of the church. Foundation soils, below shallow units of made ground (FY) and a clayey silt (ML), are constituted by a medium to dense sand and gravel level (DS/DG) with a thickness of about 9 m. At a depth of 13 m (10 m a.s.l.), the basal limestone formation, with increasing stiffness and strength properties with depth (UCL-HP, UCL, MCL), is found.



Figure 2. Structural model of the church (SAP2000 code).

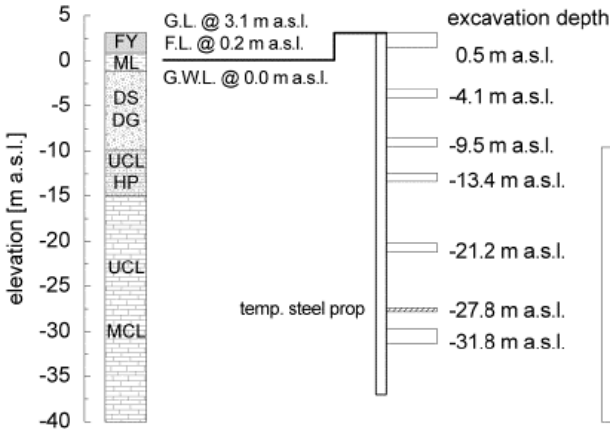

Figure 3. Soil profile and top-down excavation stages in front of the church.

Figure 4 shows the three-dimensional (3D) FEM computational mesh of the geotechnical model of both the excavation and the church. The church is modelled by an equivalent embedded linear elastic solid (Rampello et al., 2012), on which the average dead loads obtained from the structural analysis are applied. The HSM nonlinear, plasticity hardening model (Schanz et al., 1999) was used for soil and rock units. Calculation steps of the analysis followed, after the in-situ stage and the simulation of retaining walls construction, the top-down sequence depicted in Figure 3. Predicted maximum settlements of the Church were very small: about 0.5 mm due to retaining wall construction and about 1.7 mm at the end of excavation stages. Full details on soil parameters, numerical modelling approach and results of the 3D numerical soil-structure interaction analysis (class A prediction) are described in Soccodato and Tropeano (2021).

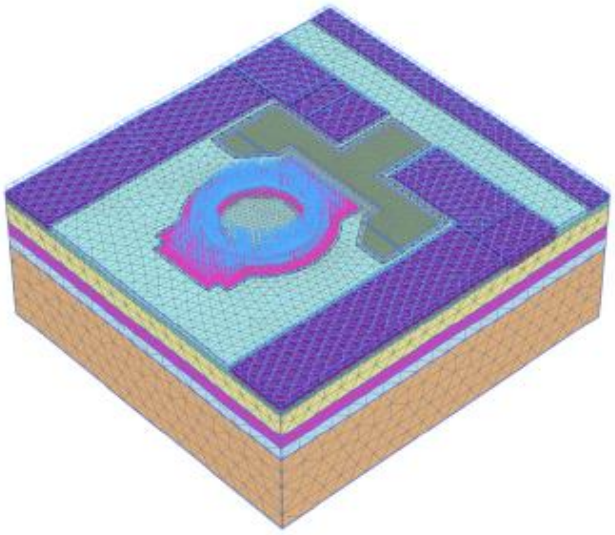

Figure 4. Geometry and mesh of the geotechnical model (PLAXIS 3D code).

3.3 Monitoring system

The project included a detailed monitoring plan, with an automatic remote acquisition system (KRONOS) to provide real-time information about the effects of construction activities. Precision levelling points were placed on the church structure and inclinometers were installed inside the retaining walls and in the soil behind (Figure 5).

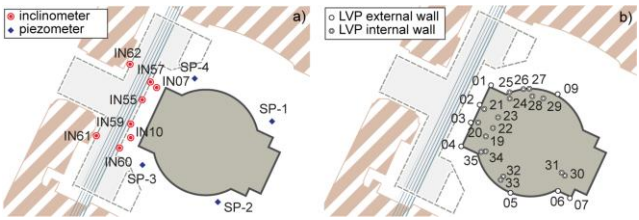

Figure 5. Monitoring system: a) inclinometers and piezometers; b) levelling points.

3.4 Evaluating the effects of construction

Settlement fields applied to the bottom nodes of the structural model of the church are shown in Figure 6. The reference stage is represented by the self-weight (SW) condition before the construction works. Predicted settlement field at the design stage (G1) was then applied, evaluating changes in stress and strain values.

During construction works, monitoring system recorded higher settlements than those predicted. Firstly, wall installation in front of the Church caused a maximum settlement of about 3 mm (KRONOS): a first correction to the applied settlement fields (G2) was thus considered, by adding to the actual settlement field recorded by measurements (KRONOS) the predicted settlement field induced by excavation stages. Furthermore, first excavation stages also gave rise to settlements of the church higher than those predicted. Considering the 'at time' available monitoring data compared to predictions, the settlement field obtained from numerical geotechnical analysis for the excavation stages was increased by a factor equal to 4, giving rise to the final settlement field (G3) used for BRA updating.

Maximum measured settlements of the church at the end of works were about 7 mm, in close agreement with the G3 displacement field used for BRA (Soccodato and Tropeano, 2021). It is worth noting that nearly one half of the total observed maximum settlement was due to retaining wall construction.

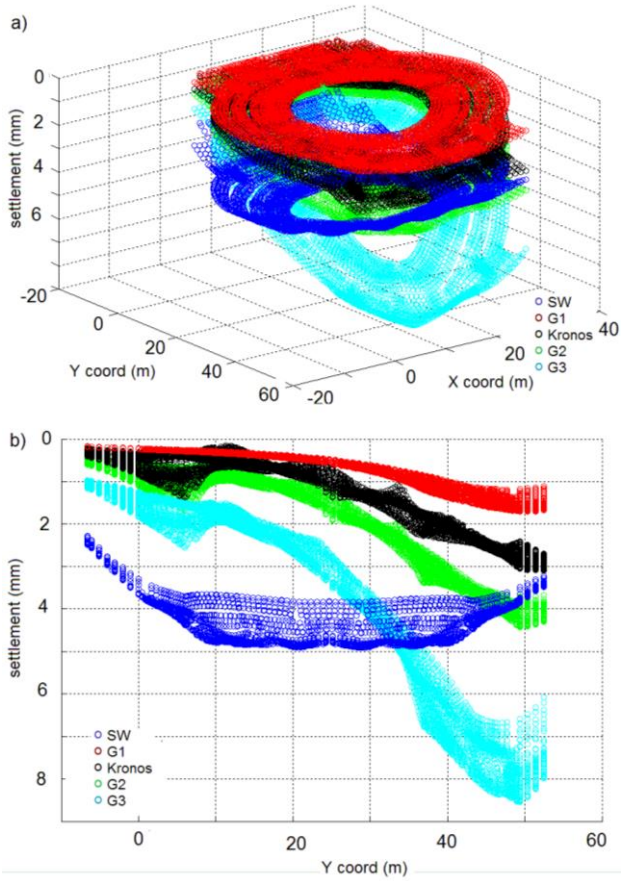

Figure 6. Foundation settlement fields used for BRA: a) 3D view; b) longitudinal view toward box station excavation.

As stated before, BRA was based on the comparison of stress and strain fields under different settlement fields, taking as reference the SW condition.

Figure 7 shows, as an example, the frequency distribution of principal tensile strain obtained from the structural model in the dome elements and in the inner structure. Maximum strain values are very small ($< 3 \cdot 10^{-4}$) and significantly lesser than those associated to 0.1 mm width cracks in masonry structures. Furthermore, changes (in value and frequency) due to construction works (both for G2 and updated G3 settlement fields) are quite limited, allowing for the

estimation of a negligible damage induced by the excavation.

Figure 8 shows the stress values for the inner structure, which allowed for a preliminary identification of the parts of the structure potentially affected by cracking.

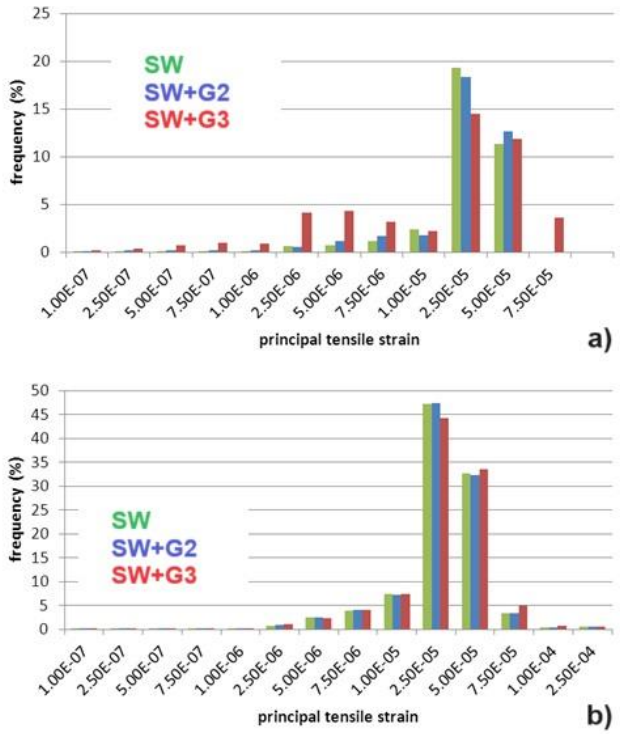

Figure 7. Distribution of principal tensile strain: a) in dome elements; b) in the inner structure (masonry).

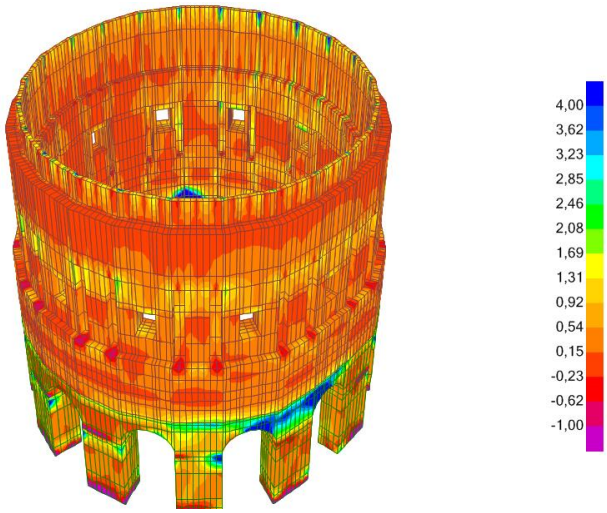

Figure 8. Inner structure, SW+G3 settlement field: maximum principal stresses (units: daN/cm², tensile if >0).

4 CONCLUSIONS

The Building Risk Assessment process carried out for MarmorKirken has been a very challenging task: archaeologist, structural and geotechnical engineers collaborated to define reliable models to be used in the evaluation of the excavation induced effects on the church. Negligible effects of construction activities on MarmorKirken were predicted at the design stage, as well as negligible damage appeared in MarmorKirken at the end of works. During construction, the real time automatic monitoring system allowed for successfully updating the Building Risk Assessment, pointing out the importance of real time measurements and of their interpretation in this kind of process.

ACKNOWLEDGEMENTS

The Authors are grateful to Metroselskabet and WeBuild for the permission to publish monitoring data.

REFERENCES

Burghignoli A., Callisto L., Rampello S., Soccodato F.M., and Viggiani, G.M.B. (2013). The crossing of the hystorical centre of Rome by the new underground Line C: a study of soil–structure interaction for historical buildings. In *Geotechnics and Heritage: Case Histories*, E. Bilotta et al. (eds), CRC PRESS, pp. 97-136.

Pascariello, M.N., Luciano, A., Bilotta, E., Acikgoz, S. and Mair, R. (2023). Numerical modelling of the response of two heritage masonry buildings to nearby tunnelling. *Tunnelling and Underground Space Technology*, 131:104845. https://doi.org/10.1016/j.tust.2022.104845.

Rampello, S., Callisto, L., Viggiani, G. and Soccodato, F.M. (2012). Evaluating the effects of tunnelling on historical buildings: the example of a new subway in Rome / Auswertung der Auswirkungen des Tunnelbaus auf historische Gebäude am Beispiel einer neuen U-Bahnlinie in Rom. *Geomechanik Tunnelbau*, 5: 275-299. http://doi.org/10.1002/geot.201200017.

Schanz, P.A., Vermeer, P.A., and Bonnier, P.G. (1999). The hardening soil model: Formulation and verification. In *Beyond 2000 in Computational Geotechnics*, pp. 281-296. Balkema, Rotterdam.

Soccodato, F. M. and Tropeano, G. (2021). Numerical analysis of a deep excavation in front of MarmorKirken, Copenhagen. In *Challenges and Innovations in Geomechanics,* M. Barla et al. (eds.), Lecture Notes in Civil Engineering, Springer, Vol. 126, pp. 223-230. https://dx.doi.org/10.1007/978-3-030-54518-3_27.

Proceedings of the XVIII ECSMGE 2024
GEOTECHNICAL ENGINEERING CHALLENGES
TO MEET CURRENT AND EMERGING NEEDS OF SOCIETY
© 2024 the Authors
ISBN 978-1-032-54816-6
DOI 10.1201/9781003431749-517
Open Access: www.taylorfrancis.com, CC BY-NC-ND 4.0 license

ECSMGE 24
XVIII EUROPEAN CONFERENCE ON SOIL MECHANICS AND GEOTECHNICAL ENGINEERING

Prediction model for strength of cement-stabilized clays for in-situ soil mixing using artificial neural network

Modèle de prédiction de la résistance des argiles stabilisées au ciment pour le mélange de sols in situ à l'aide d'un réseau neuronal artificiel

M. Swamynaidu*, A. Tyagi
Department of Civil Engineering, Indian Institute of Technology Roorkee, India,
**m_swamynaidu@ce.iitr.ac.in*

ABSTRACT: Unconfined Compressive Strength (UCS) is usually the design criterion for in-situ ground improvement projects, including deep soil mixing, mass soil stabilization, and cutter soil mixing. Unlike subgrade stabilization projects, such techniques involve cement-content as high as 50%. Thus, the paper intends to develop a prediction model for the strength of cement-stabilized clay from the laboratory test results performed on high-plastic illite clay. First, the UCS tests are performed for cement-content varying from 5% to 50% by dry weight, for two water-contents of 1.5 and 1.85 times the liquid limit (LL), and the curing time of 7, 28, and 90 days. Test results indicate that the UCS increases with the increase in curing time and cement-content while reducing with the increase in water-content. The prediction model for UCS is then developed using the artificial neural network (ANN), and the model performance is assessed based on root mean squared error (RMSE) and coefficient of determination (R^2). According to the multi-layer perceptron (MLP) approach, the developed model equation can be used to forecast the performance of the UCS for the given range of water-content, cement, and curing time. Relative importance shows that cement-content is the most significant parameter on UCS.

RÉSUMÉ: La résistance à la compression non confinée (UCS) est généralement le critère de conception pour les projets d'amélioration du sol in situ, y compris le mélange de sol en profondeur, la stabilisation massive du sol et le mélange de sol par coupe. Contrairement aux projets de stabilisation du sol de fondation, ces techniques impliquent une teneur en ciment pouvant atteindre 50%. Ainsi, l'article vise à développer un modèle de prédiction de la résistance de l'argile stabilisée au ciment à partir des résultats d'essais en laboratoire effectués sur de l'argile illite à haute plasticité. Tout d'abord, les tests UCS sont effectués pour une teneur en ciment variant de 5% à 50% en poids sec, pour deux teneurs en eau de 1,5 et 1,85 fois la limite de liquide (LL) et un temps de durcissement de 7, 28 et 90. jours. Les résultats des tests indiquent que l'UCS augmente avec l'augmentation du temps de durcissement et de la teneur en ciment, tout en diminuant avec l'augmentation de la teneur en eau. Le modèle de prédiction pour l'UCS est ensuite développé à l'aide du réseau neuronal artificiel (ANN), et les performances du modèle sont évaluées sur la base de l'erreur quadratique moyenne (RMSE) et du coefficient de régression (R). L'importance relative des variables d'entrée montre que la teneur en ciment influence l'UCS. Selon l'approche du perceptron multicouche (MLP), l'équation du modèle développée peut être utilisée pour prévoir les performances de l'UCS pour une plage donnée de teneur en eau, de ciment et de temps de durcissement.

Keywords: Deep soil mixing; mass soil stabilization; cement stabilization; UCS prediction model.

1 INTRODUCTION

Clayey soils are often characterized by low strength and high compressible characteristics. In situ ground improvement techniques viz. deep soil mixing (DSM), mass soil mixing (MSM), and jet grouting (JG) are often used to stabilise or reinforce these such problematic soils with the use of admixtures mostly by using ordinary Portland cement (OPC). The resulting improved ground produced by these techniques provides greater mechanical stability. The degree of enhancement depends on several factors, such as the type of in situ soil, in situ water-content, type of binder, curing time and conditions, etc. (Kitazume and Terashi, 2013). For such ground improvement projects, the design, quality control (QC) and quality assurance (QA) are mostly based on the UCS of cement-treated soil samples (Yohannes and Daramalinggam, 2019; BS EN 14679, 2005; Bruce et al., 2013). The prescribed design strength is often the minimum value of the field UCS obtained after testing the cement-treated soil samples (Liu et al., 2017). In recent years, nonlinear techniques such as ANN have been used successfully in the field of geotechnical engineering for e.g., to predict the UCS of cement-stabilized soil (Das et al., 2011), geopolymer-treated soil (Eidgahee et al., 2020; Maheela et al., 2023), and stabilized pond

ashes (Suthar, 2020). Eidgahee et al., (2020) and Maheela et al., (2023) reported that the ANN models can effectively improve the prediction of UCS of geopolymer-treated clayey soils. This approach has been convenient because it has acceptable nonlinear mapping capability and also prior expertise among input parameters is not required. However, the literature reporting the prediction models on UCS of cement-treated clays for in-situ mixing techniques with high cement content and longer curing periods is limited.

This study presents a laboratory investigation on UCS of cement-treated high plastic illite clay at different water-contents (1.5 LL and 1.85 LL), cement-contents (5-50%), and curing periods (7, 28, and 90 days). These mixing parameters are selected to those adopted for DSM, JG, and MSM ground improvement projects. Further, the UCS prediction model is developed using the nonlinear ANN with the Levenberg-Marquardt algorithm. The above mixing parameters are selected similarly to those adopted in DSM/MSM techniques.

2 TESTING MATERIALS AND SAMPLE PREPARATION

2.1 Materials used

The soil used in the present study is collected from a site near the Indian Institute of Technology (IIT) Roorkee, Uttarakhand, India. The soil has a liquid limit (LL) and plasticity index (PI) of 65% and 30%, respectively. As per the unified soil classification system (USCS), the soil is high-plasticity clay (CH). ASTM C150/150M type I ordinary Portland cement is used as the admixture.

2.2 Sample preparation

The method of sample preparation follows Tyagi et al., (2019). The high-plastic clay is soaked in water for about 2 days and then sieved through a 2 mm sieve to eliminate the unwanted waste. The clay slurry is then mixed in an electronic bowl mixer with a prescribed water-content of 1.5 and 1.85 times LL. The calculated amount of cement and distilled water are mixed in an electronic bowl mixer to obtain cement slurry for a given mix-ratio. This cement slurry is then mixed with the clay slurry in an electronic bowl mixer for not more than 10 minutes. After mixing, the final clay-cement slurry is poured into polyvinyl chloride (PVC) cylindrical molds of diameter and height of 50 mm × 100 mm for performing UCS tests at specified curing days. The moulds are placed horizontally submerged in a water tub at room temperature (27±3ºC). Table 1 presents the mix ratios for the present study.

Table 1. Mix ratios.

Mix ratio (s:c:w)	**cement (%)**	**water-content (%)**	**w/c**	**curing time (days)**
20:1:21	5		21	
10:1:11	10		11	
5:1:6	20		6	
10:3:13	30	(1.5 LL)*	4.33	
10:4:14	40		3.5	
2:1:3	50		3	7*, 28*,
20:1:21	5		25.2	and 90
10:1:13.2	10		13.2	
5:1:7.2	20		7.2	
10:3:15.6	30	(1.85 LL)	5.2	
10:4:16.8	40		4.2	
2:1:3.6	50		3.6	

*Test data reported from Swamynaidu and Tyagi (2024).

2.3 Test methodology

2.3.1 Unconfined compressive strength (UCS)

UCS tests following the ASTM, 2013: D2166/D2166M are performed to determine the UCS of different soil:cement:water (s:c:w) ratios. The samples are loaded under compression at a fixed vertical displacement rate of 1 mm/minute. Five samples are tested for each mixing ratio, and the average UCS is reported for each mix ratio.

2.4 ANN model development

Figure 1 illustrates the architecture of ANN with the selected inputs, number of hidden layers, and output. In the present study, Out of 36 UCS observations, 25 and 11 UCS observations are used for training and testing the model, respectively. Backpropagated neural network is trained with the Levenberg-Marquardt algorithm, which is more efficient than the gradient descent algorithm (Maheela et al., 2023). For the best performance, tan-sigmoid and purelin activation functions are selected for the single hidden and output layer. The neurons in the hidden layer is chosen by trial and error until the optimum performance. All the input and output parameters are normalized in the range of -1 to 1 before training the database.

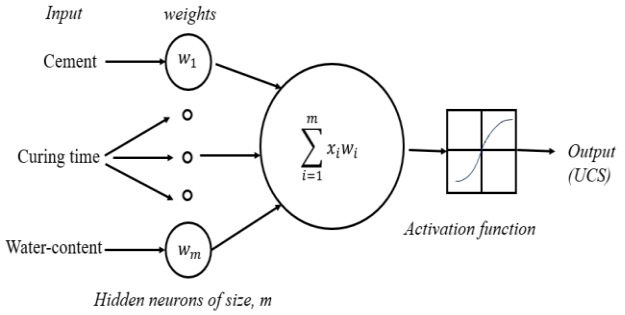

Figure 1. Showing the architecture of the ANN model.

3 RESULTS

3.1 UCS

3.1.1 Effect of cement-content differentiated by water-content and curing time

Figure 2a and 2b show the variation of obtained UCS with the water-content and cement-content after 7, 28, and 90 days of curing. The lower the water-content higher the UCS, and the extent of UCS improvement is considerably dependent on the curing time and cement (%). Figure 2(a and b) show approximately a linear variation with the increase in cement-contents irrespective of curing times and consistent with the findings of Tan et al., (2002) and Chew et al., (2004). It is seen that there is a gradual increase in UCS for a lower cement-content of 5%; however, with the increase in cement-content, a sharp increase in UCS was evident. In contrast, for a water-content of 1.85 LL, shown in Figure 2(b), the trend of increase was relatively less compared to Figure 2(a). This indicates the effective network of reactive products viz. calcium silicate hydrate (CSH) and calcium alumina silicate hydrate (CASH) for a water-content of 1.5 LL that interlocks the clay and cement grains together in the presence of water, resulting in enhanced strength over curing time. Despite this, the low UCS observations for a water-content of 1.85 LL over time were probably with the aid of weaker fabric and inconsequential cementitious reactions. As a result, more interaggregate pores are left unfilled.

Further, with increased curing time, UCS was significantly increased except for 5% of cement-content. As seen in Figure 2a and 2b for 50% of cement-content, UCS_{7d}, UCS_{28d}, UCS_{90d} were 581.27 kPa, 1132.75 kPa, and 1386.96 kPa and 377.8 kPa, 623.6 kPa, and 726.55 kPa with a water-content of 1.5 and 1.85 LL, respectively. As hydration proceeds, the resulting reactive products (principally CSH) accumulate into the void spaces, consequently causing a higher increment in UCS. Nonetheless, the rate of change in UCS was moderate after 28 days, meaning that pozzolanic reactions or hardening continued at a slower rate. Therefore, the increment in UCS reflects the structure of the treated matrix for a specified curing time.

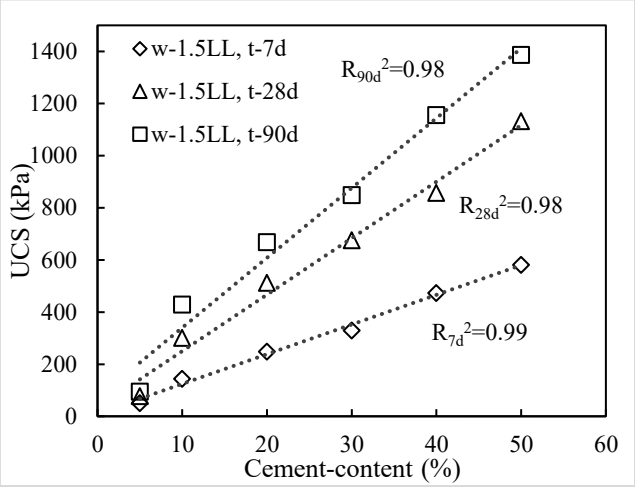

(a)

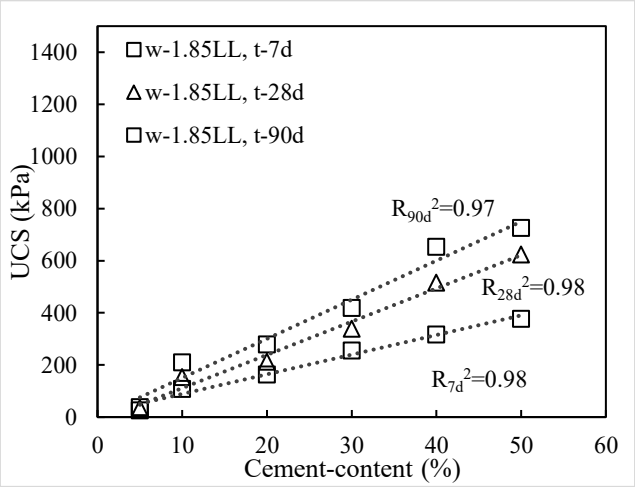

(b)

Figure 2. Showing the variation of UCS (a) 1.5 LL (Swamynaidu and Tyagi, 2024) (b) 1.85 LL.

3.1.2 ANN model

In the present study, cement-content, water-content, and curing time are considered as input variables to predict the UCS of cement-treated illite clay. Out of 36 data records, 70% and 30% are used for training and testing, respectively. After trial and error, three neurons in the single hidden layer are opted, for which the strong performance statistics (lowest RMSE and highest R^2) are achieved. Figure 3a shows the strong correlation between the predicted and experimental UCS for the training and testing databases. The performance of the model is evaluated by statistical indices such as RMSE and R^2. It is observed that the RMSE and R^2 for training and testing are 25 kPa and 0.99 and 46 kPa and 0.98, respectively.

Further, $RMSE_{all}$ and R_{all}^2 for the ANN model (32.9 kPa and 0.99) show better than the multilinear regression model (148.5 kPa and 0.84) for the same input parameters. Figure 3b compares predicted and experimental UCS to assess the reliability of the developed ANN model. Additionally, the prediction equation for UCS using connection weights is presented in eq. 1 to 1.9;

The relative importance is determined using the connection weights approach (Goh 1994; Duong and Tran 2023). Figure 3c shows the relative importance of each input variable on UCS. Accordingly, cement-content is found to be the most influential input variable, followed by curing time and water-content on the UCS. This is consistent with the experimental observations explained in the previous section 3.1.1.

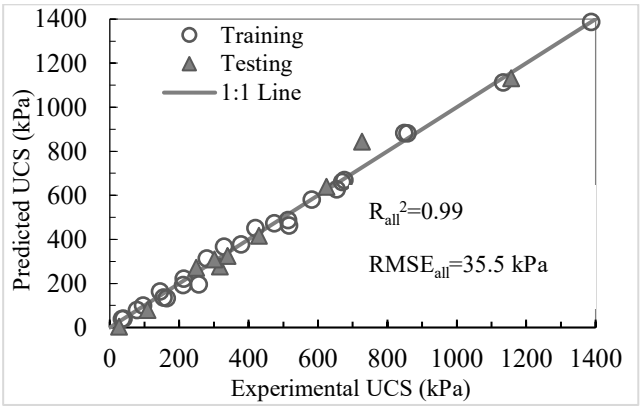

(a)

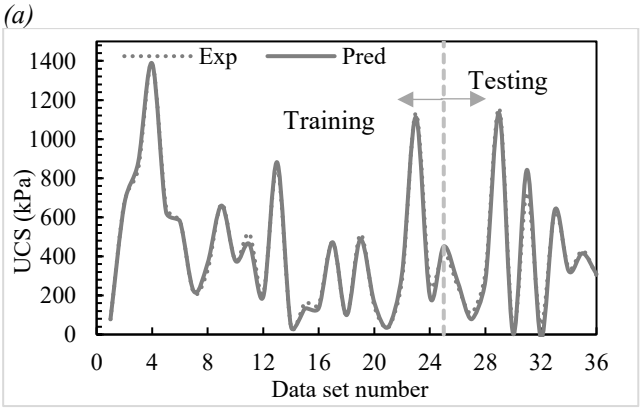

(b)

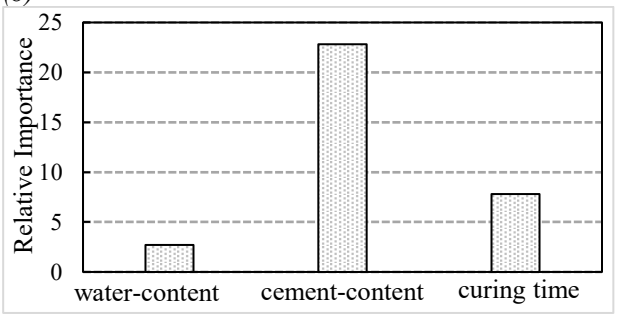

(c)

Figure 3. (a) Plot of experimental vs measured UCS for training and testing (b) comparison of experimental and predicted UCS (c) relative importance on UCS.

$$UCS_{(n)} = b_k + \sum_{j=1}^{3}\left[w_{jk} \times tansig\left(\sum_{i=1}^{m=3} w_{ij}x_i + b_j\right)\right] \quad (1)$$

$$p_1 = -5.3-0.29w-4.68c+0.20t \quad (1.1)$$

$$p_2 = -0.68-0.22w+0.46c+0.12t \quad (1.2)$$

$$p_3 = 3.59+0.27w-0.49c+2.49t \quad (1.3)$$

$$q_1 = -0.50 \times \frac{(e^{x1}-e^{-x}1)}{(e^{x1}+e^{-x}1)} \quad (1.4)$$

$$q_2 = 1.85 \times \frac{(e^{x2}-e^{-x2})}{(e^{x2}+e^{-x2})} \quad (1.5)$$

$$q_3 = 1.16 \times \frac{(e^{x3}-e^{-x3})}{(e^{x3}+e^{-x3})} \quad (1.6)$$

$$r_1 = -0.89+y_1+y_2+y_3 \quad (1.7)$$

$$UCS_n = r_1 \quad (1.8)$$

$$UCS_p = 0.5 \times (UCS_n + 1)(UCS_{max} + UCS_{min}) + UCS_{min} \quad (1.9)$$

where w_{jk} and w_{ij} are the connection weights among the input, hidden, and output layer, b_j and b_k are the biases of the hidden and output layer, tansig is the transfer function, w is water content, c is cement content, t is curing time, UCS_p is predicted UCS, UCS_n is normalized UCS, and UCS_{max} and UCS_{min} are the maximum and minimum UCS of the experimental database.

4 CONCLUSION

The study presents the UCS test results of cement-treated high plastic illite clay at different water-contents (1.5 LL and 1.85 LL), cement-contents (5-50%), and curing periods (7, 28, and 90 days). UCS at different curing times increased with decreased water-content and an increase in cement-content, and this was because of the development of more reactive products over hydration and pozzolanic activity. ANN model equation for UCS is presented as per connection weights approach. However, it should be noted that the RMSE values for both training and testing showed higher values for the ANN model, which is attributed to the lower experimental database. The developed ANN model and findings have important applications, where the field operating variables can be selected to

achieve the design UCS for JG/DSM/CSM projects in the absence of a test database. Further, considering more database and other nonlinear techniques, such as support vector regression, random forest, Gaussian process, and others may be used for future studies to improve the test observations and to select the best model for strength prediction.

ACKNOWLEDGEMENTS

This research was funded by the Faculty Initiation Grant (FIG-100851) registered at Sponsored Research and Industrial Consultancy (SRIC), IIT Roorkee. The authors would also like to thank the Ministry of Education, Govt. of India for providing funding to the first author for his Doctoral program.

REFERENCES

ASTM (2013). Standard test method for unconfined compressive strength of cohesive soil. *ASTM* D2166, West Conshohocken, PA.

Bruce, M.E.C., Berg, R.R., Collin, J.G., Filz, G.M., Terashi, M. and Yang, D.S. (2013). Deep mixing for embankment and foundation support. In: *FHWA-HRT-13-046*. Federal highway administration design manual, Washington, DC.

BS EN 14679:2005. Execution of special geotechnical works-Deep mixing. British standard institution, London, UK.

Chew, S. H., Kamruzzaman, A. H. M., and Lee, F. H. (2004). Physicochemical and engineering behavior of cement treated clays. *Journal of geotechnical and geoenvironmental engineering*, 130(7), 696-706, https://doi.org/10.1061/(ASCE)10900241(2004)130:7(696).

Das, S.K., Samui, P. and Sabat, A.K. (2011). Application of artificial intelligence to maximum dry density and unconfined compressive strength of cement stabilized soil. Geotechnical and Geological Engineering, 29, pp.329-342, DOI 10.1007/s10706-010-9379-4.

Duong, N.T. and Tran, K.Q. (2023). Estimation of seepage velocity and piping resistance of fiber-reinforced soil by using artificial neural network-based approach. Neural Computing and Applications, 35(3), pp.2443-2455.

Goh, A.T. (1994). Seismic liquefaction potential assessed by neural networks. Journal of Geotechnical engineering, 120(9), pp.1467-1480.

Kitazume, M. and Terashi, M. (2013). The deep mixing method. CRC press, Boca Raton, London. ISBN-13: 978-0-203-58963-2.

Liu, Y., Y. J. Jiang, H. W. Xiao, F. H. Lee. (2017). Determination of representative strength of deep cement-admixed clay from core strength data. *Géotechnique* 67 (4): 350–364, https://doi.org/10.1680/jgeot.16.P.105.

Maheepala, M. M. A. L. N., Nasvi, M. C. M., Robert, D. J., Gunasekara, C., and Kurukulasuriya, L. C. (2023). Mix design development for geopolymer treated expansive subgrades using artificial neural network. *Computers and Geotechnics*, 161, 105534, https://doi.org/10.1016/j.compgeo.2023.105534.

Rezazadeh Eidgahee, D., Rafiean, A. H., and Haddad, A. (2020). A novel formulation for the compressive strength of IBP-based geopolymer stabilized clayey soils using ANN and GMDH-NN approaches. Iranian Journal of Science and Technology, Transactions of Civil Engineering, 44(1), 219-229, https://doi.org/10.1007/s40996-019-00263-1.

Suthar, M. (2020). Applying several machine learning approaches for prediction of unconfined compressive strength of stabilized pond ashes. *Neural Computing and Applications*, 32(13), 9019-9028, https://doi.org/10.1007/s00521-019-04411-6.

Swamynaidu, M., and Tyagi, A. (2024). Hydraulic Conductivity of Cement-Clay Mixes by Accelerated Permeability Tests using Triaxial. Construction of Building materials (under review).

Tan, T. S., Goh, T. L., and Yong, K.Y. (2002). Properties of Singapore marine clays improved by cement mixing. *Geotechnical Testing Journal*, 25(4), 422-433, https://doi.org/10.1520/GTJ11295J.

Tyagi, A., Xiao, H., Chin, K. G., and Lee, F. H. (2019). Model for predicting the unit weight of cement-treated soils. *Soils and Foundations*, 59(6), 1921-1932, https://doi.org/10.1016/j.sandf.2019.09.002.

Yohannes, M., and J. Daramalinggam. 2019. Specifying strength proper-ties of soil mixing and jet grouting in Malaysia: A statistical approach. In Vol. 8 of Proc., 1st Malaysian Geotechnical Society and Geotechnical Society of Singapore Conference Malaysia: Malaysian Geotechnical Society. ASCE06023017-9 Int. J. Geomech.

Proceedings of the XVIII ECSMGE 2024
GEOTECHNICAL ENGINEERING CHALLENGES
TO MEET CURRENT AND EMERGING NEEDS OF SOCIETY
© 2024 the Authors
ISBN 978-1-032-54816-6
DOI 10.1201/9781003431749-518
Open Access: www.taylorfrancis.com, CC BY-NC-ND 4.0 license

ECSMGE 24
XVIII EUROPEAN CONFERENCE ON SOIL MECHANICS AND GEOTECHNICAL ENGINEERING

Setup and calibration of piles with FBG strain sensors in a geotechnical centrifuge

Configuration et calibration de pieux équipés de capteurs de deformation FBG dans une centrifugeuse géotechnique

C. Tang*, A.M. Marshall, C.M. Heron
Department of Civil Engineering, University of Nottingham, Nottingham, UK

A. Franza
Department of Civil and Architectural Engineering, Aarhus University, Aarhus, Denmark

J. Xu
School of Transportation, Southeast University, Nanjing, China

**chuanjin.tang@nottingham.ac.uk*

ABSTRACT: This paper discusses technical aspects of the experimental setup and calibration processing during centrifuge testing of single piles, instrumented with fibre Bragg grating (FBG) strain sensors, under vertical loads. Results illustrate the influence of the pile head connection method and data processing/correction of FBG readings. First, experimental data demonstrate issues encountered when adopting a rigid connection between a loading device, and how these can be tackled by adopting a point-to-surface contact. Second, the paper presents a method to minimise, in FBG strain sensor data, issues relating to pile bending during routine compression calibration and centrifuge testing.

RÉSUMÉ: Cet article aborde les aspects techniques de la configuration expérimentale et du traitement de la calibration lors des essais en centrifugeuse de pieux simples, instrumentés avec des capteurs de contrainte à réseaux de Bragg en fibre optique (FBG), sous des charges verticales. Les résultats illustrent l'influence de la méthode de connexion de la tête de pieu et du traitement/correction des données des capteurs FBG. Tout d'abord, les données expérimentales mettent en évidence les problèmes rencontrés lors de l'adoption d'une connexion rigide entre un dispositif de chargement, et comment ceux-ci peuvent être résolus en adoptant un contact ponctuel avec la surface. Ensuite, l'article présente une méthode pour minimiser, dans les données des capteurs de contrainte FBG, les problèmes liés à la flexion du pieu lors de la calibration de compression de routine et des essais en centrifugeuse.

Keywords: Centrifuge; pile; calibration; fibre Bragg grating (FBG).

1 INTRODUCTION

Geotechnical centrifuge testing is extensively used for modelling axial loading and force transfer mechanisms of piles in various scenarios, including external loading and during excavations. The configuration and calibration of model piles are crucial to ensure the reliability of the measured pile axial force.

Researchers have used a variety of methods to apply external loads to a pile head, such as fixing dead weights (Loganathan et al., 2000), or using mechanical load actuators (Song et al., 2022). The use of a rigid connection between the pile head and the load actuator components has advantages with respect to pile-load alignment and the ability to apply both driving and pulling forces to the pile. This method may, however, cause bending of the pile and/or experimental errors at the attached load cell.

FBG sensors can be used to measure strains/loads within structural elements in centrifuge tests (Li et al., 2020; Song et al., 2022). Song et al. (2022) incorporated embedded FBGs to measure pile axial force F_i using its positive correlation with FBG wavelength shift $\Delta\lambda_{B_i}$ at particular FBG strain sensors B_i (Figure 1(a)). FBG strain sensors are not affected by electrical noise and their size (diameter of 0.22 mm) makes them ideal for being glued inside hollow model piles for force measurement.

This paper presents data from a recent centrifuge modelling study concerning tunnel-pile interactions. The effect of two actuator-pile connection methods is examined first; an improved calibration method for FBG strain sensors placed inside model piles prior to and during centrifuge tests is proposed.

2 CENTRIFUGE TEST SETUP

Tests were conducted at 60 g within the 2 m radius, 50 g-tonne NCG centrifuge. Dry Leighton Buzzard Fraction E sand (0.14 mm average diameter, 1.58 uniformity coefficient, 2.65 specific gravity, 1.01/0.61 maximum/minimum void ratio, 90% relative density) and an eccentric rigid boundary mechanical tunnel model (90 mm diameter, 180 mm cover depth, 225 mm buried depth; Song et al., 2022) were adopted. The 60 g level was applied at half the tunnel's burial depth, i.e. 113 mm from the surface. The pile models, made of aluminium tube, have a 12.6 mm outer diameter (including a 0.3 mm thick layer of sand bonded to the shaft to get a rough shaft-soil interface), 9.3 mm inner diameter, and 150 mm length below the surface. Pile models were pushed vertically into the sand at 1 g using guides after the sand was prepared. The pile head load was applied by a stepper motor driven actuator during tests. FBGs were fixed on the smooth inner wall of the pile models using superglue (Figure 1). A "dummy pile" with similar specifications but with temperature sensors located inside was buried used to obtain data for temperature compensation of the FBGs.

The centrifuge test configuration represents a full-scale prototype scenario of 0.756 m diameter and 9 m deep piles located above/adjacent to a 5.4 m diameter tunnel with a 10.8 m cover depth.

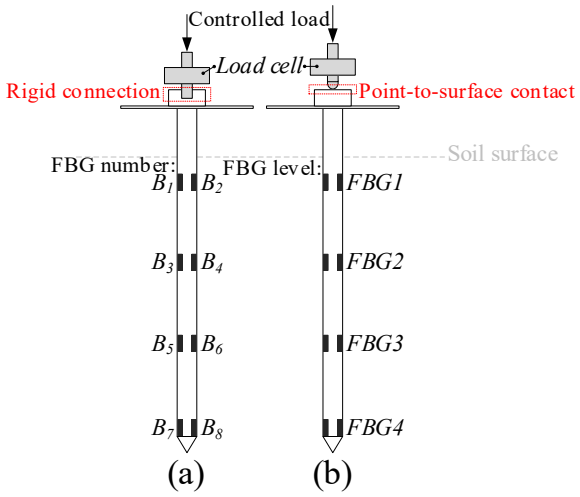

Figure 1. Diagrams of (a) rigid connection and (b) point-to-surface contact between load cell and pile head.

3 EXPERIMENTAL RESULTS

3.1 Influence of the connection at the pile head

Figure 1 illustrates the standard model piles, as well as the two types of connection methods between the pile head and the load cell above it: a "rigid connection", where the lower part of the load cell is threaded onto the pile head, and a "point-to-surface contact", where a hemispherical base of the lower part of the load cell makes contact with the top plane of the pile head. The upper end of both load cells is threaded to the loading device above, delivering only vertical force. Figure 2(a) shows the difference in pile axial forces for the two FBG sensors at each level (i.e. $\Delta F = F_i - F_{i+1}$, where i and $i+1$ refer to the FBGs on opposite faces, Figure 1(a)). The discrepancy in axial force serves as an indicator of the magnitude of pile bending.

The rigid connection increased the pile bending. In contrast, the point-to-surface contact reduced the force difference ΔF compared with the rigid connection. Whilst in theory using the average FBG readings of the two sensors on opposite faces should still provide an accurate measurement of axial force, this relies on precise positioning and alignment of the sensors, which is difficult to achieve in practice. Figure 2(b) shows that the point-to-surface contact tended to give higher FBG load readings (also described later).

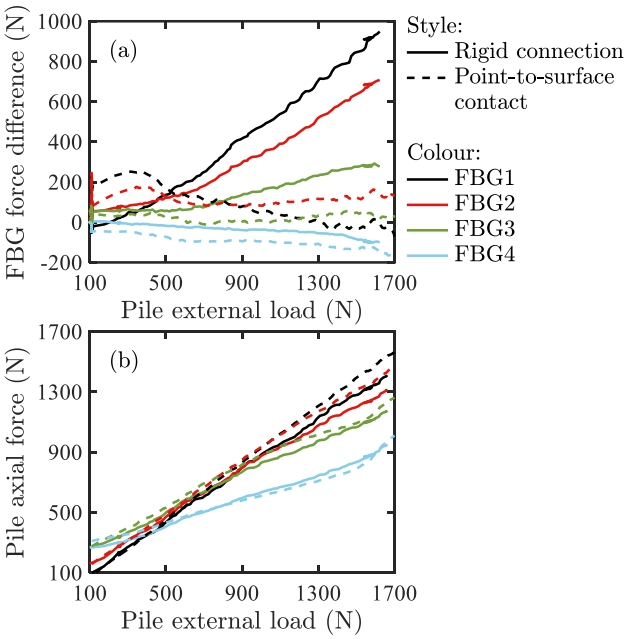

Figure 2. (a) FBG force difference between opposite positions at same level and (b) pile axial force with rigid connection and point-to-surface contact during loading.

3.2 FBG strain sensor calibration

In this paper, the axial force along the pile N_j is inferred from the average wavelength shift $\Delta\lambda_{FBG_j}$ of two FBGs at the same level (at FBG_j, Figure 1(b)) as:

$$N_j = K_{FBG_j}(\Delta\lambda_{FBG_j} - \Delta\lambda_{T_j}) + \Delta N_{exp} \quad (1)$$

where j is the FBG level reference number, K_{FBG_j} (in N/pm, pm=picometre) is FBG calibration coefficient,

$\Delta\lambda_{T_j} = K_t\,\Delta T$ is the temperature-induced wavelength offset proportional to the change in temperature ΔT by a factor K_t = 32-41 pm/°C estimated for no mechanical strains, and ΔN_{exp} is an offset introduced during centrifuge testing to correct for the disturbance resulting from the loading system. $\Delta\lambda_{T_j}$ and ΔN_{exp} are zero during K_{FBG_j} calibration tests performed at constant temperature.

3.2.1 Coefficient calibration

Table 1 shows the range, mean, and standard deviation (STD) of K_{FBG} from five sets of routine lab compression tests at 1 g within a standard loading frame (Lab C, two cycles from 0-600-0 N with an increment of ±100 N; a small cylindrical aluminium block with a conical groove matching the shape of the pile tip provides a surface for loading), two sets of compression tests using a loading/fixing system that fits on the centrifuge done at both at 1 g and 60 g (Cen 1 g, Cen 60 g, as above), and seven lab tension tests at 1 g (Lab T, from 0-200-0 N with an increment of ±20 N). After each cycle of loading-unloading, the position of the pile was altered through translation and/or rotation.

Table 1. FBG calibration coefficients from lab compression (C), centrifuge compression, and lab tension (T) tests.

		FBG1	FBG2	FBG3	FBG4
Lab C	K_{FBG}	2.5-2.6	2.5-2.6	2.5-2.6	2.4-2.6
	Mean	2.53	2.54	2.57	2.52
	STD	0.048	0.052	0.024	0.064
Cen 1 g	K_{FBG}	2.6-2.7	2.7-2.8	2.7-2.8	2.8-2.9
	Mean	2.63	2.74	2.71	2.83
	STD	0.016	0.043	0.043	0.090
Cen 60 g	K_{FBG}	~2.6	~2.7	2.6-2.7	2.7-2.8
	Mean	2.59	2.70	2.66	2.73
	STD	0.022	0.040	0.037	0.044
Lab T	K_{FBG}	2.3-3.0	2.5-2.7	2.5-2.8	/
	Mean	2.62	2.54	2.62	/
	STD	0.229	0.070	0.080	/

The deviation in 1-g lab compression coefficient K_{FBG} is likely caused by pile bending due to misalignment within the loading frame, despite attempts to reduce its effects. Overall, the values of lab compression coefficient K_{FBG} are stable and satisfactory, supported by the results of the centrifuge and tension tests discussed below.

Next, the centrifuge compression coefficient K_{FBG} under 1-g and 60-g levels are discussed. K_{FBG} at 60 g was slightly smaller (by ~2.1% on average) than the results obtained at 1 g (conducted prior to and after the 60 g tests, without adjusting any components), which implies a slight (and acceptable) overestimation of the pile axial force when using K_{FBG} from 1 g lab compression tests.

To minimise the effect of pile bending on K_{FBG}, lab tension tests were performed. The pile was fixed at the top and weights were hung from the pile via a clamp that was attached to the pile base, close to FBG4 (thus, FBG4 readings are unreliable). Neglecting the outliers for FBG1, $K_{FBG_{1-3}}$ are consistent with the compression results.

3.2.2 Offset at elevated gravity

The tunnel-pile interaction tests included "stabilisation cycles" in which the centrifuge was repeatedly spun up/down to achieve a more uniform stress distribution within the soil and at soil-structure interfaces, and ensuring consistency between tests (Song et al., 2022).

To minimise deviations in FBG readings due to misalignments and bending, $\Delta N_{exp} = \Delta N_{exp,1} + \Delta N_{exp,2}$ in Eq. (1) is estimated for each test in two steps: (i) $\Delta N_{exp,1}$ is estimated during the stabilisation cycles of a specific centrifuge test as the difference between the readings of FBG1 at 15 mm beneath the surface and the theoretical axial load at the surface (neglecting the shaft friction between FBG1 and the soil surface); next, (ii) $\Delta N_{exp,2}$ is a constant for the instrumented pile estimated at a given g-level in centrifuge calibration tests without soil to account for the (minor) effects of the self-weight of FBG sensors and the glue covering them when g-level is increased.

Figure 3 illustrates the uncorrected changes in pile axial forces (when $\Delta N_{exp} = 0$) in two centrifuge tests during stabilisation cycles from 1-60-10-60-10-60 g. Two scenarios are included: subplot (a) for a pile positioned directly above the tunnel; subplot (b) for a pile located 150 mm away from the tunnel centreline ("no tunnel"). The pile axial forces showed good repeatability subsequent to the first spin-up to 60 g. Specifically, in Figure 3(a)-(b), the axial force at FBG1 was 15/-30 N at the 1st 10 g, whereas it was 2/-60 N for the subsequent 2nd and 3rd 10 g.

In these tests, the "theoretical surface load" (i.e. theoretical pile load at the soil surface) is equal to 22 N and 110 N at 10 g and 60 g respectively: e.g. at 60 g it consists of 105 N from the self-weight of the components above the soil surface (adjusted for distance from centre of rotation of the centrifuge) and a constant load of 5 N applied by the stepper motor (controlled load in Figure 1).

The FBG correction of $\Delta N_{exp,1}$ = 20 N and 82 N were estimated, respectively, at the last spin-down to 10 g in Figure 3(a)-(b), so that the FBG1 load matched the theoretical surface load of 22 N. Note that $\Delta N_{exp,1}$

estimated for FBG1 is applied to all other FBG loads while considering $\Delta N_{exp,2} = 0$.

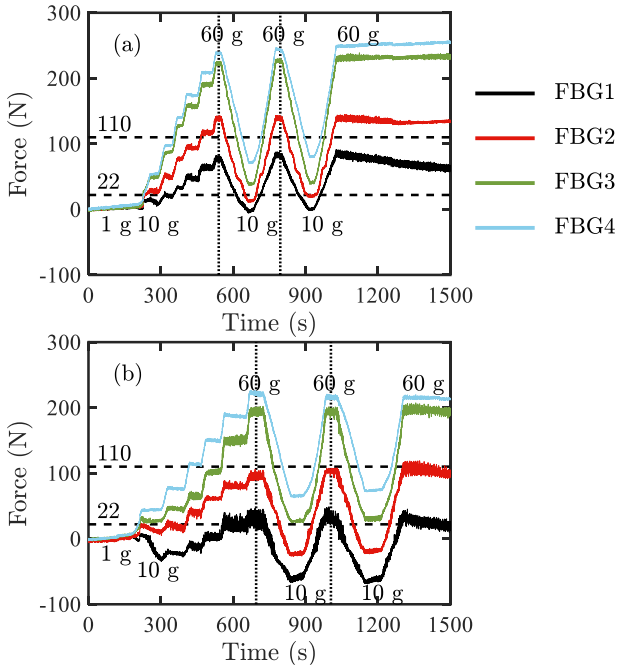

Figure 3. Changes in pile axial forces during centrifuge spin up/down for pile (a) above tunnel and (b) no tunnel.

Next, $\Delta N_{exp,2}$ is added to measurments at the end of the spin-up (or stabilisation cycles) once the final target 60 g is reached. This second offset $\Delta N_{exp,2}$ was estimated, at each FBG location, from the difference between the measured average pile axial forces and the theoretical pile self-weight in two calibration centrifuge tests at N-g without soil (while assuming $\Delta N_{exp,1} = 0$); as shown in Figure 4, $\Delta N_{exp,2}$ is within the range of 1-33 N, which is relatively small compared with the pile load capacity measured in centrifuge tests at 60 g (~1.6 kN, including base load and shaft friction).

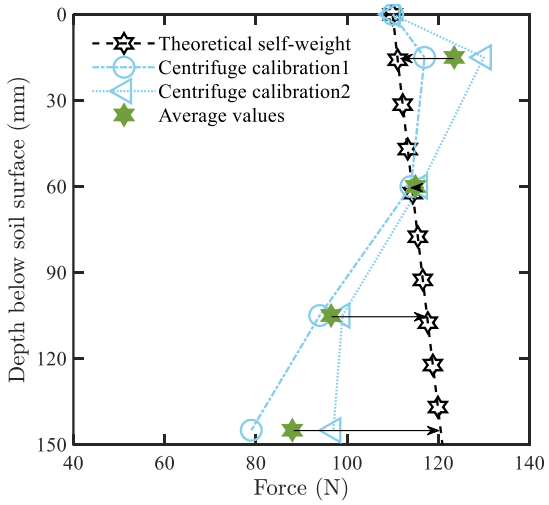

Figure 4. Pile axial force offset at 60 g

4 CONCLUSIONS

This paper summarised some "lessons learned" from recent centrifuge testing of FBG-instrumented model piles under vertical loads at the University of Nottingham Centre for Geomechanics (NCG). The following main conclusions can be drawn.

(1) The point-to-surface contact between the load actuator and pile head reduced errors in measurement of axial forces with respect to a rigid actuator-pile connection, as point-to-surface contact minimises pile bending from the misalignment between the load actuator and model pile.

(2) A systematic FBG calibration method for measuring pile axial force was applied: i) determine the calibration coefficient K_{FBG} between the axial force along pile centreline and the average wavelength shifts of two FBG strain sensors on opposite sides at the same pile level; ii) assign the theoretical load values to easily evaluated FBG positions at a stable small g-level before reaching the target gravity as a reference for correcting all pile axial forces; iii) correct the pile axial force again at the target gravity based on the deviation between the measured pile axial force in the absence of soil and the theoretical axial force from the pile self-weight. This method effectively reduces the effects of pile bending, soil movement, superglue and FBG self-weight, and other potential sources of error in the data processing.

ACKNOWLEDGEMENTS

The first author recognizes the financial support provided by the China Scholarship Council (CSC) and the University of Nottingham, UK.

REFERENCES

Li, Z. S., Blanc, M., & Thorel, L. (2020). Using FBGS to estimate the horizontal response of a monopile in a geotechnical centrifuge. *International Journal of Physical Modelling in Geotechnics*, 20(3), 164-174. https://doi.org/10.1680/jphmg.19.00022.

Loganathan, N., Poulos, H. G., & Stewart, D. P. (2000). Centrifuge model testing of tunnelling-induced ground and pile deformations. *Geotechnique*, 50(3), 283-294. https://doi.org/10.1680/geot.2000.50.3.283.

Song, G., Xu, J., Heron, C. M., Marshall, A. M., Correia, R., & Korposh, S. (2022). Centrifuge application of fibre Bragg gratings: pile axial loads and wall bending moments. *International Journal of Physical Modelling in Geotechnics*, 22(4), 192-207. https://doi.org/10.1680/jphmg.20.00078.

Proceedings of the XVIII ECSMGE 2024
GEOTECHNICAL ENGINEERING CHALLENGES
TO MEET CURRENT AND EMERGING NEEDS OF SOCIETY
© 2024 the Authors
ISBN 978-1-032-54816-6
DOI 10.1201/9781003431749-519
Open Access: www.taylorfrancis.com, CC BY-NC-ND 4.0 license

ECSMGE 24
XVIII EUROPEAN CONFERENCE ON SOIL MECHANICS AND GEOTECHNICAL ENGINEERING

Finite element simulation of biocement precipitation in soils

Simulation par éléments finis de la précipitation de biociment dans les sols

V.S. Terra*
Instituto Superior Técnico, Lisbon, Portugal

F.M.F. Simões, R. Cardoso
Instituto Superior Técnico and CERIS, Lisbon, Portugal

**victor.terra@tecnico.ulisboa.pt*

ABSTRACT: Microbially induced calcite precipitation is a soil reinforcement technique where bacteria are used to produce calcium carbonate, precipitated after the hydrolysis of urea promoted by the enzyme urease present in the microorganisms. This biocement clogs the soil pores and bonds its grains, increasing the soil strength and stiffness and decreasing its permeability. A two-phase porous medium model is created to analyse the precipitation process, where each phase has several species. The solid phase is composed by soil particles, bacteria and calcite while the fluid phase contains water, urea and other dissolved species that are present in the biochemical reaction. A finite element formulation embodying water seepage, advective diffusion of species and soil deformation is proposed to compute the generation of solid mass (the biocement), and a numerical simulation is presented to analyse the process under a given set of boundary conditions.

RÉSUMÉ: La précipitation de calcite induite par les micro-organismes est une technique de renforcement des sols dans laquelle des bactéries sont utilisées pour produire du carbonate de calcium, précipité après l'hydrolyse de l'urée promue par l'enzyme uréase présente dans les micro-organismes. Ce biociment obstrue les pores du sol et lie ses grains, entraînant une augmentation de la résistance et de la rigidité du sol et une diminution de sa perméabilité. Un modèle d'un milieu poreux à deux phases est créé pour analyser le processus de précipitation, où chaque phase est composée de plusieurs espèces. La phase solide est constituée de particules de sol, de bactéries et de calcite, tandis que la phase fluide contient de l'eau, de l'urée et d'autres espèces dissoutes présentes dans la réaction biochimique. Une formulation d'éléments finis incorporant l'écoulement d'eau, la diffusion advective des espèces et la déformation du sol est proposée pour calculer la génération de masse solide (le biociment), et des simulations numériques sont présentées pour analyser le processus sous certaines conditions aux limites.

Keywords: Chemo-hydro-mechanical coupled model; microbially-induced calcium carbonate precipitation; biocementation.

1 INTRODUCTION

Biocementation, also referred as microbially-induced calcite precipitation (MICP), is a ground improvement technique that involves the use of microorganisms (such as bacteria, and micro-algae) to precipitate calcium carbonate ($CaCO_3$) in the predominant form of calcite. This mineral precipitates subsequent to the urea ($CO(NH_2)_2$) hydrolysis by the urease enzyme present in the microorganisms, according to (1), and in the presence of a calcium source supplied in the feeding solution (2):

$$CO(NH_2)_{2\,(aq.)} + 2H_2O_{(l)} \xrightarrow{\text{urease}} 2NH_{4\,(aq.)}^{+} + CO_{3\,(aq.)}^{2-} \quad (1)$$

$$Ca_{(aq.)}^{2+} + CO_{3\,(aq.)}^{2-} \rightarrow CaCO_{3\,(s)}. \quad (2)$$

This research presents a chemo-hydro-mechanical coupled finite element model developed to predict precipitated calcite content in soils during biocementation and subsequent changes on soil's hydromechanical properties. The need for such type of models is justified by the fact that biocementation processes must be simulated in order to help predicting the improvement achieved with this treatment.

The formulation developed encompasses: (i) hydrogeologic aspects, as in (van Wijngaarden et al., 2011), (Minto et al., 2019) and (Faeli et al., 2023), addressing only diffusion couplings that involve water seepage and water advective diffusion of ionic species, and (ii) geomechanical aspects, as in (Fauriel and Laloui, 2012), that address hydromechanical couplings and where soil deformation is accounted for.

2 FORMULATION

A two-phase porous media is considered (assuming full saturation), where each phase has several species. The solid phase (S) contains soil particles and bacteria, denoted by symbol (s) and calcite (c). In this model, calcite is the only calcium carbonate morphotype that is considered as resulting product of the ureolysis induced calcium carbonate precipitation process. The fluid phase (W) contains water (w), urea (u), and ions calcium (Ca), chloride (Cl), and amonium (a).

The main hypotheses of the model are: (i) mass balance is required for each species; (ii) momentum balance is required for the porous medium as a whole; (iii) species in the fluid phase are endowed with their own velocities, being the velocity of the species in the solid phase equal to the velocity of that phase ($\mathbf{v}_{k\mathrm{S}} = \mathbf{v}_{\mathrm{S}}, k \in$ S); (iv) the urea hydrolysis reaction creates bicarbonate and ammonium ions; and (v) calcium and bicarbonate ions in the fluid phase precipitate forming calcite in the solid phase.

2.1 Mass balance of the species

The conservation mass law of the species can be written as (Loret and Simões, 2017):

$$\frac{\mathrm{d}^k \rho^{kK}}{\mathrm{d}t} + \rho^{kK}\,\mathrm{div}(\mathbf{v}_{kK}) = \hat{\rho}^{kK}, \qquad (3)$$

where the suffix kK is a designation for the species k in phase K; $\mathrm{d}^k/\mathrm{d}t$ is the derivative following the particles of the species k, $\rho^{kK} = M_{kK}/V$ is the apparent density of the species, M_{kK} is the mass of the species, V is the total volume of the porous medium, $\mathbf{v}_{kK}$ is the velocity of the species, and $\hat{\rho}^{kK}$ is the rate of mass of the species per unit volume that is created or lost during the reactions. Eq. (3) can be alternatively written as (Loret and Simões, 2017):

$$\frac{\mathrm{d}v_{kK}}{\mathrm{d}t} + \mathrm{div}(\mathbf{J}_{\mathrm{kK}}) = \frac{\hat{m}^{kK}}{\rho_k}, \qquad (4)$$

where $\mathbf{J}_{kK} = n_{kK}(\mathbf{v}_{kK} - \mathbf{v}_{\mathrm{S}})$ is the flux of the species through the solid skeleton, $v_{kK} = V_{kK}/V_0$ is the volumetric content of the species, $n_{kK} = V_{kK}/V$ is the volume fraction of the species, V_{kK} is the volume of the species, ρ_k is the intrinsic density of the species, V_0 is the initial volume of the porous medium and $\hat{m}^{kK} = \hat{\rho}^{kK}\det\boldsymbol{F}$.

Summing (4) for all the species $k \in$ W and for all the species $k \in$ S, and since $\frac{\mathrm{d}}{\mathrm{d}t}(\sum_{k\in\mathrm{W}} v_{k\mathrm{W}} + \sum_{k\in\mathrm{S}} v_{k\mathrm{S}}) = \mathrm{div}(\mathbf{v}_{\mathrm{S}})$, it is possible to obtain a global equation of mass balance:

$$\mathrm{div}(\mathbf{v}_{\mathrm{S}}) + \mathrm{div}(\mathbf{J}_{\mathrm{W}}) = \sum_{k\in\mathrm{W}} \frac{\hat{m}^{k\mathrm{W}}}{\rho_k} + \sum_{k\in\mathrm{S}} \frac{\hat{m}^{k\mathrm{S}}}{\rho_k}, \qquad (5)$$

where $\mathbf{J}_{\mathrm{W}} = \sum_{k\in\mathrm{W}} \mathbf{J}_{k\mathrm{W}}$ is the flux of water. The rates of mass created or lost during the reactions are defined by:

$$\frac{\hat{m}^{k\mathrm{W}}}{\rho_k} = v_k^{(M)} n_w m_k r, \qquad (6)$$

where $v_k^{(M)}$ is the molar volume of the k species, n_w is the porosity of the medium, m_k is the stoichiometric constant for the k species (according to (1) and (2), m_{u}=-1, m_{a}=2, m_{Ca}=-1, m_{Cl}=-1 and m_{c}=1) and r is the reaction rate for calcite precipitation.

The reaction rate for both urea hydrolysis and calcite precipitation, according to the Michaelis-Merten kinetics, is defined as in (van Wijngaarden et al., 2011):

$$r = v_{máx}\frac{C_{u\mathrm{W}}}{K_m + C_{u\mathrm{W}}}\left(1 - \frac{t}{t_{max}}\right), \qquad (7)$$

where $v_{máx}$ and K_m are constants that dictate, respectively, the maximum velocity of the reaction and the half-saturation of the medium, and t_{max} represents the bacteria lifespan.

The rate of loss of urea mass is equal to the sum of the rate of creation of bicarbonate and ammonium ions $\left(-\hat{m}^{uW} = \hat{m}^{bW} + \hat{m}^{aW}\right)$, and the rate of precipitation of calcite mass is equal to the sum of the rate of loss of calcium and bicarbonate ions ($\hat{m}^{cS} = -\hat{m}^{CaW} - \hat{m}^{bW}$). Although bicarbonate ions are involved in the reactions, bicarbonate concentration is not a part of the model since the mass that is formed during urea hydrolysis immediately precipitates when calcite is formed.

2.2 Global balance of linear momentum

The global equation for the balance of the linear momentum is given by:

$$\mathrm{div}(\boldsymbol{\sigma}) + \rho\mathbf{g} = 0\,, \tag{8}$$

where $\boldsymbol{\sigma} = \boldsymbol{\sigma}' - P_{\mathrm{w}}\mathbf{I}$ is the total stress tensor, $\boldsymbol{\sigma}'$ is the effective stress tensor, P_{w} is the pore-water pressure (the negative sign is introduced as it is a general convention to take tensile components of stress as positive (Zienkiewicz et al., 1999)), $\mathbf{I}$ is the identity matrix, $\mathbf{g}$ is the gravity acceleration and $\rho = \sum_{k\in \mathrm{W,S}} \rho^{kK}$.

2.3 Diffusion of the ionic species

The diffusive flux of the ionic species $\mathbf{J}^{\mathrm{d}}_{k\mathrm{W}} = n_{kW}(\mathbf{v}_{k\mathrm{W}} - \mathbf{v}_{\mathrm{wW}})$ is defined by Fick's law as:

$$\mathbf{J}^{\mathrm{d}}_{k\mathrm{W}} = -v_k^{(M)} n_w \mathbf{D}\cdot\boldsymbol{\nabla} C_{k\mathrm{W}}\,, \tag{9}$$

where $\mathbf{D}$ is the diffusion matrix and $C_{k\mathrm{W}}$ is the concentration of the *k* species in the water phase.

2.4 Water phase flux

Water flow is governed by Darcy's law:

$$\mathbf{J}_{\mathrm{w}} = -\mathbf{k}\cdot(\boldsymbol{\nabla} P_{\mathrm{w}} + \rho^{\mathrm{w}}\mathbf{g})\,, \tag{10}$$

where $\mathbf{k}$ is the permeability matrix, assumed to be constant and isotropic.

3 NUMERICAL MODEL

The finite element formulation is obtained by multiplying the global momentum balance equation (8), the global mass balance equation (5), the aqueous species mass balance equations and the calcium carbonate mass balance equation (4) by the virtual displacement ($\mathbf{u}^*$), water pressure (p^*), concentration (c^*) and mass per unit volume (m^*) fields, and integrating by parts over the element volume (Ω) providing the weak form of the problem as presented on eq. (11)-(14):

$$\int_\Omega \boldsymbol{\nabla}\mathbf{u}^* : \boldsymbol{\sigma}\mathrm{d}V - \int_\Omega \mathbf{u}^*\cdot\rho\mathbf{g}\mathrm{d}V = \int_{\partial\Omega}\mathbf{u}^*\cdot\boldsymbol{\sigma}\cdot\mathbf{n}\mathrm{d}S\,, \tag{11}$$

$$\int_\Omega \left[p^*\mathrm{div}(\boldsymbol{v}_{\mathrm{s}}) - \boldsymbol{\nabla}p^*\cdot\mathbf{J}_w - p^*\left(\sum_{k\in\mathrm{W}}\frac{\widehat{m}^{k\mathrm{W}}}{\rho_k} + \sum_{k\in\mathrm{S}}\frac{\widehat{m}^{k\mathrm{S}}}{\rho_k}\right)\right]\mathrm{d}V = -\int_{\partial\Omega} p^*\,\mathbf{J}_w\cdot\mathbf{n}\mathrm{d}S\,, \tag{12}$$

$$\int_\Omega c^* n_{\mathrm{w}}\frac{\mathrm{d}C_{k\mathrm{W}}}{\mathrm{d}t}v_k^{(M)}\mathrm{d}V + \int_\Omega c^*\left[\left(\sum_{k\in\mathrm{W}}\frac{\widehat{m}^{k\mathrm{W}}}{\rho_k}\right)C_{k\mathrm{W}}v_k^{(M)} - \frac{\widehat{m}^{k\mathrm{W}}}{\rho_k}\right]\mathrm{d}V + \int_\Omega \boldsymbol{\nabla}c^*\cdot\boldsymbol{\alpha}_k\mathrm{d}V + \int_\Omega c^*\mathbf{J}_w\cdot\boldsymbol{\nabla}C_{kW}v_k^{(M)}\mathrm{d}V = -\int_{\partial\Omega} c^*\,\boldsymbol{\alpha}_k\cdot\mathbf{n}\mathrm{d}S, \tag{13}$$

$$\int_\Omega m^*\left(\frac{\mathrm{d}\boldsymbol{m}_{c\mathrm{S}}}{\mathrm{d}t} - \widehat{m}^{c\mathrm{S}}\right)\mathrm{d}V = 0, \tag{14}$$

where $\partial\Omega$ is the element surface, $\boldsymbol{n}$ its unit normal vector and $\boldsymbol{\alpha}_k = -\sum_{l\in\mathrm{W}}\left(\mathbf{I}_{kl} - C_{k\mathrm{W}}v_k^{(M)}\right)\mathbf{J}^{\mathrm{d}}_{l\mathrm{W}}$.

The solid displacements, water pressure, concentration of the ionic fluid species and calcite mass per unit volume are approximated inside the finite element by using shape functions and node values and the final equation to be solved is:

$$\mathbf{F}^{\mathrm{int}}(\mathbf{X},\mathbf{V}) = \mathbf{F}^{\mathrm{ext}}, \tag{15}$$

where $\mathbf{F}^{\mathrm{ext}}$ is the vector of external forces, and $\mathbf{F}^{\mathrm{int}}$ is the vector of internal forces that depends on the global unknown vector $\mathbf{X}$ of nodal primary variables (displacements, water pressure, concentration of ionic species (u, a, Ca and Cl) and mass of calcite per unit of volume):

$$\mathbf{X} = [\mathbf{U}\quad \mathbf{P}_{\mathrm{w}}\quad \mathbf{C}_{\mathrm{uW}}\quad \mathbf{C}_{\mathrm{aW}}\quad \mathbf{C}_{\mathrm{CaW}}\quad \mathbf{C}_{\mathrm{ClW}}\quad \mathbf{m}_{\mathrm{cS}}] \tag{16}$$

and on its velocity $\mathbf{V} = \dot{\mathbf{X}}$.

The formulated semi-discrete equations are integrated in time. A midpoint scheme is employed for the integration, signifying that, at each increment the equations are computed at time $\mathrm{t}_{n+\alpha} = \mathrm{t}_n + \alpha\Delta\mathrm{t}$, with $\alpha = 0.5$ and $\Delta\mathrm{t} = \mathrm{t}_{n-1} - \mathrm{t}_n$.

Within each step, several iterations are performed until the system's convergence is reached, that is, the residual force is zero:

$$\mathbf{R}_{n+\alpha} = \mathbf{F}^{\mathrm{ext}}_{n+\alpha} - \mathbf{F}^{\mathrm{int}}_{n+\alpha} \simeq 0. \tag{17}$$

A linearization of the equations around the solution in the current iteration, through the development of the internal forces into a Taylor series, results in:

$$\mathbf{F}^{\mathrm{ext}}_{n+\alpha} - \mathbf{F}^{\mathrm{int}}_{n+\alpha} \simeq \mathbf{R}^{i+1}_{n+\alpha} - \mathbf{C}^{*\,i+1}_{n+\alpha}(\alpha\Delta\mathbf{V}) = 0, \tag{18}$$

where $\mathbf{C}^* = \mathbf{C} + \alpha\Delta\mathrm{t}\mathbf{K}$, $\mathbf{C} = \mathrm{d}\mathbf{F}^{\mathrm{int}}/\mathrm{d}\mathbf{V}$ and $\mathbf{K} = \mathrm{d}\mathbf{F}^{\mathrm{int}}/\mathrm{d}\mathbf{X}$, which gives the increment of velocity $\Delta\mathbf{V}$ that is used to update $\mathbf{V}$ and $\mathbf{X}$.

4 NUMERICAL SIMULATION

A one-dimensional version of the model was initially developed. The domain of the analysis comprises a soil column with a height of 6 cm and diameter of 2 cm. The adopted soil constants were: void ratio (e) = 0.44;

specific gravity (Gs) = 2.636; bulk density (ρ_d) = 1500 kg/m^3; initial solid mass (m_{s0}) = 0.0283 kg and hydraulic conductivity (k_h) = 1e-5 m/s. Regarding the chemical constants, the values used for the molar volume and molar mass of calcite were 36.9e-6 m^3/mol and 100.1e-3 kg/mol, respectively. The 1-D diffusive constant utilized was $D = \alpha_L \|\mathbf{v}_{wW}\|$, where α_L=0.01 (van Wijngaarden et al., 2011) and $\mathbf{v}_{wW}$ is the water velocity vector. The reaction rate coefficients used were: K_m = 10 mol/m^3 and v_{max} = 0.09 mol/(m^{3}s).

The soil column is discretized with a total of 40 bar (1-D) uniform finite elements with three nodes per element regarding the displacement variable and two nodes per element regarding the other primary variables, comprising a total of 327 global degrees of freedom.

Initially, it is assumed that the soil column is saturated and without presence of urea, calcium, chloride and calcite in the medium. At the bottom of the column the displacement is zero and there is no change in the pore-water pressure, from the beginning until the end of the analysis. At the top of the column, a constant raise in concentration of urea and calcium from 0 until 1 kmol m^{-3}, a raise in the chloride concentration from 0 until 2 kmol m^{-3} and a raise of the water pressure from 0 to 2 kPa, are applied during the first 10 seconds. Subsequently, all the concentrations remain constant until the end of the analysis.

Figure 1 presents the mass of calcite per unit of volume along the column in different instants of time. As it is expected, the formation of calcite can be seen first at the top of the domain (elevation 0. 06 m) due to the presence of urea and calcium ions in this region. As time goes by, as the ionic species are carried out deeper into the soil mass, the precipitation of calcite occurs in the whole domain.

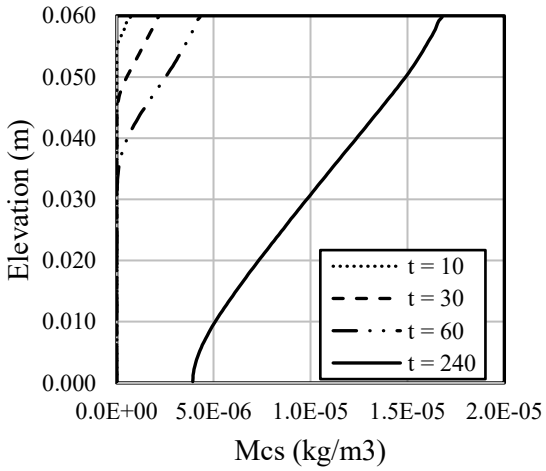

Figure 1. Mass of calcite per volume unit generated through the specimen along time (s).

5 CONCLUSIONS

This study gives an insight on the biocementation process and the main factor that controls the amount of precipitated calcite, which is the reaction rate. Therefore, more experimental research will be needed to improve the definition of the reaction rate equation and of the corresponding materials parameters. No calcite transport is considered in the model. In practice, this is a simplification, since non-attached calcite can be formed and transported along the pores. Further research will also be necessary to improve this aspect of the model, so that it can be used in the future to support the biocementation technique, in particular to predict the amount of biocement precipitated for specific treatment dosages and protocols.

ACKNOWLEDGEMENTS

The authors are grateful for the financial support provided by the Fundação para a Ciência e Tecnologia (FCT). The project presented in this article is supported by the FCT scholarship (Ref.: 2022.10441.BD) and is a part of the Project Calcite (Ref.: PTDC/ECI-EGC/1086/2022).

REFERENCES

Faeli, Z., Montoya, B.M., Gabr, M.A. (2023). Elucidating factors governing MICP biogeochemical processes at macro-scale: A reactive transport model development. *Computers and Geotechnics*, 160. doi: https://doi.org/10.1016/j.compgeo.2023.105514.

Fauriel, S., Laloui, L. (2012). A bio-chemo-hydro-mechanical model for microbially induced calcite precipitation in soils. *Computers and Geotechnics*, 46, pp. 104-120 doi: https://doi.org/10.1016/j.compgeo.2012. 05.017.

Loret, B., Simões, F.M.F. (2017). Biomechanical aspects of soft tissues, CRC Press, Taylor & Francis Group, Boca Raton, USA.

Minto, J.M., Lunn, R.J., El Mountassir, G. (2019). Development of a reactive transport model for field-scale simulation of microbially induced carbonate precipitation. *Water Resources Research*, 55(8), 7229-7245. doi: https://doi.org/10.1029/2019WR025153.

van Wijngaarden, W., Vermolen, F., Meurs, G. v., Vuik, C. (2011). Modelling Biogrout: A New Ground Improvement Method Based on Microbial-Induced Carbonate Precipitation. *Transp. Porous Med.*, pp. 397-420. https://doi.org/10.1007/s11242-010-9691-8.

Zienkiewicz, O.C., Chan, A.H.C., Pastor, M., Schrefler, B.A., Shiomi, T. (1999). Computational Geomechanics, John Wiley & Sons, Chichester, USA.

Proceedings of the XVIII ECSMGE 2024
GEOTECHNICAL ENGINEERING CHALLENGES
TO MEET CURRENT AND EMERGING NEEDS OF SOCIETY
© 2024 the Authors
ISBN 978-1-032-54816-6
DOI 10.1201/9781003431749-520
Open Access: www.taylorfrancis.com, CC BY-NC-ND 4.0 license

ECSMGE 24
XVIII EUROPEAN CONFERENCE ON SOIL MECHANICS AND GEOTECHNICAL ENGINEERING

Design and modelling for groundwater engineering and control

Conception et modélisation pour l'ingénierie et le contrôle des eaux souterraines

S.D. Thomas*, G. French, J. Watson
OGI Groundwater Specialists Ltd, City of Durham, UK

B. Casal
Sondagens Casal Lda, Sintra, Portugal

**stephen.thomas@ogi.co.uk*

ABSTRACT: Groundwater engineering and control is regularly used to lower the water table and pore pressure beneath and surrounding deep excavations for the construction of shafts, tunnels and other deep structures. The construction methodology will greatly influence the type of groundwater control system most appropriate. There is a different groundwater control system required for an open-cut excavation, than that required for an impermeable steel sheet pile, secant or diaphragm wall. Similarly, the type of groundwater control system designed can greatly influence the type of construction required. A professionally designed dewatering system can result in a substantial reduction in cost and carbon emitted. If mathematical modelling is used during the design, the groundwater control system can be optimised. This paper presents recommended stages in the design, modelling and construction of a groundwater control dewatering system. Examples are presented of efficient design and modelling for both abstraction and recharge systems. Presented is a case study where a groundwater control system was designed to lower the water table below a deep detention shaft, an open-face pipe jack operation, and a smaller reception shaft in a mature garden. Modelling resulted in the final design only requiring boreholes around the deep shaft, eliminating unnecessary construction of boreholes and pipework around other structures.

RÉSUMÉ: L'ingénierie et le contrôle des eaux souterraines sont régulièrement utilisés pour abaisser la nappe phréatique et la pression interstitielle sous et autour des excavations profondes pour la construction de puits, de tunnels et d'autres structures profondes. La méthodologie de construction influencera grandement le type de système de contrôle des eaux souterraines le plus approprié. Il existe un système de contrôle des eaux souterraines différent de celui requis pour une palplanche en acier imperméable, un sécant ou un mur moulé. De même, le type de système de contrôle des eaux souterraines conçu peut grandement influencer le type de construction requis. Un système d'assèchement conçu par des professionnels peut entraîner une réduction substantielle des coûts et des émissions de carbone. Si la modélisation mathématique est utilisée lors de la conception, le système de contrôle des eaux souterraines peut être optimisé. Cet article présente les étapes recommandées pour la conception, la modélisation et la construction d'un système d'assèchement des eaux souterraines. Des exemples de conception et de modélisation efficaces pour les systèmes d'abstraction et de recharge sont présentés. Une étude de cas a été présentée dans laquelle un système de contrôle des eaux souterraines a été conçu pour abaisser la nappe phréatique sous un puits de rétention profond, une opération de vérin à tuyau à face ouverte et un puits de réception plus petit dans un jardin mature. La modélisation a abouti à la conception finale ne nécessitant que des trous de forage autour du puits profond, éliminant ainsi la construction inutile de trous de forage et de tuyauteries autour d'autres structures.

Keywords: Groundwater control; construction dewatering; deep excavations; tunnels; shafts.

1 INTRODUCTION

The control of groundwater during construction of deep excavations, shafts and tunnels, is critical to the safety of the project and the individuals working on the project. Groundwater control utilising the abstraction of groundwater (known as construction dewatering), is a complex operation requiring skill and knowledge of the disciplines of geology, hydrogeology, geotechnical and civil engineering. Examples of groundwater control systems implemented on-site across the world have been published previously (Bock and Markussen, 2007; Goodfellow and Thomas, 2018; Margat and van der Gun, 2013; Powrie and Roberts, 1995). The objective of a groundwater control operation is to achieve the aims of reducing the water table (phreatic surface) or the pore water pressure to acceptable levels to reduce the risks from groundwater (Figures 1, 2) Another requirement is to mitigate the impact of dewatering on the surrounding infrastructure and

environment. This impact can involve the settlement of surrounding structures resulting from consolidation and reduction of groundwater resources caused by over-abstraction. Industry guidance is available outlining how to mitigate these risks (Powers, Schmall, 2007; Preene, Roberts, Powrie, 2016).

The safest and most cost-effective approach is to have a well-planned groundwater control operation, that is integral to both the temporary and permanent works design. This is best achieved by employing specialists with expertise and experience in this field.



Figure 1. A site without any groundwater control.

Controlling groundwater during a construction project, however, can have significant costs. It also takes up valuable project time and available space. For this reason, risks from groundwater are often ignored by a project team, with hazards and delays still emerging despite wishing otherwise.



Figure 2. A site with appropriate groundwater control.

A principal contractor who requires the control of groundwater for their deep excavation project, often chooses an expensive deep cut-off wall system instead of a more effective and efficient dewatering system, principally because of their familiarity. Construction dewatering is often seen as a complex art, in which the outcome, particularly the final cost, is uncertain. To remedy this uncertainty, the authors recommend the presentation of the dewatering process in colourful clear sequence drawings. This provides clarity and confidence to the contractor, who, as a result, is more likely to choose dewatering as a preferred option.

This paper does not aim to present to the reader all the expertise in this field, but instead serves to present understandable guidance in the form of key stages required to produce a safe and robust groundwater control system for a major construction project that requires excavation below groundwater levels.

2 GROUNDWATER CONTROL GUIDANCE

To provide a simple-to-understand guidance for the development of a safe and robust groundwater control system when constructing below the water table, or potentiometric surface, the following presents key stages in the process. Some of the stages can be undertaken by the principal contractor, some by the sub-contractor, and some by the consultant.

Whilst stages can be the responsibility of different parties, each stage must be managed by experienced and capable persons. All stages are to be integrated so that there are no gaps and shortfalls in the overall operation.

The following provides guidance that the authors have developed over decades of experience. The guidance is not to provide a strict specification, nor a construction standard, but is offered here as support to other guidance available within the industry.

2.1 Initial review of construction operation

A conceptual model of the ground and groundwater conditions is first required. An outline of the building structure can then be overlaid on the conceptual model to provide clarity of the risks during and after construction. It is then required to establish hydraulic boundary conditions to enable analysis and modelling.

Based on this information, an experienced and skilled groundwater engineer can then identify the critical risks to the construction process and provide an outline of groundwater control design. An example of a first-stage conceptual model is depicted in Figure 3.

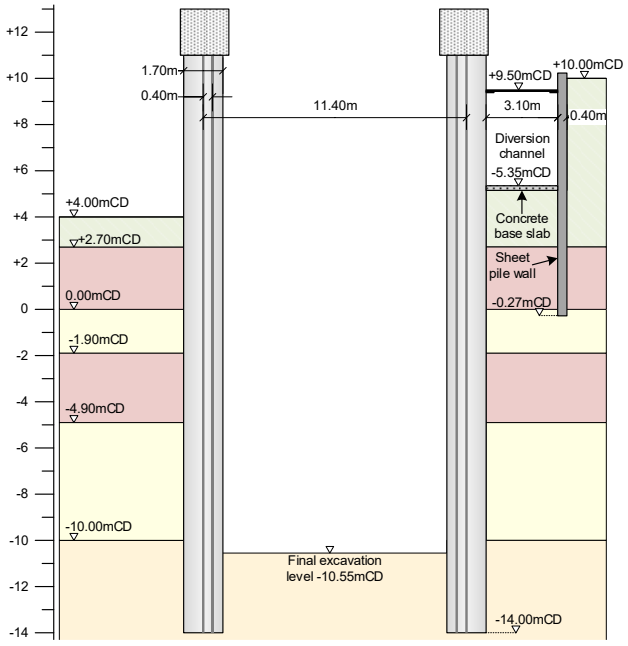

Figure 3. A conceptual model of the ground and structure.

2.2 Identification of critical success factors

With a first-stage conceptual model prepared, an initial dewatering design can be produced by an experienced designer. However, it is essential at this stage to further identify critical parameters that need to be quantified to enable a detailed design of a robust groundwater control system. Such parameters include: permeability, transmissivity, anisotropy, elevation of aquifer base, isolated artesian layers, and critical boundary conditions. Other factors can include (i) the ground compressibility if there are sensitive structures nearby, (ii) water supply wells or other water bodies that could be affected by the abstraction of groundwater, and (iii) factors that can affect the operation such as boulders, access, etc.

2.3 Preliminary groundwater control strategy

When developing a groundwater control design, it is good practice to produce a preliminary groundwater control strategy that includes an outline design based on a range of hydrogeological conditions established from the available groundwater information (Figure 4).

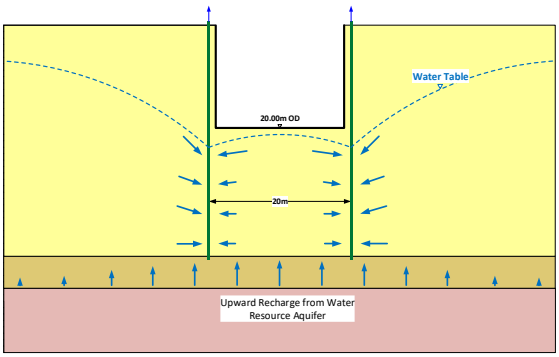

Figure 4. Preliminary groundwater control strategy.

In the authors' experience, information available from a standard site investigation is normally most inadequate as a basis for a final groundwater control design, especially in the case of the critical parameter of permeability. As a consequence, this preliminary strategy must emphasise that the design is based on a range of ground conditions, and that it is essential to undertake further specific pumping tests, together with additional groundwater-specific site investigation.

2.4 Design, implementation, analysis of project specific pumping test operation

Critical to the design of a groundwater control system, a pumping test and analysis is required, especially to establish the expected abstraction rate when applying for a permit from the UK environment agencies. Such tests normally require a minimum of constructing a groundwater pumping well, together with a series of piezometers to observe drawdown during pumping. It is good practice to undertake a series of tests, rotating the pumping from different wells and observation piezometers. Figure 5 provides an example plot of groundwater drawdown versus time, matched by a mathematical model, from which the required aquifer parameters can be back-calculated.

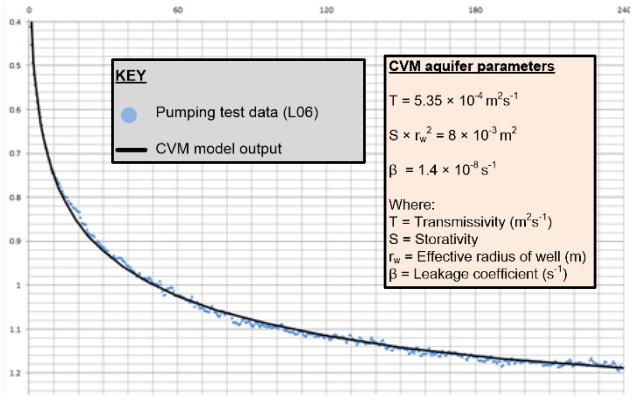

Figure 5. Pump test analysis to establish aquifer properties, where the x-axis is time, and the y-axis is drawdown.

With the site-based parameters calculated from a mathematical model, the same model can be used to calculate the range in expected abstraction rates based on the range of values obtained from the tests.

2.5 Development of mitigation strategies

Mitigation strategies are often required to mitigate the impacts that can result from groundwater abstraction. Strategies can include the deepening of cut-off walls to reduce groundwater inflow, or using recharge wells to provide a hydraulic barrier to reduce the radius of influence from the dewatering operation. Figure 6 depicts the proposed dewatering from boreholes inside a secant pile wall, with the abstracted groundwater pumped back to the ground to protect water resources.

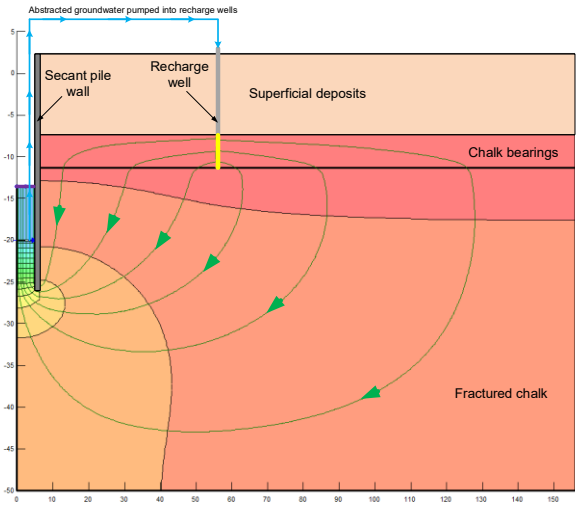

Figure 6. Groundwater pumping and recharge.

2.6 Detailed design and value engineering

Following the analysis of the pumping test results and any additional ground investigations, detailed design and value engineering are then undertaken. All parties then work together to value engineer the system in a collaborative manner. This value engineering takes into account constraints of working space, programme, geology, hydrogeology, and mitigation strategies. All play a part in the final detailed design (Figures 7 and 8).

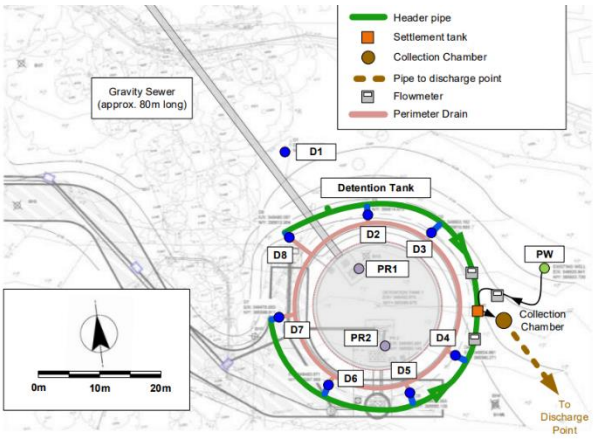

Figure 7. Location plan for dewatering boreholes.

After value engineering, the preliminary strategy document is updated to a strategy for construction. This document contains the detailed specifications for drilling and pumping, but always retains the flexibility to revise designs in light of the actual geology and hydrogeology encountered on site.

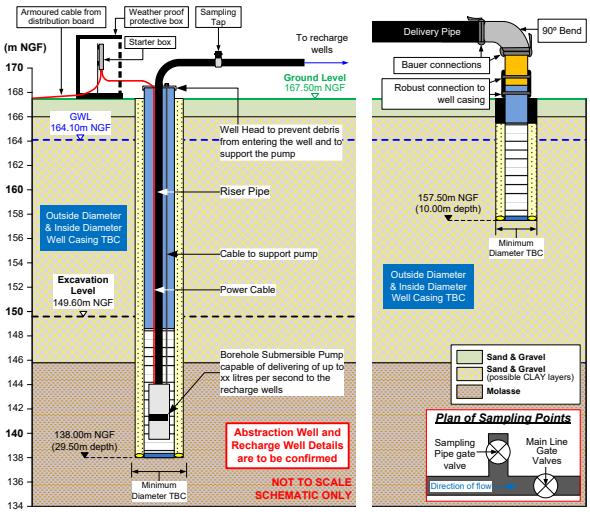

Figure 8. Drilling, pumping and recharge specifications.

2.7 Groundwater control system construction

Construction of a groundwater control system on site is required by an experienced, accomplished and specialist contractor (Figures 9 and 10). Drilling dewatering boreholes requires different skills to water supply boreholes, requiring experience in working on busy construction sites in close proximity to other trades.



Figure 9. Drilling of deep dewatering borehole.



Figure 10. Series of pressurised recharge boreholes.

2.8 Mathematical modelling of groundwater

Mathematical modelling uses computer software to solve the equations governing groundwater flow in a saturated or partially saturated porous material. The outputs are hydraulic heads, pore pressures and Darcy velocity. Modelling is highly valuable in predicting the groundwater behaviour of a dewatering operation.

Mathematical modelling of groundwater through soil or rock can be a major undertaking, with time and cost resources needed. It is recommended here to use a model only of sufficient complexity to solve a site situation. It is not recommended to use, for example, a fully three-dimensional model to apply to a simple pumping test operation from a single borehole.

For most applications, a multi-well analytical model is sufficient in a homogeneous aquifer, with most more complex transient and inhomogeneous aquifers being solved using a two-dimensional finite element model.

Figure 11 depicts the application of the finite element model SEEP/W to a shaft/tunnel project near Liverpool. Modelling was undertaken in advance of

the dewatering operation and during the pumping test. This enabled the ground properties, and the model boundary conditions to be established. Modelling was also undertaken in "real-time" during the dewatering operation to refine the dewatering design. The benefits of this procedure included a prediction of a wide drawdown, which determined that after some time, no groundwater control was then required in the reception shaft in a mature garden, and so mitigating operations.

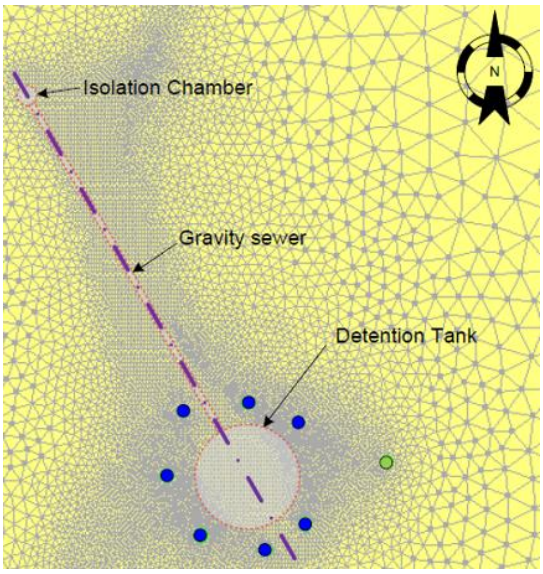

Figure 11. Finite Element modelling using Seep/W.

Another benefit to the project was the cost savings by predicting when additional pumps would be required. Only half the number of pumps was required for the dewatering operation, with pumping from boreholes only required for the deep shaft (Figure 12).

Using the groundwater model to enable the calculation of transmissivity, accurate predictions of the final groundwater abstraction could be made. This assisted with the application of licences and permits and enabled early appropriate pump selection.

2.9 Multi-well analytical modelling

To model a multi-borehole dewatering operation under steady-state conditions, OGI has developed efficient and effective models which use analytical solutions. These analytical models are extremely beneficial as they are simple to set up and fast to provide results.

Figure 13 depicts the conceptual model for an underground metro station, platform and tunnels, with Figure 14 depicting the simulated drawdown using a 2-D analytical groundwater model in plan.

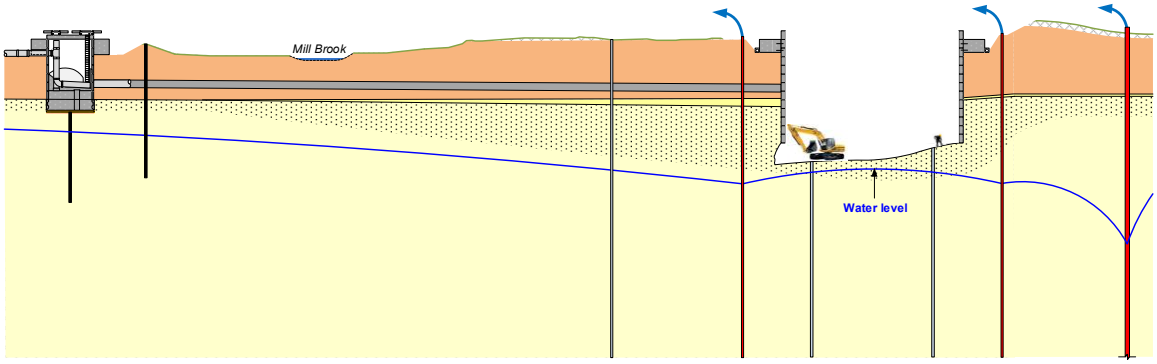

Figure 12. Simulation of dewatering from boreholes around a deep shaft, with drawdown reaching a smaller shaft.

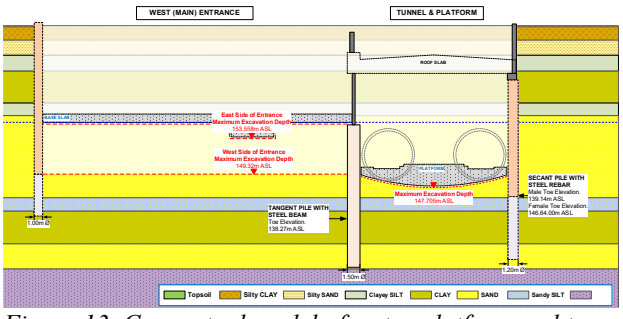

Figure 13. Conceptual model of metro platform and tunnel.

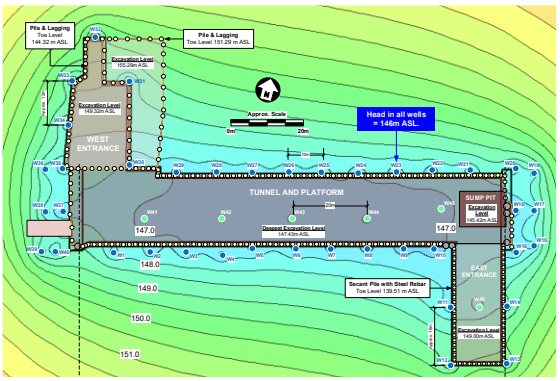

Figure 14. Simulated head using analytic modelling.

This analytical modelling enabled the simulation of abstraction wells and passive pressure relief wells in advance to the start of the dewatering operation. This capability greatly contributed to an efficient and effective groundwater control operation. At the start of pumping from only a few boreholes, drawdown was observed from non-pumping wells, after which aquifer properties were back-calculated using the analytical model to refine the design in real-time.

This enabled the additional pumping boreholes to be accurately positioned to provide the maximum impact. This was particularly valuable as the operation took place during the COVID-19 pandemic, where drilling crews were scarce, and optimisation was critical. Figure 15 demonstrates a successful outcome in challenging ground conditions.



Figure 15. Drawdown achieved beneath the metro station.

3 CONCLUSIONS

The principal stages in producing a groundwater control system are paramount within the Groundwater Engineering Industry. This paper outlines these stages and how their presence enhances a groundwater control system, and therefore, a project's success.

Conceptual models provide a visualisation of the subsurface and the proposed structures, which contribute to a preliminary groundwater control strategy. While useful, these strategies will always signify a requirement for further investigations to supplement the final design produced for a project.

Vital to these investigations are pumping tests and their subsequent analysis, which is inclusive of sensible mathematical modelling. The authors advocate that sensible modelling, encompassing only the required complexity, is needed to solve in advance the groundwater flow in the aquifer. The calculations using the aquifer properties feed into implementing mitigation strategies into the system design.

When these stages have been completed, they will augment the production of a detailed design that can be utilised to specify a robust groundwater control system to lower the water table to an acceptable level at a site, and so reduce the water risks accordingly.

REFERENCES

Bock, M., & Markussen, L. M. (2007). Dewatering control in central Copenhagen. In Proceedings 14th Conference on Soil Mechanics and Geotechnical Engineering 2 (bls. 715-720). Amsterdam: Geotechnical Engineering in Urban Environments.

Cashman, P. M., & Preene, M. (2013). Groundwater Lowering in Construction: A Practical Guide to Dewatering 2nd edition. CRC Press. Boca Ranton. https://doi.org/10.4324/9780203476321.

Goodfellow, T. L. & Thomas, S. D. (2018). Groundwater resource protection from construction groundwater control in Lincolnshire chalk. Engineering in Chalk: Proceedings of the Chalk 2018 Conference (bls. 669-674). London: ICE Publishing. https://doi.org/10.1680/eiccf.64072.669.

Margat, J., & van der Gun, J. (2013). Groundwater around the world. Lisse, The Netherlands: Balkema.

Powers, J., A, C., & Schmall, P. (2007). Construction dewatering and groundwater control: new methods and applications. John Wiley & Sons.

Powrie, W., & Roberts, T. O. (1995). Case history of a dewatering and recharge system in chalk. Geotechnique 45(4), 599-609. https://doi.org/10.1680/geot.1995.45.4.599.

Preene, M; Roberts, T; Powrie, W. (2016). Groundwater Control: Design and Practice, 2nd Edition. Construction Industry Research and Information Association. London: CIRIA Report C750.

Thomas S., Watson J., Goodfellow T. (2020). The Role of Temporary Groundwater Control Recharge Systems in Water Conservation. Abrunhosa M. et al. GEOETH&GWM'20. Springer.

Watson J. and Thomas S. (2020) Geoethics in the Design and Implementation of Temporary Groundwater Control Systems. Abrunhosa M. et al. GEOETH&GWM'20. Springer.

Proceedings of the XVIII ECSMGE 2024
GEOTECHNICAL ENGINEERING CHALLENGES
TO MEET CURRENT AND EMERGING NEEDS OF SOCIETY
© 2024 the Authors
ISBN 978-1-032-54816-6
DOI 10.1201/9781003431749-521
Open Access: www.taylorfrancis.com, CC BY-NC-ND 4.0 license

ECSMGE 24
XVIII EUROPEAN CONFERENCE ON SOIL MECHANICS AND GEOTECHNICAL ENGINEERING

Square shallow foundation on four rigid inclusions subjected to uncentered vertical load: Centrifuge modelling

Semelle carrée sur quatre Inclusions Rigides sous chargement vertical excentré: Modèle réduit centrifugé

L. Thorel*, M. Blanc, A. Neel, A. Jagu, Ph. Audrain, P. Gaudicheau, S. Lerat
University Gustave Eiffel, GERS-CG Lab., Nantes, France

**luc.thorel@univ-eiffel.fr*

ABSTRACT: The load eccentricity effect of a square foundation resting on 4 Rigid Inclusions is investigated with small scale centrifuged models. 3 tests have been performed on instrumented models with the robot of Uni Eiffel Centrifuge laboratory. The kinematics of the foundation and the load transfer towards the Rigid Inclusions are presented.

RÉSUMÉ: L'effet d'un chargement excentré sur une fondation carrée reposant sur 4 Inclusions Rigides est étudié sur des modèles réduits centrifugés. 3 essais ont été réalisés sur des modèles instrumentés en utilisant le robot téléopérateur du laboratoire Centrifugeuses Géotechniques de l'Uni Eiffel. La cinématique de la fondation et le transfert des charges vers les Inclusions Rigides sont présentés.

Keywords: Rigid inclusions; centrifuge; kinematics; load transfer; eccentricity.

1 INTRODUCTION

In the framework of the French National Project ASIRI+ devoted to the reinforcement of soft soils by rigid inclusions (https://asiriplus.fr), the behaviour of a square foundation on 4 Rigid Inclusions (RI) is studied with centrifuged models. This "composite foundation" includes, from top to bottom in Figure 1: 1) a shallow foundation; 2) a granular Load Transfer Platform (LTP); 3) deep foundations (RIs) installed in a soft clay; 4) a sand layer where the RI tips penetrate. The forces transmitted to the RIs as well as the kinematics of the shallow foundation are presented, for three different eccentricities.

2 EXPERIMENTAL SETUP

The set of experiments is inspired from in field tests' geometry (Briançon *et al.*, 2000). The scaling laws (*e.g.* Garnier *et al.*, 2007) applied for designing the centrifuge tests leaded to a reduced scale of 1/16.9, corresponding to a g-level of N=16.9. The results are presented at model scale.

The reconstituted soil mass includes, from the bottom to the top: 1) a filtration geotextile to avoid sandy particles to move towards the drainage circuit; 2) a dense saturated Hostun HN31 sand; 3) the soft soil, prepared in 3 layers with a loading programme adapted to a slightly over consolidated clay, is made of a mixture of kaolin clay and Fontainebleau sand NE34 (Baudouin, 2010); 4) the LTP, made of dense well-graded Hostun sand (Baudouin *et al.*, 2008). The rigid inclusions are jacked at 1mm/min, in the lab (under earth gravity), guided accurately together 4 by 4.

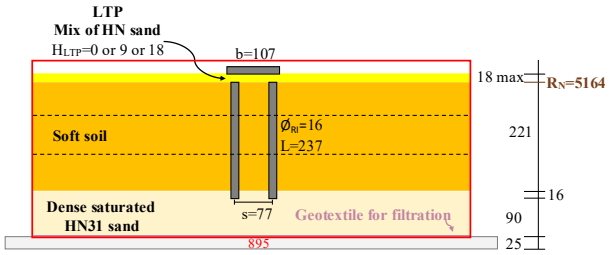

Figure 1. Scheme in elevation of the composite foundation in the circular container tested in the centrifuge (in mm).

The model foundation is made of aluminium (Figure 2), as well as the instrumented RIs (Figure 3). The foundation includes an upper part, with a T-shape, used to be hanged and downward loaded, inducing only a main rotation around the x-axis.

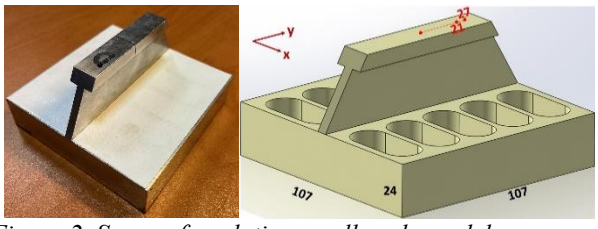

Figure 2. Square foundation small scale model.

A (white) scotch tape is stuck on the top surface.

The RIs are instrumented with a force sensor intimately linked to the top surface cap (Figure 3).

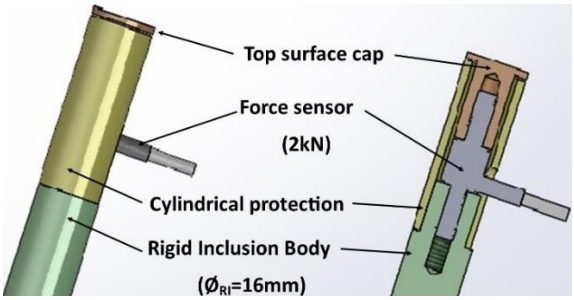

Figure 3. Drawings of Instrumented Rigid Inclusion.

To optimise the clay consolidation time in centrifuge, 4 tests are performed during the same centrifuge flight, thanks to the Uni Eiffel Robot (Gaudicheau *et al.*, 2014). A special tool has been developed for the foundation carriage and loading (Figure 4). The 4 foundations are stored on a board fixed on the container, and are installed on the expected location (where the RIs have been pre-installed) before being loaded (Figure 5).

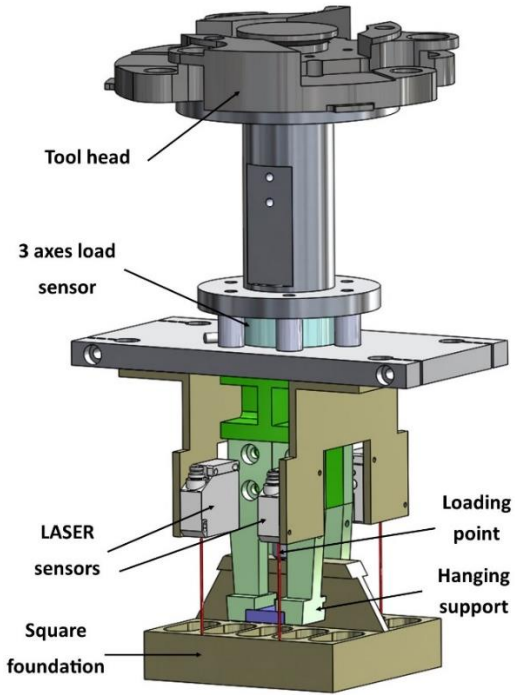

Figure 4. Multi-use tool for the centrifuge robot.

3 EXPERIMENTAL PROGRAMME

The centrifuge tests are performed in the same circular container, with an LTP height of 18mm (0.3m in prototype scale), and with 3 eccentricities e reported to the spacing s: e/s = 0, 0.27 & 0.35 (or to the foundation width b: e/b = 0, 0.19 & 0.25).

After a consolidation phase during about 2 hours in flight, the series of foundation loading start. The vertical loading of the foundations is performed in displacement control conditions at a velocity of 1mm/min. If the eccentricity is positive, the vertical loading generates a negative rotation around the x-axis (θ_x). The data acquisition is performed at a frequency of 10Hz, thanks to HBK Quantum DAS.

The laser sensors installed on the multi-use tool are pointed towards the foundation to access to its solid rotation. The distance between the laser rays is 100mm in the x direction and 40mm in the y direction. This induces a better accuracy of the rotation around y-axis (θ_y) than x-axis (θ_x).

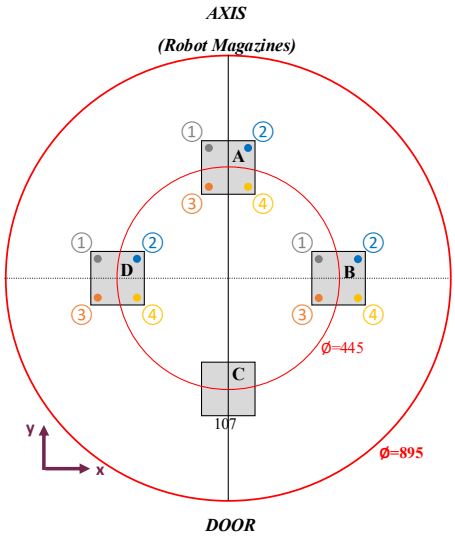

Figure 5. Top view implementation in the container (mm).

The load tests (Table 1) are devoted to eccentric loading, for investigation the load repartition and the kinematics of the square foundation.

Table 1. Load test configuration.

Test	e/s	Comment
A	0.35	
B	0.27	
C	NA	H loading, not included
D	0	

4 DISCUSSION

The results of loading (Figure 6) show the behaviour up to a settlement of 1/10th of the foundation width (107mm), at model scale. The settlement is calculated at the centre of the foundation.

For the vertical centred load, it can be seen that the loads are almost the same on the RIs until the symmetry is lost, generating a slight rotation towards RI 2 and 4.

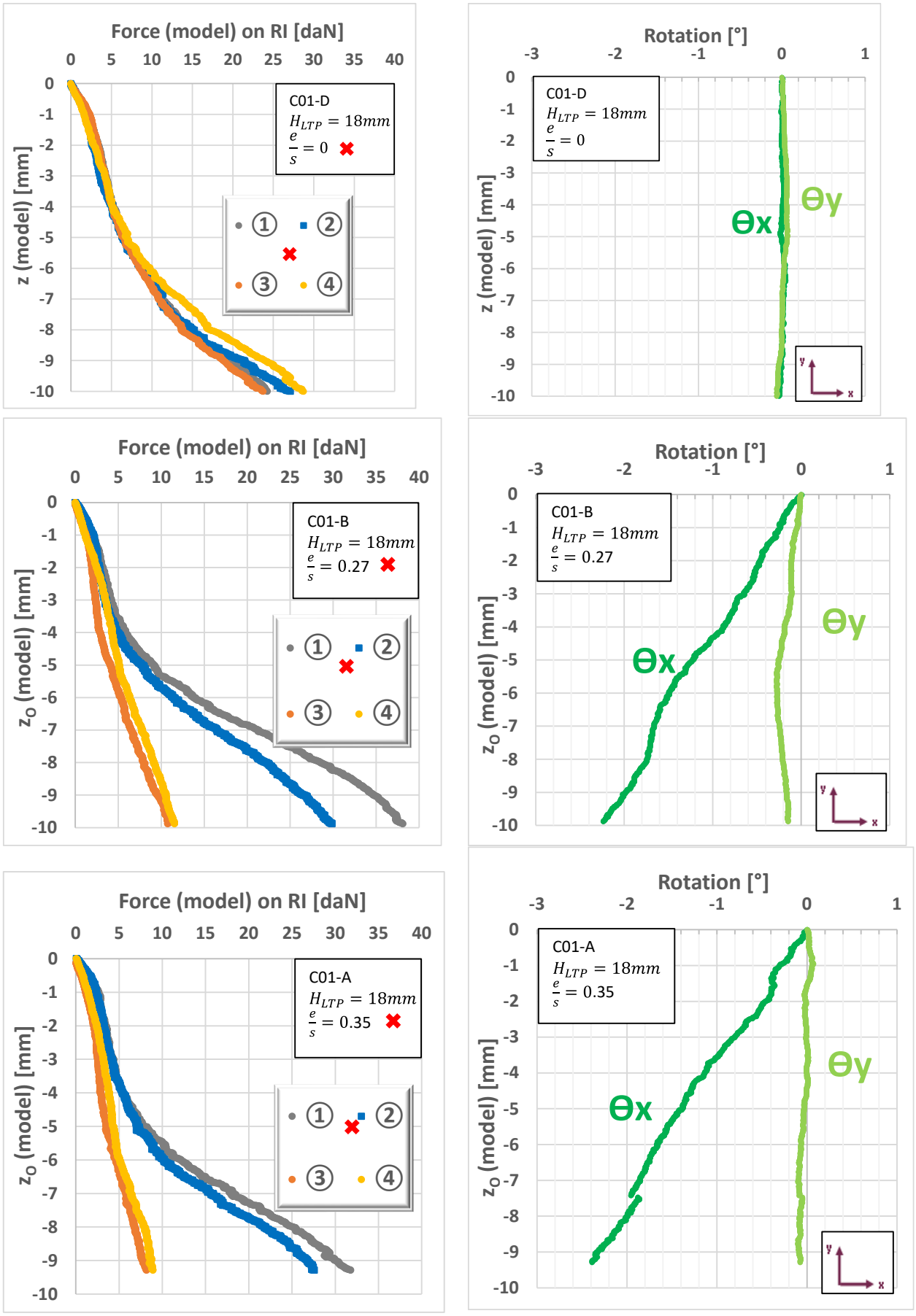

Figure 6. Forces transmitted to the Rigid inclusions(left) and rotations (right) versus settlement for 3 eccentricities: 0 (top), 0.27 (middle), 0.35 (bottom).

When an eccentric load is applied, the rotation of the foundation is immediately visible. The load transfer towards RIs 1 and 2 is emphasised after a settlement of few millimeters, showing a complex behaviour that includes first a mechanism inside the LTP and then the mobilisation of the RIs in an asymetrical way.

It can be observed that, even if a careful process has been followed in the preparation of the soil model, the RIs installation and the location of the loading points, very small rotations are observed on the y axis. This shows that there is small uncertainties relative to the loss of symetry.

The total load variation applied on the foundation is in the same proportion than to the sum of the load variation on RIs (Figure 7), whatever the eccentricity is. Two distinct mechanisms of load transfer may be identified. The initial slope for small settlements (and loadings) is about 0.38, when the final slope is close to 0.74, showing a progressive mobilisation of the RIs. For a similar settlement of the foundation center (*e.g.* the end of the curves correspond to the Service Limit State, 10% of the foundation width), loads decrease with the increase of the eccentricity, both for the total load and the transfered loads to the RI.

It could be said that to reach the same settlement at the centre of the foundation: 1) stronger force is required for centred load than for eccentred; 2) similar load proportion is transfered to the soft soil. In any case, the load transmitted to the RIs is smaller than the load applied to the foundation, but the ratio does not seem to be affected by the eccentricity.

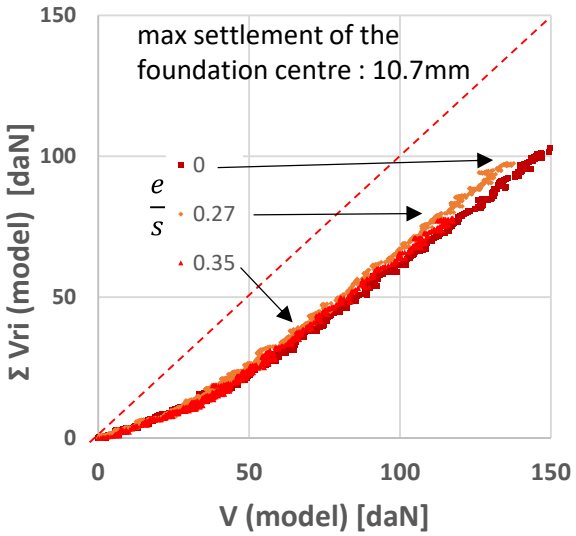

Figure 7. Total force variation applied on the RIs vs the total force variation applied on the foundation.

5 CONCLUSIONS

A series of centrifuge tests has been developed to investigate the eccentricity effect on complex foundation system made of a shallow square foundation resting on four rigid inclusions.

The first results show that for a settlement of 10% of the width of the foundation, the rotation reach a value of about 2 degrees, and that the rear RIs are overloaded up to 3 times the front RIs.

During the loading of each foundation, two mechanisms seem to appear: 1) load transfer mainly in the LTP; 2) a load transfer more active towards the RIs.

Additional investigation is under process for other test configuration such as the LTP height.

ACKNOWLEDGEMENTS

The authors are grateful for the financial support provided by the French National Project ASIRI+.

REFERENCES

Briançon, L., Bohn, C., Szymkiewicz, F. (2020), Semelles sur inclusions rigides – Plan d'auscultation. Rapport PN ASIRI+, tâche 4, T4-04, ASI+/R/001, 15p.

Baudouin, G., 2010. Modélisation Physique en centrifugeuse des sols renforcés par Inclusions rigides, Ph.D. Univ. Nantes. https://www.theses.fr/2010NANT2046.

Baudouin G., Rosquoët F., Canou J., Dupla J.C., Thorel L., Rault G., Andria-Ntoanina I. (2008). Caractérisation mécanique d'un mélange de sables d'Hostun. Journées Nationales de Géotechnique et de Géologie de l'Ingénieur, Nantes 18-19 juin JNGG08. ISBN 9782720825204. pp 491-498. https://www.geotech-fr.org/download.php?type=pdf&doc=jngg-2008.

Garnier, J., Gaudin, C., Springman, S.M., Culligan, P.J., Goodings, D., Konig, D., Kutter, B., Phillips, R., Randolph, M.F., Thorel, L. (2007). Catalogue of scaling laws and similitude questions in geotechnical centrifuge modelling. *Int. J. Phys. Mod. Geotechnics* 7(3), 1-24. doi.org/10.1680/ijpmg.2007.070301.

Gaudicheau, P., Thorel, L., Néel, A., Audrain, Ph., Lozada, C., Monroy, J. (2014). Improvement of the IFSTTAR robot control system, 8th ICPMG Int. Conf. Phys. Mod. Geotech., Perth 14-17 jan., pp.221-226.

Proceedings of the XVIII ECSMGE 2024
GEOTECHNICAL ENGINEERING CHALLENGES
TO MEET CURRENT AND EMERGING NEEDS OF SOCIETY
© 2024 the Authors
ISBN 978-1-032-54816-6
DOI 10.1201/9781003431749-522
Open Access: www.taylorfrancis.com, CC BY-NC-ND 4.0 license

ECSMGE 24
XVIII EUROPEAN CONFERENCE ON SOIL MECHANICS AND GEOTECHNICAL ENGINEERING

Mechanical properties of a gravel soil injected with a polyurethane binder

Propriétés mécaniques des sols graveleux injectés avec un liant polyuréthane

G. Tintelnot
Gtcs Chemical Solutions GmbH, Hamburg, Germany

G. Spagnoli*
Sweco, Essen, Germany

**giovanni.spagnoli@sweco-gmbh.de*

ABSTRACT: Chemical grouts refer to the use of polyurethane foams and gels, acrylates and epoxies. The usage of polyurethane (PU) is expanding for joint sealing in concrete construction work as well as for controlling seepage in cracked rock and concrete. As part of an experimental investigation, tests were carried out in soils with a constant granulometry (with grain diameter 1-4mm) grouted with a polyurethane binder. A hydraulic permeability of $k = 5.10^{-3}$m/s was specified as the target variable for the soils to be examined. Grouting tests were performed at a maximum pressure of 150kPa. After the grouting of the soils samples, three unconfined compressive strength and triaxial tests were performed in soils with relative densities of 1. Different binder quantities were injected into the soil. Results show that unconfined compressive strength values was about 6MPa. Triaxial tests performed on seven samples at relative densities between 0.89 and 0.94 showed peak deviatoric stress between 5.2 and 6.9MPa. PU binder is therefore suitable for permeation grouting in high permeable soils.

RÉSUMÉ: Les coulis chimiques font référence à l'utilisation de mousses et de gels de polyuréthane, d'acrylates et d'époxy. L'utilisation du polyuréthane (PU) se développe pour l'étanchéité des joints dans les travaux de construction en béton ainsi que pour contrôler les infiltrations dans la roche et le béton fissurés. Dans le cadre d'une investigation expérimentale, des essais ont été réalisés dans des sols à granulométrie constante (diamètre des grains 1-4 mm) injectés avec un liant polyuréthane. Une perméabilité hydraulique de $k = 5.10^{-3}$ m/s a été spécifiée comme variable cible pour les sols à examiner. Les tests d'injection ont été effectués à une pression maximale de 150 kPa. Après l'injection des échantillons de sols, trois essais de résistance à la compression libre et triaxiaux ont été réalisés dans des sols de densité relative 1. Différentes quantités de liant ont été injectées dans le sol. Les résultats montrent que les valeurs de résistance à la compression non confinée étaient d'environ 6 MPa. Les tests triaxiaux effectués sur sept échantillons à des densités relatives comprises entre 0.89 et 0.94 ont montré une contrainte déviatorique maximale comprise entre 5.2 et 6.9 MPa. Le liant PU convient donc aux injections de perméation dans des sols très perméables.

Keywords: Grouting; polyurethane; gravel; mechanical properties.

1 INTRODUCTION

The injection of a grout into a highly porous, granular soil to saturate and bind the particles together is known as permeation grouting. In general, the procedure is utilized to build a structural, load-bearing structure, a stabilized soil zone for tunnelling, and water cut-off barriers.

Chemical grouting is a technique where materials are fully dissolved in a fluid, i.e. called also solutions (Nicholson, 2015).

Chemical grouting is a technique used in geotechnical engineering to stabilize and strengthen soil or rock formations. It involves injecting chemical grout into the ground to fill voids, consolidate loose soil, or create impermeable barriers. Chemical grouts typically consist of a liquid or gel-like material that solidifies after injection.

Chemical grouting has various applications, including foundation repair, soil stabilization, tunnelling, and groundwater control. It is commonly used to address issues such as sinkholes, water infiltration, and unstable slopes. The process is relatively quick and can be performed in various soil and rock conditions (Karol, 2003). Among the different binder types used in chemical grouting (e.g. Fraccica et al., 2022), grouting with polyurethane (PU) resins is an efficient means of improving the mechanical and sealing qualities of soils and rocks (Bodi et al., 2012).

PU grouting materials are classified into three major classes based on their chemistry (Bodi et al., 2012):

- two-component (PU) organic resins;
- one-component organic resins;
- two-component organic-mineral resins (OMR).

In this paper a two-component PU binder was injected in a gravel sand (1-4mm grain) under low pressure (max. 150kPa injection pressure). Unconfined compressive strength and triaxial test values are presented. Similar tests were done in sand and presented by Spagnoli et al. (2023).

2 MATERIAL AND METHODS

The investigations were carried out with the injection of a two-component, fast-reacting, slightly flexible, silicate-based injection foam equipped with flame retardants.

2.1 Binder

The A component is based on a water glass solution (silicic acid) which has a density of 1.3 g/cm^3 and a dynamic viscosity of 30 mPas at a temperature of 23°C. The B component is based on an isocyanate mixture, which is characterized by a density of 1.21 g/cm^3 and a dynamic viscosity of 120 mPas at a temperature of 23°C.

The two components are mixed together for the reaction in a volume ratio of 1:1. At room temperature, there is a reaction between the two components about 30 seconds after mixing. A slowly hardening foam is formed. The foam volume is significantly larger than that of the two individual components (formation of air bubbles).

2.2 Soil

A hydraulic permeability of k = 5.10^{-3}m/s was specified as the target value for the soils to be examined. Table 1 shows the properties of the soil used in the experiment.

2.3 Grouting set up

The test stand consists of a 50cm long commercial PVC pipe (DN 110), which is sealed airtight with an associated socket plug on the bottom (see Figure 1). To fix it, the pipe was screwed to a wooden structure using pipe clamps.

Table 1. Properties of the soil used in the test

Property	Value
Grain dimension	1-4mm
High dry density	1.877g/cm^3
Low dry density	1.608g/cm^3
Grain specific gravity	2.76
Low k-value	$6.03 \cdot 10^{-3}$m/s
High k-value	$1.81 \cdot 10^{-2}$m/s
D_{60}	2.8mm
D_{30}	2.0mm
D_{10}	1.7mm

Small holes were drilled through the wall at the bottom of the tube to avoid uplift as a result of the injection. The air displaced by the foam could escape through these holes. In addition, a grid was fixed over the built-in soil on the pipe to produce test specimens with a constant volume. This prevented heaves due to volume expansion of the foam.

A cartridge gun operated with compressed air was used for the injection. The two individual components of the injection material were mixed and homogenized using commercially available static mixers.

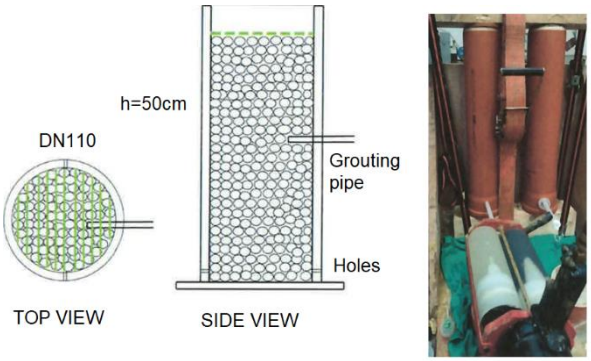

Figure 1. Set up for the grouting tests.

To investigate the vertical expansion behaviour of PU, 300ml, 400ml and 600ml of the mixed injection material were injected into soils, which had previously been installed in dense storage in the pipe, with an injection pressure of approx. 1.5 bar. The installation densities of the soils used were determined before the injection and ranged between 1.85 and 1.88 g/cm^3.

3 RESULTS AND DISCUSSION

Figure 2 shows the results for the grouted material injected into the 1-4mm gravel soil for 300, 400 and 600ml. The red arrow indicated the point of injection.

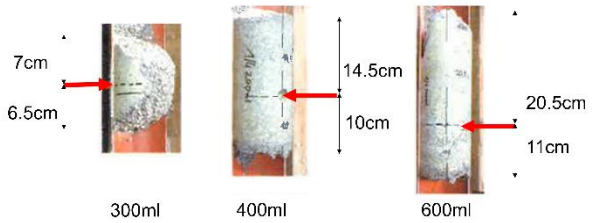

Figure 2. Results from the grouting test for 300ml, 400ml and 600ml injection material (from left to right).

Approximately 30 seconds after the start of the injection, the injected material hardens and foams at the lower end of the injection front. It forms the basis of the injected soil body.

Mechanical tests on the grouted samples were performed on 7 days curing age.

Three uniaxial compression tests according to DIN EN ISO 17892-7 (DIN, 2018a) were carried out on specimens (height-to-diameter ratio of 2) made from soil-foam mixtures. The installed soil dry density was 1.88 g/cm^3 (relative density Dr = 1.0).

The specimens were subjected to uniaxial loading and shearing at a constant rate of 0.2% of the initial height of the specimens per minute in accordance with DIN EN ISO 17892-7.

The determined stress-strain relationships of the three uniaxial compression tests on the soil-foam mixtures carried out under the same boundary conditions are shown in Figure 3. In addition, the test results are listed in Table 2.

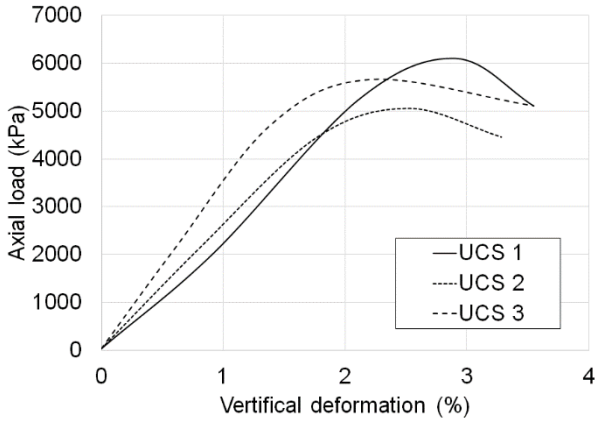

Figure 3. Results of UCS tests.

The modulus of elasticity secant E50 was determined in the stress range between 0kPa and 50% of σ_1 (i.e. the axial load).

Table 2. Data of UCS tests

Test	UCS (kPa)	E50 (MPa)
UCS 1	5100	269
UCS 2	5700	372
UCS 3	6100	239

The mean UCS and E50 values are respectively 5.6MPa and 293MPa.

Furthermore, triaxial tests were carried out on dry test specimens according to DIN EN ISO 17892-9 (DIN, 2018b). The specimens prepared with dry density between 1.84 and 1.86 g/cm^3. The cylinder samples (height 20cm, diameter 10cm) were sheared at a constant rate of 0.2% of the specimen height per minute (approx. 0.4mm/min).

A total of seven specimens were tested under triaxial conditions and sheared at different lateral pressures σ_3. The test boundary conditions are listed in Table 3.

Table 3. Data of triaxial tests

Test	Dr soil	σ_3 (kPa)	E50 (MPa)	Dr
TX 1	0.94	100	206	0.94
TX 2	0.94	200	293	0.94
TX 3	0.93	300	255	0.93
TX 4	0.93	500	282	0.93
TX 5	0.89	200	213	0.89
TX 6	0.89	300	216	0.89
TX 7	0.89	500	288	0.89

The triaxial tests show values of σ_1 - σ_3 between 5.2MPa and 6.9MPa, which occur at axial strains ε between 2.6% and 3.8% (see Figure 4). The stiffness E50 of the specimen varies between 200 MPa and 300 MPa. A clear increase in the strength and stiffness of the soil-foam mixtures with the lateral pressure σ_3 is not recognizable. The foam density is around 0.4 g/cm^3. A dependence of the results on the foam density cannot be determined given the small differences in foam density here.

To roughly determine the shear parameters of the soil-foam mixture, the results of the three uniaxial compression tests and the seven triaxial tests were transferred together into an t-s diagram (see Figure 5). For each individual test, the maximum value of the deviator stress ($t = \sigma_{1,max} - \sigma_3 /2$) and the associated mean principal stress ($s = \sigma_{1,max} + \sigma_3 /2$) are plotted in the t-s diagram. In the uniaxial compression test, $\sigma_3 = 0$. The black dots are the UCS tests, whereas the white dots the triaxial tests.

A regression line was then drawn through the points. Using the parameters α (angular coefficient) and b (intercept) according to Figure 5, the cohesion c and the angle of friction φ can be calculated as:

$$c = \frac{b}{cos\varphi} \quad (1)$$

$$sin\varphi = tan\alpha \quad (2)$$

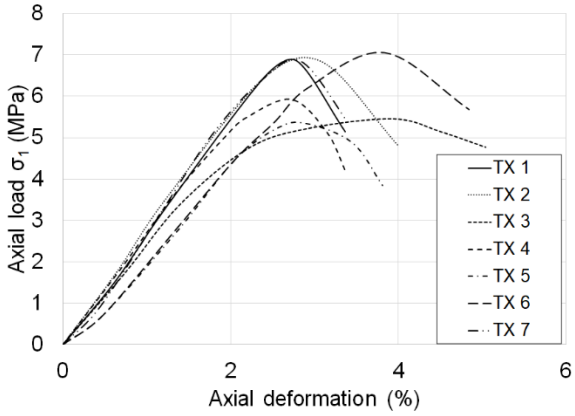

Figure 4. Results of the triaxial tests.

From the results of Figure 5, the cohesion is 887.5kPa and the friction angle φ is 48.7°, considering a value α of 36.9° and a value b of 585.5kPa.

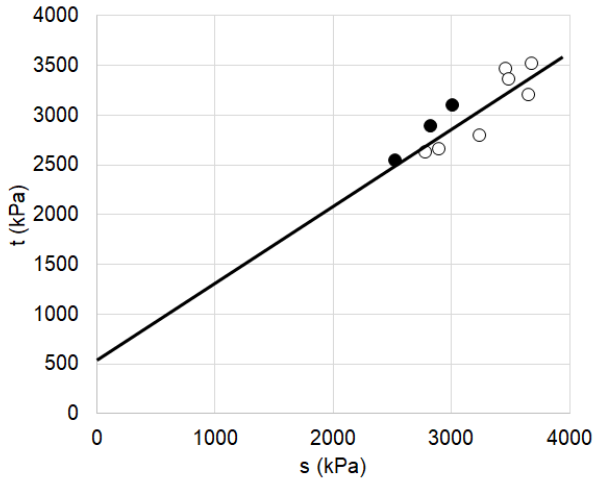

Figure 5. Results of the triaxial and UCS tests into the t-s diagram. Black dots are the UCS tests, white dots the triaxial tests.

4 CONCLUSIONS

The note showed some mechanical tests performed on a gravel soil with 1-4mm grains at a k value of $5 \cdot 10^{-3}$m/s. Axial load values for UCS tests range between 4 and 6MPa. Triaxial tests performed under different lateral pressure and relative density values demonstrate no discernible improvement in the strength and stiffness of the soil-foam combinations with lateral pressure σ_3. Given the modest changes in foam density here, a dependency of the results on foam density cannot be detected.

REFERENCES

Bodi, J., Bodi, Z., Scucka, J. and Martinec, P. (2012). Polyurethane Grouting Technologies. In *Polyurethane*, F. Zafar, and Sharmin, E. (eds.), pp. 307-336. London: IntechOpen. http://dx.doi.org/10.5772/35791.

DIN (2018a). *Geotechnische Erkundung und Untersuchung - Laborversuche an Bodenproben - Teil 7: Einaxialer Druckversuch (ISO 17892-7:2017)*. Berlin: Beuth Verlag GmbH.

DIN (2018b). *Geotechnische Erkundung und Untersuchung - Laborversuche an Bodenproben - Teil 9: Konsolidierte triaxiale Kompressionsversuche an wassergesättigten Böden* (ISO 17892-9:2018). Berlin: Beuth Verlag GmbH.

Fraccica, A., Spagnoli, G., Romero, E., Arroyo, M. and Gomez, R. (2022). Permeation grouting of silt-sand mixtures. *Transportation Geotechnics*, 35, 100800. https://doi.org/10.1016/j.trgeo.2022.100800

Karol, R. H. (2003). *Chemical Grouting and Soil Stabilization*. CRC Press.

Nicholson, P. G. (2015). *Soil Improvement and Ground Modification Methods.* Elsevier.

Spagnoli, G., Collico, S. and Tintelnot, G. (2023). Mechanical behavior of grouted sands with acrylates and polyurethane resins. *Proceedings of the Institution of Civil Engineers - Ground Improvement*. https://doi.org/10.1680/jgrim.23.00005.

Proceedings of the XVIII ECSMGE 2024
GEOTECHNICAL ENGINEERING CHALLENGES
TO MEET CURRENT AND EMERGING NEEDS OF SOCIETY
© 2024 the Authors
ISBN 978-1-032-54816-6
DOI 10.1201/9781003431749-523
Open Access: www.taylorfrancis.com, CC BY-NC-ND 4.0 license

ECSMGE 24
XVIII EUROPEAN CONFERENCE ON SOIL MECHANICS AND GEOTECHNICAL ENGINEERING

Excavation, retaining wall and deep foundations solutions for an office building at Alcântara – Lisbon

Excavation, mur de soutènement et fondations profondes pour un immeuble de bureaux à Alcântara – Lisbonne

R. Tomásio*
JETsj Geotecnia, Lisbon, Portugal

F. Veloso
Rockbuilding, Lisbon, Portugal

N. Rosa
Alves Ribeiro, Lisbon, Portugal

**rtomasio@jetsj.com*

ABSTRACT: This paper presents the proposed solutions for the excavation works, retaining wall and deep foundations necessary for the construction of 4 underground floors of two office buildings at Alcântara, adjacent to Avenida da Índia, in Lisbon. The main existing constraints were archeological, geological, hydrogeological, geotechnical and the neighbourhood conditions, which determined the choice of the retaining wall solution and respective horizontal support. Diaphragm wall technology was used for the retaining wall combined with a top-down sequence to assure the horizontal support. The solutions adopted for the deep foundations are also described, namely the use of high-capacity base grouted bored piles. Particular emphasis is given to archaeological aspects, which strongly determined the top-down solution and construction sequence. Finally, the main results of the monitoring devices are presented as well as the changes implemented during the works determined by differences between the measurements and the design estimations.

RÉSUMÉ: Cet article présente les solutions proposées pour les travaux d'excavation, de mur de soutènement et de fondations profondes nécessaires à la construction de 4 étages souterrains de deux bâtiments de bureaux à Alcântara, adjacents à l'Avenida da Índia, à Lisbonne. Les principales contraintes existantes étaient les conditions archéologiques, géologiques, hydrogéologiques, géotechniques et de voisinage, qui ont déterminé le choix de la solution du mur de soutènement et son support horizontal. La technologie des parois moulées a été utilisée pour le mur de soutènement, combinée à une séquence descendante pour assurer le support horizontal. Les solutions adoptées pour les fondations profondes sont également décrites, à savoir l'utilisation de pieux forés de grande capacité avec injection the coulis de ciment dans la base. Un accent particulier est accordé aux aspects archéologiques, qui ont fortement déterminé la solution et la séquence constructive. Enfin, les principaux résultats des dispositifs de suivi sont présentés ainsi que les changements mis en œuvre au cours des travaux déterminés par les différences entre les mesures et les estimations de conception.

Keywords: Diaphragm wall; bored piles; top-down; excavation; ground anchor.

1 INTRODUCTION

The foundation, excavation and retaining wall solutions developed for the construction of the underground levels of the Alcântara Riverside project, located on Avenida da Índia in Alcântara, Lisbon, were defined to enable the construction of 4 underground levels under safe conditions and to guarantee the minimisation of the impact on the existing constraints in the surroundings (Figure 1).

Considering the location of the building, there was a set of extremely important natural and anthropogenic constraints that strongly determined the conceptual design of the works, namely: the proximity to the River Tagus, which determined the existence of a high water table; the existence of very permeable sandy alluvium which, together with the high water table, recommended that ground anchors should (prudently) not be used below the water table; and the existence of important archaeological findings scattered throughout the intervention area, which needed to be preserved and/or recorded before they suffered any affect resulting from the works.

To take into account all the existing constraints, a diaphragm wall solution was defined, anchored at the

top level (at the capping beam) and propped at the level of floors -1 and -3 by slab strips and metal struts.



Figure 1. Site location.

The foundation solution consisted of Ø1000mm and Ø1200mm high-capacity base grouted bored piles, embedded at the basalt rock and injected through the cross-hole tubes at a depth of 3.0m below the base.

2 MAIN CONSTRAINS

2.1 Geological and geotechnical scenario

An in-depth analysis of the geological conditions revealed sedimentary materials overlying volcanic formations, requiring specialized geotechnical solutions (Figure 2).

A first step in comprehending the geological and geotechnical intricacies scenario of the Alcântara region involved deploying advanced subsurface exploration techniques. The deployment of Cone Penetration Tests (CPT), borehole drilling, and geophysical surveys played a central role in mapping the subsurface layers and soils distribution. This section delves into the methodologies employed, emphasizing the importance of obtaining accurate and high-resolution data to support subsequent design phases.

The Alcântara site exhibited a diverse range of sedimentary layers, ranging from loose soils to compacted clays. Understanding these layers was fundamental to devising foundation strategies. The paper expounds on the challenges posed by the variability in sediment types and how these challenges were addressed in the selection of foundation elements. The stability of basalt formations, identified at deeper levels, provided a robust material for foundational elements.

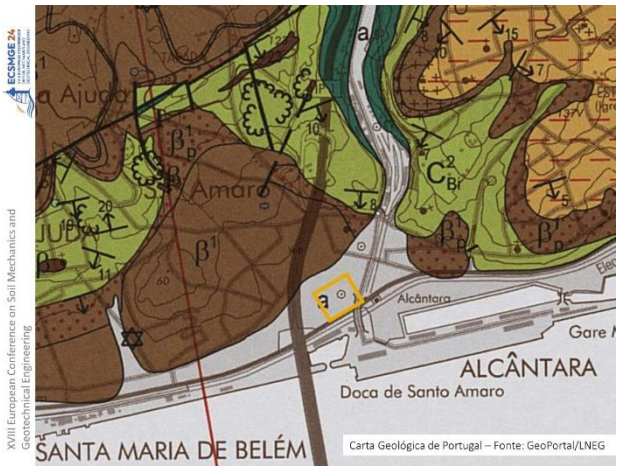

Figure 2. Portuguese geological map.

2.2 Hydrogeological scenario

The altered water flow resulting from human interventions demanded a thorough evaluation of hydrogeological conditions. In the present case, to assess the impact of the 4 basements on the underground flow regime, a global hydrogeological study was developed by LNEC (2018), in accordance with the provisions of PP Alcântara Poente (Figure 3). The result of the study indicates that the impact on the ground water table was neglectable and that no mitigation measures were needed.

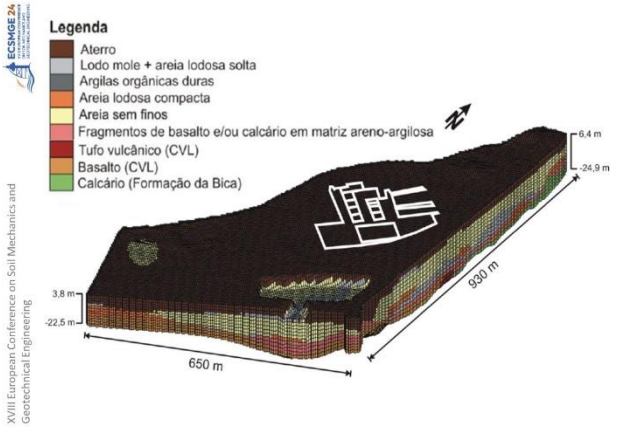

Figure 3. Hydrogeological study – Global model (LNEC 2018).

2.3 Archaeological factors

The existence of archaeological remnants, up to a depth of at least 6,0m, including several well-preserved quay walls, added an extra layer of complexity to the project (Figure 4).

Of all the structures identified, it was considered that the existing quay wall along the entire southeast alignment should be preserved in situ, with the remaining archaeological structures being demolished after proper registration.

In this context, the peripheral retaining wall, combined with temporary ground anchors allowed an unconditioned archaeological excavation to a general depth of 6.0m and an additional excavation up to 9.0m deep in the central area of the excavation.

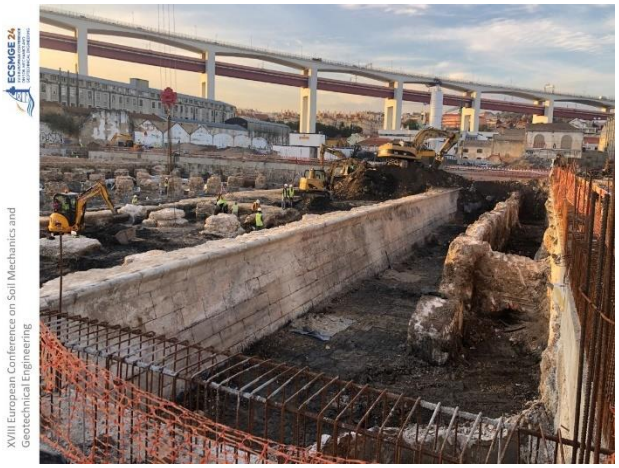

Figure 4. Archaeological remains.

3 SOLUTIONS

This section provides a detailed insight of the chosen geotechnical solutions. It includes the rationale behind opting for reinforced concrete bored piles, the structural considerations in designing a substantial raft foundation, and the application of diaphragm walls supported by temporary anchors and slab bands. The flexibility and adaptability of these solutions to address unforeseen challenges are emphasized.

3.1 Deep foundations

The selection of reinforced concrete bored piles as foundation elements was supported in a meticulous understanding of the geological strata. The Ø1000mm and Ø1200mm piles were designed to pass through the heterogeneous sedimentary layers and anchor firmly into the stable basalt formations. Detailed geotechnical analysis, combined with high pressure grouting of the pile bases, guided the precise placement of these piles, and allowed to maximize their load-bearing capacity (Figure 5).

The design of the raft foundation emerged as a critical aspect, considering the hydrogeological challenges inherent in the project site. A robust prestressed raft was designed to distribute loads uniformly and mitigate the impact of hydrostatic pressure.

In this context, the foundation piles were designed for two extreme scenarios: one in which the water table could reach 1.20m above the ground surface (in the long term due to sea level rise); and another in which the water table could not determine the installation of significant water pressure under the slab (in the short term and dependent on the permeability of the soil involved).

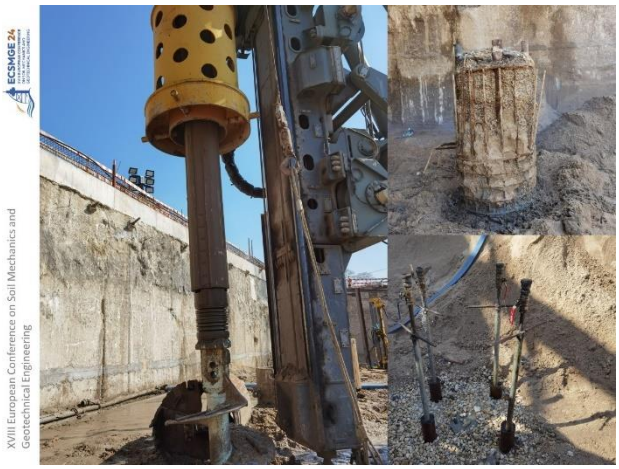

Figure 5. Bored piles drilling and base grouting.

3.2 Retaining wall and support system

The implementation of diaphragm walls as earth retaining solution was imperative for this project since it ensures high quality results, minimizing the number of joints between panels, reducing the vertical deviation of the wall, and decreasing the risk of water inflow into the excavation area. These aspects are quite important due to the height of the wall (up to 32,0m), the presence of high permeability sandy alluvium soils, and the existence of several important and settlement-sensitive city infrastructures (Figure 6).

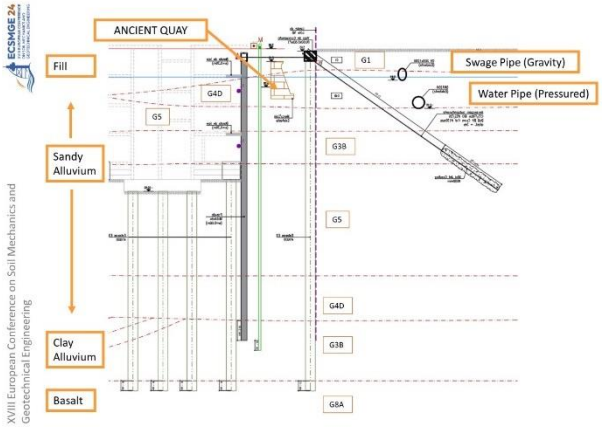

Figure 6. Cross Section of the retaining wall.

The design of the horizontal support of the wall was defined to use temporary ground anchors at the capping beam and two levels of slab bands (floor -1 and floor -3). The self-drilling ground anchors were made of tubular profiles ANP 52/26 with 10m to 17m of free lengh and 7.0m of pressure grouted lengh.

The execution of these anchors allowed the full excavation until the depth of 6.0 m and the necessary registry of all archaeological artefacts, ensuring compliance with the archaeological heritage preservation critiria. After that, the foundation piles were executed, including the teporary collumns to support the slab bands (Figure 7).

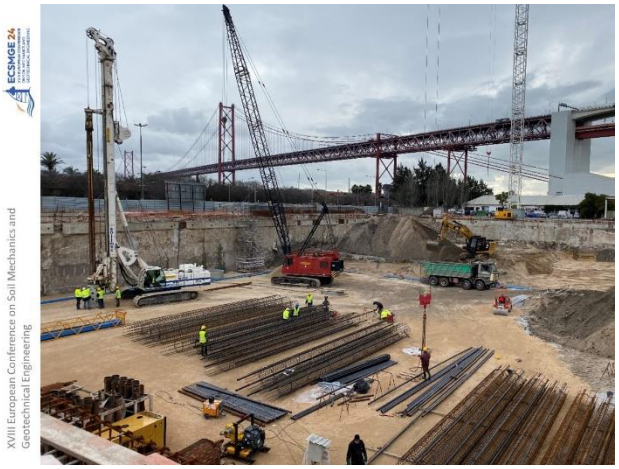

Figure 7. Excavation works at 6.0m depth.

The general design of the slab bands account not only the resistance and stiffness necessary to guarantee safety conditions of the retaining wall, but also the associated construction process, both the excavation phase and the construction phase. In this sense, the geometry of the slab bands was defined in such a way as to interfere as little as possible with the execution of the vertical elements of the structure of the building.

During the excavation phase, the slab bands were supported by the retaining wall at the external perimeter and HEB200 steel collumns sealed into the foundation piles of the definitive columns (Figure 8).



Figure 8. Execution of slab bands.

4 NUMERICAL MODELING

Advanced numerical modelling tools, such as PLAXIS 2D (Figure 9) and SAP2000 (Figure 10) were used to analyse the structural and geotechnical behaviour of the earth retaining system. The behaviour of the soil was simulated using the Hardening Soil constitutive model. The retaining walls and metallic profiles were modelled using “Plate” beam-type elements, with elastic behaviour. The anchors were modelled with spring-type elements, namely “node-to-node anchor”, while the slab bands were modelled using “Fixed-end anchor” spring-type elements. Finally, the foundation piles were modelled using “Embedded Beam Row” elements.

Regarding the high water table and the high permeability of several aluvium soil layers the Plaxis analysis were performed considering a steady state water flow and the flow rate was estimated to design the temporary water pumps.

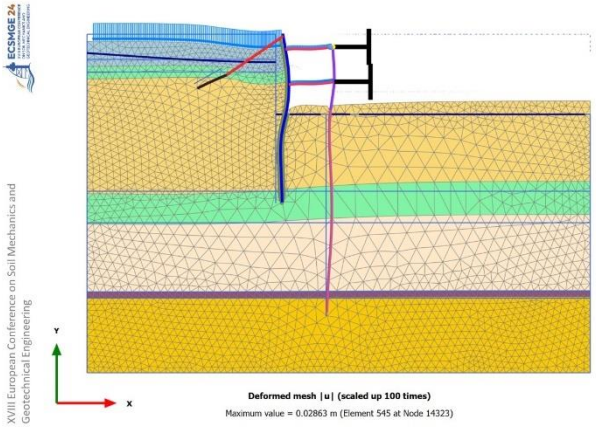

Figure 9. Plaxis 2D model. Final phase of excavation.

The slab strips on floors -1 and -3 and the additional steel struts, were analysed using the automatic structure calculation program SAP2000. The actions acting on the slab strips were determined in the PLAXIS 2D model and their stiffness was also incorporated in that model.

5 MONOTORING AND OBSERVATION PLAN

Figure 10 presents the monitoring plan implemented during construction, which involved various instruments to track displacements (inclinometers), rotations (tiltmeters), settlements (settlement marks), and groundwater levels (piezometers).

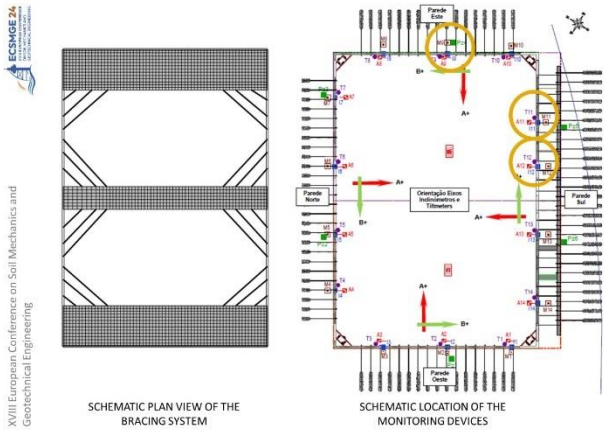

Figure 10. Monitoring devices (Inclinometer I9, I11 and I12).

During the progress of the excavation works, there was a general tendency to measure horizontal displacements of the wall greater than those foreseen in the design, particularly along the elevation supported by steel struts which are more deformable than the strip slabs.

The inclinometer graphs on Figure 11 allows the identification of much higher deformations (75mm) on I11 and I12 which are placed in a location where the diaphragm wall is supported by steel struts, than on I9 (20mm) which was placed in a location where the diaphragm wall is supported by a strip of the floor slab.

The estimated horizontal deformation of the wall for both section was 22mm and 27mm, respectively.

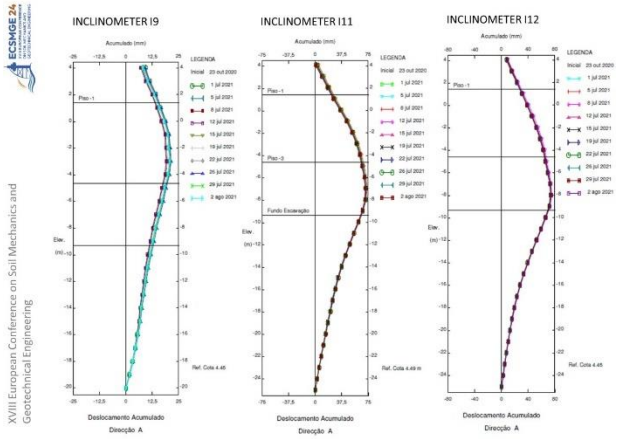

Figure 11. Inclinometer graphs.

The comparison of the wall deformation presented in Figure 9 with the real deformation measured by the inclinometers (Figure 11), and the retroanalysis performed during the construction works, indicated that the most probable cause of the higher deformation was a combination for two aspects:

- Overestimation of the steel struts' stiffness due to an underestimation of the slab strips stiffness. The smaller deformation of the slab strips decreases the induced deformation of the corner struts which reduces the efficiency of the struts on the perpendicular elevation;
- Underestimation of the stiffness reduction of the clean sand alluvial formations located at the passive zone of the wall.

6 CONSTRUCTION CHALLENGES AND ADAPTATIONS

Unforeseen challenges, including higher-than-expected deformations and anomalies in foundation pile tests, are addressed in this section.

Several steel struts were encased in reinforced concrete to increase their stiffness and, indirectly, to minimise the horizontal deformations of the retaining wall.

During the execution of the cross-hole integrity tests, planned for all foundation piles, the existence of some anomalies was detected, namely lack of covering, enlargements of the section, concrete segregation, and intercalation of soil pockets (Figure 12).



Figure 12. Foundation piles anomalies.

In some situations, where the pathologies were relevant for the future performance of the piles, due to their position on the building layout or the expect stress level, some reinforcement measures were implemented. In the most demanding situations, namely in a structural alignment where there was only one pile under each column, it was necessary to enhance the load capacity through the execution of additional large capacity self-drilling micropiles of 3200kN ultimate load.

During the excavation works, through the quantification of the flow rates pumped daily, it was possible to confirm that the inflow of water into the excavation area was extremely low when compared to

the estimates from the design phase (conditioned by the various permeability tests carried out during the initial surveys). Based on these results and previous experience (Pita, 2012), the planed raft foundation was replaced by a drainage mattress and individual pile caps connected by foundation beams (Figure 13).

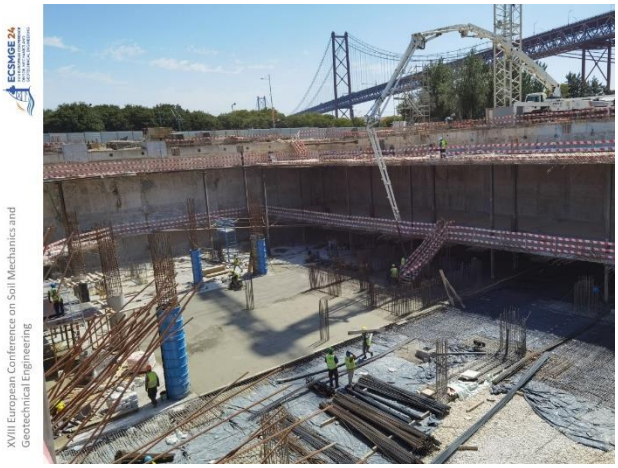

Figure 13. Bottom drainage gravel layer.

7 CONCLUSION

The success of the project is attributed to the careful integration of geological, hydrogeological, and archaeological considerations.

The adaptability of the proposed solutions, supported by systematic monitoring of the retaining wall was determinant in the timely implementation of corrective measures and cost optimization decisions.

ACKNOWLEDGEMENTS

The authors would like to thank the Owner of the building for authorising the writing and publication of this paper. They also would like to emphasise that the success of the solutions implemented was the result of teamwork of the following companies: JETsj Geotecnia as designer, Rockbuilding as project and supervision manager, Alves Ribeiro / HCI as general contractor, and Teixeira Duarte as geotechnical subcontractor.

REFERENCES

Pita, X.; Pinto, A.; Borges, R. (2012). Retaining wall and foundation solutions for Agencies pump station in Lisbon ”In Portuguese“. In: 13º Congresso Nacional de Geotecnia, Lisbon, Portugal, pp. 33–34. ISBN 978-972-98781-8-3.

LNEC (2018). Hidrogeological study for the Alcântara office buildings. Evaluation of potential impacts ”In Portuguese“, LNEC, Lisbon, Portugal.

Proceedings of the XVIII ECSMGE 2024
GEOTECHNICAL ENGINEERING CHALLENGES
TO MEET CURRENT AND EMERGING NEEDS OF SOCIETY
© 2024 the Authors
ISBN 978-1-032-54816-6
DOI 10.1201/9781003431749-524
Open Access: www.taylorfrancis.com, CC BY-NC-ND 4.0 license

ECSMGE 24
XVIII EUROPEAN CONFERENCE ON SOIL MECHANICS AND GEOTECHNICAL ENGINEERING

Analysis of the influence in soil permeability, with the use of high-density drilling fluids applied in the internal edge of drilling rows

Analyse de l'influence sur la perméabilité du sol, avec l'utilisation de fluides de forage à haute densité appliqué dans le bord interne des lignes de forage

A.H.P. Toyoshima, C.C. Soares
Chammas Engenharia, Belo Horizonte, Brazil

G.C. Alvarez
Walm BH Engenharia, Belo Horizonte, Brazil

G.C.L.R. Costa*
Chammas Engenharia, Belo Horizonte, Brazil

**giovani.costa@chammas.com.br*

ABSTRACT: Among the most useful methods of gathering geotechnical information from soils beneath the surface are drilling and applying permeability tests in it. The results obtained from such methods provide relevant data that can be used to predict and avoid natural and geotechnical disasters, such as slope and dam failures. A very common practice in drilling tropical soils is the usage of high viscosity fluids, in order to cool down the drilling row, provide stability to the borehole walls and ease the retrieval of samples. However, the use of such fluids causes impermeability in the borehole walls and impacts the hydraulic parameters obtained when the water is injected during the permeability test. A solution for this problem could rely on applying high-density fluids only in the internal edge of the sampling row, implying that no contact between the fluid and the borehole walls occurs. Therefore, this study aims to compare the results from permeability tests executed in the same geological layer, with and without the use of drilling fluids. The expected results indicate that there should not be relevant differences in the results of both methods, hence the fluid will not overflow to the borehole walls.

RÉSUMÉ: Parmi les méthodes les plus utiles pour collecter des informations géotechniques sur les sols sous la surface figurent le forage et l'application de tests de perméabilité. Les résultats obtenus grâce à ces méthodes fournissent des données pertinentes qui peuvent être utilisées pour prédire et éviter les catastrophes naturelles et géotechniques, comme les ruptures de pentes et de barrages. Une pratique très courante dans le forage des sols tropicaux consiste à utiliser des fluides à haute viscosité, pour refroidir la rangée de forage, d'assurer la stabilité des parois du trou de forage et de faciliter la récupération des échantillons. Cependant, l'utilisation de tels fluides provoque l'imperméabilité des parois du forage et impacte les paramètres hydrauliques obtenus lors de l'injection de l'eau pendant le test de perméabilité. Une solution à ce problème pourrait consister à appliquer des fluides à haute densité uniquement sur le bord interne de la rangée d'échantillonnage, ce qui implique qu'aucun contact entre le fluide et les parois du trou de forage n'est établi. Cette étude vise donc à comparer les résultats de plusieurs tests de perméabilité réalisés dans les mêmes strates géologiques, avec et sans utilisation de fluides de forage. Les résultats attendus sont qu'il ne devrait pas y avoir de différences significatives dans les résultats des deux méthodes, raison pour laquelle le fluide ne débordera pas vers la paroi du forage.

Keywords: Permeability test; hydraulic conductivity coefficient; high-density fluids; "quadrilátero ferrífero"; drilling.

1 INTRODUCTION

In order to determine the *in-situ* hydraulic conductivity coefficient (k) of soils, different permeability test methods can be applied, such as the tests executed inside of boreholes or standpipe piezometers (field testing).

In general, the methodology of execution of those tests consists of applying a variation in the water column (rising or falling) through injection or removal of water and measuring the absorbed/removed water volume due to time.

In both engineering and environmental geology study fields, those tests are systematically executed to establish permeability conditions and enable the

design and implementation of civil engineering works and environmental projects. Therefore, they are often employed in dams and tunnels projects, also for landfill conceptions, and investigation of contaminated sites, among many other types of projects (ABGE, 2020).

Due to the relation between the execution of field permeability tests and the prospection method applied, it is certain that operational factors may interfere in hydraulic conductivity results. As example, the use of drilling fluids can be mentioned. Under those circumstances, it is common to be required the non-utilization of those fluids in boreholes which are destinated to permeability tests execution.

On the other hand, the use of those fluids is essential to ensure effective drilling operation, since it provides better drilling rates and lower operational costs. Some of the advantages of the usage of drilling fluids stands out: lubrification and cooling of the drilling tools during rotary drilling process; efficient removal of debris inside the borehole; better recovery rates of unconsolidated materials; avoiding overcoming obstructions; and avoiding damages to drilling equipment.

A solution for this matter could rely on applying high density fluids only in the internal edge of the sampling row, implying that no contact between the fluid and the borehole walls is made.

Still, there are few published studies which intend to investigate the relation between the use of drilling fluids and hydraulic conductivity results.

Therefore, the present paper intends to compare the results from permeability tests made in the same geological layer, with and without the use of drilling fluids.

2 OBJECTIVES

The present study aims to stablish and understand the influence of using high density fluids in drilling operations, and the results obtained with permeability tests applied at the same geological layer.

The expected results indicate there should be no relevant differences in the results of both methods, hence the fluid will not overflow to the borehole wall. The methodology consisted of applying the following steps:

- Perforation of two boreholes, with a length of 19.0 m each: SM-01, with non-material recovering and without using high density fluid materials; SM-02, sibling borehole, with material recovering and using high density fluid;
- Execution of geological visual-tactile description of the SM-02 drilling soil samples;
- Carrying out permeability tests inside both boreholes, according to preestablished depth intervals;
- Calculation of the soil hydraulic conductivity coefficient (k) for each test, according to Zangar (1953);
- Comparison of the results obtained for each geological layer, in order to verify how the usage of high-density fluid influenced the k coefficient.

The study area belongs to a mining complex located at “Quadrilátero Ferrífero” geological province, more specifically at Itabirito city, Minas Gerais state, Brazil. Figure 1 illustrates the location of the two boreholes inside the study area.

The boreholes were executed using an hydraulic rotary drilling equipment. The equipment and tools employed at the permeability tests development are listed below:

- Water pump with a minimum 40 L/min capacity;
- 2 water meters (flow range: 10 to 40 L/min);
- Graduated cylinder;
- Threaded funnel attachable to the liner;
- Electric water level meter;
- Graduated bucket;
- Certified metal ruler;
- Stopwatch.

.

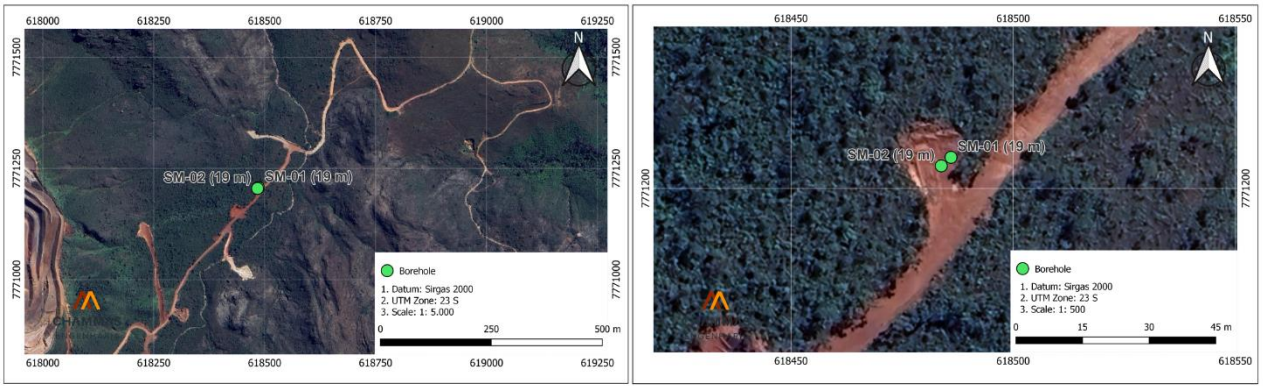

Figure 1. Location of the two boreholes inside the study area (left:1:5.000 scale; right: 1:500 scale).

The tests were carried out holding the water level column inside the borehole through water addiction. The equations proposed by Zangar (1953) allow obtaining the hydraulic conductivity coefficient (k).

For unsaturated strata, k coefficient is calculated using the Equation 1 below:

$$k = \frac{Q}{2\pi L_A\,(2h_1 - L_A)} \cdot \left[sinh^{-1}\left(\frac{L_A}{r_1}\right) - \left(\frac{L_A}{h_1}\right)\right] \quad (1)$$

For saturated strata, k is calculated using the Equation 2 below:

$$k = \frac{1}{C_s r_1} \cdot \frac{Q}{h_1}, where\ C_s = \frac{L_A}{r_1} \cdot \frac{2\pi}{ln\frac{L_A}{r_1}} \quad (2)$$

where k is the hydraulic conductivity coefficient (cm/s), Q is the steady state flow (cm³/s), h_1 is the head on well (cm), r_1 is the well radius (cm), L_A is the active or uncased length of well (cm) and C_s is the saturated strata conductivity coefficient.

3 RESULTS

Table 1 shows the permeability test results for both drilling holes. The geological description of the soil drilling samples is presented at Table 2 below.

Table 1. Permeability tests results for SM-01 and SM-02.

Test nº	Depth (m)	SM-01	SM-02
1	3.00 – 4.00	1.79E-04	1.51E-05
2	6.00 – 7.00	-	5.20E-06
3	9.00 – 10.00	-	-
4	12.00 – 13.00	2.29E-04	4.00E-05
5	15.00 – 16.00	7.44E-05	1.65E-05
6	18.00 – 19.00	2.49E-07	4.25E-05

Table 2. Geological description of the soil drilling samples (SM-02).

Depth (m)	Description
3.00 – 4.00	Clayey silt
12.00 – 13.00	Fine-to-medium silty sand
15.00 – 16.00	
18.00 – 19.00	Fine-to-medium silty sand (altered rock – quartzite)

Due to operational reasons, it was not possible to execute the test in SM-01 at depths 6.00 m to 7.00 m (test number 2) and 9.00 m to 10.00 m (test number 3- in this case, at both drillholes). Hence, these two intervals were not taken for analysis purposes, since there is no data related. Once the tests executed at the range 18.00 m to 19.00 m (test number 6) covers an altered rock layer, this must be taken in consideration. Figure 2 illustrates the permeability coefficients obtained for each range.

In general, it is possible to notice that the results obtained from permeability tests executed in SM-02 were influenced using high-density fluids, showing a reduction trend of permeability coefficient when high-density fluids were used at the drilling process.

Although, the same pattern was not observed in tests number 6 results (executed between 18.00 m and 19.00 m, covering the altered rock layer). In that case, the permeability coefficient for SM-01 (with high-density fluids) was higher than the result obtained for SM-02 (without using high-viscosity fluids).

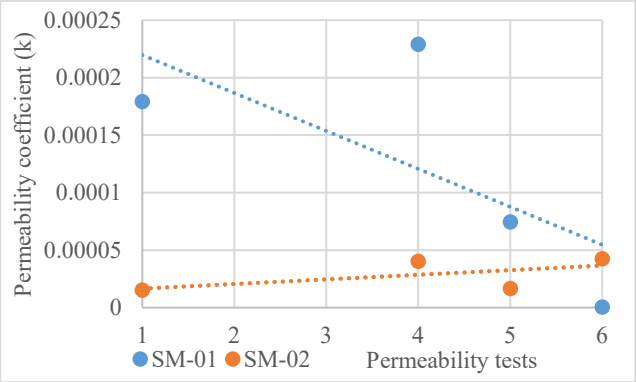

Figure 2. Results of permeability coefficients (k) obtained for SM-01 and SM-02.

4 CONCLUSIONS

Based on the obtained results, it is possible to conclude that using high-density fluids in drilling operations may compromise the permeability test results. The hydraulic conductivity coefficient results, calculated for tests made at SM-01 drilling, show a decrease rate around 10 times when compared to the same tests carried out in SM-02, which highlights the influence of using such fluids.

In order to deepen the analysis of the relation between using of high-density fluids and their influence in borehole walls permeability and hydraulic parameters, more data is necessary. Thus, the authors recommend the study to be continued, applying the same methodology in more samples.

ACKNOWLEDGEMENTS

The authors are grateful for the financial and executional support provided by Chammas Engenharia.

REFERENCES

Brazilian Association for Engineering Geology (ABGE) (2020). Permeability tests in soils – Guidelines for field execution. In: Geological-Geotechnical Investigations – Guidelines [In Portuguese], 1st ed., São Paulo, Brazil, pp. 246-300.

Zangar, C.N. (1953). Theory and Problems of Water Percolation. *Engineering Monographs*, nº 8, Bureau of Reclamation, United States Department of the Interior, Denver, Colorado.

Proceedings of the XVIII ECSMGE 2024
GEOTECHNICAL ENGINEERING CHALLENGES
TO MEET CURRENT AND EMERGING NEEDS OF SOCIETY
© 2024 the Authors
ISBN 978-1-032-54816-6
DOI 10.1201/9781003431749-525
Open Access: www.taylorfrancis.com, CC BY-NC-ND 4.0 license

ECSMGE 24
XVIII EUROPEAN CONFERENCE ON SOIL MECHANICS AND GEOTECHNICAL ENGINEERING

De-construction as part of life cycle management

La déconstruction dans le cadre de la gestion du cycle de vie

A. Tuomela*, J. Majava, T. Luukkonen, P. Leviäkangas
University of Oulu, Oulu, Finland

**anne.tuomela@oulu.fi*

ABSTRACT: Finland has committed to utilizing 70% of construction and demolition waste (CDW) by 2020. However, the current re-utilization rate is still below 60%. Altogether 85% of the total CDW is generated by repair projects and demolished buildings, while the remaining 15% is coming from new construction. Hence, the main emphasis should be on the recycling of demolished or repaired buildings and constructs. Construction in urban areas start often with the demolition of old buildings and structures. At the same time, there is a need to construct new or upgrade old infrastructure such as streets, footpaths and bicycle lanes, parking areas, and noise barriers. The demolition materials should be utilized *in situ*, near the demolition site. This would result in apparent economic savings in terms of heavy transportation and thereby and lower emissions. Also, the strain on existing road structures and congestion on the city's street network would be relieved. Finally, the need for virgin raw materials would be less. This paper presents a novel operating model that combines demolition operations and construction operations by optimizing material quantities, quality, work scheduling, and site operations. Various demolishing aggregates, side flows and other fraction flows will be tested in experimental structures with the aim of finding out whether they meet the regulatory requirements and standards for infrastructure construction.

RÉSUMÉ: La Finlande s'est engagée à utiliser 70 % des déchets de construction et de démolition (CDW) d'ici 2020. Cependant, le taux de réutilisation actuel est toujours inférieur à 60 %. Au total, 85 % des déchets CDW sont produits par des projets de réparation et des bâtiments démolis, et les 15 % restants proviennent de nouvelles constructions. L'accent devrait donc être mis principalement sur le recyclage des bâtiments et constructions démolis ou réparés. Dans les zones urbaines, la construction commence souvent par la démolition de vieux bâtiments. Dans le même temps, il est nécessaire de construire de nouvelles infrastructures ou de moderniser les anciennes infrastructures telles que les rues, les sentiers piétonniers et les pistes cyclables, les aires de stationnement et les écrans antibruit. Les matériaux de démolition peuvent être utilisés à proximité du site de démolition. Cela se traduirait par des économies économiques apparentes en termes de transport lourd et donc par une réduction des émissions. De plus, la pression sur les structures routières existantes et la congestion du réseau routier de la ville seraient réduites. Enfin, le besoin de matières premières vierges serait moindre. Cet article présente un nouveau modèle d'exploitation qui combine les opérations de démolition et les opérations de construction en optimisant les quantités de matériaux, la qualité, la planification des travaux et les opérations sur le site. Différents agrégats de démolition, écoulements latéraux et autres flux de fractions seront testés dans des structures expérimentales dans le but de déterminer s'ils répondent aux exigences réglementaires et aux normes relatives à la construction d'infrastructures.

Keywords: Construction; demolition; waste; infrastructure; recycling.

1 INTRODUCTION

Construction and demolition waste (CDW) accounts more than a third of all waste generated in the European Union (EU). CDW contains a wide variety of materials such as concrete, bricks, wood, glass, metals, plasterboard, and plastic. EU set an ambitious target for 2020: recovery, re-use, and recycling of non-hazardous CDW materials should be increased to at least 70% by weight (Directive, 2008). Many countries are behind the target, including Finland in which the recycling rate is still less than 60% (Figure 1) (Statistics Finland, 2023).

The Finnish National Waste Plan for 2027 has objectives for CDW waste management as follows: a) the total amout of CDW waste should be decreased, b) CDW utilization rates should reach the level of 70%, and c) the high-quality recovery of CDW waste is increased by managing the risks (Ministry of Environment, 2022). The forthcoming risk management objective will be an important part in the circulation of CDW waste. The same principle has been followed in the rehabilitation of contaminated soils for a decade.



Figure 1. In Finland the recycling of construction waste is behind the recycling target set by the EU (green line) (Statistics Finland, 2023.

Ginga et al. (2020) considered the importance of future research in exploring new construction applications for CDW waste. Menegaki and Damigos (2018) collected data on the factors enhancing and hindering CDW waste recovery. More specifically, Kourmpanis et al. (2008) collected data on the challenges and benefits of on-site crushing and sorting. Disadvantages included, for example, noise and dust emitted in urban areas. However, today‘s technologies and machines are more advanced, as was the case almost 20 years ago. Also, the readiness to change many working practices and processes has increased.

This paper introduces the preliminary framework to be tested and evaluated in PURKU project. The project, Demolition as part of urban construction - eco-efficient utilization of demolition material in infrastructure and building construction, start in the beginning of 2024. The project is funded by the EU‘s Just Transition Fund (JTF). In addition, the paper introduces effective measures that will be executed in the project to enhance CDW waste recovery and recycling.

2 DATA AND METHODS

The PURKU project is divided into seven work packages including value network and life cycle analysis, development of project practices and operation methods, laboratory studies, demolition pilots, support for the industry change, and project management and communication. The main objective is to create new operating model that will be studied and tested at the test sites (demolition pilots). Particular attention is paid to new working methods for crushing rock to be suitable for reuse at or in the vicinity of the site, without the materials being transported to be processed away from the demolition sites and back after treatment. On the other hand, attention is paid to project management and that in the future demolition would be better managed in the life cycle of construction. Laboratory studies aim to investigate the properties of structures and the conversion of harmful substances to a less harmful form. The workshops will bring together different stakeholders to learn about sustainable demolition. Together with various actors the operation model is developed and implemented.

2.1 Value chain and project management practices

The project develops a new kind of value chain and project management practices for construction that assume that demolition is at the beginning of the value chain and life cycle models. Traditionally, demolition has been the end point of construction (e.g., Yeheyis et al., 2013). The construction industry involves various stakeholders at different stages of a building's life cycle. These include, for example, legislators, authorities, city planners, customers, designers, contractors, material suppliers, subcontractors, demolition companies, material, and waste handlers. The construction industry's operating models and practices are well-established and regulated in many ways, but the transition to a circular economy (CE) poses new challenges and needs for change. The transition to a more efficient material life cycle and the utilization of side streams and demolition material requires value chain and project practice development to comply with CE principles.

To achieve the goals above, our project will analyse the construction value chain and its development opportunities from building aggregates’ perspective by using life cycle, stakeholder, and business model analysis as tools. The analysis will be conducted on previous demolition-construction cases in Oulu area as well as the demolition pilots implemented in the project. Furthermore, the analysis will cover project management practices (including processes, actors, decision-making, tools) with the aim of identifying development opportunities in different phases of the project's extended life cycle (conceptualization, planning, implementation, operational phase). The use of CE thinking and strategies in case projects will be utilized to develop a project management model and a business model that integrates demolition with construction. The aim is to develop stakeholder management, procurement management, and risk management, as well as replicable project management procedures that take CE principles into account. Finally, demolition-construction related operating models, practices and material management will be developed. Figure 2 shows the current and

target life cycles and practices in the construction value chain.

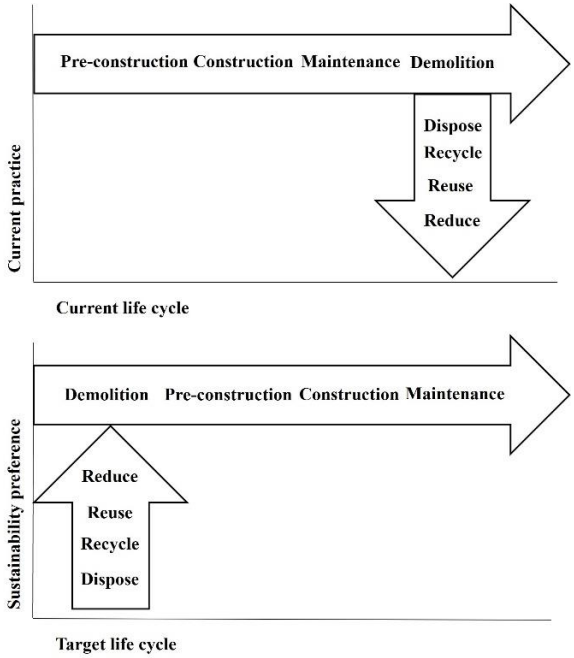

Figure 2. Current and targeted construction value chain.

2.2 Demolition pilots

The research pilots are in Oulu region, Finland. Oulu is home to Finland's largest demolition site, the old University Hospital, which is one of the selected research and pilot sites. In addition, there are other pilot sites coming from the area, but they are smaller.

The purpose of the pilots is to change the crushing activities of the materials so that the mineral based structures are crushed on-site in the urban area. During the crushing, the following parameters are monitored 1) dust, 2) vibration and 3) noise generated by on-site demolition pilots, and 4) other emissions that are harmful to the environment and the populations.

In Finland, a large part of the year is worked in winter conditions and it brings its own challenges e.g., to dust-binding. Water has typically been used for dust-binding, but water freezes, so other additives must be used economically end enviromentally wise for winter dust-binding. To achieve the best possible results, it is possible to test new additional equipment and alternative bio-based dust-binding methods at the sites.

Crashing and demolition is generally known to be loudly processes. Efforts are made to identify noise-sensitive activities at the site and find ways to prevent noise and vibration. Pilots require from contractors' equipment to be used to reach the permitted noise and vibration levels.

The non-hazardous CDW waste from the pilots are planned to be use in the sites or nearby infrastructure construction sites, like the foundation of bridges. Still, contaminated CDW waste is generated. The purpose is to build test fields in which those hardly utilized materials are used for bottom structures. The fields will be monitored for several years to provide information on environmental impacts. Similar smaller laboratory scale test structures will be built in parallel, in which climate conditions can be modified and accelerated to obtain information on the environmental impact of materials.

2.3 Laboratory studies

The laboratory-scale studies of the project support the demolition pilots but also make some completely new research openings (e.g., related to asbestos waste). The topics are (1) dissolution studies of asbestos fibres to render them non-hazardous; (2) studies of Polycyclic Aromatic Hydrocarbons (PAH) and heavy metal containing demolition waste fractions; (3) dust suppression during demolition; and (4) seepage water studies. For asbestos, the aim is to utilize additives enhancing the dissolution of the fibres with potential to utilize the dissolved asbestos (rich in silica (Si), calcium (Ca), magnesium (Mg), and iron (Fe)) as a raw material to the development of new recycled construction materials. PAH and heavy metal quantities and distribution in demolition materials are studied with their solubility under different conditions, which supports the material choices for the pilots. In terms of dust suppression, the goal is to conduct preliminary studies with enhanced dust-binding chemicals. The aim of seepage water experiments is to build laboratory-scale model systems simulating the behaviour of the materials when exposed to outdoor conditions.

2.4 Workshops

During the project training events and workshops will be arranged together with stakeholders to achieve new value chain-based operation model. In addition to public training events and seminars, the joint collaborative workshops will be organized with the key stakeholders that are involved in de-construction and construction value chain. The objective is to verify and elaborate the change requirements that are caused by the transition to more sustainable de-construction and life cycle management practices based on circular economy methods. The analyses of earlier de-construction projects and experiences gained during the de-construction pilots will be used as inputs in the work conducted in the workshops. The intended outcome of the workshops is to create a joint regional development plan to advance the use of de-

construction materials and circular economy in the construction industry overall.

3 RESULTS AND CONCLUSIONS

The project will officially start at the beginning of 2024. The first demolition sites will be started during the spring or summer. Preparations have already been commenced and will continue throughout winter 2024. The project will demonstrate how on-site demolition can make sense, by utilising life cycle calculation methods and narrating practical examples.

Direct positive effects are expected to be observed for example regarding reduced heavy truck traffic. This would improve road safety and reduce the load stress of the local roads and streets, as well as minimize emissions from heavy traffic.

Alternative project management concepts can be applied to enhance wider use of demolition materials. For instance, the project attempts to find new synergies between local construction projects to create local mass/material balance. This will improve local material circularity. The main ambition is to demonstrate that materials from demolition are valuable and usable building material, and it makes both economic and environmental sense to make maximum use of them.

ACKNOWLEDGEMENTS

The authors are grateful for the financial support provided by funding agency Just Transition Fund (JTF) of EU. In addition, many thanks for the French translation assistance to the researcher Mahtab Akbarzadeh Khoei.

REFERENCES

Directive. (2008) Directive 2008/98/EC of the European Parliament and of the Council, Fundamental Texts on https://eur-lex.europa.eu/legal-content/EN/TXT/PDF/?uri=CELEX:02008L0098-20180705&from=SV.

Ginga, C.P., Ongpeng, J.M.C., Daly, M.K.M. (2020) Circular economy on construction and demolition waste: A literature review on material recovery and production, *Materials*, 13(13), pp. 1–18. https://doi.org/10.3390/ma13132970.

Kourmpanis B., Papadopoulos A., Moustakas K., Stylianou M., Haralambous K.J., Loizidou M. (2008) Preliminary study for the management of construction and demolition waste, *Waste Management and Research*, 26(3), pp. 267–275. https://doi.org/10.1177/0734242X07083344.

Menegaki, M., Damigos, D. (2018) A review on current situation and challenges of construction and demolition waste management, *Current Opinion in Green and Sustainable Chemistry*, 13, pp. 8–15. https://doi.org/10.1016/j.cogsc.2018.02.010.

Ministry of the Environment. (2022) From Recycling to Circular Economy, *National Waste Plan to 2027*.

Statistics Finland. (2023) *Waste statistics*. Available at: https://stat.fi/index_en.html.

Yeheyis M., Hewage K., Alam M.S., Eskicioglu C., Sadiq R. (2013) An overview of construction and demolition waste management in Canada: A lifecycle analysis approach to sustainability, *Clean Technologies and Environmental Policy*, 15(1), pp. 81–91. https://doi.org/10.1007/s10098-012-0481-6.

Proceedings of the XVIII ECSMGE 2024
GEOTECHNICAL ENGINEERING CHALLENGES
TO MEET CURRENT AND EMERGING NEEDS OF SOCIETY
© 2024 the Authors
ISBN 978-1-032-54816-6
DOI 10.1201/9781003431749-526
Open Access: www.taylorfrancis.com, CC BY-NC-ND 4.0 license

ECSMGE 24
XVIII EUROPEAN CONFERENCE ON SOIL MECHANICS AND GEOTECHNICAL ENGINEERING

3D small-scale tests on steel-reinforced piled embankments

Essais sur modèles réduits en 3D de remblais sur pieux renforcés par une nappe de treillis soudés

S.J.M. van Eekelen*
Deltares, Netherlands

M. Schneider
Technical University of Darmstadt, Institute of Geotechnics, Germany

B. Wittekoek
Deltares, Netherlands

M. Hell, P. Pandrea
Keller, Germany

P. Schauber
Keller, France

M. Topolnicki
Keller, Poland

K. Makowska
SHM System, Poland

K. Zdanowicz
SHM System, Poland / FOLAB GmbH, Germany

R. Sieńko
SHM System, Poland

H. Zachert
Technical University of Darmstadt, Institute of Geotechnics, Germany

suzanne.vaneekelen@deltares.nl

ABSTRACT: This paper looks at the behaviour of welded steel mesh-reinforced piled embankments through a series of small-scale tests. Findings reveal that reinforcement axial and bending stiffnesses have minimal influence on soil arching. In contrast, the friction angle of the embankment fill plays a more significant role in shaping soil arching. The Concentric Arches (CA) model, adopted in CUR226 (2016), tailored for geosynthetics, matches the measured soil arching well. The study introduces the use of Distributed Fibre Optic Sensing (DFOS) technology, providing a 3D view of reinforcement and fill deformations.

RÉSUMÉ: Cet article examine le comportement de remblais en pieux renforcés par treillis soudés à travers une série de tests à petite échelle. Les résultats révèlent que la rigidité du renforcement a une influence minimale sur les transferts de charges. En revanche, l'angle de frottement du matériau de remblai joue un rôle plus significatif dans les mécanismes de transferts de charges. L'effet d'arche du modèle 'Concentric Arches' (CA), utilisé dans CUR226 (2016), dédiée aux géosynthétiques correspond bien aux mesures obtenues. L'étude introduit également l'utilisation de la technologie de détection par fibre optique répartie (DFOS), offrant une vision tridimensionnelle des déformations du renforcement et du remblai.

Keywords: Piled embankments; steel basal reinforcement; model scale tests; soil arching.

1 STEEL MESH BASAL REINFORCEMENT IN PILED EMBANKMENTS

Pile-supported (PS) embankments with basal geosynthetic reinforcement (GR) are commonly built in soft soil areas (van Eekelen and Han, 2020). Steel mesh reinforcement (SR) is particularly appealing for high embankments (Topolnicki et al., 2019). Its high axial stiffness, in comparison to geosynthetic, reduces horizontal deformation at the embankment base, minimizes bending moments in the piles, ultimately enhancing the embankment stability.

This paper presents a small-scale test series on steel-reinforced piled embankments, conducted in the Deltares laboratory. The tests are part of a broader research initiative called Piled Embankments with Basal Steel Reinforcement (PEBSTER), which also includes a large-scale test (Schneider et al., 2024).

The research aims to address the following questions:

1. Does the soil arching in a piled embankment differ if SR is used instead of GR?
2. Are deformations different with SR instead of GR?
3. What is the influence of flexible vs. rigid piles?
4. Can the current design methods for piled embankments using GR be applied for SR or do they require a modification?
5. Do the answers on these questions depend on the scale of model tests?

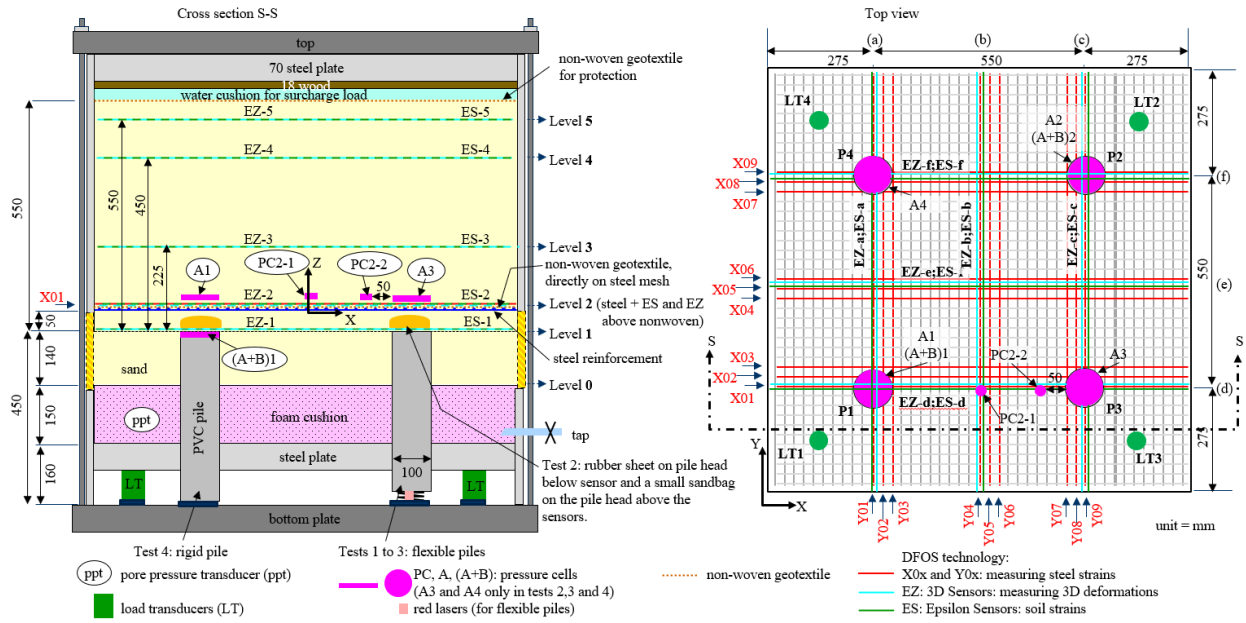

Figure 1. Test set-up small scale test steel-reinforced pile-supported embankments.

2 SET-UP SMALL SCALED TESTS

Figure 1 shows the test set-up, which is an extended version of the test set-up described by Van Eekelen et al. (2012a, 2024a). A steel plate supports a foam cushion, that is sealed and soaked. A tap allows for drainage of the foam cushion, simulating the consolidation of the subsoil between the piles. Four piles with a 0.1 m diameter pass through the steel plate.

The welded steel mesh-reinforcement was placed 50 mm above the pile heads. It consists of 43 bars in each direction. These bars have a 5 mm diameter and a centre-to-centre spacing of 25 mm, resulting in the axial stiffness EA = 164934 kN/m and bending stiffness EI = 0.2577 kN·m^2.

The fill material used is 'Darmstadt sand', sediments from the river Main, characterized as medium coarse sand. Table 1 lists test details, where the values of φ'_{cv} were derived from the relative density (RD) of the fill, using an empirical correlation obtained from 15 triaxial tests.

Table 1. Test details of the four small-scale tests.

Test no.	**1**	**2**	**3**	**4**
Fill height above steel (m)	0.55	0.55	0.55	0.56
Unit weight γ (kN/m^3)	16.7	16.9	17.0	16.6
Relative density RD (%)	68	72	75	64
Friction angle φ'_{cv} (°)	33.8	34.0	34.1	33.7

An equally distributed surcharge load is applied using a water cushion. A rubber sheet greased with Vaseline minimises the friction between fill, box walls, foam cushion and piles. The load distribution is measured by pressure cells and load transducers.

Soil strains and displacements were monitored at five elevations within the fill (Figure 1), utilizing distributed fibre optic sensing (DFOS) technology from the Nerve-Sensors family, as depicted in Figure 2. Additionally, the steel mesh reinforcement was extensively instrumented with optic fibres. In the x-direction, X01 to X09 were glued to the top of the top steel bars, while in the y-direction, Y01 to Y09 were attached to the bottom of the bottom steel bars.

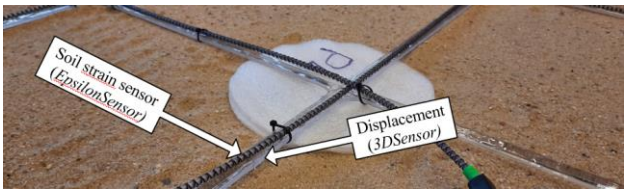

Figure 2. DFOS sensors (connected to a LUNA OBR 4600 reflectometer with 15-channel optical switch).

The series of four tests included:

Test 1: With SR, flexible piles (utilizing springs with a stiffness of 4605 kN/m below the piles) and stepwise consolidation;

Test 2: As Test 1, but continuous consolidation (the tap of the foam cushion was kept open permanently). This test closely aligns with the large-scale test described by Schneider et al., 2024.;

Test 3: As Test 1, but without SR;

Test 4: As Test 1, but with rigid piles (no springs).

3 MEASURED LOAD DISTRIBUTION

When the area between the piles deforms more than the piles, soil arching develops. In a piled embankment

with basal reinforcement, this results in a non-uniform distribution of the vertical load on the reinforcement. A significant portion of the vertical load (labelled as 'A' in Figure 3) is directly transferred to the piles since they deform less than the reinforcement. The residual load, 'B+C' in Figure 3, is supported by the subsurface between the piles.

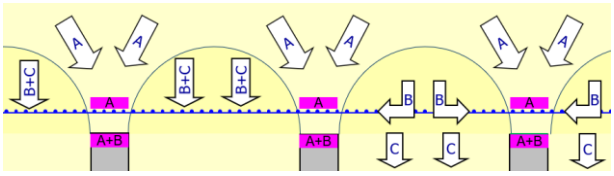

Figure 3. Load distribution in a PS embankment.

Several design guidelines and standards, such as BS8006 (2010), EBGEO (2011), ASIRI (2012), CUR226 (2016), and Topolnicki and Kłosiński et al. (2022), provide equations to divide the total vertical load into A and B+C. These guidelines then offer methods for calculating the strain in the reinforcement from B+C, considering the load-deflection behaviour of the reinforcement.

Many researchers have analysed how the geometry and material properties affect soil arching. Van Eekelen et al. (2012b) showed that the soil arching quickly develops, even when the deflection of the GR is minimal. In line with this finding, they showed that the GR tensile stiffness has a limited impact on soil arching, while the shear properties of the fill (internal friction angle) play a significant role.

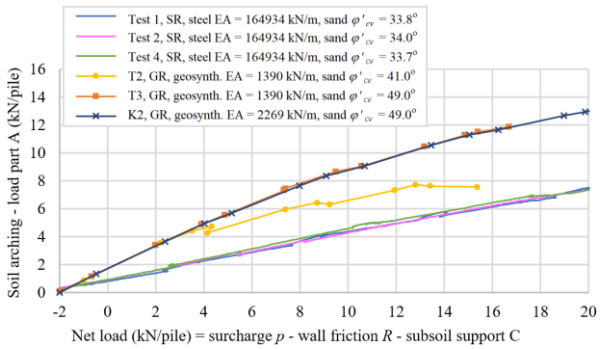

Figure 4. Measured soil arching A in the current tests with SR, compared to previous tests with GR in the same test box (van Eekelen et al., 2012).

These conclusions were valid for GR. An important question is whether the high axial and bending stiffnesses of the SR affect the soil arching.

Figure 4 compares Tests 1, 2 and 4 with SR with three previous tests with GR, conducted in the same test box. The data show much less soil arching in the SR tests than in the GR tests. The fill friction angle, however, seems to have a major impact on the soil arching, where the reinforcement stiffness does not show the same level of influence.

Since only one combination of SR stiffness and fill friction angle was tested, the pure test results cannot confirm this conclusion. However, it is possible to validate the impact of the fill and SR stiffness by comparing the measured and calculated soil arching, using three analytical methods, as shown in Figure 5 for four conducted tests.

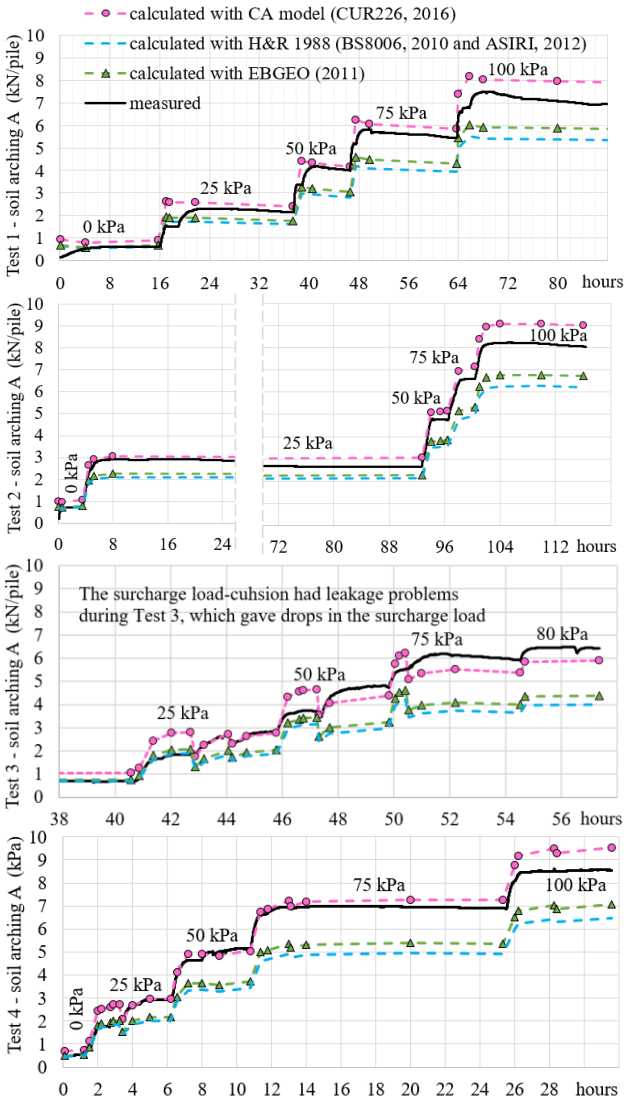

Figure 5. Measured and calculated soil arching A, using three European models. H&R refers to the model of Hewlett & Randolph 1988. Surcharge loads are indicated (0 to 100 kPa). Input parameters from Table 1.

The CA model (CUR226, 2016) consistently matches the measurements well, specifically for $p \leq 75$ kPa. It can therefore be concluded that the axial and bending stiffnesses of the reinforcement do not play a significant role because they are not considered in the soil arching part of the CA model.

4 MEASURED FILL DEFORMATIONS

For each test, the model was rebuilt. Some DFOS ruptured during testing (due to high local strains above 4%), and not all of them could be replaced in the next test. For this reason, this section focuses on Test 1, although Tests 1, 2 and 4 exhibit similar trends. This becomes evident when comparing Figure 6 and Figure 7, for example.

Figure 6 and Figure 7 show the settlements measured at different levels in the fill. The most significant differential settlements occur in the steel bars that bridge adjacent piles, denoted by lines (a), (c), (d) and (f).

The bars running through the centre of the test setup, represented by lines (b) and (e), show slightly more settlement, but notably less differential settlement. After the consolidation phase under a surcharge load of 25 kPa, the maximum settlement of the steel mesh (level 2), in the centre between four piles, is on average 8.6% greater than the settlement in the middle between adjacent piles. This finding is in line with the 3D FEM analysis of Zhang et al. (2019), who reported 6 to 8% difference. In contrast, the field measurements of Van Eekelen et al. (2020) showed a difference of approximately 25%.

The differential deflection of the steel mesh (level 2) between the piles causes soil arching. At level 3, located 225 mm above the pile heads, the differential settlement is noticeably less. At levels 4 and 5, it was only possible to reliably assess the deformations along lines (b) and (e). The settlements at these lines (b) and (e) at levels 4 and 5 are uniform. This does not prove that the 'plane of equal settlement' has been found, as there is no information about lines (a), (c), (d) and (f) at these high elevations, and these are the lines where most differential settlement occur.

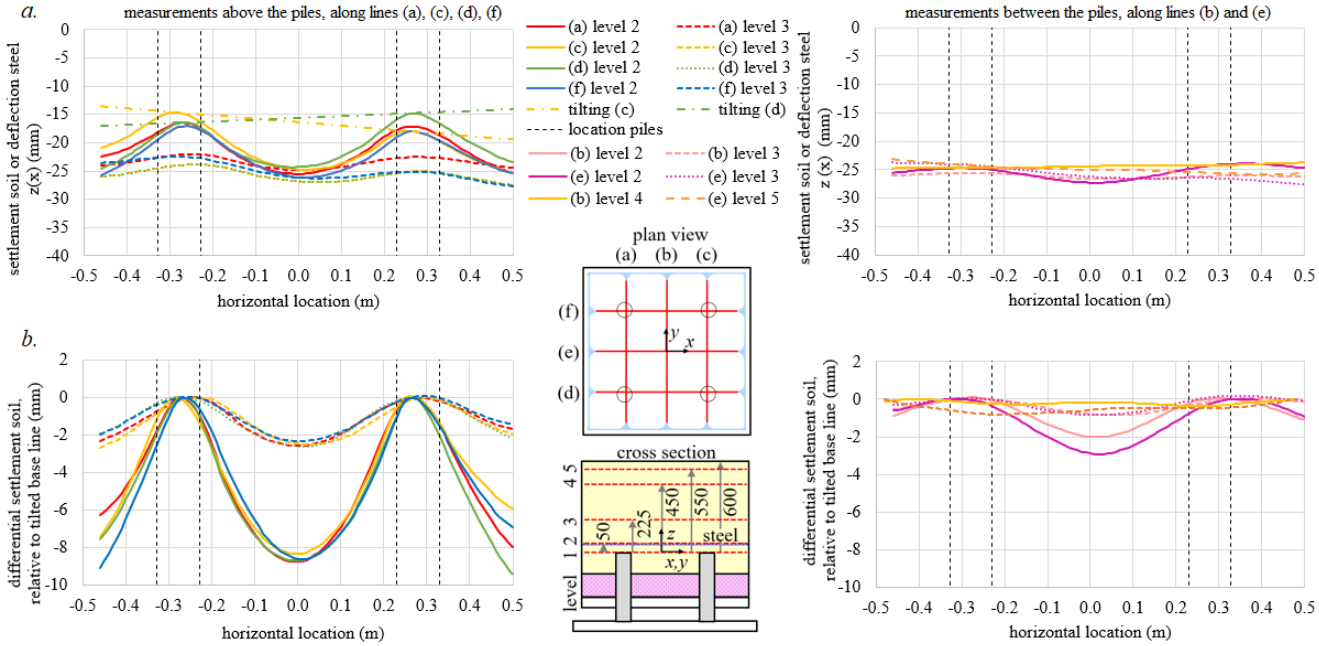

Figure 6. Test 1. Measured settlement in the fill at various levels under a 25 kPa surcharge load, after a consolidation phase. a. Measured settlements b. Settlement relative to the tilting baselines of each grid, as illustrated in top-left graph.

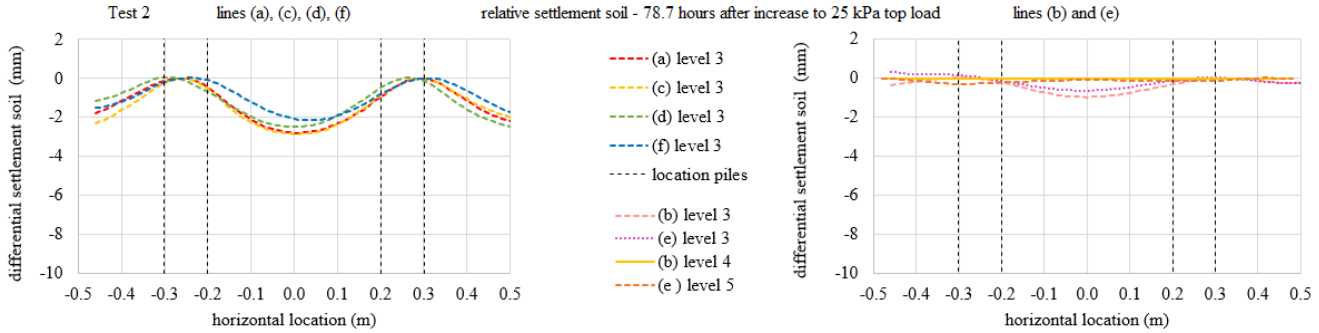

Figure 7. Test 2. Measured settlement in the fill at different levels at 25 kPa surcharge load after a consolidation phase. No data available for Test 2 – level 2.

5 MEASURED STEEL STRAINS

Figure 8 shows the strain at the top of the upper bars, all in x-direction. The left-side graphs show significantly higher strains in the steel bars above the piles, compared to those located between the piles, as shown in the right-side graphs. Bar X03 lies just next to a pile, resulting in 17 – 35% less tensile strain than the average strain in X01, X02 and X07 to X09 for the phases depicted in Figure 8.

Above the piles, we observe tensile strain in the top of the upper bars, indicated by positive values. These strains result from the bending of the steel bars above the piles. In Figure 8*b*, the maximum tensile strain reaches around 0.2%, while the maximum compression strain is around 0.06%. The presence of a 5 cm layer of sand between the steel mesh and pile heads facilitates a 'smooth' bending of the steel bars, contrasting a scenario where the SR has been installed directly on the pile heads.

In the area between the piles, we observe compression strain, represented by negative values in the top of the top bars. This is also caused by the bending of the steel (visible in Figure 7). This behaviour differs from GR, which experiences only tensile strain. Towards the edges of the piles, the steel bars exhibit an increasing tensile strain.

The alternation of compression and tensile strain underscores the importance of considering axial and bending stiffness of the steel mesh when performing calculations to simulate this situation.

The local spikes in Figure 8 are strain reading anomalies (SRAs), which are disturbances in the DFOS fibres. The higher the local bending, the more SRAs were found in the DFOS measurements. Van Eekelen et al. (2024b) further analysed these SRAs in the DFOS measurements.

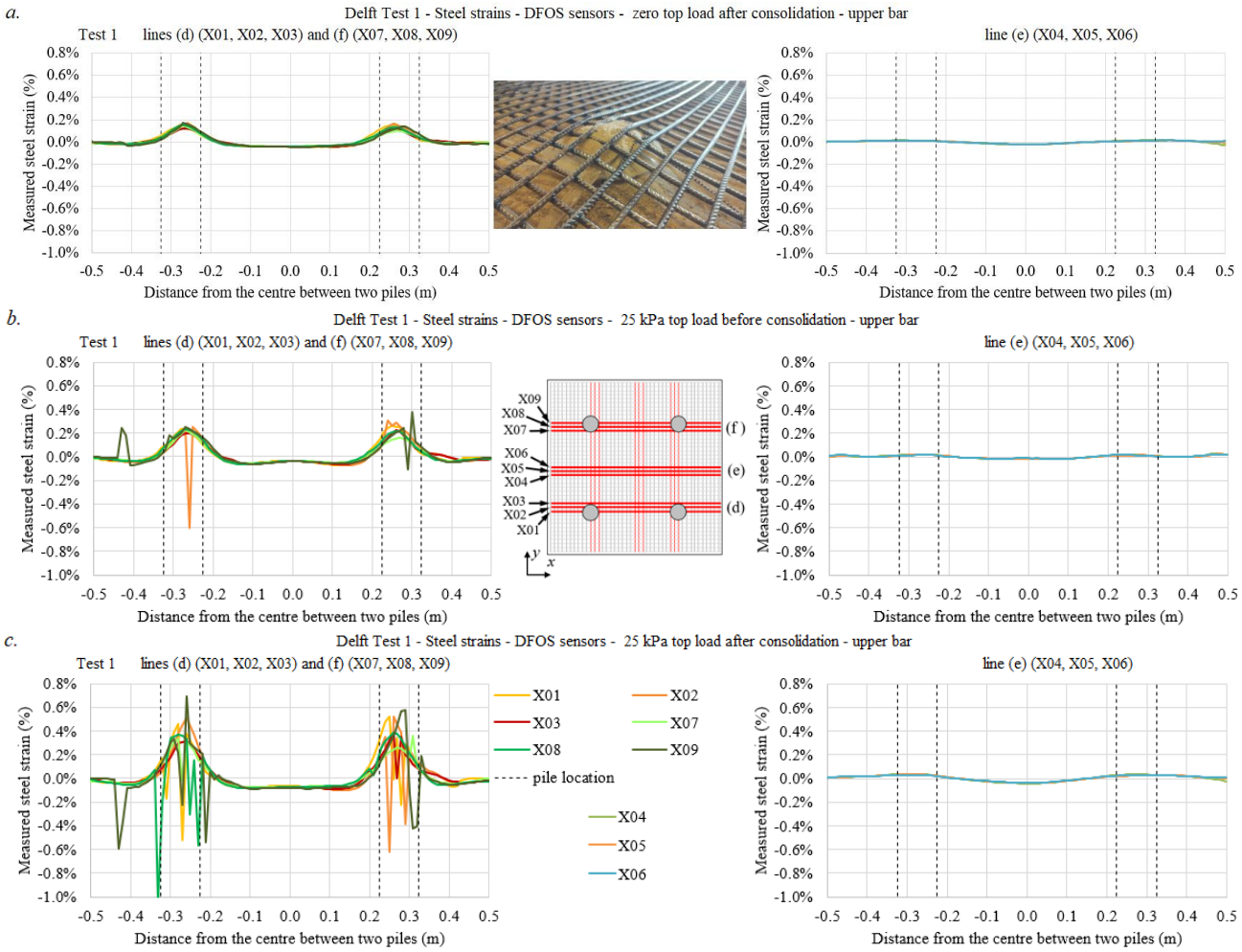

Figure 8. Test 1. Steel strains, measured on top of the top steel bar in x-direction. a. after consolidation without surcharge load, b. after increasing the surcharge load to 25 kPa, and c. after consolidation with surcharge load at 25 kPa.

6 CONCLUSIONS

This paper presents four small-scale tests on steel-reinforced (SR) piled embankments. This is part of a larger research, that also includes a large-scale test and numerical analyses. Based on the test results presented in this paper, we draw the following preliminary conclusions.

- The axial and bending stiffnesses of the SR do not significantly affect the soil arching in the fill above the piles. Consequently, the load part that is transferred to the piles directly (load part A) is similar for both types of basal reinforcement: geosynthetic and welded steel mesh reinforcement.
- The friction angle of the embankment fill has much more influence than the reinforcement type.
- Three main European design methods for GRPS embankments closely align with the measured soil arching, with the CA model exhibiting the best match.
- The DFOS sensors provide continuous and a unique 3D picture of the deformations of the reinforcement and the fill.
- The steel mesh reinforcement shows significant differential deflection and strain in the bars that bridge adjacent piles. The bars running through the centre of the square between the four piles, show slightly more settlement, but much less differential settlement and steel strain. This is in line with the deformation pattern observed in geosynthetic-reinforced piled embankments.
- Tensile strains due to bending are observed above the piles in the top bars of the reinforcement. Compression strains due to bending occur in the area between adjacent piles. This indicates that load-deflection design models for steel mesh and geosynthetic reinforcements should be different.

ACKNOWLEDGEMENTS

The authors are grateful for the funding received from the European Union's Horizon 2020 research and innovation program under Grant Agreement No. 101006512 for the transnational GEOLAB project PEBSTER, the TKI-PPS funding of the Dutch Ministry of Economic Affairs and the financial and practical support of Keller.

REFERENCES

ASIRI (2013). *Recommendations for the design, construction and control of rigid inclusions ground improvements* (French version is of 2012).

BS8006-1 (2010). *Code of practice for strengthened/reinforced soils and other fills*. British Standards Institution, UK.

CUR226 (2016). See van Eekelen and Brugman (2016).

EBGEO (2011). *Recommendations for Design and Analysis for Earth Structures using Geosynthetic Reinforcements* (German version is of 2010).

Hewlett, W.J. and Randolph, M.F. (1988). Analysis of piled embankments. *Ground Eng.,* 21(3): 12-18.

Schneider, M., Hell, M., Wittekoek, B., Pandrea, P., van Eekelen, S.J.M., Topolnicki, M., Makowska, K., Sieńko, R. and Zachert, H. (2024). Large-scale test on the load bearing and deformation behaviour of basal steel-reinforced piled embankments. In: *Proc. ECSMGE 24*, Lisbon, Portugal.

Topolnicki, M., Sołtys, G. and Brzozowski, T. (2019). Performance and modelling of road embankment supported on rigid inclusions and a transfer platform with steel geogrid, *Proc. ECSMGE 2019*, Iceland.

Topolnicki, M., Kłosiński, B. et al. (eds.) (2022). *Recommendations for Ground Improvement with Rigid Inclusions - Design, Execution and Control* (in Polish). PWN SA. ISBN 978-83-01-22578-0.

van Eekelen, S.J.M., Bezuijen, A., Lodder, H.J. and van Tol, A.F. (2012a). Model experiments on piled embankments Part I. *Geotextiles and Geomembranes*, 32: 69-81. DOI: 10.1016/j.geotexmem.2011.11.002.

van Eekelen, S.J.M., Nancey, A. and Bezuijen, A. (2012b). Influence of fill material and type of geosynthetic reinforcement in a piled embankment, model experiments. In: *Proc. Eur. Geosynthetic Congress.,* Valencia, Spain, Vol 5, 167-171.l.

van Eekelen, S.J.M. and Brugman, M.H.A., Eds. (2016). *Design Guideline Basal Reinforced Piled Embankments* (CUR226). CRC press, Delft, Netherlands.

van Eekelen, S.J.M. and Han, J. (2020). Geosynthetic-reinforced pile-supported embankments: state of the art. *Geosynthetics International* 27 (2) 112-141. DOI: 10.1680/jgein.20.00005.

van Eekelen, S.J.M., Venmans, A.A.M., Bezuijen, A. and van Tol, A.F. (2020). Long term measurements in the Woerden geosynthetic-reinforced pile-supported embankment. *Geosynthetics International,* 27 (2) 142-156. DOI: 10.1680/jgein.17.00022.

van Eekelen, S.J.M., Wittekoek, B., Zwaan, R., Bezuijen, A. and Nancey, A. (2024a). Groundwater in geosynthetics-reinforced pile-supported embankments. *Proc. ECSMGE24*, Lisbon, Portugal.

van Eekelen, S.J.M, Schneider, M., Hell, M., Wittekoek, B., Makowska, K., Zdanowicz, K., Wittekoek, B., Pandrea, P., Sieńko, R., Schauber, P., Topolnicki, M., Zachert, H. (2024b). Distributed Fibre Optic Sensing (DFOS) in 3D small-scale tests on steel-reinforced piled embankments. In: *Proc. ECPMG 2024*, Delft, Netherlands.

Zhang, Z., Wang, M., Ye, G. B. and Han, J. (2019). A novel 2D-3D conversion method for calculating maximum strain of geosynthetic reinforcement in pile-supported embankments. *Geotextiles and Geomembranes*, 47 (3) 336–351. DOI: 10.1016/j.geotexmem.2019.01.011.

Proceedings of the XVIII ECSMGE 2024
GEOTECHNICAL ENGINEERING CHALLENGES
TO MEET CURRENT AND EMERGING NEEDS OF SOCIETY
© 2024 the Authors
ISBN 978-1-032-54816-6
DOI 10.1201/9781003431749-527
Open Access: www.taylorfrancis.com, CC BY-NC-ND 4.0 license

ECSMGE 24
XVIII EUROPEAN CONFERENCE ON SOIL MECHANICS AND GEOTECHNICAL ENGINEERING

Groundwater in geosynthetics-reinforced pile-supported embankments, 3D Experiments

Nappe phréatique affleurant les remblais renforcés par géosynthétiques sur pieux, Expérimentations en 3D

S.J.M. van Eekelen*, B. Wittekoek, R.A. Zwaan, A. Bezuijen
Deltares, Delft, Netherlands

A. Nancey
Solmax, Paris, France

**suzanne.vaneekelen@deltares.nl*

ABSTRACT: This paper investigates the influence of groundwater on geosynthetic-reinforced pile-supported (GRPS) embankments. 3D experiments showed that groundwater primarily reduces the load, mainly through uplift forces, but also causes a slight reduction in soil arching. However, the soil arching quickly recovers when the groundwater level decreases again. The Concentric Arches (CA) model (CUR226, 2016), combined with Archimedes' principle, provides the most accurate match compared to two other main calculation models. No significant correlation between groundwater levels and geosynthetic reinforcement strains was observed.

RÉSUMÉ: Cet article examine l'impact du niveau de la nappe phréatique sur les remblais renforcés par des géosynthétiques et des pieux (GRPS). Les expériences 3D montrent que la présence d'eau réduit principalement la charge par des forces de soulèvement, avec une légère réduction de l'effet de voûte de sol. Cependant, cet effet se rétablit rapidement lorsque le niveau d'eau souterraine diminue. Le modèle des arcs concentriques (CA) (CUR226, 2016), combiné avec le principe d'Archimède, offre la meilleure correspondance parmi les modèles de calcul. Aucune corrélation significative entre les niveaux d'eau et les déformations du renforcement géosynthétique n'a été observée.

Keywords: Groundwater; geosynthetic-reinforced pile-supported embankments; soil arching.

1 GROUNDWATER IN GEOSYNTHETIC-REINFORCED PILED EMBANKMENTS

The calculation model in the CUR226 (2016) design guideline for geosynthetic-reinforced pile-supported (GRPS) embankments was validated with over 100 measurements in experiments and field (van Eekelen et al., 2015). The validated application of a guideline is limited to circumstances like the ones from which the validation measurements were obtained. For GRPS embankments, this means for example that the entire embankment must be located above the groundwater table.

However, infrastructure needs to remain usable during or after heavy rain. In addition to that, in low, flat, subsidence-prone areas, it is often desirable to install the embankment at least partly below groundwater level. Therefore, insight is required in the influence of groundwater on the behaviour of GRPS embankments.

Limited research was done on the influence of water in a piled embankment. Briançon and Simon (2012), Sloan (2011), and Van Eekelen et al. (2020) observed that heavy rainfall affects measurements.

Song et al. (2018) presented small-scale 2D trapdoor tests with sand and concluded that water can degrade the soil arching. Wang et al. (2019), however, showed with full-scale 3D model experiments that the soil arching strengthened with an increasing water level.

In contrast, Van Eekelen et al., (2023) found no significant correlation between the groundwater table and GR strains during four years monitoring in a partly submerged GRPS embankment.

Various mechanisms can play a role when the groundwater rises in a GRPS embankment:

- An increase in uplifting forces, resulting in a reduction of effective stress. This study investigates whether this affects the soil arching mechanism, deformations and GR tensile strains.
- Swelling of the subsoil underneath the reinforcement, as measured by van Eekelen et al. (2020). The subsoil swelling reduces strain

in the reinforcement and the load on the piles. This situation is not addressed in this study.

- Dynamic liquefaction. It is essential to determine whether fill layers in the design may be liquefiable. This phenomenon is also not considered in this study.

The study aims to investigate the influence of high and changing groundwater levels in a GRPS embankment, addressing the following questions: How does the changing groundwater table in a GRPS embankment affect the soil arching in the fill, the deformations and the GR strains? For this purpose, the paper presents 3D laboratory experiments, analyses the results, and compares these with analytical calculations.

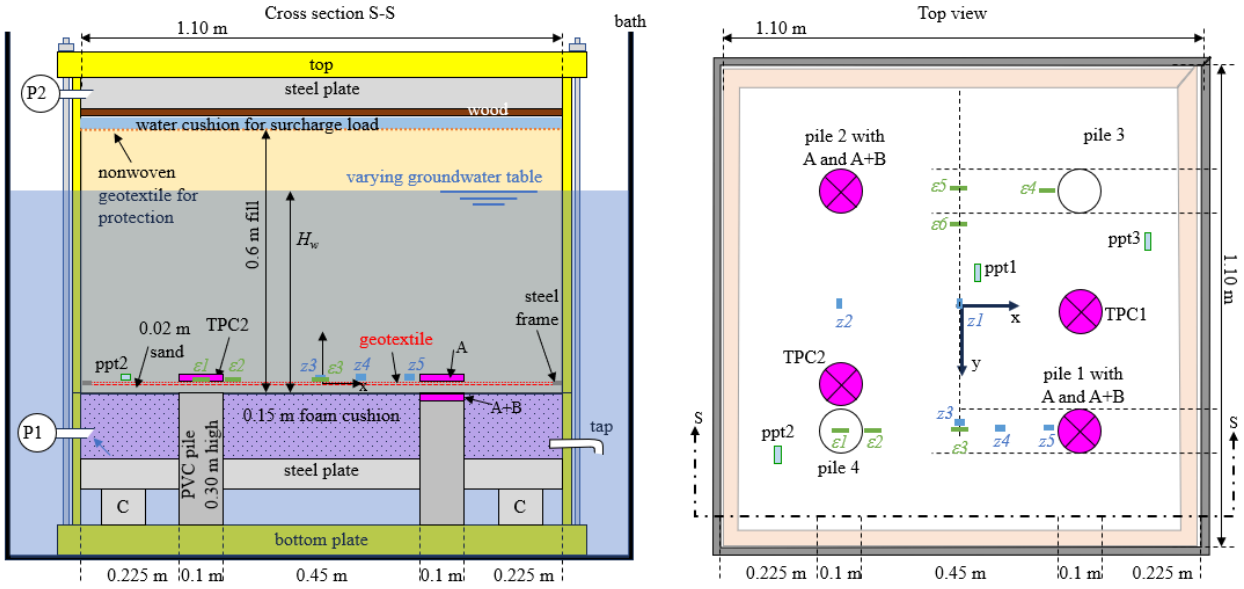

Figure 1. Test setup GRPS embankment in bath to induce a varying groundwater table in the fill.

2 SCALED EXPERIMENTS

Figure 1 shows the test setup (van Eekelen et al., 2012a, 2024). A steel plate supports a foam cushion, that is sealed and soaked. A tap allows for the drainage of the foam cushion. Four PVC piles with a 0.1 m diameter pass through the steel plate.

Two layers of Geolon 100-50 woven geotextile were placed perpendicular to and directly on top of each other. They were attached to a rigid steel frame. The combined geotextiles had a tensile strength of 100+50 = 150 kN/m and a tensile stiffness at 2% strain of $J_{2\%}$ = 1200 kN/m and 1013 kN/m for 10 and 1000 hours loading, respectively.

An equally distributed surcharge load was applied on the fill surface, using a water cushion. A rubber sheet greased with Vaseline minimised the wall-soil friction. The load distribution in the fill was measured by total pressure cells, GR deflection with a liquid levelling system (water pressure cells in a tube filled with water and connected to a reference box with water), and the GR strains were measured using cables (van Eekelen et al., 2024).

Two types of mixed demolition waste granulate were used; one with fine content (d/D = 0/31.5 mm) and one without fine content (d/D = 4/31.5 mm), where d and D are the lower and upper sieve sizes (EN13242, 2015). Table 1 lists fill details. The values of $\varphi'_{15\%}$ were obtained from four drained large-scale triaxial tests with a sample diameter of 0.45 m.

Table 1. Test details of the three small-scale tests.

Test no.	1	2	3
Fill height above steel (m)	0.65	0.60	0.60
Limiting sieve sizes d/D (mm/mm)	4/31.5	0/31.5	4/31.5
Median particle size D_{50} (mm)	18.8	7.0	18.8
Unit weight dry fill γ_d (kN/m^3)	13.19	14.60	13.20
Unit weight saturated fill γ_s (kN/m^3)	18.11	19.00	18.12
Unit weight initial fill γ_i (kN/m^3)	13.90	15.39	13.91
Porosity n (V_{pores}/ V_{total})	0.50	0.45	0.50
Friction angle unsaturated fill $\varphi'_{15\%}$ (°)	41.0	39.4	41.0
Friction angle saturated fill $\varphi'_{15\%}$ (°)	40.5	39.6	40.5

After the installation of the reinforcement, sensors and the fill, the box was closed and placed in a bath (Figure 1). Then, the subsoil support was removed by sucking the foam cushion vacuum.

Subsequently, the bath was filled. The groundwater table in the fill followed the water level in the bath easily. Then, (in Tests 2 and 3) the groundwater table was lowered again. After that, the surcharge load was increased in steps. After each surcharge load step, a groundwater cycle was applied again. In Test 1, the phreatic line was kept constant.

3 CALCULATIONS

The three main European design methods for GRPS embankments are:

- the Concentric Arches model of van Eekelen et al., (2013, 2015, adopted in CUR226, 2016);
- the model of Zaeske (2001), adopted in EBGEO, (2011);
- the model of Hewlett and Randolph (1988) adopted in both the French ASIRI (2012) and the British Standard (BS8006, 2010).

The first calculation step of these models divides the vertical load into two parts (Figure 2). Part A (kN/pile) is directly transferred to the piles and is relatively large, due to soil arching. The residual load, 'B+C' (kN/pile) is supported by the subsurface between the piles.

The second calculation step calculates the GR strain, and implicitly also divides B+C further into B and C. In the tests presented in this paper, the foam cushion underneath the GR was sucked vacuum, so that for all tests the subsoil support was zero during the entire test, so that C = 0.

3.1 Input parameters

Figure 1 gives the geometry properties, and Table 1 the fill properties. The groundwater table H_w was derived from the measured pore pressures (ppt 1, 2 and 3). The weighted value of γ in equations (2) to (5) was derived from γ_d below groundwater level (combined with Archimedes' p_{uplift} for the grains) and γ_i (kN/m^3) above groundwater level. γ_i is the initial fill unit weight that includes the 5.4% moisture content of the sand above the phreatic line.

The wall-soil friction R was 20-25% of the total load and was derived by subtracting the measured A+B+C from the total effective load. R was subtracted from the surcharge load. There was no subsoil support, so the subgrade reaction k = 0 kN/m^3. The geotextile tensile stiffness $J_{2\%}$ was chosen in line with the test duration: $J_{2\%}$ = 1106 kN/m.

3.2 Water in the calculations

Archimedes' principle states that a body immersed in a fluid is subject to an upward force equal to the weight of the displaced fluid. This aligns Terzaghi's effective stresses, which are the difference between the total stress and the water pressure.

In this paper, Archimedes' upward pressure (p_{uplift}) is used to bring into account the water in the fill. This upward pressure is defined as:

$$p_{uplift} = (1\text{-}n) \cdot H_w \cdot \gamma_w \text{ (kPa)} \quad (1)$$

where n (-) is the porosity, H_w (m) is the groundwater table above the piles, and γ_w is the unit weight of water (9.81 kN/m^3).

This p_{uplift} is integrated in the CA calculations by reducing surcharge load p with p_{uplift}. Theoretically, this aligns Terzaghi's effective stress calculations. However, using the Terzaghi's effective stresses is not possible for the CA model. This is explained as follows for the CA model (van Eekelen et al., 2013), but also applies for EBGEO:

Firstly, the CA model calculates the load distribution A% and (B+C)% without including the surcharge load (p = 0). This results in $A_{p=0}$ and $(B+C)_{p=0}$. So far, the calculation only uses the soil weight above the arches (besides geometry and material properties). Therefore, using Terzaghi's effective stress-approach would only impact the calculation for the fill part above the arches.

Secondly, the CA model includes the surcharge load:

$$A_{p>0} = \frac{\gamma H+p}{\gamma H} \cdot A_{p=0} \text{ and} \quad (2)$$

$$(B+C)_{p>0} = \frac{\gamma H+p}{\gamma H} \cdot (B+C)_{p=0} \quad (3)$$

In this study, we account for the groundwater by adjusting the equations as follows:

$$A_{p>0} = \frac{\gamma H+p-p_{uplift}}{\gamma H} \cdot A_{p=0} \text{ and} \quad (4)$$

$$(B+C)_{p>0} = \frac{\gamma H+p-p_{uplift}}{\gamma H} \cdot (B+C)_{p=0} \quad (5)$$

4 IMPACT GROUNDWATER

4.1 Impact groundwater on soil arching

Figure 2 compares the measured and calculated soil arching for Test 2. We observe the following:

- A rising groundwater level gives a limited decrease in both A and B.
- This decrease is primarily attributed to the uplift forces of Archimedes' principle rather than a change in soil arching. This is demonstrated by the calculations, which closely match the measurements. The calculations included the Archimedes uplift but did not reduce the soil arching due to a higher groundwater level.
- Figure 2c shows a slight decrease in soil arching A% due to groundwater. This shows that the decrease in A is not solely attributable to the Archimedes uplift, even though this remains the most significant mechanism at play.

The soil arching almost immediately rebounds when the phreatic line decreases. The soil arching (A)

changes less than 3.5% due to groundwater cycles, both up and down. The only exception is the first groundwater cycle which decreases the arching by 26%. At that stage, the arching had not found its equilibrium yet.

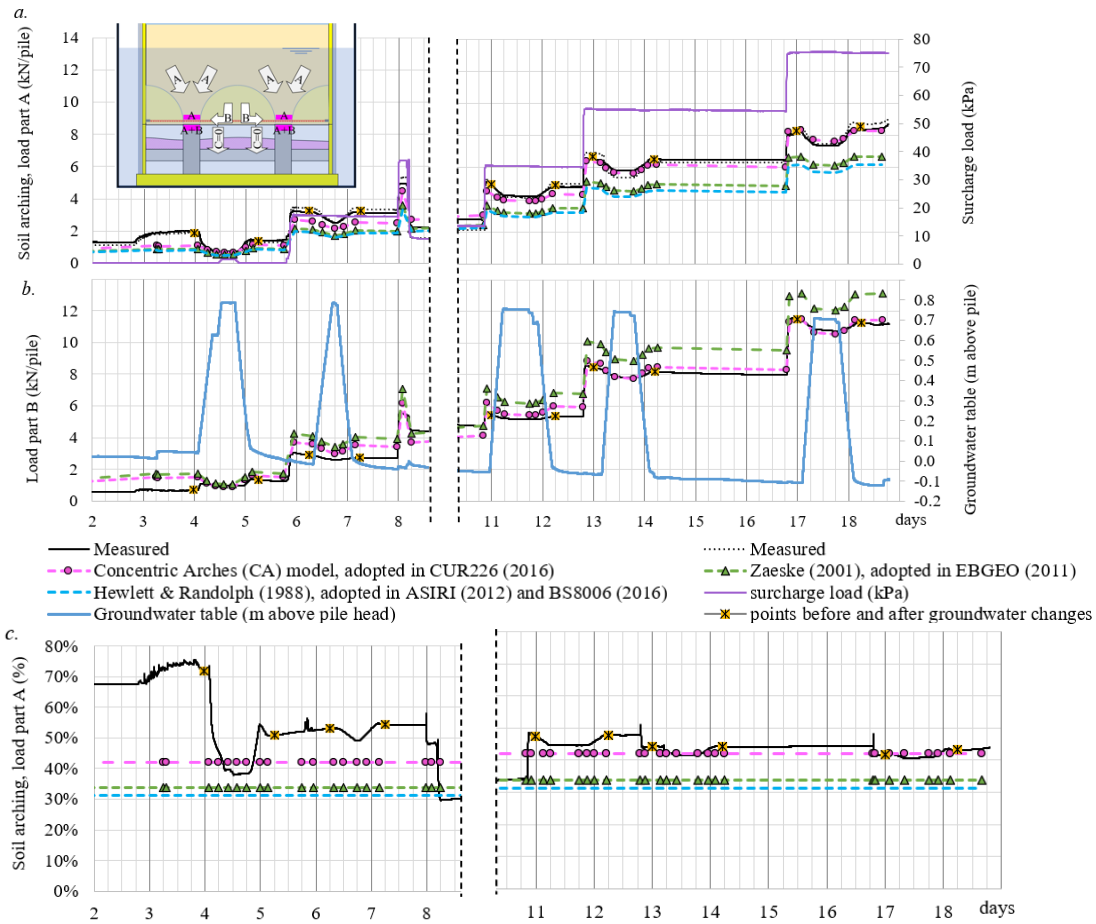

Figure 2. Comparison measured and calculated load distribution for Test 2. a. Soil arching (load part A). b. Load part B. c. Load part A in % of the total load. The 'measured' value of B was derived from the average measured values of A+B and A. p_{uplift} was integrated in all calculations by reducing surcharge load p with p_{uplift}. Between days 8 and 11, the surcharge load cushion leaked.

- The CA model matches the measurements better than the other two calculation models. Both EBGEO and Hewlett and Randolph (1988) underestimate the soil arching.

4.2 Impact groundwater on GR strains

Strain cables ('strain' or 'ε'), made from bicycle brake cables, were attached to the geotextile using tie wraps. The twisted steel wire that runs through an outer sleeve was pulled out by roughly 10 mm and fixed to the geotextile. A displacement transducer registered the difference between displacement of the twisted steel wire and the outer sleeve. This system provides only a qualitative result: many measured values are unrealistically large (van Eekelen et al., 2024): larger than the rupture strain, without rupture observed. Nevertheless, the measurements seem qualitatively reliable as in Figure 3a and Table 2, they match our expectations: the highest GR strains were measured in the strips between adjacent piles. The closer to the pile, the higher the strain. Outside the GR strip between adjacent piles (ε6), we observe much lower strains, typically around zero.

The GR strains do not show any significant response to changes in the groundwater level. This matches the findings of van Eekelen et al., 2023, who also found no convincing correlation between water and GR strain in field measurements. Temperature appeared to show a stronger correlation with the GR strain.

4.3 Impact groundwater on settlements

Figure 3b compares the measured and calculated GR deflection at the midpoint between two piles. The calculations were done for the middle of two adjacent piles. The CA model matches the measured deflection

nicely. Some settlement transducers show heave due to rising groundwater, specifically sensor z2. The calculations also show this effect, although to a lesser extent.

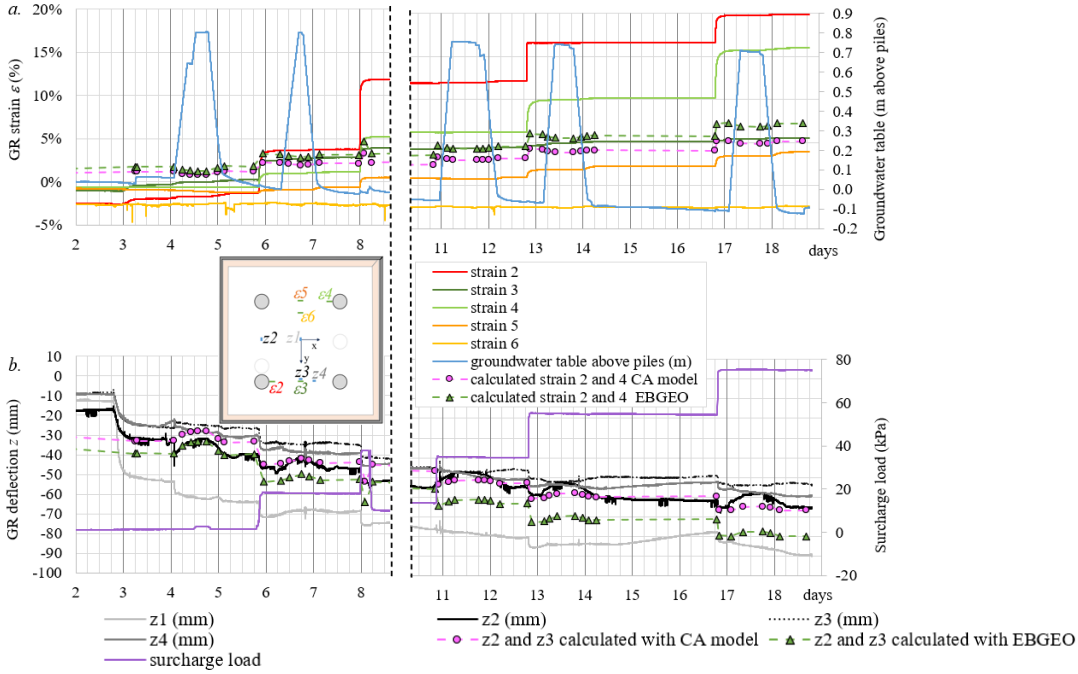

Figure 3. Measured and calculated deformations and strains. a. GR strains ε, and b. GR deflection z.

5 FILL WITH FINES OR NO FINES

Table 2 compares the measured and calculated values for Tests 1 to 3, for two surcharge loads (~ 17 and 55 kPa) and with and without groundwater.

The loading patterns of Tests 2 and 3 were comparable (after each surcharge load step a groundwater cycle), while Test 1 had surcharge load steps during one high groundwater period.

The deformations of Tests 2 and 3 match well, both with each other and with the CA calculations. The fill difference does not seem to have an impact.

The measured values of load part A, however, seem too high in the fill without fines of Tests 1 and 3. This difference is not in line with the measured GR deflections. Possibly, the issues that arose during Tests 1 and 3 play a role, such as leaks and malfunctioning sensors and pressure vessels. However, the high values of A in Tests 1 and 3 remain not fully explained.

As explained in Section 2, the strain measurements should only be considered qualitatively, they tend to be too large, sometimes larger than the rupture strain. In the average values of Table 2, these high values were not included.

All tests respond similarly to groundwater rise: a reduction in load and GR deflection, with a quick rebound after the high-water period. The CA calculations match the impact of groundwater well, if the uplift forces are taken into account.

Table 2. Comparison measurements and calculations for Tests 1, 2 and 3.

		Test 1	**Test 2**	**Test 3**	**Test 1**	**Test 2**	**Test 3**	**Test 1**	**Test 2**	**Test 3**	**Test 1**	**Test 2**	**Test 3**
	Time (day)	7.00	7.90	10.83	8.50	6.80	11.75	N/A	16.00	17.75	10.18	13.42	19.00
	Water table (m above pile)	0.00	0.00	0.00	0.65	0.60	0.55	N/A	0.00	0.00	0.65	0.60	0.60
	Surcharge load (kPa)	17.0	16.7	17.7	17.1	16.8	17.2	N/A	54.5	56.7	54.5	55.0	56.6
A (kN/pile)	Measured	4.9	3.2	4.6	3.7	2.5	3.7	N/A	6.4	9.1	7.7	5.6	8.5
	CA model (CUR226)	2.7	2.5	2.7	2.4	2.2	2.2	N/A	6.1	6.6	7.0	5.7	6.1
	Zaeske (EBGEO)	2.3	2.0	2.2	2.0	1.7	1.8	N/A	4.9	5.3	5.8	4.6	4.9
	Hewlett & Randolph 1988	2.2	1.9	2.0	1.9	1.6	1.6	N/A	4.5	4.9	5.6	4.2	4.5
GR deflection between two piles	Measured [1]	-43	-40	-37	-51	-38	-37	N/A	-55	-51	-67	-53	-52
	CA model (CUR226)	-44	-44	-44	-42	-42	-41	N/A	-60	-60	-61	-58	-58
	Zaeske (EBGEO)	-52	-52	-52	-50	-50	-49	N/A	-71	-72	-72	-70	-70
GR strain between two piles	Measured [2]	-	2.6%	1.6%	-	2.4%	1.6%	N/A	5.9%	3.0%	-	5.6%	3.1%
	CA model (CUR226)	2.1%	2.1%	2.1%	1.9%	1.9%	1.8%	N/A	4.1%	4.1%	4.2%	3.9%	3.9%
	Zaeske (EBGEO)	3.1%	3.1%	3.1%	2.8%	2.8%	2.7%	N/A	5.8%	5.8%	5.9%	5.5%	5.5%

[1] *Test 1: z4, Tests 2 and 3: average of z1, z2, z3.*

[2] *Clearly wrong measured strain values excluded (i.e. negative strain values and > 10%)*

6 CONCLUSIONS

Experiments were conducted to investigate the impact of groundwater in a GRPS embankment. The following conclusions were drawn:

- Groundwater gives a reduction of load, due to uplift forces.
- The reduction of load part A, which expresses soil arching, is mainly caused by the uplift forces, but a groundwater increase also leads to a slight reduction in soil arching.
- The soil arching immediately recovers when the groundwater level decreases again.
- The CA model provides a closer match to the measurements than the other two considered calculation models (EBGEO and Hewlett and Randolph (1988)), both of which underestimate the soil arching.
- The response on groundwater rise is similar for both fill types, with and without fines.
- An increase of groundwater gives some heave of the GR, due to the uplift forces. This heave disappears upon lowering the groundwater again.
- The presented experiment did not reveal any significant response of GR strains to changes in groundwater. This is in line with the field measurements of van Eekelen et al., 2023, who observed a correlation between air temperature and GR strain, and not between the groundwater table and GR strain. However, some authors, like Briançon and Simon (2012) and van Eekelen et al. (2020) reported changes in deformation and load distribution after heavy rain. It is possible that changes in temperature resulting from such heavy rain showers played a role in those cases, or by swelling of the subsoil due to the increase in water content.

ACKNOWLEDGEMENTS

The authors are grateful for the support of Solmax-TenCate, both financially and practically, and the support of the TKI-PPS funding of the Dutch Ministry of Economic Affairs.

REFERENCES

ASIRI (2013). *Recommendations for the design, construction and control of rigid inclusions ground improvements* (French version is of 2012).

Archimedes. (circa 250 BCE). Archimedes' Principle.

Briançon, L. and Simon, B. (2012). Performance of Pile-Supported Embankment over Soft Soil: Full-Scale Experiment, *J. of Geotech. and Geoenv. Eng.*, 138: 551-561. DOI: 10.1061/(ASCE)GT.1943-5606.0000561.

BS8006-1 (2010). Code of practice for strengthened/reinforced soils and other fills. British Standards Institution, UK.

CUR226 (2016). See Van Eekelen and Brugman (2016).

Hewlett, W.J. and Randolph, M.F. (1988). Analysis of piled embankments. Ground Eng. 21(3): 12-18.

NEN-EN 13242 (2015) *Hydraulic bound and unbound aggregates*.

Song, J., Chen, K., Li, P., Zhang, Y. and Sun, C. (2018). Soil arching in unsaturated soil with different water table. *Granular Matter*, 20: 78. DOI: 10.1007/s10035-018-0849-3.

van Eekelen, S.J.M., Bezuijen, A., Lodder, H.J. and van Tol, A.F. (2012a). Model experiments on piled embankments Part I. *Geotextiles and Geomembranes*, 32: 69-81. DOI: 10.1016/j.geotexmem.2011.11.002.

van Eekelen, S.J.M., Bezuijen, A. van Tol, A.F., (2013). An analytical model for arching in piled embankments. Geotextiles and Geomembranes 39: 78-102. DOI: 10.1016/j.geotexmem.2013.07.005.

van Eekelen, S.J.M., Nancey, A., Bezuijen, A. (2012b). Influence of fill material and type of geosynthetic reinforcement in a piled embankment, model experiments. In: *Proc. Eur. Geosynthetic Congres.,* Valencia, Spain, Vol 5, 167-171.

van Eekelen, S.J.M., Bezuijen, A. and Van Tol, A.F. (2015). Validation of analytical models for the design of basal reinforced piled embankments. *Geotextiles and Geomembranes*, 43(1): 56 - 81. DOI: 10.1016/j.geotexmem.2014.10.002.

van Eekelen, S.J.M. and Brugman, M.H.A., Eds. (2016). *Design Guideline Basal Reinforced Piled Embankments* (CUR226). CRC Press, Delft, Netherlands.

van Eekelen, S.J.M., Venmans, A.A.M., Bezuijen, A. and van Tol, A.F. (2020). Long term measurements in the Woerden geosynthetic-reinforced pile-supported embankment. *Geosynthetics International,* 27(2): 142-156. DOI: 10.1680/jgein.17.00022.

van Eekelen, S.J.M., Zwaan, R.A., Nancey, A., Hazenkamp, M. and Jung, Y.H. (2023). Four years field measurements in a partly submerged woven geotextile-reinforced pile-supported embankments. *Geosynthetics: Leading the Way to a Resilient Planet*, 1072-1077. DOI: 10.1201/9781003386889-133

van Eekelen, S.J.M., Wittekoek, B., Zwaan, R.A., Bezuijen, A., Nancey, A. (2024). 3D Experiments in bath: groundwater in geosynthetics-reinforced pile-supported embankments. In: *Proc. ECPMG 2024,* Delft, Netherlands.

Wang, H.-L., Chen, R.-P., Cheng, W., Qi, S. and Cui., Y.-J. (2018). Full-scale model study on variations of soil stress in geosynthetic-reinforced pile-supported track bed with water level change and cyclic loading. *Can. Geot. J.* 56(1): 60-68. DOI: 10.1139/cgj-2017-0689.

Proceedings of the XVIII ECSMGE 2024
GEOTECHNICAL ENGINEERING CHALLENGES
TO MEET CURRENT AND EMERGING NEEDS OF SOCIETY
© 2024 the Authors
ISBN 978-1-032-54816-6
DOI 10.1201/9781003431749-528
Open Access: www.taylorfrancis.com, CC BY-NC-ND 4.0 license

ECSMGE 24
XVIII EUROPEAN CONFERENCE ON SOIL MECHANICS AND GEOTECHNICAL ENGINEERING

Effect of the variable discharge capacity of prefabricated vertical drains on the behaviour of an embankment built on soft soils

Effet de la capacité de décharge variable des drains verticaux préfabriqués sur le comportement d'un remblai construit sur des sols mous

P.J. Venda Oliveira*
Department of Civil Engineering, University of Coimbra, Coimbra, Portugal
**pjvo@dec.uc.pt*

ABSTRACT: In the past, the design of vertical drain systems considered an infinite discharge capacity. Although this hypothesis is suitable for sand drains with high coefficient of permeability, when prefabricated vertical drains (PVDs) are used, the decrease of the discharge capacity with elapsed time cannot be ignored. In this paper, a formula that relates the discharge capacity of PVDs to the consolidation time and the confining pressure around the drains is used to analyse the behaviour of an embankment built on a soft soil. The vertical and horizontal displacements predicted numerically considering infinite, reduced and variable discharge capacity of the PVDs are compared with one another and with field data. In general, the results show that the use of the formula proposed improves the numerical predictions of the settlement during the intermediate phases of consolidation. In terms of the horizontal displacement, the effect of the discharge capacity of the vertical drains seems to be negligible.

RÉSUMÉ: Dans le passé, la conception des systèmes de drains verticaux considérait une capacité de décharge infinie. Bien que cette hypothèse convienne aux drains de sable avec un coefficient de perméabilité élevé, lorsque des drains verticaux préfabriqués (PVD) sont utilisés, la diminution de la capacité d'évacuation avec le temps écoulé ne peut être ignorée. Dans cet article, une formule qui relie la capacité de décharge des PVD au temps de consolidation et à la pression de confinement autour des drains est utilisée pour analyser le comportement d'un remblai construit sur un sol mou. Les déplacements verticaux et horizontaux prédits numériquement en considérant une capacité de décharge infinie, réduite et variable des PVD sont comparés entre eux et avec les données de terrain. En général, les résultats montrent que l'utilisation de la formule proposée améliore les prévisions numériques du tassement pendant les phases intermédiaires de consolidation. En ce qui concerne le déplacement horizontal, l'effet de la capacité de décharge des drains verticaux semble être négligeable.

Keywords: Geosynthetics; soft soil; discharge capacity; PVDs.

1 GUIDELINES

The design of vertical drain systems has been based on the classical theoretical solution (Barron, 1948), in which the drains were considered as ideal drains, that is, with infinite discharge capacity. Although this hypothesis is suitable for sand drains with high permeability (Hansbo et al., 1981), when PVDs with low discharge capacity are used, the decrease of the discharge capacity with elapsed time cannot be ignored (Holtz et al., 1988).

The progressive blockage of the water flow inside the drain is due to the following issues (Chai and Miura, 1999; Indraratna and Redana, 2000; Indraratna et al., 2003; Karunaratne, 2011; Deng et al., 2013): (i) folding and crimping of the drain induced by excessive settlement, which happens in very compressible soils; (ii) reduction of the section of the drain core due to the increases of the confining pressure at depth; (iii) infiltration of fine particles of soil (silt and clay) through the filter; (iv) the existence of air bubbles inside the drainage path. Another issue that affects the consolidation rate of vertical drains arises from the reduction of the permeability in the soil around the PVDs (smeared zone) due to the disturbance induced by the method of installing the PVDs. In fact, this depends on of the characteristics of the mandrel (shape and size) and the dimensions of the anchor plate (Lin and Chang, 2009; Tripathi and Nagesha, 2010; Karunaratne, 2011).

In order to improve the numerical predictions of the behaviour of the PVDs, an empirical formula to evaluate the changes in the discharge capacity over time and with the confining pressure of the soil is

presented in this work. This formula was included in a three-dimensional (3D) finite-element (FE) code, which was used to predict the behaviour of an embankment built on a soft soil improved with PVDs. The ability of this formula to simulate real cases is examined by comparing the numerical results obtained with the numerical predictions using ideal vertical drains (i.e. with infinite discharge capacity) and using PVDs with a reduced discharge capacity constant over time. All the numerical predictions are compared with the field data in terms of settlement and horizontal displacement.

This investigation was carried out using a 3D FE code developed at the University of Coimbra (Almeida e Sousa, 1998; Venda Oliveira, 2013; Cruz, 2008). It allows elastoplastic analyses to be carried out with coupled consolidation and it incorporates several constitutive laws.

2 PROPOSED FORMULA

Regarding the experimental results obtained previously (Chai and Miura, 1999; Chai et al., 2004; Kim et al., 2011; Deng et al., 2013; Bergado et al., 1996; Karunaratne, 2011; Asha and Mandal, 2012), a new empirical formula to evaluate the discharge capacity of PVDs (q_w) is proposed, to evaluate the change of q_w with the confining pressure and the consolidation time:

$$q_w = q_{w,max} \cdot [r + (1-r)\exp(-a\frac{t}{t_1}).(1-m\frac{\overline{\sigma}_h}{\sigma_{h1}})] \quad (1)$$

where $q_{w,max}$ is the maximum discharge capacity of the PVD in m^3/s (defined as the rate of discharge of the drain under a unit hydraulic gradient); $\overline{\sigma}_h$ is the average total horizontal soil pressure (i.e., the confining pressure) surrounding the PVD in kPa; σ_{h1} is the total reference horizontal pressure (usually =100 kPa); t is the consolidation time expressed in days; t_1 is the reference time (usually t_1 = 1 day); r is the reduction factor which states the minimum discharge capacity ($q_{w,min} = r \cdot q_{w,max}$); m and a are the parameters that control the decay of q_w with $\overline{\sigma}_h$ and t, respectively. Parameter m is related to the structure and the stiffness of the PVD, while parameter a depends on the shape of the core of the PVD, the characteristics of the filter of the PVD and the soil characteristics around the PVD. r, a and m are dimensionless parameters, which can be evaluated from sensibility studies in order to approximate the variation of the q_w of the PVDs over time and with the confining stress obtained from formula (1) with the experimental results obtained from laboratory tests or field data.

Formula (1) does not consider the effect of the hydraulic gradient on the drainage capacity since the results published are not totally in agreement. Indeed, some studies show a reduction of drainage capacity over time for a lower hydraulic gradient (Chai et al., 2004; Müller et al., 2008; Asha and Mandal, 2012; Ali and Huat, 1992; Karunaratne, 2011), while others works describe the opposite, i.e., the discharge capacity increases when the hydraulic gradient decreases (Bergado et al., 1996; Tran-Nguyen et al., 2010).

3 CHARACTERISTICS AND NUMERICAL MODELLING OF THE EMBANKMENT

3.1 General description

The site studied is located in Portugal, at km 7.775 on the A14 motorway. The geotechnical profile of this cross-section (Figure 1) shows alluvial sandy-silts and clay-silts over limestone (Venda Oliveira et al., 2010). The water table changes with time, between 0.5 metres above and 1.5 metres below the surface.

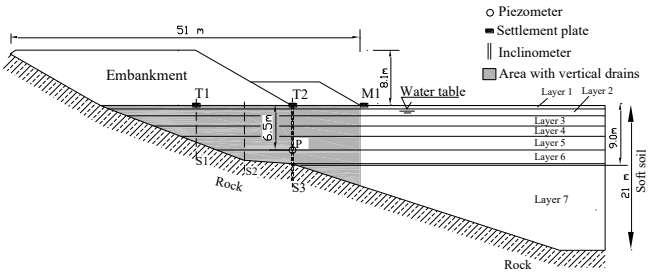

Figure 1. Geotechnical profile of the section of the embankment (based on Venda Oliveira, 2013).

The geotechnical characterisation of the foundation soils (Venda Oliveira et al., 2010) is shown in Table 1, where the mean physical and mechanical characteristics of the layers are presented. To account for permeability anisotropy, a ratio of k_h/k_v of 3 was considered. The embankment (Figure 1) was instrumented with: a sub-vertical inclinometer tube placed at the foot of the main embankment's slope and three settlement plates (T_1, T_2 and M_1).

To accelerate the consolidation of the soft soil, PVDs were installed down to the bottom of the soft soil deposit, in a square pattern with a spacing of 2.2 meters. In accordance with the manufacturer's specifications, the PVDs have a discharge capacity of about 25×10^{-6} m^3/s for a confining pressure of 200 kPa in a buckled condition.

The construction of the embankment is described by six sub-layers with elevations of 1.1, 1.85, 3.45, 4.7, 7.55 and 8.1 metres, applied at 0, 80, 240, 290, 385 and 420 days, respectively.

Table 1. Characteristics of soil layers (based on Venda Oliveira et al., 2010).

Layer	Depth (m)	γ (kN/m^3)	OCR	K_0	e_0
Emb.	------	22.0	-----	-----	-----
1	0.0 - 0.5	15.0	7.5	0.87	2.0
2	0.5 - 1.5	15.0	5.5	0.76	2.0
3	1.5 – 3.0	14.8	3.5	0.62	2.0
4	3.0 - 4.5	14.5	1.8	0.47	2.2
5	4.5 - 6.5	14.5	1.0	0.40	2.1
6	6.5 - 8.5	15.2	1.0	0.40	1.8
7	8.5 - 21.0	15.0	1.0	0.40	1.9

Layer	Parameters of MCC model				k_v (m/s) [x 10^{-9}]
	$e_{\lambda o}$	λ	κ	M	
Emb.	-----	-----	-----	-----	-----
1	2.57	0.217	0.027		-----
2	2.72	0.217	0.027		1.50
3	2.88	0.261	0.035		6.02
4	3.05	0.304	0.060	1.48	10.0
5	3.13	0.304	0.060		2.00
6	2.45	0.178	0.025		0.50
7	2.76	0.217	0.026		0.60

3.2 Numerical model

The mesh used in the 3D analyses consists of 10,406 nodal points and 1,917 twenty-noded isoparametric quadrilateral elements. Due to symmetry, only a row of half of the drains in the direction of the axis of the motorway is modelled.

To simulate the consolidation phenomenon in the soft soil, a coupled analysis of fluid flow and deformation is considered below the water table (at 0.5 metres of depth). Thus, each of the 3D elements have sixty eight nodal degrees of freedom, allowing the calculation of the displacement at twenty nodes and the excess pore pressure at eight corner nodes. The elements used provide quadratic interpolation of displacement and bilinear interpolation of pore pressure values. The boundary conditions are such that the right vertical side is restrained from horizontal movement, while the bottom and left boundaries of the soft soil have zero displacement both vertically and horizontally. In addition, the movement in the direction parallel to the axis of the motorway is also restrained. In terms of hydraulic boundary conditions, the top boundary, corresponding to the water table, is permeable. The other boundaries are impermeable. Above the water table, no water flow was considered in the numerical analyses.

3.3 Simulation of vertical drains

In the numerical analyses, the PVDs are simulated by equivalent square drains with a 52 mm edge to obtain the same draining surface. The smear zone is considered as a square area around the PVDs corresponding to an equivalent radius of 99.3 mm (r_s/r_w =3), where there is a reduction in the horizontal permeability of the soil surrounding the drain to $k_s=k_h/2$ (Hard et al., 1992).

Six cases of the discharge capacity for the PVDs are analysed, three cases with a constant discharge capacity (q_w= infinite; q_w= 1.0x10^{-6} m^3/s; q_w= 1.0x10^{-7} m^3/s) are compared with three other cases, which consider the variation of q_w with the following parameters of proposed formula (1): $q_{w,max}$ = 60x10^{-6} m^3/s, r = 0.001, m = 0.1, t_1= 1 day, σ_{h1}= 100kPa (usual reference value). Additionally, the variation of the parameter a (0.02, 0.03 and 0.04) is analysed.

The FE code evaluates the variation of the discharge capacity of the PVDs by changing the permeability of the FE elements of the vertical drains ($k_w = q_w/A_w$) with the current effective stress state and the time of consolidation. The FE code performs a recalculation of the current permeability of the PVDs at all steps (iterations) of the numerical computation. As the FE code uses a coupled consolidation analysis, the total horizontal pressure ($\bar{\sigma}_h$) is continuously evaluated by the FE code from the horizontal effective pressure and the pore water pressure.

During the calculation, the coefficients of permeability of the soil change with the void ratio, in accordance with the following expression (Taylor, 1948):

$$k = k_0 \times 10^{\frac{e-e_0}{C_k}} \qquad (2)$$

where e_0 represents the initial void ratio, k_0 is the coefficient of permeability corresponding to e_0, k is the current coefficient of permeability relative to the current void ratio e, and C_k is a constant equal to $e_0/2$ (Tavenas et al., 1983).

3.4 Mechanical characteristics

The behaviour of the soil foundation is predicted using the Modified Cam Clay (MCC) model and the parameters are shown in Table 1. The embankment material is characterized by an isotropic linear elastic law, with ν' equal to 0.3 and E' assuming the values of 30, 25, 20, 15, 10 and 5 MPa, from the bottom to the upper layer. This variation aims to reflect the lesser confinement of the upper layers (Venda Oliveira, 2010).

4 ANALYSIS OF RESULTS

4.1 Settlement

Figure 2 compares the evolution over time of the settlement (plate T2) measured in the field and predicted numerically. The numerical results show that the use of an infinite discharge capacity for PVDs induces a higher settlement rate, which originates a reasonable prediction of the settlement for t < 200 days. When a lower and constant discharge capacity for the PVDs is considered (q_w=1.0x10^{-7} m^3/s), the settlement rate predicted numerically decreases, which induces a poor prediction of the settlement during the initial phases, but induces a slight improvement with elapsed time (t > 200 days). This fact reveals that the discharge capacity of the PVDs changes over time, therefore the use of a constant value of q_w is not very suitable to predict the settlement during the consolidation phase.

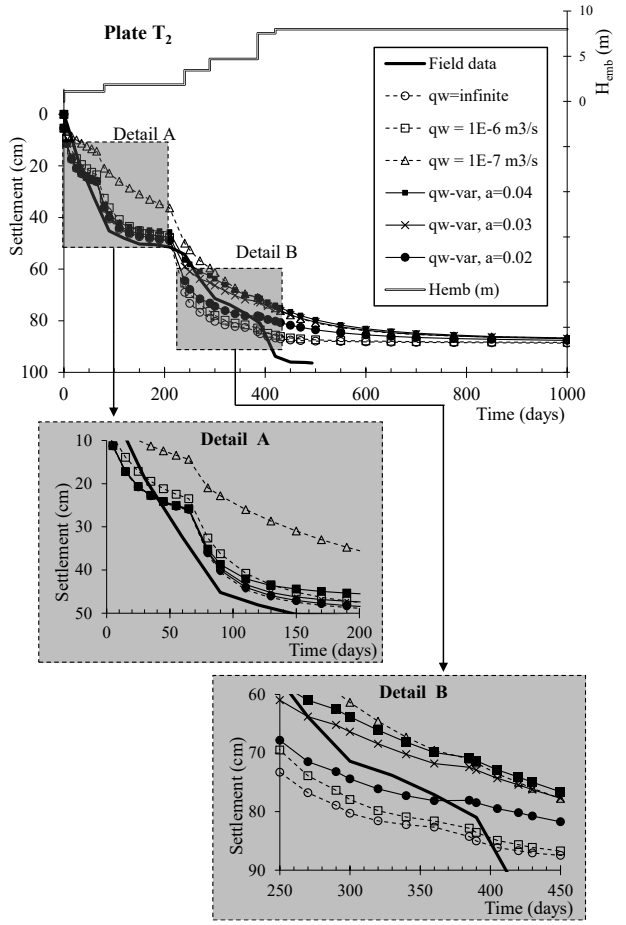

Figure 2. Evolution of the settlements with time (plate T2) (based on Venda Oliveira , 2013).

As expected, Figure 2 also shows that the use of a variable discharge capacity for the PVDs over time induces a decrease in the settlement rate with elapsed time. Thus, for time less than 200 days the effect of changing parameter *a* is negligible, however this effect is clearly visible with increasing time. This behaviour is due to the fact that the decreases of parameter *a* induces an accentuated reduction of q_w with elapsed time. The numerical results show that the value of parameter *a*, which best matches the field data for a time of up to 400 days, is between 0.02 and 0.03. As expected, for times higher than 800 days the differences between the diverse numerical predictions tend to be attenuated.

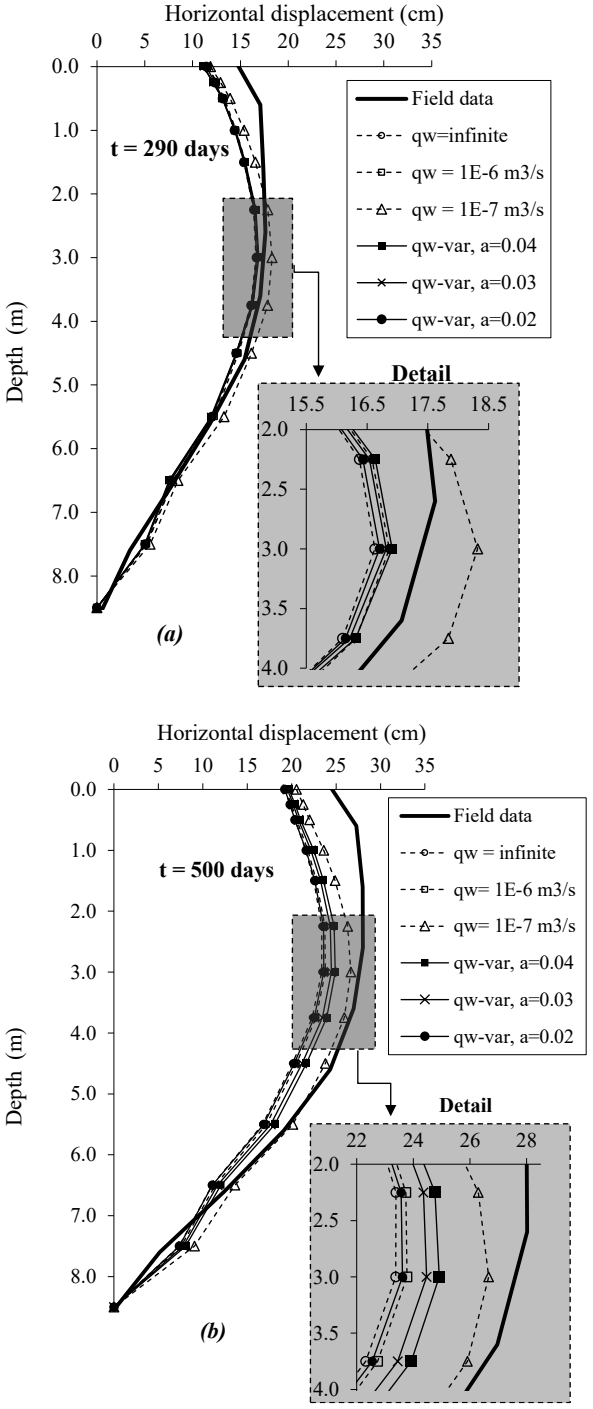

Figure 3. Horizontal displacements for: (a) 290 days; (b) 500 days (based on Venda Oliveira , 2013).

4.2 Horizontal displacement

Figure 3 illustrates the evolution of the horizontal displacement with depth under the foot of the main embankment slope, for 290 and 500 days. In general, the horizontal displacement predicted numerically for the six calculations are similar to the field data. The reduction of the discharge capacity of the PVDs, when q_w is constant over time, increases the horizontal displacement slightly. This effect is more marked for the variation of q_w from $1x10^{-6}$ m^3/s to $1x10^{-7}$ m^3/s (Δy_{max}= 8.6% and 12.2% for 290 and 500 days, respectively) in relation to the reduction of q_w from infinite to $1x10^{-6}$ m^3/s (Δy_{max} = 1.4% and 1.6% for 290 and 500 days, respectively). This behaviour is in accordance with the findings of Indraratna et al. (2003).

The reduction of parameter *a* [equation (1)] induces a slight decrease of the horizontal displacement with time, i.e., this is little affected by the variation of q_w. Thus, independently of the parameter *a* used, the horizontal displacement values predicted numerically by an infinite discharge capacity of the PVDs are quite similar to those obtained with variable q_w.

5 CONCLUSIONS

This paper proposes a formula to predict the variation of the discharge capacity of prefabricated vertical drains due to confining pressure and with consolidation time. This formula simulates the progressive blockage of the PVDs due to the clogging, folding and crimping effects.

The ability of the proposed formula to replicate the behaviour of the PVDs in-situ is analysed using the case study of an embankment built on soft soils improved with PVDs. The numerical results presented show that the use of a variable discharge capacity of the PVDs, improves the numerical prediction for the settlement for the time period between 200 and 400 days (intermediate phases of the consolidation), when the effect of the blockage of the PVDs is most significant, However, the use of a variable discharge capacity of the PVDs does not significantly affect the evolution of horizontal displacement.

Naturally, the effect of the variable discharge capacity of the PVDs would be more significant if longer PVDs were used.

ACKNOWLEDGEMENTS

The authors would like to express their thanks to the institutions that financially supported the research: project research grant FCT (POCI-01-0145-FEDER-028382) and ACIV. This work was partly financed by FCT/MCTES through national funds (PIDDAC) under the units ISISE (UIDB/04029/2020), and ARISE (LA/P/0112/2020).

REFERENCES

Ali, F.H. j. and Huat, B.B.K. (1992). Performance of composite and monolithic prefabricated vertical drains. *Pertanika*, 15(3): 255-262. [http://www.pertanika.upm.edu.my/pjtas/browse/regular-issue?article=PERT-0745-1992, accessed: 1/12/2023]

Almeida e Sousa, J.N. (1998). *Tunnels in soils: Behaviour and numeric modelling*. Ph.D. thesis, Department of Civil Engineering, University of Coimbra (in Portuguese).

Asha, B.S. and Mandal, J.N. (2012). Absortion and discharge capacity tests on natural prefabricated vertical drains. *Geosynthetics International*, 19(4): 263-271. https://doi.org/10.1680/gein.12.00013.

Barron, R.A. (1948). Consolidation of fine-grained soils by drain wells, *Trans. Am- Soc. Civ. Engrs*, 113: Paper No. 2346. https://doi.org/10.1061/TACEAT.0006098.

Bergado, D.T., Manivannan, R. and Balasubramaniam, A.S. (1996). Proposed criteria for discharge capacity of prefabricated vertical drains. *Geotextiles and Geomembranes*, 14: 481-505. https://doi.org/10.1016/S0266-1144(96)00028-3.

Chai, J.C. and Miura, N. (1999). Investigation of factors affecting vertical drain behaviour. *Journal of Geotechnical and Geoenvironmental Engineeering*, 125(3): 216-226. https://doi.org/10.1061/(ASCE)1090-0241(1999)125:3(216) .

Chai, J.C., Miura, N. and Nomura, T. (2004). Effect of hydraulic radius on long-term drainage capacity of geosynthetics drains. *Geotextiles and Geomembranes,* 22: 3-16. https://doi.org/10.1016/S0266-1144(03)00048-7.

Cruz, F.P.M.L. (2008). *Implementation of 3D consolidation in finite element program*. M.Sc. thesis, Department of Civil Engineering, University of Coimbra (in Portuguese).

Deng, Y.B. , Xie, K.H., Lu, M.M., Tao, H.B. Lui, G.B. (2013). Consolidation by prefabricated vertical drains considering the time dependent well resistance. *Geotextiles and Geomembranes*, 36: 20-26. https://doi.org/10.1016/j.geotexmem.2012.10.003.

Hansbo, S., Jamiolkowski, M. and Kok, L. (1981). Consolidation by vertical drains. *Geotéchnique*, 41(1): 45-66. https://doi.org/10.1680/geot.1981.31.1.45.

Hard, C.C., Pyrah, I.C. and Russel, D. (1992). Finite element modelling of vertical drains beneath embankments on soft ground. *Geotéchnique*, 42(3): 499-511. https://doi.org/10.1680/geot.1992.42.3.499.

Holtz, R.D., Jamiolkowski, M., Lancellotta, R. and Pedroni, S. (1988). Behaviour of bent prefabricated vertical drains. *Proceedings of the 12th International Conference of Soil Mechanics and Foundation Engineering*, Rio de Janeiro, Vol. 3, pp. 1657–1660.

Indraratna, B. and Redana, I.W. (2000). Numerical modelling of vertical drains with smear and well resistance installed in soft clay. *Canadian Geotechnical Journal,* 37: 132-145. https://doi.org/10.1139/t99-115.

Indraratna, B., Bamunawita, C., Redana, I.W. and Mcintosh, G. (2003). Modelling of prefabricated vertical drains in soft clay and evaluation of their effectiveness in practice. *Ground Improvement*, 7(3): 127-137. https://doi.org 1680/grim.2003.7.3.127.

Karunaratne, G.P. (2011). Prefabricated and electrical vertical drains for consolidation of soft clay. *Geotextiles and Geomembranes*, 29: 391-401. https://doi.org/10.1016/j.geotexmem.2010.12.005.

Kim, R., Hong, S.J., Lee, M.J. and Lee, W. (2011). Time dependent well resistance factor of PVD. Marine. *Georesources and Geotechnology*, 29(2): 131-144. https://doi.org/10.1080/1064119X.2010.525145.

Lin, D.G. and Chang, K.T. (2009). Three-dimensional numerical modelling of soft ground improved by prefabricated vertical drains. *Geosynthetics International*, 16(5): 339-353. https://doi.org/10.1680/gein.2009.16.5.339.

Müller, W.W., Jakob, I. andTatzky-Gerth, R. (2008). Long-term water flow capacity of geosynthetic drains and structural stability of their drain cores. *Geosynthetics International*, 15(6): 437-451. https://doi.org/10.1680/gein.2008.15.6.437.

Tavenas, F., Jean, P., Leblond, P. and Leroueil, S. (1983). The permeability of natural soft, part II: permeability characteristics. *Canadian Geotechnical Journal*, 20(4): 645-660. https://doi.org/10.1139/t83-073.

Taylor, D.W. (1948). *Fundamentals of Soil Mechanics*. John Wiley and Sons, Inc., New York.

Tran-Nguyen, H.H., Edil, T.B. and Schneider, J.A. (2010). Effect of deformation of prefabricated vertical drains on discharge capacity. *Geosynthetics International*, 17(6): 431-442. https://doi.org/10.1680/gein.2010.17.6.431.

Tripathi, K.K. and Nagesha, M.S. (2010). Discharge capacity requirement of prefabricated vertical drains. *Geotextiles and Geomembranes*, 28: 128-132. https://doi.org/10.1016/j.geotexmem.2009.09.004.

Venda Oliveira, P.J., Lemos, L.J.L. and Coelho, P.A.L.P. (2010). Behavior of an atypical embankment on soft soil: field observations and numerical simulation. *Journal of Geotechnical and Geoenvironmental Engineering*, 136(1): 35-47. https://doi.org/10.1061/(ASCE)GT.1943-5606.0000183.

Venda Oliveira, P.J. (2013). A formula to predict the effect of the variable discharge capacity of prefabricated vertical drains. *Geosynthetics International*, 20(6): 408-420. https://doi.org/10.1680/gein.13.00028.

Proceedings of the XVIII ECSMGE 2024
GEOTECHNICAL ENGINEERING CHALLENGES
TO MEET CURRENT AND EMERGING NEEDS OF SOCIETY
© 2024 the Authors
ISBN 978-1-032-54816-6
DOI 10.1201/9781003431749-529
Open Access: www.taylorfrancis.com, CC BY-NC-ND 4.0 license

ECSMGE 24
XVIII EUROPEAN CONFERENCE ON SOIL MECHANICS AND GEOTECHNICAL ENGINEERING

Research on the formation mechanism and application of curtain for ground drilling grouting in water-rich sand layer

Mécanisme de formation et étude de l'application des rideaux par injection de coulis de forage dans le sol du strate de sable riche en eau

X.S. Wang*, Z.S. Yao, C.X. Rong, X.J. Wang, B. Tang
School of Civil Engineering and Architecture, Anhui University of Science and Technology, Huainan, China
xswang@aust.edu.cn

ABSTRACT: The theoretical formula of the cylindrical diffusion model of radial tube flow for sand layer penetration grouting, considering the tortuous effect, was embedded in COMSOL Multiphysics to explore the curtain formation mechanism of ground drilling grouting in a water-rich sand layer. The grouting of three adjacent grouting holes during a ground drilling grouting project for the main shaft of Guotun Coal Mine was numerically simulated. Moreover, the formation of a grouting curtain and the distribution law of the pressure isosurface and velocity field during slurry diffusion were analyzed. The results revealed that the volume fraction of cement slurry gradually decreased along the diffusion direction, and slurry volume fractions of (0.6, 0.8] corresponded to the key areas for grouting reinforcement. The isosurface of formation pressure changed from dense to sparse along the direction of slurry diffusion, indicating that slurry pressure rapidly and slowly attenuates near and far from the grouting pipe, respectively.

RÉSUMÉ: Afin d'explorer le mécanisme de formation du rideau d'injection dans le forage souterrain d'une couche de sable riche en eau, nous considérons la formule théorique du modèle de diffusion cylindrique de la canalisation de rayonnement de coulis d'infiltration de couche de sable avec effet tortueux intégré dans COMSOL Multiphysics, et simulons numériquement le processus de coulis de trois trous de coulis adjacents dans le projet de forage de surface et de coulis du puits principal de la mine de charbon de Guotun, et analysons la loi de distribution du champ de surface et de vitesse équivalente à la pression pendant le processus de formation du rideau de coulis et de la diffusion de boue. Les résultats montrent que la fraction volumique de la boue de ciment diminue progressivement le long de la direction de diffusion, et que la région de la fraction volumique de la boue à (0,6, 0,8] est la région clé du renforcement de l'injection. Les isosurfaces de pression stratigraphique vont de denses à éparses le long de la direction de diffusion de la boue, ce qui indique que la pression de la boue diminue fortement près du tuyau d'injection et diminue lentement dans la région éloignée du tuyau d'injection.

Keywords: Water-rich sand layer; ground drilling grouting; penetration grouting; cylindrical diffusion; grouting curtain.

1 INTRODUCTION

Water leakage accidents often occur when servicing coal mine shafts, which severely threaten the safety of underground workers and lower production efficiency. Common measures for shaft seepage treatment are grouting after wall and ground drilling grouting. However, the shaft wall of the water-rich sand layer is at a high risk of water inrush after grouting and fails to meet current coal mine safety regulations. Accordingly, ground drilling grouting is preferred instead. Ground drilling grouting results in the formation of a grouting curtain around the shaft, which prevents disruption to normal shaft production. By isolating the groundwater seepage around the shaft wall, this method can effectively improve the deformation coefficient of the stratum and the stress state of the shaft.

Existing research on the formation of the grouting curtain has focused on tunnel engineering. Taking the curtain grouting reinforcement of Nanshibi Tunnel as an example, Yin et al. (2022) studied the creep behavior of grouting stone based on nonlinear Burgers' model and numerically simulated the grouting process of the operating tunnel. Chai and Cui (2012) validated the theory of optimal grouting curtain thickness via finite element numerical simulation based on one- and two-dimensional seepage models. Zhang et al. (2015) explored the influence of curtain grouting on the pore pressure field, stress field, and plastic zone rock surrounding tunnels using the fluid–solid coupling method and numerical simulation method. Taking a water-rich loess tunnel as an example, Wei et al. (2021) verified that curtain

grouting can effectively control surrounding rock deformation and surface settlement. Li et al. (2021) studied the propagation law of tunnel cracks under different curtain grouting parameters and described the characteristics of water inrush caused by excavation. These research efforts demonstrated the complex diffusion of slurry in a complex formation environment. These studies obtained grouting results under specific working conditions and captured the dynamic diffusion of slurry in the layer. These provide some reference for guiding grouting construction and optimizing grouting parameters.

The development of numerical calculation software has facilitated the numerical simulation of grouting. Han et al. (2022) used COMSOL multiphysics multifield coupled numerical simulation software to study the diffusion law of cement slurry in the surrounding rock of a tunnel by considering time-varying gravity and viscosity. Pan et al. (2022) and Guo et al. (2021) used similar methods to study the influence of different grouting parameters on the grouting effect. Zhang et al. (2018) and Yang et al. (2021) used discrete element numerical methods, such as PFC2D and EDEM, to simulate grouting in a soft coal seam and obtain the slurry diffusion range under given grouting pressures. Wang et al. (2021) used finite difference software FLAC3D to optimize the grouting parameters of an ultrashallow buried double-arch tunnel with a large section.

Therefore, reports on the curtain formation process of a coal mine shaft during ground drilling curtain grouting are few. As such, research is urgently needed to guide the selection of grouting parameters to control leakage in a coal mine shaft wall during ground drilling. The grouting process of three adjacent grouting holes in the main shaft during a ground drilling grouting project in Guotun Coal Mine, Shandong Province, was numerically simulated using COMSOL Multiphysics. The pressure isosurface and velocity field distribution during grouting curtain formation and slurry diffusion were analyzed. Notably, the results have reference value for shaft water disaster control in water-rich sand layers.

2 PROJECT OVERVIEW

The water inflow of the Guotun Coal Mine in Shandong Province is shown in Figure 1. During shaft construction, the water inflow is 50–60 m^3/h, whereas it was 500–600 m^3/h during coal mine production, an increase of approximately 10-fold. This resulted in uneven ground subsidence and shaft deflection of the industrial square, and the maximum shaft deflection of the main shaft and the auxiliary shaft were 348 mm and 336 mm, respectively, which pose a risk for coal mine production. Therefore, to maintain normal mine production, surface drilling grouting was used to control the unevenness and settlement of the shaft.

According to the water pressure, grouting, and core indoor geotechnical tests, as well as the results obtained from the test and grouting holes were distributed on the circumference, with a radius of 30 m and the wellbore center serving as the center. The pressure relief holes were distributed on the circumference, with a radius of 16 m and the wellbore center serving as the center. The grouting holes and pressure relief holes were misplaced, and the design grouting diffusion radius was 8 m. The layout of the boreholes around the main shaft are shown in Figure 2. The 12 grouting holes were spaced 13.84 m apart. Seven pressure relief holes (including the main hole and the main inspection hole) were arranged, with hole spacings of 9.81–16.00 m. Moreover, 9 directional drilling holes were arranged.

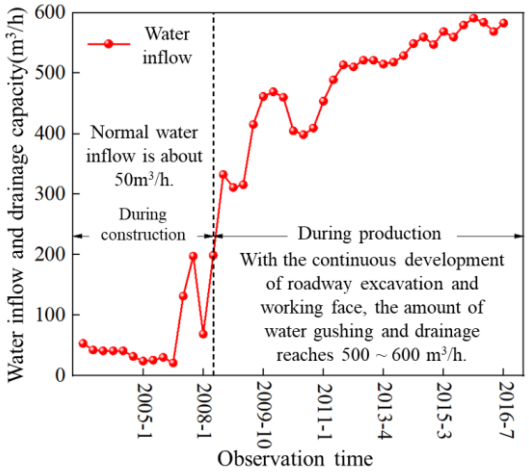

Figure 1. Statistics of water inflow in mining area.

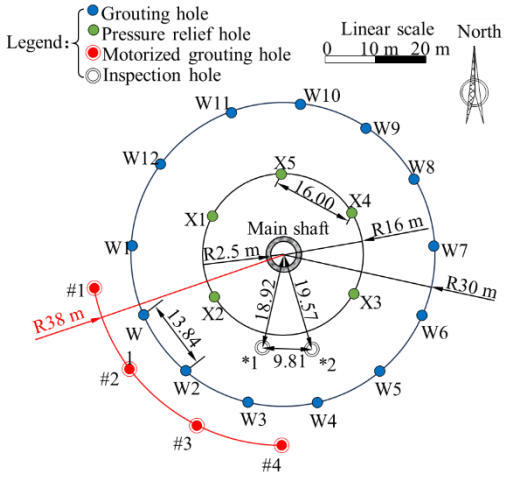

Figure 2. Layout plan of drilling hole.

3 NUMERICAL SIMULATION

To verify the rationality of the design parameters of the curtain grouting scheme and grout diffusion law, as well as the formation mechanism of the curtain, the grouting processes of holes W1, W2, and W3 in the main well were taken as the research object. Moreover, the slurry cylindrical diffusion theory formulas derived from the literature (Wang, 2022a, 2022b) were embedded into COMSOL Multiphysics. A numerical simulation of cylindrical diffusion of ground borehole grouting was then conducted.

3.1 Basic assumptions

1) The distance between the three grouting holes selected for the simulation was relatively small, and the stratum in the grouting section is a whole, the soil layer is incompressible, and the physical parameters are isotropic.

2) The slurry is an incompressible Bingham fluid, and the flow pattern does not change during grouting.

3) The percolation of slurry and water satisfies the generalized Darcy's law.

3.2 Model parameters and meshing

The grouting model is shown in Figure 3. The size of the model was 80 m × 80 m × 40 m. The three grouting holes were located on the circumference with a radius of 30 m and the center of the main shaft as the center. The same spatial positions as holes W1, W2, and W3 in the main shaft were used, and the distance between adjacent grouting holes was 13.84 m. Additionally, the length of the grouting pipe was 36 m, which does not penetrate the simulated formation, and the slurry flows into the formation along the radial flow after flowing out of the grouting pipe.

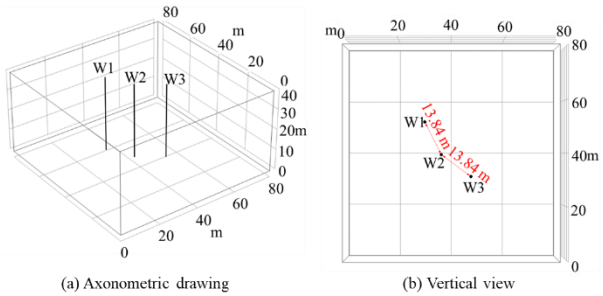

Figure 3. Grouting model.

The results of laboratory geotechnical tests of the sand revealed a density of 2000 kg/m^3, volume modulus of 100 MPa, shear modulus of 20 MPa, cohesion of 5 Pa, internal friction angle of 35°, lateral pressure coefficient of 0.42, and porosity of 0.35. The density of water was 1000 kg/m^3, and the dynamic viscosity was 1.0 mPa·s. The slurry density was 1310 kg/m^3, and the dynamic viscosity was 11.0 mPa·s. The Biot coupling coefficient was 1.0.

The meshing of the model is shown in Figure 4. First, a virtual grid domain was used to divide the vicinity of the grouting hole, the edges of the box were then encrypted, and the tetrahedral mesh was used to divide the model. Finally, the remainder of the model was refined. The complete mesh consisted of 479,102, 21,742, and 4080 domain, boundary, and edge elements, respectively.

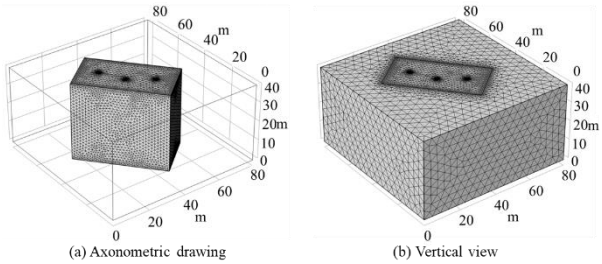

Figure 4. Model meshing diagram.

4 RESULTS AND ANALYSIS

4.1 Slurry Diffusion Form

Under the action of slurry pressure, the cement slurry permeates and diffuses within the saturated sandy soil, sequentially forming the cement slurry, slurry–water mixing, and pore water zones along the diffusion direction. The volume fraction method was used to characterize the slurry–water mixing zone to characterize the volume percentage of the slurry occupying the slurry–water mixing zone with a continuously varying numerical interval (0,1). The process of cement slurry replacing pore water in the pore space of sandy soil via osmotic diffusion was simulated via the "two-phase Darcy's law" interface of COMSOL Multiphysics.

First, the two-phase Darcy's law physical field was accessed, and the theoretical formula of the cylindrical diffusion model of radial tube flow obtained from the literature (Wang, 2022a, 2022b) was embedded into COMSOL Multiphysics. Holes W1 and W3 were slurried first, and the pressure boundary conditions in holes W1 and W3 were set, with a measuring line arranged at the connecting line of holes W1 and W3. The time variable was controlled via transients, and slurry injection was stopped when the predetermined slurry radius was reached. Slurry injection was then repeated for hole W2 and stopped when the slurry body intersected the circle to form a complete curtain. The slurry diffusion form is shown in Figure 5.

Figure 5 shows that the slurry diffusion region of a

single slurry injection hole was approximated as a cylinder. The cement slurry volume fraction was higher near the grouting pipe and gradually decreased along the diffusion direction. In this study, the region where the volume fraction of the cement slurry was greater than 0.4 was taken as the effective slurry diffusion region, and the interface where the volume fraction of the slurry was equal to 0.4 was the slurry diffusion frontal surface (Cai, 2018). The distance from the diffusion frontal surface to the axis of the slurry pipe was the slurry diffusion radius.

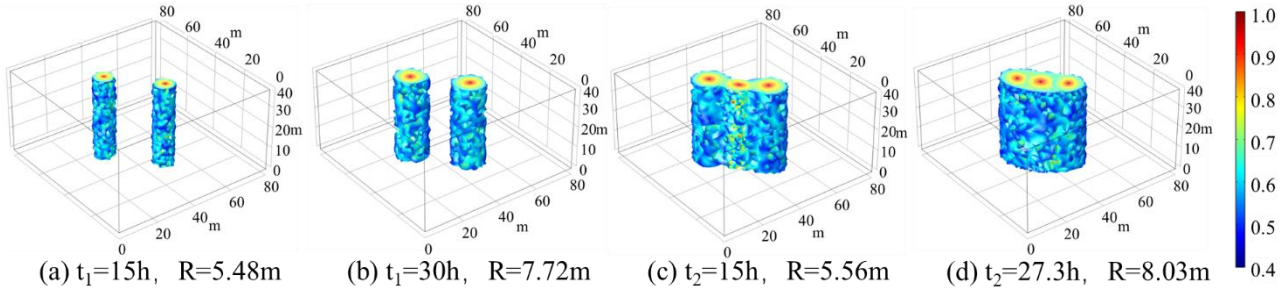

(a) t_1=15h, R=5.48m (b) t_1=30h, R=7.72m (c) t_2=15h, R=5.56m (d) t_2=27.3h, R=8.03m

Figure 5. Slurry diffusion form.

The volume fraction of cement slurry can be divided into four regions along the radial distribution. The area with a slurry volume fraction of (0, 0.4] was the ineffective reinforcement area, which was omitted from the figure. The cement content in this area was too low to achieve water plugging or reinforcement effects. The area with a slurry volume fraction of (0.4, 0.6] was located at the outer edge of the effective reinforcement area, and the width of this area was small relative to the width of the slurry curtain. The region with a slurry volume fraction of (0.6, 0.8] had a higher cement content, with good water plugging and reinforcement effects, and was the primary region of slurry reinforcement. The region with a slurry volume fraction of (0.8, 1.0] was concentrated near the slurry pipe and accounts for a low percentage of the entire slurry diffusion region. This suggests that the cement slurry was diluted with pore water soon after flowing from the slurry pipe.

The radius of diffusion was 5.48 m when holes W1 and W3 were slurried for 15 h; when slurried for 30 h, the radius of diffusion was 7.72 m, which was close to the design value of 8 m, and the slurring was stopped at this time. After 18 h of grouting in hole W2, the slurry front was tangent to the grouted stones in holes W1 and W3, and the radius of diffusion at this time was 6.12 m. Afterward, the diffusion of the slurry in the tangent direction of the circumference of the grouted holes was hindered by the slurry stones in holes W1 and W3, and the diffusion of the slurry in the direction of the circumference of the slurry holes was dominated by slurry diffusion in the tangent direction of the circumference of the grouted holes. Therefore, the diffusion process gradually increased the width of the slurry curtain after the slurry front of hole W2 was tangent to the slurry nodule body of holes W1 and W3. After 27.3 h of slurry injection in hole W2, the width of the slurry curtain was relatively uniform (approximately 16 m). In this study, only three slurry holes were selected for simulation. Because the distribution of slurry holes had spatial symmetry, if skip-hole slurrying is performed over the entire circle diameter, a circular slurry curtain with a width of approximately 16 m will be formed at the periphery of the wellbore.

4.2 Pressure isosurface and velocity field distribution laws

The distribution of pressure isosurfaces and the velocity field in the slurry diffusion is shown in Figure 6. The arrows in the figure represent the velocity field, and their direction is the velocity field direction. The isosurfaces represent the pressure field, and the direction of the outer normal of the isosurfaces is the pressure direction. Figure 6 shows that the pressure isosurface is denser near the slurry pipe and sparser away from it, indicating that the slurry pressure is sharply attenuated near the slurry pipe. Attenuation was slow in the region away from the grouting pipe and gradually close to the formation stress. This change rule is consistent with the results in the literature (Wang, 2022a, 2022b) regarding the slurry pressure attenuation law.

Figures 6(a) and 6(b) show that the slurry pressure influence range is only in the vicinity of the slurry pipe during preslurrying in holes W1 and W3. The pressure was higher near the slurry pipe, and the pressure decayed faster near the slurry pipe. Almost no interaction occurred between the two grouting pipes, and the influence range of grouting pressure was not prominent. As slurry injection proceeded, the slurry pressure gradually affected the surrounding strata through the slurry in the formation. Meanwhile, the

pressure field between the two grouting pipes gradually began to interact, and the pressure dissipated faster in the slurry body and slower in the formation. Finally, a pressure fault was formed at the interface between the grouted caking body and the sandy soil, as shown in Figures 6(c) and 6(d).

As shown in Figures 6(e)–6(h), the slurry pressure was concentrated in the vicinity of the slurry pipe at the beginning of slurry injection in hole W2, and the influence of slurry injection in hole W2 on the change of formation stress was not prominent. As the slurry injection proceeded, the slurry diffusion was affected by the slurry injection nodule body of holes W1 and W3 after the slurry front was tangent to the slurry injection nodule body of the holes. The slurry and water need to bypass this region, and the slurry pressure equivalent surface and velocity field distribution were reduced to only one axis of symmetry. The influence range of the grouting pressure mainly acted on the nodule body; that is, the slurry pressure decayed toward the vicinity of the slurry nodule body, it was less than the shear force provided in the formation, and slurry spreading stopped. The pressure decay rate on the outside of the nodule body slowed, and the pressure was more evenly distributed within the formation.

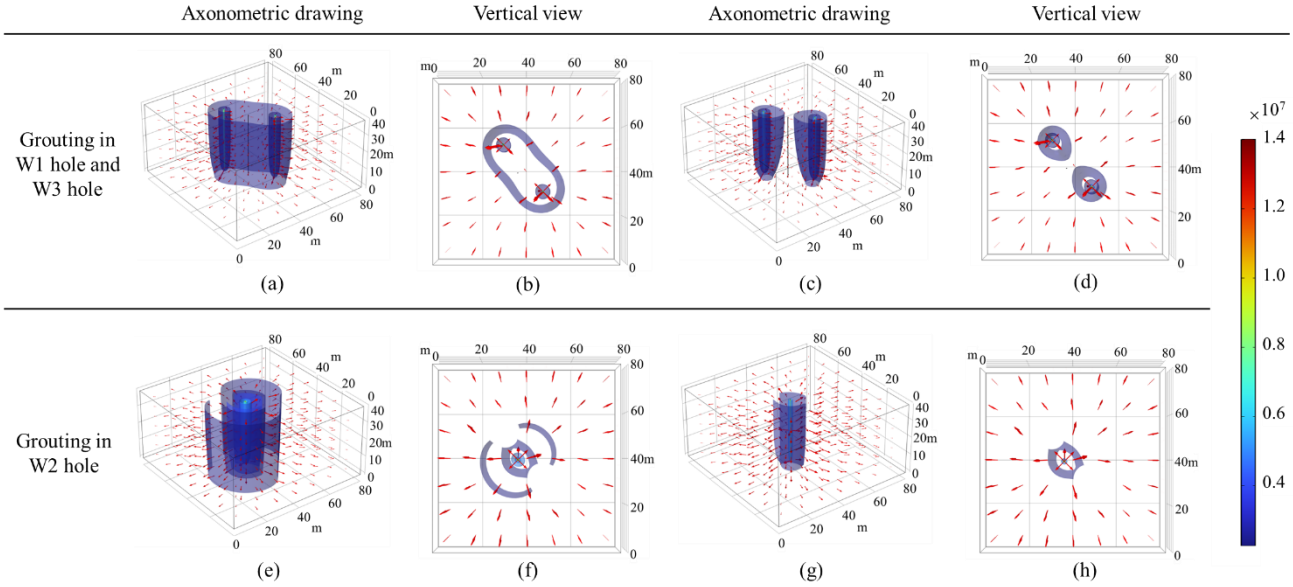

Figure 6. Pressure isosurface and velocity field distribution.

5 CONCLUSIONS

(1) The theoretical formula of the cylindrical diffusion model of radial tube flow was embedded in COMSOL Multiphysics, and the grouting process of holes W1, W2, and W3 holes in the ground drilling grouting project of the main shaft of Guotun Coal Mine was numerically simulated. The grouting construction involved designing a circle and determining the hole spacing, and a grouting curtain with a thickness of approximately 16 m was formed around the shaft.

(2) Cement slurry was gradually diluted by pore water along the direction of grouting diffusion. Only the area near the grouting pipe has a slurry volume fraction of (0.8, 1.0], and the area with a slurry volume fraction of (0.6, 0.8] was the key area for grouting reinforcement, accounting for the highest proportion of grouting curtain width.

(3) The slurry affects the pressure field around the injected formation. The pressure isosurface was dense near the grouting pipe, but sparse far from the grouting pipe. The slurry pressure decayed sharply near the grouting pipe and slowly far from the grouting pipe, gradually approaching the formation stress.

ACKNOWLEDGEMENTS

The project presented in this article is supported by the Anhui University of Science and Technology Research Fund for the Introduction of Talents (2023yjrc15).

REFERENCES

Cai, Y. J. (2018). Study on Grouting Diffusion Mechanism of Loose Bottom Aquifer in Guotun Coal Mine. Master thesis, Anhui University of Science and Technology, Huainan, Anhui. (In Chinese).

Chai, J. R. and Cui, W. J. (2012). Optimum thickness of curtain grouting on dam foundation with minimum seepage pressure resultant. Structural and multidisciplinary optimization, 45(2): 303-308. https://doi.org/10.1007/s00158-011-0699-7.

Guo, T. T. Zhang, Z. W. Yang, Z. Q. Zhu, Y. Y. Yang, Yi. Guo, Y. H. Wang, R. C. Zhang, B. H. Fang, Y. C. Yu, D. L. Mi, Y. P. Su, J. K. Liu, H. Zhang, J. Guo, Y. F. and Wang, H. L. (2021). Penetration Grouting Mechanism of Time-Dependent Power-Law Fluid for Reinforcing Loose Gravel Soil. Minerals (Basel), 11(12): 1-17. https://doi.org/10.3390/min11121391.

Han, X. L. Li, C. Y. Wang, G. Yang, Z. Q. Feng, C. C. Li, M. Zhao, C. S. Zhang, Z. H. He, N. Wang, X. P. Ye, C. W. Yuan, L. W. Yang, T. Q. Xi, W. F. Li, X. H. (2022). Study on Diffusion Laws for Cement Slurry in Surrounding Rock of Tunnels Considering Gravity and Time-Varying Viscosity of Slurry. Industrial Construction, 52(03): 38-43. https://doi.org/10.13204/j.gyjzg21090708 (In Chinese).

Li, G. Ma, W. B. Tian, S. M. Zhou, H. B. and Fan, H. B. (2021). Groundwater Inrush Control and Parameters Optimization of Curtain Grouting Reinforcement for the Jingzhai Tunnel. Geofluids, 2021: 1-10. https://doi.org/10.1155/2021/6634513.

Pan, W. D. Liang, S. Y. Liu, S. Y. Zhao, Z. N. and Zha, D. S. (2022). Numerical Simulation of Diffusion Regularity and Parameter Optimization of Shaft Grouting Slurry. PROCESSES, 10(5): 1-15. https://doi.org/10.3390/pr10050803.

Wang, J. X. Cao, A. S. Wu, Z. Wang, H. R. Liu, X. T. Li, H. B. Q. and Sun, Y.W. (2021). Experiment and Numerical Simulation on Grouting Reinforcement Parameters of Ultra-Shallow Buried Double-Arch Tunnel. Applied sciences, 11(21): 10491. https://doi.org/10.3390/app112110491.

Wang, X. S. Cheng, H. Yao, Z. S.Rong, C. X. Huang, X. W. and Guo, L.H. (2022a). Theoretical Research on Grouting in Deep Loose Layers Based on the Cylindrical Diffusion Model of Radial Tube Flow. Geofluids, 2022: 1-12. https://doi.org/10.3390/w14071028.

Wang, X. S. Cheng, H. Yao, Z. S.Rong, C. X. Huang, X. W. and Liu, X. Y. (2022b). Theoretical Research on Sand Penetration Grouting Based on Cylindrical Diffusion Model of Tortuous Tubes. Water (Basel), 14(7): 1028. https://doi.org/10.3390/w14071028.

Wei, Z. D. Zhu, Y. P. Bin, G. and Gong, B. (2021). Seepage in Water-Rich Loess Tunnel Excavating Process and Grouting Control Effect. Geofluids, 2021: 1-13. https://doi.org/1-13. 10.1155/2021/5597845.

Yang, C. W. Guo, J. H. Wei, S. W. Zhang, L. Li, S. F. and Liu, Y. (2021). Study on the Calculation Method of the Diffusion Range of Grouting Slurry for a High-speed Railway Ballastless Track Subgrade. Advances in Civil Engineering, 2021: 1-8. https://doi.org/10.1155/2021/5279479.

Yin, Z. C. Zhang, X. Li, X. H. Zhang, J. Q. and Zhang, Q. S. (2022). Modified Burgers model of creep behavior of grouting-reinforced body and its long-term effect on tunnel operation. Tunnelling and underground space technology, 127: 104537. https://doi.org/10.1016/j.tust.2022.104537.

Zhang, Q. S. Li, P. Wang, G. Li, S. C. Zhang, X. Zhang, Q. Q. Wang, Q. Liu, J. G. and Kala, Z. (2015). Parameters Optimization of Curtain Grouting Reinforcement Cycle in Yonglian Tunnel and Its Application. Mathematical problems in engineering, 2015: 1-15. https://doi.org/10.1155/2015/615736.

Zhang, Z. L. Shao, Z. S. Fang, X. B. and Liang, X. J. (2018). Research on the Fracture Grouting Mechanism and PFC Numerical Simulation in Loess. Advances in materials science and engineering, 2018:1-7. https://doi.org/10.1155/2018/4784762 .

Proceedings of the XVIII ECSMGE 2024
GEOTECHNICAL ENGINEERING CHALLENGES
TO MEET CURRENT AND EMERGING NEEDS OF SOCIETY
© 2024 the Authors
ISBN 978-1-032-54816-6
DOI 10.1201/9781003431749-530
Open Access: www.taylorfrancis.com, CC BY-NC-ND 4.0 license

ECSMGE 24
XVIII EUROPEAN CONFERENCE ON SOIL MECHANICS AND GEOTECHNICAL ENGINEERING

The geotechnical works for the construction of the Travis Brow link road, Stockport, UK

Les travaux géotechniques pour la construction de la route Travis Brow link, Stockport, Royaume-Uni

A. Willoner*, L. Allievi
Mott MacDonald, Sheffield, UK
**Alan.Willoner@mottmac.com*

ABSTRACT: The Travis Brow to A6 link road created a new highway connection in Stockport. The construction of the two-lane dual carriageway required the implementation of a variety of geotechnical construction techniques, including soil nailing, contiguous pile walls and the installation of prestressed rock anchors with hard facing to support the rock beneath the foundations of two piers of the Grade II* listed Stockport viaduct, which carries the West Coast main line rail service. This paper describes the design and construction of the geotechnical works carried out for the scheme, focussing particularly on the undercutting of the viaduct footings, which was carried out following a staged construction sequence, with excavation works carried out in bays both horizontally and vertically. The results of rock anchor testing are also discussed.

RÉSUMÉ: La route de liaison Travis Brow à A6 a créé une nouvelle connexion autoroutière à Stockport. La construction de la route à deux voies à deux voies a nécessité la mise en œuvre d'une variété de techniques de construction géotechniques, y compris le clouage du sol, des murs de pieux contigus et l'installation d'ancrages rocheux précontraints avec un revêtement dur pour soutenir la roche sous les fondations de deux piliers du viaduc de Stockport, classé Grade II*, qui transporte le service ferroviaire de la ligne principale de la côte ouest. Cet article décrit la conception et la construction des travaux géotechniques réalisés pour le projet, en se concentrant particulièrement sur la sous-découpe des piles du viaduc, qui a été réalisée selon une séquence de construction par étapes, avec des travaux d'excavation réalisés dans les travées horizontalement et verticalement. Les résultats des essais d'ancrage rocheux sont également discutés.

Keywords: Ground anchor; finite element analysis; stress testing.

1 INTRODUCTION

The new Travis Brow highway provides a link from the M60 Junction 1 to the A6 in Stockport. The project has several challenges associated with urban developments and steep topography as illustrated in Figure 1, as well as presence of contaminated soil and fitting works around an old buried cut and cover tunnel and buried masonry wall.

A variety of geotechnical works were required for the construction of the highway. A short initial section within traditional cutting is followed by a 100m long section supported by 555 No. soil nails with flexible complex facing and green finishing on a 45 degrees slope with a gravity wall at the toe of the slope. As the cutting deepens, contiguous pile walls are used as earth retention system for a 150m long section, with retained height between 5 and 8m, after which the road reaches the Stockport Viaduct.

The new carriageway bisects the Stockport Viaduct, with the alignment undercutting the pad foundations of the 1840s Grade II* listed structure, which carries the West Coast Main Line.



Figure 1. Image of the New Link Road looking east towards the Stockport Viaduct, with the M60 to the south.

Undercutting of the Viaduct pad footings was essential to achieve a safe gradient and standard highway width, but it also presented a complex geotechnical challenge and required approval from Network Rail, the owner and maintainer of the Viaduct.

2 THE STOCKPORT VIADUCT

Having been widened to accommodate four tracks in the 1880s, the Viaduct is founded at two significantly different levels featuring stepped profiles, with the foundations of the extension being deeper than the foundations of the original structure. The new road passes between span 23, where the piers are 3m thick and 12.2m high. An 'Archie-M' structural analysis of arch and piers carried out to assess the load at foundation level indicates that under live train loading, a trapezoidal pressure distribution develops under each pad with peak bearing pressure of 1220kPa.

The excavation for the construction of the proposed highway required undercutting the footings for a depth of up to 2.5m in temporary conditions and 1.7m permanently, with a 70-degrees rock slope as illustrated in Figure 2.

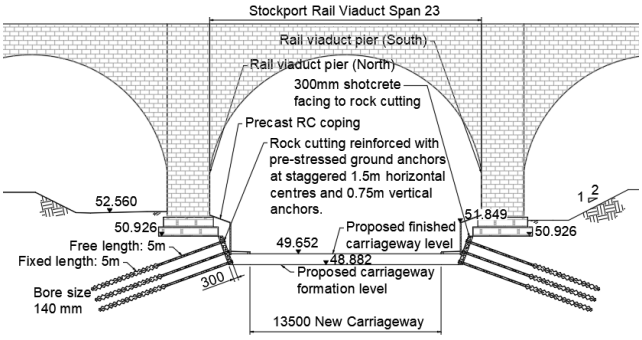

Figure 2. Section at span-23 illustrating anchor layout.

3 GROUND CONDITIONS

The formation to the viaduct pad footings comprises the Chester Pebble bed formation of the Triassic Sherwood Sandstone unit. This rock is typically very weak medium to closely bedded red SANDSTONE, with bedding dipping typically 20-degrees to the west. A less persistent steeply inclined joint set is also encountered in this formation. Project specific investigation revealed extrapolated Standard Penetration Test (SPT) N values in the range of 231 to 945. Point Load and Unconfined Compressive Strength laboratory testing verified the SPT results and gave an average UCS of 3.5MPa to be used for 'best estimate' SLS prediction of ground movement. Some judgement was applied to establish a worst credible UCS of 1.9MPa. The data on rock quality and strength was processed through the RSData software to obtain the equivalent Mohr-Coulomb strength parameters using the Hoek-Brown criteria, and provided best estimate ϕ_p' 49^0, c' 40kPa and E_r' 750MPa, and worst credible ϕ' 40^0, c' 20kPa and E_r' 400MPa, where ϕ_p' is effective peak friction angle, c' is effective cohesion and E_r' is drained rock mass modulus.



Figure 3. Trial trench perpendicular to pier at Arch 23 illustrating the quality of the rock and bedding.

4 DESIGN & CONSTRUCTION

A robust design solution was required due to the high bearing pressures of the Viaduct footings, the critical importance of the structure hosting 4 overhead tracks of the West Coast Mainline and its heritage value.

Conceptual design options considered were i) Top-down excavation after installation of a 450mm diameter contiguous piled wall with either propping in front of the walls below the new road or by means of ground anchors behind, ii) Pre-stressed rock anchors and hard facing with each unsupported excavation being confined to as small an area as practical.

The Contractor's preference was the second option due to cost and programme savings and for similarity with historical works at Pier 20 (Golders, 1977).

The design of the viaduct undercutting was carried out in accordance with BS EN 1997-1:2004, using the finite element software Plaxis 2D. Some judgment was required to analyse a 3D problem in a 2D FE program.

Several sensitivity tests were run to establish the optimum anchor pre-stress level, which was identified as the value of pre-stress above which there was very little improvement in reduction in SLS elastic deformation. The tightest practical anchor spacing was used to reduce the risk of large inelastic movement along unfavourably orientated rock discontinuities exposed by the excavation.

The Plaxis analyses predicted a distribution of elastic rock mass deformation as illustrated in Figure 4. This assumed plane strain conditions, with each anchor being stressed before excavating below.

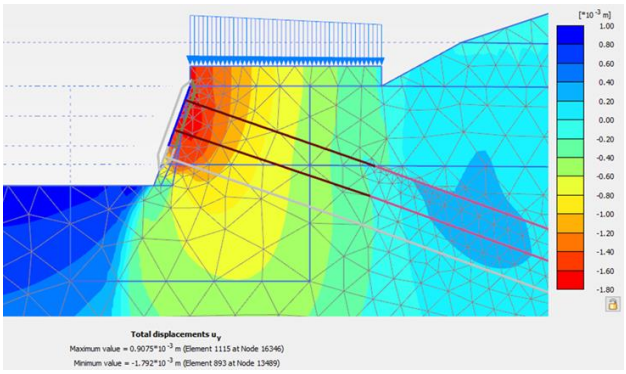

Figure 4. Output of SLS predicted elastic rock movements at finished excavation, before installation and prestressing of the bottom row of anchors.

However, in order to keep the sub-contractor working continuously, two vertical levels of anchors were installed at the same time with adjacent support being provided from a rock buttress (as illustrated in Figure 5) or by recently installed and stressed anchors, with the gang working on a horizontal 'hit-and-miss' basis across 5 bays on each side of the arch and then working down and along the bottom line of anchors.



Figure 5. Placing hard facing to the initial working bay below the north footing of arch 23.

The best estimate and worst credible predictions of elastic rock deformation on the cut face were 0.5 and 2.0mm respectively. The associated rotations of the base of the viaduct pier were also estimated, which were 1:10,000 and 1:4,000 for best estimate and worst credible cases respectively, hence acceptable.

The final design comprised on 32 anchors per footing at 1.5m horizontal and 0.75m vertical spacing. Anchors were 10m long with 5m fixed and 5m free (unbonded) length, inclined at 20-degrees to the horizontal and comprising a 40mm Gewi bar with double corrosion protection in a 140mm diameter grout filled bore. Design prestress was 250kN per anchor.

Anchors installation was carried out in accordance with BS EN 1537:2013 and BS 8081:2015.

5 INSTRUMENTATION & TESTING

Each face of the viaduct had 45 mini prisms installed to monitor the movement of the viaduct and establish baseline movement levels due to wind, temperature change and rail traffic.

Background movements of the Viaduct were greater than predicted movements due to the Works. It was therefore essential to directly measure the ground movements to understand if, and how much, these affected the superstructure.

Extensometers were installed into the new rock faces. These recorded maximum ground movements of 0.5mm beneath the north pier and 0.8mm beneath the south pier, as illustrated in Figure 6.

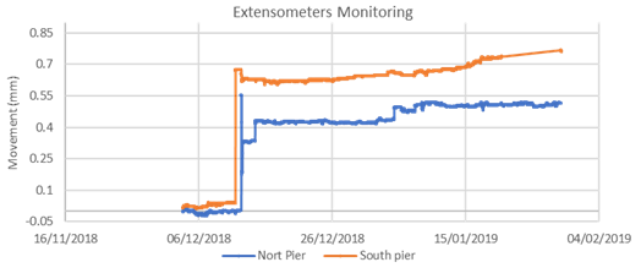

Figure 6. Extensometer results validating SLS predictions.

Selective anchors were fitted with load cells for future monitoring. During the first reading of the load cells, in June 2019, a measured load up to 60% less than the specified lock-off load was noted in all monitored anchors. The cause of the reduced load was investigated by an expert sub consultant.

Increased monitoring of the load cells was implemented, and lift-off tests were carried out on all accessible anchors. The tests confirmed that all anchors held a lower load than specified, with a

reduction ranging from 30% to 65% of the nominal 250kN lock-off load.

Following the results of the lift-off tests, restressing of two anchors, subsequent increased monitoring, and a review of the anchor drilling reports, it was established that the likely cause of the reduced load was the procedure adopted for the initial lock-off of the anchors, which did not allow for any lock-off loss due to transfer of load from the jack to the nut. The consequence was that all the anchors were likely to have load at levels significantly less than specified, including the lower row of anchors no longer accessible because buried beneath the finished road level.

As a remedial measure, all accessible anchors were re-tested for acceptability and locked-off at 275kN, 110% of the original design SLS load, in January 2020, thus increasing the average load imposed to the rock face to an average force of 205kN closer to the original design value and equivalent to 1mm of lock off loss. No adverse effects on the viaduct have been recorded to date.

6 CONCLUSIONS

The design of the Stockport Viaduct undercutting provided Network Rail, owner of the asset, with confidence that the Viaduct footings could be undercut by a 70-degress slope to 2.5m depth with works being monitored and contingency strutting implemented between the two footings if ground movements exceeded predictions.

The ground conditions encountered were generally as expected. There was one small wedge failure from unfavourably oriented joints which was addressed quickly by sprayed gunite dentition.

Low anchor stress was identified during monitoring and in turn investigations revealed non-confirmances with the locking-off methodology. It is important to establish what amount of additional stress is required to provide allowance for lock-off losses, especially for short anchors in competant rock where lock-off losses can be very significant. This should be done by immediate lift-off checks to confirm the specified load is locked into each anchor.

The anchor testing was carried out in accordance with BS EN ISO 22477-5:2018 Test Method 1, as per standard UK pratice, which prescribes that the anchor is loaded in steps on one or more load cycles increasing to proof load, with measurement of displacement carried out over a prescribed fixed period at each load step.

ACKNOWLEDGEMENTS

The authors are grateful for the support and collaboration from the main project stakeholders Stockport Council, Graham Construction and Network Rail.

A specific acknowledgement is also made to Jim Martin of Byland Engineering for his expert forensic investigation into the cause of the low anchor stresses and for assisting with a practical solution.

REFERENCES

British Standards Institution (2013), BS EN 1537:2013 Execution of special geotechnical works – ground anchor, BSI Standards Publications, London, UK.

British Standards Institution (2020), BS 5930:2015 + A1:2020 Code of practice for ground investigations, BSI Standards Publications, London, UK.

British Standards Institution (2015), BS 8081:2015 Code of practice for grouted anchors (+A2:2018), BSI Standards Publications, London, UK.

British Standards Institution (2018), BS EN ISO 22477-5:2018 Geotechnical investigation and testing - Testing of geotechnical structures, Part 5 - Testing of grouted anchors, BSI Standards Publications, London, UK.

Golders Associates (1977). Stockport Viaduct Stabilisation of Pier 20. Rep L77003.

Proceedings of the XVIII ECSMGE 2024
GEOTECHNICAL ENGINEERING CHALLENGES
TO MEET CURRENT AND EMERGING NEEDS OF SOCIETY
© 2024 the Authors
ISBN 978-1-032-54816-6
DOI 10.1201/9781003431749-531
Open Access: www.taylorfrancis.com, CC BY-NC-ND 4.0 license

ECSMGE 24
XVIII EUROPEAN CONFERENCE ON SOIL MECHANICS AND GEOTECHNICAL ENGINEERING

Forensic examination of gravity block walls

Évaluation forensique des murs en blocs de gravité

M.G. Winter*
Winter Associates, Kirknewton, Scotland, United Kingdom

M. Duffy-Turner, I.M. Nettleton
Coffey Geotechnics, Manchester, United Kingdom

P. Liew
National Highways, Birmingham, United Kingdom

**mwinter@winterassociates.co.uk*

ABSTRACT: The effective design, specification and construction of geotechnical assets or Special Geotechnical Measures (SGMs) are critical to the efficient operation of the National Highways Strategic Road Network (SRN) in England. Given the required performance of the SRN in terms of resilience, reliability, redundancy and recovery it is essential that SGMs are themselves reliable in terms of performance and life; resilient to external conditions such as earthworks deterioration and extraordinary conditions (e.g. climate change). Around 100 different types of SGMs are used on the SRN and the early installations of some SGMs are approaching the end of their design life; the design, specification and application of many of these techniques are based on limited studies. A detailed account of issues identified on the Strategic Road Network (SRN) is given resulting from the inspection of Block Walls of various types and in various settings. The results were used to develop advice on the design, construction, inspection, maintenance and decommissioning of such structures and to make a series of recommendations for their future use. Principle amongst these is that the evidence suggests that when properly designed, specified, constructed and maintained, including an appropriate inspection regime, Gravity block walls can meet the required design life of such SGMs.

RÉSUMÉ: La conception, la spécification et la construction efficaces d'actifs géotechniques ou de mesures géotechniques spéciales (SGM) sont essentielles au fonctionnement efficace du réseau routier stratégique national (SRN) en Angleterre. Compte tenu des performances requises du SRN en termes de résilience, de fiabilité, de redondance et de récupération, il est essentiel que les SGM soient eux-mêmes fiables en termes de performances et de durée de vie ; résistant aux conditions externes telles que la détérioration des terrassements et les conditions extraordinaires (par exemple, le changement climatique). Environ 100 types différents de SGM sont utilisés sur le SRN et les premières installations de certains SGM approchent de la fin de leur durée de vie ; la conception, la spécification et l'application d'un grand nombre de ces techniques reposent sur des études limitées. Un compte rendu détaillé des problèmes identifiés sur le réseau routier stratégique (SRN) est donné à la suite de l'inspection de murs en blocs de divers types et dans divers contextes. Les résultats ont été utilisés pour élaborer des conseils sur la conception, la construction, l'inspection, l'entretien et le démantèlement de ces structures et pour formuler une série de recommandations pour leur utilisation future. Le principe parmi ceux-ci est qu'il n'y a aucune preuve convaincante que lorsqu'ils sont correctement conçus, spécifiés, construits et entretenus, y compris un régime d'inspection approprié, les murs en blocs de gravité ne peuvent pas respecter la durée de vie requise de ces SGM.

Keywords: Geotechnical; asset; retaining; wall; block.

1 INTRODUCTION

This paper provides a brief summary of a study that investigated gravity block walls. Typically, Block Walls are used on the Strategic Road Network (SRN) in England as low-height walls around features such as telecommunication housings and at the base of embankments. However, drystone and mortared stone walls are also prevalent on the network in both free-standing and retaining form.

This work forms part of a wider study (Duffy-Turner et al., 2022a) of the performance of geotechnical asset types, known as Special Geotechnical Measures (SGMs), including block walls (Winter et al., 2022), gabion walls (Duffy-Turner et al, 2022b), counterfort drains (Nettleton et al, 2022), and soil nails (Duffy-Turner et al., 2022c).

An account is given of issues identified from inspections of gravity block walls on the SRN along with issues for their design, construction, maintenance and recommendations for future use.

2 ISSUES IDENTIFIED

A wide variety of issues was identified during the inspection of 10 gravity block walls on the network. These included but were not restricted to the issues described in the following paragraphs.

Deterioration and loss of mortar of the exposed top course (coping) and or the lower courses, most likely due to the effects of salt spray; this often included the complete loss of blocks. Cracking of blocks was also commonly observed (Figure 1).

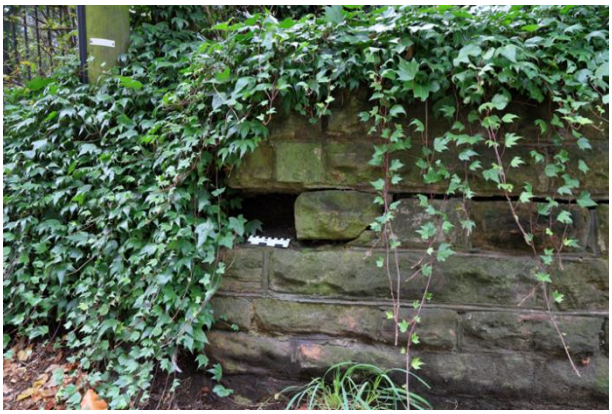

Figure 1. Deterioration of the lower courses of a stone block mortared wall most likely due to salt spray. The deterioration of this wall at this location is through the full height with the loss of block(s) in the central area (A52).

Vehicle damage to the upper free-standing part of a retaining wall was observed (Figure 2).



Figure 2. Upper free-standing part of a dry-stone retaining wall (mortared coping) showing the effects of vehicle impact. The wall below the carriageway retains a height of between 2m and 3m below the road. (A628).

Bulging and leaning were commonly observed, as were sagging and hogging of both modular concrete block (mortar free) and stone (mortared or otherwise) walls (Figure 3).

The provision of weepholes to block walls was relatively uncommon, with seepage taking place through the wall itself, and no instances of an identifiable drainage layer behind the wall were encountered (although this is difficult to establish definitively). Where weepholes were provided, they generally appeared to be working although the washout of gravel particles suggests that construction materials are also being washed out (Figure 4), indicating that there was a lack of a suitable filter/separator in the construction of the wall/drainage. The lack of adequate drainage is a factor that may cause deterioration and subsequent failure and is an area of potential concern that ought to trigger further evaluation of the Block Wall.



Figure 3. Stone block mortared wall showing significant signs of instability: substantial mortar loss, sagging and bowing of the wall and that, in places, has led to substantial misalignment of the individual blocks with the potential for individual blocks, or groups of blocks, to be lost (A303).

Block walls, whether mortar or dry stone, have the potential to fail with blocks falling to the ground surface often from the top course (coping) and the potential to cause injury and blockage of, for example, footpaths causing the public to enter the highway in order to pass. Cracking, bulging, leaning and seepage/lack of drainage provision are indicators of potential failure but do not necessarily indicate that the risk associated with that failure merits intervention. Ownership may also be uncertain.

Evidence of efflorescence was observed at some locations; this was largely at a level considered to be aesthetic issue, with preventative or remedial measures needed only in visually sensitive areas.

Changes to the spatial relationship between walls and the infrastructure can also occur when the asset has been developed around older walls, leading to suboptimal configurations (O'Reilly and Perry, 2009). Some walls thought to have been constructed as free-standing were found to be retaining for at least part of their height, in some instances explaining the absence of weepholes.

Block walls often form the boundary to third party properties and there can be doubt as to the ownership

of the walls. This may in part explain the change in function over time while the build-up of detritus can also form a backfill.



Figure 4. Weepholes (80mm internal diameter at 6m centres) in a 78m long, 0.75m high stone block mortared wall. The gravel particles in front of the wall appear to have been washed out of the weepholes indicating that they are functional but possibly washing out material that forms part of the construction (A30, January 2021).

Notwithstanding the issues outlined above, dry stone walls in particular can be a relatively resilient form of structure.

3 DESIGN

Published design, specification and construction guidance, while limited is summarised by Winter et al. (2022). Key issues include:

- Ensuring that the layout is such as to maximise internal stability, typically stretcher bond, and where that is not possible ensure that vertical joints do not coincide over more than two courses (Haramy et al., 2006).
- That the design takes account of any mechanical interlock.
- Weepholes and an effective drain and filter should be provided to the rear face of the wall allowing water to flow to a suitable outlet. This should be designed in the context of the prevailing surface/ground water conditions.
- That the block materials are considered with respect to their durability. This is particularly the case with stone blocks located in parts of England where weak sandstones and limestones predominate, and competent material may have been in short supply. Argillaceous rocks, and other materials potentially susceptible to weathering, should not be used to construct gravity block walls of any type on the SRN.
- Coping protection may be necessary.
- Where possible block walls should be located so as to minimise the effects of salt spray from de-icing salts as this may cause deterioration in the fabric of the lower parts of the wall.

4 CONSTRUCTION

All blocks and mortar used must maintain integrity in the light of the mechanical and environmental stresses that it might face during its design life. These can include contact stresses in the case of dry-stone walls and the effects of de-icing salts for all forms of wall.

High contact stresses can be caused by incorrect handling during transport and construction such that concentrated loads are generated rather than the blocks being placed square on top of each other, or by subsequent movement of the retained material or deterioration of the block(s).

Drainage provision is essential and must be as detailed in the design. The drainage media must be durable over the design life of the asset with adequate inspection and maintenance built into the plan to manage the asset.

Adequate and competent personnel for construction and supervision are essential for what is often an artisanal form of construction.

Provision should be made for handover inspection and subsequent snagging prior to the removal of any traffic management and the contractor leaving the site.

5 MAINTENANCE

Maintenance (and demolition) of the wall should be considered throughout the design, specification and construction process and plans should be prepared and incorporated into handover documentation.

O'Reilly and Perry (2009) give cost comparisons of various forms of reconstruction and repair techniques for different heights of dry-stone walls and also note that the annual costs of maintenance of such walls are around 0.75% of their replacement cost. While the actual costs date back to around 1995 the relative comparisons are considered to remain valid with those of pressure pointing and soil nailing being around 12% and 50% of replacement structures.

Maintenance of dry stone and many stone block mortared walls must be taken in the context of the history and the natural and cultural heritage of their setting. Amongst the walls inspected during the site visits was a wall retaining an ancient cemetery within the Peak District National Park. It should be clear that a degree of sensitivity and consultation will be required prior to any major maintenance works and

that this will be particularly so if any intrusive repair (e.g. soil nail repair) or reconstruction is considered.

6 CONCLUSIONS AND RECOMMENDATIONS

Different types of wall are not always differentiated in the asset management system, with masonry walls and stone walls all being described as block walls.

The evidence suggests that when properly designed, specified, constructed and maintained, including an appropriate inspection regime, block walls can meet the required design life (120 years) of such SGMs.

Advice in standards and other related documents for Block Walls is clearly limited. Through the course of this work a number of key issues have been identified and these are set out as recommendations for action in the following paragraphs.

Recommendation 1: The design of block walls should take due cognisance of manufacturer's information, where relevant, as well as fundamental design principles.

Recommendation 2: The provision of adequate and appropriate drainage for block walls should be addressed through the design, specification, construction and approval phases.

Recommendation 3: The use of argillaceous rock, or other material susceptible to weathering, to form block walls is not recommended, due to the possibility of rapid deterioration, in particular in locations of high exposure.

Recommendation 4: Contractor acceptance, or self-certification, of block walls is not recommended as part of the findings from the wider work undertaken (Duffy-Turner et al., 2022a).

Recommendation 5: Any inspections for the acceptance of constructed block walls should be undertaken prior to the site becoming fully-operational and while items are visible and remedial measures can be readily implemented; it is recommended that provision for early inspection should be built into the contract.

Recommendation 6: Inspection of SGMs should be certified by a Geotechnical Advisor in accordance with CD 622 .

Recommendation 7: A formal risk-based approach to the inspection and maintenance of block walls should be developed. This would assign values to attributes during assessment to allow prioritisation of actions including maintenance and replacement. Attributes to be considered include but are not limited to, wall type, condition, provision and effectiveness of drainage, proximity to road users; a draft scheme with examples is described by Winter et al. (2022).

ACKNOWLEDGEMENTS

This work was undertaken through the National Highways Designated Fund scheme in support of the Geotechnical Resilience and the Geotechnical Climate Change Adaptation Programmes.

REFERENCES

CD 622. Managing geotechnical risk. Design Manual for Roads and Bridges, Revision 1, March 2020. https://www.standardsforhighways.co.uk/tses/attachments/ff5ed991-71ed-4ff2-9800-094e18cd1c4c?inline=true.

Duffy-Turner, M, Winter, M G, Nettleton, I M and Butler, G. (2022a). Forensic examination of Critical Special Geotechnical Measures. PPR 1032. TRL, Wokingham.

Duffy-Turner, M, Winter, M G and Nettleton, I M. (2022b). Forensic examination of Critical Special Geotechnical Measures: Gabion Wall Information Note. PPR 1036. TRL, Wokingham.

Duffy-Turner, M, Nettleton, I M, Winter, M G and Webber, I. (2022c). Forensic examination of Critical Special Geotechnical Measures: Soil Nail Information Note. PPR 1033. TRL, Wokingham.

Haramy, K Anderson, S, Alzamora, D, Barrows, R, Mohamed, K and Surdahl, R. (2006). Rockery design and construction guidelines. Publication No FHWA-CFL/LTD-06-006, November. FHA, Washington DC.

Nettleton, I M, Winter, M G and Duffy-Turner, M. (2022a). Forensic examination of Critical Special Geotechnical Measures: Counterfort Drain Information Note. PPR 1034. TRL, Wokingham.

O'Reilly, M P and Perry, J. (2009). Dry stone retaining walls and their modifications – condition appraisal and remedial treatment. CIRIA Report RP723. CIRIA, London.

Winter, M G, Duffy-Turner, M. and Nettleton, I M. (2022). Forensic examination of Critical Special Geotechnical Measures: Gravity Block Wall Information Note. PPR 1035. TRL, Wokingham.

Proceedings of the XVIII ECSMGE 2024
GEOTECHNICAL ENGINEERING CHALLENGES
TO MEET CURRENT AND EMERGING NEEDS OF SOCIETY
© 2024 the Authors
ISBN 978-1-032-54816-6
DOI 10.1201/9781003431749-532
Open Access: www.taylorfrancis.com, CC BY-NC-ND 4.0 license

ECSMGE 24
XVIII EUROPEAN CONFERENCE ON SOIL MECHANICS AND GEOTECHNICAL ENGINEERING

Experimental and numerical study on the compaction of granular soils by vibrations

Etude expérimentale et numérique du compactage de sols granulaires par vibrations

M. Wotzlaw*, D. Aubram, F. Rackwitz
Technische/Universität Berlin, Germany

**moritz.wotzlaw@tu-berlin.de*

ABSTRACT: The paper deals with the influence of vibrations, i.e. cyclic excitations with large acceleration amplitudes, on dry granular materials like sand. The inertial stresses induced by the accelerations cause a temporary loss of shear strength as well as a permanent compaction of the material. Although this phenomenon is known for a long time and plays an important role in many geotechnical construction processes like deep vibrocompaction and vibrodriving of piles, only few systematic studies on the fundamental relations exist. The investigations at TU Berlin focus on the relationship between the static and dynamic stress states in the material during vibrations and the achieved compaction. An experimental setup was developed which allowed for the compaction of sand under small effective stresses and large acceleration amplitudes. As the dynamic stresses determining the compaction behaviour vary within the sample, a simple method to evaluate the vertical distribution of void ratio is applied. The results of these tests are presented and a simple model for estimating the compaction based on the stress state and acceleration amplitude is proposed. This model is applied to the results of numerical simulations of deep vibrocompaction, to gain an estimate of the amount of compaction caused by the cyclic accelerations.

RÉSUMÉ: Ce document traite de l'influence des vibrations, c'est-à-dire des excitations cycliques avec de grandes amplitudes d'accélération, sur les matériaux granulaires secs comme le sable. Les contraintes inertielles induites par les accélérations provoquent une perte temporaire de la résistance au cisaillement ainsi qu'un compactage permanent du matériau. Bien que ce phénomène soit connu depuis longtemps et qu'il joue un rôle important dans de nombreux processus de construction géotechnique tels que le vibrocompactage en profondeur et le vibrofonçage de pieux, il n'existe que peu d'études systématiques sur les relations fondamentales. Les recherches menées à l'Université technique de Berlin se concentrent sur la relation entre les états de contrainte statiques et dynamiques dans le matériau pendant les vibrations et le compactage obtenu. Un dispositif expérimental a été mis au point pour permettre le compactage du sable sous de faibles contraintes effectives et de grandes amplitudes d'accélération. Comme les contraintes dynamiques qui déterminent le comportement du compactage varient à l'intérieur de l'échantillon, une méthode simple est appliquée pour évaluer la distribution verticale du taux de vide. Les résultats de ces essais sont présentés et un modèle simple d'estimation du compactage basé sur l'état de contrainte et l'amplitude d'accélération est proposé. Ce modèle est appliqué aux résultats des simulations numériques du vibrocompactage en profondeur, afin d'obtenir une estimation de l'ampleur du compactage causé par les accélérations cycliques.

Keywords: Vibrocompaction; granular soils; cyclic accelerations; experimental tests; numerical simulations.

1 INTRODUCTION

Granular material like sand can be efficiently compacted with the use of vibrations, which we define as alternating deformations of the grain skeleton and sufficiently large acceleration amplitudes. Although the first findings were published early on (Barkan, 1962), the underlying mechanisms are still poorly understood. There have been repeated attempts to investigate the phenomenon (Youd, 1968; Norman-Gregory and Selig, 1989; Bement, 1996; see also Denies, 2014 for an overview) but these have remained isolated and have not led to a systematic theory of vibrocompaction of granular materials. The experimental set-ups of the works mentioned are always comparable: A sample of granular material is placed inside a test container with rigid walls, loaded vertically via a load stamp and vibrated in vertical or horizontal direction using a shaking table. The change of density over time is determined by measuring the settlement of the load stamp.

Irrespective of the exact experimental set-up and the intensity or direction of vibrations applied, the following basic observations were made: Starting from the initial value e_0, the void ratio decreases non-

linearly and asymptotically approaches the limit value e_Γ (also called the equilibrium void ratio, Figure 1 above), which is defined as the minimum void ratio that can be achieved under the given surcharge p_z and non-dimensional acceleration amplitude $\Gamma = a/g$, where a is the acceleration amplitude and g is the acceleration due to gravity. With an increasing value of Γ the equilibrium void ratio e_Γ decreases towards the minimum void ratio achievable for this material by vibrations (Figure 1 below).

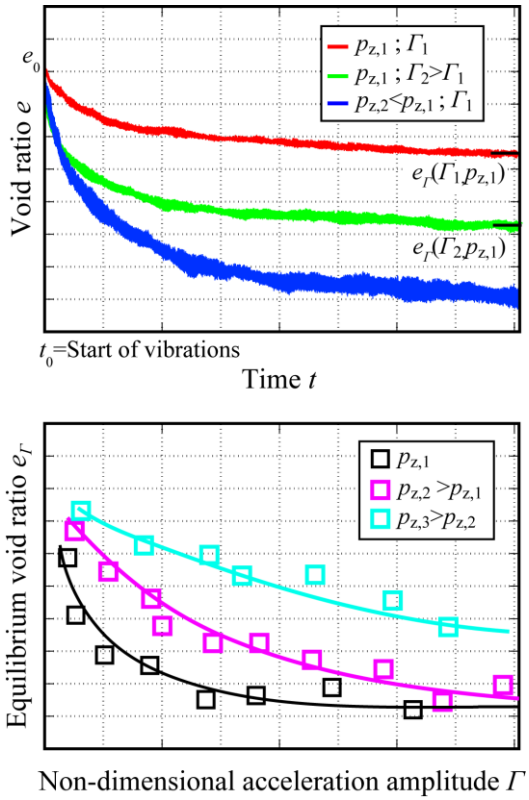

Figure 1. Time history of void ratio during compaction with constant surcharge p_z and dimensionless acceleration amplitude Γ (above). Dependence of the equilibrium void ratio e_Γ on the acceleration amplitude Γ (below).

Obviously the void ratio e_Γ isn't solely dependent on the acceleration amplitude but also the static surcharge p_z. It does not seem reasonable to use Γ as the only non-dimensional number characterising the compaction behaviour, as has been common practice up to now (Youd, 1968; Bement, 1996). Accordingly, a new non-dimensional number is introduced here, which we call the local stress ratio κ. It is defined as the ratio of the dynamic (destabilising) stress amplitude σ_{dyn} to the static (stabilising) stress σ_{stat}. For the specific test conditions applied in this study, it is assumed to take the form:

$$\kappa = \frac{\sigma_{\mathrm{dyn}}}{\sigma_{\mathrm{stat}}} = \frac{\Gamma \cdot g \cdot m/A}{p_z + g \cdot m/A} \qquad (1)$$

where m and A are the sample's mass and sectional area respectively. The dynamically excited mass increases with the depth z of the sample (starting from the sample's top surface), so that κ is a function of z and increases with depth. It will be shown that the dimensionless number controlling densification is κ rather than Γ.

As the stress ratio defined in eq. (1) increases with depth and the equilibrium void ratio depends on κ, one hypothesis is that the distribution of void ratio inside the sample also correlates to the stress ratio, i.e. the density in the lower area of the sample is greater than in the upper area after compaction.

2 EXPERIMENTAL SETUP

The experimental setup depicted in Figure 2 is used for the tests carried out at TU Berlin. Here the sample is placed in a cylindrical container having rigid walls. The surface is straightened and covered by a load stamp. The specimen has a diameter of $d = 80$ mm and initial height h_{ini} ranging from 60 mm to 80 mm, depending on the installed mass and initial density.

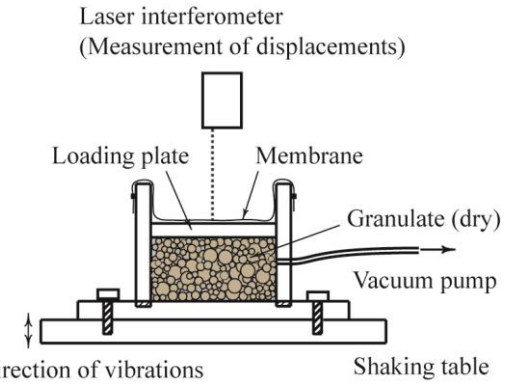

Figure 2. Experimental setup for vibrocompaction tests. The container is cylindric and has an inner diameter of 8 cm.

The container is then sealed by a thin latex membrane, so that an underpressure p_0 can be created inside the sample with the aid of a connected vacuum pump. It follows that the resulting static surcharge is given by $p_z = p_{\mathrm{atm}} - p_0$.

On the one hand this way of load application makes it possible to create a very small static stress level so that even with relatively small accelerations a large value of κ can be achieved. On the other hand, the surcharge itself is not dependent on inertia, as would be the case for example, if the load was applied via weights.

The tested material was a Toyoura sand, with a coefficient of uniformity of $C_{\mathrm{U}} = 1.3$, a minimum/maximum void ratio of $e_{\mathrm{min}} = 0.569$ and $e_{\mathrm{max}} = 0.907$ respectively. After placing the test cell

on a shaking table, it was vibrated at a frequency of 50 Hz in vertical direction, where the acceleration can be regulated by adjusting the displacement amplitude.

In order to determine the local distribution of void ratio and to check on the hypothesis formulated in the introduction, the following simple procedure is applied: After compaction, the sample is removed in layers using a vacuum pump. Height and mass of each layer is measured so that the locally averaged void ratio can be calculated afterwards.

3 EXPERIMENTAL RESULTS

The distributions of the locally averaged void ratios after compaction e_κ over the sample height are shown in Figure 3. For reference an exemplary initial (i.e. pre-compaction) distribution is also shown in black. The average initial void ratio was around 0.9 in all of the tests, which is close to the sand‘s maximum void ratio.

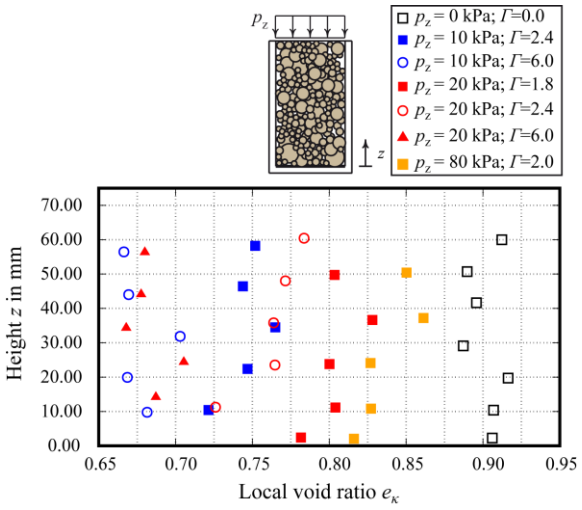

Figure 3. Distribution of void ratios after compaction over the sample height for various combinations of surcharge and acceleration amplitude.

Some already known properties can be identified: The larger the acceleration amplitudes (at constant surcharge), the more the sample is compacted over the entire height. The larger the surcharge, however, the weaker the compaction, given the same or comparable acceleration. There seems to be at least a tendency for the sand to be denser in the lower areas than in the upper areas, although this is not clearly pronounced in all cases. However, this is consistent with the observations by Norman-Gregory and Selig, 1989.

If these test results are plotted over the assumed local dynamic stress ratio κ, a correlation of both quantities is visible (Figure 4). The black curve in Figure 4 is given by equation (2), with the vibratory minimum void ratio $e_\infty = 0.65$, the maximum void ratio $e_{\max} = 0.907$ and a coefficient $\lambda = 0.015$:

$$e(\kappa) = e_\infty + (e_{\max} - e_\infty) \cdot \frac{1}{1+\kappa/\lambda} \qquad (2)$$

4 NUMERICAL SIMULATIONS

We will now demonstrate briefly, how these findings could be used to estimate the compaction of sand due to cyclic accelerations caused by vibroflotation, a well-established method for the compaction of granular (see Kirsch and Kirsch, 2010 for details). For this we use results obtained by simulations with the CEL method. The numerical model is shown in Figure 5.

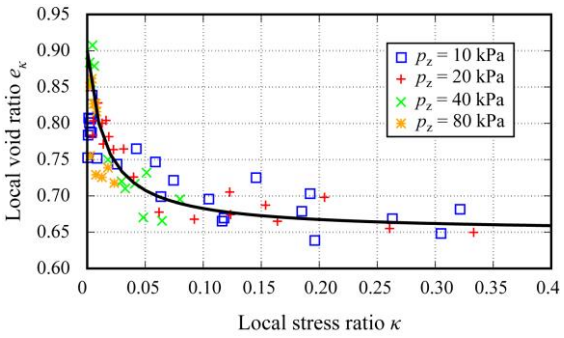

Figure 4. Dependence of the locally averaged void ratio after compaction on the local stress ratio, for which a linear distribution is assumed.

The mechanical soil behaviour is modelled using the hypoplastic constitutive model with intergranular strains (von Wolffersdorff, 1996; Niemunis and Herle, 1997) using the parameters shown in the table in Figure 5. The model and its validation were described in detail by Wotzlaw et al., 2023. It has a height of 30 m and a diameter of 25 m. In our simulations the vibrator is operating at a depth of 11 m below ground level (referring to the vibrator tip). The initial void ratio is given by $e_0 = 0.907$.

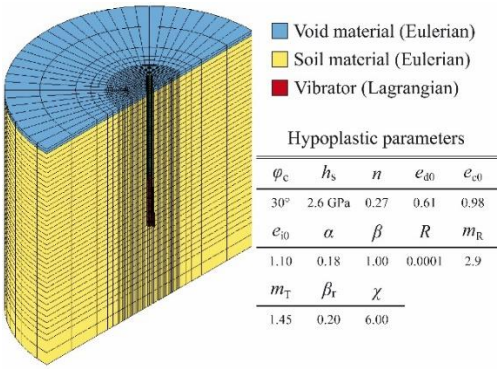

Figure 5. Numerical model and hypoplastic parameters after Herle (1997).

By using this fully fledged CEL model described above, the time history of vertical stress could be evaluated. From this and the local static vertical stress,

a time-averaged local stress ratio has been determined for each finite element in order to apply eq. (2) (Figure 6). In a radial distance of approximately 1 m from the vibrator axis, the stress ratio has a value of up to 0.5 and then quickly decreases in a larger distance to the vibrator. However, as can be seen from Figure 4, the degree of compaction does not increase significantly for stress ratios larger than approximately 0.2.

Accordingly, the distribution of minimum void ratio due to vibrations in Figure 7, which we get solely by applying Eq. (2) on the distribution of average stress ratio, shows that the soil can be compacted efficiently from an initial relative density of $I_D = 0$ to a densities after compaction ranging from $I_D = 0.6$ in a distance of 3 m from the vibrator axis to $I_D = 0.76$ within a radius of 1 m around the vibrator.

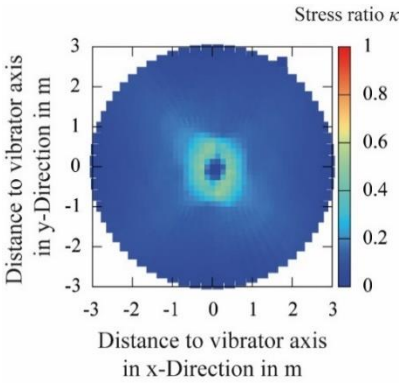

Figure 6. Average local stress ratio in a depth of 9.6 m below ground level caused by vibrocompaction.

5 CONCLUSIONS

We have shown experimentally, that the void ratio after vibrations e_κ depends on the local stress ratio κ inside the vibrated granulate. Further research on this matter has to be performed, especially the influence of the direction of vibration and the effect of vibrations on the shear resistance have to be considered.

We included numerical simulations to show how these findings can be used to estimate the amount of compaction solely by application of the proposed eq. (2). In later works, the effect of simultaneous cyclic shear deformations has to be included. However, even with all simplifications, this example shows that the impact of cyclic accelerations on the relative density of granular soils should be taken into account in numerical simulations. Utilising the dependence on the local stress ratio can be one way of doing so.

ACKNOWLEDGEMENTS

Funded by the Deutsche Forschungsgemeinschaft (DFG, German Research Foundation) – project number 461480840. The authors are grateful for this financial support.

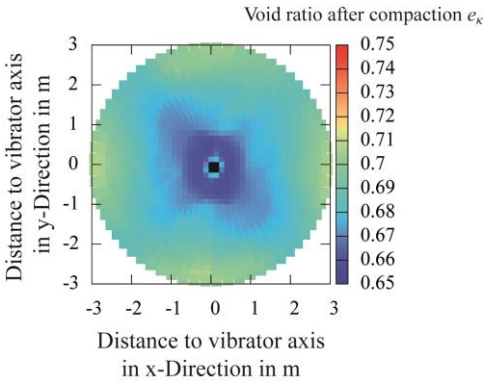

Figure 7. Minimum void ratio e_κ due to vibrations caused by vibrocompaction.

REFERENCES

Barkan, D. D. (1962): Dynamics of Bases and Foundations. McGraw-Hill, New York.

Bement, R. A. P. (1996): Ground compaction due to vibrodriving of piles. Dissertation, Durham University. http://etheses.dur.ac.uk/5182.

Denies, N., Canou, J., Roux, J.-N., Holeyman, A., (2014): Vibrocompaction properties of dry sand, Canadian Geotechnical Journal, 51, 409-419, dx.doi.org/10.1139/cgj-2012-0436.

Herle, I. (1997): Hypoplastizität und Granulometrie einfacher Korngerüste (Hypoplasticity and granulometry of simple grain skeletons). Dissertation. No. 142 in Publications of the Institute of Soil Mechanics and Rock Mechanics of the University Fridericiana in Karlsruhe, University of Karlsruhe (TH), Faculty of Civil Engineering of the University of Karlsruhe (in German).

Kirsch, K., Kirsch, F. (2017): Ground Improvement by Deep Vibratory Methods, Second Edition, CRC Press/Taylor & Francis Group, USA, 234 Pages.

Niemunis, A. and Herle, I. (1997): Hypoplastic model for cohesionless soils with elastic strain range. Mechanics of Cohesive-Frictional Materials 2:279-299.

Norman-Gregory, G.M. and Selig, E.T. (1989): Volume change behavior of vibrated sand columns, Journal of Geotechnical Engineering, 115(3): 289-303.https://doi.org/10.1061/(ASCE)0733-9410(1989)115:3(289).

von Wolffersdorff, P.-A. (1996): A hypoplastic relation for granular materials with a predefined limit state surface. Mechanics of Cohesive-frictional Materials 1(3):251-271.https://doi.org/10.1002/(SICI)1099-1484(199607)1:3<251::AID-CFM13>3.0.CO;2-3

Wotzlaw, M., Aubram, D., Rackwitz, F. (2023): Numerical analysis of deep vibrocompaction at small and full scale, Computers and Geotechnics, vol. 157, Elsevier.

Youd, T. L. (1967): The engineering properties of cohesionless materials during vibration. Dissertation. Iowa State University. https://lib.dr.iastate.edu/rtd/322

Proceedings of the XVIII ECSMGE 2024
GEOTECHNICAL ENGINEERING CHALLENGES
TO MEET CURRENT AND EMERGING NEEDS OF SOCIETY
© 2024 the Authors
ISBN 978-1-032-54816-6
DOI 10.1201/9781003431749-533
Open Access: www.taylorfrancis.com, CC BY-NC-ND 4.0 license

ECSMGE 24
XVIII EUROPEAN CONFERENCE ON SOIL MECHANICS AND GEOTECHNICAL ENGINEERING

Interpretation of ion exchange in soil-bentonite mixtures

Interprétation de l'échange d'ions dans les mélanges sol-bentonite

R. Yu*
Graduate School of Global Environmental Studies, Kyoto University, Kyoto, Japan
A. Takai, T. Kato, T. Katsumi
Graduate School of Global Environmental Studies, Kyoto University, Kyoto, Japan
**yu.rongguang.36t@st.kyoto-u.ac.jp*

ABSTRACT: This study investigated the Ca^{2+}-Na^{+} exchange within soil-bentonite (SB) mixtures, commonly employed in the construction of vertical cut-off walls, with a primary focus on the Ca^{2+} sorption and Na^{+} desorption processes. Batch tests were conducted using sodium bentonite, decomposed granite soil, and SB (7.5% mass fraction of bentonite), in $CaCl_2$ solutions with concentrations ranging from 0.5 to 50 mmol/L. The results revealed a significant impact of the water-absorbing swell of bentonite on the volume of the bulk solution, which interfered the calculation of Ca^{2+} sorption. Notably, Na^{+} desorption ceased when the bulk Ca^{2+} concentration exceeded 4 mmol/L, simplifying the development of Ca^{2+}-Na^{+} exchange into Ca^{2+} sorption process. The sorption isotherms of SB, Soil, and bentonite are proportional to their respective bentonite mass fractions. By incorporating parameters related to volume change and sorption isotherms, an average concentration of montmorillonite interlayer space (C_{in}) was proposed. Correlations were founded between C_{in} and the hydraulic conductivity of SB, offering insights into permeability changes based on batch test results.

RÉSUMÉ: Cette étude explore le comportement d'échange Ca^{2+}-Na^{+} dans les mélanges de sol-bentonite (SB) couramment utilisés dans la construction de murs de confinement verticaux. L'accent est mis sur l'sorption du Ca^{2+} et la désorption du Na^{+} dans le mélange SB. Des essais en lots ont été effectués avec de la bentonite sodique, du sol de granite décomposé, et du SB (7,5 % en masse de bentonite), en utilisant des solutions de $CaCl_2$ de 0,5 à 50 mmol/L. Les résultats montrent un impact significatif du gonflement de la bentonite sur le volume de la solution en vrac, influençant le calcul de l'sorption de Ca^{2+}. La désorption du Na^{+} cesse lorsque la concentration en Ca^{2+} dépasse 4 mmol/L, simplifiant le comportement d'échange d'ions en un processus d'sorption de Ca^{2+}. Les isothermes d'sorption du SB, du sol, et de la bentonite sont proportionnelles à leurs fractions massiques respectives de bentonite. En incorporant des paramètres liés au changement de volume et aux isothermes d'sorption, une concentration moyenne de l'espace interlamellaire de montmorillonite (C_{in}) est proposée. Des corrélations sont établies entre C_{in} et les conductivité hydrauliques du SB, offrant des perspectives sur les changements de perméabilité basés sur les résultats des essais en lots.

Keywords: Soil-bentonite; ion-exchange; batch test; sorption; free swell.

1 INTRODUCTION

Soil-bentonite (SB), a mixture of parent soil and sodium bentonite, is widely utilized in constructing vertical cut-off walls because of its exceptional impermeability and self-healing properties (Evans, 1993; Takai et al., 2013) attributed to the added bentonite (Bradshaw & Benson, 2014; Gleason et al., 1997).

The ion exchange of sodium bentonite involves the replacement of Na^{+} within the montmorillonite lattice with other cations from the bulk solution, thereby weakening the barrier performance of bentonite. While previous research has delved into the ion exchange of pure sodium bentonite (Egloffstein, 2001; Whittaker et al., 2019), less attention has been given to the ion exchange behavior of SB, which contains only small quantities of bentonite. Furthermore, challenges persist in assessing material permeability through ion exchange analysis.

Batch test offers an effective means of evaluating ion exchange by subjecting sodium bentonite to multivalent cation solutions (Kaya & Ören, 2005; Meneguin et al., 2017). Existent sorption theories have been found to align well with the characteristics of bentonite when the bulk cation concentration was below 1 g/L. However, its sorption behavior when bulk cation concentrations resembling those found in real-world contaminated leachate (Naveen et al., 2017) is not comprehensively understood.

The aim of this study is to examine the Ca^{2+}-Na^{+} ion exchange behavior of SB and compare it with the behavior in pure bentonite and parent soil. This investigation involves conducting batch tests with pure

Table 1. Physical properties of soil materials.

		Na-bentonite	Decomposed granite soil	SB	Note
Particle density	(g/cm^3)	2.79*	2.65	2.66	JIS A 1202
Montmorillonite content	(%)	48*	-	-	* Komine et al., 2009
CEC Na^+	(meq/g)	0.631*	-	-	
CEC Ca^{2+}	(meq/g)	0.464*	-	-	
Plastic limit	(%)	26.55	NP	NP	JIS A 1205
Liquid limit	(%)	522.0	NP	25.03	

bentonite, SB, parent soil and free swell tests with bentonite in $CaCl_2$ solutions over a concentration range from 0.5 to 50 mmol/L. Additionally, the study seeks to establish a correlation between ion exchange behavior and the permeability of SB.

2 MATERIALS AND METHODS

2.1 Soil materials

The physical properties of soil materials are listed in Table 1. Decomposed granite soil (Soil), which is a sandy soil widely distributed in the subsurface throughout Japan (Ham et al., 2010), was used as the parent soil. Kunigel V1, one of the sodium bentonites collected in Japan (Komine et al., 2009), was used as the bentonite added to the parent soil.

In order to simulate the SB that have been used in Japan (Takai et al., 2016), moisture content of prepared SB is designed as 29%, and mass fraction of sodium bentonite in SB is controlled at $n_{bent.}$ = 7.5%:

$$n_{bent.} = m_{bent.} / (m_{bent.} + m_{soil}) \quad (1)$$

where m_x (g) represents the dry mass of bentonite or decomposed granite soil.

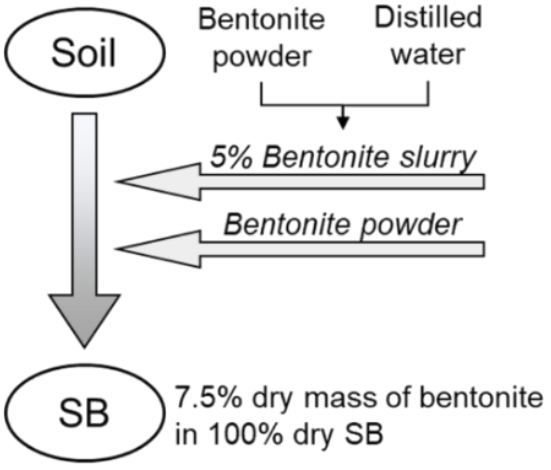

Figure 1. SB mixing procedures.

The procedures of SB preparation is given in Figure 1. The Soil was first passed through 2 mm sieve and then dried by 110 °C oven, while the bentonite powder was air dried with 7.2% initial moisture content, and the 5% bentonite slurry was prepared by mixing bentonite powder with distilled water at a mass ratio of 1:20 for 20 minutes using an aqueous mixer. The slurry was first added into the dried Soil, where the bentonite mass in the slurry was counted in the total $m_{bent.}$. Then, the input of bentonite powder was divided into several times. After all the bentonite powder and water were inputted, the soil mixer will continue to run for 5 minutes to ensure uniform mixing.

2.2 Batch tests

All batch tests were carried out in 250 mL-PP bottles contain 200 mL $CaCl_2$ with different initial concentrations, the initial Ca^{2+} concentrations for each test were listed in Table 2. The solid inputs in bentonite and SB batch systems were designed to have 0.75 ± 0.01 g bentonite, hence ≈12.9±0.1 g SB were placed in SB batch systems, the actual mass of SB input depends on its measured moisture content. And for batch tests of soil, 10 ± 0.1 g were placed in each test.

Table 2. Designed conditions of batch tests.

	Initial Ca^{2+} (mmol/L)									
	0.5	**1**	**5**	**10**	**15**	**20**	**25**	**30**	**40**	**50**
Bentonite	✓	✓	✓	✓	✓	✓	✓	✓	✓	✓
Soil	✓	✓	✓	✓		✓	✓			
SB	✓	✓	✓	✓	✓	✓	✓			

After adding the solids, the bottles were secured on an oscillator and agitated at 3.33 Hz for 24 hours. Following agitation, the bottles were left undisturbed for 15 minutes. The solution was then extracted and centrifuged at 3000 rpm for 10 minutes and filtrated through 0.2 μm filter to collect the supernatant for ionic measurement. Each test was triplicated.

The widely known mass conservation for batch system stands as below:

$$q_e = (V_0 C_0 - V_e C_e) / m_s \quad (2)$$

where q_e (mmol/g) is the sorption or desorption amount of specific component at the end of test; V_0 and V_e (L) are the volumes of bulk solution at initial and final states; C_0 and C_e (mmol/L) are the molarities of

specific component in the bulk solution at initial and final states; m_s (g) is the dry mass of solid.

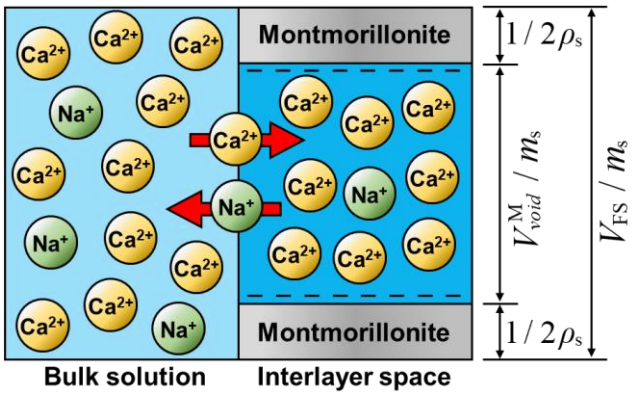

Figure 2. Schematic of montmorillonite unit in bentonite batch system.

Generally, V_0 and V_e are treated as equal. However, in bentonite batch system, the border line between bulk solution and solid particle become ambiguous, the water molecule as well as cations in the solution will be attracted into interlayer space of montmorillonite lattices and be restrained by electrostatic force (Figure 2). In an unfree state, the solution in the interlayer space, strictly speaking, is in a different state than the bulk solution. Therefore, the interlayer space should be eliminated to obtain the volume of bulk solution precisely, the final volume of bulk solution can be calculated by:

$$V_e = V_0 - V_{void}^M + w \cdot m_s / \rho_w = r \cdot V_0 \qquad (3)$$

where V_{void}^M (mL) is the volume of the montmorillonite interlayer in batch system; $w \cdot m_s / \rho_w$ (mL) is the volume of water previously present in the soil; w is gravimetric moisture content. Simplifying V_e as V_0 multiplied by a numerical coefficient r, the mass conservation becomes:

$$q_e = V_0 \cdot (C_0 - r \cdot C_e) / m_s \qquad (4)$$

It has to be noted that in a batch system of bentonite and $CaCl_2$ solution, for Ca^{2+} sorption, the value of q_e is positive, it represents the sum of Ca^{2+} amount that directly contact to the solid particles and those trapped in the interlayer of montmorillonite lattice; and for Na^+ desorption, the value of q_e is negative since $C_0 = 0$, it only represents the Na^+ amount in the bulk solution at the end. According to Eq (4), the diversity of q_e between taking volume change into account or not rises when either the r is not approximately equal to one or the value of C_e is very large, the comparison between sorption/desorption isotherms obtained using coefficient r or not had also been conducted in this study.

2.3 Free swell tests

The free swell tests correspond to ASTM D5890 (2019) were conducted in order to find the volume of interlayer space of montmorillonite under different $CaCl_2$ concentrations. The designed initial Ca^{2+} molarities were consistent with the batch conditions.

The tests were conducted in 100 mL graduated cylinders. Initially, each cylinder was filled with a solution up to 90 mL. Next, 2 g of dry bentonite powder were carefully added without touching the cylinder's walls. The cylinder was then topped up to 100 mL with a solution and left undisturbed for 24 hours. The results were obtained when the bentonite volume reading in the cylinder remained unchanged for 6 hours, at which point the supernatant was collected and the equilibrium concentrations of Na^+ and Ca^{2+} were measured.

The volume of the montmorillonite interlayer space per unit mass of bentonite was calculated by:

$$V_{void}^M / m_s = V_{FS} / m_s - 1/\rho_s \qquad (5)$$

where V_{FS} / m_s (mL/g) is the free swell volume per gram observed from the test; ρ_s (g/cm^3) is the particle density of bentonite.

2.4 Measurement of ionic compositions

The molarities of Ca^{2+} and Na^+ in the supernatants collected from batch tests and free swell tests, and their initial concentrations in every test were measured by an atomic emission spectrometer (SHIMADZU, ICPE-9800). All fluids were collected in 15 mL centrifuge tubes and stored at 4°C previous to the measurement.

3 RESULTS

3.1 Montmorillonite interlayer space

The change of montmorillonite interlayer space of unit mass V_{void}^M / m_s at different Ca^{2+} concentrations obtained from free swell tests according to the Eq (5) are given in Figure 3, the bulk concentrations in the figure are the concentrations when the free swell volumes were read. It can be seen that the V_{void}^M / m_s decrease significantly as the increase of Ca^{2+} molarity in the solution, and the V_{void}^M / m_s at any Ca^{2+} molarity in bulk solution less than 50 mmol/L can be precisely estimated.

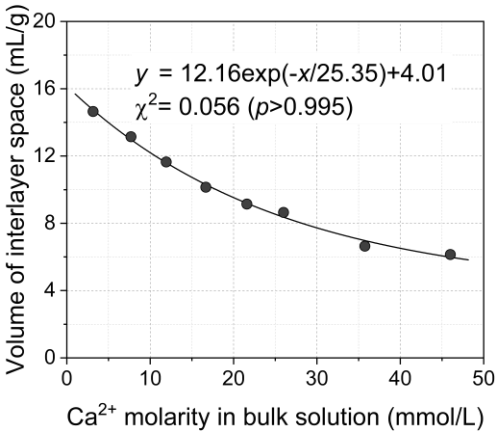

Figure 3. Interlayer space of bentonite in different Ca^{2+} concentrations.

3.2 Sorption and desorption isotherms

All isotherms in this study were plotted with an independent variable of Ca^{2+} molarity in bulk solution, the isotherms obtained without considering the volume change were labelled as Ordinary, while isotherms obtained using Eq (4) were labelled as Modified.

The sorption and desorption isotherms in bentonite and SB batch systems are given in Figure 4, the isotherms in the two systems exhibited same characteristics. For Ca^{2+} sorption, the ordinary isotherms shared a trend of decreasing when the Ca^{2+} concentration in bulk solution exceeded 10 mmol/L while the modified isotherms tended to remain unchanged. The differences between two kinds of isotherms gradually increased with the increase of Ca^{2+} concentration in bulk solution. In Figure 4, when the Ca^{2+} concentration closed to 50 mmol/L, the modified q_e was almost 3 times of the ordinary q_e, meanwhile the estimated interlayer space for 0.75 g bentonite at 50 mmol/L Ca^{2+} was about 3.75 mL, which was only approximately 1.88% of the V_0. Such differences between ordinary isotherms and modified isotherms indicate that when the calculation of bentonite sorption based on mass conservation of batch system was proceeded, the volume changes of bulk solution can be eliminated only when the concentration of bulk solution is very low (at least < 4 mmol/L for Ca^{2+}).

On the other hand, the change of bulk volume did not generate huge diversities in Na^+ desorption isotherms. Recallling Eq (4), when C_0 = 0, the differences between two kinds of isotherms would only depend on the value of r, hence slightly change in bulk volume only have slightly effect to the calculated Na^+ desorption amount. The Na^+ desorption isotherms indicating that the original Na^+ in bentonite were quickly and completely replaced by Ca^{2+} meanwhile the Ca^{2+} sorption were still developing, the development of so-called Ca^{2+}-Na^+ exchange were dominated by the extent of Ca^{2+} sorption when bulk Ca^{2+} exceeded 4 mmol/L. Thus, the binary process of ion exchange in bentonite and SB batch systems could be simplistically described, to a large extent, by single process of Ca^{2+} sorption.

The isotherms in the Soil batch systems are given in Figure 5. Neither Ca^{2+} nor Na^+ had illustrated obvious sorption or desorption, confirmed that decomposed granite soil did not undergo significant ion exchange process, and the isotherms of SB were mostly contributed by the properties of bentonite.

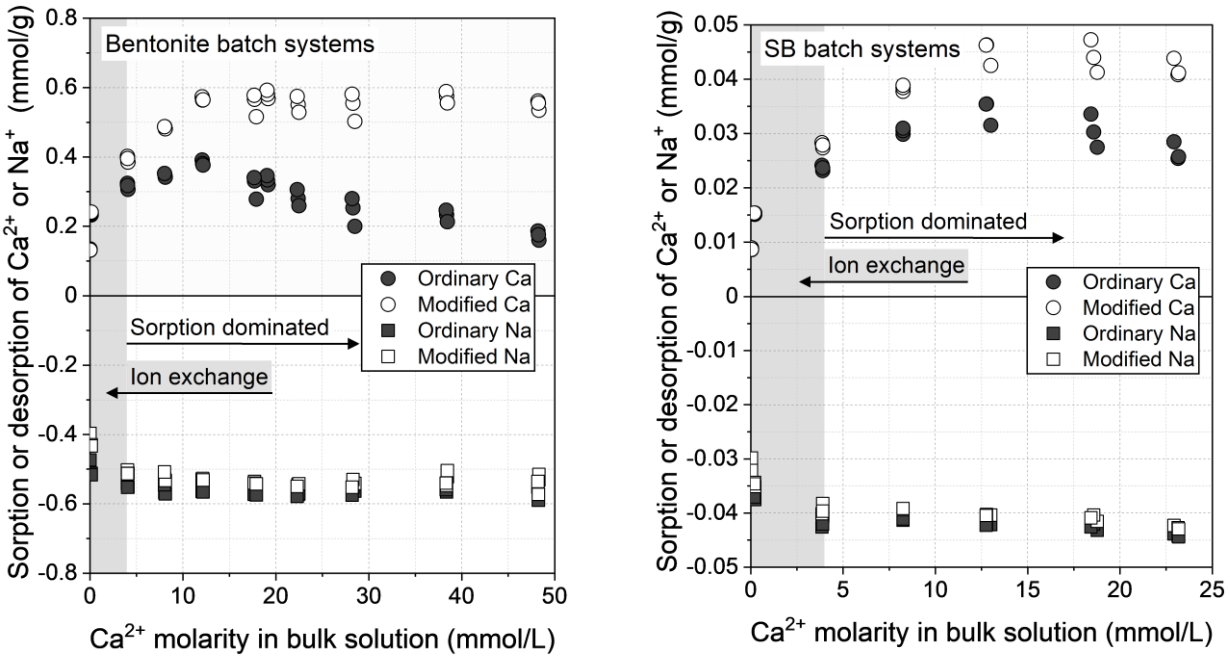

Figure 4. Sorption/desorption isotherms in bentonite (left) and SB (right) batch systems.

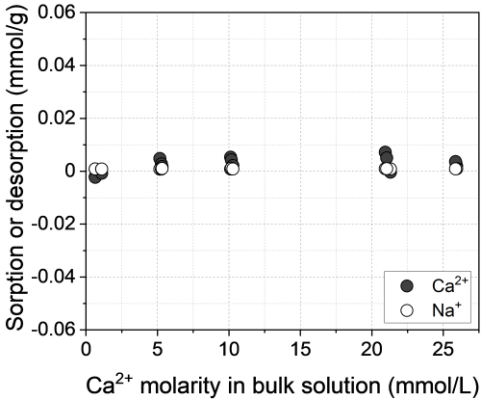

Figure 5. Sorption/desorption isotherms in decomposed granite soil batch systems.

4 DISCUSSION

For the obtained Ca^{2+} sorption isotherms of bentonite, Soil, and SB, quantitative relation based on mass fractions therotically exist as below:

$$q_{\mathrm{SB}} = n_{bent.} \cdot q_{bent.} + (1 - n_{bent.}) \cdot q_{soil} \qquad (6)$$

where q_{sub} is the numerical function of sorption isotherm of specific substance; $n_{bent.}$ = 7.5% in SB mixture, and $q_{soil} = 0$ is approximated. In Figure 6, $q_{bent.}$ was well fitted by Exponential model, and the plots of SB were in line with the calculated q_{SB}, indicating that Soil and bentonite did not interact to each other in batch tests, the Ca^{2+} sorption potential of bentonite can be fully exploited in SB with a 7.5% mass fraction.

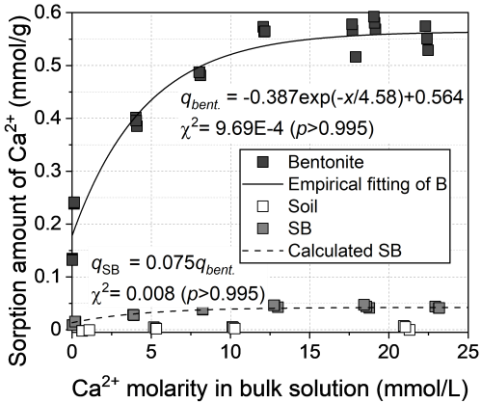

Figure 6. The relation between modified Ca^{2+} sorption isotherms of bentonite, Soil and SB.

Though the ion exchange can be simplfied as Ca^{2+} sorption process, the increase of Ca^{2+} sorption amount were observed converged when bulk Ca^{2+} molarity reached 25 mmol/L, while the permeability of bentonite materials will continue to increase in higher cation molarities (Norris et al., 2018), which has revealed the limitation of using sorption isotherms to estimate permeability changes.

In physical sense, it is the particle surface area and volume of interlayer space that mostly determine the sorption capacity of bentonite (Figure 2). But 1 g bentonite could have different volume of interlayer space under different conditions, which brings insufficiencies to the description of q_e (mmol/g) for bentonite and SB. By considering both the mass and volume, a sufficient description of average molarity in bentonite interlayer space C_{in} is proposed as below:

$$C_{\mathrm{in}} = (q_e / n_{bent.}) / (V_{void}^{\mathrm{M}} / m_s) \qquad (7)$$

where the intensive variable C_{in} (mmol/L) links the results of batch test and the free swell test. Since the scope of C_{in} is only the interlayer space in bentonite, C_{in} is actually independent to the $n_{bent.}$ (q_e is not). The relation between Ca^{2+} molarity in bulk solution and C_{in} is given in Figure 7. C_{in} of Ca^{2+} keeps increasing as bulk concentration and is linearly related to the Ca^{2+} molarity in bulk solution. It can be inferred that the convergence trend of sorption isotherms is limited by the decrease of volume.

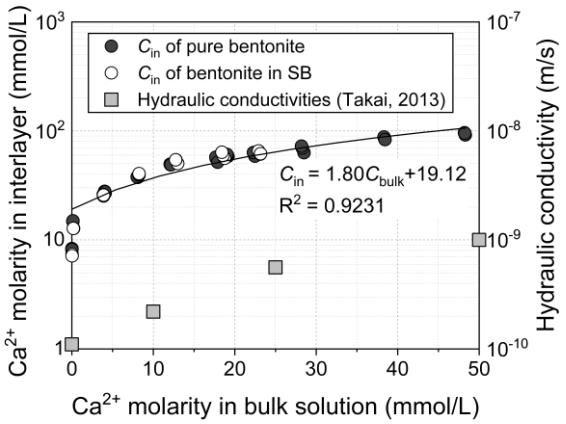

Figure 7. The relations between Ca^{2+} molarity in bulk solution and C_{in} or hydraulic conductivity.

Comparing the C_{in} with hydraulic conductivity of SB prehydrated with $CaCl_2$ solutions, under same concentration range by flexible-wall permeability test (Takai et al., 2013), the increase in hydraulic conductivity was a macroscopic phenomenon that occured simultaneously with the increase of C_{in}. In addition, it is possible to estimate the permeability changes of SB based on the value of C_{in}.

5 CONCLUSIONS

By analysing the results of batch test and the free swell test, the following conclusions were obtained.

(1) In bentonite and SB batch systems, the bulk volume changed as the osmotic swell of bentonite, when bulk Ca^{2+} molarity was closed to 50 mmol/L, the

1.88% of the volume change resulted in an error of nearly 300% in the Ca^{2+} sorption amount.

(2) The developments of Ca^{2+}-Na^{+} exchange process observed in bentonite and SB batch systems were dominated by the extent of Ca^{2+} sorption, when Ca^{2+} bulk concentrations were >4 mmol/L.

(3) The bentonite with 7.5% mass fraction in SB can fully exploit its Ca^{2+} sorption potential as pure bentonite. The measured Ca^{2+} sorption isotherms of bentonite, Soil, and SB are proportional to their respective bentonite mass fractions.

(4) Average molarity in bentonite interlayer space (C_{in}) was proposed, based on the sorption isotherms and results of free swell test. C_{in} was observed to be linearly related to the bulk Ca^{2+} concentration and can be used to estimate the permeability change of SB.

ACKNOWLEDGEMENTS

The authors are grateful for the financial support provided by JSPS KAKENHI 21H01426 and 22H00227. This research is supported by Mr. G. Araki (Raito Kogyo Co., Ltd.) and his colleagues.

REFERENCES

ASTM D5890. (2019). *Standard Test Method for Swell Index of Clay Mineral Component of Geosynthetic Clay Liners has been revised to D5890-11*. American Society for Testing and Material.

Bradshaw, S. L., & Benson, C. H. (2014). Effect of Municipal Solid Waste Leachate on Hydraulic Conductivity and Exchange Complex of Geosynthetic Clay Liners. *Journal of Geotechnical and Geoenvironmental Engineering*, *140*(4). https://doi.org/10.1061/(asce)gt.1943-5606.0001050.

Egloffstein, T. A. (2001). Natural bentonites - Influence of the ion exchange and partial desiccation on permeability and self-healing capacity of bentonites used in GCLs. *Geotextiles and Geomembranes*, *19*(7), 427–444. https://doi.org/10.1016/S0266-1144(01)00017-6.

Evans, J. C. (1993). Vertical cutoff walls. In *Geotechnical Practice for Waste Disposal* (pp. 430–454). Springer US. https://doi.org/10.1007/978-1-4615-3070-1_17.

Gleason, M. H., Daniel, D. E., & Eykholt, G. R. (1997). Calcium and Sodium Bentonite for Hydraulic Containment Applications. *Journal of Geotechnical and Geoenvironmental Engineering*, *123*(5), 438–445. https://doi.org/10.1061/(ASCE)1090-0241(1997)123:5(438).

Ham, T.-G., Nakata, Y., Orense, R., & Hyodo, M. (2010). Influence of Water on the Compression Behavior of Decomposed Granite Soil. *Journal of Geotechnical and Geoenvironmental Engineering*, *136*(5), 697–705. https://doi.org/10.1061/(asce)gt.1943-5606.0000274.

Kaya, A., & Ören, A. H. (2005). Adsorption of zinc from aqueous solutions to bentonite. *Journal of Hazardous Materials*, *125*(1–3), 183–189. https://doi.org/10.1016/j.jhazmat.2005.05.027.

Komine, H., Yasuhara, K., & Murakami, S. (2009). Swelling characteristics of bentonites in artificial seawater. *Canadian Geotechnical Journal*, *46*(2), 177–189. https://doi.org/10.1139/T08-120.

Meneguin, J. G., Moisés, M. P., Karchiyappan, T., Faria, S. H. B., Gimenes, M. L., de Barros, M. A. S. D., & Venkatachalam, S. (2017). Preparation and characterization of calcium treated bentonite clay and its application for the removal of lead and cadmium ions: Adsorption and thermodynamic modeling. *Process Safety and Environmental Protection*, *111*, 244–252. https://doi.org/10.1016/j.psep.2017.07.005.

Naveen, B. P., Mahapatra, D. M., Sitharam, T. G., Sivapullaiah, P. V., & Ramachandra, T. V. (2017). Physico-chemical and biological characterization of urban municipal landfill leachate. *Environmental Pollution*, *220*, 1–12. https://doi.org/10.1016/j.envpol.2016.09.002.

Norris, A., Di Emidio, G., Malusis, M. A., & Replogle, M. (2018). Modified bentonites for soil-bentonite cutoff wall applications with hard mix water. *Applied Clay Science*, *158*(November 2017), 226–235. https://doi.org/10.1016/j.clay.2018.03.030.

Takai, A., Inui, T., & Katsumi, T. (2016). Evaluating the hydraulic barrier performance of soil-bentonite cutoff walls using the piezocone penetration test. *Soils and Foundations*, *56*(2), 277–290. https://doi.org/10.1016/j.sandf.2016.02.010.

Takai, A., Inui, T., Katsumi, T., Kamon, M., & Araki, S. (2013). Hydraulic barrier performance of soil bentonite mixture cutoff wall. *Coupled Phenomena in Environmental Geotechnics: From Theoretical and Experimental Research to Practical Applications - Proceedings of the International Symposium, ISSMGE TC 215*, *December*, 707–714. https://doi.org/10.1201/b15004-96.

Whittaker, M. L., Lammers, L. N., Carrero, S., Gilbert, B., & Banfield, J. F. (2019). Ion exchange selectivity in clay is controlled by nanoscale chemical-mechanical coupling. *Proceedings of the National Academy of Sciences of the United States of America*, *116*(44), 22052–22057. https://doi.org/10.1073/pnas.1908086116.

Proceedings of the XVIII ECSMGE 2024
GEOTECHNICAL ENGINEERING CHALLENGES
TO MEET CURRENT AND EMERGING NEEDS OF SOCIETY
© 2024 the Authors
ISBN 978-1-032-54816-6
DOI 10.1201/9781003431749-534
Open Access: www.taylorfrancis.com, CC BY-NC-ND 4.0 license

ECSMGE 24
XVIII EUROPEAN CONFERENCE ON SOIL MECHANICS AND GEOTECHNICAL ENGINEERING

A review of DFOS sensors installation methods for curved surfaces in tunnels

Examen des méthodes d'installation des capteurs DFOS pour les surfaces courbes dans les tunnels

S.Q. Zhang
University College Cork, Cork, Ireland

K. Zhang
China University of Mining and Technology, Xuzhou, China

Z.L. Li*
University College Cork, Cork, Ireland

**zili.li@ucc.ie*

ABSTRACT: This paper reviews previous published articles on structural health monitoring (SHM) of tunnels using distributed fibre optic sensing (DFOS). The installation of DFOS sensors onto curved surfaces in tunnels, such as the transverse cross section of a tunnel, is a major challenge for the effectiveness of SHM of tunnels. The state-of-the-art DFOS sensors installation methods currently used for monitoring surface strains in tunnels are summarized, with emphasis on evaluating the applicability scenario of each method and their advantages and disadvantages.

RÉSUMÉ: Ce document est un recueil d'articles publiés précédemment sur le contrôle de la santé structurelle (SHM) des tunnels au moyen de la détection distribuée par fibre optique (DFOS). L'installation de capteurs DFOS sur des surfaces courbes dans les tunnels, telles que la section transversale d'un tunnel, est un défi majeur pour l'efficacité du SHM des tunnels. Les méthodes d'installation des capteurs DFOS actuellement utilisées pour contrôler les contraintes de surface dans les tunnels sont résumées, en mettant l'accent sur l'évaluation du scénario d'applicabilité de chaque méthode et sur leurs avantages et inconvénients.

Keywords: Distributed fibre optic sensing; tunnel engineering; structural health monitoring.

1 INTRODUCTION

Tunnel engineering has been one of the most vital aspects of underground infrastructure over recent decades, serving an important function in the urban transportation network. By the end of 2020 in China, there were already 16,789 tunnels in operation, with a total length of about 19,630km; 2,746 tunnels under construction, with a total length of about 6,083km; and 6,354 tunnels under planning, with a total length of about 16,255km (Tian et al. 2021). With the increase of construction and service time, tunnel defects are unavoidable (e.g. settlement deformation, lining cracking and tunnel leakage) due to adverse factors such as extreme weather and material deterioration. Recently, distributed fibre optic sensing (DFOS) is emerging as an innovative monitoring tool for measuring continuous strain development by a single fibre optic cable in civil infrastructures (Li et al., 2018). However, DFOS sensors need to be closely attached to the monitored structure so that they can deform simultaneously with the monitored structure and provide accuratemeasurement. Such close attachment can be easily achieved in monitoring flat operational structures such as piles, pipelines, and bridge decks, but it is rarely seen on curved surfaces. The lack of suitable methods for installing DFOS sensors on curved surfaces has been a major obstacle to promoting this innovative technology in tunnel engineering. This paper presents the state-of-the-art methods for installing DFOS sensors on curved surfaces, mainly by comparing the advantages and disadvantages of each method and briefly suggesting improvement measures. It aims to promote the further application of DFOS in tunnel engineering and beyond.

2 EMBEDDED INSTRUMENTATION

Regarding tunnels under construction, DFOS sensors are mainly embedded in the monitored structure, which ensures that DFOS sensors deform simultaneously with the monitored structure by a solid bond, allowing reliable deformation to be transmitted to the sensitive glass fibre core (Monsberger and Lienhart, 2017). Figure 1 shows the typical embedding positions of DFOS sensors.

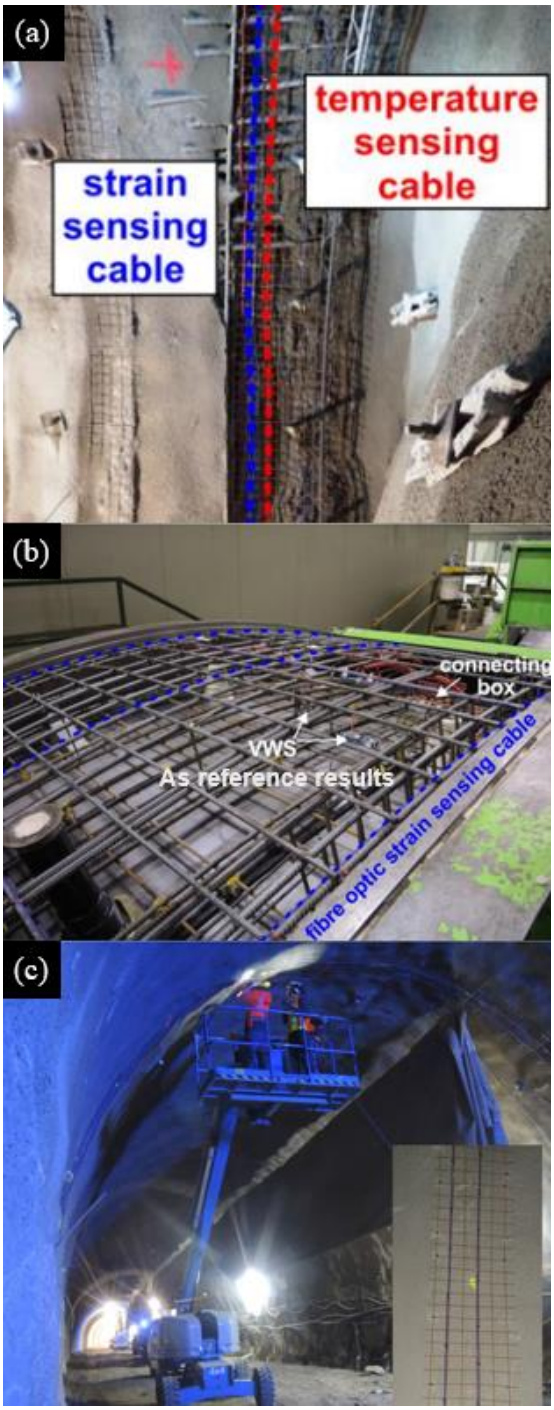

Figure 1. Typical embedding position of DFOS sensors, (a) in shotcrete lining, (b) in tunnel segments and (c) along the shotcrete lining.

Regardless of the tunnel construction methods used (e.g., the New Austrian Tunneling Method (NATM) or prefabricated tunnel segments, as shown in Figure 1(b)), embedding DFOS sensors into the monitored structure in tunnels generally involves two steps:

1) The sensors are first attached directly to the monitored structure at regular intervals (15-20 cm) along the reinforcement bars using some fixing materials, including epoxy resins, eye-bolts, buckles and cable ties.
2) A solid bond between DFOS sensors and the monitored structure is obtained by concrete.

Pre-tension of DFOS sensors has also been shown to be not necessary in a demonstration case reported by Monsberger et al. (2018). A comparative analysis of tunnel lining deformation measurements using vibrating wire sensors (VWS) and non-prestrained DFOS demonstrated that the data obtained from both methodologies exhibited a high degree of congruence in terms of their magnitude and geometric profiles. This finding underscores the reliability and compatibility of non-prestrained DFOS in parallel with traditional vibrating wire sensor measurements for assessing tunnel lining deformations.

For existing tunnels, embedding DFOS sensors directly into the structure at the initial stage is often not possible. In these scenarios, the attachment of DFOS sensors to the cross-section of the tunnel can be achieved via a supplementary structure applied to the tunnel lining, utilizing elements like custom-designed clamps (Muley et al., 2011; Monsberger et al., 2021). After the DFOS sensors installation, additional shotcrete is applied to the area of the secondary structure to ensure a solid bond between the DFOS sensors and the existing tunnel lining. A major limitation of this DFOS sensors installation method is the robustness of DFOS sensors since the DFOS sensors are placed in harsh tunnel construction environment by workers in limited working space. For example, in a NATM construction project, shotcrete is often sprayed onto reinforcement grids under high pressure, the DFOS sensor has to be able to withstand the high pressure and the grid vibrations caused by the high pressure to avoid partial dislodgement of the DFOS sensors from the reinforcement bars. Therefore, DFOS sensors often require additional protective layers and corresponding experimental investigation in the laboratory to examine the influence of site construction on the DFOS robustness and measurement accuracy.

The absence of a requirement for pre-tensioning the DFOS sensors and the ability to accurately track the monitored structural deformations stand as the principal advantages of the embedment instrumentation. However, the construction phase

presents a significant risk of damages the DFOS sensors, resulting post-embedment repairs or replacements changelling without significant intervention in the structure. Consequently, the implementation of supplementary protective measures is advocated to safeguard the integrity of DFOS sensors during installation.

3 SURFACE INSTRUMENTATION

For most existing tunnels, the installation of DFOS sensors on the surface of the monitored structure is more popular due to feasibility, tunnel integrity and serviceablity. The DFOS sensors can be either installed onto tunnel surface using a continuous bonding method or a fixed-point method. Figure 2 summarises the common materials and tools used to attach the DFOS sensors to the surface of the monitored structure.

3.1 Continuous bonding method

In theory, the continuous bonding method shown in Figure 2(a) is the most effective method for attaching the DFOS sensors on the surface of the monitored structure to exploit the continuous strain sensing capacities of DFOS sensors (Sui et al., 2021). Gue et al. (2015) attached the DFOS sensors via continuous gluing to obtain a continuous strain profile along the entire cross section for a cast iron tunnel over a period of 11 months and representative strains of the behaviour of the cast iron ring were measured. However, in order to achieve effective bond between the DFOS sensors and the surface of the monitored structure, a comprehensive treatment of the surface is necessary, including fluting, smoothing, grinding, cleaning, bottoming, sticking, checking etc. These installation techniques severely limit the application of the continuous bonding method. Also, the performance of adhesive (usually a thin layer of epoxy resin) in the long term is vital since the effective contact between the DFOS sensors and the surface of the monitored structure are achieved mainly by the adhesive. According to Gomez et al. (2020), additional protective measures could be taken to avoid possible damage of the DFOS sensors as shown in Figure 2(b).

3.2 Fixed-point method

In many practical situations, a major challenge is that the continuous bonding method can not be used due to the constraints of the construction and service environment. In response to this challenge, the fixed-point method has been advocated. This approach acknowledges the inherent limitation that strain measurements are only representatively for the gauge length. Consequently, rigorous consideration of gauge length is necessary as the computation of deformation hinges on the product of strain and this precisely defined interval length. The hook-and-pulley system shown in Figure 2(c) is currently the most widely reported fixed-point method for installing DFOS sensors (Mohamad et al., 2012). Briefly, the hooks are fixed at different locations on the surface of the monitored structure, with the DFOS sensors passing along the pulleys. Zhu et al. (2022) reported that fixing clamps, designed for installation on tunnel linings through the use of external expansion screws as illustrated in Figure 2(d), are also efficacious in gripping the DFOS snesors. Regardless of the tool used to fix the DFOS sensors to a number of discrete points on the surface of the monitored structure, the DFOS sensors need to be pre-strained to avoid any slack sections. The selected fixation kit should have a suitable curvature to avoid excessive optical signal loss and minimize the distance between the DFOS sensors and the surface of the monitored structure.

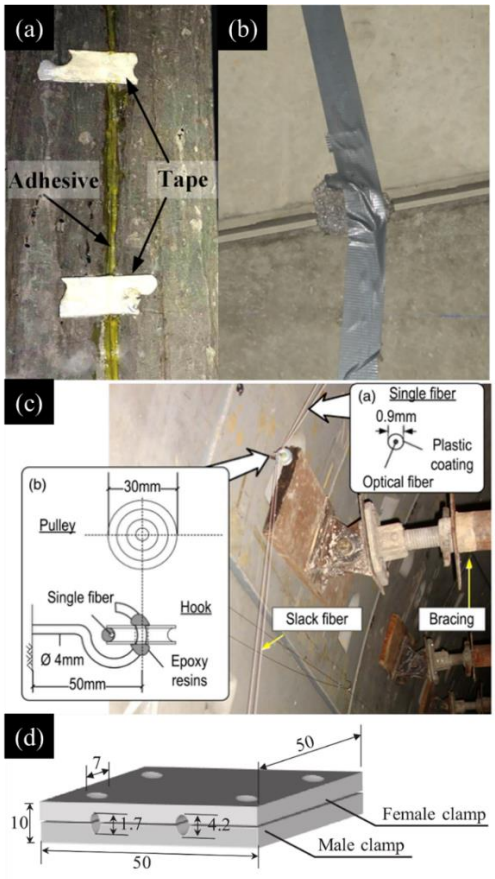

Figure 2. Common materials and tools for attaching the DFOS sensors to the surface of the monitored structure.

Compared with embedded instrumentation, surface instrumentation provides a straightforward and minimally invasive method for structural health

monitoring, offering better flexibility for sensor maintenance, adjustments, and replacements without compromising structural integrity. However, deploying DFOS sensors on the curved surfaces introduces unique challenges, particularly in maintaining consistent contact between the sensors and the curved surfaces, which is crucial for accurate deformation measurement. The complexities introduced by curved surfaces need to be addressed by emphasizing the need for careful method selection, development of innovative attachment solutions and data correction techniques.

4 CONCLUSION

In recent years, a large number of field monitoring projects have been conducted to successfully demonstrate the great potential of DFOS in structural health monitoring. Nevertheless, the capability of DFOS for monitoring structures with curved surface has always been restricted by the reliable DFOS sensor installation method. The present work summarized the DFOS sensors installation method for curved surface, aiming to enhance the applicability of this innovative monitoring technology in tunnel engineering and beyond.

ACKNOWLEDGEMENTS

The authors are grateful for the financial support provided by Science Foundation Ireland Frontiers for the Future Programme, 21/FFP-P/10090.

REFERENCES

Gue, C.Y., Wilcock, M., Alhaddad, M.M., Elshafie, M.Z.E.B., Soga, K., Mair, R.J. (2015) The monitoring of an existing cast iron tunnel with distributed fibre optic sensing (DFOS), *Journal of Civil Structural Health Monitoring*, Vol. 5, pp. 573–586. https://doi.org/10.1007/s13349-015-0109-8.

Li, Z., Soga, K., Kechavarzi, C. (2018) Distributed fibre optic sensing of a deep excavation adjacent to pre-existing tunnels, *Geotech Lett*, Vol. 8, pp. 171–177. https://doi.org/10.1680/jgele.18.00031.

Tian S.M., Wang W., Gong J.F. (2021) Development and prospect of railway tunnels in China (including statistics of railway tunnels in China by the end of 2020), *Tunnel Construction*, 41(2): 308. https://doi.org/10. 3973 / j. issn. 2096-4498. 2021. 02. 018.

Mohamad, H., Soga, K., Bennett, P.J., Mair, R.J., Lim, C.S. (2012) Monitoring Twin Tunnel Interaction Using Distributed Optical Fiber Strain Measurements, *Journal of geotechnical and geoenvironmental engineering*, Vol. 138, pp. 957–967. https://doi.org/10.1061/(asce)gt.1943-5606.0000656.

Monsberger, C., Lienhart, W. (2017) In-situ deformation monitoring of tunnel segments using high-resolution distributed fibre optic sensing, In: *Proceedings of the 8th international conference on structural health monitoring (SHMII-8),* Brisbane, Australia, pp. 149–160.

Monsberger, C.M., Buchmayer, F., Lienhart, W. (2021) Autonomous Integrity Monitoring of Shotcrete Tunnel Linings using Distributed Fiber Optic Sensing, In: *Proceedings of the 10th International Conference on Structural Health Monitoring of Intelligent Infrastructure, SHMII*, pp. 1489–1495.

Monsberger, C.M., Lienhart, W., Kluckner, A., Wagner, L., Schubert, W. (2018) Continuous strain measurements in a shotcrete tunnel lining using distributed fibre optic sensing, In: *Proceedings of the 9th European workshop on structural health monitoring*, Manchester, UK, pp. 10-13.

Muley, P.S., Yang, Y., Sham, W.L. (2011) Stability and reliability of fiber optic measurement systems: basic conditions for successful long term structural health monitoring, *Nondestructive Characterization for Composite Materials, Aerospace Engineering, Civil Infrastructure, and Homeland Security 2011*, Vol. 7983, pp. 383-393. https://doi.org/10.1117/12.881147.

Sui, Y., Cheng, X., Wei, J. (2021) Distributed fibre optic monitoring of damaged lining in double-arch tunnel and analysis of its deformation mode, *Tunnelling and Underground Space Technology*, Vol. 110, p. 103812. https://doi.org/10.1016/j.tust.2021.103812.

Zhu, H.H., Wang, D.Y., Shi, B., Wang, X., Wei, G.Q. (2022) Performance monitoring of a curved shield tunnel during adjacent excavations using a fiber optic nervous sensing system, *Tunnelling and Underground Space Technology*, Vol. 124, p. 104483. https://doi.org/10.1016/j.tust.2022.104483.

E - Environment, water and energy
E - Environnement, eau et énergie

Proceedings of the XVIII ECSMGE 2024
GEOTECHNICAL ENGINEERING CHALLENGES
TO MEET CURRENT AND EMERGING NEEDS OF SOCIETY
© 2024 the Authors
ISBN 978-1-032-54816-6
DOI 10.1201/9781003431749-535
Open Access: www.taylorfrancis.com, CC BY-NC-ND 4.0 license

ECSMGE 24
XVIII EUROPEAN CONFERENCE ON SOIL MECHANICS AND GEOTECHNICAL ENGINEERING

Concrete piles with lowest carbon emissions and optimised environmental impact

Pieux en béton avec les émissions de carbone les plus faibles et un impact environnemental optimisé

K.A. Abushama*, W. Hawkins, L. Pelecanos, T. Ibell
University of Bath, Bath, United Kingdom

**kaa71@bath.ac.uk*

ABSTRACT: Many studies have addressed the embodied carbon of superstructures, however, the carbon footprint of substructures has only been investigated to a limited extent. This study aims to optimize the design of reinforced concrete piles through finding the best combination of concrete design parameters, this is done using a hybrid-optimization algorithm that uses a genetic algorithm to find the optimal pile design. Moreover, the optimization algorithm is used to test the effect of pile geometry on the embodied carbon. Results show that for solid piles, utilizing the optimal design parameters leads to a significant cut in the total embodied carbon compared to common pile designs. However, solid piles proved to be the least efficient environmentally compared to other geometries.

RÉSUMÉ: De nombreuses études se sont penchées sur le carbone incorporé des superstructures, cependant, l'empreinte carbone des infrastructures a été peu étudiée. Cette étude vise à optimiser la conception des pieux en béton armé en trouvant la meilleure combinaison de paramètres de conception du béton, cela est réalisé en utilisant un algorithme d'optimisation hybride qui utilise un algorithme génétique pour trouver la conception optimale du pieu. De plus, l'algorithme d'optimisation est utilisé pour tester l'effet de la géométrie du pieu sur le carbone incorporé. Les résultats montrent que pour les pieux pleins, l'utilisation des paramètres de conception optimaux entraîne une réduction significative du carbone incorporé total par rapport aux conceptions de pieux courantes. Cependant, les pieux pleins se sont avérés être les moins efficaces sur le plan environnemental par rapport à d'autres géométries.

Keywords: Embodied carbon; reinforced concrete; hollow and tapered piles.

1 INTRODUCTION

Concrete is the most widely used construction material, the pillar of modern infrastructure, and a symbol of human inventiveness. It has played a decisive role in shaping our municipal scenes, from skyscrapers to bridge designs. Yet, behind its long-lasting strength lies a hidden environmental cost and a major threat to our planet (UN report, 2022). As modern societies grapple with the urgent need to mitigate climate change and reduce greenhouse gas emissions, the construction industry is under inspection, and urgent interventions are being taken to cut carbon emissions by 70% by the end of 2030 a milestone towards achieving the net-zero by 2050 (Allwood, J. et al., 2019). Over the past few years, there has been an evolving interest in optimizing the environmental impact of superstructures through introducing new cleaner material-production techniques as well as seeking new structural systems able to resist applied loads utilizing less material and emitting less carbon to the environment (Hawkins et al., 2020). However, researchers have been less devoted to the environmental impact of substructures although foundations are responsible for a considerable share of the total embodied carbon for any structure, including low-rise buildings and lightweight structures such as fences and horizontal structures (Zolotuchin et al., 2018), as well as 14% of the amount of concrete consumed in some of the well-known high-rise landmarks such as Burj Khalifa (Poulos H., 2016). In the United Kingdom, the latest UK FIRES report shows that foundations account for nearly half of the ready-mix concrete consumption and account for 2.5 $MtCO_2e$ emissions annually.

This research focuses mainly on optimizing the environmental impact of reinforced concrete piles, a genetic algorithm optimization method is used to find the optimal pile design parameters as well as testing the effect of pile geometry on its environmental impact. This work is part of a research program that aims at optimizing the design of substructures including building carbon and cost models.

2 METHODOLOGY

2.1 Calculating pile capacities

The structural capacity of a pile N is calculated as shown in equation (1) and according to BS EN 1991-1-1:2008, while equation (2) determines the geotechnical capacity of piles Q_t subjected to compressive loads according to EN 1997-1:2004: The skin friction of tapered piles is calculated using the cavity expansion theory discussed by Khan et al. (2008) and as shown in equation (4).

$$N = 0.4\, f_{ck}\, A_c + 0.75\, f_y\, A_s \quad (1)$$

$$Q_b = q_{soil}.\pi.r_{base}^2 \quad (2)$$

$$Q_s = 2\pi \int_0^L L\,.\,r_i.\tau_s\, d(L) \quad (3)$$

$$\tau_{st} = k_s.k_t.\sigma_v'.tan\delta \quad (4)$$

where:

- A_c and A_s = concrete cross-sectional area and reinforcement steel area.
- f_{ck} and f_y = compressive strength of concrete and yield strength of steel
- Q_t, Q_b, and Q_s = total capacity, base bearing capacity, and shaft friction resistance.
- q_{soil} = soil bearing capacity
- r_i and r_b = pile radius and pile base radius.
- τ_s = pile's surface friction
- δ = the concrete-soil friction angle
- k_s *and* k_t= lateral earth pressure and taper modification coefficients.

2.2 Calculating pile settlement and serviceability limit state

The force-displacement method (t-z method) is used for theoretically calculating the pile's settlement; the pile body is divided into a number of discrete sections with assigned properties, and the pile-soil interaction is modeled using nodal springs with a predefined nonlinear stiffness as calculated by Randolph & Wroth (1978), the nodal stiffness values are then used to form the global stiffness matrix and solve for the pile's settlement as shown in equations (5-7) (Craig and Knappett, 2012):

$$\{F\} = [K_n + K_s] \cdot \{u\} \quad (5)$$

$$\{u\} = [K_n + K_s]^{-1} \cdot \{F\} \quad (6)$$

$$k_s = \frac{G}{r \cdot ln\left(2.5\, L\frac{1-\nu}{r}\right)} \quad (7)$$

where:

- $\{F\}$ and $\{u\}$ = vectors of known axial force and unknown vertical displacements.
- $[K_n]$ and $[K_s]$ = stiffness matrices of pile and soil.
- G and ν = shear modulus and Poisson's ratio of the soil.
- L and r = length and radius of the pile.

The settlement limit is set to match the Eurocode 7 settlement limit of 10% of the pile diameter.

2.3 Calculating the embodied carbon

The embodied carbon at stages A1-A3 is calculated using equation (8) as proposed by Orr et al. (2020): a more detailed study addressing A4 and A5 stages will be published shortly.

$$\sum EC = (m_s)(ECF_s) + (m_c)(ECF_c) \quad (8)$$

where:

- $\sum TEC$ = total embodied carbon (kg)
- m_s = reinforcement steel mass (kg)
- m_c = concrete mass (kg)
- ECF_s = embodied carbon factor for steel (kgCO2e/kg)
- ECF_c = embodied carbon factor for concrete (kgCO2e/kg)

2.4 The optimization algorithm

A genetic-algorithm-based optimization method is used to allocate the optimal values of design parameters; concrete grade (f_{ck}), steel-to-concrete ratio (A_s/A_c) and slenderness ratio and (L/D) corresponding to pile designs with minimal embodied carbon. Afterward, a local minimization function is used to check the genetic algorithm results. Figure 1 summarizes the adopted optimization algorithm. The optimization algorithm is used to fulfill the following research aims:

1. Allocate the optimal dimensions and design parameters for cylindrical solid piles: a cylindrical solid pile is the most popular pile geometry in the industry, however, solid pile designs are barely optimized due to different reasons discussed by Abushama et al. (2023). The algorithm is used to investigate the optimal design parameters for solid piles at different load capacities.
2. Compare different pile geometries: the embodied carbon associated with solid piles, tapered piles, hollow cylindrical piles and hollow tapered piles are all compared at different pile capacities.

Table 1. Soil properties tested by Craig 2012.

Property	Symbol	Value
Unit weight	γ	15 (kN/m^3)
Angle of friction	φ	18^0
Poisson's ratio	ν	0.2
Shear modulus	G	$5000 + 500\,Z$ (kPa)

The soil properties used are as tested by Craig and Knappett (2012) and summarized in Table 1.The tested pile geometries are shown in Figure 2.

3 RESULTS

3.1 Optimizing the embodied carbon of solid piles

Figure 3 shows the optimal values of concrete grade (f_{ckc}) and slenderness ratio $(L/D)_c$ for solid piles of different capacities, the optimal steel-to-concrete ratio was always found to be the minimum allowable ratio set in Eurocode 2 (0.004). It is observed that low-capacity piles prefer very slender piles at high concrete grades, while high-capacity piles prefer stockier piles at lower concrete grades (a large volume of low-grade concrete). These optimization results agree with the basic pile design principles as long thin piles provide higher friction resistance which is favourable in the case of low-capacity piles. However, for high-capacity piles, low-grade concrete provides a bigger concrete volume and consequently higher bearing resistance. Nevertheless, it should be noted that the range of optimal pile slenderness ratios calculated [115-133] is far from industry-common design slenderness ratios [10 - 35] which justifies solid piles not being an optimal solution, therefore, better pile geometries are to be tested.

3.2 Effect of pile geometry on the total embodied carbon

Figure 4 shows the optimal amount of embodied carbon associated with four different pile geometries (solid piles, tapered piles, hollow cylindrical piles, and hollow tapered piles) at different loads. A separate study was performed to find the optimal outer-to-inner diameter ratio (D_i/D_o = 0.87) for hollow-cylindrical piles as well as the optimal pile taper angle ($\alpha = 1.70^0$). Figure 4 shows a significant 77% cut in the total embodied carbon between the common solid piles and the optimal tapered-hollow piles. Moreover, it is observed that optimal hollow-cylindrical piles provide a very good alternative to tapered-hollow piles as hollow-cylindrical piles managed to provide the required pile capacities at 60% less carbon than common solid piles. However, building voids inside piles is a construction concern addressed by a contracting company Keltbray in their latest pile design HIPER Pile (2021).

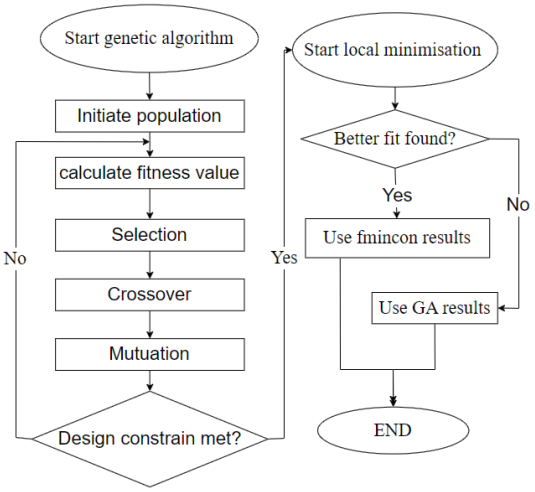

Figure 1. the adopted optimization algorithm.

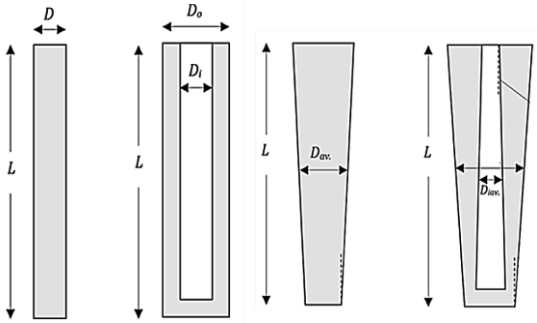

Figure 2. tested pile geometries.

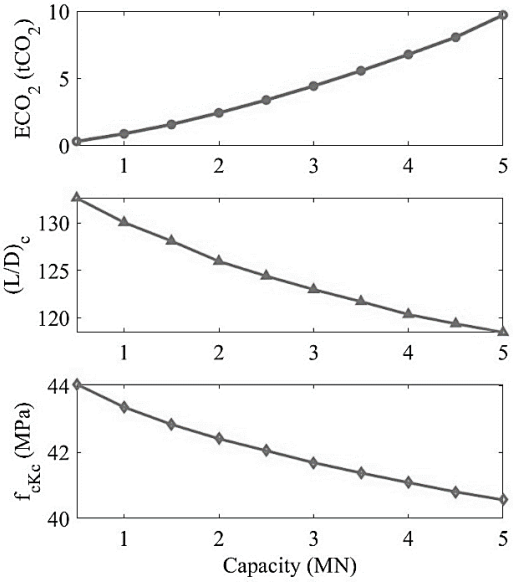

Figure 3. Optimization results for solid piles.

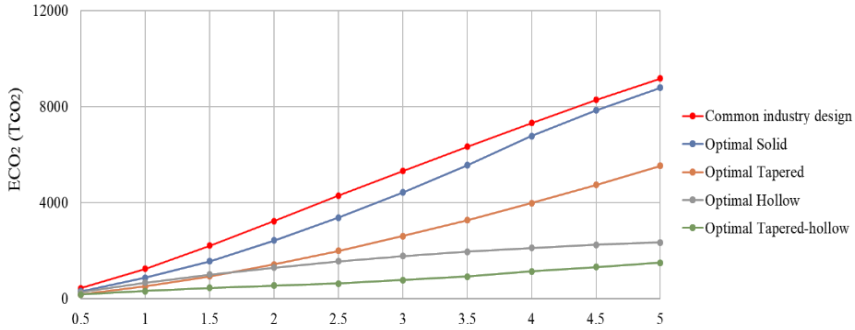

Figure 4. comparing the total embodied carbon for different pile geometries at different load capacities.

4 CONCLUSIONS

To summarize, the environmental impact of reinforced concrete foundations has been barely addressed in the literature. This research introduces a genetic algorithm method that can be used to optimize the design of solid cylindrical piles through calculating the optimal concrete grade, steel-to-reinforcement ratio, and slenderness ratio. Moreover, the algorithm was further used to compare the embodied carbon of different pile geometries at different pile loading capacities, The following are the main concluded points:

- The common solid pile designs are far from optimal as optimal piles acquire higher slenderness ratios than those used in industry.
- Tapered piles with inner voids proved to be the best pile geometry and provided 77% less carbon emissions compared to common solid piles.
- Hollow cylindrical piles provide an adequate solution as they can provide less embodied carbon than solid piles and the adequacy of constructability compared to tapered piles. However, more analysis is needed to quantify the bending capacities of optimal pile designs.
- This research highlights a deficiency in our current pile design standards and policies which should be further covered in more studies.

REFERENCES

Abushama, K., Hawkins, W., Pelecanos, L. and Ibell, T., 2023, December. Minimizing the embodied carbon of reinforced concrete piles using a multi-level modelling tool with a case study. In *Structures* (Vol. 58, p. 105476). Elsevier. Doi: https://doi.org/10.1016/j.istruc.2023.105476.

Allwood, J. et al. (2019) *Absolute Zero*. Apollo - University of Cambridge Repository. Doi:10.17863/CAM.46075.

Hawkins, W., Orr, J., Ibell, T. and Shepherd, P. (2020) 'A design methodology to reduce the embodied carbon of concrete buildings using thin-shell floors.' *Engineering Structures*. Elsevier, 207(January) p. 110195. Doi: 10.1016/j.engstruct.2020.110195.

Keltbray (2021) 'HIPER ® Pile Brochure' pp. 1–4.

Khan, M.K., El Naggar, M.H. and Elkasabgy, M., 2008. Compression testing and analysis of drilled concrete tapered piles in cohesive-frictional soil. Canadian Geotechnical Journal, 45(3), pp.377-392. Doi: 10.1139/T07-107.

Knappett, J., & Craig, R. F. (2012). Craig's soil mechanics. Florida: CRC Press LLC. doi: https://doi.org/10.1201/b12841.

Orr, J., Gibbons, O. and Arnold, W. (2020) 'A brief guide to calculating embodied carbon.' *The Structural Engineer*, (June) pp. 22–27. doi: https://doi.org/10.17863/CAM.53699.

Poulos, H.G. Tall building foundations: design methods and applications. *Innov. Infrastruct. Solut.* **1**10(2016). https://doi.org/10.1007/s41062-016-0010-2.

United Nations Environment Programme (2022). 2022 Global Status Report for Buildings and Construction: Towards a Zero-emission, Efficient and Resilient Buildings and Construction Sector. Nairobi.

Zolotuchin, S. N., Novikova, K. K. and Kim, M. S. (2018) 'New Method for the Construction of Pile Foundations in Low-Rise Constructions Using Micro-Piles in the Knocked-Out Wells.' *IOP Conference Series: Materials Science and Engineering*, 463(2). Doi: 10.1088/1757-899X/463/2/022067.

Proceedings of the XVIII ECSMGE 2024
GEOTECHNICAL ENGINEERING CHALLENGES
TO MEET CURRENT AND EMERGING NEEDS OF SOCIETY
© 2024 the Authors
ISBN 978-1-032-54816-6
DOI 10.1201/9781003431749-536
Open Access: www.taylorfrancis.com, CC BY-NC-ND 4.0 license

ECSMGE 24
XVIII EUROPEAN CONFERENCE ON SOIL MECHANICS AND GEOTECHNICAL ENGINEERING

Long-term horizontal cyclic loading model test results of monopile for offshore wind turbines

Résultats de l'essai sur modèle de chargement horizontal cyclique à long terme d'un monopieu pour éoliennes offshore

C.T. Akdag*, F. Rackwitz
Technische Universität Berlin, Berlin, Germany
**akdag@tu-berlin.de*

ABSTRACT: In this study, a $1g$ model monopile test was conducted under long-term horizontal cyclic loading. The focus of the study is to understand the effect of the number of cycles on the response of the monopile which is mainly used for large $8-9\ MW$ offshore wind turbines OWTs. The monopile was tested in a saturated very dense sand and subjected to a sinusoidal cyclic horizontal load H. The H is approximately 3.5% of the ultimate load capacity H_u. Unidirectional one-way cyclic loading $N = 2{,}000$ with a loading frequency of $f = 0.2\ Hz$ was applied considering the typical frequency range for OWTs. The head of the model pile was equipped with the transducers to obtain the lateral pile head displacement, pile head rotation, and the lateral stiffness evaluation during cyclic loading. The results show that the pile head displacement and rotation accumulation continue to increase with the increase of the number of cycles. In particular, the displacement accumulation during the first few load cycles is clearly larger than the subsequent displacement accumulation. Besides, the lateral secant stiffness k_s decreases with increasing number of loading cycles. The test results indicate that pile head displacement, head rotation, and the lateral stiffness are considerably affected by the number of load cycles.

RÉSUMÉ: Dans cette étude, un essai sur un modèle de monopieu de 1g a été réalisé sous une charge cyclique horizontale à long terme. L'objectif de l'étude est de comprendre l'effet du nombre de cycles sur la réponse du monopieu qui est principalement utilisé pour les grandes éoliennes offshores de $8-9\ MW$. Le monopieu a été testé dans un sable saturé très dense et soumis à une charge horizontale cyclique sinusoïdale H. La H est approximativement 3,5% de la capacité de charge ultime H_u. Une charge cyclique unidirectionnelle $N = 2\ 000$ avec une fréquence de chargement de $f = 0{,}2\ Hz$ a été appliquée en tenant compte de la gamme de fréquence typique des OWT. La tête du pieu modèle a été équipée de transducteurs pour obtenir le déplacement latéral de la tête du pieu, la rotation de la tête du pieu et l'évaluation de la rigidité latérale pendant la charge cyclique. Les résultats montrent que le déplacement de la tête du pieu et l'accumulation de la rotation continuent d'augmenter avec l'augmentation du nombre de cycles. En particulier, l'accumulation de déplacement pendant les premiers cycles de charge est nettement plus importante que l'accumulation de déplacement suivante. En outre, la rigidité latérale sécante k_s diminue avec l'augmentation du nombre de cycles de chargement. Les résultats des essais indiquent que le déplacement de la tête du pieu, la rotation de la tête et la rigidité latérale sont considérablement affectés par le nombre de cycles de charge.

Keywords: Monopile; offshore wind turbines; long-term cyclic loading; 1 g model test.

1 INTRODUCTION

A large number of OWTs with large wind turbines of $8-10\ MW$ rated power are planned to be installed in water depths greater than $40\ m$ over the next few decades (Figure 1). The monopiles, which are the most used foundation type for OWTs, has also been chosen to design OWTs in deeper waters in the current years. The foundations are subjected to large wind and wave loadings with million number of cycles over the duration of OWTs service lifetime in offshore circumstances. It is required to investigate the response of large monopile foundation systems of such OWTs under long-term cyclic loadings.

Several experimental studies have been conducted to understand the behaviour of pile foundation under lateral cyclic loading (Little and Briaud, 1988; Long and Vanneste, 1994; Lin and Liao, 1999). It is stated in almost all investigations that the amplitude and the number of lateral loading cycles have significant influence on the response of pile. The results of 34 cyclic field lateral load tests and 20 full-scale pile lateral cyclic load tests were taken into consideration in the studies of Long and Vanneste (1994) and Lin and Liao (1999), respectively. The researchers indicated that soil-pile stiffness and lateral pile head displacement accumulation are considerably affected

by the number of loading cycles. It should be noted that the cycle number of the considered field tests in these studies are less than 100. A series of centrifuge tests were carried out in dry dense sand under one-way lateral cyclic loading ($20 < N < 50$) in the study of Verdure et al. (2003). The authors stated that secant stiffness under cyclic loading increases slightly with the increase of number of cycles and is obtained 1.5 to 3.0 times larger than the stiffness in monotonic loading condition. It was found that the pile head displacement increases with the increase of cycle number. Similar findings were also reported in the study of Rosquoët et al. (2007). However, the study presented from Rosquoët et al. (2007) was also performed under few loading cycles up to $N = 40$.

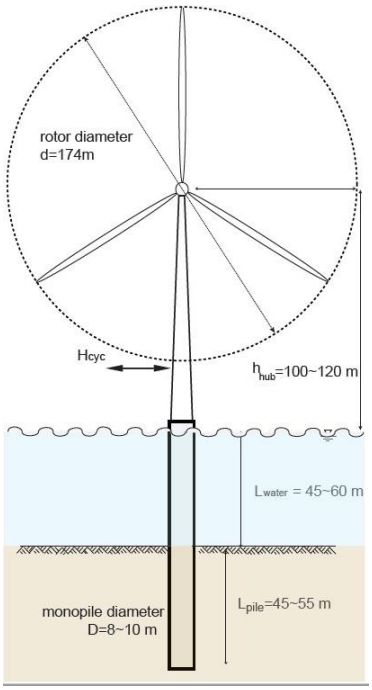

Figure 1. Sketch of a large OWT (8-10 MW).

Model test and field test studies have been implemented on monopiles for OWTs under lateral cyclic loading especially in the last decade. Field test was performed in dense sand with a saturation degree 70% above the ground level under one-way loading up to $N = 5000$ (Li et al., 2015). $1g$ model tests were conducted in saturated loose to dense sand under one-way and two-way cyclic loading between number of cycles $3000 < N < 80{,}000$ (Peralta and Achmus, 2010; Tasan et al., 2011; Nicolai and Ibsen, 2014). The $1g$ tests presented in the study of Nanda et al., (2017) were carried out for open and closed end pile, in dry dense sand under one-way and two-way cyclic loading with $N = 1000$. Centrifuge tests were executed in dry dense sand condition under one-way cyclic loading with $N = 1000$. The results of the above cited investigations on monopile tests in cohesionless soil for OWTs show that the pile head displacement and head rotation accumulation are strongly dependent on the number of cycles, loading type (one-way, two-way), and the amplitude of the cyclic loading.

In this study, the results of the model test are presented. The test was conducted on open-end monopile under unidirectional and one-way lateral loading with N = 2000 number of cycles in saturated very dense sand. The effect of the number of cycles on lateral pile head deformation and rotation accumulation, and lateral stiffness evaluation are investigated and assessed.

2 MODEL TEST

In this investigation, $1g$ model test was conducted to investigate the response of a large OWT with a capacity of $8 - 9\ MW$ under long-term lateral cyclic loading. The large-scale model monopile test was performed for a large OWT supported by a monopile with a large diameter $D = 9\ m$, a diameter-to-wall thickness ratio $D/t = 75$, and an embedded length $L = 50\ m$, and hence an aspect ratio of 5.55. The utilized scaling approach with implemented relations and equations are stated in detail in the study by Akdag and Rackwitz (2023). The testing system involves test pit, subgrade material, loading mechanism, model pile, pile head instrumentation, and lateral load mechanism. The testing system illustration with dimensions are given in Figure 2 and Figure 3.

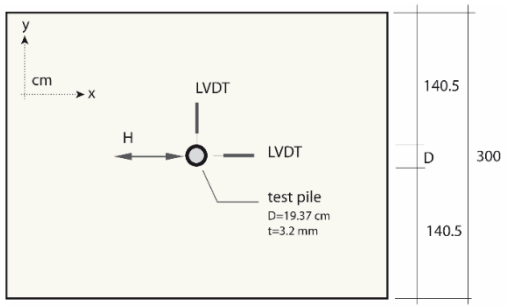

Figure 2. Plan view of 1g model test system.

The large scaled $1g$ model test was conducted on a scaled open-ended steel pile with dimensions of $D = 0.194\ m$, $D/t = 60.53$, and $L = 3.03\ m$.

Poorly graded (SP) “Cottbuser sand” with a grain size among $63\mu m$ and $2\ mm$ was utilized as the subgrade material for the $1g$ model test. It was obtained from the Cottbus area in Germany and the characteristics of the sand is given in the study by (Akdag et al., 2023). The sand was placed in the test pit at its natural moisture content through a repeatable compaction procedure using a vibration plate. First, the sand was placed and compacted to a height equal

to 4 times the pile diameter D to set the soil under the pile. The model monopile was then positioned in the centre of the test pit (Figure 3). Then, sand was located around the pile in layers of 15 cm thickness which are compacted dynamically.

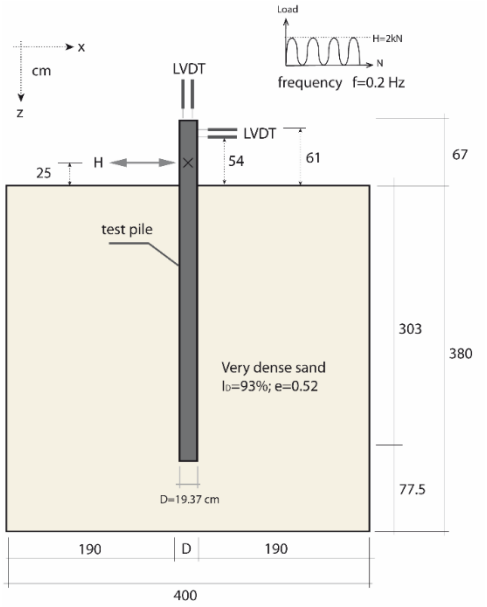

Figure 3. Cross section of model test system.

The average effective unit weight of the sand was found to be $\gamma' = 10.50\ kN/m^3$. The average relative density of the sand was found to be $I_D = 93\%$, which corresponds to very dense sand state. The average void ratio was obtained to be $e = 0.52$. Direct shear test was conducted under normal stresses of $\sigma = 100, 200, and\ 400\ kPa$ to obtain the peak angle of internal friction φ of the sand with a relative density of $I_D = 93$. It was found to be $\varphi = 45.8°$.

During the model test a unidirectional one-way lateral cyclic loading $N = 2000$ was conducted with a constant maximum load value of $H_{max_{cyc}} = 2\ kN$. Applied load amplitude is almost $\xi_b = 3.5\ \%$ of the ultimate load capacity H_{us} of the monopile-soil system in the model test. Two normalised parameters $\xi_b\ and\ \xi_c$ were recommended by LeBlanc et al. (2010) to identify the utilized horizontal cyclic loading characteristics are given in Eq. 1 and Eq. 2.

$$\xi_b = \frac{H_{max}}{H_{us}};\ cyclic\ load\ magnitude \quad (1)$$

$$\xi_c = \frac{H_{min}}{H_{max}};\ cyclic\ load\ ratio \quad (2)$$

Because of one-way cyclic loading application cyclic load ratio is $\xi_c = 0$ in this study.The monotonic ultimate lateral load capacity H_{us} of the model pile was estimated according to the three-dimensional finite element model analysis, which was found to be $H_{us} \cong 60\ kN$ corresponding to the pile head rotation $\theta = 2°$ (Akdag and Rackwitz, 2023).

A load-controlled test was performed in this study, and the horizontal loading mechanism was not fixed to the pile head as shown in Figure 4. Sinusoidal cyclic horizontal loading with a loading frequency of $f = 0.2\ Hz$ was performed considering the typical frequency range for OWTs, as reported in the literature (Lesny and Hinz, 2009; Bhattacharya et al., 2013). The horizontal load was carried out to the pile head at a height $h = 1.30D$ above the sand surface (Figure 3).



Figure 4. Lateral cyclic loading mechanism.

The pile head horizontal displacement accumulation u_x was obtained from the displacement transducers which are instrumented at the pile head in the loading direction. The data recorded from the two transducers oriented in the loading direction were used to obtain the pile head rotation θ accumulation during lateral cyclic loading. Pile lateral stiffness k_s evaluation was found using horizontal load (ΔH) - pile head displacement (Δu) relationship.

3 TEST RESULTS EVALUATION

In this section, the pile head lateral displacement accumulation, pile head rotation accumulation, and pile lateral stiffness evolution are assessed based on the test results.

The accumulation of lateral pile head displacements u_x in the loading direction with maximum $u_{x_{max}}$ and minimum $u_{x_{min}}$ values for increasing numbers of loading cycles up to $N = 2000$ is shown in Figure 5. The test results indicate that the lateral displacement accumulation continues to increase as the number of cycles increases. The

minimum lateral displacement values show the permanent accumulation occurred and increased with the number of loading cycle. Remarkably, $u_{x_{max}}$ accumulation up to $N = 100$ is almost 25% of the maximum pile head accumulations obtained after $N = 2000$.

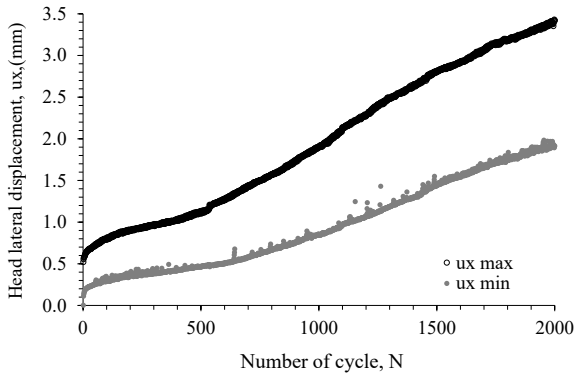

Figure 5. Pile head lateral deformation accumulation.

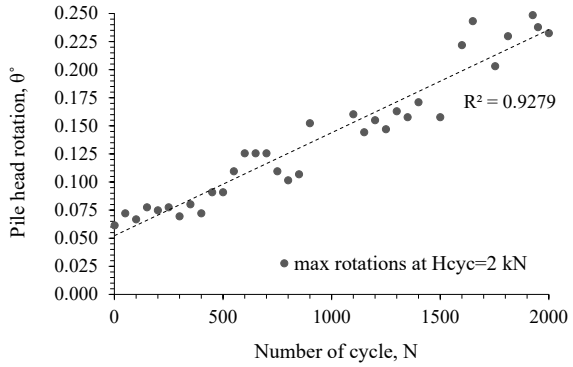

Figure 6. Pile head rotation accumulation.

In Figure 6, the model test results as the pile head rotation accumulation at maximum lateral load level in specific load cycles up to $N = 2000$ is presented. It can be seen from the test results that the accumulation of maximum rotation at $H_{max_{cyc}}$ continues to increase as the number of cycles increases. Notably, the behaviour of the increase in pile head rotation can be evaluated to be linear as shown in the Figure 6. In addition, the maximum rotation reached almost $\theta \cong 0.25°$ after $N = 2000$, which is stated as serviceability limit state SLS according to Det Norske Veritas offshore guideline (DNV, 2018).

The evaluation of pile lateral stiffness during the loading cycles was obtained according to the horizontal load (ΔH) - pile head displacement (Δu) relationship using Eq.3 in Figure 7. The unloading and reloading lateral secant stiffness of the soil-monopile with increasing number of cycles up to $N = 2000$ is given in Figure 8. The test results show that the k_s decreases as the number of load cycles increases. In addition, the rate of decrease in the stiffness alters with increasing N. The rate of reduction in k_s decreased significantly between $N = 1000 - 1400$ with an increasing number of cycles. Subsequently, the change in secant stiffness after the cycles $N = 1400$ is trivial and can be considered almost constant. The stiffness, which reaches an approximately constant value after $N = 1400$, is approximately 3.5 times lower than the stiffness in the initial cycles.

$$k_s = \frac{\Delta H}{\Delta u} \quad (3)$$

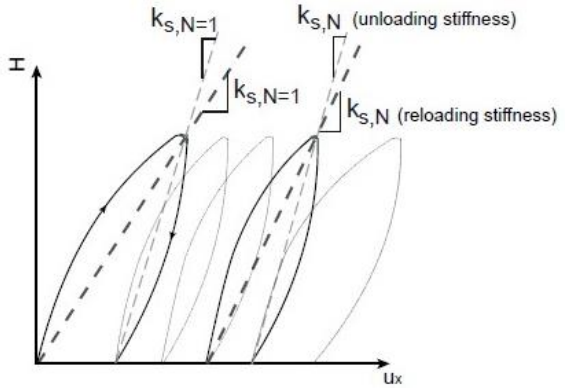

Figure 7. Illustration of secant stiffness determination.

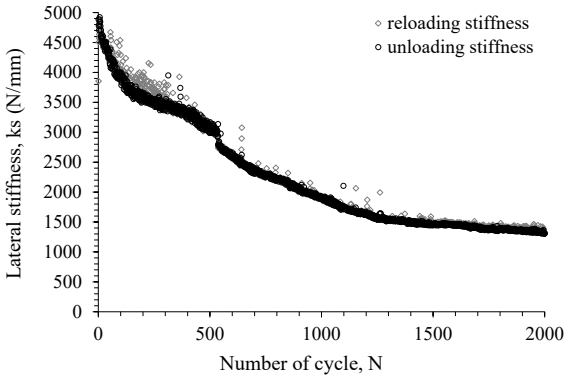

Figure 8. Secant stiffness evaluation.

4 CONCLUSIONS

In this study, the results of the large-scale $1g$ model test is presented. Test was conducted on open-end monopile under unidirectional and one-way lateral loading with N = 2000 number of cycles in saturated very dense sand. The results of the test indicate that the pile head displacement and rotation accumulation continue to increase with the increasing number of cycles. Besides, the lateral secant stiffness k_s decreases with increasing number of loading cycles. Consequently, the test results indicate that pile head displacement, head rotation, and the lateral stiffness are considerably affected by the number of load cycles.

REFERENCES

Akdag C.T., Isik N., Le V.H., Rackwitz F. (2023) Test results for a monopile in medium dense sand subjected to unidirectional lateral cyclic loading. *European Journal of Environmental and Civil Engineering*,27(5):1957-1988. https://doi.org/10.1080/19648189.2022.2107576.

Akdag C.T., Rackwitz F., (2023) Model test and finite element analysis results of a monopile in very dense sand under unidirectional horizontal cyclic loading. *Ocean Engineering*, 288, https://doi.org/10.1016/j.oceaneng.2023.116053.

Bhattacharya, B., Cox, J. A., Lombardi, D., & Wood, D. M. (2013). Dynamics of offshore wind turbines supported on two foundations. *Geotechnical Engineering*,166(GE2):159–169. https://doi.org/10.1680/geng.11.00015.

Det Norske Veritas - DNV (2018). DNV-ST-0126 – Support Structures for Wind Turbines. Oslo, DNV-GL, 208.

LeBlanc, C., Byrne, B. W., Houlsby, G. T. (2010). Response of stiff piles to random two-way lateral loading. *Géotechnique,* 60(9): 715–721. https://doi.org/10.1680/geot.09.T.011.

Lesny, L., & Hinz, P. (2009). Design of monopile foundations for offshore wind energy converters. *International Foundation Congress and Equipment Expo 2009*, Orlando, FL, pp. 512–519. https://doi.org/10.1061/41021(335)64.

Li, W., Igoe, D., & Kenneth, G. (2015). Field tests to investigate the cyclic response of monopiles in sand. Geotechnical Engineering, 168: 407–421. https://doi.org/10.1680/jgeen.14.00104.

Lin, S.-S., & Liao, J. C. (1999). Permanent strains of piles in sand due to cyclic lateral loads. *Journal of Geotechnical and Geoenvironmental Engineering*, 125(9):798–802 https://doi.org/10.1061/(ASCE)10900241(1999)125:9(798).

Little, R. L., & Briaud, J. (1988). Full scale cyclic lateral load tests on six single piles in sand. *Geotechnical Division*, Texas A&M, 121.

Long, J. H., & Vanneste, G. (1994). Effects of cyclic lateral loads on piles in sand. *Journal of Geotechnical Engineering*, 120(1): 225–243. https://doi.org/10.1061/(ASCE)07339410(1994)120:1(225).

Nanda, S., Arthur, I., Sivakumar, V., Donohue, S., Bradshaw, A., Keltai, R., Gavin, K., Mackinnon, P., Rankin, B., & Glynn, D. (2017). Monopiles subjected to uni- and multilateral cyclic loading. *Geotechnical Engineering*, 170: 246–258. https://doi.org/10.1680/jgeen.16.00110.

Nicolai, G., & Ibsen, L. I. (2014). Small-scale testing of cyclic laterally loaded monopiles in dense saturated sand. *Journal of Ocean and Wind Energy*, 1, 240–245.

Peralta, P., & Achmus, M. (2010). An experimental investigation of piles in sand subjected to lateral cyclic loads. *7th International Conference on Physical Modeling in Geotechnics*, Zurich. Taylor & Francis Group (pp. 985–990).

Rosquoët, F., Thorel, L., Garnier, J., Canepa, Y. (2007). Lateral cyclic loading of sand-installed piles. *Soils and Foundations*, 47(5): 821–832. https://doi.org/10.3208/sandf.47.821.

Tasan, E., Rackwitz, F., Savidis, S. (2011). Experimentelle Untersuchungen zum Verhalten von zyklisch horizontal belasteten Monopiles. *Bautechnik*,88(2):102–112. https://doi.org/10.1002/bate.201110010.

Verdure, L., Garnier, J., & Levacher, D. (2003). Lateral cyclic loading of single piles in sand. *International Journal of Physical Modelling in Geotechnics*,3(3):17–28. https://doi.org/10.1680/ijpmg.2003.030303.

Proceedings of the XVIII ECSMGE 2024
GEOTECHNICAL ENGINEERING CHALLENGES
TO MEET CURRENT AND EMERGING NEEDS OF SOCIETY
© 2024 the Authors
ISBN 978-1-032-54816-6
DOI 10.1201/9781003431749-537
Open Access: www.taylorfrancis.com, CC BY-NC-ND 4.0 license

ECSMGE 24
XVIII EUROPEAN CONFERENCE ON SOIL MECHANICS AND GEOTECHNICAL ENGINEERING

Machine learning to expedite concept monopile design

Apprentissage automatique pour accélérer la conception de monopieux conceptuels

J.S. Alexander*
Geowynd/University of Glasgow, Glasgow, UK

R.M. Buckley
University of Glasgow, Glasgow, UK

S.A. Whyte
Geowynd, London, UK

**jal@geowynd.com*

ABSTRACT: Offshore wind turbine generators (WTG)s are typically supported by monopile foundations in shallow water (<50m). The design of monopile foundations is usually conducted using rule-based soil reaction curves (SRC)s in a 1D or 0D model. For the derivation of SRCs, WTG location-specific 3D finite element analysis (FEA) is now typically adopted in industry to ensure optimised foundation design. However, this approach is time consuming to calibrate to new sites and hence not well suited for early-stage structural design and load simulations where thousands of calculations are performed to finalise the offshore wind farm layout. This paper presents a novel approach for early stage monopile design (i.e. concept or pre-FEED), in which a concept design surrogate model was trained on a database of 2000 3D FEA simulations using a machine learning algorithm. The surrogate model provides rapid estimations of monopile design for Natural Frequency Analysis (NFA) and Fatigue Limit State (FLS) conditions, while also intrinsically incorporating the fidelity of the 3D FEA simulations. The surrogate model predicts results close to that of 3D FEA, over 10000 times faster, for layered soil profiles and a wide range of monopile dimensions inside the training space. Published monopile lateral response results from field testing were used to further validate the model. Use of such a tool in practice will speed up the process of preliminary monopile design and load simulations, reducing risks and time for developers, whilst improving site feasibility studies and cost estimates.

RÉSUMÉ: Les générateurs d'éoliennes offshore (WTG) sont généralement soutenus par des fondations monopieux. La conception des fondations monopieux est généralement réalisée à l'aide de courbes de réaction du sol (SRC) basées sur des règles dans un modèle 1D ou 0D. Pour la dérivation des SRC, la FEA 3D spécifique à l'emplacement WTG est désormais généralement adoptée dans l'industrie pour garantir une conception optimisée des fondations. Cependant, cette approche prend du temps à calibrer sur de nouveaux sites et n'est donc pas bien adaptée à la conception structurelle et aux simulations de charges à un stade précoce, où des milliers de calculs sont effectués pour finaliser la configuration du parc éolien offshore. Cet article présente une nouvelle approche de la conception de monopieux à un stade précoce (c'est-à-dire concept ou pré-FEED), dans laquelle un modèle de substitution de conception de concept a été formé sur une base de données de 2000 simulations FEA 3D à l'aide d'un algorithme d'apprentissage automatique. Le modèle de substitution fournit des estimations rapides de la conception de monopieux pour les conditions d'analyse de fréquence naturelle (NFA) et d'état limite de fatigue (FLS), tout en intégrant intrinsèquement la fidélité des simulations FEA 3D. Le modèle de substitution prédit des résultats proches de ceux de la FEA 3D, plus de 10 000 fois plus rapides, pour des profils de sol en couches et une large gamme de dimensions de monopieux à l'intérieur de l'espace d'entraînement. Les résultats publiés de la réponse latérale du monopile du PISA JIP ont été utilisés pour valider davantage le modèle. L'utilisation pratique d'un tel outil accélérera le processus de conception préliminaire du monopieu et de simulations de charge, réduisant ainsi les risques et le temps pour les développeurs, tout en améliorant les études de faisabilité du site et les estimations de coûts.

Keywords: Offshore wind; monopiles; machine learning; concept design; finite element analysis.

1 INTRODUCTION

The offshore wind industry is currently experiencing a period of rapid growth and innovation due to the threat of the climate crisis and the finite supply of fossil fuels. As the scale of wind generating structures grows, impetus to optimise their construction increases. This is especially true for foundations, which can represent up to 30% of the total offshore wind farm (OWF)

CAPEX cost. Monopiles are the most common foundation type for WTGs and are typically used in water depths up to 60m, with diameters up to 12m and length to diameter ratios of 2.5-6. Identifying suitable locations where WTGs can be constructed economically at an early stage in the design process can lead to significant cost and time savings for developers. The approach explored herein, named the Rapid Monopile Design Surrogate (RMDS) tool, employs modern machine learning methods to allow NFA and FLS design assessments at proposed WTG locations to be carried out faster than is currently possible whilst retaining accuracy. The outputs can be easily integrated into established workflows to estimate the optimum monopile dimensions, and subsequently foundation cost, for the given location.

2 BACKGROUND

2.1 Current methods for NFA and FLS design

The monopile diameter and wall thickness, and hence feasibility, is typically driven by the NFA and FLS design; therefore, it is critical this is assessed at the early stage of the project. The current industry practice for early stage NFA and FLS assessments and aeroelastic WTG load simulations uses a combination of 3D FEA and SRCs. However, this is a slow process which is computationally expensive, and can demand a considerable amount of time and expertise to set-up. A macro element 0D model, consisting of a coupled three-spring configuration, is an alternative approach, suitable for early stage design. This simplifies the monopile by replacing it with a lateral spring (K_L), a rotational spring (K_R) and a cross-coupling spring (K_{LR}), where the springs represent the stiffness of the monopile at mudline. Vertical stiffness is generally omitted from calculations as it is large enough that zero displacement can be assumed. The values of the three springs can then be used directly as inputs for calculation of natural frequency and deformation of the monopile in the small displacement zone. To obtain values of each spring, empirical equations have been proposed. Arany (2017) provides a summary of commonly used equations. However, these equations can only be applied to idealised soil conditions and have been shown to lead to overly stiff designs .

2.2 Machine learning models

Few attempts have been made to predict monopile response using ML. Suryasentana (2020) showed that Gaussian Progress regression was effective in predicting *p-y* springs down the length of a monopile.

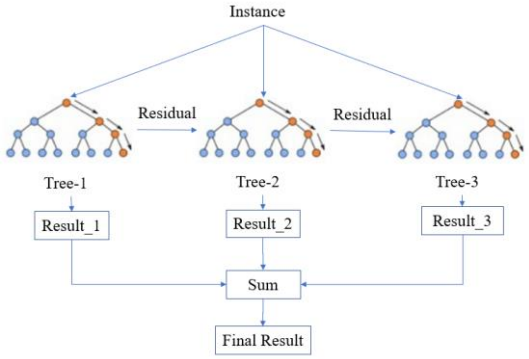

Figure 1. Simplified XGBoost model visualised (Wang et al., 2020).

Suryasentana notes that in their work the dataset was small and specific to one site and therefore, randomised 3D FEA would be a more suitable method to generate a database of monopile responses capable of generalising to a wider variety of soil conditions.

The ML model chosen for this study was the open-source package XGBoost (Chen *et al.* 2016). The algorithm is based on the concept of decision trees; a series of conditions are applied to the inputs of the tree (i.e., is depth greater than 15m?), to improve predictions of an output (Figure 1). XGboost is widely used in datascience due to its scalability and relatively low computational intensity and is increasingly used for regression problems in geotechnical engineering (see Kardani, 2020).

3 METHODOLOGY

3.1 Dataset formulation

The database on which the RMDS tool was trained consisted of results from 2000 FEA simulations with monopile dimensions, loading conditions and soil profiles as outlined in Table 1. These properties were randomly generated at small intervals to reduce the effects of overfitting to input parameters. This process was automated using a python script and employed the commercial FEA software PLAXIS 3D.

Table 1. Parameter space for dataset.

Header	Range	Step
Diameter (m)	6-12	0.25
Embedment length (m)	25-45	1
Lever arm (m)	20-120	1
Initial shear modulus (MPa)	1-350	1
Layer thickness (m)	2-10	1
Poisson's ratio	0.495	Constant
Diameter/pile wall thickness	120	Constant

NFA/FLS calculations are influenced by behaviour in the very small strain region where the behaviour is often close to linear. As a result, the FEA employed a linear elastic soil constitutive model. Two values were extracted from each simulation to train the RMDS tool, these are referred to as the target variables:

$$K_H = \frac{F_x * D}{u_x} \quad (1)$$

$$K_M = \frac{M_y}{\theta_y} \quad (2)$$

Where K_H is the uncoupled lateral stiffness (GN), F_x is the shear at mudline (GN), u_x is the lateral displacement at pile head (m), K_M is the uncoupled rotational stiffness (GNm/rad), M_y is the overturning moment and θ_y (GNm) is the pile rotation at mudline (rad).

Prior to model training, the format of the soil profile was altered to improve resolution and readability for training. This was accomplished by taking values of initial shear modulus (G_{max}) at 30 equally spaced points down the pile length, where each G_{max} value would be an individual input to the ML model.

3.2 Training of machine learning models

The RMDS tool consists of two XGBoost models that were trained using the same 33 input features: diameter, embedment length, lever arm and 30 G_{max} values. For one model K_H was the target variable and for the other it was K_M. The dataset was partitioned so that of the 2000 samples, 80% was used for training and 20% was held out for testing. A grid search was used to return the optimal hyperparameters (these are XGBoost parameters set by the user which govern how the model learns) for both models. It was found that no regularisation hyperparameters were required other than subsampling the data. This is likely because there is very little noise in the database generated by FEA, which is an advantage of using FEA for ML model training.

As a result of training the RMDS tool with different lever arms, the values of each spring in the three spring model can be calculated. This is achieved by solving for each term in the stiffness matrix using two different lever arms:

$$\begin{bmatrix} F_x \\ M_y \end{bmatrix} = \begin{bmatrix} K_L & K_{LR} \\ K_{RL} & K_R \end{bmatrix} \cdot \begin{bmatrix} u_x \\ \theta_y \end{bmatrix} \quad (3)$$

Due to small errors, the cross-coupling terms were not exactly equal, therefore an average of K_{LR} and K_{RL} can be taken as the value of the cross-coupling term.

4 RESULTS

4.1 Model fit

Figure 2 highlights the effectiveness of the RMDS tool in predicting both target variables (uncoupled lateral and uncoupled rotational stiffness) for 20% of the database that was set aside for testing. As shown by the high r^2 value, the variance in the target variables is explained very well by both ML models, and the mean absolute percentage error (MAPE) is very low for both models, most notably the rotational model.

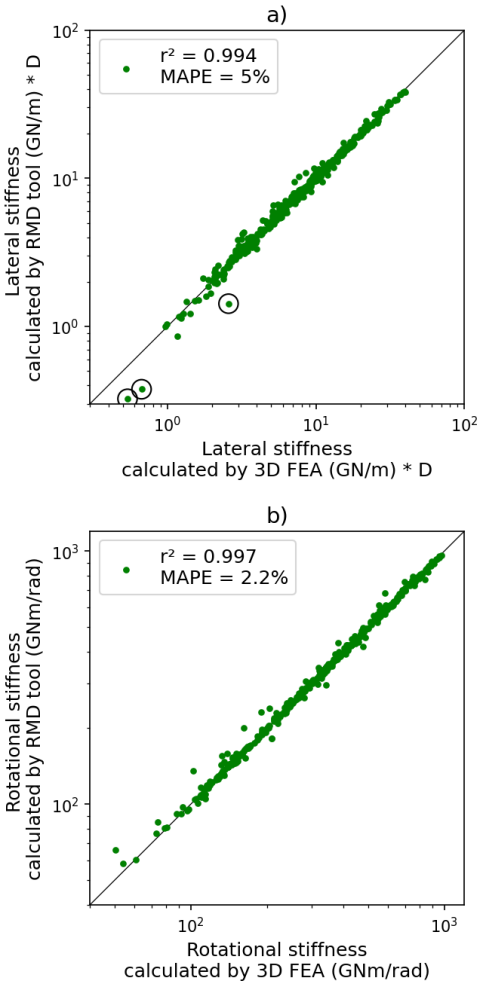

Figure 2. RMDS tool predictions versus 3D FEA predictions for a) uncoupled lateral stiffness and b) uncoupled rotational stiffness. Three poor predictions are circled in a) which corresponded to cases with unrealistic soil profiles.

It was found that the poorest predictions corresponded to an FEA simulation in which the randomised soil profile was unrealistically low. For example the circled points in Figure 2 had a median

G_{max} of 20MPa or lower down the length of the monopile.

The RMDS tool was able to predict both the lateral and rotational stiffness in 0.017 seconds, in comparison to 20 minutes, which is a representative time for the 3D FEA analysis. This highlights the potential time savings of implementing the RMDS tool in concept design. A benefit of the ML approach is that the tool can be continually improved by adding more training data and retraining the model.

4.2 Validation

To further establish the reliability of the RMDS tool, it was compared with 3D finite element calibration analysis conducted within the PISA JIP as presented in Byrne *et al*. (2020), which serves as the basis for industry-standard design methods. Specifically, the RMDS tool was compared to calibration analyses, and design cases for which there was data available and pile diameter and embedment length were within 25% of the corresponding ranges as outlined in Table 1. More details can be found in (Byrne *et al.*, 2020).

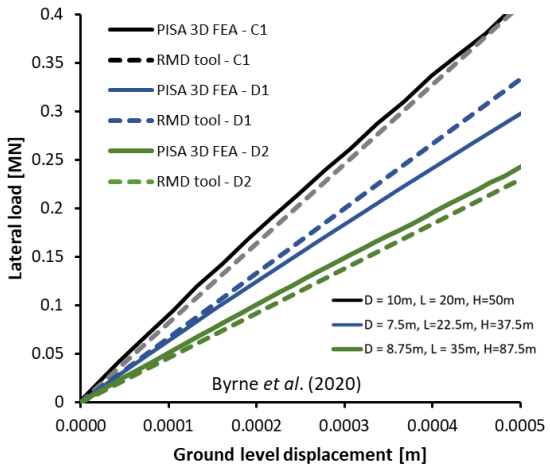

Figure 3. RMDS tool predictions of uncoupled lateral stiffness in the very small strain region, compared to 3D FEA results from PISA calibration analysis C1 and design cases D1 and D2 presented in Byrne et al. (2020).

Generally, very good agreement with the initial lateral stiffness is observed as shown in Figure 3. Therefore, the results provide confidence that the FEA set-up used to create the training database was accurate and that the RMDS tool was able to effectively learn the trends of the database to act as a surrogate FEA model.

5 CONCLUSIONS

The RMDS tool was developed using modern machine learning techniques to act as a surrogate model for 3D FEA, allowing rapid, accurate predictions of monopile stiffness in the very small strain region. This capability could result in significant time and cost savings for concept NFA and FLS assessments. However, unlike 3D FEA, the RMDS tool can only be used within its calibration range and in some instances, may overfit to its input parameters. The demonstrated proof-of-concept tool shows good predictive capabilities on results from well-established published field tests and can be continually improved by retraining the model on new data. This paper has focused on the small strain region, using a simplified linear elastic constitutive model; however, techniques presented in this study could also be used to train ML models for predicting non-linear soil response, using more advanced constitutive models, or predicting *p-y* springs along the length of a monopile.

REFERENCES

Arany, L., Bhattacharya, S., Macdonald, J., and Hogan, S. J. (2017). Design of monopiles for offshore wind turbines in 10 steps. *Soil Dynamics and Earthquake Engineering*, *92*, 126-152. https://doi.org/10.1016/j.soildyn.2016.09.024 [DOI].

Byrne, B. W., Houlsby, G. T., Burd, H. J., Gavin, K. G., Igoe, D. J., Jardine, R. J., & Zdravković, L. (2020). PISA design model for monopiles for offshore wind turbines: application to a stiff glacial clay till. *Géotechnique*, *70*(11), 1030-1047. https://doi.org/10.1680/jgeot.18.P.255 [DOI].

Chen, T., & Guestrin, C. (2016, August). Xgboost: A scalable tree boosting system. *22nd acm sigkdd international conference on knowledge discovery and data mining*, 785-794. https://doi.org/10.1145/2939672.2939785 [DOI].

Kardani, N., Zhou, A., Nazem, M., & Shen, S. L. (2020). Estimation of bearing capacity of piles in cohesionless soil using optimised machine learning approaches. *Geotechnical and Geological Engineering*, *38*, 2271-2291. https://doi.org/10.1007/s10706-019-01085-8 [DOI].

Suryasentana, S. K., Burd, H. J., Byrne, B. W., Aghakouchak, A., & Sørensen, T. (2020). Comparison of machine learning models in a data-driven approach for scalable and adaptive design of laterally-loaded monopile foundations. ISFOG. Texas.

Wang, W., Chakraborty, G., & Chakraborty, B. (2020). Predicting the risk of chronic kidney disease (ckd) using machine learning algorithm. *Applied Sciences*, *11*(1), 202. https://doi.org/10.3390/app11010202 [DOI].

Proceedings of the XVIII ECSMGE 2024
GEOTECHNICAL ENGINEERING CHALLENGES
TO MEET CURRENT AND EMERGING NEEDS OF SOCIETY
© 2024 the Authors
ISBN 978-1-032-54816-6
DOI 10.1201/9781003431749-538
Open Access: www.taylorfrancis.com, CC BY-NC-ND 4.0 license

ECSMGE 24
XVIII EUROPEAN CONFERENCE ON SOIL MECHANICS AND GEOTECHNICAL ENGINEERING

Raising the standard of flood protection in Hull: the Humber Hull Frontages flood defence scheme

Relever le niveau de protection contre les inondations à Hull: le projet de défense contre les inondations des Humber Hull Frontages

L. Allievi*, A. Willoner
Mott MacDonald, Sheffield, UK
**Lorenzo.Allievi@mottmac.com*

ABSTRACT: The Humber Hull Frontages flood defence scheme reduced the risk of flooding from the Humber estuary for 113,000 properties and it consists of more than seven kilometres of tidal flood defences along the estuary frontage. This paper describes the design of a variety of flood defences in challenging ground conditions, typically comprising deep fill deposits associated with the pre-existing flood defences and with large areas of reclaimed land overlying normally consolidated soft tidal flat deposits. The solutions provided to overcome multiple design and construction constraints due to the current and historical use of the project setting are presented in this paper.

RÉSUMÉ: Le projet de défense contre les inondations des Humber Hull Frontages a réduit le risque d'inondation par l'estuaire de l'Humber pour 113,000 propriétés et il comprend plus de sept kilomètres de défenses contre les inondations maritimes le long du front de mer. Ce document décrit la conception de diverses défenses contre les inondations dans des conditions de sol difficiles, comprenant généralement des dépôts de remblai profonds associés aux défenses contre les inondations préexistantes et de grandes zones de terres récupérées recouvrant des sols alluviaux mous normalement consolidés. Les solutions apportées pour surmonter les multiples contraintes de conception et de construction dues à l'utilisation actuelle et historique du cadre du projet sont présentées dans ce document.

Keywords: Flood defence; soft soil; sheet piles; seepage.

1 INTRODUCTION

The city of Hull lies on the north bank of the Humber Estuary and is protected from tidal flooding by the River Hull Barrier and a combination of raised defences of varying age, condition and height along the Humber Estuary frontage. The objective of the Humber Hull Frontages (HHF) project was to improve the existing tidal flood defences so that they would provide a flood defence for 2040 tidal flood event levels with provision to install future additional defences for 2115 tidal flood event levels.

The £42 million scheme reduced the risk of flooding for 113,000 properties upgrading more than seven kilometres of tidal flood defences, from St Andrew's Quay Retail Park in the west to Victoria Dock Village in the east, as shown in Figure 1.

A wide range of defences were proposed for the scheme, ranging from installation of driven piles, construction of new piled or gravity walls, raising of the existing flood defences and improvement of the existing flood defences.



Figure 1. Plan overview of the Humber Hull Frontages scheme.

This paper focuses on the works at Victoria Pier (Zone 6) and Victoria Dock Village East (Zone 8), where the challenges posed by both historical and current land use had the greatest impact on the design and construction of the flood defences.

2 GROUND CONDITIONS

Like many UK east coast estuaries, the geology of the superficial deposits along the Humber is complex. The wide range of environmental conditions and sea levels has resulted in the deposition of a varied and discontinuous sequence of glacial, fluvioglacial and tidal flat deposits (TFD) consisting of sands, gravels, silts and peats.

A conceptual ground model of the River Hull Barrier, which is also applicable to the HHF project, is depicted in Figure 2.

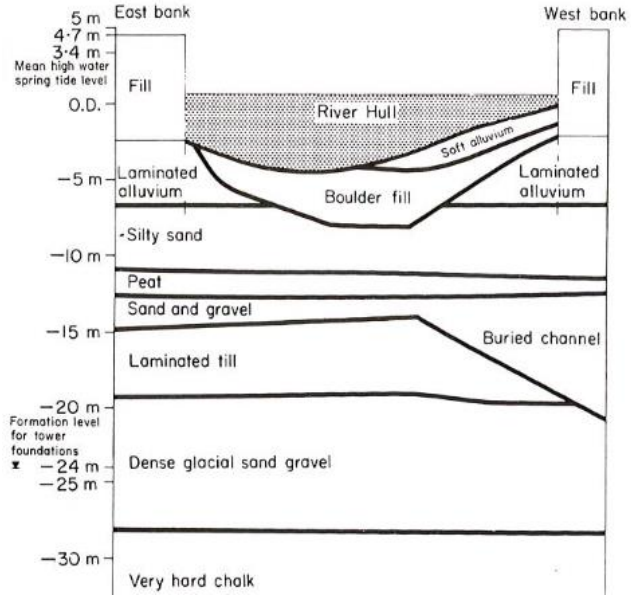

Figure 2. Conceptual ground model of the River Hull Barrier (Fleming et al., 1980).

In general, the ground conditions at the scheme comprise a variable thickness of made ground overlying TFD. Notably, along the Humber frontage vast areas have been reclaimed from the estuary through time and flood defences were built on top of the reclaimed land, resulting in the presence of sections of deep fill, mostly consisting of reworked TFD, overlying a starter layer of gravel to cobble sized chalk. Typically, a 1.0 to 1.5m thick firm to stiff desiccated crust is found at the top of the TFD, where this has not been removed by historical anthropogenic activities. The underlying TFD generally consists of normally consolidated low-strength and low-stiffness silty clay and clayey silt with organic content and peat layers.

The deeper geology comprises mostly glacial till overlying bedrock of the Burnham Chalk Formation from the Upper Cretaceous.

Groundwater associated with the chalk is sub-artesian, with a significant rise noted following the installation of deep boreholes. Groundwater in drift deposits is tidal and is also influenced by the pressure in the Chalk aquifer locally.

3 VICTORIA PIER

Victoria Pier, built in 1825, is a disused ferry terminus named after a Royal visit by Queen Victoria in 1854. The existing structure is a timber pier and jetty, with existing river walls consisting of tied sheet piles.

The new flood defences required complex piling works as the poor condition of the existing tied sheet pile wall indicated minimal residual life to support a new gravity flood wall constructed on the land.



Figure 3. Construction works at Victoria Pier.

Key features and challenges include the following:

- The existing timber pier required partial demolition to fit new sheet piles in front of it.
- The existing sheet piles along the upstream end of the quay wall were inclined at 6 degrees, so the new piles had to be raked to avoid a clash at depth.
- The rake of the new sheet piles had to avoid conflicting with the deep vertical timber piles to the pier.
- The quay wall at the mouth of the River Hull was vertical, so the new sheet-piled wall had to change inclination from raking to vertical. This was also necessary to avoid conflict with the vertical ‘dolphin’ pier to the footbridge.
- New sheet piles had to be installed within 2m of an existing structure, therefore a minimal vibration method was required to install piles.
- Presence of known (and unknown) buried obstructions.
- The ground conditions were highly variable and included very soft organic soils to 22m depth, a buried sand-filled channel and sub-artesian groundwater.
- The site was less than 100m from the location of a 1999 tunnel collapse (Grose et al 2005), which resulted in the largest claim (£50M) ever made under a Contractors ‘all risk’ policy.

- Working through the covid pandemic.

Clearly this was a site that required a comprehensive ground investigation and management of ground risk.

A schematic ground model of this area is shown in Figure 4. The SPTs did not exceed N10 until 22.5m depth in the central area, however adjacent CPT investigation indicated higher soil stiffness and it was likely that the high-water pressures caused piping at the base of the boreholes.

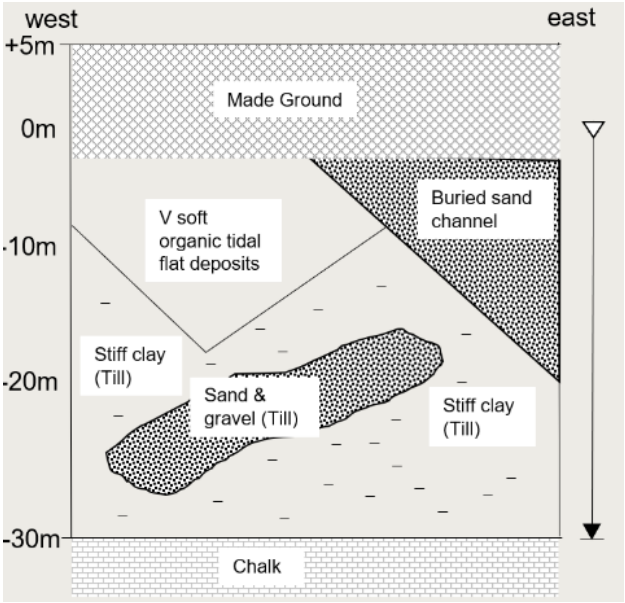

Figure 4. Schematic ground model at Victoria Pier.

Historical records indicated that there would be a high density of buried obstructions. To avoid the need for the installation of ties or anchors to support the sheet piles, the initial proposal was to carry out a wet soil mixing operation to the upper part of the passive wedge, working in 6x6x6m cubic zones during each 'window' of low tide.

Unfortunately, the time required for the regulatory approval process for mixing cement into the mud flats proved to be too long to fit into the programme and the scheme had to revert to an alternative solution. A tied wall was considered lower risk than an anchored wall as the ties could be threaded between and beneath existing timbers and services in open excavations.

Works commenced with the upstream piles, installed at a 3-degree rake 2m in front of the existing wall and 15m in length to avoid conflict with the exiting piles at depth. Although small, the rake on the sheet piles made the design of the wailing beam complex and a double UKB was needed to resist eccentric loading.



Figure 5. Installation of raked piles along the Humber.

As the wall turned the corner from the River Humber to the River Hull, a bespoke triangular pile was installed to transition to vertical piles along the River Hull face. This was vital to enable piles to be pressed rather than driven near existing buildings.



Figure 6. Installation of pressed piles along the River Hull.

As expected, the installation of anchor piles was complex. Some had to be pressed in proximity to a grade II listed toilet block, several were realigned due to obstructions with the tie roads being lengthened, and towards the upstream end of the works, several anchor piles refused at very short depths, potentially due to the original masonry quay wall, and were replaced with a balanced gravity RC wall constructed in open excavation to 3m depth.

4 VICTORIA DOCK VILLAGE EAST

The proposed flood defences at Victoria Village East consisted of a reinforced concrete flood wall up to 1.5m high running at the back of the gardens of the residential properties along the estuary.

The 1856 Ordnance Survey map of Hull shows that the High Water Spring Tide line at Victoria Dock Village East was about 150m to the north of the existing coastline. Land reclamation took place in the second half of the 1800s, consequently, a 7 to 8 metres thick layer of made ground was encountered.

The main challenge for the works in this area was represented by the historical use of the site.



Figure 7. Aerial photograph showing historical timber pond, slipways and shipbuilding yard.

Historical maps and pictures show the presence of the following features:

- a timber pond located to the east of the half tide and outer basins; this basin was then infilled and residential buildings were constructed over it.
- two slipways and a historical tidal dock were located within the area of the proposed works. This was confirmed by an obstruction and locally different ground conditions encountered during the investigation at the location of one of these slipways.
- the area east of Harbour Way used to be a shipbuilding yard, where ships were built on the groynes onto a basic slipway.

The main issue presented by these historical features was related to the potential for seepage paths existing underneath the new flood defences. While the typical infill used for reclaimed land in the area consisted of reworked TFD silty clay or clayey silt, hence with low permeability and low risk of seepage during flood events, the ground investigation confirmed that coarser soil was used to infill these features at a later date than the surrounding area.

Seepage analyses were carried out for the area, considering both the typical ground conditions and ground models specific to the infill recorded at the location of the buried historical features. The analyses showed that if a material with hydraulic conductivity greater than 10^{-5}m/s was encountered below the flood wall foundation level, seepage could have occurred below the walls. Sheet piles for seepage cut-off were therefore installed in the areas where the proposed flood walls encountered permeable infill.

5 CONCLUSIONS

The Humber Hull Frontages scheme provided a high standard of flood protection for 113,000 properties along the estuary of the Humber, in Hull. A wide range of geotechnical works were constructed for the scheme, the majority of which were successfully completed between 2019 and 2021, with the project being officially opened to the public in 2022.

The design and construction of the proposed works faced several challenges, mostly related to the constraints posed by the historical and existing urban context of the works and the onerous ground conditions, comprising a great thickness of made ground and soft TFD.

Two particularly challenging areas of the scheme were Victoria Pier, where the design of the new piled wall had to adapt to the presence of buried obstructions, existing sheet piles and listed structures, and Victoria Dock Village East, which historically was the site of features such as slipways and artificial basins.

A good understanding of the impact of these constraints on the proposed works and flexibility in the design approach, adapting to modifications required during construction, allowed the successful delivery of the scheme.

REFERENCES

Environment Agency (2022), Humber: Hull Frontage Flood Defence Improvements. Available at: https://consult.environment-agency.gov.uk/yorkshire/humber-hull-frontages/, accessed: 21/11/2023.

Fleming, J. H., McMilllan, P. H., Williams, B.B. (1980). The River Hull tidal surge barrier, In: *Proceedings of the Institution of Civil Engineers*, 68 (3), ICE, London, pp. 417-454, https://doi.org/10.1680/iicep.1980.2244.

GOV.UK (2021), Vital Hull tidal flood defence scheme complete. Available at https://www.gov.uk/government/news/vital-hull-tidal-flood-defence-scheme-complete, accessed: 20/11/2023.

Grose W.J and Benton L (2005). Hull wastewater transfer tunnel: tunnel collapse and causation investigation, In: *Geotechnical Engineering,* 158 (4), ICE, London, pp. 179-185, https://doi.org/10.1680/geng.2006.159.2.125.

Proceedings of the XVIII ECSMGE 2024
GEOTECHNICAL ENGINEERING CHALLENGES
TO MEET CURRENT AND EMERGING NEEDS OF SOCIETY
© 2024 the Authors
ISBN 978-1-032-54816-6
DOI 10.1201/9781003431749-539
Open Access: www.taylorfrancis.com, CC BY-NC-ND 4.0 license

ECSMGE 24
XVIII EUROPEAN CONFERENCE ON SOIL MECHANICS AND GEOTECHNICAL ENGINEERING

Influence of spatial variability of ground conditions on energy pile thermal yield

Influence de la variabilité spatiale des conditions du sol sur le rendement thermique des pieux énergétiques

Q.I. Alqawasmeh, G.A. Narsilio
University of Melbourne, Melbourne, Australia

M.J. Kreitmair*
University of Surrey, Guildford, United Kingdom

**m.kreitmair@surrey.ac.uk*

ABSTRACT: Energy piles are a cost-effective alternative to conventional boreholes in shallow geothermal systems as they can lower capital investment while maintaining efficient heat exchanging capability when properly designed. Among a range of parameters that affect the thermal yield of energy piles, ground thermal and hydraulic properties have a decisive influence. Studies on energy pile thermal yield usually consider homogeneous ground conditions, or, to a lesser extent, horizontally layered ground conditions. However, spatial geological heterogeneity exists not only between the soil-stratified layers in the vertical direction but also within each horizontal layer. This study investigates the impact of spatial hydro-geological heterogeneity on heat transfer within the ground. A three-dimensional numerical model is developed to solve for heat transport considering several numerically generated lognormal autocorrelated random fields of ground thermal conductivity and permeability values, transformed from geostatistical random Gaussian distributions based on their statistical distributions. Results show that the assumption of homogeneous ground characteristics has a marginal effect, up to ~6% in energy provision, when the variations in thermal and hydraulic properties are small, making it a pragmatic assumption in such cases. However, the uncertainty in energy yield prediction becomes considerable, in between ~13% to ~25%, for significant ground variability. Moreover, accounting for the variability in hydraulic properties such as the permeability is more detrimental than the thermal conductivity.

RÉSUMÉ: Les pieux énergétiques sont une alternative rentable aux forages conventionnels dans les systèmes géothermiques peu profonds, car ils peuvent réduire l'investissement en capital tout en maintenant une capacité d'échange de chaleur efficace lorsqu'elles sont correctement conçues. Parmi une gamme de paramètres qui influent sur le rendement thermique des pieux énergétiques, les propriétés thermiques et hydrauliques du sol ont une influence décisive. Les études sur le rendement thermique des pieux énergétiques considèrent généralement des conditions homogènes du sol, ou, dans une moindre mesure, des conditions du sol en couches horizontales. Cependant, il existe une hétérogénéité géologique spatiale non seulement entre les couches stratifiées du sol en direction verticale, mais aussi au sein de chaque couche horizontale. Cette étude examine l'impact de l'hétérogénéité hydro-géologique spatiale sur le transfert de chaleur dans le sol. Un modèle numérique tridimensionnel est développé pour résoudre le transport de chaleur en considérant plusieurs champs aléatoires lognormaux autocorrélés numériquement générés de conductivité thermique et perméabilité du sol, transformées à partir de distributions gaussiennes aléatoires géostatistiques basées sur leurs distributions statistiques. Les résultats montrent que l'hypothèse de caractéristiques homogènes du sol a un effet marginal, jusqu'à environ ~6% dans la fourniture d'énergie, lorsque les variations des propriètès thermiques et hydrauliques sont faibles, ce qui en fait une hypothèse pragmatique dans ce cas. Cependant, l'incertitude dans la prédiction du rendement énergétique devient considérable, entre environ ~13% et ~25%, pour une variabilité significative du sol, en particulier à de faibles vitesses d'écoulement des eaux souterraines. Prendre en compte la variabilité des propriétés hydrauliques telles que la perméabilité est plus préjudiciable que la conductivité thermique.

Keywords: Spatial variability; autocorrelated random fields; permeability; thermal conductivity; energy piles.

1 INTRODUCTION

Energy piles are a type of shallow geothermal energy system where the heat exchanger is built into structural pile foundations, to heat and cool buildings through heat exchange with the surrounding soil. Therefore, the energy piles serve a dual purpose: to carry structural load and to harvest energy from the ground. Using pile foundations contributes to a reduction in the high initial costs commonly associated with other

traditional shallow geothermal systems that rely on the drilling of boreholes down to a few hundred meters (Lu and Narsilio, 2019). Shallow geothermal systems rely on the fact that the ground temperature is close to stable throughout the year at depths greater than a few metres from the ground surface, regardless of the air temperature. This makes the ground an efficient medium of heat, such that it can act as both a heat sink and a source (Banks, 2012).

In energy piles, a circulation pump is used to circulate a carrier fluid inside ground heat exchanging (GHE) pipes, attached to the cage of the pile before casting. The carrier fluid enters the heat exchanging pipes, losing or gaining heat via heat exchange with the ground adjacent to the pile, and returns with a lower or higher temperature than at inlet. The heat is then distributed to the building via a ground source heat pump (GSHP).

Optimising the thermal design of energy piles is crucial to their wider adoption. Among the different ground properties that affect the rate of heat exchange, and therefore the system's thermal design, the ground hydrothermal properties (thermal conductivity and permeability) act as primary geological parameters that control ground heat transport rates and thus the thermal yield of energy piles. Energy pile design has been studied extensively with the assumption of homogeneous ground, where average values of ground hydrothermal properties are used. Few studies consider horizontally layered soil, and ground spatial heterogeneity is rarely discussed in the literature, even though conditions vary significantly not only between the soil-stratified layers in the vertical direction but also within each horizontal layer. Using a single average value for the hydrothermal parameters may not always lead to accurate estimation of energy pile thermal yield due to wide ranges in parameter values (Zhao et al., 2022).

Further research is needed to understand the impact of ground heterogeneity on the thermal yield of geothermal energy piles, and to compare it to the widely used assumption of homogeneity. This study investigates the influence of spatial variability in ground thermal and hydrogeological properties (namely, thermal conductivity and permeability) on energy pile thermal yield. To this end, the thermal yield from an energy pile determined using uniform values for the ground properties is compared against that determined from spatially varying properties but with the same mean values. Cases of low-to-high spatial variablity, in terms of coefficient of variation (COV), are considered.

2 METHODOLOGY

In this study, hydrothermal ground heterogeneity is characterised in terms of spatial variability in the ground thermal conductivity, λ [W/ m·K], and the intrinsic permeability κ [m^2], as these are influential energy pile design parameters. The spatial variability of permeability is considered rather than that of hydraulic conductivity as the latter depends not only on the permeability but also the fluid properties such as density and viscosity.

Synthetic 3D autocorrelated random fields for ground thermal conductivity (solid part) and permeability are created using a geostatistical Gaussian randomisation method implemented in the GSTools python library (Müller et al., 2022). A lognormal transformation for the random fields is performed, as it is a preferred option for hydrothermal soil properties distribution since it ranges from zero to infinity. The cross correlation between λ and κ is assumed to be zero, following published findings (Mielke et al., 2010). Figure 1 illustrates a realisation of the random fields.

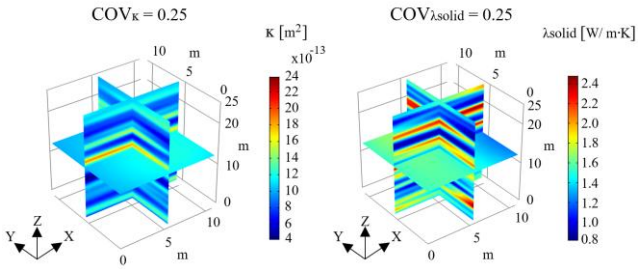

Figure 1. Ground permeability and solid thermal conductivity random field realisations for COV=0.25.

Typical COV values reported in literature are between 0.05 and 0.25 for thermal conductivity, and between 0.25 and 4 for permeability, across a range of materials. Hence, values of $COV_\lambda = 0.25$, and $COV_\kappa =$ (0.25, 0.5, 1, 2, 4) are assumed for the study.

A further important aspect in characterising the spatial variation of ground properties is the scale of fluctuation (SOF) in the horizontal and vertical directions. The SOF describes the distance over which parameters are correlated. In the available literature, the SOF of κ is more widely reported on than that of λ. Therefore, giving the layered nature of the ground, a typical value of horizontal $SOF_h = 10$ m and vertical $SOF_v = 1$ m is adopted for both λ and κ.

The random fields generated are exported as a point cloud and implemented in a 3D numerical model, previously validated by the authors (Alqawasmeh et al., 2024), to solve for conduction-convection heat transfer around energy piles. In the numerical model, λ and κ are assigned to the ground material.

This study assumed characteristics found in the literature typical for a sandy soil: the mean value of permeability is $\mu_\kappa = 1 \times 10^{-12}$ m^2, that of solid thermal conductivity is $\mu_{\lambda solid} = 1.5$ W/ m·K, the porosity $n = 0.4$, and the seepage velocity $v =$ 0.3 m/day. Therefore, the mean effective thermal conductivity is $\mu_\lambda = 1.13$ W/ m·K, given that $\lambda_{fill} = \lambda_{water} = 0.586$ W/ m·K inside voids, following

$$\lambda = (1-n) \cdot \lambda_{solid} + n \cdot \lambda_{fill} \quad (1)$$

The numerical model solves for carrier fluid temperature from inlet to outlet through the GHE. The average fluid temperature, T_{avg}, between inlet and outlet is calculated and compared across the cases considered. In the homogeneous case, i.e., $\kappa = 1 \times 10^{-12}$ m^2, and $\lambda = 1.13$ W/ m·K, T_{avg} is calculated from a single model run. This is compared to the mean value of T_{avg} for the heterogeneous cases, arising from 50 realisations of the random fields, for each case. This number of realisations was found to give a reasonable COV of less than 0.05 for the T_{avg} values, and keeping the pile's energy yield unaffected.

The energy pile considered in this paper is initially designed under the assumption of a homogeneous ground, such that it rejects 1 kW of heat to the ground for three months (cooling), followed by three months of rest (shutting off), before operating again for another three months to extract 1 kW from the ground (heating), followed by another three months of resting, and so on. After that, the design capacity of the energy pile is investigated considering spatial variation in λ and κ, and compared to the 1 kW of the homogeneous case. Figure 2 shows the details of the numerical model setup, boundary conditions in presence of groundwater flow (GWF), and the impeded 4U-loop GHE. The dimensions of the model were chose so as to ensure that boundary effects are negligible.

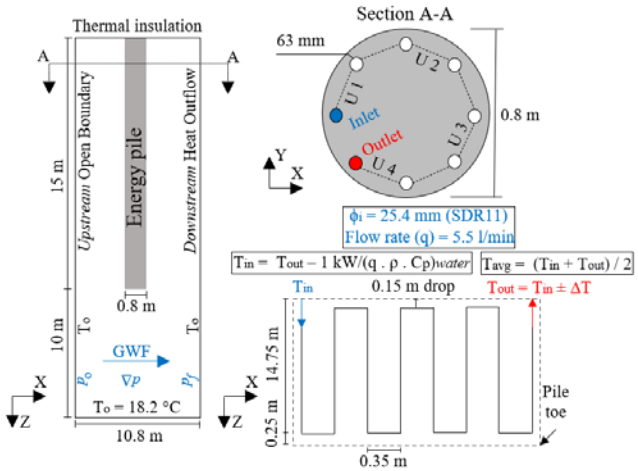

Figure 2. Numerical model setup of the energy pile.

3 RESULTS AND DISCUSSION

The parametric study involves analyses of three different cases:

(i) λ is varying spatially (COV_λ = 0.25) and κ is deterministic (1 x 10^{-12} m^2),

(ii) κ varies spatially (COV_κ = 0.25, 0.5, 1, 2, and 4) and λ is deterministic (1.13 W/ m·K), and

(iii) κ is spatially variable (COV_κ = 0.25, 0.5, 1, 2, and 4) and λ is spatially variable (COV_λ = 0.25).

In all cases, a groundwater flow (Darcy) velocity of 0.3 m/day and ground porosity value of 0.4 are used.

Figure 3 shows the average fluid temperatures resulting from different cases. Each violin plot represents the distribution of the resulting T_{avg} from the 50 realisations, with red dots denoting the mean value of the distribution to be compared with the dashed red line which represents the T_{avg} of the deterministic (homogeneous) case.

Generally, the cases where both permeability and solid thermal conductivity are varied (blue plots) exhibit results very similar to the cases when only the permeability is varied, and the solid thermal conductivity is deterministic (i.e., $COV_{\lambda solid}$ = N/A). This implies that the variability of κ is more influential on the fluid temperature than that of λ. Differences in T_{avg} are evident with increase in variability. For COV_κ values lower than 1, only minor differences arise between the heterogeneous and homogeneous cases, indicating that the assumption of homogeneity can be acceptable in practice for low levels of ground variability. However, when the value of COV_κ is greater than 1, significantly higher values of T_{avg} can be seen compared to that of the homogeneous case. Further, the higher COV_κ, the greater the dispersion of the distribution of the predictions of the thermal yield and, consequently, the lower the probability of getting the deterministic T_{avg} from random realisations.

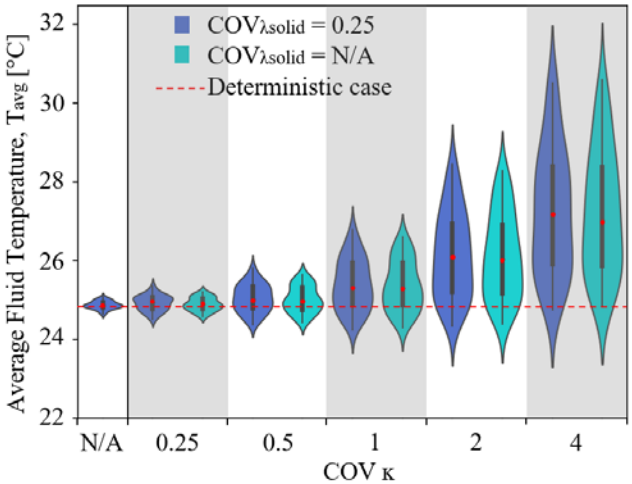

Figure 3. Spatial variability influence on average fluid temperature (each violin plot represents 50 realisations).

Table 1. The difference in energy provision compared to the base thermal load for all considered cases.

	$COV_{\lambda solid}$ = N/A			$COV_{\lambda solid}$ = 0.25		
COV_κ	**$\Delta T^\dagger$ °C**	**ΔEP %**	**Pr %**	**$\Delta T^\dagger$ °C**	**ΔEP %**	**Pr %**
N/A	*Deterministic*			0.03	0.31	6
0.25	0.05	0.52	8	0.05	0.52	12
0.50	0.17	1.80	14	0.20	2.10	18
1.00	0.52	5.40	24	0.55	5.70	24
2.00	1.27	13.20	40	1.29	13.40	38
4.00	2.37	24.70	46	2.40	25.0	46

$^\dagger\Delta T$ is the difference between T_{avg} in the homogeneous (deterministic) ground case and the mean of T_{avg} of 50 realisations for the hetrogeneous ground case realisations.

Table 1 lists the change in average fluid temperature for each of the cases considered, given by the mean over the 50 realisations, compared to that of the homogeneous (deterministic) case. To investigate the influence of the uncertainty associated with the average fluid temperature due to neglect of spatial variability, the expected thermal yield for each case was calculated and the percentage change in energy provision (EP) from the energy pile determined. Finally, the probability (Pr) of the deterministic case overpredicting the thermal yield by ΔEP is quantified.

To illustrate this, Figure 4 shows an example of the difference in the energy provision due to the variation in average fluid temperature for the case when COV_λ = 0.25 and COV_κ = 4. The difference in average fluid temperature within the enclosed area represents the difference in energy provision in this case (i.e., the percentile decrease in the base thermal load, 1 kW cooling/heating, needed to make the solid curves align with the dashed one represents the energy provision difference percentile from the base thermal load).

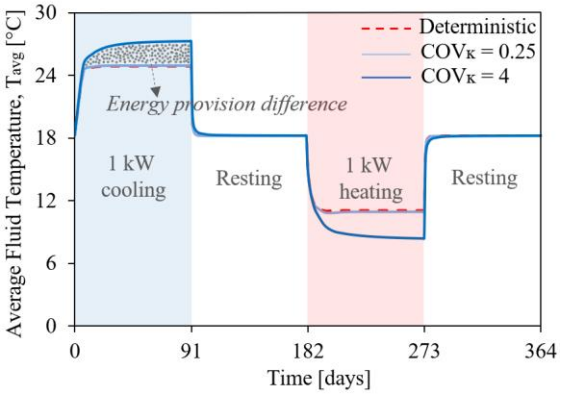

Figure 4. Spatial variability impact on energy provision.

Due to the higher variability that κ can have than λ_{solid}, nearly similar behaviour is exhibited, regardless whether spatial variability of λ_{solid} is considered. This indicates that the spatial variability in permeability is more impactful than that of the thermal conductivity. In addition, when COV_κ is less than 1, the energy provision difference is less than 6%. However, higher ground variability enhances the difference, which can reach up to ~25% when COV_κ=4. Moreover, the chance of getting similar outcomes to the deterministic case out of the random realisations becomes lower with increasing coefficient of variation. In other words, the probability of significant differences in temperature and overpredicting the energy yield becomes higher.

4 CONCLUSION

This study shows that the assumption of homogeneous ground thermal and hydrogeological properties, made in energy pile design, is an appropriate one at low levels of ground heterogeneity, with only a small level of uncertainty in the energy yield exhibited in such cases. However, when ground variability is high, significant variability arises in the calculated average fluid temperature in the energy piles, leading to uncertainty in energy provision of up to ~25% with high chance of occurrence. Further research on the influence of other factors such as seepage velocity and thermal load scheme is encouraged.

REFERENCES

Alqawasmeh, Q. I., Narsilio, G. A., Makasis, N., and Kreitmair, M. J. (2024) The impact of soil layering and groundwater flow on energy pile thermal performance. *Geomechanics for Energy and the Env.*, 38, 100538. https://doi.org/10.1016/j.gete.2024.100538.

Banks, D. (2012). *An introduction to thermogeology: ground source heating and cooling*, 2nd ed., John Wiley & Sons. http://doi:10.1002/9781118447512.

Lu, Q., and Narsilio, G. A. (2019) Cost effectiveness of energy piles in residential dwellings in Australia, *Current Trends in Civil & Structure Eng.*, 3, 1-6, https://doi:10.33552/CTCSE.2019.03.000564.

Mielke, P., Bignall, G., and Sass, I. (2010). Permeability and thermal conductivity measurements of near surface units at the Wairakei Geothermal Field, New Zealand, In: *Proceedings of the World Geothermal Congress*, Bali, Indonesia. Available at: https://core.ac.uk/download/pdf/357301166.pdf.

Müller, S., Schüler, L., Zech, A., and Heße, F. (2022) GSTools v1.3: a toolbox for geostatistical modelling in Python. *Geoscientific Model Development*, 15, 3161-3182, https://doi.org/10.5194/gmd-15-3161-2022.

Zhao, Z., Lin, Y. F., Stumpf, A., and Wang, X. (2022) Assessing impacts of groundwater on geothermal heat exchangers: A review of methodology and modeling, *Renewable Energy,* 190, 121-147, https://doi.org/10.1016/j.renene.2022.03.089.

Proceedings of the XVIII ECSMGE 2024
GEOTECHNICAL ENGINEERING CHALLENGES
TO MEET CURRENT AND EMERGING NEEDS OF SOCIETY
© 2024 the Authors
ISBN 978-1-032-54816-6
DOI 10.1201/9781003431749-540
Open Access: www.taylorfrancis.com, CC BY-NC-ND 4.0 license

ECSMGE 24
XVIII EUROPEAN CONFERENCE ON SOIL MECHANICS AND GEOTECHNICAL ENGINEERING

Are construction errors in the placement of ground heat exchanging loops in energy piles important to consider?

Les erreurs de construction dans le placement des boucles d'échange de chaleur au sol dans les pieux énergétiques sont-elles importantes à prendre en compte?

Q.I. Alqawasmeh, G.A. Narsilio*
The University of Melbourne, Melbourne, Australia

N. Makasis
University of Cambridge, Cambridge, United Kingdom

**narsilio@unimelb.edu.au*

ABSTRACT: Shallow geothermal energy is considered as an efficient and sustainable green technology to heat and cool buildings. Incorporating the ground heat exchanging loops (GHEs) inside structural piles, known as energy piles, largely reduces the capital cost. Despite the extensive literature on loops connected in series inside energy piles, optimal distribution or lack of thereof of loops connected in parallel remain largely unexplored. For this purpose, a 3D numerical model has been built to undertake parametric analyses on an energy pile equipped with GHEs connected in parallel. The impact of GHEs misplacement due to construction errors on thermal yield is explored, considering the influence of pile diameter, pile length, pile-to-pile spacing, flow rate, pipe diameter, and ground thermal conductivity. Results show that the GHEs placement generally has a marginal effect of less than 3% on the total thermal yield of the energy pile. However, the heat transfer share between individual loops is highly dependent on its distribution, particularly for certain pile diameters. This may affect maintaining the equilibrium thermal performance. Moreover, in symmetrical loop distributions, an insignificant thermal performance penalisation was observed for a range of separation-to-shank distance ratios from 0.5 to 1.5. While symmetrical and evenly spaced distribution is recommended, the latter result indicates that there is flexibility when installing the GHEs loops, with deviations from design during construction rendering low impacts on overall thermal performance.

RÉSUMÉ: La géothermie superficielle est considérée comme une technologie verte efficace et durable pour chauffer et refroidir les bâtiments. L'intégration des boucles d'échange de chaleur au sol (GHE) à l'intérieur de pieux structurels, appelés pieux énergétiques, réduit considérablement le coût en capital. Malgré la littérature abondante sur les boucles connectées en série à l'intérieur de pieux d'énergie, la distribution optimale ou l'absence de celle-ci des boucles connectées en parallèle restent largement inexplorées. Pour cela, un modèle numérique 3D a été construit pour entreprendre des analyses paramétriques sur une pieu énergétique équipée de GHE connectés en parallèle. L'impact du mauvais positionnement des GHEs en raison d'erreurs de construction sur le rendement thermique est exploré, en tenant compte de l'influence du diamètre du pieu, de la longueur du pieu, de l'espacement pieu à pieu, du débit, du diamètre du tuyau et de la conductivité thermique du sol. Les résultats montrent que le placement des GHE a généralement un effet marginal de moins de 3% sur le rendement thermique total de la pieu énergétique. Cependant, la part du transfert de chaleur entre les boucles individuelles dépend fortement de sa répartition, en particulier pour certains diamètres de pieux. Cela peut affecter le maintien des performances thermiques d'équilibre. De plus, dans les distributions de boucles symétriques, une pénalisation insignifiante des performances thermiques a été observée pour une plage de rapports séparation/distance de tige allant de 0.5 à 1.5. Bien qu'une distribution symétrique et uniformément espacée soit recommandèe, ce dernier résultat indique qu'il existe une flexibilité lors de l'installation des boucles GHE, avec des écarts par rapport à la conception pendant la construction ayant un faible impact sur les performances thermiques globales.

Keywords: Energy piles; loops in parallel; GHEs configuration; GHEs optimisation; GHEs spacing.

1 INTRODUCTION

Energy piles are a sort of shallow geothermal energy system (Brandl, 2006) in which conventional pile foundations are incorporated with high density polyethylene (HDPE) pipes filled with circulating fluid, known as ground heat exchangers (GHEs); therefore, they serve dual purposes: to carry the structural load and to heat and cool buildings.

Nowadays, this green technology has become popular as it contributes to green gas emission reduction due to higher yearly efficiencies than traditional electrical systems (Banks, 2012). A proper design of the GHEs loops within the energy pile is crucial. Wide research studies compared some popular heat exchanger designs to harvest as much energy from the ground as possible, these have been recently reviewed in (Cui et al., 2022). The U-tube loop configuration is widely used due to its simplicity in terms of design, transportation, and construction (Mohamad et al., 2021). Most of the investigated layouts rely on connecting the pipes *in series* to create a longer path for the moving fluid inside the pipes to exchange heat compared to the parallel connection, assuming the performance is the same. However, if faults occur in the serially-connected pipes during their lifetime (such as leakage), this results in the loss of a portion of the geothermal system. In addition, the pumping cost may be greatly different (Banks, 2012).

Some numerical and experimental studies have considered *parallel* loop connection within energy piles and show the importance of accounting for thermal interference between adjacent loops (Park et al., 2022; Cui et al., 2020). Most studies consider an even number of loops, and all of them consider only a symmetrical GHE distribution. However, a design with an odd number of loops can add a zone of potential thermal interferance between two adjacent inlets and outlets (i.e., a colder fluid is running besides a hot fluid). A misplacement of loops from the symmetrical distribution may occur during construction as well. In addition, the optimised distribution of loops in terms of the shank spacing of the same loop and the separation spacing from the adjacent loops is rarely discussed in literature.

This study aims to investigate the thermal performance of a set of energy pile diameters that accommodate three U-tube loops connected in parallel at different placements around the pile perimeter. In addition, the optimal ratio between the separation distance of individual loop legs (shank spacing) and the separation distance of adjacent loops is examined. The study also investigates the impact of various influencing design parameters, including the thermal conductivity of the ground, the length of the pile, the carrier fluid flow rate within the GHEs, the pipe diameter, and the pile-to-pile spacing. The study helps widen the practical design knowledge of such a promising green and sustainable technology.

2 METHODOLOGY

A three-dimensional numerical model, previously validated by the authors (Alqawasmeh et al., 2024), is used to solve for conduction-convection heat transfer. The heat within the wall of the ground heat exchanger, the concrete of the pile body, and the soil mass is mainly transported by conduction. Wherase the heat is transferred by convection through the running carrier fluid inside the GHEs.

Figure 1 shows the energy piles numerical model setup with details of their boundary conditions (a), the considered three U-tube loops (b), and the different placements of one of the loops (L2) around the pile perimeter (c). The misplacement is assumed to likely happen in one loop (e.g., L2). The angle (β) represents the angle that separates the three loops symmetrically, while (α), separates loop L2 and L3. A "*Rotation Factor"* is defined as the ratio of both angles.

The study covers two sets of analyses. The first set is performed on three selected pile diameters (0.5 m, 0.6 m, and 0.7 m), considering site-specific conditions (Arden site) located in Melbourne, Australia. The pile length is 40 m with 5 m of pile-to-pile spacing, representing an isolated pile from a pile array for simplicity and computational cost efficiency. A flow rate of 5.5 l/min running through a 25.4 mm (SDR11) inner pipe diameter is considered for each of the three U-tube loops. The average ground properties of the Arden site are 2.5 W/(m·K) for thermal conductivity, 1,881 kg/m^3 for density, and 1,284 MJ/(m^3·K) for heat capacity (Jensen-Page, 2019).

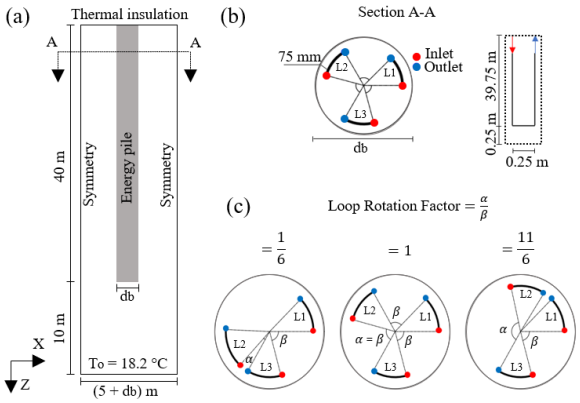

Figure 1. Schematic (not to scale) of: the numerical model setup and boundary conditions (a), three U-loop GHE details (b), and different GHE placements by moving L2 (c).

The inlet temperature entering the system is taken as 32.2°C in cooling mode and 10.7 °C in heating mode follwoing (Kavanaugh , 2008). The system is assumed to operate continuously during 3 months in winter and 3 months in summer and be turned off during the other six months of the year.

The second set of analyses aims to generalise the findings of the site-specific study (Arden site) for 0.5 m pile diameter (where the chance of thermal interference is maximum), taking into account some influential parameters on energy pile thermal performance, including (i) ground thermal conductivity, (ii) pile length, (iii) fluid flow rate, (iv) inner pipe diameter, and (v) pile-to-pile spacing.

3 RESULTS

3.1 The Arden site case

Figure 2 shows the total heat transfer per pile throughout the annual building cooling period for various pile diameters: $P_{0.5m}$, $P_{0.6m}$, and $P_{0.7m}$, Results for the heating period are analogous (not shown).

It is evident that the maximum total heat transfer occurs when the GHEs loops are symmetrically distributed around the pile's circumference ($\alpha/\beta = 1$). Moreover, marginal differences exits for other rotation factors (e.g., for $P_{0.7m}$, the worst-case scenarios at 1/6 and 11/6, results in a heat transfer reduction of ~133 kW h or ~ 2.7% compared to the symmetrical distribution over the annual building cooling period.).

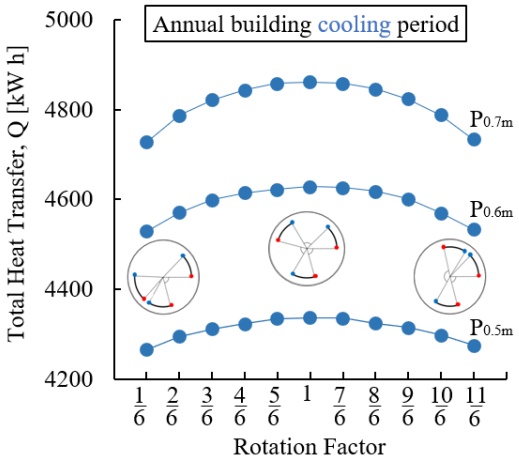

Figure 2. Total heat transfer from all loops for $P_{0.5m}$, $P_{0.6m}$, and $P_{0.7m}$ energy piles for different Rotation Factors, for the three months annual building cooling period.

Moreover, as the pile diameter increases, the separation between loops increases, which decreases the thermal interaction, yielding a higher heat transfer capacity for the same GHEs configuration design.

Furthermore, to examine the individual loops response, Figure 3 depicts the proportionate contribution of each individual loop (L1, L2, and L3) to the total heat transfer. In general, the share of the total heat transfer between loops is nearly equal when loops are symmetrically arranged, but a deviation from this symmetry, potentially arising from human error during construction, can disrupt the total heat transfer share balance between loops. These relatively minor differences increase as the loops' distribution strays further from the symmetrical distribution. The uneven temperature distribution within the pile may induce some thermo-mechanical strains. In the case of the 0.5 m pile's diameter ($P_{0.5m}$), the variation in loop shares, even under symmetrical distribution, reaches up to 2% (~ 30 kW h per pile over the annual building cooling period). This might be attributed to the smaller pile diameter, resulting in reduced separation distance

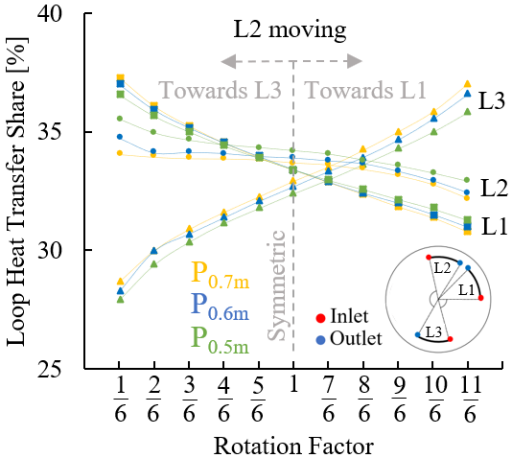

Figure 3. Loop heat transfer share from the total heat transfer for $P_{0.5m}$, $P_{0.6m}$, and $P_{0.7m}$ energy piles for different Rotation Factors of L2.

between individual loops (considering a 25 cm shank spacing between the individual loop's legs), and consequently, higher thermal interference between adjacent loops. However, even for the small pile diameter, the differences are within an acceptable range (less than 5%) as long as the loop distribution does not deviate significantly from symmetry.

From the previous discussion, minor differences in the thermal performance among parallel loops at different relative placements allow for design flexibility and reduce the risk of having significant efficiency decline due to installation uncertainties, although the symmetrical loop distribution is recommended during installation.

The separation distance between loops in a symmetrical arrangement depends on the shank spacing between the legs of individual loops. To further maximise the thermal performance of the energy pile, optimising the shank spacing while all loops are in symmetric distribution is investigated.

Figure 4 shows the total heat transfer considering different separation-to-shank distance ratios (S/K). A similar total heat transfer is achieved for $0.5<S/K<1.5$, suggesting great flexibility in designing the GHEs distribution inside energy piles while maintaining their

thermal performance. Yet, it is still practical to design for an equally spaced arrangement (i.e., S/K = 1).

3.2 Generalised case

To further generalise results, we consider the cases listed in Table 1. Each case focuses on one influencing parameter, with subcase (a) representing the Arden site, and subcases (b) and (c), a smaller or larger value parameter than Arden's (and all others, kept the same).

Results confirm that the highest total heat transfer occurs when the loops are symmetrically distributed (not shown). The maximum differences between loop

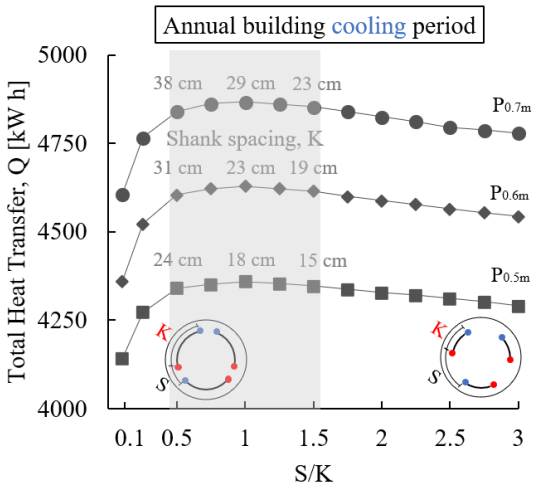

Figure 4. Total heat transfer from all loops for $P_{0.5m}$, $P_{0.6m}$, and $P_{0.7m}$ for different separation-to-shank distance ratios (S/K) over the annual building cooling period.

placements near the symmetry condition ($\alpha/\beta < 3/6$) and in the highly non-symmetric condition ($\alpha/\beta > 10/6$) are summarised in Figure 5.

Table 1. Parametric analysis cases for worst-case $P_{0.5m}$.

Case		Description	Value
1	a	Thermal conductivity (ground) [W/(m·K)]	~ 2.5
	b		1
	c		4
2	a	Pile length [m]	40
	b		15
	c		25
3	a	Fluid flow rate [l/min]	5.5
	b		7.5
	c		10
4	a	Inner pipe diameter [mm]	25.4
	b		12.7
	c		38.1
5	a	Pile spacing [m]	5
	b		2
	c		3.5

4 CONCLUSION

The study demonstrates great flexibility in designing parallel-connected GHEs loops in energy piles and the relatively small impact of misplacing loops during construction. A drop of less than 3% in the overall thermal performance and less than 5% in the total heat transfer share between loops for limited deviations from symmetrical placements has been calculated. Only highly non-symmetric configurations show deviations of ~ 8%. In addition, the marginal drop in thermal performance when the symmetrical separation-to-shank distance ratios range from 0.5 to 1.5 allows for more design flexibility and to increase pile thermal yield by increasing the number of loops.

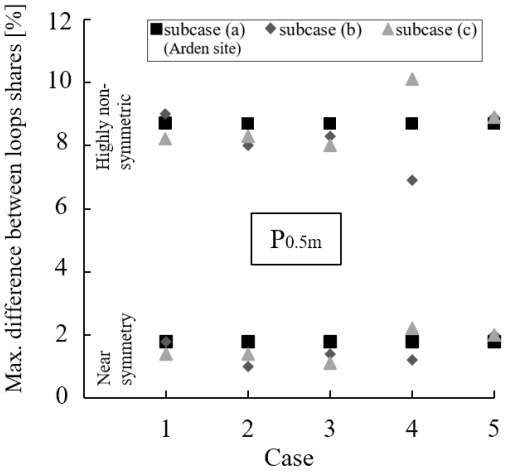

Figure 5. Maximum difference in total heat transfer share between loops for all cases in Table 1 (0.5 m pile diameter).

Installing the loops in a symmetrical and evenly spaced pattern, on the other hand, results in the best overall performance and is thus recommended.

REFERENCES

Alqawasmeh, Q. I., Narsilio, G. A., Makasis, N., and Kreitmair, M. J., (2024) The impact of soil layering and groundwater flow on energy pile thermal performance. *Geomechanics for Energy and the Env.*, 38, 100538. https://doi.org/10.1016/j.gete.2024.100538.

Banks, D. (2012). *An introduction to thermogeology: ground source heating and cooling*, Wiley & Sons. https://doi.org/10.1002/9781118447512.

Brandl, H., (2006) Energy foundations and other thermo-active ground structures. *Géotechnique*, 56(2), 81-122. https://doi.org/10.1680/geot.2006.56.2.81.

Cui, P., Jia, L., Zhou, X., Yang, W., and Zhang, W., (2020) Heat transfer analysis of energy piles with parallel U-Tubes. *Ren. Energy*, 161, 1046-58. https://doi.org/10.1016/j.renene.2020.07.149.

Cui, P., Yang, W., Zhang, W., Zhu, K., Spitler, J. D., and Yu, M., (2022) Advances in ground heat exchangers for

space heating and cooling: review and perspectives. *Energy Built Env.*, 5, 255-269. https://doi.org/10.1016/j.enbenv.2022.10.002.

Jensen-Page, L. C. (2019). *Measurement of ground thermal properties for shallow geothermal applications,* PhD thesis, University of Melbourne.

Kavanaugh, S. P. (2008). A 12-step method for closed-loop ground heat-pump design source. *ASHRAE Trans.,* 114.2, 328-337. ISBN: 978-1-936504-12-1.

Mohamad, Z., Fardoun, F., and Meftah, F., (2021) A review on energy piles design, evaluation, and optimization. *Journal of Cleaner Production*, 292, 125802. https://doi.org/10.1016/j.jclepro.2021.125802.

Park, S., Lee, S., Park, S., and Choi, H., (2022) Empirical formulas for borehole thermal resistance of parallel U-type cast-in-place energy pile. *Renewable Energy*, 97, 211-227. https://doi.org/10.1016/j.renene.2022.07.077.

Proceedings of the XVIII ECSMGE 2024
GEOTECHNICAL ENGINEERING CHALLENGES
TO MEET CURRENT AND EMERGING NEEDS OF SOCIETY
© 2024 the Authors
ISBN 978-1-032-54816-6
DOI 10.1201/9781003431749-541
Open Access: www.taylorfrancis.com, CC BY-NC-ND 4.0 license

ECSMGE 24
XVIII EUROPEAN CONFERENCE ON SOIL MECHANICS AND GEOTECHNICAL ENGINEERING

Improving the remoulded shear strength of a quick clay using biochar

Améliorer la résistance au cisaillement remodelée d'une argile rapide à l'aide de biochar

E.W. Ånes*
Norwegian Geotechnical Institute (NGI), Oslo, Norway
Oslo Metropolitan University, Oslo, Norway

J.I. Loshelder
University of Arkansas, Fayetteville, Arkansas, USA

S. Hov, P. Paniagua
NGI & Norwegian University of Science and Technology (NTNU), Trondheim, Norway

S. Ritter
NGI & Oslo Metropolitan University, Oslo, Norway

**eivind.wiik.aanes@ngi.no*

ABSTRACT: In the pursuit of finding a less carbon-intensive binder alternative to cement, an ongoing research project in Norway is investigating the effect on properties of various soft soils when substituting parts of the cement with industrial by-products and biochars. This paper considers how three biochars influence the soil properties of a Norwegian quick clay when acting as the only binder. The practical application would first and foremost be to ease the handling and transportation of excavated quick clay by increasing its remoulded shear strength. The laboratory study determined that the biochar that yielded the lowest shear strength when added alongside cement had the distinctly largest positive influence when added alone. At a quantity of 100 kg/m^3, this particular biochar, made from calcinated sewer sludge, increased the fall cone shear strength of the remoulded clay from an average of 2.3 kPa to 85.0 kPa after 28 days of storage, and to above 100 kPa after 90 days. The follow-up unconfined compression tests only revealed shear strengths of 19.5-31.4 kPa, indicating serious method-dependency. Nevertheless, the calcinated sewer sludge biochar appears as a sustainable binder option to lime and cement when aiming at improving the shear strength of already excavated sensitive soils.

RÉSUMÉ: Dans la recherche d'une alternative de liant moins intensive en carbone que le ciment, un projet de recherche en cours en Norvège étudie l'effet sur les propriétés de divers sols souples lors du remplacement de parties du ciment par des sous-produits industriels et des biochars. Cet article examine comment trois biochars influencent les propriétés du sol d'une argile rapide norvégienne lorsqu'ils agissent comme seul liant. L'application pratique serait principalement de faciliter la manipulation et le transport de l'argile rapide excavée en augmentant sa résistance au cisaillement remaniée. L'étude en laboratoire a déterminé que le biochar qui a donné la plus faible résistance au cisaillement lorsqu'il était ajouté avec du ciment a eu l'influence positive la plus marquée lorsqu'il était ajouté seul. À une quantité de 100 kg/m^3, ce biochar particulier, issu de la calcination des boues d'égout, a augmenté la résistance au cisaillement du cône de chute de l'argile remaniée d'une moyenne de 2,3 kPa à 85,0 kPa après 28 jours de stockage, et à plus de 100 kPa après 90 jours. Les tests de compression non confinée de suivi n'ont révélé que des résistances au cisaillement de 19,5 à 31,4 kPa, indiquant une sérieuse dépendance à la méthode. Néanmoins, le biochar de boues d'égout calcinées apparaît comme une option de liant durable par rapport à la chaux et au ciment lorsqu'on vise à améliorer la résistance au cisaillement des sols sensibles déjà excavés.

Keywords: Quick clay; biochar; remoulded shear strength; fall cone test; unconfined compression test.

1 INTRODUCTION

Quick clays, recognized by their collapsible nature when disturbed or loaded beyond the yield strength, are found in urbanised areas in Scandinavia and Canada, as well as in parts of Russia. Groundworks in these areas typically require the soil to be stabilised, and often the dry deep mixing method is preferred. An ongoing research project in Norway investigates whether various industrial by-products and biochars may replace parts of the lime and cement to reduce the considerable CO_2 impact of the method. To be used in

dry deep mixing, the alternative binders however should not degrade the engineering performance, and at the very least the resulting shear strength should surpass the in-situ undisturbed shear strength. In practice, this excludes several of the alternative binders and limits the amount of lime and cement that may be replaced. However, there are other uses that do not require the same engineering performance. In projects which include excavation of soil, the quick or soft clay above the final excavation level is sometimes mixed with a reduced binder (typically lime and cement) quantity to facilitate easier excavation and transport to a landfill. For these cases, the shear strength is only required to increase to a level where the soil becomes plastic rather than liquid, and easy and safe to handle and transport.

Biochars are materials made from heating organic masses in the absence of oxygen. Contrary to most industrial by-products proposed to be used as alternative binders, biochars sequester carbon that would otherwise have been emitted to the atmosphere. Thus, the use of biochars to stabilise soils can even have a carbon-negative footprint if enough of the cement and/or lime is replaced (Hov et al., 2023). This makes biochars especially interesting as alternative binders.

Findings from unconfined compression tests by Hov et al. (2023) and Ritter et al. (2023a) highlight that the effect of biochars on the strength and stiffness of soft soils depends heavily on the biochar and soil type, as well as on the added cement and biochar quantities (with both having an optimal amount).

Of the in total five tested biochars in the two studies, none were found to give more than a modest strength increase compared to when cement was added alone. Also, two of the biochars were found to have a negative influence. Hov et al. (2023) discussed that the water adsorption ability of the biochars is likely important to the stabilising effect when added alongside cement. While only one biochar was added without cement by Ritter et al. (2023a), none of the four biochars used by Hov et al. (2023) were added without cement. Thus, the knowledge of the individual effect of biochars on the properties of remoulded quick clays is limited.

The described research investigated how three of the biochars used along with cement by Hov et al. (2023) impacted the fall cone shear strength, $s_{u,FC}$, of the tested quick clay when added alone. The study was initiated as a cost- and material-effective way to provide a reference for the cement and biochar stabilised samples as well as to compare the individual effect of the different biochars.

2 METHODOLOGY

2.1 Materials

The soil used was a quick clay from the Norwegian GeoTest Site (NGTS) at Tiller-Flotten, Trondheim, in Norway. The clay from this site was well characterised by L'Heureux et al. (2019) and has previously been used for similar research (e.g. Hov et al., 2022, 2023; Paniagua et al., 2023; Ritter et al., 2022, 2023a). Tube samples from 14-18 m depth were mixed until visually homogenised. The quick clay from this depth has a clay content of around 50-60%, organic content < 1%, water content w = 40-45%, bulk density 18-18.5 kN/m^3, plasticity index I_P between 10-15%, liquidity index I_L around 1.5-2.0, undisturbed shear strength s_u (from unconfined compression and fall cone tests) approximately between 50 and 85 kPa, sensitivity S_t > 30. A stiffness E_{50} of around 2.5 MPa has been measured for this clay (Ritter et al., 2023a).

All three biochars were produced at temperatures around 470-600 °C in a full-scale micro-wave-assisted pyrolysis (MAP) unit with a residence time of ~20 minutes (Hov et al. 2023). The three biochars (BC) originated from: BC1 - demolition wood such as wood panels, furniture etc., containing some metals and glue remains; BC2 - slightly decayed bottom sludge from municipal sewage with around 39wt.% of limestone, $CaCO_3$, added for hygenisation and workability before the sludge was used for biochar production; BC3 - sewage and food waste, with iron chloride ($FeCl_3$) added for flocculation. Before mixing, the biochars were sieved to grain sizes < 1 mm and oven-dried at 100 °C over night. Their respective specific surface areas (SSA) were measured to be 38.5, 54.8 and 51.3 m^2/g by adsorption of gas and calculated according to Brunauer-Emmet-Tellet theory (Hov et al., 2023). In terms of major elements present, determined by X-ray fluorescence, the most notable differences were high contents of CaO ($CaCO_3$) in BC2, and ferric oxide (Fe_2O_3) in BC3 (Hov et al., 2023).

2.2 Sample preparation and lab testing

For the main testing regime in which the shear strength was tested by the fall cone (FC) method, 29 samples were prepared. The quick clay and biochars were mixed by a Kenwood kitchen mixer according to standard Norwegian lime-cement stabilisation lab procedures (NGF, 2012). Seven mixtures were prepared: two of each biochar, with quantities of 50 and 100 kg/m^3, and one without binder. Following the mixing, around 150 g samples were prepared by pouring/scooping the mixtures into small aluminium containers (see Figure 1). The samples were then sealed and left for storage in room temperature (around

20 °C). For each of the biochar-stabilised mixes, four samples were prepared: three to be tested after 28 days of storage, and one to be tested after 90 days. The test regime consisted of calculating water content (NS-EN ISO 17892-1:2014, NS, 2014), performing fall cone shear strength tests in stored undisturbed and remoulded states (Norwegian correlation developed for testing natural soils, NS 8015:1988; NS, 1988), as well as determining the liquid (w_L) and plastic (w_P) limits (NS-EN ISO 17892-12:2018; NS, 2018). The Atterberg limits were only tested after 28 days of storage, on material from two of the prepared FC samples after FC testing.

Because the BC2 gave unexpectedly high fall cone strengths, three 10 cm unconfined compression (UC) samples were prepared with 100 kg/m^3 of BC2 to provide strength and stiffness values directly comparable to those from Hov et al. (2023). They were tested after 14, 28 and 90 days of curing at room temperature, using a strain rate of 3.8% of the height per minute (NS-EN ISO 17892-7:2017; NS, 2017).

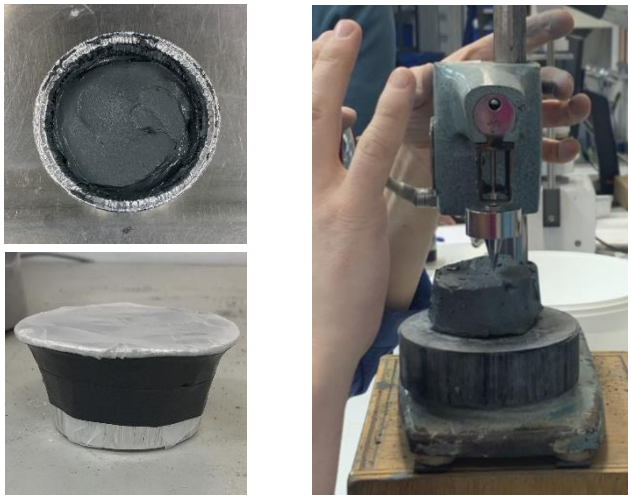

Figure 1. (Upper left) a prepared sample before storage, (lower left) a sealed, prepared sample, and (right) an extracted sample being tested in "undisturbed" state.

3 RESULTS AND DISCUSSION

Figure 2 presents the water contents and liquid and plastic limits. The FC samples with no added binder had a water content varying from 39.6% (1 day) to 37.5% (90 days), indicating that the latter sample might have experienced some drying. For the other samples, this trend was not observed, and the water contents varied insignificantly. The lower water contents when the biochars were added can be explained by the increased dry mass while keeping the amount of water constant. The higher water contents measured for the UC samples can likely be explained by less water being evaporated during mixing and storing.

Considering the Atterberg tests, BC2 had a considerably more prominent effect than BC1 and BC3, both in terms of increasing the liquid (w_L) and plastic (w_P) limits as well as the plasticity index. Although the BC1 and BC3 performed similar, BC1 was the least effective. Even when adding 100 kg/m^3 BC1, the samples still had a water content $w > w_L$.

Figure 3 presents key results from the fall cone (FC) and unconfined compression (UC) tests. Table 1 summarizes all shear strength test results. Every biochar increased the FC shear strengths compared to the non-stabilised remoulded samples. However, BC2 had a greater effect than BC1 and BC3, corresponding with the respective influences on the plasticity. The strength increase caused by BC2 began immediately upon mixing. While all biochars gave a larger strength increase at 100 kg/m^3 than at 50 kg/m^3, the effect was most pronounced for BC2 and BC3, where s_u more than doubled.

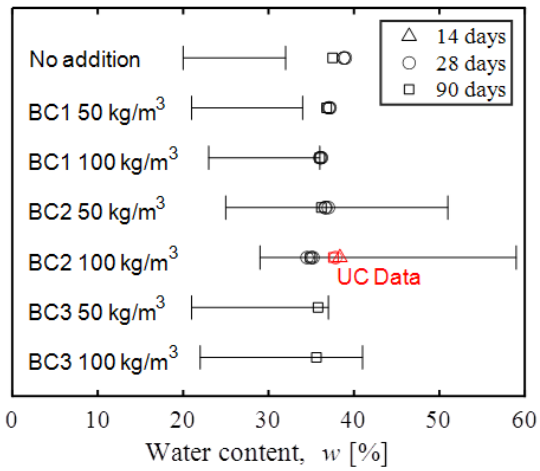

Figure 2. Measurements of w (symbols), and w_P and w_L.

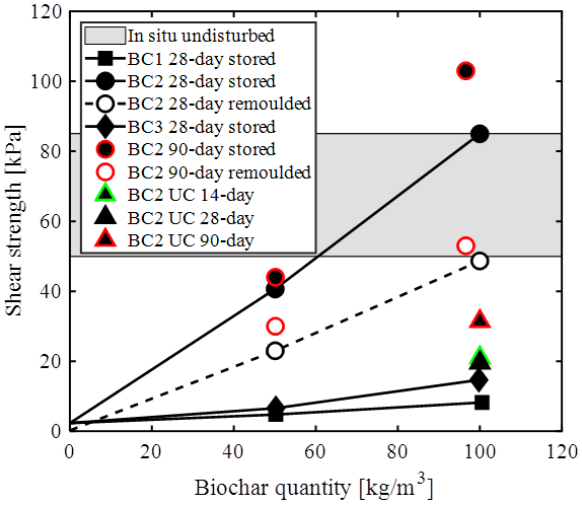

Figure 3. Key shear strength results.

Table 1. Fall cone and unconfined compression test results. Triplicate FC samples were tested after 28 days. All other shear strength results were from one sample/test. Shear strength from UC tests were derived as half the unconfined compression strength (UCS /2).

Binder	Quantity	Fall cone (FC) Stored		After remoulding		Unconfined compression (UC) Stored	
		s_u	St. dev.	s_u	St. dev.	*UCS/2*	*E50*
		28 / 90 days	28 days	28 / 90 days	28 days	14 / 28 / 90 days	14 / 28 / 90 days
[-]	[kg/m3]	[kPa]				[kPa]	
None	-	2.3 / 3.3	0.12	0.2 / 0.6	0.05		
BC1	50	4.8 / 7.7	0.24	1.4 / 3.6	0.24		
	100	8.2 / 15	1.58	2.2 / 7.5	1.58		
BC2	50	40.7 / 44	1.70	23 / 30	1.70		
	100	85 / 103.0	2.83	48.7 / 53	2.83	21 / 19.5 / 31.4	220 / 450 / 1600
BC3	50	6.6 / 15	0.43	3.6 / 9	0.43		
	100	14.7 / 27	1.70	7.9 / 16	1.70		

The reasons why BC2 had a greater effect than the other two biochars have not yet been understood. Some aspects which may explain the observed differences will be discussed in the following.

3.1 Remoulding and time-dependency

Every FC sample experienced a decrease in shear strength upon remoulding. However, all stabilised samples retained a shear strength above the quick clay threshold of 0.5 kPa. As every sample was essentially remoulded upon storing, the reduction indicated a time-dependent strength increase during storing, even for the non-stabilised samples. This thixotropic tendency was also indicated by comparing FC and UC results after 28 and 90 days of storage. Only one sample from each series was tested after 90 days, but the fact that an increase was seen for all series, and that the loss of water content was negligible, strongly implies that there were active processes that increased the strength of the particle structures also after 28 days. How the binders themselves contributed to these processes are difficult to assess based on the results presented herein. It is nevertheless worth noting that percentagewise, both BC1 and BC3 provided a larger increase in stored shear strength from 28 to 90 days than BC2 (83 and 84% vs. 21% for the FC samples, respectively, and 61% for the UC samples). This could indicate that the processes providing the immediate (or short-term) and the time-dependent strength increase are not the same. Alternatively, the processes caused by additions of BC1 and BC3 may have initially been moving slower than when BC2 was added. The stabilising effects of BC2 are further discussed in Section 3.3.

3.2 Fall cone vs. unconfined compression tests

Studies have determined the correlation between unconfined compression tests and fall cone tests to be strongly soil dependent (e.g. Tanaka et al., 2012). From the results presented in this paper, it is also observed that the correlation is distant from 1:1. For example, the average $s_{u,FC}$ of the BC2 100 kg/m^3 samples after 28 days of storage was around 4×*UCS/2*. Part of the discrepancy is likely due to differences in sample preparation, sample size, and test method. Also, the fact that the framework for determining shear strength from fall cone tests was developed for natural soils, and not reconstituted ones, might be part of the explanation.

3.3 Biochar and cement vs. biochar

Not surprisingly, the biochar-stabilised samples exhibited much lower shear strengths than when 50 kg/m^3 of cement was included in the binder mixture (Hov et al., 2023, see Table 2). For BC2-stabilised samples after 28 days of storage, the addition of cement gave approximately a 20-fold increase of *UCS/2* compared to when only the biochar was used (396 kPa vs. around 20 kPa). The stiffness, E_{50}, of the BC2 samples was between 220 – 450 kPa, less than 1/50 of the BC2- and cement samples and less than the in-situ stiffness (2 500 kPa). After 90 days of storage, the *UCS/2* and E_{50} increased to 31.4 kPa and 1 600 kPa respectively which was still below the in-situ values.

Table 2. Extract of results from (Hov et al., 2023). Average shear strength and stiffness values from unconfined compression tests performed after 28 days of storage.

Cement	Biochar	*UCS/2* [kPa]	E_{50} [kPa]
50 kg/m^3	-	460	118 000
50 kg/m^3	100 kg/m^3 BC1	396	102 000
50 kg/m^3	100 kg/m^3 BC2	166	25 000
50 kg/m^3	100 kg/m^3 BC3	217	41 000

Possibly the most surprising finding when comparing the two studies was that BC2 was the least effective biochar when used together with cement but

the most effective one when added alone. It is unclear whether this is related to the biochar properties, such as water retention, or the constituents available for chemical reactions. Considering the latter, it may imply that the chemical compounds in BC2 are more active than those from the other biochars, and that the chemical compounds, or the chemical reactions which they are involved in, may obstruct the curing of the cement. However, Hov et al. (2023) discussed that the BC2 had no cementitous properties, as calcium is only present as calcite ($CaCO_3$) and not calcium oxide (CaO). Microstructural analyses, e.g. with a scanning electron microscope, could provide further insight into the mechanisms involved.

3.4 Implications for the use of the biochars

The calcinated sewer sludge biochar (BC2) notably increased the shear strength and plasticity of the remoulded Tiller-Flotten quick clay. As the strength increase began immediately after mixing in the lab, this biochar could be used as an alternative to lime and cement to stabilise already excavated soft and quick clays. Even at 50 kg/m^3 (or even lower), the instant improvement of the Tiller-Flotten clay would likely be enough to quickly make the clay safe and practical to handle and transport. While the other biochars could in theory also be used for this purpose, a larger quantity of biochar would be required. Further analyses should look at the economic implications due to the actual costs of biochar production.

Recently, the possibility to reuse excavated soils, instead of depositing them at landfills, has gained some attention. For example, an ongoing research project in Norway is investigating whether excavated lime and cement stabilised clays may be utilised as compacted clay liners at landfills (Ånes et al., 2024; Ritter et al., 2023b). In this regard, it could be interesting to explore how clays stabilised with biochars or other alternative binders compare to clays stabilised with lime and cement. If alternative binders are found to be better for this or other purposes, thus increasing the usability of the excavated mass, it could be an incentive for construction projects to rather use such binders to stabilise soft and quick clays after excavation.

4 CONCLUSION

All three biochars had a positive effect on the shear strength of the remoulded quick clay. Additions of 50 and 100 kg/m^3 of BC2 and BC3 stabilised the clay to above the quick clay threshold of $s_{u,\ remoulded} > 0.5$ kPa, as well as $w > w_L$. Samples with BC1 only surpassed the first criterion. BC2 had the distinctly most positive effect and increased the average fall cone shear strength after 28 days of storage from 2.3 kPa to 85 kPa, and *UCS/2* to around 20 kPa.

BC2 seems to be a viable climate-friendly alternative to lime and cement to improve the handling and transportation of quick and soft clays after excavation. The field performance including environmental and economic aspects of using BC2 as an alternative binder to improve remoulded quick clay should be studied further.

The reasons for the superior effects caused by BC2 compared to BC1 and BC3 have not yet been determined. Potential explanations could be a higher water retention capacity of BC2, or that BC2 contains constituents that react chemically when added to clay. However, from the performed chemical and mineralogical analyses by Hov et al. (2023), there are no obvious differences between BC2 and the other biochars to suggest this. Scanning electron microscope should be used to study the microstructure of stabilised samples to help expose the mechanisms.

ACKNOWLEDGEMENTS

This research was funded by Research Council of Norway, grant number 328767 "GOAL – Green soil stabilisation". The authors are especially grateful to Ingrid Peikli, Karl Sigmundstad Halse, and Maria Cansignia at the NGI geotechnical laboratory in Oslo for performing the laboratory tests.

REFERENCES

Ånes, E. W., Ritter, S., Pabst, T., Stridal, A. C., Nilsen, N. G., Hovland, K., & Okkenhaug, G. (2024). Utilisation of geological surplus masses in landfill cover: percolation results from pilot test. *Proceedings of the XVIII ECSMGE 2024*.

Hov, S., Paniagua, P., Sætre, C., Rueslåtten, H., Størdal, I., Mengede, M., & Mevik, C. (2022). Lime-cement stabilisation of Trondheim clays and its impact on carbon dioxide emissions. *Soils and Foundations*, *62*(3). https://doi.org/10.1016/j.sandf.2022.101162.

Hov, S., Paniagua, P., Ritter, S., Sætre, C., Long, M., & Cornelissen, G. (2023). Stabilisation Of Soft Clay, Quick Clay And Peat By Industrial By-Products And Biochars. *Applied Sciences*, *13(16).*

L'Heureux, J.-S., Lindgård, A., & Emdal, A. (2019). The Tiller-Flotten research site: Geotechnical characterization of a very sensitive clay deposit. *AIMS Geosciences*, *5*(4), 831–867. https://doi.org/10.3934/geosci.2019.4.831.

NGF (Norwegian Geotechnical Society) (2012) Veiledning for grunnforsterkning med kalksementpeler. Guidelines for ground improvement with lime- and cement-piles (in Norwegian). Oslo, Norway.

NS (Standard Norge) (1988) 8015:1988 Geoteknisk prøving – Laboratoriemetoder – Bestemmelser av udrenert skjærstyrke ved konusprøving. Geotechnical testing – Laboratory methods – Determination of undrained shear strength by fall cone (in Norwegian). Standard Norge, Lysaker, Norway.

NS (2014) ISO 17892-1 Geotechnical investigation and testing – Laboratory testing of soil – Part 1: Determination of water content. Standard Norge, Lysaker, Norway.

NS (2017) ISO 17892-7 Geotechnical investigation and testing – Laboratory testing of soil – Part 7: Unconfined compression test. Standard Norge, Lysaker, Norway.

NS (2018) ISO 17892-12 Geotechnical investigation and testing – Laboratory testing of soil – Part 12: Determination of liquid and plastic limits. Standard Norge, Lysaker, Norway.

Paniagua, P., Ritter, S., Moseid, M., & Okkenhaug, G. (2023). Bioashes and Steel Slag as Alternative Binders in Ground Improvement of Quick Clays. *Proceedings Geo-Congress 2023*, 25–34. https://doi.org/doi.org/10.1061/9780784484661.003.

Ritter, S., Paniagua, P., Hansen, C. B., & Cornelissen, G. (2022). Biochar amendment for improved and more sustainable peat stabilisation. *Proceedings of the Institution of Civil Engineers: Ground Improvement*. https://doi.org/10.1680/jgrim.22.00023.

Ritter, S., Paniagua, P., & Cornelissen, G. (2023a). Biochar in Quick Clay Stabilization: Reducing Carbon Footprint and Improving Shear Strength. *Geo-Congress 2023*.

Ritter, S., Wiik Ånes, E., Hovland, K., Stridal, A. C., Hansen, H., Henriksen, T., & Okkenhaug, G. (2023b). Sustainable impermeable landfill barriers: The potential of using geological waste and surplus masses. *9th International Congress on Environmental Geotechnics (ICEG2023)*. https://doi.org/10.53243/ICEG2023-102.

Tanaka, H., Hirabayashi, H., Matsuoka, T., & Kaneko, H. (2012). Use of fall cone test as measurement of shear strength for soft clay materials. *Soils and Foundations*, *52*(4), 590–599. https://doi.org/10.1016/j.sandf.2012.07.002.

Proceedings of the XVIII ECSMGE 2024
GEOTECHNICAL ENGINEERING CHALLENGES
TO MEET CURRENT AND EMERGING NEEDS OF SOCIETY
© 2024 the Authors
ISBN 978-1-032-54816-6
DOI 10.1201/9781003431749-542
Open Access: www.taylorfrancis.com, CC BY-NC-ND 4.0 license

ECSMGE 24
XVIII EUROPEAN CONFERENCE ON SOIL MECHANICS AND GEOTECHNICAL ENGINEERING

Utilisation of geological surplus masses in landfill cover: percolation results from pilot test

Utilisation de matériaux d'excavation dans les systèmes de recouvrement des sites d'enfouissement: résultats de percolation d'un essai pilote

E.W. Ånes*, S. Ritter
Norwegian Geotechnical Institute (NGI), Oslo, Norway
Oslo Metropolitan University, Oslo, Norway

T. Pabst
NGI, Oslo, Norway

A.C. Stridal, N.G. Nilsen, K. Hovland
NOAH, Holmestrand, Norway

G. Okkenhaug
NGI, Oslo, Norway
Norwegian University of Life Sciences, Ås, Norway

**eivind.wiik.aanes@ngi.no*

ABSTRACT: To minimize the generation of leachates and thus the contamination of the environment, landfills are usually closed using a cover system which includes a low-permeable hydraulic barrier. For landfills for ordinary and hazardous wastes, a common requirement is that the hydraulic conductivity of this layer must be less than $1x10^{-9}$ m/s. Compacted soil layers with natural dry crust clays have been used for this purpose in Norway. However, these soils are not always available within reasonable transport distances of landfills. An ongoing field-scale pilot test conducted at a landfill site in southern Norway therefore aims to evaluate whether a press filter residue from a soil-washing plant or an excavated cement stabilised clay could be used instead of natural-occurring clays. These two materials are normally considered wastes and currently have no application. Their reuse would therefore contribute to reduce the environmental footprint and the costs associated with their deposition in a landfill. Field results for a 6-month period (May 1st to October 31st, 2023) are presented and discussed in this article. These initial results indicate that the cover made of compacted dry crust clay is the most effective, but that the two alternative materials also fulfil the hydraulic conductivity target of 1×10^{-9} m/s. Overall, field measurements match well characterisation and hydraulic conductivity tests conducted in the laboratory. However, the difference in hydraulic conductivity between the dry crust clay and the reused materials is smaller in the field than in the lab. The environmental aspects regarding the reuse of these materials are yet to be evaluated.

RÉSUMÉ: Afin de minimiser la génération de lixiviats et donc la contamination de l'environnement, les décharges et sites d'enfouissement sont généralement restaurés au moyen d'un système de recouvrement comprenant une couche de faible perméabilité. En Norvège, les installations de stockage de déchets ordinaires et dangereux doivent normalement être recouverts d'une couche d'argile compactée ayant une conductivité hydraulique inférieure à 1×10^{-9} m/s. On emploie souvent des argiles glacio-marines altérées à cette fin, mais les matériaux adéquats ne sont pas toujours disponibles dans un rayon de transport raisonnable des décharges. Un essai pilote est donc en cours sur une décharge du sud de la Norvège afin d'évaluer si un résidu filtré provenant d'une usine de lavage de sols et une argile stabilisée au ciment excavée pourraient être utilisés à la place des argiles conventionnelles. Ces deux matériaux sont généralement considérés comme des déchets et n'ont actuellement aucune autre application. Leur réutilisation permettrait donc de réduire l'empreinte environnementale et les coûts liés à leur entreposage. Cet article présente les résultats de terrain pour une période de 6 mois, du 1er mai au 31 octobre 2023. Ces premiers résultats indiquent que la couverture constituée d'argile est la plus efficace, mais que les deux matériaux recyclés remplissent également le critère 1×10^{-9} m/s. Les résultats de ces essais de terrain confirment bien les caractérisations et tests de perméabilité réalises au laboratoire. Cependant, la différence de perméabilité entre l'argile et les matériaux recyclés est plus faible sur le terrain qu'au laboratoire. Les aspects environnementaux liés à la réutilisation de ces matériaux restent cependant à évaluer.

Keywords: Landfill; final cover; low-permeable barrier; compacted soil; reuse.

1 INTRODUCTION

Reducing the water percolation in a landfill is an important part of minimizing the generation of leachates and thus reduce the risk of contamination of the surrounding environment. Landfills are usually reclaimed using a cover system that includes a low-permeable hydraulic barrier, for example consisting of compacted clayey soil. For landfills for ordinary and hazardous wastes, the environmental authorities in Norway typically require this barrier to have a hydraulic conductivity lower than 1×10^{-9} m/s. This criterion is usually assumed to ensure that the annual percolation does not exceed 20 to 50 mm/yr (Avfall Norge, 2015).

A landfill for inorganic ordinary and hazardous industrial wastes, located in southern Norway, is currently planning its closure. Dry crust clays (DCCs), the weathered upper metres of marine clay deposits, have been used for the construction of a compacted soil layer (called sealing layer in previous associated papers) within the cover system for a closed part of the landfill. However, the availability of DCCs in the region is limited, and the landfill company therefore investigates possible alternative materials for the closure of the last part. Two clayey materials that are normally considered as wastes and deposited as such have been identified as potential alternatives. These include a clayey press filter residue (PFR) from a soil-washing plant, and a cement-stabilised clay (CSC) excavated from a construction site in the region. Several preliminary lab and field studies have, indeed, showed, that these two materials can achieve the target of 1×10^{-9} m/s, provided a sufficient compaction effort is applied (e.g., Kristensen, 2017; Pedroni et al., 2018; Ritter et al., 2023).

A large-scale pilot test is therefore being conducted in the field, complemented by a laboratory characterisation test program, to evaluate the in-situ hydraulic conductivity and properties of these two alternative materials as well as a dry crust clay (DCC). Pilot design and field results are presented in this article.

2 METHODOLOGY

2.1 Materials

Three materials were evaluated in this research: the DCC, the PFR and the CSC. The DCC was obtained from a construction site in Oslo, Norway. The PFR was produced at a soil-washing plant, being the clay- and silt-fractions separated from the coarser fractions of various excavated lightly contaminated sediments. The CSC came from another construction project in Oslo. All three materials have been characterised as part of this study, and earlier by Ritter et al. (2023). The particle size distribution was determined by the falling drop method (NS-EN ISO 17892-4:2016; NS, 2016), water content by loss on drying (NS-EN ISO 17892-1:2014; NS, 2014), compaction properties were determined from the Standard Proctor test (AASHTO T99-10; AASHTO, 2022), consistency limits were evaluated by Atterberg tests (NS-EN ISO 17892-12:2018; NS, 2018), the shear strength was determined from fall cone (NS-EN ISO 17892-6:2017; NS, 2017) and minature vane (ASTM D4648; ASTM, 2016), whereas the hydraulic conductivity was measured in oedometer and triaxial cells (NS-EN ISO 17892-11:2019; NS, 2019). Table 1 summarises the results from these tests. All lab hydraulic conductivities presented herein were measured at 40 kPa, equivalent to the 1.8-2 m overburden the compacted soil layers were subjected to. The entirety of permeability test results are presented by the companion paper by Kim et al. (2024).

Table 1. Hydrogeotechnical properties of tested materials (partly adapted from Kim et al. (2024) and Ritter et al. (2023)). Averages are in parantheses (). DCC = dry crust clay, PFR = press filter residue, CSC = cement stabilised clay.

Parameter	DCC	*PFR*	CSC
Clay content	42-48% (45%)	19-30% (25%)	4.5 – 35% (31%)
Water content	27 – 30% (28%)	31-38% (35%)	23-30% (29%)
Optimum water content	~22-25%	~28-30%	~24-27%
Plasticity index	17 – 22% (20%)	25%	18 – 31% (25%)
Liquid limit	42 – 45% (43%)	53 – 56% (55%)	41 – 65% (53%)
Remoulded shear strength	95 kPa	20 kPa	-
Hydraulic conductivity at 40 kPa	2.4 – 3.0 $\times10^{-10}$ m/s (2.7×10^{-10})	1.0 – 4.9 $\times10^{-9}$ m/s (1.8×10^{-9})	1.9×10^{-7} – 6.2×10^{-10} m/s (4.3×10^{-8})

The used DCC had a clay content of around 45%, a shear strength of around 95 kPa and an average (of 3 oedometer samples) hydraulic conductivity at 40 kPa of 2.7×10^{-10} m/s. The clay content of the PFR varied between 19 and 30%, with an average at 25%. Its shear strength was considerably lower than that of the DCC, with an average of around 20 kPa. Its average hydraulic conductivity (6 oedometer and 2 triaxial samples) was 1.8×10^{-9} m/s. The CSC was characterized by a significant variability of both its geotechnical and hydrogeological properties. For

example, the measured hydraulic conductivity of undisturbed samples from the field (5 oedometer and 2 triaxial samples) was between 6.2×10^{-10} m/s and 1.9×10^{-7} m/s, over 300 times higher.

This heterogeneity may be attributed to the nature of the material, a mixture of cement, cement stabilised clay lumps and non-stabilised natural clay. The various parts were mixed during excavation, handling, and transportation, but seemingly far from homogenised.

2.2 Pilot design, construction and instrumentation

Four test cells were constructed as one continuous final cover about 14 m wide and 35 m long, with a cross-section as shown in Figure 1. A lysimeter, consisting of a permeable gravel placed on top of an impermeable geomembrane with a drain at the bottom, was installed at the base of each cell. All lysimeters were nearly quadratic and varied from about 11.5 m^2 to 14.5 m^2. The percolated water volumes were measured using tipping buckets (Campbell Scientific, 2023). The compacted soil layer was constructed (in three lifts/layers) by laying out the loose materials and compacting with a Cat D6 bulldozer (Caterpillar, 2023). A 13-ton rolling machine was then used to further compact and smoothen the surface of the third lift. The surface of the compacted soil was slightly inclined (approx. 1:16) towards the side of the cells (not towards the neighbouring cell). The compacted soil was covered by a 1.8-2.0 m thick protection layer of crushed limestone against climatic conditions and exterior alterations (freeze/thaw and drying/wetting cycles especially). The four different compacted soil layer designs consisted of (1) the DCC, (2) the PFR, (3) one lift of PFR and two overlying lifts of CSC, and (4) CSC alone.

A tipping bucket and temperature sensor was installed on top of the protection layer to measure the precipitation and air temperature. Teros 12 and 21 sensors (Teros, 2023) and a PT100 temperature sensor were installed at different depths in all cells to monitor temperature, volumetric water content, electrical conductivity, and matric suction. The construction and design of the pilot tests are described in more detail by Ånes et al. (2023).

Daily monitoring data from the 6-month period May 1st to October 31st (2023) were collected and analysed. Measured field percolation was compared with the laboratory characterization conducted on undisturbed samples (Kim et al., 2024).

3 RESULTS

Percolation volumes measured by the tipping buckets were normalised by the lysimeter area and expressed in equivalent millimetres.

The total precipitation during the considered 6-month period was 390 mm. The weather through the period was variable (Figure 2). Only 35 mm of precipitation were recorded in May and June, i.e., 1/5 of the total precipitation for the period. In contrast, July and August were particularly wet with 260 mm in total, while September-October experienced 95 mm. The average temperatures for the three two-month periods were 14.7, 15.9 and 10.9°C, respectively.

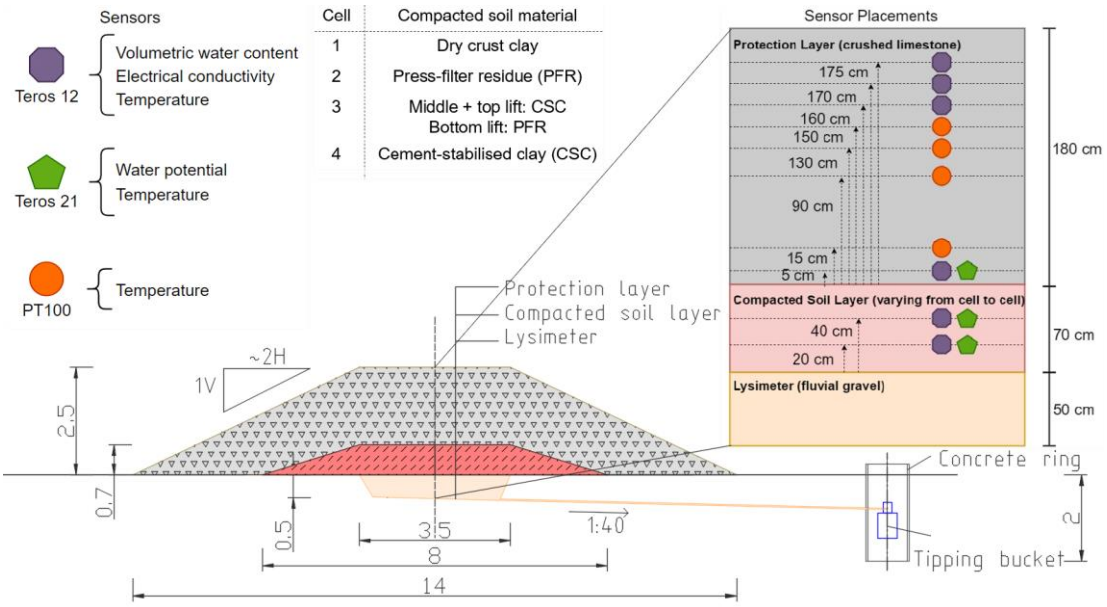

Figure 1. Cross-section drawing of the pilot final cover, including instrumentation. Dimensions for the final cover are in meters. Modified from Ånes et al. (2023).

The percolation through the alternative compacted soil layers (cells 2, 3 and 4) was around 7 mm (1.8% of precipitation), more than 2 times greater than in the cell with DCC (3 mm, 0.8% of precipitation). With an annual precipitation around 1000 mm (2.5 times the recorded precipitation for the monitoring period), the total percolation in cells 2, 3 and 4 was therefore expected to be between 8 and 18 mm/yr, i.e., below the target criteria (Avfall Norge, 2015).

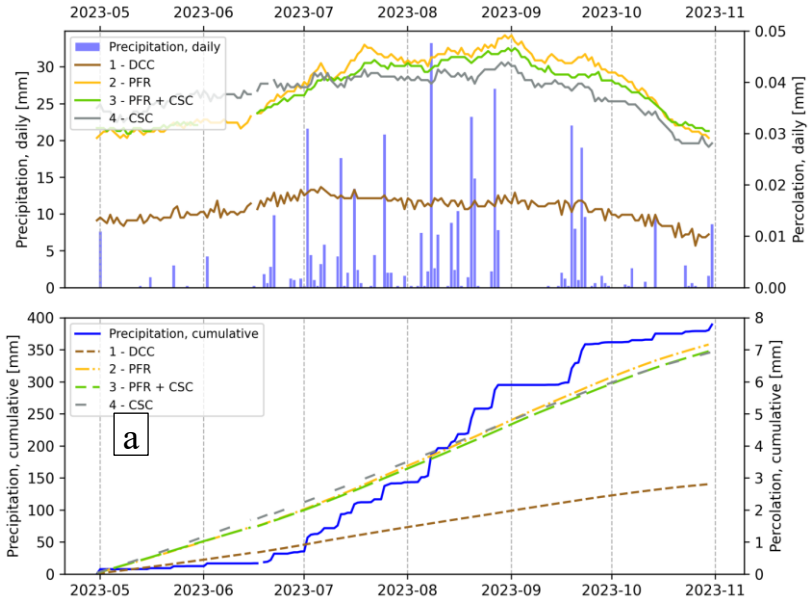

Figure 2. (a) Daily and (b) cumulative percolation and precipitation in each of the instrumented pilot cells from May 1st to October 31st. DCC = Dry crust clay, PFR = Press filter residue, CSC = Cement stabilised clay.

Considering the daily variations (Figure 2a), it may be noted that the effect of precipitation was different for the various compacted soil layers. The percolation through cell 1 plateaued early after the onset of the wet period (beginning of July), whereas the percolation through cell 2 and 3 continued to increase until the end of August when the wet period ended. The percolation in cell 4 varied less than in cell 2 and 3, being higher in the dry period May-June, and lower in July-October. It is not clear what caused this, but differences in material properties and degrees of saturation, and continuous reactions involving cement in the stabilised clay, are possible explanations. Additional tests and analyses are currently ongoing to further investigate potential mechanisms.

The degree of saturation of the compacted soil layers, measured using the water content probes installed in the pilot, was between 85% and 95%. Based on suction measurements, a conservative downward hydraulic gradient of 1 was assumed for all cells, leading to an estimation of the hydraulic conductivity between 2×10^{-10} m/s (cell 1) to around 4×10^{-10} m/s (cell 2-4).

The difference in hydraulic conductivity between the DCC and the PFR and CSC in the pilot was around 2 (towards 3 during the summer and fall), i.e. lower than in the laboratory where the average measured hydraulic conductivity of PFR and CSC were, respectively, 7 and 159 times greater than that of the DCC. The variability of the materials (especially CSC) may at least in part be the cause for these differences between lab and field results. The slightly lower degree of saturation in the field and/or variations in porosity in the laboratory may also be part of the explanation. Further investigations may be required to evaluate if the representativity of the lab samples and their size may be another reason for the observed differences.

4 CONCLUSION

A pilot test has been constructed at a landfill site in Norway to quantify the field-performance of final cover compacted soil layers consisting of various reused clayey soils.

Percolation and precipitation results from May 1st to October 31st showed that all the proposed compacted soil layers had a hydraulic conductivity lower than 1×10^{-9} m/s, and thus satisfied the criteria of hydraulic conductivity for compacted soil layers. The compacted soil layer with dry crust clay had the lowest hydraulic conductivity, which corresponded well with hydraulic conductivity tests conducted in the laboratory (Ritter et al. (2023) and Kim et al. (2024)) as well as with the higher clay content compared to the other materials. The compacted soil layers with the

press filter residues and excavated cement stabilised clay were slightly more permeable than the DCC, but suitable, nevertheless. The hydraulic conductivities of CSC evaluated in the field were notably lower than the lab average, most probably because of the heterogeneity of the materials and scale effects influencing the lab results. Additional lab tests are ongoing to further assess the variations in field and lab, as well as the variation between lab samples of the same material.

ACKNOWLEDGEMENTS

This work was supported by the earthresQue centre for research driven innovation, Rescue of Earth Materials and Wastes in the Circular Economy, partly funded by the Research Council of Norway, project number 310042/F40. The authors thank Taehon Kim, Yusuke Suzuki, Karoline Helen Løvlie and Geir Wold Åsli for all the valuable help with the laboratory work at NGI. Erling Singstad Paulsen, Kristoffer Heian and Ola Paaske Gulbrandsen at the instrumentation group at NGI are also acknowledged for their tedious work with installing sensors as well as facilitating the handling of field data. Lastly, personnel from Kjeldaas entrepreneurs deserve acknowledgement for their skilled and cautious construction of the final cover.

REFERENCES

AASHTO (American Association of State Highway and Transportation Officials) (2022). AASHTO T 99-10 Standard method of test for moisture-density relations of soils using a 2.5-kg (5.5-lb) rammer and a 305-mm (12-in) drop. American Association of State Highway and Transportation Officials, Washington DC, USA.

Ånes, E. W., Ritter, S., & Okkenhaug, G. (2023). Use of numerical modelling when designing a full-scale field test of landfill top covers. *9th International Congress on Environmental Geotechnics (ICEG2023)*. https://doi.org/10.53243/ICEG2023-402.

ASTM (2016). D4648/D4648M-16 Standard test methods for laboratory miniature vane shear test for saturated fine-grained clayey soil. ASTM International, West Conshohocken, PA, USA.

Avfall Norge (2015). Veileder for avslutning og etterdrift av deponier. Guidelines for closure and post-operation of landfills (in Norwegian).

Campbell Scientific (2023). Product specifications for tipping bucket 52202-L. Available at: https://www.campbellsci.com/pn52202, accessed: 28/11/2023.

Caterpillar (2023). Product specifications for D6T. Available at: https://www.cat.com/en_MX/products/new/equipment/dozers/medium-dozers/18331763.html, accessed: 28/11/2023.

Kim, T. H., Ritter, S., Ånes, E. W., Åsli, G. W., & Suzuki, Y. (2024). The permeability characteristics of compacted recycled materials for landfill geo-barriers in Norway. *Proceedings of the XVIII ECSMGE 2024*.

Kristensen, E. C. (2017). Nyttegjøring og gjenbruk av kalk-/sementstabilisert leire i deponier. Utilization and re-use of lime cement stabilized clay in landfills (in Norwegian). Master's thesis, Trondheim, Norwegian University of Science and Technology (NTNU).

NS (Standard Norge) (2014) ISO 17892-1 Geotechnical investigation and testing – Laboratory testing of soil – Part 1: Determination of water content. Standard Norge, Lysaker, Norway.

NS (2016) ISO 17892-4 Geotechnical investigation and testing – Laboratory testing of soil – Part 4: Determination of particle size distribution. Standard Norge, Lysaker, Norway.

NS (2017) ISO 17892-6 Geotechnical investigation and testing – Laboratory testing of soil – Part 6: Fall cone test. Standard Norge, Lysaker, Norway.

NS (2018) ISO 17892-12 Geotechnical investigation and testing – Laboratory testing of soil – Part 12: Determination of liquid and plastic limits. Standard Norge, Lysaker, Norway.

NS (2019) ISO 17892-11 Geotechnical investigation and testing – Laboratory testing of soil – Part 11: Permeability tests. Standard Norge, Lysaker, Norway.

Pedroni, L., Kristensen, E. C., Okkenhaug, G., & Baardvik, G. (2018). Reuse of excavated lime and cement stabilized soft and quick clay. *10th International Conference on the Environmental and Technical Implications of Constriction with Alternative Materials (WASCON 2018)*, pp. 6–8.

Ritter, S., Wiik Ånes, E., Hovland, K., Stridal, A. C., Hansen, H., Henriksen, T., & Okkenhaug, G. (2023). Sustainable impermeable landfill barriers: The potential of using geological waste and surplus masses. *9th International Congress on Environmental Geotechnics (ICEG2023)*. https://doi.org/10.53243/ICEG2023-102.

Teros (2023). Product specifications Teros 12 and 21. Available at: https://www.metergroup.com/en/meter-environment/products/, accessed: 28/11/2023.

Proceedings of the XVIII ECSMGE 2024
GEOTECHNICAL ENGINEERING CHALLENGES
TO MEET CURRENT AND EMERGING NEEDS OF SOCIETY
© 2024 the Authors
ISBN 978-1-032-54816-6
DOI 10.1201/9781003431749-543
Open Access: www.taylorfrancis.com, CC BY-NC-ND 4.0 license

ECSMGE 24
XVIII EUROPEAN CONFERENCE ON SOIL MECHANICS AND GEOTECHNICAL ENGINEERING

Effect of setback distance of leachate recirculation systems on the slope stability of bioreactor landfills

Effet de la distance de recul des systèmes de recirculation des lixiviats sur la stabilité des pentes des décharges de bioreacteurs

L.S. Avinash, A. Mishra*
Indian Institute of Technology Roorkee, Roorkee, India

**anumita.mishra@ce.iitr.ac.in*

ABSTRACT: The present study investigates the impact of leachate recirculation on stability of landfills by conducting numerical modelling using finite element analysis. The validation of the model was carried out and the results were subsequently compared with the previous literature. The leachate recirculation was simulated using the horizontal trench of 1 m × 1 m. The effect of leachate injection on the pore water pressure and slope stability was examined for heterogeneous and anisotropic waste conditions for various injection pressures and slope configurations. The performance of horizontal trenches with different setback distances varying between 5 m - 50 m for various injection pressures was compared, and their effects on landfill slope stability were evaluated. A setback distance of less than 25 m has a significant impact on landfill stability under high injection pressures, primarily because of the influence of pore water pressure on the slope. The results showed that a factor of safety greater than 1.5 was achieved for the optimum range of setback distance of 30 m - 40 m and was found to be suitable across various injection pressures (49 kPa, 98 kPa,147 kPa, and 196 kPa). The outcomes of the present research would help in better understanding the influence of setback distance of leachate recirculation on slope stability and contribute to the improvement of the design of landfills.

RÉSUMÉ: La présente étude examine l'impact de la recirculation des lixiviats sur la stabilité des décharges en réalisant une modélisation numérique à l'aide de l'analyse par éléments finis. La validation du modèle a été effectuée, et les résultats ont ensuite été comparés avec la littérature précédente. La recirculation des lixiviats a été simulée en utilisant la tranchée horizontale de 1 m × 1 m. L'effet de l'injection de lixiviats sur la pression interstitielle et la stabilité des pentes a été examiné dans des conditions de déchets hétérogènes et anisotropes, pour différentes pressions d'injection et configurations de pentes. La performance des tranchées horizontales avec différentes distances de recul variant de 5 m à 50 m pour différentes pressions d'injection a été comparée, et leurs effets sur la stabilité des pentes de la décharge ont été évalués. Une distance de recul inférieure à 25 m a un impact significatif sur la stabilité de la décharge sous des pressions d'injection élevées, principalement en raison de l'influence de la pression de l'eau interstitielle sur la pente. Les résultats ont montré qu'un facteur de sécurité supérieur à 1,5 a été atteint pour la plage optimale de distance de recul de 30 m à 40 m et s'est avéré adapté à différentes pressions d'injection (49 kPa, 98 kPa, 147 kPa et 196 kPa). Les résultats de la présente recherche contribueront à une meilleure compréhension de l'influence de la distance de recul de la recirculation des lixiviats sur la stabilité des pentes et contribueront à l'amélioration de la conception des décharges.

Keywords: Horizontal trench; bioreactor landfill; factor of safety; leachate recirculation; landfill stability.

1 INTRODUCTION

Bioreactor landfills utilize the leachate recirculation mechanism to increase moisture levels, thereby accelerating the biodegradation process and enhancing the stabilization rate of municipal solid waste (MSW). The concept of bioreactor landfills has attracted global interest due to their significant benefits, and they are recognized as an environmentally sustainable approach to waste management (Reddy et al., 2017; Avinash et al., 2023a). Leachate recirculation is facilitated through various leachate recirculation systems (LRS) such as horizontal trenches (HT), drainage blankets, and vertical wells (Reddy et al., 2020; Avinash and Mishra, 2023a). The injection of leachate through HT systems is a preferred choice in new landfills because these can be installed during active landfilling operations without disrupting landfill activities (Avinash et al., 2023b). Leachate injection near the slope has the potential to impact the stability of landfill slopes by leading to the development of excess pore water pressures (PWP). This phenomenon results in a reduction of effective stress, consequently decreasing the shear strength of waste. The failures attributed to excess PWP near

slopes resulting from inadequate leachate operations have been documented in previous studies (Koerner and Soong, 2000). USEPA (2007) recommends a setback distance of 15-30 meters to prevent leachate seepage from side slopes and to ensure the safety of the landfill against slope failure. Giri and Reddy (2014a) investigated the influence of waste anisotropy and heterogeneity under various injection pressures on moisture and PWP distribution within the landfill, as well as its effect on stability. Xu et al. (2012) investigated the impact of pressurized leachate injection on landfill stability under different operational strategies. These include variations in the permeability of MSW with depth, high injection pressures, low permeable cover within the landfill body, and clogging of the leachate extraction system. Based on previous studies, it is evident that the effect of PWP generated from the LRS significantly affects slope stability. Furthermore, limited research is available on the investigation of the setback location for injection in relation to injection pressures and the configuration of landfill slopes.

This study conducts a numerical modelling to investigate the influence of setback distance on the landfill stability. Further, the influence of variation in MSW properties with depth, side slope, and injection pressures were also investigated. The leachate recirculation was performed using a HT system. The optimum setback distance was proposed based on the observations of PWP distribution and its effect on landfill slope.

2 MODELLING

2.1 Landfill Geometry

A two-dimensional numerical analysis was conducted for a 50 m high bioreactor landfill with two landfill configurations (1V:4H, 1V:3H). The landfill model was assumed to be symmetric, and the MSW within the landfill cell was layered with a thickness of 5 m for all ten layers. The landfill widths for the two different slope configurations were 240 m and 190 m, respectively. It was assumed that the leachate collection and removal system (LCRS), which had a thickness of 0.3 m and comprised free-draining granular soil, would be situated at the base of the landfill. In this study, the leachate recirculation was simulated by using a HT of 1 m × 1 m and was assumed to be filled with gravel. The HT system was positioned at a height of one-third of the overall height measured from the landfill surface (Avinash and Mishra, 2023b). The setback distance of the LRS from the slope, which varied from 5 m – 50 m was installed in each numerical simulation.

2.2 Numerical Model

The numerical modelling of landfill stability and leachate infiltration was carried out using GeoStudio to observe the changes in landfill stability and PWP. The infiltration using transient analysis was carried out for a run time of five years in SEEP/W. The boundary conditions type was chosen as hydraulic for landfill modelling. Zero flux was assigned to the landfill bottom, side slope, and top surface to simulate the impermeable boundary. The leachate extraction from LCRS was simulated by using the zero-pressure head. In this study, the Morgenstern-Price method was employed for stability calculations because of its ability to satisfy both force and moment equilibrium conditions of the selected slip surface. Figure 1 shows the bioreactor landfill configuration with boundary conditions for a slope of 1V:3H.

2.3 Input Parameters

The landfilled waste considered for modelling was heterogeneous and anisotropic. The variation in hydraulic conductivity and unit weight with depth was modelled based on relationships proposed in earlier studies, which account for the increase in effective stress caused by overlying MSW layers in simulating the heterogeneous and anisotropic waste (HTAW) conditions (Zekkos et al., 2006; Reddy et al., 2009). These properties of MSW are shown in Figure 1 (Giri and Reddy, 2014b). Unsaturated properties considered for modelling were taken from the previous literature (Breitmeyer and Benson, 2011). The anisotropy of 10, shear strength parameters (friction angle 35°, cohesion 15 kPa), and the properties of the granular material used in LCRS were taken from the previous literature (Xu et al., 2012).

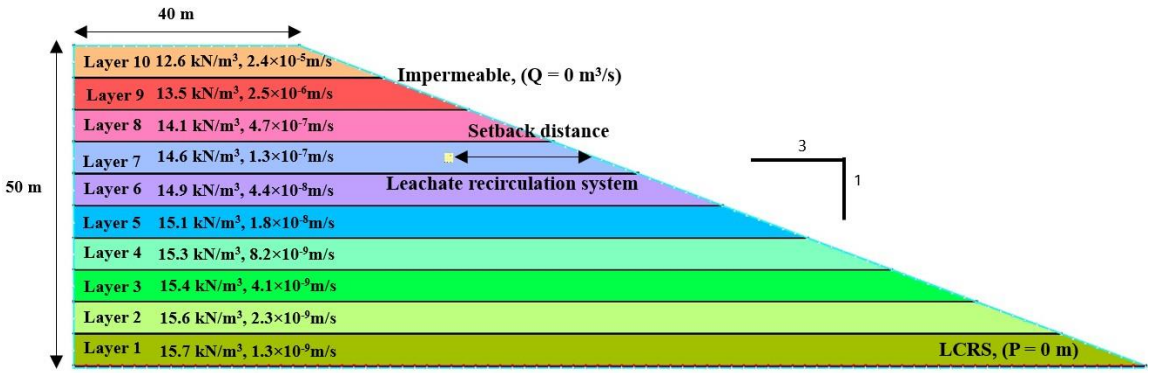

Figure 1. Bioreactor landfill configuration with HT under HTAW conditions.

The pressurized injection was simulated by using water pressure heads ranging from 5 m - 20 m, corresponding to pressures of 49-196 kPa. Table 1 shows the landfill geometry and parameters considered for modelling the leachate recirculation using the HT system.

Table 1. Details of numerical analysis conducted in this study.

Parameter	Value
Slope configuration	1V:3H, 1V:4H
Landfill height (m)	50
Landfill width (m)	190, 240
Setback distance	5-50 m with an interval of 5 m
Injection pressure (kPa)	49, 98, 147, and 196

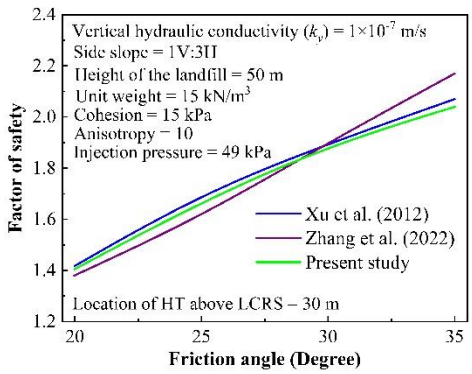

Figure 2. Comparison of FOS for various friction angles of the present study with previous literature.

3 RESULTS

3.1 Validation of Model

The landfill geometry of the numerical model was validated for slope stability under homogeneous anisotropic waste conditions. The leachate injection was conducted using the HT system with an injection pressure of 49 kPa over a 10-year period. The results of factor of safety (FOS) of the present study were compared with the previous studies as shown in Figure 2 (Xu et al., 2012; Zhang et al., 2022). The results were in good agreement with Xu et al. (2012) and a deviation of 6 % with Zhang et al. (2022) was observed due to the difference in computational software and analysis.

3.2 Pore Water Pressure

The monitoring of PWP is an important aspect of bioreactor landfill operations. The magnitude of the injecting pressure varies depending on the type and location of the injecting system. Figure 3 shows the contour of PWP distribution resulting from leachate injection using the HT system.

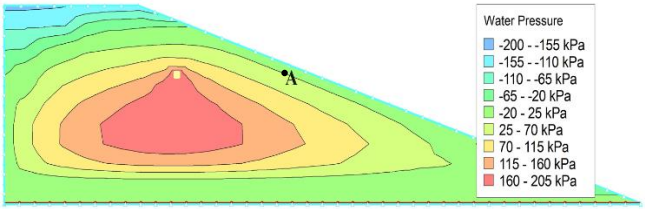

Figure 3. Results of PWP distribution contours due to leachate recirculation.

The observations of PWP were taken at point A, as shown in Figure 3, which is located 5 m from the side slope towards the injection system for all the cases. This location is chosen to monitor the distribution of PWP near the slope in order to safeguard landfill stability and manage lateral seepage effectively for bioreactor landfill operations through pressure control. The maximum PWP was observed at point *A* for the low setback distance of 5 m from the slope and tends to decrease as the setback distance increases. Figure 4 shows the distribution of PWP with time for the different setback distances (10 m, 20 m, 30 m, and 40 m) considered in this study. The PWP distribution observations were found to be nearly the same for both slope configurations. The decrease in PWP as we move away from the injected location is because of the anisotropic nature of the MSW considered in this

study. It was observed that over 85% of the PWP was dissipated upon reaching point *A* for setback distances greater than or equal to 30 m.

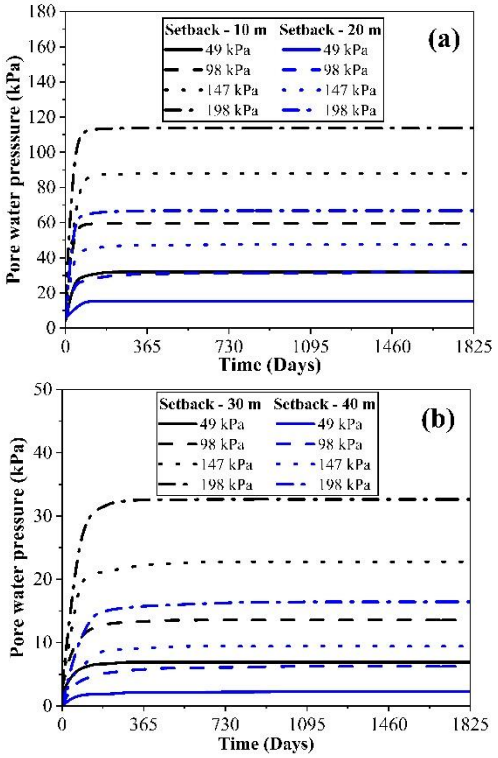

Figure 4. Comparison of PWP with time for various setback distances (a) 10 m and 20 m (b) 30 m and 40 m.

3.3 Slope Stability

Table 2 demonstrates the effect of leachate injection through the HT system on landfill stability by varying the setback distances for all the modelled cases. Figure 5 shows the variation in FOS over time for setback distances of 30 m and 40 m, as they undergo varying injection pressures for various landfill slope configurations. The variation in the stability of landfills is due to changes in the distribution of PWP. The results of this study regarding leachate injection in bioreactor landfills are specifically relevant when the stability design adheres to the safety limit FOS≥1.5, as suggested by Giri and Reddy (2014c) for executing safe landfill operations. The FOS observations in Table 2 indicate that setback distances of 25 m or less are unsuitable for high injection pressures of 147 and 196 kPa, primarily due to the influence of PWP on the slope. However, this influence of PWP decreases with an increase in setback above 25 m, and the recommended safety limit is achieved for any injecting pressure in both slope configurations. The FOS exhibited a notable increase from 0.5 to 1.9, when the setback location was adjusted from 5 m – 50 m, while maintaining an injecting pressure of 196 kPa.

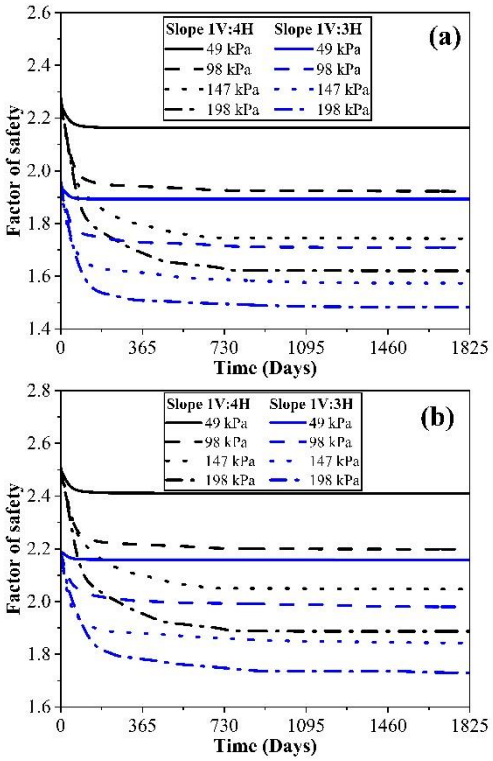

Figure 5. Factor of safety with time (a) setback 30 m (b) setback 40 m.

Therefore, the setback location of injection system proves to be a critical factor in regulating the FOS. The outcomes of the present study suggest that setback distances of 30 m – 40 m are sufficient to carry leachate recirculation in landfill operations.

Table 2. Comparison of FOS for different landfill slope configurations.

Set-back (m)	1V:4H				1V:3H			
	Injection Pressure (kPa)							
	49	98	147	196	49	98	147	196
5	1.3	1.2	0.9	0.6	1.2	1.0	0.7	0.5
10	1.5	1.4	1.0	0.8	1.4	1.2	0.9	0.7
15	1.7	1.5	1.2	1.0	1.5	1.3	1.0	0.9
20	1.9	1.7	1.4	1.3	1.6	1.5	1.2	1.1
25	2.0	1.8	1.6	1.5	1.8	1.6	1.4	1.3
30	2.2	1.9	1.7	1.6	1.9	1.7	1.6	1.5
35	2.3	2.1	1.9	1.8	2.1	1.9	1.7	1.6
40	2.4	2.2	2.1	1.9	2.2	2.0	1.8	1.7
45	2.5	2.3	2.2	2.0	2.3	2.0	2.0	1.8
50	2.6	2.3	2.2	2.0	2.3	2.1	2.0	1.9

4 CONCLUSIONS

In the current study, a numerical modelling was carried out to investigate the impact of PWP on landfill slope stability. The analysis also includes the variations in the side slope configuration and injecting pressures. The conclusions of the present study are as follows.

The PWP in the observed point *A* decreases as the setback distance increases, significantly improving the landfill stability. Furthermore, the slope configuration plays a crucial role in stability, and it is not recommended to provide slopes steeper than 1V:3H. High injecting pressures should not be used for setback distances less than 25 m in leachate recirculation. However, the results of FOS reveal that changing the setback location from 5 m to 50 m enhances the stability of the landfill by 25-75% in relation to the recommended limit, and the required performance is achieved with setbacks greater than or equal to 30 m for all injecting pressures under leachate recirculation. Therefore, this study recommends an optimum setback of 30 m - 40 m for leachate recirculation, making it suitable even for high leachate injecting pressures in conjunction with steep slopes of 1V:3H.

REFERENCES

Avinash, L. S. Mishra, A. and Ojha, C. S. P. (2023a) Effects of Leachate Recirculation using Drainage Blanket and Horizontal Trenches on Slope Stability of Bioreactor Landfills. In Proceedings of the 8th International Congress on Environmental Geotechnics, Chania, Greece, pp 65-74. https://doi.org/10.53243/ICEG2023-330.

Avinash, L. S. Mishra, A. Kami, V. B. and Ojha, C. S. P. (2023b). A Critical Appraisal of Leachate Recirculation Systems in Bioreactor Landfills. Journal of Hazardous, Toxic, and Radioactive Waste, 27(3), 03123002. https://doi.org/10.1061/JHTRBP.HZENG-1186.

Avinash, L. S. and Mishra, A. (2023a). Slope Stability Analysis of Bioreactor Landfills with Combined Horizontal Trench and Vertical Well Systems. In Proceedings of the Indian Geotechnical Conference 2023: IGC-2023, Spinger Nature.

Avinash, L. S. and Mishra, A. (2023b). Effects of Leachate Recirculation Systems on Slope Stability of Bioreactor Landfills. Geo-Congress 2023, 141–151. https://doi.org/10.1061/9780784484661.015.

Breitmeyer, R. J. and Benson, C. H. (2011). Measurement of Unsaturated Hydraulic Properties of Municipal Solid Waste. Geo-Frontiers 2011, 1433–1442. https://doi.org/10.1061/41165(397)147.

Giri, R. K. and Reddy, K. R. (2014a). Slope stability of bioreactor landfills during leachate injection: Effects of heterogeneous and anisotropic municipal solid waste conditions. Waste Management and Research, 32(3), 186–197. https://doi.org/10.1177/0734242X14522492.

Giri, R. K. and Reddy, K. R. (2014b). Slope stability of bioreactor landfills during leachate injection: Effects of unsaturated hydraulic properties of municipal solid waste. International Journal of Geotechnical Engineering, 8(2), 144–156. https://doi.org/10.1179/1939787913Y.0000000013.

Giri, R. K. and Reddy, K. R. (2014c). Design Charts for Selecting Minimum Setback Distance from Side Slope to Horizontal Trench System in Bioreactor Landfills. Geotechnical and Geological Engineering, 32(4), 1017–1027. https://doi.org/10.1007/s10706-014-9777-0.

Koerner, R. M. & Soong, T.-Y. (2000). Leachate in landfills: the stability issues. Geotextiles and Geomembranes, 18(5), 293–309. https://doi.org/10.1016/S0266-1144(99)00034-5.

Reddy, K. R. Hettiarachchi, H. Parakalla, N. Gangathulasi, J. Bogner, J. and Lagier, T. (2009). Hydraulic Conductivity of MSW in Landfills. Journal of Environmental Engineering, 135(8), 677–683. https://doi.org/10.1061/(ASCE)EE.1943-7870.0000031.

Reddy, K. R. Kulkarni, H. S. Giri, R. K. and Khire, M. V. (2017). Horizontal trench system effects on leachate recirculation in bioreactor landfills. Geomechanics and Geoengineering, 12(2), 115–136. https://doi.org/10.1080/17486025.2016.1181793.

Reddy, K. R. Kumar, G. and Kulkarni, H. S. (2020). Two-Phase Flow Modeling to Evaluate Effectiveness of Different Leachate Injection Systems for Bioreactor Landfills. Environmental Modeling & Assessment, 25(1), 115–128. https://doi.org/10.1007/s10666-019-09663-z.

USEPA. (2007). Bioreactor Performance. EPA530-R-07-007.

Xu, Q. Tolaymat, T. and Townsend, T. G. (2012). Impact of Pressurized Liquids Addition on Landfill Slope Stability. Journal of Geotechnical and Geoenvironmental Engineering, 138(4), 472–480. https://doi.org/10.1061/(ASCE)GT.1943-5606.0000609.

Zekkos, D. Bray, J. D. Kavazanjian, E. Matasovic, N. Rathje, E. M. Riemer, M. F. and Stokoe, K. H. (2006). Unit Weight of Municipal Solid Waste. Journal of Geotechnical and Geoenvironmental Engineering, 132(10), 1250–1261. https://doi.org/10.1061/(ASCE)1090-0241(2006)132:10(1250).

Zhang, P. Chai, J. Cao, J. Dang, M. Geng, K. Qin, Y. and Xu, Z. (2022). Study of leachate recharge model and vertical well design method for bioreactor landfills. Environmental Science and Pollution Research, 30(12), 35170–35188. https://doi.org/10.1007/s11356-022-24622-0.

Proceedings of the XVIII ECSMGE 2024
GEOTECHNICAL ENGINEERING CHALLENGES
TO MEET CURRENT AND EMERGING NEEDS OF SOCIETY
© 2024 the Authors
ISBN 978-1-032-54816-6
DOI 10.1201/9781003431749-544
Open Access: www.taylorfrancis.com, CC BY-NC-ND 4.0 license

ECSMGE 24
XVIII EUROPEAN CONFERENCE ON SOIL MECHANICS AND GEOTECHNICAL ENGINEERING

Effect of saline water on the strength behavior of beach sand from northeastern Brazil coastline

Effet de l'eau saline sur la résistance du sable de plage du littoral nord-est du Brésil

G.F. Azevedo*
Universidade de Brasília, Brasília/DF, Brasil

A.S. Moura, F.C.S. Filho, R.F. Leme
Universidade Federal do Ceará, Fortaleza/CE, Brasil

D.R.L. Gonçalves, R.P. Cunha
Universidade de Brasília, Brasília/DF, Brasil

**gabrielaazevedotn@hotmail.com*

ABSTRACT: This study addresses the effect of saline water on the strength of Pacheco Beach sand, located on the northeast coast of Brazil. Although several studies in the literature deal with the influence of saline water on the behavior of soils in coastal areas, information regarding the behavior of Brazilian coastal sands is scarce, justifying the need for this current research. The study is particularly important for maritime works, such as foundations for offshore wind towers in new exploration potential areas like the northeast coast of Brazil. For this purpose, two samples were collected and subjected to characterization tests and direct shear tests at normal stresses of 50, 100, and 200 kPa. The specimens were saturated with distilled water and saline water for the loose state. The results demonstrate that the presence of salts in water significantly influences the shear strength of sands, as well as the values of friction angles, indicating alterations in the mechanical properties of these soils. In direct shear tests, saturating a sample in saline water resulted in a 6% increase in friction angles compared to samples saturated in distilled water.

RÉSUMÉ: Cette étude aborde l'effet de l'eau salée sur la résistance du sable de la plage de Pacheco, située sur la côte nord-est du Brésil. Bien que plusieurs études dans la littérature traitent de l'influence de l'eau salée sur le comportement des sols dans les zones côtières, les informations concernant le comportement des sables côtiers brésiliens sont rares, justifiant ainsi la nécessité de cette recherche actuelle. L'étude est particulièrement importante pour les travaux maritimes, tels que les fondations des tours éoliennes en mer dans de nouvelles zones à fort potentiel d'exploration comme la côte nord-est du Brésil. Dans ce but, deux échantillons ont été prélevés et soumis à des tests de caractérisation et des tests de cisaillement direct à des contraintes normales de 50, 100 et 200 kPa. Les spécimens ont été saturés d'eau distillée et d'eau salée pour l'état lâche. Les résultats démontrent que la présence de sels dans l'eau influence significativement la résistance au cisaillement des sables, ainsi que les valeurs des angles de frottement, indiquant des altérations dans les propriétés mécaniques de ces sols. Dans les essais de cisaillement direct, la saturation d'un échantillon dans de l'eau salée a entraîné une augmentation de 6% des angles de frottement par rapport aux échantillons saturés dans de l'eau distillée.

Keywords: Coastal soils; saline water; direct shear tests; salinity influence.

1 INTRODUCTION

Knowledge about the variables that can affect soil strength plays an extremely important role in geotechnical engineering. One of the key properties governing structure stability is the soil's shear strength, influenced by several factors, including soil genesis, particle distribution and shape, degree of preconsolidation, saturation level, as well as the nature of the fluid present in the subsurface.

It's worth noting that the water saturation level of soils is subject to constant changes due to seasonal activities, climate variations, and numerous human interventions that can alter the physical, chemical, and mechanical properties of the soil. Studies indicate that the solution's pH strongly influences the geotechnical characteristics of the soil (Osuolale et al., 2012; Sunil, et al., 2006). Rahman and Nahar (2015) demonstrated that the shear strength of sandy soil increases with an increase in the soil's pH value. Moreover, the type and

concentration of the solution affect the soil's shear properties (Naeini and Jahanfar, 2011).

As noted by several studies, the presence of saline solution in the soil increases shear strength (Ajalloeian et al., 2013; Elsawy and Lakhouit, 2020; Geng et al., 2022) and frictional resistance (Geng et al., 2022; Taha and Fall, 2014). However, other studies indicate that this shear strength increases to a certain point and then decreases afterward, as highlighted by Naeini and Jahanfar (2011) and Wilson and Vasudevan (2021).

Regarding the effect of seawater on the consistency limits of clayey soils, there are discrepancies in the literature: Mahasneh (2004) observed an increase in liquid and plastic limits with the use of saline water. However, according to Nguyen et al. (2019), the liquid and plastic limits decrease when the soil is submerged in seawater. Arasan and Yetimoglu (2008) state that high saline concentrations can either reduce or increase the plastic limit depending on the clay classification.

Concerning water salinity, numerous studies analyze the influence of saline solution on soil (Emami Azadi, 2008; Mahasneh, 2004; Tiwari et al., 2005; Yukselen-Aksoy et al., 2008). However, in Brazil, particularly in coastal regions, there is a scarcity of studies addressing this issue, highlighting the need for additional research to fill this knowledge gap.

Therefore, it's observed that the presence of salinity significantly influences the resistance properties and behavior of soils. This factor should be further analyzed, especially concerning coastal, maritime, and offshore structures, which are directly subjected to saline water. Even in these cases, such as in maritime construction projects during the foundation design phase, shear tests are commonly conducted only with distilled water, which may not accurately represent the soil's actual behavior. In this regard, this study investigates the resistance of coastal sand under the influence of saline water compared to distilled water through direct shear tests.

2 MATERIALS AND METHODS

The studied sands were collected from the northeastern coast of Brazil, specifically at Pacheco Beach, in the municipality of Caucaia, Ceará. The tests were conducted on disturbed samples, and for the direct shear tests, the specimens were reconstituted. Initially, characterization tests were performed, determining the maximum and minimum void ratios, X-ray fluorescence, and determining the pH of the saline water (collected from the sea at the same location as the soil collection). It is important to note that distilled water is free from salts and any impurities, with a neutral pH (close to 7), while seawater is naturally saline and composed of various salts.

To study the influence of water salinity, 12 direct shear tests were conducted on two samples of Pacheco soil, PCH1 and PCH2, in their loose state, that is, with void proportions close to the maximum value. Six tests used distilled water, and six used saline water, under normal tensions of 50, 100, and 200 kPa. Additionally, three direct shear tests were performed on PCH2 samples saturated with saline water in the compacted state. In this procedure, the soil sample was previously saturated in either saline (S) or distilled (D) water before being subjected to shear stress under a determined rupture plane, with controlled normal tension. The rupture speed was adjusted to 0.2 mm/min to ensure effective drainage during the shear test.

3 RESULTS AND DISCUSSIONS

3.1 Soil properties

Samples PCH1 and PCH2 are classified as well-graded sand (SW) and well-graded sand with silt (SW-SM), respectively, according to the Unified Soil Classification System (USCS). The particle size distribution curve are presented in Figure 1. The elemental composition of the samples obtained from the X-ray fluorescence test can be verified in Table 1, and the geotechnical characterization is presented in Table 2. The pH of the collected seawater showed a more alkaline content with a value of 7.48.

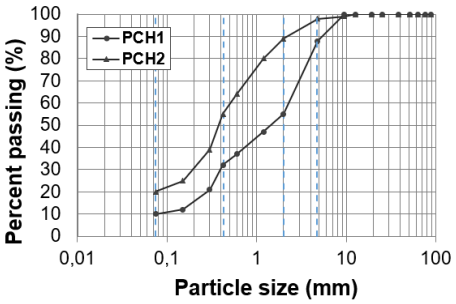

Figure 1. Grain size distribution curves of Pacheco sand (PCH1, PCH2).

3.2 Direct shear test

3.2.1 Saline water effect

In Figures 2(a) and 2(b), the stress-strain curves of shear stress versus horizontal displacement of samples (PCH1 and PCH2, respectively) saturated with saline water and distilled water are compared. It can be observed that sample saturation with saline water resulted in higher shear stresses for both samples and

studied stress levels, supporting the results presented by Tiwari et al. (2005).

Table 1. Mineralogical composition of Pacheco Sands (samples PCH1 and PCH2).

Composition (%)	PCH1	PCH2
Al_2O_3 - Aluminum Oxide	14.89	15.51
SiO_2 – Total Silica	52.55	52.32
dFe_2O_3 – Oxide of iron	2.99	3.78
K_2O - Potash	2.96	3.07
Rb_2O - Rubidium Oxide	1.64	-
SrO - Strontium Oxide	1.12	-
Ta_2O_5 - Tantalum Pentoxide	-	0.96
CaO - Lime	0.89	0.85
TiO_2 – Oxide of Titanium	0.78	0.85
Cl - Chlorine	0.54	0.36
P_2O_5 - Phosphorus Pentoxide	0.4	0.42
ZrO_2 - Zirconium Dioxide	0.17	0.15
MoO_3 - Molybdenum Trioxide	0.21	-

Table 2. Geotechnical properties (PCH1 and PCH2).

		PCH1	PCH2
Grain density (G_s)	g/cm³	2.61	2.64
Maximun void ratio ($e_{máx}$)	-	0.78	0.81
Minimun void ratio ($e_{mín}$)	-	0.53	0.52
Specific weigth ($\rho_{mín}$)	g/cm³	1.51	1.51
Specific weigth ($\rho_{máx}$)	g/cm³	1.69	1.8

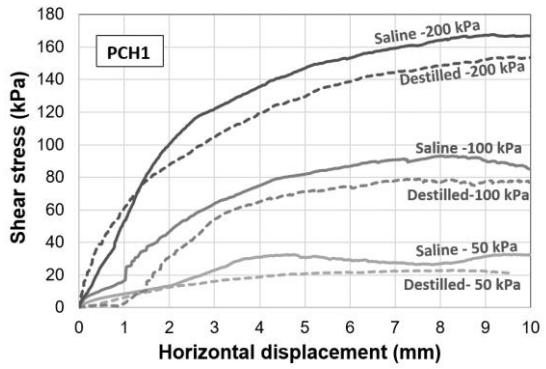

(a)

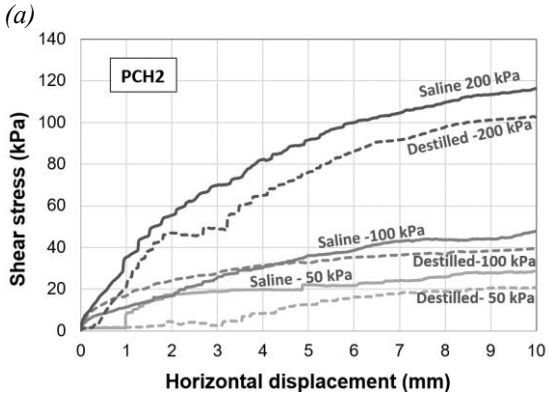

(b)

Figure 2. Variation of the shear strength versus horizontal displacement, of samples saturated with saline water and distilled water in the loose state (a) PCH1 (b) PCH2.

In the analysis of the rupture envelopes presented in Figure 3, it is observed that there was no significant variation in the friction angle for the PCH1 sample with the use of saline water. However, for the PCH2 sample saturated with saline water, there was an increase of 6% in the friction angle compared to saturation in distilled water, with values of 31° and 29°, respectively. These results indicate a possible influence of salinity on the shear strength of the soil, which is especially relevant in coastal and maritime works. Furthermore, it is important to highlight that this analysis refers to low normal voltages. It is also observed an increase in the difference in shear stresses between samples saturated with saline water and distilled water as the normal stress increases. Therefore, it is necessary to carry out studies at higher normal stresses to confirm this trend and to evaluate its impact on more sensitive geotechnical applications.

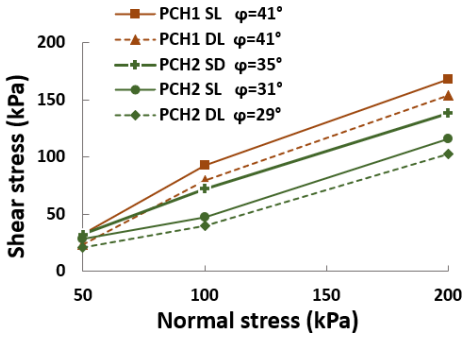

Figure 3. Rupture envelope of samples PCH1 and PCH2 saturated in saline water (S) and distilled water (D) in the loose (L) and dense (D) states.

3.2.2 Saline water effect on relative compaction

In Figures 4(a) and 4(b), the results of the direct shear test for sample PCH2 saturated in saline water, in loose and compact states, can be observed. It can be seen that for the normal stress of 200 kPa, both the dense and loose states behaved similarly, showing a reduction in vertical displacement. As expected, the most compacted soil exhibited a 13% increase in friction angle compared to the loose soil (Figure 3), with 35° for the dense state and 31° for the loose state.

4 CONCLUSIONS

This study addressed the impact of water salinity on the shear strength properties of the soil, based on direct shear tests. The results revealed an increase in the friction angle of samples saturated in saline water compared to distilled water. Specifically, one of the samples showed a 6% increase in the friction angle when saturated in saline water.

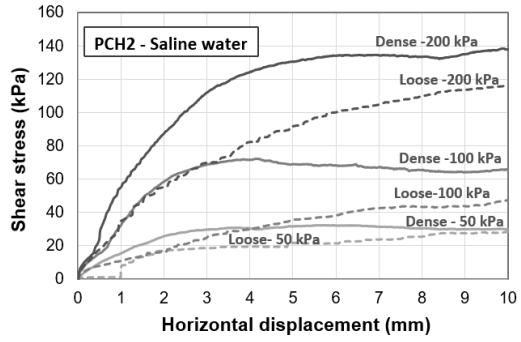

(a)

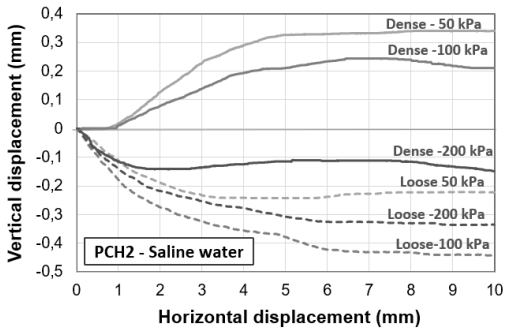

(b)

Figure 4. Sample PCH2 saturated in saline water in loose and dense states (a) Variation of shear strength versus horizontal displacement, (b) Variation of vertical displacement versus horizontal displacement.

Furthermore, the results point to a greater influence of water salinity at higher normal stresses, which is evidenced by the observed increase in the difference between the shear stresses of samples saturated in saline water and distilled water as the normal stress increases. It is of fundamental importance, however, to conduct more studies under higher normal stress conditions to confirm this trend, especially for coastal and marine geotechnical works.

Thus, it is necessary to carefully consider water salinity in soil behavior, especially when designing geotechnical structures exposed to salt water, aiming to guarantee the safety and durability of these structures in marine environments.

ACKNOWLEDGEMENTS

This study received financial support from the Coordenação de Aperfeiçoamento de Pessoal de Nível Superior – Brasil (CAPES) – through Finance Code 001 – and the Conselho Nacional de Desenvolvimento Científico e Tecnológico (CNPq). The authors express their sincere appreciation for the generous funding provided by PETROBRAS. Special thanks are also extended to the postgraduate program in the DEHA department at Universidade Federal do Ceará (UFC) for their invaluable support.

REFERENCES

Ajalloeian, R.; Mansouri, H.; Sadeghpour, A. H. (2013) Effect of saline water on geotechnical properties of fine-grained soil. Electronic Journal of Geotechnical Engineering, v. 18, p. 1419–1435.

Arasan, S.; Yetimoglu, T. (2008) Effect of inorganic salt solutions on the consistency limits of two clays. Turkish Journal of Engineering and Environmental Sciences.

Elsawy, M. B. D.; Lakhouit, A. (2020) A review on the impact of salinity on foundation soil of coastal infrastructures and its implications to north of Red Sea coastal constructions. Arabian Journal of Geosciences, v. 13, n. 13, p. 555. https://doi.org/10.1007/s12517-020-05601-6.

Emami Azadi, M. R. (2008) The effects of Urmieh Lake salt water on the proctor compaction and CBR test results of well graded gravel-sand mixed with clay (GSCW) soil samples.

Geng, W.; Han, W.; Yin, J.; Lu, Z. (2022) Salinity effects on the strength and morphological indices of soft marine clay. Scientific Reports. https://doi.org/10.1038/s41598-022-22627-w.

Mahasneh, B. (2004) Dead Sea water as a soil improvement agent.

Naeini, S.; Jahanfar, A. (2011) Effect of salt solution and plasticity index on undrain shear strength of clays. World Academy of Science, Engineering and Technology.

Nguyen, N. T.; Nguyen, D. T.; Nguyen, P. V. (2019) The effects of salt contents on the geotechnical properties of some soft soils in the coastal area of Vietnam. v. 60.

Osuolale, O. M.; Falola, O. D.; Ayoola, M. A. (2012) Effect of PH on Geotechnical Properties of Laterite Soil Used in Highway Pavement Construction. Civil and Environmental Research, v. 2, n. 10, p. 23. https://doi.org/10.1016/j.enggeo.2005.09.039.

Rahman, M.; Nahar, T. T. (2015) Effect of pH on Shear Strength Behavior of Granular Soil. Recent Trends in Civil Engineering & Technology.

Sunil, B. M.; Nayak, S.; Shrihari, S. (2006) Effect of pH on the geotechnical properties of laterite. Engineering Geology, v. 85, n. 1–2, p. 197–203. https://doi.org/10.1016/j.enggeo.2005.09.039.

Taha, A.; Fall, M. (2014) Shear behavior of sensitive marine clay–steel interfaces. Acta Geotechnica, v. 9, n. 6. https://doi.org/10.1007/s11440-014-0321-4.

Tiwari, B.; Tuladhar, G. R.; Marui, H. (2005) Variation in Residual Shear Strength of the Soil with the Salinity of Pore Fluid. Journal of Geotechnical and Geoenvironmental Engineering, v. 131, n. 12.

Wilson, A.; Vasudevan, A. K. (2021) Strength and Stiffness of Soils Under Salinity Conditions. Em: Patel, S.; Solanki, C. H.; Reddy, K. R.; Shukla, S. K. (Eds.). Proceedings of the Indian Geotechnical Conference 2019. Lecture Notes in Civil Engineering. Singapore: Springer Singapore.

Yukselen-Aksoy, Y.; Kaya, A.; Oren, A. (2008) Seawater effect on consistency limits and compressibility characteristics of clays. Engineering Geology. https://doi.org/10.1016/j.enggeo.2008.07.005.

Proceedings of the XVIII ECSMGE 2024
GEOTECHNICAL ENGINEERING CHALLENGES
TO MEET CURRENT AND EMERGING NEEDS OF SOCIETY
© 2024 the Authors
ISBN 978-1-032-54816-6
DOI 10.1201/9781003431749-545
Open Access: www.taylorfrancis.com, CC BY-NC-ND 4.0 license

ECSMGE 24
XVIII EUROPEAN CONFERENCE ON SOIL MECHANICS AND GEOTECHNICAL ENGINEERING

Experimental assessment of adsorbed water for geomechanical applications

Évaluation expérimentale de l'eau adsorbée pour les applications géomécaniques

S. Babiy*, A. Tuttolomondo, L. Laloui
Laboratory of Soil Mechanics (LMS), Ecole Polytechnique Fédérale de Lausanne (EPFL), Lausanne, Switzerland

**svetlana.babiy@epfl.ch*

ABSTRACT: One of the major factors controlling behavior of clays is their chemical structure. Active clays in particular are notable for their high-swelling and hydro-isolating properties, which make them valuable in various geotechnical applications, including deep repositories for nuclear waste and landfills. The properties mentioned above arise from the water that is physically attracted to clay particles. This water, often described as "adsorbed" or "physisorbed," can exhibit an ordered structure, greater density, and a distinct dielectric constant compared to water in its bulk liquid form. The attracted water is influenced – among other factors – by salinity of the pore water, degree of saturation, temperature of the waste repositories. The mechanical response of the material, like swelling upon hydration, can be predicted by advanced modelling approach accounting for the physical-chemical interactions between water and clay particles. Such complex multi-physical predictions require precise microstructural investigations, which are critical for understanding the active clays behavior. This work proposes a novel methodology for quantitatively assessing the adsorbed water in active clays using Thermogravimetric Analysis (TGA). Following the proposed methodology, new insights into the types and amounts of water retained at various saturation levels of MX-80 bentonite are provided. These insights can be integrated into mechanical prediction models to enhance their accuracy.

RÉSUMÉ: La structure chimique des argiles est un facteur clé dans la compréhension de leur comportement. Les argiles actives se distinguent par leur capacité à gonfler et à isoler l'eau, ce qui les rend utiles dans diverses applications géotechniques, notamment le stockage souterrain des déchets radioactifs et autre projets d'enfouissement. Ces propriétés sont dues à la forte interaction et attraction entre l'eau et les particules d'argile. Cette eau, qualifiée d'"adsorbée" ou de "physio-absorbée ", possède des caractéristiques différentes de l'eau libre, notamment une structure ordonnée et une densité plus élevée. Les propriétés de l'eau attirée sont notamment influencées par la salinité, le degré de saturation et la température des dépôts de déchets. Une approche de modélisation avancée prenant en compte les interactions physico-chimiques entre l'eau et les particules d'argile permet de prédire le comportement mécanique du matériau. Le développement d'un modèle multi-physique complexe nécessite une étude poussée de la microstructure des argiles, essentielle à la compréhension du comportement des argiles actives. Cette étude propose une nouvelle méthodologie utilisant l'analyse thermogravimétrique (TGA) pour quantifier l'eau adsorbée dans les argiles actives. Elle permet notamment une meilleure quantification de l'eau retenue dans la bentonite MX-80 à différents degrés de saturation, ainsi qu'une caractérisation du type d'eau. Ces informations peuvent être intégrées dans les modèles de prédiction mécanique pour améliorer leur précision.

Keywords: Bentonite; expansive clay; adsorbed water; thermogravimetry.

1 INTRODUCTION

Bentonite is a widely used material in waste disposal, (Laine, Karttunen, 2010). Its favorable properties for waste disposal include swelling and reduced hydraulic permeability upon wetting, preventing the migration of contaminants from waste disposals. Bentonite acts as a "seal" for nuclear waste (Pusch et al. 1998; Laine, Karttunen, 2010).

Presence of salts in the environment affects physicochemical interactions between clay particles and bulk water, leading to changes in hydro-mechanical behavior, such as decreased swelling and increased permeability (Slade, 1991; Likos, 2004; Tester et al, 2016). However, those interactions are not fully understood (Wang et al, 2020).

Understanding water adsorption in clay is vital for assessing changes in mechanical properties. Existing modeling approaches allow predicting hydration isotherms of bentonite by combining different mechanisms connected to types of water adsorbed

(e.g., Wang et al, 2022). Existing experimental assessments of adsorbed water are limited to platelets spacing assessment by X-Ray Powder Diffraction (XRPD) and it is assumed the space between platelets is filled with water. Moreover, XRPD requires fine powders and is unable to detect amorphous structure (such as water or randomly located surface cations) (Cockcroft and Fitch, 2008).

Montmorillonite, a key mineral in bentonite, attracts water in two forms: tightly bonded crystalline hydrates and weakly bonded osmotic hydrates. Mercury Intrusion Porosimetry (MIP) is unable to capture crystalline hydration (e.g. Norrish, 1962), occurring at humidities above 25% (Cases et al, 1992). Additionally, at low humidity levels, most of the surface area remains vacant from water layers.

Thermogravimetric Analysis (TGA) is a technique that allows to obtain the change of mass of a small specimen as a function of temperature (dynamic heating) or time (Tajeddine et al, 2015). Each temperature level corresponds to the energy needed for sublimation/evaporation of certain molecules in the sample (Vieillard, Tajeddine L, 2015). Thus, higher-level bonds removal would be visible at a higher temperature.

In case of clays, similar processes were distinguished to take place in kaolinite, montmorillonite, saponite and other clay minerals during heating from 30°C to 950°C: first step – evaporation of adsorbed water; second one – dehydroxylation – the release of structural OH in the form of water molecules, third – silica phase transformation. It is generally assumed that by the start of dehydroxylation no adsorbed water is left (Vieillard et al, 2016; Saadatkhah et al, 2020, Zeng et al, 2022), however, that assumption remains not proved. Additionally, there is no consensus between authors on the temperature levels when all adsorbed water is removed.

Discrepancies between water retention mechanisms in literature require development of new experimental tools capable of detecting water-clay particle interactions at the nanoscale across different chemo-hydro-mechanical states. These tools are essential for later implementation into accurate modeling approaches.

In the present contribution, a new methodology for quantifying the different types of water retained by active clays is proposed. The proposed methodology involves using thermogravimetric analysis (TGA) on active clay specimens at different hydration stages, as well as using TGA on water samples having the chemical composition of the active clay specimens of interest.

2 MATERIALS AND METHODS

2.1 Tested material

Bentonite MX-80 mixture was obtained by mixing the grains of fractions up to 4 mm with Fuller granulometry distribution. Smectite content of the material is 85%, Specific Surface Area (SSA) is 523m^2/g, specific gravity 2.74 (Seiphoori et al, 2014). Liquid and plastic limits are 544% and 110% respectively. Hygroscopic water content of the resulting mixture under laboratory conditions (imposed total suction 140 MPa, T=25°C) is 5.9%, dry density – 1.3 Mg/m^3.

2.2 Methodology

The proposed methodology involves, after an initial specimen preparation phase, performing TGA on clay and water samples (using the same heating programme for all samples). A comparison of the temperature-water content curves of the clay specimens and of the water specimens reveals the temperature ranges required to remove a certain type of retained water and allows the corresponding water content to be quantified.

2.2.1 Hydration procedure

Bentonite was placed into 3 “Microcells” (cells made of brass able to create constant volume conditions with small openings) for confined hydration in desiccators with the imposed total suction values of 1, 26, 59 MPa (D, C, B states on Figure 1a.) Total suction of bentonite was measured by WP4C dew point chilled-mirror potentiometer (Leong et al, 2003). Total suction value of 1 MPa was measured on fully saturated bentonite (saturation was performed in Microcell in a chamber with water pressure 2.5 MPa for 2 days until no change in water volume in the pump was observed).

2.2.2 Thermogravimetric analysis

Experimental part of TGA consists of 2 sub-parts: testing of bentonite samples and of distilled water (Figure 1b).

Bentonite samples, taken immediately after opening microcells, are put in ceramic crucibles in the heating chamber of a Perkin Elmer TGA 4000 apparatus (Figure 1c). The following heating (for all heating steps the rate is 10°C/min) is adopted: (i) isothermal step for 1 min at 30°C for equilibration; (ii) heating from 30 to 80°C; (iii) isothermal step for 15 min at 80°C; (iv) heating from 80 to 950°C; (v) isothermal step 1 min at 950°C. Bentonite samples included also those oven-dried (105°C) for more than 1 month to ensure the evaporation of all water in the

sample. These long-dried samples are taken as reference state later in the analysis.

Water samples are put into crucibles in a form of a drop using syringe. The initial mass varied from 2mg to 21mg (Figure 1d). The following heating program is adopted: (a) isothermal step for 1 min at 30°C; (b) heating from 30 to 80°C; (c) isothermal step at 80°C; (d) heating from 80 to 150°C.

2.2.3 Accuracy of measurements

The Perkin Elmer TGA 4000 apparatus makes measurements with accuracy of the balance 0.01% (for most of samples 0.005mg), temperature accuracy 0.8°C.

Additionally, the influence of total mass of sample and granulometry on accuracy was measured. Mass of samples influences the first part of the normalized curves (30...450°C) with coefficient of variation 0.53% (standard deviation 0.57%). Granulometry of the sample influences predominantly the part between 600 and 800°C with coefficient of variation 0.42%, standard deviation 0.4%.

2.3 Results analysis

The experimental results are analyzed implementing the following procedure: (i) normalization of all bentonite TGA curves with respect to the final mass; (ii) combination of water evaporation curve with the long-dried sample TGA curve (Figure 1e), representing the change of mass of bentonite without adsorption phenomena; (iii) difference between the actual sample with adsorbed water and the modelled curve. The combined curve is modelled in a way that it has the same water content as the samples in hydration path (Figure 1a), in this way, the only difference between actual and modelled curve is the mass of water bonded to clay platelets. That mass is expressed as the mass of water per unit mass of dry clay on Figure 1f (the normalisation changed to initial mass for interpretation of results).

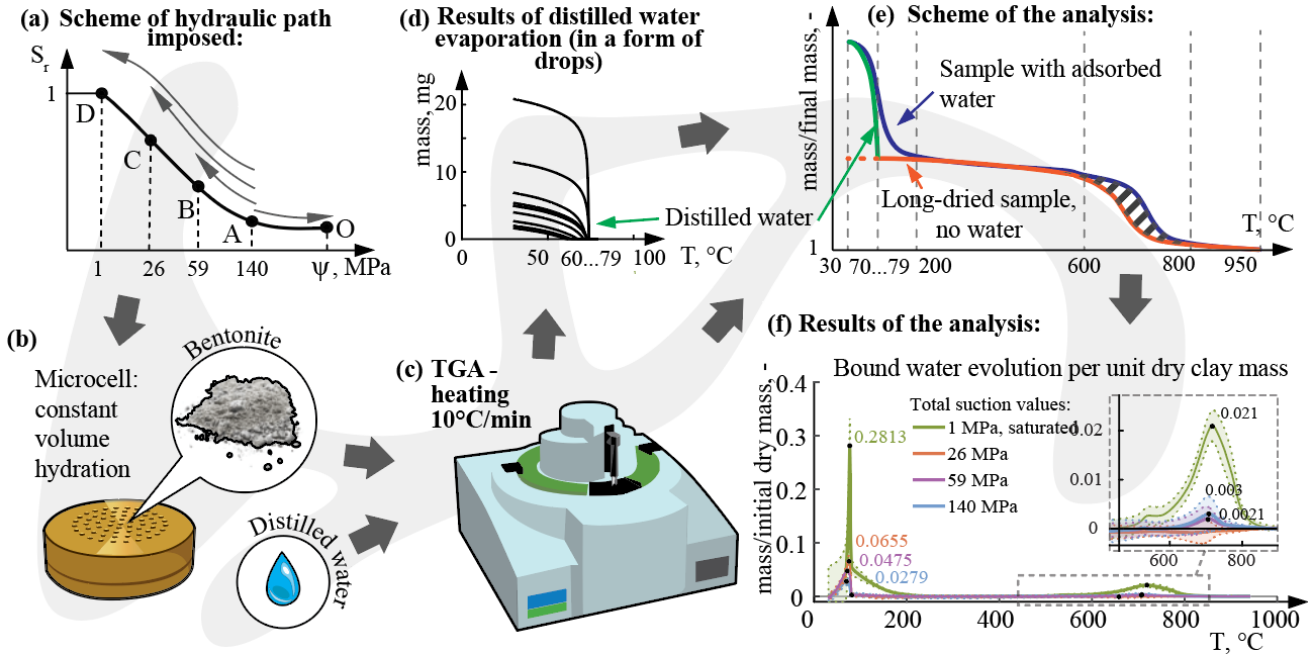

Figure 1. Methodology and results of the present work.

3 RESULTS AND DISCUSSIONS

Figure 1f represents the results of presented methodology. Two main regions could be identified: (i) 30...200°C with sharp peaks at around 80°C and (ii) 600°C...800°C with peaks starting from 0 to 0.021. The first region of the difference represents the water bonded to clay, thus, this region corresponds to adsorbed water (bulk water was removed by difference operation). According to the second region, the states of total suction 26, 59 and 140MPa show peaks of around zero, and the saturated sample has a higher value of 0,021. That fluctuation most probably corresponds to the change of fabric during saturation, as the accuracy evaluation due to granulometry was the highest at similar temperature zone. As samples from the mixture were picked randomly, most probably the variation in grain size and in the amount of water retained by big and small grains resulted in scatter data. Therefore, this methodology should be targeted on the grain size of interest.

Overall, the values of adsorbed water obtained in present analysis is similar to some of the other methodologies (Warr and Berger, 2007 reported half of water stored in adsorbed form). On Figure 2 the interpretation of results is presented in a form of soil water isotherm, representing the water types' amounts change upon hydration (capillary and adsorbed).

4 CONCLUSIONS

In present work a novel thermogravimetric methodology for experimental quantification of adsorbed water was developed for the first time. The advantage of this methodology lies in its reliance on energy-based measurements.

It was found that the adsorbed water and capillary water are present simultaneously and vary upon hydration. The abovementioned water types were quantified and a water isotherm was presented based on the findings. The results were presented as a soil water isotherm.

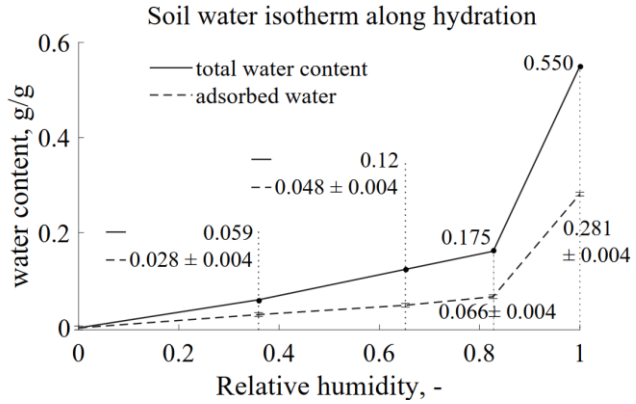

Figure 2. Outcome of the analysis.

ACKNOWLEDGEMENTS

The authors are grateful for the financial support provided by Swiss National Science Foundation (financial support No. 200021_204099, Division II).

REFERENCES

Leong, E.-C., Tripathy, S. & Rahardjo, H. (2003). Total suction measurement of unsaturated soils with a device using the chilled-mirror dew point technique. *Géotechnique* 53, No. 2, 173–182, http://dx.doi.org/10.1680/geot.2003.53.2.173.

Tajeddine, L., Gailhanou, H., Blanc, P., Lassin, A., Gaboreau, S., and Vieillard, P. (2015). Hydration–dehydration behavior and thermodynamics of MX-80 montmorillonite studied using thermal analysis. *Thermochimica Acta*, 604: 83–93. http://dx.doi.org/10.1016/j.tca.2015.02.002.

Vieillard, P.H., and Tajeddine, L. (2015). Thermo-Analytical Techniques on MX-80 Montmorillonite: A Way to Know the Behavior of Water and its Thermodynamic Properties during Hydration – Dehydration Processes. *Pharmaceutica Analytica Acta,* **07**(02). http://dx.doi.org/10.4172/2153-2435.1000462.

Wang, H., Shibue, T., and Komine, H. 2020. Hydration and dehydration of water of bentonite: A solid-state 1H magic-angle spinning NMR study. *Chemical Physics*, 536: 110796.http://dx.doi.org/10.1016/j.chemphys.2020.110796.

Wang, Y., Hu, L., Luo, S., and Lu, N. 2022. Soil water isotherm model for particle surface sorption and interlamellar sorption. *Vadose Zone Journal*, 21(5): e20221. http://dx.doi.org/10.1002/vzj2.20221.

Cockcroft, J.K., and Fitch, A.N. 2008. Chapter 2. Experimental Setups. In *Powder Diffraction*. Edited by R.E. Dinnebier and S.J.L. Billinge. Royal Society of Chemistry, Cambridge. pp. 20–57.

Warr, L.; Berger, J. 2007. Hydration of Bentonite in Natural Waters: Application of "Confined Volume" Wet-Cell X-Ray Diffractometry. *Physics and Chemistry of the Earth*, Parts A/B/C 2007, 32 (1–7),247–258. http://dx.doi.org/10.1016/j.pce.2006.02.048.

Proceedings of the XVIII ECSMGE 2024
GEOTECHNICAL ENGINEERING CHALLENGES
TO MEET CURRENT AND EMERGING NEEDS OF SOCIETY
© 2024 the Authors
ISBN 978-1-032-54816-6
DOI 10.1201/9781003431749-546
Open Access: www.taylorfrancis.com, CC BY-NC-ND 4.0 license

ECSMGE 24
XVIII EUROPEAN CONFERENCE ON SOIL MECHANICS AND GEOTECHNICAL ENGINEERING

Investigating foundation damping for OWTs using small strain hardening model calibrated with element scale tests

Étude de l'amortissement des fondations pour les OWT à l'aide d'un modèle d'écrouissage aux petites déformations calibré avec des tests à l'échelle des éléments

M. Barzan*, S. Kasyap, D. Igoe
Trinity College Dublin, Dublin, Ireland
**momohamm@tcd.ie*

ABSTRACT: Offshore wind turbines (OWTs) are subjected to cyclic excitations from the environmental and mechanical loads which control the fatigue lifetime of the structural components and can govern the overall design optimisation of the OWT. The growth of OWT size in recent years has led to a greater need to accurately quantify the different sources of damping that significantly influence the dynamic response of offshore wind turbines. Incorporating total damping in integrated numerical analysis will yield more realistic values of structural loads and bending moments which can be used to produce cost effective structural support design for modern size OWTs. One source of damping that is often overlooked is the contribution of the foundation to attenuate the dynamic response through the hysteretic behaviour of the surrounding soil. Thus, this research aims to accurately calculate the global foundation damping for a reference 15 MW OWT through calibrating a constitutive soil model to cyclic triaxial tests, and then implementing full 3D finite element FE analyses to capture the evolution of soil damping with monopile displacement at the mudline level. The small strain hardening soil model (HSsmall) was chosen due to its capability to exhibit non-linearity and stress-strain loops upon load reversals. Time domain free-decay analyses are executed in order to evaluate soil damping through logarithmic-decrement approach.

RÉSUMÉ: Les éoliennes offshore (OWT) sont soumises à des excitations cycliques dues à des charges environnementales et mécaniques qui contrôlent la durée de vie en fatigue des composants structurels et peuvent régir l'optimisation globale de la conception de l'OWT. La croissance de la taille des OWT ces dernières années a conduit à un besoin accru de quantifier avec précision les différentes sources d'amortissement qui influencent de manière significative la réponse dynamique des éoliennes offshore. L'intégration de l'amortissement total dans l'analyse numérique intégrée produira des valeurs plus réalistes des charges structurelles et des moments de flexion qui pourront être utilisées pour produire une conception de support structurel rentable pour les OWT de taille moderne. Une source d'amortissement souvent négligée est la contribution de la fondation à atténuer la réponse dynamique via le comportement hystérétique du sol environnant. Ainsi, cette recherche vise à calculer avec précision l'amortissement global des fondations pour un OWT de référence de 15 MW en calibrant un modèle de sol constitutif pour des essais triaxiaux cycliques, puis en mettant en œuvre des analyses FE par éléments finis 3D complètes pour capturer l'évolution de l'amortissement du sol avec le déplacement du monopile au niveau du sol. niveau de la ligne de boue. Le modèle d'écrouissage aux petites déformations (Hssmall) a été choisi en raison de sa capacité à présenter des boucles de non-linéarité et de contrainte-déformation lors d'inversions de charge. Des analyses de désintégration libre dans le domaine temporel sont exécutées afin d'évaluer l'amortissement du sol par une approche de décrémentation logarithmique.

Keywords: Monopile; offshore wind turbine; small strain hardening soil model; foundation damping.

1 INTRODUCTION

Due to the power production potential offered by offshore wind when compared to its onshore counterpart, this source of renewable energy has become a key technology to help overcome climate change challenges and to create sustainable energy sources for future generations. However, the cost associated with offshore wind development remains a significant issue that restricts its growth. While significant cost reductions in OWTs have been achieved through technological advancements and installations of larger size turbines, further reductions are needed to increase the economic viability of building new wind farms in less favourable conditions. One area that is receiving significant attention within the geotechnical engineering community is optimising the foundation design via understanding the interaction between the foundation

and the wind turbine tower. This is because the cost associated with the foundations can contribute up to 30% of the overall development cost (Bhattacharya, 2019).

OWTs are inherently characterised as flexible structures which are very sensitive to the frequency of the mechanical and environmental applied loads. The behaviour is often determined by carrying dynamic simulations using aeroelastic programs such as FAST. However, the results of these simulations are only valid when the damping contribution of each source is correctly taken into account. The soil-structure interaction affects the eigenmodes and the overall damping ratios, hence, the dynamic amplification that takes place. Several research studies pointed out that integrating foundation damping could lead to reducing the structural demands. Carswell et al., (2015) showed that including the foundation damping as a lumped rotational dashpot at the mudline level reduced the maximum and standard deviation of the mudline moment by 7-9% respectively during storm conditions. Although, the importance of soil damping is recognised in design guidelines such as DNV (2014), there are no standardised procedures for accurate determination.

This research paper aims to calculate foundation damping for the IEA 15 MW (Gaertner et al., 2020) reference wind turbine using 3D FE analysis with a constitutive model that is calibrated to cyclic triaxial results. The results show the global damping ratio against the mudline displacement of the monopile. The novelty of this work lies in the calibration procedure which focuses primarily on the soil element damping while also attempting to properly fit the monotonic tests.

2 METHODOLOGY

The FE numerical analysis is carried out using the software package Plaxis 3D which allows dynamic simulations to be performed. For modelling the soil behaviour, the small strain hardening model (HSsmall) is used and calibrated using the soil test facility that allows recreating common laboratory tests under different scenarios. The damping ratio is determined by displacing the OWT at the RNA level and then removing the load to allow the structure to freely decay and then calculate the damping based on the logarithmic-decrement equation.

The triaxial tests were conducted on sand samples taken from Blessington site in Ireland. The cyclic tests were performed and analysed according to ASTM (D3999).

3 NUMERICAL MODEL

The model mainly consists of beam and plate elements. The monopile is modelled using plate elements while the tower above the mudline is modelled with beam elements. A weightless plate with very large young's modulus is created 1m above mudline (so no soil is in contact with the plate) and is connected to the beam elements to allow the transfer of shear and bending moment between the tower and the foundation. The 3D FE model and its dimensions is shown in Figure 1. Viscous boundaries are activated to prevent wave reflections.

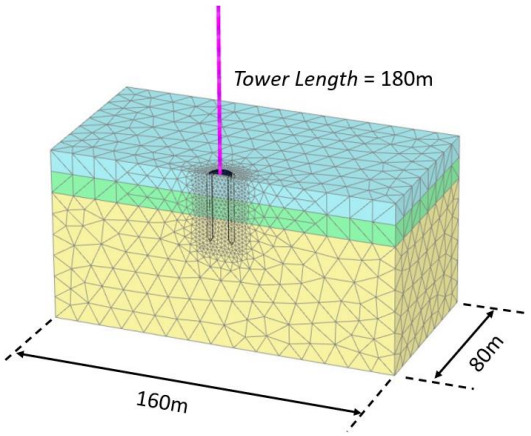

Figure 1. The 3D FE Model.

The mass at the RNA level is represented by modelling a small beam element with an equivalent unit weight. The mesh is generated fine enough to obtain accurate results with reasonable calculation time. The diameter of the monopile is 10m and the embedment depth is 30m. The dimensions of the tower and the mass of the RNA were taken from IEA Wind TCP 37 technical report (Gaertner et al., 2020).

4 SOIL INPUTS

The stratigraphy is divided into three layers. The model parameters are summarised in Table 1 and 2. The relative density of the soil is 60%. The soil is isotopically consolidated to effective confining stresses of 50, 150, and 300 kPa. Parameters that are not mentioned are maintained as the standard values in Plaxis 3D

Table 1. Soil input parameters.

Soil layer	Depth (m)	γ' (kN/m³)	φ' (deg)	ψ (deg)
1	0-10	9.74	46.9	14.9
2	10-20	9.74	43.8	11.0
3	20-80	9.74	39.3	5.4

Table 2. Soil input parameters.

Soil layer	E_{50ref} (kPa)	E_{oedref} (kPa)	E_{urref} (kPa)	G_{oref} (kPa)	$\gamma_{0.7}$ (-)
1	45000	30000	90000	83690	.00020
2	45000	30000	90000	83690	.00036
3	45000	30000	90000	83690	.00057

The two parameters that control damping in the HSsmall soil model are $\gamma_{0.7}$ and the ratio of G_{oref}/E_{urref} which acts as a cutoff. Figure 2 shows the calibrated Plaxis output curves with respect to the triaxial results curve fittings. Since the ratio of G_{oref}/E_{urref} is the same for all three layers, the maximum value of damping remains constant. The damping curves are shifted to the right by increasing $\gamma_{0.7}$ value. The Plaxis outputs match very well with the tests until 0.04% cyclic shear strain. The calibration involved varying the stiffness parameters until the Plaxis output matched the damping ratio and the monotonic test graphs. Figure 3 compares the monotonic response obtained from the laboratory tests and the Plaxis simulations. The monotonic tests were carried out in drained condition in order to find the angle of shearing resistance and the angle of dilation.

The initial stiffness from Plaxis triaxial simulations match well with the laboratory results as can be seen from Figure 3. Furthermore, the peak deviatoric stresses are also very similar which provides further validation for the input values. The axial LVDTs can measure displacements in the small and medium strain range. Thus, the maximum axial strain measured by the LVDTs before reaching their limit is roughly around 3% as shown in figure 3. The tests are further continued to determine the critical angle of shearing resistance which is approximately 35 degrees for the sand used in this research.

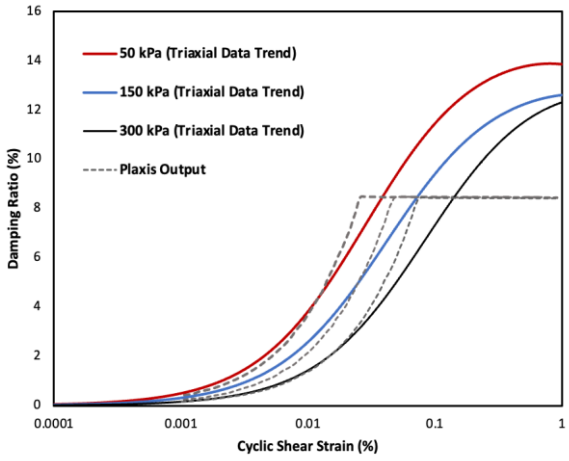

Figure 2. Calibrated damping curves.

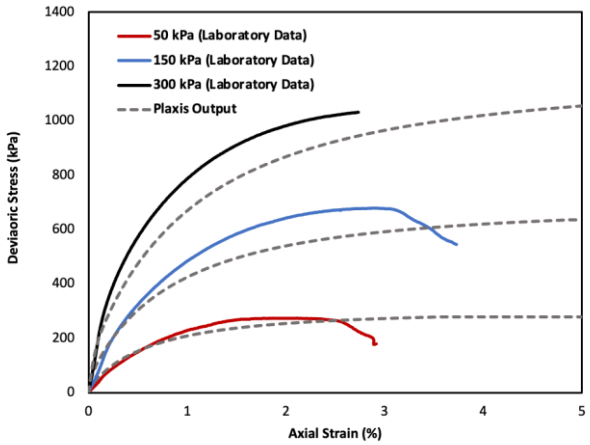

Figure 3. Monotonic triaxial test results and simulations.

5 RESULTS

The free vibration of the tower at the RNA level for different displacements is shown in Figure 4. The following equations are used for calculating the logarithmic decrement ratio (δ) and the damping ratio (ξ):

$$\delta = \frac{1}{n} \cdot ln\left(\frac{A_0}{A_1}\right) \quad (1)$$

$$\xi = \frac{1}{\sqrt{1+\left(\frac{2\pi}{\delta}\right)^2}} \quad (2)$$

where A_0 and A_1 are two successive amplitudes at the RNA level and n is number of cycles apart. The second cycle for each time history is used for the damping calculation. The damping ratio against the mudline translation is shown in Figure 5.

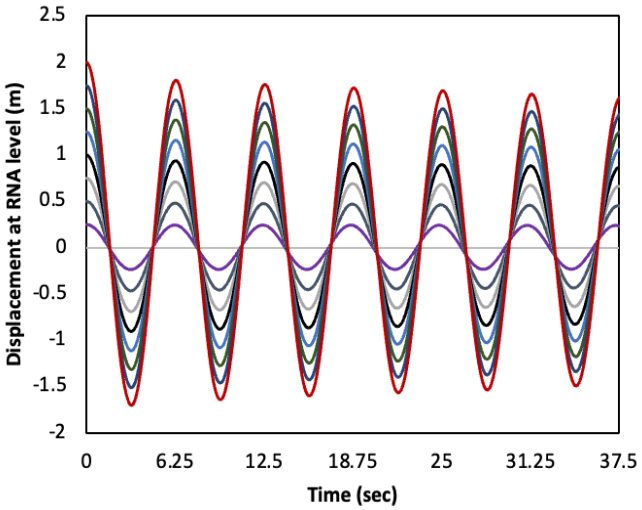

Figure 4. Free vibration of the tower.

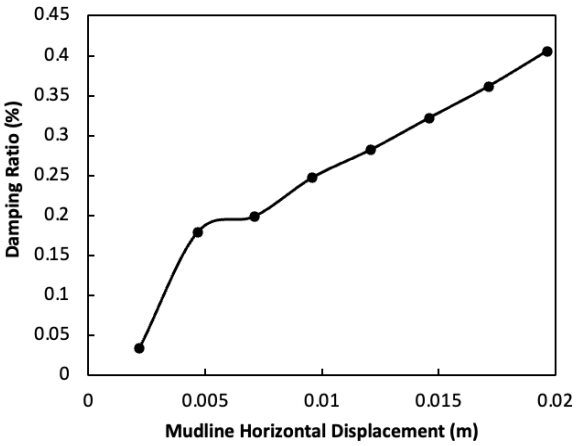

Figure 5. Damping ratio against mudline translation.

Since the 3D FE model contains no other form of damping, the decay of displacements in Figure 4 is only due to the hysteretic behaviour of soil. This has been validated by running the same simulations with a linear elastic soil model and no damping was observed (results not shown here). Figure 5 shows that as the mudline displacement increases, the damping ratio also becomes higher. This is consistent with the behaviour of soil at the element level shown in Figure 2. The damping ratio results obtained in this study falls within the range of ratios (0.15% - 1.5%) determined in previous studies as summarised by Malekjafarian et al., (2021). Several studies (such as Damgaard et al., 2013; Shirzadeh et., 2013; Versteijlen., 2011) back calculated soil damping from the total damping ratio observed during rotor-stop tests on actual OWTs. However, the accuracy of these results depends on whether the damping ratios of the other sources are correctly accounted for and the validity of the assumption of linear combination of different damping sources.

6 CONCLUSION

The primary aim of this paper was to determine the hysteretic foundation damping for the reference IEA 15 MW OWT through carrying out 3D FE analyses and using soil parameters from dynamic triaxial tests. The geometry of the monopile represents the current dimensions employed to support OWTs. The soil was medium-dense and was tested at different mean effective stresses to obtain the variation of damping at different depths. The damping ratio values determined from the FE analyses can be considered reliable and conservative when compared to previous studies and can help design engineers to gain a perspective of the damping ratio that can be expected from the monopile.

ACKNOWLEDGEMENTS

The authors are grateful for the financial support provided by the funding agency Sustainable Energy Authority of Ireland (SEAI).

REFERENCES

ASTM D3999/D3999M-11 (2013). Standard test methods for the determination of the modulus and damping properties of soils using the cyclic triaxial apparatus, West Conshohocken, PA.

Bhattacharya, S. (2019). *Design of Foundations for Offshore Wind Turbines*. Wiley, ISBN 9781119128151

Carswell, W., Johansson, J., Løvholt, F., Arwade, S. R., Madshus, C., DeGroot, D. J., and Myers, A. T. (2015). Foundation damping and the dynamics of offshore wind turbine monopiles. *Renewable Energy*, Vol. 80, pp. 724-736. https://doi.org/10.1016/j.renene.2015.02.058.

Damgaard, M., Ibsen, L. B., Andersen, L. V., and Andersen, J. K. F. (2013). Cross-wind modal properties of offshore wind turbines identified by full scale testing. *Journal of Wind Engineering and Industrial Aerodynamics*, Vol. 116, pp. 94-108. https://doi.org/10.1016/j.jweia.2013.03.003.

DNV-OS, D. (2014). J101 Design of offshore wind turbine structures. DNV GL: Oslo, Norway, 212-214.

Gaertner, E.O., Rinker, J., et al., (2020). IEA Wind TCP Task 37: Definition of the IEA 15-Megawatt Offshore Reference Wind Turbine. Technical Report NREL/TP-5000-75698, National Renewable Energy Lab. (NREL), Golden, CO (United States).

Malekjafarian, A., Jalilvand, S., Doherty, P., and Igoe, D. (2021). Foundation damping for monopile supported offshore wind turbines: A review. *Marine Structures*, Vol. 77, 102937. https://doi.org/10.1016/j.marstruc.2021.102937.

Shirzadeh, R., Devriendt, C., Ahmadi Bidakhvidi, M., and Guillaume, P. (2013). Experimental and computational damping estimation of an offshore wind turbine on a monopile foundation. *Journal of Wind Engineering and Industrial Aerodynamics*, Vol. 120, pp. 96-106. https://doi.org/10.1016/j.jweia.2013.07.004.

Versteijlen, W. G., Metrikine, A., Hoving, J., Smidt, E., and de Vries, W. (2011). Estimation of the vibration decrement of an offshore wind turbine support structure caused by its interaction with soil. *Knowledge, Technology & Policy.*

Proceedings of the XVIII ECSMGE 2024
GEOTECHNICAL ENGINEERING CHALLENGES
TO MEET CURRENT AND EMERGING NEEDS OF SOCIETY
© 2024 the Authors
ISBN 978-1-032-54816-6
DOI 10.1201/9781003431749-547
Open Access: www.taylorfrancis.com, CC BY-NC-ND 4.0 license

ECSMGE 24
XVIII EUROPEAN CONFERENCE ON SOIL MECHANICS AND GEOTECHNICAL ENGINEERING

Generalized P-y curves for monopile design using the PISA methodology

Courbes P-y généralisées pour la conception de monopieux avec la méthodologie PISA

L. Berenguer Todo Bom*
COWI A/S, Hamburg, Germany

**lbbm@cowi.com*

ABSTRACT: The PISA design model is rapidly becoming the standard methodology for the design of offshore monopile foundations supporting wind turbine structures. The PISA model allows designers to either derive from finite element models (FEM) or use rule-based equations, to obtain normalized parameters. Despite the clear benefits, due to the relatively high computational cost and specialist knowledge required to calibrate advanced constitutive models from specialized soil testing, FEM-based PISA calibrations are only adopted during detailed design stages. On the other hand, the rule-based approach has documented limitations namely in new provinces, for soils with distinct geological histories than those tested as well as in layered soil profiles. Since binding monopile geometry decisions are, however, made at earlier project phases, this presents a dilemma for practising engineers. This paper presents an alternative approach of the P-y curve components of the PISA method. It can used at both early stages of design, to derive the normalized parameters in layered profiles, and at detailed design stage to inform the best-fit procedure of the normalized curves. The input soil profiles may contain both coarse and fine-grained formations, either exhibiting drained or undrained behaviour. The new formulation takes into account physical principles of the soil resistance components, to define the PISA normalized parameters.

RÉSUMÉ: Le modèle de conception PISA est rapidement en train de devenir la méthodologie standard pour la conception des fondations de monopieux offshore supportant des structures d'éoliennes. Le modèle PISA permet aux ingénieurs de dériver à partir de modèles d'éléments finis (FEM) ou d'utiliser des règles pour obtenir des paramètres normalisés. Malgré les avantages clairs, en raison du coût de calcul relativement élevé et des compétences spécialisées nécessaires pour calibrer les modèles constitutifs avancés à partir d'essais de sol spécialisés, les calibrations PISA basées sur les éléments finis sont uniquement adoptées au cours des étapes de conception détaillée. D'autre part, l'approche basée sur des règles a des limites connues, notamment dans les nouvelles géographies, pour les sols ayant une histoire géologique différente de celle des sols testés, ainsi que dans les profils de sol stratifiés. Comme les décisions relatives à la géométrie des monopieux sont prises dès les premières phases du projet, cela pose un dilemme aux ingénieurs en exercice. Cet article présente une approche alternative des composantes de la courbe P-y de la méthode PISA. Elle peut être utilisée à la fois aux premiers stades de la conception, pour dériver les paramètres normalisés dans les profils en couches, et au stade de la conception détaillée pour informer la procédure de meilleur ajustement des courbes normalisées. Les profils de sol utilisés peuvent contenir des formations sableuse ou argileuse, présentant un comportement drainé ou non drainé. La nouvelle formulation prend en compte les principes physiques des composantes de la résistance du sol, pour définir les paramètres normalisés PISA.

Keywords: Offshore engineering; finite element modelling (FEM); monopiles; PISA methodology.

1 INTRODUCTION

The modelling of soil-structure interaction in pile foundations has advanced substantially in the field of offshore geotechnical engineering. The developments to tackle the technical challenges have been driven by a need to improve the existing P-y method approaches and also to integrate additional lateral soil resistance components which became relevant in larger foundation sizes. As monopile diameters increase to ranges beyond the basis of the standard method, designers optimize foundation geometries by adopting the benefits of a larger structure in all resistance components.

For detailed design of offshore monopile foundations, FEM-based methods have become the industry practice, Burd et al. (2020). Due to the complexity, time constraints and high computational costs, however, pile geometry design iterations are not typically performed within FEM software. These rather rely on 1D Beam-in-Elastic Foundation (BEF) simplifications, resorting to soil-structure interaction models consisting of non-linear interaction curves. Moreover, at earlier stages in design, solely the design

of certain positions in the offshore wind farm will be FEM-based, while the remainder rely on extrapolated normalized parameters to define the soil-structure interaction models. For both these cases, normalization methods as well as rule-based parameters to determine the soil interaction curves are required. This paper presents a methodology to derive P-y curves, based on the PISA design model, proposed by Byrne et al. (2017), and supported on soil mechanics principles, to better address the design challenge of monopile foundations.

2 CURRENT METHODS

The traditional design methodologies provided in API RP 2GEO (2014) and DNVGL-ST-0126 (2018), and which can be used for pile foundations subject to lateral loading, were not developed for the large diameter structures currently adopted in the offshore wind industry. The work undertaken by the PISA group aimed to close this gap, as presented in Byrne et al. (2017), and has become the standard design methodology for monopile design. It provides a framework to both include additional lateral components of resistance but mainly a normalization approach to define soil interaction curves in normalized space with a simple mathematical formulation of a conic function. Normalization factors of the P-y curve components, as shown in Table 1, are proposed for both effective and total stress-based soil responses, typically named representative for sand (coarse-grained) and clay (fine-grained) soil materials, respectively.

Table 1. Normalization of P-y curves, Byrne et al. (2017).

Normalized variable	**Clay**	**Sand**
Lateral displacement, $\bar{\boldsymbol{v}}$	$\frac{v}{D}\frac{G_0}{S_u}$	$\frac{v}{D}\frac{G_0}{\sigma'_{vi}}$
Distributed load, $\bar{\boldsymbol{p}}$	$\frac{P}{S_u D}$	$\frac{P}{\sigma'_{vi} D}$

Based on these curve normalization functions and in-situ large diameter pile load testing, Burd et al. (2019) and Byrne et al. (2019) propose a rule-based approach where normalized PISA parameters are defined for both the sand and clay frameworks, respectively. The rule-based approach, however, has been shown to perform poorly namely in new geographies, for soils with distinct geological histories from those tested as well as in layered soil profiles with relevant stiffness contrast, as shown in Burd et al. (2020), among other limitations.

3 MODEL DESCRIPTION

The proposed P-y model approach comprises an improved normalization function for the 'sand framework', a methodology to model the undrained behaviour of sand as well as a soil mechanics'-based analytical approach within the PISA framework.

3.1 Effective stress normalization

The PISA sand framework normalization functions of the p-value solely normalize to the effective stress and pile diameter. This limits its applicability to derive global PISA parameters per unit for sites where the same unit may have distinct strength parameters. More importantly, the normalization does not relate the normalized parameters to other physical quantities. The latter is due to the missing strength parameters and in situ confinement stress definition for it to be compatible with critical state soil mechanics. The proposed modification serves to complement the effective stress normalization, based on Leonards (1962), to normalize by the shear stress as follows:

$$\bar{v} = \frac{v}{D}\frac{G_0\,(1-sin\phi')}{\sigma'_{vi}\,sin\phi'} \quad (1)$$

$$\bar{p} = \frac{P}{D}\frac{(1-sin\phi')}{\sigma'_{vi}\,sin\phi'} \quad (2)$$

where ϕ' is the friction angle. The rule-based formulation in the PISA sand framework also limits its applicability for other sands than those tested in the PISA project. The main parameter selected is ill conceived since relative density (D_r) is not a good indicator of soil behaviour nor of its critical state. Different soils behave differently at the same relative density. Based on the new normalization formulation, a total stress rule-based approach, which is by definition conservative, is defined in Section 3.2. The conservativism of such an approach can be seen by comparing the results of two laterally loaded monopile PLAXIS 3D FE models, in two sand profiles, one adopting effective stress parameters and a second with maximum shear stress, both adopting the Hardening Soil Small-Strain model, according to equations (1) and (2). An additional result for an undrained modelling, adopting the NGI-ADP model, is also shown in Figure 1. The model has a pile diameter of 9m and a pile embedment of 28m. Soil parameters were derived following correlations given in the PLAXIS MoDeTo Manual (2018). The slight difference in secant stiffness is due to limitations on the constitutive model parameter definition when selecting a very low friction angle in PLAXIS. The ultimate capacity is underestimated as expected for

both the total and undrained modelling, since from the constitutive model perspective, this results from the underestimation of the frictional contribution of the resistance during loading as the positive contribution of the increase in horizontal stress is not considered.

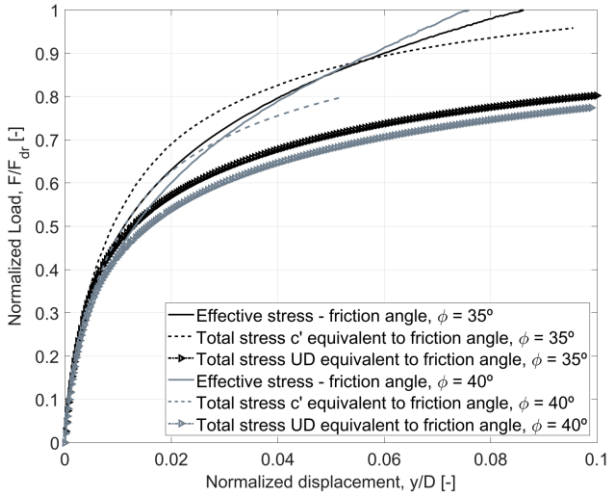

Figure 1. Comparison of 3D FEM effective, total and undrained stress models, where F_{dr} is the effective stress resistance.

3.2 Total stress / Shear stress approach

The sand framework formulation, and its respective rule-based formulation, has been found to be the least representative to be used in design. This is due to several reasons. One of the foremost is the fact that the extreme loading condition of offshore foundations is due to rapid individual loading events, such as wind and waves, for which the soil behaviour may be either undrained or partially drained, rather than fully drained, as is the basis of the PISA formulation. An assessment of the drainage type, using the dimensionless velocity ratio proposed by Finnie and Randolph (1994), indicates that the soil behaviour during the wave impact is not fully drained. Furthermore, the generation of excess pore-pressure will be greater in the vicinity of the pile, which most impacts the soil resistance components.

A pragmatic approach to extend the PISA formulation to an undrained loading of sands is to resort to the total stress approach, i.e., the PISA clay framework, where the undrained shear strength of sands is determined from triaxial extension as:

$$S_{u-sand} = \sigma'_{vi} \cdot \frac{sin\phi' \left(1-A_f+K_0\,A_f\right)}{1-sin\phi'+2\,A_f\,sin\phi'} \qquad (3)$$

where A_f is the Skempton pore-water pressure parameter A at failure. Janbu (1985) defines for triaxial compression tests on saturated soils the dilatancy parameter D as:

$$D = \frac{1}{3} - A_f \qquad (4)$$

where $D = 0$ represents elastic behaviour, $D < 0$ contractive behaviour and $D > 0$ dilatant behaviour. The determination of A_f in sands depends on several factors namely relative density, confinement pressure and loading stress path. This parameter should ideally be determined from constant normal stiffness shear tests or directly from available undrained testing of soil samples. Care should be taken when calibrating from undrained tests since these simulate perfectly rigid boundary conditions. Hence, the increase in effective confinement stress, which in turn increases the shear stress resistance, observed in the laboratory, will not be present in situ. A possible approach to estimate the A_f parameter is through the state parameter ψ, as defined in Jefferies and Been (2006). This parameter can be either directly or indirectly determined from the cone penetration test (CPT). The standard CPT correlations, when inverted, provide a relationship to the commonly derived relative density, shown in Figure 2, for different vertical stress intervals.

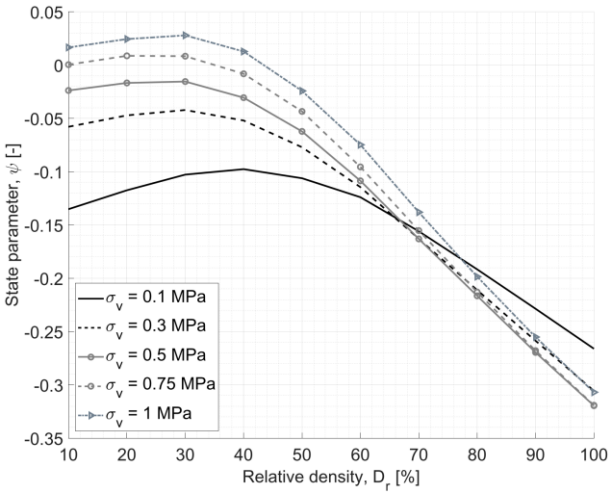

Figure 2. Inverted CPT correlations between D_r and ψ.

This approach implies that the behaviour of sands and parameter usage are in the same context as the undrained shear of clays, which is consistent with critical state soil mechanics' principles. Adopting the formulation given in Wroth (1984), the normalized ratio of both the undrained shear strength of loose sands and clays to the reference level of $\psi = 0.05$ and over-consolidation ratio (OCR) of 1.0, respectively, can be determined, as shown in Figure 3 for the stress path of isotropic triaxial compression. The starting point of both lines is so defined since, as discussed in Jefferies and Been (2006), while the state parameter and over-consolidation are different entities, the

undrained shear strengths of loose sands ($\psi \approx 0.05$) are comparable to normally consolidated clays (OCR=1).

In Figure 3, the red line represents the OCR effect on clay undrained shear strength, given in Wroth (1984), while the black line represents the peak friction angle relation to the state parameter in sands, as given in Jefferies and Been (2006). The different rates of variation are due to the distinct relationship between OCR and ψ to volumetric behaviour of fine- and coarse-grained materials.

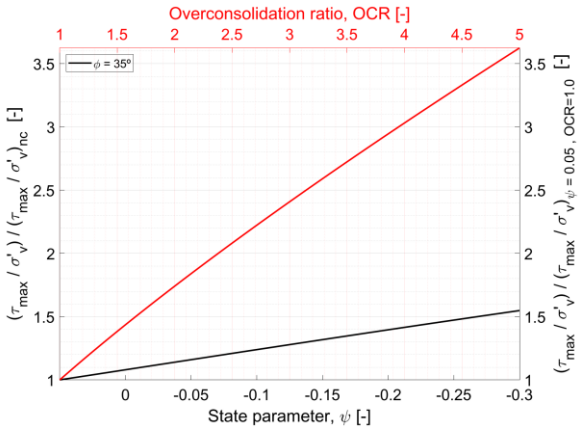

Figure 3. Variation in normalized undrained strength ratio.

This section summarized an analytical approach to determining the undrained shear strength for both fine- and coarse-grained materials for different initial stress conditions and loading histories.

4 RULE-BASED FORMULATION

The proposed formulations in the previous sections are defined based on maximum shear stress, therefore, can be directly incorporated within the PISA clay framework. The normalization functions proposed for the 'clay framework', based on a total stress approach, are simpler and broadly based on analytical solutions. The approach defined results in the normalized P-y PISA parameters ($\bar{p}_u, \bar{v}_{pu}, n_p$ and k_p) having a physical basis from soil mechanics. As shown in the following equations, for example, $\bar{p}_u$ can be seen to be the bearing capacity factor N_p, while k_p is the multiplying factor to G_0, the small-strain shear modulus, to define the initial stiffness of the P-y curve.

$$P_u = \bar{p}_u S_u D\,, \qquad \bar{p}_u = N_p \tag{5}$$

$$k_i = k_p G_0, \qquad k_i = \frac{P_i}{v_i} \tag{6}$$

For both these parameters several analytical solutions exist, such as Jeanjean et al. (2017), Ashford and Juirnarongrit (2003) and Suryasentana and Lehane (2016), respectively, providing a robust rule-based approach for these values. The curvature parameter n_p can be derived from backbone curves such as Darendeli (2001), assuming a shear strain displacement relationship from several simplified approaches summarized in Zhang and Andersen (2017). Finally, the $\bar{v}_{pu}$ parameter can be estimated from rigidity index values at failure, typically varying between 5 to 15% of the ratio of lateral displacement to pile diameter, as per Jeanjean and Zakeri (2023).

5 FINITE ELEMENT ANALYSIS OF P-Y RESPONSE

The comparison between the proposed rule-based method, for both effective and total stress approaches is performed by comparison of the $\bar{p}_u$ and k_p PISA parameters, calibrated to match the P-y curves from the effective stress and undrained load-displacement curves, calculated in FEM presented in Figure 1. The PISA calibration procedure ensures a near perfect match per soil curve extracted which in turn result can replicate the overall pile behaviour. The results obtained are plotted in Figure 4 and Figure 5. Alongside the calibrated PISA parameters, the analytical PISA parameters as per equations (5) and (6) are also plotted for comparison. The rule-based approach is shown to be conservative, both in stiffness and strength, when compared to FEM results. For detailed design stages, multiplication factors, as shown in the right of Figure 4 and Figure 5, can be applied to the formulation to obtain a better match to the FEM model and thereby define global PISA parameters.

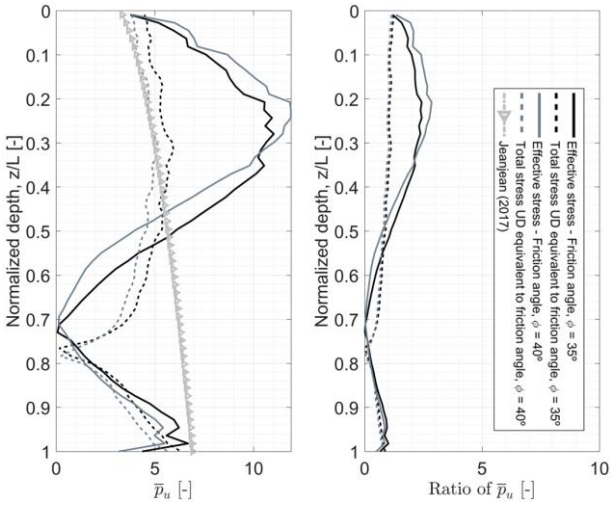

Figure 4. Left - FEM calibrated, analytical $\bar{p}_u$ PISA parameter as given in Eq. (5); Right - ratio between numerical and analytical values.

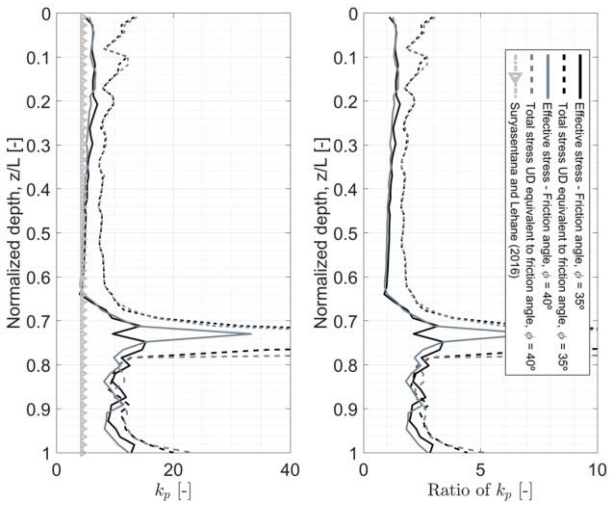

Figure 5. Left - FEM calibrated, analytical k_p PISA parameter as given in Eq. (6); Right - ratio between numerical and analytical values.

6 CONCLUSIONS

The proposed formulation to determine P-y curves for both coarse and fine-grained formations, exhibiting either drained or undrained behaviour has been presented. The method comprises an alternative normalization for coarse-grained materials in the PISA framework and a methodology to determine the failure shear stress of sands under undrained behaviour and a soil mechanics'-based rule-based approach. A comparison to FEM results indicates the rule-based approach proposed to be adequately conservative for early-stage designs.

REFERENCES

API RP 2GEO (2014), Geotechnical and Foundation Design Considerations. First Edition. American Petroleum Institute, April 2011 + Addendum 1.

Ashford, S. and Juirnarongrit, T. (2003). Evaluation of Pile Diameter Effect on Initial Modulus of Subgrade Reaction. J. Geotech. Geoenvironmental Eng. 129, 234–242. https://doi.org/10.1061/(ASCE)1090-0241(2003)129:3(234).

Burd et al. (2019): PISA Design Model for Monopiles for Offshore Wind Turbines: Application to a Marine Sand, Géotechnique 2020 70:11, 1048-1066. https://doi.org/10.1680/jgeot.18.p.277.

Burd et al. (2020). PISA: Application of the PISA design model to monopiles embedded in layered soils, Géotechnique 2020 70:11, 1067-1082. https://doi.org/10.1680/jgeot.20.PISA.009.

Byrne et al. (2017). PISA: New Design Methods for Offshore Wind Turbine Monopiles. Proc. 8th Int. Conf. for Offshore Site Investigation and Geotechnics, London.

Byrne et al. (2019): PISA Design Model for Monopiles for Offshore Wind Turbines: Application to a Stiff Glacial Clay Till. Géotechnique, 70:11, 1030-1047. https://doi.org/10.1680/jgeot.18.p.255.

Darendeli M.B. (2001). Development of a New Family of Normalized Modulus Reduction and Material Damping Curves. Ph.D. Dissertation, University of Texas at Austin, 362 pp.

DNVGL-ST-0126 (2018). Support structures for wind turbines. DNV.

Finnie, I. M. S. & Randolph, M. F. (1994). Punch-through and liquefaction induced failure of shallow foundations on calcareous sediments. In 7th International conference on behaviour of offshore structures (ed. C. Chryssostomadis), pp. 217–230. Oxford, UK: Pergamon Press.

Janbu N. (1985). Soil models in offshore engineering. Géotechnique, 35:3, 241-281. https://doi.org/10.1680/geot.1985.35.3.241.

Jeanjean, P., Zhang, Y., Zakeri, A., Andersen, K.H., Gilbert, R. and Senanayake, A.I.M.J. (2017). A framework for monotonic p-y curves in clays. In Offshore Site Investigation Geotechnics 8th International Conference Proceeding (Vol. 108, No. 141, pp. 108-141). Society for Underwater Technology.

Jeanjean, P. and Y., Zakeri (2023). Efficiencies and challenges in offshore wind foundation design. In Offshore Site Investigation Geotechnics 9th International Conference Proceeding (Vol. 109, pp. 700-141). Society for Underwater Technology.

Jefferies, M., and Been, K. (2006). Soil Liquefaction: A Critical State Approach (1st ed.). CRC Press. https://doi.org/10.4324/9780203301968.

Leonards, G.A. (Ed.), (1962), Foundation Engineering, McGraw-Hill, New York, 1136 p.

Plaxis. Plaxis 3D Reference Manual CONNECT Edition V22.

PLAXIS MoDeTo Manual, 2018.

Suryasentana, S. and Lehane, B. (2016). Updated CPT-based p – y formulation for laterally loaded piles in cohesionless soil under static loading. Géotechnique. 66. 1-9. https://doi.org/10.1680/jgeot.14.P.156.

Wroth C. P. (1984). The interpretation of in situ soil tests, Géotechnique 34:4, 449-489. https://doi.org/10.1680/geot.1984.34.4.449

Zhang, Y. and Andersen, K. (2017). Scaling of lateral pile p-y response in clay from laboratory stress-strain curves. Marine Structures. 53. 124-135. https://doi.org/10.1016/j.marstruc.2017.02.002.

Proceedings of the XVIII ECSMGE 2024
GEOTECHNICAL ENGINEERING CHALLENGES
TO MEET CURRENT AND EMERGING NEEDS OF SOCIETY
© 2024 the Authors
ISBN 978-1-032-54816-6
DOI 10.1201/9781003431749-548
Open Access: www.taylorfrancis.com, CC BY-NC-ND 4.0 license

ECSMGE 24
XVIII EUROPEAN CONFERENCE ON SOIL MECHANICS AND GEOTECHNICAL ENGINEERING

Evaluation of the geomechanical properties of lime-treated silt samples extracted from an experimental levee 6 years after construction

Évaluation des propriétés géomécaniques d'échantillons de limons traités à la chaux extraits d'une digue expérimentale 6 ans après construction

F. Bertola, F. Klotz
Lhoist Research & Development, Nivelles, Belgium

P. Gerard
BATir Department, Laboratory of GeoMechanics (LGM), Université libre de Bruxelles (ULB), Brussels, Belgium

B. François*
Department of Urban and Environmental Engineering, University of Liège, Liège, Belgium

**bertrand.francois@uliege.be*

ABSTRACT: In recent decades, multiple research projects have shown the positive impact of lime treatment on the construction or improvement of hydraulic structures. Both the hydraulic and the mechanical properties of lime-treated soils can be improved allowing for new design techniques and potential resource saving. In July 2015, as part of the DigueELITE project, a full-size experimental levee was built in a meander of the Vidourle River (Gard, France). The structure comprises a first section with a platform and a settling basin at the toe of the slope constructed with silty soil treated with 2% lime, and a second section built with the same soil untreated. As a primary objective, the resistance to external erosion of the lime-treated soil was quantified by performing overflow tests in 2016 and 2017. Then, the monitoring of the durability of the structure treated with lime was carried out. For this latter purpose, a test campaign took place in June 2021; samples were extracted from the core of the structure on the platform in lime-treated soil and characterized. This paper provides a brief description of the experimental levee, the experiments previously carried out, and the procedure implemented to study the geomechanical behavior of the samples extracted. Finally, the results of permeability, UCS, shearing strength, and oedometric compressibility tests, performed 6 years after the construction, are presented, and compared with those acquired just after the construction of the levee on samples prepared in the laboratory and cured for 7 to 28 days.

RÉSUMÉ: Récemment, de multiples projets de recherche ont montré l'impact positif du traitement à la chaux pour la construction ou l'amélioration des ouvrages hydrauliques. L'amélioration des propriétés hydrauliques et mécaniques des sols traités à la chaux, permet d'envisager des nouvelles techniques de conceptions plus économes en ressources. En juillet 2015, dans le cadre du projet DigueELITE une digue expérimentale de taille réelle a été construite dans un méandre du fleuve Vidourle (Gard, France). Le démonstrateur est constitué d'une première section construite avec un limon traité à 2% de chaux et d'une seconde section construite avec le même limon non traité. L'ouvrage comprend aussi une plateforme et un bassin de décantation construits en limon traité. L'objectif premier du projet était de quantifier la résistance à l'érosion externe du sol traité à la chaux à l'aide d'essais de surverse réalisés en 2016 et 2017. Un second sujet d'intérêt concerne le suivi de la durabilité des ouvrages traités à la chaux. A ce titre, une campagne d'essais a eu lieu en juin 2021 et des prélèvements en cœur d'ouvrage ont été réalisés. Ce papier fournit une brève description de la digue et des expérimentations précédemment réalisés puis présente les moyens mis en œuvre pour étudier le comportement géomécanique des échantillons prélevés. Finalement les résultats obtenus en termes de perméabilité, de résistance à la compression simple et au cisaillement, et de compressibilité œdométrique sur le matériau extrait à 6 ans de cure sont présentés et comparés à ceux acquis lors d'une étude antérieure datant de la construction de l'ouvrage et réalisée sur des échantillons préparés en laboratoire et consolidés de 7 à 28 jours.

Keywords: Silty soil; lime; durability; compressive strength; shear strength; permeability.

1 INTRODUCTION

The chemical treatment of soils with lime is a technique widely used on earthworks to improve poor-quality soils containing a clay fraction. The benefits of treating fine silty-clay soils with lime are twofold. Firstly, the addition of lime allows for better control and improves the physical characteristics of the soil and its compaction behaviour during processing, making it much easier to reuse. Secondly, over and above the short-term improvement effect, the addition of lime in sufficient quantity enables the development of improved geotechnical properties compared with untreated soil, particularly in terms of compressive and shear strength (Bell, 1996; Little, 1995). Recent research programs have also demonstrated the positive effects of treating soils for hydraulic structures, thanks to the increased resistance to erosion provided by the treatment, and the adaptation of treatment processes to meet low permeability requirements (Herrier et al., 2012; Nerincx et al., 2018; Herrier et al., 2018). The behaviour of treated soils is widely studied at the laboratory level, but only a few real structures have been monitored years after their construction (Haas et al., 2019, Das et al., 2021; Chabral et al., 2023).

This paper reports the monitoring of the properties of an experimental levee built on a meander of the river Vidourle in France. After a brief presentation of the experimental structure and the initial project, the method for taking and preparing the samples for the laboratory investigation is described. Finally, the results of permeability, UCS, shear strength, and oedometric compressibility tests, performed 6 years after the construction are presented and compared with those acquired on samples prepared and cured in a laboratory for 7 and 28 days.

2 PRESENTATION OF THE EXPERIMENTAL LEVEE

The construction of the experimental levee for the DigueELITE research program was completed in July 2015. Located on the edge of the Vidourle River, the structure is part of the work to improve the network of local levees. With a length of 50 m, a crest height of 3.5 m and a slope of 1.5H/1V, the demonstrator comprises a section of lime-treated soil and a section of untreated soil, and it is shown in Figure 1. The soil used is a locally extracted silt (Plasticity Index = 5), treated in a mobile plant with 2% quicklime. The slopes are not covered with topsoil, so the soil is directly exposed to the environment. The levee concerned by the experiments faces south and is therefore subject to wide temperature variations. The levee is not in direct contact with the Vidourle, which is several meters below; the water table is 2 to 3 meters below the structure.

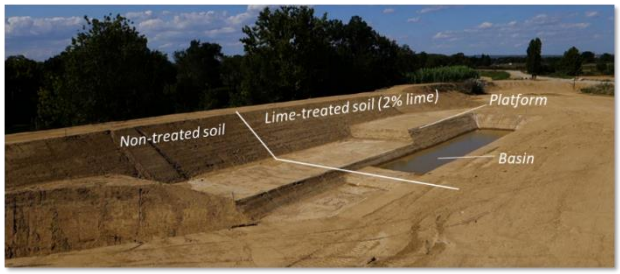

Figure 1. Aerial view of the Vidourle experimental levee. The platform and basin were also made with lime-treated soil and used for overflow test purposes.

This demonstrator was built to conduct overflow tests to quantify and compare the erosion resistance of treated and untreated soil on a real scale. Details of the tests and the overflowing simulator are presented in Bonelli et al. (2018). The project also made it possible to confirm the procedures for using treated soils in the construction of hydraulic structures, which differ from conventional treatment procedures. Thanks to its well-known construction history, the structure can now be used to conduct tests aimed at assessing the durability of the lime treatment solution.

3 SAMPLE COLLECTION AND PREPARATION

In 2021, the external erosion resistance of the treated and untreated soil was assessed using the JET test (Nicaise et al., 2024). This was also an opportunity to take samples from the body of the lime-treated levee on the platform part to assess its geomechanical performance. As for the experimental backfill in Rouen (Saussaye et al., 2020), blocks were extracted with a mechanical shovel using a small bucket to dig two narrow trenches 30 cm wide, 1 m apart from each other. The blocks were then lifted out from the backfill by planting the teeth of a wide bucket in the interlayers identified, with the mechanical shovel overhanging the platform. The extracted pieces were then carefully handled and cut on site using a floor saw to reduce their size and facilitate the handling (Figure 2). The final blocks obtained were approximately 40x40x30 cm in size and showed no visible cracks caused by the handling. After identification, the blocks were sealed in watertight plastic sheets. The material sampled corresponded to layer 6 and layer 7 of the lime-treated silt platform as shown in Figure 3.

The samples for the œdometric tests were obtained by machining the blocks using a milling machine to obtain a diameter of 5 cm and a height of 1.5 cm

(Figure 2). While to carry out direct shear and permeability tests, the samples were obtained by dry coring over a diameter of 10 cm with a height of about 10 cm. For simple compression tests, the same process was implemented, but the ratio length/diameter of the samples varied between 1 and 1.6. The high resistance of the treated soils made them fragile, and the sporadic presence of pebbles did not allow to obtain longer samples with a good yield.



Figure 2. Left: View on the two trenches and the mechanical shovel. Middle: An extracted block re-sized using a floor saw for conditioning. Right: A re-sized block used to shape a sample by milling.

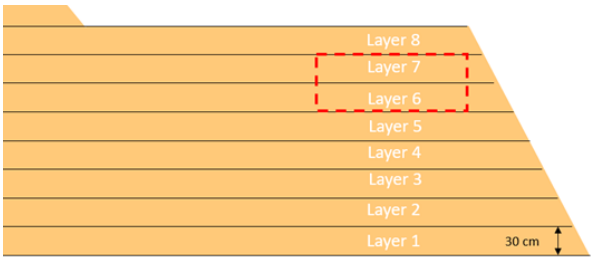

Figure 3. Schematic cross-visualization of the location of layer 6 and layer 7 of the material extracted from the platform in the lime-treated soil.

4 GEOMECHANICAL PROPERTIES AFTER 6 YEARS

4.1 Oedometric compressibility

The œdometric tests were performed by placing the milling-shaped samples between two porous stones in œdometric cells. After a period of saturation in water, loading and unloading tests were carried out in saturated conditions, and the vertical displacement of the samples was measured after stabilization. Ten loading/unloading bearings were applied in the following sequence: 25, 50, 100, 200, 400, 800, 1600 kPa, then 400, 100, and 25 kPa. Three samples from layer 6 were tested in loading up to 800 kPa, and six samples from layer 7 were tested three with loads up to 800 and three with loads up to 1600 kPa. The objective was to verify potential heterogeneities between layers, but also within the same layer.

The results of the compressibility tests are presented in Figure 4 and compared with the results obtained on samples prepared in the laboratory in 2015.

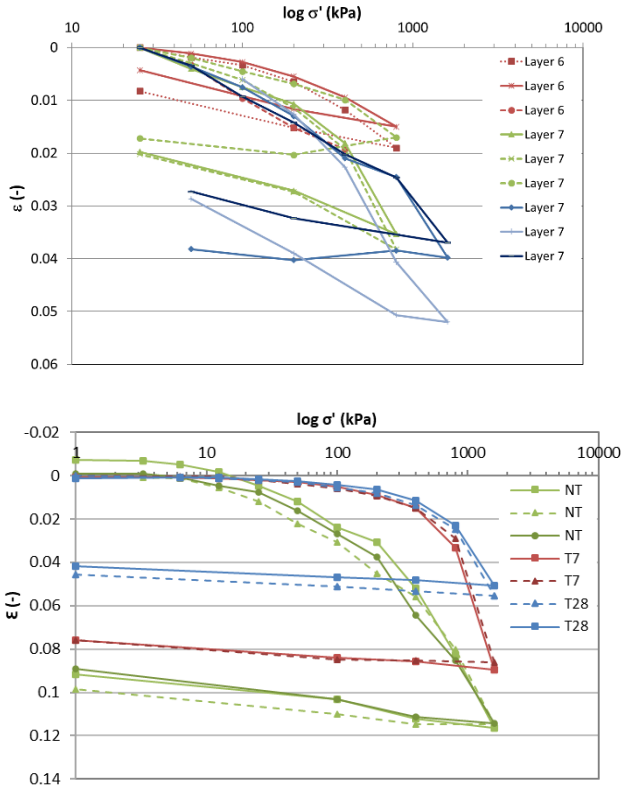

Figure 4. Top: Compression curves of the specimen extracted after 6 years. Bottom: Compression curves of the specimen non-treated (NT) and treated in the laboratory after 7 (T7) and 28 (T28) days of curing.

Table 1 summarizes the various parameters calculated from the compression curves.

Table 1. Parameters measured during the compressibility tests on the samples extracted from the Vidourle levee after 6 years of aging (onsite samples) and compared to values obtained on laboratory samples tested at younger ages.

Study	Soil - Cure	Compressibility index	Swelling index	Pre-consolidation stress σ' (kPa)
This study *(onsite samples)*	Layer 7 (2% treated soil) - 6 years	0.0205	0.0041	> 600
	Layer 6 (2% treated soil) - 6 years	0.0092	0.0040	200 - 600
2015 study *(laboratory samples)*	Untreated soil	0.0415	0.0030	109
	2% treated soil – 7 days	0.0527	0.0016	565
	2% treated soil – 28 days	0.0292	0.0012	503

According to the results, the treated soil, sampled after 6 years of weathering, maintains, or even improves, its compressibility characteristics. Layer 7 shows a compressibility behaviour similar to that of the laboratory-treated soil after 7 and 28 days of curing, significantly improved in comparison with the behaviour of the untreated soil.

A significant difference between layer 6 and layer 7 is observed as layer 6 is less compressible. Furthermore, layer 6's material shows an improved behavior compared to that of the soil tested in the lab at a shorter curing time. Its pre-consolidation stress probably exceeds 600 kPa but remains non-calculable as it is doubtful that the plastic range is reached at 800 kPa. In general, the results obtained within the same layer are close and reproducible.

4.2 Unconfined compressive strength (UCS)

The unconfined compressive strength (UCS) of the samples from both the layers was measured on cylindrical drilled samples. The length/diameter ratio of the samples being systematically lower than 2, a corrective factor on the measured resistance was applied, under the recommendations of the ASTM C42 standard. The tests were carried out at the natural water content, without resaturation; the samples were placed between two horizontal plates and the vertical movement of the upper plate was controlled at a speed of 0.3 mm/min. The vertical deformations were deduced from the measurements of the top plate displacement through two external displacement sensors (LVDT). Table 2 summarizes the corrected UCS values obtained for both layers and compares them to the values obtained on the laboratory samples of the same treated and untreated soil.

Table 2. UCS measured on the samples extracted from the Vidourle levee after 6 years of aging (onsite samples), compared to values obtained on laboratory samples at younger ages.

Study	Curing	UCS (MPa)
This study *(onsite samples)*	Layer 7 – 6 years	0.82
	Layer 6 – 6 years	1.77
2015 study *(laboratory samples)*	Untreated soil	0.21
	7 days	0.32
	28 days	0.39
	60 days	0.44
	90 days	0.53
	180 days	0.73
	365 days	1.20

These results show a similar trend to that already observed; the results are reproducible and relatively homogeneous. Layer 7 displays lower UCS values than layer 6 and comparable with the values obtained for a soil compacted and tested in laboratory after 180 days of cure. Layer 6 exhibits higher strength and stiffness with an improved resistance compared to the one measured on laboratory samples after 1 year, probably reflecting the good development and conservation of pozzolanic reaction products.

4.3 Permeability

Permeability tests were performed on the samples intended for direct shear tests. Samples of 10 cm of diameter and +/- 10 cm of height were wrapped in a latex membrane with two porous stones placed on both free sides. The whole specimen was installed in a confining cell fixing the membrane against the sample. The lower porous stone was connected to a pressure/volume controller to impose pressure and measure the volume of water injected. The upper porous stone was connected to a drainage circuit allowing water to drain to the open air. A pressure of 1 bar (= 100 kPa) was imposed on the base while the pressure at the top of the sample corresponded to the atmospheric pressure.

Table 3 summarizes the permeability coefficients obtained. Overall, the results are reproducible, and the permeability measured is very low for both layers.

Table 3. Permeability measured on the samples extracted from the Vidourle levee after 6 years of aging.

Soil - Cure	Permeability k (m/s)
Layer 7 (2% treated soil) - 6 years	$1.9.10^{-10}$
	$1.8.10^{-8}$
	4.10^{-9}
Layer 6 (2% treated soil) - 6 years	$1.61.10^{-8}$
	$3.38.10^{-8}$
	$1.06.10^{-8}$
	$2.41.10^{-9}$
	$8.52.10^{-9}$
	$2.99.\ 10^{-9}$

4.4 Shear strength

The same saturated samples that led to the permeability measurements were used to perform direct shear tests under the following normal stresses: 50 kPa, 100 kPa and 200 kPa. The rate of shearing was fixed low enough, at 6 mm/hour, to maintain drained conditions during shearing. According to ASTM D3080, with a coefficient of consolidation of 2E-5 m^2/s (deduced from the permeability and the stiffness), a thickness of specimen of 10 cm and a failure occurring at 3 mm of displacement, the maximum speed should be 9 mm/hour. The evolutions of shear stress versus tangential displacement are reported in Figure 5. The peak state is defined as the maximum

ratio of shear (τ) versus the normal (σ_N) stress, while the residual state corresponds to the minimum of this ratio (τ/σ_N) after passing the peak.

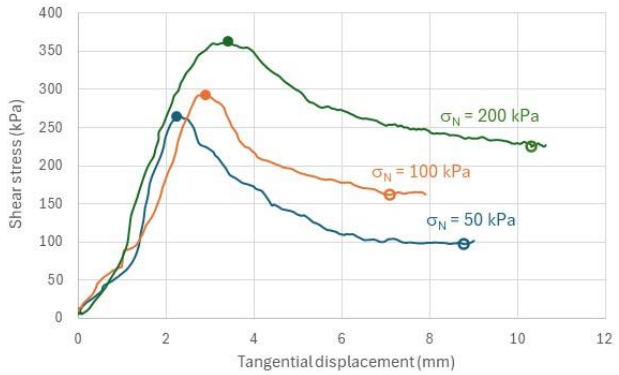

(a)

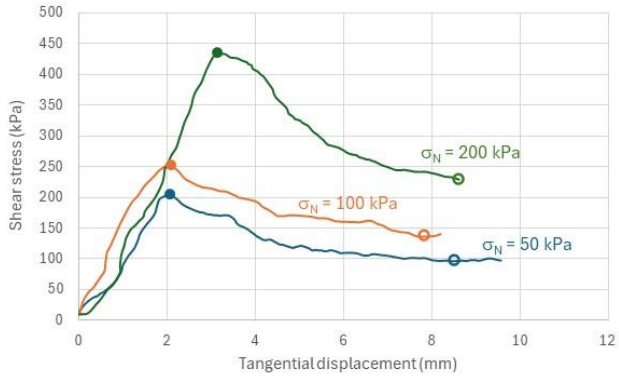

(b)

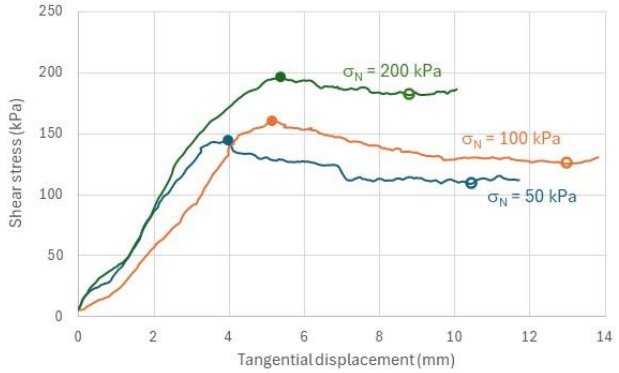

(c)

Figure 5. Direct shear tests performed on the specimens extracted after 6 years, at normal stress of 50 kPa, 100 kPa and 200 kPa. (a) 1st series on layer 6, (b) 2nd series on layer 6, (c) series on layer 7. Peak and residual states are reported by full and empty circles, respectively.

The peak and residual cohesion (c) as well as the associated friction angles (ϕ) measured are presented in Table 4. The peak values are compared with those obtained on laboratory samples cured for 7, 14 and 28 days, tested in consolidated undrained triaxial compression.

As for the other geomechanical properties measured, the layer 7 shows lower values than layer 6, with a significant drop in the friction angle. However, in both cases there is a positive change in cohesion which has greatly increased compared to that developed by samples produced and tested in laboratory at younger ages with values multiplied by a factor of 4 to 6. When compared to the natural soil, the treated soil exhibits values 10 to 20 times higher demonstrating a far greater resistance.

5 CONCLUSIONS

The objective of the present study was to carry out a series of geomechanical tests on samples of soil extracted from the Vidourle levee to assess the characteristics and the durability of the lime-treated soil after 6 years of weathering. Based on the results presented above, the following considerations can be drawn:

- the permeability measured on the soil treated with lime is consistently low;
- the soil treated with 2% of lime and then subject to weathering for 6 years has shown to maintain enhanced geomechanical properties if compared to the same natural soil tested in the laboratory (untreated);
- the geomechanical properties of the soil treated with lime tend to increase with the sample depth in the body of the levee;
- the geomechanical properties are significantly improved for the deeper layer (layer 6) demonstrating the positive impact of the pozzolanic reaction in the long term.

The upper layer considered in the study is located at a depth between 30 and 60 cm from the surface. Its position closer to the surface and the fact that the Vidourle levee is subjected to strong variations in temperature and humidity throughout the years, can possibly explain its worse behaviour. Deterioration due to weathering, or a different kinetics of development compared to the deeper material, more protected, could have caused this phenomenon. To verify this hypothesis, an additional monitoring campaign including sampling and testing is planned for 2024 to better investigate this topic.

Table 4. Parameters measured during the shearing tests performed on the samples extracted from the Vidourle levee after 6 years of aging (onsite samples) (from consolidated drained direct shear test) and compared to values obtained on laboratory samples tested at younger ages (from consolidated undrained triaxial tests).

Study	Soil - Cure	Peak resistance		Residual resistance	
		c (kPa)	Φ (°)	c (kPa)	Φ (°)
This study *(onsite samples)*	Layer 7 (2% treated soil) – 6 years	126	18	78	24
	Layer (2% treated soil) – 6 years	157 – 230	32 – 43	54 – 65	36 – 37
2015 study *(laboratory samples)*	Untreated soil	11	33	(residual state not measured from CU triaxial tests)	
	2% treated soil – 7 days	25	48		
	2% treated soil – 14 days	28	46		
	2% treated soil – 28 days	40	42		

REFERENCES

Bell, F.G. (1996). Lime stabilization of clay minerals and soils, Eng. Geol. 42, 223–237. https://doi.org/10.1016/0013-7952(96)00028-2.

Little, D.N. (1995). Stabilization of Pavement Subgrades and Base Courses with Lime.

Herrier, G., Lesueur, D., Puiatti, D., Auriol, J.-C., Cuisinier, O., Chevalier, C., Haghighi, I., Bonelli, S. (2012). Principles and properties of soils treated by lime for hydraulic earthen structures, 3rd Int. Seminar on Earthworks in Europe, Berlin, Germany.

Nerincx, N., Bonelli, S., Nicaise, S., Herrier, G., Lesueur, D., Tachker, P., Puiatti, D., Cornacchioli, F. (2018). The DigueELITE project: lessons learned and impact on the design of levees with lime-treated soils, International Journal on Hydropower & Dams, 25 (6): 10.

Herrier, G., Bonelli, S., Cornacchioli, F., Nerincx, N., Nicaise, S., Puiatti, D., Tachker, P., Richard, J.-M. (2018). Erosion resistant dikes thanks to soil treatment with lime, 3rd International Conference on Protection against Overtopping, Grange-over-Sands, UK.

Haas, S., Hammerschmidt, S., Shtiza, A., Denayer, C., Scutt, D. (2019). Soil improvement with quicklime - quantification of the carbonation rate in an embankment after 34 years, XVII European Conference of Soil Mechanics and Geotechnical Engineering, Reykjavik, Island.

Das, G., Razakamanantsoa, A., Herrier, H., Saussaye, L., Lesueur, D., Deneele, D. (2021). Evaluation of the long-term effect of lime treatment on a silty soil embankment after seven years of atmospheric exposure: Mechanical, physicochemical, and microstructural studies, Engineering Geology, 281. https://doi.org/10.1016/j.enggeo.2020.105986.

Chabrat, N., Cuisinier, O., Masrouri, F. (2023). In Situ Alteration of the Hydro-Mechanical Behaviour of a Compacted Stabilised Expansive Soil, Geotechnics, 3 (3), 921–936. https://doi.org/10.3390/geotechnics3030049.

Bonelli, S., Nicaise, S., Charrier, G., Chaouch, N., Byron, F., Grémeaux, Y. (2018). Quantifying the erosion resistance of dikes with the overflowing simulator, 3rd International Conference on Protection against Overtopping, Grange-over-Sands, UK.

Nicaise, S., Klotz, F., Bertola, F., Byron, F., Chaouch, N., Grémeaux, Y., Aubriet, J., Ozturk, T., Doghmane, A., Bonelli, S. (2024). Performance trends for lime-treated dikes in a Mediterranean climate, Digues 2024, Aix-en-Provence, France.

Saussaye, L., Das, G, et al., 2020, Experimental dikes in silty soil treated with quicklime and untreated: Evaluation avec 7 years, 10th JNGG, Lyon, France.

Proceedings of the XVIII ECSMGE 2024
GEOTECHNICAL ENGINEERING CHALLENGES
TO MEET CURRENT AND EMERGING NEEDS OF SOCIETY
© 2024 the Authors
ISBN 978-1-032-54816-6
DOI 10.1201/9781003431749-549
Open Access: www.taylorfrancis.com, CC BY-NC-ND 4.0 license

ECSMGE 24
XVIII EUROPEAN CONFERENCE ON SOIL MECHANICS AND GEOTECHNICAL ENGINEERING

Solving challenges of operational areas for renewable energy infrastructure

Relever les défis des zones opérationnelles pour les infrastructures d'énergie renouvelable

M. Beuße
GTU Ingenieurgesellschaft mbH, Hamburg, Germany

L. Vollmert*
Naue GmbH & Co. KG, Espelkamp, Germany

**lvollmert@naue.com*

ABSTRACT: The renewable energy sector requires new infrastructure for development, prefabrication, storage, installation and operation. Most often, the subsoil conditions of the construction facilities, roads and working platforms are characterised by weak clay, organic soil or sand deposals of low density or a combination thereof. The size of loads from e.g. turbine parts, foundation- or tower segments or cranes for installation are challenging. Resulting loads from e.g. low motion vehicles and crane hardstandings are characterised by high deviator-stresses. Anyhow, only limited differential settlements are accepted. To scope with these issues, a wide range of foundation techniques are used as e.g. floating platforms, dynamic compaction, vertical bearing elements or piling. For all techniques, special attention has to be paid on local bearing capacity on the surface, in combination with total and differential settlement. The paper presents a major project on the example of a large nacelle factory, and addressing requirements on working platforms, making use of the combination of different foundation techniques. The geotechnical design by combining analytic models and numerical analysis are presented and discussed.

RÉSUMÉ: Le secteur des énergies renouvelables nécessite de nouvelles infrastructures pour le développement, la préfabrication, le stockage, l'installation et l'exploitation. Le plus souvent, les conditions du sous-sol des installations de construction, des routes et des plates-formes de travail sont caractérisées par des dépôts d'argile faible, de sol organique ou de sable de faible densité, ou par une combinaison de ces éléments. La taille des charges provenant, par exemple, des pièces de l'éolienne, des segments de la fondation ou de la tour, ou des grues pour l'installation, est un défi. Les charges résultant, par exemple, de véhicules à faible mouvement et de grues sont caractérisées par des contraintes de déviation élevées. Quoi qu'il en soit, seuls des tassements différentiels limités sont acceptés. Pour faire face à ces problèmes, un large éventail de techniques de fondation est utilisé, comme par exemple les plates-formes flottantes, le compactage dynamique, les éléments porteurs verticaux ou les pilotis. Pour toutes ces techniques, une attention particulière doit être accordée à la capacité portante locale de la surface, en combinaison avec le tassement total et différentiel. L'article présente des projets majeurs sur l'exemple d'une grande usine de nacelles, et aborde les exigences sur les plates-formes de travail, en utilisant la combinaison de différentes techniques de fondation. La conception géotechnique par la combinaison de modèles analytiques et d'analyses numériques sont présentés et discutés.

Keywords: Working platforms; dynamic soil compaction; geogrids; case study; renewable energy.

1 INTRODUCTION

The south-eastern port area of the city of Cuxhaven in Northern Germany is being planned as the German Offshore Industry Centre, where several production facilities for offshore wind turbines and other components are based. The development of the south-eastern harbour extension was carried out by pumping sands from the North Sea several years ago. Due to the original topography and genesis, the flushing fields in the area of the harbour extension have special geotechnical features. In the tidally influenced area of the river Elbe, there is a soft to pulpy clay layer with widely varying thicknesses on medium-density tidal sands. This is covered by the approximately three metre thick layer of sand, which is loosely to densely compacted (Figure 1).

The eastern area of the harbour extension is used for a production facility for offshore wind turbines. The high stresses of up to 180 kN/m² from the construction and production in combination with low permissible settlements and a subsoil with a 2.0 m to

3.0 m thick layer of clay made special foundation engineering measures unavoidable. Following the evaluation of the ground investigation, the foundation concept envisaged a foundation for the base slab of the production hall, the office and restaurant building, the outbuildings and the circulation areas on a geogrid-reinforced foundation pad over a columnar ground improvement. Despite the high loads in some areas, the client wanted to do without a shallow deep foundation. The highly loaded column foundations, the crane runways and the sprinkler tank were piled.

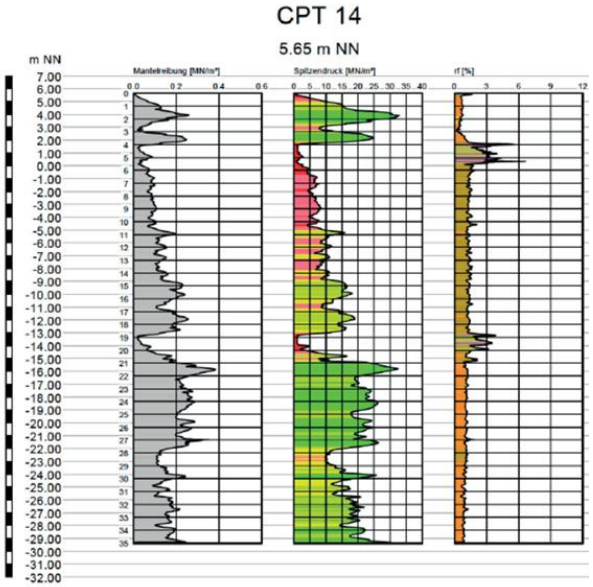

Figure 1. Cone penetration Test Profile, exemplarily.

The columnar soil improvement measure was carried out in the area of the existing access road and the parallel rainwater channel (DN 2,000, GRP material) using vibro-compaction (approx. 200 RSV columns) and in the majority of the area by means of dynamic deep compaction (approx. 5,300 DYNIV® columns) over an area of approx. 130,000 m².

Additional, Cuxhaven is preferred also for monopile production. Monopiles are to be temporarily until they are used in offshore construction. Due to the very large dimensions of the monopiles with diameters of 12 m to 14 m, a length of up to 130 m and a total weight of up to 3,500 tonnes, an economical foundation concept had to be developed for the total available area of just under 330,000 m². In addition to the aforementioned soil conditions of the south-eastern area, the inhomogeneous soil conditions in the area of the formerly approx. 4.00 m deep drainage ditch, which was backfilled in the course of backfilling, required special attention for a floating working area. The surface is to be designed in such a way that it can be driven over by the special transport vehicles for the monopiles.

From a geological perspective, the construction sites are located in the area of Holocene mixed mudflat deposits, which are strongly influenced by their proximity to the water and by the tides. There are Holocene, backfilled sands with a thickness of around 1.70 m to 4.00 m and a very heterogeneous bedding density (very loose to dense).

Below the fill, the subsoil exhibits a typical sequence of Holocene tidal deposits, which can be visualised as follows:

- locally existing lenses of tidal sands with a maximum thickness of 3.50 metres.
- upper clover horizon of varying thickness up to 10.00 m with a soft to stiff consistency. This clay is described as clayey silt with varying degrees of organic content and has low permeability.
- 5.00 m to approx. 17.00 m thick tidal sand layer in loose to medium-dense bedding,
- locally occurring, lower, up to 15.00 m thick clover layer with a soft to stiff consistency,
- From about 18.00 m below ground level, Pleistocene sands in medium-dense to dense compaction.

2 CONSTRUCTION OF NEW PRODUCTION FACILITYS

2.1 Requirements and foundation concept

In total, for the production of wind turbines, an area of 133,000 m² had to be improved. This was divided into six sub-areas, which were differentiated according to their subsequent use. The design load on the individual areas varies significantly between 40 kN/m² and 180 kN/m². Just 60,000 m² of the area is accounted for by the production hall, for which the settlements occurring were to be limited to such an extent that settlement differences incompatible with the structure could be avoided.

The foundation concept envisaged a vertical transfer of the large individual loads in the area of the columns via piles into the Pleistocene layers and a shallow-founded hall base in the other areas. Due to these different foundation systems, large settlement differences were to be expected, which could not be withstood without further geotechnical measures. It was therefore necessary to improve and homogenise the settlement-relevant clays.

In addition to the challenging technical constraints, the time pressure was a decisive factor in

this construction project. For this reason, consolidation using vertical drains and ballast fill, which can be used in similar construction projects, was not an option. As the planned construction period fell between the winter months of November and March, downtimes due to weather conditions had to be minimised.

After a variant test, dynamic intensive compaction with a diameter of over 2.50 m and the addition of foreign material was selected.

As part of a calibration field, a grid dimension of 7.00 m was defined in two phases. This results in a centre distance of 4.95 m. Figure 2 shows the corresponding grid scheme.

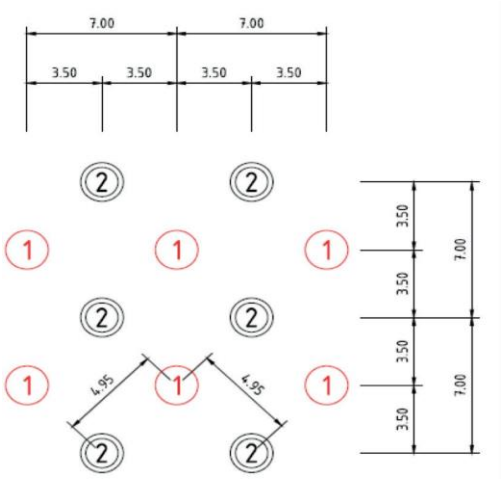

Figure 2. DYNIV® column grid with two offset phases.



Figure 3. Execution of dynamic compaction.

The work sequence provided for the removal of the partially very firm layer of cover sand layer by means of a preliminary excavation and the compaction of the underlying clay with the addition of coarse-grained material. The crater was then backfilled with the pre-excavated material and comparable sand, whereby the installation was carried out in layers. A total of around 5,300 DYNIV® columns were produced, with five machines achieving a peak output of 3,400 m² per day (Figure 3). The amount of material added was adapted to the soil parameters. While between 5 m³ and 10 m³ of crushed stone (base course material with crushed material, 0/32 mm grain size) was usually added to a compaction point, up to 51 m³ of crushed stone was added in areas where high water content was encountered.

2.2 Design of the load distribution layer

In order to ensure optimum load transfer into the compacted columns, a two-layer geogrid-reinforced foundation pad with a total thickness of 75 cm was designed as load and settlement distribution layer. This adaptable, ductile system can compensate for settlement differences resulting from different loads. The design required a long term design yield strength of 1,680 kN/m (per layer) considering creep and installation damage, which could be covered by a biaxial polyester geogrid Secugrid 120/120 Q6 with a short-term strength of 120 kN/m² (md and cmd) to be sufficient to ensure load transfer.

The serviceability verification could not be performed according to EBGEO, as the predefined boundary conditions (significant difference in bedding modulus of rigid column to soft soil > 75) were not met by the DYNIV® columns. Thus, the design was based on the differential equation as provided by Zaeske (2001), documented by Geduhn & Vollmert (2005), taking the column and subsoil stiffness into consideration.

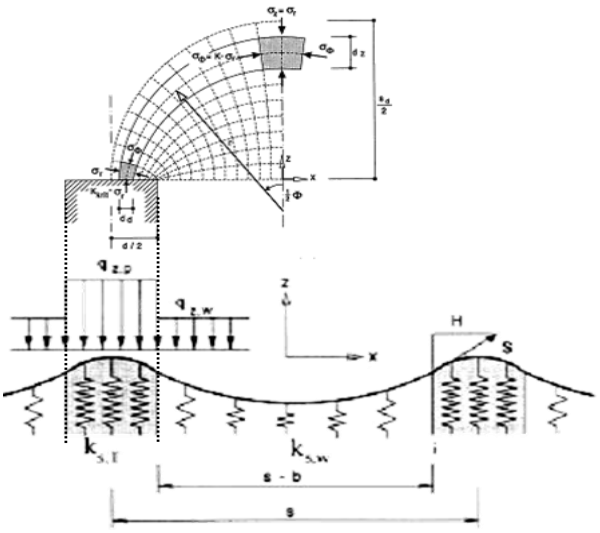

Figure 4. Principle model of the elastic embedded geosysnthetic between vertical bearing elements prone to settlement, arching model according to EBGEO.

Figure 4 shows the model, taking the stiffness of the vertical bearing elements into account. The verification of the static system resulted to a degree

of utilisation of 0.54 << 1.0, thus the ultimate limit state (ULS) was verified.

Beside ULS, the serviceability limit state (SLS) had to be focussed, as the allowable differential settlement was limited to less than 1.5 cm. The finite element method (PLAXIS 2D and PLAXIS 3D) was used, taking into account a linear elastic, ideally plastic model with the Mohr-Coulomb failure criterion. Beside taking into account the long-term design yield stiffness, the calculation of the two biaxial geogrids was carried out with a predefined plasticity limit. For other, more powerful material models, with which more realistic deformation predictions would have been possible, it was not possible to determine further material parameters due to the tight deadlines.

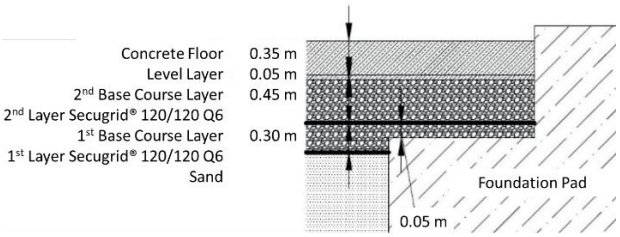

Figure 5. The two-layer, biaxial geogrid in the area of a reinforced concrete foundation (Dr Beuße).

In the area of the hall foundations, the biaxial geogrid layers were arranged as shown in Figure 5, so that notch and shear stresses within the concrete floor are reduced and avoided.

2.3 Installation



Figure 6. Interlocking of base course material and geogrid, compaction with the help of plate compactors (2nd installation level).

During the tender phase, the general contractor had specified Secugrid® 120/120 Q6 from Naue GmbH & Co. KG, as geogrid reinforcement and stabilisation in the first and second layer. Compaction test in a test environment verified the compatibility of the base course material crushed gravel 0/45 mm up to a bearing capacity (plate load test) of 150 MN/m². For this bearing capacity, a compaction of $D_{Pr} \geq 100\,\%$ was verified. The installation guideline required the installation of the base course material by introducing shear forces, so that the geogrid is slightly prestressed and the gravel will be pushed into the open grid structure to ensure proper interlocking of the stiff geogrid structure with the base course grain structure. Figure 6 gives an impression of the interlocking effect.



Figure 7. 1st installation level of the geogrid reinforcement.

The first geogrid layer was laid on the post-compacted sand subgrade (Figure 7). As shown in Figure 8, the second layer of the foundation pad was placed over the individual foundations up to the rising structural elements on a gravel base course.



Figure 8. 2nd installation level of the geogrid reinforcement in the production hall area.

2.4 Safety of construction and transport equipment

The projects in Cuxhaven indicate exemplarily, that weak subsoils covered by relatively thin medium-

dense to dense compacted sandy layers are sensitive to differential settlement. Furthermore, the stability of heavy equipment against ground bearing failure as well as against punching has to be ensured. In some cases, especially in large operational areas for the renewable energy sector as Cuxhaven, extraordinary loads have to be considered from the components itself, or transport vehicles to handle components as e.g. offshore tower segments with dimensions of e.g. 130 m length and 15 m diameter. The dimensions can even exceed the example as given in Figure 9, which represents an equalized load of approx. 110 kPa. Loads like these, demand a special attention to consider weak soil layers even in higher depth, as typically needed for road vehicles.

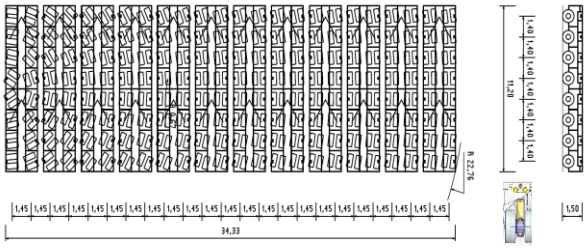

Figure 9. Example of transport vehicle dimensions 34m x 11m with heavy loading up to 120 kPa equalized load.

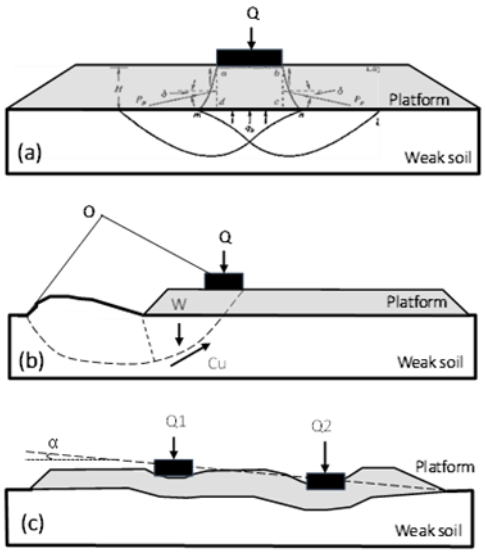

Figure 10. Failure modes to be considered for working platforms as well as for transport devices with large dimensions.

Thus, the punching resistance of the entire structure had to be checked by appropriate measures. Khansari et al. (2023) discussed several aspects of designing operational areas and working platforms, taking thin cover layers and weak subsoil conditions into consideration. Figure 10 outlines the three most relevant aspects, which are considered in design.

Complementing analytical approaches, finite element methods, 2D as well as 3D, allow to calculate the safety level by phi-c-reduction. Therewith, deformation-consistency can be considered more appropriate than using analytical models only. Strain conditions calculated, e.g. on the bottom of asphalt pavements, allow to discuss not only the absolute strain, but also the level of prestressing the system and, comparing with failure strains of asphalt, the tolerance for long term use.

CONCLUSION

Operational areas for renewable energy demand the development of large areas, often placed in locations sensitive to settlements. The presented project has been successfully designed and installed by a combination of soil improvement and stabilized base course layers, reinforced with geogrids of high long term stiffness characteristic. The requirements of the contractor using loads up to 180 kPa could have been met successfully.

REFERENCES

EBGEO - Recommendations for Design and Analysis of Earth Structures using Geosynthetic Reinforcements. *Translation of the 2nd German Edition*. Published by German Geotechnical Society. Ernst & Sohn, 2012. 978-3-433-02950-3.

Geduhn, M. and Vollmert, L. (2005). Deformation-dependent stress states in horizontal geosynthetic reinforcements over pile elements in the dam base. In German. *Bautechnik*, Wiley, 82 (2005), 9, S. DOI 10.1002/bate.v82:9, page 657-662.

Khansari, A., Vollmert, L. and Klompmaker, J. (2023): Evaluation of the available design models for the analysis of geosynthetic-reinforced working platforms. Proceedings of GeoAfrica, 2003.

Zaeske, D. (2001): On the function of unreinforced and reinforced mineral base courses over piles. In German. *Schriftenreihe Geotechnik*, Universität Kassel, 10. ISBN 3897920484.

Proceedings of the XVIII ECSMGE 2024
GEOTECHNICAL ENGINEERING CHALLENGES
TO MEET CURRENT AND EMERGING NEEDS OF SOCIETY
© 2024 the Authors
ISBN 978-1-032-54816-6
DOI 10.1201/9781003431749-550
Open Access: www.taylorfrancis.com, CC BY-NC-ND 4.0 license

ECSMGE 24
XVIII EUROPEAN CONFERENCE ON SOIL MECHANICS AND GEOTECHNICAL ENGINEERING

Physical models of mechanical root-soil interaction

Modèles physiques de l'interaction mécanique entre les racines et le sol

A. Boiero*, M. Arroyo, E. Romero
Department of Civil and Environmental Engineering, Universitat Politècnica de Catalunya, Barcelona, Spain
**alvaro.boiero@upc.edu*

ABSTRACT: In geotechnical bioengineering, living plant material is used to perform engineering functions. In this context, one of the most complex aspects of the soil-root interaction problem is the interplay between the mechanical reinforcement effect and the hydraulic effect, mediated by suction. Soil-root mechanical interaction has been investigated on 1-g models and at scale, using centrifuge tests. The characteristics of model roots have been explored as well, by means of tensile and direct shear tests, in which the soil-root interface response under different loading conditions was studied. However, in most cases these studies were developed for extreme saturation conditions (dry or fully saturated state). This paper summarizes the advances made so far in the field of physical models applied to the analysis of soil-root interaction, and presents the general characteristics of the models currently under development at the UPC-BarcelonaTECH for the study of soil-root interaction under different saturation conditions, highlighting the advantages and limitations of such experimental methodologies.

RÉSUMÉ: Dans la bio-ingénierie des sols, le matériel végétal vivant est utilisé pour remplir des fonctions d'ingénierie. Dans ce contexte, l'un des aspects les plus complexes du problème de l'interaction sol-racine est l'interaction entre l'effet de renforcement mécanique et l'effet hydraulique, médié par la succion. L'interaction mécanique sol-racine a été étudiée sur des modèles à 1 g et à l'échelle, à l'aide d'essais en centrifugeuse. Les caractéristiques des racines modèles ont également été explorées au moyen d'essais de traction et de cisaillement direct, dans lesquels la réponse de l'interface sol-racine sous différentes conditions de charge a été étudiée. Cependant, dans la plupart des cas, ces études ont été développées pour des conditions de saturation extrêmes (état sec ou complètement saturé). Cet article résume les progrès réalisés jusqu'à présent dans le domaine des modèles physiques appliqués à l'analyse de l'interaction sol-racine, et présente les caractéristiques générales des modèles actuellement en cours de développement à l'UPC-BarcelonaTECH pour l'étude de l'interaction sol-racine dans différentes conditions de saturation, en soulignant les avantages et les limites de ces méthodologies expérimentales.

Keywords: Bioengineering; unsaturated soils; root-soil interaction; interface direct shear tests; 1-g root-soil models.

1 INTRODUCTION

The engineered use of vegetation is referred to as "bioengineering" (Coppin & Richards, 2007; Norris et al., 2008). One of the applications of soil bioengineering is the use of vegetation for slope stabilization. However, although vegetation began to be used for this purpose in ancient times, the formal adoption and development of this technology has been very slow, mainly due to the difficulties faced by engineers when trying to quantify its beneficial effects on slope stability (Coppin & Richards, 2007; Świtała et al., 2018).

The mechanisms of root influence on slope stability can be grouped into hydrological effects and mechanical reinforcement effects (Reubens et al., 2007). From a hydrological point of view, the presence of roots in the soil mass implies a reduction in moisture content do to the evapotranspiration process (which implies an increase in suction), and the generation of macropores during root growth (which results in a greater infiltration capacity). However, it should be noted that these effects occur at different times: the greatest infiltration occur during and immediately after rainfall events, while evapotranspiration predominates between rainfall events. In terms of mechanical reinforcement, it is possible to distinguish three types of root-mediated stabilization mechanisms (see Figure 1): A) *basal reinforcement*, provided by roots crossing a potential failure surface, similar to that provided by an anchor system; B) *lateral reinforcement* provided by the soil-root interface strength when the roots do not reach the failure plane and are located either in the sliding wedge (downstream of the tensile crack) or in the stable part of the ground (above the tensile crack); and C) *soil stiffening* due to the presence of roots in the sliding mass, particularly when there is an interaction between neighboring root systems (Reubens et al.,

2007; Wu et al., 2015; Schwarz et al., 2015; Giadrossich et al., 2017).

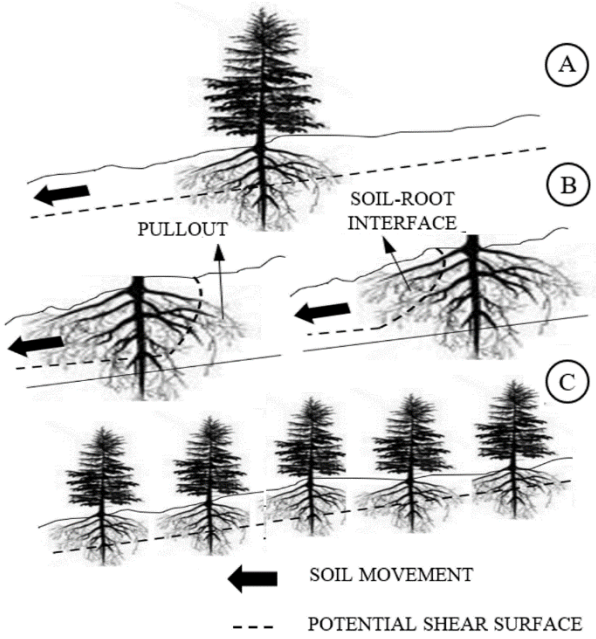

Figure 1. Root stabilization mechanisms: A) basal reinforcement; B) lateral reinforcement; C) stiffening.

Although root systems can penetrate up to 3m into the soil, 80% to 90% of tree roots are concentrated in the upper 0.9m of soil (Coppin & Richards, 2007; Norris et al., 2008). As a consequence, most of soil-root interaction phenomena occur in a low confining stress environment. Thus, during slope failure the unstable soil mass applies a passive pressure or thrust on the wedge soil downstream of the tensile crack and, at the same time, active thrust conditions are generated upstream, when the sliding mass separates from the tensile crack and the soil disaggregates in the form of blocks. This mechanism implies a progressive increase in volume (associated with an increase in void space) and a consequent decrease in total density, leading to a progressive failure.

According to the above, considering that the plant moves together with the sliding mass (because it is rooted in it), when the root system crosses the potential failure surface (Figure 1-A) it will experience displacements that mainly generate bending and predominantly pull-out axial loads. At the same time, lateral roots (Figure 1-B) will mobilize pull-out (when the plant is downstream of the tensile crack) or tensile resistance (when the plant is upstream of the tensile crack), which will depend on the roots themselves and the soil-root interface.

One of the most complex aspects of the soil-root interaction problem is that mechanical reinforcement and hydraulic effects, mediated by suction, interact with each other within a complex root system (Pollen, 2007; Stubbs et al., 2019). This fact seriously complicates purely empirical approaches. However, it must be considered in any soil-roots physical model for an adequate simulation of field conditions.

2 SOIL-ROOT PHYSICAL MODELS

The effects of plant roots on slope stability have been extensively studied over the last 40 years. Early studies on root reinforcement of soil focused on quantifying the mechanical behaviour of roots (O'Loughlin, 1974). In their pioneering work, Wu et al. (1979) studied the increase in shear strength ($\Delta\tau$) provided by a root system using a conventional direct shear test apparatus (63mm square box and 150mm in diameter circular box) to perform drained direct shear tests under constant load conditions (DST_{CNL}), both on natural moisture content and saturated soil-root samples. In addition, measurements of the tensile strength of roots by means a device based on the deformation of a calibrated spring were done.

In the following years, several studies were developed using physical models to analyze the effect of the root morphology and properties, under vertical uprooting stresses and under lateral loads (and moments) associated to wind action. Stokes et al. (1996) conducted a series of 1-g mechanical tests on model young tree root systems made of copper-coated steel wire (1-3 mm thick) and embedded in sand. Each root system was placed in a cylindrical container 300 mm high and 200 mm wide where manually placed damp sand was placed around it. Roots´ anchorage effects were quantified by measuring the pull-out resistance before failure in sand. Operstein & Frydman (2000) developed a simple dead-load application system in which roots were held at each end by specially developed 30 mm in diameter anchor grips, to obtain tensile stress-strain curves for real roots of different plants and diameters. Sonnenberg et al. (2007) performed centrifuge tests applying a scale factor n=15, using a 500x800x500mm height rigid box, with two transparent methacrylate faces. Several sensors were installed in the model: linear variable differential transducers (LVDT), pore pressure transducers (PPT), miniature tensiometers (Ten), and strain gauges attached to woody root analogues. Image processing techniques (Particle-image-velocimetry - PIV) were applied to obtain deformation fields. The model roots were fabricated with lime wood, as a pivoting root structure of L=100mm and A_m=3x3mm^2 size.

Subsequently, some research groups have idealised real root geometries and created artificial roots to assess pull-out strength and quantify the contribution

of roots to slope stabilization. This led to the development of scaled tests using centrifuge (Sonnenberg et al., 2012; Ng et al., 2016; Zhang et al., 2020), 1-g modelling (Zhang et al., 2020), and analysis of the hydromechanical behaviour of rooted soils under partially saturated conditions, both in shear apparatus and in centrifuge (Fraccica et al., 2022; Ng et al., 2016). In general, these investigations corroborate the beneficial effect of roots on slope stability, as well as the influence of the geometry and properties of the soil-root interface at low confining stresses, both under static and earthquake conditions. The importance of the scale factor in 1-g models was also highlighted, in order to consider the effect associated with the lack of confinement on such tests.

Some laboratory and field tests (Leung et al., 2015; Ng et al. 2013) have shown that vegetated soil could retain a suction of up to 10-20kPa within the root zone for rainfall with a return period of less than 10 years. However, most of the above-mentioned research has generally ignored the hydrological effects of evapotranspiration and the resulted induced soil suction.

3 MODELS AT UPC-BARCELONATECH

Computational simulation is now considered as key to accelerating research on soil-root system interaction, as it allows to generalize empirical research findings through virtual models (Stubbs et al., 2019). In relation with this, an experimental programme is under development at UPC-BarcelonaTECH with the following main objectives: a) to document the failure modes of the soil-root system under overturning/pull-out tests in a 1-g physical model, using root analogues; and b) to measure the strength at the soil-real root interface under partial saturated conditions, by means DST_{CNL}. The obtained data will be used in the development of new soil-root interaction simulation tools based on the G-PFEM platform (Geotechnical Particle Finite Element Method; Carbonell et al. 2022).

3.1 Materials

In this research, two soils are being used: a mixture of 70% BR37 quartz sand and 30% UQ12 silt (Material A); and a silty clay from the Agropolis batch, located in Barcelona (Material B). Particle size distributions are shown in Figure 2, while their physical properties are summarised in Table 1.

Two different 3D root analogue models used in previous studies (Liang et al. 2015; Liang & Knappett 2017; Zhang et al., 2020) are considered in this research (Figure 3a): one with a relatively narrow and deep architecture (ND), and another with a wider and shallower architecture (WS). Both models were created from root architecture data obtained from Pinus pinaster trees grown on predominantly sandy soils in France (Danjon & Reubens 2008). Root models will be printed on Acrylonitrile Butadiene Styrene (ABS) plastic, a material that exhibits similar behaviour to that of real roots (Liang et al., 2015).

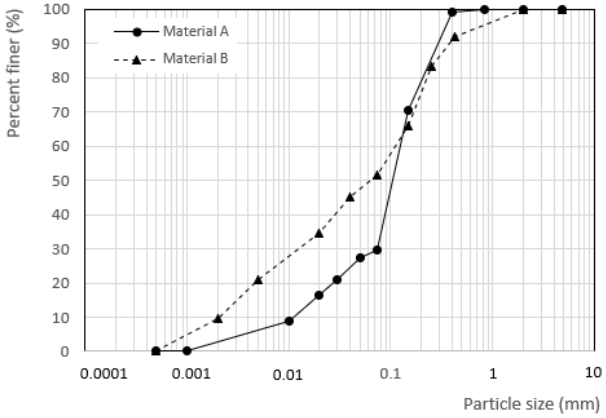

Figure 2. Particle size distribution of materials A and B.

Table 1. Physical properties of materials A and B.

	Material	
	A	**B**
Mean grain size, d_{50} (mm)	0.11	0.07
Density of solids, ρ_s (Mg/m^3)	2.65	2.70
Dry density, ρ_d (Mg/m^3)	1.61	1.80
Maximum void ratio, e_{max}	0.849	-
Minimum void ratio, e_{min}	0.440	-
Plastic limit, PL	NP	16.5
Liquid limit, LL	NP	28.9
Hydraulic conductivity, k_{ws} (m/s)(*)	$5x10^{-6}$	$9x10^{-9}$

(*) Under saturated conditions

Considering a weighted average diameter of the printed root model ($d_{r,\,ave}$) equal to 2 mm, an optimum value of N=20 was selected as scale factor for the tree analogues. Such selection is supported on the rate $d_{r,ave}/d_{50}$ (=17 for material A; =28 for material B), which must be graeter than a minimum threshold of 15 to avoid soil-structure interferences in physical models (Wood, 2004).

For the interface tests in the direct shear apparatus, two types of wood samples were used in order to consider the effect of root´s roughness: a) samples of real roots from Pinus halapencis, obtained in the Collserola mountain range, located near Barcelona (relatively high roughness); and b) samples of a commercial treated pine wood (relatively low roughness).

3.2 Overturning/pull-out tests (1-g model)

According to the failure mechanisms outlined above (see Figure 1), it seems appropriate to assume that the overturnig/pull-out tests allow the analysis of the root extraction scenario from a stable soil, analogous to a surface landslide initiating above the tree line, or to tree uprooting associated with wind action.

A rigid box of dimensions 250x700x400 mm in height, constructed with methacrylate, will be used for 1-g physical models (Figure 3). A 10 mm layer of gravel will be placed on the bottom of the box to facilitate drainage, and a 100 mm layer of BR37 sand on top of it. A 1:20 root model will be installed in the central part of the container, and then the soil will be placed around it by compacting successive layers until reaching void ratios of 0.645 for material A (corresponding to a dry density of 1.61 Mg/m^3) and 0.467 for material B (corresponding to a dry density of 1.80 Mg/m^3). The tests will be performed at variable saturation levels {0-40-70-95}%, which will be reached by ascending saturation from the base of the box, and will be controlled by the installation of a METER Group tensiometer TEROS-31, and several SEN0193 sensors for soil moisture measurement. Readings from these devices will be analysed with the SWCC curve of each material, in order to verify the reached saturation degree.

Subsequently, overturning/pull-out tests will be performed. For the overturning tests, the load will be applied at a point located 60 mm above the surface of the model, through a RS Pro 100N Electric Linear Actuator motor, working at a constant speed of 0.15mm/min (material A) and 0.08mm/min (material B). It will be recorded: i) the load applied on the trunk, by means of a CTCM load cell of 15 kg capacity; and ii) the lateral movement, through a CONTROLS displacement transducer of 25 mm capacity. In the case of pull-out tests, the loading system arrangement will be modified, as illustrated in Figure 3b, and the root of the model will be extracted under the same parameters indicated for the overturnig tests, recording the following: i) the load applied on the top of the trunk; and ii) the vertical displacement. For this, the same sensors mentioned above will be used.

Relative root-soil stiffness ratio is being considered to compensate for the lack of confinement in the 1-g model.

3.3 Soil-root interface tests

When trees are above the tensile crack, as occurs in the case of clearings, riverbanks, or cuts for railroads and roads (Giadrossich et al., 2019), the activated force depends mainly on the friction at the soil-root interface, which can be studied from interface direct shear tests.

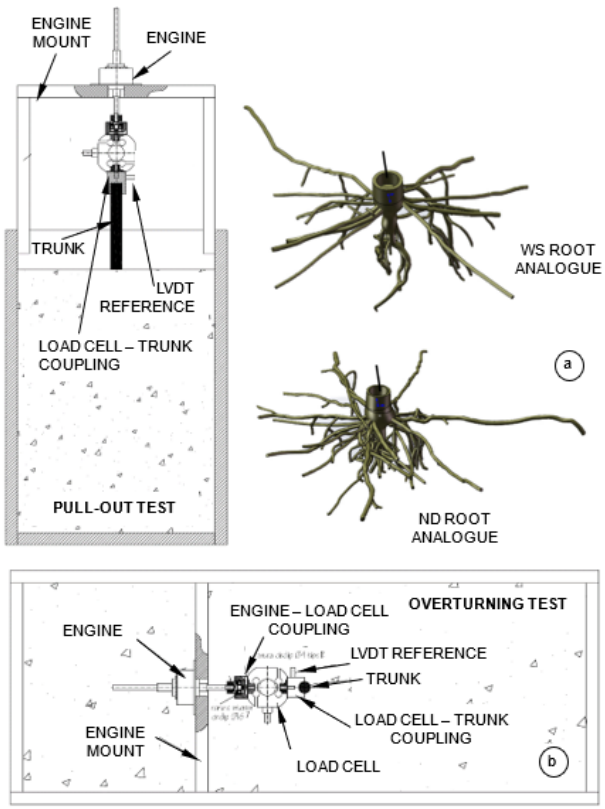

Figure 3. 1-g physical model arrangement: a) root analogues; b) model components.

The research is being conducted on a Wykeham Farrance model 27-WF2160 AUTOSHEAR direct shear machine. The vertical and horizontal displacements in the specimen, and the shear force during the test, are recorded through LVDTs and a 5kN horizontal load cell, using data acquisition software incorporated in the direct shear apparatus. Samples from soils A and B were prepared at the same initial conditions contemplated in the 1-g model. The height of the soil samples was 20mm. For the interface tests, a 14.5mm high and 60x60mm size wood sample was placed in the lower half of the shear box. Then, the soil sample was placed on it. The DST_{CNL} were performed using three initial normal stresses σ_o={7-15-24.5}kPa, on the two types of wood samples mentioned above. The horizontal displacement rate was set at 0.15mm/min (material A) and 0.08mm/min (material B). Figure 4 shows preliminary results obtained in the interface tests on Material A, considering the extension of the Mohr-Coulomb model for partially saturated soils proposed by Fredlund et al. (1978), and the variation of shear strength (τ) as a function of water ratio ($e_\omega=S_{rf}e_f$). This parameter is appropriate as volumetric state variable

because it tends to void ratio (e) under nearly saturated states (Romero & Vaunat, 2000).

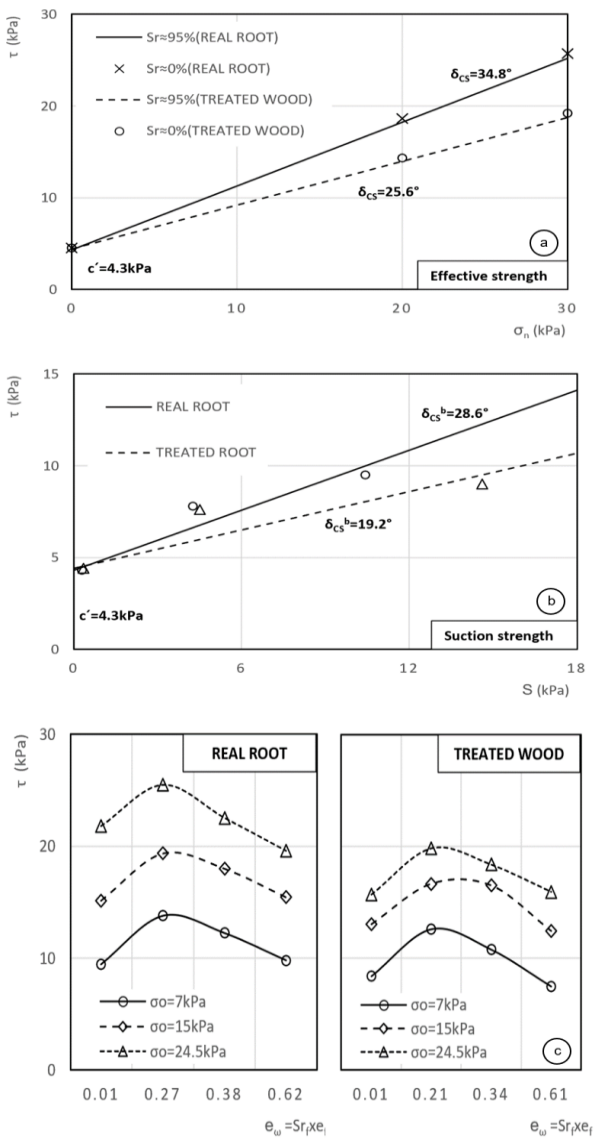

Figure 4. Preliminary results soil-real root interface tests on Material A.

According Figure 4a, from the τ-σ_n graph, the soil-real root (high roughness) effective interface friction angle at the ultimate shear strength is δ_{sc}=34.8º, with an effective soil-root adhesion of 4.3kPa; while the soil-treated wood (low roughness) effective interface friction angle at the ultimate shear strength is δ_{sc}=25.6º, with an effective soil-root adhesion of 4.3kPa. The effect of suction can be seen in Figure 4b. For the real root-soil interface, $\delta_{sc}{}^{b}$=28.6º, while for the treated wood-soil interface, $\delta_{sc}{}^{b}$=19.2º. Finally, from Figure 4c it is evident that for rougher roots, the shear strength at the interface (including the effect of the degree of saturation) is higher than for treated wood, representative of less rough roots.

4 CONCLUSIONS

A review of the physical models used over the last 40 years to study the effect of roots on slope stability, shows the evolution of research from simple root analogues tested in 1-g physical models, to 3D printed root analogous with mechanical properties like those of real roots, employed in 1-g and scaled centrifuge physical models. In addition, direct shear apparatus looks like a useful tool to study the soil-root interface. There is also a trend towards the use of computational simulation in research, as it allows to generalize empirical research findings through virtual models. At the UPC-BarcelonaTECH experimental research is currently underway, which will serve to validate a soil-root interaction simulation tools based on the G-PFEM platform.

ACKNOWLEDGEMENTS

The authors are grateful for the financial support provided by MCIN/AEI/10.13039/501100011033 and Union EuropeaNextGenerationEU/PRTR.

REFERENCES

Carbonell, J. M., Monforte, L., Ciantia, M., Arroyo, M., Gens, A. (2022). The Geotechnical Particle Finite Element Method for the modelling of soil-structure interaction under large deformation conditions. *Journal of Rock Mechanics and Geotechnical Engineering* 14 3: 967-983. https://doi.org/10.1016/j.jrmge.2021.12.006

Coppin, N. J., Richards, I. G. (2007). Use of vegetation in civil engineering. CIRIA. London, UK.

Danjon F., Reubens, B. (2008) Assessing and analysing 3D architecture of woody root systems, a review of methods and applications in tree and soil stability, resource acquisition and allocation. *Plant Soil* 303:1 - 34. https://doi.org/10.1007/s11104-007-9470-7. .

Fraccica A., Romero E., Fourcaud, T. (2022) Tensile strength of a compacted vegetated soil: laboratory results and reinforcement interpretation. *Geomechanics for Energy and the Environment* 30, 100303:1-100303:14 https://doi.org/10.1016/j.gete.2021.100303.

Fredlund D., Morgenstern N., Widger R. (1978) The shear strength of unsaturated soils. Canadian Geotechnical Journal, volumen 15(número 3): 313-321.

Giadrossich, F., Schwarz, M., Cohen, D., Vergani, C., Hubble, T., Phillips, C., Stokes, A. (2017) Methods to measure the mechanical behaviour of tree roots: a review. *Ecological Engineering* 109: 256-271. http://dx.doi.org/10.1016/j.ecoleng.2017.08.032.

Leung, A., Garg, A., Ng, C. (2015) Effects of plantroots on soil-water retention and induced suction in vegetated soil. *Engineering Geology*, 193, 183–197. https://doi.org/10.1016/j.enggeo.2015.04.017.

Liang T., Knappett, J., Duckett, N. (2015) Modelling the seismic performance of rooted slopes from individual root ‐ soil interaction to global slope behaviour. *Géotechnique* 65:995 ‐ 1009. https://doi.org/10.1680/jgeot.14.P.207.

Liang, T., Knappett J. (2017) Centrifuge modelling of the influence of slope height on the seismic performance of rooted slopes. *Géotechnique* 67:855 ‐ 869. https://doi.org/10.1680/jgeot.16.P.072.

Ng, C., Kamchoom, V., Leung, A. (2016) Centrifuge modelling of the effects of root geometries on the transpiration-inducedsuction and stability of vegetated slopes. *Landslides*, 1–14 http://dx.doi.org/10.1007/s10346-015-0645-7.

Ng, C., Woon, K., Leung, A., Chu, L. (2013).“Experimental investigation of induced suction distributions in agrass-covered soil.”Ecol. Eng., 52, 219–223 https://doi.org/10.1016/j.ecoleng.2012.11.013.

Norris, J., Stokes, A., Mickovski, S., Cammeraat, E., van Beek, R., Nicoll, B., Achim, A. (Eds.). (2008). Slope Stability and Erosion Control: Ecotechnological Solutions. Springer Netherlands. https://doi.org/10.1007/978-1-4020-6676-4.

O’Loughlin, C., 1974. The effect of timber removal on the stability of forest soils. *J. Hydrol. (NZ)* 13 (2), 121–134.

Operstein, V. & Frydman, S. (2000) The influence of vegetation on soil strength. *Ground improvement* 4:81-89.

Pollen, N. (2007) Temporal and spatial variability in root reinforcement of streambanks: accounting for soil shear strength and moisture. *Catena*; 69(3),197–205. http://dx.doi.org/10.1016/j.catena.2006.05.004.

Reubens, B.; Poesen, J.; Danjon, F.; Geudens, G.; Muys, B. (2007) The role of fine and coarse roots in shallow slope stability and soil erosin control with focus on root system architecture: a review. *Trees* 21:385-402. http://:doi.org/10.1007/s00468-007-0132-4.

Romero, E. & Vaunat, J. (2000) Retention curves on deformable clays. In: *Experimental Evidence and Theoretical Approaches in Unsaturated Soils, Tarantino & Mancuso* (eds) Balkema, Rotterdam, ISBN 90 5809 1864.

Schwarz, M., Rist, A., Cohen, D., Giadrossich, F., Egorov, P., Büttner, D., Stolz, M., Thormann, J.-J., (2015) Root reinforcement of soils under compression. *J. Geophys. Res.: Earth Surf.* 120 (10), 2103–2120. http://dx.doi.org/10.1002/2015JF003632.

Sonnenberg, R., Bransby, M., Bengough, A., Hallett, P., Davies, M. (2012). Centrifuge modelling of soil slopes containing model plant roots. *Canadian Geotechnical Journal*, 49(1), 1-17. https://doi.org/10.1139/t11-081.

Sonnenberg, R.; Davies, M.; Bransby, M.; Hallet, P.; Bengough, A.; Mickovski, S., Hudacsek, P. (2007) Centrifuge modelling of slope reinforcement by vegetation. In: *XIV European Conference on Soil Mechanics and Geotechnical Engineering.* Madrid, Spain.

Stokes, A.; Ball, J.; Fitter, A.; Brain, P. & Coutts, M. (1996) An experimental investigation of the resistance of model root systems to uprooting. *Annals of Botany Company*. 78: 415-421. http://dx.doi.org/10.1006/anbo.1996.0137.

Stubbs, C., Cook, D., Niklas, K. (2019). A general review of the biomechanics of root anchorage. *Journal of Experimental Botany*, 70(14), 3439-3451. https://doi.org/10.1093/jxb/ery451.

Świtała, B. M., & Wu, W. (2018). Numerical modelling of rainfall-induced instability of vegetated slopes. *Géotechnique*, 68(6), 481-491. http://dx.doi.org/10.1680/jgeot.16.P.176.

Wood, D. (2004). Geotechnical modelling. Spon Press - Taylor & Francis Group. London, UK.

Wu, T., W. McKinnell, Swanston, N. (1979) Strength of tree roots and landslides on Prince of Wales Island, Alaska, *Can. Geotech. J.*, 16, 19-33. https://doi.org/10.1139/t79-003.

Wu, W., Switala, B., Acharya, M., Tamagnini, R., Auer, M., Graf, F., Kamp, L., Xiang, W. (2015). Effect of vegetation on stability of soil slopes: numerical aspect. *Recent Advances in Modeling Landslides and Debris Flows*. Published by Springer International Publishing. (pp. 163-177). https://doi.org/10.1007/978-3-319-11053-0_15.

Zhang, X., Knappett, J., Leung, A., Ciantia, M., Liang, T., Danjon, F. (2020). Small-scale modelling of root-soil interaction of trees under lateral loads. *Plant and Soil*, 456(1-2), 289-305. https://doi.org/10.1007/s11104-020-04636-8.

Proceedings of the XVIII ECSMGE 2024
GEOTECHNICAL ENGINEERING CHALLENGES
TO MEET CURRENT AND EMERGING NEEDS OF SOCIETY
© 2024 the Authors
ISBN 978-1-032-54816-6
DOI 10.1201/9781003431749-551
Open Access: www.taylorfrancis.com, CC BY-NC-ND 4.0 license

ECSMGE 24
XVIII EUROPEAN CONFERENCE ON SOIL MECHANICS AND GEOTECHNICAL ENGINEERING

Revisiting the effect of coefficient of thermal expansion in energy pile–soil interactions

L'effet du coefficient de dilatation thermique dans les interactions pieu énergétique-sol: une revue

T.M. Bodas Freitas*, P.J. Bourne-Webb
CERIS, Instituto Superior Técnico, Lisbon, Portugal

M. Fernandes
Ródio, Alenquer, Portugal (formerly Instituto Superior Técnico)

D. Sterpi
Politecnico di Milano, Milan, Italy

**teresabodas@tecnico.ulisboa.pt*

ABSTRACT: When pile foundations and the ground around them are thermally-activated as part of a shallow geothermal energy system, new and somewhat complex changes in pile-soil interaction occur. In this paper, the influence of the relative expansion and contraction between the pile and surrounding soil, as expressed via the ratio of the coefficient of thermal expansion (CTE) of the soil to that of the pile, is revisited. Previous steady-state thermo-mechanical analysis by the authors suggested that this may be a very significant parameter especially when the CTE ratio was somewhat greater than 1 but more recent work has shown there are a number of other factors which may work to either mitigate or exacerbate this effect. This paper brings together recent work relating to this effect, to provide guidance on the impact of the form of the thermal loading in time and the initial mobilisation of the pile shaft resistance on when the CTE ratio may be significant in the functioning of thermally-activated pile foundations.

RÉSUMÉ: Lorsque les fondations sur pieux et le sol qui les entoure sont thermiquement activés dans le cadre d'un système d'énergie géothermique peu profond, des changements nouveaux et quelque peu complexes dans l'interaction pieu-sol se produisent. Dans cet article, l'influence de la dilatation et de la contraction relatives entre le pieu et le sol environnant, exprimée par le rapport du coefficient de dilatation thermique (CTE) du sol à celui du pieu, est revisitée. Une précédente analyse thermomécanique en régime permanent par les auteurs a suggéré que cela pouvait être un paramètre très important, mais des travaux plus récents ont montré qu'il existe un certain nombre de d'autres facteurs susceptibles d'atténuer ou d'exacerber cet effet. Cet article rassemble des travaux récents relatifs à cet effet, pour fournir des indications sur l'impact de la forme du chargement thermique dans le temps et la mobilisation initiale de la résistance du fût du pieu lorsque le rapport CTR peut être significatif dans le fonctionnement des fondations sur pieux.

Keywords: Piles; thermal; interactions; safety

1 INTRODUCTION

In order to reduce humanity's reliance on carbon intensive energy and to reduce overall energy demand, many countries are looking to source energy via sustainable technologies. An example of this type of technology are shallow geothermal energy (SGE) systems, which can be used to heat and cool buildings. SGE systems have been widely used since the oil-shocks of the 1970s, especially in North America and Northern Europe and have been demonstrated to reduce environmental impact, have low operational costs and save on primary energy expenditure.

For the implementation of SGE, especially in urban areas, the utilization of the pile foundations as a substitute for borehole heat exchangers, has received increasing attention over the past 20 years, amidst efforts to establish renewable and sustainable, heating and cooling systems within the construction industry. A significant number of experimental studies both in the field and laboratory, supplemented by numerical studies, have been undertaken to examine the technical issues associated with the use of thermally-activated pile foundations (TAPS). When pile foundations and the ground around them are thermally-activated as part of an SGE system, new and somewhat complex changes in pile-soil interaction occur. These effects are

a function of a number of factors, especially the restraint of the pile along its shaft and at the ends, in addition to the thermal characteristics of the soil and pile. In this paper, the influence of the relative expansion and contraction between the pile and surrounding soil, as expressed via the ratio of the linear coefficient of thermal expansion (CTE) of the soil to that of the pile, is examined.

While the CTE of construction materials like steel (11-13 με/K) are well defined, the CTE of concrete is somewhat more variable depending primarily on the mineralogy of the aggregates; e.g. Bonnell & Harper (1951) report values of 6.1-8.5, 8.6-10.4 and 12.2-13.7 με/K for limestone-, granite- and quartzite-based concretes. The CTE of granular soils will also depend largely on the mineralogy of the soil particles with e.g. Bonnell & Harper (1951) reporting values of 4.0- 6.5, 5.4 – 9.0 and 11 – 12.6 με/K for limestone, granite and quartzite aggregates. For concrete piles, in granular soils, the range of values for the CTE ratio is likely to be in the range of 0.5 to 2. In fine-grained soils, the volumetric response to drained thermal loading not only depends on mineralogy but also the over-consolidation ratio. Broadly speaking, in normally and lightly over-consolidated clay, the soil will contract irrecoverably during heating (thermally-induced consolidation) but as the soil becomes over-consolidated, recoverable thermal expansion is observed. In this latter case, indications from experimental data (e.g. Cekerevac & Laloui, 2004) suggest the CTE ratio could be in excess of two.

The potential influence of the CTE ratio in the response of thermally-activated (TA) piles was previously explored by Bodas Freitas et al. (2013), Bourne-Webb et al. (2016) and Bourne-Webb et al. (2019) for a TA pile in a cohesive medium and based on steady state thermal conditions. This suggested a strong effect with the thermal axial stress change becoming increasingly tensile as the CTE ratio increased, as illustrated in Figure 1 where the max. thermal stress in the pile, normalised by the thermal stress in a perfectly restrained pile, is plotted against the pile head thermal movement, normalised by the expansion of a perfectly unrestrained pile.

Rotta Loria & Laloui (2016), illustrated a similar effect when examining the influence of CTE ratio on the interactions between pairs of piles, and Gawecka et al. (2017) found that in back-analysing a TA pile test in over-consolidated London Clay, a CTE ratio of 1.8 was needed to achieve good agreement.

Recognising that steady state thermal conditions or long-periods of sustained thermal loading were not necessarily representative of realistic seasonal thermal loadings, and following the review of cyclic thermal loading of TA piles in Bourne-Webb & Bodas Freitas (2020), further work was undertaken using numerical analysis to explore how balanced periodic thermal loads impact on the behaviour of TA piles and the influence of CTE ratio within this.

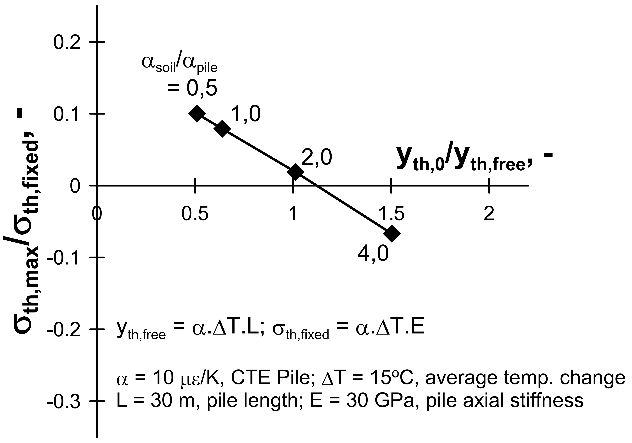

Figure 1. Influence of CTE for a pile in a cohesive medium under thermal steady state conditions (Bourne-Webb et al., 2019)

Bourne-Webb et al. (2022a, 2022b) highlighted how the response of TA piles to cyclic thermal loading was linked to the proportion of the available shaft resistance that was initially mobilised under mechanical loading (quantified by the factor M, the ratio between the shaft resistance mobilised at working load and the ultimate shaft resistance) which was a function of the load itself and pile spacing in groups. Bodas Freitas et al. (2021) modelled the response of a cyclically TA pile in a cohesive medium with the initial shaft mobilisation, M ≅ 50% and 90%, and with varying CTE ratio. In comparison to the steady state case previously examined, it was shown that the effect was much reduced, Figure 2.

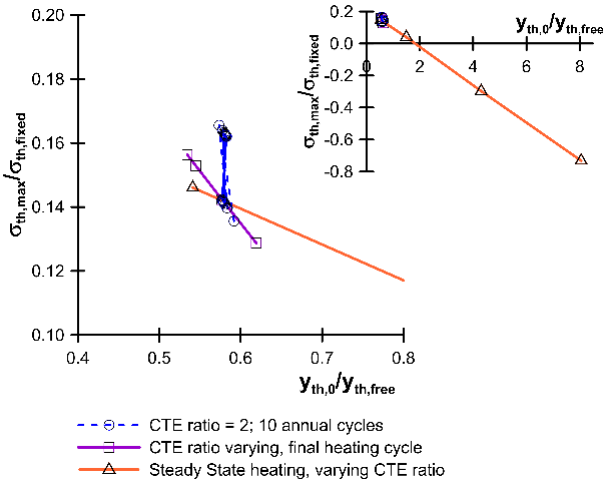

Figure 2. Influence of CTE for a pile in a cohesive medium under transient thermal loading, (Bodas Freitas et al., 2021)

To further explore these results, the work presented herein expands on that in Bourne-Webb et al. (2022a) by examining the role of the CTE ratio in the response of TA piles in granular media at differing levels of initial shaft resistance mobilisation.

2 BASIS FOR ANALYSES

In the axisymmetric finite element analyses presented here, a single reinforced concrete pile with a diameter of 1 m and a length of 30 m was considered, and Figure 3 illustrates the geometry used for the analysis domain. The radius of the model domain was varied between 30 m and 2 m. The reduced radial dimensions permit the behaviour of an infinite pile group to be examined based on a unit cell approach with the pile spacing being equivalent to 2x the radius.

The pile was modelled as a linear elastic material and the soil was modelled as linear elastic-perfectly plastic with a Mohr-Coulomb failure criterion, using the program ABAQUS 2016 (Dassault Systèmes, 2021), with the mechanical and thermal properties outlined in Table 1. The soil stiffness is shown graphically in Figure 3 and averages 129 MPa over the length of the pile.

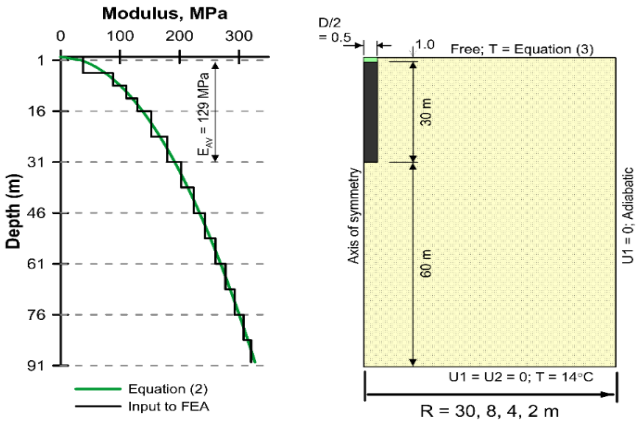

Figure 3. FE Model geometry and soil stiffness variation.

The modelling sequence and temperature boundary conditions were applied as follows: i) the initial stress and temperature fields were established based on the K_0 and T_0 values in Table 1; ii) a periodic temperature function, Eqn. (1) was applied at the ground surface over a period of 10 years, to mimic the initial temperature profile in the near-surface region (T_0 = 14°C, ΔT = 11°C; t is the time in years); iii) The pile was wished-in-place and then mechanically loaded; iv) 10 years of TA pile operation was modelled by applying a temperature change based on Eq. (1) along a line extending over the length of the pile shaft, at a radius of 0.4 m (T_0 = 14°C, ΔT = 12°C). During this period the surface temperature was switched to 23±2°C, to represent the climate-controlled building atop the foundation.

$$T = T_0 + \Delta T.sin[2\pi(t)] \quad (1)$$

Mechanical loads were imposed on in order to generate different levels of initial shaft resistance mobilisation, M which are quoted alongside the respective results in Figures 4 to 6.

3 RESULTS & DISCUSSION

In the following, the results of a parametric analysis utilising the model described in the previous section are presented.

Figure 4 presents the baseline case for an isolated, cyclically TA pile (domain radius, R = 30 m) with a shaft mobilization M = 100% and shows the evolution of thermally-induced pile head settlement, $y_{0,th}$ and axial load, N_{th} for soil:pile CTE ratios of 1:1, 1:2 and 2:1, over 10 years. All start with pile heating, except CTE 1:1c which started with pile cooling. It is apparent that whether the TA starts with heating or cooling only affects the first couple of years, after which the response converges.

In all cases, during the first pile cooling phase, significant additional settlement developed: around 10 mm with CTE ratios of 1:1 and 2:1, after which it is almost stable, and about 20 mm when the CTE ratio was 1:2 (pile expands more than the soil) which continues to exhibit increasing settlement across the 10 years simulated. Thermally-induced axial load changes follow a similar pattern with an initial increase in compression followed by quasi-stable load variations with CTE ratios of 1:1 and 2:1 but a steady increase in load when the CTE ratio was 1:2.

Figure 5 illustrates the effect of cyclic TA for cases where the domain radius is reduced to R = 4 and 2 m, to capture TA pile group effects in an approximate manner. Again, CTE raios of 1:1 (C03, C10), 1:2 (C04, C13) and 2:1 (C07, C37) were considered. With R = 4 m, M remains close to 100% but when R = 2 m, M reduced to about 90%.

Compared to the isolated pile case, a clear reduction in induced thermal movement is seen and the effect of the CTE ratio variation is also progressively eliminated. Broadly speaking, the response is similar to those reported by (Bourne-Webb et al., 2022a). In terms of the thermal load changes, the case where the CTE of the pile is twice that of the soil continues to lead to significant increases (R = 4 m) or much larger amplitude (R = 2 m).

Although not shown here, when the value of M is reduced (moving from a factor of safety on shaft

resistance of 1 to 2 with respect to the mechanical load), the increase in initial stability (reduced M) of the TA pile leads to the thermal ratcheting in R = 4 m cases being eliminated. Again, the main effect of the variation in CTE ratio is in the thermally-induced axial load changes which are smaller than the cases with high initial shaft mobilisation.

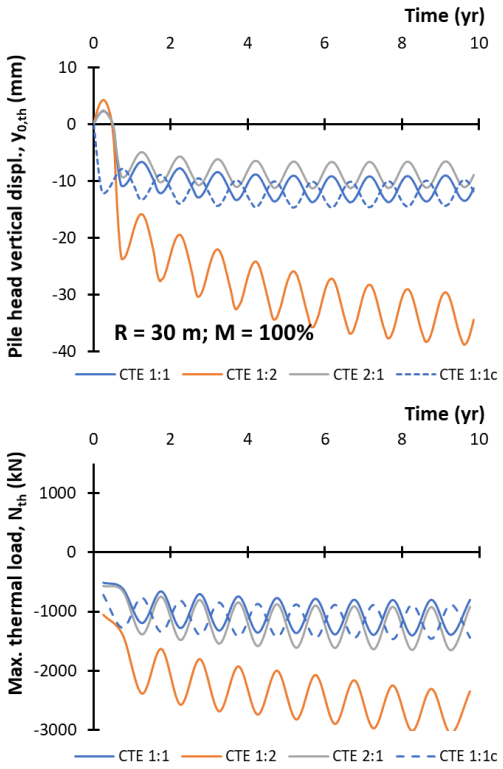

Figure 4. Isolated TA pile (R = 30) with high M.

4 CONCLUSIONS

The work presented in this paper continues to build on the understanding of the response of TA piles: the influence of the geometric layout of the pile(s), mechanical loading and key thermal parameters, i.e. CTE.

While under steady state thermal conditions the CTE has been shown to have a profound effect on pile-soil interactions, when balanced cyclic thermal loading is considered, the resulting effect depends on other factors as discussed above – namely, pile spacing and the initial shaft mobilisation under mechanical loading.

If piles are largely isolated, then care needs to be exercised when cyclic thermal loading is applied on piles with high initial mobilisation of the shaft. More so, if the CTE of the pile is larger than that of the soil.

Depending on the degree of mechanical interaction between piles within a group, which affects the initial shaft mobilisation, the effect of CTE variations in the cyclic thermal response can be reduced or even eliminated.

ACKNOWLEDGEMENTS

The work presented was financed by the *Fundação para a Ciência e a Tecnologia*, Portugal, via grants PTDC/ECI-EGC/29083/2017 (DEEPCOOL) and UIDB/04625/2020. The authors would like to express their gratitude to the funding institution.

REFERENCES

Bodas Freitas, T.M., Cruz Silva, F., Bourne-Webb, P.J. (2013). The response of energy foundations under thermo-mechanical loading, in: *Proc. 18th Intl. Conf. on Soil Mech. and Geotech. Eng'g*. Paris, France, pp. 3347–3350.

Bodas Freitas, T.M., Zito, M., Bourne-Webb, P.J., Sterpi, D. (2021). Thermal performance of seasonally, thermally-activated floating pile foundations in a cohesive medium. *Engineering Structures* 243, 112588. https://doi.org/10.1016/j.engstruct.2021.112588

Bonnell, D.G.R., Harper, F.C. (1951). *The thermal expansion of concrete*. Building Research Station, Garston, Watford, UK.

Bourne-Webb, P.J., Bodas Freitas, T.M., Freitas Assunção, R.M. (2016). Soil–pile thermal interactions in energy foundations. *Géotechnique* 66, 167–171. https://doi.org/10.1680/jgeot.15.T.017

Bourne-Webb, P.J., Bodas Freitas, T.M., Freitas Assunção, R.M. (2019). A review of pile-soil interactions in isolated, thermally-activated piles. *Computers and Geotechnics* 108, 61–74. https://doi.org/10.1016/j.compgeo.2018.12.008

Bourne-Webb, P.J., Bodas Freitas, T.M. (2020). Thermally-activated piles and pile groups under monotonic and cyclic thermal loading–A review. *Renewable Energy* 147, 2572–2581. https://doi.org/10.1016/j.renene.2018.11.025

Bourne-Webb, Peter J., Lupattelli, A., Bodas Freitas, T.M., Salciarini, D. (2022a). The influence of initial shaft resistance mobilisation in the response of seasonally, thermally-activated pile foundations in granular media. *Geomechanics for Energy and the Environment* 32, 100299. https://doi.org/10.1016/j.gete.2021.100299

Bourne-Webb, Peter J, Freitas, T.M.B., Zito, M., Lupattelli, A., Sterpi, D., Salciarini, D. (2022b). Outstanding issues in understanding the behaviour of thermally-activated pile foundations. *DFI-EFFC Intl. Conf. on Deep Foundations and Ground Improvement*, Berlin, Germany, p. 10.

Cekerevac, C., Laloui, L. (2004). Experimental study of thermal effects on the mechanical behaviour of a clay. Int. J. Numer. Anal. Meth. Geomech. 28, 209–228. https://doi.org/10.1002/nag.332

Dassault Systèmes, (2021). Abaqus 2016 Software Documentation. Dassault Systèmes Simulia Corp., Providence, RI, USA

Gawecka, K.A., Taborda, D.M.G., Potts, D.M., Cui, W., Zdravković, L. Haji Kasri, M.S., (2017). Numerical modelling of thermo-active piles in London Clay. *Proc. ICE - Geotechnical Engineering* 170, 201–219. https://doi.org/10.1680/jgeen.16.00096

Rotta Loria, A.F., Laloui, L. (2016). The interaction factor method for energy pile groups. *Computers and Geotechnics* 80, 121–137. https://doi.org/10.1016/j.compgeo.2016.07.002

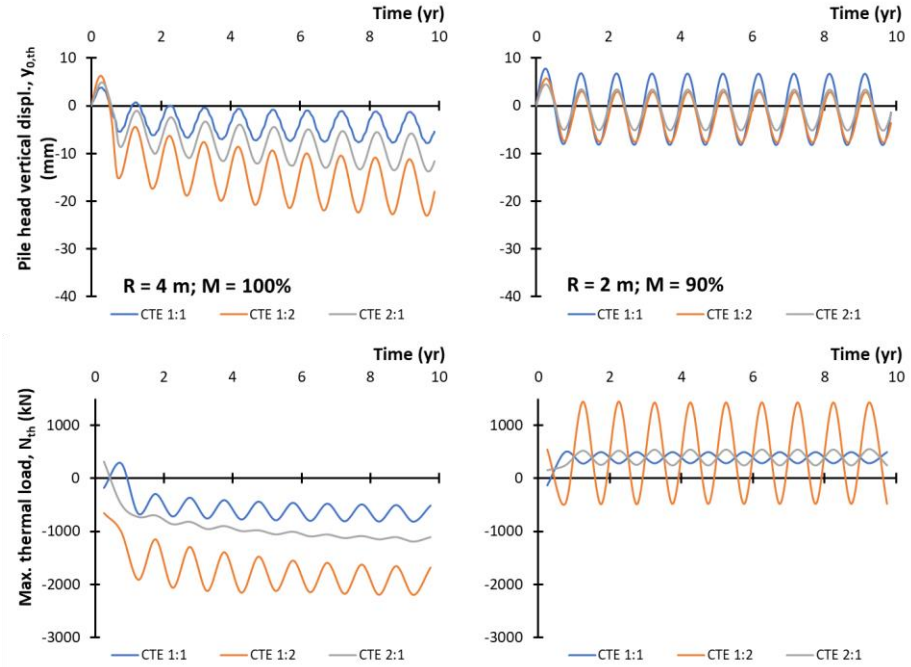

Figure 5. Pile group (unit cell: R = 4 & 2 m) with high M.

Table 1. Material parameters used in analysis

Parameter	Pile	Frictional soil
Density, ρ (kg/m^3)	2500	1900
Young's modulus, E (MPa)	30000	Figure 6
Poisson's ration, ν (-)	0.2	0.3
Angle of shearing resistance, φ' (deg.)	-	38
Angle of dilation, ψ (deg.)	-	0.1
Cohesion, c' (kPa)	-	0.1
Pile-soil interface friction, δ (deg.)	-	32
Pile-soil adhesion, a (kPa)	-	0
Pile-soil friction coeff., μ (-)	-	0.624
Relative displacement, y_{rel} (m)	-	0.0020
At-rest earth pressure coeff., K_0 (-)	-	0.429
Thermal conductivity, k (W/m.K)	2	2
Specific heat, c_s (J/kg.K)	940	800
Initial temperature, T_0 (°C)	14	14
Linear coeff. thermal expansion, α (με/K)	10 or 20	10 or 20

Proceedings of the XVIII ECSMGE 2024
GEOTECHNICAL ENGINEERING CHALLENGES
TO MEET CURRENT AND EMERGING NEEDS OF SOCIETY
© 2024 the Authors
ISBN 978-1-032-54816-6
DOI 10.1201/9781003431749-552
Open Access: www.taylorfrancis.com, CC BY-NC-ND 4.0 license

ECSMGE 24
XVIII EUROPEAN CONFERENCE ON SOIL MECHANICS AND GEOTECHNICAL ENGINEERING

Back-analysis of a small-scale (1g) energy pile test using the finite element method

Rétro analyse avec la méthode des éléments finis d'un test de pieux énergétique à petite dimension (1g)

P.J. Bourne-Webb*, T.M. Bodas Freitas
CERIS, Instituto Superior Técnico, ULisboa, Lisbon, Portugal

D. Abrantes
Helica, Tomar, Portugal (formerly Instituto Superior Técnico)

**peter.bourne-webb@tecnico.ulisboa.pt*

ABSTRACT: Previous work by the authors reviewed the reported response of full- and small-scale piles in tests in granular soils where they were subject to cyclic thermal loading. In the case of the former, largely stable behaviour has been reported but amongst the latter, the reported response consistently reveals irrecoverable settlement and increase in axial compression stress. This later is reported to be a function of the applied load with greater irrecoverable settlement occurring at lower global factor of safety and has been attributed to a variety of possible mechanisms. A hypothetical mechanism based on the initial mobilisation of the pile shaft resistance was proposed to explain this and then tested by undertaking numerical analysis. This confirmed the stable behaviour of the full-scale piles was likely due to low mobilisation (high margin of safety) with respect to the shaft resistance, while in the small-scale tests, the reverse was true. In this paper, a small-scale test on a thermally-activated pile has been back-analysed. In the test, the mechanical load-displacement behaviour along with the response to three cycles of heating and cooling were reported in sufficient detail to provide a good basis for the analytical work. It is shown that by matching the mechanical response, reasonable agreement between the thermal part of the test and finite element back-analysis can be achieved, and that the agreement can be further improved through calibration of the coefficient of thermal expansion of the pile and soil.

RÉSUMÉ: Des travaux antérieurs des auteurs ont examiné la réponse rapportée des pieux à grande et petite échelle lors d'essais dans des sols granulaires où ils étaient soumis à une charge thermique cyclique. Dans le cas des premiers, un comportement largement stable a été rapporté, mais parmi les seconds, la réponse rapportée révèle systématiquement un tassement irrécupérable et une augmentation de la contrainte de compression axiale. Ce dernier est signalé comme étant une fonction de la charge appliquée avec un tassement irrécupérable plus important se produisant à un facteur de sécurité global inférieur et a été attribué à une variété de mécanismes possibles. Un mécanisme hypothétique basé sur la mobilisation initiale de la résistance du fût du pieu a été proposé pour expliquer cela, puis testé en entreprenant une analyse numérique. Cela a confirmé que le comportement stable des pieux à grande échelle était probablement dû à une faible mobilisation (marge de sécurité élevée) par rapport à la résistance de l'arbre, alors que dans les essais à petite échelle, l'inverse était vrai. Dans cet article, un essai à petite échelle sur un pieu activé thermiquement a été rétro-analysé. Dans le test, le comportement mécanique de charge-déplacement ainsi que la réponse à trois cycles de chauffage et de refroidissement ont été rapportés de manière assez détaillée, fournissant une bonne base pour le travail analytique. Il est démontré qu'en faisant correspondre la réponse mécanique, un accord raisonnable entre la partie thermique de l'essai et la rétro-analyse par éléments finis peut être obtenu, et que l'accord peut être encore amélioré par l'étalonnage du coefficient de dilatation thermique du pieu et du sol.

Keywords: Piles; thermal; interactions; safety.

1 INTRODUCTION

In the last decade, numerous (more than 50) experimental studies examining the response of thermally-activated (TA) piles either at 1-g or in the centrifuge at N-g acceleration have been published. Such testing is promoted as being able to provide valuable insights into the response of geotechnical structures in a more controlled and cost-effective manner than e.g. full-scale tests in the field.

Bourne-Webb et al. (2019) and Bourne-Webb & Bodas Freitas (2020) collated the results for such studies, along with full scale tests on TA piles and found a distinct discrepancy between the reported behaviours, especially with respect to the normalised maximum axial thermal stress response ($\sigma_{th,max}/\sigma_{th,fixed}$

where $\sigma_{th,fixed} = \alpha\Delta T.E$; and α = Pile CTE; ΔT = Temp. change; E = pile stiffness; L = pile length) and the likelihood of the pile head movement ($y_{th,0}$) exceeding the free thermal expansion of the pile ($y_{th,free} = \alpha\Delta T.L$), i.e. $y_{th,0}/y_{th,free} > 1$, Figure 1. Reduced axial thermal stress was attributed to the low confining stress acting in 1-g and the very small thermal displacements generated on the model pile interfaces irrespective of scale, due to the short length of the piles. Pile head movement exceeding $y_{th,free}$ was attributed to effects that led to irrecoverable settlement: namely, reduction of available shaft restraint during cooling and load transfer to the pile base, Figure 2.

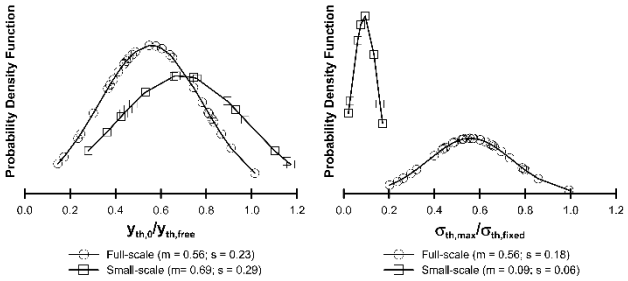

Figure 1. Stress-displacement response of full- and small-scale TA pile tests.

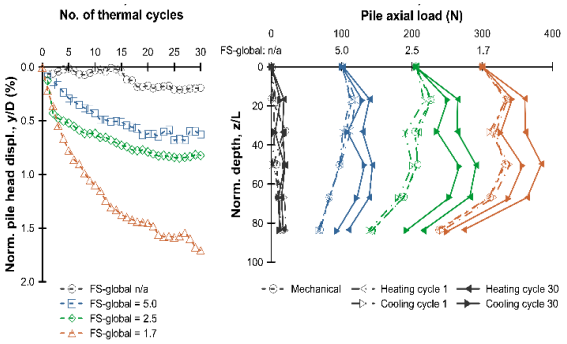

Figure 2. Settlement & axial load response in small-scale cyclically TA pile, Nguyen et al. (2017).

2 BASIS FOR ANALYSES

The model tests used as the basis for this study were those reported by Wang et al. (2016, 2017) in which a single, 104 mm diam., 1.4 m long pile embedded in dry sand was loaded mechanically and then subject to heating and cooling cycles. Specifically, the behaviour of Pile 4 which had a W-shaped heat exchanger tube layout is examined here. In this study, the finite element analysis (FEA) program PLAXIS 2D 2023.1 was employed to undertake the back-analysis of the model test.

The geometry used is based on the physical dimensions of the rectangular test tank which was 1.75 m deep and had plan dimensions of 8 x 8 m^2. While it is possible that the proximity of the lower boundary may have influenced the test results, for this exercise it is not so important as the FEA is replicating the test boundary conditions. The test piles were installed 1 m from the side boundaries and the FEA simplified the geometry to be axisymmetric with a domain radius of 1,0 m (c. 10 pile diameters), Figure 3.

Basic characteristics of the sand used in the testing were reported, along with details of the preparation method and the target initial state: a relative density of about 63%. These details were used to infer suitable parameters to be employed in the back-analysis, Table 1. The stress-dilatancy approach developed by Bolton (1986a, b) was employed to assess the peak angle of shearing resistance that might be applicable in the sand at the very low confining stress in the tank. This suggested a peak angle of shearing resistance of about 40° and thus, a value of φ' = 34° was used in conjunction with an angle of dilation, ψ of 6°, in the FEA. Iwasaki & Tatsuoka (1977) and Mayne (2000) were used to provide an initial estimate for the stiffness parameters, reflecting the confining pressures and level of mobilisation within the model. In the FEA, the Mohr-Coulomb (MC) model available in PLAXIS was employed. These values were then calibrated in order to better reproduce the reported load-displacement of the test piles – primarily through adjusting the soil stiffness and initial stress state.

The thermal and mechanical properties for the model pile were less clearly defined and quoted values in Wang et al. (2016, 2017) appear to be generic rather than model specific, e.g. the quoted coefficient of thermal expansion (CTE) is $10x10^{-6}$ K^{-1} with no mention of their having tested the pile to obtain the value. Likewise, the applicable pile Young's modulus.

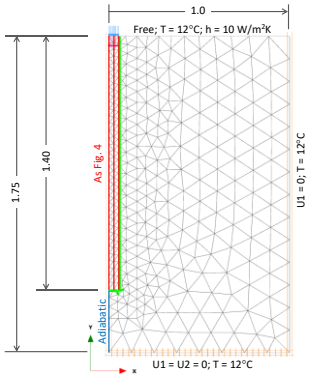

Figure 3. Geometry used in FEA.

Standard mechanical boundary conditions were applied, i.e. fully-fixed on bottom, horizontal fixity on sides and free on the top surface. Regarding temperature boundary conditions, the bottom and outer edge were held constant at 12°C; below the pile, the centreline was set as adiabatic; the surface was set to be convective with a thermal conductance of

10 W/m^2.K and an air-temperature of 12°C. Within the pile, temperatures following the average pile temperaure reported by Wang (2016, 2017) were imposed along lines at x = 0, r/2 and r, where r is the pile radius, Figure 4. This ensured that the pile volume underwent a constant temperature change.

The back-analysis of the model tests was undertaken in two stages: first, the mechanical load-displacement response was evaluated with initial stress, soil shear strength & stiffness parameters calibrated to approximate the response reported by Wang (2016, 2017), then the thermo-mechanical response was evaluated (assuming the above parameters were not affected) with variations in the thermal properties detailed in Section 3. In reproducing the mechanical load-displacement response, the set of parameters finally arrived at included an At-rest Earth Pressure coefficient, K_0 = 1 this is higher than e.g. that given by the Jaky-formula (K_0 = 1-sinφ', Jaky (1948)) but data from Boulon & Foray (1986) show that at low vertical stress, in small scale tests on piles, it is possible to have K_0 values inexcess of 1.0, depending on the density of the soil. So the value used as considered reasonable.

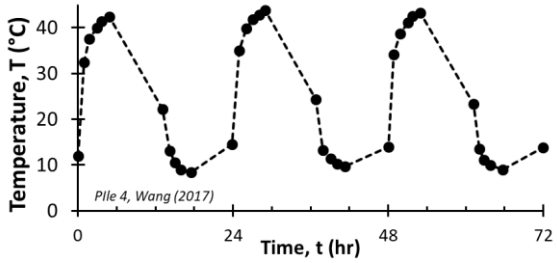

Figure 4. Average pile temperature imposed in FEA, adapted from Wang (2017).

3 RESULTS & DISCUSSION

3.1 Load-displacement response

In Wang et al. (2016, 2017), one model pile was tested in order to define the mechanical behaviour of the pile under axial load. The results were consistent and used to define a working load of 10 kN which was applied to the other test piles before the thermal part of the test was carried out.

After only small alterations in the initiallly assessed soil parameters, acceptable agreement between the reported behaviour and the FEA using both the MC and HS soil models was obtained, Figure 5. This mainly involved, adjustments in the distribution between φ‘ and ψ, and the soil stiffness. From this analysis, it was possible to examine the underlying response which revealed that the available shaft resistance was only a small proportion of the total, around 1,5 to 2 kN, with the remainder derived from the pile base. Thus, a working load of 10 kN, as used by Wang et al. (2016, 2017), implies that the shaft resistance is fully mobilised prior to thermal loading.

3.2 Thermo-mechanical behaviour

Before examining the thermo-mechanical (TM) response, the predicted temperature variation was validated against the radial temperature field reported in Wang (2017). Figure 6 shows this comparison which is very good, confirming that the model is providing an acceptable reproduction of the thermal response. Figure 7 shows the temperature contours for a steady state thermal analysis, to illustrate the effect of the boundary conditions on the temperature field. These fields were the same irrespective of the soil model employed.

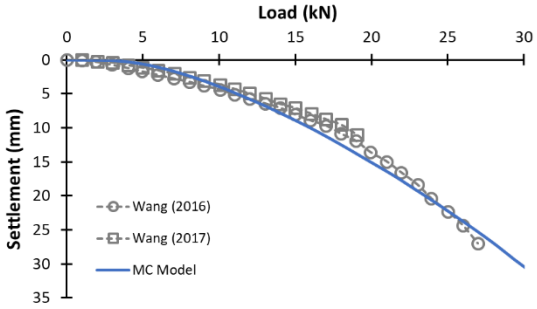

Figure 5. Load-displacement response of model pile as reported in Wang (2016. 2017) and predicted by FEA.

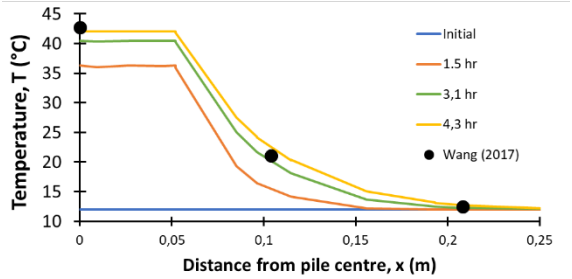

Figure 6. Radial temperature profile at about pile mid-depth, and at the end of first heating stage, reported by Wang (2017) and predicted by FEA.

Having established that the imposed temperature field was acceptable, the thermo-mechanical response was examined via the comparison with reported thermally-induced axial strain (ε_{th}) and stress changes (σ_{th}), and pile head displacement ($y_{0,th}$), and Figure 8 to 10 illustrate the various responses.

Initially, the MC model was employed in conjunction with the CTE of the pile equal to the soil, i.e. 10 x10^{-6} K^{-1}or case "CTE 10/10". First, the axial strain response at a depth of about 0.65 m (0.46L) is compared in Figure 8 and it is apparent that when the

pile CTE is 10 x10^{-6} K^{-1} (cases CTE 10/10 & 10/05), the agreement is very good, irrespective of the soil CTE but using a CTE for the pile of 15 x10^{-6} K^{-1} (case CTE 15/10) overestimates the thermal axial strain. This confirms that the value quoted by Wang et al. (2016, 2017) is reasonable. Also shown is the blocked strain, ε_{blkd} (Eq. 1) obtained in the FEA which are rather small and only a few-percent of $\alpha\Delta T$, confirming a lack of restraint on the shaft;

$$\varepsilon_{blkd} = [\varepsilon_{th} - \alpha(T - T_0)] \quad (1)$$

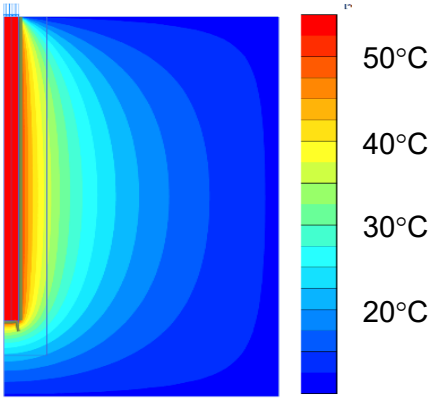

Figure 7. Steady State temperature field for imposed pile temperature of 53 ℃ (ΔT = 41 ℃).

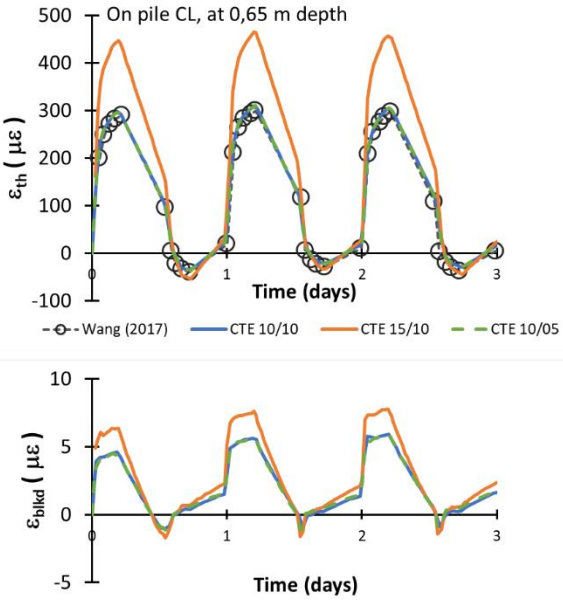

Figure 8. Thermal axial strain reported by Wang et al. (2017) and predicted by FEA using MC soil model.

The associated thermal stress response is shown in Figure 9 where clear discrepancies between the reported values and the FEA can be noted. This belies the good agreement between the reported and back-analysed results presented above. However, given that the thermal stress is evaluated using Eq. (2) in which errors accumulate through each of the experimental input parameters (ε_{th} & T), and the difference inside the square brackets (ε_{blkd}) is small (see Figure 8), large differences can be expected;

$$\sigma_{th} = E[\varepsilon_{th} - \alpha(T - T_0)] \quad (2)$$

To test this further, the 800 to 900 kPa axial stress reported by Wang (2017) implies an axial load of 6.8 to 7.7 kN which is higher than the total available shaft resistance implied by the load test discussed earlier (less than 2 kN). Based on Wang (2016) and other works, the maximum thermal stress will occur a depth of 0.5L to 0.7L. Thus, to generate the axial restraint required, friction equivalent to about 32 kPa and 23 kPa, respectively, would need to be mobilised on the shaft. This is highly unrealistic given the very low confining pressures acting on the pile shaft and based on Eq. (3), implies β = 2.9 – 5.7, values only likely to be found for large-displacement piles in sand;

$$\beta = {}^{q_{s,u}}/_{\bar{\sigma}'_v} \quad (3)$$

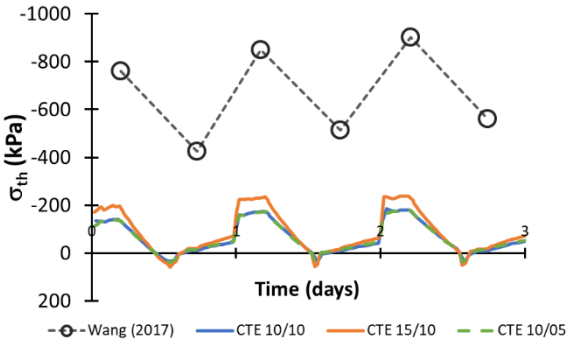

Figure 9. Thermal axial stress response reported by Wang et al. (2017) and predicted by FEA using MC soil model.

The other key parameter in TA pile response is the pile head movement and the reported values are compared with those predicted by the FEA in Figure 10. It is apparent that in terms of $y_{0,th}$, in the first cycle and subsequent heating stages, the agreement is good for case CTE 10/10. However, in the cooling stages, while the behaviour is qualitatively similar, the accumulated settlement diverges from and is less than that reported.

To assess this, a series of analyses were undertaken to investigate how the CTE affected the results. In Figure 10, results from analyses where the CTE of the pile was increased by 50% (CTE 15/10) and where the CTE of the soil was reduced by 50% (CTE 10/05) with respect to the initial values, are also shown. Again, the same pattern of accumulated settlement occurs: increasing the pile CTE improves the agreement with later cycles but at the cost of poor agreement in the

first. Halving the soil CTE only affects the 2nd and 3rd cycles and marginally improves the predicted behaviour. Reducing the soil CTE further improves the match in the cooling cycles but the agreement during heating cycles deteriorates, underpredicting the reported values.

Table 2 and Figure 11 examine the reported thermally-induced pile settlement a little further. Table 2 summarises the incremental pile head movement and temperature change during each temperature change stage, i.e. Initial → H1 → C1 →… Also tabulated is the associated free thermal expansion, $y_{th,free}$ based on the average pile temperature and CTE reported by Wang et al. (2017).

What is clear in Table 2 is that within each cooling cycle, the pile head moves down by an amount approximately equal to $y_{th,free}$, while in the heating stages the pile head moves up and the proportion of $y_{th,free}$ mobilised increases with each heating stage. Figure 11 illustrates schematically what is thought to be happening; when heated the pile expands, reversing the friction in the upper part of the pile and thus, $y_{0,th} < y_{th,free}$. At the base of the pile, the pile expansion leads to downwards movement. When cooled, additional shaft resistance cannot be mobilised, and to maintain equilibrium, the pile base settles some more. After the first cycle, this repeats throughout the test, leading to the thermal ratcheting effect that was reported in Wang et al. (2016, 2017) and predicted by the FEA.

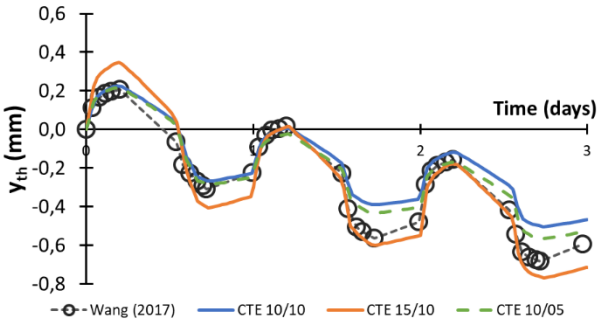

Figure 10. Thermal pile head displacement reported by Wang et al. (2017) and predicted by FEA using MC soil model.

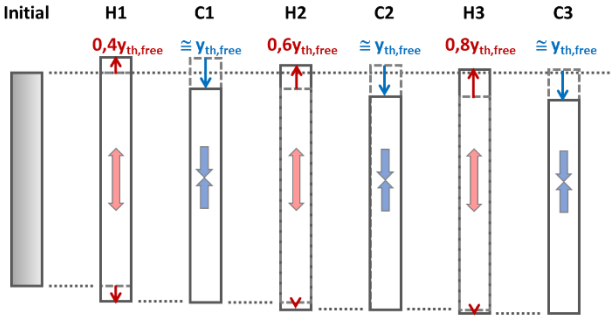

Figure 11. Schematic of pile thermal ratcheting mechanism.

.

Table 1. Material parameters used in analysis.

Parameter	Units	Pile	Sand
			MC Model
Density, ρ	kg/m^3	2500	1600
Young's modulus, E_{ref}	MPa	30000	20
Modulus increment, E_{inc}	MPa		14
Poisson's ratio, ν	-	0.2	0.3
Angle of shearing resistance, φ'	deg.	-	34
Angle of dilation, ψ	deg.	-	6
Cohesion, c'	kPa	-	0
Pile-soil interface friction, δ	deg.	-	29
Interface factor, R_{inter} = tanδ/tanφ'	-	-	0.822
At-rest earth pressure coeff., K_0	-	-	1.0
Thermal conductivity, k	W/m.K	1.6	0.3
Specific heat, c_s	J/kg.K	880	830
Linear coeff. thermal expansion, α	x10^{-6} K^{-1}	varies	10
Initial temperature, T_0	°C	12	12

Table 2. Analysis of thermally-induced incremental pile head displacements.

Stage	Initial	H1	C1	H2	C2	H3	C3
$y_{0,th}$ (mm)	-	+0.21	-0.52	+0.33	-0.58	+0.41	-0.53
T (°C)	12.0	42.4	8.5	43.7	9.7	43.3	9.1
ΔT (°C)	-	+30.4	-33.9	+35.3	-34.0	+33.6	-34.2
L = 1600 mm, α = 10 x10^{-6} K^{-1}							
αΔT.L (mm)	-	+0.43	-0.48	+0.49	-0.48	+0.47	-0.48
$y_{0,th}$/αΔT.L	-	0.43	0.96	0.59	1.07	0.76	0.97

4 CONCLUSIONS

In this work, the behaviour of a small scale thermally-activated pile has been examined using the finite element method, employing two well known and commonly employed soil models. The following points have been demonstrated in this work:

- The mechanical load-displacement of the pile must be reproduced accurately in order to be able to reproduce the correct thermo-mechanical response.
- Good agreement between the test and analysis was found in terms of the thermal axial strains and pile head movements during heating.
- The results diverged in the cooling stages beyond the first cycle. The cause of this is not yet apparent, as e.g., a mechanism involving thermal compaction of the soil adjacent to the pile might improve this comparison but would likely no longer capture the movements during heating.
- The comparison between reported and predicted thermal stress was also poor. This may be due to the low levels of restraint on the pile shaft which means slight errors greatly exaggerate the blocked thermal strain and thus, the thermal stress reported. It is shown that the reported axial stress is likely to be unreliable.

ACKNOWLEDGEMENTS

The work presented was financed by the *Fundação para a Ciência e a Tecnologia*, Portugal, via grants PTDC/ECI-EGC/29083/2017 (DEEPCOOL) and UIDB/04625/2020. The authors would like to express their gratitude to the funding institution

REFERENCES

Bolton, M.D., (1987). Discussion: The strength and dilatancy of sands. *Géotechnique* 37, 219–226. https://doi.org/10.1680/geot.1987.37.2.219.

Bolton, M.D., (1986). The strength and dilatancy of sands. *Géotechnique* 36, 65–78. https://doi.org/10.1680/geot.1986.36.1.65.

Boulon, M., Foray, P., (1986). Physical and numerical simulations of lateral shaft friction along offshore piles in sand, in: *Proc. 3rd Int. Conf. on Numerical Methods in Offshore Piling*. Nante, France, pp. 127–147.

Bourne-Webb, P.J., Bodas Freitas, T.M., Freitas Assunção, R.M., (2019). A review of pile-soil interactions in isolated, thermally-activated piles. *Computers and Geotechnics* 108, 61–74. https://doi.org/10.1016/j.compgeo.2018.12.008.

Bourne-Webb, P.J., Bodas Freitas, T.M., (2020). Thermally-activated piles and pile groups under monotonic and cyclic thermal loading–A review. *Renewable Energy* 147, 2572–2581. https://doi.org/10.1016/j.renene.2018.11.025.

Bourne-Webb, P.J., Lupattelli, A., Bodas Freitas, T.M., Salciarini, D. (2022a). The influence of initial shaft resistance mobilisation in the response of seasonally, thermally-activated pile foundations in granular media. *Geomechanics for Energy and the Environment* 32, 100299. https://doi.org/10.1016/j.gete.2021.100299.

Bourne-Webb, P.J, Freitas, T.M.B., Zito, M., Lupattelli, A., Sterpi, D., Salciarini, D., (2022b). Outstanding issues in understanding the behaviour of thermally-activated pile foundations. *DFI-EFFC Intl. Conf. on Deep Foundations and Ground Improvement*, Berlin, Germany, p. 10.

Iwasaki, T., Tatsuoka, F. (1977). Effects of Grain Size and Grading on Dynamic Shear Moduli of Sands. Soils and Foundations 17, 19–35. https://doi.org/10.3208/sandf1972.17.3_19.

Jaky, D.J. (1948). Pressure in silos. Proc. 2nd Intl. Conf. Soil Mech. and Fdtn. Eng'g, Rotterdam, Vol. 1, 103-107. https://www.issmge.org/uploads/publications/1/43/1948_01_0021.pdf (accessed: 04/03/2024).

Mayne, P.W. (2000). Enhanced geotechnical site characterization by seismic piezocone penetration tests. *4th Intl. Geotech. Conf.*, Cairo, Egypt, pp. 95–120.

Nguyen, V.T., Tang, A.M., Pereira, J.-M. (2017). Long-term thermo-mechanical behavior of energy pile in dry sand. *Acta Geotech.* 12, 729–737. https://doi.org/10.1007/s11440-017-0539-z.

Rotta Loria, A.F., Donna, A.D., Laloui, L. (2015). Numerical Study on the Suitability of Centrifuge Testing for Capturing the Thermal-Induced Mechanical Behavior of Energy Piles. *J. Geotech. Geoenviron. Eng.* 141, 04015042. https://doi.org/10.1061/(ASCE)GT.1943-5606.0001318.

Wang, C., Liu, H., Kong, G., Ng, C.W.W., Wu, D. (2016). Model tests of energy piles with and without a vertical load. *Environmental Geotechnics* 3, 203–213. https://doi.org/10.1680/jenge.15.00020.

Wang, C., Liu, H., Kong, G., Wang Wai Ng, C. (2017). Different types of energy piles with heating–cooling cycles. *Proceedings of the Institution of Civil Engineers - Geotechnical Engineering* 170, 220–231. https://doi.org/10.1680/jgeen.16.00061.

Proceedings of the XVIII ECSMGE 2024
GEOTECHNICAL ENGINEERING CHALLENGES
TO MEET CURRENT AND EMERGING NEEDS OF SOCIETY
© 2024 the Authors
ISBN 978-1-032-54816-6
DOI 10.1201/9781003431749-553
Open Access: www.taylorfrancis.com, CC BY-NC-ND 4.0 license

ECSMGE 24
XVIII EUROPEAN CONFERENCE ON SOIL MECHANICS AND GEOTECHNICAL ENGINEERING

Climate change impacts on geotechnical infrastructure

Impacts du changement climatique sur les infrastructures géotechniques

C.A. Bridges*
Queensland University of Technology, Brisbane, Australia
**chris.bridges@hdr.qut.edu.au*

ABSTRACT: When undertaking designs for developments and infrastructure, geotechnical engineers now need to account for uncertainty due to climate change. For many years engineers have designed considering historical precedent, such as rare long-term flood events. Now, however, we have to accept these may be more frequent. In other areas climate change may result in periods of long duration drought with less frequent, but higher intensity, rainfall. These effects mean that geotechnical engineers must now consider different conditions which take account of a constantly changing environment over the lifetime of the structure. Geotechnical engineers must also be careful in material selection in order to achieve a required design life when ultimately, the conditions encountered now and are designed for, will change. This paper discusses these issues and how geotechnical engineers can take account of climate change in their designs.

RÉSUMÉ: Lorsqu'ils entreprennent la conception d'aménagements et d'infrastructures, les ingénieurs géotechniques doivent désormais tenir compte de l'incertitude due au changement climatique. Depuis de nombreuses années, les ingénieurs conçoivent en tenant compte des précédents historiques, tels que les rares inondations à long terme. Aujourd'hui, cependant, nous devons accepter que ces phénomènes soient peut-être plus fréquents. Dans d'autres régions, le changement climatique peut entraîner des périodes de sécheresse de longue durée accompagnées de précipitations moins fréquentes mais de plus forte intensité. Ces effets obligent désormais les ingénieurs géotechniques à considérer différentes conditions qui tiennent compte d'un environnement en constante évolution tout au long de la durée de vie de l'ouvrage. Les ingénieurs géotechniciens doivent également être prudents dans la sélection des matériaux afin d'atteindre une durée de vie de conception requise lorsqu'en fin de compte, les conditions rencontrées actuellement et pour lesquelles elles sont conçues changeront. Cet article aborde ces questions et comment les ingénieurs géotechniques peuvent prendre en compte le changement climatique dans leurs conceptions.

Keywords: Climate change; risk.

1 INTRODUCTION

In Queensland, Australia during the winter of 2022 the dry season was anything but dry. In both Queensland and the southern state of New South Wales in 2022 they were areas of flooding and in some cases repetitive flooding. At the time of writing, at the start of the 2023 – 2024 summer we are now seeing the first bush fires in Queensland. With historical global temperature records falling year after year, and weather patterns changing, it must be asked whether the basis of design for a lot of the infrastructure we build today – which is derived from historical precedent - will be relevant over the lifetime of that infrastructure.

With a constantly evolving climate, we need to consider whether our codes, standards and specifications are fit for purpose and ask how this uncertainty is going to be managed in the future.

2 GEOTECHNICAL RISKS

Geotechnical failures typically occur due to a small number of reasons:

- design – the structure is analysed incorrectly, or the design fails to account for the likely ground or loading conditions during the life of the structure
- construction – slopes are cut too steep, ground support may not be installed in time, or the incorrect materials are used
- loading changes – unforeseen changes in loading are not uncommon. Examples include: higher groundwater levels due to extreme rainfall; a new structure applying an additional

load; or, new construction such as excavation in front of a retaining wall
- change of material properties – these could include conditions such as erosion or shrink-swell

How these types of failure are impacted by climate change is discussed in the following sections.

3 CLIMATE IMPACTS AND RISKS

Geotechnical structures are typically sensitive the environment they are in. For example, groundwater levels and surface water flows impact most inground structures and earthworks.

Climate change impacts can be divided into two major groupings:
- precipitation - extreme rain, storm and floods
- increasing temperature - drought and wildfire

However, there are obvious overlaps between the two groupings. For example, hurricanes are caused by elevated sea temperatures and can result in increased precipitation and flooding (due to storm surges).

A summary of potential impacts of climate change on geotechnical structures is provided in Table 1 and examples of impacts on an earth embankment is shown on Figure 1.

3.1 Precipitation

Extreme precipitation is often associated with storms and hurricanes (cyclones) which are of relatively short duration, but high intensity, or from weather systems that continue deposit rain over a number of days or even weeks.

In general, it would be anticipated that increasing precipitation (based on Varallyay, 1990) will result in:
- surface runoff in sloping areas, especially if little or sparse vegetation is present, and the water carrying capacity of the soil is limited
- higher water infiltration and storage, recharging of the groundwater, where water carrying capacity of the soil is not limited

The consequences include an increase in instability of retaining walls and slopes (natural and manmade) which are often observed in the form of landslides (Bracko et al., 2022; The Earthworks Management Task Force, 2021; Toll, 2001).

Increased surface water flows can overwhelm existing drainage systems increasing erosion and making slopes susceptible to infiltration and surficial instability in following rain events. In addition, this could block culverts and undermine structural foundations.

The impact of rising groundwater may also bring naturally occurring sulfates and chlorides from their dry states into solution causing faster deterioration of substructures (Mallick et al., 1989). Alternatively, lowering groundwater tables expose timber piles to aerobic conditions and subject them to biodegradation (Toll et al., 2012).

Short or long-term rises of groundwater can impact foundations and basements reducing bearing capacity, causing uplift or increasing seepage. For retaining walls, increased water pressures will be observed.

3.2 Increasing temperature

Increasing temperatures can influence soils and ground conditions – drying out soils and if long-term can cause a reduction in the groundwater level. In general, it would be anticipated that increasing temperature (based on Varallyay, 1990) will result in:
- decreasing surface runoff, infiltration and recharging of the groundwater, if accompanied by low precipitation
- modification of the extent and depth of permafrost, resulting in increasing groundwater storage and movement

Lower groundwater levels may adversely impact the settlement of structures and increase loads on piles due to negative skin friction (Toll et al., 2012) or through by reducing buoyancy. Areas of karst geology, where the ground is supported by flooded caverns may be severely impacted by lowering groundwater levels resulting in collapse and sinkholes forming (Chen et al., 2021; He et al., 2022; Toll et al., 2012).

In northern latitudes rising temperatures have had the greatest impact on ground conditions. It is typical for settlements in these areas to be built on permafrost - the situation where groundwater near the surface is permanently frozen. As temperatures have increased, whole settlements - and their road accesses - are being flooded due to the recent release of groundwater making the areas marshy or swamp like. Even those areas not as significantly impacted, are facing buildings sinking due to lower bearing capacities. Slopes are also failing due to the release of groundwater.

In Alaska there are long-term concerns about the impact to infrastructure – roads, rail and pipelines – as well as former defence bases where melting permafrost may lead to contamination spread (U.S. Arctic Research Commission Permafrost Task Force, 2003).

Recent examples of hot weather influencing ground conditions are in the UK where the hot weather has resulted in an increase in the number of subsidence claims and have resulted in a number of large-scale coastal rock falls (Menteth, 2022).

Table 1. Summary of potential impacts on geotechnical infrastructure due to climate change (after Bridges, 2023; based on Vardon, 2015).

Climate change feature	Potential impact on geotechnical structure	Potential failure mode
Existing infrastructure		
Increased temperature (incl. fire)	Reduction of vegetation Hydrophobic soil	Erosion, slope stability Erosion
Decreased precipitation (drought)	Soil desiccation Soil shrinkage Reduction of vegetation / soil erosion Lower groundwater level	Piping, internal erosion, slope stability Piping, subsidence Piping, slope stability Overloaded piles, serviceability failure
Increased mean precipitation	Some soil erosion / loss of soil quality Change in water table leading to instability	Erosion, piping Slope stability
Intense precipitation	Significant soil erosion Rapid soil wetting, highly dynamic pore pressure changes potentially Flooding	Piping, slope stability Slope stability Piping, internal erosion, slope stability
Freeze/thaw cycles (incl. reduced permafrost)	Loss of soil structure Expansion of rock joints	Slope stability, bearing capacity, serviceability failure Rockfall
New infrastructure		
Drought	Reduction of moisture content of fill (compaction more difficult) and mixing of fill with water is expensive	Cost, serviceability failure
Increased precipitation / intense precipitation	Collapsing of some fill material due to wetting	Slope stability, serviceability failure

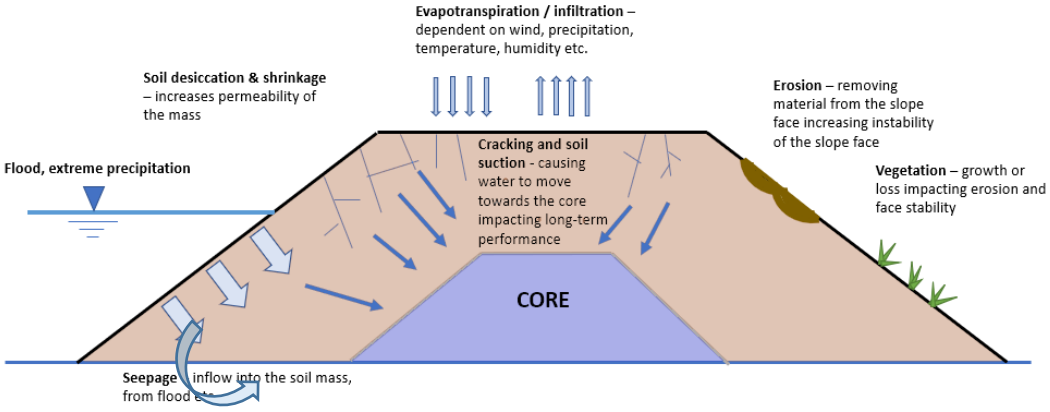

Figure 1. Influence of climate impacts on soil moisture and erosion (NTS) (based on Bridges, 2023; Vardon, 2015).

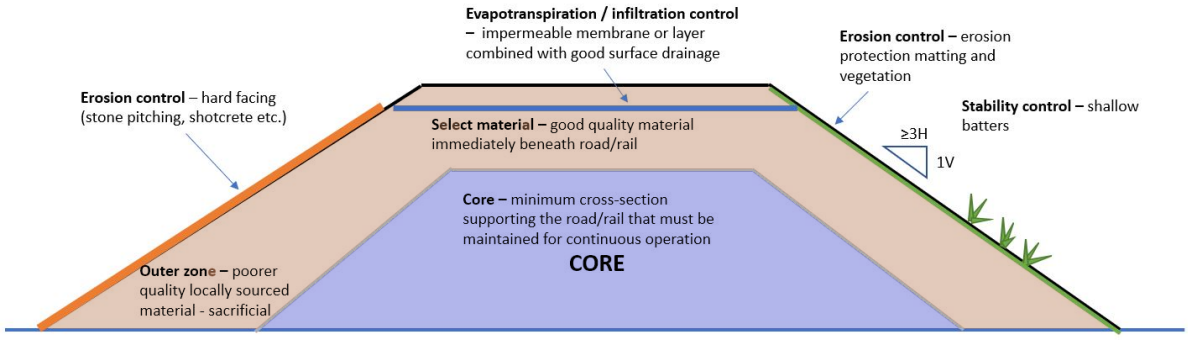

Figure 2. Influence of climate impacts on soil moisture and erosion (NTS) (Bridges, 2023).

Hot, dry conditions can also have an impact on forest or wildfires. Apart from destroying vegetation which can increase erosion, soils become hydrophobic in the period immediately after a fire, which can also increase the susceptibility to erosion (Movasat and Tomac, 2021).

4 ENGINEERED SOLUTIONS

There are a number of solutions that can be adopted to provide long-term performance of geotechnical structures. For example, for embankments some options include (Figure 2):

- wider and shallower embankment shoulders
- soft erosion protection for shallower slope batters and harder protections for steeper batters
- surface and interior drainage
- higher embankment heights to keep the infrastructure above flood levels

For cut slopes erosion protection and surface drainage are primary elements to address, combined with sub-horizontal drains to reduce groundwater levels.

Pile foundation design need to consider additional loads due to rising or falling groundwater levels. It is more difficult to address all the possible scenarios for shallow foundations, such as higher groundwater levels impacting bearing capacity) and this may lead to the adoption of more piled foundations in future.

5 CONCLUSIONS

Codes, standards and specifications are retrospective by nature and climate change impact challenges the geotechnical engineer to develop solutions not based on precedence but to think through the possible environmental conditions their structures will face.

REFERENCES

Bracko, T., Žlender, B., and Jelušic, P. (2022). Implementation of Climate Change Effects on Slope Stability Analysis. *Applied Sciences*, *12*(16). https://doi.org/10.3390/app12168171.

Bridges, C. (2023). Long-term geotechnical impacts of climate change on projects. *Proceedings of the 14th Australia and New Zealand Conference on Geomechanics (ANZ2023)*, Cairns, QLD, Australia.

Chen, X., Guo, R., Tang, L., and Zhang, X. (2021). Study on Ground Collapse of Covered Karst Soil Caves by Sudden Drop of Groundwater [Research Article]. *Advances in Civil Engineering*, *2021*, Article 7796401. https://doi.org/10.1155/2021/7796401.

He, Q., Tan, F., Peng, Z., Tao, L., Jiao, Y., Liu, S., and Peng, H. (2022). Genesis Analysis of Ground Collapse in Wuhan Based on 3D Geological Model. *Frontiers in Earth Science*, *10*, Article 934452. https://doi.org/10.3389/feart.2022.934452.

Menteth, T. (2022). Devon cliff collapses for second time during August heatwave. *Ground Engineering*(October), 8.

Movasat, M., and Tomac, I. (2021). Assessment of Physical Properties of Water-Repellent Soils [Technical Note]. *Journal of Geotechnical Geoenvironmental Engineering*, *147*(9). https://doi.org/10.1061/(ASCE)GT.1943-5606.0002604.

The Earthworks Management Task Force. (2021, February). *A review of earthworks management*. Network Rail. Retrieved 1 November 2023 from https://www.networkrail.co.uk/wp-content/uploads/2021/03/Network-Rail-Earthworks-Review-Final-Report.pdf.

Toll, D. G. (2001). Rainfall-induced landslides in Singapore [Briefing]. *Proceedings of the Institution of Civil Engineers - Geotechnical Engineering*, *149*(4), 211-216.

Toll, D. G., Abedin, Z., Buma, J., Cui, Y., Osman, A. S., and Phoon, K. K. (2012). *'The impact of changes in the water table and soil moisture on structural stability of buildings and foundation systems: systematic review CEE10-005 (SR90)*. Collaboration for Environmental Evidence.

U.S. Arctic Research Commission Permafrost Task Force. (2003, December). *Climate change, permafrost, and impacts on civil infrastructure*. U.S. Arctic Research Commission. Retrieved 1 November 2023 from https://www.arctic.gov/uploads/assets/permafrost.pdf.

Varallyay, G. Y. (1990). Influence of climate change on soil moisture regime, texture, structure and erosion. In H. W. Scharpenseel, M. Schomaker, & A. Ayoub (Eds.), *Soils on a warmer earth* (pp. 39-49). Elsevier Science Publishers B.V.

Vardon, P. J. (2015). Climatic influence on geotechnical infrastructure: a review. *Environmental Geotechnics*, *2*(EG3), 166-174. https://doi.org/10.1680/envgeo.13.00055.

Proceedings of the XVIII ECSMGE 2024
GEOTECHNICAL ENGINEERING CHALLENGES
TO MEET CURRENT AND EMERGING NEEDS OF SOCIETY
© 2024 the Authors
ISBN 978-1-032-54816-6
DOI 10.1201/9781003431749-554
Open Access: www.taylorfrancis.com, CC BY-NC-ND 4.0 license

ECSMGE 24
XVIII EUROPEAN CONFERENCE ON SOIL MECHANICS AND GEOTECHNICAL ENGINEERING

Site selection and early-stage design of trenchless submarine cable landings

Sélection de site et conception préliminaire d'un atterrage de câble sous-marin sans tranchée

L.J. Burley
Cathie Group, Newcastle, United Kingdom

V.A. Terente*, H.K. Waterston, H.J.B. Bryan, D. Hinxman
Cathie Group, Newcastle, United Kingdom

**victor.terente@cathiegroup.com*

ABSTRACT: There is an increasing need for offshore wind developments and submarine interconnector projects. The selection of the landing area has a major influence in construction techniques, drilling equipment requirements, construction schedule, project risks and costs. Often offshore wind cable landings are under prioritised during the project design until a late stage but are crucial for project viability. This paper illustrates what processes and data are required to select an adequate coastal area for landing using trenchless installation technologies including Horizontal Directional Drilling and Direct Pipe. Once a landfall site has been selected through methodologies such as constraint mapping and BRAG assessments, the site investigation and early-stage design works required to complete a successful project can be scoped and undertaken.

RÉSUMÉ: Le besoin de développer des projets d'éoliennes en mer et d'interconnexions sous-marines va croissant. Or, le choix de la zone d'atterrage exerce une influence majeure sur les techniques de construction, les exigences en matière d'équipement de forage, le calendrier de construction, les risques et les coûts du projet. Souvent, les atterrages de câbles éoliens offshore ne sont pas prioritaires lors de la conception du projet, et ce jusqu'à un stade avancé, mais ils sont cruciaux pour sa viabilité. Cet article illustre les processus et les données nécessaires pour sélectionner une zone côtière adéquate pour l'atterrage à l'aide de technologies d'installation sans tranchée, comme le forage directionnel horizontal et les conduites directes, qui sont discutés. Une fois qu'un site d'atterrage a été sélectionné grâce à des méthodologies de cartographie des contraintes et des risques, l'étude du site et les travaux d'ingénierie préliminaires nécessaires pour mener à bien un projet réussi peuvent être définis et entrepris.

Keywords: Landfall; installation; site selection; HDD; direct pipe; trenchles; subsea cables.

1 INTRODUCTION

There is an increasing need for offshore wind power developments and submarine interconnector projects, which need to connect to the onshore electrical grid system. The selection of the landing area has a major influence in construction techniques, drilling equipment requirements, construction schedule, project risks and costs.

Landfall installation techniques can be categorised into;

1. Surface lay – which may include external protection such as rock bags, cable protection Systems (CPS) etc.
2. Trenched – continual cable burial on to shore e.g., with plough, jet sled. This may include additional onshore techniques such as backhoe etc.
3. Trenchless – Horizontal Directional Drilling (HDD) and Direct Pipe/Micro tunnelling (which this paper focuses on).

This paper summarises what processes and data are required to select an adequate coastal area for landing and the survey and preliminary engineering works required to complete a successful trenchless landfall project, illustrated with examples.

2 TRENCHLESS LANDFALL INSTALLATION TECHNIQUES

For Trenchless landfall installation techniques there are two main methodologies; Direct Pipe and Horizontal Directional Drilling (HDD) which are summarised below.

Direct pipe construction and HDD are two different trenchless techniques used in the installation of

underground pipelines. They each have their own advantages and disadvantages presented in Table 1, and the choice between them depends on various factors such as the specific project requirements, geological conditions, and budget.

2.1 Direct pipe (pipe jacking)

Direct pipe installation encompasses microtunelling (using a microtunnel boring machine, MTBM) and pipe jacking methods benefitting from simultaneous hole creation and pipeline insertion. This is facilitated by direct attachment of the pre-fabricated steel pipeline to the MTBM machine creating a permanently supported bore throughout installation and minimising the risk of collapse, Figure 1.

In contrast to conventional microtunelling, this method is steerable and allows for precise control when creating inclines, slopes and curves across an installation trajectory (Stein, 2005).

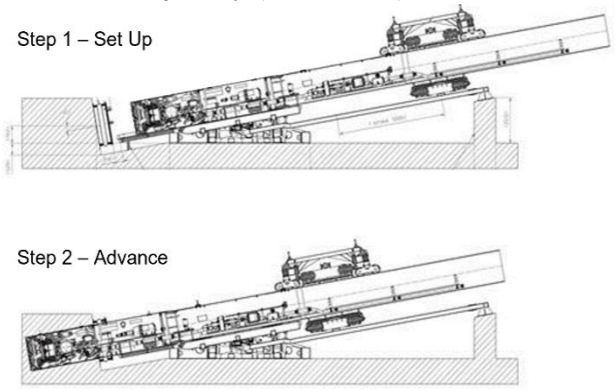

Figure 1. Illustrative direct pipe set-up and advancement (Stockton drilling, 2023).

A small trench may need to be excavated at the punching out point location. The MTBM terminates into the trench and then is remotely disconnected. The microtunnelling machine is then recovered at the exit point, usually by a jack up equipped with a suitable crane. This method is significantly more expensive than conventional microtunnelling and requires a large area to accommodate the jacking and pipe equipment.

2.2 Horizontal Directional Drilling (HDD)

HDD is a trenchless technique using a remotely operated steerable drill head which can accommodate a large range of complex alignments. Pre-construction works include a detailed chainage design of HDD route (entry, exit and trajectory), assessment of drill and pulling requirements, blowout assessments (due to the high drilling fluid pressures used) , duct stresses and cable pull force assessments (Stein, 2005, Willoughby, 2005).

Pipeline and cable installation using HDD comprises a multi-staged approach presented in Figure 2.

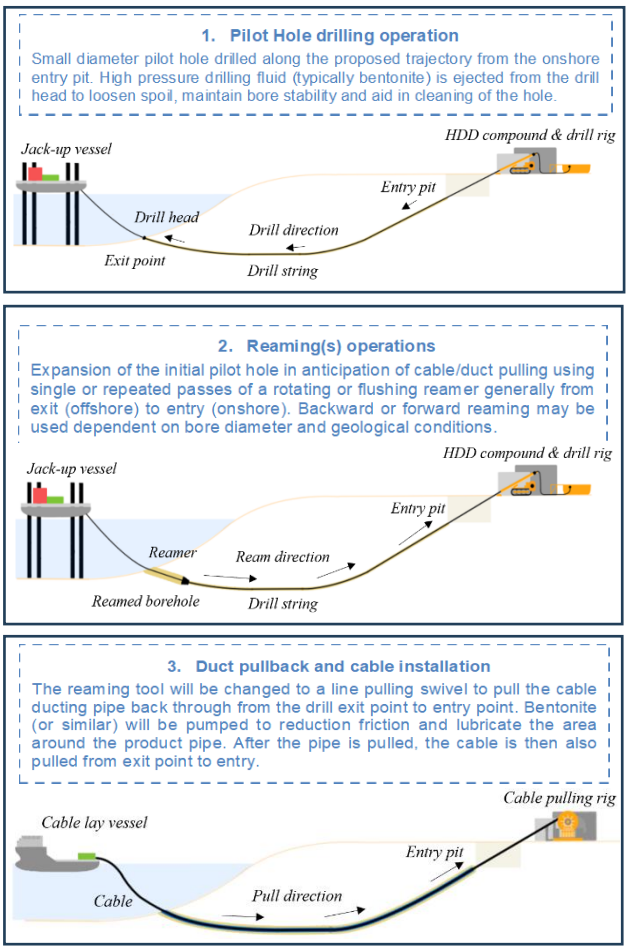

Figure 2. HDD Installation Methodology.

Table 1 summarises considerations of both HDD and Direct Pipe techniques.

Table 1. Installation technique considerations.

Technique	Consideration
HDD	• Need sufficient clearance for operations HDD rig etc. at drill site including access for vehicles etc. • Gravels and fractured rocks are generally not suitable/challenging. • Generally restricted to <2km. • Usually requires deep burial (risk of cable overheating)
Direct Pipe	• Expensive solution as it is requiring tunnelling equipment and recovery. • Need sufficient clearance for operations tunnelling equipment etc. May need personnel to enter duct for maintenance.

2.3 Overall process – concept development

There are varying levels of detail required at each stage. At an early stage a key understanding of project

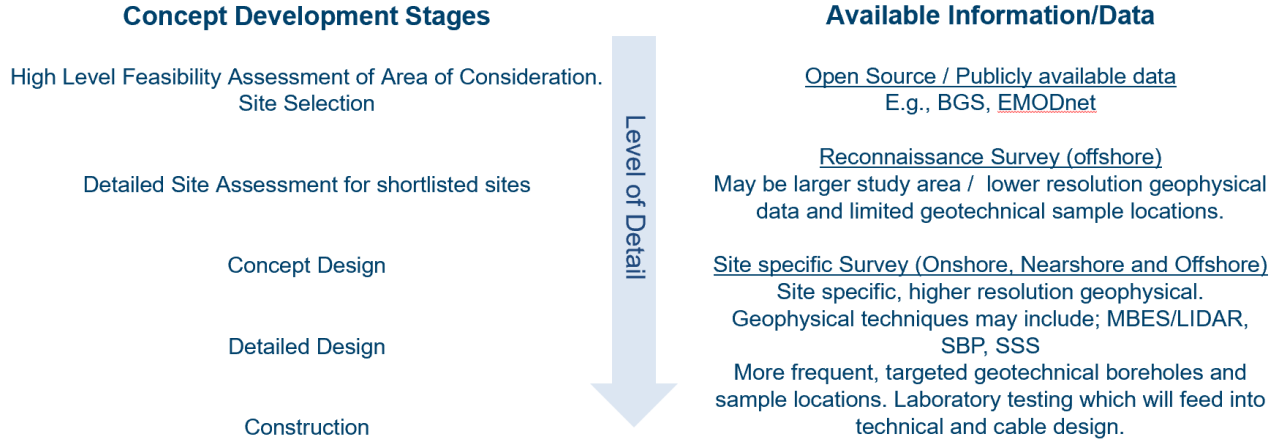

Figure 3. Flow chart presenting Concept Design Development and Associated Available Data.

requirements, risk management and stakeholder engagements is key to a viable landfall selection and a robust concept design. The concept development stages generally follow the sequence presented in Figure 3.

As each stage progresses the required engineering workload increases, as does the available site data. In initial studies such as site selection generally only open-source data and walkover data are available.

The initial studies will aid the survey strategy and inform geotechnical borehole locations. The survey strategy is described in more detail in Section 3.

2.4 Site selection – constraint mapping

The initial site selection is based on numerous factors including onshore grid connection considerations, offshore development distance and site conditions (coastal erosion, environmental constraints, land uses and MetOcean conditions, etc.).

Often the initial landfall location will be defined by the development team and may include a large area(s) which can often be over 5km. The next stage would be to identify specific constraints in the area to define the most appropriate landing points, prior to available site-specific survey data being acquired.

Constraints would be separated into hard constraints which must be avoided, and soft constrains which should be avoided if practicable. Examples of hard constraints may include identified UXO, wrecks, certain land uses, environmental restrictions, etc. Soft Constraints may include certain shallow geology, seabed features etc.

An example of a theoretical landfall selection is shown in Figure 4. Assuming the large study area, there are numerous constraints resulting in only two areas fit for the next stage on the basis of environmental constraints, build up areas and the presente of a fish farm.

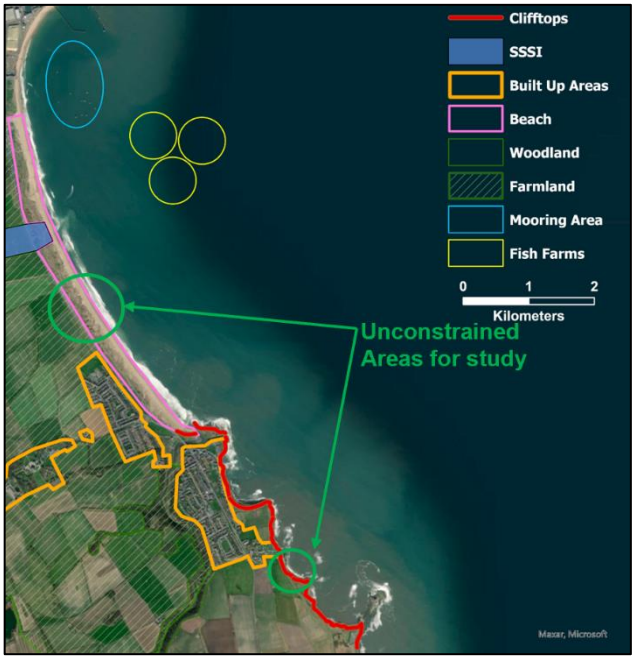

Figure 4. Example of Constraint Identification.

2.4.1 Site Selection – BRAG Assessment

Should there be multiple locations, a further initial study may be undertaken in the form of an optioneering exercise, comparing multiple sites prior to engineering. This may be in the form of a BRAG assessment (black, red, amber, green) where black shows: Significant constraints prohibiting development, red: High potential for the development to be constrained, amber: Intermediate potential for the development to be constrained and green: Low potential for the development to be constrained.

This assessment can include installation techniques in order to shortlist the most suitable installation methodology prior to detailed engineering e.g. should there be a steep cliff present this would rule out trenched methods.

This exercise would generally be undertaken following a constraint mapping exercise compiled from opensource data and prior to detailed engineering.

2.5 Engineering considerations

A series of design checks are required for both Direct Pipe and HDD installation to check feasibility of the design. These are elaborated on below:

1. Settlement Evaluation

Surface settlements are a critical consideration particularly in soft soils when crossing beneath sensitive infrastructure such as railways, roads, underground services, or buildings. Simple analytical tools or FE methods can be used to quantify ground movements above tunnels (O'Rielly & New, 1982, CIRIA, 1996). These are generally classified under two components:

a) Surface (vertical) settlement
b) Resultant horizontal ground movement

Guidance for limiting values of settlement are presented in Eurocode 7 Part 1, Annex H (BSI, 2004) for routine structures. Sensitive infrastructure such as utilities or railways have specific requirements which are set by asset owners and are not covered in general standards.

2. Cable / Duct Pulling Evaluation

Pulling forces are largely dependent on the nature of the HDD/DP trajectories, terrain and cable characteristics. A combination of analytical static pull calculations and specialist software models, such as OrcaFlex (Orcina, 2022) can be used to estimate anticipated pulling forces (Maidla, 1987, Stein, 2005, Willoughby, 2005). This is critical to assess the suitability of the duct and cable in terms of its working load limit and the pulling capacity of plant machinery.

3. Duct Stress Evaluation

Evaluation of duct stresses throughout installation is key to understanding the potential risk of buckling. Curvature of the trajectory, radial stresses from surrounding soils and drill fluids contribute to the overall risk. The right choice of duct material (Steel, HDPE, etc) and internal ballasting helps to combat this issue. The resultant stresses are then compared to the pipes maximum safe bending and tension stress to account for the maximum curvature along the profile (Stein, 2005, Willougby, 2005).

4. Hydrofracture Evaluation

Hydrofracture is the term used to describe fracturing originated from large pressures acting against a borehole wall which exceeds the maximum allowable pressure of the surrounding ground. For HDD, this may occur due to pressurization of the mud slurry within the bore annulus (Bennett et al, 2008).

The maximum allowable pressure is calculated based upon the cavity expansion model (Kuelen, 2001).

5. Thermal Rating Evaluation

Thermal rating of the known site conditions via site investigation and detailed characterisation is crucial to landfall design. Thermal rating is key to deriving the separation distance between cables, burial depths and number of cables required.

2D calculations can be undertaken, however can often be conservative with FE modelling required for complex topography and subsurface conditions. Knowledge of the subsurface, ground water level, thermal conductivity, and ground temperature along the profile are essential to providing a robust evaluation (IEC, 2014, IEC, 2015).

3 SITE INVESTIGATION AND CHARACTERISATION

3.1 Site investigations

Site investigations are crucial to the early-stage design of cable landings. Site investigations need to obtain sufficient information to permit safe and economical design of the duct installation and permanent works, and viability of the cable pulling operations.

Prior to site investigation works, site walk overs are key for early identification of ground, installation and maintanece hazards not easily identifiable from just desk-based studies or historic ground investigation data.

Site investigations are staged into geophysical (non-intrusive) and geotechnical (intrusive) campaigns (BSI, 2020, Eurocode 7, 2012).

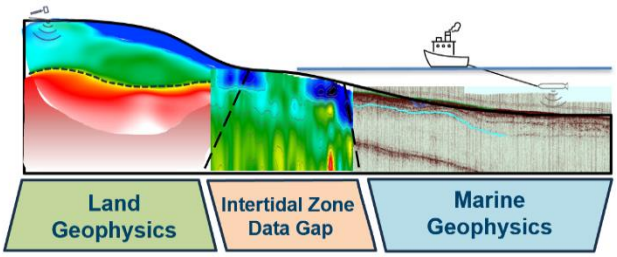

Figure 5. Data acquisition and integration requirements of different landing zones.

1. Geophysical Campaigns (Non-Intrusive)

Geophysical Investigations aim to better understand the ground conditions aiming to profile the shallow subsurface through identifying soil/rock units and geological structure, and allow for identification of seabed features at an early stage.

2. Geotechnical Campaigns (Intrusive)

Geotechnical investigations aim to ground truth the geophysical model and test samples for the design of both the chosen installation methodology as well as the duct and cable itself.

Table 2 presents a summary of common investigation techniques utilised.

Table 2. Summary Table presenting common geophysical and geotechnical investigation techniques.

Location	**Geophysical**	**Geotechnical**
Land	• Seismic Refraction and Reflection • Electrical Resistivity Tomography • Ground Penetrating Radar • LiDAR	• Trial pits • Boreholes • In-situ testing (e.g. geophysical logging, high pressure dilatometer) • Soil and rock laboratory testing
Marine	• Multibeam Echosounder • Sub-Bottom Profiler • Magnetometry • Sidescan Sonar	• Boreholes • Cone Penetration Testing • Vibrocore • In-situ testing (e.g. geophysical logging, high pressure dilatometer) • Soil and rock laboratory testing

Obtaining both geophysical and geotechnical data are sub-divided into three areas: onshore, nearshore and offshore, which maybe undertaken during multiple campaigns.

Often the intertidal region is underprioritised with limited site investigation and characterisation between the land and the marine based survey methods, resulting in a common data gap. This is illustrated in Figure 5. This can be mitigated using established geophysical techniques such as LiDAR, drone magnetometer surveys and geotechnical techniques such as tracked CPT rigs, etc to allow for good data integration between land and marine surveys.

Early-stage site investigation is recommended to confirm open source information or assumptions, and identify ground hazards.

3.2 Site characterisation

Following data acquisition through the required site investigations, early integration of geophysical and geotechnical data is key for a robust site characterisation.

Early construction of a well developed integrated ground model can identify ground hazards which can be mitigated through an adequate conceptual design and planning.

Figure 6 presents an example HDD profile through an integrated ground model. This incorporates site selection, engineering considerations (Section 2.4 and 2.5), and an advanced understanding of the site geological conditions reducing associated installation risk at an early stage.

The trajectory of such drills is designed to specific low angles for launching and punch through (generally between 5-10^0) and high curvature ratios for trayectory changes (in the order of 500m). A minmum level of soil cover is then selected on the basis of blow up risks, cable overheating and more complex geological considerations.

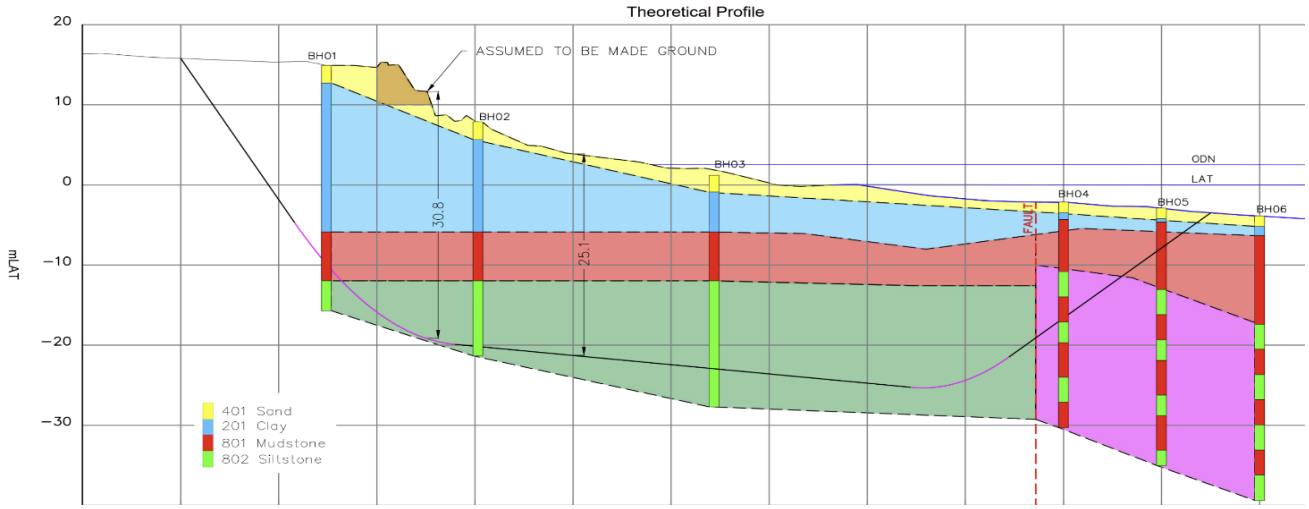

Figure 6. Theoretical HDD Profile Incorporating an Integrated Ground Model.

4 CONCLUSIONS

Landfall selection and concept design are crucial for the project viability of marine cables.

A proactive site selection strategy with good understanding of project requirements, risk management and stakeholder engagements is key to a viable landfall selection and to providing a robust concept design at an early stage.

The identification of a preferred landfall area through methodical constraint mapping and BRAG assessments will inform the possible installation methodologies, allowing for targeted and efficient site investigation stages.

Successful site investigation of trenchless cable landings will, in turn, inform the most adequate design, mitigating ground hazards and reducing installation risks.

REFERENCES

Bennett, D. and Wallin, K., (2008). Step by step evaluation of hydrofracture risks for horizontal directional drilling projects. In Pipelines 2008: Pipeline Asset Management: Maximizing Performance of our Pipeline Infrastructure (pp. 1-10).

BSI (2020). BS 5930:2015 Code of practice for ground investigations, BSI Standards Limited.

BSI (2004). BS EN 1997-1 Eurocode 7: Geotechnical design – Part 1: General rules, British Standards Institution, London.

CIRIA. (1996). PRJ PR 30 Prediction and effects of ground movements caused by tunnelling in soft ground beneath urban areas. CIRIA, London.

Eurocode 7. (2012). Geotechnical Design to Eurocode 7. Springer Science and Business Media, London.

IEC (2015). IEC 60287-2-1 Thermal resistance - Calculation of thermal resistance, International Electrotechnical Commission.

IEC (2014). IEC 60287-1-1 Current rating equations and calculation of losses – General, International Electrotechnical Commission.

Keulen, B (2001). Maximum allowable pressures: Maximum allowable pressures during horizontal directional drillings focussed on sand, Doctoral dissertation, Delft University of Technology. [online] Available at: https://repository.tudelft.nl/islandora/object/uuid:ad91dad8-b958-481b-82d8-c7395d1a3874?collection=education, accessed: 24/10/2023.

Maidla, E. E. (1987). Borehole Friction Assessment and Application to Oilfield Casing Design in Directional Wells, Louisiana State University [online] Available at: https://repository.lsu.edu/cgi/viewcontent.cgi?article=5460&context=gradschool_disstheses, accessed: 24/10/2023.

Orcina (2022). OrcaFlex (11.3) [computer program] Available at: https://www.orcina.com/orcaflex/, accessed: 24/10/2023.

O'Reilly & New. (1982). Settlements above tunnels in the United Kingdom – their magnitude and prediction. Crowthrone, England.

Stein, D. (2005). Trenchless technology for installation of cables and pipelines, 1st ed., Stein & Partner, Germany.

Stockton Drilling. (2023). Available at: https://stocktondrilling.com/, accessed: 24/10/2023.

Willoughby, D. (2005). Horizontal directional drilling: utility and pipeline applications, 1st ed., McGraw-Hill Education, USA.

Proceedings of the XVIII ECSMGE 2024
GEOTECHNICAL ENGINEERING CHALLENGES
TO MEET CURRENT AND EMERGING NEEDS OF SOCIETY
© 2024 the Authors
ISBN 978-1-032-54816-6
DOI 10.1201/9781003431749-555
Open Access: www.taylorfrancis.com, CC BY-NC-ND 4.0 license

ECSMGE 24
XVIII EUROPEAN CONFERENCE ON SOIL MECHANICS AND GEOTECHNICAL ENGINEERING

Different jacket foundation installation methods for three offshore substations

Différentes méthodes d'installation de fondations de type jacket pour trois sous-stations électriques offshore

A. Cardoso*, J. Leplat, N. Van Damme, S. Raymackers
DEME Offshore, Zwijndrecht, Belgium

**cardoso.alexandra@deme-group.com*

ABSTRACT: Following the world demand for clean energy, the development of Offshore Windfarms (OWF) has been in constant growth with more challenging sites being considered for the construction of these OWF. Three Offshore Substations (OSS) of three different OWF located off the North and West coast of France, are installed on four-legged jackets founded on piles. For each of the OSS, the installation method of the pile foundations was different due to the soil conditions found on site: Rock Socket Drilling (RSD), Drill and Grouted (DG) and Drive-Drill-Drive (DDD). For all the three OSSs a pre-pilling template was deployed on the seabed. For the RSD method, for each pile a casing was oscillated into the seabed. Afterwards the rock socket was drilled to target depth and the casing retrieved after grouting. Then the pile was installed in the socket and the annulus between the pile and socket was grouted. For the DG method, first a pile was driven to the shallowest hard layer. Next a socket was drilled to target depth and the pile inserted. Afterwards, the inserted pile was grouted in the socket and in the driven pile. For the DDD method, first the pile was driven until initial refusal. Then a pilot hole was drilled and afterwards the pile was driven to target depth. In this paper, a more detailed description and challenges of these installation methods are discussed.

RÉSUMÉ: Suite à la demande mondiale d'énergie propre, le développement des parcs éoliens offshore (OWF) n'a cessé de croître et des sites de plus en plus difficiles sont envisagés pour la construction de ces OWF. Trois sous-stations offshore (OSS) pour trois parcs éoliens offshore différents situés au large des côtes nord et ouest de la France ont été installées sur des jackets à quatre pieds fondés sur des pieux. Pour chacun des OSS, la méthode d'installation des fondations sur pieux était différente en raison des conditions de sol rencontrées sur le site Forage de la roche (RSD), Forage et coulis (DG) et battage-forage-battage (DDD). Pour les trois méthodes OSS, un gabarit de préforage a été déployé sur le fond marin. Pour la méthode RSD, un tubage a été oscillé dans le fond marin pour chaque pieu. Ensuite, la cavité rocheuse a été forée jusqu'à la profondeur cible et le tubage a été récupéré après injection de coulis. Le pieu a ensuite été installé dans l'alvéole et l'espace annulaire entre le pieu et l'alvéole a été jointoyé. Pour la méthode DG, un pieu a d'abord été battu jusqu'à la couche dure la moins profonde. Ensuite, une alvéole a été forée jusqu'à la profondeur cible et un deuxième pieu a été inséré. Ensuite, le pieu inséré a été jointoyé dans l'alvéole et le pieu battu. Pour la méthode DDD, le pieu a d'abord été battu jusqu'au refus initial. Ensuite, un trou pilote a été foré et le pieu a été battu jusqu'à la profondeur cible. Dans cet article, une description plus détaillée et les défis de ces méthodes d'installation sont discutés.

Keywords: Pre-pilling; driving; drilling; grouting; offshore.

1 INTRODUCTION

Three Offshore Wind Farms (OWFs) located off the North and West coast of France were planned to be constructed and be commissioned by 2023. For each of these OWFs an offshore substation (OSS) needed to be installed. The OSSs are installed on a four-legged jacket with 26m x 26m footprint, which were founded on four piles. The piles were installed prior to the installation of the jacket (pre-piling) using a piling template deployed on the seabed. The installation method for the piles of each of the OSSs was different and the selection was based on the soil conditions found specifically at the OSS locations: Calcarenite overlying sand (Site 1), sand overlying chalk interbedded with flint layers (Site 2) and sand/clay overlying calcarenite and calcilutite (Site 3). The presence of rock at these sites presented a challenge for the pile installation as the standard/normal installation method (drive only) would not have been able to install the piles at these sites.

The piles were installed using the jack-up platform (JUP) "Sea Installer". A picture of the JUP, at Site 2, is shown in Figure 1.

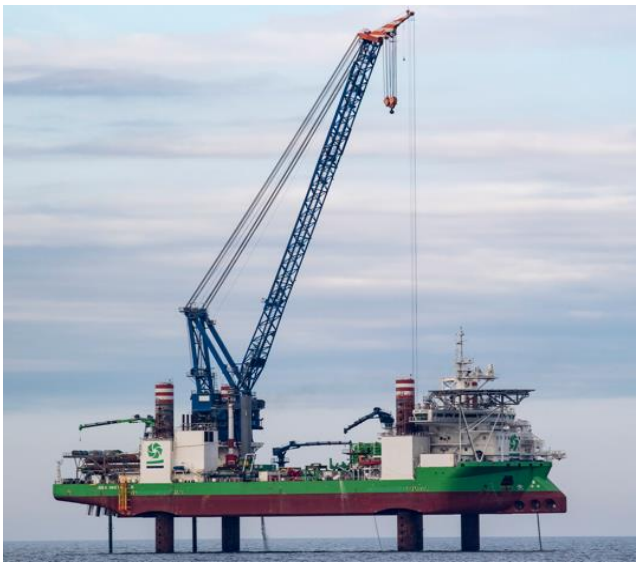

Figure 1. Jack-up platform Sea Installer at Site 2.

2 SOIL CONDITIONS

Rock is present at the three sites. However, the characteristics and depth at which the rock occurs varies between them. The general soil conditions at each of the sites and soil profiles, up to the pile embedment depth, considered for installation assessment, are described below, and depicted in Table 1, 2 and 3.

At Site 1, rock (calcarenite) is found at seabed, with thicknesses around 19m. The rock presents Unconfined Compressive Strength (UCS) values ranging from 2MPa and 24MPa.

Table 1. Soil profile at Site 1.

Stratum Type	Top depth (mbsb*)	Bottom depth (mbsb*)	Range of UCS (MPa)
Calcarenite	0.0	18.8	2.2-24.0

Note: *mbsb – meters below seabed

At Site 2, a thin layer of sand overlies the rock. The rock consists of low to medium density chalk becoming high density with depth. Several flint layers/cobbles were detected within the chalk at different depths below seabed level, the first occurrence being at 13.9mbsb.

Table 2. Soil profile at Site 2.

Stratum Type	Top depth (mbsb*)	Bottom depth (mbsb*)	Range of UCS (MPa)
Sand	0.0	0.4	-
Chalk	0.4	28.5	1.0-4.0

At Site 3, the rock (limestone: calcarenite and calcilutite) is found at around 7mbsb depth overlain by a thin layer of sand and a thick layer of clay.

Table 3. Soil profile at Site 3.

Stratum Type	Top depth (mbsb*)	Bottom depth (mbsb*)	Range of UCS (MPa)
Sand	0.0	0.9	-
Clay	0.9	7.0	-
Calcarenite	7.0	18.8	2.2-24.0
Calcilutite	18.8	21.1	3.5-6.0
Clay	21.1	23.1	-
Calcilutite	23.1	28.9	6.0-9.0
Calcarenite	28.9	31.0	12.0-20.0

The layering considered for these soil profiles, is based on the boreholes performed at the centre of the jacket. The top level of the different stratum types was expected to show some variability between the borehole and the pile locations. Due to this variability, especially for the shallowest flint layer at Site 2 (where driving refusal was expected) and the calcarenite layer at 28.9m depth at Site 3 (where the piles needed to be founded to ensure the pile capacity), contingency measures had to be foreseen to ensure the integrity of the piles (safe driving) and that the piles would reach the necessary embedment depth to obtain the pile design capacity. These measures are explained in Chapters 4.2 and 4.3, respectively.

3 PILE DESIGN

The general pile dimensions for the three sites are given in Table 4, Table 5 and Table 6, respectively.

Table 4. General characteristics of the installed piles at Site 1.

Pile section	Pile length (m)	Pile embedment (mbsb)	Pile diameter (m)	Bottom WT* (mm)
1	9.5	4.5	2.3	80
2	9.5	9.0	2.3	60

*WT – Wall Thickness

Table 5. General characteristics of the installed piles at Site 2.

Pile section	Pile length (m)	Pile embedment (mbsb)	Pile diameter (m)	Bottom WT* (mm)
Driven	16.5	13.5	3.0	75.0
Insert	28.5	28.5	2.4	50.0

Table 6. General characteristics of the installed piles at Site 3.

Pile length (m)	Pile embedment (mbsb)	Pile diameter (m)	Bottom WT* (mm)
35.0	31.0+	3.0	100

Note: + Including 2m contingency length due to variability of the top level of the calcarenite found at 28.9mbsb

4 INSTALLATION METHODS

Based on the soil conditions described in Chapter 2, for the three sites, three pile installation methods were used:

- Site 1 Rock socket drilling (RSD)
- Site 2 Drill and grouted (DG)
- Site 3 Drive-drill-drive (DDD)

Although the installation method was different, all methods used a piling template as a piling guide for placing the jacket piles within tolerances into the ground. One single piling template was custom-made for the projects as the jacket footprints are identical. A picture of the template while being tested is shown in Figure 2.



Figure 2. View of the template used.

The drilling equipment consisted of a Wirth PB 928 for site 1 and LD2500 for sites 2 and 3.

For Sites 2 and 3, adding to the drilling operations, driving operations were necessary as part of the installation method. For that purpose, IQIP impact hammers S-800 and S-2000, for site 2 and 3 respectively, and a follower, were used. A picture of the impact hammer and follower is shown in Figure 3.

4.1 Rock socket drilling – Site 1

Due to the presence of rock at seabed and up to 19mbsb, the installation method chosen for Site 1 was rock socket drilling. This method consisted of deploying the piling template and stabbing a casing in the template sleeve. The casing was then oscillated into the seabed. Afterwards, the drill rig was mounted directly on the top of the casing and the BHA was lowered inside the casing, enabling the rock socket to be drilled to target depth. The drilling methodology is based on the reverse circulation drilling (RCD) process. After drilling operations were completed, the BHA and drill rig were recovered and put back on deck and the casing was cut just above the seabed, leaving the casing shoe (sacrificial) to stabilize the top rock layer. Finally, the pile was lowered into the drilled socket and the annulus between the socket and the pile was grouted. Ultimately, the casing was removed and the template recovered. A view of the drilling set-up (BHA and drill rig) and the oscillator is shown in Figure 4.



Figure 3. Impact hammer and follower.

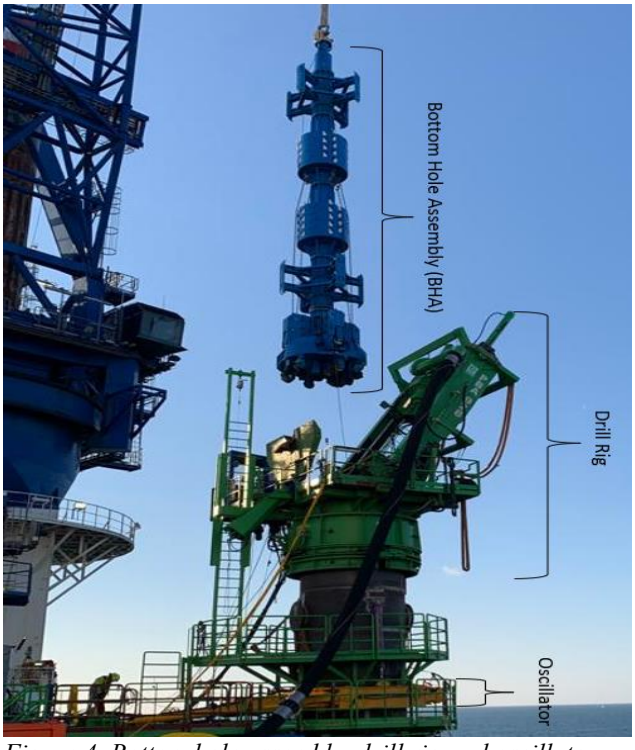

Figure 4. Bottom hole assembly, drill rig and oscillator.

4.2 Drill and grouted – Site 2

Due to the presence of high-density chalk, it was estimated that the pile could not be driven up to target depth. It was also considered that the presence of the flint layers would pose a risk with regards to pile tip damage. Hence, the drill and grouted installation method was chosen.

The drill and grouted method consisted of driving a 3m diameter pile up to the top of the shallowest flint layer (13.9mbsb) with an 800kJ impact hammer. In the case the shallowest flint layer was encountered at depths shallower than the expected 13.9mbsb, and to ensure that the driven pile would have sufficient embedment depth for loads to be transferred from the driven to drilled and grouted casings, a drilling spread was mobilized for a drive-drill-drive contingency. After driving the 3m diameter pile, a casing was stabbed and supported on the template. Then the drill rig was mounted directly on top of the casing and the BHA was lowered inside the casing and a socket was drilled to target depth (the drilling method was the same as for Site 1). Afterwards the BHA and the drill rig were recovered on deck. Finally, the pile was lowered through the driven pile into the drilled socket and the annulus between the socket and the pile and between the insert and driven pile were grouted. At the end, the casing and the piling template were recovered.

4.3 Drive-Drill-Drive – Site 3

At Site 3, due to the presence of rock with UCS values up to 24MPa below 7mbsb depth, it was estimated that the pile could not be driven to target depth with an impact hammer, unless a pilot hole was drilled to reduce the shaft friction and end bearing. Hence the DDD method was considered for this site. The method consisted of driving the pile with a 2000kJ impact hammer through the template sleeve, until refusal (top of calcarenite) occurred. Afterwards a casing was installed, and the drill rig was mounted directly on top of the casing. The BHA was lowered inside the pile and a pilot hole with 80% of the outside diameter of the pile was drilled up to 29mbsb (the drilling method was the same as the one mentioned for Site 1 and Site 2). Then the drill rig was recovered and put back on deck. Afterwards, the pile was driven to target depth with the 2000kJ impact hammer. At the end, the piling template was recovered.

In the case that the stratum required to ensure pile capacity, expected at 29mbsb depth, would be at deeper depths, pile length was increased and a pile cutting spread was mobilized on board. At the end three out of the four piles were cut.

5 PILE DRIVING MONITORING

Hard driving conditions were expected at Sites 2 and 3. The axial stresses on the pile, and particularly at the pile tip, were to be limited to prevent the risk of pile tip damage by means of pile driving monitoring. The instrumentation consisted of two deep-sea underwater accelerometers and four deep-sea underwater strain transducers per pile. Sensors were bolted on the pile external shaft at 5m from the top. All jacket piles on both sites were instrumented.

Monitoring measures the compressive stresses at sensor level. Based on a Safe Tip analysis done prior to installation (defining a safe driving criterion), the stresses at pile tip were estimated. The driving criterion consisted of intervals alert function of a compressive stress limit, taken 80% of the steel yield stress: pre-alert limits (80% of stress limit), alert limits (90% of stress limit) maximum limits (equal to stress limit).

At the sites, the stresses remained below the alert limits which allowed for safe driving operations to take place and mitigate the risk of pile damage.

6 CONCLUSIONS

Soil conditions offshore are becoming more challenging, preventing the use of the “standard” drive only installation method to be used. Also, the fact that there is rock on site does not mean that one method should fit all rock sites. The type of rock, and more particularly the strength and layering encountered at the sites, have a major impact on the method chosen to install the piles.

For the three sites here presented, where rock occurs within the embedment depth of the piles, an active cooperation between designer and installation contractor led to the selection of the optimal design and installation method, that allowed for a safe and economical installation of the piles.

ACKNOWLEDGEMENTS

The authors would like to acknowledge EDF for allowing publishing these data.

Proceedings of the XVIII ECSMGE 2024
GEOTECHNICAL ENGINEERING CHALLENGES
TO MEET CURRENT AND EMERGING NEEDS OF SOCIETY
© 2024 the Authors
ISBN 978-1-032-54816-6
DOI 10.1201/9781003431749-556
Open Access: www.taylorfrancis.com, CC BY-NC-ND 4.0 license

ECSMGE 24
XVIII EUROPEAN CONFERENCE ON SOIL MECHANICS AND GEOTECHNICAL ENGINEERING

Soil treatment solutions for the construction of steel storage tanks: Design and behaviour

Solutions de traitement des sols pour la construction de réservoirs de stockage en acier: Conception et comportement

E. Carvajal Diaz*
Keller SWE, Madrid, Spain

P. Barros, P. Matos
Keller Portugal, Lisbon, Portugal

enmanuel.carvajal@keller.com

ABSTRACT: Presentation of soil treatment solutions by vibro stone columns and rigid inclusions for the construction of steel storage tanks with references to the defined solutions for this type of structures considering the existing soil conditions, design loads and structural requirements, as well as references to the time and magnitude of the settlements. The main design aspects of steel tank foundations to guarantee permissible settlements were described, remarking the importance of the types of differential settlement to be controlled according to API Standards. Also, some considerations are made regarding the monitoring of those structures either in hydrotest or operation situations.

RÉSUMÉ: Présentation des solutions de traitement des sols par vibro colonnes ballastées et inclusions rigides pour la construction de réservoirs de stockage en acier avec des références aux solutions définies pour ce type de structures en tenant compte des conditions du sol existantes, des charges de conception et des exigences structurelles, ainsi que des références au temps et ampleur des tassements. Les principaux aspects de conception des fondations de réservoirs en acier pour garantir les tassements admissibles ont été décrits, en soulignant l'importance des types de tassements différentiels à contrôler selon les normes API. En outre, certaines considérations sont faites concernant la surveillance de ces structures, que ce soit dans des situations d'essais hydroélectriques ou d'exploitation.

Keywords: Steel tanks; hydrotest; ground improvement; settlements; API Standards.

1 INTRODUCTION

The steel tanks represent one of the most important facilities for industrial developments within the oil and gas sector. In many cases, the construction of their foundations supposes a critical task to achieve the project success. Frequently, the soil conditions impose the need of special works like soil improvement or deep foundation which affect the project schedule, type of tank foundation (e.g.: ring footing, slab foundation), interaction with other facilities (e.g.: pipeline racks) and possibly maintenance tasks for tanks during their life cycle. This paper presents some case studies and key aspects for the tanks analysis and selection of ground treatments.

2 ANALYSIS OF TANK FOUNDATIONS

The analysis of tank foundation should focus on meeting an allowable bearing capacity and appropriate differential settlements, which can cause large damages to the steel structure of tanks. Typically, the analysis is performed considering two different phases of quasi-permanent loading.

Firstly, a hydrotest is carried out by filling up the tank with water to check any leakage or failure of the steel structure. It supposes a preloading to the soil profile, due to afterwards tank should be emptied. Thereafter the piping should be connected to the empty tank. The second loading phase corresponds to the operational loading, imposed by the weight of the storage product in the long term, which have typical densities between 7 to 8,5 kN/m^3. Thus, according to the corresponding standard, different hypothesis and load cases can be considered for loading combination, of wind, seismic, snow, and other special loading.

2.1 Typical tank settlements according to API Standards

The API Standards highlight the following types of settlements to be checked:

Uniform Settlements which represent the uniform descent of the entire tank base. These types of settlements do not suppose a significant risk to the tank structure, and only must be considered to plan the connections between the external pipes and the tank.

Settlements that cause tank to tilt as a rigid body (Rigid body – planar tilt)- which can cause damage to the tank structure. They are generally associated with a failure mechanism due to lack of bearing capacity and/or large differential settlements.

Differential settlements outside the plane of inclination as a rigid body (Out-of-plane settlement), which represent the measured settlements along the tank perimeter. Those settlements are the difference between the settlements corresponding to the possible plane of inclination as a rigid body and the measured settlement in the perimeter. Excessive values of differential settlements on the perimeter would cause significant damage to the structure of the tanks (mainly to the walls of the tank).

Differential settlements in the bottom plate (Bottom plate settlement), which represent the maximum differential settlement under the tank footprint. Usually, the differential settlement between the centre of perimeter of tank bottom-plate.

Figure 1 shows the diagrams that correspond to these types of settlements. Figures 2 shows the methodology indicated by API Standards to evaluate differential settlements along the tank perimeter (Out-of-plane settlements – Appendix B, API 653), indicating the settled location of the tank shell, after rigid body tilt, represented by a cosine wave with respect to its original position in a horizontal plane. In Figure 2 the vertical distances between the irregular curve (measured settlements) and the optimum cosine curve represent the out-of-plane settlement.

The common method to get this cosine curve consists of solving the constants a, b and c, to find the optimum curve of the form: $Elev_{pred} = a + b \cdot \cos(\theta + c)$; where $Elev_{pred}$ is the elevation predicted by the cosine curve at angle θ. The optimum cosine curve is considered the one that fits adequately the measured settlements for $R^2 > 0{,}9$; being $R^2 = (S_{yy} - SSE)/S_{yy}$; where S_{yy} is the sum of the squares of the differences between average measured elevation and the measured elevations, and SSE is the sum of the square of the differences between the measured and predicted elevations. As a reference to be validated by either tank manufacturer or purchaser (or both of them), the allowable out-of-plane can be estimated by Eq. (1) when cosine curve fits the measured curve with $R^2>0{,}9$, otherwise Eq. (2) should be used (Andreani and Carr, 2007; API 653, 2014) and centre of tank settlements can be estimated by Eq. (3):

$$S_{max,ft} = \frac{(L^2 \cdot Y \cdot 11)}{(E \cdot H)} \quad (1)$$

$$S_{max,in} = min\left[K \cdot S_{arc} \cdot \left(\frac{D}{H}\right) \cdot \left(\frac{Y}{E}\right); 4\right] \quad (2)$$

$$W = \left[W_e^2 + \frac{0{,}37 \cdot \sigma_f \cdot D^2}{FS \cdot E}\right]^{0{,}5} \quad (3)$$

where:

$S_{max,ft}$: permissible out-of-plane settlement, in feet
$S_{max,in}$: permissible out-of-plane settlement, in inch
S_{arc}: effective settlement arc (see API 653; Annex B, Section B.2.2.5.1), in feet
W: Deflection or settlement in centre of tank
We: initial camber
FS: Factor of safety (FS ≤ 4 for localized yielding; FS ≤ 2 for severe overstress and possible yielding)
L: length between measurement points, in feet
Y: yield strength of the shell material, in psi
E: Young's modulus of the shell material, in psi
H: tank height, in feet
D: tank diameter, in feet
K: factor estimated according to Table 1

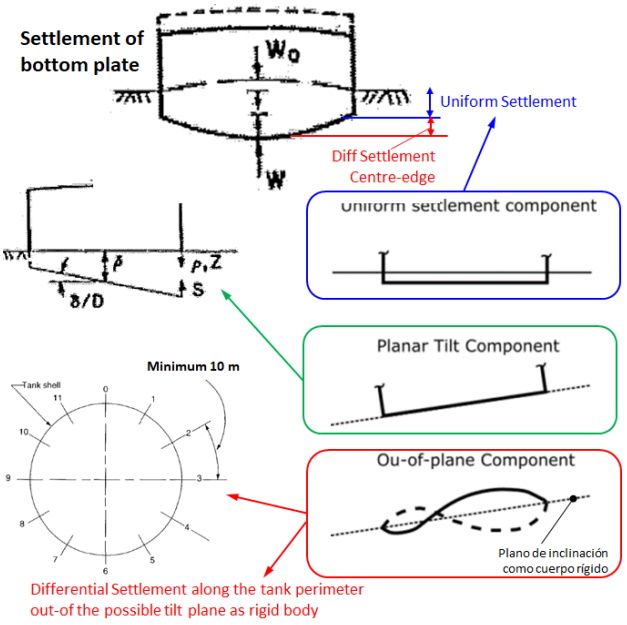

Figure 1. Types of settlement below steel tanks foundation.

Table 1. Factor K for out-of-plane settlement Eq. (2).

Tank Diameter	K, Open Top	K, Fixed Roof
D ≤ 50	28.7	10.5
50 < D ≤ 80	7.8	5.8
80 < D ≤ 120	6.5	3.9
120 < D ≤ 180	4.0	2.3
180 < D ≤ 240	3.6	NA
240 < D ≤ 300	2.4	NA
300 < D	NA	NA

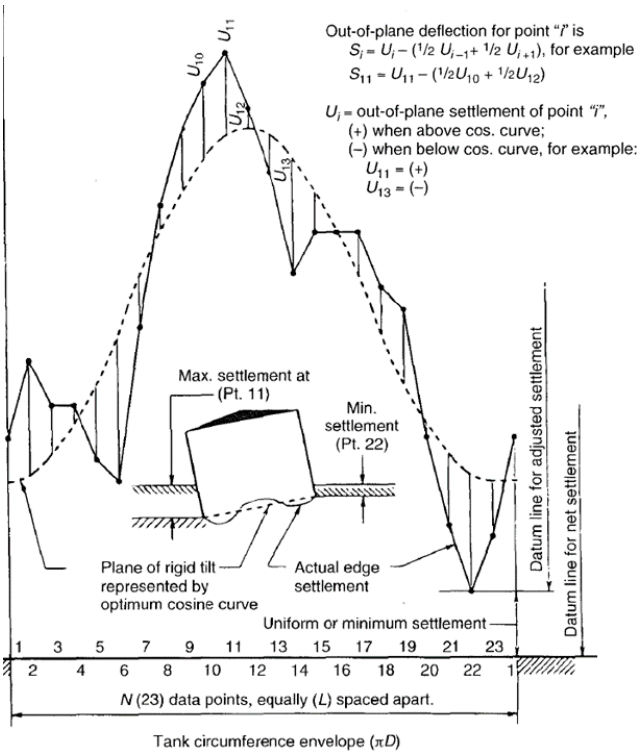

Figure 2. Methodology for analysis of differential settlement along tanks perimeter, according to Standard API 653.

3 CASE STUDY 1: STONE COLUMNS

For the construction of a new terminal of fuel storage tanks in the State of Puebla (Mexico), ground improvement by vibro stone columns was necessary to support the tanks and other facilities.

The soil profile comprises non plastic silts and silty sands below the water table, overlying medium to dense soils beyond 12 m depth. The site location presents high seismicity (Mw=7,2; PGA=0,47g) which suppose high risk of soil liquefaction.

The tanks terminal encompasses 9 fuel storage tanks and 1 fire water tank (Figure 4). The foundation for the structure of all the tanks foresees edge-ring footings of reinforced concrete and granular backfilling inside the ring and right below the tanks).

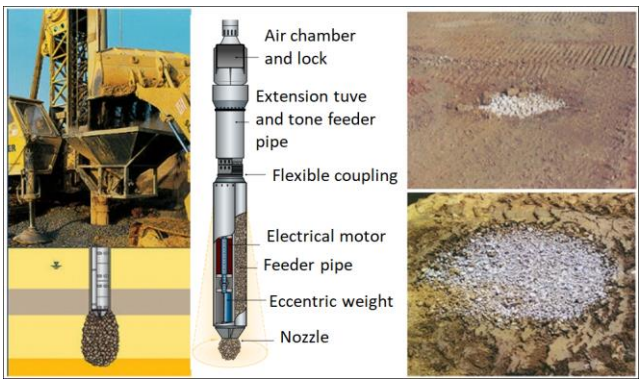

Figure 3. Ground improvement by vibro stone column.

The vibro stone columns installed by deep vibrators have been used successfully in numerous projects since the 1960s to reinforce soft or loose soil with high compressibility, speed up the consolidation process, decrease settlement, increase bearing capacity, and mitigate soil liquefaction. This deep vibro technique has a specific European Standard (EN 14731:2005, Ground treatment by deep vibration). In this project was used the bottom-feed method, which consists of gravel insertion into the ground through a system of tubes attached to a vibrator at the bottom. The whole rod is introduced into the ground aided by lateral displacement, vibration, vertical pull-down force and compressed air. Once the required depth is reached, the tubes stabilize the cavity and allow the gravel feeding. The general motions of deep vibrator compact the gravel by successive lowering and uplifting moves until the column is finished with variable diameter in in the range of 0,6 to 1,0 m depending on the soil stiffness. (Figure 3).

Figure 5 shows a typical borehole with the corrected SPT blow-count with the depth and the factor of safety against soil liquefaction (Boulanger an Idriss 2014) depicting the high risk of liquefaction until 12 to 15 m depth, approximately. Figure 6 shows the foundation details of the tanks, and the stone columns as were installed until 15 to 18 m depth.

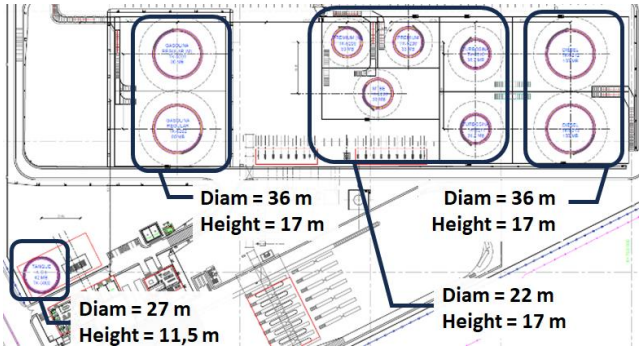

Figure 4. Project layout. Diameter and height of tanks.

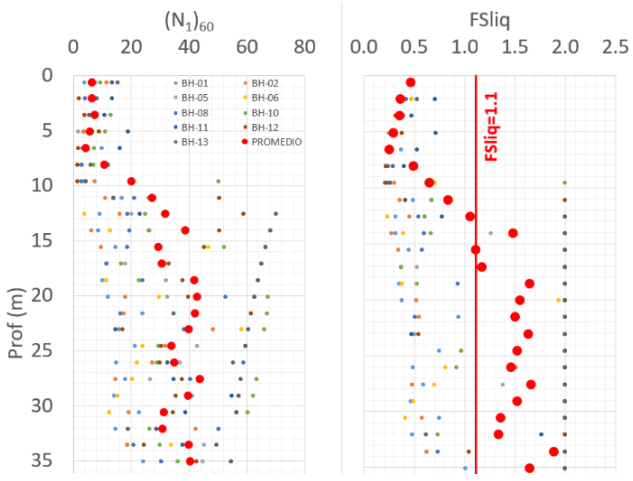

Figure 5. Factor of safety against soil liquefaction.

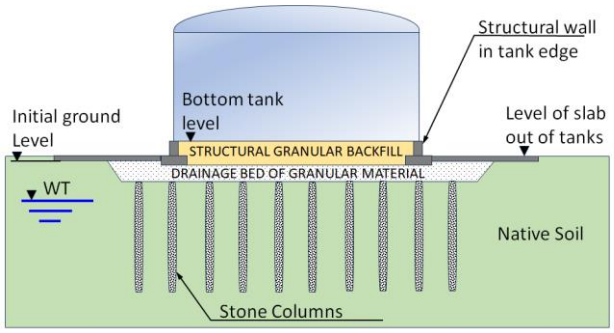

Figure 6. Details of tanks foundation.

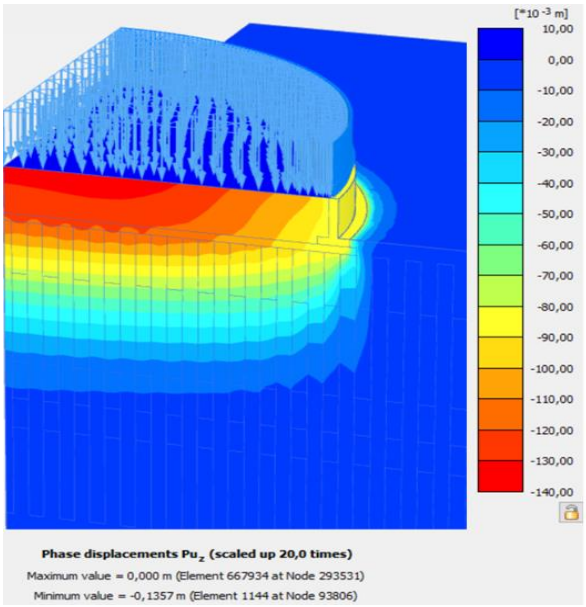

Figure 7. Settlement estimation of tank by FEM analysis.

Figure 7 shows the settlement estimation done by finite element analysis for the hydrotest phase of one of the biggest tanks (diameter of 36 m), resulting a maximum settlement of 13,5 cm in the centre and 9 cm in the perimeter. On the other hand, Figure 8 shows the measured settlements for all the points in the perimeter which match very well the estimated settlements.

Regarding the liquefaction mitigation, Figure 9 shows the results of the pore pressure ratio ($r_u=\Delta u/\sigma'_v$) as a function of depth and earthquake duration. It can be noted that Ru < 0,55, which corresponds to FS>1,1 (Marcuson et al., 1990). In Figure 6 an additional width of ground improvement beyond the rig-wall footing can be noticed to ensure the soil stability against possible liquefaction in the unimproved areas, following the recommendations by JGS (1998).

4 CASE STUDY 2: COMPACTION RIGID INCLUSIONS

Whitin the development of a large industrial project in México, there were built two steel tanks with 85 m in diameter and 15 m height, for fuel storage. The seismic design is characterized by Mw = 6,5 and PGA = 0,19g.

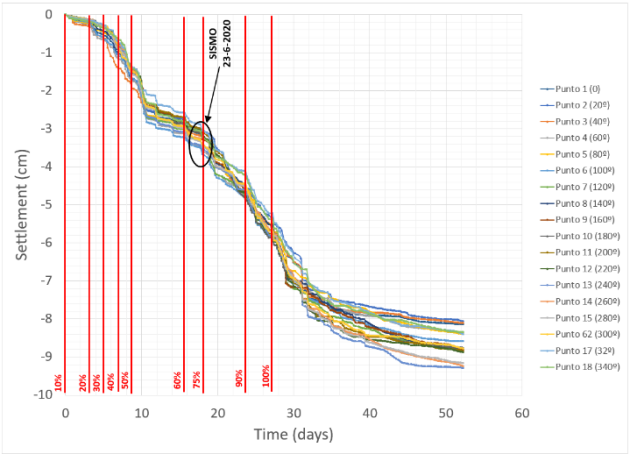

Figure 8. Settlements measured during hydrotest.

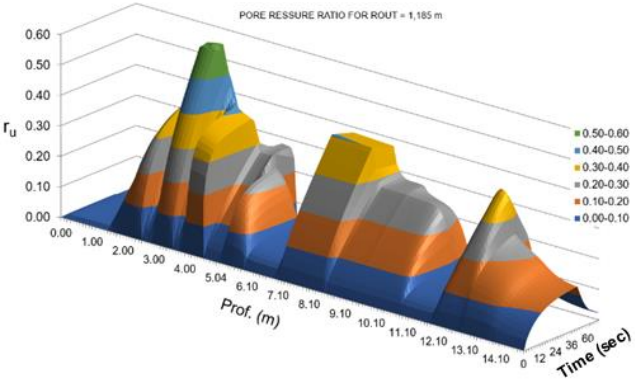

Figure 9. Pore pressure ratio of improved soil.

The soil profile comprises 8 to 12 m of liquefiable sands in the upper layers (qc = 3 to 8 MPa; Ic = 1,6 to 2,1) overlying a very soft clay layer (qc= 1 to 2 MPa; Ic > 3) with 4 to 6 m thickness, and below medium dense sand until 30 m depth was encountered.

After the analysis of the possible solutions, it was adopted as the optimum treatment the ground improvement by Compaction Rigid Inclusions (CRI). This kind of treatment was able to meet the technical requirements which basically were liquefaction mitigation, control of settlement and reaching allowable bearing capacity.

The Compaction Rigid Inclusions (CRI) are performed by means of drillings with full displacement augers (FDA) to avoid massive extraction of soil spoil; once reaching the foreseen depth, the grouting phase initiates by feeding the concrete through the extension tubes coupled to the displacement auger which outflow by the bottom. In those layers which need liquefaction mitigation the grouting is carried out by applying higher pumping pressure until maximum values of 4 to 7 MPa, with the objective to enlarge the column

diameter by displacement process, and this way densify the surrounding soil.

Figure 11 shows a sketch of the adopted solution. In the liquefiable layers until 12 m depth, the CRIs reached an average diameter of 0,6 m, whereas at higher depths there were not liquefiable soils and the mean diameter reach 0,4 m, very similar to the diameter of the drilling auger.

The pattern consists of two overlapped grids of rigid inclusions. The first grid has 2,1 m spacing between columns with compaction grouting process until 12 m. The second grid corresponds to the columns in between the first grid and until the maximum depth of 27 m. In this 2nd grid all the columns have the smallest diameter in the bottom and the highest one in the top where liquefaction needs to be mitigated. So that the column spacing in the top become in 1,5 m, and in the bottom remains of 2,1 m.

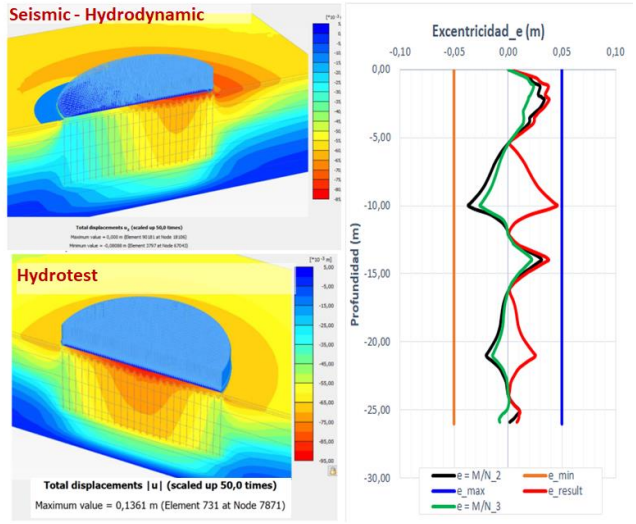

Figure 10. FEM analysis of hydrotest (SLS) and accidental action due to seismic-hydrodynamic loading (ULS).

Figure 11 also shows the pre and post CPTU testing performed in a field trial carried out at the beginning of the treatment. In can be observed the increase of tip resistance by a factor of 2 to 3, that implies improved tip resistances higher than 10 MPa, which meet the required cyclic strength to mitigate the liquefaction.

Figure 10 shows the maximum settlement of 16 cm estimated by FEM analysis of the hydrotest. Figure 10 also shows the results of the seismic-hydrodynamic analysis, that was done by applying the equivalent pseudo-static forces in the bottom of the tanks, which produce vertical stress concentration. The right side of Figure 10 shows the verification of internal forces in rigid inclusions produced by this seismic-hydrodynamic analysis.

5 CASE STUDY 3: RIGID INCLUSIONS

The construction of terminal tanks located in Huelva, south-west of Spain, is developed to facilitate the development of a petrochemical complex.

The soil profile presents predominantly loose to medium dense silty-sand materials until 5 to 7 m depth, overlying a dense gravely sand. The water table was found between 2 and 3 m depth.

The layout includes 8 tanks with 17 m of diameter, and 2 tanks 24 m in diameter. All of them have 28,5 m height and foundation slabs with octagonal configuration and a variable thickness of between 1,4 and 1,0 m. According to the chemical product to be storage, the design load for both hydrotest and operational phases was 287 kPa. Technical requirements foresee differential settlements below 5 mm in 5 m along the perimeter, and 85 mm from centre to edge. Tilt distortion should be below 1/1000, and minimum factor of safety of 3 against bearing capacity. Figure 12 shows an overview of the solution.

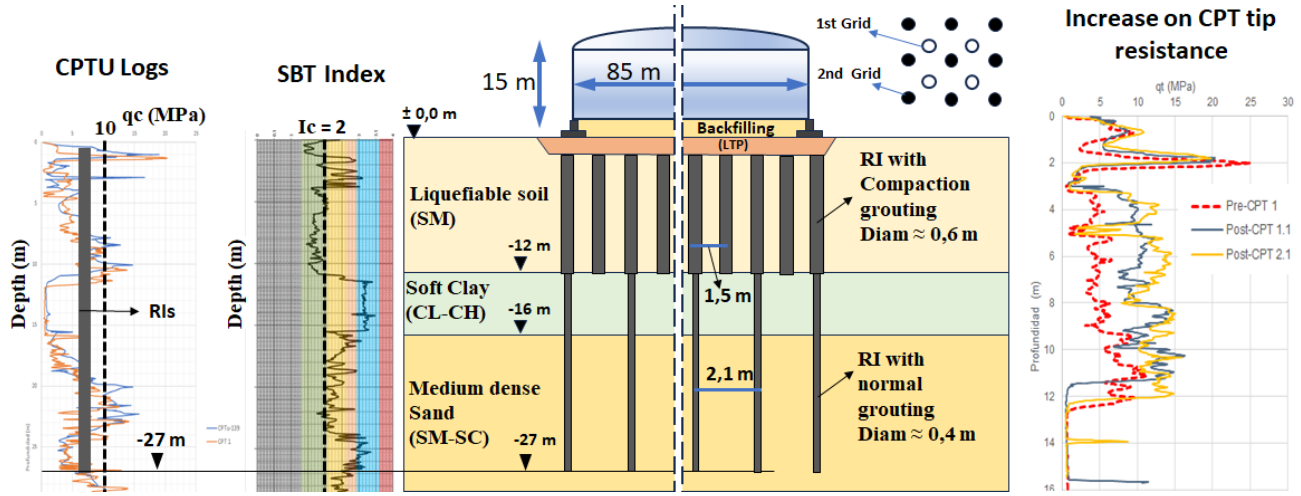

Figure 11. Soil profile, sketch of ground improvement cross section and CPTU verification of liquefaction mitigation.

Figures 13 shows settlement estimation of 5,5 cm in the centre and 3,5 cm in perimeter for the tank of 24 m in diameter. Figure 14 depicts the settlements measured for each loading stage, which match very well the settlement estimation for the last consolidation phase with 100% of loading. Figure 15 shows the analysis of differential settlements measured in the perimeter and the plane of rigid tilt represented by an optimum cosine curve as described in Section 2.1 according to API 653. It was checked an allowable cosine curve to validate the tilt requirement.

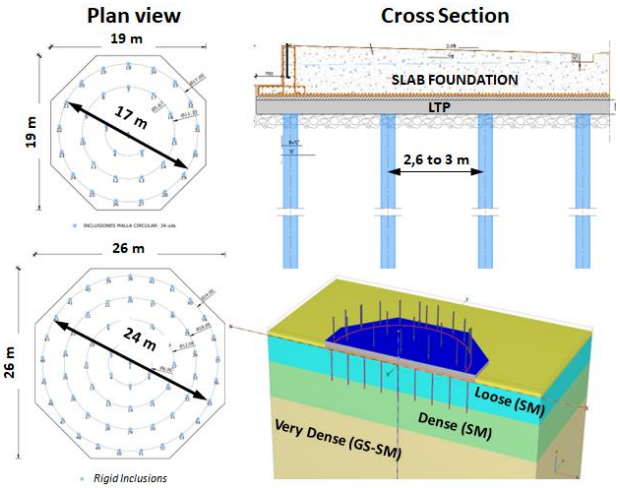

Figure 12. Rigid inclusions solution.

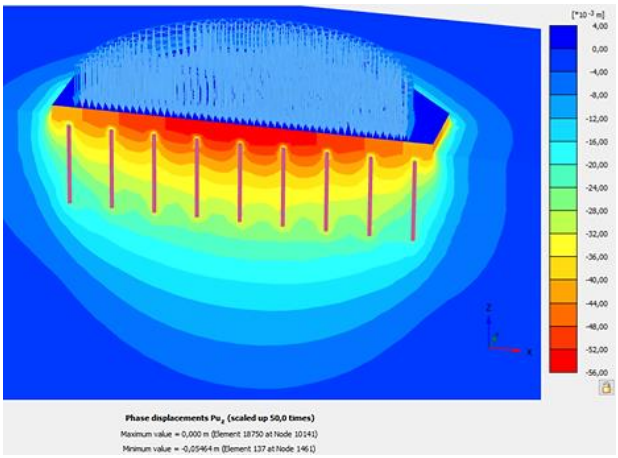

Figure 13. Settlement estimation for tank with 24 m diam.

6 CONCLUSIONS

The main design aspects of steel tank foundations to guarantee permissible settlements were described, remarking the importance of the types of differential settlement to be controlled according to API Standards. As optimal (cost-effective) solutions, it was presented 3 case studies with successfully implementation of ground improvement by vibro stone columns, rigid inclusions, and compaction rigid inclusions. Thus, the presented ground improvement methods demonstrate their capabilities to speed up the consolidation process, decrease settlement, increase bearing capacity, and mitigate soil liquefaction.

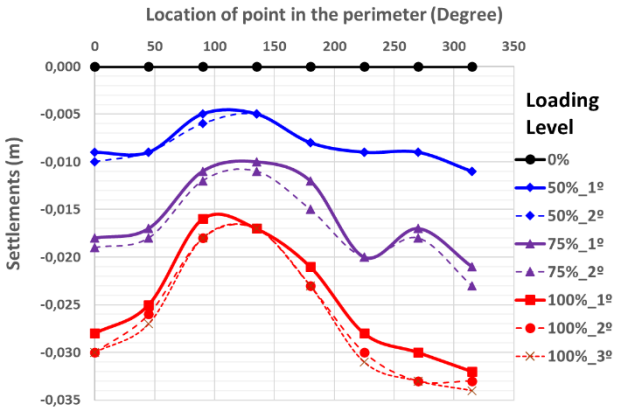

Figure 14. Settlement measurement for each loading stage.

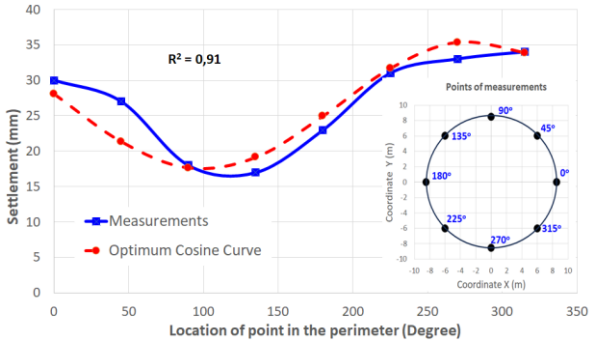

Figure 15. Analysis of diff settlement and rigid body tilt.

REFERENCES

Andreani, J. L. and Carr, N. A. (2007). Final report on the study of out-of-plane tank settlement. API SCAST, SCI. Washington, D.C.

American Petroleum Institute (2014). API Standard 653. Tank Inspection, Repair, Alteration, and Reconstruction, 5th Ed., Washington, 2014.

EN-14731 (2005). Execution of special geotechnical works–Ground treatment by deep vibration. European Standard.

Boulanger R.W. and Idriss I.M. (2014). CPT and SPT based liquefaction triggering procedures. Report No. UCD/CGM-14/01. Center for Geotechnical Modelling, CA Univ., Davis.

Japanese Geotechnical Society (1998). Remedial measures against soil liquefaction, From investigation and design to implementation, A.A.

Marcuson, W. F., Hynes, M. E., and Franklin, A. G., (1990). Evaluation and use of residual strength in seismic safety analysis of embankments, Earthquake Spectra. 6(3), 529-72.

Proceedings of the XVIII ECSMGE 2024
GEOTECHNICAL ENGINEERING CHALLENGES
TO MEET CURRENT AND EMERGING NEEDS OF SOCIETY
© 2024 the Authors
ISBN 978-1-032-54816-6
DOI 10.1201/9781003431749-557
Open Access: www.taylorfrancis.com, CC BY-NC-ND 4.0 license

ECSMGE 24
XVIII EUROPEAN CONFERENCE ON SOIL MECHANICS AND GEOTECHNICAL ENGINEERING

Effect of the concentration of the activator on the mechanical properties of the geopolymer stabilized soil

Effet de la concentration de l'activateur sur les propriétés mécaniques du sol stabilisé par géopolymère

D. Chami*, A. Cuccurullo, P. Gerard
Université libre de Bruxelles (ULB), BATir department, Brussels, Belgium
**diana.chami@ulb.be*

ABSTRACT: Geopolymers are the result of a reaction between a precursor (material rich in silica and alumina) and an activator (alkaline solution responsible for the dissolution of the precursor). Optimizing the quantity of activator is crucial to guarantee the strength development of the geopolymer while limiting the use of chemical substances. This study investigates the effect of different concentrations of the activator, in the range from 1 to 12M with a constant precursor content of 10% of the dry mass of the soil, on the mechanical properties of a geopolymer stabilized silty clay soil. A by-product calcium-rich granulated ground blast furnace slag (GGBS) is used as precursor and sodium hydroxide is used as an activator. Cylindrical stabilized samples compacted at the standard proctor optimum moisture content and maximum dry density and cured in sealed conditions for 7, 28, 60 and 90 days are tested for unconfined compressive strength. A set of unstabilized and slag-stabilized samples are manufactured and tested for comparison. First, the results showed that geopolymers can be used efficiently to enhance the strength of the soil. Also, increasing the concentration of the activator do not necessarily increase the strength of the stabilized soil. The optimum compressive strength corresponds to a concentration of 2M.

RÉSUMÉ: Les géopolymères sont le résultat d'une réaction entre un précurseur (matériau riche en silice et alumine) et un activateur (solution alcaline responsable de la dissolution du précurseur). Optimiser la quantité d'activateur est très important pour combiner le développement de la résistance du géopolymère avec un usage limité de substances chimiques. Cette étude analyse l'effet de différentes concentrations de l'activateur, dans la gamme de 1 à 12M avec une teneur constante en précurseur de 10 % de la masse sèche du sol, sur les propriétés mécaniques d'un sol argilo-limoneux stabilisé par géopolymère. Un laitier broyé et granulé de haut fourneau riche en calcium est utilisé comme précurseur et de l'hydroxyde de sodium est utilisé comme activateur. Des échantillons cylindriques stabilisés compactés à la teneur en eau optimale et à la densité sèche maximale standard Proctor scellés pendant 7, 28, 60 et 90 jours de temps de cure sont testés pour leur résistance à la compression simple. Un ensemble d'échantillons non stabilisés et stabilisés par du laitier de haut fourneau (sans activateur) sont fabriqués et testés à des fins de comparaison. Premièrement, les résultats ont montré que les géopolymères peuvent être utilisés efficacement pour améliorer la résistance du sol. De plus, l'augmentation de la concentration de l'activateur n'augmente pas nécessairement la résistance du sol stabilisé. La résistance optimale à la compression correspond à une concentration de 2M.

Keywords: Soil stabilization; geopolymers; mechanical testing.

1 INTRODUCTION

Soil stabilization is of huge importance in civil engineering practice since it aims at improving the physical and mechanical properties of naturally weak soils. While typical soil stabilization techniques involve the use of additives such as lime and cement (Khemissa and Mahamedi, 2014), their production leads to high emissions of CO_2 into the atmosphere. Geopolymer soil stabilization is emerging nowadays to provide a more sustainable alternative. Geopolymers were first introduced in the 1970s to refer to alkali-activated materials (Davidovits, 2002). Geopolymers are synthesized by the dissolution of a precursor (a by-product rich in silica and alumina) by an activator (an alkaline solution) to form a gel that solidifies and hardens. The properties of the geopolymer binder itself were widely studied in the literature while its application for soil stabilization is emerging recently and no standards exist yet to regulate its use.

While the activator is the key component in the geopolymerization reaction and thereafter essential for the strength development of the geopolymer binder, it is the most expensive and non-eco-friendly

component. Hence, finding the optimum concentration of the activator to reach the desired strength without overusing it is very important. Ghadir and Ranjbar (2018) reported that increasing the concentration of the activator from 4 to 12M increases the mechanical strength of volcanic-ash-based geopolymer stabilized clayey soil by around 50%. On the other hand, Cristelo et. al (2012) showed that for a low in calcium fly-ash (class F) based geopolymer stabilized silty sand, an optimum concentration exists, and it depends on the mass ratio of the precursor to the activator. The variation in the conclusions available in the literature can be attributed to the differences in the precursor properties, curing conditions or type of soil. Hence, additional research on the controlling parameters is necessary.

This research focuses on exploring the effect of the concentration of a sodium hydroxide (NaOH) activator on the short and long-term mechanical strength of a ground granulated blast furnace slag (GGBS) based geopolymer-stabilized clayey silt soil. To this end, unconfined compressive strength tests were performed on geopolymer-stabilized soil with varying concentrations of the activator after 7, 28, 60 and 90 days of curing sealed at ambient temperature. Unstabilized and slag-stabilized samples were tested as well for comparison purposes.

2 MATERIALS AND METHODS

2.1 Materials

A clayey silt (CL-ML, according to the Unified Soil Classification System) obtained from Marche-Les-Dames (MLD) region in Belgium was used in the present study. Initially, the MLD soil was oven-dried for 24 hours before being used. The grain size distribution of the soil, showing 93% of fines passing through 75 µm sieve, is presented in Figure 1. The clayey fraction represents 23%, the silty one about 67% and the sandy one about 10%. According to the ASTM D 4318, the liquid limit (LL), plastic limit (PL) and plasticity index (PI) of the soil were measured as 28.4%, 19.6% and 8.8% respectively. The Standard Proctor optimum moisture content (OMC) and the maximum dry density (MDD) of the soil were obtained to be 15.5% and 1.82 g/cm^3 respectively, in accordance with ASTM D 698.

Ground granulated blast furnace slag (GGBS) provided by VVM cement company in Belgium was used as a precursor. All GGBS grains were smaller than 75 µm. It was stored in tightly sealed containers.

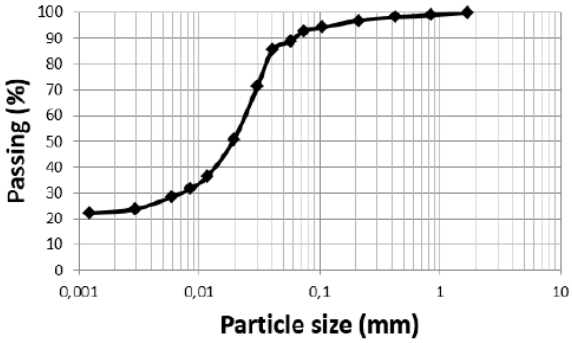

Figure 1. Grain size distribution of the MLD soil.

The chemical compositions obtained from the X-ray fluorescence analysis of the MLD clayey silt and the GGBS are presented in table 1.

As for the activation of the precursor, sodium hydroxide (NaOH) solution was used as the alkali solution. The NaOH solution with the required concentration was prepared in the laboratory by dissolving NaOH pellets with 99% purity in distilled water 24 hours prior to use to enable the release of the hydration heat.

Table 1. Chemical composition of GGBS and MLD soil.

Chemical composition	**Percentage by mass (%)**	
	GGBS	MLD soil
Calcium oxide (CaO)	43.15	0.69
Silicon oxide (SiO_2)	36.27	71.43
Aluminum oxide (Al_2O_3)	10.47	13.89
Magnesium oxide (MgO)	5.98	1.17
Sulphur oxide (SO_3)	1.51	0.02
Potassium oxide (K_2O)	0.67	2.52
Ferric oxide (Fe_2O_3)	0.58	4.27
Titanium oxide (TiO_2)	0.54	0.87
Manganese oxide (Mn_2O_3)	0.29	0.05
Sodium oxide (Na_2O)	0.26	0.77

2.2 Mix proportion and samples preparation

To study the effect of the concentration of the activator on the behavior of the geopolymer stabilized soil, a fixed precursor content of 10% of the dry mass of the soil (MLD) is used with different concentrations of the activator (1, 2, 4, 6, 8, 10 and 12M). To compare, a set of unstabilized soil samples and slag stabilized soil (without activator) samples were tested. For the preparation of the stabilized soil, GGBS and soil were initially mixed under dry conditions for 1 min and a half at low speed in the MATEST mortar mixer to attain uniformity. Then, the NaOH solution of the required concentration (for geopolymer stabilized soil) or distilled water (for slag stabilized soil) was added to the mix and the mixing process continued for 2 more minutes at high speed. NaOH solution or distilled

water is then added to reach the standard Proctor optimum moisture content for the mixture composed of the MLD soil and GGBS. The sample IDs and mix proportions are presented in table 2.

Table 2. Sample IDs and properties.

Sample ID	GGBS (%)	NaOH (M)	MDD (g/cm^3)	OMC (%)
MLD	-	-	1.82	15.5
MLD10	10	-	1.76	17
MLD10M1	10	1	1.76	17
MLD10M2	10	2	1.76	17
MLD10M4	10	4	1.76	17
MLD10M6	10	6	1.76	17
MLD10M8	10	8	1.76	17
MLD10M10	10	10	1.76	17
MLD10M12	10	12	1.76	17

The quantity of the stabilized soil in each sample is obtained based on the MDD of the mixture of the MLD soil and the GGBS. 72 mm height and 36 mm in diameter cylindrical samples were dynamically compacted in three equal layers. After the manual extrusion of the compacted samples from the molds, the soil samples were wrapped in plastic and aluminum films in order to avoid any moisture loss. The samples were cured sealed for 7, 28, 60 and 90 days in at a controlled room temperature of $\pm$ 18 ℃ until the day of testing.

2.3 Experimental procedure

Unconfined compressive strength (UCS) tests were performed on unstabilized and stabilized cylindral samples. During compression, the soil samples were wrapped in an impermeable membrane to avoid altering the composition of the samples during the test. The UCS tests were performed at an axial displacement rate of 0.1 mm/min. Each test continued until the failure surfaces were clearly visible or until an axial strain of 20% was attained.

To ensure consistency and reproducibility, three identical samples, with the same mix proportion and curing time, were tested each time and the average results were reported.

3 RESULTS AND DISCUSSION

Unconfined compressive strength tests on stabilized and unstabilized samples were performed at 7, 28, 60 and 90 days. The results of the UCS tests are shown in Figure 2 where the error bars provide the minimal and maximal strength observed experimentally. The results show a good reproducibility of the experimental data. Overall, regardless of the stabilization technique (slag or geopolymer) and the concentration of the activator, the compressive strength of the stabilized soil increased with the curing time. Although, the variation of the strength between 60 and 90 days is not significant for higher concentrations of activator (4, 6, 8, 10 and 12M). The slag-stabilized soil experienced none to very low strength improvement compared to the unstabilized soil. However, the GGBS-based geopolymer stabilized soil experienced a significant increase in the UCS compared to unstabilized soil even at 7 days.

MLD10M2 specimens reached the highest strength compared to all other concentrations of NaOH. The UCS of MLD10M2 specimens reached 1.4, 2.5, 4.0 and 4.7 MPa at 7, 28, 60 and 90 days respectively compared to 0.13 MPa for the unstabilized soil. The strength development is associated with the dissolution of the silica and alumina ions from the GGBS leading to the formation of a geopolymeric gel

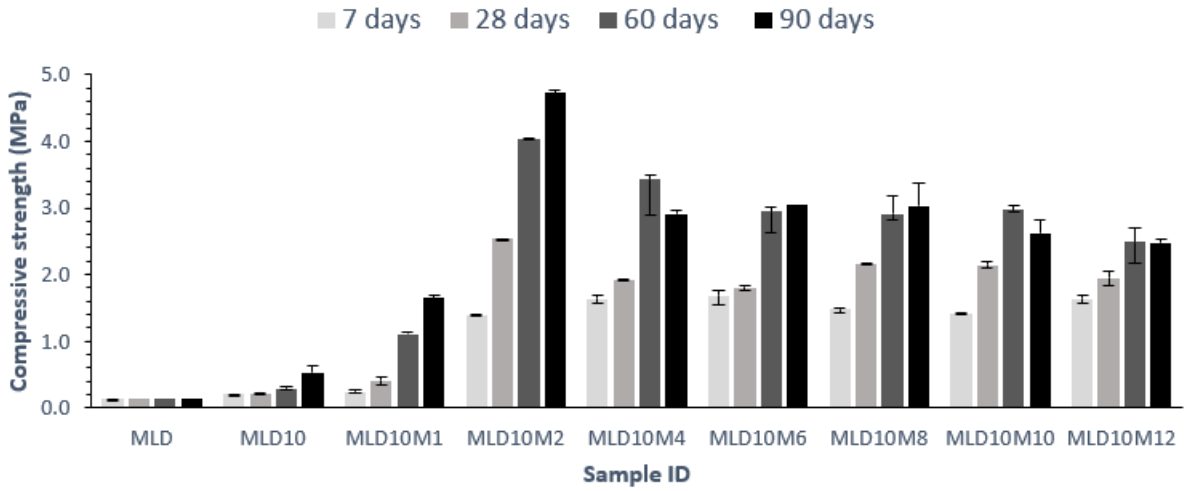

Figure 2. Unconfined compressive strength tests results.

and ultimately hydrated products (Sahoo and Prasad Singh, 2022). However, MLD10M1 attained lower strength increment at all curing times which may be attributed to the lack of alkali in the mixture causing a poor geopolymeric network in the matrix (Sahoo and Prasad Singh, 2022). Furthermore, samples with higher concentrations (4, 6, 8, 10 and 12M) showed lower workability during mixing and difficulties in compaction which may be the cause of the drop in the UCS especially at 60 and 90 days (Cristelo et. al, 2012).

The effect of the curing time on the stress-strain behavior of the geopolymer-stabilized soil with a concentration of 2M during the UCS test is reported in Figure 3. A transition from ductile (for unstabilized soil) to a brittle behavior (for geopolymer-stabilized soil) is observed. This change in behavior can be attributed to the formation of cementitious products that reach their maximum stress level just before experiencing sudden failure (Abdullah et al., 2019). Furthermore, it can be observed that the stiffness of the stabilized soil is independent of the curing time. The Young's modulus of MLD10M2 specimens varies from 190 to 290 MPa with the curing time.

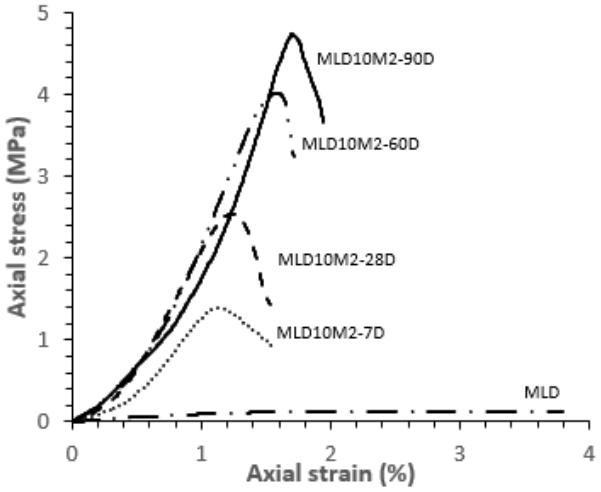

Figure 3. Effect of the curing time on the stress-strain behavior of MLD10M2 samples.

4 CONCLUSION

This study investigated the effect of the concentration of the most expensive geopolymer component (the activator) on the mechanical properties of a GGBS-based geopolymer-stabilized clayey silt soil.

- Geopolymer soil stabilization is an efficient soil stabilization technique. The UCS of the stabilized soil increases with the curing time.
- For a precursor content of 10%, a concentration of 2M of the activator increased the UCS of the soil almost 10 times at short term and 36 times at long term, compared to the unstabilized soil.
- Based on the mechanical strength, a concentration of 2M seems to be an optimum concentration of the activator for a GGBS content of 10%.

In order to better explain the existence of an opitmum activator concentration for the strength development and validate some explanations proposed in this paper (e.g. impact of workability loss at high concentrations), further microstructural analysis such as Scanning Electron Microscopy (SEM) and Mercury Intrusion Porosimetry (MIP) might be of interest.

REFERENCES

Abdullah, H.H., Shahin, M.A. and Walske, M.L. (2019). Geo-mechanical behavior of clay soils stabilized at ambient temperature with fly-ash geopolymer-incorporated granulated slag, *Soils and Found*ations. 59 (6) 1906–1920, https://doi.org/10.1016/j.sandf.2019.08.005.

Cristelo, N., Glendinning, S., Miranda, T., Oliveira, D. and Silva, R. (2012). Soil stabilization using alkaline activation of fly ash for self-compacting rammed earth construction, *Construction and Building Materials.* 36, 727–735. https://doi.org/10.1016/j.conbuildmat.2012.06.037.

Davidovits, J. (2002). 30 years of successes and failures in Geopolymer Applications. Market Trends and Potential Breakthroughs. *Geopolymer 2002 Conference,* October 2002, 28–29.

Ghadir, P. and Ranjbar, N. (2018). Clayey soil stabilization using geopolymer and Portland cement. *Construction and Building Materials*, 188, 361–371. https://doi.org/10.1016/j.conbuildmat.2018.07.207.

Khemissa, M. and Mahamedi, A. (2014). Cement and lime mixture stabilization of an expansive overconsolidated clay, *Applied Clay Science*. 95, 104–110, https://doi.org/10.1016/j.clay.2014.03.017.

Sahoo, S. and Prasad Singh, S. (2022). Strength and durability properties of expansive soil treated with geopolymer and conventional stabilizers. *Construction and Building Materials*. 328(January), 127078. https://doi.org/10.1016/j.conbuildmat.2022.127078.

Proceedings of the XVIII ECSMGE 2024
GEOTECHNICAL ENGINEERING CHALLENGES
TO MEET CURRENT AND EMERGING NEEDS OF SOCIETY
© 2024 the Authors
ISBN 978-1-032-54816-6
DOI 10.1201/9781003431749-558
Open Access: www.taylorfrancis.com, CC BY-NC-ND 4.0 license

ECSMGE 24
XVIII EUROPEAN CONFERENCE ON SOIL MECHANICS AND GEOTECHNICAL ENGINEERING

Improving mechanical performance of soil-bentonite by slag cement addition

Amélioration des performances mécaniques du sol-bentonite par ajout de ciment de laitier

J. Chen*, Y. Masaki, A. Takai, T. Kato, T. Katsumi
Graduate School of Global Environmental Studies, Kyoto University, Japan

chen.ji.68s@st.kyoto-u.ac.jp

ABSTRACT: Soil bentonite (SB) mixtures generally presents inadequate mechanical properties compared to other cutoff wall materials. Since both deformability and a certain level of strength properties need to be achieved for static loads or in situations of dynamic loads, the cement amendment is adopted to improve the engineering performance and ensuring the long-term effectiveness of SB cutoff walls. This study investigated the strength properties and deformation characteristics of soil-bentonite mixtures amended with slag cement using Consolidated-Undrained (CU) triaxial tests. The contents of slag cement powder considered were 25, 50, and 75 kg/m^3. The test results indicate that the undrained shear strength, residual shear strength and effective strength parameters are significantly influenced by the integration of cementation and consolidation. As compared in different cement addition, the 25 kg/m^3 cement amended specimens shows strain-hardening behaviours, 42.7 to 65.1 kPa undrained shear strength in ductile failure mode with no discernible cracks, which signifying plastic deformation with high deformability under triaxial loading. This implies that, although the contents of the slag cement were not so high, such as 25 kg/m^3, the amended soil-bentonite performed high strength and deformability.

RÉSUMÉ: Les mélanges de bentonite du sol (SB) présentent généralement des propriétés mécaniques insuffisantes par rapport aux autres matériaux de mur de séparation. Étant donné que la déformabilité et un certain niveau de propriétés de résistance doivent être atteints pour des charges statiques ou dans des situations de charges dynamiques, l'amendement au ciment est adopté pour améliorer les performances techniques et assurer l'efficacité à long terme des murs de séparation SB. Cette étude a examiné les propriétés de résistance et les caractéristiques de déformation de mélanges sol-bentonite amendés avec du ciment de laitier à l'aide d'essais triaxiaux consolidés-non drainés (CU). Les teneurs en poudre de ciment de laitier considérées étaient de 25, 50 et 75 kg/m^3. Les résultats des tests indiquent que les paramètres de résistance au cisaillement non drainé, de résistance résiduelle au cisaillement et de résistance effective sont significativement influencés par l'intégration de la cimentation et de la consolidation. Comparés à différents ajouts de ciment, les échantillons modifiés au ciment de 25 kg/m^3 présentent des comportements d'écrouissage, une résistance au cisaillement non drainé de 42,7 à 65,1 kPa en mode de rupture ductile sans fissures perceptibles, ce qui signifie une déformation plastique avec une déformabilité élevée sous chargement triaxial. Cela implique que, même si la teneur en ciment de laitier n'était pas si élevée, par exemple 25 kg/m^3, le sol-bentonite amendé présentait une résistance et une déformabilité élevées.

Keywords: Soil-bentonite; slag cement amendment; consolidated-undrained triaxial test; mechanical performance.

1 INTRODUCTION

Soil-bentonite (SB) is widely applied in vertical cutoff walls for preventing the migration of contaminants to the aquifer, owing to extremely low hydraulic conductivity and high deformability (Takai, A. et al., 2016). However, SB exhibits relatively low shear strength, and the effectiveness will be influenced in situations of high hydraulic or seismic loads.

Cementitious additives are often utilized to enhance certain mechanical properties, such as internal friction angle, cohesion coefficient and unconfined compressive strength, of soft soils (Luis, A.L. et al., 2019). The slag cement, as one type of eco-friendly material in cementitious additives, are often applied to improve the engineering properties and ensuring the long-term effectiveness of soft soils. In the application of vertical cutoff walls, it is worthy to investigate the enhanced mechanical performance and the variations in deformability in instances of relatively low content ratio of slag cement. Previous studies evaluated the compressive strength properties coupled with hydraulic performance of soil-cement-bentonite, but the deformation mode as the effect of cement amount was not studied (Ata, A.A., et al, 2015; Huang, X., et al., 2021).

In this paper, a series of Consolidated-Undrained (CU) triaxial tests on soil-bentonite (SB) and soil-bentonite with slag cement (SB-C) was conducted to investigate the variations in residual shear strength properties and effective strength parameters. Moreover, Young's modulus E_0 and secant modulus E_{50}, combining with three typical failure modes were summarised to further investigate the deformation modes and classify the capacities of SB and SB-C to simultaneously maintain both comprehensive shear strength and high deformability.

2 MATERIALS AND METHODS

2.1 Materials

Decomposed granite soil, which is widely distributed in Japan, was selected as the host soil. The bentonite used in this paper was sodium bentonite provided from Kunimine Industries Co., Ltd., Japan. For the cement amendment, the Portland Blast-Furnace Slag Cement was taken as the cement additive. The dry density of the decomposed granite soil, sodium bentonite and slag cement are 2.73, 2.60 and 3.04 g/cm^3, respectively.

2.2 Methods

Before the triaxial test, cylindrical specimens with a height of 100 mm and a diameter of 50 mm were prepared and cured for 7 D. The summary of test scheme has been presented in Table 1.

Table 1. Summary of test scheme.

	Bentonite slurry (L/m^3)	**Bentonite powder (kg/m^3)**	**Slag cement (kg/m^3)**	**Effective confining pressure (kPa)**
C0	350	97.5	0	40, 80, 160
C25			25	
C50			50	
C75			75	

The specimen mixing process of SB-C mixtures can be divided into four steps. Firstly, the bentonite slurry (5% bentonite by weight) was prepared 24 h ahead of time for sufficient hydration. Then, the dry decomposed granite soil was mixed with distilled water and bentonite slurry for 5 mins. The third step was adding the bentonite powder in two batches and mixing for 5 mins respectively. Finally, the slag cement powder was added and mixed for 10 mins. To ensure the homogeneity, the specimens were prepared with the target dry density of 1.30 g/cm^3. After the mixing process, the mixtures were poured into plastic cylinder with vibration to eliminate air voids and bubbles in the specimens. Summary of test scheme The specimens were then sealed immediately with plastic wrap and aluminum foil to minimize possible moisture change and cured at 20 ℃ for 7 days.

To evaluate the mechanical performance of SB and SB-C specimens, a series of consolidated-undrained (CU) triaxial test as per ASTM D4767-11 (ASTM International, 2020) were conducted. The schematic of the triaxial test apparatus is shown in Figure 1.

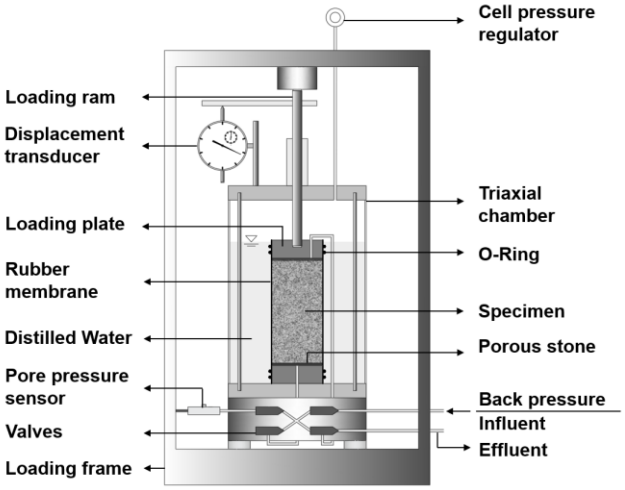

Figure 1. Schematic view of triaxial test apparatus.

For C0 specimens, after the third step of specimen mixing process, the soil-bentonite mixture was poured into a specially manufactured metal cylinder and installed in the triaxial chamber for saturation process. After 7 days curing, the C25/50/75 specimen was dissembled from the plastic cylinder and installed on the apparatus. In CU tests, specimens were saturated under a confining pressure of 10 kPa (i.e., a difference of 10 kPa between cell pressure and back pressure) until the B value is higher than 0.95. The specimens were then consolidated under different isotropic effective confining pressures (i.e., σ_3 =q 40, 80 and 160 kPa) and sheared at an axial strain rate of 0.05 mm/min until reaching approximately 15% axial strain.

3 RESULTS AND DISCUSSION

3.1 Undrained shear strength properties

The results of the undrained shear strength (S_u) and failure axial strain obtained from the triaxial CU test as a function of cement addition under different effective confining pressure are presented in Table 2, where the value of S_u is equal to one half the deviator stress at failure. As according to the ASTM D4767-11 (ASTM International, 2020), the failure of specimen is corresponding to the maximum deviator stress (q_{max}) or deviator stress at 15% axial strain, whichever is the

first obtained during the test. The deviator stress (q) is determined using equation (1),

$$q = \sigma_1' - \sigma_3' \quad (1)$$

where σ_1' is the effective major stress and σ_3' is the effective minor principal stress.

Table 2. Undrained shear strength and failure axial strain.

	40 kPa		80 kPa		160 kPa	
	S_u (kPa)	ε_{peak} (%)	S_u (kPa)	ε_{peak} (%)	S_u (kPa)	ε_{peak} (%)
C0	10.5	15.0	17.5	15.0	30.4	15.0
C25	42.7	15.0	43.2	15.0	65.1	15.0
C50	94.1	13.1	89.6	11.7	117.6	12.6
C75	142.0	7.9	153.9	6.3	190.8	7.4

In Table 2, it can be seen that the value of S_u increases as the cement addtion augments with almost double increment, which suggestes the effect of cementation during curing process. The S_u value of C0 presents over half percent increasing from 10.5 kPa to 17.5 kPa under 40 and 80 kPa effective confining pressure, respectively. As the effective confining pressure rising from 40 kPa to 80 kPa, the value of S_u increases slightly in cement amended cases except for C50 with 4.5 kPa decrease. On the contrary, the S_u value of all the cases pronounce ascending trend when the effective confining pressure doubled from 80 kPa to 160 kPa.

It is indicated that, influenced by cementitious bonding, lower effective confining pressure exerts a reduced impact on the value of S_u. Moreover, all of the C0 and C25 specimens were sheared to S_u at the failure axial strain ε_{peak} of 15%. For C50, the ε_{peak} values were varying from 11.7% to 13.1%, while the ε_{peak} values of C75 were comparatively lower, from 6.3% to 7.4% and 7.9%. Figure 2 shows the variation of residual undrained shear strength (S_r) as the function of cement addtion.

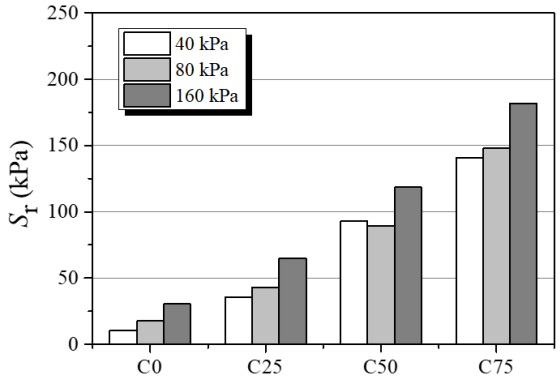

Figure 2. Residual undrained shear strength.

In Figure 2, the S_r is defined as half value of the deviator stress at 15% axial strain. It can be observed that the S_r increases with the increasing of confining pressure at a given cement amount except for the C50. Similar upward variation trend of S_r with the augment of cement addtion can be found, as the variation trend of S_u in Table 2. Moreover, when comparing S_r with S_u, for C0 and C25, the S_r is about the same with S_u. For C50 and C75, the S_r is exceeding 90% on average the S_u, which points to high strength retention characteristics after failure.

3.2 Effective stress path and strength envelope

The results of the effective stress path and strength envelope are plotted in Figure 3. The mean effective stress p' is defined in equation (2):

$$p' = \frac{\sigma_1' + 2\sigma_3'}{3} \quad (2)$$

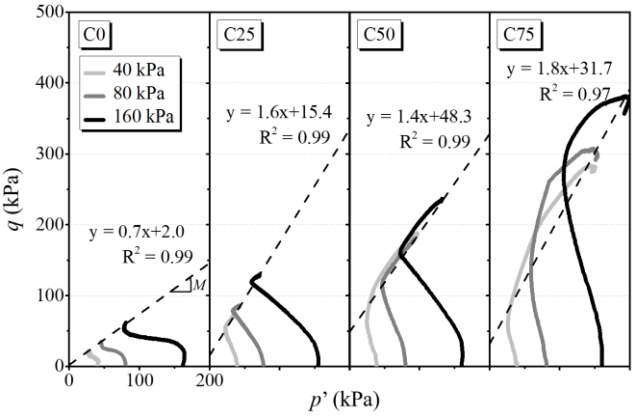

Figure 3. Effective stress path and strength envelope.

In Figure 3, the slope M of linear strength envelopes for SB (C0) and SB-C (C25, C50, C75) specimens were determined to estimate the effective strength parameters (c' and φ'). The relationship between the internal friction angle φ'_{peak} and the parameter M is expressed in equation (3) (Luis, A.L. et al., 2019):

$$M = \frac{6sin\varphi'_{peak}}{3 - sin\varphi'_{peak}} \quad (3)$$

The effective cohesion (c') is determined using equation (4):

$$c' = \frac{c}{M} \quad (4)$$

where the c is the intercept with the q axis of the linear envelopes in Figure 3. The results of c' and φ' are summarized in Table 3.

Table 3. Effective strength parameters (c' /kPa, φ' /°).

C0		C25		C50		C75	
c'	***φ'***	***c'***	***φ'***	***c'***	***φ'***	***c'***	***φ'***
2.0	35.8	15.4	58.2	48.3	55.0	31.7	61.0

As shown in Figure 3, the gradients of these envelopes are similar in SB-C specimens as the φ' were ranging from 55.0° to 61.0°, which represents high shear strength. With low cement amount amended, the φ' of C25 is 58.2 kPa, higher than C50 and close to C75. The c' of C25 is 15.4 kPa, as 2.0 kPa of C0 with high deformability, and over 30 kPa for C50 and C75.

3.3 Elastic moduli and failure modes

To evaluate the deformation mode, the results of Young's modulus E_0 and secant modulus E_{50} (defined at 50% of the peak strength) are illustrated in Figure 4.

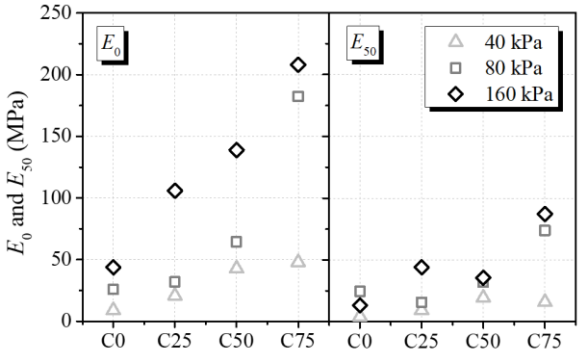

Figure 4. Young's modulus E_0 and secant modulus E_{50}.

It is observed that the moduli (E_0, E_{50}) increase with the augment of cement addition. When comparing the E_0 to E_{50}, it is evident that, the E_{50} is less than 50% of E_0 in all instances. It is noteworthy that this value does not align with that of typical elastic material, which tends to be significantly higher. It is also indicated the propensity for plastic deformation. Moreover, three typical failure modes are summarized in Figure 5.

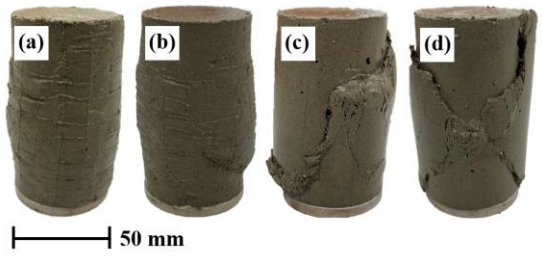

Figure 5. Typical failure modes

Figure 5 (a) was strain-hardening ductile failure in C0 and C25, while (b) presented planar failure in C50 under 40 kPa effective confining pressure. Figure 5 (c) and (d) are planar failure with larger failure angle in C50 specimens, and split failure in all C75 specimens. This point can be explained by the hydration and pozzolanic reactions of cement, which result in the igidity of specimens (Luis, A.L. et al., 2019).

4 CONCLUSIONS

In this paper, the slag cement amended SB-C specimens exhibit diverse mechanical performance.

The results indicate that C25 displays 42.7 to 65.1 kPa undrained shear strength with strain-hardening behaviours. No discernible cracks are observed at ductile failure, signifying plastic deformation with a high degree of deformability when subjected to triaxial loading. Comparing with C25, C0 presents the same failure mode with lower S_u, while planar failure and split failure can be observed in C50 and C75 with excessively higher S_u but lower deformability.

ACKNOWLEDGEMENTS

The authors are grateful for Mr. G. Araki (Raito Kogyo Co., Ltd.) and his colleagues for their great assistance on this research.

REFERENCES

ASTM D4767-11 (2020), Standard Test Method for Consolidated Undrained Triaxial Compression Test for Cohesive Soils, ASTM International, West Conshohocken, PA, the United States.

Ata, A.A., Salem, T.N., Elkhawas, N.M. (2015) Properties of soil–bentonite–cement bypass mixture for cutoff walls. *Construction and Building Materials*. 93: 950-956. http://doi.org/10.1016/j.conbuildmat.2015.05.064.

Huang, X., Li, J.S., Guo, M.Z., Xue, Q., Du, Y.J., Wan, Y., Liu, L., and Poon C.S. (2021) Using MgO activated slag and calcium bentonite slurry to produce a novel vertical barrier material: Performances and mechanisms. *Construction and Building Materials*. 291: 1-14. http://doi.org/10.1016/j.conbuildmat.2021.123365.

Luis, A.L. Deng, L. Shao, H.L. (2019) Triaxial behaviour and image analysis of Edmonton clay treated with cement and fly ash, *Construction and Building Materials*. 197: 208-219. https://doi.org/10.1016/j.conbuildmat.2018.11.222.

Takai, A., Inui, T., Katsumi T. (2016) Evaluating the hydraulic barrier performance of soil-bentonite cutoff walls using the piezocone penetration test, *Soils and Foundations*. 56(2): 277-290. http://dx.doi.org/10.1016/j.sandf.2016.02.010.

Proceedings of the XVIII ECSMGE 2024
GEOTECHNICAL ENGINEERING CHALLENGES
TO MEET CURRENT AND EMERGING NEEDS OF SOCIETY
© 2024 the Authors
ISBN 978-1-032-54816-6
DOI 10.1201/9781003431749-559
Open Access: www.taylorfrancis.com, CC BY-NC-ND 4.0 license

ECSMGE 24
XVIII EUROPEAN CONFERENCE ON SOIL MECHANICS AND GEOTECHNICAL ENGINEERING

Applying electrokinetic technology coupled with enzyme-induced carbonate precipitation treatment to Cu- and Pb-contaminated loess remediation

Application de la technologie électrocinétique associée à un traitement par précipitation de carbonate induit par des enzymes à l'assainissement du loess contaminé par le Cu et le Pb

W.C. Cheng*
School of Civil Engineering/Xi'an University of Architecture and Technology, Xi'an, China
L. Wang, Z.F. Xue
School of Civil Engineering/Xi'an University of Architecture and Technology, Xi'an, China
M.M. Rahman
UniSA STEM, ScaRCE, University of South Australia, Mawson Lakes, Australia
**w-c.cheng@xauat.edu.cn*

ABSTRACT: Excessive copper (Cu) or lead (Pb) in soils can cause serious threats to surrounding environments and human health. In the present work, a modified EK (electrokinetic) reactor was proposed where the single and multiple EICP (enzyme-induced carbonate precipitation) treatments were incorporated into a permeable reactive barrier (PRB) for the first time to remove Cu and Pb metals. Results showed that the EK-PRB technology outperformed the EK technology. The PRB worked with the cathode electrolyte well to reduce the remaining Pb^{2+} by about 35%. The effect of multiple EICP treatments increased the potential of combining Cu^{2+}/Pb^{2+} with CO_3^{2-}, which caused difficulty in performing the electromigration and electroosmosis during the EK remediation. It, however, depressed the focusing effect. The higher cathode pH, induced by the effect of a single EICP treatment, was accompanied by the copper-ammonia complex formation, improving the fraction of Cu^{2+} removed by the cathode electrolyte well. The Pb removal behaved similarly to the Cu removal.

RÉSUMÉ: Un excès de cuivre (Cu) ou de plomb (Pb) dans les sols peut constituer de graves menaces pour l'environnement et la santé humaine. Dans le présent travail, un réacteur EK (électrocinétique) modifié a été proposé dans lequel les traitements EICP (précipitation de carbonate induite par des enzymes) simples et multiples ont été incorporés pour la première fois dans une barrière réactive perméable (PRB) afin d'éliminer les métaux Cu et Pb. Les résultats ont montré que la technologie EK-PRB surpassait la technologie EK. Le PRB a bien fonctionné avec l'électrolyte cathodique pour réduire le Pb^{2+} restant d'environ 35 %. L'effet de plusieurs traitements EICP a augmenté le potentiel de combinaison de Cu^{2+}/Pb^{2+} avec CO_3^{2-}, ce qui a rendu difficile la réalisation de l'électromigration et de l'électroosmose pendant l'assainissement EK. Cependant, cela a diminué l'effet de focalisation. Le pH cathodique plus élevé, induit par l'effet d'un seul traitement EICP, s'est accompagné de la formation d'un complexe cuivre-ammoniac, améliorant la fraction de Cu^{2+} éliminée par le puits d'électrolyte cathodique. L'élimination du Pb s'est comportée de manière similaire à l'élimination du Cu.

Keywords: Electrokinetic remediation; permeable reactive barrier; enzyme-induced carbonate precipitation; loess.

1 INTRODUCTION

The electrokinetic (EK) technology is applied to a variety of contaminated sites due to its good maneuverability (Han et al., 2021). Despite that, the electromigration and electroosmosis require a period of time and their energy consumption may be extremely high to achieve a satisfactory remediation efficiency (Song et al., 2022). Thus, a combination of the EK technology and other technologies may provide a pathway to address the mentioned problems. The enzyme-induced carbonate precipitate (EICP) has drawn great attention as bacterial cultivation is not required prior to catalyzing urea hydrolysis (Sun et al., 2021). Permeable reactive barriers (PRB) are often applied to adsorb heavy metals in water bodies (Ma et al., 2022). The EICP technology may be incorporated into PRB to not only eliminate the discharge of NH_4^+ into surrounding environments but also improve the removal of heavy metals. Despite that, its interplay

with EK process is still unclear. In addition, OH^- can combine with Cu^{2+} or Pb^{2+} to develop the hydroxide precipitation surrounding the cathode, clogging the electroosmosis and electromigration during the EK remediation (Li et al., 2012). The main objectives of this study are to: (1) propose an EK reactor where the multiple EICP treatments are incorporated into PRB, (2) mitigate the focusing effect, and (3) explore the inherent mechanism affecting the removal efficiency.

2 METHODOLOGY

2.1 Electrokinetic reactor

The EK reactor was proposed and applied to the removal of Cu and Pb in the loess soil, as shown in Figure 1. The soil compartment containing five soil sections, namely A1 to A5, was separated from the anode and cathode electrolyte wells using a graphene plate. The Cu- or Pb- contaminated loess was loaded into A1, A2, A4, and A5, respectively, while a PRB was deployed into A3.

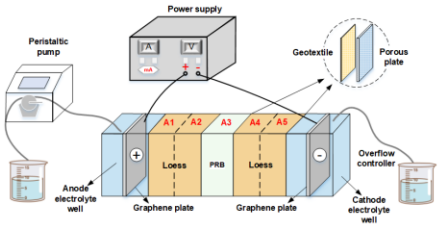

Figure 1. Schematic illustration of electrokinetic reactor.

2.2 Materials

The loess was taken from Jingyang County, Shaanxi Province, China, which is classified as low plasticity clay (CL). Copper nitrate ($Cu(NO_3)_2$) and lead nitrate ($Pb(NO_3)_2$) of analytical pure as a contaminant were applied to prepare Cu- or Pb-contaminated loess. Their concentration was manipulated to 500 mg/kg. In addition, PRB mainly consisted of urea, urease, and chitosan addition. The use of chitosan isolated the urease from Cu^{2+} or Pb^{2+}, preventing its inactivation.

2.3 Experimental design

The experimental design mainly consisted of the control group (CG) and test group-2 (TG-2). CG neglected PRB. TG-2 took PRB into account where the multiple EICP treatments intervened in the EK remediation. The concentration of Cu or Pb was measured in accordance with the Tessier's sequential extraction procedure (Tessier et al., 1979). Five fractions (EXC: Exchangeable state, CAR: Carbonate combination state, OX: Fe-Mn oxides state, ORG: Organic state, RES: Residue state) denoted different species of Cu or Pb.

3 RESULTS

3.1 EK remediation

Figure 2a shows the temporal relationships of electric conductivity applied to Cu removal using the EK technology. In CG test, the changes in electric conductivity fall within a 300 to 2000 μs/cm range. The electric conductivity in A5 goes into a decline at 4 h after the commencement of CG test, which is earlier than A4. Similar phenomena can also be seen in the temporal relationships of electric conductivity applied to Pb removal (see Figure 2b). Figures 2c and 2d show the temporal relationships of pH applied to Cu and Pb removals. As CG test progresses, the difference in pH between the anode and cathode becomes much more significant.

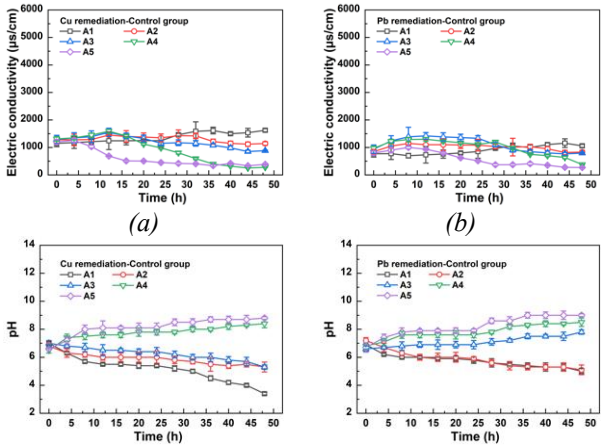

Figure 2. Temporal relationships of: (a) EC applied to Cu removal, (b) EC applied to Pb removal, (c) pH applied to Cu removal, and (d) pH applied to Pb removal.

Figures 3a and 3b show the temporal relationships of cumulative EOF (electroosmotic flow) and electric current applied to Cu and Pb removals. EOF increases very quickly to above 900 mL/h at 15 h for Cu removal and then remains a small change until the end of CG test. The electric current for Cu removal behaves similarly to Pb removal.

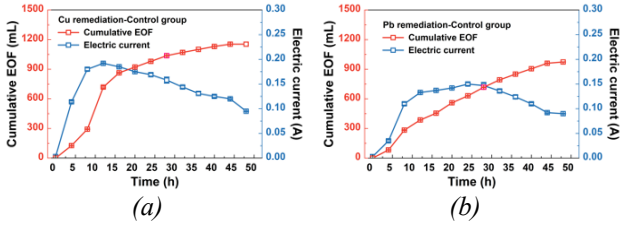

Figure 3. Temporal relationships of cumulative EOF and electric current applied to: (a) Cu removal and (b) Pb removal.

The relationships of removal efficiency versus soil section (A1 to A5) are shown in Figure 4. The removal efficiency decreases in a gentle manner from A1 to A5. The highest removal efficiency of 16% is attained in A1, while the lowest removal efficiency of 2% is attained in A5, most likely because of the hydroxide precipitation in the vicinity of the cathode.

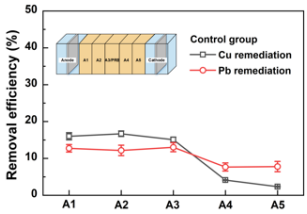

Figure 4. Variations of removal efficiency against soil section.

3.2 EK-PRB remediation considering the effect of multiple EICP treatments

Figure 5 shows the temporal relationships of electric conductivity applied to Cu and Pb removals respectively considering the effect of multiple EICP treatments. The multiple EICP treatments applied to TG-2 test encourage the sequential discharge of NH_4^+ and OH^-. Some of the EC curves lie above those in CG test (see Figures 5a and 5b). In CG test, the difference in pH between the anode and cathode enlarges with time (see Figures 2c and 2d). Here this phenomenon is not as pronounced as that in CG test (see Figures 5c and 5d).

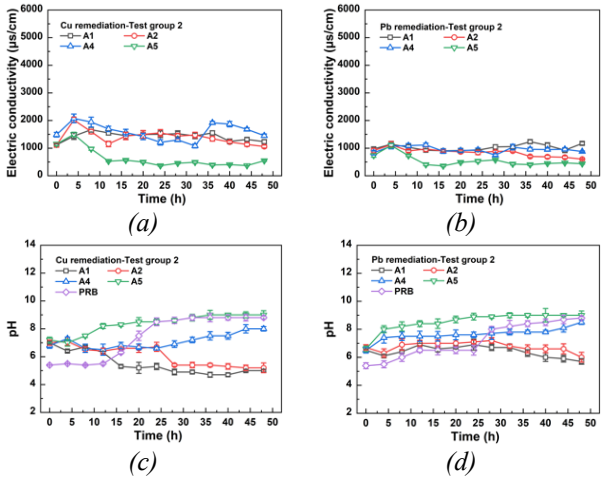

Figure 5. EK remediation (multiple EICP treatments) - Temporal relationships of EC applied to: (a) Cu removal and (b) Pb removal, - Temporal relationships of pH applied to: (c) Cu removal and (d) Pb removal.

Unlike CG test, EOF in TG-2 test starts increasing after a period of time (see Figure 6). The maximum EOF for Cu removal is higher in CG test than in TG-2 test. The maximum EOF for Pb removal is also higher in CG test than in TG-2 test. Although the effect of multiple EICP treatments depresses the focusing phenomenon, it causes a side effect to prevent EOF from going higher. More details would be presented later in this paper.

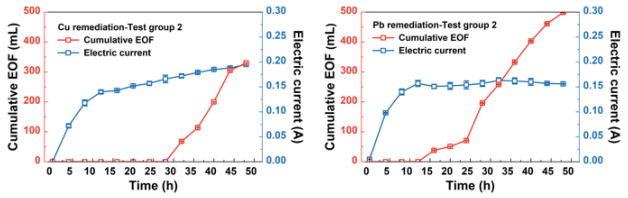

Figure 6. EK remediation (multiple EICP treatments) - Temporal relationships of cumulative EOF and electric current applied to: (a) Cu removal and (b) Pb removal.

The relationships of removal efficiency versus soil section (A1 to A5) are shown in Figure 7. In TG-2 test, the closer the soil section to the cathode, the higher the removal efficiency, meaning that Cu^{2+} or Pb^{2+} can migrate toward the cathode with no difficulty due to the absence of hydroxide precipitation. Despite that, the aforesaid side effect raises up the possibility of combining Cu^{2+} or Pb^{2+} with CO_2^{3-} that is heading toward the anode.

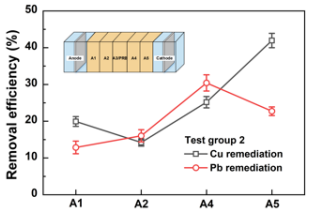

Figure 7. Variations of removal efficiency against soil section.

4 DISCUSSION

Compared to the initial CAR-Cu, CAR-Cu in A1 and A2 in CG test presents a small decrease (see Figure 8), indicating that a part of CAR-Cu desorbs due to exposure to acidic environments in the vicinity of the anode and migrates toward the cathode electrolyte well to achieve their removal (see Figure 9a). CAR-Cu in A4 and A5 in CG test shows a small change compared to the initial CAR-Cu. Alkaline environments around the cathode impede their desorption, causing CAR-Cu in A4 and A5 in CG test to remain nearly the same. In TG-2 test, CAR-Cu in A1 and A2 does not present a further decrease but an increase compared to CAR-Cu in A1 and A2 in TG-1 test (see Figure 8). TG-1 has been omitted herein due to limited space and takes the effect of a single EICP treatment intervenes into account. The effect of multiple EICP treatments increases the possibility of combining Cu^{2+} with CO_3^{2-}

and causes malachite ($Cu_2(OH)_2CO_3$) and azurite ($Cu_3(CO_3)_2(OH)_2$) to precipitate, reducing the fraction of Cu^{2+} removed by PRB (referred to also as the 'side effect'). CAR-Cu in A4 in TG-2 test also presents an increase rather than a further decrease. Since the effect of multiple EICP treatments narrows pH ranges in CG-2 test (see Figure 5), the lower pH of about 8 prevents copper-ammonia complex from developing (Xie et al., 2023), reducing the fraction of Cu^{2+} removed by the cathode electrolyte well. It is worth noting that the fraction of Cu^{2+} removed by the cathode electrolyte well is higher than that removed by PRB (see Figure 9a). In spite that the effect of multiple EICP treatments results in the side effect, it, however, mitigates the focusing effect, improving the fraction of Cu^{2+} removed by the cathode electrolyte well. Pb removal behaves similarly to Cu removal (see Figures 9b and 10).

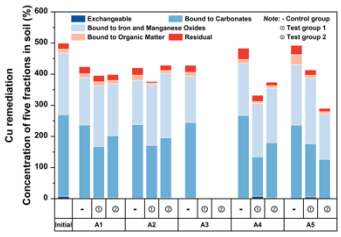

Figure 8. Distributions of five species applied to Cu removal.

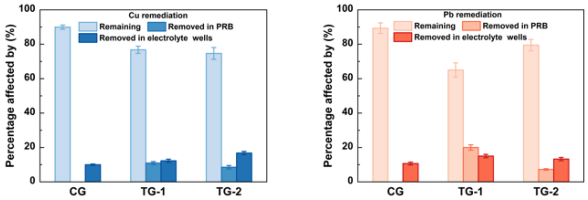

(a) *(b)*

Figure 9. Mass balance calculation: (a) Cu removal and (b) Pb removal.

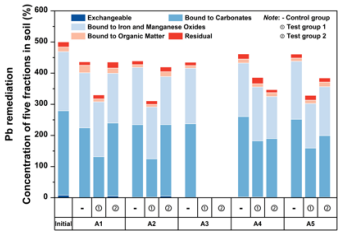

Figure 10. Distributions of five species applied to Pb removal.

5 CONCLUSIONS

Based on the results and discussion, some main conclusions can be drawn as follows:

(a) In this study, the bio-PRB that incorporates the EICP treatment applies to the EK technology as an adsorbent. The EK-PRB technology outperforms the EK technology regarding the Cu and Pb removals.

(b) PRB reduces the remaining Cu^{2+} and Pb^{2+} by 10% and 20% respectively. PRB works with the cathode electrolyte well to reduce the remaining Pb^{2+} by 35%. The above highlights the role of PRB in the EK-PRB technology.

(c) The effect of multiple EICP treatments reduces the fraction of Cu^{2+} or Pb^{2+} removed by PRB. This, in turn, encourages the formation of azurite and malachite precipitation. Due to this reason, only a small number of Cu^{2+} or Pb^{2+} can migrate toward the cathode, reducing the focusing effect. Pb removal behaves similarly to Cu removal, although Pb^{2+} is more willing to combine with CO_3^{2-}.

REFERENCES

Han, D., Wu, X., Li, R., Tang, X., Xiao, S., and Scholz, M. (2021). Critical review of electro-kinetic remediation of contaminated soils and sediments: Mechanisms, performances and technologies, *Water Air and Soil Pollution*, 232, 335. http://doi.org/10.1007/s11270-021-05182-4.

Li, G., Guo, S.H., Li, S.C., Zhang, L.Y., and Wang, S.S. (2012). Comparison of approaching and fixed anodes for avoiding the 'focusing' effect during electrokinetic remediation of chromium-contaminated soil. *Chemical Engineering Journal*, 203, 231–238. http://doi.org/10.1016/j.cej.2012.07.008.

Ma, L., Zhang, C., Liu, S., Luo, Q., Zhang, R., and Qian, J. (2022). Sensitivity analysis of factors influencing pollutant removal from shallow groundwater by the PRB method based on numerical simulation, *Environmental Science and Pollution Research*, 29, 82156-82168. http://doi.org/10.1007/s11356-022-21406-4.

Song, P., Xu, D., Yue, J., Ma, Y., Dong, S., and Feng, J. (2022). Recent advances in soil remediation technology for heavy metal contaminated sites: A critical review, *Science of the Total Environment*, 838, 156417. http://doi.org/10.1016/j.scitotenv.2022.156417.

Sun, X., Miao, L., Wang, H., Yuan, J., and Fan, G. (2021). Enhanced rainfall erosion durability of enzymatically induced carbonate precipitation for dust control, *Science of the Total Environment*, 791, 148369. http://doi.org/10.1016/j.scitotenv.2021.148369.

Tessier, A., Campbell, P.G.C., and Bisson, M. (1979). Sequential extraction procedure for the speciation of particulate trace metals, *Analytical Chemistry*, 51(7), 844-851. http://doi.org/10.1021/ac50043a017.

Xie, Y.X., Cheng, W.C., Wang, L., Xue, Z.F., Rahman, M.M., and Hu, W. (2023). Immobilizing copper in loess soil using microbial-induced carbonate precipitation: Insights from test tube experiments and one-dimensional soil columns, *Journal of Hazardous Materials*, 444, 130417. http://doi.org/10.1016/j.jhazmat.2022.130417.

Proceedings of the XVIII ECSMGE 2024
GEOTECHNICAL ENGINEERING CHALLENGES
TO MEET CURRENT AND EMERGING NEEDS OF SOCIETY
© 2024 the Authors
ISBN 978-1-032-54816-6
DOI 10.1201/9781003431749-560
Open Access: www.taylorfrancis.com, CC BY-NC-ND 4.0 license

ECSMGE 24
XVIII EUROPEAN CONFERENCE ON SOIL MECHANICS AND GEOTECHNICAL ENGINEERING

Waste valorisation in landfill barriers: Opportunities and challenges

Valorisation des déchets en tant que barrières d'étanchéité de décharge: Opportunités et défis

F. Chihi*, G. Varga
Department of Engineering Geology and Geotechnics, Faculty of Civil Engineering, Budapest University of Technology and Economics, Budapest, Hungary

**chihi.feten@emk.bme.hu*

ABSTRACT: Landfill barriers play a fundamental role in environmental protection, mitigating the migration of contaminants into the surrounding environment. This review provides an in-depth analysis of the potential of diverse waste types as substitutes or amendments for conventional landfill liners and covers. Outlined from extensive literature, the study highlights the dual advantage of waste utilization in landfill barriers: conservation of natural resources and waste recycling enhancement. While certain waste products have shown promise due to their improved geotechnical and mechanical characteristics, concerns about the leaching of hazardous contaminants remain paramount. This review evaluates the optimal use of waste in landfill barriers. It emphasizes the necessity of comprehensive chemical and bioassay evaluations to accurately predict long-term leaching behavior and environmental compatibility. Research indicates the prospective utility of waste-derived materials in landfill barrier applications, aligned with environmental sustainability objectives. However, this approach mandates a heightened emphasis on safety, necessitating comprehensive, site-specific evaluations.

RÉSUMÉ: Les barrières d'étanchéité de décharge jouent un rôle fondamental dans la protection de l'environnement, en atténuant la migration des contaminants dans l'environnement environnant. Cette revue fournit une analyse approfondie du potentiel de divers types de déchets en tant que substituts ou amendements pour les revêtements et couvertures de décharge conventionnels. Décrit à partir d'une vaste littérature, l'étude met en évidence le double avantage de l'utilisation des déchets dans les barrières de décharge: la conservation des ressources naturelles et l'amélioration du recyclage des déchets. Bien que certains produits de déchets se soient montrés prometteurs en raison de leurs caractéristiques géotechniques et mécaniques améliorées, les préoccupations concernant la lixiviation des contaminants dangereux restent primordiales. Cette revue évalue l'utilisation optimale des déchets dans les barrières de décharge. Elle souligne la nécessité d'évaluations chimiques et bioessais complètes pour prédire avec précision le comportement de lixiviation à long terme et la compatibilité environnementale. La recherche indique l'utilité prospective des matériaux dérivés des déchets dans les applications de barrière de décharge, alignée avec les objectifs de durabilité environnementale. Cependant, cette approche exige un accent accru sur la sécurité, nécessitant des évaluations complètes et spécifiques au site.

Keywords: Landfill barriers; geotechnical characteristics; recycling.

1 INTRODUCTION

In recent decades, incineration, recycling, and composting have increasingly enhanced solid waste management strategies in contemporary societies. However, landfilling persists as a globally predominant method for waste disposal. A significant portion of industrialized nations, including numerous European Union (EU) member states and the United States of America (US), continue to incorporate landfilling as a fundamental component of their solid waste management systems.

The primary environmental concern with landfilling is the contamination of the surrounding environment due to landfill leachate. To prevent this, engineered landfills are equipped with impermeable multi layered barriers, including a cover and bottom liner systems, which consist of natural geological barriers, technical barriers, and drainage systems. These systems serve to reduce rainfall infiltration, control gas emissions, and protect soil and water contamination.

EU regulations stringently govern landfill specifications, mandating a combination of geological and artificial barriers along with bottom liners from the construction phase till the closure and post-closure phase. It should be mentioned that the affordability and technological feasibility of such landfill lining technologies is often beyond the reach of low-income

countries. Consequently, a diverse range of alternative materials, both natural and waste-derived, have gained attention as potential substitutes.

The application of waste materials in landfill linings is believed to have economic benefits. It conserves natural resources and conforms to essential international environmental policies that emphasize waste reduction, the reuse of materials, and recycling efforts. Moreover, incorporating waste materials can potentially enhance liner characteristics and performance. However, the application of these unconventional materials is not without controversy.

Despite extensive research on the use of wastes material in landfill barrier construction, results still present poorly definitive conclusions on the suitability of each waste material for such applications. Therefore, this paper provides a comparative analysis of various waste materials suggested in literature publications for use in engineered hydraulic barriers within landfills. It discusses the geotechnical (Figure 1) and hydraulic conductivity (k)properties (Table 1), advantages, and disadvantages of these materials, with a focus on environmental protection issues, adhering to international global regulatory norms and guidelines.

2 RED MUD

In waste management, the application of Red Mud, a byproduct of alumina extraction from bauxite, has garnered significant interest for its potential in environmental remediation, particularly as a liner material for landfills. Several studies, demonstrated the Red Mud's efficacy in reducing contaminants like iron (Fe), sulphate (SO_4), cooper (Cu), Zinc (Zn), and bacteria in leachate (Duchesne and Doye, 2005; Çoruh and Ergun, 2010). Field investigation conducted by Ujaczki *et al.*, (2016) evaluated the use of red mud-soil mixtures as potential additives for landfill cover layers. Using a comprehensive set of chemical, biological, and ecotoxicity metrics, it was concluded that these mixtures could be safely used in poor-quality subsoils at concentrations up to 20% by weight without causing ecological toxicity. Based on these findings, red mud-soil mixtures were advocated to be incorporated into the surface layers of landfill cover systems.

Kalkan (2006) found that red mud improves the density and strength of compacted clay liners while reducing their expansibility and permeability (k<10-9m/s). Rubinos et al. (2015, 2016, 2017) studied red mud in landfill liners, examining its geotechnical qualities, low permeability, chemical stability, and environmental safety. They also noted its ability to capture mercury from leachates. Their findings show that red mud has a low permeability (10-9 m/s), high friction angle (38°), and cohesion (79.5 kPa), enhancing shear resistance on slopes. However, organic solvents and acids affect its properties, suggesting the need for more research on its chemical and environmental effects.

Nonetheless, the studies also highlighted that desiccation significantly affect red mud's permeability, raising concerns about its direct application in landfill cover systems. Panda et al., (2017) highlighted that red mud bioneutralization using microbial action with various carbohydrate sources could improve its geotechnical properties. While red mud's resistance to chemical attack and contaminant retention are notable, concerns about its alkalinity, the need for effluent management, and the potential release of radionuclides and trace metals under varying conditions necessitate careful consideration (Rubinos and Barral, 2013; Hegedűs et al., 2016). Field validation red mud liners remains essential. Given these factors, the use of red mud liners might be best suited for industrial or mining waste landfills. While red mud shows promise as a landfill liner material, its application should be carefully evaluated, considering its narrow operational range, potential environmental impacts, and the need for effective effluent management.

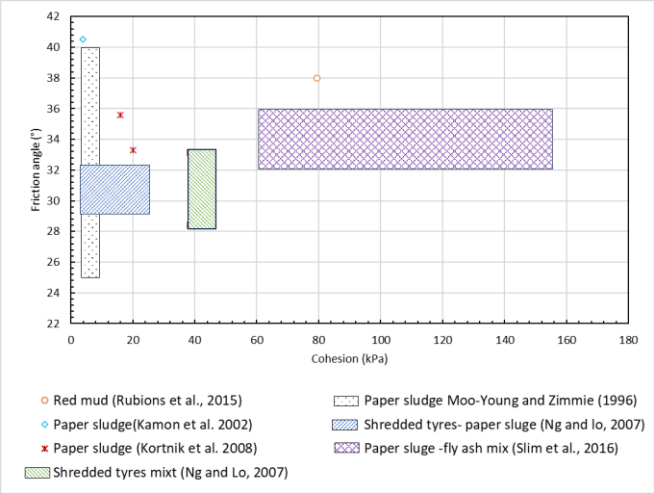

Figure 1. Shear parameter of wastes studied in the review.

3 PAPER SLUDGE

In recent decades, the utilization of waste materials from the paper industry, particularly paper sludges, gathered considerable consideration in the context of sustainable landfill engineering. These by-products, often described as paper sludge, have been increasingly recognized as viable alternatives to traditional clays for the construction of landfill liners.

Table 1. Waste material characteristics and its hydraulic Conductivity.

Material	Hydraulic Conductivity	Advantages	Limitation	Reference
Red Mud	9 x 10^{-10} to 5.13 x 10^{-10} m/s	- Good for reducing contaminants like Fe, SO4, Cu, Zn, and bacteria. - Enhances geotechnical properties when used in clay liners. - Can withstand shear forces on landfill slopes.	-Susceptible to desiccation affecting permeability. -Concerns about alkalinity, need for effluent management, and potential release of radionuclides and trace metals.	Rubinos et al. (2015); Panda et al. (2017)
Paper Sludge	3.4 x 10^{-10} to 5.3 x 10^{-8} m/s	- Effective as hydraulic barriers due to low *k*. - Contains organic fibers enhancing cohesion and friction angle. -Environmental compatibility confirmed for landfill applications.	-Susceptibility to desiccation and freeze-thaw cycles. - Requires high *w* during compaction.	Moo-Young and Zimmie (1996); Kamon et al. (2002); Kraus et al. (1997); Kortnik et al. (2008)
Paper Sludge - Wood Ash	5.0 x 10^{-9} m/s	-Potential enhancement of geotechnical properties.	-Requires further study for comprehensive understanding.	Kortnik et al. (2008)
Shredded Tyres - Paper Sludge	4.15 x 10^{-9} m/s	- Improves shear strength. - High ability of Pb retardation.	-Potential increase in *k*. -Variable concentrations of heavy metals in leachates.	Ng and Lo (2007)
Shredded Tyres Mixture	4.01 x 10^{-7} to 1.0 x 10^{-10} m/s	-Reduces dry density and compressive strength beneficially. -Enhances contaminant sorption capacity.	-May lead to an undesirable elevation in *k*.	Ng and Lo (2007)
Cement Kiln Dust - Black Cotton Soil	1.0 x 10^{-8} to 1.5 x 10^{-10} m/s	-Elevates maximum dry density and reduces optimum *w*. -Improves vertical strain and unconfined compressive strength.	-Concerns about caustic nature and potential leachates containing harmful compounds.	Oriola and Moses (2011)
Cement Kiln Dust - Lateritic Soil	9 x 10^{-9} to <1.0 x 10^{-10} m/s	-Reduction in plasticity index and vertical strain. -Notable increase in unconfined compressive strength.	-Concerns about caustic nature and potential leachates containing harmful compounds.	Amadi and Ebermu (2013)

Investigations identified the potential of paper sludge to achieve a state of low *k*, thereby serving effectively as hydraulic barriers (Rubinos and Spagnoli, 2018).Moo-Young and Zimmie, (1996) investigated the geotechnical characteristics of various paper mill sludges, revealing their high water content (*w*: 150 – 250%), plasticity index (77–191), and compressibility. These studies highlighted the impact of *w* on the compaction and hydraulic properties of paper sludge, noting the trade-off between water content and hydraulic performance although the shear strength varied based on the contents of organic matter and the fibres. However, challenges such as the susceptibility of the paper sludge to desiccation and freeze-thaw cycles, which can significantly influence its *k*, were also identified.

Further laboratory and field investigations focused on the long-term efficiency of paper sludge as an hydraulic barrier layer in landfill covers by Kraus *et al.*, (1997) and Moo-Young and Zimmie, (1997), demonstrated that paper sludge could maintain acceptable hydraulic barrier properties over extended periods ($k < 10^{-9}$ m/s). Kamon *et al.*, (2002), confirmed these results by conducting a comprehensive assessment of paper sludge for landfill cover applications, emphasizing its potential to maintain low *k* under a large range of *w* (50–200%) and for 10 years, and its high friction angle (40.5˚) and cohesion of 3.9 kPa due to the presence of organic fibres.

The environmental compatibility of paper sludge has been the subject of studies by Boni *et al.* (2004) that have evaluated the leaching potential of heavy metals from paper sludge, finding concentrations to be within acceptable environmental thresholds. Zule *et al.* (2007) and Kortnik *et al.* (2008) extended these analyses to include chemical and biodegradability assessments, further validating the environmental suitability of paper sludge for landfill applications.

Studies by Slim *et al.*, (2016), have experimented with paper sludge mixtures and, incorporating class C fly ash to enhance their geotechnical properties while maintaining low *k*. These studies suggest that with appropriate modification, paper sludge could serve as an effective component in alternative landfill liner designs.

Paper sludge appears to be a viable option for landfill barrier construction as its primary benefits include its suitable *k* and geotechnical characteristics, which have been verified in operating municipal solid waste landfills across the United States, Finland,

Canada, and Japan. It`s considered relatively safe regarding the leaching of trace metals (Rubinos and Spagnoli, 2018). However, its significant vulnerability to drying out and freeze-thaw cycles presents a notable drawback.

4 CEMENT KILN DUST

Cement kiln dust, a fine, alkaline material by-product captured through electrostatic precipitators during cement clinker manufacture, has been increasingly investigated for its potential as a soil stabilization agent, particularly in the construction of waste containment barriers(Kunal, et al., 2012). Research conducted by Mohamed (2002) in which cement kiln dust was utilized at an optimal ratio of 6% in soil barriers formulation specifically for hazardous waste in arid environments, led to a significant reduction in k, to below 10^{-9} m/s, and simultaneously improved the soil's shear strength. Parallel findings were reported by Oriola and Moses, (2011), who examined the effects of integrating 4 –16% cement kiln dust (by dry weight) into "black cotton" expansive soils. The research indicated that cement kiln dust generally elevates the maximum dry density and reduces the optimum w. Soils with 4–12% cement kiln dust content achieved satisfactory k levels below 10^{-9} m/s. However, it was noted that the 4% cement kiln dust concentration was particularly effective in improving soil k, while higher cement kiln dust proportions tended to be counterproductive. Additionally, significant improvements in vertical strain and unconfined compressive strength were observed, surpassing 200 kN/m^2, for up to 16% cement kiln dust treatment. This enhancement is attributed to the pozzolanic properties of cement kiln dust.

Amadi and Eberemu, (2013) extended this research to compacted lateritic soils derived residually, stabilized with up to 16% cement kiln dust. They reported a reduction in plasticity index (from 20 to 30%) and maximum unit weight, alongside a decrease in vertical strain (consistently below 4%) and a notable increase in unconfined compressive strength with rising cement kiln dust content. Osinubi *et al.* (2015) outlined the optimal zone for cement kiln dust cured lateritic soil, specifying 10% cement kiln dust content, prepared with w ranging between 13.5 and 21.3%, and compacted using British Standard Heavy (BSH) energy.

Collectively, these studies advocate for the potential application of cement kiln dust as a soil stabilizer in the construction of waste containment barriers, especially considering its geotechnical properties and influence on k. However, it is crucial to address concerns regarding the potential environmental hazards posed by cement kiln dust leachates, which may contain harmful compounds and exhibit a caustic nature. Hence, a definitive assessment of cement kiln dust's suitability for such applications necessitates a detailed understanding of these environmental implications.

5 SHREDDED TYRES

The integration of shredded tyres in landfill hydraulic barriers, either alone or in conjunction with natural soil or other waste materials, has been the focus of numerous research. Al-Tabbaa and Aravinthan, (1998) examined the engineering and leaching attributes of compacted clay mixed with up to 20% shredded tyres. The findings indicated that the addition of shredded tyres resulted in reduced dry density, unconfined compressive strength, and k. Natural clay-shredded tyres mixtures with varying percentages and particle sizes when permeated with different liquids such as paraffin, acidic water, and distilled water, exhibited interesting adhering dynamics between shredded tyres and clay. The study found that k increased when permeated with water or acidic water, but decreased significantly when permeated with paraffin by more than 50 times, attributed to the absorption by tyre particles and their consequent swelling (up to 600 kPa). This property was seen as beneficial, as it mitigated the negative impact of organic chemicals with low dielectric constants on clays. However, the leaching tests indicated variable concentrations of heavy metals, necessitating site-specific assessments.

Ng and Lo (2007) adopted a different approach by creating a combination of waste tyre aggregates with paper sludge for use as daily landfill covers. The research demonstrated that the mixed paste, being significantly lighter and less permeable than conventional soil covers, improved shear strength. Additionally, the paste displayed a high ability of Pb retardation (retardation factor D = 19.0–59.0), suggesting its effectiveness as a landfill cover system (Ng and Lo, 2010).

A study focusing on the geotechnical characteristics of sand-bentonite mixtures reinforced with tyre chips (5 - 15%) for a potential use as liner material, revealed a reduction in maximum dry density from 1.69 to 1.76 g/cm³ with an increase in tire content from 0% to 15% (Mukherjee and Mishra, 2017). Up to 10% tyre content the consolidation coefficient exhibited a slight decrease, but then rose to 0.110 with further addition (15%). The optimum water content remained largely stable at approximately 16%. Additionally, the swelling index improved across all tire content levels (from 0.023 to 0.089), attributable to the tires elastic properties. The inclusion of tire

material positively influenced the unconfined compressive strength, as evidenced by a growth in the Improvement factor. This enhancement was also seen in the cohesion (from 28.4 kPa to 49.1 kPa) up to 10% tire content, and in the friction angle (from 27.3° to 33.1°) for all tire contents. These findings suggest that the integration of tire chips into soil base can significantly reduce the probability of failure. Despite improving the shear strength, the addition of tyre chips adversely affected hydraulic conductivity, necessitating careful consideration of the tyre content to maintain desired permeability values.

Overall, these studies collectively indicate that shredded tyres can be an effective reinforcement additive for clay liners, mitigating issues like cracking due to desiccation and enhancing contaminant sorption capacity. Conversely, concerns regarding increased *k* and potential leaching of contaminants from the tyres remain.

6 COMPARATIVE CONCLUSION

The examination of the previously mentioned waste materials demonstrates that a significant proportion exhibit technical attributes appropriate for the landfill barriers. Nonetheless, it is imperative to acknowledge that every distinct waste type possesses unique properties, and its deployment offers both benefits and drawbacks relative to conventional materials employed in landfill liners and covers. These considerations predominantly pertain to geotechnical and hydraulic efficacy, economic implications, and environmental safety concerns.

Bauxite residue (red mud) is characterized by a suite of beneficial properties for application as a liner, predominantly due to its robust mechanical resistance, considerable capacity of acid neutralization, resilience to chemical degradation, and notably, its superior adsorption capabilities for a large spectrum of contaminants, comprising toxic trace metalloids, organic chemicals, phosphorus, and bacteria. Conversely, its limitations are marked by a restricted range of acceptable *k*, vulnerability to desiccation, inherently caustic nature, the presence of radionuclides and trace metalloids, its alkalinity leaching and its sensitivity to desiccation. These factors necessitate a cautious approach, recommending the use of red mud primarily for reactive bottom liners in industrial or mining wastes landfills.

Pulp and paper mill sludges present viable options for landfill cover system, attributed to their low *k*, acceptable slope stability, and controlled metal leaching during landfilling operations. The primary challenges associated with paper sludge include the necessity for high *w* during compaction and the risk of biodegradation. However, the most critical limitation of paper sludge is its heightened susceptibility to desiccation and freeze-thaw cycles and oxidative and microbiological degradation. This characteristic strongly suggests the implementation of a protective top layer to mitigate the risk of structural compromise due to cracking.

Cement Kiln Dust is beneficial as a conditioner for clays or clayey soils, enhancing the geotechnical properties, density, and vertical settlement properties of barrier materials. However, limitations exist in the permissible proportions of in the mixture, and its occasional adverse impact on k presents technical challenges. The most notable concerns with Cement Kiln dust use are its acidic properties and its leachate hazardous materials.

End-of-life shredded tires demonstrate functional efficacy in reinforcing liners, attributable to their swelling and elastic characteristics. The incorporation of such materials enhances the geotechnical characteristics and contaminant retention capabilities of the natural barriers. Significantly, their incorporation mitigate the detrimental effects of low dielectric constant organic chemicals on clays. However, this approach is not without weaknesses, as it may lead to an undesirable elevation in hydraulic conductivity and an increased risk of contaminant leaching.

The utilization of waste in engineering landfill barriers offers common advantages, such as reducing landfill space and environmental impacts, decreasing costs, and enhancing waste recycling rates. However, there is a necessity for more comprehensive research on the chemical compatibility and environmental impact of these wastes, particularly regarding their contaminant leaching characteristics.

REFERENCES

Al-Tabbaa, A. and Aravinthan, T. (1998) 'Natural clay-shredded tire mixtures as landfill barrier materials', *Waste Management*, 18(1), pp. 9–16. https://doi.org/10.1016/S0956-053X(98)00002-6.

Amadi, A.A. and Eberemu, A.O. (2013) 'Potential Application of Lateritic Soil Stabilized with Cement Kiln Dust (CKD) as Liner in Waste Containment Structures', *Geotechnical and Geological Engineering*, 31(4), pp. 1221–1230. https://doi.org/10.1007/s10706-013-9645-3.

Boni, M. (2004) 'Environmental quality of primary paper sludge', *Journal of Hazardous Materials*, 108(1–2), pp. 125–128.https://doi.org/10.1016/j.jhazmat.2003.11.017.

Çoruh, S. and Ergun, O.N. (2010) 'Use of fly ash, phosphogypsum and red mud as a liner material for the disposal of hazardous zinc leach residue waste', *Journal of Hazardous Materials*, 173(1–3), pp. 468–473.

https://doi.org/10.1016/j.jhazmat.2009.08.108.

Duchesne, J. and Doye, I. (2005) 'Effectiveness of Covers and Liners Made of Red Mud Bauxite and/or Cement Kiln Dust for Limiting Acid Mine Drainage', *Journal of Environmental Engineering*, 131(8), pp. 1230–1235. https://doi.org/10.1061/(ASCE)0733-9372(2005)131:8(1230).

Hegedűs, M. *et al.* (2016) 'Radiological characterization of clay mixed red mud in particular as regards its leaching features', *Journal of Environmental Radioactivity*, 162–163, pp. 1–7. https://doi.org/10.1016/j.jenvrad.2016.05.002.

Kalkan, E. (2006) 'Utilization of red mud as a stabilization material for the preparation of clay liners', *Engineering Geology*, 87(3–4), pp. 220–229. https://doi.org/10.1016/j.enggeo.2006.07.002.

Kamon, M. *et al.* (2002) 'Evaluation of Waste Sludge Compatibility for Landfill Cover Application', *Soils and Foundations*, 42(4), pp. 13–27. https://doi.org/10.3208/sandf.42.4_13.

Kortnik, J., Černec, F. and Hrast, K. (2008) 'Paper Sludge Layer as Low Permeability Barrier on Waste Landfills', *Soil and Sediment Contamination: An International Journal*, 17(4), pp. 381–392. https://doi.org/10.1080/15320380802146586.

Kraus, J.F. *et al.* (1997) 'Freeze-Thaw Cycling and Hydraulic Conductivity of Bentonitic Barriers', *Journal of Geotechnical and Geoenvironmental Engineering*, 123(3), pp. 229–238. https://doi.org/10.1061/(ASCE)1090-0241(1997)123:3(229).

Kunal, Siddique, R. and Rajor, A. (2012) 'Use of cement kiln dust in cement concrete and its leachate characteristics', *Resources, Conservation and Recycling*, 61, pp. 59–68. https://doi.org/10.1016/j.resconrec.2012.01.006.

Mohamed., A.M.O. (2002) 'Hydro-mechanical evaluation of soil stabilized with cement-kiln dust in arid lands', *Environmental Geology*, 42(8), pp. 910–921. https://doi.org/10.1007/s00254-002-0590-3.

Moo-Young, H.K. and Zimmie, T.F. (1996) 'Geotechnical Properties of Paper Mill Sludges for Use in Landfill Covers', *Journal of Geotechnical Engineering*, 122(9), pp. 768–775. https://doi.org/10.1061/(ASCE)0733-9410(1996)122:9(768).

Moo-Young, H.K. and Zimmie, T.F. (1997) 'Waste Minimization and Re-Use of Paper Sludges in Landfill Covers: a Case Study', *Waste Management & Research: The Journal for a Sustainable Circular Economy*, 15(6), pp. 593–605. https://doi.org/10.1177/0734242X9701500605.

Mukherjee, K. and Mishra, A.K. (2017) 'The Impact of Scrapped Tyre Chips on the Mechanical Properties of Liner Materials', *Environmental Processes*, 4(1), pp. 219–233. https://doi.org/10.1007/s40710-017-0210-6.

Ng, K.T.W. and Lo, I.M.C. (2007) 'Mechanical behaviors of a synthetic paste of tire chips and paper sludge in MSW landfill daily cover applications', *Canadian Geotechnical Journal*, 44(8), pp. 928–941. https://doi.org/10.1139/T07-041.

Ng, K.T.W. and Lo, I.M.C. (2010) 'Effects of Design Mix and Porosity of Waste-Derived Paste as Landfill Daily Covers on Lead Retardation', *Practice Periodical of Hazardous, Toxic, and Radioactive Waste Management*, 14(3), pp. 195–204. https://doi.org/10.1061/(ASCE)HZ.1944-8376.0000033.

Oriola, F. and Moses, G. (2011) 'Compacted black cotton soil treated with cement kiln dust as hydraulic barrier material', *American Journal of Scientific and Industrial Research*, 2(4), pp. 521–530. https://doi.org/10.5251/ajsir.2011.2.4.521.530.

Osinubi, K.J., Moses, G. and Liman, A.S. (2015) 'The Influence of Compactive Effort on Compacted Lateritic Soil Treated with Cement Kiln Dust as Hydraulic Barrier Material', *Geotechnical and Geological Engineering*, 33(3), pp. 523–535. https://doi.org/10.1007/s10706-014-9837-5.

Panda, I. *et al.* (2017) 'Characterization of red mud as a structural fill and embankment material using bioremediation', *International Biodeterioration & Biodegradation*, 119, pp. 368–376. Available at: https://doi.org/10.1016/j.ibiod.2016.11.026.

Rubinos, D.A, Spagnoli, G. and Barral, M.T. (2015) 'Assessment of bauxite refining residue (red mud) as a liner for waste disposal facilities', *International Journal of Mining, Reclamation and Environment*, 29(6), pp. 433–452. https://doi.org/10.1080/17480930.2013.830906.

Rubinos, D.A. and Barral, M.T. (2017) 'Sorptive removal of Hg II by red mud (bauxite residue) in contaminated landfill leachate', *Journal of Environmental Science and Health, Part A*, 52(1), pp. 84–98. https://doi.org/10.1080/10934529.2016.1229938.

Rubinos, D.A. and Spagnoli, G. (2018) 'Utilization of waste products as alternative landfill liner and cover materials–A critical review', *Critical Reviews in Environmental Science and Technology*, 48(4), pp. 376–438. https://doi.org/10.1080/10643389.2018.1461495.

Rubinos, D.A., Spagnoli, G. and Barral, M.T. (2016) 'Chemical and environmental compatibility of red mud liners for hazardous waste containment', *International Journal of Environmental Science and Technology*, 13(3), pp. 773–792. Available at: https://doi.org/10.1007/s13762-015-0917-8.

Slim, G.I. *et al.* (2016) 'Optimization of Polymer-Amended Fly Ash and Paper Pulp Millings Mixture for Alternative Landfill Liner', *Procedia Engineering*, 145, pp. 312–318. https://doi.org/10.1016/j.proeng.2016.04.079.

Ujaczki, É. *et al.* (2016) 'The potential application of red mud and soil mixture as additive to the surface layer of a landfill cover system', *Journal of Environmental Sciences*, 44, pp. 189–196. Available at: https://doi.org/10.1016/j.jes.2015.12.014.

Zule, J., Černec, F. and Likon, M. (2007) 'Chemical properties and biodegradability of waste paper mill sludges to be used for landfill covering', *Waste Management & Research: The Journal for a Sustainable Circular Economy*, 25(6), pp. 538–546. https://doi.org/10.1177/0734242X07079188.

Proceedings of the XVIII ECSMGE 2024
GEOTECHNICAL ENGINEERING CHALLENGES
TO MEET CURRENT AND EMERGING NEEDS OF SOCIETY
© 2024 the Authors
ISBN 978-1-032-54816-6
DOI 10.1201/9781003431749-561
Open Access: www.taylorfrancis.com, CC BY-NC-ND 4.0 license

ECSMGE 24
XVIII EUROPEAN CONFERENCE ON SOIL MECHANICS AND GEOTECHNICAL ENGINEERING

Simulation of pile installation in chalk: Discrete and continuum approaches

Simulation de pose de pieux dans la craie: Approches discrètes et continues

M.O. Ciantia*
University of Dundee, Dundee, UK; Università Degli Studi di Milano Bicocca, Milan, Italy

J. Zheng, M. Previtali, J.A. Knappett
University of Dundee, Dundee, UK

m.o.ciantia@dundee.ac.uk; matteo.ciantia@unimib.it

ABSTRACT: Chalk is a type of porous rock formed from cemented calcite grains. It is widely found in areas across the UK, and is present beneath the North Sea where offshore wind turbines are being installed. Large piles are often driven into chalk to support these turbines. However, the installation process can cause the intact rock below the pile to crush, creating a putty-like material with different mechanical properties from the original rock. This unpredictability has made it difficult to design piles that are appropriate for use in chalk. This paper presents two approaches to modelling open-ended pile installation in chalk. The first approach is based on the Discrete Element Method (DEM), which represents the rock as separate particles bonded together. A new contact model is proposed for highly porous rocks. The second approach uses the Geotechnical Particle Finite Element Method (GPFEM), which has been adapted to account for the large displacements and nonlinearities of the problem. With GPFEM the coupled hydromechanical effects developing during pile installation are investigated using a robust and mesh-independent implementation of an elasto-plastic constitutive model at large strains. With DEM the micromechanical features of pile plugging are explored and the mechanisms behind radial stress distributions inside and outside the plug are unveiled. Although both approaches have their challenges, they have been successful in modelling pile installation experiments at model scale. This offers the potential for a closer examination and improved understanding of the mechanisms underlying open-ended pile installation in chalk.

RÉSUMÉ: La craie est un type de roche poreuse formée de grains de calcite cimentés. Elle est largement répandue au Royaume-Uni et se trouve sous la mer du Nord, où des éoliennes offshore sont installées. De grands pieux sont souvent enfoncés dans la craie pour soutenir ces éoliennes. Cependant, le processus d'installation peut entraîner l'écrasement de la roche intacte située sous le pieu, créant ainsi un matériau semblable à du mastic dont les propriétés mécaniques sont différentes de celles de la roche d'origine. Cette imprévisibilité a rendu difficile la conception de pieux adaptés à une utilisation dans la craie. Cet article présente deux approches pour modéliser l'installation de pieux ouverts dans la craie. La première approche est basée sur la méthode des éléments discrets (DEM), qui représente la roche comme des particules séparées liées entre elles. Un nouveau modèle de contact est proposé pour les roches très poreuses. La seconde approche utilise la méthode des éléments finis à particules géotechniques (GPFEM), qui a été adaptée pour tenir compte des grands déplacements et des non-linéarités du problème. Avec la GPFEM, les effets hydromécaniques couplés qui se développent pendant l'installation des pieux sont étudiés en utilisant une implémentation robuste et indépendante du maillage d'un modèle constitutif élasto-plastique à grandes déformations. Avec le DEM, les caractéristiques micromécaniques du colmatage des pieux sont explorées et les mécanismes qui sous-tendent les distributions radiales des contraintes à l'intérieur et à l'extérieur du colmatage sont dévoilés. Bien que les deux approches présentent des difficultés, elles ont permis de modéliser avec succès des expériences d'installation de pieux à l'échelle du modèle.

Keywords: Displacement piles; DEM; GPFEM; Chalk.

1 INTRODUCTION

Designing foundations in soft, cemented porous rocks presents a significant challenge due to the material's complex mechanical behaviour. Upon loading soft rocks may crush and collapse and, if saturated, consequent pore water pressure build up would further reduce the effective stress. Material behaviour would then change from stiff elastic to a non-linear irreversible soil-like one, characterised by completely different hydraulic properties. Whilst for low levels of loading, an elastic response may facilitate design, the insertion of a rigid body like a steel pile will definitively remould the rock (Buckley et al., 2017) and therefore suffer from the above-mentioned consequences. Small scale physical modelling in soft

rocks has revealed that the damage process is completely different when comparing a closed-ended cone shaped pile with an open-ended tubular one (Alvarez-Borges et al., 2018). For this reason, the post-installation stress field will change depending on the geometry of the penetrating object. To incorporate installation effects, current practice for pile design in soft rocks is moving towards cone penetration test (CPT) methods (Jardine et al., 2023) where radial stress profiles around open-ended piles pushed into soft rocks are inferred from the CPT response.

In recent years, several numerical methods able to overcome difficulties related to large deformations and various types of non-linearities (e.g. material, contact) have been developed. On one side, the Discrete Element Method (DEM), often used to investigate elemental soil behaviour, has been shown to be an appropriate tool that with reasonable computational power can be used to simulate boundary value problems (BVPs). Several boundary value problems including pile penetration (Cerfontaine et al., 2023; Ciantia et al., 2019) and screw piles (Sharif et al., 2021) have been investigated using the DEM.

On the other hand, amongst various continuum approaches (CEL, MPM, SPH), the Geo-Particle Finite Element Method (GPFEM) has been shown to be able to manage large deformations and address the complexities of nonlinear soil behaviour (Carbonell et al., 2022). GPFEM has been shown to be suitable to investigate CPT installation and interpretation in structured ground (Oliynyk et al., 2021). Thanks to its robust large deformation hydro-mechanically-coupled formulation it was used to study installation problems in chalk in partially drained conditions (Previtali et al., 2023).

Both DEM and GPFEM have advantages and disadvantages. For example, whilst DEM only requires calibration of simple physical parameters to capture soil behaviour quite realistically at the macroscale, it is computationally demanding, particularly if hydro-mechanical problems need to be modelled. In contrast, continuum approaches were developed from the outset to solve BVPs, but strongly depend on the ability of the constitutive relationship used to accurately simulate soil behaviour. In this work DEM and GPFEM are used to investigate the installation process of an open-ended pile in a soft rock. Reference experimental data by Alvarez-Borges et al. (2018) that used X-ray tomography will be used as a validation dataset.

2 NUMERICAL FRAMEWORKS

2.1 DEM for highly porous rocks

The behaviour of rocks has been historically modelled in DEM by introducing cohesive bonds through the Bonded Particle Method (BPM) (Potyondy & Cundall, 2004). Zheng et al. (2023) recently developed a bond-softening damage model able to capture the complex pressure dependent behaviour of weakly cemented porous rocks. Such a contact model, which is used in this study, is defined within the macro-element framework characterized by a generalized force-displacement failure envelop:

$$f = \left|\frac{\tilde{M}}{\bar{M}}\right|^{1.001} + \left(\frac{N}{\bar{N}}\right)^2 + \left(\frac{V}{\bar{V}}\right)^4 \left[1 - \left(\frac{N}{\bar{N}}\right)^2\right]^{-1} - 1 \quad (1)$$

The behaviour in the (i) normal (N), (ii) tangential (V) and (iii) bending direction ($\tilde{M}$) is linear elastic within the yield surface, according to Euler beam theory. The overbar symbols $\bar{M}, \bar{N}$ and $\bar{V}$ represent the size of the yield surface on a given axis and are function of the bond tensile (σ_{t0}), compressive (σ_{c0}) and shear (τ_0) strength. Unlike in the BPM, the bond does not instantaneously fail once the combined load reaches the yield surface but starts accumulating damage. This damage variable (D_d) then affects the size of the yield surface modifying σ_0 and τ_0 through plastic softening. D_d depends on the irreversible displacements in the normal u_n^p and tangential u_s^p direction and the irreversible rotation θ_b^p:

$$D_d = 1 - e^{-\left(\frac{\left|u_n^p\right|}{u_n^c} + \frac{u_s^p}{u_s^c} + \frac{\theta_b^p}{\theta_b^c}\right)} \quad (2)$$

Table 1. Chalk DEM parameters (see. Zheng et al. (2023)).

Parameter	Value	Parameter	Value
$\bar{E}^*[GPa]$	1.7	θ_b^c[rad]	6e^{-3}
$\bar{\kappa}^*[-]$	5	$\sigma_{c0}[MPa]$	50
$u_n^c[m]$	2e^{-5}	$\sigma_{t0}[MPa]$	1
$u_s^c[m]$	2e^{-5}	$\tau_0[MPa]$	2

2.2 GPFEM of structured soils

The GPFEM is based on a standard FEM framework that, through continuous remeshing, mitigates mesh distortion issues. The efficiency of the numerical approach lies in the use of low-order triangular elements which simplify the remeshing process. To avoid interlocking issue, a mixed formulation is used. The constitutive model used in this work is an extension of Modified Cam Clay to incorporate bonding (Monforte et al., 2019). In addition to the standard preconsolidation pressure of the unbonded material p_s, an extra internal variable related to the

tensile strength of the rock (p_t) is used to account for bonding. The shape of yield surface is controlled by M_f while $M_g$controlles the plastic flow. The hardening internal variables evolve with deviatoric and volumetric plastic strains. $\rho_{s,t}$ and $\xi_{s,t}$ are constitutive model parameters controlling the rate of hardening and softening. The material parameters listed in Table 1 and 2 were calibrated against a combination of literature data and element tests on Saint Nicholas at Wade (SNW) chalk (Riccio et al., 2023). Refer to Previtali et al, (2023) for further details.

Table 2. Constitutive model parameters for chalk.

Parameter	Value	Parameter	Value
$\boldsymbol{e_0}$ [−]	0.83	p_{s_0} $[kPa]$	3000
$\boldsymbol{\rho'}$ $[\boldsymbol{Mgm^{-3}}]$	1.4	p_{t_0} $[kPa]$	200
$\boldsymbol{\nu}$ [−]	0.12	E $[GPa]$	1
$\boldsymbol{\rho_s}$ [−]	19	ρ_t [−]	15
$\boldsymbol{\xi_s}$ [−]	0.5	ξ_t [−]	0.5
$\boldsymbol{M_f}$ [−]	1.0	M_g [−]	1.2

3 MODEL PILE SIMULATIONS

Figure 1 shows the numerical model reproducing the experimental set up for the model pile installation tests in SNW chalk by Alvarez-Borges et al. (2018). In the experiment a tubular pile with external diameter of 8 mm and wall thickness of 1 mm was jacked to a depth of 2 cm in a cylinder of diameter 100 mm and length of 120 mm. The axisymmetric simplification of the geometry along with some geometrical quantities are represented in Figure 1. The figure also shows the DEM and GPFEM numerical model initial conditions.

Axisymmetric conditions for DEM models are extremely challenging due to the particles on the symmetry axis and therefore a 3D model is used. The rock domain is generated using the periodic cell replication method PCRM (Ciantia et al., 2018) . It consists of a combination of different techniques aimed at speeding up large DEM models generation. To reduce the computational burden, the PSD of destructured chalk was upscaled by a factor of 2.1 near the pile (<0.6D) increasing to a factor of 4.8 at 2.5D. Considering that the damage model is framed to be scale independent the scaling used does not affect the calibrated parameters (Zheng et al. 2023). The maximum and minimum particle size was 0.18 mm and 0.066 mm, respectively, with a d50 of 0.116 mm. To limit scale effects on potential plugging behavior (Cerfontaine et al., 2023), this scaling value was chosen to provide a sufficient number of particles in contact with the pile whilst keeping the computational burden manageable. Pile wall thickness (t_w) to d50 ratio is 4.0.

To mitigate computational load and prevent boundary effects, the edges of the DEM domain are coupled with a Finite Difference Model (FDM). Additional details on DEM-FDM model coupling are available in Zheng et al. (2023). Given the significant stiffness contrast between the pile and the rock, the pile representation is simplified by using a rigid, non-deformable wall and the installation force is obtained as the sum of the vertical contact forces.

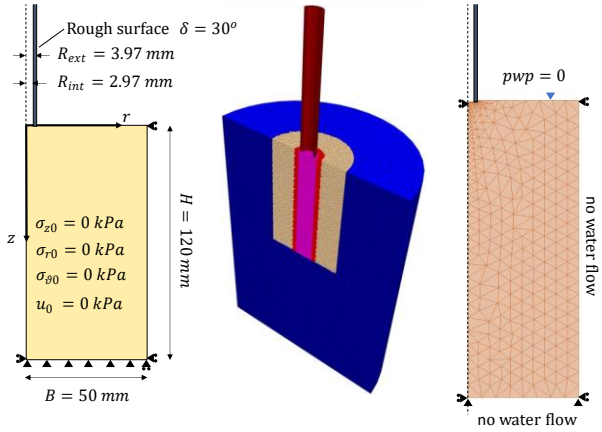

Figure 1. (left) Model pile tests experimental setup by Alvarez-Borges et al. (2018) along with geometrical quantities and snapshots of the discrete (middle) and continuum (right) numerical model initial states.

The GPFEM model generation is much simpler as initial conditions can be directly assigned as for classic FE models. Moreover, axisymmetric conditions are easily modelled with continuum methods and are hence here used. Although the experiments were performed pushing the pile slow enough to attain drained conditions, the simulations were carried out using a coupled hydro-mechanically formulation. As with the DEM model, the pile is simplified as a perfectly rigid wall and the installation force is measured as the sum of the contact forces. Boundary conditions are represented in Figure 1.

4 RESULTS AND DISCUSSION

Figure 2a compares the experimental results against the load displacement curve predicted by the two numerical models. The general trend is very similar although the GPFEM simulation seems to underpredict the penetration force. There are several reasons for such discrepancy. These include for example, the constitutive model softening parameters or the approximation of the flat tip with a curved geometry to avoid the sharp corners. Figure 2b shows contours of the radial stresses close to the pile tip. Whilst the continuum and discrete model results appear very similar a more quantitative comparison would be required for a proper comparison.

5 CONCLUSIONS

Two different numerical approaches, namely the DEM and GPFEM have been used to simulate open- ended pile installation in a soft chalk. Both procedures were able to overcome the difficulties associated with large displacements, large strains as well as geometrical, material and contact nonlinearities. The good agreement between the two methods and the experimental data indicates that both approaches are adequate for the investigation of open-ended pile installation in chalk.

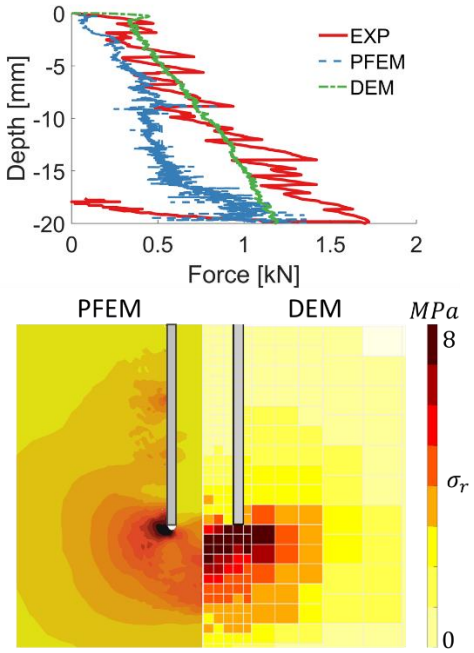

Figure 2. (top) Force displacement curves and (bottom) radial stress contours at the end of installation.

ACKNOWLEDGEMENT

This work is funded by EPSRC EP/W00013X/1 project and the CSC Scholarship (202008330363).

REFERENCES

Alvarez-Borges, F. J., Richards, D. J., Clayton, C. R. I., et al. (2018). Application of X-ray computed tomography to investigate pile penetration mechanisms in chalk. *Proceedings of the Chalk 2018 Conference*, pp. 565–570.

Buckley, R. M., Jardine, R. J., Kontoe, S., et al. (2017). Ageing and cyclic behaviour of axially loaded piles driven in chalk. *Géotechnique*, 68(2):146–161. 10.1680/jgeot.17.P.012.

Carbonell, J. M., Monforte, L., Ciantia, MO., et al. (2022). Geotechnical particle finite element method for modeling of soil-structure interaction under large deformation conditions. *JRMGE*, 14(3): 967-983. 10.1016/j.jrmge.2021.12.006.

Cerfontaine, B., Ciantia, M. O., Brown, M. J., et al. (2023). DEM study of particle scale effect on plain and rotary jacked pile behaviour in granular materials. *Computers and Geotechnics*, 161, pp. 105559. 10.1016/j.compgeo.2023.105559.

Ciantia, M. O., Boschi, K., Shire, T., et al. (2018). Numerical techniques for fast generation of large discrete-element models. Proceedings of the Institution of Civil Engineers: Engineering and Computational Mechanics, 171(4), 147–161. 10.1680/jencm.18.00025.

Ciantia, M. O., O'Sullivan, C., & Jardine, R. J. (2019). Pile penetration in crushable soils: Insights from micromechanical modelling. *Proceedings of the 17th European Conference on Soil Mechanics and Geotechnical Engineering*, pp. 298–317.

Jardine, R. J., Buckley, R. M., Liu, T., et al. (2023). The axial behaviour of piles driven in chalk. *Geotechnique*, pp. 1–45. 10.1680/jgeot.22.00041.

Monforte, L., Ciantia, M. O., Carbonell, J. M., et al. (2019). A stable mesh-independent approach for numerical modelling of structured soils at large strains. *Computers and Geotechnics*, 116, pp. 103215. 10.1016/j.compgeo.2019.10321.

Oliynyk, K., Ciantia, M. O., & Tamagnini, C. (2021). A finite deformation multiplicative plasticity model with non–local hardening for bonded geomaterials. *Computers and Geotechnics*, 137, pp. 104209. 10.1016/j.compgeo.2021.104209.

Potyondy, D. O., & Cundall, P. A. (2004). A bonded-particle model for rock. *International Journal of Rock Mechanics and Mining Sciences*, 41(8): 1329–1364. 10.1016/j.ijrmms.2004.09.011.

Previtali, M., Ciantia, M. O., & Riccio, T. (2023). Numerical installation of OE piles in soft rocks within the GPFEM framework. *Proceedings of the 10th European Conference on Numerical Methods in Geotechnical Engineering*. pp. 1-6.

Riccio, T., Previtali, M., Ciantia, M.O., et al. (2023). The soft-oedometer: a simple test to calibrate advanced constitutive models for CPT simulations in soft socks. *CNRIG 2023*, 477–484.

Sharif, Y. U., Brown, M. J., Ciantia, M. O., et al. (2021). Using discrete element method (Dem) to create a cone penetration test (cpt)-based method to estimate the installation requirements of rotary-installed piles in sand. Canadian Geotechnical Journal, 58(7): 919–935. 10.1139/cgj-2020-0017.

Zheng, J., Previtali, M., Ciantia, M.O., et al. (2023). Micromechanical numerical modelling of foundation punching in highly porous cemented geomaterials in a virtual Centrifuge environment. *CNRIG 2023*, pp. 390–397.

Proceedings of the XVIII ECSMGE 2024
GEOTECHNICAL ENGINEERING CHALLENGES
TO MEET CURRENT AND EMERGING NEEDS OF SOCIETY
© 2024 the Authors
ISBN 978-1-032-54816-6
DOI 10.1201/9781003431749-562
Open Access: www.taylorfrancis.com, CC BY-NC-ND 4.0 license

ECSMGE 24
XVIII EUROPEAN CONFERENCE ON SOIL MECHANICS AND GEOTECHNICAL ENGINEERING

Initial design and testing of a new site investigation tool for the direct determination of *p-y* soil reaction curves: ROBOCONE

Conception initiale et expérimentation d'un nouveau dispositif d'investigation de site pour la détermination directe des courbes de réaction du sol *p-y*: ROBOCONE

J. Creasey*, A.E. Hajjar, A.T. Conn, E. Ibraim, A.H. Bateman, G. Mylonakis, G. Martin, A. Diambra
University of Bristol, Bristol, United Kingdom

K. Wen, B.P.J. Cerfontaine, S.M. Gourvenec, D.J. White
University of Southampton, Southampton, United Kingdom

D. Igoe, S.S. Kasyap
Trinity College Dublin, Dublin, Republic of Ireland

**james.creasey@bristol.ac.uk*

ABSTRACT: This paper presents the initial design, specification, testing and calibration of a new site investigation tool aiming to provide direct characterisation of the '*p-y*' soil reaction curves. This tool, developed within the ROBOCONE project consists of a dedicated '*p-y*' module to be attached behind the cone of a conventional CPT. The proposed module is capable of horizontal translation with respect to the CPT rod, imposing kinematic conditions different from those of the conventional pressuremeter and dilatometer, and fully resembling those of a miniature laterally loaded pile. Beyond the main design features and performance specification of this innovative module, this paper presents some initial preliminary tests to investigate the capability and output of the device in addition to its sensor calibration. Initial testing has been performed in a miniature calibration chamber. It is shown that the module can be used to apply both monotonic and complex displacement-loading histories, while obtaining the expected shape of soil reaction. The potential for implementation in 'whole-life' geotechnical design approaches will be discussed, however development of the theoretical framework for the full interpretation of the module results is outside the scope of this paper.

RÉSUMÉ: Cet article présente la conception initiale, les spécifications, les essais et l'étalonnage d'un nouvel outil d'investigation de site visant à fournir une caractérisation directe des courbes de réaction du sol "*p-y*". Cet outil, développé dans le cadre du projet ROBOCONE, consiste en un module "*p-y*" destiné à être installé derrière le cône d'un CPT conventionnel. Le système proposé est capable de subir un mouvement latéral par rapport à la tige du CPT, imposant des conditions cinématiques différentes de celles du pressiomètre et du dilatomètre conventionnels, et ressemblant totalement à celles d'un pieu miniature soumis à une charge latérale. Au-delà des principales caractéristiques de conception et des spécifications de performance de ce dispositif innovant, cet article présentera les premiers essais visant à étudier la capacité et le rendement de l'appareil, ainsi que l'étalonnage de ses capteurs. Les premiers essais ont été réalisés dans une chambre d'étalonnage miniature. Il sera démontré que le module peut être utilisé pour appliquer des séquences de force-déplacement monotones et complexes, tout en obtenant la réaction attendue du sol. Le potentiel de mise en œuvre dans les approches de conception géotechnique "tout au long de la vie" sera discuté, mais le développement du cadre théorique pour l'interprétation complète des résultats du module n'entre pas dans le cadre de cet article.

Keywords: ROBOCONE; site; investigation; tool; offshore.

1 ROBOCONE: CONTEXT AND OPPORTUNITY

To meet future net zero carbon emission targets by 2050, global installed offshore wind capacity must be increased by a factor of ~5 over the next 25 years (GWEC, 2023). This acceleration of offshore wind deployment requires a compression of typical project timelines (HMG, 2022). A key stage which could be streamlined is the typically lengthy and expensive site investigation where soil samples are obtained and returned to shore for determination of geotechnical

parameters via laboratory testing. An alternative approach could utilise specifically designed in-situ soil testing procedures to generate these parameters earlier in the project cycle, speeding up the design process.

Recent developments in both robotic and sensing technologies offer techniques that could improve the speed, and also the quality of the site investigation stage supporting advanced 'whole-life' design of ocean structures over a complete strain range (Gourvenec, 2020; Mayne, 2001; White, 2022).

The ROBOCONE project presented in this paper introduces an innovative new device with the capability of smart in-situ soil testing, aiming to improve the efficiency and quality of offshore geotechnical design and other applications.

2 THE ROBOCONE PROJECT

2.1 Overview

The ROBOCONE research project is a collaboration between the University of Bristol, University of Southampton and Trinity College Dublin. The aim of the ROBOCONE project is to develop an intelligent robotic tool which upon insertion within the ground, can mimic the loading histories experienced by soil elements around geotechnical infrastructure. The device is designed to fit behind a standard 15cm^2 cone penetrometer, consisting of three modules, each capable of smart and controlled probing of the soil in three different active sensing directions (vertical, horizontal and torsional) demonstrated in Figure 1 (Creasey et al, 2023). The device aims to infer soil mechanical characteristics over an entire strain range relevant to design through the application of whole life stress paths, an example of which is also shown in Figure 1. The current focus of the project has been to develop the *p-y* module, capable of horizontal translation described in the next section.

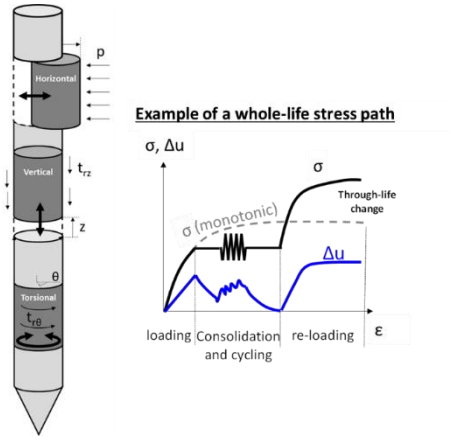

Figure 1. The ROBOCONE device and an example of a whole-life stress path that can be applied to the soil.

2.2 The *p-y* module

The ROBOCONE *p-y* module, is a cylindrical section of cone with the ability to translate horizontally within soil as highlighted by Figure 2a. The module translation aims to mimic the force and displacement history imposed by a laterally loaded pile element, so that the in-situ measured response can be scaled for pile design or used to determine soil constitutive parameters. An initial concept design for an aluminium prototype of the *p-y* module has been built at the University of Bristol (Figure 2b) with design specifications shown in Table 1. The device is capable of horizontal translation through an internal straight-line mechanism that converts vertical to horizontal linear motion driven via a motorised lead screw actuator fitted within the shaft above the module.

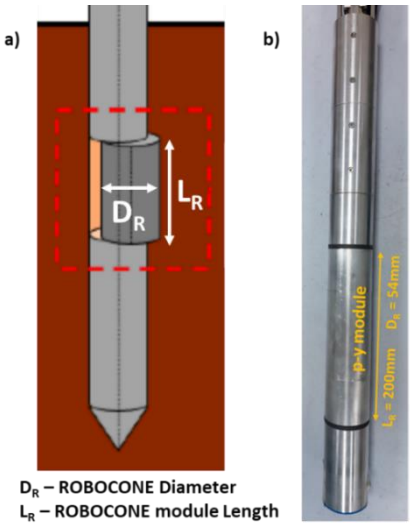

Figure 2. The ROBOCONE p-y module: (a) schematic; (b) initial aluminium prototype.

Table 1. Initial ROBOCONE p-y module specification.

Module diameter	54 mm
Module height	200 mm
Horizontal displacement range	0-13 mm
Displacement resolution	< 0.1 μm
Force capacity	~ 5-6 kN

The module is designed to fit within an enlarged section of cone with diameter 54 mm compared to the standard 44 mm cone penetrometer, enabling the housing of components of the internal mechanism, miniature sensors and cables. This enlarged section, occasionally included on a standard cone penetrometer acts as a friction reducer during soil penetration, easing resistance on the remaining cone length to be pushed to greater depths.

3 INITIAL *P-Y* MODULE TESTING

3.1 Bench verification and testing

Prior to testing the *p-y* module within soil, correct functioning of the device has been checked to ensure accuracy and reliability of both force and displacement measurements.

Measuring the total force acting on the module face as it displaces has been a challenge during the device development. All points of contact between the internal mechanism used to push the module must be connected to the shell via a load cell, so that all the load required to displace the module is measured. Figure 3 shows the method used to check the load cell configuration within the device. A central portion of the *p-y* module is placed in a loading frame and displaced up and down against an external load cell. The force measured by the external cell is then compared to the combined force measured by two internal load cells connecting the two points of contact between the internal mechanism and the outer shell. Comparison between external and internal load shows very good accuracy during both loading and unloading stages (Figure 4), a feature which was repeatable and not present in early design attempts due to the development of friction and unforeseen parallel contact points within the system, shown by the grey lines in Figure 4.

Due to space limitations only the vertical displacement imposed by the electrical motor could be measured through an LVDT placed inside the ROBOCONE. Therefore, a calibration process has been carried out to convert the vertical displacement of inner mechanism to the horizontal module translation, leading to a repeatable conversion factor of 2.52 as shown in Figure 5.

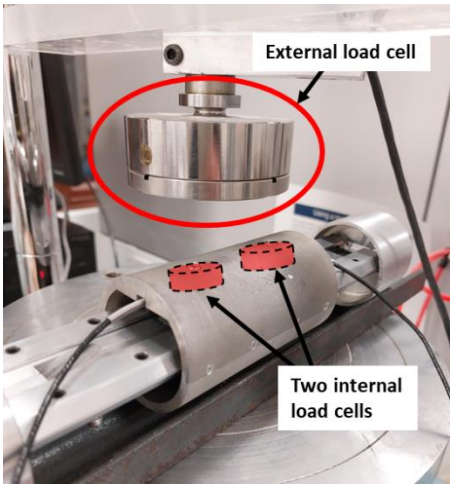

Figure 3. Test configuration for load cell investigation within the ROBCONE p-y module.

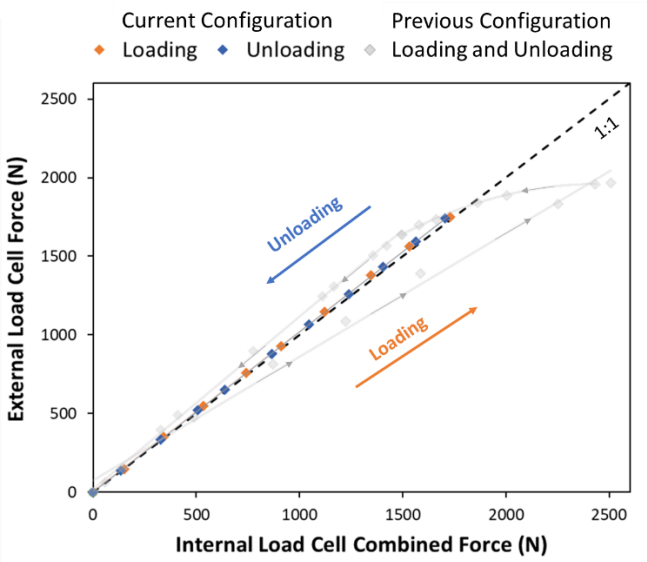

Figure 4. Comparison of external and internal load cell measurements.

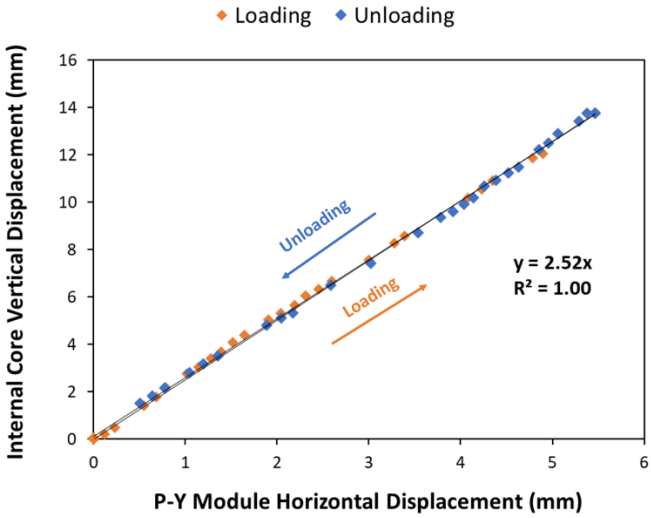

Figure 5. Comparison of vertical core displacement and horizontal p-y module displacement.

3.2 Calibration chamber testing

To investigate the capability and output of the ROBOCONE *p-y* module, initial small-scale tests have been conducted within a calibration chamber (Figure 6).

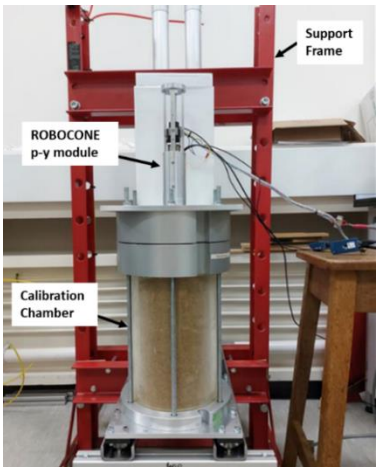

Figure 6. Initial small-scale testing of p-y module within a calibration chamber.

Within the chamber, the *p-y* module was displaced in dry Redhill sand (D_{50} = 0.17mm) with different vertical stresses applied. Varying load and unload loops were trialled and measurements of lateral force on the module face and lateral displacement were recorded. A typical force-displacement curve obtained is shown in Figure 7, where the module was displaced with two unload-reload loops during loading. The data shows load-displacement trends as expected and demonstrates the system capability to apply complex load histories.

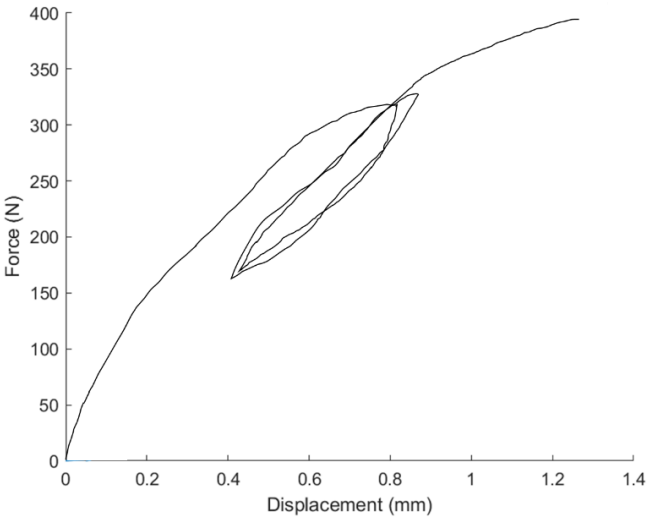

Figure 7. A typical force-displacement curve obtained within Redhill sand.

During testing, an assessment of the device's mechanical operation showed that the internal mechanism successfully transferred force to displace the module within sands and the sealing effectively prevented ingress of small dry sand particles.

4 CONCLUSIONS

Within the context of offshore wind design, the opportunity for an intelligent robotic site investigation tool has been highlighted. The initial design and specification of a horizontal (*p-y*) modular section of ROBOCONE has been presented, alongside preliminary bench verification and chamber tests in sand that validate its ability to impose complex stress paths and obtain force-displacement curves. It is essential that these tests are carried forward using a fully developed device with a larger range of soil types to obtain 'whole-life' soil reaction curves, supporting the advanced design of complex infrastructure.

ACKNOWLEDGEMENTS

The authors would like to acknowledge the financial support from the EPSRC (Ref: EP/W006235/1) and SFI (Ref: 21/EPSRC/3787). SG is supported by the RAEng through the Chair in Emerging Technologies scheme. DW is supported by the EPSRC Supergen ORE Hub, grant (Grant EP/S000747/1).

REFERENCES

Creasey, J., Hajjar, A.E., Diambra, A., et al. (2023). Motivation and demonstration of robotic tooling for ground characterization: the ROBOCONE. Proc. 9th Int. Conference on Offshore Site Investigation and Geotechnics 2023.

Gourvenec, S. (2020). Whole-life geotechnical design: What is it? What's it for? So what? And what next? Proc. 4th Int. Symp. Frontiers in Offshore Geotechnics. 206-246.

GWEC. (2023). Global Wind Report 2023. Global Wind Energy Council.

HM Govt. (2022). British Energy Security Strategy: Secure, clean and affordable British energy for the long term. 4/22.

Mayne, P. (2001). Stress-strain-strength-flow parameters from enhanced in-situ tests. Proc, Int. Conf. In-Situ Measurement of Soil Properties & Case Histories, Bali, Indonesia, 27-48.

White, D. (2022). CPT equipment: Recent advances and future perspectives. Proc. 5th Int. Symp. on Cone Penetration Testing, CPT22.

Proceedings of the XVIII ECSMGE 2024
GEOTECHNICAL ENGINEERING CHALLENGES
TO MEET CURRENT AND EMERGING NEEDS OF SOCIETY
© 2024 the Authors
ISBN 978-1-032-54816-6
DOI 10.1201/9781003431749-563
Open Access: www.taylorfrancis.com, CC BY-NC-ND 4.0 license

ECSMGE 24
XVIII EUROPEAN CONFERENCE ON SOIL MECHANICS AND GEOTECHNICAL ENGINEERING

Effects of stabilization on the behaviour of Finnish sensitive soils

Effets de la stabilisation sur le comportement des sols sensibles Finlandais

M. Di Sante*, G. Di Luigi, I. Bellezza, F. Mazzieri, E. Fratalocchi
Università Politecnica delle Marche, Ancona, Italy

B. Di Buò, T. Länsivaara
Tampere University, Tampere, Finland

**m.disante@univpm.it*

ABSTRACT: The proposed note presents the results of an experimental activity aiming at studying the hydraulic and mechanical behaviour of a Finnish sensitive soil treated by fly ash and lime. A laboratory testing program was carried out both on treated and untreated soil; soil-binders samples were prepared by wet mixing of the components and by Standard Proctor compaction. Hydraulic conductivity tests were carried out in flexible wall permeameters; the compressibility was studied by incremental load oedometric tests. The results have shown a general increase of the hydraulic conductivity and a significant reduction in compressibility after binders addition; the extent of modification of soil properties was observed to depend upon the compaction water content of the soil. The soil treatment is generally economically convenient if compared to disposal in waste landfills, which would represent the only alternative for the soil type of concern. In addition, if a by-product such as fly-ash is able to act as effective binder in the mixture, this surely constitutes a promising perspective in terms of sustainability in the field of earthen structures.

RÉSUMÉ: La note proposée présente les résultats d'une activité expérimentale visant à étudier le comportement hydraulique et mécanique d'un sol finlandais sensible traité aux cendres volantes et à la chaux. Un programme d'essais en laboratoire a été réalisé sur du sol traité et non traité. Les échantillons de sol modifié aux liants ont été préparés par mélange humide des composants et compactage Standard Proctor. Les tests de conductivité hydraulique ont été réalisés avec des perméamètres à parois flexibles; la compressibilité a été étudiée par des essais oedométriques à charges incrémentales. Les résultats ont montré une augmentation générale de la conductivité hydraulique et une réduction significative de la compressibilité après l'ajout de liants; les degré de modification des propriétés du sol a été différent en fonction de la teneur initiale en eau du sol. Généralement, le traitement du sol est économiquement avantageux par rapport à la mise en décharge, qui représenterait la seule solution alternative pour le type de sol concerné. De plus, si un sous-produit tel que la cendre volante est capable d'agir comme liant efficace dans le mélange, cela constitue sûrement une perspective prometteuse en termes de soutenabilité dans le domaine des constructions en terre.

Keywords: Soil reuse; sensitive soils; stabilization.

1 INTRODUCTION

Fostered by the objectives of the recent European Green Deal, global societies share the target of implementing reuse practices and search for innovative technical solutions to reduce overall waste generation thus limiting landfilling and carbon emissions. Environmental geotechnics, in particular the field of ground improvement techniques, can surely contribute to reach these goals allowing for the reuse of treated excavated soils in earthen structures.

Several studies (e.g. Blengini et al., 2010) indicate that the re-use of excavated soils and rocks saves up to 14 kg CO_2 per ton and 250 MJ/ton of non-renewable energy as transport, landfilling and collection from quarries are reduced. Soil stabilization allows for the reuse of excavated soil by treating it with different additives. If the binder used in the mixture is a by-product from industrial processes, this will additionally contribute to the sustainability goal.

1.1 Soil stabilization by lime

Lime is nowadays commonly used as binder for clayey soil stabilization. In addition to the need of extracting limestone for lime production, the process itself causes the emission of 1006.5 kg CO_2/ton of lime (Zhang et al., 2019). On the other hand, its potentiality is well known and testing standards and construction procedures have been fully finalized (e.g., Di Sante et al., 2014; Beetham et al., 2014).

When treating a clayey soil with lime, cation exchange reaction firstly develops (and consequent aggregation of clayey particles) and then lime reacts with silica and alumina producing long-term pozzolanic products (reaction fostered by high pH environment).

The treatment improves the mechanical characteristics of a soil (increase in strength and reduction in compressibility), whereas, hydraulic conductivity usually increases taking into account the compaction water content effect (Bhattacharia et al, 2003; Bellezza et al.,2006; Di Sante et al., 2016).

1.2 By-products for soil stabilization

Developing a strategy to employ production scraps as binding agents for soil stabilization unquestionably constitutes a significant stride within the context of sustainable methodologies. By-products currently studied for soil stabilization include rice husk ash, mushroom waste, wet olive pomace, marble powder, ground granulated blast furnace slag or fly ash (Devi et al., 2020). The latter develops cementitious products if alkali activated with hydroxides acting as strong bases in the soil-binders-water system (Costa et al., 2023). The high alkaline environment fosters the dissolution of silicates and aluminates coming both from the ash and from the clay fraction of the soil, thus cementation reactions.

1.3 Soft sensitive soils

Soft sensitive clays can be found in the coastal areas of Scandinavia, as well as in some part of North America and Asia. The high compressibility, low undrained shear strength and high sensitivity shown by these soils make the geotechnical design often rather challenging. The degree of sensitivity is expressed by the ratio between the undrained shear strength of an undisturbed specimen and the strength of the same specimen at the same water content but in a remoulded condition (Torrance, 1974; Rosenqvuist, 1953; Bjerrum, 1954). The essential factors for development of high sensitivities can be divided into depositional and post-depositional factors (Torrance 1974). Of depositional factors most important is inter-particle flocculation, which is necessary to create open structure high water content sediments. Most of these clays are deposited in marine to brackish environment, where the ions in salty water reduce the repulsive forces between the soil particles allowing flocculation. In fresh water similar response may be due to sufficiently high concentrates of calcium. Out of post depositional factors the one having most impact is leaching. When the salinity decreases the open structure remains, but repulsive forces between the soil particles increase, reducing the liquid limit and remolded shear strength. Such high sensitivity clays with a remoulded shear strength below 0.5 kPa are often classified as quick clays.

Soft sensitive clay deposits are mainly located along the coastal regions of southern Finland. Inland, various local conditions manifest, such as the presence of intermediate soils like clayey silt or silt. While these soils might arise from similar geological processes, they exhibit distinct mechanical behaviors and mineral compositions.

In the present note, experimental results on soil-lime-fly ash mixtures are presented, focusing on hydraulic conductivity and compressibility. Results are discussed also in comparison with those of the untreated compacted soil. The present work is the result of an established research cooperation between Università Politecnica delle Marche, Ancona – Italy and Tampere University, Tampere – Finland.

2 MATERIALS AND TEST METHODS

2.1 Materials

The studied soil is a clayey silt of low plasticity, characterized by a medium-high sensitivity (Sensitivity index=31.4 - Rankka et al., 2004) taken from the Kouvola site in the southern part of Finland, 135 km east of Helsinki. It is worth highlighting that the remoulded strength of the soil is equal to5 kPa, higher than the usual values registered for sensitive clays (<1 kPa). Soil characteristics are summarized in Table 1.

Table 1. Soil properties(ICL=Initial Consumption of ime).

Property	Value	STANDARD
sand (%)	22	ASTM D422-63(07)
fine (%)	78	ASTM D422-63(07)
clay (<2μm,%)	24	ASTM D422-63(07)
Liquid Limit (%)	28	CEN ISO/TS17892-12
Plasticity Index (%)	16	ASTM D4318-05
ICL - %CaO	3	ASTM C977-00
CEC (meq/100g)	8.6	CUR n.33 EUBA2002
Specific surf. (m^2/g)	77	CUR n.33 EUBA2002

The X-Ray diffraction spectrum (Philips diffractometer, PW1730 X-ray generator, PW 1050/70 goniometer and CuK radiation) is displayed in Figure 1: the main mineralogical components include Quartz, Albite, Muscovite, Chlinochlore (chlorite group), Amphibole and Sanidine (potassium Feldspar).

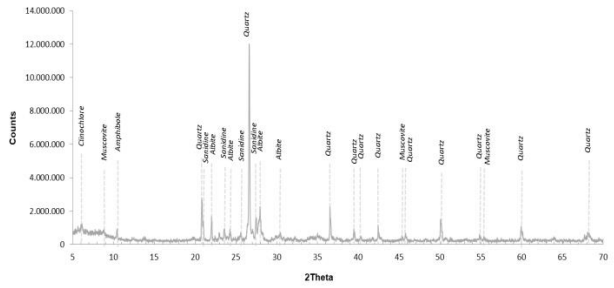

Figure 1. X-Ray diffraction spectrum of the soil.

The amounts of sulphate and organic matter are 0.01% and 1.31% by dry mass of soil, respectively. The studied soil fully matches the requirements for the suitability for lime treatment.

The lime used (QL) is a fine calcic quicklime, classified as CL80-Q dp (UNI EN 459-1).

The Fly Ash (FA) is a high pozzolanic fly ash (supplied by General Admixtures SpA). Its unit weight is 2200 kg/m^3. Microstructural and chemical investigation was performed on the FA by means of SEM observations and Energy Dispersive X-Ray Spectroscopy, EDS (FESEMSUPRA40–ZEISS), after air dewatering of samples and their gilding (by an Emitech K550 sputter coater). SEM image of spheroidal particles of the FA is displayed in Figure 2. EDS highlighted the presence of 45% Silicon, 23% Aluminum, 10% Iron, 10% Calcium, 4% Potassium and 7% other components (% by weight, excluding Oxygen).

The X-Ray diffraction spectrum highlights the presence of silicon dioxide (quartz), calcium oxide and mullite ($Al_{4.56}$ $Si_{1.44}$ $O_{9.72}$) as main components.

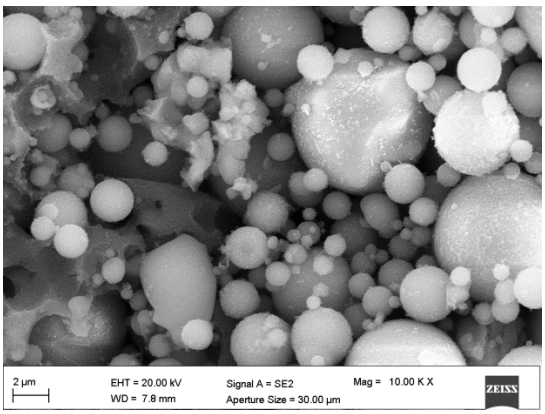

Figure 2. SEM images of the FA (Magnification:2000x).

2.2 Test methods

All the specimens for the laboratory geotechnical tests were prepared by crumbling the air dried soil (to 2 mm in size), adding the amount of water necessary to reach the desired moisture content, then mixing binders and soil at the wet state (as usually done in the field) until a uniform distribution was achieved. The only exception was done for the soil at w_{Nat}, for which lime was added "as is". The soil mixtures was then compacted according to the Standard Proctor procedure (ASTM D698-12) in one layer, obtaining samples of 101 mm in diameter and 40 mm in height. The samples were then cured in sealed plastic containers at a temperature of 20±1°C.

One-dimensional incremental load consolidation tests (ASTM D24345-11) were performed on specimens after 7 days of curing.

Permeability tests (ASTM D5084-10) were carried out in flexible walls permeameters at 35 kPa of effective confining stress with tap water as permeant. The tests on the treated specimens were carried out for 20 days of curing.

Also pH trend with time is monitored by daily measuring pH in the slurry of the mixture of concern (20g of dry soil+2%FA+2%QL+100ml of distilled water).

3 RESULTS AND DISCUSSION

In order to set the mix design for the experimental program, being the ICL value equal to 3% by dry weight of soil (Table 1) and given that ICL+1-2% is usually the promising value to be tested in lab phase of lime stabilization studies, a total amount of 4% of binders was fixed. Aim of the present research work is to test the efficacy of the use of by products as binders for soil stabilization. For this reason soil was treated with 2% of FA combined with 2% of QL. The latter has the double function of acting both as a stabilizer and as activator of the FA.

The first important experimental results is that the soil lost its sensitive behaviour once treated.

3.1 Compaction

Compaction curves of the untreated soil and of soil treated with binders are shown in Figure 3.

Binders addition slightly reduces the optimum water content from 20% to 19%. In Figure 3 it is possible to identify in 14-23% the range of water contents able to guarantee a sufficiently high dry unit weight (considered higher than 95% of the γ_{dmax}, as reported in most of technical specifications for construction works).

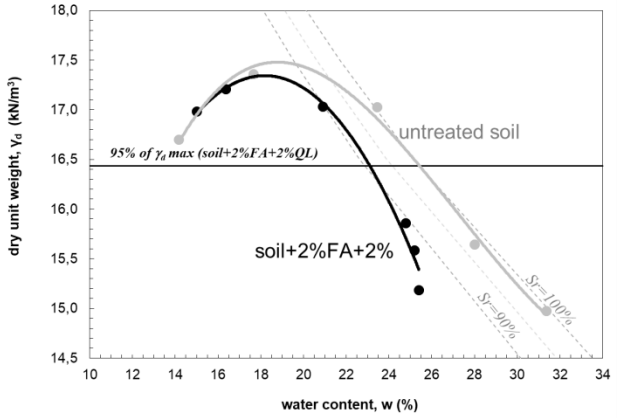

Figure 3. Proctor compaction curves of treated and untreated soil.

It is worth noticing that binder addition systematically reduces of 2-4 percent points the water content mainly due to CaO hydration process (oxide coming from both QL and FA).

3.2 Compressibility

Figure 4 shows the results of the one-dimensional compression tests performed starting from 7 days of curing on specimens of soil-FA-QL mixtures and of untreated soil, both compacted at w_{Nat}.

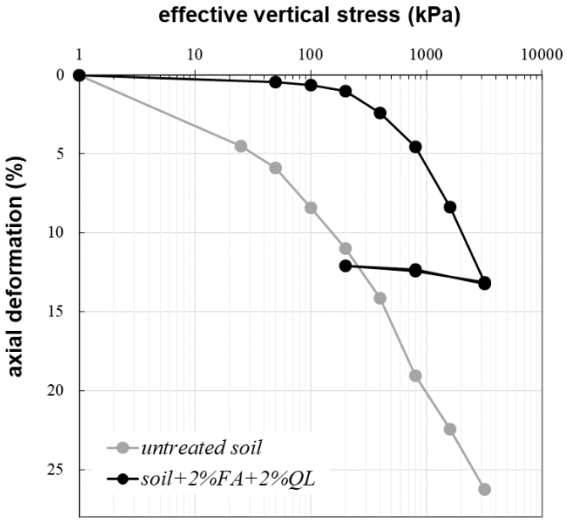

Figure 4. Compressibility curves of the untreated soil: and treated with 2%FA+2%QL (7days of curing).

The significant reduction in compressibility caused by binders addition is evident. In particular, at the range of 50-100 kPa of effective vertical stress (typical values for designing of earthworks, e.g. road embankments) axial deformation of the treated specimen is almost 10 times lower than that of the untreated compacted soil (8% deformation at 100kPa). When the vertical confining stress is increased, the untreated soil showed a maximum axial deformation of 26% that is reduced to 13% after FA+QL addition. The yield stress of the treated soil is 200 kPa while it is not possible to identify any yeld stress for the untreated compacted soil.

3.3 Hydraulic conductivity

Hydraulic conductivity values, k, are shown in Figure 5 as a function of the curing time. An increase in k values due to binders addition is evident when comparing data for treated and untreated soil compacted at w_{Nat} (grey and black circles in Figure 5). This increase is probably due to the aggregation of clay particles after cation exchange reaction. For the sample compacted at w=18% (w=15% after binder addition) k values (blak diamonds in Figure 5) are 2 order of magnitude higher than those of the treated sample compacted at w_{Nat}.

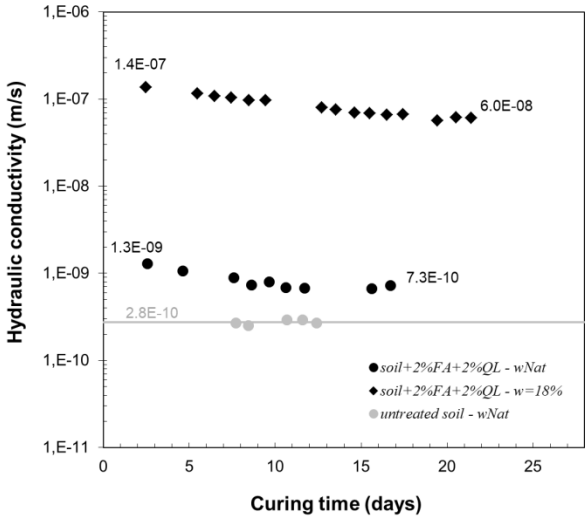

Figure 5. Hydraulic conductivity of treated and untreated compacted samples.

In addition, the treated samples show significant decreasing trend with curing (k values attained after 14 days of curing is half of the initial k). This trend is typically caused by gel form of pozzolanic products that partially fill the inter-aggregate porosity resulting from cation exchange (Beetham et al., 2014). Pozzolanic products are formed due to both hydration of fly ash and reaction of calcium ions supplied by lime and silicates and aluminates from clay fraction of the soil.

Measurements of pH of slurry of the mixture soil+2%FA+2%QL (Figure 6) corroborates this findings showing a continuously decreasing trend. In fact, in pozzolanic reactions, each calcium ion reacting with SiO_2 links 2 hydroxil ions thus causing the decrease in pH values.

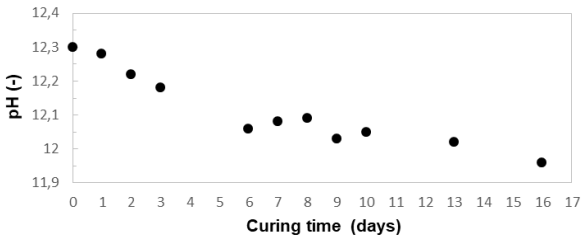

Figure 6. pH values - slurry of soil+2%FA+2%QL.

4 CONCLUSIONS

The combined use of fly ash and lime demonstrated to be a sustainable solution for the stabilization of the Finnish soil of concern. In particular, for the considered soil-fly ash-lime mixture, a general increase in hydraulic conductivity due to the addition of binders is observed. Permeability turns out to be very sensitive to a reduction in water content showing an increase of 2 orders of magnitude. Pozzolanic reaction development contributes to reduce the permeability in the long term (within 1 order of magnitude). Compressibility is significantly reduced 7 days after the treatment.

The soil treatment is generally economically convenient if compared to disposal in waste landfills, which would represent the only alternative for the soil type of concern. In addition, if a by-product such as fly-ash is able to act as effective binder in the mixture, this surely constitutes a promising perspective in terms of sustainability in the field of earthen structures.

The present work represent a preliminary feasibility study that should be completed with micro-structural investigation, strength tests and an in-situ test-pad.

REFERENCES

Beetham P., Dijkstra T., Dixon N., Fleming P., Hutchinson R., Bateman J. (2014). Lime stabilisa-tion for earthworks: a UK perspective. *Proc. Inst, Civ. Eng. – Ground Improvement*, 168(GI2): 81-95. https://doi.org/10.1680/grim.13.00030

Bellezza, I and Fratalocchi, E (2006). Effectiveness of cement on hydraulic conductivity of compacted soil–cement mixtures. *Proc. Inst, Civ. Eng. – Ground Improvement,* 10(2):77–90. https://doi.org/10.1680/grim.2006.10.2.77

Bhattacharia S., Bhatty J.I. and Todres H.A (2003). *Stabilization of clay soils by Portland cement or lime - A critical review of literature*. PCA R&D Serial No. 2066, Portland Cement Associ-ation, Skokie Illinois USA, 60.

Bjerrum, L.(1954). Geotechnical properties of Norwegian marine clays. *Geotechnique* 4(2): 49-69.

Blengini and Garbarino, (2010). Resources and waste management in Turin (Italy): the role of recycled aggregates in the sustainable supply mix. *J Clean. Prod.* 18: 1021–1030. https://doi.org/10.1016/j.jclepro.2010.01.027

Costa, L.T., Vitale, E., Cappelletti, P., Graziano s.f., Rispoli, C. and Russo, G. (2023). Alkaline activation of volcanic ash as binder for soil improvement. *Proceedings of the 8th Italaian Conference of researchers in Geotechnical Engineering*, Ferrari Rosone Ziccarelli Gottardi (eds.), Springer, pp. 792-799.

Devi, k., Chhachhia, A. and Kumar, A. (2020). Soil Improvement using waste materials: a review. *J. of Build. Mat.Sci*. 2(1): 11-17. https://doi.org/10.30564/jbms.v2i1.2641

Di Sante, M., Fratalocchi, E., Mazzieri, F. and Pasqualini, E.(2014). Time of reaction in a lime treated clayey soil and influence of curing conditions on its microstructure and behaviour. *Appl. Clay Sci*. 99: 100-109. https://doi.org/10.1016/j.clay.2014.06.018

Di Sante, M., Fratalocchi, E., and Mazzieri, F. (2016). Effects of variation in compaction water content on geotechnical properties of lime-treated clayey soil. *Procedia Eng*., 158:63-68. https://doi.org/10.1016/j.proeng2016.08.406

Rankka, K., Andersson-Sköld, Y., Hultén, C., Larsson, R., Leroux, V., and Dahlin, T. (2004) Quick clay in Sweden. SGI. Linköping.

Rosenqvist, I.T.(1953). Considerations on the sensitivity of Norwegian quick-clays. *Geotechnique* 3(5): 195-200.

Torrance, J.K. (1974). A laboratory investigation of the effect of leaching on the compressibility and shear strength of Norwegian marine clays. Norwegian Geotechnical Institute Publication N.104

Zhang, R., Long, M. and Zheng,J.(2019). Comparison of Environmental Impacts of two alternative stabilization Techniques on expansive soil slopes. *Advances in Civ. Eng*. 19: 1-13. https://doi.org/10.1155/2019/9454929

Proceedings of the XVIII ECSMGE 2024
GEOTECHNICAL ENGINEERING CHALLENGES
TO MEET CURRENT AND EMERGING NEEDS OF SOCIETY
© 2024 the Authors
ISBN 978-1-032-54816-6
DOI 10.1201/9781003431749-564
Open Access: www.taylorfrancis.com, CC BY-NC-ND 4.0 license

ECSMGE 24
XVIII EUROPEAN CONFERENCE ON SOIL MECHANICS AND GEOTECHNICAL ENGINEERING

Class A predictions for centrifuge modelling of uplift induced instabilities of river embankments

Prévisions de classe A pour la modélisation en centrifugeuse des instabilités des berges induites par les pressions de soulèvement

E. Dodaro*, G. Gottardi
University of Bologna, Department of Civil, Chemical, Environmental and Materials Engineering, Bologna, Italy

M. Pirone, C. Mancuso
University of Napoli Federico II, Department of Civil, Building and Environmental Engineering, Napoli, Italy

R. Ventini
Ministry of Infrastructures and Transport, Interregional Public Works Department, Firenze, Italy

D. Giretti
University of Bergamo, Department of Engineering and Applied Science, Dalmine, Italy

C.G. Gragnano
Laboratoire Navier, Ecole des Ponts ParisTech, Gustave Eiffel University, CNRS, Marne-la-Vallée, France

V. Fioravante
University of Ferrara, Engineering Department, Ferrara, Italy

F. Zarattini, F. Gabrieli
University of Padova, Department of Civil, Environmental and Architectural Engineering, Padova, Italy

**elena.dodaro2@unibo.it*

ABSTRACT: Flood events caused by the collapse of water-retaining earthworks are recognized as one of the most impactful natural disasters, affecting both urban and rural environment, as well as society and economy. The understanding of the peculiarities of different failure mechanisms is crucial for explaining the causes of breaching and assessing the safety of both new and existing earth infrastructures, under different hydraulic loading scenarios. This paper investigates the potential instability of the landside slope induced by high uplift pressures beneath the toe of a river embankment. This complex failure mechanism is largely influenced by the stratigraphy of the foundation soil and it might occur when embankment is constructed on alluvial plains with silty or clayey blankets overlying sandy soil strata, which act as preferential flow channel between the water basin and the landside. Results of a numerical predictive study carried out with the finite element method (FEM) on an unsaturated river embankment model, characterized by this peculiar subsoil layout, are presented and discussed. The impact of different thickness of the fine-grained layer on the potential failure mechanism has been evaluated, showing that this mainly affects the onset time of failure and the hydrometric level associated with its triggering. The analyses here presented provided fundamental insights for the design of a physical model test in a centrifuge.

RÉSUMÉ: Les inondations provoquées par l'effondrement des ouvrages de retenue d'eau sont parmi les catastrophes naturelles les plus dévastatrices, affectant tant les milieux urbains que ruraux, ainsi que la société et l'économie. Comprendre les divers mécanismes de défaillance est crucial pour expliquer les ruptures et évaluer la sûreté des infrastructures existantes et nouvelles, en tenant compte des conditions hydrauliques changeantes. Cet article se penche sur l'instabilité potentielle des talus terrestres, déclenchée par des pressions de soulèvement sous le pied d'une digue fluviale. Ce mécanisme complexe est largement influencé par la stratigraphie du sol de fondation et survient souvent lorsque la digue est érigée sur des plaines alluviales, avec des couches limoneuses ou argileuses recouvrant des strates de sol sableux, servant de voies de circulation privilégiées entre le bassin hydrographique et le talus. Les résultats d'une étude numérique utilisant la méthode des éléments finis sur un modèle de digue non saturée sont présentés, fournissant des orientations essentielles pour la conception de tests en centrifugeuse. L'impact de différentes épaisseurs de la couche de grains fins sur le mécanisme de défaillance est évalué, démontrant que l'épaisseur influe principalement sur le moment et le niveau de déclenchement de la défaillance. Ces analyses sont cruciales pour la conception de tests en centrifugeuse afin d'étudier les phénomènes physiques à petite échelle.

Keywords: River embankments; FEM numerical modelling; uplift pressure.

1 INTRODUCTION

Due to its profound impacts on the population, communication infrastructures, and economic and productive fabric, hydrogeological instability associated with the collapse of water-retaining earth structures constitutes a relevant issue for European countries. Therefore, identifying the main factors that adversely affect river embankment stability and trigger failure conditions is of particular concern for researchers and geotechnical engineers and represents a fundamental step for the optimal design and assessment of this critical infrastructure.

River embankment failure, defined as the inability to prevent the inundation of the area surrounding a watercourse, may occur due to various hydraulic and structural causes, such as overtopping, seepage flow through the embankment body and foundation layers, internal and external erosion, macro-instabilities of the slopes, scour and liquefaction (Van et al., 2022). Among macro-instabilities, it is possible to distinguish two mechanisms induced by the development of uplift pressures underneath the toe of the embankment that might lead to collapse: *(i)* backward erosion piping, involving the erosion and transportation of sand particles from the aquifer underlying a water-retaining structure, driven by underseepage forces; *(ii)* instability of the external slope of the embankment, due to a localized reduction in soil shear strength within the foundation.

This paper focuses on the second mechanism, which might occur when the subsoil is characterized by a shallow soft fine-grained layer, overlying a highly permeable sandy one, directly connected with the river and acting as a preferential channel between the reservoir and landside. In particular, if the water level increases, high pore water pressures can build up at the interface between the fine-grained and sandy layers, exceeding the overburden stress of the blanket on the landside. This circumstance may result in localized toe uplift and, simultaneously, favour the progression of a slip surface in the embankment body, resulting in a potential collapse, as evidenced in ICOLD (2013).

Despite the increasing occurrences of river embankment failures, there is a shortage of well-documented case studies of embankment collapse triggered by pore pressure build-up at the toe, with the exception of notable investigations carried out on some specific events. These include the embankment failure at Dartfort Lock (UK) in 1953, attributed by Cooling and Marsland (1953) to fine fissuring, as consequence of the abnormally high tides, which caused the development of high pore-water pressure in the underlying permeable sandy gravel layer. In the same year, a flood embankment collapsed at Crayford Marshes, on the south side of the River Thames, due to excessive pressures beneath the stratum of peaty clay alluvium, leading to slope instability of the outward face. In the Netherlands, the collapses of Wolpherense and Streefkerk river embankments in 1981 and 1984, respectively, have been also attributed to uplift pressures (Van et al., 2005), as well as the instability of a segment of the Adige river embankment near to San Floriano (Italy) in 1981, as reported by Amabile et al. (2020). In 2013 an embankment failure near Breitenhagen (Germany), was triggered by a localized weakness of the soil and to unexpected high water pressures, due a connection between a pond on the riverside of the earth structure and the aquifer (Kool et al., 2021).

To shed light on this complex failure mechanism, fully coupled flow-deformation analyses have been carried out using the software PLAXIS 2D (2021), on a river embankment model, subjected to a simulated river stage increment. The earthwork is characterized by an unsaturated silty sand embankment, supported by a fine-grained foundation overlying a sandy aquifer. Parametric analyses have been conducted by varying the thickness of the clayey silt foundation layer to explore its influence on the onset time of failure and to predict the critical hydraulic head, able to trigger the embankment failure. The results of the simulations are presented and discussed hereafter.

These findings provided crucial insights for the design of a centrifuge model test, executed at the Istituto Sperimentale Modelli Geotecnici - ISMGEO (Bergamo, Italy). To this aim, numerical simulations have been performed by considering the reduced physical model dimensions, to replicate the stress states expected during all the stages of the experiment. Further seepage and stability analyses were carried out at the prototype scale using various software on the same river embankment model and the outcomes of these studies are detailed in Girardi et al. (2023).

2 NUMERICAL MODELLING

2.1 Geometry and materials

The geometry of the river embankment numerically analysed is shown in Figure 1, along with control points for displacements. It refers to a small-scale physical model. In centrifuge modelling the geometrical similitude (Garnier et al., 2007) is expressed by Eq. (1):

$$L_m/L_p = 1/N \quad (1)$$

where N is the scale factor for acceleration (i.e. $a_m=N\,a_p$), L_m and L_p are characteristic lengths of model and prototype, respectively. In the present case the model acceleration, a_m, has been assumed equal to 50 times the gravity. The embankment body is characterized by a height of 150 mm, a 60 mm wide crown and slopes inclination of 1H:1V and 1H:1.5V for the riverside and the landside, respectively (Figure 1). The model has been numerically discretized with 4864 fifteen-triangular elements, with an average element size of 0.01 m. The foundation consists of a clayey silt deposit underlying a sandy layer, which extends beyond the landside toe and is hydraulically connected to the water basin on the riverside.

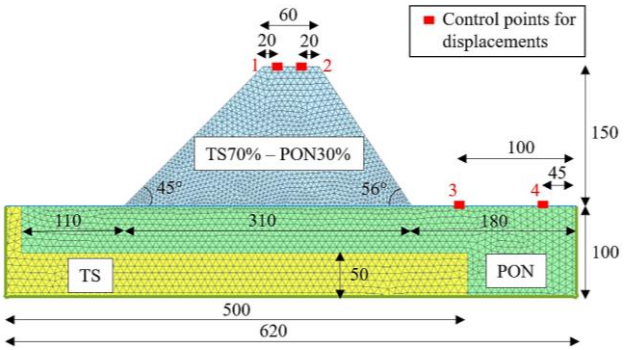

Figure 1. Geometry of the embankment section numerically analysed (in the case of 2.5 m-thick PON layer) in PLAXIS 2D - length unit at the model scale (in mm).

The filling material selected for the embankment body, typically constituted by a heterogeneous mix of sands and silts, is a compacted mixture of 70% by weight of Ticino Sand (TS, a uniform, coarse to medium, clean sand) and 30% of Pontida Clay (PON, a sandy clayey silt), while for the upper layer of the subsoil, which frequently consists of clayey and silty strata, deposited in a floodplain environment, a homogeneous consolidated layer of PON is considered. For the aquifer a compacted TS layer has been adopted. The main index and physical properties of the three materials can be found in Fioravante and Giretti (2016) and Ventini et al. (2021). The optimum moisture content (w = 8.8%) and dry density (γ_d = 20.60 kN/m^3), determined using the Standard Proctor compaction energy, are taken as reference for the initial state (at 1g, i.e. before centrifuge acceleration) of the TS70% - PON30% mixture, while a pre-overburden vertical effective stress of 800 kPa has been considered for the PON layer. A relative density equal to 80%, with a water content of 5%, has been assumed to define the initial conditions of the TS layer.

2.2 Mechanical and hydraulic soil properties

The mechanical behaviour of the materials is modelled with the hardening soil (HS) constitutive model, developed by Duncan and Chang (1970) under the framework of the plasticity theory. Soil strength and stiffness parameters, calibrated based on specific laboratory procedures - extensively discussed in Ventini et al. (2021) - and assumed as input in the finite element analyses, are listed in Table 1.

Table 1. Mechanical properties of the embankment and foundation units, according to HS constitutive models.

Soil		TS	TS70%-PON30%	PON
E	-	0.644	0.314	0.440
k_{sat}	m/s	$3.45\cdot10^{-5}$	$1.23\cdot10^{-7}$	$4.34\cdot10^{-9}$
γ_{dry}	kN/m^3	15.89	20.36	18.85
γ_{sat}	kN/m^3	20.00	22.30	21.09
N	-	0.256	0.233	0.200
c'	kPa	0.1	5.0	4.0
φ'	°	41	46	33
$E_{50,\,ref}$	kPa	19800	22000	6000
$E_{oed,\,ref}$	kPa	14143	15000	4500
$E_{ur\,ref}$	kPa	59400	60000	20000
m	-	0.5	0.5	1.0
$K_{0,NC}$	-	0.344	0.287	0.455
OCR	-	1.0	1.0	6.9
POP	kPa	0	0	800

Hydraulic and retention properties of the mixture and PON, accurately estimated from constant head permeability tests, evaporation tests and high-range psychrometric measurements (Dodaro, 2023) are listed in Table 2, together with the saturated hydraulic conductivity of TS. The non-hysteretic van Genuchten (1980) model was adopted for the fitting of the experimental data, through the parameters g_n, g_a, g_l. It is noted that the constitutive model adopted is able to take into account the influence of suction on soil shear strength, nevertheless, the dependence of compression index, C_c, on suction and the phenomena of wetting collapse, that distinguish the behaviour of unsaturated soils, are neglected.

Table 2. Hydraulic and retention parameters considered for the fully coupled flow-deformation analyses.

Unit	k_{sat} (m/s)	S_{res} (-)	S_{sat} (-)	g_n (-)	g_a (1/m)	g_l (-)
TS 70% - PON 30%	$1.23\cdot10^{-7}$	0.057	1.000	1.240	0.821	-3.350
PON	$4.34\cdot10^{-9}$	0.000	1.000	1.455	0.070	-0.584
TS	$3{,}45\cdot10^{-5}$	-	-	-	-	-

2.3 Initial, boundary conditions and calculation stages

Imposing realistic initial conditions in terms of pore water pressure distributions is a crucial aspect when conducting transient seepage analyses of water-retaining earth structures. In the present numerical

study, a uniform value of matric suction of about 5 kPa has been initially assigned to the embankment, to reproduce the physical model preparation state. In addition, an initial water head of 0.03 m (1.5 m at the prototype scale) has been applied for the time required to attain the equilibrium of pore water pressures in the whole model and to lead the aquifer to a saturated state (Figure 4a). Regarding boundary conditions, since the model is expected to be contained in a rigid steel box, in the FE analysis, the bottom horizontal, right, and left vertical sides of the subsoil are assumed to be impermeable, with fully and horizontally fixed constraints, respectively. A zero head hydraulic condition has been assigned to the top surface of the foundation on the landside, to simulate a water outlet zone. Furthermore, to model the interaction between the foundation soil and the container walls and to account for potential flow channels, three interface elements have been included. These last are characterized by a stiffness equal to the Young modulus of the steel and a hydraulic conductivity of 10^{-5} m/s. The progressive drying of the model due to evapo-transpiration phenomena has been neglected.

To replicate the centrifuge test plot, the following five calculation stages were considered: *I*) generation of initial stresses; *II*) construction of embankment; *III*) acceleration to the target; *IV*) self-weight equilibrium; *V*) river level rise. Details concerning each phase are reported hereafter and a scheme is provided in Figure 2. Vertical and horizontal effective stress-fields have been initialized in *phase I* with the '*K0 procedure*' (PLAXIS 2D, 2021). To generate the preconsolidation stress state of the foundation strata at 1g, during the initial phase of the simulation, only the foundation layer has been activated and a pre-overburden pressure (POP) of 800 kPa has been imposed. During *phase II*, the 1g embankment construction has been simulated by means of an elastic-plastic deformation analysis ('*Plastic analysis' in* PLAXIS), in which the foundation is modelled as an undrained material, thus, excess pore water pressures have been calculated. The *'spin-up'* of the model, characterized by the gradual increase in the angular speed of centrifuge has been simulated through '*Consolidation analyses'*, by setting two different multiplier factors (*ΣM weight* equal to 24.3 and 50.6 g), uniformly applied on the whole numerical model, thus neglecting the distortion of the centrifugal field (*phase III*). Then, *'Fully coupled flow-deformation analyses'* have been carried out to simulate the dissipation of excess pore water pressure, resulting from the increase in the angular speed (*self-weight equilibrium stage, phase IV*) and to investigate the triggering of the failure mechanism caused by the rising of the water level (*flooding stage, phase V*) and the subsequent increase in the pore water pressure beneath the toe of the embankment. To identify the critical hydraulic head which would likely trigger a toe uplift mechanism, a time-dependent hydrometric condition, has been imposed on the riverside of the embankment (Figure 2). Each water level was incrementally reached at a rate of about 14 mm/min and maintained for a period of 30 minutes, corresponding to about 50 days at the prototype scale, according to centrifuge scaling laws (Garnier et al., 2007), to guarantee the establishment of a steady-state flow regime within the embankment body at each step (Figure 3). The parametric study has been conducted by varying the fine-grained layer thickness, among 0.04 m, 0.05 m, and 0.06 m, while maintaining a constant dimension for the foundation (0.1 m). Consequently, the thickness of the sandy layer was adjusted accordingly.

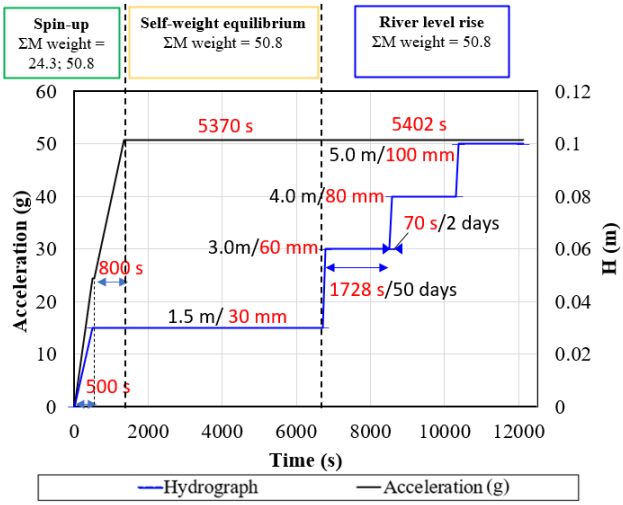

Figure 2. Time histories of the acceleration and water levels applied during the stages of the test (in red at the model scale and in black at the prototype scale) and calculation phases.

3 RESULTS AND DISCUSSION

Figure 3 shows FE numerical results, considering a 0.05 m-thick PON layer (2.5 m at the prototype scale) with reference to three significant time steps: a) at the beginning of the flooding stage (H = 0.03 m); b) at the end of the persistence of the first river stage; c) in correspondence of the triggering of the failure mechanism, occurred at H* = 0.073 m (3.65 m at the prototype scale). Following the first water level increment, a sudden increase of pore water pressures occurs in the aquifer. Then, the water level persistence leads to a progressive saturation of the lower part of the embankment body and, simultaneously, to a gradual rise in pore pressures, even in the fine-grained layer. The total deviatoric strains, initially extremely low and concentrated at the interface between PON

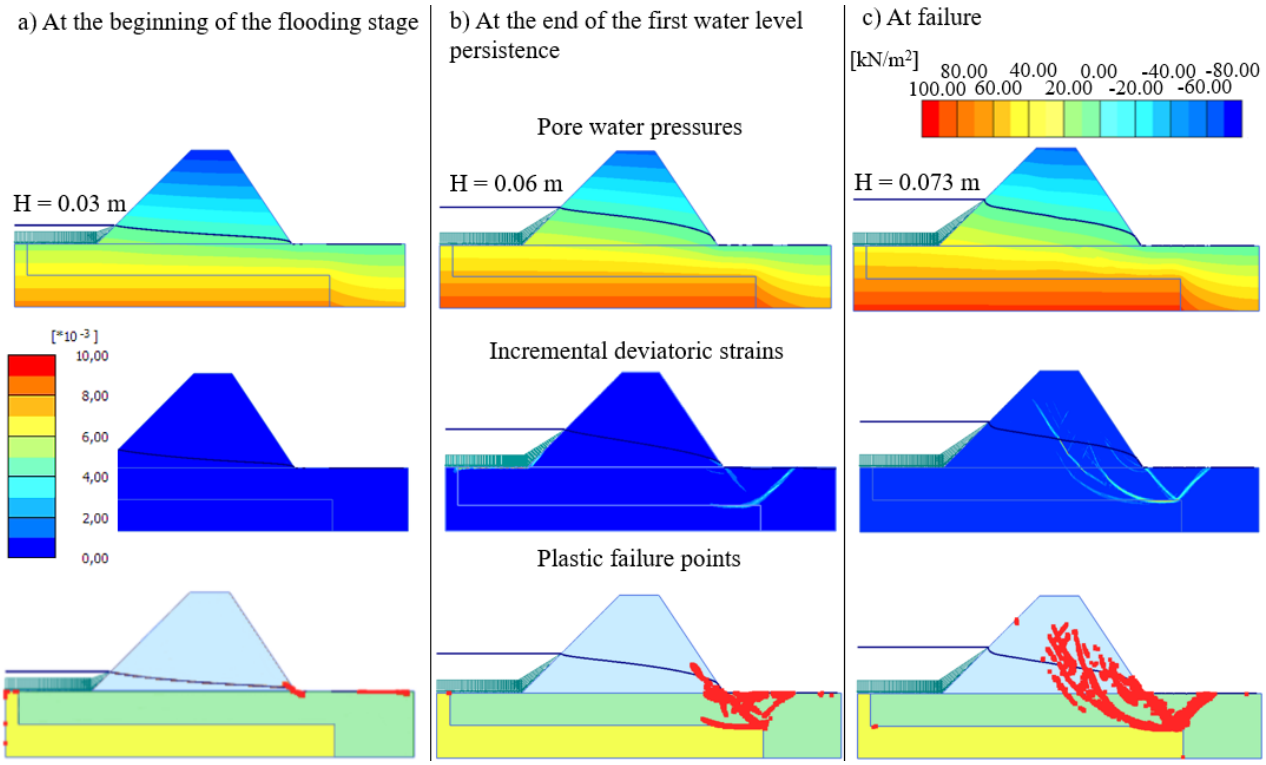

Figure 3. Pore pressures, total deviatoric strains and plastic failure points at different stages during FE analysis, considering a PON layer thickness of 0.05 m. Isoline increment = 10 kPa, phreatic surface in blue line.

and TS, gradually increase, as the phreatic surface advances within the earthfill. This progression is accompanied by a contextual decrease in vertical effective stresses in the PON layer, highlighting the shape of an instabile wedge and of potential slip surfaces within the embankment body, on the landside. Even the number of plastic failure points dramatically increase, as the hydrometric level rises to 0.073 m, suggesting a significant weakening of the embankment section, especially in correspondence of the landside toe, ultimately resulting in the collapse of the earth structure. Figure 4 reports the vertical displacement, u_y, calculated at the nodes highlighted in Figure 1, throughout all stages of the analysis conducted with the 0.05 m-thick PON layer. During the centrifuge spin-up and the self-weight equilibrium stage, a gradual ground settlement associated with the consolidation of the PON layer was observed at nodes 1 and 2, located on the crest of the embankment. The settlement tendency diminished during the persistance of the first river stage, while at the critical head H*, displacements approached a vertical asymptote, evidencing the collapse of the embankment. After an initial settlement, during the second increment in water level, the ground surface on the landside began to ascend, with node 3 experiencing a higher rate of rise than node 4, indicating the occurrence of an uplift phenomenon near the toe of the embankment.

The correlation between the thickness of the PON layer and the critical hydrometric level for the three stratigraphy investigated is notably apparent in Figure 5. In particular, the 0.04 m thick PON layer reaches a critical condition towards the end of the first water level persistence. Conversely, for thicknesses of 0.05 m and 0.06 m, the critical hydraulic heads, H*, are higher, i.e., 0.073 m (3.65 m at the prototype scale) and 0.08 m (4.0 m at the prototype scale), respectively. The foundation stratigraphy also influences the timing of failure onset. As the thickness of the PON layer increases, the time to reach conditions of potential instability also rises, as clearly highlighted by the trend depicted in red in Figure 5. Pore pressures changes and deformations detected in the FE analyses, suggest an appropriate layout for the monitoring sensors.

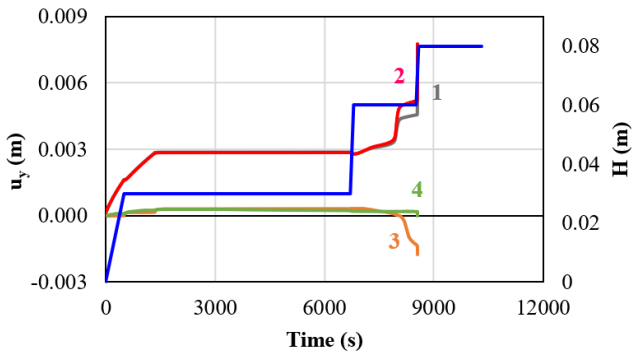

Figure 4. Vertical displacement calculated during the FE analysis on the crest of the embankment (1-2) and on the ground level on the landside (3-4). Settlements correspond to positive displacements.

This layout should include tensiometers within the embankment body; pore pressure transducers in the foundation soils, concentrated at the interface between the the fine-grained and sandy layer, and displacement sensors positioned on the crest, the outward face and near the toe of the embankment.

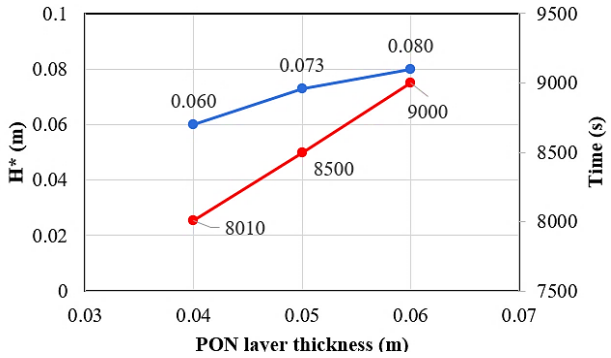

Figure 5. Effect of the PON thickness on the critical hydrometric level H (in blue) and on the time of failure onset (in red).*

4 CONCLUSIONS

This paper presents and discusses the results of a numerical study carried out to investigate a failure mechanism for river embankments caused by uplift pressures beneath the toe. The main aim was to support the design of a centrifuge test. The study examines the influence of different foundation stratigraphy on the timing of failure and the hydrometric level associated to the collapse of the earthwork. In particular, as the thickness of the PON layer increases, the critical water level rises, and collapse occurs after a longer persistence of the flood event. Additionally, recommendations regarding an appropriate instrumentation layout for the centrifuge test were provided based on the outcomes of Finite Element Method (FEM) analyses.

ACKNOWLEDGEMENTS

The Authors would like to acknowledge the financial support from MIUR (RedReef - PRIN 2017, Grant agreement 2017YPMBWJ). We would also like to thank Prof. Claudio Mancuso, our friend and colleague and tireless PI of this project, who recently passed away.

REFERENCES

Amabile, A., Pozzato, A. and Tarantino, A. (2020) Instability of flood embankments due to pore-water pressure build-up at the toe: lesson learned from the Adige River case study, *Canadian Geotechnical Journal*, 57(12), pp. 1844–1853. https://doi.org/10.1139/cgj-2018-0372.

Cooling, L. F., and Marsland, A. (1953). Soil Mechanics Studies of Failures in the Sea Defence Banks of Essex and Kent. In: *Conference on the North Sea floods of 31 January/1 February, 1953*, London, United Kingdom.

Dodaro, E. (2023). *A comprehensive experimental and numerical approach for assessing the hydro-mechanical behaviour of river embankments*, Ph.D. Thesis, University of Bologna, Italy.

Duncan, J.M. and Chang, C.-Y. (1970) Nonlinear analysis of stress and strain in soils, *Journal of the Soil Mechanics and Foundations Division*, 96(5), pp. 1629–1653. https://doi.org/10.1061/JSFEAQ.0001458.

Fioravante, V. and Giretti, D. (2016) Unidirectional cyclic resistance of Ticino and Toyoura sands from centrifuge cone penetration tests, *Acta Geotechnica*, 11(4), pp. 953–968. https://doi.org/10.1007/s11440-015-0419-3.

Garnier, J., Gaudin, C., Springman, S.M., Culligan, P.J., Goodings, D., Konig, D., Kutter, B., Phillips, R., Randolph, M.F., Thorel, L. (2007) Catalogue of scaling laws and similitude questions in geotechnical centrifuge modelling, *International Journal of Physical Modelling in Geotechnics*, 7(3), pp. 1–23. https://doi.org/10.13140/2.1.1615.3281.

Girardi, V., Dodaro, E., Ventini, R., Pirone, M., Gragnano, C.G., Giretti, D., Zarattini, F., Gabrieli, F. (2023). Numerical study of uplift induced levee failure for the design of a centrifuge test. In: *Lecture Notes in Civil Engineering*, Vol. 305, Springer, Cham, pp. 213–221. https://doi.org/10.1007/978-3-031-20172-1_20.

ICOLD (2013) Internal erosion of existing dams, levees and dykes, and their foundations. International Commission on Large Dams, Paris, France, Bulletin 164, Vol. 1: Internal Erosion Processes and Engineering Assessment.

Kool, J. J., Kanning, W., Jommi, C., Jonkman, S.N. (2021) A Bayesian hindcasting method of levee failures applied to the Breitenhagen slope failure, *Georisk: Assessment and Management of Risk for Engineered Systems and Geohazards*, 15(4), pp. 299–316. https://doi.org/10.1080/17499518.2020.1815213.

PLAXIS Connect Edition V21 (2021). *Reference manual*. Bentley Systems Incorporated. Delft, The Netherlands.

Van Genuchten, M.T. (1980) A closed-form equation for predicting the hydraulic conductivity of unsaturated soils, *Soil Science Society of America Journal*, 44(5), pp.892–898.

Van, M.A., Koelewijn, A.R., Barends, F.B. (2005) Uplift phenomenon: model, validation, and design, *International Journal of Geomechanics*, 5(2), pp. 98-106. https://doi.org/10.1061/(ASCE)1532-3641(2005)5:2(98).

Van, M.A., et al. (2022). Failure paths for levees. ISSMGE Technical Committee TC201 'Geotechnical aspects of dikes and levees'.

Ventini, R. et al. (2021) 'Experimental and Numerical Investigations of a River Embankment Model under Transient Seepage Conditions', *Geosciences*, 11(5), pp. 192. https://doi.org/10.3390/geosciences11050192.

Proceedings of the XVIII ECSMGE 2024
GEOTECHNICAL ENGINEERING CHALLENGES
TO MEET CURRENT AND EMERGING NEEDS OF SOCIETY
© 2024 the Authors
ISBN 978-1-032-54816-6
DOI 10.1201/9781003431749-565
Open Access: www.taylorfrancis.com, CC BY-NC-ND 4.0 license

ECSMGE 24
XVIII EUROPEAN CONFERENCE ON SOIL MECHANICS AND GEOTECHNICAL ENGINEERING

Design and construction carbon reductions for HS2 station road network rail overbridge with polymer geogrid reinforced soil wall abutments and wingwalls on shallow foundations

Réductions de carbone dans la conception et la construction du pont ferroviaire du réseau routier de la station HS2 avec culées de murs en sol renforcé par géogrille polymère et murs en aile sur des fondations peu profondes

C. Doulala-Rigby*, M. Dalwadi
Tensar, a Division of CMC, Blackburn, UK

J. Belton, M. Duffy-Turner
Coffey Geotechnics, Manchester, UK

R. Blackmore
Arcadis, Warrington, UK

G. Katsigiannis
Ferrovial Construction, UK

H.M.B. Al-Hashemi
Geofem, Cyprus

**crigby@tensar.co.uk*

ABSTRACT: Tensar International Limited was subcontracted by Arcadis Setec COWI (ASC) DJV working for Eiffage Kier Ferrovial BAM (EKFB) JV delivering the design and construction of Britain's High Speed Rail Main Works Civils Contract C23, to carry out the design of the load bearing bridge abutments and wing walls that will support an overbridge over Network Rail tracks at Station Road. The original concept design comprised reinforced concrete (RC) bridge abutments and L-Shaped wing walls, all founded on piled foundations. The alternative design replaced the piled RC bridge abutments and wing walls with polymer geogrid reinforced soil bridge abutments and wing walls founded on shallow foundations. Coffey Geotechnics Ltd subsequently partnered with Tensar to undertake a comparative assessment of a reinforced soil wall system against the original piled RC retaining system. This paper presents the technical solution eventually adopted by EKFB and a comparison of the embodied carbon related to the two design options. The carbon emissions compared in this assessment includes the embodied carbon at the factory gate for the main materials and carbon emissions associated with transportation, on-site construction activities and waste disposal. The paper also presents cost savings from adopting the alternative retaining system both in design and construction.

RÉSUMÉ: Tensar International Limited a été sous-traité par Arcadis Setec COWI (ASC) DJV travaillant pour le groupement d'Eiffage Kier Ferrovial BAM (EKFB), pour la conception et la construction du contrat civil C23 des principaux travaux ferroviaires à grande vitesse britanniques, pour réaliser la conception des supports de charge. Les culées du pont et les murs en aile qui soutiendront un pont supérieur au-dessus des voies du Network Rail à Station Road. Le concept original comprenait des culées de pont en béton armé (BA) et des murs d'aile en forme de L fondés sur des fondations sur pieux. La conception alternative a remplacé les culées de pont sur pieux RC et les murs en aile par des culées de pont en sol renforcé de géogrille polymère et des murs en aile fondés sur des fondations peu profondes. Coffey Geotechnics Ltd s'est ensuite associée à Tensar pour entreprendre une évaluation comparative du système de murs en sol renforcé par rapport au système de soutènement RC sur pieux d'origine. Cet article présente la solution technique finalement adoptée par l'EKFB et une comparaison du carbone incorporé lié aux deux options de conception. Les émissions de carbone comparées dans cette évaluation incluent le carbone incorporé à la sortie de l'usine pour les principaux matériaux et les émissions de carbone associées au transport, aux activités de construction sur site et à l'élimination des déchets. Le document présente également les économies de coûts résultant de l'adoption du système de retenue alternatif, tant au niveau de la conception que de la construction.

Keywords: Reinforced soil; sustainability; carbon; bridge abutments; high speed rail.

1 INTRODUCTION AND BACKGROUND

The High Speed Two (HS2) project is a High-Speed Railway Line currently under construction in the UK. Phase 1 of HS2 runs between London and Birmingham across the English Midlands. This scope is part of the HS2 Main Works Civils Contract C23, awarded to Eiffage Keir Ferrovial Bam (EKFB) JV in partnership with the design JV of Arcadis Setec COWI (ASC).

Station Road, which joins the village of Quainton to the A41 in Buckinghamshire is to be realigned to the northwest of its current location. The bridge currently carrying Station Road (Quainton Road Overbridge, MCJ2/184A) over the Marylebone to Claydon Junction (MCJ) is to be replaced to provide access to the Buckinghamshire Railway Centre (BRC) and car park.

Two new overbridges, and associated earthworks, are required to cross over the HS2 supporting earthworks and the existing Aylesbury Link Railway (MCJ) which is being replaced as part of the HS2 works. As the route is used to transport locomotives to the BRC on low-loaders, all new structures must be designed to accommodate SV100 loading. Fiddlers Field Road and Quainton Road will also be realigned.

2 DESIGN PHILOSOPHY AND DEVELOPMENT

The original scheme design of the new Station Road National Rail Overbridge comprised prestressed concrete u-beam deck fully integral with reinforced concrete (RC) abutments and wingwalls, founded on RC piles, in keeping with HS2's design philosophy of minimising maintenance over the structure design life. In order to comply with the highway alignment requirements, the bridge was skewed at 36.8 degrees.

A value engineering exercise was carried out to reduce cost and programme and improve the sustainability performance of the structure. The piled RC abutments and wingwalls were replaced with polymer geogrid reinforced soil bridge abutments and wing walls parallel to the Network Rail track and supported on shallow foundations. The original RC load bearing bridge abutments replaced with bank seats sat on top of the reinforced earth retaining wall fill.

2.1 Reinforced concrete structure

A piled solution was proposed for the structure to manage the magniture of settlement expected due to the presence of a thick deposit of firm to very stiff clay of the Oxford Clay Formation.

Each abutment was founded on a group of 8no. 1050mm diameter RC piles of 23m length. The pile caps measured 14m in length by 7.2m in width and were 1.5m deep. The abutment walls measured 14m in length by 7.2m in height. The abutment wall thickness was 2.3m

Wingwalls either side of the bridge abutments were also proposed to be founded on two rows of 1050mm diameter piles measuring 20m in length, totalling 39 piles for both sides. The wingwalls varied from 12.8m to 17.7m.in length to suit the approach embankment earthworks, accounting for the skew of the structure. The wingwall pile caps measured 1.5m in depth in 5m in width. The wingwall stem was trapezoidal in shape, with a minimum width of 300mm at the top and a 7degree slope on the back of the wall. The width of the bottom of the stem varied along the length of the structure.

The total volume of concrete required to construct the abutments, wingwalls and piles was 1,885m^3.

2.2 Reinforced soil load bearing bridge abutments and wing walls

Tensar was appointed in April 2020 to carry out the detailed design of the reinforced soil structures proposed to support Station Road Network Rail Overbridge. Reinforced soil retaining walls with near vertical faces were chosen as the preferable to form the bridge abutments and adjoining wingwalls to minimise the bridge span.

The Tensar*tech*® TW3 geogrid reinforced soil retaining wall system was used to create the near vertical face (1° incline). The system comprises four major components, namely the concrete modular face block, the HDPE uniaxial geogrid, the polymeric mechanical block connector and high quality, granularreinforced fill material.

The facing units are produced in an automated factory process in the UK using a semi-dry concrete mix with a minimum crushing strength at 28 days of 40 MPa.

The uniaxially orientated high-density polyethylene (HDPE) geogrids are produced in the UK and are subjected to all internationally recognised standards such as ISO and ASTM. The geogrids carry the European CE registration and the independent HAPAS (ex-British Board of Agrément (BBA)) certification.

The mechanical polymeric connectors are also made of HDPE to provide a high level of load transfer at the grid-block connection whilst allowing the transfer of horizontal shear loads between adjacent blocks. The shape and feature of these connectors is designed specifically for the system, is durable in all conditions and provides high efficiency connection strength.

The shear strength properties for the various soil types used for design are as shown in the table 1 below.

Table 1. Design parameters for reinforced soil wall.

Soil Type	ϕ' (°)	c' (kPa)	γ' (kN/m^3)
Reinforced Fill type 6I*[1]	42	0	20
Retained fill 6N	38	0	20
Foundation Treatment Fill Class 1A	38	0	20

*[1] Series 600 of Highways Works Specification in the UK & Maximum particle size not more than 75 mm, Percentage by mass passing 63 micron sieve (0.075 mm) less than 15%, Uniformity Coefficient – higher than 10, pH value of reinforced fill between 4-12

An added advantage of the modular block retaining system was that the individual component parts of the system listed above could be easily transported to the site seperately. In addition, the individual components are all dry laid so no curing time or formwork is necessary, minising construction programme.

2.3 Design Method

Reinforced soil modular block walls have been constructed internationally for more than 35 years. In the UK, reinforced soil structures used in bridge applications are designed in accordance with BS8006-1:2010+A1:2016. Retaining wall structures designed in accordance with this standard, incorporating polymeric geogrids, are classified as 'extensible' reinforcement and utilize a tie-back wedge design method.

Internal stability comprises two fundamental checks: failure against rupture and failure against pull-out of geogrid or adherence check. Internal stability provides the geogrid strengths and spacing that are required for a stable design.

In accordance to BS8006, an additional internal stability check was also carried out to make sure that the geogrids will not strain more than 1% under the sustained working load that they will be subjected to over their 120 year design life.

2.4 External Stability & Shallow Foundation Design

Tensar, in collaboration with Geofem Limited, developed the foundational designs of the reinforced soil abutment and wing walls for Station Road National Rail Overbridge. A two-dimensional (2D) plane strain finite element analysis (FEA) was performed using Plaxis 2D Version 22, capitalizing on the uniform geometry of the abutment and wing walls. This approach facilitated the simultaneous evaluation of potential failure modes and prediction of foundation settlement.

The modelling work aligns with the protocols set out in published papers (Lees, 2016), ensuring the adopted methods adhere to recognised industry standards.

A division of the Oxford Clay at 74.7mAOD introduced varied strength and stiffness characteristics. Boundary constraints minimized boundary effects, and groundwater levels were set at the formation level. Initial findings pointed to potential sliding, bearing failures under undrained conditions, and bearing failures in drained conditions without ground modifications. For an optimal safety margin, we implemented the following measures:

- Foundation soil replacement with Class 1A $\varphi'=38°$ and $\gamma=20kN/m^3$ material, 3.7m in depth.
- Geogrid Reinforcement length of 10m and 7.8m for the abutment and wing walls, respectively.

Fill materials adhered to the standardised Linear Elastic Perfectly Plastic (Mohr-Coulomb) constitutive models. The FEA model integrated Geogrid specifications from Tensar, accounting for the material's long-term resilience. Load assessments incorporated the fill material's self-weight density and mechanical properties FEA modelling unfolded over several phases, each contemplating diverse loading and soil scenarios for a thorough evaluation. Adjustments in soil and fill strengths were predicated on foundation soil drainage conditions, with strategies ranging from stepwise reduction to equilibrium attainment without discernible failure routes. Drained ULS (with partial factors applied only on the loads in the drained case) assessments for both structures yielded a safety factor (via shear strength reduction) exceeding 1.25 (Figure 1). Figure 2 depicts the wing wall's slip surface. For undrained ULS, partial factors modified the soil parameters, with the model converging smoothly (safety factor > 1.0). Post-construction predictions include a wall displacement of approximately 12mm, a bankseat shift close to 13mm, horizontally, vertically of ~28mm shown in Figure 3, and a peak geogrid tensile axial force of around 20kN/m in any SLS analysis. Notably, an

average additional post-construction tensile strain of 0.12% is anticipated in the lowermost geogrid layer due to prolonged foundation consolidation, remaining within accepted boundaries.

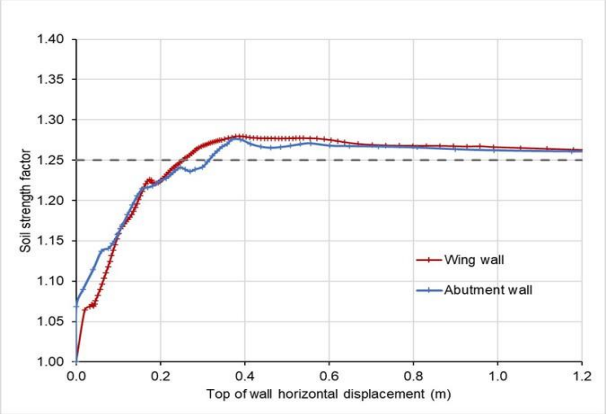

Figure 1. Drained ULS Safety Analysis.

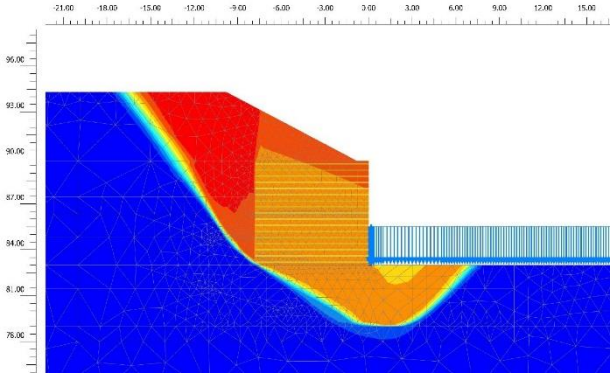

Figure 2. Slip Surface at the Wing Wall.

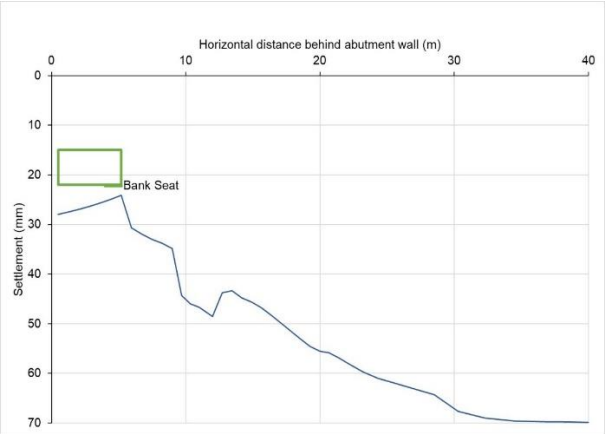

Figure 3. Deformation behind the Wall and underneath the Bank Seat.

3 CARBON CALCULATIONS

3.1 Background

The Climate Change Act 2008 committed the UK to an 80% reduction in carbon emissions by 2050, compared to 1990 levels and in 2019 this was updated to 100% reduction (Institute for Government, 2020). This made the UK the first major economy to set legally binding carbon budgets which require emissions, including those from transport, to be Net Zero by 2050. This commitment is supported by HS2's Environmental Sustainability Vision and Net Zero Carbon Plan and EKFB's target to reduce carbon emissions by 50%.

The call to measure and reduce carbon dioxide emissions comes from two directions: regulatory and commercial. Regulatory pressures arise from government drives to reduce greenhouse gas emissions in the UK and commercial pressures arise from increased client demand for information to demonstrate steps taken to limit carbon emissions.

Following the change in the design of Station Road Network Rail Overbridge, a comparison of the carbon emissions arising from the construction of RC bridge abutments and wing walls supported on piled foundations against polymer geogrid reinforced soil bridge abutments and wing walls founded on shallow foundations, was undertaken.

For the purpose of this paper, only the carbon emissions of the major elements of the wall construction have been considered, it does not take into account other things that may be included in a life cycle assessment such as storage, on site movements, removals and land use change.

3.2 System Boundaries

It is important when communicating carbon dioxide emissions that the boundaries of the calculation are known. Comparison of carbon dioxide emissions for different products can only be made if they are based within a similar set of boundaries.

This approach is in line with EKFB's Carbon Management Plan and based on PAS 2050:2011 (BSI, 2011) and BS EN 17472:2022 (BSI, 2022) and considers cradle to end of construction. The boundaries cover 'Product' module stages: 'Raw Material Supply' (A1); 'Transport'; (A2) and 'Manufacturing' (A3). It also considers 'Construction Process' module stages: 'Transport' (A4); and 'Construction Installation' (A5). The 'Use' and 'End of Life' module stages have not been considered in the calculations. Emissions have been calculated separately for the 'Product' stages (A1 to A3), 'Transport' stage (A4), and 'Construction Installation' stage (A5), and are then combined for assessment and comparison.

3.3 Process

Process maps were derived for each structural option detailing the requirements of each stage in the process. For the 'Product' modules this included manufacturing/production of the wall components including, geogrids, modular blocks and connectors, concrete, reinforcing steel and aggregate. The 'Construction Process' modules included transport of all the components (by a variety of vehicles either by train or road) and the construction elements included, but were not limited to, boring of piles, excavation of foundation, pouring of concrete for the piles, pile cap, walls, levelling pad and bankseat and placement and compaction of aggregate for the different fill types (i.e. Class 1A, 6I1 and 6N).

3.4 Collecting Data

A combination of primary and secondary data sources was used in the calculations, with primary data sources such as design drawings, details of specific transport vehicles and Environmental Product Declarations (EPDs) from manufacturers being the preferred option. Emission factors that convert activity data into carbon emissions were typically from secondary sources including the Inventory of Carbon and Energy database (Circular Ecology, 2019) and UK Government GHG Conversion Factors 2023.

3.5 Calculating the Emissions

Total CO_2 equivalent emissions to the end of construction were calculated for both bridge supports. The RC wall option was not considered at detailed design, therefore, assumptions have been made on the material quantities based on reasonable engineering judgement and typical construction practices. The concrete bankseat has been included in the Reinforced Soil wall calculations to ensure a comparable design up to the level of the bridge bearings. It is assumed that the deck construction and its ancillaries would be the same in both cases, therefore this has been omitted from the carbon emission calculation.

3.6 Results

The potential reductions in carbon dioxide equivalent emissions available by constructing a Reinforced Soil wall in comparison to a RC wall have been calculated and are shown in Figure 4.

The total calculated carbon emissions for the Reinforced Soil wall are 663 tCO2e of which 58% is in the 'Products', 35% in the 'Transport' and 7% in the 'Construction Installation'. For the RC wall there is 2,002 tCO2e of which 91% is the embodied carbon in the 'Products', 6% in the 'Transport' and 3% in the 'Construction Installation'.

The direct comparison between these two equivalent structures demonstrates that the Reinforced Soil design contributes a 66% carbon saving in comparison to the RC design.

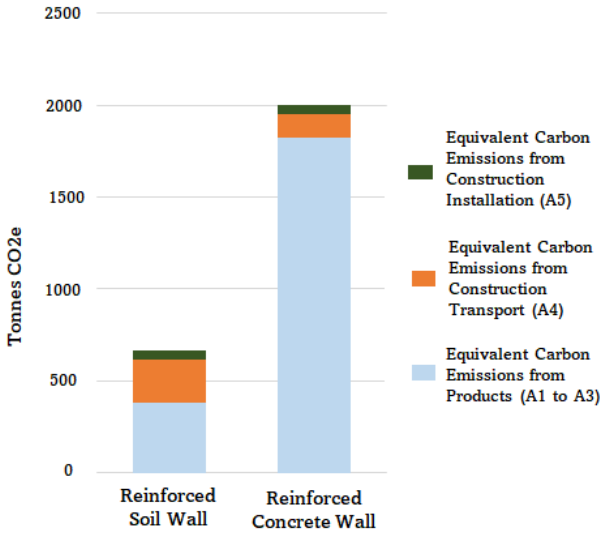

Figure 4. A comparison of the equivalent carbon emissions in both the Reinforced Soil Wall and Reinforced Concrete Wall.

3.7 Discussion

The majority of the embodied carbon in the RC wall comes from the concrete (842 tCO2e) and steel (898 tCO2e) making up 95% of the 'Product' emissions with only 5% coming from the structural fill element (85 tCO2e). Both concrete and steel production are very carbon-intensive with steel being the largest industrial source of CO_2 emissions in the UK (E&T, 2021) and cement being the largest single industrial emitter of CO_2 emissions globally (Ellis et al, 2019). These high value CO_2 emissions for concrete and steel also contribute to the Reinforced Soil wall results with the concrete reinforced bankseat comprising 36% of the embodied carbon within the 'Products' for a component which makes up only 2% of the overall volume. The remaining CO_2 emissions attributed to the embodied carbon in the 'Products' for the Reinforced Soil wall include 21% in the Reinforced Fill, 20% in the Class 1A foundation, 2% in the Class 6N behind the bankseat and 21% combined from the geogrid, modular blocks and connectors.

The CO_2 emissions calculated for 'Transport' were higher for the Reinforced Soil wall (230 tCO2e) due to the movement of a larger amount of aggregate required for the construction of the 3.7m deep foundation. Material is to be sourced from UK quarries up to 295km away from site.

The CO2 emissions for 'Construction Installation' were similar for both wall options with the Reinforced Soil wall being slightly higher at 49 tCO2e compared to 48 tCO2e for the RC wall. For the RC wall the majority of the emissions relating to construction came from the boring of 1,148 linear metres of 1050mm diameter piles. This equated to 95% of the carbon emissions in the 'Construction Installation'.

For the Reinforced Soil wall, the majority of the emissions relating to construction came from the disposal of the excavated soils for the foundation. This equated to 93% of the carbon emissions in the 'Construction Installation'. In both cases the carbon emissions generated by construction activities are small in comparison to the carbon in the 'Products' and 'Transport'.

4 COST COMPARISON

The direct comparison between the two equivalent structures demonstrates that the Reinforced Soil bridge abutment option resulted in savings of the order of 35% in comparison with the Reinforced Concrete bridge abutment supported on piled foundation.

5 CONCLUSIONS

Within the last 40+ years, polymeric geogrid reinforced structures have become established as reliable alternatives to conventional reinforced concrete structures and have been successfully used in high-risk applications like bridge abutments. This paper, through a direct comparison between two equivalent structures, has proven that a Reinforced Soil design contributes up to 66% savings in carbon in comparison with a Reinforced Concrete design, when assessing emissions from cradle to end of construction, and savings in cost of the order of 35%. Additionally, significant extra savings will be achieved in programme, personnel and plant movements.

In conclusion, in this project, by replacing the traditional RC bridge abutment construction solution with polymer geogrid-reinforced soil wall alternative, a robust, cost and carbon effective solution was provided, while championing HS2's legacy as one of the world's most sustainable high speed rail network.

ACKNOWLEDGEMENTS

The authors are grateful to High Speed 2 Ltd. for allowing us to publish this case study.

REFERENCES

British Standards Institution, 2016, *Code of practice for strengthen/reinforced soils and other fills*, BS8006-1:2010+A1:2016, HMSO, London.

British Standards Institution. 2011. PAS 2050: 2011 *Specification for the assessment of the life cycle greenhouse gas emissions of goods and services*. British Standards Institution, London.

British Standards Institution. 2022. BS EN 17472:2022. *Sustainability of construction works. Sustainability assessment of civil engineering works. Calculation methods.* British Standards Institution, London.

Circular Ecology. 2019. *ICE (Inventory of carbon & Energy) V3.0* [ONLINE] Available at: https://circularecology.com/embodied-carbon-footprint-database.html [Accessed 05 September 2023].

Ellis, L. D., Badel, A. F., Chiang, M. L., Park, R. J.-Y. & Chiang, Y.-M. 2019. *Toward electrochemical synthesis of cement—An electrolyzer-based process for decarbonating CaCO3 while producing useful gas streams*. Proc. Natl Acad. Sci. USA 117, 12584–12591 (2020).

Engineering and Technology. 2021. *EU set to race ahead of UK in green steel production* [ONLINE] Available at: https://eandt.theiet.org/content/articles/2021/05/eu-set-to-race-ahead-of-uk-in-green-steel-production/ [Accessed 08 November 2023].

Institute for Government. 2020. *UK net zero target* [ONLINE] Available at: https://www.instituteforgovernment.org.uk/article/explainer/uk-net-zero-target. [Accessed 26 September 2023].

Lees, Andrew. 2016. *Geotechnical finite element analysis: a practical guide*. ICE publishing.

Proceedings of the XVIII ECSMGE 2024
GEOTECHNICAL ENGINEERING CHALLENGES
TO MEET CURRENT AND EMERGING NEEDS OF SOCIETY
© 2024 the Authors
ISBN 978-1-032-54816-6
DOI 10.1201/9781003431749-566
Open Access: www.taylorfrancis.com, CC BY-NC-ND 4.0 license

ECSMGE 24
XVIII EUROPEAN CONFERENCE ON SOIL MECHANICS AND GEOTECHNICAL ENGINEERING

A laboratory study of freeze-thaw effects on hydraulic conductivity of kaolin-sand mixtures

Une étude en laboratoire des effets du gel-dégel sur la conductivité hydraulique des mélanges kaolin-sable

S. Feng*
Birmingham City University, Birmingham, United Kingdom

E. Ibraim, P.J. Vardanega
University of Bristol, Bristol, United Kingdom

**shuyin.feng@bcu.ac.uk*

ABSTRACT: Freeze-thaw effects on subgrade soils are of relevance to geotechnical and pavement engineering given the potential for increased road construction in colder regions due to climate change. The freezing and thawing cycles can result in changes to some soil parameters, therefore, for design processes, there is a need to characterize such progressive changes. This paper gives an overview of a laboratory experimental campaign on fine-grained soil and clay-sand mixture soil samples under multiple freezing and thawing cycles. The effects of freezing and thawing conditioning processes on the hydraulic and properties of tested soil samples were investigated. The experimental observations were used to develop transformation models for fine-grained soil and soil mixtures tested.

RÉSUMÉ: Les effets gel-dégel sur les sols de fondation sont importants pour l'ingénierie géotechniques et des chaussées, étant donné le potentiel d'augmentation du volume des routes dans les régions plus froides en raison du changement climatique. Les cycles de gel-dégel peuvent entraîner des modifications de certains paramètres du sol. Par conséquent, dans les processus de conception, il est nécessaire de caractériser ces changements progressifs. Cet article donne un aperçu d'une campagne expérimentale d'essais en laboratoire sur des échantillons de sol à grains fins et de mélanges argile-sable sous plusieurs cycles de gel et de dégel. Les effets d'application de ces cycles sur les propriétés de conductivité hydraulique des échantillons de sol testés ont été étudiés. Les observations expérimentales ont été utilisées pour développer des modèles de transformation pour les sols à grains fins et les mélanges de sols testés.

Keywords: Freeze-thaw effects; soil mixtures; hydraulic conductivity.

1 INTRODUCTION

Hydraulic conductivity (k) is used in many aspects of geotechnical engineering to understand the flow of fluids through soils and has been the subject of much geotechnical research (e.g. Chapuis, 2012). Freeze thaw effects have been reported in various studies showing some effect on intrinsic soil parameters (e.g. Benson and Othman, 1993; Othman and Benson, 1993; Feng et al. 2023).

For many geotechnical applications, including road construction, soils are found as a mixture comprising coarse and fine-grained materials and this can affect k values (e.g. Sivapullaiah et al. 2000). Various forms of empirical equations linking k to soil void ratio (e_s) (e.g. Nagaraj et al. 1993; Sivapullaiah et al. 2000; Vardanega et al. 2017; Feng and Vardanega, 2019) have been reported for fine-grained soils.

The important study of Sivapullaiah et al. (2000) compared k data for different percentages of Bentonite mixed with different sand and silt materials. Sivapullaiah et al. (2000) showed a log(k) versus e_s fitting for the datasets studied: in this paper this assumption will be tested for Kaolin-Leighton Buzzard Sand (K-LB) mixtures subjected to various numbers of freeze-thaw cycles (FTC). This paper will study the influence of FTC on the k function.

2 SAMPLE PREPARATION & TESTING

The kaolin sample preparation followed the procedure outlined in Feng (2022) and Feng et al. (2023). Reconstituted kaolin samples were prepared in a floating cylinder type consolidometer. The samples were then subjected to incrementally to the following vertical pressures, 30 kPa, 60 kPa, 120 kPa and 180 kPa. The first three pressures were continuously applied for 48 hours, and the final pressure for 120 hours. The samples were then allowed to swell for 48

hours after the consolidation phase. The extruded soil samples were sliced horizontally and then cut into oedometer samples of approximately 20mm in height and 75 mm in diameter. These samples had a pre-conditioned e_s of around 1.30. Further details on this testing are detailed in Feng (2022) and Feng et al. (2023).

In this paper, data from tests on Kaolin-sand mixtures are presented. The sand used in the mixtures was Leighton Buzzard Sand with: the sieve sizes through which ten percent (and fifty percent) of the material would pass are (D_{10}) of 1.28mm and (D_{50}) of 1.5mm respectively; coefficient of uniformity (C_U) of 1.26; coefficient of curvature (C_Z) of 0.97. The Kaolin-sand mixture samples were prepared using a moist tamping method to minimize the potential nonuniformity and inhomogeneity of the mixtures. The Kaolin was mixed with water, and then sand was added to form a mixture consisting of 50% kaolin and 50% sand (by mass) with an initial water content of 35%. The soil mixtures were then tamped in the oedometer cell to a pre-conditioned e_s of around 0.56.

The conditioning process was similar to the procedure described in the recent paper of Feng et al. (2023). In summary, samples were saturated with de-ionized water in the oedometer cell for 24 hours, then frozen at a temperature set at -20°C in a freezer. After 24 hours of freezing, the oedometer cells were then allowed to thaw with access to water in a bucket at room temperature (approximately 20°C) for 24 hours. After applying FTC, the specimens were placed in an oedometer cell and consolidated under vertical stresses of approximately 50 kPa, 110 kPa, 220 kPa, 440 kPa, and 110 kPa applied incrementally (following BSI 1990). The k values were found by the 'square root of time fitting method' (Taylor, 1948).

3 ANALYSIS RESULTS

3.1 Selection of empirical function

Figures 1 to 8 show the hydraulic conductivity (k) versus (e_s) data for both the pure kaolin data from Feng (2022) and Feng et al. (2023) and the new data for Kaolin-Leighton Buzzard (KL-B) sand mixtures fitted with various empirical functions. The statistical measures: number of data-points (n), coefficient of determination (R^2), standard error (SE) and p-value of the correlation (cf. Paradine and Rivett 1953) are also shown on the Figures 1 to 8.

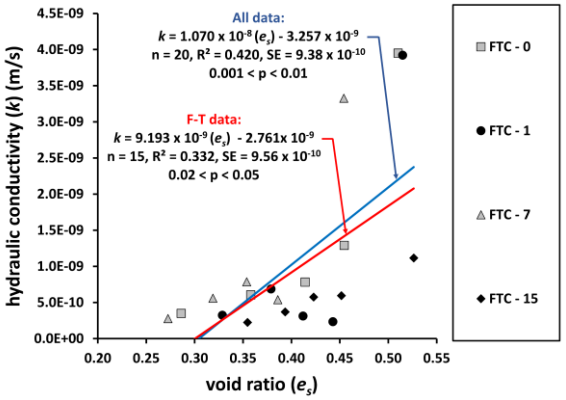

Figure 1. k versus e_s for the studied K-LB mixes.

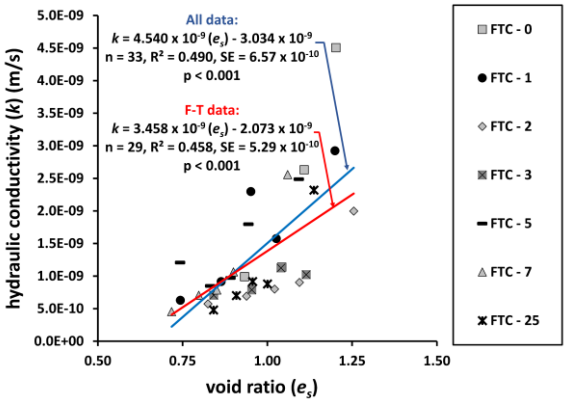

Figure 2. k versus e_s for the studied kaolin tests.

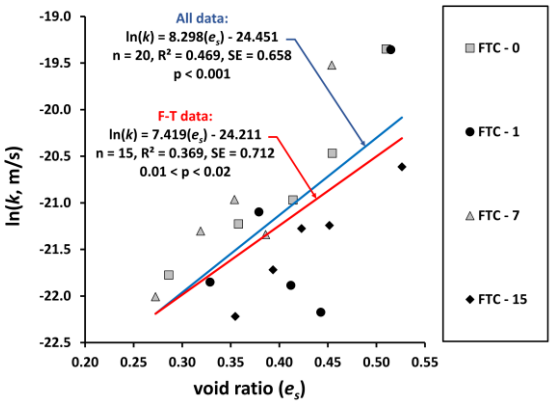

Figure 3. ln(k) versus e_s for the studied K-LB mixes.

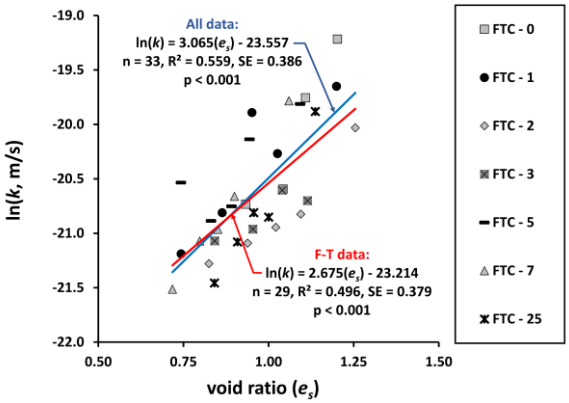

Figure 4. ln(k) versus e_s for the studied kaolin tests.

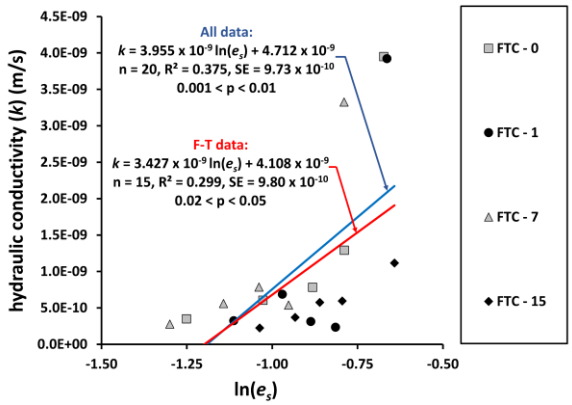

Figure 5. k versus ln(e_s) for the studied K-LB mixes.

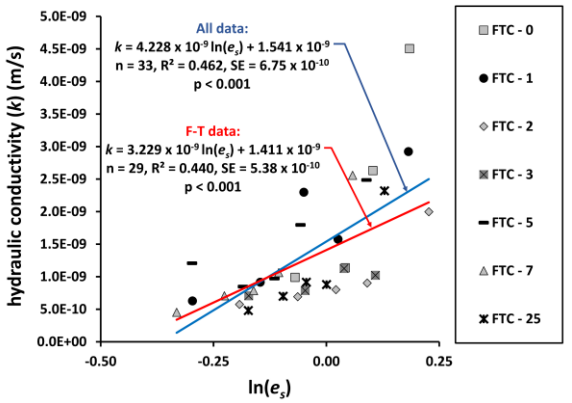

Figure 6. k versus ln(e_s) for the studied kaolin tests.

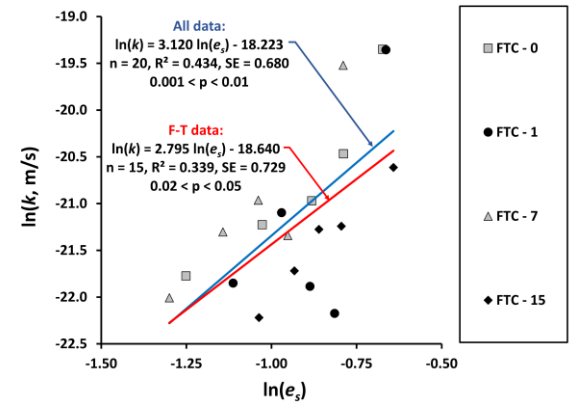

Figure 7. ln(k) versus ln(e_s) for the studied K-LB mixes.

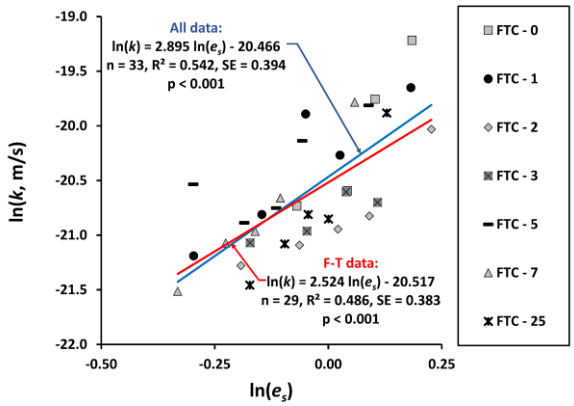

Figure 8. ln(k) versus ln(e_s) for the studied kaolin tests.

Figures 1 and 2 show a linear fitting to the K-LB mixtures and the pure kaolin tests series. The linear fittings considering only samples with FT conditioning give similar trends as the combined datasets albeit with consistently lower R^2 values. The correlations shown on Figures 1 and 2 have $R^2 = 0.420$ ($0.001 < p < 0.01$) (K-LB) and $R^2 = 0.490$ ($p < 0.001$) (Kaolin). Figures 3 and 4 show a semi-log fitting to the K-LB mixtures ($\ln(k)$ vs. e_s) and the pure kaolin tests series. The correlations shown on Figures 3 and 4 have $R^2 = 0.469$ ($p < 0.001$) (K-LB) and $R^2 = 0.559$ ($p < 0.001$) (Kaolin). Figures 5 and 6 also show a semi-log fitting to the K-LB mixtures (k vs. $\ln(e_s)$) and the pure kaolin tests series. The correlations shown on Figures 5 and 6 have $R^2 = 0.375$ ($0.001 < p < 0.01$) (K-LB) and $R^2 = 0.462$ ($p < 0.001$) (Kaolin). Figures 7 and 8 present a log-log fitting to the K-LB mixtures ($\ln(k)$ vs. $\ln(e_s)$) and the pure kaolin tests series. The correlations shown on Figures 7 and 8 have $R^2 = 0.434$ ($0.001 < p < 0.01$) (K-LB) and $R^2 = 0.542$ ($p < 0.001$) (Kaolin).

3.2 $\ln(k) - e_s$ equation

The best fitting was obtained for both kaolin and kaolin-sand data sets (see Figures 1 to 8) was the $\ln(k)$ versus (e_s) fitting of the form shown as Eq. (1) (see also Sivapullaiah et al. 2000) which can be rearranged to Eq. (2):

$$\ln(k) = \alpha(e_s) - \beta \quad (1)$$

$$k = e^{-\beta} e^{\alpha e_s} \quad (2)$$

where α and β are fitting parameters. For the K-LB data series (Figure 3):

$$\ln(k) = 8.298(e_s) - 24.451 \quad (3)$$
$$[n = 20, R^2 = 0.469, SE = 0.658, p < 0.001]$$

For Eq. 3 the R^2 value indicates that 46.9% of the variation in $\ln(k)$ can be explained by e_s (cf. Montgomery et al. 2004, p.273). Eq. 3 can further be rearranged to the following format:

$$k = 2.405 \times 10^{-11} e^{8.298 e_s} \quad (4)$$

For the kaolin data series (Figure 4):

$$\ln(k) = 3.065(e_s) - 23.557 \quad (5)$$
$$[n = 33, R^2 = 0.559, SE = 0.386, p < 0.001]$$

For Eq. 5 the R^2 value quoted means that 55.9% of the variation in $\ln(k)$ can be explained by e_s. Eq. 5 can be rearranged to:

$$k = 5.879 \times 10^{-11} e^{3.065 e_s} \quad (6)$$

3.3 Freeze-thaw effect

Table 1 shows the fitted α values for Kaolin samples with 0% and 50% sand after various numbers of FTC. The α parameter increases consistently with the addition of sand. A decrease in α is seen when comparing the 'All data' to the 'FTC samples' dataset. The small sizes of single FTC value datasets (e.g. 1 FTC, 2 FTC etc) are not sufficient to establish if the α values are influenced by the number of FTC.

Table 1. α-values for data series from this study.

Mixture	0% Sand		50% Sand	
	α	n	α	n
All data	3.065	33	8.298	20
FTC samples	2.675	29	7.418	15
0 FTC	5.973	4	10.14	5
1 FTC	3.348	5	10.86	5
2 FTC	2.820	5		
3 FTC	1.641	4		
5 FTC	2.657	5		
7 FTC	5.006	5	12.21	5
15 FTC			9.022	5
25 FTC	5.137	5		

4 SUMMARY AND CONCLUSIONS

This paper has presented some new k data of Kaolin-sand mixtures. The new data has been compared with k tests on kaolin reported in Feng et al. (2023). A semi-log function was found to be the best fit to the data studied in this paper. The α value increases considerably with the addition of 50% sand to kaolin, compared to the tests on pure kaolin. However, the effect of the number of FTC was not detected in this study.

ACKNOWLEDGEMENTS

The authors thank Mr G. Martin for technical support and Dr El Hajjar for assistance with the French translation.

Data availability: the new experimental data are available from the first author upon reasonable request.

REFERENCES

Benson, C.H. and Othman, M.A. (1993). Hydraulic Conductivity of Compacted Clay Frozen and Thawed In Situ. *Journal of Geotechnical Engineering (ASCE)*, 119(2): 276-294. https://doi.org/10.1061/(ASCE)0733-9410(1993)119:2(276).

British Standards Institution (BSI) (1990). Methods of test for soils for civil engineering purposes - Part 5: Compressibility, permeability, and durability tests. *BS 1377–5:1990*. BSI, London, UK.

Chapuis, R.P. (2012). Predicting the saturated hydraulic conductivity of soils: a review. *Bulletin of Engineering Geology and the Environment,* 71(3): 401-434. https://doi.org/10.1007/s10064-012-0418-7.

Feng, S. (2022). Hydraulic Conductivity of Road Construction Materials: with a Focus on Freeze-thaw Effects. *Ph.D. thesis*, University of Bristol, Bristol, UK.

Feng, S. and Vardanega, P.J. (2019). Correlation of the Hydraulic Conductivity of Fine-Grained Soils with Water Content Ratio Using a Database. *Environmental Geotechnics*, 6(5): 253-268. https://doi.org/10.1680/jenge.18.00166.

Feng, S., Ibraim, E. and Vardanega, P.J. (2023). Hydraulic conductivity of fine-grained soils subjected to freeze-thaw cycles. *Cold Regions Science and Technology*, 213: [103902]. https://doi.org/10.1016/j.coldregions.2023.103902.

Montgomery, D.C., Runger, G.C. and Hubele, N.F. (2004). *Engineering Statistics*. 3rd Edition, John Wiley & Sons, New York.

Nagaraj, T.S., Pandian, N.S. and Narashimha Raju, P.S.R. (1993). Stress state–permeability relationships for fine-grained soils. *Géotechnique*, 43(2): 333–336. https://doi.org/10.1680/geot.1993.43.2.333.

Othman, M.A. and Benson, C.H. (1993). Effect of freeze-thaw on the hydraulic conductivity and morphology of compacted clay. *Canadian Geotechnical Journal,* 30(2): 236-246. https://doi.org/10.1139/t93-020.

Paradine, C.G. and Rivett, B.H. (1953). *Statistics for technologists*. English Universities Press, London, UK.

Sivapullaiah, P.V., Sridharan, A. and Stalin, V.K. (2000). Hydraulic conductivity of bentonite-sand mixtures. *Canadian Geotechnical Journal,* 37(2): 406-413. https://doi.org/10.1139/t99-120.

Taylor, D.W. (1948). *Fundamentals of Soil Mechanics*. John Wiley & Sons Inc., New York.

Vardanega, P.J., Feng, S. and Shepheard, C.J. (2017). Some recent research on the hydraulic conductivity of road materials. In: *Bearing Capacity of Roads, Railways and Airfields,* A. Loizos et al. (eds.), CRC Press/Balkema, Leiden, the Netherlands, pp. 135-142.

Proceedings of the XVIII ECSMGE 2024
GEOTECHNICAL ENGINEERING CHALLENGES
TO MEET CURRENT AND EMERGING NEEDS OF SOCIETY
© 2024 the Authors
ISBN 978-1-032-54816-6
DOI 10.1201/9781003431749-567
Open Access: www.taylorfrancis.com, CC BY-NC-ND 4.0 license

ECSMGE 24
XVIII EUROPEAN CONFERENCE ON SOIL MECHANICS AND GEOTECHNICAL ENGINEERING

Sustainable erosion control in geotechnical structures – case study

Contrôle écologique de l'érosion dans les structures géotechniques - étude de cas

A. Ferreira*, J. Sousa, J. Dias, A. Neves
Ascendi IGI, Porto, Portugal

**aferreira@ascendi.pt*

ABSTRACT: Bearing in mind that surface erosion is one of the most recurrent pathologies in geotechnical structures, and its occurrence has become more and more common with greater structural consequences due to climate change, Ascendi has worked to find more sustainable and innovative solutions to prevent and resolve this type of pathology using bioengineering methodologies. The solution presented, in this case study, is limited to the projection of a mixture with a specific formulation, with species of reticulated root, appropriate to the active and adjusted to the geographical location, not requiring the previous existence or application of a layer of vegetable soil. The embankment slope under analysis, located at PK 201+000 of the A13 was presumably composed by silty sand intercalations of black schist (slate) and quartz-feldespar brown schist soils from excavations carried out near the site, very susceptible to erosion, and difficult to stabilize with the application of hydroseeder with vegetable soil. The traditional solution for this pathology would resort to filling the eroded strata with rock material. This new approach reduces the consumption of materials, water and fuels, preserving existing ecosystems and favoring biodiversity through the application of native species. The creation of a uniform vegetation cover on the slope face and the establishment of the reticulated roots allow a stabilization of the slope and increased resilience to Natural Hazard.

RÉSUMÉ: Sachant que l'érosion de surface est l'une des pathologies les plus récurrentes dans les structures géotechniques, et que son occurrence est devenue de plus en plus courante avec des conséquences structurelles plus importantes en raison du changement climatique, Ascendi s'est efforcé de trouver des solutions plus durables et innovantes pour prévenir et résoudre ce type de pathologie en utilisant des méthodologies de bio-ingénierie. La solution présentée, dans cette étude de cas, se limite à la projection d'un mélange avec une formulation spécifique, avec des espèces de racines réticulées, appropriées à l'actif et adaptées à la situation géographique, ne nécessitant pas l'existence préalable ou l'application d'une couche de sol végétal. Le talus analysé, situé au PK 201+000 de A13, était vraisemblablement constitué de phyllites grises et de métagraviers brunâtres provenant d'excavations réalisées à proximité du site, très sensibles à l'érosion et difficiles à stabiliser par l'application d'un hydroseeder avec un sol végétal. La solution traditionnelle pour cette pathologie consisterait à remplir les strates érodées avec du matériel rocheux. Cette nouvelle approche réduit la consommation de matériaux, d'eau et de combustibles, tout en préservant les écosystèmes existants et en favorisant la biodiversité grâce à l'utilisation d'espèces indigènes. La création d'une couverture végétale uniforme sur la face de la pente et l'établissement de racines réticulées permettent une stabilisation de la pente et une résilience accrue aux risques naturels.

Keywords: Geotechnical structures; erosion; sustainability; bioengineering; natural hazard.

1 INTRODUCTION

Nowadays, as result of climate change, there is a greater frequency of very high and concentrated rainfall in short periods of time. These phenomena, usually associated with other factors (quality of geotechnical materials, slope geometries that are not in line with the geology, insufficient drainage systems, construction problems, among others), can lead to serious pathologies in geotechnical structures and ultimately to instabilisation and rupture phenomena.

Ascendi, aware of this fact, has researched, studied, and implemented more sustainable solutions from an ecological point of view, that allow pathologies to be resolved and increase the resilience of its assets against Natural Hazards.

This document presents a practical case study in which a sustainable solution was implemented using bioengineering to correct and mitigate the surface erosion phenomena observed.

2 TRADITIONAL VS SUSTAINABLE SOLUTION

To treat or prevent this type of pathology, there are different solutions which can be implemented, all with a set of advantages and disadvantages.

To treat pathologies related to surface erosion, the most common and traditional solution is often to fill these surfaces with stone material.

Figure 1 shows an example of a traditional solution, where the surface ravine was repaired by using rockfill.



Figure 1. Example of a traditional solution - repaired by using rockfill.

Although it is a very effective and easy-to-implement solution, promoting stabilization of the geotechnical structure and increasing resistance to erosion phenomena, it has a number of disadvantages in environmental terms when compared to other more sustainable solutions, such as hydro-sowing.

Solutions using stone material generally require more labor and mechanical resources, and consume more non-renewable natural resources such as water, energy and fossil fuels. As a result, they have a higher economic and environmental cost and more negative impacts on the ecosystem. Other solutions can be considered, such as:

- Application of geotextile for erosion control;
- Surface coating;
- Construction of containment barriers;
- Reinforcement of the drainage system
- Slope re-profiling

As less traditional but more sustainable solutions, Chemical Stabilisation and the application of hydro-sowing can also be considered.

Figure 2 shows an example of the implementation of a sustainable solution, where the surface was treated by applying a hydro-sowing.



Figure 2. Example of a sustainable solution – applying hydro-sowing.

3 CASE STUDY

The slope that is the subject of this study was built in 2013, with a slope gradient of 1.0V:1.5H and a total height of 52.0 metres. It was initially built with 3 benches, and in 2022 it was supplemented with a backfill with two more benches.

The material that makes up the embankment comes from excavations carried out to build a short-distance overpass and is highly susceptible to erosion due to its composition.

The body of the embankment was built according to Elsamex (2021) and the Detailed Design with black and dark grey phyllites, with a very variable state of alteration (from decomposed to moderately altered) and a generally high state of fracture; reddish-brown, greyish, black and greenish-grey shales, sometimes with quartz fillets, sometimes with oxidised fractures and clay fillings, with a very variable state of alteration (from decomposed to moderately altered) and a generally high state of fracture; dark grey metagrauvaques with a generally high state of alteration and fracture.

In 2016, the first longitudinal cracks were seen in the embankment pavement. In 2020, several pathologies were observed on the same slope. Pathologies related to the displacements and instability phenomena observed in the structures. In order to guarantee the stability of the structure and stop the instability phenomena, a new support slope was built at the foot of the embankment.

After the construction of the new reinforcement earth structure, which was completed in February 2023, a landscape integration and surface protection

solution - hydro-sowing - was studied with the aim of protecting the embankment against surface erosion agents. This will act as a preventative measure, avoiding the occurrence of future pathologies associated with erosion phenomena, promoting the growth of native vegetation, biodiversity and the preservation of ecosystems. This solution also adds value in economic terms and is more environmentally sustainable.

Hydro-sowing is a landscaping and protection technique that consists of spreading a mixture of seeds, fertiliser, mulch, fixatives and water on the surface. All these materials are mixed and applied according to set proportions. This mechanical process makes it possible to firmly fix the seeds and create a favourable environment for germination in the most adverse weather conditions and on poor, hard-to-reach land.

The hydro-sowing system implemented is adapted to the region, considering soil conditions and water availability. A mixture of 90 per cent herbaceous plants (grasses and legumes) and 10 per cent shrubs was considered.

The mix will thus be made up of grasses, whose fasciculate roots actively contribute to fixing the soil, legumes that will act as green manure and a portion of shrubs that will make up the stable and permanent autochthonous scrub communities.

The composition of the hydro-sowing is as follows:

- Grasses and Legumes 35g/m2 (90% of the total seed mixture)
  - 55% Lolium multiflorum;
  - 18% Lolium perenne;
  - 10% Brisa maxima;
  - 10% Festuca arundinácea;
  - 5% Dactilis glomerata;
  - 1% Trifolium repens;
  - 1% Vicia spp.
- Shrubs 3,5g/m2 (10% of the total seed mixture)
  - 50% Lavandula stoechas;
  - 40% Ulex. Sp.;
  - 10% Caluna vulgaris.

The study considered two solutions:

A. Solution adopted for the two lower levels:
   a. Covering the areas with a layer of vegetable soil;
   b. Application of hydro-sowing as described above.

Figure 3 shows the application of solution A during phase b.



Figure 3. Solution A - Application of the hydro-sowing (December 2022).

Figure 4 shows the evolution of the solution A.

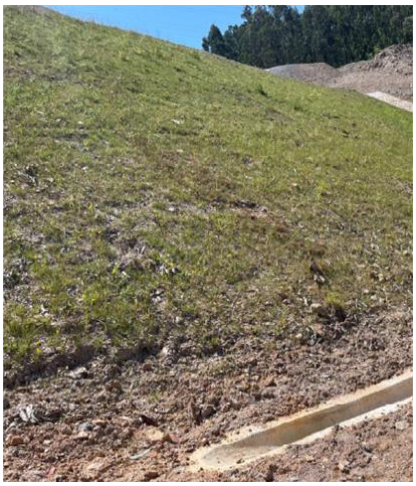

Figure 4. Evolution of Solution A.

B. Solution adopted in the upper level:
   a. Scarifying the surface;
   b. Application of hydro-sowing as described above.

Figure 5 shows the application of solution B during phase b.



Figure 5. Solution B - Application of the hydro-sowing (March 2023).

Figure 6 shows the evolution of the solution B.



Figure 6. Evolution of Solution B.

The two solutions were adopted, A - with a layer of vegetable soil and B - without the soil layer, to compare the results of both. As the entire landfill was made using material from the same geological formation, it is possible to compare the results obtained. Solution A achieved a better uniformity of vegetation cover, but only one growing cycle has been completed so it is too early to reach any final conclusions. It is also necessary to take into account the time difference between the application of both solutions (3 months).

Figure 7 shows the record in December 2023.



Figure 7. Results of the hydro-sowing application (December 2023).

4 CONCLUSIONS

The case study, for both solutions presented in the previous point, proved to be effective in controlling surface erosion on embankment slopes.

The application of a layer of vegetable soil can be an advantage in the early stages of vegetation growth. The advantages or disadvantages in later stages are still being analyzed. We're expecting that solution B might be the most attractive overall, and at a lower cost.

This type of solution - the application of hydro-sowers - with species and formulation studied for the location of the geotechnical structure to be treated, is a more sustainable natural engineering solution that stands out:

- Less consumption of non-renewable natural resources;
- Control of invasive species by using native species;
- Lower water and energy consumption compared to traditional solutions using stone and/or blankets;
- Less consumption of fossil fuels;
- Promotion of biodiversity;
- Greater landscape integration;

All these indicators encourage the preservation of ecosystems. This solution mitigates the surface erosion of geotechnical structures, helping to increase resilience to Natural Harazds.

As future challenges, we intend to extend the methodologies to other Embankment and Excavation Slopes with other geotechnical formations and geographical locations within the Ascendi network.

REFERENCES

Elsamex (2021), Historical analysis - embankment at PK 201+400 (Análise histórica – aterro ao PK 201+400), Elsamex Portugal, Portugal.

Viaponte (2012), Project - Coimbra/Condeixa Sub-section (Lot 3) (Projeto de Execução – Sublanço Coimbra/Condeixa (Lote 3)), Viaponte, Portugal.

Proceedings of the XVIII ECSMGE 2024
GEOTECHNICAL ENGINEERING CHALLENGES
TO MEET CURRENT AND EMERGING NEEDS OF SOCIETY
© 2024 the Authors
ISBN 978-1-032-54816-6
DOI 10.1201/9781003431749-568
Open Access: www.taylorfrancis.com, CC BY-NC-ND 4.0 license

ECSMGE 24
XVIII EUROPEAN CONFERENCE ON SOIL MECHANICS AND GEOTECHNICAL ENGINEERING

Enhancement of soil mechanical properties with biopolymers

Amélioration des propriétés mécaniques des sols avec des biopolymères

N. Fradj*, I. Kádár, K. Kopecskó, A. Németh
Department of Engineering Geology and Geotechnics, Faculty of Civil Engineering, Budapest University of Technology and Economics, Budapest, Hungary

**nourhenmohcen.fradj@edu.bme.hu*

ABSTRACT: The utilization of biopolymers in geotechnical engineering to enhance soil properties has garnered significant interest owing to their environmentally friendly, biodegradable, and sustainable characteristics. Various biopolymers, including chitosan, alginate, pectin, cellulose, and starch, have been explored for soil improvement purposes. Notably, guar and xanthan gums have emerged as prominent biopolymers for soil stabilization applications. The primary objective of employing biopolymers is to augment mechanical properties such as shear strength, stability, and permeability of soils. Evaluations of treated soils have consistently demonstrated the effectiveness of guar gum and xanthan gum in enhancing soil behavior, rendering them suitable for diverse geotechnical applications. Moreover, they represent a sustainable and eco-friendly alternative to conventional chemical and mechanical soil improvement techniques, which may entail adverse environmental consequences. In the research, several laboratory tests, including Atterberg limits, Proctor, and direct shear tests, were conducted on Hungarian soils treated with guar and xanthan gums to observe their mechanical behavior after treatment. Specifically focusing on uniformly graded sandy soil, the research delves into shear test parameters discussion and microscopic visualizations depicting the bonds between guar and xanthan gums and the sand particles.

RÉSUMÉ: L'utilisation de biopolymères dans l'ingénierie géotechnique pour améliorer les propriétés des sols a suscité un grand intérêt en raison de leurs caractéristiques écologiques, biodégradables et durables. Divers biopolymères, dont le chitosane, l'alginate, la pectine, la cellulose et l'amidon, ont été étudiés à des fins d'amélioration des sols. Les gommes de guar et de xanthane se sont notamment imposées comme des biopolymères de premier plan pour les applications de stabilisation des sols. L'objectif premier de l'utilisation des biopolymères est d'augmenter les propriétés mécaniques telles que la résistance au cisaillement, la stabilité et la perméabilité des sols. Les évaluations des sols traités ont constamment démontré l'efficacité de la gomme guar et de la gomme xanthane dans l'amélioration du comportement des sols, ce qui les rend appropriés pour diverses applications géotechniques. En outre, elles représentent une alternative durable et écologique aux techniques conventionnelles d'amélioration chimique et mécanique des sols, qui peuvent entraîner des conséquences néfastes sur l'environnement. Dans la recherche actuelle, plusieurs tests de laboratoire, y compris les limites d'Atterberg, les tests Proctor et les tests de cisaillement direct, ont été effectués sur des sols hongrois traités avec des gommes de guar et de xanthane afin d'élucider leur comportement mécanique. En se concentrant spécifiquement sur les sols sableux à granulométrie uniforme, la recherche examine les résultats des tests de cisaillement et les visualisations microscopiques décrivant les liens formés entre les gommes de guar et de xanthane et les particules de sable.

Keywords: Biopolymers; soil stabilization; shear strength; stability; permeability.

1 INTRODUCTION

Over time, several approaches have been developed to enhance the geotechnical characteristics of soil. These include chemical stabilization, dewatering, natural and synthetic soil reinforcement, and the provision of drains.

The type of soil, the project's requirements, the budget, the available expertise, and other considerations all play a role in the technique selection. One of the most often used methods for improving the quality of the ground is the use of different admixtures and additives to change the properties of the soil. But there's also reason for considerable concern over how this stabilizing method affects the soil ecosystem.

When it comes to improving the strength of soil, chemical techniques that include adding cementitious additives, such as cement, lime, etc., work incredibly well, but they also permanently change the soil's environment. Furthermore, throughout the cement product's production process, significant greenhouse gasses such as carbon dioxide are released (Chang et al., 2016)

The use of cement and lime is often seen as less ecologically benign than the use of industrial by-products. Industrial by-products are fundamentally more sustainable because they constitute a beneficial

reuse application that is an alternative to landfilling or another comparable by-product disposal. Because of the high Ca $(OH)_2$ concentration of the stabilizer, traditional additive stabilization typically elevates soil pH following treatment, which may have negative environmental impacts such as affecting groundwater quality or limiting vegetation growth. Traditionally treated soils are also overly brittle, which can have an impact on the performance and stability of structures (Chang et al., 2015).

The review of existing literature has shown that numerous studies have explored the use of gum and xanthan gum to stabilize soil across various soil types, yielding promising outcomes. For instance, Chang et al. (2015) observed that the inclusion of guar gum enhanced soil aggregate stability and mitigated soil erosion, while Mendonça et al. (2021) noted that xanthan gum improved the rheological properties and resistance to erosion in silty clay soil. Both studies focused on assessing the impact of biopolymers on the geotechnical characteristics of loess soil. Jiang (2022) discovered that injecting guar gum significantly elevated the unconfined compressive strength of loess soil while decreasing its permeability. Similarly, xanthan gum was found to enhance the elastic modulus and shear strength of loess soil, with its effectiveness being linked to the concentration used.

In a laboratory trial, the addition of 0.2% guar gum led to a notable increase of up to 50% in the unconfined compressive strength of loess soil compared to untreated soil (Bagheri, 2023). Another study revealed that incorporating 0.2% xanthan gum resulted in substantial enhancements of up to 180% in elastic modulus and 77% in shear strength of loess soil (Jiang, 2022). It's important to note that the precise improvements in soil properties depend on various factors such as soil type and concentration of biopolymer, and curing duration, thus these effects may differ across different soils and biopolymers. Further research is necessary to fully grasp the impacts of biopolymer treatment on soil properties and to validate its efficacy in improving soil mechanical properties.

Biopolymers are naturally occurring polymers with remarkable tensile strength that are non-toxic and biodegradable. Because of potential cost savings, low environmental impact, non-toxicity, and non-secondary pollution, biopolymers are acknowledged as a viable alternative to traditional chemical polymers (Aminpour and O'Kelly, 2015).

2 MATERIALS

2.1 Soil

The soil was obtained from a construction site in Göd, Hungary originated from a mine of Dűne Szektor Kft. (October 2022).

It is greyish-black in color and does not contain any organic content.

The grain size distribution curve of the soil as measured by hydrometer and sieve tests and following the ASTM D, 2487-06 ASTM International (2021), indicates that the soil is a uniformly graded sand, as shown in Figure 1. The percentages of different soil components are presented in Table 1 and the grading characteristics of the soil are shown in Table 2.

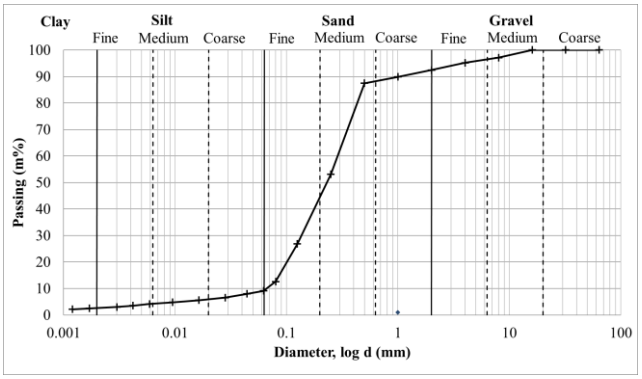

Figure 1. Grain size distribution curve of sand.

Table 1. Soil composition.

Soil Fractions m (%)	
Gravel K(Gr)	7.57%
Sand H(Sa)	83.17%
Silt I(Si)	6.63%
Clay A(Cl)	2.63%

Table 2. Grading characteristics of the soil.

Soil characteristics			
D90	1.059 mm	Cu	4.50
D60	0.300 mm	Cc	0.98
D30	0.140 mm	w	1.3%
D10	0.067 mm	γ_s	2.65 kN/m^3

2.2 Guar Gum (GG)

Guar gum, scientifically identified as Cyamopsis tetragonolobus, is a natural biopolymer obtained from the endosperm polysaccharide of guar seeds, classified within the Leguminosae family, and categorized as a seed gum. Its composition comprises D-galactose and D-mannose polymers in a 1:2 ratio (Sujatha and Saisree, 2019).

Upon complete hydration, guar gum transforms a thixotropic, viscous, colloidal dispersion. The borate ions inherent in guar gum serve as cross-linking agents, facilitating the formation of cohesive and thick gels.

2.3 Xanthan Gum (XG)

Xanthan gum is a polysaccharide that is extensively used as a food additive and rheology adjuster; it is generated by the Xanthomonas campestris bacteria by fermentation of glucose or sucrose. Xanthan gum's ($C_{35}H_{49}O_{29}$) fundamental chemical structure is a linear linked b-D glucose backbone with a trisaccharide side chain on every other glucose. Using hydrogen bonds, the trisaccharide side chain is aligned with the backbone, providing stability and overall shape.

3 METHODS

3.1 Sample preparation

The soil samples are oven-dried at 100 °C to 110 °C for 24 h. The guar gum and xanthan gum-treated soil samples are prepared by adopting the dry mixing procedure. Initially, the biopolymer in powder form is mixed with the required amount of soil at percentages of 0.5% and 1% by weight of the soil.

The biopolymer powder is mixed thoroughly with the soil sample in a plastic bag to be sure that the fine particles of powder won't be wasted in the air, and then the required water amount is added. In this experiment, the optimum water content was added for the mixing, which is 9.5% of the total mass of the dry mixture. With the first contact of the biopolymer with water, the galactose, and the mannose present in the biopolymer hydrate at a faster rate by absorbing the water rapidly, and the soil becomes coated with the biopolymer.

3.2 Experimental investigation

3.2.1 Microscopic observations

The interaction of sand with the biopolymer was investigated microscopically using a transmitted illumination optical microscope (Olympus BH2 PLM Asbestos Polarizing Microscope) see Figure 2.

This Olympus BH2 microscope is equipped with a binocular head featuring a pair of CWHK 10x eyepieces, with one eyepiece incorporating a crossline reticle. The Bertrand lens module includes a rotating analyzer and is furnished with a 530 nm wave plate.

The nosepiece, offering four positions, is fitted with D Plan PO objectives of 10x, 20x, 40x, and a Central Stop Dispersion 10x A PO objective. The stage is capable of 360-degree rotation and is accompanied by a set of stage clips. Additionally, the flip-out condenser is complemented by an attached rotating polarizer (Microscope central, 2023).

For this research, samples were prepared in small portions immediately and observed by the microscope. The two types of biopolymers were observed independently to analyze their microscopic structure, then mixed dry with sand particles, Finally, some water drops were added to the mix to visualize the created bonds between the powders and the sand grains.



Figure 2. Olympus BH2 PLM Asbestos Polarizing Digital Microscope.

3.2.2 Shear box test

After finishing the preparation of the sample and where homogeneity was achieved, the direct shear test was conducted using the machine in Figure 3.



Figure 3. Direct shear test (The Laboratory of Geotechnics and Engineering Geology at BME University, Hungary).

This test is among the most frequent and simple methods to determine the shear strength of soils. It was

performed on five specimens with 5 different mixtures: an untreated sandy sample and four treated samples with the ratios, respectively: 0.5%GG, 1%GG, 0.5%XG, and 1%XG. The amount of water was specified to be the optimum water content, which is 9.5%. The shear tests were done with three loading points each (50, 100, and 150 kPa) to get enough outputs to compare.

The setting inputs of the shear box test are resumed in Table 3.

Table 3. Direct shear box parameters used in geotechnical engineering laboratory (BME university).

DEVICE DATA		
Frame length (L):	60	mm
Frame width (B):	60	mm
Frame area (A):	3600	mm^2
LOADING PARAMETERS		
Shear velocity	0.5	mm/min
Max. displacement	6.5	mm
Loading type	Constant rate	
Consolidated	yes	

4 DISCUSSION

The preference for guar gum and xanthan gum as stabilizing agents was driven by their natural abundance and sustainable characteristics, leading to enduring positive impacts. Extensive experimental tests were carried out to investigate the feasibility of utilizing these biopolymers for enhancing the geotechnical characteristics of soil, and the findings from these tests are detailed in the study.

4.1 Microscope

According to the results obtained using the Olympus microscope at different magnifications, the granules displayed an interesting diversity of morphologies ranging from oval, spherical, and polygonal to irregular forms depending on the type of the utilized biopolymer. In this phase of research, the Olympus microscope provided a simple visualization of the GG and XG powders on a bigger scale which also allowed us to compare the shapes and forms of these biopolymers, see Figures 4 and 5.

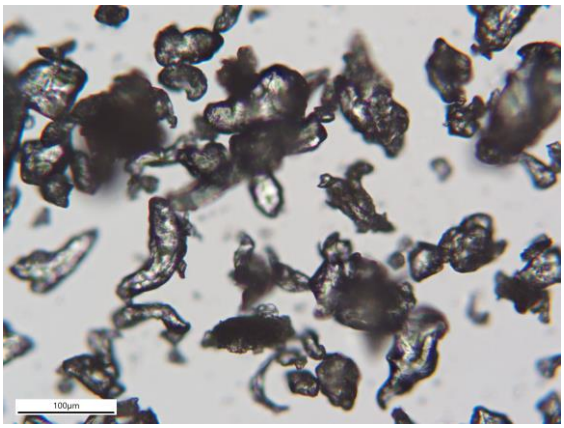

Figure 4. Guar gum at 200X magnification.

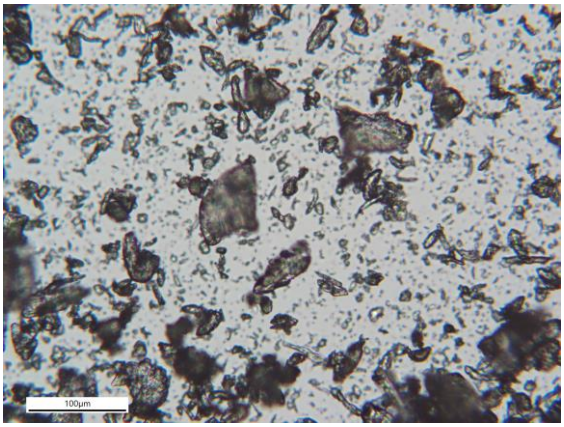

Figure 5. Xanthan gum at 200X magnification.

For instance, at the same 200X magnification, it is clear that GG has bigger particles than the XG particles, they are more fine and dense, it is also shown that the particle quantity of XG is more than the one of GG, as a result, it was mostly the reason why it works more with granular soils proving the results found by previous literature (Bagheri, 2023; Chang et al., 2015). However, GG was proved more efficient with cohesive soils (Bagriacik et al., 2021). Under the microscope, the raw soil in this study—which is sand—also revealed an intriguing shape with shades of brown and yellow colors. Refer to Figure 6.

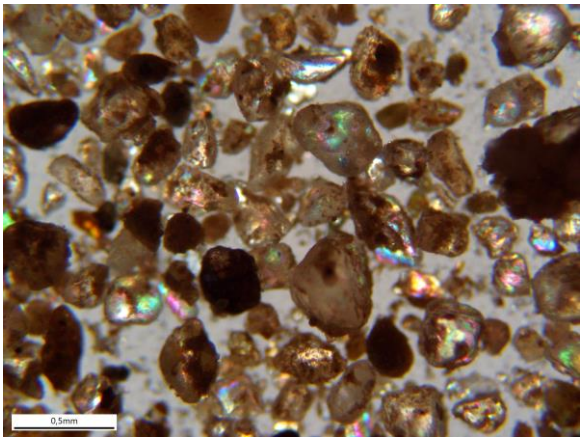

Figure 6. Sand sample with 40X magnification.

Observing the behavior of the soil in dry form with the two different powders and the entire mixture after adding water was the most fascinating aspect. It was shown by the microscopic magnification that the hydrogen linkages formed the instantaneous bonds between the biopolymer grains and soil crystals.

The water filled the voids, and the powder created a coating on the sand particles, the white-colored shapes are the gel-like structure created by water plus powder.

Figures 7 and 8 show both dry and wet mixtures of soil with GG and XG biopolymers at 40X magnification.

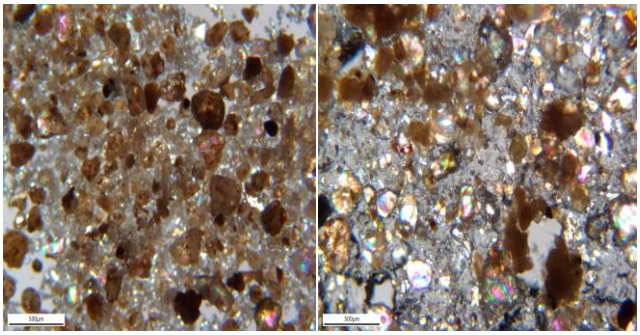

Figure 7. Dry (left) and wet(right) mixtures of soil with GG at 40X magnification.

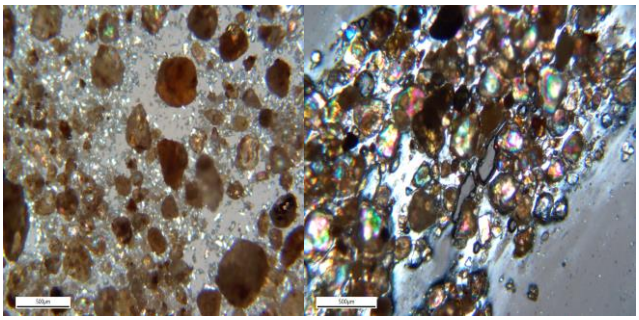

Figure 8. Dry (left) and wet(right) mixtures of soil with XG at 40X magnification.

4.2 Shear test

The initial soil exhibits a friction angle with a peak value of 33° and 0 kPa cohesion, characteristic of sandy soil. Subsequent treatment with Guar Gum (GG) and Xanthan Gum (XG) at varying ratios results in notable changes in soil properties. Simultaneously, cohesion experiences substantial improvement, with the peak value reaching 18.4 kPa, after being initially cohesionless, this result was achieved with just a 0.5% addition of GG. A parallel evolution is observed with a 1% addition of the same powder.

On the other hand, XG-treated sand demonstrates significant improvements in cohesion, exceeding the GG, results are shown in Table 4. This observation is consistent with current literature findings (Chang et al., 2020), indicating that XG is more commonly employed for granular soils, such as the soil under investigation in the present research.

Biopolymers like guar gum and xanthan gum can act as lubricants between soil particles, reducing inter-particle friction. This lubricating effect can lead to a slight decrease in friction angle as the soil particles experience less resistance to sliding past each other. However, this decrease is typically minimal compared to the increase in cohesion. The addition of biopolymers may also influence the arrangement of soil particles. The formation of a cohesive matrix can promote closer packing of particles, leading to improved interlocking and a slight reduction in friction angle.

Table 4. Shear Test results.

	Friction angle (°)		Cohesion (kPa)	
(%)	**Peak**	**Residual**	**Peak**	**Residual**
0.5% GG	23.5	26.5	18.4	6.9
1% GG	26	27	9.8	6.4
0.5% XG	27.5	25	18.4	16.6
1% XG	28.5	27	11.9	11.4

5 CONCLUSIONS

The research delves into an examination of guar gum and xanthan gum biopolymers concerning the stabilization of sand soil, aiming to enhance geotechnical properties while preserving mineral compositions. The findings reveal observable modifications in geotechnical properties with the addition of 0.5% and 1% concentrations of both guar gum and xanthan gum. This study provides valuable insights into the underlying mechanisms of stabilization between biopolymers and soil, as uncovered through various laboratory tests, including meticulous microscopic investigations.

Key conclusions drawn from the study highlight a change in the behavior of the granular soil;

- In Xanthan-treated granular soil, the enhanced strength primarily arises from the formation of the Xanthan matrix on the soil's surface and within voids. This matrix notably contributes to the increased shear strength of the soil.
- When water, guar gum, or xanthan gum is added to improve sandy soil, cohesion increases due to enhanced particle bonding facilitated by these substances. This results in higher overall shear strength. However, the friction angle may remain steady or increase slightly due to changes in particle arrangement and interlocking.
- Determining the optimal dosage of biopolymers is crucial and contingent on specific purposes,

such as stabilization, enhancing dam permeability, or improving the plasticity of a given soil.

Future studies aimed at precisely quantifying the use of xanthan and guar gum in soil stabilization would significantly enhance our understanding of stabilization mechanisms and improve overall process efficacy. Embracing these microbial enhancers opens avenues for altering biopolymer stabilization and modifying soil characteristics in ways not achievable with conventional stabilizers like cement.

ACKNOWLEDGEMENTS

The Laboratory of Geotechnics and Engineering Geology of the Budapest University of Technology and Economics and the technicians are acknowledged.

REFERENCES

Aminpour, M., & O'kelly, B. C. (2015). *Applications of biopolymers in dam construction and operation activities*. https://www.researchgate.net/publication/304088221

ASTM International. (2021, June 10). *Test Method for Particle-Size Distribution (Gradation) of Fine-Grained Soils Using the Sedimentation (Hydrometer) Analysis*. https://doi.org/https://doi.org/10.1520/d7928-21e01

Bagheri P, I. G. M. R. (2023). Effects of Xanthan Gum Biopolymer on Soil Mechanical Properties. *Applied Sciences*, *13*(2), 887. https://doi.org/https://doi.org/10.3390/app13020887

Bagriacik, B., Ok, B., & Kahiyah, M. T. M. A. (2021). An experimental study on improvement of cohesive soil with eco-friendly guar gum. *Soils and Rocks*, *44*(2). https://doi.org/10.28927/SR.2021.060020

Chang, I., Im, J., & Cho, G. C. (2016). Geotechnical engineering behaviors of gellan gum biopolymer treated sand. *Canadian Geotechnical Journal*, *53*(10), 1658–1670. https://doi.org/10.1139/cgj-2015-0475

Chang, I., Im, J., Prasidhi, A. K., & Cho, G. C. (2015). Effects of Xanthan gum biopolymer on soil strengthening. *Construction and Building Materials*, *74*, 65–72. https://doi.org/10.1016/j.conbuildmat.2014.10.026

Chang, I., Jeon, M., & Cho, G. C. (2015). Application of microbial biopolymers as an alternative construction binder for earth buildings in underdeveloped countries. *International Journal of Polymer Science*, *2015*. https://doi.org/10.1155/2015/326745

Chang, I., Lee, M., Tran, A. T. P., Lee, S., Kwon, Y. M., Im, J., & Cho, G. C. (2020). Review on biopolymer-based soil treatment (BPST) technology in geotechnical engineering practices. In *Transportation Geotechnics* (Vol. 24). Elsevier Ltd. https://doi.org/10.1016/j.trgeo.2020.100385

Chang, I., Prasidhi, A. K., Im, J., Shin, H. D., & Cho, G. C. (2015). Soil treatment using microbial biopolymers for anti-desertification purposes. *Geoderma*, *253–254*, 39–47. https://doi.org/10.1016/j.geoderma.2015.04.006

Mendonça, A., Morais, P. V., Pires, A. C., Chung, A. P., & Oliveira, P. V. (2021). A review on the importance of microbial biopolymers such as xanthan gum to improve soil properties. In *Applied Sciences (Switzerland)* (Vol. 11, Issue 1, pp. 1–14). MDPI AG. https://doi.org/10.3390/app11010170

Microscope central. (2023, November). *Olympus BH2 PLM Asbestos Polarizing Microscope*. https://microscopecentral.com/products/olympus-bh2-plm-asbestos-polarizing-microscope

Sujatha, E. R., & Saisree, S. (2019). Geotechnical behaviour of guar gum-treated soil. *Soils and Foundations*, *59*(6), 2155–2166. https://doi.org/10.1016/j.sandf.2019.11.012

Jiang, J.Z.T. and J.Z. (2022). Splitting tensile strength and microstructure of xanthan gum-treated loess. *Scientific Reports*, *12*(9921). https://doi.org/https://doi.org/10.1038/s41598-022-14058-4

Proceedings of the XVIII ECSMGE 2024
GEOTECHNICAL ENGINEERING CHALLENGES
TO MEET CURRENT AND EMERGING NEEDS OF SOCIETY
© 2024 the Authors
ISBN 978-1-032-54816-6
DOI 10.1201/9781003431749-569
Open Access: www.taylorfrancis.com, CC BY-NC-ND 4.0 license

ECSMGE 24
XVIII EUROPEAN CONFERENCE ON SOIL MECHANICS AND GEOTECHNICAL ENGINEERING

Experimental study on the elasticity modulus of RCA–RTW mixtures

Étude expérimentale du module d'élasticité des mélanges RCA–RTW

K. Gabryś*, W. Sas
Water Centre WULS, Warsaw University of Life Sciences – WULS, Warsaw, Poland
**katarzyna_gabrys@sggw.edu.pl*

ABSTRACT: The present study aims to show the possibility of soft rubber tire waste (RTW) application in rigid recycled concrete aggregate (RCA) by evaluating the mechanical properties of the large concrete aggregates with a grain diameter size up to 4.0 mm mixed with small ground rubber with diameter 0–2 mm, with weight percentages between 0 and 50%. The paper presents the results of drained monotonic triaxial tests on compacted RCA–RTW mixtures. The test results prove that the inclusion of rubber in the RCA significantly reduces the elastic modulus (*E*). From the perspective of the utilization of the studied material in road construction, a less rigid (stiff) material is obtained.

RÉSUMÉ: La présente étude vise à démontrer la possibilité d'utiliser des déchets de pneus en caoutchouc mou (RTW) dans des agrégats rigides de béton recyclé (RCA) en évaluant les propriétés mécaniques de gros agrégats de béton d'un diamètre de grain allant jusqu'à 4,0 mm mélangés à du petit caoutchouc broyé d'un diamètre de 0 à 2 mm, avec des pourcentages de poids compris entre 0 et 50%. L'article présente les résultats d'essais triaxiaux monotones drainés sur des mélanges compactés RCA–RTW. Les résultats des essais prouvent que l'inclusion de caoutchouc dans le RCA réduit de manière significative le module d'élasticité (*E*). Du point de vue de l'utilisation du matériau étudié dans la construction routière, on obtient un matériau moins rigide.

Keywords: Mechanical properties; anthropogenic soil; recycled concrete aggregate; rubber waste.

1 INTRODUCTION

The primary goal of the solid waste management system is to protect public health, safety, and welfare effectively. Recycled materials are mostly used for non-structural applications. However, a large number of industrial and municipal waste can be used in the construction industry. The sustainable management of tire rubber waste is a major challenge for industry and the public sector. This is due to the following reason: landfill disposal of scrap tires is legally prohibited in all countries due to the negative environmental impact (Al-Rkaby, 2019).

Given this problem, various academic research studies are proposing to investigate the feasibility of the re-use of this waste through reliable and viable long-term solutions (Benjelloun et al., 2021). Examples may include road engineers who tried incorporating tire rubber into asphalt pavements (Carlson and Zhu, 1999). The desirable properties of rubber waste in geostructures over geomaterials include compressibility, lightness, high thermal insulation, and good durability (Saberian et al., 2018). Many experiments using triaxial and direct shear tests have been carried out so far to understand the strength properties of tire shreds, tire chips, and their mixtures with sand. Notable among these is a study by Rao and Dutta (2006) who found that mixtures of sand with 20% of tire chips could be a potential material for highway and embankment construction, due to the improved load-bearing characteristics compared to sand only. Earlier research by Ghazavi (2004) indicates that the addition of 10 to 20% rubber to the sand is optimal for the highest friction angle, with these rubber materials alone giving a friction angle of 31°. Other previous studies demonstrated that scrap tire particles ranging in size from 50 to 100 mm give the highest shear strength parameters (Moo-Young et al., 2003). Wu et al., (1997) performed triaxial tests on pure tire chips including rubber powder, and reported that rubber waste improved shear strength and internal friction angle in blends. The value of Young's modulus varied from 420 to 840 kPa.

More recent studies carried out by e.g. Bali Reddy et al. (2016) indicate that shear strength increases with increasing rubber shred content up to 30–40% by weight and then decreases. Similar observations were made by Tiwari et al. (2017) who showed that shear strength increased to an optimum value of 25% of the

volume and weight of the rubber aggregates and then decreased above 25%. Even more recent studies, such as the work of Balaban et al. (2019) reduce this optimum level of rubber waste in the mix to 20%, when an improvement in mix strength can be observed. A summary of previous work on sand reinforcement by adding crushed rubber can be found in the work of (Benjelloun et al., 2021).

The authors have explored the effect of the addition of waste rubber on the strength parameters, using different waste materials, i.e. fine recycled concrete (particles ≤ 2 mm) (Gabryś et al., 2021). The research was part of an ongoing extensive program of experimental trials carried out at the Warsaw University of Life Sciences (WULS), Poland, and at the Vytautas Magnus University Agriculture Academy (VMU), Lithuania. According to the triaxial tests conducted, the largest improvement in shear strength occurred for the mixture with 10% recycled tire waste (RTW).

It is also important to note that, among other rubber properties, the modulus of elasticity (E) has a significant effect on the mechanical behavior of soil–rubber compounds (Aksoy et al., 2021). The results of laboratory tests on this parameter of granular rubber–sand mixture, in addition to the previously mentioned work by Wu et al., (1997), can be found, e.g., in the research of Guler and Enunlu (2009). The inclusion of rubber waste in the sand was found to reduce the E–modulus significantly.

Regarding the state of the art discussed above, this work aims to study the mechanical behavior, particularly the elasticity modulus of compacted anthropogenic soil modified with recycled tire waste (RTW). This research focuses on the use of man-made soil material–recycled concrete aggregate (RCA), which in its unbound state can be placed as a subbase in road structures.

2 MATERIALS AND METHODS

The materials used in this work are recycled concrete aggregate (RCA) and rubber aggregates from waste car tires (RTW), their characteristics are summarized below.

2.1 RCA

The RCA adopted in the present study was the reference material in many of the authors' previous research (e.g. Gabryś et al., 2023). The physical characteristics of this RCA were determined in our laboratory (Table 1). The RCA belongs to the category of gravel with sand (saGr), according to PN-EN ISO 14688-1:2018-05, with uniform and spherical grains after crushing. The RCA has an average grain size of D_{50}=2.0 mm; the void ratio can vary between e_{min}=0.201 and e_{max}=0.405, and the specific density of the grains is ρ_s=2.17 g/cm^3. The particle size distribution curve of this RCA, together with its image after grinding and mixing, is presented in Figure 1. From Figure 1 it can be seen that the RCA is a non-uniformly well-graded coarse material. This classification was obtained by estimating the uniformity (C_U) and curvature (C_C) coefficients.

Table 1. Physical characteristics of used recycled concrete aggregate and recycled rubber aggregate.

Materials Under Study	RCA	RTW
D_{10} (mm)	0.25	0.68
D_{30} (mm)	1.00	0.84
D_{50} (mm)	2.00	1.00
D_{60} (mm)	2.30	1.10
C_U (/)	9.20	1.62
C_C (/)	1.74	0.94
ρ_s (g/cm^3)	2.17	1.19
$\rho_{d,\,min}$ (g/cm^3)	1.545	0.464
$\rho_{d,\,max}$ (g/cm^3)	1.735	0.565

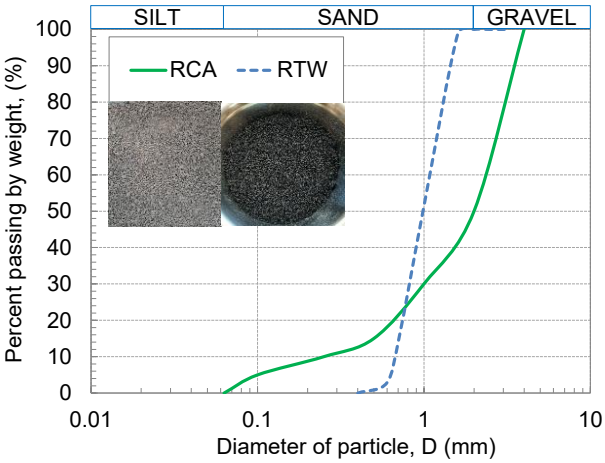

Figure 1. Particle size distribution of testing materials and their images.

2.2 RTW

The ground rubber used in this study is a by-product of the scrap tire shredding process. Rubber particles were sieved to obtain a uniform size. The rubber material is angular and irregularly shaped and has a diameter varying from 0.5 to 2 mm with an average diameter of D_{50}=1.0 mm. The specific density of the rubber grains is 1.19 g/cm^{3,} which falls within the range of values given by, e.g., Akbulut et al. (2007). The determined maximum and minimum values of the

void ratio are e_{max}=1.565 and e_{min}=1.106. The particle size distribution curve of the RTW is shown in Figure 1, whereas the basic parameters of tire waste are presented in Table 1. The values of the coefficients C_U and C_C indicate rubber materials with uniform granulation. No amounts of textile parts or steel strapping were found in this rubber additive. The applied rubber waste is not harmful to human health, and has a stable composition, posing no risk during storage and transport (according to the manufacturer), with a positive health assessment.

2.3 Mixtures preparation and testing procedure

In this study, a triaxial apparatus is used to perform all standard isotropic CD triaxial tests on samples with different mixing ratios of the RCA and RTW. The testing program is summarized in Table 2. A total of 9 samples, consisting of ground rubber tires and recycled concrete aggregate, mixed in a ratio of 0:100, 25:75, and 50:50 by weight, are employed in laboratory tests. Generally, the volumetric proportion of the geotechnical mixture controls the mechanical behavior of the mix. Thus, the mixing ratios by volume (a_v) of the RTW and the RCA are tabulated in Table 2. The a_v values were calculated based on the volume of particles for each mix as follows (Youwai and Bergado, 2003):

$$a_v = \frac{1}{\frac{G_{RTW}}{R_m}\left[\frac{(100-R_m)}{G_{RCA}}+\frac{R_m}{G_{RTW}}\right]} \quad (1)$$

where R_m is the mixing ratio by dry weight of the RTW in the mixture (%), G_{RTW} is the specific gravity of the RTW, and G_{RCA} is the specific gravity of the RCA. An isotropic confining pressure is applied at three different values, 90, 180, and 270 kPa, to cover the range of stresses in applications such as road construction or off-road lightweight fill used in embankment construction.

A standard triaxial cell is used in a temperature-controlled room, capable of handling samples 70 mm in diameter and 140 mm in height (Figure 2). It was important to avoid any segregation when preparing the mixtures that could affect the results obtained. Therefore, to obtain a reasonably uniform, non-segregated mixture, special care is taken to mix the RCA and RTW thoroughly from the beginning to the point of pouring into the mold. After mixing the appropriate amount of dry crushed concrete aggregates and rubber aggregates, the specimens are carefully constructed in five layers using undercompaction (Ladd, 1978). Every layer is subsequently tamped using a metal rod tamper providing a relative density between 70 and 80%. To ensure a uniform compaction energy in each layer, the number of blows per layer varies from 21 blows for the first layer to 25 for the fifth layer.



Figure 2. Triaxial apparatus available at WULS.

After each compound is set up in the triaxial cell with the vacuum pressure (~10 kPa), the chamber is filled with de-aired water, and the saturation process is carried out by applying different values of back pressure while keeping a constant initial effective stress of 50 kPa until obtaining a Skempton's *B*-value greater than 0.93. Thereafter, every mixture is isotropically consolidated by increasing the effective confining pressure to the appropriate value according to Table 2. At the end of consolidation, the axial load is increased at a constant axial strain rate until failure occurs. A controlled shear rate of 0.033 mm/min is applied during testing.

3 RESULTS

This section presents the results and analysis of the mechanical properties of the RCA–RTW mixtures from triaxial consolidation and drainage (TXCD) tests, where the shear of the specimens follows a standard path, i.e. with a constant chamber pressure and increasing vertical stress. In this article, the authors focus primarily on the analysis of the elastic modulus (alternatively elasticity modulus or Young's modulus).

During the standard triaxial shear stage, when the total confining stress is held constant, Young's modulus is usually calculated from the equation:

$$E = \frac{\Delta q}{\Delta \varepsilon_v} \quad (2)$$

where Δq is the deviatoric stress increment, and $\Delta \varepsilon_v$ is the vertical (axial) strain increment. All soil moduli can be calculated as secant or tangent, similar to Young's modulus. In Figure 3, schemes for

determining the secant (E_S) and tangent (E_t) modulus at two selected points X and Y are presented, from stress–strain curve measured in drained monotonic triaxial tests. The authors are particularly interested in two characteristic moduli, namely E_0 and E_{50}. E_0 is the initial (maximum) stiffness value in the very small strain range (< 10^{-5}). E_{50} is evaluated as secant stiffness for the interval between deviatoric stress q = 0 and q = $q_{failure}/2$ (Wichtmann et al., 2017).

Table 2. Summary of the testing program.

No	Designations	Mixing ratio		Preshear mean stress (kPa)	Preshear dry unit weight (kPa)	Preshear void ratio (/)
		RTW: RCA by weight (%)	RTW by volume (%)			
1	MIX1_A	0:100	0	90	16.68	0.30
2	MIX1_B	0:100	0	180	16.68	0.30
3	MIX1_C	0:100	0	270	16.68	0.30
4	MIX2_A	25:75	0.38	90	11.71	0.85
5	MIX2_B	25:75	0.38	180	11.85	0.83
6	MIX2_C	25:75	0.38	270	11.90	0.82
7	MIX3_A	50:50	0.65	90	9.35	1.32
8	MIX3_B	50:50	0.65	180	9.36	1.32
9	MIX3_C	50:50	0.65	270	9.38	1.31

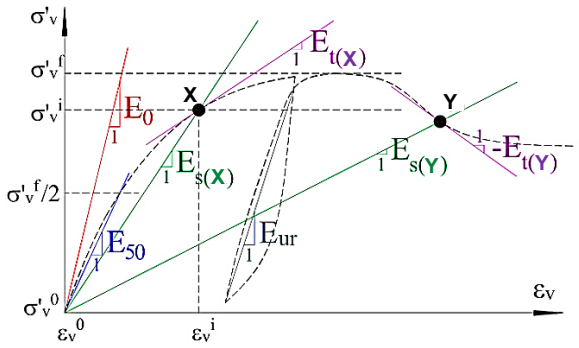

Figure 3. Evaluation of elastic modulus based on stress–strain characteristics (Wichtmann et al., 2017).

The stress–strain relationships of the anthropogenic soil–ground rubber compounds at different mix ratios are plotted in Figures 4–6. For mixtures with rubber waste (MIX2 and MIX3), the relationships between q and ε_S are relatively linear when the distortional strain is less than 15% for MIX 2 (Figure 5) and 20% for MIX 3 (Figure 6). Despite the high deformability of the ground rubber particles used, it is possible to obtain a failure in the mixes with rubber. It can be observed that the distortional strain magnitude increases with increasing rubber waste content in the specimen. In contrast, by comparing Figures 5 and 6, ca. 20% decrease of the deviatoric stress (e.g. from ~ 645 kPa to ~ 434 kPa for MIX2_C and MIX3_C, respectively) with increasing RTW content is evident.

Overall, the deformation characteristics of the studied RCA–RTW blends are quite similar to the pure RCA. Regarding the RCA, the peak strength (up to even ~ 860 kPa) develops at distortional strains ε_S=3.33, 2.76, and 2.53% for the confining stress at 90, 180, and 270 kPa, respectively. It can be seen that adding 25% rubber to the RCA results in an average 16% increase in distortional strains.

Based on the results in Table 3, the shear strength of the non-reinforced RCA and RCA–RTW mixes increases significantly with increasing normal stress, and the shear strength of the mix is greater at higher normal stresses. This increase is due to the modification of the microstructure of the blends, which produces an improvement in the contacts between the particles, namely the friction angle.

The results obtained have been attempted to compare with the mechanical properties of pure rubber waste found in the literature, see e.g. Guler and Enunlu (2009). In the case of pure rubber specimens, no internal friction angle can be determined, as the rubber shows no signs of yield, even when approaching 20% strain. Consequently, the E_S modulus can be only defined from the slope of the stress–strain curve, which is more and less straight.

Regarding the elastic moduli, the RCA containing 25 and 50% of RTW are characterized by moduli E_0 averaging between 80 and 113 MPa lower and E_{50} averaging around 64–66 MPa lower in comparison to Young's modulus E_0 and E_{50} of the pure RCA. Among all tested mixtures, the largest stiffness values are recorded for crushed concrete.

In Table 3, there are also the assumed values of E_{50} (designated as $E_{assum.}$) representing the arithmetic average of the three values obtained for a given mixture. The comparison between $E_{assum.}$ and the

E–moduli of pure rubber waste indicate that the RTW has over 90% less stiffness than the RCA. Moreover, for the blend with a mixing ratio of 50:50, the influence of the confining stress on Young's modulus is rather negligible. For the mixes MIX3_A, B, and C very similar values of E_0 and E_{50} are derived.

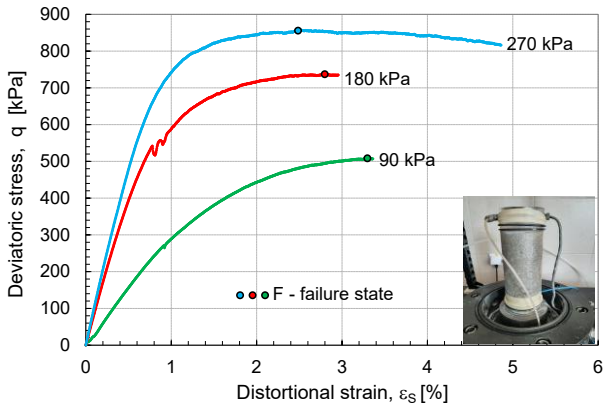

Figure 4. Deviatoric stress curves of the RCA–RTW mixtures: MIX1 (RTW=0% by weight).

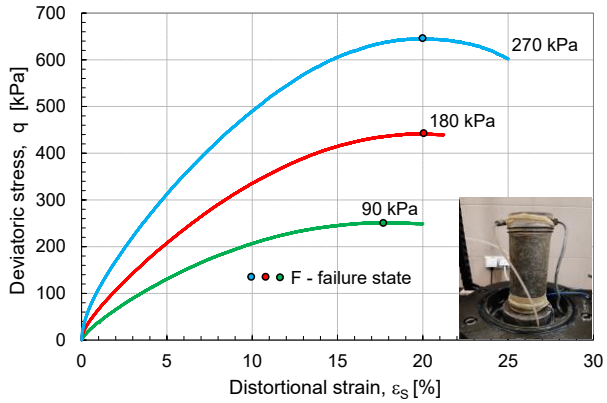

Figure 5. Deviatoric stress curves of the RCA–RTW mixtures: MIX2 (RTW=25% by weight).

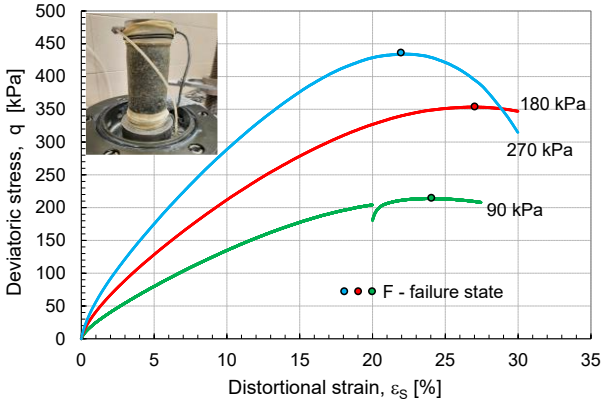

Figure 6. Deviatoric stress curves of the RCA–RTW mixtures: MIX3 (RTW=50% by weight).

4 CONCLUSIONS

The introduction of new or alternative (recycled waste) materials in geotechnical engineering applications may have many various benefits, but a proper understanding of their geomechanical properties is essential to correctly evaluate their performance. Because of the above, this article attempts to verify selected mechanical parameters of recycled concrete aggregate blended with recycled rubber inclusions.

The results obtained in this study can be summarized as follows. The friction angle and shear stress at the failure of the RCA-RTW mixtures generally decrease with increasing rubber content. As is the case of gravelly soils, and conversely to sandy soils, the addition of rubber does not enhance the strength of the RCA. Available experimental data demonstrate that the rubber-reinforced RCA has the *E*–moduli lower in comparison with the pure RCA. This reduces the possibility of using the tested mixes

Table 3. Summary of selected mechanical properties of the tested RCA–RTW mixtures.

No	Designations	φ (°)	σ failure (kPa)	ε failure (%)	E_0 (MPa)	E_{50} (MPa)	$E_{assum.}$ (MPa)
1	MIX1_A		507.45	3.33	95.73	30.17	
2	MIX1_B	34.22	736.45	2.76	134.35	79.47	69.04
3	MIX1_C		856.96	2.53	140.18	97.48	
4	MIX2_A		251.25	17.87	10.39	2.65	
5	MIX2_B	32.05	441.38	19.57	51.89	4.06	4.29
6	MIX2_C		644.95	19.97	67.39	6.16	
7	MIX3_A		213.92	24.00	8.05	1.46	
8	MIX3_B	25.90	353.51	26.94	10.03	2.29	2.33
9	MIX3_C		434.30	22.02	12.20	3.23	
10	Pure rubber*	-	-	-	-	0.89	

* Data taken from Guler and Enunlu (2009).

in road construction, where the stiffness of the material seems to be a key value. Finally, as the rubber itself is characterized by the elasticity modulus ca. 70 times lower than that of the RCA, the applicability of this material is expanding. The addition of rubber to the RCA thus creates opportunities for the potential use of such mixtures as a barrier to absorb pressure waves caused by earthquakes.

REFERENCES

Akbulut, S., Arasan, S. and Kalkan, E. (2007) Modification of Clayey Soils Using Scrap Tire Rubber and Synthetic Fibers. *Appl. Clay Sci*. 2007, 38:23–32. https://doi.org/10.1016/j.clay.2007.02.001.

Aksoy, H.S., Taher, N. and Awlla, H.A. (2021) Shear strength parameters of sand-tire chips mixtures. *Gümüşhane Üniversitesi Fen Bilimleri Enstitüsü Dergisi*,11:713–720. https://doi.org/10.17714/gumusfenbil.865490.

Al-Rkaby, A.H.J. (2019). Strength and Deformation of Sand-Tire Rubber Mixtures (STRM): An Experimental Study. *Stud. Geotech. Mech*., 41(2): 74-80. https://doi.org/10.2478/sgem-2019-0007.

Balaban, E., Smejda, A. and Onur, M.I. (2019). Influence of tire crumbs on mechanical properties of sand-fine soil mixtures. *Geomech. Geoengin.,* 1-16. https://doi.org/10.1080/17486025.2019.1688870.

Bali Reddy, S., Pradeep Kumar, D. and Murali Krishna, A. (2016). Evaluation of the optimum mixing ratio of a sand-tire chips mixture for geoengineering applications. *J. Mater. Civ. Eng.*, 28,06015007.https://doi.org/10.1061/(ASCE)MT.1943-5533.0001335.

Benjelloun, M., Bouferra, R., Ibouh, H., Jamin, F., Benessalah, I. and Arab, A. (2021). Mechanical Behavior of Sand Mixed with RubberAggregates.*Appl.Sci.,*11,11395.https://doi.org/10.3390/app112311395.

Carlson, D.D. and Zhu, H. (1999). Asphalt-rubber, an anchor to crumb rubber markets. Third joint UNCTAD/IRSG workshop on rubber and the environment international rubber forum Veracruz, Mexico.

Ladd, R.S. (1978). Preparing test specimens using undercompaction. *Geotech. Test. J.*, 1(1): 16–23.

Gabryś, K., Dołżyk-Szypcio, K., Szypcio, Z. and Sas, W. (2023). Stress–Strain Behavior of Crushed Concrete as a Special Anthropogenic Soil. *Materials*,16,7381.https://doi.org/10.3390/ma16237381

Ghazavi, M. (2004). Shear strength characteristics of sand-mixed with granular rubber. *Geotech. Geol. Eng.*, 22: 401-416.

Guler, E. and Enunlu, A.K. (2009). Mechanical properties of granular rubber - sand mixtures determined by triaxial tests. In Proceedings of 2nd International Conference on New Developments in Soil Mechanics and Geotechnical Engineering, 28-30 May 2009, Near East University, Nicosia, North Cyprus.

Moo-Young, H., Sellasie, K., Zeroka, D. and Sabnis G. (2003). Physical and Chemical Properties of Recycled Tire Shreds for Use in Construction. J. Environ. Eng., ASCE, 129 (10): 921-929.

PN-EN ISO 14688-1:2018-05; Rozpoznanie i Badania Geotechniczne—Oznaczanie i Klasyfikowanie Gruntów—Część 1: Oznaczanie i Opis. PKN: Warsaw, Poland, 2018. Available:https://sklep.pkn.pl/pn-en-iso-14688-1-2018-05e.html (accessed on 22 February 2018).

Rao, G. V. and Dutta, R.K. (2006). Compressibility and strength behaviour of sand–tyre chip mixtures. *Geotech. Geol. Eng.*, 24: 711-724.

Saberian, M., Mehrinejad Khotbehsara, M., Jahandari, S., Vali, R. and Li, J. (2018). Experimental and phenomenological study of the effects of adding shredded tire chips on geotechnical properties of peat. *Int. J. Geotech. Eng.*, 12(4): 347–356. https://doi.org/10.1080/19386362.2016.1277829.

Tiwari, S.K., Sharma, J.P. and Yadav, J.S. (2017). Geotechnical Properties of Dune sand-Waste Tires Composite. *Mater. Today Proc*., 4: 9851–9855. https://doi.org/10.1016/j.matpr.2017.06.280.

Wichtmann, T., Kimmig, I. and Triantafyllidis, T. (2017). On correlations between “dynamic” (small-strain) and “static” (large-strain) stiffness moduli – An experimental investigation on 19 sands and gravels. *J. Soil Dyn*., 98(4): 72–83. https://doi.org/10.1016/j.soildyn.2017.03.032.

Wu, W., Benda, C. and Cauley, R. (1997). Triaxial determination of shear strength of tire chips. *J. Geotech. Eng. ASCE,* 123(5): 479–482.

Youwai, S. and Bergado, D.T. (2003). Strength and deformation characteristics of shredded rubber tire – sand mixtures. *Can. Geotech. J*., 40: 254–264. https://doi.org/10.1139/T02-104.

Proceedings of the XVIII ECSMGE 2024
GEOTECHNICAL ENGINEERING CHALLENGES
TO MEET CURRENT AND EMERGING NEEDS OF SOCIETY
© 2024 the Authors
ISBN 978-1-032-54816-6
DOI 10.1201/9781003431749-570
Open Access: www.taylorfrancis.com, CC BY-NC-ND 4.0 license

ECSMGE 24
XVIII EUROPEAN CONFERENCE ON SOIL MECHANICS AND GEOTECHNICAL ENGINEERING

The impact of geotechnical spatial variability on the installation of suction caisson anchors

L'impact de la variabilité spatiale géotechnique sur la conception des ancrages de caissons d'aspiration

E. Gallagher*
Trinity College Dublin, Dublin, Ireland
Gavin and Doherty Geosolutions (GDG), Dublin, Ireland

S. Buykx
Gavin and Doherty Geosolutions (GDG), Utrecht, The Netherlands

C. Reale
University of Bath, United Kingdom

D. Igoe
Trinity College Dublin, Dublin, Ireland

**gallage7@tcd.ie*

ABSTRACT: Over the past decade, the offshore wind industry has evolved with significant technological advances. These have been driven by the need for offshore wind energy to provide cost-competitive renewable energy. The economics of offshore wind necessitates lean and efficient designs and nowhere is this more prevalent than in anchors for floating wind turbines. This paper examines the impact of geotechnical spatial variability on the installation of suction caisson anchors for floating offshore wind turbines (FOWTs). Monte Carlo simulations are used to examine the probability of failure of the suction caissons to reach its target depth during installation.

RÉSUMÉ: Au cours de la dernière décennie, l'industrie éolienne offshore a évolué grâce à des avancées technologiques significatives. Celles-ci ont été motivées par la nécessité de l'énergie éolienne offshore pour fournir une énergie renouvelable à un coût compétitif. L'aspect économique de l'éolien offshore nécessite des conceptions simples et efficaces, et cela n'est nulle part plus répandu que dans les ancrages des éoliennes flottantes. Cet article examine l'impact de la variabilité spatiale géotechnique sur l'installation d'ancrages à caissons à succion pour les éoliennes offshore flottantes (FOWT). Les simulations Monte Carlo sont utilisées pour examiner la probabilité de défaillance des caissons d'aspiration pour atteindre leur profondeur cible lors de l'installation.

Keywords: Suction caisson anchor; offshore geotechnics; suction installation; floating offshore wind turbine; Monte-Carlo simulations.

1 INTRODUCTION

The offshore wind sector has undergone significant advancements in recent years, and there is now particular focus on the development of floating offshore wind turbines (FOWTs) for deep water. Better understanding of the uncertainty in their design, can help reduce the cost of suction caisson anchors (SCAs) for FOWTs. One aspect of uncertainty can be related to geotechnical variability and the complexity of the soil across a wind farm site. Moreover, the high costs associated with offshore geotechnical surveys can lead to overly cautious SCA designs, primarily due to the lack of detailed, site-specific geotechnical data. This paper aims to outline an approach for addressing this issue using Monte-Carlo simulations to examine the probability of failure to achieve the target penetration of a SCA during installation.

2 SUCTION CAISSON INSTALLATION DESIGN

The installation of a SCA takes places over two stages: (1) touchdown and self-weight penetration followed by (2) suction penetration. The penetration resistance, R, of a SCA can be calculated using two standard approaches: the bearing capacity (alpha/beta) or Cone

Penetration Test (CPT) based approach. This paper will focus on the latter.

Penetration resistance is determined using equation 1 (DNV, 2017):

$$R = A_p k_p q_{c,L} + A_{si} \int k_f q_{c,z} dz + A_{so} \int k_f q_{c,z} dz \quad (1)$$

where A_p (m^2) is the anchor skirt tip area, k_p(-) is an empirical coefficient relating the CPT tip resistance to the unit-end bearing resistance, $q_{c,L}$is the CPT cone tip resistance at the anchor embedded length, L (m), A_{si} (m) is the caisson inner perimeter, k_f (-) is an empirical coefficient relating the CPT tip resistance to the unit skin friction resistance, $q_{c,z}$ is the CPT cone tip resistance at depth z (m) and A_{so}(m) is the caisson outer perimeter.

3 ANALYSIS INPUTS

A simple suction caisson anchor model was developed to assess the probability of failure during installation due to geotechnical variability in the soil. A diameter of 10m, skirt wall thickness of 50mm and a range of lengths from 10-20m (in 1m increments) were assumed for the anchor geometry. To estimate the anchor weight, padeye dimensions of 1m x 1m with a thickness equal to twice the wall thickness of the skirt were assumed. The thickness of the top plate was assumed equal to that of the padeye. To maintain model simplicity, the mass contributions of internal or external stiffeners were omitted.

3.1 Maximum installation force

The maximum available installation force was defined as the sum of the force due to the maximum pump pressure and the weight of the caisson for each length considered. The maximum pump pressure was assumed to be 500kPa, or 5bar, and was transformed to a force by multiplying it across the area of the anchor lid. The weight of the caisson was computed by multiplying the sum of the volume of the skirt, top plate and padeye by the submerged density of steel, taken to be 6,850 kg/m^3.

3.2 Soil parameters

In the calculation of penetration resistance, this study adopted a lognormal distribution of the k_p and k_f parameters to account for the model uncertainty in these empirical coefficients. The mean and 95th percentile parameters of the resulting lognormal distributions were adopted as the 'Most probable' and 'Highest expected' values, respectively, as reported in DNV (2017) and shown in Table 1.

Table 1. Values of k_f and k_p for SAND from (DNV, 2017).

Coefficient	Most Probable (R_{prob})	Highest Expected (R_{max})
k_f	0.001	0.003
k_p	0.3	0.6

Firstly, the underlying normal distribution parameters, mean and standard deviation, were derived, and these were exponentiated to obtain a lognormal distribution dataset. The standard deviation (SD) of the lognormal distribution can be determined from equation 2:

$$SD = \sqrt{(e^{\sigma^2} - 1)(e^{2\mu + \sigma^2})} \quad (2)$$

where σ and μ are the standard deviation and mean of the underlying normal distribution, respectively. The lognormal distribution had a standard deviation of 0.0639 for k_p and 0.000344 for k_f.

For each Monte Carlo realisation, a unique value for k_p and k_f was sampled from a lognormal distribution of 10,000 values. Local seepage effects in sand during installation were ignored.

3.3 Monte-Carlo simulation inputs

In the study, geotechnical spatial variability was examined using spatially varying CPT cone resistance profiles, generated using the random field approach. The method used to develop these profiles is outlined in Igoe and Reale (2023). A summary of the procedure is provided in this section.

The CPT profiles were assumed to be normally distributed, and the random field was defined using three parameters: mean, standard deviation, and scale of fluctuation (θ). At first a mean CPT profile is derived to which noise can then be added. The mean CPT cone resistance profile, $\bar{q}_t$ (corrected for pore pressure effects), was derived based on a constant relative density of 70% using correlations proposed by Kulhawy and Mayne (1990). A scale of fluctuation value of θ = 5m was assumed in this analysis. Using the Markov correlation structure, a correlation matrix can be developed from equation 3:

$$\rho(\tau_j) = exp\left(\frac{-2|\tau_j|}{\theta}\right) \quad (3)$$

where j = 0, 1,…, n-1 with n being the number of data points, $\tau_j = j\Delta\tau$ is the lag distance between the two data points and ρ is the correlation matrix. Given that

the correlation matrix is positive definite, it can be decomposed into upper (L^T) and lower (L) triangular forms via Cholesky decomposition:

$$\rho = LL^T \quad (4)$$

Subsequently, the spatially correlation normal random field, G, is derived by multiplying the lower triangular matrix with a matrix of independent normal random numbers with a mean of zero and a standard deviation of one, denoted as U, as per equation 5:

$$G = LU \quad (5)$$

Finally, by adjusting the normal random field, G, using the mean and standard deviation, stochastic CPT profiles are produced using equation 6:

$$q_t = \bar{q}_t + \sigma G \quad (6)$$

For the corrected cone resistance in this paper, a coefficient of variation of 30% was assumed meaning $\sigma = 0.3\bar{q}_t$.

4 RESULTS AND DISCUSSION

Firstly, an acceptable probability of failure (p_f) was defined at 5%. 10,000 CPT profiles were developed to represent the geotechnical variability across a site. The result of this analysis is shown in Figure 1.

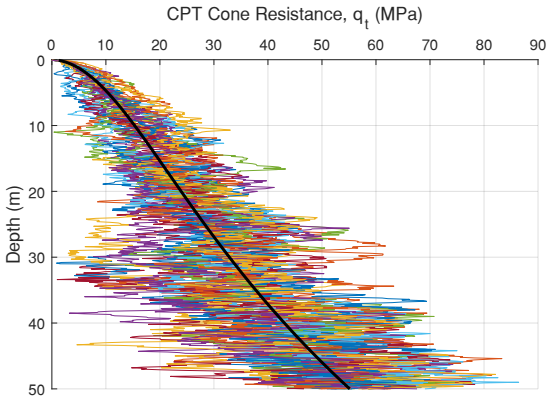

Figure 1. Cone resistance versus depth below seabed (mean profile represented by black line).

For each CPT profile, values of kf and kp were sampled from their distribution and the penetation resistance of the SCA was computed using equation 1. No uncertainty in the geometrical properties of the caisson was considered. Figure 2 shows the total soil installation resistance of the anchor with respect to depth below seabed for a range of pile embedded lengths. The weight of the anchor (black line), maximum installation force including self weight (red line) and total resistance using the mean CPT profile and 'Most probable' (dashed blue line) and 'Highest expected' (dashed black line) k_f and k_p parameters are also included in Figure 2.

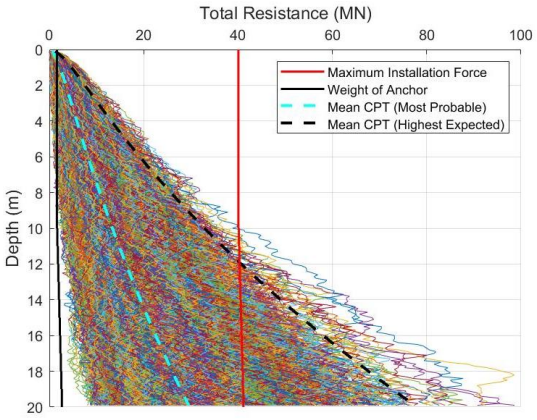

Figure 2. Total installation resistance versus depth below seabed.

Figure 3 shows a box plot of the total resistances across for a range of anchor lengths from 10 – 20m. The mean is shown as a horizontal red line across the centre of each box, with the top and bottom of each box representing +/- one standard deviation from this mean. The whiskers extending from the box show the minimum and maximum values of total resistance at each anchor length. The horizontal stepped green line above each box represents the maximum installation force for that anchor length.

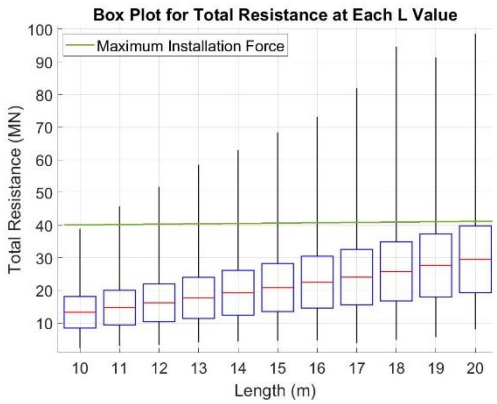

Figure 3. Box plot of total resistance for each anchor length.

The probability of failure in this paper is estimated using Monte-Carlo simulation. The failure criterion was defined using the inequality shown in equation 7:

$$R > maximum\ installation\ force \quad (7)$$

This failure included any instance up to and including the length increment, as the anchor may fail

during installation prior to reaching the target penetration depth.

The probability of failure across all CPT profiles for each length can be determined as N_f/N where N_f is the number of realisations which fail and N is the total number of realisations. A sensitivity analysis was conducted to confirm that 10,000 realisations was adequate to maintain a stable probability of failure for each iteration. Figure 5 shows this analysis for each increment in length. A summary of the maximum installation force and percentage failure for each anchor length is provided in Table 2.

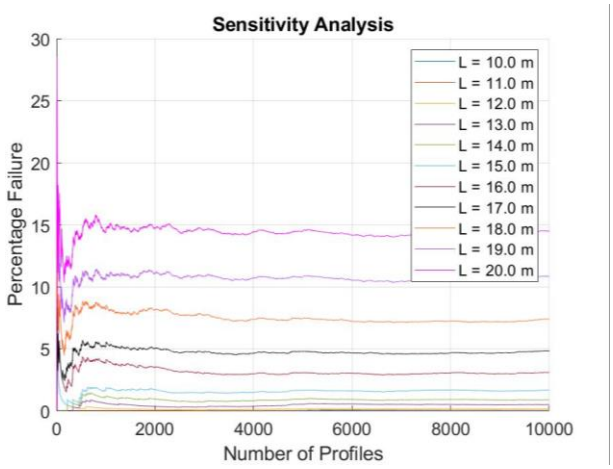

Figure 5. Sensitivity analysis for each anchor length, L.

Table 2. Summary of results.

Length (m)	Maximum Installation Force (MN)	Percentage Failure (%)	Mean Resistance (MN)
10	40.08	0.00	13.30
11	40.18	0.07	14.72
12	40.29	0.19	16.19
13	40.40	0.51	17.70
14	40.50	0.95	19.28
15	40.61	1.91	20.87
16	40.71	3.29	22.52
17	40.82	5.05	24.06
18	40.92	7.57	25.80
19	41.03	10.97	27.64
20	41.13	14.47	29.52

5 CONCLUSIONS

This paper explores the potential impact of geotechnical spatial variability on the installation of suction caisson anchors for floating offshore wind turbines. The probability of failure of a range of anchor lengths was investigated using Monte-Carlo simulation with 10,000 realisations. This paper presented an approach to the preliminary installation design of suction caisson anchors from CPT data to account for site-specific variations in ground conditions. This study has shown that Monte-Carlo simulations can be used effectively to enhance quantitative understanding of the impact of geotechnical variability on the suction installation failure/success rate. This work will be developed to incorporate the in-place capacity of an anchor to include an estimation of the site-specific operational probability of failure of suction caisson anchors.

ACKNOWLEDGEMENTS

The research presented in this article is funded by the Irish Research Council Postgraduate Employment-based Programme under the grant number EBPPG/2022/209.

REFERENCES

Igoe, D.J.P., and Reale, C. (2023). The effect of geotechnical uncertainty on the preliminary design of large diameter monopiles. *14th International Conference on Applications of Statistics and Probability in Civil Engineering*, ICASP14, Dublin, Ireland.

DNV (2017). *Offshore soil mechanics and geotechnical engineering*, Recommended Practice. DNVGL-RP-C212.

Brinkgreve, R.B.J., Engin, E., Engin, H.K. (2010). Validation of empirical formulas to derive model parameters for sands. *7th NUMGE*, Trondheim, Norway.

Kulhawy, F.H., and Mayne, P.W. (1990). Manual on Estimating Soil Properties for Foundation Design. EPRI-EL-6800.

Proceedings of the XVIII ECSMGE 2024
GEOTECHNICAL ENGINEERING CHALLENGES
TO MEET CURRENT AND EMERGING NEEDS OF SOCIETY
© 2024 the Authors
ISBN 978-1-032-54816-6
DOI 10.1201/9781003431749-571
Open Access: www.taylorfrancis.com, CC BY-NC-ND 4.0 license

ECSMGE 24
XVIII EUROPEAN CONFERENCE ON SOIL MECHANICS AND GEOTECHNICAL ENGINEERING

Insight into modelling offshore monopiles via 3D finite element analyses

Considérations pour la modélisation de monopieux par élément finis 3D

D. Gaudio*
Dipartimento di Ingegneria Strutturale e Geotecnica, Sapienza Università di Roma, Rome, Italy

A.B. Batilas, L.M. Lapastoure, A. Loukas, J. Lee, T. Joseph, I. Thusyanthan
Gavin & Doherty Geosolutions, Dublin, UK

**domenico.gaudio@uniroma1.it*

ABSTRACT: Offshore wind farms have been attracting the attention of both researchers and practitioners over the past few decades, due to the growing interest in renewable energy. The choice of a particular foundation, which depends on several factors such as the mechanical properties of soil, depth to bedrock and bathymetry, may influence the overall wind farm cost by up to about 20%. Monopiles are the most used foundation system in the market, whose design can be further refined with advanced numerical analyses, provided that input parameters are properly calibrated. This paper shows the main results of a nonlinear static analysis of a monopile subjected to a horizontal load and embedded in a layered deposit. The analysis was performed using a 3D Finite Element model, where the foundation was represented with *plate* elements, and the soil mechanical behaviour was described with advanced constitutive models. The obtained pushover curves are shown and discussed, from which a reference design condition was selected. Then, the bending moment profile was obtained following three approaches, listed in a descending order of complexity: (1) integration of the stresses at the soil-*plate* interface; (2) derivation of the monopile rotation profile of the *plate* elements; (3) direct output from a *dummy beam* element located at the centreline of the monopile. It is shown that the *dummy beam* provides results in good agreement with those from the other two approaches, suggesting that it may be successfully adopted in practice to speed up the post-processing in the design of monopiles. The methodology presented in this paper would be useful for industrial projects.

RÉSUMÉ: Le développement des parcs éoliens en mer s'est accéléré au cours des dernières décennies grâce aux politiques publiques en matière d'environnement. Les monopieux sont le type de fondation le plus courant. Leur optimisation nécessite des modèles numériques avancés. Cet article présente les principaux résultats de la modélisation par éléments finis 3D d'un monopieu soumis à une charge horizontale. Dans cet exemple, le monopieux est installé dans un sol stratifié composé d'argile et de sable. Les résultats sont présentés en termes de déplacement et rotation du pieu sous l'effet du chargement latéral. L'évolution du moment de flexion le long du pieu est extrait de trois manières différentes: (1) par intégration des efforts à l'interface sol-pieu; (2) par dérivation du profil de rotation calculé à partir du déplacement des éléments coques qui modélisent le pieu; (3) à l'aide d'une poutre fictive modélisée au centre du pieu et qui permet de faciliter l'extraction des résultats. Cet exemple montre que les trois approches mènent à des résultats équivalents. Cela suggère que l'utilisation d'une poutre fictive peut être adoptée afin de faciliter et accélérer la modélisation des monopieux.

Keywords: Offshore wind turbines; monopiles; pushover analysis; 3D Finite Element model; *dummy beam.*

1 INTRODUCTION

Wind energy has emerged as a promising alternative energy source over the last few decades, to fill the world's energy supply and overcome some of the key issues associated with traditional fossil fuels, such as global warming. Particularly in Europe, offshore wind energy shows immense potential thanks to the presence of substantial portions of sea that are ideally suited for the construction of offshore wind farms (OWFs). Thanks to advancements in technology, OWFs have become profitable enough, despite their high construction costs, which depend not only on governmental subsidies, but also on private support. Most of the OWFs budget is allocated to foundation design, construction, and installation. Despite other solutions being under development, monopiles are still the most used type of substructure.

In this paper, the main preliminary results of a nonlinear static (*i.e.*, pushover) analysis of a monopile embedded in a layered deposit are presented. The analyses were carried out with the Finite Element (FE) code *Plaxis 3D* (Bentley, 2023a), considering advanced constitutive models, capable of capturing the nonlinear and irreversible behaviour of the soil. The

results of the analyses are first given in terms of force-displacement and force-rotation curves, together with the bending moment profile developed in the monopile. The latter was computed following three approaches, namely: (1) integration of the stresses at the soil-*plate* interface; (2) derivation of the rotation profile obtained from the *plate* elements representing the monopile; (3) extraction of direct output from a *dummy beam* element located at the centreline of the monopile. It is shown that the *dummy beam* provides results in good agreement with the other two strategies, which may suggest adopting it in the practice to speed up the post-processing step in the design of monopiles.

2 PROBLEM DEFINITION

Figure 1 shows the soil profile considered in the study, together with the geometry of the monopile. The soil profile is composed of two units, namely a clayey and a sandy layer. The layer thickness is equal to 5.2 m for the clay layer and 9.3 m for the sand layer. The water table is located 0.6 m below ground level.

The monopile is a hollow steel pile with an outer diameter $D = 2.0$ m, a wall thickness $t = 0.035$ m, a length $L = 11$ m ($L/D = 5.5$), and an embedment depth $H = 10.0$ m. Although the above dimensions are slightly smaller than those typically adopted for monopiles, they were considered in the numerical study for ease of numerical runs.

3 3D FINITE ELEMENT MODELLING

The Finite Element Analysis (FEA) was performed using the *Plaxis 3D* software to simulate the monotonic test under undrained conditions with a horizontal load applied atop the monopile, with a level arm $e = 0.5$ m with reference to the ground surface.

The mechanical clay behaviour was modelled using the *NGI-ADP* constitutive model (Grimstad *et al.*, 2012), while the sand was simulated using the *HS-small* (*HSS*) model (Benz *et al.*, 2009). The *NGI-ADP* constitutive model has been tailored to model the undrained behaviour of clays, matching both the undrained shear strength and strains at failure for three different stress paths *i.e.*, Active (s_u^A), Direct Simple Shear (s_u^{DSS}), and Passive (s_u^P). The *HSS* model is simple to calibrate and yet capable of capturing the key soil behaviour for the problem under consideration, such as a good representation of the stiffness at small strains and the non-linear stiffness behaviour with increasing strain.

The monopile was modelled using linear elastic, homogeneous and isotropic 6-node triangular *plate* elements with five degrees of freedom per node and quadratic shape functions, characterised by a wall thickness 0.035 m, a unit weight $\gamma = 78.5$ kN/m^3, a Young's modulus $E = 199.2$ GPa, and a Poisson's ratio $\nu = 0.3$. The modulus is slightly lower than that of steel, as a consequence of the code interpreting the input diameter as a centreline diameter: hence, the Young's modulus was corrected so that the bending stiffness *EI* remained unaffected.

The behaviour of the interface within the soil-monopile zone was modelled with linearly elastic-perfectly plastic *interface* elements, whose coefficient of reduction of the shear strength was equal to $R_{inter} = 0.7$ along the shaft and to $R_{inter} = 1.0$ at the base. The FE model consisted of 18117 elements, extending by 40 m along the *y*-axis and by 16 m along the *x*-axis (Figure 2), corresponding to $20 \cdot D$ and $16 \cdot D/2$, while the depth of the model was equal to 14.5 m. These model dimensions resulted from a preliminary sensitivity analysis, which showed that the boundaries did not affect the results when horizontal loads are applied atop the monopile. Also, they are in agreement with previous analyses performed on caisson foundations and onshore wind turbines under seismic loading (Gaudio *et al.*, 2016; 2023).

In the analysis, the monopile was applied a horizontal force at the top, along the *y*-direction: therefore, half of the domain was only modelled, due to the symmetry of the problem.

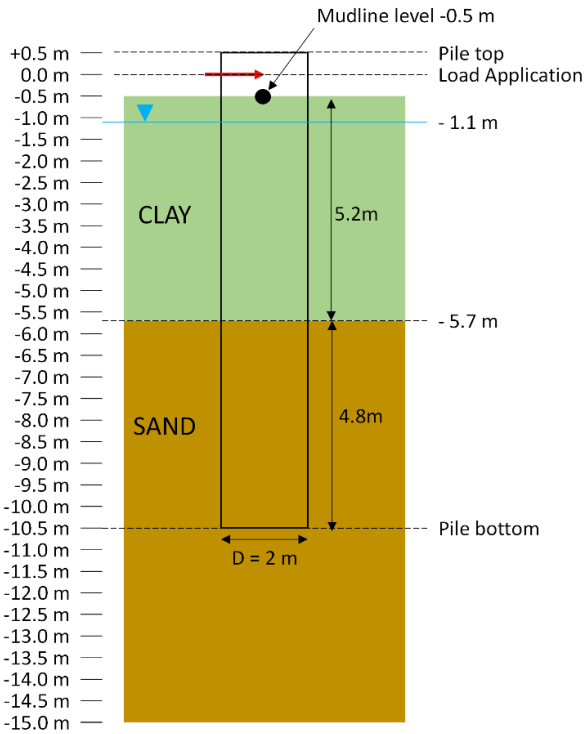

Figure 1. Soil profile and monopile geometry.

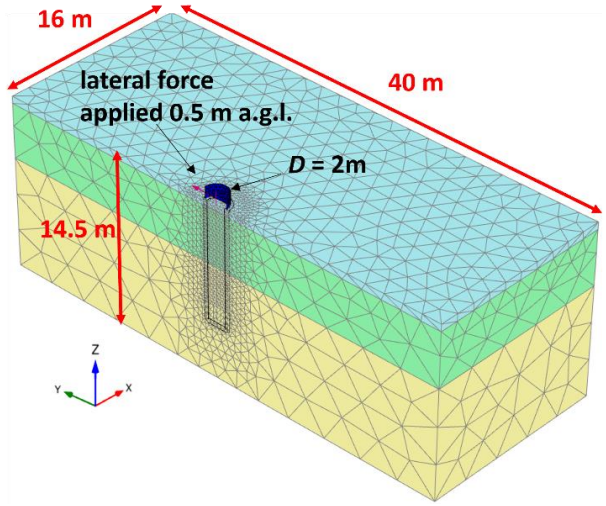

Figure 2. 3D Finite Element model adopted in the study.

3.1 Constitutive model soil parameters

The soil parameters of the constitutive models adopted in the FE analysis are listed in Table 1 and 2 for the *NGI-ADP* and the *HSS* models, respectively, which are representative of the mechanical behaviour of the clayey and sandy layers.

Table 1. NGI-ADP parameters for the clay layer.

Soil parameter	Value	Units
γ_{sat}	17	[kN/m^3]
γ'	7	[kN/m^3]
G_0/s_u^A	500	[-]
$s^A_{u,ref}$	60	[kPa]
$s^A_{u,inc}$	0	[kPa/m]
s_u^p/s_u^A	0.50	[-]
s_u^{DSS}/s_u^A	0.75	[-]
γ_f^C	12	[%]
γ_f^E	24	[%]
γ_f^{DSS}	18	[%]
τ_0/s_u^A	0	[-]
k_0	1	[-]

Table 2. HS-small parameters for sand layer.

Soil parameter	Value	Units
γ_{sat}	18	[kN/m^3]
γ'	8	[kN/m^3]
E_{50}^{ref}	69.6	[MPa]
E_{oed}^{ref}	69.6	[MPa]
E_{ur}^{ref}	208.7	[MPa]
G_0^{ref}	200	[MPa]
ν^{ur}	0.25	[-]
m	0.5	[-]
$\gamma_{0.7}$	0.015	[%]
φ'	40.0	[°]
φ'_{cv}	32.0	[°]
ψ	9.9	[°]
k_0	0.357	[-]
OCR	6	[-]

4 PUSHOVER CURVES

The results obtained from the nonlinear static analysis are discussed in this paragraph, which was performed as a *Plastic* calculation in Plaxis 3D. The monotonic response of the monopile is presented in Figure 3 in terms of the lateral load against the horizontal pile displacement and rotation of the monopile at the mudline level (see Figure 1).

As expected, the non-linear behaviour of the soil-monopile system was triggered from low levels of horizontal displacement. The displacement $y = D/10 = 0.20$ m is also marked in Figure 3, which was taken as a reference design condition for the assessment of the bending moment acting into the monopile, to compare against the yield moment, M_y, as discussed in the following section. The horizontal load $H_{0.1D} = 3076$ kN was computed for this design condition, which corresponded to a rotation $\theta = 1.49°$.

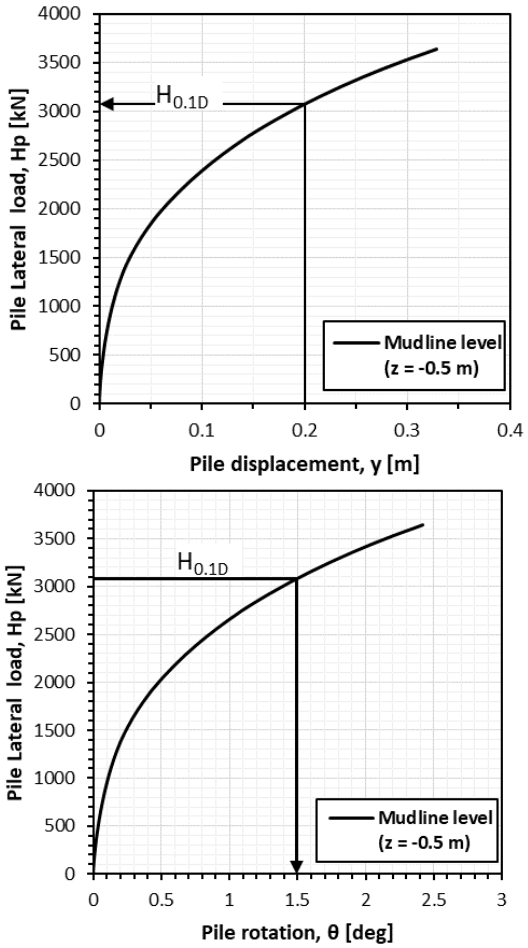

Figure 3. Monotonic pile response at the mudline level.

5 BENDING MOMENT PROFILES

The structural checks of the foundation were made by comparing the maximum bending moment

experienced by the monopile for the reference design condition mentioned above. To this end, the bending moment profile was first evaluated, following three different approaches, such as: (1) integration of the stresses at the soil-*plate* interface; (2) derivation of the rotation profile of the *plate* elements simulating the monopile; and (3) extraction of a direct output from the *dummy beam* element located at the centreline of the monopile.

The results obtained with the three approaches are compared in the next sections, after introducing them in a descending order of complexity.

5.1 Stress integration at the soil-*plate* interface

The bending moment profile was first calculated from the integration of stresses acting at the soil-*plate* interface as below:

$$M_{i,s} = H_p \times e + \int_0^{z_i} \left[p(z) \times \Delta z \right] \cdot dz + \int_0^{z_i} m(z) \cdot dz \quad (1)$$

where subscript i represents a depth counter (i = 1 m, 0.5 m, 0,…,-10.5 m), H_p is the lateral force applied atop the monopile, e = 0.5 m is the distance between the lateral load and the mudline level, $p(z)$ and $m(z)$ are the distributed lateral reaction and moment applied by the soil to the monopile, respectively, and Δz = 0.5 m is the depth interval selected for integration (Figure 4). The distributed lateral reaction $p(z)$ was computed from the integration of the interface forces along the y-direction, while the distributed moment, $m(z)$, was obtained from the integration of forces along the z-direction, multiplied by the respective lever arm $y = D/2$ = 1 m:

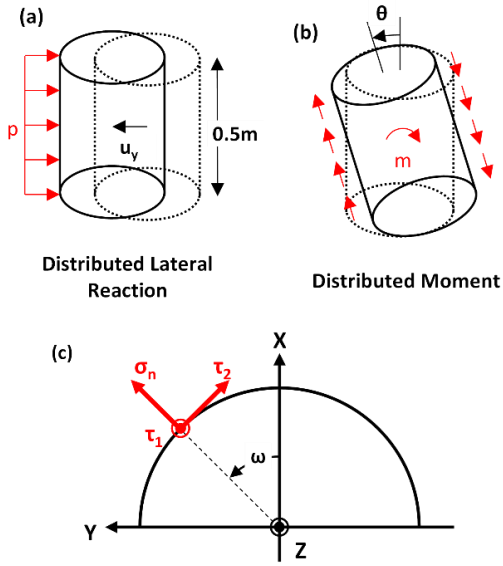

Figure 4. Distributed (a) lateral load p(z) and (b) moment m(z); (c) local coordinate system.

$$p(z) = \frac{\int_{z-\Delta z/2}^{z+\Delta z/2} F_y(z) \cdot dz}{\Delta z} \quad (2)$$

$$m(z) = \frac{\int_{z-\Delta z/2}^{z+\Delta z/2} F_z(z) \times y \cdot dz}{\Delta z} \quad (3)$$

where F_y and F_z are the forces along the y and z-direction, respectively.

Only stresses in local coordinates are accessible rather than forces F_y and F_z in the FE analysis, where σ_n is the stress normal to the interface, while τ_1 and τ_2 are the vertical and horizontal tangential stresses, respectively (Figure 4). The stresses were translated into forces as in eqs. (4) and (5) below, for every stress point, *i.e.*, for a given pair of coordinates, x and y, element area, A, and integration weight, w (Bentley, 2023b):

$$F_y(z) = w \cdot A \cdot \left[\sigma_n(z) \sin\omega - \tau_2(z) \cos\omega \right] \quad (4)$$

$$F_z(z) = w \cdot A \cdot \tau_1(z) \quad (5)$$

5.2 Derivative of rotations of *plate* elements

The bending moment profile was also calculated from the *plate* elements representing the monopile. To this end, the steps reported below were followed, starting from the vertical displacement of the two ends of the plates, whose sign convention is depicted in Figure 5:

- extraction of the back and front vertical displacement of the plate, $u_{z,i}^{front}$ and $u_{z,i}^{back}$, respectively;
- calculation of the pile rotation, θ_i, at the ith depth (i = 1 m, 0.5 m, 0,…,-10.5 m) as:

$$\theta_i = \tan^{-1}\left(\frac{u_{z,i}^{back} - u_{z,i}^{front}}{D} \right) \quad (6)$$

- computation of the bending moment at the ith depth (i = 1 m, 0.5 m, 0,…,-10.5 m), $M_{i,p}$, from the derivative of the pile rotation with depth (*i.e.*, curvature), where EI represents the bending stiffness of the monopile (E = Young's modulus, I = moment of inertia around the vertical axis) as:

$$M_{i,p} = EI \cdot \frac{d \tan\theta_i}{dz} = EI \cdot \left(\frac{\theta_i - \theta_{i+1}}{z_i - z_{i+1}} \right) \quad (7)$$

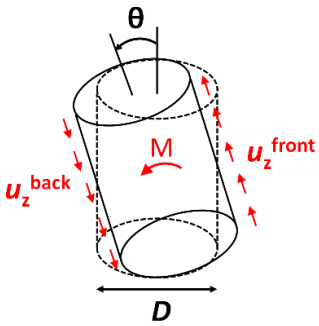

Figure 5. Calculation of the bending moment from plate elements.

5.3 Direct output from the *dummy beam*

Finally, the bending moment profile of the monopile was also obtained from a *dummy beam*, which was introduced at the centreline of the monopile. It is worth noting that this approach has already been routinely followed for excavation wall simulations in 2D conditions, when using continuum elements to model the wall and postprocessing the wall bending moments (Lam, 2018).

The stiffness of the *dummy beam* was selected to be low (*i.e.*, $E_{real}/E_{dummy} \approx 1000$) in order to not affect the results, as this beam was only used as a trick to avoid either integrating stresses acting along the shaft of the monopile or differentiating the *plate* rotation profile. Therefore, a Young's modulus $E_{dummy} = 210$ MPa was assigned to the *dummy beam* element, since the "real" Young's modulus of the monopile was the one of steel, $E_{real} = 199.2$ GPa (see § 3). As for the moment of inertia of the dummy beam, only half of the monopile inertia was considered thanks to the symmetry of the problem, *i.e.*, for the original diameter $D = 2$ m, the moment of inertia of the *dummy beam* was $I = 1/2 \cdot \pi/64 \cdot [D^4 - (D - 2t)^4] = 0.05216$ m^4. The bending moment profile was then extracted as follows:

$$M_{i,b} = \frac{(EI)_{real}}{(EI)_{dummy}} \times M_{dummy,i} = 1897 \times M_{dummy,i} \quad (8)$$

5.4 Comparison of bending moments profiles

A comparison of the bending moment profiles obtained with the three strategies above is made in Figure 6. The bending moments were computed for the design at the reference condition of a horizontal displacement $y = D/10 = 0.20$ m at mudline level. In the figure, the bending moment at yield, $M_y = 33.9$ MN·m, is also plotted.

From Figure 6 it is evident that the three solutions provide quite similar results, both in terms of the bending moment profile and its maximum value. In

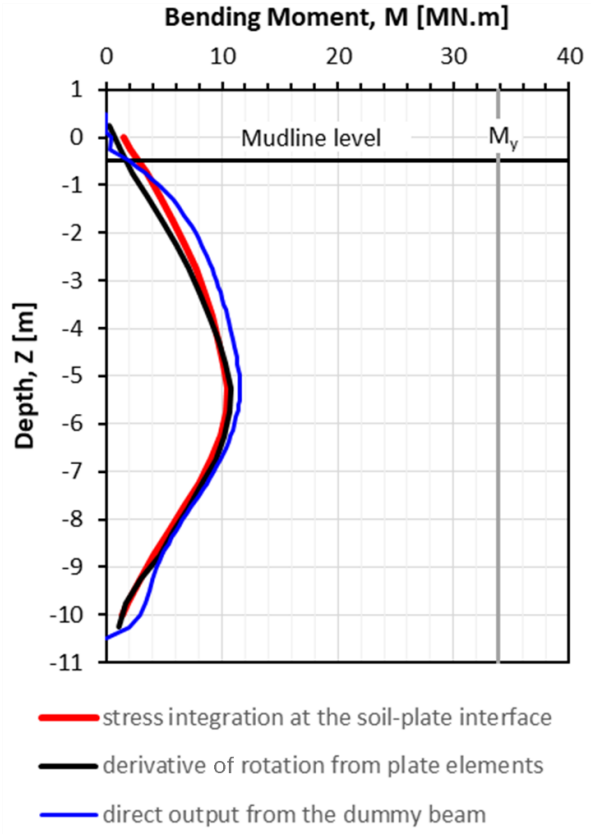

Figure 6. Bending moment profiles along the monopile computed with the three approaches adopted in the study.

particular, it is shown that the maximum bending moment from the stress integration (red line) was equal to $M_{max,\,s} = 10.4$ MN·m, while the one from the derivative of the monopile rotation (black) was equal to $M_{max,\,p} = 10.8$ MN·m, with negligible deviation of about 4.0%. As for the profile from the *dummy beam* (blue), the peak bending moment is equal to about $M_{max,\,b} = 11.5$ MN·m, which corresponded to an overestimation of 1.1 MN·m (~ 9.6%) and 0.7 MN·m (~ 6.1%) from the maximum values obtained from the stress integration and the derivative of rotations from the plate elements, respectively. This result shows that the *dummy beam* provides results in a good agreement with the other two strategies, which may suggest adopting it in the practice in the design of monopiles. Based on project experience of the Authors, the best method to derive the bending moment profile was the derivative of rotation from *plate* element method. The results above are summarised in Table 3.

Table 3. Summary of maximum bending moments (MN·m).

Approach	**Value [MN·m]**	***Comparison with the dummy beam***
stress integration	10.4	– 9.6%
rotation derivative	10.8	– 6.1%
dummy beam	11.5	/

6 CONCLUSIONS

The market of offshore wind turbines has been expanding over the last decades due to climate change, thereby increasing focus on the design of the foundation system, which can represent up to about 20% of the cost of the entire wind farm. Innovative solutions and design methods have therefore been sought to reduce costs of the foundation system.

In this paper, the results of a 3D Finite Element pushover analysis conducted on a monopile embedded in a layered deposit have been presented. In the analyses, the monopile was simulated through *plate* elements and subject to a horizontal force applied to the top of the foundation. The resulting force-displacement and force-rotation pushover curves have been first shown and discussed to detect a reference design condition for the monopile, corresponding to a horizontal displacement at the mudline level equal to one tenth of the outer diameter.

Then, the bending moment profile developed in the monopile has been computed. For the design condition, three different approaches have been used to determine this profile which include the integration of the stresses at the soil-*plate* interface, the derivation of the rotation profile obtained from the *plate* elements representing the monopile, and the extraction of direct output from a *dummy beam* located at the centreline of the monopile. It has been shown that the *dummy beam* provides results in good agreement with the other two strategies, which may suggest adopting it in the practice to speed up the post-processing step in the design of monopiles. It is worth noting that the Timoshenko's beam theory has been adopted in this study, which means that the beam deflection comes both from bending and shearing. This is expected to be well representative of the real behaviour for the monopile at hand. A discussion on the pitfalls of the deterministic approach followed for the *dummy beam* is given in Beck and Silva Jr. (2011).

The capability of 3D Finite Element models of capturing the main features of the soil-monopile behaviour under consideration would always involve a level of uncertainty. It is recommended that these models and results are validated using field-test results or case histories from existing literature.

ACKNOWLEDGEMENTS

The first author is grateful for the financial support provided by Ministero dell'Università e della Ricerca (Italy) through the project PON "Ricerca e Innovazione" 2014-2020.

REFERENCES

Beck, A. T., da Silva Jr, C. R. (2011). Timoshenko versus Euler beam theory: Pitfalls of a deterministic approach. *Structural Safety*, 33(1): 19-25, https://doi.org/10.1016/j.strusafe.2010.04.006.

Bentley (2023a). *PLAXIS 3D 2023.1: General Information Manual 3D* (Available at: https://communities.bentley.com/cfs-file/__key/communityserver-wikis-components-files/00-00-00-05-58/PLAXIS_5F00_3D_5F00_2023.1_5F00_3D_5F00_0_5F00_-General-Information-Manual.pdf, accessed: 12/03/2024).

Bentley (2023b). *PLAXIS 3D 2023.1: Scientific Manual 3D* (Available at: https://communities.bentley.com/cfs-file/__key/communityserver-wikis-components-files/00-00-00-05-58/PLAXIS_5F00_3D_5F00_2023.1_5F00_3D_5F00_4_5F00_-Scientific-Manual.pdf, accessed: 12/03/2024).

Benz, T., Vermeer, P. A., Schwab, R. (2009). A small-strain overlay model. *International Journal for Numerical and Analytical Methods in Geomechanics*, 33(1): 25-44, https://doi.org/10.1002/nag.701.

Gaudio, D., Rampello, S. (2016). Dynamic soil-structure interaction of bridge-pier caisson foundations. In *Geotechnical engineering in multidisciplinary research: from microscale to regional scale CNRIG2016. VI Italian Conf. of Researchers in Geotechnical Engineering, Procedia Engineering*, Elsevier, 158: 146-151, https://doi.org/10.1016/j.proeng.2016.08.420.

Gaudio D., Seong J., Haigh S., Viggiani G. M. B., Madabhushi G. S. P., Shrivatsava R., Veluvolu R., Padhy P. (2023). Boundary effects on dynamic centrifuge modelling of onshore wind turbines on liquefiable soils. *International Journal of Physical Modelling in Geotechnics*, ICE Publishing, 23(1): 16-34, ISSN: 1346-213X, https://doi.org/10.1680/jphmg.21.00085.

Grimstad, G., Andresen, L., Jostad, H. P. (2012). NGI-ADP: Anisotropic shear strength model for clay. *International Journal for Numerical and Analytical Methods in Geomechanics*, 36(4): 483-497, https://doi.org/10.1002/nag.1016.

Lam, A. K. (2018). An engineering solution for a hillside project in Hong Kong. *Geotechnical Research*, ICE Publishing, 5(3), 170-181, https://doi.org/10.1680/jgere.18.00008.

Proceedings of the XVIII ECSMGE 2024
GEOTECHNICAL ENGINEERING CHALLENGES
TO MEET CURRENT AND EMERGING NEEDS OF SOCIETY
© 2024 the Authors
ISBN 978-1-032-54816-6
DOI 10.1201/9781003431749-572
Open Access: www.taylorfrancis.com, CC BY-NC-ND 4.0 license

ECSMGE 24
XVIII EUROPEAN CONFERENCE ON SOIL MECHANICS AND GEOTECHNICAL ENGINEERING

Technical solutions for reducing CO_2 footprint in MSE wall constructions

Solutions techniques permettant de réduire l'empreinte carbone des murs en terre armée

A. Grandclerc*, T. Joussellin
Terre Armée, Rueil-Malmaison, France

**anais.grandclerc@terre-armee.com*

ABSTRACT: Today, the construction industry represents 6 to 8% of total GWP emission worldwide (Lee and Romero, 2023). Actions have been taken for several years to reduce these emissions, but progress is still being made to reach the global greenhouse gas emission reduction targets. MSE walls are mainly composed of a facing made of concrete or welded mesh panels with a backfill reinforced by metallic or geosynthetic elements. They are one of the least CO_2 intensive earth retaining structures. This article deals with the proposal of technical solutions to reduce each component's carbon footprint of a MSE wall (facing, reinforcement, backfill) and to estimate the CO_2 emission reduction at the construction project level (calculations based on a specific and real construction project). Concerning the concrete panels, the replacement of ordinary Portland concrete by low carbon concrete is a key parameter in the reduction of CO_2 emissions of the construction of a MSE wall (estimation of CO_2 emission reduction between 15% and 30% on the total CO_2 emission for this project). Regarding the backfill reinforcement, using geosynthetic reinforcement instead of steel reinforcement is also a way to reduce CO_2 emissions. Indeed, steel reinforcement accounts for around 20% of total CO_2 emissions for this project, while geosynthetic reinforcement accounts for around 5%. Finally, regarding backfill, its carbon impact represents about 45% of this project's overall CO_2 emissions, considering the materials and their transportation. Thus, using recycled materials as backfill or marginal backfill to reduce transportation distance are essential.

RÉSUMÉ: De nos jours, l'industrie de la construction représente 6 à 8% des émissions mondiales de GES (Lee and Romero, 2023). Des actions ont été entreprises depuis plusieurs années pour réduire ces émissions, mais des efforts doivent encore être fournis pour atteindre les objectifs de réduction des émissions de gaz à effet de serre. Les murs en terre armée sont composés de panneaux en béton ou en treillis soudé et d'un remblai renforcé par des éléments métalliques ou géosynthétiques. Ils sont l'un des ouvrages de soutènement à l'empreinte carbone la plus réduite. Cet article porte sur la proposition de solutions permettant de réduire l'impact de chaque élément constituant un mur en terre armée (parement, renforcement, remblais) et d'estimer la réduction d'émission de CO_2 à l'échelle d'un réel projet de construction. Concernant les panneaux en béton, le remplacement des bétons à base de ciment Portland par des bétons bas carbones est un paramètre clé dans la réduction de l'empreinte carbone d'un mur en terre armée (réduction comprise entre 15 et 30% sur l'émission totale de CO_2 du projet). Par ailleurs, l'utilisation de bandes en géosynthétiques à la place des renforcements métalliques pour le remblai est aussi une solution pour réduire l'impact carbone des projets. En effet, les renforcements métalliques représentent 20% des émissions totales du projet, tandis que les renforcements en géosynthétiques représentent uniquement 5%. Concernant le remblai, son impact représente environ 45% des émissions carbones totales. Ainsi, il est essentiel d'utiliser des matériaux recyclés comme remblais et de réduire les distances de transport.

Keywords: Carbon footprint; MSE wall; low-carbon solutions.

1 INTRODUCTION

Progress is still being made to reach the global greenhouse gas emission reduction targets in the construction industry which represents 6 to 8% of total GWP emission worldwide (Lee and Romero, 2023).

MSE wall (Reinforced Earth® wall) components are divided into three parts (Figure 1):

- Facing made of concrete reinforced by steel or welded mesh panels.
- Backfill
- Steel or geosynthetic reinforcements for the backfill.

MSE walls are one of the least CO_2 intensive earth retaining structures.

For this study, a real construction project is considered. The carbon footprint of the components used in the project but also the transportation from the

plants to the construction site, are calculated. A scheme of MSE wall is presented in Figure 2.

In the following, the CO_2 emissions associated with this construction project will be calculated, and then alternatives will be proposed with technical solutions that emit less CO_2.



Figure 1. Description of MSE wall.

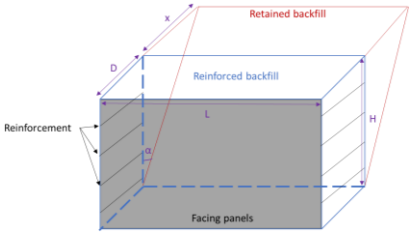

Figure 2. Schematic representation of MSE wall.

2 DESCRIPTION OF THE MSE WALL CONSIDERED FOR THIS STUDY

The construction project considered for this study is a MSE wall composed of reinforced concrete panels as facing, geosynthetic straps as reinforcements of the backfill and backfill.

In this study, the manufacturing of the components, and the transportation of components from the factories to the construction site are considered. The quantities used for this project are presented in Table 1 and in Table 2 and are calculated for 1 m² of wall. The weights of reinforced backfill and retained backfill are calculated from geometrical dimensions of the wall section (Figure 2). The emission factors used to calculate the carbon footprint of this project are presented in Table 3.

Table 1. Geometrical dimensions of the wall and quantity of material for 1 m² of wall.

Designation	Quantity
Surface considered	1 m²
Average height	4 m
Average depth	5 m
Steel reinforcement ratio of the panels	5 kg/m²
% of recycled steel for the panel reinforcement	99%
Total length of backfill reinforcements	14 linear meters
Weight of reinforced backfill	7.5 t
Weight of retained backfill	3 t

Table 2. Transportation of materials from the plants to the construction site.

Materials	Type of transportation	Distance (km)
Facing panels	Truck	150
Geosynthetic reinforcements	Truck	500
Backfill	Truck	20

Table 3. Emission factors used in this study.

Materials	Emission factors	Unit	Database
Concrete	300	$kgCO_2e/m^3$	Exegy solutions, 2022
First cast steel in concrete	1.99	$kgCO_2e/kg$	ICE Database V3, 2019
Recycled steel in concrete	0.565	$kgCO_2e/kg$	EcoInvent v3.10, 2023
Geosynthetic reinforcements	0.30	$kgCO_2e/lm$	EPD GeoStrap, 2021
Backfill	4	$kgCO_2e/t$	Base carbone (V22), 2023
Steel straps (galvanized steel)	2.67	$kgCO_2e/kg$	LCI study, 2021

The result obtained for this construction project is equal to **99 $kgCO_2e$ for 1 m² of MSE wall**.

CO_2 footprints of components (manufacturing and transportation of components to the construction site) of MSE wall are broken down as follows (Figure 3):

- 47% for concrete reinforced by steel panels.
- 4% for reinforcement of backfill.
- 49% for backfill itself.

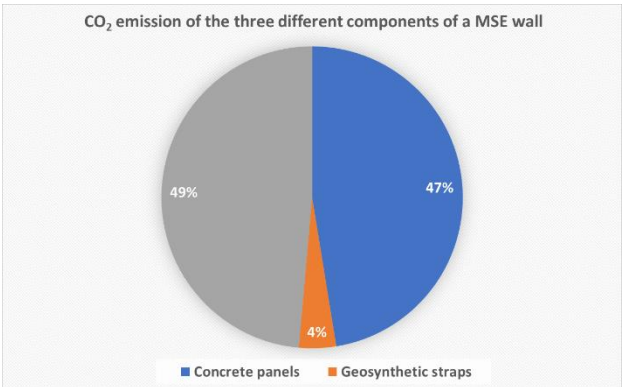

Figure 3. Breakdown of CO_2 emission of a MSE wall specific project.

3 TECHNICAL SOLUTIONS TO REDUCE CARBON FOOTPRINT

3.1 Facing panels

In this part, the impact of using low carbon concrete is studied. Three categories of low carbon concretes are defined in terms of emission factors for concrete with a compressive class strength between C35/45 to C45/55 (MPa), which is the most common strength classes used for concrete panels in MSE applications (Table 4). The emission factors are extracted from Exegy solutions, 2023.

Table 4. Emission factors for three low carbon concrete categories according to Exegy solutions, 2023.

Category	Emission factors minimum	Emission factors maximum	Unit
Classic concrete	240	-	$kgCO_2e/m^3$
Low carbon concrete	175	240	$kgCO_2e/m^3$
Very low carbon concrete	120	175	$kgCO_2e/m^3$
Ultra-low carbon concrete	-	120	$kgCO_2e/m^3$

The impact of using low carbon, very low carbon and ultra-low carbon categories on total CO_2 emission of a MSE wall is proposed in Table 5.

Table 5. Impact of using low carbon concretes on the CO_2 emission of a MSE construction project.

Category	Emission factors ($kgCO_2/m^3$)	Total CO_2 emission ($kgCO_2e$) for 1m² of MSE wall
Classic concrete	300	99.35
Low carbon concrete	200	85.35
Very low carbon concrete	150	78.35
Ultra-low carbon concrete	100	71.35

The use of low-carbon concrete reduces the carbon footprint of the entire structure by 14% for low carbon concrete, 21% for very low carbon concrete and 28% for ultra-low carbon concrete.

3.2 Reinforcements of backfill

In this part, the impact of using steel straps with 50% of recycled steel instead of geosynthetic straps is studied. The results are presented in Table 6.

Table 6. Impact of using steel straps instead of geosynthetic straps on the CO_2 emission of a MSE construction project.

Type of reinforcement	Emission factors ($kgCO_2/kg$)	Total CO_2 emission ($kgCO_2e$) for 1m² of MSE wall
Steel straps (50% recycled)	1,62*	109.16
Geosynthetic straps	3,3**	99.35

** from steel with 50% recycled, from [EcoInvent v3.1, 2014].*
***from [EPD GeoStrap, 2021].*

The use of geosynthetic straps reduces the carbon footprint of the entire structure by 9% compared to the use of steel strips with 50% of recycled steel.

3.3 Backfill

This section examines the CO_2 footprint impact of the distance of transportation for the backfill.

As mentionned in section 2, backfill represents 49% on the total CO_2 emission of the specific MSE wall construction project considered in this study and 15% of the CO_2 emission from the backfill is occupied by the transportation to the construction site.

Table 7 presents the study of the impact of transportation distance on the CO_2 footprint of the structure.

Table 7. Impact of transportation distance of backfill on the CO_2 emission of a MSE construction project.

Distance of backfill transportation (km)	Total CO_2 emission ($kgCO_2e$) for 1m² of MSE wall
20	99.35
50	108.75

It is important to use a fill material from the closest possible source to the construction site, as increasing the transportation distance from 20 to 50 km increases the project's CO_2 emissions by 8.6%.

4 CONCLUSIONS

The three alternatives proposed have a significant impact on the total CO_2 footprint of a MSE wall. Indeed, the calculation of the carbon footprint of a project with the most polluting assumptions (steel straps, conventional concrete for the panels, 50 km for the transportation of the backfill) results in a total CO_2 emission of 118.56 $kgCO_2e$, while for a project with the least polluting assumptions (geosynthetic straps, Ultra-low-carbon concrete, and 20 km for the transportation of the backfill), the total emission is equal to 71.35 $kgCO_2e$. Using low carbon concretes

seems a key parameter to reduce CO_2 emission of this type of construction.

This study demonstrates that feasible solutions can significantly reduce the carbon emissions of a MSE wall.

Other alternatives exist, such as increasing the amount of recycled steel in steel strips or replacing the steel reinforcement in panels with glass or basalt fibers reinforcement or using recycled materials such as crushed concrete as backfill.

ACKNOWLEDGEMENTS

This study has been performed inside TERRE ARMEE company. No external financial support was provided.

REFERENCES

Agence de la transition écologique (2024). Base Carbone V22, [online] Available at: Base carbone® - data.gouv.fr, accessed: 24/03/2024.

Circular Ecology (2019). ICE Database V3, [online] Available at: ICE Database V3 Launched - Circular Ecology, accessed: 10/06/2019.

EcoInvent (2023). EcoInvent V3.10, [online] Available at: ecoinvent v3.10 - ecoinvent, accessed: 10/11/2023.

Lee, H., and Romero, J. (2023). Sections. In: Climate Change 2023: Synthesis Report. Contribution of working groups I, II and III to the Sixth Assessment Report of the Intergovernmental Panel on Climate Change, IPCC, Geneva, Switzerland, pp. 35-115, doi: 10.59327/IPCC/AR6-9789291691647.

Terre Armée (2021). Environmental product declaration of GeoStrap, [online] Available at: https://www.terre-armee.com/geostrap-reinforcements-now-certified-by-rts-for-an-environmental-product-declaration-epd/, accessed: 7/10/2021.

Vinci Construction (2022). Exegy-solutions, [online] Available at: EXEGY (exegy-solutions.com), accessed: 2022.

World Steel Association (2021). Seventh global LCI study for steel products, Available at: Life cycle inventory (LCI) study (worldsteel.org), accessed: 05/2021.

Proceedings of the XVIII ECSMGE 2024
GEOTECHNICAL ENGINEERING CHALLENGES
TO MEET CURRENT AND EMERGING NEEDS OF SOCIETY
© 2024 the Authors
ISBN 978-1-032-54816-6
DOI 10.1201/9781003431749-573
Open Access: www.taylorfrancis.com, CC BY-NC-ND 4.0 license

ECSMGE 24
XVIII EUROPEAN CONFERENCE ON SOIL MECHANICS AND GEOTECHNICAL ENGINEERING

Why natural log of soil permeability is a linear function of void ratio for 0-400µm soils having a sandy-silty-clayey matrix?

Pourquoi le logarithme décimal de la perméabilité des sols est une fonction linéaire de l'indice des vides pour des sols 0-400µm ayant une matrice sablo-limono-argileuse ?

J.C. Gress*
Ecole Nationale des Travaux Publics de l'Etat, Vaulx en Velin, France

M. Ferreira
Hydrogeotechnique, Rouen, France

J.M. Cuinet
Hydrogeotechnique, Nancy, France

**jeanclaude.gress@gmail.com*

ABSTRACT: Many authors working on soil permeability put forward the proportionality of its value with the term $e^3/(1+e)$, where e is the void ratio. Others working on soils having a sandy-silty-clayey matrix, consider that the natural logarithm of their permeability is proportional to e. These two relations are very different. The link between them will be presented. Then, the way to calculate the soil permeability through that of the 0-400µ fraction will be detailed.

RÉSUMÉ: De nombreux auteurs travaillant sur la perméabilité des sols avancent que leurs perméabilités est proportionnelle au terme $e^3/(1+e)$, où e est leur indice des vides. D'autres travaillant sur des sols à matrice sablo-limono-argileuse considèrent que le logarithme décimal de leurs perméabilités est proportionnel à e. Ces relations sont très différentes. Le lien qui les relie est présenté. Puis sera détaillée la manière de calculer la perméabilité du sol au travers de celle de la fraction 0-400µ.

Keywords: Soil permeability; void index; liquidity limit; plasticity index; volume-specific area.

1 INTRODUCTION

When working on soil permeability k, geotechnical engineers use relationships linking its value to void ratio e. Chapuis, for example propose its proportionality to the term $e^3/(1+e)$ and Tavenas put forward a linear relationship between the natural logarithm of k and e.

In order to make the comparison possible between the two relationships, a general geotechnical framework is at first proposed in order to classify the type of soil we are working on. Then, the importance of the notion of the equivalent vertical stress σ'_{eq} will be presented. Comparing the correlation for 0-400µm soils due to Terzaghi between compressibility index Cc and the liquidity limit wl to the relationship in a oedometer test between Cc and the vertical pressures σ'_1 and $\sigma'_{7,5}$ explaining water-contents equal to liquidity limit and 7,5% will be deduced the value of $\log\sigma'_{7,5.}$ Then, still in an oedometer test diagram, we will develop a relationship between void ratio at a vertical pressure of σ'_{eq} defined in paragraph 3 and a relationship between soil dry density and liquidity limit and $\sigma_{eq.}$. It will then imply a linear relationship between $\log(e^3/(1+e))$ and e for 0-400µm soils. For 0-D soils, a difficulty will remain, that is the evaluation of the volume-specific surface as proposed by Chapuis and appearing in the general relationship giving k. Will then be presented improved ways compared with those suggested by Chapuis and Locat,soil permeability being deduced from the assesmnent of the permeability of the 0-400µ fraction.

2 PROPOSED GENERAL GEOTECHNICAL FRAMEWORK.

We work on soils having a 0-D particle size distribution curve, D being the lowest diameter of the

maximum particle size. The passing value at 400µ is written %400µ.
It is then important to distinguish those where D is equal to or less than 400µm, and when D is greater than 400µm, those for which 400µ-D grains are scattered in the 0-400µ matrix and those where they are in contact. When scattered, then a consolidation process explais their density. In both cases, we can notice that soil permeability of the 0-D soil is the permeability of the 0-400µ fraction, adjusted by the surface of the 0-400µ fraction passed through by the waterflow:

$$k_{0\text{-}D} = \%400\mu(\gamma_{d0\text{-}D}/\gamma_{0\text{-}400\mu})\, k_{0\text{-}400\mu} \quad (1)$$

Secondly, the dry density of the total soil $\gamma_{d0\text{-}D}$, of the 0-400µ fraction $\gamma_{d0\text{-}400\mu}$and of the grains γ_s are linked in both cases by the relationship:

$$1/\gamma_{d0\text{-}D} = \%400\mu / \gamma_{d0\text{-}400\mu} + (1\text{-}\%400\mu)/\gamma_s \quad (2)$$

For 0-400µm soils, grains 400µ-D scattered, they are generated by a consolidation process, through a first loading at a preconsolidation pressure σ'_p followed by an unloading at σ'_{v0} kPa, vertical effective pressure. The soils are supposed not to be cemented. They don't include organic matters and are not saline. Their sensitivity St is lower than 4.

3 EQUIVALENT VERTICAL PRESSURE

The equivalent pressure σ'_{eq} is the vertical pressure that would lead through a normally consolidated process to the same soil void ratio than that due to the loading and unloading process. Its value is linked to σ'_p and σ'_{V0} through the relationship:

$$\sigma'_{eq} = \sigma'^{(Cs/Cc)}_{vo}\, \sigma'^{((Cc-Cs)/Cs)}_{p} \quad (3)$$

Cc compression index and *Cs* recompression index, measured by an oedometer test, then for *D* less than 3,2mm.

4 DRY DENSITY, LIQUIDITY LIMIT AND EQUIVALENT VERTICAL PRESSURE

For 0-400µm soils, one correlation is well known between Cc compressibility index and liquidity limit wl due to Terzaghi:
Cc = 0,009 (wl - 10) that can be written with little difference:

$$Cc = 0{,}0085(wl - 7{,}5),\ wl \text{ in } \% \quad (4)$$

Looking at an oedometer diagram, we can write:

$$Cc = \gamma_s/\gamma_w\ (wl - 7{,}5)/100/\log(\sigma'_{7,5}/\sigma'_1) \quad (5)$$

where σ'_1 and $\sigma'_{7,5}$ are vertical effective stresses leading to void ratios corresponding to a saturated water content equal to liquid limit and to 7,5%, γ_s and γ_w being grains and water density.

Comparing (4) with (5), it appears that for $\log\sigma'_1=1$ corresponding to σ'_1 = 10 kPa, then $\log\sigma'_{7,5}$ = 4,2. We can then write, using the second relationship hereafter:

$$Cc = \gamma_s/\gamma_w\ (wnoc - 7{,}5)/100/\ (\log\sigma'_{7,5} - \log\sigma'_{eq}) \quad (6)$$

$$\gamma_w/\gamma d = \gamma_w/\gamma_s + 0{,}075 + 0{,}00315(wl-7{,}5)(4{,}2-\log\sigma'_{eq}) \quad (7)$$

or, with σ'_{eq} in kPa:

$$eoc = \gamma_s/\gamma_w\ (0{,}075 + 0{,}00315(wl-7{,}5)(4{,}2-\log\sigma'_{eq})) \quad (8)$$

or:

$$eoc = 0{,}20 + 0{,}0085\ (wl-7{,}5)\ (4{,}2-\log\sigma'_{eq}) \quad (9)$$

For 0-D soils, we will have to make a correction on γ_d through relationship (2).

5 GENERAL RELATIONSHIP GIVING k

For a water at a temperature of 10 degrees Celsius, Kozeny and Carman general equation giving k in m/s is:

$$k = 1{,}5\ 10^{-6}\ (1/vssa)^2\ e^3/\ (1+e) \quad (10)$$

where vssa is the volume-specific surface area (m^{-1}), calculated through the gradation curve as proposed by Chapuis and Locat, and developed in paragraph 7.

For a water at a temperature t, k given by (9) must be multiplied by the expression:

$$\alpha = 0{,}737 + 0{,}025\ t + 0{,}00016\ t^2 \quad (11)$$

due to the water dynamic viscosity variation with temperature. In Martinique island, for a water at 30 degrees, k must be multiplied by 1,63.

6 CALCULATION OF log(e^3/(1+e)) AS A FUNCTION OF wl AND e FOR 0-400µ SOILS

Through relationship (9), we calculate values of e for varying values of σ'_{eq} and liquid limit wl. Then we calculate log (e^3/(1+e)) and compare its value to e.

The results are summarized in Table 1.

Table 1. values of e for varying values of σ'eq and liquid limit wl.

wl	σ'eq kPa	50	100	150	200
0,20	E	0,46	0,43	0,41	0,40
	log(e^3/(1+e))	-1,16	-1,24	-1,30	-1,33
0,40	e	0,89	0,81	0,76	0,72
	log(e^3/(1+e))	-0,43	-0,53	-0,60	-0,66
0,60	e	1,32	1,18	1,10	1,05
	log(e^3/(1+e))	-0,007	-0,12	-0,19	-0,25
0,80	e	1.74	1.56	1.45	1.37
	log(e^3/(1+e))	0,28	0,17	0,09	0,03
1,00	e	2,17	1,93	1,79	1,69
	log(e^3/(1+e))	0,51	0,39	0,31	0,26

Looking at the values displayed in Table 1 and shown in Figure 1, it appears that they obey to the general relationship:

$$log(e^3/(1+e)) = A + Be \qquad (12)$$

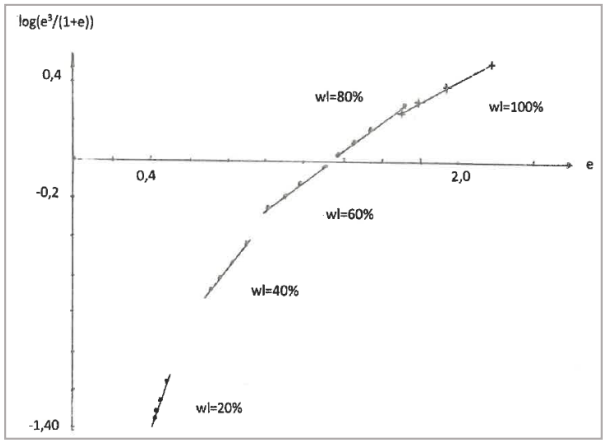

Figure 1. Relations between log (e^3/(1+e)) and e.

Table 2. Values of A and B

wl	0,20	0,40	0,60	0,80	1,00
A	-2,444	-1,658	-1,200	-0,884	-0,638
B	2,762	1,382	0,907	0,710	0,528

It appears that A and B are hyperbolic functions of wl, as shown by Figure 2:

$$A = - 0,706/ (wl + 0,0883) \qquad (13)$$

$$B = 0,529/ (wl – 0,009) \qquad (14)$$

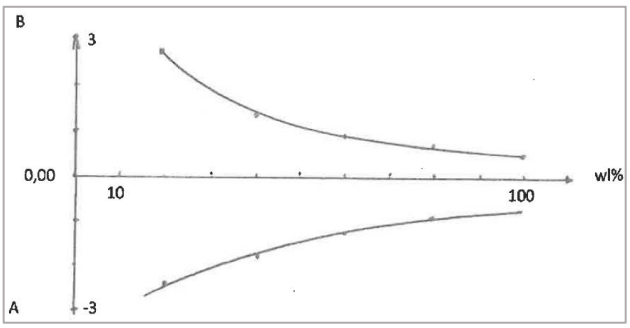

Figure 2. Values of A and B function of wl.

Then taking the natural logarithm of each member, relationship (10) becomes:

$$logk = 6,176 - 2log\ vssa + log(e^3/(1+e)) \qquad (15)$$

and using expressions (12), (13) et (14):

$$logk=6,176-0,706/(wl+0,0883)-2logvssa+0,529e/(wl-0,009) \qquad (16)$$

In the proposed framework of thinking, it appears that the natural logarithm of permeability is indeed a linear function of void ratio e for 0-400µm soils.

7 CHAPUIS AND LOCAT CALCULATION OF VSSA

We need to have the soil particle size distribution and the soil dry density $\gamma d_{0\text{-}D}$. We will use relationships (1) and (10),and for the latter vssa and e are those of the 0-400µ fraction.

7.1 Soils having a non-plastic matrix, PI of the 0-400µ fraction being less than 10.

Chapuis and Legaré (1992), suggest to calculate vssa through the grain size curve, and the expression:

$$vssa = 6\ \Sigma\ (Pnod_i – Pnod_{(i+1)})/(d_{(i+1)} \qquad (17)$$

($Pnod_i$ – $Pnod_{(i+1)}$) is the difference between the percentage by weight smaller than size d_i and that larger than next size $d_{(i+1)}$, vssa unit being m2/m3. The grain size curves always have a minimum measurable particle size dmin. In the method of Chapuis and Legaré, an equivalent size deq must be defined for all particles smaller than dmin through the expression:

$$deq^2 = dmin^2/3 \qquad (18)$$

the percentage in weight dedicated to deq being the difference between 100% and the percentage value

corresponding to dmin. Secondly (figure 3), in the fine size zone, the grain size distribution has to be modified to follow a minimum slope of 20% (Chapuis).

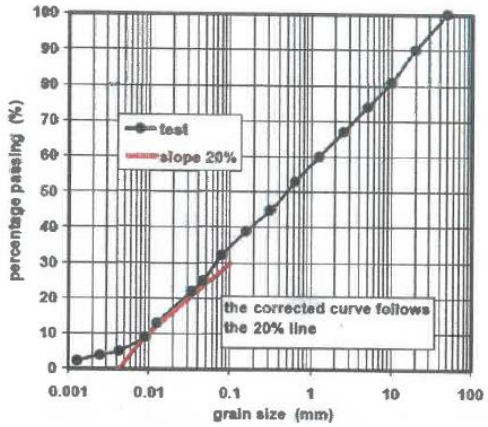

Figure 3. Chapuis proposed modification if slope flatter than 20%.

The assessment of vssa is made on the 0-400µ fraction. The void index is that of the 0-400µ fraction, equal to the void index of the 0-D soil,divided by the volume of the 0-400µ grains:

$$e_{0\text{-}400\mu} = (\gamma_s/\gamma_{dO\text{-}D} - 1)/(\%400\mu\ \gamma d_{0\text{-}D}/\gamma_s) \quad (19)$$

7.2 Soils having a plasticity index of the 0-400µ fraction greater than 10.

The mssa value is that of the 0-400µ fraction calculated through Locat (1984) proposals. Chapuis gives on Figure 4, Locat correlation between mass specific surface area and percentage smaller than 2µm. Based on this suggestion, we propose the underlying correlation:

$$mssa \text{ in } m^2/kg = 10^3(5+1.2\ PI) \quad PI \text{ in } \% \quad (20)$$

We know (Gress) that:

$$PI = -4(1-\%2\mu) + 4.5\ \%2\mu\ VB2\mu \quad (21)$$

VB2µ being the methylene blue value of the 0-2µ fraction.

(20) can then be expressed as:

$$mssa = 10^3\ (0.2 + \%2\mu\ (4.8 + 5.4\ VB2\mu)) \text{ in } m^2/kg \quad (22)$$

Figure N°4 gives the link between mssa value of the 0-400µ fraction , the passing at 2µ and the blue methylene value of the 0-2µ fraction VB 2µ.

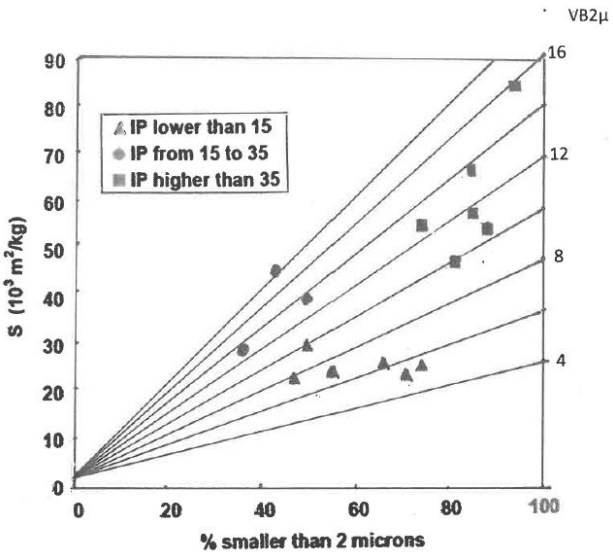

Figure 4. Locat highlighted by VB2µ values.

The link between vssa and mssa is given by:

$$vssa = \rho_s\ mssa,\ \rho_s \text{ given in kg/m}^3 \quad (22)$$

8 CONCLUSIONS

The reason why the natural logarithm of permeability is a linear function of void ratio for 0-400µ soils has been explained.

Furthermore, ways to estimate the soil permeability have been given in order to calculate the permeability of all 0-D soils through Kozeny- Carman expression, through that of the 0-400µ fraction.

All these proposals are valid in the general framework of working, we have detailed. Difficulties will still be due to the quality of the samples on which we will measure dry densities and determine grain size curves.

REFERENCES.

Carman, P.C. (1939) Permeability of saturated sands, silts and clays. *Journal of Agricultural Science.* 29: 263-273. DOI:10.1017/S0021859600051789 Corpus ID: 85222206.

Chapuis, R.P. (2003). Predicting the coefficient of permeability using the Kozeny-Carman equation. Ecole Polytechnique de Montréal.

Fair, G.M. and Hatch, L.P. (1933) Fundamental factors governing the steam line flow of water through sands. *Journal of American Water Works association.*25(11)1551-1565. DOI:10.1002/J.1551-8833.1933.TB18342.X Corpus ID: 108144981

Proceedings of the XVIII ECSMGE 2024
GEOTECHNICAL ENGINEERING CHALLENGES
TO MEET CURRENT AND EMERGING NEEDS OF SOCIETY
© 2024 the Authors
ISBN 978-1-032-54816-6
DOI 10.1201/9781003431749-574
Open Access: www.taylorfrancis.com, CC BY-NC-ND 4.0 license

ECSMGE 24
XVIII EUROPEAN CONFERENCE ON SOIL MECHANICS AND GEOTECHNICAL ENGINEERING

Theoretical assessment of the advective-diffusive transport of contaminants through landfill composite liners

Évaluation théorique du transport advectif-diffusif de contaminants permis les barrières composites des décharges

N. Guarena*, A. Dominijanni, M. Manassero
Polytechnic University of Turin, Turin, Italy

**nicolo.guarena@polito.it*

ABSTRACT: Composite liners consisting of a geomembrane, placed over a low-permeability clay layer, are used throughout the world for the lining of waste disposal facilities, with the aim to prevent the groundwater quality from being compromised, and an unacceptable risk for the human health and the environment from occurring. Despite the importance of developing a rational approach to calculate the contaminant transport rate through composite liners, for both the design of new landfills and the risk assessment of the existing ones, limited attention has been paid so far to the derivation of analytical, numerical, or hybrid analytical-numerical solutions, which can help designers assess the containment performance of lining systems. After an overview of the simplified calculation approaches that are currently adopted for the performance-based design of composite liners, a novel theoretical framework is presented in this paper, which allows the advective-diffusive transport of inorganic contaminants to be modelled considering imperfect contact conditions between the geomembrane and the underlying clay layer.

RÉSUMÉ: Les barrières composites constituées d'une géomembrane, placée sur une couche d'argile à faible perméabilité, sont utilisés dans le monde pour l'isolement des installations de stockage des déchets, pour éviter que la qualité des eaux souterraines ne soit pas compromise et ne présente pas un risque inacceptable pour la santé et l'environnement. Malgré l'importance de développer une approche rationnelle pour calculer le taux de transport des contaminants permis les barrières composites, pour la conception de nouvelles décharges et pour l'évaluation des risques des décharges existantes, une attention limitée a été accordée jusqu'à présent à l'élaboration de solutions analytiques, numériques ou hybrides analytiques-numériques, qui peuvent aider les ingénieurs à évaluer les performances de confinement des systèmes d'isolement. Après un aperçu des approches de calcul simplifiées actuellement adoptées pour la conception basée sur les performances des barrières composites, un nouveau cadre théorique est présenté dans cet article, qui permet de modéliser le transport advectif-diffusif des contaminants inorganiques en considérant des conditions de contact imparfaites entre la géomembrane et la couche d'argile sous-jacente.

Keywords: Contaminant transport; geosynthetics; landfills; performance-based design; risk assessment.

1 INTRODUCTION

Composite liners that include a high-density polyethylene (HDPE) geomembrane (GM), placed over a compacted clay liner (CCL), are prescribed throughout the world for the bottom lining systems of waste disposal facilities, with the goal of minimising the migration of contaminants from the waste fill to the surrounding environment (Giroud and Cazzuffi, 1989). Furthermore, the use of alternative lining systems, such as those in which the CCL is replaced with a geosynthetic clay liner (GCL), is permitted in most regulations, provided that equivalency with the prescribed composite liner is demonstrated on the basis of a selected performance criterion. The most widely adopted approach is to assume that equivalency is demonstrated if the steady-state advective travel time through the proposed alternative liner is lower than that through the prescribed liner, but this approach fails to recognise that diffusion is a significant, if not the dominant, contaminant transport mechanism within low-permeability clay liners (Manassero and Shackelford, 1994; Foose et al., 2002; Shackelford, 2014). For such a reason, the performance criteria that account for the combined effect of advection and diffusion on contaminant transport, under either steady-state or transient-state conditions, are preferable over the advective travel time criterion (Shackelford, 1990; Manassero et al., 2000; Katsumi et al., 2001; Rowe and Brachman, 2004).

Although several analytical, numerical, and empirical solutions have been developed, since the pioneering study of Giroud and Bonaparte (1989), to calculate the liquid flux through landfill composite liners, relatively few studies have been aimed at quantifying the advective-diffusive transport of contaminants in the presence of defects in the GM layer (e.g., defective seams between adjacent panels, punctures caused by sharp materials beneath and above the GM, and tensile failures induced by the landfilling operations). The latter issue is particularly relevant in the case of inorganic compounds, which, unlike many organic compounds, do not readily diffuse through intact portions of the GM and, therefore, their transport should be recognised as a three-dimensional (3D) process that involves migration through the GM defects, through the interfacial zone between the GM and the underlying low-permeability mineral layer and, finally, through the mineral layer itself, via a combination of advection and diffusion.

A simplified approach to model the advective-diffusive transport of inorganic contaminants through composite liners was proposed by Katsumi et al. (2001), who identified an equivalent one-dimensional (1D) system for which analytical solutions to the contaminant breakthrough time and mass flux exist. This approach, which has since been implemented in a number of analytical studies that have dealt with the performance-based design of landfill lining systems, allows both steady-state (Foose, 2010; Guarena et al., 2020; Dominijanni and Manassero, 2021; Dominijanni et al., 2021) and transient-state contaminant transport analyses (Foose et al., 2001; Kandris and Pantazidou, 2012; Dominijanni et al., 2023) to be carried out using typical spreadsheet applications and hand-held calculators. Despite being particularly attractive because of its versatility, the Katsumi et al. (2001) approach is not devoid of drawbacks, the most serious of which can probably be ascribed to neglecting the mass conservation condition for the solute phase. The objective of this paper is thus to illustrate a novel theoretical framework, which has recently been developed by Guarena et al. (2023) with the aim of covering the aforementioned modelling gap.

2 THEORETICAL FRAMEWORK

The theoretical framework outlined herein has been developed under the assumption that inorganic contaminants preferentially migrate through holes that are located in correspondence to the wrinkles of the GM layer, rather than through holes that occur in flat areas. Therefore, only the case of a damaged wrinkle of width $2b_w$ is referred to in this paper, which is perfectly analogous to the case of a cut, tear, or defective seam of width $2b_w$ occurring in a flat area of the GM if the liquid and contaminant transport rates are not controlled by the size of the actual holes in the wrinkle (Figure 1). Moreover, if the length of the defect, L_w, is much greater than its width (i.e., defect of uniform width and infinite length), the liquid and contaminant transport analyses can be treated as two-dimensional problems (Touze-Foltz et al., 1999; Giroud and Touze-Foltz, 2005).

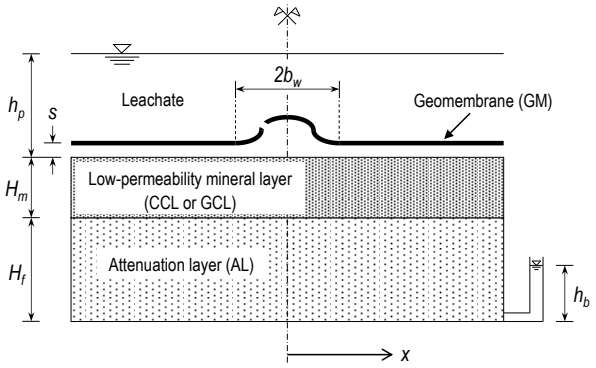

Figure 1. Reference scheme for the liquid and contaminant transport analyses through a composite liner with a defect of uniform width and infinite length in the GM layer and imperfect contact conditions between the GM and the low-permeability mineral layer (not to scale).

2.1 Katsumi et al. (2001) approach

The approach that was proposed by Katsumi et al. (2001), with the aim of providing a simple calculation tool to analyse the transport of inorganic contaminants through composite liners when the leachate flow is at steady state, consists in computing an equivalent area, A_e, which conducts the same (total) leachate flow rate as the considered defect for the same hydraulic head drop across the composite liner. If Rowe's (1998) analytical model for non-interacting defects of uniform width and infinite length is adopted to assess the leachate flow rate, the equivalent area is expressed as follows:

$$A_e = 2b_w L_w \left(1 + \frac{1}{\alpha b_w}\right) \tag{1}$$

The α parameter that appears in Equation 1 can be interpreted as the exponential decay constant of the hydraulic head beneath the GM, and is given by:

$$\alpha = \sqrt{\frac{k_s}{\left(H_f + H_m\right)\theta_h}} \tag{2}$$

where θ_h is the hydraulic transmissivity of the interfacial zone between the GM and the low-permeability mineral layer, and k_s is the equivalent hydraulic conductivity corresponding to the low-permeability mineral layer (saturated hydraulic conductivity k_m) and the attenuation layer (AL) (saturated hydraulic conductivity k_f):

$$k_s = \frac{H_f + H_m}{\frac{H_f}{k_f} + \frac{H_m}{k_m}} \tag{3}$$

Once the equivalent area has been computed, the contaminant mass flow rate through the GM defect, J_e, can be obtained as the product of A_e and the contaminant mass flux, which in turn is calculated according to the existing analytical solutions to the partial differential equation that governs the 1D solute transport through multi-layerd barriers via advection, diffusion, sorption, and degradation. When steady-state conditions are achieved for both the liquid and solute transport, the dimensionless contaminant mass flow rate through the GM defect, J_e^*, which is defined as the ratio of J_e to the advective component of the mass flow rate occurring below the defect, is given by:

$$J_e^* = \left(1 + \frac{1}{\alpha b_w}\right) \frac{\exp(P_L) - \chi_b}{\exp(P_L) - 1} \tag{4}$$

where P_L is the Péclet number and χ_b is the ratio of the contaminant concentration at the bottom of the composite liner to that in the leachate drainage layer.

The Péclet number can be assessed as follows:

$$P_L = \frac{i_s k_s}{\Lambda} \tag{5}$$

where i_s is the maximum mean hydraulic gradient through the low-permeability mineral layer and the attenuation layer, and Λ is the equivalent diffusivity:

$$i_s = 1 + \frac{h_p - h_b}{H_f + H_m} \tag{6}$$

$$\Lambda = \frac{1}{\frac{H_f}{n_f D_f^*} + \frac{H_m}{n_m D_m^*}} \tag{7}$$

being n_m and n_f the porosities of the low-permeability mineral layer and the attenuation layer, respectively, and D_m^* and D_f^* the effective diffusion coefficients of the low-permeability mineral layer and the attenuation layer, respectively, which are obtained as the product of the apparent tortuosity factor, τ (< 1), and the free-solution diffusion coefficient of the contaminant, $D_{s,0}$.

2.2 Guarena et al. (2023) approach

According to the theoretical framework which has recently been developed by Guarena et al. (2023), the 3D advective-diffusive transport of inorganic contaminants within the composite liner is conceptualised as a horizontal flow along the interface between the GM and the low-permeability mineral layer and then a vertical flow in the low-permeability mineral layer, in a similar way to the reference scheme that was considered by Rowe (1998) and Touze-Foltz et al. (1999, 2001) with a view to approximating the actual leachate flow network under imperfect contact conditions at the GM/CCL or GM/GCL interface.

If steady-state conditions are achieved for both the liquid and solute transport, the contaminant concentration profile beneath the GM satisfies the following homogeneous, second-order, linear ordinary differential equation with non-constant coefficients:

$$\frac{\mathrm{d}^2\chi}{\mathrm{d}\xi^2} - \frac{\Theta}{\exp(\xi)}\frac{\mathrm{d}\chi}{\mathrm{d}\xi} + \\ - \frac{\Theta}{\exp(\xi)\left[\exp\left(\frac{P_L}{\exp(\xi)}\right) - 1\right]}(\chi - \chi_b) = 0 \tag{8}$$

which has to be solved for $0 \le \xi < +\infty$ in conjunction with the following set of boundary conditions:

$$\begin{cases} \chi(0) = 1 \\ \lim\limits_{\xi \to +\infty} \dfrac{\mathrm{d}\chi}{\mathrm{d}\xi}(\xi) = 0 \end{cases} \tag{9}$$

In Equation 8, χ is the ratio of the contaminant concentration beneath the GM to that in the leachate drainage layer, ξ is the dimensionless distance from the GM defect, $\xi = \alpha(x - b_w)$, and Θ is the transmissivity number, which is a measure of the relative importance of advection compared to diffusion through the GM/CCL or GM/GCL interface:

$$\Theta = \frac{i_s \theta_h (H_f + H_m)}{\theta_d} \tag{10}$$

where θ_d the diffusive transmissivity of the interface.

Once the steady-state contaminant concentration profile beneath the GM has been determined, the

dimensionless contaminant mass flow rate through the GM defect, J_s^*, is given by:

$$J_s^* = \frac{\exp(P_L) - \chi_b}{\exp(P_L) - 1} + \frac{1}{\alpha b_w}\left[1 - \frac{1}{\Theta}\frac{d\chi}{d\xi}(\xi = 0)\right] \quad (11)$$

3 EXAMPLE ANALYSIS

With the aim of quantifying the error in the predicted steady-state contaminant mass flow rate, due to the use of the Katsumi et al. (2001) approach relative to the novel theoretical framework outlined in this paper, and referred to as the Guarena et al. (2023) approach, the lining system described in Table 1 has been considered herein. Such lining system comprises, from top to bottom, a GM, a 1-cm-thick GCL, and a 4-m-thick AL. Cadmium (Cd^{2+}) has been selected to represent the inorganic leachate constituent of interest ($D_{s,0}$ = $7.17 \cdot 10^{-10}$ m^2/s), and the half-width of the GM defect, b_w, has been assumed equal to 0.1 m. The GM-GCL interface has been assigned a value of the hydraulic transmissivity ($\theta_h = 3.5 \cdot 10^{-11}$ m^2/s), which is consistent with the range of variation measured through laboratory-scale experiments (Rowe and Brachman, 2004).

Table 1. Properties of the layers comprising the landfill composite liner, which is referred to for the purposes of the example analysis.

	AL	GCL	
n	0.3	0.69	(-)
τ	0.25	0.31	(-)
k	$1 \cdot 10^{-7}$	$1 \cdot 10^{-11}$	(m/s)

Perfect flushing boundary conditions have been adopted at the base of the composite liner (i.e., $\chi_b = 0$), while the diffusive transmissivity of the GM-GCL interface, in the absence of experimental studies devoted to its measurement, can be tentatively estimated as follows:

$$\theta_d = D_{s,0} s \quad (12)$$

where s is the thickness of the GM/GCL interface, which in turn can be related to θ_h, if Newton's viscosity law for the flow between two parallel plates applies to the transmissive layer (Giroud and Bonaparte, 1989):

$$s = \sqrt[3]{\frac{12\theta_h \mu_w}{\gamma_w}} \quad (13)$$

being γ_w (10 kN/m^3) and μ_w (10^{-6} kPa·s) the unit weight and viscosity of water, respectively.

According to Equation 12, the θ_d parameter varies between $1 \cdot 10^{-15}$ and $1 \cdot 10^{-14}$ m^3/s, and the associated range of variation of the transmissivity number can be assessed through Equation 10 as a function of the hydraulic gradient. As shown in Figure 2a, even when diffusion represents the dominant transport mechanism within the multi-layered soil profile (i.e., $P_L \ll 1$), contaminant transport through the GM/GCL interface may be controlled by advection due to the high values of the transmissivity number (i.e., $\Theta \gg 1$) corresponding to the estimated values of the diffusive transmissivity.

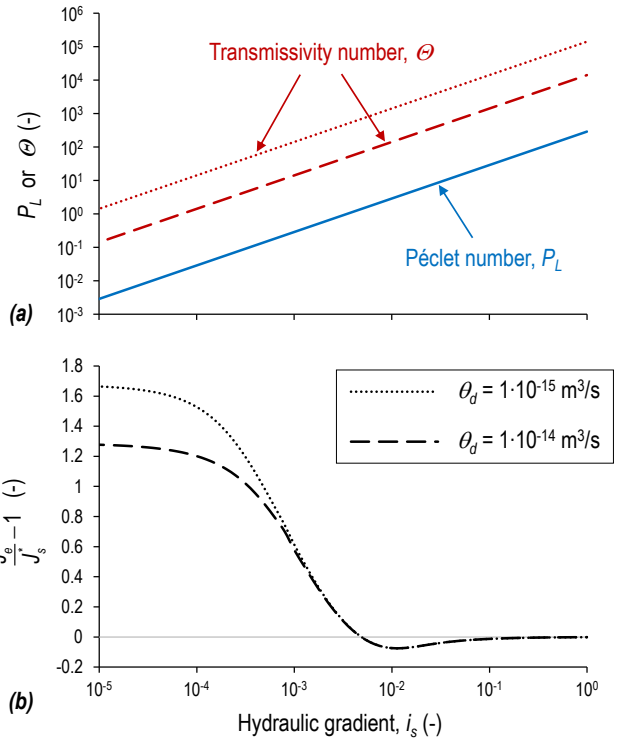

Figure 2. Results of the example calculation: (a) Péclet and transmissivity numbers as a function of the hydraulic gradient across the composite liner, and (b) error in the predicted contaminant mass flow rate due to the use of the Katsumi et al. (2001) approach.

The error in the predicted steady-state contaminant mass flow rate, which is associated with the use of the Katsumi et al. (2001) approach, can be finally assessed for the considered range of variation of both the hydraulic gradient and the diffusive transmissivity. Equations 4 and 11 have been used to calculate J_e^* and J_s^*, respectively, the latter of which has been determined after solving numerically Equation 8 according to the finite difference method.

As shown in Figure 2b, two asymptotic conditions clearly emerge from the example analysis:

- at the highest hydraulic gradients ($i_s > 10^{-2}$), when advection dominates over diffusion through both the multi-layered soil profile ($P_L \gg 1$) and the GM/GCL interface ($\Theta \gg 1$), the Katsumi et al. (2001) approach leads to a prediction of the contaminant mass flow rate that can be regarded as the rigorous one from the mass conservation condition viewpoint, for both the liquid and solute phases;
- at the lowest hydraulic gradients ($i_s < 10^{-3}$), when the importance of diffusion is comparable to ($\Theta \sim 1$) or greater than ($P_L \ll 1$) that of advection through the GM/GCL interface and the multi-layered soil profile, respectively, neglecting the mass conservation condition for the solute phase causes an error, whose magnitude depends to a large extent on the diffusive transmissivity of the GM/GCL interface.

4 CONCLUSIONS

An original theoretical framework has recently been developed by Guarena et al. (2023) to calculate the steady-state mass flow rate of inorganic contaminants through landfill composite liners, which are made up of a GM overlying a low-permeability mineral layer. The transport of both the liquid and the solute has been assumed to only occur through GM defects of uniform width and infinite length (e.g., holed wrinkles and defective seams), with the additional restriction that all the soil layers maintain fully-saturated conditions. The migration pathway within the lining system has been conceptualised as a horizontal flow along the interfacial zone between the GM and the underlying mineral layer, and then as a vertical flow in the mineral layer itself, as in the reference scheme considered by Rowe (1998) and Touze-Foltz et al. (1999, 2001) for the calculation of the leachate flow rate. The theoretical framework developed by Guarena et al. (2023) can thus be interpreted as an attempt to take a step forward with respect to the simplified calculation approach, which was originally conceived by Katsumi et al. (2001) and is routinely being used for the performance-based design of landfill lining systems.

The error associated with the use of the simplified calculation approach proposed by Katsumi et al. (2001) has been quantified in the present paper with the aid of an example analysis. In the case of purely advective transport, the latter approach has been proven to be consistent with the mass conservation condition for both the solvent and solute phases, while satisfaction of the mass conservation condition for the solute phase is no longer guaranteed when diffusion represents the main transport mechanism, leading to an error that greatly depends on the diffusive properties of the interface between the GM and the mineral layer.

Further research is recommended on the aspects dealt with in the present paper. From a theoretical viewpoint, solutions to the contaminant mass flow rate should be developed for shapes of the geomembrane defects (e.g., circular holes in a flat GM), boundary conditions (e.g., parallel interacting damaged wrinkles), transport properties of the soil layers (e.g., change in the degree of saturation for positive suction heads), and chemical types (e.g., organic contaminants diffusing through intact GMs) that differ from the working hypotheses of this study. From an experimental viewpoint, the laboratory investigation of the relative role of advection and diffusion in the transport of contaminants through the GM/CCL and GM/GCL interfaces is of the utmost importance. Finally, it would be advisable to validate the outlined theoretical framework through comparison of the model predictions with actual field measurements, e.g., the contaminant concentration in the secondary leachate collection system of a double composite liner.

REFERENCES

Dominijanni, A. and Manassero, M. (2021). Steady-state analysis of pollutant transport to assess landfill liner performance. *Environmental Geotechnics*, 8(7): 480-494. https://doi.org/10.1680/jenge.19.00051.

Dominijanni, A., Guarena, N. and Manassero, M. (2021). Risk assessment procedure for the performance-based design of landfill lining systems and cutoff walls. *Japanese Geotechnical Society Special Publication*, 9(5): 199-204. https://doi.org/10.3208/jgssp.v09.cpeg028.

Dominijanni, A., Guarena, N. and Manassero, M. (2023). A systems engineering and risk assessment-based approach for the design of landfills. *Proceedings of the 12th International Conference on Geosynthetics*, Rome, Italy, pp. 1520-1526. https://doi.org/10.1201/9781003386889-198.

Foose, G.J. (2010). A steady-state approach for evaluating the impact of solute transport through composite liners on groundwater quality. *Waste Management*, 30(8-9): 1577-1586. https://doi.org/10.1016/j.wasman.2010.02.027.

Foose, G.J., Benson, C.H. and Edil, T.B. (2001). Analytical equations for predicting concentration and mass flux from composite liners. *Geosynthetics International*, 8(6): 551-575. https://doi.org/10.1680/gein.8.0206.

Foose, G.J., Benson, C.H. and Edil, T.B. (2002). Comparison of solute transport in three composite liners. *Journal of Geotechnical and Geoenvironmental Engineering*, 128(5): 391-403. https://doi.org/10.1061/(ASCE)1090-0241(2002)128:5(391) .

Giroud, J.P. and Bonaparte, R. (1989). Leakage through liners constructed with geomembranes - Part II. Composite liners. *Geotextiles and Geomembranes*, 8(2): 71-111. https://doi.org/10.1016/0266-1144(89)90022-8.

Giroud, J.P. and Cazzuffi, D. (1989). Uses of geosynthetics for environmental control. *Proceedings of the 12th International Conference on Soil Mechanics and Foundation Engineering*, Rio de Janeiro, Brazil, Vol. 5, pp. 3119-3125.

Giroud, J.P. and Touze-Foltz, N. (2005). Equations for calculating the rate of liquid flow through geomembrane defects of uniform width and finite or infinite length. *Geosynthetics International*, 12(4): 191-204. https://doi.org/10.1680/gein.2005.12.4.191.

Guarena, N., Dominijanni, A. and Manassero, M. (2020). From the design of bottom landfill liner systems to the impact assessment of contaminants on underlying aquifers. *Innovative Infrastructure Solutions*, 5: 2. https://doi.org/10.1007/s41062-019-0251-y.

Guarena, N., Dominijanni, A. and Manassero, M. (2023). Contaminant transport through landfill composite liners due to geomembrane defects. *Proceedings of the 12th International Conference on Geosynthetics*, Rome, Italy, pp. 1413-1422. https://doi.org/10.1201/9781003386889-182.

Kandris, K. and Pantazidou, M. (2012). Landfill base liners: Assessment of material equivalency and impact to groundwater. *Geotechnical and Geological Engineering*, 30(1): 27-44. https://doi.org/10.1007/s10706-011-9447-4

Katsumi, T., Benson, C.H., Foose, G.J. and Kamon, M. (2001). Performance-based design of landfill liners. *Engineering Geology*, 60(1-4): 139-148. https://doi.org/10.1016/S0013-7952(00)00096-X.

Manassero, M. and Shackelford, C.D. (1994). The role of diffusion in contaminant migration through soil barriers. *Rivista Italiana di Geotecnica*, 28(1): 5-31.

Manassero, M., Benson, C.H. and Bouazza, A. (2000). Solid waste containment systems. *Proceedings of GeoEng2000: An International Conference on Geotechnical & Geological Engineering*, Melbourne, Australia, Vol. 1, pp. 520-642.

Rowe, R.K. (1998). Geosynthetics and the minimization of contaminant migration through barrier systems beneath solid waste. *Proceedings of the 6th International Conference on Geosynthetics*, Atlanta, Georgia (USA), Vol. 1, pp. 27-103.

Rowe, R.K. and Brachman, R.W.I. (2004). Assessment of equivalence of composite liners. *Geosynthetics International*, 11(4): 273-286. https://doi.org/10.1680/gein.2004.11.4.273.

Shackelford, C.D. (1990). Transit-time design of earthen barriers. *Engineering Geology*, 29(1): 79-94. https://doi.org/10.1016/0013-7952(90)90083-D.

Shackelford, C.D. (2014). The ISSMGE Kerry Rowe Lecture. The role of diffusion in environmental geotechnics. *Canadian Geotechnical Journal*, 51(11): 1219-1242. https://doi.org/10.1139/cgj-2013-0277.

Touze-Foltz, N., Rowe, R.K. and Duquennoi, C. (1999). Liquid flow through composite liners due to geomembrane defects: Analytical solutions for axi-symmetric and two-dimensional problems. *Geosynthetics International*, 6(6): 455-479. https://doi.org/10.1680/gein.6.0160.

Touze-Foltz, N., Rowe, R.K. and Navarro, N. (2001). Liquid flow through composite liners due to geomembrane defects: Nonuniform hydraulic transmissivity at the liner interface. *Geosynthetics International*, 8(1): 1-26. https://doi.org/10.1680/gein.8.0184.

Proceedings of the XVIII ECSMGE 2024
GEOTECHNICAL ENGINEERING CHALLENGES
TO MEET CURRENT AND EMERGING NEEDS OF SOCIETY
© 2024 the Authors
ISBN 978-1-032-54816-6
DOI 10.1201/9781003431749-575
Open Access: www.taylorfrancis.com, CC BY-NC-ND 4.0 license

ECSMGE 24
XVIII EUROPEAN CONFERENCE ON SOIL MECHANICS AND GEOTECHNICAL ENGINEERING

The effect of soil type on the temperature-dependent strength parameters

L'effet des types de sol sur les paramètres de résistance dépendant de la température

M. Guner*, S. Polat, U.C. Erginag, O. Cinicioglu
Bogazici University, Istanbul, Turkey

M. Sutman
University of Edinburgh, Edinburgh, United Kingdom

A. Hashemi
Heriot-Watt University, Edinburgh, United Kingdom

**mert.guner@boun.edu.tr*

ABSTRACT: The mechanical behaviour of soils under non-isothermal conditions is a crucial factor in the analysis and design of energy geostructures. To investigate this behaviour, thermal direct shear tests were conducted in this study within the practical operational temperature range (8-45°C) of energy geostructures. Normal stress was applied in the range of 100 and 400 kPa. Within the scope of the study, continuous heating and cooling was adopted as thermal loading protocol and therefore, the effect of creep was not examined. Furthermore, the impact of soil type on the temperature-dependent shear strength parameters of soils was investigated. Results show that hardening behaviour was observed for normally consolidated (NC) clays while there was no change in the behaviour of sand. There was an increase in apparent cohesion for both heating and cooling episodes. Angle of friction remained unchanged for sand during tests while in NC clays lower friction angle is observed at higher temperatures. Obtained experimental results are reported and used to discuss the practical implication of the dependency of soil strength parameters on temperature in design and performance of energy geostructures.

RÉSUMÉ: Le comportement mécanique des sols dans des conditions non isothermes est un facteur crucial dans l'analyse et la conception des géostructures énergétiques. Pour étudier ce comportement, des essais de cisaillement thermique direct ont été réalisés dans cette étude dans la plage de température opérationnelle pratique (8 à 45 °C) des géostructures énergétiques. Une contrainte normale a été appliquée dans la plage de 100 à 400 kPa. Dans le cadre de l'étude, un chauffage et un refroidissement continus ont été adoptés comme protocole de chargement thermique et donc, l'effet du fluage n'a pas été examiné. De plus, l'impact du type de sol sur les paramètres de résistance au cisaillement dépendant de la température du sol a été étudié. Les résultats montrent qu'un comportement de durcissement a été observé pour les argiles normalement consolidées (NC) tandis qu'il n'y a eu aucun changement dans le comportement du sable. Il y a eu une augmentation de la cohésion apparente pour à la fois les épisodes de chauffage et de refroidissement. L'angle de frottement est resté inchangé pour le sable pendant les tests, tandis que dans les argiles NC, un angle de frottement plus bas est observé à des températures plus élevées. Les résultats expérimentaux obtenus sont rapportés et utilisés pour discuter de l'implication pratique de la dépendance des paramètres de résistance du sol à la température dans la conception et les performances.

Keywords: Shear strength; temperature; silica sand; normally consolidated clay.

1 INTRODUCTION

The impact of thermal influences on soil shear strength has been a subject of exploration over several years (Laloui et al. 2014, Maghsoodi et al. 2020, Laloui & Sutman 2021). Investigations into the shear strength of clay soils have yielded varied results, without a definitive consensus on the precise effect. Some studies suggest that higher temperatures can enhance the shear strength of clays (Graham et al. 2001, Abuel-Naga et al. 2007), while others indicate a decrease in strength at elevated temperatures (Chiu 1996, Maghsoodi et al. 2020). In contrast, assessments of temperature changes on sand's shear strength parameters reveal an independence of interface shear strength from temperature (Di Donna et al. 2015, Vasilescu et al. 2019, Maghsoodi et al. 2020, Laloui & Sutman 2021).

This study aimed to gain a deeper comprehension of temperature-dependent soil strength parameters by conducting thermal direct shear tests on both sand and clay soils.

2 TESTING PROCEDURE

2.1 Tested materials

In the present study, thermal direct shear tests were conducted for both sand (silica sand) and clay (Polwhite-E type kaolin). Physical properties of the silica sand are shown in Table 1. The soil classification for the sand used in the tests is SP according to the Unified Soil Classification System (USCS).

Table 1. Silica sand properties.

Property	Value
D_{50} (mm)	0.140
C_u	1.596
C_c	0.906
AFS (Average Fineness Number)	99.53

Polwhite-E type kaolin is a non-active temperature-sensitive clay and classified as CH according to USCS. Corresponding properties are shown in Table 2. Water content for the tested kaolin clay was 30%.

Table 2. Clayey soil properties.

Property	Value
Specific Gravity (G_s)	2.61
LL (%)	50.71
PI (%)	18.67
w_{opt} (%)	26.8
Maximum dry unit weight ($\gamma_{d,max}$ kN/m^3)	13.94

2.2 Experimental set-up

The experiments for silica sand and kaolin clay were conducted with different direct shear devices. Thermal direct shear device shown in Figure 1 was used for the silica sand, while a modified standard direct shear device was used for the kaolin clay, as show in Figure 2 (Hashemi et al., 2022). Shear box dimensions for the silica sand and kaolin clay are 100x100x20 mm and 60x60x20 mm, respectively.



Figure 1. Thermal direct shear device used for silica sand.

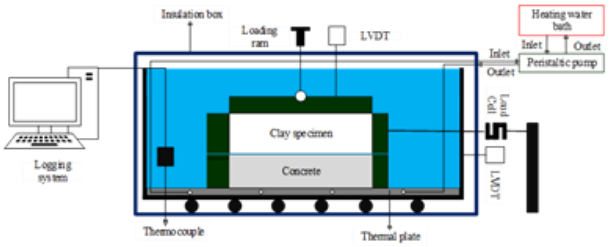

Figure 2. Thermal direct shear device used for kaolin clay.

2.3 Thermal loading protocol

In this experimental study, the loading path applied for the silica sand before shearing is shown in Figure 3. Sand samples initially loosely placed in the shear box with the pouring method. The dry density of the sand placed in the shear box was set to be the same for each test and 14.52 kN/m^3. Next, specimens were immersed in distilled water at a temperature of 24°C to ensure complete saturation. Subsequently, consolidation was carried out at normal stress levels of 100 and 400 kPa in the corresponding paths of A-B and A-C, respectively. Prior to initiating the shearing process, thermal loading was applied to selected samples. For both normal stress conditions, the samples were subjected to thermal loading at temperatures of 8°C (path B-D and C-F) and 45°C (path B-E and C-G). The samples experienced a temperature variation of 15°C within a span of approximately 30 minutes, corresponding to 0.5°C/min heating and cooling rate. Since the thermal loading was rapid, the sample was kept at constant temperature for 3 hours after reaching the designated temperature to allow for the dissipation of any excess pore water pressure that may occur, although it is not very likely. Upon achieving the desired temperature and the associated deformation, the shearing phase was initiated. Since silica sand is a granular soil, the shearing rate was determined as 0.5 mm/min based on the standards (ASTM,1998).

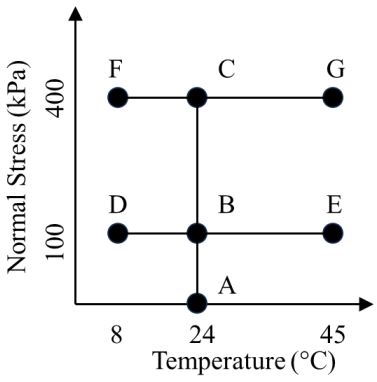

Figure 3. Loading paths.

Kaolin clay samples were subjected to the same thermo-mechanical (TM) paths as those shown in

Figure 3. The kaolin samples were immersed in distilled water for at least 48 hours at a temperature of 24°C. This immersion period ensured a degree of saturation exceeding 95% before testing commenced. To confirm this, a series of separate immersion and saturation degree tests were conducted beforehand on multiple samples. The mixture was stored in an airtight container for a minimum of three days to achieve moisture equilibrium (Ravera et al., 2020). Subsequently, the soil was statically compacted within the shear box. This involved applying a gradual and variable static force via a piston in the strain-controlled press until the target void ratio was reached.

The water level was maintained above the samples throughout the testing period. Next, the samples were consolidated to the desired mechanical load (100 or 400 kPa). Unlike silica sand samples, the heating/cooling rate was limited to 3°C/hr to maintain drained conditions (Hashemi and Sutman, 2023). Once the desired temperature and associated deformation were stable, the shearing phase was initiated at a rate of 0.005 mm/min to ensure drained shearing (Di Donna et al., 2016; Hashemi et al., 2022).

3 EXPERIMENTAL RESULTS

3.1 Silica sand

The outcomes derived from experimental investigations on silica sand are shown in Figures 4-6. In all tests conducted at three different temperatures and under two different normal stresses, shear stress increased as the horizontal displacement increased. Maximum shear strength did not change with temperature and was found to be a function of normal stress. As shown in Figure 4, soil contracted at low horizontal displacement and then, it exhibited a dilative behaviour. Angle of friction is obtained as 34° and it is independent of temperature.

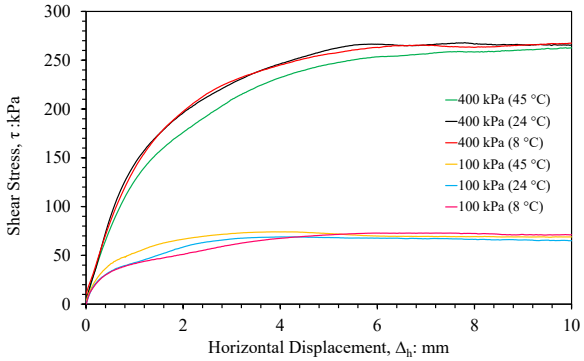

Figure 4. Experimental results on sand: shear stress versus horizontal displacement.

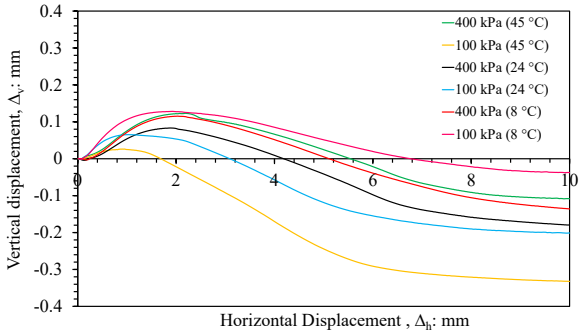

Figure 5. Experimental results on sand: vertical displacement versus horizontal displacement.

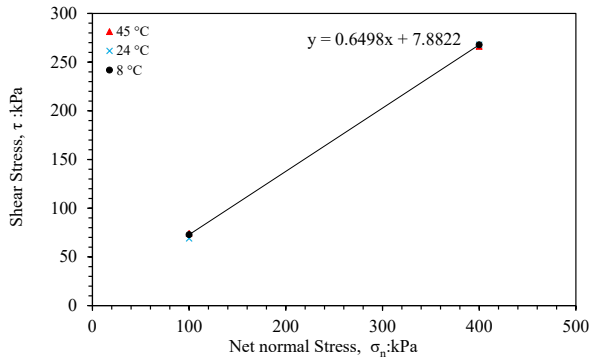

Figure 6. Failure envelope of sand.

3.2 Kaolin clay

Figures 7 and 8 show the results of direct shear tests on kaolin clay, with respect to shear stress and vertical displacement evolution with horizontal displacement. At the low normal stress of 100 kPa, heating and cooling induced insignificant changes in the shear strength of the sample. However, by increasing the normal stress to 400 kPa, the heated sample showed lower shear strength than the interfaces either cooled or sheared at room temperature. This suggests that the impact of thermal loading on shear strength is governed by normal stress, at least for the clay tested in this study (Hashemi et al. 2023).

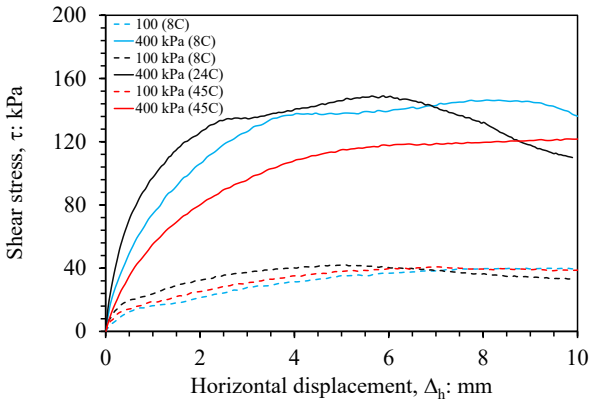

Figure 7. Experimental results on clay: shear stress versus horizontal displacement.

Temperature also has a significant impact on the volumetric behaviour of the clay during shearing. As shown in Figure 7, the thermally loaded samples showed a less contractive behaviour during the shearing stage, regardless of the normal load. This behaviour can be attributed to thermal deformation of the samples prior to shearing, with cooled and heated samples experiencing an elastic or plastic contraction, respectively (Hashemi and Sutman, 2022).

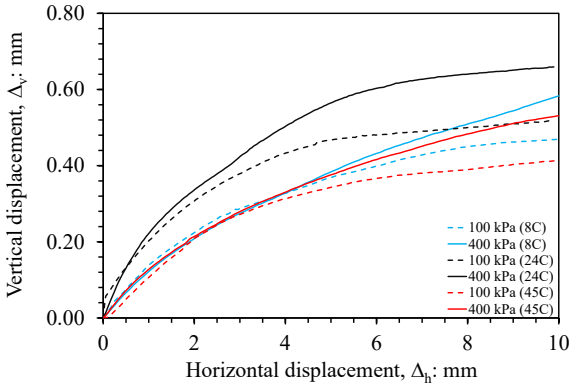

Figure 8. Experimental results on clay: vertical displacement versus horizontal displacement.

Figure 8 presents the failure envelopes at varying temperature, revealing a downward shift towards lower shear stresses upon heating. While a higher cohesion and an identical friction angle are determined upon cooling, a higher cohesion is coupled with a lower friction angle for the heated samples. For the kaolin samples studied here, the relationship between thermal loading and strength parameters is summarised in Table 3.

Table 3. Shear strength parameters of kaolin clay (c_a: cohesion; φ: interface friction angle).

Temperature (°C)	c_a (kPa)	φ (°)
8	6	19.8
24	3	19.8
45	12	15.1

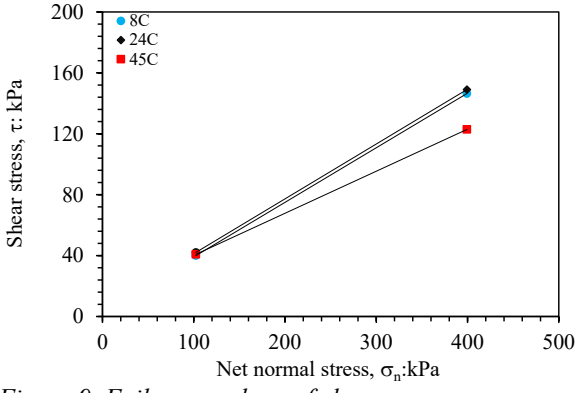

Figure 9. Failure envelope of clay.

4 DISCUSSIONS

Results from the tests on silica sand indicate strong consistency in terms of shear stress with respect to horizontal displacement. However, the consistency for vertical displacement versus horizontal displacement is not as evident. Vertical displacement is correlated with the volume of the sheared zone, which can vary for each test. A linear function can be successfully employed to establish a correlation between shear strength and normal stress, which facilitates the determination of the friction angle. These findings highlight the reliability of the obtained results.

According to obtained results, the effect of temperature on silica sand strength and angle of friction is almost negligible, which was also shown by previous research (Di Donna et al. 2015, Vasilescu et al. 2019, Maghsoodi et al. 2020, Laloui & Sutman 2021). Upon achieving larger horizontal displacements, residual shear strength remained unchanged.

The effect of temperature on the friction angle of soils is generally insignificant. However, for cohesive soils tested at high temperatures, the friction angle can either increase or decrease, depending on the specific soil and the testing conditions (Di Donna et al. 2015, Maghsoodi et al. 2020). In the current study on kaolin clay, plastic thermal deformation in response to heating and ensured drained shearing caused by a low heating rate are likely the main reasons for the observed temperature effects on friction angle, which might be absent in other studies (Hashemi et al., 2023).

To understand the effect of temperature on cohesion, it is important to study the mechanisms that contribute to cohesion in non-isothermal conditions. Two main mechanisms that determine cohesion force are solid-solid and liquid-mediated contacts (Bhushan, 2003). In this study, both mechanisms contributed to higher cohesion at higher temperatures caused by increased number of contacts due to thermal contraction and higher viscous force, respectively (Li et al., 2019; Hashemi et al., 2022).

5 CONCLUSIONS

In this study, the impact of soil type on the temperature dependent shear strength parameters of soils was investigated through thermal direct shear tests. To achieve this, tests were conducted on both sandy and clayey soils under two different normal stresses (100 and 400 kPa) at various temperatures (8, 24 and 45 °C). It was observed that the effect of temperature on the shear strength of sand was negligible in the applied temperature range. At large horizontal displacements, the residual shear strength did not change.

This study also investigated the effect of temperature on the shear strength of normally consolidated (NC) clay. The results showed that heating NC clay leads to a decrease in shear strength, which is more pronounced at higher normal loads. Cooling, on the other hand, does not have a significant effect on shear strength. The decrease in shear strength upon heating is attributed to the plastic contraction of the soil. For the NC clay, the plastic contraction due to heating and the elastic contraction due to cooling resulted in less contractive behaviour during shearing and contributed to a lower friction angle at higher temperatures and higher cohesion at both low and high temperatures.

ACKNOWLEDGEMENTS

The authors are grateful for the financial support provided by the Cost Action CA21156.

REFERENCES

Abuel-Naga, H. M., Bergado, D. T., Bouazza, A., and Ramana, G. V. (2007) Volume change behavior of saturated clays under drained heating conditions: Experimental results and constitutive modeling, *Can. Geotech. J.*, 44(8), 942–956. https://doi.org/10.1139/t07-031.

ASTM (1998). Standard test method for direct shear test of soils under consolidated drained conditions. ASTM standard D3080-98, ASTM International, West Conshohocken, Pa.

Bhushan, B. (2003) Adhesion and stiction: mechanisms, measurement techniques, and methods for reduction, *Journal of Vacuum Science & Technology B: Microelectronic sand Nanometer Structures Processing, Measurement, and Phenomena*, 21(6):2262–2296. http://dx.doi.org/10.1116/1.1627336.

Chiu, S. L. (1996). *Behaviour of normally consolidated clay at elevated Temperature*, Ph.D. thesis, Univ. of Sydney, Sydney, Australia.

Di Donna, A., Laloui, L. (2015) Response of soil subjected to thermal cyclic loading: experimental and constitutive study, *Eng. Geol.,* 190 (1), pp. 65-76. https://doi.org/10.1016/j.enggeo.2015.03.003.

Graham, J., Tanaka, N., Crilly, T., and Alfaro, M. (2001) Modified Cam-clay modeling of temperature effects in clays, *Can. Geotech. J.*, 38(3), 608–621. https://doi.org/10.1139/t00-125.

Hashemi, A., Sutman, M., Medero, G.M. and Buckman, J. (2023) Compressibility and microstructure of kaolin in varying thermo-hydro-mechanical states imposed by energy geostructures, Engineering Geology, 324, p.107248.https://doi.org/10.1016/j.enggeo.2023.10724.

Hashemi, A., Sutman, M. and Abuel-Naga, H. (2022) Thermomechanical response of kaolin clay–concrete interface in the context of energy geostructures, Canadian Geotechnical Journal, 60(3), pp.380-396. https://doi.org/10.1139/cgj-2022-0172.

Hashemi, A. and Sutman, M. (2022) Thermo-hydro-mechanical behaviour of partially saturated fine-grained soils in the context of energy geostructures, Soils and Rocks, 45. https://doi.org/10.28927/SR.2022.076821.

Hashemi, A., Sutman, M. And Medero, G.M. (2023) A review on the thermo-hydro-mechanical response of soil–structure interface for energy geostructures applications, Geomechanics for Energy and the Environment, p.100439. https://doi.org/10.1016/j.gete.2023.100439.

Hashemi, A. and Sutman, M., (2023). A direct shear setup for studying the THM shear response of the soil-structure interface in the context of energy geostructures, In: Symposium on Energy Geotechnics, Delft, Netherlands, (pp. 1-2). https://doi.org/10.59490/seg.2023.504.

Laloui, L., Olgun, C.G., Sutman, M., McCartney, J.S., Coccia, C.J., Abuel-Naga, H.M. and Bowers, G.A. (2014) Issues involved with thermoactive geotechnical systems: characterization of thermomechanical soil behavior and soil-structure interface behavior, *DFI Journal-The Journal of the Deep Foundations Institute*, 8(2), pp.108-120. https://doi.org/10.1179/1937525514Y.0000000010.

Laloui, L., Sutman, M. (2021) Experimental investigation of energy piles: From laboratory to field testing, *Geomechanics for Energy and the Environment*., Vol. 27, pp. 200214. http://dx.doi.org/10.1016/j.gete.2020.100214.

Li, C., Kong, G., Liu, H., and Abuel-Naga, H. (2019) Effect of temperature on behaviour of red clay–structure interface, *Canadian Geotechnical Journal*, 56(1):126–134. https://doi.org/10.1139/cgj-2017-0310.

Maghsoodi, S., Cuisinieri O., Masrouri, F. (2020) Thermal effects on mechanical behaviour of soil–structure interface, *Canadian Geotechnical Journal,* 57 (1), pp. 32-47. http://dx.doi.org/10.1139/cgj-2018-0583.

Ravera, E., Sutman, M. and Laloui, L. (2020) Cyclic thermomechanical response of fine-grained soil–concrete interface for energy piles applications, *Canadian Geotechnical Journal*, 58(8), pp.1216-1230. https://doi.org/10.1139/cgj-2020-0437.

Vasilescu, R., Yin, K., Fauchille, A. L., Kotronis, P., Dano, C., Manirakiza, R. & Gotteland, P. (2019). Influence of thermal cycles on the deformation of soil-pile interface in energy piles, *E3S Web of Conferences*. https://doi.org/10.1051/e3sconf/20199213004.

Proceedings of the XVIII ECSMGE 2024
GEOTECHNICAL ENGINEERING CHALLENGES
TO MEET CURRENT AND EMERGING NEEDS OF SOCIETY
© 2024 the Authors
ISBN 978-1-032-54816-6
DOI 10.1201/9781003431749-576
Open Access: www.taylorfrancis.com, CC BY-NC-ND 4.0 license

ECSMGE 24
XVIII EUROPEAN CONFERENCE ON SOIL MECHANICS AND GEOTECHNICAL ENGINEERING

Preliminary study of the influence of marble dust on clayey soils improvement depending on the characteristics of the natural soil

Etude préliminaire de l'influence de la poussière de marbre sur l'amélioration des sols argileux en fonction des caractéristiques du sol naturel

E. Gutierrez*, J.L. Pastor, M. Cano, A. Santos
University of Alicante, Alicante, Spain

T. Hino
Saga University, Saga, Japan

**erick.gutierrez@ua.es*

ABSTRACT: Some soils are not suitable to support the application of loads or to be used for embankment construction due to their low strength and/or high deformability. However, with proper treatment, these soils can improve their geotechnical properties to fulfil the requirements needed for this use. Building on or with problematic soils usually requires the use of traditional stabilizers like lime and cement which drives up construction and environmental costs. Alternatives have been studied to avoid or reduce these costs associated with soil improvement. Marble dust or Limestone powder obtained as waste from cutting and polishing activities of the natural stone industry has shown great potential in stabilizing expansive soils. Nevertheless, the effect of limestone waste on the properties of the mixed soil depends on the characteristics of the natural soil. In this work, the effect of limestone powder has been studied on three types of clayey soils to evaluate the geotechnical properties of the mixed soil and their relation to some properties of the natural soil such as grain size, plasticity and calcium carbonate content. Preliminary results show that as the addition of limestone powder waste to clayey soils can increase the unconfined compressive strength and the CBR index, reducing the swelling potential of the soil. The level of improvement depends on the type of soil, being influenced by its grain size distribution and mineralogy, although a clear match between parameters has not been obtained.

RÉSUMÉ: Certains sols ne sont pas adaptés pour supporter l'application de charges ou pour être utilisés dans la construction de remblais en raison de leur faible résistance et/ou de leur grande déformabilité. Cependant, avec un traitement approprié, ces sols peuvent améliorer leurs propriétés géotechniques pour répondre aux exigences nécessaires à cette utilisation. Construire sur des sols problématiques ou avec eux nécessite généralement l'utilisation de stabilisateurs traditionnels tels que la chaux et le ciment, ce qui augmente les coûts de construction et environnementaux. Des alternatives ont été étudiées pour éviter ou réduire ces coûts liés à l'amélioration des sols. La poudre de calcaire obtenue en tant que déchet des activités de découpe et de polissage de l'industrie de la pierre naturelle a montré un grand potentiel dans la stabilisation des sols expansifs. Néanmoins, l'effet des déchets de calcaire sur les propriétés du sol mélangé dépend des caractéristiques du sol naturel. Dans ce travail, l'effet de la poudre de calcaire a été étudié sur trois types de sols argileux pour évaluer les propriétés géotechniques du sol mélangé et leur relation avec certaines propriétés du sol naturel telles que la granulométrie, la plasticité et la teneur en carbonate de calcium. Les résultats préliminaires montrent que l'ajout de déchets de poudre de calcaire aux sols argileux peut augmenter la résistance à la compression non confinée et l'indice CBR, réduisant le potentiel de gonflement du sol. Le niveau d'amélioration dépend du type de sol et est influencé par sa distribution granulométrique et sa minéralogie, bien qu'il n'y ait pas de correspondance claire entre les paramètres.

Keywords: Limestone powder; soil improvement; soft ground; geotechnical properties; laboratory test.

1 INTRODUCTION

The strength and deformability of a soils are crucial for the suitability of a material in construction. Expansive soils, not meeting the required quality standards in embankment construction, often undergo treatments to improve their geotechnical properties (Chu et al., 2009; Mitchell, 1981), resulting in increased construction costs and energy consumption in the production of hydraulic binders (Sharma et al., 2018).

Alternatives have been investigated to reduce soil improvement costs using industrial byproducts (Kar, 2021; Uma Maguesvari et al., 2023)

On the other hand, mining activity continues to grow due to its economic utility. Spain is one of the leading producers of natural large amounts of waste stone (Trio Maseda and Guillermo Ortuño, 2018). Approximately 25% of a marble block becomes slurry (Kuoribo and Mahmoud, 2022; Saygili, 2015), and another 15% becomes solid waste (Founti et al., 2010). Limestone dust (LD), being inert and non-biodegradable, is often disposed of in landfills without treatment (Aukour and Al-Qinna, 2008), causing negative environmental impacts (Çınar and Kar, 2018).

Limestone dust could serve as a stabilizing agent in road embankments (Thirumalai et al., 2017). Jassim et al., (2022) found that the plasticity index decreased by approximately 22% with increased limestone dust content. Cabalar and Omar, (2023) demonstrated that the unconfined compressive strength (UCS) of a silty specimen with 30% of limestone dust reached 500 kN/m^2, twice the UCS without limestone dust. Additionally, an increase in the CBR index was observed with 17% limestone dust in a clayey soil (Niraj and Sharma, 2023).

2 MATERIALS AND METHODS

To perform the tests, ornamental rock residue and three types of clayey soils were used.

2.1 Soil

The clayey soil was extracted from the localities of Novelda (S1), Almería (S2), and Fortuna (S3), all of which are located in sutheast Spain. The properties of the materials are detailed in Table 1. Sample S1 is classified as low-plasticity silty clay. Sample S2 is classified as low to medium-plasticity clay. Sample S3 is classified as medium to high-plastic clay.

2.2 Limestone dust

The limestone dust (LD) residue was collected from the landfill of a natural stone factory located west of the province of Alicante. The calcium carbonate content in the limestone powder samples was 90.9%.

Table 1. Materials properties.

Properties	**S1**	**S2**	**S3**	**LD**
0.4 mm (% passing)	100.0	100.0	100.0	100.0
0.08 mm (% passing)	76.3	92.0	85.0	99.7
Liquid Limit	39.5	37.5	51.0	22.8
Plasticity Index	14.0	14.6	15.9	4.3
% Carbonates	7.05	15.6	44.7	90.9
Na_2O	0.431	0.919	1.380	0.135
MgO	3.170	5.290	3.790	0.386
Al_2O_3	20.800	13.902	8.810	0.818
SiO_2	57.700	36.669	31.800	1.180
P_2O_5	0.256	0.316	0.175	0.091
SO_3	0.133	2.760	3.190	0.069
Cl	0.163	0.248	0.846	0.015
K_2O	5.990	2.907	2.350	0.039
CaO	1.130	14.722	42.700	97.100
Fe_2O_3	8.640	5.461	4.0700	0.127
SrO	0.024	0.175	0.147	0.028
TiO_2	1.350	0.644	0.657	-
Cr_2O_3	0.020	0.018	-	-
MnO	0.025	0.070	0.065	-
Co_3O_4	0.017	-	-	-
NiO	0.014	0.009	0.020	-
Rb_2O	0.023	0.016	0.010	-
Y_2O_3	0.003	0.003	0.004	-
ZrO_2	0.033	0.025	-	-
CeO_2	0.055	-	-	-
CuO	-	-		-
ZnO	-	0.020		-
BaO	-	0.042		-
WO_3	-	0.024		-
PbO	-	0.012		-

3 METHODOLOGY

3.1 Sample preparation

The clayey soil and the residue were prepared by crushing them with a rubber mallet without breaking the particles, and placed in an oven at a temperature of 50º C until a constant weight, and a homogeneous mixture was prepared. Standard Proctor tests were used to obtain the optimum moisture content and maximum dry density for specimens with and without limestone dust. Once the optimum moisture content was defined, test specimens were prepared for further testing with the optimum moisture content and the compaction energy of the Standard Proctor.

3.2 Free swelling test

Three specimens with a diameter of 50 mm and a thickness of 25 mm were manufactured. Each clayey soil sample has its corresponding specimen with added residue, prepared with the respective optimum moisture content for each type of soil, and soil mixed with limestone dust. The determination of swelling of a specimen was carried out on an oedometer bench following Spanish regulations (AENOR, 1996).

3.3 Unconfined compressive strength

The specimens for the Unconfined compressive strength (UCS) test were manufactured with a diameter of 50 mm and a height of 100 mm using compaction energy according to the standard Proctor method. The maximum axial stress that a cylindrical specimen can withstand before its failure is defined as the UCS This test was conducted in accordance with Spanish regulations (AENOR, 1993).

3.4 CBR index

To determine the California bearing ratio (CBR) index, tests were conducted following the relevant standard (AENOR, 1995). The manufactured specimens underwent a four-day curing period in a humidity and temperature-controlled chamber (>95% RH and 20 ± 2º C).

4 RESULTS

4.1 Atterberg limits

The liquid limit (LL) of each sample is shown in Figure 1. There is a significant reduction in the liquid limits of the Novelda (S1) and Fortuna (S3) samples; however, the LL remains approximately constant in the case of the Almería sample (S2) after adding limestone dust (LD).

4.2 Free swelling

The results of the free swelling potential for the prepared samples, natural soil (NS) and natural soil with limestone dust (NS+LD) by adding 20% of the residue weight of dry soil are shown in Figure 2. The free swelling of the samples decreased when limestone dust was added.

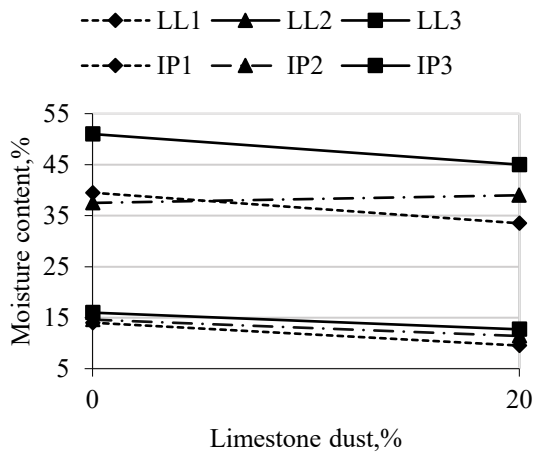

Figure 1. Liquid limit of samples containing limestone dust.

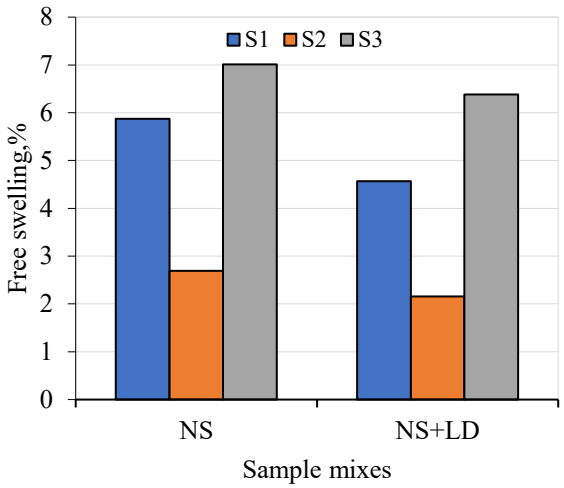

Figure 2. Free swelling of clay samples with limestone dust.

4.3 Unconfined compressive strength

The unconfined compressive strength of the analysed samples without the addition of residue can be seen in Figure 3. The results of the specimens with 20% limestone dust are shown in Figure 4. The strength of the specimens increased to a greater extent with the clay from Almería (S2). Nevertheless, the limestone dust did not have a positive effect on the Fortuna soil (S3).

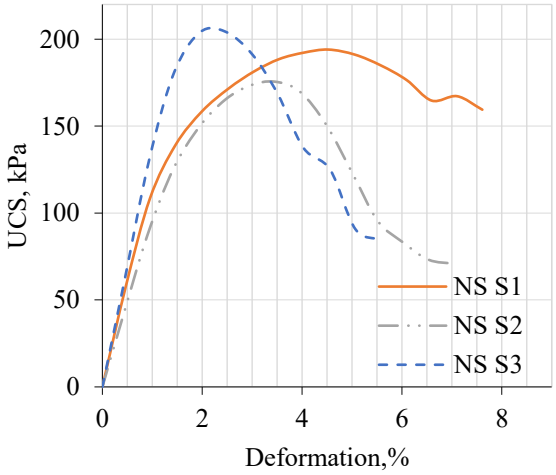

Figure 3. Unconfined compressive strength of natural soil (NS).

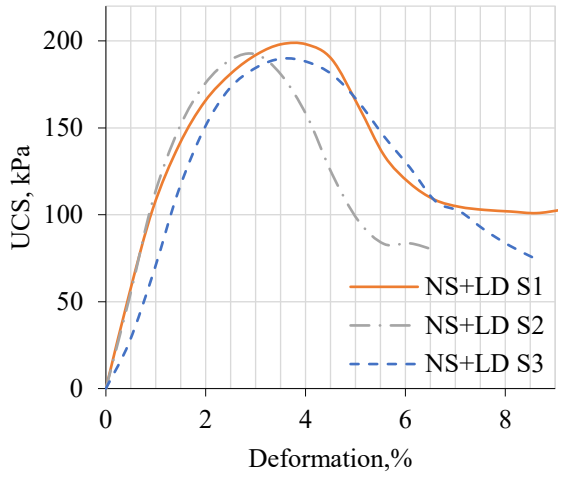

Figure 4. Unconfined compressive strength of natural soil (NS) with limestone dust (LD) of each clay sample.

4.4 California bearing ratio

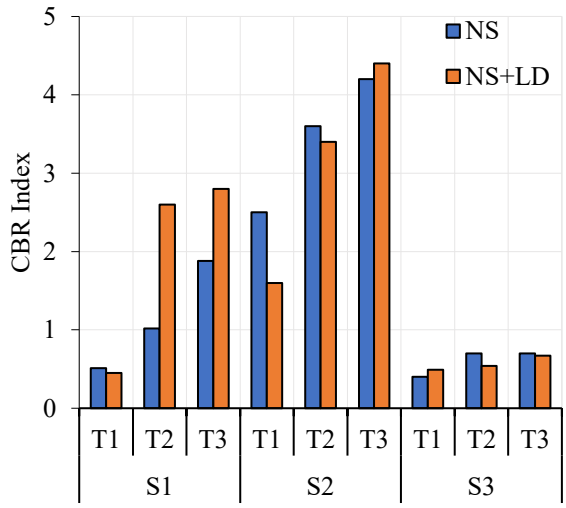

Figure 5. CBR index of the samples with and without LD.

The California bearing ratio (CBR) index was obtained using the normal Proctor energy, and the results are shown in Figure 5. The ornamental rock dust has not had a positive effect on the Fortuna soil (S3). The greatest increase in the CBR index occurred in the soil from the Novelda (S1) locality.

5 DISCUSSION

The results obtained show, in the first instance, positive effects when adding the limestone waste to the natural soils. Nevertheless, the effect was different for the three soils. A decrease in the consistency limits is observed for soils S1 and S3, however, it remains approximately constant for S2. In the case of sample S3, the reduction in the consistency limits would imply a change in position on the Casagrande chart, shifting from an MH-OH classification to ML-OL. Ali et al., (2014) obtained a similar result by reducing the LL by 12% and changing the classification of their samples from CH to CL.

Swelling is reduced with the addition of limestone residue, similar to the results obtained by Ali et al., (2014). A reduction in free swelling is observed in all three types of clayey soils, with a greater effect on the Novelda soil (S1) and Fortuna soil (S3), with a decrease of 23% and 20%, respectively. The Almería soil (S2) experienced a 9% reduction compared to the maximum swelling obtained.

The UCS results do not show a general tendency. The UCS of sample S2 increased by 7.5% compared to the maximum obtained for the natural soil. However, the UCS of soil S3 decreased slightly. Chore et al., (2023) reported an increase of the UCS of a clayey soil when adding marble powder. Similar results to those obtained by Ahirwar and Chore (2021), although in this case the maximum UCS was obtained for a 15% addition of limestone dust, decreasing the UCS when adding 20%. The UCS obtained when adding LD could depend not only on the type of soil but also on the final LD content. As it looks like there is a threshold of LD addition, after this threshold the UCS could decrease.

Regarding the CBR, soils S1 and S2 showed an increase in the CBR index. Being S1 the soil which showed the greatest gain. Similar results were obtained by Niraj and Sarma (2023) after adding 17% of limestone dust, although a decrease was observed when adding 21%. This could mean that the optimal limestone powder content may fall within this range. The greatest improvement observed for soil S1 when adding limestone powder waste could be related to the lowest content of carbonates observed on this soil before adding the limestone powder waste.

6 CONCLUSIONS

Different improvement has been observed by adding limestone dust to three different clayey soils. This could be due to the different chemical compositions of the three soils. Limestone dust is primarily composed of carbonates. However, the carbonate content in Soils S1, S2 and S3 is different. On the other hand, the content of silicon oxide and aluminum oxide is higher in soil type S1. The relationship between the chemical compounds of each soil and the improvement of their properties is not entirely clear. The addition of limestone dust to clayey soils reduces the free swelling and improves the consistency of the clays. The improvements are quite remarkable in the CBR index. In general, in most of the test conducted,

improvements are observed, both in strength and in expansiveness.

ACKNOWLEDGEMENTS

This work has been supported by Conselleria de Innovación, Universidades, Ciencia y Sociedad Digital (Generalitat Valenciana) under the project CIBEST/2022/52 and Conselleria de Innovación, Universidades, Ciencia y Sociedad Digital within the framework of the project CIAICO/2021/335. This project has been supported from the European Union's Horizon 2020 research and innovation programme Marie Skłodowska-Curie Actions – Staff Exchange (SE) Grant agreement No. 101131146.

REFERENCES

AENOR. (1993). *UNE 103400. Simple compression rupture test in soil test specimens (in Spanish)*.

AENOR. (1995). UNE 103502:1995 Test laboratory method for determining in a soil the C.B.R. index. In *http://www.aenor.es/*. https://www.une.org/encuentra-tu-norma/busca-tu-norma/norma?c=N0007852.

AENOR. (1996). *UNE 103601. Test for free swelling of soil in oedometer device (in Spanish)*.

Ahirwar, A. D., and Chore, H. S. (2021). *Effect of Curing on Strength of Clayey Soil Stabilized with Marble Dust*. https://doi.org/10.1007/978-981-19-4739-1_48.

Ali, R., Khan, H., and Shah, A. A. (2014). Expansive Soil Stabilization Using Marble Dust and and Bagasse Ash. *International Journal of Science and Research (IJSR)*, *3*(6), 2812–2816.

Aukour, F. J., and Al-Qinna, M. I. (2008). Marble Production and Environmental Constrains: Case Study from Zarqa Governorate, Jordan. *Jordan Journal of Earth and Environmental Sciences*, *1*(1).

Cabalar, A. F., and Omar, R. A. (2023). Stabilizing a silt using waste limestone powder. *Bulletin of Engineering Geology and the Environment 2023 82:8*, *82*(8), 1–16. https://doi.org/10.1007/S10064-023-03302-4.

Chore, H. S., Khadse, A. M., and Ahirwar, A. D. (2023). Unconfined Compressive Strength of Clayey Soil Stabilized with Marble Dust. *Lecture Notes in Civil Engineering*, *280*, 601–605. https://doi.org/10.1007/978-981-19-4739-1_57.

Chu, J., Varaksin, S., Klotz, U., and Mengé, P. (2009). Construction processes. *Proceedings of the 17th International Conference on Soil Mechanics and Geotechnical Engineering: The Academia and Practice of Geotechnical Engineering*, *4*, 3006–3135. https://doi.org/10.3233/978-1-60750-031-5-3006.

Çınar, M. E., and Kar, F. (2018). Characterization of composite produced from waste PET and marble dust. *Construction and Building Materials*, *163*, 734–741. https://doi.org/10.1016/J.CONBUILDMAT.2017.12.155.

Founti, M. A., Giannopoulos, D., and Laskaridis, K. (2010). Environmental management aspects for energy saving in natural stone quarries. *Global Stone Congress*, 1–6. https://www.academia.edu/download/42829909/ENVIRONMENTAL_MANAGEMENT_ASPECTS_FOR_ENE20160219-19988-1bjfqsr.pdf.

Jassim, N. W., Hassan, H. A., Mohammed, H. A., and Fattah, M. Y. (2022). Utilization of waste marble powder as sustainable stabilization materials for subgrade layer. *Results in Engineering*, *14*, 100436. https://doi.org/10.1016/J.RINENG.2022.100436.

Kar, K. K. (2021). Handbook of Fly Ash. In *Handbook of Fly Ash*. https://doi.org/10.1016/B978-0-12-817686-3.00035-9.

Kuoribo, E., and Mahmoud, H. (2022). Utilisation of waste marble dust in concrete production: A scientometric review and future research directions. *Journal of Cleaner Production*, *374*, 133872. https://doi.org/10.1016/J.JCLEPRO.2022.133872.

Mitchell, J. K. (1981). *Soil Improvement — State-of-the Art Report | ISSMGE*. In: Proceedings of the 10th International Conference on Soil Mec. https://www.issmge.org/publications/publication/soil-improvement-state-of-the-art-report.

Niraj, B., and Sharma, T. (2023). Experimental study on stabilization of clayey soil using agricultural and industrial waste. *Materials Today: Proceedings*. https://doi.org/10.1016/J.MATPR.2023.08.290.

Saygili, A. (2015). Use of waste marble dust for stabilization of clayey soil. *Medziagotyra*, *21*(4), 601–606. https://doi.org/10.5755/j01.ms.21.4.11966.

Sharma, L. K., Sirdesai, N. N., Sharma, K. M., and Singh, T. N. (2018). Experimental study to examine the independent roles of lime and cement on the stabilization of a mountain soil: A comparative study. *Applied Clay Science*, *152*, 183–195. https://doi.org/10.1016/J.CLAY.2017.11.012.

Thirumalai, R., Babu, S. S., Naveennayak, V., Nirmal, R., Lokesh, G., Thirumalai, R., Babu, S. S., Naveennayak, V., Nirmal, R., and Lokesh, G. (2017). A Review on Stabilization of Expansive Soil Using Industrial Solid Wastes. *Engineering*, *9*(12), 1008–1017. https://doi.org/10.4236/ENG.2017.912060.

Trio Maseda, M., and Guillermo Ortuño, Mi. (2018). *Panorama Minero 2018-20*. https://www.igme.es/PanoramaMinero/actual/PANORAMA MINERO 2019.pdf.

Uma Maguesvari, M., Muthaiyan, P., and Yugasini, S. (2023). Stabilization of soil using kenaf fibre and rice husk ash. *Materials Today: Proceedings*. https://doi.org/10.1016/J.MATPR.2023.06.261.

Proceedings of the XVIII ECSMGE 2024
GEOTECHNICAL ENGINEERING CHALLENGES
TO MEET CURRENT AND EMERGING NEEDS OF SOCIETY
© 2024 the Authors
ISBN 978-1-032-54816-6
DOI 10.1201/9781003431749-577
Open Access: www.taylorfrancis.com, CC BY-NC-ND 4.0 license

ECSMGE 24
XVIII EUROPEAN CONFERENCE ON SOIL MECHANICS AND GEOTECHNICAL ENGINEERING

The use of LCA in a slope stability study for a quay rehabilitation assessment

L'utilisation de l'ACV dans l'évaluation de la stabilité globale d'une remédiation de quai

E. Hafstad*
AFRY/KTH, Stockholm, Sweden

G. Waldheim*
COWI/KTH, Stockholm, Sweden

A.B. Lundberg
ELU Konsult/KTH, Stockholm, Sweden

S. Larsson
KTH, Stockholm, Sweden

**elin.hafstad@afry.com; gewa@cowi.com*

ABSTRACT: The increasing construction activity along the shoreline of the Stockholm region has intensified the use of existing quay structures. The geotechnical stability is a major issue for the condition assessment of the quays and normally requires geotechnical rehabilitation to retain the usage. However, such methods can entail a large carbon footprint, which needs to be considered in the preliminary design phases. This paper presents a systematic evaluation of five geotechnical remediation methods at an early design stage to facilitate the selection of an appropriate method. The methods are applied to a quay with insufficient stability to reach a target safety factor. The climate impact for each method was evaluated through a life cycle assessment (LCA) based on data from environmental product declarations (EPD). The result shows that the method with the lowest climate impact is the support berm, and the one with the highest is the piled embankment with steel piles. The paper also discusses uncertainties regarding the methods' applicability in real-life conditions, the impact of later life-cycle stages, and the influence of cost on the choice of remediation.

RÉSUMÉ: L'activité croissante de construction le long du littoral de la région de Stockholm a intensifié l'utilisation des structures de quai existantes. La stabilité géotechnique est un problème majeur pour l'évaluation de l'état des quais et nécessite généralement une remédiation géotechnique pour maintenir leur utilisation. Cependant, de telles méthodes peuvent entraîner une empreinte carbone importante, qui doit être prise en compte dès les phases de conception préliminaire. Cet article présente une évaluation systématique de cinq méthodes de remédiation géotechnique à un stade précoce de la conception pour faciliter le choix d'une méthode appropriée. Les méthodes sont appliquées à un quai dont la stabilité est insuffisante pour atteindre un facteur de sécurité cible. L'impact climatique de chaque méthode a été évalué à travers une analyse de cycle de vie (ACV) basée sur des données provenant de déclarations environnementales de produits (EPD). Les résultats montrent que la méthode ayant l'impact climatique le plus faible est la berme de support, tandis que celle ayant le plus élevé est le remblai en pieux avec des pieux en acier. L'article aborde également les incertitudes concernant l'applicabilité des méthodes dans des conditions réelles, l'impact des étapes ultérieures du cycle de vie et l'influence des coûts sur le choix de la remédiation.

Keywords: Quay structure; slope stability; climate impact; life-cycle assessment.

1 INTRODUCTION

The increasing construction activity along Stockholm's coastal areas has intensified the use of the existing quays. Different and more extensive land use with higher loads requires a re-examination of the bearing capacity, and the geotechnical total stability can be a significant issue. Geotechnical rehabilitation methods can be used in cases where renovation is required. These methods often entail a large climate impact, which therefore should be included in the early design phase.

One method for assessing climate impact is through a life cycle assessment (LCA). LCA in geotechnical engineering is a relatively new field with limited research conducted and there is no standardized

framework for the implementation (Samuelsson et al., 2021; Song et al., 2020; Das et al., 2018, Maas et al., 2011).

Consequently, there exists a need to investigate how climate impact, with an LCA, can be included and facilitate the selection of remediation methods for quay renovations. The aim of the paper is to provide a systematic evaluation of remediation methods through the assessment of climate impact at an early design stage to facilitate the selection of an appropriate method.

2 METHOD

A case study has been carried out where five geotechnical rehabilitation methods have been applied to a clay slope with a gravity-wall quay structure. The rehabilitation methods have been compared through a total stability analysis performed in the LE-program GeoStudio SLOPE/W.

The calculation process is shown in Figure 1, with an initial total factor ($SF_{initial}$) of the slope, in this case SF=1.0. With each rehabilitation method, the goal was to achieve a final sufficient safety factor (SF_{target}) to evaluate the quantities of materials needed. The target safety factor was 1.5, for undrained analysis, and 1.3, for combined analysis.

The climate impact of the different methods has subsequently been evaluated through a life cycle analysis (LCA) based on climate data from environmental product declarations (EPD) and the material quantities. The climate data originates from *Klimatkalkyl*, a tool developed by The Swedish Transport Administration. The LCA was limited to include only the product stage of the life cycle (A1-A3) which includes raw material supply, transport, and manufacturing. Input data for the general slope and quay was based on Munkbrokajen in Stockholm (see Figure 2). Input data and characteristic values are shown in Table 1.

In addition to the case study, a sensitivity analysis was carried out to investigate the impact of slope inclination and undrained clay shear strength on the results. For the slope, steeper inclinations of 30° and 40° were implemented, as well as varying undrained shear strengths 15, 18, 22 and 25 kPa.

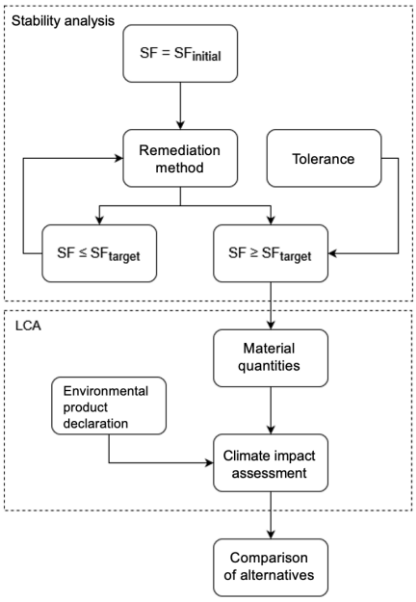

Figure 1. The working process.

Table 1. Input data for soil layers.

Material	γ [kN/m³]	ϕ [°]	c_u [kPa]
Gravel fill	18	33	(18)
Clay	17	(30)	20+1.5 kPa/m*
Sand/Gravel	21	35	-
Gravity wall	24	-	-
Wooden piles	17	-	$9 \times c_{u,clay}$

*Increasing undrained shear strength with depth.

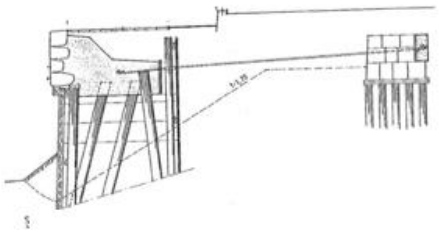

Figure 2. Munkbrokajen in central Stockholm.

2.1 Rehabilitation methods

The case study has included stability analysis of the following methods.

2.1.1 Ground improvement

Ground improvement with lime-cement columns aims to increase the strength of the soil volume under the fill. The emission factor was weighted where a 50/50 distribution was assumed of cement and lime, the amount of mixing 90 kg/m^3 and a coverage rate in the soil of 50%. The cement was adopted to be of the CEM II type.

2.1.2 Lightweight fill

Lightweight fill increases the slope stability by decreasing the weight on the slope and therefore

decreasing the driving force. The lightweight fill consists of expanded cellular plastic with a density of 30 kg/m^3. The friction angle was assumed to be 33°, the same as the original fill.

2.1.3 Support berm

The support berm increases the resisting moment and therefore the overall stability (see Figure 3). It consists of crystalline uncompacted rock fill with a weight of 20 kN/m^3 and a friction angle of 45°. The rock fill was assumed to be collected from a project nearby, whereby a limited amount of processing is required.

2.1.4 Piled embankment

The piled embankment aims to decrease the destabilizing force in the slope by countering the traffic load and the load from the filling. Two cases are examined, one with concrete piles and another with steel piles. The piled embankment is constructed of 13.5 m long piles with concrete pile caps and a load-distributing layer (see also Figure 4). The reinforced concrete piles have a diameter of 235 mm while the steel piles are of the type RD 170/10 filled with unreinforced concrete. The concrete pile caps have the dimensions 1.6 x 1.6 x 0.5 m and are reinforced with a quantity of 200 kg/m^3.

2.1.5 Sheet pile wall

The sheet pile wall is installed in front of the gravity wall structure and back-anchored to a 5 m retaining wall (see also Figure 5). The area between the gravity wall and the sheet pile wall is filled with soil fill. The sheet pile is made of structural steel of the type LX, PU16 with a density of 7850 kg/m^3. The wale band is assumed to consist of two UPE 330 beams.

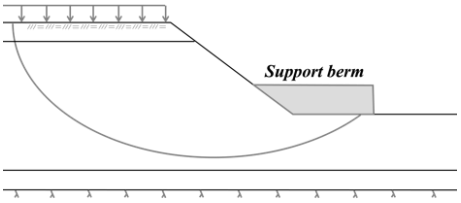

Figure 3. Cross-section of the support berm structure.

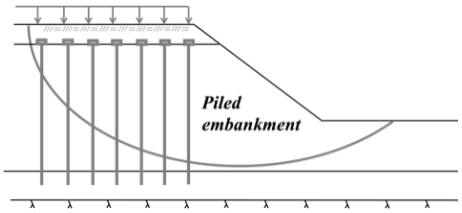

Figure 4. Cross-section of the piled embankment.

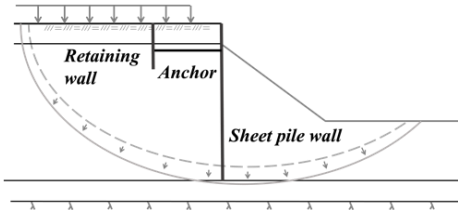

Figure 5. Cross-section of the sheet pile wall structure.

3 RESULTS

The result from the assessment of the total climate impact for each remediation method is shown in Table 2 and Figure 6. The piled embankment with steel piles gives the largest emission of greenhouse gases and thus the largest impact on the climate in the product stage of the life cycle. Furthermore, the sheet pile wall, the lime-cement columns, and the piled embankment with concrete piles result in a similar climate impact value. The light-weight fill has the second lowest climate impact of all the methods, regardless of its relatively high emission factor. The support berm with the largest volume is ultimately the method with the lowest climate impact.

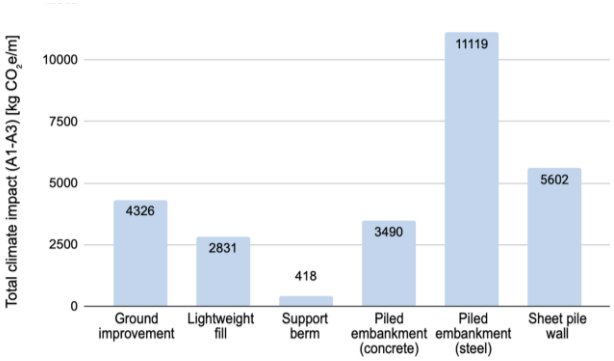

Figure 6. Calculated total climate impact for each method.

Table 2. Climate impact assessment for each method. The emission factor is expressed either per mass or length unit.

Method	Material	Length [m]	Mass [kg/m]	Volume [m^3/m]	Emission factor /kg [kg CO_2e/kg]	Emission factor /m [kg CO_2e/m/m]	Total climate impact [kg CO_2e/m]	
Ground improvement	Lime-cement columns	*a*=50%	3915	43.5	1.1	-	4326	**4326**
Lightweight fill	EPS	-	1191	39.7	2.4	-	2823	**2831**
	Geotextile	22.3	5.8	-	1.4	-	8.3	
Support berm	Rock fill	-	1045540	52.3	0.004	-	418	**418**
Piled embankment (concrete)	Conc. piles (SP1, 7pc)	13.5	-	0.06	-	26.3	1184	**3490**
	Pile caps (7pc)	1.6	-	1.28	-	430.7	2297	
	Geotextile	23	5.98	-	1.4	-	8.6	
Piled embankment (steel)	Steel piles (SP1, 10pc)	13.5	-	-	-	93.0	7172	**11119**
	Pile caps (10pc)	1.6	-	1.28	-	430.7	3938	
	Geotextile	23	5.98	-	1.4	-	8.6	
Sheet pile wall	Sheet pile	15	-	-	-	268.4	4026	**5602**
	Ret. sheet pile	5	-	-	-	268.4	1342	
	Wale beam	-	53.2	-	2.2	-	234.1	
	Anchor (cc=3)	18	0.1	0.007	2.2	-	0.1	
	Soil fill	-	18360	10.2	0.0003	-	0.003	

3.1 Sensitivity analysis

With steeper slope inclinations, several of the rehabilitation methods are not applicable. The support berm and the sheet pile wall can be used in slopes with steeper inclinations. The sheet pile wall is dependent on the depth of the clay layer rather than the inclination of the slope.

Assessing the sensitivity of the undrained shear strength value the lightweight fill, lime-cement columns, and the piled embankment are not applicable at a shear strength of 15 kPa or lower due to a non-sufficient safety factor. The impact from the sheet pile wall and the piled embankment with concrete remains constant with varying shear strengths. This results in a shift in the relative ranking of some of the different methods, which otherwise have a relatively constant relation to one another (see Figure 7).

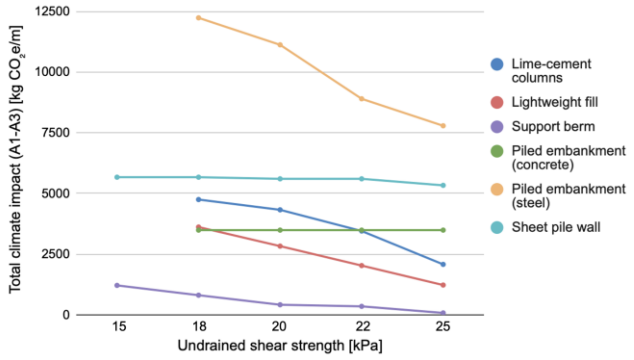

Figure 7. Climate impact with varying undrained shear strength for the clay.

4 DISCUSSION AND CONCLUSIONS

The results clearly show, as expected, that the support berm has the lowest climate impact, while the piled embankment with steel piles has the highest impact. It should be noted that the support berm's low climate impact comes from its low emission factor due to the assumption that it is a by-product. This is consistent with other studies by Song et al. (2021) and Samuelsson et al. (2023). The result for the lime-cement columns will be different in the future with the development of fossil-free steel or alternative materials such as cement kiln dust (CKD) or blast furnace slag.

For a more comprehensive result, the practical feasibility of each method and additional climate data should be included. Additional climate data combined with a project-specific study could lead to the inclusion of additional life cycle stages. The result of the support berm can, e.g., be significantly affected by the inclusion of the production due to its large weight, therefore requiring more transportation.

In addition, it can also be important to consider whether all the methods are practically feasible or how they can be combined to optimize the usage of materials. The analysis shows that with steeper slopes and lower strength in the clay, the methods aiming to reduce the driving moment or change the soil properties are generally not applicable in this case.

When deciding which alternative to choose, other factors can also influence the choice, where financial cost can be a crucial factor. Therefore, it is suggested to complement the LCA with a life cycle cost analysis (LCCA), preferably considering the uncertainties in the final assessment of the remediation method.

Despite these limitations, it can be considered sufficient to achieve the goal of evaluating the climate impact of the measures at an early design stage.

REFERENCES

Das, J. T., Puppala, A. J., Bheemasetti, T. V., Walshire, L. A., & Corcoran, M. K. (2018). Sustainability and resilience analyses in slope stabilisation, In: *Proceedings of the Institution of Civil Engineers – Engineering Sustainability*, 171, pp. 25–36. https://doi.org/10.1680/jensu.16.00054.

Maas, T., De Gijt, J., & Dudok Van Heel, D. (2011). Comparison of quay wall designs in concrete, steel, wood and composites with regard to the CO2-emission and the Life Cycle Analysis, In: *International Maritime-Port Technology and Development Conference (MTEC)*, pp. 129–134. https://doi.org/10.3850/978-981-08-7617-3.

Samuelsson, I., Larsson, S., & Spross, J. (2021). Life cycle assessment and life cycle cost analysis for geotechnical engineering: review and research gaps. *IOP Conference Series: Earth and Environmental Science*, 710. https://doi.org/10.1088/1755-1315/710/1/012031.

Samuelsson, I., Spross, J., & Larsson, S. (2023). Integrating life-cycle environmental impact and costs into geotechnical design. *Proceedings of the Institution of Civil Engineers - Engineering Sustainability*, Ahead of Print.

Song, X., Carlsson, C., Kiilsgaard, R., Bendz, D., & Kennedy, H. (2020). Life Cycle Assessment of Geotechnical Works in Building Construction: A Review and Recommendations. *Sustainability*, 12. https://doi.org/10.3390/su12208442.

Song, X., Iqbal, H., Rankka, W., Kiilsgard, R., & Bolin, P. (2021). Jämförande livscykelanalys av stabilitetshöjande åtgärder: Fallstudier Göta älv. Swedish Geotechnical Institute (SGI).

Proceedings of the XVIII ECSMGE 2024
GEOTECHNICAL ENGINEERING CHALLENGES
TO MEET CURRENT AND EMERGING NEEDS OF SOCIETY
© 2024 the Authors
ISBN 978-1-032-54816-6
DOI 10.1201/9781003431749-578
Open Access: www.taylorfrancis.com, CC BY-NC-ND 4.0 license

ECSMGE 24
XVIII EUROPEAN CONFERENCE ON SOIL MECHANICS AND GEOTECHNICAL ENGINEERING

Large-scale soil bio-cementation: insights into homogeneity, quality control, and waste handling

Sur l'effet des paramètres et des techniques d'injection pour obtenir une bio-amélioration homogène des sols: aperçus d'une expérience à grande échelle

R. Harran, D. Terzis, M. Büyüklü*, L. Laloui
Laboratory of Soil Mechanics/ Swiss Federal Institute of Technology (EPFL), Lausanne, Switzerland
**merih.buyuklu@epfl.ch*

ABSTRACT: This paper deals with challenges in large-scale soil bio-cementation. Introducing a novel treatment strategy with ex-situ hydrolysis in a 1000 L bioreactor, the study employs a state-of-the-art installation to inject hydrolyzed solutions into a 40 m^2 area of 0–4 mm sand. A comprehensive multilevel quality control system monitors chemical and hydraulic processes across cycles, resulting in reaction efficiencies exceeding 80%. The paper discusses the gradual increase in pressure at the injection inlet, correlating with higher calcification levels. Findings indicate improved resistance in zones with higher injection pressure, demonstrating the efficacy of ex-situ bio-cementation. The study also explores the mechanical improvements, suggesting comparable results to traditional in-situ methods. Additionally, the paper addresses the monitoring of microbially induced calcium precipitation (MICP) at the geotechnical scale, highlighting the issue of residual ammonium reaching absorbed quantities of 4 mol/L.

RÉSUMÉ: Cet article traite des défis liés à la bio-cimentation des sols à grande échelle. Introduisant une nouvelle stratégie de traitement avec l'hydrolyse ex-situ dans un bioréacteur de 1000 L, l'étude utilise une installation de pointe pour injecter des solutions hydrolysées dans une zone de 40 m2 de sable de 0 à 4 mm. Un système complet de contrôle de la qualité à plusieurs niveaux surveille les processus chimiques et hydrauliques à travers les cycles, aboutissant à des efficacités de réaction dépassant 80%. L'article discute de l'augmentation graduelle de la pression à l'entrée de l'injection, corrélée à des niveaux de calcification plus élevés. Les résultats indiquent une résistance améliorée dans les zones avec une pression d'injection plus élevée, démontrant l'efficacité de la bio-cimentation ex-situ. L'étude explore également les améliorations mécaniques, suggérant des résultats comparables aux méthodes traditionnelles in-situ. De plus, l'article aborde le suivi de la précipitation calcique induite par les micro-organismes (MICP) à l'échelle géotechnique, mettant en lumière le problème de l'ammonium résiduel atteignant des quantités absorbées de 4 mol/L.

Keywords: MICP; upscaling; quality control; dynamic penetrometer; field testing.

1 INTRODUCTION

Nearly two decades since its inception, Microbially Induced Calcium Carbonate Precipitation (MICP) has gained attention as a sustainable alternative for ground improvement. Utilizing urease-bearing microorganisms, urea hydrolysis induces carbonate ion creation, leading to solid calcium carbonate precipitation. This biochemical process enhances soil properties, impacting permeability, stiffness, compressibility, and shear strength. The technique has been explored in controlled setups and natural environments, addressing diverse geotechnical challenges (Terzis & Laloui, 2019).

2 MATERIALS & METHODS

To validate the ex-situ treatment strategy, a bench-scale campaign was conducted. Sand columns, representing the tank's porosity, underwent treatment with hydrolyzed and calcium-rich solutions. Analysis of liquid samples assessed precipitation efficiency through calculations involving influent and effluent reactant concentrations. The laboratory-scale investigation provided insights into the chemical efficiency of the treatment strategy, microstructural comparisons, and its potential for improving soil mechanics.

A reinforced concrete container, 8.0 m × 10.0 m × 2.5 m, was constructed with two compartments for repeated experiments (Harran et al., 2022).



Figure 1. Testing set-up.

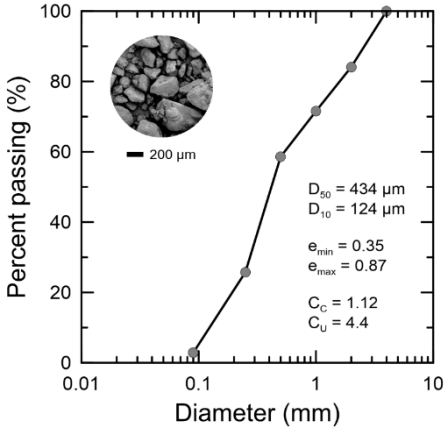

Figure 2. Particle size distribution and properties of the chosen sand.

Unlike previous impermeable setups, this design incorporated draining tubes in the tank's bottom, preventing reactant accumulation. This setup allowed control over water table levels, simulating real environmental conditions. Eight injection wells (Figure 1) per compartment facilitated the bio-cementation protocol's implementation. The design prioritized preventing ammonium leaching and maximizing liquid circulation.

Both compartments were filled with 0–4 mm sand from the Catellani quarry (Switzerland), exhibiting a diverse grain size distribution and composed of 70% quartz and 30% natural carbonate minerals. The sand is labelled SP according to ASTM D2487 but still covers a range of contents from fine (2.9% < 0.1 mm diameter) to coarse (15.9% > 2 mm diameter). (Figure 2). The bio-cementation protocol involved 11 days of successive cycles injecting hydrolyzed carbonate solution followed by immediate cementation solution injection. Sporosarcina pasteurii was used for urea hydrolysis, and both solutions were prepared in 1000 L batches.(Table 1) The protocol aimed for full pore volume coverage, and drainage tubes simulated a draining bottom surface, collecting effluents for monitoring. This setup enabled control over injection pressure and offered insights into the bio-cementation process.

In-situ testing utilized an instrumented dynamic penetrometer (Panda, Solsolution) across treated and untreated sand volumes. Tests at various locations, chosen for spatial heterogeneity representation, assessed the bio-cementation effect on cone tip resistance. The results provided a detailed understanding of the treatment‘s impact on the soil‘s mechanical properties.

Mechanical performance assessment involved Unconfined Compressive Strength (UCS) tests on lab-treated samples. The samples were compared to conventionally bio-cemented ones. Testing included controlled axial strain rates and subsequent determination of calcium carbonate contents, offering insights into the treatment‘s impact on mechanical behavior.

Samples from both laboratory and large-scale experiments underwent Scanning Electron Microscopy (SEM) for textural and geometrical characterization of the precipitated calcium carbonate. This microscopic analysis provided visual insights into the structure and morphology of the cemented material.

Table 1. Treatment solution constituents.

	Bioreactor Solution (BS)	Cementation Solution (CS)
Peptone (kg/m^3)	1	-
Lyophilized bacteria (L/m^3)	1	-
Urea (kg/m^3)	50	-
Calcium chloride (kg/m^3)	-	200

3 RESULTS

The precipitation efficiencies were computed based on the excess reactant species found in each injection cycle, using either calcium or TIC excess. For each injection cycle, two effluent samples were taken. Remarkably, high completion rates exceeding 70% were achieved with reaction times as short as 4 hours between injections. The effluent predominantly exhibited a richness in calcium in five out of eight injection cycles.

The use of pre-hydrolyzed urea played a pivotal role in this efficiency, as calcium carbonate precipitated immediately upon the contact of BS and CS solutions. This process demonstrated comparable efficiency to conventional Microbially Induced Calcium Carbonate Precipitation (MICP). Notably, it boasted faster precipitation times and the advantage of

introducing a solution into the ground with known characteristics, concentrations, and stability.

UCS (Figure 3) values increased with rising bond contents, reaching as high as 2.1 Mpa for 10% $CaCO_3$. Young's modulus (E) varied between 180 Mpa and 480 Mpa, increasing with higher bond content. Despite some observed scattering associated with the measured heterogeneity in gravimetric contents within the same sand column, the results were consistent. Generally, higher $CaCO_3$ contents resulted in a brittle response, characterized by distinctive peak strength followed by sharp softening.

SEM observations of precipitates formed in liquid batches after mixing the ex-situ BS and CS solutions are provided in Figure 4. The crystals exhibited a typical rhombohedral calcite morphology, reaching a size of 20 µm when precipitated without a sand matrix.

When ammonium concentrations exceed the water's natural self-purification capacity, it triggers various environmental concerns, notably eutrophication. Eutrophication, in turn, leads to the decline of aquatic life, such as fish, degradation of water quality, and disturbance of biodiversity. Therefore, it is crucial to monitor and mitigate ammonium concentrations arising from the bio-cementation process, to maintain them below acceptable thresholds. The recirculation of ammonium, combined with the levels produced with every new hydrolyzed batch, led to an increase in influent NH4+ concentrations throughout the treatment, as illustrated in Figure 5. At the end of the 20,800 L treatment, the effluent NH4+ concentration stabilized at around 1 mol/L.

Considering the average NH4+ concentration in the 11 cycles, accounting for dilution, the residual recorded ammonium aligned with the theoretical value. This suggests that to bring NH4+ within acceptable limits, substantial volumes and pumping times are needed in large-scale projects. The potential retention of NH4+ on soil particles and dissolution in groundwater observed in previous literature works further underscores the challenges associated with NH4+ elimination through MICP-induced ureolysis.
Hence, the study postulates that byproduct extraction from treatment solutions prior to injection into the ground using ex-situ hydrolysis remains a promising alternative. This approach aims to enable NH4+ elimination and minimize operational constraints, ultimately producing soil admixtures or grouts for bio-cementation that align with environmental norms.The results of dynamic penetrometer tests revealed varying heterogeneity in the treated section. Figure 6 presents a typical penetrogram result with a discrepancy at a depth of 1.2m attibuted to the well‘s outlet.

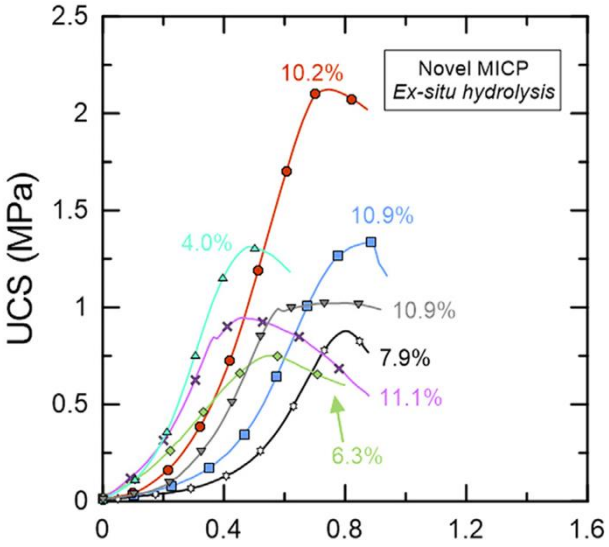

Figure 3. UCS determination on samples produced using ex-sity hydrolysis.

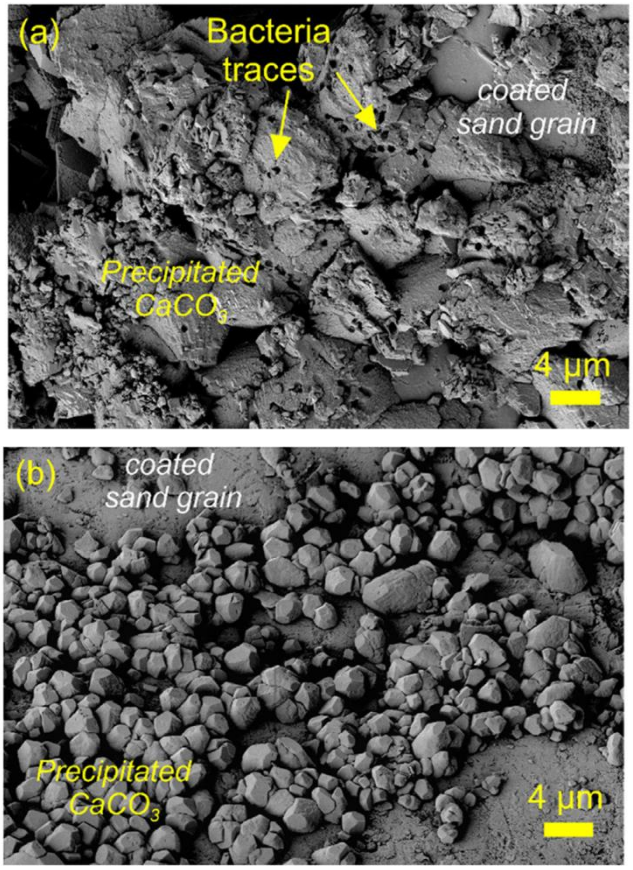

Figure 4. SEM observations of calcium carbonate precipitated on the surface of sand grains using (a) traditional MICP with in-situ hydrolysis and (b) novel MICP with ex-situ hydrolysis.

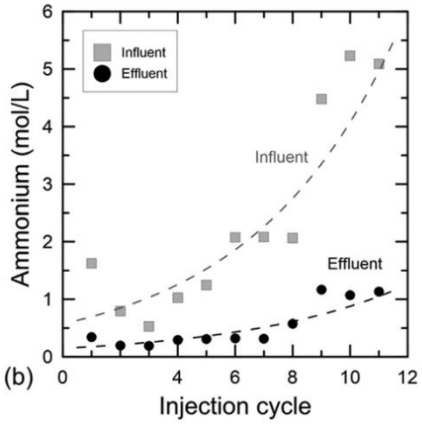

Figure 5. NH4+ concentrations during recirculation of enriched treatment batches.

All tests in the untreated compartment demonstrated overall homogeneity in cone resistance (qd) across depth, with values ranging between 0.5 and 1 MPa. A follow-up experiment using a slited pipe, i.e. without outlets every 50cm across the well‘s depth, yielded more homogenous results (Figure 7).

4 CONCLUSIONS

The ex-situ hydrolysis approach demonstrated high precipitation efficiencies and comparable mechanical properties to traditional MICP. The microscopic analysis revealed changes in mineralization processes at the pore scale. Chemical monitoring confirmed the efficiency of the precipitation reaction, with implications for the treatment of residual ammonium. The dynamic penetrometer campaign provided spatial insights into the effectiveness of bio-cementation, highlighting areas of significant improvement. Overall, the study contributes to bridging laboratory advancements with large-scale implementation of bio-cementation, providing a comprehensive multi-level quality monitoring system for real-world applications.

ACKNOWLEDGEMENTS

The authors would like to acknowledge the financial support of the European Research Council (ERC) under the European Union’s Horizon 2020 research and innovation program (grant agreement No. 788587).

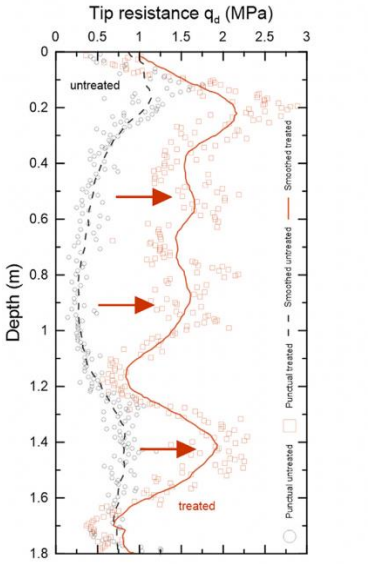

Figure 6. Penetrograms for both treated and untreated states using a sleeved tube.

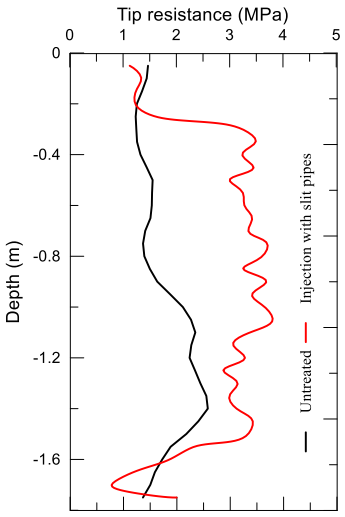

Figure 7. Penetrogram for both treated and untreated states using a slit tube.

REFERENCES

Harran, R., Terzis, D. and Laloui, L. (2023) Addressing the challenges of homogeneity, quality control and waste handling in soil bio-cementation: A large-scale experiment. *Soils and Foundations*, Volume 63, Issue 4, p.101332. https://doi.org/10.1016/j.sadndf.2023.101332.

Terzis, D. and Laloui, L. (2018) 3-D micro-architecture and mechanical response of soil cemented via microbial-induced calcite precipitation, *Scientific reports*, 8(1), p.1416.

Terzis, D., and Laloui, L. (2019) A decade of progress and turning points in the understanding of bio-improved soils: A review. *Geomechanics for Energy and the Environment*, Volume 19, p.100116. https://doi.org/10.1016/j.gete.2019.03.001.

Proceedings of the XVIII ECSMGE 2024
GEOTECHNICAL ENGINEERING CHALLENGES
TO MEET CURRENT AND EMERGING NEEDS OF SOCIETY
© 2024 the Authors
ISBN 978-1-032-54816-6
DOI 10.1201/9781003431749-579
Open Access: www.taylorfrancis.com, CC BY-NC-ND 4.0 license

ECSMGE 24
XVIII EUROPEAN CONFERENCE ON SOIL MECHANICS AND GEOTECHNICAL ENGINEERING

Thermal soil properties as a basis for design of underground high voltage cables

Propriétés thermiques du sol comme fondement pour la conception des câbles souterrains haute tension

K. Hendler*, C. Meier, S. Kleiber
Boley Geotechnik GmbH, Munich, Germany

J. Stegner
TenneT TSO GmbH, Bayreuth, Germany

C. Drefke
TransnetBW GmbH, Stuttgart, Germany

C. Boley
University of the Bundeswehr, Munich, Germany

k.hendler@boleygeotechnik.de

ABSTRACT: The dimensioning of underground extra-high voltage direct current (HVDC) power lines, requires detailed knowledge of the ground and its thermal conductivity. For this purpose, a laboratory test using transient methods with the needle probe, to determine reproducible values of the thermal conductivity of soils was developed for the construction of the 700 km long SuedLink underground power line in Germany. The unique approach of this test not only yielded precise thermal conductivity measurements but also allowed for the depiction of the thermal conductivity to water content relationship, covering the entire range from saturated to oven-dried soil states. This allows site specific groundwater conditions to be considered during the design. Additionally, the gravel content of the soil was also taken into account.The results of the thermal conductivity tests of the soil samples form the basis of the thermal ground model which governs the thermal design of HVDC underground cables. The thermal design is crucial for optimising the spacing between cables in order to minimise the project costs and the environmental impact. In this paper the process from laboratory testing to the creation and analysis of the thermal ground model is presented. Furthermore, insights into the thermal design of HVDC cables are provided focussing on horizontal directional drilling (HDD) methods.

RÉSUMÉ: Le dimensionnement des lignes électriques souterraines à courant continu à haute tension (HVDC) nécessite une connaissance détaillée du sol et de sa conductivité thermique. À cet effet, un test en laboratoire utilisant des méthodes transitoires avec une sonde à aiguille, pour déterminer des valeurs reproductibles de la conductivité thermique des sols, a été développé pour la construction de la ligne électrique souterraine SuedLink de 700 km de long en Allemagne. L'approche unique de ce test a non seulement permis d'obtenir des mesures précises de la conductivité thermique, mais a également permis de représenter la relation entre la conductivité thermique et la teneur en eau, couvrant toute la gamme des états du sol, de saturé à séché au four. Cela permet de prendre en compte les conditions spécifiques au site en ce qui concerne les niveaux d'eau souterraine lors de la conception. De plus, la teneur en gravier du sol a également été prise en compte. Les résultats des tests de conductivité thermique des échantillons de sol constituent la base du modèle thermique du sol qui régit la conception thermique des câbles souterrains HVDC. La conception thermique est cruciale pour optimiser l'espacement entre les câbles afin de minimiser les coûts du projet et l'impact environnemental. Dans cet article, le processus allant des tests en laboratoire à la création et à l'analyse du modèle thermique du sol est présenté. De plus, des informations sur la conception thermique des câbles HVDC sont fournies en mettant l'accent sur les méthodes de forage directionnel horizontal (HDD).

Keywords: Soil thermal conductivity; underground cables; extra-high voltage direct current; water content; renewable energy.

1 INTRODUCTION

In line with the Renewable Energy Sources Act (BMWK, 2021), all electricity in Germany should be carbon-neutral by no later than 2050. The extra-high voltage direct current (HVDC) underground cable project SuedLink will contribute to this goal by making

it possible to transmit wind energy from the northern parts to the southern parts of the country.

Most of the 700 km route of the SuedLink power line consists of the so-called trunk-line where four HVDC cables will be installed underground at various distances to one another, see Figure 1. This will be done by means of open excavations as well as using trenchless construction techniques (such as HDD) along significant lengths of the project.

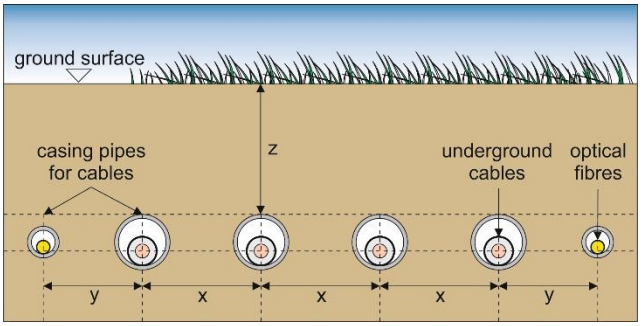

Figure 1. Sketch of HVDC underground cables constructed using HDD.

Some of the electrical energy transported along the cables is converted to heat energy due to the resistance of the cables. As each of the HVDC cables emits a certain amount of heat, they need to be spaced sufficiently far apart from one another in order to avoid overheating and thereby reducing their performance. This is why the thermal conductivity (TC) of the ground plays a crucial role in the thermal design of underground HVDC cables.

As part of the SuedLink project a novel method for determining the water content dependant TC of soils was developed and applied. The results of these tests were used to develop thermal ground models which formed the basis of the thermal design of the HVDC cables.

Different methodologies can be applied in order to determine the TC of soils as explained by Banks (2012). Typically, these fall into either the category of employing the steady state solution to Fourier's law in several variants or by using a transient method. In laboratory settings, steady-state methods entail subjecting a specimen to unidirectional heat flow. The power input and temperature difference across the specimen are then measured once a steady state is achieved. Transient methods require the application of heat to the specimen, with subsequent monitoring of temperature changes throughout a specified duration.

Clarke et al. (2008) described a steady state test method for TC of soils where heat is applied to one end and assumed to have one-directional flow, since the sample is insulated radially and at the base. Low et al. (2017) performed an error analysis on the Clarke et al. (2008) setup by performing physical laboratory tests and then comparing these to a finite element model of the tests. Low et al. (2017) conclude that significant radial heat losses occur through the sides of the thermal cell which significantly impacts the calculated TC. Low et al. (2017) proceed to recommend using transient testing techniques. Furthermore Schedel et al. (2019) argue that a valid measurement of the TC on a partially saturated material, using steady state methods, is also not possible. This is because the displacement of the water content along the temperature gradient, due to uneven heat distribution, can also lead to significant inaccuracies.

Other literature on TC of soils is typically found in the context of ground source heat pumps or energy foundations. Here the thermal response test to determine the effective TC along the length of a borehole is described in Banks (2012) and VDI 4640 (2010). However, the results of these tests are applied in the design of ground source heat pump systems and are not directly applicable for determining the TC of specific soil samples and their representative layers. VDI 4640 (2010) does, however, provide typical values of thermal conductivities for various soil types at different water contents which can be useful as indicative values to use during a pre-design.

Currently no standard exists for determining the characteristic TC value of soils in the field or in the laboratory using transient test methods. Only the configuration of the needle probe and the subsequent measurement to determine the TC are described in standards ASTM D5334:22a and IEEE Std 442-2017. With the participation of numerous experts, the processes of sampling, sample transport and measuring across various water contents up to evaluation were developed into a project specification, which has been adopted by the four major energy grid operators in Germany.

2 THERMAL CONDUCTIVITY (TC) TEST

In the SuedLink project, the investigation of thermal properties of soils is carried out on samples taken during the ground investigation. The TC of a soil is highly dependent on its water content as well as the degree of compaction. The latter is adjusted to the in-situ density when samples are prepared for TC measurements. The water content of soils is subject to natural (seasonal, land use) and operational (drying due to heat radiation of cables) changes. To take this into account, the samples are dried out in the laboratory over a defined period of time, starting from the saturated state and ending in the oven-dried state. During this drying process the TC is continuously measured and recorded. The results of the laboratory

tests yield a relationship between TC and water content for a specified density. In contrast to only having measurements at single points, this continuous measurement allows the entire process to be partially automated, thus avoiding external influences and providing very detailed data on the TC.

2.1 Test setup

In the laboratory test the sample is air dried, from an initially saturated state, in an open topped cylinder. During this drying period, the TC is measured using the needle probe method, as per ASTM D5334:22a, while simultaneously measuring the water content gravimetrically. The basic procedure of this continuous TC measurement and the use of 50 mm high cylindrical soil samples is based on investigations by Markert (2012) and Drefke et al. (2017) and further adapted by Stegner et al. (2017).

Figure 2 shows the experimental set-up for the continuous measurement of TC and water content on a cylindrical soil sample.

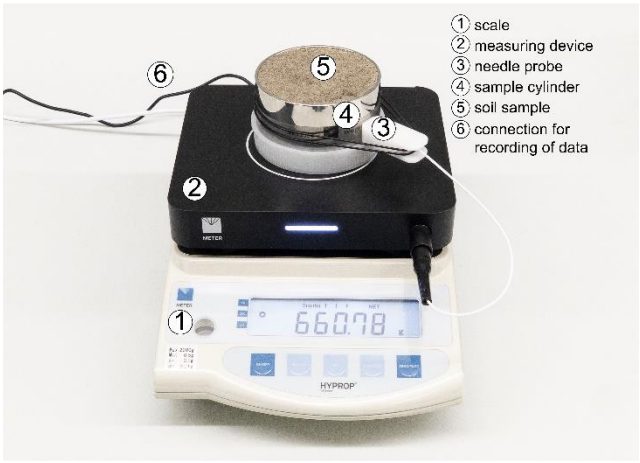

Figure 2. Experimental setup for continuous measurement of TC and water content of a cylindrical soil sample, adapted from METER Group AG (2021).

The laboratory test is carried out with standardised 250 cm³ steel cylinders (inner diameter = 80 mm; height = 50 mm). Three openings are arranged at 120° to each other along the middle of the cylinder. One of these is used to insert the needle probe into the soil sample.

In the SuedLink project, the TR-3 Inline needle probe from METER Group AG with a length of 70 mm and a diameter of 2.4 mm is used. The needle probe complies with the specifications of the relevant electrical engineering standards (ASTM D5334:22a; IEEE Std 442-2017).

For determining the relationship between TC and water content, the VARIOS measuring system (Meter Group AG) was further developed in cooperation with the manufacturer and the laboratory based on the measurement specification provided by the client. The special feature of this measuring system is the fully automated continuous measurement and recording of the TC data using the line source test method (ASTM D5334:22a) and the water content via weighing. The samples remain in position on the scales during the entire test procedure, so that disturbances during sample handling and thus falsification of measurement results can be ruled out.

2.2 Sample extraction and preparation

Both disturbed and undisturbed samples can be used for the laboratory test to determine the TC. In the case of high coarse grain contents, disturbed samples are preferred to undisturbed samples, as these allow the so called “oversize grains” (d > 6.3 mm) to be separated during sample preparation. This may be necessary if the insertion of the needle probe into the soil samples is hindered by these oversize grains.

If the samples from the ground investigation are mostly gravel free, it is favourable to take undisturbed soil samples by means of modified stainless-steel liners, specifically intended for the TC tests (see Figure 2). Undisturbed soil samples have the in-situ density and thus reflect the natural state more accurately than disturbed soil samples which are subsequently packed. It is therefore favourable to use undisturbed soil samples, since the TC of a soil is dependent on the density.

In the case of disturbed samples (bucket samples), first the water content of the soil is determined and, if necessary, oversized granular material is separated. By knowing the water content as well as the natural density of the soil, the sample can be installed into the cylinder as close as possible to the in-situ conditions. If no density information is known, the sample is compacted to a density that matches the packing density or consistency as per DIN 4220:2020-11 (2020). In the case of undisturbed samples, no special preparation is necessary before carrying out the test, as these samples are already in a near to in-situ state.

In the next step, the entire sample is covered by a filter paper and permeable caps on both sides and then saturated in a water bath for at least 30 hours.

2.3 Testing

After saturation, the needle probe is inserted and fixed in one of the three lateral openings. The test is started once the sample with the needle probe and the TC measuring device are placed on the scale and connected to the needle probe.

The system automatically measures the TC of the sample at intervals of 60 minutes. Simultaneously the

corresponding weight of the experimental set-up, i.e., the continuous weight loss, is recorded via the scales. The exact water content at each measurement can only be assigned after the sample is oven dried at the end of the test. Both the sample preparation and the measurements are carried out at constant room temperatures under controlled laboratory conditions.

Normally the test would be terminated once the sample has reached a constant mass. However, depending on the soil type, this could take between a few days up to weeks. A termination criterion of 8 days from start of test, has proven to be sufficient to record the water content relevant for HVDC cable dimensioning. The sample is then dried in an oven at 65 °C for 48 hours. After cooling in a desiccator, the so-called "oven-dried" TC is measured. Hereby the theoretically possible driest condition of the soil directly around the cables is simulated. Finally, the sample is dried at 105 °C in order to assign the corresponding water contents and dry density to the recorded sample weight measurements. The procedure described above is represented in the flow chart in Figure 3.

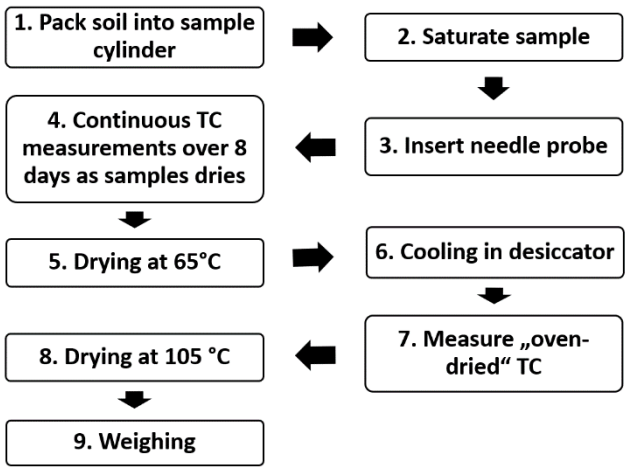

Figure 3. Laboratory test procedure for determining soil TC.

3 THERMAL CONDUCTIVITY RESULTS

3.1 Raw Data

A laboratory test result of the TC to water content of a sand sample is shown in Figure 4. The (almost) fully saturated sample has a volumetric water content of about 47% with a corresponding TC of approximately 1.5 W/(m·K). As drying progresses, the TC decreases to about 0.9 W/(m·K) at a volumetric water content of about 15%. This range is recorded during the continuous measurements of 8 days. In this case the "oven-dried" TC was determined to be approximately 0.35 W/(m·K) at a volumetric water content of 2%.

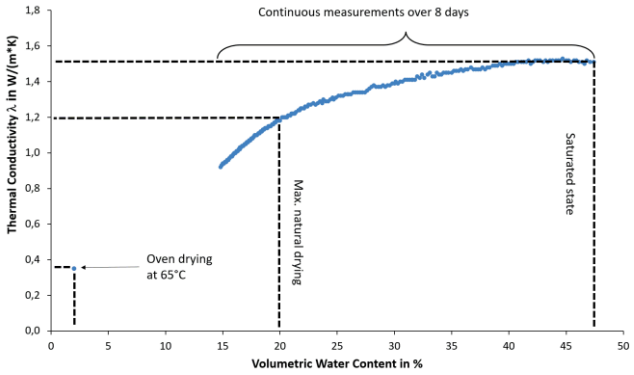

Figure 4. Exemplary TC test result of a sand sample measured from complete saturation to oven drying.

The above example clearly illustrates the tendency of the TC to decrease as drying progresses. At low water contents further drying by evaporation takes longer than at high water contents, which is why the 8-day cut-off criteria was defined. The gap between the oven dried reading and the last reading after 8 days can be bridged with sufficient precision by linear interpolation.

Generally, the TC decreases as the soil dries out. However, occasionally cohesive soils show an increase in TC with increased drying over a certain period of time. This observation correlates with a shrinkage observed in these samples during the initial phase of heating and subsequent drying-out (Laloui, 2001).

3.2 Evaluation of raw data

To ensure a uniform evaluation and a minimisation of human errors of the TC laboratory results within the SuedLink project, the geo-data management software GeODin was used, for which a specific TC-plug-in was developed by Fugro GmbH.

For the evaluation, all relevant subsoil data, such as stratigraphic logs, information on the TC samples, and so on need to be entered into GeODin. The software imports and reads the raw data of the TC test results. The GeODin plug-in corrects the discrepancy that arises from the non-measurement of the oversize grains during the TC tests, by geometric means (Woodside & Messmer, 1961; Farouki, 1986). This is done because rocks have a higher TC than soils, which is why the oversize grains fraction that was separated before the test (see section 2.2) has a positive influence on the overall TC of a stratigraphic soil layer. In addition to this the relevant water contents and corresponding thermal conductivities of the soil are determined by the plug-in. This whole process is semi-automated.

In the next step of the evaluation, the measurement gap between the continuous measurement and the "oven dried" TC (see Figure 4) is closed by linear interpolation.

In a further evaluation step, the TC value of the minimum natural water content is determined. This is based on the results of site-dependent, multi-year water balance models. In the example in Figure 4, the minimum natural water content is 20% which corresponds to a TC of approx. 1.2 W/(m·K), as per Figure 4. Under certain conditions, it can also be necessary to apply a water content that accounts for technically induced drying. Ultimately the evaluation of the TC test with the GeODin-TC-Plugin yields the TC associated with the typical drying of the soils (saturated, natural drying/damp, technically induced cable drying, oven-dry) for each sample.

4 THERMAL GROUND MODEL AND DESIGN

For the thermal design of the cable above groundwater, the relevant thermal conductivities are comprised of a pair of TC values corresponding to the water content of the soil in its natural state and the soil dried by the cable. Below groundwater the TC corresponding to the saturated water content of a soil is adopted. For each sample these thermal conductivities are integrated into a thermal ground model where areas of comparable thermal properties (thermal zones) are defined. An example of a thermal ground model is displayed in Figure 5.

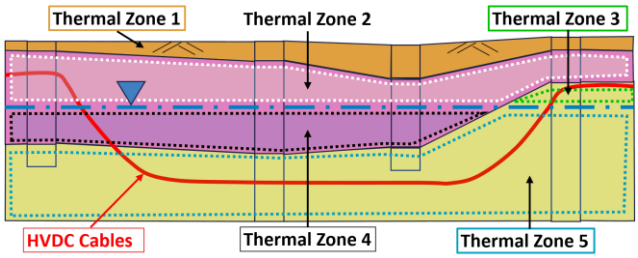

Figure 5. Example of a thermal ground model with demarcated thermal zones.

Within a soil layer, different thermal conductivities due to different water contents can become relevant for the design. For example, when a soil layer extends from above the water table to below the water table. This is why, for example, the thermal zone 2 is differentiated from the thermal zone 4 in Figure 5. The lowest groundwater level expected over the lifetime of the cable must always be used during design.

The closer the cables are laid to each other, the greater their mutual thermal influence. The maximum operating temperature of 70 °C in the cable conductor limits the minimum centre-to-centre spacing between the cables for a given cable type and local thermal soil properties. In the thermal design the minimum centre-to-centre spacing is calculated iteratively as a function of the depth of the cable.

The thermal design calculations are performed by means of Finite Element modelling for stratified ground using a two-layer model according to the Cigre Study Committee 21 (1992). The primary input parameters for the thermal design calculations are the TC value-pairs.

The results of these calculations were developed into a set of tables for the SuedLink project that cover the vast majority of cases encountered when performing a thermal design. This not only stream-lined, but also created a transparent and reproducible designs. Specific cases that were not covered by the tables had to be calculated individually.

At the same installation depth, changes in soil type and water content can result in large differences in the required cable spacing, which can in some cases differ by a factor of four.

The detailed TC investiagtions have led to signficant optimisations in cable-spacing, as can be seen by the following example. Conventionally a very conservative TC-Pair corresponding to the „damp“ and „cable-dried“ water contents, of 1 W/(m*K) and 0.4 W/(m*K), is assumed. At 8 m cable depth this would lead to a required cable spacing of approximately 27 m along the trunk-line. Comparing this to a true TC-Pair of 1 W/(m*K) and 1 W/(m*K), which has often proved to be the case for various soils, a cable spacing of only 9 m is required.

For the thermal design, various boundary conditions such as heat-emitting underground cables (from third parties), pipelines and topographic changes in ground level need to be carefully considered.

Various technical solutions can be adopted and considered in the design in order to reduce the required spacing between the cables installed by means of trenchless construction. This included improving the TC in the area of the cable by filling the casing pipes with a conductive material such as a gel or water. Alternatively, the standard casing pipe diameter (280 mm) was increased and also filled with a conductive material. In certain cases, the construction tolerance for the HDD was reduced.

5 CONCLUSIONS

The partially automated testing and evaluation processes described here has been established and used on over 6000 soil samples in the SuedLink project. The creation and understanding of the thermal ground model require detailed evaluation with corresponding expertise due to complex stratigraphy’s as well as various external boundary conditions. Similarly, a

good understanding of soil thermal conductivity principles, in the context of HVDC cables, are essential for an efficient design.

Looking forward, European energy grid operators envision the development of a comprehensive database incorporating the soil TC test results from the SuedLink project. Coupled with pedotransfer functions, this database would streamline ground exploration for future underground cable projects, contributing to more efficient and cost-effective designs.

REFERENCES

ASTM D5334:22a (2022) Standard Test Method for Determination of Thermal Conductivity of Soil and Rock by Thermal Needle Probe Procedure. West Conshohocken, United States: ASTM International.

Banks, D. (2012) An Introduction to Thermogeology: Ground Source Heating and Cooling. Second ed. Oxford: Wiley-Blackwell.

BMWK (2021) Renewable Energy Sources Act (EEG). Berlin: Federal Ministry for Economic Affairs and Climate Action.

Cigre Study Committee 21 (1992) Determination of a value of critical temperature rise for a cable backfill material. s.l.:Electra.

Clarke, B. G., Agab, A. & Nicholson, D. (2008) Model specification to determine thermal conductivity of soils. Proceedings of the Institution of Civil Engineers - Geotechnical Engineering, GE3, 161-168. https://doi.org/10.1680/geng.2008.161.3.161.

DIN 4220:2020-11 (2020) Pedologic site assessment – Designation, classification and deduction of soil parameters (normative and nominal scaling). Berlin: Beuth.

Drefke, C., Schedel, M., Stegner, J. Balzer, C., Hinrichsen, V., Sass, I. (2017) Measurement Method of Thermal Properties of Cementitious Bedding Materials and Unsaturated Soils: Hydraulic Influence on Thermal Parameters. Geotechnical Testing Journal, 40(1), 160-170. https://doi.org/10.1520/GTJ20160027.

Farouki, O. (1986) Thermal properties of soils. New Hampshire, U.S.A.: United States Army Corps of Engineers.

IEEE Std 442-2017 (2017) IEEE Guide for Thermal Resistivity Measurements of Soils and Backfill Materials. New York, USA: The Institute of Electrical and Electronics Engineers.

Laloui, L. (2001) Thermo-mechanical behaviour of soils. Revue Française de Génie Civil, 5(6), 809-843. https://doi.org/10.1080/12795119.2001.9692328

Low, J., Loveridge, F. & Powrie, W. (2017) Error analysis of the thermal cell for soil thermal conductivity measurement. Proceedings of the Institution of Civil Engineers - Geotechnical Engineering, 170(3), 191-200. https://doi.org/10.1680/jgeen.16.00137.

Markert, A. (2012) Einfluss von Substrateigenschaften auf die Wärmeleitfähigkeit von Böden – Bodenphysikalische Nutzungsaspekte von Erdwärmekollektoren. Influence of substrate properties on the thermal conductivity of soils - Soil physical utilisation aspects of geothermal collectors. (in German). Berlin: Technische Universität Berlin.

METER Group AG (2021) Photo documentation of a measuring stand for determining the thermal conductivity. Munich: s.n.

Schedel, M., Drefke, C. & Sass, I. (2019) Comment on the paper "Temperature dependency of the thermal conductivity of porous heat storage media" by Henok Hailemariam and Frank Wuttke in Heat and Mass Transfer (2018) 54:1031–1051. Heat Mass Transfer 55, 2689–2691 (2019). https://doi.org/10.1007/s00231-019-02603-3.

Stegner, J., Drefke, C., Hailemariam, H., Anbergen, H., Wuttke, F., Sass, I. (2017) Messtechnik für den Erdkabeltrassenbau – Ermittlung der Wärme-leitfähigkeit von Bettungsmaterialien. Measuring technique for underground cable routes – Determination of the thermal conductivity of bedding material (in German). Bauphysik, 39(1), 41-48. https://doi.org/10.1002/bapi.201710003.

VDI 4640 Part 1:2010-06 (2010) Thermal use of the underground - Fundamentals, approvals, environmental aspects. Düsseldorf: Verein Deutscher Ingenieure e.V.

Woodside, W. & Messmer, J. (1961) Thermal Conductivity of Porous Media. I. Unconsolidated Sands. Journal of Applied Physics, Volume 32, pp. 168-1699.

Proceedings of the XVIII ECSMGE 2024
GEOTECHNICAL ENGINEERING CHALLENGES
TO MEET CURRENT AND EMERGING NEEDS OF SOCIETY
© 2024 the Authors
ISBN 978-1-032-54816-6
DOI 10.1201/9781003431749-580
Open Access: www.taylorfrancis.com, CC BY-NC-ND 4.0 license

ECSMGE 24
XVIII EUROPEAN CONFERENCE ON SOIL MECHANICS AND GEOTECHNICAL ENGINEERING

Validation of the applicability of the PS logger borehole probe for diverse geotechnical scenarios

Validation du système PS Logger dans divers scénarios géotechniques

R.M. Hen-Jones*, P. Worthington, G. Comber, S. Garantini
Robertson Geo, Deganwy, North Wales, United Kingdom

P.J. Vardanega
University of Bristol, Bristol, United Kingdom

**rhjones@robertson-geo.com*

ABSTRACT: The PS logger is a low frequency dipole-based sonic logging probe which is used widely to measure P- and S- wave velocities of earth materials. It is of particular interest to offshore environments where the latter can be used to derive the small-strain stiffness G_{max}, an important measurement in offshore construction. The method relies on the indirect excitation of the borehole via a dipole pressure wave excited in the borehole fluid, allowing shear wave velocity (V_s) to be measured in both fast and slow formations. In this study, the theoretical basis for the PS logger is presented, alongside the results of recent field projects which provide answers to key questions regarding the viability of the tool for a range of situations, and to the interpretation of results for widely ranging ground conditions. These include a comparison of results from both uncased (open) and cased boreholes, and from a wide range of ground velocities ($V_s \approx$ 220m/s to 3760m/s), and for varying borehole sizes. Full waveform analysis of time-series data is undertaken and underlines the need for consideration of theoretical principles in data interpretation. Ultimately, the results demonstrate the wide applicability of the tool beyond the geotechnical limits of traditional logging tools, which is attributed largely to the low frequency nature of the PS logger.

RÉSUMÉ: Le système PS Logger est une sonde de diagraphie sonique utilisant un émetteur basse fréquence de type dipôle, utilisée pour générer et mesurer les vitesses des ondes de compression P et de cisaillement S dans les sols. La sonde est particulièrement intéressante dans la conception de structures offshore où elle peut être utilisée pour calculer le module de cisaillement G_{max}, qui est une mesure majeure dans ce domaine. La méthode repose sur l'émission d'une onde de compression dans le fluide qui au contact de la paroi du forage génère une onde flexurale permettant de mesurer la vitesse de l'onde de cisaillement (Vs) dans les formations rapides mais surtout dans les formations lentes. Dans cette étude, le principe théorique de fonctionnement de l'outil PS logger est présenté, ainsi que les résultats de chantiers récents qui éclairent sur les capacités de l'outil dans différentes situations et montrent des résultats dans des conditions de sol très variés. Également présentés: - une comparaison des résultats en forages non tubés (ouverts) et tubés, - des mesures dans une gamme très large de vitesses de terrain (Vs ≈ 220 m/s à 3760 m/s) et dans différents diamètres de forage. Une analyse complète des trains d'ondes a été réalisée utilisant l'ensemble des principes théoriques régissant la propagation des ondes P et S dans les sols. En conclusion, les résultats présentés démontrent la large applicabilité de l'outil PS Logger et ses capacités bien supérieures aux outils de diagraphie traditionnels de type FWS grâce à son système d'émission dipolaire flexural.

Keywords: Suspension logging; dipole source; flexural wave; seismic velocity.

1 SONIC LOGGING

Sonic logging methods are used to obtain velocity data in boreholes with depths ranging from a few metres to several kilometres. Variations exist on logger configurations, which have evolved to overcome problems including measurement in slow formations and poor measurement resolution (Close et al., 2009). The propagation velocities of body waves in a medium are a complex function of several factors, including density, porosity, and mineralogy (Rafavich, 1984). Sonic logs utilise acoustic sources operating within a frequency spectrum, exciting waves in the surrounding formation of wavelength λ (m) determined by Eqn. 1, where f (Hz) is excitation frequency within the source spectrum, and V (m/s) is the velocity of the wave:

$$V = f\lambda \quad (1)$$

Traditional monopole tools use critical refraction of compressional (P) and shear (S) waves to measure velocities, causing symmetric borehole displacement (Figure 1.a), but are impeded by the fact that shear refraction is not possible in slow formations. Dipole tools overcome this issue by generation of the flexural

(bending) mode (Figure 1.b), which, at sufficiently low source frequencies travels at the formation shear velocity (but technically constituting a surface mode) (Close et al., 2009).

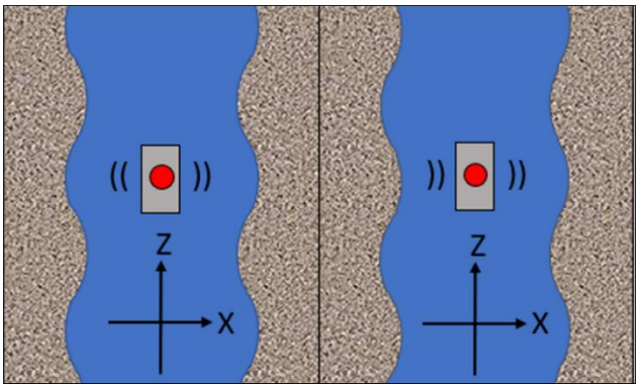

Figure 1. Side view of fundamental borehole movement resulting from (a) monopole; (b) dipole forces.

1.1 PS Logger

The principal features of the PS logger (a suspension-type logger) are a dipole hammer source, separated from two receivers by acoustic damping tubes. The hammer source constitutes a solenoid-operated shuttle housed within a steel cylinder. Firing causes the shuttle to strike the inner surface of the steel cylinder, indirectly exciting the borehole fluid, exciting both P and S_f (flexural) waves along the borehole in both fast and slow formations (Robertson Geo, 2023). Measurements are made in two horizontal directions (left and right), producing flexural modes 180˚ out of phase. The source centre frequency is approx. 1.5kHz.

As the hammer strikes the cylinder, a momentary imbalance in push/pull action between the struck/ opposite sides causes bulging (Figure 2a), creating a monopole in the fluid, exciting P and Stoneley waves. As the opposite side reacts, a pressure doublet is set up, such that a pressure increase in the fluid on one side of the cylinder is matched by a pressure decrease in the fluid on the other side (Figure 2b), exciting the flexural mode, generating dipole P waves and flexural waves. The PS logger is fitted with hydrophones and geophones, which are configured to measure P and S_f (flexural) wave velocities, respectively.

In this paper, widely ranging ground conditions are considered, in order to evaluate the viability of the PS for diverse geotechnical conditions. The particular focus is on measurement of shear wave velocities, generally harder to resolve than compressional waves.

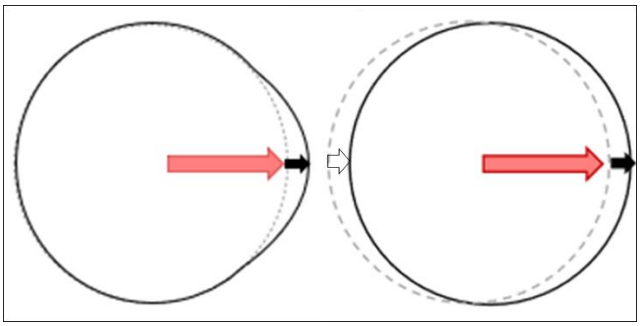

Figure 2. Planar view of steel cylinder primary displacement modes. (a) Bulging caused by initial imbalance; (b) flexural mode displacement.

2 CASE STUDIES

Anonymised Robertson Geo archives provided the data for the following case studies, allowing the following geotechnical scenarios to be investigated. Recorded waveforms were obtained using the geophone receivers.

2.1 Open (uncased) versus cased borehole

A 146mm diameter borehole was drilled and PS logging undertaken along a 17m profile, at 0.5m intervals, whilst the borehole was open (uncased).

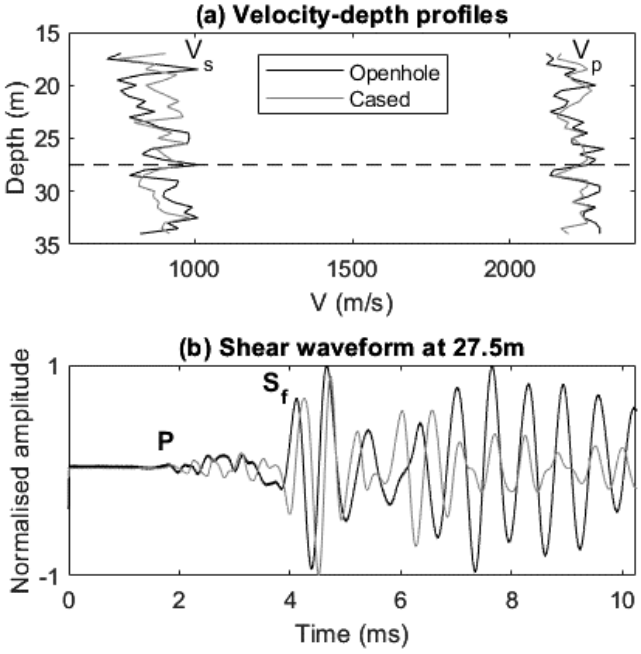

Figure 3. Openhole versus PVC cased borehole comparison. (a) Velocity-depth profile averaged from right and left hammer shot results (V_s obtained from geophone channels, V_p from hydrophone channels); (b) Geophone-recorded waveforms (data from right hammer shot only). "P" and "S_f" indicate the arrival of compressional and flexural waves, respectively.

The PS logger was removed and the borehole lined with PVC casing, reducing the diameter to 90mm, and the measurements repeated with the casing in place. Figure 3. shows reasonable agreement between datasets, summarising relative differences in Table 1.

Table 1. Summary of openhole versus cased (PVC-lined) borehole comparison.

Velocity type	Min. diff (%)*	Max. diff (%)*	Mean diff (%)*
V_p	0.0	5.4	1.6
V_s	0.0	21.6	8.1

*Calculated with respect to openhole data. Describes absolute difference.

2.2 Varying formation velocity

Waveforms pertaining to the extremes of shear velocities were obtained from the data archives, describing very slow shear velocities of 223m/s and 3759m/s respectively. In the slow formation, both P and S_f waves are observed on both near and far receivers, whilst in the fast formation, only S_f waves are observed (Figure 4).

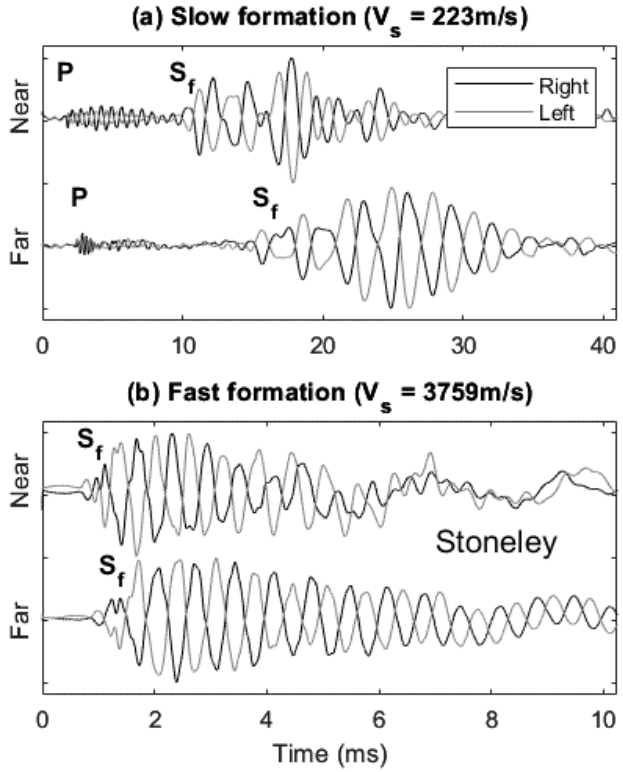

Figure 4. Geophone-recorded waveforms for (a) slow; (b) fast formations. Data from both right and left hammer shots are shown, illustrating clear reversals of amplitudes. Note, different time axes reflect different sampling rates. "P" and "S_f" indicate the arrival of compressional and flexural waves, respectively. Calculated Poisson's ratio for the slow formation waveform is 0.49.

2.3 Borehole size

Waveforms pertaining to the extremes of industry borehole sizes were obtained from the data archives describing borehole diameters of 250mm (large), 146mm (medium) and 76mm (small). Figure 5 demonstrates that in all three cases, clear waveforms have been obtained, resolving both P and S arrivals.

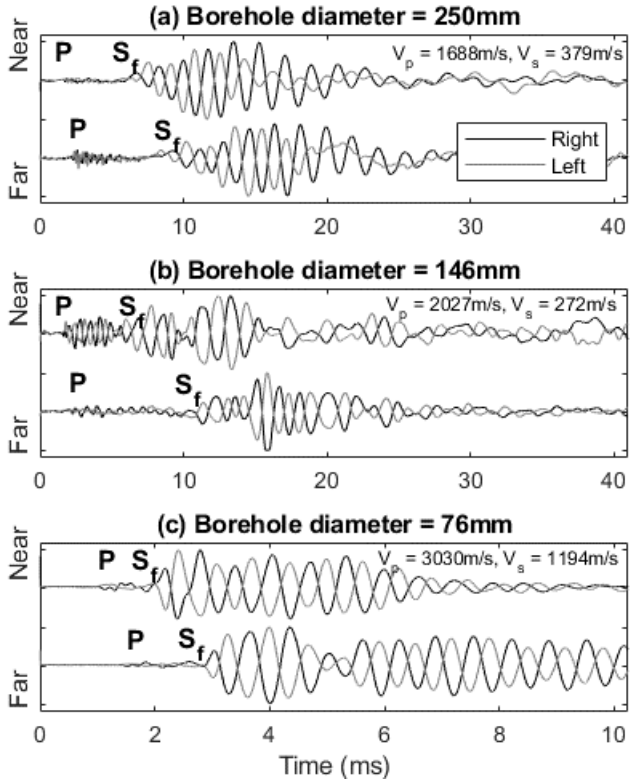

Figure 5. Geophone-recorded waveforms for (a) large, (b) medium and (c) small borehole diameters. Data from both right and left hammer shots are shown, illustrating clear reversals of amplitudes. Note, different time axes reflect different sampling rates. "P" and "S_f" indicate the arrival of compressional and flexural waves, respectively. Poisson's ratios are 0.47 (a), 0.49 (b) and 0.41(c).

3 DISCUSSION

Generally, the PS logger is recommended for use in uncased boreholes, however, manufacturers do provide specifications for casing installation and grouting such that the tool should operate regardless (Robertson Geo, 2023). Figure 3.a shows velocity-depth profiles of a borehole with and without PVC casing, where V_p values are in strong agreement, and V_s sees deviations of up to 21.6%. It should be noted that the two datasets were obtained one month apart, such that ground conditions may have changed, affecting measured velocities, and it is possible that the installation of the casing may have disturbed the borehole. According to Eqn. 1, the wavelength of P

waves will be greater than that of the flexural waves (as compressional waves arrive first) for a source centre frequency of 1.5kHz, therefore, it is reasonable to consider that they would be less affected by near-borehole disturbance, however, there is still good agreement between V_s profiles (mean diff. 8.1%).

One principal issue of traditional monopole tools is that they cannot refract a shear wave in slow formations (Schmitt, 1988). Figure 4 shows a comparison of waveforms recorded using the geophone channels ("S-channels") in slow and fast formations, where the flexural mode has allowed shear wave velocity to be inferred in the slow formation. In the fast formation, a refracted S wave will also be present, and indistinguishable from the flexural arrival. Time axes demonstrate the requirement for different sampling rates, and show that in the fast formation, the P arrival cannot be observed, which usually only appears in slow formations. In Figure 4b, a low frequency oscillation is present, in phase between right and left hammer shot traces, likely to be a Stoneley wave generated by the monopole component of the logger.

Under ideal conditions, the same material would be tested for varying borehole diameters, however, because the borehole diameter is largely dictated by the formation material (larger boreholes in softer, slower formations) and client constraints and specifications, this is usually only possible using modelling techniques (e.g., Wang et al., 2022). Figure 5 shows waveforms from three slow formations (V_s < 1500m/s) where full waveforms have been successfully obtained in boreholes with diameters ranging from 76mm to 250mm. A general consideration of any invasive measurement method is disturbance to the material. For borehole logging, the ratio of the wavelength to the borehole diameter is considered key in determining the degree of disturbance but is difficult to quantify. Kurkjian (1986) cites a minimum ratio of 10, however, in Wang et al. (2022), simulated experiments demonstrated that at sufficiently low source frequencies, the borehole size has relatively little influence on the radiated acoustic. Because of its relatively low operating frequency, the required wavelength to borehole diameter ratio to avoid borehole effects is likely to be considerably lower than 10, however, greater understanding of the ratio effects would be beneficial.

Since the development of dipole-based logging tools which generate the flexural mode, the problem of measurement of shear velocities in slow formations has been overcome, however, many tools operate at relatively high frequencies, where dispersion correction is required (Cheng, 2015) if source frequencies exceed a cutoff value estimated to be 3.5kHz (Schmitt, 1988). With a source centre frequency of 1.5kHz, observed flexural arrivals can be assumed to travel at the formation shear velocity.

4 SUMMARY AND CONCLUSIONS

The PS logger is most often used in offshore geotechnics applications, where measured shear velocities are combined with density info (samples or log data) to derive the small-strain stiffness (G_{max}) important for offshore wind turbine construction. In such situations, formations are usually slow (e.g. unconsolidated sands) and boreholes are uncased with typical diameters of 150mm. The PS logger can successfully be deployed in geotechnical scenarios beyond these conditions, overcoming some of the problems of traditional tools including measurement in slow formations and avoiding the need for dispersion correction, rendering it highly versatile in its applicability. Although it has successfully been deployed in large boreholes, borehole effects may be important; more research is needed to fully understand these implications on seismic velocity estimates.

REFERENCES

Cheng, A.C.H. (2015). Can we ever trust the shear-wave log? The Leading Edge (Special Section: Borehole geophysics and sonic logging), 34(3), pp. 278-284. https://doi.org/10.1190/tle34030278.1.

Close, D., Cho, D., Horn, F., Edmundson, H. (2009). The sound of sonic: a historical perspective and introduction to acoustic logging, *CSEG Recorder*, 34 (May), pp. 34–43.

Kurkjian, A.L. (1986). Theoretical far-field radiation from a low-frequency horizontal acoustic point source in a vertical borehole. *Geophysics*, 51(4), pp. 930-939. https://doi.org/10.1190/1.1442150.

Rafavich, F., Kendall, C.H. St.C., Todd, T.P. (1984). The relationship between acoustic properties and the petrographic character of carbonate rocks. *Geophysics*, 49(10), pp. 1622-1636. https://doi.org/10.1190/1.1441570.

Robertson Geo, 2023. PS Logger User Manual, version 3.7.

Schmitt, D.P., 1988, Shear wave logging in elastic formations: *Journal of the Acoustical Society of America*, 84(6), pp. 2215–2229. https://doi.org/10.1121/1.397015.

Wang, H., Wang, C., Liu, Y., Xia, S. Fu, H., Yuan, Y. Bie, K., Li, X. (2022). Influencing Factors of Shear Wave Radiation of a Dipole Source in a Fluid-Filled Borehole. *Energies*, 15(18), [6789]. https://doi.org/10.3390/en15186789.

Proceedings of the XVIII ECSMGE 2024
GEOTECHNICAL ENGINEERING CHALLENGES
TO MEET CURRENT AND EMERGING NEEDS OF SOCIETY
© 2024 the Authors
ISBN 978-1-032-54816-6
DOI 10.1201/9781003431749-581
Open Access: www.taylorfrancis.com, CC BY-NC-ND 4.0 license

ECSMGE 24
XVIII EUROPEAN CONFERENCE ON SOIL MECHANICS AND GEOTECHNICAL ENGINEERING

Impact of soil parameters on cyclic pull-out capacity of offshore screw anchors

Impact des paramètres du sol sur la capacité d'arrachement cyclique des vis d'ancrage offshore

C.F. Ho, A.P. Dyson, A. Tolooiyan*
Computational Engineering for Sustainability Lab (CES-Lab), School of Engineering, University of Tasmania, Hobart, 7005, Australia

**ali.tolooiyan@utas.edu.au*

ABSTRACT: This paper presents a comparison of the cyclic behaviour of offshore screw anchors for various soils using the Simplified UnDrained Cyclic Accumulation Model (UDCAM-S). In producing the required stress-strain contours for UDCAM-S, a new correction procedure proposed in previous research with reference to a database of Drammen clay is followed and performed on Gulf of Mexico clay, the results of which are compared with the physical soil test results of the same clay. Stress-strain contours are also constructed for a Kaolin clay following the same procedure. Thereafter, modelling of the screw anchor is performed using the finite element method to investigate its pull-out capacity under cyclic tension, for each of the selected clays. Based on a chosen failure criterion, the bearing capacity is determined and normalised. According to the stress-displacement curves of the simulated screw anchor for each given clay, the validity of the correction procedure is investigated by comparing the corrected and experimental test results, and the effects of plasticity index are assessed to determine the associated impact on the anchor cyclic behaviour.

RÉSUMÉ: Cet article présente une comparaison du comportement cyclique des ancrages à vis offshore pour divers sols grâce à l'utilisation du modèle d'accumulation cyclique simplifié non drainé (UDCAM-S). Lors de la production des contours contrainte-déformation requis pour UDCAM-S, une nouvelle procédure de correction proposée dans des recherches antérieures en référence à une base de données d'argile de Drammen est suivie et réalisée sur l'argile du Golfe du Mexique, dont les résultats sont comparés avec le sol physique. Résultats des tests de la même argile. Des contours contrainte-déformation sont également construits pour une argile Kaolin en suivant la même procédure. Par la suite, une modélisation de la cheville à vis est réalisée par la méthode des éléments finis afin d'étudier sa capacité d'arrachement sous tension cyclique, pour chacune des argiles sélectionnées. Sur la base d'un critère de rupture choisi, la capacité portante sous contrainte de rupture est déterminée et normalisée. Selon les courbes contrainte-déplacement de la vis d'ancrage simulée pour chaque argile donnée, la validité de la procédure de correction est étudiée en comparant les résultats des tests corrigés et expérimentaux, et les effets de l'indice de plasticité sont évalués pour déterminer l'impact du cycle sur le comportement de l'ancrage.

Keywords: Screw anchors; cyclic behaviour; UDCAM; clay; plasticity index.

1 INTRODUCTION

Offshore screw anchors are becoming more common in offshore energy production because of their obvious advantages due to the low costs of installation. These ground anchor systems are often fixed to the seabed, which is saturated. In the case of offshore clays, for example, their behaviour is assumed to be undrained (Andersen, 2015), because the excess pore water pressures are not able to dissipate with the fast progression of load cycles. Cyclic shear stresses trigger the accumulation of pore pressure due to the compressive behaviour of the clay in shearing (Rasch, 2016).

To better understand the behaviour of such clays, a cyclic constitutive soil model named the Simplified UnDrained Cyclic Accumulation Model (UDCAM-S) is used in this project. While UnDrained Cyclic Accumulation Model (UDCAM) requires less modelling time due to its ability to model soil cyclic degradation without modelling individual cycles, UDCAM-S is a simplified model that can put the sophisticated UDCAM into practical applications (Rasch, 2016). In the modelling of this research, UDCAM-S serves as the constitutive model using the Finite Element Method (FEM).

The equivalent number of cycles at failure (N_{eq}) is determined by pore pressure accumulation or strain

accumulation (Andersen, 2015). To obtain the necessary input clay parameters for UDCAM-S, the results of relevant cyclic tests such as Direct Simple Shear (DSS), Triaxial Compression (TXC), and Triaxial Extension (TXE) are required.

To compare the effects of different clay parameters on the cyclic behaviour of offshore screw anchors, this project presents several offshore clays for comparison based on the differences in plasticity index (I_p) and undrained shear strength (s_u), with reference to a procedure proposed by Andersen et al. (2023) for establishing cyclic parameters for clays from a database of Drammen clay.

2 DATA SOURCE

Three offshore clays are chosen for comparison, namely Drammen clay, Kaolin clay, and Gulf of Mexico (GoM) clay, which have different values of I_p and s_u. Drammen clay is treated as the principal clay given the calibration procedure (Andersen et al. 2023) is largely based on the database of stress-strain contours of Drammen clay, which were determined using a procedure that assumed the pore pressure at the start of each load cycle was equal to that at the end of the previous cycle (Andersen, 2015). Cyclic DSS test results of GoM clay are available from a previous study (Liedtke et al., 2019), allowing comparison with the calibration procedure.

Table 1 gives a summary of the properties of the selected clays in this research. Drammen clay has the lowest I_p, given by Andersen et al. (1988, 2023). GoM clay has the largest I_p, given by Liedtke et al. (2019). The I_p and s_u^C values of Kaolin clay are based on previous simple shear test results (Huang B. et al., 2023) and research (Zografou, 2018), respectively.

Table 1. Properties of the selection of offshore clays.

Clay	I_p	Undrained compressive shear strength (s_u^C, kPa)
Drammen	27	126.5
Kaolin	34	30.0
GoM	47	31.2

3 METHODOLOGY

The numerical simulations were performed using the FEM with PLAXIS 2D (Bentley Systems, 2021). As for the other two clays in comparison with Drammen clay, some extra steps are taken to determine their corresponding stress-strain contours for UDCAM-S.

The procedure to develop relevant soil contours for UDCAM-S (Andersen et al., 2023) is specified below.

- Determine the equivalent over-consolidation ratio (OCR) of the specified clay for Drammen clay given the measured normalised monotonic DSS strength, using the SHANSEP equation:

$$\frac{(\frac{s_{uD}}{\sigma'_{ref}})_{OC}}{(\frac{s_{uD}}{\sigma'_{ref}})_{NC}} = OCR^m \quad (1)$$

  where s_{uD}/σ'_{ref} is the normalised monotonic DSS strength and m is a laboratory test-specific constant.
- From the database of Drammen clay contour diagrams for OCR of 1, 4 and 40 (Andersen et al., 1988), determine which of the three values is the closest to the previously determined equivalent OCR.
- Correct the Drammen clay contour diagrams using the correction factor calculated below:

$$F_{I_p} = 0.41 * \frac{{I_p}^{0.224}}{27^{0.224}} \quad (2)$$

  where, F_{Ip} is the plasticity index correction factor, and I_p is the plasticity index of the specified clay.
  The correction is performed by dividing the shear strains on the vertical axis of the contour diagrams by the correction factor.

To identify the impact of clay properties on the cyclic behaviour of offshore screw anchors, an axisymmetric FEM model has been developed in PLAXIS 2D to simulate the cyclic pull-out behaviour of a 3-helix screw anchor in each of the selected offshore clays.

Figure 1(a) shows the geometry of the offshore screw anchor, in which B is the helical diameter (equal for all helices), D is the shaft length from the top helix to the top of the anchor, t is the thickness of each helix (equal for all helices), S is the spacing between helices (equal for all helices), d is the shaft diameter, y is the distance from the bottom of the bottom helix to the bottom of the anchor. Figure 1(b) presents the geometry of the axisymmetric FEM model in PLAXIS 2D. The simulated screw anchor has a helix diameter of 0.5 m and a shaft length of 2 m.

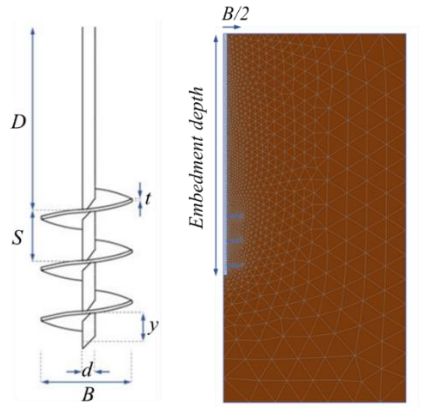

Figure 1. (a)Screw anchor geometry; (b)model geometry.

4 RESULTS

4.1 Stress-strain contours

Using Equation 1, the closest OCR value of Drammen clay for both GoM and Kaolin clays is 1, which is the reference OCR for this research and determines the corresponding stress-strain contours of Drammen clay in the database for the subsequent correction.

Comparison of stress-strain contour diagrams between Drammen and the other two offshore clays is given in Figure 2. The presented stress-strain contours correspond to an N_{eq} of 10, assuming an isotropic soil behaviour.

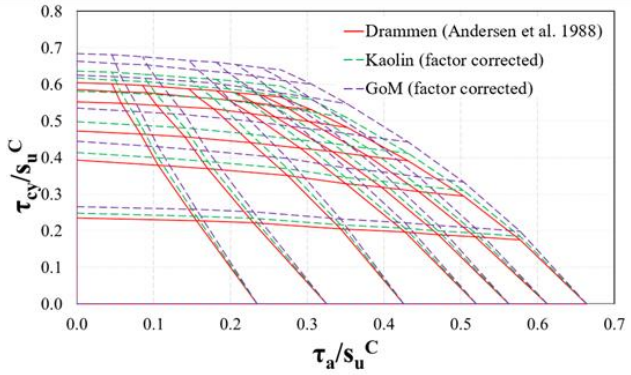

Figure 2. comparison of stress-strain contours between Drammen clay and factor corrected clays.

The original contour diagrams in the database have the average and cyclic shear stresses normalised by undrained DSS shear strength (s_u^{DSS}) (Andersen et al. 1988). In PLAXIS 2D, shear stresses are normalised by undrained compressive shear strength (s_u^{C}) for the cyclic accumulation calculations in UDCAM-S. Therefore, the original contour diagrams from the data base have to be converted for modelling in PLAXIS 2D. According to the laboratory test results, the ratio of s_u^{DSS} to s_u^{C} is 0.664, which has been applied when constructing stress-strain contours of Drammen clay.

The correction procedure proposed by Andersen et al. (2023) only applies the correction on the vertical axis of the stress-strain contours, which is the cyclic shear stress normalised by s_u^{C}. An alternative approach is specified in the procedure to perform the correction by applying two other factors on the derived stress-strain curves from the contours. In this research, however, correction has been performed using the correction factor in Equation 2 only. As I_p increases, the horizontal contour lines are shifted upwards, dragging the vertical contour lines slightly rightwards.

Since cyclic soil test results are available for GoM clay (Liedtke et al. 2019), the experimental stress-strain contours are provided with the factor corrected contours in Figure 3. Similarly, the original contour diagrams are based on cyclic DSS tests and the shear stresses normalised by s_u^{DSS}. Given the monotonic DSS and triaxial test results on GoM clay, the ratio of s_u^{DSS} to s_u^{C} is 0.8774, which has been applied when constructing the stress-strain contours of GoM clay (from cyclic DSS tests) in Figure 3.

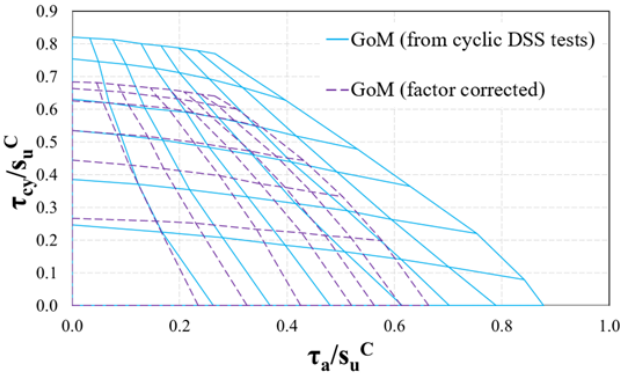

Figure 3. comparison of stress-strain contours between GoM clay based on cyclic DSS tests and factor corrected GoM clay.

As shown in Figure 3, there are obvious differences between the two sets of contours of GoM clay ranging from 10% to 25%.

One possible reason for such differences is that the corrected stress-strain contours of GoM clay are corrected with F_{Ip} given in Equation 2 only. As mentioned previously, the alternative correction approach using two other factors is not adopted in this research. Although there is this alternative option, it is applied to the derived stress-strain curves or calculated load-displacement curves. As a result, the stress-strain contours will still not reflect any differences directly, even if the alternative approach has been used instead.

Another possible explanation for the differences in contours in Figure 3 is that the determined ratio of s_u^{DSS} to s_u^{C} of 0.8774 is based on the trendlines drawn on the corresponding normalised shear strength scatter plots with an assumed ratio of vertical consolidation stress

to atmospheric pressure of 1. Considering that the trendlines cannot fully represent the scattered data points, the calculated ratio of s_u^{DSS} to s_u^C is, therefore not totally accurate.

4.2 FEM simulations

The stress-strain contours for each of the selected clays are inputed into PLAXIS 2D for modelling the cyclic uplift behaviour of the simulated screw anchor. The "total analysis" of UDCAM-S deals with ultimate limit state calculations for bearing capacity (Rasch, 2016) and is thus considered in this research.

With force captured at the displacement (s) corresponding to 10% of the helix diameter (B), the bearing capacity ($q_{0.1}$) is calculated by dividing the force by the helix area, then normalised by undrained compressive shear strength. As seen in Figure 4, the normalised stress (q/s_u^C) curves of the simulated screw anchor in each of the four cases only have minimal differences. Considering only the factor corrected clays and Drammen clay, the slope of the normalised stress curve is the greatest for GoM clay and the smallest for Drammen clay, with Kaolin in the middle, at displacements below 2% of the helical diameter. This is in line with the order of their I_p values, suggesting that the stiffness of the clay increases with increasing I_p.

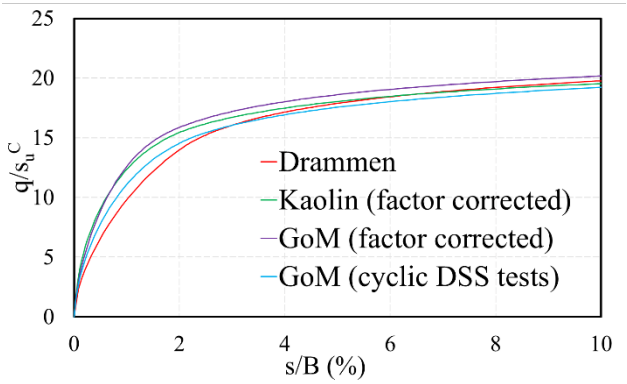

Figure 4. stress-displacement curves of the simulated screw anchor in each of the three offshore clays.

Comparing the actual values of normalised bearing capacity for the factor corrected GoM clay and the GoM clay from cyclic DSS test results in Table 2, it can be seen that $q_{0.1}/s_u^C$ for these two cases differs by 4.8%. Although there are large differences in their stress-strain contours, the small difference in normalised bearing capacity suggests that the correction procedure proposed above is applicable, producing comparable results with the same clay based on cyclic soil test results.

Table 2. Normalised bearing capacity in each of the offshore clays.

Clay	$q_{0.1}/s_u^C$
Drammen	19.77
Kaolin (factor corrected)	19.54
GoM (factor corrected)	20.19
GoM (cyclic DSS tests)	19.22

5 CONCLUSION

The results of the FEM simulation suggest that the clay stiffness increases with increasing I_p, and that the correction approach can produce results comparable with those based on experimental soil test results.

REFERENCES

Andersen, K. H., Kleven, A., & Heien, D. (1988). Cyclic soil data for design of gravity structures. Journal of Geotechnical Engineering, 114(5), 517-539. https://doi.org/10.1061/(ASCE)0733-9410(1988)114:5(517).

Andersen, K. H. (2015). Cyclic soil parameters for offshore foundation design. 3rd ISSMGE McClelland Lecture. In *Frontiers in Offshore Geotechnics III, ISFOG'2015*, Meyer. Taylor & Francis Group, London, 978-1-138-02848-7. Proc., 5-82. Revised version available from http://www.issmge.org/committees/technical-committees/applications/offshore.

Andersen K. H., Engin H. K., D'Ignazio M., & Yang S. (2023). Determination of cyclic soil parameters for offshore foundation design from an existing data base. *Ocean Engineering*, 267(5), Article 113180. https://doi.org/10.1016/j.oceaneng.2022.113180.

Bentley Systems. (2021). Material Models Manual. The Netherlands: Bentley Systems.

Huang B., Cai S., Li J., Wu K., & Yang W. (2023). Undrained strength of clay determined from simple shear test. In *Frontiers in Earth Science*. https://doi.org/10.3389/feart.2022.1098846.

Liedtke, E., Andersen, K. H., Zhang, Y., & Jeanjean, P. (2019). *Monotonic and Cyclic Soil Properties of Gulf of Mexico Clays*. Paper presented at the Offshore Technology Conference, Houston, Texas. https://doi.org/10.4043/29622-MS.

Rasch, C. (2016). *Modelling of cyclic soil degradation - Development of a cyclic accumulation model and the application to a gravity based foundation*. MSc thesis, Delft University of Technology, Netherlands.

Zografou D. (2018). *Investigation of shallow skirted foundations under undrained cyclic loading*. PhD thesis, The University of Western Australia. Available at: https://api.research-repository.uwa.edu.au/ws/portalfiles/portal/34391104/THESIS_DOCTOR_OF_PHILOSOPHY_ZOGRAFOU_Dimitra_2018.pdf, accessed 12/09/2023. https://doi.org/10.26182/5ba491df5348e.

Proceedings of the XVIII ECSMGE 2024
GEOTECHNICAL ENGINEERING CHALLENGES
TO MEET CURRENT AND EMERGING NEEDS OF SOCIETY
© 2024 the Authors
ISBN 978-1-032-54816-6
DOI 10.1201/9781003431749-582
Open Access: www.taylorfrancis.com, CC BY-NC-ND 4.0 license

ECSMGE 24
XVIII EUROPEAN CONFERENCE ON SOIL MECHANICS AND GEOTECHNICAL ENGINEERING

Improving soil dry compaction by adding granular material

Amélioration du compactage à sec en ajoutant du gravier

Y. Hocini*, A. Medjnoun, R. Bahar
Faculty of Civil Engineering, LEEGO / University of Sciences and Technology Houari Boumediene, Bab Ezzouar, Algiers, Algeria

*yhocini@usthb.dz

ABSTRACT: In the arid and semi-arid zones, where about eighty percent of Algeria is covered, the earthworks are more difficult because of the rarity of water sources and their transportation which is commonly expensive. Increasing compaction energy was suggested in previous research as the best solution to compensate for the lack of water. This paper is an experimental study carried out in the laboratory on fine-grain soil. It consists of compacting soil with optimal water content and low water content. To improve the maximum dry densities and the California bearing ratio values at low water content, this work also shows that it's necessary to add coarse materials, such as gravel, to the fine-grained soil, in order to improve the values of compaction characteristics at low water content. The obtained results showed that it's possible to reach the maximum normal and modified dry densities at low water content. And, the existence of optimal gravel content refers to optimal compaction behavior.

RÉSUMÉ : Dans les zones arides et semi-arides, qui couvrent environ quatre-vingts pour cent du territoire algérien, les travaux de terrassement sont plus difficiles en raison de la rareté des sources d'eau et de leur transport généralement coûteux. L'augmentation de l'énergie de compactage a été suggérée dans des recherches antérieures comme la meilleure solution pour compenser le manque d'eau. Cet article est une étude expérimentale réalisée en laboratoire sur les sols fins. Il consiste à mesurer la compacité d'un sol avec une teneur en eau optimale et faible teneur en eau. Pour améliorer les densités sèches maximales et l'indice portant californien à faible teneur en eau. Ce travail montre également qu'il est nécessaire d'ajouter des matériaux grossiers, tels que le gravier, au sol fin, afin d'améliorer la compacité à faible teneur en eau. Les résultats obtenus ont montré qu'il est possible d'atteindre les densités sèches maximales normales et modifiées à faible teneur en eau. Ils montrent aussi l'existence d'une teneur en gravier optimale qui fait référence à un compactage optimal.

Keywords: Dry compaction; fine grained soil; low water content; maximum dry density; gravel material.

1 INTRODUCTION

The development of southern regions in Algeria requires the construction of numerous road infrastructures to develop its economy. However, this latter is very expensive given the extremely severe climatic conditions, the difficulty of reusing local materials, and the non-availability of water sources and transportation. This research aims to improve soil compacity by addition granular material on arid soils at their low natural water content. This solution is considered widely economic and environmental, owing to the fact of preserving water sources and avoiding high water transportation costs.

According to literatures, various materials have been added to different soils such as lime; cement, fly ash (Kolias, et al 2005) , (Ige and Ajamu 2015) ; stone dust (Suresh et al, 2009.) (Mishra.S et al 2019) , etc...(Al-naje et Al-Taie 2020).

However not so many researchers investigated the improvement of the soil's geotechnical properties at the dry side of the compaction curves. In general, compaction at the dry side of the optimum, exhibit higher CBR values than those of soil compacted on the wet side of optimum.

In order to improve the geotechnical characteristics of lateritic fine soil different percentages of crushed granite were added. It appears that the optimal water content decreased. The soaked CBR values increased from 14 to 37% with the addition of 20 to 30% (Mbengue et al. 2022).

Marginal base soil was stabilized mechanically by the addition of gravels with sand or crushed stones with sand. It appears that The CBR values were improved by the addition of gravel from 15% to 20%; and for crushed stones from 12% to 15%. (Zumrawi 2012)

I.Goual et al 2012, tested compaction and bearing capacity of tuff and quarry dust mixture showed that OMC decreases and MDD increase. The bearing capacity indexes showed the existence of an optimal

mixture formulation, equivalent to 30% to 40%, respectively for the immediate indices and after 4 days of soaking.

The present work aims to improve soil compaction at low water content through a series of laboratory tests (proctor and CBR tests). At first, the influence of the low water content is studied on silty-sand soil, the effect of the addition of grained material on the silty sands in terms of the impact of compaction at low water content, maximum dry density (MDD), and CBR test are also studied in the second part of this work.

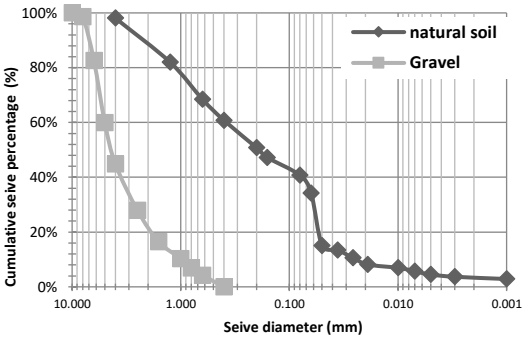

Figure 1. Sieve analysis curve of the studied soil and gravel.

2 MATERIALS AND METHODS

2.1 Methods

The studied soil went through several laboratory tests like sieve analysis (NF P094-056 and NF P094-057), Atterberg's limits (NF P094-051), specific gravity (G). The compaction parameters are also determined according the French standards for both standard and modified proctor test (NF P94-AFNOR).

The soil specimens were compacted using a proctor and CBR mold with the modified compaction energy. Each specimen was compacted in five layers ; 56 blows per layer, with a hammer of4,5 kg. The CBR test was also determined immediately after the compaction process to evaluate the immediate Californian bearing index. The classification of the used soil is done according to the Unified Soil Classification System (USCS).

2.2 Materials

The chosen soil is similar to that of the Algerian desert in the aim to better evaluate the behavior of dry compaction at lower water content. This soil was extracted from Jijel by *SOALKA Company* in the northern east of Algeria.

The gravel material was chosen from a local supplier according to its granular classes (0/3) and (3/8) and its angular shape. The sieve analysis for both natural soil and gravel are presented in Figure 1.

The soil physical parameters and the gravel properties are presented in the Table 1.

The process of adding the different amounts of gravel in order to study the effect of its addition on the dry density and the CBR Index was done by a path of 5% to the natural soil by dry weight.

3 RESULS AND DISCUSSIONS

3.1 Soil characterization

The results of soil physical properties are shown in Table 1. The used soil contained 38,2% of silts and 43,3% of sand with small amounts of clay and gravel (Figure 1). A plasticity index of 11,25 % and 39,80% for the liquid limit. The soil was classified according to the USCS standards as fine well-graded silty sand. Whereas the crushed gravel used in this study was classified as well graded clean gravel.

Table1. Soil and gravel physical properties.

Parameter	soil	Gravel
Specific gravity	2,65	2,7
Gravel (%)	15,4	78
Sand (%)	43,3	15,2
Silt (%)	38,2	6.8
Clay (%)	3,1	-
Uniformity coefficient (Cu)	15,38	5
Coefficient gradation (Cc)	0,34	1,8
BMV	0,53	-
Natural moisture content (%)	7,83%	-
Liquid Limit LL (%)	39,80%	-
Plasticity Limit PL (%)	28,55%	-
Plasticity Index PI (%)	11,25%	-

3.2 Effect of water content on dry density and CBR index

The results of Figure **2** present the soil's dry density versus moisture content for standard and modified proctor test. The lower dry density is obtained for the standard proctor energy at low and optimum water content, whereas; the maximum dry density is obtained for the modified proctor energy at the optimum water content.

The maximum dry density increases from 16.7 to 18.80 KN/m^3 respectively with a decrease of water content from 15.85% to 11.50% in standard and modified compaction energy test.

The growth of the maximum dry density is negligible (12%) and relative to the decrease of the optimal moisture content of about 15 %. The compaction process helps the soil particles to rearrange closely resulting in a reduction in air voids existing in the soil.

The complete compaction curves shape of studied fine soil is irregular and similar to those studied by (Ellis,1980) and (Faure et Fiès, 1972), and it's particularly for the dry compaction side. The figure also shows that it is possible to achieve a dry compaction test with high values of maximum dry density (>15%) for low water content at 2% and 4% of water.

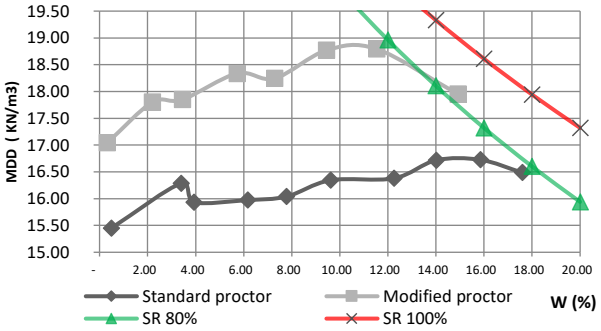

Figure 2. Soil compaction curve for standard and modified proctor test.

The compacted soil samples are submitted immediately to the CBR test, the CBR values are shown in Figure 3.

The maximum value of CBR index was noticed for the optimal water content and it is about 35.

At 4% of water content an acceptable value of CBR (24,40) was also noticed. This value is approximately near to that of optimum water content about 30% but relative to a reduction of 65% in water content.

At 2 % the CBR value is lower than the recorded values at OMC and W= 4%. This decrease is due to the low hydration of studied soil as observed.

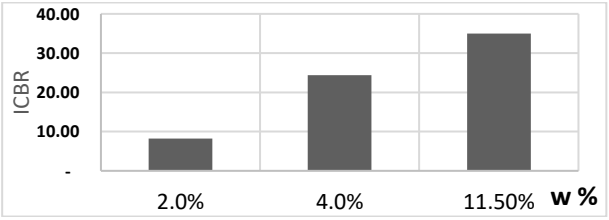

Figure 3. CBR index evolution as function as water content.

3.3 Effect of gravel addition on soil compaction parameters

Since the tested theory of the dry compaction process had satisfactory results on dry density and CBR values, another compaction tests are examined at 4% of water content by adding various amount of gravel to the natural soil by dry weight (5%, 15%, 20%, and 25%). The effect of gravel addition on the soil's dry density is shown in Figure 4.

It was noticed that even though the low moisture content (4%), the MDD values of 18.38 KN/m^3 and 18.6 KN/m^3; respectively for 20% and 25% of gravel addition were closely higher or the same of that obtained at the optimum water content with no additives (18.47 kN/m^3). Owing to the gravel angular shape and its large particles that interlocks the soil fine particles increasing its compactness and density (Mustafa 2018).

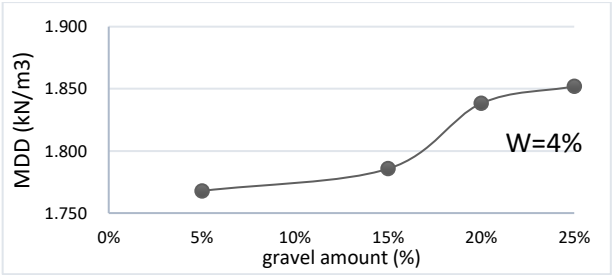

Figure 4. The evolution of maximum dry density at 4% of water content as function as gravel content.

These results are confirmed by the results of the bearing capacity tests represented in Figure 5.

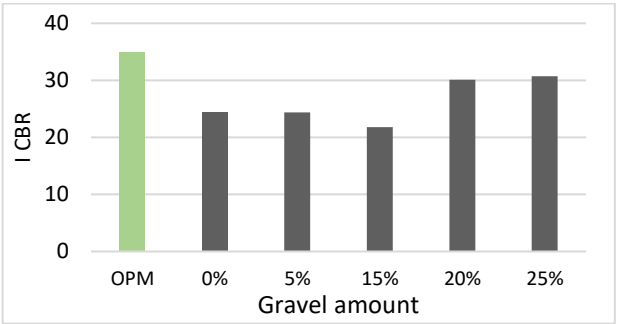

Figure 5. The evolution of CBR index at 4% of water content as function as gravel content.

The Figure 5 shows interesting results considering the low water content. It can be seen that a slight difference in the CBR values was measured between the optimal moisture content and low moisture content at 4% with no addition. In contrast, the gravel addition to the soil allowed obtaining high CBR values when adding 20% and 25% of gravel reaching a peak value of 30.12 And 30,70 respectively.

According to figures 4 and 5, it can be considered that the amount of **25%** of gravel addition as an optimal gravel content. This optimal amount strengthens the soil structure by providing a more rigid and stable structure, that contributes to improve the soil's bearing capacity. This may be due to the gravel high density.

4 CONCLUSIONS

The present study shows that soil compaction at low water content reduce its bearing capacity and dry density. To overcome this, reduce, the soil is treated with gravel. The results showed a significant increase of the CBR Index and of the maximum dry density more than the one obtained at Optimum moisture content.

However, the present compaction results need a complementary study as the Unconfined Compressive Strength UCS to confirm the satisfactory results of the CBR values of the studied soil at 4%of water content.

ACKNOWLEDGEMENTS

The authors of this paper wish to thank ***Kaolin's Society of Algeria*** SOALKASPA-Jijel for their help and furniture of the materials.

REFERENCES

Al-Naje, Farah Qais, Abed, Alaa Hussein, et al-Taie, Abbas Jawad. (2020). A Review of Sustainable Materials to Improve Geotechnical Properties of Soils. Al-Nahrain Journal for Engineering Sciences, Vol.23, No.3, p.289-305. http://doi.org/10.29194/NJES.23030289

Coduto, D. P., Yeung, M. C. R., & Kitch, W. A. (2011). Geotechnical Engineering: Principles and Practices. Upper Saddle River: Pearson, c201, 2nd Edition ISBN-13: 978-0-13-135425-8

Ellis, C.I. (1980). Soil Compaction at Low Moisture Content - Field Trials in Sudan. 7th Regional Conference for Africa on Soil Mechanics and Foundation Engineering, Accra, Ghana, p.331–340 http://worldcat.org/isbn/906191079X

Faure, A. & Fies, J. C. (1972). Experimental Study of the Sensitivity to Compaction of Loose Materials as a Function of Their Granulometric Composition. Ann. Agron., Vol. 23, No. 3

Goual, I., Goual, M. S., Taibi, S., & Abou-Bekr, N. (2012). Amélioration des propriétés d'un tuf naturel utilisé en technique routière saharienne par ajout d'un sable calcaire. European Journal of Environmental and Civil Engineering, 16(6), 744-763. https://doi.org/10.1080/19648189.2012.667653

Ige, J. A., & Ajamu, S. O. (2015). Unconfined Compressive Strength Test of a Fly Ash Stabilized Sandy Soil. International Journal of Latest Research in Engineering and Technology, 1(3), 1-11. ISSN: 2454-5031

Kolias, S., Kasselouri-Rigopoulou, V., & Karahalios, A. (2005). Stabilisation of Clayey Soils with High Calcium Fly Ash and Cement. Cement and Concrete Composites, 27(2), 301-313. https://doi.org/10.1016/j.cemconcomp.2004.02.019

Mbengue, M. T. M., Gana, A. L., Messan, A., & Pantet, A. (2022). Geotechnical and Mechanical Characterization of Lateritic Soil Improved with Crushed Granite. Civil Engineering Journal, 8(5), 843-862. https://doi.org/10.28991/cej-2022-08-05-01

Mishra, S., Sachdeva, S. N., & Manocha, R. (2019). Subgrade Soil Stabilization Using Stone Dust and Coarse Aggregate: A Cost-Effective Approach. International Journal of Geosynthetics and Ground Engineering, 5, 1-11. https://doi.org/10.1007/s40891-019-0171-0

Mustafa, W. S., Najmaddin, D. Y., Hassan, H. J. A., & Arbili, M. M. (2018). Effect the Shape of Gravel on Improving CBR and Compaction Behaviour of Clayey Soil. Journal of Duhok University, 21(2), 154-164. https://doi.org/10.26682/sjuod.2018.21.2.12

Suresh, K., Padmavathi, V., & Sultana, A. (2009). Experimental Study on Stabilization of Black Cotton Soil with Stone Dust and Fibers. Indian Geotechnical Society, IGS, 2009, p.502-506.

Zumrawi, M. M., & Abdalla, E. A. (2018, December). Stabilization of Expansive Soil Using Marble Waste Powder. In Conference Proceedings Civil Engineering 2018.

Proceedings of the XVIII ECSMGE 2024
GEOTECHNICAL ENGINEERING CHALLENGES
TO MEET CURRENT AND EMERGING NEEDS OF SOCIETY
© 2024 the Authors
ISBN 978-1-032-54816-6
DOI 10.1201/9781003431749-583
Open Access: www.taylorfrancis.com, CC BY-NC-ND 4.0 license

ECSMGE 24
XVIII EUROPEAN CONFERENCE ON SOIL MECHANICS AND GEOTECHNICAL ENGINEERING

Moisture content distribution in a dike cross-section – A case study of a geophysical investigation

Distribution de la teneur en eau dans une section transversale de digue - Étude de cas d'une investigation géophysique

Zs. Illés*, G. Nagy, L. Nagy
Budapest University of Technology and Economics, Faculty of Civil Engineering, Department of Engineering Geology and Geotechnics, Budapest, Hungary

A. Kovács
KBFI-Triász Kft., Budapest, Hungary

**zsombor.illes@edu.bme.hu; illes.zsombor@emk.bme.hu*

ABSTRACT: Due to long spells of droughts, embankments can desiccate. Dikes constructed of high plasticity clays can crack. These cracks can be detected by visual inspection, site investigation, or geoelectric resistivity. We aimed to identify areas with geoelectric measurements that are desiccated and vulnerable to fissuring. To better understand the cracks' cause, geophysical measurements and traditional geotechnical investigations were carried out on a dike section where cracks on the paved crest were already visible. A soil moisture monitoring system was already installed at one of the investigated sections. Geophysical measurements can identify large areas of desiccated embankment slopes, while geotechnical drillings and sensors can only be at point locations. Geophysical measurements can only be used to identify desiccated areas if it is known that the investigated embankment is relatively homogeneous. Electric resistivity and moisture content correlation were done based on the field measurements.

RÉSUMÉ: En raison de longues périodes de sécheresse, les digues peuvent se dessécher. Les digues construites avec des argiles à haute plasticité peuvent se fissurer. Ces fentes de dessiccation peuvent être détectées par une inspection visuelle, une étude du site ou par résistivité géoélectrique. Dont l´objectif d´identifier les zones vulnérables aux risques de desséchement, des mesure géoélectriques ont été prélever. Pour mieux comprendre ce phénomène, l´étude geoélectrique a été couple par une études géotechniques traditionnelles sur un tronçon de digue où des fissures sur la crête pavée étaient déjà visibles. Un système de surveillance de l'humidité du sol avait déjà été installé sur l'une des sections étudiées. Les mesures géophysiques permettent d`acquérir une identification continue sur la totalité de la surface de zone étudier, alors que l´identification des forages et des capteurs n´est que ponctuels. L'approche géophysique ne peut être utiliser pour identifier les zones à risque de dessiccation que dans les cas où le talus étudier est relativement homogènes. La corrélation de la résistivité électrique et de la teneur en eau a été effectuée sur la base des mesures de terrain.

Keywords: Dikes; geophysics; high plasticity clays; soil moisture sensors; shrink-swell behaviour.

1 INTRODUCTION

Flood protection embankments, also known as dikes, are built to protect floodplains and the population of their areas along rivers and lakes from inundation. In Hungary, dikes along the Tisza River and its tributaries are mainly constructed from locally available cohesive materials such as silt and clay (Illés and Nagy, 2022). Most of them were built before the development of modern soil mechanics in the middle of the 19th century (Nagy 2006). At that time, construction standards were more permissive than today, and materials available near the site were utilised. Historical methods, namely cross transportation, were used as the primary construction mode (Dyer et al., 2009). The material was extracted from ditches at the waterfront and then piled onto the dike. The soil was moderately or not compacted at all.

Wide-spread cracking has been identified on the dikes of the Great Hungarian Plain, along the Tisza and its tributary rivers (Szepessy 1991; Lazányi and Horváth 1997). The same phenomena have been identified in North England (Dyer et al. 2009).

The desiccation of clay (and fine-grained) layers in lake and river beds has been studied since the middle of the 20th century (Neal 1968; Walker 1986).

The desiccation and cracking of these high plasticity and mainly high montmorillonite content

earthworks are triggered by long spells of droughts as a consequence of climate change.

2 METHODS

2.1 Location

The examined dike section is located on the Szolnok-floodplain, north of Szolnok, Great Hungarian Plain (Figure 1). The surface of the area is covered by Holocene sediments (silt and clay) transported by the Zagyva and Tisza rivers from the North Hungarian Mountain range.

The site was selected based on a dike crest pavement survey (Illés and Nagy, 2022) and on-site visits. The nationwide study aimed to identify the natural and human causes of the dike pavement fissure and deterioration (Illés 2023). The cracks on the pavement and the grass slopes indicate that clays susceptible to volume change are present.



Figure 1. Location of the water retention monitoring system in the dike.

2.2 Dike materials

The dike, according to ISO 14688-2:2017, is constructed of high plasticity clays ($w_L = 56.1\%$ and $I_p = 33.7\%$), while the subsoil under the dike has higher Atterberg limits ($w_L = 70.5\%$ and $I_p = 43.8\%$). The dike contains considerable fine content ($Si > 50\%$ and $Cl > 20\%$) based on the grain size distribution measurements (ISO 17892-4:2016).

The shrinkage limit, according to Krabbe's empirical relationship from 1958 (Schultze and Muhs 1967):

$$w_s = w_L - 1.25 \cdot I_P \qquad (1)$$

Based on the equation for the dike and the subsoil the shrinkage limits are 14 % and 16% respectively.

2.2.1 Unsaturated soil properties

Dikes saturate during flooding until the seepage line, or the upper parts of the cross-section after heavy showers. Apart from these events most of the dike section is unsaturated. The measurements presented by Illés and Antal (2022) support this statement, however under the paved crest the dike is almost constantly saturated. The volumetric behaviour of compacted unsaturated soils is particularly complex due to the co-existence of three different phases: solid, liquid and air (Kieu and Mahler 2018). It is influenced by soil suctions. Laboratory and in-situ soil suction measurements are conducted and compared to better understand the state of the dike (Illés and Antal 2022).

2.3 Monitoring system

It is essential to monitor soil moisture content to determine the health state of an embankment (Utili et al. 2015). An established method is to create a water content profile from disturbed samples when signs of shrinkage cracks are visible on an embankment (Nagy and Illés 2016). However, we aimed to continuously monitor a flood protection embankment's water content at as many points as possible.

2.3.1 Sensors

The monitoring system is composed of 17 sensors: 14 TEROS 11 soil moisture sensors, 3 TEROS 21 water potential sensors and 3 ZL6 data loggers, all supplied by METER Group. The instruments are located at Doba (North of Szolnok city), section 87+620 and installed in 4 borings; flood side slope, flood side of the crest, crest axis, and at the protected side charging bench (see Figure 2.). The soil moisture sensor (TEROS 11) has a range of 0.00 – 0.70 m^3/m^3 volumetric water content (METER Group, Inc. 2018a), while the water potential sensor (TEROS 21) has a range of −5 to −100,000 kPa (METER Group, Inc. 2018b). Both instruments are equipped with thermocouple, measuring temperature; their detailed data sheets are available in the manuals.

The installation procedure and the initial results are described by Illés and Antal (2022).

2.4 Geophysical measurements

In-situ electric resistivity tomography (ERT) measurements are a useful tool for engineers to assess the soil properties along a section and not just from drilling. It can be used to identify soil water deficit (Chrétien et al. 2014), to detect desiccation cracking (Nagy et al. 2008; Sentenac and Zielinski 2009; Jones et al. 2014) and the presence of dispersive clays (Nagy et al. 2021). We aimed to identify the areas with different moisture content and, if present the location, of possible cracks.

Multielectrode site geophysical measurements were conducted in the cross-section of the monitoring

system, and in other two cross-sections before and after it. Furthermore, the dike was examined in three longitudinal sections, on the flood side. Altogether a total length of 535 m was measured with a 0,5 m electrode arrangement. Three longitudinal (90 m) and three cross-sections (55 m).

Resistivity (P) measurements by the ERT and soil moisture measurements by the sensors can be related by using the Waxman and Smits (1968) model:

$$Pws = \frac{a}{\varphi^m {S_r}^n}\left(\frac{1}{\rho_w} + \frac{BQ_v}{S_r}\right)^{-1} \qquad (2)$$

where S_r is the degree of saturation, φ is the porosity, a is the tortuosity factor, m is the cementation, while n is the saturation exponent, ρ_w is the pore water density, B is the average ionic mobility, Q_v is the cation concentration per unit pore volume in (meq/cm^3). The material density (ρ_s) and dry density (ρ_d) of the samples are measured. The void ratio ($e = \rho_s/\rho_d - 1$), and the porosity ($\varphi = 1 - \rho_d/\rho_s$) are calculated. The void ratio are used for the calculation of the saturation (S_r).

3 RESULTS AND DISCUSSION

Temperature and soil moisture distribution of the examined cross-section is presented along resistivity measurements in Figure 2. High resistivity areas on the flood and protected side are matched by areas of low water content. The dike crest is paved, it acts as a seal. A stretch of high moisture content can be found under the dike crest. The installation depth of the soil moisture sensors was limited by the installation tool, provided by the manufacturer. From the resistivity map it can be seen that the core of the dike has a homogenous resistivity indicating a stable water content.

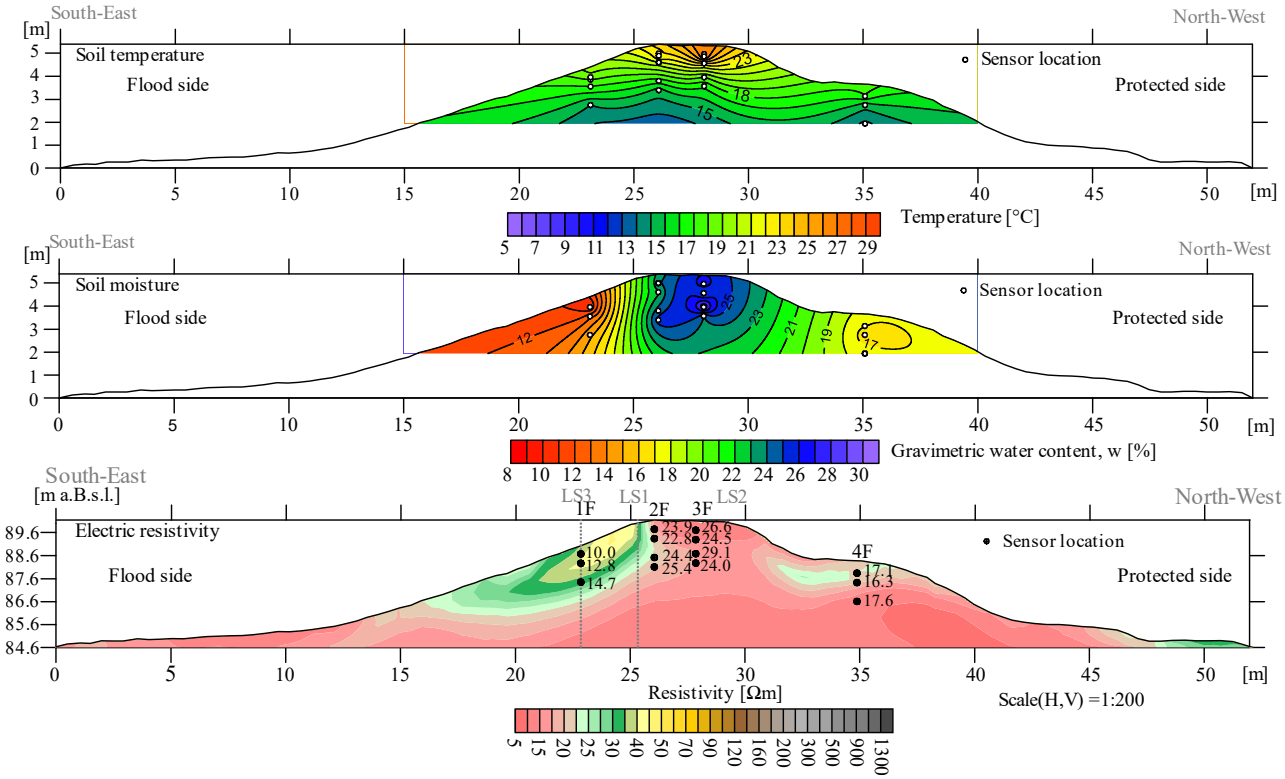

Figure 2. Dike cross-section; soil temperature and moisture distribution, resistivity measurement.

The data of the soil moisture sensors and electric resistivity measurements are pared (same location and time), to analyse the connection in between them.

The Waxman-Smits model was fitted on these measurements (see Figure 3). The used parameters are summarised in Table 1. The cation exchange capacity (CEC) value is based on a literature review. Csillag et al. (1995), measured 39.0 meq/100g near the Hungarian town Szolnok. Furthermore, Yilmaz (2004) proposed a connection between liquid limit and cation exchange capacity; the proposed equation resulted in a similar value, somewhat higher. In general, clays have a higher CEC value than 30 meq/100g.

Table 1. Waxmann-Smith parameters.

Parameters		Value	Notes	Units
Tortuosity factor	α	2.56	Fitted	-
Cementation exponent	m	2.82	Fitted	-
Saturation exponent	n	1.58	Fitted	-
Pore water resistivity,	P_w	14.00	Estimated	Ωm
Pore water density,	ρ_w	1.00		g/cm^2
Solid density,	ρ_s	2.70		g/cm^3
Average ionic mobility	B	2.00	Estimated	(Sm^{-1}) cm^3/meq
Cation exchange capacity,	C	39.00	Estimated	meq/100g

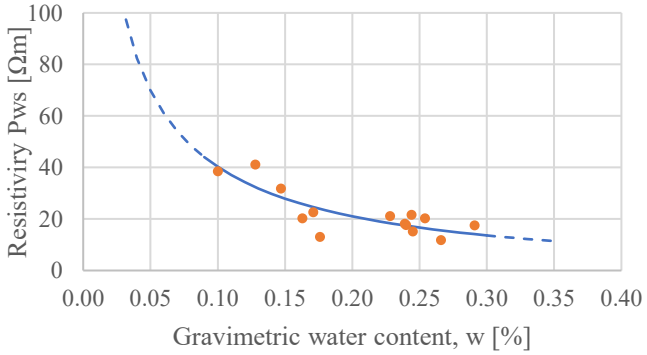

Figure 3. Waxman-Smits model, correlation of in-situ resistivity measurements versus gravimetric moisture content.

As only the in-situ measurements were used (soil with natural water content), we could not capture the whole phenomena, the exponential increase of resistivity with the decrease of soil moisture content.

Glendinning et al. (2014) used laboratory resistivity and gravimetric moisture content measurements to fit the Waxman-Smits model. The gained curve was used to calculate the volumetric water content distribution of the test embankment at the times of the ERT resistivity measurements.

The resistivity measurements of this conference paper (5-120 Ωm) and Glendinning et al. (2014) (10-150 Ωm) are in the same range, the two major differences are; i) the embankment at Tisza river is paved, due to it the moisture content is relatively high under the crest, ii) the slopes desiccate to much deeper extent in Hungary, due to the more severe droughts.

4 CONCLUSIONS

Electric resistivity tomography is a useful tool to distinguish areas with different moisture content. It can be applied to identify stretches with considerable moisture deficit, on dike slopes or just on the open field. For different kinds of soils, resistivity moisture content calibrations are needed to be able to use geophysical measurements on their own. In our case, with 0,5 m electrode distribution the cracks were not visible on the sections. However, areas with high resistivity indicate a highly unsaturated state (pores mainly filled with air) and an area with a possible hairline crack system. The results were correlated with the Waxman-Smits model, indicating reasonable agreement.

ACKNOWLEDGEMENTS

"Prepared with the Professional Support of the Doctoral Scholarship Program of the Co-operative Doctoral Program of the Ministry for Innovation and Technology from the source of the National Research, Development and Innovation Fund."

The authors would like to acknowledge the financial support from the General Directorate of Water Management (OVF) and VIZITERV-Environ Ltd. to install the monitoring system.

The authors are grateful to Begidsán Anna (KBFI-TRIÁSZ Ltd.) for evaluating the multielectrode geophysical measurements.

REFERENCES

Chrétien M, Lataste JF, Fabre R, Denis A (2014) Electrical resistivity tomography to understand clay behavior during seasonal water content variations. Engineering Geology 169:112–123. https://doi.org/10.1016/j.enggeo.2013.11.019.

Csillag J, Tóth T, Rédly M (1995) Relationships between soil solution composition and soil water content of Hungarian salt-affected soils. Arid Land Research and Management. https://doi.org/10.1080/15324989509385893.

Dyer M, Utili S, Zielinski M (2009) Field survey of desiccation fissuring of flood embankments. Proceedings of the Institution of Civil Engineers - Water Management 162(3):221–232. https://doi.org/10.1680/wama.2009.162.3.221.

Glendinning S, Hughes P, Helm P, Chambers J, Mendes J, Gunn D, Wilkinson P, Uhlemann S (2014) Construction, management and maintenance of embankments used for road and rail infrastructure: implications of weather induced pore water pressures. Acta Geotech 9(5):799–816. https://doi.org/10.1007/s11440-014-0324-1.

Illés Zs (2023) Causes of dike deterioration – environmental and anthropogenic effects. ScientSec 3(3):205–218. https://doi.org/10.1556/112.2022.00123.

Illés Zs, Antal Ö (2022) Installation of a flood protection embankment's monitoring system. In: 11th International Symposium Field Monitoring in Geomechanics. London, pp 1–9.

Illés Zs, Nagy L (2022) Effect of climate change on earthworks of infrastructure: statistical evaluation of the cause of dike pavement cracks. Geoenviron Disasters 9(1):20. https://doi.org/10.1186/s40677-022-00221-6.

ISO 14688-2:2017 (2017) Geotechnical investigation and testing — Identification and classification of soil — Part 2: Principles for a classification.

ISO 17892-4:2016 (2016) Geotechnical investigation and testing — Laboratory testing of soil — Part 4: Determination of particle size distribution.

Jones G, Sentenac P, Zielinski M (2014) Desiccation cracking detection using 2-D and 3-D Electrical Resistivity Tomography: Validation on a flood embankment. Journal of Applied Geophysics 106:196–211. https://doi.org/10.1016/j.jappgeo.2014.04.018.

Kieu MT, Mahler A (2018) The, K.M. A Study on the Relationship Between Matric Suction and the Void Ratio and Moisture Content of a Compacted Unsaturated Soil. Period Polytech Civil Eng. https://doi.org/10.3311/PPci.11974.

Lazányi I, Horváth G (1997) Deterioration of flood protection dikes due to shrinkage cracking. In: Proceedings of the 14th International Conference on Soil Mechanics and Foundation Engineerings. Hamburg, pp 351–357.

METER Group, Inc. (2018a) TEROS 11/12 Manual.

METER Group, Inc. (2018b) TEROS 21 GEN 2 Manual.

Nagy G, Illés Zs, Nagy L, Kovács A (2021) Geotechnics and Soil Sciences: multidisciplinary investigation of a saline lakebed. 6th International Conference on Geotechnical and Geophysical Site Characterisation :8. https://doi.org/10.53243/ISC2020-1.

Nagy L (2006) Dike breaches in the Carpathian basin. Periodica Polytechnica Civil Engineering 50(2):115–124.

Nagy L, Illés Zs (2016) Árvízvédelmi töltések száradási repedései (Drying Cracks on Embankments). Erdélyi Magyar Műszaki Tudományos Társaság (EMT), Csíksomlyó, Romania.

Nagy L, Kovács A, Varga M (2008) Cracked Dikes Investigation with Geoelectrical Tomography. In: 4th International Symposium on Flood Defence. Toronto, Ontario, Canada, p 152/1–9.

Neal JT (1968) Playa Surface Morphology: Miscellaneous Investigation. Air Force Cambridge Research Laboratories, L. G. Hanscom Field, Bedford, Massachusetts.

Schultze E, Muhs H (1967) Untersuchungen am fertigen Bauwerk. Springer, Berlin, Heidelberg.

Sentenac P, Zielinski M (2009) Clay fine fissuring monitoring using miniature geo-electrical resistivity arrays. Environ Earth Sci 59(1):205–214. https://doi.org/10.1007/s12665-009-0017-5.

Szepessy J (1991) Árvízvédelmi gátak töltésének repedései - a kúszási repedés (Cracks in flood levees, the creep crack). Hidrológiai Közlöny 71(6):321–331.

Utili S, Castellanza R, Galli A, Sentenac P (2015) Novel Approach for Health Monitoring of Earthen Embankments. J Geotech Geoenviron Eng 141(3):04014111. https://doi.org/10.1061/(ASCE)GT.1943-5606.0001215.

Walker JD (1986) Cracks in a surface look intricately random but actually develop rather systematically. Scientific American.

Waxman MH, Smits LJM (1968) Electrical Conductivities in Oil-Bearing Shaly Sands. Society of Petroleum Engineers Journal 8(2):107–122. https://doi.org/10.2118/1863-A.

Yilmaz I (2004) Relationships between liquid limit, cation exchange capacity, and swelling potentials of clayey soils. Eurasian Soil Science 37(5):506–512.

Proceedings of the XVIII ECSMGE 2024
GEOTECHNICAL ENGINEERING CHALLENGES
TO MEET CURRENT AND EMERGING NEEDS OF SOCIETY
© 2024 the Authors
ISBN 978-1-032-54816-6
DOI 10.1201/9781003431749-584
Open Access: www.taylorfrancis.com, CC BY-NC-ND 4.0 license

ECSMGE 24
XVIII EUROPEAN CONFERENCE ON SOIL MECHANICS AND GEOTECHNICAL ENGINEERING

Using grain size distribution to estimate permeability

Utiliser granulometry pour estimer la perméabilité

E. Imre*, Á. Bálint, D.Q. Houng, L. López, Cs. Kollár, L. Répássy, D.K. Mwinken
Óbuda University, Budapest, Hungary

Zs. Illés
Budapest University of Technology and Economics, Budapest, Hungary

M. Datcheva
Institute of Mechanics., Bulgarian Academy of Sciences, Sofia, Bulgaria

W. Baille
Ruhr-Universität Bochum, Bochum, Germany

D. Barreto, J. Leak
Edinburgh Napier University, United Kingdom

S. Feng
Birmingham University, United Kingdom

**imre.emoke@uni-obuda.hu*

ABSTRACT: This study examines the saturated water permeability using samples of loose and dense 2-fraction coarse sand mixtures. Besides the non-normalised entropy variables, some additional parameters like void ratio or relative density are used to characterize the pore sizes. Two variable pairs the (Cu and d10) and the non-normalised entropy variables (ΔS and S0) are found to have similar role, to describe the mean and the maximum controlling pore diameter sizes, resp.

RÉSUMÉ: Cette étude examine la perméabilité à l'eau saturée à l'aide d'échantillons de mélanges de sable grossier à 2 fractions lâches et denses. Outre les variables d'entropie non normalisées, certains paramètres supplémentaires tels que la densité (trouve important) sont utilisés pour caractériser la taille des pores. Deux variables paires (Cu et d10) and d'entropie non normalisées (ΔS et S_0) ont similaire role pour decrire la moyenne et maximum de contrôle diameter des pore, resp.

Keywords: Grading entropy; saturated permeability; coarse sand; model fitting; specific surface area; harmonic mean.

1 INTRODUCTION

A study has been started within the context of a large research project related to the various physical model parameters of granular matter as a function of the grading curve (Imre et al., 2021, 2022, 2023).

The space of the grading curves with N fractions is isomorphic to the space of the unit-sided simplex with dimension N-1 (Imre et al., 2014). The image of the simplex by the entropy map is the 2-dimensional grading entropy diagram. Instead of the interpolation over the simplex based on j^{N-1} interpolation points (j in each coordinate direction), the interpolation is made on the grading entropy diagram, using about 2j such points where the entropy map is unique (eg., on the image points of mean grading curves).

This paper is related to the saturated water permeability prediction in terms of the grading curve. A model discrimination was started to be made. The models contained traditional and new diameter type variables (the specific surface variables, the d_{10} and C_u, the grading entropy parameters), the void ratio and the relative density as a new parameter. According to the results, without the density parameters no acceptably good fit was attainable. Moreover, an acceptably good fit needed both mean pore size and maximum pore size related parameters.

2 MATERIALS AND METHODS

2.1 New permeability variables

The base entropy S_o and its normalised form, A, are defined by Lőrincz (Lőrincz,1986; Singh, 2014) as:

$$S_o = \sum_{i=1}^{N} x_i S_{oi} \text{ and } A = \frac{S_o - S_{o\min}}{S_{o\max} - S_{o\min}} \quad (1)$$

where x_i is the relative frequency of fraction i, $S_{0i} = i$ is the ith fraction entropy (see Table 1), and N is the number of fractions. The entropy increment ΔS:

$$\Delta S = -\frac{1}{\ln 2}\sum_{i=1}^{N} x_i \ln x_i \text{ and } B = \frac{\Delta S}{\ln(N)} \quad (2)$$

The harmonic mean diameter (being similar to d_{10}) and the specific surface area per volume are related to the mean pore size (Imre et al., 2014):

$$d_h = \frac{1}{\sum_{i=1}^{N} \frac{x_i}{d_i}} \text{ and } S_{sv} = 6/[(1+e)d_h] \quad (3)$$

The tested density variables were the void ratio e and the relative density $R_d = (e_{max} - e)/(e_{max} - e_{min})$.

2.2 Data

In this paper, an existing granular database (Imre et al., 2021, Figure 1a) is started to be extended onto the coarse sand range of granular soils. The four fractions: 0.25 – 0.50 mm, 0.5 – 1.0 mm, 1.0 – 2.0 mm and 2.0 – 4.0 mm, are illustrated in Figure 1b.

Constant head permeability tests were made on the samples comprising 15 finite fractal 2-fraction mixtures, with two different sample preparation methods to obtain loose densities (15 samples) and dense densities (45 samples, 3 repetitions).

In Figure 1c, the maximum void ratios were assessed from earlier research of Lőrincz (1986) with different sand materials but the same composition, e_{min} was computed from e_{max}/e_{min} (Imre et al., 2011).

2.3 Regression models

The equations for k_{sat} were as follows, extending the approach of Feng et al. (Feng et al., 2019):

$$k = \exp(C_3)\Delta S^{C_1} S_0^{C_2} \quad (4)$$

$$k = \exp(C_4)\Delta S^{C_1} S_0^{C_2} e^{C_3} \quad (5)$$

$$k = \exp(C_4)\Delta S^{C_1} S_0^{C_2} p^{C_3} \quad (6)$$

where C_1,C_2, C_3 and C_4 are model parameters to be identified, p can be the relative density, specific surface area per unit volume or other variable. The grading entropy parameter pair was interchanged by d_{10} and C_u, the Ren and Santamarina (2017) equation:

$$k = \frac{e^{C_1}}{(S_{sv})^2} \quad (7)$$

where S_{sv} is the specific surface area per unit volume of the soil (mm^{-1}), parameter C_1 is identified.

Table 1. Definition and properties of fraction j.

j	**1**	**23**	**24**
Limits in d_0	1 to 2	2^{22} to 2^{23}	2^{23} to 2^{24}
S_{0j} *[-]*	1	23	24

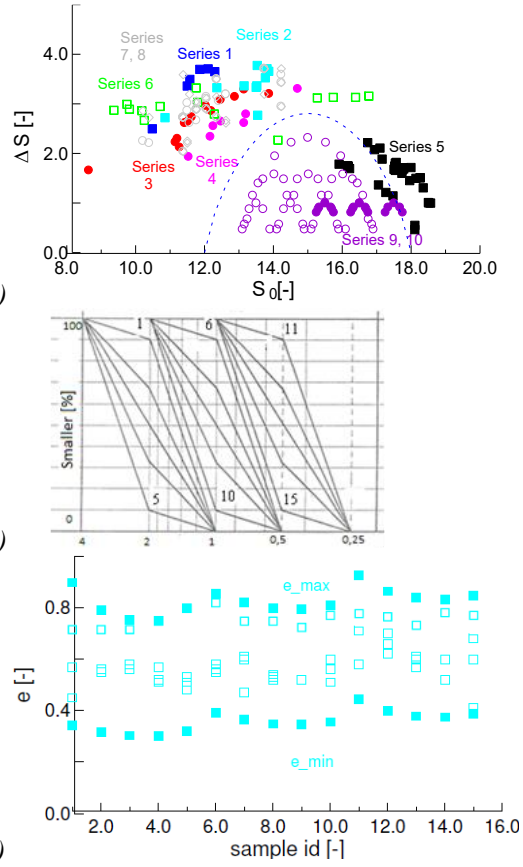

Figure 1. (a) Series 9 in the database (i.e. new samples 1 to 15) in purple closed symbol. Blue, light blue, red, pink, green, black, purple open: old series 1, 2, 3, 4, 5, 6, and planned mixtures, resp. (b) Particle size distributions of the 2-fraction fractal mixtures in Series 9. (c) void ratio for 15 mixtures in terms of id number, shown in Figure 1(b).

3 RESULTS

The k_{sat} of the 15 optimal 2-fraction soil mixtures with finite fractal gradings was between about 0.01 to 1 cm/s. The data were separated considerably for loose and dense samples in terms of specific surface area per volume (Figure 2a) or d_{10} relations.

In contrast, the measured data did not separate within series when the relative density or when the Ren and Santamarina variable (Figures 2b, c) were used. Since one sample was tested at a low relative density value, and three samples were tested at higher relative density values, the repetition of the former could reduce the difference, some further data are needed.

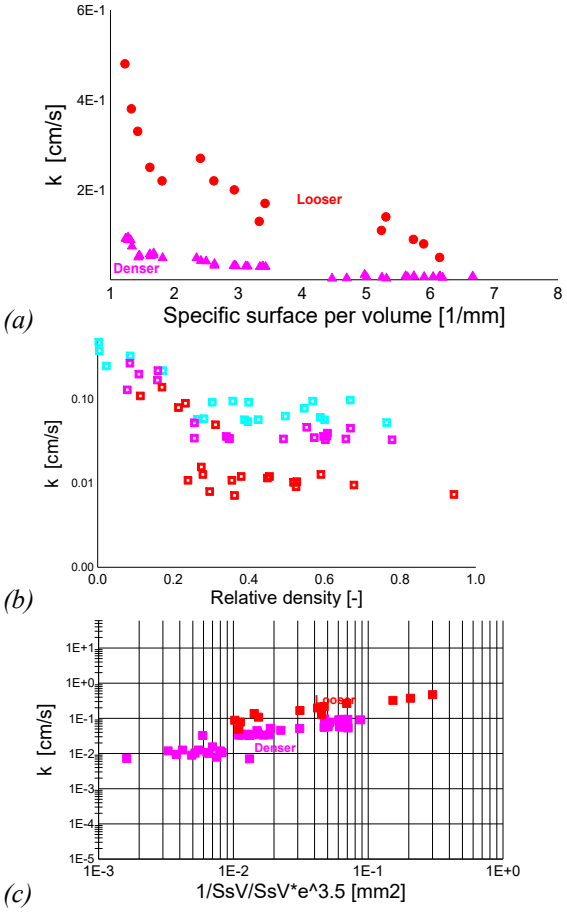

Figure 2. Permeability in terms of (a) specific surface per unit volume and (b) relative density, (c) Ren and Santamarina variable. Colours in (b): sub-series 1, 2 and 3 in turquoise, pink, and red, respectively.

The parameters of the empirical equations were determined using the Gauss Normal Equations approach (Press et al., 2007). The results of the Least-Squares fitting process was evaluated through the coefficient of determination value (R^2) – expressing what fraction of the variance is explained.

Referring to Table 2, by using only entropy parameters for the 2-fraction soils with small C_u, the R^2 is not satisfactory having identical gradings with different density. When additional density parameters were considered (i.e. void ratio e, relative density R_d) the models showed higher values of R^2. The highest values of R^2 were found with the relative density, this result need confirmation with new data.

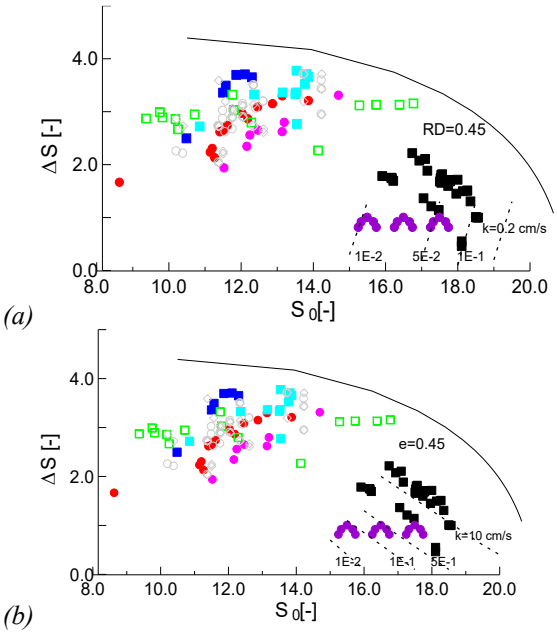

Figure 3. Approximate constant permeability level lines in the edge of diagram (a) assuming constant void ratio e, (b) constant relative density R_d. The shape of the level lines is finalized once series 5 data are completed with R_d.

Table 2. 2-fraction mixtures with R^2 values.

Variable	R^2
Entropy parameters, relative density	0.8847
d_{10}, C_u and relative density	0.8733
d_{10}, C_u with specific surface area	0.7709
Entropy parameters with void ratio, e	0.7701
Entropy parameters, S_{sv}	0.7476
Ren and Santamarina, 2017	0.7362
Entropy parameters only	< 0.5

Approximate k-level lines for series 9 were constructed in the non-normalised diagram using the identified parameters by fixing the R_d and the e values. The constant void ratio and the constant relative density R_d level lines qualitatively differed (Figure 3).

4 DISCUSSION

The grading entropy parameter pair was interchanged by pair d_{10} and C_u, (the latter were suggested by Nagy, 2011), and the fit had a similar R^2 as in the case of the grading entropy coordinates.

These parameter pairs were compared by using a series of mean grading curves (Imre et al., 2022). The mean C_u - ΔS relation (Figure 4) is not unique, having two close branches: in $0<A<2/3$ and $1>A>2/3$ (see more in Imre et al., 2022). The base entropy S_o or A has a unique relation with d_{10} (Figure 5). These relations may explain the similar results in Table 2.

The identified exponent of e was greater than 2 in in every empirical equation and for the other parts of

the database (Figure 1(a), Imre et al., 2021). The relative density was established from the ratio of e_{max}/e_{min} (Imre et al., 2011, Kabai, 1974) and the e_{max} data of Lőrincz (1986).

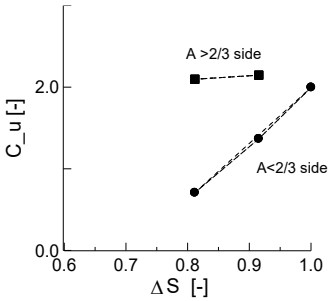

Figure 4. The relation of $C_u \Delta S$, N= 2, all tested data.

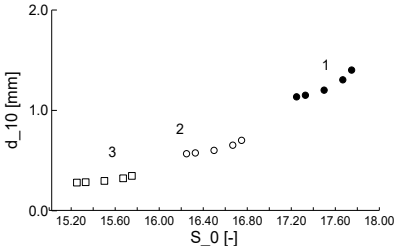

Figure 5. The relation of d_{10} and S_o, N= 2, all tested data.

The e_{max} at fixed A is decreasing with increasing fraction diameter range (since larger fractions have wider diameter range allowing a denser configuration). The void ratio is not related to the maximum pore channel size, being important in describing the k_{sat}. besides the mean pore size.

5 CONCLUSION

Theoretically, to assess for k_{sat}, the relevant problem is to assess the mean and the maximum controlling diameters of the pore channels (Imre et al., 2008).

The permeability variables can be divided into various groups and are either related to the mean controlling pore size variables (Imre et al., 2014) as d_{10}, d_h, S_{sA}, S_0, or to the maximum controlling pore size variables as C_u and ΔS, scaled by the relative density or the void ratio or the $e/(1+e)$ porosity term.

The result of the model fitting was acceptable in case of the tested 2-fraction coarse sands (identical composition, different densities) if one variable from each class was included. The best density parameter was the relative density.

The statement is supported by the facts that the S_0, ΔS and the d_{10}, C_u pairs were similar in mean grading curves relations, moreover these pairs were interchangeable in the equations. Further measurements and research are suggested, e.g., on the role of the the relative density.

ACKNOWLEDGEMENTS

M. Datcheva acknowledges the partial support by Grant No BG05M2OP001-1.001-0003-C01 financed by the Science and Education for Smart Growth OP (2014-2020) and co-financed by the EU through the ESI funds. D. Barreto acknowledges the financial support by the Royal Academy of Engineering Leverhulme Trust Fellowship (LTRF2223-19-134).

REFERENCES

Feng, S., Vardanega, P.J., Ibraim, E., Widyatmoko, I. and Ojum, C. (2019). Permeability assessment of some granular mixtures, *Géotechnique*, 69(7): 646–654. https://doi.org/10.1680/jgeot.17.T.039.

Imre, E., Fityus, S., Keszeyné, E. and Schanz, T. (2011). A comment on the ratio of the maximum and minimum dry density for sands. *Geotechnical Engineering,* 42(4): 77-82.

Imre, E., Lőrincz, J., Hazay, M., Juhász, M., Rajkai, K., Schanz, T., Lins, Y., Singh, V.P., Hortobagyi, Zs. (2014). Sand mixture density. *Proc. 6th UNSAT*, Sydney, pp. 691-697.

Imre, E., Bálint, Á., Nagy, L., Lőrincz, J. and Illés, Z. (2021). Examination of saturated hydraulic conductivity using grading curve functions, *Proc. ISC6*, Budapest, Hungary, https://doi.org/10.53243/ISC2020-373.

Imre, E., Hortobágyi, Z., Illés, Z., Nagy, L., Talata, I., Barreto, D., Fityus, S. and Singh, V.P. (2022). Statistical parameters and grading curves. *Proc. 20th ICSMGE,* Sydney, Australia, pp. 713-718.

Imre, E., Firgi, T., Baille, W., Datcheva, M., Barreto, D., Feng, S. and Singh, V., (2023). Soil parameters in terms of entropy coordinates. *E3S Web of Conf.* (Vol. 382, p. 25003). UNSAT 2023.

Kabai, I. (1974). The effect of grading on the compactibility of coarse grained soils. *Periodica Polytechnica*, 18 (4): 255-275.

Lőrincz, J. (1986). *Grading entropy of soils*. Doctoral Thesis, BME, Budapest, 1986.

Lőrincz, J., Tarnai, T., Trang, Q. P., Imre, E., Talata, I., Telekes, G., Scheuermann, A., Semar, O., Witt, K. (2008). The Characterization of the Grains and the Pores, Applications. 12. IACMAG. 976-983.

Nagy, L. (2011). Permeability of graded soils. *Periodica Polytechnica Civil Engineering,* 55 (2):199-204. https://doi.org/10.3311/pp.ci.2011-2.12.

Press, W.H., Teukolsky, S.A., Wetterling, W.T. and Flannery, B.P. (2007). *Numerical recipes Cambridge*, UK; ISBN 978-0-511-33555-6.

Ren, X.W. and Santamarina, J.C. (2017). The hydraulic conductivity of sediments: A pore size perspective, *Engineering Geology*, 233: 48–54.

Singh, V. P (2014) Entropy Theory in Hydraulic Engineering New York (NY), ASCE, 656 p. ISBN: 9780784412725.

Proceedings of the XVIII ECSMGE 2024
GEOTECHNICAL ENGINEERING CHALLENGES
TO MEET CURRENT AND EMERGING NEEDS OF SOCIETY
© 2024 the Authors
ISBN 978-1-032-54816-6
DOI 10.1201/9781003431749-585
Open Access: www.taylorfrancis.com, CC BY-NC-ND 4.0 license

ECSMGE 24
XVIII EUROPEAN CONFERENCE ON SOIL MECHANICS AND GEOTECHNICAL ENGINEERING

The potential use of shallow geothermal systems to urban acclimatization – how to evaluate and how to implement?

L'utilisation potentielle des systèmes géothermiques peu profonds pour l'acclimatation urbaine - Comment évaluer et comment mettre en œuvre?

M. Inácio*, C. Pinto
Câmara Municipal de Lisboa, Lisbon, Portugal

A. Vieira
Laboratório Nacional de Engenharia Civil, Lisbon, Portugal

I. Moitinho de Almeida
Faculdade de Ciências da Universidade de Lisboa, Lisbon, Portugal

**ext.miguel.inacio@cm-lisboa.pt*

ABSTRACT: The research project GeoSustained, funded by the Portuguese Foundation for Science and Technology (PTDC/ECI-CON/1866/2021), aims to study sustainable solutions for using shallow geothermal systems for buildings and infrastructure acclimatization. Lisbon Municipality is a partner in the consortium, playing a particularly important role in the implementation and regulation of the mandatory elements for installing the system. For this purpose, a working group was created to collaborate with the responsible entities, namely Direção-Geral de Energia e Geologia (DGEG, a public energy and geology institution). Two priorities were established: (1) definition of the best practices for the implementation of shallow geothermal solutions; (2) development of a guide with the flow to implement the systems licensing procedure. This information will be integrated into the Municipal Regulation for Urbanization and Construction in Lisbon (Regulamento Municipal para a Urbanização e Edificação de Lisboa). It is also expected that the collaboration with DGEG will contribute to improve the implementation of this type of solution at a national level, being a critical approach to more sustainable and resilient cities to climate change.

RÉSUMÉ: Le projet de recherche GeoSustained, financé par la Fondation Portugaise pour la Science et la Technologie (PTDC/ECI-CON/1866/2021), vise à étudier des solutions durables pour l'utilisation de systèmes géothermiques peu profonds pour l'acclimatation des bâtiments et des infrastructures. La municipalité de Lisbonne est un partenaire du consortium, jouant un rôle particulièrement pertinent dans la mise en œuvre et la régulation de ce type de système à l'échelle locale. À cette fin, un groupe de travail a été créé pour collaborer avec les entités compétentes, à savoir la Direção-Geral de Energia e Geologia (DGEG, une institution publique d'énergie et de géologie). Trois priorités ont été établies: (1) définition des meilleures pratiques pour la mise en œuvre de solutions géothermiques peu profondes; (2) élaboration d'un guide avec le flux à adopter pour permettre la licence de ces systèmes. Ces informations seront intégrées dans le Règlement Municipal pour l'Urbanisation et la Construction de Lisbonne (Regulamento Municipal para a Urbanização e Edificação de Lisboa). Il est également prévu que la collaboration avec la DGEG contribuera à améliorer la mise en œuvre de ce type de solution au niveau national, étant une approche critique pour des villes plus durables et résilientes face au changement climatique.

Keywords: GeoSustained project; sustainable urban acclimatization; climate resilient cities; geothermal potential map.

1 INTRODUCTION

The GeoSustained project (CML, 2023), "Sustainability assessment of shallow geothermal systems for Lisbon. Characterization studies of the city soils thermal and thermomechanical behavior" is funded by the Portuguese Foundation for Science and Technology (FCT). Laboratório Nacional de Engenharia Civil (LNEC) leds the Consortium and Lisbon Municipality (CML), Universidade de Aveiro (UA), and Agência de Energia e Ambiente de Lisboa, Lisboa E-NOVA are partners. The GeoSustained project has two general objectives:

- To understand the thermal and thermomechanical behavior of geological formations in Lisbon through in situ and laboratory tests and mathematical modeling.
- To evaluate and contribute to the sustainability of shallow geothermal systems, considering Lisbon's geological and climatic characteristics.

This project is aligned with three Sustainable Development Goals (United Nations, 2015):

Goal 7: Affordable and Clean Energy – Ensure access to affordable, reliable, sustainable, and modern energy for all. Characterizing the thermal conductivity of Lisbon's geological formations will contribute for using shallow geothermal resources in the city, or others with similar soils and weather conditions, making it easier and more accessible for project developers to carry out feasibility studies.

Goal 9: Industry, Innovation, and Infrastructure – build resilient infrastructure, promote inclusive and sustainable industrialization, and foster innovation. Thermomechanical characterization of Lisbon's soils will increase the knowledge about their behavior and how temperature affects it, particularly their strength and deformability. In addition, buildings that use shallow geothermal systems are less energy dependent infrastructures and, therefore, more resilient.

Goal 13: Climate Action – take urgent actions to combat climate change and its impacts. Shallow geothermal is a clean energy source of great importance in reducing greenhouse gas emissions and, consequently, in combating climate change.

2 APPROACH

Lisbon Municipality, as the organization in charge of managing the city of Lisbon and a partner of the GeoSustained Project, has a fundamental role in encouraging and regulating the implementation of geothermal systems. To achieve that, three significant outputs must be considered:

1. Standards for the use of shallow geothermal resources in an urban context: a guide is being developed with relevant information to encourage and simplify the evaluation of the feasibility to use geothermal resources, namely a regulatory document, references for real estate developers interested in using these systems, and information on the prospecting work to be carried out, including relevant tests.

2. Procedural workflow and licensing documents: a working group has been set up, which includes technicians of the GeoSustained project and technicians from Direção-Geral de Energia e Geologia (Directorate-General for Energy and Geology). This group's mission is to develop a guide with the procedural workflow to be adopted to simplify the licensing of these operations and a list of instructional elements to be presented by those that need to develop an urban licensing procedure. This information will soon be included in Regulamento Municipal para a Urbanização e Edificação de Lisboa (Lisbon Municipal Regulations for Urbanization and Building).

3. Geothermal Potential Map: this dynamic map will be a decision-support tool integrated into the Lisbon Geotechnical Map, making it possible to identify the shallow geothermal systems potential. The geothermal potential map is a critical output for increasing the implementation of shallow geothermal systems in Lisbon, and it is the main topic covered in this paper.

3 GEOTHERMAL POTENTIAL MAP

The Geothermal Potential Map will indicate, for each area in the city, the differences in the potential for exploiting the geothermal resource in depth, considering factors such as geology, thermal conductivity, the existence of water in-depth, and also subsoil occupation, a fundamental aspect in a densely urbanized area such as Lisbon (Figure 1). The purpose of this map is to support the preliminary assessment of the viability of shallow geothermal systems for new buildings and urban rehabilitation in Lisbon. The possibility for project developers and planners to conduct this quick assessment by consulting the geothermal potential map will incentivize them to consider using this clean energy resource in their projects.



Figure 1. Considered components of the Lisbon Geothermal Potential Map.

The Geothermal Potential Map is made up of different components that complement each other:

Three-dimensional modeling of geological formations of Lisbon: this task is being carried out using RockWorks software. It is based on the information available on the 1:10,000 scale geological

map and Lisbon Municipality's GeoSIG platform. This platform gathers geotechnical data obtained from boreholes in Lisbon and currently includes more than 13,000 entries. This information will allow the geometry of Lisbon's geological formations to be modeled at depth.

Determination of the thermal conductivity of the modeled geological formations: this task is underway and is based on a three-scale approach (Figure 2): macroscale, in which thermal conductivity values are obtained from the literature; mesoscale, in which conductivity values measured in local geological formations are used and whose values are extrapolated to other points where the geothermal potential is to be assessed; microscale, with conductivity values measured directly on representative samples of the site to be evaluated.

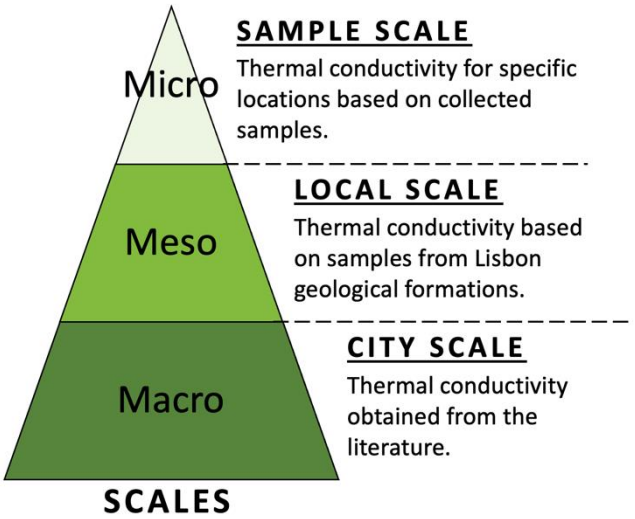

Figure 2. Three-scale approach to obtain thermal conductivity values for the Lisbon Geothermal Potential Map.

In the macroscale approach, Vieira *et al.* (2023) compiled thermal conductivity values for soils and rocks like the ones in Lisbon, allowing cartography to be drawn up on the scale of the municipality. This work assigned minimum and maximum thermal conductivity values and recommended estimates to the formations, which were grouped into ten systems based on their lithostratigraphy and mineralogy. The result was represented in a distribution of surface values (Inácio *et al.*, 2023). At this stage, parameters as compaction and water saturation were not considered.

At the microscale, where the information is being refined, the actual thermal and thermomechanical characteristics of samples collected in the project's scope are considered. Three boreholes were made in three different locations within the municipality to reach the microscale, aiming to intercept most of the Lisbon's geological formations (Figure 3).

A 65 m deep borehole was drilled in Parque da Quinta das Conchas e dos Lilases, in which 8 m of alluvium and 57 m of Lower Miocene formations were intersected. The second borehole was drilled at the Lisbon Municipality's Sewage Brigades, where is intended to install a shallow geothermal system for climatization and water heating in the framework of a rehabilitation process. An 80 m borehole was drilled at this site, in which 15 m of alluvium and 60 m of Middle Miocene formations were intersected. Finally, the third borehole was drilled at Doca de Pedrouços, next to the future "Hub do Mar" complex, where the feasibility of using shallow geothermal systems is also being studied. A 50 m borehole was drilled at this site, in which 38 m of alluvium and 12 m of the Complexo Vulcânico de Lisboa (Lisbon Volcanic Complex) were intersected. Undeformed samples were also collected at these sites and are being analyzed in laboratory to determine the thermal and thermomechanical characteristics of these formations. In addition, temperature and thermal conductivity measuring sensors were installed along the drilled depths (every 5 m) to detect seasonal and in-depth temperature variations.

Finally, to gather more information on the characteristics of Lisbon geological formations, a sampling plan is also being carried out on construction sites that are underway in the municipality, whether carried out by private or public entities, namely in the context of Plano Geral de Drenagem de Lisboa (Lisbon Drainage Master Plan). The aim is to cover possible data gaps on geological formations that were not intercepted in the boreholes. The samples will be submitted to the same tests as the ones collected in the boreholes.

The mesoscale approach will be possible considering the modeled geology, as well as the tests, carried out on the samples collected as part of the project, consisting of extrapolating the conductivity values obtained for the locations of these same formations elsewhere in the city, considering the local conditions in which these formations are present, namely depth, compaction, and saturation. Regarding water levels, existing data on the GeoSIG platform will be considered, which will also be complemented with data from Lisbon Municipality on the existence of underground structures that could influence water circulation, which has been updated through ModSub 3D Project.

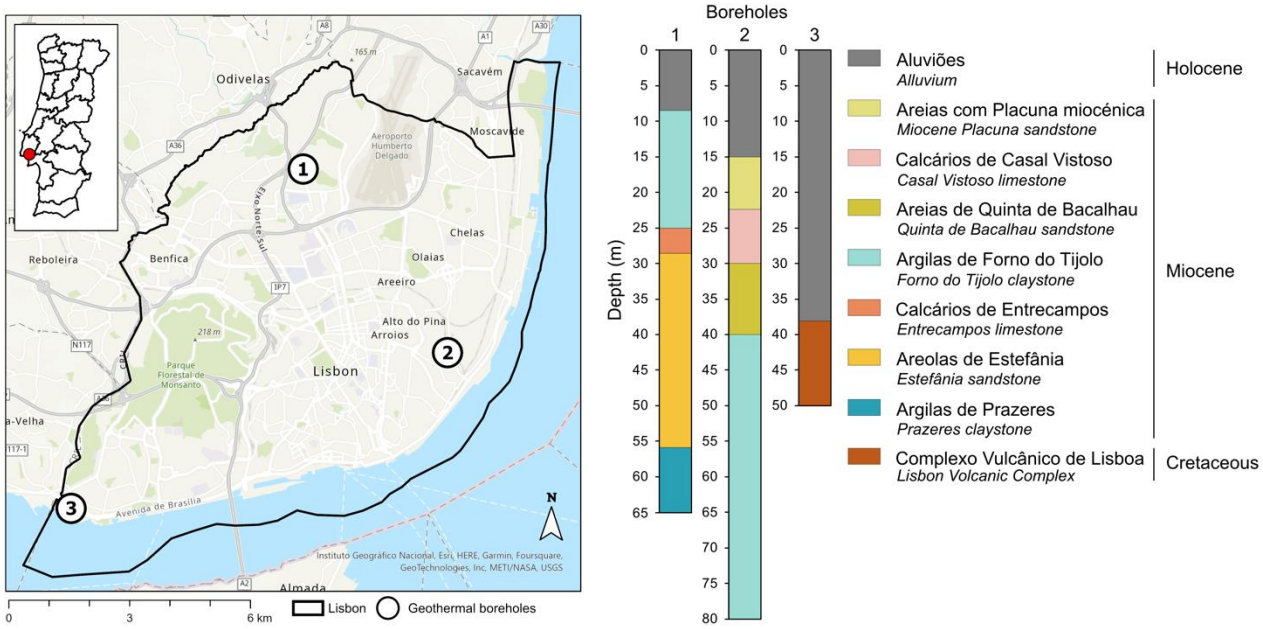

Figure 3. Location and geological logs of the boreholes performed in the scope of the GeoSustained Project.

4. CONCLUSION

The GeoSustained Project is actively contributing to increasing the use of shallow geothermal resources in Lisbon, namely through the Geothermal Potential Map. This map is currently being drawn up, and a preliminary version has already been presented on a macroscale approach with superficial information. Transposing this information in depth will be the next step, as well as assessing the potential of the Lisbon geological formations based on samples collected as part of this project. At the same time, the work being done on writing a guide to good practices and establishing regulations for projects using geothermal energy will, in the short term, make its application in a real context much simpler and faster.

Finally, the work carried out under this project can be extrapolated to other municipalities, being Lisbon a pilot city for defining the best approaches to increase the use of geothermal energy in Portugal. DGEG is also a strategic partner that will enable similar strategies to be implemented at a national level, and this approach is aligned with the best practices ongoing in other European countries.

ACKNOWLEDGMENTS

The authors are grateful for the financial support provided by the Portuguese Foundation for Science and Technology through the GeoSustained Project (PTDC/ECI-CON/1866/2021).

REFERENCES

CML (2023). GeoSustained – Informações e Serviços. Câmara Municipal de Lisboa. Available at: https://informacoeseservicos.lisboa.pt/prevencao/resiliencia-urbana/projetos/geosustained, accessed: 5/12/2023. (GeoSustained – Information and Services in Portuguese).

Inácio, M., Pinto, C., Vieira, A., Almeida, I. M., Ferreira, A., Leonardo, P. and Frias, A. (2023). Contribuição da geologia na localização dos furos geotérmicos do Projeto GeoSustained, In: *Atas do 18º Congresso Nacional de Geotecnia (18CNG)*, Évora, Portugal, pp 331-340 (Geology's contribution to the location of geothermal boreholes of GeoSustained Project in Portuguese).

United Nations (2015). Transforming our world: the 2030 Agenda for Sustainable Development. United Nations General Assembly, New York, UK. Available at: https://sdgs.un.org/2030agenda, accessed: 5/12/2023.

Vieira, A., Pinto, C., Aljundi, K., Inácio, M., Almeida, I. M. and Pereira, C. (2023). Estudo da condutividade térmica dos solos de Lisboa, In: *Atas do 18º Congresso Nacional de Geotecnia (18CNG)*, Évora, Portugal, pp 1387-1396. (Study of the thermal conductivity of Lisbon's soils in Portuguese).

Proceedings of the XVIII ECSMGE 2024
GEOTECHNICAL ENGINEERING CHALLENGES
TO MEET CURRENT AND EMERGING NEEDS OF SOCIETY
© 2024 the Authors
ISBN 978-1-032-54816-6
DOI 10.1201/9781003431749-586
Open Access: www.taylorfrancis.com, CC BY-NC-ND 4.0 license

ECSMGE 24
XVIII EUROPEAN CONFERENCE ON SOIL MECHANICS AND GEOTECHNICAL ENGINEERING

Behaviour of model pipe piles jacked in calcarenite

Comportement de pieux tubulaires modèles vérinés dans la calcarénite

M. Jafari*
Former affiliation: UCLouvain, Louvain-La-Neuve, Belgium, Current affiliation: COWI A/S, Hamburg, Germany

H. Gharsallaoui
Former affiliation: UCLouvain, Louvain-La-Neuve, Belgium, Current affiliation: Jan De Nul nv Belgium

A. Holeyman
UCLouvain, Louvain-La-Neuve, Belgium

**jafari.researchgate@gmail.com*

ABSTRACT: Evaluation of pile driving feasibility in weak carbonate rocks such as calcarenite requires an estimation of the penetration resistance. Results from an experimental programme are presented during which open-ended model pipe piles were jacked into large intact calcarenite blocks. The failure mechanisms at the pile toe and shaft were characterized. A significant feature of the penetration resistance was its oscillations with trough values as low as 10% of the peak values. Heterogeneity of the block was ruled out as a possible cause of the oscillations after a careful examination. Such behaviour was attributed to repeated calcarenite failures inside the pipe after some incremental penetrations of the pipe. The failure mechanism was confirmed by observing that disk-like fragments were generated inside the pile. At the outer pile-calcarenite interface, a region of crushed material formed. Contributions of pipe shaft and toe annulus to the jacking resistance were evaluated.

RÉSUMÉ: Évaluation de la faisabilité du battage de pieux dans des roches carbonatées faibles telles que la calcarénite nécessite une estimation de la résistance à la pénétration. Les résultats d'un programme expérimental sont présentés au cours duquel des pieux modèles à extrémité ouverte ont été introduits par vérinage dans de grands blocs de calcarénite intacts. Les mécanismes de rupture au niveau de la base du pieu et de son fût ont été caractérisés. Une caractéristique significative de la résistance à la pénétration était ses oscillations avec des valeurs de creux aussi basses que 10% des valeurs de crête. L'hétérogénéité du bloc a été exclue comme possible cause des oscillations après un examen attentif. Un tel comportement a été attribué à des ruptures répétées de la calcarénite à l'intérieur du pieu après quelques pénétrations incrémentales du pieu. Le mécanisme de rupture a été confirmé en observant que des fragments en forme de disque étaient générés à l'intérieur du pieu. À l'interface externe pieu-calcarénite, une région de matériau concassé s'est formée. Les contributions du fût du pieu et de l'anneau de la base à la résistance au vérinage ont été évaluées.

Keywords: Pile driving; weak rocks; open-ended model pipe piles.

1 INTRODUCTION

Recent developments in the domain of renewable energy have led the industry to go offshore on the continental shelf where winds are stronger and steadier for harnessing green energy. One of the challenges in this new environment is the presence of soft carbonate rocks. Pipe piles may have to be driven through hard layers to ensure lateral stability at the design depth. Pile piles must survive the installation process. Wide discrepancies have been reported in the description of cemented carbonate deposits. The term “calcarenite” is often used in the literature to describe cemented carbonate formations (Le Tirant and Nauroy, 1994).

Several studies investigated the shaft and base response of pipe piles in cemented formations through model tests (Jafari et al., 2019; Holeyman, 2017; Montargès, 1988; Settgast, 1980). Results from an experimental programme are presented during which model pipe piles were jacked into calcarenite blocks to investigate jacking resistance and failure mechanisms at the pile toe and shaft.

2 SPECIMEN PREPARATION

Model pipe piles were jacked into four calcarenite blocks extracted from Saint-Maximin Quarries in France. The calcarenite is locally referred to as “Roche Douce” or “Roche Saint Leu”. The supplier was Ouachée et Corpechot. Mechanical properties are listed in Table 1. Information regarding microstructure

of similar materials can be found elsewhere (Baud et al., 2017; Stavropoulou et al., 2021). It consists of calcite (60%) and quartz (40%) embedded into a calcite matrix and frequent fossils. Each block was an octagonal prism with the diameter of the inscribed cylinder equal to 0.45m, a height of 0.5m, and a mass of about 137kg. Each block was confined with a steel tube of an outer diameter (D_o) of 508mm and a wall thickness (t) of 7.9mm. The gap between the calcarenite block and the confining steel tube was filled with non-shrinking grout.

Table 1. Mechanical properties of the calcarenite (Bosco and Vander Elst, 2018).

	Units	Mean (SD*)
Bulk density	kg/m^3	1772 (45)
Particle density	kg/m^3	2692 (9)
Uniaxial compressive strength (σ_{ci})	MPa	6.8 (1.7)
Splitting tensile strength	MPa	1 (0.2)
Elastic modulus	GPa	7.2 (1.3)
Porosity	%	39
Poisson's ratio	-	0.22 (0.04)
Shear modulus	GPa	2.9

*SD: Standard deviation.

Five jacking tests of model piles with diameter D_o and length L were conducted at various locations as shown in Figure 1c. For tests with shallow penetration depth on one face (face 1), the block was turned upside down and another test was conducted on the intact face (face 2). Information regarding pile geometries, test locations, and the final penetration depth for each test are listed in Table 2.

Table 2. Description of the model pipes and jacking tests.

Model Pile	D_o [mm]	L [mm]	Block	Face	Location	Final depth [mm]
P4	60	200	B	2	W	137
P5	60	200	B	2	C	158
P6	60	200	A	1	S	157
P8	110	300	E	1	N	171
P9	110	300	D	1	S	242

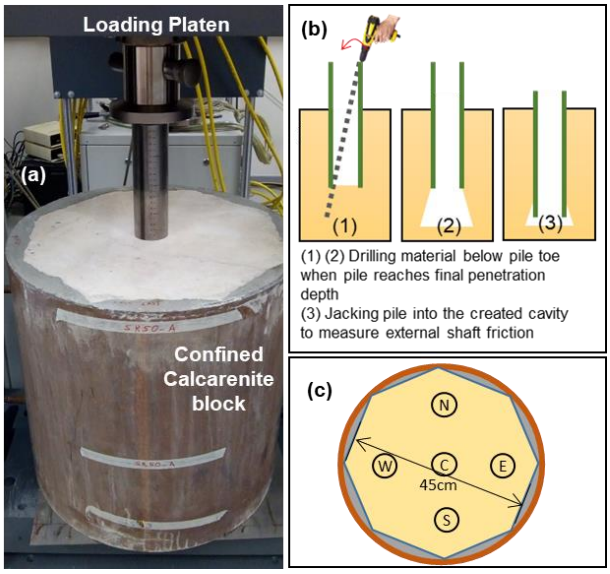

Figure 1. (a) Typical test configurations for P5 (b) procedure for measuring shaft resistance at the end of the test (c) possible locations on a block for conducting jacking tests.

3 TEST PROCEDURE

In the jacking tests, to avoid development of resistance due to the material accumulating inside the pipe (plug), the pipe was regularly emptied at penetration intervals of about 20mm for the 60mm piles and 35mm for the 110mm piles. Large calcarenite fragments (Figure 2) were recovered by hand or with a drill bit. The remaining fines and smaller fragments were vacuum cleaned from the inside the model piles.

After each pipe had been jacked to the desired depth, a cavity was created at the base of the model piles with a hand drill (Figure 1b). Then the pipe head was further jacked downwards to measure the external friction on pipe wall (Figure 1b). Later, the model pile was filled with non-shrinking grout.



Figure 2. Disk-like fragments recovered from P4.

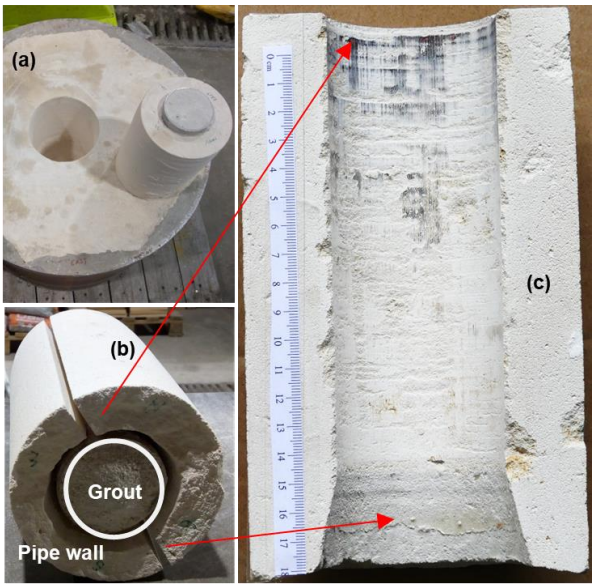

Figure 3. (a) Model pile (P5) filled with hardened grout cored out of the block (b) core sawn longitudinally to the remove the pipe (c) half of the core showing the pipe-calcarenite interface.

To analyse the interface of pipe and calcarenite, the pipe and the adjacent calcarenite for P5 was cored out with the aid of a concrete coring bit (Figure 3a). The core was cut longitudinally to detach the pipe from the interface. One half of the core showing the pipe-calcarenite interface can be seen in Figure 3c. The other half was placed inside gypsum to preserve the interface. It was then sawn transversally to see the pipe calcarenite interface as shown in Figure 4. Test setup is shown in Figure 1a. The pile head was axially jacked downwards via strokes of 1mm followed by unloading to below 500N. The velocity was 0.3 mm/min during loading. The force-displacement curve of P4 is shown in Figure 5. The unloading-reloading cycles are removed for visual clarity. Further details on the results and tests can be found in (Jafari, 2021; Jafari et al., 2019).

4 RESISTANCE MECHANISM

The force-displacement curves of all model piles exhibited an increasing trend with considerable variations (see e.g., Figure 5). The applied force can decrease down to 10% of the peak values. The Force-displacement curve in Figure 5 exhibits a constant linear part at the end beyond a depth of 137mm. This part is due to the removal of the calcarenite at the pile toe, which leaves only the shaft resisting the pile downward movement. Knowing the shaft skin friction at the end of the test, one can reasonably argue that increasing trend of the applied force is due to the increasing skin resistance with further pile penetration.

As the cause of the oscillations, the heterogeneity of the calcarenite was ruled out after a careful examination of the blocks did not reveal any signs of stratification.

Similarly, sudden reductions followed by build-up of the applied forces were reported during penetration of model pipe piles in sand (Paikowsky,1990). This behaviour was attributed to the destruction of arches inside the plug. In our experiments, the plug was regularly removed. The only remaining component of jacking resistance, which can be responsible for the oscillations is the annulus resistance. This is confirmed by the failure mechanism at the pile base.

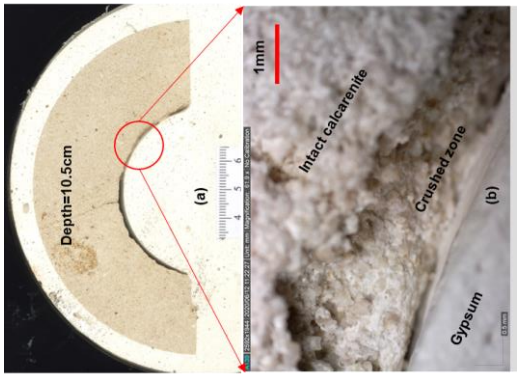

Figure 4. (a) Transversal cross section of pipe-calcarenite interface for P5 (b) close-up showing crushed region adjacent to external pile wall.

4.1 Failure mechanism at pile base and shaft

During the tests, it was observed that pile penetration into the calcarenite block generated disk-like calcarenite fragments popping up inside the pipe. Figure 2 shows the fragments recovered for P4. The jacking resistance decreased significantly upon formation of a disk-like fragment inside the pipe. Jafari et al. (2019) reported similar Behaviour. This process will be hereafter referred to as "chipping". The annulus resistance depended on the "chipping type" at the pile toe. In general, the chipping type was either "full chipping" (Figure 2d) or "partial chipping" (Figure 2abc). In full chipping, a full disk-like calcarenite fragment is created inside the pipe after a peak is reached. The penetration resistance was highest prior to full chipping.

Failure patterns at the external shaft of model piles can be seen in Figure 4. A crushed compressed zone was seen to form around the pipe wall as seen in transversal cross-sections (Figure 4). The thickness of the crushed zone is almost equal to the pipe wall thickness. With help of an air blow gun, some of the crushed material could be blown away so that the extent of the crushed zone could be assessed.

The chipping mechanism can be expected to

influence the thickness of the crushed zone around the model pile (Figure 4). The pipe penetration results in the volumetric compression of the calcarenite at the pipe tip. The compressed region consists of compacted finely crushed calcarenite forming a doughnut-shape. Intuitively, it could be expected that the radius of the circular cross section of this doughnut increases with penetration depth until some critical embedment d_{crit} is reached. At that point, chipping occurs allowing the pipe to cut through the doughnut and to leave a region of dense fine material at the external and internal faces of the pipe. This process repeats itself with further penetration. The compacted crushed region has a maximum thickness (hence maximum normal stress) at a depth when chipping occurs. At that depth, the calcarenite tends to stick to pipe (leaving a dent on calcarenite interface) when one separates the pipe and calcarenite as seen in Figure 3c.

4.2 Periodicity of oscillations in jacking resistance

To understand the frequency content each resistance curve (F_0) was decomposed as follows:

1. F_0 was de-trended by fitting a fifth order polynomial to find $F_{detrended}$ (Figure 6a)
2. Low frequency content (F_{smooth}) is obtained by smoothing $F_{detrended}$ with a moving average filter (Figure 6b).
3. High frequency oscillations (F_{oscill}) were obtained as $F_{oscill}=F_{detrended}-F_{smooth}$ (Figure 6b)
4. Scalograms of both high and low frequency contents were constructed (Figure 6b-c).

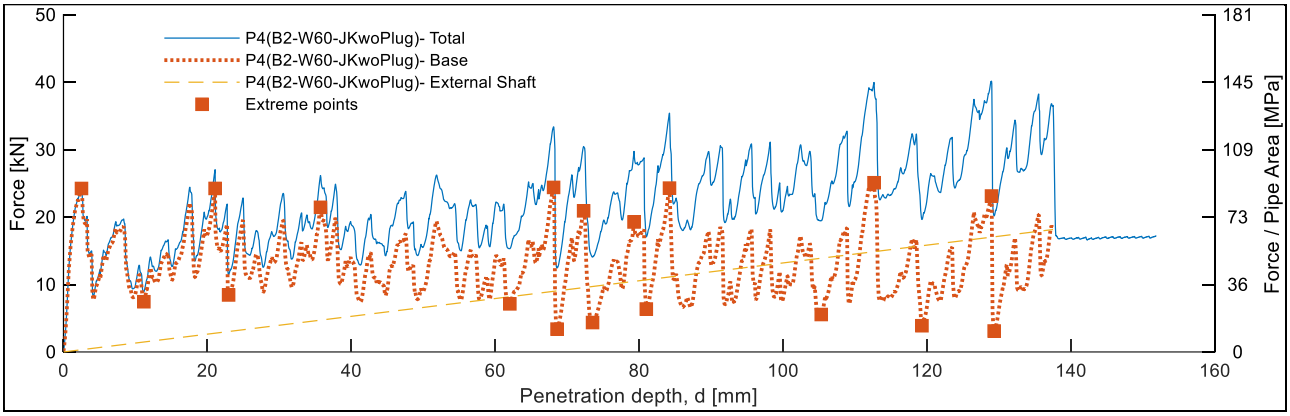

Figure 5. Typical force-displacement curves for test P4 with the estimated shaft and annulus components.

The peaks in the F_{smooth} curve corresponded to when full chipping occurred in the tests. On the other hand, the peaks in the F_{oscill} corresponded to when partial chipping occurred.

From the scalograms, it was found out that on average:

- The high frequency component has a period of 4mm for the 60mm-piles while it has a period of 8mm for the 110mm-piles. These periods are about $0.07D_o$.
- The low frequency content has a period of 12mm for the 60mm-piles while it has a period of 27mm for the 110mm-piles. These periods are about $0.23D_o$.

The period of the low and high frequency components of the signals from 110mm-piles is about two times that of the 60mm-piles. These results indicate that the resistance oscillations depend on the pile diameter rather than the pile wall thickness in contrast to what was reported by Jafari et al. (2019).

4.3 Shaft resistance

External shaft resistance at the end of the tests was measured by jacking the pipe into a cavity created below the pipe tip (Section 4). Assuming a linear increase of shaft resistance with penetration depth (Figure 5), one can compute an average shear stress τ_{ave} on the pipe outside wall. τ_{ave} is 440 kPa and 405 kPa for the 60mm and 110mm piles, respectively. These values are about 6% of σ_{ci}.

These values are consistent with laboratory experiments by ARGEMA (Association de Recherche en GEotechnique MArine) in which small piles were *driven* in limestone with 5MPa< σ_{ci} <25MPa. Skin friction values were between 7 to 9 percent of σ_{ci}. In addition, pullout tests of driven piles in cemented carbonate formations exhibited skin friction values reaching 300 kPa in formations with σ_{ci} ranging from 3.5 to 5MPa according to Le Tirant and Nauroy (1994). High shaft friction values seem to be typical of model pipe piles installed in carbonate rocks. These results may be used combined with the investigation of rock-steel interfaces after Ziogos et al. (2023) to

better understand the skin friction of crushed calcarenite and the model steel pipe pile.

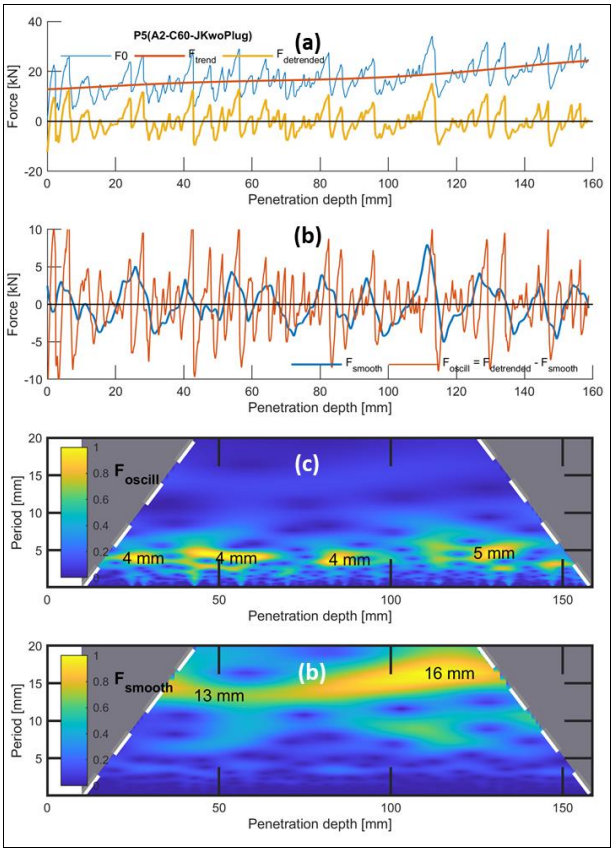

Figure 6. (a) De-trending of penetration resistance for P5 (b) decomposition of detrended curve into high frequency and low frequency curves (c) (d) scalograms of Foscill and Fsmooth.

4.4 Annulus resistance

By subtracting the shaft resistance from the total jacking resistance, one can obtain the annulus resistance. The estimated annulus resistance falls in a band of peak and residual values (Figure 5). For the peaks with the highest prominence, full chipping occurred (Section 4.1). The *findpeaks* function of Matlab® was used to identify all the peaks and troughs of a curve with a prominence equal to 30% of the maximum annulus resistance. This criterion proved relatively effective in capturing the peaks and troughs associated with full chipping as seen in Figure 5. Mean peak annulus stress of all the model piles is 85MPa = $12.5\sigma_{ci}$ while mean residual annulus stress is 23MPa = $3.4\sigma_{ci}$. No discernible scale effects were observed between the annulus capacity of the 60mm and 110mm model piles. The estimated residual annulus stress is close to upper bound suggestion by Le Tirant and Nauroy (1994), which is the minimum of $4.5\sigma_{ci}$ and 12 MPa. The authors (Jafari, 2021; Jafari et al., 2019) investigated numerically the bearing capacity of open-ended pipe piles in intact rock. The annulus bearing capacity did not depend on the D_o/t for the common ranges in practice ($D_o/t < 100$). With increasing embedment depth, a maximum annulus capacity q_b was approached. A fit to those numerical results leads to an annulus bearing capacity of $11.8\sigma_{ci}$. This value is in good agreement with the mean peak stress of the jacked model pile which is $12.5\sigma_{ci}$. Prediction of the residual bearing capacity in terms of the intrinsic properties of the medium is an area open to further research.

5 CONCLUSIONS

Model pipe piles were jacked into relatively large blocks of a reference calcarenite. The model piles were jacked down to 1.5 to 2.5 times pipe diameter. Penetration resistance was measured. During jacking, the material accumulating inside the pipe was removed at regular intervals. The total jacking resistance was split into annulus and shaft resistance components. Annulus resistance exhibited important oscillations, which was attributed to calcarenite chipping mechanisms inside the pipe. The period of the oscillations depended on the pile diameter rather than pile wall thickness. At the pile-calcarenite interface, a region of compacted crushed material formed over a thickness of the order of that of the pipe wall.

ACKNOWLEDGEMENTS

Calcarenite samples used for penetration testing were graciously supplied by EDF Renouvelables, thanks to Ms. Elisabeth Palix. Contributions from members of LEMSC laboratory in particular Ms. Catherine Doneux, who facilitated the experiments are also appreciated.

REFERENCES

Baud, P., Schubnel, A., Heap, M., Rolland, A., 2017. Inelastic Compaction in High-Porosity Limestone Monitored Using Acoustic Emissions. J. Geophys. Res. Solid Earth 122, 9989–10,008. https://doi.org/10.1002/2017JB014627.

Bosco, J., Vander Elst, M., 2018. Calcarenite used as foundation material for windmills, Master thesis. UCLouvain, Louvain-La-Neuve.

Holeyman, A., 2017. Battage de pieux métalliques dans la roche. Rev. Fr. Géotechnique 1. https://doi.org/10.1051/geotech/2017014.

Jafari, M., 2021. Numerical and experimental investigation of monopile driving resistance in carbonate rocks. PhD thesis, UCLouvain.

Jafari, M., Gharsallaoui, H., Victor, K.H., Holeyman, A., 2019. End bearing response of open-ended pipe piles

embedded in rock. Int. J. Rock Mech. Min. Sci. 119, 46–57. https://doi.org/10.1016/j.ijrmms.2019.04.008.

Le Tirant, P., Nauroy, J.-F., 1994. Foundations in carbonate soils. Editions Technip.

Montargès, R., 1988. Frottement des pieux battues dans les formations carbonatées cimentées. (No. IFP 36018).

Paikowsky, S.G., 1990. The mechanism of pile plugging in sand, in: Offshore Technology Conference. Offshore Technology Conference.

Settgast, R.H., 1980. Marine pile load testing in carbonate rocks, in: Offshore Technology Conference. Offshore Technology Conference.

Stavropoulou, E., Dano, C., Boulon, M., 2021. Shear Response of Wet Weak Carbonate Rock/Grout Interfaces Under Cyclic Loading. Rock Mech. Rock Eng. https://doi.org/10.1007/s00603-021-02406-1.

Ziogos, A., Brown, M. J., Ivanović, A., & Morgan, N. (2023). Understanding Rock-Steel interface properties for use in offshore applications. Proceedings of the Institution of Civil Engineers: Geotechnical Engineering, 176(1), 27-41. https://doi.org/10.1680/jgeen.20.00183.

Proceedings of the XVIII ECSMGE 2024
GEOTECHNICAL ENGINEERING CHALLENGES
TO MEET CURRENT AND EMERGING NEEDS OF SOCIETY
© 2024 the Authors
ISBN 978-1-032-54816-6
DOI 10.1201/9781003431749-587
Open Access: www.taylorfrancis.com, CC BY-NC-ND 4.0 license

ECSMGE 24
XVIII EUROPEAN CONFERENCE ON SOIL MECHANICS AND GEOTECHNICAL ENGINEERING

Les tunnels de drainage de Lisbonne: Enjeux et spécificités

The drainage tunnels of Lisbon: Challenges and specificities

C. Jassionnesse*, G. Euzen
Spie Batignolles Génie Civil, Nanterre, France

F. Rocha
Spie Batignolles Portugal, Lisboa, Portugal

**christophe.jassionnesse@spiebatignolles.fr*

RÉSUMÉ: Le projet des tunnels de drainage « Monsanto-Santa Apolonia » (TMSA) et « Chelas-Beato » (TCB) vise en priorité à maitriser les inondations qui se produisent en plusieurs endroits de la ville de Lisbonne. Le marché attribué en Conception-Réalisation au groupement Mota-Engil – Spie Batignolles International (constructeurs), Spie Batignolles Génie Civil – LCW – Aqualogus (concepteurs) comprend la construction des deux tunnels - le TMSA de 4,4 km de longueur, et le TCB de 1,1 km. Il comprend également la réalisation des travaux de dérivation des ruisseaux canalisés en amont des tunnels, de trois chambres d'interception du réseau existant avec les puits de chute associés et les ouvrages de décharge dans le Tage. Le TMSA recoupera deux grands ensembles géologiques, de longueur équivalente. En partie nord-ouest, le tunnel recoupera des calcaires crétacés et les tufs et basaltes du complexe volcanique de Lisbonne. En partie Sud-Est le tunnel recoupera des terrains sablo-argileux compacts à indurés, de la série du Miocène de Lisbonne, Le TCB recoupe uniquement les couches supérieures du Miocène. Les ouvrages de décharge seront réalisés dans des remblais de remodelage des rives du Tage. Le contexte urbain du TMSA est très dense sur les deux tiers sud-est du tracé, avec le croisement de trois lignes de métro sous une faible couverture et le passage sous des quartiers anciens d'une grande valeur architecturale. Le contexte urbain du TCB est moins dense mais comprend le passage sous deux voies ferrées importantes.

ABSTRACT: The «Monsanto-Santa Apolonia» (TMSA) and «Chelas-Beato» (TCB) Drainage Tunnels Project is aimed primarily at controlling flooding in several areas of the city of Lisbon. The design & build contract attributed to the joint-venture Mota-Engil – Spie Batignolles International (builder), Spie Batignolles Génie Civil – LCW – Aqualogus (designer) includes the achievement of the two tunnels - TMSA of 4,4 km long and TCB of 1,1 km. It also includes the work of capturing the canalized streams upstream of the tunnels, three interception chambers of the existing network with the associated shafts and works of the outlets in the Tagus. The TMSA will intersect two large geological units of equivalent length. In the northwest part, the tunnel will intersect Cretaceous limestones and tuffs and basalts of the Lisbon volcanic complex. In part South-East the tunnel will intersect sandy-clay soils, compact to indurated, of the series of the Miocene of Lisbon, TCB only intersects the upper layers of the Miocene. The outlets works will be embedded in the embankments of the Tagus shore. The urban context of the TMSA is very dense on the south-eastern two thirds of the route, with the crossing of three metro lines under a weak cover and the passage under old districts of great architectural value. The urban context of TCB is less dense but includes the crossing under two major railways.

Keywords: Urban tunnelling; drainage; Lisbon.

1 INTRODUCTION

Le projet général des tunnels de drainage s'inscrit dans le cadre du plan général de drainage de la ville de Lisbonne pour la période 2016-2030 (Câmara Municipal de Lisboa, 2015). Ce projet vise à la maîtrise des inondations qui se produisent en plusieurs endroits de la ville. Outre la construction de deux tunnels - le tunnel Monsanto - St. Apolónia (TMSA) d'une longueur de 4,4 km, et le tunnel Chelas - Beato (TCB) d'une longueur de 1,1km (Figure 1) le marché comprend notamment la réalisation des ouvrages de dérivation des rivières d'Alcântara et de Chelas, des chambres d'interception des réseaux d'eau pluviale, (Av. da Liberdade, R. St Marta et Av. Almirante Reis), avec les puits de chute associés, qui envoient les débits déviés dans le TMSA et les ouvrages de rejet à l'estuaire du Tage. En outre, le marché comprend la construction d'un bassin antipollution à l'entrée amont du tunnel TMSA, et d'un réservoir d'eau traitée, ainsi que la mise en œuvre du système de drainage des eaux usées de la zone basse du bassin de St. Apolónia, dans la zone entourant le rejet du TMSA.



Figure 1. Plan général de localisation des tunnels de drainage de la ville de Lisbonne.

Le système formé par les tunnels et les réseaux existants garantit ainsi le transport des débits pour des périodes de précipitations supérieures à 100 ans. Le TMSA a été dimensionné pour une capacité d'écoulement de 170m3/s et le TCB de l'ordre de 147m3/s. Dans le cas de débits dépassant la capacité des tunnels, les débits excédentaires continuent en aval (par "by-pass") et sont transportés par les infrastructures existantes. Les effluents du système de drainage, par temps sec, seront traités par les stations d'épuration existantes. Par temps de pluie, le déchargement vers les tunnels n'aura lieu qu'à partir d'un débit assurant une dilution élevée. Compte tenu de la profondeur d'implantation des tunnels, les débits interceptés dans ces chambres de dérivation sont conduits à des ouvrages de chute en vortex qui assurent une bonne dissipation d'énergie. Il est également prévu que les tunnels permettent le transport d'effluents traités pour des utilisations d'arrosage d'espaces verts et de nettoyage urbain.

2 LES OUVRAGES DE DERIVATION

2.1 Les ouvrages de dérivation amont (TM1, TC1)

Les ouvrages de dérivation du Caneiro de Alcântara (TM1), en amont du TMSA, se situent à Campolide, dans le bassin de la rivière d'Alcântara canalisée et couverte. Aujourd'hui, les eaux du collecteur de l'Alcântara coulent jusqu'au Tage. L'ouvrage de dérivation des collecteurs de la vallée de Chelas (TC1), en amont du TCB, est implanté dans le lit majeur du ruisseau de Chelas, aujourd'hui canalisé et couvert.

Les ouvrages de dérivation amont incluent fonctionnellement les principaux organes suivants:

- Un chenal d'intersection et de déviation des collecteurs existants;
- Un puits de décharge des gros éléments charriés et des fosses de tamisage/dessablage;
- Des bassins de dépollution et une station de pompage vers une station d'épuration (TM1);
- Un chenal latéral (TM1) ou une chambre (TC1) d'amené du débit de crue au tunnel;
- Divers dispositifs d'écrêtage et de contrôle du flux (seuils, vannes-écluses etc.) entre les organes.

Les débits de temps sec et les débits de pluie (jusqu'à 2 fois le débit de pointe) sont détournés en amont des ouvrages de dérivation et amenés vers une station d'épuration.

Il s'agit d'ouvrages majoritairement enterrés, avec quelques émergences (bâtiment de contrôle-commande etc.). Ainsi, les structures du TM1 sont implantés à 20m sous le terrain naturel. Elles sont constituées de piliers, de dalles massives et de murs en béton armé. Sur le TC1, la structure est enterrée à environ 15m de profondeur. Compte tenu des contraintes de site, il a été retenu des solutions de soutènement périphérique par rideaux de pieux en béton armé avec différents niveaux d'ancrages provisoires, qui seront en définitif remplacés par les dalles des niveaux enterrés.

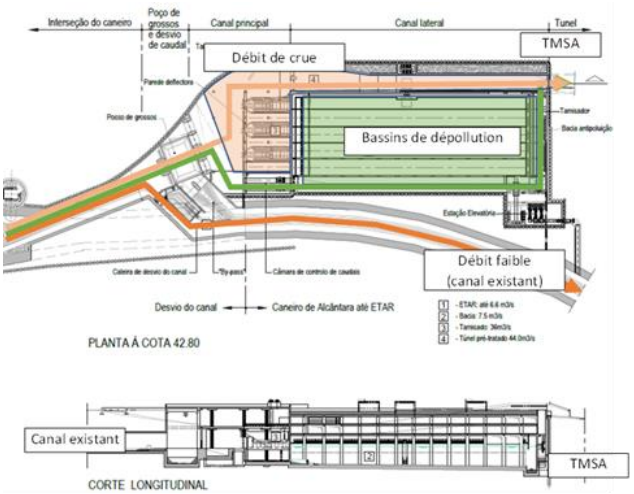

Figure 2. Ouvrage d'interception et de dérivation du collecteur d'Alcantara (TM1).

Les excavations du TM1 constituent la tranchée de départ du tunnelier pour le creusement du TMSA en pente descendante. En revanche, le tunnelier sortira de terre dans la tranchée du TC1, à la fin du creusement du TCB en attaque montante.

2.2 Les ouvrages d'interception des réseaux existants (TM2, TM3, TM4)

Ces ouvrages ne sont présents que le long du TMSA. Les ouvrages TM3 et TM4 sont implantés sur la rue St. Marta et l'Av. Almirante Reis respectivement, au droit des deux principaux thalwegs du centre

historique de Lisbonne qui se rejoignent dans la ville basse (Baixa de Lisboa) et débouchent dans le Tage au niveau de la Place du Commerce (Praça do Comercio). L'ouvrage TM2 est implanté sur l'Av. da Liberdade, sur le flanc ouest du thalweg de St. Marta.

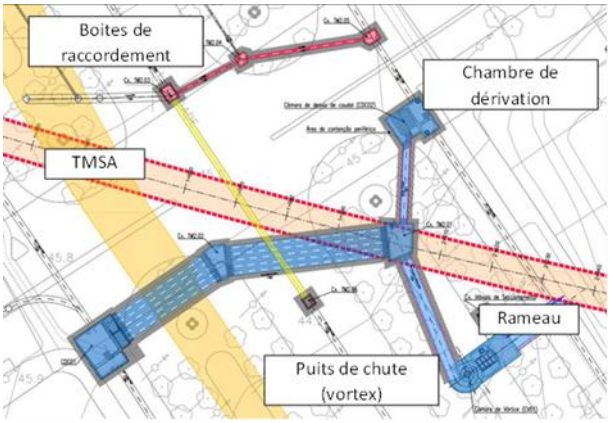

Figure 3. Ouvrage d'interception de l'Av. da Liberdade (TM2).

Les ouvrages de dérivation amont incluent fonctionnellement les principaux organes suivants:

- Des boîtes de raccordement qui interceptent les débits des collecteurs existants;
- Des chambres de dérivation qui dirige le débit de crue vers un puits de chute et les débits courants vers la station d'épuration à travers le réseau existant;
- Un puits de chute en vortex;
- Une chambre de dissipation;
- Un rameau de raccordement au TMSA.

Les puits de chute en vortex sont constitués par une rampe hélicoïdale en pente à 20% environ, à l'intérieur de l'enceinte cylindrique du puits, de 6m (puits TM2, TM3) à 8,6m de diamètre (puits TM4).

L'enceinte des puits TM3 et TM4, de 20m de profondeur environ, est constituée par des pieux en béton armé, complétée par un béton projeté armé et des anneaux de renforcement en béton armé. L'enceinte du puits TM2 est également constituée par des pieux descendus jusqu'au toit du rocher (CVL, voir § 5), et, en dessous, par un soutènement au rocher par boulonnage, béton projeté avec des anneaux de renforcement en béton armé. La base des puits et l'amorce des rameaux en section élargie (hauteur x largeur = 8m x 5m) constitue la chambre de dissipation de l'énergie de chute. Les rameaux ont une longueur de 20m environ sur TM2 et TM3 et de 75m sur TM4. Ils sont excavés en méthode conventionnelle puis revêtus en béton coffré après la réalisation de la jonction au tunnel.

3 LES TUNNELS MONSANTO-SANTA APOLONIA ET CHELAS-BEATO

3.1 Géométrie et structure

Le tunnel Monsanto-Santa Apolónia (TMSA) a une longueur de 4,4km. Il présente une pente de 0,8% sur la majeure partie de son linéaire. La couverture varie de 4m à 85m et la pression hydrostatique maximale des eaux souterraines est de 320 kPa. Il sera excavé dans le sens descendant.

Le tunnel Chelas-Beato (TCB) a une longueur de 1,1km. Il présente une pente constante de 0,5%, permettant de diriger les flux d'eaux de pluie vers l'aval. La couverture varie de 7m à 45m et la pression hydrostatique maximale des eaux souterraines est de 100 kPa. Il sera excavé dans le sens montant.

Le revêtement final est constitué d'anneaux universels composés de 6 voussoirs rhomboïdaux.

Les principaux paramètres géométriques sont listés ci-dessous:

- Diamètre intérieur: 5,50m;
- Diamètre extérieur: 6,10m;
- Epaisseur du revêtement: 0,30m;
- Longueur nominale des anneaux: 1,80m.

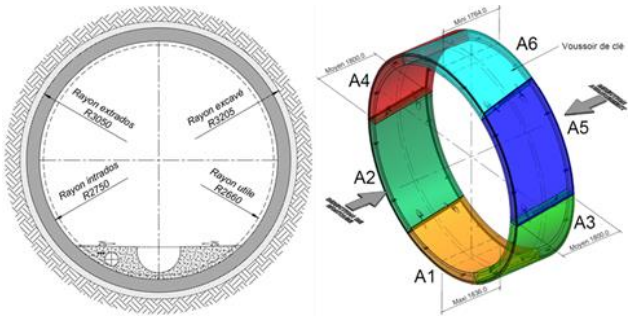

Figure 4. Géométrie du revêtement.

3.2 Contraintes de conception

Le dimensionnement du revêtement intègre des contraintes particulières:

- Le revêtement doit être en mesure de suivre une courbe de rayon 200m (courbe la plus serrée du projet). Les anneaux de voussoirs présentent donc un pincement important;
- La partie avale des tunnels peut être en contact avec l'eau de mer (zone de marnage). Cela conduit à des enrobages non courants afin d'éviter la corrosion induite par les chlorures;
- Le revêtement doit pouvoir reprendre une pression hydrostatique interne de 1 bar;
- Les tunnels sont situés en zone sismique.

4 LES OUVRAGES DE RESTITUTION

Les ouvrages de restitution dans l'estuaire du Tage (TM5 pour le TMSA, TC2 pour le TCB) sont constitués par des cadres fermés en béton armé, enterré, avec un nombre variable de cellules intérieures, et une largeur et une hauteur variables qui augmente avec le nombre de cellules, destinées à réduire les vitesses d'écoulement en sortie.

L'ouvrage TM5 à St. Apolónia, se développe sur une longueur de 180 m et l'ouvrage TC2 sur 320m à Poço do Bispo, avec une pente de l'ordre de 0,5%. Le niveau de restitution au Tage étant inférieur de quelques mètres au niveau moyen de l'estuaire, les ouvrages reçoivent le flux de la marée remontante.

L'ouvrage TM2 s'inscrit dans un site contraint, avec un passage au-dessus du tunnel de la ligne bleue du métro, avec une très faible couverture. L'ouvrage sera alors porté par des pieux descendus sous le tunnel. Le contexte géologique de ces ouvrages est caractérisé par la présence d'alluvions lâches et de remblais, d'épaisseur croissante vers l'aval.

La présence des terrains de faible compacité sous la nappe, nécessite la réalisation de rideaux de soutènements par pieux sécants, sur une grande partie du linéaire de ces ouvrages, avec la mise en place de tirants provisoires.

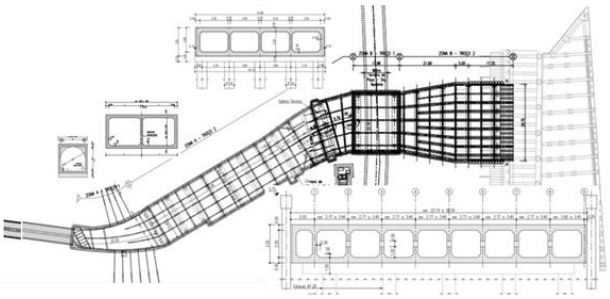

Figure 5. Ouvrage de restitution (TM5) – plan et coupes-types.

Compte tenu de la forte exposition au risque sismique de liquéfaction, ces terrains feront l'objet de traitement d'amélioration en place (colonnes ballastées etc.).

5 GEOLOGIE ET GEOTECHNIQUE

Le TMSA traverse dans sa moitié nord-ouest une structure rocheuse anticlinale, localement faillée, avec des calcaires et des calcaires marneux du Crétacé, recouverts par le complexe volcanique de Lisbonne (CVL) constitué d'une alternance de basaltes et de tufs volcaniques. Sur ce tronçon, le TMSA pourrait traverser une zone de failles avec la présence de roches altérées et fracturées, avec des passages argileux et d'éventuelles cavités karstiques.

Dans sa moitié sud-est, le tunnel interceptera une partie de la série sédimentaire miocène de Lisbonne (MI à MIVb), évoluant de l'Aquitanien au Burdigalien, constituée de terrains compacts de nature sablo-argileuse dominante avec la présence d'horizons rocheux peu nombreux et discontinus de résistance faibles de calcarènites et d'argilites.

Toutes ces assises sont légèrement basculées d'environ 5º à 10º vers le Tage.

Le contexte hydrogéologique du tronçon rocheux est déterminé par l'état de fissuration et d'altération des roches. La charge hydraulique peut atteindre quelques dizaines de mètres au-dessus du tunnel mais les flux souterrains sont généralement faibles comme le montre l'expérience sur les travaux dans ces formations, sauf potentiellement au droit des failles.

Le contexte hydrogéologique du tronçon en terrain meuble est caractérisé par la présence d'un système multicouche avec des communications latérales et verticales et des variations importantes des conditions hydrogéologiques. Les perméabilités mesurées dans les essais de perméabilité réalisés sont variables, mais généralement faibles (10^{-6} à 10^{-9} m/s).

Les calcaires du Crétacé présente une résistance moyenne, de l'ordre de 45 MPa. On observe une grande dispersion des résistances obtenues sur les roches du CVL: les basaltes sains correspondent à des roches très résistantes et très rigides et les tufs volcaniques correspondent à des roches peu résistantes et peu rigides.

Les sols de la série miocène vont des sables silteux peu plastiques aux argiles très plastiques avec des sols intermédiaires (silts ou sables silteux à très silteux peu à moyennement plastique).

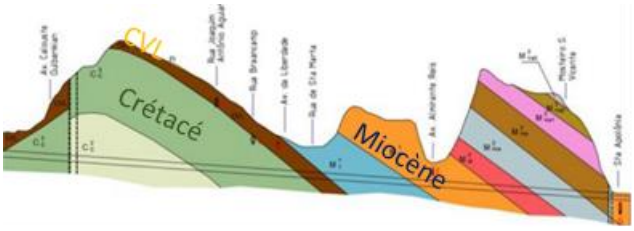

Figure 6. Profil en long géologique du TMSA.

Les terrains traversés par le TCB appartiennent à la série miocène finale, du Burdigalien Supérieur au Serravalien. Sur les deux tiers ouest, le tunnel s'inscrit dans des terrains à dominante sableuse, avec de nombreux niveaux indurés gréso-carbonatés, sous une faible charge hydraulique de quelques mètres en radier. Sur le tiers est, les terrains sont majoritairement argileux avec des niveaux marno-calcaires ou de calcarènites. La charge hydraulique peut atteindre une

dizaine de mètres sur ce tronçon. Les derniers mètres du tunnel s'inscrivent dans la formation des Grès de Grilos, affectée de phénomènes karstiques importants.

6 LES METHODES DE REALISATION DES TUNNELS

Le TMSA sera excavé par un tunnelier à confinement par pression de terre (EPB). Le TCB, initialement prévu d'être excavé en méthode conventionnelle, sera également excavé par le même tunnelier, à la suite du TMSA. La roue de coupe est de type mixte, équipée de 40 molettes 17'' et de couteaux, avec un taux d'ouverture de près de 30% Le diamètre du bouclier est de 6,4m environ, pour une longueur de 10m. La poussée totale de 38000 kN est assurée par 24 vérins au contact des voussoirs.

Le tunnelier fonctionnera selon plusieurs modes de pilotage du confinement:

- En mode « ouvert », la vis fonctionne en extraction à la pression atmosphérique;
- En mode « chambre mi-pleine » avec confinement à l'air en partie supérieure et injections de bentonite le long du bouclier éventuelles;

Le mode « ouvert » est réservé aux tronçons en terrain rocheux, hors zone de failles, prévisible sur 40% du linéaire du TMSA.

En mode « chambre pleine », avec injection de bentonite le long du bouclier.



Figure 7. Réception en atelier du tunnelier « Oli ».

Le mode « chambre mi-pleine » est prévu en terrain meuble (partie du TMSA et totalité du TCB). Le mode « chambre pleine » est réservé aux tronçons sous faible couverture (thalwegs…) sur la base d'un pilotage observationnel par les tassements en surface et une instrumentation en forage. L'injection de remplissage du vide annulaire, de type « coulis bi-composants » est également pilotée en pression-volume sur la base des observations.

La pression de consigne maximale est de 3,8 bars sur le TMSA et de 2,6 bars sur le TCB.

7 LES POINTS SENSIBLES

7.1 Les thalwegs et les passages sous le metro

Le tunnel Monsanto-Santa Apolónia passe successivement sous deux thalwegs:

- Le thalweg de l'ancienne rivière de Valverde où se trouve aujourd'hui la rue St. Marta;
- Le thalweg de l'ancienne rivière de Arroios au niveau de l'actuelle av. Almirante Reis.

Dans ces zones, la couverture est d'environ 13m (2Ø) et le contexte urbain est dense.

Sous le versant ouest du thalweg de Valverde, le tracé du TMSA croise successivement la ligne jaune du métro sous une couverture de 20m et la ligne bleue sous une couverture de 14m. Sous le thalweg de l'av. Almirante Reis, le tracé du TMSA croise la ligne verte sous une couverture réduite à 6m.

En cours de creusement, le suivi des déplacements sur ces ouvrages et le bâti environnant fera l'objet d'un monitoring renforcé, avec notamment la mise en place d'une instrumentation en forage sur le premier thalweg franchi.

7.2 Les intersections tunnel - rameaux

Au droit des intersections tunnel - rameaux, les ouvertures à réaliser dans le revêtement de voussoirs sont relativement importantes (environ 5m de largeur pour 3,5m de hauteur). Par ailleurs, les structures provisoires de reprise doivent impacter le moins possible le gabarit tunnel pendant les travaux de celui-ci. Afin de répondre à cette problématique, les structures provisoires de reprise sont constituées de deux linteaux en UPN (inférieur et supérieur) connectés par deux piédroits cintrés en HEB. Les linteaux inférieurs et supérieurs sont connectés aux anneaux par le biais de scellements et de bèches.

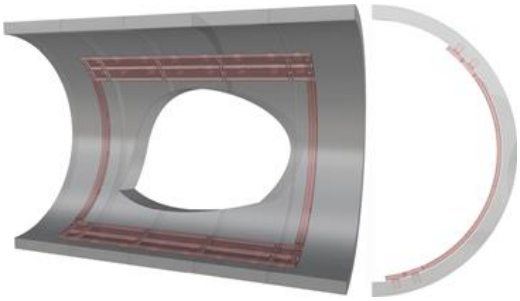

Figure 8. Structure provisoire de reprise au droit des intersections tunnel – rameaux.

7.3 La sortie du tunnelier à St. Apolónia

Le site de sortie du tunnelier à Santa Apolónia est situé au pied de la colline de l'Alfama. Le site est caractérisé par une forte pente. Les avoisinants sont constitués par un bâti très dense, de construction ancienne en

maçonnerie, de deux à quatre niveaux habitables, séparé par des ruelles étroites et des escaliers. Le bâtiment le plus proche du tympan du tunnel, avec une très faible couverture de 3m sous les fondations, est particulièrement sensible en raison de son revêtement de façade en carrelage (« Casa do Azulejo »). Le seuil de déformation admissible (« Limiting Tensile Strain, d'après Boscardin et Cording, 1989), pour un niveau de dommage "léger" est alors de 4.10^{-4}, correspondant aux paramètres de contrôle suivants:

- Tassement différentiel: $\Delta S < 25$ mm
- Angle de distorsion: $\beta < 1/350$

Compte tenu de la faible couverture, le respect de ces seuils ne permet pas d'envisager la sortie du tunnelier en mode "confinement en pression de terre".

En effet, ce mode de confinement ne permet pas une régulation suffisamment précise de la pression, notamment le long du bouclier.

Par ailleurs, le contexte géotechnique présente une forte variabilité des faciès au sein des « Sables de la Quinta do Bacalhau » et des remblais hétérogènes d'épaisseur variable, en lien avec les vestiges archéologiques de la « Muralha Fernandina ».



Figure 9. Vue de la Casa do Azulejo et élévation des cibles de suivi des déplacements.

Le principe retenu est la réalisation en méthode traditionnelle avec présoutènement par voûte parapluie, d'une galerie en demi-section supérieure, en contre-attaque à partir du tympan de la tranchée couverte du TM5 (voir § 4). La longueur de cette galerie est conditionnée par la présence d'un niveau rocheux plurimétrique de calcarénites, remontant en voûte du tunnel à 26m du tympan et constituant un toit suffisant pour abaisser en sécurité la pression de confinement du tunnelier. Une fois la section inférieure excavée par le tunnelier, le revêtement définitif de la galerie sera constitué par les voussoirs.

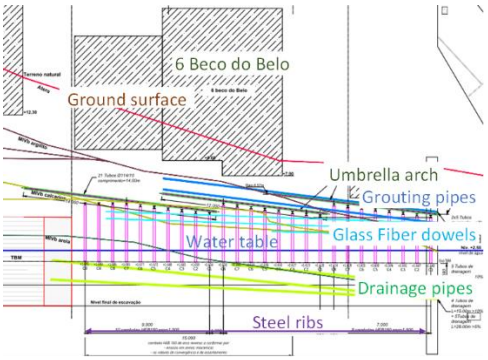

Figure 10. Profil en long de la galerie de contre-attaque.

Le vide entre l'extrados des voussoirs et l'intrados de la galerie de contre-attaque, sera comblé par des injections de mortier, à partir de conduits disposés préalablement à l'intrados de la galerie.

Une évaluation des dommages engendrés sur la « Casa do Azulejo » a été menée à l'aide d'un modèle aux éléments finis de la façade, afin de vérifier le respect du critère de déformation admissible. En cours de creusement, le suivi des déplacements sur la façade sera réalisé par un théodolite, à l'aide d'un réseau dense de cibles de mesures optiques (voir Figure 10).

8 CONCLUSION

La maitrise des inondations urbaines est un des enjeux de l'adaptation au changement climatique, auquel répond la construction des tunnels de drainage de Lisbonne. Le projet associe des ouvrages hydrauliques complexes à des tunnels de longueur et de diamètre importants, qui justifient l'utilisation d'un tunnelier. Malgré un contexte géologique relativement favorable, les contraintes en site urbain ont nécessité des études approfondies de l'impact du chantier et des solutions techniques au cas par cas, comme le recours à un tunnelier à confinement de type pression de terre, diverses solutions de traitements de terrains ou la réalisation d'une galerie de contre-attaque pour la sortie du tunnelier. Après une phase d'étude de trois ans dans le cadre du contrat de Conception-Réalisation, l'année 2023 verra le démarrage du chantier, avec un objectif de mise en service en 2026.

REFERENCES

Boscardin, M., & Cording, E. (1989). Building Response to Excavation-Induced Settlement. Journal of Geotechnical Engineering, 115(1), pp. 1-21.

Plano Geral de Drenagem de Lisboa - Câmara Municipal de Lisboa (2015). hhtps://planodrenagem.lisboa.pt/noticias https://youtu.be/yWG4t8m2tHU.

Proceedings of the XVIII ECSMGE 2024
GEOTECHNICAL ENGINEERING CHALLENGES
TO MEET CURRENT AND EMERGING NEEDS OF SOCIETY
© 2024 the Authors
ISBN 978-1-032-54816-6
DOI 10.1201/9781003431749-588
Open Access: www.taylorfrancis.com, CC BY-NC-ND 4.0 license

ECSMGE 24
XVIII EUROPEAN CONFERENCE ON SOIL MECHANICS AND GEOTECHNICAL ENGINEERING

Jet grouting experience in river borne materials (RBM)

Expérience en jet grouting dans les matériaux fluviaux (RBM)

A.C. Joshi*, Arvind
Koldam hydro power station, NTPC Limited, India

V.A. Sawant
Department of Civil Engineering, IIT Roorkee, India

**akhilesh_cj@ce.iitr.ac.in*

ABSTRACT: This paper elaborates a real-time, full-scale, hands-on field experience of jet grouting in river borne materials (RBM). An earthen dyke of approximately 320 m length and15 m height was constructed with available river borne material (RMB) on riverbed and riverbanks. The key function of this dyke was to isolate the working front in the spillway and plunge pool area from flowing river water just downstream of a rock fill dam of a hydropower project in India. Sieve analysis of RBM showed it as gravely sand with very less fine. To check the efficacy of jet grouting the cylindrical cores are drilled and tested. Unconfined compressive strength of cylindrical cores varies from 8 to 10 MPa, which is well comparable to similar results reported worldwide. Analysis of jet grouting parameters e.g. grouting rate and pressure, properties of grout and spoil, UCS of grout and spoil, cement intake etc. is done across the length of the dyke. Jet grouting methodology, materials, test results, effectiveness, challenges faced, comparison with similar works are detailed in this paper. This experience shall reinforce the confidence of practicing engineers and academician in adopting jet grouting technology in highly variable and porous materials like RBM.

RÉSUMÉ: Cet article élabore une expérience pratique en temps réel, à grande échelle, du jet grouting dans des matériaux fluviaux (RBM). Une digue en terre d'environ 320 m de longueur et 15 m de hauteur a été construite avec des matériaux fluviaux (RMB) disponibles sur le lit et les berges de la rivière. La fonction clé de cette digue était d'isoler le front de travail dans la zone du déversoir et du bassin profond de l'eau de la rivière qui coule juste en aval d'un barrage en enrochement d'un projet hydroélectrique en Inde. L'analyse par tamisage du RBM a montré qu'il s'agissait de sable graveleux très moins fin. Pour vérifier l'efficacité du jet grouting, les noyaux cylindriques sont forés et testés. La résistance à la compression non confinée des noyaux cylindriques varie de 8 à 10 MPa, ce qui est tout à fait comparable aux résultats similaires rapportés dans le monde entier. Analyse des paramètres de jet grouting, par ex. Le taux et la pression d'injection, les propriétés du coulis et des déblais, l'UCS du coulis et des déblais, l'apport de ciment, etc. sont effectués sur toute la longueur de la digue. La méthodologie du jet grouting, les matériaux, les résultats des tests, l'efficacité, les défis rencontrés, la comparaison avec des travaux similaires sont détaillés dans cet article. Cette expérience renforcera la confiance des ingénieurs et des académiciens en exercice dans l'adoption de la technologie de jet grouting dans des matériaux très variables et poreux comme le RBM.

Keywords: Jet grouting; earthen dyke; river borne material; hydro power plant; grout and spoil properties.

1 INTRODUCTION

Jet grouting had been accepted as a well-established ground improvement technique since decades. In the present case jet grouting has been used as mainly as a seepage channel barrier to secure a dry working area. The jet grouting process involves the erosion of the in-situ soil, by a jet of fluid projected at very high velocity from a small diameter nozzle. The eroded soil is then mixed with a fluid (generally cement grout) to form a mixture, which after hardening is called soil-cement element. However, to efficiently implement this technique, it is imperative to carefully arrange the jet grouting equipment and methodically execute the process.

Apart from the technical know-how, the other bigger challenge was to execute a series of interdependent tasks of dyke construction, jet grouting, dewatering, concrete back filling etc. in very small frame and before onset of monsoon season; and to manage a huge machinery and manpower at very congested work front. Planning and monitoring of this strengthening activity without hindering the operation of hydropower generation was a rare management lesson.

2 PROJECT DESCRIPTION

Koldam Hydro Power Station (Koldam HPS) is situated on river Satjuj in district Bilaspur, Himachal Pradesh, India. The Koldam HPS is basically a run-of-the river scheme with additional storage facility for the initial 30 years. Koldam HPS envisages utilization of a head of about 140 m by constructing a 167m high (from the deepest foundation) rock/ gravel fill dam with impervious central clay core and a dam toe powerhouse with an installation of 4 units of 200 MW each. The Gross capacity at full reservior level (FRL) is 576 million cumec (MCM) and the dead storage capacity is 486 MCM. Figure 1 shows the panaromic view of Koldam HPS.



Figure 1. Panoramic View of Koldam HPS.

3 DYKE CONSTRUCTION AND JET GROUTING

An earthen dyke of approximately 320 m length and 15 m height was constructed with available river borne material (RMB). The key function of this dyke was to isolate the working front in the spillway and plunge pool area from flowing river water just downstream of a rock fill dam of a Koldam HPS in Himachal.The purpose of dyke and jet grout column is to create a impervious cut-off wall so that dewatering and further excavation & concreting works are taken up in the Plunge Pool. Dyke was made up of river bed materials by cut and fill method with the available materials nearby. Figure 2 depicts the dyke constructed along Sutlej river.



Figure 2. Dyke Constructed along Sutlej River.

4 JET GROUTING PARAMETERS

Jet grouting technique was introduced in the late 1960s in Japan and is based on the principle of injecting high-velocity fluids into the subsoil. This process requires high-velocity grout for breaking up the soil matrix, with or without water jet along with the addition of cement.

Soil improvement works using high pressure jet grouting method involves injecting a continuous selected mix of cement grout at high pressure from nozzles to cut and break into the surrounding subsoil, mixing and replacing it with cement slurry to form a hardened cemented mass. This soil improvement method modifies and improves the mechanical properties of the treated soil, most notable its shear strength, stiffness while reducing its permeability.

The high-pressure jet grouting using double tube system was implemented at site for soil improvement works presented in this paper. Jet grouting was performed with a Casagrande C7 hydraulic crawler rig and grout pump assembly with double tube system with grout pumping pressure of 400 bar with water cement ratio of 1(ordinary portland cement OPC). Depth of jet grouting was varying from 8 to 20 m based on depth of dyke and spacing of drilling holes with steel casing of 168 mm diameter for grouting was kept as 1m. Based on the jet grouting trials it was observed that the diameter of jet grouting column varies from 1.2 to 1.6 m in diameter leading to an overlap of 200 mm to 600mm. An average cement consumption of 700 to 750 kg was observed per m length of jet grout column.

5 ANALYSIS OF EXPERIMENTAL AND JET GROUTING DATA

The unconfined compressive strength (UCS) of cylindrical cores of jet grouting column is tested in site laboratory. 75 mm diameter cylindrical cores of L/D ratio about 2 were taken for different modes and ages of the jet grout column e.g. trial jet grouting column after 28 days, jet grouting column after 28 days, remains of jet grouting column parts after 7 months.

The plot of UCS shown below in fig 3 demonstrates that the UCS of jet grouting columns cores vary in the range of 4.5 MPa to 18 MPa. As expected highest UCS is observed for trail jet grouting column cores. The UCS of remains of jet grouting column after 7 months is higher than that of initial UCS values after 28 days. That is

probably due to washing of weaker zones and increase in strength with depth of column. An average UCS of 9.32 MPa is indicative of excellent quality of jet grouting works.

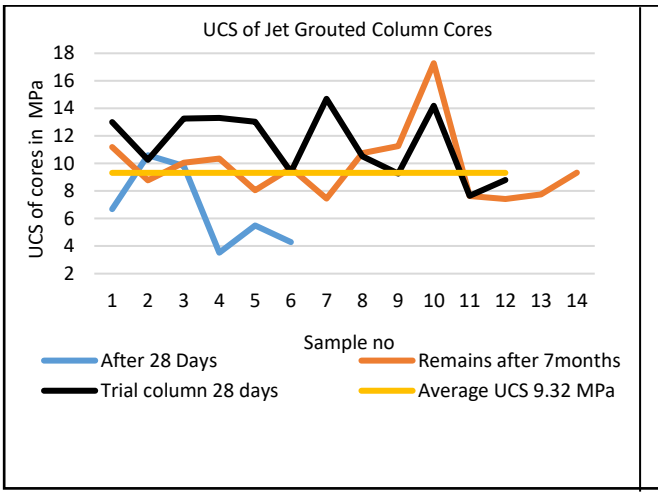

Figure 3. Variation of UCS of Jet grouted columns cores.

5.1 UCS of Grout mix

Grout mix of water cement ratio of 1:1 (ordinary portland cement OPC) was used for jet grouting of earthen Dykes. Cylindrical grout samples of diameter about 60 mm and L/D ratio 2 were tested for UCS at the age of 7 days and 28 days. The analysis of test datashown in fig 4 revealed that the 28 days strength of grout samples is about 30 to 80% higher than that of 7 days; with an average increase value of 46%. Minimum and maximum 28 days UCS values are 10.5 MPa and 20.1 MPa respectively showing a variance of about 91%.

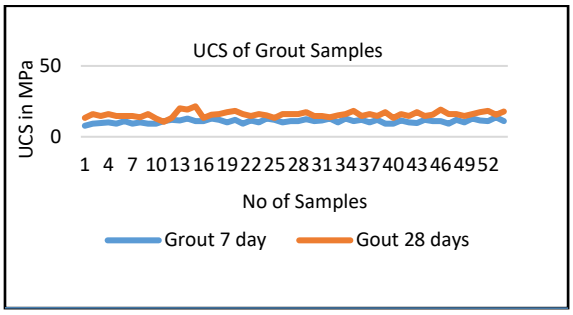

Figure 4. Variation of UCS of grout mix samples.

Comparison of UCS of grout and spoil cylindrical samples were also performed. Based on the analysis of more than 50 data sets, it can be concluded that the UCS of grout samples was always higher than UCS of spoil samples. The 28 days strength of spoil samples was quite matching to 7 days UCS value of grout sample (shown in Fig 5). Estenban Diaz et al. (2023)[2]has analyzed the 854 UCS test result data of UCS of jet grouting columns and arrived at an average UCS of 5.85 MPa. In current case study the average UCS value of 9.32 MPa is observed. In view of this extensive data base analysis also the current test results and analysis both are well validated.

The physical properties of a jet grout column are the function of the in situ properties of the soil before treatment, the properties of the grout and the operational parameters of the jetting which are injection pressure, nozzle size, monitor rotation and withdrawal rates.[3]

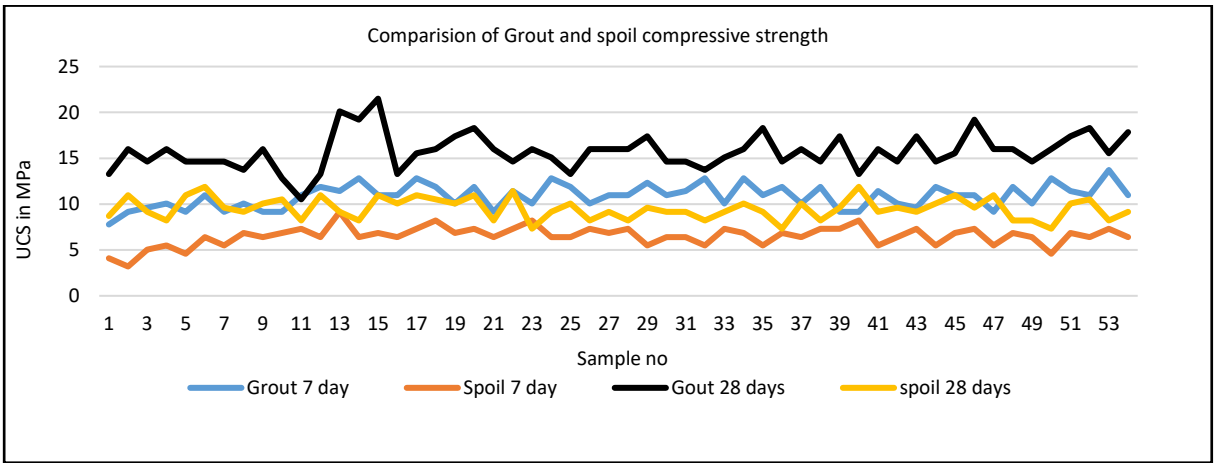

Figure 5. Comparison of UCS of Grout and Spoil Samples.

5.2 DENSITY OF GROUT AND SPOIL

The density of grout and spoil was monitored continuously. A part of data analysis shown in figure 6 shows that the density of spoil always exceeded the density of grout. At some points of time the spoil density dropped down to the level of grout density; which indicated that no grout intake was taken by underground medium in that reach. Analysis of more than 400 test data reveals that spoil density is about 4 to 19% higher than that of cement grout.

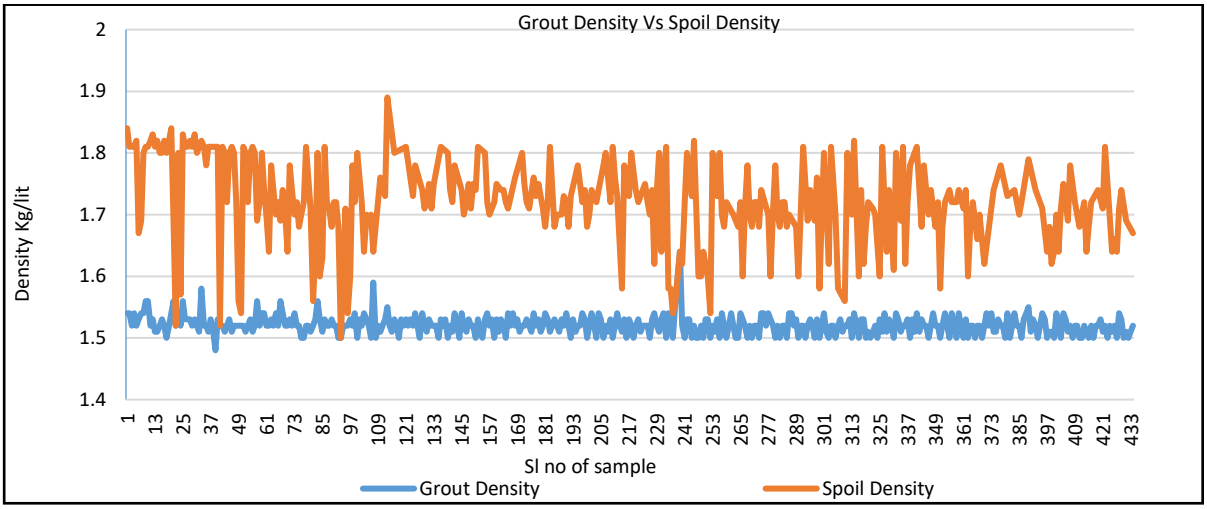

Figure 6. Variation of Grout Density and Spoil Density.

6. CONCLUSIONS

In the current case there was no direct way to establish the extent of ground improvement and seepage barrier provided by jet grouting.Efficacy of jet grouting was proven as it kept the work front practically seepage free even under the varying water depth of 3 to 12 m along the one side of dyke and river discharge of 100 to 1200 cumec in non-monsoon season.

This experience shall reinforce the confidence of practicing engineers and academician in adopting jet grouting technology in highly variable and porous materials like RBM.

It can be safely concluded that the jet grouting techniques can be deployed as effective and reliable seepage control measure and sufficient strength (up to 8 to 10 MPa) of jet grout column can also be achieved even in the variable alluvial deposited material like RBM. The grout density and viscosity were observed to be lower than spoil density and viscosity respectively.

Scope of further research includes permeability tests on the cylindrical specimen of jet grout column. Further, direct shear and triaxial tests are planned on the jet grouting column cores to have an insight of its geotechnical properties. Authors are working on detailed Analysis and comparison of similar works carried out in India and abroad.

REFERENCES

Pierre Guy AtanganaNjock, Jun Chen, Giuseppe Modoni, ArulArulrajah, Yong-Hyun Kim, "A review of jet grouting practice and development" *Arabian Journal of Geosciences (2018)*.

Esteban Díaz, Edgar Leonardo Salamanca-Medina, Roberto Tomás, "Assessment of compressive strength of jet grouting by machine learning" *Journal of Rock Mechanics and Geotechnical Engineering (2023)*.

E Guler and G GumusSecilen, "Jet grouting technique and strength properties of jet grout columns"Journal of Physics: *Conference Series. 1928 Deep Foundations and geotechnical problems of territories (DFGC 2021)*.

Proceedings of the XVIII ECSMGE 2024
GEOTECHNICAL ENGINEERING CHALLENGES
TO MEET CURRENT AND EMERGING NEEDS OF SOCIETY
© 2024 the Authors
ISBN 978-1-032-54816-6
DOI 10.1201/9781003431749-589
Open Access: www.taylorfrancis.com, CC BY-NC-ND 4.0 license

ECSMGE 24
XVIII EUROPEAN CONFERENCE ON SOIL MECHANICS AND GEOTECHNICAL ENGINEERING

Accelerated implicit cyclic loading with the hypoplastic sand

Chargement cyclique implicite accéléré avec le sable hypoplastique

T. Kadlíček*, D. Mašín
Faculty of Science, Charles University, Czech Republic
**tomas.kadlicek@natur.cuni.cz*

ABSTRACT: Numerical simulations of the cyclic loading can be distinguished of two types, implicit and explicit. While the implicit cyclic loading approach integrates each individual cycle in its full length separately, the explicit cyclic loading simulation is concerned only with average values of the loading cycles. Consequently, performing a robust implicit cyclic loading simulation spanning over tens or hundreds of cycles is very time consuming and therefore, the explicit cyclic loading provides a suitable alternative. Nonetheless, the explicit cyclic loading provides only accumulation of strains and related state variables. This paper introduces a new approach to the implicit cyclic loading designated as accelerated which can significantly reduce computational time. The proposed approach is applied on a simple axisymmetric numerical model first. Later a simple model of monopile subjected to the cyclic loading is performed with the fully implicit and accelerated approach and compared.

RÉSUMÉ: Les simulations numériques du chargement cyclique peuvent être distinguées en deux types, implicites et explicites. Alors que l'approche implicite du chargement cyclique intègre séparément chaque cycle individuel sur toute sa longueur, la simulation explicite du chargement cyclique ne s'intéresse qu'aux valeurs moyennes des cycles de chargement. Par conséquent, la réalisation d'une simulation de chargement cyclique implicite robuste couvrant des dizaines ou des centaines de cycles prend beaucoup de temps et le chargement cyclique explicite constitue donc une alternative appropriée. Néanmoins, le chargement cyclique explicite ne fournit qu'une accumulation de déformations et de variables d'état connexes. Cet article présente une nouvelle approche du chargement cyclique implicite désigné comme accéléré, qui peut réduire de manière significative le temps de calcul. L'approche proposée est d'abord appliquée à un modèle numérique axisymétrique simple. Ensuite, un modèle simple de monopieu soumis à une charge cyclique est réalisé avec l'approche entièrement implicite et accélérée et comparé.

Keywords: Cyclic loading; implicit; accelerated; hypoplastic sand; monopile.

1 INTRODUCTION

Numerical and experimental investigation of a cyclic loading received a significant attention due a rapid development of wind turbines installations. This process was started due to a transformation to the green energy to which the wind energy is a significant part of.

The common approach to the simulation of the cyclic loading, designated as implicit, is based on integrating each cycle in its full length. While this approach is appropriate in the case of low number o cycles, typically 1-1000 cycles, it loses its relevance once we approach tens of thousands of cycles due to its significant computational time. Furthermore, undesired consequence of the implicit approach is accumulation of the integration error when subjected to large number of cycles which can impact the results.

Alternative approach, called explicit (Niemunis, 2005), focuses on integration of average values of the cyclic loading and thus significantly decrease computational time. However, the constitutive models used for the explicit cyclic loading provides only accumulation of the strains and state variables and thus can be viewed as a type of creep-like constitutive model, where integration is performed with respect to number of cycles instead of time. Therefore, any change of stress state is related to the soil/structure interaction. This fact can hinder a proper analysis at the failure state.

In this paper we introduce a new approach to the cyclic loading simulation designated as accelerated implicit. This approach tries to remedy problems associated with both implicit and explicit modelling approaches, namely: decreasing computational time of implicit cyclic loading, and enabling stress accumulation during the cyclic loading while guaranteeing that the failure condition is satisfied. On the other hand, any shortcoming of cyclic modelling at the constitutive model level will be inherent to the accelerated implicit approach as well.

2 ACCELETERATED CYCLIC LOADING

The main idea of the accelerated cyclic loading originates in the extrapolation of the accumulated properties such as stresses, strains and other state variables. The extrapolation is performed on the local level in the integration points as well as on the global level on the finite element (FE) mesh.

The accelerated cyclic loading is performed in three steps:

1. First, the implicit cyclic loading is performed.
2. At the designated cycles, the accumulated stresses $\Delta\boldsymbol{\sigma}_{acc}$, strains $\Delta\boldsymbol{\varepsilon}_{acc}$ and other state variables are recorded in the integration points (local level) and also the displacements of the FE mesh $\Delta\mathbf{u}_{acc}$ in the nodes (global level). The accumulation can be recorded for one or multiple cycles for more precise extrapolation.
3. The displacements are extrapolated in the FE nodes for the desired number of cycles. These displacements are converted to strains in the integration points. During the acceleration, different than the constitutive model stiffness tensor $\boldsymbol{\mathcal{M}}$ has to be used since the response of the constitutive model would not match the desired extrapolation. Therefore, the acceleration stiffness tensor $\boldsymbol{\mathcal{M}}_{acc}$ must be expressed from the extrapolated strains and stresses. In general, the constitutive equation can be expressed as follows:

$$\Delta\boldsymbol{\sigma}_{acc} = \boldsymbol{\mathcal{M}}_{acc} : \Delta\boldsymbol{\varepsilon}_{acc}, \qquad (1)$$

in this case, however, the unknown is the acceleration stiffness tensor $\boldsymbol{\mathcal{M}}_{acc}$ and therefore, the $\boldsymbol{\mathcal{M}}_{acc}$ has to be derived as

$$\boldsymbol{\mathcal{M}}_{acc} = \Delta\boldsymbol{\sigma}_{acc} \otimes \Delta\boldsymbol{\varepsilon}_{acc} / (\Delta\boldsymbol{\varepsilon}_{acc} : \Delta\boldsymbol{\varepsilon}_{acc}). \qquad (2)$$

The tensor $\boldsymbol{\mathcal{M}}_{acc}$ is strain-rate direction dependent, that is, it can be applied only for the loading direction from which it was derived.

In the present study, only a linear extrapolation is used based on one implicit cycle, however, a nonlinear extrapolation can be applied too when fit through multiple recorded cycles.

Tremendous benefit of the accelerated approach is that the entire acceleration can be performed in one step without any iteration needed since all the FE nodes are loaded with prescribed displacements. It should be also noted that the numerical simulation of the cyclic loading can be performed while combining implicit, accelerated and explicit approaches in sucession.

3 CONSTITUTIVE MODELS

In this paper, two constitutive models are used. The hypoplastic sand model (Von Wolffersdorff, 1996) defines the behaviour of the soil and linear elastic model is applied to the structure of a monopile.

3.1 Hypoplastic sand model

The hypoplastic sand is a nonlinear constitutive model defined in the form of rate equation and defines these 8 parameters:

h_s – Granular hardness
n – Exponent of normal compression line
e_{i0} – Initial void ratio of the isotropic state
e_{c0} – Initial void ratio of the critical state
e_{d0} – Initial void ratio of the densest state
α – Peak state controlling exponent
β – Stiffness controlling exponent
φ_c – Critical state friction angle

The small strain enhancement (Niemunis, 1997) defines additional state variable δ designated as intergranular strain and 5 parameters:

R – Elastic strain range
m_T – Stiffness factor for 90° strain path change
m_R – Stiffness factor for 180° strain path reversal
χ – Controls stiffness degradation
β_r – Controls nonlinearity of small strain evolution

The simulations undertaken in this paper were conducted with the parameters presented in Table 1 and Table 2. Unit weight of the soil was defined as $\gamma = 20\ \mathrm{kN/m^3}$.

Table 1. Hypoplastic sand parameters.

h_s [kPa]	n [-]	e_{i0} [-]	e_{c0} [-]	e_{d0} [-]	α [-]	β [-]	φ_c [°]
3×10^6	0.2	1.2	1.0	0.6	0.3	3.0	30

Table 2. Small strains enhancement.

R[-]	m_T[-]	m_R[-]	χ[-]	β_r[-]
1×10^{-5}	2.5	5.0	5.0	1.0

3.2 Elastic model

The monopile is assigned a linear elastic constitutive model which defines two parameters, namely: Young's modulus E and Poisson's ratio ν. The parameters values are gathered in Table 3.

Table 3. Linear elastic model.

E [kPa]	ν [-]
3.10^7	0.25

4 VALIDATION

4.1 SIMPLE AXISYMMETRIC CASE

The proposed approach was first tested with the axisymmetric elements test subjected to various loading conditions in FE model discretised to 64 FE elements.

The example of drained triaxial with a strain driven loading is shown in Figure 1. Initially, the sample was isotropically consolidated to 100 kPA. The cyclic loading was performed with the vertical strain amplitude $\Delta\varepsilon_{ax}$ = 0.05%. As a benchmark, 100 implicit cycles were undertaken (red). The accelerated cyclic loading was performed with a combination of 10 implicit cycles and 10 (green) and 20 (black) accelerated cycles, respectively. The extrapolation was based on the accumulation of the last implicit cycle. While the differences in strains and void ratios between the implicit and accelerated loading are relatively small, the evolutions of the accelerated axial stresses σ_{ax} show initially significant deviations. Nonetheless, accelerated σ_{ax} asymptotically converge at 100th cycle due to a well approximated void ratios e.

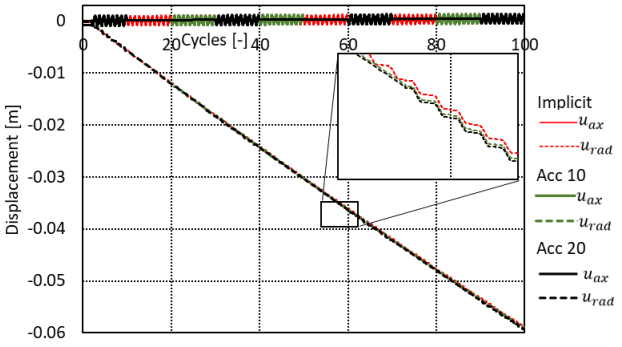

a) Axial and radial displacements

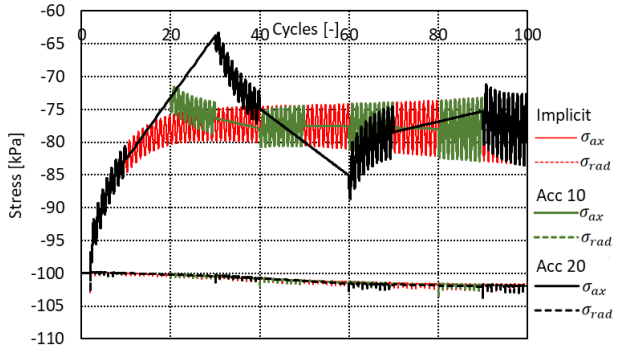

b) Axial and radial stresses

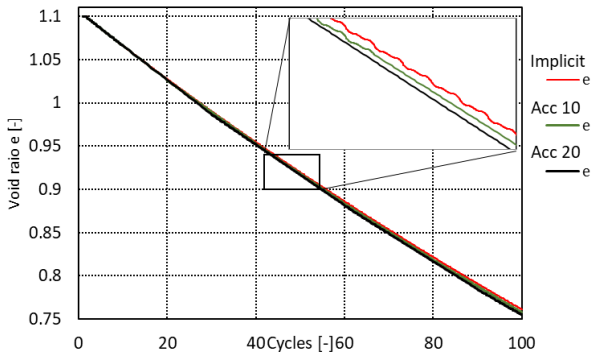

c) Void ratio e

Figure 1. Element testing of the accelerated approach.

4.2 MONOPILE SIMULATION

We chose to simulate a monopile under a cyclic loading corresponds well with a current focus on wind farms and renewable energy. It is important to note that there was no contact defined on the soil/structure boundary since all constitutive models used during the acceleration must be implemented as accelerated. To remedy a problem with local tension at the soil/pile boundary, additional hypoplastic parameter p_t = 50 kPa was used, which extends admissible states to tension.

The geometry of the monopile is depicted in Figure 2 with rather coarse mesh counting 4004 tetrahedral elements. The pile is loaded on the top in the direction of the x-axis with force amplitude.

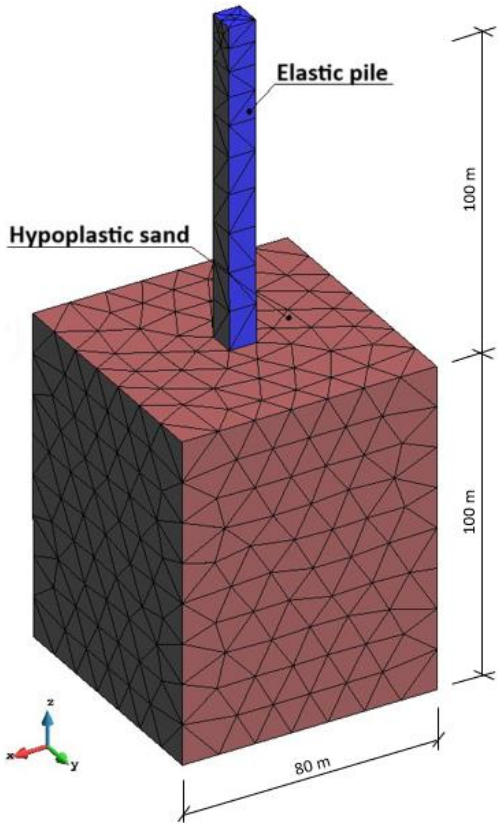

Figure 2. Geometry of the simple monopile model

As a benchmark, a fully implicit cyclic loadings were performed. Furthermore, different combinations of the implicit and accelerated cycles were simulated. In this study, a combination of 10 accelerated and 5 implicit loading cycles is presented with the cyclic amplitude 10 kN. At the beginning, 20 cycles were performed fully implicit in order to stabilize values of state variables. Comparison of the accelerated cyclic loading and the fully implicit cyclic loading is displayed in Figure 3.

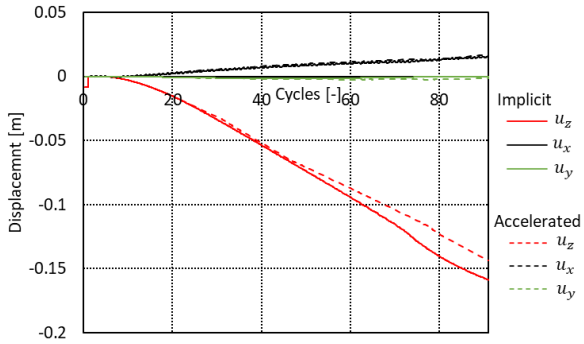

a) Horizontal and vertical displacements

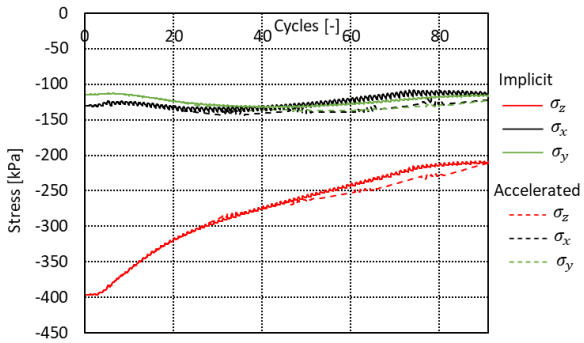

b) Horizontal and vertical stresses

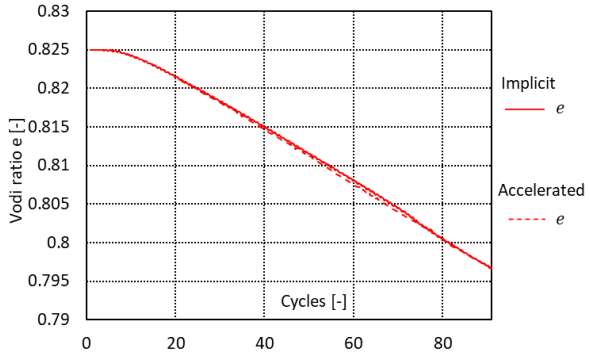

c) Void ratio e

Figure 3. Simple monopile model.

Simulating results are plotted for a point with coordinates P [55, 40, 80]. Similarly to the elements testing, the extrapolation is based on the accumulation over one cycle, which resulted in small deviations of the explicit loading from the implicit loading. The intergranular strain tensor δ is shown in Figure 4. For the sake of clarity only components δ_{11}, δ_{22} and δ_{33} are displayed. It was shown that after 15-20 initial cycles the intergranular strains values at the end of cycles stabilize and thus can be extrapolated with a constant value since the fully implicit and accelerated intergranular strains reach comparable values.

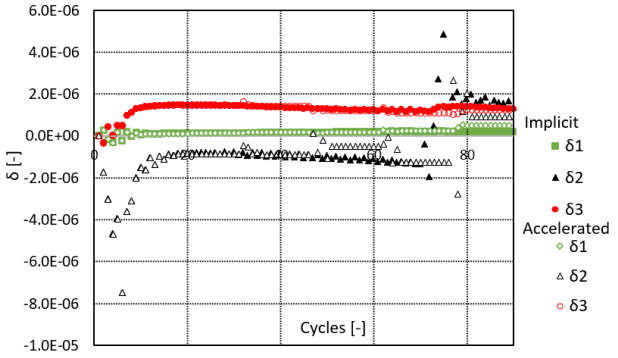

Figure 4. Small strains δ.

5 CONCLUSIONS

In this paper, a new approach to the simulation of cyclic loading was introduced which can significantly reduce computational time of the implicit cyclic loading. The approach is based in extrapolation of displacement, stresses, strains and state variables over prescribed number of cycles.

ACKNOWLEDGEMENT

This research was supported by the Johannes Amos Comenius Programme (P JAC), project No. CZ.02.01.01/00/22_008/0004605, Natural and anthropogenic georisks and Czech Science Foundation grant No. 21-35764J.

REFERENCES

Niemunis, A., & Herle, I. (1997). Hypoplastic model for cohesionless soils with elastic strain range. *Mechanics of Cohesive-frictional Materials: An International Journal on Experiments, Modelling and Computation of Materials and Structures*, 2(4), 279-299, https://doi.org/10.1002/(SICI)1099-1484(199710)2:4<279::AID-CFM29>3.0.CO;2-8.

Niemunis, A., Wichtmann, T., & Triantafyllidis, T. (2005). A high-cycle accumulation model for sand. *Computers and geotechnics*, 32(4),245-263, https://doi.org/10.1016/j.compgeo.2005.03.002.

Von Wolffersdorff, P. A. (1996). A hypoplastic relation for granular materials with a predefined limit state surface. *Mechanics of Cohesive-frictional Materials: An International Journal on Experiments, Modelling and Computation of Materials and Structures*, 1(3), 251-271, https://doi.org/10.1002/(SICI)1099-1484(199607)1:3<251::AID-CFM13>3.0.CO;2-3.

Proceedings of the XVIII ECSMGE 2024
GEOTECHNICAL ENGINEERING CHALLENGES
TO MEET CURRENT AND EMERGING NEEDS OF SOCIETY
© 2024 the Authors
ISBN 978-1-032-54816-6
DOI 10.1201/9781003431749-590
Open Access: www.taylorfrancis.com, CC BY-NC-ND 4.0 license

ECSMGE 24
XVIII EUROPEAN CONFERENCE ON SOIL MECHANICS AND GEOTECHNICAL ENGINEERING

Discrete element modelling of axial load testing on piles under the influence of ageing

Modélisation par éléments discrets d'essais de charge axiale sur pieux sous l'influence du vieillissement

S.S. Kasyap*, M.B. Mohammed, D. Igoe
Trinity College Dublin, Dublin, Ireland

**sarvades@tcd.ie*

ABSTRACT: Pile ageing has shown to increase the axial shaft capacity of piles by up to 250% within 9 months of installation. Incorporating ageing effects in the design of offshore wind turbine foundations could significantly reduce pile length, and therefore material and installation costs. However, this requires a deeper understanding of the underlying mechanisms through systematic investigations. Numerous researchers have investigated the influence of ageing on the axial capacity of piles using physical models at field and laboratory scales. The time and costs of undertaking parametric studies are much higher in physical testing, and have therefore been limited to date. Discrete Element Modelling (DEM) has shed light on micro-to-macro scale mechanisms of various complex geomechanical problems. This paper is a pilot study using DEM (Particle Flow Code software) for axial pile testing, where the ageing phenomenon is simulated using bonds at the soil-pile interface. Field-scale axial loading tests on aged piles performed in Blessington, Ireland, are used as a reference in this study. This study provides an innovative DEM approach to simulate the effects of pile ageing phenomenon and explore the axial load behaviour of piles.

RÉSUMÉ: Il a été démontré que le vieillissement des pieux augmente la capacité axiale des pieux jusqu'à 250 % dans les 9 mois suivant l'installation. L'intégration des effets du vieillissement dans la conception des fondations des éoliennes offshore pourrait réduire considérablement la longueur des pieux, et donc les coûts de matériaux et d'installation. Cependant, cela nécessite une compréhension plus approfondie des mécanismes sous-jacents grâce à des enquêtes systématiques. De nombreux chercheurs ont étudié l'influence du vieillissement sur la capacité axiale des pieux à l'aide de modèles physiques à l'échelle du terrain et du laboratoire. Le temps et les coûts nécessaires pour entreprendre des études paramétriques sont beaucoup plus élevés dans les tests physiques et ont donc été limités à ce jour. La modélisation par éléments discrets (DEM) a mis en lumière les mécanismes à l'échelle micro-macro de divers problèmes géomécaniques complexes. Cet article est une étude pilote utilisant le logiciel DEM (Particle Flow Code) pour les essais de pieux axiaux, où le phénomène de vieillissement est simulé à l'aide de liaisons à l'interface sol-pieu. Des essais de chargement axial à l'échelle du terrain sur des pieux vieillis effectués à Blessington, en Irlande, sont utilisés comme référence dans cette étude. Cette étude propose une approche DEM innovante pour simuler les effets du phénomène de vieillissement des pieux et explorer le comportement des pieux en charge axiale.

Keywords: Offshore foundations; pile ageing; DEM; micro-to-macro.

1 INTRODUCTION

Axially loaded steel tubes are used as foundations for various types of offshore structures. Anchor systems for floating structures and foundations for jacket structures use large-diameter axially loaded steel tubes where the shaft resistance plays as critical role in their stability. The shaft resistance of these steel piles installed in sand increases with time following their installation due to the phenomenon known as pile ageing. The knowledge of the ageing phenomenon and its associated effects is still incoherent owing to the variability in the results obtained by various researchers (Zhang and Wang, 2014) and the understanding of the mechanism leading to the ageing phenomenon itself.

Chow (1997) suggested three different mechanisms for pile ageing: (i) Physio-chemical reaction at the pile-soil interface, (ii) Creep-induced stress redistribution, and (iii) Confined dilation of sand in the shear zone. Addressing these mechanisms, a significant amount of research has been carried out to investigate the effects of ageing in piles on their axial capacity, predominantly using field- and laboratory-scale model tests. Gavin and Igoe (2021), Lim and Lehane (2014), and Jardine et al. (2006) are a few

noteworthy works discussing the steel pile axial capacity aged in sand.

Discrete element modelling (DEM) is gaining popularity, particularly among offshore geotechnics research groups. Simulation of pile driving in finite element modelling leads to mesh distortion near the pile due to large deformation (Yang et al., 2020). A Coupled Eulerian-Lagrangian (CEL) method was developed (over the classically used Lagrangian methods) to address this issue (Qiu et al. 2011) but inaccuracies due to state variable mapping upon re-meshing were observed (Phuong et al., 2016). DEM on the other hand simulates each rigid grain's movement under the influence of surrounding forces and provides numerical stability and accuracy to the model even at large deformations. Cerfontaine et al. (2023) and Duan et al. (2018) investigated the effects of different installation methods of piles using DEM simulations. Li et al. (2021), Liu et al. (2019), and Zhang and Wang (2015) used DEM to examine plugging effect and other micromechanical aspects of the open-ended steel pile foundations.

This paper attempts to provide a background and an innovative methodology to simulate aspects of pile ageing in open-ended piles while examining the capabilities of DEM for modelling pile installation.

2 MODELLING PROCEDURE

A commercial 3D DEM software, Particle Flow Code 3D, was used in this study. The numerical model was created based on the field-scale pile testing series performed by Gavin and Igoe (2021) in Blessington, Ireland. The *Hertz contact model* (HCM) was used for defining the behaviour of grain-grain and grain-wall contacts. Also, the *Linear parallel bond model* (LPBM) was used for pile wall-grain contacts within the bonded zone (discussed in Section 4). Unlike HCM, LPBM gives a provision to define the bond strength between the contacting elements.

2.1 Calibration of DEM Microparameters

The sand from the Blessington pile testing site was simulated here. DEM triaxial test simulations were performed, and the microparameters were calibrated (trial-and-error) to match the simulation results with laboratory test results based on stress-strain responses. The calibrations were performed at two different relative densities (R_d of 30% and 60%), and this was achieved by changing the interparticle friction coefficient of the DEM sample during sample generation and consolidation. The comparison of stress-strain responses (60% R_d at 50kPa) is shown in Figure 1, and the calibrated microparameters are shown in Table 1.

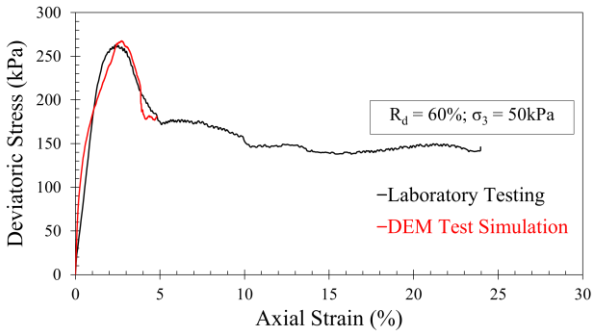

Figure 1. Comparison of stress-strain curves from DEM and physical triaxial testing.

Table 1. Microparameters of DEM model without ageing.

Parameter	Value	Units
Grain Size		
D_{50}	0.36	mm
Minimum Diameter	0.126	mm
Maximum Diameter	0.800	mm
Hertz Contact Model		
G	2e9	Pa
Poisson Ratio	0.3	-
$\mu_{grain\text{-}grain}$	0.375	-
$\mu_{grain\text{-}wall}$	0.20	-
Linear Parallel Bond Model		
E_{mod}	5e7	Pa
Stiffness ratio	1.00	-
μ	Vary with ageing period simulation.	-
Tensile strength and Cohesion		Pa

2.2 Model Preparation

The DEM model was prepared at a 100g scale compared to the field-scale tests performed by Gavin and Igoe (2021). The open-ended pile was modelled as a rigid single-walled cylinder of diameter 3.4mm and length 75mm (340mm internal diameter and 7.5m long in field-testing scale). The procedure for model preparation described here is based on the DEM work by Sharif et al. (2020). The soil domain boundary is made as a rigid wall cylinder with a diameter of 70mm and 120mm in length. The model extent to pile diameter ratio is greater than 20, so no significant boundary effects can be expected. The soil bed was prepared with particle size distribution scaling, with the scale increasing from the centre of the domain to the boundaries. The soil bed is divided into four coaxial zones with central core zone PSD as two times the Blessington sand, and the consecutive zones had a ratio of 5, 7, and 10 (Figure 2). The maximum grain diameter of the smaller fraction is kept lower than the average grain diameter of the immediate larger

fraction to ensure no overlap of zones occurs in the model. The central core zone has a diameter of pile to D_{50} ratio of more than 5, assuring that a significant number of contacts are formed around the pile, and the model instabilities are minimized. The grains are consolidated under gravity (100g), and the model is brought to equilibrium until the unbalanced force ratio becomes minimum (<1e-5).

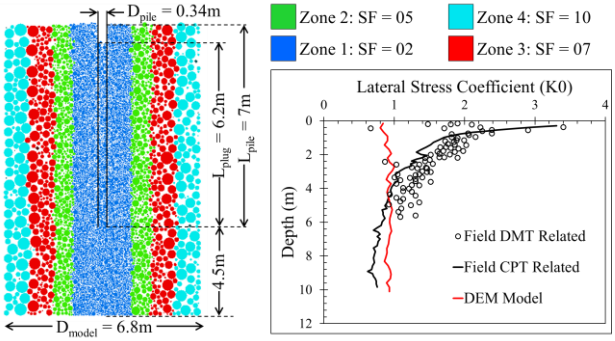

Figure 2. Cross-section of DEM model; Comparison of lateral stress coefficient values between DEM and field tests.

The variation of lateral stress coefficient, K_0, with dept, is shown in Figure 2. The K_0 trends observed from the field testing (Dilatometer Test, DMT; Cone Penetration Test, CPT) are also plotted in Figure 2 for comparison. Except for the initial 2m depth, where significantly large K_0 values were observed in-situ, the DEM model and field profiles are in a similar range. The top 2m of Blessington geotechnical testing site is considered over-consolidated in its geological history (Doherty et al., 2012).

3 PILE DRIVING AND TENSION TESTS

The field tests aimed to replicate in this numerical study used impact driving of piles. However, a simple constant velocity jacking was used here to make the pile driving simulations simple and quick. The authors acknowledge several numerical and experimental studies investigating the installation effects (Duan et al., 2018, Zarrabi and Eslami, 2016). A slow rate of jacking with 0.05m/sec was adopted in this study, with an approximate penetration of $4x10^{-5}$ mm/dt. This penetration rate resulted in a computational time of about 9.5 days (for an i9-13900K 24-core processor) for a penetration of 70mm in model scale.

The field tests showed that the piles were fully plugged over the first meter of installation and then partially plugged over the end of installation (with a final plug length of around 4.6m). In the present DEM simulations, the final plug length was higher than the field test values of around 6.2m (Figure 2). Better agreement might be possible if the similar installation mode as field tests (impact driving) was simulated in DEM, and it needs further investigation.

After installation, servo-controlled vertical translation in the upward direction was applied on the pile wall at a slow rate to stabilize the stresses generated due to pile driving. Axial tension test simulations were also performed in a displacement-controlled manner. Unlike the field tests, no holding time was exercised in these DEM simulations. As discussed in Section 2, LPBM was used to simulate bonding in the model. The HCM contacts between the pile and soil are modified to LPBM within the range of the targeted pile section, and then the model is stabilized.

3.1 No-ageing Condition

No-ageing tension test simulation was performed with no contact model changes. The force-displacement curve related to the no-ageing tension test simulation is shown in Figure 3. The peak force was observed at 440kN. The field tension test results for different ageing periods from Gavin and Igoe (2021) are also shown in Figure 3 for comparison. The DEM simulation of the no-ageing tension test is in the range of a two-day tension test from the field. The DEM simulation response is much stiffer than the field test response, owing to the rigid pile wall behaviour, unlike the steel pile's elastic behaviour in the field tests.

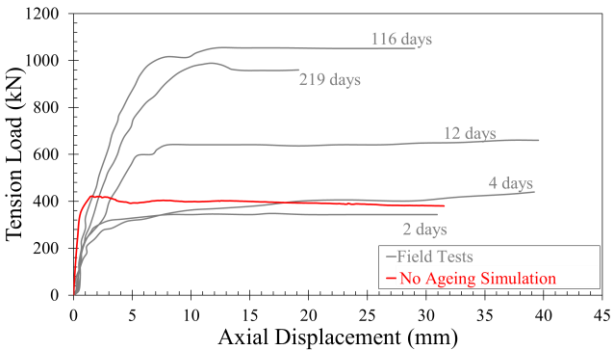

Figure 3. Comparison of DEM no ageing test DEM simulation with field tests by Gavin and Igoe (2021).

3.2 Simulation of pile ageing effects in DEM

The effects of ageing in piles were simulated in the present model by creating bonds at grain-wall contacts, i.e., soil-pile interface contacts. Hertz contact model was used initially for pile driving simulations and the no ageing tension test simulations. The contact model for a certain range of pile length was changed to the Linear Parallel Bond contact model, and tension test simulations were performed with different bond capacities. From field-scale aged pile testing by Gavin and Igoe (2021), the soil-pile interface bonding (crust

formation) was observed only in the bottom 2-3m of a 7m pile after exhuming them. Following this observation, bonding was created at the grain-wall interface for a finite part of the pile bottom (~3m) with certain bond strength (cohesion and tensile strength). In the present study, the effects of pile ageing phenomenon were simplified by applying a uniform bond strength for the pile-soil contacts in the bonded zone, which may not be the case in the actual pile ageing phenomenon. Given the lack of information on the actual bond strength characteristics of the pile-soil interface, a large range of bond strengths was simulated (50kPa to 10MPa), and the corresponding peak tension force values were examined (Figure 4). The lower bound value of 50kPa was based on the peak tension load from no ageing test simulations. The upper bound of 10MPa was based on the ultimate peak tension load capacity, where the bond capacities of 1MPa and 10MPa resulted in the same peak tension force.

Figure 4 shows the peak tension force for cohesion values in the bonded zone and for different interface friction values. Apart from the crust formation in the bottom section of the pile, the soil-pile interface friction also changes through the length of the pile over time. Starting from the calibrated interface friction coefficient of 0.1, minute increments were simulated, and the corresponding peak tension forces are plotted in Figure 4.

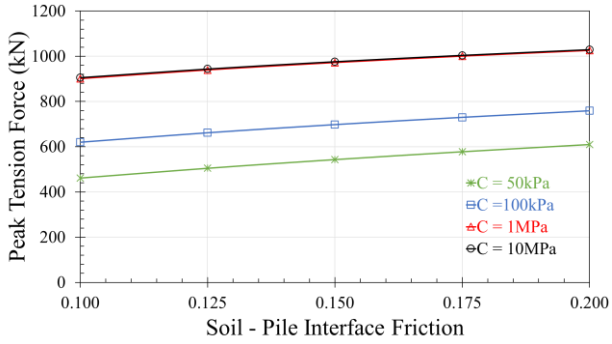

Figure 4. Variation of peak tension force for different cohesion and interface friction coefficient values of soil-pile contacts.

The authors acknowledge that the phenomenon of pile ageing is not just because of the changes in soil-pile interface properties (bonding and friction) but also changes in the stress regime around the pile due to creep effects. But as a pilot study, this simple way of generating a condition of the aged pile with increased tensile load capacity can bring new insights into the aged pile testing. Further developments would be needed to simulate the ageing conditions in DEM more accurately.

Despite certain limitations in the present DEM simulation of tension tests on aged piles, some interesting micromechanical observations were noted. One of the mechanisms leading to increased tension capacity of aged piles is the dilation of the surrounding soil. Two diametrical cross-sections of the DEM models with extreme cases of (i) no bonding and (ii) maximum bond strength are shown in Figure 5. These cross-sections show the displacements of grains in the model during the tension test (~15mm of axial displacement). The movement of grains outside the pile was minimal for the no ageing condition. On the other hand, strong bond conditions showed displacement zones with grains closer to the pile having larger displacement values, indicating enhanced dilation as the aged pile is pulled upwards. Further work is required in understanding the effects of particle and pile scaling on the dilation behaviour in DEM.

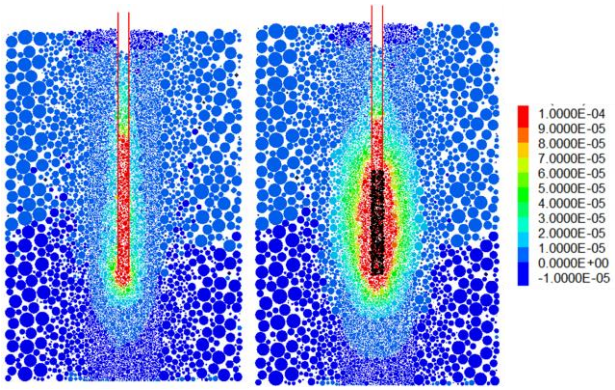

Figure 5. Cross-section of DEM model showing grain displacements during a tension test for no-ageing (left) and maximum bond strength (right) conditions.

4 CONCLUSIONS

Three-dimensional DEM simulations of pile driving and tension tests were performed in this study. Field tests on open-ended monopiles performed by Gavin and Igoe (2021) were used as basis here. For the first time, DEM was used to simulate the effects of pile ageing and the corresponding observations are reported in this paper.

- Particle size distribution scaling and 100g centrifuge scaling was employed to decrease computational costs involved with DEM.
- The K_0 variation with depth from DEM model and field tests correlations showed comparable values; except for highly over-consolidated top 2m of soil.
- Displacement-controlled jacking of pile was simulated unlike impact driving in field tests.

Hence, slightly higher plug length was observed in DEM compared to field tests.

- Tension tests were also performed in displacement-controlled manner, and no-ageing condition showed peak tension load in the vicinity of 2-day and 4-day aged pile tests in field.
- The effects of pile ageing was simulated by creating bonds at the grain-wall contacts (soil-pile contacts). Increasing bond strength and interface friction coefficient resulted in higher peak tension load.
- The range of peak loads observed from varying bond strength and friction values are within the limits of capacities observed at field tests for 2 to 219 days aged piles.
- The aspect of dilation in the bonded zone of pile-soil interface was also observed in the DEM simulations.
- Accurate calibration of interface properties of aged piles/ aged soil-pile interfaces would provide further confidence in the DEM simulation results, and prediction of the pile ageing effects in arbitrary situations. Performing various load combinations of static and cyclic loading would then be feasible, offering scope for extension of this study.

ACKNOWLEDGEMENTS

The authors would like to acknowledge the financial support from Science Foundation Ireland (Ref: 21/EPSRC/3787). The project presented in this article is supported by EPSRC-SFI Joint Research Grants Programme (EPSRC – Ref: EP/W006235/1). The authors also acknowledge Dr. Huan He (Southeast University, China) for providing PFC software access.

REFERENCES

Cerfontaine, B., Ciantia, M.O., Brown, M.J., White, D.J., Sharif, Y.U. (2023) DEM study of particle scale effect on plain and rotary jacked pile behaviour in granular materials, *Computers and Geotechnics,* 161, 105559, https://doi.org/10.1016/j.compgeo.2023.105559.

Chow, F. (1997) *Investigation into behaviour of displacement piles for offshore structures,* Ph.D., University of London, Imperial College , London, UK, Available at https://spiral.imperial.ac.uk/handle/10044/1/7894, accessed: 14/09/2023.

Duan, N., Cheng, Y.P., Liu, J.W. (2018) DEM analysis of pile installation effect: comparing a bored and a driven pile, *Granular Matter,* 20, 36, https://doi.org/10.1007/s10035-018-0805-2.

Gavin, K., Igoe, D. (2021) A field investigation into the mechanisms of pile ageing in sand. *Géotechnique*, 71(2), pp. 120-131, https://doi.org/ 10.1680/jgeot.18.P.235.

Jardine, R., Standing, J., Chow, F. (2006) Some observations of effects of time on the capacity of piles driven in sand. *Géotechnique,* 55(4), pp. 227-244, https://doi.org/10.1680/geot.2006.56.4.227.

Li, L., Wu, W., Liu, H., Lehane, B. (2021) DEM analysis of the plugging effect of open-ended pile during the installation process, *Ocean Engineering,* 220, 108375, https://doi.org/10.1016/j.oceaneng.2020.108375.

Lim, J.K., Lehane, B.M. (2014) Characterisation of the effects of time on the shaft friction of displacement piles on sand. *Géotechnique*, 64(6), pp. 476-485, https://doi.org/10.1680/geot.13.P.220.

Liu, J., Duan, N., Cui, L., Zhu,N. (2019) DEM investigation of installation responses of jacked open-ended piles. *Acta Geotechnica,* 14, 1805-1819, https://doi.org/10.1007/s11440-019-00817-7.

Phuong, N.T.V., van Tol, A.F., Elkadi, A.S.K., Rohe, A. (2016) Numerical investigation of pile installation effects in sand using material point method. *Computers and Geotechnics,* 73, 58-71.

Qiu, G., Henke, S., Grabe, J. (2011) Application of a Coupled Eulerian–Lagrangian approach on geomechanical problems involving large deformations. *Computers and Geotechnics,* 38(1), 30-39.

Sharif, Yang, Z.X., Gao, Y.Y., Jardine, R.J., Guo, W.B., Wang, D. (2020) Large deformation finite-element simulation of displacement-pile installation experiments in sand. *Journal of \Geotechnical and Geoenvironmental Engineering*, 146(6), 04020044, https://doi.org/10.1061/(ASCE)GT.1943-5606.0002271.

Zarrabi, M., Eslami, A. (2016) Behavior of piles under different installation effects by physical modelling. *International Journal of Geomechancis (ASCE),* 16(5), 04016014.

Zhang, Z., Wang, Y.H. (2014) Examining setup mechanisms of driven piles in sand using laboratory model pile tests. *Journal of Geotechnical and Geoenvironmental Engineering*, 141(3), 04014114, https://doi.org/10.1061/(ASCE)GT.1943-5606.0001252.

Zhang, Z., Wang, Y.H. (2014) Three-dimensional DEM simulations of monotonic jacking in sand. *Granular Matter,* 17, pp. 359-376, https://doi.org/10.1007/s10035-015-0562-4.

Proceedings of the XVIII ECSMGE 2024
GEOTECHNICAL ENGINEERING CHALLENGES
TO MEET CURRENT AND EMERGING NEEDS OF SOCIETY
© 2024 the Authors
ISBN 978-1-032-54816-6
DOI 10.1201/9781003431749-591
Open Access: www.taylorfrancis.com, CC BY-NC-ND 4.0 license

ECSMGE 24
XVIII EUROPEAN CONFERENCE ON SOIL MECHANICS AND GEOTECHNICAL ENGINEERING

The effect of polypropylene fibre content on the mechanical properties of mass-stabilised soils

L'effet de la teneur en fibres de polypropilène sur les propriétés mécaniques des sols stabilisés en masse

L.C. Kelly, S.B. Mickovski*, A. Gonzalez-Ollauri
Glasgow Caledonian University, Glasgow, Scotland, UK

**Slobodan.Mickovski@gcu.ac.uk*

ABSTRACT: Mass mixing or deep soil mixing involves cement being used as a binder within a weak or soft soil, with scope to turning it into a stable foundation. In this study, we investigate the effect polypropilene fibres have when introduced within a mass stabilised soil in order to improve the soil strength and potentially be used in production of pipework, bricks, insulation, window frames, or as a substitute to bitumen acting as a binder. In order to investigate this, polypropylene fibres were added to a soil mix originating from a site in the Scottish Central Belt. The fibres were added at different contents (0%, 0.5% and 2%) and lengths (3mm and 12mm), they were then put through a series of laboratory tests (direct shear, unconfined compressive strength and oedometer consolidation) at an accredited soil testing laboratory. The data obtained from the tests show that there is a significant strength gain if polypropilene fibres are added in large quantity. However, these strength levels are achievable at relatively high strains. The results also show that the volume compressibility of the soil reinforced with plastics increases with the polypropilene fibre content, although this may depend on the length of the fibres mixed in the soil. In conclusion, the polypropilene fibres do showcase a much more ductile failure compared to the soil only, which could possibly be used and have some limited benefits. Further testing of different plastic additions and soil mixes should be carried out to explore other effects.

RÉSUMÉ: Le stabilisation de masse ou le mélange de sol en profondeur implique l'utilisation de ciment comme liant dans un sol faible ou mou, avec la possibilité de le transformer en une fondation stable. Dans cette étude, nous étudions l'effet des fibres lorsqu'ils sont introduits dans un sol stabilisé en masse afin d'améliorer la résistance du sol et potentiellement être utilisés dans la production de tuyauterie, de briques, d'isolation, de châssis de fenêtre, ou comme substitut au bitume agissant comme liant. Afin d'étudier cela, des fibres de polypropylène ont été ajoutées à un mélange de sol provenant d'un site de la ceinture centrale écossaise. Les fibres ont été ajoutées à différentes teneurs (0%, 0,5% et 2%) et longueurs (3mm et 12mm), elles ont ensuite été soumises à une série d'essais en laboratoire (cisaillement direct, résistance à la compression libre et consolidation oedométrique) dans un sol accrédité laboratoire d'essais. Les données obtenues à partir des tests montrent qu'il y a un gain de résistance significatif si les fibres sont ajoutés en grande quantité. Cependant, ces niveaux de résistance sont réalisables à des contraintes relativement élevées. Les résultats montrent également que le taux de tassement du sol renforcé avec des fibres augmente avec la teneur en fibres, bien que cela puisse dépendre de la longueur des fibres mélangées dans le sol. En conclusion, les fibres plastiques présentent une défaillance beaucoup plus ductile par rapport au sol uniquement, ce qui pourrait éventuellement être utilisé et présenter des avantages limités. Des tests supplémentaires de différents ajouts de fibres plastiques et de mélanges de sol devraient être effectués pour explorer d'autres effets.

Keywords: Recycling; plastics; organic soils; strength; permeability.

1 INTRODUCTION

Improving the ground stability conditions is an ongoing challenge in the construction industry worldwide. Action to improve ground stability is particularly needed in soft soils, such as peat, very soft to soft clays, or loose sands and gravels, which have very low strength and high capacity for deformation under loads which result in short and long-term settlements. These soils can be reinforced and thus made acceptable for construction through the use of in situ mass mixing method which can be costly (Topolnicki, 2004) and is limited to relatively shallow depths. The creation of soil composites through adding reinforcing, structural elements into the soil, is a well-known technique to promote ground stability and has recently been proven effective in the case of nature-based solutions (e.g. Gonzalez-Ollauri and Mickovski, 2016). However, the development of plant roots in the soil profile tends to have limitations (e.g. Tardio et al., 2016), and it is not immediate. An alternative, cost-effective soil reinforcement approach is the insertion

of biodegradable plastic fibres into the soil. Previous research has shown that different shapes and types of plastics have varying effects on the mechanical properties of the soil-plastic mix (Russell et al., 2017).

The aim of this study is to investigate the effect of adding plastics during the process of mass soil mixing on the mechanical strength properties of the treated soil. To this end, the shear strength, the unconfined compressive strength, and the consolidation capacity of soil undergoing mass mixing were investigated through standard laboratory tests. The results will allow a critical assessment of the benefits and disadvantages of adding plastics into mass soil mix processes seeking to improve ground stability in construction projects.

2 MATERIALS AND METHODS

2.1 Soil samples

The soil samples were taken from a site of proposed residential development in the Scottish Central Belt, where large bulk earthworks and ground improvement were required in order to enable construction of new roads and houses. As part of the proposed construction design, deep soil mixing was envisaged down to 4 metres below ground level (b.g.l) as foundation for the earthworks and roads, as well as for improving the bearing capacity of the soil where the residential properties were to be built. During the ground investigation works, large areas of organic clays (i.e., soil organic content, SOC > 5 %), mineral clays (i.e., SOC < 5 %), and peat were found within several areas of the proposed development and, as a result, these areas were to be treated by deep soil mixing. During the ground investigation, large bulk samples of organic clays, peat, and mineral clays from the topmost 4 m of the ground were taken in order to assess their potential for mass mixing. The samples retrieved during these investigations were used for soil laboratory testing in this study.

The bulk samples of organic clay were mixed in the laboratory using a mechanical mixer in order to create a homogenous soil sample which was then sieved through a 2 mm sieve (99% mass passed). The same process was followed for the mineral clay and peat bulk samples (97.5% mass passed). Some key mechanical properties of each soil are shown in Table 1.

Once homogenised, the three separate soil samples (i.e., organic clay, mineral clay, peat) were then subsampled for further testing. The masses of these subsamples were as follows: 5 kg organic clay, 5 kg inorganic clay, and 3.4 kg peat.

Table 1. Properties of the materials sampled from the development site.

Material	Moisture content (%)	Liquid limit (%)	Plastic limit (%)	Plasticity index (%)	Soil organic content (%)
Organic clay	35	43	22	21	5.7
	39	51	26	25	4.5
	39	48	25	23	6.8
Mineral clay	38	46	25	21	3.3
Peat	180	204	86	118	17.3

2.2 Soil mass mixing and testing

Cement binder (15% of the bulk unit weight of the soil) was added to the soil after this initial mixing/homogenisation in an attempt to replicate the process to be followed during soil improvement on site. The soils used in the mixes comprised 5 kg organic clay, 5 kg inorganic clay, 3.4 kg peat, and 5 kg sand. The latter, by bulk unit weight, replicated the worst case scenario identified on site. In total, four testing mixes were created using a combination of manual and mechanical mixing with 30 minute duration in the laboratory.

First, the cement was mixed with water (1:1.5 ratio) before incorporating them into the test mixes using a mechanical mixer. In three out of the four testing samples, plastic fibres were added after the cement-water mix and mixed until distributed throughout the sample. The three samples containing plastic comprised:

- 12mm polypropylene fibres at 0.5% of bulk unit weight of the soil sample.
- 3mm polypropylene fibres at 0.5% of bulk unit weight of the soil sample.
- 12mm polypropylene fibres at 2% bulk unit weight of the soil sample

When the samples were homogenous, they were transferred into cylindrical, cubical or ring-shaped moulds (i.e., one mould type for each mechanical test; see below) while trying to avoid/remove any air voids. The moulds were then sealed to prevent evaporation and water loss. The samples were left to cure in the laboratory at a temperature comprised between 15-18°C which, although lower than the ideal for the curing of cement, was considered acceptable as all of the samples were cured at the same temperature.

The description and classification of the soil mixes was carried out in accordance with current British Standards. The mechanical properties were investigated on the four mixes (3 mixes with plastic added and one without polypropilene fibres - i.e., control) and comprised: unconfined compressive strength (UCS) at 7 days (4 samples), 14 days (4

samples), and 28 days (8 samples), direct shear (4 samples), and consolidation (4 samples) tests in accordance with BS 1377 parts 6 and 7. The UCS tests were carried out on the samples cured in the cylindrical moulds of 200mm in height and 100mm in diameter at a displacement rate of 1mm/min. Moisture content samples were taken from every tested sample after completing each test. Direct shear tests at normal stresses of 50, 100, and 200 kPa, were carried out on 100mm x 100 mm x 20mm samples after 28 days of curing. The shearing rate was 1.5mm/min and moisture content samples were taken from every tested sample after completing each test. Consolidation tests were carried out using an oedometer at 6 loading steps on each soil mix at 28 days of curing. A small pressure was applied to the sample before starting the test. The tests were run at increasing normal pressure sequences of 12 kPa, 25 kPa, 50 kPa, 100 kPa, 200 kPa, and 400 kPa. The vertical displacement was measured during each loading stage until the primary consolidation was complete, then, the next loading step was applied. After the primary consolidation was completed at 400kPa, the unloading stage to 25kPa was initiated and the water was drained from the sample cell. After disassembling the apparatus, the final height and mass of the sample were measured before placing the sample in the oven at 105°C overnight in order to measure the final moisture content.

3 RESULTS

The liquid limit of the soil only mix was found to be 57% and the plastic limit was calculated at 35%, with a plasticity index of 22%, classifying the soil mix as a silt of high plasticity. The particle size distribution analysis showed that the sand added into the soil mix can be described as poorly graded, slightly silty sand.

The results of the UCS tests are shown in Table 2. The peak compressive strength of the 2% plastic mix sample showed a greater strength than the others, in particular the 14 day test. The 28 day tests for the 2% plastic mix were not run until failure at a peak load due to the excessive strain required to reach the peak; they were stopped at axial strains of 36% and 28%.

Table 2. Peak compressive strength (kPa).

Mix	7 days	14 days	21 days	28 days
Control	83.65	-	105.74	115.65
0.5%, 12mm	72.20	-	123.97	101.95
0.5%, 3mm	92.77	-	141.84	124.91
2%, 12mm	513.00	4924.00	-	514.57

The significant axial strain (74%) of a 2% plastic sample at peak compressive strength is shown in Table 3, the difference in peak compressive strength, with the exception of the 2% 12mm length plastic samples at 28 days of curing which were stopped before reaching their peak compressive strength.

Table 3. Peak compressive strength (kPa).

Mix	7 days	14 days	21 days	28 days
Control	2.42	-	2.76	3.37
0.5%, 12mm	4.10	-	11.61	3.58
0.5%, 3mm	4.79	-	6.13	4.71
2%, 12mm	34.41	74	-	32.63

In order to have a more relevant comparison, the compressive strength at serviceability limit was derived. Figure 1 shows that the 0.5% 3mm plastic mix generally has a higher compressive strength than the 'No plastics' sample. On the other hand, the 0.5% 12mm plastic specimen is shown to be weaker than the mix containing no fibres, this is both unexpected and unexplained. This may be down to a poor-quality mix or any deformities within the 0.5% 12mm length plastic samples. More tests would need to be carried out to explain this fully.

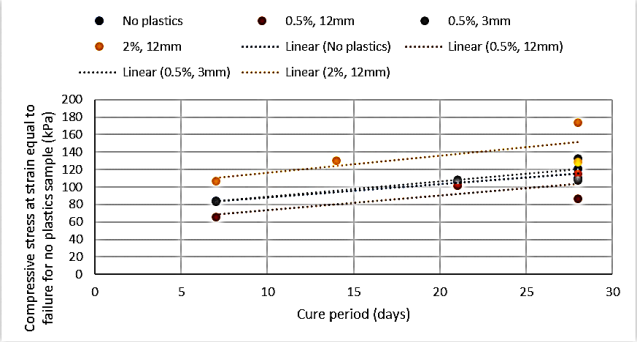

Figure 1. Compressive strength at serviceability limit.

Direct shear tests resulted in a failure of the 'No plastics' samples. Upon completion of the direct shear test on 'No plastics' samples, it was observed that it would have been beneficial to run the tests to a greater horizontal displacement. However, this was not possible due to the limitations of the standard direct shear testing apparatus. The results obtained for the 'No plastics' mix showed that the peak shear stress was either reached or was very close to be reached when the data acquisition had to stop. When carrying out the tests on the plastic mix samples, the true peak strength was not reached. This was due to the horizontal travel limit of the shear box being 15mm and, in turn, the sample was unable to be sheared beyond this limit and the peak shear strength was taken as the shear stress observed at the displacement limit. The peak stress results obtained for all of the samples can be seen in Table 4. To capture the behaviour at low

and high stresses, only the 50kPa and 200kPa normal stress tests were carried out for the plastic mix samples. The plastic mixes were shown to have higher shear strength than the 'No plastics' samples; similarly to the results of the UCS tests, this occurring at large displacements. A serviceability check was therefore carried out for analysing the shear stress for each of the tests in order to view the shear stress of the plastic mixes at the same horizontal displacement or strain as when the non-plastic samples at the same normal pressure reached their peak strength.

Table 4. Shear strength parameters of the tested samples.

Mix / normal load	50 kPa	100 kPa	200 kPa	Cohesion (kPa)	Angle of friction (°)
Control	55.7	92	136.2	33.7	27.6
0.5%, 12mm	97.0	-	186.0	67.2	30.8
0.5%, 3mm	84.3	-	208.6	42.87	42.9
2%, 12mm	112.1	-	213.3	12.60	34.0

The results of this check are shown in Table 5, where it can be seen that the plastic mixes are at least as strong as the non-plastic mix at the strain level that caused failure for the 'No plastics' sample.

Table 5. Shear strength of the tested samples at serviceability limit.

Mix	Normal stress (kPa)	
	50	200
Control	55.7	136.2
3mm 0.5%	63.6	184.5
12mm 0.5%	59.8	187.3
12mm 2%	62.2	188.2

The coefficient of volume compressibility results are shown in Table 6.

Table 6. Coefficient of volume compressibility.

Pressure (kPa)	Coefficient of volume compressibility m_v, (m^2/kN)			
	Control	0.5%, 12mm	0.5%, 3mm	2%, 12mm
12	0.171	0.412	0.246	0.392
25	0.084	0.157	0.160	0.313
50	0.065	0.115	0.097	0.165
100	0.067	0.101	0.086	0.098
200	0.094	0.111	0.109	0.055
400	0.097	0.093	0.095	0.032

4 CONCLUSIONS

Although the 2% plastic mix strength was far superior in terms of compressive strength to the others, the axial strain required to reach the strength of the sample meant that there could possibly be no practical use for this strength due to the possible serviceability issues. The behaviour of this mix resembles the one of root-permeated soil (Gonzalez-Ollauri and Mickovski, 2016). When the compressive strength was compared within the serviceability limits, it was shown that more, and shorter plastic inclusions would contribute better to the compressive strength. The shear test results showed that the cohesion and friction angle of the plastic mixes are greater than these of the 'No plastics' samples. It was observed that the 2% fibre addition has the greatest effect on the strength parameters of the soil mix. It is believed that in order to get a clearer idea of which mix would be most suitable for use, the test would need to be repeated and run to completion to understand the true peak stress of the samples containing plastic. However, due to the limitations of the standard apparatus it may not be possible to successfully test plastic mixes in the shear box. All samples tested at 50 kPa normal load had a very similar shear stress at the serviceability limit; however, for 200 kPa normal load, the samples with polypropilene fibres exhibited significantly higher shear stresses. This resulted in a steeper gradient of the best fit line for the plastic mixes. When the samples are subject to higher stresses they are all have very similar m_v values; however, when low stresses are applied, it can be seen that the 'No plastic' samples exhibit significantly lower volume compressibility than those containing polypropylene fibres. However, carbon reductions in using fibre reinforced soil may outweigh the setbacks in terms of strength and compression of such soils so more research is needed in quantifying the properties and application for soils stabilised with plastic fibres.

REFERENCES

González-Ollauri, A. and Mickovski, S.B. (2016). Using the root spread information of pioneer plants to quantify their mitigation potential against shallow landslides and erosion intemperate humid climates. *Ecological Engineering* 95: 302-315.

Russell, A.R., Chapman, M., Teh, S.H. and Wiedmann, T. (2017). Cost and embodied carbon reductions in cutter soil mix walls through fibre reinforcement. Geosynthetics International.pp.1-13.

Tardio, G., González-Ollauri, A. and Mickovski S.B. (2016). A non-invasive preferential root distribution analysis methodology from a slope stability approach. *Ecological Engineering* 97: 46-57. DOI: 10.1016/j.ecoleng.2016.08.005.

Topolnicki, M. (2004). *In Situ Soil Mixing* Chapter 9. In: Moseley, M.P, Kirsch, K ed., Spon Press, pp. 340-437.

Proceedings of the XVIII ECSMGE 2024
GEOTECHNICAL ENGINEERING CHALLENGES
TO MEET CURRENT AND EMERGING NEEDS OF SOCIETY
© 2024 the Authors
ISBN 978-1-032-54816-6
DOI 10.1201/9781003431749-592
Open Access: www.taylorfrancis.com, CC BY-NC-ND 4.0 license

ECSMGE 24
XVIII EUROPEAN CONFERENCE ON SOIL MECHANICS AND GEOTECHNICAL ENGINEERING

3D and 1D modelling of monitored monopiles located in the Belgian North Sea

Modélisation 3D et 1D de monopieux monitorés situés en Mer du Nord Belge

A. Kheffache*
Ghent University, Ghent, Belgium

B. Stuyts, C. Sastre Jurado
Ghent University/OWI-lab , Ghent, Belgium

W. Weitjens, C. Devriendt
Vrije Universiteit Brussel/OWI-lab, Brussels, Belgium

*Anis.kheffache@ugent.be

ABSTRACT: Offshore Wind Turbines (OWTs) located in the Belgian North Sea have been monitored for several years using different monitoring setups (accelerometers, strain gauges and Fiber Bragg Gratings). The monitoring data reveals that OWTs do not perform as expected, as they were designed using recommendations that were not adapted for large diameter and longer piles such as the API/DNV p-y methods. These design methodologies were extensively used due to their low numerical cost when compared to 3D- Finite Element (FE) simulations. Both 3D and 1D FE analyses of a laterally loaded monopile are carried in this paper. First, a 3D site-specific model of a monitored OWT is developed. The model consists of a monopile and the soil medium which is simulated using calibrated hypoplastic models. The monopile model is then subjected to representative lateral loadings then bending moments are extracted. Similar analyses are done using 1D rule-based PISA models and API/DNV models. Numerical results of a comparative study between the 3D-FE, 1D-PISA, 1D-API/DNV and the monitoring data are presented and discussed.

RÉSUMÉ: Les éoliennes offshores situées au large de la côte Belge en Mer du nord ont été monitorés depuis plusieurs années en utilisant différents appareillages (accéléromètres, gauges de déformations et Fibres). Les données issues du monitoring révèlent un comportement non-prévu des éoliennes, surement due au fait qu'elles aient été dimensionnés en utilisant des recommandations non adaptés au pieux de grand diamètre tel que les courbes p-y formulés par l'API/DNV. Ces méthodes ont été utilisés extensivement due à leurs faible cout numérique comparé aux simulations en éléments finis (EF)-3D. Des analyses EF en 3D et 1D d'un monopieu sous chargement latéral sont effectués. Tout d'abord, nous établissons un modèle de site 3D d'une éolienne soumises au monitoring. Le modèle est constitué d'un monopieu et du sol avoisinant qui est simulé en utilisant une loi de comportement hypoplastique. Le monopieu est ensuite soumis à des charges latérales représentatives des charges in situ puis les courbes de moment fléchissant son extraites. Des analyses similaires sont effectués en utilisant un modèle 1D ou les courbes de réactions sont issues de recommandations PISA et API/DNV. Une étude comparative est effectué sur les résultats numériques et les données issues du monitoring.

Keywords: Monitoring; reaction-curves; bending moment; finite element; monopile.

1 INTRODUCTION

The recently adopted consensus is to reach 120 GW and 300 GW of total power output from offshore wind in the North Sea. Offshore wind turbines can be supported by many types of support structures, for example: gravity base foundations, suction buckets and jacket foundations. However, monopiles are still the preferred type of foundations in shallow coastal waters as they represent not less than 80% of the total installed foundations for offshore wind turbines (WindEurope, 2020). Monopiles are large-diameter hollow steel piles that are designed to support the upper wind turbine structure under multiple loads such as thrust load, wind shear, waves, currents and seismic loads (in earthquake-prone regions). These loads can be induced under normal operational or extreme conditions (such as storms and earthquakes).

Monopiles are typically designed using 1D beam-column models where the soil adjacent to the pile is modelled using discrete linear or non-linear springs.

Different non-linear spring functions exist in the literature, such as the API p-y method (API, 2011) that considers a set of lateral reactions along the pile. This method has been extensively used for the design of pile foundations in the oil and gas (O&G) industry. The more recent PISA methodology (Burd et al., 2020; Byrne et al., 2020) is reputed to be more adequate for the design of laterally loaded monopiles. 3D Finite Element approaches are known to be numerically more costly than the 1D ones, however they are better at simulating the complex soil-monopile interactions, and have been used successfully in the literature for the simulation of more complex problems (Kementzetzidis et al., 2018; Kheffache et al., 2023).

Monitoring data on wind turbines can help understand and gain insight on their real in situ behaviour (Stuyts et al., 2023). The different types of monitoring data that can exist on a wind turbine are listed below:

- Supervisory Control And Data Acquisition (SCADA) data; which gives the basic wind turbine outputs such as wind speed at the hub level, wind direction and rotations per minute (rpm)
- Acceleration measurements; which can be transformed into resonance frequencies
- Strain measurements from strain gauges (SGs) /Fiber Bragg gratings (FBGs); which can be transformed into bending moments
- Pore pressures;

In this work, both 3D and 1D numerical analyses of a monitored monopile located in the Belgian North Sea are performed. The 1D analyses are done following both the API/DNV (DNV, 2014) and PISA approaches while the 3D ones are done using the ABAQUS Finite Elements (FE) software in which the soil is simulated using advanced constitutive models that are calibrated to the available laboratory test/in situ data. The approaches are compared to each other and to the monitoring data.

2 MODELING OF LATERALLY LOADED PILES

2.1 API/DNV

The first versions of API/DNV reaction curves were initially developed by Cox et al (1974) and Matlock (1970). The API sand p-y reaction curves were derived directly from the results of laterally loaded piles which had a diameter of 610mm and a penetration depth of 21m, for a corresponding L/D ratio of 33.84.

The basic input parameters of the API method for both sands and clays are listed below:

- Unit weight γ' (sand/clay)
- Pile diameter D (sand/clay)
- Undrained shear strength (clay)
- Empirical constant J (clay)
- Strain parameter ϵ_{50}(clay)
- Friction angle φ' (sand)
- Loading factor A (sand)

The mathematical formulation is not given for the sake of brevity. This method has been proven to be unreliable for the design of monopiles as they are of bigger diameter than the ones used in the API pile tests (Doherty & Gavin, 2012)

2.2 PISA method

The PISA project formulated a new design methodology for laterally loaded monopiles in clays and sands; by taking into consideration 3 new sets of reaction curves on top of the lateral p-y ones, as shown in Figure 1.

The full methodology was established through lateral pile testing on piles with an L/D ratio that is between 2 and 6 and that is comparable to the ratio of monopiles. The pile tests were simulated using a 3D-FE model from which the 1D reaction curves were then extracted, the rule-based method was then formulated in which the basic mathematical functions of every reaction curve was established. The basic input parameters of the rule-based method are listed below:

- Relative density D_R (sand)
- Small strain stiffness G_{max} (sand/clay)
- Vertical effective stress σ_v' (sand)
- Undrained shear strength S_u (clay)
- Pile diameter D (sand/clay)

By comparing the input parameters for both methods, we can see that the PISA methodology takes into account both parameters at small and large strain.

2.3 FEM

The Finite Element Method is generally not used for design but rather as a design-verification tool. It allows the soil and pile mediums to behave according to a more advanced mathematical formulation (constitutive models) when compared to 1D approaches. This method is however more computationally costly both in terms of computational time and input parameters, depending on the complexity of the constitutive models used.

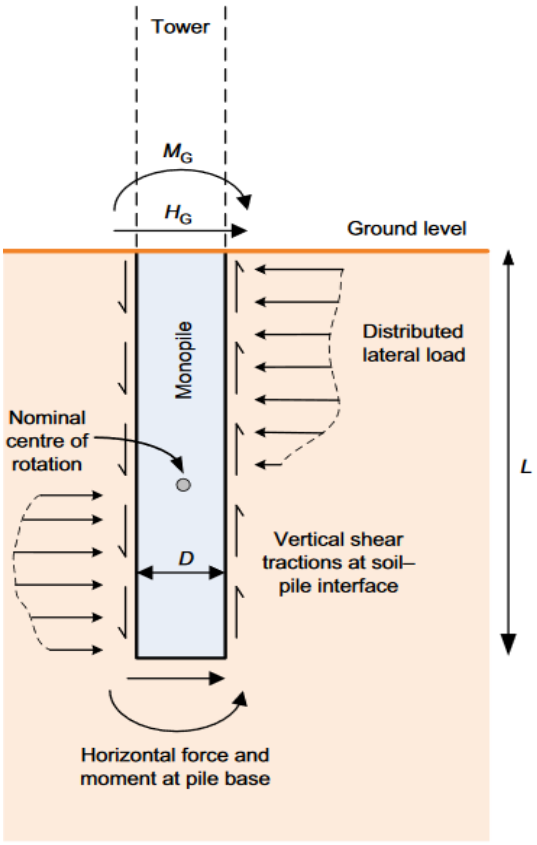

Figure 1. Different reaction curves considered in the PISA methodology (Byrne et al., 2020).

3 SITE CONDITIONS

3.1 Monopile

The studied monopile is located in the Belgian North Sea, some of the data was already presented in previous works (kheffache et al., 2022). The FBGs on the lower monopile part are shown in Figure 2

3.2 Soil conditions

The monitored wind turbine is located in the Belgian North Sea. The monopile is embedded in multilayered soil profile made of sand and clay layers. The Cone Penetration Test result and the soil layering at the wind turbine's location are shown in Figure 2.

3.3 Loads

Representative sets of loadings were extracted from the monitoring data (10-minutes strain measurements) available on the upper structure (above mudline part of the wind turbine). The derived loading consists of a point force and moment applied at the head of the monopile. A total of 23 load conditions are considered in this work. It is worth mentioning that the loads are considered to be quasi-static; the loads were exctracted

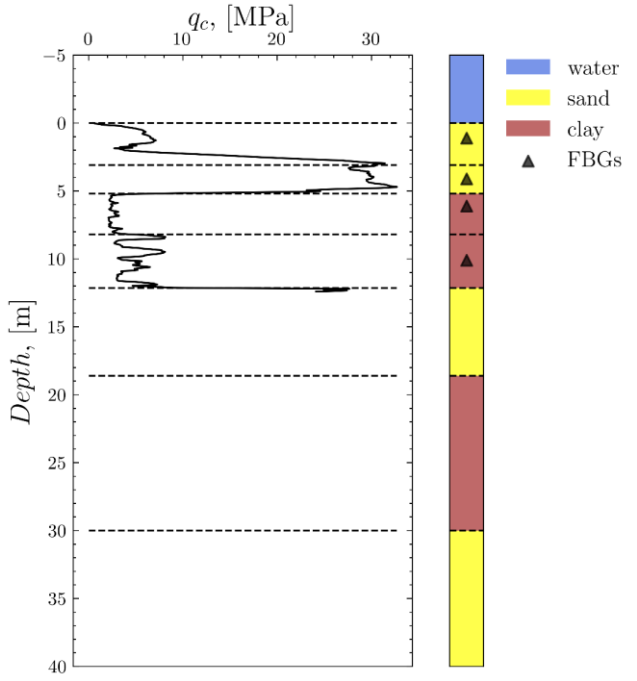

Figure 2. CPT, FBGs and soil layering at the wind turbine's location.

from episodes where the wind turbine was operating under normal conditions and where the strain measurements were seen to have relatively small variations.

4 FE MODELLING

4.1 1D models

The 1D modelling is done using an in-house beam-column model. Both API and PISA reaction curves can be assigned to the monopile. All of the PISA input parameters can be calibrated directly from in situ test results where as for the API ones; ϵ_{50} and γ' are generally calibrated from laboratory test data.

4.2 3D models

4.2.1 Soil

The sand and clay hypoplastic models are assigned to sand and clay layers respectively (Mašín, 2013; von Wolffersdorff, 1996), and are calibrated to advanced laboratory test data which consists of oedometric, triaxial, DSS, resonant column and bender element tests. The calibration methodologies discussed by Mašín, (2019) are followed. The inputs for both models have been discussed and some values have been presented in previous works (kheffache et al., 2022), the calibration is not repeated here for the sake of brevity. The calibration is further optimised using the in situ data such as Seismic Cone Penetration Tests (SCPT). The calibrated G_{max} profile is show in Figure 3.

The soil stress is initialized by considering a K_0 initial stress state, where K_0 is the earth pressure coefficient at rest and is given by the following equations:

$$K_{0,sand} = 1 - sin(\varphi_c) \quad (1)$$

$$K_{0,clay} = (1 - \sin(\varphi_c))OCR^{\sin(\varphi_c)} \quad (2)$$

where φ_c is the critical friction angle and OCR is the overconsolidation ratio interpreted from a nearby borehole. A slightly higher K_0=0.8 was assigned for the upper sand layer to take into consideration overconsolidation. The initial void ratio e_0 was derived from a nearby borehole. A drained and undrained behviour is assigned to the sand and clay layers respectively.

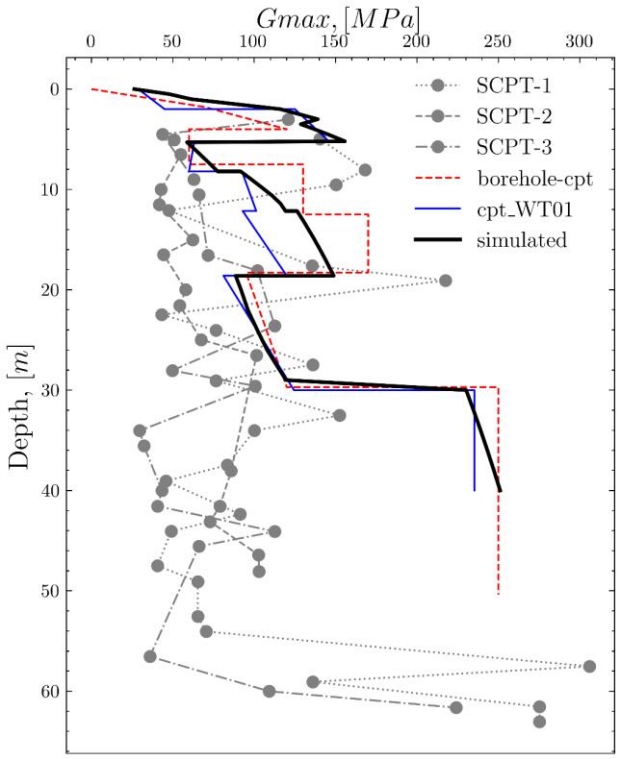

Figure 3. G_{max} profile.

4.2.2 Monopile

The monopile is modelled using C3D8I mesh elements which are incompatible 3D continuum 8 noded fully integrated linear brick elements, recommended for solid elements subject to bending (Abaqus, 2011). A comparative study was done by comparing C3D8I elements to S4R (shell) bending moments, negligeable differences were observed.

4.2.3 Boundary conditions

Only half of the model is simulated by taking into account symmetry in the y direction. The model is fixed in all direction at the bottom, while it is fixed only in the x and y directions at the edge.

4.2.4 Contact

The general contact algorithm which allows for the automatic detection of interfaces is used. The pile-soil contact is modelled by considering a Mohr-Coulomb frictional coefficient μ. A sensitivity study was conducted on the effect of the friction coefficient on the results. No significant effects were observed. A constant friction coefficient of 0.5 is assigned along the monopile-soil interface.

5 RESULTS

The results are investigated in terms of bending moments as mentioned before. 23 bending moment profiles were generated (corresponding to the 23 load cases), however only 4 profiles are shown in Figure 4 for brevity. The bending moments are normalised to the highest value, whereas the depth is normalised to the monopile's diameter. It can be seen that for the 4 load cases, the FEM-based bending moments are the closest to the monitored ones, translating a stiffer behaviour when compared to the API/PISA-based bending moments. If we compare the bending moments that result from 1D approaches, we notice that the PISA-based ones are the closest to the monitoring data (and also relatively close to the FEM ones). In all of the analyses (FEM, API and PISA), the simulated bending moments are always at the right hand side of the monitored ones (overprediction), which means that the monopile is laterally stiffer in reality compared to the simulations.

The results can also be quantified in terms of Mean Relative Error (MRE), where MRE is given by the following equation:

$$MRE_M = \frac{1}{n}\sum_{i=0}^{n-1}\frac{M_m^{z,i} - M_s^{z,i}}{M_m^{z,i}} \quad (3)$$

where n is the total number of considered load cases (23), $M_m^{z,i}$ is the monitored bending moment at the z-th sensor depth for the i-th load case, $M_s^{z,i}$ is the simulated bending moment at the same depth and for the same load case. According to the previous MRE definition, a positive value translates into an underestimation whereas a negative value translates into an overestimation of the bending moments when compared to the monitored ones.

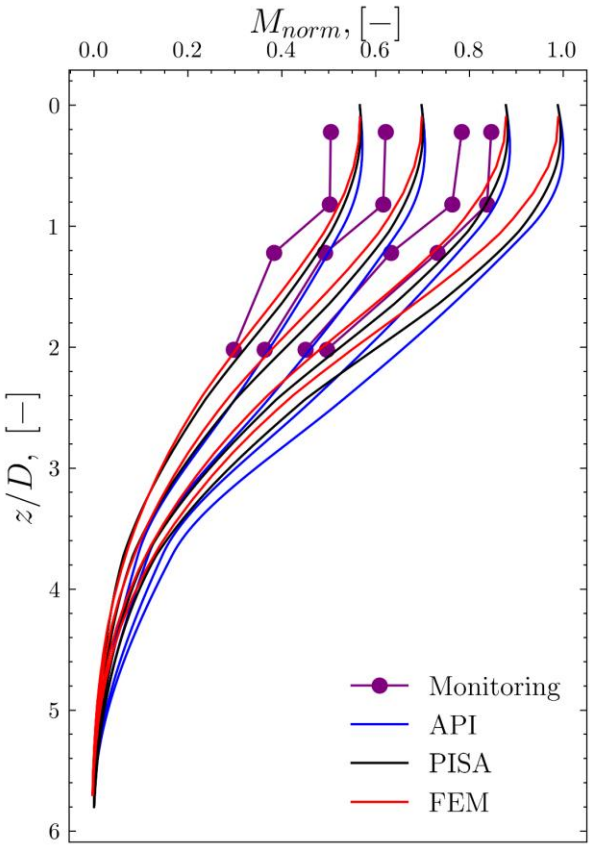

Figure 4. Bending moment versus depth.

Figure 5 represents the MRE for all the simulated cases at each sensor depth below mudline. We can see that for all the sensors depths, the MRE is always the lowest for the FEM approach, while it takes the highest values for the API one, confirming the previous observations. We can also see that the MRE difference between the approaches is larger at the lowest sensor depth when compared to the shallowest sensor depth. When comparing between the results in terms of Global MRE (GMRE, the mean of MRE for every method) given in Table 1, we see that the API method overpredicts the results by 20%, almost twice as much as the FEM approach.

Table 1.Global MRE for the different modelling approaches

Approach	API	PISA	FEM
GMRE (%)	-20.04	-14.70	-10.48

6 CONCLUSIONS

In this work, a monitored wind turbine located in the Belgian North Sea was studied. 3 different design-methodologies were used:

- API guidelines
- PISA method
- FEM.

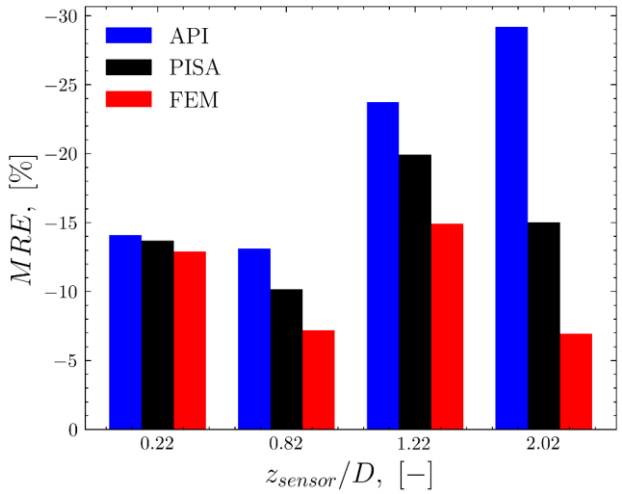

Figure 5. MRE at different sensor depths.

The monopile was subjected to representative sets of quasi-static loads extracted from the monitoring data on the wind turbine. The monitored and simulated bending moments using the different approaches were compared. All the methods were seen to overpredict the bending moment on the monopile which is due to the fact that the monopile behaves stiffer than expected, probably due to the missing contribution of the scour protection in the simulations, and the missing installation effects. The PISA rule-based method was seen to give satisfactory results, almost matching the FEM ones, while the API approach gave the least accurate ones.

ACKNOWLEDGEMENTS

The authors would like to acknowledge the support of the Belgian Ministry of Economic Affairs through the EFT project WINDSOIL project. The Support of VLAIO through the De Blauwe Cluster SBO SOILTWIN project is also acknowledged.

REFERENCES

Abaqus, G. (2011). Abaqus 6.11. Dassault Systemes Simulia Corporation, Providence, RI, USA, 3.

API. (2011). API RP2 GEO Geotechnical and Foundation Design Considerations.

Burd, H. J., Taborda, D. M. G., Zdravković, L., Abadie, C. N., Byrne, B. W., Houlsby, G. T., Gavin, K. G., Igoe, D. J. P., Jardine, R. J., Martin, C. M., McAdam, R. A., Pedro, A. M. G., & Potts, D. M. (2020). PISA design model for monopiles for offshore wind turbines: Application to a marine sand. Géotechnique, 70(11), 1048–1066. https://doi.org/10.1680/jgeot.18.P.277.

Byrne, B. W., Houlsby, G. T., Burd, H. J., Gavin, K. G., Igoe, D. J. P., Jardine, R. J., Martin, C. M., McAdam, R. A., Potts, D. M., Taborda, D. M. G., & Zdravković, L. (2020). PISA design model for monopiles for offshore

wind turbines: Application to a stiff glacial clay till. Géotechnique, 70(11), 1030–1047. https://doi.org/10.1680/jgeot.18.P.255.

Cox, W. R., Reese, L. C., & Grubbs, B. R. (1974). Field testing of laterally loaded piles in sand. Offshore Technology Conference, OTC-2079. https://onepetro.org/OTCONF/proceedings-abstract/74OTC/All-74OTC/46408.

DNV. (2014). DNV-OS-J101 Design of Offshore Wind Turbine Structures.

Doherty, P., & Gavin, K. (2012). Laterally loaded monopile design for offshore wind farms. Proceedings of the Institution of Civil Engineers - Energy, 165(1), 7–17. https://doi.org/10.1680/ener.11.00003.

Kementzetzidis, E., Versteijlen, W. G., Nernheim, A., & Pisano, F. (2018). 3D FE dynamic modelling of offshore wind turbines in sand: Natural frequency evolution in the pre– to after-storm transition. 2, 1477–1484.

kheffache, A., Stuyts, B., Jurado, C. S., Weijtjens, W., & Devriendt, C. (2022). 3D FE simulation of an instrumented monopile under quasi-static loading. ISSMGE. https://doi.org/10.53243/NUMGE2023-344.

Kheffache, A., Stuyts, B., Sastre Jurado, C., Devriendt, C., & Weijtjens, W. (2023). Coupled simulations of a monitored wind turbine monopile subject to lateral loading. OSIG2023.

Mašín, D. (2013). Clay hypoplasticity with explicitly defined asymptotic states. Acta Geotechnica, 8(5), 481–496. https://doi.org/10.1007/s11440-012-0199-y.

Mašín, D. (2019). Modelling of Soil Behaviour with Hypoplasticity: Another Approach to Soil Constitutive Modelling. Springer International Publishing. https://doi.org/10.1007/978-3-030-03976-9.

Matlock, H. (1970). Correlation for design of laterally loaded piles in soft clay. Offshore Technology Conference, OTC-1204. https://onepetro.org/OTCONF/proceedings-abstract/70OTC/All-70OTC/110538.

Stuyts, B., Weijtjens, W., Gkougkoudi-Papaioannou, M., Devriendt, C., Troch, P., & Kheffache, A. (2023). Insights from in-situ pore pressure monitoring around a wind turbine monopile. Ocean Engineering, 269, 113556. https://doi.org/10.1016/j.oceaneng.2022.113556.

von Wolffersdorff, P.-A. (1996). A hypoplastic relation for granular materials with a predefined limit state surface. Mechanics of Cohesive-Frictional Materials, 1(3), 251–271. https://doi.org/10.1002/(SICI)1099-1484(199607)1:3<251::AID-CFM13>3.0.CO;2-3.

WindEurope. (2020). Offshore Wind in Europe: Key trends and statistics 2019. https://windeurope.org/wp-content/uploads/files/about-wind/statistics/WindEurope-Annual-Offshore-Statistics-2019.pdf.

Proceedings of the XVIII ECSMGE 2024
GEOTECHNICAL ENGINEERING CHALLENGES
TO MEET CURRENT AND EMERGING NEEDS OF SOCIETY
© 2024 the Authors
ISBN 978-1-032-54816-6
DOI 10.1201/9781003431749-593
Open Access: www.taylorfrancis.com, CC BY-NC-ND 4.0 license

ECSMGE 24
XVIII EUROPEAN CONFERENCE ON SOIL MECHANICS AND GEOTECHNICAL ENGINEERING

The permeability characteristics of compacted recycled materials for landfill barriers in Norway

Les caractéristiques de perméabilité des matériaux recyclés compactés pour les barrières d'étanchéité des décharges de déchets en Norvège

T. Kim*
NGI, Oslo, Norway

E.W. Ånes, G.W. Åsli, Y. Suzuki
NGI, Oslo, Norway

S. Ritter
Oslo Metropolitan University, Norway

**taeheon.kim@ngi.no*

ABSTRACT: Recycling waste materials for barrier system of landfills has more recently been increasingly considered in geotechnical engineering to improve sustainability. Among various geomechanical parameters, hydraulic conductivity is one of the essential factors to be evaluated when designing landfill liners. With such motive, three types of materials were studied in our ongoing research: press filter residue (PFR), cement stabilized clay (CSC) and dry crust clay (DCC). The three recycled materials were compacted in a field pilot project to investigate their applicability as landfill liners. Compacted samples from the pilot project were then cored in tube samplers and transported to the laboratory for hydraulic conductivity measurements. Permeability was measured using oedometer, flexible wall permeameter and triaxial permeability cells. Permeability measurements were made on horizontal and vertical directions to investigate potential permeability anisotropy characteristics at a wide range of consolidation stress levels (15 kPa to 650 kPa). The hydraulic conductivity measured on the samples was in the range of 2×10^{-7} m/s to 10^{-10} m/s. For most of the samples, permeability decreased to below 10^{-9} m/s with increasing stresses, where Norwegian regulations and practice recognises that it is suitable for, liners of landfills containing non-hazardous and hazardous waste. Moreover, the hydraulic conductivity of the materials was anisotropic, and the anisotropy changed with increasing consolidation stresses.

RÉSUMÉ: Le recyclage des déchets pour les systèmes de barrières d'étanchéité des décharges a plus récemment été de plus en plus pris en compte dans l'ingénierie géotechnique pour améliorer la durabilité. Parmi les différents paramètres géomécaniques, le coefficient de perméabilité est l'un des facteurs essentiels à évaluer lors de la conception des barrières d'étanchéité des décharges. C'est pour cette raison que trois types de matériaux ont été étudiés dans nos recherches en cours: les résidus de filtres presses (PFR), les argiles stabilisées au ciment (CSC) et les argiles à croûte sèche (DCC). Les trois matériaux recyclés ont été compactés dans le cadre d'un projet pilote sur le terrain pour étudier leur applicabilité en tant que barrières d'étanchéité des décharges. Les échantillons compactés du projet pilote ont ensuite été carottés dans des tubes d'échantillonnage et transportés au laboratoire pour des mesures de conductivité hydraulique. La perméabilité a été mesurée à l'aide d'un œdomètre, d'un perméamètre à paroi flexible et de cellules de perméabilité triaxiale. Des mesures de perméabilité ont été effectuées dans les directions horizontale et verticale pour étudier les caractéristiques potentielles d'anisotropie de perméabilité dans une large gamme de niveaux de contrainte de consolidation (15 kPa à 650 kPa). Le coefficient de perméabilité mesuré sur les échantillons était compris entre 2×10^{-7} m/s et 10^{-10} m/s. Pour la plupart des échantillons, la perméabilité a diminué jusqu'à moins de 10^{-9} m/s avec des contraintes croissantes, là où la réglementation et la pratique norvégiennes reconnaissent qu'elle convient aux barrières d'étanchéité des décharges contenant des déchets non-dangereux et dangereux. De plus, la conductivité hydraulique des matériaux était anisotrope, et l'anisotropie changeait avec l'augmentation des contraintes de consolidation.

Keywords: Permeability; recycled materials; landfill liners; vertical and horizontal permeability.

1 INTRODUCTION

A research project called earthresQue on reusing waste soils from various origins was laid out by the Norwegian centre for research-based innovation (SFI). The main purpose of earthresQue is to improve the sustainability of treating waste and surplus earth materials from the building and construction industry. One work package investigates recycled earth materials as alternative, more sustainable materials for

landfill liners. As part of this, there has been constructed a final cover pilot test at a landfill site in southern Norway, using two such materials: PFR (Press Filter Residue) and CSC (Cement Stabilized Clay). These are compared to a DCC (Dry Crust Clay), a type of raw material that is a common surplus mass from construction projects in parts of Norway and has been used as barrier materials. This paper presents results from permeability tests conducted on undisturbed, compacted samples of these materials. Initial results from the pilot test itself is presented in the other paper of this conference (Ånes et al., 2024).

Norwegian regulations require barrier materials for bottom liners in hazardous and non-hazardous waste landfills to have hydraulic conductivity lower than 10^{-9} m/s(Ministry of Climate and Environment, 2004), which is classified as impermeable according to Casagrande and Fadum (1940). Typically, the environmental authorities also set the same permeability requirement to final cover for these landfills. The materials that match the criteria are usually rich in clay minerals (and clay-sized particles) and have homogenous internal structure.

The work presented in this paper aims to evaluate the suitability of the three materials as landfill liners and to characterize their hydraulic conductivity.

2 EXPERIMENTAL PROGRAMME

2.1 Materials

The press filter residual (PFR) is the clay and silt fractions of excavated, lightly contaminated soils that have been washed and sorted at a soil washing plant. The cement stabilized clay (CSC) is a marine clay that was stabilized with cement and cement-kiln dust before excavation at a construction site in Oslo. The dry crust clay (DCC), being the upper, weathered part of a clay deposit, was excavated from another construction site in Oslo. The soil properties of the tested materials are listed in Table 1. For further description of PFR and CSC, refer to (Ritter et al., 2023). Based on the index properties of the soils, hydraulic conductivity lower than 10^{-9} m/s is expected to be achievable (Benson et al., 1994).

The three materials were compacted in the field at the final cover pilot site. The samples were then cored using a 72 mm diameter Shelby tube sampler. Cored samples were sealed and sent to the laboratory at the Norwegian Geotechnical Institute (NGI) for permeability tests.

Table 1. Soil composition and index properties of three recycled materials.

Sample	Soil fraction (%)			Atterberg limit (%)			Particle density (Mg/m^3)
	Sand	Silt	Clay	Plastic limit, w_p	Liquid limit, w_l	Plasticity index, I_p	
PFR	4.2	67.3	28.5	28	53	25	2.74
CSC	1.2	63.7	35.1	23	41	18	2.76
DCC	2.5	49.3	48.2	23	43	22	2.80

2.2 Permeability measurements

Three different testing types were used for hydraulic conductivity measurements: oedometer cell, flexible wall permeameter and triaxial cell. Both vertical (normal to the bedding plane) and horizontal (parallel to the bedding plane) permeability measurements were investigated. The specimens for vertical permeability were trimmed as per normal triaxial specimens, while the specimens for horizontal permeability were sub-sampled horizontally of the vertical cores using a horizontal extruder and cradle built in-house.

Constant head method was adopted for all three types of tests (NS-ISO, 2019). Three measurements were made with different hydraulic gradients for each stage of the permeability test. The permeability was measured when the flow rate became linear assuming it reached a steady state. The three values were then averaged to obtain hydraulic conductivity at each stage.

2.2.1 Oedometer

One-dimensional incremental loading oedometer cells were used for the permeability measurements. A nominal initial specimen height of 20 mm and diameter of 67 mm was used. Vertical stress was increased step by step and permeability was measured at designated vertical stresses. Back pressure was not applied for the oedometer test.

For the permeability measurement, a VPC (Volume Pressure Controller) was connected at the bottom reservoir whilst the top reservoir was opened to the atmosphere. A small constant head difference was applied between the bottom and the top of the specimen.

To simulate a range of relevant overburdens (road embankment, final cover to bottom liner), the vertical stress range at which permeability was measured was between 20 kPa and 650 kPa.

2.2.2 Flexible wall permeameter

Flexible wall permeameter was used for measuring the horizontal permeability. Unlike the typical triaxial samples, a height to diameter (H/D) ratio of 1.0 (H = D = 50 mm) was used.

The stress conditions were always isotropic as a deviator load was not applied or measured. The mean effective stress range at which the permeability was measured was between 15 kPa and 650 kPa and the deformation was traced monitoring the pore volume and a Linear Variable Differential Transformer (LVDT) mounted externally on the piston. For the permeability test, two VPCs were connected to the top and bottom reservoirs allowing the control over the pore pressure. The permeability was measured by applying differential pressures at bottom and top reservoirs.

2.2.3 Triaxial cell

Permeability was measured as a part of triaxial testing. Initial triaxial specimens had a H/D ratio of about 2 (either H = 140 mm and D = 72 mm or H = 108 mm and, D = 54 mm). The stress conditions were isotropic, and the deformation was measured using the pore volume change and the LVDT measurements. The stress range at which permeability tests were carried out was between 20 kPa and 640 kPa. The permeability measurements were done the same way as in the flexible wall permeability test.

3 RESULTS

Figure 1 plots the hydraulic conductivity with respect to void ratio, density and vertical effective stress. With increase in effective stress the soil compacts leading to decreased void ratio and increased bulk density and finally a decrease in hydraulic conductivity. Most of the samples reached hydraulic conductivity lower than 10^{-9} m/s when the effective stress exceeded above 150 kPa. Note that the effective stress of oedometer tests is the vertical effective stress and that of the flexible wall permeameter and triaxial test are mean effective stresses.

It can also be seen from the plots that the permeability measurements are widely distributed unlike soils reconstituted in the laboratory under well controlled environments. Table 2 lists the initial

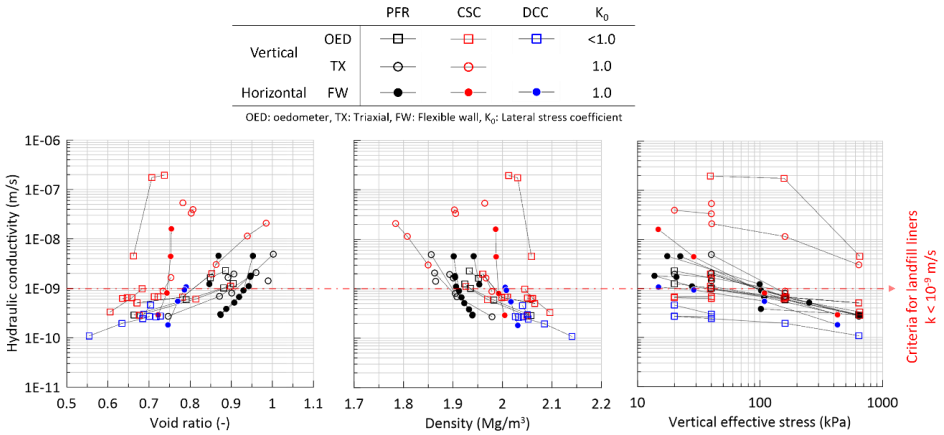

Figure 1. Hydraulic conductivity with respect to void ratio, density and vertical effective stress.

properties of each material compacted in-situ (In Table 2, k_v is the vertical hydraulic conductivity, e is the void ratio and ρ is the density). Large variability was detected for initial vertical hydraulic conductivity, void ratio and bulk density. PFR and CSC results showed large scatter, whereas the DCC results were more constant. Such a distinction seems to be from the origin of the specimens compacted and sampled in the field, noting that DCC were from a single core and PFR and CSC samples were from multiple cores extracted from various locations.

Table 2. Range of initial properties of intact materials.

Material	k_v (m/s)	e (-)	ρ (Mg/m³)
PFR	4.9×10^{-9} – 1.2×10^{-10}	1.00 – 0.67	1.86 – 1.96
CSC	1.9×10^{-7} – 6.4×10^{-10}	0.98 – 0.65	1.78 – 2.05
DCC	2.7×10^{-10} – 4.6×10^{-10}	0.73 – 0.70	2.03 – 2.04

Comparing the vertical and horizontal permeabilities, the horizontal permeability was not necessarily larger than the vertical which is often reported for reconstituted consolidated soils (Adams et al., 2013; Clennell et al., 1999; Zhang et al., 2019).

The evolution of horizontal permeability was more significant than the vertical permeability with the equivalent amount of void ratio decrement (Figure 1 left) and increase in bulk density (Figure 1 centre). This may be due to the anisotropic structure of the compacted soils. Similar to the vertical hydraulic conductivity, the value dropped below 10^{-9} m/s satisfying the Norwegian criteria for landfill liners for non-hazardous and hazardous waste after loading to high stresses.

4 FINAL REMARKS AND DISCUSSION

This paper observed the hydraulic conductivity characteristics of three materials, using three different apparatuses in the laboratory. The following points summarize and discuss the observations made:

- The field compacted PFR and CSC initial properties such as void ratio and bulk density had a wide variability. For the DCC, the initial properties varied less compared to others.
- Most of the recycled samples (PFR and CSC) did not satisfy the criteria for landfill liners ($k \leq 1.0\times10^{-9}$ m/s) at the low consolidation stresses (approx. below 100 kPa). Increasing the effective stress led to a large drop in hydraulic conductivity; with effective stresses exceeding 150 kPa the hydraulic conductivity decreased satisfying the criteria. The criteria may be met with sufficient deposition of landfills; however, this does not guarantee the suitability of landfill barriers and may require further improvement to ensure impermeability.
- The evolution of hydraulic conductivity with respect to void ratio change was more significant on the horizontal direction than on the vertical direction. Such behaviour may be attributed to the anisotropic soil structure of the compacted soils. This observation suggests that the horizontal flow should be considered for sidewalls of landfill liners.
- The permeating fluid was deionized water that does not necessarily represent the field conditions as permeating leachates tend to have high salt content. Changes in salt content/species of the permeant has the possibility of changing the permeability in orders of magnitude (Das & Bharat, 2021). Therefore, the effect of salt concentration of permeants on the hydraulic conductivity of these materials should be investigated prior to implementing to the field.

ACKNOWLEDGEMENTS

The research activities carried out and the study presented in the paper are financially supported by the Research Council of Norway through NGI's research project SP14: Characterisation of Permeability on Geomaterials at NGI (SFI earthresQue RCN grant 310042/F40).

REFERENCES

Adams, A. L., Germaine, J. T., Flemings, P. B., & Day-Stirrat, R. J. (2013). Stress induced permeability anisotropy of Resedimented Boston Blue Clay. *Water Resources Research*, *49*(10), 6561-6571. https://doi.org/https://doi.org/10.1002/wrcr.20470.

Ånes, E. W., Ritter, S., Pabst, T., & Okkenhaug, G. (2024). *Initial results from a landfill final cover pilot test utilising waste soils (forthcoming)* ECSMGE2024, Portugal.

Benson, C. H., Zhai, H., & Wang, X. (1994). Estimating Hydraulic Conductivity of Compacted Clay Liners. *Journal of Geotechnical Engineering*, *120*(2), 366-387. https://doi.org/doi:10.1061/(ASCE)0733-9410(1994)120:2(366).

Casagrande, A., & Fadum, R. E. (1940). Notes on soil testing for engineering purposes.

Clennell, M. B., Dewhurst, D. N., Brown, K. M., & Westbrook, G. K. (1999). Permeability anisotropy of consolidated clays. *Geological Society, London, Special Publications*, *158*(1), 79-96. https://doi.org/doi:10.1144/GSL.SP.1999.158.01.07.

Das, P., & Bharat, T. V. (2021). Kaolin based protective barrier in municipal landfills against adverse chemo-mechanical loadings. *Scientific Reports*, *11*(1), 10354 https://doi.org/10.1038/s41598-021-89787-z.

Ministry of Climate and Environment, N. (2004). *Regulations relating to recycling and treatment of waste (Waste Regulations)*. Norway Retrieved from https://lovdata.no/dokument/SF/forskrift/2004-06-01-930.

NS-ISO. (2019). Geotechnical investigation and testing. In *Laboratory testing of soil* (pp. 20) https://online.standard.no/nb/ns-en-iso-17892-11-2019.

Ritter, S., Ånes, E. W., Hovland, K., Stridal, A. C., Hansen, H., Henriksen, T., & Okkenhaug, G. (2023). *Sustainable impermeable landfill barriers: The potential of using geological waste and surplus masses* 9th International congress on Environmental Geotechnics, Chania, Greece. https://doi.org/10.53243/ICEG2023-102.

Zhang, F., Cui, Y.-J., Zeng, L., & Conil, N. (2019). Anisotropic features of natural Teguline clay. *Engineering Geology*, *261*, 105275 https://doi.org/10.1016/j.enggeo.2019.105275.

Proceedings of the XVIII ECSMGE 2024
GEOTECHNICAL ENGINEERING CHALLENGES
TO MEET CURRENT AND EMERGING NEEDS OF SOCIETY
© 2024 the Authors
ISBN 978-1-032-54816-6
DOI 10.1201/9781003431749-594
Open Access: www.taylorfrancis.com, CC BY-NC-ND 4.0 license

ECSMGE 24
XVIII EUROPEAN CONFERENCE ON SOIL MECHANICS AND GEOTECHNICAL ENGINEERING

Identifying porosity distribution and swell anisotropy of laboratory sedimented high plasticity clay through NMR imaging

Identification de la distribution de la porosité et de l'anisotropie du gonflement de l'argile à haute plasticité sédimentée en laboratoire grâce à l'imagerie RMN

E.M. Kinslev*, I. Rocchi, L.T.P. Meireles
Technical University of Denmark, Kgs. Lyngby, Denmark
*emki@dtu.dk

ABSTRACT: When studying fundamental features of soil behaviour it is common to resediment or remould "artificial" soil samples under well-defined conditions to limit uncertainties caused by variability in soil structure. Therefore, the laboratory sedimented sample is a useful reference state for a given soil. However, the sedimentation process inevitably causes anisotropy which is previously linked to sedimentation structure. This is related to the anisotropic stress state of oedometric confinement used in laboratory sedimentation. As such anisotropy is unavoidable it is necessary to identify it. More troublesome is the potential unwanted heterogeneity caused by the separation of constituents during the sedimentation process. To investigate these two features, large (Ø20cm x 6cm) laboratory sedimented high plasticity clay discs were prepared. On both vertically and horizontally oriented subsamples at different locations in these discs, the porosity distribution was mapped through low field Nuclear Magnetic Resonance (NMR) imaging. This allowed verification of the level of homogeneity achieved by the laboratory sedimentation procedure. Further, the anisotropy of the discs was studied by measuring the free swell of the subsamples at the two orientations. The obtained results provide insights into the effectiveness of laboratory sedimentation for creating homogeneous reference soil samples and further exemplify the usefulness of NMR imaging in identifying initial porosity distribution and porosity evolution during swelling.

RÉSUMÉ: Lors de l'étude des caractéristiques fondamentales du comportement du sol, il est courant de resédimenter ou de remouler des échantillons de sol « artificiels » dans des conditions bien définies afin de limiter les incertitudes causées par la variabilité de la structure du sol. Par conséquent, l'échantillon sédimenté en laboratoire constitue un état de référence utile pour un sol donné. Cependant, le processus de sédimentation provoque inévitablement une anisotropie qui est auparavant liée à la structure de la sédimentation. Ceci est lié à l'état de contrainte anisotrope du confinement oedométrique utilisé en sédimentation en laboratoire. Une telle anisotropie étant inévitable, il est nécessaire de l'identifier. Plus gênante est l'hétérogénéité potentiellement indésirable provoquée par la séparation des constituants au cours du processus de sédimentation. Pour étudier ces deux caractéristiques, de grands disques d'argile sédimentés en laboratoire (Ø20 cm x 6 cm) à haute plasticité ont été préparés. Sur des sous-échantillons orientés verticalement et horizontalement à différents endroits de ces disques, la distribution de la porosité a été cartographiée par imagerie par résonance magnétique nucléaire (RMN) à faible champ. Cela a permis de vérifier le niveau d'homogénéité atteint par la procédure de sédimentation en laboratoire. De plus, l'anisotropie des disques a été étudiée en mesurant le gonflement libre des sous-échantillons aux deux orientations. Les résultats obtenus donnent un aperçu de l'efficacité de la sédimentation en laboratoire pour créer des échantillons de sol de référence homogènes et illustrent en outre l'utilité de l'imagerie RMN pour identifier la distribution initiale de la porosité et l'évolution de la porosité au cours du gonflement.

Keywords: Resedimentation; sample homogeneity; swelling anisotropy; nuclear magnetic resonance (NMR).

1 INTRODUCTION

Soil behaviour depends both on the material properties (i.e. mineralogical and particle size distribution, and particle size and morphology) as well as its state (porosity and its distribution, particle arrangement, bonding/cementation, etc.). Burland (1990) devised a reference state, namely a remoulded conditions, which represents the intrinsic material behaviour by providing a term of comparison and thereby allowing to distinguish between behavioural features linked to material properties and those linked to soil "structure", defined by Cotecchia and Chandler (2000), as the

combination of fabric (i.e. particle orientation) and bonding. Although the remoulded sample starts from an isotropic state (no preferential particle orientation), the anisotropic stress state experienced during oedometric compression, which is used for laboratory preparation of fine-grained samples, induces a preferred particle orientation. Furthermore, when using resedimentation rather than remoulding as a preparation method, Stallebrass et al. (2007) observed particle sorting caused by the sedimentation process (similar to the effects utilized when determining particle size distributions, see e.g. ASTM D7928). This led to a parallel shift of the compression line relative to the intrinsic one, based on the reconstitution method proposed by Burland (1990).

It is apparent, that laboratory produced soil samples will inevitably contain some degree of anisotropy and potentially some unwanted heterogeneity. A large laboratory resedimented disc (D=20cm x H=6cm) of Røsnæs Clay was created and several small (D=2cm x H=2cm) specimens were taken at different locations to investigate these aspects. The degree of heterogeneity was determined through measurements of the pore size distribution and porosity at these varying positions through Nuclear Magnetic Resonance (NMR). The degree of anisotropy was estimated by exposing both vertical and horizontal plugs to demineralised water and monitoring the free swell process also through NMR measurements.

The combination of these observations provides an assessment of laboratory resedimentation procedures for creating relevant reference soil samples.

2 METHODS AND MATERIALS

The material used as the basis of the study is the already mentioned disc of resedimented Røsnæs Clay. The details of the resedimentation procedure are described by Kinslev et al. (2022) and are briefly summarised as: The soil is mixed into suspension with artificial pore water (composition) ensuring a water content of 500%, after which it is sedimented in a purpose build consolidometer and compressed to 1000 kPa. The final product (the disc) is removed and stored in several layers of waxed cling film while not being sampled.

The specimens are sampled in plastic confining rings to enable NMR measurements since metal rings would interfere with the magnetic field. These confining rings have a perforated base, on which is placed a filter paper, resulting in uptake of water from both ends but one-sided swelling once exposed to demineralised water. In total seven specimens were sampled from the disc, positioned as illustrated in Figure 1.

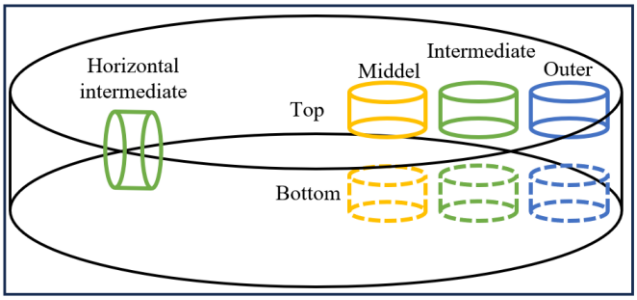

Figure 1. Position of specimens in the resedimented disc.

The Røsnæs Clay used in this study originates from core samples taken during the ground investigation campaign performed for the Fehmarn Belt tunnel project and has properties as listed in Table 1.

Table 1. Selected properties of Røsnæs Clay. Data from Awadalkarim 2014, Di Remigio 2021 and Kinslev 2022.

Grain density	[-]	2.75-2.85
Liquid limit	[%]	93-181
Plastic limit	[%]	26-39
Clay mineral content	[%]	64-68
Kaolinite	[%]	11-18
Illite	[%]	13-15
Smectite	[%]	33-43
Specific surface area	[m^2/g]	56-68

The Røsnæs Clay formation was deposited in the North Sea during the Palaeogene period. In Table 1 only the clay mineralogy is detailed but it should be added, that the remaining mineralogy is dominated by very fine particles (primarily quartz) as nothing is retained by a 63 micron sieve.

The NMR measurements are based on T_2 relaxation; hence the exponentially decaying relaxation of the nuclear angular momentum of hydrogen nuclei to an external magnetic field after tilting by 90 degrees via a timed magnetic pulse. This relaxation is governed by three mechanisms: Bulk relaxation, diffusion and surface relaxation. At the fast diffusion limit (almost all soils), relaxation is dominated by the surface relaxation and T_2 relaxation times correlate linearly to pore size.

Bulk NMR measurements were taken for each specimen to determine the relative pore size distribution as well as total porosity. Subsequently the specimens were exposed to a 0.18M NaCl solution and allowed to free swell for 800 min, while NMR bulk measurements were taken at relevant time intervals (more closely spaced initially, when the free swell process is fastest).

3 RESULTS AND DISCUSSION

The homogeneity of the produced disc is evaluated comparing porosity distributions. The total porosity in Figure 2 is obtained as the area under the curve (also reported in legend), while the T_2 relaxation time distribution is a proxy for pore size distribution. Figure 2 shows the values for each of the vertical specimens (see Figure 1).

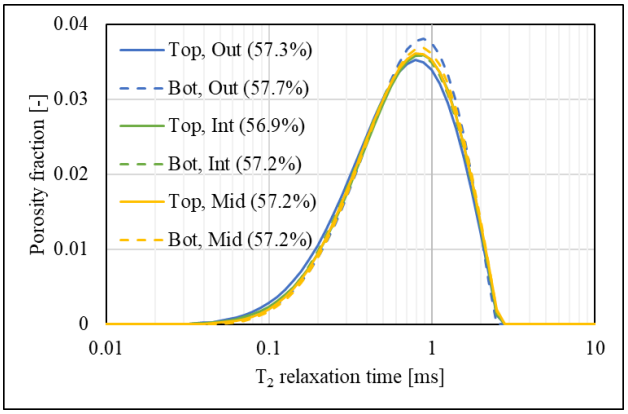

Figure 2. Distribution of porosity fractions with T_2 relaxation times for the six vertical specimens with their total porosity noted in the legend.

From Figure 2 it may be seen that the porosity varies between 56.9 and 57.7% across the disc, which is deemed to be minimal. Further, since there is no consistent trend in the total porosity distribution between the positions in the disc (from middle to outer or top to bottom) the variations in porosity are more likely related to the accuracy of the NMR measurements as well as potential small disturbances during the sampling process. In addition to the consistent total porosity between the specimens, Figure 2 also shows that the pore size distribution is almost identical between them. They all display a similar build up from 0,05 ms to a single peak at 8-9 ms and a maximum relaxation time of approx. 2.5 ms. Altogether this indicates that particle segregation was minimal and that the applied sedimentation procedure resulted in a homogenious sample. This sucess is of course related to the particular soil in this study as another attempt of laboratory sedimentation by Stallebrass et al. (2007) was visibly heterogenous. However, it is worth noting that Røsnæs Clay is a natural material with a heterogenious mineralogy albeit with limited partice size varriation.

In the assessment of sample anisotropy generated by the oedometric compression the development of total porosity with time during free swell is plotted in Figure 3.

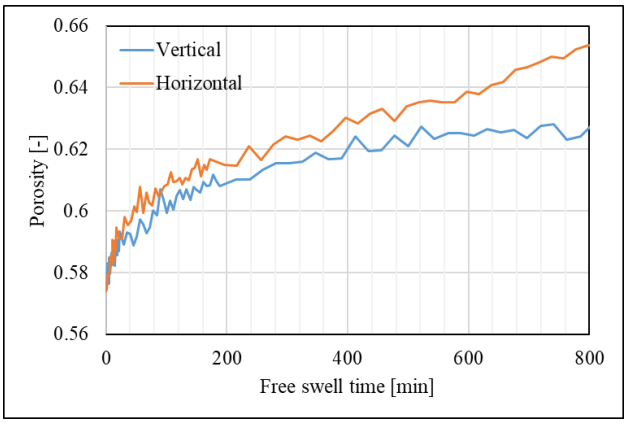

Figure 3. Time development of porosity in the vertical and horizontal specimens subjected to free swell.

From Figure 3 it may be seen that the horizontal specimen swells faster and more compared to the vertical one. At the 800 min mark the vertical specimen has a porosity of 62.8% relative to the 65.4% for the horizontal one, resulting in roughly 50% more swelling (relative to the starting point at 57.4%) of the later. Despite the horizontal specimen swelling slightly faster than the vertical one, the porosity development between the two is very comparable up to the 600 min mark, where the vertical plug plateaus while the horizontal one keeps swelling at a close-to-constant rate. This indicates, that the free swell should have been allowed to continue for a longer period of time to ensure stability of the results. However the overall trend is still clearly evident from the tests.

The clear swelling anisotropy of the sample shows that the anisotropic stress state during compression caused particle rearrangement, which is retained after release of this stress state (during dismantling where the stress state becomes isotropic). The NMR free swell tests can be used to quantify the degree of anisotropy, however for a more direct assessment of the particle arrangement, these results must be compared to e.g. molecular dynamic modelling or scanning electron microscopy performed on planes positioned at different height along the specimens.

While Figure 3 shows the development of porosity during free swell, no information is gained about how the pore space changes to accommodate this increase of porosity. To illustrate this, the pore size distribution before and after free swell are compared in Figure 4. Here it may be seen, that the pore size distribution retains its general shape during the free swell regardless of the specimen orientation. The curves expand in the direction of the largest pores, such that the initial build up of the porosity distribution is completely unchanged, while the front moves to larges relaxation times.

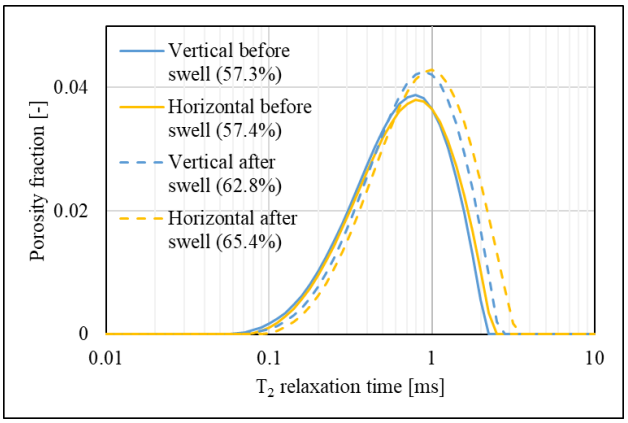

Figure 4. Bulk porosity before and after free swelling with their total porosity noted in the legend.

Because the size of the smallest pores are almost unchanged, the particle interactions occur at the same positions (hence the electro-static repulsion is unchanged) and the stress release causes "only" an elastic rebound of the entire soil skeleton. Since this process is the same in both the horizontal and vertical directions, the anisotropy must be related to boundary conditions of the plugs hence which plane (vertical or horizontal) allowed to deform.

4 CONCLUSIONS

The presented investigations confirm the usefulness of laboratory resedimentation for creating representative reference samples with minimal heterogeneity, provided particle size is below 63 microns. After laboratory sedimentation and compression of a high plasticity clay (Røsnæs Clay) a homogeneous pore size distribution, as measured through NMR T_2 relaxation, was observed throughout the sample. Only minimal variations occurred, which fall within the accuracy of the measurement method. In addition to the particular presented case, the study illustrates the usefulness of NMR measurements in evaluating sample homogeneity. Although applied destructively in this study (by sub-sampling), the method also has potential for being applied non-destructively through imaging or slice selective bulk measurements. Beyond the evaluation of the homogeneity, the investigations showed that significant sample anisotropy emerges from the sedimentation and compression process as a 4% increase of free swell is observed in the horizontal relative to vertical direction. This quantification represents a key step in understanding the development of stress induced anisotropy.

ACKNOWLEDGEMENTS

The authors are grateful for the financial support provided by DTU offshore, through the Carbon Storage Program. The results presented were performed as part of the CO_2 Seal Integrity project.

REFERENCES

ASTM D7928 (2021). Particle-size distribution (gradation) of fine-grained soils using the sedimentation (hydrometer) analysis. ASTM International. 10.1520/D7928-21E01.

Awadalkarim, A. (2014). *Petrophysics of Palaeogene sediments*. PhD thesis, Technical University of Denmark, Kgs. Lyngby, DK.

Burland, J. B. (1990). On the compressibility and shear strength of natural clays. *Géotechnique* 40(3), 329-378. doi.org/10.1680/geot.1990.40.3.329.

Cotecchia, F. and Chandler, R. J. (2000). A general framework for the mechanical behaviour of clays. *Géotechnique* 50(4), 431-447. doi.org/10.1680/geot.2000.50.4.431.

Di Remigio, G. (2022). *Multiscale assessment of swelling and compressibility of fine grained geomaterials*. PhD thesis, Technical University of Denmark, Kgs. Lyngby, DK.

Kinslev, E. M. (2022). *Efficient performance of large infrastructure: a geomechanical approach towards sustainable design*. PhD thesis, Technical University of Denmark, Kgs. Lyngby, DK.

Kinslev, E. M., Hededal, O., Rocchi, I. and Zania, V. (2022). Influence of pore water composition on the compressibility of a Danish high plasticity Paleogene clay during sedimentation. *Proceedings of the 20th Internatinal Conference on Soil Mechanics and Geotechnical Engineering.*

Stallebrass, S. E., Atkinson, J. H. and Mašin, D. (2007). Manufacture of samples of overconsolidated clay by laboratory sedimentation. *Géotechnique* 57(2), 249-253. doi.org/10.1680/geot.2007.57.2.249.

Zhao, B. and Santamarina, J. C. (2022). Fine-Grained Sediment Characterization and Process Monitoring Using Nuclear Magnetic Resonance (NMR). Geotechnical Testing Journal 45(4), 877-890. doi.org/10.1520/GTJ20210144.

Proceedings of the XVIII ECSMGE 2024
GEOTECHNICAL ENGINEERING CHALLENGES
TO MEET CURRENT AND EMERGING NEEDS OF SOCIETY
© 2024 the Authors
ISBN 978-1-032-54816-6
DOI 10.1201/9781003431749-595
Open Access: www.taylorfrancis.com, CC BY-NC-ND 4.0 license

ECSMGE 24
XVIII EUROPEAN CONFERENCE
ON SOIL MECHANICS AND
GEOTECHNICAL ENGINEERING

Study on carbon-neutral ground improvement using recycled concrete fines

Étude sur l'amélioration des sols neutres en carbone en utilisant des fines de béton recyclées

T. Kono*, S. Nishiie
Takenaka R &D institute Takenaka corporation, Chiba, Japan

M. Sugimoto
Takenaka Nagoya brunch Takenaka corporation, Aichi, Japan

**koono.takao@itakenaka.co.jp*

ABSTRACT: Reducing carbon dioxide (CO_2) emissions is an important aspect of global climate change. In Japan, CO_2 emissions from cement production account for approximately 5% of total CO_2 emissions. A technology system for the substantial reduction of CO_2 emissions was developed. In this system, high-slag cement with a slag content of over 60% was newly developed. Carbonate-demolished recycled concrete fine powders (RCFs) have also been developed. RCFs contain cement hydrates, that react with CO_2 and transforms into calcium carbonate. They can be used as carbon capture and utilization (CCU) materials. New cement and carbonate RCFs have been used for soil stabilization. The new cement has a reduction performance of 70% and 40% compared whit Ordinary Portland Cement (OPC) and conventional Blast furnace cement type B (BB cement). The RCFs were carbonated under dry conditions to form a CCU material that could fix 10% CO_2 by mass. This study presents the properties of RCFs and carbonate RCFs. Subsequently, in laboratory tests, the fluidity before hardening and the compressive strength of soil stabilization were investigated. The fluidity decreased when carbonate RCFs were used, requiring the use of a chemical admixture. The compressive strength of mixtures containing carbonated RCFs was found to be 1.1 to 1.5 times higher than those without it. Based on these findings, we conclude that these new materials can be applied as environmentally friendly ground improvement solutions.

RÉSUMÉ: La réduction des émissions de CO_2 est une question importante en ce qui concerne le changement climatique mondial. Au Japon, les émissions de CO_2 liées à la production de ciment représentent environ 5% des émissions totales de CO_2 japonaises. Un système technologique permettant une réduction substantielle des émissions de CO_2 a été développé. Dans ce système, un ciment à haute teneur en laitier avec une teneur en laitier supérieure à 60% a été nouvellement développé. De plus, une poudre fine de béton recyclé décarbonatée (RCFs) a été développée. Les RCFs contiennent de l'hydratation de ciment, qui réagit avec le CO_2 et se transforme en carbonate de calcium. Ils peuvent être utilisés comme matériau de capture et d'utilisation du carbone (CCU). Le nouveau ciment et les RCFs à base de carbonate ont également été utilisés pour la stabilisation des sols. Le nouveau ciment présente une performance de réduction de 70% et 40% respectivement par rapport au ciment Portland ordinaire et au ciment de type haut fourneau conventionnel (ciment BB). Les RCFs ont été carbonatés dans des conditions sèches pour former un matériau de CCU capable de fixer 10% de CO_2 en masse. Cet article présente les propriétés des RCFs et des RCFs à base de carbonate. Ensuite, lors d'essais en laboratoire, la fluidité avant durcissement et la résistance à la compression de la stabilisation des sols ont été étudiées. Il a été observé que la fluidité diminuait lors de l'utilisation de RCFs à base de carbonate, nécessitant l'utilisation d'un adjuvant chimique. La résistance à la compression des mélanges contenant des RCFs carbonatés s'est avérée être de 1,1 à 1,5 fois supérieure à celle des mélanges sans RCFs. Sur la base de ces résultats, nous concluons que ces nouveaux matériaux peuvent être utilisés comme solutions d'amélioration des sols respectueuses de l'environnement.

Keywords: Recycled concrete fines; carbon capture and utilization; soil stabilization.

1 INTRODUCTION

Recently, reduction in CO_2 emissions has been required as a countermeasure against global warming, and in the field of geotechnics, decarbonization is additionally required because a significant amount of cement is consumed during soil stabilization, which emits a considerable amount of CO_2. Some studies have been conducted to reduce environmental impact of soil stabilization, such as adding ground- granulated blast-furnace slag, which is a by-product of steel production that serves as a binder (Kawamura and Kasai, 1999), and performing soil stabilization using

ladle furnace slag and the application of cement with a high blast furnace slag content cement had been carried out for soil stabilization (Kono et al. 2016). improvement. However, it is not possible to achieve carbon neutrality by achieving a 100% slag substitution rate, because there are limitations to the extent of substitution.

One countermeasure to achieve carbon neutrality in soil–cement stabilization is the use of recycled concrete fines (RCFs). A significant amount of RCFs is generated during the production of recycled fine and coarse aggregates from demolished concrete, and these RCFs contain cement hydrates, such as calcium hydroxide and dicalcium silicate (Jiang et al., 2022). Therefore, the use of RCFs as a carbon capture and utilization (CCU) materials are being considered because RCFs can absorb CO_2 when the powder is soaked in water containing a high concentration of CO_2 (Ho et al., 2021).

In this study, a soil stabilizer composed of cement and carbonated and CO_2-fixed RCFs was introduced to further reduce the environmental impact of soil stabilization. The RCFs were carbonated, and the amount of CO_2 fixed in the RCFs was investigated using thermogravimetric differential thermal analysis (TG/DTA). To clarify the changes in the amounts and types of hydrates in the RCFs before and after carbonation, X-ray diffraction (XRD) analyses of the uncarbonated and dry-carbonated RCFs were conducted. To confirm the fluidity of the cement slurry and the change in the strength properties owing to the addition of uncarbonated and carbonated RCFs, P-funnel and unconfined compressive tests were conducted.

2 RECYCLED CONCRETE FINES

2.1 RCFs material

The RCFs used in this study were demolished from an office building in Tokyo. The average compressive strengths of the cores were 27.4 N/mm^2. The concrete was blasted under dry conditions, which resulted in the formation of recycled fine and coarse aggregates and RCFs.

2.2 Carbonation methods

In this study, the dry RCFs method (Nishiie et al., 2023) was used. Figure 1 shows the dry carbonation system used in this study. In the dry carbonation method, naturally dried RCFs were exposed for 9 days in a chamber with a CO_2 concentration of 10%, temperature of 20 °C, and relative humidity of 60%, and they were stirred and weighed every 3 days. When the mass change of the RCFs stabilized, the carbonation of the RCFs was regarded as complete.



Figure 1. Dry carbonation system.

2.3 Physicochemical properties of RCFs

Figure 2 shows the particle size distributions of the carbonated RCFs obtained via laser diffraction analysis. The median diameters of the carbonated RCFs were 33.4 μm. Table 2 lists the densities of the RCFs before and after carbonation obtained using the gas replacement method. The density of the carbonated RCFs is approximately equal to that of the uncarbonated RCFs.

Figure 3 shows the XRD patterns of uncarbonated and dry-carbonated RCFs. Regarding the uncarbonated RCFs, the peaks of cement hydrates, such as calcium hydroxide and ettringite, appeared; however, these peaks disappeared after carbonation. This indicated that the cement hydrates reacted with CO_2 to form calcium carbonate, whereas after carbonation, cement hydrates did not appear in the RCFs.

2.4 Mass of CO_2 fixed in RCFs

The mass of CO_2 fixed in the RCFs was investigated via thermogravimetric/differential thermal analysis (TG/DTA). The relationship between the change in sample weight loss and temperature was determined via TG/DTA. In this study, weight loss occurred at temperature from 550 °C to 950 °C owing the decomposition of calcium carbonated (CaCO3), and the percent weight loss in this temperature range was regarded as the mass percentage of fixed CO_2 (Chang & Chen, 2006). The weight loss percentages in these temperature ranges were 8.2% and 11.1%, respectively. RCFs had already fixed 8% CO_2 by mass before the carbonation process, and after carbonation, the mass of CO_2 fixed in RCFs increased by 3%; hence using carbonated RCFs, approximately 10% of CO_2 by mass could be fixed, including CO_2 fixed prior to carbonation. The uncarbonated RCFs had already absorbed CO_2 because they reacted with atmospheric CO_2 in the months following production.

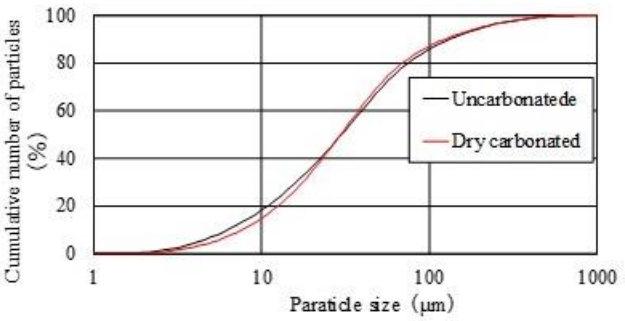

Figure 2. Particle size distribution of RCFs.

Table 1. Density of RCFs.

Type of RCFs	Density (Mg/m^3)
Uncarbonated	2.46
Dry carbonated	2.45

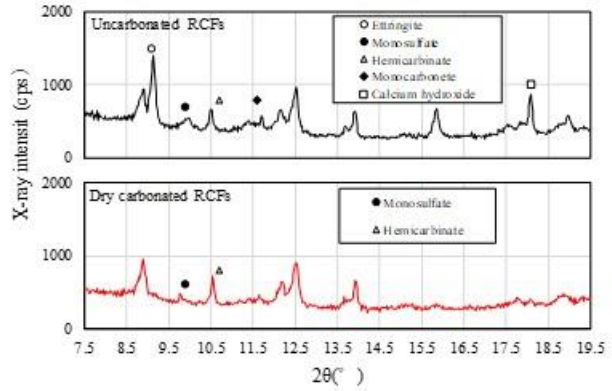

Figure 3. XRD pattens of RCFs.

3 SOIL STABILIZATION USING RCFS

3.1 Test specimens

To investigate the applicability of carbonated RCFs for soil stabilization, test specimens with simulated soil–cement columns were prepared. The type of cement used in this study was blast-furnace slag cement type B (based on the Japanese Industrial Standard), the mass of cement per unit volume (1 m^3) of soil was set to 300 kg, and the water–cement ratio was set to 1.0 The sandy soil used in the experiment was composed of silica sand and Gairome clay at a mass ratio of 9:1 and a water content of 18%. All the specimens were cylindrical with a radius of 50 mm and a height of 100 mm.

Table 1 lists the mix proportions and masses of each specimen. The effects of the type and amount of carbonated RCFs added to the soil–cement column on its physicochemical properties were investigated. In addition, to investigate the effect of the reduced water–powder ratio owing to powder addition on the strength of the soil–cement column, specimens with sandstone powder, which featured low reactivity and a particle size distribution similar to that of the RCFs, were prepared. Uncarbonated and carbonated RCFs and sandstone powder were added at 30%, 60%, and 90% of the cement mass.

Table 1. Mix proportion.

No	Mass of cement (kg/m^3)	Mass of water (kg/m^3)	Type of add material	Mass of add material (kg/m^3)
1	300	300	-	-
2	300	300	Uncarbo. RCFs	90
3	300	300	Uncarbo. RCFs	180
4	300	300	Uncarbo. RCFs	270
5	300	300	Carbo. RCFs	90
6	300	300	Carbo. RCFs	180
7	300	300	Carbo. RCFs	270
8	300	300	Stone powder	90
9	300	300	Stone powder	180
10	300	300	Stone powder	270

3.2 Fluidity of cement slurry

In this study, the CDM method was used to construct soil stabilization using RCFs. The fluidity of the cement slurry was evaluated using the P-funnel flow time. Using a Hobart mixer, cement, added material, and water were mixed for 5 min to produce a cement slurry. Figure 4 shows the P-funnel flow time of the cement slurry. It was found that adding RCFs increased the P-funnel flow time compared to the addition of sandstones. In particular, for dry carbonated RCFs, the impact on the increase in the P-funnel flow time was significant. Furthermore, when 90% of the RCFs had been added, the test could not be conducted.

In the CDM method, the pumping of the cement slurry is possible if the P-funnel flow time is less than 15 s (Ban et al., 1995). Therefore, if the water-cement ratio of the cement slurry is 100%, it would be necessary to use chemical admixtures to improve the fluidity and add RCFs in a proportion greater than 30%.

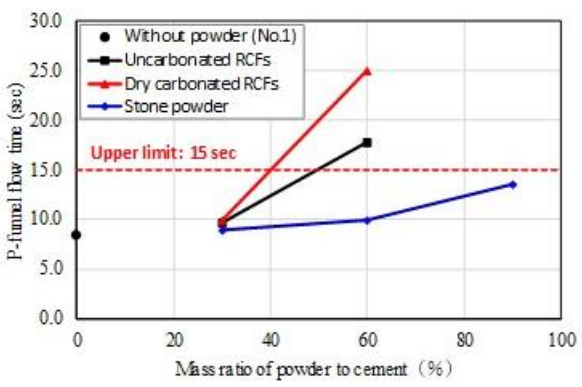

Figure 4. Test results of P- funnel flow time.

3.3 Unconfined compressive strength

Figure 5 shows the compressive strength after curing period of four weeks. The compressive strengths of the specimens containing sandstone powder were 1.05 to 1.13 times higher than those without powder. In the specimens containing uncarbonated RCFs, the compressive strengths were 1.24 to 1.39 times higher than those without powder. The compressive strengths of the specimens containing dry carbonated RCFs were 1.15 to 1.52 times higher.

Based on these results, a greater increase in compressive strength was observed in the specimens containing uncarbonated and carbonated RCFs than in those containing sandstone powder, confirming the effectiveness of adding RCFs in increasing the strength of the soil stabilization, and an increase in the RCFs ratio increased the strength of the soil stabilization.

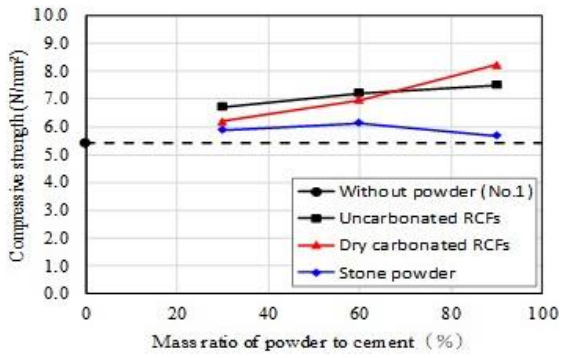

Figure 5. Compression strength of soil stabilization.

4 CONCLUSION

In this study, the physicochemical properties of the RCFs generated during the crushing of waste concrete with CO_2 fixed and the applicability of soil stabilization with carbonated RCFs were investigated. The density of the RCFs slightly increased after wet carbonation, whereas it did not change after dry carbonation, and the particle size distribution did not change regardless of the carbonation condition. The RCFs absorbed CO_2 and were fixed at a 10% CO_2 mass. By adding carbonated RCFs, the compressive strength of the soil stabilization was 1.2 to 1.5 times higher than that of the soil stabilization without using RCFs. The impact of the RCFs' carbon dioxide fixation capacity of RCFs and the strength of soil stabilization are influenced by properties such as the strength of the dismantled concrete; therefore, it will be necessary to investigate this variability. Furthermore, it is necessary to investigate the alkaline properties and hexavalent chromium leaching characteristics of carbonated RCFs as well as soil stabilization using carbonated RCFs.

ACKNOWLEDGEMENTS

This study was supported by the “Development of Technologies for Producing Concrete and Cement Using CO_2” project (JPNP21014) of the New Energy and Industrial Technology Development Organization (NEDO).

REFERENCES

Ban K., Asano Junichi and Takahashi K. (1995). Mixture Proportions for Deep Mixing Method Using Fly Ash (FGC) and Engineering Characteristics of FGC Treated Soil, Cement Science and Concrete Technology, Proceedings of Annual Conference of The Japan Society of Civil Engineers, No.50, 1536-1537. (in Japanese).

Chang, C. & Chen, J. (2006). The experimental investigation of concrete carbonation depth. Cement and Concrete Research, 36, 1760-1767. https://doi.org/10.1016/j.cemconres.2004.07.025.

Ho, H., Iizuka, A., Shibata, E., Tomita, H., Takano, K., & Endo, T. (2021). Utilization of CO_2 in direct aqueous carbonation of concrete fines generated from aggregate recycling: Influences of the solid–liquid ratio and CO_2 concentration. Journal of Cleaner Production, 312, 127832. https://doi.org/10.1016/j.jclepro.2021.127832.

Jiang, Y., Li, B., Liu, S., He, & J., Hernandez, A. G. (2022). Role of recycled concrete powder as sand replacement in the properties of cement mortar. Journal of Cleaner Production, 371, 133424. https://doi.org/10.1016/j.jclepro.2022.133424.

Kawamura, M. and Kasai, Y. (1999). An experimental study on the mix proportion, strength and densities of soil–cement concrete substituted cement with a granulated blast furnace slag. Concrete Research and Technology, 10(1), 123-132. (in Japanese) https://doi.org/10.3151/crt1990.10.1_123.

Kono T., Aoki M. and Yonezawa T. (2016). Development of Low CO_2 Emission Soil Improvement Using High-Slag Cement, Civil Engineering Conference in the Asia Region CECAR7 (CD-ROM).2-1279.

Nishiie, S., Kono, T. and Sugimoto M. (2023). Reducing the environmental impact of soil cement stabilization using fine powder generated during crushing waste concrete with carbon dioxide fixed, Proceedings of the 9ICEG, 325-332.

Wang, L., Wang, J., Wang, H., Fang, Y., Shen, W. & Chen, P. (2022). Eco-friendly treatment of recycled concrete fines as supplementary cementitious materials. Construction and Building Materials, 322, 126491. https://doi.org/10.1016/j.conbuildmat.2022.126491.

Proceedings of the XVIII ECSMGE 2024
GEOTECHNICAL ENGINEERING CHALLENGES
TO MEET CURRENT AND EMERGING NEEDS OF SOCIETY
© 2024 the Authors
ISBN 978-1-032-54816-6
DOI 10.1201/9781003431749-596
Open Access: www.taylorfrancis.com, CC BY-NC-ND 4.0 license

ECSMGE 24
XVIII EUROPEAN CONFERENCE ON SOIL MECHANICS AND GEOTECHNICAL ENGINEERING

Formulation of a practical multi-surface plasticity model for sands

Formulation d'un modèle pratique de plasticité multi-surfaces pour les sables

D. Konstantinidis*, H.J. Burd, C.M. Martin
Department of Engineering Science, University of Oxford, Oxford, UK

**dimitrios.konstantinidis@eng.ox.ac.uk*

ABSTRACT: This paper presents a new effective stress constitutive model for sands subjected to either monotonic or cyclic loading; the model is referred to as 'PIMSS' (Parallel Iwan Multi-Surface Sand). PIMSS has been developed for geotechnical design applications with an emphasis on the simulation of offshore wind turbine (OWT) monopile foundations in sand. The model employs a parallel Iwan approach, comprising multiple elastoplastic micro-models; it is capable of predicting Masing-type nonlinear hysteretic response without the need for translating surfaces and kinematic hardening rules. From an industry perspective, an attractive feature of the PIMSS model is that it can readily be calibrated via standard geotechnical laboratory testing procedures. An advantage of this modelling concept is that each micro-model is numerically implemented as a single-surface plasticity model; this eases the model implementation process. The theoretical framework and calibration processes for the model are explained. Single-element simulations and comparisons with available test data are described.

RÉSUMÉ: Cet article présente un nouveau modèle constitutif de contrainte effective pour les sables soumis à un chargement monotone ou cyclique; le modèle est appelé « PIMSS » (Parallel Iwan Multi-Surface Sand). PIMSS a été développé pour les applications de conception géotechnique en mettant l'accent sur la simulation des fondations monopieux d'éoliennes offshore (OWT) dans le sable. Le modèle utilise une approche Iwan parallèle, comprenant plusieurs micro-modèles élastoplastiques; il est capable de prédire la réponse hystérétique non linéaire de type Masing sans avoir besoin de surfaces de translation et de règles de durcissement cinématique. Du point de vue de l'industrie, une caractéristique intéressante du modèle PIMSS est qu'il peut être facilement calibré via des procédures d'essais géotechniques standard en laboratoire. Un avantage de ce concept de modélisation est que chaque micro-modèle est implémenté numériquement comme un modèle de plasticité à surface unique; cela facilite le processus de mise en œuvre du modèle. Le cadre théorique et les processus d'étalonnage du modèle sont expliqués. Des simulations à élément unique et des comparaisons avec les données de test disponibles sont décrites.

Keywords: Constitutive model; monotonic and cyclic loading; sands; multi-surface plasticity; parallel Iwan approach.

1 INTRODUCTION

Consideration of cyclic loading is crucial for designing offshore wind turbine (OWT) foundations, necessitating the use of appropriate constitutive models for accurate numerical simulations of their response. Over the past decades, there has been a proliferation of advanced constitutive models that have been proposed and effectively employed in the simulation of the monotonic loading of sandy soils. However, these models exhibit limitations in their ability to replicate faithfully the behaviour of sands under cyclic loading conditions (Konstantinidis et al., 2023). Moreover, these models often require extensive calibration procedures and frequently prove insufficient for accurately representing all loading conditions using a single set of parameters.

This paper intends to present further details of a recently-developed effective stress model, 'PIMSS' (Konstantinidis et al., 2023), for monotonic and cyclic loading. This model has been developed for the simulation of OWT monopile foundations in sand, aiming to predict the behaviour during representative storm loading. The predictability of the PIMSS model is assessed with single-element simulations and comparisons with experimental data from laboratory tests performed on Karlsruhe fine sand (Wichtmann & Triantafyllidis, 2016a, 2016b).

2 DESCRIPTION OF THE PIMSS MODEL

The PIMSS model is classified within the multi-surface model category and is based on the parallel approach. The multi-surface plasticity concept originated with Iwan (1967), who proposed two one-dimensional models, termed as 'parallel-series' and 'series-parallel' respectively, for brevity replaced by

'parallel' and 'series' in this paper. Subsequently, various three-dimensional continuum models have been developed using both the parallel (Dawson, 2013; Whyte et al., 2020) and series (Cerfontaine, 2014; Prevost, 1985) concepts as a basis.

A motivation for the development of PIMSS was the promising predictive performance of the Prevost model (Cerfontaine, 2014), which inspired an exploration into the potential performance of a parallel version of the model without kinematic hardening. When the parallel approach is employed to formulate a constitutive model, several individual micro-models are arranged in parallel and consequently experience the same strain history (Whyte et al., 2020). The resulting macro-stress tensor ($\boldsymbol{\sigma}$) is computed by aggregating the individual micro-stress tensors ($\boldsymbol{\sigma}_{micro}$) through a weighted sum, as follows:

$$\boldsymbol{\sigma} = \sum_{i=1}^{n} w_i \cdot \boldsymbol{\sigma}_{micro}; \qquad \sum_{i=1}^{n} w_i = 1 \quad (1)$$

where n is the total number of micro-models and w_i is the weight corresponding to each micro-model.

The numerical implementation of PIMSS involves the parallel arrangement of several stationary micro-models incorporating the same yield surface, plastic potential, and elasticity as the Prevost model implementation by Cerfontaine (2014). The yield surface equation of the *i*th micro-model is

$$f^i = \boldsymbol{s}^i : \boldsymbol{s}^i - \frac{2}{3}\left(p^i \cdot M^i\right)^2 = 0 \quad (2)$$

where $\boldsymbol{s}^i$and p^i are the deviatoric stress tensor and the mean effective stress respectively, and M^i is a material parameter controlling the aperture of the cone of each micro-model. The incremental plastic strain direction $\boldsymbol{P}^i$ of each micro-model is broken down into a deviatoric component, which is associative, and a volumetric component, which is non associative, as:

$$\boldsymbol{P}^i = (\boldsymbol{P}^i)' + (P^i)'' \cdot \boldsymbol{\delta} \quad (3)$$

$$\left(\boldsymbol{P}^i\right)' = \frac{2 \cdot \boldsymbol{s}^i}{\left\| \frac{\partial f^i}{\partial \boldsymbol{\sigma}^i} \right\|} \quad (4)$$

$$(P^i)'' = \frac{\psi^i}{3} \cdot \frac{(\eta^i)^2 - (\bar{\eta}^i)^2}{(\eta^i)^2 + (\bar{\eta}^i)^2} \text{ and } \eta^i = \frac{(3/2 \cdot \boldsymbol{s}^i : \boldsymbol{s}^i)^{1/2}}{p^i} \quad (5)$$

where $(\boldsymbol{P}^i)'$ is the deviatoric component of the plastic strain rate direction and $(P^i)'' \cdot \boldsymbol{\delta}$ is its volumetric component, ψ^i is a material parameter scaling the volumetric component of the plastic strain rate and $\bar{\eta}^i$ is a material parameter indicating the stress ratio at phase transformation. In terms of the elastic part of each micro-model, the dependency of stiffness on the mean effective stress is:

$$G^i(p^i) = {G_0}^i \cdot \left(\frac{p^i}{p_{ref}}\right)^{0.5} \quad (6)$$

where G^i is the shear stiffness, p_{ref} is a reference pressure, ${G_0}^i$ is the small-strain shear modulus at the reference pressure. A constant Poisson's ratio of ν=0.05 is adopted.

3 CALIBRATION OF THE PIMSS MODEL

As PIMSS is not a critical state model a specific set of parameters is needed for different sand densities. This paper examined the performance of PIMSS for both loose and medium dense Karlsruhe fine sand with corresponding relative densities D_{r0} in the range 15% to 29% and 57% to 68% respectively. The parameters adopted for these relative density ranges are listed in Table 1 and Table 2.

PIMSS was calibrated by fitting the backbone stress-strain curve of a drained triaxial compression test corresponding to each density range. This included the distribution of the stiffness and strength parameters among its components, each assigned equal weighting, following the procedure:

- The maximum shear stiffness, G_{max}, is estimated from the backbone curve.
- The amount of shear stiffness decrease for each micro-model, from its maximum value, G_{max}, is equal to $G_{step} = G_{max}/\text{NMM}$ (where NMM is the total number of micro-models).
- The shear stiffness of each micro-model is calculated as:

$$G^1 = G_{max}$$
$$G^N = G^{N-1} - G_{step} \quad (7)$$

- The deviatoric strain values, ${\varepsilon_q}^i$, corresponding to the yield of each micro-model are selected.
- The deviatoric yield stresses, q_i, are found as:

$$q^i = 3G^i \times {\varepsilon_q}^i \quad (8)$$

The deviatoric yield stresses, q^i, can be used to find M^i, by solving equation (2) for each micro-model considering that $\Delta q^i / \Delta p^i = 3$. In relation to the plastic potential parameters $\bar{\eta}^i$ and ψ^i, the micro-models are grouped into two categories. Micro-models 1-7 are configured such that they lead to a purely contractive behaviour, while micro-models 8-15 initially exhibit a smaller contractive response but then a more

pronounced dilation. The combination of these two sets of micro-models results in an appropriate overall response. As indicated in Table 1 and Table 2, $\bar{\eta}^i$ and ψ^i required adjustments for the cyclic simulations, and therefore, the values within parentheses were used, which differ from the values used in the monotonic simulations.

4 SINGLE-ELEMENT SIMULATIONS

Figure 1 illustrates simulations of monotonic drained triaxial compression tests conducted on loose ($15\% \leq D_{r0} \leq 25\%$) and medium dense sand samples ($57\% \leq D_{r0} \leq 68\%$) under different initial stress conditions (cell pressures of 50, 100, 200 and 400 kPa). Concerning the looser densities, PIMSS can reproduce all stress-strain curves quite accurately. However, PIMSS overestimates the shear strength of the medium dense sand samples at large strain levels as its current formulation does not account for softening. Regarding the volumetric response, PIMSS performs well overall, however it slightly overestimates contraction for the loose sands and underestimates dilation for the denser ones.

Figure 2 depicts simulations of monotonic undrained triaxial compression tests conducted on loose ($D_{r0} = 29\%$) and medium dense sand samples ($60\% \leq D_{r0} \leq 64\%$) under various initial stress conditions (cell pressures of 100, 200, 300 and 400 kPa). PIMSS captures the stress-strain response of the undrained tests well, overpredicting slightly the dilative tendency of the looser sample. Good agreement between the simulations and the laboratory data can also be deduced regarding the stress paths. However, for the density of $D_{r0} = 29\%$ the initial contractive tendency of the sample was underestimated.

Figure 3 shows simulations of undrained cyclic triaxial tests on loose ($D_{r0} = 29\%$) and medium dense ($64\% \leq D_{r0} \leq 66\%$) sand samples after isotropic consolidation. Large strain amplitudes are applied to the samples. From the stress-strain responses, it is seen that PIMSS can predict adequately the stiffness degradation that occurs in the sand sample. However, PIMSS cannot predict liquefaction of the samples as shear locking occurs.

5 CONCLUSIONS

A practical multi-surface effective stress model, PIMSS, employing a parallel arrangement of stationary micro-models, has been presented. This study compared single-element simulations with test data, yielding promising results under both monotonic and cyclic conditions under different densities. As the core PIMSS model framework is flexible, it can be adapted to address specific geotechnical problems through extensions and customized calibration, aligned with the design application at hand. Future modifications of the model will further improve its predictive capability.

ACKNOWLEDGEMENTS

The first author gratefully acknowledges the financial support of Fugro GB Marine Limited.

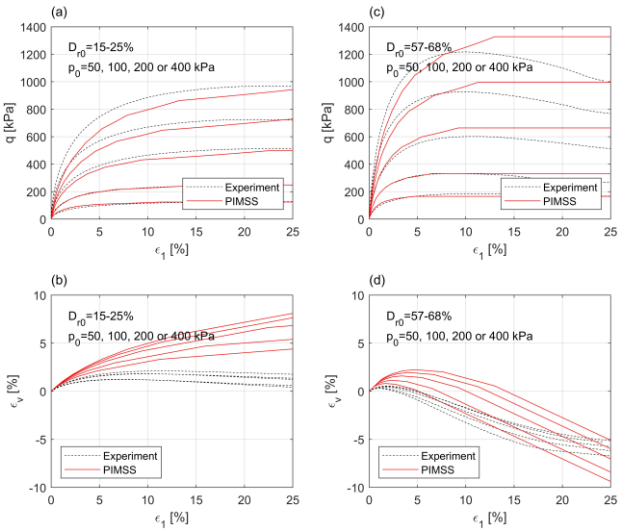

Figure 1. Simulations of drained monotonic triaxial tests on loose and medium dense Karlsruhe fine sand samples with different initial stresses (Wichtmann & Triantafyllidis, 2016a).

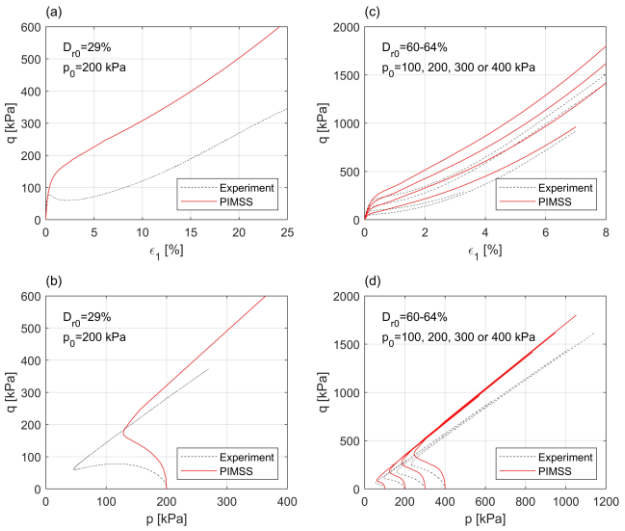

Figure 2. Simulations of undrained monotonic triaxial tests on loose and medium dense Karlsruhe fine sand samples with different initial stresses (Wichtmann & Triantafyllidis, 2016a).

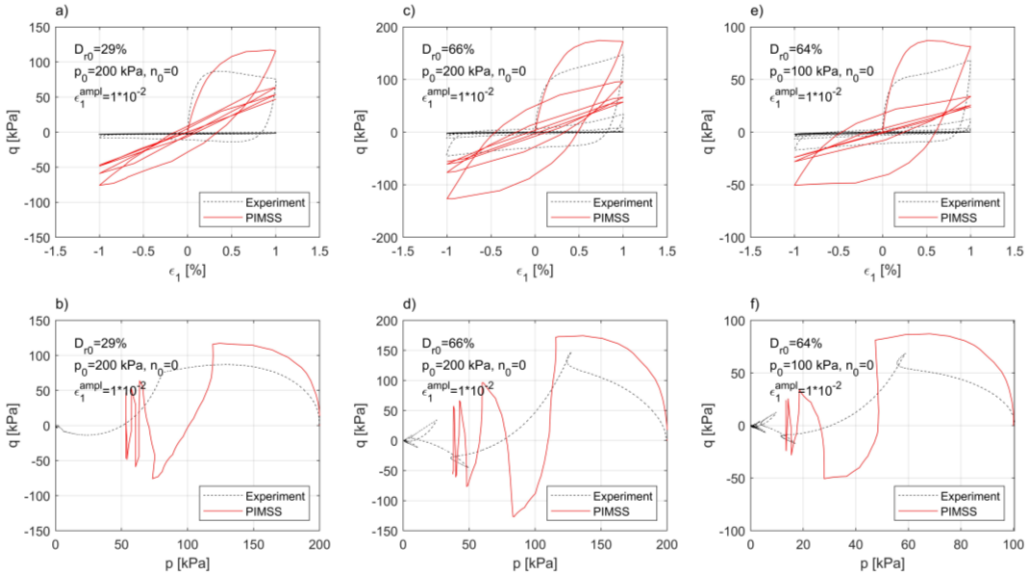

Figure 3. Simulations of undrained cyclic triaxial tests on loose and medium dense Karlsruhe fine sand samples with different initial stresses (Wichtmann & Triantafyllidis, 2016b).

Table 1. PIMSS model parameters for Karlsruhe fine sand with a relative density D_{r0} in the range 15 to 29%.

Surface	**1**	**2**	**3**	**4**	**5**	**6**	**7**	**8**	**9**	**10**	**11**	**12**	**13**	**14**	**15**
w^i [-]	0.062	0.067	0.067	0.067	0.067	0.067	0.067	0.067	0.067	0.067	0.067	0.067	0.067	0.067	0.067
M^i [-]	0.108	0.196	0.293	0.414	0.647	0.75	0.818	1.04	1.235	1.4	1.65	1.8	1.9	2	2.15
$G_0{}^i$ [kPa]	25	23.33	21.67	20	18.33	16.67	15	13	11.67	10	8.33	6.67	5	3.33	1.67
Micro-models 1-7	$\bar{\eta}^i$ [-]				ψ^i [-]				**Micro-models 8-15**	$\bar{\eta}^i$ [-]			ψ^i [-]		
	$1.5M^i$ ($3M^i$)				0.9					$0.65M^i$ ($2M^i$)			0.9		

Table 2. PIMSS model parameters for Karlsruhe fine sand with a relative density D_{r0} in the range 57 to 68% (Konstantinidis et al., 2023).

Surface	**1**	**2**	**3**	**4**	**5**	**6**	**7**	**8**	**9**	**10**	**11**	**12**	**13**	**14**	**15**
w^i [-]	0.062	0.067	0.067	0.067	0.067	0.067	0.067	0.067	0.067	0.067	0.067	0.067	0.067	0.067	0.067
M^i [-]	0.124	0.211	0.4	0.64	0.838	1.0	1.2	1.4	1.5	1.6	1.8	2.0	2.05	2.15	2.3
$G_0{}^i$ [kPa]	37	34	33	32	30	28	25	20	19	17	15	13	10	7	5
Micro-models 1-7	$\bar{\eta}^i$ [-]				ψ^i [-]				**Micro-models 8-15**	$\bar{\eta}^i$ [-]			ψ^i [-]		
	$2M^i$ ($2.5M^i$)				1.7 (0.9)					$0.5M^i$ ($1.3M^i$)			1.1 (0.9)		

REFERENCES

Cerfontaine, B. (2014). *The cyclic behaviour of sand, from the Prevost model to offshore geotechnics*, Doctoral Dissertation, Université de Liège.

Dawson, E. M. (2013). A parallel Iwan model for 3D cyclic loading of frictional materials. In: *Proceedings of the 3rd International FLAC/DEM Symposium*.

Iwan, W. D. (1967). On a class of models for the yielding behavior of continuous and composite systems. *J. Appl. Mech.*, 34(3), 612–617. https://doi.org/10.1115/1.3607751.

Konstantinidis, D., Martin, C. M., & Burd, H. J. (2023). Evaluation of three advanced constitutive models for cyclic loading of sands. In: *10th European Conference on Numerical Methods in Geotechnical Engineering (NUMGE2023)*.

Prevost, J. H. (1985). A simple plasticity theory for frictional cohesionless soils. *Int. J. Soil Dyn. Earthquake Eng.*, 4(1), 9–17. https://doi.org/10.1016/0261-7277(85)90030-0.

Whyte, S. A., Burd, H. J., Martin, C. M., & Rattley, M. J. (2020). Formulation and implementation of a practical multi-surface soil plasticity model. *Computers and Geotechnics*, 117. https://doi.org/10.1016/j.compgeo.2019.05.007.

Wichtmann, T., & Triantafyllidis, T. (2016a). An experimental database for the development, calibration and verification of constitutive models for sand with focus to cyclic loading: part II—tests with strain cycles and combined loading. *Acta Geotechnica*, 11(4), 763–774. https://doi.org/10.1007/s11440-015-0412-x.

Wichtmann, T., & Triantafyllidis, T. (2016b). An experimental database for the development, calibration and verification of constitutive models for sand with focus to cyclic loading: part I—tests with monotonic loading and stress cycles. *Acta Geotechnica*, 11(4), 739–761. https://doi.org/10.1007/s11440-015-0402-z.

Proceedings of the XVIII ECSMGE 2024
GEOTECHNICAL ENGINEERING CHALLENGES
TO MEET CURRENT AND EMERGING NEEDS OF SOCIETY
© 2024 the Authors
ISBN 978-1-032-54816-6
DOI 10.1201/9781003431749-597
Open Access: www.taylorfrancis.com, CC BY-NC-ND 4.0 license

ECSMGE 24
XVIII EUROPEAN CONFERENCE ON SOIL MECHANICS AND GEOTECHNICAL ENGINEERING

Adaptation of a constitutive model for sand to account for non-plastic fines

Adaptation d'un modèle constitutif du sable pour tenir compte des fines non plastiques

D. Konstantinidis*, C.M. Martin, H.J. Burd
Department of Engineering Science, University of Oxford, Oxford, UK
**dimitrios.konstantinidis@eng.ox.ac.uk*

ABSTRACT: With the continued development of offshore wind farms in the North Sea it is apparent that seabed sand layers often incorporate a significant fines content within the sand grain skeleton. The presence of fines can alter the mechanical behaviour of the soil from the 'clean sand' case. When modelling sand with fines it is common industry practice to employ constitutive models for clean sand, either by re-calibrating the models to account for the presence of fines or by disregarding the influence of fines. This paper describes modifications to an existing constitutive model for sand, 'Ta-Ger', so that it is able to predict the behaviour of sand with a range of fines contents, f_c. The influence of the fines is addressed via equivalent granular state theory (EGST). The resulting model is shown to capture the effects of initial void ratio and stress level as well as being able to account for a varying fines content. Comparisons with some available test data are described.

RÉSUMÉ: Avec le développement continu des parcs éoliens offshore en mer du Nord, il apparaît clairement que les couches de sable des fonds marins incorporent souvent une teneur importante en fines dans le squelette des grains de sable. La présence de fines peut altérer le comportement mécanique du sol du cas « sable propre ». Lors de la modélisation du sable contenant des fines, il est courant dans l'industrie d'utiliser des modèles constitutifs pour le sable propre, soit en recalibrant les modèles pour tenir compte de la présence de fines, soit en ignorant l'influence des fines. Cet article décrit les modifications apportées à un modèle constitutif existant pour le sable, « Ta-Ger », afin qu'il soit capable de prédire le comportement du sable avec une gamme de teneurs en fines, f_c. L'influence des fines est abordée via la théorie de l'état granulaire équivalent (EGST). Il est démontré que le modèle résultant capture les effets de l'indice de vide initial et du niveau de contrainte, tout en étant capable de prendre en compte une teneur variable en fines. Des comparaisons avec certaines données de test disponibles sont décrites.

Keywords: Constitutive model; sand; fines; critical state; equivalent granular state theory.

1 INTRODUCTION

Over the past decades, constitutive modelling for clean sand has advanced significantly. One notable achievement has been the incorporation of critical state theory (Roscoe et al., 1958) together with the state parameter framework (Been & Jefferies, 1985) within the core formulation of constitutive models for sand. Models based on this approach (e.g. Li & Dafalias, 2000) attempt to unify the prediction of dense and loose sand behaviour, accounting for the effects of void ratio and stress level with a single set of material parameters.

However, natural sand deposits often contain significant quantities of fines within the sand grain skeleton. Hence, a need for predicting the behaviour of sand with different fines contents, f_c, has arisen. In terms of constitutive modelling, this suggests that a model should be able to simulate the behaviour of a sand with different percentages of fines, without the need to adjust the model constants for each specific case. This has been achieved via equivalent granular state theory (EGST) (Rahman, 2021) for sands with non-plastic or low-plasticity fines. Specifically, the void ratio e and state parameter ψ in a 'clean sand' state-dependent model are replaced by an equivalent granular void ratio e^* and equivalent granular state parameter ψ^* (Lashkari, 2014; Rahman et al., 2014; Rahman & Dafalias, 2022). This paper evaluates whether EGST can be used to develop a sand-with-fines model based on the state-dependent sand model 'Ta-Ger', specifically its 'formulation B' (Tasiopoulou & Gerolymos, 2016), denoted here as 'Ta-Ger B'. The predictive capability of the proposed model is assessed via single element simulations and comparisons with data from laboratory tests on mixtures of Sydney sand and Majura silt (Rahman et al., 2011).

2 MODEL DEVELOPMENT

2.1 Equivalent granular void ratio e^* and state parameter ψ^*

This study concerns sand-silt mixtures that fall under the 'fines-in-coarse' category (Thevanayagam & Martin, 2002). To account for the participation of fines in load-bearing microstructure and the density state of 'fines-in-coarse' mixtures, the equivalent granular void ratio e^* was defined by Thevanayagam & Martin (2002) as:

$$e^* = \frac{e+(1-b)f_c}{1+(1-b)f_c} \quad (1)$$

where b is the fraction of fines that actively takes part in force transmission in the soil skeleton. For the calculation of b, this study adopts a semi-empirical equation proposed by Rahman & Lo (2008):

$$b = \left[1 - exp\left(-0.3\frac{1}{1-\chi^{-0.25}}\frac{f_c}{f_{thre}}\right)\right]\left(\frac{1}{\chi}\frac{f_c}{f_{thre}}\right)^{1/\chi} \quad (2)$$

where χ is the particle size ratio, defined as D_{10}/d_{50} (D_{10} is the effective size of the host sand and d_{50} is the median size of the fines). f_{thre} is the threshold fines content, which delimits a 'fines-in-sand' from a 'sand-in-fines' mixture (Thevanayagam & Martin, 2002), and can be determined either from empirical relationships (Rahman & Lo, 2008) or experimentally.

As described by the state parameter framework (Been & Jefferies, 1985), the mechanical behaviour of clean sands depends on the combined effects of the void ratio and the mean effective normal stress. Been and Jefferies proposed a state parameter $\psi = e - e_c$, where e_c is the void ratio on the critical state line (CSL) corresponding to the current mean effective stress p. Accordingly, with EGST, an equivalent granular state parameter ψ^* can be defined in terms of the equivalent granular void ratio as $\psi^* = e^* - e_c^*$ (note that $e_c^* = e_c$, as the equivalent granular CSL coincides with the CSL for $f_c = 0$).

2.2 Constitutive formulation

The Ta-Ger model is based on a framework that combines perfect elastoplasticity with smooth hysteresis by introducing a Bouc-Wen motivated hardening law. The main deviation of this approach from classical plasticity is the introduction of a plastic modulus which scales the plastic part of the incremental stiffness matrix instead of being defined as an additive term in the denominator (Tasiopoulou & Gerolymos, 2016):

$$\boldsymbol{E}_h^{ep} = \boldsymbol{E}^e\left[\boldsymbol{I} - \frac{\boldsymbol{\Phi}_g\boldsymbol{\Phi}_f{}^T\boldsymbol{E}^e\boldsymbol{H}}{\boldsymbol{\Phi}_f{}^T\boldsymbol{E}^e\boldsymbol{\Phi}_g}\right] \quad (3)$$

where $\mathbf{E}^e$ is the elastic stiffness matrix, $\boldsymbol{\Phi}_f$ and $\boldsymbol{\Phi}_g$ are the gradients of the yield surface and plastic potential surface, and $\mathbf{H}$ is the matrix playing the role of the plastic modulus. $\mathbf{H}$ is defined as $\mathbf{H} = \zeta^n\mathbf{I}$, where ζ is responsible for the hardening/softening through a mapping rule and n is a hardening parameter.

In line with the approach suggested by Rahman et al. (2014), all the constitutive equations of Ta-Ger B are retained as originally proposed (Tasiopoulou & Gerolymos, 2016) with no further reformulation, except for the substitution of e^* and ψ^* for e and ψ. Other variables affected by this substitution will also be denoted with a superscripted star. For brevity, only the modified equations will be shown. The elastic matrix $\mathbf{E}^e$ of Ta-Ger B is composed of terms that are functions of non-linear shear (G) and bulk (K) moduli (Li & Dafalias, 2000), giving:

$$G^* = G_0 p_a \frac{(2.97-e^*)^2}{1+e^*}\left(\frac{p}{p_a}\right)^m \quad (4)$$

where G_0 and m are dimensionless material parameters, and p_a is atmospheric pressure. The bulk modulus K^* is obtained from $K^* = 2G^*(1+v)/3(1-2v)$ assuming a constant Poisson's ratio, v. Rahman et al. (2012) showed that the influence of fines on the shear modulus G can be adequately captured by substituting e^* for e as shown in equation (4). Critical state compatibility is achieved via the phase transformation stress ratio, M_{pt}, and the bounding surface stress ratio, M_s, which are modified via the substitution of ψ^* for ψ:

$$M_{pt}^* = M_{cs}e^{n_d\psi^*},\ M_s^* = M_{cs}e^{-n_b\psi^*} \quad (5)$$

where M_{cs} is the critical state stress ratio, and n_d, n_b are positive material constants. The dilatancy, d, and hardening parameter, ζ, are also affected as they depend on M_{pt} and M_s correspondingly:

$$d^* = R_d\left(\sqrt{\frac{2}{3}}M_{pt}^* - \frac{\boldsymbol{s}}{p}:\boldsymbol{n}\right) \quad (6)$$

$$\zeta^* = \frac{|\boldsymbol{r}-\boldsymbol{r}_p|}{\sqrt{\frac{2}{3}}M_s^* - n_p} \quad (7)$$

where R_d is a parameter capturing densification effects, $\boldsymbol{s}$ is the deviatoric stress tensor, $\boldsymbol{n}$ is a normalised stress ratio tensor, $\boldsymbol{r}$ is the current deviatoric stress ratio tensor, $\boldsymbol{r}_p$ is a deviatoric stress

tensor that plays the role of the 'back-stress' ratio in conventional bounding surface models, and n_p is an inner tensor product obtained as $n_p = \boldsymbol{n}:\boldsymbol{r}_p$.

3 TRIAXIAL TEST SIMULATIONS

The predictive capability of the proposed model was evaluated against experimental data on Sydney sand mixed with Majura silt (Bobei, 2004). The parameters used for the simulations are shown in Table 1. Parameters related to elasticity, critical state, bounding surface, dilatancy, and fines content are taken from previous work (Lashkari, 2014). The hardening exponent parameter, n, has been calibrated by fitting the stress-strain curves of drained monotonic triaxial tests (Bobei, 2004) on the sand-silt material studied by Rahman et al. (2011). These tests were conducted with different initial void ratios (e_0 of 0.780, 0.749, 0.732 and 0.722) and mean effective stresses (p_0 of 100, 300, 400 and 600 kPa), but covered only a single fines content (f_c of 10%). The results from the experiments and the simulations are shown in Figure 1. The proposed model can reproduce all stress-strain curves quite accurately, despite slightly overpredicting the deviator stress at lower strains. Regarding the volumetric response, the model also performs well overall.

Figure 2 shows a second set of model predictions, for undrained monotonic triaxial tests (Rahman et al., 2011). Specifically, subfigures (a) and (b) concern samples with different fines contents (f_c of 0, 15 and 20%), initial void ratios (e_0 of 0.743, 0.535 and 0.573) and initial mean effective stresses (p_0 of 350 and 600 kPa). Subfigures (c) and (d) relate to samples with a single fines content (f_c of 15%) but different initial void ratios (e_0 of 0.645, 0.569 and 0.535) and mean effective stresses (p_0 of 600, 1100 and 1300 kPa). Generally, model prediction works best for flow (contractive) behaviour, but the quality of the prediction reduces as the behaviour changes to limited flow (dilative response) and non-flow (strongly dilative response). Discrepancies between predictions and observations for samples with denser behaviour are primarily attributed to the fact that the parameters utilised were determined from tests showcasing looser behaviour. Nevertheless, the simulations generally align reasonably well with the experimental data. The significance of the model's ability to capture the responses of the sand-silt material reliably can be appreciated by studying the response of the sample with $f_c = 20\%$ and $e_0 = 0.573$ (subfigures (a), (b)). Focusing solely on the negative initial value of the state parameter ($\psi_0 = -0.236$) would misleadingly imply a tendency for the sample to dilate. However, in adherence to EGST, the modified model considers the equivalent state parameter ψ^* instead of the state parameter ψ. With the equivalent state parameter taking a positive initial value ($\psi_0^* = 0.064$), the model correctly predicts liquefaction triggering rather than strain hardening.

4 CONCLUSIONS

A constitutive model for sand containing varying proportions of non-plastic fines has been proposed. The present work involved the modification of a state-dependent model for clean sands, Ta-Ger B, by replacing the void ratio e and state parameter ψ with the equivalent granular void ratio e^* and equivalent granular state parameter ψ^*. It has been shown that, with a single set of parameters, the model can predict the drained and undrained monotonic behaviour of sand with fines over a range of initial mean effective stresses, void ratios, and fines contents. Additional modifications and enhancements of the core formulation of the model could further improve its predictive capability. However, this could compromise the model's straightforwardness, its small number of input parameters, and the simplicity of the calibration procedure.

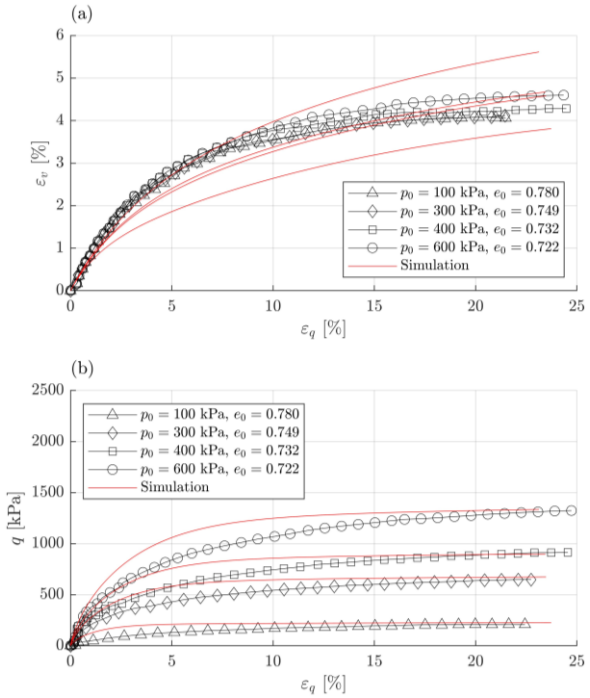

Figure 1. Calibration of parameters using drained monotonic triaxial tests on Sydney sand mixed with Majura silt ($f_c = 10\%$) (Bobei, 2004).

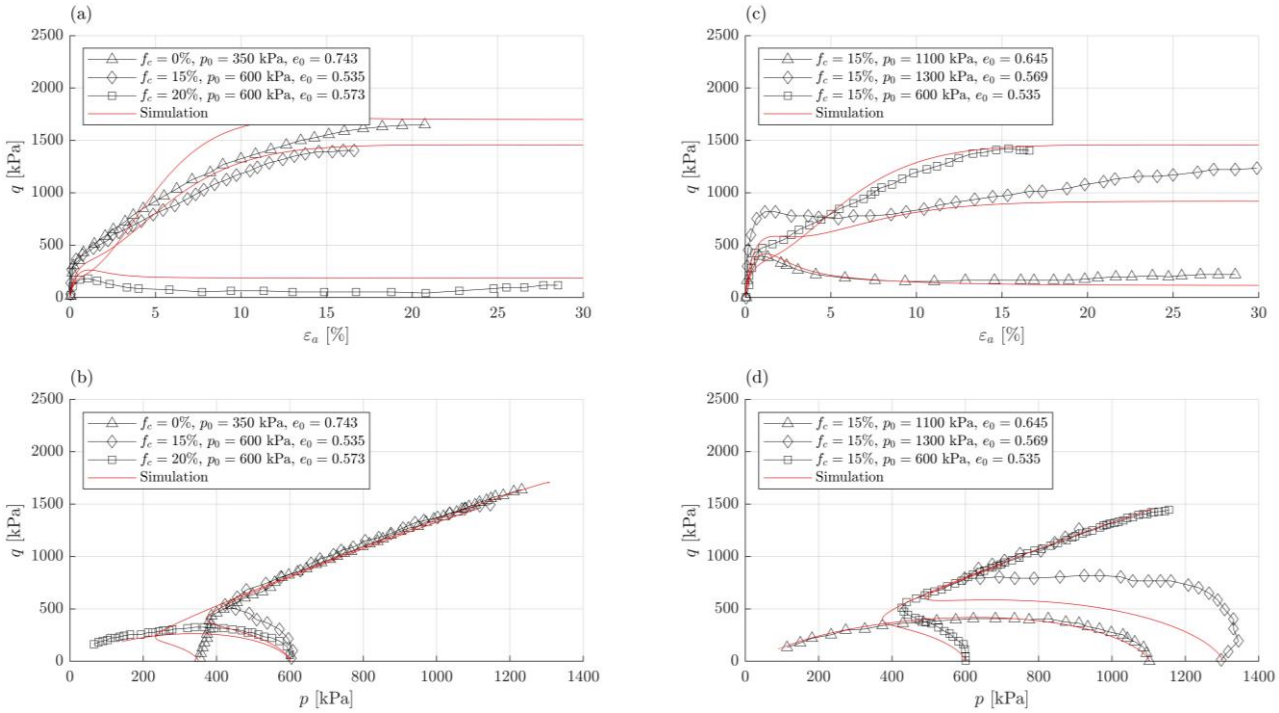

Figure 2. Simulations of undrained monotonic triaxial tests on Sydney sand mixed with Majura silt (Rahman et al., 2011).

Table 1. Model parameters for Sydney sand mixed with Majura silt.

Elasticity			Critical state line				Bounding Surface & Dilatancy		Hardening	Fines content	
G_0 [-]	ν [-]	m [-]	M_{cs} [-]	e_0 [-]	λ [-]	ξ [-]	n_b [-]	n_d [-]	n [-]	f_{thre} [-]	χ [-]
90	0.15	0.5	1.305	0.0375	0.6	0.92	0.8	2.5	0.25	0.40	37

ACKNOWLEDGEMENTS

The first author gratefully acknowledges the financial support of Fugro GB Marine Limited.

REFERENCES

Been, K., & Jefferies, M. G. (1985). A state parameter for sands. *Géotechnique*, 35(2), 99–112. https://doi.org/10.1680/geot.1985.35.2.99.

Bobei, D. (2004). *Static liquefaction of sand with a small amount of fines*, PhD thesis, UNSW Sydney.

Lashkari, A. (2014). Recommendations for extension and re-calibration of an existing sand constitutive model taking into account varying non-plastic fines content. *Soil Dyn. Earthq. Eng.*, 61–62, 212–238. https://doi.org/10.1016/j.soildyn.2014.02.012.

Li, X. S., & Dafalias, Y. F. (2000). Dilatancy for cohesionless soils. *Géotechnique*, 50(4), 449–460. https://doi.org/10.1680/geot.2000.50.4.449.

Rahman, M. M. (2021). The State of Art on Equivalent State Theory for Silty Sands. In: *Latest Developments in Geotechnical Earthquake Engineering and Soil Dynamics*, T. G. Sitharam, R. Jakka & S. Kolathayar (Ed.), Springer Singapore, (pp. 225–246).

Rahman, M. M., Cubrinovski, M., & Lo, S. R. (2012). Initial shear modulus of sandy soils and equivalent granular void ratio. *Geomech. Geoengin.*, 7(3), 219–226. https://doi.org/10.1080/17486025.2011.616935.

Rahman, M. M., & Dafalias, Y. F. (2022). Modelling undrained behaviour of sand with fines and fabric anisotropy. *Acta Geotech.*, 17(6), 2305–2324. https://doi.org/10.1007/s11440-021-01410-7.

Rahman, M. M., Lo, S. C. R., & Dafalias, Y. F. (2014). Modelling the static liquefaction of sand with low-plasticity fines. *Géotechnique*, 64(11), 881–894. https://doi.org/10.1680/geot.14.P.079.

Rahman, M. M., & Lo, S. R. (2008). The prediction of equivalent granular steady state line of loose sand with fines. *Geomech. Geoengin.*, 3(3), 179–190. https://doi.org/10.1080/17486020802206867.

Rahman, M. M., Lo, S. R., & Baki, M. A. L. (2011). Equivalent granular state parameter and undrained behaviour of sand-fines mixtures. *Acta Geotech.*, 6(4), 183–194. https://doi.org/10.1007/s11440-011-0145-4.

Roscoe, K. H., Schofield, An., Wroth, & P, C. (1958). On the yielding of soils. *Géotechnique*, 8(1), 22–53. https://doi.org/10.1680/geot.1958.8.1.22.

Tasiopoulou, P., & Gerolymos, N. (2016). Constitutive modeling of sand: Formulation of a new plasticity approach. *Soil Dyn. Earthq. Eng.*, 82, 205–221. https://doi.org/10.1016/j.soildyn.2015.12.014.

Thevanayagam, S., & Martin, G. R. (2002). Liquefaction in silty soils—screening and remediation issues. *Soil Dyn. Earthq. Eng.*, 22(9), 1035–1042. https://doi.org/10.1016/S0267- 7261(02)00128-8.

Proceedings of the XVIII ECSMGE 2024
GEOTECHNICAL ENGINEERING CHALLENGES
TO MEET CURRENT AND EMERGING NEEDS OF SOCIETY
© 2024 the Authors
ISBN 978-1-032-54816-6
DOI 10.1201/9781003431749-598
Open Access: www.taylorfrancis.com, CC BY-NC-ND 4.0 license

ECSMGE 24
XVIII EUROPEAN CONFERENCE ON SOIL MECHANICS AND GEOTECHNICAL ENGINEERING

Reclamation of former brown coal mines: determining shear strength

Remise en état d'anciennes mines de lignite: détermination de la résistance au cisaillement

J. Kostal*
Czech Technical University in Prague, Faculty of Civil Engineering, Prague, Czech Republic
Division of Power Engineering, INSET s.r.o., Czech Republic

P. Cernoch
CEZ Energy side-products, Hostivice, Czech Republic
Czech Technical University in Prague, Faculty of Civil Engineering, Prague, Czech Republic

**kostal.jiri@inset.com*

ABSTRACT: In the process of a hydraulic recultivation of former brown coal mines, it is necessary to address the issues related to the subsequent stability of the retaining slopes. It is evident that the determination of the design value of the shear strength of the soil will be crucial and decisive, particularly in relation to the contact between the clay and the coal seam in their natural position after being flooded with water. The determined values of the shear strength of the affected soils were used in stability calculations for the retaining slopes. In the first step a large-scale shear apparatus was designed and constructed. The test results provided the peak strength before the sample collapsed and the residual strength value determined by the movement of the soil along the shear plane. The large-scale shear field test provided a more precise view of soil behaviour, especially under lateral stress, on a larger scale. The determination of the actual values of the soil shear parameters can then be used for modelling the stability of the original/retaining slopes from the end of mining to lake filling.

RÉSUMÉ: Dans le processus de recultivation hydraulique des anciennes mines de charbon brun, il est nécessaire de s'attaquer aux problèmes liés à la stabilité ultérieure des pentes de retenue. Il est évident que la détermination de la valeur de conception de la résistance au cisaillement du sol sera cruciale et déterminante, en particulier par rapport au contact entre l'argile et la veine de charbon dans leur position naturelle après avoir été inondées d'eau. Les valeurs déterminées de la résistance au cisaillement des sols affectés sont ensuite utilisées dans les calculs de stabilité pour les pentes de retenue. Dans une première étape, un appareil de cisaillement à grande échelle a été conçu et construit. Les résultats des tests ont fourni la résistance de pointe avant que l'échantillon ne soit détruit et la valeur de résistance résiduelle déterminée par le déplacement du sol le long du plan de cisaillement. Le test de cisaillement sur le terrain à grande échelle a fourni une vision plus précise du comportement du sol, en particulier sous contrainte latérale, à une plus grande échelle.

Keywords: Large-scale shear device; clay; geomechanical parameters.

1 INTRODUCTION

As part of the anticipated flooding (hydraulic reclamation) of surface brown coal quarries, the question of the subsequent stability of their retaining slopes arises. It is necessary to address the final form and reclamation of residual pits in broader relationships and correlations, especially in terms of the process of creating dump bodies and the shape of the resulting retaining slopes of the quarry. Subsequent hydraulic reclamation must be carried out without major technical problems and within hydraulically, ecologically, and economically tolerable limits.

Practically no study has so far dealt with the stability of the slopes of anticipated lakes (with a depth of up to 200 m). The knowledge of the design values of the contact shear strengths of individual soils, which subsequently enter the model calculations, can be considered completely significant. This mainly concerns the contact surfaces of original materials (claystone and coal layer), this contact is crucial for the project of residual pits and prediction of their changes. Before the design work, which among other things, includes proper deformation and stability calculations, it is necessary to establish real values of input geotechnical parameters (especially values of shear strength).

For this purpose, it was necessary to perform engineering geological survey. The research included

the following activities: research; development of a large-scale shear device for use in situ; the application of a large-scale shear device in situ at the coal x subsoil (bedrock) contact; determination of geomechanical parameters for subsequent stability calculations. The research area is situated on the north part of the bohemia (Figure 1).



Figure 1. Research area.

2 SCOPE AND METHODOLOGY OF WORK PERFORMED

The performance of the large-scale shear test was preceded by excavation of large-profile notches and exposure of problematic sections. The tests provided a more accurate view of soil behaviour, especially under lateral stress, on a larger scale. The monitored areas contained more heterogeneity than what can be captured in a laboratory test performed on undisturbed samples of soils/rocks, including the inclusion of possible discontinuities across the tested area and the possibility of testing in situ. Therefore, the natural deposition and natural degree of saturation of the observed contact was guaranteed.

2.1 History of the device

Shear strength of soils is a basic property for slope stability evaluation. The box shear test is the oldest method for determining shear strength. Traditionally, a soil sample is placed in a rigid metal box, subjected to a vertical force, and sheared along a horizontal plane between the two halves of the shear box.

Large-scale shear frames were originally designed to test drained materials containing large particles, such as gravelly soils, industrial slag, rubble, or mining spoil. Regarding the history of direct field shear tests in former Czechoslovakia, large shear tests were already conducted in the 1960s, for example on rock blocks measuring 500 x 500 mm^2 x 150 mm during surveys for the construction of the Czech Television building at Pankrác plain.

Various engineers performed field measurements to determine the shear strength parameters of the rock mass, e.g., Hudek in 1980, Líbal in 1983, Hanák and Horák in 1988, and Mencl in 1992. Typical frame dimensions were 500 x 500 mm^2 x 300 mm or less frequently 700 x 700 mm^2 x 305 mm. Shift-controlled loading allowed evaluation of both maximum and residual shear strength. Hydraulic jack introducing normal stress into the sample could be supported by the surrounding rock in the rock mass.

Líbal, based on his previous experience in 1991, performed a set of in situ shear tests at the Nástup Tušimice Mine with Seyček to evaluate the contact of the coal seam and its substrate consisting of clay and claystone. The 500 x 500 mm2 x 145 mm sample was loaded using a hydraulic jack supported by an anchored load bridge. The study of the shear strength of deeply located coal and rock interfaces for stability analysis requires a large-scale device capable of transmitting the large stresses that occur in the deep contact layers of extensive slopes. One of the largest shear devices in the world was developed at the University of Newcastle in 2013 for testing square samples of up to 720 mm edge under high vertical stress of up to 4 MPa. In this case, this shear device was designed for laboratory testing, so it was possible to use a massive loading frame to ensure normal pressures that occur in large rock dams and high spoil heaps. In addition to these unique devices, some traditional manufacturers also offer large-scale devices for soil and rock testing again for use in laboratories, such as Wille with their shear boxes up to 1,000 x 1,000 mm^2 and normal stress up to 1 Mpa (in Molina at all, 2020).

2.2 Technical requirements for the device

The purpose of the large-scale shear device is to determine the cohesion coefficient c and the shear friction angle ϕ of the geological environment in situ from Mohr-Coulomb diagrams. A necessary premise for the development of a device enabling field shear strength tests was the ability of the device to apply a normal force of 120 kN and a tangential force of 35 kN to a test sample of dimensions 500 x 500 x 150 mm. The loading must be displacement-controlled in the tangential direction, with a shearing speed of 0.05 mm/min in the first phase (reaching peak strength) and 0.5 mm/min in the second phase. In the four corners of the spreader plate, four displacement sensors will be placed in the normal direction and three displacement sensors in the tangential direction.

2.3 Proposed solution

The first variant was designed with a spreader frame. Here, a groove about 2 m deep and about 4 m wide was considered. The spreader frame would be anchored into the coal seam using spiral anchors. The load

capacity of spiral anchors depends on the depth of the anchor and also on the distance of the anchor from the free edge. This law affects the stiffness of the spreader frame and its weight, which is decisive for manipulation and the necessary presence of a crane, thus increasing the cost and time of performing the shear test. A static stress calculation of the beam loaded with a normal force of 112.5 kN was carried out by the finite element method. From the results, it was clear that near the middle of the beam and at both ends, stress was already occurring close to the slip (deformation about 6 mm). The weight of the beam without the spreading consoles was 120 kg. With the spreading consoles, the weight would increase to about 200 kg. This option was rejected due to manipulation and the results of the strength calculation.

The attempt to reduce the weight of the loading frame and its manageability led to the idea of using a truss. In principle, it is a similar variant as the variant with a beam, but the difference is that the weight decreased but there was still no improvement in the stiffness of the device. Therefore, another variant was approached.

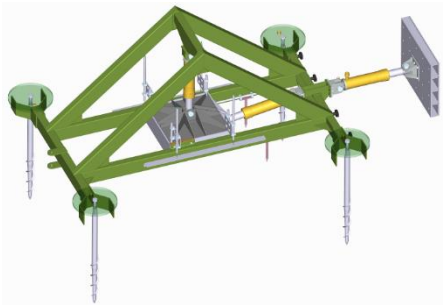

Figure 2. Final shear test device.

The final variant of the large-scale shear device meets the requirements of easy manipulation, appropriate weight, and sufficient stiffness. The advantage of this variant is the fixation (anchoring) of the frame to the clay subsoil, an open area where there is no danger of the operator being buried by the coal layer sliding into the deep groove. Another advantage is the small size of the frame. The Figure 2 shows a frame placed over the test sample together with a support box, spreader plate, and hydraulic cylinders for vertical and horizontal directions.

An industrial computer, Getac, equipped with the WinMost program (INSET) and an 80-channel measuring card from National Instruments, was used to measure displacements and loads.

Inductive LVDT sensors DH_100 with a spring-loaded tip and a measuring range of 0 to 100 mm were used for displacement measurement with resolution 10^{-3} mm and extended combined uncertainty U(k=2) = 5 * 10^{-2} mm. Vertical measurement was carried out between the fixed frame and the movable spreading plate resting on the soil sample (coal layer). For measuring the displacement of the test sample in the horizontal direction, a boxed sensor holder equipped with a tip, hammered into the clay subsoil, was used. An alternative (which was used in most cases) was anchoring into the bedrock using drilled earth spiral anchors, with a concrete filling. For this purpose, test breakout tests of anchors were conducted to declare the required pull - an equivalent necessary counterforce, which is to be used for the large-scale shear device. Control tests demonstrated sufficient load-bearing capacity.

2.4 Preparation of the test field

The creation of the test field by machine mechanization had several phases. First, the entire area around the test field was revealed down to the coal by a bucket ripper, then the coal layer was lowered to a height of 1 m. After the longitudinal and transverse grooves were marked out, they were machine-made using a tractor excavator to create transverse and longitudinal grooves in the coal, and finally the terrain was adjusted for the movement of workers and equipment - creating drivable and handling areas for the purpose of manually separating future samples from the rock mass. An indispensable condition was to preserve the natural deposition of the rock environment (there could be no predisposition to damage the shaped body). A combination of a disc saw with water cooling, a jackhammer, and especially a chainsaw with water cooling served as a manual tool. The sample was manually formatted to the necessary size of 500 x 500 x 150 mm. This was followed by the positioning of the loading device (large-scale shear device).

2.5 Result of the large-scale shear test

Large-scale in-situ shear tests (Figure 3) were performed in groups with varying normal stress, specifically 50, 200 and 350 kPa. Analogous to the laboratory evaluation of box shear tests, it was then possible to obtain the values of the friction angle ϕ and the cohesion c. In total, three groups of tests were carried out and evaluated, which can be considered a statistically evaluable sample of material (coal layer - underlay contact), from which the average values of geomechanical parameters were derived.



Figure 3. Large-scale shear test.

The results of the realised large-scale tests are provided in Table 1.

Table 1. Results of the conducted large-scale tests.

Group	ϕ [°]	c [kPa]
I	34.6	29.0
II	38.0	40.0
III	25.8	88.0

3 CONCLUSION

The conducting of a large-scale shear test was preceded by the excavation of large-profile notches and the exposure of problematic sections, i.e., the contact of the brown coal seam with the underlying claystones. The excavation work for the large-scale tests (experiments) allowed a spatial view of the observed contact of the affected soils, their documentation, and collection of undisturbed samples of the observed soils. The large-scale shear field test provided a more accurate view of soil behaviour, especially under lateral stress on a larger scale. The observed place contained more heterogeneities than the laboratory test, including the inclusion of possible discontinuities across the test area within in situ testing. Thus, the natural positioning and the natural degree of saturation of the observed contact were guaranteed. The concept of the shear test device for a large-scale in situ shear test was based on the traditional laboratory box shear device.

During the large-scale shear test, all the data needed to determine the values of shear parameters determine the values of shear parameters, the size of deformation, normal stress, shear stress, and pore pressure, were recorded. The result of the test was determining the peak strength before breaking the sample and determining the value of the residual strength given by the movement of the soil over the created shear face. Also, a statistically evaluable set of large-scale shear tests was carried out in a total of 9. This provided a sufficient set of shear parameter values at the observed coal layer - claystone contact in its natural positioning. The values of shear parameters obtained from the performed large-scale shear tests will subsequently be compared with the data obtained from the literature review and the laboratory results. A literature review will be conducted using a set of samples collected over the last 3 years during mining exploration, feasibly exploration, and drilling exploration in interest. At the same time, drilling work was carried out as part of the field tests, including the collection of undisturbed samples at the contact of the brown coal layer with the overburden and the substrate for subsequent laboratory tests. After evaluating these three sets of data, the characteristic values of shear strengths will be determined. The determination of real values of shear parameters of soils will be used for the modelling of the stability of original/final slopes from the end of mining to the filling of the lake. The calculations will simulate the prediction of the behaviour of individual stages and the overall slope of the spoil body during the gradual filling of the lake. Eventually, the real values of shear strengths (obtained particularly from the field) will influence the design of technical measures to ensure the stability of the studied area as part of the planned study of filling lakes (hydraulic reclamation).

REFERENCES

Cernoch, P. and Kostal, J. (2019). Preparations for remediation of a former surface mine a technical reclamation area. *Acta Polytechnica CTU Proceesings.* 23. pp 14-19. https://doi.org/10.14311/APP.2019.23.0014.

Liu, F. Yang, K. Yang, T. Gao, Y. Li, J. Liu and Q. Fu, Q. (2022). Pumped storage hydropower in an abandoned open-pit coal mine: Slope stability analysis under different water levels. *Earth Sci.* 10:941119. https://doi.org/10.3389/feart.2022.941119.

Molina, S. L. Bradfield, L. Fityus, S. G. Simmons, J. V. and Lizcano, A. (2020). Design of a 720-mm Square Direct Shear Box and Investigation of the Impact of Boundary Conditions on Large-Scale Measured Strength. *ASTM International. Geotech. Test*. 43(6): 1463–1480. https://doi.org/10.1520/GTJ20190344.

Vrablikova, J. Wildova, E. and Vrablik, P. (2016). Sustainable development and restoring the landscape after coal mining in the northern part of the Czech Republic. *Journal of Environmental Protection.* 7. pp 483-1496. https://doi.org/10.4236/jep.2016.711125.

Proceedings of the XVIII ECSMGE 2024
GEOTECHNICAL ENGINEERING CHALLENGES
TO MEET CURRENT AND EMERGING NEEDS OF SOCIETY
© 2024 the Authors
ISBN 978-1-032-54816-6
DOI 10.1201/9781003431749-599
Open Access: www.taylorfrancis.com, CC BY-NC-ND 4.0 license

ECSMGE 24
XVIII EUROPEAN CONFERENCE ON SOIL MECHANICS AND GEOTECHNICAL ENGINEERING

Thermal activation of sewers and embedding in a heating-cooling network

Activation thermique des canalisations d'eaux usées et intégration dans un réseau de chaleur et de froid

T. Kugler*, Ch. Moormann
University of Stuttgart, Institute of Geotechnical Engineering, Stuttgart, Germany
**till.kugler@igs.uni-stuttgart.de*

ABSTRACT: The thermal activation of foundation elements through the installation of absorbers in components being in contact with the underground has become state-of-the-art. A new approach involves the thermal activation of sewers as a part of the urban hydraulic infrastructure. These so called ´hybrid sewers´ enable energy extraction or storage from both the inner sewer climate and the subsoil in which the sewer is embedded. The wastewater flow continuously supplies thermal energy, so that a higher thermal energy can be obtained than from usual activated foundation elements. Consequently, the system is base load-capable and is therefore suitable as the basic system of a regenerative heating network. The thermal performance of hybrid sewers, previously unexplored, has now been validated using numerical simulations and measurements.

RÉSUMÉ: L'activation thermique des éléments de fondation consiste à installer, dans les éléments en contact avec le sol, des absorbeurs qui sont traversés par un liquide caloporteur et qui absorbent l'énergie thermique. L'activation thermique des égouts hybrides est particulièrement judicieuse, car l'énergie thermique provient à la fois du sol et de la terre. Les eaux usées qui s'écoulent fournissent de l'énergie thermique en continu, ce qui permet de récupérer une quantité d'énergie thermique nettement plus importante et plus constante que dans le cas d'un simple contact avec le sol. Le système peut donc supporter une charge de base et convient donc comme système de base d'un réseau de chaleur régénératif. Le comportement thermique du canal hybride était jusqu'à présent inconnu et a maintenant été validé par des simulations numériques et des mesures.

Keywords: Hybrid sewer; district heating; wastewater heat absorber; hydrothermal coupled numerical simulation.

1 INTRODUCTION

Renewable energy sources, unlike fossil energy sources are widely accessible based on local applications. However, they may have a limited capacity to provide a consistent base load capacity in certain cases. Therefore, it is logical to integrate different renewable energy sources within a heating network.

The thermally activated “hybrid sewer”, investigated in the research project “IWAES” offers the benefit of being able to extract and supply thermal energy from the surrounding subsoil, the inner sewer climate and the wastewater. In this context, the term “hybrid” denotes the sewer’s capability of the to simultaneously transport wastewater and gain thermal energy. Moreover, the hybrid sewer can enable bidirectional compensation among various consumers due to additional transport functions. In order to heat and cool, the individual users do not necessarily produce solely their own thermal energy; instead, they can use the waste heat and cooling energy of other users within the network.Thus, the users within the network become both producers and consumers of thermal energy. The efficient integration of energy sources and storage facilities into the heating network should also considered.

2 ENERGY GEOSTRUCTURES

An “energy geostructure” refers to the incorporation of absorber pipes, typically made of copper or plastic, into construction elements which serve a structural primary purpose. These pipes facilitate heat transfer through fluid flow (see Figure 1) (Laloui & Rotta Loria, 2020). The heat transfer fluid absorbs thermal energy while flowing through the component and then transfers the energy to a heat pump or heat exchanger. The heat pump increases the temperature to the desired level with the aid of electrical energy.

Theoretically, all foundation elements can be thermally activated, so there are thermally activated diaphragm walls (u. a. Sterpi et al., 2017), tunnelling

structures (u.a. Moormann et al 2019), piled fondations and also mixed in placed methods (Brandl, 2006). To prevent the water in the concrete from freezing, the flow temperature should not fall below the freezing point for all statically effective foundation structures. Water should mainly be used as the heat transfer fluid instead of a water-glycol mixture.

Typically, shallow geothermal systems can only operate efficiently for a certain period of time before requiring deactivation to regenerate. Foundation elements that border both the subsoil and a flowing medium are permanently self-regulating and can therefore efficiently generate thermal energy almost indefinitely. Such elements include tunnelling structures, sheet pile walls and sewers.

The thermal activation of underground infrastructure diminishes the necessity for additional resources typically required for constructing alternative geothermal systems like geothermal probes or collectors. Additionally, the ground that has already been heated by anthropogenic use (such as sewers) undergoes subsequent cooling.

3 HYBRID SEWER

3.1 General

The thermal activation of sewers represents a logical progression of the thermal activation of structurally necessary components.



Figure 1. Thermally activated sewer `hybrid sewer´.

The term “hybrid sewer” refers to a sewer segment that effectively carries out the primary task of transporting wastewater. By incorporating externally helically arranged absorbers, thermal activation enables the extraction of thermal energy from the surrounding soil, sewer air and wastewater (Figure 1). The three-dimensional design of the hybrid sewer depicts a section of an activated sewer with a length of 6 m made of plastic. Alternatively, other prefabricated lengths of the sewer sections are conceivable. Additional transport lines installed above enables the thermal energy to be transported through the district at varying temperature levels (Figure 2). In an optimal scenario, the transported thermal energy does not require a heat pump to raise the temperature level, thus eliminating the need for additional electrical energy.

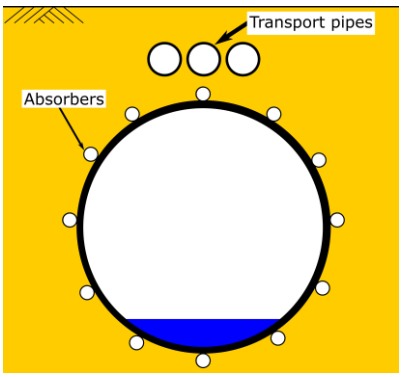

Figure 2. Schematic section of a hybrid sewer.

3.2 Thermal performance

The advantage of the thermally activated sewer over foundation elements surrounded exclusively by soil, e.g. piles, lies in the permanent thermal regeneration facilitated by the downstream wastewater. Unlike conventional energy geostructures that are not installed in flowing groundwater, the continuous thermal regeneration due to the wastewater flow leads to a certain base load capacity. The thermal energy from the wastewater can be harnessed not only in the sewer but also within the building and in the sewage treatment plants. While existing methodologies and effective implementations for this have already been established, as indicated in reference Nagpal et al, (2021), comprehensive dimensioning aids have not yet been developed.

There are mathematical models to determine the effects of heat extraction on wastewater temperature (Dürrenmatt & Wanner, 2014). However, there are currently no models available to infer the heat extraction capacity from the wastewater temperature and volume flow.

It is also known that the wastewater flow (l/s), as well as the filling level (cm) and the wastewater temperature have an influence on the performance of thermally activated wastewater absorbers (weighting increases with sequence) (Adam & Markiewicz, 2009).

To assess the thermal performance, new approaches and calculations are required. The approach of calculating the sum of all heat flows acting on the absorber is challenging, as the heat flux that directly impacts on the absorber is crucial for its performance. This heat flux is influenced by various heat flows, such as solar, geothermal heat flow that act within and in the vicinity of the hybrid sewers. There

are interdependencies between the different heat flows. Additionally, heat flows must be categorised according to their specific mode of heat transfer (conductive, convective). Since a closed analytical solution is not available, numerical simulations are carried out. For these simulations, all thermal-hydraulic parameters must be known. With regard to the climate inside sewers, hardly any reliable measured data have been published. Existing publications on the topic take a stochastic approach to the topic, as seen in reference (Abdel-Aal et al. 2021). Therefore, field measurements were carried out in selected sewers to gather necessary data.

3.3 Sewer air investigations

Investigations on thermally activated tunnel structures have revealed a significant influence of the tunnel air on the possible heat extraction (Schneider, 2011; Schneider, 2013; Buhmann 2019). Similarly, to assess the thermal performance of hybrid sewers, it is crucial to have accurate information about the temperature and flow of the sewer air. To achieve this, sewers with different diameters and gradients were equipped with measurement sensors and investigated (Figure 3).

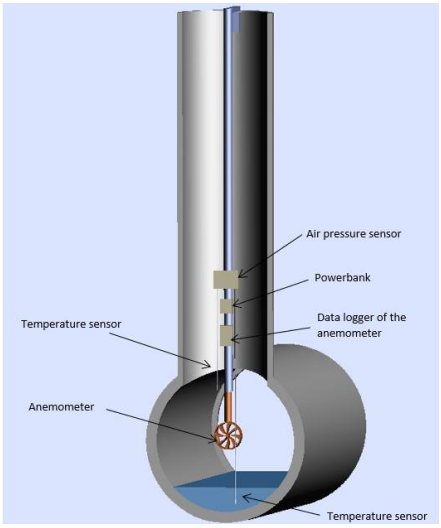

Figure 3. Sewer equipped with measurement technology.

Figure 4 illustrates the presence of an airflow within the sewer, which can occur independently of the direction of wastewater flow. Concequently, it can be inferred that the heat transfer between the sewer air and the inner sewer surface primarily occurs through convection. This fact is additionally supported by literature (Bischofberger, 1984). The dimensionless convective heat transfer coefficient is significantly higher than the heat transfer coefficient solely from conduction. Since wastewater in the sewer flows continuously, there is no direct thermal coupling between energy extraction and water temperature. The heat transfer, which is the product of the temperature gradient and the heat transfer coefficient, is therefore significantly higher than for foundation elements with pure soil contact.

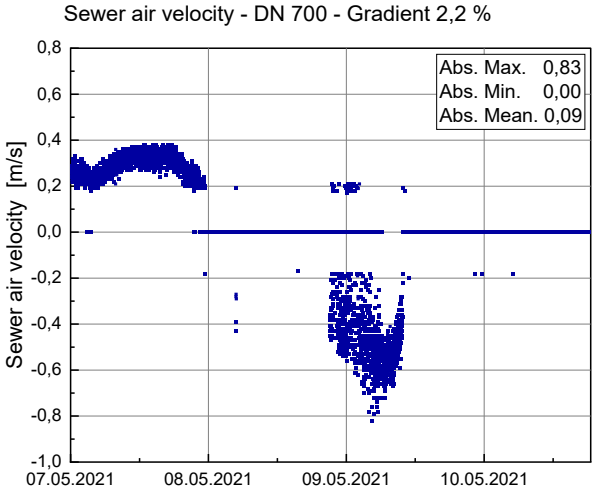

Figure 4. Measurement of the sewer air velocity.

3.4 Numerical investigations

The thermal performance of the hybrid sewers was evaluated through conducting numerical simulations, both two- and three-dimensional, which involved coupled thermal-hydraulic calculations. The simulations were carried out using the COMSOL® simulation software and the model used is depicted in Figure 5. To mitigate boundary effects arising from unsuitable geometry and network effects, extensive sensitivity analyses were carried out beforehand. In this study, the factors influencing the individual heat flows were quantified in order to identify those requiring further investigation. The analysis revealed that the velocity and temperature of the wastewater and the sewer air in particular are crucial for the performance of the absorber. Additionally, the atmospheric heat input, especially convective heat flow due to wind, has an influence that must be considered. The dimensionless convective heat transfer coefficient, which acts as a result of air currents on terrain surfaces, was calculated according to Beisel (1999) by means of the average wind speed (v), as shown in Equation (1). The average wind speeds and surface temperatures were obtained from the test reference years of the German Weather Service for the year 2045.

$$\alpha = \begin{cases} 1{,}8 + 4{,}1 \cdot v & v \leq 5\frac{m}{s} \\ 7{,}3 \cdot v^{0{,}73} & v > 5\frac{m}{s} \end{cases} \quad (1)$$

All pertinent parameters required to generate the thermal load profile were derived from the urban

planning design. The thermal load profile illustrates when the analysed user requires what amount of thermal energy. The thermal effects of the wastewater temperature were evaluated using the hourly temperature measurements at the main wastewater treatment plant in Stuttgart.

The diameters, lengths and expected flow velocity of the wastewater could be taken from the conceptualised wastewater network.

The flow within the absorbers exhibits a slightly turbulent flow (Re = 3000), represting the energetic optimum between the pump flow used and the heat energy extracted (VDI 4640, 2019). The findings from the aforementioned investigations were utilised for the sewer air data. Initially, a non-cohesive, homogeneous soil without groundwater flow was assumed for simulation of the soil continuum. The applied thermal load curve was developed within the project for a typical building block.

In the initial step, a supply temperature of +2°C of the heat carrier fluid is provided to the numerical model. The simulation then calculates the outflow temperature of the absorber. According to Equation (2), the required performance $\dot{Q}$, the volumetric flow $\dot{V}$ and the return temperature ϑ_{Outlet} can be used to calculate the supply temperature ϑ_{Inlet}. The heat capacity and density are given by c_p, ρ.

$$\dot{Q} = \dot{V} \cdot c_p \cdot \rho \cdot (\vartheta_{Inlet} - \vartheta_{outlet}) \qquad (2)$$

The thermal energy requirement for each hour is determined from the thermal load profile. By adjusting the formula based on the temperature differential, it becomes feasible to calculate the temperature difference at which the heat transfer medium needs to be cooled in order to 4ulfil the thermal energy demand. Subsequently, the new inlet temperature is calculated by subtracting the temperature difference from the determined outlet temperature.

The result of the numerical investigation represents the average thermal performance of the hybrid sewer. The average thermal performance of the hybrid sewer was determined using the following equation and divided by the number of annual full load hours (heating load hours: 1240 h, cooling load hours: 360 h) are shown in Table 1. Applied to a district with a high population density, the hybrid sewer can cover approximately 15% of the total thermal demand (heating and cooling) of the district. The degree of energy coverage here is in line with the literature (DWA M 114, 2020).

Table 1. Numerical results for the thermal performance of the investigated sewers.

Diameter [mm]	Heating [W/m²]	Cooling [W/m²]
300	140	830
400	130	700
800	115	640

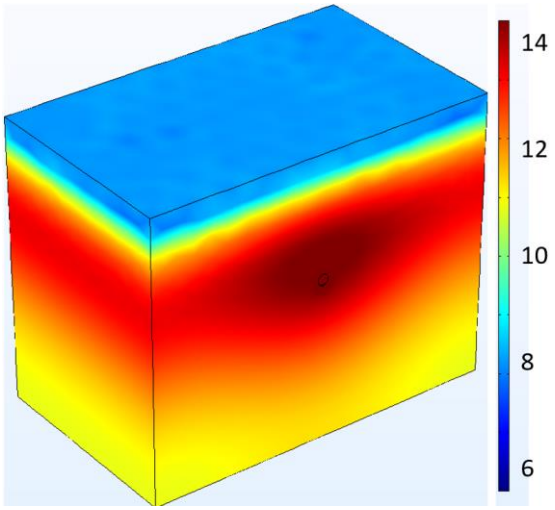

Figure 5. Three-dimensional thermo-hydraulically coupled model of the hybrid sewer [°C].

For comparison, the performance of thermally activated diaphragm walls and floor slabs is between 10 W/m² and 35 W/m².

4 VALIDATION

To facilitate further parameter studies, it is imperative to validate the simulation model using monitored real hybrid sewers. Therefore, an experimental test setup under laboratory conditions and a pilot plant were developed within the framework of the IWAES project. The parameter studies carried out by the simulation model validated by back-analysis of the results of the experimental tests and of the pilot plant will serve as the basis of a thermal resistance-capacity model. This model, in turn, will provide the foundation for a simplified design concept for the engineering practice.

4.1 Experimental tests under laboratory conditions

The experimental setup exists of a 4.0 m long hybrid sewer which is embedded in a test box (width: 2.8 m, length: 4.8 m, height: 1.5 m) filled with moist sand (see Figure 6). The hybrid sewer, has an internal diameter of 200 mm and is continuously flowed through by water. The "waste water" is consistently heated by a flow heater, while the absorber fluid is

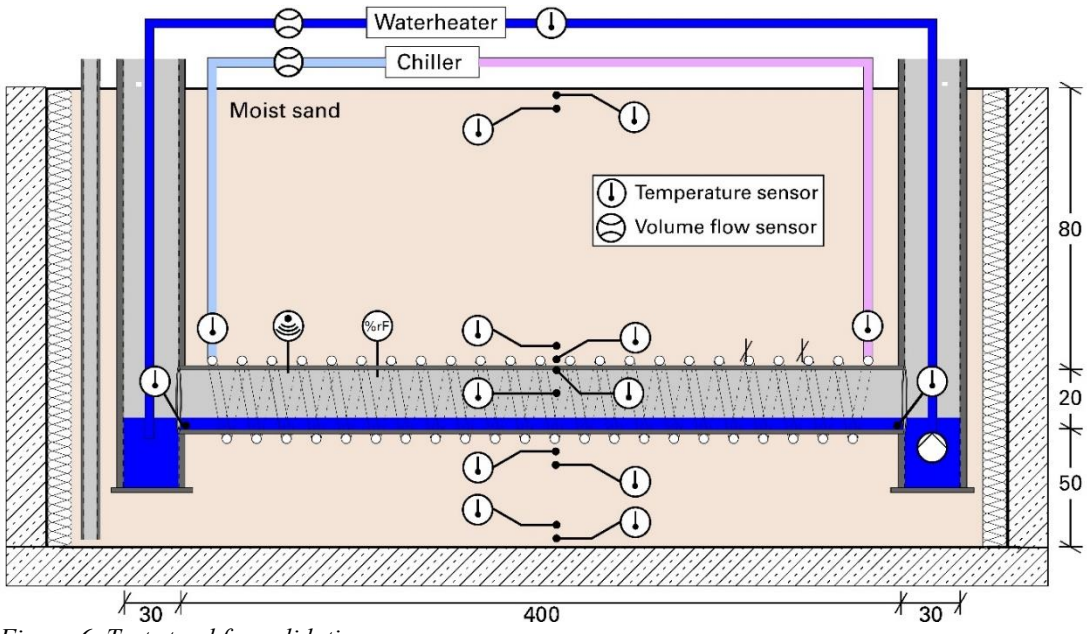

Figure 6. Test stand for validation.

cooled by a flow cooler, mimicking the evaporator of a heat pump. The absorber fluid will cool down as it flows through the absorber pipe, as in a real hybrid sewer.

The numerical model precisely replicates the physical system described. Validation of the numerical model will be based on the congruence between the numerically determined and measured return flow temperature.

The temperatures as well as the volume flow can be varied. In addition, a sewer air flow can be simulated by applying a blower.

4.2 Pilot plant

In Bavaria, a hybrid sewer is repurposed as a penstock for a small hydropower plant. The pressure tunnel links a spring pond with a water turbine, and the channel cross-section is fully filled. All pertinent variables are measured and logged and used for back-analysis.

Figure 7 illustrates the temperature of the flow and return for a six-metre-long section of the sewer. Despite continuous operation, the difference between the flow and return is around 2 K, with a flow rate of 25 litres/min. Using Equation 2, this results in a performance of 220 W/m² concerning to the length of the sewer. Compared to thermally activated piles, which typically have extraction capacities of 18-32 W/m², the extraction capacity of the hybrid sewer is significantly higher. The conductivity of thermally activated floor slabs and diaphragm walls is also significantly lower (Brandl, 2006). The reason for this is the convective heat transfer between the flowing water and the sewer´s walls.

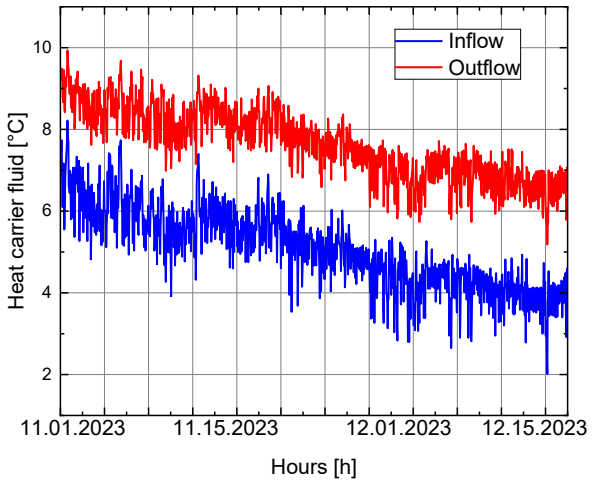

Figure 7. Measurement of the flow and return temperature of the heat carrier fluid for a 6 m long segment, volume flow 25 l/min.

The measurement data gained are currently being used to validate the numerical model developed.

5 THERMAL NETWORK

Since the concept of the hybrid sewer cannot fulfill the entire thermal demand of an urban district with a high population density, additionaly renewable energy sources are required to achieve self-sufficient heat management. These additional energy sources, as along with the exchange of surplus energy, must be facilitated by an interconnected network.

The developed concept aims to achieve equilibrium between thermal demands and surpluses at the district level, obviating the need for additional energy

generation. To accomplish this, the transport network must be capable of bidirectional operation, meaning it must be able to both absorb and release heat. Heat networks with these characteristics are termed as “5th generation heat networks” (Wirtz, 2022). Within the developed transport network, a three-pipe system is implemented for this purpose, comprising of one supply pipe each for "heat" and "cold" along with a common return pipe. The hybrid sewer serves as the fundamental component of the integrated thermal network. The concept of the heat network is further elaborated in Kugler et al, (2022).

6 CONCLUSION

The hybrid sewer can extract thermal energy from both the ground and the waste water. The waste water leads to continuous thermal regeneration of the surrounding soil due to its continuous outflow.

The thermal conductivity of the hybrid channel was determined through numerical analyses. To validate the numerical model, a real hybrid sewer and a real-scale test-setup were equipped with measurement devices. The numerical model, validated by back analysis of the measurement results, is subsequently utilized to develop a design aid that enables rapid pre-dimensioning.

The results obtained thus far demonstrate that the heat extraction capacity is significantly higher compared to conventional thermally activated foundations.

ACKNOWLEDGEMENT

The IWAES research project is funded by the German Federal Ministry of Education and Research (BMBF) as a part of the research program RES:Z under grant number 033W106A. Their support is gratefully acknowledged.

REFERENCES

Abdel-Aal, M., Tait, S., Mohamed, M., Schallart, A. (2021). Using long term simulations to understand heat transfer processes during steady flow conditions in comined sewers, *Water*, 13(570).

Adam, D., Markiewicz, R. (2009). Energy from earth-coupled structures, foundations, tunnels and sewers, *Géotechnique,* 59(3), 229-236.

Brandl, H.(2006). Energy foundations and other thermo-active ground structures, *Géotechnique,* 56(2), 81-122.

Beisel, S. (1999). *Vermessung, Modellierung und Bewertung des Erdreichwärmeübertragers beim Passiv-Solarhaus Cölbe*, Diploma-Thesis, University of Marburg (in German).

Bischofberger, W., Seyfried, C.F. (1984). Wärmeentnahme aus Abwasser. Berichtshefte des Lehrstuhls für Wassergütewirtschaft der Technischen Universität München, Germany, Rep. 56 (in German).

Buhmann, P., Moormann, Ch., Westrich, B., Pralle, N., Friedemann, W. (2016). Tunnel geothermics - a German experience with renewable energy concepts in tunnel projects, *Geomechanics for Energy and the Environment*, 8, 12/2016, pp. 1-7.

Buhmann, P. (2019). *Energetisches Potential geschlossener Tunnelgeothermiesysteme.* Stuttgart: PhD-Thesis, Proc. of the Institute of Geotechnical Engineering at University of Stuttgart, Vol. 73, (in German).

Dürrenmatt, D., Wanner, O. (2014). A mathematical model to predict the effect of heat recovery on the wastewater temperature in sewers*, Water Research*, 48, 548- 558

DWA – M 114. (2020). *Merkblatt Abwasserwärmenutzung,* DWA-Guideline, Hennef (in German).

Kugler, T., Schittenhelm, C., Volkmer, S., Ryba, M., Moormann, C., Koenigsdorff, R., Kurth, D. (2022). Sustainable heating and cooling management of urban quarters. *Sustainability*, 14, 4353.

Kugler, T., Moormann, C. (2023). Thermal activation of sewers and embedding in a heating-cooling network. In: *Symposium on Energy Geotechnics (SEG23)*, Delft, the Netherlands.

Laloui, L., Rotta Loria, A.F. (2020). *Analysis and design of energy geostructure*, 1th ed., Elsevier, London, ISBN: 978-0-12-820623

Moormann, Ch., Buhmann, P., Pralle, N., Friedemann, W., Homuth, S. (2016). Tunnel geothermics - International experience with renewable energy concepts in tunnelling ´ 65. Geomechanik Kolloquium, 12.-14. Oktober 2016, Salzburg, Geomechanik und Tunnelbau 10/2016; 9(5): 467-480.

Nagpal, H., Spriet, J., Murali, M., McNabola, A. (2021). Heat recovery from wastewater – A review of available resource*, Water*, 13, 1274.

Schneider, M., Vermeer, P.A., Moormann, Ch. (2011). Tunneling as a contribution to sustainable energy. *Proc. XVth ECSMGE 2011: Geotechnics of Hard Soils – Weak Rocks*, Anagnostopoulos, A. Et al. (eds.): Amsterdam, IOS Press BV, 2011, Part 3, 1815-1820

Schneider, M. (2013). *Zur energetischen Nutzung von Tunnelbauwerken – Messungen und numerische Berechnungen am Beispiel Fasanenhof*. Stuttgart: PhD-Thesis, Proc. Of the Institute of Geotechnical Engineering at University of Stuttgart, Volume 68, (in German).

Sterpi, D., Coletto, A., Mauri, L. (2017). Investigation on the behaviour of a thermo-active diaphragm wall by thermo-mechanical analyses*, Geomechanics for Energy and the Enviroment*, 9.

VDI 4640 Blatt 2 (2019). Thermische Nutzung des Untergrunds – Erdgekoppelte Wärmepumpenanlagen (in German).

Wirtz, M. (2022). Survey of 53 5th Generation District Heating and Cooling (5GDHC) Networks in Germany, *Energy Technology*, 10(11)

Proceedings of the XVIII ECSMGE 2024
GEOTECHNICAL ENGINEERING CHALLENGES
TO MEET CURRENT AND EMERGING NEEDS OF SOCIETY
© 2024 the Authors
ISBN 978-1-032-54816-6
DOI 10.1201/9781003431749-600
Open Access: www.taylorfrancis.com, CC BY-NC-ND 4.0 license

ECSMGE 24
XVIII EUROPEAN CONFERENCE ON SOIL MECHANICS AND GEOTECHNICAL ENGINEERING

Accelerated stabilization of municipal solid waste in bioreactor landfills

Stabilisation accélérée des déchets solides municipaux dans les décharges de bioréacteurs

G. Kumar
Geosyntec Consultants, Austin, USA

K.R. Reddy*, J.K. Janga
University of Illinois Chicago, Chicago, USA

**kreddy@uic.edu*

ABSTRACT: In recent years, bioreactor landfills, which involve leachate recirculation/injection operations to enhance the moisture levels within the municipal solid waste (MSW) landfills and facilitate rapid waste decomposition and early waste stabilization have emerged as a promising MSW management option. However, unlike conventional landfills, there is a lack of well-established procedures/methods for an effective design and operation of such landfills primarily due to a limited understanding of the physical, chemical and biological processes and their coupled interactions that influence the MSW behaviour in landfills. Several researchers have developed numerical models to simulate MSW behaviour in landfills but only a few models have comprehensively considered the simultaneous interactions of hydraulic, mechanical, biochemical, and thermal processes within the waste in their numerical models. In this study, a brief overview of the past studies at University of Illinois Chicago (UIC) including laboratory, field, and numerical investigations regarding MSW behaviour in bioreactor landfills is presented. Further, a numerical modelling framework newly developed at UIC that incorporates the coupled thermo-hydro-bio-mechanical processes in MSW landfills is briefly discussed. Finally, the predictive capabilities of the developed coupled numerical model in demonstrating the accelerated stabilization of MSW and associated long-term performance of bioreactor landfills are highlighted.

RÉSUMÉ: Ces dernières années, les décharges de bioréacteurs, qui impliquent des opérations de recirculation/injection des lixiviats pour augmenter les niveaux d'humidité dans les décharges de déchets solides municipaux (MSW) et faciliter la décomposition rapide des déchets et la stabilisation précoce des déchets, sont apparues comme une option prometteuse de gestion des DSM. Cependant, contrairement aux décharges conventionnelles, il existe un manque de procédures/méthodes bien établies pour une conception et une exploitation efficaces de telles décharges, principalement en raison d'une compréhension limitée des processus physiques, chimiques et biologiques et de leurs interactions couplées qui influencent le comportement des DSM dans les décharges conventionnelles. décharges. Plusieurs chercheurs ont développé des modèles numériques pour simuler le comportement des DSM dans les décharges, mais seuls quelques modèles ont pris en compte de manière exhaustive les interactions simultanées des processus hydrauliques, mécaniques, biochimiques et thermiques au sein des déchets dans leurs modèles numériques. Dans cette étude, un bref aperçu des études antérieures menées à l'Université de l'Illinois à Chicago (UIC), y compris des enquêtes en laboratoire, sur le terrain et numériques concernant le comportement des DSM dans les décharges de bioréacteurs, est présenté. En outre, un nouveau cadre de modélisation numérique intégrant des processus couplés thermo-hydro-bio-mécaniques développés à l'UIC est présenté. Enfin, les capacités prédictives du modèle numérique couplé développé pour décrire la stabilisation accélérée des DSM dans les décharges ont été mises en évidence.

Keywords: Municipal solid waste; bioreactor landfills; leachate recirculation; coupled processes.

1 INTRODUCTION

Bioreactor landfills are emerging as a promising alternative to conventional MSW landfills due to enhanced waste decomposition rates facilitating early waste stabilization and numerous other short-term and long-term benefits (e.g., enhanced methane gas production rates, reduced leachate treatment and disposal costs, reduced post-closure monitoring costs). However, unlike the conventional landfills, the procedures/methods for the design, construction, and effective operation of bioreactor landfills are not well-established in that there needs be careful consideration towards the flow and distribution of the injected leachate within the landfill, the liquid and gas

pressures developed and their influence of the structural stability of the landfill slopes, the heat generation and temperature distribution within the landfill, and the differential settlement of waste and its influence on the integrity of the landfill components, among others (Reddy, 2006). The holistic behaviour of the abovementioned aspects of bioreactor landfills on their long-term performance is not well-understood primarily due to an incomplete understanding of the fundamental coupled processes that dictate the MSW behaviour. In this regard, several researchers have performed large-scale laboratory experiments, pilot-scale experiments, full-scale field investigations, and numerical modelling studies to develop a greater understanding of the different landfill processes and their interactions on the MSW behaviour in bioreactor landfill conditions. A comprehensive review of the previous investigations by other researchers on various aspects of landfill processes is summarized in Reddy et al. (2017) and Kumar and Reddy (2019).

In this paper, an overview of the previous work involving field-scale investigations, lab-scale experiments, and development of numerical model performed at UIC, which formed the basis of a more comprehensive coupled thermo-hydro-bio-mechanical model (CTHBM) presented in this paper, is reviewed and summarized. Additionally, the application of the developed model to demonstrate the accelerated stabilization of MSW in bioreactor landfills as compared to conventional landfills and the representative results from those analyses are discussed. Finally, the ongoing research in the development of the CTHBM model are highlighted.

2 PREVIOUS INVESTIGATIONS AT UIC

2.1 Field-scale investigations

Extensive field investigations were performed at Orchard Hills (OH) landfill located in Davis Junction, Illinois, USA where leachate recirculation was carried out in one of the landfill cells. The various field investigations performed included but not limited to:

- Monitoring of leachate recirculation and in situ moisture conditions using a comprehensive electrical resistivity tomography to non-invasively assess the zone of influence by the leachate recirculation systems (LRS) implemented (Grellier et al. 2007b).
- Optimization of leachate recirculation and moisture distribution at the OH landfill by interior imaging of the landfill using electromagnetic conductivity and ground penetrating radar (Carpenter et al. 2008).
- Seismic imaging using P-waves and S-waves through the landfilled waste to identify spatial and temporal changes and to evaluate the effects of leachate recirculation and degradation on the dynamic properties of MSW (Carpenter et al. 2013).
- Extensive sampling of both fresh waste from working face of the landfill and landfilled waste at different waste depths (Grellier et al. 2007a). The field waste samples collected from the OH landfill were sorted to identify the waste fractions and for waste characterization and further investigated in the laboratory as discussed in the section below.

2.2 Laboratory-scale investigations

Fresh waste samples, the landfilled waste samples, and the leachate samples collected from the OH landfill were transported to laboratory for additional comprehensive geotechnical testing to determine the engineering properties of MSW. These laboratory investigations (Grellier et al. 2007a, Reddy et al., 2009a-d) included but not limited to:

- Determining engineering properties such as particle size distribution, moisture content, organic content, specific gravity, hydraulic conductivity, compressibility, shear strength parameters, and biochemical properties such as the biochemical methane potential (BMP) of the waste.
- Long-term anaerobic bioreactor column tests on representative bulk samples of fresh waste and landfilled waste subjected to leachate recirculation. Waste samples were exhumed from the anaerobic bioreactors at different stages of degradation, based on gas composition and gas volumes, and tested for engineering properties.
- Analysis of moisture content, organic content, and BMP of the landfilled waste at different distances form the LRS to assess the effectiveness of LRS in moisture distribution at the OH landfill.
- Laboratory testing was performed on synthetic MSW (SMSW) simulating typical fresh waste composition of MSW generated in the United States to systematically evaluate the reproducibility of the test results for identical SMSW composition. Statistical analyses of the test results were performed to validate the laboratory test results.

2.3 Numerical modelling

With a better understanding on the engineering properties of waste developed from the abovementioned comprehensive field and laboratory investigation, numerical modeling efforts were carried out to further understand the complex coupled behaviour of MSW on the performance of bioreactor landfills. The intent of the modelling efforts was to develop guidance and/or recommendations that can be used by landfill owners and operators to designing safe and effectively operating bioreactor landfills in practice. These modelling efforts are summarized in Kumar (2021) and include but not limited to:

- Modelling of the mechanical behaviour of MSW for the prediction of long-term settlement of waste in MSW landfills, using a new constitutive model developed based on the concept of critical state soil mechanics (Babu et al. 2010).
- Hydraulic modelling of bioreactor landfills to evaluate the effectiveness of different LRS in enhancing the moisture distribution in bioreactor landfills (Reddy et al. 2020).
- Coupled hydro-mechanical (CHM) modelling to evaluate the stability of landfill slopes under different MSW slope and leachate injection configurations (Reddy et al., 2015). Coupled hydro-bio-mechanical (CHBM) modelling of bioreactor landfills by incorporating the effects of biodegradation on the engineering properties of MSW (Reddy et al. 2018).
- Incorporating the effects of temperature on the biodegradation rates of MSW to evaluate long-term performance of MSW landfills (Kumar et al. 2021).

3 COUPLED THERMO-HYDRO-BIO-MECHANICAL (CTHBM) MODEL

Although the previous numerical modelling efforts at UIC progressively advanced the comprehensiveness of the numerical model to simulate MSW behaviour landfills, there were several important limitations in the developed CHBM model, and the numerical models developed by other researchers (Reddy et al. 2017) including but not limited to the following:

- Ignoring the effects of coupled fluid-mechanical interactions and the interdependencies of biochemical and thermal processes
- Ignoring the effects of creep behaviour and if considered using a highly empirical approach to simulate the phenomenon
- Incorporating the effects of biodegradation on waste settlement using an empirical approach instead of a fundamental constitutive approach.
- Ignoring the large-strain kinematics.
- Inability of the models to assess broader performance aspects of MSW landfill systems (e.g., slope stability, liner/cover stability and integrity).

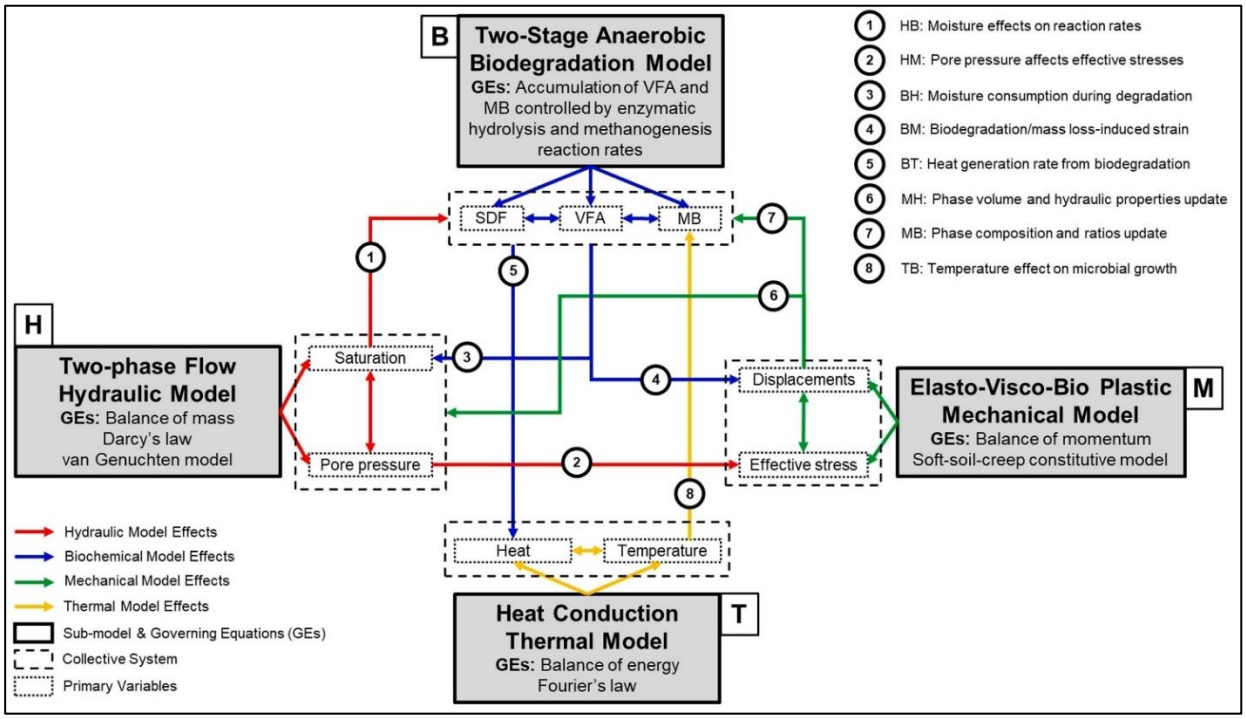

Figure 1. Conceptual CTHBM model.

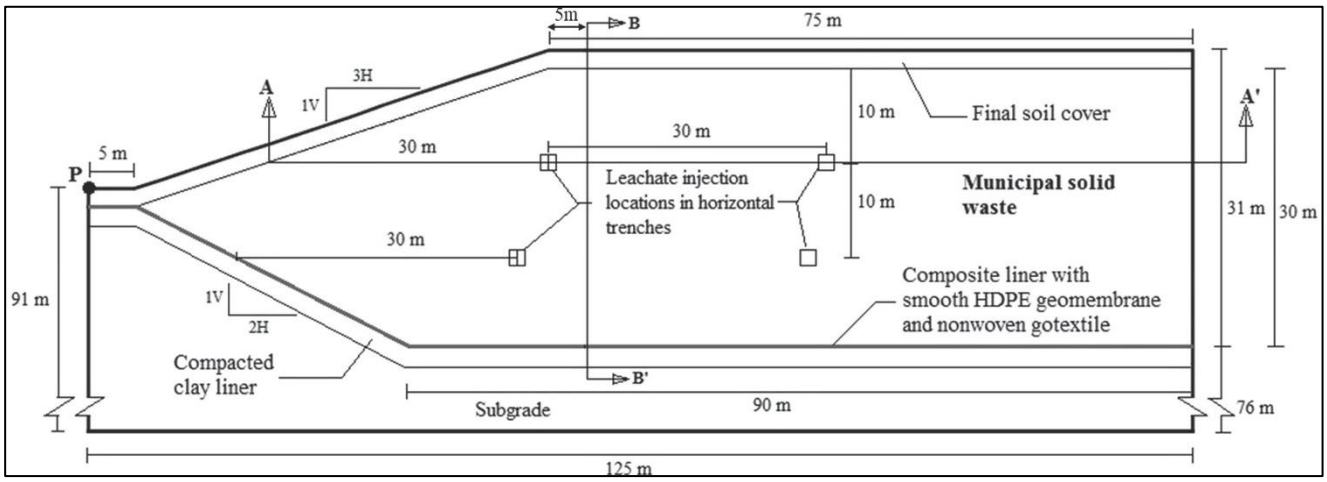

Figure 2. Schematic of landfill cell configuration.

Incorporating the abovementioned limitations, a new CTHBM model is developed to realistically simulate the coupled thermo-hydro-bio-mechanical processes in MSW landfills and thereby evaluate the holistic short-term and long-term performance of MSW landfills under conventional and bioreactor conditions. The CTHBM model is implemented in Fast Lagrangian Analysis of Continuum (FLAC), a finite difference code. A schematic of the CTHBM conceptual model mentioning the governing equations used for each of the landfill processes and the interdependencies incorporated within the CTHBM model is presented in Figure 1 below. For brevity, detailed description of the CTHBM model components and its implementation algorithm in FLAC is not presented in Kumar and Reddy (2021).

4 ACCELERATED STABILIZATION OF MSW IN BIOREACTOR LANDFILLS

To demonstrate the applicability of the CTHBM model for assessing long-term performance of MSW landfills under conventional and bioreactor conditions, a deterministic analysis was performed by running two simulations of a full-scale realistic landfill cell configuration as shown in Figure 2.

The two numerical simulations performed (i.e., one for conventional landfill conditions and another for bioreactor landfill conditions) included same landfill construction sequence, same material models and properties for soil and MSW, same boundary, initial, and interior conditions, with the only difference between the two simulations being the simulation of leachate (for simplicity assumed to be water) injection through horizontal trenches (HTs) at an injection pressure of 50 kilo pascal (kPa) in the bioreactor simulation. The simulation process, material and numerical parameters/properties, boundary, initial, and interior conditions for the two simulations are described in detail in Kumar and Reddy (2021).

Figure 3 below presents the comparison of certain long-term hydraulic, mechanical, biochemical, and thermal characteristics between the conventional and bioreactor simulations.

Figure 3(a) depicts that the model can enable landfill designers to evaluate different leachate injection configurations including different leachate recirculation/injection systems to evaluate the anticipated pore pressures near side slopes and thereby develop design guidance for safe injection pressures and spacing for effective distribution of moisture. Figures 3(b) and 3(c) demonstrate that the model can be used to realistically simulate and predict the spatial and temporal variation in the anticipated surface settlement and methane (CH_4) gas generation, which in-turn demonstrates the accelerated stabilization of MSW in landfills, thus assisting landfill operators to effectively plan bioreactor landfill operations, waste capacity, and maintaining the integrity of the landfill components (final cover). Figure 3(d) demonstrates that enhanced degradation rates through leachate injection can accelerate anaerobic heat generation leading to relatively higher temperatures than conventional landfills with similar waste conditions. Detailed description of the comparison of short-term and long-term performance characteristics along with a discussion on their influence on the stability/integrity of landfill liner and cover components derived from the two conventional and bioreactor landfill simulations are discussed in Kumar and Reddy (2021). However, the results presented in this study clearly indicates that leachate recirculation into landfills indeed enhances the waste stabilization rates in bioreactor landfills.

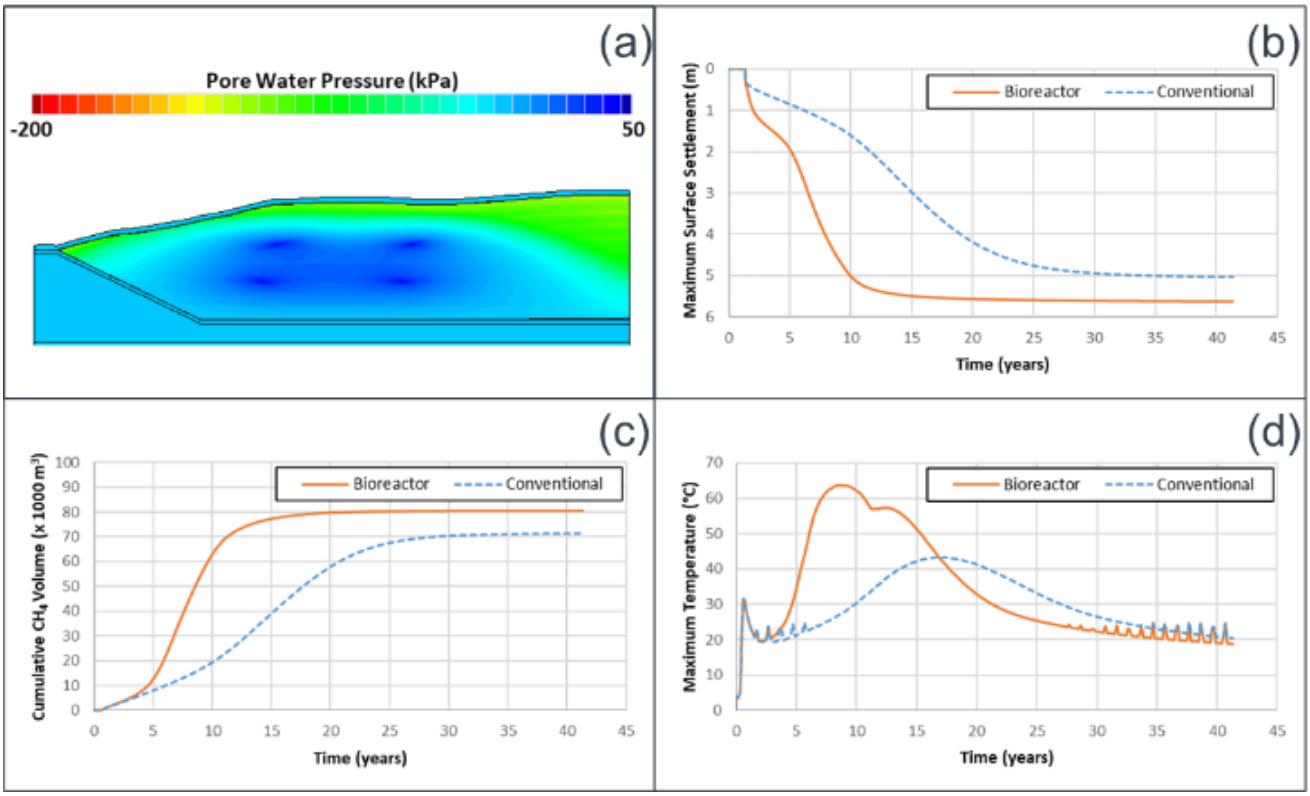

Figure 3. (a) Pore water pressure distribution in bioreactor landfill at the end of 40 years, and (b) maximum surface settlement, (c) cumulative CH_4 gas generation, and (d) maximum waste temperatures, with time.

5 CONCLUSIONS AND ONGOING RESEARCH

The newly developed CTHBM model has been successfully validated and demonstrates it's ability to accurately and realistically simulate the observed trends in the hydraulic (leachate distribution), mechanical (waste settlement), biochemical (gas generation), and thermal (temeprature distribution) characteristics observed in laboratory experiments and full-scale landfill cell under conventional and bioreactor conditions. Additionally, the CTHBM model can be used to perform parametric analyses on different landfill configurations to develop design recommendations for effective deisgn and operation of bioreactor landfills. Finally, the CTHBM model can be used to perform probabilistic analysis by considering spatial variability in the MSW properties acorss landfills and assist with creating realistic bounds for the predicted long-term characteristics of bioreactor landfills.

Continued research is ongoing at UIC to futher develop the CTHBM model by incorporating other importat processes such as convective heat transport, leachate characteristics, alternative heat generation mechanisms, liner interface shear behavior, among others.

ACKNOWLEDGEMENT

This research was funded by the National Science Foundation (NSF) (CMMI #1537514) and the University of Illinois Chicago (UIC). Any opinions, findings, conclusions, and recommendations expressed in this material are those of the authors and do not necessarily reflect the views of the NSF or UIC.

REFERENCES

Babu, G.L.S., Reddy, K. R., Chouksey, S. K. (2010). Constitutive model for municipal solid waste incorporating mechanical creep and biodegradation-induced compression. *Waste Management*, 30(1): 11-22. https://doi.org/10.1016/j.wasman.2009.09.00.

Carpenter, P.J., Grellier, S., Reddy, K.R., Adib, R., Peters, C., Gangathulasi, J. (2008). Investigating the interior of a landfill cell with leachate injection using electromagnetic conductivity and ground-penetrating radar surveys. In: *21st Symposium on the Application of Geophysics to Engineering and Environmental Problems*, Environmental and Engineering Geophysical Society, Denver, CO, USA, pp. 212-222. https://doi.org/10.3997/2214-4609-pdb.177.130.

Carpenter, P.J., Reddy, K.R., Thompson, M.D. (2013). Seismic imaging of a leachate recirculation landfill: Spatial changes in dynamic properties of municipal solid waste. *Journal of Hazardous, Toxic, and Radioactive*

Waste, 17(4): 331-41. https://doi.org/10.1061/(ASCE)HZ.2153-5515.0000175.

Grellier, S., Reddy, K.R., Gangathulasi, J., Adib, R., Peters, C. (2007a). US MSW and its biodegradation in a bioreactor landfill. In: *11th International Waste Management and Landfill Symposium*, S. Margherita di Pula, Cagliari, Italy, 10p.

Grellier, S., Reddy, K., Gangathulasi, J., Adib, R., Peters, C. (2007b). Correlation between electrical resistivity and moisture content of municipal solid waste in bioreactor landfill. In: *GeoDenver 2007*, Geotechnical Special Publication No. 163, ASCE, Reston, VA. https://doi.org/10.1061/40907(226)11.

Kumar, G. (2021). *Coupled Thermo-Hydro-Bio-Mechanical Model for Holistic Performance Assessment of Municipal Landfills*. Doctoral Thesis, University of Illinois Chicago. Avaiable at: https://indigo.uic.edu/articles/thesis/Coupled_Thermo-Hydro-Bio-Mechanical_Model_for_Holistic_Performance_Assessment_of_Municipal_Landfills/15272364/1/files/29254938.pdf. Accessed 19/01/2024.

Kumar, G., Reddy, K.R.. Constitutive models for municipal solid waste in landfills. In: *Proceedings of the XVI Pan-American Conference on Soil Mechanics and Geotechnical Engineering*, Cancun, Mexico. https://doi.org/10.3233/STAL190096.

Kumar, G., Reddy, K.R. (2021). Comprehensive coupled thermo-hydro-bio-mechanical model for holistic performance assessment of municipal solid waste landfills. *Computers and Geotechnics*, 132: 103920. https://doi.org/10.1016/j.compgeo.2020.103920.

Kumar, G., Kopp, K.B., Reddy, K.R., Hanson, J.L., Yeşiller, N. (2021). Influence of waste temperatures on long-term landfill performance: Coupled numerical modeling. *Journal of Environmental Engineering*, 147(3): 04020158. https://doi.org/10.1061/(ASCE)EE.1943-7870.0001855.

Reddy, K.R. (2006). Geotechnical aspects of bioreactor landfills. In: *Indian Geotechnical Conference*, IIT Madras, India, pp. 79-94.

Reddy, K.R., Hettiarachchi, H., Gangathulasi, J., Parakalla, N., Bogner, J.E., Lagier, T. (2009a). Compressibility and shear strength of municipal solid waste under short-term leachate recirculation operations. *Waste Management & Research*, 27(6): 578-587. https://doi.org/10.1177/0734242X09103825.

Reddy, K.R., Hettiarachchi, H., Gangathulasi, J., Bogner, J.E., Lagier, T. (2009b). Geotechnical properties of synthetic municipal solid waste. *International Journal of Geotechnical Engineering*, 3(3): 429-438. https://doi.org/10.3328/IJGE.2009.03.03.429-438.

Reddy, K.R., Hettiarachchi, H., Parakalla, N., Gangathulasi, J., Bogner, J.E., Lagier, T. (2009c). Hydraulic conductivity of MSW in landfills. *Journal of Environmental Engineering*, 135(8): 677-683. https://doi.org/10.1061/(ASCE)EE.1943-7870.0000031.

Reddy, K.R., Hettiarachchi, H., Parakalla, N.S., Gangathulasi, J., Bogner, J.E. (2009d). Geotechnical properties of fresh municipal solid waste at Orchard Hills landfill, USA. *Waste Management Journal*, 29(2): 952-959. https://doi.org/10.1016/j.wasman.2008.05.011.

Reddy, K. R., Giri, R. K., Kulkarni, H. S. (2015). Modeling coupled hydromechanical behavior of landfilled waste in bioreactor landfills: Numerical formulation and validation. *Journal of Hazardous, Toxic, and Radioactive Waste*, 21(1): D4015004. https://doi.org/10.1061/(ASCE)HZ.2153-5515.0000289.

Reddy, K.R., Kumar, G., Giri, R.K. (2017). Modeling coupled processes in municipal solid waste landfills: An overview with key engineering challenges. *International Journal of Geosynthetics and Ground Engineering*, 3(1): 6. 2017. https://doi.org/10.1007/s40891-016-0082-2.

Reddy, K. R., Kumar, G., Giri, R. K. (2018). Modeling coupled hydro-bio-mechanical processes in bioreactor landfills: Framework and validation. *International Journal of Geomechanics*, 18(9): 04018102. https://doi.org/10.1061/(ASCE)GM.1943-5622.0001164.

Reddy, K.R., Kumar, G., Kulkarni, H.S. (2020). Two-phase flow modeling to evaluate effectiveness of different leachate injection systems for bioreactor landfills. *Environmental Modeling & Assessment*, 25: 115-128. https://doi.org/10.1007/s10666-019-09663-z.

Proceedings of the XVIII ECSMGE 2024
GEOTECHNICAL ENGINEERING CHALLENGES
TO MEET CURRENT AND EMERGING NEEDS OF SOCIETY
© 2024 the Authors
ISBN 978-1-032-54816-6
DOI 10.1201/9781003431749-601
Open Access: www.taylorfrancis.com, CC BY-NC-ND 4.0 license

ECSMGE 24
XVIII EUROPEAN CONFERENCE ON SOIL MECHANICS AND GEOTECHNICAL ENGINEERING

Basic characteristics of environment-friendly soil-cement material with added biochar

Caractéristiques de base d'un matériau sol-ciment écologique avec biochar ajouté

Y. Kurimoto*, Y. Asaka
Institute of Technology/Shimizu Corporation/Tokyo, Japan
**yuhei.kurimoto@shimz.co.jp*

ABSTRACT: This paper describes research in which carbon-rich biochar is added to a soil-cement slurry in the laboratory with the purpose of offsetting the carbon emissions of the stabilizer used in cement-treated soil. The effect of the biochar on strength development and resistance to material separation is investigated. Blast furnace cement type B is used as the stabilizer, which is added to solidify the soil. Specimens with five different ratios of stabilizer relative to the volume of the soil-water mixture are tested (40, 80, 120, 150 and 300 kg/m^3) and different proportions of biochar are added to offset and more than offset the CO_2 emissions of the stabilizer. The assumed CO_2 sequestration resulting from biochar addition is 2.51 kg-CO_2/kg, based on methodologies used for the addition of biochar to mineral soil in cropland/grassland. The unconfined compression strength of the soil-cement with biochar after curing for 28 days tends to be higher than that of the material without biochar, except for the 40 kg/m^3 cases. The maximum ratio of increase in unconfined compression strength is 1.04, 1.43, 1.37, 1.36 and 1.16 for the 40 to 300 kg/m^3 cases. The material segregation resistance of the soil-cement is also improved when the amount of biochar added exceeds 30 kg/m^3, regardless of the amount of stabilizer added.

RÉSUMÉ: Cet article décrit des recherches dans lesquelles du biochar riche en carbone est ajouté à une boue sol-ciment en laboratoire dans le but de compenser les émissions carbone du stabilisateur utilisé dans le sol traité au ciment. L'effet du biochar sur le développement de la résistance mécanique et sur la résistance à la séparation des matériaux est étudié. Du ciment de haut fourneau de type B est utilisé comme stabilisateur, qui est ajouté pour solidifier le sol. Des échantillons avec cinq ratios différents de stabilisateur par rapport au volume du mélange sol-eau sont testés (40, 80, 120, 150 et 300 kg/m^3) et différentes proportions de biochar sont ajoutées afin de compenser et faire plus que compenser les émissions de CO_2 du stabilisateur. La séquestration de CO_2 supposée résultant de l'ajout de biochar est de 2,51 kg-CO_2/kg, sur la base des méthodologies utilisées pour l'ajout de biochar à un sol minéral dans des terres cultivées/prairies. La résistance à la compression monoaxiale du sol-ciment avec biochar après 28 jours de durcissement tend à être supérieure à celle d'un matériau sans biochar, à l'exception des cas à 40 kg/m^3. Le ratio d'augmentation maximum de la résistance à la compression monoaxiale est de 1,04, 1,43, 1,37, 1,36 et 1,16 pour les cas allant de 40 à 300 kg/m^3. La résistance à la ségrégation des matériaux du sol-ciment est également améliorée lorsque la quantité de biochar ajoutée dépasse 30 kg/m^3, indépendamment de la quantité de stabilisateur ajoutée.

Keywords: Carbon sequestration; biochar; cement-treated soil; unconfined compression strength; bleeding.

1 INTRODUCTION

The building and construction industry accounts for around 37% of global energy usage and process-related CO_2 emissions (UNEP, 2022). Emissions from the manufacture of concrete, aluminium and steel used in the construction of buildings are estimated to represent around 2.3 Gt-CO_2 globally. Other materials used in the construction of buildings, such as bricks and glass, are estimated to account for a further 1.2 Gt-CO_2 of emissions globally. NILIM (2008) reported that CO_2 emissions associated with construction (embodied carbon) and demolition account for approximately 30% of the life cycle CO_2 emissions of a building. Meanwhile, research and development related to carbon capture and storage (CCS) and carbon capture, utilization and storage (CCUS) is being pursued in the field of geotechnical engineering. Furthermore, both artificial and natural low-carbon building materials, such as recycled concrete fines and bio-improved soils, are being investigated. The use of wood in construction projects is also being actively promoted (e.g., Kuittinen, 2013) to increase carbon accumulation and mitigate climate change. Moreover, carbon-rich materials, such as wood and biochar, have attracted attention in recent years not only in the agriculture field but also among geotechnical engineers. Biochar is a solid material

generated by heating biomass to a temperature in excess of 350°C under conditions of controlled and limited oxidant concentration to prevent combustion. Senadheera (2023) summarized comprehensively the physicochemical properties of biochar when added to cementitious materials, considering both the environmental and economic impact.

In this paper, the effect of adding biochar to soil-cement used as a material for backfilling, earth retaining and ground improvement is studied through laboratory tests.

2 TEST OVERVIEW

2.1 Materials

A soil-water mixture consisting of silica sand in air-dried condition, a 1:1 mix of Kibushi clay and Kaolin clay by mass, and water with a mass ratio of 4:1:2.15 was used as the original mud. Blast furnace cement type B (symbol: BB) complying with the Japan Industrial Standard (JIS R 5211, 2019) was used as the stabilizer; its characteristics are density 3.04 g/cm^3, specific surface area 3950 cm^2/g, ignition loss 1.39%, SO_3 2.14%, and addition ratio of blast furnace slag 40%. The cement used was of the type generally distributed in Japan with ingredients stipulated by JIS, bearing in mind that cement ingredients differ among countries.

Biochar was used as an admixture to improve the segregation resistance of the soil-cement material. It was manufactured by Nara Tanka Industries Co., Ltd. and had been sieved to a grain size of 5 mm or less. The original feedstock for this biochar is sawdust produced while cutting coniferous and broad-leaved trees. The sawdust is compression-molded into briquettes, then carbonized, pulverized, and sieved for use as biochar. Biochar can be highly porous depending on the original feedstock and pyrolysis conditions, and the specific surface area differs by three orders compared to the stabilizer. The water absorption of the biochar is 21-25%. Other basic physical properties of the biochar are available in Kurimoto (2023).

2.2 Mix proportions

Five amounts of stabilizer (40, 80, 120, 150 and 300 kg/m^3) were used relative to the volume of the soil-water mixture. The target water content of both the soil-water mixture and the soil-cement was 43%. The target unconfined compression strength of the soil-cement was set to 100-3000 kPa.

Based on the CO_2 emissions inventory data of the stabilizer (MLIT, 2017), the amount of biochar used was adjusted to offset the CO_2 emissions of the stabilize or more than offset them. Note that the amount of CO_2 sequestration by the biochar was assumed to be the ratio of organic carbon content for this type of biochar (0.77) × fraction of biochar carbon remaining after 100 years (0.89) × relative molecular mass ratio of carbon dioxide to carbon (44/12) = 2.51 kg-CO_2/kg, based on methodologies used in regard to biochar addition to mineral soil in cropland/grassland (J-Credit Scheme, 2023). Biochar was added as a material percentage at the beginning of mixing. In this experiment, CO_2 emissions related to the manufacture and transport of the biochar were not considered.

2.3 Mixing and testing

The soil-cement material was prepared by kneading for three minutes in a small mixer. Details of the process are given in Kurimoto (2023). Immediately after kneading, the temperature, density, flow, and bleeding characteristics of the soil-cement in a slurry state were measured. Test specimens were prepared with a size of 50 mm in diameter and 100 mm in height and these were demolded at the age of 28 days. The specimens were then tested for shear wave velocity and unconfined compression. Sher wave velocity was measured by bender element test. Shear wave velocity and unconfined compression strength results are the averages of three test specimens.

3 EXPERIMENTAL RESULTS

Table 1 shows the physical properties and unconfined compression strength of the soil-cement specimens. Test IDs consist of "type of stabilizer - amount of stabilizer added - ratio of CO_2 fixation in biochar to CO_2 emissions of stabilizer." For example, "BB-80-1" represents the case in which the stabilizer is blast furnace cement type B, the amount of stabilizer added is 80 kg/m^3, and biochar is added to exactly offset the CO_2 emissions of the stabilizer. Figures 1 to 4 show the results for all test specimens. The vertical axes in Figure 1 and Figure 2 are normalized by the value for the soil-cement without biochar in each case.

Table 1 and Figure 1 show that, although there is no effect of adding biochar on the density of the soil-cement after kneading, the flow and bleeding tend to decrease as the amount of biochar increases, except for BB-40-0 to BB-40-3. In other words, the material segregation resistance of the soil-cement is improved when the amount of biochar added exceeds 30 kg/m^3, regardless of the amount of stabilizer added.

Table 1 and Figure 2 demonstrate that the unconfined compression strength of the soil-cement without biochar in five cases is 169-2695 kPa, which satisfies the target strength. By contrast, the unconfined compression strength of the soil-cement with biochar is

Table 1. Physical properties and unconfined compression strength of the soil-cement material.

Test ID	Biochar (kg/m^3)	CO_2 emissions of stabilizer (kg/m^3)	CO_2 fixation in biochar (kg/m^3)	Density (g/cm^3)	Flow (mm)	Bleeding (%)	Unconfined compression strength (kPa)
BB-40-0	0	20	0	1.77	254	1.19	169
BB-40-0.5	4	20	10	1.78	234	1.17	149
BB-40-1	8	20	20	1.77	235	1.21	154
BB-40-1.5	12	20	30	1.78	249	1.18	161
BB-40-2	16	20	40	1.78	260	1.47	141
BB-40-2.5	20	20	50	1.77	263	1.39	159
BB-40-3	24	20	60	1.79	261	1.20	158
BB-40-3.5	28	20	70	1.80	237	0.84	162
BB-40-4	32	20	80	1.79	240	0.70	175
BB-80-0	0	40	0	1.77	238	0.75	223
BB-80-0.5	8	40	20	1.77	264	0.85	238
BB-80-1	16	40	40	1.76	240	0.48	259
BB-80-1.5	24	40	60	1.77	229	0.34	266
BB-80-2	32	40	80	1.78	198	0.23	269
BB-80-2.5	40	40	100	1.79	185	0.49	286
BB-80-3	48	40	120	1.79	198	0.41	298
BB-80-3.5	56	40	140	1.80	198	0.26	314
BB-80-4	64	40	160	1.78	197	0.28	320
BB-120-0	0	60	0	1.78	264	0.81	465
BB-120-0.5	12	60	30	1.79	221	0.22	486
BB-120-1	24	60	60	1.79	241	0.57	481
BB-120-1.5	36	60	90	1.78	223	0.43	456
BB-120-2	48	60	120	1.78	232	0.32	504
BB-120-2.5	60	60	150	1.79	200	0.19	499
BB-120-3	72	60	180	1.80	200	0.28	525
BB-120-3.5	84	60	210	1.78	198	0.13	639
BB-120-4	96	60	240	1.80	174	0.00	536
BB-150-0	0	75	0	1.76	270	0.79	744
BB-150-0.5	15	75	37	1.76	265	0.72	817
BB-150-1	30	75	75	1.78	250	0.51	781
BB-150-1.5	45	75	112	1.78	242	0.33	855
BB-150-2	60	75	150	1.78	216	0.17	947
BB-150-2.5	75	75	187	1.78	207	0.21	975
BB-150-3	90	75	225	1.76	190	0.05	950
BB-150-3.5	105	75	262	1.77	183	0.00	1015
BB-150-4	120	75	300	1.77	169	0.00	1001
BB-300-0	0	150	0	1.71	254	0.01	2695
BB-300-0.5	30	150	75	1.73	264	0.00	2570
BB-300-1	60	150	150	1.75	247	0.00	2722
BB-300-1.5	90	150	225	1.75	234	0.00	2836
BB-300-2	120	150	300	1.76	206	0.00	2981
BB-300-2.5	150	150	375	1.74	209	0.00	2781
BB-300-3	179	150	450	1.75	186	0.00	3127
BB-300-3.5	209	150	525	1.75	171	0.00	3015
BB-300-4	239	150	600	1.77	156	0.00	3126

slightly higher, except for BB-40. The maximum ratio of unconfined compression strength increase in each case is 1.04 for BB-40, 1.43 for BB-80, 1.37 for BB-120, 1.36 for BB-150 and 1.16 for BB-300. This slight increase in strength is because the highly porous biochar absorbs water over time, thereby reducing the water-cement ratio of the soil-cement (Kurimoto, 2023). On the other hand, the water-cement ratio of the soil-cement in BB-40 is larger than in the other cases; consequently, the water absorption of biochar has little effect on strength of the soil-cement. Figure 3 shows that when the unconfined compression strength of the soil-cement is in range of 141-3127 kPa, the corresponding deformation modulus is in the range 26-712 MPa. The ratio of the deformation modulus E_{50} and the unconfined compression strength q_u is in the range 180-260. The unconfined compression strength exhibits a unique relationship with shear wave velocity

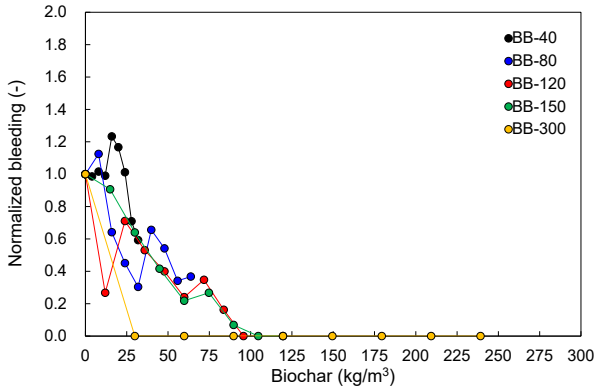

Figure 1. Normalized bleeding results.

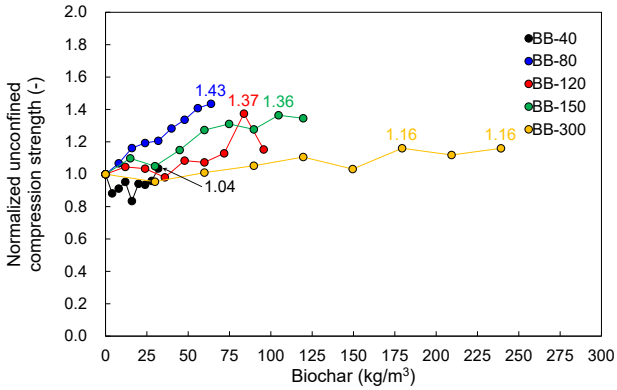

Figure 2. Normalized unconfined compression strength results.

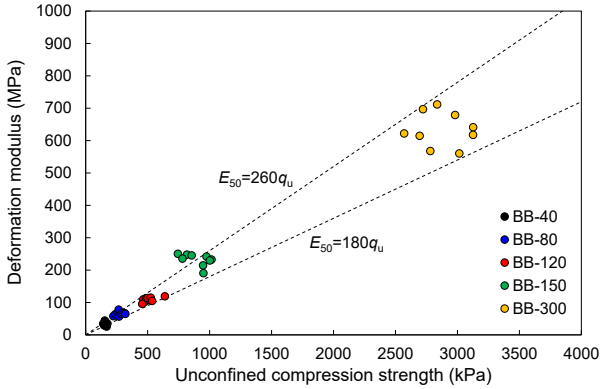

Figure 3. Relationship between deformation modulus and unconfined compression strength.

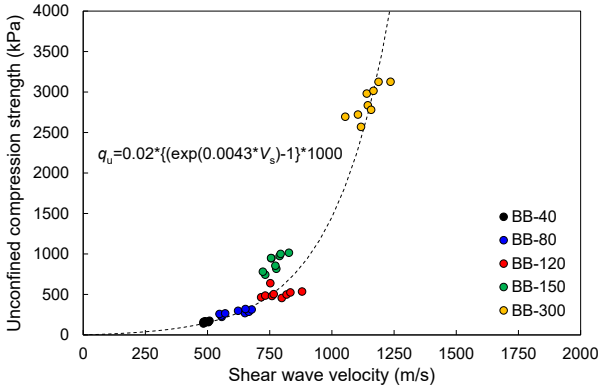

Figure 4. Relationship between unconfined compression strength and shear wave velocity.

regardless of the presence or absence of biochar and can be expressed as an exponential of the shear wave velocity, as shown in Figure 4. This relation is very similar to a description by Asaka (2011).

4 CONCLUSIONS

Biochar was used as an admixture to sequester the CO_2 in the soil-cement, and its effect on the physical and mechanical properties of the soil-cement was evaluated by laboratory tests.

As a result of adding biochar to reduce the emissions resulting from the soil-cement stabilizer, the unconfined compression strength of the material increased with the amount of stabilizer (80, 120, 150 and 300 kg/m^3) while material segregation resistance improved when the amount of biochar added exceeded 30 kg/m^3. Additionally, it was found that the relationship between the unconfined compression strength, deformation modulus and shear wave velocity was not affected by the addition of biochar.

REFERENCES

Asaka, Y. and Abe, T. (2011). Non-destructive technique for assessing cement-treated ground. *Proceedings of the Institution of Civil Engineers - Ground Improvement*, Vol. 164, No. 3, pp. 179-187. https://doi.org/10.1680/grim.2011.164.3.179.

Japanese Industrial Standards (2019). Portland blast-furnace slag cement (JIS R 5211). (in Japanese)

J-Credit Scheme (2023). Biochar addition to mineral soil in cropland/grassland (AG-004). (in Japanese)

Kuittinen, M., Ludvig, A. and Weiss, G. (2013). Wood in Carbon Efficient Construction: Tools, Methods and Applications. CEI-Bois.

Kurimoto, Y., Yoda, Y., Kojima, K. and Asaka, Y. (2023). Carbon sequestration using biochar in cement-treated ground. *Proceedings of the 9th International Congress on Environmental Geotechnics*, Vol. 4, pp. 216-221. https://doi.org/10.53243/ICEG2023-351.

Ministry of Land, Infrastructure, Transport and Tourism (2017). Global Warming Countermeasures in the Field of Construction. (in Japanese).

National Institute for Land and Infrastructure Management (2008). Project Research Report, No. 21. (in Japanese).

Senadheera, S. S., Gupta, S., Kua, H. W., Hou, D., Kim, S., Tsang, D. C. W. and Ok, Y. S. (2023). Application of biochar in concrete - A review. *Cement and Concrete Composites*, 143, pp. 105204-1-16. https://doi.org/10.1016/j.cemconcomp.2023.105204.

United Nations Environment Programme (2022). 2022 Global Status Report for Buildings and Construction: Towards a Zero-emission, Efficient and Resilient Buildings and Construction Sector.

Proceedings of the XVIII ECSMGE 2024
GEOTECHNICAL ENGINEERING CHALLENGES
TO MEET CURRENT AND EMERGING NEEDS OF SOCIETY
© 2024 the Authors
ISBN 978-1-032-54816-6
DOI 10.1201/9781003431749-602
Open Access: www.taylorfrancis.com, CC BY-NC-ND 4.0 license

ECSMGE 24
XVIII EUROPEAN CONFERENCE ON SOIL MECHANICS AND GEOTECHNICAL ENGINEERING

Prediction of short piles response to lateral monotonic load in dense sand at Blessington

Prédictions de la réponse de pieux courts sous charge monotonique latérale dans le sable dense de Blessington

L.-M. Lapastoure*
Department of Civil, Structural and Environmental Engineering, Trinity College Dublin, Dublin, Ireland Gavin and Doherty Geosolutions, Dublin, Ireland

D. Igoe
Department of Civil, Structural and Environmental Engineering, Trinity College Dublin, Dublin, Ireland

**lapastol@tcd.ie*

ABSTRACT: This paper presents some initial results of an experimental campaign aimed at extending the existing database of pile lateral field tests. Monopiles with low slenderness ratios (L/D, ratio of pile embedment to pile diameter) less than 4.5 are deemed to be representative of current and future monopile foundation designs for the offshore wind industry. The monopile field testing consisted of both monotonic and cyclic tests with slenderness ranging from 2.2 to 4.4. A total of 6 piles with an outer diameter of 457 mm were driven and tested in dense sand at the Blessington test site, located south to Dublin in Ireland. Three different approaches were used to predict the monotonic pile responses. Traditional approaches (API and PISA rule) were found to significantly underestimate both piles stiffness and ultimate capacity. A novel set of CPT based correlations of HS-small parameters for three-dimensional finite-element analyses recently developed by Trinity College Dublin was found to provide very accurate predictions of both stiffness and ultimate reaction.

RÉSUMÉ: Cet article présente les premiers résultats d'une campagne expérimentale visant à étendre la base de données existante d'essais in-situ de pieux chargés latéralement. Des rapports d'élancement (L/D, rapport entre la profondeur et le diamètre du pieu) plus faibles sont plus représentatifs des dimensions des fondations monopieux supportant actuellement les éoliennes en mer. Des pieux avec des rapports d'élancement allant de 2.2 à 4.4 ont été testés sous charges monotoniques et cycliques. Au total, 6 pieux d'un diamètre extérieur de 457 mm ont été battues et testés dans du sable dense sur le site d'essai de Blessington, situé au sud de Dublin en Irlande. Trois approches différentes ont été utilisées pour prédire la réponse des pieux sous chargement monotone. Les approches traditionnelles (API et PISA rule) ont sous-estimé de manière significative la rigidité et la capacité ultime des pieux. Trinity College Dublin a récemment développé un jeu de corrélations basées sur le CPT pour les paramètres du model de sol constitutif HS-small, populaire pour les analyses éléments finis 3D. Cette approche s'est avérée fournir des prédictions très précises de la rigidité et de la réaction ultime des pieux.

Keywords: Offshore wind; geotechnical engineering; monopiles; field tests.

1 INTRODUCTION

This paper outlines the preliminary findings from an experimental initiative aimed at expanding the current repository of lateral field tests for low L/D monopiles. Monopiles are large diameter open ended steel pipe piles which are typically impact driven into the seabed and are the most commonly used foundation for offshore wind turbines. As the offshore wind industry matures, larger wind turbines are being designed which require monopiles with diameters in excess of 10 m. These XL monopiles typically have slenderness ratios (L/D, where L is the embedded length and D the diameter) less than 4.5. In this paper, the results from one of the monotonic field test piles with L/D=3.3 is compared to three different approaches for predicting the lateral responses of the piles. The paper shows that current rule-based beam-spring approaches such as API (2011) and PISA-rule based method (Burd et al. 2020) both significantly underestimate the stiffness and ultimate capacity of these small scale piles. In contrast, a 3D Finite Element approach developed at Trinity College Dublin, using CPT-based correlations, provides highly accurate predictions for the entire load-displacement response.

2 METHODOLOGIES

This section presents 3 different approaches to predict the response of piles subjected to monotonic lateral loading in sands.

2.1 API

The traditional industry practice used to follow the oil and gas industry design standard (API, 2014). The 'p-y approach' involves modelling the pile by means of one-dimensional elastic beam elements. At each depth, a 'p-y curve' defines the non-linear relationship between the soil resistance, p, mobilised as a result of the pile lateral displacement, y. The soil layers are assumed to behave independently, therefore the curves are uncoupled. API RP 2GEO (API, 2014) provides basis for the formulation of the non-linear p-y curves in sands, soft clays and stiff clays. In sands, it takes the form of a hyperbolic tangent as shown by equation (1):

$$p = Ap_u \tanh\left(\frac{kz}{Ap_u} y\right) \quad (1)$$

where:

- $A = \left(3 - 0.8\frac{z}{D}\right) \geq 0.9$ for monotonic loading.
- p_u is the ultimate lateral resistance at depth z.
- k is the rate of increase with depth of initial modulus of subgrade reaction at depth z.
- y is the lateral pile deflection at depth z.
- z is the depth below ground level.

The interested reader is invited to refer to API (2014) section 8.5.6 for additional information, including basis for calculation of p_u and k.

2.2 PISA rule

The PISA design model (Burd et al., 2020) represents the state-of-the-art design methodology for monopiles and is now used globally in the industry. Like API, the PISA approach rely on one-dimensional finite-element analyses. However, PISA considers three other soil reaction components in addition to the distributed lateral load: the distributed moment, the base shear and the base moment (see Figure 1). The soil reaction curves can be constructed from a set of equations referred to as 'depth variation functions' (DVFs). The DVFs provide basis to generate nornalised soil reaction curves. The soil inputs required to un-normalised the curves in sand are the soil realtive density, small strain shear modulus, and unit weight. Following the PISA rule-based approach, the DVFs from the Generalised Dunkirk Sand Model (GDSM) developed by Burd et al. (2020) is considered in this study.

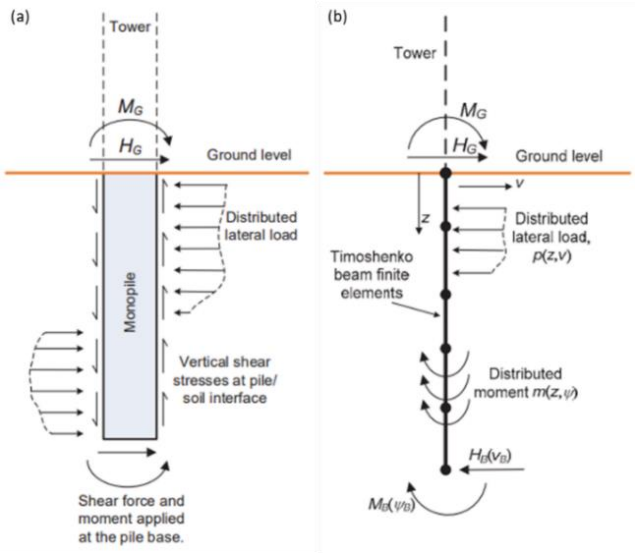

Figure 1. PISA design model: (a) soil reaction components acting on the pile; (b) implementation in 1D FE (after Burd et al., 2019).

2.3 3D FEA

With the development of computational power, it is now standard practice to use three-dimensional finite element analyses for monopile design.

In this study, the piles were modelled at full scale and half-space in Plaxis 3D. The pile structure is modelled using linear-elastic isotropic plate elements with standard steel properties (Young's modulus of 210 GPa and Poisson's ratio of 0.3). The pile is weightless since the focus is on lateral loading. Interfaces at the outside and inside of the pile capture the soil-structure interactions.

The sand is modelled with the Hardening soil model with small strain stiffness (HS-small) assuming drained conditions. All the inputs required for the constitutive models were calibrated from site specific CPTs following the approach recently developed in Trinity College Dublin and presented in Igoe and Jalilvand (2020). The approach has already been validated against a large database of lateral pile field tests, including the PISA test in Dunkirk.

3 EXPERIMENTAL CAMPAIGN

The test site is located in Blessington, in an active quarry approximately 25 km south-west of Dublin, Ireland. Prior to pile installation, cone penetration testing (CPT) was undertaken at each desired pile location. Relevant CPT profiles are plotted on Figure 2 demonstrating minimum vertical or lateral soil variability. The site comprises of homogenous dense sand deposits.

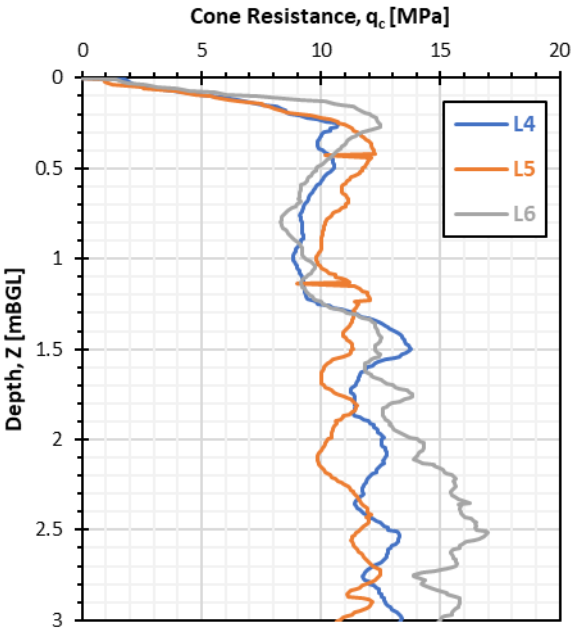

Figure 2. CPT profiles in terms of cone tip resistance (after Lapastoure and Igoe, 2024).

A total of 6 piles with an outer diameter (D) of 457 mm were driven at CPT locations. Pile embedded lengths (L) are ranging from 1 m to 2 m (L/D ranging from 2.2 to 4.4). The piles were installed in a 3x2 grid with the longer piles installed at the centre as shown on Figure 3. The longer piles were used as reaction piles to test the shorter piles. A stick-up length of 1.5 m was left out to ensure the lateral load could be applied with sufficient eccentricity to be representative of offshore conditions. The loads were applied at an eccentricity of 1.37 m (about 3*D).

During each test, both piles were instrumented with inclinometers and linear variable differential transducer at ground level. The lateral load was applied with a hydraulic jack and measured with a tension load cell. The experimental campaign consisted of 5 field tests:

- Test 1: Monotonic test between L6 (L/D=2.2) and L5 (L/D=4.4).
- Test 2: Monotonic test between L4 (L/D=3.3) and L5 (L/D=4.4).
- Test 3: Cyclic test (4000 cycles in total) followed by monotonic push over between L3 (L/D=3.3) and L2 (L/D=4.4).
- Test 4: Cyclic test (3670 cycles in total) followed by monotonic push over between L1 (L/D=2.2) and L2 (L/D=4.4).
- Test 5: Cyclic test (3160 cycles in total) between L2 (L/D=4.4) and L5 (L/D=4.4).

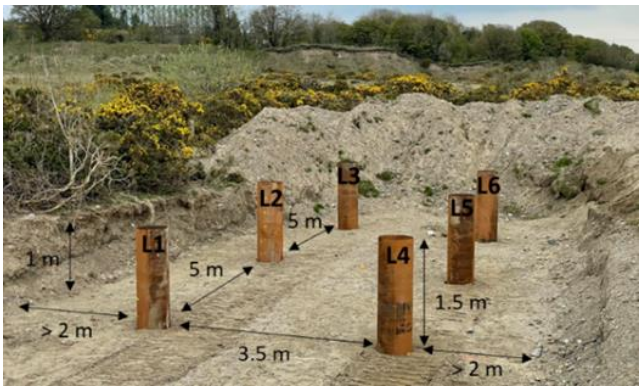

Figure 3. Piles arrangement (after Lapastoure and Igoe, 2024).

Only the results of the monotonic tests are considered for this study (Test 1 and Test 2). The interested reader is invited to refer to Lapastoure and Igoe (2024) for more information.

4 PRELIMINARY RESULTS

Figure 4 presents a comparison of experimental and predicted load-displacement response at ground level for pile L4 (L/D=3.3). For consistency, all three approaches (API, PISA rule and 3D FEA) are based on the soil parameters correlated from the CPT based approach presented in section 2.3 (all parameters provided in Igoe & Lapastoure, 2024). The predictions based on the API and PISA rule approaches are found much softer than the actual pile response. The 3D FEA approach is found to provide a very good prediction.

Figure 4 presents a comparison of experimental and predicted load-displacement response at ground level for pile L4 (L/D=3.3). For consistency, all three approaches (API, PISA rule and 3D FEA) are based on the soil parameters correlated from the CPT based approach presented in section 2.3 (all parameters provided in Igoe & Lapastoure, 2024). The predictions based on the API and PISA rule approaches are found much softer than the actual pile response. The 3D FEA approach is found to provide a very good prediction.

Table 1 compares the blind predicitons to the experimental response for piles L4 (L/D=3.3), L5 (L/D=4.4) and L6 (L/D=2.2) in terms of initial stiffness and ultimate reaction. The initial stiffness is defined as the secant stiffness for a pile displacement of D/1000 at ground level, where D is the pile diameter. The ultimate reaction is defined for a pile displacement of D/10 at ground level for the numerical models, and as the maximum lateral load reached for the experimental tests. Ultimate reaction could not be reached during the test for L5 due to limitations with the loading system.

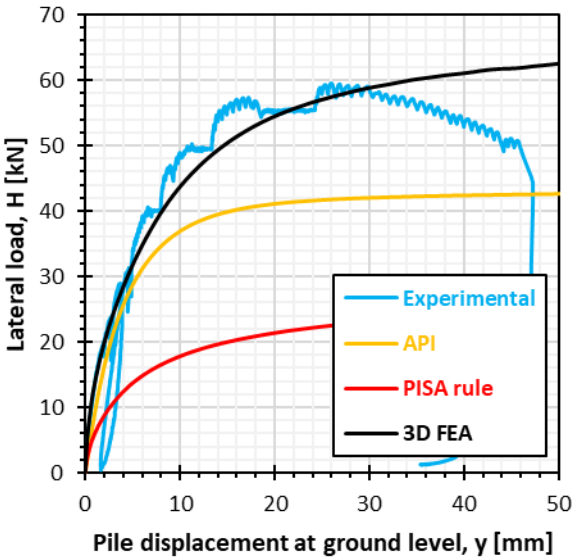

Figure 4. Comparison of experimental and predicted load-displacement response at ground level for pile L4 (L/D=3.3).

PISA rule is found to largely underestimate the stiffnesses and the ultimate reactions by more than 50%. This is because the depth variation functions from the General Dunkirk Sand Model (GDSM) are being used outside of their calibration space. Indeed, Burd et al. (2020) calibrated the GDSM against three-dimensional finite element analyses with pile diameters ranging from 5 m to 10 m. In this experimental study, piles have a diameter of 457 mm.

Although the API 'p-y' approach was developed for long and flexible piles, it is found to perform slightly better than PISA rule for these short and rigid piles. However, it still significantly underestimates stiffnesses (37% to 53%) and ultimate reactions (about 30%).

3D FEA is found to provide very good matches with the experimental data, the average error being less than 5% accross the different pile penetrations. These results further validate the CPT based correlations of HS-small parameters developed by Igoe and Jalilvand (2020).

Table 1. Comparison of blind predictions to experimental piles response in terms of initial stiffness and ultimate capacity.

Approach	Initial stiffness relative error [%]			Ultimate capacity relative error [%]		
	L4	L5	L6	L4	L5	L6
Field test	Ref	Ref	Ref	Ref	-	Ref
API	-44.4	-36.9	-53.3	-28.6	-	-30.6
PISA rule	-50.9	-48.8	-57.9	-59.2	-	-57.3
3D FEA	8.8	4.5	5.6	3.9	-	-2

5 CONCLUSION

This paper presents the initial results of a recent campaign of pile lateral field tests. 6 piles with diameter of 457 mm and penetration ranging from 1 m to 2 m were driven into dense sands at the Blessington test site in Ireland and subjected to monotonic and cyclic loading.

The piles response to monotonic loading were predicted ahead of testing using three approaches: API 'p-y curve' approach, PISA rule-based approach and three-dimensional finite-element analysis with a novel set of CPT based correlations for all the input parameters to the soil constitutive model. The API and the PISA rule approaches were found to largely underestimate both initial stiffness and ultimate reaction for all piles. The 3D FEA prediction with CPT based input parameters were found to match very well with the experimental monotonic response for all piles.

These results further validate the CPT based correlations developed by Igoe and Jalilvand (2020) and suggest that the approach can be used for monopile foundations design supporting offshore wind turbines which are characterised by low slenderness ratios (L/D). The full list of correlations and parameters used in the 3D FE modelling is provided in Igoe and Lapastoure (2024).

ACKNOWLEDGMENT

The research conducted in this publication was funded by the Irish Research Council employment-based postgraduate programme under grant number EBPPG/2019/4.

REFERENCES

API (2014). ANSI/API Recommended Practice 2GEO. First edition, April 2011 + addendum 2014.

Burd, H.J., Taborda, D.M., Zdravković, L., Abadie, C.N., Byrne, B.W., Houlsby, G.T., Gavin, K.G., Igoe, D.J., Jardine, R.J., Martin, C.M. and McAdam, R.A. (2020). PISA design model for monopiles for offshore wind turbines: application to a marine sand. *Géotechnique*, 70(11), 1048-1066. https://doi.org/10.1680/jgeot.18.P.277

Igoe, D. and Jalilvand, S. (2020). 3D Finite Element Modelling of Monopiles in Sand Validated against Large Scale Field Tests. In: *4th International Symposium on Frontiers in Offshore Geotechnics (ISFOG)*, Austin, US.

Igoe, D. and Lapastoure, L.-M. (2024). Field lateral load tests on monopiles in dense sand at Blessington – Part 1 – Monotonic loading. *Submitted to Geotechnique*.

Proceedings of the XVIII ECSMGE 2024
GEOTECHNICAL ENGINEERING CHALLENGES
TO MEET CURRENT AND EMERGING NEEDS OF SOCIETY
© 2024 the Authors
ISBN 978-1-032-54816-6
DOI 10.1201/9781003431749-603
Open Access: www.taylorfrancis.com, CC BY-NC-ND 4.0 license

ECSMGE 24
XVIII EUROPEAN CONFERENCE ON SOIL MECHANICS AND GEOTECHNICAL ENGINEERING

Microbial biopolymer-based soil treatment (BPST) effectiveness on the soil hydraulic erosion reduction assessed via laboratory to field scale methods

Efficacité du traitement des sols à base de biopolymères microbiens (BPST) sur la réduction de l'érosion hydraulique du sol évaluée via des méthodes à l'échelle du laboratoire et du terrain

S. Lee, I. Chang*
Ajou University, Suwon, Republic of Korea

M. Lee
Korea Atomic Energy Research Institute, Daejeon, Republic of Korea

Y.M- Kwon
Northwestern University, Evanston, IL, USA

G.C- Cho
Korea Advanced Institute of Science and Technology, Daejeon, Republic of Korea

ilhanchang@ajou.ac.kr

ABSTRACT: Biopolymers have been emerged as an innovative and environmentally friendly construction material due to their significant strengthening effect, causing minimal environmental pollution when compared to traditional binders. This research examines the viability of using a biopolymer to enhance resistance against erosion. The impact of biopolymer treatment was assessed through laboratory tests, including hole erosion and hydraulic flume tests. The earthen levee models treated with a 1% biopolymer-to-soil mass ratio demonstrated remarkable resistance to piping erosion. In conclusion, this study suggests that implementing biopolymer treatment would be effective in practical applications.

RÉSUMÉ: Les biopolymères sont apparus comme un matériau de construction innovant et respectueux de l'environnement en raison de leur effet fortifiant significatif, provoquant une pollution environnementale minimale par rapport aux liants traditionnels. Cette recherche examine la viabilité de l'utilisation d'un biopolymère pour améliorer la résistance à l'érosion. L'impact du traitement aux biopolymères a été évalué par des tests en laboratoire, notamment des tests d'érosion des trous et des canaux hydrauliques. Les modèles de digues en terre traitées avec un rapport massique de biopolymère/sol de 1% ont démontré une résistance remarquable à l'érosion des canalisations. En conclusion, cette étude suggère que la mise en œuvre d'un traitement par biopolymère serait efficace dans des applications pratiques.

Keywords: Sustainable geotechnical engineering; biopolymer; biological ground improvement; Xanthan gum; Biopolymer-based soil treatment (BPST).

1 INTRODUCTION

This study investigates the efficacy of biopolymer-soil treatment (BPST) in reducing erosion. Recently introduced in geotechnical engineering as a biological ground improvement method, microbial biopolymer-based soil treatment (BPST) aligns with the global demand for sustainable engineering technologies. Leveraging its interparticle bonding characteristic and high yield point (shear strength), BPST is anticipated to elevate the critical shear stress in hydraulic erosion situations.

While earthen levees play a crucial role in safeguarding inhabited and cultivated lands, their susceptibility to failure primarily stems from external erosion (overtopping, 34%) and internal erosion (piping, 28%). Consequently, numerous researchers have endeavoured to comprehend piping behaviour and explore mitigation technologies (Foster & Fell, 2001; Masannat & Hydrogeology, 1980; Ojha, Singh, & Adrian, 2003). The potential effectiveness of biopolymer-soil treatment (BPST) lies in the assumption that coagulating particles enhance erosion resistance.

Two experimental programs were performed. In detail, the effectiveness of BPST was assessed in terms of critical shear stress by Hole Erosion Test (HET) and the laboratory-scale model test was carried out in order to verify applicability on the earthen levee structures.

2 MATERIALS AND METHOD

2.1 Soils

The employed soil is Sydney sand, categorized as SP (Poorly graded soil) according to the Unified Soil Classification System (USCS). The mean diameter (d_{50}), maximum void ratio (e_{max}), and minimum void ratio (e_{min}) are 0.36, 0.92, and 0.6, respectively. The coefficient of curvature (C_c) and uniformity (C_u) are 0.96 and 1.18. The specific gravity (G_s) is 2.6. Kaolinite, derived from weathered feldspar and mica, has a structural composition comprising a silica layer and an alumina layer via hydrogen bonding. Research-grade kaolinite (Walker Ceramics, CAS number: 1332-58-7) was used in this study.

2.2 Xanthan gum biopolymer

This study incorporates a polysaccharide-based biopolymer, xanthan gum, chosen for its workability and notable bonding characteristics. Xanthan gum is derived from the bacterium *Xanthomoas campestris* and features a primary repeating structure consisting of two glucose units, two mannose units, and one glucuronic acid unit. In this study, research-grade xanthan gum (Merck, CAS number: 11138-66-2) was used.

2.3 Sample preparation in common

To create a xanthan gum hydrogel, powdery xanthan gum and deionized water were admixed at a specified mass ratio ($m_{biopolymer}/m_{water}$). Subsequently, a xanthan gum-soil mixture was formulated by blending oven-dried soils with the xanthan gum hydrogel, maintaining a designated moisture ratio ($m_{moisture}/m_{soil}$). Concurrently, the mass ratio of xanthan gum content to soil ($m_{biopolymer}/m_{soil}$) was controlled.



Figure 1. Hole erosion test (HET) apparatus.

2.4 Laboratory hole erosion test

2.4.1 Sample preparation

Soil mixtures, comprising Sydney sand and kaolinite clay, were prepared according to Table 1. Following the incorporation of xanthan gum hydrogel into the soil mixture, the resultant samples were poured into a cylindrical acrylic mould (10 cm in a diameter and 10 cm in a height) featuring a vertical rod with a 6 mm diameter. The vertical rod was strategically positioned to simulate a pre-drilled hole throughout the duration of the experiment. Subsequently, the prepared samples were saturated under a 5 kPa confinement for a period of 24 hours.

2.4.2 Test method

Laboratory hole erosion test (HET) apparatus was manufactured based on the specifications from previous studies (Lüthi, Fannin, & Millar, 2012; Wan & Fell, 2004). While Wan and Fell (2004) suggested a horizontal HET apparatus, our design deviated by adopting a vertical arrangement to minimize the impact of sedimentation following the pre-drilled hole. Illustrated in Figure 1, the apparatus consisted of upstream, specimen, and downstream components. Following the assembly of the upstream and downstream parts to the sample mould, the upstream section was connected to the pressure volume controller (GDS STDDPC) to induce a hydraulic head differential across the soil sample.

2.5 Hydraulic flume test

A hydraulic flume test was performed to simulate the semi-field scale examination. The hydraulic flume test apparatus had dimensions of 10 m in length, 0.6 m in width, and 0.9 m in height. Test samples were positioned within the hydraulic flume test device as depicted in Figure 2.

Table 1. Information of HET (Hole Erosion Test) samples.

Annotation	% of clay	% of sand	% of xanthan gum	Water content (%)	Dry density (kg/m^3)
C100	100	0	-	55	1150
C20S80	20	80	-	18	2214
C20S80XG1	20	80	1	20	2185
S100XG1	0	100	1	20	1988

Table 2. Information of Hydraulic flume test samples.

Annotation	% of clay	% of xanthan gum (ratio of cross-sectional area)	Treatment morphology
S100	0	0	-
S90C10-XG0	10	0	-
S90C10-XG10	10	10	Surface
S90C10-XG25	10	25	Surface

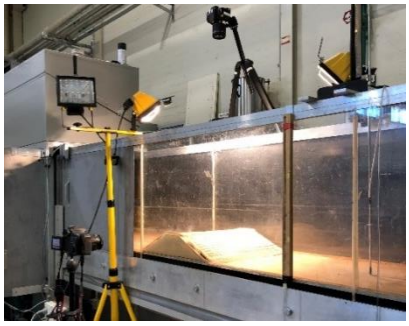

Figure 2. Hydraulic flume test device.

3 RESULTS AND DISCUSSION

3.1 Experimental results from HET

C100 demonstrated a critical shear stress of 99 Pa and an erosion rate index of 3.2. In contrast, C20S80 exhibited a critical shear stress of 7.8 Pa and an erosion rate index of 3.3. However, the critical shear stress increased to 18.8 Pa while the erosion rate index remained at 2.54 when xanthan gum was added (C20S80XG1). It affirms that the application of xanthan gum to soils induces inter-particle bonding, leading to an enhancement in critical shear stress. In short, the xanthan gum treatment, by delaying erosion initiation, contributes to an overall improvement in structural stability. Meantime, S100XG1 achieved a critical shear stress of 14.9 Pa, whereas pure sand typically exhibits negligible critical shear stress.

Table 3. Critical shear stress from laboratory HET.

Test specimen	Critical shear stress (Pa)
C100	99
C20S80	7.8
C20S80XG1	18.8
S100XG1	14.9

3.2 Hydraulic flume test results

In the case of S100, monitoring the progression of piping erosion proved challenging as seepage rapidly developed throughout the soil specimen. Concurrent with seepage, the pre-drilled hole collapsed rather than propagating as intended, leading to the collapse within a minute. Conversely, S90C10 displayed evident piping erosion corresponding to the pre-drilled hole, resulting in overall structure instability.

S90C10-XG10 and S90C10-XG25 exhibited a backward erosion behaviour which refers erosion proceeding to upstream direction. Furthermore, turbulent flow developed following the rapid xanthan gum-treated layer in the case of S90C10-XG25.

The improvement in erosion resistance can be attributed to inter-particle bonding (Khatami & O'Kelly, 2012; Renault, Sancey, Badot, & Crini, 2009), and disturbance in soil particle movement caused by biopolymer dissolution, coupled with the dampening behaviour of the viscous pore-fluid (Fujino, Sun, Pacheco, & Chaiseri, 1992).

4 CONCLUSIONS

The objective of this study is to evaluate the impact of biopolymer-based soil treatment (BPST) on erosion mitigation using the hole erosion test (HET), and hydraulic flume test. The application of xanthan gum to treated soil enhances critical shear stress, and the corresponding earthen levee model exhibits turbulence development following the rigid xanthan gum-treated layer during surface treatment.

The experimental findings suggest that the introduction of biopolymers contributes to the stability of earthen levee models by alleviating surface erosion.

Through fostering interparticle bonding among sand particles, biopolymers impart resistance against external shear forces induced by water flow.

It is extensively documented that conventional earthen levee structures often fail as a result of piping or overtopping during events such as hurricanes, Katrina, and other natural disasters (Briaud, 2008). The application of xanthan gum treatment emerges as a potentially effective mitigation method, noteworty for its ability to address these concerns without posing environmental risks.

ACKNOWLEDGEMENTS

This research was supported by Basic Science Research Program through the National Research Foundation of Korea (NRF) funded by the Ministry of Education (grant number: RS-2023-00274813).

REFERENCES

Briaud, J.-L. (2008). Case histories in soil and rock erosion: Woodrow wilson bridge, Brazos river meander, normandy cliffs, and New orleans levees. *Journal of Geotechnical and Geoenvironmental Engineering, 134*(10), pp. 1425-1447. http://doi.org/ [10.1061/(ASCE)1090-241(2008)134:10(1425)].

Foster, M., Fell, R. (2001). Assessing embankment dam filters that do not satisfy design criteria. *Journal of Geotechnical and Geoenvironmental Engineering, 127*(5), pp. 398-407. http://doi.org/ [10.1061/(ASCE)1090-0241(2001)127:5(398)].

Fujino, Y., Sun, L., Pacheco, B. M., Chaiseri, P. (1992). Tuned liquid *damper* (TLD) for suppressing horizontal motion of structures. *Journal of Engineering Mechanics, 118*(10), pp. 2017-2030. http://doi.org/ [10.1061/(ASCE)0733-9399(1992)118:10(2017)].

Khatami, H., O'Kelly, B. (2012). Improving mechanical properties of sand using biopolymers. *Journal of Geotechnical and Geoenvironmental Engineering, 139*(8), pp. 1402-1406. http://doi.org/ [10.1061/(ASCE)GT.1943-5606.0000861].

Kwon, Y.-M., Cho, G.-C., Chung, M.-K., Chang, I. (2021). Surface erosion behavior of biopolymer-treated river sand. *Geomechanics and Engineering, 25*(1), pp. 49-58. https://doi.org/[10.12989/gae.2021.25.1.049].

Lüthi, M., Fannin, R. J., Millar, R. G. (2012). A modified hole erosion test (HET-P) device. *Geotechnical Testing Journal, 35*(4), pp. 660-664.

Masannat, Y. M. (1980). Development of piping erosion conditions in the Benson area, Journal of Engineering Geology and Hydrogeology, *13*(1), pp. 53-61. http://doi.org/[10.1144/GSL.QJEG.1980.013.01.0].

National Institute of Environmental Research. (2020, 2021.01.19). Water environment information system.

Ojha, C., Singh, V., Adrian, D. (2003). Determination of critical head in soil piping. *Journal of Hydraulic Engineering, 129*(7), pp. 511-518. https://doi.org/ [10.1061/(ASCE)0733-9429(2003)129:7(511)).

Renault, F., Sancey, B., Badot, P. M., Crini, G. (2009). Chitosan for coagulation/flocculation processes – An eco-friendly approach. *European Polymer Journal, 45*(5), pp. 1337-1348. https://doi.org/ [10.1016/j.eurpolymj.2008.12.027].

Wan, C., Fell, R. (2004). Laboratory tests on the rate of piping erosion of soils in embankment dams. *Geotechnical Testing Journal, 27*(3), 295-303. https://doi.org/ [10.1520/GTJ11903].

Proceedings of the XVIII ECSMGE 2024
GEOTECHNICAL ENGINEERING CHALLENGES
TO MEET CURRENT AND EMERGING NEEDS OF SOCIETY
© 2024 the Authors
ISBN 978-1-032-54816-6
DOI 10.1201/9781003431749-604
Open Access: www.taylorfrancis.com, CC BY-NC-ND 4.0 license

ECSMGE 24
XVIII EUROPEAN CONFERENCE ON SOIL MECHANICS AND GEOTECHNICAL ENGINEERING

Modelling hysteretic damping of soils for monopiles

Modélisation de l'amortissement hystérétique des sols pour les monopieux

A.R. Leon Bal*, M. Jafari, L.A. Berenguer Todo Bom, M. Goodarzi
COWI A/S, Hamburg, Germany

*arbl@cowi.com

ABSTRACT: This paper proposes a new method to evaluate the hysteretic soil damping in offshore wind turbines (OWT) with monopiles. Soil damping is a key factor affecting the design of OWT and its fatigue life span. Dynamic 3D finite element analyses incorporating the Hardening Soil-small model are performed. The OWT damping is obtained from the decay of tower displacements. Depending on the expected monopile deflections and soil stiffness, it is found that the widely adopted Cook and Vandiver (1982) method from the oil and gas industry, can underestimate the soil hysteretic damping.

RÉSUMÉ: Cet article propose une nouvelle méthode pour évaluer l'amortissement hystérétique du sol dans les éoliennes offshore (OWT) avec des monopieux. L'amortissement du sol est un facteur clé qui affecte la conception de l'éolienne et sa durée de vie en fatigue. Des analyses dynamiques par éléments finis en 3D intégrant le modèle Hardening Soil-small ont été réalisées. L'amortissement de l'OWT est obtenu à partir de la décroissance des déplacements de la tour. En fonction des déflexions attendues du monopieu et de la rigidité du sol, on constate que la méthode Cook et Vandiver (1982), largement adoptée dans l'industrie pétrolière et gazière, peut sous-estimer l'amortissement hystérétique du sol.

Keywords: Soil damping; offshore wind turbines; finite element analyses; hardening soil model; decay test.

1 INTRODUCTION

The impact of damping in the performance of offshore wind turbines with monopile foundations cannot be understated, as it helps in the reduction of peak displacements of the structure, steel quantities and costs (Versteijlen et al., 2011) and the extension of its life span (Malekjafarin et al., 2022). Therefore, accurate representation of the soil-structure interaction is crucial for the achievement of optimized designs.

Although different damping sources affecting the dynamic response of OWT have been identified, namely, aerodynamic, hydrodynamic, structural and foundation damping, foundation damping remains as one of the major contributors (Malekjafarin et al., 2022). Foundation damping includes radiation, seepage, and hysteretic components, where the soil hysteretic damping is more relevant for OWT and will be the focus of this paper.

2 METHOLOGY

A series of dynamic 3D finite element analyses (FEA) were conducted with Plaxis 3D. The tower geometry in terms of the outer diameter (OD) and wall thickness is also shown in Figure 1 (left). The model setup as well as the FE mesh are shown in Figure 1 (right). Viscous absorbing boundary conditions are used to model the energy dissipation into the far field (radiation damping). The tower was modelled as linear elastic using plate elements. The Rotor-Nacelle Assembly (RNA) was modelled using a rigid circular plate with a fictive density at the tower top to give a mass of 809 tons. Half symmetry in the fore-aft direction was also employed to reduce the model size and hence, the simulations time. The soil behaviour was captured with the Hardening Soil model with small strain stiffness (HS-small). The soil properties are presented in Table 1. Due to the expected low levels of pile deformations under fatigue limit state conditions, the stress dependency of the stiffness parameters of the HS-small model are ignored.

Table 1. Soil parameters of the numerical model.

Unit	Depth [m]	γ_{sat} [kN/m3]	γ_{70} [-]	G_0 [MPa]	E_{50} [MPa]	*Eur [MPa]
A	0-2	19	1.37E-04	25.1	8.6	25.6
B	2-16	19.6	3.90E-04	76.7	22.8	68.4
C	16-49	19.4	3.23E-04	234	41.6	125

*G_{ur} was computed based on E_{ur} and assuming a Poisson's ratio of $\nu = 0.25$.

As discussed in Brinkgreve et al. (2007), the γ_{70} parameter in HS-small is calibrated so that the Plaxis damping ratio curve agrees well with the resonant column test results. The HS-small model employs a shear strain-dependent reduction curve for the shear modulus, which allows for the development of hysteresis loops but yields zero hysteretic damping at very small strains. However, resonant column tests in general show a certain amount of damping even at very small strain levels. Such damping cannot be captured using HS-small model. As a result, Rayleigh damping is often added to the finite element models. Resonant column tests of the soil units in Table 1 indicate that a Rayleigh damping ratio amounting to 1.5% should be added to get a better match of the Plaxis soil damping curves to that of the lab tests. The Raleigh damping coefficients are set to α = 0.01257 and β = 0.01592. These set of parameters result in a Raleigh damping of 1.5% at the natural frequency of the structure (0.17 Hz). Nevertheless, the authors found that the contribution of the Rayleigh damping is negligible due to the extremely low natural frequency of the structure (below 0.2 Hz) and resulting low tower velocity during the structural vibrations.

To observe the free lateral vibrations of the tower in the first mode, the tower head is displaced from the initial position (x = 0 m) to one side (e.g., x = 0.25 m) in a static phase. Then, the tower head is released in a dynamic phase and allowed to vibrate freely. The total duration of dynamic phase is 100 seconds with a step size 0.4 seconds. Several dynamic analyses with different initial lateral displacements (x = 0, 0.5, 1 and 1.5 m) are considered.

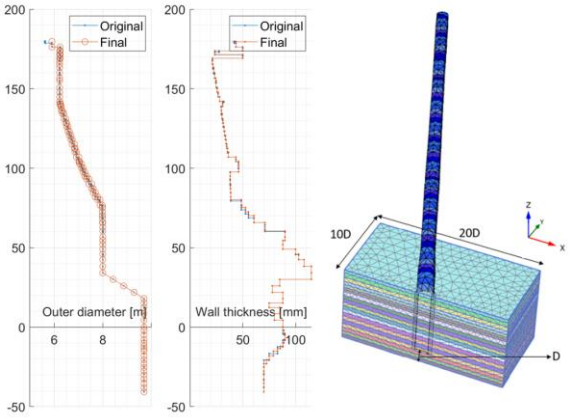

Figure 1. FE model in Plaxis: (left) Final geometry of the tower and pile and (right) FE mesh and soil layering. Very short cans are merged in the final geometry.

3 RESULTS AND DISCUSSION

Time histories of the computed displacement at the mudline for maximum displacements in x-direction of u_{max} = 1.14, 2.34, 5.17 and 8.70 mm are depicted in Figure 2 (left), considering various initial cycle amplitudes at tower top (A_0 = 0, 0.5, 1 and 1.5 m).

A Fast Fourier Transform (FFT) was also performed to extract the frequency content of the displacement time history at the tower head. As seen in Figure 2 (right), the FFT reveals that the natural frequency of the modelled structure is 0.17 Hz.

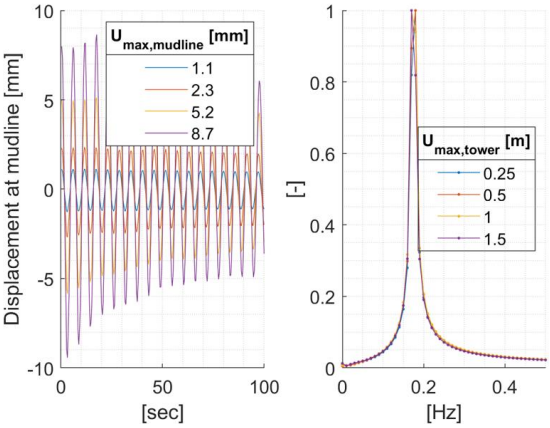

Figure 2. Computed time history of the displacement at the (left) mudline and (right) Fast Fourier Transform of the tower top displacement.

From each displacement time history, cycle peaks are extracted to evaluate the decay of the displacement amplitude. In order to obtain a representative damping ratio coefficient ζ (%) of the system, an exponential decay function $u(t) = A_0 e^{-\zeta 2\pi f_n t}$ is fitted to the extracted cycle peaks of the tower top in which t (s) is the time, A_0 (m) is the displacement amplitude at t = 0 (s) and f_n (Hz) is the natural frequency of the system. The fitted curves can be seen in Figure 3 (left). The back-calculated damping ratios are plotted against the initial mudline displacement in Figure 3 (right).

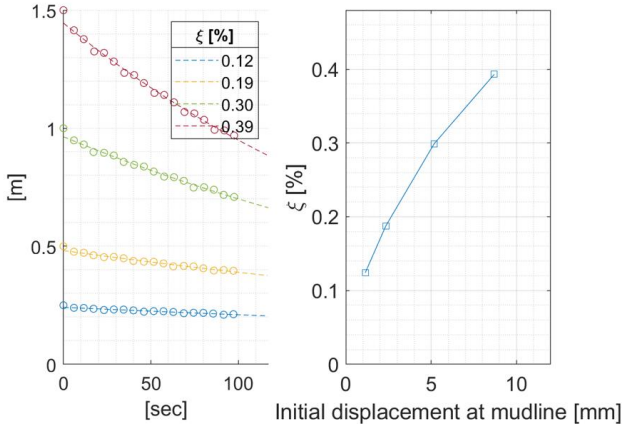

Figure 3. Fitting the exponential decay function to the tower head displacement to find the soil hysteretic damping: (left) Source data from Plaxis and (right) fitted ζ values for the selected cycle amplitudes (0.25, 0.50, 1, and 1.5 m) in correlation to the initial mudline displacement.

The FE-based damping ratio values are compared against those computed using the Cook and Vandiver method (Cook and Vandiver, 1982) for the first vibration mode of the structure. In this method, the pile is discretized into n nodes to which soil reaction springs are connected. The damping ratio ζ is calculated as

$$\zeta = \frac{1}{\omega_n^2 M}\sum_{i=1}^{n} K_s(z_i)\Psi_i(z_i)\zeta_{smd}(z_i) \quad (1)$$

in which $\omega_n = 2\pi f_n$ is the circular natural frequency, M is the modal mass of the structure, $K_s(z_i)$ is the soil spring stiffness for node i at depth z_i, $\Psi_i(z_i)$ is the mode shape of the node for the first deformation mode and $\zeta_{smd}(z_i)$ is the specific soil damping.

The first mode shape and modal mass are obtained by conducting an eigen frequency analysis of the structure, for which the soil interaction springs are extracted from the FE model at every meter along the embedded pile length. The $\zeta_{smd}(z_i)$ is interpolated from the calibrated damping ratio versus shear strain curve, considering the shear strain γ calculated after (Skempton, 1951)

$$\gamma = \frac{1+\upsilon}{2.5\,OD}\cdot y(z_i) \quad (2)$$

in which υ is the soil Poisson's ratio, and $y(z_i)$ is the lateral monopile deflection at z_i computed from a static push-over analysis of a 1-D beam model of the monopile. The soil stiffness K_s is calculated assuming two scenarios:

- K_s is taken as the initial stiffness of the soil reaction springs.
- K_s is taken as a linearized secant stiffness of the soil springs. The linearization level is determined by a static push-over analysis of the 1-D beam model of the monopile, where the mudline is laterally pushed to a certain amount u_{max}. For the analyses u_{max} = 1.14, 2.34, 5.17 and 8.70 mm.

Figure 4 displays the calculated damping ratio as a function of the normalized initial mudline displacement (u_{max}/OD = 0.01, 0.02, 0.05 and 0.09%) considering the two scenarios for the calculation of the soil spring stiffness. In general, the FE-based and the Cook and Vandiver method compares well up to u_{max}/OD = 0.02%, beyond which the Cook and Vandiver method underestimates the soil damping. Therefore, using the secant soil spring stiffness in the Cook & Vandiver method results in very conservative damping ratios. However, taking K_s as the initial stiffness of the springs, a plateau is reached with increasing u_{max}/OD. A plateau indicates that the maximum damping ratio for all the soil damping curves for each node along the monopile has been reached.

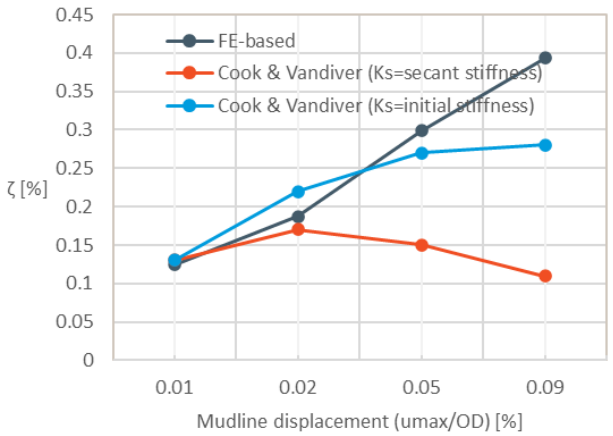

Figure 4. Damping ratio vs. maximum normalized mudline displacements according to (Cook and Vandiver, 1982) and FE calculations.

The increase of damping ratio values with increasing amplitudes of cyclic loading has been also reported in the literature (Malekjafarin et al., 2022). The Cook and Vandiver method, on the other hand, cannot capture this increasing trend properly due to the following factors:

- Utilization of the soil secant stiffness K_s instead of the stiffer loading/unloading K_{ur} stiffness. The stiffness. K_{ur} is more representative of the soil behaviour. For fatigue limit state conditions where pile displacements are very low, K_{ur} is relatively close to the initial stiffness of the springs (K_{ini}). As the mudline displacement increases, the secant stiffness reduces. This reduction is more pronounced for large u_{max}/OD ratios and does not compensate the increase in specific damping ratio ζ_{smd} with increasing strains, leading to an overall decrease of the soil damping ratio.
- Inherent uncertainties in the calculation of shear strains from pile displacements. The correct estimation of the soil shear strains is of paramount importance for the accurate determination of the specific damping ratio and in turn, the soil hysteretic damping.
- The influence of the pile diameter. While the Cook and Vandiver formulation was calibrated and tested against typical pile foundations in the oil and gas industry decades ago, current monopiles with smaller length to diameter ratios behave more rigidly, exhibiting a different deformation mode characterized by rotations along the shaft as well as rotations and lateral

displacements along the base (Burd et al., 2020). By extending Eq. (1) with additional rotational and pile base terms (e.g., rotational stiffness, modal rotations, etc.), more realistic hysteretic damping values could be attained.

4 CONCLUSIONS

In this contribution, a new FE-based methodology based on a free vibration analysis of the wind turbine structure is presented for the estimation of hysteretic soil damping in OWT's. The FE-based damping ratio is compared with that of the Cook and Vandiver methodology. The utilization of the Cook & Vandiver method can result in an underestimation of the hysteretic soil damping depending on the expected monopile deflections and the assumed soil stiffness in its formulation. The main characteristics of the proposed numerical strategy are the following:

- A 3D FE model comprising the tower, monopile and the rotor nacelle assembly.
- The incorporation of the Hardening Soil model with small strain stiffness, capable of reproducing hysteresis loops in the soil via the strain-driven degradation of the small-strain shear modulus.
- Performing dynamic analysis as part of numerical decay tests with selected initial cycle amplitudes at the tower top.
- The generation of damping curves (for each cycle amplitude) from the tower peak displacements and the subsequent exponential fitting to extract the damping ratio.
- Transforming tower displacements to mudline displacements and finding the damping ratio at the desired mudline displacement from the resulting damping ratio-mudline displacement curve.

For the assessed mudline displacements, the proposed methodology consistently predicted increasing damping ratios for increasing cycle amplitudes. To have a baseline, results computed with the Cook and Vandiver method were presented. Results from this method but using instead the secant soil stiffness calculated from the smallest cycle amplitude were also included. For larger mudline displacements, the Cook and Vandiver method failed to capture the positive correlation between cycle amplitudes and damping ratios. On the other hand, by using the soil secant stiffness from the smallest cycle amplitude (u_{max}/OD = 0.01), the gap with the FE-based results was substantially reduced.

Finally, the utilization of the secant or the initial soil spring stiffness, the transformation from pile displacements to soil shear strains and the pile diameter, were identified as potential factors hindering the accuracy of the Cook and Vandiver method for large mudline displacements.

REFERENCES

Brinkgreve, R. B. J., Kappert, M. H. and Bonnier, P. G., (2007). Hysteretic damping in a small-strain stiffness model. In: *Proc. of Num. Mod. in Geome*ch., NUMOG X, Rhodes, Greece, pp. 737-742.

Burd, H. J., Taborda, D. M., Zdravković, L., Abadie, C. N., Byrne, B. W., Houlsby, G. T., ... and Potts, D. M. (2020). PISA design model for monopiles for offshore wind turbines: application to a marine sand. *Géotechnique*, 70(11), pp. 1048-1066, https://doi.org/10.1680/jgeot.18.P.277.

Cook, M. F., and Vandiver, J. K. (1982). Measured and predicted dynamic response of a single pile platform to random wave excitation. In: *Offshore Technology Conference (OTC)*, Houston, Texas, USA, pp. 637-643., https://doi.org/10.4043/4285-MS.

Malekjafarian, A., Jalilvand, S., Doherty, P., and Igoe, D. (2021). Foundation damping for monopile supported offshore wind turbines: A review. *Marine Structures*, 77(102937), pp. 1-22, https://doi.org/10.1016/j.marstruc.2021.102937.

Skempton, A.W., (1951). The bearing capacity of clays. *Selected papers on soil mechanics*, pp. 50-59., https://doi.org/10.1680/sposm.02050.0008.

Versteijlen, W. G., Metrikine, A., Hoving, J. S., Smid, E., and De Vries, W. E. (2011). Estimation of the vibration decrement of an offshore wind turbine support structure caused by its interaction with soil. In: *Proceedings of the EWEA offshore 2011 conference*, Amsterdam, The Netherlands.

Proceedings of the XVIII ECSMGE 2024
GEOTECHNICAL ENGINEERING CHALLENGES
TO MEET CURRENT AND EMERGING NEEDS OF SOCIETY
© 2024 the Authors
ISBN 978-1-032-54816-6
DOI 10.1201/9781003431749-605
Open Access: www.taylorfrancis.com, CC BY-NC-ND 4.0 license

ECSMGE 24
XVIII EUROPEAN CONFERENCE ON SOIL MECHANICS AND GEOTECHNICAL ENGINEERING

Analysis of different temporary anchor points for construction of 380 kV high-voltage transmission masts

L'analyse des points d'ancrages différentes temporairement pour la construction des pylônes à haute tension de 380 kV

S. Leppla*, J.C. Paninski, R. Freund
Frankfurt University of Applied Sciences, Frankfurt/Main, Germany
**steffen.leppla@fb1.fra-uas.de*

ABSTRACT: For the construction of new high-voltage transmission lines and the improvement of existing lines temporary anchor points are necessary. In engineering practice, basically three different systems are used: deadman structures, counterweights and the so-called Spinnanker. Deadman structures are wood or steel beams or steel pipes, which are buried in the subsoil. The resistance occurs due to the passive earth pressure. For counterweights, large concrete blocks are used to activate the sliding resistance. The Spinnanker consists of an anchor plate and threaded steel bars, which are screwed into the subsoil. The resistance results from the skin friction of the steel bars. Deadman structures and counterweights are two well-known systems, but they cause a lot of tillage and use of material thus have a massive impact on the environment. The Spinnanker is a new construction system, which is minimally invasive especially with regard to soil mixing and soil compaction. Based on a real construction project in Germany these three different temporary anchor systems are analyzed regarding the design and safety concept. Finally, recommendations for the field of application, the construction and the secure and economic design are given.

RÉSUMÉ: En raison de la transition énergétique, la construction de nouvelles lignes électriques à haute tension et l'amélioration des lignes existantes sont nécessaires. Dans la pratique de l'ingénierie, trois systèmes différents sont utilisés : les constructions « homme mort », des blocs en béton et ce qu'on appelle le « Spinnanker ». Les constructions « homme mort » se composent de poutres en acier ou de tuyaux en acier enfouis dans le sous-sol. La résistance est due à la pression passive du sol. Les blocs en béton sont utilisés pour activer la résistance au glissement. Le « Spinnanker » se compose d'une plaque d'ancrage et de tiges filetées vissées dans le sous-sol. La résistance est une combinaison du frottement superficiel de la pression passive du sol. Les constructions « homme mort » et les blocs en béton sont deux systèmes bien connus, mais ils nécessitent beaucoup de travail du sol et d'utilisation de matériaux et ils ont un impact élevé sur l'environnement. Le « Spinnanker » est un système de construction peu invasif, surtout en ce qui concerne le mélange et le compactage du sol. Basés sur un projet de construction réel en Allemagne, ces trois différents systèmes d'ancrage temporaires sont analysés en termes de conception et de concept de sécurité. Enfin, des recommandations concernant le domaine d'application, la construction et la conception sécurisée et économique sont données.

Keywords: Temporary anchor; safety; resource reduction; Spinnanker.

1 INTRODUCTION

Just in Germany, 4,000 km of new high-voltage transmission lines will be approved until the middle of 2025. Therefore, a lot of temporary anchor points are necessary during construction time. These anchor points should be environmentally neutral as possible to save resources, time and money and to avoid unnecessary CO_2-emission. For the design and construction of overhead electricity lines, the regulations in the standard EN 50341 (CEN 2013) have to be considered. This standard deals with the basics for design and dimensioning for the structure of the masts including the different loading cases, electrical requirements, materials to be used, the foundation and requirements for the components. It does not include a preliminary design or the dimensioning of temporary anchor points for all construction stages. Regarding the geotechnical aspects of the design and construction of the masts the standard EN 1997-1 (CEN 2014) has to be considered.

According to EN 1997-1 all relevant geotechnical boundary conditions including the ground and groundwater situation and the regulations for the safety concept have to be considered in all analyses of stability and serviceability. The standard is also to be applied for the design and the construction of temporary anchor points of electricity masts.

2 DEADMAN STRUCTURE

Deadman structures are wood or steel beams or steel pipes, which are buried in the subsoil. The design of deadman structures is not fully covered by the standard EN 1997-1. In engineering practice there exists a design procedure which refers partly to EN 1997-1. Furthermore it is based on a design approach which may overestimate the resistance of the soil.

Due to this, the following design procedure based on ranking domain is recommended. This procedure includes the analysis of all possible geotechnical failure mechanisms:

- horizontal stability
- vertical stability
- inclined sliding stability

Figure 1 shows the principle layout of a deadman structure with the geometric parameters and the characteristic tensions force F_k (kN), which results from permanent and variable loads. Regarding the impact, for a conservative approach the partial factor $\gamma_Q = 1{,}3$ is used.

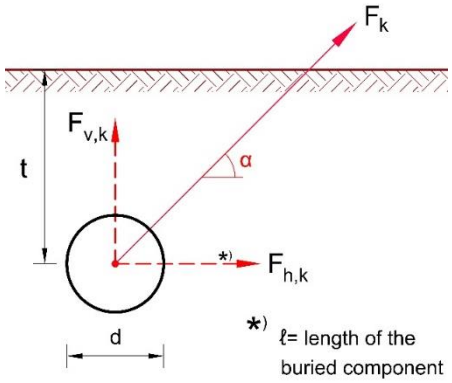

Figure 1. Principle layout of a deadman construction (sectional view).

2.1 Analysis of the horizontal stability

For the analysis of the horizontal stability, the horizontal impact $E_{h,d}$ (kN) is compared to the horizontal earth resistance $R_{h,d}$ (kN). The horizontal impact consists of the horizontal component $F_{h,k}$ (kN) of the tension force F_k (kN) and the active earth pressure $e_{ah,k}$ (kN/m²). All forces are shown in Figure 2.

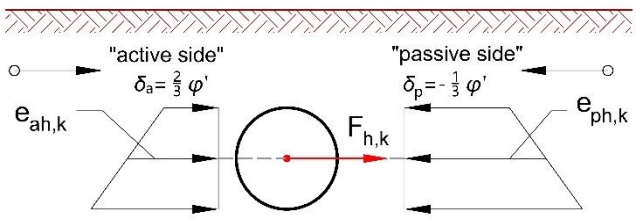

Figure 2. Horizontal components (sectional view).

The total impact $E_{h,d}$ is explained by Equation (1), using the partial factor $\gamma_G = 1{,}2$ for the earth pressure.

$$E_{h,d} = F_{h,k} \cdot \gamma_Q + e_{ah,k} \cdot d \cdot l \cdot \gamma_G \qquad (1)$$

In the analysis of the horizontal stability the resistance $R_{h,d}$ is the passive spatial earth pressure $e_{ph,k}$ (kN/m²), which depends on the length l (m) and the diameter d (m) of the buried component and the friction angle φ' (°) of the soil. The effective length l^{Er} (m) for the spatial earth pressure is defined for the dead load of the soil by Equation (2) and for the cohesion by the Equation (3).

$$l_{pg}^{Er} = l + 0{,}6 \cdot d \cdot \tan\varphi' \qquad (2)$$

$$l_{pc}^{Er} = l + 0{,}3 \cdot d \cdot (1 + 1{,}5 \cdot \tan\varphi') \qquad (3)$$

The design value of the resistance $R_{h,d}$ is described by the Equation (4). The partial factor is $\gamma_{R,e} = 1{,}3$.

$$R_{h,d} = \frac{R_{h,k}}{\gamma_{R,e}} = \frac{e_{pgh,k} \cdot d \cdot l_{pg}^{Er} + e_{pch,k} \cdot d \cdot l_{pc}^{Er}}{\gamma_{R,e}} \qquad (4)$$

The final proof in the analysis of the horizontal stability is as follows:

$$E_{h,d} \leq R_{h,d} \qquad (5)$$

2.2 Analysis of the vertical stability

For the analysis of the vertical stability, the vertical impact $E_{v,d}$ (kN) is compared to the vertical earth resistance $R_{v,d}$ (kN). The vertical impact consists of the vertical component $F_{v,k}$ (kN) of the tension force F_k and of the vertical component of the passive earth pressure $E_{pv,k}$ (kN). The vertical earth resistance $R_{v,d}$ consists of the dead load of the soil G_k (kN) and of the friction force $R_{s,k}$ (kN) in the shear zone above the buried component. All forces are shown in Figure 3.

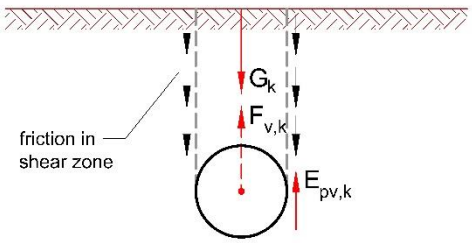

Figure 3. Vertical components (sectional view).

The total impact $E_{v,d}$ is explained by the Equations (6) and (7).

$$E_{v,d} = F_{v,k} \cdot \gamma_Q + E_{pv,k} \cdot \gamma_G \quad (6)$$

$$E_{pv,k} = R_{h,k} \cdot tan\left(\frac{1}{3}\varphi'\right) \quad (7)$$

The dead load of the soil G_k is characterized by the geometry above the buried component, the weight of the buried component $G_{bc,k}$ (kN) and the weight of the soil γ (kN/m³), Equation (8). In the case of groundwater, the weight of the soil changes to γ'.

$$G_k = (\gamma \cdot d \cdot (t-d) \cdot l) + G_{bc,k} \quad (8)$$

The friction force $R_{s,k}$ results from the horizontal earth pressure at rest E_0 (kN) which exists in the shear zone above the buried component. The area of the shear zone is the circumference of the ground view of the buried component. The earth pressure at rest E_0 and the resulting friction force $R_{s,k}$ are defined by the Equations (9) and (10).

$$E_0 = \gamma \cdot (1 - sin\,\varphi') \cdot \left(t - \frac{d}{2}\right) \cdot \frac{t - d/2}{2} \cdot (2 \cdot l + 2 \cdot d) \quad (9)$$

$$R_{s,k} = E_0 \cdot tan\,\varphi' \quad (10)$$

The total resistance $R_{v,d}$ is as follows:

$$R_{v,d} = \frac{G_k + R_{s,k}}{\gamma_{R,e}} \quad (11)$$

The final proof in the analysis of the vertical stability is as follows:

$$E_{v,d} \leq R_{v,d} \quad (12)$$

2.3 Analysis of the inclined sliding stability

For the analysis of the inclined sliding stability, the activated soil body is simplified, not proven, formed as a wedge where the basic side is in the direction of the tension force F_k (kN). At this activated soil body the impact E_d (kN) is compared to the sliding resistance R_d (kN). The impact consists of the tension force F_k and of the inclined component of the active earth pressure $E_{a,\|,k}$ (kN/m). The impact E_d is explained in Equation (13) and (14).

$$E_d = F_k \cdot \gamma_Q + E_{a,\|,k} \cdot \gamma_G \cdot l \quad (13)$$

$$E_{a,\|,k} = E_{ah,k} \cdot cos\,\alpha \quad (14)$$

The sliding resistance R_d consists of the

- friction force $R_{s,G,k}$ (kN) in the sliding surface, which results from the dead load of the soil $G_{\perp,k}$ (kN)
- downslope force of the dead load of the soil $G_{\|,k}$ (kN)
- friction force $R_{s,Ea,k}$ (kN) in the sliding surface, which results from the inclined component of the active earth pressure $E_{a,\perp,k}$ (kN/m)
- friction force $R_{s,c,k}$ (kN) in the sliding surface, which results from the cohesion
- friction force $R_{s,E0,k}$ (kN) in the area A (m²), which results from the earth pressure at rest E_0 (kN)

All forces and the geometry of the sliding block are shown in the Figures 4 and 5.

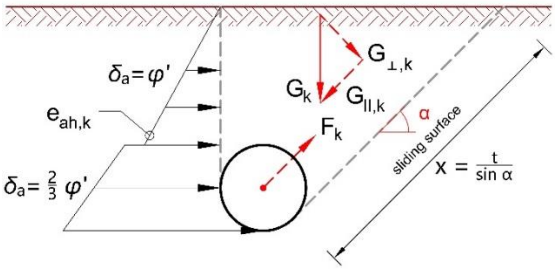

Figure 4. Sliding block (sectional view).

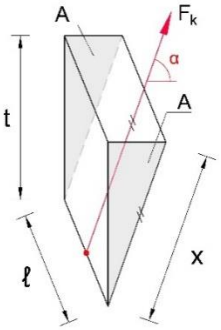

Figure 5. Sliding block (3-dimensional view).

The components of the total resistance R_d are described by the Equations (15) to (20).

$$R_{s,G,k} = G_{\perp,k} \cdot tan\,\varphi' \quad (15)$$

$$G_{\perp,k} = G_k \cdot cos\,\alpha \quad (16)$$

$$R_{s,Ea,k} = E_{a,\perp,h} \cdot tan\,\varphi' \cdot l \quad (17)$$

$$E_{a,\perp,k} = E_{ah,k} \cdot sin\,\alpha \quad (18)$$

$$R_{s,c,k} = c'_k \cdot x \cdot l \quad (19)$$

$$R_{s,E0,k} = 2 \cdot A \cdot E_0 \cdot tan\,\varphi' \quad (20)$$

The total resistance R_d is as follows:

$$R_d = \frac{R_{s,G,k}+R_{s,Ea,k}+R_{s,c,k}+R_{s,E0,k}+G_{\parallel,k}}{\gamma_{R,h}} \quad (21)$$

$$G_{\parallel,k} = G_k \cdot \sin\alpha \quad (22)$$

The final proof in the analysis of the inclined sliding stability is as follows:

$$E_d \leq R_d \quad (23)$$

2.4 Safety and quality assurance

The real load-displacement behavior of deadman structures has not be analyzed completely. This includes small scale and large scale tests in soil for high loads. Regarding the regulations in EN 1997-1 the deadman structure has to be treated as an anchor system. Due to this, in-situ load-displacement tests on each construction site are necessary, if no comparable information is available. For the necessary testing load the regulations for pre-stressed anchor systems have to be considered.

3 COUNTERWEIGHTS

Counterweights consist of large concrete blocks which are positioned on a steel frame on the bottom. To increase the friction between the counterweights and the subsoil, a bedding of gravel material is often installed. For the design procedure the regulations for single foundation elements in EN 1997-1 have to be considered. The main part of the stability is given by the dead load of the counterweight and the friction in the subsoil. Due to this, the following design procedure is recommended. This procedure includes the analysis of all possible geotechnical failure mechanisms:

- uplifting
- sliding stability
- limitation of the eccentricity
- bearing resistance

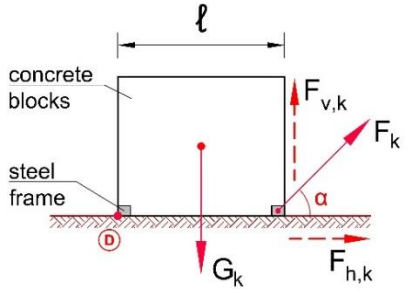

Figure 6. Principle layout of a counterweight.

Figure 6 shows the principle layout of a counterweight with the geometric parameters and the characteristic tensions force F_k (kN), which results from permanent and variable loads. For a conservative approach the partial factor $\gamma_Q = 1{,}3$ is used.

3.1 Uplift

For the analysis of the uplift, the vertical component $F_{v,k}$ (kN) of the tension force F_k is compared to the dead load G_k (kN) of the counterweight. For the design level the partial factors $\gamma_{G,stb} = 0{,}95$ and $\gamma_{Q,dst} = 1{,}30$ are used in the Equation (24) and (25).

$$E_{v,d} = F_{v,k} \cdot \gamma_{Q,dst} \quad (24)$$

$$R_{v,d} = G_k \cdot \gamma_{G,stb} \quad (25)$$

The final proof in the analysis of the uplifting is as follows:

$$E_{v,d} \leq R_{v,d} \quad (26)$$

3.2 Sliding stability

For the analysis of the sliding stability, the horizontal component $F_{h,k}$ (kN) of the tension force F_k is compared to the friction resistance $R_{h,k}$ (kN) below the counterweight. The horizontal impact is as follows:

$$E_{h,d} = F_{h,k} \cdot \gamma_Q \quad (27)$$

The friction resistance is influenced by the angle of friction δ_k in the subsoil below the surface:

$$R_{h,d} = \frac{(G_k - F_{v,k}) \cdot \tan\delta_k}{\gamma_{R,h}} \quad (28)$$

Regarding the plain surface of the prefabricated concrete blocks and the steel frame, the angle of friction in the subsoil should be limited to $\delta_k = 2/3 \cdot \varphi'$. For the partial safety factor of the friction resistance $\gamma_{R,h} = 1{,}1$ should be used. The final proof in the analysis of the sliding stability is as follows:

$$E_{h,d} \leq R_{h,d} \quad (29)$$

3.3 Limitation of the eccentricity

For the analysis of the limitation of the eccentricity, the moments in point D in Figure 6 are calculated. The moments occur due to the vertical component $F_{v,k}$ of the tension force F_k and due to the dead load of the counterweight G_k. The impact moment and the resistance moment are as follows:

$$M_{E,d} = F_{v,k} \cdot l \cdot \gamma_{Q,dst} \quad (30)$$

$$M_{R,d} = G_k \cdot \frac{l}{2} \cdot \gamma_{G,stb} \quad (31)$$

The partial safety factors are $\gamma_{Q,dst}$ = 1,05 and $\gamma_{G,stb}$ = 0,90. Equation (32) shows the final proof. In addition the eccentricity e should not exceed l/3 on the level of the characteristic loads (Eq. 33).

$$M_{E,d} \leq M_{R,d} \quad (32)$$

$$\frac{F_{v,k} \cdot l/2}{G_k - F_{v,k}} \leq \frac{l}{3} \quad (33)$$

3.4 Bearing resistance

The bearing resistance failure is caused by excessive stress in the ground due to the applied load. Very important is to consider the eccentricity e which shortens the length l to l'. This shortened length is the effective length l' = l – (2 · e). The impact V_k (kN) is the dead load of the counterweight G_k reduced by the vertical component $F_{v,k}$ of the tension force F_k. The impact on the design level is described by equation (34).

$$V_d = \left(G_k - F_{v,k}\right) \cdot \gamma_Q \quad (34)$$

The bearing resistance $R_{v,k}$ is influenced by the effective base area of the counterweight, the angle of friction φ' (°), the cohesion c' (kN/m^2) and the inclination of the load. The counterweight does not have any embedment depth. The design value of the bearing resistance is

$$R_{v,d} = \frac{R_{v,k}}{\gamma_{R,v}} \quad (35)$$

4 SPINNANKER

The Spinnanker is a new type of foundation and anchorage system consisting of threaded steel bars that are screwed into the soil. It can be easily installed in both cohesive and non-cohesive soils using a hand-held turning machine. The common models have 6 to 18 threaded bars, which are screwed into the subsoil through a circular anchor plate. Figure 7 shows a Spinnanker type XII / 2.0 / 15. Bars with different diameters 15, 18, 20 and 26 mm can have a length from 2.0 to 8.0 m and are installed with different inclinations. The diameter of the plate, the number and the length of the bars depend on the soil condition and the load. The possible applications are described in Katzenbach et al. (2019a). Figure 8 shows for example the anchoring for installing a new 380 kV high-voltage line.



Figure 7. Spinnanker XII / 2.0 / 15 (12 threaded bars with a length of 2.0 m and a nominal diameter of 15 mm).



Figure 8. Anchoring with Spinnankers for a new 380 kV high-voltage line in Germany.

4.1 Load-deformation behaviour

The load-deformation behavior of the Spinnanker can easily be described by vertical pull-out tests. Figure 9 shows a typical load-displacement curve obtained from a pull-out test. The maximum load was in this case 180 kN at a displacement of only 2.5 mm.

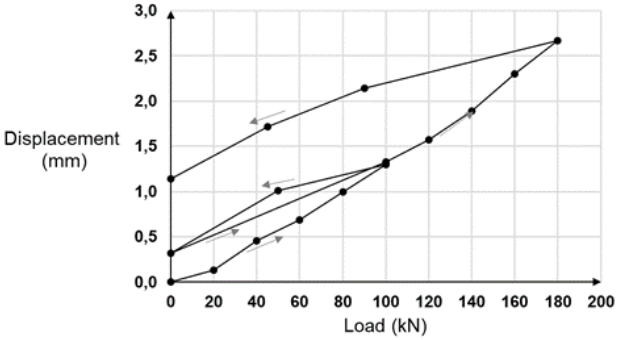

Figure 9. Vertical pull-out test on a Spinnanker XII / 3.0 /15 in fine and medium sand with medium density.

4.2 Design and safety concept

The first step is a preliminary design based on the large number of former load tests. The second step is the final design based on suitability load tests in-situ which leads to the characteristic value of the bearing

capacity $R_{t,k}(\vartheta, n_{Sp})$ in (kN) for an inclined load (inclination ϑ) and/or for a group of multiple Spinnankers (amount n_{Sp}). For the ultimate limit state, the design value of the load bearing capacity is calculated using partial safety factors according to EN 1997-1:

$$R_{d,\vartheta} = \frac{R_{t,k}(\vartheta, n_{Sp})}{\gamma_{s,t}} = \frac{R_{t,k}}{\gamma_{s,t}} \cdot k_\vartheta \cdot k_n \qquad (36)$$

In Eq. (36) the correction factors k_ϑ for the inclination of the load and k_n for the amount of Spinnankers in a group are included. The partial factor for the resistence is $\gamma_{s,t} = 1.15$ based on the results of in-situ load tests. The design resistance $R_{d,\vartheta}$ (kN) should be higher than the design load $E_{d,\vartheta}$ (kN) which correspond to a resulting force in the direction $\vartheta = \alpha$ (°):

$$E_{d,\vartheta} \leq R_{d,\vartheta} \qquad (37)$$

For a conservative approach for the design load $E_{d,\vartheta}$ the partial factor γ_Q = 1,3 is used. A detailed description of the design and safety concept is given in Katzenbach et al. (2019b) and Leppla et al. (2022).

5 COMPARISON OF ANCHOR POINTS

Based on an example from engineering practice the three different temporary anchor points are designed. The boundary conditions are as follows:

- tension force F_k = 120 kN, inclination α = 60 °
- medium dense sand/gravel:
  γ = 19 kN/m^3, φ' = 32.5 °, no groundwater

The results of the design of the three different anchor points are as follows:

- deadman structure:
  steel pipe, diameter d = 406 mm,
  length l = 4 m, depth t = 3 m
- counterweight:
  concrete blocks, total volume 13.8 m^3 and 31.8 tons, ground area a/b = 2.4 m / 2.4 m
- Spinnanker:
  1 x XII / 4.0 / 15 with only 120 kg of steel

6 CONCLUSIONS

As shown, the design concepts of the three different temporary anchor points are significantly different. Regarding the level of safety it has to be pointed out, that for deadman structures and for counterweights no in-situ load tests are carried out in engineering praxis. This leads to uncertainty in the design and the resulting lower level of safety.

In addition, the different efforts for construction regarding the necessary use of resources have to be focused. An optimized design and construction leads to the minimization of the CO_2-emission.

For the design and construction of temporary anchor points, the following aspects and requirements have to be considered:

- All necessary geotechnical parameters have to be detected by a professional soil and groundwater investigation.
- The construction of deadman structures and of counterweights leads to a heavy impact on the environment.
- The design of a Spinnanker is based on in-situ load tests. This leads to a well defined level of safety and an economic optimization.
- Compared to other systems, the Spinnanker leads to a lower emission of CO_2.
- Regarding the technical regulations in EN 1997-1 the bearing capacity of all anchor systems has to be verified by in-situ load tests. Therefore, load tests for deadman structures and counterweights are necessary.

REFERENCES

CEN European Committee for Standardization (2013). EN 50341-1:2012 – Overhead electrical lines exceeding AC 1 kV – Part 1: General requirements – Common specifications.

CEN European Committee for Standardization (2014). EN 1997-1:2004 – Eurocode 7: Geotechnical design – Part 1: General rules.

Katzenbach, R., Rochée, S., Leppla, S., Okonek, P., Guerra, L. (2019a). Spinnanker – Technische Entwicklungen eines neuartigen Verankerungs- und Fundamentierungssystems. In: *12. Österreichische Geotechniktagung*, Wien, Österreich, 223-234.

Katzenbach, R., Rochée, S., Leppla, S. Okonek, P., Guerra., L. (2019b). Spinnanker – Technical developments of an innovative foundation and anchor system, In: *17th European Conference on Soil Mechanics and Geotechnical Engineering*, Rejkjavik, Island, 8 p. https://doi.org/10.32075/17ECSMGE-2019-0272.

Leppla, S., Katzenbach, R., Rochée, S., Okonek, P., Guerra, L (2022). Spinnanker – technical development of a new foundation and anchor system. In: *20th International Conference on Soil Mechanics and Geotechnical Engineering*, Sydney, Australia, 4959-4964.

Proceedings of the XVIII ECSMGE 2024
GEOTECHNICAL ENGINEERING CHALLENGES
TO MEET CURRENT AND EMERGING NEEDS OF SOCIETY
© 2024 the Authors
ISBN 978-1-032-54816-6
DOI 10.1201/9781003431749-606
Open Access: www.taylorfrancis.com, CC BY-NC-ND 4.0 license

ECSMGE 24
XVIII EUROPEAN CONFERENCE ON SOIL MECHANICS AND GEOTECHNICAL ENGINEERING

Geotechnical characterization of a test site in Zeebrugge for large scale tests of monopiles in the framework of the SAGE-SAND project

Caractérisation géotechnique d'un site d'essai à Zeebruges pour des tests à grande échelle de monopieux dans le cadre du projet SAGE-SAND

N. Letizia, G. Anoyatis
KU Leuven, Bruges, Belgium

L. Simonin, H. Rattez
UC Louvain, Louvain-la-Neuve, Belgium

F. Collin
University of Liege, Liège, Belgium

S. François*, H. Claes, J. Soete
KU Leuven, Leuven, Belgium

**stijn.francois@kuleuven.be*

ABSTRACT: This paper reports on large scale tests of monopile foundations for Offshore Wind Turbines (OWT) to be conducted in test site in Zeebruges, Belgium, in the framework of the SAGE-SAND project (*Soil ageing around OWT foundations – from operational response to decommissioning*). The project aims to investigate the evolution of the soil mechanical properties with time, and the alternative use of vibratory driving, to hammering, for installation and decommissioning of monopiles. Four hollow steel monopiles will be installed, by impact hammering and by vibratory driving, at a location where the soil conditions are representative of the Belgian sector of the North Sea. At selected time intervals during the project, the piles will be subjected to lateral loading at a fraction of their lateral capacity. Both the soil ageing effects and the influence of the installation method will be investigated. Herein an overview of the SAGE-SAND field testing program is presented, along with geotechnical information obtained from standard in-situ tests. Cone Penetration Tests (CPTs), as well as geological information and existing boreholes in the vicinity of the project are shown. Available correlations and empirical relationships from the Belgian practice are used to infer the soil stratigraphy and relate CPT data to soil properties necessary to perform predictive numerical simulations. Continuous in-situ tests such as cross hole tests and CPTs to the proximity of the piles throughout the duration of the project will allow the examination and the analysis of the soil ageing process.

RÉSUMÉ: Ce document rend compte de tests à grande échelle de fondations monopieux pour les éoliennes offshore (OWT) à réaliser sur un site d'essai à Zeebruges, en Belgique, dans le cadre du projet SAGE-SAND (vieillissement du sol autour des fondations OWT - de la réponse opérationnelle à la mise hors service). Le projet vise à étudier l'évolution des propriétés mécaniques du sol avec le temps, ainsi que l'utilisation alternative du battage vibratoire, par rapport au martelage, pour l'installation et la mise hors service des monopieux. Quatre monopieux en acier creux seront installés, par martelage et par battage vibratoire, dans un endroit où les conditions du sol sont représentatives du secteur belge de la mer du Nord. À des intervalles de temps sélectionnés pendant le projet, les pieux seront soumis à une charge latérale correspondant à une fraction de leur capacité latérale. Les effets du vieillissement du sol et de la méthode d'installation seront tous deux étudiés. Une vue d'ensemble du programme d'essais sur le terrain SAGE-SAND est présentée ici, ainsi que des informations géotechniques obtenues à partir de tests in situ standard. Des essais de pénétration au cône (CPT), ainsi que des informations géologiques et des sondages existants à proximité du projet, sont également présentés. Des corrélations disponibles et des relations empiriques issues de la pratique belge sont utilisées pour déduire la stratigraphie du sol et relier les données CPT aux propriétés du sol nécessaires à la réalisation de simulations numériques prédictives. Des tests in-situ continus tels que des essais de trou traversant et des CPT à proximité des pieux tout au long de la durée du projet permettront l'examen et l'analyse du processus de vieillissement du sol.

Keywords: Offshore geotechnics; mono-pile foundations; site investigation; large-scale tests.

1 INTRODUCTION

Offshore wind energy, decisive in the global shift towards green energy, is marked by ambitious plans worldwide to expand wind farms for a sustainable, long-term renewable energy supply. The wind farms, consisting of large turbines, hold significant potential to generate multi-gigawatts of electricity. The focus on minimizing costs for offshore turbines is crucial for achieving this long-term vision and requires advanced engineering approaches for design and site-specific optimization, especially for the foundations, that constitute approximately 30% of the total cost (Gavin et al., 2016).

Monopiles are the most commonly used foundation system for Offshore Wind Turbines (OWTs): large-diameter steel tubes which are either impact- or vibratory driven into the seabed. Recent studies conducted to advance design methodologies for monopiles for OWTs result from the findings of the PISA project. As such, a new design method has been developed by combining numerical modelling approaches and findings from large-scale monopile tests conducted at two sites, namely Dunkirk (dense sand) (Byrne et al., 2020) and Cowden (stiff clay) (Burd et al., 2020). The tests mainly focused on monotonic lateral loading and explored the rate effects and cyclic loading. However, previous research efforts have suggested the need for investigating the effect of soil ageing and installation method on the monopiles' response, as described in the following.

The soil ageing phenomenon, often referred to as "set-up," has been studied in the context of driven piles in clay, where the dissipation of excess pore pressures induced by driving leads to a positive gain in capacity with time (Gavin et al., 2016). However, the understanding of the mechanisms of ageing for piles in sand, as well as the quantification of its effect on the monopile's stiffness and lateral capacity, remains still much less explored. Field studies were conducted by researchers at Imperial College London (IC), the Norwegian Geotechnical Institute (NGI), and University College Dublin (UCD), to shed light on the behaviour of monopiles subjected to ageing processes.

All these studies revealed that ageing effects on steel pipe piles may be responsible for an increase in axial capacity with time (Jardine et al., 2005), although with variable growth rates. Karlsrud et al. (2014) attributed this variability to local soil conditions, emphasizing the need for site-specific considerations in understanding ageing effects.

On top of such considerations, environmental concerns regarding noise emissions during pile driving have led to the development of alternative installation methods to mitigate the impact on marine ecosystems.

The Vibro project conducted a major field trial at Cuxhaven involving six instrumented monopiles. The project's findings, as presented by Achmus et al. (2020), indicate that when monopiles in sand are installed by vibro-driving without specific requirements, reduction factors for stiffness during primary loading and unloading should be considered in the design. The study concludes the need for further research to identify optimum installation parameters.



Figure 1. Experimental site for large scale pile testing established for the SAGE-SAND project in Zeebruges, Belgium.

The SAGE-SAND project *"Soil ageing around offshore wind turbine foundations - from operational response to decommissioning"* aims to study the interaction between soil and pile for OWTs, in order to understand the effects of the soil ageing and of the installation process on the lateral behaviour of the foundation system during its lifetime, up to the decommissioning of the pile. For this purpose, an experimental site has been selected at the Port of Antwerp-Bruges in Zeebruges, Belgium (Figure 1).

The main aim of this paper is to show preliminary findings from the research project's initial stage, focusing on the CPT measurements to enhance understanding of the reference site.

2 OVERVIEW OF THE PROJECT

The experimental campaign provides for: an extensive geotechnical site investigation, the pile installation, lateral pile load tests, and at the end, the pile extraction. The geotechnical site characterization includes borings to identify the soil stratigraphy and retrieve samples for laboratory tests (e.g., soil classification, triaxial test), cross-hole tests, inclinometer measurements, Cone Penetration Tests (CPTs), seismic CPTs, and the geophysical method Multichannel Analysis of Surface Waves (MASW).

The piles have a diameter of 2.0 m and an embedded length of 18 m. According to the initial plan

two piles will be vibratory installed, and two piles will be hammered. The dynamic pile response during driving will be measured using accelerometers. The strains along the pile will be continuously measured using optical Fiber Bragg Gratings (FBG's). Piezometric pore water pressures in the vicinity of the piles will detect overpressures, that arise during the driving and can induce liquefaction of the surrounding soil. As the heat from the driving process may influence the chemical and ageing processes in the foundation soil, the temperature distribution will be measured using thermocouples, and the soil plug inside the piles will be monitored.

The long-term monitoring plan includes regular CPTs at the proximity of the piles, repeated cross-hole tests, and pile impedance measurements. The continuous monitoring will be carried out at selected time intervals, following lateral load tests. This way it aims to capture the evolution of soil properties with time, to provide insights crucial to achieve the project's objectives. The present paper focuses on the analysis and interpretation of the CPT campaign.

3 GEOLOGICAL INFORMATION

Preliminary information about the local geology has been obtained from the Databank Ondergrond Vlaanderen (DOV). This is a database that provides geological and geotechnical information from the Flemish subsurface, available via the online DOV Portal (DOV, 2023). The subsoil at the test site consists of Quaternary deposits up to a depth of 22.50 m, Tertiary (Eocene) and Quaternary layers up to a depth of 27.5 m, on top of Tertiary layers. The groundwater is saline. A complete set of data is retrieved from an existing borehole, near the test site (borehole: 1439-BB69-1818, DOV portal).

The samples extracted during the execution of this borehole are available in the Geotheek, the Flemish repository for samples from the subsurface (DOV, 2023). This helped gain an initial understanding of the stratigraphy at the nearby test location. In this regard, eight layers have been identified (starting from the ground surface): silt, fine sand interspersed by silt, silty clay, peat, silty sand, medium sand interspersed by thin lenses of fine sand.

4 CONE PENETRATION TESTS

4.1 Description of the equipment and test locations

Four electrical cone penetration tests (e-CPTs) were conducted at the locations of the piles, as shown in Figure 2. The probes were performed using a 10 cm^2 electric cone. The cone resistance, q_c, and the friction resistance, f_s, are measured at depth intervals of 1 cm. Their ratio, expressed as a percentage, yields the parameter R_f, friction ratio.



Figure 2. CPTs performed at the locations of the piles.

4.2 CPT data and soil layering

The CPTs data are used to determine the stratigraphy of the subsoil and estimate its properties. In particular, the acquired data are interpreted using available empirical methods to estimate the soil engineering parameters, such as strength and stiffness, that are required to conduct installation and lateral load analyses of the test piles. In particular, the subsoil at the test location has been idealized as a layered deposit, where each layer is considered homogeneous, and it is characterised by average constant q_c and R_f values. These values are calculated by omitting the extreme peaks, identified using the statistical method called "interquartile range" to find the outliers of a dataset. Figure 3 shows the CPT data in terms of q_c and R_f, at the four investigated locations S1, S2, S3 and S4, as well as the idealized soil layers. The complete set of the CPT data will be made available on the database titled Databank Ondergrond Vlaanderen (URL:https://www.dov.vlaanderen.be/portaal/?module=verkenner).

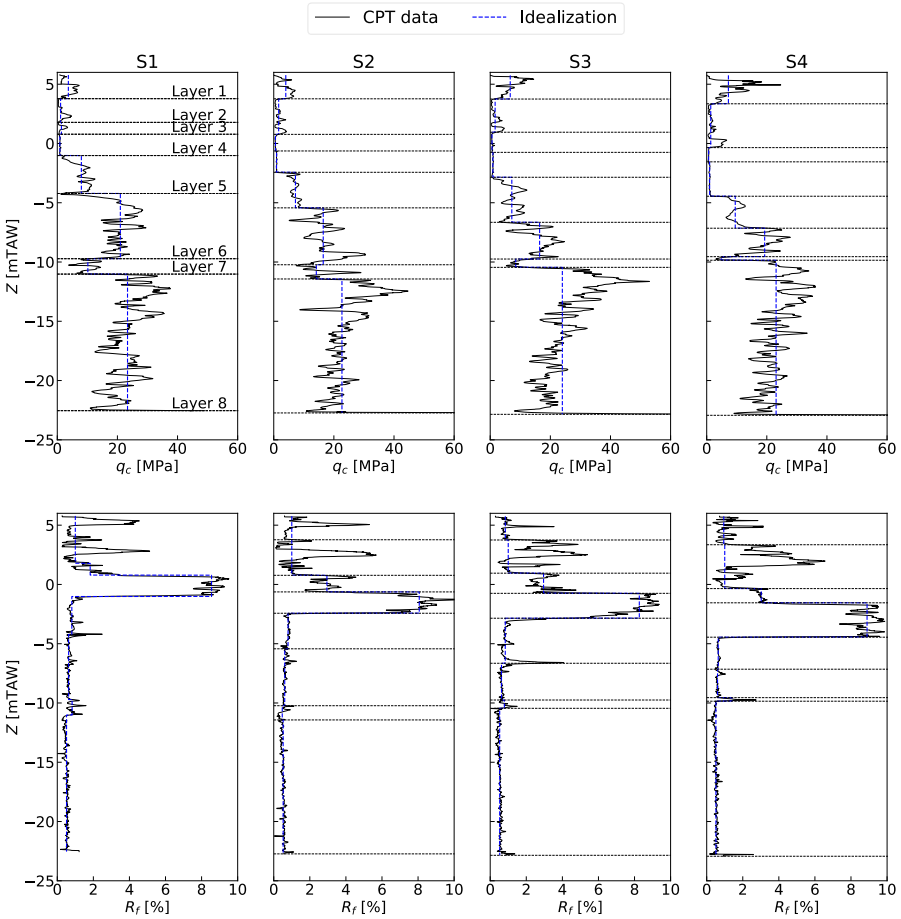

Figure 3. CPT data and layer idealization at the 4 investigated locations.

Table 1. Average values of q_c and f_s per soil layer at the 4 investigated locations.

	S1		S2		S3		S4	
Layer	q_{cm} (MPa)	f_{sm} (MPa)	q_{cm} (MPa)	f_{sm} (MPa)	q_{cm} (MPa)	f_{sm} (MPa)	q_{cm} (MPa)	f_{sm} (MPa)
1	3.69	0.040	4.01	0.040	6.66	0.061	7.22	0.057
2	1.10	0.019	1.63	0.020	1.64	0.027	1.36	0.032
3	1.38	0.020	0.57	0.016	0.59	0.02	0.64	0.019
4	0.87	0.076	0.93	0.074	0.90	0.073	0.98	0.088
5	8.01	0.066	7.22	0.056	7.19	0.060	9.49	0.061
6	20.98	0.133	16.46	0.103	16.43	0.112	19.29	0.117
7	10.17	0.079	14.16	0.064	8.48	0.068	4.85	0.069
8	23.37	0.118	22.69	0.118	23.98	0.120	23.09	0.117

5 BELGIAN GUIDELINES FOR CPT DATA INTERPRETATION

The recommendations by the Belgian standard 'NBN EN 1997-1 ANB' were adopted to identify the mechanical properties of the soil layers. The average q_c and f_s values are used to provide such estimates. Table 2 presents the soil effective unit weight γ', the friction angle φ', the undrained shear strength c_u, and effective cohesion c'.

Table 2. Soil mechanical properties per layer according to the Belgian practice (NBN EN 1997-1 ANB).

Layer	γ' (kN/m^3)	φ' (°)	c_u (kPa)	c' (kPa)
1	9	28	-	-
2	8	25	25	2
3	7	23	14	2
4	2	15	20	5
5	9	30	-	-
6	10	35	-	-
7	10	30	-	-
8	10	35	-	-

6 GEOTECHNICAL CORRELATIONS USING CPT DATA

Suitable correlations from the literature have been selected to provide additional CPT-based predictions of the soil parameters.

The total unit weight, γ, was estimated from CPT data using the relationship proposed by Robertson and Cabal (2015):

$$\frac{\gamma}{\gamma_w} = 0.27\ logR_f + 0.36\ log\left(\frac{q_t}{p_a}\right) + 1.236 \quad (1)$$

where γ_w is the unit weight of water, p_a is atmospheric pressure, q_t is the CPT corrected total cone resistance.

To estimate the peak friction angle, φ', the expression by Uzielli et al. (2013), valid for clean quartz sands, was adopted:

$$\varphi' = 25\left[\frac{(q_t/p_a)}{\sqrt{\sigma'_{v0}/p_a}}\right]^{0.1} \quad (2)$$

where σ'_{v0} is the in-situ vertical effective stress.

The soil relative density, D_R, was estimated by the formula proposed by Jamiolkowski et al. (2003), which is valid for clean silica sands:

$$D_R = 100\left[-0.675 + 0.268\ ln\left(\frac{q_c/p_a}{\sqrt{\sigma'_{v0}/p_a}}\right)\right] \quad (3)$$

The overconsolidation ratio, OCR, was evaluated as the ratio between the soil effective yield stress, σ'_p, and σ'_{v0}. To estimate σ'_p, the correlation provided by Mayne (2013) valid for all soils was adopted:

$$\sigma'_p = 0.33(q_t - \sigma_{v0})^m (p_a/100)^{1-m} \quad (4)$$

where σ_{v0} is the total vertical stress, m can be calculated by Eq. (5) as suggested by the author:

$$m = 1 - \frac{0.28}{1 + (I_c/2.65)^{25}} \quad (5)$$

where I_c is the soil behaviour type index as reported in Robertson and Wride (1998) and Robertson (2009).

The following relationship between c_u and OCR, valid for fine-grained soils, was adopted, considering that the compression indices and φ' are not known with confidence (Ladd and DeGroot, 2003):

$$c_u = \sigma'_{v0} 0.22 OCR^{0.8} \quad (6)$$

To estimate the small strain shear modulus, G_0, the well-known relationship between G_0 and the shear wave velocity, V_s, provided by the elasticity theory, has been considered. A number of empirical correlations to estimate the V_s profile using CPT data are available in literature. Herein, the in-situ V_s profiles were estimated using the equation derived by Mayne (2006) which was obtained from a well-documented experimental dataset of saturated clay, silt, and sand sites:

$$V_s = 118.8 \log f_s + 18.5 \quad (7)$$

where V_s is in (m/s) and f_s in (kPa).

A more accurate estimation of G_0 will result from the interpretation of the MASW data and cross-hole tests data.

Table 3 presents the estimated values of the layers' physical and mechanical properties, namely the soil effective unit weight, γ', peak friction angle, φ', relative density, D_R, overconsolidation ratio, OCR, undrained shear strenght, c_u, and small strain shear modulus, G_0.

Table 3. Soil mechanical properties per layer according to correlations for the CPT interpretation at the test site.

Layer	γ' (kN/m³)	φ' (°)	D_R (%)	OCR (-)	c_u (kPa)	G_0 (MPa)
1	9	-	-	18	20	89
2	7	-	-	3	13	66
3	7	-	-	3	23	59
4	8	-	-	5	42	104
5	9	39	53	3	-	98
6	10	42	70	3	-	130
7	9	38	49	2	-	104
8	10	42	69	2	-	132

Note that values for the soil mechanical properties are not reported for the layer types that fall outside the applicability range of the adopted correlations. Detailed analyses are included in the geotechnical report titled "Interpretation of CPT results for the SAGE-SAND test site in Zeebrugge" (Letizia et al., 2023). By comparing the estimated parameters presented in Tables 2 and 3, large differences in values can be observed. This discrepancy can be attributed to the fact that the Belgian guidelines provide a rather conservative estimation of the soil parameters to be used in design based on the experience of the local soils.

7 CONCLUSIONS

This study presents an analysis of geotechnical data obtained from the SAGE-SAND project's site CPT campaign. Specifically, the geotechnical interpretation of four CPTs conducted at the site in Zeebruges, Belgium, is presented. The research project aims to quantify the impact of the soil ageing and installation process, namely impact hammering and vibratory driving, on the lateral capacity and stiffness of monopiles for offshore wind turbines, as well as on extractability of such foundations during the decommissioning phase. This work focuses on the geotechnical characterization of the test site, and provides its soil stratigraphy by interpreting CPTs using the Belgian design guidelines and correlations from the existing literature. Additional tests which include geophysical methods (MASW), cross-hole tests, seismic CPTs and extensive laboratory tests are currently ongoing to best identify the soil properties to be used consequently to simulate the pile installation and make predictions of the lateral monopile response.

ACKNOWLEDGEMENTS

The academic consortium KU Leuven – UCLouvain – ULiege is grateful for the financial support provided by the Energy Transition Fund (Energietransitiefonds, ETF2022), via the project SAGE-SAND Soil ageing around OWT foundations – from operational response to decommissioning.

REFERENCES

Achmus, M., Schmoor, K. A., Herwig, V., & Matlock, B. (2020). Lateral bearing behaviour of vibro-and impact-driven large-diameter piles in dense sand, *geotechnik*, 43(3), pp. 147-159. https://doi.org/10.1002/gete.202000006.

Burd, H. J., Taborda, D. M., Zdravković, L., Abadie, C. N., Byrne, B. W., Houlsby, G. T., ... & Potts, D. M. (2020). PISA design model for monopiles for offshore wind turbines: application to a marine sand, *Géotechnique*, *70*(11), pp. 1048-1066. https://doi.org/10.1680/jgeot.18.P.277.

Byrne, B. W., Houlsby, G. T., Burd, H. J., Gavin, K. G., Igoe, D. J., Jardine, R. J., ... & Zdravković, L. (2020). PISA design model for monopiles for offshore wind turbines: application to a stiff glacial clay till, *Géotechnique*, *70*(11), pp. 1030-1047. https://doi.org/10.1680/jgeot.18.P.255.

DOV (2023). Databank ondergrond vlaanderen, Available at: [https://www.dov.vlaanderen.be/], accessed: 30/09/2023.

Gavin, K., Igoe, D., Sorensen, K. K., & Huybrechts, N. (2016). Research and Development Activities on Pile Foundations in Europe. In: *Proceedings of the ISSMGE-ETC 3 International Symposium on Design of Piles in Europe,* Leuven, Belgium.

Jamiolkowski, M., Lo Presti, D. C. F., & Manassero, M. (2003). Evaluation of relative density and shear strength of sands from CPT and DMT. In: *Soil behaviour and soft ground construction*, Cambridge, Massachusetts, pp. 201-238. https://10.1061/40659(2003)7.

Jardine, R. J., Chow, F. C., Overy, R. F., & Standing, J. R. (2005). *ICP procedures for driven piles in sands and clays*. Thomas Telford, London, England.

Karlsrud, K., Jensen, T. G., Lied, E. K. W., Nowacki, F., & Simonsen, A. S. (2014). Significant ageing effects for axially loaded piles in sand and clay verified by new field load tests. In: *Offshore Technology Conference*, Houston, Texas. https://doi.org/10.4043/25197-MS.

Ladd, C. C., & DeGroot, D. J. (2003). Recommended practice for soft ground site characterization: Arthur casagrande lecture. In: *12th Panamerican Conference on Soil Mechanics and Geotechnical Engineering*, Massachusetts Institute of Technology, Cambridge, MA, USA.

Letizia, N., Anoyatis, G., François S., Claes H., & Soete, J. Interpretation of CPT results for SAGE-SAND site in Zeebrugge, KU Leuven, Brugge, Belgium, Rep. SAGE-SAND R-GEO-CPT.

Mayne, P. (2006). Undisturbed sand strength from seismic cone tests. The 2nd James K. Mitchell lecture, *Geomechanics and Geoengineering*, 1(4), 239–258. https://doi.org/10.1080/17486020601035657.

Mayne, P. W. (2013). Evaluating yield stress of soils from laboratory consolidation and in-situ cone penetration tests. In: *Sound geotechnical research to practice: Honoring robert d. holtz II*, San Diego, California, pp. 405–419.

NBN (2014). NBN EN 1997-1 ANB: Eurocode 7: Calcul géotechnique – Partie 1: Règles générales - Annexe nationale. Bureau de Normalisation, Brussels, Belgium.

Robertson, P. K., & Wride, C. (1998). Evaluating cyclic liquefaction potential using the cone penetration test, *Canadian geotechnical journal*, 35(3), pp. 442–459. https://doi.org/10.1139/t98-017.

Robertson, P. K. (2009). Cpt-dmt correlations, Journal of geotechnical and geoenvironmental engineering, 135(11), pp. 1762–1771. https://doi.org/10.1061/(ASCE)GT.1943-5606.0000119.

Robertson, P., & Cabal, K. (2015). *Guide to cone penetration testing for geotechnical engineering*, 6th ed., Gregg Drilling Testing, Inc., Signal Hill, California.

Uzielli, M., Mayne, P., & Cassidy, M. (2013). Probabilistic assignment of design strength for sands from in-situ testing data. In: *Modern geotechnical design codes of practice: Implementation, application and development*, Vol. 1, IOS Press, Amsterdam, Netherlands, pp. 214–227. https://doi.org/10.3233/978-1-61499-163-2-214.

Proceedings of the XVIII ECSMGE 2024
GEOTECHNICAL ENGINEERING CHALLENGES
TO MEET CURRENT AND EMERGING NEEDS OF SOCIETY
© 2024 the Authors
ISBN 978-1-032-54816-6
DOI 10.1201/9781003431749-607
Open Access: www.taylorfrancis.com, CC BY-NC-ND 4.0 license

ECSMGE 24
XVIII EUROPEAN CONFERENCE ON SOIL MECHANICS AND GEOTECHNICAL ENGINEERING

A novel mechanical energy storage solution using underground CO_2 hydrate capsules

Une nouvelle solution de stockage mécanique d'énergie utilisant des capsules d'hydrate de CO_2 souterraines

O. Lev Yehudi
Technion – Israel Institute of Technology, Haifa, Israel

A. Franza*
Aarhus University, Aarhus, Denmark

N. von Solms
Technical University of Denmark, Lyngby, Denmark

A. Klar&
Technion – Israel Institute of Technology, Haifa, Israel

**anfr@cae.au.dk; &klar@technion.ac.il*

ABSTRACT: Mechanical energy storage can cope with the intermittent power supply of renewable energy sources (e.g. solar and wind). Concurrently, the green transition requires carbon capture and utilization technologies. This paper presents a novel concept of underground impermeable capsules formed by CO_2 hydrates, which can be used to pressurize gas and/or fluids (water, air, and/or carbon dioxide) for energy storage. Such capsules can be used for Pumped-Hydro Compressed Carbon Dioxide Energy Storage; in which water is compressed against pressurized gas in the capsule. This "green" use of gas hydrates can deliver both energy storage and carbon utilization objectives, in onshore and offshore applications. The paper first presents the construction phases and working principles of this underground mechanical energy storage. Next, temperature-pressure requirements for CO_2 gas hydrate stability are outlined, identifying a depth range of 30 m – 200 m as ideal for hydrate capsule creation. Finally, a simplified mechanical model based on elasticity is developed to quantify energy storage as a function of capsule geometry and material behavior.

RÉSUMÉ: Le stockage mécanique de l'énergie peut faire face à l'alimentation électrique intermittente des sources d'énergie renouvelables (par exemple, solaire et éolienne). Parallèlement, la transition verte nécessite des technologies de captage et d'utilisation du carbone. Cet article présente un nouveau concept de capsules souterraines imperméables formées d'hydrates de CO_2, qui peuvent être utilisées pour pressuriser du gaz et des fluides (eau, air et/ou dioxyde de carbone) en vue du stockage d'énergie. De telles capsules peuvent être utilisées pour le stockage d'énergie du dioxyde de carbone comprimé-hydro-pompé; dans lequel l'eau est comprimée contre le gaz sous pression dans la capsule. Cette utilisation « verte » des hydrates de gaz peut atteindre à la fois les objectifs de stockage d'énergie et d'utilisation du carbone, tant dans les applications terrestres qu'offshore. Le document présente d'abord les phases de construction et les principes de fonctionnement de ce stockage mécanique souterrain d'énergie. Ensuite, les exigences de température et de pression pour la stabilité des hydrates de CO_2 sont décrites, identifiant une plage de profondeur de 30 m - 200 m comme idéale pour la création de capsules d'hydrates. Enfin, un modèle mécanique simplifié basé sur l'élasticité est développé pour quantifier le stockage d'énergie en fonction de la géométrie de la capsule et du comportement des matériaux.

Keywords: Energy storage; gas hydrates; geotechnical engineering; carbon utilization.

1 INTRODUCTION

The EU has set a target of achieving a minimum of 40% renewable energy by 2030. Such movement towards renewable sources requires a capability of energy storage to accumulate surplus production, to be discharged when demand is greater than output (Guney and Tepe, 2017).

One sustainable way to store renewables is Underground Mechanical Energy Storage (UMES), which could level demand and production by pumping/discharging pressurized fluids into/from an

underground natural or man-made reservoir. There are two main approaches for underground energy storage: (*i*) Underground Pumped Hydroelectric Storage (UPHS), in which surplus production is stored as gravity (potential) energy by lifting a manmade soil mass ("overburden") when inflating with water a buried geomembrane-lined bag (Norlyk et al., 2020; Olsen et al., 2015); (*ii*) Compressed Air Energy Storage (CAES) using compressors to convert renewables into exergy as compressed air reservoirs at constant volume (isochoric) or constant pressure (isobaric) that is, then, expanded across a turbine to recover electricity (Budt et al., 2016). Proof-of-concept studies have investigated UPHS for shallow man-made membrane-lined reservoirs in sandy overburden, with difficulties in preventing straining of the lining used for the man-made reservoir (Olsen et al., 2015). On the other hand, CAES using underground air reservoirs is not competitive due to geological restrictions and uncertainties/variabilities of underground spaces affecting its airtightness (Budt et al., 2016). A hybrid approach of Pumped-Hydro Compressed Air Energy Storage (PH-CAES) has been studied (Pottie et al., 2020). Concurrently, recent studies proposed innovative thermo-mechanical closed-cycle energy storage having Carbon Dioxide (CO_2) as working compressed fluid in Compressed Carbon Dioxide Storage (CCDS) (Manzoni et al., 2022). Thus, there is scope to combine Carbon Capture, Utilization, and Storage (CCUS) with UMES to reduce the carbon dioxide in the atmosphere and mitigate climate change.

This paper presents a novel concept for energy storage based on man-made CO_2 hydrate capsules that serve as pressurized underground reservoirs for compressed fluids; this unites the objectives of UMES and CCUS. The paper is composed of four sections. Firstly, the construction and working principle are conceptually presented. Secondly, the feasibility of the CO_2 hydrate capsules is studied. Thirdly, the relative portion of energy storage in the domain is analyzed by a simple mechanical model. Finally, the key research questions required for further advancement of the suggested approach are presented.

2 PROPOSED UMES CONCEPT

Figure 1 illustrates the steps of construction and operation of the proposed concept of UMES using pressurized CO_2 gas hydrate capsules to store energy. While illustrated for offshore conditions, this solution can also be employed onshore.

To overcome the shortcomings of natural reservoirs, it is proposed to construct a (nearly) impermeable capsule using CO_2 gas hydrate in permeable porous soil deposits at intermediate depths of 10 m – 200 m. First, a spherical (filled) body is formed of CO_2 hydrate from the "creation" well through seepage in a porous medium (e.g. coarse-grain soil with an appropriate coefficient of permeability), as shown in Figure 1a. Then, the inner volume of the spherical hydrate body is dissociated to remain with soil and water within an external thick and relatively impermeable boundary, illustrated in Figure 1b. The disassociation would be triggered by a reduction in pore pressures and/or heat conduction through the well; the thermal-pressure conditions under which CO_2 gas hydrate can form and remain stable are discussed in the subsequent section. The thickness of the hydrate layer (forming the capsule) may be regulated by both the duration of a controlled hydrate formation and later dissociation processes.

As hydrates can reduce the permeability of sandy soil by a factor of 1000 for a volumetric hydrate saturation of 50% (Minagawa et al., 2005), the spherical hydrate shell structure practically forms an impermeable barrier.

Prior to standard operations, the man-made vessel (i.e., the capsule embedded in the deformable ground) may be internally pressurized to increase the energy storage capability of the system. The water inside the man-made hydrate structure can be pressurized or replaced by compressible gas (Figure 1c) depending on the storage approach: namely, (*i*) entire water removal and gas injections for the deploying compressed gas storage; (*ii*) water injections to use the capsule for underground pumped hydro storage; (*iii*) the water in the inner volume is partially replaced by pressurized gas, allowing for a hybrid solution in which water is compressed against gas to allow the use of hydraulic turbines. Thus, there are multiple possible applications of CO_2 gas hydrate capsules.

Furthermore, either air or CO_2 may be used as working gas. The use of CO_2 instead of air offers a four-fold advantage: CO_2 can serve as a self-healing material (recreating and sealing hydrate within tension-induced cracks), it will enhance efficiency (minimizing exergy losses) as it has ease of compression compared to air (Astolfi et al., 2022) and minimal dissolution in water at the operating pressure and temperature ranges (Shindo et al., 1995). Also,

using CO_2 as a construction material may benefit the carbon footprint.

The optimal envisioned application would be hybrid Pumped-Hydro Compressed Carbon Dioxide Energy Storage. During operations, see Figure 1d, the injection of water into the well would store mechanical energy in the compressed gas and water, and strain energy in the deformable capsule and ground (i.e. the vessel components). The stored energy is recovered by discharging the pressurized water across a turbine, exploiting efficient turbine/pump systems currently used in above-ground pumped hydro storage.

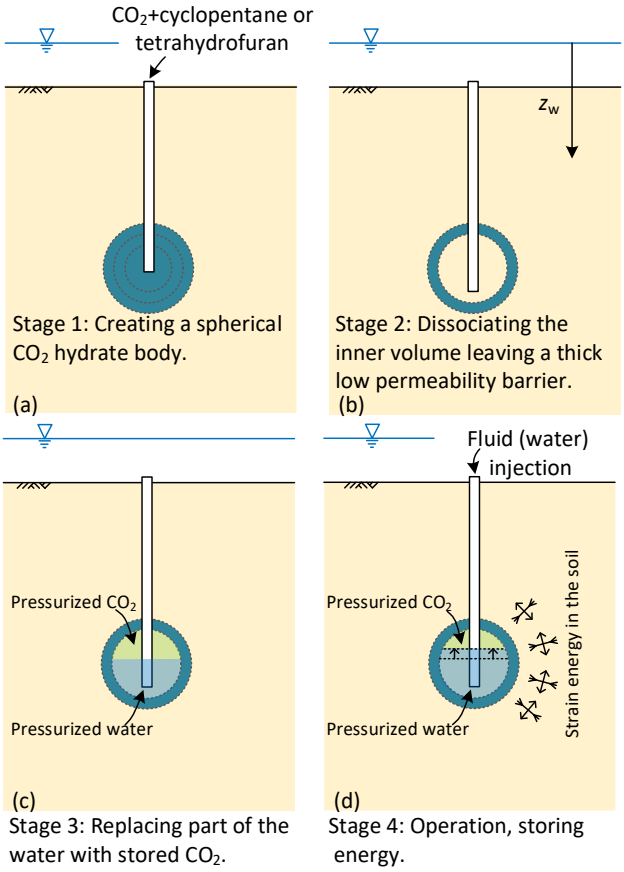

Figure 1. Hydrate capsule formation and operation.

3 STABILITY REQUIREMENTS OF CO_2 GAS HYDRATES

CO_2 gas hydrates require high pressures and low temperatures to be stable, with an exponentially increasing trend between dissociation pressure and temperature. For instance, Herslund et al. (2012) reported CO_2 gas hydrates being stable at 10°C for pressures greater than 4 MPa. This stability condition would not be compatible with the envisioned application at intermediate depths. However, the use of promoters such as cyclopentane or tetrahydrofuran (or a mixture of which) with concentrations of up to about 5 % of the water by mass, can reduce the hydrate formation pressure to values less than 1 bar (=100 kPa) at 13 °C (Herslund et al., 2014) and less than 4 bar (=400 kPa) at 19 °C.

Figure 2 shows the hydrate phase equilibrium together with the pressure-temperature profile of the groundwater in an offshore environment for a location in the North Sea with seabed depth H_w = 10 m or 80 m: the hydrate is stable when water pressure is greater than the disassociation pressure at a given temperature. As can be seen, pressure and temperature conditions for the stability of CO_2 gas hydrate capsules are met for a depth, below water table (z_w), ranging from 30 m to 400 m, approximately. On the other hand, CO_2 gas hydrates with promoters may not be stable at shallow depths (due to a combination of high temperatures and low pressures) or at water depths greater than 500 m (due to the increase in water temperature with depth and the exponential increase in dissociation pressure with temperature).

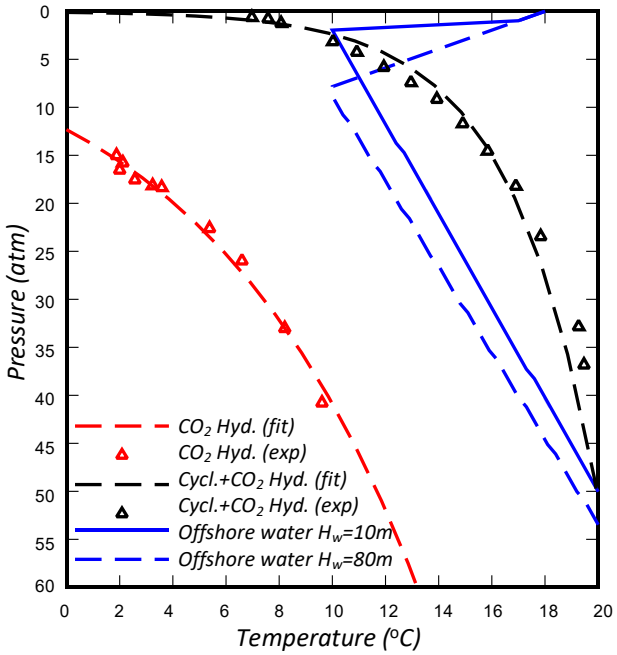

Figure 2. CO_2 hydrate stability condition versus offshore water and temperature profiles.

Therefore, when adopting cyclopentane or tetrahydrofuran promoters, vessel systems based on CO_2 gas hydrates are suitable for intermediate depths only. Furthermore, the internal temperature conditions within the vessel must be kept within the bounds of the hydrate's phase transformation curves throughout the operation to avoid impacting the formed capsule. Also, for offshore applications, water salinity and shallow

water temperature need to be considered. Jensen et al. (2011) reported that salinity (3.5 wt % NaCl solution) shifted the P-T curve by 2°C (leftwards in Figure 2); if considering a similar shift in CO_2 gas hydrates, the feasible depth range for capsule creation will reduce to 200 m. Future works will explore feasibility depths for onshore conditions.

4 A SIMPLIFIED MODEL FOR ENERGY DIVISION

This section presents a simple model to evaluate the energy storage ratios among the various system components.

To this aim, we assume that the entire system is elastic, and does not involve yielding. In addition, we assume that the internal soil (enclosed by the capsule) is found under homogenous and isotropic state. This condition could be considered correct for fully air or water saturated, and a fair estimation for the mixed condition. Under these conditions, one can consider a four-part system, as illustrated in Figure 3.

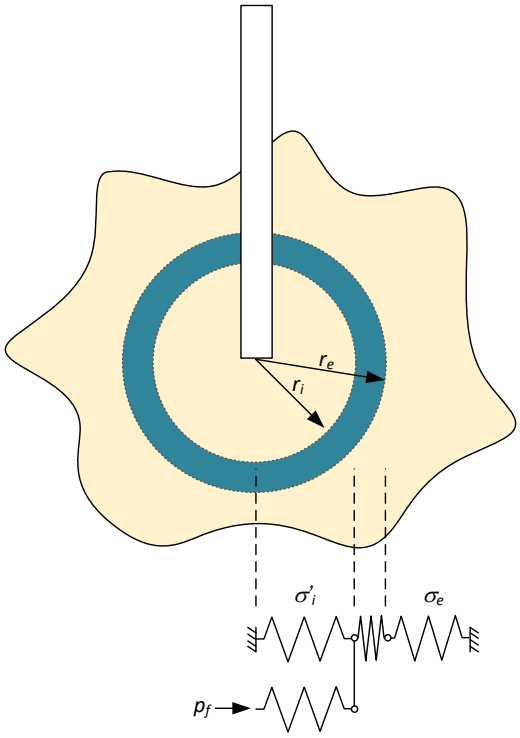

Figure 3. Simple model for evaluating the stress condition.

Considering an infinite elastic domain beyond the external boundary of the capsule, one can relate the pressure change at the boundary to the displacement of the outer boundary as follows:

$$u_e = \frac{\Delta\sigma_e}{4G_s} r_e \qquad (1)$$

where u_e is the displacement at the outer boundary at the distance r_e, $\Delta\sigma_e$ is the change of radial stress at the outer boundary (positive in compression), G_s is the shear modulus of the soil. Note that no volumetric strains develop at this outer region, and consequently no changes in pore pressure occur.

Applying the governing equations of elasticity to the hydrate bearing soil section, with the total stress boundary condition at its two boundaries results in:

$$u_h(r) = \frac{r_e^3 r_i^3 (\Delta\sigma_i - \Delta\sigma_e)(1+\nu) + 2r^3(1-2\nu)(r_i^3\Delta\sigma_i - r_e^3\Delta\sigma_e)}{4\,G_h r^2 (r_e^3 - r_i^3)(1+\nu)} \qquad (2)$$

where G_h is the shear modulus of the hydrate bearing soil. In general hydrate bearing soils exhibit significantly larger stiffness (e.g. Klar et al., 2010; Uchida et al., 2012) as well as dilatancy (e.g. Pinkert, 2016; Cohen and Klar, 2019), although this is somewhat irrelevant to the elastic solution presented here.

Assuming a uniform and isotropic stress condition in the inner region results in the following equation:

$$u_i = -\frac{\Delta\sigma'_i}{3\,K_s} r_i = -\frac{\Delta\sigma_i - \Delta p_f}{3\,K_s} r_i \qquad (3)$$

where p_f is the uniform fluid or gas pressure, and K_s is the bulk stiffness of the soil skeleton in the internal body. Overall, there are 4 unknowns ($u_i, u_e, \Delta\sigma_i, \Delta\sigma_e$) and 4 equations that allow for a solution to be established (Eq. 1., Eq. 2 applied at $r = r_i$ and at $r = r_e$ with the values of u_i and u_e, and Eq. 3).

Eq. 4 and 5 (below) provide the solution for the case in which the Poisson's ratio of the hydrate bearing soil is 1/2 (representing an impermeable undrained in terms of total stresses):

$$\Delta\sigma_i = \frac{4\left(G_s r_i^3 + G_h\left(r_e^3 - r_i^3\right)\right)}{(4G_h + 3K_s) r_e^3 - 4(G_h - G_s) r_i^3} \Delta p_f \qquad (4)$$

$$\Delta\sigma_e = \frac{4G_s r_i^3}{(4G_h + 3K_s) r_e^3 - 4(G_h - G_s) r_i^3} \Delta p_f \qquad (5)$$

The final displacement, u_i and u_e can be calculated by substituting the above stress changes in to Eqs. 1 and 3, or alternatively in to Eq. 2 with the associated radii. The strain energy stored in each region is as follows. For the inner zone:

$$E_{inner} = \frac{6K_s \pi r_e^6 r_i^3}{\left((4G_h + 3K_s) r_e^3 - 4(G_h - G_s) r_i^3\right)^2} \Delta p_f^2 \qquad (6)$$

For the hydrate bearing soil:

$$E_{hbs} = \frac{8G_h\pi r_e^3 r_i^3 (r_e^3 - r_i^3)}{\left((4G_h+3K_s)r_e^3 - 4(G_h-G_s)r_i^3\right)^2}\Delta p_f^2 \qquad (7)$$

and for the outer region:

$$E_{outer} = \frac{8G_s\pi r_e^3 r_i^6}{\left((4G_h+3K_s)r_e^3 - 4(G_h-G_s)r_i^3\right)^2}\Delta p_f^2 \qquad (8)$$

Again, these expressions assume a Poisson's ratio of 1/2 only for the hydrate bearing soil. At the limit cases where only water (or other fluid) is pressurized the energy stored in the fluid would be:

$$E_{fluid} = \frac{2\pi r_i^3}{3\frac{K_f}{n}}\Delta p_f^2 \qquad (9)$$

where K_f is the bulk stiffness of the fluid and n is the soil porosity. Eq. 9 is a rough estimate of the change in the stored energy of gas if the change in pressure (p_f) is small and K_f is taken as p_g (for ideal gas).

For partially water and gas filling conditions, K_f can be replaced by an equivalent stiffness of $K_{eq} = K_w K_g / \left(S_w K_g + S_g K_w\right)$ where K_w and K_g are the bulk stiffnesses of the water and gas, and S_w and S_g are the volumetric fractions of water and gas in the capsule ($S_w + S_g = 1$). Under this condition, there is still a clear proportionality between the components of energy storage that can be examined.

Figure 4 shows the relative part of each region in energy storage as a function of the radii of the hydrate boundaries for material properties relevant for water saturated inner region and for mixed filling condition with $K_{eq}/n = 0.5G_s$. In practice r_e/r_i would be close to 1 for large capsules and in the range of 1.2 to 2 for small capsules, suggesting that for water saturated inner region most of the energy will be stored in the soil for large capsules, and largely in the hydrate bearing soil for small capsules. Clearly, Figure 4 does not reveal information about the storage capacity but merely on the division between the components.

When K_f is associated with fully gas saturated, the ratios effectively become such that all the energy is stored in the gas, with almost no contribution from the soil. This is also true for the mixed water-gas condition, as any small amount of gas greatly reduces the equivalent stiffness (as can be evaluated by K_{eq}, or in Figure 4 for the mixed condition in which the gas stores more than 90% of the energy). This suggests that for gas storage the suggested approach simply results in a subsurface porous gas container.

The above spherical 'elastic' model is limited but could be the basis for the extension and inclusion of hydrate fracturing, soil yielding, and even healing aspects (by recreation of hydrates in formed cracks).

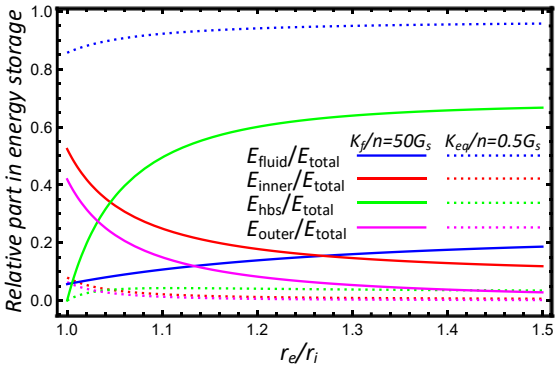

Figure 4. Relative part in energy storage for case in which $\frac{K_f}{n} = 50G_s$ *(full) and* $\frac{k_{eq}}{n} = 0.5G_s$ *(dashed),* $G_h = 10G_s$, $K_s = 1.67G_s$.

It is expected that it would be beneficial to induce high pressure, as part of the construction stage, to crack the hydrate and allow for reformation of hydrate in the formed fractures. Upon release of the induced pressure, the hydrate capsule (shell structure) would become prestressed, allowing for substantial pressure containment capacity during the operational stage. Therefore, during the first pressurization cycle, yielding of soil can increase the maximum operational fluid pressure for greater storage capacity.

5 SUMMARY AND DISCUSSION

This paper introduced a novel approach for Underground Mechanical Energy Storage (UMES) systems using CO_2 hydrates to create an impermeable vessel that can be internally pressurized by a mix of fluids (water, air, and/or carbon dioxide). The proposed concept of Pumped-Hydro Compressed Carbon Dioxide Energy Storage has the ambition to unite energy storage and carbon utilization objectives for the construction of the pressurized vessel, while exploiting efficient turbine/pump systems currently used in above-ground pumped hydro storage.

The construction phases, working principles, and requirements for hydrate stability were outlined. Then, a simplified mechanical model based on elasticity was suggested and used to quantify energy storage as a function of capsule geometry and material behavior. This may be considered a first step for the preliminary design of case studies.

To further advance this innovative concept and address critical knowledge gaps, the following research questions must be explored: (*i*) can spherical

hydrate be formed in real condition or gas buoyancy will hinder the ability to form capsules, (*ii*) what are the limits on pressurization in terms of hydrate and soil yielding, and can those be mitigated by healing processes of hydrate reformation in fractures, (*iii*) how large can the capsules be and what is the duration of their construction, (*iv*) does the thermal changes associated with gas storage impact the hydrate structure and to what extent, (*v*) what is the energy efficiency during operations as the result of the pressure-volume relationship at the inlet. To address these aspects, future works will span small-scale experiments and computer simulations.

It is worth noting that over the last 20 years extensive research has been carried out on geomechanical aspects of gas hydrates bearing sediments, although for a completely different objective of gas production. It is believed that the research knowledge and numerical tools developed in these prior studies (e.g. Klar et al., 2013) could be fostered towards analyzing the innovative energy storage solution presented in this paper.

ACKNOWLEDGEMENTS

The authors would like to express their deep appreciation to DTU Offshore and the BIRD Foundation for their interest and financial support. The authors would also like to thank Hans Horikx and Charlotte Nørgaard Larsen for the discussion on the topic and for providing the environmental data.

REFERENCES

Astolfi, M., Rizzi, D., Macchi, E., and Spadacini, C. (2022). A novel energy storage system based on carbon dioxide unique thermodynamic properties. *Journal of Engineering for Gas Turbines and Power*, 144(8): 081012. https://doi.org/10.1115/1.4054750.

Budt, M., Wolf, D., Span, R., and Yan, J. (2016). A review on compressed air energy storage: Basic principles, past milestones and recent developments. *Applied energy*, Vol. 170: 250-268. https://doi.org/10.1016/j.apenergy.2016.02.108.

Cohen, A. and Klar, A. (2019). A cohesionless micromechanical model for gas hydrate bearing sediments. *Granular Matter*, 21: 36. https://doi.org/10.1007/s10035-019-0887-5.

Guney, M.S. and Tepe, T. (2017). Classification and assessment of energy storage systems. *Renewable and Sustainable Energy Reviews*, 75: 1187-1197. https://doi.org/10.1016/j.rser.2016.11.102.

Herslund, P. J., Daraboina, N., Thomsen, K., Abildskov, J., and von Solms, N. (2014). Measuring and modelling of the combined thermodynamic promoting effect of tetrahydrofuran and cyclopentane on carbon dioxide hydrates. *Fluid Phase Equilibria*, 381: 20-27. https://doi.org/10.1016/j.fluid.2014.08.015.

Herslund, P. J., Thomsen, K., Abildskov, J., and von Solms, N. (2012). Phase equilibrium modeling of gas hydrate systems for CO_2 capture. *The Journal of Chemical Thermodynamics*, 48: 13-27. https://doi.org/10.1016/j.jct.2011.12.039.

Jensen, L., Thomsen, K., and von Solms, N. (2011). Inhibition of structure I and II gas hydrates using synthetic and biological kinetic inhibitors. *Energy & fuels*, 25(1): 17-23. https://doi.org/10.1021/ef100833n.

Klar, A., Uchida, S., Soga, K. and Yamamoto, K. (2013). Explicitly coupled thermal-flow-mechanical formulation for gas hydrate sediments. *SPE Journal*, 18(2): 196-206. https://doi.org/10.2118/162859-PA.

Klar, A., Soga, K. and Ng, M.Y.A. (2010). Coupled deformation-flow analysis for methane hydrate extraction. *Geotechnique*, 60(10):765-776. https://doi.org/10.1680/geot.9.P.079-3799.

Manzoni, M., Patti, A., Maccarini, S., and Traverso, A. (2022). Analysis and comparison of innovative large scale thermo-mechanical closed cycle energy storages. *Energy*, 249: 123629. https://doi.org/10.1016/j.energy.2022.123629.

Minagawa, H., Ohmura, R., Kamata, Y., Ebinuma, T., Narita, H. and Masuda, Y. (2005). Water permeability measurements of gas hydrate-bearing sediments. *Proc. 5th Int. Conf. Gas Hydrates*, Trondheim, Norway 1, 398–401.

Norlyk, P., Sørensen, K., Andersen, L. V., Sørensen, K. K., and Stutz, H. H. (2020). Holistic simulation of a subsurface inflatable geotechnical energy storage system using fluid cavity elements. *Computers and Geotechnics*, 127, 103722. https://doi.org/10.1016/j.compgeo.2020.103722.

Olsen, J., Paasch, K., Lassen, B., and Veje, C. T. (2015). A new principle for underground pumped hydroelectric storage. *Journal of Energy Storage*, 2: 54-63. https://doi.org/10.1016/j.est.2015.06.003.

Pinkert, S. (2016) Rowe's stress-dilatancy theory for hydrate-bearing sand. *Int. J. Geomech.* 17: 06016008. https://doi.org/10.1061/(ASCE)GM.1943-5622.0000682.

Pottie, D.L.F., Ferreira, R.A.M., Maia, T.A.C. and Porto, M.P. (2020). An alternative sequence of operation for Pumped-Hydro Compressed Air Energy Storage (PH-CAES) systems, *Energy*, 191: 116472. https://doi.org/10.1016/j.energy.2019.116472.

Shindo, Y., Fujioka, Y., Takeuchi, K., and Komiyama, H. (1995). Kinetics on the dissolution of CO_2 into water from the surface of CO_2 hydrate at high pressure. *International journal of chemical kinetics*. 27(6): 569-575, https://doi.org/10.1002/kin.550270607.

Uchida, S., Soga, K., and Yamamoto, K. (2012) Critical state soil constitutive model for methane hydrate soil, *J. Geophys. Res.*, 117: B03209. https://doi.org/10.1029/2011JB008661.

Proceedings of the XVIII ECSMGE 2024
GEOTECHNICAL ENGINEERING CHALLENGES
TO MEET CURRENT AND EMERGING NEEDS OF SOCIETY
© 2024 the Authors
ISBN 978-1-032-54816-6
DOI 10.1201/9781003431749-608
Open Access: www.taylorfrancis.com, CC BY-NC-ND 4.0 license

ECSMGE 24
XVIII EUROPEAN CONFERENCE
ON SOIL MECHANICS AND
GEOTECHNICAL ENGINEERING

Three-dimensional characterization of non-uniform deformation in drying fine sediments: An x-ray CT study

Caractérisation tridimensionnelle de la déformation non uniforme dans le séchage des sédiments fins: Une étude par tomographie à rayons X

L. Li*, B. Zhao
School of civil engineering, University College Dublin, Dublin, Ireland
**ludi.li@ucdconnect.ie*

ABSTRACT: Desiccation-induced cracks in fine sediments comprises soil strength, elevate hydraulic permeability, and undermine the integrity of geotechnical structures. The drying-induced shrinkage is typically constrained at boundaries, fostering non-uniform shrinkage and promoting desiccation crack formation. This study employs sequential X-ray computed tomography (CT) scans to investigate non-uniform deformation in saturated bentonite during the drying process. Internal glass bubbles serve as markers, enabling the characterization of three-dimensional (3D) internal deformation. A particle tracking algorithm, enhanced by using an Artificial Neural Network, facilities the estimation of glass bubbles displacement fields between scans. Results indicate that sidewall adhesion contributes to non-uniform deformation during drying, fostering desiccation crack formation near the sidewall.

RÉSUMÉ: Les fissures induites par la dessiccation dans les sédiments fins compromettent la résistance du sol, augmentent la perméabilité hydraulique et sapent l'intégrité des structures géotechniques. Le retrait dû au séchage est généralement contraint aux limites, favorisant un retrait non uniforme et encourageant la formation de fissures de dessiccation. Cette étude utilise des balayages séquentiels en tomographie par rayons X (CT) pour étudier la déformation non uniforme dans le bentonite saturé pendant le processus de séchage. Des bulles de verre internes servent de marqueurs, permettant la caractérisation de la déformation interne en trois dimensions (3D). Un algorithme de suivi de particules, renforcé par un réseau neuronal artificiel, facilite l'estimation des champs de déplacement des bulles de verre entre les balayages. Les résultats indiquent que l'adhésion de la paroi latérale contribue à la déformation non uniforme lors du séchage, favorisant la formation de fissures de dessiccation près de la paroi latérale.

Keywords: Desiccation crack; fine sediments; x-ray CT; particle tracking.

1 INTRODUCTION

Desiccation cracks in fine sediments form due to the drying-induced shrinkage and weaken the functionality of various geotechnical structures (Novak et al., 2000), such as embankment dams (Atique et al., 2009), shallow foundations (Lozada et al., 2015), and landfill liners (Omidi et al., 1996). More frequent severe drought events are expected to occur due to climate change and will intensify desiccation cracks.

For the last few decades, researchers have adopted laboratory tests (Corte & Higashi, 1964), numerical simulations (Amarasiri et al., 2011), and field characterization (Philip et al., 2002) to develop a better understanding of desiccation crack formation. Soil shrinkage is driven by elevated matric suction and influenced by boundary constrictions. At pore-scale, desiccation crack is formed by air invasion in water-saturated fine sediments (Shin & Santamarina, 2011; Zhao & Santamarina, 2020). It is anticipated that boundary restrictions induce non-uniform deformation, lead to local pore enlargement, and promote desiccation crack formation (Weinberger, 1999). Laboratory tests adopted digital camara to characterize the morphology of desiccation cracks and quantify the impact of substrate friction on desiccation crack formation (Decarlo & Shokri, 2014). Results show that more extensive cracks form due to the increased substrate friction (Costa et al., 2008). However, there is limited experimental studies on the internal non-uniform deformation within drying fine sediments.

This study adopts X-ray computed tomography (CT) to quantify internal deformation within drying fine sediments. Micron glass bubbles were embedded in a saturated bentonite sample to serve as tracking markers. During drying, multiple X-ray scans were collected to characterize the internal deformation. We adopted a particle tracking method enhanced by using

an Artificial Neural Network (ANN) to link glass bubbles between scans based on their location and morphology information. The three-dimensional (3D) displacement fields offer insights into non-uniform deformation resulted from sidewall adhesion and its impact on desiccation cracks formation.

2 EXPERIMENTAL METHOD

2.1 Material and sample preparation

We adopted bentonite with a liquid limit of *LL*=375%, as determined by fall-cone tests. Bentonite powders were hydrated by deionized water to achieve an initial water content of 375%. Glass bubbles were adopted to serve as tracking markers to monitor the internal deformation during the drying process. These glass bubbles are hollow glass spheres with a diameter ranging from 40 to 80 μm with a bulk density of 0.1 to 0.15 g/cm^3 (Gurit). Glass bubbles were mixed with saturated bentonite at a mass ratio of about 1.67%. The mass ratio was chosen to have an average distance between glass bubbles equals to three times the bubble diameter. Glass bubbles were gently mixed with saturated bentonite to avoid damage.

The container for drying tests had an inner diameter (*d*) of 8mm, a thickness (*t'*) of 2mm, and a height (*h*) of 10mm, as illustrated in Figure 1(a). The container is made of acrylic, which is transparent to X-ray. The sidewall was treated to increase the adhesion with bentonite sample. We polished sidewall using 400CW sandpaper and then coated it with PVA (Polyvinyl alcohol) to change the surface wettability from hydrophobic to hydrophilic(Trantidou et al., 2017). Subsequently, the mixture of bentonite and glass bubbles was injected into the container slowly using a small syringe to minimise the trapped gas bubbles.

2.2 Scanning procedure

The sample underwent drying in an environmental chamber at a constant temperature of 23℃ and at a relative humidity around 50%. Figure 1(b) shows the evolution of water content with drying time. Three high-resolution X-ray CT scans were conducted at pre-defined water contents to investigate the non-uniform deformable characteristics. The water content for scanning was selected based on preliminary tests to investigate non-uniform deformation before and after desiccation crack. The sample was covered during X-ray CT scans so that the water content remained unchanged.

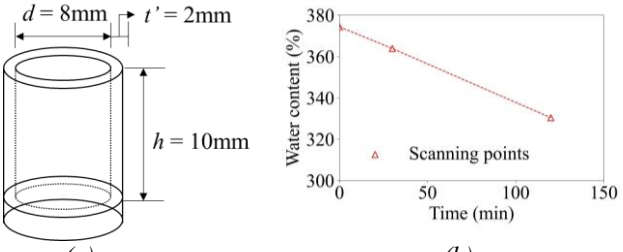

Figure 1. (a) Container for drying tests. (b) Drying curve and three scanning points.

2.3 Image processing

Figure 2 (a-c) shows grey-scale slices of the X-ray CT image for Scan-1 to Scan-3. A noticeable contrast was evident among the glass bubbles (air), bentonite, and acrylic container. To minimize image noise, we applied a median filter of size 3×3×3 voxels twice. Then, glass bubbles were separated from both bentonite and container with the threshold determined from Otsu's method (Otsu, 1979). The three-dimensional morphology and location of individual glass bubbles were obtained. The location data of each glass bubble is defined by the *x*, *y*, and *z* coordinates of its centroid. The morphology was quantified for both particle size and particle shape. Particles size parameters include volume (*V*) and surface area (*SA*), where particle shape parameters are sphericity (*SP*), aspect ratio (*AR*). More details of image processing and shape analysis were described by Zhao and Wang (Zhao & Wang, 2016).

2.4 Particle tracking algorithm

This study adopted the particle tracking algorithm enhanced by using an Artificial Neural Network (ANN) (Xu et al., 2023). The algorithm adopts both particle location and morphology to link bubbles between scans. A summary of the procedure is shown as follows:

First, we defined the unified coordination systems based on the base of container and six bubbles near the base. Then, the centroid parameters of all bubbles were consistently adjusted to ensure a unified coordinate system for three scans. After that, we manually linked 1,098 pairs of glass bubbles to set up the trained ANN model by using the parameter combination including *x*, *y*, *z*, *V* and *SP*, which has a highest accuracy 97.58%. The trained ANN model was applied to link bubbles between three scans, with a spatial position threshold to efficiently track all the glass bubbles (total 28,504) involved in our research. The ANN particle tracking successfully linked the majority of glass bubbles. A flittering was employed to the displacement data to remove tracking errors.

3 RESULTS

The first drying stage induced primarily vertical shrinkage in Scan-2 (Figure 2a – 2b). Due to the existence of sidewall adhesion, the vertical displacement in the middle of the sample is much larger. Eventually, a crack formed at near the sidewall and resulted in the horizontal shrinkage in Scan-3 (Figure 2c).

Figure 2 (d) displays the projection of displacement vectors on the vertical plane (x-z) at the middle section between Scan-1 and Scan-2. Vertical displacement reduced gradually from the sample surface to the base of container. Also, more pronounced displacement occurred in the centre, especially near the sample surface. The mean vertical displacement within the top 10% of the sample decreased from 0.36 mm at the centre to 0.17 mm near the sidewall. These results underlined the evident non-uniform displacement occurring on the sample surface with significant sidewall adhesion prior to crack formation. Figure 2 (e) shows a three-dimensional view of the displacement field between Scan-1 and Scan-2. The pronounced displacement was especially evident in the central of the surface, while there were smaller displacement on both sides due to the adhesion between the sidewall and the sample.

Figure 2 (f) shows the projection of displacement vectors on the vertical plane (x-z) at the middle section between Scan-2 and Scan-3. The crack formed on the left side of the sample resulted in large horizontal displacement in addition to the vertical displacement. For instance, within the top 10% of the sample, the horizontal displacement near the crack varied between 0.05mm and 0.10mm. The horizontal displacement gradually decreased as it approached the right side. Also, significant vertical displacement was observed, with the absence of sidewall adhesion influence on the left side due to the crack formation. The overall displacement field indicated a shrinkage towards the lower right corner.

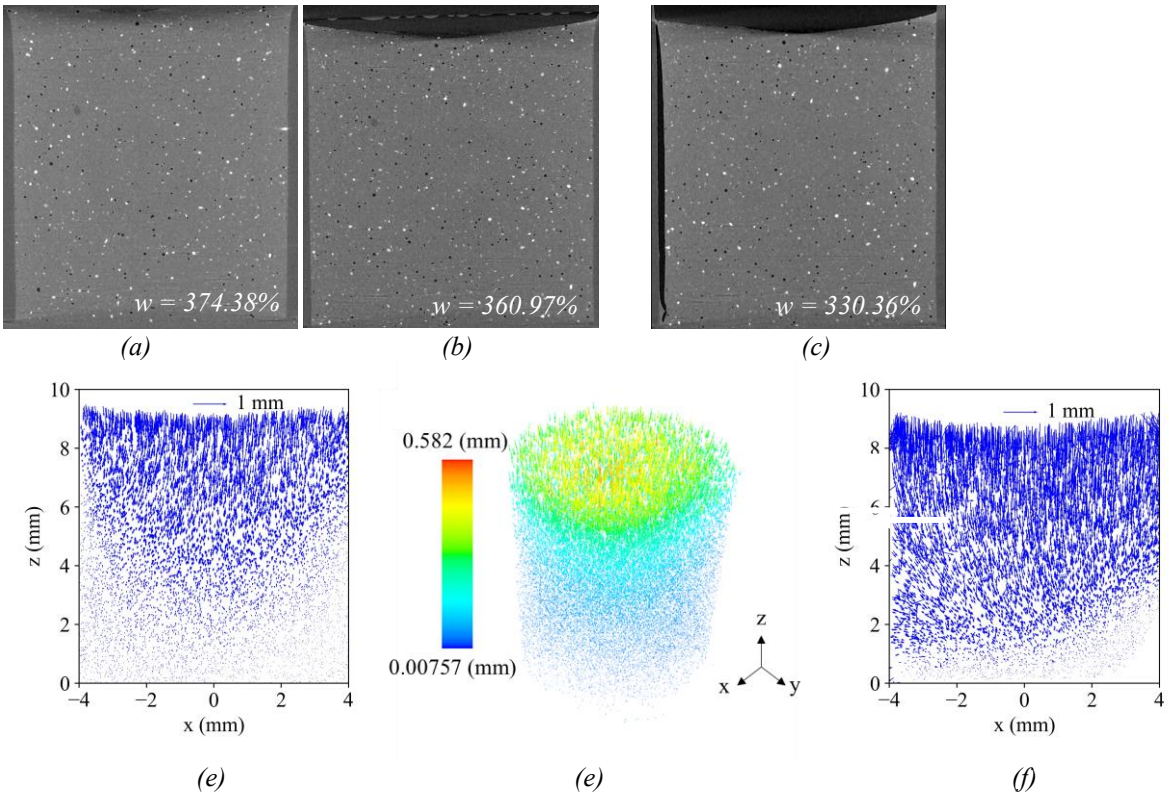

Figure 2. Non-uniform deformation and desiccation crack formation. (a)~(c) Vertical slices of Scan-1 to Scan-3. (d) Vertical projection of displacement field from Scan-1 to Scan-2. (e) 3D view of displacement vectors from Scan-1 to Scan-2 (f) Vertical projection of displacement field from Scan-2 to Scan-3.

4 CONCLUSIONS

This study investigated the non-uniform deformation of a drying bentonite sample. Glass bubbles were embedded in saturated bentonite to serve as tracking markers, while X-ray CT scans was employed to monitor internal deformation. The glass bubbles were tracked with an ANN model to quantify the three-dimensional displacement field before and after desiccation crack formation. The internal deformation before desiccation crack is dramatically affected by the adhesion between the bentonite and the container sidewall. A much larger vertical displacement

occurred in sample centre, while the vertical displacement was constrained at the sidewall. Desiccation crack formed near the sidewall lead to significant horizontal displacement, in addition to the vertical shrinkage observed in the sample.

ACKNOWLEDGEMENTS

L. Li acknowledges the financial support through the China Scholarship Council (CSC no. 202206280040) as a PhD student at the School of Civil Engineering, University College Dublin.

REFERENCES

Amarasiri, A. L., Kodikara, J. K., & Costa, S. (2011). Numerical modelling of desiccation cracking. *International Journal for Numerical and Analytical Methods in Geomechanics*, 35(1), 82–96. https://doi.org/10.1002/nag.894.

Atique, A., Sánchez, M., & Romero, E. (2009). Investigation of crack desiccation in soil from a flood protection embankment. *Unsaturated Soils, Two Volume Set: Experimental Studies in Unsaturated Soils and Expansive Soils (Vol. 1) & Theoretical and Numerical Advances in Unsaturated Soil Mechanics (Vol. 2)*, 2, 413.

Corte, A., & Higashi, A. (1964). *Experimental research on desiccation cracks in soil* (No. CRREL-RR-66 Final Rpt.).

Costa, S., Kodikara, J., & Thusyanthan, N. I. (2008). Modelling of desiccation crack development in clay soils. *Proc. 12th International Conference of IACMAG, Goa, India*, 1099–1107.

Decarlo, K. F., & Shokri, N. (2014). Effects of substrate on cracking patterns and dynamics in desiccating clay layers. *Water Resources Research*, 50(4), 3039–3051. https://doi.org/10.1002/2013WR014466.

Lozada, C., Caicedo, B., & Thorel, L. (2015). Effects of cracks and desiccation on the bearing capacity of soil deposits. *Géotechnique Letters*, 5(3), 112–117. https://doi.org/10.1680/jgele.15.00021.

Novak, V., Šimåunek, J., & Genuchten, M. T. van. (2000). Infiltration of water into soil with cracks. *Journal of Irrigation and Drainage Engineering*, 126(1), 41–47. https://doi.org/10.1061/(ASCE)0733-9437(2000)126:1(41).

Omidi, G., Thomas, J., & Brown, K. (1996). Effect of desiccation cracking on the hydraulic conductivity of a compacted clay liner. *Water, Air, and Soil Pollution*, 89, 91–103. https://doi.org/10.1007/BF00300424.

Otsu, N. (1979). A threshold selection method from gray-level histograms. *IEEE Transactions on Systems, Man, and Cybernetics*, 9(1), 62–66. https://doi.org/10.1109/TSMC.1979.4310076.

Philip, L., Shimell, H., Hewitt, P., & Ellard, H. (2002). A field-based test cell examining clay desiccation in landfill liners. *Quarterly Journal of Engineering Geology and Hydrogeology*, 35(4), 345–354. https://doi.org/10.1144/1470-9236/2001-37.

Shin, H., & Santamarina, J. C. (2011). Open-mode discontinuities in soils. *Géotechnique Letters*, 1(4), Article 4. https://doi.org/10.1680/geolett.11.00014.

Trantidou, T., Elani, Y., Parsons, E., & Ces, O. (2017). Hydrophilic surface modification of PDMS for droplet microfluidics using a simple, quick, and robust method via PVA deposition. https://doi.org/10.1038/micronano.2016.91. *Microsystems & Nanoengineering*, 3(1), 1–9.

Weinberger, R. (1999). Initiation and growth of cracks during desiccation of stratified muddy sediments. *Journal of Structural Geology*, 21(4), 379–386. https://doi.org/10.1016/S0191-8141(99)00029-2.

Xu, S., Lai, J., O'Kelly, B. C., & Zhao, B. (2023). 3D deformation and strain fields in drying kaolinite obtained from tracking internal bubbles using X-ray CT and ANN. *Acta Geotechnica* , 1-15. https://doi.org/10.1007/s11440-023-01948-8.

Zhao, B., & Carlos Santamarina, J. (2020). Desiccation crack formation beneath the surface. *Geotechnique*, 70(2), 181–186. https://doi.org/10.1680/jgeot.18.T.019.

Zhao, B., & Wang, J. (2016). 3D quantitative shape analysis on form, roundness, and compactness with μCT. *Powder Technology*, 291, 262–275. https://doi.org/10.1016/j.powtec.2015.12.029.

Proceedings of the XVIII ECSMGE 2024
GEOTECHNICAL ENGINEERING CHALLENGES
TO MEET CURRENT AND EMERGING NEEDS OF SOCIETY
© 2024 the Authors
ISBN 978-1-032-54816-6
DOI 10.1201/9781003431749-609
Open Access: www.taylorfrancis.com, CC BY-NC-ND 4.0 license

ECSMGE 24
XVIII EUROPEAN CONFERENCE ON SOIL MECHANICS AND GEOTECHNICAL ENGINEERING

Axial resistance of piles during driving in chalk

Résistance axiale des pieux lors du battage dans la craie

T. Liu*
University of Bristol, Bristol, UK

S. Kontoe
University of Patras, Patras, Greece; Imperial College London, London, UK

R.M. Buckley
University of Glasgow, Glasgow, UK

R.J. Jardine, K. Vinck
Imperial College London, London, UK

B.W. Byrne
University of Oxford, Oxford, UK

R.A. McAdam
Ørsted Power Ltd, London, UK

**tingfa.liu@bristol.ac.uk*

ABSTRACT: The driveability and axial capacity of driven piles depend critically on their geometry, end conditions and the degree of drainage they experience during driving. This paper summarises the installation characteristics of 41 impact-driven piles driven for the ALPACA joint industry project (JIP). The installed piles covered open- and closed-ended steel tubular, sheet and reinforced square concrete piles with a wide range of diameters (from 139 mm to 1.8 m), wall thickness ratios (14 to 72), and embedment length-to-diameter ratios (6 to 40). Analyses that applied parameters interpreted from parallel piezocone penetration and dissipation tests indicated that pore-pressures of several MPa developed beneath large open-ended piles during rapid driving and led to surprisingly low shaft resistances. However, the slower driving of the closed-ended concrete and sheet piles permitted far higher degrees of dissipation and led to far greater shaft resistances. Signal matching analyses demonstrate how the End of Driving (EoD) shaft resistances were affected strongly by de-structuration of the chalk and the relative depth of the pile tip. The EoD shaft resistances corresponded closely with predictions made applying the short-term Chalk ICP-18 Soil Resistance to Driving (SRD) formulae. An updated base resistance formula was proposed that correlates with pile wall thickness ratio.

RÉSUMÉ: La capacité de battage et la capacité axiale des pieux battus dépendent essentiellement de leur géométrie, de conditions d'extrémité et du degré de drainage pendant le battage. Cet article résume les caractéristiques d'installation de 41 pieux battus par impact pour le projet industriel commun ALPACA, incluant des pieux tubulaires en acier à extrémités ouvertes et fermées, des tôles et des pieux carrés en béton armé, avec des diamètres (139 mm à 1,8 m), des rapports d'épaisseur de paroi (14 à 72) et de longueur d'ancrage par diamètre (6 à 40). Des analyses utilisant des paramètres interprétés à partir d'essais de pénétration et de dissipation de piézocônes parallèles ont indiqué que des pressions interstitielles de plusieurs MPa se développaient sous de grands pieux à extrémité ouverte lors d'un battage rapide et conduisaient à des résistances d'arbre étonnamment faibles. Cependant, l'enfoncement plus lent des palplanches et du béton à extrémité fermée a permis des degrés de dissipation beaucoup plus élevés et a conduit à des résistances d'arbre bien plus grandes. Les analyses d'appariement des signaux démontrent comment les résistances de l'arbre en fin de battage (EoD) ont été fortement affectées par la déstructuration de la craie et la profondeur relative de la pointe du pieu. Les résistances des arbres EoD correspondaient étroitement aux prédictions faites en appliquant les formules à court terme de Chalk ICP-18 Soil Resistance to Driving (SRD). Une formule de résistance de base mise à jour a été proposée, en corrélation avec le rapport d'épaisseur de paroi du pieu.

Keywords: Chalk; impact driving; chalk resistance to driving (CRD); axial capacity; signal matching.

1 INTRODUCTION

Chalk is a high-porosity, calcareous, variable soft biomicrite found in large areas of North West Europe and other regions worldwide (Mortimore, 2012).

Large open-ended driven piles are employed to support a wide range of onshore and offshore infrastructure at chalk sites. However, their driveability has proven challenging to predict. Refusal has been reported on driving through high density chalk while strikingly low average shaft resistances (sometimes well below 20 kPa) can be developed on driving through low-to-medium density chalk, attributing to uncontrolled self-penetration (or 'runs') to far greater-than-expected depths (Carotenuto et al., 2018). Buckley et al. (2021) proposed a short-term 'Chalk ICP-18' Resistance to Driving (CRD) approach based on back-analyses of onshore and offshore

driving records of open-ended piles with respective length-to-diameter and wall thickness ratios of $5 \leq L/D \leq 40$ and $17 \leq D/t_w \leq 67$ driven in structured low-to-medium density chalks with corrected cone resistances (q_t) broadly between 10 and 20 MPa. They also suggested that the annular base resistances (q_b) developed during driving amount to around $0.6q_t$.

Jardine et al. (2023a, b) report how the significant uncertainties and challenges involved in designing driven pile foundations to sustain axial and lateral, monotonic and cyclic loading in chalk were addressed in the major ALPACA (Axial-lateral pile analysis for chalk applying multiscale field and laboratory testing) and ALPACA Plus joint industry research projects. Forty-one instrumented piles were driven at the well-characterised St Nicholas at Wade low-to-medium density chalk site in Kent, UK (Vinck et al., 2023) and comprehensive testing undertaken that led to new design guidelines for all the above loading cases.

This paper summarises the key phenomena observed during driving with dynamic instruments mounted on all piles and the findings obtained from rigorously conducted stress wave record numerical matching analyses. The performance of the Chalk ICP-18 CRD predictive approach was checked against the extended dataset, and the base driving resistance formula updated to account for wall thickness ratio.

2 PILE INSTALLATION OBSERVATIONS

Table 1 summarises the ALPACA and ALPACA Plus ranges for pile diameter D (139 mm – 1.8 m), slenderness ratio (L_p/D) (6 – 40), wall thickness ratio (D/t_w) (14 – 72), tip conditions, geometry and shaft materials. Also listed are the hammer masses, non-dimensional average velocities V (= vD/c_h), upper bound full drainage elapsed times and end-of-driving average shaft resistances (τ_{avg}^{EoD}) back analysed from stress-wave matches. All piles were monitored with above-ground pile driving analyser (PDA) strain gauges and accelerometers; 16 were instrumented with paired Fibre Bragg Grating optical strain gauge strings embedded along their shafts (Buckley et al., 2020).

All the open-ended piles drove in a fully coring manner with internal chalk columns that extruded and rose well above ground level at the end of driving, confirming relatively little outward volume displacement into the stiff surrounding chalk mass. Figure 1 shows how the volume displaced above ground compared to that of the embedded steel, V_{pag}/V_{steel}, fell systematically with L_p/D; open-pile cores rarely rise above ground level in sands and clays.

Driving the open-tubular LD and SD piles to target depths with the employed hammers required 9 to 55 blows per 250 mm and total driving times of 2 to 14 minutes. Relatively hard driving was required for (i) the 200 mm square concrete piles, with up to 308 blows/250 mm over up to 81 minutes and (ii) the sheet piles with up to 100 blows/250 mm and ≈ 20-minute driving times, leading to relatively low V values. These piles' slow driving is likely to have led to greater degrees of drainage that attributed to higher τ_{avg}^{EoD} (83.3 and 37.1 kPa respectively) average shaft resistances than the 24.8 kPa of open-ended piles.

Table 1. ALPACA and ALPACA Plus driven pile installation: pile geometries, conditions, hammer details, ranges of normalised velocity V, upper bound full drainage elapsed times and end-of-driving (EoD) average shaft resistances (τ_{avg}^{EoD}).

Pile numbers, codes and material	D (mm)	t_w (mm)	R^* (m)	L_p (m)	L_p/D	Hammer (ram mass)	Norm. V (= vD/c_h)	Upper bound t_{95} (min)	τ_{avg}^{EoD} (kPa)
12 'LD' open-ended steel	508	20.6	0.100	10.16	20	Juntann SHK-4 (4 ton)	1.54 – 2.09	27.9	15.6 – 28.0
2 'LD' open-ended steel	508	20.6	0.100	3.05	6	HHK-5A (5 ton) for LD14	0.79 – 1.67	27.9	19.8 – 31.3
16 'SD' open-ended steel, including 2 stainless steel	139	8.0 – 10.3	0.035	4.9 – 5.5	38 – 40	Delmag (1.4 ton)	0.52 – 1.50	3.4	18.1 – 27.4
2 'SD' closed-ended steel	139	9.4 – 9.7	0.070	5.4 – 5.5	39 – 40		0.36 – 1.20	13.4	19.7
2 concrete square	226	NA	0.113	4.9 – 5.4	22 – 24		0.10 – 0.16	35.5	83.3
2 SM-J steel sheet piles	290	11 – 12.2	0.057	5.4	18.6		0.24	9.0	37.1
TP1 open-ended steel	1800	25	0.211	18	10	BSP CG240 (16 ton)	2.74	123.4	26.2
TP2 and R1 open-ended steel	1220	24.6	0.171	7.3	6	BSP CX110 (9 ton)	1.64 – 2.48	81.8	22.1 – 31.3
R2 open-ended steel	1220	24.6		18	14.8				24.2
TP3 open-ended steel	508	12.5	0.079	18	35.4		0.50	17.2	26.9

Notes: D listed for concrete and sheet piles based on equivalent area; t_w: pile wall thickness; R: equivalent radius for open-ended piles ($= (R^2 - R_i^2)^{0.5}$); R and R_i: outer and inner radius, respectively; c_h: coefficient of horizontal consolidation.*

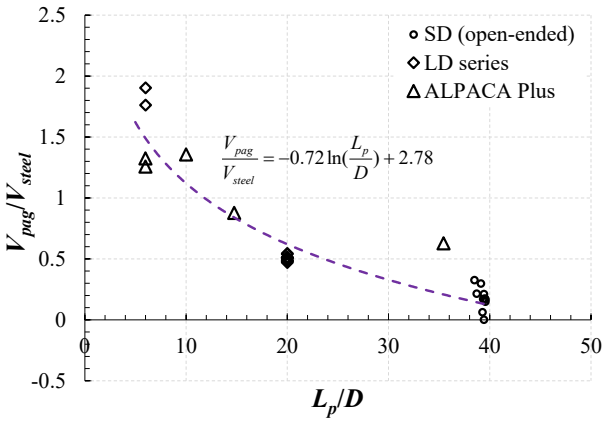

Figure 1. Variation of the ratio between the above-ground chalk plug volume (V_{pag}) and embedded steel volume (V_{steel}) against L_p/D.

3 DRIVING RESISTANCE PREDICTIONS

3.1 ALPACA shaft and base CRD formulae

Buckley et al. (2020) show that internal shaft resistances are likely to be far lower than apply externally to piles driven in chalk. The overall shear resistances are therefore considered in Chalk ICP-18 as the sum of the external and internal shaft stresses and treated as applying only on the external pile shaft. The overall shear resistances available at any level on the shaft, τ_{rzi}, are determined through Equation (1), in which σ_{ri}' denotes radial effective stress during installation and δ_{ult}' interface shear resistance angle determined from Bishop ring shear interface tests and typically taken as 32° (Vinck, 2021).

$$\tau_{rzi} = \sigma_{ri}' tan\delta_{ult}' \quad (1)$$

The local radial effective stress (σ_{ri}') and base bearing pressure (q_b) are defined as functions of relative pile tip depth (h), corrected cone resistance (q_t), equivalent radius (R^*) and D/t_w:

$$\sigma_{ri}' = 0.031 q_t \left(\frac{h}{R^*}\right)^{-0.481\left(\frac{D}{t_w}\right)^{0.145}} \quad (h/R^* \geq 6) \quad (2)$$

$$R^* = \left(R^2 - R_i^2\right)^{0.5} \quad (3)$$

$$q_b = q_t (D/t_w)^{-0.175} \quad (4)$$

3.2 Performance of the method in predicting field behaviour

The performance of the Chalk ICP-18 shaft CRD method was assessed systematically against the dynamic stress-wave matches of the ALPACA and ALPACA Plus piles' instrumented driving records, as well as independent cases collated and analysed by Vinck (2021).

Overall comparison of the total EoD shaft load between the predictions for shaft resistance Q_s integrated from the above expressions and the signal-matching outcomes, indicated a fortuitously unbiased mean calculated-to-measured (Q_c/Q_m) ratio of 1.00 and a coefficient of variation (CoV) of 0.38 for the open-ended piles listed in Table 1. The latter CoV, which should be recognised when developing upper and lower bound CRD profiles for hammer selection and pile fatigue analyses, reflects natural variabilities of chalk conditions and driving operations as well as uncertainties inherent in stress wave matching.

Further testing of the approach by Vinck et al. (2023) at the Sauchay medium density chalk test site near Dieppe in France also showed good agreement with mean Q_c/Q_m of 0.99 and CoV of 0.19.

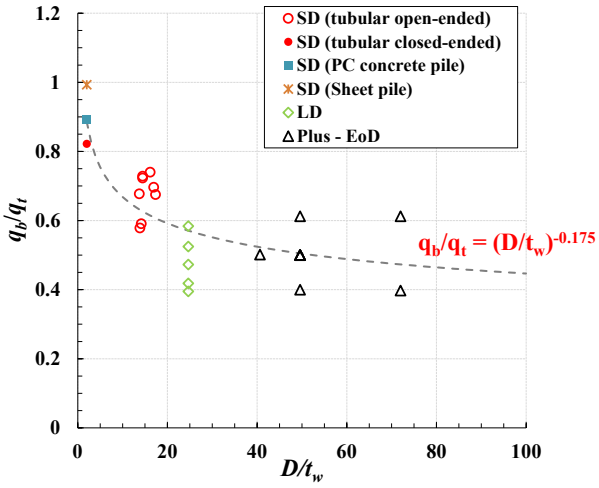

Figure 2. Normalised bearing pressure (q_b/q_t) against piles' D/t_w at end-of-driving (Note: q_b evaluated over closed-ended piles' full areas and open-ended piles' steel annuli; D/t_w taken as 2 for closed-ended piles).

However, Jardine et al. (2023b) and Vinck et al (2023) proposed from their analyses that the base driving resistance formula required updating. Figure 2 plots the signal-matched End-of-Driving base resistance (q_b) values normalised by q_t against D/t_w, showing a declining trend that can be expressed by power-law Equation (4). This updated method leads to

a better and more conservative fit to the data than the Chalk ICP-18's tentatively suggested $q_b/q_t \approx 0.6$.

Two examples from the signal matching analyses are shown in Figure 3. The shaft resistance profiles derived from signal matching back analyses are compared with predictions from Equations (1)-(3) for both relatively long (L_p/D = 20) and short (L_p/D = 6) open steel, 508mm outside diameter piles (LD5 and 13 respectively). Two q_t profiles are also shown, as established in CPT soundings made close to both piles.

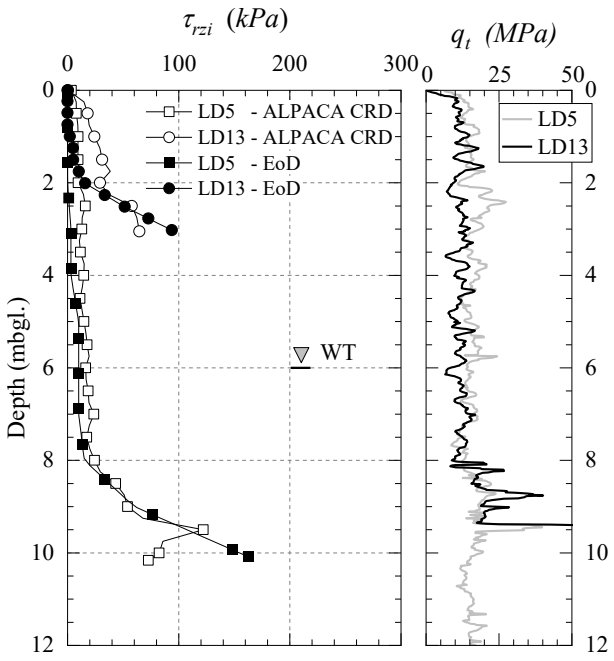

Figure 3. Profiles of CPT resistance and shaft friction from EoD PDA analysis against CRD prediction for two LD piles (D =508 mm, D/t_w =25).

4 CONCLUSIONS

(1) Predicting pile's driveability in chalk is crucial to many onshore and offshore projects.

(2) Comprehensive research was undertaken in the ALPACA and ALPACA Plus campaigns on 41 instrumented piles to (i) improve fundamental understanding of driving resistances and (ii) calibrate new predictive approaches. Axial driving resistances were found to depend critically on pile geometry, end conditions, CPT resistance and any drainage during installation.

(3) Closed-ended sheet and concrete piles experienced relatively hard driving that permitted higher degrees of drainage and higher driving resistances.

(4) Rigorous stress wave analyses confirmed that the Chalk ICP-18 resistance to driving (CRD) method led to unbiased shaft predictions for the St Nicholas at Wade (SNW) piles and generally good matches in other independent cases. The test analysis also allowed an improvement of the method's formulation for base resistance to driving.

ACKNOWLEDGEMENT

The Authors gratefully acknowledge support from UK grants from EPSRC (EP/P033091/1), Royal Society (NA160438) and Supergen ORE Hub 2018 (EPSRC EP/S000747/1). Byrne is supported by the Royal Academy of Engineering under the Research Chairs and Senior Research Fellowships scheme, while Vinck was supported by EPSRC Grant EP/L016826/1, DEME and Imperial College. Financial and technical support by the following project partners is also acknowledged gratefully: Atkins, Cathies, Equinor, Fugro, GCG, LEMS, Ørsted, Parkwind, RWE, Siemens-Gamesa, Scottish Power Renewables and Vattenfall. The Authors also wish to acknowledge Socotec UK Ltd as the principal contractor for the ALPACA and ALPACA Plus field testing campaigns.

REFERENCES

Buckley, R.M., McAdam, R.A., Byrne, B.W., Doherty, J.P., Jardine, R.J., Kontoe, S., and Randolph, M.F. (2020). Optimisation of impact pile driving using optical fibre Bragg grating measurements. *Journal of Geotechnical and Geoenvironmental Engineering*, 146(9). https://doi.org/10.1061/(ASCE)GT.1943-5606.0002293.

Buckley, R.M., Kontoe, S., Jardine R.J., Barbosa, P. and Schroeder, F.C. (2021). Pile driveability in low- to medium-density chalk. *Canadian Geotechnical Journal*, 58(5): 650-665. https://doi.org/10.1139/cgj-2019-0703.

Carotenuto, P., Meyer, V., Strøm, P.J., Cabarkapa, Z., St. John, H. and Jardine, R.J. (2018). Installation and axial capacity of the Sheringham Shoal offshore wind farm monopiles–a case history. Proceedings of the Engineering in Chalk Conference (Lawrence J.A., Preene M., Lawrence U.L. and Buckley R.M.(eds)), Institution of Civil Engineers (ICE) Publishing, London https://doi.org/10.1680/eiccf.64072.117.

Jardine, R.J., Buckley, R.M., Liu, T., Byrne, B.W., Kontoe, S., McAdam, R.A., Schranz, F. and Vinck, K. (2023a). The ALPACA and ALPACA Plus Joint Industry studies of driven pile behaviour in low-to-medium density chalk. Proceedings of 9th International Offshore Site Investigation and Geotechnics Conference, London. The Society for Underwater Technology.

Jardine, R.J., Buckley, R.M., Liu, T., Andolfsson, T., Byrne, B.W., Kontoe, S., McAdam, R.A., Schranz, F. and Vinck, K. (2023b). The axial behaviour of piles driven in chalk. *Géotechnique*, Ahead of Print. https://doi.org/10.1680/jgeot.22.00041.

Lord, J.A., Clayton, C.R.L. and Mortimore, R.N. (2002). Engineering in chalk, CIRIA, C574.

Vinck, K. (2021). Advanced geotechnical characterisation to support driven pile design at chalk sites. PhD thesis, Imperial College London.

Vinck, K., Liu, T., Jardine R.J., Kontoe, S., Ahmadi-Naghadeh, R., Buckley, R.M., Byrne, B.W., Lawrance, J.A., McAdam, R.A. and Schranz, F. (2022). Advanced in-situ and laboratory characterisation of the ALPACA chalk research site. *Géotechnique*, Ahead of Print. https://doi.org/10.1680/jgeot.21.00197.

Vinck, K., Liu, T., Mawet, J., Kontoe, S. and Jardine, R.J. (2023). Field tests on large scale instrumented piles driven in chalk: results and interpretation. *Canadian Geotechnical Journal*, 60(10), 1475-1490: https://doi.org/10.1139/cgj-2022-0441.

Proceedings of the XVIII ECSMGE 2024
GEOTECHNICAL ENGINEERING CHALLENGES
TO MEET CURRENT AND EMERGING NEEDS OF SOCIETY
© 2024 the Authors
ISBN 978-1-032-54816-6
DOI 10.1201/9781003431749-610
Open Access: www.taylorfrancis.com, CC BY-NC-ND 4.0 license

ECSMGE 24
XVIII EUROPEAN CONFERENCE ON SOIL MECHANICS AND GEOTECHNICAL ENGINEERING

The contribution of ductile cast-iron piles to a more sustainable deep foundations industry

La contribution des pieux en fonte ductile à une industrie plus durable des fondations profondes

F. Lopez*, E. Steinlechner
Tiroler Rohre GmbH, Hall in Tirol, Austria

**freddy.lopez@trm.at*

ABSTRACT: As addressed by the UN Secretary-General, António Guterres, at the opening of the Climate Implementation Summit at COP27 (Sharm el-Sheikh, Egypt) in 2022, climate change is not only an essential challenge of our century but the defining issue of our age. Any hope of limiting temperature rise to 1.5°C means achieving global net-zero emissions by 2050. The built environment and with it the construction industry is worldwide responsible for 39% of greenhouse gas emissions (CO_2), therefore it is our responsibility as part of the construction industry to take stronger actions and effective accountability. Wherever we are and whichever our position might be, our actions can produce large positive changes. The following technical paper presents an overview of the contribution of ductile cast-iron piles to achieve a more sustainable deep foundations industry, by reducing considerably the embodied carbon footprint of the implemented solutions. It is not too late yet, but we all need to redouble efforts in order to bend the global emissions curve. It is the fight of our lives and we will lose, unless we work together. The use of innovative and sustainable materials can definitely help the building sector to face successfully today´s existential challenges.

RÉSUMÉ: Comme l'a déclaré le Secrétaire général des Nations unies, António Guterres, lors de l'ouverture de la conférence sur les changements climatiques dite COP 27 (Charm el-Cheikh, Égypte), le changement climatique n'est pas seulement un défi essentiel de notre siècle, mais aussi l'enjeu fondamental de notre époque. Tout espoir de limiter la hausse de la température globale à 1.5°C implique d'atteindre zéro émission nette mondiale d'ici 2050. L'environnement bâti et avec lui l'industrie de la construction sont responsables à hauteur de 39% des émissions de gaz à effet de serre (CO2) dans le monde. C'est donc notre responsabilité, en tant qu'acteur de l'industrie de la construction, de prendre des mesures plus fermes et de rendre compte de manière efficace. Où que nous nous situions et quelle que soit notre position, nos actions peuvent produire d'importants changements positifs. Cet article technique présente l'ensemble des contributions des pieux battus en fonte ductile pour parvenir à une industrie plus durable des fondations profondes, en réduisant considérablement l'empreinte carbone intrinsèque des solutions mises en œuvre. Il n'est pas encore trop tard, mais nous devons tous redoubler d'efforts pour infléchir la courbe des émissions mondiales. C'est le combat de notre vie et nous le perdrons si nous ne travaillons pas ensemble. L'utilisation de matériaux innovants et durables peut indiscutablement servir le secteur du bâtiment dans le but de relever avec succès les défis existentiels d'aujourd'hui.

Keywords: Sustainability; reduction of carbon footprint; ductile cast-iron piles.

1 GREENHOUSE GAS EMISSIONS AND CLIMATE CHANGE

The work of scientists and researchers around the world report changes beyond the natural variation of temperatures on land and in the ocean, as well as abnormal trends in the timing of seasons, rainfall patterns and occurrence of extreme climate events, which affect millions of people globally. The scientific community acknowledges the irrefutable link between the human-caused greenhouse gas (GHG) emissions and the global climate change, observed in the last decades.

In response to this, a legally binding international treaty on climate change - the *Paris Agreement* - was adopted by 196 parties in 2015, pursuing efforts to limit global warming to 1.5 °C by the end of the 21st century (compared to preindustrial levels). To achieve this goal, global emissions must reach net-zero by 2050 (Climate Watch, 2023).

2 THE ENVIRONMENTAL IMPACT OF THE BUILT ENVIRONMENT

The built environment, consisting of buildings and infrastructure, is responsible for a large share of the

human-made global environmental impact, including approx. 40% of the global energy consumption, 50% of all raw material extraction, 33% of all potable water usage and 35% of all waste generation, as well as 39% of the carbon emissions (AIB and IGBC, 2022).

2.1 GHG emissions

It is estimated that the world emissions reach approx. 48 billion metric tons of GHG (measured in CO_2e) each year and the built environment accounts for almost 39% of them (Figure 1), a figure comprising both *operational carbon* (resulting from heating, cooling, lighting, etc.) and *embodied carbon*, or emissions resulting from the manufacturing of materials, construction processes and end of life cycle phases of all buildings and infrastructure (Figure 2).

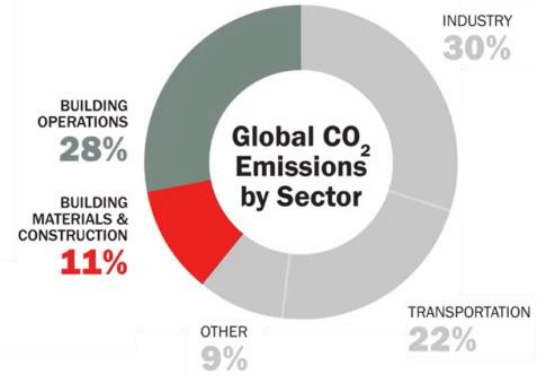

Figure 1. Breakdown of operational and embodied carbon (Architecture 2030, 2023).

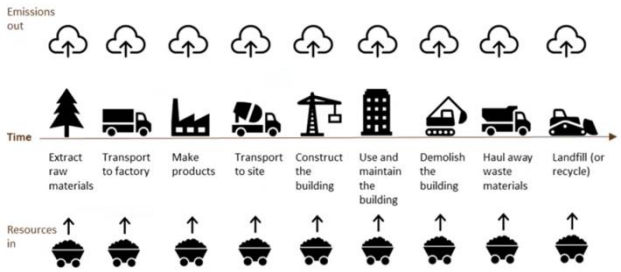

Figure 2. Life cycle phases of a building (Athena Institute, 2019).

2.2 Importance of embodied carbon

The embodied carbon emissions have largely been overlooked historically but contribute around 11% of all global carbon emissions (Figure 1). Carbon emissions released before the building or infrastructure begins to be used, sometimes called *upfront carbon*, will be responsible for half of the entire carbon footprint of new construction between now and 2050 (WGBC, 2019). Taking into account the embodied carbon, the construction industry is the biggest offender when it comes to global emissions.

While the construction industry has made great strides on the *operational front* in recent years (decarbonisation of electricity and gas grids, more efficient heating/cooling systems, etc.), the *embodied carbon front* will be responsible for the majority of the carbon emissions associated with global new building and infrastructure (Architecture 2030, 2023).

2.3 The response of the construction industry

Parallel to the reduction of operational carbon, the construction industry has acknowledged that efforts must now rapidly increase to tackle embodied carbon emissions at a global scale, too. In this context, different global initiatives such as *Advancing Net Zero* (World Green Building Council), *Envision* (Institute for Sustainable Infrastructure, USA), *Level(s)* (European Commission), etc. originated within the construction sector to decarbonize the construction industry by 2050.

Because the embodied emissions of a building or infrastructure project are locked-in once the project is constructed and cannot be taken back or reduced, the focus of the construction industry is being set on minimizing the upfront carbon to the greatest extent possible and to reduce, or as a last resort, offset all remaining embodied carbon in order to achieve net zero across the life cycle of any building or infrastructure asset (WGBC, 2019). Although Emissions can be reduced at any point of a project development stage; the opportunities to limit and/or reduce upfront embodied carbon are greater at the earliest stages (HM Treasury, 2013). As a project progresses, it becomes more challenging to make design changes to obtain the same outcome (Figure 3).

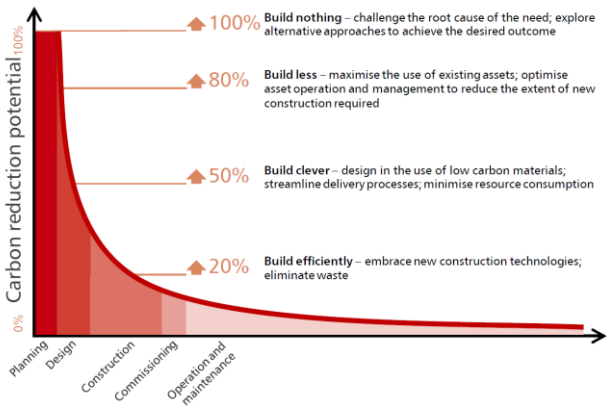

Figure 3. Carbon reduction curve (HM Treasury, 2013).

While it is not always possible to follow the "*build nothing*" approach, interventions to existing building and infrastructure assets to re-use them ("*build less*" approach) can result in considerable

reductions. The "*build clever*" and "*build efficiently*" approaches, mainly related to the selection of lower carbon materials and the adoption of new techniques that eliminate waste (such as off-site manufacturing), are applicable to new buildings and infrastructure and result in important reductions (HM Treasury, 2013).

3 EMBODIED CARBON IN DEEP FOUNDATIONS

Deep foundations are integral to the built environment and the broader civil engineering and construction industry. The positive impacts of reducing carbon emissions are commendable reasons to change the way the deep foundation industry operates (Martin, 2022). The first step to reduce the embodied carbon in deep foundations is to quantify the carbon footprint of the designed and built solutions. Based on the quantification, it is possible to compare and contrast different technical approaches within a project, identifying the sources that drive the upfront carbon emissions (i.e. materials) and to implement optimizing measures to effectively reduce them and/or mitigate their impact. A very helpful tool is the *Carbon Calculator*, developed by the European Federation of Foundation Contractors (EFFC, UK) and the Deep Foundations Institute (DFI, USA), using verifiable and standardised data to estimate the upfront carbon of special geotechnical works.

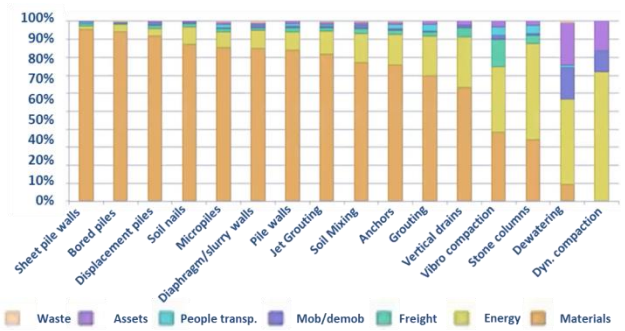

Figure 4. Contribution of different emission categories to the total carbon footprint of special geotechnical works (Martin, 2022).

The assessment of different case studies (Figure 4) shows that for most techniques in the deep foundation industry, the largest impact on the total carbon footprint of the implemented solutions came from materials (Martin, 2022), such as cement and steel, both materials with a high global warming potential (Figure 5).

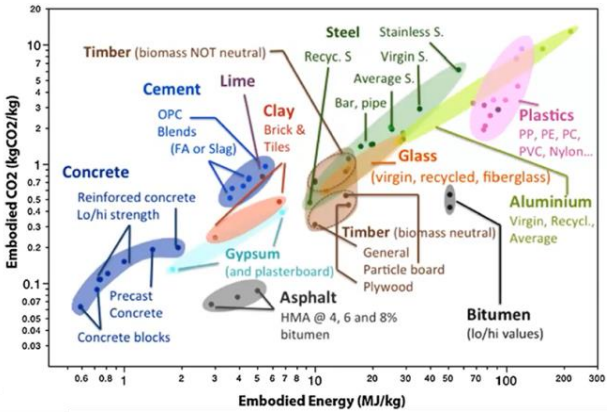

Figure 5. Embodied Carbon and embodied energy for different construction materials (Barcelo et al, 2014).

4 DUCTILE IRON PILES

Ductile iron piles (DIPs) are low vibration, driven, full-displacement piles, installed using a medium-sized excavator and a hydraulic breaker hammer with a modified shank that seats into the pile socket (bell) for driving, using the hammer's percussive energy (Figure 6). DIPs are used to transfer loads from the superstructure into the lower soil layers and/or to limit deformations, developing skin friction and end-bearing capacity (Lopez and Steinlechner, 2023).



Figure 6. Execution of ductile iron piles (DIPs).

4.1 Embodied carbon of DIPs

The pile elements are produced using 100% of recycled materials (steel scrap), which are smelted in a furnace with the help of coke as a reaction and reduction agent (Bau EPD GmbH, 2022). Due to the use of 100% recycled materials in the production and the potential implementation of additional measures to reduce the carbon intensity of the manufacturing process (i.e. re-use of waste heat, exhaust air and water treatment, use of renewable energy, etc.) result in further reductions of the system´s total carbon footprint, enabling DIPs to fall under the category of low carbon materials.

4.2 A comparative analysis

In 2017, two technical proposals for the deep foundations of a new production and logistics warehouse in Germany (Figure 7) were compared.

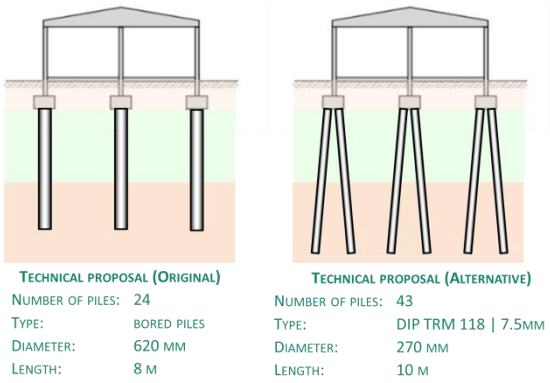

Figure 7. Technical proposals for the comparative analysis (modified after Gschösser, 2018).

The results of a life cycle analysis for both alternatives (bored piles and grouted DIPs) are summarized in Table 1. Compared to the bored pile solution, the execution of DIPs presented a reduction of about 29% in the embodied carbon emissions. In addition, the DIP proposal saved approx. 25% of construction costs and 60% of execution time.

Table 1. Embodied carbon analysis (Gschösser, 2018).

Cast-in-place bored piles			
Phase	**Description**		**Ton CO_2e**
A1-A3	Material production	Concrete	15.97
		Rebars	3.20
A4	Transport to project site [1)]	Concrete	0.69
		Rebars	0.04
A5	Construction	Total	4.45
Total			**24.35**
Ductile iron piles (DIPs)			
Phase	**Description**		**Ton CO_2e**
A1-A3	Material production	Concrete	6.20
		DIP	9.59
A4	Transport to project site [2)]	Concrete [2)]	0.27
		DIP	0.29
A5	Construction	Total	0.93
Total			**17.28**

[1)] Transport Concrete: 30 km / transport rebars: 100km
[2)] Transport concrete: 30 km / transport DIPs: 300km

5 SUMMARY AND FINAL REMARKS

Buildings and infrastructure are currently responsible for 39% of global carbon emissions, thus, decarbonising the construction sector is one of the most cost effective ways to mitigate the worst effects of climate breakdown, however, the pace and scope of decarbonisation efforts must be radically increased, collaborating across the whole construction value chain to develop and deploy more low embodied carbon alternatives, required to achieve the scale of change needed (WGBC, 2019). Deep foundations are an integral part of the built environment; therefore sustainability should also be a key consideration in the industry. Ductile iron piles fall into the category of low carbon materials, due to the use of 100% recycled materials and the implementation of potential improvements in their manufacturing process. DIP solutions comply with the core philosophy of embodied carbon reductions (Figure 4), allowing to build clever and efficiently, contributing to a more sustainable deep foundations industry.

REFERENCES

AIB and Irish Green Building Council (2022), Sustainability and commercial real estate, available at: www.igbc.ie/resources/sustainability-and-commercial-real-estate/, accessed: 20/10/2023.

Architecture 2030 (2023), available at: www.architecture2030.org/, accessed: 19/10/23.

Athena Institute (2019), About whole-building LCA and embodied carbon, available at: www.athenasmi.org/resources/about-lca/technical details/, accessed: 30/09/2023.

Barcelo, L., Kline, J., Walenta, G., and Gartner, E. (2014), Cement and carbon emissions, *Materials and Structures*, 47(6), pp. 1055–1065, available at: https://doi.org/10.1617/s11527-013-0114-5.

Bau EPD GmbH (2022), Environmental Product Declaration TRM Piling Systems, Vienna, Austria, Rep. Bau EPD-TRM-2022-1-ECOINVENT-Pfahlsysteme, available at: www.bau-epd.at/en/epd/data/trm-pyling-systems-2022-ecoinvent, accessed: 23/10/2023.

Climate Watch (2023), available at: www.climatewatchdata.org/, accessed 10/05/2023.

Gschösser, F. (2018), LCA study. Comparison of deep foundations systems consisting of bored piles and ductile cast-iron piles.

HM Treasury (2013), Infrastructure carbon review, London, UK, Rep. PU1593, available at: www.gov.uk/government/publications/infrastructure-carbon-review, accessed: 13/09/2023.

Lopez, F. and Steinlechner, E. (2023). A new approach for the calculation of the external load-bearing capacity of ductile iron piles. In: *Proceedings of the 18th Portuguese Congress of Geotechnical Engineering*, Évora, Portugal.

Martin, K., (2022), The EFFC/DFI Carbon Calculator: Why and how to use it, Deep Foundations, Nov/Dec 2022, 47(6), pp. 87–90

World Green Building Council (2019), Bringing embodied carbon upfront, available at: www.worldgbc.org/reports/, accessed: 12/09/2023.

Proceedings of the XVIII ECSMGE 2024
GEOTECHNICAL ENGINEERING CHALLENGES
TO MEET CURRENT AND EMERGING NEEDS OF SOCIETY
© 2024 the Authors
ISBN 978-1-032-54816-6
DOI 10.1201/9781003431749-611
Open Access: www.taylorfrancis.com, CC BY-NC-ND 4.0 license

ECSMGE 24
XVIII EUROPEAN CONFERENCE ON SOIL MECHANICS AND GEOTECHNICAL ENGINEERING

3D Thermo-mechanical analysis of a real-world thermally activated piled foundation

Analyse thermo-mécanique 3D d'une fondation en pieux activés thermiquement d'un cas d'étude réel

A. Lupattelli, D. Salciarini*
Department of Civil and Environmental Engineering, University of Perugia, Perugia, Italy
**diana.salciarini@unipg.it*

ABSTRACT: The work presents the results of a Three-Dimensional (3D) thermo-mechanical analysis, carried out through the COMSOL Multiphysics finite-element code, to investigate the effects of the heating/cooling cycles on the response of a real case of bored and cast-in-place piled foundation, where all the piles have been equipped with pipes to operate as heat exchangers with the ground. Referring to the available data on the building design and to the results of thermal property tests performed on soil samples, a 3D model of the soil-foundation system has been reconstructed. To obtain realistic operational conditions, a uniform mechanical pressure acting on the slab top surface has been imposed, while a transient heat conduction simulation has been conducted by adopting a simplified temperature harmonic function, representing the average air temperature in the Italian area, both on piles and at the ground surface. By dividing the foundation piles into subgroups, two configurations of pile thermal activation have been analyzed to optimize the system performance. The comparison between layouts reveals very similar trends, with pile's stresses and displacements predominantly influenced by the mechanical load. Energetically, the heat flux per unit of pile surface remains almost unchanged in the two considered cases, despite one layout experiencing alternate years of inactivation, with the soil temperature restores to the initial conditions.

RÉSUMÉ: Le travail présente les résultats d'une analyse thermo-mécanique tridimensionnelle (3D) réalisée à travers le code aux éléments finis COMSOL Multiphysics afin d'étudier les effets des cycles de chauffage/refroidissement sur la réponse d'un cas concret de fondation en pieux forés et coulés en place, où tous les pieux ont été équipés de tuyaux pour fonctionner comme échangeurs de chaleur avec le sol. En se référant aux données disponibles sur la conception du bâtiment et aux résultats des tests de propriétés thermiques effectués sur des échantillons de sol, un modèle 3D du système sol-fondation a été reconstruit. Pour obtenir des conditions opérationnelles réalistes, une pression mécanique uniforme agissant sur la surface supérieure de la dalle a été imposée, tandis qu'une simulation de conduction de chaleur transitoire a été réalisée en imposant une fonction harmonique de température simplifiée, représentant la température moyenne de l'air en saison chaude dans la région italienne, tant sur les pieux qu'à la surface du sol. En subdivisant les pieux de fondation en sous-groupes, deux configurations d'activation thermique des pieux ont été analysées pour optimiser les performances du système. La comparaison entre les configurations révèle une tendance cohérente, avec des valeurs principalement influencées par la charge mécanique. Énergétiquement, le flux de chaleur par unité de surface de pieu reste relativement stable, malgré une configuration connaissant des années alternées d'inactivation, lorsque la température du sol revient aux conditions initiales inchangées.

Keywords: Thermo-active piles; energy geostructures; numerical modeling; thermo-mechanical analysis; pile groups.

1 INTRODUCTION

Nowadays the growth in the consumption of fossil fuels in the building sector has become increasingly impacting. Therefore, numerous efforts are being made to find alternative technologies that allow the use of renewable energy. The heat contained in the most superficial layers of the Earth's crust, called low-enthalpy geothermal energy, can be effectively exploited as renewable and available energy in various applications: among these, Energy Piles (EPs) associate the traditional mechanical function to the energetical one by exchanging heat with the ground (Brandl, 2006; Ravera et al., 2024), allowing for satisfying a large part of the energy needs of a building, and providing for heating and cooling according to seasonal needs (Rotta Loria et al., 2020; Gerola et al., 2023). Extensive research, experimental sites, and real project monitoring demonstrated the feasibility of EPs (Bourne-Webb et al., 2022; Cecinato and Salciarini, 2022; Lupattelli et al., 2023a, 2023b, 2024), leading to the adaptation of this solution for a large number of buildings. Nevertheless, this technology's potential remains underestimated,

hindering its wider adoption: key barriers include the limited availability of specific technical information and lack of long-term performance assessments. It is essential to demonstrate the EPs' suitability in terms of thermal efficiency and geo-mechanical impact: pilot case studies could draw lessons from existing small-scale or community-scale projects, applying these insights to improve future projects on a larger scale.

Based on this perspective, a real case study of an energy-piled foundation located in Umbria (central Italy) has been modeled and analyzed to examine the soil-foundation Thermo-Mechanical (TM) response under the hypothesis of different activation layouts.

2 DESCRIPTION OF THE CASE STUDY

The case study of a private building located in Umbria (central Italy) is presented, whose project has been provided by the Owner (Figure 1).

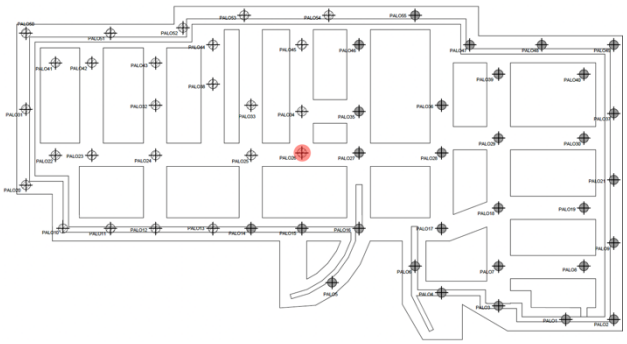

Figure 1. Plan of the building foundation: piles of 8.5 m length in light grey; piles of 10 m length in dark grey; reference pile highlighted in red.

The building, a two-story house, is founded on n. 55 bored and cast-in-place concrete piles, characterized by length varying from 8.50 m (n. 25 piles) to 10 m (n. 30 piles), and a diameter of 0.50 m. Besides the structural function, to supply the heating and cooling needs of the building for about 290 m^2 living area, all the piles have been equipped with pipes for the circulation of a heat-carrying fluid.

2.1 Soil properties

The foundation soil consists of a homogeneous layer of clayey silt with medium consistency. Given the presence of a water table close to the ground surface, the soil is assumed to be fully saturated. To study the thermal characteristics of the soil involved in the heat exchange process during the EGs operation, Thermal Property (TP) tests have been conducted on soil samples by means of two experimental facilities: a Hot Disk TPS 2500S apparatus, and an ATT DM 340 SR climatic chamber. Thermal conductivity λ_s, and volumetric specific heat $C_{p,s}$ (with nominal error of 3%, and 7%, respectively) of the samples have been measured according to the ISO 22007-2 standard. The soil thermal expansion coefficient β_s, and the thermal diffusivity α_s have been derived from the literature for typical fine-grained soils.

3 THERMO-MECHANICAL ANALYSIS

3.1 Geometry and discretization

Using the *"COMSOL Multiphysics"* Finite Element (FE) numerical code, the geometry of the entire foundation has been modeled in the central part of a homogeneous soil volume, and it has been discretized with 502588 tetrahedral elements (Figure 2), using mesh refinement for the foundation.

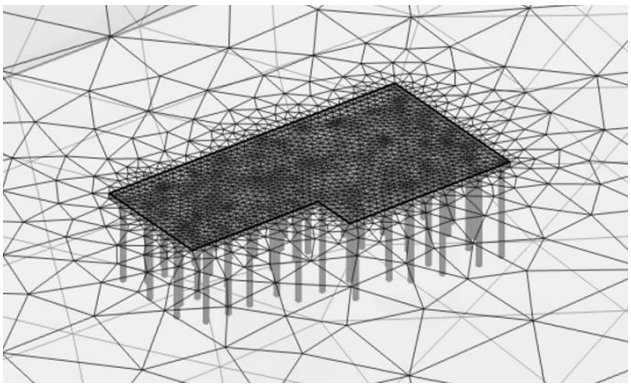

Figure 2. 3D View of domain spatial discretization.

The bottom and later boundaries of the domain have been placed at a depth of 50 m from the ground surface and at 100 m from the slab lateral edges, respectively. Piles have been modeled as a linear elastic material, while the soil has been modeled as a linear elastic-perfectly plastic material. To simulate fully saturated conditions in the fine-grained soil, the material has been characterized by thermo-physical properties accounting for the fluid and solid phases.

3.2 Initial and boundary conditions

The pile-soil interface has been considered as perfectly rough (full adhesion), and no soil-pile interface elements have been introduced. Fixed displacements have been assumed at the base of the soil volume, and horizontal displacements have been constrained for the symmetry vertical planes. A uniform pressure of 25 kPa has been applied to the slab (according to the actual project), to simulate the weight of the elevated structure. Thermal insulation has been adopted on the symmetry vertical planes, as well as at the bottom of the soil volume, and at the slab top surface.

To simulate the seasonal operation of the EPs, a simplified balanced seasonal variation of the carrier fluid temperature has been considered, since the real thermal needs of the building have not been made available. The temperature of each pile has been increased and decreased by applying a harmonic function (15±10°C), according to two different scenarios of activation (Figure 3): *i)* the entire foundation is thermally activated, and *ii)* the foundation is divided into two pile subgroups A (25 piles), and B (30 piles).

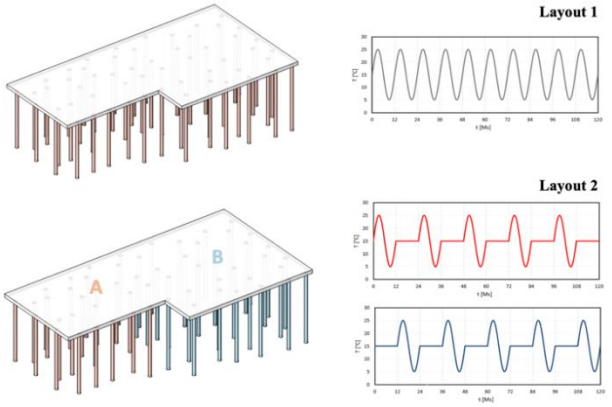

Figure 3. Pile subgroup activation according to two different scenarios (layouts 1 and 2).

3.3 Numerical simulation program

A 3D, FE model of the soil-foundation system has been prepared to conduct long-term analyses. Two simulations have been carried out to assess the influence of the adopted EP activation layout (Figure 3):

- layout 1 (reference case): all foundation piles are heated and cooled for 10 consecutive years (6 months of heating and 6 months of cooling);
- layout 2: the two subgroups are alternate-year activated, *i.e.*, pile subgroup A is activated in years 1, 3, 5, 7, and 9 (6 months of heating and 6 months of cooling), while pile subgroup B is activated in years 2, 4, 6, 8, and 10 (6 months of heating and 6 months of cooling).

4 RESULTS AND DISCUSSION

The mechanical response of a central pile of the foundation slab has been analyzed in terms of vertical stress and displacements along the pile axis, and at depths of z_1=2.5 m, z_2=5 m, and z_3=7.5 m. Also, the energy performance has been analyzed in terms of the time evolution of the conductive heat flux across the pile lateral surface. The following sign convention is used here: compressive stress, upward displacements, and heating flux are considered positive.

4.1 Effect of activation of layout 1

The TM effects induced in the soil-pile system by the operation of the energy foundation according to layout 1 are presented in the following for the selected pile (Figure 4a,b).

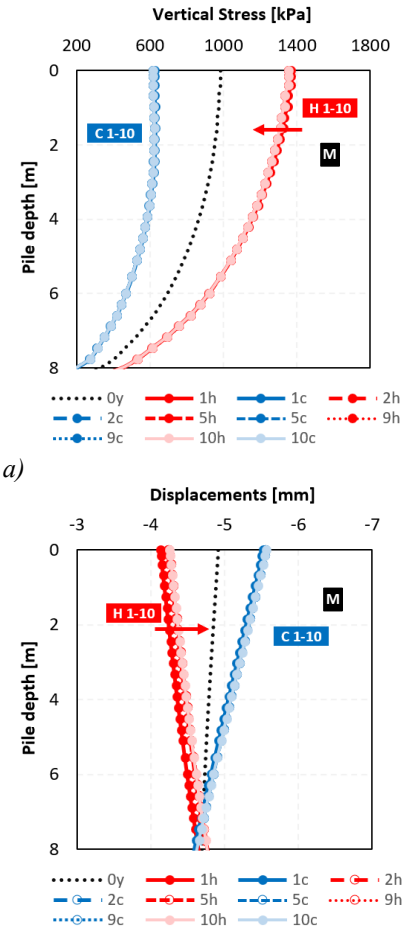

Figure 4. a) Vertical stresses, and b) displacements distribution along the reference pile axis during thermal cycles.

The initial application of the mechanical load results in a pile compression of about 1000 kPa and induces a downward displacement of 5 mm (represented by the black dashed curves, labeled with M). At the end of the first heating and cooling cycles, the temperature in the near soil reaches 20°C and 10°C, respectively, and then stabilizes due to the progressive cycles. Heating, along with the rigid constraint offered by the foundation slab and the mechanical load applied, determines a significant increase in global vertical compression (+400 kPa) within the pile (black dashed curves, labeled with M). During the first cooling phase, the process is reversed, and the pile experiences a reduction in the vertical stress, while remaining under compression (–400 kPa). Heating is responsible for a partial uplift of the

pile due to the expansion (of about +1 mm), while the opposite occurs during cooling, as pile displacements start increasing downward (of about –0.5 mm).

4.2 Effect of activation of layout 2

This second set of numerical simulations aimed at assessing the influence of the thermal activation of layout 2 (Figures 5 and 6). The results are shown for a reference pile, belonging to subgroup B.

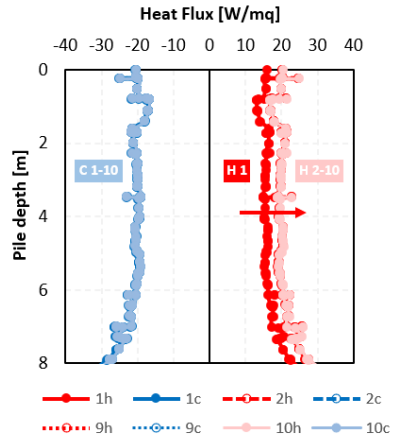

a)

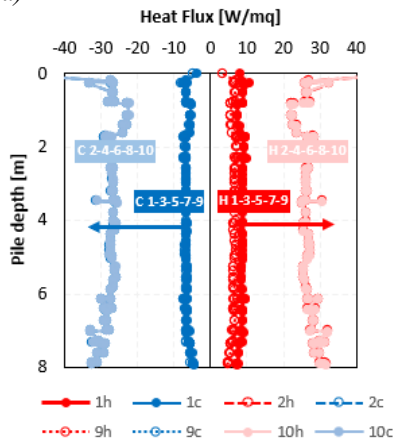

b)

Figure 5. Heat flux along the pile lateral surface during thermal cycles for a) layout 1, and b) layout 2.

From a first comparison, and from an energy point of view, there are no substantial changes between the two scenarios. Heat flux per unit pile surface taken at soil-pile interface, during years 2-4-6-8-10 (when the pile is active for both layouts), shows increased values for heating (+25 W/m^2) and cooling phases (–25 W/m^2) in layout 2 with respect to layout 1 (+22 W/m^2 and –22 W/m^2, respectively). This difference is very limited likely due to the same temperature distribution registered within the soil. The slight increase of the heat flux can be attributed to the temperature recovery to unchanged initial conditions during the years of pile inactivity in layout 2, which brings thermal exchange benefits in the following year of thermal activation.

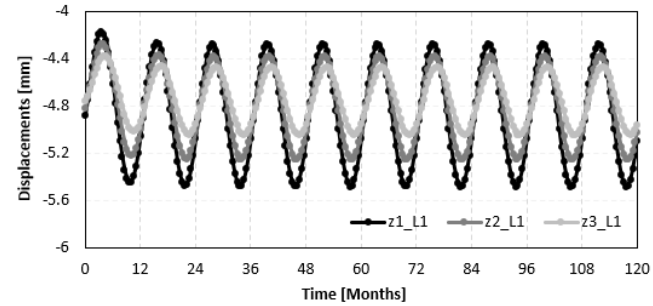

a)

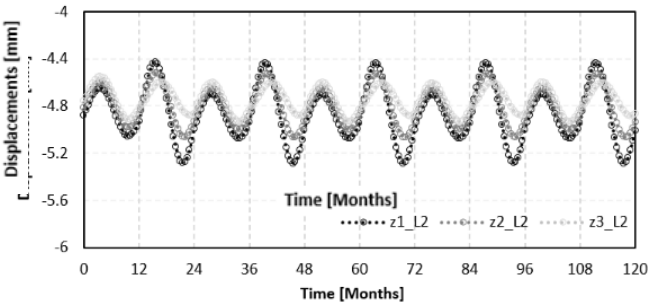

b)

Figure 6. Time evolution of vertical displacements at selected pile depths z_1, z_2, and z_3 for a) layout 1, and b) layout 2.

From a mechanical perspective (Figure 6), layout 1 exhibits higher displacements during the first thermal cycle. At the beginning of the analysis the soil volume has a uniform initial temperature T_0, and because of variations in temperature distribution between the cycles, the thermal field undergoes significant modifications, leading to a change in the initial conditions for the subsequent heating and cooling cycles. The better mechanical performance can be attributed to the case of alternate activation (layout 2). Indeed here the thermal induced displacements are slightly lower compared to layout 1, with about ± 0.6 mm of displacements compared to ± 0.4 mm of layout 1 (Figure 6).

5 FINAL REMARKS

A 3D model of an energy-piled foundation case study has been shown, and the TM response of a reference pile has been analyzed in two activation scenarios.

The recorded values of vertical stress and displacements were observed to be primarily influenced by the applied mechanical load, with the thermal load contributing to a comparatively minor values fluctuation. From the comparison, the heat flux per unit of pile surface does not change significantly, although the pile and soil in layout 2 are subjected to alternate years of temperature recovery due to the

inactivation. Considering the pile lateral surface, which varies according to its length, the global heating and cooling thermal power, extracted for each cycle, will be certainly greater preferring layout 1. Conversely, the mechanical performance of layout 2 is slightly better in terms of vertical displacements during cycles. However, stresses and displacements registered in layout 1 fit perfectly into the capacity of the single pile.

Improved predictions might be obtained by knowing the actual energy needs of the building, which is currently not available.

ACKNOWLEDGEMENTS

The Authors would thank CIRIAF of Perugia, for support in carrying out laboratory thermal tests. Part of the work presented was carried out within the scope of COST Action CA21156 "FOLIAGE", PRIN 2022 Project "GEOREFIT" (CUP: E53D23002670006), and CETP 2022 "LEG-DHC" (CUP: B97G22000940003).

REFERENCES

Brandl, H. (2006) Energy foundations and other thermo-active ground structures, *Géotechnique*, 56(2), pp. 81–122. https://doi.org/10.1680/geot.2006.56.2.81

Bourne-Webb, P.J., Lupattelli, A., Bodas Freitas, T.M., Salciarini, D. (2022) The influence of initial shaft resistance mobilisation in the response of seasonally, thermally-activated pile foundations in granular media, *Geomechanics for Energy and the Environment*, 32, n. 100299. https://doi.org/10.1016/j.gete.2021.100299

Cecinato, F., Salciarini, D. (2022) Energy performance assessment of thermo-active micro-piles via numerical modeling and statistical analysis, *Geomechanics for Energy and the Environment*, 29, n. 100268. https://doi.org/10.1016/j.gete.2021.100268

Gerola, M., Lupattelli, A., Cecinato, F., Salciarini, D., Arola, T. (2023). Numerical Analysis of the Behaviour of Energy Micropiles Used for Heat Storage: A Case Study in Turku (Finland), *Springer Series in Geomechanics*, Proc. of: *National Conference of the Researchers of Geotechnical Engineering "CNRIG 2023: Geotechnical Engineering in the Digital and Technological Innovation Era"* pp. 808–815. https://doi.org/10.1007/978-3-031-34761-0_97

Lupattelli, A., Bourne-Webb, P.J., Bodas Freitas, T.M., Salciarini, D. (2023a) A numerical study of the behaviour of micropile foundations under cyclic thermal loading, *Applied Sciences,* 13, n. 9791. https://doi.org/10.3390/app13179791

Lupattelli, A., Cernuto, E., Brunelli, B., Cattoni, E., Salciarini, D. (2023b) Experimentation of the Thermo-Mechanical Behavior of the Soil-Concrete Interface, In: *Geotechnical Engineering in the Digital and Technological Innovation Era: Springer Series in Geomechanics and Geoengineering*, 1st ed., Springer, Cham, pp. 343–350. Springer, Cham. https://doi.org/10.1007/978-3-031-34761-042

Lupattelli, A., Salciarini, D., Cecinato, F., Bodas Freitas, T.M., Bourne-Webb, P.J. (2024) Temperature dependence of soil-structure interface behaviour in the context of thermally-activated piles: A review, *Geomechanics for Energy and the Environment*, 37, n. 100521. https://doi.org/10.1016/j.gete.2023.100521

Ravera, E., Rotta Loria, A.F., Laloui, L. (2024) Performance of complex energy geostructures, *Geomechanics for Energy and the Environment*, 38, n. 100536. https://doi.org/10.1016/j.gete.2024.100536

Rotta Loria, A.F., Bocco, M., Garbellini, C., Muttoni, A., Laloui, L. (2020) The role of thermal loads in the performance-based design of energy piles, *Geomechanics for Energy and the Environment*, 21, n. 100153. https://doi.org/10.1016/j.gete.2019.100153

Proceedings of the XVIII ECSMGE 2024
GEOTECHNICAL ENGINEERING CHALLENGES
TO MEET CURRENT AND EMERGING NEEDS OF SOCIETY
© 2024 the Authors
ISBN 978-1-032-54816-6
DOI 10.1201/9781003431749-612
Open Access: www.taylorfrancis.com, CC BY-NC-ND 4.0 license

ECSMGE 24
XVIII EUROPEAN CONFERENCE ON SOIL MECHANICS AND GEOTECHNICAL ENGINEERING

Soil stabilization with plastic waste and sisal fibres

Stabilisation des sols avec des déchets plastiques et des fibres de sisal

R. Luzia*, D. Gardete, D. Monteiro, M. Sousa
Instituto Politécnico de Castelo Branco, Castelo Branco, Portugal
**rluzia@ipcb.pt*

ABSTRACT: In Portugal, road pavements as well as their foundation are mostly built with natural aggregates, usually crushed, with high economic and environmental impacts. However, the attempt to use excavation materials has become more frequent, whenever they meet the requirements for that use, either in the foundation or in the granular layers of road pavements. Nevertheless, it often happens that the materials found on the construction site do not meet the requirements to be reused, in many situations because they are fine clayey materials. One way to make it possible to reuse those materials is to improve their properties to fulfil the requirements of use. In this work, two clayey sand soils were characterized, in its natural state and after mixing it with plastic waste and sisal fibres, respectively. Mixtures with 1%, 2% and 3% of plastic waste and with 0.5%, 1.0% and 1.5% of sisal fibres with 15 mm length were characterized. Laboratory tests were performed to assess their ability to improve soil properties for embankment construction and pavement layers. The bearing capacity ratio was determined using California Bearing Ratio (CBR) test. An increase in the bearing capacity ratio was achieved with plastic waste stabilization. Reduction in the bearing capacity ratio was observed in the specimens stabilized with sisal fibres. Increase in the bearing capacity ratio was more effective for high penetration values. The dry unit weigh decreased with the increase in plastic waste / sisal fibre content.

RÉSUMÉ: Au Portugal, les revêtements routiers ainsi que leurs fondations sont pour la plupart construits avec des granulats naturels, généralement concassés, avec des impacts économiques et environnementaux élevés. En revanche, la tentative d'utiliser des matériaux d'excavation est devenue plus fréquente, chaque fois qu'ils répondent aux exigences de cet usage, soit dans les fondations, soit dans les couches granulaires des revêtements routiers. Cependant, il arrive souvent que les matériaux trouvés sur la ligne ne répondent pas aux exigences pour être réutilisés dans les travaux. Une façon de rendre possible la réutilisation de ces matériaux est d'améliorer leurs propriétés pour répondre aux exigences d'utilisation. Dans ce travail, deux sols argilo-sableux ont été caractérisés, respectivement à l'état naturel et après mélange avec des déchets plastiques et des fibres de sisal. Des mélanges contenant 1%, 2% et 3% de déchets plastiques et 0,5%, 1,0% et 1,5% de fibres de sisal d'une longueur de 15 mm ont été caractérisés. Des tests en laboratoire ont été effectués pour évaluer leur capacité à améliorer les propriétés du sol pour la construction de remblais et les couches de chaussée. La capacité portante a été déterminée à l'aide du test CBR. Une augmentation de la capacité portante a été obtenue grâce à la stabilisation des déchets plastiques. Une réduction de la capacité portante a été observée sur les échantillons stabilisés avec des fibres de sisal. Le poids unitaire sec a diminué avec l'augmentation de la teneur en déchets plastiques/fibres de sisal.

Keywords: Soil stabilization; CBR test; plastic waste; sisal fibres; road embankments.

1 INTRODUCTION

There is a need to significantly reduce waste production and increase recycling rates. Many wastes and industrial by-products can benefit from more reuse and recycling solutions reducing the life cycle impacts. However, since natural fibres are readily available and less expensive, soil can also be stabilized with them.

Soil stabilization using waste materials or natural fibres as an additive can have technical and environmental advantages. Some researchers have studied the use of waste materials, mainly produced from plastic wastes (Paramkusam et al. 2013) and natural fibres (Fonseca da Silva, et al., 2019) in soil stabilization.

The plastic wastes can be used for stabilization as plastic strips, plastic flakes, or fibres. Plastic wastes included, as example, plastic strips of HDPE or PET from bottles (Rawat and Kumar 2016; Babu and Chouksey 2011), shredded labels of PE and PP from packages (Gardete et al. 2017), flakes from grounded PET bottles (Gardete and Luzia 2017).

Natural fibres can have different origins, such as sisal, coconut, jute, rice straw, bamboo, linen, and cut into different lengths, from 5 mm (Wu, et al., 2014) to 75 mm (Fonseca da Silva, et al., 2019) and used in different percentages, from 0.25% (Manjunath et al., 2013) to 2.0% (Mohammed, et al., 2022).

From the stabilization with several types of waste materials, it was observed that the percentages of

waste addition achieving best results are generally lower than 2% (Choudhary et al. 2010; Rawat and Kumar 2016; Paramkusam et al. 2013). From stabilization with natural fibers it was observed that the percentages of fiber addition that achieve better results are, generally, less than 1% (Nguyen and Indraratna, 2023). Nevertheless, some authors refer percentages up to 1.5% (Mohammed et al., 2022). With regard to fiber length, the optimal value varies between 10 mm (Maity et al., 2018) and 15 mm (Mohammed et al., 2022).

Stabilization with plastic waste materials and with natural fibres increased the resistance and the shear strength parameters of the soil measured in CBR tests, unconfined compression tests and simple shear tests (Hejazi et al. 2012, Nguyen and Indraratna, 2023).

2 MATERIALS

2.1 Soils

Two clayey sand soils (A and B) were used. Visually, the soils are reddish-brown with a significant quantity of fines and evident plastic behaviour. Plastic waste was mixed with the clayey sand soil A, with nearly 50% passing the No. 200 sieve. Sisal fibres were mixed with the clayey sand soil B, with nearly 37% passing the No.200 sieve.

At this point it should be said that for each of the tests referred to in the following sections, two specimens were tested. The results presented correspond to the average of the results for each of the specimens.

The gradation for both soils is presented in Figure 1 (LNEC, 1966a).

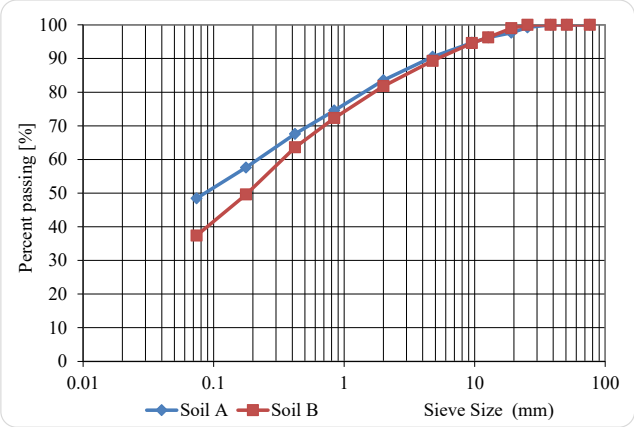

Figure 1. Gradation curves.

The following properties of the soils were characterized, liquid limit, plastic limit, sand equivalent, organic matter content and methylene blue value. The results are presented in Table 1.

Table 1. Soil properties.

Property	Standard	Soil A	Soil B
Liquid Limit [%]	NP 143 (IGPAI, 1969)	31.6	27.2
Plastic Limit [%]		20.6	20.7
Sand Equiva-lent [%]	LNEC E 199 (LNEC, 1967a)	14.4	44.6
Organic Matter Content [%]	NLT-117 (IRANOR, 1977)	2.48	3.00
Methylene Blue Value [g/100g]	NF P18-592 (AFNOR,1990)	0.8	0.5

Table 2 presents the classification of the two soils according to USCS (ASTM, 2006). and AASHTO (LNEC, 1970) classifications.

Table 2. Soil classification.

Classification	Soil A	Soil B
USCS (ASTM, 2006).	SC- Clayey sand	SC-SM – Silty clay sand
AASHTO (LNEC, 1970)	A-6-(3)	A-4(1)

Modified Proctor compaction test was used to determine MDD (Maximum Dry Density) and OMC (Optimum Moisture Content) of the soils. The test procedures followed standard LNEC E 197 (LNEC, 1966b). Soil A presented an OMC of 12.7% and MDD of 19.2 kN/m^3 and Soil B presented an OMC of 11.6% and MDD of 19.6 kN/m^3, Figure 2.

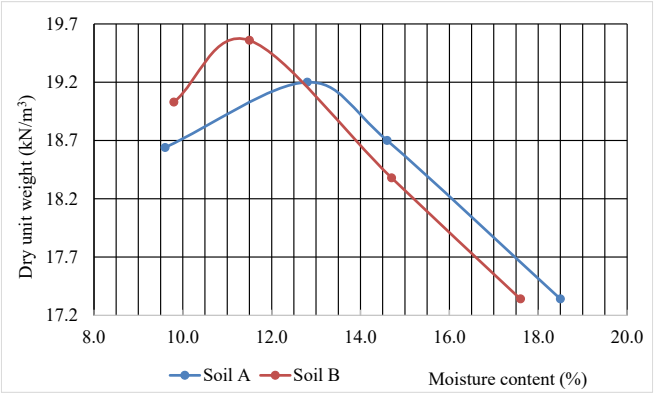

Figure 2. Modified Proctor test results.

2.2 Plastic waste and sisal fibres

2.2.1 Plastic waste

Plastic waste came from the industry and is used as it was provided without any modification. It was selected for having low recycling and reuse value. The plastic waste used was provided by plastic recycling

company Ecoiberia - Reciclados Ibéricos, S.A.. The plastic waste used was made from shredded labels in PE and PP. The flakes are highly flexible, very thin (estimated thickness from 30 to 60 µm), irregular shape and size mostly between 1.0 and 2.0 cm^2, some flakes are creased, Figure 3. The flakes are made from assorted materials and colors, therefore this type of waste has low interest for recycling.

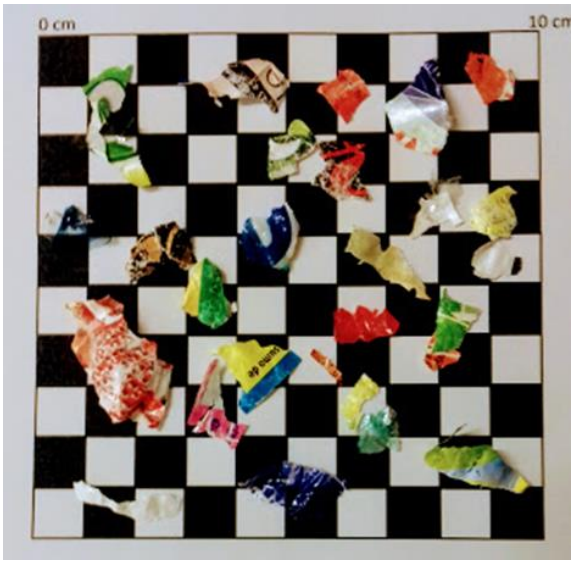

Figure 3. Waste plastic flakes.

2.2.2 Sisal fibres

The sisal fibers used were purchased in a commercial store and are generally used for civil construction work associated with plaster. Sisal fibers generally have an average diameter of 150 µm and a density of 1.35 g/cm^3 (Mohammed et al., 2022) and were cut to 15 mm in length, Figure 4.

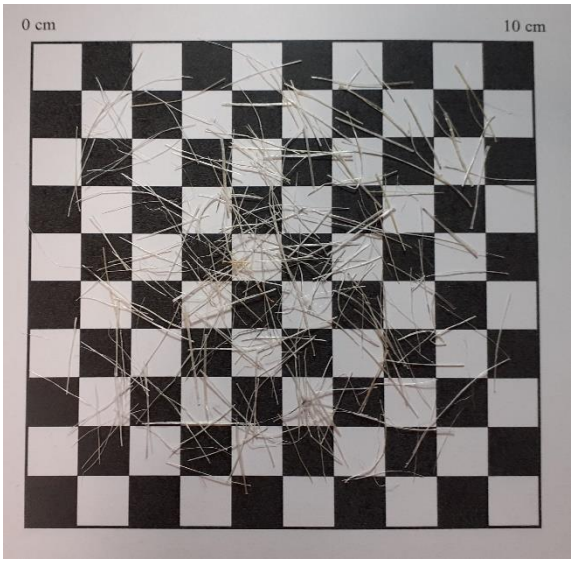

Figure 4. Sisal fibres.

3 SOIL STABILIZATION

3.1 Mixing

The soils were mixed with both plastic waste and sisal fibres by hand. The contents of plastic waste used were 1%, 2% and 3%, weight of waste / dry weight of soil and for sisal fibre were 0.5%, 1.0% and 1.5%, weight of sisal fibre / dry weight of soil. The values for 0% waste / sisal fibre content are referred to the original soils without stabilization. For the stabilization plastic waste / sisal fibres were added to the dry soils. These were mixed until a visually homogeneous mixture was observed. The water content for all specimens compacted corresponded to the OMC of the original soils (soil A for plastic waste and soil B for the sisal fibers). Water was added and mixture proceeded until a good dispersion of the water in the mixture was observed.

A homogeneous mixture was easy to achieve when using the waste plastic flakes. Flakes are easily dispersed in the soil and a visually homogeneous dispersion was observed.

With sisal fibers it was a little more complicated to mix, particularly for the higher percentage of fibre. Even so, a mixture with good homogeneity was achieved.

All specimens were compacted with 55 blows/layer (like the Modified Proctor Test specimens).

Two specimens were tested for each waste plastic / sisal fibre percentage.

3.2 CBR test results

CBR test procedures followed standard LNEC E 198 (LNEC, 1967b). In Figure 5 are presented the relative compaction (dry density of the specimen / MDD) values for CBR specimens. As expected, higher plastic waste/sisal fibre content lead to lower relative compaction.

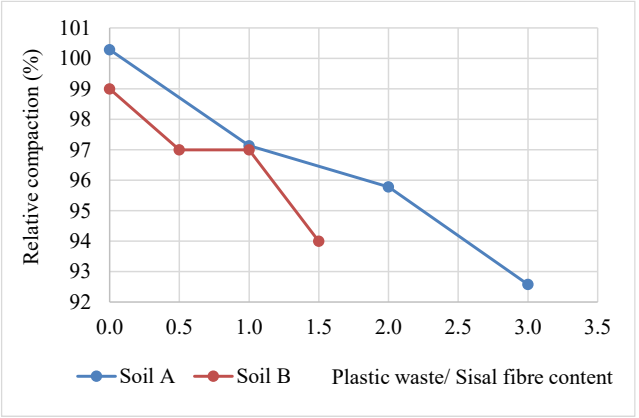

Figure 5. Relative compaction in CBR specimens.

In Figure 6 and Figure 7 the Force-Penetration curves from the CBR test are presented. The effect of the stabilization is more evident for high penetrations. For penetration values higher than 10 mm stabilization with 1% and 2% of plastic flakes provided better result than the original soil. Stabilization with sisal fibres shows that the original soil presented better performance until 6.0 mm of penetration. After 6.0 mm it was observed a change in the trend with a reduction of performance. Whereas mixtures with 1.0% and 1.5% of fibres maintained a practically linear trend up to 12 mm of penetration.

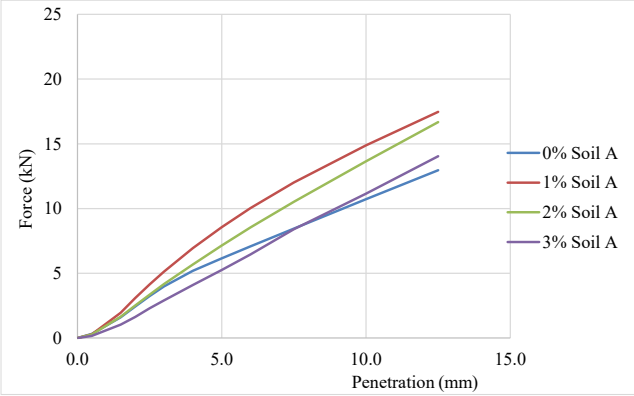

Figure 6. Force-penetration curves for soil A stabilized with waste plastic flakes.

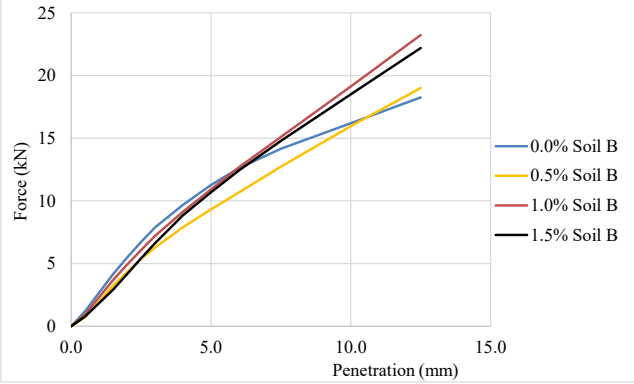

Figure 7. Force-penetration curves for soil B stabilized with sisal fibres.

The CBR values obtained for 2.5 mm and 5.0 mm penetration are presented in Figure 8. For both soils CBR values for 5.0 mm penetration were higher. Stabilization with plastic waste increased CBR values until 1% content but after this value CBR values decreased with increasing plastic waste content. For 1% plastic waste content CBR at 5.0 mm penetration increased from 14% to 19% (36% increase), and CBR at 2.5 mm penetration increased from 11% to 14% (27% increase). No increase in CBR was observed for sisal fibre stabilization. The original soil achieved higher CBR2.5 and CBR5.0 values. The CBR values decrease for 0.5% of sisal fibers, increasing to 1%, to 55%, very close to the natural soil, and decreasing again to 1.5%.

The results obtained in Figure 6 and Figure 7 show that the improvement in soil behavior obtained by stabilization with plastic waste / sisal fiber is more evident for high penetration values (greater than 5 to 6 mm). Therefore, this improvement in behavior is not captured in the CBR values (determined for 2.5 and 5 mm of penetration), Figure 8. As a consequence, it is also observed that the CBR values for 5 mm present a more favorable trend than those for 2.5mm. Despite observing an improvement in soil behavior through the analysis of force-penetration curves, in the CBR values only for stabilization with plastic waste, an increase in CBR values was obtained compared to the original soil, in this case to a percentage of 1%.

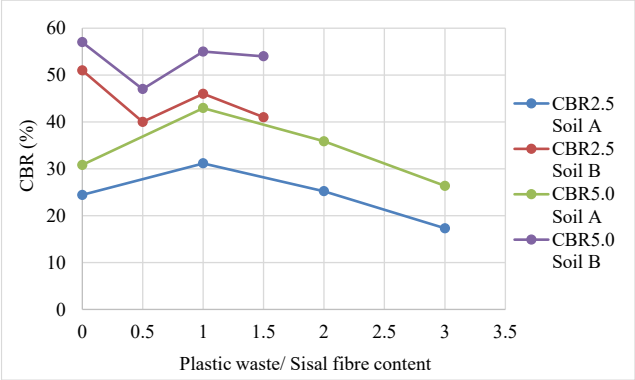

Figure 8. CBR2.5 and CBR 5.0 values.

4 CONCLUSIONS

Waste plastic flakes and sisal fibres were used for the stabilization of two clayey sand soils, Soil A and Soil B. Contents of 1%, 2% and 3% of plastic waste and 0.5%, 1.0% and 1.5% of sisal fibres were used. Results show a decrease in the relative compaction with increasing plastic waste or fibre content. Stabilization with waste plastic flakes increased CBR by more than 20% when compared to the original soil. Optimum waste plastic flakes content was 1%. CBR values decreased for higher contents. CBR values generally decreased with the addition of sisal fibres. However, for 1% of fibers the CBR value, 55%, is close to the CBR of natural soil, 57%. For 1.5% the CBR decreases again. This maybe could be explained by the fact that the mixture with sisal fibers is less homogeneous.

The use of waste materials and natural fibres for soil stabilization can be interesting options. Waste plastic flakes showed better results, the dispersion in the soil was easy and increased CBR values for percentages close to 1%. Sisal fibres were more complicated to mix, with low homogeneity achieved and CBR values generally decreased.

REFERENCES

AFNOR (1990). Granulats. Essai au bleu de méthylène. Méthode à la tache. NF P 18-592, Association Française de Normalisation, France.

ASTM (2006). Standard Practice for Classification of Soils for Engineering Purposes (Unified Soil Classification System), D2487-06, Annual Book of ASTM Standards, Vol. 04.08, American Society for Testing and Materials, USA.

Babu, G., Chouksey, S. (2011). Stress–strain response of plastic waste mixed soil, *Waste Management* **3**, 481-488. doi: 10.1016/j.wasman.2010.09.018.

Choudhary, A.K., Jha, J.N., Gill, K.S. (2010). A Study on CBR Behavior of Waste Plastic Strip Reinforced Soil, *Emirates Journal of Engineering Research* 15 (1), 51-57.

Fonseca da Silva, H. E., Camargos, C. S., Viana de Souza, M., Gongora, I. M. A. (2019). Estudo da viabilidade do uso de fibras naturais como reforço de solos. Geotechnical Engineering in the XXI Century: Lessons learned and future challenges, N. P. López-Acosta et al. (Eds.). doi:10.3233/STAL190200.

Fonseca da Silva, H., Camargos, C., Souza, M., Gongora, I. (2019). Estudo da viabilidade do uso de fibras naturais como reforço de solos. XVI Pan-American Conference on Soil Mechanics and Geotechnical Engineering (XVI PCSMGE). doi:10.3233/STAL190200.

Gardete, D., Luzia, R. (2017). Soil Stabilization with Flexible and Rigid Plastic Waste, *International Scientific-Technical Conference "Prospects of Road Transport and Engineering – Communication Infrastructure"*, 24-25 November, Tashkent, Uzbekistan.

Gardete, D., Sousa, M. (2017). Melhoramento de Solos Utilizando Resíduos Plásticos Provenientes de Etiquetas de Embalagens, *Proc. ICEUBI2017 Internacional Congress in Engineering*, 5-7 December, Covilhã, Portugal. ISBN: 978-989-654-403-4.

Hejazi, S., Sheikhzadeh, M., Abtahi, S., Zadhoush, A. (2012). A simple review of soil reinforcement by using natural and synthetic fibers, *Construction and Building Materials* 30, 100-116, doi:10.1016/j.conbuildmat.2011.11.045.

IGPAI (1969). Determinação dos Limites de Consistência. NP – 143, Inspeção Geral dos Produtos Agrícolas e Industriais, Lisboa.

IRANOR (1977). Determinación con agua oxigenada del contenido de materia orgánica en los suelos. UNE 7-368-77, Instituto Nacional de Racionalización y Normalización, Madrid.

LNEC (1966a). Análise Granulométrica. E 196, Laboratório Nacional de Engenharia Civil, Lisboa.

LNEC (1966b). Ensaio de Compactação. E 197, Laboratório Nacional de Engenharia Civil, Lisboa

LNEC (1967a). Ensaio de Equivalente de Areia. E 199, Laboratório Nacional de Engenharia Civil, Lisboa.

LNEC (1967b). Determinação do CBR. E 198, Laboratório Nacional de Engenharia Civil, Lisboa.

LNEC (1970). Classificação para fins Rodoviários. E240, Laboratório Nacional de Engenharia Civil, Lisboa.

Maity, J., Chattopadhyay, B., Mukherjee, S. (2018). Improvement of Characteristics of Clayey Soil Mixed with Randomly Distributed Natural Fibers, Journal of The Institution of Engineers (India): Series A, 99 (1), 55–65, doi:10.1007/s40030-017-0244-9.

Manjunath K. R, Venugopal G, Rudresh A. N. (2013). Effect Of Random Inclusion Of Sisal Fibre On Strength Behavior Of Black Cotton Soil, International Journal of Engineering Research & Technology, 02 (07). ISSN: 2278-0181.

Mohammed, H., Assefa, E., Shantveerayya, K. (2022). Utilization of Sisal Fiber as a Subgrade Soil Reinforcement: A Case Study of Alem Tena Town Along Modjo-Meki Expressway. International Journal of Mechanical Engineering, Vol. 7 (Special Issue, Jan.-Feb. 2022).

Nguyen, T. T., Indraratna, B. (2023). Natural Fibre for Geotechnical Applications: Concepts, Achievements and Challenges. Sustainability, 15, 8603, https://doi.org/10.3390/su15118603.

Paramkusam, B., Prasad, A., Arya, C. (2013). "A Study on CBR Behaviorof Waste Plastic (PET) on Stabilized Red Mud and Fly Ash, *Int. J. Struct. & Civil Engg. Res,* 2 (3). ISSN 2319 – 6009.

Rawat, P., Kumar, A. (2016). Study of CBR Behaviour of Soil Reinforced with HDPE Strips, *Indian Geotechnical Conference IGC2016*, 15-17 December, IIT Madras, Chennai, India. doi: 10.17577/IJERTV2IS70815.

Wu, Y., Li, Y., Niu, B. (2014). Assessment of the Mechanical Properties of Sisal Fiber-Reinforced Silty Clay Using Triaxial Shear Tests. TheScientificWorldJournal. Volume 2014, http://dx.doi.org/10.1155/2014/436231.

Proceedings of the XVIII ECSMGE 2024
GEOTECHNICAL ENGINEERING CHALLENGES
TO MEET CURRENT AND EMERGING NEEDS OF SOCIETY
© 2024 the Authors
ISBN 978-1-032-54816-6
DOI 10.1201/9781003431749-613
Open Access: www.taylorfrancis.com, CC BY-NC-ND 4.0 license

ECSMGE 24
XVIII EUROPEAN CONFERENCE ON SOIL MECHANICS AND GEOTECHNICAL ENGINEERING

Geomechanical evaluation of analogs of reservoirs for geological storage of CO_2

Évaluation géomécanique d'analogues de réservoirs pour le stockage géologique du CO_2

D. Manzanal*, C.B. Laskowski, M. Cortés, P. Vidal
Universidad Politécnica de Madrid, Madrid, Spain

C.B. Laskowski, M. Cortés, P. Vidal, J. Allard
Universidad Nacional de la Patagonia San Juan Bosco, Comodoro Rivadavia, Chubut, Argentina

**d.manzanal@upm.es*

ABSTRACT: Anthropic activities significantly contribute to the release of CO_2 into the atmosphere, which worsens global warming and accelerates climate change. To address these issues, geological storage in depleted oil reservoirs is seen as a potential solution to mitigate these effects. However, there is a lack of information on the application of this technique in the Golfo San Jorge Basin in Argentina, as well as geomechanical studies on its rocks. This study aims to characterize the geomechanical properties of rocks from the Salamanca, Castillo and Pozo D-129, formations under the influence of supercritical carbon dioxide injection. The studied samples were obtained from reservoir analogues exposed at the outcrop. Core plugs were used to assess the variation in the rock's mechanical behaviour when exposed to a CO_2-rich environment during 30-day periods, by performing Uniaxial Compressive Tests in both pristine and carbonated states. Additional analyses including X-ray diffraction (DRX) and mercury intrusion porosimetry (MIP) were conducted to evaluate the modifications produced in the microstructure. Notably, significant variations in mechanical parameters and porosity were observed in the studied formations. This article discusses the interaction between rock and supercritical CO_2, considering its chemical composition, to contribute to a better understanding of the potential for geological storage in the Golfo San Jorge Basin.

RÉSUMÉ: Les activités anthropiques contribuent de manière significative à la libération de CO_2 dans l'atmosphère, ce qui aggrave le réchauffement de la planète et accélère le changement climatique. Le stockage géologique dans des réservoirs de pétrole épuisés est considéré comme une solution potentielle pour atténuer ces effets. Cependant, on manque d'informations sur l'application de cette technique dans le bassin du Golfo San Jorge en Argentine, ainsi que d'études géomécaniques sur ses roches. Cette étude vise à caractériser les propriétés géomécaniques des roches des formations de Salamanca, Pozo D-129 et Castillo sous l'influence de l'injection de dioxyde de carbone supercritique. Les échantillons étudiés ont été obtenus à partir d'analogues de réservoirs exposés à l'affleurement. Des carottes ont été utilisées pour évaluer la variation du comportement mécanique de la roche lorsqu'elle est exposée à un environnement riche en CO_2 pendant des périodes de 30 jours, en effectuant des essais de compression uniaxiale à l'état vierge et à l'état carbonaté. Des analyses supplémentaires, notamment la diffraction des rayons X (DRX) et la porosimétrie par intrusion de mercure (MIP), ont été effectuées pour évaluer les modifications produites dans la microstructure. Notamment, des variations significatives des paramètres mécaniques et de la porosité ont été observées dans les formations étudiées. Cet article traite de l'interaction entre la roche et le CO_2 supercritique, compte tenu de sa composition chimique, dans le but de contribuer à une meilleure compréhension du potentiel de stockage géologique dans le bassin du Golfo San Jorge.

Keywords: Carbon dioxide geological storage; supercritical CO_2; Golfo San Jorge Basin; depleted oil and gas reservoirs; geomechanical property evolution.

1 INTRODUCTION

According to the Intergovernmental Pannel on Climate Change, during the past 100 years, an increase of 1.1ºC has been produced in the World's mean temperature (IPCC, 2023). Bearing in mind that climate change is produced due to the increase in the emission of greenhouse effect gases (GHG), and that at least 75% of them are represented by carbon dioxide (CO_2), it would be reasonable to think that by reducing the emissions of CO_2, this phenomenon would be mitigated. Among the available alternatives, capturing and storing CO_2 in the subsurface, is being considered as a way of reducing the concentration of this GHG in the atmosphere, while replacements for fossil fuels are developed.

CO_2 underground storage consists of capturing the CO_2 directly from its emission source (industries) for its further injection into an underground rock stratum. The formation chosen as reservoir, must be studied deeply enough to assure it is adequate. The feasibility of using a certain stratum as a CO_2 reservoir is determined by the evolution of the rock's geomechanical and hydro-chemical properties when exposed to a supercritical CO_2 ($scCO_2$) rich environment. The final objective is to ensure the reservoir's integrity in both short and long terms. Among the properties looked after in a possible CO_2 store, porosity, permeability, composition, and strength are of special interest (Bradshaw et al., 2007, and Hawkes et al., 2004).

In Argentina, there are several underground formations considered as possible CO_2 stores. Some of the potential underground reservoirs are Neuquina Basin, Claromecó Basin and Golfo San Jorge Basin (GSJB) (Grasetti et al., 2022, Laskowski et al., 2023). The three of them are characterized for being oil and gas reservoirs, being of particular interest for this study the Golfo San Jorge Basin (GSJB), since it stands out for containing reservoir rocks in different formations such as Salamanca, Castillo and Pozo D-129.

The main aim of the presented research is to fill the lack of information available in terms of geomechanical and chemical characterization of some GSB Basin formations and to technically consider their potential as possible CO_2 reservoirs. In this context, the results obtained from developing a series of laboratory tests on both pristine and carbonated rocks are presented, showing the evolution produced in their properties after the 30-day and 60-day aging.

2 MATERIALS AND METHODS

2.1 Geological context

The three different groups of rocks studied correspond to Salamanca, Castillo, and Pozo D-129 formations, which are all part of the Golfo San Jorge Basin (GSJB). Figure 1 shows a resume of the geological context of GSJB. The Pozo D-129 Fm. is the basal unit of the Chubut Group, which contains some tight reservoirs that serves as a source of oil and gas (Paredes et al. 2022). The depositional environment is associated with lacustrine and deltaic systems (Allard et al., 2018). The overliying Castillo Fm. represents traditional reservoirs of the petroleum system associated to the Chubut Group, consisting mainly of fluvial and paleosoils deposits (Paredes et al. 2015). A common feature of both rocks is the presence of varying amounts of tuffaceous material, associated with resedimented volcanic ash. The main lithologies are tuffaceous sandstone and tuff. (Cortes et al., 2024). On the other hand, the Salamanca Fm. is the shallowest oil reservoir of the basin, depleted at present and formed of marine sediments. The analyzed rock is a well-sorted glauconitic sandstone (Foix 2009).

These reservoir rocks are proposed as possible CO_2 stores as they meet the properties mentioned by Bachu (2000), presenting high porosity and permeability values (Cortés et al. 2024). Besides, the contrasting geological framework allows for the evaluation of different controls like the lithological composition and the diagenetic evolution.

2.2 Pristine and carbonated cores

To analyse the evolution produced in the properties of the different rocks due to their exposure to a CO_2-rich environment, it is necessary to obtain a group of representative specimens. Even when it would be ideal to obtain reservoir depth samples, this was economically not feasible, so it was proposed as a first approach, to obtain outcrop samples. Once in the laboratory, from these samples, cores with a 38 mm diameter and 76 mm height were obtained following the ASTM D 4543 – 01 specifications. From the samples obtained, half of them were separated and stored as pristine samples, and the other half were selected to expose them to $scCO_2$. Having completed the separation of the cores, the ageing process began.

Firstly, the cores were saturated in water by submerging them for 24 hours. This is an important step since water inside the rock facilitates the diffusion of CO_2. Secondly, they were disposed of in a tray holder, and introduced in the carbonation cell (Figure 2), where the CO_2-aging procedure was meant to be completed. Thirdly, the gas inlet was allowed until the carbonation cell was filled, a moment in which the temperature and pressure conditions were established to ensure the supercritical state of the CO_2 (60ºC temperature and 10 MPa pressure). The cell's conditions were maintained constant for 30 days. Finally, both the temperature and pressure were taken to environmental conditions carefully, to avoid the cracking or even fracture of the carbonated cores due to abrupt changes. The extracted cores were stored in a constant temperature and humidity chamber, covered in 40 μm polyethylene film, to maintain their properties invariant in time.

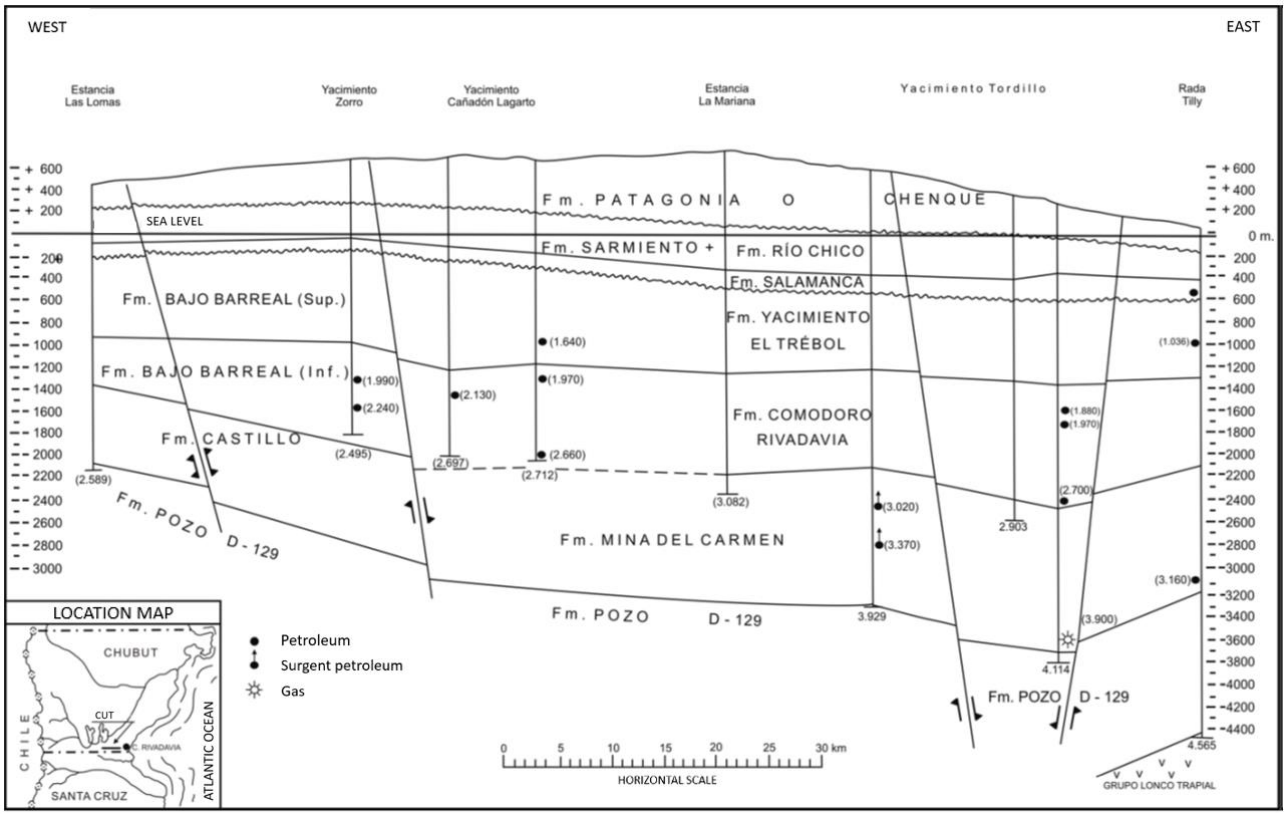

Figure 1. Golfo San Jorge Basin distribution of studied Formations (Sciutto et al., 2008).



Figure 2. Specimens in tray holder and carbonation cell.

2.3 Mechanical properties determination

The importance of analysing the evolution produced in the mechanical behaviour of the reservoir rock proposed as CO_2 underground storage, lies in verifying its long-term integrity. It is in this context, that a series of Uniaxial Compressive Tests, following the ASTM D 3148 – 02 specifications, were performed in both pristine and carbonated rock cores corresponding to the three formations. The results obtained from these tests were tenso-deformational curves which allowed making a complete comparison between the mechanical and elastic properties of the rocks before and after their exposure to $scCO_2$.

2.4 Microstructural properties determination

To reach a better understanding of the results obtained from performing the Uniaxial Compressive Tests, the variation produced in the microstructural properties due to CO_2 injection was analysed. The tests chosen for this research were the Mercury Intrusion Porosimetry (MIP) and the X-Ray Diffraction (XRD). With the results derived from the first group of tests, the available pore volume for CO_2 storage would be estimated, giving this a first approach to determine if the rock is a good reservoir alternative or not. On the other hand, the results obtained from the XRD, would allow to understand the trapping mechanisms being developed in each rock.

3 RESULTS AND DISCUSSION

3.1 Uniaxial compressive strength

The stress–strain curve obtained from performing Uniaxial Compressive Tests on Salamanca Fm. shows a significant reduction of Uniaxial Compressive Strength in carbonated cores at 30 days as is shown in Figure 1. Also is observed that the sample becomes more ductile after the $scCO_2$-aging.

Figure 3 shows the comparison for all lithologies, and formations, showcasing the evolution of Uniaxial Compressive Strength (UCS) for both pristine and

carbonated cores. After subjecting the Sandstone from the Salamanca Fm. to ageing with supercritical carbon dioxide for 30 days, a notable decrease of approximately 40% in Uniaxial Compressive Strength (UCS) is evident. However, in the Tuffaceous Sandstone samples and the Tuff from Castillo and D-129 Fms., this reduction is less pronounced, ranging from 20 to 22%. The trend of UCS reduction persists in rock samples aged for 60 days, though the results remain inconclusive due to the limited number of tests conducted. Various authors have highlighted variations in strength, which depend upon the composition of the rocks. Typically, carbonates exhibit more significant alterations, while results for carbonate-cemented sandstone appear ambiguous, and silica-cemented sandstone tends to undergo minor changes (Vilarrasa et al., 2019). The predominance of carbonate cement within the Salamanca Fm. (Laskowski et al., 2024) and the identification of zeolitic cement in the D-129 Fm. (Olazabal, pers. com.) and samples from the Castillo Fm. (Tunik et al., 2015), explains the variations in strength observed, both before and after $scCO_2$ carbonation, between the studied formations.

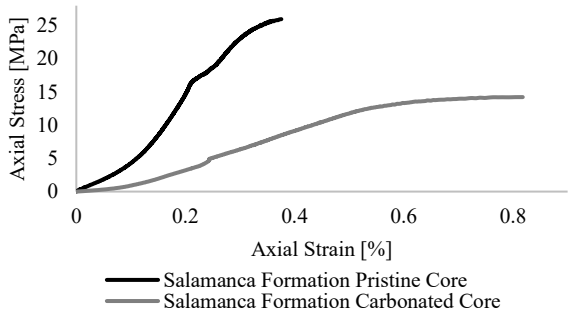

Figure 2. Example of results of stress – strain curve obtained from performing Uniaxial Compressive Tests on Salamanca, in both pristine and carbonated cores at 30 days.

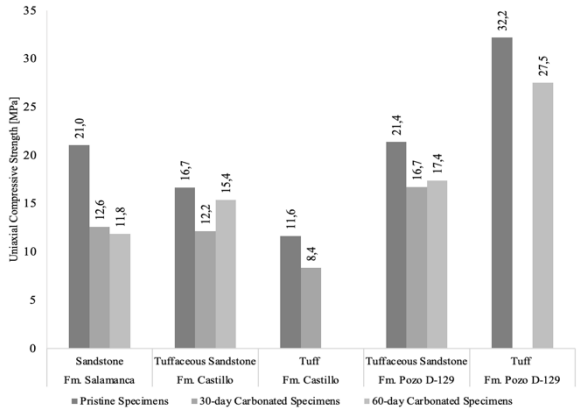

Figure 3. UCS on Salamanca, Castilla and Pozo D-129 Fms, in both pristine and carbonated cores at 30 and 60 days.

3.2 Porosity variations after $scCO_2$-exposure

Mercury Intrusion Porosimetry (MIP) tests were carried out to examine the porosity changes in the chosen reservoir rock induced by supercritical carbon dioxide ($scCO_2$). In general, the sandstone demonstrated a reduction in porosity following exposure to a CO_2-rich environment as is shown in Table 1. MIP porosity of sandstone from Salamanca Fm. is approximately 10.66%, while post-aging porosity is 9.65%. The tuffaceous sandstone from the Castillo Formation and the Tuff of the D-129 Formation exhibit mean values of MIP porosity of approximately 19%, with post-aging porosity measuring 17%.

A detailed examination of Figure 4 revealed changes in the pore size distribution of sandstone from Salamanca Fm. The Differential Intrusion-Pore Diameter curves indicated a notable increase in the volume of smaller pores (40-90 nm), rising from 30% to 45%, alongside a decrease in the larger pores (800-4000 nm) from 30% to 10%.

Table 1. Porosities were obtained for the different rocks studied.

Specimen Characterization		CO_2 exposure time [days]	
		0	30
Formation	Lithology	Porosity [%]	
Fm. Salamanca	Sandstone	10,66	9,65
Fm. Castillo	Tuffaceous Sandstone	19,79	17,05
Fm. Pozo D-129	Tuff	19,30	17,05

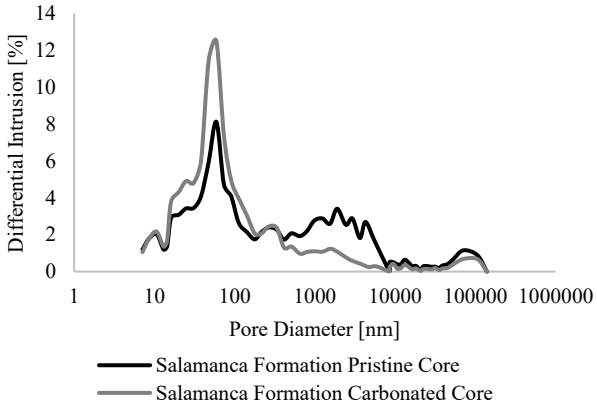

Figure 4. Results of Differential Intrusion-Pore Diameter obtained from performing MIP tests on Sandstone from Salamanca Fm. in both pristine and carbonated cores.

3.3 X-Ray diffraction

XRD analysis demonstrated that the rocks from Castillo and D-129 Fm. generally contain variable amounts of quartz, potassic feldspar, plagioclase, and clays such as kaolinite and illite. Small amounts of

jarosite and analcime are also present in some of the samples.

The treated samples exhibited insignificant changes in potassic feldspar, kaolinite, and illite, except for a 2% reduction in illite observed only in the tuffaceous sandstone of the Castillo Fm. Similarly, analcime displayed minimal changes, but the variation was almost 7%.

The most significant alterations were observed in quartz and plagioclase. In most cases, quartz content decreased, while plagioclase increased in the treated samples. This trend aligns with the measurements of silica and aluminium obtained by portable XRF (Cortés et al., 2024). The reduction in silica and quartz content in the carbonated samples, as determined by XRF and XRD measurements, respectively, may be attributed to the corrosion of quartz crystals (Rathnaweera et al., 2015) or the dissolution of clay minerals (Rathnaweera et al., 2015). However, it is more conventional for feldspars to react before quartz.

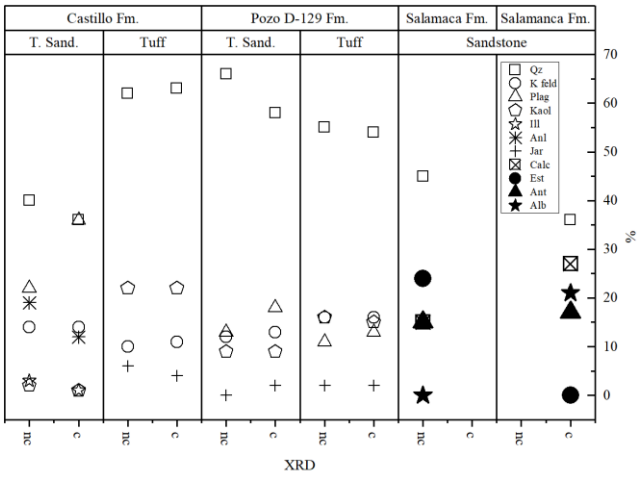

Figure 5. Mineral composition of carbonated and non-carbonated samples determined by XRD. Qz= Quartz, K feld= Potassium feldspar, Plag= Plagioclase, Kaol=Kaolinite, Ill=Illite, Anl=Analcine, Jar=Jarosite. Cal = magnesic calcite, Est = sodic estilbita, Ant = anorthite, Alb=albite.

Remarkably, the quantity of potassic feldspar remained relatively stable, while the amount of plagioclase increased. Both observations pose geological inconsistencies due to the inert nature of quartz and the exclusive magmatic genesis of plagioclase. This increase is attributed to the dissolution of minerals more soluble than plagioclase, leading to an increase in its relative content as stated by Yang et al. (2022). This also could be attributed to the sampling process, which may be influenced by the potential heterogeneity of the formation. Another aspect to remark on is the high quartz content which is inconsistent with previous petrographic studies as stated by Cortés et al. (2024).

The treated samples of Sandstone from Salamanca Fm. exibihit changes in magnesic calcite, sodic estilbita and albite. The effects of glauconite reaction to CO_2 may be a major control in the associated geochemical process (Fu et al. 2015). These changes are affecting the porous matrix and its strength. Further clarity on this uncertainty will be obtained through in-depth analyses, such as thin sections or Scanning Electron Microscope images.

4 CONCLUSIONS

The research emphasizes findings across mechanical, petrophysical, and chemical evolution of the glauconitic sandstone of Salamanca Fm. and tuff and tuffaceous sandstone Castillo and Pozo D-129 Fms for pristine and supercritical CO_2-aged samples at 30 and 60 days.

The evident alteration in the chemical composition of the treated specimens indicates a consequential influence on both mechanical strength and porosity. The drop in mechanical strength is evident across all three analyzed lithologies following CO_2-aging. However, despite the impact on mechanical strength, the samples exhibit a decrease in porosity. Further examination, particularly through thin sections and Scanning Electron Microscopy (SEM), is imperative to elucidate the underlying geochemical reactions and mineralogical changes. The scope of tests is being broadened, encompassing triaxial tests, to delve deeper into the mechanical behaviour and explore the evolution of microstructures under conditions mimicking CO_2 underground storage.

ACKNOWLEDGEMENTS

The authors would like to express their gratitude to Prof. Foix, Prof. Battaglia (UNPSJB) and Ph.D. Mauro Muñiz-Menéndez (CEDEX), for the advice received. The author thanks PhD fellowship of the Fundación José Entrecanales Ibarra (second author) and CONICET (third author). The authors also acknowledge the European Commission's (H2020 MSCA-RISE 2020 Project DISCO2-STORE, Grant Agreement No 101007851), the Universidad Nacional de la Patagonia San Juan Bosco (Project PI1614 80020190200006 IP), and the Agency of Scientific and Technological Promotion from the Argentinian Republic (PICT 2020–0288) financial support.

REFERENCES

Allard, J.O., Foix, N., Bueti, S.A., & Olazábal, S.X. (2018). Variabilidad petrofísica, geomecánica y geoquímica de deltas volcaniclásticos de la Formación Pozo D-129 en la Sierra Silva, cuenca del Golfo San Jorge. *Proceedings of X Congreso de Explor. y Desarrollo de Hidrocarburos. Argentina.*

Bachu, S. (2000). Sequestration of CO2 in geological media: criteria and approach for site selection in response to climate change. Energy Conversion & Management, 41:953-970. https://doi.org/10.1016/S0196-8904(99)00149-1.

Bradshaw, J., Bachu, S., Bonijoly, D., Burruss, R., Holloway, S., Christensen, N. P. & Mathiassen, O. M. (2007). CO_2 storage capacity estimation: Issues and development of standards. *International Journal of Greenhouse Gas Control* I: 62-68. http://dx.doi.org/10.1016/S1750-5836(07)00027-8.

Cortés, M., Manzanal, D., Vidal P., Allard, J. & Orlandi, S. (2024). Mechanical and Petrophysical Variations Induced by Supercritical CO2 interaction in the Castillo and Pozo D-129 Formations, San Jorge Gulf Basin. Proc. of EUROCK 2024, Alicante, Spain. July 15-19, 2024.

Foix, N. (2009). Doctoral Thesis. Tectónica de sedimentación del registro paleógeno (Formaciones Salamanca y Río Chico), Cuenca del Golfo San Jorge, Argentina. Univ. Nac.de la Patagonia San Juan Bosco, Com. Riv., Argentina.

Fu, Y., van Berk, W., Schulz, H., Mu N. (2015). Berthierine formation in reservoir rocks from the Siri oilfield as result of fluid–rock interactions: Part III. Determining mineral stability and CO2-sequestering capacity of glauconitic sandstones. Marine and Petr. Geol. 65: 327-333.

Grasetti, C., Piqué, T., Noya, M., Vila, G., Manoni, R., Brisson, I., De Leo, D., Dzelalija, F., Canale, N., Zalazar, M., Cabana, C., Tunik, M., Fortunatti, N., Lebinson, F., Bahía, M. and Grill, S. (2022). Atlas AR-CO_2. An Argentinian atlas for underground CO_2 storage potential. Proc. of 16th International Conf. on Greenhouse Gas Control Technologies.

Hawkes, C., Mclellan, P. & Bachu, S. (2004). Geomechanical factors affecting geological storage of CO2 in depleted oil and gas reservoirs. Journal of Canadian Petroleum Technology 44 (10). http://dx.doi.org/10.2118/05-10-05.

Hawkes, C., Mclellan, P. & Bachu, S. (2004). Geomechanical factors affecting geological storage of CO2 in depleted oil and gas reservoirs. Journal of Canadian Petroleum Technology 44 (10). http://dx.doi.org/10.2118/05-10-05.

IPCC. (2023). Climate Change 2023: Contribution of WG I, II and III to the Sixth Assessment Report of the Intergovernmental Panel on Climate Change. doi: 10.59327/IPCC/AR6-9789291691647.

Laskowski, C.; Manzanal, D.; Muñíz-Menéndez, M.; Orlandi, S.; & Allard, J. (2023). Carbon dioxide impact on the mechanical properties of a sandstone from San Jorge Gulf Basin (Argentina). Proc. from the 15th Int. ISRM Congress 2023. 9-14 of october 2023; Salzburg, Austria.

Laskowski, C.; Manzanal, D.; Muñíz-Menéndez, M.; Orlandi, S.; & Allard, J. (2024). Evolution of microstructural and chemical properties of the CO_2-aged Banco Verde sandstone. Proc. 28th European Young Geotechnical Engineers Conf. Macedonia, Albania.

Paredes, J.M., Foix, N., Allard, J.O., Colombo, F., & Tunik, M.A. (2015). Alluvial architecture of reworked pyroclastic deposits in peri-volcanic basins: Castillo Formation (Albian) of the Golfo San Jorge basin, Argentina. *Revista de la Asociación Geológica Argentina*, 72 (1), 42-62.

Paredes, M.J., Foix, N., & Allard, J.O. (2022). Estratigrafía Cretácica de la Cuenca del Golfo San Jorge. *Proc. of XXI del Cong. Geológico Arg.*

Rathnaweera, T., Ranjith, P., Perera, M., Haque, A., Lashin, A., Al Arifi, N., Chandrasekharam, D., Yang, S., Xu, T., Wang, S. & Yasar, E. (2015). CO_2-induced mechanical behaviour of Hawkesbury sandstone in the Gosford basin: An experimental study. *Mat. Sc. & Eng.* 641: 123-137.

Sciutto, J. C., Césari, O. & Iantanos, N. (2008). Hoja Geológica 4569-IV, Escalante, provincia del Chubut. *Instituto de Geología y Recursos Minerales. Servicio Geológico Minero Argentino, Boletín 351, 76 p. Buenos Aires. Argentina.*

Tunik, M., Paredes, J., Fernandez, M., Foix, N., Allard, J.O. (2015) Análisis Petrográfico de areniscas de la Fm. Castillo. Rev. Asoc. Geol. Arg. 72(1):63-80).

Vilarrasa, V., Makhnenko, R. Y., & Rutqvist, J. (2019). Field and laboratory studies of geomechanical response to the injection of CO_2. In Science of carbon storage in deep saline fms (209-236).

Yang, K., Zhou, J., Xian, X., Zhou, L., Zhang, C., Tian, S., Lu, Z., & Zhang, F. (2022). Chemical-mechanical coupling effects on the permeability of shale subjected to supercritical CO_2-water exposure. *Energy* 248. http://dx.doi.org/10.1016/j.energy.2022.123591.

Proceedings of the XVIII ECSMGE 2024
GEOTECHNICAL ENGINEERING CHALLENGES
TO MEET CURRENT AND EMERGING NEEDS OF SOCIETY
© 2024 the Authors
ISBN 978-1-032-54816-6
DOI 10.1201/9781003431749-614
Open Access: www.taylorfrancis.com, CC BY-NC-ND 4.0 license

ECSMGE 24
XVIII EUROPEAN CONFERENCE ON SOIL MECHANICS AND GEOTECHNICAL ENGINEERING

Testing methodologies to evaluate waste-based liners

Méthodologies de test pour évaluer les revêtements à base de déchets

L. Marchiori*
GeoBioTec, Civil Engineering and Architecture Department, University of Beira Interior, Covilhã, Portugal
M.V. Morais, A. Albuquerque, L. Andrade Pais, V. Cavaleiro
GeoBioTec, Civil Engineering and Architecture Department, University of Beira Interior, Covilhã, Portugal
**leonardo.marchiori@ubi.pt*

ABSTRACT: Improper waste disposal and management due to industrial activity may lead to soil and groundwater contamination. Thus, the development of methodologies for mitigating waste generation and its valorisation should be investigated to reduce environmental impacts, create waste-based products, and fulfil sustainable development goals. When malfunctioning, earthworks can negatively impact the environmental, besides clayey soils have mechanical issues, and represent high costs of logistics depending on the region, in addition to geosynthetics being still a costly solution. Therefore, recent investigations are using industrials by-products for construction purpose. This research reviews the literature of the main wastes used as liner materials, and their laboratorial tests program to evaluate their potential for liner. Furthermore, a flowchart was designed to optimize the valorisation process depending on the waste availability, and a table developed within the tests over the literature available.

RÉSUMÉ: Une élimination et une gestion inappropriées des déchets dues à l'activité industrielle peuvent entraîner une contamination des sols et des eaux souterraines. Ainsi, le développement de méthodologies pour atténuer la production de déchets et leur valorisation devrait être étudié pour réduire les impacts environnementaux, créer des produits à base de déchets et atteindre les objectifs de développement durable. En cas de dysfonctionnement, les terrassements peuvent avoir un impact négatif sur l'environnement, de plus les sols argileux présentent des problèmes mécaniques, et représentent des coûts logistiques élevés selon les régions, de plus les géosynthétiques restent une solution coûteuse. Par conséquent, des études récentes utilisent des sous-produits industriels à des fins de construction. Cette recherche passe en revue la littérature sur les principaux déchets utilisés comme matériaux de revêtement, ainsi que leur programme d'essais en laboratoire pour évaluer leur potentiel pour l'imperméabilisation des terrassements. De plus, un organigramme a été conçu pour optimiser le processus de valorisation en fonction de la disponibilité des déchets, et un tableau a été développé pour organiser les tests selon la littérature disponible.

Keywords: Industrial wastes; methodology for liner material; laboratory and in-situ tests; geotechnical applications.

1 INTRODUCTION

Liner materials are usually made of compacted clay liners (CCL) or geosynthetic clay liners (GCL), mainly used as layers of low hydraulic conductivity (k) and environmental protection barriers in landfilling, roads, channels, dams, reservoirs, and wastewater lagoons and ponds (Bouazza, 2002; Kerry Rowe et al., 2022). Suitable liners' properties can be summarized mainly as having low k, less than or equal to 10^{-9} m/s, enough strength to support the weight of the disposed/transported solid/liquid materials, deformation during service without cracking or rupture, self-healing properties, and chemical compatibility with the materials.

Depending on the region, natural clays exploration creates logistics' issues and environmental impacts, besides, geosynthetics still represents a costly solution, justifying the use of alternative materials, for use as waterproofing in earthworks. Furthermore, there are several industrial by-products as mining tailings (Maritsa et al., 2016; Pastore 2003; Marchiori et al., 2022a), furnace slags (Masri et al., 2019; Bennett et al., 2011; Liu et al., 2022; Herrmann et al., 2010), fly ashes (von Maubeuge et al., 2015; Marchiori et al., 2023b), and water treatment sludges (Baghbani et al., 2023, Marchiori et al., 2021, 2022b), which seem to have chemical and mechanical properties for that application. The reuse or valorisation of industrial by-products is within the circular economy directives and United Nations' Agenda for Sustainable Development Goals since it allows reduction of construction costs, helps preserve natural resources, decreases the production of synthetic materials and lead to sustainable new geomaterials design.

In addition, there was identified lack of specific methodologies to classify certain types of waste materials as geomaterials (Kerry Rowe et al., 2022), mainly over geotechnical, chemical, and environmental characterization, long-term behaviour of materials, mechanical properties, chemical and mineralogical composition, and leaching evaluation (Agamuthu, 2013; Devarangadi and Shakar M, 2021; Marchiori et al., 2020). Thus, this paper aims to review the literature, select the main laboratorial and in-situ test programs, and propose a laboratorial program to evaluate industrial by-products as liner geomaterial.

2 METHODOLOGY

A review of the literature was performed gather testing methodologies used for producing and assessing liner alternative materials. The chosen database was Scopus, and the main tests were selected in order to create Figure 1 and Table 1.

3 RESULTS

The process to qualify a waste material as a sustainable barrier should comprise careful sampling, identification, and characterization according to physical, chemical, mechanical, and hydraulic parameters, and the need of additives and/or geosynthetics materials to mitigate environmental impact without performance loss. The following subsections present the main concerns on the mentioned characteristics. Table 1 summarizes testing programs used by different authors. The flowchart in Figure 1 organizes the proposed methodology for waste valorisation as liner material.

3.1 Sampling and identification

The most concern about sampling is due to contamination, all the care with the samples must be done in order to do not contaminate it. It is very important to understand and analyze all the industrial processes that generate the by-products to understand some components in further identification (Kerry Rowe et al, 2022). Sample treatment can be included, like dehydration and sieved, but calcination should be avoided due to gas release.

Chemical compactibility and potential negative environmental impacts are the most important worries when dealing withh waste containment facilities. The composition through X-ray fluorescence (XRF) and mineralogical composition with X-ray diffractures (XRD) should be done to identify the possiblity of contamination in the sample. Besides, microstructure assessment with scanning electron microscopy (SEM), computed tomography (CT) scan and mercury intrusion porosimeter (MIP), in addition to thermogravimetric analysis (TGA) and Fourier transformed infrared (FTIR) linked to leaching potential for chemical detections (Marchiori et al., 2020). Physical identification includes the analysis of particle size distribution by sieve or laser equipment, and material classification, besides specific gravity measurements (Herrmann et al., 2010; Liu et al., 2022). The soil characterization should assess Atterberg limits and compaction characteristics within Proctor tests (Maritsa et al., 2016).

3.2 Geocomposite development

Specific gravity plays an important role in the chosen ratios of soil-waste when is searching for a suitable waste-based liner. Waste incorporation percentage must be defined according to the parameters to reach linked to its density (Marchiori et al., 2023a).

Table 1. Test program for liner material.

Characterization	References
Chemical	
Composition	1,3,5,6,7
Mineralogy	1,3,5,6,7
Leaching	1,2,3
Microstructure	1,3,6,7
Geotechnical	
Particle Size	1,5,6,7
Atterberg Limits	1,5,6,7
Specific Gravity	3,4,5,6,7
Compaction	1,4,5,6,7
Consolidation	6,7
Triaxial CU	6,7
Permeability	1,3,4,5,6,7
In-situ	
Intelligent Compaction	4
Permeability Control	4

1. Maritsa *et al.* (2016); 2. Pastore (2003); 3. Liu *et al.* (2022); 4. Herrmann *et al*. (2010); 5. Marchiori *et al.* (2021); 6. Marchiori *et al.* (2022b); 7. Marchiori *et al.* (2023b).

3.3 Geotechnical assessment

3.3.1 Mechanical performance

With those preliminary physical and chemical identification, and further geocomposite design, the mechanical evaluation can be done, basically understanding deformation over tension application, and the main tests to be develped are one-dimensional oedometric consolidation and consolidated-undrained (CU) triaxial shearing test to simulate liner conditions (Marchiori et al., 2022b, 2023b).

3.3.2 Hydraulic conductivity

The main parameter of liners is the hydraulic conductivity (k), permeability characterization must be comprised due to the required low k, less than or equal to 10^{-9} m/s. Intermediate- to large-scale experiments can be done, and the methodology for experimental liner development should be designed according to hydrogeological and geotechnical aspects of the selected site, besides economical and environmental impact of the area. Intelligent compaction should be addressed and permeability testing must be conducted (Bouazza, 2002).

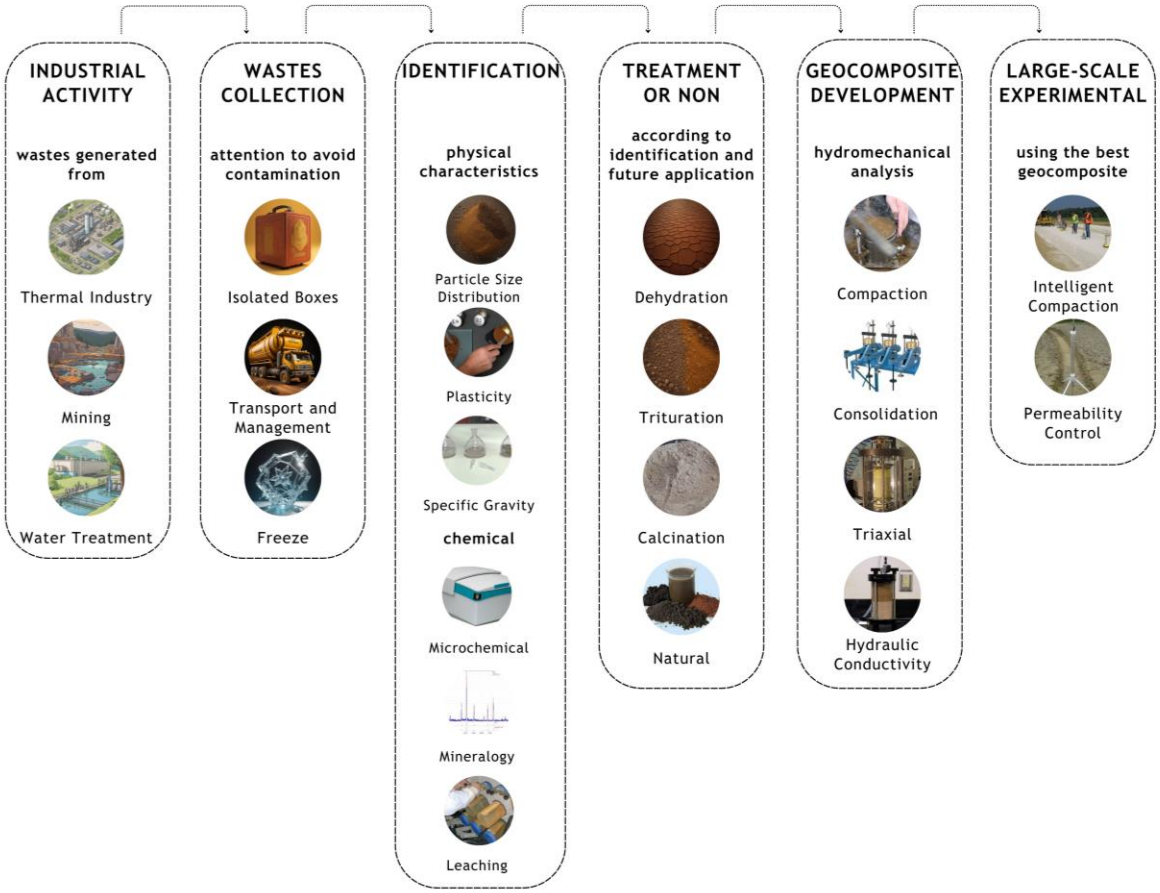

Figure 1. Schematic process for waste-based liner material evaluation.

4 CONCLUSIONS

The flowchart presented here aims to complement rather than invalidate other methods. It focuses on reducing the need for repeated laboratory work and emphasizes key factors and parameters for creating waterproof liners from waste materials. As a result, the information provided in this study, which covers environmental, physicochemical, and geomechanical tests, appears to facilitate the use of wastes with soils for liner production as alternative geomaterials.

ACKNOWLEDGEMENTS

The authors are grateful for the financial support provided by FCT (Fundação para a Ciência e Tecnologia), supported by the strategic project GeoBioTec (UIBD/04035/2020).

REFERENCES

Agamuthu, P. (2013). Landfilling in developing countries. *Waste Management Resistance,* 31(1), pp.1-2. http://doi.org/10.1177/0734242X12469169.

Baghbani, A., Nguyen, M.D., Kafle, B., Baghbani, H., Faradonbeh, R.S. (2023). AI grey box model for alum sludge as a soil stabilizer: an accurate predictive tool. *International Journal of Geotechnical Engineering*. https://doi.org/10.1080/19386362.2023.2258749.

Bennett, J., Sridhar, S., Nakano, J., Kwong, K.-S., Lam, T., Kaneko, T., Fernandez, L., Komolwit, P., Thomas, H., Krabbe, R. (2011). Slag Characterization for the Development of New and Improved Service Life Materials in Gasifiers using Flexible Carbon Feedstock.

Advances in Materials Science for Environmental and Nuclear Technology II, 227.

Bouazza, A. (2002). Geosynthetic clay liners. *Geotextiles and Geomembranes.* 20(1), pp. 3-17. https://doi.org/10.1016/S0266-1144(01)00025-5.

Devarangadi, M., Shakar M, U. (2021). Correlation studies on geotechnical properties of various industrial byproducts generated from thermal power plants, iron and steel industries as liners in a landfill- a detailed review. *Journal of Cleaner Production.* 261. pp. 121207 https://doi.org/10.1016/j.jclepro.2020.121207.

Herrmann, I., Andreas, L., Diener, S., Lind, L. (2010). Steel slag used in landfill cover liners: laboratory and field tests. *Waste Management & Research,* 28(12), pp. 1114-1121. https://doi.org/10.1177/0734242X10365095.

Kerry Rowe, R., Jefferis, S., Abdelaal, F., Dominijanni, A., Legge, K., Palmeira, E., Scheirs, J. , Shackelford, C.D., Scalia IV, J., Zhan, T.L.T., Benson, C.H., Bouazza, A., Di Emidio, G.,Evans, J.C., Fratalocchi, E., Gardoni, M.G., Katsumi, T., Manassero, M., Parra, D. (2022) State of the Art Lecture on Environmental Geotechnics. Protecting the environment from contamination with barrier systems: advances and challenges. *in Proceedings of 20th International Conference on Soil Mechanics and Geotechnical Engineering.* Sydney, Australia, Australian Geomechanics Society, pp. 187-293.

Liu, Y., Lu, H., Wang, C., Liu, Y., Ma, J., Liu, M. (2022). Mechanical Strength,Water Seepage and Microstructure of a Novel Landfill Solidified Sludge Liner Material. *Processes,* 10(8), p.1641. https://doi.org/10.3390/pr10081641.

Marchiori, L. & Albuquerque, A. (2020). Critical review of industrial solid wastes as barrier material for impermeabilization of storage waste facilities. *In Proceedings of the 5th Symposium on Urban Mining and Circular Economy.* Venice, Italy, CISA Publisher.

Marchiori, L., Albuquerque, A. & Cavaleiro, V. (2022a). *Granitic mining waste feasibility for liner material production.* In Proceedings of the 7th World Congress on Civil, Structural, and Environmental Engineering (CSEE'22). Lisbon, Portugal. https://doi.org/10.11159/iceptp22.203.

Marchiori, L., Morais, M.V., Albuquerque, A., Cavaleiro, V. (2023a). Geotechnical Characterization Methodology of Water Treatment Sludge for Production of Liner Material. *in Yukselen-Aksoy, Y., Reddy, K.R., Agnihotri, A.K. (eds) Sustainable Earth and Beyond. EGRWSE 2022. Lecture Notes in Civil Engineering, vol 370. Springer, Singapore.* https://doi.org/10.1007/978-981-99-4041-7_41.

Marchiori, L., Studart, A., Albuquerque, A., Cavaleiro, V., Boscov, M.E.G. (2022b). Mechanical and chemical behaviour of water treatment sludge and soft soil mixtures for liner production. *The Open Civil Engineering Journal,* 16. https://doi.org/10.2174/18741495-v16-e221115-2022-27.

Marchiori, L., Studart, A., Albuquerque, A., Cavaleiro, V., Silva, A. (2021). Geotechnical characterization of water treatment sludge for liner material production and soft soil reinforcement. *Materials Science Forum,* 1046, pp. 83-88. https://doi.org/10.4028/www.scientific.net/MSF.1046.83.

Marchiori, L., Studart, A., Morais, M.V., Albuquerque, A., Cavaleiro, V. (2023b). Geotechnical Characterization of Vegetal Biomass Ashes Based Materials for Liner Production. *In: Chastre, C., et al. Testing and Experimentation in Civil Engineering. TEST&E 2022.* RILEM Bookseries, 41. Springer, Cham. https://doi.org/10.1007/978-3-031-29191-3_6.

Maritsa, L., Tsakiridis, P.E., Katsiotis, N.S., Tsiavos, H., Velissariou, D., Xenidis, A., Beazi-Katsioti, M. (2016). Utilization of spilitic mining wastes in the construction of landfill bottom liners. *Journal of Environmental Chemical Engineering,* 4, pp. 1818-1825. https://doi.org/10.1016/j.jece.2016.03.011.

Masri, N., Kusin, F., Daud, N., Man, H. (2019). Strength assessment of mining soil treated with steel slag as liner material for retention pond. *Pertanika Journal of Science and Technology,* 27(4), pp. 2305-2315. e-ISSN: 2231-8526.

Pastore, E. (2003). Impacts of organic waste liner. *Bulletin of Engineering Geology and the Environment,* 62, pp. 269-277. https://doi.org/10.1007/s10064-003-0193-6.

Rubinos, D. A., Spagnoli, G. (2018). Utilization of waste products as alternative landfill liner and cover materials – A critical review. *Critical Reviews in Environmental Science and Technology,* 48(4), pp. 376-438. https://doi.org/10.1080/10643389.2018.1461495.

von Maubeuge, K., Egloffstein, T. & Vollmert, L. (2015). Road noise barriers as longitudinal waste deposits - lined slopes with geosynthetics protecting the environment. *Japanese Geotechnical Society Special Publication*, 2(69), pp. 2347-2351. https://doi.org/10.3208/jgssp.IGS-31.

Proceedings of the XVIII ECSMGE 2024
GEOTECHNICAL ENGINEERING CHALLENGES
TO MEET CURRENT AND EMERGING NEEDS OF SOCIETY
© 2024 the Authors
ISBN 978-1-032-54816-6
DOI 10.1201/9781003431749-615
Open Access: www.taylorfrancis.com, CC BY-NC-ND 4.0 license

ECSMGE 24
XVIII EUROPEAN CONFERENCE ON SOIL MECHANICS AND GEOTECHNICAL ENGINEERING

Numerical analysis of monopiles supporting offshore wind turbines exposed to scour and cyclic loading

Analyse numérique des monopieux supportant des éoliennes offshores exposées à l'affouillement et aux charges cycliques

C. Menéndez-Vicente*, S. López-Querol
University College London, London, United Kingdom
**carlos.vicente.19@ucl.ac.uk*

ABSTRACT: Offshore wind turbines founded on monopiles are exposed to geohazards such as scour that threaten their long-term stability and serviceability. An active seabed changes the foundation conditions of these structures, which directly affects the soil-structure stiffness and its performance under environmental (cyclic) loading composed of wind and sea waves. This study aims to investigate the effects of scour under cyclic loading. A numerical approach with finite element analysis in Abaqus was applied. To simulate the long-term strain accumulation with load cycles, a hypoplastic constitutive model to reproduce the sand behaviour was implemented. Through these simulations, the ratcheting phenomenon based on increasing deformations with the number of cycles, has been simulated for sandy soils. The results quantify the effect of higher scour depths causing an increase of the displacement incremental rate per load cycle, which leads to larger maximum and residual displacements. This evidences the long-term risk for monopiles exposed to scour and cyclic loading in terms of serviceability and economic viability, due to a potential lifetime reduction given their vulnerability to excessive tilt. This study intends to raise awareness about the importance of considering scour during the design and operation of offshore wind turbines exposed to an active seabed.

RÉSUMÉ: Les éoliennes offshore fondées sur des monopieux sont exposées à des géorisques tels que l'affouillement, qui menacent leur stabilité et leur fonctionnalité à long terme. Un fond marin actif modifie les conditions de fondation de ces structures, ce qui affecte directement la rigidité du système sol-structure et son comportement sous une charge environnementale (cyclique) composée de vent et de vagues. Cette étude vise à examiner les effets de l'affouillement sur un monopieu soumis à une charge cyclique. Une approche numérique avec une analyse par éléments finis dans Abaqus a été appliquée. Pour simuler l'accumulation de déformations à long terme avec cycles de charge, un modèle constitutif hypoplastique simulant le comportement du sable a été implémenté. Ainsi, le phénomène de ratcheting de sols sableux, qui est basé sur l'augmentation des déformations avec l'augmentation du nombre de cycles, a été simulé. Les résultats quantifient l'effet que des profondeurs d'affouillement plus importantes entraînent une augmentation du taux de déplacements incrémentiels par cycle de charge, ce qui conduit à des déplacements maximaux et résiduels plus importants. Ceci met en évidence le risque à long terme pour les monopieux exposés à l'affouillement et aux charges cycliques en termes d'aptitude au service et de viabilité économique, en tenant compte d'une réduction potentielle de la durée de vie en raison de leur vulnérabilité à un basculement excessif. Cette étude vise à sensibiliser à l'importance de la considération de l'affouillement lors de la conception et de l'exploitation d'éoliennes offshore exposées à un fond marin actif.

Keywords: Offshore wind turbines; scour; monopiles; soil-structure interaction; finite elements analysis.

1 INTRODUCTION

Offshore Wind Turbines (OWT) are rapidly being installed worldwide due to the high demand for clean and renewable energy. These structures are exposed to waves and currents, which cause scour around piled foundations. Normally, scour protection such as rock armour is installed to prevent erosion. Nonetheless, non-protected foundations may develop scour holes, which reduce the embedment length and weaken the lateral capacity of monopiles. Cyclic loading caused by wind-wave loads leads to a degradation of the foundation material (often sands), which produces long-term strain accumulation and ultimately irreversible tilting (i.e. serviceability and structural damage). Moreover, this stiffness reduction may lead to a shift in the natural frequency towards the forcing frequencies and an increase in fatigue damage.

To numerically simulate OWT monopiles exposed to cyclic loading, complex constitutive models to replicate the long-term stress-path dependent strain accumulation of granular materials such as sands are needed. Hypoplasticity (von Wolfersdorff, 1996;

Niemunis and Herle, 1997) was implemented successfully by Askarinejad et al. (2022) for sands to reproduce their results obtained through centrifuge testing for a monopile with scour protection. The present paper intends to analyse the opposite: the effect of scour on monopiles exposed to cyclic loading. With a series of simulations for different scour depths S, the impact of cyclic loading is analysed through a hypoplastic constitutive law of the sand surrounding the scoured piled foundation.

2 METHODOLOGY

2.1 Numerical model

A finite element (FE) model based on the study of Askarinejad et al. (2022) was developed in Abaqus. The domain consists of a symmetric half soil-pile system with a pile diameter of $D = 1.8$ m (Figure 1). For comparison purposes, a further FE model with a large-diameter monopile ($D = 7.5$ m) was also modelled. Regarding the boundary conditions, the lateral faces were constrained in normal direction, whereas the bottom plane was fixed in all directions. The pile was modelled for simplicity with an elastic constitutive behaviour using solid bodies (instead of tubular structures) with equivalent masses and flexural stiffnesses (López-Querol et al., 2020). Table 1 shows the material properties, where D is the diameter of the pile, t is the thickness of the tubular profile, ρ is the density, v is the Poisson's ratio, E is the Young's modulus, and I is the moment of inertia. For the pile embedded in the soil, a sand fill of the tubular section was considered, whereas the upper part was modelled as a hollow cylinder. Dry densities were considered in analogy to Askarinejad et al. (2022); nonetheless, the findings are also applicable to submerged conditions. For the soil-pile interface, a fully rough condition was applied. The scour hole was modelled for simplicity as an inverted cone with a range of scour depths $S = \{0; 0.5D; 1.0D\}$ that may be found on the field (Whitehouse et al., 2011) and a slope angle equivalent to the soil's friction angle.

Table 1. Pile elastic properties.

Type	D [m]	t [m]	ρ [t/m^3]	v [-]	E [GPa]	I [m^4]
pile filled with sand						
tubular	1.8	0.031	7.86	0.2	210	0.0674
solid	1.8	-	2.397	0.2	27.51	0.5153
hollow structure						
tubular	1.8	0.031	7.86	0.2	210	0.0674
solid	1.8	-	0.532	0.2	27.47	0.5153

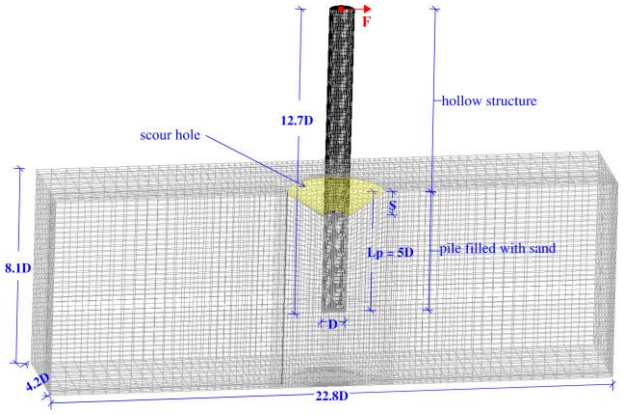

Figure 1. Mesh of the scoured soil-pile system used for FE analysis in Abaqus (adapted from Askarinejad et al., 2022).

2.2 Constitutive model

To reproduce the cyclic soil response, a hypoplastic constitutive model was implemented. This allows a strain and stress-path dependent stiffness adaptation for the simulation of strain accumulation under loading, unloading and reloading stress paths (von Wolfersdorff, 1996; Niemunis and Herle, 1997). With the hypoplastic model, the ratcheting phenomenon (i.e. cumulative plastic deformation, with a constant increment per cycle; Cuéllar, 2011) in sand was simulated. Readers are referred to Askarinejad et al. (2022) for further details about the implementation of hypoplasticity. A drained Geba sand was used with the parameters shown in Table 2 (Azúa-González et al., 2019). These parameters correspond to a fine sand with a d_{50} of 0.12 mm and a relative density of 0.63.

Table 2. Hypoplastic model for Geba sand (Azúa-González et al., 2019).

von Wolffersdorff´s model parameters							
φ'	h_s	n	α	β	e_{i0}	e_{c0}	e_{d0}
[°]	[MPa]	[-]	[-]	[-]	[-]	[-]	[-]
34	2500	0.3	0.11	2	1.28	1.07	0.64
IS model parameters							
m_R	m_T	R	β_R	χ			
[-]	[-]	[-]	[-]	[-]			
5.5	3.9	10^{-4}	0.3	0.7			

2.3 Validation

The results obtained through centrifuge testing in Askarinejad et al. (2022) were used for validation. The numerical model described previously was subjected to a horizontal cyclic load applied on the top of the structure with a magnitude of 100 kN and a load frequency of 1 Hz with $N = 10$ load cycles.

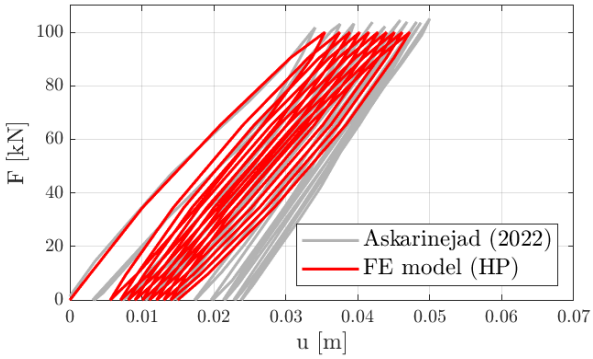

Figure 2. Validation results with hypoplasticity vs. centrifuge results from Askarinejad et al. (2022).

The FE model with hypoplasticity yielded similar results compared to those presented by Askarinejad et al. (2022). Figure 2 shows the horizontal displacements u at the top of the structure (loading point) plotted against the loading force F. A good agreement of the results with the centrifuge data is found, especially for the first load cycles. Hence, the hypoplastic model was considered validated and applied for further investigations of scour affecting the lateral soil-pile response under cyclic loading.

3 RESULTS AND DISCUSSION

The FE model described previously was subjected to a cyclic load with an amplitude of $F = 50$ kN at the top of the structure and a frequency of $f = 1$ Hz during $N = 10$ cycles as a simplified horizontal load representing a wind-wave resultant. For simplicity, only one-way load cycles were considered. Figure 3 and Figure 4 show the dimensionless load-displacement curve for different scour depths $S = \{0; 0.5D; 1.0D\}$ for the small and the large diameter monopiles respectively. A similar behaviour is observed for both models. In Figure 4 it is seen that the higher scour depth ($S = 1.0D$) moves away from the cases with $S = \{0; 0.5D\}$, evidencing the (large diameter) monopile vulnerability to scour compared to the small diameter monopile. The scour depth is linked with D, i.e. a higher D causes a higher absolute S. The displacements were recorded at the loading point (i.e. the top of the structure). The load was normalized by the dead load of the tubular pile ($V = m_{pile}\, g$) and the displacement was normalized by D. Figure 6 shows the soil horizontal stresses (σ_{11}) and the horizontal displacements (u_1) for $S = 0.5D$. Figure 5 shows the evolution of the maximum displacements with N. As expected, the accumulated displacements increase with increasing scour depth due to the loss of lateral bearing capacity given the shorter embedment length and the material degradation with increasing cycling.

It is seen from Figure 5 that the displacement accumulation increases at a higher rate with increasing scour depth. The incremental rate $(u_{N=10} - u_{N=1})/u_{N=1}$ increases from 13% (for $S = 0$) to 19% (for $S = 1.0D$) in the first ten cycles. This confirms that scoured monopiles are more vulnerable to cyclic loading compared to non-scoured monopiles or those with scour protection. Figure 6 (u_1) shows that plastic displacements remain after a series of cycles at the top and bottom of the pile, suggesting a permanent tilt for a combined action of scour and cyclic loading. The simulations are limited by the computational power required, which restricts the number of cycles that can be simulated in a reasonable amount of time.

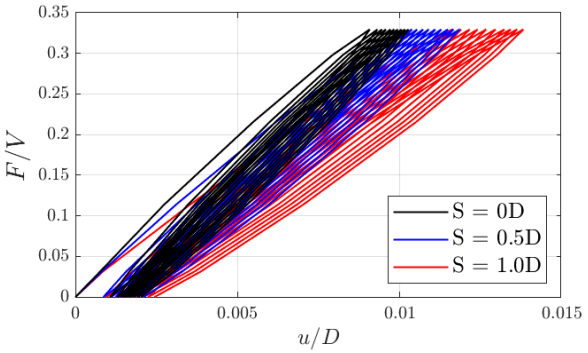

Figure 3. Load-displacement curve for S = {0; 0.5D; 1.0D} with D = 1.8 m.

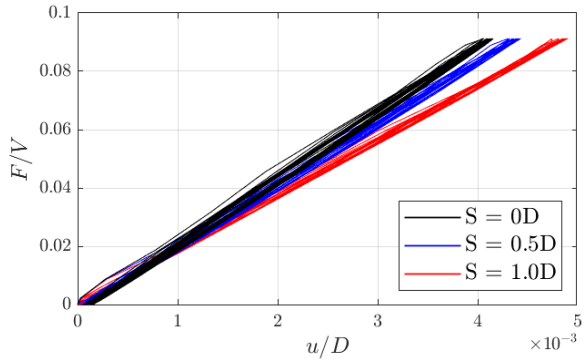

Figure 4. Load-displacement curve for S = {0; 0.5D; 1.0D} with D = 7.5 m.

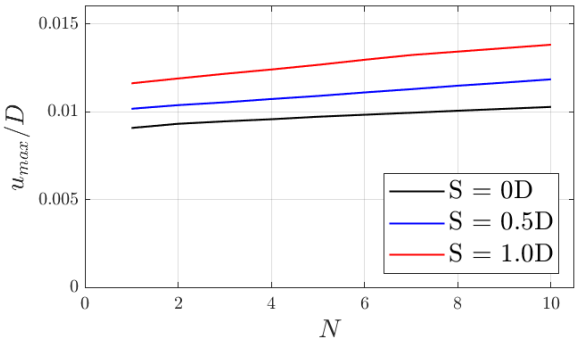

Figure 5. Evolution of maximum displacements with load cycles N for S = {0; 0.5D; 1.0D} with D = 1.8 m.

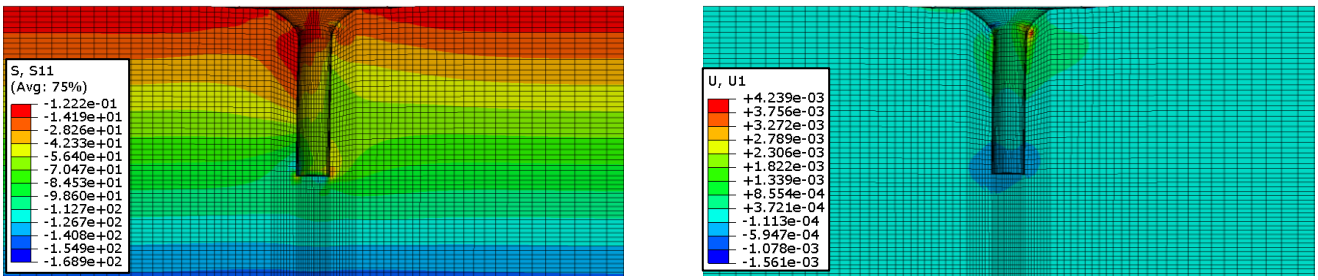

Figure 6. (l) Horizontal stresses (σ_{11}) in kPa; and (r) displacements (u_1) in m for S = 0.5D (scale factor: 50).

Future work will focus on investigating the long-term tendency of cycling and scour. To this end, Niemunis et al. (2005) proposed the high-cycle accumulation (HCA) model for number of cycles $>10^3$ and moderate or small strains, which may also be appropriate for offshore applications.

4 CONCLUSIONS

This paper studied the combined action of scour and cyclic loads obtaining the following conclusions:

- Hypoplasticity has shown to be an appropriate constitutive law to simulate cyclic loading in sands, including cycle-dependent permanent displacements and the ratcheting phenomenon for the explored cyclic loading conditions.
- As expected, the maximum and residual displacements increase with increasing *S*. However, this study demonstrates that also the displacement incremental rate increases with *S*. For the analysed monopile (S = 1.0D), during the first cycles the displacement incremental rate $(u_{N=10} - u_{N=1})/u_{N=1}$ reaches 19%, compared to only 13% for the S = 0 case.
- This study shows the vulnerability of scoured monopiles in terms of serviceability and economic viability. Hence, it is concluded that scour requires substantial consideration during design and, particularly, close monitoring of scour development and corresponding structural performance during operation.

ACKNOWLEDGEMENTS

The authors would like to gratefully acknowledge the expertise provided by Prof R. Simons (UCL), Dr J. Harris, and Dr N. Tavouktsoglou (HR Wallingford).

REFERENCES

Askarinejad, A., Wang, H., Chortis, G., Gavin, K. (2022) Influence of scour protection layers on the lateral response of monopile in dense sand, *Ocean Engineering*, 244(110377), https://doi.org/10.1016/j.oceaneng.2021.110377.

Azúa-González, C. X., van Zeben, J. C. B., Álvarez-Grima, M., van't Hof, C., Askarinejad, A. (2019). Dynamic FE analysis of Soft Boundary (SB) effects on impact pile driving response in centrifuge tests, In: *Proceedings of the XVII EXSMGE-2019*, Reykjavik, Iceland, https://doi.org/10.32075/17ECSMGE-2019-0821.

Cuéllar, P. (2011). *Pile foundations for Offshore Wind Turbines: Numerical and experimental investigations on the behaviour under short-term and long-term cyclic loading*, Doctoral thesis, TU Berlin. Available at: https://depositonce.tu-berlin.de/items/baebdda2-4a78-4db7-8986-ed6c9149d747/full, accessed: 29/08/2023.

López-Querol, S., Spyridis, M., Moreta, P. J. M., Arias-Trujillo, J. (2020) Simplified numerical models to simulate hollow monopile wind turbine foundations, *Journal of Marine Science and Engineering*, 8(11), pp. 1-25, https://doi.org/%20doi:10.3390/jmse8110837.

Niemunis, A., Herle, I. (1997) Hypoplastic model for cohesionless soils with elastic strain range, *Mechanics of cohesive-frictional materials*, 2(4), pp. 279-299, https://doi.org/10.1002/(SICI)1099-1484(199710)2:4%3C279::AID-CFM29%3E3.0.CO;2-8.

Niemunis, A., Wichtmann T., Triantafyllidis, Th. (2005) A high-cycle accumulation model for sand, *Computers and Geotechnics*, 32(4), pp. 245-263, https://doi.org/10.1016/j.compgeo.2005.03.002.

von Wolffersdorff, P.-A. (1996) A hypoplastic relation for granular materials with a predefined limit state surface, *Mechanics of cohesive-frictional materials*, 1(3), pp. 251-271, https://doi.org/10.1002/(SICI)1099-1484(199607)1:3<251::AID-CFM13>3.0.CO;2-3.

Whitehouse, R.J., Harris, J.M., Sutherland, J., Rees, J. (2011) The nature of scour development and scour protection at offshore windfarm foundations, *Marine Pollution Bulletin*, 62(1), pp. 73-88, https://doi.org/10.1016/j.marpolbul.2010.09.007.

Proceedings of the XVIII ECSMGE 2024
GEOTECHNICAL ENGINEERING CHALLENGES
TO MEET CURRENT AND EMERGING NEEDS OF SOCIETY
© 2024 the Authors
ISBN 978-1-032-54816-6
DOI 10.1201/9781003431749-616
Open Access: www.taylorfrancis.com, CC BY-NC-ND 4.0 license

ECSMGE 24
XVIII EUROPEAN CONFERENCE ON SOIL MECHANICS AND GEOTECHNICAL ENGINEERING

Physical modelling of the behaviour of buried gas pipe under surface loading

Modélisation physique du comportement de conduites de gaz enterrées sous chargement de surface

A. Mertz*, C. Dano, F. Emeriault, O. Jenck
Université Grenoble Alpes, CNRS, Grenoble INP, 3SR, Grenoble, France

C. Fernandez, A. Lebrun, M. Polo
GRTgaz, Bois-Colombes, France

**antoine.mertz@3sr-grenoble.fr*

ABSTRACT: This communication focuses on the behaviour of buried steel pipes submitted to surface loading such as traffic loading. A laboratory small-scale model has been developed to better understand the soil-pipe interaction. The final objective is to assess the existing design method, and develop them if required.The test set-up consists in a rigid tank with metric dimensions, filled with sand. Real steel pipes are scaled down at 1/3 on the length, leading to the relevant use of 100 mm diameter aluminium pipes. No gas pressure is simulated within the pipes, as it is then an unfavourable condition regarding the effect of surface loading on the pipe. Surface loading with up to 1000 cycles is applied using a vertical actuator acting on a plate. The procedure includes an extensive instrumentation, in particular strain gauges on the pipe and inner displacement sensors,. The experimental campaign permitted to assess the effect of the pipe radial stiffness (by varying the pipe thickness) on the pipe response due to monotonic then cyclic surface loading. The small-scale experimental results were upscaled at the real structure scale and compared to the existing design practice, to highlight its limits and the importance of taking the soil-pipe interaction into account.

RESUME: Cette communication porte sur le comportement des canalisations en acier enterrées soumises à des charges de surface telles que les charges de trafic. Un modèle réduit de laboratoire a été développé pour mieux comprendre l'interaction sol-canalisation. L'objectif final est d'évaluer les méthodes de dimensionnement existantes et de les améliorer si nécessaire. Le dispositif d'essai consiste en une cuve rigide de dimensions métriques, remplie de sable. Les canalisations en acier prototypes sont réduites à 1/3 de leur longueur, ce qui conduit à l'utilisation de canalisations en aluminium de 100 mm de diamètre. Des charges de surface jusqu'à 1000 cycles sont appliquées sur une plaque par un verin vertical. La procédure comprend une instrumentation extensive, en particulier par des jauges de déformation sur la canalisation et des capteurs de déplacement interne. La campagne expérimentale a permis d'évaluer l'effet de la rigidité annulaire de la canalisation (en variant son épaisseur) sur la réponse de la canalisation due aux charges de surface monotones puis cycliques. Les résultats expérimentaux en échelle réduite ont été extrapolés à l'échelle de la structure réelle et comparés aux méthodes de dimensionnement existantes afin d'en mettre en évidence les limites et l'importance de prendre en compte l'interaction sol-canalisation.

Keywords: Physical modeling; soil structural interaction; buried structures; gas transportations pipelines.

1 INTRODUCTION

Most of gas infrastructures are buried. During their lifetime, they can be affected by additional loads (roads, railways or embankments) compared to the design load cases, transmitted through the ground. Pipeline network operators then have to guarantee the integrity of the pipes and to accurately assess the stress increase in the pipe due to these additional surface loads. Based on the pioneering works by Marston & Anderson (1913) on rigid pipes and Spangler & Shafer (1938) on flexible pipes, it is well-known that the stress assessment is highly related to a soil – pipe interaction problem.

More recent improvements in the design methods lie on the reliable determination of the horizontal earth pressure (Scarino, 2003) or in the introduction of a parabolic distribution of the vertical load (Tian et al., 2015). Some of these improvements are in use nowadays, such as in the in-house software RAMCES from GRTgaz (one the French gas operator) used to predict the internal stresses inside a pipe, as well as its deformations to decide acceptability of various overloads. The results of the current experimental

study will be compared to the results from RAMCES predictions.

2 MATERIAL AND METHODS

The main interest of carrying lab testing (contrary to field testing) is to ensure controlled environnement and variables, with a good repeatability from one test to another. Subsequent sections will describe briefly the protocol and the materials used in the tests, while more details can be found in Mertz, 2023.

2.1 Test tank

The experimental campaign is carried out in a test tank (Figure 1), with dimensions 1 × 0.93 × 1.90 m^3, filled with sand and equipped with a vertical electric jack to apply a model surface loading.

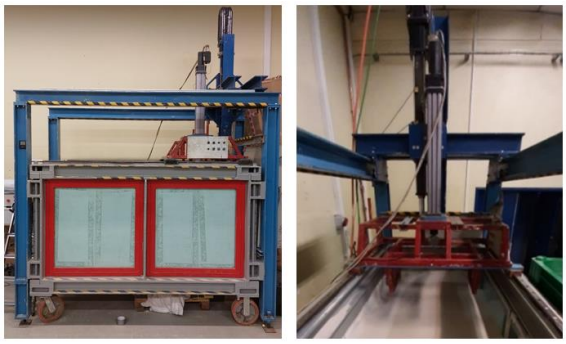

Figure 1. Tank (left) and loading system (right).

The soil used to fill the tank is a siliceous fine sand, uniform and poorly graded, denominated as Fontainebleau NE34 sand. Some of the sand characteristics are presented in Table 1, after Andria-Ntoanina et al. (2010). Filling is done by multiple layers, three of 0.2 m and one of 0.15 m, for a total sand thickness of 0.75 m, with he pipe center being 30 cm deep. Compaction is achieved for each layer using a vibrating plate, as shown on Figure 2, reaching a relative density of around 72 %.

2.2 Pipes

The pipelines used by GRTgaz are mainly made of steel, with nominal diameters ranging from 80 mm to 1200 mm, and thicknesses from 3 mm up to 30 mm. Such structures are not convenient to work with in lab conditions (in term of weight and size for handling, as well as required force to be applied during experiments). Thus, the choice has been made to work with small-scale model. Such scaling needs to be done with care, to avoid introducing bias in the model (scale-effect).

Table 1. Fontainebleau NE34 characteristics.

$d_{50}(mm)$	C_u	$\rho_{s\,(g/cm^3)}$	$e_{\min}$	$e_{\max}$
0.206	1.49	2.65	0.510	0.882

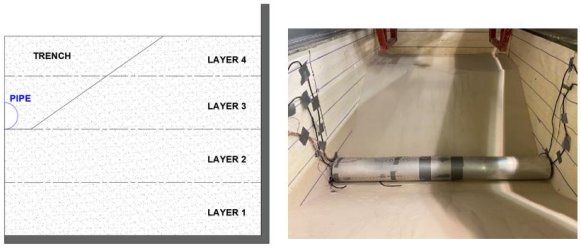

Figure 2. Scheme of the trench in half geometry (left), and pipe installed in the tank (right).

The scaling has been carried out using dimensional analysis, coming from the Vashy-Buckingham Theorem that describes the relationship between the properties of the model and the properties of the prototype, which takes the form of a scale factor λ (Garnier et al., 2007) such as:

$$\lambda = \frac{\text{model property}}{\text{prototype property}} \quad (1)$$

The scale factor on geometry is set to 1/3, meaning that all lengths of the prototype will be divided by 3 in the model scale. The reference prototype pipe, from GRTgaz catalogue, has a diameter of 300 mm. Therefore, a model pipe of 100 mm outside diameter and three different thicknesses (2 ± 0.05 mm, 1.75 ± 0.1 mm, and 1.35 ± 0.1 mm, respectively), have been considered, to investigate a wide range of annular rigidity of the pipe.

Dimensionnal analysis gives the scale factor on other metrics of the model, such as the stresses, that should also be 1/3 of the one of prototype pipes. This also runs for the Young‘s modulus. Thus, because prototype pipe are made of steel TUE360, with a Young‘s modulus of 210 MPa: the model pipes will then be made of aluminium 6060, with a Young‘s modulus of 69.5 MPa.

The resulting annular rigidity is presented in Figure 3, in which the error bar corresponds to the uncertainty resulting from the measured thickness deviation.

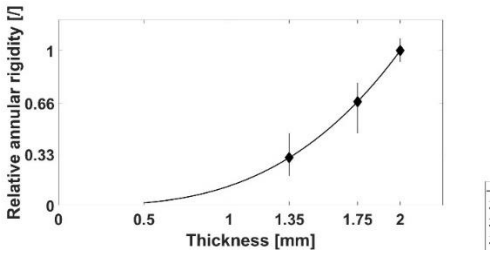

Figure 3. Pipe relative annular rigidity as a function of pipe thickness.

2.3 Loading

An EXLAR IX-40 electric jack ensures a vertical force, which is measured using a 20 kN S-shaped load cell. The load is distributed to the soil through a a 0.1 ×0.1 m² rigid aluminum plate, with four LVDT sensors, measuring the settlement and the tilting of the plate. Loading was applied with a constant velocity of the jack (0.05 mm/s) until the average stress under the loading plate reaches 100 kPa in model configuration (300 kPa in the prototype configuration), with unloading/reloading loops for everytime the loading exeed the previous maximum by 25 kPa. Preliminary tests showed that the bearing capacity of the soil with this surface plate geometry was reached for an average stress of around 110 kPa.

2.4 Instrumentation

This study uses a wide range of instrumentation, for both the pipe and the soil.

Bi-directional 350 Ω strain gauges are placed on the external surface of the pipe, with 45° of spacing between each, see Figure 4, in order to retrieve deformations in both longitudinal and ortho-radial directions at different pipe orientations.

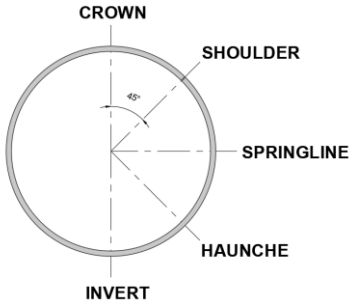

Figure 4. Placement of strain gauges.

Two flexure gauges AU/1 inside the pipe and miniaturized stress sensors placed 20 mm away from the pipe in the soil were also used, for measuring the pipe ovalisation and evolution of stresses in the sand respectively. However, these results will not be presented hereafter.

3 RESULTS AND DISCUSSION

3.1 Pipe stresses and evolution during cycles

The deformations on the pipe given by the strain gauges allow to calculate the acting stresses, in both directions (ortho-radial and longitudinal), assuming that the pipe behaves elastically. For a surface loading of 100 kPa, Figure 5 shows a maximum stress around 5 MPa (far below the yield stress of 60 MPa) for the ortho-radial stress at the springline of the 1.35 mm pipe (relative annular rigidity of 0.33).

Ortho-radial stress plot shows that the pipe is under compression at crown and invert, while experiencing tension at springline, compatible with an ovalisation of the pipe. Shoulders are in tension as well, indicating that the change from tension to compression is happening between shoulders and crown.

It can be seen that decreasing the pipe annular stiffness led to a significant increase in stress in the upper part (crown, shoulders), while variations are small to non-existent at haunches and invert. Longitudinal stresses indicate that the pipe experiences flexion, with compression at crown and tension at invert, as expected by the loading configuration (load concentrated on a small 0.1× 0.1 m² plate). Reducing the pipe thickness does not impose strong variation of the longitudinal stress, due to the fact that the longitudinal flexure rigidity is depending strongly on the diameter, but only marginally on the thickness.

The evolution of stresses during the application 100 cycles of loading between 1 and 100 kPa is presented in Table 2.

Table 2. Stress changes during cyclic loading.

Pipe thickness [mm]	***Max stress [MPa]***		***Stress change for 1000 cycles [%]***	
	Tension	*Compression*	*Tension*	*Compression*
2	0.91	-2.3	+11.7	+2.2
1.35	2.5	-4.5	+18.9	-28.2

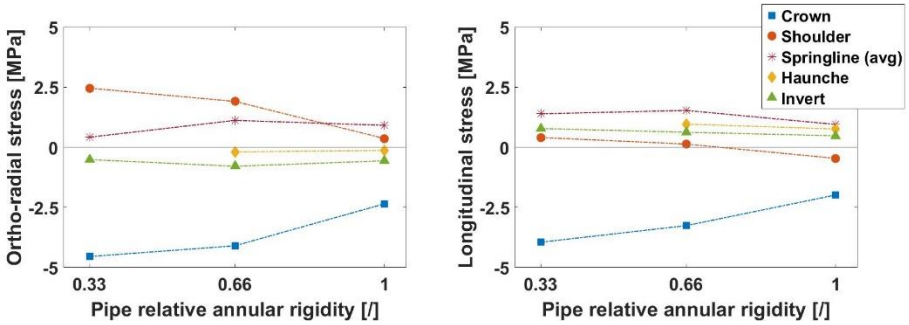

Figure 5. Measured ortho-radial (left) and longitudinal (right) pipe stress, for a surface loading of 100kPa (compression is negative).

Data from the 1.75 mm pipe are excluded due to a malfunction of the strain gauges during cyclic loading. The 2 mm pipe exhibits smaller changes in stresses when compared to the 1.35 mm one, which indicates that the relative stiffness between the soil and the pipe affects the cyclic behaviour.

3.2 Comparison with design models

Results were compared to the predictions made according to the RAMCES software. However, since this software is working at prototype scale, experimental data were upscaled, according to equation 1. This scaling also includes a corrective coefficient for the soil non-linear behaviour, based on numerical simulations, (see details in Mertz, 2023). The prototype situation thus corresponds to 4.25/5.25/6 mm thick steel pipes, with a diameter of 300 mm, loaded with 300 kPa on a 0.30 × 0.30 m² surface.

The metric used for the comparison is the safety factor F_s, defined as the ratio of the calculated stress to the experimental stress. A safety factor above 1 indicates that the model overestimates the actual stress of the pipe, leading to an opportunity of optimisation on the calculation method. The detailed analysis (Mertz, 2023) showed that RAMCES software captured the pipe behaviour quite well, but with F_s around 1.4.

4 CONCLUSIONS

Small-scale pipes with different annular rigidities have been tested in laboratory conditions, in which they were buried and subjected to a controlled surface loading. It appears that reducing annular rigidity increases recorded stresses in the pipe on some locations (crown and shoulder mainly), but also changes the observed behaviour during cyclic loading.

Comparisons with the RAMCES code show that there is an opportunity for optimisation, by improving the physical model used, which can lead to higher safety (by better representation of the pipe behaviour), as well as a more efficient design.

This work will be enriched with additional data, such as the pipe displacement and recorded soil stresses near the pipe, both radially and in the horizontal plane above it, and assessment of the soil-structural interaction will be done.

ACKNOWLEDGEMENT

We want to give special thanks to Grenoble Civil Engineering Department at IUT for their always-helpful assistance.

REFERENCES

Andria-Ntoanina, I., Canou, J. and Dupla, J.-C. (2010). Mechanical characterization of Fontainebleau NE34 sand with monotonic triaxial test CERMES, ENPC/LCPC, France. (In French).

Garnier, J., Gaudin, C., Springman, S.M., Culligan, P.J., Goodings, D., Konig, D., Kutter, B., Phillips, R., Randolph, M.F. and Thorel L. (2007). Catalogue of scaling laws and similitude questions in geotechnical centrifuge modelling. *Int. J. of Physical Modelling in Geotechnics,* 7(3), pp. 1-23. https://doi.org/10.1680/ijpmg.2007.070301.

Marston, A. and Anderson, O. (1913). The theory of loads on pipes in ditches. Bull 3I, Iowa Engineering Station, USA.

Mertz, A. (2023). Behavior of model buried gas pipelines under patch surface PhD dissertation, University Grenoble Alpes, France (in French).

Spangler, M. and Shafer, G. (1938). The structural design of flexible pipe culverts. *Highway Research Board Proceedings,* 17, pp. 235–239.

Scarino, H. (2003). Reappraisal of Marston's Formula. *Journal of Transportation Engineering*, 129(6), pp. 703-712. https://doi.org/10.1061/(ASCE)0733-947X(2003)129:6(703).

Tian, Y., Liu, H., Jiang, X. and Yu, R. (2015). Analysis of stress and deformation of a positive buried pipe using the improved Spangler model. *Soils and Foundations*, 55(3), pp. 485-492. https://doi.org/10.1016/j.sandf.2015.04.001.

Proceedings of the XVIII ECSMGE 2024
GEOTECHNICAL ENGINEERING CHALLENGES
TO MEET CURRENT AND EMERGING NEEDS OF SOCIETY
© 2024 the Authors
ISBN 978-1-032-54816-6
DOI 10.1201/9781003431749-617
Open Access: www.taylorfrancis.com, CC BY-NC-ND 4.0 license

ECSMGE 24
XVIII EUROPEAN CONFERENCE ON SOIL MECHANICS AND GEOTECHNICAL ENGINEERING

Bervie Braes at 10 years: critical review of the effectiveness of slope stabilisation measures

Bervie Braes à 10 ans: bilan critique de l'efficacité des mesures de stabilisation des pentes

S.B. Mickovski*
Glasgow Caledonian University, Glasgow, Scotland, UK
**Slobodan.Mickovski@gcu.ac.uk*

ABSTRACT: Bervie Braes is a 750 m long, and up to 55 m high coastal slope above a residential area and harbour in Stonenaven, Scotland, with a history of instability mostly associated with the road traversing the slope. Slope stabilisation works in terms of soil nailing, contour drains and seeding/planting were carried out in 2012 to minimise the risks posed to the former trunk road bisecting the Braes. In this paper, I critically review the effectiveness of the stabilisation measures using an established sustainability assessment tool. Through interviews with the local authority representatives, I am also detailing the timeline of monitoring and maintenance actions in the past ten years and mapping them against the global best practice in terms of sustainability and resilience. Based on the results of our investigation, I am concluding this paper with recommendations for future actions and research that will lead towards more efficient slope stabilisation and use of vegetation for civil engineering purposes.

RÉSUMÉ: Bervie Braes est une pente côtière de 750 m de long et jusqu'à 55 m de haut au-dessus d'une zone résidentielle et d'un port à Stonenaven, en Écosse, avec une histoire d'instabilité principalement associée à la route traversant la pente. Des travaux de stabilisation des talus en termes de clouage du sol, de drains de contour et d'ensemencement/plantation ont été réalisés en 2012 afin de minimiser les risques posés à l'ancienne route nationale coupant en deux le Braes. Dans cet article, J'examine de manière critique l'efficacité des mesures de stabilisation à l'aide d'un outil d'évaluation de la durabilité établi. Grâce à des entretiens avec les représentants des autorités locales, je détaille également le calendrier des actions de surveillance et de maintenance au cours des dix dernières années et les comparons aux meilleures pratiques mondiales en termes de durabilité et de résilience. Sur la base des résultats de notre enquête, Je conclus cet article par des recommandations pour des actions et des recherches futures qui conduiront à une stabilisation plus efficace des pentes et à l'utilisation de la végétation à des fins de génie civil.

Keywords: Sustainability; resilience; erosion; landslides; eco-engineering; slope stability.

1 INTRODUCTION

Bervie Braes is a 750 m long, and up to 55 m high coastal slope above the old harbour in Stonehaven, north-east Scotland. The slope is bisected by a former trunk road (Bervie Road) which once served as a main access route to Stonehaven. Since being downgraded in the 1980s, this road serves mainly as the tourist route that connects Stonehaven with the nearby War Memorial and Dunnottar Castle to the south.

Bervie Braes has historically suffered from instability, often demonstrated as shallow landslides, debris or mud flows, and erosion (Mickovski et al., 2013). These instabilities, together with the risk they posed to the residential properties at the toe of the slope, were the main reason for procuring and completing slope stabilisation measures in the period 2007-2012. The funding for these measures came from the Scottish Government and Local Authority (LA) with the stabilisation works focussing on the slope sections below Bervie Road which were most at risk of instability and failure (Mickovski et al., 2016).

The works carried out in 2012 comprised soil nailing of different sections of the lower slope, drainage works on the road and lower slope, as well as ground bio-engineering works on the lower slope (Mickovski 2014a,b).

After the completion of the works in 2012 (Figure 1), Bervie Road was reopened subject to restrictions while there was no formal programme of inspection and monitoring of the performance or efficiency of the constructed stabilisation measures.

The aim of this study is to critically review the changes occurring at Bervie Braes in the ten years immediately after the completion of the stabilisation works with a view of assessing the efficiency and

success of the stabilisation measures from sustainability aspect. An objective of this study is to also look at the future of Bervie Braes not only from the stability but also sustainability. It is hoped that this review and assessment can be used as a 'lessons learned' tool for projects with a similar context.

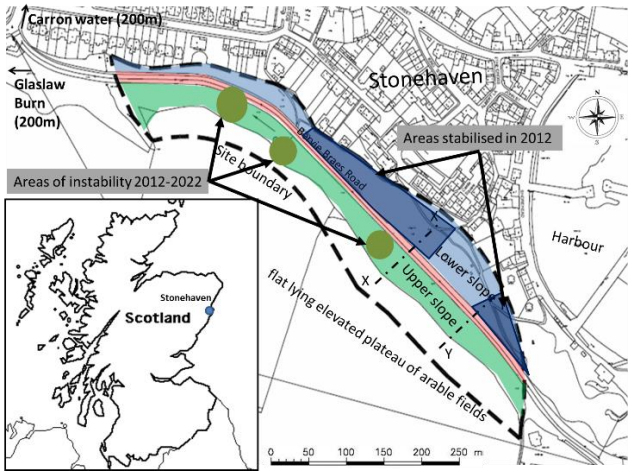

Figure 1. Plan of Bervie braes showing areas of completed works and issues in the last 10 years.

2 MATERIALS AND METHODS

Several methodological approaches were used for this study. Firstly, periodic site visits were carried out of the Bervie Braes site and it surroundings with a focus on the functioning of the constructed measures. These, mostly visual, surveys took place at different seasons. Secondly, three interviews with the LA representative were carried out in the period 2012-2023 in order to collect information on any reported issues on the site but also to query the strategic and tactical planning considerations concerning the site (Mickovski and Thomson 2016). Finally, the information from the site visits and interviews with the LA was used to assess the sustainability of the post-construction stages of the Bervie Braes slope stabilisation project. This assessment was carried out using an established sustainability assessment framework (Mickovski and Thomson, 2017) with a view of providing more objective view of the post-construction activities/works as well as a guideline of what can be done to make the operation and maintenance stage more sustainable.

3 RESULTS

3.1 Site visits

The site visits were focussed on visual assessment and identification of any issues with the installed soil nails, drainage network, and planted/seeded vegetation. Due to the nature of the measure, it was not possible to visually inspect the actual soil nails which were buried so only selected number of soil nail heads, erosion protection cover and protective mesh were inspected on 16 occasions in the period 2012-2024 (Figure 2). There were no major structural defects in either the concrete heads or protective mesh detected, suggesting the nails were functioning as per the design. During the first 3 years after construction it was easier to locate and inspect the soil nail heads because of the size and extent of vegetation (Figure 3). After this period, the erosion protection cover (coir blanket) started to degrade and can now only be seen in few smaller areas which is also in accordance with the design.



Figure 2. South end of Bervie Road in 2012 (left),2014 (centre), and 2022 (right).

The drainage network visually surveyed included the drains on Bervie Road, the raking drains within the slope and the contour drain along the footpaths on the lower slope. During all site visits, all of the inspected appeared to be functioning with no standing water or visible contamination in the network. Although the contour drain covers appeared to collect gravel from the footpaths (Figure 4) on several occasions, the water within them appeared to flow without problems. Similarly, the road drains appeared to be functioning during all site visits despite the fine material deposited within them (noted on few occasions). Not all of the raking drains were seen to drain water through the pipes - only the ones in the zones where high ground water table was recorded during construction.



Figure 3. Results of hydroseeding and tree planting in 2012 (left),2014 (centre), and 2022 (right).

As designed, the vegetation cover on the stabilised slope increased from 0% after construction to around 50% in the two growing seasons after the completion of the works, around 90% after five seasons, to almost 100% in 2022 (Figure 3). The area with slower ground cover recovery was the southernmost part, which is higher than the crowns of the trees on the lower slope and most exposed to the elements. The trees and

shrubs planted in the more exposed areas grew slower than the ones planted in more protected zones. The planting success rate was around 80% with several trees being windthrown and quite a few vandalised over the past 10 years. It is worth noting that the windthrown/broken trees were reported to the LA after inspection and were replaced by the contractor during the defect rectification period.

3.2 Interviews

The interviews with the LA were used to clarify the timeline of actions/events post construction. In summer 2013 Bervie Road was re-opened (April to October only) with installation of orange/white barriers, a 2 tonne weight limit and 1.8 m width restriction for all vehicles. In autumn 2014 a cyclepath was constructed on the seaward side of the road to make the vehicle width reduction permanent. A gate at the southernmost end of the road was also constructed to allow for winter and/or emergency closure. The existing footway construction was left in place to minimise works close to the crest of the lower slope and plastic kerbs were used to minimise the load on the lower slope. In 2022 concrete surfacing and handrails were constructed to footpath on the lower slope leading from the harbour. The contour and raking drains were kept as constructed in 2012.



Figure 4. Controur drain along the stabilised exposed section in 2012 (left),2015 (centre), and 2023 (right).

There was no maintenance carried out in the nailed areas (Figure 5). Slope drains were inspected sporadically but there was no need for maintenance. The road drainage was jetted regularly and specifically after slips on the upper slope in order to keep it functioning. In 2022, the filter drain on the landward side of Bervie Braes was inspected with CCTV – it was found that the pipework was clear and functioning over the whole length although there has been weed growth in the filter material which will have to be cleared.

The interviews also revealed issues associated with the history of instability at Bervie Braes: a landslip on the upper slope in 2014 blocked the inlet to the drain pipe in a storm which resulted in water flowing down the road into Stonehaven. After this, inlet headwall was moved further up the gully on the upper slope, with the extension of the pipe constructed as a large filter drain, to drain the area of the upper slope and prevent any similar blockages to the inlet. The upper slope area slope was cleared up and regraded. There have been some further minor slips in the gully during heavy rainfall events but the drain has not been blocked again.



Figure 5. Nailed section in 2012 (left) and 2022 (right).

There were no further slips on the upper slope until winter 2022 when there was a surface slip (Figure 6). The barriers contained the slip as intended however the road has remained closed to traffic since the slip pending investigation and implementation of a remedial stabilisation scheme. Ground investigation has established that the cause is buildup of groundwater in the slope causing surface failures, exacerbated by a potential failure of a historic drainage system on the slope. Since there was no evidence of deeper failure risk, a remedial scheme to construct filter drains in the affected area is being prepared and should be completed by Summer 2023. When that is complete the road is planned to re-open to traffic.

Cracking in carriageway in the northern, unnailed section of Bervie Road, was noted in 2021 and has been monitored since. This was a section that showed movement prior to the main works and was excavated and reinstated at that time. Investigation was carried out by installing boreholes and inclinometers but no movement was detected during the three month monitoring period. The boreholes are being left in place and further long-term monitoring both visually and with inclinometer will be carried out to determine if any remedial works are required.



Figure 6. Upper slope instability (left) and cracks in the road indicative of deeper-seated instability (right).

Finally, the interviews revealed that in the last ten years the LA worked on Bervie Braes (and other

similar projects in their portfolio) under a significant resource restraint. All the actions/works at Bervie Braes were carried out with LA funding, usually as a reactive mechanism after a significant issue has been reported.

3.3 Sustainability assessment

The two post-construction stages (Monitoring and Long-term considerations) were re-assessed in terms of sustainability key performance indicators of an existing framework (Mickovski and Thomson, 2017). The average score for the monitoring stage was 2.0 (cf. 2.9 in 2012), while the average score for the Long-term stage was 2.8 (cf. 3.0 in 2012) – both of which indicate detriment to the baseline sustainability value (3.0; where 1.0 is very detrimental and 5.0 is very beneficial to sustainability). This is mainly due to the lack of monitoring plan (which, in itself is partly due to the lack of funding and partly due to the traditional reactive approach by the LAs) and lack of focus on future sustainability, ecosystem/biodiversity, and resilience (Mickovski et al., 2022).

4 CONCLUSIONS

The slope stabilisation measures installed in 2012 appear to be functioning as designed. While no major structural damage or deterioration has been noted with the soil nails, the drainage network and the vegetation cover were subject to minor maintenance works in the last 10 years, which helped in keeping them functional and effective. These findings are in line with similar projects in Europe (Mickovski et al., 2022).

No landslips or erosion events occurred on the lower slope (especially not in the stabilised sections) in the past 10 years. However, several landslips occurred on the upper slope and there is an indication that a bigger mass movement may have been reactivated under the Bervie Road in 2022, at a section which has not been stabilised in 2012. The interview with the LA representative revealed that resourcing issues both in terms of physical and financial resources were the major obstacle to extending the stabilisation works and pro-active management of the risks on the braes.

While the above occurrences highlight the stability brought to the braes by the works in 2012, they also confirm that instability may still occur in the areas which have not been stabilised (Mickovski, 2018). In order to mitigate these risks, there is a need for more formal monitoring plan, especially for the upper slope and the sections which have not been stabilised, targeting the links between the climate, precipitation, ground water, slope stability and the vegetation as the basis for increasing ecosystem services provision, sustainability and resilience (Mickovski, 2021).

ACKNOWLEDGEMENTS

I am grateful for the help of Mr James Black (Aberdeenshire Council, retired) for access to information, Dr Alejandro Gonzalez-Ollauri during the site visits, and the financial support provided by the Civil Engineering and Environmental Management Department at Glasgow Caledonian University.

REFERENCES

Mickovski, S.B. and Thomson, C.S. 2016. Innovative Approach in the Stabilisation of Coastal Slopes. Engineering Sustainability, 171(1): 15–24, DOI: 10.1680/jensu.16.00047.

Mickovski, S.B. and Thomson, C.S. 2017. Developing a framework for the sustainability assessment of eco-engineering measures. Ecological Engineering, 109: 145-160. DOI: 10.1016/j.ecoleng.2017.10.004.

Mickovski S.B., Black J.D. and Smith M.J. 2013. Innovative use of ECC (NEC3) for procurement and management of infrastructure projects with limited funding: Bervie Braes case study *In:* Smith, S.D and Ahiaga-Dagbui, D.D (Eds) *Procs 29th Annual ARCOM Conference,* 2-4 September 2013, Reading, UK, Association of Researchers in Construction Management, 799-808.

Mickovski, S.B. Gonzalez-Ollauri, A. Thomson, C.S. Gallagher, C.E. and Tardio, G. 2022. Assessment of the Sustainability Performance of Eco-Engineering Measures in the Mediterranean Region. Land, 11(4), 533, DOI:10.3390/land11040533.

Mickovski, S.B., Lindsay, F.M., and Smith, M.J. 2016. Construction and testing of self-drilled soil nails. Geotechnical Engineering, 169(6): 541–553. DOI: 10.1680/jgeen.15.00149.

Mickovski S.B. 2014. Stabilisation of former trunk road embankment using combined structural and eco-engineering strategies. In Lakušić, S (ed.) Proc. 3rd Int'l Conf. on Road and Rail Infrastr. CETRA2014, Split, Croatia 28-30April, 2014.

Mickovski, S.B. 2014. Resilient design of landslip prevention measures: a case study. Proceedings of the ICE - Forensic Engineering. 168(2):96-106. DOI: 10.1680/feng.14.00001.

Mickovski, S.B. 2018. Risk-based framework accounting for the effects of vegetation in geotechnical engineering. CE / Papers. 2, 2-3, p. 377-382. DOI:10.1002/cepa.700.

Mickovski, S.B. 2021. Re-Thinking Soil Bioengineering to Address Climate Change Challenges. Sustainability 2021, 13(6), 3338; DOI: 10.3390/su13063338.

Proceedings of the XVIII ECSMGE 2024
GEOTECHNICAL ENGINEERING CHALLENGES
TO MEET CURRENT AND EMERGING NEEDS OF SOCIETY
© 2024 the Authors
ISBN 978-1-032-54816-6
DOI 10.1201/9781003431749-618
Open Access: www.taylorfrancis.com, CC BY-NC-ND 4.0 license

ECSMGE 24
XVIII EUROPEAN CONFERENCE ON SOIL MECHANICS AND GEOTECHNICAL ENGINEERING

Experimental tests to evaluate skirt penetration resistance in scour protection for offshore foundations

Essais expérimentaux pour évaluer la résistance à la pénétration de la jupe dans la protection contre affouillements pour les fondations offshore

M. Miranda, J. Castro*, E. Varela, M. Jahanshahinowkandeh
Universidad de Cantabria, Santander, Spain

J. Sarmiento, R. Guanche
IH Cantabria, Santander, Spain

**castrogj@unican.es*

ABSTRACT: Full scale experimental tests were performed to evaluate the penetration resistance of steel plates (skirts), which are present in different types of offshore foundations, like mud-mat foundations. This research is motivated by the design of the jacket foundation for the DolWin kappa offshore substation, within the framework of DolWin6 project Penetration resistance is well-studied in clays and sands, but there is limited information on penetration in coarse granular materials, which are typically used as scour protection. Direct extrapolation of penetration resistance in sands is not possible because of the grain-size effect. Several plate thicknesses and gravel sizes were used to study the influence of the grain-size effect on the penetration resistance. The results of the experimental tests showed a strong dependence of penetration resistance on penetration depth as expected, but also a significant dependence on skirt thickness and gravel grain size. A good agreement with experimental results has been found when analytically interpreting the penetration resistance using traditional bearing capacity formulas, but with an equivalent skirt thickness related to the real skirt thickness and to the grain size, to account for the grain-size effect.

RÉSUMÉ: Des essais expérimentaux à grande échelle, ont été réalisés pour évaluer la résistance à la pénétration des jupes, qui sont présentes dans différents types de fondations offshore, telles que les fondations de type mud-mat. La résistance à la pénétration est bien étudiée dans les argiles et les sables, mais il y a peu d'informations sur la pénétration dans les matériaux granulaires grossiers, qui sont généralement utilisés comme protection contre l'affouillement. L'extrapolation directe de la résistance à la pénétration dans les sables n'est pas possible en raison de l'effet de la taille des grains. Plusieurs épaisseurs de plaques et tailles de graves ont été utilisées pour étudier l'influence de l'effet de la taille des grains sur la résistance à la pénétration. Les résultats des essais expérimentaux ont montré une forte dépendance de la résistance à la pénétration par rapport à la profondeur de pénétration, comme prévu, mais aussi une dépendance significative par rapport à l'épaisseur de la jupe et à la taille des grains de graves. Un bon accord avec les résultats expérimentaux a été trouvé lors de l'interprétation analytique de la résistance à la pénétration en utilisant les formules traditionnelles de capacité portante, mais avec une épaisseur de jupe équivalente liée à l'épaisseur réelle de la jupe et à la taille des grains, pour tenir compte de l'effet de la taille des grains.

Keywords: Offshore; foundations; experimental test; skirt; penetration.

1 INTRODUCTION

Offshore wind has a key role in the path towards a net-zero energy mix, it has a large potential for further development and for supplying cheap, clean and safe energy. In fact, offshore wind offers the opportunity to exploit 80% of Europe's offshore wind resource by unlocking shallow to deep water sites. Besides, in the coming years, the power from offshore wind is expected to become cheaper than that from onshore wind because of the larger turbine sizes and the fact that the consistent winds out on the sea allows higher load factors (UK Department for Business, Energy and Industrial Strategy, 2020).

The foundation of offshore wind structures, and in particular critical structures like offshore substations, poses new challenges to a wide range of engineering disciplines like offshore geotechnics. In some cases, such as in skirted or mud-mat foundations, penetration of steel elements into the sea bottom is required to ensure structure stability (e.g., Lu and Maclaren, 2016).

The foundation of offshore structures sometimes requires a scour protection system, which traditionally

is composed of a combination of an armour layer and a filter layer (e.g., Sonneville et al., 2014; Escribano and Brennan, 2017). They are commonly installed in advance and then penetration of foundation steel elements (skirts, shear keys...) must be ensured into the scour protection.

Some existing standards and recommended best practices, namely API RP 2GEO (2011) and DNVGL (2017), provide guidance in evaluating the penetration resistance, by means of bearing capacity formulae (Figure 1) or correlations with cone penetration resistances, respectively. Also, some authors (e.g., Andersen et al., 2008; Houlsby and Byrne, 2005) have further studied the penetration resistance of skirted elements. However, all these studies are focused either on cohesive soils or on sandy soils (fine-grained, non-cohesive soils). Hence, there is limited experience or information in the literature about penetration resistance in gravels, which are the base of scour protection systems.

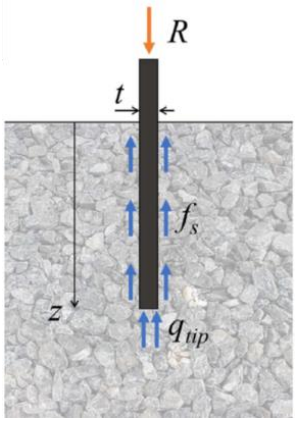

Figure 1. Plate penetration problem and calculation based on bearing capacity.

As presented in the following, extrapolation of formulations for sandy soils to gravels by adjusting the friction angle is not possible due to the influence of the gravel grain size. When the mean grain size (d_{50}) starts to be comparable to the steel plate thickness (t), the grain size increases the penetration resistance. Bolton et al. (1999) studied this particle size effect for cone penetration testing (CPT) in sands and found that the effect appears when the t/d_{50} ratio falls below about 20. More recently, Miyai et al. (2019) presented a notable contribution on the influence of the particle size on plate penetration.

This paper is aimed to study this plate penetration problem accounting for the influence of the gravel grain size and the proposed methodology is based on several full-scale tests. In this manner, this paper further analyses the data presented in Varela et al. (2022) and adds new relevant information, namely the results of direct shear tests on the gravel using a large box (300x300 mm).

2 TEST SET-UP

A 5x5x2.5 m^3 container was designed for the field tests in order to minimize the required volume of gravel and to facilitate the allocation of a 1,000-kN jack. The container was buried in the ground, so that its top part was approximately at the ground surface level. A loading frame was rigidly connected to the container and an auxiliary crane was installed in order to ease the manoeuvring of loads (Figure 2).



Figure 2. Testing container, loading frame and auxiliary crane.

The scour protection required a high-density gravel in this case, and thus an eclogite gravel from Norway was chosen. Two grain size distributions were used, a 0.5-1.5 in. gravel, with a mean grain size (d_{50}) of around 1 in. (25 mm), and 1-3 in. gravel, with a d_{50} of 2 in. (50 mm). Details of some gravel physical properties, grain size distribution and the controlled pouring process to reach the in situ density may found in Varela et al. (2022).

Two steel skirt thicknesses were tested, namely 15 and 80 mm. An additional case with a beveled tip may be found in Varela et al. (2022).

A total of 13 tests were carried out with both gravels and both skirts. The repetitiveness of the tests was ensured through four per test. A summary of the tests performed is given in Table 1. The test procedure was identical for all the configurations. Once the gravel was in place, each skirt was pushed (jacked) into the gravel by means of a hydraulic jack (Figure 3). Both, vertical displacement and vertical load, were measured during each test. The displacement of the skirt was recorded using two ultrasonic displacement sensors (Point 3 in Figure 3).

The hydraulic jack had a maximum capacity of 1,000 kN and a maximum stroke of 500 mm. Thus, for tests with the 80-mm-thick skirt, which had a target maximum penetration depth of 950 mm, the test

procedure was a step-based one, combining the available stroke with coupling steel extensions to the hydraulic jack. Therefore, an unloading-loading cycle is visible in the results.

Table 1. Summary of field tests. Test repetitions and penetration depth for the different test configurations.

Particle size	t=15 mm	t=80 mm
d_{50}=25 mm	4 (z<350 mm)	0
d_{50}=50 mm	4 (z<300 mm)	4 (z<950 mm)
	1 (z<500 mm)	

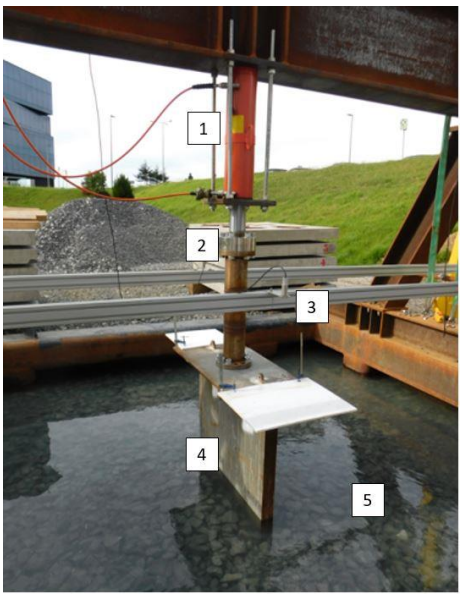

Figure 3. Test set-up. 1-hydraulic jack; 2-load cell; 3-displacement sensor; 4-steel plate; 5-eclogite gravel.

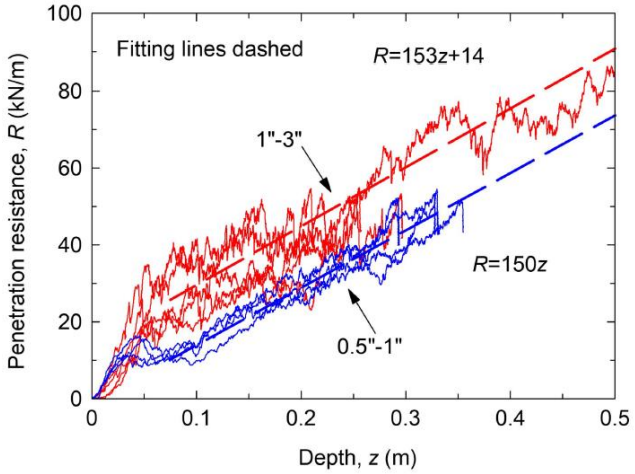

Figure 4. Penetration resistance of 15-mm-thick skirt in both gravels.

3 EXPERIMENTAL RESULTS

Figure 4 presents the penetration resistance versus penetration depth and their linear fittings for the 15-mm-thick skirt in both gravels. As expected, the load required to jack the skirt through the gravel with the larger grain size was higher and it increases with the penetration depth. Besides, the penetration resistance notably oscillated (noise), which was mainly a consequence of the grain-size effect (larger oscillations in the 1-3 in. gravel).

Figure 5 shows the results of the penetration of the 80-mm thick plate in the 1-3 in. gravel. As already explained, there is an unloading-reloading loop at 0.5 m of penetration. Obviously, the penetration resistance is larger for the 80 mm-thick plate than for the 15-mm thick one, but the penetration resistance is increased by a factor of around 2-2.5 times, while the ratio between plate thicknesses is larger.

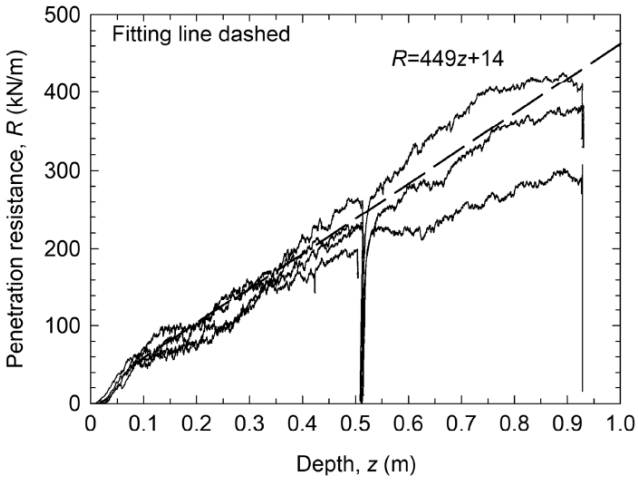

Figure 5. Penetration resistance of 80-mm-thick skirt in 1-3 in. gravel.

The theoretical background for the linear fittings is that the tip resistance is clearly the major component of the penetration resistance (around 98% for these cases, see Varela et al., 2022), while the contribution of the shaft resistance, which increases with the square of the penetration depth, is limited in comparison. From these linear fittings, the back-calculated values of the friction angle for each case using the real and equivalent thicknesses are summarized in Table 2.

It is also worth highlighting that there is a penetration depth beyond which the penetration resistance reduces its increase, e.g., around 0.4 m for the 15-mm-thick skirt and 0.8 m for the 80-mm-thick skirt. This agrees with the limit usually considered for the pile tip resistance of a depth around 20 times the pile diameter (e.g., Tomlinson and Woodward, 2008).

Table 2. Friction angles obtained from back analysis for real and equivalent skirt thicknesses (lengths in mm).

Particle size	t=15	t=80	t=15 + d_{50}	t=80 + d_{50}	t=15 + d_{99}	t=80 + d_{99}
d_{50}=25	54°	--	49°	--	47°	--
d_{50}=50	56°	51°	48°	48°	46°	46°

4 DIRECT SHEAR TESTS

Direct shear tests in a large equipment (300x300 mm box) were performed at different normal pressures, in samples of the smallest gravel (d_{50} =25mm). As expected, peak friction angles obtained decrease with normal stress (Table 3). The high values found, especially for low pressures, might be influenced by the scale factor, as the size of the particles is bigger than 1/6 of the box height. In addition, for loose gravel, the direct shear test results give also higher friction angles than the ones obtained under triaxial conditions, as shown in Varela et al. (2022). Comparing the values of friction angles estimated using the theoretical approaches and those obtained from the direct shear tests, most of them are in the same range, but the friction angles estimated using the equivalent plate thickness are more consistent.

Table 3. Friction angles obtained from direct shear tests at each normal stress for the gravel with d_{50}=25 mm.

σ'=	***25 kPa***	***50 kPa***	***100 kPa***	***200 kPa***	***300 kPa***	***450 kPa***
ϕ	67°	65°	55°	53°	49°	44°

5 CONCLUSIONS

The results of the experimental tests confirm that the penetration resistance increases with the penetration depth, the skirt thickness and the gravel grain size. Tip resistance component is the highest, being the frictional part just around 2% of the total. A good agreement is found between experimental data and semi-empirical approaches when using the equivalent skirt thickness hypothesis proposed by Miyai et al. (2019), in traditional approximations like Andersen et al. (2008). Therefore, this equivalent skirt thickness is the suggested calculation method. In future studies, a wider range of gravel sizes and skirt thicknesses should be tested, in order to increase the reliability of this approach.

ACKNOWLEDGEMENTS

This work is part of the R&D project "Advanced methodology for foundation of critical structures in offshore wind farms (CREMA)" funded by MCIN/ AEI /10.13039/501100011033. This study also forms part of the ThinkInAzul programme and is supported by Ministerio de Ciencia e Innovación with funding from European Union NextGenerationEU (PRTR-C17.I1) and by Comunidad Autónoma de Cantabria through the project entitled: "Tools for the analysis of the interaction between the seabed and the foundations of offshore renewable energy structures (CIMA)".

REFERENCES

Andersen, K. H., Jostad, H. P. and Dyvik, R. (2008). Penetration resistance of offshore skirted foundations and anchors in dense sand. *Journal of Geotechnical and Geoenvironmental Engineering* 134: 106-116. https://doi.org/10.1061/(ASCE)1090-0241(2008)134:1(106) .

API (American Petroleum Institute). (2011). Petroleum and natural gas industries—Specific requirements for offshore structures, Part 4—*Geotechnical and foundation design considerations*. API RP 2GEO.

Bolton, M. D., Gui, M. W., Garnier, J., Corte, J. F., Bagge, G., Laue, J. and Renzi, R. (1999). Centrifuge cone penetration tests in sand. *Geotechnique* 49: 543-552. https://doi.org/10.1680/geot.1999.49.4.543.

DNVGL. (2017). *Recommended Practice DNVGL-RP-C212. Offshore soil mechanics and geotechnical engineering*.

Escribano, D. E. and Brennan, A. J. (2017). Stability of scour protection due to earthquake-induced liquefaction: Centrifuge modelling. *Coastal Eng.* 12: 50-58. https://doi.org/10.1016/j.coastaleng.2017.08.015.

Houlsby, G. T. and Byrne, B. W. (2005). Design procedures for installation of suction caissons in sand. *Proc. ICE – Geotechnical Eng.* 158: 135-144. https://doi.org/10.1680/geng.2005.158.3.135.

Lu, P. and Maclaren, D. (2016). Geotechnical challenge of offshore mudmat foundation stability: Combining analytical and finite investigation of bearing capacity of sand overlying soft clay. *Geomech. Energy and the Environment* 6, 58-69. https://doi.org/10.1016/j.gete.2016.02.004.

Miyai. S., Kobayakawa. M., Tsuji. T. and Tanaka, T. (2019). Influence of particle size on vertical plate penetration into dense cohesionless granular materials (large-scale DEM simulation using real particle size). *Granular Matter* 21: 1-21. https://doi.org/10.1007/s10035-019-0961-z.

UK Department for Business, Energy and Industrial Strategy. (2020). The UK government expects offshore wind to become cheaper than onshore wind by the mid-2030s. *BEIS electricity generation cost report*. 24.08.2020.

Sonneville, B., van Velzen, G. and Wigaard, J. (2014). Design and optimization of scour protection for offshore wind platform DolWin beta. *Proc. ASME 2014* 33rd International Conference on Ocean, Offshore and Artic Engineering OMAE 2014. June 8-13, 2014, San Francisco, California, USA. https://doi.org/10.1115/OMAE2014-23154.

Tomlinson, T. and Woodward, J. (2008). *Pile design and construction practice*. Taylor and Francis.

Varela, E., Miranda, M., Castro, J., Sarmiento, J. and Guanche, R. (2022). Full-Scale Tests of Skirt Penetration Resistance in Gravel for Offshore Wind Structures. *J. Geotech. Geoenvironmental Engineering* 148(11): 04022084. https://doi.org/10.1061/(ASCE)GT.1943-5606.0002889.

Proceedings of the XVIII ECSMGE 2024
GEOTECHNICAL ENGINEERING CHALLENGES
TO MEET CURRENT AND EMERGING NEEDS OF SOCIETY
© 2024 the Authors
ISBN 978-1-032-54816-6
DOI 10.1201/9781003431749-619
Open Access: www.taylorfrancis.com, CC BY-NC-ND 4.0 license

ECSMGE 24
XVIII EUROPEAN CONFERENCE ON SOIL MECHANICS AND GEOTECHNICAL ENGINEERING

Impact of transport distance in life cycle assessments of geosynthetic reinforced soil walls

Impact de la distance de transport dans l'analyse du cycle de vie des murs en sol renforcé par géosynthétiques

A. Moncada*, S. Olivella
Universitat Politècnica de Catalunya·BarcelonaTech (UPC) and International Centre for Numerical Methods in Engineering (CIMNE), Barcelona, Spain

I.P. Damians
Universitat Politècnica de Catalunya·BarcelonaTech (UPC), International Centre for Numerical Methods in Engineering (CIMNE), and VSL International Ltd, Barcelona, Spain

R.J. Bathurst
Royal Military College of Canada, Kingston, Ontario, Canada

**anibal.moncada@upc.edu*

ABSTRACT: A prevailing methodology to evaluate the environmental impact and subsequent sustainability assessment of structures is the life cycle assessment (LCA). In civil engineering, LCA methodologies allow for the quantification and evaluation of environmental impacts of comparable structures, considering different materials, processes, and manufacturing. For a valid comparison, structures must satisfy the same function or need. Regarding geotechnical engineering field, particularly for retaining structures, previous studies have shown the reduced environmental impact of reinforced soil walls (RSW) over solutions such as gravity or cantilever walls. RSWs are constructed with polymeric or steel soil reinforcement materials with different geometries (e.g., straps, grids, or sheets). Aside from a structural point of view, the selection of reinforcement can be of lasting impact, as geosynthetic materials can play an important role in meeting the United Nations sustainability goals regarding counting carbon mitigation and adapting to the impacts of climate change. The present work details the LCA of geosynthetic RSWs with concrete panel facings. Environmental impact assessments consider various wall heights, with special emphasis on the sensitivity to transport distances on the overall scoring, considering local and worldwide scenarios. Results show transport activities can be the second to third most impactful factor for RSW LCA

RÉSUMÉ: L'évaluation du cycle de vie (ACV) est une méthodologie courante pour évaluer l'impact environnemental et la durabilité des structures. En génie civil, les méthodologies d'ACV permettent de quantifier et d'évaluer les impacts environnementaux de structures comparables, en tenant compte des différents matériaux, processus et procédés de fabrication. Pour que la comparaison soit valable, les structures doivent répondre à la même fonction ou au même besoin. Dans le domaine de l'ingénierie géotechnique, en particulier pour les structures de soutènement, des études antérieures ont montré la réduction de l'impact environnemental des murs en sol renforcé (RSW) par rapport à des solutions telles que les murs gravitaires ou les murs en porte-à-faux. Les murs de soutènement sont construits avec des matériaux de renforcement du sol en polymère ou en acier de différentes géométries (par exemple, des sangles, des grilles ou des feuilles). Outre le point de vue structurel, le choix du renforcement peut avoir un impact durable, car les matériaux géosynthétiques peuvent jouer un rôle important dans la réalisation des objectifs de durabilité des Nations Unies concernant l'atténuation des émissions de carbone et l'adaptation aux impacts du changement climatique. Le présent travail détaille l'ACV des murs de soutènement géosynthétiques avec parements en panneaux de béton. Les évaluations de l'impact sur l'environnement prennent en compte différentes hauteurs de murs, en mettant l'accent sur la sensibilité des distances de transport à la note globale. Sur la sensibilité des distances de transport sur la note globale, en considérant des scénarios locaux des scénarios locaux et mondiaux.

Keywords: Geosynthetics; reinforced soil wall; life cycle analysis; environmental impact; sensitivity analysis.

1 INTRODUCTION

Reinforced soil walls (RSWs) (also known as mechanically stabilized earth (MSE) walls) are a proven technology which compete with gravity and concrete cantilever walls to perform the same soil retaining wall function. RSWs are characterized by compacted soil layers with embedded longitudinal

reinforcing elements attached to the wall facing elements. The reinforcement can be of the extensible geosynthetic (polymeric) type with different geometries (e.g., straps, grids, or sheets) or relatively inextensible steel type (e.g., strips, grids, and ladders). Life cycle analysis (LCA) has shown that geosynthetic RSWs have significant advantages over gravity and cantilever walls with respect to environmental impact, particularly as structure height increases (Damians et al. 2017, Heerten 2012, Rafalko et al. 2010, Stucki et al. 2011, Zhu et al. 2022). This is largely due to the use of soil as the main structural component, rather than reinforced concrete.

In this study, LCAs were carried out to evaluate the environmental impact of transportation distances of the structural components employed in geosynthetic RSWs. Analyses used a detailed environmental inventory composed of construction materials, transportation to the project site, and construction activities (e.g., excavation, placement and compaction of soil materials) obtained from an environmental database.

2 LIFE CYCLE ANALSIS AND STUDY CASE DESCRIPTION

There are several commercially available software packages to perform LCA. This study used SimaPro v9.4.0.2 (PRé sustainability, 2022), together with ecoinvent v3.8 (Wernet et al. 2016) database (allocation, cut-off classification). There are many environmental impact calculation methods. The ReCiPe 2016 v1.1 (Huijbregts et al. 2017) and CED v1.11 (Frischknecht et al. 2003) methods were selected. The ReCiPe method allows for the evaluation of midpoint and endpoint indicators. For midpoint environmental indicators, 18 categories are calculated in parallel, including global warming potential (GWP), stratospheric ozone depletion, and mineral resource scarcity, among others. Endpoint indicators are the aggregate result of the 18 midpoint categories. The cumulative energy demand (CED) method calculates the consumption of energy throughout the proposed life cycle. As a first approach, the present study uses GWP (measured in equivalent emissions – CO_2 eq.) and CED (measured of consumed energy - J) to compare the effect of transportation distances in a life cycle analysis.

The functional unit was defined as a 1- m of running length of wall with a design life of 100 years. Problem boundaries include cradle-to-gate considerations and three height scenarios (3- m, 6- m, and 9- m tall). Table 1 shows the environmental inventory. Backfill material consisted of a quarried (not washed), high quality granular soil with $\phi = 36^o$, c = 0 kPa, and γ = 1800 kg/m^3. Reinforcements were assumed as polymeric (polyester) straps with 3.6 straps/m in the running wall face direction. Construction activities were included based on diesel or other energy consumptions. Spreading and compaction of the backfill material assumed an energy consumption of 1.97 MJ/m^3 (Stucki et al. 2011). Precast facing panels assumed an installation rate of 0.04 h/m^2 of wall face (Damians et al. 2017)

The main focus of this study is the effect of transportation distances on LCA results. Table 2 shows the modal, minimum, and maximum distance values. Fresh concrete for the levelling pad considered a maximum distance of 60 km, which takes into consideration that, usually, concrete mix-trucks must discharge their load within two hours. Transport distances for geosynthetic reinforcements reflect local and global supplier warehouse locations. Maximum distances were chosen to reflect viable options regarding construction logistics (e.g., maximum distance of 20 km for the backfill material).

Table 1. Structural components inventory for three wall heights.

Item	Wall height		
	3 m	6 m	9 m
Precast panels [a] [m^2]	3	6	9
Concrete [b] [m^3]	0.05	0.05	0.05
Polymeric straps [m]	29.87	119.47	268.8
Granular soil [c] [m^3]	11.5	45.2	101.3

Notes: [a]: includes concrete and steel; [b]: material for levelling pad for the vertical facing; [c]: includes material for drain layers.

Table 2. Proposed modal, minimum, and maximum values for transport distances.

Item	Transport distance [km]		
	Modal	Min.	Max.
Precast panels	50[a]	5[a]	60[a]
Concrete	50[b]	5[b]	100[b]
Polymeric straps	100[a] & 200[c]	50[a]	200[a] & 10000[d]
Granular soil	10[a]	5[a]	20[a]

Notes: [a]: transported by truck; [b]: transported by mix-truck; [c]: transported by train; [d]: transported by sea freight.

3 ENVIRONMENTAL IMPACT RESULTS

Figure 1a and 1b show the relative impact of each component (backfill material, construction activities, concrete and steel, geosynthetics, and transportation activities) and the total values with respect to wall

height from a LCA using modal transport distances (see Table 2). Concrete, steel and backfill materials are the highest contributors to CO_2 eq. and cumulative energy demand, followed by transportation activities. For a height of 3 m, transport activities constitute 13.8% of total CO_2 eq. (Figure 1a) and 19.3% of the total required energy (Figure 1b). For wall heights of 6 m and 9 m, the relative impact of transport-related emissions increases to 17.3% and 19.3%, respectively, for GWP, while CED values increase to 21.7% and 22.8%, respectively. Overall, as wall height increases, the relative impact of concrete and steel is reduced, while the impact of the remaining categories increases. Transport-related impacts are more noticeable for CED than for GWP.

Figure 1c shows the relative GWP impact of each inventory component with respect to transport-related emissions considering modal distances. The input for transportation-related emissions is based on mass and distance (units of metric tonnes×km), meaning that the larger the distance and/or the mass, the higher the impact. Most of the transport related emissions are, as expected, due to the backfill material transportation, since most of the mass of the inventory is soil. As wall height increases, the relative mass of the soil increases more than that of the other materials (e.g., concrete and steel). Polymeric straps are a small fraction of the total mass in the environmental inventory, which results in a negligible contribution to GWP emissions, as seen in Figure 2c.

Figure 2 shows total GWP emissions and CED requirements for all weight hights considering modal, minimum, and maximum transportation distances (see Table 2). At 3 m of height, impact scores vary from -8.2% to +13.4% for GWP, and from -11.4% to +10% for CED, between the mean and minimum or maximum distance scenarios. For 9 m of height, impact scores variations are of -10.4% and +19.3% for GWP, and -12.3% and 10% for CED. Transport-related emissions also depend on mass quantities, thus, for lower height walls (which require less material), the overall impact of distance of transport related activities is slightly lower than in higher walls. Regardless, results show a significant effect on calculated transport-related GWP and CED values due to transportation distance. Clearly, the selection of material suppliers, must take shipping distances into consideration and not only technical considerations and material costs at point of sale. With this in mind, differences between the local and global suppliers for polymeric strap reinforcement had a 4% or less impact on GPW and CED, which is attributed to the low mass of required polymeric straps.

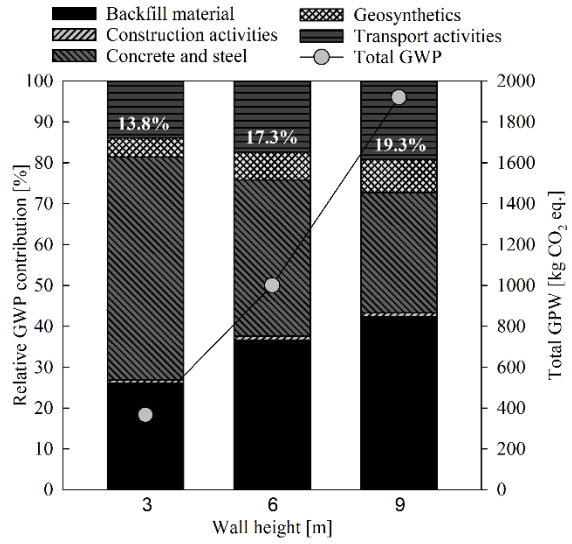

(a)

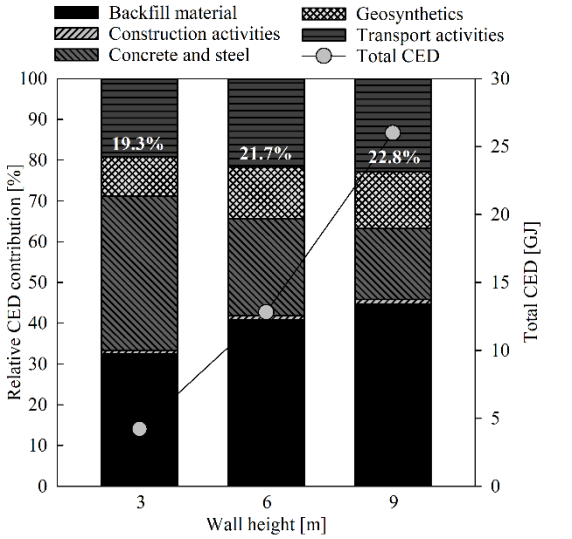

(b)

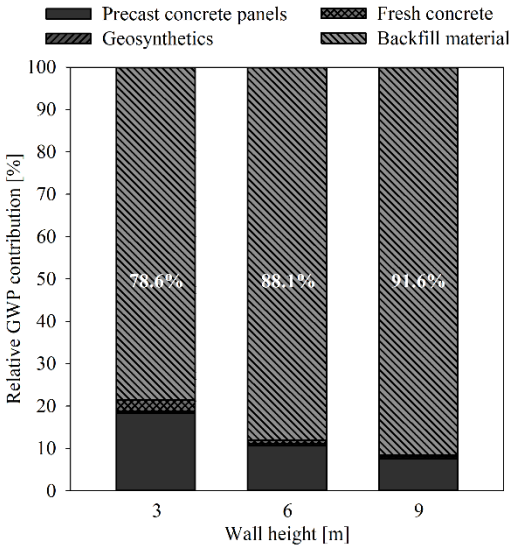

(c)

Figure 1. Relative impact [%] of inventory components and total values for (a) GWP [kg CO_2 eq.], (b) CED [GJ], and (c) with respect to transport-related emissions

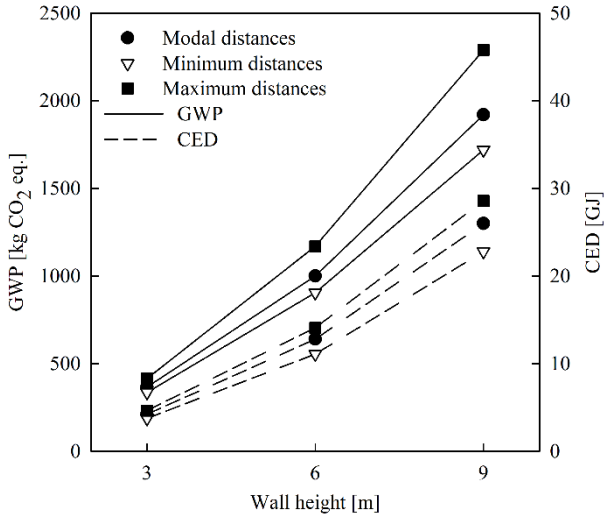

Figure 2. GWP and CED values considering modal, minimum and maximum transport distance values.

4 CONCLUSIONS

Life cycle analyses (LCA) were carried out to quantify the environmental impact of reinforced soil walls with polymeric straps. Analyses were focused on the impact of transport distances in the environmental inventory, using CO_2 eq. and cumulative energy demand as environmental indices. The main findings are:

- transport activities can be the third to second most impactful factor for RSW LCA, depending on the structure height.
- the environmental impact of transport activities will depend on distance and transported mass (or weight).
- backfill material transportation is the most significant contributor. Reducing soil transport distance or using an on-site soil could greatly reduce the environmental footprint.

The present work should be expanded by considering different backfill materials and reinforcement solutions, as well as probabilistic (Monte Carlo) simulations to widen the number of different scenarios. However, it is important to recall that a LCA is only one of several pillars of a proper sustainability assessment, which should also include economic, and social components (e.g., Damians et al. 2018).

ACKNOWLEDGEMENTS

The authors wish to acknowledge the support of GECO Industrial (Rep. of Korea), the Department of Civil and Environmental Engineering (DECA) of the Universitat Politècnica de Catalunya·BarcelonaTech (UPC) and the International Centre for Numerical Methods in Engineering (CIMNE), and the funding received from the Spanish Ministry of Economy and Competitiveness through the "Severo Ochoa Programme for Centres of Excellence in R&D" (CEX2018-000797-S-20-4).

REFERENCES

Damians, I.P., Bathurst, R.J., Adroguer, E.G., Josa, A., and Lloret A. (2017). Environmental assessment of earth retaining wall structures. *Environmental Geotechnics*, 4(6): 415-431. https://doi.org/10.1680/jenge.15.00040

Damians, I.P., Bathurst, R.J., Adroguer, E.G., Josa, A., and Lloret, A. (2018). Sustainability assessment of earth retaining wall structures. *Environmental Geotechnics*, 5(4):187-203. http://dx.doi.org/10.1680/jenge.16.00004

Frischknecht, R., Jungbluth, N., et.al. (2003). Implementation of Life Cycle Impact Assessment Methods. Final report ecoinvent 2000, Swiss Centre for LCI. Duebendorf, CH.

Heerten, G. (2012). Reduction of climate-damaging gases in geotechnical engineering practice using geosynthetics. *Geotextiles and Geomembranes* 30: 43–49. https://doi.org/10.1016/j.geotexmem.2011.01.006

Huijbregts, M.A.J., Steinmann, Z.J.N., Elshout, P.M.F et al. (2017). ReCiPe2016: a harmonised life cycle impact assessment method at midpoint and endpoint level. *Int. Journal of Life Cycle Assessment* 22: 138–147. http://doi.org/10.1007/s11367-016-1246-y

PRé sustainability B.V. (2022) SimaPro Multiuser (v9.4.0.2.) Amersfoort, Netherlands. Available at: https://simapro.com/, accessed: 01/10/2023

Rafalko, S.D., Sankey, J.E., and Freitag, N. (2010). Sustainability measures for MSE walls and baseline environmental impact evaluations. *Proceedings of the 2010 Earth Retention Conference*, Bellevue, Washington, USA. Geo-Institute of the American Society of Civil Engineers, Reston, VA, USA. https://doi.org/10.1061/41128(384)48

Stucki, M., Büsser, S., Itten, R. Frischknecht R., and Wallbaum, H. (2011). Comparative Life Cycle Assessment of Geosynthetics versus Conventional Construction Materials. European Association of Geosynthetics Manufacturers, ESU-services, Uster, ETH Zürich, Switzerland.

Wernet, G., Bauer, C., Steubing, B., Reinhard, J., Moreno-Ruiz, E., and Weidema B. (2016). The ecoinvent database version 3 (part I): overview and methodology. *Int. Journal of Life Cycle Assessment*, 21(9): 1218–1230. http://doi.org/10.1007/s11367-016-1087-8

Zhu, Y., Zhang, F., and Jia, S. (2022). Embodied energy and carbon emissions analysis of geosynthetic reinforced soil structures. *Journal of Cleaner Production*, *370*: 133510. https://doi.org/10.1016/j.jclepro.2022.133510

Proceedings of the XVIII ECSMGE 2024
GEOTECHNICAL ENGINEERING CHALLENGES
TO MEET CURRENT AND EMERGING NEEDS OF SOCIETY
© 2024 the Authors
ISBN 978-1-032-54816-6
DOI 10.1201/9781003431749-620
Open Access: www.taylorfrancis.com, CC BY-NC-ND 4.0 license

ECSMGE 24
XVIII EUROPEAN CONFERENCE ON SOIL MECHANICS AND GEOTECHNICAL ENGINEERING

An introduction to shared anchor in weak rock for floating systems

Une introduction à l' ancrage en partage de charges dans les roches faibles pour les systèmes flottants

L. Montalti, F. Moreno, V. Terente*
Cathie, Newcastle, UK

**victor.terente@cathiegroup.com*

ABSTRACT: Floating offshore wind is currently going through a significant expansion. However, there are existing gaps between naval architects and geotechnical experts that need to be bridged to achieve cost effective solutions. In this paper, Cathie presents a holistic methodology to cover some of these gaps. This paper investigates the opportunity of novel shared anchor concepts with specific reference to anchoring in rock. This solution not only offers a potential significant reduction on overall number of anchor points but also could allow a substantial reduction of the CAPEX/OPEX and the associated risk mitigation strategies. The study focuses on multiple lines anchor system simulations of anchor forces generated with example semisubmersible structure and a 15 MW wind turbine. The anchors in rock are assessed via state-of-the-art design methods for drilling and grout foundation and driven pile solutions with particular attention to the global capacity based on multi load cases.

RÉSUMÉ: L'éolien offshore flottant connaît actuellement une expansion significative. Cependant, il existe des écarts entre les architectes navals et les experts géotechniques qui doivent être comblés pour parvenir à des solutions rentables. Dans cet article, Cathie présente une méthodologie holistique pour combler certaines de ces lacunes. Cet article étudie l'opportunité de nouveaux concepts d'ancrage partagés avec une référence spécifique à l'ancrage dans la roche. Cette solution offre non seulement une réduction potentielle significative du nombre total de points d'ancrage, mais pourrait également permettre une réduction substantielle des CAPEX/OPEX et des stratégies d'atténuation des risques associées.
L'étude se concentre sur des simulations de systèmes d'ancrage à lignes multiples des forces d'ancrage générées avec un exemple de structure semi-submersible et une éolienne de 15 MW. Les ancrages dans la roche sont évalués via des méthodes de conception de pointe pour les solutions de forage et de coulis de fondations et de pieux battus, avec une attention particulière à la capacité globale basée sur des cas de charges multiples.

Keywords: Offshore floating; shared anchor; weak rock; multiple line anchor.

1 INTRODUCTION

Mooring systems are designed to ensure station keeping capabilities. Motions, both platform translation and rotation responses, must remain within operational boundaries and allow permissible peak anchor loads distributions, separated into horizontal, vertical and torsional components.

Shared anchors solutions for floating system will be a key driver to reduce the overall costs of floating wind farms. However, because of the novelty of shared mooring solutions, no applicable design approaches already exist to guide their application in floating offshore wind turbines (FOWT).

Sloan (2022) and Fontana (2019), evaluated novel multiline anchoring concepts for potential implementation in a real floating offshore wind farm; they assessed the limits on the number of lines per anchor determining the unique load characteristics of a multiline anchor and the cost benefit of the multiline system. However, both authors, did not include specific information on which type of anchors for particular soil condition could be used in a mooring shared anchors system.

With particular attention to foundations, based on the latest offshore leasing areas, and with specific interest for floating wind, it is expected that many of these development areas will be located in regions where rock at or near seabed is present. Therefore, for this paper, a solution for anchors in shallow rock geology is selected.

2 DESIGN MODEL METHODOLOGY

2.1 Case study model

The present study utilizes reference technology that is regularly used for multiple roles within the offshore wind community. The model chosen employs the most commonly studied platform type (semisubmersible) and mooring system type (catenary) in current FOWT technological stages.

The University of Maine (UMaine) Volturn US-S reference floating model designed to support the IEA Wind 15 MW WTG was modelled in OrcaFlex software (see IEA Wind, 2020).

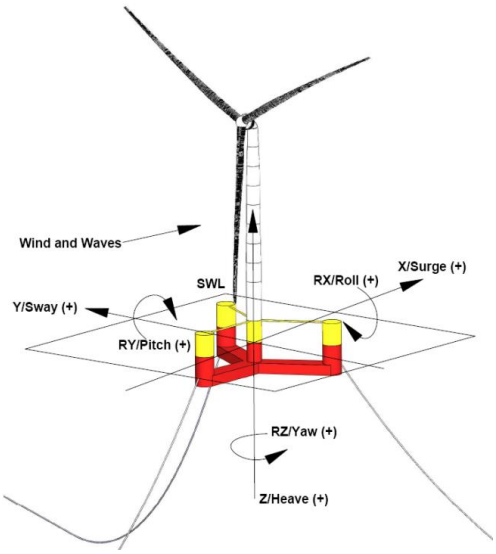

Figure 1. View of the floating system.

2.1.1 Simulation framework

It is important to evaluate the dynamics of the net force over a significant range of environmental and operational conditions. Through an engineering assessment and according to floating wind turbine structure standard - DNV-ST-0119, the most relevant design load cases (DLCs), combined with wind, waves and currents, includes DLC 1.6 and DLC 6.1.

2.1.2 Site characterization

The water depth in the present study associated with the lowest astronomical tide (LAT) is 200.0 m. The tidal water levels for this generic location have been considered.

2.1.2.1 Seabed conditions

The soil stratigraphy at the location predominantly comprises of dense to very dense sands overlying a band of extremely weak to very weak rock strength of mudstone and sandstone, UCS ranges from 2.6 MPa to 4.5MPa with selected values for the rock mass modulus from 44.8 MPa to 72.9 MPa.

2.1.3 Turbine and floating platform

The turbine chosen for this study is the IEA Wind 15 MW is a Class IB. It is composed of a direct drive generator in an upwind configuration. This WTG is coupled with the reference floater UMaine Volturn-U US. The coordinate systems used is shown in Figure 1, courtesy of University of Maine.

2.1.4 Mooring system definition

The use of 3 mooring lines per floater was selected as it is considered as a basic configuration for an initial study, see Figure 2.

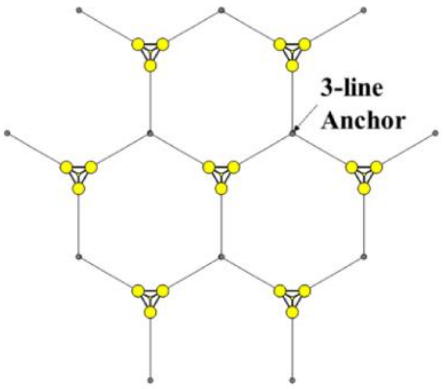

Figure 2. 3-Line anchor layout scheme, Fontana (2019).

2.2 Results

Multiline anchor loading is subjected to loading from any direction over the course of its design life, as the average direction of multiline anchor net force is aligned with the direction of the environmental load. Spatial layout of the multiline anchor for 3-line anchors with colour codes for each of the mooring tensions (Figure 3).

The maximum plan view misalignment angle assumed is ±10°. This is a typical inaccuracy value in the industry. The resolved mooring line load distribution is the characteristic for a catenary mooring system, separated into horizontal, vertical and torsional components. The multiline anchor net force is found using vector summation in each of the mooring line directions.

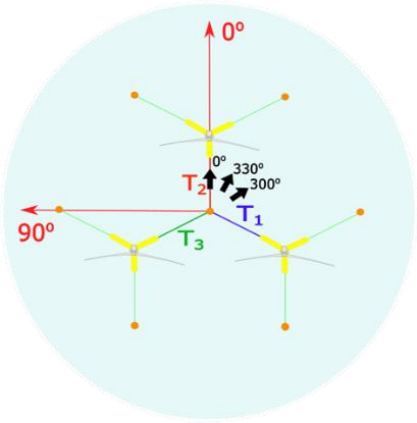

Figure 3. Line anchors.

2.2.1 Design load envelope

The design tension and moment are the sum of two factored characteristic components, the mean and the dynamic. The maximum loads (factored) calculated were a horizontal load of 4.89 MN and a vertical load of 1.05 MN for DLC 1.6 Rated-005, and a torsion load of 2.88 MN·m for DLC 1.6 Rated-011.

3 ANCHORS FOUNDATION CHECK

Based on the mooring system defined in the previous sections, for the shared anchors solution, a single pile foundation was selected which will be connected to 3 mooring lines. Due to the rocky geology condition and rock strength, the foundation was assumed to be installed via drill and grouted (D&G) solution.

3.1 Anchor geometry and assumptions

The anchor pile was selected having a diameter of 2.3 m and thickness of 45 mm with a total length of the pile of 16.5 m. The stick up from the seabed level is assumed approximately of 1.5 m high.

Figure 4 also shows some key considerations and assumptions for the concept design check discussed in this paper.

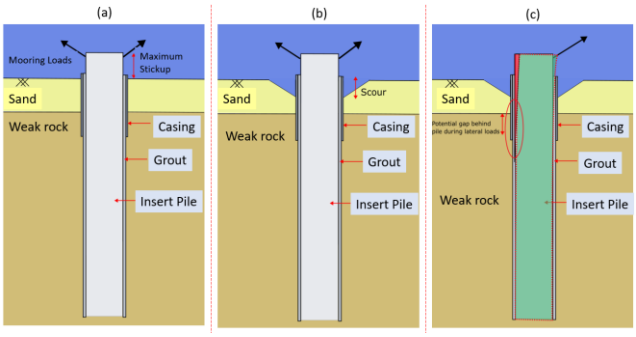

Figure 4. (a) anchor information (b) scour (c) potential presence of a gap behind the lateral loaded pile.

3.2 Axial Capacity check for D&G piles

The axial anchor capacity was estimated based on the methodology proposed by Seidel and Collingwood (2001). Such approach has a theoretical background and accounts for key effects that affect the shaft capacity of D&G piles in rock, i.e. - rock strength (intact drained and residual strength parameter), socket roughness and the general geometry of the interface resulting from the drilling process (rock mass modulus with its Poissons ratio, socket diameter, construction practice). Although the method considers key effects which influence the piles shaft capacity, the ultimate shaft resistance, f_s, remains expressed through the traditional simple relationship as expressed in the following equations:

$$f_s = \alpha \cdot UCS \quad (1)$$

$$SRC = \eta_c \cdot \frac{E_m}{UCS \cdot (1+v)} \cdot \frac{\Delta r}{d_s} \quad (2)$$

Where:
UCS = is the Unconfined Compressive Strength.
α = derived from plots provided by Seidel and Collingwood (2001) based on UCS and SRC values.
Δr = is the mean roughness height defined using Monash model; see Seidel and Collingwood (2001).
d_s = is the socket diameter.
η_c = is the construction method reduction factor, see Seidel and Collingwood (2001).
E_m = rock mass stiffness.
v = rock Poissons ratio.

Figure 5 shows the results for axial factored capacity against the design load for the worst case under DLC 1.6.

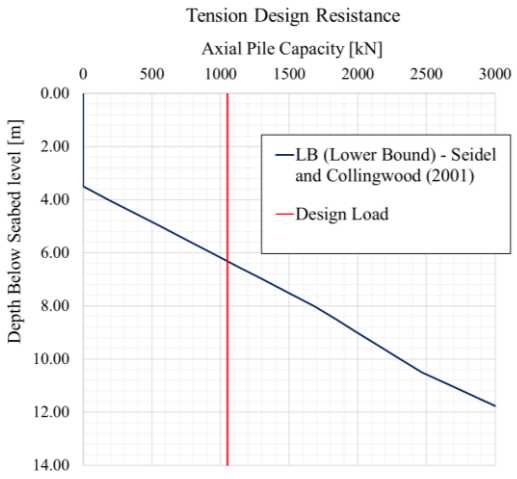

Figure 5. Tension axial capacity check based on Seidel and Collingwood (2001), factored load.

3.3 Lateral design check

3.3.1 PY curves based on Reese, Fragio and Abbs

Three different PY methodologies were used to evaluate the lateral response of the anchor, Fragio et al. (1985), Abbs (1983) and Reese (1997).

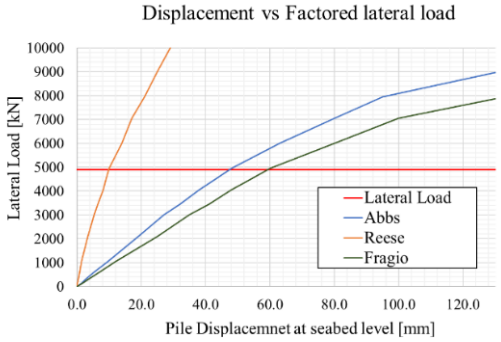

Figure 6. Horizontal displacements at mudline vs lateral load.

The PY curves were included in a 1D model and the Figure 6 show the results for this initial analysis. As expected, and as discussed from various authors, it can be observed how the PY curves from Reese give a stiff response compared to the other methods. Therefore, for a more detailed design is suggested to couple the method from Reese (1997) with the initial stiffness formulation proposed by Liang (2009) where a parametrical study based on 3D FE models was used to study various factors influencing the initial stiffness including the shaft diameter, the stiffness properties of the drilled shaft, the Poisson's ratio and the rock mass modulus.

3.3.2 Torsion check

The torsional response of a pile or anchor embedded in soil (or rock) is a subject which has received little attentions in the past. However, any pile foundation which is loaded laterally is liable to undergo some degree of torsion due to eccentricity of the applied load. Inadequate design against torsion may seriously affect the serviceability and safety of the foundation with catastrophic consequences.

As discussed in the previous sections, the proposed anchors solution with 3 mooring lines converging in a single pile foundation could lead in torsional forces applied to the pile. Structural misalignments, imperfections and anchor position are some of the main sources which will create a torsion force at the anchor. This was also discussed by Fontana et al. (2019), and Pillai et al. (2022), who stated that shared moorings or mooring misalignment during installation can lead to torsion loading.

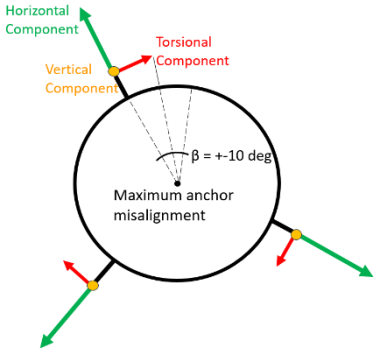

Figure 7. Torsional force from assumed mooring/structure misalignments.

Torsional failure is expected to begin from the surface and then progress down. For a rigid shaft the failure mode for torsion will be rapid where the peak torsion shear resistance is mobilised almost simultaneously everywhere along the shaft. However, for more flexible shafts the progress of slip down the shaft will occur more slowly and the situation may arise where the interface near the top of the shaft has reached a residual condition before the bottom of the shaft has reached a peak. In practical situations, the flexibility of the pile will lead to a gradual reduction in the angle of twist down the length of the pile (Carter & Kulhawy 1988).

Many design methods for check against torsion are available but in general they lack in critical details and justifications regarding the assumptions involved.

In general, the development of the maximum torsional resistance of the foundation involves a complicated interaction between the concrete-rock bonding at the sidewalls and at the tip, the roughness of the interface, and the relative stiffness and strength and surrounding rock mass Carter & Kulhawy (1988). At the moment there are no available full-size tests in weak rock where anchors are loaded under torsion.

There is also a key discussion which needs to be considered for future projects, in relation to the inadequate design of piles against the cyclic torsional loading which may affect the safety and serviceability of the foundation, leading to potential severe consequences (Vickery, 1979; Barker and Puckett, 1997). This discussion will not be part of this paper (which is mainly focused on ULS loads).

The cyclic load initiates the reversal of soil-pile interface shear stress, thus producing a progressive deterioration in strength and stiffness of the surrounding soil and consequently, pile soil interactive performance undergoes significant degradation (Basack, 2015).

There are some available analytical methods which can be used to assess the torsional response of piles, O'Neill (1964-a), Randolph (1981), Chow (1985),

Hache & Valsangkar (1988), Guo & Randolph (1996), Lin (1996), Carter & Kulhawy (1988). However, the majority of these methods were mainly focused on soils, sand/clay strata with some of them with clear limitations as discussed by Nasairat et at (2004). In this initial check the methodology proposed by Stuedlein et al. (2016), which is based on pile torsional response for cohesionless soil was used.

For anchors in weak rock, when the pile is under both axial, lateral and torsion loading there are no specific design methodologies. Further research is needed, also to confirm if the same assumption used for axial capacity, which is based on the working principle for lateral rigidity to prevent dilatancy (Seidel and Collingwood, 2001) could be also used for torsion and how the rock mass condition could affect the torsional response. The figure below clearly illustrates how small variations in assumptions (or methods) can influence the torsional response.

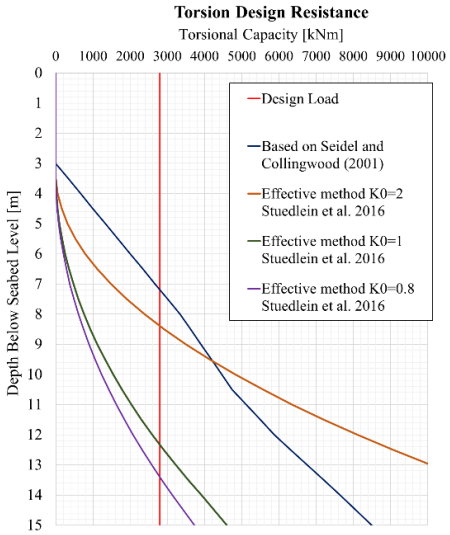

Figure 8. Torsional capacity (factored) vs anchor depth.

4 CONCLUSIONS

The majority of global offshore wind resource lies in water depths exceeding 60 meters, which are not suited to conventional bottom-fixed turbines (WFO, 2022). For example the 2022 ScotWind seabed leasing round has 60% floating capacity i.e. 15 GW of 25 GW total (Crown Estate Scotland, 2022), compared to zero farm-scale floating in previous UK leasing rounds. Floating foundations are therefore necessary to maximize this potential. However, the high capital cost of the support systems remains a primary obstacle. As discussed by Cerfontaine et al. (2023), to meet the expected target installation capacity for floating, the quantities of requited anchors are far beyond the current supply chain capacity, and create motivation for anchor optimization, or anchor sharing (Fontana et al., 2019), to reduce the overall demand. Therefore, the costs could be contained by minimazing the number of required anchors in the system via sharing anchors.

There are many new OWF leases in the East of Scotland and in many other areas for floating where it is expected rocky geology conditions. For these conditions, drilling and grouting could be one of the main option available for anchor solutions. Therefore, in this paper we have covered a conceptual level assessment, including the estimation of loads and the discussion on the effects of such loads on the dimensioning of a drilled and grouted anchor for lateral, torsion and tension capacity purposes.

The paper gives an initial understanding on the importance to provide and integrated approach based on naval architect inputs and geotechnical design in order to optimize wind farm layouts and achieve cost effective solutions via multiple mooring lines attached to a single anchor.

As also stated by Nuerberg et al. (2023), anchor sharing can also reduce the overall net forces acting on the anchors, as the forces from different turbines are "counteracting in direction, therefore the effect partially cancels each other".

With regards to the selected anchor foundation, a future study to be included as part of this line of research will be to investigate the effect of cyclic degradation present during multilateral loading, for instance. Mooring misalignment could also result in two-way cyclic loading (Fontana et al., 2019, and Pillai et al., 2022) which will be a key input to assess final anchor resistance degradation.

REFERENCES

Abbs, A.F. 1983. Lateral pile analysis in weak carbonate rocks. In Geotechnical Practice in Offshore Engineering, *Proceedings, Offshore Technology Conference*, Austin, Tex. Paper OTC 4852.

Barker, R. M., and Puckett, J. A. (1997). Design of Highway Bridges Based on AASHTO LRFD Bridge Design Specification. New York, NY: Wiley.

Basack, S. (2015). Design recommendations for pile subjected to cyclic load. *Marine Geores. Geotech*. 33, 356–360.

Carter, J.P. & F.H. Kulhawy. 1988. Analysis and design of drilled shaft foundations socketed into rock. *Report EL-5918*. Palo Alto: Electric Power Research Institute.

Cerfontaine et al., 2023. Anchor geotechnics for floating offshore wind: Current technologies and future innovations. Ocean Engrineering 279 (2023) 114327.

Chow, Y. K., (1985) “Torsional Response of Piles in Non-Homogeneous Soil,” Journal of Crown Estate, 2022. Offshore Wind Report 2021.

Dutt, R. N. and O'Neill, M. W. (1983). Torsional behavior of model piles in sand. Geotechnical Practice in Offshore Engineering, ASCE, New York, 315–334.

Fontana, Casey, "A Multiline Anchor Concept for Floating Offshore Wind Turbines" (2019). Doctoral Dissertations. 1486.

Fragio, A. G., Santiago, J. L., and Sutton, V. J. R. (1985), Load Tests on Grouted Piles in Rock, Offshore Technology Conference, 1985.

Geotechnical Engineering, ASCE, Vol. 111, pp. 942-947.

Liang, R., Yang, K. and Nusairat, J. (2009). P-y criterion for rock mass. J. Geotech. & Geoenviron. Eng., ASCE, 135(1), 26-36.

Lin, S.S., and AlKhaleefi, A.L. (1996) "Torsional Behavior of Cracked Reinforced Concrete Piles in Sand," Journal of The Chinese Institute of Engineers, Vol.19: (6), pp. 689-696.

Lovera. PhD. Cyclic lateral design for offshore monopiles in weak rocks. Environmental Engineering. Université Paris-Est, 2019.

Nimbalkar, S., and Indraratna, B. (2016). Improved performance of ballasted rail track using geosynthetics and rubber shockmat. J. Geotech. Geoenviron.

Nusairat, J., Liang, R., Engel, R., Hanneman, D., AbuHejleh, N., and Yang, K. (2004). "Drilled shaft design for sound barrier walls, signs, and signals." Rep. No. CDOT-DTD-R-2004-8, Colorado Dept. of Transportation, Denver.

Nuerberg et al., 2023. Advanced Hydrodynamics of Floating Offshore Structures.

Pillai, A.C., Gordelier, T.J., Thies, P.R., Dormenval, C., Wray, B., Parkinson, R., 2022. Anchor loads for shallow water mooring of a 15 MW floating wind turbine — Part I : chain catenary moorings for single and shared anchor scenarios. Ocean Eng. 111816.

Randolph, M. F. (1981) "Piles Subjected to Torsion," Journal of the Geotechnical Engineering

Reese, L. C. (1997). "Analysis of laterally loaded piles in weak rock." J. Geotech. Envir. Engrg., ASCE, 123(11), p. 1010-1017.

Seidel and Collingwood. A new socket roughness factor for prediction of rock socket shaft resistance (2001).

Tawfiq, Kamal. 2000. "Drilled Shaft under Torsional Loading. TRID (the TRIS and ITRD database). Florida State University, Tallahassee. Report/Paper Numbers: WPI 0510704, Final Report.

Vickery, B.J. 1979. Wind effects on building and structures-critical unsolved problems. In IAHR/IUTAM Practical Experiences with Flow induced Vibrations Symposium, Karlsruhe, Germany, pp. 823-828.

Word Forum Offshore Wind, Mooring Systems for Floating Offshore Wind: Integrity Management Concepts, Risks and Mitigation. White paper (2022).

Proceedings of the XVIII ECSMGE 2024
GEOTECHNICAL ENGINEERING CHALLENGES
TO MEET CURRENT AND EMERGING NEEDS OF SOCIETY
© 2024 the Authors
ISBN 978-1-032-54816-6
DOI 10.1201/9781003431749-621
Open Access: www.taylorfrancis.com, CC BY-NC-ND 4.0 license

ECSMGE 24
XVIII EUROPEAN CONFERENCE ON SOIL MECHANICS AND GEOTECHNICAL ENGINEERING

Ballast degradation under different cycles and rotational speeds in micro-Deval equipment

Dégradation du ballast sous différents cycles et vitesses de rotation dans un équipement micro-Deval

N.S. Montero-Cubillo*, J. Estaire, E. Marull
LG-CEDEX, Madrid, Spain

**natalia.montero@cedex.es*

ABSTRACT: The ballast layer plays a crucial part in transmitting and distributing the wheel load from sleepers to the underlying sub-ballast and subgrade at a reduced and acceptable level. Upon repeated train loading, ballast becomes degraded. The amount of degraded ballast is directly connected with the load and velocity of the train, and the type of rock. This paper shows the results of 14 Ballast Degradation in micro-Deval equipment (BDMD) tests carried out at different rotation velocities (13, 25, 50, 63, 75, 100 y 120 rpm) and at different number of cycles (0, 1000, 3000, 6000, 9000, 15000, 21000, 69000 y 105000) with samples of two types of railway ballast. The first is gneiss ballast, one of the most common in the High-speed Spanish railways, and the second one is a limestone ballast, forbidden in Spain. For each one of the mentioned cycles, a grain size distribution test is performed. The main objective of this paper is to analyse the influence of the rotational speed and the number of applied cycles on the degradation of the ballast.

RÉSUMÉ: La couche de ballast joue un rôle crucial dans la transmission et la distribution de la charge des roues des traverses au sous-ballast et à la plate-forme sous-jacente à un niveau réduit et acceptable. Le ballast se dégrade sous l'effet de la charge répétée des trains. La quantité de ballast dégradé est directement liée à la charge et à la vitesse du train, ainsi qu'au type de roche. Cet article présente les résultats de presque 11+3 tests de dégradation du ballast dans un équipement de micro-dégradation (BDMD) effectués à différentes vitesses de rotation (13, 25, 50, 63, 75, 100 et 120 tr/min) et à différents nombres de cycles (0, 1000, 3000, 6000, 9000, 15000, 21000, 69000 et 105000) avec des échantillons de deux types de ballast de chemin de fer. Le premier est un ballast de gneiss, l'un des plus courants dans les chemins de fer espagnols à grande vitesse, et le second est un ballast de calcaire, interdit en Espagne. Pour chacun des cycles mentionnés, un test de distribution de la taille des grains est effectué. L'objectif principal de cet article est d'analyser l'influence de la vitesse de rotation et du nombre de cycles appliqués sur la dégradation du ballast.

Keywords: Railway ballast degradation; micro-Deval test; number of cycles; rotational speed.

1 INTRODUCTION

One of the tests used to estimate the degradation resistance of ballast particles is the micro-Deval test. The standard (EN-103450 standard "Aggregates for Railway Ballast) dedicates a specific annex to the testing of railway ballast.

In addition, there are numerous references in which the micro-Deval test is used to quantify the degradation of railway ballast as a function of intrinsic parameters of the ballast particles. The following should be highlighted:

- Bach (2013) investigates the influence of pattern rock type on degradation resistance.
- Nålsund (2014) studies the influence of certain rock textural parameters (such as roughness, mineral grain size, quartz content, and soft mineral content) on the value of the micro-Deval coefficient.
- Moaveni et al. (2014) use a particle image analyser to visualize the changes in particle morphology after micro-Deval testing.

During the micro-Deval test, the ballast particles collide with each other and with the drum walls, producing an accelerated degradation, especially through the mechanisms of abrasion and chipping, which implies the breakage of vertices and edges (Estaire and Montero-Cubillo, 2022), of greater magnitude and homogeneity, than occurred in real tracks. For example, Deiros et al. (2016) estimate that, in some areas of the drum, friction work reached, a maximum value of 10,000 J/mm^2 during a micro-Deval cycle, while at the passage of a train axle in real track a maximum friction work of only 0.1 J/mm^2 under sleeper is produced.

However, although the energy magnitude and the degradation mechanism are not identical between the test and the real track, the energy-degradation relationship in the test has allowed us to obtain certain qualitative and quantitative conclusions applicable to the real track, as can be seen in Estaire et al. (2023). Also, according to several authors (Deiros et al., 2016) and Gupta et al., 2022), the appearance of the particles at the end of the micro-Deval test is very similar to that observed in ballast particles collected from high-speed tracks after a long period in operation. This fact is also corroborated in the tests performed for this paper.

A new procedure was developed in this study when compared with the conventional micro-Deval test. The new test is named Ballast Degradation in micro-Deval equipment (BDMD test). The test was designed to study the relationship between degradation and: a) rotational speed and number of cycles, and b) power and energy supplied by the equipment to the specimen. Also, the variation of particle size distribution of the ballast specimens, along the test, can be analysed.

2 MATERIALS AND METHOD

2.1 Ballast samples

Two types of railway ballast were tested: a) a gneiss (Figure 1a), of metamorphic origin and one of the most common in the high-speed Spanish railways, and b) a limestone, of sedimentary origin (Figure 1b), forbidden in Spain but allowed in other countries, like UK or USA. Both materials were tested to demonstrate the difference in terms of degradation and to establish certain parameters dependent on the rock strength and the degradation.



Figure 1. a) Gneiss ballast particle, b)Limestone ballast particle.

2.2 Test equipment

The equipment used for the BDMD test is an adaptation of the equipment used for the micro-Deval test (EN 1097-1), as shown in Figure 2, in such a way that its standard rotation system is used, but the standard drums are modified. A 304 mm high drum was used, joining two drums of the standard equipment (Figure 2). Also, a variable-frequency drive was connected to the rotation system to vary the rotational speeds and to quantify the applied energy.

Additionally, sieves to perform complete particle size distribution tests were used: 100; 63; 50; 40; 40; 31.5; 22.4; 12.5; 10; 6.3; 5 and 1.25 mm.



Figure 2. BDMD test equipment of LG-CEDEX and joined drums.

2.3 Test procedure

The application of micro-Deval test for ballast is regulated by Annex E of EN-103450 "Aggregates for Railway Ballast". For this study, BDMD tests were performed under different conditions than the standard usual, as can be seen in Table 1.

Table 1. Differences between micro-Deval and BDMD tests.

Test magnitude	Test	
	micro-Deval[a]	BDMD
Initial load (kg)	10	3.8
Cycles	14,000	1,000 to 105,000
Rotational speed (rpm)	100	13 to 120
Water	Yes	No
Degradation (Passing sieve)	1.6 mm (micro-Deval coefficient)	22.4 mm
Complete PSD[b]	No	Yes

[a] According to Annex E/EN-103450
[b] PSD: Particle Size Distribution test

The accumulation of fine material in ballast layers is known as ballast fouling. For assessing the need for ballast treatment, the European Rail Research Institute (ERRI D182/RP3) proposed a ballast fouling level upper or equal to 30%, at which the mechanical properties of railway ballast begin to be altered dramatically. In this study, degradation (Table 1) is considered as ballast fouling (or soiling in ERRI), defined as the percentage by weight of the specimen material that falls through a 22.4 mm sieve.

The procedure followed in BDMD tests was as follows:

a) Specimen preparation. Selection of 10 kg of new ballast particles between 50 and 31.5 mm in size and subsequent drying in an oven at 110 ºC, until constant mass.

b) Selection of 3800 ± 200 g of the specimen prepared in the previous stage, creating the following approximate initial particle size: 20% of 31.5 mm size and 80% of 40 mm size.

c) Selection of the test frequency in variable-frequency drive (which is related to the rotational speed).

d) Reset the energy consumption counter.

e) Place the ballast specimen inside one of the drums.

f) Close the open end using the other hollow drum and tighten the nuts. Additionally, a resin had to be added to the joint area of both drums to avoid dust loss during the test.

g) Place the drums in the equipment

h) Selection, in the control device of the equipment, of the required test time (calculated from the desired number of cycles according to the test rotational speed).

i) Start-up.

j) When the selected time is reached the test stops.

k) Read and note the energy consumed after the number of cycles applied.

l) Separation of the drums and overturning of the specimen in one of them.

m) Weigh the drum with the contained specimen to asses possible dust losses and note.

n) Extraction of the specimen from the drums taking care not to release too much dust when the specimen is poured.

o) Weigh the resulting specimen without the drum and note.

p) Sift, weigh, and take readings for the different fractions mentioned above.

q) Repetition of steps e) to p) until the final number of cycles required is reached, with the same specimen.

2.4 Performed tests

Unlike the test established in the standard, in this study, the cycles were applied in steps: 1,000, 3,000, 6,000, 9,000, 15,000, 21,000, 69,000, and 105,000 cycles. In each of these steps, the specimen was extracted from the drum, and its complete particle size distribution was determined, to evaluate the modification of the original sizes of the particles and the generation of new particles.

Additionally, to analyse the influence of the rotational speed on the degradation mechanisms of the ballast particles, tests were carried out with different rotational speeds of the drums by installing a variable-frequency drive in the original equipment. Almost 11 tests were performed with the gneiss ballast, with 7 different velocities (13, 25, 50, 63, 75, 100, and 120 rpm) and 8 different consecutive applied cycles for each velocity. Also, 3 tests were carried out with the limestone ballast, with 3 different velocities (13, 50, and 100 rpm) and 8 different consecutive applied cycles for each speed.

3 RESULTS AND DISCUSSION

3.1 Degradation, number of cycles, and rotational velocity

The results obtained from these BDMD tests are shown in Figure 3, where the values of the degradation of the ballast particles in the tests performed with different rotational speeds of the equipment are plotted as a function of the number of cycles applied in each test step. The degradation is measured as the percentage by weight of the material passing through the 22.4 mm sieve with respect to the weight of the total specimen.

It should be noted that some of the tests were repeated, using the same rotational speed, to corroborate or disprove some anomalous trends. These anomalous variations, in terms of degradation for the same test speed, may be related to the variability of the shape of the ballast particles of each specimen, randomly chosen.

The curves considered as the most representative of all the tests performed are shown in Figure 3a, for gneiss ballast and Figure 3b for limestone ballast.

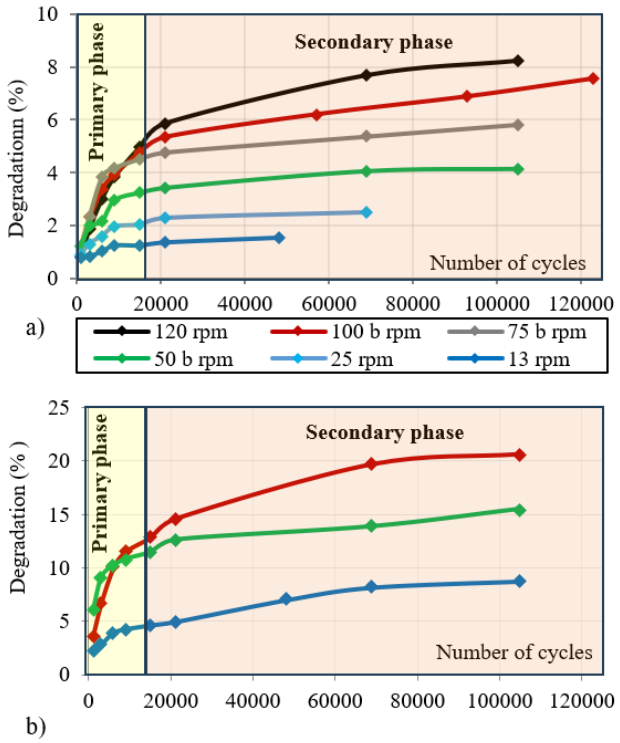

Figure 3. Degradation of ballast particles as a function of the number of cycles at different speeds: a) gneiss ballast and b) limestone ballast.

In Figures 3a and b, two phases of degradation can be seen:

- Primary phase: the initial degradation increases rapidly with the number of cycles. Depending on the rotational speed of each test, the primary phase ends between 10,000 and 20,000 cycles, with an approximate average value of 15,000 cycles. Although it is difficult to specify, it seems intuitive that the primary phase ends earlier the lower the rotational speed used in the test. During this phase, the particles still have a high roughness and angularity due to the presence of sharp vertices and edges, so degradation by abrasion and breakage of vertices and edges is much higher.
- Secondary phase: a second and more linear step is observed (from between 10,000 and 20,000 cycles, depending on the speed), with a constant slope in each test, in which degradation continues to increase with the applied cycles, but more slowly than during the primary phase. In this phase, the ballast particles have less roughness and angularity to break and it is increasingly difficult to generate degradation, since the particles are already more rounded and polished, so the degradation rate decreases.

In any case, the cumulative degradation increases with the rotational speed used in the test and with the number of cycles. It was also possible to verify that degradation accelerates with increasing speed, both in the primary and secondary phases, increasing the slope of the degradation-number of cycles curve.

Also, comparing Figure 3a and Figure 3b, the following differences between gneiss and limestone ballasts can be highlighted.:

- At a velocity of 100 rpm and an accumulated cycles of 1,000 BDMD degradation was: 1.2% in the case of gneiss and 3.5% in the case of limestone.
- At a velocity of 100 rpm and an accumulated cycles of 100,000 BDMD degradation was: 7% in the case of gneiss and 20% in the case of limestone.

Both cases reveal a degradation difference in the order of 3 times more for limestone than for gneiss ballast particles. For this study, some Point Load Tests (PLT) with these two types of ballast were performed. The results showed that the PLT strength is also in the order of 3 times more for limestone (Is_{50} = 3 MPa) than for gneiss (Is_{50} = 7.8 MPa). So the BDMD degradation parameter could be inversely proportional to the PLT strength of the pattern rock which constitutes the ballast particles.

Additionally, an approximate micro-Deval coefficient can be estimated from the BDMD test. Micro-Deval coefficiente was: 4% in the case of gneiss ballast and 11% in the case of limestone ballast. Should be noted that this value was calculated from tests at 100 rpm and 15,000 cycles with the differences between both tests (micro-Deval and BDMD) shown in Table 1.

On the other hand, considering the curves in Figure 3a, the degradation for certain numbers of cycles has been plotted as a function of rotational speed, in Figure 4.

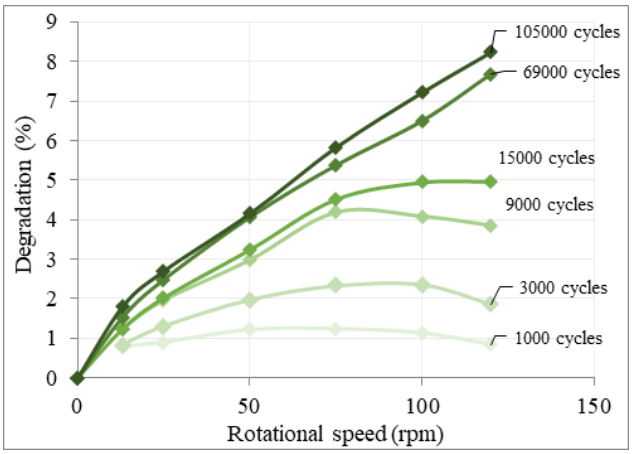

Figure 4. Degradation of ballast particles as a function of rotational speed at a given number of cycles.

The following conclusions can be drawn from Figure 4:

- For the same rotational speed the degradation increases with the number of cycles (also appreciable in Figure 3). The higher the speed, the greater the difference in degradation between 1,000 and 105,000 cycles.
- The degradation does not increase significantly with speed until the number of cycles applied exceeds approximately 1,000. As can be seen, when the number of cycles is low (1,000) the degradation is almost the same regardless of the rotational speed of the test.
- This fact can also be observed in Figure 3, in which at cycles close to 1,000 all the curves overlap, starting at approximately the same degradation value.
- This can be interpreted as if there is an initial degradation energy threshold of about 1,000 cycles. The first degradations that occur in the particles do not seem to require high energy and/or power, so even the test with the lowest energy and power (associated with 13 rpm and 1,000 cycles) manages to produce this degradation and it does not cause more breakage by rotating faster.
- From 1,000 cycles onwards, the effect of rotational speed on degradation starts to be

noticed, and degradation starts to increase linearly with speed for high cycles, from 15,000 onwards.

3.2 Energy - degradation relationship

Another way to appreciate the relationship between degradation, rotational speed and number of cycles is to graph a plot degradation - energy. The energy was estimated as the rotational speed (v) squared multiplied by the number of cycles applied (N) of each test step.

Figure 5 shows that the regression coefficient of this potential expression is very high, proximate to 1 and equal to 0.92. This fact reveals the clear relationship between these three parameters for measuring degradation with the micro-Deval or the BDMD tests and probably when the degradation is measured at the real railways. For more details about the extrapolation of the BDMD results to the railways, see Estaire et al. (2023).

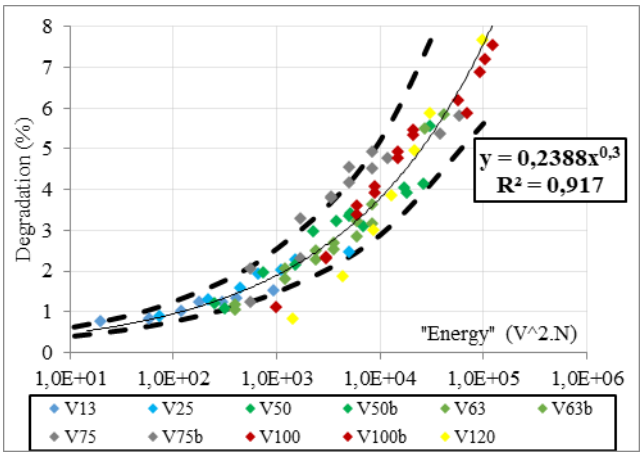

Figure 5. Degradation as a function of applied cycles and rotational speed.

3.3 Particle size distribution and visual analysis

The particle size distributions of all samples before and after BDMD tests were performed. As can be seen in Figure 6, the main generated sizes in this type of test were fine particles under 1.25 mm of diameter, related to abrasion mechanism, and, in a minor proportion, particles of 22.4 or 10 mm, related to chipping mechanism.

Comparing Figure 6a and Figure 6b, the following differences between gneiss and limestone ballasts can be highlighted:

- The percentage of particles with a diameter of 1.25 mm or lower increases, from 0 to 105,000 applied cycles: from 0 to 6% in the case of gneiss ballast and from 0 to 16% in the case of limestone ballast.
- The percentage of particles with a diameter between 22.4 and 12.5 mm increases, from 0 to 105,000 applied cycles: from 0 to 1% in the case of gneiss ballast and from 0 to 3% in the case of limestone ballast.

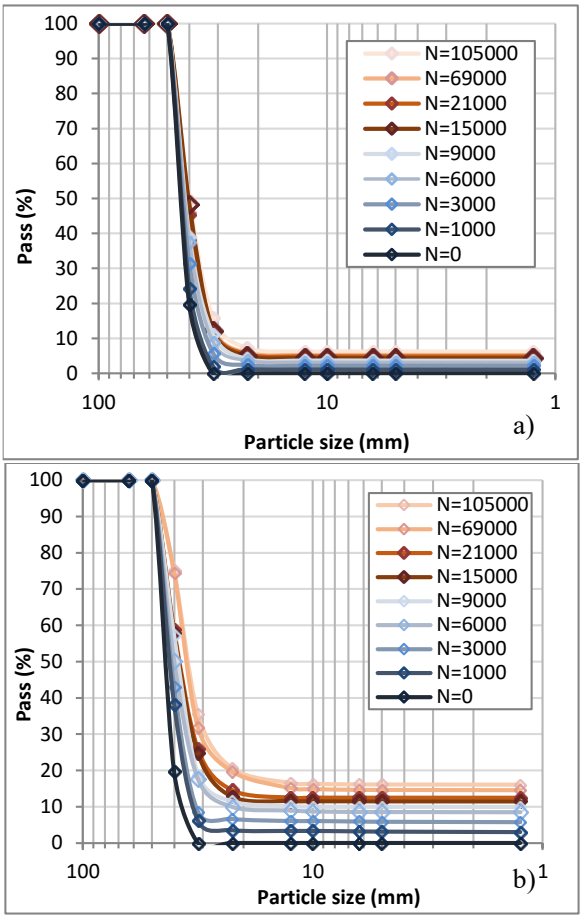

Figure 6. Particle size distribution after tests: a) ballast from gneiss, and b) ballast from limestone.

In Figure 7, the appearance of ballast particles after the application of 15,000 cycles in BDMD test is compared to the aspect of particles collected at real railways. As it can be seen, and other authors indicate (Deiros et al., 2016 and Gupta et al., 2022), the aspect of the ballast particles of the two samples (coming from real track and from BDMD test) are similar, in qualitative terms of roughness and angularity.



Figure 7. Appearance of ballast particles: degraded ballast in track (left) and degraded ballast in BDMD test (15,000 cycles)(right).

4 CONCLUSIONS

The main conclusions of this paper drafts the following highlighted aspects:

- During the primary phase of the BDMD test, the particles still have a high roughness and angularity due to the presence of sharp vertices and edges, so degradation by abrasion and breakage of vertices and edges is much higher and rapidly increases with the number of cycles. In the secondary phase of the BDMD test, the ballast particles have less roughness and angularity to break and it is increasingly difficult to generate degradation, since the particles are already more rounded and polished, so the degradation rate decreases, remaining approximately constant.
- The cumulative degradation increases with the rotational speed used in the test and with the number of cycles. It was also possible to verify that degradation accelerates with increasing speed, both in the primary and secondary phases, increasing the slope of the degradation-number of cycles curve.
- The degradation does not increase significantly with speed until it exceeds approximately 1000 cycles applied. At cycles close to 1000, all the curves overlap, starting at approximately the same degradation value. This can be interpreted as if there is an initial degradation energy threshold of about 1,000 cycles. The first degradations that occur in the particles do not seem to require high energy and/or power, so even the test with the lowest energy and power (associated with 13 rpm and 1,000 cycles) manages to produce this degradation and it does not produce more breakage by rotating faster.
- The BDMD degradation parameter could be inversely proportional to the Point Load Test strength of the pattern rock which constitutes the ballast particles. However, more types of rocks should be studied to set a clear trend.
- In this type of test, particles with 1.25 mm of diameter or lower are mainly generated related to abrasion as the most important performer mechanism.
- The aspect of ballast particles after 15000 applied cycles in DBMD tets is similar to the aspect of particles collected at real railways, as other authors indicate in the case of the micro-Deval test.

ACKNOWLEDGEMENTS

The authors would like to acknowledge the collaboration of the following persons: Felipe García and Elías Roces. The authors are grateful for the ballast samples provided by Rosa Casquero and Franciso Cabrera, from ADIF.

REFERENCES

Bach, H. (2013). Evaluation of attrition tests for railway ballast. July 2013, 109. PhD Thesis. Graz University of Technology. Institute for Railway Engineering and Transport Economy.

ERRI, European Rail Research Institute (1991b). Assessment of ballast condition in the track. ERRI Report D182/RP2. Utrecht. 33p., 44 app.

Estaire, J. and Montero-Cubillo, N.S. (2022). Informe del CEDEX "Análisis de la degradación de balasto mediante ensayos en equipo micro-Deval - Parte 2: Interpretación". Septiembre 2022, Clave CEDEX: 89-422-5-003.

Estaire, J., Montero-Cubillo, N. and Crespo-Chacón, I. (2023) "Simulation model of ballast degradation". European Conference 2023. Rail Track Ballast Management. Global Rail Group. Dusseldorf. November 2023

EN 1097-1:1997. Tests for mechanical and physical properties of aggregates. Part 1: Determination of the resistance to wear (micro-Deval).

EN 13450:2004. Aggregates for railway ballast.

Gupta, A., Madhusudhan, B. N., Zervos A., Powrie, W., Harkness, J. and Le Pen, L. (2022). Grain characterisation of fresh and used railway ballast. Granular Matter, Vol 24, article number 96.

Deiros I., Voivret, C., Combe, G. and Emeriault, F. (2016). Quantifying Degradation of Railway Ballast using Numerical Simulations of Micro-Deval Test and In-situ Conditions. Advances in Transportation Geotechnics 3. The 3rd International Conference on Transportation Geotechnics (ICTG 2016). Volume 143, Pages 1016–1023.

Nålsund R. (2014). Railway ballast characteristics, selection criteria and performance. PhD Thesis. December 2014. NTNU – Trondheim. Norwegian University of Science and Technology. Moaveni et al (2014).

Proceedings of the XVIII ECSMGE 2024
GEOTECHNICAL ENGINEERING CHALLENGES
TO MEET CURRENT AND EMERGING NEEDS OF SOCIETY
© 2024 the Authors
ISBN 978-1-032-54816-6
DOI 10.1201/9781003431749-622
Open Access: www.taylorfrancis.com, CC BY-NC-ND 4.0 license

ECSMGE 24
XVIII EUROPEAN CONFERENCE ON SOIL MECHANICS AND GEOTECHNICAL ENGINEERING

Influence of different seasonal snow cover on thermal regime of the ground

Influence de la couverture neigeuse saisonnière sur le régime thermique du sol

Z. Motamedi*
Soil Mechanics, Mining and Geotechnical Engineering, Luleå University of Technology, Sweden

H. Mattsson, J. Laue, S. Knutsson
Soil Mechanics, Mining and Geotechnical Engineering, Luleå University of Technology, Sweden

J. Casselgren
Experimental Mechanics, Luleå University of Technology, Sweden

**Zahra.Motamedi@ltu.se*

ABSTRACT: Ground thermal regime in cold regions is influenced by seasonal snow cover, which acts as an insulating layer influencing the heat transfer between the atmosphere and the underlying soil. The thermal properties of the snow change with different environmental conditions, playing a crucial role to determine the thermal state of the sub-surface soil. Previous research in this field have faced challenges to accurately characterize thermal properties of seasonal snowpacks under varying spatial and meteorological conditions. To address this issue, two experimental field setups were constructed in Luleå, Sweden, to observe the temperature distribution of the snowpack and the ground sub-surface soil. The first experiment studied a naturally accumulated, undisturbed snowpack. The second experiment was conducted on a roadside ditch where the snowpack consists of a combination of natural accumulated snow and plowed snow from the adjacent road. In this research, heat transfer processes at both field sites were monitored over a winter season each to better understand the complex relationship between snow cover properties and sub-surface thermal regime. Furthermore, thermal conductivity of a basal layer in each snowpack was calculated over a time period, based on the field measurements. The results showed that the history of snow deposition, meteorological conditions, and changes in soil moisture impact the metamorphism process within the snowpack, thereby altering the structure of the layers of snowpack and its influence on the thermal regime of the sub-surface soil. The findings of this research have important applications in various sectors, from mining to road maintenance and agriculture.

RÉSUMÉ: Le régime thermique du sol dans les régions froides avec une couverture neigeuse saisonnière est influencé par la couche isolante de neige, qui agis sur le transfert de chaleur entre l'atmosphère et le sol sous-jacent. Les propriétés thermiques de la neige changent en fonction de différentes conditions environnementales, jouant un rôle crucial dans la détermination de l'état thermique du sous-sol. Des recherches antérieures dans ce domaine ont rencontré des défis pour caractériser de manière précise les propriétés thermiques des manteaux neigeux saisonniers dans différentes configurations spatiales et des conditions météorologiques variables. Pour résoudre ce problème, deux dispositifs expérimentaux ont été construits à Luleå, en Suède, afin d'observer la distribution de la température dans le manteau neigeux et le sol. La première expérience a étudié un manteau neigeux accumulé naturellement et non perturbé. La deuxième expérience a été menée dans un fossé en bordure de route où le manteau neigeux est constitué d'une combinaison de neige accumulée naturellement et de neige déblayée de la route adjacente. Dans cette recherche, les processus de transfert de chaleur sur chacun des sites ont été surveillés pendant une saison hivernale pour mieux comprendre la relation complexe entre les propriétés de la couverture neigeuse et le régime thermique en sous-sol. De plus, la conductivité thermique d'une couche de base dans chaque manteau neigeux a été calculée sur une période donnée, en fonction des mesures sur le terrain. Les résultats ont montré que l'historique du dépôt de neige, les conditions météorologiques et les variations de l'humidité dans le sol affectent le processus de métamorphose au sein du manteau neigeux, modifiant ainsi la structure des couches du manteau neigeux et son influence sur le régime thermique du sous-sol. Les conclusions de cette recherche sont applicables dans divers secteurs, de l'exploitation minière à l'entretien des routes et à l'agriculture.

Keywords: Ground thermal regime; thermal properties; seasonal snow cover.

1 INTRODUCTION

The ground thermal regime in cold regions is strongly influenced by the presence of seasonal snow cover, which acts as an insulating layer during the cold season. Alterations in snow cover conditions have a significant influence on the correlation between meteorological conditions and the thermal state of the soil beneath the snow. Scientific research conducted in the Arctic and sub-Arctic regions has revealed that the seasonal snow cover is composed of distinct layers with varying physical and thermal characteristics (Benson & Sturm, 1993). Of particular interest in recent years is the formation of a basal layer of snowpack known as the depth hoar, which has important implications for the properties of the snowpack and interacts closely with the soil beneath the snow. Depth hoar crystals are characterized by their large size, hollow facets, and poor interconnectivity, resulting in layers of low density and low thermal conductivity. These crystals play a significant role in the thermal insulation of the snowpack.

Domine et al. (2018) emphasized that the formation of depth hoar is primarily influenced by soil moisture and wind conditions. Understanding this relationship is crucial to simulate snow properties accurately, particularly thermal conductivity, in order to effectively model the ground thermal regime.

To explore this matter, two experimental test sites were established in Luleå, located in the northern part of Sweden. The objective of the experimental configurations at the sites was to investigate and analyze how two types of seasonal snowpack, each characterized by a unique thermal conductivity in their basal layer, affect the thermal regime of the ground.

2 FIELD MEASUREMENT

Measurements were conducted at two distinct experimental field sites: Experimental Site 1 (ES1) during the winter of 2021-2022, and Experimental Site 2 (ES2) during the subsequent winter of 2022-2023, as illustrated in Figure 1 and Figure 2.

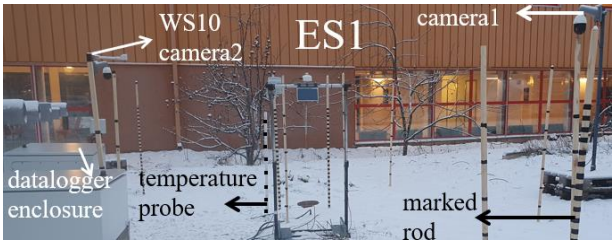

Figure 1. ES1 during the winter 2021-2022.

ES1, was situated within the premises of Luleå University of Technology. The site was specifically selected for studying a naturally accumulated and undisturbed snowpack. ES2 was located near the Luleå airport on a roadside ditch, where the snowpack consisted of a mixture of naturally accumulated snow and plowed snow from the adjacent road. At both field sites, meteorological data was collected using a WS10 weather station (Lufft Mess und Regeltechnik GmbH, 2019). To quantify snow depth, a system was implemented where two cameras were stationed at each site. The cameras captured images of rods, marked at 5 (cm) intervals, providing clear reference points for measurement. Images were taken at 4-hour intervals. Additionally, a temperature measurement probe equipped with thermocouples type T produced by Pentronic were utilized to measure the temperature of the soil sub-surface at a depth of 40 (cm), the temperature at the soil-snow interface and the temperature of 15 (cm) above the interface within the snowpack. Furthermore, thermal conductivity of the

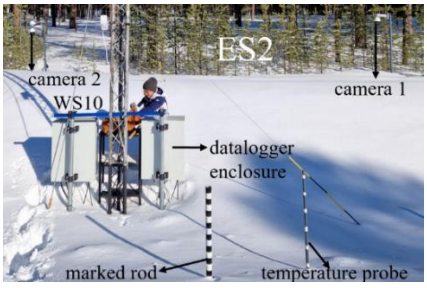

Figure 2. ES2 during the winter 2022-2023.

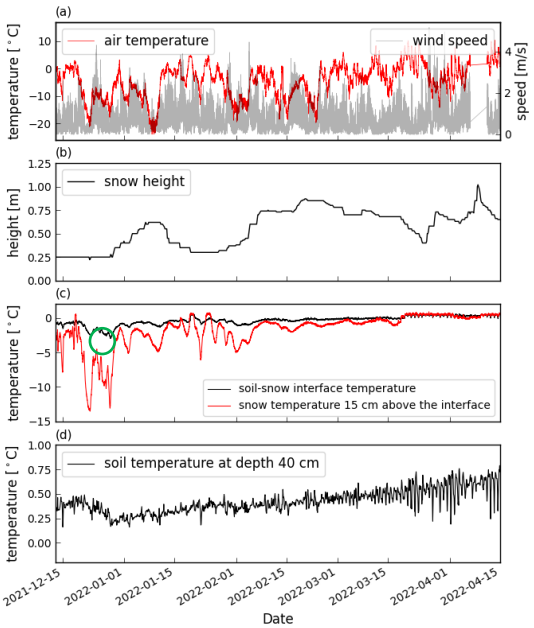

Figure 3. Recorded measurements at ES1 a) air temperature and wind speed, b) snow depth, c) temperature at the soil-snow interface and within the snowpack at a height of 15 cm above the interface, and d) soil sub-surface temperature at a depth of 40 cm.

sub-surface soil at a depth of 40 (cm) was measured using a TP01 thermal sensor. The sensors were connected to a CR1000X datalogger, manufactured by Campbell Scientific. The datalogger was housed in an enclosure equipped with additional insulation to ensure that the measured junction temperature was representative of the entire terminal block.

Figure 3 and Figure 4 present the recorded measurements at ES1 and ES2, respectively. These figures show the measurement results spanning two winter seasons, from December 13 to April 18. During the measurement period at ES1, the air temperature fluctuates between -23.7 (ºC) and 14.8 (ºC), with an average temperature of -4.5 (ºC). Similarly, at ES2, the air temperature ranges from -23.6 (ºC) to 9.9 (ºC), with an average temperature of -6.9 (ºC). However, the wind speed at ES2 is higher than at ES1.

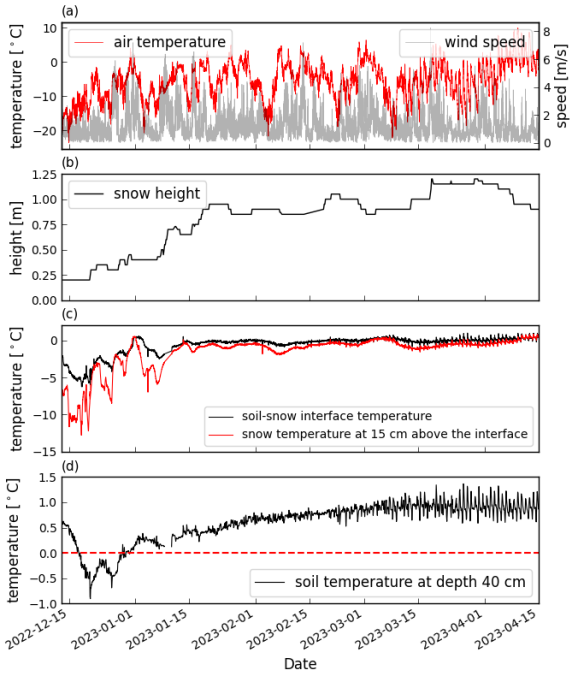

Figure 4. Recorded measurements at ES2 a) air temperature and wind speed, b) snow depth, c) temperature at the soil-snow interface and within the snowpack at a height of 15 cm above the interface, and d) soil sub-surface temperature at a depth of 40 cm.

2.1 Seasonal freeze/thaw development

The air temperature at ES1 exhibits fluctuations around the freezing point during the initial phase of the measurement period, Figure 3(a), contrasting with ES2 that initially just experiences negative air temperature, Figure 4(a). Nevertheless, within a few days, the air temperature at ES1 converges to a comparable range as that recorded at ES2. Furthermore, the data presented in Table 1, along with Figure 3(b) and Figure 4(b), highlights that the snow cover height at ES1 surpasses that at ES2 by a margin of 5 (cm) at the onset of the measurement.

Figure 3(c) and Table 1 highlight a distinct trend at the ES1 soil-snow interface in the beginning of the winter. Here, the interface temperature maintains stable just below 0 (ºC) for an extended period, characterized as the "zero-curtain" and illustrated in the figure by a green circle, before gradually dropping to -3 (ºC). This stability coincides with a phase transition from water to ice in the soil moisture, leading to the release of latent heat. Meanwhile, Figure 4(c) and Table 1 indicate a -6 (ºC) temperature decrease at the ES2 interface.

ES1 is characterized by sandy loam soil, whereas ES2 consists of poorly graded sand. Thermal conductivity measurements conducted at the sites revealed that ES1 demonstrated an average thermal conductivity of 0.57 ($Wm^{-1}K^{-1}$), while ES2 exhibited a slightly higher value of 0.8 ($Wm^{-1}K^{-1}$). The water table beneath ES1 is situated 2 (m) below the soil surface, while the water table beneath ES2 is found at a depth of 10 (m) below the soil surface. Thus, it is expected that the soil moisture content at ES1 will be higher than that at ES2, owing to both the proximity of the water table to the soil surface and the differing soil compositions.

As shown in Table 1, the initial temperature of the sub-surface soil at ES2 is 0.4 (ºC) higher than that of ES1 at the start of the measurement period. Nevertheless, unlike ES2, the sub-surface soil at ES1 remained unfrozen throughout the entire season, as shown in Figure 3(d). Conversely, the corresponding sub-surface soil at ES2 experienced approximately 10 days of freezing after one full day of the zero-curtain phenomenon at that depth. While thawing at ES2, the sub-surface soil experienced a full-day period of zero-curtain before it fully thawed. This sequence is outlined in Table 1 and visually represented in Figure 4(d).

The air temperature at both experimental sites typically remains within a similar range, with only a brief variation noted at the onset of the measurements. Furthermore, the difference in snow depth covering the sites is merely 5 (cm) at the commencement of the study. Despite a marginal difference of 0.23 ($Wm^{-1}K^{-1}$) in the thermal conductivity of the soil between ES2 and ES1, the higher moisture content in the soil at ES1 prevents the subsurface from freezing throughout the measurement period. This can be attributed to the significant latent heat energy released during the transition of water to ice. However, the subsurface soil at ES2 experienced a short period of "zero curtain" before undergoing freezing and subsequent thawing. This phenomenon can be attributed to the low moisture content of the soil at ES2.

2.2 Snow depth

Based on the analysis by Sokratov and Barry (2002), snow depth affects the soil surface energy balance, from beginning of the active layer freezing until the snow depth reaches its maximum level. Sturm and Holmgren (Zhang, 2005) conducted field measurements on November 17, 1998 in Ivotuk, Alaska. It was observed that the influence of snow depth on soil-snow interface temperature becomes less significant when the snow depth exceeds 40 (cm).

Table 1. Variation of critical temperature with snow height during the winter season at soil-snow interface and sub-surface soil at a depth of 40 cm at ES1 and ES2.

	Temperatue (ºC)	Snow height (cm)	Date
Soil-snow interface			
ES1	-0.7	25	2021-12-13
	-2.9	25	2021-12-28
	almost stable at 0	60	2022-02-06
ES2	-1.9	20	2022-12-13
	-6.3	20	2022-12-18
	almost stable at 0	65	2023-01-13
Sub-surface soil at a depth of 40 cm			
ES1	0.3	25	2021-12-13
	0.1	25	2021-12-28
ES2	0.7	20	2022-12-13
	zero-curtain	20	2022 -12-17 2022-12-18
	-1	25	2022-12-20
	zero-curtain	40	2022-12-28- 2022-12-29

Zhang (2005) underscores the significant impact of snow thickness variations on soil-snow interface temperatures, particularly when the snow depth is below approximately 50 (cm). Nevertheless, the data from the sites ES1 and ES2 demonstrate that when the snow depth reaches 60 (cm), the soil-snow interface temperature remains consistently at 0 (ºC), as depicted in Table 1 and Figure 1(b) and (c), as well as Figure 2 (b) and (c).

3 HEAT TRANSFER

3.1 Depth hoar formation

Seasonal snow cover usually consists of a coarse depth hoar layer at the base of the snowpack. This layer is characterized by its low-density and low-thermal conductivity < 0.2 ($Wm^{-1}K^{-1}$) (Sturm, et. al, 2002, Domine, et.al, 2016). Depth hoar typically forms through the metamorphism of snow exposed to a temperature gradient > 20 (Km^{-1}) (Marbouty, 1980).

A study conducted by Domine et al. (2018) has demonstrated the significance of wind as the primary factor influencing depth hoar formation in the polar desert. Investigations on subarctic snowpack, where wind is weak and uncompacted snow accumulates, have revealed that such snow exhibits high permeability, facilitating convection through the pore spaces (Sturm & Benson, 1997) leading to water vapor movement that encourages the growth of depth hoar crystals.

Davesne et al. (2022) have shown that snow pits in humid sites exhibit lower thermal conductivity values and less variability in the basal layer compared to dry sites. In regions characterized by higher humidity, the depth hoar crystals typically exhibit a coarser texture compared to drier locations. A lower soil moisture level leads to less latent heat released during the freezing process, speeding up the freezing of the active soil layer and consequently soil cooling. This, in turn, reduces the temperature gradient within the snowpack, resulting in decreased water vapor flux and slower snow metamorphism.

3.2 Heat transfer at soil-snow interface

As the snow accumulates and reaches a specific height, the soil-snow interface temperature stabilizes at 0 (ºC), as shown in Figure 3(c) and Figure 4(c). Therefore, the energy balance at the soil-snow interface can be expressed as

$$Q_s + Q_{sn} + I_0 = 0 \quad (1)$$

where Q_s(Wm^{-2}) represent the heat flux coming from sub-surface soil layer, Q_{sn}(Wm^{-2}) denote the heat flux within the basal layer of snowpack, and, I_0(Wm^{-2}) indicate the amount of solar radiation absorbed at the interface.

Due to the relatively small pore sizes compared to the overall volume of the soil structure, heat conduction is considered to be the dominant heat transfer mechanism within the soil.

As a result of sufficient height for the accumulated snow, the snowpack basal layer and a layer above are no longer exposed to a significant temperature gradient. Consequently, the rate of metamorphism becomes relatively slow, and the local impact of released latent heat can be disregarded. This is due to the presence of a highly conductive ice network that connects the ice volume enabling rapid heat conduction away from the layer. Furthermore, under a

sufficient depth of snow cover, solar radiation at the soil-snow interface becomes insignificant.

The energy balance at the soil-snow interface when the snow reaches a sufficient height, can be depicted as follows:

$$k_s \frac{T_{1S}-T_0}{h_s} = k_{sn} \frac{T_{1Sn}-T_0}{h_{sn}} \quad (2)$$

where $k_{s/sn}$ (Wm^{-1}K^{-1}) denotes the thermal conductivity of soil/snow, $h_{s/sn}$ (m) represents the thickness of the respective soil/snow layer, T_{1S} (ºC) signifies the soil sub-surface temperature at the depth of h_s, T_0(ºC) indicates the soil-snow interface temperature, and T_{1Sn} (ºC) represents the temperature of the snow layer above the interface at the height of h_{sn}. Figure 5 provides a comprehensive view of the heat transfer mechanisms within the soil/snow layer.

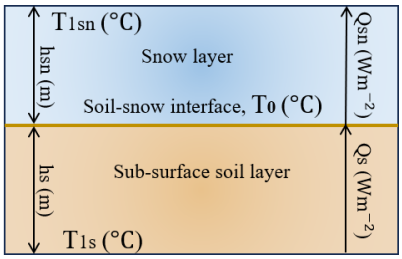

Figure 5. Heat transfer within the soil/snow layer.

3.3 Thermal conductivity of basal depth hoar layer

During the final eight days of February for the two consecutive winter seasons in ES1 and ES2, the measured temperature close to the soil-snow interface does not change very much, as shown in Figure 6(b) and (d), as well as Figure 7(b) and (d).

The heat flow from the soil to the snowpack at the interface was evaluated at both research sites by analyzing the temperature measurements and the thermal conductivity of the soil. Using Eq.(2), the thermal conductivity of the snowpack basal layer situated above the soil-snow interface was estimated, relying on the recorded temperature data. The computed thermal conductivity illustrated in Figure 6(a) and Figure 7(a) indicating that the snowpack basal layer at ES2 exhibits higher thermal conductivity.

In Section 2.1, it is evident that the soil moisture at ES2 is lower than that at ES1. This lower moisture content has led to a faster freezing of the active soil layer, resulting in a reduced temperature gradient with the atmosphere. Consequently, the rate of metamorphism in the snowpack basal layer has been affected. Figure 3(c) and Figure 4(c) illustrate this phenomenon, showing that, at the beginning of the measurement period, the temperature difference between the measured temperatures is more pronounced at ES1 than at ES2.

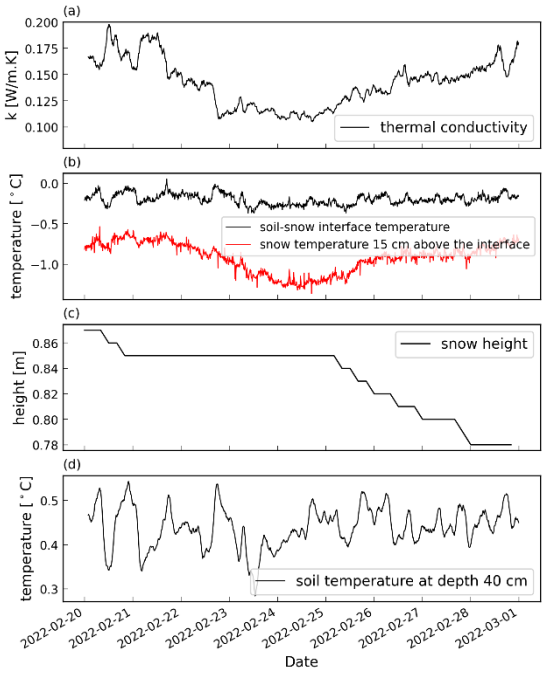

Figure 6. ES1, a) calculated thermal conductivity of snow layer above the soil-snow interface b) soil-snow interface temperature and snow temperature at 15 cm above the interface c) snow height d) soil sub-surface temperature at a depth of 40 cm.

In the ES1 area, the wind speed mostly remained below 4 (ms^{-1}), see Figure 3(a). In contrast, ES2 experiences higher wind speed up to 6 (ms^{-1}), as illustrated in Figure 4(a). The lower wind speed at ES1 compared to ES2 is expected to result in increased porosity and decreased density in the basal layer. Additionally, at ES2 the snowpack consists of a combination of naturally accumulated snow and plowed snow from the adjacent road, leading to a more compacted snowpack with reduced porosity and increased density in the basal layer.

The examination of the estimated thermal conductivity within the basal layer of the ES2 snowpack indicates that a depth hoar layer has not formed at the base of the snowpack. This is attributed to the fact that the thermal conductivity of this layer falls outside the typical range associated with depth hoar formation. This absence significantly affects the thermal regime of the ground, resulting in a diminished insulating effect, as summarized in Table 1.

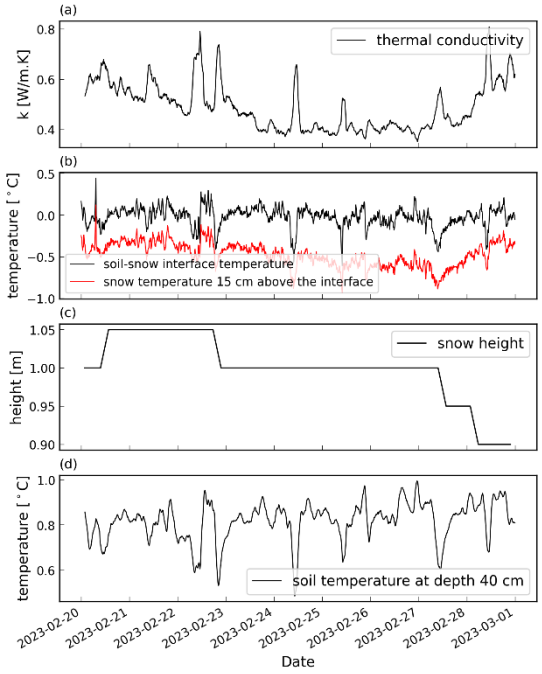

Figure 7. ES2, a) calculated thermal conductivity of snow layer above the soil-snow interface b) soil-snow interface temperature and snow temperature at 15 cm above the interface c) snow height d) soil sub-surface temperature at a depth of 40 cm.

4 CONCLUDING REMARKS

The present study underscores the vital role of snow metamorphism in shaping the structure of the layers of the snow cover. This metamorphic process, influenced by factors such as snow deposition history, meteorological conditions, and soil moisture content, results in alterations of the thermal properties of snow, particularly its thermal conductivity. Consequently, the varying thermal conductivity of different types of snow cover leads to diverse heat transfer effects on the thermal regime of the ground. However, accurately measuring snow thermal conductivity poses challenges due to the variability in snow properties across different spatial and environmental conditions. Consequently, physical models of snow struggle to adequately simulate snow properties and in particular thermal conductivity.

These findings hold implications for various maintenance sectors, for instance road maintenance, in planning both cost-effective and environmentally friendly operations. Nevertheless, it is essential to recognize that the existing body of research on the influence of different types of seasonal snow cover on seasonally frozen ground remains limited.

ACKNOWLEDGEMENTS

The authors are grateful for the financial support provided by the Swedish Transport Administration (Trafikverket) within the research program “Make Way for the Future” (Bana Väg För Framtiden – BVFF).

REFERENCES

Benson, C., & Sturm, M. (1993). Structure and wind transport of seasonal snow on the Arctic slope of Alaska. *Annals of Glaciology*, 18, 261-267. https://doi.org/10.3189/S0260305500011629.

Davesne, G., Domine, F., & Fortier, D. (2022). Effects of meteorology and soil moisture on the spatio-temporal evolution of the depth hoar layer in the polar desert snowpack. *Journal of Glaciology*, 68(269), 457-472. https://doi.org/10.1017/jog.202021.105.

Domine, F., Barrere, M., & Sarrazin, D. (2016). Seasonal evolution of the effective thermal conductivity of the snow and the soil in high Arctic herb tundra at Bylot Island, Canada. *The Cryosphere*, 10(6), 2573-2588. https://doi.org/10.520194/tc-10-2573-2016.

Domine, F., Belke-Brea, M., Sarrazin, D., Arnaud, L., Barrere, M., & Poirier, M. (2018). Soil moisture, wind speed and depth hoar formation in the Arctic snowpack. *Journal of Glaciology*, 64(248), 990-1002. https://doi.org/10.1017/jog.2018.89.

Lufft Mess und Regeltechnik GmbH. (2019, 09 23). Manual weather station WS10. Retrieved 05 23, 2023, from : www.lufft.com/fileadmin/lufft.com/07_downloads/1_manuals/Manual_WS_10_EN_V1-5_01.pdf.

Marbouty, D. (1980). An experimental study of temperature-gradient metamorphism. *Journal of Glaciology*, 26(94), 303-312. https://doi.org/10.3189/S0022143000010844.

Sokratov, S. A., & Barry, R. G. (2002). Intraseasonal variation in the thermoinsulation effect of snow cover on soil temperatures and energy balance. *Journal of geophysical research*, 107(D10), ACL-13. https://doi.org/10.1029/2001JD000489.

Sturm, M., & Benson, C. (1997). Vapor transport, grain growth and depth-hoar development in the subarctic snow. *Journal of Glaciology*, 43(143), 42-59. doi.org/10.3189/S0022143000002793.

Sturm, M., Perovich, D. K., & Holmgren, J. (2002). Thermal conductivity and heat transfer through the snow on the ice of the Beaufort Sea. *Journal of Geophysical Research: Oceans*, 107(C10), SHE-19. https://doi.org/10.1029/2000JC000409.

Zhang, T. (2005). Influence of the seasonal snow cover on the ground thermal regime: An overview. *Reviews of Geophysics*, 43(4). https://doi.org/2010.1029/2004RG000157.

Proceedings of the XVIII ECSMGE 2024
GEOTECHNICAL ENGINEERING CHALLENGES
TO MEET CURRENT AND EMERGING NEEDS OF SOCIETY
© 2024 the Authors
ISBN 978-1-032-54816-6
DOI 10.1201/9781003431749-623
Open Access: www.taylorfrancis.com, CC BY-NC-ND 4.0 license

ECSMGE 24
XVIII EUROPEAN CONFERENCE ON SOIL MECHANICS AND GEOTECHNICAL ENGINEERING

COOP Project: Energy piles under combined loading

Projet COOP: Pieux énergétiques sous sollicitations combinées

H. Mroueh*
University of Lille, IMT Lille Douai, Univ. Artois, Yncrea Hauts-de-France, ULR 4515 - LGCgE, Laboratoire de Génie Civil et géo-Environnement, Lille, France,

T. Badinier, M. Blanc, T. Dubreucq, J. de Sauvage, F. Szymkiewicz
Univ Gustave Eiffel, GERS-SRO, Marne-la-Vallée, France

J.-M. Pereira, A.-M. Tang
Navier, Ecole des Ponts, Univ Gustave Eiffel, CNRS, Marne-la-Vallée, France

R. Vasilescu
ENTREPRISE PINTO, Fougères, France

**hussein.mroueh@univ-lille.fr*

ABSTRACT: The growing energy needs of urban areas and the environmental context are leading to the development of new geothermal technologies. In this context, energy geostructures, such as thermo-active (or energy) piles, were developed in the early 1980s and consist of heat exchanger tubes fixed to the reinforcement cages of foundation piles to extract/inject heat from/into the ground to meet the heating and cooling needs of buildings. Their specificity lies in their dual function: structural support and energy exchanger. Therefore, two aspects can be critical and should be considered in their design. The first is the nature of the cyclic thermal load acting along the energy pile, which can affect its mechanical response. Consequently, the cyclic thermal loading can cause a variation in the shear stresses at the soil-pile interface, thereby affecting the pile's load-bearing capacity. The second aspect concerns the adaptation of the design under combined lateral and axial loading, i.e. the interaction between lateral (or axial) loading and the axial (or lateral) behaviour of the energy piles, coupled with volumetric thermal loading acting on the surrounding soil and along the pile. These configurations are the most favourable for the installation of heat exchange tubes, as they mechanically require reinforcement cages along the entire lenght of the pile. The objective of the COOP project, funded by the French National Research Agency (ANR), is to improve the knowledge of the behaviour of energy piles under these complex load configurations by proposing different research topics, from real experimental case studies to physical centrifuge modelling and numerical modelling, with the final aim of providing engineers with a relevant tool for the design of energy piles under combined loading.

RÉSUMÉ: Les besoins énergétiques croissants des zones urbaines et le contexte environnemental conduisent au développement de nouvelles technologies de géothermie. Dans ce contexte, les géostructures énergétiques, telles que les pieux thermoactifs (ou énergétiques), ont été développées au début des années 1980 et consistent en des tubes échangeurs de chaleur fixés aux cages de renforcement des pieux de fondation pour extraire/injecter de la chaleur du/dans le sol afin de répondre aux besoins de chauffage et de refroidissement des bâtiments. Leur particularité réside dans leur double fonction : rôle structural et échangeur d'énergie thermique. Par conséquent, deux aspects peuvent être critiques et doivent être pris en compte dans leur dimnesionnement. Le premier est la nature de la charge thermique cyclique, qui agit sur toute la longueur du pieu et qui peut affecter sa réponse mécanique. Par conséquent, une charge thermique cyclique peut entraîner une modification des contraintes de cisaillement à l'interface sol-pieu et donc impacter la capacité portante du pieu. Le deuxième aspect concerne l'adéquation de la méthode de calcul à une charge transversale et axiale combinée, c'est-à-dire l'interaction entre la charge transversale (ou axiale) et le comportement axial (ou latéral) des pieux énergétiques, associée à une charge thermique volumétrique agissant sur le sol environnant et le long du pieu. Ces configurations sont les plus favorables à l'installation de tubes d'échange de chaleur, car elles nécessitent mécaniquement des cages de renforcement sur toute la hauteur du pieu. L'objectif du projet COOP, financé par l'Agence Nationale de la Recherche (ANR), est d'améliorer la connaissance du comportement des pieux énergétiques sous ces configurations de charge complexes en proposant différents thèmes de recherche, allant d'études de cas expérimentaux réels à la modélisation physique en centrifugeuse et à la modélisation numérique, dans le but final de fournir aux ingénieurs un outil pertinent pour le dimnesionnement de pieux énergétiques sous chargements combinés.

Keywords: Energy piles; combined loading; in situ experiment; centrifuge modelling.

1 INTRODUCTION

The growing energy needs of urban areas and the environmental context lead to the development of new energy technologies. In particular, since the 1980s, a new geothermal method has been developed: energy geostructures, consisting in fixing heat exchanger pipes to the reinforcement cages of geotechnical structures like foundations to extract/inject the heat from/into the ground with the purpose of meeting the building heating and cooling demands. Among them, Energy Piles (EP) have been widely studied because their thermal behaviour is quite similar to the one of usual Ground Source Heat Pumps installations, with the specificity of a dual function: structural support and energy exchanger (Loveridge et al. 2020). These studies provide knowledge about mechanical behaviour upon mainly the axial direction and about the assessment of the energy performance of the system. Despite all economic and ecological advantages of this technology, EP installation in France is still held back by some uncertainties, which among them one concerns the thermo-mechanical behaviour under complex loading.

Indeed, based on the application, EP may be mechanically subjected to predominantly vertical loading due to a supported superstructure, and lateral loading if used in a bridge abutment or embankment stabilization, or combined vertical-horizontal loading (and potentially moment too) in buildings subjected to pile eccentricity (figure 1). Moreover, although wind and earthquakes induce dynamic loads, in common engineering practice their effects are considered as horizontal static loads applied to the pile head (NF EN NF P 94-262, 2017).

All these configurations, where combined vertical-horizontal loading is encountered, are the most favourable for installing heat exchanger pipes since, from a purely mechanical point of view, they require reinforcement cages all along the pile height. It is then crucial to offer to engineers a relevant knowledge to design energy piles under combined loading and this project aims at characterizing the effect of combined loading on energy piles and at the development of open-source and easy-to-use design tools for energy piles, capable of **constructing an overall failure envelope including thermal cycling loading effects**.

2 STATE OF THE ART

In the current design practice, the response of conventional pile under combined axial and horizontal loading is separately analysed and then superposed. This approach neglects the coupling effect of the combined loads while the optimum design of pile foundations requires consideration of the influence of axial loads on their horizontal response. Most previous studies have investigated the behaviour of conventional piles under pure horizontal loads and only a limited number have considered combined axial and horizontal loading (Heidari et al., 2022). Moreover, these studies gave contrasted results and the coupling effects of combined axial and lateral loads still raise complexities and uncertainties, even regarding conventional piles. This might be intensified in the case of energy piles because the thermal variations could affect the pile properties, the behaviour of the surrounding soil, lead to creep effects, or cause ratcheting phenomena in heavily-loaded piles subjected to cyclic thermal loads. Accordingly, it is necessary to identify the influence mechanism of combined axial and compression loads on the global behaviour of energy piles.

Descriptive diagram of combined loads in geothermal piles supporting a building.

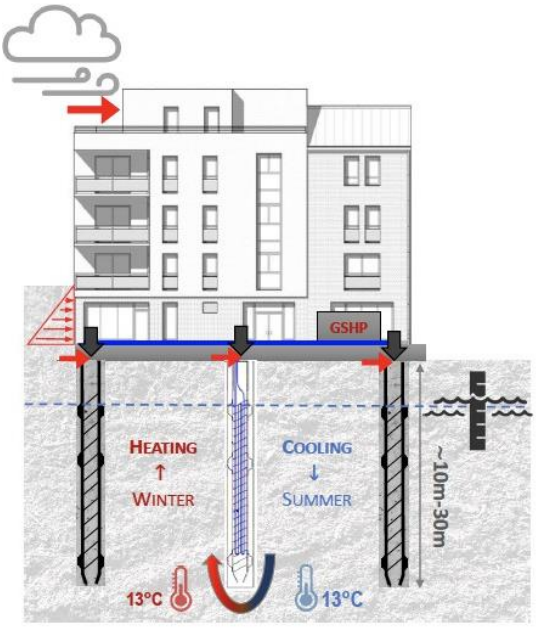

Figure 1. Combined loads acting on energy piles.

Many researchers have put a lot of effort into better understanding the thermo-mechanical behaviour of energy piles during monotonic heating or cooling and one or multiple thermal cycles. The work of Vitali et al. (2021) could be considered as the only available study using centrifuge model tests to investigate the influence of monotonic heating on the flexural behaviour of horizontally-loaded energy piles. Several studies have been performed to assess the behaviour of axially-loaded energy piles during multiple thermal cycles through field scale tests (Sutman et al. 2019), 1-g small-scale physical model tests (Nguyen et al., 2020) and centrifuge model tests (Ng et al. 2015).

A recent critical review of knowledge upon energy piles (Cunha and Bourne-Webb, 2022) draws an accurate picture of the experiments realised until now. It appears that very few experiments have been carried out on real scale energy piles considering combined mechanical loadings. This lack of experiments should be fulfilled even if centrifuge modelling offers alternative results.

The centrifuge modelling approach to characterize the transient thermo-mechanical response of energy foundations during heating-cooling cycles has been first used by Stewart and McCartney (2014). During successive cycles, slight decreases in upward thermal head displacement were observed. Later, Ng et al. (2020) have assessed rigorously scaling effects on the centrifuge modelling of floating energy piles by the so-called 'modelling of models' technique (two centrifuge models tested at two different *g* levels simulating the same prototype). Recently, Zhao et al. (2022) have presented the study on the thermally-induced ratcheting under a constant horizontal load. Yet, this first study has been performed in a dry sample without measurement of the pile strain to compare with numerical modelling.

Complementary to experimental results, numerous numerical studies have been performed to investigate the Thermo-Hydro-Mechanical THM behaviour of energy piles. The key findings are: (i) Heating/cooling of the pile induces stress changes in the pile and at the pile-soil interface; (ii) Heating/cooling cycles can degrade the side friction at the pile-soil interface; (iii) Thermal loads can induce irrecoverable displacement if the mechanical load is high; (iv) Irreversible and accumulating settlement over yearly thermal cycles, with a ratcheting phenomenon, also seems to take place in the long term during cyclic continuous loading. It should be noted that these findings were obtained exclusively from studies investigating piles subjected to axial mechanical load. The unique numerical study investigating the behaviour of energy pile subjected to sustained lateral load, from our knowledge, is Zhao et al. (2022). This study, based on finite-element simulations showed that ratcheting was evident in laterally-loaded piles in sand and its extent was more significant when the working horizontal load was higher. The ratcheting phenomenon was attributed to the accumulation of soil plastic strain due to the cyclic mechanical loading induced by pile thermal horizontal expansion and contraction, soil dilation upon soil-pile interface shearing, and creep. Beside these studies, we can't find any numerical study investigating the mechanical behaviour of energy piles, subjected to thermal cycles, under sustained combined lateral-axial loads. It should be noted that investigating the mechanical behaviour of pile subjected to combined lateral-axial loads itself already requires advanced numerical methods including 3D mesh and soil-pile interface models (Achmus & Thieken, 2010; Suryatriyastuti et al., 2013a-b, 2016; Hazzar et al., 2017).

The experimental and numerical studies mentioned above are focused on the behaviour of energy piles. To transfer this knowledge to the practice, it is crucial to develop engineering tools allowing the design of energy piles. Numerous works have been driven (Knellwolf et al., 2011; Mimouni and Laloui, 2013), but none of them have integrated the effect of lateral component of load in the axial response of pile. Mroueh and Shahrour (2009) have shown that combined load acting on pile may have great effect on its axial response and therefore on its design.

3 OVERALL METHODOLOGY

3.1 Organisation of the project

To investigate the questions raised hereby, the French National Research Agency (ANR) funded a project, called *Combined lOading Of energy Piles* (COOP), driven by Université de Lille and involving Université Gustave Eiffel, Ecole des Ponts ParisTech and the Pinto company. It aims to offer to engineers a relevant tool to design energy piles under combined loading. To achieve this objective, a specific organisation has been designed including a multiscale study of the thermo-mechanical behaviour of energy piles relying on three Work Packages (WP1, 2 and 3) and a Work Package dedicated to the transfer of knowledge to engineering practice (WP4). In addition, the WP0 is dedicated to project management.

The WP1 will allow to study the behaviour of energy piles under lateral loading through testing two experimental energy piles (0.42 m in diameter and 12.0 m in length), which have been installed in the campus of Ecole des Ponts ParisTech (Vasilescu, 2019). They are equipped with PE tubes for the circulation of the heat transfer fluid, PT 100 temperature sensors and optical fibre sensors. Temperature sensors are also installed in the soil, around the piles. The piles will be initially subjected to axial static compressive load (10, 20, or 40% of the ultimate axial load) and then in the subsequent stage, horizontal static load will be incrementally applied (30, 50, or 70% of the ultimate horizontal load), while the axial load is kept constant. The horizontal load will be applied by an actuator between two piles to ensure they are submitted to the same loading. At each level of horizontal load, to simulate the actual operating condition of energy piles, ten thermal cycles with

temperature variation of -/+ 10 °C will be repeatedly applied to one of the piles while the mechanical loads are maintained constant. The unheated pile will be used as a control experiment. The principle of this testing is represented on Figure 2.

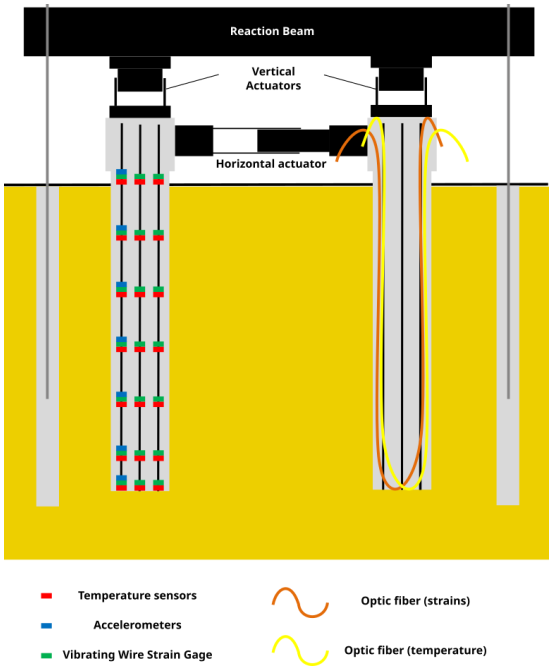

Figure 2. Principle of the real-scale testing.

In WP2, the behaviour of energy piles subjected to lateral loading will be studied through smallscale model tests performed in centrifuge. The advantage of placing these small-scale models in a macro-gravity field is to generate on this model the same stress state that is applied to the prototype in real size. In the perspective of energy piles, the second advantage of the physical modelling in centrifuge is to also reduce the time scale. Thus, the time scale (for diffusion) of a 1/N model subjected to N×g is reduced by N^2 (at 100×g), 1 hour of centrifuge test represents 14 months in the prototype scale ("real scale"). In this way, centrifuge tests can model several years of cyclic thermal loading. Moreover, in the framework of this project, the tests performed in centrifuge are particularly well suited to calibrating the numerical model developed in the WP3. Indeed, in centrifuge, the boundary conditions, the soil homogeneity and the different loadings are very well established and controlled which gives valuable data up to failure.

For this study, the centrifuge test principle consists in applying a thermal cyclic loading inside the pile while the mechanical loads (horizontal and vertical) remain constant. The accumulation of lateral displacement (the ratcheting effect) will be monitored. Several couples of thermal and mechanical loadings will be studied. A parametric study will be conducted on key aspects governing the energy pile response subjected to lateral loading will be studied: i) the pile slenderness ratio, ii) the soil saturation and iii) the soil density. Using a system adapted from (Ouzzine et al., 2023) for the thermal loading, initial tests have been carried out including only horizontal mechanical loading (Figure 3).

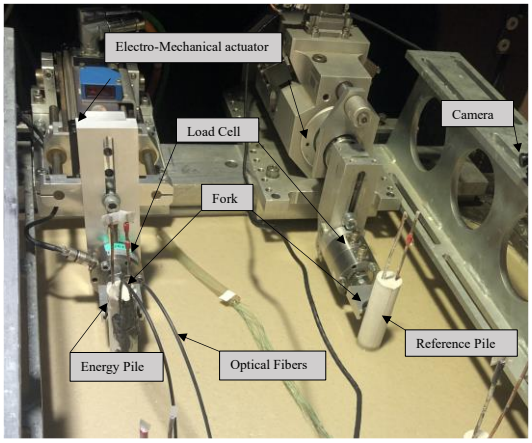

Figure 3. Initial centrifuge tests.

WP3 aims to investigate the thermo-mechanical behaviour of energy pile subjected to thermal cycles under sustained combined lateral-axial loads. This goal will be achieved by using complex 3D modelling on CESAR-LCPC software (Humbert et al, 2005). It is a Finite Element software dedicated to the modelling and analysis of civil engineering projects, particularly well-suited to geotechnical problems and continuously developed by Université Gustave Eiffel. It integrates a wide range of calculation capabilities for extending the analyses to heat transfers and THM couplings.

WP4 will focus on the development of a simplified design tool, accounting for combined loading, which is of paramount importance in the industry uptake and large-scale deployment of energy piles. Drawing from the results obtained from the real scale (WP1) and centrifuge tests (WP2) as well as the results of the parametric study performed in the WP3, an open-source simplified design tool will be developed to bridge the gap between research and engineering practice. The principal goal of this application will be to determine the stresses and displacements resulting from a set of combined thermomechanical loads and a 3D failure envelope corresponding to the energy pile combined axial and lateral response and accounting for thermal cyclic loading.

4 CONCLUSIONS

The first steps towards characterization of the effect of combined loading on energy piles have been hereby

presented as well as the organisation of the project COOP whose final goal is the development of an open-source user-friendly design tool.

The development and dissemination of such tool is essential to maximize the development and deployment of energy pile technology in the construction sector. Providing access to such tools to building contractors, design engineers, and control offices will allow to easily design and control energy pile solutions without resorting to complex 3D modelling and experimented engineers. We believe that the easy access to design tools will promote a virtuous cycle of energy geostructures' development, multiplying the examples and proving the performance and necessity of such solution.

ACKNOWLEDGEMENTS

The project presented in this article is supported by the project COOP, funded by the French National Research Agency (ANR) and coordinated by University of Lille.

REFERENCES

Achmus, M. and Thieken, K. (2010). On the behavior of piles in non-cohesive soil under combined horizontal and vertical loading. Acta Geotech, 5(3): 199-210.

Cunha, R.P. and Bourne-Webb, P.J. (2022). A critical review on the current knowledge of geothermal energy piles to sustainably climatize buildings, Renewable and Sustainable Energy Reviews, 158.

Hazzar, L., Hussein, M. and Karray, M. (2017). Influence of vertical loads on the lateral response of pile foundations in sands and clays, J Rock Mech Geotech Eng, 9(2):291-304.

Heidari B., Garakani A.A., Mokhtari Jozani S. and Tar P.H. (2022). Energy piles under lateral loading: Analytical and numerical investigations, Renewable Energy, 182, 172-191. 10.1016/j.renene.2021.09.125.

Humbert, P., Dubouchet, A., Fezans, G., & Remaud, D. (2005). CESAR-LCPC, un progiciel de calcul dédié au génie civil. *Bulletin des laboratoires des ponts et chaussées*, *256*, 7-37.

Knellwolf, C., Peron, H., and Laloui, L. (2011). Geotechnical analysis of heat exchanger piles. Journal of Geotechnical and Geoenvironmental Engineering, 137(10), 890-902. 10.1061/(ASCE)GT.1943-5606.0000513.

Loveridge, F., McCartney, J. S., Narsilio, G. A. a,d Sanchez, M. (2020). Energy geostructures: a review of analysis approaches, in situ testing and model scale experiments. Geomechanics for Energy and the Environment 22, 100173. 10.1016/j.gete.2019.100173.

Mimouni, Thomas & Laloui, Lyesse. (2013). Towards a secure basis for the design of geothermal piles. Acta Geotechnica. 9. 10.1007/s11440-013-0245-4.

Mroueh, H. and Shahrour, I. (2009). Numerical analysis of the response of battered piles to inclined pullout loads, International Journal for Numerical and Analytical Methods in Geomechanics, 33(10), 1277-1288. 10.1002/nag.765.

NF EN NF P 94-262 (2017). Guide pieux. AFPS - Cahier technique N° 38.

Ng, C. W. W., Shi, C., Gunawan, A., Laloui, L. and Liu, H. L. (2015). Centrifuge modelling of heating effects on energy pile performance in saturated sand. Can. Geotech. J., 52(8), 1045–1057. 10.1139/cgj-2014-0301.

Ng, C.W.W., Zhang, C., Farivar, A. and Gomaa, S.M.M.H. (2020). Scaling effects on the centrifuge modelling of energy piles in saturated sand. Géotechnique Letters 10(1) 57-62. 10.1680/jgele.19.00051.

Nguyen, V. T., Wu, N., Gan, Y., Pereira, J. M. & Tang, A. M. (2020). Long-term thermo-mechanical behaviour of energy piles in clay. Environmental Geotechnics, 7(4), 237-248, 10.1680/jenge.17.00106.

Ouzzine B, de Sauvage J, Madabhushi G, Viggiani G, Reiffsteck P. (2023). Centrifuge modelling of an energy pile group with ground water flow. International Journal of Physical Modelling in Geotechnics. May 30:1-25

Stewart, M.A. and McCartney, J.S. (2014). Centrifuge modeling of soil-structure interaction in energy foundations. Journal of Geotechnical and Geoenvironmental Engineering, 140(4). 10.1061/(ASCE)GT.1943-5606.0001061.

Suryatriyastuti, M.E., Mroueh, H., Burlon, S., Habert, J. (2013a). Numerical analysis of the bearing capacity of thermoactive piles under cyclic axial loading. Energy Geostructures: Innovation in Underground Engineering. 139-155, 10.1002/9781118761809.ch7.

Suryatriyastuti, M.E., Mroueh, H. and Burlon, S. (2013b). Impact of Transient Heat Diffusion of a Thermoactive Pile on the Surrounding Soil. In Energy Geostructures (eds L. Laloui and A. Di Donna), https://doi.org/10.1002/9781118761809.ch10.

Suryatriyastuti, M.E., Mroueh, H. and Burlon, S. (2016). On the understanding of cyclic mechanisms in an energy pile group. International Journal for Numerical and Analytical Methods in Geomechanics, 40(1), 3–24.

Sutman, M., Brettmann, T. and Olgun, G. (2019). Full-scale in-situ tests on energy piles: Head and base-restraining effects on the structural behaviour of three energy piles. Geomechanics for Energy and the Environment 18, 56-68, https://doi.org/10.1016/j.gete.2018.08.002.

Vasilescu A.R. (2019). Design and execution of energy piles : Validation by in-situ and laboratory experiments. PhD Dissertation, Ecole Centrale de Nantes.

Vitali, D., Leung, A., Feng, S., Knappett, J. A. and Ma, L. (2021). Centrifuge modelling of the use of discretely-spaced energy pile row to reinforce unsaturated silt. Géotechnique, In press https://doi.org/10.1680/jgeot.20.P.157.

Zhao, R., Leung, A.K. and Knappett, J.A. (2022). Thermally-induced ratcheting of a thermo-active reinforced concrete pile in sand under sustained lateral load. Géotechnique. 10.1680/jgeot.21.00299.

Proceedings of the XVIII ECSMGE 2024
GEOTECHNICAL ENGINEERING CHALLENGES
TO MEET CURRENT AND EMERGING NEEDS OF SOCIETY
© 2024 the Authors
ISBN 978-1-032-54816-6
DOI 10.1201/9781003431749-624
Open Access: www.taylorfrancis.com, CC BY-NC-ND 4.0 license

ECSMGE 24
XVIII EUROPEAN CONFERENCE ON SOIL MECHANICS AND GEOTECHNICAL ENGINEERING

Back-analysis of a full-scale dyke stress test with advanced models for soft soils

Rétro-analyse d'un essai de contrainte sur digue en grandeur réelle à l'aide de modèles avancés pour les sols mous

S. Muraro*, C. Chao
Delft University of Technology, Delft, The Netherlands

L. Su, C. Jommi
Delft University of Technology, Delft, The Netherlands
Politecnico di Milano, Milano, Italy

**s.muraro@tudelft.nl*

ABSTRACT: Advanced models for soft organic layers encountered in the shallow subsoils in the Netherlands have been developed recently at TU Delft. The models are based on high-quality laboratory data on peats and soft organic clays. The constitutive effort mostly focussed on some partially unexplored features, such as the role of fibres, extension stress conditions, and the dependence of hardening on deviatoric plastic strains, besides anisotropy. Although the models have proven to be able to reproduce and predict the behaviour over a variety of triaxial probe tests, validation at the field scale is lagging behind. On the one hand, field soil response encompasses diverse stress paths and histories not replicable in the laboratory. On the other hand, the role of the advanced features introduced in the models on the engineering structure response needs to be quantified. We back-analyse a well-documented full-scale test performed in the Netherlands, the Leendert de Boerspolder stress test, where the role of different soft soil layers both on the pre-failure and failure response has been investigated. Comparison between numerical simulations and available monitoring data is used to demonstrate the contribution of advanced models to the understanding of the engineering response of soft soils.

RÉSUMÉ: Des modèles avancés pour les couches organiques molles trouvées dans les sous-sols superficiels aux Pays-Bas ont été développés récemment à TU Delft. Les modèles sont basés sur des données de laboratoire de haute qualité sur les tourbes et les argiles organiques molles. L'effort constitutif s'est principalement concentré sur certaines caractéristiques partiellement inexplorées, telles que le rôle des fibres, les conditions de contrainte d'extension et la dépendance de l'écrouissage aux déformations plastiques déviatoriques, en plus de l'anisotropie. Bien que les modèles se soient avérés capables de reproduire et de prédire le comportement lors d'une variété d'essais à la sonde triaxiale, la validation à l'échelle du terrain est à la traîne. D'une part, la réponse du sol sur le terrain englobe diverses chemins de contraintes et histoires qui ne peuvent être reproduites en laboratoire. D'autre part, le rôle des caractéristiques avancées introduites dans les modèles sur la réponse de la structure d'ingénierie doit être quantifié. Nous rétro-analysons un essai en échelle réelle bien documenté réalisé aux Pays-Bas, l'essai de contrainte de Leendert de Boerspolder, où le rôle de différentes couches de sol mou a été étudié à la fois sur la réponse avant rupture et sur la réponse à la rupture. La comparaison entre les simulations numériques et les données de surveillance disponibles est utilisée pour démontrer la contribution des modèles avancés à la compréhension de la réponse d'ingénierie des sols mous.

Keywords: Soft soils; advanced constitutive modelling; numerical simulation; case-history.

1 INTRODUCTION

The Netherlands relies on an extensive network of primary and secondary flood defence embankments. Many dykes, especially in the western part of the country, lie on thick deposits of peat and organic clay, prone to settlement and shear deformation. Assessing the serviceability and safety of these dykes is challenging due to the complex behaviour of soft soils under general stress paths.

To better understand the engineering response of these soils, advanced models for the soft organic layers encountered in the shallow subsoils in the Netherlands have been recently developed at TU Delft. These models include non-associated plastic flow rule, anisotropy described by a rotational hardening law, and a generalised hardening rule, which depends on both deviatoric and volumetric plastic strains. While the models have proven to be able to replicate the

response of the soils in a variety of triaxial stress paths, validation at the field scale is lagging behind.

In this study, we back-analyse a well-documented full-scale stress test performed in the Netherlands, the Leendert de Boerspolder stress test (De Gast, 2020; Jommi et al., 2021). Finite element simulations incorporating standard and new advanced models for soft soils are carried out, and the results of the numerical simulations are compared with in-situ monitoring data.

2 OVERVIEW OF THE FIELD TEST

The Leendert de Boerspolder dyke was a regional dyke located north of Leiden (Figure 1). Under service conditions, the water levels in the canal and polder were regulated with little variations: the canal regulating system kept the water level on the canal side at constant h = - 0.6 m NAP, in which the NAP (Normaal Amsterdams Peil) is used as the reference for the vertical coordinate. On the polder side, it was managed by pumping stations at h = - 2.3 m NAP.



Figure 1. Plane view of the test area at the Leendert de Boerspolder before the start of the failure test (https://www.stabialert.nl/nl/projecten/ldeb-polder/).

The stress test consisted of a series of excavation and dewatering stages operated at the toe of the dyke to induce the failure. The schematisation of the cross-sectional view of the dyke, along with the geometry of the excavations and the position of monitoring instrumentation, are presented in Figure 2.

In the first stage, a trench was excavated at the toe of the dyke while maintaining the water level in the trench unchanged. Subsequently, the water level was lowered by one meter in two steps. At the end of the first stage, the water was refilled back to the same water level as at the start. Similar operations were performed in the following second and third excavation stages, with a more extensive portion of soil being removed. The dyke failed during the last dewatering step between Section Centre and Section South (Figure 1).

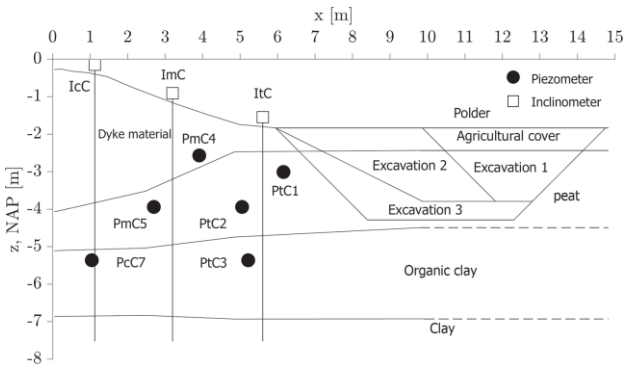

Figure 2. Schematisation of the central cross-sectional profile of the dyke and monitoring instrumentation.

2.1 Subsoil properties

To characterise the soil layers at the test site, an extensive site and laboratory investigation program was carried out including CPTu, triaxial, simple shear and oedometer tests on undisturbed soil samples (Ponzoni, 2017). The reconstructed soil profile consists of: (i) highly heterogeneous dyke material; (ii) peat layer with a varying thickness between 1.5 – 2.5 m; (iii) organic clay deposit with a thickness of about 2.0 m; (iv) deep clay layer above the Pleistocene sand. The dry density, void ratio, hydraulic conductivity, and over-consolidation ratio estimated from oedometer and triaxial tests on undisturbed samples, are summarised in Table 1. For the peat layer, the dependence of the hydraulic conductivity on the void ratio is reported by Zhao and Jommi (2023). For the in-situ void ratio, the hydraulic conductivity is in the range between 10^{-6} m/s to 10^{-7} m/s.

Table 1. Material properties for each layer.

Layer	ρ_d [kg/m^3]	e [-]	k [m/s]	OCR [-]
Dyke	1290	1.3	5×10^{-8}	1.0-1.6
Peat	150	9.0-13.0	$k\,(e)$	1.0-3.0
Organic clay	610	2.8	5×10^{-9}	1.0-3.0
Clay	900	1.0	5×10^{-9}	1.0

2.2 Monitoring instrumentation

The in-situ instrumentation was designed with the two primary purposes of providing sufficient data on the pre-failure response of the system, during excavation, dewatering, refilling, and collecting as much information as possible during the failure. It included: (i) 25 piezometers; (ii) 5 automatic two-axis inclinometers; and (iii) 9 vertical rod-type extensometers allowing to automatically record settlement and heave of the different soil layers. The sensors were installed at three cross-sections along the longitudinal direction, namely Section North, Centre, and South. Figure 2 reports the

position of the instrumentation in the Section Centre which was the most instrumented one.

3 CONSTITUTIVE MODELS

Different constitutive models are chosen for the different soil layers. In all the numerical simulations, the dyke material and the deep clay layer are modelled as linear-elastic perfect plastic material with the Mohr-Coulomb failure criterion. For the peat layer and the organic clay layer, the results of the two analyses are compared. In the first one, the Modified Cam Clay (MCC, Roscoe and Burland, 1968) was used. The second one was run adopting the advanced models developed at TU Delft.

For the peat layer, the model proposed by Muraro and Jommi (2021) is adopted. It includes a non-associated isotropic yield surface and plastic potential and a mixed volumetric and distortional hardening law derived from triaxial probe tests. For the organic clay layer, the recently proposed model by Chao (2024) is adopted. The model extends the generalised expression of yield locus proposed by McDowell and Hau (2003) to account for anisotropy. The evolution of anisotropy in the model is described by an amended version of the rotational hardening rule proposed by Dafalias and Taiebat (2013) to better capture the stress-strain response observed in the extension domain. The proposed expression for the rate of evolution of the rotation hardening variable, α, and the corresponding asymptotic values, α_b, are defined as

$$\delta\alpha = \langle L \rangle c p_{atm} \frac{p'}{p'_c} (\alpha_b - \alpha) \tag{1}$$

$$\alpha_b = \begin{cases} \frac{M_{g,c}}{z_c}\left[1 - \exp\left(-s\frac{|\eta|}{M_{g,c}}\right)\right]^y, \eta \geq 0 \\ -\frac{M_{g,e}}{z_e}\left[1 - \exp\left(-s\frac{|\eta|}{M_{g,e}}\right)\right]^y, \eta < 0 \end{cases} \tag{2}$$

with $M_{g,c}$, $M_{g,e}$ critical stress ratio in compression and extension, η stress ratio, p_{atm} atmospheric pressure, p' mean effective stress, p'_c preconsolidation stress, L plastic multiplier, and z_e, z_c, c, s, y model constants. Both constitutive models are implemented in ABAQUS in UMAT subroutines.

The model parameters adopted in the numerical simulations for each soil layer and summarised in Table 2, Table 3, and Table 4 were calibrated on triaxial stress probe tests (Ponzoni, 2017; Muraro and Jommi, 2021; Chao 2024). The compression parameters for the peat and organic clay in the new models remain as in the MCC.

For the organic clay, the constants of the rotational hardening rule (Equations (1) and (2)) are z_c = 1.6, z_e = 1.2, c = 50, s = 2.2, y = 2. The initial inclination of the yield locus and plastic potential was determined following the procedure described by Dafalias et al. (2006), assuming K_0 conditions for the stress state of the sample in the field. The calculated initial inclination is α_i = 0.50.

Table 2. Input parameters for dyke and deep clay.

Layer	E [kPa]	ν [-]	φ [°]	ψ [°]	c [kPa]
Dyke	5600	0.3	30.0	3.0	5.0
Clay	5200	0.3	31.0	6.0	5.0

Table 3. Input parameters for peat and organic clay modelled with the MCC.

Layer	κ^* [-]	ν [-]	λ^* [-]	M [-]	K [-]
Peat	0.08	0.3	0.36	1.75	0.8
Organic clay	0.009	0.2	0.09	1.42	0.8

Table 4. Input parameters for peat and organic clay modelled with the new advanced models.

Layer	$M_{g,c}$ [-]	$M_{g,e}/M_{g,c}$ [-]	$M_{f,c}$ [-]	χ_f [-]	χ_g [-]
Peat	1.75	0.80	1.5	2.0	0.98
Organic clay	1.42	0.80	1.0	1.25	2.0

4 NUMERICAL MODEL

The field stress test is modelled as a 2D plane-strain, hydro-mechanical coupled problem in the finite element software ABAQUS, and its geometry is presented in Figure 3. The model consists of 10128 type "CPE8RP" elements.

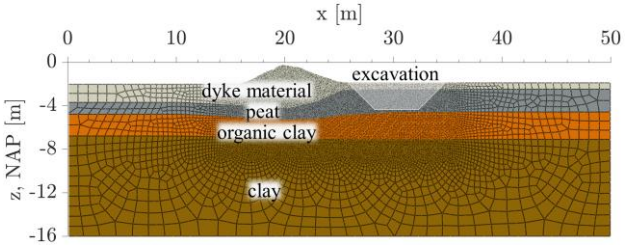

Figure 3. Geometry and mesh of the FE model.

4.1 Boundary and initial conditions

The following boundary constraints are imposed: (i) the two lateral vertical boundaries are fixed in the horizontal direction; (ii) the lower boundary is fixed in the horizontal and vertical directions; (iii) hydrostatic

pore pressure profile is applied to the lateral boundaries corresponding to the water level in the canal and the water table at the polder; (iv) drainage-only flow condition is imposed on the outer slope of the dyke.

To simulate the excavation process underwater the module "Model Change" is used which reduces gradually the forces/fluxes exerted by the region to be removed. In the dewatering step, a drainage-only flow condition is applied to the lateral boundaries of the excavation trench, which enables the reduction of pore pressure to the desired value. The boundary conditions applied during the excavation and dewatering steps are displayed in Figure 4.

To reflect the different stress history and stress levels in the foundation layers, an initial profile of OCR changing in the x-direction is assigned to the peat and the organic clay layer as shown in Figure 5. The chosen OCR profile simplifies the interpolation of oedometer data from undisturbed samples.

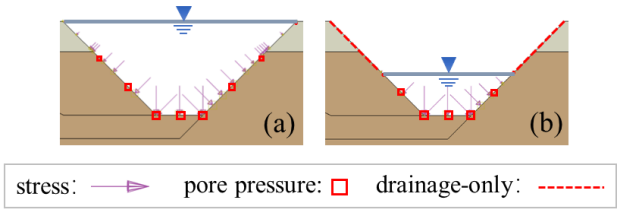

Figure 4. Schematization of the boundary conditions: (a) at the end of excavation; (b) at the end of the dewatering.

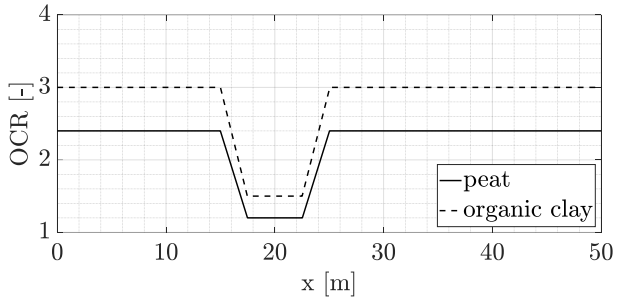

Figure 5. OCR profile in peat and organic clay layer.

4.2 Analysis phases

The analysis steps defined in the numerical simulations are presented in Table 5. The so-called "geostatic step" at the beginning of the analysis is used to establish equilibrium before the loading stage with the applied loads, boundary conditions and initial conditions. Each other step replicates one operation of the stress test. It should be noted that the third dewatering step (on 10-14, Table 5) involved three sub-steps, each pumping 0.5 meters of water with a 30-minutes consolidation period in between.

Table 5. Analysis steps in the simulations.

Operation	Label	Start (mm-dd)	Duration (h)
Initial State	-	-	-
Excavation 1	E1	09-28 09:20	6.9
Dewatering 1	D1	09-30 09:20	2.7
Filling 1	F1	10-01 12:45	1.3
Excavation 2	E2	10-05 08:00	9.5
Dewatering 2	D2	10-07 09:05	4.3
Filling 2	F2	10-08 08:00	2.1
Excavation 3	E3	10-12 07:20	9.4
Dewatering 3	D3	10-14 00:30	5.6

5 NUMERICAL RESULTS

In this section, the numerical results in terms of horizontal displacements and pore pressure response are presented and compared with in-situ measurements. The attention is given to the prediction of different constitutive models, MCC and the new advanced models for peat and organic clay layers.

5.1 Horizontal displacements

Figure 6 shows the resultant displacement predicted at the end of the final dewatering step from both the MCC and the advanced models. Both simulations predict a failure mechanism characterized by the outward bulging of the peat layer at the toe. This pattern, typical for peat (Landva and La Rochelle, 1983) is consistent with the field monitoring data.

Figure 7 presents the numerical predictions and the inclinometer measurements installed at the crest (IcC), mid-slope (ImC) and toe (ItC). The layering is indicated with the letters D, P, and OC which stand for dyke material, peat and organic clay. The data for the first, second, and third dewatering steps are plotted in black, red, and blue, respectively. The comparison in Figure 7 shows better qualitative and quantitative prediction of the horizontal displacement profile by the new advanced models compared to the MCC. Very good agreement is observed for the organic clay layer at the toe and mid-slope of the dyke where the MCC underestimates the magnitude of the displacement. Reconstruction of the failure mechanics from in-situ measurements revealed that the failure originated initially in the organic clay layer at the toe (Jommi et al., 2021). It is worth remarking that the inclinometer ImC was working down to – 5.5 m (NAP) only.

The benefit of the new models is also evident for the peat layer with a bulging profile predicted at the toe very close to the observed one. The simulation with the advanced models yields a maximum displacement of 0.086 m, compared to 0.065 m predicted by the

MCC, thus very close to the observed one, 0.1 m. The difference in predicted and observed displacements increases towards the upper peat layer, likely due to different mechanical properties of the surficial and deep peat layer as indicated by laboratory tests. Good agreement is also observed in the peat layer at the mid-slope of the dyke (ImC). For the inclinometer IcC, the final horizontal displacement is slightly overestimated. Laboratory tests indicated slightly stiffer peat and organic clay samples below the crest of the dyke compared to the polder side.

It is worth noticing that the difference between the MCC and the new models predictions is not evident in the first two dewatering stages but becomes clear in the last dewatering stage (blue lines in Figure 7). In the early dewatering stage, the soil stress state remains mostly inside the elastic domain, given the initial OCR profile. The difference becomes dominant as the stress state enters the plastic domain. The initial yield locus rotation and progressive reorientation during the last stages of dewatering improved the predictions for the organic clay layer, particularly at the toe of the dyke. Additionally, adopting a non-associated flow rule calibrated on experimental data helped to better replicate the plastic deformation mode in the peat layer.

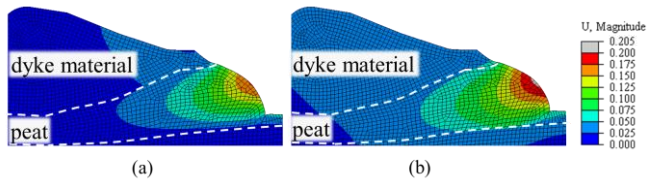

Figure 6. Displacement contour at the end of the third dewatering step: (a) MCC; (b) new models (units in m).

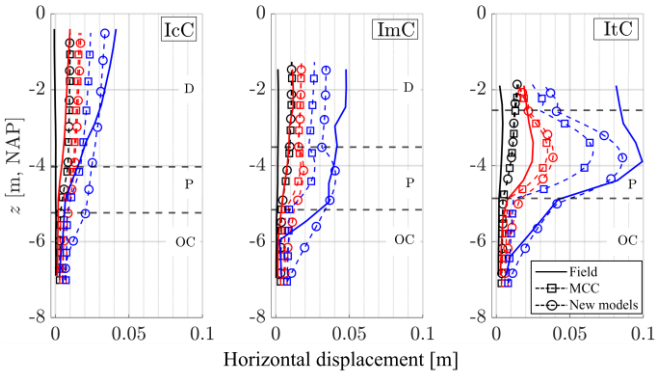

Figure 7. Measured and simulated horizontal displacement along inclinometer IcC, ImC, and ItC at the end of three dewatering stages.

5.2 Hydraulic response

The hydraulic response predicted by the numerical simulations and the comparison with field measurements is presented in Figure 8 in terms of variation of the excess pore pressure at piezometers PtC1, PtC2, PtC3, and PmC4 located at the toe of the dyke and in the dyke material (Figure 1) throughout the different steps. The timing of each operation is indicated by the labels E, D, and F as indicated in Table 5. The excess pore pressure is calculated based on the pore pressure before the first excavation stage.

The changes in pore water pressure during the initial excavation and dewatering step (E1, D1) are minimal due to the limited extent of excavation and the relatively small drawdown during the first operation stage. Small differences are observed in the numerical prediction for PmC4 during refilling after the first excavation and dewatering, with the new models better replicating the measurements.

The reduction in pore water pressure observed during the second and third excavation and dewatering phases (E2, D2, E3, and D3) is well captured.

Despite the difference in the displacement profile previously outlined, the variation of pore water pressure between the simulations, using the MCC and advanced models, is nearly identical. This suggests that the compressibility coefficient dominates the pore pressure response. In addition, it is relevant to mention that the dyke failure took place between Section Centre, here considered as representative cross-section, and Section South. Additional examination of the piezometer measurements at both Section South and Section North will be necessary to fully assess the model predictions in terms of hydraulic response.

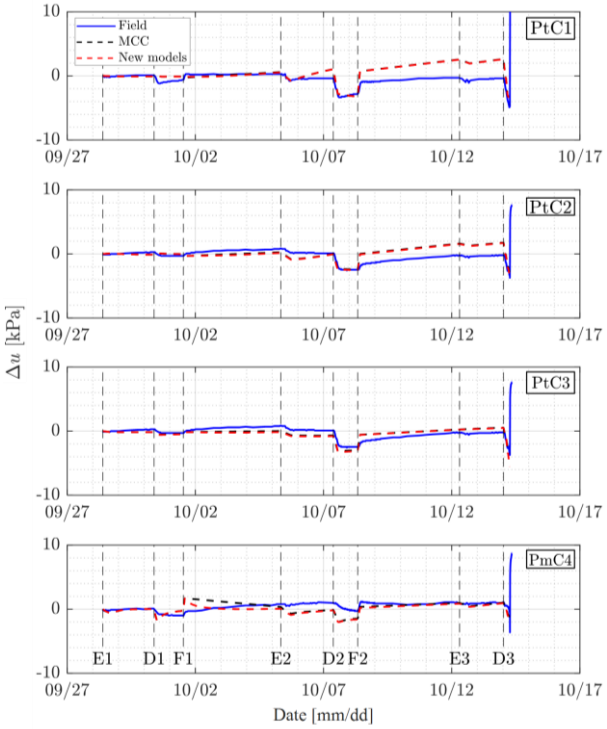

Figure 8. Measured and simulated time history of excess pore pressure at piezometer PtC1, PtC2, PtC3, and PmC4.

6 DISCUSSION AND CONCLUSIONS

This study presents a comparison between finite element simulations and in-situ measurements of a well-documented case study of a full-scale dyke stress test conducted on a regional dyke in the Netherlands. Particular attention is given to analysing the behaviour of the foundation layers consisting of peat and organic clays. Hydro-mechanical coupled finite element simulations are conducted with both traditional and new advanced constitutive models developed at TU Delft to better capture the complex behaviour of organic soft soils.

The numerical simulations show the benefits of the advanced models in better replicating both qualitatively and quantitatively the observed displacement field. In particular, the new models show a more diffusive displacement profile in the organic clay layer, where failure originated and a more pronounced lateral bulging profile very characteristic of peat.

The evolution of pore water pressure at different positions is well captured, with variations nearly identical in simulations using both MCC and advanced models possibly due to the dominant role of the compressibility coefficient in the overall volumetric response.

The comparison between the predicted displacement field along the entire cross-section profile with the in-situ data and laboratory data suggests possible variations of the compression coefficients within the foundation layers along the horizontal direction which should be accounted for a further refinement of the geotechnical model used in the numerical simulations. In addition, given the very small effective stress level which characterises regional dykes on soft soils, a proper initialisation of the in-situ stress state and OCR profile is of paramount importance to assess the engineering response of geo-infrastructure on soft soils.

ACKNOWLEDGEMENTS

The financial support of STOWA and the Dutch organisation for scientific research NWO, under the project “Reliable Dykes 13864“ is acknowledged. Thanks are due to Tom de Gast, who managed the design of the stress test in the field as part of his PhD research.

REFERENCES

Chao, C.Y. (2024). A comprehensive journey on Dutch organic clays. From element testing through constitutive modeling towards a novel cyclic multidirectional shear device. PhD Thesis, Delft University of Technology.

Dafalias, Y. F. and Taiebat, M. (2013). Anatomy of rotational hardening in clay plasticity. Geotechnique, 63(16), pp. 1406-1418. https://doi.org/10.1680/geot.12.P.197.

De Gast, T. (2020). Dykes and Embankments: a Geostatistical Analysis of Soft Terrain. PhD Thesis, Delft University of Technology, Delft. https://doi.org/10.4233/uuid:4ce3b4ec-0a6a-4886-9a82-5945a1f9ea50.

Jommi, C., Chao, C.Y., Muraro, S., and Zhao, H.F. (2021). Developing a constitutive approach for peats from laboratory data. Geomechanics for Energy and the Environment, 27, pp. 100-220. https://doi.org/10.1016/j.gete.2020.100220.

Landva, A.O., and La Rochelle, P. (1983). Compressibility and Shear Characteristics of Radforth Peats. ASTM International. pp. 157-191. https://doi.org/10.1520/STP37341S.

McDowell, G.R., and Hau, K.W. (2003). A simple non-associated three surface kinematic hardening model. Geotechnique, 53(4), pp. 433-437. https://doi.org/10.1680/GEOT.2003.53.4.433.

Muraro, S., and Jommi, C. (2021). Pre-failure behaviour of reconstituted peats in triaxial compression. Acta Geotechnica, 16(3), pp. 789-805. https://doi.org/10.1007/S11440-020-01019-2.

Ponzoni, E. (2017). Historical constructions on natural silty soils accounting for the interaction with the atmosphere. PhD thesis, Università degli Studi di Brescia.

Roscoe, K.H., and Burland, J.B. (1968). On the generalized stress-strain behaviour of wet clay. In Engineering plasticity, pp. 535-609. Cambridge University Press.

Zhao, H., and Jommi, C. (2023). Consequences of drying on the engineering properties of fibrous peats: compression behaviour. Canadian Geotechnical Journal, 60(4), pp. 438–452. https://doi.org/10.1139/cgj-2020-0086.

Proceedings of the XVIII ECSMGE 2024
GEOTECHNICAL ENGINEERING CHALLENGES
TO MEET CURRENT AND EMERGING NEEDS OF SOCIETY
© 2024 the Authors
ISBN 978-1-032-54816-6
DOI 10.1201/9781003431749-625
Open Access: www.taylorfrancis.com, CC BY-NC-ND 4.0 license

ECSMGE 24
XVIII EUROPEAN CONFERENCE ON SOIL MECHANICS AND GEOTECHNICAL ENGINEERING

Type-curves to assess seepage under sheet-piles for dewatering geotechnical works in limited 2D geometries

Courbes types pour évaluer l'infiltration sous palplanche pour les travaux géotechniques de drainage dans des géométries 2D limitées

S. Navarro Carrasco, J.A. Jiménez-Valera*, I. Alhama Manteca
Mining and Civil Engineering Department, Technical University of Cartagena, Spain
jose.jvalera@upct.es

ABSTRACT: Graphical methods based on flownets or numerical modelling are two procedures traditionally used to estimate groundwater flow under different geotechnical structures (dams, sheet-piles, diaphragm walls, among others). In this work, both methods are combined with dimensionless analysis to set out and verify the dimensionless groups that govern the groundwater discharge. The results are a set of type-curves charts easy-to-use to assess seepage per metre transversal length of sheet-pile. The chart is applied to flow under sheet-piles for maritime or fluvial shored scenarios, where permanent dewatering is required in the enclosure. Geometrical parameters like sheet-pile height, depth of sheet-pile embedment, impervious bedrock depth, excavation width, horizontal stretch in the back face and water levels and physical parameters as hydraulic conductivity are input data in the chart, all of them included in the monomials. The physical scenario assumes isotropic medium and cross-section symmetry.

RÉSUMÉ: Les méthodes graphiques basées sur les flownets ou la modélisation numérique sont deux procédures traditionnellement utilisées pour estimer le mouvement des eaux souterraines sous différentes structures géotechniques (barrages, palplanche, paroi moulée, entre autres). Dans ce travail, les deux méthodes sont combinées avec une analyse adimensionnelle pour définir et vérifier les groupes adimensionnels qui régissent le mouvement des eaux souterraines. Les résultats sont un ensemble de courbes types faciles à utiliser pour évaluer l'infiltration par mètre de longueur transversale de palplanche. Les courbes est appliqué au mouvement sous les palplanches pour des scénarios de berges maritimes ou fluviales, où un assèchement permanent est nécessaire dans la tranchée. Les paramètres géométriques tels que la hauteur des palplanches, la profondeur d'encastrement des palplanches, la profondeur du substratum rocheux imperméable, la largeur de l'excavation, l'étirement horizontal et les niveaux d'eau, ainsi que les paramètres physiques tels que la conductivité hydraulique, sont des données d'entrée dans le diagramme, toutes incluses dans les monômes. Le scénario physique suppose un milieu isotrope et une symétrie de la section transversale.

Keywords: Numerical modelling; dimensionless monomial; seepage; dewatering.

1 INTRODUCTION

Most civil engineering construction sites requires working under the ground surface. The stability of the excavation is, in many cases, supported by geotechnical structures like sheet pile walls, steel sheeting, diaphragm walls, cut-off walls, or cofferdams. The design of them relies on soil mechanics properties and on the presence of groundwater. The groundwater flowing under the retaining structure and into the excavation (seepage) is conditioned by the geometry, the specific boundary conditions and the hydraulic conductivity.

In this work, we focus on the calculus of seepage in a 2D isotropic scenario outlined in Figure 1. The 2D geometry of the aquifer is constrained by "*H*" and "*L*", both having finite values. The solution is given as a set of abacuses and the type curves depicted in them relates dimensionless monomials (groups of parameters involved in the solution).

Similar solutions are found in technical or scientific literature. For example, in Puertos del estado and Ministerio de Fomento (2005) and Graham (2006), the solution was given for a non-horizontal limited scenario (length "*L*" was not included). In Preene et al. (2014), the horizontal and vertical extend "*L*" and "*H*", respectively, were not defined. This last case was also studied in Navarro Carrasco et al. (2023), but considering anisotropic media. A problem we found in some of these works is the lack of explanation about the meaning of some parameters required to use the abacuses. Most of them are not even defined in the documents, what make them difficult to understand.

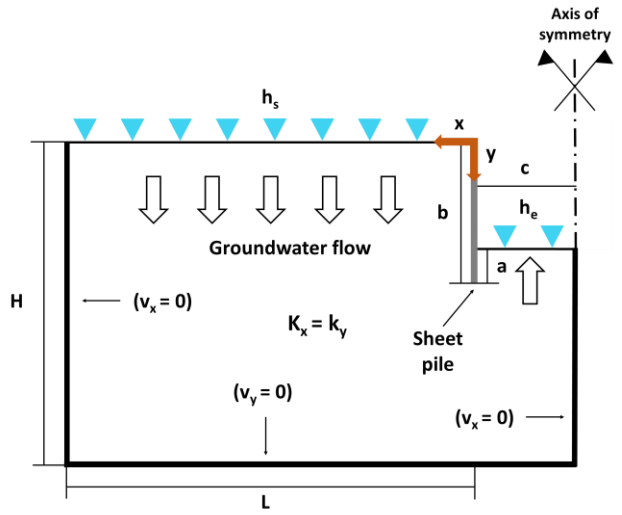

Figure 1. 2D schema of the problem with geometric data and boundary conditions.

This work is a first step before further studies with anisotropic media or heterogeneous layered substratum. A theoretical example of application is given at the end of section 3, to illustrate the use of the abacuses.

2 PHYSICAL MODEL AND GOVERNING GROUPS

The list of parameters that define the problem are shown in Figure 1: piezometric heads at the back of the wall (h_s) and inside (h_e) the excavation, the horizontal (L) and vertical (H) extend, the depth of the retaining structure in contact with groundwater b, the embedment a, half of the horizontal extend of the excavation c, and the isotropic hydraulic conductivity K. The transversal extend of the excavation is large enough to neglect effects at the edge and axis-symmetry is assumed. To ensure that the horizontal and vertical extension are short enough to influence on the solution, the concept of characteristic lenghts previously studied in Navarro Carrasco et al. (2023) and Martínez-Moreno (2022), is applied. This concept relates to specific vertical (T^*) and horizontal (L^*) lengths: if $H > T^*$ and $L > L^*$ the solution is similar to an infinite scenario (not the case here we are dealing with), and if $H < T^*$ and $L < L^*$ the solution is that of a finite scenario. In section 3 it will be clarified with and example.

As shown in Figure 1, water is flowing from the surface to the bottom of the excavation and under the geotechnical structure. The boundary conditions are Dirichlet condition (constant head) at the ground surface and bottom of the excavation and Neumann condition (impervious limits) at the geotechnical structure, vertical limits ($v_x = 0$) and at the bottom ($v_y = 0$). As it can be apreciated, the ground located over the prehatic level is not conditioning the seepage.

Each monomial (group of parameters involved in the solution) is obtained from classical dimensional analysis techniques (Palacios, 1964). The values of the 4 monomials obtained govern the solution. It means that, as long as the values of the monomial remain constant, the solution is the same irrespective of the values of the parameters included in the groups. The monomials are:

$$\pi_1 = a/b \quad (1)$$

$$\pi_2 = b/c \quad (2)$$

$$\pi_3 = b/H \quad (3)$$

$$\pi_4 = c/L \quad (4)$$

$$\pi_Q = \frac{Q}{(h_s - h_e)\cdot k} \quad (5)$$

According to Pi Theorem (Buckingham, 1914), the group π_Q with the unknown Q is a function of the rest of groups (1-4) and its value was previously set by Martinez-Moreno (2021). A total number of 72 simulations with MODFLOW (Harbaugh et al., 2000), each of them taking an average of less than 15 second to compute, were carried out to depict the abacuses and type curves, so the function π_Q was defined. The procedure required keeping three monomials constant and while changing the values of the fourth, so the variation π_Q can be drawn as a function of the fourth. The process is repeated by taking turns with all the monomials.

3 RESULTS: TYPE CURVES

4 abacuses containing 3 type curves each one, are shown in Figure 2.

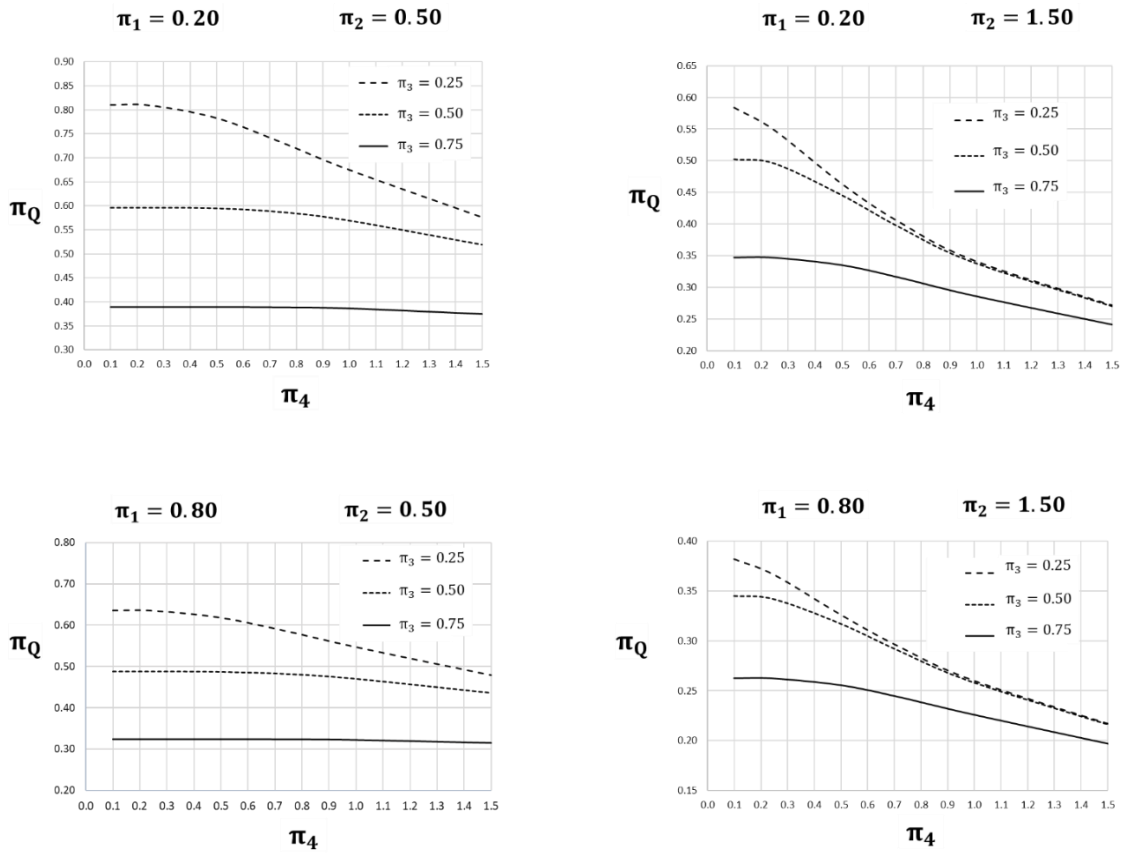

Figure 2. Type curves to calculate seepage under a retaining structure and into the excavation.

The curve parameter is π_3 and the values considered are 0.25, 0.50 and 0.75. The abacus parameters are π_1(0.2-0.8) and π_2 (0.5-1.5). On each graph, π_4 ranges from 0.1 to 1.5. These values were chosen to consider aspect related to stability or heave.

To illustrate the use of the abacuses, a theoretical application based on example 3.3 of Berry and Reid (1993) is solved. The parameter values and the monomials are shown in Table 1.

Table 1. values of the variables in the theoretical example.

Parameter/monomial	Value	Units
a	4.0	m
b	5.0	m
c	3.0	m
L	12.0	m
H	9.0	m
$\boldsymbol{h_s - h_e}$	4.0	m
k	$7 \cdot 10^{-5}$	m/s
$\boldsymbol{\pi_1 = a/b}$	0.80	dimensionless
$\boldsymbol{\pi_2 = b/c}$	1.67	dimensionless
$\boldsymbol{\pi_3 = b/H}$	0.56	dimensionless
$\boldsymbol{\pi_4 = c/L}$	0.25	dimensionless

The steps that must be followed are:

Step 1: Check if the values of L and H are lower than those of the characteristic legths L^* and T^*, so that the type-curves of Figure 3 can be used. Figures 3 and 4 are used in this step.

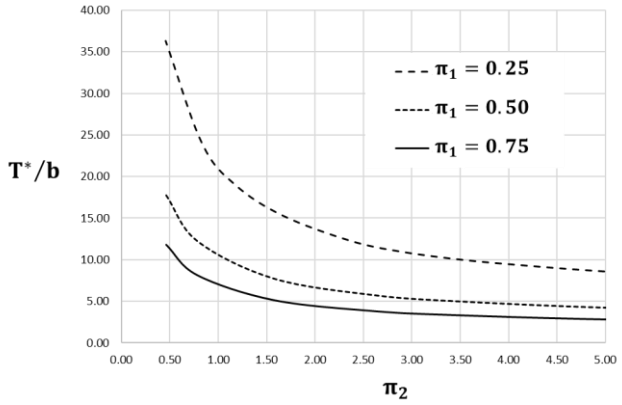

Figure 3. Type curves to calculate the vertical characteristic length T^*. Modified from Navarro Carrasco et al. (2023).

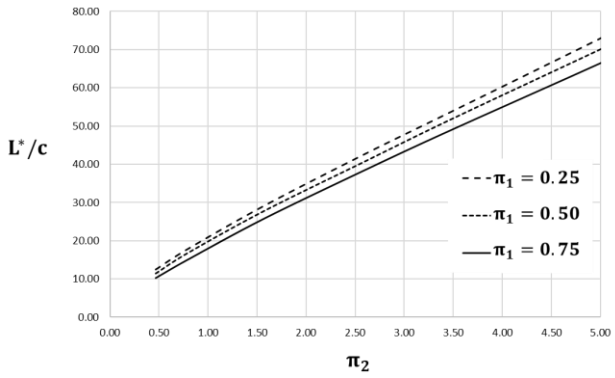

Figure 4. Type curves to calculate the horizontal characteristic length L^*. Modified from Navarro Carrasco et al. (2023).

According to values in Table 1, L^* = 84 m and T^* = 25 m, both greater than L = 12 m and H = 9 m, so the abacuses in Figure 3 can be used.

Step 2. We select the abacus according to the values of the monomials, in this case, the one with π_2 = 1.5 (the closest) and π_1 = 0.8. With the value of π_4 = 0.25 and π_3 = 0.56, the function containing the unknown is π_Q = 0.33.

Step 3. With the values of π_Q = 0.33, we obtain Q from equation 5: $Q = 9.24 \cdot 10^{-5}$ m^3/s/m.

In Berry and Reid (1993), the result for $L = \infty$ (in our variant we have considered L = 12 m) is $Q = 8.96 \cdot 10^{-5}$ m^3/s/m. Simulating the example of Berry and Reid with L = 12 m in MODFLOW, $Q = 9.14 \cdot 10^{-5}$ m^3/s/m.

4 CONCLUSIONS

In this work, we provide 12 type-curves distributed in 4 abacuses to calculate seepage under embedded retaining structures from geometrical and physical data. Each graph depicts the monomial containing the unknown π_Q, as a function of the 4 dimensionless groups. The conditions are isotropic hydraulic conductivity and limited horizontal and vertical extension of the scenario, so that the geometry is conditioning groundwater flow.

To illustrate the use of the type-curves, a modified example has been carried out. The first verification compares by using two charts, the vertical (H) and horizontal (L) length of the scenario with the characteristic lengths T^* and L^*, respectively. It allows to differentiate between limited and infinite scenarios, those where the geometry is not conditioning the seepage.

ACKNOWLEDGEMENTS

The authors want to thank Doctor Francisco Javier Alhama López for his advice in this research.

REFERENCES

Berry, P. L., & Reid, D. (1993). *Mecánica de suelos*. McGraw-Hill, Santafé de Bogotá, Colombia.

Buckingham, E. (1914). On physically similar systems; illustrations of the use of dimensional equations. *Phys. Rev*., 4(4), 345.

Graham, J. (2006). *Canadian Foundation Engineering Manual*., Canadian Geotechnical Society, Saskatoon, Canada.

Harbaugh, A. W., Banta, E. R., Hill, M. C. and McDonald, M. G. (2000). *MODFLOW-2000, the U. S. Geological Survey Modular Ground-Water Model—User Guide to Modularization Concepts and the Ground-Water Flow Process*; U.S. Geological Survey: Reston, VA, USA, p. 121. https://doi.org/10.1103/PhysRev.4.345.

Martínez Moreno, M. E. (2021). *Characterization and numerical verification of seepage scenarios in anisotropic soils under retaining structures and in unconfined aquifers due to pumping wells*, Doctoral thesis, Universidad Politécnica de Cartagena. Available at: [http://hdl.handle.net/10317/9466], accessed: 27/10/2023.

Navarro Carrasco, S., Jiménez-Valera, J. A. and Alhama, I. (2023). A Universal Graphical Solution to Calculating Seepage in Excavation of Anisotropic Soils and Non-Limited Scenarios, *Geotechnics*, 3(3), 719–730. https://doi.org/10.3390/geotechnics3030039.

Palacios J. F. (1964). Dimensional Analysis. MacMillan & Co. Ltd. St Martin's Press, New York, USA.

Preene, M., Roberts, T. O. L. and Powrie, W. (2014). *Groundwater Control: Design and Practice*. CIRIA, London, UK.

Puertos del Estado and Ministerio de Fomento (2005). Recommendation for maritime works. Rom 0.5-05. Geotechnical recommendations for the design of maritime and harbour works. Isbn 978-84-88975-62-2. Ministerio de fomento (Spanish Goverment), Spain.

Proceedings of the XVIII ECSMGE 2024
GEOTECHNICAL ENGINEERING CHALLENGES
TO MEET CURRENT AND EMERGING NEEDS OF SOCIETY
© 2024 the Authors
ISBN 978-1-032-54816-6
DOI 10.1201/9781003431749-626
Open Access: www.taylorfrancis.com, CC BY-NC-ND 4.0 license

ECSMGE 24
XVIII EUROPEAN CONFERENCE ON SOIL MECHANICS AND GEOTECHNICAL ENGINEERING

Producing pore pressure due to heat for bentonite-sand mixture with difference dry densities

Production d'une pression interstitielle due à la chaleur pour un mélange bentonite-sable avec des densités sèches différentes

T. Nishimura*
Ashikaga University, Tochigi, Japan
**nishimura.tomoyoshi@g.ashikaga.ac.jp*

ABSTRACT: Radioactive waste has to be isolated from the human habitat for absolutely so long time period until its radioactivity has decayed to an innocuous situation. Many researchers have reported and demonstrated the interpretation of thermal hydration mechanical chemical couple phenomena (i.e. THMC phenomena) for unsaturated-saturated bentonite. There is lack to measure the pore pressure, and discuss the fluid pressure phenomena. This study represents pore pressure associated to heat, and have used in developed steel mold accomplished crucial pressure sensor within the high resistance to temperature. The materials used in this test program are bentonite and sand, and the bentonite is sodium type and sand are classified into silica. The bentonite sand mixture remains a ratio of 70% and 30% in dry weight. The specimen variety from 0.80 Mg/m^3 to 1.80 Mg/m^3 in dry density. The specimen closed in the steel mold have received heat performance, and the temperature achieve to 80 degrees Celsius. The pore pressures result that all of specimens with the difference dry densities describe more than 10 kPa in the pressure, and the dense specimens verify the high pore pressures.

RÉSUMÉ: Les déchets radioactifs doivent être isolés de l'habitat humain pendant une période de temps absolument longue jusqu'à ce que leur radioactivité soit devenue inoffensive. De nombreux chercheurs ont rapporté et démontré l'interprétation des phénomènes de couple mécanique-chimique d'hydratation thermique (c'est-à-dire les phénomènes THMC) pour la bentonite insaturée-saturée. Il manque de mesurer la pression interstitielle et de discuter des phénomènes de pression des fluides. Cette étude représente la pression interstitielle associée à la température de la chaleur et a utilisé dans le moule en acier développé un capteur de pression crucial dans la haute résistance à la température. Les matériaux utilisés dans ce programme de test sont la bentonite et le sable, et la bentonite est de type sodium et le sable est classé en silice. Le mélange de sable bentonite reste dans une proportion de 70% et 30% en poids sec. La variété spécimen de 0,80 Mg/m3 à 1,80 Mg/m3, en densité sèche. Les échantillons fermés dans le moule en acier ont reçu des performances thermiques et la température atteint 80 degrés Celsius. Les pressions interstitielles font que tous les échantillons avec des densités sèches différentes décrivent une pression supérieure à 10 kPa, et les échantillons denses vérifient les pressions interstitielles élevées.

Keywords: Pore pressure; bentonite-sand mixture; unsaturated soil; shear strength; heating.

1 INTRODUCTION

Many researchers have reported and demonstrated the interpretation of thermal hydration mechanical chemical couple phenomena (i.e. THMC phenomena (Huertas and Santiago, 1997) for unsaturated-saturated bentonite, and the variety in the mechanical of bentonite sand mixture caused by THMC phenomena. Lloret et al., (2004) reported the results of the thermo-hydro-mechanical (THM) in the laboratory test and established the calibration of the models. It is verified the influence of the microstructure changes in bentonite. Sellin et al., (2020) explained the key objective of Beacon, and verified the tools for the assessment of the mechanical evolution of installed bentonite components and the eventual performance of the barrier. There is lack to measure the pore pressure, and discuss the fluid pressure phenomena. It is often understood as gas migration and gas generation in the arterial barrier system.

2 PURPOSE OF THIS STUDY

This study represents pore pressure associated to heat temperature, and have used in developed steel mold accomplished crucial pressure sensor within the high resistance to temperature. The materials used in this test program are bentonite and sand, and the bentonite is sodium type and sand are classified as silica. The bentonite sand mixture remains a ratio of 70% and 30% in dry weight. The specimen variety from 0.80 Mg/m^3 to 1.80 Mg/m^3, in dry density. The specimen closed in the steel mold have received heat

performance, and the temperature achieve to 80 degrees Celsius. The pore pressures result that all of specimens with the difference dry densities describe more than 10 kPa in the pressure, and the dense specimens verify the high pore pressures.

3 TEST PRODUCER

3.1 Soil material

This testing program have the purpose such as deformation, strength and pore fluid pressure under heat produce. Considering, Kunigel V1, a sodium bentonite, is used in a series of three testing programs to confirm the Thermal-Hydro-Mechanical properties in experimental laboratory studies. Majority of chemical components are as following; SiO_2 is 70.2%, Al_2O_3 is 14.2%, Fe_2O_3 is 2.5% and CaO is 2.0%.

3.2 Specimens

The bentonite sand mixture is put into the stiffness steel mold with an inner diameter of 38.0 mm, a thickness of 18.0 mm and a height of 76.0 mm. In term of friction stress at inner surface and soil material, it is assumed to be neglection, because of density distribution is equal in previous experimental works. Then, the pre-consolidation pressure is measured at processing the compaction, as result, approximately 10 MPa is estimated through consolidation test.

3.3 Apparatus

This testing programs consist of five testing programs. These test programs are divided categories into thermal-hydration and thermal-mechanics. The developed steel mold and thermal heating triaxial compression apparatus are used to appear the key futures for unsaturated bentonite-sand mixture specimen.

3.4 Testing program

This testing programs consist of five testing programs. These test programs are divided categories into thermal-hydration and thermal-mechanics.

3.4.1 Measurement of relative humidity

Testing program (A) measure the relative humidity in steel mold under heating that use miniature relative humidity and temperature sensor. Some salt solutions are put into the steel mold, subsequently, the steel mold is completely closed that is undrained conditions. The controlling relative humidity is following the vapor pressure technique that is common in suction measurement method.



Figure 1. Developed steel mold wit sensor.

3.4.2 Heating under free deformation

Testing program (B) conducted out heating for unsaturated specimens in the steel mold. All of specimens produce the deformations (i.e., axial direction and horizontal directions). After heating, all of specimens are measured compressive strength.

3.4.3 Heating under confirmation of lateral deformation

Testing program (C) attempted the heating application and measure unconfining compressive strength. All of specimens in the steel mold prevent the expansion deformations in the horizontal way. Other hand, free deformations allowed in axial way.

3.4.4 Triaxial compression tests with heating for saturated specimen

Testing program (D) produce the triaxial compression test used for saturated specimens., which are prepared due to apply the vacuum in the water bath. Either distilled water or salinity water is supplied in the bath and the concentration is 3.5% for salinity water. Applied temperature is 80 degrees Celsius.

3.4.5 Measurement of pore pressure due to heating

Considering of pore pressure increment is employed in Testing program (E). The steel mold is used as shown in Fig 1, which installed two pressure sensors (PHF-S-3MPS3B manufactured by KYOWA) with high temperature resistance. Calibrations are often investigated through this testing programs. Some specimens with variation dry densities are prepared for measurement of pore pressures under heating.

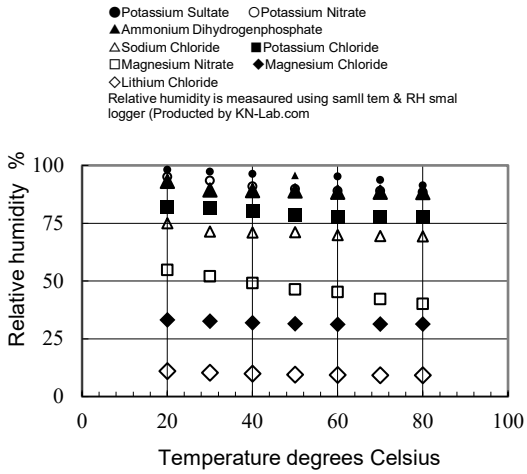

Figure 2. Change of relative humidity.

4 TEST RESULTS

4.1 Changing of relative humidity

The steel mold is prepared that some salt solutions are installed in order to investigate relative humidity changing in Testing program (A). Whole the mold was placed in thermostat oven, in which controlled a range from 20 degrees Celsius to 80 degrees Celsius. Variations of salt solutions are used to create relative humidity ranges, and the results is described as shown in Figure 2. Determined relative humidity has a range from 95% to 9.0%. All of chemical substances have common tendency which is reduction with increment of temperature regardless of relative humidity at 20 degrees Celsius. Much reductions of relative humidity are indicated in such tendency when Magnesium Nitrate is place in the mold, that it is from 54.7% to 40.2% in relative humidity.

4.2 Unconfined compressive strength subjected to deformations

All specimens, are equivalent to given temperature s and relative humidity as above mentioned in Section 4.1 that used for determination of unconfined compressive strength according to unconfined compression test (Figure 3). While compression process in the triaxial compression cell, reproduce the temperature at 20, 40, 60 and 80 degrees Celsius remaining. As mechanical component, removing of unconfined compressive strength for unsaturated bentonite subjected to heating and developed relative humidity is significant factor. The specimens except of 20 and 40 degrees Celsius have some cracks. All specimens derive that the unconfined compressive strength decrease according to heat, are smooth tendency in plotted strength with temperatures. Particularly, the specimens with equivalent to relative humidity of 75% that describe the further reduction by heat, and the different in strength is over 500 kPa between 20 degrees Celsius and 80 degrees Celsius.

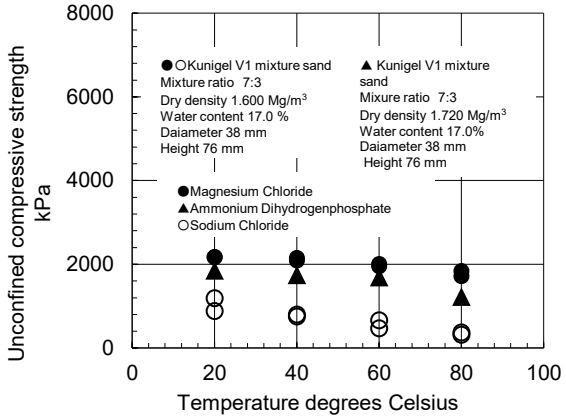

Figure 3. Reduction of shear strength (Test (B)).

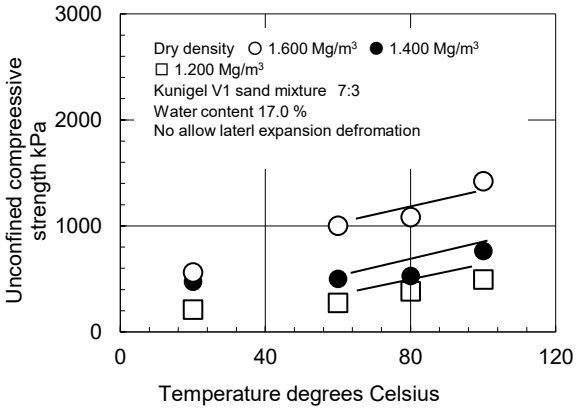

Figure 4. Increment of shear strength (Test (C)).

4.3 Unconfined compressive strength considering axial strains

Three different dry densities are selected that are 1.200 Mg/m^3, 1.400 Mg/m^3 and 600 Mg/m^3, and all of these specimens are common the water content of 17.0% and bentonite-sand ratio is 7:3. All specimens present the shrinkage phenomena at beginning of test air surrounding of 20 degrees Celsius. Contrast, exchange axial strain with increment temperature that are coincident regardless of different of dry density, axial strain stays in remaining expansion deformation.

The relationship between temperature and unconfined compressive strength is produced as shown in Figure 4. Investigation of the unconfined compressive strength used the thermal triaxial compression apparatus. It obviously confirms that measured unconfined compressive strength increase with the dry density regardless of the temperature. Even if increment of temperature is applied to the

specimens, the influence of dry density on strength is remained and the increasing of temperatures. The difference in strength varied from 563 kPa to 1421 kPa through changing of temperature for dry density of 1.600 Mg/m^3, and describe further increment beyond 60 degree Celsius. For both two dry densities (i.e. 1.200 Mg/m^3 and 1.400 Mg/m^3) the strength increases smoothly with heat, and verified the lines are seem to be straight with some slopes. These slopes are closely at range from 60 degrees Celsius and 100 degrees Celsius. Case of dry density of 1.600 Mg/m^3 compare, the large slope is provided that are 10.5 kPa per degree Celsius. Other two lines have a slope of 6.5 and 5.5 kPa per degree Celsius. Figures. 3 and 4 show the contradictory results that the cause is suggested deformation characteristic properties. The results shown in Figure 3 related to all direction deformation and the results for Figure 4 is allowable deformations in limitations.

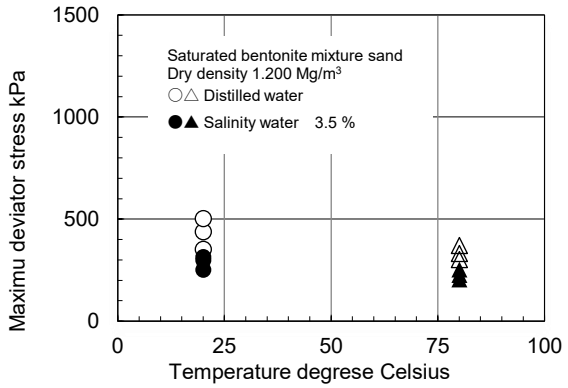

Figure 5. Change of maximum deviator stress.

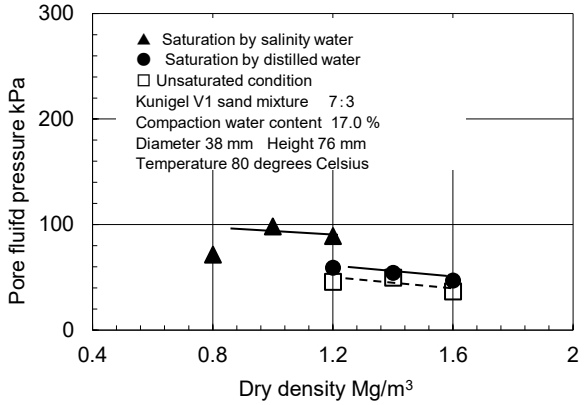

Figure 6. Produced pore pressures.

4.4 Shear strength for saturated specimen under heating

This study appear the shear strength obtained from thermal triaxial compression test that all of specimens are saturated condition, and the applied lateral confining pressures are 100 kPa, 300 kPa and 600 kPa. Also, soaking waters are distilled water and salinity water, the salinity water has the concentration is 3.5%. The saturated shear strength has the influence of temperatures as shown Figure 5 that the increment of temperature causes the reduction shear strength.

4.5 Producing of pore pressure by heating

Above mentioned, it is obviously that the heating actions is significant factors such as THMC phenomena. This study measures the produced pore pressures due to heating that the relationship between temperature and pore pressures is shown in Figure 6. The investigation is conducted out under 80 degrees Celsius s for unsaturated specimen and saturated specimens. According to be increase the dry density, the pore pressure decreases regardless of dry density.

5 CONCLUSIONS

This study represents pore pressure associated to heat temperature, and unconfined compressive strength in other subjection.

1. The relative humidity decreases with associated to be heating. The unconfined compressive strength changes due to application of heating that is close related to deformation characteristic properties due to heat.
2. The pore pressures are induced by increment of temperatures, and the measured pore pressures decrease with dry density.

REFERENCES

Huertas, F., and Santiago, J. L. (1997). The FEBEX Project. General Overview, *MRS Online Proceedings Library (OPL)* 506. 343. https://doi.org/10.1557/PROC-506-343 [DOI].

Lloret, A., Romero, E., and Villar, M. V. (2004). FEBEX II Project Final report on thermo-hydro-mechanical laboratory tests. *Diseno y production: TransEdit.*

Sellin, P., Westermark, M., Leupin, O., Norris, S., Gens Solé, A., Wieczorek, K., and Swahn, J. (2020). Beacon: bentonite mechanical evolution. *EPJ nuclear sciences & technologies*, 6, 23-1. 10.1051/epjn/2019045 [DOI].

Proceedings of the XVIII ECSMGE 2024
GEOTECHNICAL ENGINEERING CHALLENGES
TO MEET CURRENT AND EMERGING NEEDS OF SOCIETY
© 2024 the Authors
ISBN 978-1-032-54816-6
DOI 10.1201/9781003431749-627
Open Access: www.taylorfrancis.com, CC BY-NC-ND 4.0 license

ECSMGE 24
XVIII EUROPEAN CONFERENCE ON SOIL MECHANICS AND GEOTECHNICAL ENGINEERING

Database of measured shear wave velocity profiles for Icelandic soil sites

Base de données des profils de vitesse des ondes de cisaillement mesurés pour les sites de sols islandais

E.A. Olafsdottir*, S. Erlingsson, B. Bessason
Faculty of Civil and Environmental Engineering, University of Iceland, Reykjavik, Iceland
**elinasta@hi.is*

ABSTRACT: MASW (Multichannel Analysis of Surface Waves) is an active-source surface wave method that provides information on shear wave velocity (V_S) distribution down to 10–30 m depth. The technique has been found well-suited for profiling of Icelandic soil sites, including gravelly sites and sites with partly cemented materials or mixed soils containing cobbles or boulders. This paper introduces a database where results of MASW measurements conducted in Iceland can be accessed. The database is available in open-access online and provides the user with an interface which allows results from different sites to be viewed simultaneously and compared in terms of dispersion curves, V_S profiles and time-averaged V_S.

RÉSUMÉ: MASW est une méthode d'onde de surface à source active qui fournit des informations sur la distribution de la vitesse des ondes de cisaillement (V_S) jusqu'à 10 à 30 m de profondeur. La technique s'est avérée bien adaptée au profilage des sites de sols islandais, y compris les sites graveleux et les sites avec des matériaux partiellement cimentés ou des sols mixtes contenant des galets ou des rochers. Cet article présente une base de données où les résultats des mesures MASW effectuées en Islande peuvent être consultés. La base de données est disponible en libre accès en ligne et offre à l'utilisateur une interface permettant de visualiser simultanément les résultats de différents sites et de les comparer en termes de courbes de dispersion, de profils V_S et de V_S moyenné dans le temps.

Keywords: Iceland; shear wave velocity; surface wave analysis; MASW; database.

1 INTRODUCTION

Seismic site characterization is a fundamental aspect of engineering design of structures in seismically active areas. The seismic hazard in Iceland is considered moderate to high, with the largest earthquakes occurring within two complex fracture zones: the South Iceland Seismic Zone (SISZ) in the south and the Tjörnes Fracture Zone (TFZ) in the north (Einarsson, 2008). The soil site conditions in Iceland are shaped by a combination of volcanic activity, glacial drift, and sea level variations through the ages. The soil deposits largely consist of coarse-grained granular materials of basaltic origin (i.e., coarse silt, sand, gravel, and coarser grains), although thick peat deposits exist in some locations. Clayey materials are uncommon in Iceland (Erlingsson, 2019).

Surface wave methods have been found well-suited for profiling of Icelandic soil sites, including gravelly sites and sites characterized by conglomerated materials or mixed soils containing cobbles or boulders. From 2013 to 2021, MASW (Multichannel Analysis of Surface Waves) measurements were conducted in 19 areas in Iceland. Together, the tested sites represent the three most commonly encountered types of natural soil deposits in Iceland, in addition to engineered fills. This paper describes the first efforts made to create a database where the measurement results, along with supporting data, can be accessed. The database is accessible in open access at https://serice.hi.is. The user interface allows results from different sites to be viewed simultaneously and compared in terms of dispersion curves and measured shear wave velocity (V_S) profiles. The V_S profiles are further presented as time-averaged shear wave velocity ($V_{S,z}$) in line with the site categorization in the current Eurocode 8 [EC8] (CEN, 2004).

2 ANALYSIS PROCEDURE

The term MASW describes a linear data acquisition layout where a vertical impact source is applied in-line with an array of equally spaced receivers that are placed on the surface. The interval V_S profile of the underlying soil stratum is then obtained by inverting the dispersion characteristics of the recorded Rayleigh waves.

The same data acquisition and analysis approach was used for all the sites that are currently included in the database (Figure 1). The in-situ measurements were generally conducted using 24 vertical 4.5 Hz geophones with a spacing of 0.5 m, 1 m, and/or 2 m, depending on site conditions. In exceptional cases, the number of receivers was 12 or 16. Rayleigh waves were generated with a sledgehammer that was struck at various distances (usually in the range of 3–30 m) from one or both ends of each geophone array. Several shot gathers were recorded for each array length and impact point location. Each multi-channel record was analysed separately to quantify the variability of the dispersion curve estimates prior to the inversion. Comparison of dispersion curves obtained at different impact points (i.e., different source offset lengths and forward/reverse shot gathers) was further used during the data analysis for detection of possible near-field effects at certain source offsets and for validation of the 1D assumption adopted in the inversion process. For each test site, the resulting dataset was merged into a single composite curve by adding up the elementary dispersion curves within log-spaced wavelength bands. The composite experimental dispersion curve is subsequently referred to by the abbreviation EDC. A Monte Carlo global search process was then used to identify a set of V_S profiles that fit the observed data, given the uncertainty of the mean EDC and the assumed ground model. A comprehensive description of the data processing and inversion procedures is provided in Olafsdottir et al. (2023).

3 DATABASE OF MEASURED V_S PROFILES

The soil site database currently stores measured dispersion curves, V_S profiles and $V_{S,z}$ from 19 sites in Iceland. Between one and seven measurements are available for each site with an inter-profile distance below 1.1 km and an investigation depth between 10 m and 30 m (Olafsdottir et al., 2023).

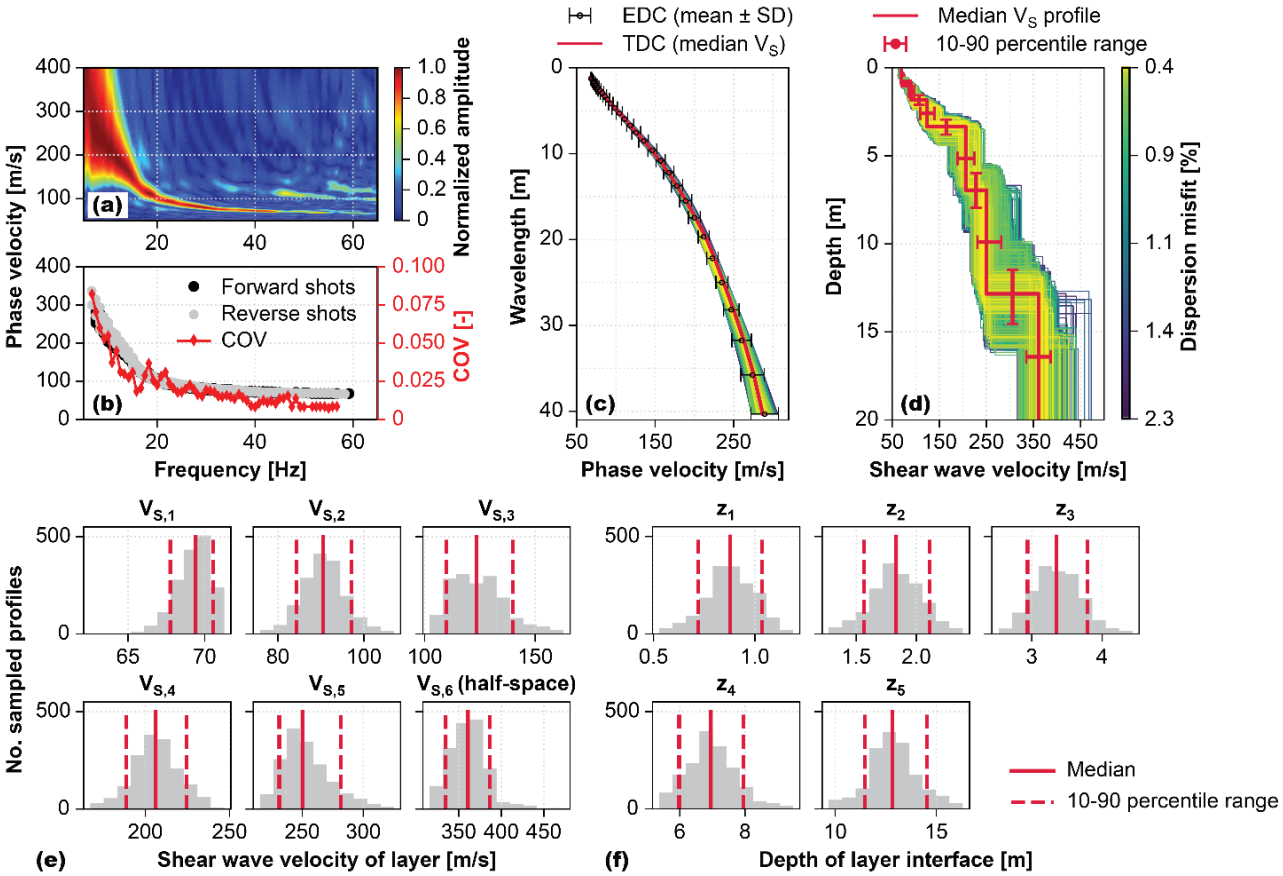

Figure 1. MASW survey by the Ölfus River in South Iceland, illustrating the workflow used for all sites. (a) Spectral image of a single shot gather. (b) Dispersion curves identified from repeated shot gathers (left-hand axis) and variation of the phase velocity values (right-hand axis). (c,d) Sampled V_S profiles (six-layered model) whose theoretical dispersion curves (TDC) fall within the boundary EDCs. The median and 10th to 90th percentile range of the V_S models, and the TDC corresponding to the median V_S profile, are shown in red. (e) Distribution of the shear wave velocity in the i-th layer, $i \in \{1, \dots, 6\}$, and (f) the depth of the i-th layer interface, $i \in \{1, \dots, 5\}$, for the set of velocity models shown in (d).

The user interface is based on an interactive map that shows the surveyed sites (Figure 2). By clicking on a specific map marker, the measurement locations at the given site are displayed (Figure 3a) and the profile(s) of interest can be selected by clicking their unique identifiers (IDs) (Figure 3b). The data are presented in figure form as shown in Figures 3d–f. Results from an unlimited number of measurements (from any survey sites) can be viewed simultaneously. The selected measurements are managed using the check boxes (view/hide) and cross marks (remove) by their profile IDs (Figure 3c).

The interval V_S profile shown for each measurement (Figure 3e) is the median of the subset of sampled V_S profiles whose associated theoretical dispersion curves fall within the boundary EDCs at all wavelengths. The 10th and 90th percentiles of $V_{S,i}$ and z_i are further provided (here $V_{S,i}$ and z_i denote the shear wave velocity in the i-th layer and the depth of the i-th layer interface, respectively).

The mean EDC and its boundary curves are presented as shown in Figure 3d. The boundary EDCs are defined as one standard deviation (SD) above and below the mean curve, except for measurements conducted on top of earth-rockfill dams with a central core, where they are specified as 1.5 SDs from the mean EDC. In those cases, the acquired multi-channel time series likely represent a mixture of the response of the core and shell materials. The theoretical dispersion curve of the median V_S profile is given, thus allowing the user to visually evaluate its fit to the EDC.

The median V_S profile is also given as time-averaged shear wave velocity ($V_{S,z}$, Figure 3f), defined by Eq. (1) where $V_{S,i}$ and h_i are the velocity and thickness of the i-th layer for a total of N layers down to depth z:

$$V_{S,z} = \frac{z}{\sum_{i=1}^{N}\left(\frac{h_i}{V_{S,i}}\right)} \quad (1)$$



Figure 2. The map interface of the soil site database. The current test sites are shown with red markers.

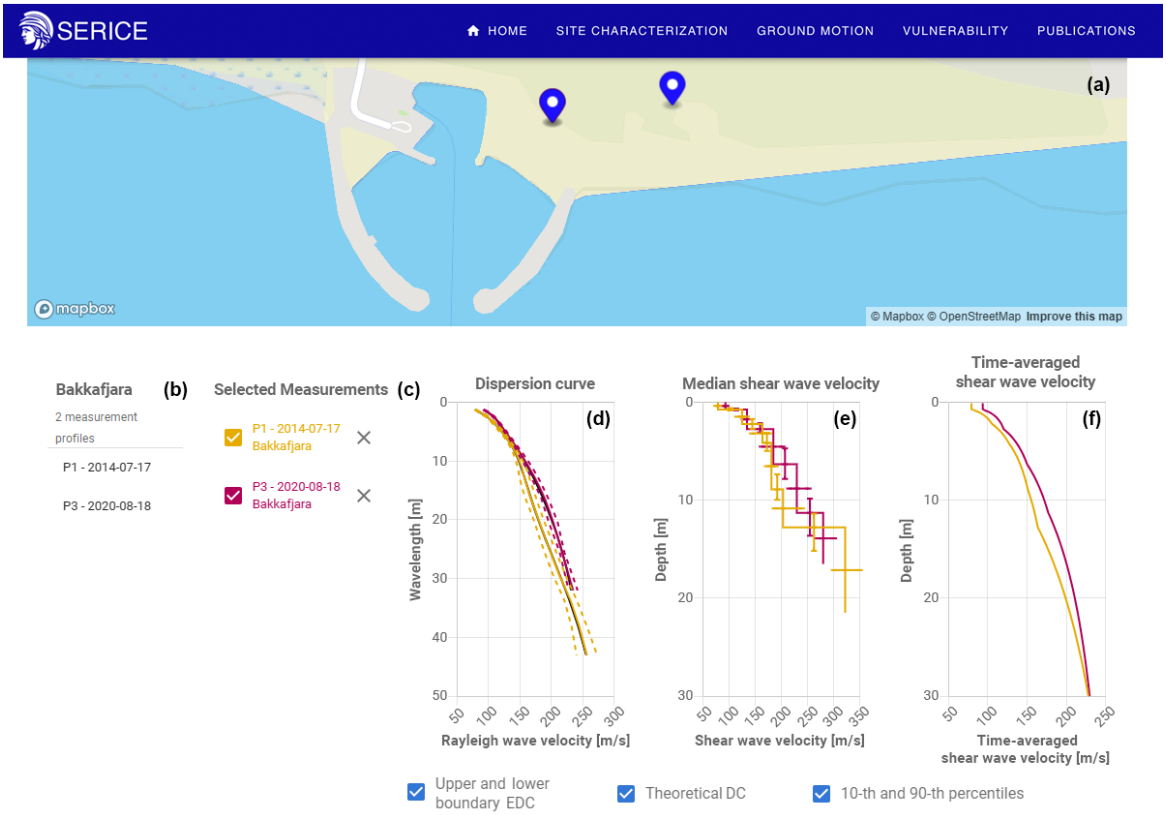

Figure 3. The user interface of the soil site database. (a) Measurement locations and (b) their profile IDs. (c) List of selected measurements. Results presented in terms of (d) dispersion curves, (e) median V_S profiles, and (f) time-averaged V_S.

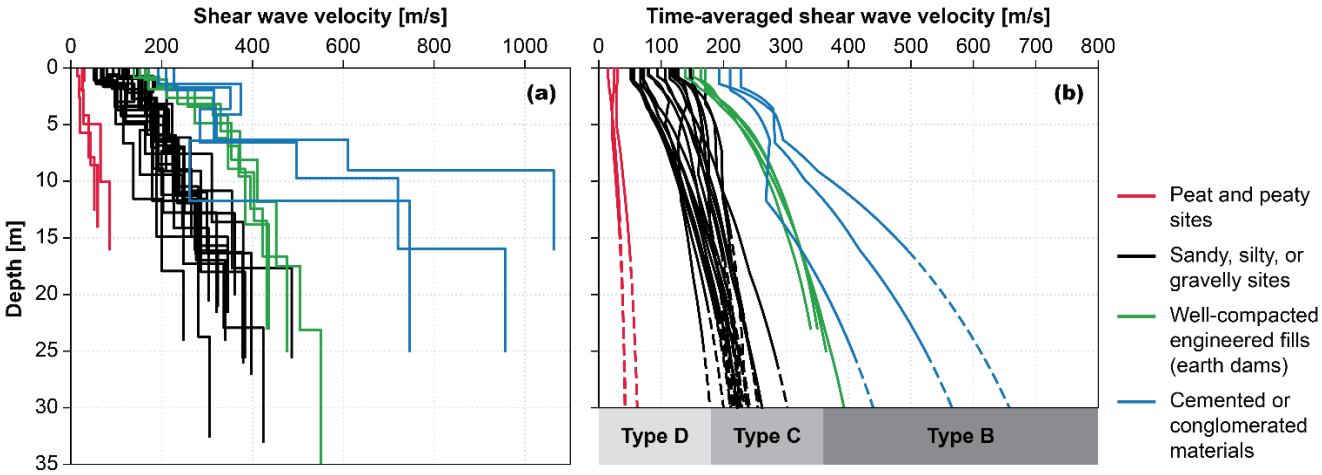

Figure 4. (a) Shear wave velocity (V_S) and (b) time-averaged shear wave velocity ($V_{S,z}$) profiles in the database. The $V_{S,z}$ profiles are shown with dashed lines at depths $z > z_{max}$ for natural sites with a survey depth of $z_{max} < 30$ m. The grey shaded areas in (b) illustrate the $V_{S,30}$ ranges defining ground types B, C, and D in the current EC8 (CEN, 2004).

The $V_{S,z}$ profile of each natural soil site is evaluated down to 30 m. In instances where the survey depth (z_{max}) is less than 30 m, the median V_S is extended to 30 m using the half-space velocity for calculation of $V_{S,z}$ at $z > z_{max}$. When V_S increases with depth, as is expected for all the sites currently included in the database, this approach provides a conservative estimate of $V_{S,30}$.

Figure 4 shows the current collection of median V_S profiles and the corresponding $V_{S,z}$. The tested sites are classified by general soil characteristics as (i) peat and peaty sites, (ii) silty, sandy, or gravelly sites, (iii) well-compacted engineered fills, and (iv) cemented or conglomerated materials. As shown, there is a distinct separation between the four classes. The estimated $V_{S,30}$ values further provide a general indication of the expected EC8 site category of sites within each class. It is though worth mentioning that a $V_{S,30}$ categorization of the peat and peaty sites included in this work is considered uncertain as they might also be categorized as type E or, in some cases, type S_1 or S_2.

4 CONCLUSIONS

Here we present a database (https://serice.hi.is) of surface wave measurements conducted in Iceland. The main purpose is to give researchers and professional engineers access to data and interpreted velocity profiles for design and further analysis.

Future work is aimed at extending the database by adding results from additional sites, as well as adding information on key site effect proxies. Future surveying efforts will also be aimed at assessing the depth of the seismic bedrock formation or the fundamental frequency of the soil deposits, which are required for site categorisation according to the 2nd gen. EC8 (CEN/TC250/SC8, 2021). Further research in this field is believed to be of high value for professional engineers to implement the new site classification scheme and aid simplified identification of site categories in cases where little (or no) site-specific information is available.

ACKNOWLEDGEMENTS

This work was supported by the Icelandic Research Fund (grant no. 206793-053, 218149-053), the Icelandic Road and Coastal Administration, and the Energy Research Fund of the National Power Company of Iceland.

REFERENCES

CEN (2004). *Eurocode 8: Design of structures for earthquake resistance. Part 1: General rules, seismic actions and rules for buildings*, European Committee for Standardization, Brussels, Belgium.

CEN/TC 250/SC 8 (2021). *Eurocode 8: Earthquake resistance design of structures. prEN_1998–1–1_2021_ENQ 2022-01-11*.

Einarsson, P. (2008). Plate boundaries, rifts and transforms in Iceland, *Jökull*, 58, pp. 35-58.

Erlingsson, S. (2019). Geotechnical Challenges in Iceland. *Proceedings of the XVII European Conference on Soil Mechanics and Geotechnical Engineering,* Reykjavik, Iceland, pp. 27-51. https://doi.org/10.32075/17ECSMGE-2019-1109.

Olafsdottir, E. A., Bessason, B., Erlingsson, S. (2023). Gagnagrunnur fyrir skúfbylgjuhraða í jarðsniðum byggður á yfirborðsbylgjumælingum, *Icelandic Journal of Engineering*, 29(1) [in Icelandic]. https://doi.org/10.33112/ije.29.3.

Proceedings of the XVIII ECSMGE 2024
GEOTECHNICAL ENGINEERING CHALLENGES
TO MEET CURRENT AND EMERGING NEEDS OF SOCIETY
© 2024 the Authors
ISBN 978-1-032-54816-6
DOI 10.1201/9781003431749-628
Open Access: www.taylorfrancis.com, CC BY-NC-ND 4.0 license

ECSMGE 24
XVIII EUROPEAN CONFERENCE ON SOIL MECHANICS AND GEOTECHNICAL ENGINEERING

Assessment of soil constitutive models to predict the response of offshore wind turbines subjected to lateral cyclic loads

Évaluation des modèles constitutifs des sols pour prédire la réponse des éoliennes offshore soumises à des charges cycliques latérales

O. Orakci
KU Leuven, Bruges, Belgium
The University of Melbourne, Melbourne, Australia

G. Anoyatis*
KU Leuven, Bruges, Belgium

S. François
KU Leuven, Leuven, Belgium

S. Chow, Y. Tian
The University of Melbourne, Melbourne, Australia

**george.anoyatis@kuleuven.be*

ABSTRACT: Monopiles are the frequently used foundation types for offshore wind turbines (OWTs) to withstand the cyclic loads from wind and waves ensuring safe and reliable operation. Under such cyclic loads, strain accumulation occurs while the soil undergoes repeated loading and unloading cycles throughout the OWT's lifespan. Such a mechanism, referred to as "ratcheting", causes changes in soil properties and affects the performance of the OWT. Large accumulative displacements and rotations can cause fatigue damage and serviceability problems which may result in structural failure and operational disruptions. While a wide range of methods is available to predict the monotonic monopile response, limited advanced soil models are available to capture the complex mechanism of cyclic strain accumulation. Such models have different levels of accuracy, complexity, and parameter calibration process. Prior to assessing any boundary value problem, it is important to evaluate the performance of the soil constitutive models at the soil material level. This work presents a comparative numerical study of two state-of-the-art constitutive models for sands i.e., SANISAND-MS and PM4SAND, under triaxial test conditions via OpenSees and PLAXIS. A discussion on the model parameters, analysis settings, and the effect of the number of cycles in the response is presented.

RÉSUMÉ: Les monopieux sont les types de fondations fréquemment utilisés pour les éoliennes offshore afin de résister aux charges cycliques dues au vent et aux vagues, garantissant ainsi un fonctionnement sûr et fiable. Sous de telles charges cycliques, une accumulation de contraintes se produit pendant que le sol subit des cycles répétés de chargement et de déchargement tout au long de la durée de vie de l'éolienne. Un tel mécanisme, appelé "ratcheting", provoque des changements dans les propriétés du sol et affecte les performances de l'éolienne. De grands déplacements et rotations cumulatifs peuvent causer des dommages par fatigue et des problèmes de service qui peuvent entraîner une défaillance structurelle et des interruptions opérationnelles. Bien qu'une large gamme de méthodes soit disponible pour prédire la réponse monotone des monopieux, il existe peu de modèles avancés de sol pour capturer le mécanisme complexe d'accumulation de déformations cycliques. Ces modèles ont différents niveaux de précision, de complexité et de processus d'étalonnage des paramètres. Avant d'évaluer tout problème de valeur limite, il est important d'évaluer les performances des modèles constitutifs du sol au niveau du matériau du sol. Ce travail présente une étude numérique comparative de deux modèles constitutifs de pointe pour les sables, à savoir SANISAND-MS et PM4SAND, dans des conditions d'essai triaxial via OpenSees et PLAXIS. Une discussion sur les paramètres du modèle, les paramètres d'analyse et l'effet du nombre de cycles sur la réponse est présentée.

Keywords: Monopiles; cyclic lateral loads; strain accumulation; constitutive models for sands.

1 INTRODUCTION

Soil constitutive models describe the mechanical behavior of soils by defining the entire incremental stress-strain response under different loading conditions. The description of the soil behavior is particularly important for sands surrounding OWT monopiles. The pore water pressure buildup increases and affects cyclic mobility (Wichtmann et al. 2019). The strain accumulates resulting in tilting of OWTs and affecting structures' fatigue life (Liu et al., 2019).

Single element tests are commonly used to calibrate and verify soil constitutive models. Assessment of these models on their predictive capability of element tests gives an intuition about their use in boundary value problems (Duque et al., 2021). Wichtmann et al. (2019) and Duque et al. (2021) inspected triaxial simulations of different soil models on Karlsruhe fine sand (KFS). Both studies have concluded that there were deficiencies in accurately replicating some important attributes, such as pore pressure reproduction and accumulation of plastic strains. Since the results showed relative density (D_r) dependence, it is inferred that the bounding surface cannot be adequately characterized solely by the mean effective stress and void ratio for all stress-strain paths. Duque et al. (2021) claimed that a comprehensive model capable of addressing all these challenges has yet to be developed.

This paper compares the predictive power of two cutting-edge soil constitutive models: SANISAND-MS (Liu et al., 2019) and PM4SAND (Boulanger and Ziotopoulou, 2015) with SANISAND04 (Dafalias and Manzari, 2004) by numerical simulations of triaxial tests in OpenSees (Zhu et al., 2018) and PLAXIS (Bentley, 2020). The objective of the paper is to obtain insights for practical offshore foundation applications by gaining a deeper understanding of the capabilities and limitations of these models to capture strain accumulation at long-lasting cyclic loading events.

2 TRIAXIAL SIMULATION

An 8-node hexahedral linear isoparametric fully coupled *u-p* element with a single point integration point (SSPbrickUP) is used for effective stress analyses in saturated soils. Rayleigh damping with $\mathbf{C} = 0.05\,\mathbf{M} + 0.00032\,\mathbf{K}$ is defined to damp out the waves. For the shearing, each cycle is comprised of compression (1/4 of a full cycle), extension (2/4 of a full cycle), and compression again (1/4 of a full cycle). Cyclic loading continues until the predefined number of loading cycles is reached.

SANISAND04 is the first member of the SANISAND family. SANISAND-MS includes a memory surface to better control large strains. PM4SAND is formulated under plane strain conditions and features a revised fabric formation requiring three primary model input parameters: G_0, h_{p0}, and D_r, which are most important for model calibration. Secondary parameters are set to default values, which typically align with observed trends.

KFS was extensively tested in monotonic/cyclic, drained/undrained triaxial test conditions by Wichtmann and Triantafyllidis (2016). The soil model parameters calibrated in former studies are held for the comparison study (Wichtmann et al., 2019 for SANISAND04 and Liu et al., 2019 for SANISAND-MS). Although these models share 13 parameters in their model formulation, it is observed in the literature that model parameters for the same sand might be calibrated to arrive at a different set of parameters. For PM4SAND, G_0 is adopted from SANISAND-MS, and h_{p0} is calibrated by the PLAXIS Soil Test parameter optimization tool via SANISAND-MS predictions. The selected parameters are presented in Table 1.

Table 1. Parameters for Karlsruhe fine sand (KFS).

	SANI-04	SANI-MS	PM4-S	Tests
Elasticity				
G_0	150	95	90	DMT, UCT
ν	0.05	0.05	-	OED
Critical state				
M_c	1.34	1.35	-	UMT
c	0.7	0.81	-	UMT
λ_c	0.122	0.055	-	DMT, UMT, CS
e_c	1.103	1.035	-	OED, CS
ξ	0.205	0.36	-	DMT, UMT, CS
Yield surface				
m	0.05	0.01	-	-
Kinematic hardening				
h_0	10.5	7.6	-	DMT, UCT
c_h	0.75	0.97	-	DMT
n^b	1.2	1.2	-	DMT
Dilatancy				
A_0	0.9	0.74	-	DMT
n^d	2.0	1.79	-	DMT
Fabric dilatancy				
z_{max}	20	-	-	UCT
c_z	10000	-	-	UCT
Memory surface				
μ_0	-	82	-	UCT
ζ	-	0.0005	-	UCT
β	-	4	-	UCT
Contraction				
h_{po}	-	-	0.4	CPT, SPT

OED oedometric test, DMT drained monotonic triaxial test, UMT undrained monotonic triaxial test, UCT undrained cyclic triaxial test, SPT standard penetration test, CPT cone penetration test.

3 RESULTS AND DISCUSSION

OpenSees simulations are compared against the soil tests simulated by the commercial software PLAXIS, which uses a single-point algorithm. In this section, each model will be examined separately.

3.1 SANISAND04

While the model can predict the butterfly-shaped last cycles, it shows inadequate performance in realistically capturing the excess pore pressure development rate and the subsequent pace of effective stress reduction (Figure 1). Although the strain expands to both sides in the triaxial experiment, it accumulates more on the extension side. However, the prediction shows a stronger accumulation on the tension side with a pace different than the actual soil test data (Figure 2).

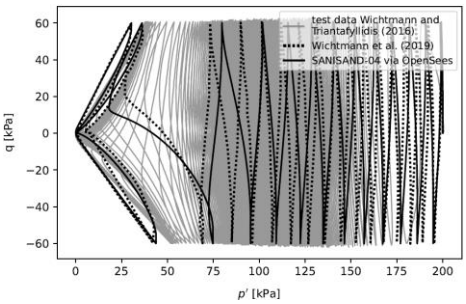

Figure 1. UCT results for q_{amp}=60 kPa, p_0=200 kPa, and D_{r0}=87%: deviatoric stress vs. effective mean pressure.

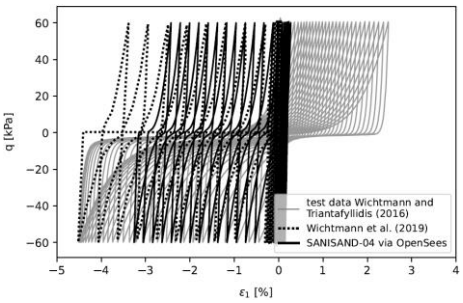

Figure 2. UCT results for q_{amp}=60 kPa, p_0=200 kPa, and D_{r0}=87%: deviatoric stress vs. axial strain.

3.2 SANISAND-MS

The model has been compared against SANISAND-04 since PM4SAND is formulated in plane strain conditions. For the drained analysis (Figure 3), SANISAND-MS appears to represent the triaxial test data more accurately than SANISAND-04, as it exhibits a trend that aligns more closely with the test results. Since both model parameters are calibrated towards cyclic loading tests, and it is known that one set of parameters for both cyclic and monotonic loading tests are not attainable, such results were anticipated.

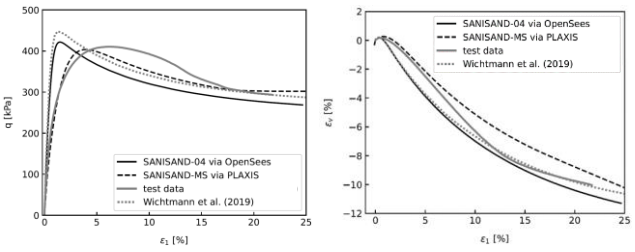

(a) (b)

Figure 3. DMT results for p_0=100 kPa and D_{r0}=85%: (a) deviatoric stress vs. axial strain and (b) volumetric strain vs. axial strain.

For the undrained analysis (Figure 4), SANISAND-MS shows slightly better (but still higher in terms of stress ratio q/p) predictions considering the larger displacements it can predict under deviatoric stress. However, in terms of stress paths, none of the models could predict the dense-sand dilatant behavior as we expect from the triaxial tests. This proves the previous findings stating that the bounding surface cannot be adequately characterized solely by the mean effective stress and void ratio for all stress-strain paths.

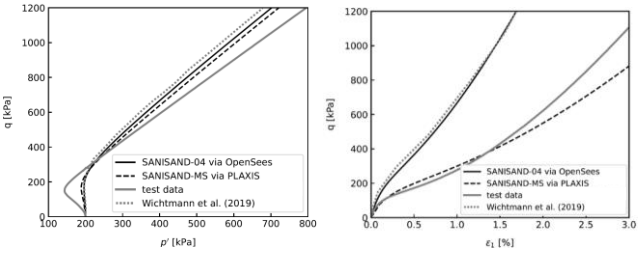

(a) (b)

Figure 4. UMT results for p_0=200 kPa and D_{r0}=87%: (a) deviatoric stress vs. effective mean pressure and (b) deviatoric stress vs. axial strain.

Since a stress-controlled test was not possible for PLAXIS simulations, comparisons are held for a strain-controlled test. The differences are evident in the cyclic tests shown as can be seen in Figure 5 and Figure 6. The model predictions are similar yet deviate from the triaxial test data.

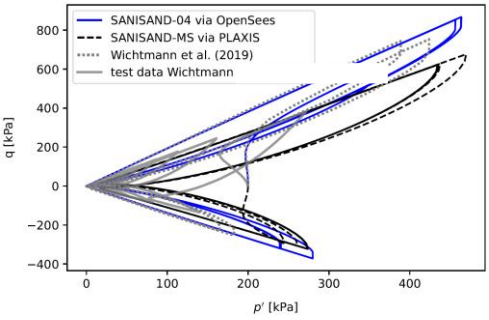

Figure 5. UCT results for ε_{amp}=1%, p0=200 kPa, and D_{r0}=94%: deviatoric stress vs. effective mean pressure.

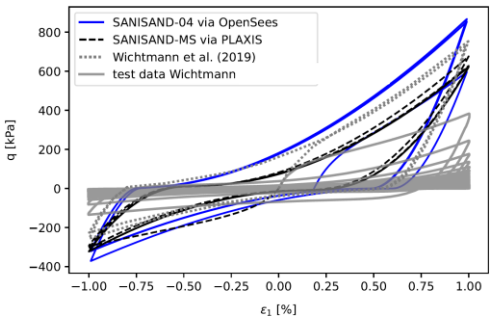

Figure 6. UCT results for ε_{amp}=1%, p_0=200 kPa, and D_{r0}=94%: deviatoric stress vs. axial strain.

3.3 PM4SAND

Figure 7 shows that SANISAND-04 and MS models exhibit similar stiffness degradation and damping with shear strain (with a higher dissipated energy for SANISAND-MS). PM4SAND predicts different behavior than these two models mostly attributed to parameter selection. This underscores the importance of secondary parameter calibration for the model.

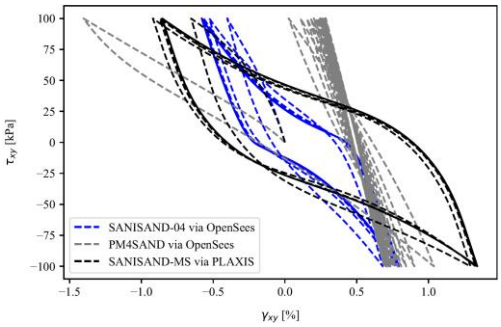

Figure 7. CDSS results for p_0=200 kPa and D_{r0}=94%: shear strain vs. shear stress.

4 CONCLUSIONS

This study aims to conduct a comparative analysis of two state-of-the-art constitutive models for sandy soils: SANISAND-MS and PM4SAND, with their predecessor SANISAND-04. The main findings of this work can be summarized as follows:

Despite the fact that the models can predict the butterfly-shaped loading path, the excess pore pressure development rate is not realistic.

Models are not that accurate in reproducing the strain development pace. This is more pronounced in high cyclic loading.

Since the models are engineered to accommodate certain conditions, when subjected to more complex loading scenarios, the models could yield results that are not in agreement with physical observations. As such, overshooting following immediate reloading or reverse loading can be attributed to the physics imposed within the mathematical formulations of the models.

ACKNOWLEDGEMENTS

This research was supported by the *Cyclic soil-structure interaction framework for the foundations of offshore renewable energy structures* project, funded by the "KU Leuven Global PhD Partnerships with The University of Melbourne" scheme (GPUM/21/023) and "The University of Melbourne Chancellery Strategic International Research Collaboration funds".

REFERENCES

Bentley (2020). PLAXIS 2D-Reference Manual CONNECT Edition V20.02.

Boulanger, R. W., & Ziotopoulou, K. (2015). PM4Sand (Version 3): A sand plasticity model for earthquake engineering applications. *Center for Geotechnical Modeling Report No. UCD/CGM-15/01, Department of Civil and Environmental Engineering, University of California, Davis, Calif.*

Dafalias, Y. F., & Manzari, M. T. (2004). Simple plasticity sand model accounting for fabric change effects. *Journal of Engineering mechanics, 130*(6), 622-634. https://doi.org/10.1061/(ASCE)0733-9399(2004)130:6(622).

Duque, J., Yang, M., Fuentes, W., Mašín, D., & Taiebat, M. (2021). Characteristic limitations of advanced plasticity and hypoplasticity models for cyclic loading of sands. *Acta Geotechnica,* 1-23. https://doi.org/10.1007/s11440-021-01418-z.

Liu, H. Y., Abell, J. A., Diambra, A., & Pisanò, F. (2019). Modelling the cyclic ratcheting of sands through memory-enhanced bounding surface plasticity. *Géotechnique, 69*(9), 783-800. https://doi.org/10.1680/jgeot.17.P.307.

Wichtmann, T., & Triantafyllidis, T. (2016). An experimental database for the development, calibration and verification of constitutive models for sand with focus to cyclic loading: part I—tests with monotonic loading and stress cycles. *Acta Geotechnica, 11*, 739-761. https://doi.org/10.1007/s11440-015-0402-z.

Wichtmann, T., Fuentes, W., & Triantafyllidis, T. (2019). Inspection of three sophisticated constitutive models based on monotonic and cyclic tests on fine sand: Hypoplasticity vs. Sanisand vs. ISA. *Soil Dynamics and Earthquake Engineering, 124*, 172-183. https://doi.org/10.1016/j.soildyn.2019.05.001.

Zhu, M., McKenna, F., & Scott, M. H. (2018). OpenSeesPy: Python library for the OpenSees finite element framework. *SoftwareX, 7*, 6-11. https://doi.org/10.1016/j.softx.2017.10.009.

Proceedings of the XVIII ECSMGE 2024
GEOTECHNICAL ENGINEERING CHALLENGES
TO MEET CURRENT AND EMERGING NEEDS OF SOCIETY
© 2024 the Authors
ISBN 978-1-032-54816-6
DOI 10.1201/9781003431749-629
Open Access: www.taylorfrancis.com, CC BY-NC-ND 4.0 license

ECSMGE 24
XVIII EUROPEAN CONFERENCE ON SOIL MECHANICS AND GEOTECHNICAL ENGINEERING

Lignin used as stabilizer in an expansive unsaturated soil

Lignine utilisée comme stabilisateur dans un sol expansif non saturé

S. Orlandi*
Universidad Nacional de la Patagonia San Juan Bosco, Comodoro Rivadavia, Argentina
D. Manzanal, C. Laskowski
ETSI de Caminos, Canales y Puertos, Universidad Politécnica de Madrid, Madrid, Spain
L.G. Libardi, L. Oldecop
Instituto de Investigaciones Antisísmicas, Universidad Nacional de San Juan, San Juan, Argentina
**sandra.orlandi@gmail.com*

ABSTRACT: The most important pathologies that occur in civil constructions are a consequence of the foundations. Expansive soils are among the most problematic soils, being the cause of some of these pathologies. It is possible to design foundations that can resist and restrict the action of expansive soils. One of the alternatives that could be applied to some constructions is to mix the soil with an additive. In this paper, the additive used to modify the swelling properties of an expansive Patagonian soil is lignin, a calcium lignosulphonate (CLS). CLS was analysed considering its influence on the behaviour of the soil. A series of tests were carried out to get a better understanding of the impact the addition of lignin produces on the soil. Tests performed were focused on the physicochemical and microstructure characterization (XR diffractometry, mercury intrusion porosimeter and scanning electronic microscope), volumetric behaviour upon wetting (free swelling), hydraulic behaviour (water retention test using dew-point potentiometer and permeability test) and mechanical behaviour (uniaxial compression test). Time of contact clay-CLS was considered as a variable to analyse the stability of the mixture.

RÉSUMÉ: Les pathologies les plus importantes qui surviennent dans les constructions civiles sont la conséquence des fondations. Les sols expansifs sont parmi les sols les plus problématiques, étant la cause de certaines de ces pathologies. Il est possible de concevoir des fondations capables de résister et de limiter l'action des sols expansifs. L'une des alternatives pouvant être appliquée à certaines constructions consiste à mélanger le sol avec un additif. Dans cet article, l'additif utilisé pour modifier les propriétés de gonflement d'un sol expansif de Patagonie est la lignine, un lignosulfonique de calcium (CLS). Le CLS a été analysé en fonction de son influence sur le comportement du sol. Les essais réalisés ont porté sur la caractérisation physico-chimique et de la microstructure (diffractométrie XR, porosimètre à intrusion de mercure et microscope électronique à balayage), le comportement volumétrique lors du mouillage (gonflement libre), le comportement hydraulique (essai de rétention d'eau à l'aide d'un potentiomètre à point de rosée et de la technique du papier filtre, essai de perméabilité) et le comportement mécanique (essai de compression uniaxiale). Le temps de contact argile-CLS a été considéré comme une variable pour analyser la stabilité du mélange.

Keywords: Expansive clay; calcium lignosulfonate; stabilizing additive; biopolymer.

1 INTRODUCTION

For a long time, the additives have been used as stabilizers in expansive soils. Lime is one of the most common additives, but it has a negative impact over the environment, reason why, nowadays, new, and more eco-friendly biopolymers are being studied to replace it. Some examples of alternative stabilizers being studied are waste tire rubber fibre (Bekhiti et al. 2019), burned olive waste (Attom and Al-Sharif, 1998), seeds and starches (Orlandi et al. 2021), ultrafine palm oil fuel ash (Pourakbar et al. 2015), rice hush ash (Brooks, 2009) and gypsum (Yilmaz and Civelekoglu 2009), among others.

All around the world, the paper pulp industry produces lignin in large quantities, and its disposal has become an environmental global problem (Ijaz and Dai, 2020). Some researchers have been studying this waste as an expansive soil stabiliser for the last decade (Alazigha et al., 2018, Orlandi et al., 2019, Fernandez et al., 2021). Significant advancements have been made in analysing the mechanical and hydraulic behavior of CRclay with varying additions of calcium lignosulfonate (CLS) ranging from 3% to 10%, along with the microstructural changes induced (Orlandi et al., 2019, Fernandez et al., 2021).

This article studies the influence of different curing ages (1 day, 1 month, 3 and 6 months and 1 year) of a Patagonian soil (CRclay) mixed with 10%CLS. The efficacy of the 10% CLS added to CRclay was studied considering the changes in microstructure and the hydraulic and mechanical behaviour. Using 10% CLS was shown to be effective in reducing the swelling potential of CRclay (Orlandi et al., 2019).

2 MATERIALS: CRCLAY - CLS

CRclay is Patagonian expansive soil located in Comodoro Rivadavia (Argentina) classified as MH by Unified Soil Classification System (USCS). Table 1 shows the CRclay properties (Manzanal et al., 2019). CRclay is a soil with a high swelling potential (LL=74.5%, PI= 35.3%, Contraction limit = 24.2%), and high surface area (563 m^2/g). The active clay mineral smectite (Sm), known for its swelling behaviour upon hydration was identified within the XRD diffractogram of CRclay (Fernandez et al., 2021). Additionally, impurities such as calcium (Ca^{2+}) and feldspar (F) were also observed.

Table 2. CRclay properties.

Properties	CRclay
% clay	76.64
% silt	21.4
% sand	1.96
pH 1:2,5	8:51
EC [dS/m] (electrical conductivity)	10.81
Organic matter content [%]	0.6
Carbon content [%]	0.3
Available phosphorus [mg/kg]	11
SO^{4-} [mg/kg]	3608
Ca [meq/100g]	16.0
Mg [meq/100g]	1.5
K [meq/100g]	7.8
Na [meq/100g]	28.5
CEC (cation exchange capacity)	55
XRD mineralogical identification	Mostly smectite

CLS was a commercial biopolymer which was provided by Norlig® which has a degradation temperature of 300ºC, a glass transition temperature, Tg = 80ºC, and 10.33% ash content (Orlandi et al., 2021).

3 METHODS

Utilizing their prior expertise in determining optimal CLS content (Orlandi et al., 2019; Fernandez et al., 2020), this study explores the influence of curing time on CRclay samples and CRclay-10%. All samples were uniformly prepared by static compaction at a dry unit weight of 13 kN/m^3. The natural water content of 18% was maintained for samples of various tests, including free swelling, uniaxial compression, mercury intrusion porosimetry (MIP), and scanning electron microscopy (SEM). Variable Charge Permeameter (VCP) tests were conducted on samples compacted at a moisture content of 33%. Samples were sealed with film to prevent moisture fluctuations and stored under controlled temperature and humidity until testing. Different ages of testing were adopted for each type of test: free swelling tests were carried out on samples of 1 day and 9 months and uniaxial compressive tests were performed over samples with ages of 1 day, 1 month, 3 months, 6 months, 9 months, and 1-year. The microstructure (MIP and SEM) was analysed for samples aged at 1 day and 1 year. Water retention (WP4: dew-point potentiometer), and permeability tests were conducted on samples aged 1 day.

4 RESULTS AND DISCUSSION

The water retention capacity of the unsaturated compacted samples of CRclay and CRclay+10%CLS were obtained using dew-point potentiometer (WP4) as is illustrated in Figure 1. When comparing samples with equal degrees of saturation in terms of water content and dry unit weight ($13kN/m^3$), it was observed that the addition of CLS increases suction in the sample. This trend is more pronounced in samples with saturation degrees higher than 50% (similar to the molding moisture content of 18%). Comparable findings were also reported using other techniques (Fernandez et al., 2021, Orlandi, 2021). The evolution of unsaturated compacted samples at the water content of 18% was evaluated with the VCP test and free swelling test.

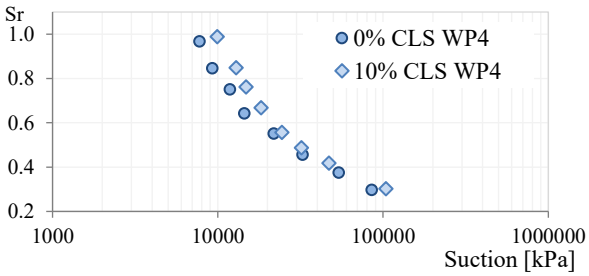

Figure 1. Suction obtained by using WP4 for 0%CLS and 10%CLS.

The VCP test demonstrates that the addition 10% CLS increases the permeability compared to CRclay, as illustrated in Figure 1. This is attributed to the change in inter-aggregate porosity caused by CLS

(Fernandez et al., 2021). Moreover, we note a gradual decrease in VCP permeability over two months of testing due to specimen expansion at constant volume, and the sequential saturation processes of inter-pore, intra-pore, and eventual development of the diffuse double layer (Delage, 2007).

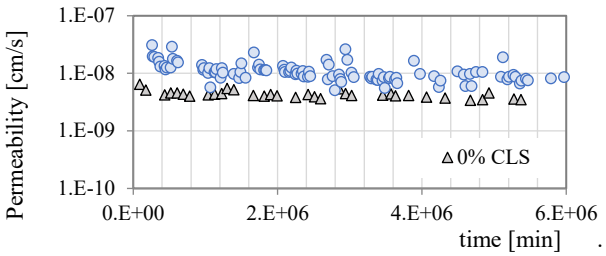

Figure 1. Permeability evolution for 0%CLS and 10%CLS.

The volumetric behaviour of both CRclay and CRclay-10%CLS samples upon wetting is shown in Figure 2. Results reveal a substantial reduction in free swelling for specimens with CLS, with a decrease of 84% observed for samples tested one day after moulding and 83% for those tested after 9 months, compared to the volumetric behaviour of CRclay.

The time evolution of free swelling depicted in Figure 2 displays three clear periods. The initial swelling is attributed to the saturation of interaggregate porosity, followed by primary swelling associated with the ongoing saturation of intra-aggregate porosity, culminating in secondary swelling once the double-layer expansion is fully saturated.

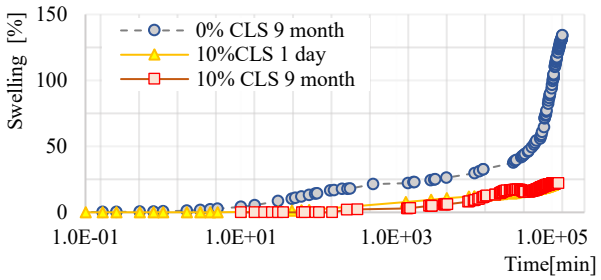

Figure 2. Free swelling for 0% CLS and 10% CLS, at 1 day and 9 months aged samples.

The unconfined compressive stress-strain behaviour of CRclay (Figure 3a) and CRclay-10%CLS (Figure 3b) illustrates the impact of varying sample ages. Overall, the results indicate a slight increase in UCS for samples with the addition of 10% CLS, accompanied by enhanced ductility. The additive does not modify the mechanical behaviour as a function of time but follows the trend shown by the compacted soil.

The variation of stress-strain curves with the age of the sample could be related to gradual water redistribution after the sample compaction stage is finalized. This migration within a sample induces changes in the distribution of interaggregate porosity and porosity with time (Figure 4), which are contingent upon the initial moisture content and dry density of the mixtures. This redistribution may account for the time-dependent fluctuations observed in permeability and simple compressive strength (Delage, 2007, Fernandez et al., 2021).

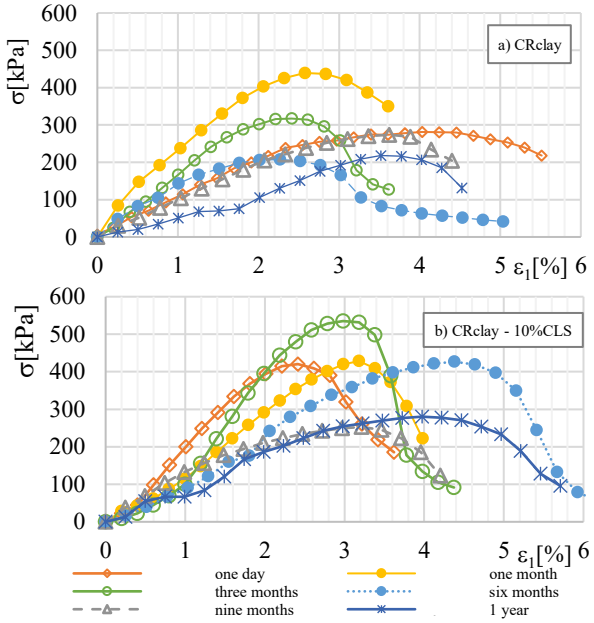

Figure 3. Unconfined Compressive test for nine different curing ages for a) CRclay and b) CRclay-10%CLS samples.

The physicochemical interaction mechanisms between CRclay and CLS are illustrate in Figure 4 (right), revealing the emergence of new lamellar and elongated linear structures within the soil matrix. However, due to the inability to analyse the composition of these structures, assessing their impact on the overall behaviour is not feasible. Furthermore, the presence of spores, known for their natural ability to polymerize lignins, may generate effects which were not evaluated in this study (Orlandi, 2021).

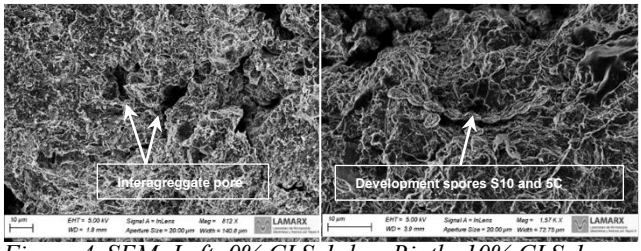

Figure 4. SEM: Left: 0% CLS-1 day. Rigth: 10% CLS-1 year SEM.

Upon further analysis of the influence of sample age on pore distribution using MIP for CRclay-10% CLS samples, we observe significant in the bimodal

distribution between samples aged 1 day and 1 year, with a notable variation in intrapore density increasing with age. Interporosity shows an increase in total pore volume but a decrease in characteristic pore diameter.

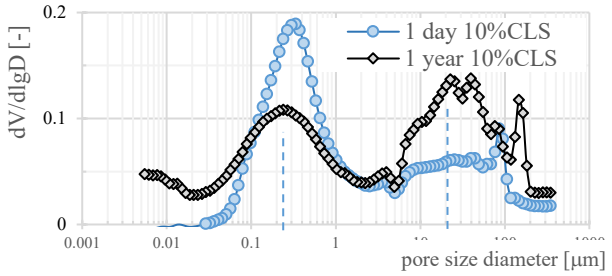

Figure 5. MIP: *Pore size diameter distribution* for CRclay+ *10% CLS* sample.

5 CONCLUSION

The stabilization mechanisms formed between CRclay, and calcium lignosulphonate (CLS) induce mechanical, hydraulic, and microstructural changes in the soil. The incorporation of 10% CLS yields positive effects on soil behaviour, and these changes persist over time. The additive does not alter the mechanical behaviour over time; rather, it mirrors the trend exhibited by the compacted CRclay. This phenomenon could be attributed to the redistribution of water within the soil pores in an unsaturated state.

It can be highlighted:

- The impact on water retention capacity is more pronounced in samples with water content exceeding the natural moisture for the dry unit weights studied.
- The saturation process of the samples in constant volume tests (VCP) and volume change upon wetting confirms the three stages studied by other authors: The initial swelling is attributed to the saturation of interaggregate porosity, followed by primary swelling associated with the ongoing saturation of intra-aggregate porosity, culminating in secondary swelling once the double-layer expansion is fully saturated.
- The effect of time on both CRclay and CRclay+10% CLS samples follows a similar trend in the unconfined compression tests. Variations in porosity observed in SEM and MIP analyses confirm a time-dependent effect in both the CRclay and CLS mixture, signifying an increase in interporosity in the CLS samples, indicating a tendency to disrupt clay aggregation.

The mechanical results should be validated through triaxial tests to verify the contraction-dilatant behaviour of the CLS samples.

REFERENCES

Alazigha, D. P., Indraratna, B. J., Vinod, S. and Heitor, A. (2018). Mechanisms of stabilization of expansive soil with lignosulfonate admixture. Transportation Geotechnics, 14, 81–92. https://doi.org/10.1016/j.trgeo.2017.11.001.

Attom M. F. and Al-Sharif M. M. (1998). Soil stabilization with burned olive waste. Applied Clay Science, 13(3), 219–230.

Bekhiti, M., Trouzine, H., Rabehi,. M. (2019). Influence of waste tire rubber fibers on swelling behavior, uniaxial compressive test and ductility of cement stabilized bentonite clay soil. Const. and Building Materials, 208, 304–313.

Brooks, R. M. (2009). Soil stabilization with fly-ash and rice husk ash. International Journal of Research and Reviews in Applied Sciences.

Delage, P. (2007) Microstructure Features in the Behaviour of Engineered Barriers for Nuclear Waste Disposal. In: Schanz T. (eds) Experimental Unsaturated Soil Mechanics. Springer Proceedings in Physics, vol 112. https://doi.org/10.1007/3-540-69873-6_2.

Fernández, M., Orlandi, S., Codevilla, M., Piqué, T., Manzanal, D. (2021) Performance of calcium lignosulfonate as a stabiliser of highly expansive clay, Transp. Geotechnics, Vol. 27, https://doi.org/10.1016/j.trgeo.2020.100469.

Ijaz, N. and Dai, F. (2020). Paper and wood industry waste as a sustainable solution for environmental vulnerabilities of expansive soil: A novel approach. Journal of Environmental Management, 262.

Manzanal, D., Orlandi, S., Miranda, E., Robinson, M., Barría, J. C. (2019). Swell characterization of expansive clays from Comodoro Rivadavia city. PANAM XVII. Cancún. México 2019. Doi: 10.3233/STAL190107.

Orlandi, S., Manzanal, D. Miranda, E., Robinson, M. (2019). Use of lignin as stabilizer in expansive soils. PANAM XVII. Cancún. México 2019. Doi:10.3233/STAL190295.2291-2298.

Orlandi, S., et al. (2021). Additives based on vegetable biomass to improve the stabilization of expansive clay Soil. Environmental Geotechnics, https://doi.org/10.1680/jenge.20.00066.

Orlandi, S. (2021). Use of calcium lignosulphonate as an expansive soil stabilizer. Doctoral Thesis: Universidad Nacional de la Patagonia San Juan Bosco. (In Spanish)

Pourakbar, S., Asadi, A., Huat, B. B. K., Fasihnikoutalab, M. H. (2015). Stabilization of clayey soil using ultrafine palm oil fuel ash (POFA) and cement. Transp. Geotech, 3, 24–35.

Yilmaz, I., Civelekoglu, B. (2009). Gypsum: An additive for stabilization of swelling clay soils. App. Clay Sci. 44, 166–172.

Proceedings of the XVIII ECSMGE 2024
GEOTECHNICAL ENGINEERING CHALLENGES
TO MEET CURRENT AND EMERGING NEEDS OF SOCIETY
© 2024 the Authors
ISBN 978-1-032-54816-6
DOI 10.1201/9781003431749-630
Open Access: www.taylorfrancis.com, CC BY-NC-ND 4.0 license

ECSMGE 24
XVIII EUROPEAN CONFERENCE ON SOIL MECHANICS AND GEOTECHNICAL ENGINEERING

Application of a new real-time analysis of the size distribution of rock fragments

Application d'une nouvelle analyse en temps réel de la distribution de la taille des fragments de roche

J. Ortuta*
Amberg Engineering Slovakia, s.r.o., Bratislava, Slovakia

V. Greif
Comenius University Bratislava, Department of Engineering Geology, Bratislava, Slovakia

**jortuta@amberg.sk*

ABSTRACT: The open-pit mining process is generally made up of a sequence of unit operations including drilling, blasting, loading, hauling, and crushing. Drilling and blasting can have a major impact on the performance and cost of subsequent operations. The prime objective of these two operations is to obtain optimum fragmentation within safe and economical limits. As a result, a quick and accurate evaluation process is required to assess its effectiveness. Today, the most accurate method of measuring fragment size is sieving analysis. The drawback of this method is that it is a time-consuming and labor-intensive process. The disadvantage of the prediction methods is the lack of actual measurement of the fragments which may result in inaccurate assessment. There is a need for a more reliable and effective way of obtaining grain size distribution than by sieving analysis while providing more accurate results than the predictive methods. The problem of determining the grain size distribution of blast fragmentation from the surface of a pile of fragments has been studied by many researchers. This paper discusses the application of Doppler radar (Semi-automatic method) as the possibility of fragmentation material measurements during the blasting and the direct possibility of its further use in building other construction such as road embankments where grain size plays a decisive role. With this refinement, it is possible to omit additional crushing of the material, which is associated with financial costs. Effective use of residual material as well as mitigation of environmental impact by associated technologies would be achieved.

RÉSUMÉ: Le processus d'exploitation minière à ciel ouvert est généralement constitué d'une séquence d'opérations unitaires comprenant le forage, l'abattage à l'explosif, le chargement, le transport et le concassage. Le forage et le dynamitage peuvent avoir un impact majeur sur les performances et le coût des opérations suivantes. L'objectif premier de ces deux opérations est d'obtenir une fragmentation optimale dans des limites sûres et économiques. Par conséquent, un processus d'évaluation rapide et précis est nécessaire pour évaluer leur efficacité. Aujourd'hui, la méthode la plus précise pour mesurer la taille des fragments est l'analyse par tamisage. L'inconvénient de cette méthode est qu'il s'agit d'un processus qui prend du temps et nécessite beaucoup de main-d'œuvre. L'inconvénient des méthodes de prédiction est l'absence de mesure réelle des fragments, ce qui peut entraîner une évaluation inexacte. Il est nécessaire de trouver un moyen plus fiable et plus efficace d'obtenir la distribution de la taille des grains que l'analyse par tamisage, tout en fournissant des résultats plus précis que les méthodes prédictives. Le problème de la détermination de la distribution granulométrique des fragments d'explosion à partir de la surface d'une pile de fragments a été étudié par de nombreux chercheurs. Cet article traite de l'application du radar Doppler (méthode semi-automatique) pour mesurer la fragmentation des matériaux pendant le dynamitage et de la possibilité directe de l'utiliser dans la construction d'autres ouvrages tels que les remblais routiers, où la taille des grains joue un rôle décisif. Grâce à ce raffinement, il est possible d'éviter le concassage supplémentaire du matériau, qui est associé à des coûts financiers. L'utilisation efficace des matériaux résiduels et l'atténuation de l'impact sur l'environnement par les technologies associées seraient ainsi réalisées.

Keywords: Doppler radar; fragmentation; blasting; grain size distribution.

1 INTRODUCTION

The open-pit mining process is generally made up of a sequence of unit operations including drilling, blasting, loading, hauling and crushing. Drilling and blasting, being the first unit operations, can have a major impact on the performance and cost of subsequent operations. The prime objective of these two operations is to obtain optimum fragmentation within safe and economical limits.

The output from the blasting process depends on many parameters such as rock composition, layer thickness, type of explosives, etc. As a result, a quick and accurate evaluation process is required to assess its effectiveness. In addition, this evaluation process can be used to monitor blasting, optimize the blast design and assess loading conditions for scoops and shovels. One of the key indicators of the effectiveness of a blast is the size of the resulting fragments. Today, the most accurate method of measuring fragment size is sieving analysis. The drawback of this method is that it is a time consuming and labor-intensive process. This has led many researchers to use blasting parameters and rock mass properties to predict the fragment size distribution.

2 ACTUALITY AND IMPORTANCE OF THE WORK

Most open-pit mining operations employ blasting for primary breakage of the rocks. Since blasting is a major cost factor, both cases (under and over breakage) create additional costs reflected in the increase of the operation and maintenance of the machinery. To establish optimum cost values, it is important that the combined performance of the blast controllable parameters be acknowledged, complying with the ultimate goals of the overall mining operation. This is usually accomplished with the definition of a set of conditions minimizing total production cost per ton of rock blasted. The blasting process has been described in the Literature as a nonlinear process in which several parameters, often difficult to evaluate, dictate the outcome. Generally speaking, these parameters can be grouped into two categories: controllable parameters (explosives parameters), and uncontrollable parameters (rock parameters).

Fragmentation is one of the major parameters that affect the performance of the loading and hauling equipment deployed in a mine. Fragmentation is a relative term, and its desired values are equipment specific.

Since there are conflicting requirements (Figure 1) of drilling-blasting and loading-hauling equipment's deployed in a mine, the situation poses a difficult proposition. The whole scenario has been discussed by several workers and can be described in terms of optimization. For enacting an optimization schedule, it is essential to understand the level i.e. the system or sub-system level at which the optimization is anticipated. If the whole system is considered, the scenario becomes quite complicated, particularly, when costs of individual components of the system are to be considered.

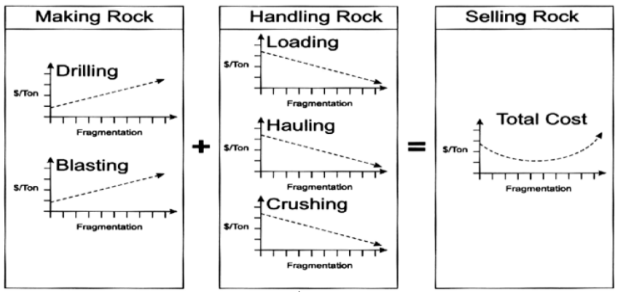

Figure 1. Relation of individual system components in mine system and the optimum thereof.

3 NEW IDEA FOR GRAIN SIZE MEASUREMENT

The key objective of production blasting is to achieve optimum rock fragmentation. The degree of rock fragmentation plays an important role in order to control and minimize the overall production cost including loading, hauling, and crushing costs (Figure 2). Optimum rock fragmentation improves the energy efficiency of crushing processes and thousands of kilowatt-hours energy per year can also be saved.

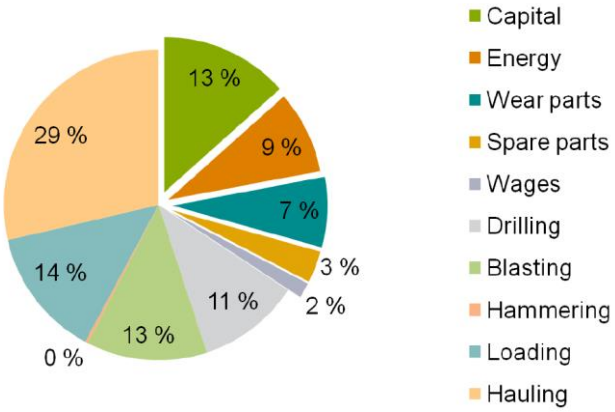

Figure 2. Example of quarrying costs (Product 0-20mm).

Blasting is the first step of the size reduction in mining, and it is followed by crushing and grinding unit operations (Figure 3). The efficiency of these unit operations is directly related to the size distribution of muck pile. Therefore, reliable evaluation of fragmentation is a critical mining problem. Production of finer fragments in blasting operation reduces the workload of primary crushers; therefore, increasing the crusher efficiency and reducing the crushing cost. Also crushing rate per hour will increase (Figure 4).

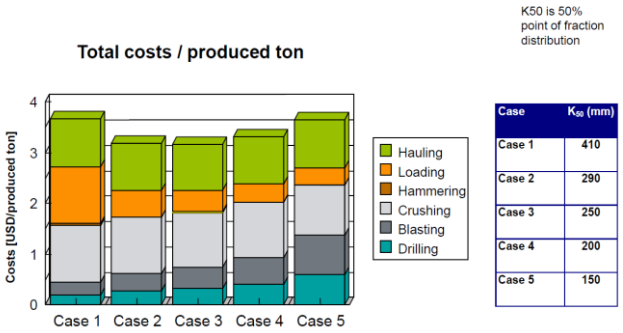

Figure 3. Comparison of different blasted fragmentations.

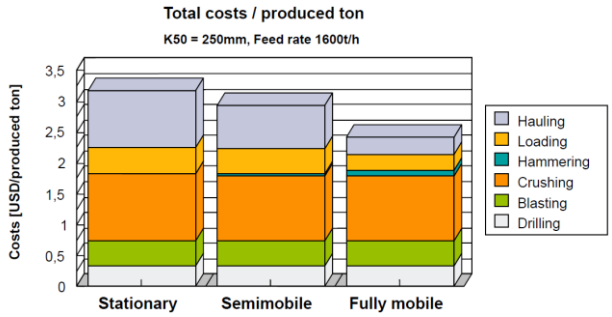

Figure 4. Comparison of different crushing methods.

The problem of determining the true size distribution of blast fragmentation from the surface of a pile of fragments has been studied by many mining researchers. In this thesis, an attempt is made to derive a reliable measure of fragments, based on Doppler radar measure of reflectivity of flying stones during blasting.

4 USING RADAR REFLECTIVITY TO DETERMINE GRAIN SIZE

The reflectivity, Z is the ratio between reflected and incident intensity as the size of energy for example electromagnetic waves (light current) or sound waves (sound pressure, sound field size).

Reflectivity is defined as the total reflecting area of small particles per cubic meter with a dielectric constant greater than zero. This value is proportional to the sixth power of the diameter of an object with a spherical surface. The reflectivity is the sum of all individual objects in a space of one cubic meter by a model of the distribution of the different grain sizes.

For our measurement was used modified micro rain radar MRR-2 was by the company METEK (Figure 5).

The relationship between waveform and blasting characteristics becomes clear when one looks more closely at the theoretical spectra of elementary results.

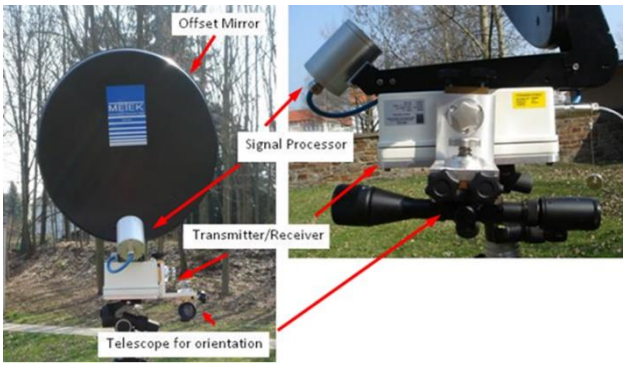

Figure 5. Setup of a radar station with additional schematic arrangements.

The example shows less idealized situation. There will be a directed blasting, in which the particles with speeds of 15 to 25 m/s fly at an opening angle of ± 50° around the radar beam (Figure 6).

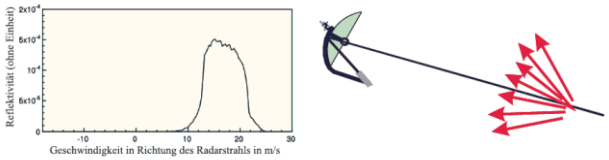

Figure 6. The theoretical spectrum of a directed explosion.

This example can be seen as a prototype of the spectrum for blasting. By blowing up the energy of the explosion is limited to a range of angles. Blasting is directed almost horizontally.

5 MEASUREMENT AND RESULT

Based on the experiments, it was possible to describe the dependence between reflectivity, velocity, and grain size.

The results of these measurements created a relationship between grain size (D) and reflectivity (Z) (Figure 6). Due to possible measurement error were determined the maximum and minimum values of reflectivity for measured grain size.

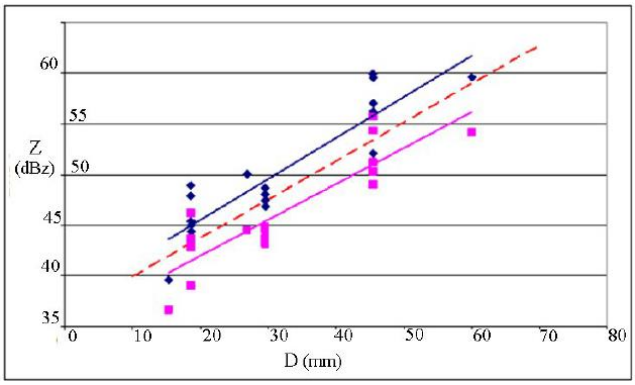

Figure 6. Change of reflectivity depends on changes in grain grains.

6 CHANGE OF THE WALL´S STRUCTURE DURING THE BLAST

Pulse period of Doppler radar is in all cases, 1 s. This means that the grain size distribution can be determined every second of the initiation of blasting and thus track the change of structure of the blast wall.

As an example, the measurement in the quarry Seifsdorf. This measure was supplemented by scanning the blasting wall with high-speed camera. The result is in Figure 7. It seems that the size of material changes every second. This change influences the quantities of the energy from the use of explosives.

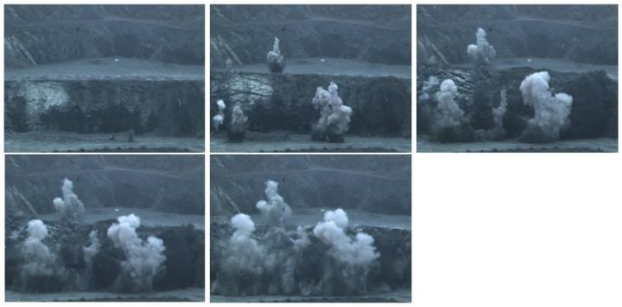

Figure 7. The progress of the blasting captured by a high-speed camera (the blast duration is 5 seconds).

Surface grain size analysis expresses the absolute value of the sum of all the measured reflectivity of flying particles, for the duration of the blasting from t = 1s to t + t_n (Figure 8).

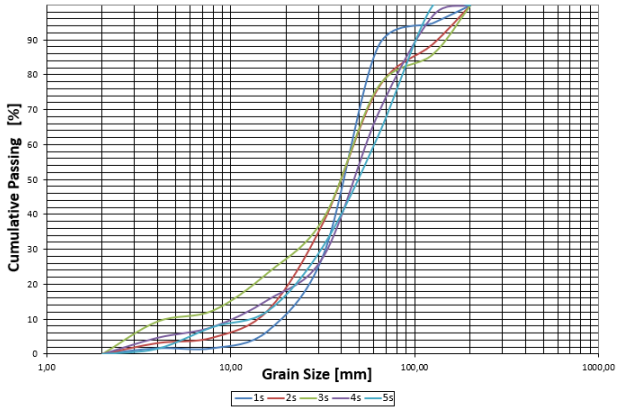

Figure 8. Complete analysis of blasting second after second.

7 USING OF CORRELATION RELATIONSHIP FOR GRAIN SIZE DISTRIBUTION

After the evaluation and comparison of the in situ measurement was possible to convert recorrections for the dependence of grain size and reflectivity. The result of this correction is introduced in Figure 9. The graphs represent the different geological environment. Comparison is in a log-linear coordinate system. The Red line is measured by Radar during the blast, the brown line is a measurement of surface grain size distribution with photo analysis, and the green line measurement by Radar after equipment correction.

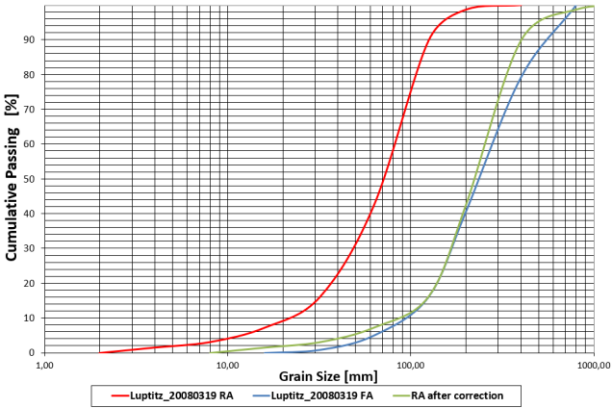

Figure 9. Grain size distribution for blast in rhyolite.

8 CONCLUSION

The idea of using a Doppler effect to detect objects in space is old more than one hundred years. Based on physical theories, its use can also be extended because its variability is currently not limited in any way.

In situ measurements were conducted in places with different material structures, which were conducted and analysed over 60 blasting with a very positive correlation result. After the establishment of a computational algorithm, the total time determining the grain size distribution decreased to about 2 minutes after the blast.

After setting the blasting parameters, it is possible to do a grain size analysis right after blasting and determine its use without unnecessary crushing. This optimization would be able not only to save financial resources, but also to a large extent mitigate the impact on the environment, which is represented by cyclic blasting.

REFERENCES

Ortuta, J. (2012): Use Radar Reflectivity as the possibility to determine the Blasting Fragmentation, *Scientific Reports on Resource Issues*, TU Bergakademie Freiberg, Vol. 1, 2012, S. 207 - 214 (ISSN 2190-555X).

C. Drebenstedt, J. Ortuta (2009): New Approach for Energy Efficient Blast Calculation, *SWEMP*, Banff, Canada.

J. Ortuta, C. Drebenstedt (2012): Use Radar Reflectivity as possibility for Measurements of Fragmentation during the blasting, *Fragblast 10*, New Delhi, India.

C. Drebenstedt, J. Ortuta (2010): Using measurements of the optical sensors and Doppler radar to minimize the impact of blasting, *Blasting Techniques 2010*, Stará Lesna, Slovakia.

Proceedings of the XVIII ECSMGE 2024
GEOTECHNICAL ENGINEERING CHALLENGES
TO MEET CURRENT AND EMERGING NEEDS OF SOCIETY
© 2024 the Authors
ISBN 978-1-032-54816-6
DOI 10.1201/9781003431749-631
Open Access: www.taylorfrancis.com, CC BY-NC-ND 4.0 license

ECSMGE 24
XVIII EUROPEAN CONFERENCE ON SOIL MECHANICS AND GEOTECHNICAL ENGINEERING

Laboratory testing and numerical modelling of seepage in building materials

Essais en laboratoire et modélisation numérique de l'infiltration dans les matériaux de construction

M. Pap*
National University of Public Service, Budapest, Hungary

A. Mahler, Zs. Illés, S.G. Nehme
Budapest University of Technology and Economics, Budapest, Hungary

**pap.miklos@uni-nke.hu*

ABSTRACT: This paper focuses on the importance of understanding and modelling water flow through concrete. To achieve this, the water retention curve (WRC) was determined for various concrete mixtures with different cement quantities and water-cement ratios. The pore system of concrete is complex and consists of open macropores and capillary pores, making it essential to use a bimodal function such as Fredlund and Xing (1994) bimodal model for WRC fitting. The theory of lateral shift was applied to estimate the wetting water retention curve from the drying WRC. The curves obtained are then used to calculate the permeability functions applying the Fredlund et al. (1994) model. To validate our results, finite element modelling of the standard test for watertightness was performed with Plaxis 3D, utilizing the calculated functions. The results of this study provide valuable information for investigating and modelling seepage through the pores of concrete, which is crucial for life-span analyses of underground structures such as hazardous waste storages.

RÉSUMÉ: Cet article met l'accent sur l'importance de comprendre et de modéliser l'écoulement de l'eau à travers le béton. Pour ce faire, la courbe de rétention d'eau (WRC) a été déterminée pour divers mélanges de béton avec différentes quantités de ciment et des rapports eau-ciment différents. Le système de pores du béton est complexe et se compose de macropores ouverts et de pores capillaires, ce qui rend essentiel l'utilisation d'une fonction bimodale telle que le modèle bimodal de Fredlund et Xing (1994) pour l'ajustement de la WRC. La théorie du décalage latéral a été appliquée pour estimer la courbe de rétention d'eau de mouillage à partir de la WRC de séchage. Les courbes obtenues sont ensuite utilisées pour calculer les fonctions de perméabilité en appliquant le modèle de Fredlund et al. (1994). Pour valider nos résultats, une modélisation par éléments finis du test standard d'étanchéité à l'eau a été réalisée avec Plaxis 3D, en utilisant les fonctions calculées. Les résultats de cette étude fournissent des informations précieuses pour l'investigation et la modélisation de l'infiltration à travers les pores du béton, ce qui est crucial pour les analyses de durée de vie des structures souterraines telles que les installations de stockage de déchets dangereux.

Keywords: Concrete; water retention curve; permeability function; lateral shift; numerical modelling.

1 INTRODUCTION

Numerous studies in existing literature demonstrate the applicability of unsaturated soil mechanics theories in computing and analysing water flow within various unsaturated porous materials, such as concrete, asphalt, and geotextile (Park and Fleming, 2006; Renken et al., 2016; Pap et al., 2018). This paper focuses on measuring the drying water retention curve and estimating the wetting water retention curve using the lateral shift technique (Fredlund, 2000; Pham, 2002; Pham et al., 2003; Zhai et al., 2015) for six distinct concrete mixtures. Additionally, the unsaturated permeability function, a crucial input for modelling water flow in concrete, was obtained based on the measured water retention curves.

Direct experimental measurements of the unsaturated permeability coefficient for porous media pose challenges due to their difficulty and time-consuming nature. Various estimation methods have been developed to calculate the permeability function, categorised into empirical, statistical, correlation, and regression models. Statistical models apply a physical model of pore channel arrangements through which water flows, relying on known saturated permeability coefficients and water retention curves (Fredlund et al., 2012). These models assume a close relationship between permeability function, water retention curve,

and pore-size distribution of the soil (van Genuchten, 1980; Fredlund et al., 1994; Zhai and Rahardjo, 2015).

The configuration of the water retention curve in certain porous mediums deviates from the unimodal characteristic. Some soils possess not only a single series of pores but also larger and smaller pores, resulting in at least two peaks in their grain size distribution curve (e.g., gap-graded soils) (Imre et al., 2012). These soils exhibit a bimodal or multimodal characteristic in the water retention curve (Figure 1).

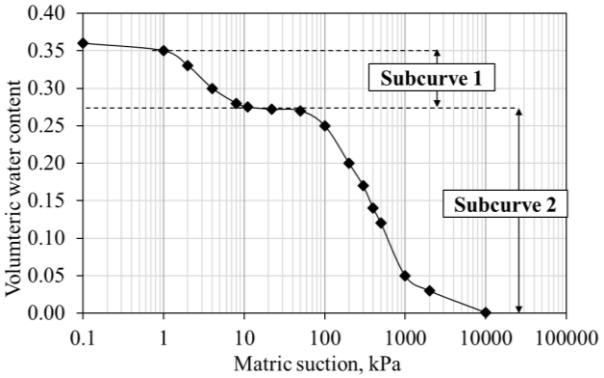

Figure 1. Characteristic of a bimodal water retention curve after Satyanaga et al. (2013).

In laboratory tests, only specific points on the water retention curve are typically measured precisely. Therefore, it becomes necessary to fit a mathematically descriptive function to the measured points for practicality. Various closed-form, empirical equations have been recommended to optimally align with laboratory data for water retention curves (Mualem, 1976; van Genuchten, 1980; Fredlund and Xing, 1994; Satyanaga et al., 2013).

The aim of this study was to furnish substantial input data, such as the water retention curve, unsaturated permeability function and saturated permeability coefficient, for the modelling of seepage in concrete. To evaluate the suitability of the measured data, we simulated the standard watertightness test using finite element software. During this test, a concrete specimen measuring 150×150×150 mm is subjected to a water pressure of 500 kPa on a circular part (75 mm in diameter) of one surface of the specimen for 72 hours. After this period, the specimen is sectioned, and the depth of water penetration is determined through visual inspection.

2 MATERIALS AND METHODS

2.1 Concrete types

We prepared six concrete mixtures for the laboratory tests, varying the water-cement ratio between 0.45 and 0.50. Portland cement composite (CEM II) with a strength class of 42.5 N was utilized.

The aggregates included washed, segregated, and dried sand, along with gravelly sand. The aggregate composition comprised 40% of 0/4 mm, 25% of 4/8 mm, and 35% of 8/16 mm fractions. For M5 and M15 concrete mixtures, polymer fiber was introduced to expand the range of concrete properties, with a fiber content of 0.35% by volume.

To achieve the desired consistency, a superplasticizer based on polycarboxylic solution was added to the concrete mix. For the M7 concrete mix, Penetron Admix, an integrated crystalline additive, served as a waterproofing admixture. The composition details of the tested concrete mixtures can be found in Table 1.

Table 1. Summary of concrete mixtures tested.

Mix No.	Cement (kg/m^3)	w/c ratio	Fiber used	Penet-ron
M1	360	0.50	-	no
M5	400	0.45	polymer	no
M7	360	0.50	-	yes
M13	360	0.40	-	no
M15	400	0.50	polymer	no
M17	400	0.45	-	no

2.2 Measuring methods for water retention curves

The drying water retention curve was determined using three different methods, chosen to accommodate the extensive range of suction values. Consequently, core samples were prepared from each concrete type, with a height ranging from 25 to 50 mm and a diameter of 50 mm, for the measurement. These samples were extracted and cut from concrete cubes measuring 150×150×150 mm. To prevent any mass changes resulting from healing during the tests, the prepared concrete specimens underwent testing after reaching an age of 100 days. At this point, the concrete exhibits recovered residual properties.

In a sand/kaolin box, water content was measured at pF 0, pF 1, pF 1.5, pF 2.0, and pF 2.5 (0.1 kPa, 1 kPa, 3.2 kPa, 10 kPa, and 31.6 kPa) suction values. Suction values were controlled during measurement by adjusting the water surface relative to the position of the tested samples. The determination of water content was conducted through weighing.

Water content at pF 3.4 and pF 4.2 (251.2 kPa and 1584.9 kPa) suction values was determined in a pressure membrane extractor using the axis translation technique. During the test, water pressure was controlled, creating an overpressure in the apparatus.

For high suction ranges, additional procedures are required to control suction. The vapor equilibrium technique, utilizing diverse chemicals and salts, allows for relative humidity control (Ng and Menzies, 2007). The principle involves equilibrium development between the water content of the samples and the surrounding relative humidity. In our measurements, four different chemicals were used to achieve relative humidity values of 95.6%, 90.0%, 75.3%, and 31.0% in a desiccator. Table 2 outlines the chemicals used and their corresponding pF values.

Table 2. Chemicals and corresponding suction values.

Chemicals	Temperature [°C]	Relative humidity (%)	pF value	Suction (kPa)
Sulfuric acid	20.0	95.6	4.79	6 208
Zinc sulphate	20.0	90.0	5.16	14 537
Sodium chloride	25.0	75.3	5.59	38 905
Calcium chloride	24.5	31.0	6.21	161 588

2.3 Determination of saturated permeability coefficient

The permeability coefficients were established through constant head permeability tests conducted in triaxial cell on concrete samples measuring 50 mm in diameter and 50 mm in height. Each sample undergoing three tests at head differences of 100 kPa, 300 kPa and 600 kPa. The average values of the permeability coefficients are summarized in Table 3.

The measured permeability coefficient values exhibited a range from 3.06×10^{-11} m/s and 4.85×10^{-10} m/s, indicating a relatively narrow span considering the diverse range of concrete types.

Table 3. Measured average permeability coefficients.

Mix No.	Average permeability coefficients, k (m/s)
M1	4.97×10^{-10}
M5	1.97×10^{-10}
M7	3.06×10^{-11}
M13	2.20×10^{-10}
M15	4.46×10^{-10}
M17	4.85×10^{-10}

3 INTERPRETATION OF WATER RETENTION CURVES

3.1 Fitting method of water retention curves

As previously mentioned, the water retention curve test allows for the measurement of only a limited number of points in the function. Therefore, it becomes imperative to fit a function to the measured points, facilitating the determination of the permeability function (Leong and Rahardjo, 1997). Analyzing the measured data and the complex pore size distribution of concrete reveals the potential bimodal characteristic in the water retention curve. This implies that formulas such as Satyanaga et al. (2013) or modified procedures (Zhang and Chen, 2005), capable of considering both large-pore and small-pore series, should be employed to accurately fit the measured data. Consequently, the fitting of the WRC to the measured data utilized the bimodal version of the Fredlund and Xing (1994) function, and the fitting process was executed using the Solver Add-in in Excel software.

The model developed by Fredlund and Xing (1994) has proven to be applicable for describing water retention curves not only in soils but also in non-soil materials (Park and Fleming, 2006). This formula incorporates a correction factor that extends the suction range from residual suction to a fully dry state. The bimodal model by Fredlund and Xing (1994) is as follows:

$$\theta(\psi) = \theta_{sl} \cdot \left[1 - \frac{ln\left(1+\frac{\psi}{\psi_{rl}}\right)}{ln\left(1+\frac{10^6}{\psi_{rl}}\right)}\right] \cdot \frac{1}{\left\{ln\left[e+\left(\frac{\psi}{a_l}\right)^{n_l}\right]\right\}^{m_l}} + \theta_{ss} \cdot \left[1 - \frac{ln\left(1+\frac{\psi}{\psi_{rs}}\right)}{ln\left(1+\frac{10^6}{\psi_{rs}}\right)}\right] \cdot \frac{1}{\left\{ln\left[e+\left(\frac{\psi}{a_s}\right)^{n_s}\right]\right\}^{m_s}} \quad (1)$$

where $\theta(\psi)$ is the volumetric water content at the given suction value (kPa), ψ is the suction value, θ_{sl} and θ_{ss} are the saturated volumetric water content for the large-pore and the small-pore series, a_l, n_l and m_l are fitting parameters for the large-pore series component, ψ_{rl} and ψ_{rs} is the value of suction to the residual volumetric water content for the large-pore and small-pore series (kPa), a_s, n_s and m_s are fitting parameters for the small-pore series component.

In Figure 2 the normalized volumetric water content is presented as a function of suction for the M1 concrete mixture, employing the bimodal equation by Fredlund and Xing (1994). Notably, the water content appears to decrease in two distinct steps. This characteristic in the water retention curve of concrete is attributed to the complex pore system inherent in

concrete, comprising both open macropores and capillary pores. At lower suction levels, the water is rapidly expelled from the open macropores due to the influence of gravity on water movement within the concrete.

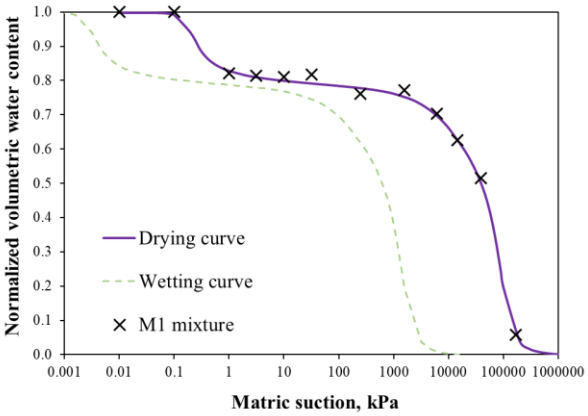

Figure 2. Drying and wetting water retention curve for M1 concrete mixture.

3.2 Estimation of wetting WRCs

The initial curve typically determined for a material is the drying water retention curve, given the quicker attainment of equilibrium on the drying side compared to the wetting side. Estimating the wetting curve often involves assuming a suitable lateral shift for the drying curve. Additionally, it is common to assume that the drying and wetting curves are parallel in the inflection point segment of the curves (Fredlund et al., 2011; Pham et al., 2003).

Consequently, the estimation of the wetting water retention curve involves a horizontal translation to the left in semi-logarithmic space. The fitting parameter *a* in the WRC equations typically governs the lateral shift of both drying and wetting curves.

The percent lateral shift of the WRCs, expressed as ξ, is mathematically represented as follows (Fredlund et al. 2011):

$$\xi = 100[log(\psi_{ad}) - log(\psi_{aw})] \qquad (2)$$

where ψ_{ad} is the suction at any point along the drying WRC (kPa), and ψ_{aw} is the suction at any corresponding water content on the wetting WRC (kPa). With the former formula, the lateral shift can be determined from any point at the curve.

Equation (2), which expresses the lateral shift of the water retention curve, can be rearranged to allow for the computation of suction on a congruent WRC from the drying curve. Subsequently, the modified form of Equation (2) is presented as follows (Fredlund et al. 2011):

$$\psi_w = 10^{(log\,\psi_d - \frac{\xi}{100})} \qquad (3)$$

In an analysis by Pham et al. (2003), the lateral shift between drying and wetting WRCs was examined for published data from various researchers. The results indicated the most substantial shift between drying and wetting curves for clay soils (50-100) and the smallest shift for uniform sand soils (15-35).

For the determination of wetting WRCs in concrete mixtures, previous studies were referenced. Pap et al. (2018) utilized the theory of lateral shift to estimate wetting WRCs. The findings revealed a higher lateral shift in concrete compared to soils, ranging between 145 and 215 for concrete prepared with CEM II AS 42.5 N. Based on this investigation, a mean value of 180 was employed as the lateral shift to estimate wetting curves from the measured drying curves. Figures 2 depicts the estimated wetting WRCs.

3.3 Determination of permeability function

Methods for estimating permeability functions can be categorized into various groups, with proposed models often relying on statistical assumptions regarding pore distributions and interpretation of the water retention curve. In this recent study, the model introduced by Fredlund et al. (1994) was utilized. Their procedure involves numerical integration along the WRC, performed using PTC Mathcad software. The equation is expressed in the following form:

$$k_r(\psi) = \frac{\int_{ln\,(\psi)}^{b} \frac{\theta(e^y)-\theta(\psi)}{e^y}\theta\prime(e^y)dy}{\int_{ln\,(\psi_{aev})}^{b} \frac{\theta(e^y)-\theta_s}{e^y}\theta\prime(e^y)dy} \qquad (4)$$

where *b* is the upper limit of integration, *y* is a dummy variable of integration representing the logarithm of suction, θ' is the derivative of the WRC equation, e^y is the natural number raised to the dummy variable power.

Figure 3 illustrates the normalized permeability functions for M1 concrete mix, revealing a substantial reduction in permeability with increasing suction by several orders of magnitude. This result emphasizes that it is crucial to have more measured points in the very low suction region and the transition zone. Additionally, due to the significant hysteresis of the curves, the permeability coefficient of concrete is notably smaller during the wetting process at the same suction value.

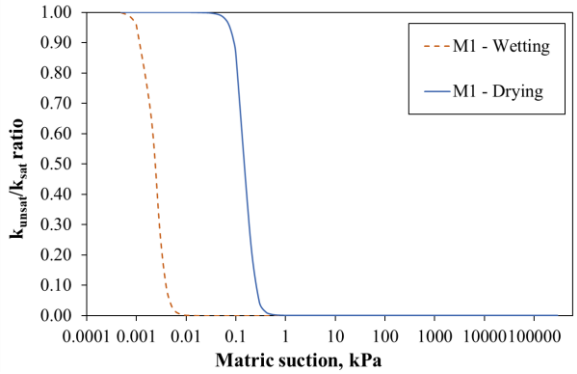

Figure 3. Normalized permeability functions for M1 concrete mixture.

4 NUMERICAL MODELLING OF STANDARD TEST FOR WATERTIGHTNESS

4.1 Geometry

Numerical analysis was conducted utilizing the Plaxis 3D Ultimate finite element software. To expedite calculations, the geometry was simplified by taking advantage of symmetry, modelling only a quarter of the sample (Figure 4). Tetrahedron finite elements were employed during mesh generation, with refinement determined by the water penetration location, as per previous studies. Specifically, refinement occurred on the vertical sides in the upper part of the model and on the horizontal plane on the quarter circle where water pressure was applied. In total, the model was divided into 24210 finite elements.

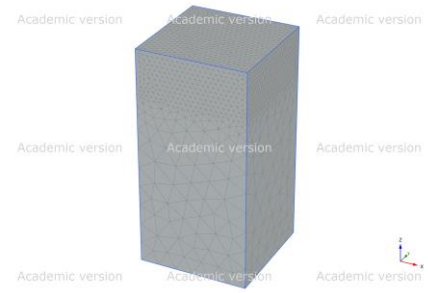

Figure 4. Model geometry of concrete specimen.

4.2 Material properties

Seepage analysis requires specific material properties, including saturated permeability coefficient, initial water conditions, and concrete functions such as WRC and permeability function. These parameters must be calibrated to ensure that the numerical model produces results consistent with the measured data. In the modelling process, the measured saturated permeability values were utilized, and isotropic seepage behaviour was assumed. For hydraulic model, the user-defined dataset was used.

Ensuring the accurate determination of the initial water condition, specifically the initial suction value, is crucial for obtaining appropriate results. In this study, the initial suction value was set to 200 kPa based on sensitivity analysis.

4.3 Boundary conditions

A water pressure of 5 bar was designated as the boundary condition on the quarter circle within the model, while closed seepage boundaries were assigned to the symmetry axes. Seepage within the concrete was computed as a transient flow, requiring specified time intervals. Given that the standard test for watertightness has a duration of 72 hours, the ultimate time step has already been established as 72 hours.

4.4 Results

The depth of water penetration, delineating the boundary between the saturated and unsaturated zones, was determined based on computed pore water pressure values. Figure 5 illustrates the negative pore water pressure values, defining the shape of water penetration for the M1 mix. Despite the model's arrangement suggesting that the maximum penetration depth would occur along the middle axis, the shape of penetration is irregular, resulting in the maximum depth being observed in a different section. Additionally, numerical uncertainties are evident along the boundary of the saturated and unsaturated zones and at the edge of the model. Therefore, further clarification of initial conditions and model setting is still needed.

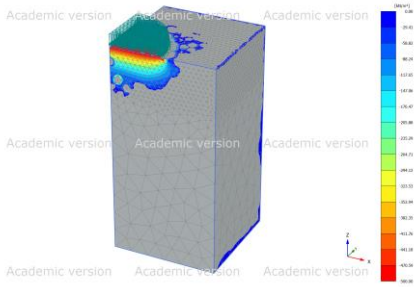

Figure 5. Shape of water penetration for M1 mix based on pore water pressure.

5 CONCLUSIONS

This study aims to furnish input data for modelling water flow in building materials, particularly concrete. A series of laboratory tests were conducted, examining different concrete mixtures for water retention using the sand/kaolin box method, pressure membrane

extractor, and vapor equilibrium technique. Due to the intricate pore system of concrete, the bimodal form of the Fredlund and Xing (1994) model was employed to approximate the water retention curve based on measured data points.

To establish the wetting water retention curve, a lateral shift was implemented, employing a shift value determined from prior studies. It has been demonstrated that the unsaturated permeability function for concrete can be defined using the Fredlund et al. (1994) model. The results emphasized that even a minor alteration in suction can lead to a significant reduction in permeability for concrete.

The numerical modelling has led to the conclusion that both the measured data and the calculated functions are applicable for modelling water flow in concrete. However, further investigations are required to address the effect of changes in initial suction value on the results of modelling.

REFERENCES

Fredlund, D. G. (2000). The 1999 R.M. Hardy Lecture: The implementation of unsaturated soil mechanics into geotechnical engineering. *Canadian Geotechnical Journal*, 37(5): 963–986. https://doi.org/10.1139/t00-026.

Fredlund, D. G., and Xing, A. (1994). Equations for the soil-water characteristic curve. *Canadian Geotechnical Journal*, 31(4): 521–532. https://doi.org/10.1139/t94-061.

Fredlund, D. G., Rahardjo, H., and Fredlund, M. D. (2012). *Unsaturated Soil Mechanics in Engineering Practice*. John Wiley & Sons, New Jersey. https://doi.org/10.1002/9781118280492.

Fredlund, D. G., Sheng, D., and Zhao, J. (2011). Estimation of soil suction from the soil-water characteristic curve. *Canadian Geotechnical Journal,* 48: 186-198. https://doi.org/10.1139/T10-060.

Fredlund, D. G., Xing, A., and Huang, S. Y. (1994). Predicting the Permeability Function for Unsaturated Soils Using the Soil-Water Characteristic Curve. *Canadian Geotechnical Journal*, 31(4): 533-546. https://doi.org/10.1139/t94-062.

Imre, E., Rajkai, K., Firgi, T., Laufer, I., Genovese, R., and Jommi, C. (2012). Modified grading curve - SWCC relations. In: *2nd European Conference on Unsaturated Soils*, pp. 39-46. Napoli, Italy. http://doi.org/10.1007/978-3-642-31343-1_5.

Leong, E. C., and Rahardjo, H. (1997). A review of soil–water characteristic curve equations. *J. Geo. Geo. Eng.*, 123(12): 1106–1117. https://doi.org/10.1061/(ASCE)1090-0241(1997)123:12(1106).

Mualem, Y. (1976). A new model for predicting hydraulic conductivity of unsaturated porous media. *Water Resources Research*, 12(3): 513–522. https://doi.org/10.1029/WR012i003p00513.

Ng, C. W. W., and Menzies, B. (2007). *Advanced Unsaturated Soil Mechanics and Engineering*. Taylor and Francis, London, and New York. https://doi.org/10.1201/9781482266122.

Pap, M., Mahler, A., and Nehme, S. G. (2018). Analysis and Finite Element Modelling of Water Flow in Concrete. *Periodica Polytechnica Civil Engineering*, 62(4): 1052-1059. https://doi.org/10.3311/PPci.13005.

Park, K. D., and Fleming, I. R. (2006). Evaluation of a geosynthetic capillary barrier. *Geotextiles and Geomembranes*, 24: 64-71. https://doi.org/10.1016/j.geotexmem.2005.06.001.

Pham, H. Q. (2002). *An engineering model of hysteresis for soil-water characteristic curves*. M.Sc. thesis, University of Saskatchewan, Saskatoon.

Pham, H. Q., Fredlund, D. G., and Barbour, S. L. (2003). Estimation of the hysteretic soil-water characteristic curves from the boundary drying curve. In: *56th Canadian Geotechnical Conference*. Winnipeg, Canada.

Renken, L., Oeser, M., Milatz, M., and Grabe, J. (2016). Measurement of hydraulic properties of unsaturated permeable polyurethane bound asphalt materials. In: *Unsaturated Soil Mechanics - from Theory to Practice: Proceedings of the 6th Asia Pacific Conference on Unsaturated Soils*. pp. 407-412. Guilin, China. http://doi.org/10.1201/b19248-66.

Satyanaga, A., Rahardjo, H., Leong, E. C., and Wang, J. Y. (2013). Water Characteristic Curve of Soil with Bimodal Grain Size Distribution. *Computers and Geotechnics*, 48: 51-61. https://doi.org/10.1016/j.compgeo.2012.09.008.

van Genuchten, M. T. (1980). A closed form equation for predicting the hydraulic conductivity of unsaturated soils. *Soil Sc. Soc. Am J.,* 44(5): 892-898. https://doi.org/10.2136/sssaj1980.03615995004400050002x.

Zhai, Q., and Rahardjo, H., (2015). Estimation of permeability function from the soil-water characteristic curve. *Eng. Geol.*, 199: 148–156. https://doi.org/10.1016/j.enggeo.2015.11.001.

Zhang, L., and Chen, Q. (2005). Predicting bimodal soil-water characteristic curves. *Jour. of Geo. and Geo. Eng.*, 131(5): 666-670. https://doi.org/10.1016/j.compgeo.2014.01.004.

Proceedings of the XVIII ECSMGE 2024
GEOTECHNICAL ENGINEERING CHALLENGES
TO MEET CURRENT AND EMERGING NEEDS OF SOCIETY
© 2024 the Authors
ISBN 978-1-032-54816-6
DOI 10.1201/9781003431749-632
Open Access: www.taylorfrancis.com, CC BY-NC-ND 4.0 license

ECSMGE 24
XVIII EUROPEAN CONFERENCE ON SOIL MECHANICS AND GEOTECHNICAL ENGINEERING

Assessment of waste dump affected area and its stability analysis for sustainable utilization of land and waste materials - a case study from the Sisdol dumpsite, Nepal

Évaluation de la zone affectée par la décharge et analyse de sa stabilité pour une utilisation durable des terres et des déchets - une étude de cas de la décharge de Sisdol, Népal

D.R. Pathak*
Engineering Study & Research Centre, Kathmandu, Nepal
M. Rijal
Maccaferri (Nepal) Pvt. Ltd, Kathmandu, Nepal
**drpathak@esarcnepal.com*

ABSTRACT: The volume of solid waste has immensely increased over the last decades in Kathmandu Valley (KTMV), the main urban center of Nepal. The Sisdol site was initially developed as a sanitary landfill site in 2005 to accommodate only 150 thousand tons of municipal solid waste (MSW) for 2.5 years however it received more than 3 million tons (~6 million cubic meters) of MSW over the period of 14 years until it turned into a vulnerable dumpsite. When extending more than 300 m horizontal distance, about 80 m high waste dump has already been reached, which created multiple problems in surrounding areas. Therefore, a slope stability analysis of the waste dump was carried out using SLOPE/W before designing the post-closure and land utilization plan of the dumpsite and surrounding area. The factor of safety (FoS) was calculated in three different critical sections of the dumpsite for both static and seismic loading cases. The FoS obtained in sections for the earthquake loading case confirms the slope of the waste dump seems unstable, which is also in compliance with the observation made at the site. The findings of the slope stability analysis in this study indicate the risk of sliding of the dumpsite along the road connecting the new Bancharedanda Landfill, which needs to be minimized with proper stabilization measures before post-closure and sustainable utilization of land in the Sisdol dumpsite.

RÉSUMÉ: Le volume de déchets solides a énormément augmenté au cours des dernières décennies dans la vallée de Katmandou (KTMV), le principal centre urbain du Népal. Le site de Sisdol a été initialement développé comme site d'enfouissement sanitaire en 2005 pour accueillir seulement 150 000 tonnes de déchets solides municipaux (MSW) pendant 2,5 ans, mais il a reçu plus de 3 millions de tonnes (~ 6 millions de mètres cubes) de MSW au cours de la période de 2005. 14 ans jusqu'à ce qu'il se transforme en une décharge vulnérable. En s'étendant sur plus de 300 m de distance horizontale, on a déjà atteint une décharge d'environ 80 m de haut, ce qui a créé de multiples problèmes dans les zones environnantes. Par conséquent, une analyse de stabilité de la pente de la décharge a été réalisée à l'aide de SLOPE/W avant de concevoir le plan de post-fermeture et d'utilisation des terres de la décharge et de ses environs. Le facteur de sécurité (FoS) a été calculé dans trois sections critiques différentes de la décharge pour les cas de chargement statique et sismique. Le FoS obtenu par coupes pour le cas de chargement sismique confirme que la pente de la décharge semble instable, ce qui est également conforme à l'observation faite sur le site. Les résultats de l'analyse de stabilité des pentes dans cette étude indiquent le risque de glissement de la décharge le long de la route reliant la nouvelle décharge de Bancharedanda, qui doit être minimisé par des mesures de stabilisation appropriées avant la post-fermeture et l'utilisation durable des terres de la décharge de Sisdol.

Keywords: Dumpsite stability; municipal solid waste; leachate; post closure; SLOPE/W.

1 INTRODUCTION

Solid waste management (SWM) has become a major concern for municipalities of developing countries, like Nepal. With rapid and uncontrolled urbanization, lack of public awareness and poor management by municipalities has intensified environmental problems in towns of developing countries, where waste management is still limited to inadequate disposal (dumpsites on non-sanitary waste disposal sites) (Kaza et al., 2018; Ferronato and Torretta, 2019; Ma et al., 2022). For example, the 18

municipalities of Kathmandu Valley (KTMV), the main urban center of Nepal generates 1,262 tons per day (t/d) of municipal solid waste (MSW), roughly 25 percent of total MSW of Nepal, and 15 percent of KTMV's MSW is still uncollected (World Bank, 2023). At present, more than 800 tons/day of MSW from KTMV is being disposed of at the Sisdol dumpsite, which is about 63 percent of total produced solid waste (World Bank, 2023). The site was initially developed as a short-term sanitary landfill site in 2005 for two and half years as shown in Figure 1a. However, in the name of the capacity extension, waste was disposed of without a liner, leachate collection, treatment facilities and landfill gas management facilities for nearly 14 years until it was turned into a highly unstable vulnerable dumpsite as shown in Figure 1b (Pathak and Shahi, 2021).

Dumping of solid waste in non-engineered landfills is very common in developing countries. It generates leachate, a toxic by-product that can migrate into surface water and percolate into the groundwater (Costa et al., 2019; Ma et al., 2022). As the dominant waste fractions in the cities of developing countries is organic waste with high moisture content, it has more leachate generation potential (Zairi et al., 2014). Moreover, poor surface water management also adds the leachate volume significantly in such a dumpsite. A similar case can be observed in the Sisdol dumpsite, where the spring water sources were not diverted during the expansion of the dumpsite area and hence entered into the dumpsite, which is not only deteriorating the water quality and surrounding environment (Figure 1c) but also leads instability and sliding failure in dumpsite due to increase of pore pressure, increase unit weight and decrease the strength of body of waste.

Slope failure in MSW dumpsites is a common environmental disaster that poses serious ecological and health risks (Shu et al., 2022). In several cases poorly designed and operated landfills without considering several aspects of MSW mechanical behavior have caused landfill failures. The landfills of Rumpke in the USA (Zekkos, 2005), Dona Juana in Columbia (Caicedo et al., 2002), Payatas in Philippines (Merry et al., 2005) and Leuwigajah dumpsite in Indonesia (Koelsch et al., 2005) are examples of such catastrophic events, which doesn‘t only cause heavy economic losses and human casualties but also create immense sources of environmental pollution. A similar situation may have happened in the Sisdol dumpsite, which needs to be analysing the slope stability of the dumpsite before severe consequences in the surrounding environment. As the Sisdol dumpsite has already been saturated and overloaded, its post-closure management is needed and should be carried out soonest possible.

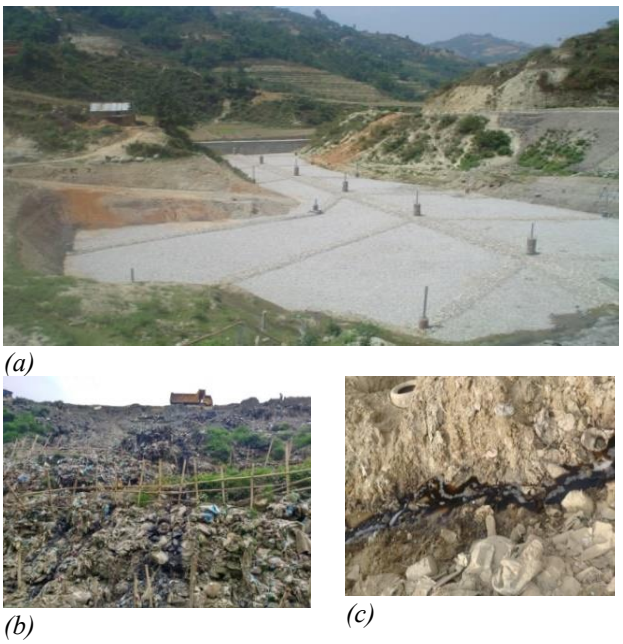

(a)

(b)

(c)

Figure 1. Sisdol Landfill site before operation in 2005(a), Existing situation of Sisdol dumpsite (b), Leachate flow at Sisdol dumpsite (c)(Source: SWMTSC/GoN).

For post-closure management, stabilizing the steep slope of the Sisdol dumpsite is required. Therefore, this paper applies the SLOPE/W to carry out the slope stability analysis of the Sisdol dumpsite. For this purpose, we calculated the factor of safety (FoS) in three critical sections of the waste dump for both static and seismic cases using the procedures of slices method as described by Morgenstern-Price.

2 METHODS

2.1 Study Area

The dumpsite is located at Ward 2 of Kakani Rural Municipality about 18 km north-west from Kathmandu city centre, which is located very close to the Kolpu River.

Figure 2 shows the status of the Sisdol dumpsite before the start and after operation over the period of 2003 to 2022. When extending nearly 300 m horizontal distance, more than 80 m vertical height has already been reached. Moreover, there is an access road to connect the Bancharedada landfill site, a new landfill site about 3 km from this dumpsite. About 200 m length of road section lies on the existing dumpsite. Based on the topographic map of the original ground, it seems about 20m to 25 m compacted old solid waste fill below the existing

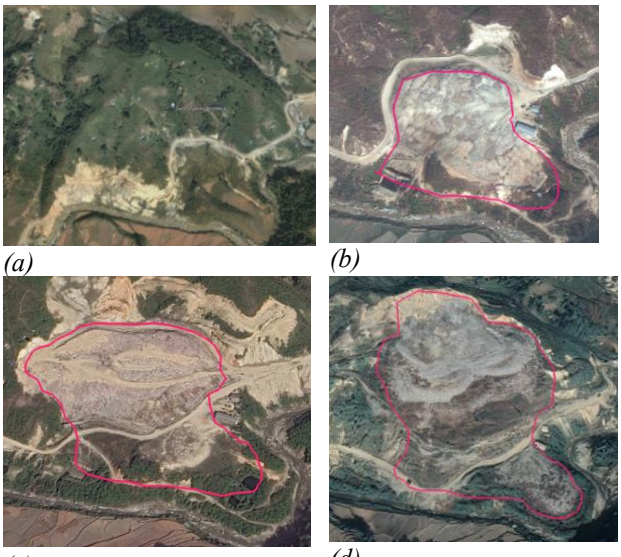

(a) *(b)* *(c)* *(d)*

Figure 2. Google image showing status of Sisdol dumpsite before and after operation over the period of 2003 to 2022-October, 2003- before construction (a), April 2010 (b), October, 2014- extension of dumpsite (c), November, 2022- turned into highly vulnerable dumpsite (d). Red line is boundary of dumpsite.

access road as shown in Figure 2d. In addition to this, the road is further critical due to the steep slope of the solid waste dump above access road. The protection of a slope of about 80 m high solid waste dump above the access road is very important for the use of this access road in an uninterrupted way for a long time.

2.2 Topographic survey of an existing dumpsite

A detailed topographic survey was conducted using a total station to capture and record the topography of the dumpsite together with both manmade and natural features which enabled in carrying out detailed assessment of slope failures of dumpsite and roadside slope.

2.3 Slope stability analysis of dumpsite

The geometry of the dump changes continuously due to the decay of organic materials, degradation of inorganic solids, and addition of waste daily. The top part is a relatively unconsolidated mix of waste and soil, whereas the bottom layer consists of the slightly consolidated and degraded solid waste mixed with soil. The slope stability issues on the Sisdol dumpsite are analyzed using SLOPE/W for both static and seismic loading cases as the study area is highly vulnerable to earthquakes. It was carried out in the three different critical sections as shown in Figure 3.

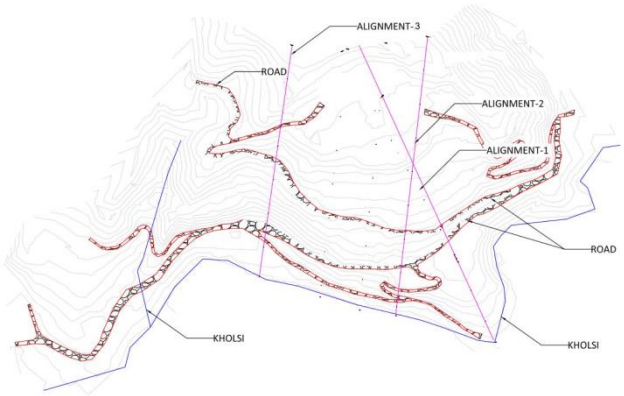

Figure 3. Topographic map of Sisdol dumpsite and three critical sections for stability analysis.

The geometry for the stability analysis is prepared based on the recent survey conducted on the dumpsite. In the Sisdol dumpsite, the MSW was disposed of from 2005 and deposited till 2007 to reach about 20 m high before its closure. In 2011, disposal of MSW again was continued at the same place due to the lack of alternative disposal sites and extended till 2022 to reach its total height of up to 80 m. Therefore, the dumpsite in the model has been divided into four layers, including the geological layer, depending upon the age of deposited MSW (Table 1).

Table 1. Summary of soil properties used in stability analysis of dumpsite.

Solid waste layer	**Unit Weight (kN/m^3)**	**Eff. Cohesion, c' (kPA)**	**Eff. Friction Angle (ϕ')**
Top layer (<20 m)	8.6	29.1	15
Middle layer (20 m - 50m)	12	18.3	22
Bottom Layer (>50m)	14	17	32
Geological layer	18	12	38

As no geotechnical explorations are carried out during this study, literature review and experience with similar waste materials of similar regions have been used to adopt the pertinent shear strength properties and unit weight of the MSW (Feng et al., 2017; Machado et al., 2010; Ramaiah et al., 2017; Iqbal et al., 2022). Feng et al. (2017) reported that the friction angle and cohesion varied from (15.7 degrees, 29.1 kPa) to (21.9 degrees, 18.3 kPa) as the depth increased from 4 to 16 m, while the unit weight increased from 7.2 and 12.5 kN/m3. According to Ramaiah et al. (2017), with the aging of the solid waste, a decrease in cohesion and an increase in

friction angle were observed in the MSW samples collected from the Ghazipur and Okhla dumps at Delhi. The shear strength of the MSW obtained in the above studies was lower than the reported values in developed countries because of the less fibrous materials and more organic materials in the MSW in the cities of developing countries, which is a similar case in our context and very relevant to use these geotechnical properties of MSW for stability analysis of Sisdol dumpsite.

3 RESULTS AND DISCUSSION

3.1 Existing situation of Sisdol dumpsite

Google imagery and field observations show nearly 300 meters of extension from the center of the previous landfill site. Although the government initially developed a sanitary landfill site to accommodate only 150 thousand tons of MSW for 2.5 years, it received more than 3 million tons (~6 million cubic meters) of MSW over 14 years (Figure 4) until turning into a vulnerable dumpsite. Disposal of an immense volume of MSW with high organic fractions and poor operation of the Sisdol dumpsite not only polluted water and soil in surrounding areas but also adversely affected the people in nearby communities due to the unpleasant odor and diseases borne vectors from the dumpsite.

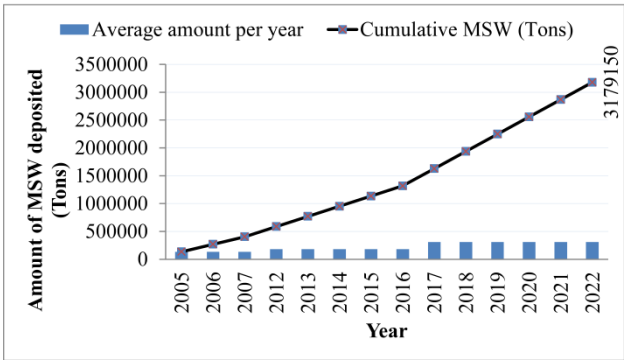

Figure 4. Annual and cumulative volume of MSW disposed at Sisdol dumpsite over 14 years period.

NAST (2020) reported a high concentration of toxic metals (heavy metals) such as arsenic and cadmium. The reason for the maximum arsenic and cadmium concentration in surface water may be probably due to the direct discharge of leachate in the river (Kolpu River). Similarly, BOD and COD values have also significantly increased from 2009 to 2018 in the leachate of the Sisdol dumpsite. Amano et al. (2021) also reported high levels of Cadmium (Cd) and turbidity in surface and groundwater sources within the surrounding area of the waste landfill site in Kumasi, Ghana. The test results of soil samples near the Sisdol dump site also reveal that cadmium, lead, and nickel in the soil are beyond the recommendations required for agricultural land.

3.2 Findings of stability analysis

The result of the stability analysis is presented in Figures 5(a-g) for two cases using MSW shear strength parameters respectively. During the monsoon season, after MSW gets saturated mass movement has been frequently observed.

As shown in the following figures, the slope profiles under static loading conditions seem stable since FoS is above 1 for all sections. And, for section-2, the FoS is higher than 1 even in seismic loading case. However, FoS in the section-1 and section-3, the FoS for the seismic loading case is less than 1, indicating unstable during earthquake, which is also in compliance with the observation made at the site.

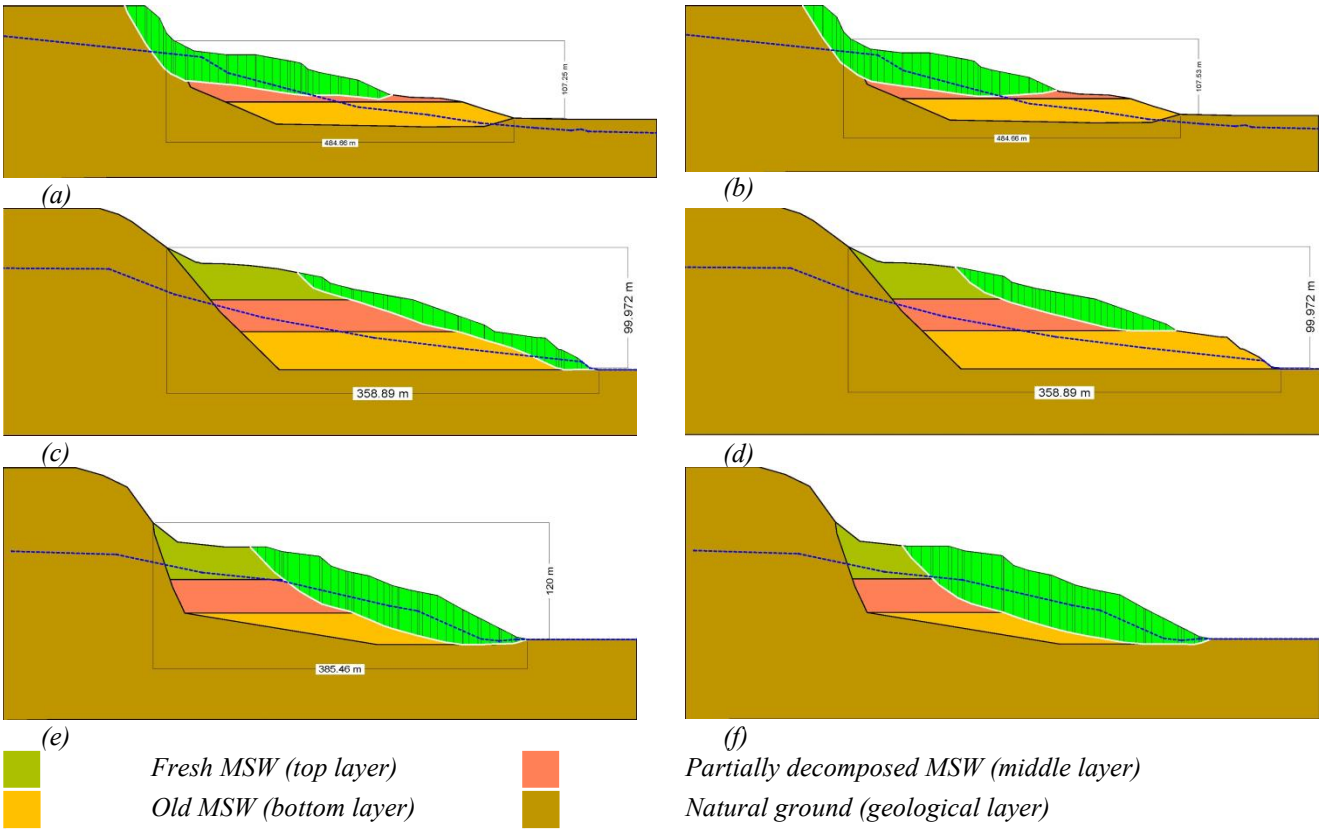

Figure 5. Stability analysis at different critical sections of the Sisdol dumpsite using Morgenstern-Price method-Factor of Safety (FoS) at section-1 for static loading case=1.37 (a), FoS at section-1 for seismic loading case=0.89 (b), FoS at section-2 for static loading case=1.96 (c), FoS at section-2 for seismic loading case=1.28 (d), FoS at section-3 for static loading case=1.52(e), FoS at section-3 for seismic loading case=0.96 (f).

Over the last few years, there was a frequent slope failure along section-3 in line with the modelling results. This supports the assumption of the materials parameters of the landfill material for stability analysis. However, the properties of dump materials change with depth and time. The geometry of the slope modelled may change in a short time span. A detailed geotechnical analysis is required to evaluate the exact geotechnical and other field properties of solid waste layers in different depths and locations of the Sisdol dumpsite for precise stability analysis which helps for both stabilizing road section on the existing dumpsite and sustainable post-closure plan. The slope stability analysis in this study indicates the risk of sliding the dumpsite along the road connecting the new Bancharedanda landfill site, which needs to be minimized with proper stabilization measures before post-closure and sustainable utilization of land in the Sisdol dumpsite.

4 CONCLUSIONS

This paper assessed how a sanitary landfill site has been gradually turned into a highly vulnerable dumpsite over the period of 2005 to 2022 with the help of satellite images, field data and observation. The adverse impacts on agricultural land, water and the surrounding communities due to poorly managed dumpsites were assessed. Moreover, slope stability analysis of the Sisdol dumpsite was also carried out using the limit equilibrium software, SLOPE/W from Geostudio before developing post-closure and land utilization plans for the dumpsite and surrounding area. The factor of safety obtained at the section (section-1 and section-3) with a steep slope seems unstable. In recent years there was a slope failure along the same section indicated by modelling results, which supports the assumption of the properties of waste materials in this study. However, detailed investigations for the evaluation of the geotechnical properties of materials in waste dumps are recommended.

The slope stability analysis in this study indicates the risk of sliding the dumpsite along the road connecting the new Bancharedanda landfill site. The risk should be minimized with proper stabilization measures along the slope profile as well as within the road itself. The steep slope at the hillside of the road as in the critical section should be trimmed to flatten the slope. The flattened slope should be supported by a gabion wall at the toe and a series of wooden or

concrete posts are to be driven to reinforce the outer layer of the waste fill before post-closure design.

REFERENCES

Amano, K. O. A., Danso Boateng, E., Adom, E., Kwame Nkansah, D., Amoamah, E. S., and Appiah Danquah, E. (2021). Effect of waste landfill site on surface and ground water drinking quality. Water and Environment Journal, 35(2), 715-729. https://doi.org/10.1111/wej.12664.

Caicedo, B., Yamin, L., Giraldo, E., Coronado, O. (2002). Geomechanical properties of municipal solid waste in Dona Juana sanitary landfill. In: Proceedings of the Fourth International Congress on Environmental Geotechnics, Brazil, vol. 1, pp. 177–182.

Costa, A. M., Alfaia, R. G. D. S. M., and Campos, J. C. (2019). Landfill leachate treatment in Brazil–An overview. Journal of environmental management, 232, 110-116. https://doi.org/10.1016/j.jenvman.2018.11.006.

Feng, S. J., Gao, K. W., Chen, Y. X., Li, Y., Zhang, L. M., & Chen, H. X. (2017). Geotechnical properties of municipal solid waste at Laogang Landfill, China. Waste Management, 63, 354-365. https://doi.org/10.1016/j.wasman.2016.09.016.

Ferronato, N., and Torretta, V. (2019). Waste mismanagement in developing countries: A review of global issues. International journal of environmental research and public health, 16(6), 1060. https://doi.org/10.3390/ijerph16061060.

Iqbal, M.R., Piumali, A.B.K.T., Priyankara, N.H., Alagiyawanna, A.M.N., Kurukulasuriya, L.C., & Kawamto, K (2022). Characterization of Physicochemical and Mechanical Properties of Dumped Municipal soild waste in Sri Lanka as affected by the climate zone and dumping age. Sustainability MDPI, 14, 4706. https://doi.org/10.3390/su14084706.

Kaza, S., Yao, L., Bhada-Tata, P., and Van Woerden, F. (2018). What a waste 2.0: a global snapshot of solid waste management to 2050. World Bank Publications.

Koelsch, F., Fricke, K., Mahler, C., Damanhuri, E. (2005). Stability of landfills – the Bandung dumpsite disaster. In: CISA (Hrsg.): Proceedings of the 10th International Landfill Symposium, Cagliari, Italy.

Ma, S., Zhou, C., Pan, J., Yang, G., Sun, C., Liu, Y., ... and Zhao, Z. (2022). Leachate from municipal solid waste landfills in a global perspective: Characteristics, influential factors and environmental risks. Journal of Cleaner Production, 333, 130234. https://doi.org/10.1016/j.jclepro.2021.130234.

Merry, S.M., Kavazanjian Jr., E., Fritz, W. (2005). Reconnaissance of July 10, 2000, Payatas landfill failure. Journal of Performance of constructed Facilities 19 (2), 100–107. https://doi.org/10.1061/(ASCE)0887-3828(2005)19:2(100).

Nepal Academy of Science and Technology (NAST) (2020). A Study Report on Impact Assessment of Affected Areas of Sisdol Landfill Site. A Report Submitted to Kathmandu Metropolitan City (KMC), 2020.

Pathak, D.R. and Shahi, A. (2021). Identification of Sisdol Landfill Site affected areas and land utilization plan of Sisdol-Banchare area. Final Report submitted Engineering Study & Research Centre to Kathmandu Metropolitan City, Unpublished.

Ramaiah, B. J., Ramana, G. V., and Datta, M. (2017). Mechanical characterization of municipal solid waste from two waste dumps at Delhi, India. Waste Management, 68, 275-291. https://doi.org/10.1016/j.wasman.2017.05.055.

Shu, S., Li, Y., Sun, Z., and Shi, J. (2022). Effect of gas pressure on municipal solid waste landfill slope stability. Waste Management & Research, 40(3), 323-330. https://doi.org/10.1177/0734242X211001414.

World Bank (forthcoming 2023). Catalyzing Sustainable and Inclusive Urban Development in Kathmandu Valley: SWM Diagnostic and Policy Implications in KTMV. The World Bank.

Zairi, M., Aydi, A., and Dhia, H. B. (2014). Leachate generation and biogas energy recovery in the Jebel Chakir municipal solid waste landfill, Tunisia. Journal of Material Cycles and Waste Management, 16, 141-150. https://doi.org/10.1007/s10163-013-0164-3.

Zekkos, D. P. (2005). Evaluation of static and dynamic properties of municipal solid-waste. University of California, Berkeley.

Proceedings of the XVIII ECSMGE 2024
GEOTECHNICAL ENGINEERING CHALLENGES
TO MEET CURRENT AND EMERGING NEEDS OF SOCIETY
© 2024 the Authors
ISBN 978-1-032-54816-6
DOI 10.1201/9781003431749-633
Open Access: www.taylorfrancis.com, CC BY-NC-ND 4.0 license

ECSMGE 24
XVIII EUROPEAN CONFERENCE ON SOIL MECHANICS AND GEOTECHNICAL ENGINEERING

Groundwater control during metro construction in urban areas – the Cityringen experience

Contrôle des eaux souterraines lors de la construction d'un métro en zone urbaine - l'expérience de Cityringen

E. Paulatto
Metroselskabet, Copenhagen, Denmark

L.M. Markussen
Rambøll, Copenhagen, Denmark

J. Damgaard
COWI, Copenhagen, Denmark

F. Petrella, J. Flink*
Arup, Copenhagen, Denmark

**jenny.flink@arup.com*

ABSTRACT: Groundwater lowering in the inner city of Copenhagen, Denmark, is generally not permitted due to the sensitive nature of the foundations of existing buildings, and to avoid spreading existing groundwater contamination. Outside the inner-city, groundwater lowering is often undesirable due to risks towards settlement of infrastructure, nature and contamination. To ensure dry conditions during construction of shafts and other large excavations, and to protect nearby buildings as well as the environment, groundwater control systems have been established in each of the 28 underground stations/shafts of the Cityringen metro, including the Nordhavn and Sydhavn extensions. The temporary groundwater control systems have comprised of cut-off walls and a network of pumping and recharge wells. There is often a notable discrepancy between the discharge rates predicted by modelling in the design phase, and those measured during construction. Possible explanations for this discrepancy include differences between the modelled design and the actual constructed dewatering system, quality of the cut-off wall, inadequate ground investigations or misinterpreted results, pressure-dependent ground permeability and uncertain assumptions regarding anisotropy. This paper describes the basis for the dewatering activities and the outcome of the three-dimensional (3D) groundwater models developed during the detailed design and compares this with the observed groundwater monitoring data. Inconsistencies between the design and observed behaviour of the groundwater control systems are reviewed and the potential reasons are investigated.

RÉSUMÉ: Le rabattement de nappe dans le centre-ville de Copenhague n'est généralement pas autorisé en raison de la nature sensible des fondations des bâtiments existants et pour éviter la propagation de contamination existante des eaux souterraines. A l'extérieur du centre-ville, le rabattement de nappe est souvent indésirable en raison du risque vis-à-vis d'affaissement d'infrastructure, des zones naturelles et de la contamination. Pour garantir des conditions sèches lors de la phase de construction de puits et d'autres larges excavations, et pour protéger des bâtiments avoisinants ainsi que l'environnement, des systèmes de contrôle des eaux souterraines comprenant à la fois des parois étanches et un réseau de forages de pompage et de réinfiltration ont été établis dans chacune des 28 stations souterraines/puits du métro « Cityringen », incluant les extensions Nordhavn et Sydhavn. Il existe souvent un écart notable entre les débits de pompage prédits par modélisation dans la phase de conception et ceux observés pendant la construction. Les explications possibles pour cet écart comprennent des différences entre le design modélisé et le système de rabattement de nappe construit, la qualité de la paroi étanche, des investigations inadéquates du sous-sol ou des résultats mal interprétés, une perméabilité du sol dépendante de la pression et des hypothèses erronées concernant l'anisotropie. Cet article décrit le fondement pour les activités de rabattement de nappe et le résultat des modélisations 3D d'écoulement des eaux souterraines développées pendant la conception détaillée, et compare cela avec les données de suivi de niveaux des eaux souterraines observés. Les inconsistances entre la conception et le comportement observé des systèmes de contrôle des eaux souterraines sont examinées et les raisons potentielles sont étudiées.

Keywords: Groundwater control; 3D groundwater modelling; Copenhagen metro; limestone, urban hydrogeology.

1 INTRODUCTION

The expansion of the metro network in Copenhagen has taken place over the last 12 years, has entailed the construction of 28 underground structures (stations and shafts), with abstraction and recharge of groundwater via dedicated groundwater control systems. A large amount of data has been collected in the monitoring database (Kronos) that was in operation during and after construction. This paper aims to analyse the information gathered, and then give a first evaluation of the substantial discrepancy between the yield rates predicted by modelling in the detail design phase and those measured during construction. This paper also offers some explanations and hypotheses that can be further confirmed and extended in future ad-hoc papers/studies. Previous publications on this topic include Bonde et al. (1997), Raben-Levetzau et al. (2004), Bock and Markussen (2007) and Markussen et al. (2019).

2 COPENHAGEN GROUND CONDITIONS

The geology of Copenhagen, see Figure 1, comprises glacial clay till and meltwater sand/gravel deposits overlying Paleocene limestone (Copenhagen Limestone and Bryozoan Limestone). This geology forms the main geological unit in which the metro tunnels and stations are constructed.

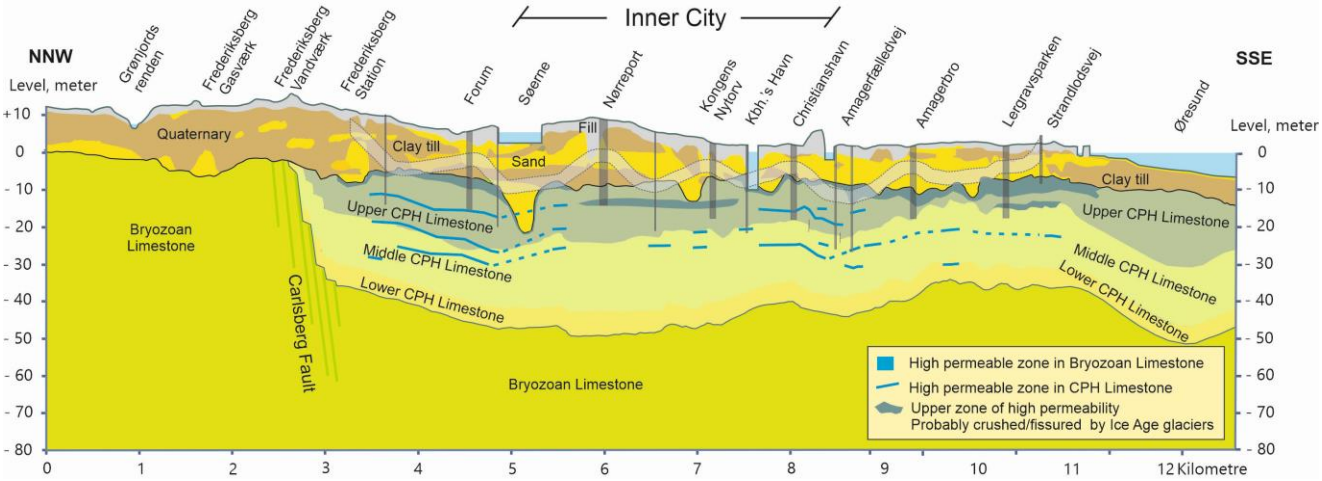

Figure 1. Copenhagen ground conditions in a profile along the M1 metro line.

The primary aquifer in the region is the upper part of the limestone, together with sand and gravel deposited directly above the limestone. The average hydraulic conductivity of the limestone generally falls in the range from 10^{-6} m/s to 10^{-4} to m/s with the majority of the flow occurring in fractures. The piezometric level of the aquifer is typically a few meters below the ground surface. Secondary aquifers are present in the overlying glacial and marine sand and gravel deposits and within the fill. Because the metro stations are situated below the groundwater table, significant dewatering works have been required for their construction.

There are several NNW-SSE oriented faults and folds in the region, the most notable in Copenhagen being the Carlsberg Fault and the Svanemølle Fault. These are known to have significant impact on limestone transmissivity (Frederiksen et al., 2002).

The primary aquifer is a source for domestic water supply with abstraction taken place in the Carlsberg fault zone where the water bearing-capacity is high. Parts of the metro alignment lie within the catchment zone associated with this abstraction.

3 COPENHAGEN METRO

The Copenhagen metro is a light rail system running 24/7 within the municipalities of Copenhagen, Frederiksberg and Tårnby. There are presently four operational lines. M1 and M2 opened in 2002 with further extensions completed in 2003 and 2007. Seventeen stations were then added in 2019, together with the M3 'circle line' (referred to as Cityringen, i.e. CR). Two of the M4 line stations opened in 2020 (referred to as Nordhavn, i.e. NH) while the remaining five stations are under construction and due to become operational in 2024 (referred to as Sydhavn, i.e. SH). This paper focuses on the M3 and M4 underground stations, and describes the temporary dewatering required to enable their construction.

The typical underground station footprint in plan is 60x20m though larger footprints are needed for crossovers or run-over tracks. The typical excavation

depth is between 18m to 25m, though a few CR stations and shafts are as deep as 35m such as the Marmorkirken and Nørrebroparken stations.

4 GROUNDWATER CONTROL SYSTEM

The city of Copenhagen was founded more than 800 years ago. It is situated at the coast, and large parts of the inner city are founded on fill as the city reclaimed land from the sea. Many residential and public buildings are old and are often listed as historical monuments. The old harbour, and the many lakes and canals, form an important part of the city identity.

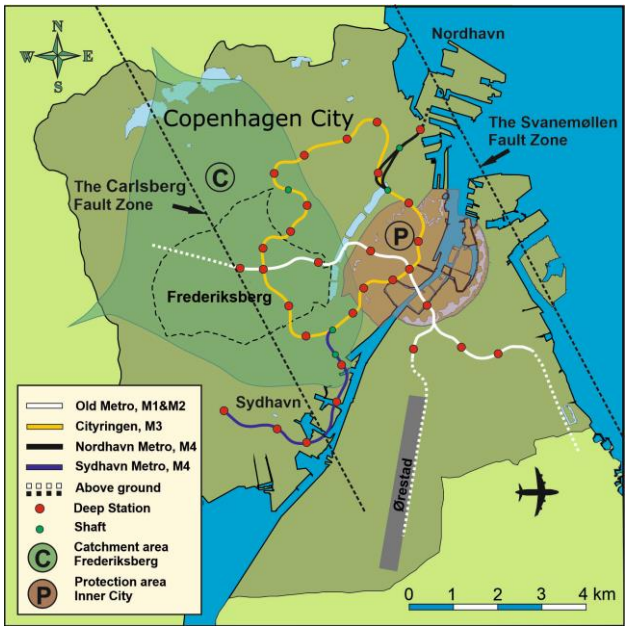

Figure 2. Copenhagen metro system.

Dewatering of deep excavations can cause:

- Settlement damage to buildings which are founded directly in fill.
- Damage to buildings which are founded on timber piles or other wooden constructions.
- Draining of city lakes
- Damage to urban drinking water interests due to pollution spreading and saltwater intrusion.
- In 1991 the Copenhagen city authorities decided to limit groundwater lowering in the entire inner city area where the risk of settlements and deterioration of wooden foundations is greatest, see Figure 2. In this area, any lowering of the upper groundwater to more than 0.3m above sea level is not allowed.

To ensure dry conditions in excavations during metro construction, and to avoid groundwater lowering in the surrounding area, a groundwater control system was established for each deep excavation. The system comprised of cut-off walls and a network of pumping and recharge wells; see conceptual layout in Figure 3.

Groundwater levels were primarily controlled by the installation of impermeable reinforced concrete secant pile cut-off in the quaternary layers and the upper part of the limestone, constructed to below excavation level. This provided a complete cut-off in the glacial layers and resulted in seepage into the excavation only occurring from the limestone. The actual cut-off depth was determined by results from pumping tests and flow logs combined with groundwater modelling.

The amount of water pumped from the sites had to be balanced by pumping back a similar amount of abstracted water into the limestone outside the secant pile wall, via the construction of recharge wells.

Monitoring was an important part of the groundwater control operation. The purpose of monitoring was twofold. Firstly, the monitoring was necessary for the actual groundwater control. Regular monitoring of groundwater levels in monitoring wells, combined with data on dewatering pumping and recharge volumes were necessary to evaluate the effect of groundwater lowering. These data were also a necessary input to the calibration of the groundwater model. Secondly, an efficient system of regular reporting to the authorities was necessary both to meet demands and to ensure efficient and professional communication with the authorities. The monitoring used the Kronos monitoring database system developed by Geodata (Rabensteiner et al. 2015).

5 DATA SET SUMMARY

Ground investigations (GI) were planned by Metroselskabet (MS) and/or their consultants to form the basis for concept design, Environmental Impact Assessment (EIA) and tender design. All the metro projects were tendered as “design and build” and therefore the contractors have often supplemented with additional GI.

For a standard station on CR, NH and SH the dewatering-related GI typically included three cored boreholes to well below the base of the excavation, one or two long-duration pumping tests, complete with multiple observation wells, three short duration pumping tests and four flow logs. These were typically made both in open hole and in the screened borehole. The GI was interpreted by both the consultants and the contractors.

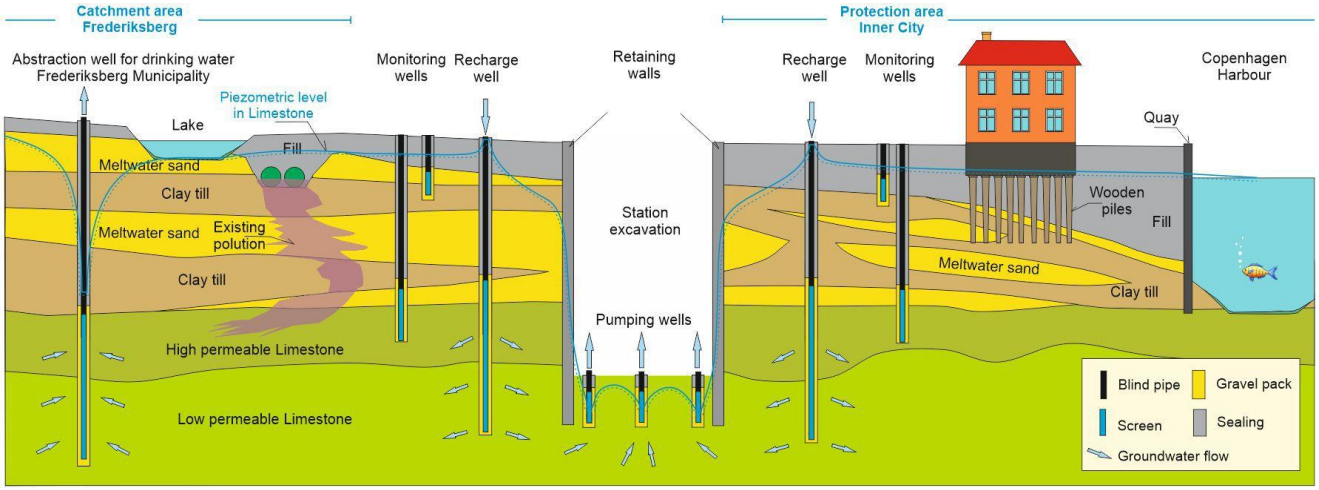

Figure 3. Typical dewatering system for metro station/shaft construction in Copenhagen.

For approximately half the stations on CR, the contractor supplemented the GI with additional boreholes and one long-duration pumping test. For NH and SH only limited additional investigations were made by the contractor.

Both MS's consultants and contractors developed their own 3D groundwater models for EIA, tendering and detailed design respectively. All models were calibrated in transient mode against the long duration-pumping tests. For CR and SH the consultant used GMS Modflow, while the contractor used Feflow for CR and GMS Modflow for SH.

The consultant used the models to determine the required minimum depth of retaining walls, expected yields, requirements of recharge rate, and locations to be reserved for recharge etc.

The contractors used the models as part of their detailed design of the dewatering system with respect to quantity and location of pumping and recharge wells, expected yields to be used for the design of water treatment, and authority applications.

6 COMPARISON OF YIELD RATES

The simulated yields (from Hydrogeological Design Reports) and measured yields (from Kronos) for the 28 underground stations/shafts were compared. The relationship between the two datasets is presented in Figure 4 and Figure 5. The yields refer to the total pumped yields from all pumping wells at the different locations.

The impact of factors such as required groundwater lowering, transmissivity, depth of cut off walls below the excavation, quality of cut off walls, limestone excavation depth, number of pumping tests, size of excavation etc. was assessed.

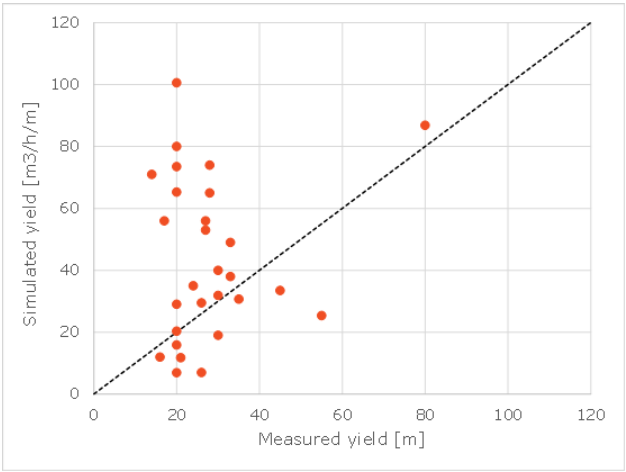

Figure 4. Relationship between simulated and measured yield.

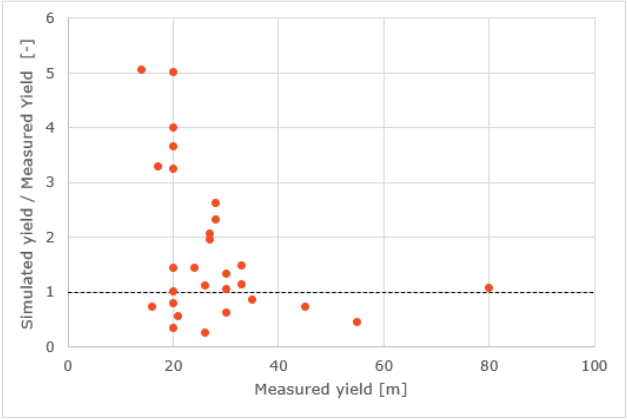

Figure 5. Relationship between simulated / measured yield and measured yield.

Figure 6 depicts the simulated and measured pumping yields when plotted against groundwater lowering.

As can be seen in the figure, the recurrent measured yield is c.20-30 m^3/h, seemingly independent of the required drawdown. The simulated yields are more variable but (besides a few exceptions) and often significantly higher than the measured ones.

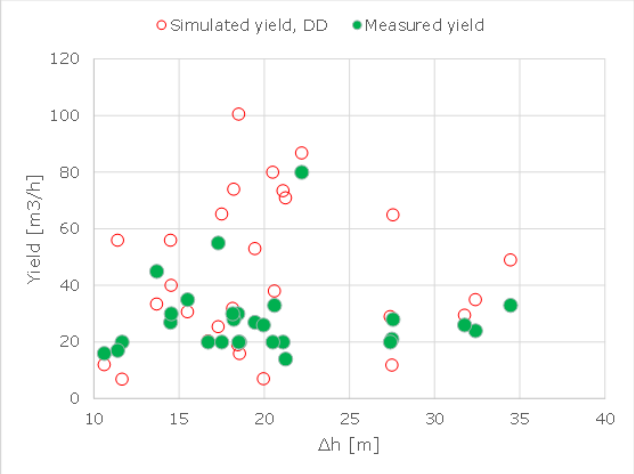

Figure 6. Relationship between simulated/measured yields and groundwater lowering.

In Figure 7, the pumping yields per meter of drawdown are plotted against groundwater lowering. No observable relationship can be seen between the yields and required drawdown.

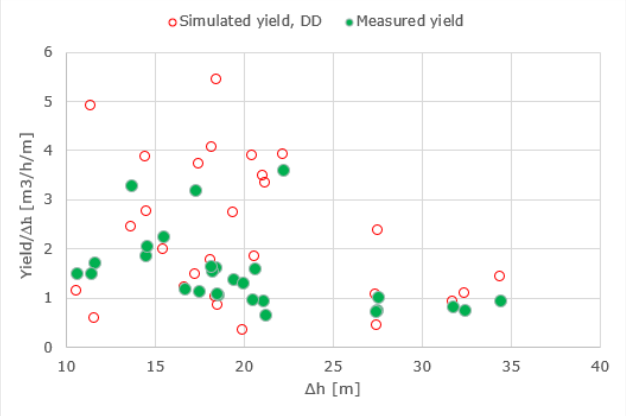

Figure 7. Relationship between simulated/measured yields per meter of groundwater lowering and groundwater lowering.

Similar to the lack of clear relationship between yield and required drawdown, no observable relationship between the yields and the other assessed factors was found.

7 DISCUSSION

A possible explanation for the recurrent 20-30 m^3/h measured yields may be that the deeper limestone, below cut-off level, is relatively homogenous across the whole Copenhagen area, in the locations where the underground metro stations have been built. The inflows are therefore steady once the upper glacially disturbed and more permeable part of the limestone is cut off. It shall be noted that the type of limestone formation being dewatered (e.g. Upper Copenhagen Limestone, Middle Copenhagen Limestone or Bryozoan Limestone) has no clear impact on the yields.

The measured yields for three stations/shafts, Mozart's Plads (45 m^3/h), Enghave Brygge/Ørestedsværket (55 m^3/h) and Sluseholmen (80 m^3/h) stations of the SH extension, exceeds the standard range. Possible explanations for the higher inflows at these locations may be proximity to geological structures (faults) and/or to the harbour.

Though no clear relationship between excavation size (area) and yield can be observed from the dataset, most excavations are of similar size with the exception of Enghave Brygge/Ørestedværket, which is twice the size of the other stations/shafts, and size is therefore likely to be part of the reason for the higher yields in this location.

At Mozart's Plads, another reason for the observed higher yields is inflow to the adjacent shallow excavation which contributed significantly to the overall yield. Investigations and dewatering design for shallow excavations in addition to the main shaft dewatering should therefore not be overlooked.

The data analysis shows that there is a notable discrepancy between simulated and measured yields. The horizontal to vertical permeability ratio (K_v/K_h) utilised in the simulation models is a key factor to estimate yields. In the Cityringen models, the assumption has typically been that K_v is a factor of 5 or 10 less than K_h which typically equates to K_v in the order of 10^{-6} m/s. Based on pumping tests and modelling of limestone in Malmø, which is similar to limestone in Copenhagen, the K_v value in the limestone has been estimated to be $3x10^{-7}$ m/s (Citytunnelkonsortiet, 2000). This could explain the deviation between simulated and measured yields. Another possible explanation is pressure dependant permeability, i.e. water bearing fissures contracting when the pressure is reduced, as postulated by Markussen et al. (2019).

8 CONCLUSIONS

Following the review of dewatering systems for the construction of 28 underground metro stations/shafts in the central part of Copenhagen, it is noted that the measured yields are relatively steady, around 20-30 m^3/h, with no observable relationship between the yields and factors such as transmissivity or required drawdown. This may be due to the deeper limestone

below cut-off level being relatively homogenous. With this in mind, determining the depth to less permeable limestone e.g. through flow logs, is considered key to assessing the required cut-off depth and thus achieving manageable yields.

The size of excavation, proximity to geological features and the harbour, are likely to be contributing causes to inflows exceeding the standard range.

Uncertain assumptions regarding anisotropy and pressure dependent permeability may explain the deviation between simulated and measured yields. Additional studies are planned to determine what 3D model parameters need to be adjusted for the models to better match the measured yields.

Despite the observed inconsistences between simulated and measured yields, 3D groundwater modelling remains a powerful tool to design groundwater control systems and provides an essential requirement to obtain the permits required by various authorities to carry out dewatering in urban areas.

ACKNOWLEDGEMENTS

The authors would like to thank Vincent Collin from COWI for translating the abstract into French.

REFERENCES

Bock, M. and Markussen, L.M. (2007) Dewatering control in central Copenhagen, In: *Proceedings 14th European Conference on Soil Mechanics and Geotechnical Engineering 2*, Amsterdam, the Netherlands, pp. 715-720.

Bonde, C., Bitsch, K., Markussen, L. (1997) Groundwater management in central Copenhagen for the construction of the fixed link across the Øresund, In: *14th International Conference on Soil Mechanics and Foundation Engineering*, Hamburg, Germany.

Citytunnelkonsortiet (2000) Numerical Geohydrological Model. Assembled Report of Technical Notes No. II, SCC-RAMBØLL JV.

Frederiksen, J.K., Eriksen, F. S., Hansen, H. K., Knudsen, C., Jørgensen, M. E., Møller, H. M. F. and Brendstrup, J. (2002) Engineering geology of Copenhagen (in Danish: Ingeniørgeologiske forhold i København), Danish Geotechnical Society Bulletin 19, Danish Geotechnical Society, Denmark.

Markussen, L.M., Hansen, S.B., Olsen, L.K. (2019) Groundwater challenges in the limestone during construction of metro and roadway tunnels to a new waterfront city district in Copenhagen, In: *Engineering in Chalk: Proceedings of the Chalk 2018 Conference*, ICE Publishing, https://doi.org/10.1680/eiccf.64072.175.

Raben-Levetzau, J., Markussen, L.M., Bitsch, K., & Nicolaisen, L. (2004) Copenhagen Metro: groundwater control in sensitive urban areas, *Tunnelling and Underground Space Technology,* 19(4-5), pp. 522, https://doi.org/10.1016/j.tust.2004.01.037.

Rabensteiner, K., Berger, P., Paulatto, E. (2015) Monitoring and integrated data management for safe urban tunneling Eurock 2015 & 64th Geomechanics Colloquium Shubert (ed.).

Proceedings of the XVIII ECSMGE 2024
GEOTECHNICAL ENGINEERING CHALLENGES
TO MEET CURRENT AND EMERGING NEEDS OF SOCIETY
© 2024 the Authors
ISBN 978-1-032-54816-6
DOI 10.1201/9781003431749-634
Open Access: www.taylorfrancis.com, CC BY-NC-ND 4.0 license

ECSMGE 24
XVIII EUROPEAN CONFERENCE ON SOIL MECHANICS AND GEOTECHNICAL ENGINEERING

Recycled red mud as an useful geotechnical material

La boue rouge recyclée comme matériau géotechnique utile

P. Pavšič*, M. Đurić, M. Košir, A. Mauko Pranjić, A. Mladenovič, P. Oprčkal, S. Seršen, V. Zalar Serjun
Slovenian National Building and Civil Engineering Institute, Ljubljana, Slovenia

primoz.pavsic@zag.si

ABSTRACT: Red mud (RM) is an extractive waste from Bayer process in alumina production. The most conventional methods of RM disposal are tailing dams, or dry storage, both of which raise environmental concerns due to the high alkalinity of RM and the presence and leaching of potentially hazardous elements (PTEs). Due to its fine-grained nature and poor mechanical properties, as well as leaching of potentially hazardous substances, RM cannot be used by itself. Properties of the RM can be improved, by mixing it with hydraulic or pozzolanic binders, such as calcareous ashes or steelmaking slag, to produce mechanically stable and durable composites for earthworks. On the other hand, RM can also serve as an immobilization additive for remediation of contaminated soils. Two different approaches for useful utilization of RM are presented based on results of laboratory research and a real case study, opening of new possibilities for conserving natural resources and reducing environmental hazards of RM deposits.

RÉSUMÉ: La boue rouge (RM) est un déchet extractif issu du procédé Bayer de production d'alumine. Les méthodes les plus conventionnelles d'élimination des MR sont les barrages à résidus ou le stockage à sec, qui tous deux soulèvent des préoccupations environnementales dues à l'alcalinité élevée des RM et au lessivage d'éléments potentiellement dangereux (PTEs). En raison de sa nature à grains fins et de ses mauvaises propriétés mécaniques, ainsi que de la lixiviation de substances potentiellement dangereuses, la RM ne peut pas être utilisée seule. Les propriétés du résidu de la RM après extraction peuvent être améliorées, en le mélangeant avec des liants hydrauliques ou pouzzolaniques, tels que des cendres calcaires ou des scories sidérurgiques, pour produire des composites mécaniquement stables et durables pour les travaux de terrassement. D'autre part, la RM peut également servir d'additif d'immobilisation pour l'assainissement des sols contaminés. Deux approches différentes pour une utilisation utile de la RM sont présentées sur la base des résultats de recherches en laboratoire et d'une étude de cas réel, ouvrant de nouvelles possibilités pour la réduction des dépôts de la RM conservant ainsi les ressources naturelles et réduisant les risques environnementaux liés aux gisements problématiques de la RM.

Keywords: Red mud; recycling; geotechnical composites; environment.

1 INTRODUCTION

Red mud (RM) is an extractive waste from Bayer process in alumina production. The process is based on digestion of the bauxite ore in a hot NaOH solution. The alumina-rich solution is then separated from the solid residues, which consist of Fe and Al (hydr)oxides and are referred to as RM. Production of RM worldwide amounts to more than 160 million tonnes annually (Zalar Serjun et al., 2018, Zeng et al., 2020, IAI, 2022). The large amount of generated RM creates several disposal problems due to the absence of appropriate storage methods (Jha et al., 2020). The most conventional methods of RM disposal are to pump the slurry into ponds behind "tailing dams", or disposal of dewatered RM by dry stacking. In both approaches, large areas of land are needed (Samal, 2021), posing a threat related to potential instability and collapsing of RM deposits and raising environmental concerns due to the high alkalinity of RM, the presence and leaching of PTEs, and alkaline airborne dust emissions (Jha et al., 2020, Samal, 2021). Potential applications for the utilisation of RM need to be explored to minimise the associated negative environmental impacts (Zalar Serjun et al., 2018, Jha et al., 2020). However, the chemical and physical properties of RM vary considerably, reflecting their different sources (differences in bauxite composition and processing plant operation). This means that the potential recycling of each deposit of RM has to be considered separately, in its own case study (Oprčkal et al., 2020). RM is not only a source for recovery of metals, such as Fe, Ti, Mn, Na, K and also rare earth elements, such as Sc, Y, Hf, Zr, and Ti (Samal, 2021), but can also be a valuable construction material (Jha et al., 2020, Samal, 2021). Due to its fine-grained nature and poor mechanical properties, as well as the environmental concerns, RM cannot be used as construction material by itself.

The properties of the RM residue can be improved, by mixing it with hydraulic or pozzolanic binders, such as calcareous ashes or steelmaking slag, to produce mechanically stable and durable composites for earthworks. On the other hand, RM can also serve as an immobilization additive for remediation of contaminated soils (Zalar Serjun et al., 2018, Oprčkal et al., 2020).

Two different approaches for the useful utilization of RM are presented, based on the results of laboratory research and a real case study, opening new possibilities for the reduction of RM deposits.

2 RED MUD AS AN ADDITIVE FOR REMEDIATION OF CONTAMINATED SOILS

Data presented in the literature show that RM's high sorption capacity for PTEs is due to the large specific surface area of its constituent mineral phases, which enables two main immobilization mechanisms: (a) surface complexation of PTEs with Fe and Al ox/hydroxides, and (b) adsorption by alumosilicates. The RM was used as an immobilisation additive for the preparation of a stable, technically and environmentally acceptable geotechnical composite. It was intermixed to contaminated soil (CS) from one of Slovenia's largest heavily contaminated areas (Zalar Serjun et al., 2018, Oprčkal et al., 2020).

2.1 Materials

The RM was sampled from an open disposal site nearby alumina plant in Podgorica, Montenegro. The RM was dried at 105 °C in a convection oven and ground to a particle size below 2 mm. The mineralogical analysis showed that the RM is composed of calcite, hematite, gibbsite, boehmite and a phase that belongs to the feldspathoid group of minerals (cancrinite / vishnevite). Goethite, quartz, ilmenite, illite/muscovite, perovskite, rutile and dolomite present its minor constituents.

Samples of contaminated soil (CS) were obtained from a 17 ha large brownfield at the Old Zinc-Works site, which is located in the central part of the town of Celje, in eastern Slovenia. According to the European Union's List of Waste (EC, 2014), excavated soil from this location was regarded as a hazardous waste. The CS consisting of silty-sandy gravel was sampled, and then crushed in a jaw crusher to a grain fraction below 16 mm.

2.2 Experimental

The geotechnical composite was prepared by blending the CS with 25 wt.% of the RM and optimal water content, followed by subsequent compaction. The optimal water content was determined by means of the Modified Proctor Compaction Test (SIST, 2013), in order to achieve maximum dry density of the composite. Monolithic test specimens of the composite were cured in a climatic chamber (20°C and 98% humidity) for 3, 7, 28, and 56 days for subsequent analyses.

To investigate the immobilization properties and efficiency of the RM, the characterisation of the RM and the CS by surface area and microstructure by X-ray fluorescence (XRF), X-ray powder diffraction (XRD), and scanning electron microscopy equipped with energy dispersive spectroscopy (SEM/EDS), as well as changes in leachate composition were studied. The BET surface areas of the RM and the CS were determined by N_2 sorption tests. Their total elemental composition was studied by XRF and corresponding phase and microstructural analyses were performed by XRD, and SEM/EDS.

The tank leaching procedure (SIST, 2002), was applied to the test specimens of the RM, CS, and composite (CS/RM). Selected PTEs in the eluates were determined by an inductively coupled plasma mass spectrometer (ICP-MS), whereas the content of Cl^- and SO_4^{2-} were investigated by the UV-Vis absorption spectrophotometry.

In addition to the basic characterization and leaching tests for environmental acceptability studies, also some basic geotechnical properties of the CS/RM composite were evaluated, namely unconfined compressive strength (SIST, 2004) and water permeability (SIST, 2019a).

2.3 Results and discussion

The most abundant PTE in the CS was Zn, which was present in concentrations of up to 15 %, whereas Si was the second most abundant element (11%), followed by Fe, Ca, Al, S, and Mg. The most problematic parameters in the eluate of the CS were water soluble Cd, Pb, and Zn, and SO_4^{2-}, which concentrations exceeded the limit values according to the present Slovenian landfilling legislation (GS, 2016) by factors of 10.5, 2.0, 16.6, and 1.35, respectively. The CS therefore has to be regarded as hazardous waste.

For the used RM a large BET specific surface area was determined, i.e. 20.1 m^2/g. According to the results of the XRF total elemental analysis, the most abundant constituent in the RM is Ca, which makes up almost 15 %. Other major constituents are Fe, Al,

Si and Ti, followed by an array of minor constituents. The results of the performed chemical analysis of the eluate indicated that, according to the present Slovenian landfilling legislation (GS, 2016), this RM is a non-hazardous waste.

The phase composition of the CS/RM composite reflects the combination of minerals from the RM and the CS, since no new mineral phases were identified by the XRD. The eluates from the CS/RM composite show a time-dependent decrease in conductivity. The measured concentrations of the PTEs in the eluates from the CS/RM were all below the limit values for inert materials (GS, 2016), which shows the immobilization effectiveness of the used RM. The immobilization of the PTEs in the investigated composite was attributed to the fact that the goethite and gibbsite mineral phases, as well as the hematite from the RM, provide numerous adsorption sites due to their large specific surface areas, resulting in the high adsorption capacity.

The unconfined compressive strength of the CS/RM composite was determined after 3, 7, 28, and 56 days of curing, and amounted to 0.5 to 0.7 MPa with no time-dependent trends. This is in agreement with findings that no new mineral phases formed in the composite that could contribute to the binding of grains. Water permeability (SIST 2019a), determined after 28 days of curing on intact monolithic test specimens, amounted to 7.88×10^{-8} m/s.

3 RED MUD AS CONSTRUCTION MATERIAL

Relatively few attempts have been made on the effective utilization of RM for the geotechnical application alone or, its combination with several chemical and waste stabilizers (Jha et al., 2020). Recycling of the RM for the production of geotechnical composite construction materials was studied. Since the applied RM residue was in a form of slurry, it needed to be treated with the addition of binder to obtain solidified, mechanically stable and the environmentally acceptable geotechnical composite material with properties suitable for use in earthworks.

3.1 Materials

In this case the RM from the Podgorica pond was first processed with gravitational and magnetic large-for extraction of metal phases, which are used as raw materials in metallurgy. The residue or the RM after extraction was in the form of slurry with a 42 wt.% of solids. The mineralogical analysis showed that it is composed of hematite, gibbsite, cancrinite, calcite, boehmite and aluminium fluoride.

Ash (PA) was obtained from a paper mill VIPAP Videm Krško, Slovenia. It is a waste that can be used as a binder with hydraulic or pozzolanic properties for soil remediation, solidification and stabilization. It is a highly alkaline material that contains a latent hydraulically active phases. The composition and properties of PA are highly dependent on the type of fuel burned, the combustion technology used, and the combustion conditions.

3.2 Experimental

The geotechnical composite (RM/PA) was prepared by mixing the RM with the PA. The amount of the PA required to achieve the appropriate consistency for compaction was determined on basis of laboratory trials. To prepare the RM/PA, 0.75 kg of PA was added to each 1 kg of RM residue slurry with a water content of 139 wt.% and homogenized. Prior to the RM/PA specimen preparation, the mellowing period of 24 hours was required to allow the chemical reactions to take place and to achieve a suitable consistency - workability of the mixture. During the mellowing period, the mixture was stored in an airtight plastic container at ambient temperature and then homogenized again. The test specimens were prepared by compaction in the molds (SIST, 2005) using the standard Proctor compaction effort (SIST, 2013). The specimens were cured at 22 °C and 98% humidity for 2, 7, and 14 days. The prepared specimens were used to determine the geotechnical, mineralogical and chemical properties of the investigated geotechnical composite at selected curing times.

Basic geotechnical properties of the composite were determined, such as unconfined compressive strength - UCS (SIST, 2004), consolidation properties - oedometer test - E_{oed} (SIST, 2017), water permeability - k (SIST, 2019a) and shear strength - ρ', c' (SIST, 2019b). Mineralogical composition was determined by XRD, while environmental acceptability by PTEs concentrations in leachate (SIST, 2002), which were determined with ICP-MS.

3.3 Results and discussion

According to the results of the XRD analysis the PA consists of calcite, lime, amorphous phase, quartz, portlandite, magnetite, gehlenite, anhydrite and feldspars. Leachate analysis of the PA showed that concentrations of all selected PTEs are below permissible levels (GS, 2022).

Mineral phase of the RM/PA composite was analysed at different time intervals, after 2, 7, and 14

days. The XRD analysis showed that during the curing new mineral phase – ettringite was formed. This phase is a member of the typical hydration products mineral group, formed in systems with latent hydraulic active materials (i.e., the used PA).

Geotechnical properties of the composite are time dependant and are presented in Table 1

Table 1. Geotechnical properties of the RM/PA composite.

Parameter	After 2 days	After 7 days	After 14 days
UCS (kPa)	144	3548	4939
E_{oed} at 100kPa (MPa)		79.4	
k at 100kPa (m/s)		5.5×10^{-11}	
ρ', c'(°, kPa)		51.5, 0,0	

From the point of view of the evaluated geotechnical properties, the investigated composite shows similar geotechnical properties as high quality natural silts, sands or gravels, that confirms its applicability as construction materials in earthworks. The results of the chemical analyses showed that the geotechnical composite RM/PA is environmentally acceptable and does not pose any risk to the environment when used as a construction material for earthworks (GS, 2022).

4 CONCLUSIONS

Two applications of the RM in construction were studied. It was shown that the RM can be effective immobilizer for PTEs in contaminated soils, thus transforming contaminated soils in useful construction material. On the other hand, the RM can also be used as construction material when stabilized with paper mill fly ash. In both cases prepared composites exhibits adequate geotechnical properties for earthworks, as well as environmental acceptability according to the Slovenian legislation.

ACKNOWLEDGEMENTS

The authors are grateful for the financial support provided through the EIT RawMaterials project, RIS-RESTORE, project no. 19269, co-funded by the European Union. The authors acknowledge the Slovenian Research and Innovation Agency core funding P2-0273 and project J1 - 4413.

REFERENCES

EC (2014). European Commission. Commission Decision Amending Decision 2000/532/EC on the list of waste pursuant to Directive 2008/98/EC of the European Parliament and of the Council 2014/955/EU. Official Journal L 370/44.

GS (2016). Government of Slovenia. Official Gazette of the Republic of Slovenia, No. 10/14, 54/15, 36/16, 37/18, 13/21 and 44/22 – ZVO-2. Decree on waste landfill.

GS (2022). Government of Slovenia. Official Gazette of the Republic of Slovenia No. 77/22. Decree on waste.

IAI (2022). International Aluminium Institute. Sustainable bauxite residue management guidance, [online] Available at: [https://international-aluminium.org/resource/sustainable-bauxite-mining-guidelines-second-edition-2022-2/], accessed: 28/10/2023.

Jha, A. K., Kumar, D, Sivapullaiah, P. V. (2020). Influence of Fly Ash on Geotechnical Behaviour of Red Mud: A Micro-mechanistic Study, *Geotechnical and Geological Engineering*, Volume (38), pp. 6157–6176, https://doi.org/10.1007/s10706-020-01425-z.

Oprčkal, P., Mladenovič, A., Zupančič, N., Ščančar, J., Milačič, R., Zalar Serjun, V. (2020). Remediation of contaminated soil by red mud and paper ash, *Journal of cleaner production*, Volume (256), pp. 1-10, https://doi.org/10.1016/j.jclepro.2020.120440.

Samal, S. (2021). Utilization of Red Mud as a Source for Metal Ions—A Review, *Materials*, Volume (14), pp. 2211, https://doi.org/10.3390/ma14092211.

SIST (2002). SIST EN 1744-3:2002 - Tests for chemical properties of aggregates - Part 3: Preparation of eluates by leaching of aggregates.

SIST (2004). SIST EN 13286-41:2004 - Unbound and hydraulically bound mixtures - Part 41: Test method for the determination of the compressive strength of hydraulically bound mixtures.

SIST (2005). SIST EN 13286-50:2005 - Unbound and hydraulically bound mixtures - Part 50: Method for the manufacture of test specimens of hydraulically bound mixtures using Proctor equipment or vibrating table compaction.

SIST (2013). SIST EN 13286-2:2010/AC:2013, Unbound and hydraulically bound mixtures - Part 2: Test methods for laboratory reference density and water content - Proctor compaction.

SIST (2017). SIST EN ISO 17892-5:2017 - Geotechnical investigation and testing - Laboratory testing of soil - Part 5: Incremental loading oedometer test.

SIST (2019a). SIST EN ISO 17892-11:2019 - Geotechnical investigation and testing - Laboratory testing of soil - Part 11: Permeability tests.

SIST (2019b). SIST EN ISO 17892-10:2019 - Geotechnical investigation and testing - Laboratory testing of soil - Part 10: Direct shear tests.

Zalar Serjun, V., Mladenovič, A., Milačič, R., Ščančar, J., Ašler, A., Zupančič, N., Nikolić, I., Oprčkal, P. (2018). Red mud as an alternative material for the production of a geotechnical composite, In: *Proceedings of the 2nd International Bauxite Residue Valorisation and Best Practices Conference*, Athens, Greece, pp. 143-149.

Zeng, H., Lyu, F., Sun, W., Zhang, H., Wang, L., Wang, Y. (2020). Progress on the Industrial Applications of Red Mud with a Focus on China, *Minerals*, Volume 10(9), pp. 773, https://doi.org/10.3390/min10090773.

Proceedings of the XVIII ECSMGE 2024
GEOTECHNICAL ENGINEERING CHALLENGES
TO MEET CURRENT AND EMERGING NEEDS OF SOCIETY
© 2024 the Authors
ISBN 978-1-032-54816-6
DOI 10.1201/9781003431749-635
Open Access: www.taylorfrancis.com, CC BY-NC-ND 4.0 license

ECSMGE 24
XVIII EUROPEAN CONFERENCE ON SOIL MECHANICS AND GEOTECHNICAL ENGINEERING

Carbon management in geotechnical engineering solutions

La gestion du carbone dans les solutions de génie géotechnique

O.J. Perttu, S.H. Vicente*, M.S. Löfman, T. Dettenborn, J. Forsman, T. Teittinen
Ramboll Finland Oy, Espoo, Finland

**saila.vicente@ramboll.fi*

ABSTRACT: The construction sector is a significant contributor to greenhouse gas (GHG) emissions, mainly because of the emission intensive construction materials. Integrating carbon accounting and management into the geotechnical design process of infrastructure projects can effectively reduce embodied carbon from land use planning through to the detailed design phases. A low-carbon geotechnical approach includes appropriate ground investigations, soil and rock mass coordination and comparisons of different foundation and soil improvement methods. In the detailed design phase, chosen foundation and soil improvement methods can be optimized for carbon emissions through material choices, transport planning, and considering life cycle durability. This paper presents the possibilities of geotechnical engineering solutions to decarbonise the infrastructure sector. Carbon emissions and costs for various ground improvement and foundation methods, including alternative solutions with recycled materials, are reported, and compared. The considered case studies and scenarios represent infrastructure projects located in Finland.

RÉSUMÉ: Le secteur de la construction est un contributeur significatif aux émissions de gaz à effet de serre (GES), principalement en raison de l'utilisation intensive de matériaux de construction émetteurs de carbone. Intégrer la comptabilisation et la gestion du carbone dans le processus de conception géotechnique des projets d'infrastructure peut efficacement réduire l'empreinte carbone dès la planification de l'aménagement du territoire jusqu'aux phases de conception détaillée. Une approche géotechnique à faible émission de carbone comprend des investigations géotechniques, une coordination des masses de sol et de roche, ainsi que des comparaisons de différentes méthodes de fondation et d'amélioration du sol. Dans la phase de conception détaillée, les méthodes de fondation et d'amélioration du sol choisies peuvent être optimisées en termes d'émissions de carbone grâce aux choix de matériaux, à la planification du transport et à la prise en compte de la durabilité sur l'ensemble du cycle de vie. Cet article présente les possibilités des solutions de génie géotechnique pour décarboniser le secteur des infrastructures. Les émissions de carbone et les coûts pour diverses méthodes d'amélioration du sol et de fondation, y compris des solutions alternatives avec des matériaux recyclés, sont rapportés et comparés. Les études de cas et les scénarios pris en considération représentent des projets d'infrastructure situés en Finlande.

Keywords: Carbon management; carbon emissions; ground improvement; low-carbon geotechnical engineering; design optimization.

1 INTRODUCTION

To align with the established net-zero greenhouse gas emissions (GHGs) target outlined in the Paris Agreement for 2050 and to address the predictions concerning climate impact as presented in the Intergovernmental Panel on Climate Change (IPCC) (2023) report, various sectors, notably the construction industry, must take proactive measures to attain net-zero emissions and to mitigate the resultant global warming effects. Built environment is a major source of greenhouse gas emissions globally – directly through the construction, operation, and maintenance of assets and indirectly through operations (Thacker et al., 2021). Further, construction affects globally available resources and infrastructure consumes more than 50% of the world's projected materials annually (IRP, 2022).

Infrastructure projects are large and long-lasting engineering projects, with associated environmental impacts throughout their lifecycle. This article investigates the significance of decarbonising infrastructure projects, focusing on the utilization of geotechnical engineering solutions in Finland to tackle emissions-intensive components and construction phases.

2 CARBON MANAGEMENT IN INFRASTRUCTURE SECTOR

2.1 Overview on carbon management

The carbon footprint of an infrastructure project is mostly determined by its embodied carbon, representing greenhouse gas (GHG) emissions

throughout the lifecycle of materials, encompassing extraction, manufacturing, transport, construction, reuse, recycling, and disposal. Materials like concrete and steel are notable contributors to embodied carbon emissions. Given the significant material consumption in infrastructure projects, key strategies to minimize embodied carbon involve reducing material usage and employing alternative materials.

Carbon management and accounting are approaches to optimise and verify low-carbon design solutions. Carbon management involves proactive reduction of project carbon footprints using carbon accounting as a numerical method. Internationally recognized standards include PAS 2080 (BSI, 2023), EN 17471 (DS, 2022), and ISO 14001 (DS, 2015). Carbon accounting identifies embodied carbon origins strategically and systematically, applicable at both project and strategic levels.

2.2 Embodied carbon in geotechnical solutions

Geotechnical solutions such as foundation engineering and ground improvement often use carbon intensive materials and thus have potential for CO_2 reduction. For instance, according to the analysis conducted by the City of Helsinki (2022a), the top five sources of embodied carbon emissions in Helsinki's infrastructure projects account for over 80% of total embodied emissions of infraconstruction projects. The primary sources of emissions are earth and aggregate materials, and transportation (36%), column stabilization (23%), natural stones (9%), concrete structures (6%), and asphalt pavements (8%).

A similar study was conducted for Espoo, another major city in the Helsinki metropolitan area (2023). In Espoo's infrastructure construction, embodied carbon arises mainly from ground improvement (including structures related to insulation, barriers, and drainage) (28%), earth cuttings and excavations (22%), pavement structures (20%), and foundations (8%). Column stabilization stands out as the largest contributor, constituting 25% of emissions, followed by steel-made sheet pile walls at 16%. The significant emissions from sheet pile walls are attributed to their widespread use and the intensive emissions from steel.

2.3 Low-carbon geotechnical engineering

Carbon management in geotechnical engineering emphasizes decarbonization and circularity principles, prioritizing reduced construction and material demand, material recycling, and the adoption of low-carbon techniques and materials. Design optimization, applicable across all design stages, serves as an efficient method to decrease embodied carbon in all lifecycle phases (FIDIC, 2023). Optimization occurs at both strategic and site-specific levels, encompassing land use planning, project scheduling, and chosen ground improvement methods. Comprehensive ground investigations further support design optimization, facilitating the development of technically sound yet resource-efficient solutions.

Emissions related to ground improvement can be reduced already during the land use planning stage by focusing on identifying optimal locations for structures according to soil conditions. Meanwhile, when construction is performed on low bearing soil conditions, geotechnical-related emissions are determined by available time. Low-carbon ground improvement methods, such as preloading embankment, require sufficient time frame.

If time-consuming ground improvement methods cannot be used the most efficient approach to reduce GHGs is to minimize material demand inside the chosen method and to seek alternative, low-carbon or recycled materials. Dosage of binder i.e., for deep mixing can be studied and reduced using multiple laboratory tests for site-specific solutions or by combining the method with lightweight aggregate structure or preloading with embankment. The carbon footprint of concrete can be reduced by up to nearly 70% by using recycled materials such as fly ash or blast-furnace slag. Similarly, steel industry aims to develop a fossil-free steelmaking process by 2030 (SSAB, 2023), which would potentially reduce significantly GHG emission arising from foundations.

The design optimization methods are being utilized in the development of a new residential area, Malminkenttä, Helsinki. Scheduled for construction between 2020 and 2050, the objective is to reduce emissions from ground improvement preconstruction activities by 50 percent by the year 2030 (City of Helsinki, 2022b).

Earthworks material coordination principles are applied in many construction projects in Finland. Coordinating soil and rock materials from earthworks inside the project and with neighbouring projects reduces virgin material extraction and related emissions, and transport emissions. Similarly, in demolition projects, concrete from demolished buildings can be used in the structural layers of street and thus reduce emissions from manufacture of stone aggregates.

3 CARBON AND COST OPTIMIZED GEOTECHNICAL SOLUTIONS

3.1 Carbon emissions and costs for different ground improvement methods

Figure 1 compares different ground improvement methods with respect to their carbon emissions and costs. Furthermore, additional preloading time before use-phase is considered, resulting in reductions in both emissions and costs. The calculation is done for a 100 × 100 m area with a 1.5 m dry crust clay layer and a 10 m soft clay layer beneath the ground surface. The fictitious site is in Helsinki. Embankment height after the construction is designed to be 2.5 m, covering the whole area. (Perttu, 2023) Emission data was gathered mainly from the Finnish national emission database (co2data.fi) and cost data from Ihku software (Ihku, 2023).

In the case example column stabilization was studied with 3 different binders: Nordkalk Terra KC50, Finnsementti CEMIII/A, and Nordkalk Terra GTC. Column stabilization was designed for both 100 mm and 300 mm use-phase settlement criteria, and preloading intervals of 0 and 9 months were considered. Lightweight aggregate (LWA, light expanded clay aggregate) was studied with preloading intervals of 0, 1, 2, and 3 years. For preloading embankments (with or without surcharge), the required preloading time was approximately 5 years. Preloading combined with vertical drains require 2-3 years of preloading. To ensure sufficient stability, staged construction is needed. In addition, a reinforced concrete slab with concrete piles was studied to compare with the ground improvement methods. The slab was designed with 2 different pile lengths, extending 3 and 10 m below the clay layer.

The study presented here focuses on both monetary and GHG parameters. A comprehensive comparison of various methods entails considering factors such as equipment availability, other environmental impacts, and long-term stability.

3.2 Emission and cost reduction potential

With column stabilization, the choice of binder has the largest impact to overall emissions. In terms of optimization, preloading time and the chosen settlement criteria affect both emissions and costs. The savings vary by clay layer depth and embankment height. With lightweight aggregates, preloading can have a significant impact on both emissions and costs. Preloading the lightweight embankment for 3 years can halve the costs compared to no preloading, as the amount of required aggregate is greatly reduced. Whether the excavated soil can be used on the site, or must be transported for further treatment, can have a significant impact on costs, as seen in Fig. 1 (Cost difference between orange and grey lines for example). Conventional preloading embankment (with or without surcharge) has the lowest costs and emissions but require a long preloading time. Vertical drains will speed up the process but require more materials and work hours.

In addition to the results in Figure 1, clay layer depths of 6.5, 16.5 and 20 meters and embankment heights of 1.5 and 4 meters were studied in the thesis (Perttu, 2023). The most emission- and cost-effective ground improvement method for a given case is determined by clay layer depth, embankment height,

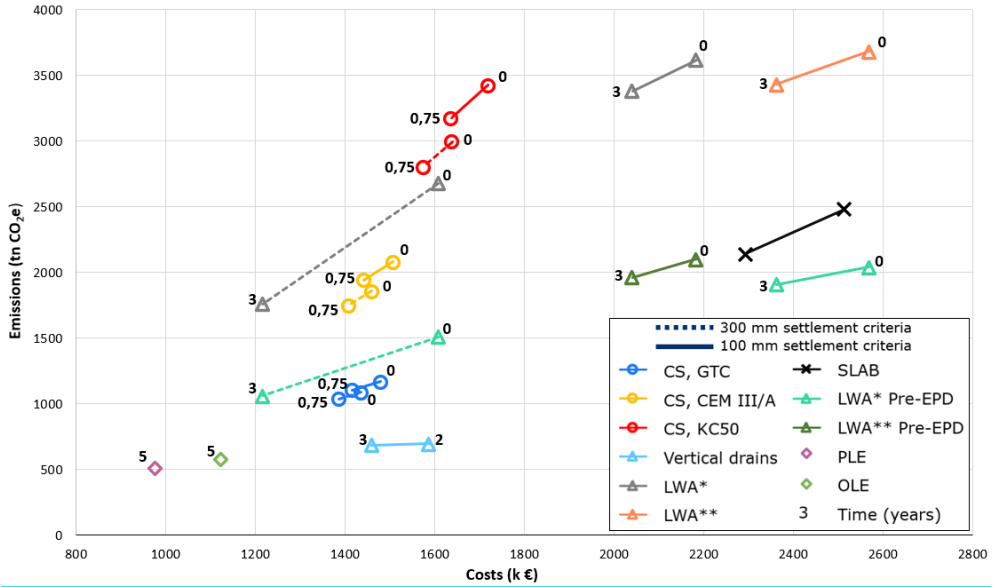

CS: Column stabilization, three different binders were studied
LWA: Lightweight aggregate embankment (=excavated soil used on site, **=excavated soil transported for disposal (60 km). Pre-EPD (Environmental Product Declarations) refers to updated but unconfirmed emission data.*
SLAB: Reinforced concrete slab & piles, chart line illustrates emission/cost increase with pile length extending below clay layer 3-10 meters
PLE: Preloading embankment, 300 mm settlement criteria
OLE: Overloading embankment, 300 mm settlement criteria
Time: Preloading time (years) between construction and use-phase. Studied preloading times vary by method.

Figure 1. Emissions (tn CO2e) vs costs (k €). Clay layer depth 11.5 m. Embankment height 2.5 m.

settlement criteria, and available preloading time as presented in Table 1. In addition to descriptive sensitivities to parameters, increase in prices and emissions by clay layer depth are depicted as functions, which are compiled from the same dataset as Fig. 1 (Perttu, 2023).

Low-carbon and cost-efficient geotechnical solutions are bound to material usage and settlement criteria. Note that the study was conducted for a site in Southern Finland, so emissions and costs can vary in other locations, as well as in the course of time as material availabilities change and technologies advance. Having more preloading time available increases the options to choose from and allows the usage of less emission- and cost-intensive solutions within a chosen method. In general, given there is time available, methods combined with pre-loading are recommended. Choosing low-carbon materials has a large impact on emissions, and recycled materials such as recycled lightweight aggregate are often also less expensive.

Table 1. Sensitivity to parameters, varying methods. Effects to prices and emissions were calculated with 100 mm settlement criteria. 1.5, 2.5 and 4 m refer to embankment height.

Method	Clay layer depth	Load (embankment height)	Settlement criteria	Effect to price (increasing clay layer thickness) €/m²	Effect to CO_2-emissions (increasing clay layer thickness) kg CO_2/m²
Pile Slab	* (pile length)	* (pile density and diameter)	-	1.5 m: 2x+175 2.5 m: 3.2x+215 4 m: 7.2x+300	1.5 m: 4.1x+165 2.5 m: 5x+190 4 m: 10x+270
Lightweight aggregate	* (LWA quantity)	** (LWA quantity)	** (LWA quantity)	1.5 m: 1.8x+120 2.5 m: 1.9x+220 4 m: 2x+380	1.5 m: 2.7x+205 2.5 m: 2.9x+405 4 m: 3.1x+730
Column Stabilization (GTC)	** (column length)	** (column spacing)	* (column spacing)	1.5 m: 5.4x+25 2.5 m: 10x+35 4 m: 11.7x+105	1.5 m: 4.2x+15 2.5 m: 10x+10 4 m: 10x+200
Column Stabilization (CEM III)	** (column length)	** (column spacing)	* (column spacing)	1.5 m: 5.5x+25 2.5 m: 10.3x+35 4 m: 12.2x+105	1.5 m: 9x+10 2.5 m: 21.6x-20 4 m: 29.6x+65
Column Stabilization (KC50)	** (column length)	** (column spacing)	* (column spacing)	1.5 m: 6.6x+25 2.5 m: 13.0x+25 4 m: 15.9x+110	1.5 m: 16x+0 2.5 m: 37.8x-60 4 m: 52.8x+70
Preloading and overloading embankments	** (time)	** (time)	** (time)	-	-
Spacing of vertical drains	-	* (time, counter embankment size)	-	1.5 m: 1.6x+80 2.5 m: 2.8x+120 4 m: 3.7x+125	1.5 m: 0.4x+40 2.5 m: 0.8x+60 4 m: 1.1x+110

Notes: Variable x in the functions refer to clay layer thickness (e.g. pile slab foundation with 1.5 m embankment and 10 m clay layer costs roughly 2*10+175=195 €/m²). - = No effect, * = Affected a little, ** = Largely affected.

4 CONCLUSIONS

Geotechnical engineering can be a crucial factor in the carbon budget of an infrastructure project, particularly when dealing with soft or challenging soil conditions. Structures like stabilized columns, and steel sheet pile walls often rely on emission-intensive materials such as cement and steel. Additionally, earthworks require a significant amount of machinery and transportation, contributing substantially to emissions in large projects.

Efficient methods for reducing greenhouse gas (GHG) emissions in geotechnical engineering during the design phase include design optimization and carbon management. Most emissions in this field stem from the use of emission-intensive materials in deep mixing, sheet piles, and other heavy foundation methods. Techniques like pre-loading and surcharge embankments, combined with the use of low-emission materials such as binders based on industrial side stream products, are effective ways to decrease the overall emissions of infrastructure projects, in soft soil conditions.

It is crucial to communicate low-emission methods within each technical field associated with the project, preferably during the early design phases. Identifying key decision-making steps and allocating sufficient resources and time for implementing low-carbon and resource-efficient solutions is essential. Integrating carbon emissions as a design consideration for geotechnical solutions can lead to reduced project costs and emissions.

Combining carbon management with design optimization is not a standard procedure, and national and international guidelines are required to incorporate GHG emissions into the decision-making process. Understanding the hotspots of GHG emissions in infrastructure is fundamental, and this knowledge should be integrated into standard practice. More research is needed to understand the mechanisms and connections from land use planning to construction and further asset management for profound low-carbon and resilient infrastructure outcomes.

ACKNOWLEDGEMENTS

The authors are grateful for the financial support provided by Ramboll Finland Oy, and for the research topic and feedback provided by UUMA4 research programme.

REFERENCES

BSI (The British Standards Institution). (2023). PAS 2080:2023 Carbon management in buildings and infrastructure, BSI Standards Limited 2023.

City of Espoo. (2023) Espoon infrarakentamisen ja kunnossapidon vuotuiset CO_2e päästöt [The annual CO_2e emissions of Espoo's infrastructure construction and maintenance.] Available at: Espoon infrarakentamisen ja kunnossapidon vuotuiset CO2e päästöt loppuraportti 2023-05-19.pdf.

City of Helsinki. (2022a). Embodied carbon and costs analysis. Unpublished report.

City of Helsinki. (2022b). Hiilineutraali Helsinki - päästövähennysohjelma [Carbon neutral Helsinki - emission reduction program], City of Helsinki, Finland, publication 2022:32. Co2data.fi (2023). Finnish national emission database. Available at: https://co2data.fi/, accessed 25/May/2023.

DS/EN 17472: 2022 Sustainability of construction works – Sustainability assessment of civil engineering works – Calculation methods.

DS/EN ISO 14001: 2015 Environmental management systems – Requirements with guidance for use.

FIDIC. (2023) Decarbonisation of the infrastructure sector. Available at: https://issuu.com/fidic/docs/fidic_glf_2023_decarbonisation_of_the_infrastructu?fr=xKAE9_zU1NQ.

Ihku. (2023). Available at: https://www.ihku-laskentapalvelu.fi/, accessed 25/May/2023.

IPCC. (2023). Summary for Policymakers. In: Climate Change 2023: Synthesis Report. Contribution of Working Groups I, II and III to the Sixth Assessment Report of the Intergovernmental Panel on Climate Change [Core Writing Team, H. Lee and J. Romero (eds.)]. IPCC, Geneva, Switzerland, pp. 1-34, doi: 10.59327/IPCC/AR6-9789291691647.001.

IRP (International Resource Panel). (2022). 2022-2025 Work Programme of the International Resource Panel. Available at: https://www.resourcepanel.org/sites/default/files/documents/document/media/2022-2025_irp_work_programme.pdf.

Perttu, O. (2023). *Pohjanvahvistuksen optimointi osana vähähiilistä esirakentamista* [Ground improvement optimization as a part of low-carbon preconstruction], master thesis, Aalto University School of Engineering.

SSAB. (2023). The road to sustainable steel, [online] Available at: https://www.ssab.com/en/fossil-free-steel/ssab-zero/the-road-to-sustainable-steel, accessed 17/October/2023.

Thacker, S., Adshead, D., Fantini, C., Palmer, R., Ghosal, R., Adeoti, T., Morgan., G., Stratton-Short S. (2021) Infrastructure for climate action. UNOPS, Copenhagen, Denmark.

Proceedings of the XVIII ECSMGE 2024
GEOTECHNICAL ENGINEERING CHALLENGES
TO MEET CURRENT AND EMERGING NEEDS OF SOCIETY
© 2024 the Authors
ISBN 978-1-032-54816-6
DOI 10.1201/9781003431749-636
Open Access: www.taylorfrancis.com, CC BY-NC-ND 4.0 license

ECSMGE 24
XVIII EUROPEAN CONFERENCE ON SOIL MECHANICS AND GEOTECHNICAL ENGINEERING

Sustainability assessment of a geotechnical site investigation in Holocene deposits: A case study from northern Germany

Évaluation de la durabilité d'une étude de site géotechnique dans les dépôts Holocènes: Une étude de cas du nord de l'Allemagne

W.T. Pfeiffer*, U. Matthiesen, M. Pohl
Federal Waterways Engineering and Research Institute, Hamburg, Germany
**wolf.pfeiffer@baw.de*

ABSTRACT: The current and projected state of earth's climate, resources and ecosystems require a substantial push towards sustainability, well above what is currently employed. The construction sector is a major contributor to the global emission of greenhouse gases and a consumer of scarce natural resources. In this work an environmental impact assessment of a geotechnical site investigation of the planned Lüneburg Lock in Northern Germany is presented. A comprehensive ground investigation was carried out comprising of 78 geotechnical exploration drillings and 81 CPTs. The total primary energy expenditure of the surveys was calculated to be 1.69×10^6 MJ. Emissions contributing to the global warming potential (GWP) are estimated at 9.77×10^4 kg CO_2-eq.

RÉSUMÉ: L'état actuel et projeté du climat, des ressources et des écosystèmes terrestres nécessitent un effort substantiel en faveur de la durabilité, bien au-delà de ce qui est actuellement mis en œuvre. Le secteur de la construction est un contributeur majeur aux émissions mondiales de gaz à effet de serre et un consommateur de ressources naturelles rares. Dans ce travail, une évaluation de l'impact environnemental d'une investigation géotechnique du site du futur écluse de Lüneburg, dans le nord de l'Allemagne, est présentée. Une enquête approfondie du sol a été réalisée, comprenant 78 forages géotechniques et 81 essais de pénétration statique. La dépense totale d'énergie primaire des enquêtes a été calculée à $1{,}69 \times 10^6$ MJ. Les émissions contribuant au potentiel de réchauffement planétaire (PRP) sont estimées à $9{,}77 \times 10^4$ kg CO_2-eq.

Keywords: Sustainability; geotechnical site investigation; life cycle assessment.

1 INTRODUCTION

International (UN 2015) and national (e. g. Bundesregierung 2021) policies are aimed at reducing our footprint on earth in terms of resource use and emissions. Environmental indicators are defined to quantify the emissions and resources used, such as the so-called global warming potential (GWP) measured in kg CO_2-eq. (UN 2023).

Based on these indicators, life cycle assessments (LCAs) can be carried out, to determine environmental impacts of products or processes, such as civil engineering projects. However, very little research has been published so far on the sustainability impact of geotechnical site investigations. Purdy et al. (2022) are the notable exception, providing an assessment of different sampling techniques and their individual impact for (generic) case studies in Canada.

In this paper an environmental impact assessment based on LCA data is carried out for the geotechnical site investigations of a planned ship lock in Northern Germany (Henze & Schulz 2019). The aim of this study is to identify and characterise missing processes and data required in order to carry out a comprehensive LCA as well as developing an understanding of the key factors contributing to emissions, resource use and energy expenditure.

2 METHOD, DATA & ASSUMPTIONS

In a first step all available data, such as field logs, were evaluated. Additional information had to be collected through personal communication with field staff and analysis of photographs to fill knowledge gaps arising from inaccurate or missing documentation.

2.1 Local geology & site investigations

The local geology is composed of holocene deposits, consisting mostly of dense to very dense sands and an interbedded cohesive silt layer of varying thickness.

Site investigations using drill-type (geotechnical exploration drillings with continuous sampling) and direct-push (Cone Penetration Tests, CPTs) techniques where launched in 2010 and 2019. The geotechnical

exploration drillings were carried out using rotary drilling techniques with continuous sampling and hydraulic loading using fresh water when drilling below the water table.

35 and 43 boreholes were drilled in 2010 and 2019 respectively. Average borehole depth was 46.7 m with the deepest borehole reaching 80.5 m. Drilling was conducted using 5 and 8 drilling rigs in 2010 and 2019 respectively. Working days across all drilling rigs were 251 in 2010 and 459 in 2019. Drilling diameter depended on the target drilling depth (219 - 512 mm). 36 of the boreholes were completed as groundwater observation wells.

CPT data was at 35 and 46 locations in 2010 and 2019, respectively. The depth ranged from 11.9 m to 68.3 m (av. 35.8 m). If advancement was not possible due to increased friction, rotary drilling with water as drilling fluid was used to clear out the already probed section. A single CPT rig was used in both campaigns.

Boreholes were backfilled using either sand, gravel, Bentonite, or a ready-to use clay-cement mixture (Brutoplast©) depending on the stratigraphy and the geohydraulic conditions. Most boreholes were at least partially grouted, using the aforementioned clay-cement mixture.

2.2 Environmental impact analysis

The environmental indicators set out in DIN EN 15804:2022-03 were used in this study, of which only a selection is shown and discussed. Process and product data were taken from the ÖKOBAUDAT 2023-I (BMWSB 2023), GaBi Professional 2023 (Sphera 2023) and ecoinvent 3.91 database (Wernet 2016, ecoinvent 2023). Unfortunately, geotechnical process data is mostly missing from databases, requiring the approximation of drilling and CPT operations. All processes used are given in Table 1.

Table 1. Process and EPD data used in this study.

Process name	Datebase
Diesel at filling station	GaBi Pro.
Diesel burned in building machine	ecoinvent
Truck	ÖKOBAUDAT
Car (Diesel) EURO 4	ÖKOBAUDAT
Pumping of concrete	ÖKOBAUDAT
Drinking water	ÖKOBAUDAT
Sand 0/2 (dried)	ÖKOBAUDAT
Bentonite granular	GaBi Pro.
Average cement D	ÖKOBAUDAT
Polypropylene pipe	ÖKOBAUDAT

The methods used in 2010 and 2019 were grouped into the categories d*rilling*, *CPT with additional drilling* and *CPT without additional drilling.* For evaluation, the geotechnical site investigations are divided into three phases of operation:

- Mobilization – the movement of equipment and people to, from and on the job site
- Advancement – the actual drilling / direct push probing incl. sampling
- Sealing & Completion – backfilling/grouting of boreholes and completion of wells

2.2.1 Mobilization

The mobilization phase includes the one-time deployment to and return from the site of each drilling and CPT rig. The remobilization between borehole/CPT locations on site was also considered, excluding the first location. Furthermore, it was assumed that each rig required a support staff of two, traveling to and from the site on each work day by car. Traveling distance of the support staff was assumed to be the distance from the company's HQ to the site.

The mobilization of the drilling and CPT rigs was calculated as a standard diesel truck, while transport/travel of the support staff was calculated assuming a EURO 4 diesel car (Table 1).

The distances between the HQs and the job site were 47.5 and 50 km in 2010 for the drilling rigs and the CPT rig, respectively. In 2019 mobilization distances were significantly greater at 169 km (drilling rigs) and 260 km (CPT rig). Mobilization distances of the support staff of more than 100 km were deemed unfeasible for daily trips. Thus for 2019 the distance to the nearest city (9 km) was taken instead, assuming overnight stays in hotels. Remobilization on the jobsite was estimated to be 500 m indifferent of the actual location. The mass of the drilling/CPT rigs were estimated at 20 tons.

2.2.2 Advancement

The amount of diesel required for and water consumed during the advancement was used in order to quantify the impact on the LCA indicators. The impact of the production of diesel fuel and the subsequent use on the job site were quantified by mass and energy, respectively. First the energy required for advancement was estimated for each drilling/probing location as:

$$\mathrm{E}_{diesel} = \frac{\mathrm{z}_{tot} \cdot P_{rig} \cdot \eta_{load} \cdot \eta_{engine}}{\bar{v}_{adv}} \qquad (1)$$

with E_{diesel} (kWh) the required energy, z_{tot} (m) the drilling/probing depth, $\bar{v}_{adv}$ (m/h) the average advancement including auxiliary work, P_{rig} (kW) the power rating of the rig's engine, η_{load} (-) the engine load as the percentage the rig's engine is running at its

nominal power rating and η_{engine} (-) the efficiency of the engine. Subsequently the mass of diesel was calculated based on the lower calorific value (LCV) of diesel, which is 11.9 kWh/kg (UN 2017).

The advancement of a CPT must be 2 cm/s (±0.5) according to DIN EN ISO 22476-1:2023-04. Factoring in auxiliary work required, e.g. adding/removing tubing, CPT advancement was set to 36 m/h. The average drilling advancement was assumed to be 2 m/h for a geotechnical exploration drilling with continuous sampling. Engine loads were set to 0.6 for rotary drilling with sampling and 0.9 for CPT advancements (including necessary drilling operations). In the absence of detailed information, a nominal power rating of 200 kW and an engine efficiency of 0.35 was assumed for all rigs.

Water was used for drilling, either to maintain a specified head (drilling with sampling) or to remove the drilling material from the borehole (CPT with drilling). For the former water use was assumed to be equal to the borehole volume, i.e. a function of the drilling depth and diameter. For the latter, water consumption was assumed to be four times the borehole volume.

2.2.3 Sealing & completion

The impact of the sealing and completion is calculated by the mass of materials used. Required interval length, dimensions of each borehole and materials used are calculated from field data (logs). The clay-cement mixture used contains 70% Kaolinite clay and 30% cement. Approx. 613 kg of dry mixture and 766 kg of water is required per m³ of void space to be grouted. The required LCA data is mostly available, using Bentonite instead of Kaolinite (Table 1). Given the very similar properties of sand and gravel in terms of their LCA data, only sand was used in the calculations. Dry bulk densities of Bentonite and sand are approximated to be 1100 and 1600 kg/m^3, respectively. The piping used for the completion of the observation wells was assumed to be of polypropylene with a wall thickness 0.01 m and a density of 930 kg/m^3. Pumping of the clay-cement mixture was estimated by the process of pumping concrete, which only quantifies the impact of the pump, not the pumped fluid mixture.

3 CASE STUDY RESULTS

Primary energy consumption of the examined geotechnical site investigations is calculated to be 1.69x10^6 MJ (Figure 1, Table 2). Most of the primary energy is required for advancement, accounting for 53.2% (9.00x10^5 MJ), followed by sealing of boreholes at 33.2% (8.52x10^4 MJ) and mobilization at 13.6% (2.3x10^5 MJ). Normalized to probing depth, energy expenditure is 379.58, 153.55 and 34.97 MJ per m for drilling, CPTs with add. drilling and simple CPTs respectively.

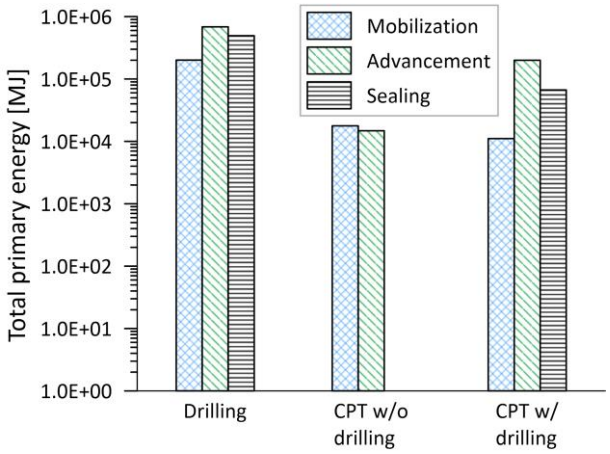

Figure 1. Total primary energy consumption of the geotechnical site investigations in 2010 and 2019.

Table 2. Results for the two surveys and selected indicators.

Indicator	Value
Renewable primary energy	9.93x10^4 MJ
Non-renewable p. energy	1.59x10^6 MJ
Global warming pot. (GWP)	9.77x10^4 kg CO_2-eq.
Acidification potential	5.56x10^2 mol H^+-eq.
Eutrophication (terrestrial)	2.53x10^3 mol N-eq.
Eutrophication (marine)	2.27x10^2 kg N-eq.
Eutrophication (freshwater)	1.26x10^0 kg P-eq.
Use of fresh water	1.19x10^3 m^3

In terms of environmental emissions, sealing is generally the largest contributor followed closely by advancement (Figure 2). For example, GWP related emissions are 4.36x10^4 kg CO_2-eq. for sealing and 3.82x10^4 kg CO_2-eq. for advancement, which is 83.7% of the total. Cement usage alone causes 1.96x10^4 kg CO_2-eq. to be emitted, which is 31% of the total GWP related emissions. Mobilization of the equipment and staff contributes 1.59x10^4 kg CO_2-eq. to the total GWP related emissions (16.3%). The same holds true to the other environmental impact indicators. However, simple CPTs require no sealing and provide efficient probing, thus mobilization becomes more important, contributing 65.9% of the GWP related emissions from this technology.

Of the resource indicators studied, only the use of fresh water is shown here, the biggest factor being the use of the clay-cement mixture (Figure 2, Table 2).

Normalized to the meters probed, drilling and CPTs with additional drilling cause emissions of 21.94 and 8.86 kg CO_2-eq. per m, respectively. The CO_2-footprint of a simple CPT is 2.01 kg CO_2-eq. per m.

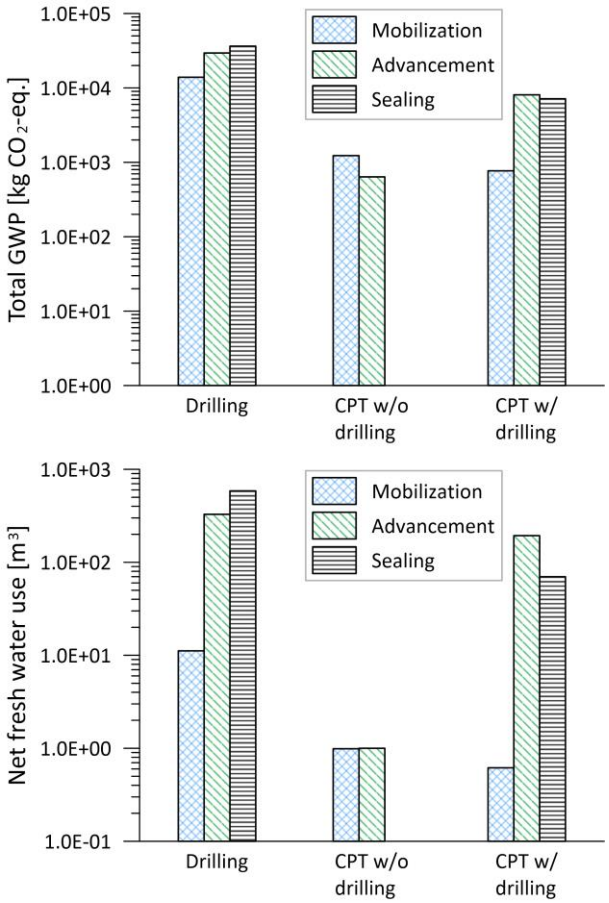

Figure 2. Total GWP and net fresh water consumption.

4 DISCUSSION & CONCLUSIONS

The results indicate that the sealing of boreholes and the actual advancement of the drilling/probing equipment are the most significant factors influencing energy expenditure, environmental emissions, and resource use. However, contributions from mobilization are not insignificant and become dominant for simple CPTs, where no sealing is required and advancement is generally quick. Given the available data, quantification of the sealing processes most likely only carries a small error. Unfortunately, calculating the impact of mobilization and advancement requires significantly more assumptions. For example, simply increasing the arbitrarily defined limit on the daily mobilization distance from 100 to 169 km to allow daily returns of the drilling crew during the 2019 campaign would make mobilization the second largest contributor to GWP related emissions with 4.07×10^4 kg CO_2-eq. The lack of knowledge on additional mobilization, such as deliveries of materials or support machinery, is a pitfall in this study. Thus, the impact of mobilization may only be considered as a lower bound estimate.

Interestingly, replacing the clay-cement mix with pure clay results in slightly increased GWP related emissions (+4.8%). This is a result of the higher bulk density of pure clay compared to the clay-cement mixture and the comparatively small difference in GWP related emissions between clay and cement.

Normalizing the results to develop an a-priori assessment tool was investigated. However, the results were not promising, showing large deviations in estimated and calculated GWP emissions. Regardless, development of such a tool might be useful for future applications. A larger and more controlled database would be favourable for such a development, which requires a more detailed logging of processes and operations on the job site, e.g. the exact amount of diesel used and actual mobilization distances covered.

REFERENCES

BMWSB (2023). ÖKOBAUDAT - Release 2023-I. Bundesministerium für Wohnen, Stadtentwicklung und Bauwesen (Federal Ministry of Housing, Urban Development and Construction), Berlin, Germany.

Bundesregierung (2021). German Sustainable Development Strategy – Update 2021. German Federal Government ecoinvent (2023). ecoinvent 3.9.1, Zurich, CH.

Henze, L., Schulz, G. (2019). Die neue Schleuse Lüneburg – Stand der Planung Teil 1. The new ship lock Lüneburg – State of planning Part 1 (in German). In: *Der Ingenieur der Wasser- und Schifffahrtsverwaltung 04/2019*. Bremen: IWSV pp. 11-15. https://doi.org/20.500.11970/108263.

Purdy, C. M., Raymond, A. J., DeJong, J. T., Kendall, A., Krage, C., Sharp, J. (2022). Life-cycle sustainability assessment of geotechnical site investigation. *Can. Geotech. J.* (59): 863-877. dx.doi.org/10.1139/cgj-2020-0523.

Sphera (2023). Professional Database Edition 2023. Managed LCA Content. Sphera, Chicago, USA.

UN (2015). Transforming our World: The 2030 Agenda for sustainable development. Resolution 70/1 adopted by the United Nations General Assembly 25.09.2015.

UN (2017). 2015 Energy Statistics Yearbook. United Nations, New York, USA.

UN (2023). The Sustainable Development Goals Report 2023. United Nations. 80 pp. ISBN: 978-92-1-101460-0.

Wernet, G., Bauer, C., Steubing, B., Reinhard, J., Moreno-Ruiz, E., Weidema, B. (2016). The ecoinvent database version 3 (part I): overview and methology. *Int J Life Cycle Assess* (21): 1218-1230. https://doi.org/10.1007/s11367-016-1087-8.

Proceedings of the XVIII ECSMGE 2024
GEOTECHNICAL ENGINEERING CHALLENGES
TO MEET CURRENT AND EMERGING NEEDS OF SOCIETY
© 2024 the Authors
ISBN 978-1-032-54816-6
DOI 10.1201/9781003431749-637
Open Access: www.taylorfrancis.com, CC BY-NC-ND 4.0 license

ECSMGE 24
XVIII EUROPEAN CONFERENCE ON SOIL MECHANICS AND GEOTECHNICAL ENGINEERING

A coupled thermo-hydro-mechanical hypoplastic model for fine-grained soils accounting small strain effects

Un modèle couplé thermo-hydro-mécanique hypoplastique pour les sols à grains fins prenant en compte les effets des petites déformations

M. Pico*, D. Mašín
Charles University, Prague, Czech Republic
**picoduam@natur.cuni.cz*

ABSTRACT: Several geotechnical applications such as nuclear waste disposal storage, buried high-voltage cables, pavements and geothermal energy are subjected to non-isothermal loading stages. The prediction of their behaviour requires constitutive models able to reproduce its response under a wide range of loading and thermal conditions. This paper is devoted to the development of a coupled thermo-hydro-mechanical hypoplastic model for fine-grained soils with the consideration of small-strain effects. Its formulation is based on the coupled-hydro-mechanical hypoplastic model by Wong and Mašín (2014) extended to account for temperature effects. The resulting constitutive model predicts large strain asymptotic behaviour and small-strain path-dependent effects on unsaturated conditions at different temperatures. Selected simulations were carried out to validate the proposed model based on the experimental results of constant water cyclic triaxial tests under suction- and temperature-controlled conditions, performed by Ng and Zhou (2014) on a completely decomposed tuff subjected to constant water cyclic triaxial loading at suction and temperature-controlled conditions. The comparison between experimental and simulation results suggests that the proposed constitutive model accurately reproduces the influence of temperature on the accumulation rates of strain under cyclic loading at partially saturated conditions.

RÉSUMÉ: Plusieurs applications géotechniques telles que le stockage des déchets nucléaires, les câbles haute tension enterrés, les chaussées et l'énergie géothermique sont soumises à des phases de chargement non isothermes. La prédiction de leur comportement nécessite des modèles constitutifs capables de reproduire leur réponse dans une large gamme de conditions de chargement et de conditions thermiques. Cet article est consacré au développement d'un modèle hypoplastique thermo-hydro-mécanique couplé pour les sols à grains fins avec prise en compte des effets de petites déformations. Sa formulation est basée sur le modèle hypoplastique couplé hydro-mécanique de Wong et Mašín (2014) étendu pour prendre en compte les effets de la température. Le modèle constitutif qui en résulte prédit le comportement asymptotique des grandes déformations et les effets dépendants du chemin des petites déformations dans des conditions non saturées à différentes températures. Des simulations sélectionnées ont été effectuées pour valider le modèle proposé sur la base des résultats expérimentaux d'essais triaxiaux cycliques à eau constante dans des conditions d'aspiration et de température contrôlées, réalisés par Ng et Zhou (2014) sur un tuf complètement décomposé soumis à une charge triaxiale cyclique à eau constante dans des conditions d'aspiration et de température contrôlées. La comparaison entre les résultats expérimentaux et de simulation suggère que le modèle constitutif proposé reproduit avec précision l'influence de la température sur les taux d'accumulation de déformation sous chargement cyclique dans des conditions partiellement saturées.

Keywords: Temperature; unsaturated fine-grained soils; hypoplasticity; cyclic loading.

1 INTRODUCTION

Given the growing demand for new alternative energy sources, energy piles have been developed as an eco-friendly solution for heating and cooling buildings. This represent an example where the soil undergoes thermo-hydro-mechanical loading, which can vary in a cyclic manner.

Constitutive models that are robust and well-validated are essential for accurately reproducing this behaviour. Among these models, the one of the first within the hypoplastic family to account for the effects of temperature and suction in soil response was developed by Mašín and Khalili (2012). In addition, for reproducing small strain stiffness effects, hypoplastic models have been enhanced with various concepts, including the intergranular strain (Niemunis and Herle, 1997; Wegener and Herle, 2014), ISA (Poblete, Fuentes, and Triantafyllidis, 2016), and the so-called ISI (Duque et al., 2020). Consequently, Wong and Mašín (2014) combined the IS concept with the formulations from Mašín and Khalili (2008) and Mašín (2010) to capture small strain stiffness effects in partially saturated fine-grained soils.

In the present work, the constitutive model by Wong and Mašín (2014) was further enhanced by incorporating the ISI concept by Duque et al. (2020) along with a new modification for capturing the effects of temperature and suction on fine-grained soils subjected to cyclic mechanical loading. The numerical model was validated by comparing the results of element tests simulations with the experimental results from Ng and Zhou (2014), who conducted constant water content cyclic triaxial tests on a silt (ML) at three suctions $s = \{0, 30, 60\}$ kPa and temperatures $T = \{25, 40, 60\}$°C. The results suggest that the model is able to capture the coupled thermo-hydromechanical effects of partially saturated fine-grained soils when subjected to cyclic loading.

2 BRIEF DESCRIPTION OF THE MODEL FORMULATION

The constitutive model presented in this paper was developed hierarchically from previous hypoplastic models. It evolves from the coupled hydromechanical hypoplastic model for predicting small strain stiffness developed by Wong and Mašín (2014). The model can reproduce asymptotic and large strain behaviour for partially saturated soils, and it predicts the effects of temperature at large strains following the formulation proposed by Mašín and Khalili (2012). The model is defined using the effective stress approach by Khabbaz and Khalili (1998) and it integrates a modified temperature-dependent smoothed hysteretic water retention curve proposed by Svoboda et al. (2023) for predicting coupled thermo-hydro mechanical effects.

Furthermore, the ISI concept by Duque et al. (2020) was modified and incorporated into the model formulation to predict small strain behaviour under different temperatures and suction magnitudes.

The general rate form of the model is given by

$$\dot{\boldsymbol{\sigma}} = [f_s(\mathcal{L}: (\dot{\boldsymbol{\varepsilon}} - \dot{\boldsymbol{\varepsilon}}^{TE}) + f_d\, \mathbf{N}\, \|\dot{\boldsymbol{\varepsilon}} - \dot{\boldsymbol{\varepsilon}}^{TE}\|] + f_u\, (\mathbf{H}_\mathrm{s} + \mathbf{H}_\mathrm{T}) \quad (1)$$

where $\dot{\boldsymbol{\sigma}}$ represents the stress rate tensor, $\mathcal{L}$ and $\mathbf{N}$ correspond to the fourth and second order hypoplastic constitutive tensors, respectively, $\dot{\boldsymbol{\varepsilon}}$ is the Euler stretching tensor, $\mathbf{H}_\mathrm{s}$ and $\mathbf{H}_\mathrm{T}$ are second order tensors for predicting wetting and heating induced collapse, respectively, and $\dot{\boldsymbol{\varepsilon}}^{TE}$ is a second order tensor that accounts for fully reversible strains resulting from thermal expansion. The latter follows:

$$\dot{\boldsymbol{\varepsilon}}^{TE} = \frac{1}{3}\, \alpha_s \dot{T} \quad (2)$$

where α_s corresponds to the thermal expansion cofficient of the soil.

2.1 Small strain stiffness effects

The constitutive model predicts small strain stiffness effects using the ISI concept by Duque et al. (2020), which allows accurate predictions of accumulation rates under cyclic loading. For its incorporation, Equation (1) can be rewritten as:

$$\dot{\boldsymbol{\sigma}} = \mathcal{M}: (\boldsymbol{\varepsilon} - \dot{\boldsymbol{\varepsilon}}^{TE}) + f_u(\boldsymbol{H}_s + \boldsymbol{H}_T) \quad (3)$$

where $\mathcal{M}$ corresponds to the tangent stiffness tensor and its calculation is given according to

$$\mathcal{M} = [\rho^{\chi_g} m_T + (1 - \rho^{\chi_g}) m_R] f_s \mathcal{L} + \begin{cases} \rho^{\chi_g}(1 - m_T) f_s\, \mathcal{L}: \widehat{\boldsymbol{\delta}}\widehat{\boldsymbol{\delta}} + \rho^{\chi_g} f_s f_d \boldsymbol{N}\widehat{\boldsymbol{\delta}} & \text{for } \widehat{\boldsymbol{\delta}}: (\boldsymbol{\varepsilon} - \dot{\boldsymbol{\varepsilon}}^{TE}) > \mathbf{0} \\ \rho^{\chi_g}(m_R - m_T) f_s \boldsymbol{\mathcal{L}}: \widehat{\boldsymbol{\delta}}\widehat{\boldsymbol{\delta}} & \text{for } \widehat{\boldsymbol{\delta}}: (\dot{\boldsymbol{\varepsilon}} - \dot{\boldsymbol{\varepsilon}}^{TE}) < \mathbf{0} \end{cases} \quad (4)$$

The ISI concept includes a function for describing the value of χ_g as follows:

$$\chi_g = \chi_0 + \Omega\, (\chi_{max} + \chi_0) \quad (5)$$

where χ_0 and χ_{max} are model parameters under saturated and ambient temperature conditions. While, Ω corresponds to an internal state variable that evolves according to the number of cycles performed. ($\Omega \to 1$) when the intergranular strain is not mobilized and becomes 0 during monotonic paths according to

$$\dot{\Omega} = C_\Omega (1 - \rho^{\gamma_g} - \Omega) \|\dot{\boldsymbol{\varepsilon}}\| \quad (6)$$

where χ_g governs the stiffness degradation of the material and the strain accumulation upon cyclic loading. The effects of temperature and partial saturation on cyclic loading were incorporated into the model by reformulating the parameter χ_{max} from Equation (5) dependent on temperature, according to the following:

$$\chi_{\max}(S_r, T) = \chi_{\max} \mathrm{S_r}^{\vartheta_w} (\ln\left(\frac{T}{T_{ref}}\right) \vartheta_\mathrm{T} + 1) \quad (7)$$

where ϑ_T is a new model parameter that captures the effect of temperature in strain accumulation during cyclic loading. In addition, ϑ_w controls the influence of partial saturation upon cyclic loading.

3 MODEL CALIBRATION AND ELEMENT TESTS SIMULATIONS

The model was calibrated and validated using experimental data available in the literature on a completely decomposed tuff (Ng et al., 2009; Ng and Xu, 2012; Ng and Zhou, 2014; Zhou, 2014). This material is classified as a low plasticity silt (ML) according to the Unified Soil Classification System.

Table 1. Calibrated parameters.

Basic model	**Thermo-hydro mechan-ical**	**WRC model**	G_{tp0} **model**	**ISI model**
φ_c	n_s	s_{en0}	A_g	R
35°	0.035	-58 kPa	4220	0.0002
λ^*	l_s	e_0	n_g	β_r
0.054	0.0001	0.568	0.55	0.06
κ^*	n_T	λ_{p0}	m_g	r_m
0.005	-0.01	0.6	0.7	0.00001
N	l_T	a_e	k_g	χ_0
0.72	0.0	0.5	0.18	0.15
ν_{pp}	m	a	m_{rat}	χ_{max}
0.3	5.0	0.118 N/m	1.0	0.31
α_G	ϑ_w	b	T_g	γ_g
1.0	0.54	-0.000154 N/mK	-1.8	7.0
	α_s	T_{ref}		C
	0.000035	298.1 K		30
				ϑ_w
				0.54
				ϑ_T
				0.6

Isotropic compression tests at three suction magnitudes were employed for calibrating the parameters corresponding to the basic hypoplastic model (λ^*, κ, N) and the parameters controlling the unsaturated mechanical effects (n_s, l_s, m). The parameters governing the smoothed hysteretic water retention model $(s_{en0}, e_0, \lambda_{p0}, a_e)$ were calibrated using water retention curves measured with a modified triaxial volumetric pressure plate system at two confining pressures. Triaxial tests under constant p^{net} conditions with bender element measurements were employed to calibrate the parameters controlling the very small strain behaviour under unsaturated conditions $(\varphi', \nu_{pp}, \alpha_G, A_g, n_g, m_g, k_g, m_{rat})$.

To calibrate the parameters related to the ISI concept $(R, \beta_r, \chi_0, \chi_{max}, r_m, \gamma_g, C_\Omega, \vartheta_w, \vartheta_T)$, six cyclic constant water content cyclic triaxial tests were used at three suction magnitudes $s = \{0, 30, 60\}$ kPa and three temperatures $T = \{25, 40, 60\}$° C. Typical values were used for the rest of the parameters as there was no available information for its calibration. The numerical model was implemented in the in-house software TRIAX (Mašín, 2023) for element tests simulations. The software also enables the user a direct incorporation of the subroutine into open-source finite element software. The final values of the calibrated parameters are presented in Table 1.

3.1 Results of element tests simulations

In this section, the results of the element tests simulations are compared with laboratory tests results.

3.1.1 Cyclic constant water content triaxial simulations

The parameters of the constitutive model controlling the behaviour under small strains were calibrated based on the experimental results of cyclic constant water content triaxial tests conducted by Ng and Zhou (2014). The experiments were performed at three constant suctions $s = \{0, 30, 60\}$ kPa and three constant temperatures $T = \{25, 40, 60\}°C$, for a total of nine experiments.

In general, the constitutive model showed reasonable predictions of the soil response under cyclic mechanical loading at various suction and temperature magnitudes. Figure 1 presents a comparison of the experimental and numerical results in terms of deviatoric stress versus shear strain for saturated conditions $\{s = 0$ kPa$\}$ at three different temperatures $T = \{25, 40, 60\}° C$, respectively. The numerical predictions are in agreement with the experimental data, as the model is able to predict an increase in the total shear strain as temperature increases.

Figure 2 presents the results of the numerical predictions and experimental tests evaluated in terms of the accumulated shear strain versus the number of cycles for each suction magnitude $s = \{0, 30, 60\}$ kPa, respectively. The shading between the lines correspond to the accumulated shear strain between the maximum and minimum strain of the applied deviatoric stress at each loading cycle. As observed, the model can qualitatively reproduce the increase in accumulated shear strain with increasing temperature under constant suction conditions. Despite consistently predicting trends, the model underpredicts the accumulated strain at a suction magnitude of 30 kPa. Additionally, at a suction of suction of 60 kPa, the highest accumulated strain was observed at a temperature of 40°C, contradicting most observed trends during the experiment.

Another important observation is the ability of the constitutive model to capture the non-linear dependency of the accumulated strain rate on the number of cycles. This is achieved through the

incorporation of the ISI concept in the model formulation, which allows the non-linear evolution of the accumulated strain with the increase on the number of cycles. See Figure 2.

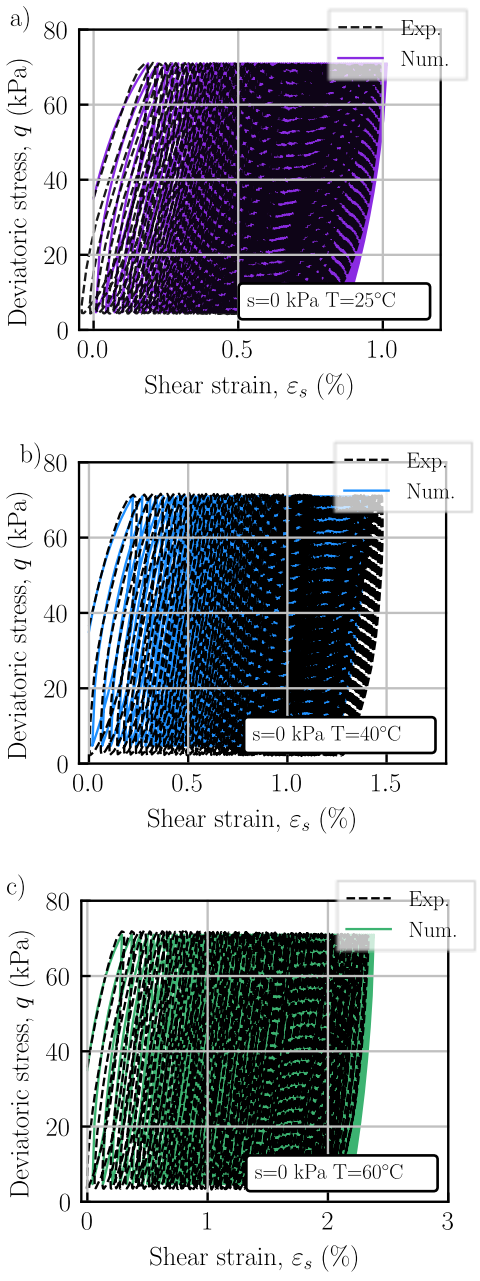

Figure 1. Results of cyclic constant water content triaxial tests at a) $T = 25°C$ b)$T = 40°$ C c) $T = 60°C$.

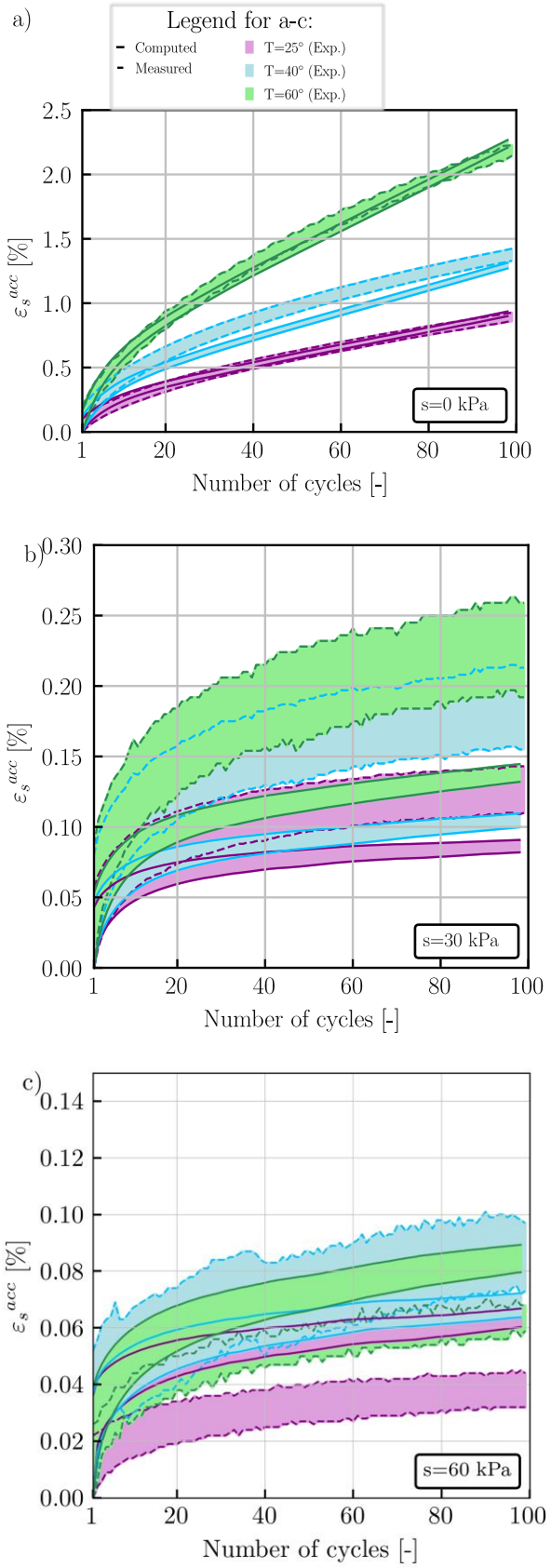

Figure 2. Comparison of accumulated shear strain vs. number of cycles at $T = \{25°, 40°, 60°\}$ at three suction magnitudes a) s= 0 kPa, b) s=30 kPa, c) s= 60 kPa.

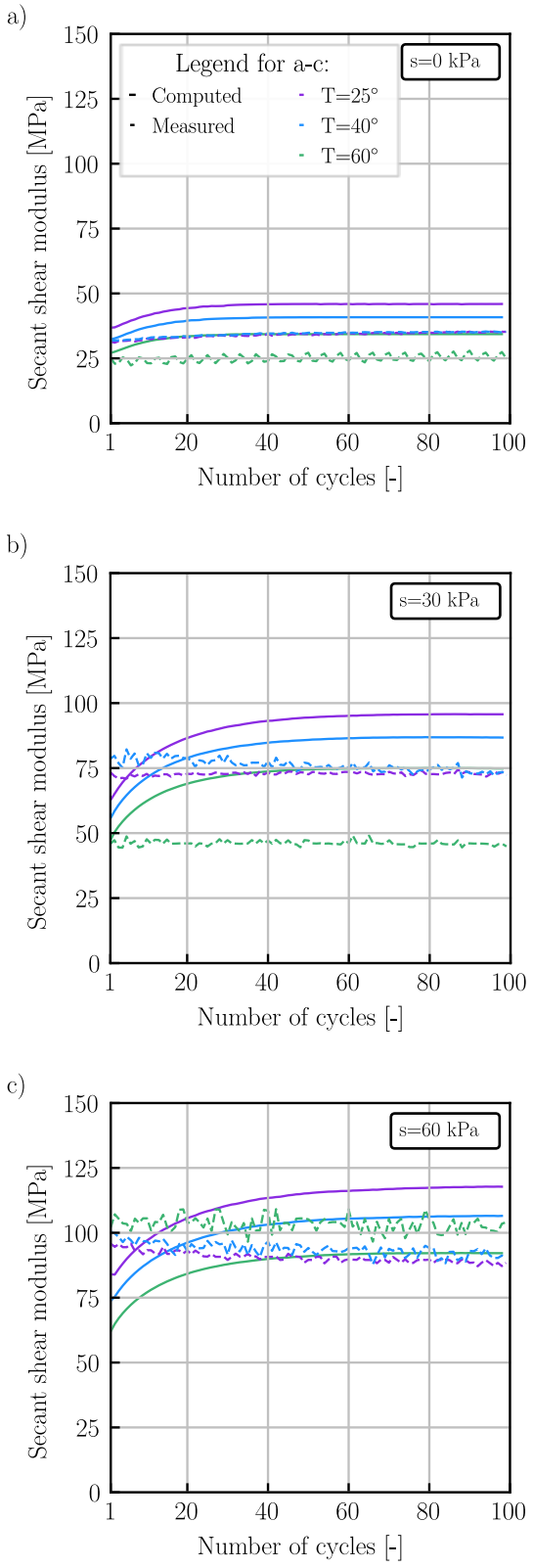

Figure 3. Comparison of secant shear modulus vs. number of cycles at $T = \{25°, 40°, 60°\}$ at three suction magnitudes a) s= 0 kPa, b) s=30 kPa, c) s=60 kPa. (C=computed, M=measured).

In addition, the values of strain at the maximum and minimum of the applied deviatoric stress in each cycle were employed to calculate the secant shear modulus. Figure 3 presents the results for each suction magnitude. The magnitude of the secant shear modulus is captured fairly well by the constitutive model. Moreover, a decreasing magnitude is predicted as temperature increases, which is in agreement with additional experimental observations (Bentil and Zhou, 2022; Zhou et al., 2015)However, the experimental data predicts and increase in the secant shear stiffness from 0 cycles to 20 cycles that is not observed in the experimental data.

4 CONCLUSION

In this work, a coupled thermo-hydro-mechanical hypoplastic constitutive model accounting for small strain stiffness effects for fine-grained soils is introduced. The constitutive model from Wong and Mašín (2014) was further enhanced to include temperatures effects on soil response. Furthermore, the ISI concept was introduced into the model with a new modification for accounting for the effects of temperature and partially saturated conditions at small strains.

The constitutive model was validated by comparing the results of element tests simulations with experimental data from constant water content cyclic triaxial test performed at three different suctions and three temperatures by Ng and Zhou (2014). The results suggest that the constitutive model reproduces fairly well the effects of temperature and suction on the soil response. The constituve model predicts higher total strains as the temperature increases, as the stiffness of the soil reduces at higher temperatures. Additionally, the consitutive model captures the non-linear dependency of the strain accumulation rate with the number of cycles. The results were also evaluated in terms of the secant shear modulus, and the consitutive model follows the decreasing trend in stiffness with the increment in temperature at each suction magnitude.

Despite the consistent predictions observed with the consitutive model, some limitations were also found. For instance, the consitutive model under-predicts the accumulated strain at a suction magnitude of 30 kPa. The ongoing efforts of the authors involve evaluating the constitutive model‘s capabitities for capturing the soil behaviour under cyclic temperature changes to further apply the constituive model for predicting the response of energy geo-structures.

ACKNOWLEDGEMENTS

The first and second authors appreciate the financial support given by the Czech Science Foundation Grant No. 21-35764J. The first author appreciates the financial support given by the Charles University Grant Agency (GAUK) with project number 260422. The first and second authors acknowledge the institutional support by the Center for Geosphere Dynamics (UNCE/SCI/006).

REFERENCES

Bentil, O. T., and Zhou, C. (2022). Effects of Temperature and Thermal Cycles on the Elastic Shear Modulus of Saturated Clay. *Journal of Geotechnical and Geoenvironmental Engineering*, *148*(7), 1–7. https://doi.org/10.1061/(asce)gt.1943-5606.0002822.

Duque, J., Mašín, D., and Fuentes, W. (2020). Improvement to the intergranular strain model for larger numbers of repetitive cycles. *Acta Geotechnica*, *15*(12), 3593–3604. https://doi.org/10.1007/s11440-020-01073-w.

Khalili, N., and Khabbaz, M. (1998). A unique relationship for chi for the determination of the shear strength of unsaturated soils. *Geotechnique*, *48*(5), 681–687.

Mašín, D, and Khalili, N. (2008). A hypoplastic model for mechanical response of unsaturated soils. *International Journal for Numerical and Analytical Methods in Geomechanics*, *30*(13), 1303–1336. https://doi.org/10.1002/nag.

Mašín, David. (2010). Predicting the dependency of a degree of saturation on void ratio and suction using effective stress principle for unsaturated soils. *International Journal for Numerical and Analytical Methods in Geomechanics*, *34*(1), 73–90. https://doi.org/10.1002/nag.808.

Mašín, David. (2023). Triax. *TRIAX User's Manual*. Prague, Czech Republic.

Mašín, David, and Khalili, N. (2012). A thermo-mechanical model for variably saturated soils based on hypoplasticity. *International Journal for Numerical and Analytical Methods in Geomechanics*, *36*(12), 1461–1485. https://doi.org/10.1002/nag.1058.

Ng, C. W. W., and Xu, J. (2012). Effects of current suction ratio and recent suction history on small-strain behaviour of an unsaturated soil. *Canadian Geotechnical Journal*, *49*(2), 226–243. https://doi.org/10.1139/T11-097.

Ng, C. W. W., Xu, J., and Yung, S. Y. (2009). Effects of wetting-drying and stress ratio on anisotropic stiffness of an unsaturated soil at very small strains. *Canadian Geotechnical Journal*, *46*(9), 1062–1076. https://doi.org/10.1139/T09-043.

Ng, C. W. W., and Zhou, C. (2014). Cyclic behaviour of an unsaturated silt at various suctions and temperatures. *Geotechnique*, *64*(9), 709–720. https://doi.org/10.1680/geot.14.P.015.

Niemunis, A., and Herle, I. (1997). Hypoplastic model for cohesionless soils with elastic strain range. *Mechanics of Cohesive-Frictional Materials*, *2*(4), 279–299;2-8.

Poblete, M., Fuentes, W., and Triantafyllidis, T. (2016). On the simulation of multidimensional cyclic loading with intergranular strain. *Acta Geotechnica*, *11*(6), 1263–1285. https://doi.org/10.1007/s11440-016-0492-2.

Svoboda, J., Mašín, D., Najser, J., Vašíček, R., Hanusová, I., and Hausmannová, L. (2023). BCV bentonite hydromechanical behaviour and modelling. *Acta Geotechnica*, *18*(6), 3193–3211. https://doi.org/10.1007/s11440-022-01689-0.

Wegener, D., and Herle, I. (2014). Prediction of permanent soil deformations due to cyclic shearing with a hypoplastic constitutive model. *Geotechnik*, *37*(2), 113–122. https://doi.org/10.1002/gete.201300013

Wong, K. S., Mašín, D., and Ng, C. W. W. (2014). Modelling of shear stiffness of unsaturated fine grained soils at very small strains. *Computers and Geotechnics*, *56*, 28–39. https://doi.org/10.1016/j.compgeo.2013.10.005.

Wong, Kwong Soon, and Mašín, D. (2014). Coupled hydro-mechanical model for partially saturated soils predicting small strain stiffness. *Computers and Geotechnics*, *61*, 355–369. https://doi.org/10.1016/j.compgeo.2014.06.008.

Zhou, C. (2014). Experimental study and constitutive modelling of cyclic behaviour at small strains of unsaturated silt at various temperatures (The Hong Kong University of Science and Technology). The Hong Kong University of Science and Technology. https://doi.org/10.14711/thesis-b1334182.

Zhou, C., Xu, J., and Ng, C. W. W. (2015). Effects of temperature and suction on secant shear modulus of unsaturated soil. *Geotechnique Letters*, *5*(July–September), 123–128. https://doi.org/10.1680/geolett.14.00096.

Proceedings of the XVIII ECSMGE 2024
GEOTECHNICAL ENGINEERING CHALLENGES
TO MEET CURRENT AND EMERGING NEEDS OF SOCIETY
© 2024 the Authors
ISBN 978-1-032-54816-6
DOI 10.1201/9781003431749-638
Open Access: www.taylorfrancis.com, CC BY-NC-ND 4.0 license

ECSMGE 24
XVIII EUROPEAN CONFERENCE ON SOIL MECHANICS AND GEOTECHNICAL ENGINEERING

Temporary cofferdam at Caniçada Dam, Portugal

Batardeau temporaire au Barrage de Caniçada, Portugal

A. Pinto*
JETsj, Geotecnia, Lisbon, Portugal

L. Caldeira
LNEC, Lisbon, Portugal

F. Cerqueira, N. Plasencia
EDP S.A., Porto, Portugal

F. Gomes
Mota Engil, Porto, Portugal

**apinto@jetsj.com*

ABSTRACT: The execution of the Caniçada dam new complementary spillway, demanded the construction of a temporary cofferdam to allow the excavation of the discharge tunnel, at the dam south side. The cofferdam with about 20m height and 135m length, intersected weathered to very weathered granite, granite residual soils, fills and sands, with medium average hydraulic conductivity. This scenario led to the execution of a hybrid cofferdam solution: 7m concrete gravity wall over a 30m maximum depth cut-off curtain, using micropiles (tube à manchette) combined with 1m diameter, spaced 0.70m, double row jet grouting columns. The main design and execution criteria are presented, as well as the main QC/QA procedures.

RÉSUMÉ: L'exécution du nouveau déversoir d'inondation complémentaire du barrage de Caniçada, a exigé la construction d'un batardeau temporaire pour permettre l'excavation du tunnel de déchargeur, du côté sud du barrage. Le batardeau, d'une hauteur d'environ 20 m et d'une longueur de 135m, a recoupé des granites altérés à très altérés, des sols résiduels granitiques et des sables, avec une perméabilité moyenne. Ce scénario a conduit à la réalisation d'une solution de batardeau hybride: un mur de gravité, en béton non armée, de 7m de hauteur, sur un écran d' étanchéité de 30 m de profondeur maximale, à l'aide de micropieux (tube à manchette) combinés avec colonnes de jet grouting 1m de diamètre, double rangée et espacés de 0.70m. Les principaux critères de conception et d'exécution sont présentés, ainsi que les principales procédures de CQ/QA.

Keywords: Cofferdam; jet grouting; micropiles; cut-off.

1 INTRODUCTION

The Caniçada dam is a double curvature concrete arch dam with a height of 76m above the foundation level and a crest length of 246m, located at the Cávado river, Peneda Gerês National Park, at Braga District, North of Portugal. The dam was built in 1955 and is resting over the granite bedrock (Figures 1 and 2).

The execution of the Caniçada dam new complementary spillway, demanded the construction of a cofferdam to allow the excavation of the new discharge tunnel portal, at the left abutment of the dam. With this objective, the cofferdam was built with about 20m height and 135m length using a hybrid solution: a concrete gravity wall over a cut-off curtain constituted by jet grouting columns (type 2) and micropiles.



Figure 1. Caniçada dam location.



Figure 2. Construction of Caniçada dam reinforced concrete arch over granite bed rock (courtesy of Rodio).

2 GEOLOGICAL SCENARIO

The geological scenario at the Caniçada dam new complementary spillway is very heterogeneous. After an intensive geological and geotechnical campaign, the following four geotechnical zones were established, from the surface (Figure 3 and 4):

- ZG4 – Fluvial beach sands and heterogeneous fills, with medium to high average permeability.
- ZG3 – Granite residual soil with boulders, with medium permeability.
- ZG2 – Granite rock mass (W3-4 and F3-2 to F3-4) with low average permeability.
- ZG1 – Granite rock mass (W2-3 and F2-3).



Figure 3. View of granite boulders at the Caniçada slopes.

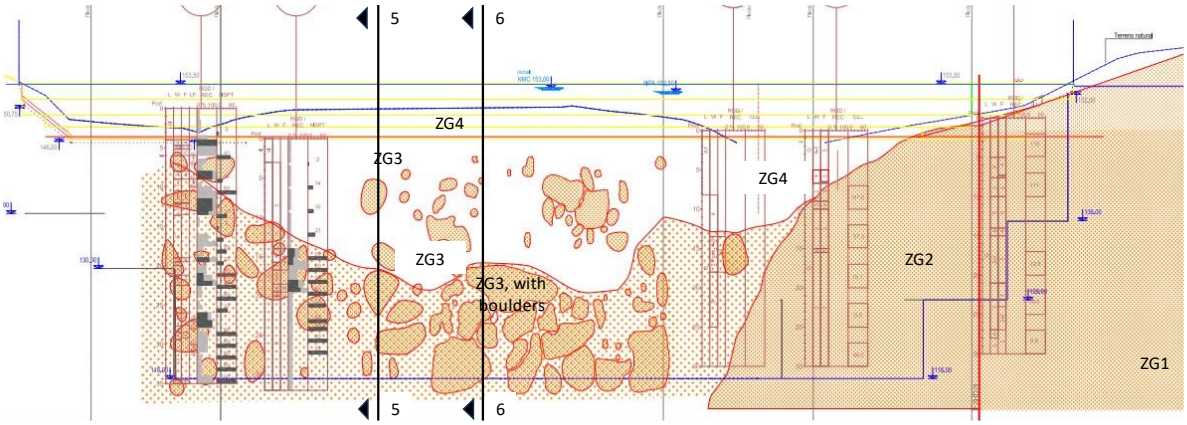

Figure 4. Geological profile (from upstream).

3 COFFERDAM SOLUTION

Considering the geological and hydrogeological complexity, as well as both cofferdam geometry and temporary nature, a cut-off curtain solution, combining jet grouting columns (Croce and Modoni, 2007) and injection micropiles (tube à manchette) with 30m maximum depth was built. A concrete gravity wall was built over the cut-off curtain with its crest level 0.5m above the dam maximum water level.

At the cofferdam most representative cross section (ZG3 intersection), the following solutions were adopted, with the double function of cut-off curtain and gravity wall foundation (Figures 5, 6 and 7):

- At the downstream side: two rows of ϕ1000mm jet grouting columns, spaced, respectively, 0.70m and 0.80m in the longitudinal and transversal alignments, with triangular distribution, were built. The micropiles were installed at the jet grouting columns intersections with sleeves at each 1m.
- At the upstream side: one alignment of inclined micropiles (HEB160 steel profiles) and vertical micropiles (HEB140 steel profiles), both spaced 1.6m.

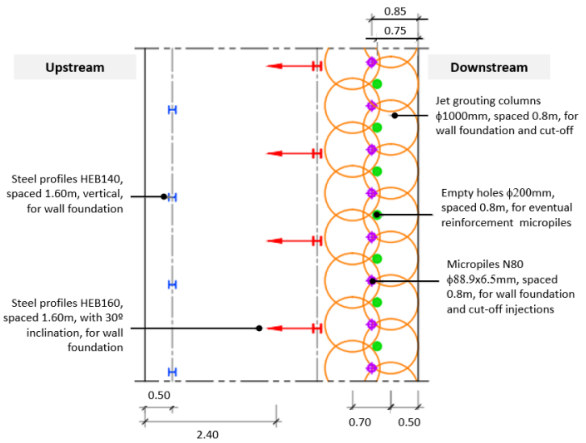

Figure 5. Plan distribution of HEB profiles and cut-off jet grouting and micropiles at the gravity wall foundation.

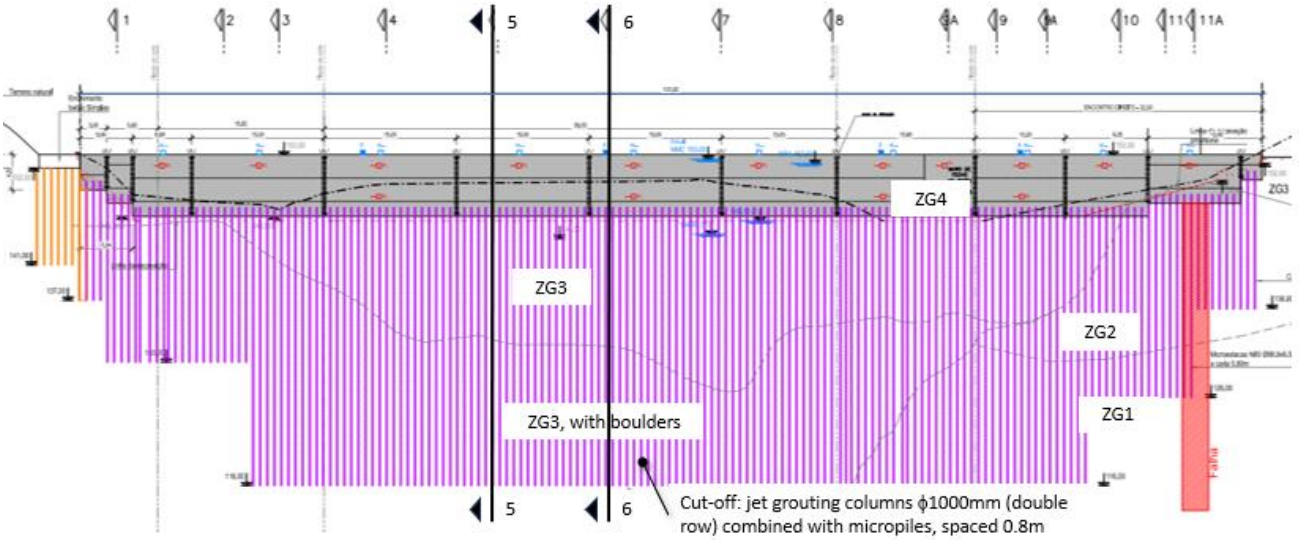

Figure 6. Cofferdam solution elevation (from upstream).

The excavation works inside protected by the cofferdam were performed with 1.25(h):1.00(v) slopes lined with shotcrete, nailed, and drained (Figures 7 and 8).

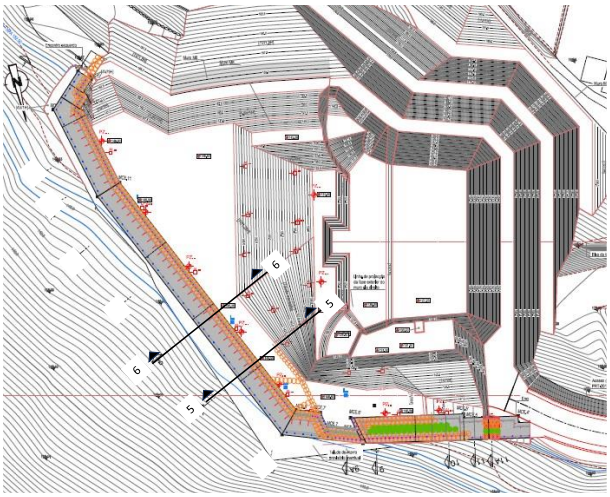

Figure 7. Cofferdam plan with the excavation slopes.

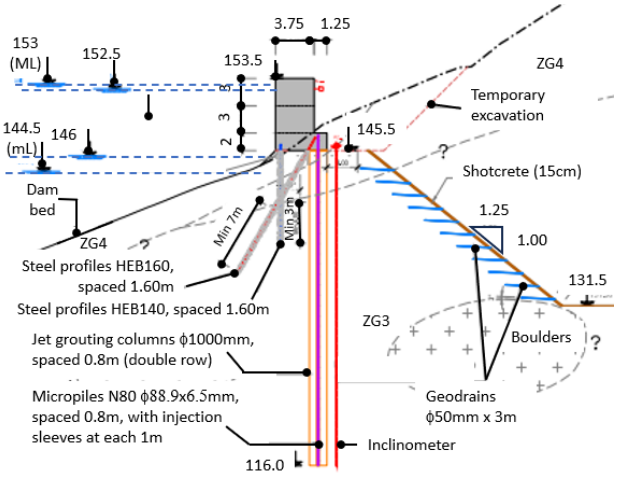

Figure 8. Cofferdam cross section 6-6 (ZG3 intersection).

4 DESIGN

4.1 Cofferdam overall stability

The cofferdam overall stability, including the excavation slope, was checked for several cross sections using SLIDE software, FEM with seepage analysis (Figure 9).

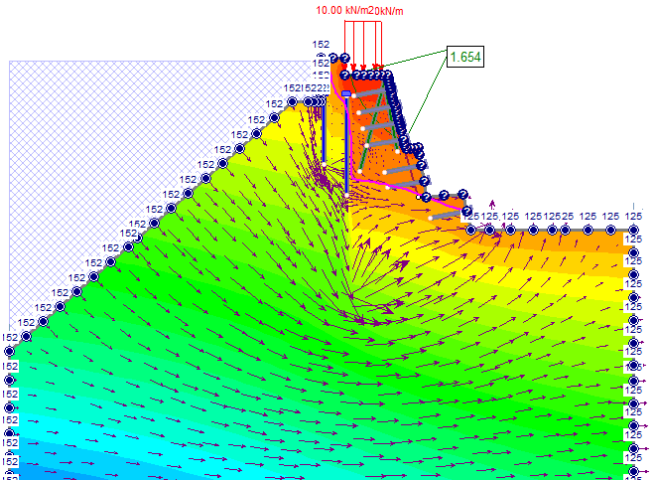

Figure 9. Safety factor for global stabiliy (1.654) at the final excavation level, considering the water inflow, cross-section 5-5.

4.2 Cofferdam hydraulic stability

The cofferdam hydraulic stability, mainly against internal erosion at the excavation base, was also checked for several cross sections using SLIDE software, FEM with seepage analysis. The safety factor for internal erosion was estimated considering the ratio between the critical hydraulic gradient (approximately 1.0) and the estimated hydraulic gradient at the excavation base exit (Figure 10).

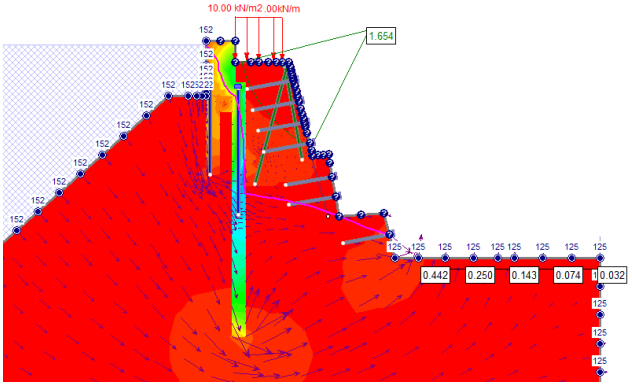

Figure 10. Hydraulic gradients at the excavation base, cross section 5-5.

5 JET GROUTING QUALIY CONTROL AND QUALITY ASSURANCE

5.1 Trial columns

Trial columns were performed to check both the columns geometry and strength at the ZG4 and ZG3. The columns strength and deformability (Young's modulus) were confirmed through UCS tests, performed at 28 days cores and compared with the design parameters: 4MPa and 1GPa, respectively, for 450kg/m^3 of cement consumption (Figure 11).



Figure 11. Trial column's view.

5.2 Execution parameters

All jet grouting execution parameters were recorded using automatic devices and compared with those established based on the trial columns.

5.3 Columns position and verticality

All jet grouting columns position and verticality were confirmed using GPS and digital inclinometer devices.

5.4 Columns integrity

Jet grouting columns integrity was checked by excavation (Figure 12), coring about 5% of the columns, sounding, cross- hole and Lugeon tests.



Figure 12. View of jet grouting excavated around columns.

6 FINAL REMARKS

The presented case study allowed to confirm the advantages of water cut-off solutions for temporary cofferdams using jet grouting columns combined with micropiles in complex geological and hydrogeological scenarios. As main advantages, compared with more conventional solutions, such as diaphragm walls, can be pointed out the following: minimum ground extraction, behaviour predictability and ease demolition (Figure 13).



Figure 13. View of the excavation final works.

ACKNOWLEDGEMENTS

The authors are grateful to EDP, Caniçada dam owner, for the permission to present this paper. The geotechnical works were performed by Keller.

REFERENCES

Croce, P. and Modoni G. (2007). Design of jet grouting cut-offs. *Proceedings of the Institution of Civil Engineers Ground Improvement*. Volume 11 Issue 1, January 2007, pp. 11-19. https://doi.org/10.1680/grim.2007.11.1.11.

Proceedings of the XVIII ECSMGE 2024
GEOTECHNICAL ENGINEERING CHALLENGES
TO MEET CURRENT AND EMERGING NEEDS OF SOCIETY
© 2024 the Authors
ISBN 978-1-032-54816-6
DOI 10.1201/9781003431749-639
Open Access: www.taylorfrancis.com, CC BY-NC-ND 4.0 license

ECSMGE 24
XVIII EUROPEAN CONFERENCE ON SOIL MECHANICS AND GEOTECHNICAL ENGINEERING

A model-scale test setup development to monitor temperature and moisture content variations around energy piles

Développement d'une configuration de test à l'échelle du modèle pour surveiller les variations de température et de teneur en humidité autour des pieux énergétiques

S. Polat*, U.C. Erginag, M. Guner, O. Cinicioglu
Bogazici University, Istanbul, Turkey

M. Sutman
University of Edinburgh, Edinburgh, United Kingdom

**semra.polat@boun.edu.tr*

ABSTRACT: Energy piles, which harness geothermal energy for efficient space heating and cooling, have gained significant popularity as a means of reducing the carbon footprint of buildings. Thermal properties of soil play a pivotal role in accurately predicting heat exchange performance, primarily contingent upon factors such as water content, temperature, and soil porosity. The drastic seasonal temperature shifts attributed to climate change, coupled with cyclic temperature variations induced by heat exchange operations, can profoundly alter soil moisture content, consequently affecting its thermal properties. Hence, it is imperative to account for moisture content variations in soils to precisely forecast the long-term efficacy of energy piles. This study aimed to develop a model setup to investigate the impact of temperature and moisture content variations around energy piles on their long-term geothermal performance. To facilitate this, a moisture content measurement sensor was developed, and a model-scale test setup was designed with several different sensor deployments to monitor changes in soil temperature and moisture content through the application of thermal cycles ranging from 5 to 50°C. The first temperature measurements from the model-scale test are presented in this study.

RÉSUMÉ: Les pieux énergétiques, qui exploitent l'énergie géothermique pour le chauffage et la climatisation efficaces des espaces, ont gagné en popularité en tant que moyen de réduire l'empreinte carbone des bâtiments. Les propriétés thermiques du sol jouent un rôle crucial dans la prédiction précise de la performance d'échange de chaleur, principalement en fonction de facteurs tels que la teneur en eau, la température et la porosité du sol. Les changements drastiques de température saisonnière attribués au changement climatique, associés aux variations cycliques de température induites par les opérations d'échange de chaleur, peuvent profondément altérer la teneur en humidité du sol, affectant ainsi ses propriétés thermiques. Il est donc impératif de prendre en compte les variations de la teneur en humidité dans les sols pour prévoir précisément l'efficacité à long terme des pieux énergétiques. Cette étude visait à développer une configuration de modèle pour étudier l'impact des variations de température et de teneur en humidité autour des pieux énergétiques sur leur performance géothermique à long terme. Pour ce faire, un capteur de mesure de la teneur en humidité a été développé, et une configuration de test à l'échelle du modèle a été conçue avec plusieurs déploiements de capteurs différents pour surveiller les changements de température et de teneur en humidité du sol grâce à l'application de cycles thermiques allant de 5 à 50 °C. Les premières mesures de température de la configuration de test à l'échelle du modèle sont présentées dans cette étude.

Keywords: Thermal cycles; energy piles; water content; model-scale test.

1 INTRODUCTION

The concept of energy piles has become increasingly recognized as an effective method for decreasing the environmental impact of buildings in recent times.
This method involves integrating circulation loops within deep foundations to efficiently harness nearby geothermal energy from the ground's surface for heating and cooling buildings (Brandl, 2006). Energy piles enable the process of transferring surplus heat into the ground during summer, effectively cooling the buildings. Conversely, energy piles extract heat from the ground during winter to provide heating for the buildings. It presents an energy-efficient substitute for traditional heating and cooling approaches (Sani et al. 2019, Sutman et al. 2020).

Thermal conductivity plays an important role in analyzing the heat transfer phenomenon, crucial for accurately predicting geothermal performance. In the context of heat transfer within porous media, such as soils, it is vital to recognize that the overall thermal conductivity of the medium stems from distinct contributions of soil grains, water, and air. Considering that the thermal conductivity of soil grains is around 10 times the one of water and 300 times the one of air, conductive heat transfer in soils highly depends on the water content and porosity (Hashemi and Sutman, 2022). During summer operation of energy piles, soil temperature increases due to heat injection into the ground. Temperature increase leads to a decrease in the viscosity and density of the water in soil pores, which may result in the water to flow away from the heat source and leading to a decrease in thermal conductivity. An inverse behaviour is expected during winter operations. Furthermore, the process of injecting heat into unsaturated soils is complex, involving the interplay of thermal energy causing both liquid and vapor water flow, coupled with the transfer of latent heat associated with phase changes (Smits et al. 2013, Lu & Dong, 2015, Moradi et al. 2016, Xu et al. 2019).

Consideration of the variations of soil thermal properties during the lifetime of energy piles is of paramount importance for the long-term analysis of their geothermal performance. Yet, most numerical simulations assume that the thermal properties are constant despite variations in water content and temperature. Thus, this study aims to develop a model-scale test setup to investigate the impact of temperature and moisture content variations around energy piles on their long-term geothermal performance.

2 TEST SETUP

A model-scale tank setup has been planned to observe the changes in the thermal conductivity of the soil based on temperature and water content variations triggered by operation of a model-scale energy pile. The dimensions of the model tank are 75×75×100 cm. The soil used in the test consists of 93% silica sand and 7% kaolin clay mixture. The hydraulic conductivity of the mixture was determined to be 1×10^{-7} m/s through the constant head permeability test. Compaction tests were conducted to determine the optimum water content value of the mixture, and a water content value of 8% was chosen for the test.

In the model-scale test, an energy pile with a diameter of 2 cm and a length of 70 cm is employed. Heat transfer is accomplished by connecting copper pipes, placed at the centre of the pile, to the thermal bath, which is capable of applying both heating and cooling episodes. Thermistors have been strategically placed for temperature measurements at both the centre and the bottom of the pile.

Within the tank, numerous sensors have been strategically positioned for measurements of water content, thermal conductivity, temperature, and suction. The employed sensors include six water potential sensors, two thermal conductivity sensors, three equitensiometer probes, eight thermocouples (one of them is placed outside of the tank to measure ambient temperature), seven thermistors, and seven water content and thermistor sensors. Before the test setup, the positions of sensors have been drawn to scale, including the cables, to ensure they do not impede the flow during the testing process, which is shown in Figure 1.

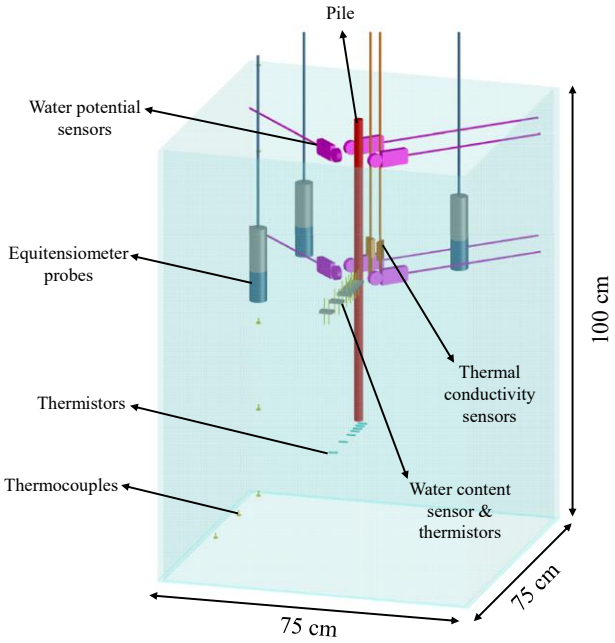

Figure 1. 3D view of the experimental setup.

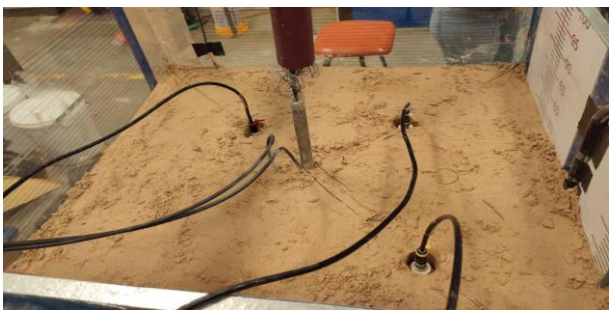

Figure 2. View of the 4th level of the setup.

In the tank setup, the soil is arranged in five levels, and the level heights are determined considering the sensor positions. A picture from the end of the 4th level of the setup can be seen in Figure 2. Compaction

was applied at each level, and sensors were placed at appropriate depths. The goal was to achieve a consistent compaction ratio by measuring the quantity and volume of material used at each level. After the compaction process at each level, the compatibility of water content values was verified with samples taken. Following the placement of piles, soil, and sensors into the tank, the top surface of the tank was insulated with suitable material to prevent evaporation. Subsequently, all surfaces of the tank were covered with thermal insulation, as illustrated in Figure 3.

In the initial stage of the test, a constant temperature of 50°C was applied.

Table 1. Locations and elevations of sensors.

Sensors	Location	Elevation (cm)
Water Potential	2 cm to the pile	55 cm
	4 cm to the pile	55 cm
	6 cm to the pile	55 cm
	2 cm to the pile	82 cm
	4 cm to the pile	82 cm
	6 cm to the pile	82 cm
Thermocouple	36 cm to the edge	0 cm
	18 cm to the edge	0 cm
	3 cm to the edge	0 cm
	3 cm to the edge	20 cm
	3 cm to the edge	40 cm
	3 cm to the edge	60 cm
	3 cm to the edge	80 cm
	Ambient	-
Thermal conductivity	2 cm to the pile	55 cm
	4 cm to the pile	55 cm
Water Content & Thermistor	1 cm to the pile	55 cm
	3 cm to the pile	55 cm
	5 cm to the pile	55 cm
	7 cm to the pile	55 cm
	10 cm to the pile	55 cm
	16 cm to the pile	55 cm
	22 cm to the pile	55 cm
Thermistor	1 cm to the pile	20 cm
	3 cm to the pile	20 cm
	5 cm to the pile	20 cm
	7 cm to the pile	20 cm
	10 cm to the pile	20 cm
	16 cm to the pile	20 cm
	22 cm to the pile	20 cm
Equitensiometer probe	16 cm to the pile	55 cm
	20 cm to the pile	55 cm
	24 cm to the pile	55 cm

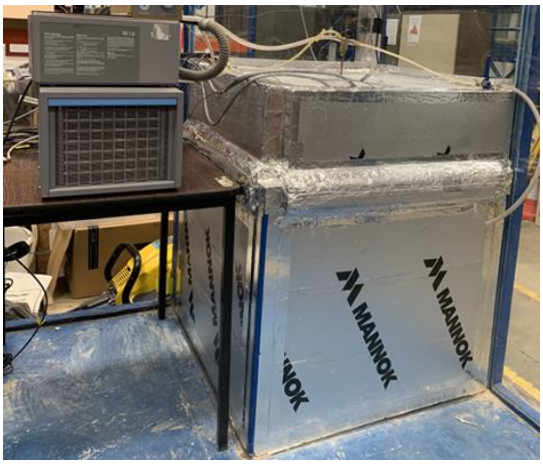

Figure 3. View of the thermally insulated tank.

3 RESULTS

Throughout the test, the temperatures measured at the pipe inlet and outlet are depicted in Figure 4. Despite the application of a constant temperature of 50°C in the test, the measured value at the pipe inlet averaged 48°C. This deviation is attributed to the fact that the connection pipe between the thermal bath and the pile is outside the tank insulation and is affected by the ambient temperature, resulting in a 2°C temperature loss. The pipe outlet temperature was measured at an average of 38°C.

The temperatures measured by the thermistors inside the pile are depicted in Figure 5. At the mid-level of the pile, the temperature values average around 42°C, while at the lower level, they have risen to an average of 36°C.

Of the eight thermocouples used in the test, seven were placed on the lower and side surfaces inside the tank. The remaining thermocouple was used to measure the ambient environment, aiming to assess insulation performance. The thermocouple measurements taken during the test are presented in Figure 6. While ambient temperatures can vary up to 6°C throughout the day, this variation is limited to approximately 1°C on the inner surfaces of the tank, close to the boundary.

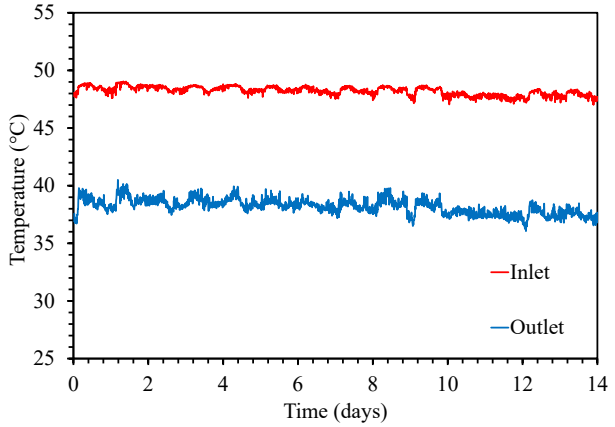

Figure 4. Inlet-outlet temperatures of the pipe.

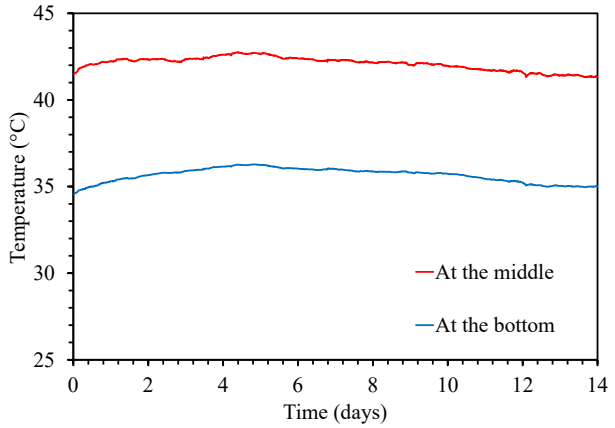

Figure 5. Temperatures at the middle and bottom of the pile.

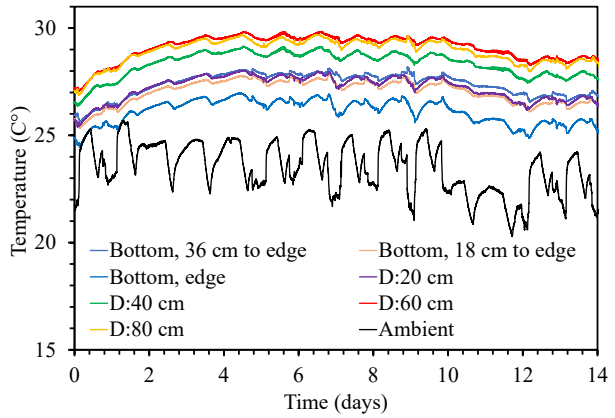

Figure 6. Temperatures at the boundaries of the tank.

4 CONCLUSIONS

Long term performance of energy piles is depended on soil thermal properties and therefore, it is a changing property with respect to the temperature and volumetric water content of the soil medium. As heating-cooling cycles occur, soil thermal conductivity might increase or decrease. Therefore, this paper develops a comprehensively instrumented model-scale test setup for long-term investigation of this phenomenon.

The test was initiated with the stabilization of the entire system by applying continuous heating. It was recorded that amount of temperature increase is different with respect to the sensor-pile relative positions. The greatest increase was observed at the vicinity of the pipe inlet while the lowest increase was obtained the bottom model boundaries, expectedly. The test is ongoing and the water potential, thermal conductivity and suction within the soil are continuously recorded, the interdependency of which will be identified by heating-cooling episodes.

ACKNOWLEDGEMENTS

The authors are grateful for the financial support provided by Cost Action CA21156. The project presented in this article is supported by the Royal Society Grant RGS\R2\202298.

REFERENCES

Brandl, H. (2006) Energy foundations and other thermo-active ground structures. *Geotechnique*, 56(2), pp. 81-122. https://doi.org/10.1680/geot.2006.56.2.81.

Sani, A., Singh, R., Amis, T., Cavarretta, I. (2019) A review on the performance of geothermal energy pile foundation, its design process and applications. *Renewable and Sustainable Energy Reviews*, 106. https://doi.org/10.1016/j.rser.2019.02.008.

Sutman, M., Speranza, G., Ferrari, A., Larrey-Lassalle, P. and Laloui, L., 2020. Long-term performance and life cycle assessment of energy piles in three different climatic conditions. Renewable Energy, 146, pp.1177-1191. https://doi.org/10.1016/j.renene.2019.07.035.

Hashemi, A. and Sutman, M., 2022. Thermo-hydro-mechanical behaviour of partially saturated fine-grained soils in the context of energy geostructures. Soils and Rocks, 45. https://doi.org/10.28927/sr.2022.076821.

Smits, K. M., Sakaki T., Howington, S. E., Peters, J. F., and Illangasekare, T. H. (2013) Temperature dependence of thermal properties of sands over a wide range of temperatures (30–70°C), *Vadose Zone J.* 12 (1): 33. https://doi.org/10.2136/vzj2012.0033.

Lu, N., Dong, Y. (2015) Closed-form equation for thermal conductivity of unsaturated soils at room temperature, *J. Geotech. Geoenviron. Eng.,* 141(6): 04015016. https://doi.org/10.1061/(ASCE)GT.1943-5606.0001295.

Moradi, A., Smits, K. M., Lu, N. and McCartney, J. S. (2016) Heat transfer in unsaturated soil with application to borehole thermal energy storage, *Vadose Zone J.,* 15 (10): 16. https://doi.org/10.2136/vzj2016.03.0027.

Xu, Y., Sun, D., Zeng, Z., and Lv, H. (2019) Effect of temperature on thermal conductivity of lateritic clays over a wide temperature range, *Int. J. Heat Mass Transfer,* 138 (Jan): 562–570. http://dx.doi.org/10.1016/j.ijheatmasstransfer.2019.04.077.

Proceedings of the XVIII ECSMGE 2024
GEOTECHNICAL ENGINEERING CHALLENGES
TO MEET CURRENT AND EMERGING NEEDS OF SOCIETY
© 2024 the Authors
ISBN 978-1-032-54816-6
DOI 10.1201/9781003431749-640
Open Access: www.taylorfrancis.com, CC BY-NC-ND 4.0 license

ECSMGE 24
XVIII EUROPEAN CONFERENCE ON SOIL MECHANICS AND GEOTECHNICAL ENGINEERING

On the influence of jack-up footprints on the dynamic behaviour of offshore foundations

Influence de l'empreinte des jack-up sur le comportement dynamique des fondations offshore

T. Pucker*
HafenCity University, Hamburg, Germany
**tim.pucker@hcu-hamburg.de*

ABSTRACT: Jack-up vessels are frequently used to install offshore structures. These vessels are shipped to the construction site and then lifted out of the water using their legs to create a stable working platform. Shallow foundations, so-called spudcans, are attached to the legs and pressed into the ground until sufficient bearing capacity is achieved. When the construction work is finished, the spudcan is pulled out of the ground again and usually a footprint remains representing a hole in the seabed. As the installation of offshore structures usually consists of several construction phases, several jack-up vessels are placed around the structure at different times and each vessel leaves several footprints. The influence of footprints on the dynamic behaviour of offshore structures is exemplified by the foundation of offshore wind turbines. The investigations were carried out with numerical simulations using the FEM. The influence of the footprint location as well as its distance to the structure is investigated. General recommendations are given and how this influence can be addressed in the design of the structure.

RÉSUMÉ: Les navires de type "jack-up" sont fréquemment utilisés pour l'installation de structures offshore. Ces navires sont transportés jusqu'au site de construction, puis soulevés hors de l'eau à l'aide de leurs pieds afin de créer une plate-forme de travail stable. Des fondations peu profondes, appelées "spudcans", sont fixées aux jambes et enfoncées dans le sol jusqu'à ce que la capacité portante soit suffisante. Lorsque les travaux de construction sont terminés, le spudcan est à nouveau retiré du sol et il ne reste généralement qu'une empreinte représentant un trou dans le fond marin. Étant donné que l'installation de structures offshore se compose généralement de plusieurs phases de construction, plusieurs navires autoélévateurs sont placés autour de la structure à différents moments et chaque navire laisse plusieurs empreintes. L'influence des empreintes sur le comportement dynamique des structures offshore est illustrée par les fondations des éoliennes offshore. Les recherches ont été menées à l'aide de simulations numériques utilisant la méthode des éléments finis. L'influence de l'emplacement de l'empreinte et de sa distance par rapport à la structure est étudiée. Des recommandations générales sont données sur la manière dont cette influence peut être prise en compte dans la conception de la structure.

Keywords: Offshore; jack-up; spudcan; FEM.

1 INTRODUCTION

Jack-up vessels are extensively used oil and gas exploration and in the offshore wind sector for the installation of wind turbines. These vessels are transported to their designated deployment sites, where they lower their legs to elevate the platform above the seawater level. This operational method ensures a higher degree of safety compared with conventional floating vessels, as the impact of sea conditions and water levels on jack-up vessels is less pronounced.

In oil and gas applications, jack-up legs can reach lengths of up to 170 m, with spudcan diameters reaching 20 m (refer to Figure 1). However, in the offshore wind industry, where water depths are shallower and the focus is solely on tower and turbine installation, the dimensions of jack-up vessels are significantly smaller. This fast-paced industry demands layout flexibility when positioning turbines offshore, considering various constraints such as seabed features such as cables and crane length limits. Consequently, it is imperative to assess the stability of jack-up vessels and load-bearing capacity of their spudcans across different soil types and layers.

On certain occasions, jack-up vessel spudcans may penetrate several meters of soft soil, significantly disturbing the soil and creating footprints with crater-like depressions. In scenarios where vessels revisit the same location for repeated jack-up activities, the necessity of reusing the same footprint for spudcan re-installation arises. This aspect has been investigated by

researchers such as Stewart and Finnie (2001), Cassidy et al. (2009), Qiu et al. (2013), and Jun et al. (2018).

All of these studies involve centrifuge testing and numerical modeling utilizing the Coupled Eulerian-Lagrangian method. They collectively conclude that spudcan resistance, both vertically and horizontally, decreases after reinstallation within a footprint area.

Additionally, researchers, including Leung et al. (2012), Liang et al. (2020) and Molina Mesa et al. (2023) have extensively evaluated the induced load on existing foundations resulting from adjacent spudcan penetrations and the impact of footprints on the vertical bearing capacity of nearby piles. Notably, this study delves into a comprehensive examination of horizontal capacity, particularly for relatively short foundations such as suction caissons.

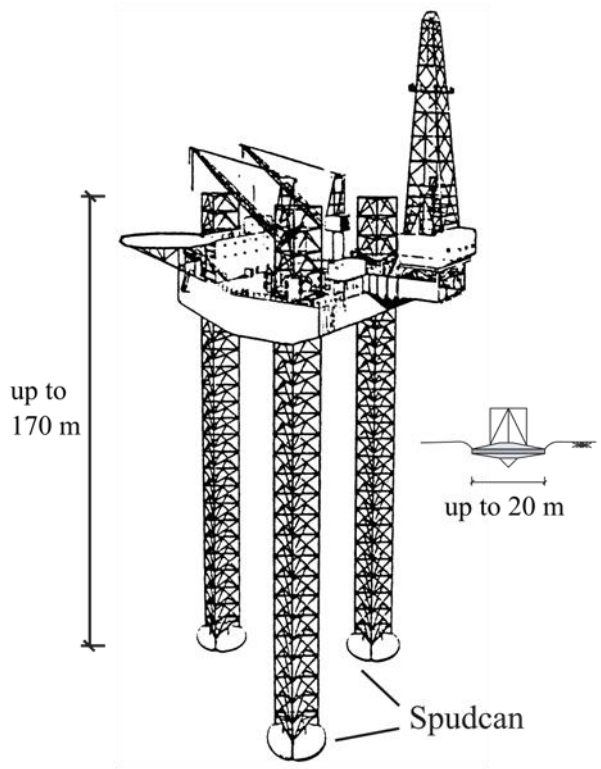

Figure 1. Illustration of a jack-up platform with three legs and spudcans including a detailed spudcan with central tip (modified after Reardon, 1986).

2 NUMERICAL MODEL

Numerical analyses are performed using the finite element software package Plaxis 3D Version 2023.2.0.1059. To save computational time, as the geometry is symmetrical, only half of the monopile and footprint is modelled.

2.1 Soil

A homogenous soil profile consisting of a single sand layer is selected for this study. The material parameters for the sand are listed in Table 1. The Hardening Soil Small Strain Model is used as material model for the sand to account for the stress dependency of the stiffness, loading history and small strain effects.

Table 1. Material parameter for the Hardening Soil Small Strain Model.

Parameter	Value
$\gamma \,/\, \gamma'$	19.6 / 9.6 kN/m^3
E_{50}^{ref}	30000 kN/m^2
E_{Oed}^{ref}	30000 kN/m^2
E_{ur}^{ref}	100000 kN/m^2
ν_{ur}	0,20
m	0,50
φ'	40°
c'	0.001 kN/m^2
ψ	0.0
G_0^{ref}	120000 kN/m^2
$\gamma_{0.7}$	0.00045
p_{ref}	100 kN/m^2

2.2 Monopile

The monopile has a penetration depth of 30 m and a free length above the seabed level of 50 m. The free length is chosen to consider a realistic combination of lateral and moment loading magnitudes at the seabed level. The outer pile diameter is 8 m. The pile is modelled using plate elements and the wall thickness is assumed to be 70 mm.

To evaluate the lateral stiffness of the monopile, the head of the monopile is moved horizontally while the reaction force is calculated. The lateral displacements at the seabed level are evaluated and compared with calculations with and without the footprint of a spudcan.

The load level of the monopile is taken as 1.5 MN in the fatigue limit state (FLS) and 10.0 MN in the ultimate limit state (ULS).

2.3 Soil pile interaction

The soil pile interaction is modelled using interface elements. The material for the interface elements is taken from the surrounding soil considering a wall friction angle of 2/3φ'.

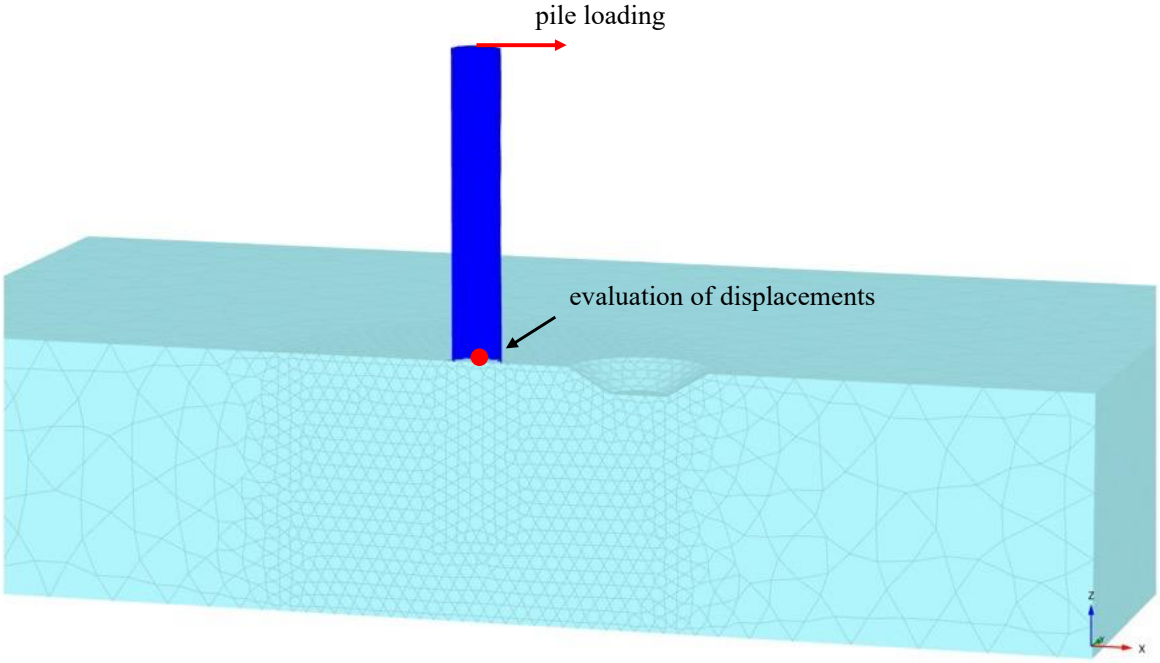

Figure 2. Numerical model of soil and pile including a footprint in 15 m distance.

2.4 Footprint

The geometry of the footprint is chosen based on offshore measurements of real footprint geometries. The geometry of the footprint is simplified as a truncated cone. The depth of the footprint is assumed to be 4 m while the diameter at the bottom of the footprint is 9.5 m and the diameter at the seabed level is 23.0 m. The distance between the footprint and monopile is varied in this study between 5.0 and 20.0 m.

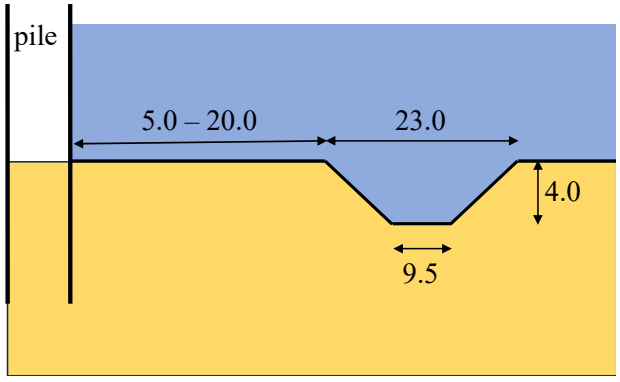

Figure 3. Geometry of the footprint and distance to monopile.

3 RESULTS

The load deflection curves for the ULS load are shown in Figure 4. As expected, decreasing the distance between the footpad and monopile increased the pile deflection at the seabed level. Hence, the horizontal stiffness of the pile soil interaction decreases resulting in a softer load response of the monopile.

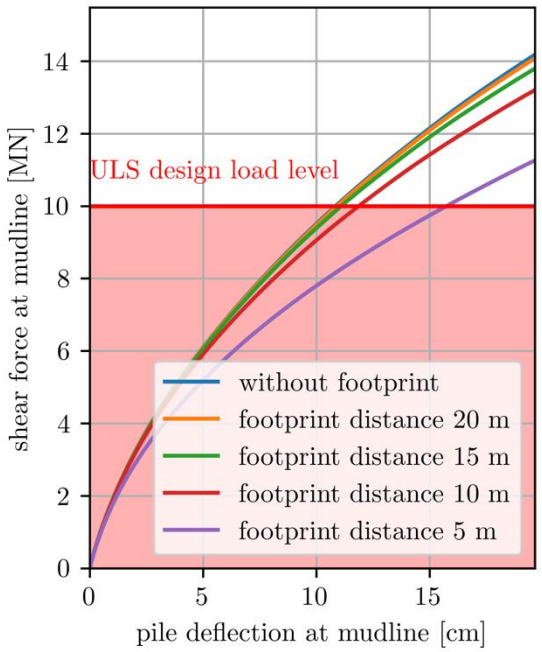

Figure 4. Load deflection curve for ULS load level considering multiple distances between monopile and footpad.

A detailed illustration of the effect of the footprint on the initial stiffness at lower load levels, such as the FLS load level, is shown in Figure 5. The influence on the initial stiffness of the pile soil interaction is much smaller than that on the stiffness at the ULS load level for distances larger than 10 m.

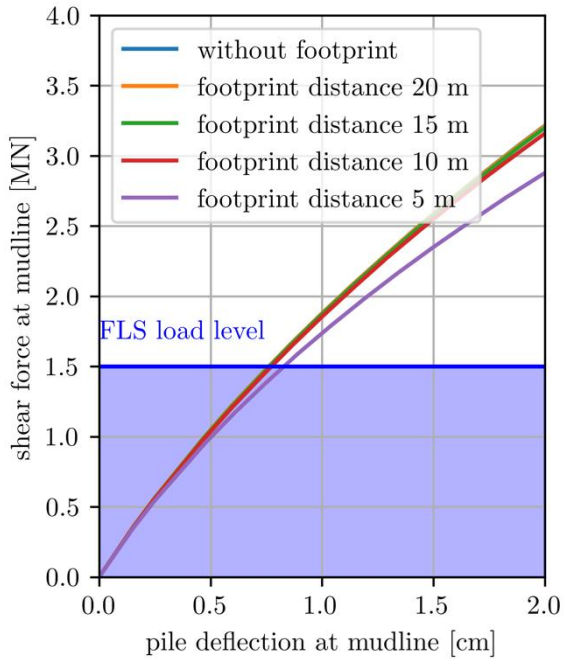

Figure 5. Load deflection curve for FLS load level considering multiple distances between monopile and footpad.

The relative change in lateral stiffness depending on the distance between the monopile and the footprint is shown in Figure 6.

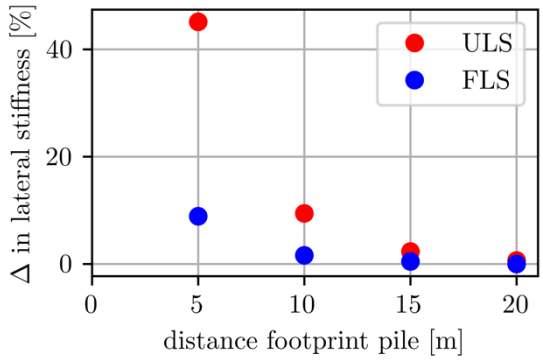

Figure 6. Change in lateral stiffness at the seabed level for multiple distances between monopile and footprint.

4 CONCLUSIONS

The present study presents an approach for estimating the influence of a spudcan footprint on the lateral stiffness response of a monopile foundation. It could be demonstrated, that for the investigated sand profile, the influence on the initial stiffness at FLS level seems to be subordiante for larger distances while the influence at the ULS level is more obvious. Nevertheless, the influence of the change in stiffness should be proven for the actual design by taking it into account for load simulations, fatigue calculations etc. In addition, it must be considered that there are several jack-up operations until the turbine is fully installed. Each operation leaves footprints that interact with a monopile foundation. Therefore, the superposition of footprints needs to be considered as well.

REFERENCES

Cassidy, M. J., Quah, C. K., and Foo, K. S. (2009). Experimental Investigation of the Reinstallation of Spudcan Footings Close to Existing Footprints. *Journal of Geotechnical and Geoenvironmental Engineering*, 135(4), 474-486. doi: 10.1061/(ASCE)1090-0241(2009)135:4(474).

Jun, Minjung & Kim, Y.H. & Hossain, M.S. & Cassidy, M.J. & Hu, Yuxia & Sim, J.W.. (2018). Numerical Investigation of Novel Spudcan Shapes for Easing Spudcan-Footprint Interactions. *Journal of Geotechnical and Geoenvironmental Engineering*. 144. doi: 10.1061/(ASCE)GT.1943- 5606.0001925.

Leung, C. F., Tho, K. K., Chow, K. Y., Xie, Y., Wong, P., Purwana, O. A. (2012). Experimental and Numerical Studies of Spudcan-Pile Interaction. *Proceedings of the Offshore Technology Conference 2012*, Houston, USA, OTC 23053.

Liang, C., Liu, R., Zhang, H., Li, C., Yuan, Y., Cao, T. (2020). The effect of spudcan footprints on the vertical bearing capacity of adjacent pile foundations. *Ships and Offshore Structures.* 16(3):1-14. doi: 10.1080/17445302.2020.1725278.

Molina Mesa, C., Pucker, T., Bubel, J. (2023). Influence of a jack-up installation near a wind turbine foundation: a numerical study. *Proceedings of the 10th European Conference on Numerical Methods in Geotechnical Engineering (NUMGE) 2023 in London*, UK. doi: 10.53243/NUMGE2023-323.

Qiu, G., Pucker, T., Grabe, J. (2013). Penetration of a spudcan near a cavity. *Proceedings of Conference on Maritime Energy (COME) 2013 in Hamburg*, Germany, 323-331, Veröffentlichungen des Instituts für Geotechnik und Baubetrieb der Technischen Universität Hamburg- Harburg, Heft 26.

Reardon, M. J. (1986). Review of the geotechnical aspects of jack-up unit operations. *Ground Eng. 19(7):* 21–26.

Stewart, D & Finnie, M. (2001). Spudcan-Footprint Interaction During Jack-Up Workovers. *Proceedings of the International Offshore and Polar Engineering Conference*. 1.

Proceedings of the XVIII ECSMGE 2024
GEOTECHNICAL ENGINEERING CHALLENGES
TO MEET CURRENT AND EMERGING NEEDS OF SOCIETY
© 2024 the Authors
ISBN 978-1-032-54816-6
DOI 10.1201/9781003431749-641
Open Access: www.taylorfrancis.com, CC BY-NC-ND 4.0 license

ECSMGE 24
XVIII EUROPEAN CONFERENCE ON SOIL MECHANICS AND GEOTECHNICAL ENGINEERING

A novel framework for modeling the vegetation and atmosphere effect on the behaviour of infrastructure embankments

Un nouveau cadre pour modéliser l'effet de la végétation et de l'atmosphère sur le comportement des remblais d'infrastructures

V. Pujević*
Department of Geotechnical Engineering/Faculty of Civil Engineering/University of Belgrade, Serbia
L. Zdravković
Department of Civil and Environmental Engineering/Faculty of Engineering/Imperial College, London, UK
**vpujevic@grf.bg.ac.rs*

ABSTRACT: The soil-vegetation-atmosphere interaction is a dynamic process, which governs the continuous change of soil hydrological conditions. These changes directly affect the seasonal and long-term performance of infrastructure cut and embankment slopes. It has been established that the combined effect of vegetation and precipitation induces seasonal cycles of shrinkage and swelling, which give rise to serviceability issues. Previous numerical studies regarding the effect of the soil-vegetation-atmosphere system interaction on the behaviour of infrastructure embankments, were unable to quantitatively reproduce the observed hydraulic behaviour. They were either based on pure hydraulic approach or in case of fully coupled analyses were employing saturated mechanical models. The framework presented in this paper is based on the fully coupled flow-deformation analysis, combined with unsaturated soil mechanics theory and sophisticated climatic boundary conditions, implemented within the ICFEP numerical code. The instrumented railway embankment located in the UK, suffering from poor track ride quality related to the presence of vegetation on the slopes, is used as a case study for this investigation.

RÉSUMÉ: L'interaction sol-végétation-atmosphère est un processus dynamique qui régit le changement continu des conditions hydrologiques du sol. Ces changements affectent directement la performance saisonnière et à long terme des talus des infrastructures et des talus. Il a été établi que l'effet combiné de la végétation et des précipitations induit des cycles saisonniers de retrait et de gonflement, qui posent des problèmes d'entretien. Les études numériques antérieures concernant l'effet de l'interaction du système sol-végétation-atmosphère sur le comportement des remblais d'infrastructures n'ont pas permis de reproduire quantitativement le comportement hydraulique observé. Soit elles étaient basées sur une approche hydraulique pure, soit, dans le cas d'analyses entièrement couplées, elles utilisaient des modèles mécaniques saturés. Le cadre présenté dans cet article est basé sur l'analyse écoulement-déformation entièrement couplée, combinée à la théorie de la mécanique des sols non saturés et à des conditions aux limites climatiques sophistiquées, mises en œuvre dans le code numérique ICFEP. Le remblai ferroviaire instrumenté situé au Royaume-Uni, souffrant d'une mauvaise qualité de roulement liée à la présence de végétation sur les pentes, est utilisé comme étude de cas pour cette enquête.

Keywords: Soil-vegetation-atmosphere interaction; coupled analysis; unsaturated constitutive model; RWUM; precipitation.

1 INTRODUCTION

The interaction between the soil, atmosphere and vegetation drives continuous movement of water in and out from the ground, affecting the distribution of subsurface water. The ability of vegetation to remove water from the soil varies seasonally, with peaks during summer drier months, and lows during the winter months, when evapotranspiration processes are diminished or ceased. These opposite processes cause cycles of drying and wetting, and associated pore water pressure variations within the soil, which in turn produce seasonal cyclic changes of effective stresses. Therefore, in embankments constructed of clay having a high-volume change potential, these are accompanied by corresponding cycles of soil shrinkage and swelling (Smethurst et al., 2015).

Due to the irregular distribution of vegetation along the embankment length as well as variations in vegetation species, sizes and densities related to water

demands, together with intrinsic heterogeneity of the clay fill, alternating volumetric deformations are nonuniform, both in longitudinal and lateral direction, thereby inducing excessive differential movements of the track and consequently poor ride quality. These are characterized as serviceability limit states (SLS) and are most frequent during late summer/early autumn, when the effects of desiccation on high-plasticity clay fills are most significant.

Magnolia Road Project is an example of an embankment that was suffering from poor track ride quality and a high rate of maintenance due to movements associated with the presence of vegetation on the slopes of the embankment (Arup Geotechnics, 2007), and is used as a case study for the evaluation of modelling framework presented in this paper.

Predicting soil-vegetation-atmosphere interaction is not straightforward, due to the complexity of both the boundary conditions involved and the hydro-mechanical behaviour of soils, which is coupled, highly nonlinear and inherently unsaturated in case of embankments. Current paper presents an advanced approach incorporating fully coupled unsaturated flow-deformation finite element analyses.

2 MAGNOLIA ROAD CASE STUDY

The instrumented embankment is located on the Shenfield–Southend Victoria railway line near Hawkwell, Essex, UK (OS grid reference TQ856923). Highly vegetated slopes at this section of the rail track, and associated excessive cyclic shrink-swell movements, negatively affected the serviceability through frequent speed restrictions and maintenance requirements.

The embankment was constructed around 1887. Along the instrumented section, its height and width are around 5.5 m and 35 m respectively. The slope of the embankment is typically around 20° steepening to around 30° at the shoulder of the embankment. This 'coat-hanger' shape, shown in Figure 1, is clear indicator that high-water demand trees were present for the prolonged period of time. The embankment consists of intermediate to high plasticity clay fill of London Clay origin covered with a layer of ash and ballast. The techniques used for embankment construction back in the 19th century involved simple tipping in one layer to the full height with practically no mechanical compaction (Skempton, 1996), forming distinctive structure often referred to as dumped clay fills. The conceptual model for the dumped clay fill, as proposed by (O'Brien et al., 2004), consists of clods of parent material that govern the compressibility and shear modulus of the soil, and the matrix which controls the permeability and shear strength.

At the start of the monitoring period in March 2006, the embankment was densely vegetated with mature and semi-mature oak and ash trees. According to (NHBC standards, 2007) oak is being classified as high water demand tree, wail ash is more of a moderate type. Beyond the embankment to the north lies predominantly agricultural land with grass vegetation.

In March 2007, the vegetation was removed over the shoulder of the embankment leaving only the vegetation near the toe. Further tree clearance occurred in March 2010, along the full length of the embankment.

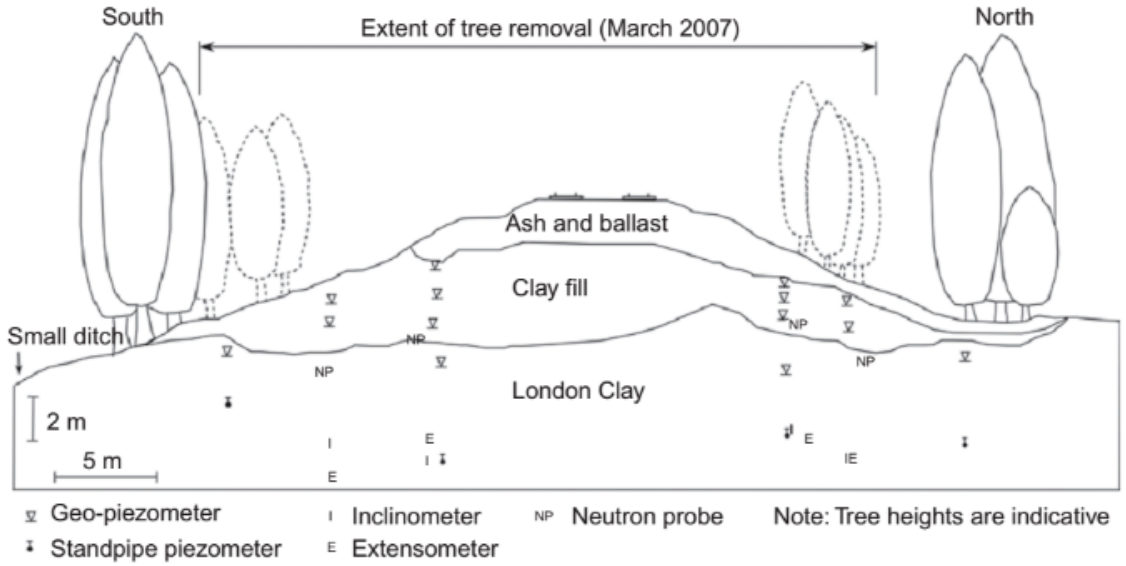

Figure 1. Cross-section view of Hawkwell embankment indicating the extent of first tree removal and location of instrumentation.

Geotechnical Interpretative Report and monitoring data were made available by (Arup Geotechnics, 2007; Geotechnical Observations, 2013). Monitoring data was available from spring 2006 until March 2011. Instrumentation was installed predominantly at two sections (Figure 1.) and consisted of: standpipe piezometers; GeO flushable piezometers (Ridley et al., 2003); neutron probe access tubes; inclinometers; extensometers; tipping bucket rain gauge.

3 NUMERICAL MODEL

Fully coupled flow-deformation analysis, combined with unsaturated constitutive model and sophisticated climatic boundary conditions, implemented within the ICFEP numerical code (Potts & Zdravković, 1999) were used to evaluate the ability of this numerical modelling approach to quantitatively reproduce the observed behaviour of the Hawkwell embankment, both prior and after vegetation removal.

The part of the finite element mesh of the northern half of the embankment and foundation soil used in plain strain analysis of the Hawkwell embankment is shown in Figure 2.

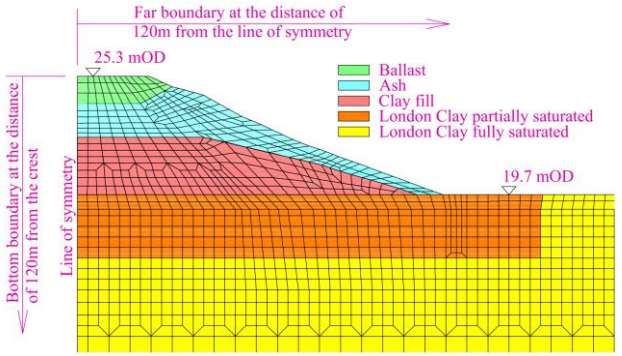

Figure 2. Zoomed in view of finite element mesh.

3.1 Hydraulic behaviour

The hydrological soil properties used in the analyses are shown in Table 1. The saturated permeability of the clay fill was adopted from the permeability testing data presented in the work of (O'Brien et al., 2004). The difference in permeability of dumped clay fill (derived from London Clay) and natural London Clay, is attributed to specific internal structure of the dumped clay fill, characterized by relatively high permeability matrix that acts as preferred flow path.

In the current analysis non-hysteretic soil water retention curve (SWRC) available in ICFEP (Melgarejo, 2004).

The gradient of the SWRC is crucial in a coupled analysis, because it affects the flow of water generated by the changes in water content. Considering that laboratory measurements of clay fill SWRC for the Hawkwell embankment were not available, the retention curve for the analysis was calibrated against in situ measurements of volumetric water content and corresponding pore water suctions.

Table 1. Hydraulic properties used in the analysis.

	Clay fill	London Clay	Ash	Balast
Isotropic/Anisotropic	Isotropic	Isotropic	Isotropic	
Saturated coefficient of permeability K_0 [m/s]	$2x10^{-9}$	$5x10^{-10}$	$4x10^{-5}$	
Nonlinear permeability model	none	logarithmic	none	Free draining
a	/	0.007	/	
Unsaturated hydraulic constitutive model	Van Genuchten type	none	none	
s_{air} *(kPa)*	20			
a	0.0125	/	/	
n	1.5			
m	0.33			

3.2 Mechanical behaviour

With regard to mechanical behaviour ash and ballast were assumed to behave as saturated materials and were therefore modelled with a linear elasto-plastic Mohr-Coulomb constitutive model. The in-situ London Clay foundation soil was also treated as saturated, except the shallow part just beneath the embankment, which is in accordance with the borehole loggings.

Table 2. Material properties used in the analysis.

	Balast	Ash[(1)]	London Clay[(2)]
Bulk unit weight γ [kN/m^3]	18,0	11,0	18,8
Shear strength parameters φ [°], c [kPa]	φ' = 40°, c' = 0 kPa	φ' = 35°, c' = 2 kPa	φ' = 20.0°, c' = 2 kPa
Angle of dilation ψ [°]	0	0	0
Elastic stiffness parameters (E,ν) or (K,G)	E = 30000 kPa ν = 0.2	E = 30000 kPa ν = 0.3	*

[(1)]Ash properties from (Arup Geotechnics, 2007)
[(2)]London Clay properties from (O'Brien, Ellis & Russell, 2004)
*Small-strain stiffness parameters used

Table 3. Parameters of the small strain stiffness model.

Shear	A	B	C [%]	α	γ	$E_{d,min}$	$E_{d,max}$	G_{min}
	970	890	0.001	1.47	0.7	0.00173	0.173	3333.3
Bulk	R	S	T	δ	μ	$\varepsilon_{v,min}$	$\varepsilon_{v,max}$	K_{min}
	772.5	712.5	0.001	2.069	0.42	0.005	0.15	4000

Pre-peak behaviour of in-situ London Clay was formulated in terms of small strain stiffness model developed by (Jardine *et al.*, 1986) and implemented into ICFEP. The model parameters are calibrated to match shear stiffness curve measured for the London clay at Terminal 5, Heathrow Airport (Hight et al., 2003), and are given in Table 3.

The Barcelona Basic type model, modified by (Georgiadis, 2003) was used to simulate the

mechanical behaviour of clay fill. The version of BBM model implemented into finite element code ICFEP requires a minimum of 23 parameters to be defined. The significantly greater number of model parameters compared to original BBM is primarily linked to the extended (Lagioia et al., 1996) expression. The calibration exercise was based on the data published in the work of (Monroy, 2005) and are provided in Table 4.

Table 4. Modified BBM model parameters values.

Model 81 parameter	Value	Description	Model 81 parameter	Value	Description
α_g	0.4	Plastic Potential function parameters	κ_s	0.07	Elastic coefficient of compressibility for suction changes
μ_g	0.9		λ_s	0.3	Coefficient of compressibility for suction changes
M_g	0.89	Slope of the critical state line in the q–p space for triaxial compression	v_1	2.75	Specific volume at unit pressure for fully saturated conditions
α_f	0.4		χ	1	Factors the coefficient κ_s
μ_f	0.9	Yield surface parameters	ω	0	Controls the effect of S_r on the coefficient κ_s
M_f	0.89		s_{air} (kPa)	20	Air-entry suction value
α_c	1.98	Characteristic stress ratio	s_0 (kPa)	1.0E+6	Yield suction
$\lambda(0)$	0.152	Coefficient of compressibility for fully saturated conditions	p_{atm} (kPa)	100	Atmospheric pressure
κ	0.02	Elastic Coefficient of compressibility (along elastic paths)	OCR	10	Overconsolidation ratio
r	0.45	Maximum soil stiffness parameter	K_{min} (kPa)	2000	Minimum bulk modulus
β	0.011	Soil stiffness increase parameter	μ	0.35	Poisson's ratio
k	SWRC	Cohesion increase parameter *r*			

3.3 Boundary conditions

The analysis stages were systematically assembled in order to replicate as closely as possible previous stress and strain history of Hawkwell embankment. The sequence of finite element analyses is illustrated in Table 5.

Table 5. Sequence of analyses.

Increment number	Description of analysis stage	Duration
0	Setting of the initial conditions	-
0	Deactivation of the elements representing the embankment	-
1-17	Construction of the embankment	6 months
18-29	Increments not used – reserved for some trial analysis steps	-
30-605	Initialisation	4 years
606-749	Seasonal flustuation stage – first year of monitoring period	1 year
750-1325	Vegetation clearance	4 years

The purpose of the initialisation stage was to cover as realistically as possible 120 years of embankment existence prior to the start of monitoring, but at the same time without overly compromising the analysis duration (Tsiampousi et al., 2017).

The bottom boundary of the mesh was assumed to be rigid, and that pore water pressures remain unchanged from the initial state (Δp_f=0). For the line of symmetry and the far boundary, the displacements were fixed at zero in the horizontal direction and free in the vertical direction. The vertical boundaries of the mesh were assumed to be impermeable (no flow boundaries). The pore water pressure profile before the embankment construction was assumed to be hydrostatic, with the groundwater table located at 1m depth, resulting in a suction of 9.81 kPa at the surface.

Precipitation is simulated via dual condition is developed by (Smith, 2003) and implemented in ICFEP, which operates either as an infiltration (specified constant flow) condition, or as a constant prescribed pressure (variable flow) condition, thereby providing automatic and continuous division of the surface reached rainwater into infiltration, run-off and ponding. The position of precipitation BCs is schematically illustrated in Figure 3. The rainfall data used in the current analysis corresponds to the Shoeburyness weather station rainfall measurements for a period 2006-2011, Figure 7.

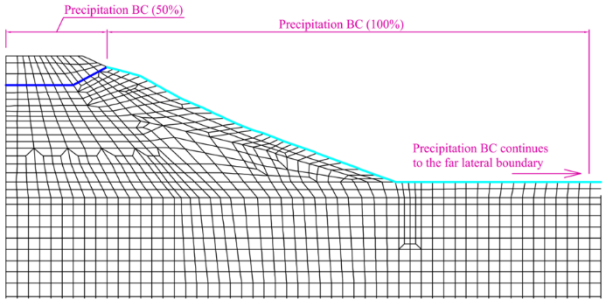

Figure 3. Contours of precipitation boundary condition.

Vegetation is simulated through non-linear root water uptake model developed by (Nyambayo & Potts, 2010). The model parameters include potential evapotranspiration, maximum root depth and reduction function. The potential evapotranspiration data for deciduous trees correspond to ones calculated using the FAO Penman-Monteith method, Figure 5. The extent over which vegetation was applied is shown in the Figure 4.

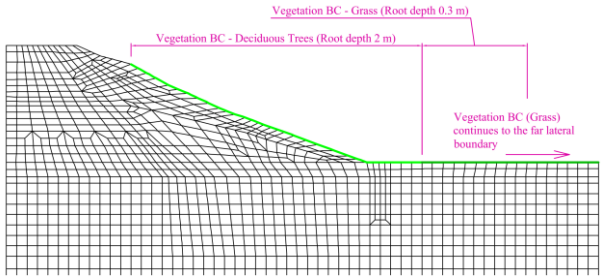

Figure 4. Contours of vegetation boundary condition.

In the present analysis the felling of large deciduous trees was modelled by reducing the root depth to 0.3 m and potential evapotranspiration rates to match the root system characteristics of the small and sparse vegetation (10% of mature trees). Trees were removed from the entire embankment slope, with the exception of zone just beyond the toe.

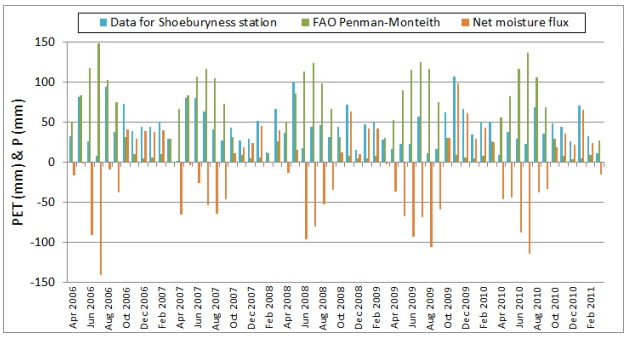

Figure 5. Potential evapotranspiration, precipitation and net rates.

3.4 Results

In the Figure 6. the comparison between the results of numerical simulation and field pore water pressure data for a midpoint of clay fill layer are presented. The obtained results, unlike some previous studies on (Briggs et al., 2016), show very good agreement with piezometers readings.

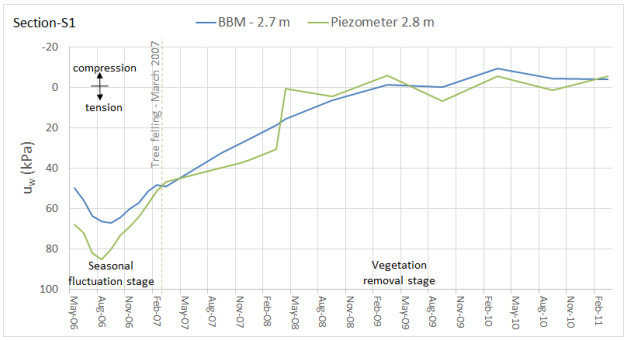

Figure 6. Comparison of numerical results and in-situ measurements of pore water pressures.

The comparison of estimated and recorded evolution of vertical displacements of a point close to the surface of section S2 is illustrated in Figure 7.

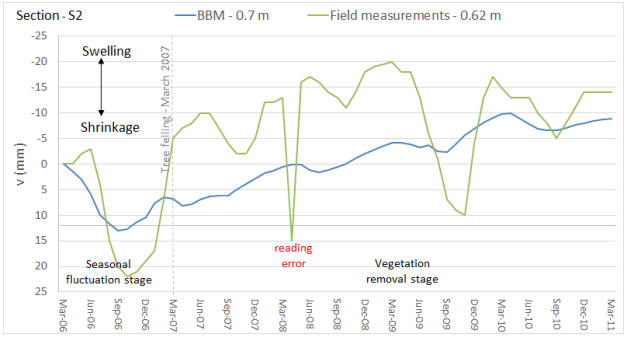

Figure 7. Comparison of numerical results and in-situ measurements of vertical displacements.

It can be seen that the numerical model somewhat underestimates the magnitudes of vertical movements. The reason for discrepancy lies in the fact that the adopted value of compressibility coefficient κ_s, that links volumetric deformation to suction changes, is based on tests on reconstituted and compacted London Clay and not the dumped clay fill.

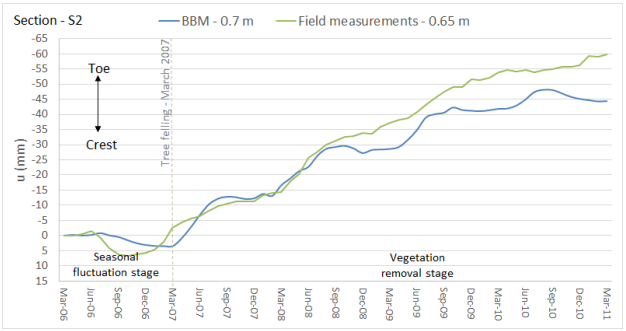

Figure 8. Comparison of numerical results and in-situ measurements of horizontal displacements.

The comparison of numerical simulations and inclinometer loggings of horizontal movements is presented in Figure 8. Both qualitatively and quantitatively, analysis predictions very accurately comply with filed observations.

4 CONCLUSIONS

The results of the presented numerical simulation prove that presented approach based on fully coupled numerical analyses combined with appropriate water retention curve, hydraulic conductivity function and advanced partially saturated constitutive model offers considerable advantages in reproducing reality. These findings will improve vegetation management, in particular the design of tree clearance schemes, and will build confidence in predictions regarding the effects of climate change.

REFERENCES

Arup Geotechnics. (2007). *Monitoring of London Clay Embankments: Geotechnical Interpretative Report*. Report number: 121286-00/GIR/SSV&SSV/01.

Briggs, K. M., Smethurst, J. A., Powrie, W., & Brien, A. S. O. (2016). The influence of tree root water uptake on the long term hydrology of a clay fill railway embankment. *Transportation Geotechnics*, *9*, 31–48. https://doi.org/10.1016/j.trgeo.2016.06.001.

Georgiadis, K. (2003). *Development, implementation and application of partially saturated soil models in finite element analysis*. PhD Thesis. Imperial College, University of London, UK.

Geotechnical Observations. (2013). *07 - 011 Magnolia Road Southend - Raw Data*.

Glendinning, S., Loveridge, F., Starr-Keddle, R. E., Bransby, M. F., & Hughes, P. N. (2009). Role of vegetation in sustainability of infrastructure slopes. *Proceedings of the Institution of Civil Engineers -*

Engineering Sustainability, *162*(2), 101–110. https://doi.org/10.1680/ensu.2009.162.2.101.

Hight, D. W., McMillan, F., Powell, J. J. M., Jardine, R. J., & Allenou, C. P. (2003). Some characteristics of London clay. *Characterisation and Engineering Properties of Natural Soils*, *2*(JANUARY 2003), 851–907.

Lagioia, R., Puzrin, A. M., & Potts, D. M. (1996). A new versatile expression for yield and plastic potential surfaces. *Computers and Geotechnics*, *19*(3), 171–191. https://doi.org/10.1016/0266-352X(96)00005-5.

Melgarejo, L. M. C. (2004). *Laboratory and numerical investigations of soil-water retention curves* (Issue June). PhD thesis, Imperial College London.

Monroy, R. (2006). *The influence of load and suction changes on the volumetric behaviour of compacted London Clay*. PhD Thesis, University of London (Imperial College), London, UK.

Nyambayo, V. P., & Potts, D. M. (2010). Numerical simulation of evapotranspiration using a root water uptake model. *Computers and Geotechnics*, *37*(1–2),175–186. https://doi.org/10.1016/j.compgeo.2009.08.008.

O'Brien, A. S., Ellis, E. A., & Russell, D. (2004). Old Railway Embankment Clay Fill - Laboratory Experiments, Numerical Modelling and Field Behaviour. *Advances in Geotechnical Engineering: The Skempton Conference*, 911–921. https://doi.org/10.1680/aigev2.32644.0020.

Potts, D. M., & Zdravković, L. (1999). Finite Element Analysis in Geotechnical Engineering: Volume One - Theory. In *Finite Element Analysis in Geotechnical Engineering: Volume One - Theory*. Thomas Telford Ltd. https://doi.org/10.1680/feaiget.27534.

Ridley, A. M., Dineen, K., Burland, J. B., & Vaughan, P. R. (2003). Soil matrix suction: some examples of its measurement and application in geotechnical engineering. *Géotechnique*, *53*(2), 241–253. https://doi.org/10.1680/geot.2003.53.2.241.

Scott, J. M., Loveridge, F., & O'Brien, A. S. (2007). Influence of climate and vegetation on railway embankments. *Geotechnical Engineering in Urban Environments: Proceedings of the 14th European Conference on Soil Mechanics and Geotechnical Engineering*, 659–664.

Skempton, A. W. (1996). Embankments and Cuttings on the early Railways. *Construction History*, *Vol. 11*, 33–49.

Smethurst, J. A., Briggs, K. M., Powrie, W., Ridley, A., & Butcher, D. J. E. (2015). Mechanical and hydrological impacts of tree removal on a clay fill railway embankment. *Géotechnique*, *65*(11),869–882. https://doi.org/10.1680/jgeot.14.P.010.

Smith, P. G. C. (2003). *Numerical Analysis Of Infiltration Into Partially Saturated Soil Slopes* (Issue June). PhD thesis, Imperial College London.

Tsiampousi, A., Zdravkovic, L., & Potts, D. M. (2017). Numerical study of the effect of soil–atmosphere interaction on the stability and serviceability of cut slopes in London clay. *Canadian Geotechnical Journal*,*54*(3),405–418. https://doi.org/10.1139/cgj-2016-0319.

Proceedings of the XVIII ECSMGE 2024
GEOTECHNICAL ENGINEERING CHALLENGES
TO MEET CURRENT AND EMERGING NEEDS OF SOCIETY
© 2024 the Authors
ISBN 978-1-032-54816-6
DOI 10.1201/9781003431749-642
Open Access: www.taylorfrancis.com, CC BY-NC-ND 4.0 license

ECSMGE 24
XVIII EUROPEAN CONFERENCE ON SOIL MECHANICS AND GEOTECHNICAL ENGINEERING

Hydraulic properties of general-shape monodisperse granular materials: An insight from pore-network perspective

Propriétés hydrauliques de matériaux granulaires monodisperses de forme générale: Un aperçu du point de vue du réseau de pores

J. Qi, W. Fei, G. Narsilio*
Department of Infrastructure Engineering, The University of Melbourne, Parkville, Australia
College of Civil Engineering, Hunan University, Changsha, Hunan, China

**narsilio@unimelb.edu.au*

ABSTRACT: The understanding of the hydraulic properties of granular materials is of fundamental importance in geotechnical engineering. These macroscopic properties are fundamentally influenced by their micro-structure. However, the understanding of the link between the microstructure and the permeability is still limited, especially for granular assemblies of irregular shapes. This study bridges the gap using a framework that incorporates Discrete Element Method (DEM) simulation, image processing, and pore-network analysis. Five assemblies of natural sand grains with different sphericity and roundness are generated in DEM based on images of real geomaterials. The 3D geometries of the assemblies are processed in OpenPNM to build their pore networks, with pores represented as nodes and pore throats represented as edges that are weighted by local hydraulic conductance. Based on complex network theory, pore network features are extracted and analysed for insight into the intrinsic links between particle shape and hydraulic properties such as permeability and tortuosity. The result shows the hydraulic properties such as permeability, tortuosity and pore structures including pore size, throat size, and weighted closeness centrality of the pore network are intrinsically influenced by the particle shape.

RÉSUMÉ: La compréhension des propriétés hydrauliques des matériaux granulaires est fondamentale dans l'ingénierie géotechnique. Ces propriétés macroscopiques sont fondamentalement influencées par leur micro-structure. Cependant, la compréhension du lien entre la microstructure et la conductivité hydraulique est encore limitée, en particulier pour les assemblages granulaires de différentes formes de grains. Cette étude comble cette lacune en utilisant un cadre qui incorpore la simulation par la Méthode des Éléments Discrets (MED), le traitement d'image et l'analyse du réseau de pores. Cinq assemblages de grains de sable naturels avec différentes sphéricités et rondeurs sont générés en MED à partir d'images de véritables géomatériaux. Les géométries 3D des assemblages sont traitées dans OpenPNM pour construire leurs réseaux de pores, les pores étant représentés comme des nœuds et les gorges entre les pores comme des arêtes pondérées par la conductance hydraulique locale. Sur la base de la théorie des réseaux complexes, les caractéristiques du réseau de pores sont extraites et analysées pour comprendre les liens intrinsèques entre la forme des particules et les propriétés hydrauliques telles que la perméabilité et la tortuosité. Le résultat montre que les structures de pores, y compris la taille des pores, la taille de la gorge et la centralité de proximité pondérée du réseau de pores, sont influencées par la forme des particules.

Keywords: Granular material; hydraulic properties; pore network; complex network theory; particle shape.

1 INTRODUCTION

The hydraulic properties of porous media are of great importance in engineering applications such as dam design, geothermal engineering (Bidarmaghz et al., 2021), CO2 geo-storage (Fei et al., 2015), and radioactive waste disposal (Brauer, 1981). Such properties are fundamentally influenced by the microstructures within the porous media(Van der Linden, 2019). The influence of particle shape on the hydraulic behaviours has been investigated through numerical simulations (Garcia et al., 2009; Zhao & O'Sullivan, 2022) and laboratory tests (Wei et al., 2021). However, the characterisation and links between the pore structures, grain shapes, and the hydraulic properties are largely unknown.

In this study, the micro-geometries of natural sand particles are obtained from CT scanning based on an established framework (Fei et al., 2021) and used to build non-spherical particle assemblies using Discrete Element Methods (DEM) (Galindo-Torres, 2013). Pore network models are constructed using Open-PNM, with maximal inscribed spheres representing the pores and cylinders representing the throats (J. T. Gostick, 2017). Complex network theory (Van der Linden et al., 2018) are utilized to analyse the intrinsic

links between the microstructures and the hydraulic properties, which is one of the first studies of its kind.

2 METHODOLOGY

2.1 Discrete element assemblies

To investigate the influence of particle shape on the microstructure and the resulting hydraulic properties, five particle shapes from CT-scanned natural sand are selected as the input for the framework proposed by this study (Table 1). Sphericity was adopted as shape descriptors to quantify the irregularity of particle shapes. In this study, only the contribution of particle shape to the microstructures of the assemblies was considered. All the particles are normalised to the same equivalent diameter of 3mm to create monodisperse assemblies.

Table 1. Particles with different sphericity.

ID	G1	G2	G3	G4	G5
Sphericity	0.895	0.863	0.790	0.719	0.588
Shape					

The monodisperse granular assemblies are generated based general-shape DEM within the open-source code Mechsys (Galindo-Torres, 2013). DEM particles are generated in a rigid box with a dimension of X×Y×Z=60×36×36mm. The irregular particles are initially placed in 6×6 horizontal matrices with random orientations and then drop to the bottom of the box driven by gravitational forces (Figure 1 (a)).

Subsequently, the generated assemblies are compressed (Figure 1 (b)) by a rigid plate from the top at a (relatively slow) speed of 0.01mm/s until reaching the target initial porosity n =0.4. Next, particles in the assembly were fixed to form a rigid assembly after particles stabilised.

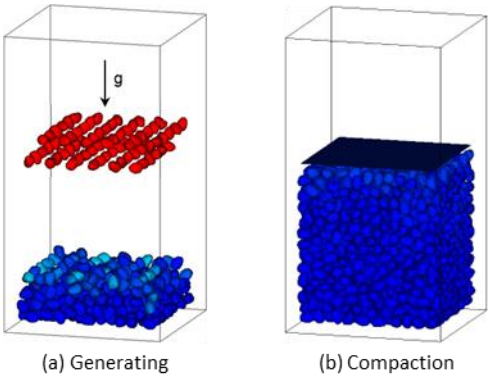

Figure 1.General-shape granular assemblies (a) DEM particle generation; (b) assembly compaction.

2.2 Pore-network construction

The pore network generator, Open-PNM, requires sequential images as inputs. Firstly, the granular assemblies generated in DEM were exported as STL meshes to obtain the geometry of the void space within the assemblies. Next, Boolean operations are conducted in Blender by subtracting the assembly meshes with a solid cube, which creates a pore geometry cube in the form of STL meshes (Figure 2(a)). The pore geometry cube was further sliced in Blender by horizontal planes along the vertical direction with evenly distributed intervals, which creates a stack of pore images (Figure 2 (b)) for the subsequent pore network construction.

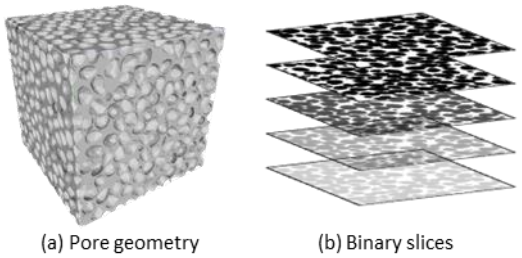

Figure 2. Pore information extraction (a) pore space geometry; (b) pore binary slicing.

To build the pore network models, the binary images (Figure 3 (a)) are processed with Open-PNM in Python. The SNOW algorithm (J. Gostick et al., 2016; J. Gostick, 2017) was applied to segment and recognize the pores (Figure 3 (b)).

To construct the pore network model, pores are represented by their maximum inscribed spheres, while the throats connecting the pores are represented by cylinders (Figure 3 (c)). By implementing these representations, the three-dimensional pore networks including the distribution and connectivity information are thus extracted from the granular assemblies (Figure 3 (d)).

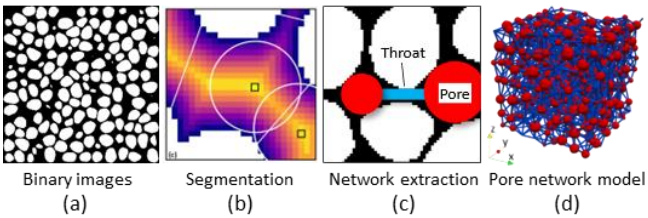

Figure 3. Construction of pore networks.

3 RESULTS

3.1 Pore and pore throat size distributions

To investigate the influence of particle shapes on the pore network structures, the probability distributions

of pore and throat sizes within assemblies of different particle shapes are statistically calculated (Figure 4). Particle shape has been observed to have a significant influence on the statistical distributions of the equivalent diameter of both the pores and throats. Rounded particles, such as G1, generally exhibited higher probability at larger equivalent diameters for both pores (0.8mm) and throats (1.7mm), compared with platy particles, such as G5.

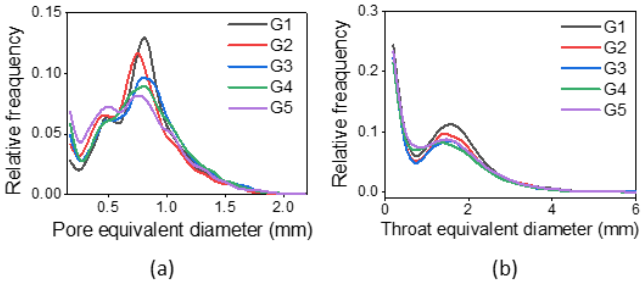

Figure 4. Pore networks size distribution:(a) pore size distribution; (b) throat size distribution.

3.2 Pore throat orientation

To further understand the impact of particle shape on pore network orientations, the edges in the networks are considered as vectors and are thus projected onto the horizontal (XY) and vertical (XZ) planes (Figure 5 (a)). The probability distribution of the orientations from the projected vectors are calculated, and here only the results for G1 and G5 are compared for simplicity. The particle shape has induced a larger difference on the XZ plane (Figure 5 (b)) compared with that on the horizontal XY plane (Figure 5 (b)). The platy particle G5 has induced structural anisotropy in pore networks, with pores having better connectivity along the horizontal direction compared to the vertical direction. Such phenomenon reals the particle shape has a significant influence on the orentation of pore networks.

3.3 Network features

Complex networks theory was uses to characterise the pore network structures. A network consists of multiple nodes connected by edges. In certain circumstances, the weights are assigned to the edges to describe the strength or importance of the connection. In this study, the pores are treated as nodes and the throats as edges. The edges are weighted by the local hydraulic conductance (Van der Linden et al., 2018) calculated from the equivalent cylindrical pores and all the connecting throats.

Network features are calculated following complex network theory, to quantify the pore networks. The *closeness centrality* measures the proximity of a node to other nodes, which has been proved to have a strong corelation with the hydraulic properties of sphere assemblies (Van der Linden et al., 2018), and thus was employed to characterise the pore network structures.

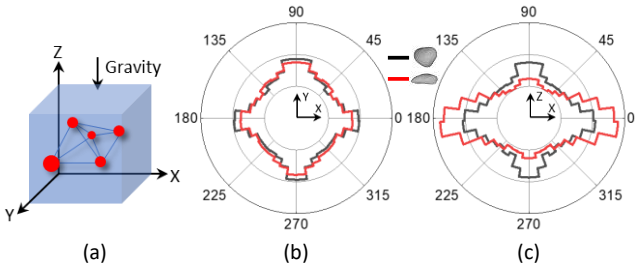

Figure 5. Pore network orientation (a) schematic of pore network projection; (b) frequency on XY plane; (c) frequency on XZ plane.

The node closeness centrality for each pore and their probability distribution are calclulated (Figure 6 (a)), which exhibits minor varation induced by particle shape. To link the pore networks with the macroscopic hydraulic properties, *weighted closeness centrality* was calculated from the local hydraulica conductance weighted pore network model (Figure 6 (b)). It is observed that the particle shape has a significant impact on the weighted closeness centrality distribution. Rounded particles, like G1, generally have higher weighted closeness centrality compared with platy particles such as G4 and G5.

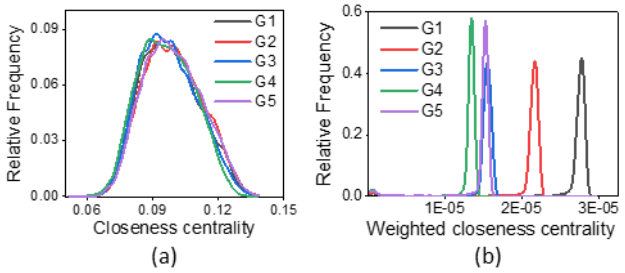

Figure 6. Probability distribution of pore network features: (a) closeness centrality (b) weighted closeness centrality from local hydraulic conductance.

3.4 Hydraulic properties

The influence of particle shape on the hydrolic properties are further investigated. Permeability along the horizontal and vertical directions was directly derived from the local hydraulic conductance within pore networks (Figure 7 (a)). Tortuosity, which quantifies the extent of distortion in flow paths along the macroscopic flow direction, was calculated from the effective diffusion path length devided by the straight-line distance along specific direction (Figure 7 (b)). Particle shape influences the permeability and tortuosity in both directions. Anisotropy was observed in permeability and tortuosity along both the horizontal and vertical directions. The platy particles

such as G5 have induced more significant anisotropy in both hydraulic properties.

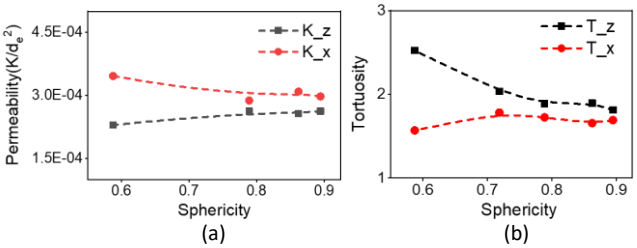

Figure 7. Influence of particle shape on hydraulic properties (a) permeability (b) tortuosity.

4 CONCLUSIONS

Based on DEM simulation, images processing, and pore network analysis, this study reveals the influence of particle shapes on the pore network and hydraulic properties of monodisperse granular assemblies.

The pore structures of granular assemblies are intrinsically influenced by the shapes of the constituent particles. Assemblies composed of more rounded particles generally exhibit larger pore and throat sizes.

The structural and hydraulic anisotropy induced particle shape are observed, which was more intensive for more platy particles such as G5.

Weighted edge closeness centrality could reflect the influence of particle shape on pore structures and hydraulic properties.

Future studies could expand the investigation to include a broader range of particle shapes, sizes and more detailed network features for pore network insight.

ACKNOWLEDGEMENTS

The authors are grateful for the financial support provided by the Australian Research Council project ARC DP210100433, the Chinese Scholarship Council (CSC) and The University of Melbourne.

REFERENCES

Bidarmaghz, A., Makasis, N., Fei, W., & Narsilio, G. A. (2021). An efficient and sustainable approach for cooling underground substations. *Tunnelling and Underground Space Technology*, *113*, 103986. https://doi.org/10.1016/j.tust.2021.103986.

Brauer, H. (1981). Two-phase flow and heat transfer in the power and process industries. VonA. E. Bergles, J. G. Colier, J. M. Delhaye, G. F. Hewitt undF. Mayinger. Hemisphere Publishing Corp., Washington - New York - London 1981. 1. *Chemie Ingenieur Technik*, *53*(9), 706–706. https://doi.org/10.1002/cite.330530907.

Fei, W. Bin, Li, Q., Wei, X. C., Song, R. R., Jing, M., & Li, X. C. (2015). Interaction analysis for CO2 geological storage and underground coal mining in Ordos Basin, China. *Engineering Geology*, *196*, 194–209. https://doi.org/10.1016/j.enggeo.2015.07.017.

Fei, W., Narsilio, G. A., van der Linden, J. H., Tordesillas, A., Disfani, M. M., & Santamarina, J. C. (2021). Impact of particle shape on networks in sands. *Computers and Geotechnics*, *137*. https://doi.org/10.1016/j.compgeo.2021.104258.

Galindo-Torres, S. A. (2013). A coupled Discrete Element Lattice Boltzmann Method for the simulation of fluid–solid interaction with particles of general shapes. *Computer Methods in Applied Mechanics and Engineering*, *265*, 107–119. https://doi.org/10.1016/j.cma.2013.06.004.

Garcia, X., Akanji, L. T., Blunt, M. J., Matthai, S. K., & Latham, J. P. (2009). Numerical study of the effects of particle shape and polydispersity on permeability. *Physical Review E - Statistical, Nonlinear, and Soft Matter Physics*, *80*(2), 1–9. https://doi.org/10.1103/PhysRevE.80.021304.

Gostick, J., Aghighi, M., Hinebaugh, J., Tranter, T., Hoeh, M. A., Forschungszentrum, |, Day, J. H., Spellacy, B., Sharqawy, M. H., Burns, A., Lehnert, W., Jülich, F., Aachen, R., & Putz, A. (2016). *OpenPNM: A Pore Network Modeling Package*. www.scipy.org.

Gostick, J. T. (2017). Versatile and efficient pore network extraction method using marker-based watershed segmentation. *Physical Review E*, *96*(2). https://doi.org/10.1103/PhysRevE.96.023307.

Van der Linden, J. H. (2019). *Pore-scale characterisation of fluid flow and heat transfer in granular geomaterials* [PhD thesis]. University of Melbourne.

Van der Linden, J. H., Sufian, A., Narsilio, G. A., Russell, A. R., & Tordesillas, A. (2018). A computational geometry approach to pore network construction for granular packings. *Computers and Geosciences*, *112*, 133–143. https://doi.org/10.1016/j.cageo.2017.12.004.

Wei, D., Wang, Z., Pereira, J. M., & Gan, Y. (2021). Permeability of Uniformly Graded 3D Printed Granular Media. *Geophysical Research Letters*, *48*(5). https://doi.org/10.1029/2020GL090728.

Zhao, B., & O'Sullivan, C. (2022). Fluid particle interaction in packings of monodisperse angular particles. *Powder Technology*, *395*, 133–148. https://doi.org/10.1016/j.powtec.2021.09.022.

Proceedings of the XVIII ECSMGE 2024
GEOTECHNICAL ENGINEERING CHALLENGES
TO MEET CURRENT AND EMERGING NEEDS OF SOCIETY
© 2024 the Authors
ISBN 978-1-032-54816-6
DOI 10.1201/9781003431749-643
Open Access: www.taylorfrancis.com, CC BY-NC-ND 4.0 license

ECSMGE 24
XVIII EUROPEAN CONFERENCE ON SOIL MECHANICS AND GEOTECHNICAL ENGINEERING

Hydraulic conductivity of bentonite amended flyash liners for MSW landfills

Conductivité hydraulique des revêtements de cendres volantes amendés à la bentonite pour les décharges MSW

K.V.N.S. Raviteja*
SRM University, Amaravati, Andhra Pradesh, India

J.K. Janga, K.R. Reddy
University of Illinois Chicago, Chicago, USA

**raviteja.k@srmap.edu.in*

ABSTRACT: This study investigates the effectiveness of bentonite-amended flyash (BAF) liners as barriers against infiltration in municipal solid waste (MSW) landfills. Laboratory experiments were conducted to evaluate the compaction properties and hydraulic conductivity (HC) of the BAF liners with varying mix proportions. Flyash, a byproduct of coal-fired power plants, amended with bentonite was utilized as a cost-effective alternative to conventional clay liners. Bentonite, a highly expandable clay mineral, was incorporated to enhance hydraulic performance. Standard Proctor compaction tests were performed to determine optimal compaction properties of different BAF mixes. Further, BAF specimens with different mix proportions were prepared by compacting at maximum dry density (MDD), and optimum moisture content (OMC). HC tests were performed on the compacted samples using a flexible-wall (triaxial) permeameter apparatus following ASTM standards. Compaction test results revealed that a mix ratio of 80:20 (Flyash: Bentonite) resulted in highest MDD and lowest OMC. Results also revealed a significant reduction in HC upon the addition of bentonite to the BAF liner. As the bentonite content increased, the HC decreased, indicating improved barrier properties. The optimal performance was achieved with a bentonite content of 20-30%, resulting in good compaction properties (high MDD and low OMC), and a HC below the regulatory limit of 10^{-7} cm/s, rendering the mix proportion optimal for barrier application. Overall, this study highlights the potential of BAF liners as efficient and cost-effective barrier systems for MSW landfills. The significant reduction in HC because of bentonite amendment, and excellent heavy metal and nutrient adsorption capabilities of flyash renders BAF effective for application as a barrier material in landfills.

RÉSUMÉ: Cette étude examine l'efficacité des revêtements de cendres volantes modifiées par de la bentonite (BAF) comme barrières contre l'infiltration de lixiviat dans les décharges de déchets solides municipaux (MSW). Des expériences en laboratoire ont été menées pour évaluer les propriétés de compactage et la conductivité hydraulique des revêtements BAF avec différentes proportions de mélange. Les cendres volantes, un sous-produit des centrales électriques au charbon, modifiées avec de la bentonite, ont été utilisées comme alternative rentable aux revêtements en argile conventionnels. De la bentonite, un minéral argileux hautement expansible, a été incorporée pour améliorer les performances hydrauliques. Des tests de compactage standard Proctor ont été effectués pour déterminer les propriétés de compactage optimales de différents mélanges BAF. De plus, des échantillons de BAF avec différentes proportions de mélange ont été préparés par compactage à une densité sèche maximale (MDD) et à une teneur en humidité optimale (OMC). Des tests de conductivité hydraulique ont été effectués sur les échantillons compactés à l'aide d'un appareil à perméamètre à paroi flexible (triaxial) conformément aux normes ASTM. Les résultats des tests de compactage ont révélé qu'un rapport de mélange de 80:20 (Flyash: Bentonite) entraînait un MDD le plus élevé et une OMC la plus faible. Les résultats ont également révélé une réduction significative de la conductivité hydraulique lors de l'ajout de bentonite au revêtement BAF. À mesure que la teneur en bentonite augmentait, la conductivité hydraulique diminuait, ce qui indique des propriétés de barrière améliorées. Les performances optimales ont été obtenues avec une teneur en bentonite de 20 à 30%, ce qui se traduit par de bonnes propriétés de compactage (MDD élevé et faible OMC) et une conductivité hydraulique inférieure à la limite réglementaire de 10 à 7 cm/s, rendant la proportion de mélange optimale pour application de barrière. Dans l'ensemble, cette étude met en évidence le potentiel des revêtements BAF en tant que systèmes de barrière efficaces et rentables pour les décharges de DSM. La réduction significative de la conductivité hydraulique due à l'amendement bentonite et aux excellentes capacités d'adsorption des métaux lourds et des nutriments par les cendres volantes rendent le BAF efficace pour atténuer la migration des lixiviats et minimiser les risques de contamination de l'environnement.

Keywords: Bentonite-amended flyash; hydraulic conductivity; leachate containment; landfill liners.

1 INTRODUCTION

Landfilling, with its aim of safeguarding the environment from potential harm due to waste disposal, addresses the critical challenge of managing the municipal solid waste (MSW). MSW, if not properly contained, poses severe risk of contaminating surface water, groundwater, soil, and air, thereby directly or indirectly affecting human health (Freeman, 1989; USEPA, 1989; Qasim and Chiang, 1994). A typical engineered landfill consists of three essential components: the top soil cover system, waste layer, and a bottom liner system (Sharma and Reddy, 2004). The bottom liner layer plays a crucial role in restricting the infiltration of leachate to groundwater. Acting as pivotal barriers, liners play an important role in effectively preventing the migration of harmful leachate substances into underground aqueducts and aquifers (Sharma and Reddy, 2004). The soil liner layer, functioning as a barrier generally consists of compacted fine-grained soil, which must adhere to specific criteria, including HC ($<10^{-7}$ cm/s), sufficient strength (Unconfined compressive strength (UCS) - 200 kPa), the absence of shrinkage/desiccation cracks, the absence of lumps/clods in compacted clay, and an adequate thickness of compacted clay (>100 cm), as outlined by Central Pollution Control Board (CPCB, 2001), and United States Environmental Protection Agency (USEPA, 1989).

Constructing liners for landfills becomes a formidable task when obtaining large quantities of low-permeable materials near the site proves challenging. In instances where suitable clayey materials are not locally available, project costs can escalate significantly due to the necessity of importing materials from external sources (Mishra and Ravindra, 2015). In addition, the high swelling characteristic of bentonite and some other low permeable clays often results in the development of desiccation cracks after several wetting and drying cycles (Gahlot et al., 2022). Nevertheless, leveraging the superior rheological and adsorption properties of bentonite, in combination with other non-plastic materials, offers a promising approach to meet the criteria of strength and permeability for effective liner materials (Daniel and Wu, 1993; Al-Badran et al., 2017; Mukherjee and Mishra, 2020; Raviteja et al., 2024).

Flyash is recognized as a potential material suitable for use as a liner when combined with bentonite or low-permeable clay. The particles of flyash exhibit a spherical shape and comprise solid spheres, cenospheres, irregular-shaped debris, and porous unburnt carbon (Buragohain et al., 2018). Past research has indicated that flyash can be effective in adsorbing a wide range of contaminants making it suitable as a component of landfill liners. However, flyash as a standalone barrier material, owing to its high permeability and non-plasticity, will not satisfy the requirements of a liner system. Hence, it is required to amend flyash with a low-permeable clayey material like bentonite in order to be employed as a barrier material. Hence, the aim of the current study is to evaluate the compaction properties and HC of different proportions of flyash and bentonite to identify the optimal mix of these materials to be employed as a landfill liner material.

2 MATERIALS AND METHODS

2.1 Flyash

In this study, class-F flyash sourced from Charlotte, NC, situated in the South-Eastern part of the USA, is utilized. Table 1 provides an overview of the physio-chemical and geotechnical properties of the flyash in accordance with ASTM standards. According to the Unified Soil Classification System (USCS), the material is classified as ML. The MDD and OMC of the flyash are observed to be 1.3 g/cm^3 and 19.1%, respectively. The saturated HC (SHC) is reported as 8.79×10^{-5} cm/s, indicating the highly porous nature of the material.

Table 1. Geotechnical and physio-chemical properties of bentonite and flyash used in this study.

Property	**Bentonite**	**Flyash**
Specific Gravity	2.49	2.27
Grain Size Distribution		
Coarse fraction	14.4	11
Silt fraction (<0.005 mm), %	30	82
Clay fraction (<0.005 mm), %	70	7
Mean diameter (D_{50}), mm	0.002	0.034
Liquid Limit (LL), %	371.7	-
Plastic Limit (PL), %	42.2	-
Plasticity Index (PI), %	329.4	NP
USCS Classification	CH	ML
Moisture-Density Relationship		
OMC, %	39.0	19.1
MDD, g/cm^3	1.24	1.30
Free Swell, ml/2g	24	-
SHC, cm/s	1.20×10^{-9}	8.79×10^{-5}
pH	9.60	7.57
Oxidation Redox Potential (ORP), mV	70.3	110.0
Electrical Conductivity (EC), µS/cm	1369	1325

2.2 Bentonite

To attain the targeted low HC levels, the utilization of bentonite as a liner material is crucial. Bentonite is composed of clay particles characterized by high plasticity and strong bonding ability. In this research, commercial sodium bentonite VOLCLAY® SOIL SEALANT CP-200, sourced from Colloid Environmental Technologies Company (CETCO), USA, is employed. Table 1 provides an overview of the physio-chemical and geotechnical properties of the bentonite. It is observed that the MDD and OMC of the bentonite are 1.24 g/cm^3 and 39%, respectively. The SHC is noted as 1.2×10^{-9} cm/s, significantly lower than that of flyash.

2.3 Compaction testing

To ensure HC and strength characteristics remain within safe limits for geomaterials employed in liners, it is crucial to identify the appropriate range of compaction parameters, including water content and dry unit weight, as emphasized by Younus and Sreedeep (2012). The desired HC was successfully achieved in both compacted and non-compacted bentonite-flyash mixes at proportions of 40-60% and 70-30%, as reported by Rashid et al. (2021). This underscores the significance of compaction in minimizing the HC of the mixed proportion. In the current research, the compaction properties of various bentonite-flyash mixes, ranging from 0-50%, were investigated. Standard proctor compaction tests as per the procedures stipulated in ASTM D698 (2021) were performed to determine the OMC and MDD of different bentonite-flyash mixtures.

2.4 Hydraulic conductivity testing

The HC of various proportions of bentonite and flyash were then determined at the optimum compaction conditions (OMC and MDD). Pre-compaction, the materials mixed with water, to achieve OMC, were kept in moisture desiccators at room temperature for 24 hours to achieve moisture equilibrium. The materials were then compacted at the predetermined MDD using a Harvard miniature compactor. Tests were conducted using triaxial flexible-wall permeameter at different mix proportions using cylindrical samples with 3.3 cm diameter and 7.1 cm height. Figure 1 shows the test setup for the HC determination. The HC of the compacted samples is determined using constant head method as per the procedure stipulated in ASTM D5084 (2016). The HC of the sample is determined after ensuring full saturation (Skempton's pore pressure coefficient – 0.986).

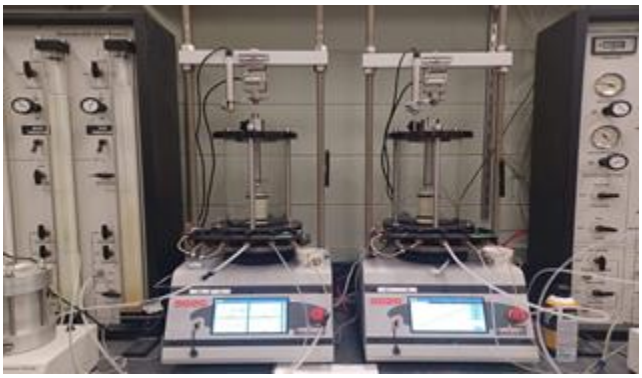

Figure 1. Flexi-wall triaxial setup used for hydraulic conductivity testing.

3 RESULTS AND DISCUSSION

3.1 Compaction testing results

A series of compaction tests were conducted on the BAF mix with proportions of bentonite varying from 5-50%. As shown in Figure 2, it is observed that the MDD has increased from 1.36 g/cm^3 to 1.47 g/cm^3 with an increase in bentonite content from 5 to 20%, and has decreased with further increase in bentonite content. The OMC has decreased from 23.2% to 19.6% with increase in bentonite content up to 20% and increased with further increase in bentonite content.

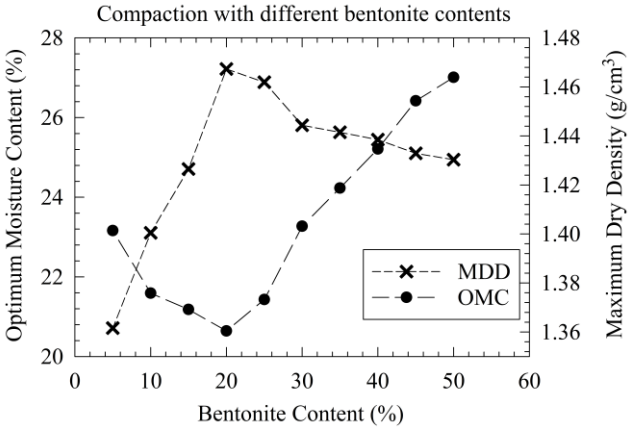

Figure 2. Influence of bentonite content on the maximum dry density (MDD) and optimum moisture content (OMC) of flyash.

It can be noted that the highest value of MDD and lowest OMC was observed at 80% flyash and 20% bentonite mix proportion. The initial increase in MDD values can be attributed to the improved compaction and packing of the soil particles due to the presence of bentonite, leading to greater dry density. Beyond a certain threshold (20%), the continued addition of bentonite may lead to excessive plasticity, hindering effective compaction. Beyond this point, the OMC

may increase, and MDD may decrease as the excess bentonite becomes more difficult to compact effectively.

The scanning electron microscopy (SEM) analysis carried out on the optimum flyash-bentonite mix (80F-20B) is shown in the Figure 3. The large spherical solids are cenospheres and other particles of flyash. Cenospheres are composed primarily of silica, alumina, and iron oxide, which can help in adsorption of inorganic pollutants. The smaller particles adsorbed onto the surface of flyash particles are the particulate matter of bentonite. As observed in the SEM image, the bentonite particles not only bonded with flyash particles, but they also helped in forming flocs of flyash particles. This flocculated structure of BAF particles can be the possible reason for excellent compaction achieved, with highest value of MDD, for 80-20 mix.

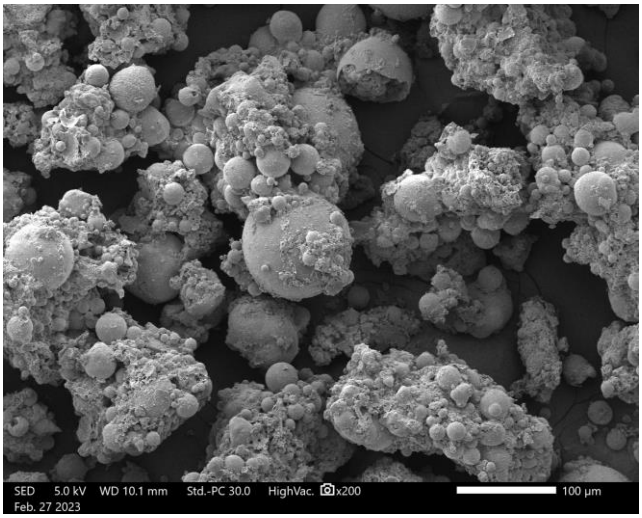

Figure 3. Scanning electron microscopy image of 80% flyash and 20% bentonite mix.

3.2 Hydraulic conductivity testing results

The HC tests were conducted at bentonite proportions varying from 10-50%. The results of the HC tests are presented in Figure 3. It is seen that for the mix proportion containing 0-10% bentonite, the HC is far higher than acceptable value of 10^{-7} cm/s. This is primarily due to the highly porous nature of flyash, which dominates the HC of the mix. The porous structure of flyash facilitates the movement of water, leading to higher HC. However, with further increase in bentonite content the HC has reduced. For a bentonite content of 20% to 30% and more, the HC has reached acceptable levels. The combination of bentonite with flyash aids in reducing HC by establishing a robust bond through pozzolanic reaction and clogging the pore spaces in flyash with swollen bentonite (Rashid et al., 2021).

The results suggest that the specific combination of 70-80% of flyash and 20-30% bentonite, by weight, provides an effective balance between the porous nature of flyash and the low permeability of bentonite. The bentonite content at this ratio sufficiently reduces the overall HC of the mixture, making it suitable for landfill liner applications.

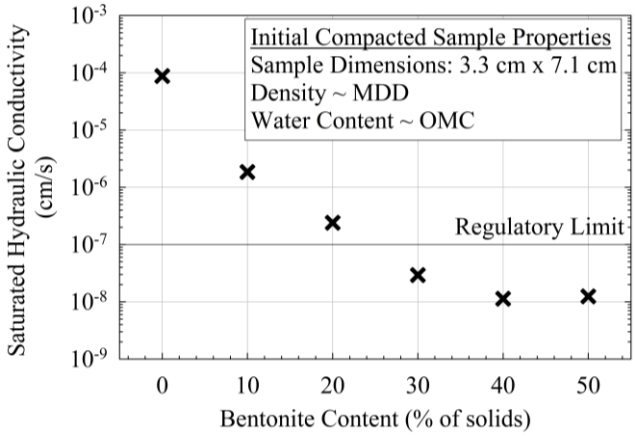

Figure 4. Influence of bentonite content on the hydraulic conductivity of flyash.

Past studies conducted to assess the performance of BAF for liner applications has resulted in similar outcomes. The optimal percentage of flyash that can be mixed with bentonite is determined to be up to 70% to ensure workability and maintain the quality of the liners as observed by Younus and Sreedeep (2012). A study conducted by Murat and Yilmaz (2001) examined the behavior of a mixture of flyash and bentonite, concluding that a combination of flyash with 20% bentonite is suitable as a liner and cover material at waste disposal sites.

4 CONCLUSIONS

Current study investigated the effectiveness of BAF as a low-permeable barrier material for application in covers/liners of MSW landfills. Laboratory experiments evaluated HC under varying conditions. Specimens with different flyash and bentonite mix proportions were prepared and compacted to optimal density. The following observations are made from the study:

- Optimal performance, in terms of compaction properties, of the proposed liner material was achieved with a bentonite content of 20% and 80% of flyash resulting in high MDD of 1.47 g/cm^3.
- Scanning electron microscopy (SEM) analysis of the optimal mix (80F-20B) revealed large

spherical solids as cenospheres of flyash and bentonite particles adhering to flyash.

- The pozzolanic reaction and the formation of a C-S-H gel matrix likely resulted in effective bonding between flyash and bentonite particles, and also resulted in a flocculated structure of particles resulting in effective compaction.
- A significant reduction in HC was observed with increased bentonite content from 0-50%.
- Bentonite content of 20-30% resulted in acceptable levels of HC for barrier applications.

Overall, this study highlights the feasibility of using BAF as efficient and cost-effective barrier material for MSW landfills. Although HC requirements can be satisfied using BAF, further studies regarding compatibility with various contaminants that can be found in landfill leachate are needed for application as a liner. Further, microstructural and chemical component analyses can help in understanding the interactions between bentonite and flyash particles at different mix proportions. In addition, field scale testing is required to assess the performance of the same in the presence of actual leachate containing diverse range of contaminants.

ACKNOWLEDGMENTS

The first author is grateful for the financial support provided in the form SERB International Research Excellence fellowship (SIR/2022/000374) by DST, Govt. of India.

REFERENCES

Al-Badran, Y., Baille, W., Tripathy, S. and Schanz, T. 2017. Swelling behavior of bentonite based backfilling materials in nuclear waste repository conditions. *J. Hazard. Toxic Radioact*. Waste, 21(1), D4015006.

ASTM D698-12. 2021. Standard Test Methods for Laboratory Compaction Characteristics of Soil Using Standard Effort. ASTM International, West Conshohocken.

ASTM D5084-16a. 2016. *Standard Test Methods for Measurement of Hydraulic Conductivity of Saturated Porous Materials Using a Flexible Wall Permeameter*. ASTM International, West Conshohocken.

Buragohain, P., Garg, A., Lin, P., Hong, M., Yi, Z. and Sreedeep, S. 2018. Exploring Potential of Fly Ash–Bentonite Mix as a Liner Material in Waste Containment Systems Under Concept of Sponge City. *Advances in Civil Engineering Materials*, 7(1), 46–70. 2018

Central Pollution Control Board (CPCB). 2001 *Criteria for Hazardous Waste Landfills*. CPCB, Delhi.

Daniel, D.E. and Wu, Y.K. 1993. Compacted Clay Liners and Covers for Arid Sites. *J. Geotech. Eng.,* 119 (2), 223 –237.

Freeman, H.M. 1989. *Standard Handbook of Hazardous Waste Treatment and Disposal*. McGraw-Hill, New York.

Gahlot, R., Verma, A. and Kumar, M. 2022. Geotechnical behavior of fly ash-coal ash and bentonite clay composite as a landfill barrier material with special emphasis on desiccation cracks. *Environmental Research*, 214(2), 113853.

Mishra, A.K. and Ravindra, V. 2015. On the Utilization of Fly Ash and Cement Mixtures as A Landfill Liner Material. *Int. J. of Geosynth. and Ground Eng*. 1, 17.

Mukherjee, K. and Mishra, A.K. 2020. Undrained performance of sustainable compacted sand-bentonite–glass fiber composite for landfill application. *Journal of Cleaner Production*, 244, 118662.

Murat, M. and Yilmaz, Y. 2001. Potential use of fly ash and bentonite mixtures as a liner or cover at waste disposal areas. *Environ Geol*., 40, 1316–1324.

Qasim, S.R. and Chiang, W. 1994. *Sanitary Landfill Leachate: Generation, Control and Treatment*. CRC Press, New York.

Rashid, H.M.A., Sardar, A. and Ismail, A. 2021. Geotechnical Characterization of Bentonite-Fly Ash Mixtures for Their Application as Landfill Liner in Pakistan. *Arab J Geosci*., 14, 1307.

Raviteja, K. V. N. S., Janga, J. K., and Reddy, K. R. 2024. Retention of Phosphate by Bentonite Amended Flyash Liners. *GeoCongress 2024*, GSP 351, ASCE, Reston, VA.

Sharma, H. D., Reddy, K. R. 2004. *Geoenvironmental engineering: site remediation, waste containment, and emerging waste management technologies*. John Wiley & Sons.

United States Environmental Protection Agency (USEPA). 1989. *Requirements for Hazardous Waste Landfill Design, Construction, and Closure.* USEPA seminar publication, Cincinnati. Report No. 625/4–89/022, 1–127.

Younus, M. and Sreedeep, S. 2012. *Evaluation of Bentonite-Fly Ash Mix for Its Application in Landfill Liners.* Journal of Testing and Evaluation, 40, 10416.

Proceedings of the XVIII ECSMGE 2024
GEOTECHNICAL ENGINEERING CHALLENGES
TO MEET CURRENT AND EMERGING NEEDS OF SOCIETY
© 2024 the Authors
ISBN 978-1-032-54816-6
DOI 10.1201/9781003431749-644
Open Access: www.taylorfrancis.com, CC BY-NC-ND 4.0 license

ECSMGE 24
XVIII EUROPEAN CONFERENCE ON SOIL MECHANICS AND GEOTECHNICAL ENGINEERING

A 4D investigation of model pile installation

Une etude 4D de l'installation de pieux modeles

T. Riccio*
University of Dundee, Dundee, United Kingdom

M.O. Ciantia, M. Previtali, M.J. Brown, L. Csetenyi
University of Dundee, Dundee, United Kingdom

**140007677@dundee.ac.uk*

ABSTRACT: Offshore wind turbines are typically fixed to the seabed via open-ended (OE) pile foundations. The risk and cost associated with OE pile installation may be reduced by performing field-scale tests to ensure adequate in-service capacity, as well as gain understanding of installation characteristics for equipment specification. However, to do so is often expensive and in most cases, highly impractical. Instead, 1*g* small-scale model tests can be used, in part, to study mechanistic behaviour which can aid in validating numerical methods which are capable of scaling to field conditions. In this paper, 1*g* pile model tests are undertaken in both sand and soft rock and the differing *in-situ* mechanisms are revealed through novel in-test X-ray techniques with time-resolve enabling a 4D study. The tests presented here are facilitated using a new compact multi-axis loading frame which is operable from within a CT bay.

RÉSUMÉ: Les éoliennes offshore sont généralement fixées au fond marin via des fondations sur pieux à extrémité ouverte (OE). Le risque et le coût associés à l'installation de pieux peuvent être réduits en effectuant des tests à l'échelle du terrain pour garantir une capacité en service adéquate, ainsi qu'en comprenant les caractéristiques d'installation pour les spécifications de l'équipement. Cependant, cela s'avère souvent coûteux et ce n'est pas pratique dans la plupart des cas. Au lieu de cela, les tests sur modèle 1*g* à petite échelle peuvent être utilisés, en partie, pour étudier le comportement mécaniste, ce qui peut aider à valider des méthodes numériques capables de s'adapter aux conditions de terrain. Dans cet article, des tests sur modèles de pieux de 1*g* sont entrepris à la fois dans le sable et dans la roche tendre et les différents mécanismes in situ sont révélés en raison de nouvelles techniques de rayons X en cours de test avec résolution temporelle permettant une étude 4D. Les tests présentés ici sont facilités à l'aide d'un nouveau bâti de chargement multi-axes compact qui peut être utilisé depuis une baie CT.

Keywords: Plugging; pile installation effects; MicroCT.

1 INTRODUCTION

Offshore structures are commonly fixed using open-ended (OE) pile foundations. These, which vary in diameter from less than 1 m to more than 8 m (Buckley et al., 2020), are designed to resist large environmental loads and to do so, require sufficient penetration defined by axial and lateral capacity requirements. Actual installation performance on site can vary, and risks such as pile run and conversely pile refusal can occur, leading to uncertain capacity. For small diameter piles, the risk of refusal is often associated with the occurrence of plugging, for which there is a greater tendency in small diameter piles due to ease of arching. This leads to an increased end bearing component as the plug forms (Fan et al., 2021) and can make reaching installation depth required for adequate lateral and axial capacity challenging. With the above in mind, novel small-scale model tests performed at 1*g* and paired with X-ray imaging are used here to investigate the occurrence of plugging on installation performance in sand and soft rock, the latter notorious for uncertainty in pile installation (Lord et al., 2002). These tests demonstrate how a blend of radiography and computed tomography (CT) can be used to track pile installation and fabric changes, offering new valuable insights which build on prior application of pile tracking through static CT (Doreau-Malioche et al., 2018). Carrying out live X-ray tomography during the installation is challenging and, in this instance, has been achieved by utilising a new multi-axis loading frame developed by Riccio et al. (2024) which is operable from within a CT bay, shown in *Figure 1*.

The tests reported in this study are not aimed to replicate real engineering application due to the limitations of the low-stress level and boundary effects. Rather, they focus on mechanistic, grain scale insight thanks to the micro level (μm) resolution of CT which may help ease the validation of new numerical

simulation techniques, like those used to study pile installation in complex geomaterials (Ciantia, 2022).

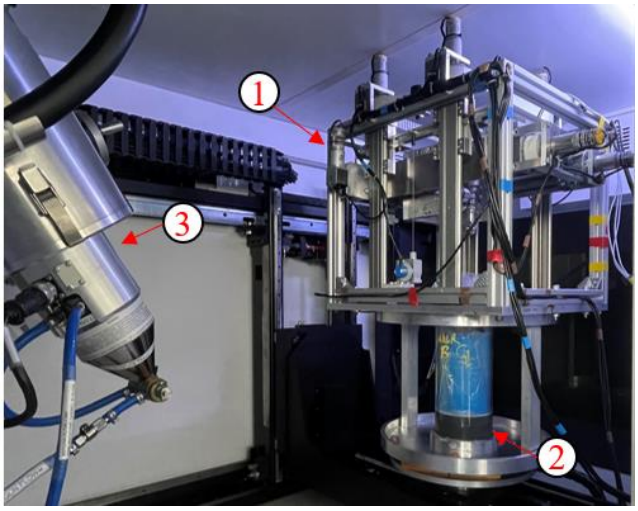

Figure 1. Multi-axis loading frame (1) with sample installed (2) positioned in lab-based X-ray CT scanner (3).

2 MATERIAL AND EXPERIMENT SET UP

2.1 Multi-axis actuator

The model tests were performed using a new multi-axis loading frame (*Figure 1*), which can apply up to 5 kN of vertical load and 400 N laterally. Actuation in the X, Y and Z plane was facilitated by DC motors controlled by a software based PID feedback which enabled both monotonic and cyclic displacement control (Riccio et al., 2024).

2.2 Sample material and preparation

Samples were prepared in a 300 mm tall acrylic chamber with a diameter of 120 mm which was fixed below the multi-axis actuator as shown in *Figure 1*. A well characterised dry sand (HST-95, see e.g., Lauder et al. (2013)) was used and pluviated from an automated hopper into the acrylic tube, achieving a relative density of $D_r = 80$ %. The soft rock sample ($\sigma_c < 2$ MPa, $d_{50} = 86$ µm) consisted of a highly porous sedimentary calcarenite rock which is widely spread along mediterranean coasts and is present at several offshore wind farms (Ciantia et al., 2015; Palix & Lovera, 2020). The cored soft rock sample, 150 mm tall and with a diameter of 100 mm, was fully saturated, notable as its strength reduces with an increasing degree of saturation (Ciantia et al., 2015).

2.3 Experimental procedure

For the soft rock a model pile of diameter Ø11.65 mm and wall thickness of $t_w = 0.74$ mm was used and for the sand a Ø15.37 mm ($t_w = 0.86$ mm). The installation depth was 100 mm in both cases, with a rate of 0.03 mm/s for the calcarenite, in order to preserve fully-drained conditions; and 0.1 mm/s for the dry sand. Following installation, tension pulls were performed on the pile installed in soft rock. During all of the aforementioned stages, live radiography was used to monitor the installation procedure. The CT scan for the soft rock test was performed following installation to study the material fabric around the pile and consisted of 8 frames per position (3141) acquired with an X-ray beam tension of 220 kV and current of 500 µA. The radiography used the same ray settings and projections were obtained every 500 ms.

3 RESULTS

3.1 Force-displacement response

In Figure 2(a) and (b), the installation force-displacement profiles for the sand (a) and the soft rock (b) are shown.

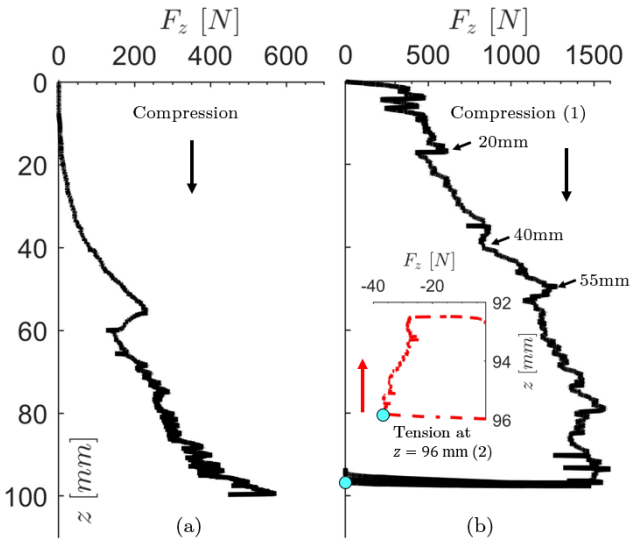

Figure 2. (a) HST-95 sand installation force profile (15.37mm pile) (b) Calcarenite installation (1) tension force profiles (2) (11.65mm pile).

The force-displacement profile of the pile penetrating the sand grew exponentially, indicative of plugging (White et al., 2000). This was likely due to the increasing internal shaft friction caused by dilation, principal stress rotation and soil-arching, sandwiching the lower portion of the plug statically (Liu et al., 2022). Between 50-100 mm the load profile was more volatile with sporadic drops, suggesting a stick-slip

mechanism within the pile plug, which may have been favoured by minor variations in the pluviated material. except for the large dip experienced at 50 mm which was a result in a brief pause in the servo actuation.

For the soft rock, the installation force profile (1) was characterised by a linear trend, with a more jagged response caused by local failures of the brittle intact material immediately below the pile toe, see Figure 2(b). The lack of an exponential force increment implies that the pile remained unplugged. However, the profile exhibited discrete step changes at 20, 40 and 55 mm and the jagged profile gradually smoothened with on-going penetration. It is hypothesised that the profile change indicated that the pile no longer experienced internal shaft stick-slip cycles and brittle failure (unplugged state) and instead transitioned to a ductile punch-like behaviour due to the closure of the pile base. This was supported by the low uplift capacity (2) (< 20 N, which was only 2.5% of the peak compressive penetration load at the same depth), a product of the material's low Poisson's ratio and damage generated around the pile during installation. This has been identified as a cause of low axial capacity of pile foundations in soft rock via large deformation simulations of fully installed close-ended model piles (Ciantia, 2022).

3.2 Post-installation visualisation

Figure 3(a) shows a 2D section through the centre of the pile following installation in the soft rock. The reconstructed image, with a resolution of 120 µm, shows the porosity distribution, obtained by calibration of the grey-values (GV) via the approximate linear relationship between GV and density (Alvarez-Borges et al., 2022). This shows that the pile did indeed plug during installation, leading to a highly densified zone of material ahead of the pile, in which the structure of the intact calcarenite rock collapsed. The bulbous failure zone (R) emphasised in Figure 3(b) extended approximately $2-3D$ ahead of the pile tip. The damage extent, previously observed in close-ended piles, is characteristic of a flat structure punching through rock (Alvarez-Borges et al., 2022; Castellanza et al., 2009). Along the pile walls the extent of damage appeared to increase with penetration depth. At ground level this extended radially by approximately the wall thickness of the pile, increasing to 2-3mm as the pile surpassed the plug initiation zone (exemplified at 2D above the pile tip, see Figure 3(c). This was likely due to the effect of the increased pile displacement which causes marked increases in radial stress, inducing failure of the surrounding material (Fan et al., 2021). The plug structure itself varied along its length as shown in Figure 3(a). At the top of the plug a mixture of intact discs and puttified material could be seen, indicative of the stick-slip mechanism. Toward the pile tip, the material progressively degraded into a dense, destructured state, in-line with the sandwiching mechanism highlighted by Liu et al. (2022).

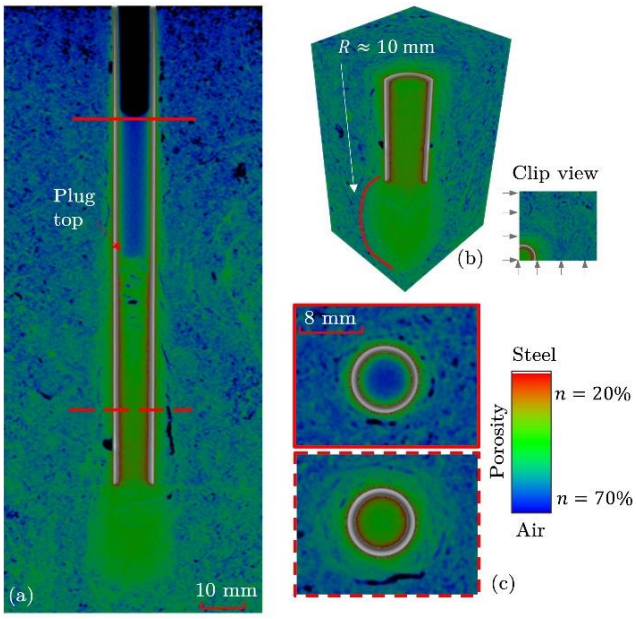

Figure 3. CT image of post installation of OE pile in calcarenite (a) 3D cross-sectional view of pile centre b) damage extent around pile annulus before plugging and after and (c) Damage bulb ahead of tip.

The plugging of this pile was unexpected, opposing a recent study in a similar soft rock (Alvarez-Borges et al., 2022), whereby the OE model pile ($D = 7.94$ mm) penetrated in full coring conditions leaving a small torus damage zone beneath the pile tip. Given that the inner diameter of the pile in this study was greater than that of Alvarez-Borges et al. (2022), a similar coring condition was anticipated. The reasons behind the different penetration mechanism appeared to stem from the variation in average pile roughness (R_a) and material grain size (d_{50}). Alvarez-Borges et al. (2022) used an acrylic pile with an $R_a \approx 0.02$ µm in conjunction with a finer grained chalk sample which had a $d_{50} \approx 5$ µm. In this study, the stainless-steel pile had an $R_a = 1.12$ µm. Combining this with the coarser-grained calcarenite resulted in a three-fold increase in R_a/d_{50}, indicative of a significantly rougher interface. This likely encouraged interlocking of the grains at the pile interface, inducing plugging.

3.3 Live installation visualisation

While it is challenging to use live radiography to assess fabric changes, it enabled real-time visualisation of the plug position for the sand example

throughout the installation, revealing real-time behaviour not attainable from the static CT scan. Figure 4(a) shows the live plug evolution during installation which was identified as the sharpest variation in the average grey-scale intensity along the pile length, e.g., Figure 4(b). This indicated that the pile cored initially and then progressively plugged corroborating with the penetration resistance, see Figure 2(a). As the pile plugged, the sand level surrounding the pile exterior rose significantly due to the increased displacement generated by the pile base closure as was evidenced between 40 and 96 mm of penetration. Although summarised briefly, the potential of live X-ray radiography has been evidenced by the ability to constantly track the pile behaviour and soil during installation.

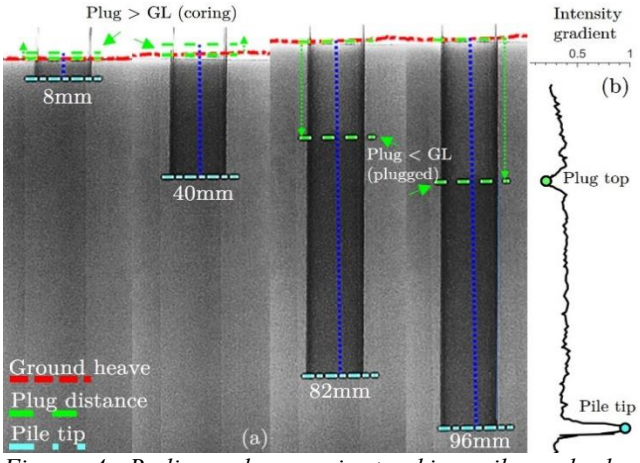

Figure 4. Radiography use in tracking pile and plug displacement during penetration for the sand example.

4 CONCLUSION

This paper has shown how the effect of plugging can alter the soil resistance to jacking. While the focus was on the plugging mechanism exhibited during installation, the CT and radiography techniques employed identified significant other mechanistic behaviour otherwise not revealed during conventional experimental or field scale studies. The new multi-axis loading frame has been highlighted as a valuable tool for researchers wishing to study 3D soil-structure problems in unison with X-ray, offering new insights into in-situ soil/rock-structure interactions.

ACKNOWLEDGMENTS

This work is an output from the ICE-PICK project, funded by the EPSRC NIA grant EP/W00013X/1.

REFERENCES

Alvarez-Borges, F., Ahmed, S., Madhusudhan, B. N., & Richards, D. (2022). Investigation of pile penetration in calcareous soft rock using X-ray computed tomography. International Journal of Physical Modelling in Geotechnics, 22(1), 38–52. https://doi.org/10.1680/jphmg.20.00031

Buckley, R. M., Jardine, R. J., Kontoe, S., Barbosa, P., & Schroeder, F. C. (2020). Full-scale observations of dynamic and static axial responses of offshore piles driven in chalk and tills. Geotechnique, 70(8), 657–681. https://doi.org/10.1680/jgeot.19.TI.001

Castellanza, R., Parma, M., Pescatore, V., & Silvestro, G. (2009). Model footing load tests on soft rocks. Geotechnical Testing Journal, 32(3), 262–272. https://doi.org/10.1520/gtj101845

Ciantia, M. O. (2022). Installation Effects on Axial Performance of Monopiles in Chalk for Offshore Renewables. Proceedings of the 2nd Vietnam Symposium on Advances in Offshore Engineering, 208 424–432. https://doi.org/10.1007/978-981-16-7735-9_47

Ciantia, M. O., Castellanza, R., & di Prisco, C. (2015). Experimental Study on the Water-Induced Weakening of Calcarenites. Rock Mechanics and Rock Engineering, 48(2), 441–461. https://doi.org/10.1007/s00603-014-0603-z

Doreau-Malioche, J., Combe, G., Viggiani, G., & Toni, J. B. (2018). Shaft friction changes for cyclically loaded displacement piles: An X-ray investigation. Geotechnique Letters, 8(1), 66–72. https://doi.org/10.1680/jgele.17.00141

Fan, S., Bienen, B., & Randolph, M. F. (2021). Effects of Monopile Installation on Subsequent Lateral Response in Sand. I: Pile Installation. Journal of Geotechnical and Geoenvironmental Engineering, 147(5), 04021021. https://doi.org/10.1061/(asce)gt.1943-5606.0002467

Lauder, K. D., Brown, M. J., Bransby, M. F., & Boyes, S. (2013). The influence of incorporating a forecutter on the performance of offshore pipeline ploughs. Applied Ocean Research, 39, 121–130. https://doi.org/10.1016/j.apor.2012.11.001

Liu, C., Tang, X., Wei, H., & Zhao, H. (2022). Visualization Investigation of the Plugging Effect on Open-Ended Pipe Pile Jacked in Transparent Sand. International Journal of Geomechanics, 22(10), 1–12. https://doi.org/10.1061/(asce)gm.1943-5622.0002455

Lord, J. A., Clayton, C. R. I., & Mortimore, R. N. (2002). Engineering in chalk CIRIA C574. CIRIA.

Riccio, T., Romero, T., Mánica, M., Previtali, M., & Ciantia, M. (2024). A 4D soil-structure interaction model testing apparatus. Submitted to Geotechnical Testing Journal, 1(1), 1–12.

White, D. D. J., Sidhu, H. H. K., Finlay, T. C. R. T., Bolton, M. D., & Nagayama, T. (2000). Press-in piling: the influence of plugging on driveability. 8th International Congerence of the Deep Foundations Institute, 299–310.

Proceedings of the XVIII ECSMGE 2024
GEOTECHNICAL ENGINEERING CHALLENGES
TO MEET CURRENT AND EMERGING NEEDS OF SOCIETY
© 2024 the Authors
ISBN 978-1-032-54816-6
DOI 10.1201/9781003431749-645
Open Access: www.taylorfrancis.com, CC BY-NC-ND 4.0 license

ECSMGE 24
XVIII EUROPEAN CONFERENCE ON SOIL MECHANICS AND GEOTECHNICAL ENGINEERING

New electric powered drill rig to meet sustainable geotechnique

Nouvelle sondeuse électrique pour atteindre une géotechnique soutenable

M. Rispal, C. Jacquard, G. de Oliveira Souza*
Fondasol, Avignon, France

P. Reiffsteck
Université Gustave Eiffel, Marne-la-Vallée, France

**guilherme-desouza@groupefondasol.com*

ABSTRACT: Drilling boreholes for geotechnical purposes such as sampling, in-situ tests and permeability testing are usually performed with the aid of drilling machines. These machines generally use internal combustion motors to provide energy to hydraulic pumps feeding the different actuators needed to push, rotate and hammer the drill bit into the ground. This results in a very noisy and polluted environment for the workers and the surrounding area. With the popularisation of electric vehicles, it's time drilling machines also make the switch to electric power. This paper presents one such prototype machine developed by Fondasol company, with the initially proposed technical specifications and the realised equipment. An autonomy up to one week has been observed on real sites, depending on the project's drilling objective. The use of electric motors allows for a new type of measuring while drilling, as the measurement of electric current and voltage is much more reliable than hydraulic pressure and flow rates. With this electric-based design, additional external sensors are no longer necessary. A first insight into this new type of measurements and its physical meaning is also given and discussed within this paper.

RÉSUMÉ: Les forages à des fins géotechniques comme le carottage, des essais pressiométriques et des essais de perméabilité sont habituellement exécutés à l'aide de machines de forage. Ces machines sont assez lourdes, généralement utilisent des moteurs thermiques pour fournir l'énergie aux pompes hydrauliques qui alimentent les différents vérins nécessaires pour pousser, tourner et marteler l'outil de forage dans le sol. Il en résulte un environnement très bruyant et pollué pour les travailleurs et les alentours. Avec la popularisation des véhicules électriques, il est temps pour les sondeuses de passer à l'énergie électrique aussi. Cette communication présente un prototype d'une telle machine, avec les spécifications proposées initialement et l'équipement réalisé. Une autonomie de plusieurs jours a été observée sur chantiers, selon l'enjeu du projet. L'utilisation de moteurs électriques permet une nouvelle forme d'enregistrement de paramètres instantanés, étant donné que la mesure du courant et de la tension électriques sont beaucoup plus fiables que les mesures de pression hydraulique et débit. Avec cette nouvelle conception, des capteurs externes additionnels ne sont pas nécessaires. Cet article montre un exemple de sondage faite avec cette sondeuse et discute de l'utilisation de ce nouveau type de mesure sa signification physique.

Keywords: Measuring while drilling; electrical drilling machine; sustainable development.

1 CONTEXT

Historically used in the energy resource fields but gaining popularity in the field of geotechnical engineering in the last decades, the method of measuring while drilling (MWD) involves monitoring and recording drilling parameters during the drilling process (Rodgers et al, 2020). In this method, a drill bit destroys the terrain as it advances downward, pushed and spun by hydraulic motors while a fluid cools down the equipment and removes loose debris from the hole (Reiffsteck, 2010).

The drilling may have multiple objectives: creating holes for sampling, in-situ tests like pressuremeter tests, installing piezometers, verifying the efficacy of soil treatments or simply gaining knowledge about the subsoil. It has the advantage of being a rapid essay giving continuous information, much like the cone penetration test, while allowing an identification of the soil (Fortunati & Pellegrino, 1998; Cardu et al, 2013).

The drill rigs used in creating these holes may vary in size and overall power but share similar architecture: they all have a mast on which translate the drilling head. The length of the mast and the characteristics of the drilling head may differ according to the project's objectives (Reiffsteck, 2010).

In addition to the translation motor, the drilling head is equipped with a rotation motor and eventually a hammer that transmit rotating forces to the drill bit underground through the drill string. Both elements are usually hydraulic. The mast has the functions of guiding and driving the drilling head vertically, pushing the drill bit into the soil. This movement is also achieved by a hydraulic system (Reiffsteck, 2010).

There are other hydraulic systems in the rig as well, such as the stabilizing cylinders, the mandible and the cylinder that folds down the mast to put the machine in displacement mode. All these systems, as well as the pump for drilling fluid, are typically powered by a hydraulic motor (ICE) (Nishi et al., 1998; Reiffsteck, 2010).

According to Reiffsteck (2010), one of the risks associated with this method is the accidental release of hydrocarbons (oils or fuel) into the soil from the various hydraulic systems or the motor, which could contaminate the water table. The combustion motor also produces polluting gases and a lot of noise which can be detrimental to the workers' health and the surrounding area, even more so when used in closed environments.

To remedy these issues and improve on the method's energy efficiency, Fondasol has developed an electric drill rig that is presented in this paper. The use of electric motors also allows a different way of measuring drilling parameters, which is also discussed in the article.

2 OBJECTIVES OF THE CLEA PROTOTYPE

The new CLEA drill rig proposes to change soil investigations by using electric motors instead of mechanic/hydraulic actuators fed by an internal combustion engine.

This allows more efficient drilling, as electric motors are more energy efficient than hydraulic systems, while producing less noise and air pollution. The drilling parameters can also be measured more reliably, as it is easier to continuously monitor electrical currents and voltages than fluid pressure or flow rate.

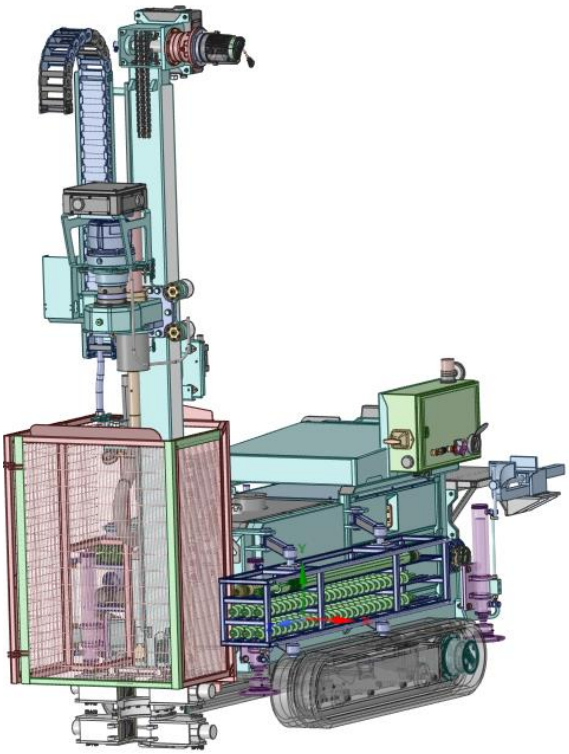

Figure 1. Electric drill rig prototype by Fondasol.

3 DRILL RIG SPECIFICATIONS

The prototype can achieve vertical speed of 900 m/h or 1500 mm/min with a maximum force of 21 kN. This movement is powered by an electric motor. The electric rotation motor allows a rotation speed of 350 rpm and a torque of 1500 Nm.

These specifications were chosen to approximate those of a conventional 32 kW hydraulic drill rig: vertical speed of 900 m/h, down force of 20 kN, rotation speed of 300 rpm and 1500 Nm of torque.

The battery bank used for the prototype is in the form of a detachable wagon and an autonomy of well over a week has been observed in the field (8 to 12% of battery used per day).

However, at this stage of development the prototype is not completely electric, it was built on the chassis of a conventional rig and still uses ICE powered hydraulic systems to operate the stabilizing cylinders and to unfold the mast. The engine is also used to power the continuous tracks while in displacement mode. A new 100% electric prototype is being built at the moment on a custom chassis with integrated power banks.

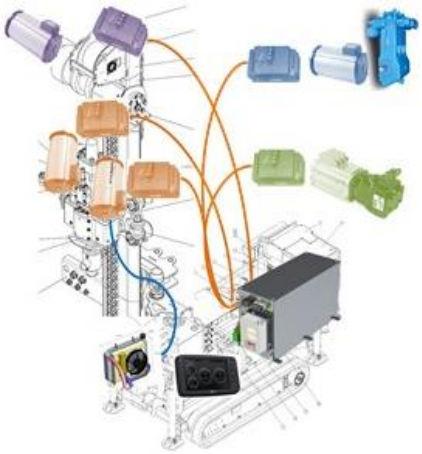

Figure 2. Scheme of all electric motors in the prototype.

4 ELECTRICAL MWD MEASUREMENT

The use of electric motors allows the monitoring of drilling parameters through the current and voltage. These electrical parameters are directly proportional to torque and rotation speed, respectively. This advantageously replaces the pressure transducers and the optical/magnetic sensors used to measure rotation speed typically used in conventional hydraulic rigs that only indirectly measure each parameter. The pressure transducers also have the disadvantage of not measuring the forces truly delivered to the drill bit as they are placed beside the pumps and cannot account for energy losses in the system (Peronne et al., 2021).

Unlike the typical measurements, the CLEA directly measures the current delivered to each motor, which is directly proportional to the torque applied on the drill bit. Instead of logging the values measured as a function of depth (typically each 2 cm), the prototype registers all the parameters as a function of time resulting in a much more detailed dataset.

The collected data can be displayed both as the conventional physical parameters in their respective units (MPa, Nm) of measurement and in terms of energy spent or power in kW delivered to the motors. Calculating the power spent by each motor also has the advantage of providing the total energy spent during the survey, which can be used to confirm the battery indicator and visualize which motor spent the most energy at a given moment.

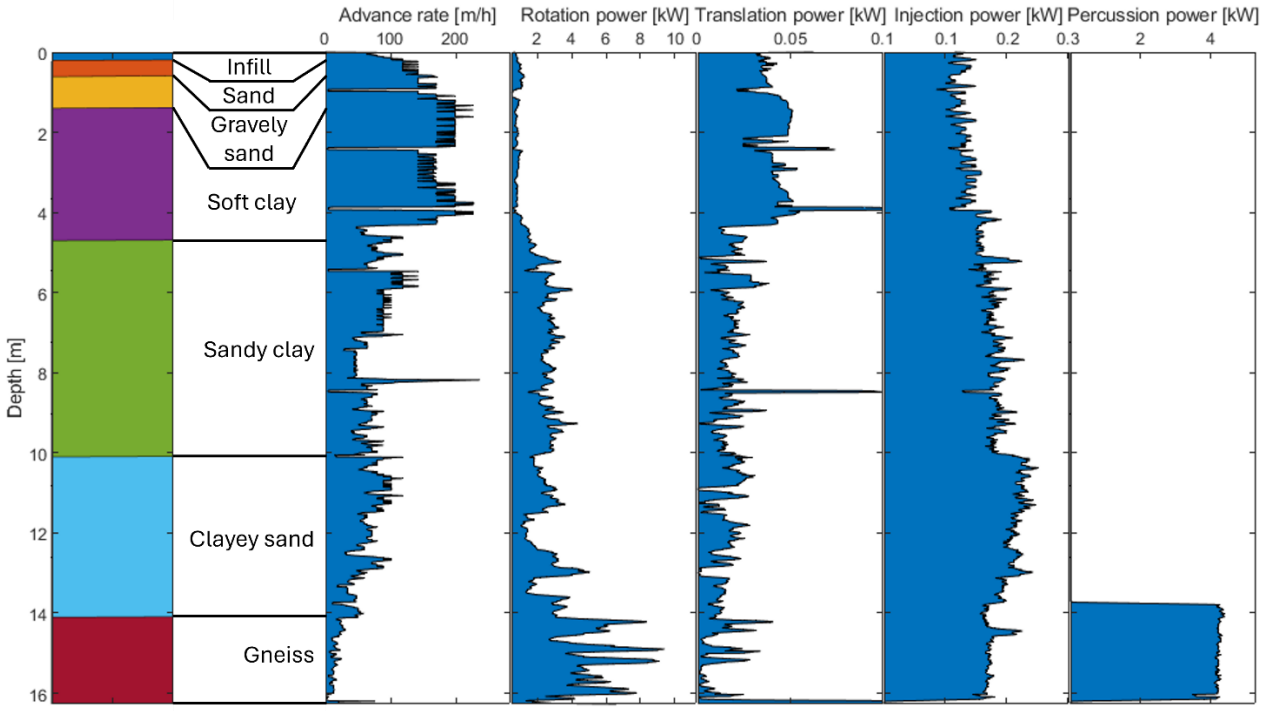

Figure 3. Example of MWD logs for electrical rig.

As shown on Figure 3, the motor responsible for vertically translating the drilling assembly (related to the down thrust parameter) consumes the least power, while the motor that rotates the rods and the hammer consume equivalent amounts of energy. Changes in soil layers are clearly visible, as indicated by the reduction in penetration rate and rise in rotation power at about 4.0 m. It can also be seen that the hammer was only used to excavate through the layer of gneiss below 14 m accompanied by a rise in rotation power. The layers of sandy clay and clayey sand above the gneiss can be differentiated by the change in injection power and larger variations in rotation power. These logs suggest that parameters based on electrical

consumption can be used to determine lithology, much like the hydraulic parameters typically recorded.

5 CONCLUSIONS

This paper has presented the architecture of a new model of drill rig that uses electrical motor instead of hydraulic ones fed by an internal combustion engine. The prototype tested in situ has performed better than expected, with autonomy for over a week of surveying without recharging, all the while being more silent and not generating greenhouse gas emissions. The data collected by logging the current and voltage used by the various motors has been shown to be as detailed or more so than the data registered while using pressure transducers in a conventional drill rig. The data can be displayed as the conventional physical parameters or in terms of power spent by each motor and can be interpreted in the same manner as regular MWD logging.

REFERENCES

Cardu, M., Oreste, P., Pettinau, D. and Guidarelli, D. (2013). Automatic measurement of drilling parameters to evaluate the mechanical properties of soil. *American Journal of Applied Sciences.* 10(7), pp. 654-663, https://doi.org/10.3844/ajassp.2013.654.663.

Fortunati, F. and Pellegrino, G. (1998). The use of electronics in the management of site investigation and soil improvement works: Principles and applications. *Geotechnical Site Caracterization,* 1st ed., Robertson & Mayne (eds), Rotterdam, Netherlands, pp.359-364.

Nishi, K., Suzuki, Y., and Sasao, H. (1998). Estimation of soil resistance using rotary percussion drill. *Geotechnical Site Caracterization,* 1st ed., Robertson & Mayne (eds), Rotterdam, Netherlands, pp.393-398.

Peronne, M., Rispal, M., Jacquard, C. and Reiffsteck, P., (2021). New Measuring While Drilling Technology ASFOREC, *6th International Conference in Geotechnical and Geophysical Site Characterisation*, Budapest, 2021. https://doi.org/10.53243/ISC2020-134.

Reiffsteck, P. (2010). Paramètres de forage en géotechnique: Méthode d'essai n° 79. Laboratoire Central des Ponts et Chaussées (LCPC), Paris, France (in french). http://doi.org/10.3829/me79-fr.

Rodgers, M., McVay, M., Horhota, D., Hernando, J. and Paris, J. (2020). Measuring while drilling in Florida limestone for geotechnical site investigation. *Canadian Geotechnical Journal*. 57(11), pp. 1733-1744. https://doi.org/10.1139/cgj-2019-0094.

Proceedings of the XVIII ECSMGE 2024
GEOTECHNICAL ENGINEERING CHALLENGES
TO MEET CURRENT AND EMERGING NEEDS OF SOCIETY
© 2024 the Authors
ISBN 978-1-032-54816-6
DOI 10.1201/9781003431749-646
Open Access: www.taylorfrancis.com, CC BY-NC-ND 4.0 license

ECSMGE 24
XVIII EUROPEAN CONFERENCE ON SOIL MECHANICS AND GEOTECHNICAL ENGINEERING

Thermal characterization of Aveiro soil for multiscale building energy simulation using shallow geothermal system

Caractérisation thermique du sol d'Aveiro pour la simulation énergétique multi-échelle des bâtiments à l'aide d'un système géothermique peu profond

R.B. Roka*
RISCO, Department of Civil Engineering, University of Aveiro, Aveiro, Portugal

A. Vieira
National Laboratory of Civil Engineering, Lisbon, Portugal

A. Figueiredo, C. Cardoso
RISCO, Department of Civil Engineering, University of Aveiro, Aveiro, Portugal

**rajeneraroka@ua.pt*

ABSTRACT: Shallow geothermal energy systems are evolving as an alternative source of energy for building space heating and cooling with notable contributions to carbon emission reduction. In this context, proper soil thermal characterization is crucial for determining the potential of these systems' use and their energy efficiency evaluation. This paper presents the results of the assessment of the physical and thermal characterization of samples retrieved in the city of Aveiro, Portugal. The thermal tests were performed in transient conditions using a needle probe and plane sensor device and the respective results were compared. The study provides some insights regarding Aveiro soil's thermal characteristics which will be further used in building energy simulation of campus buildings integrating shallow geothermal energy systems towards sustainable energy planning and development.

RÉSUMÉ: Les systèmes d'énergie géothermique peu profonde sont en train de devenir une source d'énergie alternative pour le chauffage et la climatisation des bâtiments, avec des contributions notables à la réduction des émissions de carbone. Dans le contexte de la caractérisation thermique des sols, la caractérisation est cruciale pour déterminer le potentiel d'utilisation de ces systèmes et l'évaluation de l'efficacité énergétique. L'article présente l'évaluation de la caractérisation physique et thermique d'échantillons prélevés dans la ville d'Aveiro, au Portugal. Les essais thermiques ont été effectués dans des conditions transitoires à l'aide d'une sonde à aiguille et d'un capteur plan et les résultats respectifs ont été comparés. L'étude fournit quelques informations sur les caractéristiques thermiques du sol d'Aveiro, qui seront ensuite utilisées dans la simulation énergétique des bâtiments du campus intégrant des systèmes d'énergie géothermique peu profonds pour la planification et le développement de l'énergie durable.

Keywords: Shallow geothermal energy; soil thermal conductivity; thermal probes; sustainability.

1 INTRODUCTION

For the space heating and cooling of buildings, low enthalpy ground source systems have been shown as a promising and sustainable source of renewable energy. To harness shallow geothermal energy, it is crucial to assess and determine the thermal parameters of soils as they determine the heat exchange performance between the ground and the buildings to be acclimatized (Del Pozo et al., 2021). Heat transfer processes in soils can occur, through the physical processes: conduction, convection or radiation. However, for these systems, conduction is the dominant process (Vieira et al., 2019). Thermal conductivity quantifies the ability of materials to conduct thermal energy, it is the soil´s most important factor in determining the primary circuit performance of shallow geothermal heat exchangers (Roka et al., 2023). Volumetric heat capacity indicates the amount of heat energy required to raise the temperature of a unit volume of a substance by one degree Celsius or one Kelvin. It's an important parameter when considering the thermal behavior of soil, including its ability to store or release heat (e.g. Kodesová et al., 2013). A proper knowledge of the thermal properties of soil is essential to design the geothermal system as they influence heat extraction from the soil and heat rejection to the soil as well as the performance and efficiency of the geothermal system (Vieira et al., 2017). Several factors influence the soil's thermal

conductivity and heat capacity in particular their index properties such as soil particle distribution, water content, bulk and particle density, degree of saturation, and void ratio (Zeh et al., 2021). Among these, the factors that most influence soil thermal properties are the water content (degree of saturation) and porosity. The mineralogical composition of the soil also has a significant influence on its thermal behavior.

To design an energy simulation model of the campus buildings of Aveiro University with the integration of shallow geothermal systems using whole-building energy simulation software CitySim Pro the knowledge of the heat extraction potential from the soil is crucial. The assessment of information on the thermal properties of Aveiro soils will help to fulfil this purpose.

2 LABORATORY EXPERIMENTS

2.1 Theoretical background: needle and surface probes

The needle sensor is a Transient Line Source (TLS) device for the determination of the thermal conductivity of soil in non-steady state conditions in an infinite medium (e.g. Lockmuller et al., 2003). This technique uses a line heat source, the temperature changes in soil over time are recorded when the heat of a known amount is applied to the sample soil. Carslaw and Jaeger, (1959) give the relation of temperature response at any time t (s) accordingly:

$$T = \frac{q}{4\pi\lambda}\int_x^\infty \frac{e^{-u}}{u}du \quad (1)$$

where q (W.m^{-2}) is the power input per unit area, T (K) is the temperature at any radial distance r(m) from the needle, x is $\frac{r^2}{4\alpha t}$, α (m^2.s^{-1}) is the thermal diffusivity and the thermal conductivity of soil λ (W.m^{-1}.K^{-1}).

In the TLS method, a thin needle heat source is inserted into the soil sample, simulating a linear heat source of infinitesimal radius in a semi-infinite medium. The heat flow within the soil sample follows a radial pattern. The rate of heat propagation in the soil sample is contingent on its thermal conductivity. For soils with high conductivity, the propagation time is notably shorter. Conversely, in soils with lower conductivity, the propagation time is prolonged. This distinction in propagation times provides valuable insights into the thermal characteristics of different soil types, contributing to a more comprehensive understanding of their behavior in response to heat.

When the t (s) is too large, Eq. (1) becomes:

$$T = \frac{q}{4\pi\lambda}\left(ln\frac{4\alpha t}{r^2} - \gamma\right) \quad (2)$$

Where γ represents Euler‘s constant. For a specified medium in a time-space t_1 (s) and t_2 (s) with the heat flux q (W.m^{-2}), equation 3 provides the thermal conductivity. The derived λ (W·m^{-1}·K^{-1}) value should fall within a 5% deviation from the mean value of each test (ASTM, D5334-14).

$$\Delta T = T_2 - T_1 = \frac{q}{4\pi\lambda}.ln\left(\frac{t_2}{t_1}\right) \quad (3)$$

Thermal conductivity is related to thermal diffusivity, material density and specific heat capacity. Equation 2 illustrates the relationship,

$$\lambda = \alpha.\rho.c \quad (4)$$

where ρ (kg.m^{-3}) signifies the soil density, α (m^2.s^{-1}) is thermal diffusivity, and c (J.kg^{-1}.K^{-1}) denotes specific heat capacity.

The international standards ASTM D5334-14 and IEEE 442 provide standard information regarding λ (W.m^{-1}.K^{-1}) measurement techniques for TLS. Thermal conductivity can also be measured by the surface probe or transient plane source (TPS). However, this probe is specially designed for hard soil. The surface probe sensor features elements that function both as a heat source and a temperature sensor. Comprising a robust electrical conducting pattern crafted from thick nickel foil embedded within an insulating Kapton layer, the device exhibits a dual role. The application of consistent heat through electrical power induces changes in the sensor's resistance, denoted as R_t (Ω) which is directly correlated with the corresponding increase in temperature T (K). The time-dependent resistance, R (Ω), is mathematically expressed by equation 5. Comprehensive details regarding the calculations and the specifics of the equation can be referenced in (Gustafsson, 1991).

$$R_t = R_0(1 + \phi.\Delta T_t) \quad (5)$$

where R_0 (Ω) is the initial resistance of the hot disk present in the surface probe, ϕ is the temperature coefficient of resistance (TCR) for the probe and $\Delta T_T=(T_T-T_0)$ is the temperature increase in the sensor concerning the time variable t (s). Also,

$$t = \sqrt{\left(\frac{t_0}{\theta}\right)} \text{ and } \theta = \left(\frac{\alpha^2}{\alpha}\right) \quad (6)$$

where t_o(s) is the time from the start of the transient heating, a signifies a constant that is a measure of the overall size of the resistive pattern (half the side of the hot square or the radius of the hot disk) and θ denotes the characteristic time as in equation 6 (Gustafsson, 1991).

When assuming the sample is infinitely large and has no influence from the boundaries, and the geometry of the disk consists of an n concentric ring with a radius of the outermost ring r (m) and ΔT_T can be expressed with the below equation 7,

$$\Delta T_T = \frac{P_o}{\sqrt[3]{\pi}.r\lambda}.D_T \quad (7)$$

where P_0(W) is the total output power of the probe and D_T is a dimensionless time function and can be written in equation 7 (Gustafsson, 1991).

$$D_T=(n(n+1))^{-2}.\int_0^T \frac{d\sigma}{\sigma 2}.(\sum_{h=1}^{n} h(\sum_{k=1}^{n} k.\ Exp((-h^2+k^2)/4\sigma^2n^2).l_0(h.k/2\sigma^2n^2))) \quad (8)$$

where L_0 is the modified Basel function, h(m) is the thickness of the disk, n is the number of concentric rings in the disk and σ is an integration variable. So, λ (W.m^{-1}.K^{-1}) can be obtained by fitting the experimental data to the straight line given by equation 7, and equation 6 gives thermal diffusivity.

2.2 Sampling and sample preparation

Samples were extracted at a construction site near the University of Aveiro using a tube sampler of 70mm diameter and 140mm length. The samples were extracted from excavation cuts from depths of 1m to 3.5m. After the extraction, they were wrapped with thin plastic to preserve initial moisture and carefully transported to the National Laboratory of Civil Engineering (LNEC) Soil Mechanics laboratory and stored in a temperature and moisture-controlled room. Disturbed samples were also taken from the same place as the intact ones to perform physical characterization tests namely grain size distribution, initial water content, Atterberg limits and particle density. As mentioned, some physical parameters of soil have a paramount effect on the λ (W.m^{-1}.K^{-1}). Figure 1 displays a map indicating the sampling locations. At this stage, three samples were tested. The respective results will be used in the multiscale building energy simulation. The three samples can be seen in Figure 2.

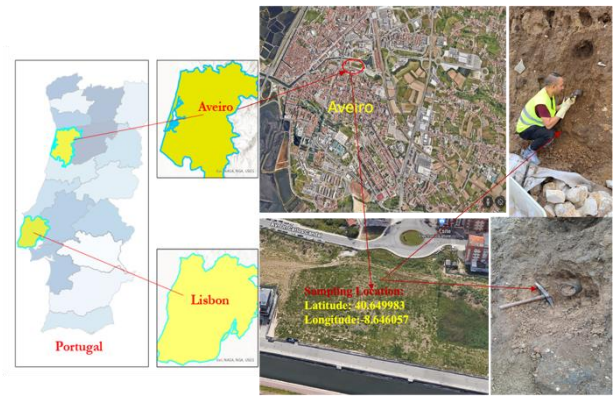

Figure 1. Location map of sampling site in Aveiro.

2.3 Equipment description

For the thermal characterization of samples, equipment comprising a measurement platform, TLS-100vCp and TLS-100 needle sensors and TPS-



Figure 2. Soil samples and their thermal tests.

4 asymmetric (single-sided) sensors were used. Both TLS have a total 100mm needle length. According to ASTM D5334-14, the specimens should be 200±30mm long and 50mm in diameter (ASTM, D5334-14). The user manual of MP-2 mentions that the minimum sample size should be 100mm long and 50mm in diameter. TPS-4 has a sensor diameter of 12.8mm and at least a 35mm diameter sample is recommended for the test recommended by the MP-2 manual (MP-2, 2022). Table 1 presents the spectrum of thermal conductivity measurements and the corresponding accuracy achieved by three distinct sensors, alongside the adhered standards.

2.4 Experimental description

Firstly, the sensor TPS-4 was calibrated by using Pyrex verification sample (λ=1.110W·m^{-1}·K^{-1}) and afterwards both needle sensors with a Polymer verification sample (λ=0.330 W.m^{-1}.K^{-1}) at room temperature 25^{0}C. Additionally, Figure 3 provides a visual representation of the MP-2 device alongside the three sensors.

Table 1. Measurement range of sensors (MP-2, 2022).

Sensor's type	Range of λ ($W \cdot m^{-1} \cdot K^{-1}$)	Accuracy	Standard followed
TPS-4	0.03-5	±5%	ASTM D5334 & IEEE 442-1981
TLS-100	0.1-5	±5%	ASTM D5334-14 & ISO 22007-2
TLS-100vCp	0.02-5	±5%	ASTM D5334-14



Figure 3. MP-2 device with three sensors.

After the calibration, some tests were carried out in a reference soil (Fontainebleau sand). Aljundi et. al., (2019) have previously measured the thermal conductivity of Fontainebleau sand under different densities and saturation degrees. The λ ($W \cdot m^{-1} \cdot K^{-1}$) value obtained at density 1715 $kg.m^{-3}$ at fully dry condition is 0.344 $W \cdot m^{-1} \cdot K^{-1}$ and fully saturated condition is 2.84 $W \cdot m^{-1} \cdot K^{-1}$. A density of 1690$kg.m^{3}$, which was missing in that study, in fully dry and fully saturated conditions was prepared and the obtained values of λ ($W \cdot m^{-1} \cdot K^{-1}$) are presented in Table 2.

Firstly, the samples were tested by using TPS-4 followed by the two-needle sensors. The top surface of the sample was levelled carefully and a weight of one kilogram was placed above the sensor in order to achieve good contact between the plane sensor and the soil sample as shown in Figure 2. Furthermore, while using the needle probes a thermal paste was used to ensure better contact with the surrounding soil. S6062 and S6063 were soft enough to insert the needle probe whereas for S6061 a hole was made with a metallic rod smaller in diameter than the needle. Special care was taken to insert the needles so as not to damage them.

A series of five measurements were performed for each sample with three sensors. The interval between each measurement should be at least 15 to 20 minutes in order to achieve a thermal equilibrium according to the manual of MP-2, though a minimum of 30 minutes was given to provide enough time for better accuracy in the results.

3 RESULTS AND DISCUSSION

Table 3 showcases information about the specific gravity of the soil particles ρ_s, moisture content w (%), void ratio e, degree of saturation S_r (%), liquid limit L_L (%), plastic limit P_L (%), particle size distribution and soil classifications of the tested samples. The particle size distribution of the three Aveiro samples is shown in Figure 4. It can be observed that S6061 has lesser fine particles with major parts of sand and gravel, whereas S6062 and S6063 have a very similar granulometric composition with more than 60% finer particles and were classified as low plasticity clays.

For the thermal tests, the calibration results with the verification sample fell below ±5% of the known value. Table 4 presents a summary of the results of the thermal tests conducted. Each value corresponds to the average of five determinations. For all cases, the repeatability R(%) obtained was excellent (with differences between measurements lower than 5%). Regarding the thermal conductivity measurements in Fontainebleau sand, as expected the value in fully saturated conditions is much higher (about 8 times more) than that in fully dry conditions. When sand is saturated with water, the air in the pore spaces is displaced. Since water has a higher thermal conductivity than air, the replacement of air with water increases the soil thermal conductivity.

In turn, in Figure 5, the values of the thermal conductivity estimated by the three probes for the different samples are shown. Globally it can be observed that the values measured with the surface probe TPS-4 are almost always inferior to the ones obtained with TLS-100 probes.

Additionally, it is noteworthy that the average difference in thermal conductivity measurements between the TLS-100 and TPS-4 sensors remained below 2% for samples 6062 and S6063. However, in the case of sample S6061, this difference exceeded 12%. The significant disparities in results between the plane source TPS-4 and TLS-100 were particularly evident in the sample with more percentage of sand and gravel. This observation may be attributed to the challenge of achieving 100% contact between the sensor and the sand and gravel, potentially allowing air to enter the gap and influencing the measurements.

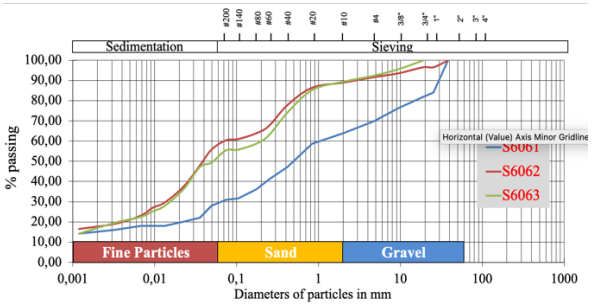

Figure 4. Particle size distribution curves.

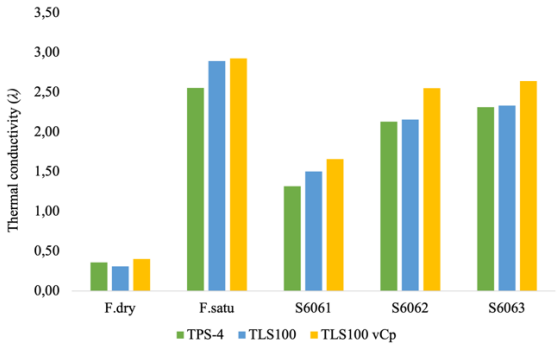

Figure 5. Test results comparison of three sensors.

Regarding measurements conducted with the two needle probes, it is notable that values obtained with probe TLS100-vCp, which incorporates heat capacity measurements, consistently exhibit higher values. On average, the differences relative to the mean are approximately 10%. The thermal conductivity of the samples is influenced by the degree of saturation. Samples S6062 (S_r=91.22%) and S6063 (S_r=92.02%) have higher thermal conductivity values than sample S6061 (S_r=67.22%). However, the relationship is complex and depends on various factors, including mineral composition, and temperature conditions. The measured values of α ($m^2.s^{-1}$) for samples are in the range of $1.0x10^{-6}$ to $3.0x10^{-6}$ $m^2.s^{-1}$. According to Hillel, (1982) the thermal diffusivity of moist soil ranges from $1.0\ x10^{-6}$ to $3.0x10^{-6}$ $m^2.s^{-1}$. Additionally, Abu-Hamdeh, (2003) obtained a volumetric heat capacity value of $1.09\text{-}3.04x10^6$ $J{\cdot}m^{-3}{\cdot}K^{-1}$ and the measured value of C_p ($J{\cdot}m^{-3}{\cdot}K^{-1}$) in this research is $1.053\text{-}2.012x10^6$ $J{\cdot}m^{-3}{\cdot}K^{-1}$ for moist soil.

Table 2 provides information on maximum density ($kg{\cdot}m^{-3}$) and their respective void ratios e^{max}, e^{min}, and e^{cal} for Fontainebleau sand.

Table 2. Maximum, minimum and calculated densities and void ratio of Fontainebleau sand.

Sample	ρ_{max} ($kg.m^{-3}$)	ρ_{min} ($kg.m^{-3}$)	ρ_{cal} ($kg.m^{-3}$)	e^{max}	e^{min}	e^{cal}
Fontainebleau sand	1750	1440	1690	0.855	0.521	0.579

Table 3. Physical properties of the Aveiro samples.

Samples	ρ_s	w (%)	e	Sr (%)	L_L-P_L (%)	Particle size distribution			Soil Classification
						Gravel (%)	Sand (%)	Fines (%)	
Aveiro-S6061	2.66	14.89	0.589	67.22	23.9-19.0	36.2	33.3	30.5	**GC** (Clayey gravel with sand)
Aveiro-S6062	2.67	14.53	0.425	91.22	20.2-12.9	10.6	31.3	58.1	**CL** (Lean clay with sand)
Aveiro-S6063	2.74	15.69	0.467	92.02	19.1-13.8	10.6	38.1	51.3	**CL-ML** (Silty clay with sand)

4 FINAL REMARKS

In this work, laboratory-measured values of the thermal properties of Aveiro soils using different thermal probes were presented. Values of the physical properties of these soils were also provided, along with data recorded on a reference soil. All measurements were conducted under non-steady-state heat flow conditions. Overall, the obtained values are typical values of the tested soil types, and very good repeatability was obtained. It was observed that the thermal conductivity values measured with the surface probe were consistently lower than those measured with the needle probes. This difference may be attributed to heat losses, contact issues, or the analytical approximations underlying this determination.

On the other hand, it is also not clear why there is a difference in measurements between the two needle probes with the probe that also allows obtaining thermal diffusivity values giving consistently higher values. According to the manufacturer, the conductivity values, in this case, are estimated based on an iterative calculation performed during the test based on the line source solution expression, which enables the simultaneous evaluation of λ ($W.m^{-1}.K^{-1}$) and α ($m^2.s^{-1}$) but not on a direct determination of λ ($W.m^{-1}.K^{-1}$). Further investigations, encompassing numerical replication of evaluation of λ ($W.m^{-1}.K^{-1}$)

Table 4. Thermal characteristics of the Aveiro soil samples by MP-2 platform with three sensors.

Samples	Thermal sensors	Thermal properties		
		λ (W.m^{-1}.K^{-1})	α (m^2.s^{-1})	C_p (J.m^{-3}.K^{-1})
Fontainebleau sand$_{dry}$	TLS-100	0.359	0.562 x10^{-6}	0.717 x10^6
	TLS-100vCp	0.402		
	TPS-4	0.310		
Fontainebleau sand$_{saturated}$	TLS-100	2.892	2.012 x10^{-6}	2.206 x10^6
	TLS-100vCp	2.926		
	TPS-4	2.556		
Aveiro - S6061	TLS-100	1.504	1.053 x10^{-6}	1.561x10^6
	TLS-100vCp	1.660		
	TPS-4	1.319		
Aveiro - S6062	TLS-100	2.158	1.423 x10^{-6}	1.792 x10^6
	TLS-100vCp	2.550		
	TPS-4	2.129		
Aveiro - S6063	TLS-100	2.332	1.575 x10^{-6}	1.679 x10^6
	TLS-100vCp	2.641		
	TPS-4	2.313		

and α (m^2.s^{-1})**.** Further investigations, encompassing numerical replication of the test, are underway as part of this study's scope.

ACKNOWLEDGEMENTS

The authors are grateful for the financial support provided by the Foundation of Science and Technology (FCT) to the first author with PhD grant number (2022.10333.BD); equipment and laboratory support from project GeoSustained (PTDC/ECI-CON/1866/2021) and National Laboratory of Civil Engineering (LNEC).

REFERENCES

Abu-Hamdeh, N. H. (2003). Thermal properties of soils as affected by density and water content. *Biosystems Engineering*, *86*(1), 97–102. https://doi.org/10.1016/S1537-5110(03)00112-0.

Aljundi, K., Vieira, A, Maranha, J. R., Lapa, J., & Figueiredo, A. (2019). Some aspects of measurement of sand thermal conductivity from laboratory tests, In: International Society for Soil Mechanics and Geotechnical Engineering, Reykjavik, Iceland. https://doi.org/10.32075/17ECSMGE-2019-0541.

ASTM (D5334-14). ASTM D5334-14, Standard Test Method for Determination of Thermal Conductivity of Soil and Soft Rock by Thermal Needle Probe Procedure, ASTM International, West Conshohocken, USA.

Carslaw and Jaeger. (1959). *Conduction of heat in solids*, Oxford Science Publications, Oxford, UK.

Del Pozo, S., Sáez-Blázquez, C., Martín Nieto, I., & Lagüela, S. (2021). Integrated approach for detecting convection effects in geothermal environments based on TIR camera measurements. *Applied Sciences*, 11(7), https://doi.org/10.3390/app11073185.

Gustafsson, S. E. (1991). Transient plane source techniques for thermal conductivity and thermal diffusivity measurements of solid materials, *Review of Scientific Instruments,* 62(3), (797–8049), https://doi.org/10.1063/1.1142087.

Hillel, D. (1982). *Introduction to Soil Physics* 1st Edition, Academic Press, California, USA.

Kodesová, R., Vlasáková, M., et.al., (2013). Thermal properties of representative soils of the Czech Republic. *Soil and Water Research*, 8(4), 141–150. https://doi.org/10.17221/33/2013-swr.

Lockmuller, N., Redgrove, J., & Kubičár, L. (2003). Measurement of thermal conductivity with the needle probe. *High Temperatures - High Pressures*, 35–36(2), 127–138. https://doi.org/10.1068/htjr099.

MP-2, (2022). Measurement platform-2, *User Manual*, Thermtest portable.

Roka, R. B., de Figueiredo, A. J. P., Vieira, A. M. C. P., & Cardoso, J. C. de P. (2023). A systematic review on shallow geothermal energy system: a light into six major barriers, *Soils and Rocks,* 46(1), https://doi.org/10.28927/SR.2023.007622.

Vieira, A., Alberdi-Pagola, M., Christodoulides, P., Javed, et.al., (2017). Characterisation of Ground Thermal and Thermo-Mechanical Behaviour for Shallow Geothermal Energy Applications, *Energies*, 10(12), (2044), https://doi.org/10.3390/EN10122044.

Vieira, A., Alberdi-Pagola, M., Barla, et.al., (2022). Site characterization for the design of thermoactive geostructures, *Soils and Rocks*, 45(1), https://doi.org/10.28927/SR.2022.001022.

Zeh, R., Ohlsen, B., Philipp, D., Bertermann, D., Kotz, T., Jocić, N., & Stockinger, (2021). Large-scale geothermal collector systems for 5th generation district heating and cooling networks, *Sustainability*, 13(11), https://doi.org/10.3390/su13116035.

Proceedings of the XVIII ECSMGE 2024
GEOTECHNICAL ENGINEERING CHALLENGES
TO MEET CURRENT AND EMERGING NEEDS OF SOCIETY
© 2024 the Authors
ISBN 978-1-032-54816-6
DOI 10.1201/9781003431749-647
Open Access: www.taylorfrancis.com, CC BY-NC-ND 4.0 license

ECSMGE 24
XVIII EUROPEAN CONFERENCE ON SOIL MECHANICS AND GEOTECHNICAL ENGINEERING

Environmental life cycle assessment of ground reinforcement using rigid inclusions

Analyse du cycle de vie du renforcement de sol par inclusions rigides

M. Saadé*
Navier Ecole des Ponts Univ Gustave Eiffel CNRS Marne-la-Vallée, France

E. Antoinet
Antea Group, Orleans, France

**myriam.saade@enpc.fr*

ABSTRACT: There are increasing societal and political concerns about the consequences of human activities on climate change and other environmental issues. In that sense, methodologies such as Life Cycle Assessment (LCA) are being developed to evaluate technical systems based on their function, considering the whole life cycle in a multi-criteria approach. Applied to the construction sector since the 1990s, particularly to buildings and other civil engineering structures, little has been done so far on geotechnical works specifically. This contribution seeks to present an application of LCA to soil reinforcement solutions in the framework of the ASIRI+ National Project. The objectives of the assessment are, first, to quantify the environmental impacts potentially generated when implementing rigid inclusions as ground improvement techniques, and second, to compare them with the impacts of other possible solutions. The study highlights the contribution of materials such as cement, lime and steel to the overall impacts, and particularly climate change, the importance of optimizing their use when designing and implementing solutions, and the need for contextualized data for such materials. It also stresses the importance of extending the limits of the assessed system to include foundations, and not to strictly focus on rigid inclusions.

RÉSUMÉ: Les préoccupations sociétales et politiques concernant les conséquences environnementales des activités humaines vont croissantes. De ce fait, les méthodologies telles que l'Analyse du Cycle de Vie (ACV) sont développées pour évaluer les systèmes techniques sur la base de leur fonction, en considérant l'ensemble du cycle de vie, dans une approche multicritère. Appliquée au secteur de la construction depuis les années 1990, peu d'études portent spécifiquement sur les ouvrages géotechniques. Cette contribution vise à présenter une application de l'ACV à des solutions de renforcement de sol, investiguées dans le cadre du Projet National ASIRI+. Les objectifs de l'analyse sont, tout d'abord, de quantifier les impacts environnementaux potentiels générés lors de la mise en œuvre des inclusions rigides comme technique de renforcement de sol, et ensuite de les comparer avec les impacts d'autres solutions envisageables. L'étude souligne la forte contribution de matériaux tels que le ciment, la chaux et l'acier aux impacts totaux, et la nécessité de données contextualisées pour ces matériaux. Elle montre également la nécessité d'étendre les limites du système étudié pour inclure les fondations, et non pas regarder strictement les inclusions rigides.

Keywords: Life cycle assessment (LCA); soil reinforcement; rigid inclusion; ASIRI+.

1 INTRODUCTION

Governmental bodies, companies and the public are increasingly concerned about the consequences of human activities on climate change and other environmental issues (depletion of resources, biodiversity loss, or degradation of human health). To translate these concerns into action, it is necessary to understand what are the impacts of such activities, how to reduce them, and/or to identify alternatives delivering the same service, with better environmental performances. In that sense, methodologies such as environmental Life Cycle Assessment (LCA) are being developed to evaluate technical systems based on their function, considering the whole life cycle (from extraction of material to end of life) in a multi-criteria approach (Jolliet et al., 2017). Applied to the construction sector since the 1990s, particularly to buildings (Peuportier et al., 1997) and other civil engineering structures (Horvath 2006; de Bortoli et al 2020), little has been done on geotechnical works specifically, until recently (Basu et al., 2013; Raymond et al., 2021).

This contribution presents an application of LCA to soil reinforcement solutions using rigid inclusions, analysed in the framework of the ASIRI+ French National Project. Its objectives are, first, to quantify

the environmental impacts potentially generated when implementing rigid inclusions as ground improvement techniques, and second, to compare them with the impacts of other solutions.

2 METHODOLOGY

2.1 Goal and scope definition

The approach adopted in this paper follows the guidelines described in ISO 14040 standards (ISO 2006) for the application of LCA (Saadé and Jolliet 2024). It consists first in defining a functional unit (FU), representing the function of the modelled system (goal and scope definition) and serving as the reference unit for the quantification of material flows and environmental impacts. For different modelled scenarios, flows of matter and energy emitted to and extracted from the environment are quantified per FU (life cycle inventory). Based on these flows, potential impacts are evaluated in different environmental categories or areas of protection (climate, human health, ecosystems…) in the life cycle impact assessment phase. During these different phases, results are being discussed and limitations described (interpretation).

2.2 Case study

The case study considered corresponds to the foundation system of the bus station attached to the multimodal transport centre of the City of Nice, France (Chen 2022), located in a moderated sismic hazard area (zone 4) according to the French regulation.

Table 1. Soil characteristics.

Level	γ [kN/m³]	p_l [MPa]	E_M [MPa]	α [-]
+6,5 to -10,5	20	0,3	5,0	½
-10,5 to 14,5	21	2,5	23,0	¼
Under 14,5	20	0,3	5,0	½

The foundation of the bus station covers a surface of 5800 m², on of B2 class soil according to the Natural Riks Prevention Plan (Table 1). The solution implemented for the foundation is a concrete slab on a soil reinforced by rigid inclusions and ductile cast iron piles. An alternative solution considered consists of a concrete slab on soil reinforced by concrete and ductile cast iron piles. Data for both solutions are provided by the company Keller Fondations Spéciales.

2.2.1 Functional unit

The functional unit is defined as the "foundation of the bus station operational for a duration of service of 50 years for the soil characteristics given in Table 1".

2.2.2 System boundaries

The system boundaries are given in Figure 1. They include the extraction of resources and the processes required for the production of materials (concrete, mortar, cast iron, reinforcing steel…), transport of materials, the use of engines on the construction site, demolition and recycling. Transportation of engines and workers are not taken into account.

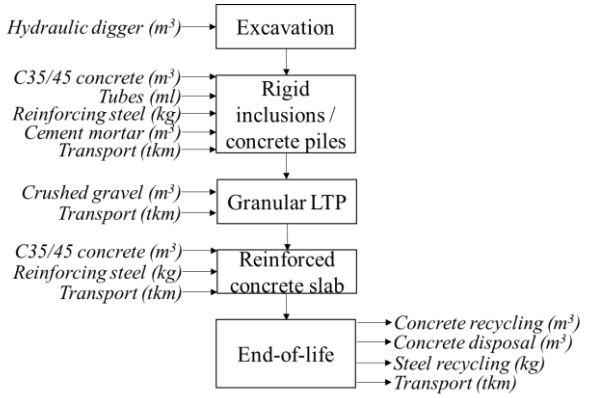

Figure 1. System boundaries.

2.2.3 Scenario definition

The two previously described scenarios are considered.

Table 2. Material quantities per scenario.

Material	Scenario 1	Scenario 2
Armed RI		
Concrete	749 m³	-
Tubes	34600 kg	-
Concrete piles		
Concrete	-	695 m³
Reinforcing steel	-	34760 kg
Ductile cast iron piles		
Tubes	16950 kg	16950 kg
Cement mortar	53 m³	53 m³
Platform	2320 m³	1740 m³
Slab		
Concrete	2030 m³	2900 m³
Reinforcing steel	111650 kg	261000 kg

The first scenario (actually implemented and proposed by the contractor) consists of a C35/45 reinforced concrete slab (0,35 m thick) + granular load transfer platform LTP (0,4 m thick) + armed rigid inclusions and ductile cast iron piles (functioning as rigid inclusions). Rigid inclusions are constituted of a

XA2 C35/45 concrete and armed with a 114 mm diameter tube; 6,2 mm thick. Ductile cast iron piles consist of tubes with a diameter of 118 mm and 9 mm thick. They are covered with a coating of cement mortar to avoid corrosion. The steel ratio in the slab is 55 kg/m^3.

The second scenario (basic solution proposed by the project manager) consists of a C35/45 reinforced concrete slab (0,5 m) + granular load transfer platform LTP (0,3 m) + concrete piles (below the structure loads) and ductile cast iron piles (functioning as rigid inclusions). In this case, the steel ratio in the slab is about 90 kg/m^3.

2.2.4 Data and assumptions, LCI database and LCIA method

Foreground data regarding the material quantities have been collected from the Keller company (Table 2). For concrete, the transport distances considered to the concrete plan are 30 km for aggregates, 49 km for cement (Portland), 232 km for blast furnace slag, 1230 km for additives. The distance between the concrete plan and the construction site is estimated at 15 km. Steel and granular material for the LTP are transported over a distance estimated at 100 km and 50 km respectively.

Background data are provided by the ecoinvent database (Frischknecht et al., 2007). The impacts are calculated using the set of indicators provided by the EN15804 standard (AFNOR 2014).

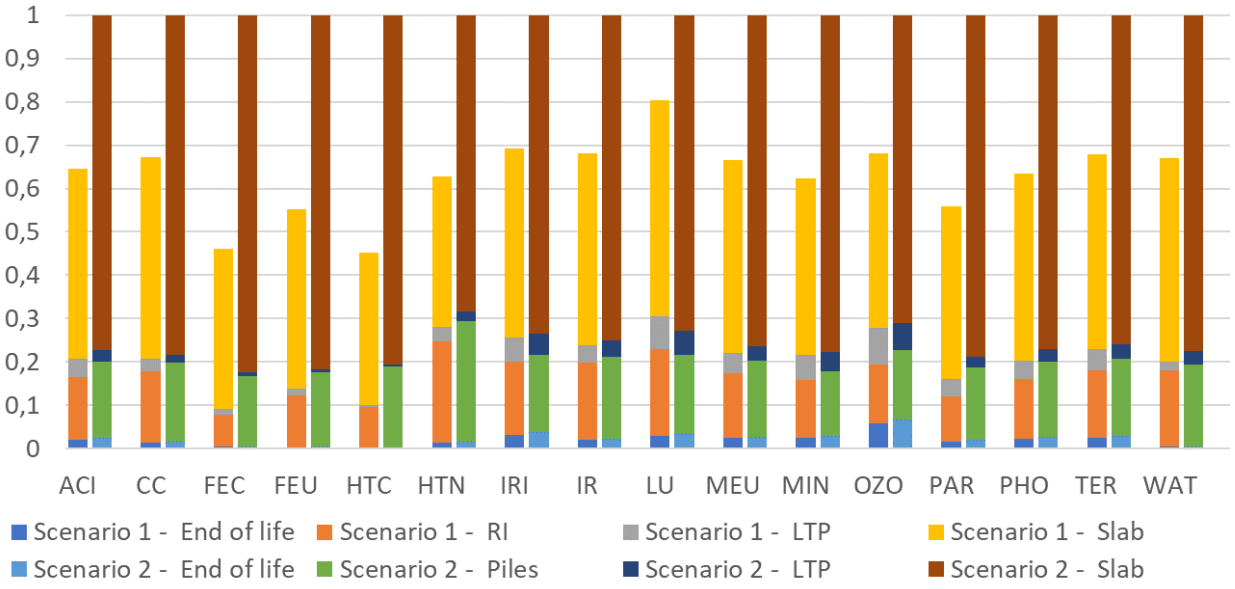

Figure 2. Comparison between the two scenarios, relative to the maximum impact score per environmental category. ACI: Acidification; CC: Climate change; FEC:Freshwater ecotoxicity; FEU: Freshwater eutrophication; HTC: Human toxicity, cancer effects; HTN: Human toxicity, non-cancer effects; IRI: Ionizing radiation E (interim); IR: Ionizing radiation HH; LU: Land use; MEU: Marine eutrophication; MIN: Mineral, fossil & ren resource depletion; OZO: Ozone depletion; PAR: Particulate matter; PHO: Photochemical ozone formation; TER: Terrestrial eutrophication; WAT: Water resource depletion.

3 RESULTS

3.1 Comparison of the two scenarios

Figure 2 compares the impacts of scenarios 1 and 2 considering the contribution of the different sub-processes of the system. Taking into account the foundation system (slab + load transfer platform + soil reinforcement solution), scenario 2 appears to have the largest impact for all categories. Most of its impact comes from the concrete slab, which explains between 70 and 80% of the overall impact, according to the environmental category. For example, respectively 45% and 35% of the climate change score are related to the production of concrete and reinforcing steel used in the slab. 20 to 30% of the impacts are related to the production and transport of the soil reinforcement solution. The granular mattress represents a few percentages of the total impact. The contribution of materials transport to the overall impact is also limited compared to materials production (Figure 3).

The impacts of scenario 1 are also dominated by the reinforced concrete slab, but in a relatively lesser extent. The relative contribution of the soil reinforcement solution is in the same order of magnitude (between 20 and 30% of the total impact depending on the environmental category). The better

environmental performance of the first scenario is explained by the lower amount of concrete and reinforcing steel used for the slab, but is still dominated by production of materials (concrete, reinforcing steel, cast iron) as illustrated by Figure 3.

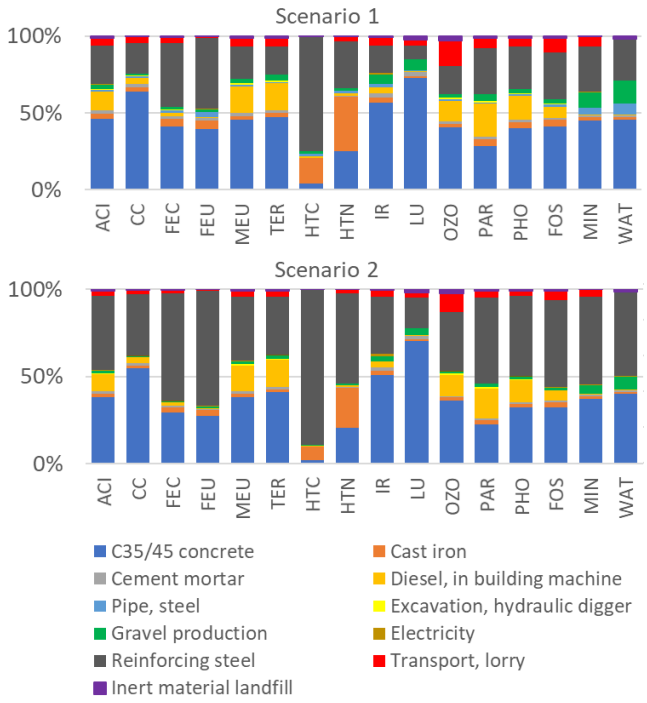

Figure 3. Scenario 1: Contribution analysis.

4 CONCLUSIONS

The study shows that materials such as cement and steel are major contributors to the overall impacts, and particularly climate change. It is therefore important to optimize their use when designing and implementing soil improvement solutions. It also stresses the need for contextualized data for such materials. The study also highlights the importance of extending the limits of the assessed system to include foundations, and not to strictly focus on soil reinforcement solutions, here rigid inclusions.

ACKNOWLEDGEMENTS

The results presented in this paper were part of the ASIRI+ National Project. The authors are grateful for the data provided by the company Keller Fondations Spéciales.

REFERENCES

AFNOR (2014) NF EN 15804+A1, Sustainability of Construction Works - Environmental Product Declarations - Core Rules for the Product Category of Construction Products. AFNOR.

Basu, D., Misra, A., Puppala, A.J., Chittoori, C.S. (2013) Sustainability in Geotechnical Engineering, In: *Proceedings of the 18th International Conference on Soil Mechanics and Geotechnical Engineering*, Paris, France, pp. 3171- 3174.

Chen, Y. (2022) *Impacts environnementaux des solutions de renforcement de sol par incusions rigides: focus sur la Plateforme de Transfert de Charge (PTC)*, Master Mécanique des sols et des roches dans leur environnement 2021-2022, Ecole des Ponts ParisTech.

de Bortoli, A., Bouhaya, L. & Feraille, A. (2020) A life cycle model for high-speed rail infrastructure: environmental inventories and assessment of the Tours-Bordeaux railway in France, *International Journal of Life Cycle Assessment*, 25:814–830. https://doi.org/10.1007/s11367-019-01727-2.

Frischknecht, R., Jungbluth, N., Althaus, H.-J., Doka, G., Heck, T., Hellweg, S., Hischier, R., Nemecek, T., Rebitzer, G., Spielmann, M., Wernet, G. (2007) Overview and Methodology. ecoinvent report No. 1, Swiss Centre for Life Cycle Inventories, Dübendorf, Switzerland.

Horvath, A. (2006) Environmental Assessment of Freight Transportation in the U.S., *International Journal of Life Cycle Assessment*, 11:229–239, https://doi.org/10.1065/lca2006.02.244.

ISO 2006a. ISO 14040: Environmental Management—Life Cycle Assessment—Principles and Framework.

Saadé, M. and Jolliet, O. (2024). *Analyse du cycle de vie, Comprendre et réaliser un écobilan*, 4th edition, EPFL Press, Lausanne, Switzerland.

Peuportier, B., Kohler, K., Boonstra, C. (1997) European project REGENER, life cycle analysis of buildings. In: 2nd International Conference "Buildings and the Environment." Paris, 9-12 Juin 1997, p 8.

Raymond, A.J., DeJong, J.T., Kendall, A., Blackburn, J.T., Rick Deschamps, R. (2021) Life Cycle Sustainability Assessment of Geotechnical Ground Improvement Methods, *Journal of Geotechnical and Geoenvironmental Engineering*, 147(12):04021161 https://doi.org/10.1061/(ASCE)GT.1943-5606.0002646.

Proceedings of the XVIII ECSMGE 2024
GEOTECHNICAL ENGINEERING CHALLENGES
TO MEET CURRENT AND EMERGING NEEDS OF SOCIETY
© 2024 the Authors
ISBN 978-1-032-54816-6
DOI 10.1201/9781003431749-648
Open Access: www.taylorfrancis.com, CC BY-NC-ND 4.0 license

ECSMGE 24
XVIII EUROPEAN CONFERENCE ON SOIL MECHANICS AND GEOTECHNICAL ENGINEERING

Centrifuge modelling of hollow heated piles in saturated sand

Modélisation centrifuge de pieux creux chauffés dans du sable saturé

G. Sabaliauskaite*, S.E. Stallebrass, A.M. McNamara, R.N. Taylor, S. Divall
City, University of London, UK

J.P. Panchal
Keltbray Piling, London, UK

**greta.sabaliauskaite@city.ac.uk*

ABSTRACT: Thermal piles are a sustainable foundation solution which support structural load whilst generating geothermal energy. Current design practice has been developed for conventional solid concrete thermal piles. This paper focusses on the use of a new innovative hollow thermal pile, the HIPER pile, developed in collaboration with Keltbray Piling. This pile is significantly more thermally efficient; leading to greater temperature gradients than could be expected with conventional thermal piles. A total of four centrifuge model tests at 50g in sand have been conducted to investigate the effects of heating and cooling cycles on pile behaviour under constant load. During testing the pile head movement, pile temperature, and soil temperature were recorded. Relationships between pile movement and thermal cycles are presented.

RÉSUMÉ: Les pieux thermiques sont une solution de fondation durable qui supporte la charge structurelle tout en générant de l'énergie géothermique. Les pratiques de conception actuelles ont été développées pour les pieux thermiques en béton massif conventionnels. Cet article se concentre sur l'utilisation d'un nouveau pieu thermique creux innovant, le pieu HIPER, développé en collaboration avec Keltbray Piling. Ce pieu est nettement plus efficace thermiquement; conduisant à des gradients de température plus importants que ceux auxquels on pourrait s'attendre avec des pieux thermiques conventionnels. Au total, quatre essais sur modèle de centrifugeuse à 50 g dans du sable ont été réalisés pour étudier les effets des cycles de chauffage et de refroidissement sur le comportement des pieux sous charge constante. Au cours des tests, le mouvement de la tête du pieu, la température du pieu et la température du sol ont été enregistrés. Les relations entre le mouvement des pieux et les cycles thermiques sont présentées.

Keywords: Centrifuge modelling; thermal piles; temperature effects.

1 INTRODUCTION

The drive towards efficiency and sustainability within the construction industry has led to an increased demand and use of energy geostructures (Laloui & Di Donna, 2013). One such structure is the thermal pile. Thermal piles use geothermal energy thereby reducing the need to use conventional energy sources, whilst also providing structural support.

Current design practice for thermal piles in the UK is presented by the Ground Source Heat Pump Association (2018). Such piles are assumed to be solid concrete. However, the HIPER (Hollow, Impression, Precast, Energy, Reusable) pile differs significantly from a solid concrete thermal pile both in geometry and thermal efficiency and the expectation is that the behaviour of this pile will not be adequately represented by the current guidance. In order to gain a better understanding of the behaviour of these piles and the effect thermal cycles have on them a short series of centrifuge tests have been undertaken.

McNamara et al. (2014) described a field study for a novel type of hollow, cast-in-situ pile, noting that this type of pile may be suited for use as a thermal pile. Adopting a large diameter hollow pile offers the prospect of energy generation from standard length bored piles that carry structural load rather than very deep dedicated energy collectors. In addition, such piles can provide high efficiency heat transfer because they are water filled with only a narrow concrete annulus, typically 200mm.

A limited number of field tests have been undertaken in order to investigate the thermal performance of HIPER piles (Ground Engineering, 2022). The available information from these tests has provided promising data on heat efficiency as noted earlier. However, the lack of control of boundary effects can lead to variability in the results of such tests making them difficult to interpret with confidence, particularly when investigating the effect of temperature cycles on pile performance.

In order to obtain reliable data from an equivalent physical event, centrifuge testing can be used to model reduced-scale piles under controlled conditions, allowing isolation of specific variables of interest. The tests reported sought to investigate the effect of thermal cycles on pile settlement and establish how these compare to typical data in the literature.

2 PREVIOUS WORK

Previous work on centrifuge modelling of heat transfer in soil (Savvidou, 1988) states that for coarse grained soils heat transfer is primarily by free convection through the pore fluid, assuming the soil is saturated. Savvidou (1988) reviewed scaling laws for heat transfer by convection and concluded that the heat transfer would occur N^2 times faster in the model than in the prototype.

Ng et al (2020) undertook a modelling of models exercise to investigate scaling effects on loaded thermal piles subjected to temperature cycles. They found that there were no scaling effects for tests in sands with a D/d_{50} greater than 92, where D is the diameter of the pile and d_{50} is the mean particle size. In the tests reported by Ng et al. (2020), 7 cycles of change in temperature of 20°C, resulted in an overall pile head settlement of 1.3%D. There have been a number of other centrifuge test results reported in the literature but these relate to dry sands and silts, for example Wang et al (2017) and Goode and McCartney (2015) where the heat transfer mechanism will be different, or tests to examine the effect of temperature on pile capacity rather than settlement, for example Ng et al. (2015).

3 OBJECTIVES

The objective was to carry out centrifuge tests at 50g using the 40g-tonne centrifuge at City, University of London, to examine the influence of cycles of temperature on the displacement of a pile under constant axial load. The length of the temperature cycles and the height of the water table were varied.

The piles were placed in a bed of dense 0.7 – 1.25 mm alluvial sand. The temperature was cycled between 17-18°C and 43-45°C for 4 cycles of 30 minutes and then 4 cycles of 60 minutes. The piles had a relatively low length to diameter ratio and were filled with water leading to a good exchange of temperature between the pile and soil; characteristics typical of those expected of a HIPER pile.

4 APPARATUS

The tests were conducted in a 375mm deep cylindrical stainless steel tub with a diameter of 420mm (Figure 1).

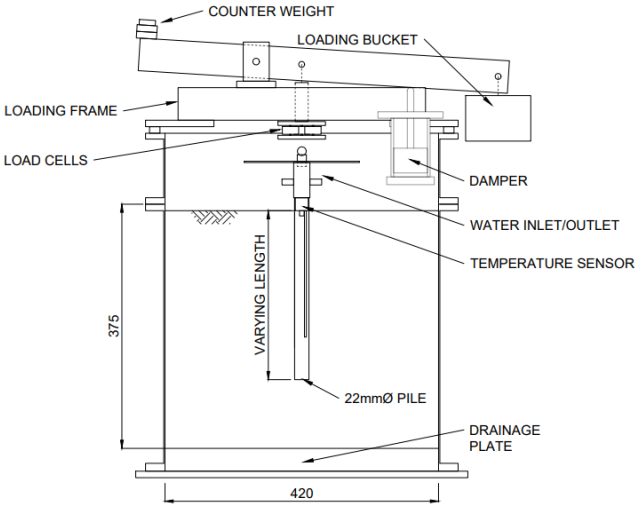

Figure 1. Model pile and loading frame set up.

The pile was modelled using 22mm outside diameter (1.10m diameter prototype) cylindrical copper tubes, coated in 0.7 – 1.25 mm alluvial sand ensuring good and consistent interface friction. This was the same sand that was used to create the soil bed. The pile cap was made from a Perspex body which housed inlet/outlet tubes for water to flow through the pile as well as a temperature sensor (Figure 2). An aluminium plate on top of the pile cap allowed LVDTs to measure vertical pile displacement.

The constant load apparatus comprised a loading beam with a water bucket at one end and a set of counterweights at the other. During the test, the loading bucket was filled with water corresponding to the desired axial load and that load was applied to the pile head. The load was measured by a load plate consisting of three load cells sandwiched between two aluminium plates ensuring that the load cells were not subjected to bending. Load was applied through a steel ball bearing at the top of the Perspex body ensuring pure axial load. To avoid a sudden movement of the bucket, and therefore an impact on the pile head, a damping mechanism was introduced.



Figure 2. Model pile embedded in sand.

5 MODEL PREPARATION AND TESTING PROCEDURE

Correct placement of the pile and soil temperature sensors was achieved with an installation guide. The pile and temperature sensors remained attached to the guide until the required height of soil was reached.

The sand was carefully placed into the tub, around the pile and soil temperature sensors, in layers of approximately 10mm, with compaction taking place after each layer of sand was placed. Pore pressure transducers were inserted through openings in the walls of the tub. A smoothing tool was used to level out the surface of the soil.

Once the top of the soil model was levelled, the installation guide was removed and the loading frame, with the load cells and LVDTs was carefully fixed onto the tub. The model was then placed on the centrifuge swing for connections to be made. A standpipe was connected to the model to establish and maintain the required water table for each test and the model was accelerated to 50g. When the water table was established the pile was loaded by filling the bucket with water to achieve the desired load. Thereafter, heating and cooling cycles began.

The pile embedment depth, water table levels, and factors of safety (FOS) for the two tests presented are summarised in Table 1.

Table 1. Summary of test variables.

Test ID	Pile embedment depth (mm)	Water table in mm below ground level	FOS
Test 1	265	129	2.6
Test 2		31	1.7

6 RESULTS

For Tests 1 and 2, the pile embedment depth was 265mm at model scale, equivalent to 13.25m at prototype scale. As noted above the first four cycles of temperature each took 30 minutes, which is equivalent to 52 days of heat transfer at prototype scale; owing to the N^2 scaling factor for heat transfer (Savvidou 1988). The second four cycles were 104 days at prototype scale. The normalised pile displacements during heating and cooling stages are shown in Figure 3.

The initial temperature of the piles was between 17 and 18°C and this was governed by the mains supply temperature. The piles were then heated to 43°C by circulating hot water through the pile, applying a temperature change of approximately 26°C between heating and cooling cycles. A slight variation in both maximum and minimum temperatures of the pile was observed owing to heat loss during cycling.

Pile heave of just under 0.3%D was observed during the first heating phase for Test 1, followed by a settlement of approximately 0.5%D during the first cooling phase. During subsequent heating and cooling cycles, ratcheting settlement of the pile was observed, with a final settlement of 0.5%D, but at this stage the net settlement at the end of a temperature cycle had reduced to 0.03%D. There was a smooth non-linear reduction in net settlement per cycle which was not affected by the length of the temperature cycle. In this test the water table was approximately half way down the pile and below the temperature sensors.

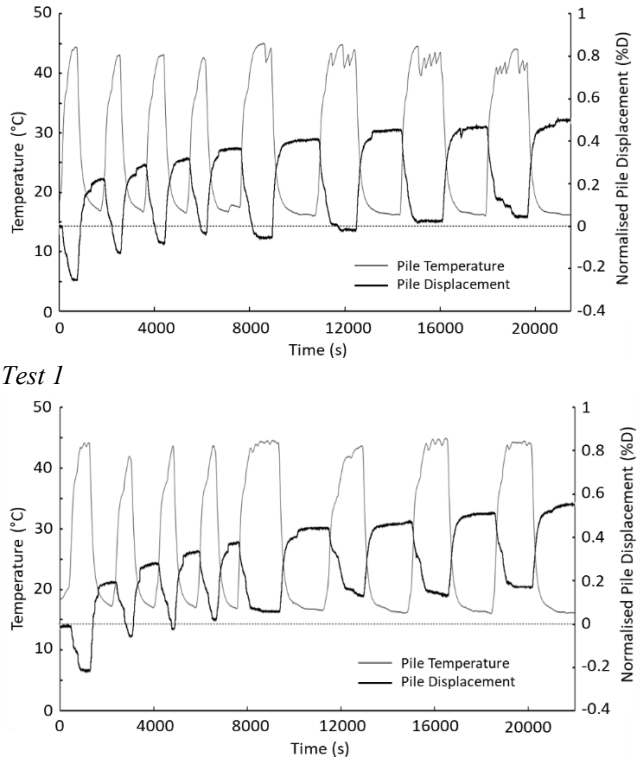

Test 1

Test 2

Figure 3. Normalised pile displacements during temperature cycles. Negative pile displacement is heave.

In Test 2 the water table was near ground surface, and pile displacement was reduced; just over 0.2%D of heave occurred when the pile was initially heated, followed by 0.45%D of settlement during the first

cooling phase. During subsequent heating and cooling cycles the net settlement increased more significantly than in Test 1 with a final settlement after 8 cycles of 0.53%D. The net settlement for the final cycle was approximately 0.03%D. In this test it appears that the cycle duration influenced the net settlement in each cycle, as there was an increase in net settlement during the first long cycle; although it is possible that this may be a function of slight disparities in the temperature cycles.

7 DISCUSSION

There was heave at the pile cap upon initial heating, followed by settlement as the pile and surrounding soil cooled and contracted. Settlement always exceeded heave but by gradually lesser amounts. The factor of safety for Test 2 was lower than that for Test 1 because the water table was near the surface and this should lead to significantly greater settlements during this test. However, the increase in settlement was marginal and this may be explained by examining the change in temperature in the soil surrounding the pile. Figure 4 shows the temperature measured at sensors placed 10, 30 and 50 mm away from the pile.

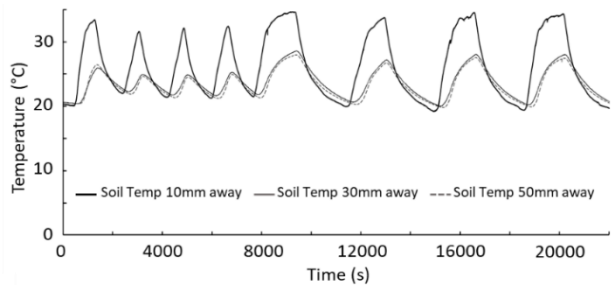

Test 1

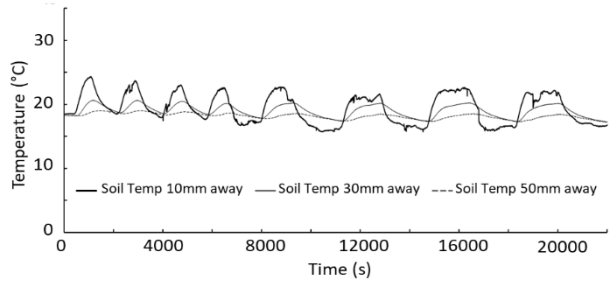

Test 2

Figure 4. Temperature variation away from the pile.

It is clear from this figure that temperature dissipates more rapidly with distance from the pile when the sand is saturated. This might be expected as the primary mechanism of heat transfer in a coarse-grained soil is convection due to motion of the pore fluid (Savvidou, 1988). In the unsaturated/dry sand at the top of the pile in Test 1 this mechanism of heat transfer will not occur and the soil surrounding the pile will be subjected to more dramatic changes in temperature leading to greater heave and settlement than might occur in a saturated sand at an equivalent factor of safety. This may also cause a pile in saturated sand to be less thermally efficient, but this is not something that could be easily established from these tests. The temperature changes are consistent with those seen by Ng et al. (2020) for thermal piles in saturated sands. Wang et al. (2017) testing piles in dry sand recorded greater temperature changes at similar distances from the pile, but in Test 1 half of the pile is in saturated soil. The overall pile head settlement after 7 cycles of temperature observed by Ng et al. (2020) was greater than in Test 2, but the pile length to diameter ratio in those tests was 19, whereas in the tests reported here it is only 12 representing a realistic geometry for a HIPER pile. A longer pile should generate greater displacement at the pile head when heated and cooled.

8 CONCLUSIONS

A short series of centrifuge testing of piles in sand has confirmed that heat transfer through saturated sand by convection within the pore fluid reduces temperature changes in the soil surrounding the pile. This in turn reduces temperature induced settlements under axial load. In comparison with similar tests on piles with higher length to diameter ratios these wider and shorter hollow piles seem to develop less net settlement, even at quite low factors of safety.

The series of tests was limited in number and further work is necessary to explore the effect of varying the water table for constant factor of safety piles.

REFERENCES

Goode, JC and McCartney, JS (2015) Centrifuge modelling of end-restraint effects in energy foundations. Journal of Geotech. and Geoenv. Eng. ASCE, 141, No 8.

Ground Engineering. “Piling: Hiper piles leave lasting impact at HS2 London Site”. July 2022.

Kramer, C. A., and P. Basu. (2014) Performance of a model geothermal pile in sand. Proc. 8th ICPMG, Perth CRC Press/Balkema.

Laloui, Lyesse, and Alice Di Donna, eds. *Energy geostructures: innovation in underground engineering*. John Wiley & Sons, 2013.

McNamara, A M., Suckling, TP, McKinley, B, Stallebrass, SE. (2014) A field trial of a reusable, hollow, cast-in-situ pile. Proc. ICE Geotechnical Engineering, Vol. 167, No 4, pp 390-401. https://doi.org/10.1680/geng.12.00102.

Ng, CWW, Shi, C, Gunawan, A, Laloui, L and Liu, HL (2015) Centrifuge modelling of heating effects on energy pile performance in saturated sand, Can. Geotech. J.,Vol. 52, No 8, pp. 1045 -1057. https://doi.org/10.1139/cgj-2014-0301.

Ng, CWW, Zhang, C, Farivar, A, and Gomaa, SMMH (2020) Scaling effects on the centrifuge modelling of energy piles in saturated sand. Geotechnique Letters, 10, pp 57-62. https://doi.org/10.1680/jphmg.22.00041.

Savvidou, C. (1988). Centrifuge modelling of heat transfer in soil. Proc. Centrifuge 88, J.-P. Corté, ed., Balkema, Rotterdam, Netherlands, 583–591.

Thermal Pile Design, Installation and Materials Standards, Ground Source Heat Pump Association, Version 2 September 2018.

Wang, C-I, Liu, H-I, Kong, G and Ng, CWW (2017) Different types of energy piles with heating-cooling cycles. Proc. ICE Geotechnical Eng, 170, GE3, pp 220-231. http://dx.doi.org/10.1680/jgeen.16.00061.

Proceedings of the XVIII ECSMGE 2024
GEOTECHNICAL ENGINEERING CHALLENGES
TO MEET CURRENT AND EMERGING NEEDS OF SOCIETY
© 2024 the Authors
ISBN 978-1-032-54816-6
DOI 10.1201/9781003431749-649
Open Access: www.taylorfrancis.com, CC BY-NC-ND 4.0 license

ECSMGE 24
XVIII EUROPEAN CONFERENCE ON SOIL MECHANICS AND GEOTECHNICAL ENGINEERING

Effects of AM fungi on root biomechanical properties

Effets des champignons AM sur les propriétés mécaniques des racines

T. Sakolpanya, V. Kamchoom*
Excellent Centre for Green and Sustainable Infrastructure, Faculty of Engineering, King Mongkut's Institute of Technology Ladkrabang (KMITL), Bangkok, Thailand

X.W. Chen
Guangdong Provincial Research Centre for Environment Pollution Control and Remediation Materials, Department of Ecology, College of Life Science and Technology, Jinan University, Guangzhou, China

A.K. Leung
Department of Civil and Environmental Engineering, Hong Kong University of Science and Technology (HKUST), Hong Kong SAR

viroon.ka@kmitl.ac.th

ABSTRACT: Arbuscular mycorrhizal (AM) fungi play a pivotal role in promoting plant growth by enhancing root biomass, cellulose content, and biomechanical properties of plant roots. The present study investigates the potential of AM fungi in conjunction with Bermuda grass (Cynodon dactylon L.) to optimize soil bioengineering methods. These environmentally friendly approaches effectively mitigate soil erosion by facilitating root adhesion to the soil matrix and reinforcing both mechanical and hydraulic properties by root biomechanical properties. The study focuses on assessing the impact of AM fungi on distinct growth and decay periods induced by controlled burning and herbicide treatments. Various parameters, including root biomass, cellulose content, and mechanical properties such as root tensile strength and root young's modulus, are measured at different temporal intervals. The findings elucidate that the presence of AM fungi significantly augments plant root biomass and root tensile strength relative to the absence of AM fungi. However, during the decay period, the influence of AM fungi on root tensile strength can increase, but it is not statistically significant. Nonetheless, these properties are notably higher in the presence of AM fungi compared to their absence, suggesting that AM fungi enhance these traits predominantly during the growth phase. The outcomes of this study underscore the profound positive effects of AM fungi on plant root properties and provide valuable insights into their potential implementation in soil bioengineering.

RÉSUMÉ: Les champignons mycorhiziens arbusculaires (AM) jouent un rôle central dans la promotion de la croissance des plantes en améliorant la biomasse des racines, la teneur en cellulose et les propriétés biomécaniques des racines des plantes. La présente étude examine le potentiel des champignons AM en conjonction avec l'herbe des Bermudes (Cynodon dactylon L.) pour optimiser les méthodes de bio-ingénierie des sols. Ces approches respectueuses de l'environnement atténuent efficacement l'érosion des sols en facilitant l'adhésion des racines à la matrice du sol et en renforçant les propriétés mécaniques et hydrauliques grâce aux propriétés biomécaniques des racines. L'étude se concentre sur l'évaluation de l'impact des champignons AM sur des périodes distinctes de croissance et de décomposition induites par des traitements de brûlage contrôlé et d'herbicides. Divers paramètres, notamment la biomasse racinaire, la teneur en cellulose et les propriétés mécaniques telles que la résistance à la traction des racines et le module de jeunesse des racines, sont mesurés à différents intervalles temporels. Les résultats montrent que la présence de champignons AM augmente considérablement la biomasse des racines des plantes et leur résistance à la traction par rapport à l'absence de champignons AM. Cependant, pendant la période de décomposition, l'influence des champignons AM sur la résistance à la traction des racines peut augmenter, mais elle n'est pas statistiquement significative. Néanmoins, ces propriétés sont nettement plus élevées en présence de champignons AM qu'en absence, ce qui suggère que les champignons AM améliorent ces caractéristiques principalement pendant la phase de croissance. Les résultats de cette étude soulignent les profonds effets positifs des champignons AM sur les propriétés des racines des plantes et fournissent des informations précieuses sur leur mise en œuvre potentielle dans la bio-ingénierie des sols.

Keywords: AM fungi; root biomechanics; growth; decay.

1 INTRODUCTION

In vegetated soil, Plant roots play a pivotal role in conferring stability to shallow slopes and preventing erosion has been underscored in previous studies (Kamchoom and Leung 2018; Ng et al. 2016). A comprehensive understanding of the biomechanical

properties of plant roots is deemed imperative for devising strategies to mitigate soil instability, particularly in regions prone to natural disasters such as landslides and erosion (Apriyono et al. 2022; Stokes et al. 2014). Consistent with this perspective, prior investigations have delved into the biomechanical properties of plant roots, aiming to elucidate their role in mitigating erosion and failures of shallow slopes. However, divergent findings have surfaced in studies exploring the period of plant root decay (Kamchoom et al. 2021; Zhu et al. 2020). It has been observed that during this phase, these biomechanical properties tend to exhibit diminished values, potentially contributing to a detrimental impact on soil stability.

During the process of plant root decay, a symbiotic association with mycorrhizal fungi can exert a significant influence, eliciting positive effects on plant roots (Basyal and Emery 2021). Specifically, Arbuscular Mycorrhizal (AM) fungi facilitate enhanced nutrient absorption by plant roots. Previous studies have indicated that AM fungi may contribute to an increase in cellulose content and even elevate the tensile strength of plant roots. It is important to note that the influence of AM fungi extends to modifications in soil properties (Chen et al. 2019; Solly et al. 2014). These alterations in soil characteristics, in turn, have implications for changes in the properties of plant roots. Nonetheless, the effect of AM fungi subsequent to decay treatment on root biomechanical properties have not been thoroughly investigated.

2 MATERIALS AND METHODS

An investigation was conducted on the roots of Cynodon dactylon, commonly known as Bermuda grass, an herbaceous species. Bermuda grass is frequently employed in soil erosion control due to its ability to develop fibrous root systems in shallow soils (Faucette et al. 2006; Ng et al. 2014). The soil selected for this study is lateritic soil, a type commonly encountered in engineering projects for landscaping purposes in tropical and subtropical regions, such as southern China and Thailand. This soil has been characterized as clayey sand. To ensure its suitability for the research, the collected soil underwent an initial sanitation process at 120 °C for 3 hours, followed by an additional two days of oven-drying at 60°C to inactivate AM fungi in situ. Subsequently, the dry soil was sieved through a 2 mm sieve, and the AM fungi were sourced from a local supplier.

To promote optimal root development, Bermuda grass seeds were germinated in nutrient-rich vermicompost one month prior to transplantation into the soil specimens. AM fungi inoculation was introduced by preparing a mixture comprising 1 kg of soil and 25 g of dry AM fungi inoculum. The soil-AM fungal inoculum underwent compaction within polyvinyl chloride cylinders (90 mm in diameter, 130 mm in depth) using the moist tamping method, resulting in a dry density of 1520 kg/m³. Following the compaction of the soil column, a 15 mm thick layer of vermicompost was applied to the upper surface.

To investigate dynamic changes in root, two distinct experimental groups were established: Soil with AM fungi (denoted as M) and Soil without AM fungi (denoted as NM). Each experimental group comprised 30 samples, meticulously maintained in a controlled glasshouse environment. Within each group, 9 samples were specifically selected for the detailed examination of root growth impact, The grass underwent cultivation for durations of 60, 120, and 180 days, collectively referred to as growth treatments. (For each treatment, a standard reference and two replicates were employed). Following 180 days of grass growth, the remaining 21 specimens underwent two distinct decay treatments: herbicide treatment and burning treatment. In the burning treatment, the entire aboveground biomass, encompassing shoots and leaves, was subjected to a 15-minute incineration using a gas torch, followed by a 3-hour smouldering period to facilitate root decay. 12 specimens were retained in the glasshouse for durations of 30, 60, 120, 180, and 360 days after burning treatment. For the herbicide treatment, two doses of Propanil (N-[3,4-dichlorophenyl] propanamide) were applied as an irrigation solution with a concentration of 36% w/v. Subsequently, 9 specimens underwent detailed assessments of root decay after intervals of 15, 30, and 60 days following the herbicide treatment.

2.1 Measurement of Root biomechanical properties

Each soil specimen containing roots was rinsed gently with running tap water and was subsequently sieved through sieves No.4 and No.10 to obtain root samples. The roots retained on the sieve were carefully collected. The saturated weight of the roots was determined by immersing them in distilled water for a period exceeding 12 hours. For tensile testing in each treatment, approximately 30 roots were chosen, ensuring the selection of root segments without any tortuosity or tissue loss. These root segments were then subjected to a uniaxial tensile test using a universal testing frame, employing a constant extension rate of 0.1 mm/s. Root segments that failed at or near the clamp margins were excluded from analysis. The root young's modulus was subsequently calculated from

stress-strain relationships derived from the tensile strength test.

2.2 Measurement of Cellulose content

The chemical composition of roots, specifically the content of lignin and cellulose, was assessed on the residual portion of each root segment using the method described by Leavitt and Danzer (1993). In general, the procedure entailed the removal of lignin polymers subsequent to the elimination of organic compounds from the root material. This process resulted in the classification of the residual constituent as a compound composed of cellulose.

3 RESULTS

3.1 Effects of AM fungi on root biomechanical properties

During the phase of normal growth, observed in the NM condition (Soil without AM fungi), there was an 18% increase in mean tensile strength from day 60 to 120. In the condition of M (Soil with AM fungi), a modest increase of 4% was noted from day 60 to 120, followed by a more substantial increase of 23% from day 120 to 180 (Figure 1a). Young's modulus demonstrated minimal impact from AM fungal inoculation at 60 and 120 days but exhibited a notable improvement of 35% at 180 days compared to the NM condition (Figure 1b).

During the decay phase, a significant decrease in mean tensile strength was observed, particularly in condition of decay due to herbicide treatment. At 60 days after decay (day 240), the mean tensile strength for NM and M was 14.9 MPa and 19.5 MPa, respectively, for herbicide treatment, and 27.6 MPa and 28.8 MPa, respectively, for burning treatment. After 180 days of burning-induced decay (day 360), AM fungi conditions displayed a clear increase in mean tensile strength, with values of 16.6 MPa for NM and 23.9 MPa for M (Figure 1a), representing a 44% increase. Regarding Young's modulus, after 60 days of decay due to herbicides (day 240), values for NM and M were 146 MPa and 160 MPa, respectively, while for decay due to burning, the values were 252 MPa and 277 MPa, respectively. A comparison of these values indicated that M condition was approximately 11-18% higher than NM condition under both decay phase.

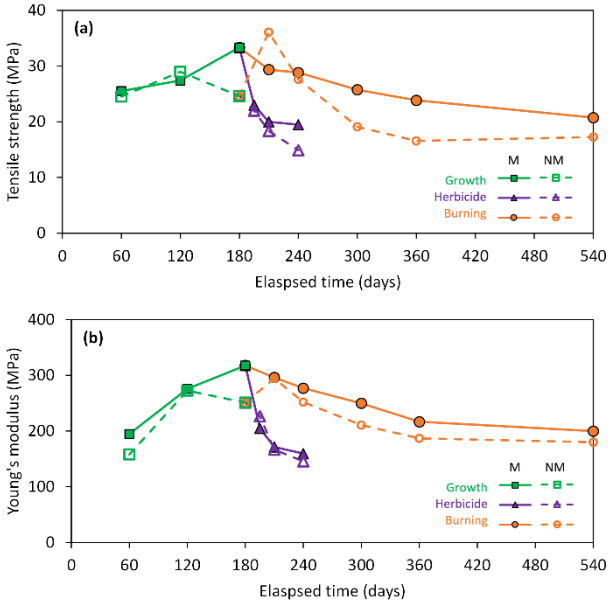

Figure 1. Variation in (a) Tensile strength and (b) Young's modulus of root with and without AM fungi.

3.2 Effects of AM fungi on root biomass and cellulose content

In the M condition, both cellulose content and root biomass exhibited higher values compared to the NM condition at each recorded time point. Throughout the growth period, cellulose content demonstrated an increasing trend. However, between days 120 and 180, a slight decrease was observed in the NM condition (Figure 2a), corresponding with the concurrent reduction in tensile strength and Young's modulus during that phase (Figure 1). During the decay phase, a decline in cellulose content and root biomass was noted, with a more pronounced reduction in the condition of herbicide-induced decay. In the presence of mycorrhizal (M), this decline in cellulose content and root biomass was mitigated, particularly in instances of decay due to herbicide (Figure 2c and d). Notably, in condition of burning treatment, although cellulose content decreased, the rate of decline was slower (Figure 2e). Root biomass also experienced a decrease, but the reduction was less pronounced (Figure 2f). The presence of mycorrhizal further attenuated the rate of decline, particularly when compared to herbicide-induced decay.

4 CONCLUSIONS

This study involved the inoculation of Arbuscular Mycorrhizal (AM) fungi to Bermuda grass, a species recognized for its resilience in revegetation stress. The primary aim was to investigate the influence of AM fungi on root biomechanical properties relevant to soil reinforcement. Preceding decay processes, AM fungi

contributed to an increase in root biomass, providing more initial root materials. In general, roots inoculated with AM fungi exhibited higher cellulose contents compared to without AM fungi. Although a positive correlation between cellulose content and root tensile strength was evident. AM fungi contributed to roots consistently demonstrated significantly higher cellulose content, tensile strength, and Young's modulus than without AM fungi. These observations were particularly pronounced during normal growth and following the burning treatment, except for the herbicide treatment, indicating that herbicide application influenced plant biochemical or physiological processes, accelerating decomposition. Furthermore, certain plant specimens managed to withstand burning while retaining intact root systems. While no significant difference in the in-situ decay rate of roots was observed between with and without AM fungi, the application of AM fungi resulted in noteworthy enhancements in root biomass, cellulose content, tensile strength, and Young's modulus. Our findings suggest that inoculating grass-rooted soils with AM fungi is an effective method for preserving their physical stability.

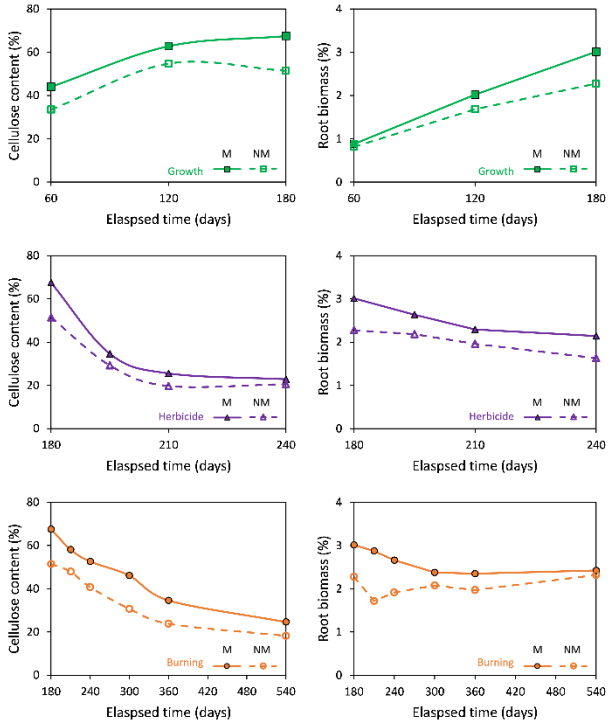

Figure 2. Variation in (a,c,e) Cellulose content and (b,d,f) Root biomass of root with and without AM fungi.

ACKNOWLEDGEMENTS

This work was supported by King Mongkut's Institute of Technology Ladkrabang.

REFERENCES

Apriyono A, Yuliana, Kamchoom V (2022) Serviceability of cut slope and embankmentunder seasonal climate variations. Acta Geophysica, 1-13. DOI: 10.1007/s11600-022-00953-x.

Basyal B, Emery SM (2021) An arbuscular mycorrhizal fungus alters switchgrass growth, root architecture, and cell wall chemistry across a soil moisture gradient. Mycorrhiza 31:251–258. https://doi.org/10.1007/s00572-020-00992-6.

Chen XW, Wu L, Luo N, et al (2019) Arbuscular mycorrhizal fungi and the associated bacte-rial community influence the uptake of cadmium in rice. Geoderma 337:749–757. https://doi.org/10.1016/j.geoderma.2018.10.029.

Faucette LB, Risse LM, Jordan CF, Cabrera ML, Coleman DC, West LT (2006) Vegetation and soil quality effects from hydroseed and compost blankets used for erosion control in construction activities. Journal of Soil and Water Conservation, 61(6): 355-362.

Kamchoom V, Boldrin D, Leung AK, Sookkrajang C, Likitlersuang S (2021) Biomechanical properties of the growing and decaying roots of Cynodon dactylon. Plant and Soil. 471: 193–210. DOI: 10.1007/s11104-021-05207-1.

Kamchoom V, Leung AK (2018) Effects of plant removal on slope hydrology and stability. In Physical Modelling in Geotechnics (pp. 1131-1136). CRC Press.

Leavitt SW, Danzer SR (1993) Method for Batch Processing Small Wood Samples to Holo-cellulose for Stable-Carbon Isotope Analysis. Anal Chem 65:87–89. https://doi.org/10.1021/ac00049a017.

Ng, CWW, Kamchoom V, Leung AK (2016) Centrifuge modelling of the effects of root ge-ometry on the transpiration-induced suction and stability of vegetated slopes. Land-slides 13(5): 925-938. DOI: 10.1007/s10346-015-0645-7.

Ng CWW, Leung AK, Woon KX (2014) Effects of soil density on grass-induced suction dis-tributions in compacted soil subjected to rainfall. Can Geotech J 51:311–321. https://doi.org/10.1139/cgj-2013-0221-.

Solly EF, Schöning I, Boch S, et al (2014) Factors controlling decomposition rates of fine root litter in temperate forests and grasslands. Plant Soil 382:203–218. https://doi.org/10.1007/s11104-014-2151-4.

Stokes A, Douglas GB, Fourcaud T, et al (2014) Ecological mitigation of hillslope instability: Ten key issues facing researchers and practitioners. Plant Soil 377:1–23. https://doi.org/10.1007/s11104-014-2044-6.

Zhu J, Wang Y, Wang Y, Mao Z, Langendoen EJ (2020). How does root biodegrada-tion after plant felling change root reinforcement to soil? Plant and Soil, 446(1–2): 211–227. https://doi.org/10.1007/s11104-019-04345-x.

Proceedings of the XVIII ECSMGE 2024
GEOTECHNICAL ENGINEERING CHALLENGES
TO MEET CURRENT AND EMERGING NEEDS OF SOCIETY
© 2024 the Authors
ISBN 978-1-032-54816-6
DOI 10.1201/9781003431749-650
Open Access: www.taylorfrancis.com, CC BY-NC-ND 4.0 license

ECSMGE 24
XVIII EUROPEAN CONFERENCE ON SOIL MECHANICS AND GEOTECHNICAL ENGINEERING

Review on carbon footprint in deep foundations: Case study for helical piles in Brasília, DF

Revue de l'empreinte carbone dans les fondations profondes: Étude de cas pour les pieux hélicoïdaux à Brasília, DF

B. Sandoval, R.P. Cunha*
University of Brasilia, Brasilia, DF, Brazil
**210008679@aluno.unb.br*

ABSTRACT: It is essential to highlight that the civil construction industry is a significant contributor to carbon emissions. The aim of this article is to develop a flowchart using the Life Cycle Assessment (LCA) methodology, which has already been employed to calculate the carbon footprint of deep foundations. This flowchart will be specifically tailored to assess the carbon footprint of helix piles used in a building project located in Brasilia, DF. Alongside this, the article will include a literature review of previous research within the foundation sector concerning carbon footprint analysis.

RÉSUMÉ: Il est essentiel de souligner que l'industrie de la construction civile est un contributeur significatif aux émissions de carbone. L'objectif de cet article est de développer un organigramme en utilisant la méthodologie d'Analyse de Cycle de Vie (ACV), qui a déjà été employée pour calculer l'empreinte carbone des fondations profondes. Cet organigramme sera spécifiquement adapté pour évaluer l'empreinte carbone des pieux hélicoïdaux utilisés dans un projet de construction situé à Brasilia, DF. En parallèle, l'article comprendra une revue de la littérature des recherches précédentes dans le secteur des fondations concernant l'analyse de l'empreinte carbone.

Keywords: LCA methodology; helix piles; deep foundations; carbon footprint.

1 INTRODUCTION

Climate change is exerting a significant impact on our environment, making it essential to adopt concrete measures to mitigate its effects. It is well known that energy consumption is the main source of greenhouse gas emissions, encompassing sectors such as transportation, electricity generation, heat generation, buildings, manufacturing, construction, fugitive emissions, and other forms of fuel combustion. For instance, in 2016, heat and electricity generation accounted for 30% of emissions, while transportation contributed 15%, and manufacturing and construction contributed 12% (WRI Brazil, 2020).

In a more specific context, greenhouse gas emissions in Brazil increased by 8.9% in 2016, reaching a total volume of 2.28 billion metric tons of carbon dioxide equivalent (CO_2e), compared to 2.09 billion recorded in 2015 (World Resources Institute Brazil, 2017). These figures position Brazil as the seventh-largest emitter of greenhouse gases globally. To meet the commitments of the Paris Agreement, the country has established ambitious climate targets, incentivizing the implementation of long-term measures to reduce emissions.

In this context, research on carbon footprint plays a crucial role. Carbon footprint, defined in 1990 (Gao et al, 2014), represents the cumulative amount of greenhouse gas emissions (GHG) generated by individuals, companies, or entities, measured in tons of carbon dioxide equivalent (CO_2eq) emitted annually. GHG encompasses a range of gaseous compounds, such as perfluorocarbons, methane, carbon dioxide, nitrous oxide, hexafluoride, sulfur, and hydrofluorocarbons. Effective measures to reduce these carbon emissions include promoting sustainable buildings, which contribute to a healthy environment in the long term, the use of renewable energies, sustainable water consumption (Okeke et al, 2018), as well as the conservation of green spaces and the development of emissions measurement tools in construction (Cheng et al, 2011).

In the field of civil construction, deep foundations, such as helical and drilled piles, play a fundamental role in environmental sustainability. They are often employed in engineering projects that require structural support in challenging soils, such as collapsible soils. However, the construction of these foundations entails significant consumption of resources, energy,

and materials, substantially contributing to the carbon footprint of a project.

Recognizing the importance of adapting deep foundations to make them more sustainable is imperative, as this can contribute to the reduction of greenhouse gas emissions. Strategies include the use of materials with lower carbon intensity, waste and resource consumption minimization, the use of energy-efficient equipment and technologies during the construction of these foundations, and effective management of construction and demolition waste, emphasizing recycling.

Therefore, when considering the construction of deep foundations, especially in challenging soils such as collapsible soils, it is crucial to adopt a sustainable approach that takes into account the environmental impact. Such an approach not only contributes to meeting carbon emission reduction goals but also results in more resilient and durable structures, providing long-term benefits to the environment and society.

Most studies emphasize the importance of assessing emissions during the construction phase of buildings (Keoleian, G et al, 2001; Junnila and Horvath, 2003; Junila et al, 2006). However, it is notable that few of these studies emphasize the construction phase of foundations, which involves the use of large volumes of steel, concrete, and heavy machinery, resulting in significant CO_2 emissions to the environment. According to the Paris Agreement, signed on December 12, 2015, and ratified on November 4, 2016, it became necessary for countries responsible for about 55% of global emissions to commit worldwide. In this context, each country established specific targets, and the European Union, along with 193 other countries, including Brazil, account for more than 90% of greenhouse gas emissions and have adhered to the treaty. The goal of this agreement is to achieve decarbonization targets by 2050 (IPCC, 2018).

Several countries have implemented emission control policies, but in Brazil, the inclusion of a carbon tax in tax reform has not yet been defined. According to a report by WRI Brazil in 2020, this document offers valuable insights into possible paths towards a transition to a low-carbon economy. The report indicates that the country is ready to adopt new economic approaches aligned with the low-carbon economy and highlights the benefits of adopting these policies (WRI Brazil and The New Climate Economy, 2020).

Based on the justifications presented above, the proposed research finds solid grounds for its realization. The gap in studies specifically addressing the construction phase of foundations, along with the need for emission control policies aligned with international commitments, such as the Paris Agreement, and the potential for a low-carbon economy, highlight the relevance of this study. Additionally, the WRI Brazil 2020 report corroborates the country's readiness to adopt sustainable economic approaches, emphasizing the importance of investigating the carbon footprint in helical piles in the region. Therefore, the proposed research is justified as a significant step towards understanding and mitigating CO_2 emissions associated with this phase of construction in Brasília-DF.

2 CARBON FOOTPRINT IN DEEP FOUNDATIONS

The carbon footprint of deep foundations can be significant due to the intensive use of construction materials, transportation of heavy materials and equipment, and the use of large machinery for drilling and excavation. The carbon footprint of these foundations can be reduced by adopting more sustainable construction techniques, such as using low-carbon construction materials and implementing more efficient transportation models. Additionally, the use of renewable energy-powered equipment and the adoption of construction techniques that reduce waste and pollution can also decrease the carbon footprint of deep foundations.

Life Cycle Assessment (LCA) is a methodology used to assess the environmental impacts of processes or products. In the case of deep foundations, LCA considers the environmental impacts of all phases of the foundation construction process, including material extraction, manufacturing, transportation, installation, and disposal. This includes an analysis of the types of materials used in the foundation, the amount of energy and water used during construction, and the emissions of greenhouse gases and other pollutants.

The Life Cycle Assessment (LCA) Matrix for Continuous Flight Auger (CFA) Pile is a tool that allows the assessment of the environmental impacts of this foundation technique. It is divided into life cycle stages of the structure, from raw material extraction to the end of the foundation's service life.

2.1 Definition of the limit for calculating the carbon footprint in continuous flight auger piles in this study

The calculation of the carbon footprint during the Installation phase of continuous flight auger piles will be carried out. In this way, the limit of the carbon footprint in the installation phase of continuous flight auger piles is established in Figures 1 and 2.

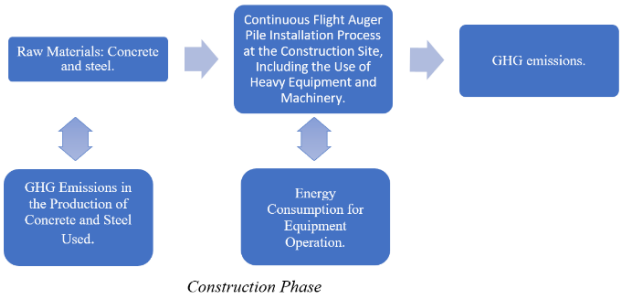

Figure 1. Limit of the carbon footprint in the construction phase of continuous flight auger piles. According with Bilec (2007).

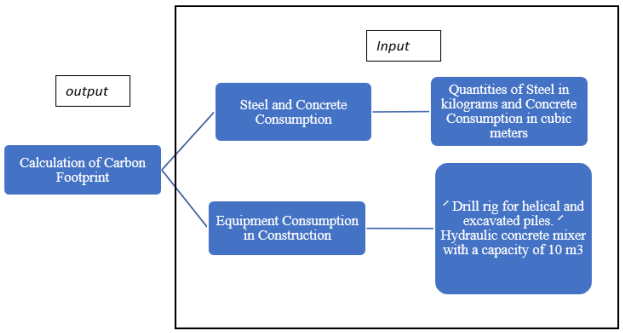

Figure 2. Helical pile limits for settlement calculation, including transport and installation phase. According with Li, et al (2019).

2.2 Calculation of emissions

In this section, we outline the methodology for calculating emissions. Our approach closely mirrors that employed by Zhang and Wang (2016). We will evaluate the carbon emissions associated with the construction of continuous flight auger piles in the collapsible soil of the Federal District. This assessment adopts methodological principles similar to those detailed by Zhang and Wang. The analysis encompasses various aspects, including quantifying carbon emissions linked to concrete transportation necessary for pile foundation, as well as emissions stemming from the production and utilization of critical materials like steel and concrete. Furthermore, we will consider specific carbon emissions generated during the construction phase of the continuous flight auger piles.

By applying this approach, in alignment with Zhang and Wang's work, we aim to ensure a consistent evaluation of the carbon emissions inherent in the implementation of these piles, thereby contributing to a comprehensive analysis of the environmental impact of this construction practice. As per the preceding paragraph, we will utilize Equations 1, 2, 3, 4, and 5, which reflect the methodology proposed by Zhang and Wang.

Manufacturing Emissions of Materials:

$$Cmat = \Sigma Ai \times FEi\ , \quad (1)$$

Emissions from On-Site Construction Activities:

$$Cact = \Sigma Aj \times FEj, \quad (2)$$

Total Carbon Footprint:

$$C_{Total}) = (Cmat + Cact), \quad (3)$$

Emissions from Concrete Transportation:

$$ETC = QCT \times FETC, \quad (4)$$

Total Carbon Footprint R:

$$RC_{Total}) = (Cmat + Cact + ETC), \quad (5)$$

The amount of carbon emissions related to materials (Cmat) is determined by the quantity of material or activity of each type, represented by Ai, multiplied by the specific carbon emission factor for that material or activity, represented by FEi. Similarly, carbon emissions associated with activities performed at the construction site (Cact) are calculated by multiplying the quantity of each type of activity, represented by Aj, by the specific carbon emission factor for that activity, represented by FEj. Therefore, the total carbon footprint (C_Total) is obtained by adding the emissions from material manufacturing (Cmat) to the emissions associated with on-site activities (Cact). Additionally, concrete transportation emissions (ETC) refer to emissions generated during the transportation of concrete from the production site to the construction site of helical piles. These emissions are determined by multiplying the quantity of transported concrete (QCT) by the specific carbon emission factor for concrete transportation (FETC). For a more comprehensive and accurate assessment of environmental impact, concrete transportation emissions are integrated into the calculation of the total carbon footprint (RC_Total), allowing for consideration of all emissions stemming from material manufacturing, on-site activities, and transportation required for helical pile foundation.

2.3 Determination of the carbon emission factor

To calculate carbon emission factors (CE) for various construction materials in civil engineering projects, we use the widely recognized and comprehensive "Carbon and Energy Inventory" (ICE) database, as referenced in Hammond and Jones (2011).

Research approach aligns with Hammond and Jones (2011) and the ICE methodology. We focus on

calculating specific CO_2 emissions for particular reference units, enabling us to determine carbon emission factors. This method offers a detailed analysis of CO_2 emissions throughout material and process life cycles, from extraction to application.

The carbon emission factor, representing CO_2 emissions per unit of activity or product, is determined as follows (Equation 6): Emission Factor = Specific Emissions / Reference Unit.

Emphasizing the importance of using reliable and up-to-date data from recognized sources, such as national emission inventories or scientific databases. In the absence of Brazilian data, reliance will be placed on the ICE database, as also done by Hendler K. J. (2020). ICE provides comprehensive information on carbon emissions related to construction materials and processes. By using ICE, the aim is to obtain accurate data on the carbon emissions of various construction components, facilitating a detailed analysis of deep foundation structures' carbon footprint. Respecting the terms of use of the ICE database, proper attribution to the authors will be provided, and access to the most recent version ensured. Regarding the environmental impact of concrete transportation, the carbon emission factor is crucial. This factor reflects greenhouse gas emissions from concrete transport vehicles. Elements like distance, vehicle type, fuel, and traffic conditions influence these emissions. Sustainable transportation practices are essential to reduce this environmental impact. Data on emission factors will be sourced from Costa (2012) and the greenhouse gas emission inventory guidelines developed by SindusCon (2022). This data will be presented in a table format to enhance understanding and support sustainable decision-making.

Table 1. Portland Cement, Steel and Concrete Emission Factor. Hammond and Jones (2011).

Material	EC ($KgCO_2/Kg$)	EC-GHG ($KgCO_2e/Kg$)
CEM I Portland Cement	0,93	0,95
Virgin bar or rod	2.58	2.74
25/30 MPa	0.106	0.113

Table 2. Emission Factors for Mixer Truck and Drill. Source: Costa (2012) and SindusCon (2022).

Equipment	EC (tCO_2/L)	EC-GHG (tCO_2e/L)
Concrete Mixer Truck e CFA Drill	**0,0032 (Costa)**	3,140 (SindusCon)

3 DATA COLLECTION

In this section, the main sources of emissions associated with concrete transportation and continuous flight auger pile installation will be presented. Aspects such as the manufacturing of materials, specifically concrete and steel used in the structure, and the energy consumption involved in the concrete transportation processes will be discussed.

3.1 Drill and mixer usage and fuel consumption in construction

Using the values related to these 79 piles, a statistical analysis was conducted, which resulted in the measures of central tendency presented in Table 3. To enable this analysis, the data was properly processed and organized.

Table 3. Statistical Measures for Drilling and Concreting Time at a Construction Site in Brasília, DF.

Statistical measures calculated for drilling and concreting of continuous flight auger piles calculated in minutes			
AM of concreting time	12,9	AM of drilling time	29,3
SD of concreting time	6,4	SD of drilling time	8.9
CV for concreting time	49,6	CV for drilling time	30,2

3.2 Helical pile material quantity

The data related to the materials used in the construction of helical piles, which have depths ranging from 15 to 23 meters and a diameter of 60 centimeters, were utilized. These details were kindly provided by SCCAP, the company responsible for the foundation project, and were directly extracted from the project's foundation plan, and can be found in Table 4.

Table 4. Average Steel and Concrete Consumption per Pile.

Data Type	Average per Pile
Steel Consumption	86,54 kg
Concrete Consumption	6,65 m^3

3.3 Data on concrete transportation to the construction site

The transportation of concrete to the construction site located in the city of Brasília, approximately 7.6 miles away from the production point. A total of 525.1 cubic meters of concrete were used in the concreting of the 79 piles. This is equivalent to 53 truck trips, each with

a concrete-carrying capacity of 10 cubic meters. The distance covered on each trip was approximately 7.6 miles, resulting in a total of 53 trips to complete the concreting process for the 79 piles. The transportation calculation for hydraulic concrete mixer trucks involves 56 trips, each covering approximately 7.6 miles, to transport 79 piles. This results in an average mileage of 5.39 miles per pile.

3.4 Labor data during the construction of helical piles

According to the information provided by the construction company, there were 3 people in the field at the time of pile construction, along with 1 supervising engineer. With this data, is it possible to estimate the carbon footprint related to the labor force.

4 RESULTS

As detailed in the previous sections, this study involved a comprehensive assessment of construction methods, soil analysis, material consumption, transportation, and equipment use. All this information was carefully collected and analysed to calculate the carbon emissions associated with this construction process.

4.1 Calculation of the carbon footprint from equipment usage

According to the emission factor of the machines, as detailed in Table 2, and the time data collected in Section 3, we will perform the calculation in Table 5 to estimate the carbon emissions associated with this equipment during the project execution according to Equation 2 for calculating emissions per activity on the construction site.

Before proceeding with the calculations, it is important to convert the volume of concrete used in each pile from cubic meters to metric tons. To convert 6.65 m^3 to metric tons, I should multiply it by 2.4 t/m^3, which would result in a value of 15.96 t.

Table 5. Calculation of emissions produced by the equipment.

Equipment	Usage Time (hours)	Fuel Consumption per Hour (L/h)	Carbon Emissions per Pile (tCO_2e)
Hydraulic Concrete Mixer	1/6	59,85	31,3215
Drilling Machine	13/30	6,4	8,7083
Total ($KgCO_2e$)			40.029,8

4.2 Carbon footprint calculation for materials used in the installation of Helical

The results of carbon emissions related to these materials will be presented in Table 6, using the emission factors of the materials found in Table 1.

Table 6. Calculation of emissions produced by the steel-reinforced concrete.

Material	Quantity of Material /Pile (kg)	Emission Factor ($KgCO_2e/Kg$)	Carbon Emissions Calculation per Pile $KgCO_2e$
30 MPa Concrete	15960	0.113	1803,48
Civil Steel	86,54	2.74	237,12
Total			2040,6

4.3 Carbon footprint calculation for transportation

To cover 5.39 miles (approximately 8.67 kilometers) with a total weight of about 21.06 metric tons and a fuel consumption rate of 0.0196 L/t.km, you would consume approximately 4.117 liters of fuel. The machine fuel consumption, as reported by SindusCon, is 4,117 liters, with an emission factor of 3.140 tCO_2e per liter. This calculation results in carbon emissions of approximately 12.927 tCO_2e per pile.

4.4 Calculation of the carbon footprint produced by the workforce

According to Li's 2019 study, during a work shift with 30 people at the construction site, a significant carbon dioxide consumption was estimated, as indicated in Table 7, where it was estimated that 460 $kgCO_2$ were produced per shift for 30 people. However, it's important to recognize that conditions and activities may vary between the two contexts. Therefore, the numbers presented here are used as an approximate estimate of carbon emissions related to the workforce in this study.

Table 7. Calculation of emissions produced by the personnel on the construction site.

Source of Consumption	Specification	Carbon Footprint per Shift ($kgCO_2$)
Office	4 people	61,33

4.5 Summary of results

Table 8 shows two key results obtained regarding the carbon footprint of continuous flight auger pile construction.

The total carbon footprint per continuous flight auger pile is calculated by summing the emissions of each component, resulting in 55,058.73 $kgCO_2e$ per continuous flight auger pile.

Table 8. Summary of Carbon Footprint Results.

Aspect Analysed	**Carbon Emissions ($kgCO_2e$/pile)**
Equipment Usage	40.029,00 (73 %)
Materials - Concrete and Civil Steel	2.040,6 (4%)
Concrete Transportation	12.927,00 (23%)
Labor (Li, 2019)	61,33 (0,1 %)
Total Carbon Footprint /pile	55.058,73

5 CONCLUSIONS

Table 8 presents a synthesis of the results obtained from the analysis of the carbon footprint associated with the construction of continuous flight auger piles in a specific project in Brasília, DF. This analysis is crucial for assessing the environmental impact of this construction process and, at the same time, provides valuable insights for the adoption of more sustainable practices in the construction industry. A notable point is the considerable impact of carbon emissions resulting from the use of equipment, especially hydraulic concrete mixers and continuous flight auger rigs, as well as bored piles in the drilling and concreting process. This finding underscores the need to consider more efficient and lower carbon footprint alternatives in the selection and use of equipment during the construction process. Additionally, concrete transportation also represents a significant portion of emissions in pile construction, emphasizing the importance of optimizing transportation logistics, exploring on-site concrete pouring options, and reducing the distance between the concrete plant and the construction site as strategies to minimize transportation-related emissions. It is important to note that most emission factors were derived from the literature and attempt to replicate the reality of the Brazilian industry, although this approach may not be entirely accurate.

ACKNOWLEDGEMENTS

We thank the National Council for Scientific and Technological Development (CNPQ) for the generous support granted during the execution of this work.

REFERENCES

Bilec, M. (2007). “A hybrid life cycle assessment model for construction process.” Ph.D. dissertation, Univ. of Pittsburgh, Pittsburgh, Estados Unidos.

Chenga J.C. (2011). A Web Service Framework for Measuring and Monitoring Environmental and Carbon Footprint in Construction Supply Chains, Procedia Engineering, Volume14 (2011) 141–147, https://www.sciencedirect.com/science/art, doi:10.1016/j.proeng.2011.07.016.

Costa, B.L.C. (2012). Quantificação das Emissões de CO_2 Geradas na Produção de Materiais Utilizados na Construção Civil no Brasil. Dissertação de Mestrado Universidade Federal do Rio de Janeiro, Rio de Janeiro, Brasil.

Hammond, G. and Jones, C. (2011). “Inventory of Carbon and Energy (ICE). University of Bath, Bath, Inglaterra, Reino Unido. 128 p.

Hendler, K.J. (2020). “Carbon Footprint of Common Quay Structures”. Master Thesis, Técnico Lisboa, Lisboa-Portugal, 105 p.

Gao T., Liu Q., Wang J. (2014). A comparative study of carbon footprint and assessment standards, International Journal Of Low-Carbon Technologies, Volume 9, 237-243. DOI: 10.1093/ijlct/ctt041.

Okeke F. ,Chinwe Sam-Amobi, Okafor, Andy N., Ani E., Okere C. and Ugwu C. Grenn Aechiteture the Nigerian Perspective ,International Journal of Agriculture, Environment and Bioresearch,Vol. 3, No. 06; 2018, www.ijaeb.org, ISSN: 2456-8643.

Sinduscon (2022). Guia metodológico para inventario de emissões de gases de efeito estufa na construção civil-setor edificações. São Paulo, Brasil.

Li, X.J., Zheng, Y. (2019). “Using LCA to research carbon footprint for precast concrete piles during the building construction stage: A china study, Jornal of Cleaner Pridction”,https://doi.org/10.1016/j.jclepro.2019.118754.

Luo, W., Sandanayake, Malindu and Zhang, G. (2019). Direct and indirect carbon emissions in foundation construction: two case studies of driven precast and *cast*-in-situ piles. Journal of Cleaner Production, 211. pp. 1517-1526. ISSN 0959-6526.

Zhang, X. and Wang, F. (2016). Assessment of embodied carbon emissions for building construction in China: Comparative case studies using alternative methods. Energy and Buildings, v. 130, p. 330-340.

Proceedings of the XVIII ECSMGE 2024
GEOTECHNICAL ENGINEERING CHALLENGES
TO MEET CURRENT AND EMERGING NEEDS OF SOCIETY
© 2024 the Authors
ISBN 978-1-032-54816-6
DOI 10.1201/9781003431749-651
Open Access: www.taylorfrancis.com, CC BY-NC-ND 4.0 license

ECSMGE 24
XVIII EUROPEAN CONFERENCE ON SOIL MECHANICS AND GEOTECHNICAL ENGINEERING

Evaluation of frost heaving in frozen foundation layers due to the transfer of water in a gaseous state

Évaluation du soulèvement par le gel des couches de fondation gelées dû au transfert d'eau à l'état gazeux

A. Sarsembayeva*
L.N. Gumilyov Eurasian National University, Astana, Kazakhastan

Ph.E.F. Collins
Brunel University London, London, UK

S. Mussakhanova
L.N. Gumilyov Eurasian National University, Astana, Kazakhastan

**assel_enu@mail.ru*

ABSTRACT: The redistribution of moisture during uniaxial freezing of the soil at the base of roads in winter is of great importance for its bearing capacity during the spring thaw. In winter, an ice lens forms directly under the road due to the higher thermal conductivity of the pavement layers. And during the spring thaw, the base of the road may become oversaturated, leading to volume changes and damage to the road structure. This article presents a theoretical calculation of moisture accumulation in frozen layers due to water migration in a gaseous state based on monitoring data. A section of the highway near Kosshy town 20 km from the capital of Kazakhstan, was monitored in the winter period of 2021-22 and 2022-23. The water mass transfer in a form of vapour 1.41-1.44·10^{-4} g/h per 1 dm³ of soil at with temperature fluctuations -5-8 °C based on monitoring data of the highway foundations in winter period. The rate of vapour transfer in the frozen soil was 0.467-0.472 m/h and caused the formation of 430-456 g of ice due to the accumulation of water in a gaseous state in every 1 m^3 of soil, which increased the humidity by 40% or more and significantly reduced the bearing road capacity during the spring thaw.

RÉSUMÉ: La redistribution de l'humidité lors du gel uniaxial du sol au pied des routes en hiver est d'une grande importance pour sa capacité portante lors du dégel printanier. En hiver, une lentille de glace se forme directement sous la route en raison de la conductivité thermique plus élevée des couches de chaussée. Et lors du dégel printanier, la base de la route peut devenir sursaturée, entraînant des changements de volume et des dommages à la structure de la route. Cet article présente un calcul théorique de l'accumulation d'humidité dans les couches gelées en raison de la migration de l'eau à l'état gazeux, basé sur des données de surveillance. Un tronçon de l'autoroute près de la ville de Kosshy, à 20 km de la capitale du Kazakhstan, a été surveillé au cours de la période hivernale 2021-22 et 2022-23. Le transfert de masse d'eau sous forme de vapeur est de 1,41-1,44·10^{-4} g/h pour 1 dm³ de sol avec des variations de température de -5-8 °C, d'après les données de surveillance des fondations routières en période hivernale. Le taux de transfert de vapeur dans le sol gelé était de 0,467 à 0,472 m/h et a provoqué la formation de 430 à 456 g de glace en raison de l'accumulation d'eau à l'état gazeux dans chaque m³ de sol, ce qui a augmenté l'humidité de 40% ou plus et a considérablement réduit la capacité portante de la route lors du dégel printanier.

Keywords: Highway construction; temperature-moisture monitoring; freezing of soils; bearing capacity; ice lens formation.

1 INTRODUCTION

Temperature effects and especially moisture content have a huge impact on the strength characteristics of road bases (Teltayev et al., 2022). Due to the continental climate, the impact of temperature changes and transitions through 0°C have a more pronounced impact on the durability of the road structure (Teltayev and Suppes, 2019). The increased thermal conductivity of pavement materials distorts the temperature field under the road, contributing to the accumulation of moisture under the influence of cryosuction forces. The gradual freezing of layers of a road structure in winter initiates the transfer of water in a gaseous state from warm layers to colder ones and, as it freezes, it captures a large suction zone (Sarsembayeva and Zhussupbekov, 2021). The formation of an ice lens under roads leads to a

significant decrease in bearing capacity when melting in the spring.

This study examined temperature and humidity monitoring data during the winter period for 2021-22 and 2022-23 at a section of the highway near Kosshy town, 20 km from the capital of Kazakhstan, Astana. The transfer of water in frozen soils in a gaseous state was considered as the main source of ice lenses formed in the foundation soils of highways in winter.

2 METHOD

The cross-section design of the highway at the experimental site is presented in Figure 1. The temperature and humidity of the highway structure was monitored at a depth of up to 3 m using sensors embedded in metal capsules and recorded by a data logger every hour.

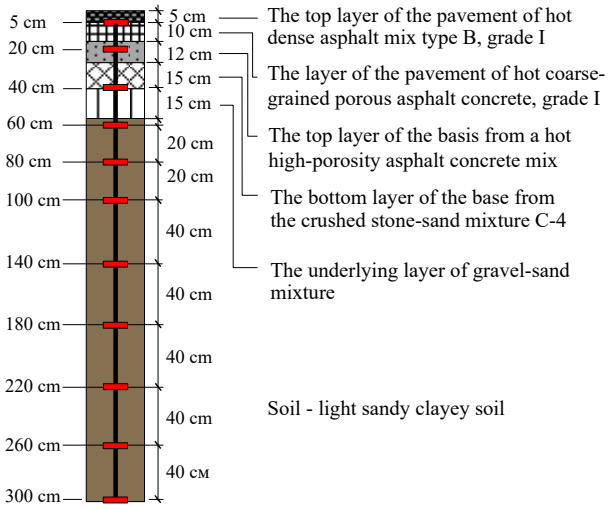

Figure 1. Design of highway structure.

Table 1. Physical and mechanical characteristics of road base soils.

Soil property	Unit	Value
Moisture content	%	20.2
Liquid Limit	%	26.5
Plastic Limit	%	15.1
Plasticity Index	%	11.6
Consistency index		0.5
Bulk density	g/cm³	2.0
Particle density	g/cm³	2.7
Void ratio		0.7
Degree of saturation		0.8
Deformation modulus	MPa	6.5
Cohesion	kPa	23.5
Angle of internal friction	degree	22

The base soil is light sandy clay loams, light brown in colour, hard, with layers of clay at a depth of 2.4 m with a thickness of up to 0.2 m. Soil samples taken from the construction site are water-bearing sediments. The amplitude of groundwater level fluctuations is 1.0-2.0 m from the ground surface, the minimum level is observed in February, the maximum at the end of May. Physical and mechanical characteristics of road base soils are presented in Table 1.

The amount of water transported in a vapour state directly depends on the type of soil and the volume of pores in the soil, the temperature gradient or temperature difference across the depth of the soil, as well as humidity at the transition through 0°C. Calculation of vapour mass using the saturated vapour pressure P_{si} over ice surface is:

$$m_{vapour,t_i} = \frac{\mu \cdot P_{si} \cdot V_{air}}{R \cdot T} \quad (1)$$

where μ - molar mass of vapour, g/mol; P_{si} - saturated vapour pressure over ice surface corresponding to the current temperature, Pa; V_{air} – volume of air in the soil, cm³; R - Universal gas constant, J/(mol·K); T – temperature; Kelvin.

The mass of ice built from the vapour passing over time period t with speed v over the cumulative air channel cross section A_{air} is calculated:

$$m_{ice} = \rho_{vapour} \cdot V_{air\ voids} = \rho_{vapour} \cdot v \cdot t \cdot A_{air} \quad (2)$$

where, m_{ice} - mass of built ice in grams; ρ_{vapour} - is taken as an average density value of the vapour densities at the start and end time point, g/cm³. The detailed calculation method was described in Sarsembayeva et al, 2022a.

3 RESULTS AND DISCUSSION

Figures 2 and 4 present temperature monitoring data in the above layers of the road structure in January 2022 and 2023. And in Figures 3 and 5 the measured moisture content of the pore space in the soil base is presented at a level of 60 cm from the surface of the road surface and below. More detailed results on monitoring temperature and humidity can be found in Sarsembayeva et al. (2022b).

The average air temperature in the winter of January 2022 was –8.12 °C, with maximum air temperatures reaching up to +6.0 °C and minimum values reaching -20.9 °C. In general, this period was characterized by higher average values compared to data from previous years. The greatest temperature fluctuations were confirmed for the upper layers of road pavement with the densest structure. There were 11 short-term transitions through 0°C in air temperature, but the layers of the road base remained in a frozen state and never crossed the 0°C, apparently

due to compensation for the heat transfer of the underlying layers with a lower temperature. Relative stabilization of the foundation soils reached a depth of -180 cm at negative temperatures ranging from -4 - 6°C. The freezing front in January 2022 occurred at a depth of -140 cm and -180 cm, as evidenced by a drop in humidity from 21 and 23%, respectively, to 17% in a frozen state.

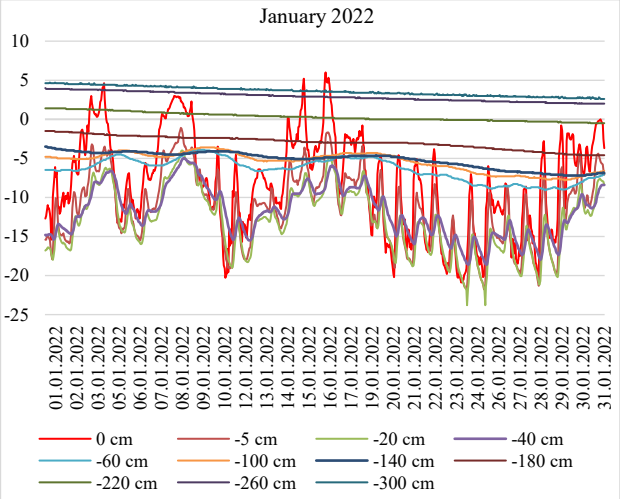

Figure 2. Temperature monitoring in January 2022.

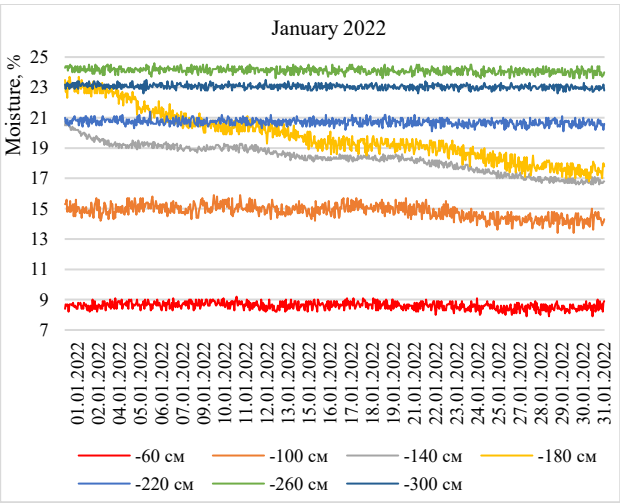

Figure 3. Monitoring of soil humidity in January 2022.

Base soil located at a depth of -60 cm consisting of light sandy clayey soil is a frost susceptible and is in a stably frozen state at a temperature of -5-8 °C. This layer acts as a moisture accumulator during the winter period, and it is there that an ice lens is formed, leading to a weakening of the bearing capacity of the road base during the spring melting period. Therefore, as an example of calculating vapor mass transfer, a soil layer at a level of -60 cm was considered. The water mass transfer in a form of vapor $1.44 \cdot 10^{-4}$ g/h per 1 dm^3 of soil. The rate of passage of vapor towards the freezing front in the soil was 0.467 m/h.

The freezing of the ground base continued for 132 days in the winter period of 2021-22 in Astana with the formation of 456.72 g of ice due to the migration of water in a gaseous state in every 1 m^3 of soil, which increases the moisture content by 40% or more comparing to the pre-freezing period and significantly reduces the bearing road capacity during the spring thaw.

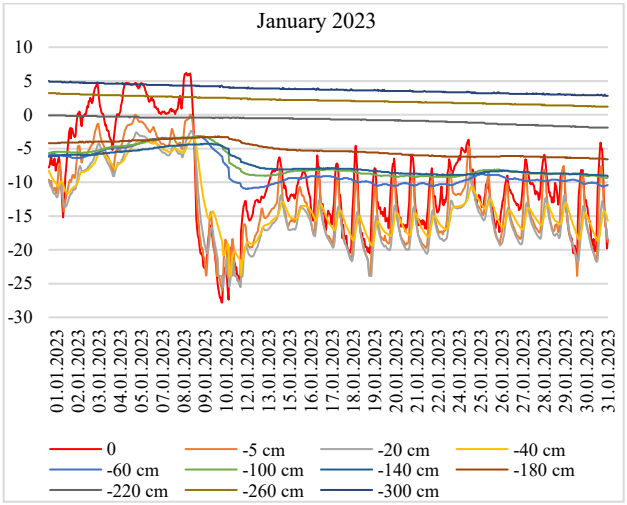

Figure 4. Temperature monitoring in January 2023.

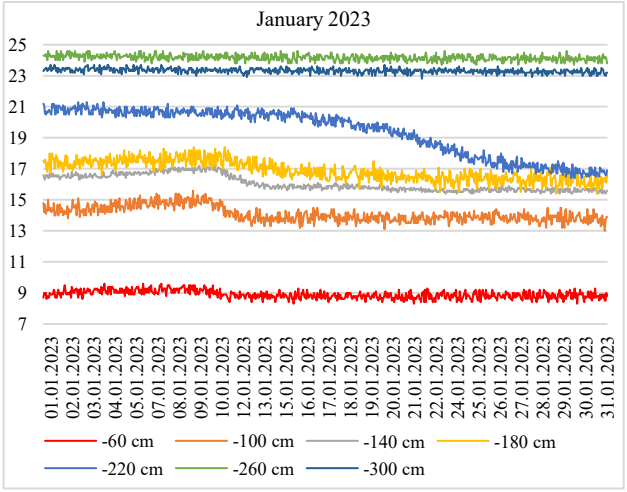

Figure 5. Monitoring of soil humidity in January 2023.

The average temperature for the month of January 2023 was -9.8 °C, with a minimum value of -27.8 °C and a maximum of +6.2 °C. The freezing front against the backdrop of a colder 2023 was deeper than in 2022, at -220 cm from the road surface. In this layer, a drop in humidity was also observed from 21% to 17% as the phase transition of water from liquid to solid state.

The duration of the frozen state of the soil under the highway was 126 days in the winter of 2022-23. The average temperature of the layer -60 cm was -9.49 °C and at a vapor transfer rate of 0.467 m/h, which led to the formation of $1.41 \cdot 10^{-4}$ g/h per 1 dm^3 of soil per day in January 2023. According to the calculations

obtained, during the period of frozen state, 426.38 g of ice per 1 m³ of base soil were accumulated in this soil layer only due to the migration and condensation of water in a gaseous state from warmer layers. An increase in humidity of up to 40% in the event of rapid melting can lead to collapse of the road structure during the spring thaw. In this area there is a restriction on cargo transportation with a large axial load, however, to prevent such risks, it is recommended to lay an additional layer of vapor barrier at a depth of -60 cm, which will also serve as thermal insulation by maintaining low humidity in the pore space of the soil.

4 CONCLUSIONS

1. Soil bases of highways, as well as layers of road pavement, remain in a stably frozen state during short-term temperature of air increases up to +6.0 °C due to sub compensation of heat (heat transfer) of the underlying layers and have a sufficient margin of safety.

2. With short-term increases in air temperature, only 25 cm from the top of the pavement are affected, which corresponds to the top layer of the base made of a hot, highly porous asphalt concrete mixture.

3. Daily temperature fluctuations in the top covering of hot dense asphalt concrete mixture average 2-5 °C with air temperature fluctuations of 6-12 °C.

4. The freezing of the layers is accompanied by a sharp drop in the humidity of the pore space from 21-23 to 11-14%, when part of the water in the gaseous state sublimates and forms a negative cryosuction pressure in these layers.

5. The base soil, located at a depth of -60 cm, consisting of light sandy clayey soil, is a frost susceptible layer and is in a stably frozen state at a temperature of -5-8 °C.

6. The water mass transfer in a form of vapour 1.41-1.44·10^{-4} g/h per 1 dm^3 of soil at with temperature fluctuations -5-8 °C based on monitoring of the highway foundations in winter period over the past 2 years. The rate of passage of vapour towards the freezing front in the soil was 0.467-0.472 m/h.

7. The freezing of the ground base continued for 126-132 days in winter periods of 2021-2023 and 2022-2023 in Astana city with the formation of 430-456 g of ice due to the accumulation of water in a gaseous state in every 1 m^3 of soil, which increased the humidity by 40% or more and significantly reduced the bearing road capacity during the spring thaw.

6. As a solution to the problem of water migration in the form of vapour, it is proposed to lay an additional layer of vapour barrier over the soil base at a depth of -60 cm.

ACKNOWLEDGMENTS

This work was supported by the Science Committee of the Ministry of Science and Higher Education of the Republic of Kazakhstan (Grant No. AP13268861). The team of authors would like to thank the RSE on REM "National Center for the Quality of Road Assets" of the Ministry of Industry and Infrastructure Development of the Republic of Kazakhstan for organizing the monitoring of the temperature and humidity condition of the highway in 2021-2023.

REFERENCES

Sarsembayeva, A., Collins, P., Saginov, Z., & Mussakhanova, S. (2022a). The impact of the temperature and humidity state of the road on heat and mass transfer in winter. *Technobius*, *2*(4), 0029. https://doi.org/10.54355/tbus/2.4.2022.0029.

Sarsembayeva A., Zhussupbekov A., Collins P.E.F. (2022b) Heat and Mass Transfer by Vapour in Freezing Soils. *Energies,* 15(4), p. 1515. https://doi.org/10.3390/en15041515.

Sarsembayeva, A. and Zhussupbekov, A. (2021) Experimental study of deicing chemical redistribution and moisture mass transfer in highway subsoils during the unidirectional freezing. *Transportation Geotechnics.* Vol. 26, 100426. https://doi.org/10.1016/j.trgeo.2020.100426.

Teltayev, B.; Oliviero Rossi, C.; Aitbayev, K.; Suppes, E.; Yelshibayev, A.; Nugmanova, A. (2022) Freezing and Thawing Processes of Highways in Kazakhstan. *Applied Sciences*, 12(23), p. 11938. https://doi.org/10.3390/app122311938.

Teltayev B.B., Suppes E.A. (2019) Temperature in pavement and subgrade and its effect on moisture. *Case Studies in Thermal Engineering,* Vol. 13, p. 100363. https://doi.org/10.1016/j.csite.2018.11.014.

Proceedings of the XVIII ECSMGE 2024
GEOTECHNICAL ENGINEERING CHALLENGES
TO MEET CURRENT AND EMERGING NEEDS OF SOCIETY
© 2024 the Authors
ISBN 978-1-032-54816-6
DOI 10.1201/9781003431749-652
Open Access: www.taylorfrancis.com, CC BY-NC-ND 4.0 license

ECSMGE 24
XVIII EUROPEAN CONFERENCE ON SOIL MECHANICS AND GEOTECHNICAL ENGINEERING

Compression characteristics of compacted sand-bentonite mixtures with and without saturation

Caractéristiques de compression des mélanges sable-bentonite compactés avec et sans saturation

S. Sato*
Obayashi corporation, Tokyo, Japan

T. Nishimura
Ashikaga University, Ashikaga, Japan

K. Nakai
Nagoya University, Nagoya, Japan

**sato.shin.ro@obayashi.co.jp*

ABSTRACT: In previous studies, the authors have demonstrated an irreversible change in void ratio with suction change of sand-bentonite mixtures after saturation, while that prior to saturation is reversible. However, it has not been clarified how the compression characteristics differ between sand-bentonite mixtures with and without pre-saturation. Therefore, in this study, one-dimensional compression tests were conducted to investigate this. As a result of the compression tests, both types of materials had nonlinear curvature of the compression line, revealing that the compression index of pre-saturated specimens increase. Furthermore, in this study a reproduction analysis of the test results using the SYS Cam - clay model which can consider the effect of soil skeleton structure was performed and good reproducibility could be obtained.

RÉSUMÉ: Dans des études antérieures, les auteurs ont démontré que le changement de l'indice de vide avec le changement de succion des mélanges sable-bentonite lorsque saturation est irréversible, tandis que celui sans saturation est réversible. Cependant, il n'a pas été clarifié en quoi les caractéristiques de compression diffèrent entre les mélanges sable-bentonite avec et sans pré-saturation. Par conséquent, dans cette étude, des tests de compression unidimensionnels ont été réalisés pour le clarifier. À la suite des tests de compression, les deux types de matériaux présentaient une courbure non linéaire de la ligne de compression, révélant que l'indice de compression de l'éprouvette pré-saturée devenait plus grand. En outre, dans cette étude, une analyse de reproduction des résultats des tests à l'aide du modèle SYS Cam-Clay qui peut prendre en compte l'effet de la structure du squelette du sol a été réalisée et il a été constaté qu'une bonne reproductibilité pouvait être obtenue.

Keywords: Sand-bentonite mixtures; suction; compression characteristic; unsaturated soil; elastoplastic.

1 INTRODUCTION

The compaction curve obtained from consolidate on tests for saturated bentonite shows nonlinear curvature and previous studies have discussed this factor. It is shown that for sand-bentonite mixtures there are two zones with different compression lines, with bentonite characteristics at low pressures and sand characteristics at high pressures (Mollins et al., 1996). Regarding the modeling of nonlinear compression lines, there are models that couple an elastoplastic model and water retention (Bosch et al., 2021), but no formulation has been proposed only an elastoplastic constitutive model behaviour. On the other hand, the area above the normal consolidation line is assumed to have be a high structure region and there are elastoplastic models that are expressed in terms of the super loading surface (Asaoka et al., 2002). This model is called SYS Cam - clay model. It is considered that the super loading surface can be used to describe the nonlinear curvature of the compression line. In this study, consolidation tests were performed using saturated and unsaturated sand-bentonite samples to determine the compaction properties. Furthermore, we reproduced the consolidation test using the SYS Cam-clay model, examined the applicability of the model, and examined its applicability to the behavior of compressed bentonite.

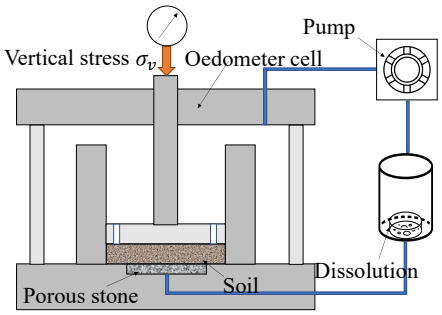

Figure 1. Schematic of the suction-controlled oedometer device using osmotic solution.

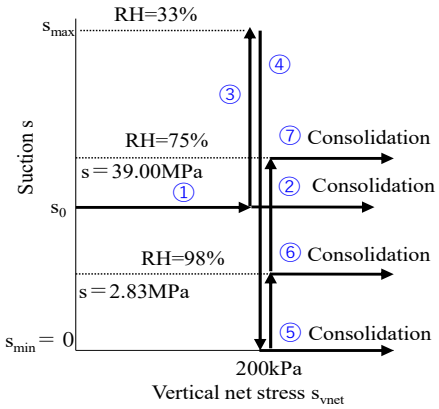

Figure 2. Test procedure.

2 MATERIAL AND EXPERIMENTAL PROCEDURES

The material used in this study is a mixture of sodium bentonite (Kunigel V1, initial water content $w_0 =$ 8.77 %) and silica sand, with a dry mass ratio of bentonite/silica sand of 7:3. The silica sand is a mixture of No. 5 and No. 7 sand in a weight ratio of 1:1. After adjusting the water content of the mixed specimens to 17 %, they were statically compacted using a high pressure hydraulic press (5 MPa) to produce specimens with a dry density of 1.600 Mg/m^3, a diameter of 60 mm and a height of 10 mm. The test apparatus is a swelling measurement device incorporating a rigid mould inside a pressure-resistant acrylic cylinder, which can also measure swelling forces and deformation by suction change under constant vertical stress loading. The test apparatus is shown in Figure 1. A porous stone is attached to the bottom plate supporting the rigid mould of the test apparatus, and the air flow in the porous stone is connected to the humidity control system through tubes connected to the bottom plate. In addition, a porous stone is attached to the pressure plate having tubular openings in contact with the upper surface of the specimen and is connected to the humidity control system through the perforations. Suction is controlled by the vapour pressure method and humidity is controlled by saturated saline solution.

Two types of specimens (with or without saturation history) were used in this study. The test procedure for this test is shown in Figure 2. First, the specimens were set in a rigid mould and subjected to a vertical stress of 200 kPa to ensure that the compressive deformation reached equilibrium. For unsaturated specimens without saturation history, the consolidation tests are carried out by increasing the vertical stress after the compression deformation has reached equilibrium. For specimens with saturation history, after the compression deformation has reached equilibrium, humidity controlled (RH 33 %) air is circulated through the porous stone at the base and the amount of shrinkage deformation resulting from increased suction is measured. After equilibrium is confirmed, the specimen is saturated by distilled water soaking through the porous stone below, while maintaining the vertical stress loading. For the specimens under saturated conditions, consolidation tests are carried out. In case of unsaturated specimens with two imposed saturation history and a specific suction that the above-mentioned compression tests were performed.

3 EXPERIMENTAL RESULTS

The compression test results for the unsaturated specimen without saturation history compared with consolidation test result for the saturated specimen are shown in Figure 3, and the consolidation test results for the saturated specimen compared with unsaturated specimen with saturation history are shown in Figure 4. For the unsaturated specimen without saturation history, the compression curve becomes straight above 2000 kPa, and for the specimen with saturation, including the saturated specimens, the compression curve becomes a straight line above 800 kPa. Therefore, the dashed line shown in Firure 3 is assumed to be the normal consolidation line in the region above this value. Comparing the unsaturated specimen without saturation history, the unsaturated specimen showed less compressibility and the saturated specimens showed greater compressibility. The slope of the NCL also increases with saturation. Therefore, the structures develop according to suction decreases. The elasto-plastic model presented by Alonso et al. (1990) also considers a model in which the compressive index decreases with decreasing suction, which is consistent with the results of this study.

For the specimens with saturation history, the compression lines tended to converge to the same

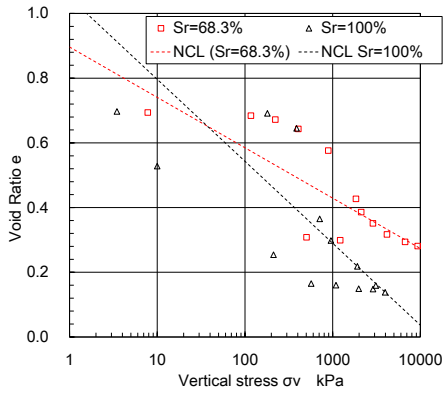

Figure 3. Compression test results of unsaturated specimen without saturation history compared with saturated specimen.

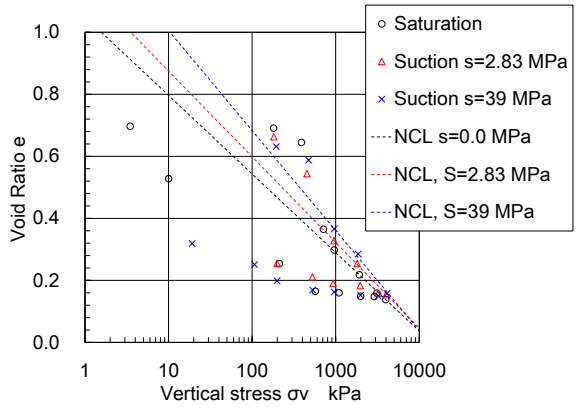

Figure 4. Consolidation results of unsaturated specimens with saturation history compared with saturated specimen.

slope regardless of suction. In terms of the structure, it tended to decrease with decreasing suction. The difference between the samples with or without saturation history is due to the evolutionary differences in the structure and the slope of the compression line under high pressure converge to same line.

4 OVERVIEW OF SYS CAM-CLAY MODEL

With regard to the behaviour of unsaturated or saturated sand-bentonite, the SYS Cam-clay model (Asaoka et al., 2002) was applied. This model was developed based on the Cam-clay model by adding the concept of "structure", "overconsolidation" and "anisotropy" as a soil skeleton structure of soils, and the changes of soil skeleton structure with ongoing plastic deformation was modeled as evolutionary rules. This model can describe the typical mechanical behavior of sand and clay using same theoretical framework, depending on the different speed of the evolutionary rules. In this study, further attempts are applied to this model to sand-bentonite mixture and confirm the effects of saturated/unsaturated condition and the saturation history on the soil skeleton structure, especially focusing on the degree of structure $1/R^*$. Here, structure refers to the bulkiness of soil (a state which can possess a larger void ratio under the same effective stress), and soil with a highly developed structure can take a stress state above the normal consolidation line. Furthermore, since structural deterioration acts as plastic compression, large volumetric compression occurs during structural deterioration. See Asaoka et al, (2002) for the detail.

5 MODELLING RESULTS

In this study, Abaqus was used as the solver and the SYS Cam-clay model was applied for analysis. The analysis method used unit elements and covered the stages from loading to the end of unloading, ignoring pore water. The parameters of the SYS Cam-clay, the initial void ratio e_0, compression index λ and swelling index κ are values obtained from experimental results. The Poisson's ratio is fixed at $\nu = 0.10$ in all cases. As a result of this study, the analysis results for the unsaturated specimen without saturation history

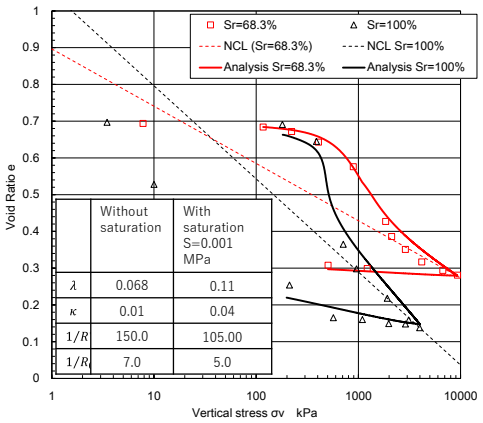

	Without saturation	With saturation S=0.001 MPa
λ	0.068	0.11
κ	0.01	0.04
$1/R$	150.0	105.00
$1/R_i$	7.0	5.0

Figure 5. Comparison between consolidation test results and reproducible analysis (specimen without saturation history).

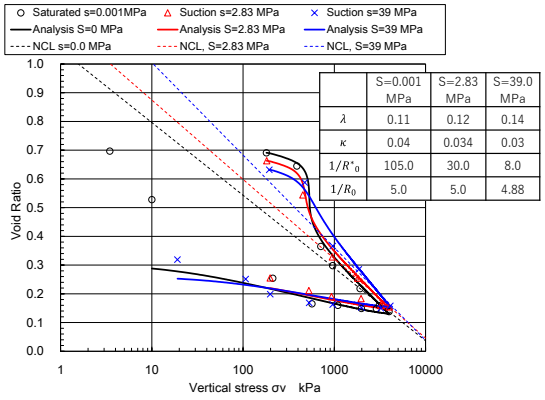

	S=0.001 MPa	S=2.83 MPa	S=39.0 MPa
λ	0.11	0.12	0.14
κ	0.04	0.034	0.03
$1/R^*_0$	105.0	30.0	8.0
$1/R_0$	5.0	5.0	4.88

Figure 6. Comparison between consolidation test results and reproducible analysis (specimen with saturation history).

compared with saturated specimen is obtained as shown in Figure 5, while the analysis results for the specimens with saturation history are compared with saturated specimen in Figure 6. The analysis results show a good agreement for the compression lines. Comparing the unsaturated and saturated specimens by Figure 5, the compressive index λ is larger for the saturated specimen, meaning that the compressive index λ increases as suction decreases. Focusing on the degree of structure $1/R^*$, it can be seen that the structure is more highly developed in unsaturated specimens than in saturated specimens. In addition to a larger compression index λ, unsaturated specimens have the characteristic of producing large volumetric compression by the collapse of the structure with ongoing increase of vertical stress. Under large vertical stress condition, the structure becomes degraded, regardless of whether it is saturated or unsaturated, and possesses a stress state on the normal consolidation line. On the other hand, the compression index λ of the specimens with saturation history was almost equal. Focusing on the degree of structure $1/R^*$, it can be seen that the lower the suction, the more significantly the structure is developed. This trend is opposite to that in Figure 5, which has no prior saturation history. From a comparison between Figure 5 and Figure 6, it was found that the presence or absence of a pre-saturation history has a great influence on the subsequent compression properties, especially on the structural development associated with the suction action. The analysis results indicate that the SYS Cam-clay model can be adapted to describe the non-linear compressive behaviour of saturated and unsaturated sand-bentonite specimens with or without saturation history.

6 CONCLUSION

The compressive behaviour of saturated and unsaturated sand-bentonite mixture was obtained by using a suction-controllable consolidation test apparatus with the vapour pressure method. As a result of the study, compression behaviour with non-linearity was obtained for both saturated and unsaturated specimens, and the compression behaviour differed depending on whether the specimens are with or without saturation history. Comparing the compression behaviour of the unsaturated and saturated specimens, the compressibility tended to be small and increased with approaching a saturation. The slope of the NCL also increases due to saturation. For the specimens with saturation history, the compression lines tended to converge to the same slope regardless of suction. In terms of the structure, it decreases with decreasing suction. Furthermore, the SYS Cam-clay model was used to perform the analysis, which showed that the compression behaviour could be reproduced by using the upper load surface. The SYS Cam-cay model can be used to describe the non-linear compression behaviour of saturated and unsaturated sand-bentonite, however a state-specific evolution law is required for the parameters such as the degree of skeletal structure for the specimen with or without saturation history.

REFERENCES

Alonso, E. E., Gens, A. and Josa, A. (1990). A constitutive moodel for partially saturated soil, *Géotechnique*, 40, (3), pp. 405-430. https://doi.org/10.1680/geot.1990.40.3.405.

Asaoka, A., Nakano, M. and Noda, T. (1994). Soil-water coupled behaviour of saturated clay near/at critical state, *Soils and Foundations*, 34 (1), pp. 91-106. https://doi.org/10.3208/sandf1972.34.91.

Asaoka, A., Noda, T., Yamada, E., Kaneda, K. and Nakano, M. (2002). An elasto-plastic description of two distinct volume change mechanisms of soils, *Soils and Foundations*, 42(5), pp. 47-57. https://doi.org/10.3208/sandf.42.5_47.

Bosch, J. A., Ferrari, A. and Laloui, L. (2021). Coupled hydro-mechanical analysis of compacted bentonite behaviour during hydration, *Computers and Geotechnics*, 140, https://doi.org/10.1016/j.compgeo.2021.104447.

Mollins, L. H., Stewart, T. I. and Cousens, T. W. (1996). Predicting the properies of bentonite-sand mixtures. *Clay Minerals* 31, pp. 243-252. https://doi.org/10.1180/claymin.1996.031.2.10.

Hashiguchi, K. (1978). Plastic constitutive equations of granular materials, Cowin, S.C. & Satake, M. (eds), *Proc. of US-Japan Seminar on Continuum Mechanics and Statistical Approaches in the Mechanics of Granular Materials*, pp. 321-329.

Hashiguchi, K. and Chen, Z.-P. (1998). Elastoplastic constitutive equations of soils with the subloading surface and the rotational hardening, *International journal for numerical and analytical methods in geomechanics*, 22, pp. 197-227. https://doi.org/10.1002/(SICI)1096-9853(199803)22:3<197::AID-NAG914>3.0.CO;2-T.

Sekiguchi, H. and Ohta H. (1977). Induced anisotropy and time dependency in clays, *Constitutive Equations of Soils (Proceedings of the 9th international conference on soil mechanics and foundation engineering, Spec. Session 9)*: 229-238. Tokyo.

Proceedings of the XVIII ECSMGE 2024
GEOTECHNICAL ENGINEERING CHALLENGES
TO MEET CURRENT AND EMERGING NEEDS OF SOCIETY
© 2024 the Authors
ISBN 978-1-032-54816-6
DOI 10.1201/9781003431749-653
Open Access: www.taylorfrancis.com, CC BY-NC-ND 4.0 license

ECSMGE 24
XVIII EUROPEAN CONFERENCE ON SOIL MECHANICS AND GEOTECHNICAL ENGINEERING

Effect of rainwater infiltration from pavement surface on base course bearing capacity

Effet de l'infiltration de l'eau de pluie à la surface de la chaussée sur la portance de la couche de base

K. Sato*, T. Fujikawa, C. Koga
Fukuoka University, Fukuoka, Japan

Y. Isobe
IMAGEi Consultant Corporation., Tokyo, Japan

**stao@fukuoka-u.ac.jp*

ABSTRACT: Japan has a huge stock of road pavements, exceeding 1.2 million km. However, road pavements require constant maintenance and repair work because they gradually progress in deterioration due to various factors immediately after the operation. In particular, the deterioration of base course bearing capacity due to rainwater infiltration through cracks from the asphalt layer is said to have a significant impact on the durability of road pavements. However, it is difficult to observe and investigate the deterioration in the base course while it is in service, and there are only a few cases where detailed investigation and analysis have been attempted. This study reports the results of CBR tests on the effects of water content ratio at the time of sample preparation and rainwater infiltration time on the bearing capacity reduction behaviour of base course using two types of pavement materials.

RÉSUMÉ: Le Japon dispose d'un énorme stock de chaussées routières, dépassant 1,2 million de km. Cependant, les chaussées nécessitent des travaux d'entretien et de réparation constants car elles se détériorent progressivement sous l'effet de divers facteurs immédiatement après leur mise en service. En particulier, la détérioration de la portance de la couche de base due à l'infiltration de l'eau de pluie à travers les fissures de la couche d'asphalte est considérée comme ayant un impact significatif sur la durabilité des chaussées routières. Cependant, il est difficile d'observer et d'étudier la détérioration de la couche de base pendant qu'elle est en service, et il n'y a que quelques cas où une étude et une analyse détaillées ont été tentées. Cette étude rapporte les résultats d'essais CBR sur les effets du rapport de la teneur en eau au moment de la préparation de l'échantillon et du temps d'infiltration de l'eau de pluie sur le comportement de réduction de la capacité portante de la couche de base en utilisant deux types de matériaux de chaussée. Je suggère d'inclure des conclusions plus détaillées si possible.

Keywords: Bearing capacity; base course; rainwater infiltration; CBR tests.

1 INTRODUCTION

Japan's road pavement stock exceeds 1.2 million km. In the future, it will be important to establish maintenance management methods for road pavements. However, in recent years, Japan has been facing a declining birth-rate and an aging population, and road maintenance and management costs are facing a very difficult situation. In the future, road managers will be required to perform maintenance management with high economic and technical effectiveness. Road pavements are structures that gradually deteriorate by the passage of years in service. In particular, the loss of base course bearing capacity due to rainwater infiltration through cracks in the asphalt layer is known to significantly affect the durability of road pavements [1].

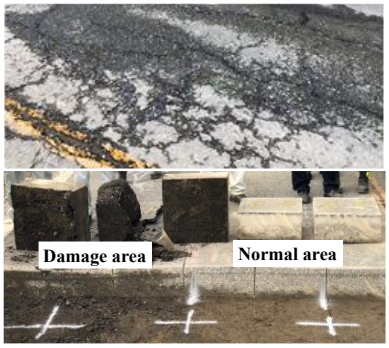

Figure 1. Early deterioration of asphalt pavement.

The process of base course bearing capacity reduction is as follows: (1) cracks occur in the asphalt layer due to age-related deterioration (Figure 1), (2) rainwater infiltrates through the cracks, (3) the fine

grains in the base course are released by the pumping phenomenon when large traffic loads act on the pavement under rainwater infiltration, and (4) Pavement bearing capacity decreases due to the change in the pore structure caused by the change in the grain size of the base course material and rainwater infiltration (Figure 1). This decrease of base course bearing capacity is a major factor in the early deterioration of road pavements. When deterioration progresses rapidly, the base course needs to be replaced. However, replacement of the base course material is rarely implemented due to traffic obstructions caused by construction regulations, construction period problems, and high repair costs. In the future, appropriate maintenance and repair technology will be required before premature deterioration of pavements progresses. However, it is difficult to understand the details of base course damage of pavements with early-stage deterioration, and very few research have attempted to investigate and analyse the damage. The water content ratio of the geomaterial at the time of base course material placement and density control after compaction are considered to have a significant effect on the base course bearing capacity [2]. Therefore, it is considered effective to obtain an experimental understanding of the mechanism of base course deterioration due to rainwater infiltration to investigate the early stage of pavement deterioration. This study reports the results of CBR tests on the effects of water content ratio at the time of sample preparation and rainwater infiltration time on the bearing capacity reduction behaviour of base course using two types of pavement materials.

2 TEST PROCEDURE

2.1 Experimental samples

Two types of pavement materials were used in this study: M-25, which was mixed and prepared from No. 4-7 crushed stone, sand, and stone dust, and RM-25, which was recycled concrete material purchased from a construction materials company. Table 1 shows the physical properties of the two materials. Figure 2 shows the particle size distribution curves of the samples before and after compaction. Figure 3 shows the compaction curve. Particularly, for RM25, particle crushing by compaction occurred, indicating that it was affected by the water content ratio. This is considered to be due to the effect of the cement content attached to the aggregate of RM-25, which was crushed by compaction.

2.2 Testing conditions

The E-b method was used in accordance with the Soil Compaction Test Method by compacting (JIS A 1210). Here, the E-b method for soil compaction is used a meld inner diameter of 15 cm (volume: 2209 cm3) and a rammer of 4.5 kg dropped from a height of 45 cm without repeated use of a soil sample with adjusted water content. In addition, the number of times of compaction was reduced to 82 times for each sample at the optimum water content ratio in order to achieve a uniform dry density of Dc=99% for each specimen. In the case of RM-25, Dc=99% was set to 1.70 x 0.99 = 1.68 Mg/m^3 at about 3% before and after the optimum water content ratio in consideration of the implementation of the project. In the same way, M-25 was set to 2.28 × 0.99 = 2.26 Mg/m^3, where Dc=99%. Table 2 shows the experimental conditions. The water content ratio of M-25 was set to 1.6 (dry side), 2.8 (optimum water content), and 3.6 (wet side) % at Dc=99%. In the case of RM-25, three different water content ratios w = 9.9 (dry side), 13.5 (optimum), and 17.4 (wet side) % at Dc=99% were used in the study.

In order to investigate the change in base course bearing capacity due to rainwater infiltration, water was sprayed from the top of the specimen after the specimen was prepared. The amount of water sprayed was set so that the water content ratio of each specimen increased by w=4.0%.

The CBR penetration tests were conducted immediately after all the sprayed water had infiltrated from the top of the specimen (t=0h) and after 6 hours(t=6h) and 24 hours (t=24h). Table 3 shows the time required to complete infiltration under each condition. The CBR penetration test was conducted after removing the water from the top of the specimen because the water did not infiltrate even after 96h in the wet side of RM-25 with 150 ml of water sprayed.

Table 1. Physical properties of base course materials.

sample	M-25	RM-25
Appearance		
Soil particle density ρ_s(Mg/m^3)	3.056	2.642
Uniformity coefficient U_c	35.10	58.37
Coefficient of curvature U_c'	2.81	1.33
Abrasion loss R(%)	14.30	30.70
Water absorption (%)	0.40	9.02

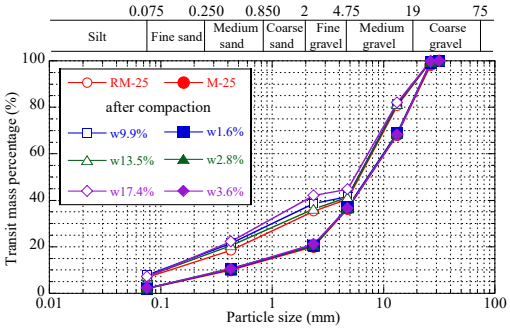

Figure 2. Grain size distribution curves of the samples before and after compaction.

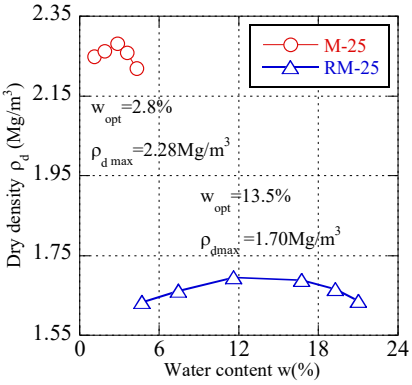

Figure 3. Compaction curve.

Table 2. Experimental conditions.

Sample	Specific water content w(%)	Compacted times	Amount of water sprinkled	Dry density ρ_d(Mg/m^3)	Standby time
M-25	1.6 (Dry) 2.8 (Optimum) 3.6 (Wet)	92times (E-b) 82times (Optimum)	0 ml 200 ml	2.26 (Dc=99%)	0 h 6 h 24 h
RM-25	9.9 (Dry) 13.5 (Optimum) 17.4 (Wet)	92times (E-b) 82times (Optimum)	0 ml 150 ml	1.68 (Dc=99%)	

Table 3. Time to the end of infiltration.

Specific water content	Sample (Amount of water sprinkled)	
	M-25 (200ml)	RM-25 (150ml)
Dry	3min	40min
Optimum	3min	1.5h
Wet	3min	96h

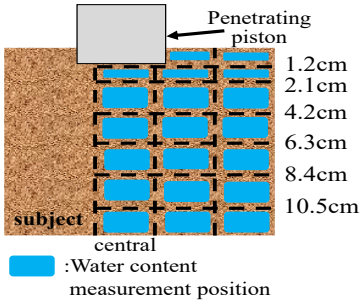

Figure 4. Location of water content measurement.

In this study, water content was measured at the locations shown in Figure 4 immediately after the CBR penetration test in order to evaluate the behaviour of bearing capacity reduction due to rainwater infiltration from the state of pore water inside the specimens. Measurements were taken at a total of 20 locations, 7 in the vertical direction and 3 in the horizontal direction, without the penetration position.

3 RESULTS AND DISCUSSIONS

Figures 5 and 6 show the distribution of water content inside the specimens after the CBR test for M-25 and RM-25 at (a) the dry side, (b) the optimum water content, and (c) the wet side, for each elapsed time after water sprayed. The average water content and saturation of the entire specimen are also shown. Figure 7 and Figure 8 show the CBR test results for M-25 and RM-25. Here, the results of experiments conducted by the authors using Decomposed granite soil under the same conditions are also shown in each figure.

3.1 Dry side

Just after water sprayed, both specimens showed a significant decrease in bearing capacity with water sprayed, similar to the results for Decomposed granite soil. This is considered to be due to the decrease in suction caused by the increase in saturation due to water infiltration. As time elapsed after water sprayed,

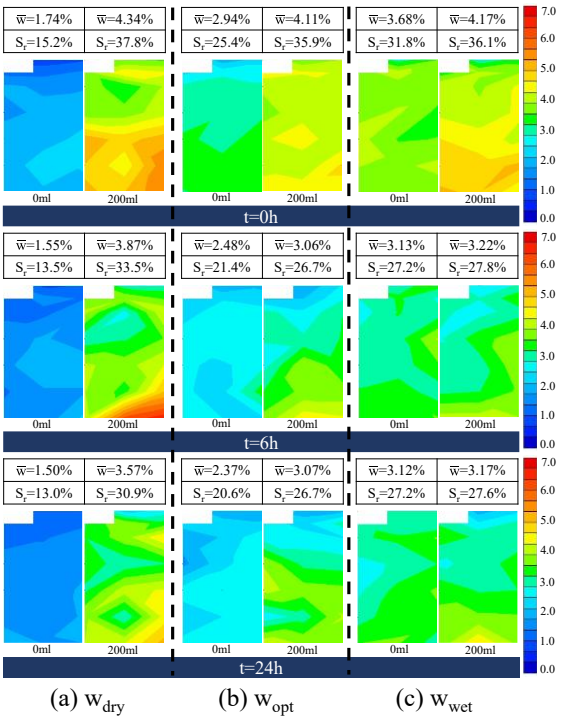

(a) w_{dry} (b) w_{opt} (c) w_{wet}

Figure 5. Distribution of water content in the specimen (M-25).

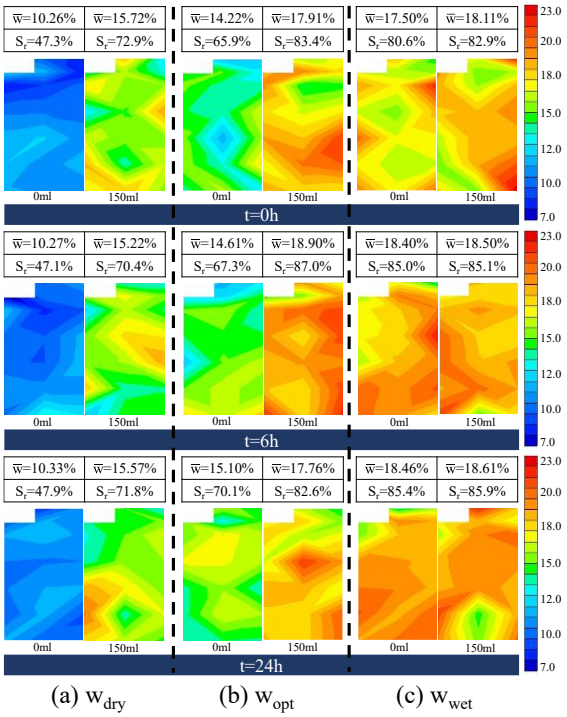

(a) w_{dry} (b) w_{opt} (c) w_{wet}

Figure 6. Distribution of water content in the specimen (RM-25).

the bearing capacity of M-25 increases compared to that of the bearing capacity just after infiltration (Figure 7(a)), similar to that of Decomposed granite soil. On the other hand, the bearing capacity of RM-25 decrease (Figure 8(a)). This is caused by the good permeability of M-25 and the decrease in water content in the upper part of the specimen with elapsed time, and the high water absorption of aggregate in RM-25 and the high water content maintained in the upper part of the specimen.

3.2 Optimum water content ratio

In both samples, the rate of decrease in bearing capacity due to water sprayed is smaller than that of the dry side. In addition, the bearing capacity of M-25 increased with the elapsed time immediately after water infiltration and approached the bearing capacity without water sprayed (Figure 7(b)), as is the case for the dry side. This is due to the assumption that the water content in the specimen approached the optimum water content with the elapsed time, as shown in the water content distribution in Figure 5(b), and that the specimen was not easily affected by the water flowing down the specimen. In comparison, the bearing capacity of RM-25 decreased after 6 hours and did not change thereafter (Figure-8(b)), as was observed for the dry side. This is considered to be due to the fact that water runoff does not occur after 6 hours and the upper part of the specimen was kept at a high water content ratio due to water absorption by the aggregate.

3.3 Wet side

M-25 shows high bearing capacity as well as other initial water content ratios, and the effect of water sprayed on the bearing capacity is similar to that of the optimum water content ratio. With the elapsed time, the bearing capacity gradually increases and recovers compared to that immediately after water sprayed (Figure-7(c)). This is caused by the distribution of the water content ratio returning to almost the same level as that before water sprayed over time, in spite of the wetted side.

On the other hand, the bearing capacity of RM-25 before water sprayed is the smallest among the other water content ratios, showing the same level of bearing water content ratios, showing the same level of bearing capacity as decomposed granite soil. This suggests that RM-25 was crushed by compaction as shown in Figure-2, causing a significant decrease in bearing capacity due to the increased water retention of the aggregate. This effect also caused a slight decrease in bearing capacity after 6 hours, after which no change was observed (Figure-8(c)). This is considered to be due to the gradually infiltrating water sprayed into the specimen, which increased the degree of saturation.

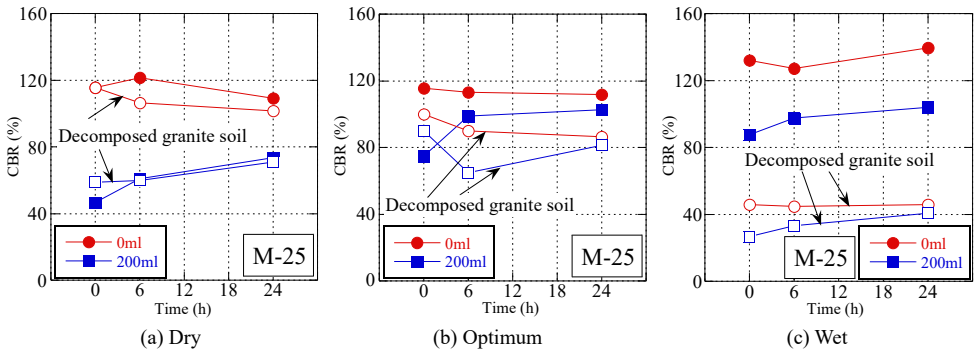

(a) Dry (b) Optimum (c) Wet

Figure 7. CBR test results (M-25).

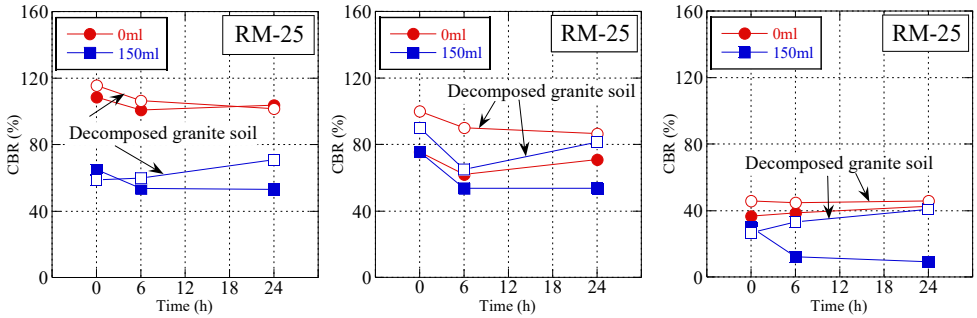

(a) Dry (b) Optimum (c) Wet

Figure 8. CBR test results (RM-25).

4 CONCLUSIONS

1) The water content of the base course at compaction has a significant effect on the strength reduction after rainwater infiltration.
2) The change of water content in the base course with the passage of time after rainwater infiltration has a significant effect on the bearing capacity behavior of the base course.

REFERENCES

Takahashi, Y.Ono and M. Sato (2015). Journal of Japan Society of Civil Engineers, Ser. E1 (Pavement Engineering), Volume 71,Issue 3.

F. Tatsuoka, K. Fujishiro, K. Tateyama, S. Kawabe and Y. Kukuchi (2015). The 15th Asian Regional Conference on Soil Mechanics and Geotechnical Engineering、242-257.

Proceedings of the XVIII ECSMGE 2024
GEOTECHNICAL ENGINEERING CHALLENGES
TO MEET CURRENT AND EMERGING NEEDS OF SOCIETY
© 2024 the Authors
ISBN 978-1-032-54816-6
DOI 10.1201/9781003431749-654
Open Access: www.taylorfrancis.com, CC BY-NC-ND 4.0 license

ECSMGE 24
XVIII EUROPEAN CONFERENCE ON SOIL MECHANICS AND GEOTECHNICAL ENGINEERING

Influence of grille spacing on the uplift behaviour of steel grillages for OHLs

Influence de l'espacement des grilles sur le comportement à l'élévation des grilles en acier pour les lignes aériennes électriques

C.J. Shepherd*, M. Brown, C. Davidson
University of Dundee, Dundee, UK

C.T.S. Beckett
The University of Edinburgh, Edinburgh, UK

S. Flint
Scottish and Southern Electricity, Glasgow, UK

c.y.shepherd@dundee.ac.uk

ABSTRACT: The increasing development of renewable energy (e.g. on and offshore wind) has increased the demand on existing electricity transmission networks in the UK. However, the remoteness of the transmission network, particularly in Scotland, makes upgrade and renewal, both economically and environmentally challenging, with often highly restrictive access constraints. Steel grillages are an alternative non-concrete foundation that can be loaded immediately post-backfill and transported to remote locations using low-ground pressure vehicles or helicopters. This paper investigates the optimisation of steel grillages for overhead line foundations such that the uplift load-displacement response is comparable to solid foundations (i.e. a concrete pad). Initial 1g uplift tests have shown that the optimal grille-spacing-to-width ratio (s/w) for a comparable ultimate uplift capacity to a solid plate lies within $1 < s/w < 2$.

RÉSUMÉ: Le développement croissant des énergies renouvelables (par exemple, les éoliennes terrestres et en mer) a augmenté la demande sur les réseaux de transmission d'électricité existants au Royaume-Uni. Cependant, l'éloignement du réseau de transmission, en particulier en Écosse, rend les travaux de modernisation et de renouvellement à la fois économiquement et environnementalement difficiles, avec des contraintes d'accès souvent très restrictives. Les grillages en acier sont une alternative aux fondations en béton qui peuvent être chargées immédiatement après le remblai et transportées vers des lieux reculés en utilisant des véhicules à basse pression au sol ou des hélicoptères. Cet article examine l'optimisation des grillages en acier pour les fondations de lignes aériennes de manière à ce que la réponse au déplacement sous charge de soulèvement soit comparable à celle des fondations solides (c'est-à-dire une dalle en béton). Les premiers tests de soulèvement à 1g ont montré que le rapport optimal entre l'espacement des grilles et la largeur (s/w) pour une capacité ultime de soulèvement comparable à une plaque solide se situe dans l'intervalle $1 < s/w < 2$.

Keywords: Grillage foundations; uplift; physical modelling; transmission infrastructure.

1 INTRODUCTION

The widespread and increasing development of both on- and offshore renewable energy in Scotland requires connection to the electrical transmission network. However, the existing network has insufficient capacity to meet future developments and new localised transmission infrastructure or upgrades are required. The current foundation design practice for new (or upgraded) overhead lines (OHLs) adopts material-heavy concrete spread foundations (e.g. concrete pads or pyramids). While these solutions have shown to be effective, they are not always practical when employed in remote and challenging terrain where limited or no access exists and often require the economically and environmentally costly operation of haul roads. Thus, recent interest in non-concrete alternatives has grown, such as those that can be heliborne or transported and installed using low-ground pressure vehicles, speeding up construction time and negating concrete's 28-day curing time before backfilling and loading. One alternative non-concrete solution is steel grillages, consisting of multiple standard steel sections (e.g. I-beams and angle sections) bolted together (Papailiou, 2017). Steel grillage foundations have been utilised extensively for steel lattice towers but fell out of fashion in the 1980s, coinciding with the

development of drilled concrete cast in-situ piles (Kulhawy *et al.*, 1983). Unfortunately, this led to a loss of knowledge and experience of these foundation types in the UK, specifically concerning their required configurations for resisting uplift forces. This paper investigates the optimum grille spacing of grillages subjected to uplift in granular soils through a series of scaled 1g uplift tests to address this knowledge gap.

1.1 Current UK design approach

The frustum method is a commonly adopted approach for determining the uplift capacity of shallow foundations for OHLs (National Grid, 2018). However, it is unclear whether the frustum method applies to grillages. Further guidance exists in BS EN 50341-1 (2012), stating that the net area of the grillage may be assumed, given that the spacing between grilles (s) does not exceed ⅓ the width (w) of the grilles and thorough backfill compaction is achieved. In addition to the uplift capacity, National Grid (2018) sets a serviceability criteria of 25 mm maximum vertical displacement.

The method assumes the resistance (Q_{FM}) is the sum of the weight of the foundation (W_f) and the weight of soil above the foundation confined within an inverted frustum (W_s) extending upwards at angle θ from the base of the foundation (Eq. 1-3):

$$Q_{FM} = W_f + W_s \quad (1)$$

$$W_s = \tfrac{1}{3}H\gamma(B^2 + B \cdot B_s + B_s^2) \quad (2)$$

$$B_s = \mathrm{B} + 2\mathrm{H}\tan\theta \quad (3)$$

where H is the embedment depth (m), B is the foundation width (m), and γ is the soil unit weight (kN/m^3). The frustum angle θ is dependent on the raw SPT N-value for granular soils, of, typically 15° for $10 \leq N < 20$ and 25° for $20 < N$.

1.2 Alternative uplift design approach

Alternative approaches for determining the uplift capacity of shallow OHL foundations have been investigated by Davidson and Brown (2021), showing that Giampa et al. (2019) best estimated the uplift capacity in granular soils. The method assumes the failure mechanism develops as an uplifted wedge at the dilation angle (ψ), mobilising shear resistance along the failure surface at the four triangular wedges along the perimeter (F_2) and conical wedges at the corners (F_3), and resistance from the weight of confined soil directly above the foundation (W_1), four triangular wedges along the perimeter (W_2), and conical wedges at the corners (W_3) (Eq. 4-9):

$$Q_G = F_2 + F_3 + W_1 + W_2 + W_3 \quad (4)$$

$$F_2 = \tfrac{1}{2}\gamma H^2 p\left(\tan\phi_{pk} - \tan\psi\right)\left[\left(\tfrac{1+k_0}{2}\right) - \tfrac{(1-k_0)\cos 2\psi}{2}\right] \quad (5)$$

$$F_3 = \tfrac{1}{3}\pi\gamma H^3\left(\tan\phi_{pk} - \tan\psi\right)\cos\left(\phi_{pk} - \psi\right) \quad (6)$$

$$W_1 = \gamma HA \quad (7)$$

$$W_2 = \tfrac{1}{2}\gamma H^2 p\tan\psi \quad (8)$$

$$W_3 = \tfrac{1}{3}\pi\gamma H^3\tan\psi \quad (9)$$

where A and p are the foundation's area (m^3) and perimeter (m^2), ϕ_{pk} is the peak friction angle, and K_0 is the lateral earth pressure coefficient (at rest).

2 PHYSICAL TESTING

The 1-g testing regime consisted of developing a reduced (1:10) plane-strain model grillage to investigate the influence of the grille-to-grille spacing ratio (s/w) where s is the spacing between grilles and w is the grille width, as illustrated in Figure 1.

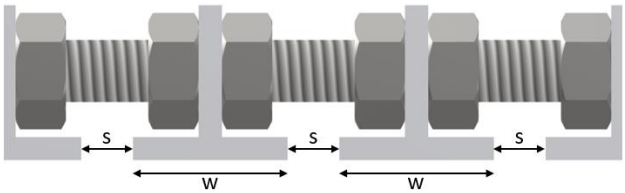

Figure 1. Illustration of grille-to-grille spacing ratio of (1:10) model grillage (s/w = ⅓ for the model shown).

2.1 Model setup

The grillage models developed allowed for multiple grille spacing (s/w = 1/2, 1/3, 1, 2, 5, and solid) while keeping the overall width of the foundation constant. The grilles were modelled using T-sections to allow for consistent compaction of sand between the grilles during sand bed preparation. The grilles were connected via three M8 threaded bars running perpendicular to an attached vertical shaft (stub connection). The positioning and spacing of individual grilles were controlled using M8 nuts placed on either side of the web. The dimensions and schematic of the model grillage are given in Table 1 and Figure 2, respectively.

The scale of the T-section, and thus the grillage, was chosen based upon the D_{50} particle size (0.14

mm (Lauder, 2010)) so that the particle scaling law requiring an opening between two embedded grilles to have a spacing ≤ 50 x D_{50}, (Garnier *et al.*, 2007), matching the smallest grille spacing (7mm). The grille length matched the box width to create plane-strain conditions for further investigation into the mechanistic behaviour.

Table 1. Grillage dimensions at model and prototype scale.

Grillage Property	Dimension	
	Model (mm)	Prototype (m)
Width, $\boldsymbol{B}$	260	2.6
Length, $\boldsymbol{L}$	440	4.4
Embedment, $\boldsymbol{H}$	260	2.6
Grille width, $\boldsymbol{w}$	20	0.2
Grille height, $\boldsymbol{h_g}$	20	0.2
Grille thickness, $\boldsymbol{t_g}$	3	0.03

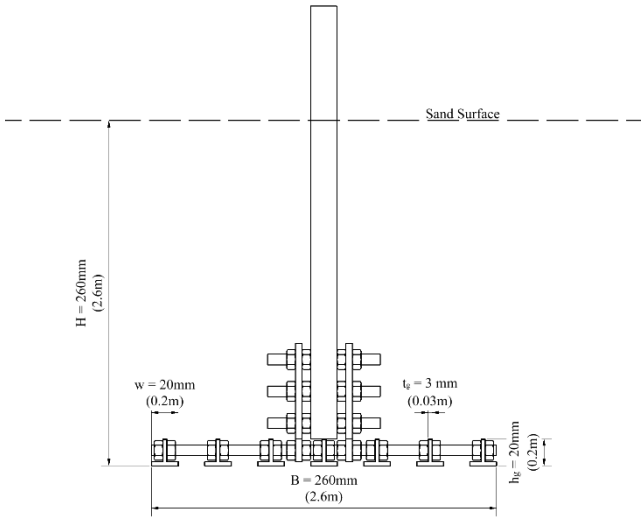

Figure 2. Dimension of assembled model grillage (assumed prototype dimensions shown in brackets).

2.2 Testing programme

The sand used for testing was dry HST95, which has been extensively characterised (Lauder, 2010). The relative densities investigated in this research are medium-dense (D_r = 42%) and dense (D_r = 82%). The properties relevant to determining the analytical capacity are given in Table 2.

Table 2. HST95 sand properties required for analytical comparison (Lauder, 2010).

Property	Relative Density, D_r	
	42%	82%
Dry unit weight, $\boldsymbol{\gamma}$ (kN/m^3)	15.8	17
Peak friction angle, $\boldsymbol{\phi_{pk}}$ (°)	37.4	45.4
Dilation angle, $\boldsymbol{\psi}$ (°)	6.5	16.9
Earth-pressure coefficient, $\mathbf{K_0}$	0.47	

The soil boxes (internal dimensions 900 x 448 x 448 mm) were prepared through pluviating sand to a bed thickness of h = 140 mm, the grillage placed at the centre of the box and sand pluviated above (i.e. wished in place) to a depth H = 260 mm (H/B = 1).

The uplift tests were conducted using an Instron-5985 UTM (Redhill 3 software) attached with a 10 kN load cell fitted with ¾ inch (19.05 mm) wedge action tensile grips fastened to the grillage stub. Uplift was tested under displacement-controlled loading at 10 mm/min, terminating after 50 mm of displacement at a logging rate of 0.1 Hz.

3 RESULTS AND DISCUSSION

3.1 Load-displacement response

Load-displacement responses at prototype scale (scale factor N = 10) are presented in Figure 3 and Figure 4, for D_r = 42% and 82%, respectively. The uplift resistances are the resistance mobilised from the soil shear and weight (i.e., excluding the grillage self-weight). At the prototype scale (i.e. Force x N^3 and displacement x N), the ultimate uplift resistance mobilised from a solid plate for D_r = 42% and 82% is 828 kN and 951 kN, respectively. Comparable uplift resistances are observed for s/w ratios of ⅓-to-1 (medium-dense) and ⅓-to-2 (dense).

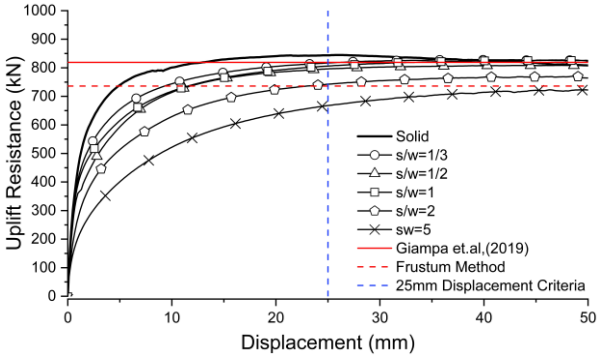

Figure 3. Uplift load-displacement response of grillages in medium-dense sand D_r = 42% at prototype scale.

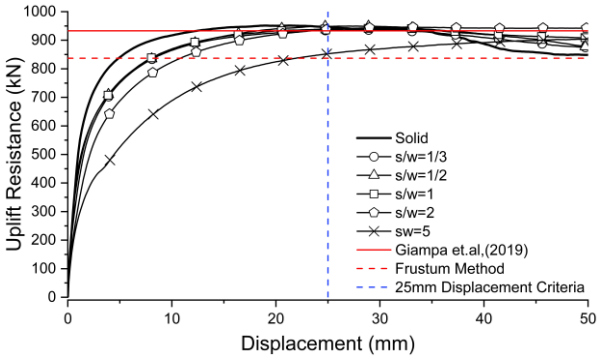

Figure 4. Uplift load-displacement response of grillages in dense sand D_r = 82% at prototype scale.

Whilst the peak uplift resistance is comparable to a solid plate (s/w = 0), the load-displacement responses reveal a reduction in stiffness with increasing s/w, as Danziger et al. (1989) observed due to soil flowthrough between the grilles. However, the reduction in stiffness is significant when assessing the design capacity against the permissible displacement of OHL foundations of 25 mm (denoted as the blue dashed line). The reduction in stiffness with increasing spacing ratio of these tests is likely suppressed by increased dilation experienced at 1g and the influence of the plain strain conditions.

The influence of grille spacing is better illustrated in Figure 5, which shows the normalised breakout factor, F_q^* = $(Q/\gamma HA)$, using a design load (Q) derived from the tangent intercept method. However, significant reductions in capacity are noted for larger s/w ratios, with an optimum spacing of s/w < 1 for D_r = 42% and s/w < 2 for D_r = 82%, in agreement with the findings of Martin (1975), who observed an optimum s/w = 1.75.

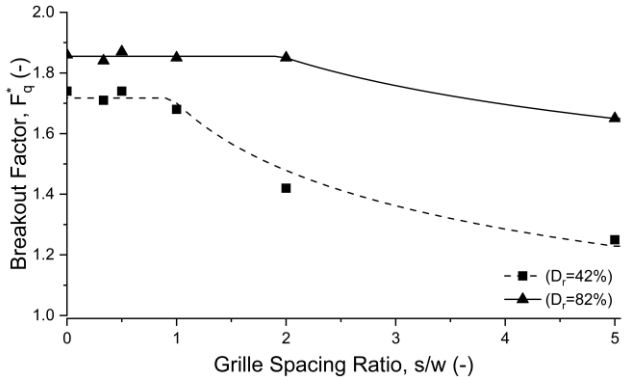

Figure 5. Influence of grille-to-grille spacing ratio (s/w) on breakout factor F_q^* for medium-dense and dense sands.

3.2 Comparison to analytical solutions

Comparing the uplift capacity to the analytical solutions (broken down into the plane-strain components, i.e. not including the wedge components along the Perspex interface), the method proposed by Giampa et al. (2019) (denoted by the solid red line in Figure 3 and Figure 4) provides a good estimate of 819 kN (-3%) and 933 kN (-2%) for D_r = 42% and 82% respectively, whereas the Frustum method (denoted by the dashed red line) underestimates the capacity, with predicted capacities of 736 kN (-13%) and 837 kN (-12%), respectively. Demonstrating that uplift capacity can be determined using existing analytical solutions assuming the net area of the grillage for spacing ratios of $1 \leq s/w < 2$. This is a significantly wider range of operation than the s/w = ⅓ specified in BS EN 50341-1 (2012), i.e. a potential for significant material savings in grillage adoption.

4 CONCLUSION

The results suggest that the optimum grille-to-width ratio in terms of uplift capacity (acting like a solid) lies between $1 \leq s/w < 2$ (density dependant), which is a wider operational range than the s/w = ⅓ proposed in BS EN 50341-1 (2012). However, an alternative design criterion may be required to consider the reduction of stiffness with increasing s/w. As these tests were undertaken at 1g, further investigation through scaled centrifuge modelling is needed to verify the observed reduction in performance in terms of stiffness.

Further investigation will focus on a series of centrifuge tests that first validate the observations of the influence of grille-to-grille spacing on both capacity and stiffness, scaling of uplift displacement, and influence of particle size before investigating means of enhancing the uplift load-displacement response (in terms of stiffness) through geogrid reinforcement and backfill compaction.

ACKNOWLEDGEMENTS

The authors are grateful for the financial support of Energy Technology Partnership (ETP) and industrial sponsor Scottish and Southern Electricity Networks.

REFERENCES

BS EN 50341-1:2012 (2012) Overhead electrical lines exceeding AC 1 kV - Part 1: General requirements - Common specifications. London, UK, p. 258.

Danziger, F.A.B. *et al.* (1989) Uplift load tests on grillages for guyed towers in Itaipu transmission system, in *XII International Conference on Soil Mechanics and Foundation Engineering*. Rio de Janeiro, Brazil, pp. 1193–1196. Available at: https://doi.org/10.1016/0266-1144(84)90012-8.

Davidson, C. and Brown, M. (2021) *Report UOD2108-1: Improved uplift capacity design methods for reassessment of existing foundations*. Dundee, UK.

Garnier, J. *et al.* (2007) Catalogue of scaling laws and similitude questions in geotechnical centrifuge modelling, *International Journal of Physical Modelling in Geotechnics*, 7(3), pp. 01–23. Available at: https://doi.org/https://doi.org/10.1680/ijpmg.2007.070301.

Giampa, J.R. *et al.* (2019) The effect of shape on the pull-out capacity of shallow plate anchors in sand, *Géotechnique*, 69(4), pp. 355–363. Available at: https://doi.org/https://doi.org/10.1680/jgeot.17.p.269.

Kulhawy, F.H. *et al.* (1983) *Transmission Line Structure Foundations for Uplift-Compression Loading*, Report EL- *Electric Power Research Institute.* Ithaca, New York.

Lauder, K. (2010) *The performance of pipeline ploughs.* PhD Thesis, University of Dundee.

Martin, D. (1975) Design of uplift foundations, *Cigre Electra*, 38(3), pp. 53–88.

National Grid (2018) *Overhead line support foundations TS 3.4.15*. Warwick, UK.

Papailiou, K.O. (2017) Overhead Lines, in *Springer Handbook of Power Systems*. 1st Edition. Springer International Publishing, pp. 611–758. Available at: https://doi.org/10.1007/978-981-32-9938-2_9.

Proceedings of the XVIII ECSMGE 2024
GEOTECHNICAL ENGINEERING CHALLENGES
TO MEET CURRENT AND EMERGING NEEDS OF SOCIETY
© 2024 the Authors
ISBN 978-1-032-54816-6
DOI 10.1201/9781003431749-655
Open Access: www.taylorfrancis.com, CC BY-NC-ND 4.0 license

ECSMGE 24
XVIII EUROPEAN CONFERENCE ON SOIL MECHANICS AND GEOTECHNICAL ENGINEERING

The SOURCE project: Quantifying and reducing the uncertainties associated with in situ stiffness measurements

Le projet SOURCE: Quantifier et réduire les incertitudes associées aux mesures de rigidité in situ

N.S. Shinde*, R.M. Buckley, L.P. Rieman
James Watt School of Engineering, University of Glasgow, U.K.
**Ninad.Shinde@glasgow.ac.uk*

ABSTRACT: Offshore wind turbine foundations account for a significant portion of a wind farm's capital cost, and design optimisation is becoming increasingly important. While the soil or rock in situ shear stiffness is a vital input parameter in several foundation design methods, the reliability of current in situ stiffness measurements and interpretation techniques is known to be variable. The SOURCE (Improved In situ Stiffness Measurement for Offshore Wind Foundation Design Considering Uncertainty Repeatability and Common Sources of Error) project is underway to quantify and reduce uncertainty in soil/rock in situ stiffness measurements and improve the predictive capability of offshore foundation design methods. The project involves multi-method geophysical and in situ field testing at three onshore sites, each having distinct ground conditions representative of offshore sites. The in situ testing is supported by advanced laboratory testing on high-quality samples. This paper reviews typical challenges and presents preliminary insights from the carefully controlled experiments, which aim to identify inter and intra-method variability in estimating the small strain in situ stiffness.

RÉSUMÉ: Les fondations des éoliennes offshore représentent une part importante du coût d'investissement d'un parc éolien, et l'optimisation de la conception devient de plus en plus importante. Bien que la rigidité au cisaillement in situ du sol ou de la roche soit un paramètre d'entrée essentiel dans plusieurs méthodes de conception de fondations, la fiabilité des techniques actuelles de mesure et d'interprétation de la rigidité in situ s'avère très variable. Le projet SOURCE (Amélioration de la mesure de rigidité in situ pour la conception des fondations d'éoliennes offshore en tenant compte de l'incertitude, de la reproductibilité et des sources d'erreur communes) est en cours pour quantifier et réduire l'incertitude dans les mesures de rigidité in situ du sol/roche et améliorer la capacité prédictive des méthodes de conception de fondations OWT. Le projet implique des essais géophysiques et in situ multi-méthodes sur trois sites terrestres, chacun présentant des conditions de sol distinctes représentatives des sites offshore. Les tests in situ sont soutenus par des tests avancés en laboratoire sur des échantillons de haute qualité. Cet article passe en revue les défis typiques et présente des informations préliminaires issues d'expériences soigneusement contrôlées, qui visent à identifier la variabilité inter et intra-méthode dans l'estimation de la rigidité in situ des petites déformations.

Keywords: In situ stiffness; seismic tests; shear wave velocity.

1 INTRODUCTION

Recent research has led to the development of new offshore wind turbine (OWT) foundation design procedures and frameworks informed by numerical modelling and field testing (Byrne et al., 2017, Jardine et al., 2023). While these advancements have led to important innovations, there remains significant uncertainty in the definition of input parameters including the small strain in situ stiffness (G_{max}). The latter is an important input into soil constitutive models for finite element analysis and simplified 1D analysis frameworks (see e.g. Byrne et al., 2020, Zdravković et al., 2020). The stiffness of the soil also influences the eigen-frequency of the turbine-tower-foundation system, which must lie outside key excitation frequencies to avoid resonance (Arany et al., 2016). As OWT foundations substantially impact the cost of wind farms, accurate measurement of G_{max} at an early stage is crucial for optimisation. The in situ stiffness is typically characterised by measurement of shear wave velocity, V_s, in seismic tests. Errors in the measurement of V_s are amplified in the subsequent calculation of G_{max}, due to the squaring of V_s in its formula ($G_{max} = \rho V_s^2$; where ρ is bulk density of soil).

Existing field and laboratory methods can exhibit significant test method dependency, data scatter, and poor correlation with laboratory measurements. The challenges in data acquisition and interpretation include e.g. source arrangements, geophone arrays and interval distance, selection of arrival time and ray path

assumptions (Parasie et al., 2022). Sampling disturbance, material anisotropy, fractures and inclusions also play a role and can lead to stark differences between laboratory and in situ stiffness (Taborda et al., 2019). Masters et al. (2019) reviewed the most common methods conducted offshore including field P-S suspension logging (PSL), seismic cone penetration testing (SCPT) and laboratory resonant column (RC) and bender element (BE) testing. Significant scatter was seen in the results. Figure 1 plots another example from a sand profile in the Ten noorden van de Waddeneilanden (TNW) wind farm zone (RVO, 2023) that highlights the difficulties in establishing consistent profiles and integrating data sets. Difficulties in accurate measurement of V_s are not unique to offshore projects. Liu et al. (2017) found variations in in situ stiffness from SCPTs of up to 50% from adjacent areas at a dense marine sand site, while large variations of up to 2GPa were observed in SCPT tests at a relatively homogenous chalk site (Vinck et al., 2022).

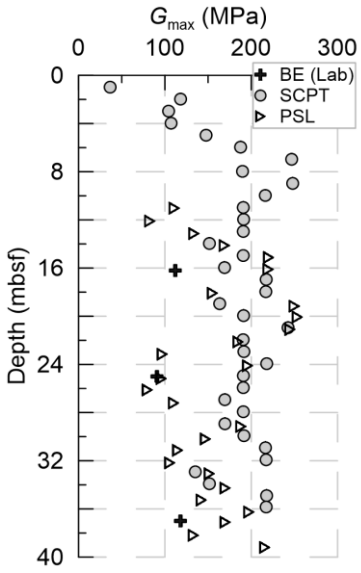

Figure 1. Example of divergence between methods to determine G_{max}: example from TNW-016-BH-CPT.

1.1 The SOURCE Project

The SOURCE (Improved insitu **S**tiffness measurements for **O**ffshore foundation design considering **U**ncertainty, **R**epeatability and **C**ommon sources of **E**rror) is a collaborative research project that aims to reduce the uncertainty associated with soil and rock in situ stiffness measurements and minimise the impact on the predictive capability of offshore foundation design methods. Comprehensive multi-method geophysical, in situ and laboratory testing is planned at three onshore test sites, in order to create benchmark datasets and develop robust, standardised guidelines for high-quality stiffness measurements. Each site involves drilling and sampling along with invasive methods including SCPTs, PSL, Down-hole (DH) and cross-hole (CH) borehole geophysics and pressuremeter tests (PMT). The field testing is supported by the extensive laboratory research undertaken at the University of Glasgow. The criteria for site selection are set to (i) be representative of typical profiles commonly encountered offshore and (ii) include sites where soil characterisation poses significant challenges. Site 1 was located at a disused chalk quarry in Kent close to the previous field-testing summarised by Jardine et al. (2023). Site 2 employed a dense sand site in Northern Germany while Site 3 will target over-consolidated clay ground conditions onshore UK.

2 IN SITU SHEAR STIFFNESS MEASUREMENTS

The in situ testing programme integrates various invasive and non-invasive methods each with unique capabilities and limitations; invasive seismic methods considered are shown in Figure 2. The SCPT and DH both work on the same principle, where a surface seismic source (a manually operated sledgehammer dropped onto a plate) generates seismic waves. These waves travel through the soil strata and are recorded by uni or multi-component sensors placed at depth. For the measurement of true interval velocity, a relative time difference between the received signals from dual receivers is calculated. Multiple shots are recorded at a particular depth to improve the signal-to-noise ratio.

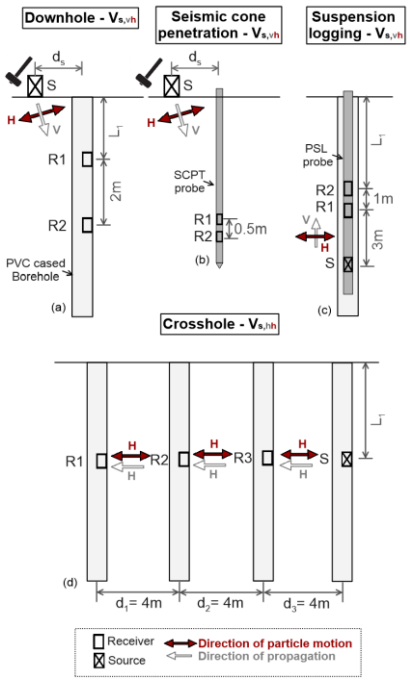

Figure 2. Invasive seismic methods considered in this study.

Cross-hole tests (CH) are conducted by placing a seismic source in one borehole and receiver(s) in another borehole(s). The PS Logging (PSL) probe consists of a seismic source together with hydrophone and geophone receivers within a single probe. The PSL system measures the compression wave velocity and formation shear-wave velocities of a portion of the soil or rock column around the borehole. PMTs determine stiffness and strength by measuring the pressure and displacement of an expanding membrane installed by self boring, placement in pre-bored holes or by pushing behind a CPT. In the laboratory, RC/BE and low-amplitude cyclic triaxial tests are performed on the high-quality samples.

3 KEY CHALLENGES

Measurements of V_s are known to be sensitive to the test procedure adopted including: (i) geophone arrays and spacing; (ii) source type, coupling and location (Koreta et al., 2022) and; (iii) testing mode e.g. DH/SCPT versus PSL, drilling versus seabed SCPT data acquisition Gibbs et al. (2018). The importance of targeting sampling frequency for a given receiver spacing is illustrated in Figure 3 for a V_s value of 450m/s (Rice, 1984). As the receiver spacing increases, the sampling frequency required to achieve a given level of accuracy in elapsed travel time, Δt, decreases which should be carefully considered when planning testing programmes.

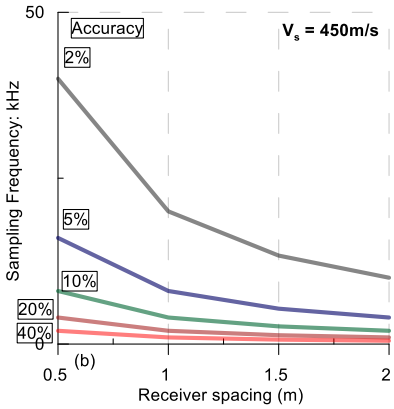

Figure 3. Relationship between sampling frequency, receiver spacing and accuracy in travel time estimation.

A comprehensive review of interpretation methods for downhole testing was provided by Stolte and Cox (2019). Classic approaches such as those that involve picking characteristic points on wave arrivals at sensors at different depths are prone to subjectivity and resist automation. The cross-correlation (CC) method (Campanella and Stewart, 1991) is often preferred where data quality allows, since it correlates information from the full signal and is less subjective to interpret. The method involves sliding one of the signals over a consecutive other signal recorded at a different depth and computing the similarity between the two signals at each time shift; CC was used for the majority of SOURCE interpretation. Once travel times have been evaluated, the analyst must make an assumption on ray path; inclined straight ray paths are typically assumed – with ray tracing based on Snell's law utilised for shallow layers and high stiffness contrasts.

Residual uncertainty in V_s due to poor data quality or ambiguous interpretation is rarely communicated to the end user of the data (Stolte and Cox 2019). There is no consensus yet on a consistent method to quantify epistemic or aleatory uncertainty. While the cross-correlation coefficient (CCC) is often used to quantify data quality, it is known to be unreliable since measurement noise is also correlated leading in some cases to unrepresentative high CCC values that can mislead investigators.

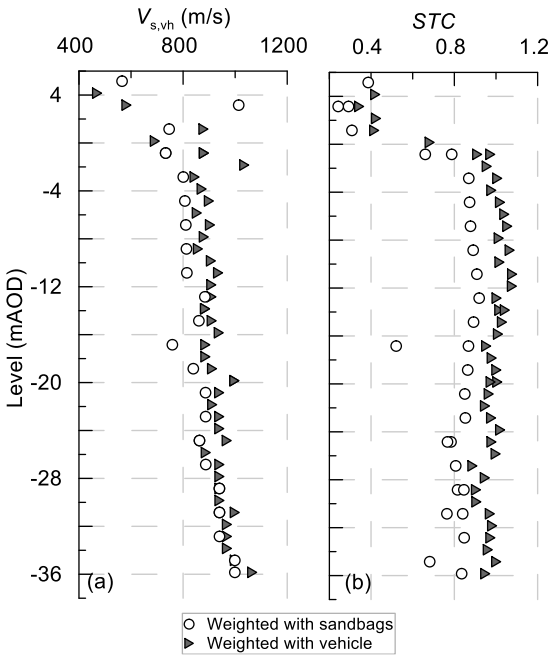

Figure 4. Influence of shear beam weighting on DH results.

Baziw and Verbeek (2017) proposed another approach: a data quality classification framework that combines CCCs with additional signal quality indicators related to linearity between receivers and the shape of the source input signal. The Seismic Trace Characterisation (STC) results in a numeric value between 0 (unacceptable) and 1 (excellent) that can be used to filter signals by flagging erroneous results and traces that require manual interpretation. Figure 4 demonstrates the usefulness of STC values when systematically assessing influence factors on (vertically propagating horizontally polarised) $V_{s,vh}$ obtained in DH testing at the chalk site. This particular

excercise assessed the influence of shear beam weighting or ground coupling on the obtained measurements. The STCs were higher, and the data less scattered where the shear beam was weighted using a vehicle (11kN) compared to when it was weighted using sandbags (1.5kN). While STC appears to be a reliable indicator of data quality, the framework alone cannot capture the complete set of uncertainties present in the shear profile and additional developments are required.

4 SUMMARY & CONCLUSIONS

The SOURCE project aims to quantify and reduce the uncertainties associated with soil and rock in situ stiffness measurements to minimise the influence on offshore foundation design. Benchmark data sets are being collected at onshore sites in the UK and Europe with ground conditions relevant to offshore ground conditions. The fieldwork is providing new insights into in situ stiffness in these materials and facilitating the development of new analysis procedures. While the focus here is on offshore foundation design, the outcomes will be equally applicable to onshore soil structure interaction problems.

ACKNOWLEDGEMENTS

The SOURCE project is supported by EPSRC through the New Investigator Award Scheme (EP/W020807/1) and industry partners including Cambridge Insitu Ltd, DNV, Fugro, In situ SI, RSK, RobertsonGeo and Vattenfall. The RVO data is made available under the Creative Commons 4.0 CC BY SA license.

REFERENCES

Arany, L., Bhattacharya, S., Macdonald, J.H. and Hogan, S.J. (2016). Closed form solution of Eigen frequency of monopile supported offshore wind turbines in deeper waters incorporating stiffness of substructure and SSI. *Soil Dynamics and Earthquake Engineering,* 83**,** 18-32. https://doi.org/10.1016/j.soildyn.2015.12.011.

Baziw, E. and Verbeek, G. (2017). Quality assessment of seismic data sets and the impact on interval velocity estimates in DST. *DFI 42nd Annual Conference on Deep Foundations*. New Orleans, USA.

Byrne, B., McAdam, R., Burd, H., Houlsby, G., Martin, C., Beuckelaer, W., Zdravkovic, L., Taborda, D., Potts, D. and Jardine, R. (2017). PISA: new design methods for offshore wind turbine monopiles. *Proc. 8th Intl. Conf. Offshore Site Investigation and Geotechnics.* London UK: Society for Underwater Technology.

Byrne, B.W., Houlsby, G.T., Burd, H.J., Gavin, K., Igoe, D., Jardine, R.J., Martin, C.M., McAdam, R.A., Potts, D.M., Taborda, D.M.G. and Zdravković, L. (2020). PISA design model for monopiles for offshore wind turbines: Application to a stiff glacial clay till. *Géotechnique,* 70**,** 1030-1047. https://doi.org/10.1680/jgeot.18.P.255.

Campanella, R. and Stewart, W. (1991). Downhole seismic cone analysis using digital signal processing. *Proc. 2nd Int. Conf. on Recent Advances in Geotechnical Earthquake Engineering and Soil Dynamics*. Missouri. USA.

Gibbs, P., Pedersen, R., Krogh, L., Christopher, N., Sampurno, B. and Nielsen, S. (2018). Challenges in marine seismic cone penetration testing. *Proc. 4th Int. Symposium on Cone Penetration Testing*, Delft, The Netherlands, 2018. CRC Press, 303.

Jardine, R.J., Buckley, R.M., Liu, T., Byrne, B., Kontoe, S., Macadam, R. and Vinck, K. (2023). Driven pile behaviour in low-to-medium density chalk: the ALPACA JIP outcomes. *9th Intl Conf Offshore Site Investigation and Geotechnics.* London, UK: SUT.

Koreta, O., Augustesen, A., Krogh, L., Lundvig, K. and Bøtker-Rasmussen, S. (2022). On the accuracy and precision of the seismic cone penetration test—a field test study on the seismic source. *Cone Penetration Testing 2022.* CRC Press.

Liu, T., Aghakouchak, A., Taborda, D.M. and Jardine, R.J. (2017). Advanced laboratory characterization of a fine marine sand from Dunkirk, France. 439-442.

Masters, T.A., Juszkiewicz, P., Mandolini, A. and Christian, H. A. (2019). Critical Appraisal of the Benefits of and Obstacles to Gaining Quality Data with Offshore Seismic CPT and PS Logging. *Offshore Technology Conference*, Houston, USA.

Rice, A.H. (1984). *The seismic cone penetrometer.* University of British Columbia.

RVO (2023). Ten noorden van de Waddeneilanden Wind Farm Zone (TNWWFZ); https://offshorewind.rvo.nl/cms/view/796048cf-12cb-4e90-8124-ae4eb73c1c49/general-information-tnw.

Stolte, A.C. and Cox, B.R. (2019). Towards consideration of epistemic uncertainty in shear wave velocity measurements obtained via SCPT. *Canadian Geotechnical Journal,* 57**,** 48-60. https://doi.org/10.1139/cgj-2018-0689.

Taborda, D.M., Zdravković, L., Potts, D.M., Burd, H.J., Byrne, B.W., Gavin, K.G., Houlsby, G.T., Jardine, R.J., Liu, T. and Martin, C.M. (2019). Finite-element modelling of laterally loaded piles in a dense marine sand at Dunkirk. *Géotechnique,* 70**,** 1014-1029. https://doi.org/10.1680/jgeot.18.PISA.006.

Vinck, K., Liu, T.F., Jardine, R.J., Kontoe, S., Ahmadi-Naghadeh, R., Buckley, R.M., Byrne, B.W., Lawrence, J.A., Mcadam, R.A. and Schranz, F. (2022). Advanced in-situ and laboratory characterisation of the ALPACA chalk research site, *Géotechnique*, online ahead of print. https://doi.org/10.1680/jgeot.21.00197.

Zdravković, L., Taborda, D.M., Potts, D.M., Abadias, D., Burd, H.J., Byrne, B.W., Gavin, K.G., Houlsby, G.T., Jardine, R.J. and Martin, C.M. (2020). Finite-element modelling of laterally loaded piles in a stiff glacial clay till at Cowden. *Géotechnique,* 70**,** 999-1013. https://doi.org/10.1680/jgeot.18.PISA.005.

Proceedings of the XVIII ECSMGE 2024
GEOTECHNICAL ENGINEERING CHALLENGES
TO MEET CURRENT AND EMERGING NEEDS OF SOCIETY
© 2024 the Authors
ISBN 978-1-032-54816-6
DOI 10.1201/9781003431749-656
Open Access: www.taylorfrancis.com, CC BY-NC-ND 4.0 license

ECSMGE 24
XVIII EUROPEAN CONFERENCE ON SOIL MECHANICS AND GEOTECHNICAL ENGINEERING

The environmental advantage of bi-directional pile testing related to traditional top-down testing

L'avantage environnemental des essais bidirectionnels sur pieux par rapport aux essais traditionnels par chargement en tête

A. Silva*
Fugro Loadtest Foundation Testing, Porto, Portugal

M. England
Fugro Loadtest Foundation Testing, London, United Kingdom

M. Profittlich
Fugro Loadtest Foundation Testing, Leidschendam, Netherlands

**a.silva@fugro.com*

ABSTRACT: Together with the constant preoccupation with the safety standards of new structure's foundations the worldwide awareness of climate change continues to increase, making these two elements together with costs the biggest parameters for any foundation project. From the beginning of any foundation project the methodology for a full-scale static load testing program can already optimise many of the requirements in terms of costs and safety, however, only now the environmental optimisation is truly valued. The bi-directional load testing method, by eliminating the reaction structures of the traditional top-down testing methodology, allows the reduction of the overall carbon footprint of the testing program in the most efficient, safe and cost-effective manner for all types of foundations, particularly for larger test loads. The benefits of using bi-directional load tests and how effective they are at reducing carbon emissions will be described. The inclusion of some case studies will illustrate the reduction of CO_2 for (bi-directional) static load testing of foundations in general.

RÉSUMÉ: Parallèlement à la préoccupation constante des normes de sécurité des fondations des nouvelles structures, la prise de conscience mondiale du changement climatique continue d'augmenter, faisant de ces deux facteurs, ainsi que des coûts, les paramètres les plus importants pour tout projet de fondation. Dès le début d'un projet de fondation, la méthodologie d'un programme d'essais de chargement statique à grande échelle permet déjà d'optimiser de nombreuses exigences en termes de coûts et de sécurité, mais ce n'est qu'aujourd'hui que l'optimisation environnementale est réellement appréciée. Du fait de l'élimination des structures de réaction nécessaires à la méthodologie d'essai traditionnelle, la méthode d'essai de chargement bidirectionnelle permet de réduire l'empreinte carbone globale de l'essai de la manière la plus efficace, la plus sûre et la plus rentable pour tous les types de fondations sur pieux, en particulier pour les charges d'essai plus importantes. Les avantages des essais de charge bidirectionnels et leur efficacité en matière de réduction des émissions de carbone seront décrits. La présentation de quelques études de cas illustrera la réduction des émissions de CO_2 pour les essais de chargement statique (bidirectionnels) des fondations en général.

Keywords: Foundation optimisation; bi-directional static load testing; Osterberg cell; decarbonisation of concrete pile foundations.

1 INTRODUCTION

When bi-directional load testing was first brought into pile testing environment, J. Osterberg (1991), predicted savings to the piling world would be in the billions of dollars with the possible reduction of pile size and concreted length for many major projects. As professor Osterberg put it, 'the most economical, functional and practical solution should be sought, followed by a study of how costs can be cut', however at that time he couldn't predict how valuable the bi-directional load testing method would be to reducing the CO_2 emissions for the construction industry.

The current paper is written with the assumption that the readers already understand the correlation between preliminary foundation testing, efficient dimensions of the foundations and the consequent reduction of CO_2 emissions. The focus will be on how the bi-directional load testing allows for a greater reduction of the CO_2 emissions in comparison to other full scale loading methods.

2 PILE DESIGN TESTING PROCESS AND FOUNDATION OPTIMISATION

Ideally, preliminary tests should be undertaken long before the working foundations are constructed, giving designers the chance to re-evaluate their designs and reduce the conservatism that is often introduced in the design due to uncertainties of construction and soil characteristics. The designs are often optimised to obtain an adequate safety factor and the most cost-effective foundations possible for the specific project. However, with the realisation of current damages to our planet provoked by the CO_2 emissions the designers should also take into consideration the environmental element of the project.

When efficiently used, the data obtained from a foundation testing program will allow the possible reduction of the foundation element dimensions and subsequently reduce the CO_2 emissions originating from the reduction of concrete used and equipment usage.

Not only during the actual foundation works are the CO_2 emissions potentially reduced. CO_2 emissions can be further reduced when the bi-directional static loading test method is selected instead of the traditional top-down testing.

3 BI-DIRECTIONAL STATIC LOAD TESTING METHODOLOGY

The bi-directional pile load testing utilises an individually calibrated hydraulic sacrificial loading device (Osterberg Cell® or O-Cell®) installed within the foundation unit. Working in two directions, upward against side-shear resistance and downward against side-shear and end-bearing resistance, the device automatically separates the resistance and displacement data for each component of the pile. By virtue of its installation within the foundation element, the load test is not restricted by overhead structural beam limits and reaction piles. Instead, the device derives all reaction from the soil. End bearing and lower side shear provide reaction for the upper side shear portion of the load test and upper side-shear provides the reaction for the end bearing and lower side-shear portion of the load test.

Once the O-Cell system has been installed within the pile shaft and the concrete has reached sufficient strength, the test can commence. Strain gauges are connected to a data logger (Figure 1) and the system can be run under computer control. When the load cells are first pressurised, the load applied will break temporary welds to prevent the cells from opening prematurely during assembly and form a horizontal separation across the pile at the load cell location.

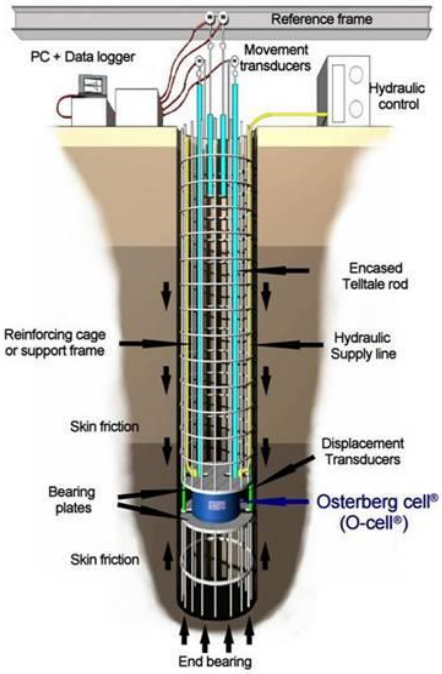

Figure 1. Schematic of a Bi-directional loading test (Fugro).

Once this is done, the test can be performed much the same as a top-down test, by applying the load in stages and measuring movements of each of the components. Testing schedules can be adopted from standard procedures or by recommendation.

4 TRADITIONAL TOP-DOWN TESTING

For the execution of a top-down test a reaction system above the foundation element has to be assembled, with the use of anchor piles combined with loading frames or the use of kentledge blocks.

For a pile/barrette with high loading, in the 10s of MN, a test might require 6 or even more anchor piles These additional anchors require drilling and constructing with steel and concrete, increasing the number of activities, material delivery and its consumption.

A traditional top-down loading system requires a large frame which needs to be constructed with multiple steel beams. The larger the test load requirement the larger these reaction structures need to be. These require to be transported from depot to site and a crane is required to erect the structure, which can be as tall as a 3 story building or more when the loads are as high as 40 to 60 MN.

5 ENVIRONMENTAL COMPARATION

In the following chapter we present a comparation from an environmental point of view between the two

foundation testing methods with the related CO_2 calculations and with project examples.

5.1 Concrete cut-off level in top-down testing

In a traditional top-down loading test the top of concrete needs to be at ground level or above, often with an additional pile cap. In contrast, for a bi-directional loading test, the CO_2 emissions can be reduced as the necessary volume of concrete can also be reduced if the concrete is not up to ground level.

As an example of this, a project executed in Switzerland included the testing of three 2800x800 mm barrettes where the concrete cut-off level was left on average at 12.3 m below ground (Figure 2, shows the empty panel is backfilled with dry sand). The possibility of leaving the concrete level at the desired cut-off elevation allowed a saving of approximately 82.66 m^3 of concrete. Assuming the Carbon Factor of 212 $kgCO_2e/m^3$ of CEM III/A GGBS (50%) based on the Inventory for Carbon and Energy (ICE) database, 17 TN of CO_2 were saved.

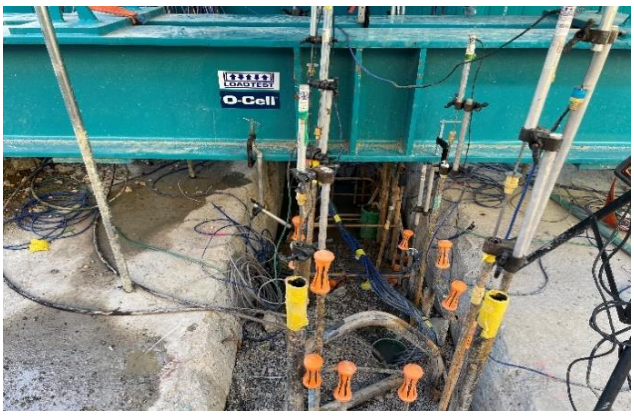

Figure 2. Bi-directional loading test on a pile with concrete cut-off level 12.3 m below ground level (Fugro).

5.2 Reaction structures and anchor piles

As described in section 4, a traditional top-down test requires external reaction structures, like a combination of anchor piles and reaction frames. The loading frame observed in yellow in Figure 3 is a good example of the dimensions and necessary material for reaction beams and anchor piles The CO_2 emissions originated by the production of these structures should be also taken into consideration.

Even if the multiple reuses of the structures on different tests can offer a sense of economic savings, the same isn't felt in terms of the environment as the transport and handling of these assemblies produces CO_2 by the combustion of fuel.

Together with transport and construction of the different reaction structures, the requirement to construct an extra number of piles to serve as anchors, increases the CO_2 emissions related with this type of test. An additional 4 anchor piles for a typical top-down test may not seem much in the total scheme of things but that might be an additional 400 m^3 for the concrete alone on deep large diameter piles, equivalent to more than 80 TN of CO_2. That is without the extra rig emissions for drilling the anchors, concrete and steel transportation and other auxiliary operations. Concrete emissions might be many times as much for high load testing of barrettes and larger piles.

Compared with a bi-directional static load testing the extra construction materials, excavation works and concrete for a top-down load test are avoidable producers of CO_2.



Figure 3. 30 MN top down reaction beams on a barrette test with multiple anchor piles (Fugro).

5.3 Transport for a kentledge test

If in the previous top-down testing method we could associate most of the unnecessary CO_2 emissions with the necessity to construct anchor piles, for a test using kentledge the CO_2 emissions originate from the transport and handling the heavy concrete blocks that will act as reaction system.

It is easily understandable by observing Figure 4 the number of trucks necessary to transport all the blocks. It is also important to note that the CO_2 emissions will directly increase with the requirements of the test load (higher the test load = more blocks needed) and added to this the distance between the depot and site. If we imagine that some remote sites can be more than 1000 km from the depot (example: Mohembo Bridge project and depot in Gaborone – Botswana), we can understand how the reduction of this transport can help reduce the CO_2 emissions.



Figure 4. Loading test using kentledge Dubai (Fugro).

In comparison, it is possible to observe in Figure 5 the equipment necessary, including O-Cells® and measuring equipment, for a bi-directional loading test designed to reach 70 MN. All the equipment was shipped via air to the closest airport and transported easily.

Figure 6, illustrates a typical test setup of a bi-directional loading test where the necessary reference beam was set over two concrete blocks. The final setup for a bi-directional pile load test may also require the use of short-term lifting equipment, it is important to notice that the same setup observed could be used in any test regardless of loading capacity, from 1 MN to over 300 MN. The test can also be performed offshore where the possibility of using top-down techniques becomes far more difficult, and substantially more expensive.



Figure 5. Instrumentation used for a designed 70 MN load test in a barrette (Fugro).



Figure 6. Bi-directional loading test underway (Fugro).

6 CONCLUSION

The bi-directional loading test was already a more economical, practical/functional and safer option over the traditional top-down loading method and with the information shared in this paper it is also noted that the bi-directional loading test is also a better environmental alternative, either when compared with a loading beam plus anchor piles or a kentledge system.

The current European and global norms have a clear goal of decreasing the CO_2 emissions and the construction sector, as one of the biggest producers of CO_2, should now give the same value to the environment as it gives to cost/profit, safety and time. For a preliminary foundation testing program or for proof tests on working piles (as post test grouting can restore the integrity of the structure) the bi-directional loading test will fulfil all those requirements, as shown in a few project examples.

ACKNOWLEDGEMENT

The authors show appreciation to all the foundation designers who have and do already take advantage of the potential design optimisation resulting from full scale static load testing using the bi-directional methodology.

REFERENCES

Osterberg, J.O. (1991). A new load testing device innovative approach to load testing of high capacity piles. *Proceedings of the International Conference on Piling and Deep Foundations*, J. B. Burland and J. M. Mitchell (eds.), Balkeman, Vol. 1, pp. 409-413.

Proceedings of the XVIII ECSMGE 2024
GEOTECHNICAL ENGINEERING CHALLENGES
TO MEET CURRENT AND EMERGING NEEDS OF SOCIETY
© 2024 the Authors
ISBN 978-1-032-54816-6
DOI 10.1201/9781003431749-657
Open Access: www.taylorfrancis.com, CC BY-NC-ND 4.0 license

ECSMGE 24
XVIII EUROPEAN CONFERENCE ON SOIL MECHANICS AND GEOTECHNICAL ENGINEERING

Portugal first HVAC submarine power transmission cable - from engineering to construction

Premier câble sous-marin de transport d'électricité CAHT au Portugal - de l'ingénierie à la construction

R. Silvano*
Cathie Group, Brussels, Belgium

V. Terente, L. Burley, R. Francos
Cathie Group, Newcastle, United Kingdom

A. Santos, M. Conceição
REN, Lisbon, Portugal

**rui.silvano@cathiegroup.com*

ABSTRACT: This paper presents the experience and some lessons learned from the design and construction of Portugal's first High Voltage Alternating Current (HVAC) submarine power transmission cable, offshore Viana do Castelo. The paper focuses on the ground conditions and the engineering solutions along the marine section of the submarine power cable, namely: 1) trenchless cable landing in hard rock, 2) the cable installation and protection requirements along a rocky seabed and 3) trenching in soil.

RÉSUMÉ: Cet article présente l'expérience et quelques enseignements tirés de la planification et de la construction du premier câble sous-marin de transport d'électricité à haute tension et à courant alternatif (CAHT) du Portugal, au large de Viana do Castelo. L'article se concentre sur les conditions du sol et les solutions d'ingénierie le long de la section marine du câble électrique sous-marin, à savoir: 1) l'atterrage du câble sans tranchée dans la roche dure, 2) l'installation du câble et les exigences de protection le long d'un fond marin rocheux et 3) le creusement d'une tranchée dans le sol.

Keywords: Submarine cable; offshore surveys; trenchless landfall; cable installation; cable protection; floating offshore wind.

1 BACKGROUND

The Windfloat Atlantic project is Europe's first floating semi-submersible offshore wind farm, located approximately 20km offshore Viana do Castelo, northern Portugal. The offshore wind farm consists of 3no. 8MW wind turbine generators on floating semi-submersible platforms anchored to the seabed at a water depth of around 100m, with an installed capacity of 25MW. These turbines are connected through a series of dynamic inter-array cables to the Portuguese grid offshore interconnection point through a Dry-Mate Connector (DMC) laid in the seabed approximately 20km offshore.

In 2015, the Portuguese government allocated to Redes Energéticas Nacionais (REN), the Portuguese Transmission System Operator, the responsibility for the design and commissioning of the Portuguese grid offshore infrastructure in Viana do Castelo, designed for a maximum nominal power of 200 MVA when operated at 150 kV. This comprises Portugal's first High Voltage Alternating Current (HVAC) submarine power transmission cable, 225mm diameter with three 1164 mm2 cores and approximately 17km. The connected generation power of the initial phase, already completed with the infrastructure operating at 60 kV is 25 MW.

For the design, supply and installation of the infrastructure, REN awarded in 2018 an EPC&Mcontract to Hengtong, who subcontracted the offshore works to DeepOcean, the landfall Horizontal Directional Drilling (HDD) to HDI, and the onshore switchyard to CME. Cathie were contracted by REN to support the offshore and landfall projects from early planning, leading the pre-tender design activities, providing tender support and the construction support.

The power transmission cable is laid along the seabed before entering the ~630m of HDD duct and connection to the national distribution grid. For protection, the cable was trenched into the seabed where possible or buried under a rock berm. This paper

focuses on the ground conditions and the engineering solutions, namely: 1) trenchless cable landing in hard rock, 2) the cable installation and protection requirements along a rocky seabed and 3) trenching in soil.

2 GROUND CONDITIONS

2.1 Geological context

The geology along the cable route can be summarised in two major sections. Section 1 (approximately 1/3 of the cable route) closer to shoreline, characterised by the presence of exposed or sub-exposed Pre-Cambrian and Palaeozoic granitoids/schist, associated with high compressive strengths and strong NNW-SSE and WNW-ESE lineations, Figure 1. The lineations are the product of the significant folding and faulting in this area.

Section 2 is generally characterised by a minimum sediment cover of 2-3m increasing towards the west. The geology of this section consists of sub-exposed cretaceous rocks and quaternary sediments (mainly fine to coarse granular materials, sandy silt becoming silt to the West of the route).

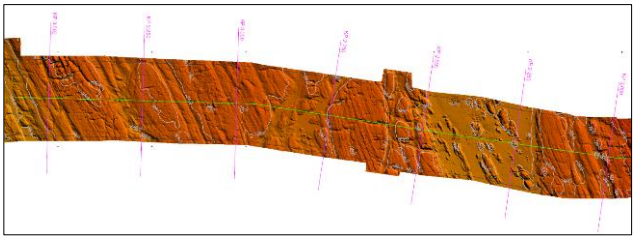

Figure 1. Bathymetry section showing rocky seabed. KP points shown every 250m.

2.2 Geophysical and Geotechnical characterisation

2.2.1 Offshore cable route

A geophysical survey of the anticipated export cable route was conducted in 2014 by GEOxyz (offshore section) and Lagoa do Ruiva Survey (nearshore section), providing multibeam echo sounder (MBES), side-scan sonar (SSS) and sub-bottom profiler (SBP) data in order to determine water depths, identifying seabed obstructions and features such as seabed sediments cover.

The nearshore survey was executed in April 2014. A zone of ~4km^2 was surveyed in the nearshore area with multibeam, where the cable was supposed to come onshore. The depth varied between +3.0m LAT and -30.0m LAT. The deepest zone was recorded in the southwestern part of the area, furthest away from the coast. This zone consists mainly of rocky outcrops.

Along the planned cable route, a corridor of 500m wide was surveyed with MBES, SSS and SBP. The first 10km of the cable route was noted to be covered with fishing gear. For this reason, side scan sonar survey was not possible in the nearshore area.

Multibeam data showed depths along the corridor varying from -10m LAT in the east, along the coast, up to -95m. Rocks were visible up to 8km from the shore, with depths up to -50m LAT. The rest of the corridor showed a smooth slope towards the west, with no rocky structures visible on the surface.

Lines for the SBP were recorded simultaneous with every multibeam or side scan line surveyed. Average penetration into the sediment resulted in 8-10m. Towards the west, the rocky structures were still visible but covered with a ~2m of sediment.

Towards the end of the corridors, rocky structures were not visible, however, in the western part of the cable route, shallow rocks were present again with only a small sediment cover. Where no rocks were visible on the surface, a mimimum of 3 meters sediment (and often more) was detected along the cable routes. Steep slopes were only visible in the rocky areas.

As part of the pre-engineering phase, an additional geophysical survey was carried out in September 2018 by MG3 under subcontract to DeepOcean, to ascertain expected free cable spans prior to finalisation of the route engineering. The scope of work involved the collection of bathymetric and geophysical data within a 200m wide corridor. The entire corridor was surveyed with MBES, SBP and seafloor dropdrown camera at certain intervals. Due to fishing activity and gear, the SSS and Magnetometer works were suspended and the MBES Backscatter Imaging was recorded as back-up in order to enable a seafloor sediment analysis.

The scope of the Export Cable geotechnical investigation, comprised a total of 32no. CPTs coupled with 32no. Vibrocore (VCs). The target penetration depth for both type of tests, was specified to be 3m to 5m below seafloor based upon the anticipated ground conditions along the cable route.

The geotechnical survey was performed by Fugro in 6 days during November-December 2016 using the MV Markab, a 63m dynamically positioned DP2 survey vessel. A 75kN Seacalf seabed CPT unit was mobilised on board of the MV Markab. Seabed CPTs were performed using a 12 tonne ROSON CPT system. Cones with a projected area of 10cm^2 and 5 tonne capacity were used for testing, with pore water measurements made on the shoulder of the cone, generally providing very good quality results, in

general, all within ISO Application Class 1 (ISO 22476-1, 2022) for ground conditions comprising loose to very dense sands and soft to very stiff clays. The CPT achieved good penetrations in the sands and occasional clays were encountered along the route up to ~10km from the shoreline, from where the CPTs recorded the presence of bedrock near surface and/or rock outcrops.

Sampling operations were performed using a high performance corer (HPC). The HPC had a base frame of 2.4m x 2.8m, an overall length of 8.1m and a weight (in air) of approximately 3.1ton. The HPC was fitted with a 6m core barre allowing for the recovery of soils samples of up to 84mm in diameter.

Only basic logging of the samples was performed offshore. Laboratory testing onshore was generally performed according to the BS 1377 (1990) procedures, including:

- Basic strength and Index laboratory Tests.
- Water content and Wet and Dry Density.
- Plasticity Index.
- Particle size distribution.
- Minimum and maximum density.
- Thermal conductivity test.
- Shear box test.
- Unconsolidated Undrained Triaxial Test.

2.2.2 Landfall

An onshore geoelectrical tomography survey supplemented by seismic refraction tomography and multichannel analysis of surface waves (MASW), calibrated with boreholes, was performed by Donié Geo-Consult in order to generate a geological model for the HDD working area. Rockhead was reported at a depth of 6-8 m, slightly inclined in the direction of the sea and underlying heterogeneous anthropogenic made ground.

Additionally, an offshore geophysical exploration in the planned landfall area was performed with MBES, SBP and electrical resistivity tomography techniques by Donié Geo-Consult and SSS and Seismic Reflection (with a boomer) by Instituto Hidrográfico. The aim of the investigation was to create a geological model for the cable landing area.

At least two to three critical sections with lengths of up to 100 m and apparently strongly fragmented hard rock were identified. On the last 100 m before the exit point, a remarkable resistivity minimum linked to a very rough surface of fractured rock according to the SBP results was identified, Figure 2. The Echo Sounder detected a strongly fractured rock surface with open fissures pointing in two main directions (NW-SE and WSW-ENE).

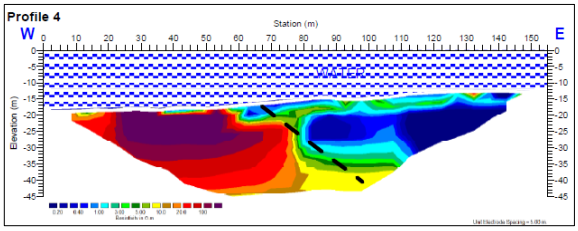

Figure 2. Geolectrical tomography of punchout area (red, high resistivity; blue low resistivity).

In 2018, a total of seven onshore rotary percussive boreholes were drilled by GeoSonda, six boreholes to a maximum depth of ~10.5m at the footprint of the switchyard building, and one borehole at the location of the HDD entry point, with total depth of 40m.

The borehole descriptions at the HDD entry point identified an upper layer of made ground, with cavities overlying solid rock composed of various types of schists, with subvertical schistosity.

Additionally, laboratory testing from five representative samples at different depths and lithologies were obtained from borehole S7 including:

- Point Load Test
- Uniaxial compressive test (UCS)
- Micro-Deval
- Cerchar Abrasivity
- D.R.I. (Drilling rate index).

Abrasivity results revealed very to highly abrasive samples, particularly in quartzitic schist. In general, medium to high D.R.I index values were obtained. Maximum values from the UCS tests ranged between ~39-80 MPa in quarzitic schist and ~12-61 MPa in andalusite schist. It was noted that the lowest values correspond to fractures along discontinuities during the test.

3 ENGINERING SOLUTION

3.1 Contractual cable burial and protection requirements

The governing basis for the design was protection for a minimum 30 year service life against fishing activity and 1:10,000 year anchoring events.

REN specified different protection requirements over two characteristic sections: rocky section (Section 1) and buried section (Section 2).

For Section 1, defined as rocky outcrops with thin or absent sediment cover, closer to shore, it was envisaged that cable armour and pinning/rock dumping compliant with environmental restrictions was required.

For Section 2, defined as minimum sediment cover, it was envisaged a minimum Depth of Cover (DoC) of

1.5m, and greater where appropriate, to guard against a 1:10,000 year anchoring damage event in accordance to Cable Burial Risk Assessment) methodology (Carbon Trust, 2015) where sufficient sediment existed.

3.2 Cable route

DeepOcean initially reviewed the GEOxyz geophysical data and the geotechnical data from Fugro 2016 to ground-truth the geophysical report and build a conceptual ground model. The cable corridor was then optimised and the route further surveyed by DeepOcean in 2018. The following items were considered in order of priority for route engineering:

- Permitted Operational Corridors.
- Avoidance of anchoring zones. An anchoring area was noted to be present to the south of the corridor. An exclusion boundary was drawn around the outside of this zone to ensure no operations were planned there.
- Avoidance of bedrock outcrops and minimisation of rock spans where possible.
- Avoidance of Archaeological excludion zones. A number of contacts with potential for archaeological content were identified. All the contacts had a 50m buffer applied to make sure that none of these buffers come within the cable corridor.
- No field infrastructure, crossings or boulders were reported to be within the corridor. Preliminary research indicated the UXO risk along the corridor to be very low.

The export cable route was designed from the Transition Joint Bay on land through the HDD westwards to the DMC. Approximately 8km consisted of subsea rock placement and ~9km corresponded to seabed trenching to a burial depth of 1.5m. Water depths along the route range from Landfall to a maximum of approximately -94m LAT.

The Cable Lay Vessel (CLV) OY Connector was used to support most offshore activities, namely rock and sandbags placement, cable lay and trenching activities. The Fall Pipe Vessel (FVP) Simon Stevin was used for the rock placement activities.

3.3 Landfall

HDD with forward reaming solution (drilling from onshore to offshore) was selected for the landfall with the use of HDI HK400 drilling rig (400t), Figure 3. The solution consisted of drilling an initial pilot hole, subsequently enlarged by a forward reaming operation, prior to the installation of a 24‘‘ steel pipeline through which the export cable was later on pulled-in.

Based on the findings from the offshore geophysical investigation, the initial HDD design trajectory was anticipated to cross an area of strongly fractured rock at exit point. The HDD trajectory was then adjusted to avoid this area and achieve an exit point 35m closer to shore.

Initial pilot hole with 12’’1/4 drill bit was aborted after 170m due to magnetic interferences afecting direction control. This pilot hole was plugged with cement grouting and abandoned. A second sucessfull pilot hole, approximately 625m long, was performed with a 9’’7/8 drill bit and with the assistance of a gyroscope to avoid magnetic interference.

Reaming was then performed in two steps, 26’’ performed to a length of 617m, and 36’’ performed to a length of 597m. Punch-out operations were performed following the same 26’’ and 36’’ drilling steps. First attempt was made with the drill bit and the 26’’ and 36’’ tools connected, in order to minimize amount of drilling fluid at sea. Shearing of a drill pipe occured during drilling; the contractor successfully engineered fishing gear to recover the drill bit, allowing to resume reaming with 26‘‘ and 36‘‘ performed separately.



Figure 3. Forward reamer and launching pit.

The final stage of the installation consisted of the installation of a 24’’steel pipeline welded on-site and pushed into the reamed hole. A messenger wire was installed at the completion of the job to allow later connection for the cable pull-in activities.

Due to the HDD exit changes to a shallower depth, approximately 40m cast iron half-shells (bend restrictors) were installed and connected to the HDD exit with diver support. Each section of half-shells incorporated a messenger wire connected to the main HDD pull in messenger wire. Thethered 4t rock bags filled with high density (3050 kg/m^3) angular quarry rock were placed over the shells to provide stability against combined wave and current loading under

extreme hydrodynamic conditions assumed for 1:50 year return period conditions.

3.4 Cable installation and protection requirements

3.4.1 Rocky seabed

A significant portion of the route along the rocky seabed involved placement of the cable on an irregular seabed with NNW-SSW ridges and NNE-SSW erosional channels, with anticipated cable free-spans. Pre-installation of rock bags and sandbags at pre-determined locations was adopted to provide support to the Export Cable, minimising free-spans along the lay route, Figure 4. After cable laying, the cable was mechanically protected by engineered rock placement.



Figure 4. Rock bags.

A Cable Protection System (CPS), consisting of half shells secured with carbon steel banding, was fitted to the portion of the cable to be laid in the rocky seabed during the cable spooling on the CLV carousel at Leixões Port in Portugal, with the purpose to provide abrasion and protection during rock placement operations.

For the cable section closer to the Port of Viana do Castelo anchorage (500-600m south of the cable route), the rock berm was designed to further protect the cable from anchoring associated with inclement weather conditions or anchor drifting in a northward direction, Figure 5. The rock berm was designed to protect against a 4000t vessel which based on the IACS rules would typically comprise an anchor of 1500kg.

Given the very low probability of an anchor strike of any size along the remaining of the cable route, assessed in the CBRA study, the rock berm design was governed by protection from fishing gear interaction and to maintain hydraulic stability.

Based on the varying governing design conditions along the route, the total rock placement length of the rocky area was subdivided into different sections, depending on the water depth. Two different rock gradings (LMA 5/40 and 1-8'') were adopted in combination with varying berm geometries and side slopes to obtain hydraulic stability. For the area adjacent to the anchorage area, a wider rock berm (1.5m) and a higher cover (total armour + cushion 1.5m) was adopted. A specific rock density of 3050kg/m³ (HD) was targeted.

For the shallowest section the rock installation placement was subject to the FPV draft limitations and was executed with the Inclined Fall Pipe system with the support of a survey support vessel. For the remainder of the rock placement scope the Fall Pipe ROV (FPROV) was used with survey systems onboard the FPV.

The rock material was mostly sourced from a quarry in the North of Spain, with some additional LMA5/40 material being sourced from Southwest Norway. The total rock weight required to create the berms protecting the cable was approximately 131,000t and involved 5 loadings at the Ferrol Port in Spain.



Figure 5. Rock berm construction operations (FPV).

3.4.2 Trenching in soil

The CBRA study concluded that there was a very low probability of an anchor strike along the buried section and the statistical analysis indicated that an unburied cable would be within REN specified target annual failure frequency of 1:10000 year. The recommended level of protection for the trenched section of the cable route was therefore governed by potential fishing gear interaction. Based on the shallow geological conditions along the route and on the varying penetration of different types of fishing gear in the region, a Minimum Depth of Cover (DoC) for protection against fishing of 0.5m was recommended by DeepOcean. For the trenching operations the following criteria was agreed:

- Target trench depth of 1.5m DoC, with results considered acceptable without further review for DoL between 1.0m and 1.5m.
- DoC between 0.5m and 1.0m: further review required between REN and DeepOcean to agree if further actions would be required based on a specific assessment of depth and lengths. This

was evidenced by an offshore field memo assessment of the TSS350 cable tracker survey results.

- DoC less than 0.5m: 2nd trenching pass required to try and achieve the above requirements.

During the pre-lay grapnel run (PLGR) along the proposed cable lay route, the grapnel train caught several fishing gear, long-lines and mono-filament tangle nets, which could prove hazardous for ROV operations during the cable lay and post-lay burial operations.

Cable trenching was completed between ~KP7.15 and ~KP16.4, with a transition zone between KP7.197 and KP7.212 where the cable was lowered into the seabed and also protected by extending the rock berm from the rocky section. From the start of trenching to approx. KP9 the trench depth was locally reduced due to the presence of bedrock within the trenching profile.

Considering the anticipated ground conditions and target burial objectives, DeepOcean selected their T1 tracked subsea jet-trencher, capable of independently loading and unloading laid product from the seabed, then digging a trench using hydraulic power whilst simultaneously burying the product behind it, Figure 6. The T1 was fitted with 3.5m jet swords which could extend to 2.2m below the seabed with the aim to lower the cable to target depth in one pass. An average speed of 200m/h was envisaged. The nozzle configuration was selected to optimise the trencher performance, with an output of 750m^3/h at 4 to 5bar.

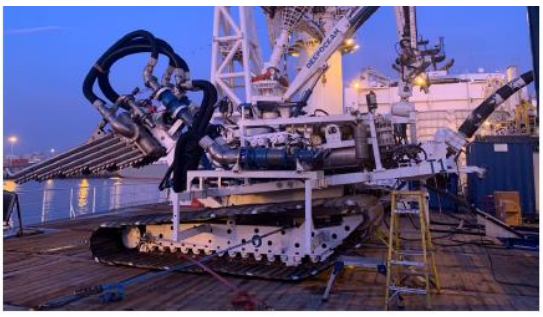

Figure 6. T1 DeepOcean Jet trencher.

Extremely low strength clay, with thickness between 0.40m and 0.6m, was noted at seabead between approx. KP14 and approx. KP15.3, overlying sand. For this section, trafficability was anticipated to be potentially difficult and several methods were employed to reduce the effective bearing pressure of the trencher and to maintain traction, namely through locking the trencher in the bullet, crane assistance to reduce the overall weight, and fitting of grousers.

At limited sections of the route, the DoC did not meet the requirements upon the trencher first pass. Following thorough review of results and consideration of potential risks and benefits of a second pass, limited sections of 1-8'' rock grading were installed to provide suitable cover where required.

At the western end of the static cable a transitioning out trenching profile was adopted until reaching the DMC position, Figure 7. A total of 31 2t rock bags were subsequently installed over the DMC and the area of exposed cable to the east of the DMC.



Figure 7. Dry-mate connector deployment.

4 CONCLUSIONS

This paper presented the experience and some lessons learned from the planning and construction of Portugal's first HVAC submarine +ower transmission cable, offshore Viana do Castelo. Operations included trenchless construction of the landing area, rocky seabed routing and free-span management, CPS fitting and deployment, rock berm construction, seabed trenching and DMC deployment and protection. The cable was successfully designed and installed and is currently operational.

ACKNOWLEDGEMENTS

The authors are grateful for REN permission to publish this paper.

REFERENCES

BS1377 (1990). Methods of test for soils for civil engineering purposes

Carbon Trust (2015). Cable Burial Risk Assessment Methodology: Guidance for the Preparation of Cable Burial Depth of Lowering Specification.

ISO 22476-1 (2022). Geotechnical Investigation and testing - Field Testing - Part 1: Electrical cone and piezocone penetration test.

Proceedings of the XVIII ECSMGE 2024
GEOTECHNICAL ENGINEERING CHALLENGES
TO MEET CURRENT AND EMERGING NEEDS OF SOCIETY
© 2024 the Authors
ISBN 978-1-032-54816-6
DOI 10.1201/9781003431749-658
Open Access: www.taylorfrancis.com, CC BY-NC-ND 4.0 license

ECSMGE 24
XVIII EUROPEAN CONFERENCE ON SOIL MECHANICS AND GEOTECHNICAL ENGINEERING

Residues' physical identification for soil-waste materials

Identification physique des résidus pour matériaux sol-résidus

A. Studart*
Civil Engineering and Architecture Department, University of Beira Interior, Covilhã, Portugal

L. Marchiori, A. Albuquerque, V. Cavaleiro, L. Andrade Pais
GeoBioTec, University of Beira Interior, Covilhã, Portugal

M.E.G. Boscov
University of São Paulo, São Paulo, Brazil

I. Strozberg
Centro Universitário Christus, Fortaleza, Brazil

**andre.studart@ubi.pt*

ABSTRACT: Climate change is demanding cleaner industrial processes besides new techniques. Waste materials, such as water treatment sludge (WS), biomass ashes (BA), mining wastes (MW), and iron slags (IS) are largely produced around the world from varied industrial activities, they represent a hazardous when incorrectly disposed due to contamination potential of soils and waters, highlighting the necessity to find new applications for them. Geotechnical engineering has been a major area for employing new materials to improve current methods. Regarding geotechnical applications, soils can have problems like high volumetric variation, high plasticity, and elevated water absorption/retention capacity, causing fissures, cracks, and low mechanical strength. Several researches have exposed the above-mentioned residues' value while improving overall aspects of the soils, successfully mitigating undesired characteristics, and making them feasible for geotechnical applications. Therefore, this paper aims to present and evaluate physical characteristics of residues alone, granular soils and mixtures of wastes-soils using varied introduction percentages of the residues into the soil, to assess their feasibility for improving the soil towards a geotechnical material for varied applications. Found results have shown all mixtures were considered as material for subgrade, according to AASHTO. Residues impacted the soil differently, WS, BA and MW led the granular soil to a finer material, while IS to a more granular material. Plasticity reduction up to 100% was achieved by WS, BA, and IS. Density was considerably increased by IS while MW sustained, and WS and BA have shown susceptibility into being light-weight materials.

RÉSUMÉ: Le changement climatique requiert l'adoption de nouvelles techniques. Les résidus, comme le boues de traitement de l'eau (WS), les cendres de biomasse (BA), les déchets miniers (MW) et les scories de fer (IS), sont générés partout le monde. Leur élimination inadéquate peut représenter un risque de contamination des sols et des eaux, soulignant la nécessité de trouver de nouvelles applications pour ces résidus. L'ingénierie géotechnique joue un rôle majeur dans l'utilisation de nouveaux matériaux pour améliorer les méthodes existantes. Les sols peuvent présenter des problèmes tels que des variations volumétriques élevées, une plasticité élevée, provoquant des fissures et une faible résistance mécanique. Diverses recherches ont révélé la valeur économique des résidus mentionnés, tout en améliorant les caractéristiques globales des sols, atténuant avec succès les caractéristiques indésirables et les rendant adaptés à des applications géotechniques. Cet article vise à présenter les caractéristiques physiques des résidus seuls, des sols granulaires et des mélanges de déchets-sols. Les résultats obtenus montrent que tous les mélanges sont considérés comme des matériaux appropriés pour les sols de fondation, selon les normes de l'AASHTO. Les WS, BA et MW transforment le sol granulaire en un matériau plus fin, tandis que les IS le transforment en un matériau plus granulaire. Une réduction de la plasticité allant jusqu'à 100% a été obtenue pour WS, IS et BA. La densité a été considérablement augmentée par les IS, tandis que les MW sont restés stables, et les WS et BA ont montré une propension à être des matériaux légers.

Keywords: Residues valorisation; geomechanical properties; circular economy; soil reinforcement.

1 INTRODUCTION

Society´s evolution requires a higher demand of natural resources to produce energy, treat the water for consumption, and create construction materials. Consequently, several residues tend to have their production to grow, due to the ever-growing demands, generating high amounts of industrial wastes. Some examples are water treatment sludges (WS), mining wastes (MW), iron slags (IS), and biomass ashes (BA)

from water treatment processes, mining activities, metallurgic and thermoelectrical industries, respectively. All of which are responsible for a large sum of these waste production while equally important for providing society the necessary resources.

Their production without a correct disposal can create several contamination problems due to the percolation of heavy metals and chemical contaminants, impacting soils and groundwater. Most of these residues are disposed in landfills, although this technique is land-consuming and could not be feasible in the long term, while demanding constant maintenance and representing a rupture risks or disasters, as in Brumadinho, Brazil (Salvador et al., 2020).

In 2016, IS generation was around 300 million tons only in China, although not reused (Guo et al., 2018). WS production in a water treatment plant (WTP) can reach up to 100.000 ton/year (Ahmad et al., 2016). MW production is estimated to be around 20 to 25 billion tons/year (Almeida et al., 2020). Although BA's exact production number is unknown, biomass is used for up to 10% of the world´s energy production, giving the magnitude order of waste generation (National Biodiesel Board, 2015).

Thus, the reuse of those residues emerges as a necessity for reducing world´s disposal and valorisation of waste materials. Regarding geotechnical engineering need for new materials, the application of waste-based materials can represent advantages for varied applications according to the wastes' characteristics.

Some soils tend to present undesired characteristics for geotechnical design, such as high volumetric variation, high water absorption-retention capacity, high plasticity, and low mechanical properties. Hence, considering the residues are materials produced by industrial processes, their introduction could mitigate these characteristics. Such characteristics are also due to the soil´s particle sizes distribution, causing variations in the particle's entanglement, water permeability and, hence, interaction of the soil skeleton within the system soil-water-air. Residues´ introduction could impact the soil skeleton, which can lead to an amelioration or enhancement of these mechanical properties.

Therefore, this paper characterizes physically four named residues, granular soils, and mixtures in varied percentages, to assess their impacts on physical properties.

2 MATERIALS AND METHODS

The tested materials were two granular soils – CB and O2 – and four industrial wastes – WS, BA, MW and IS. The soils were collected from a construction site in Castelo Branco, Portugal. The WS was collected from a WTP located in Guarda, Portugal. The BA and MW were collected in local companies from Castelo Branco and Guarda, Portugal, respectively, while IS was collected from a thermoelectrical plant in Alcochete, Portugal.

The chosen introduction ration of each residue was based on the dried masses percentages and consisted of 5, 10, 15 and 20% for WS with O2 soil while the same ratios were applicable for BA, but with CB soil. MW and IS were tested with 25 and 50% within CB soil. Mixtures were identified by the introduced percentage of the residue followed by the abbreviation of the residue.

Laboratorial geotechnical characterization was based in ISO 17892 for particle size distribution, specific gravity, and consistency limits.

3 RESULTS AND DISCUSSION

3.1 Physical identification

The analysed soils – O2 and CB – are sands with a small portion of silt and clay. O2 has a higher concentration of iron oxides´ concentration, while CB´s matrix corresponds to the region´s soil, majorly composed by schists, composed by feldspars and quartz minerals with muscovite presence and kaolinite for the clay-portion.

As for the residues, IS is highly granular, WTS and BA are silty sands, and MW is a silty-sand with low portion of clay particles. Their mineralogy are hard to assess as the several taken industrial process affect their overall characteristics and properties (Marchiori et al., 2021).

Figure 1 presents the particle size distribution of the analysed soils, residues and optimal mixtures, considered as the ones that had better workability.

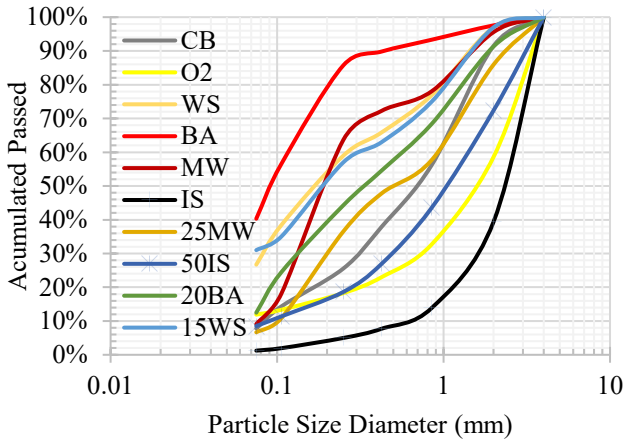

Figure 1. Particle size distribution curves.

According to USCS, both soils were characterized as silty sands. The residues vary in classification, BA, MW and WS, for example, are also classified as silty-sands, although their fine range varies considerably. Besides, IS is a well-graded gravel. Table 1 below synthetizes comparison between USCS and AASHTO classification for all materials.

Table 1. Particle size parameters.

Samples	AASHTO	USCS
O2	A-2-4	SW-SM
CB	A-2-4	SW-SM
WS	A-2-4	SW-SM
15WS	A-2-5	SW-SM
BA	A-4	SM
20BA	A-2-5	SM
MW	A-2-6	SM-SC
25MW	A-2-6	SM
IS	A-1-b	GW
50IS	A-1-b	SW-SM

Thus, both soils are well-graded sands containing silts. Each residue impacts the soil differently, BA is the finest material, being classified as a fair to poor material for subgrade application, according to AASHTO. Through USCS, BA´s granulometry is more characteristic of silty materials, causing the optimal mixture being classified as silty-sand (SM). WS is also majorly fine, although the mixture is still classified as well graduated sand with a fine portion.

MW is the residue with highest plasticity, pushing the mixtures to behave like a finer material. IS tends to push the mixture´ classification towards a more granular material. It is important to reiterate that such standards consider the analysed material as soils. Therefore, the results here exposed are an approximation of residues being treated as soils for their classification.

In addition, all the mixtures had a classification of "excellent to good" for subgrade application based on AASHTO. To further assess the impacts on the soil behaviour, Table 2 below presents specific gravity (Gs) and Atterberg limits.

MW was the only residue workable enough to do the Atterberg limits. IS lacked cohesion between the particles, while the workability of WS and BA were very low and thus, hard to properly execute the test.

Nevertheless, WS and BA tended to reduce the overall density of the mixture. MW does not seem to impact the density of the soil, although it increases its plasticity. IS is much heavier than the soil, mostly due to the high content of iron oxides, although it does not have plasticity due to its granular size. Such results indicate that WS, BA and IS can reduce plasticity, while MW could contribute for the plasticity maintenance.

Table 2. Specific gravity and Atterberg limits values.

Samples	Gs	W_L	W_P	PI
O2	2.75	35	27	8
CB	2.73	30	21	9
WS	2.00	-	-	-
15WS	2.63	42	39	3
BA	2.36	-	-	-
20BA	2.62	45	NP	NP
MW	2.63	37	25	12
25MW	2.61	37	26	11
IS	3.58	-	-	-
50IS	2.98	NP	NP	NP

Specific gravity values also could indicate the feasibility of WS and BA as light-weight material generation, while MW does not seem to impact the overall density. On the other hand, IS could lead to a harder workability and material development due to its high density.

4 CONCLUSIONS

Found results have indicated WS, MW, IS and BA are susceptible for introduction with different ratios into soils.

WS, BA and MW have led the soil to a finer material while IS led to a more granular material. Although WS and BA are finer, they seem not to contain any clayey properties, as no plasticity was found. Reduction of plasticity was achieved up to 100% for all residues, except MW which contributed for a slightly more plastic behaviour.

The major impact was on the particles´ density, being IS the one that had the highest impact, and which could affect a product or material IS-based due to its

heavy weight and possible hard workability that could difficult logistics.

Such results are part of an on-going investigation of these residues for soils´ reinforcement and liner application, which more tests shall be conducted and replicated *in-situ*, when possible, for further characterization and validation.

ACKNOWLEDGEMENTS

The authors acknowledge the companies for providing the soils and wastes here-described, namely João Tomé Saraiva, and Grupo Valor. Also, the University of Aveiro for providing the necessary support on the on-going investigation. The research was supported by national funds within UIDB/00195/2020 (FibEnTech) and UIDB/04035/2020 (GeoBioTec) projects, both funded by the Foundation for Science and Technology (FCT), Portugal.

REFERENCES

Ahmad, T., Ahmad, K., and Alam, M. (2016). Sustainable management of water treatment sludge through 3'R' concept. *Journal of Cleaner Production*, *124*, 1–13. https://doi.org/10.1016/j.jclepro.2016.02.073.

Almeida, J., Ribeiro, A. B., Silva, A. S., and Faria, P. (2020). Overview of mining residues incorporation in construction materials and barriers for full-scale application. *Journal of Building Engineering*, *29*(January), 101215. https://doi.org/10.1016/j.jobe.2020.101215.

Andrade Pais, L. (2007). *Comportamento Mecânico do Solo Residual Granítico da Covilhã com Efeito de Contaminantes*. Universidade da Beira Interior.

Carter, M., and Bentley, S. P. (1991). Correlations of soil properties. In *Correlations of soil properties*.

Guo, J., Bao, Y., and Wang, M. (2018). Steel slag in China: Treatment, recycling, and management. *Waste Management*, *78*, 318–330. https://doi.org/10.1016/j.wasman.2018.04.045.

Marchiori, L., Morais, M.V., Albuquerque, A., and Cavaleiro, V. (2023a). Geotechnical Characterization Methodology of Water Treatment Sludge for Production of Liner Material. *Lecture Notes in Civil Engineering, 370 LNCE,* pp. 461-470. https://doi.org/ 10.1007/978-981-99-4041-7_41.

Marchiori, L., Albuquerque, A., and Cavaleiro, V. (2023b). Water Treatment Sludge as Geotechnical Liner Material: State-of-Art. *Lecture Notes in Civil Engineering, 370 LNCE,* pp. 529-547. https://doi.org/ 10.1007/978-981-99-4041-7_47.

Marchiori, L., Studart, A., Morais, M.V., Albuquerque, A., and Cavaleiro, V. (2023c). Geotechnical Characterization of Vegetal Biomass Ashes Based Materials for Liner Production. *RILEM Bookseries, 41,* pp. 67-82. https://doi.org/ 10.1007/978-3-031-29191-3_6.

Marchiori, L., Studart, A., Albuquerque, A., Pais, L. A., Boscov, M. E., and Cavaleiro, V. (2022a). Mechanical and Chemical Behaviour of Water Treatment Sludge and Soft Soil Mixtures for Liner Production. *The Open Civil Engineering Journal*, *16*(1). https://doi.org/10.2174/18741495-v16-e221115-2022-27.

Marchiori, L., Albuquerque, A., and Cavaleiro, V. (2022b). Granitic Mining Waste Feasibility for Liner Material Production. *World Cngress on Civil, Structural, and Environmental Engineering, CSEE 2022.* https://doi.org/ 10.11159/iceptp22.203.

Marchiori, L., Studart, A., Alburquerque, A., Cavaleiro, V., Almeida, P. G., Boscov, M. E. G., and Andrade Pais, L. (2021a). A substituição de geossintéticos e solos através da valorização de resíduos de estação de tratamento de água em obras de terra. *17CNG - Congresso Nacional de Geotecnia*.

Marchiori, L., Studart, A., Albuquerque, A., Cavaleiro, V., and Silva, A. (2021b). Geotechnical characterization of water treatment sludge for liner material production and soft soil reinforcement. *Materials Science Forum, 1046,* p. 83-88. https://doi.org/ 10.4028/www.scientific.net/MSF.1046.83.

National Biodiesel Board, U. (2015). Introduction to Biodiesel and Glossary of Terms. In *Bioenergy* (pp. 37–40). Elsevier. https://doi.org/10.1016/B978-0-12-407909-0.00002-X.

Salvador, G. N., Leal, C. G., Brejão, G. L., Pessali, T. C., Alves, C. B. M., Rosa, G. R., and Montag, L. F. de A. (2020). Mining activity in Brazil and negligence in action. *Perspectives in Ecology and Conservation*, *18*(2), 139–144. https://doi.org/10.1016/j.pecon.2020.05.003.

Studart, A., Marchiori, L., Albuquerque, A., Cavaleiro, V., Boscov, M. E. G., Rocha, F., and Silva, E. F. (2023). *Geotechnical comparison of water treatment sludge and biomass ashes for soft soils ' application : A greener approach analysis*. https://doi.org/10.53243/ICEG2023-268.

Studart, A., Marchiori, L., Morais, M.V., Albuquerque, A., Cavaleiro, V., Boscov, M. E., and Strozberg, I. (2023). Assessment of iron slag properties for granular soil reinforcement. In *WASTES: Solutions, Treatments and Opportunities IV*.

Proceedings of the XVIII ECSMGE 2024
GEOTECHNICAL ENGINEERING CHALLENGES
TO MEET CURRENT AND EMERGING NEEDS OF SOCIETY
© 2024 the Authors
ISBN 978-1-032-54816-6
DOI 10.1201/9781003431749-659
Open Access: www.taylorfrancis.com, CC BY-NC-ND 4.0 license

ECSMGE 24
XVIII EUROPEAN CONFERENCE ON SOIL MECHANICS AND GEOTECHNICAL ENGINEERING

One dimensional static and dynamic compression behaviour of foam glass aggregate

Comportement en compression statique et dynamique unidimensionnel des granulats de verre mousse

J. Szendefy*
Budapest University of Technology and Economics, Faculty of Civil Engineering, Department of Engineering Geology and Geotechnics, Budapest, Hungary

W.S. Mustafa
Budapest University of Technology and Economics, Faculty of Civil Engineering, Department of Engineering Geology and Geotechnics, Budapest, Hungary, and Department of Survey, Akre University for applied science, Kurdistan Region, Iraq

**szendefy.janos@emk.bme.hu; waleed.sulaiman@auas.edu.krd*

ABSTRACT: Foam Glass Aggregate (FGA) has a wide particle size distribution, in addition to being lightweight and thermally insulating, which extends its potential applications to various infrastructure and construction purposes. For infrastructure projects, it can be used as a lightweight backfill material, allowing the use of soil-improvement methods to be dispensed with in soft subsoils. In buildings, it can be used as thermal insulation under floors, thus helping to improve the energy efficiency of buildings. It acts as a static load for building and earthwork structures, while vehicles or forklift cyclic loads act in case of pavements and industrial floors. It is essential to investigate the effect of different compaction ratios in order to ensure efficient use of materials. In this study, the effects of different compaction ratios (10%, 20%, 30% and 40%) on the elastic modulus (Eoed) and dynamic parameters (Resilient modulus) of the material were investigated. For cyclic loads, elastic and plastic deformations were separated to determine the short and long term behaviour of the material. Different deviator stresses were operated on the FGA for both static and cyclic loads. The results were evaluated by comparing the behaviour of FGA under static and cyclic loads.

RÉSUMÉ: L'agrégat de verre mousse (FGA) a une distribution granulométrique élevée, en plus d'être léger et thermiquement isolant, ce qui étend ses applications potentielles à diverses fins d'infrastructure et de construction. Pour les projets d'infrastructures, il peut être utilisé comme matériau de remblai léger, ce qui permet de renoncer au recours à des méthodes d'amélioration des sols dans les sous-sols mous. Dans les bâtiments, il peut être utilisé comme isolant thermique sous les planchers, contribuant ainsi à améliorer l'efficacité énergétique des bâtiments. Il agit comme une charge statique pour les structures de bâtiments et de terrassement, tandis que les charges cycliques des véhicules ou des chariots élévateurs agissent dans le cas des trottoirs et des sols industriels. Il est essentiel d'étudier l'effet de différents taux de compactage afin de garantir une utilisation efficace des matériaux. Dans cette étude, les effets de différents taux de compactage (10%, 20%, 30% et 40%) sur le module élastique (Eoed) et les paramètres dynamiques (module de résilience) du matériau ont été étudiés. Pour les charges cycliques, les déformations élastiques et plastiques ont été séparées pour déterminer le comportement à court et à long terme du matériau. Différentes contraintes de déviation ont été appliquées sur le FGA pour les charges statiques et cycliques. Les résultats ont été évalués en comparant le comportement du FGA sous charges statiques et cycliques.

Keywords: Foam glass aggregate; thermal insulating material; oedometric modulus; resilient modulus; industrial floor.

1. INTRODUCTION

The foam glass aggregate (FGA) is a new material in Hungary. Foam glass was produced from the 1930s, but it appeared in aggregate form only around the 2000s. The material is popular in the Scandinavian countries, Switzerland and the USA. In the Scandinavian countries, it is used to reduce the depth of frost penetration under road pavements, while in other places it is used as a light material filling in road and railway construction, as well as for the construction of heat-insulating bedding under industrial floors. During the production of FGA, the material is suddenly cooled, so internal stresses arise in it. Due to these internal stresses, it is broken into

more or less regular particles of the same size at the end of the manufacturing process.

Its advantageous feature is its durability. Since it does not age, regardless of environmental effects, it behaves in the same way as it did at the time of installation, even years after its installation, in terms of both its physical and chemical properties. Therefore, the material is not collapsing over time, such as polystyrene insulation materials.

Another beneficial feature - it's true that it's only the XXI. became an important aspect in the 19th century - that it is environmentally friendly. It can be produced from waste materials with low energy investment and can be recycled almost endlessly. In addition, it does not react with its environment, so no environmentally harmful substances are released from it.

Having the material's stiffness is essential for construction and infrastructure design purposes. The static and dynamic moduli are used as a design parameter to show the possibility of using the material under the impact of static and dynamic loads. In this regard, many types of recycling and manufacturing aggregates have been studied due to the increasing interest, high cost, and limited supply of high-quality naturally occurring aggregates that satisfy thermal insulation properties and get more sustainable environmental conditions. In recent years the possibility of using various types of recycled construction and demolition materials in road embankments and pavement applications such as recycled concrete (Jitsangiam et al., 2015), recycled crushed glass (Mohajerani et al., 2017) and foam glass aggregate (Arulrajah et al., 2015; Lenarta and Kaynia, 2019; Mustafa et al., 2022; Mustafa and Szendefy, 2023; Swan, Seungcheol Yeom, et al., 2016; Szendefy and Huszák, 2019) has been investigated.

The lightweight characteristics of such materials are typically due to the substantial part's low unit weight and large amounts of interconnected or nonconnected pores (Scheffler and Colombo, 2005). Different types of lightweight materials are used in civil engineering applications, including lightweight clay aggregate (Ayati et al., 2018), and foam glass aggregate (Emersleben and Meyer, 2014).

Regarding infrastructure constructions, vertical loads on soft subgrades can be reduced by using lightweight fill materials such as FGA as an alternative and in addition to bearing capacity improvement techniques (Emersleben and Meyer, 2014). FGA, as a lightweight construction material, can be used in many applications such as retaining walls, road embankments, bridge abutments, and slope stability (Szendefy et al., 2020). FGA has several technological benefits, including low density, high strength, thermal insulation, frost resistance, fire resistance, rat resistance, acoustic insulation, non-toxicity, low water absorption, and short constructing time (Hurley, 2003).

Although FGA is considered a beneficial construction material, limited studies are available on the static and dynamic behavior of the material. Therefore, more extensive research is needed to understand the factors influencing the material response under static compressional and cyclic loadings, especially the impact of different compaction ratios due to broad grain size distributions. According to the findings of (Swan, Yeom, et al., 2016), FGA has unbound compressibility behaviour. Regarding FGA, Ghafari et al. (2019) studied the resilient modulus under repeated deviatoric loads in a triaxial apparatus following the standard (AASHTO T 307-99, 2007) for the granular base and subbase materials with some particular adaptations to prepare the samples in a small triaxial scale. They concluded that the FGA resilient modulus was higher for the bigger particle size range of 20-31.5mm (Mr=150MPa) than the smaller one of 0-31.5mm (Mr= 120MPa). Depending on big-scale triaxial tests with monotonic and cyclic loading, Lenarta and Kaynia (2019) studied the properties of FGA, focusing on the stiffness and damping properties of the material. They observed a high initial stiffness, a small elastic threshold strain, and a significant modulus reduction in the first cyclic loading stage compared to other natural materials referring to a brittle structure component.

This study investigated the impact of different compaction ratios (10%, 20%, 30%, and 40%) on static and dynamic stiffness as well as the elastic and plastic strains the cyclic behavior of FGA. To determine the static compressional modulus of FGA series of loads started from 50 kPa to 300 kPa with 50 kPa intervals were applied. A sequence of uniaxial deviatoric stresses (25kPa, 100kPa, and 200kPa) with various cycle numbers were applied to the material samples. Due to the availability of high amounts of internal pored which was 92.7% for the studded FGA, this may lead to severe accumulated strains; therefore, the effect of compaction ratio and cycle numbers on accumulated plastic strains (ε_{acc}) behavior of the material have been evaluated. The resilient modulus at various compaction ratios was calculated to show the impact of elevated compaction ratios. Furthermore, this study presents a comparison between the ε_{acc} values obtained from the dynamic test and the vertical strains obtained from the static compressional test (oedometer test).

2. MATERIAL AND METHODOLOGY

2.1 Material

For the present study, the used FGA material produced by a Hungarian company has a grey color, broken-edge surface like crushed stone, while its bulk density without any compaction is around 170 kg/m3.

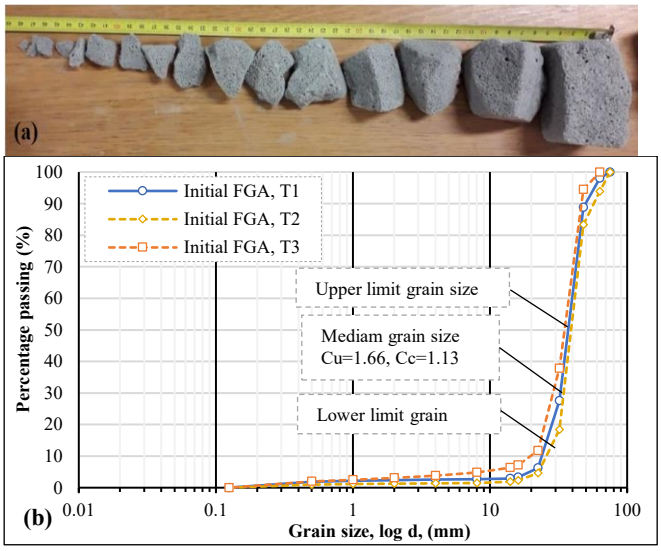

Figure 1. a) Foam glass aggregate, b) grain size distribution curve of FGA.

The material mainly contained gravel-sized particles, as shown from the particle size distribution curve of the received FGA. The initial FGA has a coefficient of uniformity Cu=1.66 and a coefficient of curvature Cc=1.13, which makes the material classified as poorly graded based on the USCS classification system, with one primary grain size range of 10-60 mm. The initial FGA material underwent over ten tests to determine its grain size distribution. However, for the purpose of clarity, only three key trials displaying significant differences in their distribution curves are included in Figure 1 (a, and b).

2.2 Methodology

A customized testing setup specifically designed for conducting static compression tests on foam glass aggregate (FGA). Since utilizing a conventional geotechnical apparatus for static compression tests on FGA samples is not feasible due to the impracticality of accommodating the individual particle size, which may exceed the conventional sample size range of 10 to 60 mm in diameter (Mustafa et al., 2022). Therefore, a cylindrical steel frame was constructed adheres to the 5D (largest particle diameter) size criterion. FGA was compacted into the mold by one layer at both 10% and 20% compaction ratios, while to reach the 30% and 40% compaction ratios the material was compacted into the mold in two layers using a heavy load plate. During the static compression test different series of static loads was tested starts at 50 kPa to 300 kPa with 50 kPa intervals were applied on samples To reach each compaction ratio, the initial FGA has been compacted into the mold till the desired mass per volume has been obtained. The 10% ration means the density is 10% higher as the origin bulk, while the weight is 20% more in case of 20% and etc.. Each loading stage was performed to the vertical strain reached the 0.01 mm/min strain value. During the tests, five trials were conducted on FGA samples to show the diversity.

To do the uniaxial dynamic compression test on the material in oedometric condition (fully side restrained) two load types of vertical stresses have been applied to FGA samples. First, a sustained conditioning load (25 kPa) was applied to the samples to represent the self-weigh of the pavement and capping layers. Then, depending on the stress distribution profile of road application sections under the pavement where FGA can be used as filling material, three different values of cyclic deviatoric vertical stresses (25 kPa, 100 kPa, 200 kPa) were selected to generate the effect of the repeated moving traffic loads. Where, the 200 kPa represent the stress at the top of the base layer, 100 kPa is at bottom of the base layer, while 25kPa is a general load in the embankment. Besides the selected deviatoric stresses, various cycle numbers have also been selected. For all compaction ratios and under the impact of 25 kPa and 100 kPa the samples were loaded for 40,000 cycles while under the impact of 200kPa the samples were loaded for 100,000 cycles. The selected cyclic stresses have been applied to the samples sequentially after the desired number of cycles has been reached.

Furthermore, because FGA contains a high amount of pores according to the nature of the structural composition of the material, in the case of the used FGA, it was 92.7%; also, there were a high amount of void ratios between the particles in their bulk condition due to the big particle size nature of the material. Therefore, the impact of long-term cycle stresses on the dynamic behavior of the material has been investigated in this study. An electro-hydraulic actuator with a 100 kN capacity was used in the axial loading condition. To measure the vertical strain (ε), a pair of linear variable displacement transducers (LVDTs) were placed on both sides at the top of FGA samples. The applied cyclic load frequency in the one-way dynamic compressional test was set to be 1.0 Hz simulating traffic loads on the roads.

3. RESULTS AND DISCUSSION

3.1. Static compressional modulus

Based on the stress-strain curves obtained from the static compressional tests conducted on five to eight FGA test samples, the compressional modulus (E_{oed}) values have been calculated. The mean values the E_{oed} under varying compaction ratios and static compressional loads ranging from 50 kPa to 300 kPa with 50 kPa intervals are presented in Table 1.

Table 1. Calculated values of Eoed (MPa) for all loading steps and compaction ratios.

Comp. ratio (%)	E_{oed} (MPa) Applied loads (kPa)					
	50	100	150	200	250	300
10	7.5	8.5	8.0	6.0	5.0	4.0
20	9.5	12.5	14.0	15.0	15.5	13.0
30	8.5	11.0	13.5	15.5	17.5	19.0
40	10.0	14.5	17.5	19.5	21.5	23.0

According to the Table 1, it is strange that the oedometric modulus was decreasing in 10% and 20% compaction ratios, while in 30% and 40% compaction ratios, the oedometric modulus continued to increase under all tested compressional loads. These findings indicate that the material at lower compaction ratios (10% and 20%) became progressively softer with higher compressional loads. Conversely, the consistently elevated oedometric modulus values suggest that the material exhibited stiffness and stability similar to conventional soils like sandy soil, which hardens. This implies that the material could be considered for geotechnical applications under similar loading conditions by providing the valuable insights for geotechnical engineers in selecting suitable compressional modulus for specific projects or applications.

As appears from the results of Table 1, the oedometric modulus of the examined FGA at 10% compaction and under the impact of 50kPa was about 7.5 MPa then it raised up to 23 MPa when compacted by 40% under the impact of 300 kPa. In this regards, the present study results is in harmony with the study of Steurer Steurer (2012) conducted a comprehensive study involving large-scaled and oedometric laboratory compression tests to investigate the load-deformation behavior of foam glass aggregates. According to his study finding, by rising the compaction ratio from 10% to 25% an increase in the stiffness modulus was also appeared. Additionally, Steurer (Steurer, 2012) observed a higher stiffness modulus compared from the long-term confined compression test ranging from 30 MPa to 43 MPa under the same compressional stress impact compared to the of the present study ranging from 100 kPa to 300 kPa. According to the authors' perspective, the higher compressional modulus observed in the mentioned study can be attributed to the greater compressive strength of the foam glass aggregate grains, which was measured at 2100 kPa. In our case, the compressional strength was approximately 1200 kPa.

3.2 Resilient modulus

The Mr values of FGA samples at different compaction ratios and under various deviatoric stresses are shown in Figure 2.

As it can be seemed from Figure 2 the decrease in Mr value was appeared parallel with an increase in the amount of compaction ratios from 10% to 40%. This considered a reverse behavior compared to other geomaterials. According to the study of Liu et al. (2019) which has been executed on dynamic and static resilient modulus of six types of sub-grade soils. They observed that dynamic and static resilient modulus was positively related to increasing the compaction degree and increased the amount of dynamic, resilient modulus by about 21%-26% when the compaction degree elevated from 90% to 93%. This behavior of FGA may be related to the impact of extra applied compaction energy to get the desired compaction ratio, which affects the material's dynamic response. FGA is considered a fragile material; this reality was practically observed by previous scholars (Lenart and Kaynia, 2019), making the material particles behave in a brittle condition under the effect of impact actions that happened during the sample preparation process. At a low compaction ratio, the material subjected to a lower amount of compaction energy saves the manufacturing properties of the particles connected at small connection areas. While to reach a high compaction ratio, a much higher amount of impact compaction energy was applied over the samples of FGA, leading to an increase in the connection area between the particles. Although, the overall skeleton of the material became stiffer to resist the applied external stresses due to better interlocking. But on the other hand, under the impact of high compaction energy, the walls, and the struts of the pores at the connection areas of FGA particles locally (completely or partially) failed and led to collect microfine deposits between the connection areas of the particles. This reality was observed clearly during the experimental work when the material was taken out from the molds. Therefore, the particles of the material were only crushed under the effect of applied impact compaction at the connection areas when the maximum strength was generated. In this regard Mustafa et al. (2022) observed from the density and porosity analysis of

foam glass material and foam glass aggregates that the total voids decreased by 4.8% compared to the material density and by 3% compared with as received bulk density after compacting FGA by 40% compaction. These were because of a decrease in the void ratios and the micro- or macropores crushing under the impact of the elevated impact compaction process. As a result, due to the material's lightweight properties, the particles' connected area behaved like a micro spring when subjected to cyclic loads and made the material gain some extra elastic recoverable strain. Since the same equation (2) was used during the calculation process for all compaction ratios, a less resilient modulus was obtained when the compaction ratio elevated due to a bigger amount of recoverable elastic strain.

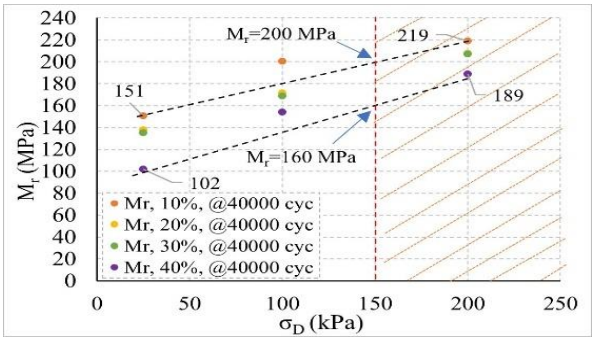

Figure 2. Boundary limits of the resilient modulus of FGA at different compaction ratios.

3.3 Elastic and plastic vertical strains

The results which obtained from both of static and uniaxial cyclic test that applied at the same boundary conditions (oedometric test) and compaction ratios (10%, 20%, 30%, and 40%) on FGA samples are presented in Figure 3. Since all samples were subjected to the same amount of loads starting from 50kPa to 300kPa with 50 kPa. Therefore, the evaluations have been made between amounts of total vertical strains obtained from both of static and dynamic tests.

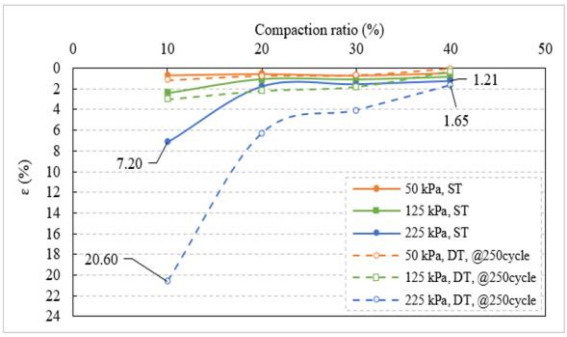

Figure 3. Effect of static and one-dimensional dynamic compression loads at various compaction ratios after 250cycles at 40,000cycle.

As appeared from Figure 3, the vertical strain exhibited by FGA in both static and uniaxial dynamic tests displayed a similar pattern of improvement. The dynamic test showed a greater disparity in strain values at lower compaction ratios of 10% and 20%, with an increase of around 15%. However, this disparity was reduced at higher compaction ratios of 30% and 40%, resulting in a difference of approximately lower than 3% at the same applied load. This condition was observed after deducting the amount of settlement obtained at the beginning 250cycles for both 30%, and 40%. This condition obtained in site under the impact of construction machine and before starting the real service life of the material as a construction material. This result considered very valuable for the practical purposes since it is more convenient to rely on static tests rather than dynamic tests to determine the final vertical strains, because static tests are easier to execute and analyse.

4. CONCLUSIONS

FGA is an extremely innovative material made from recycled glass waste. The material is durable and resistant to environmental effects, so it can be used in structures under the ground. Due to environmental protection requirements, it is a good technical solution for the thermal insulation of the underground parts of buildings, and it is also possible to reduce the amount of primary aggregate used in these places. As a light filling material, in the case of roads passing through soft, organic soils, it can be used as a filling material to avoid costly embankment foundations, which is also more beneficial from an environmental point of view. In contrast, retaining structures have advantages, where the reduction of lateral earth pressure can reduce the cross-section of structures.

When designing these structures, it is essential to know the strength characteristics of FGA. The oedometric modulus of the FGA was determined with laboratory measurements.

The compression modulus of the FGA was determined with laboratory measurements under different compaction conditions. The test results (elastic modulus) illustrated that at 10% and 20% compaction ratios, the material shows behavior similar to compressible soils, while at 30% and 40% compaction ratios, it can already provide the properties of good soils, such as sand and gravely sand soils. Based on the cyclic load tests, the material is also sufficiently resistant to dynamic loads, so it can also be designed for cyclic loads caused by vehicles using the Mr value determined by our measurements.

By comparing the settlements caused by static and dynamic loads, it was seen that the FGA is not sensitive to cyclic loading. It does not develop a larger settlement under cyclic loading in the long term than if it were statically loaded with the same pressure.

REFERENCES

AASHTO T 307-99. (2007). Standard method of test for determining the resilient modulus of soils and aggregates. Washington D.C.

Arulrajah, A., Disfani, M. M., Maghoolpilehrood, F., Horpibulsuk, S., Udonchai, A., Imteaz, M., & Du, Y. J. (2015). Engineering and environmental properties of foamed recycled glass as a lightweight engineering material. *Journal of Cleaner Production*, *94*, 369–375. https://doi.org/10.1016/j.jclepro.2015.01.080.

https://doi.org/10.1016/j.ceramint.2012.12.104.

Ayati, B., Ferrándiz-Mas, V., Newport, D., & Cheeseman, C. (2018). Use of clay in the manufacture of lightweight aggregate. *Construction and Building Materials*, *162*, 124–131. https://doi.org/10.1016/j.conbuildmat.2017.12.018

Emersleben, A., & Meyer, M. (2014). Sustainable pavement construction by the use of recycled glass. *International Journal of Geotechnical Engineering*, *8*(4), 436–440. https://doi.org/10.1179/1939787913Y.0000000030.

Ghafari, N., Segui, P., Bilodeau, J. P., Côté, J., & Doré, G. (2019). Assessment of mechanical and thermal properties of foam glass aggregates for use in pavements. *2019 TAC-ITS Canada*, *April 2020*, 1–18. https://www.tac-atc.ca/en/conference/papers/assessment-mechanical-and-thermal-properties-foam-glass-aggregates-use-pavements

Hurley, J. (2003). A UK market survey for foam glass. *Wrap*, *June 2002*, 114.

János, S., Zoltán, B., Kristóf, L., & Mustafa, W. S. (2020). Az üveghab-granulátum útépítésben való alkalmazásának vizsgálata. *Útügyi Lapok*, *8*(14), 88–104. https://doi.org/10.36246/ul.2020.2.06.

Jitsangiam, P., Boonserm, K., Phenrat, T., Chummuneerat, S., Chindaprasirt, P., & Nikraz, H. (2015). Recycled Concrete Aggregates in Roadways: Laboratory Examination of Self-Cementing Characteristics. *Journal of Materials in Civil Engineering*, *27*(10), 04014270. https://doi.org/10.1061/(asce)mt.1943-5533.0001245.

Lenart, S., & Kaynia, A. M. (2019). Dynamic properties of lightweight foamed glass and their effect on railway vibration. *Transportation Geotechnics*, *21*(May), 100276. https://doi.org/10.1016/j.trgeo.2019.100276.

Lenarta, S., & Kaynia, A. M. (2019). Dynamic properties of lightweight foamed glass and their effect on railway vibration. *Transportation Geotechnics*, *21*(August), 100276. https://doi.org/10.1016/j.trgeo.2019.100276.

Mohajerani, A., Vajna, J., Cheung, T. H. H., Kurmus, H., Arulrajah, A., & Horpibulsuk, S. (2017). Practical recycling applications of crushed waste glass in construction materials: A review. *Construction and Building Materials*, *156*, 443–467. https://doi.org/10.1016/j.conbuildmat.2017.09.005.

Mustafa, W. S., Nagy, B., & Szendefy, J. (2022). Impact of Compaction Ratio, Loading Period and Environmental Condition on Compressional Behavior of Foam Glass Aggregate. *Construction and Building Materials*, *343*(June). https://doi.org/10.2139/ssrn.4004683.

Mustafa, W. S., & Szendefy, J. (2023). Uniaxial dynamic behavior of foam glass aggregate under oedometric (fully side restrained) condition at different compaction ratios. *Construction and Building Materials*, 2023.

Scheffler, M., & Colombo, P. (2005). Cellular Ceramics: Structure, manufacturing, properties and applications. *Wiley-VCH Verlag GmbH & Co. KGaA, Weinheim*, 669.

Steurer, A. (2012). *Behavior of foam glass aggregate under static loads*. 60824. http://hdl.handle.net/20.500.12708/60824.

Swan, R. H., Seungcheol Yeom, Sjoblom, K. J., Stark, T. D., & Filshill, A. (2016). Engineering Properties of Foamed Recycled Glass as a Lightweight Fill. *Annual Book of ASTM Standards*, 11–22. https://doi.org/10.1061/9780784480151.002.

Swan, R. H., Yeom, S., Sjoblom, K. J., Stark, T. D., & Filshill, A. (2016). *Engineering Properties of Foamed Recycled Glass as a Lightweight Fill*. 11–22. https://doi.org/10.1061/9780784480151.002.

Szendefy, J., Huszák, T. (2019). Geotechnical characterization of foamglass aggregate. 17th European Conference on Soil Mechanics and Geotechnical Engineering, ECSMGE 2019 - Proceedings, 2019-Septe. https://doi.org/10.32075/17ECSMGE-2019-0589.

Liu, X., Zhang, X., Wang, H. B. J. (2019). Laboratory testing and analysis of dynamic and static resilient modulus of subgrade soil under various influencing factors. 195, 178–186. https://doi.org/doi.org/10.1016/j.conbuildmat.2018.11.061.

Proceedings of the XVIII ECSMGE 2024
GEOTECHNICAL ENGINEERING CHALLENGES
TO MEET CURRENT AND EMERGING NEEDS OF SOCIETY
© 2024 the Authors
ISBN 978-1-032-54816-6
DOI 10.1201/9781003431749-660
Open Access: www.taylorfrancis.com, CC BY-NC-ND 4.0 license

ECSMGE 24
XVIII EUROPEAN CONFERENCE ON SOIL MECHANICS AND GEOTECHNICAL ENGINEERING

Impact of stiffness properties and overconsolidation on the lateral behaviour of monopile foundations in clay deposits

Impact des propriétés de rigidité et de surconsolidation sur le comportement latéral des fondations monopieux dans les massifs argileux

D.M.G. Taborda*, A. Tsiampousi
Imperial College London, London, United Kingdom

K. Georgiadis
Aristotle University Thessaloniki, Thessaloniki, Greece

d.taborda@imperial.ac.uk

ABSTRACT: The adoption of advanced constitutive models based on the Critical State Soil Mechanics framework present both advantages and challenges. The former are well established and relate to improvements in accuracy and, due to the frequent use of the framework in explaining soil behaviour, a calibration process which is frequently simpler. However, their use in modelling of clays means that consistency between different soil properties, such as undrained shear strength and overconsolidation ratio, needs to be insured. The application of one of such models is explored in this paper in the context of offshore foundations. The influence on the lateral capacity of the foundations of different profiles of undrained shear strength, a property which is not prescribed but rather interpreted from the model parameters and initial conditions, is shown to be substantial at all values of displacement. Similarly, the use of a highly non-linear model for the shear stiffness is explored and the impact of the associated parameters is observed to be confined to the lateral stiffness of the monopile under small lateral loads.

RÉSUMÉ: L'adoption de modèles constitutifs avancés basés sur la mécanique des sols à l'état critique présente des avantages et des défis. Les premières sont bien établies et concernent l'amélioration de la précision et, en raison de l'utilisation fréquente de la mécanique des sols à l'état critique pour expliquer le comportement du sol, il est plus facile de calibrer le modèle de sol. Cependant, leur utilisation dans la modélisation des argiles signifie que la cohérence entre les différentes propriétés du sol, telles que la résistance au cisaillement non drainée et l'état de surconsolidation, doit être assurée. L'application de l'un de ces modèles est explorée dans cet article dans le contexte des fondations monopieux. La capacité latérale des fondations de différents profils de résistance au cisaillement non drainé, une propriété qui n'est pas prescrite mais interprétée à partir des paramètres du modèle et des conditions initiales, est substantielle à toutes les valeurs de déplacement. L'utilisation d'un modèle non linéaire pour la rigidité au cisaillement est explorée et l'impact des paramètres de ce modèle est limité à la rigidité latérale des fondations monopieux soumises à de faibles charges latérales.

Keywords: Monopile foundations; offshore geotechnics; numerical modelling; clays.

1 INTRODUCTION

The use in design of constitutive models based on Critical State Soil Mechanics (Schofield and Wroth, 1968), a framework employed for explaining the observed behaviour of clays prepared to a variety of initial conditions, facilitates their effective calibration, as model parameters tend to match well described properties (e.g. compressibility, shear strength at Critical State, effect of overconsolidation). However, there are considerable challenges arising from translating properties that are often measured, but are not intrinsic to the material, as they depend fundamentally on its current state, such as the undrained shear strength. This paper explores these issues using the extended version of the Modified Cam-clay model (MCC) described in Tsiampousi et al. (2023) in the context of the capacity of monopile foundations subjected to lateral loading.

2 NUMERICAL MODEL

2.1 Details of the model

A monopile foundation with diameter $D = 5\,m$ and embedment depth $L = 50\,m$ (i.e. embedment ratio $L/D = 10$) was considered in this study. The load was applied as a prescribed displacement at a height $H = 50\,m$ (i.e $H/D = 10$) The problem was simulated in

PLAXIS 3D, with the soil domain extending to $50\,m$ (i.e $10D$) either side of the monopile and down to a depth of $70\,m$ (i.e. $14D$). The soil was modelled using 193167 10-noded tetrahedral elements, with smaller elements used in the immediate vicinity of the pile. The monopile was modelled using 4402 6-noded plate elements (linear-elastic, $E = 200\,GPa$, $\nu = 0.3$), with a simulated thickness of $t = 62.5\,mm$ $(t/D = 80)$. The interaction between the monopile and the surrounding ground was modelled using 12-noded interface elements, the strength of which (denoted herein by τ_{int}) was obtained using the methodology proposed in API (2011) and DNV (2014):

$$\tau_{int} = \alpha \cdot S_{u,TXC} \quad (1)$$

$$\alpha = \begin{cases} 0.5 \cdot R^{-0.5}, & R \leq 1 \\ 0.5 \cdot R^{-0.25}, & R > 1 \end{cases} \quad (2)$$

where $R = S_{u,TXC}/\sigma'_v$, σ'_v is the vertical effective stress and $S_{u,TXC}$ is the undrained shear strength of the soil under triaxial compression loading conditions. In general, this approach produces a slight non-linear variation close to the surface, where σ'_v approaches 0. Therefore, linear profiles approximating the outcome of Equation (1) were used, described in Section 2.3. Crucially, for this type of problems, these elements are able to simulate the opening of a gap under tensile stresses that tend to be observed at the back the pile when subjected to lateral loading.

2.2 Constitutive model

An enhanced Modified Cam-clay model was used, combining the original formulation for normally consolidated and lightly overconsolidated clays with a non-linear Hvorslev surface (Tsiampousi et al., 2013) on the dry side of critical and a hypoelastic model linking the shear stiffness of the material to the stress and strain levels (Taborda et al., 2016). This model differs from that used previously in the PISA project for the simulation of Cowden till (Zdravkovic et al., 2020b) only in the fact that it employs a Mohr-Coulomb shape in the deviatoric plane, rather than a generalised shape. Therefore, the strength at Critical state, as measured by the mobilised angle of shearing resistance, is independent of the loading conditions, which means that the slight stress-induced anisotropy observed for Cowden till (Zdravkovic et al., 2020a) cannot be reproduced using the formulation adopted herein. The full formulation of the model, designated IC MAGE M06, is described in Tsiampousi et al. (2023). It has been implemented as a User-Defined Soil Model in PLAXIS within the UMIP framework (Taborda et al., 2023) and is integrated using a modified Euler scheme with automatic substepping and error control.

The model parameters adopted for Cowden till are outlined in Table 1 and are based on those reported in Zdravkovic et al. (2020a, 2020b).

Table 1. Parameters for Cowden till based on Zdravkovic et al. (2020b).

Parameters for Cowden till			
G_{ref}	$110\,MPa$	ν_1	2.200
p'_{ref}	$100\,kPa$	κ	0.021
m_G	1.0	λ	0.115
a	9.78×10^{-5}	α_{HV}	0.250
b	0.987	n	0.400
$R_{G,min}$	0.050	β_{HV}	0.200
ϕ	27.0°	m	1.000

2.3 Analysed cases

The first objective of this paper was to evaluate the impact of the assumed undrained shear strength profile. Given that properties, such as compressibility and shear strength at Critical State, are considered to be intrinsic to the material, matching a given value of undrained shear strength is achieved by determining the required value of OCR, a process which is detailed in Zdravkovic et al. (2020b). In the implementation of IC MAGE M06, this is an automatic procedure, i.e. in practice, S_u is supplied as an input parameter, though this is then converted into OCR, which varies in depth. The three profiles studied – listed in Table 2 together with the corresponding undrained shear strength profile for the interfaces – include an approximation to that assumed in Cowden, as well as two variations consisting of lower and higher values of this property ($\pm 60\,kPa$ at surface but same value at a depth of $100\,m$). Moreover, when adjusting the value of OCR, the coefficient of earth pressure at rest, K_0, is also adjusted using $K_0 = (1 - \sin\phi) \cdot \sqrt{OCR}$. The three cases are illustrated in Figure 1.

Table 2. Analysed strength soil and interface strength profiles.

Soil strength	**Interface strength**
$S_u = 90 + 3.2\,z$	$\tau_{int} = 28 + 3.2\,z$
$S_u = 30 + 3.8\,z$	$\tau_{int} = 10 + 3.3\,z$
$S_u = 150 + 2.6\,z$	$\tau_{int} = 48 + 3.0\,z$

The second objective is to analyse the effect of the non-linear law assumed for the elastic shear modulus which is described using the model proposed in Taborda et al. (2016). Of the various parameters employed in this expression, the value of a is chosen for further investigation, since it controls the value of strain at which the stiffness at very small strains

(G_{max}) reduces to half of its value (i.e. larger values of a mean larger values of shear modulus).

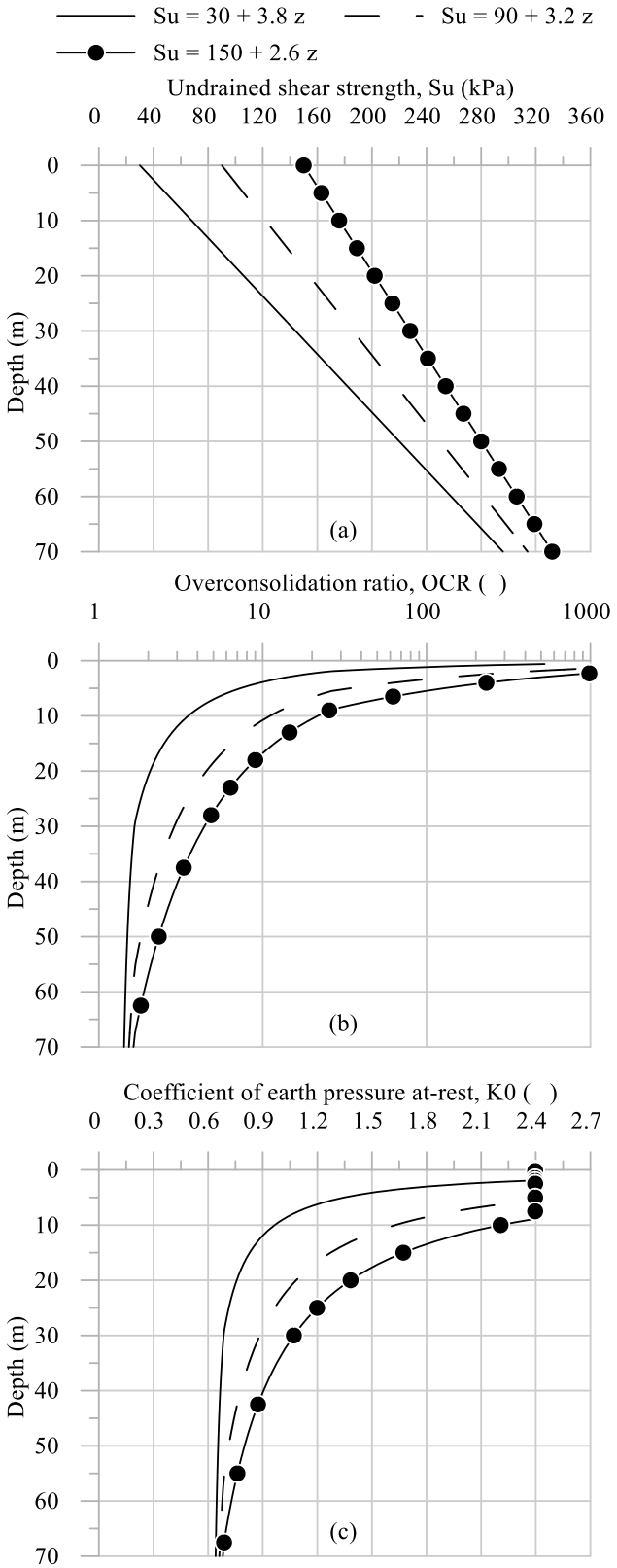

Figure 1. Profiles of (a) undrained shear strength in triaxial compression conditions, (b) overconsolidation ratio and (c) coefficient of earth pressure at-rest.

3 RESULTS

3.1 Effect of undrained strength profile

The obtained results for the three considered profiles are illustrated in Figure 2. As expected, the larger undrained shear strength leads to considerably larger capacities at failure, ranging from about 42 MN to almost 70 MN. It is also interesting to note that the shapes of the three load-displacement curves are similar at very small displacements ($< 0.1\%\ D$), suggesting that this aspect of the response is controlled by the elastic stiffness, which is identical for the three cases considered. Moreover, the capacity of the monopile is reached at different deformations: $50\%\ D$ for the lower strength profile, increasing to $100\%\ D$ for the larger strength case. This shows the difference in the hardening process associated with the various initial OCR profiles, i.e. larger $OCRs$ require larger strains to reach Critical State.

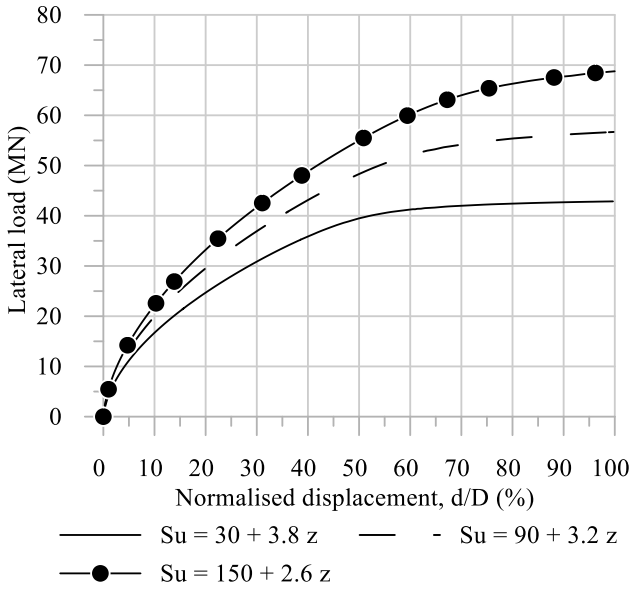

Figure 2. Lateral load-normalised displacement obtained for the various undrained shear strength profiles.

3.2 Effect of stiffness reduction parameters

The impact of varying the value of parameter a by an order of magnitude is shown in Figure 3. As expected, this parameter does not affect the ultimate capacity, though a measurable impact on the load at $10\%\ D$ is still visible ($\pm\ 1\ MN$). Clearly, a much greater impact is observed in terms of lateral stiffness, where a smaller value of a is naturally characterised by a sharper reduction in pile stiffness with lateral deformation. At very small displacements (e.g. $0.1\%\ D$), the stiffness values vary considerably.

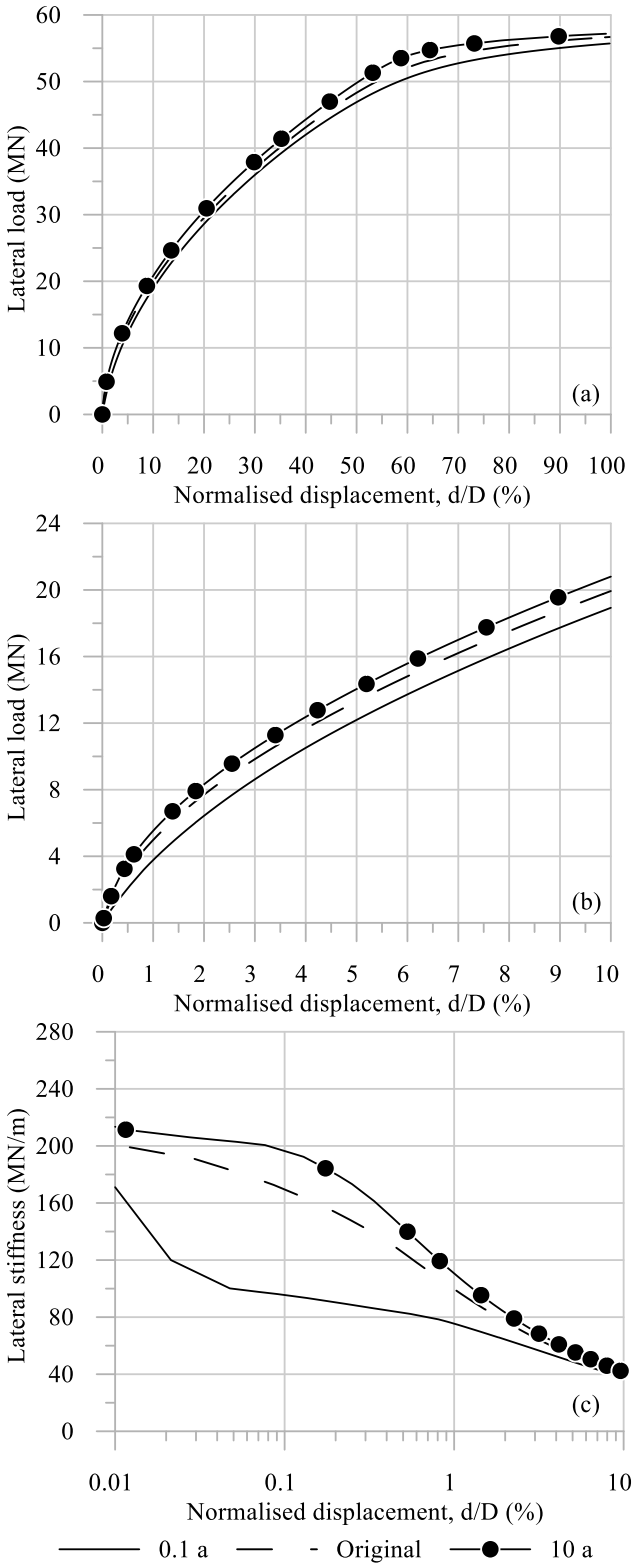

Figure 3. Effect of a on pile response for displacements up to (a) 100%D and (b) 10%D, and on (c) lateral stiffness.

4 CONCLUSIONS

Detailed finite element simulations of laterally loaded monopile foundations in clay deposits using an advanced constitutive model based on Critical State Soil Mechanics highlight the impact of the S_u profile on the pile response – not only in terms of results, but also in terms of the procedure followed to determine the initial conditions (OCR and K_0). Moreover, while the non-linear elastic shear modulus was shown to have limited impact on pile capacity, a substantial effect on monopile stiffness was observed, indicating the importance of adequately characterising and modelling this aspect of soil behaviour.

REFERENCES

API (2014) Recommended practice for planning, deigning and constructing fixed offshore platforms, American Petroleum Institute, Washington DC, Rep. No. RP 2A-WSD.

DNV (2021) Support structures for wind turbines, Det Norske Veritas, Oslo, Norway, DN-ST-0126.

Schofield, A. N., Wroth, C. P. (1968) *Critical state soil mechanics*, McGraw-Hill, London, UK.

Taborda, D. M. G., Kontoe, S., Tsiampousi, A. (2023) IC MAGE UMIP - Universal model interface for PLAXIS (Version 3.5). *Zenodo* http://doi.org/10.5281/zenodo.8226527.

Taborda, D. M. G., Potts, D. M., Zdravkovic, L. (2016) On the assessment of energy dissipated through hysteresis in finite element analysis, *Computers and Geotechnics*, 71, pp. 180-194. http://doi.org/10.1016/j.compgeo.2015.09.001.

Tsiampousi, A., Kontoe, S., Taborda, D. M. G. (2023) IC MAGE Model 06 – Modified Cam-clay model with a non-linear Hvorslev surface and isotropic small strain shear stiffness (Version 1.6). *Zenodo*. http://doi.org/10.5281/zenodo.10114909.

Tsiampousi, A., Zdravkovic, L., Potts, D. M. (2013) A new Hvorslev surface for critical state type unsaturated and saturated constitutive models, *Computers and Geotechnics*, 48, pp. 156-166. http://doi.org/10.1016/j.compgeo.2012.09.010.

Zdravkovic, L., Jardine, R. J., Taborda, D. M. G., Abadias, D., Burd, H. J., Byrne, B. W., Gavin, K. G., Houlsby, G. T., Igoe, D. J. P., Liu, T. F., Martin, C. M., McAdam, R. A., Wood, A. M., Potts, D. M., Gretlund, J. S., Ushev, E. (2020a) Ground characterisation for PISA pile testing and analysis, *Géotechnique*, 70 (11), pp. 945-960. http://doi.org/10.1680/jgeot.18.PISA.001.

Zdravkovic, L., Taborda, D. M. G., Potts, D. M., Abadias, D., Burd, H. J., Byrne, B. W., Gavin, K. G., Houlsby, G. T., Jardine, R. J., Martin, C. M., McAdam, R. A., Ushev, E. (2020b) Finite-element modelling of laterally loaded piles in a stiff glacial clay till at Cowden, *Géotechnique*, 70(11), pp. 999-1013. http://doi.org/10.1680/jgeot.18.PISA.005.

Proceedings of the XVIII ECSMGE 2024
GEOTECHNICAL ENGINEERING CHALLENGES
TO MEET CURRENT AND EMERGING NEEDS OF SOCIETY
© 2024 the Authors
ISBN 978-1-032-54816-6
DOI 10.1201/9781003431749-661
Open Access: www.taylorfrancis.com, CC BY-NC-ND 4.0 license

ECSMGE 24
XVIII EUROPEAN CONFERENCE ON SOIL MECHANICS AND GEOTECHNICAL ENGINEERING

Numerical modelling of the long-term cyclic ratcheting of monopile foundations under lateral loading

Modélisation numérique du ratcheting cyclique à long terme des fondations monopieux sous chargement latéral

P. Tantivangphaisal*, D.M.G. Taborda
Imperial College London, United Kingdom

S. Kontoe
University of Patras, Greece; Imperial College London, United Kingdom

**pt620@imperial.ac.uk*

ABSTRACT: There is growing interest to utilise advanced numerical methods by industry practitioners in the prediction of the long-term response of monopile foundations under lateral cyclic loading. One framework of interest is the High Cycle Accumulation (HCA), as it can overcome the limitations of computational expense and error accumulation encountered by conventional cycle-by-cycle finite element analyses. The authors' implementation of HCA within the finite element package PLAXIS is presented with an emphasis on the framework's key components and underlying assumptions. Furthermore, by coupling HCA with a practice oriented elasto-plastic model for sands, predictions using different HCA calibration approaches are evaluated against the field measurements of a medium sized cyclic lateral pile load test from the Pile-soil analysis (PISA) joint industry project.

RÉSUMÉ: Les professionnels de l'industrie montrent un intérêt croissant pour l'utilisation de méthodes numériques avancées afin de prédire la réponse à long terme des fondations monopieux soumises à des chargements cycliques latéraux. L'Accumulation à Haute Fréquence (HCA) est une des méthodes considérées, car elle peut surmonter les limitations de coût computationnel et les problèmes d'accumulation d'erreurs rencontrées par les analyses conventionnelles par éléments finis cycle-par-cycle. L'implémentation du HCA par les auteurs dans le logiciel de calcul par éléments finis PLAXIS est présentée ici, mettant l'accent sur les composants clés de la méthode et les hypothèses sous-jacentes. De plus, en couplant le HCA avec un modèle élasto-plastique orienté vers la pratique pour les sables, on évalue les prédictions utilisant différentes approches de calibrage du HCA par rapport aux mesures sur le terrain d'un essai de charge latérale cyclique de taille moyenne réalisé lors du projet industriel conjoint Pile-soil Analysis (PISA).

Keywords: Cyclic loading; monopile; finite element analysis; high cycle accumulation; calibration.

1 INTRODUCTION

There is a growing body of research focused on numerical methods for the prediction of long-term rotation of monopile offshore foundations subjected predominantly to regular lateral cyclic loading (Achmus et al., 2009; Staubach & Wichtmann, 2020; Abadie et al., 2023). However, translating these methods from research to design practice require both rigorous validation against large scale field tests and studies on calibration sensitivity. Greater applicability will also be found for methods whose calibration intensity can be adapted to availability of site-specific data.

The High Cycle Accumulation (HCA) framework proposed by Niemunis et al. (2005) is used here to predict the accumulated rotation of the 0.76m diameter (D) lateral cyclic pile load test in Dunkirk Sand from the PISA project (Byrne et al., 2020). Single element and field scale predictions from two calibration approaches are presented.

2 THE HCA FRAMEWORK FOR SANDS

In response to the numerical difficulties of simulating the cycle-by-cycle response of thousands of loading cycles, the HCA framework for sands proposes that the magnitude and direction of stress and strain changes due to repeated loading can be characterised directly by:

- A one-cycle cyclic strain amplitude $\|\varepsilon_{ampl}\|$,
- a history variable g^A capturing the number of cycles N and evolution of $\|\varepsilon_{ampl}\|$,
- the current (average) stress state $\{\sigma\}$,

- the current (average) void ratio e, and
- a set of material dependent properties.

When using the HCA framework in conventional finite element (FE) analyses, $\|\varepsilon_{ampl}\|$ is determined at each integration point by processing the strain path undergone over one regular loading cycle (Niemunis et al., 2005).

2.1 Low-cycle sand model

The low-cycle elasto-plastic model used herein is a non-linear elastic model capable of Masing hysteresis (Taborda et al., 2016) coupled with state-parameter driven plasticity based on the Mohr-Coulomb yield criterion (Taborda et al., 2022). Implementation details are found in Taborda et al. (2023).

2.2 High-cycle framework implementation

The incremental HCA stress-strain relation is:

$$\{\Delta\sigma\} = \left[D_{HCA}^{ela}\right]\{\Delta\varepsilon^{ela}\} \quad (1)$$

$$\{\Delta\varepsilon^{ela}\} = \{\Delta\varepsilon^{t}\} - \{\Delta\varepsilon^{acc}\} - \{\Delta\varepsilon^{p}\} \quad (2)$$

$$\{\Delta\varepsilon^{acc}\} = \left\{\frac{\partial\varepsilon^{acc}}{\partial N}\right\}\Delta N \quad (3)$$

where $\{\Delta\sigma\}$ is the local stress step, $\Delta\varepsilon^{ela}$, $\Delta\varepsilon^{t}$, $\Delta\varepsilon^{p}$, $\Delta\varepsilon^{acc}$ are respectively the elastic, total, plastic and accumulated strain steps. $\left[D_{HCA}^{ela}\right]$ is the HCA isotropic elastic stiffness matrix described by K_{HCA} and ν_{HCA}, and is dependent on e and mean effective stress (p'):

$$K_{HCA} = K_{HCA}^{ref} \cdot f_K(e) \cdot \left(\frac{p'}{100}\right)^{m_{K,HCA}} \quad (4)$$

where K_{HCA}^{ref} and $m_{K,HCA}$ are material parameters and $f_K(e) = (1.63 - e)^2/(1 + e)$ follows Wichtmann et al. (2013) as modified from Hardin & Richart (1963).

The plastic strain step is determined via standard elasto-plastic integration employing the low-cycle model yield surface and plastic potential, using a modified total strain step $\{\Delta\varepsilon^{t}\} - \{\Delta\varepsilon^{acc}\}$.

The empirical function from Wichtmann (2016) driving the prediction of the average strain change due to an increment of stress cycles (and vice-versa) is formed of a direction $\{\vec{m}\}$ and a scalar magnitude:

$$\left\{\frac{\partial\varepsilon^{acc}}{\partial N}\right\} = \{\vec{m}\} \cdot \frac{\partial f_N}{\partial N} f_{ampl} f_e f_p f_Y \quad (5)$$

where $\{\vec{m}\}$ is the unit norm of the Modified Cam Clay surface, whose size (and hence the accumulation direction) is described by a single material parameter ϕ_{HCA}. The magnitude is dependent on 9 material parameters: ϕ_{HCA}, and C_{ampl}, C_e, e_{max}, C_p, C_Y, C_{N1}, C_{N2}, C_{N3}, three state variables e, g^A and $\|\varepsilon_{ampl}\|$, and the current stress state represented by invariants p', J and θ with $\eta = J/p'$ (where J is the deviatoric stress invariant and θ the Lode-angle). The f-factors are:

$$\frac{\partial f_N}{\partial N} = C_{N1}C_{N2}\, exp\frac{-g^A}{f_{ampl}C_{N1}} + C_{N1}C_{N3} \quad (6)$$

$$f_{ampl} = \left[min\left(\frac{\|\varepsilon_{ampl}\|}{10^{-4}}, 10\right)\right]^{C_{ampl}} \quad (7)$$

$$f_e = \left(\frac{C_e - e}{C_e - e_{max}}\right)^2 \cdot \frac{1 + e_{max}}{1 + e} \quad (8)$$

$$f_p = exp\left(-C_p\left(\frac{p'}{100} - 1\right)\right) \quad (9)$$

$$f_Y = exp(C_Y \cdot Y) \quad (10)$$

where Y is a measure of stress ratio normalised by the Matsuoka-Nakai yield surface defined using ϕ_{HCA}.

$$Y = \left[\frac{9 - 3\eta^2}{1 - \eta^2 + \frac{8\sqrt{3}}{9}\eta^3\left(\sin^3\theta - \frac{3}{4}\sin\theta\right)} - 9\right] / [8\, tan^2\, \phi_{HCA}].$$

g^A initialises as 0 assuming no pre-cycling; its evolution incorporates the combined effect of ΔN and strain amplitude magnitude via f_{ampl} as follows:

$$\Delta g^A = \Delta N f_{ampl} C_{N1} C_{N2}\, exp\frac{-g^A}{f_{ampl}C_{N1}} \quad (11)$$

2.3 Implementation in PLAXIS

A user-defined soil model (UDSM) "flag" allows different integration behaviour using the same UDSM at different phases: (1) Low-cycle, no record, (2) Low-cycle, strain recorded, (3) Strain processed or 'HCA initialisation' and (4) HCA accumulation.

A two-stage modified-Euler with automatic sub-stepping and error control integration algorithm is used during (4). Given an incoming total strain step $\{\delta\varepsilon^{t}\}$, a forward $\{\delta\varepsilon^{acc}\}_1$ and a backward $\{\delta\varepsilon^{acc}\}_2$ accumulation step is first calculated using equations (3) and (5) to (11). Intermediate forward and backward stresses are then calculated, and their average and difference are used as the initial error control measure. After a suitable sub-step size is determined, a 'modified' total strain sub-step $\{\delta\varepsilon^{t}\} - \frac{\{\delta\varepsilon^{acc}\}_1 + \{\delta\varepsilon^{acc}\}_2}{2}$ is used in the conventional elasto-

plastic integration. If the underlying yield surface is inactive, the first stage suffices.

3 MODEL CALIBRATION FOR DUNKIRK SAND

3.1 Low-cycle (conventional) model

The low-cycle calibration used the laboratory and field data reported during the PISA project (Taborda et al., 2020) and followed the method outlined by Taborda et al. (2022). Material parameters used here are those reported by Pirrone and Taborda (2023).

3.2 High-cycle strain accumulation

Dunkirk sand laboratory test data for $\varepsilon_{ampl}(N)$ and $\varepsilon_{acc}(N)$ for eleven drained cyclic triaxial tests (DcycTX) is available in Liu (2018). Two parameter sets were calibrated for Dunkirk Sand:

(i): Using granulometry correlations (Wichtmann, 2016) for all $C_$ parameters and $\phi_{HCA} = \phi'_{cs}$, and

(ii): C_{ampl}, C_e, C_p, C_Y, C_{N1}, C_{N2}, C_{N3}, ϕ_{HCA} fitted to all 11 DcycTX tests.

For brevity, the simple brute-force strategy in Wichtmann et al. (2015) was used to fit (ii). 100,000 parameter combinations were picked out using a latin hypercube sampler. The value of $\|\varepsilon^{acc}\|$ was calculated using an integration driver for equation (5). A non-weighted average root mean squared error was calculated for each laboratory test at 21 cycle numbers evenly (log-) spaced between $N = 1$ and $N = 10000$. A simple mean of this error across all eleven tests is then calculated to determine the best (smallest error) set of parameters.

As expected, calibration procedure (ii) produced a better fit against strain accumulation measured in element laboratory tests. However, the granulometry correlations also gave a reasonable fit against element tests and a first estimate of HCA parameters.

Table 1. Summary of calibrated HCA parameters.

	(i)	(ii)
C_{ampl}	1.7	1.8
C_e	0.51	0.0050
C_p	0.46	0.28
C_Y	2.2	2.9
C_{N1}	7.0E-4	1.2E-4
C_{N2}	0.22	0.57
C_{N3}	4.7E-5	1.5E-5
ϕ_{HCA}(°)	32	29
e_{max}	0.91 (Liu, 2018)	
K_{HCA}^{ref} *	120,900 kPa	
ν_{HCA}^{ref} *	0.32	

*Values from Wichtmann (2016:p.211) for fine sand

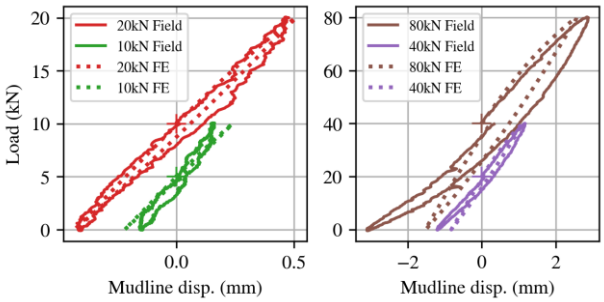

Figure 1. Low-cycle FE versus one-way field response.

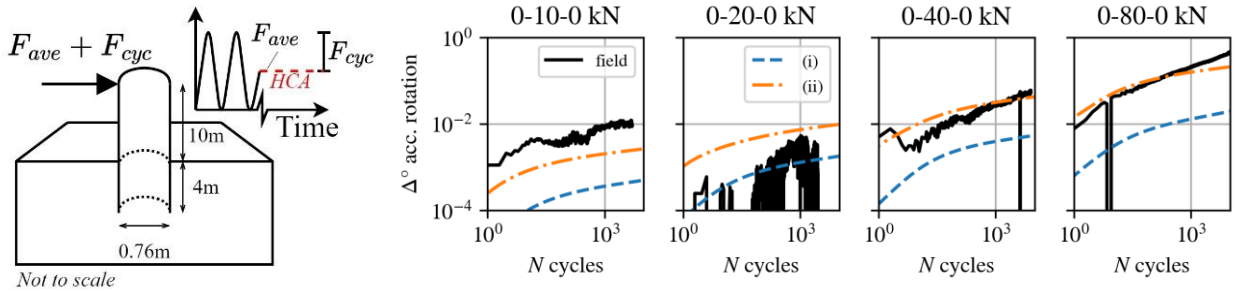

Figure 2. FE schematic and HCA simulation results compared against measured field response at mudline level.

4 FE MONOPILE PREDICTION

The initial HCA recording stage showed a reasonable match between the low-cycle model prediction and the field response (Figure 1) for the medium-sized (D=0.76m) one-way cyclic lateral pile test at Dunkirk (Byrne et al., 2020) loaded to 10 kN (N=5100), 20 kN (N=3300), 40 kN (N=8100) and 80 kN (N=11110). All analyses assumed a drained response in the sand.

In contrast to the single element response, the two calibration procedures differed by an order of magnitude in the prediction of accumulated pile head rotation (Figure 2). This is likely associated with the highly sensitive C_e parameter. The single element sensitivity reported in Wichtmann et al. (2015) seems further magnified for field-scale predictions.

5 CONCLUSION AND FURTHER WORK

A brief evaluation of the use of the HCA framework to design monopiles subjected to regular lateral loading is presented. Comparison between FE results and the field response suggests that a detailed programme of site specific drained cyclic triaxial tests is required to calibrate HCA parameters for engineering use.

Further sensitivity studies are essential to guide practitioners in the use of the HCA framework for long-term cyclic predictions, especially if calibrating using a combination of correlations and laboratory tests. An assessment of drainage effects, strain amplitude update, incorporation of sophisticated low-cycle models, and associated problems with state variable update are all keenly needed. A next step for design is to assess HCA's capability to predict soil state (e.g. void ratio distribution) and global stiffness evolution to inform dynamic and fatigue limit state design.

ACKNOWLEDGEMENTS

The authors acknowledge the financial support of the Department of Civil and Engineering, Imperial College London, through a Skempton scholarship for work undertaken during the first author's PhD.

REFERENCES

Abadie, C.N., Beuckelaers, W.J.A.P., Byrne, B.W., Houlsby, G.T., Burd, H.J. & McAdam, R. (2023) Modeling Lifetime Performance of Monopile Foundations for Offshore Wind Applications. *Journal of Geotechnical and Geoenvironmental Engineering*. 149 (8), 04023051. doi:10.1061/JGGEFK.GTENG-9833.

Achmus, M., Kuo, Y.-S. & Abdel-Rahman, K. (2009) Behavior of monopile foundations under cyclic lateral load. *Computers and Geotechnics*. 36 (5), 725–735. doi:10.1016/j.compgeo.2008.12.003.

Byrne, B.W., McAdam, R.A., Beuckelaers, W.J.A.P., Burd, H.J., Gavin, K., Houlsby, G.T., Igoe, D.J.P., Jardine, R.J., Martin, C.M., Potts, D.M., Taborda, D.M.G. & Zdravkovic, L. (2020) Cyclic laterally loaded medium scale field pile testing for the PISA project. In: *Proceedings of the Fourth International Symposium on Frontiers in Offshore Geotechnics*. 2020 Austin, Texas, U.S. pp. 1323–1331.

Hardin, B.O. & Richart, F.E. (1963) Elastic Wave Velocities in Granular Soils. *Journal of the Soil Mechanics and Foundations Division*. 89 (1), 33–65. doi:10.1061/JSFEAQ.0000493.

Liu, T. (2018) *Advanced laboratory testing for offshore pile foundations under monotonic and cyclic loading*. PhD. Imperial College London.

Niemunis, A., Wichtmann, T. & Triantafyllidis, Th. (2005) A high-cycle accumulation model for sand. *Computers and Geotechnics*. 32 (4), 245–263. doi:10.1016/j.compgeo.2005.03.002.

Pirrone, A.I. & Taborda, D.M.G. (2023) An application of machine learning to the back analysis of monopile response. In: *Proceedings of the 9th International Offshore Site Investigation and Geotechnics Conference*. 2023 pp. 2028–2035.

Staubach, P. & Wichtmann, T. (2020) Long-term deformations of monopile foundations for offshore wind turbines studied with a high-cycle accumulation model. *Computers and Geotechnics*. 124, 103553. doi:10.1016/j.compgeo.2020.103553.

Taborda, D.M.G., Pedro, A.M.G., Kontoe, S. & Tsiampousi, A. (2023) IC MAGE Model 02 – Simple state-parameter dependent model with isotropic small strain stiffness (Version 2.6). *Zenodo*. doi:10.5281/zenodo.7629677.

Taborda, D.M.G., Pedro, A.M.G. & Pirrone, A.I. (2022) A state parameter-dependent constitutive model for sands based on the Mohr-Coulomb failure criterion. *Computers and Geotechnics*. 148, 104811. doi:10.1016/j.compgeo.2022.104811.

Taborda, D.M.G., Potts, D.M. & Zdravkovic, L. (2016) On the assessment of energy dissipated through hysteresis in finite element analysis. *Computers and Geotechnics*. 71, 180–194. doi:10.1016/j.compgeo.2015.09.001.

Taborda, D.M.G., Zdravkovic, L., Potts, D.M., Burd, H.J., Byrne, B.W., Gavin, K.G., Houlsby, G.T., Jardine, R.J., Liu, T., Martin, C.M. & McAdam, R.A. (2020) Finite-element modelling of laterally loaded piles in a dense marine sand at Dunkirk. *Géotechnique*. 70 (11), 1014–1029. doi:10.1680/jgeot.18.PISA.006.

Wichtmann, T. (2016) *Soil behaviour under cyclic loading - experimental observations constitutive description and applications*. Habilitation. https://www.torsten-wichtmann.de/habil/habil-wichtmann-2016.pdf.

Wichtmann, T., Niemunis, A. & Triantafyllidis, T. (2015) Improved simplified calibration procedure for a high-cycle accumulation model. *Soil Dynamics and Earthquake Engineering*. 70, 118–132. doi:10.1016/j.soildyn.2014.12.011.

Wichtmann, T., Niemunis, A. & Triantafyllidis, T. (2013) On the "elastic stiffness" in a high-cycle accumulation model — continued investigations. *Canadian Geotechnical Journal*. 50 (12), 1260–1272. doi:10.1139/cgj-2013-0037.

Proceedings of the XVIII ECSMGE 2024
GEOTECHNICAL ENGINEERING CHALLENGES
TO MEET CURRENT AND EMERGING NEEDS OF SOCIETY
© 2024 the Authors
ISBN 978-1-032-54816-6
DOI 10.1201/9781003431749-662
Open Access: www.taylorfrancis.com, CC BY-NC-ND 4.0 license

ECSMGE 24
XVIII EUROPEAN CONFERENCE ON SOIL MECHANICS AND GEOTECHNICAL ENGINEERING

A bibliometric analysis on geotechnical research trends in floating offshore wind energy

Une analyse bibliométrique sur les tendances de la recherche géotechnique dans le domaine de l'énergie éolienne offshore flottante

A.D. Tasbasi, Y.C. Ceylan, N. Huvaj*
Middle East Technical University, Ankara, Turkey

A. Osman
Durham University, Durham, UK

**nejan@metu.edu.tr*

ABSTRACT: The objective of this study is to examine geotechnical research trends in floating offshore wind energy during a period from 1972 to 2022 via a bibliometric analysis. Using Web of Science database, 7600 articles were obtained in a variety of journals, conferences, books and series. The results indicate that the number of published articles in geotechnical engineering topics in offshore wind, and specifically on floating offshore wind, are increasing worldwide each year. Among the offshore geotechnical studies Norway, Denmark and the UK are the top contributing countries. Majority of the articles belonging to the GEO-group are about the fixed-bottom type offshore wind turbines (monopile, jacket, tripod etc.). Among the articles related to floating-type offshore wind turbines, drag embedded anchors, vertically loaded anchors, multiline anchors, pile driven plate anchors, dynamically embedded plate anchors, suction embedded plate anchors were commonly studied. As technological developments in floating offshore wind are gaining attention (e.g. seabed anchor alternatives, buried cables in seabed, shared mooring lines and shared anchors etc.) we foresee an increase in the number of articles. There seems to be a limited number of research which combines experimental and numerical modelling approaches. Research on risk, reliability-based probabilistic methods is expected to increase. Among the loading conditions, limited studies are available for seismic loading. These aspects are expected to be further investigated in the coming years. Results from this bibliometric study may highlight the current status and future trends in offshore geotechnical engineering research.

RÉSUMÉ: L'objectif de cette étude est d'examiner les tendances de la recherche géotechnique sur l'énergie éolienne offshore flottante sur une période allant de 1972 à 2022 via une analyse bibliométrique. Grâce à la base de données Web of Science, 7 600 articles ont été obtenus dans diverses revues, conférences, livres et séries. Les résultats indiquent que le nombre d'articles publiés sur des sujets d'ingénierie géotechnique liés à l'éolien offshore, et en particulier sur l'éolien offshore flottant, augmente chaque année dans le monde. Parmi les études géotechniques offshore, la Norvège, le Danemark et le Royaume-Uni sont les principaux pays contributeurs. La majorité des articles appartenant au groupe GEO concernent les éoliennes offshore de type à fond fixe (monopile, jaquette, trépied etc.). Parmi les articles relatifs aux éoliennes offshore de type flottant, les ancres encastrées par traînée, les ancres chargées verticalement, les ancres multilignes, les ancres à plaques enfoncées sur pieux, les ancres à plaques encastrées dynamiquement, les ancres à plaques encastrées par aspiration ont été couramment étudiées. À mesure que les développements technologiques dans le domaine de l'éolien offshore flottant attirent de plus en plus l'attention (par exemple, alternatives d'ancrage au fond marin, câbles enterrés dans le fond marin, lignes d'amarrage et ancres partagées, etc.), nous prévoyons une augmentation du nombre d'articles. Il semble exister un nombre limité de recherches combinant des approches de modélisation expérimentale et numérique. La recherche sur les méthodes probabilistes basées sur le risque et la fiabilité devrait se développer. Parmi les conditions de chargement, des études limitées sont disponibles pour le chargement sismique. Ces aspects devraient être approfondis dans les années à venir. Les résultats de cette étude bibliométrique peuvent mettre en évidence l'état actuel et les tendances futures de la recherche en ingénierie géotechnique offshore.

Keywords: Bibliometric analysis; offshore wind; geotechnical engineering.

1 INTRODUCTION

There is a global goal of reaching to 380 GW of offshore wind energy by 2030, as stated by The Global Offshore Wind Energy Compact (IRENA and GWEC, 2021). Fixed-bottom offshore wind has been in research forefronts, whereas research on floating offshore wind is accelerating. It is estimated that the number of floating wind turbines is expected to far exceed, by at least an order of magnitude, the number

of installed oil and gas facilities, by the end of this decade (Gourvenec et al., 2022).

The objectives of this study is to investigate the current status of geotechnical research and publications on offshore wind energy, specifically for floating offshore wind, in terms of its change over the years, classification of published articles with their topics, comparison of the countries' performance, type of foundations, research methods used in geotechnical articles, and the loading conditions studied. The analyses may highlight the current research trends and future research needs in geotechnical engineering specifically for floating offshore wind energy.

2 METHODOLOGY AND DATA

Bibliometric analysis is a quantitative method for processing and analysing data on publications in the literature. It can help identify the current status, trends and topics for guiding future studies (Tsay, 2008).

The data was obtained from Web of Science (WoS) collection as it is one of the widely used and trusted international databases on publications. Furthermore, the data can be downloaded and processed in an easy way and format. The data collection was completed in July 2022. Although, the data does not include all of the publications in 2022, it can provide sufficient information on research trends for the purposes of this study.

From 1945 to present, the Web of Science all databases system is searched with keywords and their combinations, such as: offshore wind, floating wind turbines, floating offshore wind / geotechnics / power system / energy / CFD / farm / liquefaction / platform / power plant / structure / turbine, FOWT and OFWT.

This study analyses 7600 papers which were published between 1972-July 2022. The dataset includes publication type, authors, author affiliations, article title, keywords, classification, corresponding author country, source title (journal, conference name), publication date, times-cited in WoS all databases, and their abstracts. The data is checked for duplicate information and organized via a spreadsheet, then it was analysed.

The articles are classified in seven groups which are abbreviated as ECON, ELEC, ENV, HYD, MEC, GEO, and OTHERS (see Table 1 for keywords of groups). For instance, articles in the GEO group cover geotechnical engineering related topics such as reliability of offshore wind farms with multiline anchors, lateral capacity of monopiles in sand etc. The titles, keywords and abstracts were evaluated to determine the group of the articles. The reason for this classification was to investigate the number of studies and trends in different research areas, focusing more on geotechnical engineering.

Table 1. Article groups used in classification of 7600 articles on offshore energy topics.

Article Groups	Example keywords
ECON (Economy / Planning)	Economy, resource assessment, Levelized Cost of Energy (LCOE), site selection, micro-siting, GIS, renewable energy, life-cycle assessment, policy
ELEC (Electricity / grid)	Electricity, grid, HVDC, AC-DC, transistor, automation and control, drivetrain, gear, power, computer science
ENV (Environment)	Environment, biology, sea temperature, marine life, meteorology & climate, atmosphere, global warming
HYD (Hydraulics / Hydromechanics)	Hydrodynamics, Computational Fluid Dynamics (CFD), wave model, wave energy, FAST, WASP, openFOAM, ship, tidal energy, naval
MEC (Mechanics)	Materials science, mechanical design, gear, structural stability, fatigue, wake, foil, aerodynamics
GEO (Geotechnics)	Geotechnics, foundation design, floating systems, soil, geology
OTHERS	Oil and petroleum, natural gas

3 RESULTS

3.1 Total number of publications in all floating offshore energy topics according to countries & years

The data includes 7600 articles from 85 countries. 5471 of these articles are journal articles, and the rest are published in conferences, books and series. In Figure 1, the number of published articles in each year from 1972 to July 2022 can be seen. Between 1972 and 1997 the number of publications were less than 5 per year (Figure 1). After 2000′s, the rate of increase in the number of publications increases.

Between 2020-2021, the number of published articles decreased, which might possibly be related to Covid-19 Pandemic starting in March 2020. The article search in this study was completed in July 2022, so the decrease in the number of published articles in 2022 in Figure 1 should be ignored.

Countries' contributions should be considered in bibliometric research to comprehend the global distribution of research and to identify the leading countries in the area.

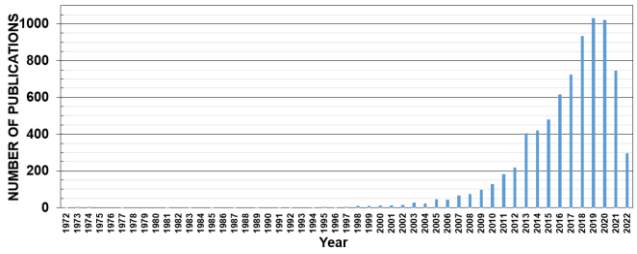

Figure 1. Number of publications about offshore wind from 1972 to 2022.

In Table 2, the top 10 contributing countries (corresponding author's country) in terms of the number of published papers on the topic of offshore wind can be seen. About 68% of 7600 articles belong to these 10 countries. Out of 7600 articles in the dataset, the highest number of articles (1424, 18.7%) is by China, followed by the USA (10.3%) and England (6.4%). The majority of the articles are in MEC (19.3% of 7600 articles), ECON (14.2%), ELEC (13%) groups/topics.

Table 2. The top 10 countries contributing to 7600 publications (percentage is out of 7600 publications).

Rank	Country	ECON	ELEC	ENV	HYD	MEC	GEO	OTHERS	Total
1	China	172	291	40	168	464	241	48	1424
2	USA	213	96	66	103	206	69	29	782
3	England	129	79	24	37	135	71	11	486
4	Norway	92	71	22	50	159	53	30	477
5	Denmark	112	102	17	25	93	43	6	398
6	Germany	97	81	28	30	105	43	10	394
7	South Korea	52	69	12	53	134	43	18	381
8	Spain	103	108	17	40	55	33	2	358
9	Scotland	78	56	6	34	46	10	5	235
10	Japan	33	37	9	50	72	19	9	229
		1081	990	241	590	1469	625	168	5164
		14.22%	13.03%	3.17%	7.76%	19.33%	8.22%	2.21%	67.95%

When we normalize the number of publications with the population [29], Norway, Denmark and the UK are the most contributing countries in terms of the number of publications normalized by population, on offshore wind topics: Norway (88 articles/one million people), Denmark (68), the UK (11), the United States (2.4). This may also be correlated with the cumulative installed offshore wind energy capacity indicating the experience in industry and in research.

3.2 Publications in offshore geotechnical engineering topics

When the articles in the GEO group are analysed (842 out of 7600 total number of articles, %11.1), the top 10 contributing countries in terms of the total number of published articles are summarized in Table 3. Out of 842 articles, the highest number of articles (28.6%) is written by researchers in China, followed by England (8.4%) and the United States (8.2%). After normalizing the total number of GEO publications with the population of the country [29], contribution ranking of countries per one million people is as Norway (9.8 articles/one million people), Denmark (7.3), the UK (1.2), the United States (0.21) and China (0.17). Norway is the most impactful country in terms of the number of published articles in the GEO group.

Table 3. Top 10 contributing countries in terms of the number of publications in GEO group.

Ranking	Countries	Number of Published Articles in GEO Group (Percentage among 842)
1	China	241 (28.6%)
2	England	71 (8.4%)
3	The United States	69 (8.2%)
4	Norway	53 (6.3%)
5	Denmark	43 (5.1%)
6	Germany	43 (5.1%)
7	South Korea	43 (5.1%)
8	Australia	37 (4.4%)
9	Spain	33 (3.9%)
10	India	31 3.7%
-	Total	664 (78.9%)

After examining the abstract, title and keywords of the articles in GEO group, they were grouped in 3 different ways:

- the type of the offshore wind turbine studied,
- the research method of the study and
- the loading condition studied.

Table 4. Number of GEO articles in terms of the offshore wind turbine types.

Type of the Offshore Wind Turbine	Number of Published Articles
Floating	295 (35%)
Fixed Bottom	469 (55.7%)
Both (Floating & Fixed Bottom)	17 (2%)
No Information	61 (7.3%)

35% of the GEO articles (295 out of 842) studied floating (Table 4) and 55.7% studied fixed bottom (monopile, suction bucket etc.) offshore wind turbines. Both types were studied in 2% of the articles and no information was found in the remaining articles.

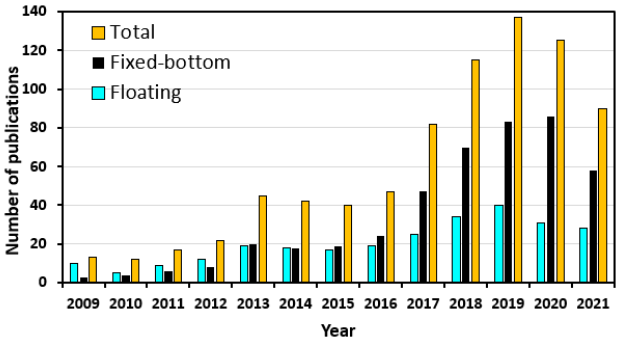

Figure 2. Among the GEO articles, number of publications on the type of wind turbines (studies that have both types and studies with no information are excluded).

In terms of the research method (Table 5), experimental methods (centrifuge test, physical modelling etc.) were used in 23.4% of the GEO articles, numerical methods (ABAQUS, PLAXIS 3D, FLAC3D, MPM etc.) in 45.6%, both experimental and numerical methods were used in 2.7% of the articles.

Table 5. Number of articles in terms of the research method.

Research Method	Number of Published Articles
Experimental	197 (23.4%)
Numerical	384 (45.6%)
Both (Experimental & Numerical)	23 (2.7%)
Probabilistic	39 (4.6%)
Seabed Soil Property	19 (2.3%)
Review	120 (14.3%)
Other	60 (7.1%)

In 4.6% of the articles, probabilistic approach (risk, reliability) was adopted, and in 2.3% seabed soil property/investigation was studied. While 14.3% of were review articles, methods other than the ones mentioned here were used in 60 articles (7.1%).

As for the loading conditions of offshore wind turbines, cyclic loading (wind, wave & current) was studied in 53.9% of 842 GEO articles; seismic loading due to earthquakes in 8.9%, and loading by floating sea ice was studied in 0.4%. Both cyclic & seismic loading and cyclic & ice loading were studied in 1.4% of the articles. For the remaining articles, no information was found.

GEO-related journal articles have been published more frequently in the journals shown in Figure 3. When we look at the individual journal articles having more than 100 citations (times cited in WoS all databases) the top-cited-articles are been published in the following journals (in order): Journal of Renewable and Sustainable Energy, Computers and Geotechnics, Journal of the Acoustical Society of America, Applied Ocean Research, Renewable Energy, Proceedings of The Institution of Civil Engineers-Geotechnical Eng., Journal of Geotechnical and Geoenvironmental Eng., Ocean Eng.

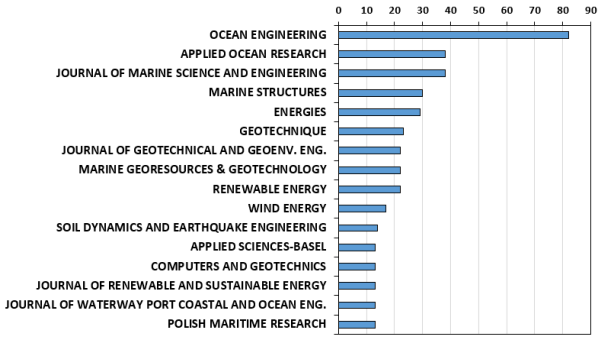

Figure 3. Journals in which GEO group articles are published in 1972 to 2021.

4 CONCLUSIONS

This bibliometric analysis gives a general idea of current research trends and future research needs in offshore wind energy based on the dataset including 7600 publications between 1972-July 2022. Norway, Denmark and the UK are the top contributing countries to total number of articles in offshore topics, as well in GEO-related topics.

Research on geotechnical engineering aspects of floating offshore wind is expected to increase in the future. Among the articles related to floating types, it is seen that drag embedded anchors, vertically loaded anchors, multiline anchors, pile driven plate anchors, dynamically embedded plate anchors, suction embedded plate anchors were studied. We foresee more studies on seabed anchor alternatives, buried cables in seabed, shared mooring lines and shared anchors etc.

There seems to be limited research which combines experimental and numerical modelling approaches. Research on risk, reliability-based probabilistic methods is expected to increase. Among the loading conditions, limited studies are available for seismic loading condition. These aspects are expected to be further investigated in the coming years.

ACKNOWLEDGEMENTS

This work is funded by the British Council under Newton Fund Institutional Link programme (Grant reference 62309484) and The Scientific and Technological Research Council of Türkiye, TUBITAK-British Council Bilateral Cooperation Program 2551, Project Number 120N973.

REFERENCES

Gourvenec, S., Sturt, F., Reid, E., and Trigos, F. (2022). Global assessment of historical, current and forecast ocean energy infrastructure: Implications for marine space planning, sustainable design and end-of-engineered-life management. Renewable and Sustainable Energy Reviews, 154, 111794, https://doi.org/10.1016/j.rser.2021.111794.

IRENA and GWEC (2021) A next Decade Action Agenda to advance SDG7 on sustainable energy for all, in line with the goals of the Paris Agreement on Climate Change, https://www.un.org/sites/un2.un.org/files/2021/09/irena_and_gwec_offshore_wind_energy_compact_-_final_1.pdf.

Tsay, M. Y. (2008). A bibliometric analysis of hydrogen energy literature, 1965–2005. Scientometrics, 75(3), 421-438, https://doi.org/10.1007/s11192-007-1785-x.

Proceedings of the XVIII ECSMGE 2024
GEOTECHNICAL ENGINEERING CHALLENGES
TO MEET CURRENT AND EMERGING NEEDS OF SOCIETY
© 2024 the Authors
ISBN 978-1-032-54816-6
DOI 10.1201/9781003431749-663
Open Access: www.taylorfrancis.com, CC BY-NC-ND 4.0 license

ECSMGE 24
XVIII EUROPEAN CONFERENCE ON SOIL MECHANICS AND GEOTECHNICAL ENGINEERING

Pisão dam. Multi-purpose hydraulic scheme of Crato - Portugal. Issues involving the natural materials availability

Barrage de Pisão. Schéma hydraulique polyvalent de Crato - Portugal. Questions liées à la disponibilité des matériaux naturels

G. Tavares*, S. Oliveira, H. Lopes, J. Camões Lourenço
TPF Consultores, Lisboa, Portugal

N. Rodrigues
Lisboa, Portugal

**goncalo.tavares@tpf.pt*

ABSTRACT: This article addresses the issues related to the geotechnical design of a zoned embankment dam, about 50 m high, located in the centre-south of Portugal. It addresses, more specifically, the issues related to the research and characterization of borrow areas for the various natural construction materials and the geometric optimization of the dam to maximize the exploitation of the various materials within the future submerged area of the reservoir, thus minimizing the environmental impacts caused by open pit exploitation outside this area, or by transport from commercial exploitations located at great distances.

RÉSUMÉ: Cet article aborde les enjeux liées à la conception géotechnique d'un barrage en remblai zoné, d'environ 50 m de hauteur, situé dans le centre-sud du Portugal. Il aborde plus spécifiquement les défis liées à la recherche et à la reconnaissance de zones d'emprunt pour les divers matériaux naturels de construction et à l'optimisation géométrique du barrage, afin de maximiser l'utilisations des différents matériaux au sein de la future zone immergée du réservoir, réduisant ainsi les impacts environnementaux résultants de l'exploitation à ciel ouvert en dehors de cette zone, ou du transport depuis des exploitations commerciales situées à de grandes distances.

Keywords: Dam; construction materials; environment.

1 INTRODUCTION

The Pisão Dam is the main asset of the Crato Multi-Purpose Hydraulic Project, whose primary objective is the establishment, in the northeast region of Alentejo, of a new strategic water reserve. Having multiple purposes, this Project will allow the supply of water for human consumption, will enable the irrigation of around 5400 ha of agricultural fields and will have an estimated installed capacity for the production of electrical energy of about 150 MW in full operation. The energy will be produced through a set of photovoltaic plants, installed on land and over the stored water.

The first studies for the dam date back to the 60s and 70s of the last century. Since then, several geological and geotechnical studies have been carried out in different phases, with emphasis not only on the site of the dam and hydraulic structures, but also on the construction materials research.

Given the geometry of the valley at the dam site, characterized by a large amplitude, the option for an embankment dam was always the only one that seemed feasible, with the solution for the dam's typical cross section being entirely conditioned by the construction materials available at the site.

2 GEOLOGICAL AND GEOTECHNICAL FRAMEWORK

The dam will be located approximately 20 km west of Vila do Crato, implanted in Ribeira de Seda. At the dam's site, the river runs on the contact between geological formations of different strengths, which results in a quite asymmetrical valley. In fact, granite formations occur on the left bank, which, due to their great strength, gives rise to more vigorous reliefs with steep slopes, whilst, on the right bank, softer schist formations occur, resulting in a relatively wavy and soft relief. About 85% of the works are located in the right bank, involving the schist rock mass.

In the right bank, dominated by schist formations, the rock mass is covered by residual soils presenting

reduced thickness. The rock mass is often observed at the surface being these soils inexistent.

Below the residual soils, grey schists predominate. Although rarely, greywacke levels have also been detected. The rock mass presents a weathering profile corresponding to a thin horizon of weathered and disaggregated rock, quickly passing to a horizon of moderately to slightly weathered and fractured rock.

In the left bank, where granite formations occur, the residual soils are more abundant, and the weathering profile is more irregular.

3 GENERAL CHARACTERISTICS OF THE DAM

The Pisão Dam, with a volume of about 2 700 000 m^3 and a crest length of 1382 m, will have a zoned embankment solution (Figure 1), with a low permeability core made of fine clayey soils (1). The upstream and downstream shells (3) will be made of soil-rockfill mixture, with a coarse sand with fines prism (2) in the transition zone between the upstream shell and the core (1). Such prism will allow the gradual reduction of permeabilities from upstream to downstream, as well as a transition in terms of stiffness.

In geometric terms, the embankment dam cross section has a maximum height of around 54 m above the foundation and a crest width of 10 m. The upstream and downstream slopes will have an inclination of 1V:2.5H and 1V:2H, respectively. The downstream slope will include three berms, 3.0 m wide, located at elevations 208.8 m, 221.8 m and 236.8 m (Figure 1).

The internal drainage system consists of a sub vertical filter, 3.0 m wide, which extends downstream at the base, through a drainage blanket. At the bottom of the valley, the 1.5 m thick drainage blancket, extends to the downstream slope face, guaranteeing the exit of the seepage. This drainage blancket is extended laterally to the abutments, and includes outlets distributed along the right bank, due to the crossing of several secondary water lines.

At the downstream shell, a rockfill toe (E2) was defined which, in addition to improving the slope stability conditions, will protect the embankment from water flooding during spillway discharges. In addition, the upstream slope face will be protected from wave-induced erosion by a protective rockfill layer (E1), beneath which a filter layer (F1) will be placed.

4 BORROW AREAS AND MATERIAL CHARACTERIZATION

4.1 General Considerations

In the initial studies (late 60s / early 70s of the 20th century), the solution considered for the dam involved a homogeneous cross section, built with residual soils from granite rock mass. Later, at the beginning of the 21st century, a review of the type of dam was carried out, in light of technological advances in dam construction, resulting in adopting a zoned cross section, with a clayey core and soil-rockfill mixture for the shells.

Since then, construction materials studies have focused, above all, on researching clayey materials for the construction of the core. To this end, the research began by essentially being confined to the future reservoir area, as required by good practices. However, given the scarcity of soils in the region with suitable characteristics for use in the dam core, namely fines content and plasticity requirements, the research was extended to areas located outside the reservoir, being the main concern the quantity assessment of the available materials.

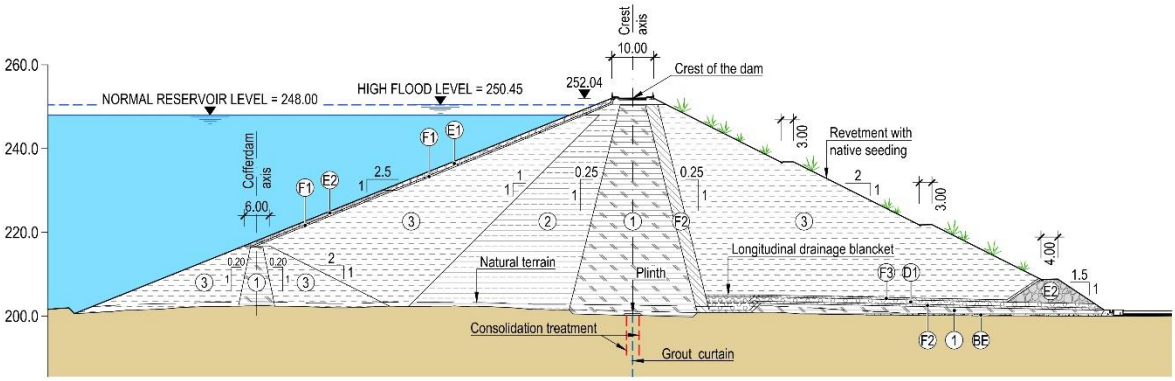

Figure 1. Typical cross-section of the da.m for the highest section (Aqualogus / TPF, 2023a).

4.2 Borrow areas

When defining the borrow areas, the main objective was to maximize the exploitation of the various materials within the future submerged area of the reservoir. Therefore, it was considered that the soil-rockfill mixtures for the shells would come from the excavations to be carried out on the right bank, whether resulting from the implementation of the bottom outlet or the creation of borrow areas inside the future reservoir, involving the highly weathered and highly fractured upper part of the rock mass as well as the residual soils cover. The coarse sand with fines prism would be made up of granitic residual soil from either the excavations for the spillway or the creation of borrow areas inside the reservoir area, on the left bank. The biggest challenge was then the identification of soils with suitable characteristics for placement in the core, and specially in sufficient quantity. With that in mind, geotechnical investigations surveys were carried out involving seismic refraction and excavation pits with sample collection. Along the different phases of the dam studies, since the late 60s / early 70s of the 20th century until 2021, a total of 57 seismic refraction tests, 48 excavation pits were executed and 90 samples were collected and submitted to laboratory testing.

Table 1 shows the distribution of the collected samples by borrow area.

Table 1. Samples submitted to laboratory testing (Aqualogus / TPF, 2023b).

Borrow area	Geological formation	Location referring to reservoir	Samples
E1	Schist	Inside	19
E2	Schist	Inside	32
E3	Ultrametamorphic rocks	Outside	17
E4	Granite	Inside	10
E3a	Schist	Outside	4
E3b	Schist	Outside	1
E3c	Schist	Outside	0
E3d	Schist	Partially inside	3
E3e	Ultrametamorphic rocks	Partially inside	4

4.3 Material characterization

Grain size distribution curves, Atterberg limits and specific gravity were determined, as well as the compaction and permeability characteristics. Table 2 presents the average values obtained in the laboratory tests.

Table 2. Average values of the index properties (Aqualogus / TPF, 2023b).

	< #200 (%)	PI (%)	w_{opt} (%)	$\gamma_{d,max}$ ($kN \cdot m^{-3}$)	G_s (.)	k ($m \cdot s^{-1}$)
1	33	10	13	18.9	2.68	10^{-9}
2	10	-	10	19.9	2.74	10^{-7}
3	12	-	9	20.0	2.67	10^{-7}

1 – Clayey soils; 2 – Sandy soils; 3 – Soil-rockfill mixtures

Regarding the mechanical properties of strength and stiffness, the materials were characterized through undrained consolidated triaxial tests (CU), with measurement of pore pressures. For soil-type materials, to be applied in the core (fine soils) and in the transition zone (coarse sand with fines prism), the specimens were tested in normal triaxial chambers (4''). In the case of soil-rockfill mixtures, it was necessary to use 230 mm chambers, to guarantee representation in relation to the maximum particle size of the mixture.

The specimens were remoulded complying with the optimal characteristics of the compaction test and were then consolidated to a pre-established stress. Finally, they were subjected to triaxial shear by increasing the deviatoric stress, q, until an axial deformation of 20% was reached.

The soils' strength (c' and ϕ') and stiffness design values were determined from the undrained triaxial tests' responses. Compatible secant drained Young modulus, E', was inferred for different levels of axial strain, namely for the axial strain associated with $q/p'max$, for 0.10% and 1% strain. The Poisson coefficient values were adopted after the literature values. Table 3 presents the considered design values.

Table 3. Design values for strength and stiffness properties (Aqualogus / TPF, 2023b).

	φ' (º)	c' (kPa)	E' (Mpa)	ν' (.)
1	32	0	40	0.35
2	37	0	50	0.30
3	40	0	70	0.30

1 – Clayey soils; 2 – Sandy soils; 3 – Soil-rockfill mixtures

5 MATERIAL AVAILABILITY AND DESIGN OPTIMIZATION

In any embankemnt dam, the most important element corresponds to the waterproofing element, which will ensure that there will be no relevant seepage through the body of the dam. In the case of the Pisão Dam, this element is materialized by the core, made up of clayey soils. Finding soil with the appropriate characteristics and in sufficient quantity for the construction of the dam core therefore became the main constraint of the material research studies.

Although initially, the site seemed very promising in terms of the presence of this type of soil since it is usually expected that schist rock masses give rise to clayey residual soils, what was found was a reduced quantity of these soils given the weathering profile of the rock mass. In fact, the schist rock mass presented a thin horizon of residual soil of about 1.0 m thickness on average (typical values between 0.5 and 1.6 m), or often inexistent. This profile was considered to lead to insufficient available volumes and important difficulties in the "clean" exploration of too thin layers of material, due to possible contamination either with top soil or with coarse material. Consequently, it was decided to search for borrow areas with better exploitation potential outside the future reservoir area, while at the same time to reduce to a minimum the need for clayey materials.

Fine materials were identified in greater abundance outside the area of the future reservoir in a radius of 1 to 3 km of the dam, corresponding to residual soil from ultrametamorphic rocks, specifically migmatite gneisses. This rock mass presented a more regular weathering profile and an average thickness of residual soils of about 1,3 m (typical values between 0.9 and 2.1 m).

Simultaneously, the core geometry was optimized, resulting in a thinner core of fine material with a minimum width of 6.0 m and 4V:1H slopes. The geometry optimization allowed the reduction in the need for fine soils from about 529 800 m^3 to 401 500 m^3.

6 CONCLUSIONS

The Crato Multi-Purpose Hydraulic Project, which includes the Pisão Dam, was considered an anchor of development by all the 15 municipalities of Alto Alentejo, by the population and by the Government, being an historical aspiration and demand dating back more than half a century.

Given this strategic importance, it became necessary to make decisions in the design stage that, although not the most desirable, would make the dam's construction viable, such as the exploitation of materials outside the future reservoir area.

However, given the thickness of exploitable material, it was considered that the implementation of current environmental recovery measures would straightforwardly reverse the impacts of this exploitation, returning the area in question to its usual use.

ACKNOWLEDGEMENTS

The AQUALOGUS - TPF Consultores Design Consortium would like to thank the Comunidade Intermunicipal do Alto Alentejo, CIMAA, for the authorization of this paper.

REFERENCES

AQUALOGUS / TPF (2023a). Assessment of the Susceptibility and Integrated Development of Water and Energy Resources of the Multi-Purpose Hydraulic Project of Crato. Component B) Study of Flow Regulation Infrastructures. Primary Infrastructures. Final Study. Volume 1 - Project Brief. Tome 1 – General Description. (In Portuguese).

AQUALOGUS / TPF (2023b). Assessment of the Susceptibility and Integrated Development of Water and Energy Resources of the Multi-Purpose Hydraulic Project of Crato. Component B) Study of Flow Regulation Infrastructures. Primary Infrastructures. Final Study. Volume 1- Project Brief. Tome 3 – Geological and Geotechnical Study. (In Portuguese).

Proceedings of the XVIII ECSMGE 2024
GEOTECHNICAL ENGINEERING CHALLENGES
TO MEET CURRENT AND EMERGING NEEDS OF SOCIETY
© 2024 the Authors
ISBN 978-1-032-54816-6
DOI 10.1201/9781003431749-664
Open Access: www.taylorfrancis.com, CC BY-NC-ND 4.0 license

ECSMGE 24
XVIII EUROPEAN CONFERENCE ON SOIL MECHANICS AND GEOTECHNICAL ENGINEERING

Numerical evaluation of the long-term performance of energy piles in hot-dominated climates

Évaluation numérique de la performance à long terme des pieux énergétiques dans les climats à dominante chaude

S. ten Bosch*, E. Ravera, L. Laloui
EPFL, Lausanne, Switzerland

**sofie.tenbosch@epfl.ch*

ABSTRACT: Using energy piles to extract geothermal energy for heating needs has been the main focus of research in energy geostructures. In hot-dominated climates, the interest is to inject heat into the ground and extract energy for space-cooling purposes. This study evaluates the feasibility of energy piles in this operation mode through 3D numerical modelling for a case study targeted to provide 40% of the total cooling demand of a typical building in Dubai. The unbalanced energy demand causes an increase in the outlet temperature of the heat carrier fluid in the geothermal pipes and the radial soil temperature over time. Observation of long-term behaviour, however, indicates that the temperature increase is most significant in the initial years and stabilizes over time. The heat pump operating limit in terms of maximum temperature is respected over 50 years due to this stabilization behaviour. The results show that energy piles are highly effective in reducing carbon emissions and supplying renewable energy to buildings in hot climates, addressing a key societal challenge.

RÉSUMÉ: L'utilisation de pieux énergétiques pour extraire l'énergie géothermique à des fins de chauffage a été le principal axe de recherche dans le domaine des géostructures énergétiques. Dans les climats chauds, l'intérêt est d'injecter de la chaleur dans le sol et d'en extraire de l'énergie pour refroidir les bâtiments. Cette étude évalue la faisabilité des pieux énergétiques dans ce mode de fonctionnement à l'aide d'une modélisation numérique en 3D pour une étude de cas visant à fournir 40 % de la demande totale de refroidissement d'un bâtiment type à Dubai. La demande d'énergie déséquilibrée entraîne une augmentation de la température de sortie du fluide caloporteur dans les tuyaux géothermiques et de la température radiale du sol au fil du temps. L'observation du comportement à long terme indique toutefois que l'augmentation de la température est plus importante au cours des premières années et se stabilise avec le temps. La limite de fonctionnement de la pompe à chaleur en termes de température maximale est respectée sur 50 ans en raison de ce comportement de stabilisation. Les résultats montrent que les pieux énergétiques sont très efficaces pour réduire les émissions de carbone et fournir de l'énergie renouvelable aux bâtiments dans les climats chauds, ce qui permet de relever un défi sociétal majeur.

Keywords: Numerical modelling; energy piles; hot-dominated climates; cooling systems; geothermal energy.

1 INTRODUCTION

The pressing challenge of providing sustainable energy for a growing global population while reducing greenhouse gas emissions emphasizes the importance of sustainable energy sources. Space cooling is a major driver of residential energy consumption in hot climates, and its demand is expected to triple by 2050 (IEA, 2018). Dubai, UAE, is a region where cooling represents a substantial portion of energy use. The need for sustainable cooling sources here is underlined by a doubling of CO_2 emissions in the UAE over the past three decades.

Energy geostructures, such as energy piles, can be used as an innovative solution for space conditioning purposes. Energy piles utilize ground-embedded structures for heating or cooling and have demonstrated strong performance in various applications (e.g., Brandl, 2006; Laloui & Rotta Loria, 2019). However, research has primarily focused on its heating applications, with less attention to cooling use in hot-dominated regions. The impact of an unbalanced energy demand has been explored by Akrouch et al. (2020), Olgun et al. (2015) and Sutman et al. (2020), but never with an only-cooling demand in the setting of an arid region.

This study aims to assess the feasibility and long-term energy performance of using energy piles exclusively for cooling in hot-dominated climates, with Dubai as a representative case. The work employs 3D time-dependent numerical modelling to simulate cooling energy extraction, offering insights into system operation in arid regions.

2 METHODOLOGY

Numerical evaluation of a representative case study in Dubai is achieved using a 3D finite element model in COMSOL Multiphysics 5.6.

2.1 Dubai case study description

An energy pile foundation with 33 20m-length and 0.8m-diameter piles is envisaged for a building in the coastal belt region of Dubai. HDPE pipes in the pile have a U-shaped configuration. A sandy soil profile characterizes the project location, and a variation in thermal conductivity over the depth of the profile is included in the study.

It is targeted to provide 40% of the total cooling demand of this building through its energy foundation. The required daily cooling load per energy pile is shown in Figure 1. The limitation of the feasibility of this technology lies in the reversed heat pump characteristics, as also identified by Alshehri et al. (2021). The outlet temperature (T_{out}) of the heat carrier fluid (HCF) in the energy pile should not reach the capacity limit temperature for the heat pump over its lifetime. The reversed heat pump employed in this study has a cooling capacity of 0.68 kW per energy pile, an energy efficiency ratio of 5.07 and the maximum allowable outlet temperature of the HCF is 45°C.

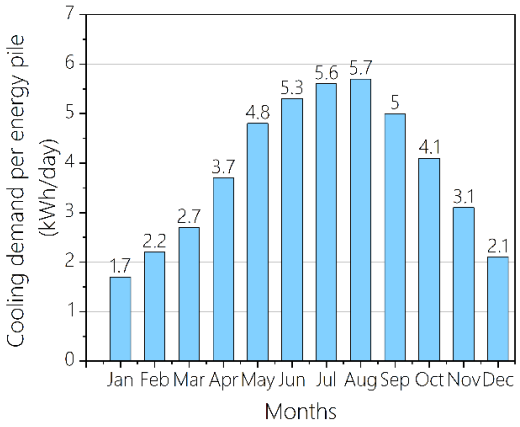

Figure 1. Monthly variation of daily cooling demand per energy pile.

2.2 Mathematical framework

This study employs a numerical modelling framework to simulate the energy piles, the ground and the geothermal pipes embedded within them. Conduction heat transfer characterizes the soil using an equivalent thermal conductivity approach, the concrete of the energy piles, and HDPE pipe wall domains. Similar frameworks have been effectively used in previous evaluations of energy geostructures (e.g., Rotta Loria, 2020) and it is thus not repeated here for concision.

The model simulates daily reversed heat pump operation, where cooling extraction continues until the calculated energy matches the daily energy demand. This approach, previously successful in prior work (Ravera, 2021; Sutman et al., 2020), is repeated for each simulated day. More information about the modelling framework can be found in Ten Bosch et al. (2024).

2.3 Numerical model description

The model, with its boundary conditions and mesh, is shown in Figure 2.

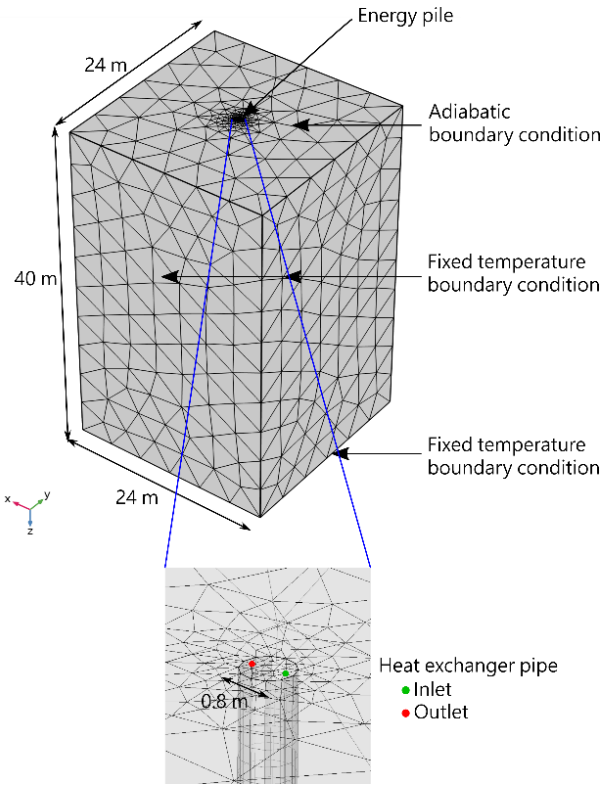

Figure 2. Setup of the numerical model for one energy pile in Dubai showing the applied boundary conditions and meshing.

Table 1. Thermal analysis model parameters.

Parameter	Value
HCF	water
Flow velocity	1.0 m/s
Ground thermal conductivity (variation over depth)	0-3 m: 0.939 W/(m·°C) 3-9 m:0.726 W/(m·°C) 9-13.5m: 1.192 W/(m·°C) >13.5m: 0.798 W/(m·°C)
Ground density	1537 kg/m^3
Ground specific heat	961 J/(kg·°C)
Pipe inner diameter	25.4 mm
Pipe surface roughness	0.0015 mm
Pipe wall thickness	3.25 mm
Pipe thermal conductivity	0.42 W/(m·°C)

Initial and boundary conditions include fixed temperature boundaries at the model's side and bottom, maintaining temperatures at the initial ground temperature of 30°C, representing Dubai's yearly average air temperature. Additionally, a thermal insulation boundary condition is applied at the model's surface. Model parameters that were used in the simulations are shown in Table 1.

3 DUBAI APPLICATION

3.1 One-year evaluation

The analysis of the system's behaviour over a year reveals fluctuations in the HCF outlet temperature. This one-year analysis is repeated with varying HCF flow velocities and internal pipe diameters, representing real-world conditions. The results are shown in Figures 3A, 3B. Daily temperature variations correspond to the activation and deactivation of the heat pump, driven by the cooling energy demand. Peak outlet temperatures coincide with higher cooling demands, notably in August. Despite these fluctuations, the HCF temperature remains within the heat pump's operating range for all model variations, indicating potential for energy-pile-based cooling.

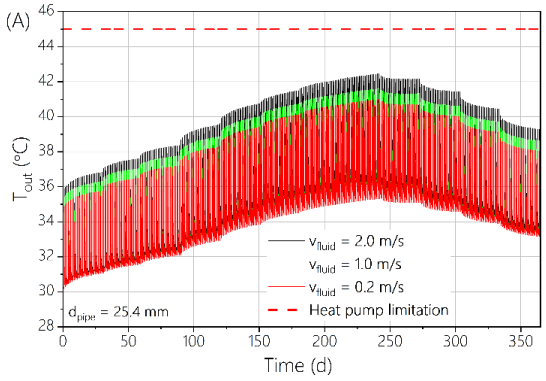

Figure 3A. One-year evaluation of the outlet temperature of the HCF fluid for variation of HCF flow velocity.

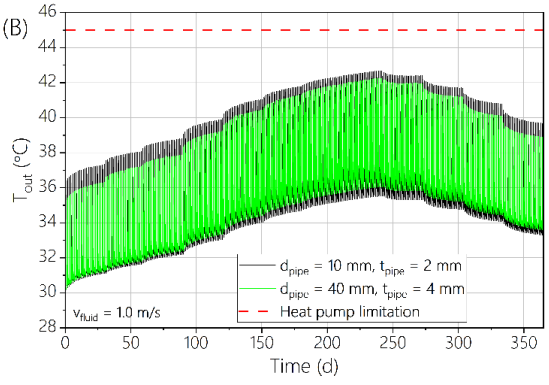

Figure 3B. One-year evaluation of the outlet temperature of the HCF fluid for variations of the pipe diameter.

Considering the sensitivity to the designs parameters, results indicate that lower flow velocities and wider pipe diameters reduce maximum outlet temperatures. Changing HCF flow velocities also affects operating costs and thus requires careful optimization.

3.2 Long term evaluation

A model with an enlarged soil domain (h = 40 m, x, y = 80 m) is used for a long-term case study evaluation to avoid boundary condition interference during the analysis.

Over a 50-year period, the system's energy performance is assessed, with Figure 4 illustrating the gradual increase in outlet water temperature. After an initial rapid response, the temperature increase stabilizes, remaining within the heat pump's capacity range.

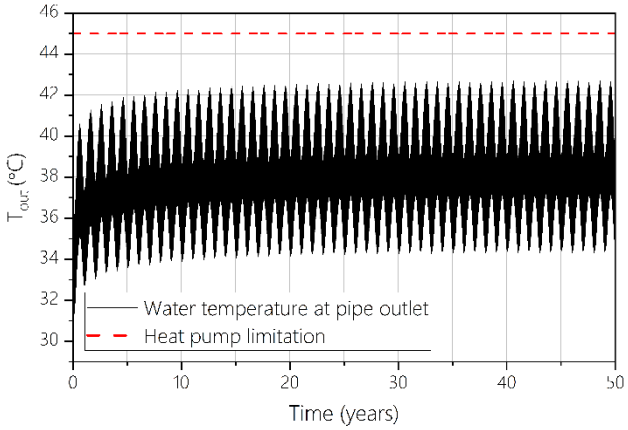

Figure 4. Long-term evaluation of the HCF outlet temperature for the Dubai case study.

Furthermore, the impact on the soil temperature around the energy pile could also be evaluated. The influence of 50 years of cooling energy extraction on soil temperature distribution at the surface level is presented in Figure 5, highlighting the highest temperatures near the pile location.

3.3 Discussion

The presented results are obtained with a single energy pile, thus, for buildings with a pile spacing exceeding the zone of influence, it is demonstrated that geothermal activation of the foundation can meet 40% of the building's energy demand. In cases where piles are closely spaced, interactions among piles should be considered. This overlapping influence can impact system performance. An assessment according to an infinite pile group model similar to Makasis & Narsilio (2022) over one year is used and indicates effects within a 10% increase of outlet temperature at the end

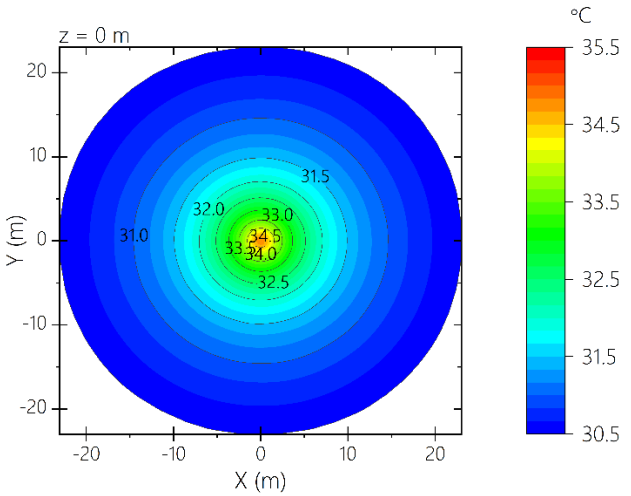

Figure 5. Ground temperature evaluation after 50 years of cooling energy extraction.

of one year for a pile spacing of 6.75 times the pile diameter using the Dubai case study settings.

Potential ground water flow is not considered in this study but is expected to have a positive influence through its cooling effect on the increasing soil temperatures surrounding the energy pile.

4 CONCLUSIONS

This work investigates the long-term behaviour of cooling energy extraction using energy piles in hot-climates. A 3D numerical model is used to assess a case study aiming to supply 40% of a typical building's cooling energy demand through the use of the energy foundation in Dubai. The unbalanced energy demand at this location causes an initial rise in heat carrier fluid and soil temperatures during operation of the energy pile. However, it is found that these increases stabilize over time, indicating the technology's viability even under such conditions. Furthermore, the numerical results for an isolated energy pile suggest it can meet 40% of the total cooling demand for the building over at least 50 years, respective heat pump functionality limitations regarding heat carrier fluid temperature.

ACKNOWLEDGEMENTS

Some of the used data inputs were inspired from measurements made available by E.construct.

REFERENCES

Akrouch, G. A., Sánchez, M., & Briaud, J. L. (2020). Thermal performance and economic study of an energy piles system under cooling dominated conditions. *Renewable energy*, *147*, 2736-2747. https://doi.org/10.1016/j.renene.2018.11.101.

Alshehri, F., Beck, S., Ingham, D., Ma, L., & Pourkashanian, M. (2021). Sensitivity analysis of a vertical geothermal heat pump system in a hot dry climate. *Renewable Energy*, *178*, 785-801. https://doi.org/10.1016/j.renene.2021.06.058.

Brandl, H. (2006). Energy foundations and other thermo-active ground structures. *Géotechnique*, *56*(2), 81-122. https://doi.org/10.1680/geot.2006.56.2.81.

IEA. (2018). *The Future of Cooling: Opportunities for energy-efficient air conditioning*. International Energy Agency. https://iea.blob.core.windows.net/assets/0bb45525-277f-4c9c-8d0c-9c0cb5e7d525/The_Future_of_Cooling.pdf.

Laloui, L., & Loria, A. F. R. (2019). Analysis and design of energy geostructures: theoretical essentials and practical application. Academic Press. https://doi.org/10.1016/C2017-0-04166-6.

Makasis, N., & Narsilio, G. A. (2022). Investigating the thermal performance of energy soldier pile walls. *Geomechanics for Energy and the Environment*, *30*, 100242. https://doi.org/10.1016/j.gete.2021.100242.

Olgun, C. G., Ozudogru, T. Y., Abdelaziz, S. L., & Senol, A. (2015). Long-term performance of heat exchanger piles. *Acta Geotechnica*, *10*, 553-569. https://doi.org/10.1007/s11440-014-0334-z.

Ravera, E. (2021). *Cyclic thermomechanical behaviour of pile-soil interface and design methods for energy pile foundations*. PhD thesis, EPFL, Lausanne, Switzerland.

Rotta Loria, A. F. (2020). Energy geostructures: Theory and application. In *E3S web of conferences* (Vol. 205, p. 01004). EDP Sciences. https://doi.org/10.1051/e3sconf/202020501004.

Sutman, M., Speranza, G., Ferrari, A., Larrey-Lassalle, P., & Laloui, L. (2020). Long-term performance and life cycle assessment of energy piles in three different climatic conditions. *Renewable Energy*, *146*, 1177-1191. https://doi.org/10.1016/j.renene.2019.07.035.

ten Bosch, S., Ravera, E., & Laloui, L. (2024). Performance of energy piles foundation in hot-dominated climate: A case study in Dubai. *Renewable Energy*, *220*, 119632. https://doi.org/10.1016/j.renene.2023.119632.

Proceedings of the XVIII ECSMGE 2024
GEOTECHNICAL ENGINEERING CHALLENGES
TO MEET CURRENT AND EMERGING NEEDS OF SOCIETY
© 2024 the Authors
ISBN 978-1-032-54816-6
DOI 10.1201/9781003431749-665
Open Access: www.taylorfrancis.com, CC BY-NC-ND 4.0 license

ECSMGE 24
XVIII EUROPEAN CONFERENCE ON SOIL MECHANICS AND GEOTECHNICAL ENGINEERING

Strength, microstructural, and leaching characteristics of phosphogypsum-fly ash mixtures

Caractéristiques de résistance, de microstructure et de lixiviation des mélanges de phosphogypse et de cendres volantes

Y. Thakur, A. Tyagi*, S. Sarkar
Department of Civil Engineering, Indian Institute of Technology Roorkee, India
**akanksha.tyagi@ce.iitr.ac.in*

ABSTRACT: Phosphogypsum (PG) is a waste product from the fertilizer industries producing phosphoric acid and phosphate fertilizers. On the other hand, fly ash (FA) is the by-product of thermal power plants. This paper presents a comprehensive study of the application of PG in combination with FA in road construction. The PG-FA mixtures are prepared in 70:30, 60:40, 50:50, and 40:60 ratios at 97% of maximum dry density (MDD) and corresponding water content. The California bearing ratio (CBR) of mixes is then evaluated after 4 days of soaking. The risk of contamination is also determined by performing Toxicity Characteristic Leaching Procedure (TCLP). In addition, Field Emission-Scanning Electron Microscopy (FE-SEM) is conducted to identify the microstructural changes and interaction of PG-FA mixtures. Results indicate that all the mix proportions have CBR values greater than 10%, while the PG:FA proportion of 50:50 was optimal. The TCLP test results suggest that the concentrations of various trace metals are within the threshold limits specified by USEPA (1992).

RÉSUMÉ: Le phosphogypse (PG) est un déchet provenant des industries d'engrais produisant de l'acide phosphorique et des engrais phosphatés. En revanche, les cendres volantes (FA) sont un sous-produit des centrales thermiques. Cet article présente une étude complète de l'application du PG en combinaison avec le FA dans la construction de routes. Les mélanges PG-FA sont préparés dans des rapports 70:30, 60:40, 50:50 et 40:60 à 97 % de la densité sèche maximale (MDD) et de la teneur en eau correspondante. Le rapport portant californien (CBR) des enrobés est ensuite évalué après 4 jours de trempage. Le risque de contamination est également déterminé en effectuant une procédure de lixiviation des caractéristiques toxiques (TCLP). De plus, la microscopie électronique à balayage par émission de champ (FE-SEM) est réalisée pour identifier les changements microstructuraux et l'interaction des mélanges PG-FA. Les résultats indiquent que toutes les proportions de mélange ont des valeurs CBR supérieures à 10 %, tandis que la proportion PG:FA de 50:50 était optimale. Les résultats des tests TCLP suggèrent que les concentrations de divers métaux traces se situent dans les limites spécifiées par l'USEPA (1992).

Keywords: Phosphogypsum; fly ash; CBR; microstructure; leaching.

1 INTRODUCTION

One of the major challenges in the field of road construction is the high demand for materials required for embankment and pavement construction. On the other hand, industries are producing a lot of waste that poses storage problems and high risks to human health and the ecosystem. For example, the phosphate and phosphoric industry generate enormous amounts of waste known as Phosphogypsum (PG). The annual production of PG is approximately 12-13 mt/yr in India, in which only about 40-50% of the PG generated is being used in the fertilizer industry, cement manufacturing, gypsum boards, and as road materials (Havanagi et al., 2018; Thakur et al., 2023a). Vast amounts of fly ash (FA) are generated as waste from thermal power plants and steel-based industries. FA has been utilized for the construction of road embankments in India for the last few decades. IRC:SP:58 (IRC, 2001) specifies the guidelines for constructing the FA embankments. However, no such guidelines exist for the use of PG for road construction. Hence, the bulk utilization of PG and FA in road construction will not only preserve natural materials but also safeguard valuable lands. The usage of PG is restricted due to the possible emission of heavy metals, fluoride, and radionuclides, as reported by several countries (Tayibi et al., 2009).

In a study conducted by Sharma and Walia (2017), it was found that the substitution of soil with 20% FA and 1-7% PG effectively met the IRC:37 (IRC, 2018) requirement of subgrade California bearing ratio

(CBR) of 2% to 10% to be used as embankment materials in flexible pavement. Havangi et al. (2018) observed the average CBR index of raw PG as 26%. The higher CBR value indicates the feasibility of using PG as a subgrade material. Recently, Thakur et al. (2023b) recently reported 4-days soaked CBR value of 31% for raw Indian PG. Ngo et al. (2022) investigated the effect of cement and lime content on various geotechnical properties, including compaction characteristics, unconfined compressive strength (UCS), modulus of elasticity, and CBR of a stabilized PG and FA mixture, in which PG was replaced with 10-20% FA and stabilized with 4-10% cement with or without the addition of lime. The UCS and CBR values remarkably improved with the increment of cement content (Ngo et al., 2022). A mixture of 80% PG, 10% FA, and 10% cement achieved a CBR value of approximately 10%, for the 7 days of curing, and more than 40%, after the 28 days of curing, at 95% and 98% relative compaction (Ngo et al., 2022).

In the last few years, extensive research has been carried out on PG-based mixes, such as PG-lime/PG-cement (Rezende et al., 2017), PG-FA/PG-FA-lime/ PG-FA-cement (Amrani et al., 2020; Meskini et al., 2021, Ngo et al., 2022), for their effective use in road construction material. However, no such studies are available on the Indian PG and FA mixtures.

Thus, this paper aims to investigate the potential utilization of Indian PG and FA mixtures for road construction by performing laboratory experiments, such as CBR. The results obtained from CBR are further explained using observations from Field Emission-Scanning Electron Microscopy (FE-SEM) images. In addition, Toxicity Characteristic Leaching Procedure (TCLP) tests are also conducted to evaluate the suitability of the PG-FA mix as subgrade material.

2 MATERIALS AND METHODOLOGY

2.1 Materials

The PG used in this study is collected from Paradeep Phosphate Limited, Paradeep, Orissa, India. FA is procured from a thermal power plant located at Hisar, Haryana, India. The particle size distribution curve of raw materials used in this study are shown in Figure 1. The PG and FA are classified as non-plastic silt based on the particle size distribution curve.

The chemical composition of raw materials was obtained from X-ray fluorescence (XRF). According to Thakur et al. (2023b), PG majorly comprises SO_3 (52-54%), CaO (42-44%), and small amounts of P_2O_5 (1-1.6%), and Al_2O_3 (0.11-0.17%). The FA majorly consisted of SiO_2 (56-59%), Al_2O_3 (25-32%), Fe_2O_3 (4-8%), and K_2O (1-1.28%) and was categorized as class F as per ASTM C-09 (ASTM, 2013).

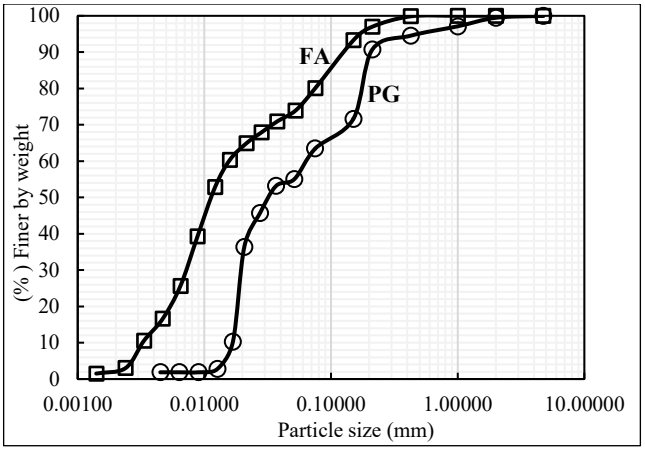

Figure 1. Particle size distribution curve of FA and PG (plot for PG taken from Thakur et al., 2023b).

2.2 Testing procedure

The California bearing ratio (CBR) is performed on different proportions of PG and FA mixtures, i.e.,70:30, 40:60, 50:50, and 60:40. All the samples are soaked under water for 4 days before conducting CBR test. The optimum mix satisfying the strength criteria is tested for TCLP. The mix proportions in this study are designated as 70PG30FA, 40PG60FA, 50PG50FA, and 40PG60FA.

2.3 Mixing procedure

To prepare the specimens, the required amounts of PG, FA, and water are weighed to 97% of maximum dry density (MDD) and corresponding moisture content. PG is replaced with different percentages of FA equivalent to 30, 40, 50, 60, and 70 % dry by weight, and then the required amounts of water are mixed. All prepared mixtures are kept in plastic bags for 24 hours for mellowing and homogeneity. Later, all prepared specimens are soaked in water for 4 days and then tested for CBR index.

2.4 Test performed

2.4.1 California bearing ratio (CBR)

The CBR test for all mix proportions is performed as per IRICEN, 2018. The samples are prepared at 97% MDD and their respective moisture content in mold diameter 152 mm and height 178 mm. All the samples are soaked under water for 4 days, then the soaked CBR test is carried out to evaluate the suitability of the mixture for road subgrade applications. The soaked CBR test is performed on PG-FA mixtures considering the adverse climate conditions on a pavement being subjected during heavy rainfall/flood.

2.4.2 Scanning electron microscopy (SEM)

For SEM analysis, samples were collected after the CBR test. A small flat piece of each specimen was then immersed into the ethanol to stop the any reactions further. Before conducting SEM, the specimens were dried in the oven at 60 ˚C for 24 hours. The specimen was coated with gold to avoid charging to the top surface. The samples' microstructure was examined using various magnifications and an acceleration voltage of 5 kV.

2.4.3 Leaching test

To assess the environmental performance of the PG-FA mixture, the TCLP test method 1311 (USEPA, 1992) test is carried out. This test is conducted only on the mixed proportion representing the optimum result (i.e., 50PG50FA). In the TCLP test, the PG-FA sample is extracted using the acetic acid solution with a pH of 4.93±0.05. This solution is prepared by adding 64.3 ml of 1M-NaOH with 5.7 ml of glacial acetic acid, then diluting to 1000 ml deionized water. The liquid-solid of 20:1 ratio is maintained for the extraction solution. Then the specimens are rotated for 18 hours at a speed of 30 rpm. After the rotation period, the leachate fluid is extracted and tested for trace element concentration using Microwave Plasma Atomic Emission Spectroscopy (MP-AES).

3 RESULTS AND DISCUSSION

3.1 California bearing ratio (CBR) results

Figure 2 illustrates the CBR test results performed on various PG-FA mixtures. All the mix proportions have values of CBR greater than 10%, which is a desirable value for sub-grade material as per IRC guidelines (IRC, 2018). Further, it is seen that the mixture containing an equal percentage of PG and FA reached the maximum CBR value, beyond which there is a significant decline (Figure 2). This reduction in CBR value may attributed to the non-cohesive nature of FA, which weakens the bond within a mixture and leads to a lower CBR value.

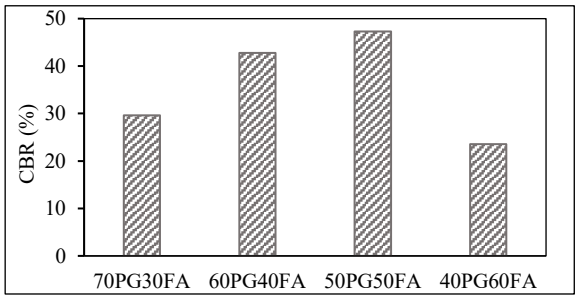

Figure 2. CBR value of different PG-FA mix at 4-day soaking corresponding to 97% relative compaction.

3.2 Microstructural characteristics

Figure 3 illustrates the SEM images of the specimens having minimum and maximum CBR values of 4 days soaking with 40,000× magnification. It is seen that the 40PG60FA specimen has a more visible pore. On the contrary, 50PG50FA shows a comparatively denser microstructure due to the formation of needle-like ettringites, which entrap the FA particles and lead to a denser microstructure. It is noted that the formation of ettringites provides early strength gain and is also known for their ability to expand. Therefore, the 50PG50FA specimen exhibits a higher CBR index than the 40PG60FA specimen. However, researchers also reported that the formation of large ettringite can cause distress and damage to the pavements (e.g., Lee et al., 2005). In this context, managing and preventing large amounts of ettringite is critical to ensure the performance and durability of a pavement. This may include careful material selection, appropriate mix design, and effective construction practices to lessen the negative impacts of ettringites.

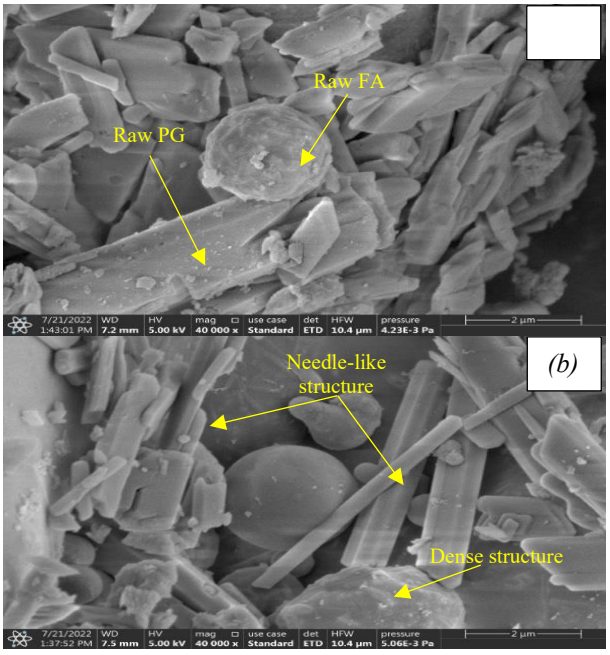

Figure 3. SEM image of (a) 40PG60FA, and (b) 50PG50FA mixes after 4 days soaked CBR test.

3.3 Leaching characteristics

Trace elements are identified by Microwave Plasma Atomic Emission Spectroscopy (MP-AES), with concentrations ranging from 0.01 mg/l to 0.70 mg/l. The selected elements are compared with the threshold limit established by the USEPA (USEPA, 1992). Table 1 shows that the obtained concentrations are below the threshold limit, which suggest that the PG-FA mixture can be used as a road subgrade material from this perspective.

Table 1 Trace element concentrations for 50PG50FA mixture.

Trace metal	Concentration (mg/l)	Threshold limit, mg/l (USEPA 1992)
Zn	0.45 ± 0.10	2.0
Cu	0.70 ± 0.05	-
Ni	0.11 ± 0.05	-
Co	Nd	-
Pb	Nd	5.0
Cr	0.37 ± 0.05	5.0
Cd	Nd	1.0
As	0	5.0
Mo	0.01 ± 0.05	-
V	Nd	-

**Nd= not detected*

4 CONCLUSIONS

The main findings of the present experimental study on PG-FA mixtures are given below:

- All the PG-FA mixtures achieved higher CBR values than the desirable value for sub-grade material, i.e., 10%. The high CBR index was obtained for equal PG and FA proportion (i.e., 50PG50FA). Further increment in FA content led to the decline in the CBR index, attributed to its non-cohesive nature.
- The 40PG60FA specimen has more visible pores, while the 50PG50FA specimen has a denser microstructure due to needle-like ettringites, resulting in a higher CBR index.
- From the TCLP test results, it can be seen that the concentrations of various trace metals are within the threshold limits specified by USEPA (1992).

ACKNOWLEDGEMENTS

Authors are thankful to the Department of Higher Education, Ministry of Education, Government of India for providing MHRD fellowship to first author for his PhD studies.

REFERENCES

Amrani, M., Taha, Y., Kchikach, A., Benzaazoua, M., & Hakkou, R. (2020). Phosphogypsum recycling: New horizons for a more sustainable road material application. Journal of Building Engineering, 30, 101267. https://doi.org/10.1016/j.jobe.2020.101267.

ASTM (2013) Committee C-09 on Concrete and Concrete Aggregates. *Standard specification for coal fly ash and raw or calcined natural pozzolan for use in concrete*. ASTM international.

Havanagi, V., Sinha, A. K., & Parvathi, G. S. (2018). *Characterization of Phosphogypsum waste for Road construction*. *In Proceedings of the Indian Geotechnical Conference,* Bengaluru, India, pp. 13-15.

IRC (Indian Road Congress). (2001). *Guidelines for use of fly ash in road embankment*. IRC:SP:58, New Delhi, India: IRC.

IRC (Indian Road Congress). (2018). *Guidelines for the design of flexible pavements (fourth revision)*. IRC:37. New Delhi, India: IRC.

IRICEN (Indian Railways Institute of Civil Engineering). (2018*). Geotechnical testing for earthwork in railway projects*. IRICEN, 2018, Pune, India.

Lee, H., Cody, R. D., Cody, A. M., & Spry, P. G. (2005). The formation and role of ettringite in Iowa highway concrete deterioration. *Cement and Concrete Research*, 35(2), 332-343. https://doi.org/10.1016/j.cemconres.2004.05.029.

Meskini, S., Samdi, A., Ejjaouani, H., & Remmal, T. (2021). Valorization of phosphogypsum as a road material: Stabilizing effect of fly ash and lime additives on strength and durability. *Journal of Cleaner Production*, 323, 129161. https://doi.org/10.1016/j.jclepro.2021.129161.

Ngo, H. T. T., Dang, V. Q., Ho, L. S., & Doan, T. X. (2022). Utilization phosphogypsum as a construction material for road base: a case study in Vietnam. *Innovative Infrastructure Solutions*, 7(1), 88. https://doi.org/10.1007/s41062-021-00695-7.

Rezende, L. R., Curado, T. D. S., Silva, M. V., Mascarenha, M. M. D. A., Metogo, D. A. N., Neto, M. P. C., & Bernucci, L. L. B. (2017). Laboratory study of phosphogypsum, stabilizers, and tropical soil mixtures. *Journal of Materials in Civil Engineering*, 29(1), 04016188. https://doi.org/10.1061/(ASCE)MT.1943-5533.000171.

Sharma, A., & Walia, B. S. (2017). Effect of Phosphogypsum and Fly ash on the CBR and UCS of clayey soil. *International Journal of Engineering Trends and Technology (IJETT)*–Volume, 50, 266-271.

Tayibi, H., Choura, M., López, F. A., Alguacil, F. J., & López-Delgado, A. (2009). Environmental impact and management of phosphogypsum. *Journal of environmental management*, 90(8), 2377-2386. https://doi.org/10.1016/j.jenvman.2009.03.007.

Thakur, Y., Tyagi, A., & Sarkar, S. (2023a). Utilization of Industrial Waste Phosphogypsum as Geomaterial: A Review. *Journal of Hazardous, Toxic, and Radioactive Waste*, 27(2), 03123001. https://doi.org/10.1061/JHTRBP.HZENG-1181.

Thakur, Y., Tyagi, A., & Sarkar, S. (2023b). Geotechnical and Leaching Characteristics of the Indian Raw Phosphogypsum. *2nd International Conference on Construction Resources for Environmentally Sustainable Technologies*, 20-22 Nov, Fukuoka, Japan.

United States Environmental Protection Agency (US EPA). (1992). *Toxicity characteristics leaching procedure, Method 1311. Test methods for the evaluation of solid waste*.

Proceedings of the XVIII ECSMGE 2024
GEOTECHNICAL ENGINEERING CHALLENGES
TO MEET CURRENT AND EMERGING NEEDS OF SOCIETY
© 2024 the Authors
ISBN 978-1-032-54816-6
DOI 10.1201/9781003431749-666
Open Access: www.taylorfrancis.com, CC BY-NC-ND 4.0 license

ECSMGE 24
XVIII EUROPEAN CONFERENCE ON SOIL MECHANICS AND GEOTECHNICAL ENGINEERING

Advances in groundwater recharge during construction dewatering

Avancées dans la recharge des nappes phréatiques lors de l'assèchement des chantiers

S.D. Thomas*, J. Watson, G.R. French
OGI Groundwater Specialists Ltd, City of Durham, UK

**stephen.thomas@ogi.co.uk*

ABSTRACT: Abstraction of groundwater for consumptive use, such as for drinking water, agriculture, and industrial purposes, regularly requires the granting of a permanent abstraction licence from environmental regulatory bodies. Temporary abstraction of groundwater required for construction, however, has not historically required an abstraction licence. More recently, due to the conservation of groundwater in Europe now being a major challenge, it is becoming more common in European countries that licensing for the temporary abstraction of groundwater during construction dewatering, known as groundwater control, is now required from the environmental regulators of each country. Due to this requirement for licensing, the development of effective techniques for reducing the overall loss of groundwater has become more important. In particular, such conservation techniques include increased use of artificial recharge of groundwater back into the same strata from which it was abstracted. This paper presents three case studies describing a number of groundwater abstraction and recharge systems implemented on major infrastructure construction projects in the United Kingdom.

RÉSUMÉ: Le captage d'eau souterraine à des fins de consommation, par exemple pour l'eau potable, l'agriculture et l'industrie, nécessite régulièrement l'octroi d'un permis de prélèvement permanent auprès d'organismes de réglementation de l'environnement. Toutefois, le prélèvement temporaire d'eau souterraine nécessaire à la construction n'a pas toujours nécessité de permis de prélèvement. Plus récemment, en raison de la conservation des eaux souterraines en Europe qui est maintenant un défi majeur, il est devenu de plus en plus courant dans les pays européens qu'une licence pour le prélèvement temporaire d'eau souterraine pendant l'assèchement des constructions, connue sous le nom de contrôle des eaux souterraines, soit désormais exigée des régulateurs environnementaux de chaque pays. En raison de cette exigence de licence, le développement de techniques efficaces pour réduire la perte globale d'eau souterraine est devenu plus important. En particulier, ces techniques de conservation comprennent l'utilisation accrue de la recharge artificielle des eaux souterraines dans les mêmes strates d'où elles ont été extraites. Cet article présente trois études de cas décrivant un certain nombre de systèmes de captage et de recharge des eaux souterraines mis en œuvre dans le cadre de grands projets de construction d'infrastructures au Royaume-Uni.

Keywords: Groundwater control; water conservation; construction dewatering.

1 INTRODUCTION

Total global groundwater abstraction was estimated to be circa 1000 km^3/annum in 2010; 72 km^3/annum of which was within Europe (Margat and van der Gun, 2013). Although significantly less than estimated global natural recharge (Dillion, Stuyfzand, and Grischeck, 2019), the concentration of abstractions in urban and dry areas has led to substantial groundwater quantity and quality deterioration in a number of regions.

Where abstraction exceeds recharge, water table lowering results in a reduction of baseflow to surface water features, ground subsidence and deterioration of water quality through mechanisms such as saline intrusion and contamination mobilization.

The rapid rise in global groundwater abstraction over the past century has resulted in groundwater resource sustainability concerns. This in turn has led to an increased drive to advance and adopt intentional artificial recharge systems, also referred to as managed aquifer recharge: MAR (Dillion, Stuyfzand, and Grischeck, 2019). This focus has generally been on long term and permanent operations, as opposed to temporary works such as construction dewatering.

Although not regularly utilised in the United Kingdom, artificial recharge during temporary construction dewatering operations is not a new concept (Bock and Markussen, 2007; Cashman and

Preene, 2013; Powrie and Roberts, 1995; Preene, Roberts, and Powrie, 2016). The additional monetary costs of implementing artificial recharge have historically been a deterrent to construction companies, unless there is a site-specific requirement.

However, in England and Wales, the Water Abstraction and Impounding (Exemptions) Regulations 2017 (Statutory instrument, 2019) came into force in January 2018. These regulations made construction dewatering a licensable activity (abstraction during engineering works was exempt from abstraction licensing prior to this date).

With construction dewatering abstraction now regulated by the Environment Agency (England) and Natural Resources (Wales), contractors are having to revise and refocus their approach to groundwater control and management.

A focus on minimising the environmental impact of construction dewatering operations, to enable a smooth licensing process, is becoming a more economically viable option. The introduction of the regulations has resulted in recharge and cut-off systems, that were previously not contemplated due to cost, now being considered more regularly.

With artificial recharge systems being increasingly designed and utilised as part of temporary construction dewatering operations, this paper aims to document the authors' experience of implementing temporary dewatering recharge systems, together with key advantages and disadvantages. Three recent case studies are also presented.

2 GROUNDWATER CONTROL RECHARGE SYSTEMS

2.1 Recharge system design

Groundwater recharge during temporary construction dewatering involves the recirculation of abstracted groundwater back into the same geological strata by reinjection (via wells) or infiltration (via trenches or shallow wells) (Preene and Fisher, 2015), generally without any intervening use. The recharge system needs to be at an appropriate distance which is logistically feasible, whilst not close enough to prevent the dewatering system from maintaining the water table below the target level.

If designed and implemented appropriately, the groundwater quality remains constant, drawdown at distance is reduced, with negligible net water abstraction from the aquifer.

Abstraction wells need designing to enable water table lowering to the target level, taking into account the reduced radius of influence due to artificial recharge. Wells need to be designed with appropriate filtration to prevent mobilization of ground fines which could clog the recharge wells or cause ground loss.

Recharge wells need careful designing to allow groundwater to readily discharge into the aquifer without causing localized flooding around the well. Wells need to have sufficient slotted length, and a free-flowing annulus filter pack. This is to mitigate water quality issues from clogging (Cashman and Preene, 2013). This becomes more critical the longer the duration of the dewatering operation.

Appropriate pipework is installed from the abstraction wells to the recharge wells. Closed pipework systems are generally utilised to reduce the clogging risks associated with the groundwater being exposed to the atmosphere (e.g. iron ochre precipitation, gas binding etc.). Discharge to recharge wells can be via gravity, or under pumped pressure. Settlement/inspection tanks, sample taps, and/or flowmeters may be installed within the connecting pipework depending on the site conditions and requirements.

A construction dewatering groundwater recharge concept is illustrated in Figure 1.

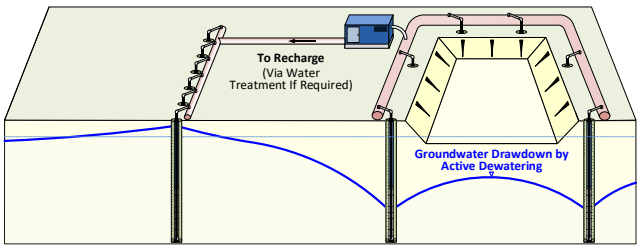

Figure 1. Concept groundwater control recharge system.

2.2 Benefits of utilising a recharge system

The primary benefits of utilising a recharge system on a temporary construction dewatering project are to adhere to legislation, protect surrounding infrastructure by mitigating settlement risk, reduce water disposal costs, conserve water and to protect vulnerable water features from drawdown impacts.

Drawdown at distance is also reduced, preventing the alteration of head gradients, which could lead to reduction in baseflow to surface water systems, deterioration of existing abstractors, and contamination/saline interface migration. A reduction in drawdown also mitigates the risk of settlement from pore water pressure reduction.

With an appropriate recharge system specified, obtaining the relevant abstraction license and discharge permit can be simplified as environmental risks are minimized. This reduces the risk of delays to the project programme.

2.3 Disadvantages of utilising a recharge system

Historically, the main disadvantage to contractors of recharge systems is the cost associated with both their installation and implementation, including their design costs. Access to suitable land to locate recharge wells can be a constraint, particularly in urban areas.

Furthermore, recharge systems are not always a feasible groundwater management strategy, as they are dependent on the hydrogeological conditions encountered. In addition, the recharge system may need to be implemented in tandem with other groundwater control methodologies such as cut-off walls, to work effectively.

Where recharge is feasible, the advantages of a recharge system can only be realised if the groundwater control system is appropriately designed and monitored by competent and experienced personnel (due to the additional risks as documented previously).

Without appropriate design, recharge systems can be overwhelmed resulting in localised flooding around the recharge wells, or the target drawdown not being met. In addition, as groundwater is being directly recharged into the aquifer, it is vital that the system is protected to prevent the possibility of contaminants entering the groundwater body.

3 GROUNDWATER RECHARGE CASE STUDIES

3.1 Tunnel boring machine drive pit, England

The River Humber gas pipeline replacement is a major infrastructure project to replace an existing gas pipeline which stretches circa 5 kilometres beneath the River Humber; a large tidal estuary on the eastern coast of Northern England.

To construct the pipeline, a slurry tunnel boring machine (Figure 2) was driven from the southern bank of the Humber. The depth of the tunnel drive pit, together with a relatively shallow water table (circa 1 m below ground level), required a temporary groundwater control system.

During the Development Consent Order stage (planning permission for developments categorized as Nationally Significant Infrastructure Projects in the UK), the sensitivity of the chalk aquifer on the southern bank of the Humber to any dewatering was identified. The primary concerns of the Environment Agency were (i) the risk of the saline interface mobilizing inland, and (ii) the regional water resource status. The Catchment Abstraction Management Strategy (CAMS) status of the south Humber bank is 'no water available for abstraction except at extremely high flows. Groundwater resources in the Lincolnshire Chalk are fully committed to existing users and the environment' (Environment Agency, 2013).



Figure 2. Tunnel boring machine used to construct the Feeder 9 gas pipeline.

The geology of the site comprised low permeability alluvial and glacial deposits (Superficial Deposits) to circa 10 m below ground level. These deposits were underlain by the Flamborough Chalk, which was highly weathered in the top several metres and recovered as a chalk gravel, and is termed by Chalk Bearings. This highly weathered stratum was highly permeable with sub-artesian groundwater encountered during the site investigation. This stratum was underlain by the intact Fractured Chalk, of significantly less permeability than the weathered chalk (Figure 3).

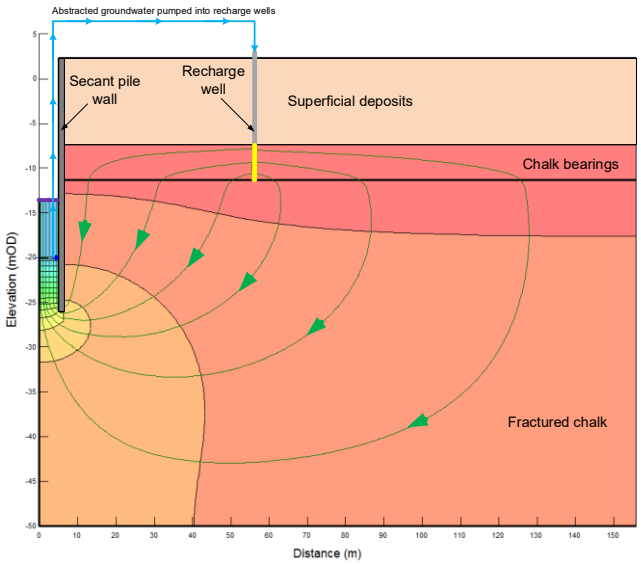

Figure 3. Finite element modelling of dewatering and recharge system for Feeder 9 gas pipeline.

To mitigate the risks, a groundwater control strategy utilising a partial cut-off and recharge system was developed (Figure 4). This resulted in abstraction

being non-consumptive, and prevented drawdown towards the River Humber, so mitigating saline water intrusion.



Figure 4. Pressurised wells to recharge abstracted groundwater back to the aquifer.

As the weathered chalk was very high permeability, a cut-off wall was required to penetrate through these deposits. Full cut-off of the weathered and underlying fractured chalk strata was originally considered; however, this was deemed impractical due to the fractured chalk extending circa 40 m to 50 m below ground level. Internal dewatering was specified within the Drive Pit (borehole pumps within designed wells). These internal wells abstracted groundwater from the more competent underlying fractured chalk.

Abstracted groundwater was then recharged back into the weathered chalk outside the Pit, reducing the radius of influence of the groundwater control operation and reducing the net abstraction from the aquifer to almost zero. The recharge system was fully enclosed, preventing the groundwater from coming into contact with the atmosphere, which helped prevent dissolved iron in the groundwater from precipitation and discolouring the groundwater.

Further project detail is described in Proceedings of the Chalk 2018 Conference (Goodfellow & Thomas, 2018; Holmes, Roberts, & Lee, 2018).

3.2 Microtunnel reception shaft Glasgow, Scotland

During construction of a Microtunnel reception shaft in Scotland, larger and more frequent boulders were encountered than expected.

These unexpected ground conditions resulted in the construction methodology being changed from jacked caisson to underpinning. The previous construction methodology could be undertaken in the wet, however the new methodology would require active dewatering.

Concerns were raised by key stakeholders about the potential risk of settlement from dewatering as the shaft was in close proximity to both a live railway, and bridge piers on frictional piles for a major road bridge spanning the River Clyde (Figure 5).



Figure 5. Photo of micro-tunnel reception shaft located close to the bridge piers.

The geology at the site generally comprised silty sands and gravels, overlying glacial till containing cobbles and boulders (Figure 6). Stakeholders were concerned with two main mechanisms for ground settlement at the site, settlement from ground loss, and settlement from a reduction in pore water pressure in shallow deposits.

To mitigate the concerns of stakeholders, a groundwater control system that included recharge was designed to minimize drawdown at a distance, as well as reduce water ingress into the shaft which could mobilise the soil.

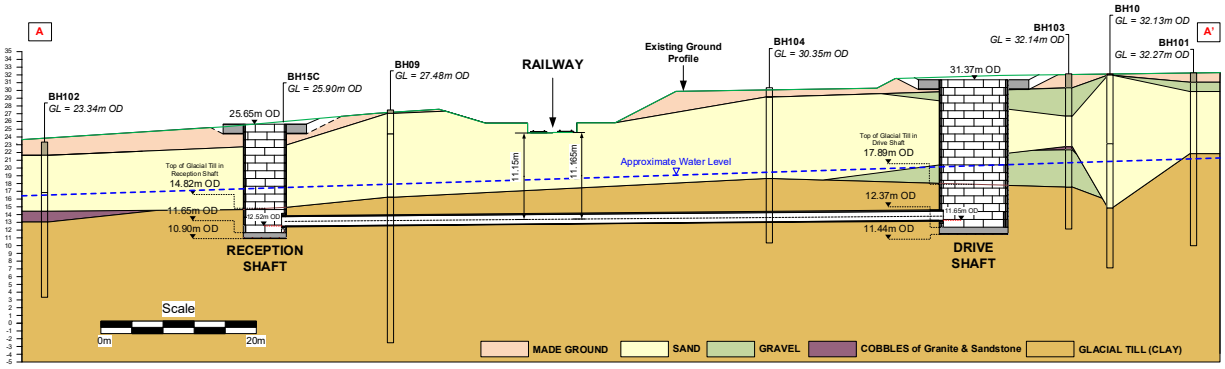

Figure 6. Conceptual model at the location of the reception shaft & drive shaft.

Site logistical constraints required recharge wells constructed within relatively close proximity to the shaft, and as such an assessment was required to confirm the system's feasibility.

Finite element modelling was undertaken to ascertain the flow rates required to minimize groundwater ingress into the shaft, and to prevent excessive drawdown below the railway and bridge piers by recharging into wells between the shaft and sensitive structures.

The finite element model head contours (Figure 7), demonstrated that a recharge system was feasible, and would prevent drawdown of more than 500 mm at the bridge piers and railway track.

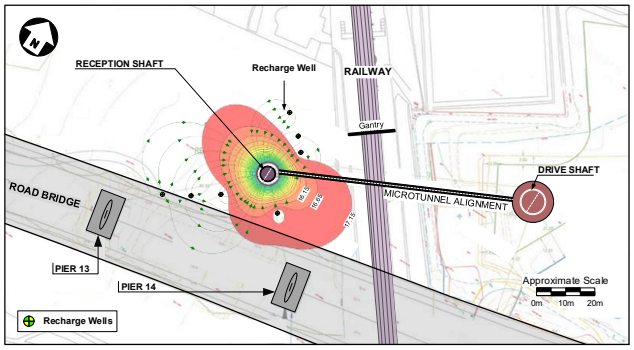

Figure 7. Finite element simulation of the dewatering and recharge system.

Figure 8 demonstrates the well design with slot sizes and filter material specified to prevent ground ingress into the wells, to mitigate ground settlement. Figures 9 and 10 depict the wellhead of a pumping well and recharge well respectively.

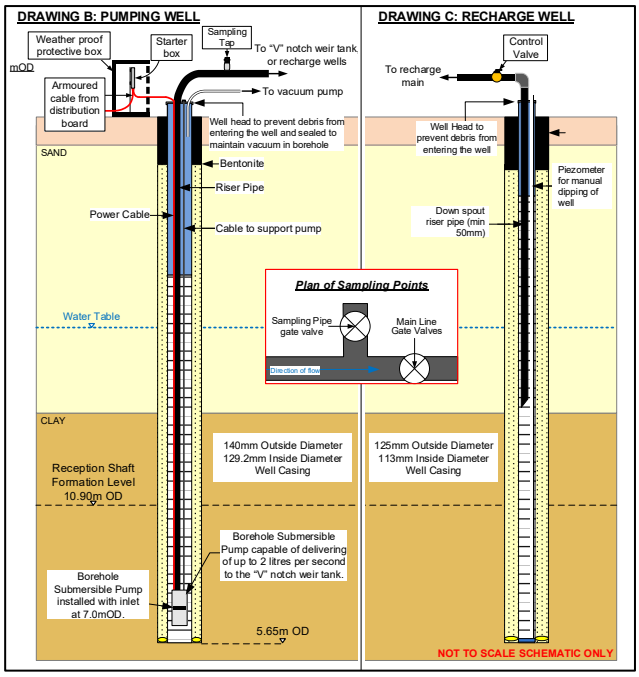

Figure 8. Specification of pumping and recharge wells.



Figure 9. Pumping well.



Figure 10. Recharge well.

3.3 The Commonwealth Games Aquatics Centre, Sandwell, Birmingham

The 2022 Commonwealth Games Aquatics Centre in Sandwell, Birmingham, was under construction over the period 2018 to 2022 (Figure 11), and required excavation for the competition pool, dive pool, plant room, down to a depth of 7 m below ground level.

The dewatering operation would have been less complex if the abstracted groundwater could be discharged directly to a watercourse. However, this approach would have resulted in the loss of groundwater from the aquifer resource in the order of 250 million litres.



Figure 11. The Birmingham Commonwealth Games Aquatic Centre during construction.

Due to the over-abstraction of groundwater from the aquifer underlying Birmingham (the Chester Formation), the Environment Agency specified a "net zero" abstraction rate during the construction of the Commonwealth Games Aquatics Centre Project. This meant that one hundred per cent of the groundwater abstracted during the construction period was required to be recharged back to the same aquifer from which it was abstracted.

The Aquatic Centre system required over 120 drilled suction abstraction wells and 50 recharge wells; with each well individually specified so that groundwater abstraction and recharge were targeted at the appropriate strata. Figure 12 presents the location of the numerous abstraction and recharge wells, and the cross-sectional output of the two-dimensional mixed confined-unconfined aquifer model GEMOS (Authors' Software).

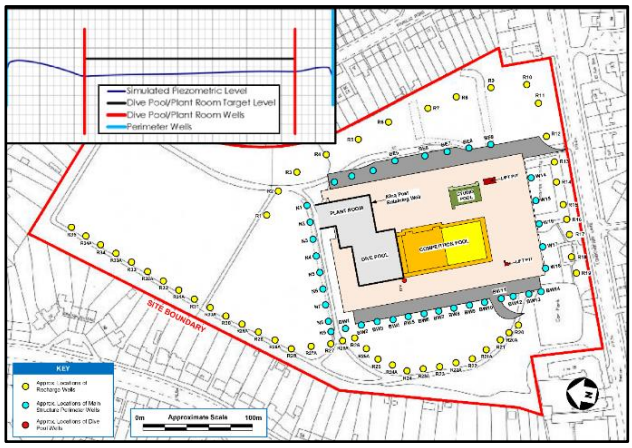

Figure 12. Location of abstraction & recharge wells during construction.

It was essential to abstract clear filtered groundwater (Figure 13), to prevent silts from being removed from the ground, and so allowing recharge of clear water to avoid frequent blockage. Note that regular maintenance and cleaning of the recharge wells was still required.



Figure 13. Abstraction of clear groundwater.

The recharge system required the pressurisation of the water with a circa 3 m head above ground level at each recharge wellhead. This was achieved by pumping the abstracted groundwater uphill to a water holding tank (Figure 14) at an elevated location. This then fed the recharge pipes to maintain a pressure of 30kPa to overcome the artesian head in the aquifer.



Figure 14. Water holding tank before discharging to the multiple-well recharge system.

REFERENCES

Bock, M., & Markussen, L. M. (2007). Dewatering control in central Copenhagen. *In Proceedings 14th Conference on Soil Mechanics and Geotechnical Engineering 2* (bls. 715-720). Amsterdam: Geotechnical Engineering in Urban Environments.

Cashman, P. M., & Preene, M. (2013). Groundwater Lowering in Construction: A Practicle Guide to Dewatering 2nd edition. *CRC Press.* Boca Ranton.

Dillion, P., Stuyfzand, O., & Grischeck, T. (2019). Sixty years of global progress in managed aquifer recharge. *Hydrogeology Journal 27(1)*, 1-30. http://dx.doi.org/10.1007/s10040-018-1841-z.

Environment Agency. (2013). *Ancholme and Louth Catchment Abstraction Management Strategy* Grimsby.

Goodfellow, T. L., & Thomas, S. D. (2018). Groundwater resource protection from construction groundwater control in Lincolnshire chalk. *Engineering in Chalk: Proceedings of the Chalk 2018 Conference* (bls. 669-674). London: ICE Publishing.

Holmes, G. J., Roberts, T. O., & Lee, M. (2018). A case study of construction dewatering in Northern Province Chalk. *Engineering in Chalk: Proceedings of the Chalk 2018 Conference* (bls. 147-153). London: ICE Publishing.

Margat, J., & van der Gun, J. (2013). *Groundwater around the world.* Lisse, The Netherlands: Balkema. http://dx.doi.org/10.1201/b13977.

Powrie, W., & Roberts, T. O. (1995). Case history of a dewatering and recharge system in chalk. *Geotechnique 45(4)*, 599-609.
https://doi.org/10.1680/geot.1995.45.4.599.

Preene, M., & Fisher, S. (2015). Impacts from groundwater control in urban areas. *Impacts from groundwater control in urban areas. Proceedings of the XVI European Conference on Soil Mechanics and Geotechnical Engineering* (bls. 2847-2852). London: ICE Publishing.

Preene, M., Roberts, T. O., & Powrie, W. (2016). *Groundwater Control: Design and Practice, 2nd Edition. Construction Industry Research and Information Association.* London: CIRIA Report C750.

Statutory instrument. (07. May 2019). *The Water Abstraction and Impounding (Exemptions) Regulations 2017*. Sótt frá legislation.gov.uk: http://www.legislation.gov.uk/uksi/2017/1044/made.

Proceedings of the XVIII ECSMGE 2024
GEOTECHNICAL ENGINEERING CHALLENGES
TO MEET CURRENT AND EMERGING NEEDS OF SOCIETY
© 2024 the Authors
ISBN 978-1-032-54816-6
DOI 10.1201/9781003431749-667
Open Access: www.taylorfrancis.com, CC BY-NC-ND 4.0 license

ECSMGE 24
XVIII EUROPEAN CONFERENCE ON SOIL MECHANICS AND GEOTECHNICAL ENGINEERING

Flood and drought mitigation using stormwater attenuation and enhanced infiltration systems

Atténuation des inondations et des sécheresses à l'aide de systèmes d'atténuation des eaux pluviales et d'infiltration améliorée

S.D. Thomas*, G.R. French
OGI Groundwater Specialists Ltd, Durham, UK

J.A. O'Meara, M.P. Dale
Groundwater Dynamics Ltd, Leamington Spa, UK

B. Casal
Sondagens Casal Lda, Sintra, Portugal

**stephen.thomas@ogi.co.uk*

ABSTRACT: Engineering systems are described for stormwater attenuation and enhanced infiltration, including the construction of trenches containing perforated attenuation pipes with a gravel surround, integrated with large numbers of drilled vertical infiltrators installed through the base of the trenches. Adding the pressure head of water in the attenuation trenches to the negative suction pressure in the unsaturated vadose zone, provides the differential pressure to force the water into the ground surrounding the infiltrators. The vertical infiltrators often encounter anisotropic ground strata where the horizontal permeability is much greater than the vertical permeability. Stormwater Attenuation and Enhanced Infiltration Systems have been used for many years in the United Kingdom to mitigate flooding and erosion, and to provide recharge to groundwater resources. With groundwater resources similarly in decline in Portugal, together with more frequent flooding conditions during intense rainfall, similar collection and enhanced infiltration systems could also be most beneficial to the hydrogeology and weather conditions of Portugal. Using this system, stormwater infiltrating into the vadose zone eventually find its way down to the water table, and so mitigate drought conditions by supplementing the aquifer water resources.

RÉSUMÉ: Des systèmes d'ingénierie sont décrits pour l'atténuation des eaux pluviales et l'infiltration accrue, y compris la construction de tranchées contenant des tuyaux d'atténuation perforés avec un entourage de gravier, intégrés à un grand nombre d'infiltrateurs verticaux forés installés à travers la base des tranchées. L'ajout de la pression de l'eau dans les tranchées d'atténuation à la pression d'aspiration négative dans la zone vadose non saturée, fournit la pression différentielle pour forcer l'eau dans le sol entourant les infiltrateurs. Les infiltrateurs verticaux rencontrent souvent des strates de sol anisotropes où la perméabilité horizontale est beaucoup plus grande que la perméabilité verticale. Les systèmes d'atténuation des eaux pluviales et d'infiltration améliorée sont utilisés depuis de nombreuses années au Royaume-Uni pour atténuer les inondations et l'érosion, et pour recharger les ressources en eaux souterraines. Les ressources en eaux souterraines étant également en déclin au Portugal, ainsi que des inondations plus fréquentes lors de pluies intenses, des systèmes similaires de collecte et d'infiltration améliorés pourraient également être très bénéfiques pour l'hydrogéologie et les conditions météorologiques du Portugal. Grâce à ce système, les eaux pluviales qui s'infiltrent dans la zone vadose finissent par se frayer un chemin jusqu'à la nappe phréatique, et atténuent ainsi les conditions de sécheresse en complétant les ressources en eau de l'aquifère.

Keywords: Stormwater attenuation; enhanced groundwater infiltration.

1 INTRODUCTION

Climate change and global warming are affecting all countries of the world, with more extreme weather events happening with greater frequency (Stott, 2016). In the United Kingdom (UK), one major impact of global warming has been the increase in hotter periods combined with an increasing frequency of high-intensity rainfall events (Kay et al., 2011, Schaller et al., 2016). With more of the UK being covered with urban developments, roads and industrial parks, the available open land to enable natural infiltration to the ground is receding (Charlesworth and Booth, 2016).

Over time this means less water is being recharged back into the ground and the major aquifers. As a consequence, the UK Government has enforced where possible the need for a developer to construct a Sustainable Drainage System (SuDS) to mitigate peak flooding that occurs from rapid runoff from hard impermeable surfaces such as roofs, roads, car parks

or other paved areas (Fletcher et al., 2015).In 2010, the UK Government published Building Regulations with Part H (Building Regulations, 2015).

Within these Regulations, Part H3 (3) describes the design of systems to manage the drainage of rainwater with the following priority:

a) An adequate soakaway or some other adequate infiltration system; or where that is not reasonably practicable,
b) A watercourse; or where that is not reasonably practicable,
c) A stormwater sewer; or where that is not reasonably practicable,
d) A foul sewer.

The building regulations guidance presented above clearly states that the priority is to discharge collected groundwater to an adequate soakaway or some other adequate infiltration system. In response to these regulations a Stormwater Attenuation and Enhanced Infiltration System (SAEIS) has been developed to provide an efficient method to collect, attenuate and infiltrate stored water into soils of variable permeability at depth. This system has been designed to infiltrate water at greater depths (typically in the range of 3 m to 12 m deep) than conventional soakaways which means this system is more suitable in areas where low permeability anisotropic soils such as laminated sandy and silty clays are more prominent (Jarvis et al., 1984).

By enabling infiltration at depth into laminated silt or sand lenses within clay soils, an enhanced infiltration system helps to mitigate local surface water flooding by reducing the flow of water to watercourses and sewers. This in turn helps to lower the peak water levels in local rivers following storm events, as illustrated in Figure 1 for a non-attenuated and attenuated concept storm hydrograph.

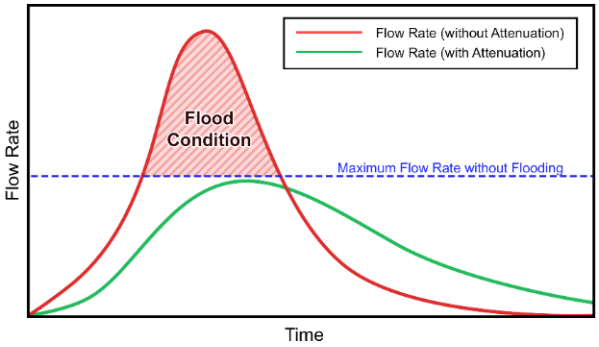

Figure 1. Illustration of two storm event hydrographs for non-attenuation and attenuation conditions respectively.

This paper describes the mathematical modelling applied to demonstrate the impact of attenuation and enhanced infiltration systems, by simulating the seepage of stormwater from the infiltrators into the surrounding anisotropic strata of mixed medium and low permeability, common in the United Kingdom.

With storm flood conditions also occurring more frequently in areas of Portugal over recent decades, enhanced infiltration techniques have the potential to mitigate the worst impact of such flooding events. Furthermore, the resulting enhanced infiltration of storm rainwater back to the unsaturated vadose zone will also serve to contribute to the mitigation of drought conditions, as the infiltrated rainwater will eventually find its way downwards to the water table.

2 STORMWATER ATTENUATION AND ENHANCED INFILTRATION SYSTEM

The enhanced infiltration system has been designed to attenuate and infiltrate large volumes of rainwater following storm events. The schematic in Figure 2 depicts how the system collects stormwater, and then how it is attenuated and infiltrated into the ground.

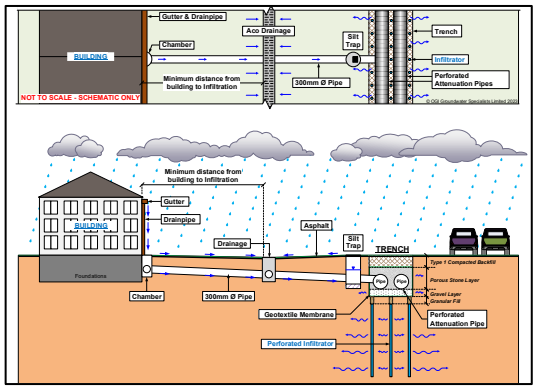

Figure 2. Attenuation and Enhanced Infiltration System.

Stormwater that lands on buildings and paved surfaces such as car parks, then enters the drainage system through a series of gutters and drains. Water then flows through a series of underground drains towards a silt trap where fine particles can settle out from the water to mitigate clogging of the infiltration system. Water then flows into a series of attenuation trenches set a minimum of 5.0 m away from any buildings. The trenches are typically in the order of 1.8 m wide and 1.7 m deep Figure 3).

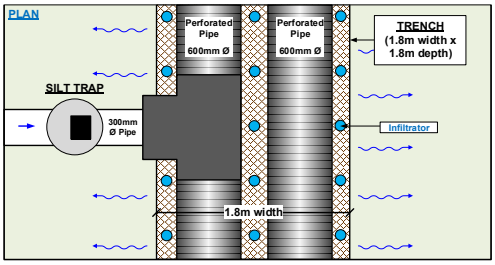

Figure 3. Schematic of the Attenuation and Enhanced Infiltration system in plan.

Each trench normally contains one or two large diameter perforated pipes, designed to provide a high storage volume to attenuate collected rainwater following a storm event. The trench is backfilled around the perforated pipes with gravel or angular stone. At the base of each trench, the pipes typically sit on a layer of 10 mm pea gravel. Gravel or stone is then backfilled around the pipes and typically to 300 mm above the crown of the pipes. Surrounding this gravel & pipe attenuation structure is a specialist nonwoven green geotextile developed to promote the growth of a microbic biofilm to absorb and digest any hydrocarbon. The nonwoven geotextile also provides stabilising of the sub-base construction. Above the attenuation structure is placed graded stone, which is compacted to provide greater bearing capacity.

Pre-drilled beneath the attenuation trenches are a series of specially designed vertical infiltrators (Figures 2 and 4), which aid the infiltration of water into the soil. Each infiltrator comprises a 90mm drilled borehole, then installed with a device that is designed to accelerate the transmission of water into the ground. The top of each infiltrator is set normally 300 mm below the base of the trench as depicted in Figure 4. The length of infiltrators normally varies between 3 m and 12 m, depending on the geology and volume rate of water that needs to be infiltrated.

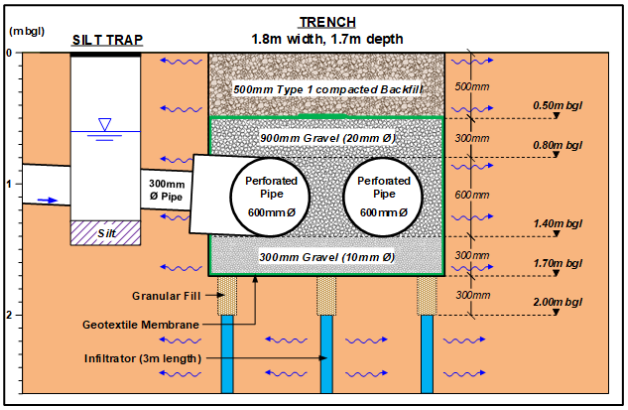

Figure 4. Attenuation and Enhanced Infiltration section.

The attenuation and enhanced infiltration system depicted above has been successfully implemented to discharge collected water at over 500 sites in the UK. The system provides an elegant and energy-efficient solution to the flooding challenges at each location.

The system has proved particularly successful in draining waterlogged sports fields, including rugby fields, cricket pitches and horse racing tracks. However, the main area of growth currently is for new-build housing and commercial construction, where city councils are legislating for 100% of the collected rainfall to be reintroduced back to ground.

To illustrate the application of this attenuation and enhanced infiltration system, Figures 5, 6 and 7 present the application at an industrial unit and car park in the northeast of England. The silty-clay ground was initially considered to be unsuitable to soakaway stormwater; but after installation, the 180m of trench, together with circa 500 infiltrators, was sufficient to manage the rainwater over a 4 Ha.



Figure 5. Perforated pipes within attenuation trenches.

Two horizontal perforated pipes are installed and then backfilled with gravel to 300 mm above the crown of the pipes. Nonwoven green geotextile wrapping of the gravel is then completed before a graded stone is infilled and compacted on top of the geotextile to provide greater bearing capacity before the construction of an asphalt finish for vehicle use.

To mitigate the potential of silts from entering the trench attenuation system, there are many silt traps and chambers constructed to intercept the silts. These structures are regularly cleaned as part of a planned maintenance program.

To degrade any possible hydrocarbon collected, the attenuation trench comprising pipes and gravel is wrapped with a specialist green nonwoven geotextile (Figure 6) before compaction of the grading layer.



Figure 6. Final backfilling of attenuation trench and wrapping with green nonwoven geotextile.

The combination of the nonwoven geotextile of a green fibre structure, with the pea gravel backfill, adds treatment for hydrocarbon contamination by

promoting the growth of a microbic biofilm which absorbs and digests the hydrocarbon.

3 RAINWATER INFILTRATION THEORY INTO UNSATURATED GROUND

Rainwater infiltration into unsaturated ground above the water-table is complex to simulate. When water fills the attenuation volume within the trenches, this water also fills the infiltrators beneath. This results in a high differential pore water pressure between the water-filled infiltrator, and the natural suction pressure in the surrounding unsaturated ground.

(i) The pressure in the infiltrators will be governed by the elevation of the water head in the attenuation storage (Figure 7). For example, if the water level fills the trenches to 600 mm above the base of the trench, and the infiltrators are installed to 3.3 m below the base of the trench, there will be a pressure of circa 38 kPa at the tip of the infiltrator.

(ii) The initial negative pore water pressure in the unsaturated ground surrounding the infiltrator (i.e., less than atmospheric pressure), is also commonly referred to as soil suction. In fine-grained soils, suction pressure can be high-negative, with values of -50 kPa regularly produced.

(iii) Combining these two conditions can result in circa 88 kPa in differential pore-water pressure between the positive pressure at the infiltrator tip and the negative suction pressure in the surrounding unsaturated soil. This results in the pressure in the infiltrator "pushing" the water into the surrounding ground, and the unsaturated ground also effectively "pulling" the water from the water-filled infiltrator.

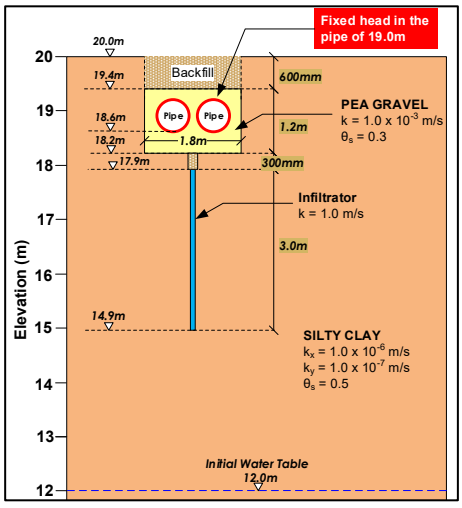

Figure 7. Conceptual model of a single infiltrator with ground properties used in the mathematical modelling.

Experience from the UK has demonstrated that the performance of a stormwater attenuation and enhanced infiltration system far exceeds the rate of infiltration from a normal and traditional soakaway trench, i.e. without the addition of drilled infiltrators.

This performance is regularly met with surprise by those who have traditionally viewed that a soakaway does not work sufficiently in silt or clay soils. However, when the concept of high anisotropy that occurs in a laminated soil, together with the fact that an unsaturated soil "pulls" the water from the infiltrator, especially when mathematical models are used to simulate and validate the performance, this innovative system is now becoming increasingly accepted in the construction industry.

Although over 500 enhanced infiltration systems have been installed in the UK, there is still always resistance to a new technique. The main opposition to the use of the system to dispose of stormwater is the view by some that this high water infiltration rate into low permeability ground is considered not feasible, despite the system having been tested and demonstrated to work in practice.

For this reason, more "science" has been required to demonstrate how it is indeed technically feasible to infiltrate high water flow rates into soils of low to medium permeability. To achieve this requirement, the authors built a non-linear finite element model to demonstrate that a carefully constructed and tested system can be proven to work scientifically.

4 FINITE ELEMENT MODELLING OF ENHANCED INFILTRATION

The movement of the collected stormwater through the infiltrator into the ground has been modelled by French and Thomas (Authors) using the GeoStudio finite element software SEEP/W (Geostudio, 2012).

The finite element model requires "discretisation" of the ground domain surrounding the infiltrators into tens of thousands of smaller zones called "elements" to geometrically simulate the groundwater behaviour using the radial version of the equation below:

$$\frac{\partial}{\partial x_i}\left(k_{rw}K_{ij}\frac{\partial h}{\partial x_j}\right) = \left(S_w S_s + \varphi\frac{\partial S_w}{\partial \psi}\right)\frac{\partial h}{\partial t} - Q_w \quad (1)$$

where k_{rw} is relative permeability, K_{ij} is Hydraulic Conductivity Tensor, h is hydraulic head, φ is porosity, S_w is water saturation, S_s is Specific Storage, ψ is pressure head, and Q_w is a point water source.

The non-linear functions used in the modelling for (i) Volumetric Water Content, and (ii) Hydraulic Conductivity, which are dependent on soil suction, are presented in Figures 8a and 8b.

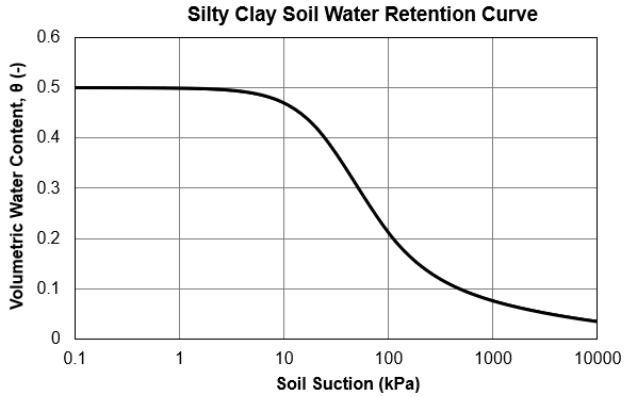

Figure 8a. Soil-water retention function curve.

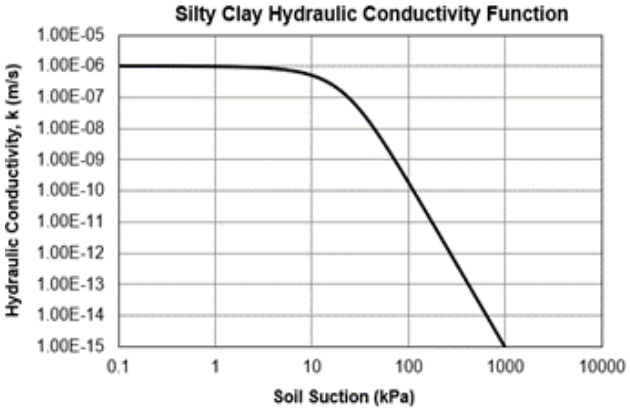

Figure 8b. Hydraulic conductivity function vs soil suction.

The finite element model then enables different properties and boundary conditions to be input in a range of locations for which the governing flow equation is solved, and heads output.

From these outputs, other information can be calculated such as pore pressure, degree of saturation and groundwater velocity.

An axisymmetric finite element computer model has been utilised to simulate two-dimensional radial steady-state flow of collected water into the vadose (unsaturated soil) zone surrounding an infiltrator.

For this scenario, a saturated sump and infiltrator have been simulated using SEEP/W. The simulated soil is based on a typical anisotropic silty clay, common to the northeast of England.

Input horizontal permeability is 1.0 x 10^{-6} m/s and vertical permeability 1.0 x 10^{-7} m/s. To simulate the unsaturated behaviour of the soil, SWRC (soil water retention curve) along with a hydraulic relative conductivity function have been selected based on typical functions for silty clays, (Figures 8a and 8b).

A fixed head boundary condition is applied to the sump, and a high permeability infiltrator is specified, to simulate the flooded sump and infiltrator.

Figure 9 presents simulated groundwater head contours (ranging from 18 m to 6 m) and the flow lines (shown by the green lines with arrows).

The dashed blue line represents the position of the water table (which is the position where pore water pressure equals 0.0 kPa and saturation equals 100%).

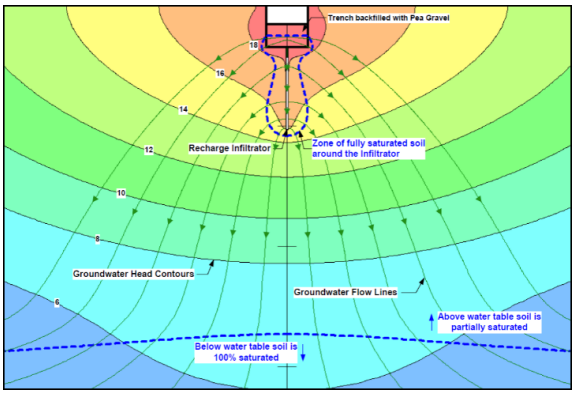

Figure 9. Simulated head contours and flow paths.

Groundwater flow velocity is driven by a gradient of hydraulic head (Darcy's Law); which explains the pattern of groundwater flow that can be seen in Figure 9. The head changes from 19.0 m at the sump to 15.0 m at the bottom of the infiltrator. This 4.0 m head differential drives the water down through the vertical infiltrator, as depicted by the green arrows.

Another driver is that the pore pressure in the unsaturated vadose zone above the water table will be negative, i.e. under suction. This means there is a greater differential head produced between the positive pressure in the infiltrators, and the negative pore-water pressure in the unsaturated vadose zone.

The collected and filtered water then enters the soil at depth, and then flows into the horizontal silt or sand layers of higher permeability. This horizontal flow into the soil results in a zone of fully saturated soil immediately surrounding the infiltrator within the upper blue water-table line in Figure 9.

Enhanced saturation enables greater groundwater flow into the surrounding soil as this increases the permeability. Radially from the infiltrator beyond the saturated zone, saturation decreases, increasing soil suction, but also reducing the effective permeability.

Whilst a reduction in the permeability of the soil occurs in the unsaturated zone, the soil suction pressure gradient, combined with the head gradient in the infiltrator, is sufficient to drive the collected water into the vadose zone surrounding the infiltrator.

The concept of transient stormwater attenuation and enhanced infiltration during and after a rainstorm event is depicted in Figure 10. Surface water during a storm event is directed to the drains and attenuation trenches. After cessation of the storm, this collected and attenuated stormwater will dissipate from the infiltrators into the surrounding unsaturated soil, and will then slowly percolate down to the water table, so ultimately restoring aquifer water resources.

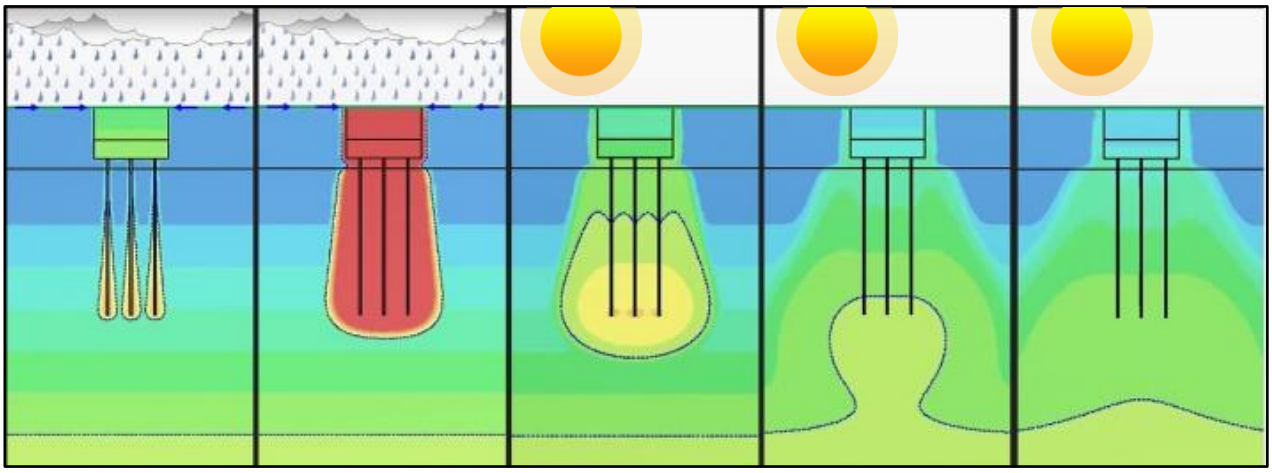

Figure 10. Various stages of attenuation and enhanced infiltration during and following a storm event.

5 CONCLUSIONS

A Stormwater Attenuation and Enhanced Infiltration System enables collection, attenuation and infiltration of stormwater back to the ground, thus mitigating surface flooding. This paper describes how this innovative attenuation and infiltration system functions in practice, and then demonstrates by mathematical modelling how water flows through the system and infiltrates water into the soil at a far greater rate than can be achieved using a conventional soakaway system. Soil characteristics used in this study are based on a typical laminated anisotropic silty clay.

Mathematical modelling conducted by the authors demonstrates that infiltration systems can be effective in both medium and low permeability ground, benefitting from the anisotropy of the ground where horizontal silt and sand bands exist within otherwise clay soil, as it enables the infiltration of stormwater at depth into more permeability soil layers.

Where stormwater has traditionally been sent to watercourses and sewers, the application of effective infiltration systems has a significant benefit by mitigating the risk of localised flooding, together with replenishing water resources. This opens the option of using enhanced infiltration systems anywhere in the world where shallow soakaway systems were once not originally thought suitable.

Stormwater attenuation and enhanced infiltration exemplify true low-carbon sustainability, contributing to the United Nations Department of Economic and Social Affairs for Sustainable Development Goal 6: ***Ensure availability and sustainable management of water and sanitation for all.***

REFERENCES

Building Regulations. (2015). "Part H - Drainage and Waste Disposal (2015 Edition)." Planning Portal.

Charlesworth, S M., Booth C. A. (2016). *Sustainable Surface Water Management*. Edited by Susanne M. Charlesworth and Colin A. Booth. *Sustainable Surface Water Management: A Handbook for SuDS*. Wiley. New Jersey. USA. http://doi.org/10.1002/9781118897690.

Fletcher, T D., Shuster W, Hunt W F., Ashley R, Butler D, Arthur S, Trowsdale S, et al (2015). "SuDS, LID, BMPs, WSUD and More – The Evolution and Application of Terminology Surrounding Urban Drainage." *Urban Water Journal* 12 (7): 525–42. https://doi.org/10.1080/1573062X.2014.916314.

GeoStudio. (2012) 'Seepage Modelling with SEEP/W: An engineering methodology (July 2012 Edition).

Jarvis, R. A, Bendelow V. C, R. Bradley I, Carroll, D. M, Furness, R. R, Kilgour, I. N. L, and. King S. J. (1984). Soils and Their Use in Northern England. Soils and Their Use in Northern England. Rothamsted Research.

Kay, A. L, Crooks S. M, Pall P, and Stone D. A. (2011). "Attribution of Autumn/Winter 2000 Flood Risk in England to Anthropogenic Climate Change: A Catchment-Based Study." *Journal of Hydrology* 406 (1–2): 97–112. https://doi.org/10.1016/j.jhydrol.2011.06.006.

Stott, P. (2016). "How Climate Change Affects Extreme Weather Events." *Science* 352 (6293): 1517 LP – 1518.

Proceedings of the XVIII ECSMGE 2024
GEOTECHNICAL ENGINEERING CHALLENGES
TO MEET CURRENT AND EMERGING NEEDS OF SOCIETY
© 2024 the Authors
ISBN 978-1-032-54816-6
DOI 10.1201/9781003431749-668
Open Access: www.taylorfrancis.com, CC BY-NC-ND 4.0 license

ECSMGE 24
XVIII EUROPEAN CONFERENCE ON SOIL MECHANICS AND GEOTECHNICAL ENGINEERING

Integration of ground energy systems for low-carbon heating and cooling of buildings

Intégration de systèmes d'énergie géothermique pour une faible émission de carbone chauffage et refroidissement des bâtiments

S.D. Thomas*
OGI Groundwater Specialists Ltd, Durham, UK

A. Vieira
LNEC (National Laboratory for Civil Engineering), Portugal

C. Pinto
CML (Lisbon City Council), Lisboa, Portugal

J. Lapa
Aveiro University (UA), Aveiro, Portugal

**stephen.thomas@ogi.co.uk*

ABSTRACT: Ground source heating and cooling is well established in many parts of the world providing a highly efficient source of low carbon heating and cooling. Given its efficiency, it is more economical to run a heat pump almost continually maintaining the minimum base heat/cool load, than it is to install a much bigger heat pump capable of reaching peak load for only short durations. For this reason, a heat pump system is most efficiently operated when integrated with other traditional or alternative energy sources to produce a hybrid system. This approach can be further enhanced by the application of other technologies, such as energy from low-carbon waste heat which can significantly improve the efficiency of heat pumps. Similarly, capturing cold night air in winter can be used to cool the ground to cool buildings in the summer in hot cities such as Lisbon. Two systems are presented to demonstrate the effectiveness of using the ground to store heat and cool energy to highlight the practical issues which may be encountered during design and installation.

RÉSUMÉ: Le chauffage et le refroidissement géothermiques sont bien établis dans de nombreuses régions du monde, fournissant une source très efficace de chauffage et de refroidissement à faible teneur en carbone. Compte tenu de son efficacité, il est plus économique de faire fonctionner une pompe à chaleur en maintenant presque continuellement la charge minimale de chauffage/refroidissement de base, que d'installer une pompe à chaleur beaucoup plus grande capable d'atteindre la charge maximale pendant de courtes durées seulement. Pour cette raison, un système de pompe à chaleur fonctionne plus efficacement lorsqu'il est intégré à d'autres sources d'énergie traditionnelles ou alternatives pour produire un système hybride. Cette approche peut être encore améliorée par l'application d'autres technologies, telles que l'énergie à partir de chaleur résiduelle à faible teneur en carbone, qui peut améliorer considérablement l'efficacité des pompes à chaleur. De même, la capture de l'air froid de la nuit en hiver peut être utilisée pour rafraîchir le sol afin de rafraîchir les bâtiments en été dans les villes chaudes comme Lisbonne. Deux systèmes sont présentés pour démontrer l'efficacité de l'utilisation du sol pour stocker la chaleur et refroidir l'énergie afin de mettre en évidence les problèmes pratiques qui peuvent être rencontrés lors de la conception et de l'installation.

Keywords: Ground source energy; heat pumps; low carbon heating and cooling.

1 INTRODUCTION

The worldwide drive towards cutting greenhouse gases and improving energy efficiency is underway. In recent years, this has resulted in the development of various new renewable technologies to generate electricity, and to produce sustainable low-carbon air and ground source systems for heating and cooling.

In the United Kingdom (UK), heating is the largest energy-consuming sector, accounting for over a third of greenhouse gas (GHG) emissions (UK Parliamentary Office of Science and Technology, 2016). In 2017, domestic heating accounted for 57% of the UK's greenhouse emissions from heating, with 20% from non-domestic (commercial) consumers, and the remainder from the industrial sector (Department for Business, 2018).

Across Northern Europe and North America, heat pump technology is used to both heat and cool buildings (Omer, 2006). However, in the UK, where gas has been traditionally used to heat homes, there is a resistance to replace a fully gas heated building with one 100% heated from ground source.

Recent advancements in technology have resulted in the design of heating and cooling systems that use ground source systems for the predominant source of heating, but with gas boilers stepping in to provide a top-up during times of extreme heating demand, and chillers being activated at times of peak cooling demand, which provides a valuable back-up system.

This paper examines the design of ground source heating and cooling systems, and describes the basic principles of a ground source system with a top-up/back-up system. Case studies are presented to show working examples of integrated ground source systems. The paper also explores how heating and cooling ground source systems can use the residual heat and coolth to operate more efficiently by storing the heat/cool energy in the ground, and so improving the efficiency of the system all year round.

Where ground source heating and cooling systems are used to replace traditional fossil fuels (i.e. gas, oil) there will be reduced carbon emissions. Using a GSHP system with a coefficient of performance (CoP) of 4.0 as an example, 75% of the thermal energy to the building is zero carbon energy abstracted from the ground. This means that there is an immediate four-fold reduction in carbon emissions. Furthermore, if the electricity used for powering the heat pump is sourced from zero-carbon energy such as wind power or photo-voltaic, then the complete system can be zero carbon.

2 TYPICAL HEAT DEMANDS OF A HEATING SYSTEM

The demand for heat in a building over a calendar year is not uniform. Clearly, there is a higher demand for heat during the winter months, than in the summer months. Additionally, heat demand varies throughout the day, during the night, and on weekends. With this, there are colder periods of weather which cannot be predicted. As a consequence of the weather variations, together with the variability of building usage and occupation, the heat demand from the heating system is highly variable.

Traditionally, a gas boiler system is sized for the maximum predicted demand, together with additional capacity. This approach is economic in that the installation cost of a gas boiler of, for example, 200 kW, is only slightly more than the installation cost of a 100 kW gas boiler. The main cost to the building is in the running costs of gas consumption per kWh. However, for a ground source system, the main costs are in the heat collection network, which comprises drilling, heat collectors, manifolds, etc. For this reason, a 200 kW ground source system can be almost twice the cost of a 100 kW ground source system.

It is for this reason that attention must be given to the most efficient sizing of the ground source system, including the size of the ground heat collection array.

In the design of a ground source heating system, it is recognised that specifying for the peak heat loading is highly inefficient regarding costs, and even carbon emissions. As an example, Figure 1 depicts a two-week period of predicted heat demand for a new hospital in the northeast of England. This figure demonstrates that if the peak building heat requirement is 1167 kW, then installing a 700 kW ground source heating system only provides 60% of the peak heating. However, the red area of the graph is the energy in kWh that is the shortfall, but the red area is substantially less than the green area, which is the total heat energy that can be provided by the ground source system. This means that the most effective system is one in which the main annual heat load is provided by the ground source, but with a top-up of peak heat, provided by a more traditional electric or gas system.

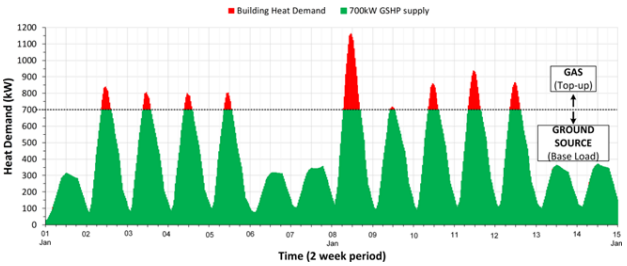

Figure. 1. Heat demand (kW) and ground source heat pump (700 kW) heat supply for a hospital.

The heat load demand for every building is always different, and the peak demand requires specification by a specialist. However, as depicted in Figure 2, the percentage of "full-load hours" of the heating demand, over an annual 8766 hours, is relatively consistent from building to building.

Based on the above, an efficient and pragmatic approach is to combine the technologies as follows:

1. Construct a ground source system to satisfy the bulk (circa 95%) of the total heat demand for a typical year, in kWh;
2. Choose the heat pump sized to maximise efficiency up to circa 60% of peak supply in kW;
3. Augment the ground source system with a gas/oil/electric boiler which provides a top-up heat supply at the point of the need. Typically, this top-up system need only provide 5% of annual demand, but can provide 100% if a back-up is required.

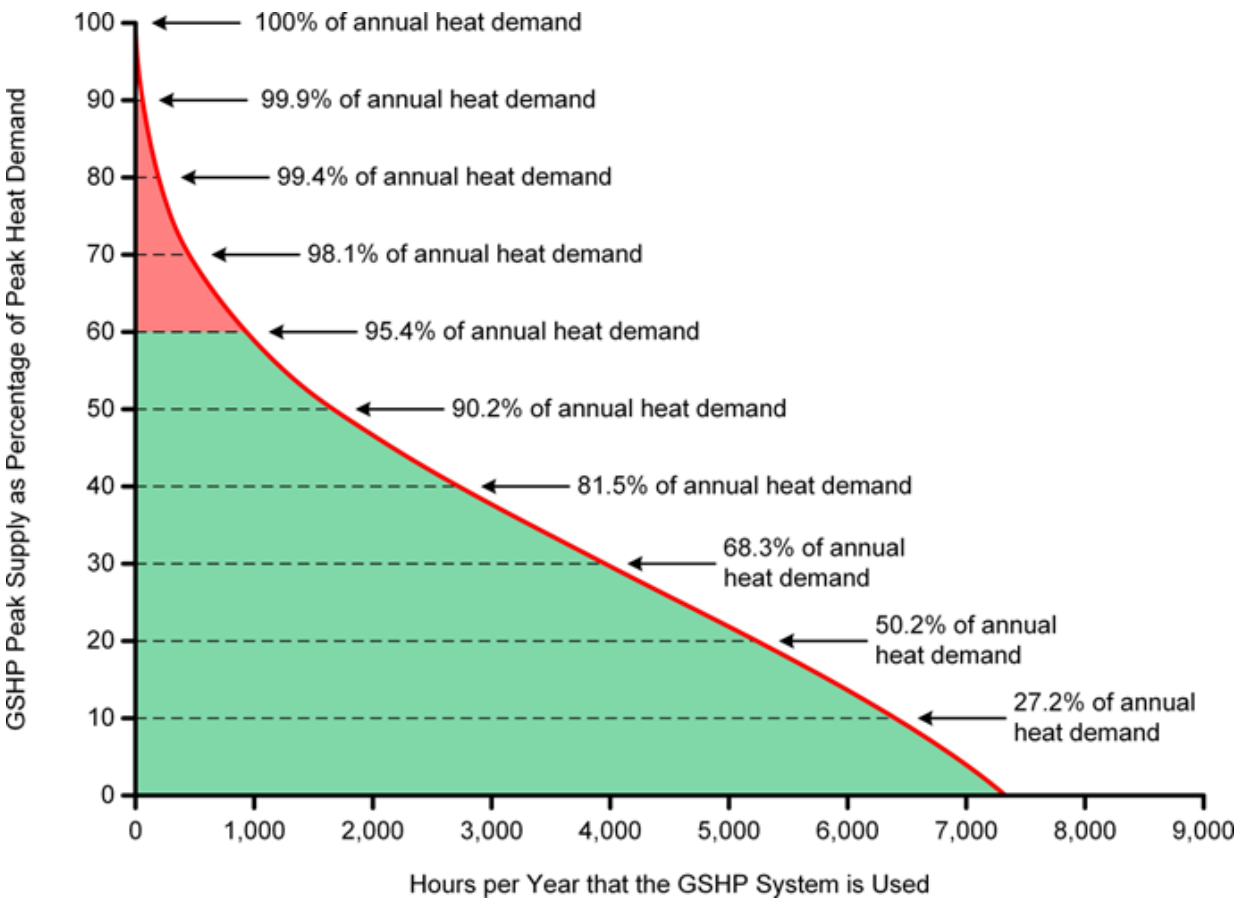

Figure 2. Graph depicting heat pump annual full load hours.

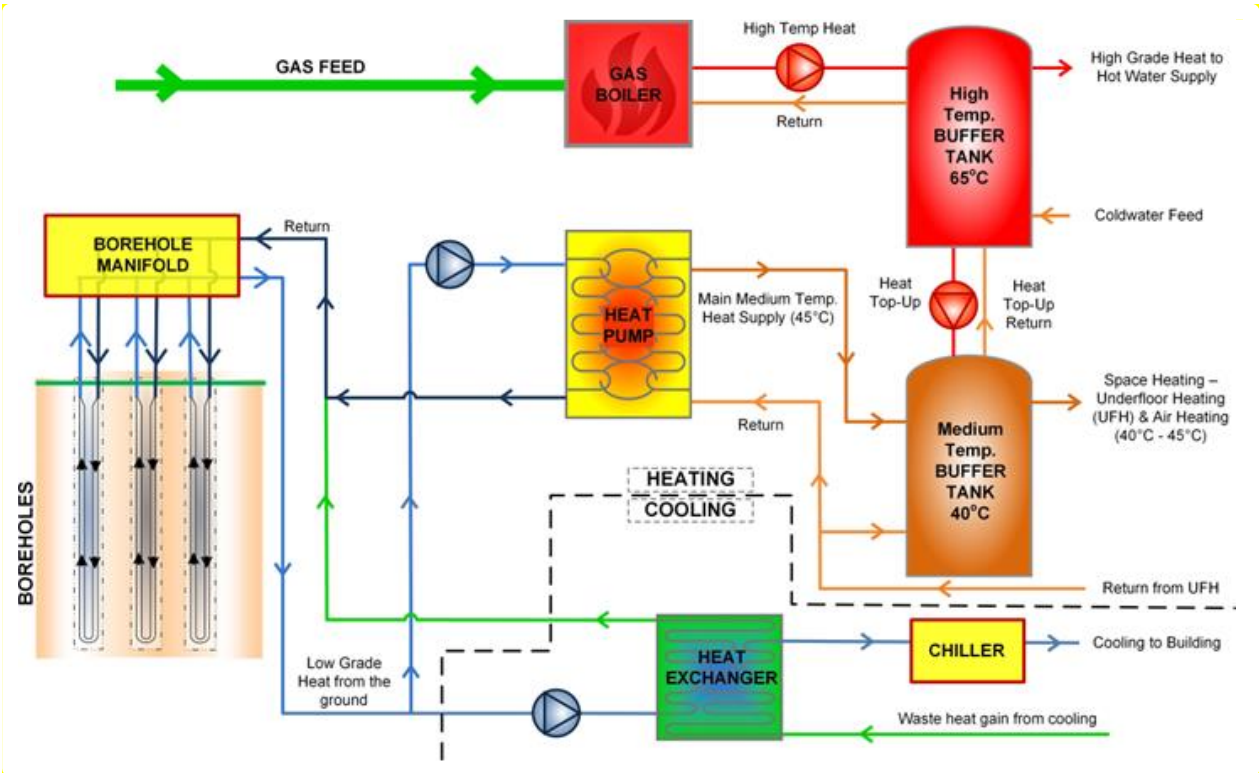

Figure 3. Schematic of ground source heating and cooling system integrated with gas boiler and electric chiller.

3 TOP-UP/ BACK-UP HEATING SYSTEM

The energy source used for top-up heating can be from a range of sources. Traditionally, this could be from natural gas, oil, LPG or electric immersion heaters. In addition, whilst heat pumps are very reliable, it can be good practice to use the top-up system as a backup (Thomas, et al. 2019). Then if there is a temporary impact on the ground source system, continued heating can be provided by the top-up system acting as backup. As the requirement for reducing carbon emission is becoming more in demand, hybrid systems depicted in Figure 3 are regularly installed to bring down the overall costs of such low-carbon heating systems.

4 CASE STUDY

The following describes details of a system designed and constructed in the north of England that has been selected to illustrate the cost and carbon reductions of a combined ground source heating and cooling system.

In 2008, a ground source heating and cooling system was designed for the new-build Stanley Primary Care Centre in County Durham, UK.

The NHS (National Health Service) Care Centre building provides an extensive range of modern medical services under one roof, including GP practices, dentistry, x-ray diagnosis and facilities to conduct minor operations. This is stated here to demonstrate that it was an essential pre-requirement for a reliable, cost-effective and low-carbon heating system to be constructed. The ground source heating system at Stanley, utilised two heat pumps, to provide heating water at 45°C used to feed the underfloor heating system and the electric fan coil ventilation system. The system generates 80 kW of peak heating, provided by two NIBE 40 kW “Fighter 1330” heat pump units. On occasions of high heating demand, the system is supplemented by integrated gas boilers, which provide up to 50 kW of heat. The gas boilers also provide heat to the building's DHW through a plate heat exchanger to the buffer vessel. The top-up system is controlled by the Building Management System (BMS) following a request for additional heat from the heat pumps.

Heat is collected from the ground via a total of 22 No. vertical boreholes and connecting trenchwork (19 No. boreholes drilled to a depth of 100 m and 3 No. boreholes drilled to a depth of 50 m). The majority of the boreholes were drilled beneath the building footprint, before construction (Figure 4).

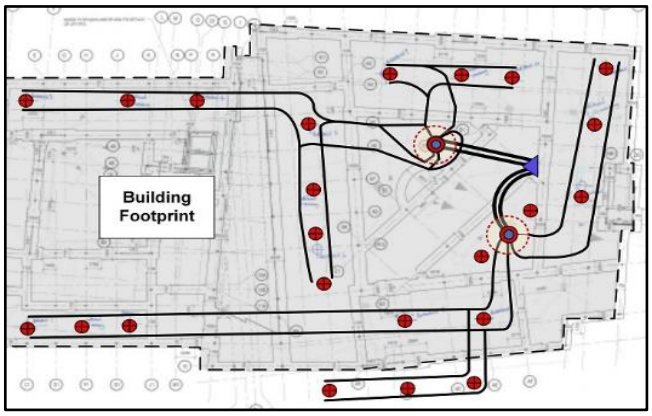

Figure 4. Stanley centre ground source collectors.

The trenches to accommodate the horizontal pipework were excavated and installed following the construction of the building superstructure.

The ground conditions beneath the site comprised interbedded sandstone, shales, and mudstone. Heat modelling was undertaken using in-house thermal software during the preliminary design stage to assess the heat replenishment of the ground (Figure 5).

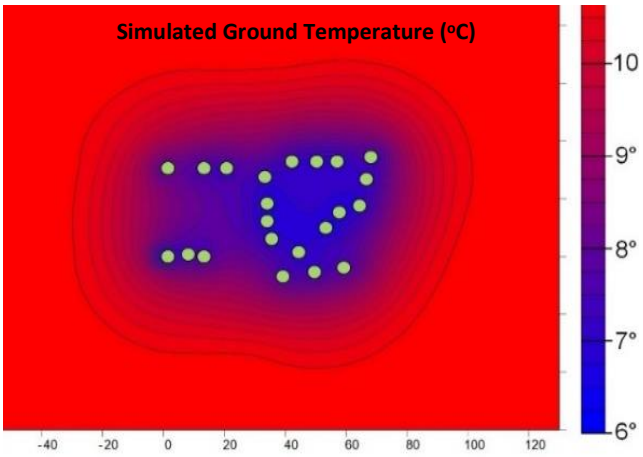

Figure 5. Thermal modelling of the ground collectors.

Each borehole has double loop collectors flow and return pipes. These are connected via underground horizontal 32 mm HDPE flow and return pipes installed within backfilled trenches to two manifold chambers. Each manifold leg is connected to a 63 mm flow and return header pipe that connects to the heat pumps located within the plant room. Manifold chambers are buried beneath ground level within the central courtyard areas of the building (Figure 6).

In summer months, the system provides 80 kW of chilled water which is stored in a chilled water accumulator. The system can do this ’passively’ (i.e. where heat transfer fluid is circulated through the ground collectors by a circulation pump but where the heat pump does not operate) or ’actively’, where the cooling water is generated by the heat pump.



Figure 6. Manifold chamber installed in the courtyard.

The heat pumps, water tanks and gas boilers are housed in the plant room on the third floor (Figure 7).

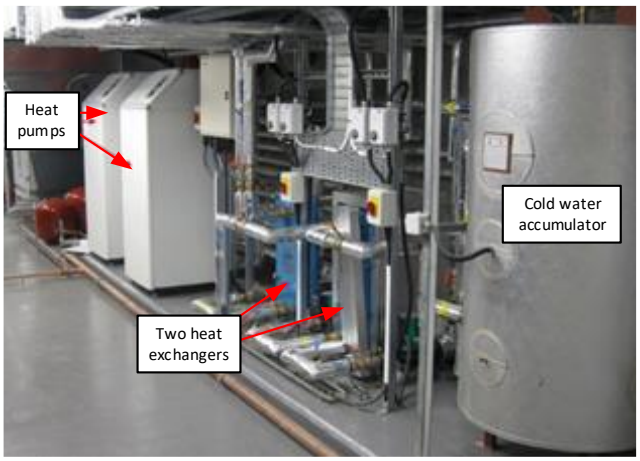

Figure 7. Stanley heat pumps, manifolds, chiller tanks.

5 FCT FUNDED PROJECTS, PORTUGAL

There has been a growing interest in the scientific and technical communities in the study of shallow geothermal systems and the assessment of their sustainability under the prevailing conditions in Southern Europe, particularly for the authors of this work, within the climatic conditions occurring in Portugal (Aljundi, et al. 2023). Between 2017 and 2021, the Portuguese National Library for Civil Engineering (LNEC) and the University of Aveiro (UA) collaborated on a research project funded by the Portuguese Foundation for Science and Technology (FCT), – ref. PTCDT/ ECM-GEO/0728/2014. In this project, the integrated behaviour of geothermal systems (primary and secondary circuits) was studied and modelled. Buildings at UA, whose climate control relies on different options of superficial geothermal systems, were used as prototypes. The project involved soil thermal characterization (Vieira et al. 2017), leading to the team gaining significant expertise. It also included extensive dynamic building modelling activities incorporating the analysis of the Shallow Geothermal System (SGE). This activity contributed to the formation of a successful collaborating working group, which is continuing and expanding.

More recently, as part of a new project, also funded by FCT – ref. PTDC/ECM-GEO/0728/2021, including in the team the Lisbon City Council (CML) and experts from the UK, there is an ongoing study on the geothermal potential of the city of Lisbon. This study has included a preliminary assessment of the thermal conductivity of the geological formations occurring in the city of Lisbon. This is presented in Figure 8, which includes the location of three testing boreholes: 1, 2, 3.

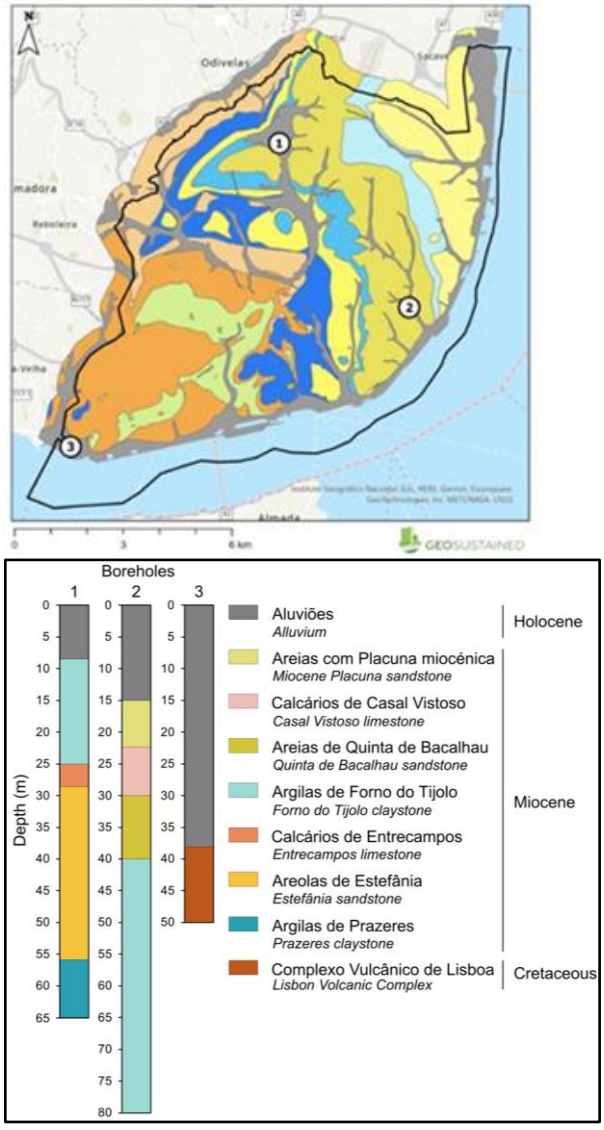

Figure 8. Lithology encountered in boreholes 1, 2, 3.

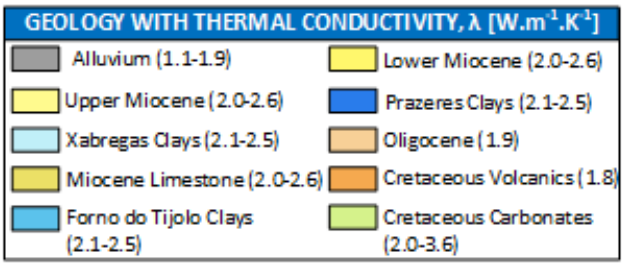

Figure 9. Lisbon thermal conductivity map, with values assessed and compiled by Vieira et al. (2023).

This comprehensive study encompasses the appraisal of the thermal characterization of the city's main geological formations, and the installation of temperature monitoring sensors at various locations in the city, allowing an understanding of the seasonal evolution of temperature to considerable depths.

The appraisal is based on bibliographic correlations that are already in the process of being validated with laboratory studies (Inácio et al, 2023; Vieira et al. 2023), as depicted in Figures 8 and 9.

Subsequent integrated studies will analyse the sustainability of these systems for different types of buildings and different SGE solutions. The entire group recognizes the importance of these studies in preparing and planning the city's evolution and addressing new challenges, particularly in the context of global warming, whose predictions indicate severe impacts on the city of Lisbon.

6 CONCLUSIONS

When designing a ground source heating and cooling system, it is ideal if there is a balance between the abstraction of heat from the ground when heating the building in the winter, and the return of the heat to the ground when cooling the building in the summer.

Similarly, the same type of ground energy balance is applied to a cooling system, whereby the ground cooling system can provide the dominant reduction in temperature through the year in kWh, with a traditional A/C unit providing a top-up system in peak demand.

When designing a balanced system for hot cities such as Lisbon, the sustainability of the ground must be considered, especially to prevent the ground temperatures from rising uncontrollably. This can be mitigated by capturing cold air during winter nights, then via heat exchangers, providing cool energy to the ground in preparation for the summer cooling period.

Meticulous testing and pilot projects are required to implement this approach sustainably. For this reason, it is encouraging to see many organisations working together to achieve this goal. This collaboration has already commenced with LNEC, the Câmara Municipal de Lisboa (CML) and UA, supported by UK-based OGI Groundwater Specialists, undertaking a research project (Project GeoSustained) to establish the thermal properties of the ground beneath the city, together with the measurements of transient ground temperatures from boreholes drilled to 80 m in depth.

Work has now started with engineers and scientists from Portugal and the UK building upon the current research to develop innovative low-carbon ground source heating, and particularly cooling systems specifically designed for the specific geology and cooling demands of the buildings in the city of Lisbon.

ACKNOWLEDGEMENTS

The authors would like to acknowledge the recent collaboration between leading scientific, engineering and governmental organisations in Portugal and the UK, and to FCT (Portuguese Foundation for Science and Technology) under the Project GeoSustained (PTDC/ECICON/1866/2021).

REFERENCES

Aljundi, K.; Figueiredo, A.; Vieira, A.; Lapa, J.; Cardoso, R. (2023): Geothermal energy system application: From basic standard performance to sustainability reflection. Renewable Energy 220 (2024)119612, https://doi.org/10.1016/j.renene.2023.119612.

Department for Business, 2018: Energy and Industrial Strategy: UK Energy in Brief 2018.

Inácio, M., Pinto, C., Vieira, A., Moitinho, I., Frias, AP. Leonardo, P. (2023). Contribuição da geologia na localização dos furos geotérmicos do projeto Geosustained. *Atas do 18º Congresso Nacional de Geotecnia*.

Omer, A. M. 2006: Ground-source heat pumps systems and application. Renewable and Sustainable Energy Reviews 12(2), 344-371. https://doi.org/10.1016/j.rser.2006.10.003.

Thomas S., Robertson J., Richardson G. (2019) Integration of Ground Source Energy Systems for Low Carbon Heating of Buildings. In: Monteiro J. et al. (eds) INCREaSE 2019. Springer.

UK Parliamentary Office of Science and Technology, 2016: Carbon Footprint of Heat Generation. Postnote No. 523.

Vieira, A.; Alberdi-Pagola, M.; Christodoulides, P. et al. (2017). Characterisation of ground thermal and thermo-mechanical behaviour for shallow geothermal energy applications. Energies, 10(12), https://doi.org/10.3390/en10122044.

Vieira, A., Pinto, C., Aljundi, K., Inácio, M., Moitinho de Almeida, I., & Pereira, C. (2023). Estudo da condutividade térmica dos solos de Lisboa. *Atas do 18º Congresso Nacional de Geotecnia.*

Proceedings of the XVIII ECSMGE 2024
GEOTECHNICAL ENGINEERING CHALLENGES
TO MEET CURRENT AND EMERGING NEEDS OF SOCIETY
© 2024 the Authors
ISBN 978-1-032-54816-6
DOI 10.1201/9781003431749-669
Open Access: www.taylorfrancis.com, CC BY-NC-ND 4.0 license

ECSMGE 24
XVIII EUROPEAN CONFERENCE ON SOIL MECHANICS AND GEOTECHNICAL ENGINEERING

Finite element modelling of wave loading on a multi-layered gassy soil seabed using complex number theory

Modélisation par éléments finis de la charge des vagues sur un fond marin à sol multicouche à l'aide de la théorie des nombres complexes

S.D. Thomas*
OGI Groundwater Specialists Ltd, City of Durham, UK
**stephen.thomas@ogi.co.uk*

ABSTRACT: Ocean wave loading on a gassy soil seabed, results in harmonic changes in stresses, displacements and pore water pressures over depth. For a multi-layered seabed soil with homogeneous properties within each layer, the behaviour of the dependent variables of displacement and pore pressure can be represented by a harmonic function in both horizontal space (x) and time (t). The amplitude of the horizontal & vertical displacement and pore-water pressure will vary over depth, dependent on the particular distribution of the multi-layered properties, together with the wave loading amplitude, wave number and angular velocity, together with the boundary conditions at the seabed, i.e. permeable or impermeable. To simulate the behaviour of the seabed in harmonic wave conditions, this paper presents a series of governing equations based on Biot theory for poro-elastic soil. These equations have been modified to represent the harmonic behaviour using real & imaginary complex number theory. The Finite Element Galerkin formulation combined with Green's Theorem is applied to these harmonic equations which result in six degrees of freedom per node, i.e. x-displacement, z-displacement and pore-water pressure, in both real (in-phase) & imaginary (out-of-phase) conditions. The harmonic finite element model can be used to match measured pore water pressure amplitude decay at various depths within a seabed, when subject to wave & tide loading.

RÉSUMÉ: La charge des vagues océaniques sur un fond marin gazeux entraîne des changements harmoniques dans les contraintes, les déplacements et les pressions de l'eau interstitielle en profondeur. Pour un sol de fond marin multicouche avec des propriétés homogènes au sein de chaque couche, le comportement des variables dépendantes du déplacement et de la pression interstitielle peut être représenté par une fonction harmonique à la fois dans l'espace horizontal (x) et dans le temps (t). L'amplitude du déplacement horizontal et vertical et de la pression de l'eau interstitielle variera en fonction de la profondeur, en fonction de la distribution particulière des propriétés multicouches, ainsi que de l'amplitude de charge des vagues, du nombre de vagues et de la vitesse angulaire, ainsi que des conditions aux limites du fond marin, c'est-à-dire perméable ou imperméable. Pour simuler le comportement des fonds marins dans des conditions de vagues harmoniques, cet article présente une série d'équations régulatrices basées sur la théorie de Biot pour les sols poro-élastiques. Ces équations ont été modifiées pour représenter le comportement harmonique à l'aide de la théorie des nombres complexes réels et imaginaires. La formulation de Galerkin par éléments finis combinée au théorème de Green est appliquée à ces équations harmoniques qui se traduisent par six degrés de liberté par nœud, c'est-à-dire le déplacement x, le déplacement z et la pression de l'eau interstitielle, dans des conditions réelles (en phase) et imaginaires (hors phase). Le modèle d'éléments finis harmoniques peut être utilisé pour faire correspondre la décroissance mesurée de l'amplitude de la pression de l'eau interstitielle à différentes profondeurs dans un fond marin, lorsqu'il est soumis à une charge de vagues et de marée.

Keywords: Wave loading; marine sediment; gassy soil; multi-layer; finite element modelling.

1 INTRODUCTION

This paper describes a Finite Element formulation of the differential equations that govern the wave-induced stresses, displacements and pore-water pressures in a multi-layered or anisotropic poro-elastic soft gassy soil seabed when subject to surface harmonic wave loading.

The harmonic stress, displacement and pore-water pressure behaviour of a gassy soil can be simulated under conditions that soil properties are homogeneous in the horizontal x and y directions, but can be variable, as in a multi-layered soil, in the vertical z-direction.

Under the condition that the total stress and water pressure loading on the seabed is harmonic in both timeand x-direction, that is a combination of a cosine and sine loading, the behaviour of each dependent variable is also harmonic in both time and the x-direction, and is governed by the wave period and wavelength of the loading wave; multiplied by the peak amplitude of the dependent variable. This is based on the equations by Yamamoto et al. (1978) and Madsen (1978).

When a combination of cosine and sine components of each dependent variable is replaced with complex

number theory, this enables application of the Galerkin Finite Element formulation combined with Green's Theorem, to the equations in the vertical dimension. This requires solving six degrees of freedom per node.

2 DIFFERENTIAL EQUATIONS FOR MULTI-LAYER & ANISOTROPIC PORO-ELASTIC SOIL CONDITIONS

Based on the Biot (1941) equations that govern the displacement, stresses and pore water pressures in a poro-elastic soil, as modified by Thomas (1987) for a Double Compressibility Gassy Soil, the equations of equilibrium in the x-direction, equilibrium in the z-direction, and continuity principles incorporating Darcy's Law of pore-fluid flow through a deformable poro-elastic medium, the following differential equations can be written for small strain conditions:

$$(\lambda + 2G)\frac{\partial^2 w_x}{\partial x^2} + G\frac{\partial^2 w_x}{\partial z^2} + \lambda\frac{\partial^2 w_z}{\partial x \partial z} + G\frac{\partial^2 w_z}{\partial z \partial x} - B\frac{\partial u_w}{\partial x} = 0 \quad (1)$$

$$(\lambda + 2G)\frac{\partial^2 w_z}{\partial z^2} + G\frac{\partial^2 w_z}{\partial x^2} + \lambda\frac{\partial^2 w_x}{\partial z \partial x} + G\frac{\partial^2 w_x}{\partial x \partial z} - B\frac{\partial u_w}{\partial z} = 0 \quad (2)$$

$$\frac{\partial}{\partial x}\left[\frac{k_{xx}}{\gamma_w}\frac{\partial u_w}{\partial x} + \frac{k_{xz}}{\gamma_w}\frac{\partial u_w}{\partial z}\right] + \frac{\partial}{\partial z}\left[\frac{k_{zx}}{\gamma_w}\frac{\partial u_w}{\partial x} + \frac{k_{zz}}{\gamma_w}\frac{\partial u_w}{\partial z}\right] = C\frac{\partial u_w}{\partial t} + B\frac{\partial}{\partial t}\left[\frac{\partial w_x}{\partial x} + \frac{\partial w_z}{\partial z}\right] \quad (3)$$

where w_x and w_z are the soil displacements in the x-horizontal and the z-vertical directions respectively, t is time, u_w the pore-water pressure within the soil matrix, k_{ij} the coefficient of permeability tensor, λ the Lame's constant and G the shear modulus. The gassy soil parameters B and C are derived from gassy soil theory (Thomas, 1987) as follows:

$$B = K^o/(K^o + K") = (1 + K"/K^o)^{-1} \quad (4)$$

$$C = (K^o + K")^{-1} + (1 - H)c_w n_w \quad (5)$$

The parameter K^o is the component of undrained bulk modulus governed by compression of the discrete gas bubbles, caused by an increase in total stress. Contributing to undrained compressibility is also water compressibility, c_w, water porosity, n_w, and Henry's constant H. The parameter $K"$ is the component of drained bulk modulus governed by consolidation of the saturated soil matrix. This results in two independent strain components, (i) caused by an increase in the total stress σ^o, and (ii) caused by an increase in the operative stress $(\sigma^o - u_w)$.

The modified equilibrium equations for a poro-elastic gassy soil are based on a Double Compressibility Model (Thomas, 1987) where the compression of the discrete gas bubbles is governed by the increase in the pressure of the gas bubbles, which in turn is governed by the average total stress within the soil. The compression of the surrounding saturated soil matrix, however, is governed by the difference between the total stress and the pore water pressure.

This difference between total stress and pore water pressure $(\sigma^o - u_w)$ is normally known as *effective stress* (Terzaghi, 1944). However, for a gassy soil, effective stress does not, on its own, govern the total volume change. For gassy soil, this difference between the mean total stress on a soil sample and the water pressure has been coined, the *operative stress* (Sills et al, 1991). This results in two independent components of strain caused by (i) an increase in the total stress σ^o, and (ii) an increase in the operative stress $(\sigma^o - u_w)$,

$$\epsilon^o = \Delta V^o/V = \Delta\sigma^o/K^o \quad (6)$$

$$\frac{\epsilon = \Delta V}{V} = \Delta\sigma"/K = (\Delta\sigma^o - \Delta u_w)/K \quad (7)$$

where ϵ^o is the volumetric strain due to the compression of the discrete gas bubbles caused by an increase in total mean stress $\Delta\sigma^o$, with $\epsilon"$ as the volumetric strain due to the compression of the soil matrix caused by an increase in operative stress $\Delta\sigma"$.

The main principle of the Double Compressibility Model (Thomas, 1987) for a gassy soil is that these two components of volumetric strain for a gassy soil, ϵ^o and, $\epsilon"$, can be added directly together to provide the total volumetric strain, as follows:

$$\epsilon = \epsilon^o + \epsilon" = \Delta\sigma^o/K^o + \Delta\sigma"/K" = \Delta\sigma^o/K^o + (\Delta\sigma^o - \Delta u_w)/K" \quad (8)$$

from which the change in total stress can be defined in terms of strain and pore pressure as:

$$\Delta\sigma^o = (\epsilon + \Delta u_w/K")/(1/K^o + 1/K") \quad (9)$$

3 HARMONIC APPROXIMATION OF GOVERNING EQUATIONS

For wave loading on the seabed when travelling in the x-direction along the surface of the seabed as depicted in Figure 1; under poro-elastic conditions, based on the equations by Yamamoto et al. (1978) and Madsen (1978), any variable ψ which is dependent on x, z and

t can be defined by a variable dependent in z only, multiplied by a harmonic function dependent on *x & t*:

$$\psi(x,z,t) = \psi_c + i\,\psi_s \tag{10}$$

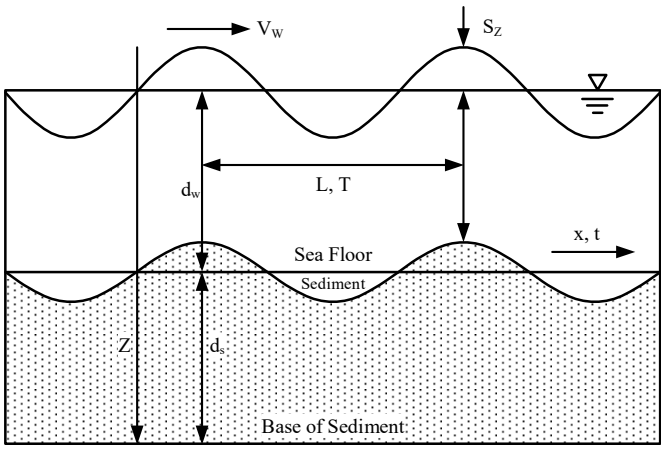

Figure. 1. Harmonic wave loading on a seabed sediment.

where:

$$\psi_c = \overline{\psi}(z)\cos(ax - \omega t) \tag{11}$$

$$\psi_s = \overline{\psi}(z)\sin(ax - \omega t) \tag{12}$$

and where $\overline{\psi}(z)$ is the peak variable function amplitude at depth z, from which:

$$\overline{\psi}(z) = \sqrt{\psi_c^2 + \psi_s^2} \tag{13}$$

$$\frac{\partial \psi}{\partial x} = +ia\psi = +ia\psi_c - a\psi_s \tag{14}$$

$$\frac{\partial \psi}{\partial t} = -i\omega\psi = -i\omega\psi_c + \omega\psi_s \tag{15}$$

where $\overline{\psi}$ is the amplitude of the harmonic variable at depth z, with a the wave number $2\pi/L$, with ω the angular velocity $2\pi/T$, and with L the wavelength and T the wave period.

This results in the harmonic displacements and pore-water pressure inhomogeneous, anisotropic soil sediment, being represented as follows:

$$w_x(x,z,t) = w_{xc} + iw_{xs} = \overline{w}_x(z)[\cos(ax - \omega t) + i\sin(ax - \omega t)] \tag{16}$$

$$w_z(x,z,t) = w_{zc} + iw_{zs} = \overline{w}_z(z)[\cos(ax - \omega t) + i\sin(ax - \omega t)] \tag{17}$$

$$u_w(x,z,t) = u_{wc} + iu_{ws} = \overline{u}_w(z)[\cos(ax - \omega t) + i\sin(ax - \omega t)] \tag{18}$$

Substituting the above three harmonic functions of x, z displacements and pore pressure into the governing equilibrium and continuity equations (1), (2) & (3), produces three differential equations, written as a mixture of real & imaginary harmonic variables:

$$-a^2(\lambda + 2G)w_x + G\frac{\partial^2 w_x}{\partial z^2} + ia(\lambda + G)\frac{\partial w_z}{\partial z} - iaBu_w = 0 \tag{19}$$

$$+(\lambda + 2G)\frac{\partial^2 w_z}{\partial z^2} - a^2 G w_z + ia(\lambda + G)\frac{\partial w_x}{\partial z} - B\frac{\partial u_w}{\partial z} = 0 \tag{20}$$

$$-a^2\frac{k_{xx}}{\gamma_w}u_w + \frac{k_{zz}}{\gamma_w}\frac{\partial^2 u_w}{\partial z^2} + ia\frac{k_{xz}}{\gamma_w}\frac{\partial u_w}{\partial z} + ia\frac{k_{zx}}{\gamma_w}\frac{\partial u_w}{\partial z} = -i\omega C u_w + a\omega B w_x - i\omega B\frac{\partial w_z}{\partial z} \tag{21}$$

4 GALERKIN FINITE ELEMENT FORMULATION

Applying the Galerkin Finite Element formulation to the above equations in the vertical dimension, combined with Green's Theorem, results in:

$$\int \left[a^2(\lambda + 2G)N_I N_J\, w_{xJ} + G\frac{\partial N_I}{\partial z}\frac{\partial N_J}{\partial z}w_{xJ} + iaG\frac{\partial N_I}{\partial z}N_J w_{zJ} - ia\lambda\, N_I\frac{\partial N_J}{\partial z}w_{zJ} + iaB\, N_I N_J\, u_{wJ}\right]dz = S_{xI} \tag{22}$$

from equilibrium in the x-direction,

$$\int \left[(\lambda + 2G)\frac{\partial N_I}{\partial z}\frac{\partial N_J}{\partial z}\, w_{zJ} + a^2 G N_I N_J\, w_{zJ} + ia\lambda\frac{\partial N_I}{\partial z}N_J w_{xJ} - iaGN_I\frac{\partial N_J}{\partial z}w_{xJ} - B\frac{\partial N_I}{\partial z}N_J\, u_{wJ}\right]dz = S_{zI} \tag{23}$$

from equilibrium in the z-direction, and

$$\int \left[\frac{k_{zz}}{\gamma_w}\frac{\partial N_I}{\partial z}\frac{\partial N_J}{\partial z} - ia\frac{k_{xz}}{\gamma_w}N_I\frac{\partial N_J}{\partial z} + ia\frac{k_{zx}}{\gamma_w}\frac{\partial N_I}{\partial z}N_J + a^2\frac{k_{xx}}{\gamma_w}N_I N_J - i\omega C\, N_I N_J\right]u_{wJ}dz + \int\left[a\omega B N_I N_J w_{xJ} - i\omega B N_I\frac{\partial N_J}{\partial z}w_{zJ}\right]dz = Q_{wI} \tag{24}$$

from continuity principles incorporating Darcy's Law.

Substituting equations 16, 17, 18 into the above three mixed real & imaginary differential equations, then separating the real & imaginary terms, results in six differential equations, each with nodal harmonic dependent variables as follows:

$$(a^2(\lambda+2G)\bar{\Gamma}_{IJ}+G\bar{A}^{zz}_{IJ})\bar{w}_{xcJ} - (aG\bar{B}^{zN}_{IJ} - a\lambda\bar{B}^{Nx}_{IJ})\bar{w}_{zsJ} - aB\bar{\Gamma}_{IJ}\,\bar{u}_{wsJ} = \bar{S}_{xcI} \quad (25)$$

$$(a^2(\lambda+2G)\bar{\Gamma}_{IJ}+G\bar{A}^{zz}_{IJ})\bar{w}_{xsJ} + (aG\bar{B}^{zN}_{IJ} - a\lambda\bar{B}^{Nx}_{IJ})\bar{w}_{zcJ} + aB\bar{\Gamma}_{IJ}\,\bar{u}_{wcJ} = \bar{S}_{xsI} \quad (26)$$

$$((\lambda+2G)\bar{A}^{zz}_{IJ} + a^2G\bar{\Gamma}_{IJ})\bar{w}_{zcJ} - (a\lambda\bar{B}^{zN}_{IJ} - aG\bar{B}^{Nx}_{IJ})\bar{w}_{xsJ} - B\bar{B}^{zN}_{IJ}\,\bar{u}_{wcJ} = \bar{S}_{zcI} \quad (27)$$

$$((\lambda+2G)\bar{A}^{zz}_{IJ} + a^2G\bar{\Gamma}_{IJ})\bar{w}_{zsJ} + (a\lambda\bar{B}^{zN}_{IJ} - aG\bar{B}^{Nx}_{IJ})\bar{w}_{xcJ} + B\bar{B}^{zN}_{IJ}\,\bar{u}_{wsJ} = \bar{S}_{zsI} \quad (28)$$

$$\left(a^2\frac{k_{xx}}{\gamma_w}\bar{\Gamma}_{IJ}+\frac{k_{zz}}{\gamma_w}\bar{A}^{zz}_{IJ}\right)\bar{u}_{wcJ} - \left(a\frac{k_{zx}}{\gamma_w}\bar{B}^{zN}_{IJ} - a\frac{k_{xz}}{\gamma_w}\bar{B}^{Nz}_{IJ} - \omega C\bar{\Gamma}_{IJ}\right)\bar{u}_{wsJ} + a\omega B\bar{\Gamma}_{IJ}\,\bar{w}_{xcJ} + \omega B\bar{B}^{Nz}_{IJ}\,\bar{w}_{zsJ} = \bar{Q}_{wcI} \quad (29)$$

$$\left(a^2\frac{k_{xx}}{\gamma_w}\bar{\Gamma}_{IJ}+\frac{k_{zz}}{\gamma_w}\bar{A}^{zz}_{IJ}\right)\bar{u}_{wsJ} + \left(a\frac{k_{zx}}{\gamma_w}\bar{B}^{zN}_{IJ} - a\frac{k_{xz}}{\gamma_w}\bar{B}^{Nz}_{IJ} - \omega C\bar{\Gamma}_{IJ}\right)\bar{u}_{wcJ} + a\omega B\bar{\Gamma}_{IJ}\,\bar{w}_{xsJ} - \omega B\bar{B}^{Nz}_{IJ}\,\bar{w}_{zcJ} = \bar{Q}_{wsI} \quad (30)$$

where:

$$\bar{A}^{zz}_{IJ} = \int \frac{\partial N_I}{\partial z}\frac{\partial N_J}{\partial z}\,dz \quad (31)$$

$$\bar{\Gamma}_{IJ} = \int N_I\,N_J\,dz \quad (32)$$

$$\bar{B}^{xN}_{IJ} = \int \frac{\partial N_I}{\partial x}N_J\,dz \quad (33)$$

$$\bar{B}^{Nx}_{IJ} = \int N_I\frac{\partial N_J}{\partial x}\,dz \quad (34)$$

5 INCORPORATION INTO A FINITE ELEMENT MODEL

A two-noded linear finite element shape function is sufficient to approximate the above matrix equations (Thomas, 1989, 1995). This simulates accurately the displacement, stress and pore water pressure, both in-phase and out-of-phase of the harmonic loading wave.

The above Galerkin Finite Element formulation has been programmed into the software WISPP (Wave Induced Stresses & Pore Pressures, Thomas, 1988).

For poro-elastic soil properties, applied boundary conditions loading, wavelength and angular velocity, WISPP produces a graphical output of the in-phase and out-of-phase x & z-displacements and pore-pressure at each of the nodes over the seabed depth, and the x-x, z-z, x-z operative stresses at each element centroid.

6 EXAMPLE OF WAVE LOADING ON A TWO-LAYERED SOIL

Figure 2 depicts finite element modelling with linear elements, of a multi-layered saturated soil with a 5m upper layer of drained bulk modulus K_1 = 1 MPa, shear modulus G_1 = 750 kPa, overlying a second 10m layer with higher stiffness of K_2 = 4 MPa & G_2 = 3 MPa.

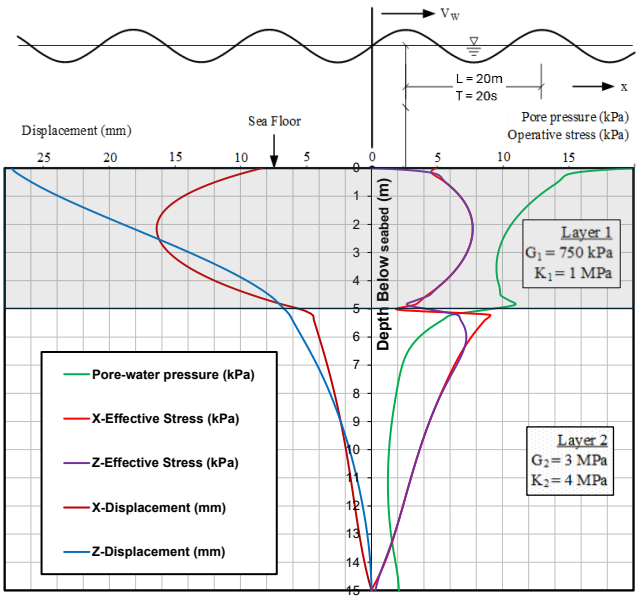

Figure. 2. Wave-induced x & z displacements, x & z operative stresses and pore-water pressures in a two-layer soil, simulated using the one-dimensional harmonic finite element WISSP model (Thomas, 1988).

A harmonic wave load of amplitude 20 kPa is applied to the soil surface with wavelength 20 m and wave period 20 s. The vertical domain has been discretised into 300 finite elements, with 100 elements in the upper layer and 200 elements in the lower layer. The permeability coefficient is 1 x 10^{-5} m/s for the upper layer, and 1 x 10^{-4} m/s for the lower layer. The output demonstrates that heterogeneity resulting from two layers with differing elastic moduli and permeability results in harmonic changes in effective stress, pore-pressure and soil displacement that are quite unexpected unless a harmonic model is applied.

7 CONCLUSIONS

Wave loading on a multi-layered poro-elastic seabed can result in unexpected displacements, stresses and pore-pressure behaviour. This is especially the case for a gassy soil seabed where undrained soil compression occurs. A Finite Element Model has been developed to simulate such behaviour under harmonic wave loading conditions using complex number theory.

REFERENCES

Biot, M.A. *(1941).* General theory of three-dimensional consolidation. J. Appl. Phys. 12 pp. 155-164. https://doi.org/10.1063/1.1712886.

Madsen, O. S. (1978). Wave-induced pore pressures and effective stresses in a porous bed. *Géotechnique*. 28 (4) pp. 377-393. https://doi.org/10.1680/geot.1978.28.4.377.

Sills, G.C., Wheeler, S.J., Thomas, S.D. & Gardner, T.N. (1991)., Behaviour of offshore soils containing gas bubbles. *Géotechnique.* 41 (2) pp. 227-241. https://doi.org/10.1680/geot.1991.41.2.227.

Terzaghi, K. (1944). *Theoretical Soil Mechanics*. John Wiley & Sons, New York, United States. http://dx.doi.org/10.1002/9780470172766.

Thomas, S.D. (1987*). The Consolidation Behaviour of Gassy Soil*. D. Phil. Thesis, University of Oxford. https://ora.ox.ac.uk/objects/uuid:f13acb0c-3e1b-4122-b497-341869846561 , accessed: 2008-03-14.

Thomas, S.D. (1988). WISPP: A finite element model for the analysis of wave-induced stresses, and pore pressures in a variably saturated seabed. University of Oxford, Department of Engineering Science, Report OUEL 1750/88. Available at http://ogi.co.uk/software.

Thomas, S.D. (1989). A finite element model for the analysis of wave-induced stresses, displacements and pore pressures in an unsaturated seabed. I: Theory. Computers & Geotechnics. 8 pp. 1-38. Elsevier Science. https://doi.org/10.1016/0266-352X(89)900 55-4.

Thomas, S.D. (1995). A finite element model for the analysis of wave-induced stresses, displacements and pore pressures in an unsaturated seabed. II: Model verification. Computers & Geotechnics. 17 pp. 107-132. Elsevier Science. https://doi.org/10.1016/0266-352X(95)91305-N.

Wheeler, S.J., Sham, W.K. and Thomas, S.D. (1990). Gas pressure in unsaturated offshore soils. *Canadian Geotechnical Journal.* 27 pp.79-89. https://doi.org/10.1139/t90-008.

Yamamoto, T., Koning, H.L., Sellmeiher, H., Hijum, E.V. (1978). On the response of a poro-elastic bed to water waves. J. Fluid Mech. 87 (1) pp. 193-206. http://dx.doi.org/10.1017/s002211207800.

Proceedings of the XVIII ECSMGE 2024
GEOTECHNICAL ENGINEERING CHALLENGES
TO MEET CURRENT AND EMERGING NEEDS OF SOCIETY
© 2024 the Authors
ISBN 978-1-032-54816-6
DOI 10.1201/9781003431749-670
Open Access: www.taylorfrancis.com, CC BY-NC-ND 4.0 license

ECSMGE 24
XVIII EUROPEAN CONFERENCE ON SOIL MECHANICS AND GEOTECHNICAL ENGINEERING

A study of soil contamination by residues of single-use face masks

Une étude de la contamination du sol par les résidus de masques faciaux à usage unique

V.A. Thomassen
Department of Civil- and Environmental Engineering, Norwegian University of Science and Technology, Instituto Superior Técnico, Ramboll Norway AS, Trondheim/Lisbon, Norway/Portugal

R.M. Singh
Norwegian University of Science and Technology, Trondheim, Norway

R. Cardoso*
Istituto Superior Técnico, University of Lisbon, Lisbon, Portugal

**rafaela.cardoso@tecnico.ulisboa.pt*

ABSTRACT: The COVID-19 pandemic has led to widespread use of single-use face masks, primarily made of plastic materials, causing significant environmental concerns, notably the potential of microplastic pollution in terrestrial and aquatic environments. This study offers a geotechnical engineering-focused examination of the environmental effects of single-use face masks on soil properties in simulated natural conditions. Soil samples compacted with different concentrations of shredded face mask fibers underwent UV radiation exposure for 6 weeks. This period was considered to be sufficient for detecting potential differences in degradation. The hydraulical properties (water retention curve and saturated permability) and the physical properties of the soil samples were measured considering the presence of shredded face mask fibers. The findings indicate a substantial decrease in soil permeability and an increase in water retention capacity upon introducing face mask fibers into the soil, suggesting potential shifts in soil structure. Additionally, prolonged UV exposure led to a reduction in the soil's void ratio, possibly due to the degradation of soil and face mask particles into smaller fragments. These outcomes underscore the need for responsible disposal of single-use face masks and inform waste management policies, as well as highlight the need for further research into the broader environmental impacts of plastic waste on soil and water systems from a geotechnical engineering perspective.

RÉSUMÉ: La pandémie de COVID-19 a entraîné une utilisation généralisée de masques jetables, principalement fabriqués en matériaux plastiques, suscitant des préoccupations environnementales importantes, notamment en ce qui concerne la pollution potentielle par les microplastiques dans les environnements terrestres et aquatiques. Cette étude propose un examen axé sur le génie géotechnique des effets environnementaux des masques jetables sur les propriétés du sol dans des conditions naturelles simulées. Les échantillons de sol ont été compactées avec différentes concentrations de fibres de masque déchiqueté, et soumis à 6 semaines d'exposition aux rayonnements UV. Cette durée a été suffisante pour détecter des différences en dégradation. Les propriétés hydrauliques (capacité de rétention et perméabilité) et physiques du sol ont été mesurées en face de la présence de fibres de masque. Les résultats indiquent une diminution substantielle de la perméabilité du sol et une augmentation de la capacité de rétention d'eau lors de l'introduction de fibres de masque dans le sol, suggérant des modifications potentielles de la structure du sol. De plus, une exposition prolongée aux UV a entraîné une réduction du rapport de vidange du sol, probablement en raison de la dégradation des particules de sol et de masque en fragments plus petits. Ces résultats soulignent la nécessité d'une élimination responsable des masques jetables et éclaire les politiques de gestion des déchets, tout en mettant en évidence la nécessité de poursuivre la recherche sur les impacts environnementaux plus larges des déchets plastiques sur les systèmes sol et eau du point de vue du génie géotechnique.

Keywords: Soil contamination; single-use face masks; COVID-19; plastic pollution.

1 INTRODUCTION

The extended use of plastic products in daily life has contributed significantly to pollution in terrestrial and aquatic ecosystems. Plastic waste is known to have slow degradation, originating microplastics (MPs), which are characterized as small plastic particles ranging from 1 micron to 5 millimeters in size (Benson et al., 2021). Annually, an astonishing 8 million metric tons of plastic waste find their way into the oceans,

primarily originating from land-based sources, thus posing a sustained threat to the environment.

The emergence of the COVID-19 pandemic prompted a surge in the use of single-use face masks as a vital tool in preventing virus transmission. By the start of the pandemic, face masks have contributed to the global plastic production by almost 370 million tons. While these masks are vital for public health, environmental concerns have arisen due to their improper disposal practices, such as littering and landfill dumping. Despite guidelines for proper disposal of the masks, numerous reports have demonstrated the commonness of improper disposal practices, notably in regions with inadequate waste management systems, leading to significant environmental accumulation of such pollutants in terrestrial ecosystems (United Nations Environment Programme), thus supporting the relevance of this study's scenario in simulating potential soil contamination outcomes. These face masks, composed of polymer-based materials, are categorized as single-use plastics. Their presence in the environment, subjected to environmental conditions like biological degradation, UV radiation, temperature fluctuations, and contact with water, can lead to fragmentation, potentially generating MPs (Kumar et al., 2020).

To address these environmental concerns, this study delves into the impact of single-use face mask fibers on soil during the COVID-19 pandemic. It includes an original laboratory experiment designed to simulate the degradation process of face masks in soil submerged in water under natural conditions. The experiment spans approximately 0 and 6 weeks, being analysed the initial and final time periods. This period was considered to be sufficient for detecting potential differences in degradation. The investigation specifically focuses on understanding how the presence of face mask fibers affects the soil, as soil represents a substantial source of plastic contamination.

2 MATERIALS AND METHODS

2.1 Materials

The soil was collected from a construction site in Lisbon, Portugal. The grading size distribution analysis revealed that approximately 82% of the particles are sand size, 15% are gravel size, and only 3% consist of fines. The soil classifies as a well-graded sand (SW) with minimal fines, accordingly with the Unified Soil Classification System.

Despite the low presence of fines, the consistency limits were determined due to the presence of clayey minerals. The liquid limit (LL) was found to be 46%, while the plastic limit (PL) was approximately 28%, resulting in a plastic index (PI) of 18%. Based on these values, the fine fraction of the soil can be classified as a low plastic clay. Mineral analysis confirmed the presence of some expanding clay minerals, including montmorillonite and illite, which suggest that the soil has swelling potential when full saturated.

The masks used in the study were commercially available, single-use face masks type IIR, made from polypropylene (PP). The middle layer of the mask was made of melt blown PP while the two other layers were made of spunbonded PP. The material was then shredded using a heavy-duty cutting mill RETCH SM 2000 with a bottom sieve of size 2 mm. The shredding process produced small fibers with sizes varying between 2 and 0.02 mm (Figure 1a) and a significant amount of dust and finer fragments.

Finally, the specific gravity (Gs) of the solid particles was 2.5 due to the presence of some organic matter. This value was used for all prepared samples in the experiment, although the real Gs of soil samples containing face mask fibers may decrease with increasing fiber content.

2.2 Sample preparation and UV treatment

To investigate the impact of shredded face masks on soil, 12 samples were prepared, 6 with the addition of face mask fibers (MH), and 6 without fibers (NM). The concentration of shredded face masks added corresponded to 5% of the solid weight. Each sample was compacted into cylindrical plastic containers (diameter 7 cm and 6 cm height). Compaction was proceeded to fit the *in situ* soil water content and dry volumetric weight. The compaction process involved three layers, each receiving 20 hammer-blows. Water content control was performed to attain the appropriate initial water content for all prepared samples The average water content, γ_d and e values, can be found in Table 1. The saturated permeability was measured in two samples compacted with and without the fibers specially prepared for that purpose. Additionally, three samples were compacted in smaller cylindrical containers, with identical water contents and void ratios (Thomassen (2023).

Table 1. Average initial water content (w), dry density (γ_d), and void ratio (e) for all samples.

Fiber concentration (%)	w (%)	γ_d (kN/m^3)	e (-)
0	18	13	1.0
5	20	12	1.1

All compacted samples were submerged in distilled water. One sample of each type was stored in a

chamber with UV exposure for 6 weeks (Figure 1b), and the other was kept in laboratorial environment for the same period. The UV exposition was an ageing test, to intending to accelerate fiber degradation.

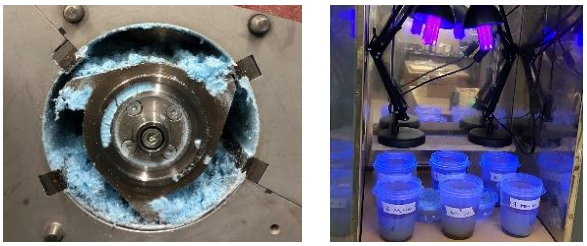

a) b)

Figure 1. a) Shredded mask fibers and b) Experimental setup of samples subjected to UV-exposure.

2.3 Measurement of hydraulic properties

The hydraulic properties of the soil samples compacted with and without the fibers were determined only for the cases after sample preparation. A variable water head test was performed to measure the saturated permeability as described by Thomassen (2023).

The water retention curve (WRC) was measured using vapor equilibrium technique, both for the wetting and drying branches. Suction was applied by vapor equilibrium. The known equation 1 was used to fit experimental data,

$$Sr = \left(1 + \left(\frac{s}{\rho}\right)^{\frac{1}{1-\gamma}}\right)^{-\gamma} \quad (1)$$

where Sr (%) is the degree of saturation computed as usual, s (MPa) is the suction and ρ and γ (MPa, -) are empirical shape-defining parameters, adjusted through curve fitting to experimental data (Thomassen, 2023).

2.4 Other tests

Mercury intrusion porosimetry (MIP) tests were performed to evaluate pore size distribution after preparation and at the end of 6 weeks submerged. An optical microscope was used to visualize the texture of the soil with and without mask fibers. Additionally, scanning electron microscopy (SEM) was used to provide information about the size, shape and morphology of the soil particles and mask fibers.

3 RESULTS AND DISCUSSION

3.1 Visual Observations

All samples experienced volume changes when submerged in water, likely due to the presence of the clay minerals previously identified. Independently from having the fibers or not, the UV-exposed samples were more disrupted because there was a larger amount of soil gathered at the bottom of their containers (Figure 2a). This was more evident in samples without mask fibers. Without UV exposition, the samples with shredded face masks exhibited more stability (Figure 2b). Both results indicate that the fibers were acting as a soil stabilizer.

These findings were corroborated by the analysis of the submersion water. Samples containing mask fibers exhibited clearer water. For samples with mask fibers exposed to UV, minimal fibers were released to the surface, suggesting that UV exposure has degraded some mask fibers (Figure 2b), even in such small period of exposure.

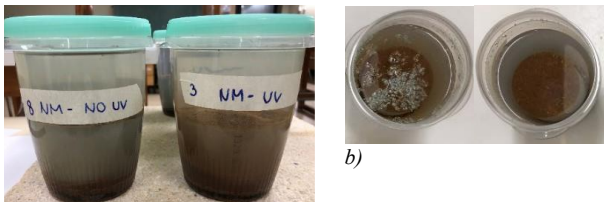

a) b)

Figure 2. a) NM samples and b) MH samples without UV exposure on the left and with UV exposure on the right.

3.2 Hydraulic properties

The saturated permeability of the samples with and without the mask fibers were, respectively, 5×10^{-7}m/s and 9×10^{-7}m/s. This small difference is probably explained by some disturbance introduced by the fibers. The WRC are presented in Figure 3, being the experimental points adjusted using Eq. 1, with ρ= 0.13 MPa and γ= 0.4 for the sample NM, and ρ= 1.0 MPa and γ= 0.4 for the sample MH.

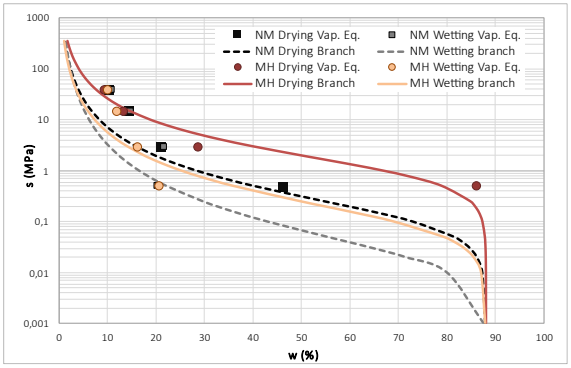

Figure 3. WRC for the samples with and without mask fibers (MH and NM, respectively).

The presence of the fibers increased the air-entry value, a result also found by Guo et al. (2022) for clays with high concentrations of MPs. It can be assumed that the presence of the impervious mask fibers increases the water retention capacity of the soil.

3.3 Other tests

The variation in pore size distribution measured in the MIP tests is presented in Figure 4.

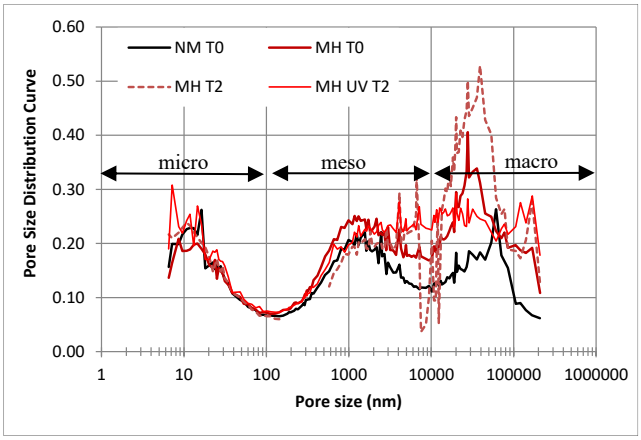

Figure 4. Distribution of pore sizes through soil samples with (MH) and without (NM) mask fibers.

The results for the samples without mask fibers (not saturated, NM_T0) served as reference. Its comparison with sample MH_T0 allows concluding that the presence of the fibers has increased macroporosity and slightly decreased microporosity. This may be explained by the formation of fiber-aggregate complexes, as shown in Figure 5a).

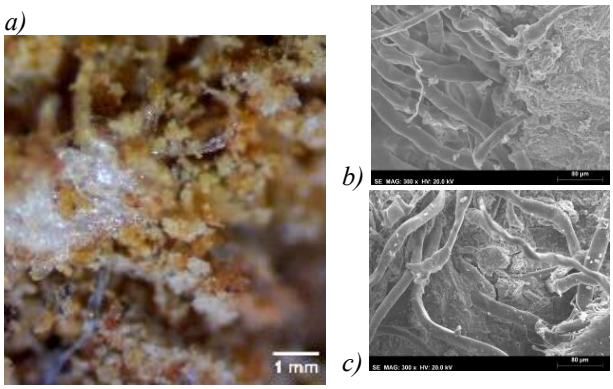

Figure 5. (a) Optical microscopy showing particles aggregation around a mask fiber; (b) SEM image of the sample without degradation and (c) with degradation after UV exposition.

Macroporosity has increased further after 6 weeks of submersion and no UV exposition (MH_T2), as well as mesoporosity. Considering the soil's low fine content, the mechanism driving these changes are not fully understood.It is hypothesized that swelling of the swelling of clay minerals present within the soil could be a factor, despite its low plasticity. However, this requires further investigation. Significant changes are observed after UV exposition (MH_UV_T2) because the amount of macropores reduce and the mesopores appear to dominate, as well as the appearance of micropores. This may be explained by some fiber degradation, producing MP that clog soil pores. Some bare degradation caused by UV exposition was observed in the fibers in SEM images presented in Figure 5a) and b), however it is not significant, probably due to the short duration of this ageing test.

Joining both results it can be concluded that the degradation of the face mask fibers with time and UV, and the formation of fiber-aggregate complexes further contributed to variations in pore size distribution and overall pore volume. Additionally, saturation also impacted the soil, being the analysis of the influence of the fibers on its volumetric behavior upon saturation not done in this paper.

4 CONCLUSIONS

This study has uncovered significant insights into the impact of shredded face mask fibers on soil properties and their response to simulated environmental conditions. The findings indicate that water and aging caused by UV exposition influenced the soil's pore structure. The presence of shredded face mask fibers in the soil led to an increase in water retention capacity, primarily due to the presence of impervious fibers, the formation of fiber-aggregate complexes, and changes in pore-size distribution due to pore clogging likely caused by fibers degradation. These findings emphasize the importance of proper disposal of face masks and the need for research on the long-term environmental consequences of face mask pollution.

REFERENCES

Benson, N. U., Bassey, D. E., & Palanisami, T. (2021). COVID pollution: Impact of COVID-19 pandemic on global plastic waste footprint. Heliyon, Vol. 7(2), e06343. http://doi.org/10.1016/j.heliyon.2021.e06343.

Guo, Z., Li, P., Yang, X., Wang, Z., Lu, B., Chen, W., Wu, Y., Li, G., Zhao, Z., Liu, G., Ritsema, C., Geissen, V., & Xue, S. (2022). Soil texture is an important factor determining how microplastics affect soil hydraulic characteristics. Environment International, Vol. 165, 107293. https://doi.org/10.1016/j.envint.2022.107293.

Kumar, M., Xiong, X., He, M., Tsang, D. C. W., Gupta, J., Khan, E., Harrad, S., Hou, D., Ok, Y. S., & Bolan, N. S. (2020). Microplastics as pollutants in agricultural soils. Environmental Pollution, Vol. 265(Part A), 114980. https://doi.org/10.1016/j.envpol.2020.114980.

Thomassen, V. (2023). A Study of Soil Contamination by Residues of Single-use Face Masks, MSc Thesis, NTNU.

Proceedings of the XVIII ECSMGE 2024
GEOTECHNICAL ENGINEERING CHALLENGES
TO MEET CURRENT AND EMERGING NEEDS OF SOCIETY
© 2024 the Authors
ISBN 978-1-032-54816-6
DOI 10.1201/9781003431749-671
Open Access: www.taylorfrancis.com, CC BY-NC-ND 4.0 license

ECSMGE 24
XVIII EUROPEAN CONFERENCE ON SOIL MECHANICS AND GEOTECHNICAL ENGINEERING

Influence of culverts on frost depth in embankments: A field study

Influence des ponceaux sur la profondeur de gel dans les remblais: Une étude de terrain

K. Tommik*, S. Knutsson, J. Laue
Luleå University of Technology, Luleå, Sweden

**karina.tommik@ltu.se*

ABSTRACT: Frost-related damages around culverts are a common problem for roads and railways built on seasonally frozen ground. Culverts create altered thermal conditions in the embankment section where they are installed, leading to deeper frost penetration around the culverts compared to the rest of the road. However, estimating the depth of frost penetration and consequential heave is difficult due to the complex thermal conditions inside culverts, which depend on various factors. To monitor the influence of culverts on the surrounding soil and assess the effect of temperature distribution inside the culvert on frost penetration in the embankment, temperatures were measured inside a 0.6 m diameter culvert and in the soil 0.30 m from the culvert in northern Sweden during the winter of 2023. Control measurements were also performed in a road section without a culvert. Temperatures were recorded in seven locations in the embankment at depths ranging from 0.1 m to 2.55 m. Effect of the temperature distribution inside the culvert on frost penetration in the embankment is assessed. The results of this study could help in the design and management of culverts in cold climates and improve our understanding of the thermal conditions around culverts. This field study is part of a larger project where collected data will be used to verify numerical models, enabling assessment of the effect of culverts of any size on temperature distribution.

RÉSUMÉ: Les dommages causés par le gel autour des ponceaux constituent un problème courant pour les routes et les voies ferrées construites sur un sol gelé de façon saisonnière. Les ponceaux créent des conditions thermiques modifiées dans la section de remblai où ils sont installés, entraînant une pénétration du gel plus profonde autour des ponceaux par rapport au reste de la route. Cependant, il est difficile d'estimer la profondeur de pénétration du gel et le soulèvement qui en résulte en raison des conditions thermiques complexes à l'intérieur des ponceaux, qui dépendent de divers facteurs. Pour surveiller l'influence des ponceaux sur le sol environnant et évaluer l'effet de la répartition de la température à l'intérieur du ponceau sur la pénétration du gel dans le remblai, les températures ont été mesurées à l'intérieur d'un ponceau de 0,6 m de diamètre et dans le sol à 0,30 m du ponceau dans le nord de la Suède au cours de la période d'essai, l'hiver 2023. Des mesures de contrôle ont également été effectuées dans un tronçon de route sans ponceau. Les températures ont été enregistrées à sept endroits du remblai à des profondeurs allant de 0,1 m à 2,55 m. L'effet de la répartition de la température à l'intérieur du ponceau sur la pénétration du gel dans le remblai est évalué. Les résultats de cette étude pourraient aider à la conception et à la gestion des ponceaux dans les climats froids et améliorer notre compréhension des conditions thermiques autour des ponceaux. Cette étude sur le terrain fait partie d'un projet plus vaste où les données collectées seront utilisées pour vérifier les modèles numériques, permettant d'évaluer l'effet des ponceaux de toute taille sur la distribution de la température.

Keywords: Culvert; frost heave; cold climate.

1 INTRODUCTION

Culverts are essential components of the road and railway embankments, facilitating drainage and the flow of water from one side of the road to the other. However, in seasonally frozen ground, the presence of culverts allows cold air to pass through the road structure. This results in frost penetration not only perpendicular to the surface of the road but also perpendicular to the surface of the culvert. Leading to increased frost depth around the culvert, which results in frost related damages if frost susceptible soil is present. Manifesting as bumps and depressions over the culvert on the surface of the road. This poses significant challenges, reducing the lifetime of road structures, increasing maintenance costs, and compromising traffic safety.

Temperature distribution inside and around culverts is influenced but not limited to the following factors: diameter, length, and material of the culvert, placement of the culvert in the embankment, outside temperature, air or water velocity inside the culvert, snow cover and solar radiation (Hua et al. 2014). Increased frost depth underneath the culvert will be

directly caused by the thermal boundary conditions established inside of the culvert due to the interaction of the previously mentioned factors.

2 METHOD

To estimate the thermal effect a culvert has on the surrounding road structure a field experiment was designed in Northern Sweden, near town of Luleå. The study area was located near the airport, allowing access to weather data from the airport weather station.

The test section comprised of an 8 m wide, two-lane road with an embankment height from the shoulder of the road to the bottom of the ditch measuring 1.5 m. The slope of the embankment is 1:4. The project specification documents of the road were unavailable. However, based on the boreholes drilled for the installation purposes it could be estimated that the road structure had around 10 cm thick asphalt layer, 20 cm of crushed rock base and the embankment as well as natural soil below terrace level were sand. The measured embankment section included a culvert with a diameter of 0.6 m and a length of 22 m, covered with an overburden of 0.84 m of soil.

One lane of the road was instrumented with seven temperature measurement probes in the vicinity of the culvert, as seen in Figure 1, each with a length of 2.5 meters and nine thermocouples at varying heights. The top of the probe is placed 5 cm under the ground surface, as the first thermocouple is at 5 cm depth, the shallowest recording takes place at 10 cm depth.

The probes form two cross-sections parallel to the culvert. One is placed close to the culvert. The second is 3 m away from the first cross-section where the thermal regime of the culvert will not influence the developing frost depth (both cross-sections marked in Figure 1). Each of the two cross-sections has a probe close to the middle of the road, in the shoulder of the road at the edge of the asphalt cover and in the ditch. The cross-section further away from the culvert has an additional 4th probe in between the wheel path of the measured lane (exact locations marked in Figure 1).

Type T thermocouples produced by Pentronic are used for the temperature measurements alongside the CR1000X datalogger and 4 Granite temp 120 thermocouple modules, produced by Campbell scientific. Resulting in relative measurement accuracy of ± 0.2 C° (based on calibration performed) and absolute accuracy of ± 0.8 C°. Recording of the temperatures started on January 14th of 2023 and will continue until probes remain operational. The data is recorded every 12 hours.

Additional thermocouples were installed inside the culvert to measure the thermal boundary conditions. However, data from the instrumentation inside the culvert was considered unreliable due to grounding errors.

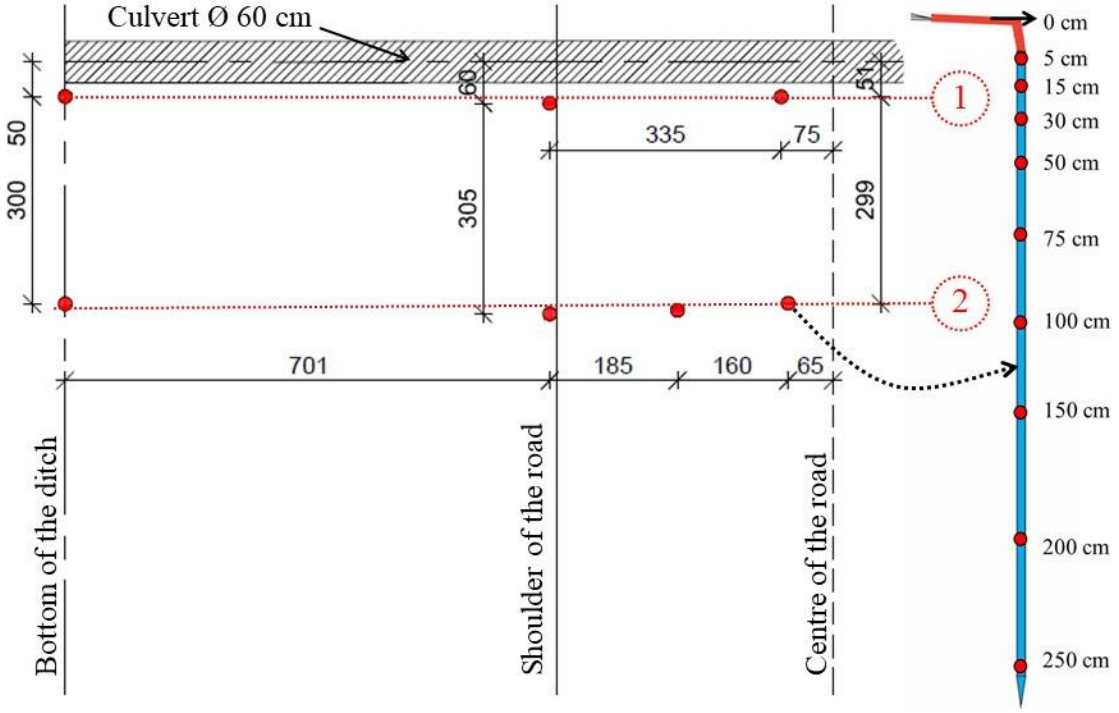

Figure 1. Top view of the installation probe locations in red, cross-section of the probe (to the right), thermocouples in red.

3 RESULTS

The results presented cover the period from Jan. 14th, when data recording commenced, to March 19th, when the maximum frost depth was reached. Frost depth was calculated by interpolating existing data using MATLAB (The MathWorks Inc., 2020). Frost depth progression at each of the probe locations through the freezing period is presented in Figure 2.

Throughout the recording period, the ground did not freeze in the ditch in either of the cross-sections due to the thick snow cover and the insulation it provided (Motamedi et al., 2024).

Frost depth in cross-section 1 (near the culvert) under the shoulder of the road was 170 cm in January, increasing to 184 cm by March, indicating a 14 cm increase over three months. In the same cross-section close to the centre of the road, frost depth increased from 184 cm in January to 193 cm in March, marking a 9 cm increase. The differences in frost depth between the shoulder and the centre of the road near the culvert were 14 cm in January and 9 cm in March. Frost depth at the shoulder is shallower due to the insulating properties of snow cover.

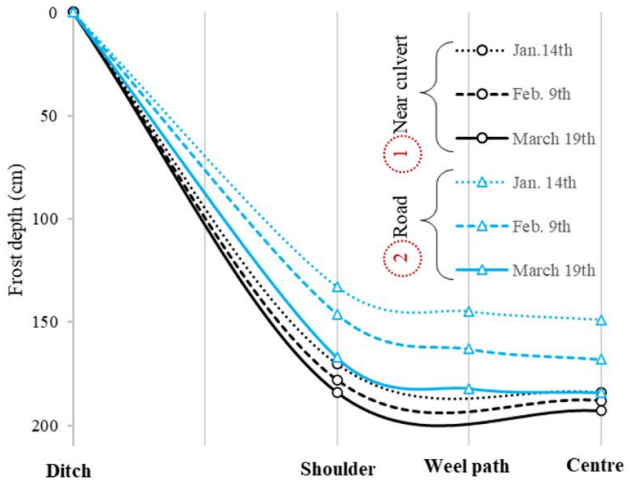

Figure 2. Frost depth progression during winter for each probe location.

Frost depth in cross-section 2 was 133 cm at the shoulder in January and increased to 167 cm in March, resulting in a 34 cm difference. For the same cross-section close to centre of the road, frost depth increased from 149 cm in January to 184 cm in March, resulting in 35 cm difference. The difference between the frost depth at the shoulder and centre of the road was 16 cm in January and 17 cm in March, with frost depth increasing towards the centre.

In cross-section 1 (near the culvert), frost penetration at the shoulder was 37 cm deeper in January and 17 cm deeper in March compared to the rest of the embankment (cross-section 2). Similarly, the difference in frost depth at the centre was 35 cm in January and 9 cm in March. Indicating that frost penetration at near the culvert is increased compared to the rest of the road. The maximum frost depth of 193 cm was recorded near the centre of the road near the culvert on March 19th. The temperature distribution in both cross-sections is seen in Figure 3, where frost depth is marked by the turquoise line. The temperature distribution and previously discussed frost depth values are obtained by interpolation between the existing measurement points.

No temperature measurements were performed in the slope of the road. Therefore, the shape of the frost

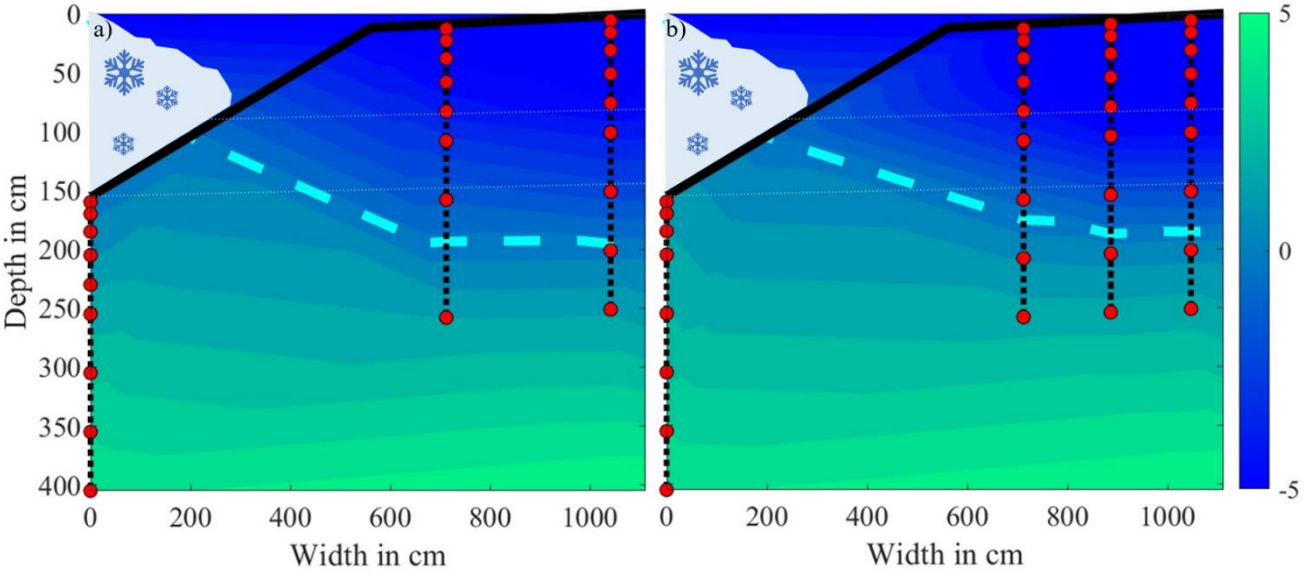

Figure 3. Temperature distribution in the embankment in a) cross-section 1 and b) cross-section 2 (temperature measurement locations in red, forst depth in turquise).

front in the slope was manually altered, to display the insulating effects of snow. As the ground never freezes in the ditch of the road and the frost depth in the shoulder is significant it is reasonable to assume that the frost front will end somewhere in the shoulder of the road, considering the volume of snow in the ditch. The increased amount of snow would increase the inclination of the line moving its end closer to the shoulder. While decrease in snow depth would lead to a flatter shape moving the end closer to the bottom of the ditch. The shape of the frost front will influence consequent frost heave as the frost heave propagation is perpendicular to the frost front line.

4 CONCLUSION AND DISCUSSION

At the start of the recording in January, frost depth near the culvert was significantly deeper (by 35 cm at the centre) compared to the rest of the road. However, this difference decreased as the winter progressed. The soil near the culvert froze faster, but the frost depth did not significantly increase during the subsequent months, while the soil in the rest of the road froze more gradually. This suggests that the increased frost depth and the speed of freezing are due to the proximity to the culvert, allowing cold air to enter the road structure before the culvert ends become covered by snow and are insulated, slowing down the frost penetration (Tommik et al., 2023).

The shoulder of the road displayed a shallower frost depth compared to the centre of the road due to the insulating properties of the snowpack in the ditch. Additionally, the ground at the bottom of the ditch did not freeze in either of the cross-sections. Frost depth differences between the shoulder and centre of the road near the culvert were smaller during the winter compared to the rest of the road, indicating that the culvert has an equalizing effect on the soil temperatures surrounding it. As a result, shape of the frost front near the culvert is flatter compared to the more bowl-shaped frost front in the rest of the road, as indicated by temperature difference between shoulder and centre of the road. This would lead to uniform heaving along the culvert rather than more severe heaving at the centre.

Presence of a culvert significantly changes the thermal balance of the road structure during the freezing period, resulting in increased frost depth around the culvert compared to the rest of the road. However, the measurements were conducted on the side of the culvert, and the deepest frost penetration in the area would be beneath the culvert itself, as frost penetration will expand radially outward from the surface of the culvert.

There is a great variation in both culvert and road dimensions as well as soil materials and weather conditions. Resulting in difficulty in knowledge regarding thermal boundaries to several locations based on one test site. Therefore, numerical models must be employed for the task. Data from such studies as presented is essential for calibrating and validating such models. Expanding the knowledge of thermal surrounding the culverts will result an improved road design in regions with seasonal frost.

ACKNOWLEDGEMENTS

The authors would like to express their gratitude to Swedish Transport Administration (Trafikverket) for the financial support of the research project within the research programme BVFF.

REFERENCES

Hua, L., Fujun, N., Yonghong, N. and Xifebg, Y. (2014.) Study on thermal regime of roadbed culvert transition section along a high-speed railway in seasonally frozen ground, *Cold Regions Science and Technology* (106-107), 216-231. https://doi.org/10.1016/j.coldregions.2014.07.008.

Motamedi, Z., Mattsson, H., Knutsson, S., Laue, J. and Casselgren, J. (2024.) Influence of different seasonal snow cover on thermal regime of ground. In *Proceedings of the XVIII ECSMGE 2024*, Portugal.

Tommik, K., Knutsson, S., Laue, J., Lintzén, N. (2023.) Air velocity and temperature distribution in culverts, *Cold Regions Science and Technology* (212) https://doi.org/10.1016/j.coldregions.2023.103888.

The MathWorks, Inc. 2020. MATLAB version R2020a. Natick, Massachusetts, United States.

Proceedings of the XVIII ECSMGE 2024
GEOTECHNICAL ENGINEERING CHALLENGES
TO MEET CURRENT AND EMERGING NEEDS OF SOCIETY
© 2024 the Authors
ISBN 978-1-032-54816-6
DOI 10.1201/9781003431749-672
Open Access: www.taylorfrancis.com, CC BY-NC-ND 4.0 license

ECSMGE 24
XVIII EUROPEAN CONFERENCE ON SOIL MECHANICS AND GEOTECHNICAL ENGINEERING

Triaxial cyclic behaviour of calcareous sand for offshore energy applications

Comportement cyclique triaxi al du sable calcaire pour les applications énergétiques offshore

N. Ullah*
KU Leuven, Department of Civil Engineering, Hydraulics and Geotechnics Section, Bruges, Belgium
The University of Melbourne, Department of Infrastructure Engineering, Offshore Geomechanics Group, Melbourne, Australia

J. Andries
Flemish Government, Department of Mobility and Public Works, Ghent, Belgium

G. Anoyatis
KU Leuven, Department of Civil Engineering, Hydraulics and Geotechnics Section, Bruges, Belgium

S. François
KU Leuven, Department of Civil Engineering, Structural Mechanics Section, Leuven, Belgium

Y. Tian, S.H. Chow
The University of Melbourne, Department of Infrastructure Engineering, Offshore Geomechanics Group Melbourne, Australia

**nazish.ullah@kuleuven.be*

ABSTRACT: Soils in the vicinity of the foundations of offshore energy systems are subjected to cyclic stresses arising from repeated environmental loads. Long-term application of such loading alters the surrounding soil's strength and deformation characteristics and subsequently may put the performance of such systems at risk. The deformation of soil i.e., strain accumulation depends on both the soil parameters and the loading conditions. This paper presents the findings from an experimental study that focuses on strain accumulation in calcareous sands subjected to long-term cyclic loading. A series of drained cyclic triaxial tests were performed on saturated calcareous sand specimens up to 10,000 loading cycles. The influence of cyclic stress amplitude and sand density on the strain accumulation is investigated. The experimental results show an increase in strain accumulation with increasing cyclic stress amplitude and void ratio. The formulations of the High Cycle Accumulation Model are calibrated based on the experimental results. The test results provide valuable information on the deformation characteristics of the calcareous sands, which can be used to predict the performance of offshore structures under cyclic loads. The triaxial test results also provide a very useful database for calibrating advanced soil models to accurately assess the performance and behavior of the foundations of offshore energy systems.

RÉSUMÉ: Les sols à proximité des fondations des systèmes d'énergie offshore sont soumis à des contraintes cycliques résultant des charges environnementales répétées. L'application à long terme de ces charges altère la résistance et les caractéristiques de déformation du sol environnant, mettant potentiellement en danger la performance de ces systèmes. La déformation du sol, c'est-à-dire l'accumulation de contrainte, dépend à la fois des paramètres du sol et des conditions de chargement. Cet article présente les résultats d'une étude expérimentale axée sur l'accumulation de contrainte dans des sables calcaires soumis à un chargement cyclique à long terme. Une série d'essais triaxiaux cycliques drainés a été réalisée sur des échantillons de sable calcaire saturé jusqu'à 10 000 cycles de chargement. L'influence de l'amplitude de contrainte cyclique et de la densité du sable sur l'accumulation de contrainte est étudiée. Les résultats expérimentaux montrent une augmentation de l'accumulation de contrainte avec l'augmentation de l'amplitude de contrainte cyclique et du rapport de vides. Les formulations du modèle d'accumulation en haute fréquence sont calibrées en fonction des résultats expérimentaux. Les résultats des essais fournissent des informations précieuses sur les caractéristiques de déformation des sables calcaires, pouvant être utilisées pour prédire la performance des structures offshore sous des charges cycliques. Les résultats des essais triaxiaux fournissent également une base de données très utile pour calibrer des modèles avancés de sol afin d'évaluer avec précision la performance et le comportement des fondations des systèmes d'énergie offshore.

Keywords: Calcareous sand; cyclic stress ratio; strain accumulation; long-term drained response.

1 INTRODUCTION

Offshore wind turbine (OWT) foundations are subjected to environmental loadings during their life span of approximately 25 to 30 years. The response of OWT foundations is influenced by the loading characteristics and the soil conditions around the foundation. During extreme events such as storms or earthquakes, the high-amplitude cyclic loads (strain amplitudes $\varepsilon^{ampl} > 10^{-3}$) can induce undrained soil behaviour. This can lead to the rapid development of excess pore pressure, posing a potential risk of liquefaction.

Under regular operational loads of small amplitude ($\varepsilon^{ampl} < 10^{-3}$), as indicated by Wichtmann et al. (2005), the excess pore water pressure dissipates, and the soil behaves in a drained fashion. However, the soil behaviour may exhibit variability across different loading frequencies and soil permeability. The cyclic loading results in hysteresis loops that are not perfectly closed leading to strain accumulation in the soil, commonly referred to as "ratcheting" (Houlsby et al., 2017). The ratcheting is a primary concern for long-term serviceability. It is responsible for settlements that can compromise the operation of the OWTs. Therefore, it is crucial to account for both the short-term undrained behaviour under extreme loads, as well as the long-term cyclic response, in the design of such foundations.

Standards and codes i.e. API (2000), and DNV (2004) provide design guidelines for typical silica sands. In the presence of calcareous sands, there is limited available knowledge due to their susceptibility to crushing (Salem et al., 2021). This becomes of increasing importance considering that calcareous sands are commonly found in the marine environment in Europe and around the globe (e.g., Southern Mediterranean Sea, the Persian Gulf, Brazil, and Australia) (Spagnoli & Doherty, 2016). The physical properties of calcareous sands are different to silica sands (Cao et al., 2020; Shi et al., 2021). The calcareous sand is formed of marine biological debris mainly composed of calcium carbonate. The particles are irregular in shape, and flaky and porous which make it prone to breaking under loading (Ding et al., 2021).

Strain accumulation in calcareous sand under long-term cyclic loading is far more limited. Jafarian & Javdanian, (2020) examined the cyclic behaviour of calcareous vs silica sands, finding that for calcareous sand, increasing effective stress led to higher shear modulus and lower damping ratio compared to silica sand. The differences were attributed to the contrasting grain shape, mineralogy, and texture of calcareous sand. Similar behaviour was also reported by Yu, (2017). Jafarian et al., (2018) compared small-strain dynamic characteristics of calcareous and silica sands. It was found that the small-strain shear modulus of calcareous sand is more affected by mean effective confining pressure than the silica sands.

This paper investigates the cyclic behaviour of calcareous sand subjected to 10,000 loading cycles. To explore the influence of stress amplitude and density state, triaxial tests have been performed at selected densities and stress amplitudes. In addition, the results are used to calibrate the High Cycle Accumulation (HCA) model parameters.

2 HIGH CYCLE ACCUMULATION MODEL

To predict the strain accumulation at a high number of loading cycles ($N \geq 1000$), Niemunis et al., (2005) proposed the High Cycle Accumulation (HCA) model. The HCA model calculates the strain accumulation by combining two different numerical strategies. They are referred to as the *implicit* (low cycle) model and the *explicit* (high cycle) model of calculation. In the *implicit* model each cycle is calculated with hundreds of small increments and the accumulation appears as a by-product due to the not perfectly closed stress or strain loops. In the explicit model, the first two cycles are calculated conventionally with strain increments. The strain accumulation due to the following cycles is calculated using a direct (explicit) formula (Figure 1).

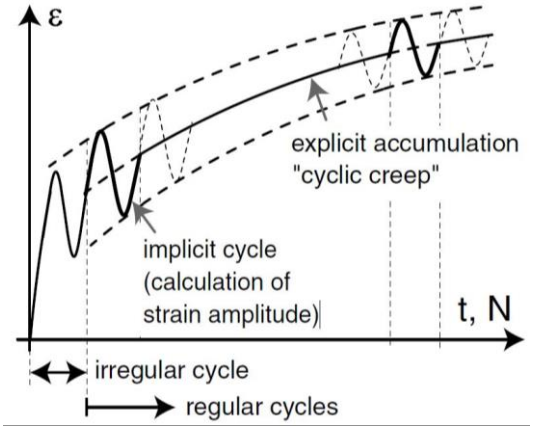

Figure 1. Calculation procedure of explicit models (Wichtmann et al., 2005).

According to the HCA model, the rate of strain accumulation can be calculated as the product of six functions (Table 1):

$$\varepsilon^{acc} = f_{ampl}\, f_N\, f_e\, f_p\, f_Y\, f_\pi \qquad (1)$$

Table 1 Summary of the functions, and material constants of the high-cycle model (Wichtmann et al., 2015)

Function	Const.
$f_{\text{ampl}} = \left(\varepsilon^{\text{ampl}}/10^{-4}\right)^{C_{\text{ampl}}}$	C_{ampl}
$\dot{f}_N = \frac{C_{N1}C_{N2}}{1+C_{N2}N} + C_{N1}C_{N3}$	C_{N1}, C_{N2}, C_{N3}
$f_p = \exp\left[-C_p\ (p^{\text{av}}/(100\ \text{kPa}) - 1)\right]$	C_p
$f_Y = \exp\left(C_Y\ \bar{Y}^{\text{av}}\right)$	C_Y
$f_e = \frac{(C_e - e)^2}{1+e}\ \frac{1+e_{\max}}{(C_e - e_{\max})^2}$	C_e

Each function considers distinctly the influence of different parameters that is strain amplitude (f_{ampl}), cyclic preloading history (f_{N}), void ratio (f_{e}), average stress (f_{p}), average stress ratio (f_{Y}), and polarization changes (f_{π}). The material constants of the functions can be obtained from drained cyclic triaxial test series. A minimum of three sets of tests are required to obtain such constants: C_e requires tests with different void ratios, keeping the same average stress and stress amplitude. C_p requires tests with different average mean pressure, under constant void ratios and average stress ratios. C_Y requires tests with different average stress ratios, under constant void ratios, average mean pressure, and stress amplitude.

Wichtmann et al. (2010) calibrated the HCA model parameters using results obtained from triaxial test results on eight different quartz sand. Further, Benoot et al. (2014) calibrated the model from cyclic tests on silica sand. However, the predictive capabilities of the HCA model had not been assessed for calcareous sands. Calcareous sands have some distinctive features, such as high void ratio, carbonate content, and crushability.

3 METHODOLOGY

3.1 Test material

The calcareous sand tested in this study was taken from a reclaimed site in the Persian Gulf. The particle size gradation of the calcareous sand is illustrated in Figure 2. The index properties are summarized in Table 2 (Shi et al., 2021), while the mean particle size (d_{50}) of the sand used in this study is much higher than for typical silica sands encountered in offshore wind projects. Figure 3 shows the grain morphology: the particles are thin, irregular, and extremely flaky, which makes them prone to breakage, and gives them an irregular shape, with some having round structures. The rough texture of the particles and the presence of more void spaces make it a highly compressible material when subjected to shearing.

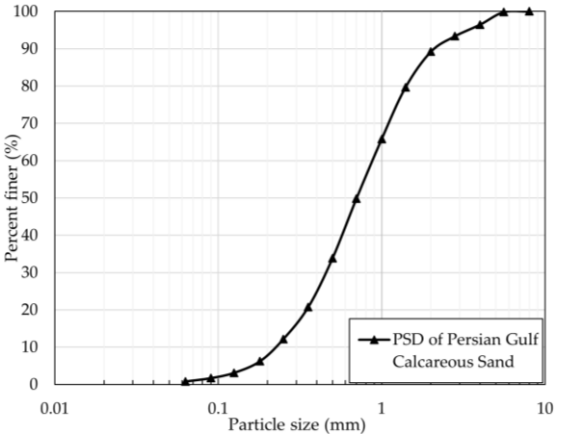

Figure 2. Particle size gradation of calcareous sand.



Figure 3. Grain morphology of calcareous sand (Shi et al., 2021).

Table 2 Basic physical and mechanical properties of calcareous sand

Property	Calcareous sand
Specific Gravity (G_s)	2.81
Maximum void ratio (e_{max})	1.21
Minimum void ratio (e_{min})	0.75
Coefficient of uniformity (C_u)	3.89
Mean particle size (d_{50}) (mm)	0.68

3.2 Triaxial apparatus

An electromechanical dynamic triaxial apparatus was used. This apparatus is comprised of pressure/volume controllers that provide cell pressure and back pressure. It includes a submersible load cell to measure the axial stress, as well as sensors for measuring displacements, and pore pressures. All components were calibrated before conducting tests.

3.3 Testing procedure

Cylindrical specimens of 50 mm in diameter and approximately 100 mm in height were tested. Soil specimens were prepared using the water pluviation technique. A pluviator equipped with five steel wire strainers, which was specifically designed to ensure

the even distribution of soil particles (Figure 4) was used. To achieve the targeted relative density and avoid sand particle breakage during the specimen preparation, the tapping of the mould from outside was employed by gently tapping the sides of the mould with a rubber hammer. Latex membranes with a thickness of 0.35 ± 0.01 mm were used.

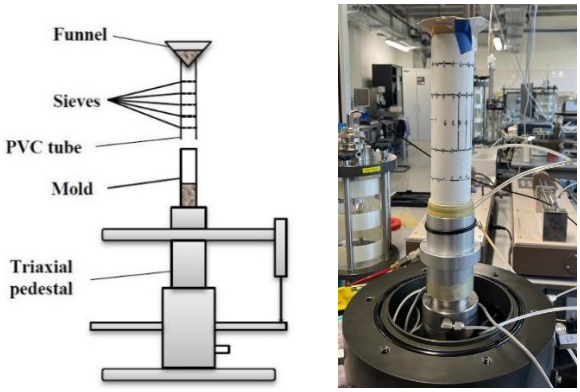

Figure 4. Water pluviation technique: (a) Schematic of pluviator, (b) pluviator with strainers used.

The specimens were saturated by flushing with de-aired water for 30 minutes and applying a back pressure of 700 kPa from 16 h to 24 h, to achieve the B-value higher than 0.95. In pre-experiment trials, it was required to apply such a high back pressure of 700 kPa to saturate the calcareous sand specimens, which was also adopted by Shi et al., (2021) using the same sand. After the saturation, the specimens were anisotropically consolidated ($K_o = 0.5$) to 100kPa initial mean effective stress levels. K_o consolidation was performed by using the Back Volume Change Measurement module in the GDS lab software. This back volume measurement is used to calculate the theoretical new height the specimen should attain to compensate for changes in volume while keeping the diameter constant.

Table 3 summarizes the stress-controlled drained triaxial tests with 10,000 load cycles conducted at a frequency of 0.5 Hz. The loading frequency of 0.5 Hz was selected based on the expectation that it would produce drained conditions based on previous studies (Ding et al., 2021; Witchmann et al., 2010). However, small fluctuations in pore water pressure of up to ±7 kPa were observed in selected tests in this study but were considered negligible relative to mean effective stress. It is also worth noting that loading frequency has minimal impact on sand deformation up to 1 Hz (Witchmann et al., 2010).

Table 3 Summary of the drained triaxial testing program.

Test ID	Void ratio	CSR= $q/2p'$	q_{ampl} (kPa)
1- CKDC	0.86	0.2	58
2- CKDC	0.89	0.2	58
3- CKDC	0.87	0.3	80
4- CKDC	0.89	0.2	58
5- CKDC	0.79	0.2	58
6- CKDC	0.79	0.3	80

4 RESULTS AND DISCUSSION

4.1 Accumulation of strain with number of cycles

Accumulation of strain with the number of cycles in sand samples subjected to cyclic loading is illustrated in Figure 5. Under cyclic loading the total strain develops in the soil sample, consisting of both recoverable (elastic) and non-recoverable (plastic/residual) components. Initial hysteresis loops showed primarily elastic behaviour with minimal plastic strain component. However, with further load cycles hysteresis loops deviated from the initial path, indicating a rise in plastic strains. The results also showed that the residual axial strain develops gradually with each additional loading cycle.

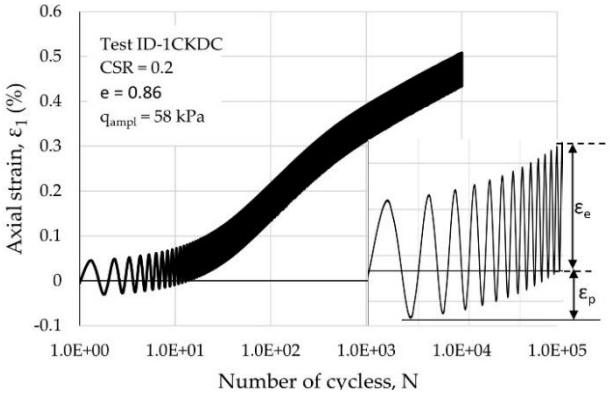

Figure 5. Axial strain progression with number of cycles, N.

4.2 Effect of cyclic stress ratio

Figure 6 presents the development of axial strain (ε_1^{acc}) versus the number of cycles (N). Four tests were conducted under selected void ratios (medium dense 0.89 and dense 0.79) and selected CSR (0.2 and 0.3). At the starting phase, a similar strain development was observed in all the curves and then, the rising rate of strain accumulation varied depending on the test conditions. For the denser specimen (tests 5 and 6), increasing the CSR from 0.2 to 0.3 resulted in higher strain accumulation. This occurred as the larger cyclic

stresses induced greater deformations with each cycle. A similar trend has been observed in the medium-dense soil specimens (tests 1 and 3). Overall, as anticipated, denser specimens exhibited lower accumulated strains than looser samples under similar CSR.

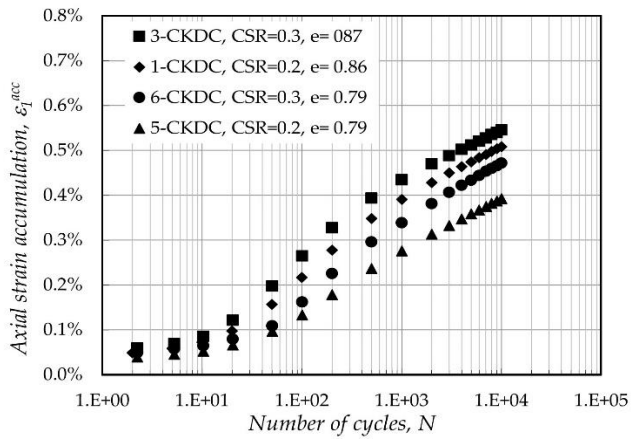

Figure 6. Axial strain accumulation with the number of cycles N in tests with different CSRs.

4.3 Effect of void ratio

Figure 7 plots the axial strain accumulation (ε_1^{acc}) as a function of the number of cycles (N). To investigate the influence of the relative density on the strain accumulation, four drained tests were performed. Tests 2 and 4 were performed under identical conditions to verify the repeatability of the test data.

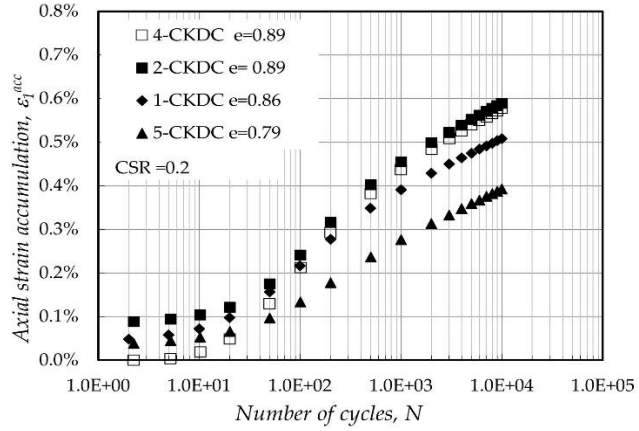

Figure 7. Axial strain accumulation with the number of cycles N in tests with varying void ratios.

A similar trend is observed for all samples in terms of strain accumulation. However, samples with higher void ratios exhibited greater accumulation of residual axial strain. Higher strain accumulation in samples with higher void ratios can be attributed to their ability to accommodate more grain arrangements under cyclic loading.

4.4 Calibration of HCA model functions

To eliminate the influence of strain accumulation on void ratio and strain amplitude, two out of six HCA model functions are used to normalize the measured strain accumulation. Function f_{ampl} accounts for the dependence of strain amplitude on the strain accumulation rate. Functions f_e accounts for the influence of the initial void ratio on the strain accumulation. In f_{ampl} and f_e functions the material constants C_{ampl} = 2 and C_e = 0.58 are determined employing non-linear regression analysis, using reference strain $\varepsilon_{ref}=10^{-4}$ and reference void ratio $e_{ref}= e_{max}=1.21$. Figure 8 and 9 show the normalized measured residual axial strain curves by f_{ampl} and f_e functions.

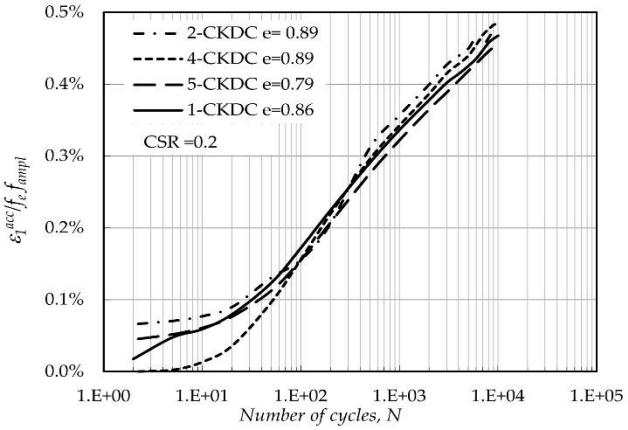

Figure 8. Normalized accumulated axial strain as a function N with different void ratios.

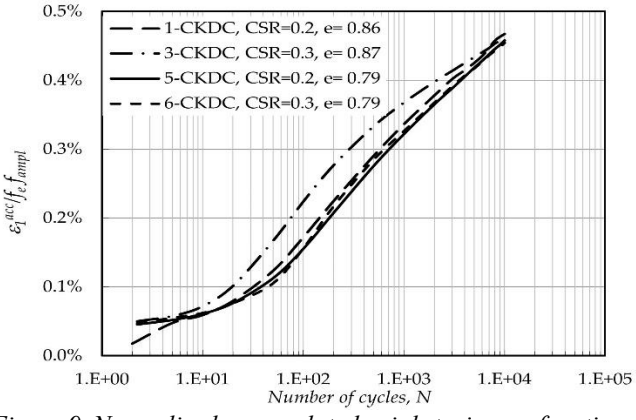

Figure 9. Normalized accumulated axial strain as a function of N with different CSRs and void ratios.

The close alignment of normalized curves suggests a close correspondence in strain accumulation behaviour. The normalization process effectively eradicated the influence of different test parameters on the strain accumulation behaviour. This suggests the HCA model functions i.e. f_{ampl} and f_e could be applied for calcareous sand, despite the Wichtmann framework being developed for silica sand.

5 CONCLUSIONS

The accumulation of strain in calcareous sand under cyclic loading was explored through a series of drained cyclic triaxial tests. The accumulated strains were normalized using the HCA model functions to facilitate comparisons across varying test conditions. The following main findings are reported:

(1) With increasing the CSR higher strain accumulation was observed. This occurred as the larger cyclic stresses induced greater deformations with each loading cycle.

(2) The strain accumulation depends strongly on the soil density. Medium dense samples ($e = 0.86, 0.87, and\ 0.89$) exhibit higher axial strains than the denser sample ($e = 0.79$).

(3) The HCA model's functions f_e and f_{ampl} are calibrated for the calcareous sand, yielded material constants $C_{ampl} = 2$ and $C_e = 0.58$. These functions were used to normalize the accumulated strain. This allowed a meaningful comparison of strain accumulation trends between tests with varying conditions. The normalization process effectively suppressed the influence of different parameters on the strain accumulation.

ACKNOWLEDGEMENTS

This research was supported by the *Cyclic soil-structure interaction framework for the foundations of offshore renewable energy structures* project, funded by the "KU Leuven Global PhD Partnerships with The University of Melbourne" scheme (GPUM/21/023) and "The University of Melbourne Chancellery Strategic International Research Collaboration funds". The authors would like to thank the Department of Mobility and Public Works (MOW) and Geotechniek Vlaanderen for providing access to the Persian Gulf sand and triaxial apparatus.

REFERENCES

Benoot, J., Haegeman, W., François, S., & Degrande, G. (2014, September). Experimental study of strain accumulation of silica sand in a cyclic triaxial test. In Proceedings of the 23rd European Young Geotechnical Engineers Conference (Vol. 1, No. 1, pp. 3-6). Universitat Politècnica de Catalunya; Barcelona.

Cai, W., Rutherford, C., Zheng, J. (2020). Monotonic Behavior of Calcareous Sands with Increasing Particle Crushing. In Geo-Congress 2020: Modeling, Geomaterials, and Site Characterization; American Society of Civil Engineers. https://doi.org/10.1061/9780784482803.023.

Cao, P., Jiang, M. J., & Ding, Z. J. (2020). Effects of particle size on mechanical behaviors of calcareous sand under triaxial conditions. *8th Japan-China Geotechnical Symposium: Challenges to Breakthrough in Geotechnic*, 182–187. https://doi.org/10.3208/jgssp.v08.c54.

Ding, Z., He, S. H., Sun, Y. F., Xia, T. D., & Zhang, Q. F. (2021). Comparative study on cyclic behavior of marine calcareous sand and terrigenous siliceous sand for transportation infrastructure applications. *Construction and BuildingMaterials*,*283*. https://doi.org/10.1016/j.conbuildmat.2021.122740.

Houlsby, G. T., Abadie, C. N., Beuckelaers, W. J. A. P., & Byrne, B. W. (2017). A model for nonlinear hysteretic and ratcheting behaviour. *International Journal of Solids and Structures*, *120*, 67–80. https://doi.org/10.1016/j.ijsolstr.2017.04.031.

Ishihara, Kenji. (1996). *Soil behaviour in earthquake geotechnics*. Clarendon Press.

Jafarian, Y., & Javdanian, H. (2020). Dynamic Properties of Calcareous Sand from the Persian Gulf in Comparison with Siliceous Sands Database. *International Journal of Civil Engineering*, *18*(2), 245–249. https://doi.org/10.1007/s40999-019-00402-9.

Jafarian, Y., Javdanian, H., & Haddad, A. (2018). Dynamic properties of calcareous and siliceous sands under isotropic and anisotropic stress conditions. *Soils and Foundations*, *58*(1), 172–184. https://doi.org/10.1016/j.sandf.2017.11.010.

Raghunandan, M. E., Juneja, A., & Benson Hsiung, B. C. (2012). Preparation of reconstituted sand samples in the laboratory. *International Journal of Geotechnical Engineering*, *6*(1), 125–131. https://doi.org/10.3328/IJGE.2012.06.01.125-131.

Salem, T. N., Elkhawas, N. M., & Elnady, A. M. (2021). Behavior of Offshore Pile in Calcareous Sand—Case Study. Journal of Marine Science and Engineering, 9, 839. https://doi.org/10.3390/jmse9080839.

Spagnoli, G., & Doherty, P. (2016). Comparison of two calcareous sands in relation to a novel offshore mixed-in-place pile. Oil Gas-Eur. Mag., 42(2), 91-94.

Shi, J., Haegeman, W., & Andries, J. (2021). Investigation on the mechanical properties of a calcareous sand: the role of the initial fabric. *Marine Georesources and Geotechnology*, *39*(7), 859–875. https://doi.org/10.1080/1064119X.2020.1775327.

Wichtmann, A. Niemunis, & Th. Triantafyllidis. (2009). *Validation and calibration of a high-cycle accumulation model based on cyclic triaxial tests on eight sands*. https://doi.org/10.3208/sandf.49.711.

Wichtmann, T., Niemunis, A., & Triantafyllidis, T. (2005). Strain accumulation in sand due to cyclic loading: drained triaxial tests. In *Soil Dynamics and Earthquake Engineering.* 25, (12). https://doi.org/10.1016/j.soildyn.2005.02.022.

Yu, F. (2017). Particle Breakage and the Drained Shear Behavior of Sands. *International Journal of Geomechanics*, *17*(8). https://doi.org/10.1061/(ASCE)GM.1943-622.0000919.

Proceedings of the XVIII ECSMGE 2024
GEOTECHNICAL ENGINEERING CHALLENGES
TO MEET CURRENT AND EMERGING NEEDS OF SOCIETY
© 2024 the Authors
ISBN 978-1-032-54816-6
DOI 10.1201/9781003431749-673
Open Access: www.taylorfrancis.com, CC BY-NC-ND 4.0 license

ECSMGE 24
XVIII EUROPEAN CONFERENCE ON SOIL MECHANICS AND GEOTECHNICAL ENGINEERING

Experimental study on the hydraulic behaviour of compacted soil mixtures in river embankments

Étude expérimentale sur le comportement hydraulique des mélanges de sol compactés dans les remblais de rivière

R. Ventini*
Ministry of Infrastructures and Transport, Interregional Public Works Department, Firenze, Italy
M. Pirone, C. Mancuso
University of Naples Federico II, Department of Civil, Building and Environmental Engineering, Napoli, Italy
**roberta.ventini@unina.it*

ABSTRACT: The hydraulic properties of compacted soils play a key role in evaluating the performance of earthworks during both design and operation. Soil hydraulic properties are influenced by compaction processes and can vary over time due to changing hydrometric and climatic conditions, significantly affecting the stability of earth structures. This study focuses on laboratory experiments aimed at determining the water retention characteristics and saturated permeability of mixtures obtained by blending different weight percentages of Ticino sand and Pontida clayey sandy silt, two Italian soils commonly used in geotechnical engineering. The interplay between soil composition and compaction conditions is systematically explored to study how these factors influence on hydraulic behaviour of river embankments.

RÉSUMÉ: Les propriétés hydrauliques des sols compactés jouent un rôle clé dans l'évaluation des performances des travaux de terrassement tant pendant la conception que pendant l'exploitation. Les propriétés hydrauliques des sols sont influencées par les processus de compactage et peuvent varier au fil du temps en raison des conditions hydrométriques et climatiques changeantes, affectant significativement la stabilité des structures terrestres. Cette étude se concentre sur des expériences en laboratoire visant à déterminer les caractéristiques de rétention d'eau et la perméabilité saturée de mélanges obtenus en mélangeant différents pourcentages pondéraux de sable du Ticino et de limon sableux argileux de Pontida, deux sols italiens couramment utilisés en ingénierie géotechnique. L'interaction entre la composition du sol et les conditions de compactage est explorée de manière systématique afin d'étudier comment ces facteurs influent sur le comportement hydraulique des digues fluviales.

Keywords: Soil mixtures; soil water retention curve; saturated permeability; earth embankments.

1 INTRODUCTION

Given the escalating frequency of catastrophic floods, there is currently a great interest in river embankments and the crucial role they play in mitigating the impact of floods. In this context, understanding and accurately assessing the hydraulic properties of compacted soils used for the construction of embankments, including water retention curve and hydraulic conductivity function, is essential for designing resilient and sustainable river infrastructure (Ventini et al., 2023a).

Compacted soils exhibit complex hydraulic behaviour due to their inherent heterogeneity and anisotropy. Various factors, such as compaction methods, soil composition, initial water content and stress history, contribute to the intricate hydraulic response of these materials (Mitchell et al., 1965, Vanapalli et al., 1999). Changes in hydrometric and climatic conditions over time further contribute to the variability of soil hydraulic properties, posing challenges in predicting and managing the performance of river embankments.

In this framework, the present study deals with laboratory investigations aimed at characterizing the hydraulic properties of different mixtures of compacted soils under controlled conditions. Specifically, the effects of the soil composition and the compaction on the hydraulic behavior of compacted soils used for river embankments construction are explored.

2 SOIL MIXTURE

The compacted heterogeneous mixtures of sand, silt and sometimes clay are typically employed in the construction of the body of the river embankments along the tributaries of the Po River (Italy). To

experimentally characterize this soil type, two well-known Italian soils were selected: Ticino sand (TS) and Pontida sandy clayey silt (PON). These soils were suitably mixed by weight in the laboratory, and three different mixtures were tested: TS50%-PON50%, TS70%-PON30% (Ventini et al, 2021, Ventini et al., 2023b), and TS85%-PON15%. The numbers in percentage represent the amount of soil by weight.

The grain size distributions and the physical properties of the tested mixtures, as well as those of TS and PON individually, are reported in Figure 1 and Table 1, respectively.

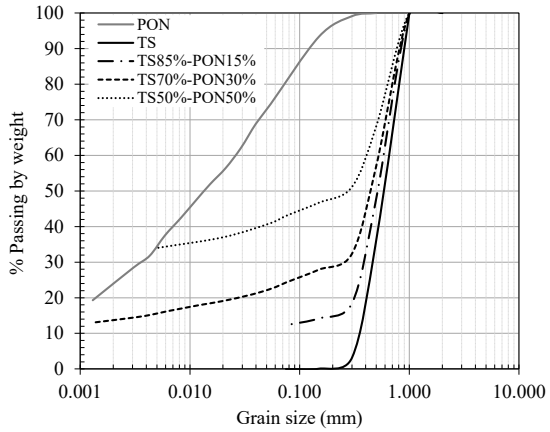

Figure 1. Grain size distributions of the tested soils.

Table 1. Average on index properties of the tested materials (G_s specific soil density, D_{50} mean particle size, U_c uniformity coefficient, LL_{cup} limit liquid from the percussion cup, PL plastic limit, PI plasticity index).

Soil	G_s	D_{50}	U_c	LL_{cup}	PL	PI
	-	mm	-	%	%	%
TS	2.671	0.574	1.83	-	-	-
PON	2.744	0.015	-	23.62	13.13	10.49
TS50%-PON50%	2.650	-	-	24.00	18.00	6.00
TS70%-PON30%	2.684	0.458	246.06	17.66	10.23	7.42
TS85%-PON15%	2.676	0.520	-	-	-	-

2.1 Compaction tests

The Proctor tests are distinguished into "standard" and "modified" and represent a compaction procedure typically used as a reference for earthworks. The Standard Proctor (SP) test results in a substantially lower degree of compaction than the Modified Proctor (MP) due to the lower compaction energy applied. Higher energy results in higher shear strength, lower void volume and lower permeability. For the mixtures considered here, the compaction curves are shown in Figure 2. The data in Figure 2 include two compaction curves for the TS70%-PON30% mixture, one for SP and another one for MP test. As mentioned before, for the same soil, the optimum dry density from MP test is higher than that from SP test and it is shown a shift of the compaction curve to the right in the γ_d - w plane when the soil is subjected to the SP effort.

Then, when the TS85%-PON15% mixture is compared to the TS70%-PON30%, determined both under the MP test, the first mixture results in both a lower variability of dry density and a significantly lower $\gamma_{d,opt}$. In contrast, the w_{opt} is almost the same for the two mixtures.

A comparison is also possible in Figure 2 between TS70%-PON30% and TS50%-PON50% mixtures, compacted under SP test (Manassero et al., 2005). These two compaction curves have a similar shape but the mixture with the same weight percentage of TS and PON records higher values at the optimum of both dry density and water content. Then, particle size analyses performed after Proctor compaction showed no significant grain breakage or particle collapsing.

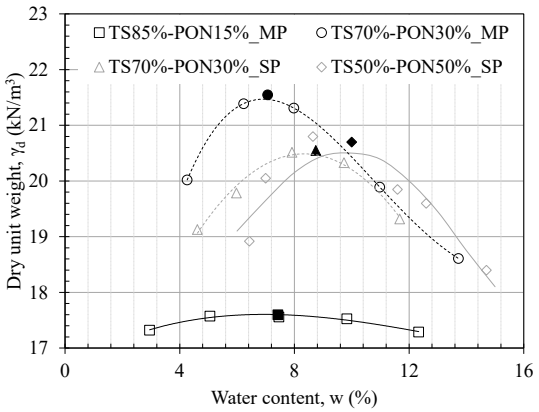

Figure 2. Proctor compaction curves of the tested soils.

2.2 Hydraulic behaviour

The hydraulic conductivity and water retention characteristics, strongly influenced by the soil texture resulting from compaction, were determined by following the procedure described in Ventini et al., (2023b). The saturated hydraulic conductivity (k_{sat}) was measured in a permeameter test at a constant load, while the hydraulic conductivity and water retention characteristics along the main drying branch were obtained using a *ku-pF* (Umwelt-Geräte-Technik GmbH) commercial apparatus and a Richards plate in series. The experimental data were then modelled by the Van Genuchten (1980) equation.

As reported in Table 2, the TS85%-PON15% mixture, characterized by a higher percentage of sand, displays significantly greater saturated permeability

than the other mixtures (about two orders of magnitude higher). This observation holds true despite the heightened compaction energy applied. When using the same compaction technique, the mixture with a higher coarse-grained component demonstrates trivially greater saturated permeability while, considering the same grain size distribution, the k_{sat} is higher for a lower initial dry unit weight.

Table 2. Optimum dry unit weight $\gamma_{d,opt}$ and water content w_{opt}, Van Genuchten model parameters for the tested specimens (saturation volumetric water content θ_{sat}, residual volumetric water content θ_r, n and α dimensionless parameters) and saturated permeability k_{sat}.

Soil	$\gamma_{d,opt}$ kN/m³	w_{opt} %	θ_{sat} -	θ_r -	n -	α 1/kPa	k_{sat} m/s
TS50%-PON50%_SP	20.70	10.00	0.16	0.13	1.50	0.06	1.10 E-08
TS70%-PON30%_SP	20.55	8.75	0.20	0.09	1.33	0.20	5.51 E-07
TS70%-PON30%_MP	21.55	7.07	0.17	0.07	1.40	0.09	6.11 E-08
TS85%-PON15%_MP	17.60	7.43	0.30	0.06	2.00	1.00	1.93 E-06

The soil water retention curves (SWRCs – θ) for the tested mixtures are depicted in Figure 3, where the TS85%-PON15% mixture, compacted with higher energy and characterized by a prevalent coarse-grained component, exhibits a low water retention capacity. This finding is consistent with the behaviour of soils dominated by sand particles.

When comparing two mixtures with the same grain size distribution (TS70%-PON30%), the role of compaction in altering soil density and subsequently affecting water retention characteristics emerges. The MP compaction technique, which results in a higher $\gamma_{d,opt}$, provide a retention curve characterized by: lower values of saturation water content (θ_{sat} -Table 2), higher air entry value (1/0.09=11 kPa), higher value of the *n* parameter, indicative of a steeper curve; lower θ_r parameter, indicating a lower ability to retain water at high suctions respect to the same mixture compacted under SP test. It results that the MP technique amplifies the hydraulic features of the finer soil component close to saturation, by providing a reduction in k_{sat} and an increase in the air entry value.

The water retention capacity demonstrated by the TS50%-PON50% mixture, characterized by a higher fine content, aligns with expectations. This mixture exhibited a hydraulic response characterized by a higher suction entry value and higher θ_r parameter respect to the TS70%-PON30% mixture obtained using the same SP technique. These two retention curves mainly differ in the high suction range.

The distinct characteristics exhibited by each mixture underscore the importance of considering both soil composition and compaction conditions in understanding water retention capacity.

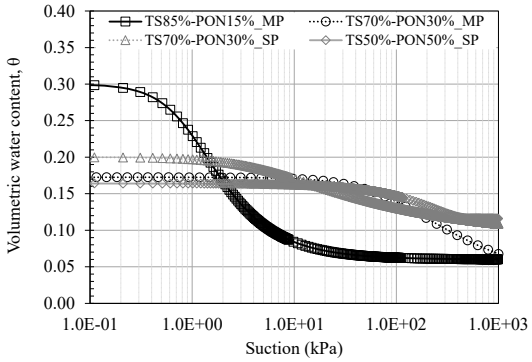

Figure 3. Soil water retention curves of the tested mixtures.

The soil hydraulic conductivity functions (*k*) obtained for the tested mixtures are shown in Figure 4.

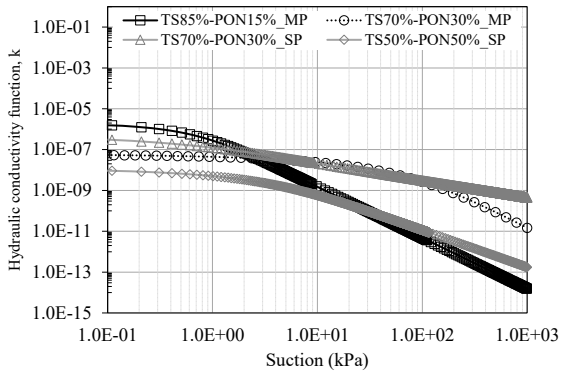

Figure 4. Soil hydraulic conductivity functions of the tested mixtures.

Generally, the hydraulic conductivity functions reflect the soil water retention curve by supporting the considerations stated above.

Comparing the mixtures TS70%-PON30%_SP and TS70%-PON30%_MP allows to observe the effects of different compaction on hydraulic conductivity. The shapes of the obtained hydraulic conductivity functions are similar, with intermediate segments running overlapping each other. However, some differences are evident close at both saturation and residual condition due to a different energy of compaction.

Then, the hydraulic conductivity of the TS85%-PON15% mixture, dominated by sand, is much higher for suction lower than 5 kPa and much lower for the

rest of the suction range than that of the TS70%-PON30%_MP.

2.3 Mechanical implications

The hydraulic response of the partially saturated material has evident implications also for the mechanical behavior. Figure 5 reports the apparent cohesion (c_a - eq.1) determined by adopting the Bishop stress approach, with χ equal to degree of saturation S_r, for soil shear strenght against suction for the TS70%-PON30% mixtures:

$$c_a = tan\varphi' \cdot S_r \cdot s \qquad (1)$$

In eq.1, φ' is the peak friction angle: 45° for the MP mixture and 41° for the SP mixture. The values of S_r (degree of saturation) and s (matric suction) have been determined by soil water retention curves (Figure 3) and by the initial soil porosity neglecting the volume variation of soil during the evaporation test. The TS70%-PON30%_MP mixture exhibits a significantly higher apparent cohesion, with a deviation that tends to approach zero at high suctions. This confirms the better performance of the MP technique, even from a mechanical point of view, making it more suitable for the construction of river embankments.

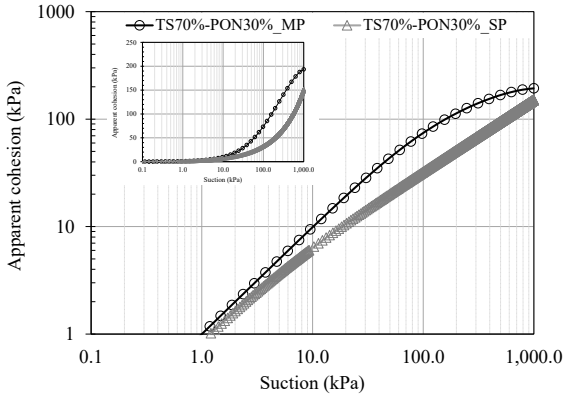

Figure 5. Apparent cohesion versus suction for the two TS70%-PON30% mixtures

3 CONCLUSIONS

The observed variations in soil hydraulic conductivity and water retention characteristics, influenced by both soil composition and compaction conditions, highlight the nuanced interplay between these factors. The greater saturated permeability exhibited by the TS85%-PON15% mixture, despite heightened compaction energy, underscores the significance of initial porosity in coarse-grained compositions. Then, the MP technique amplifies the hydraulic feature of the finer soil component close to saturation, by providing a reduction in k_{sat} and an increase in air entry value. Additionally, the notable differences in hydraulic conductivity among mixtures emphasize the need for tailored engineering solutions, recognizing that a one-size-fits-all approach may not be suitable for embankments with different soil compositions.

ACKNOWLEDGEMENTS

This research was funded under the scheme for "*PRIN 2017-REDREEF*" project, grant number 2017YPMBWJ, promoted by the Italian Ministry of University and Research (MUR). The authors dedicate a special acknowledgment to C. Mancuso, who continue to inspire us despite his premature departure.

REFERENCES

Manassero, M., Rabozzi, C., Ribotta, L. and Musso, G. (2005). On the retention properties of a polluted sand-silt mixture, In: *Advanced Experimental Unsaturated Soil Mechanics,* Tarantino, Romero & Cui (eds), Taylor & Francis Group, London, ISBN 0415383374.

Mitchell, J. K., Hooper, D. L. and Campenella, R. G. (1965). Permeability of compacted clay. *Journal of the Soil Mechanics and Foundations Division*, 91(4). https://doi.org/10.1061/JSFEAQ.0000775.

Vanapalli, S. K., Fredlund, D. G. and Pufahl, D. E. (1999). The influence of soil structure and stress history on the soil–water characteristics of a compacted till. Géotechnique, 42(2), pp. 143-159. https://doi.org/10.1680/geot.1999.49.2.143.

Van Genuchten, M.T. (1980). A closed-form equation for predicting the hydraulic conductivity of unsaturated soils. *Soil Sci. Soc. Am. J.,* 4, pp. 892–898. https://doi.org/10.2136/sssaj1980.03615995004400050002x.

Ventini, R. et al. (2023a). Analysis of transient seepage through a river embankment by means of centrifuge modelling, In: *8th International Conference on Unsaturated Soils (UNSAT 2023) Proceedings*, Milos, Greece. https://doi.org/10.1051/e3sconf/202338212008.

Ventini, R., Dodaro, E., Gragnano, C.G., Giretti, D. and Pirone, M. (2021). Experimental and numerical investigations of a river embankment model under transient seepage conditions. *Geosciences*, 11(192). https://doi.org/10.3390/geosciences11050192.

Ventini, R., Pirone, M. and Mancuso, C. (2023b). Soil water retention curves of a silty clayey sand compacted at different dry density, In: *8th International Conference on Unsaturated Soils (UNSAT 2023) Proceedings*, Milos, Greece. https://doi.org/10.1051/e3sconf/202338209007.

Proceedings of the XVIII ECSMGE 2024
GEOTECHNICAL ENGINEERING CHALLENGES
TO MEET CURRENT AND EMERGING NEEDS OF SOCIETY
© 2024 the Authors
ISBN 978-1-032-54816-6
DOI 10.1201/9781003431749-674
Open Access: www.taylorfrancis.com, CC BY-NC-ND 4.0 license

ECSMGE 24
XVIII EUROPEAN CONFERENCE ON SOIL MECHANICS AND GEOTECHNICAL ENGINEERING

Viscoplasticity and large strain consolidation modelling with converging isotaches

Viscoplasticité et grande déformation avec des isotaches convergentes

T.A. Vergote*, Y. Devrieze
DEME Group, Zwijndrecht, Belgium

**vergote.thomas@deme-group.com*

ABSTRACT: Large strain consolidation models are widely used for prediction of soft soil behavior in hydraulic filled reclamations. Large strain models typically consider an elastoplastic response with time independent constitutive relations for both permeability k(e) and compressibility e(σ'). This approach may be insufficient for soft soils subject to long consolidation times for which time dependent effects of soil are more prominent. Based on long-term column settling tests on kaolinite clay it is observed that incorporating time dependent effects (viscoplasticity) with the isotache theory improves the large strain model predictions significantly. The tests suggest changes on the amount of viscoplastic strain at high void ratio, leading to non-parallel (converging) isotaches. Therefore, a large strain converging isotache model is developed for better predictions of both settlements and pore pressures of soft soils.

RÉSUMÉ: Les modèles de consolidation par déformation importante sont largement utilisés pour prédire le comportement des sols mous dans les réhabilitations hydrauliques. Les modèles de grandes déformations considèrent une réponse élastoplastique avec des relations indépendantes du temps pour la perméabilité k(e) et la compressibilité e(σ'). Cette approche peut s'avérer insuffisante pour les longues périodes de consolidation où les effets dépendant du temps sont plus importants. Avec d'essais de tassement en colonne à long terme sur de l'argile kaolinite, il a été observé que l'incorporation de la théorie des isotaches améliore considérablement les prédictions du modèle de grandes déformation. Les tests suggèrent des isotaches non parallèles (convergentes). Par conséquent, un modèle d'isotache convergent de grande déformation est développé pour de meilleures prévisions des tassements et des pressions interstitielles de sols mous.

Keywords: Land reclamation; creep; visco-plasticity; large strain; consolidation.

1 INTRODUCTION

Recent reclamation projects are subjected to a challenge since scarcity of good quality fill material is increasing worldwide. Offshore dumping of dredged material and importing external quality fill material becomes unacceptable for both environmental and economic reasons. The reuse of soft dredged material as reclamation fill is increasing to solve these issues. From an economic and practical point of view it is interesting to hydraulically fill reclamation areas with soft dredged material, but it also leads to additional challenges in estimating the settlement behaviour of the reused dredged material with high moisture contents (100% - 300%) directly after filling.

One-dimensional consolidation of soils is conventionally analysed with the theory of Terzaghi, which is restricted to infinitesimal strains. In soils with a high moisture content this theory will be highly inaccurate. One of the most well-known large strain models (LSM) are the model of Gibson et al. (1967) and the CS2 model presented by Fox and Berles (1997). This model uses a finite difference method to calculate elastoplastic soil behaviour from the constitutive relations of the soil: permeability k(e) and compressibility e(σ'). Empirical parameters of the constitutive relations are commonly calibrated with laboratory tests. Although the model of Fox and Berles (1997) is widely used for large strain analyses, it may be insufficient for reused dredged material subject to long consolidation times for which time dependent effects of soil (creep) may be more prominent.

In recent research by Li et al. (2023), Xia et al. (2023) and Gheisari et al. (2023), time dependent effects are incorporated in a large strain model, which leads to a more accurate prediction of self-weight consolidation of soft soils when comparing the model with laboratory or large-scale tests.

In large CRS tests done by Vergote (2020) it is observed that variations in strain rate influence the loading-unloading response of soft soils. This effect is much stronger at high void ratio and low stress compared to higher stresses. This suggests that the isotaches at high void ratio do not run parallel.

The scope of this paper is to incorporate time dependent effects in the large strain model as presented in Vergote et al. (2021) by means of non-parallel isotaches (converging isotaches) and to compare the model behavior with laboratory tests.

2 LARGE STRAIN CONSOLIDATION TESTS ON SOFT SOIL

2.1 Long-term column settling tests with piezometers

Long-term column settling tests are used to evaluate the large strain model response. Large sized columns (2m high & diameter 0.2m), equipped with 4 piezometers equally distributed over their height, are filled with a slurry with predefined uniform bulk density, typically ranging between 11 and 14kN/m³. The interface between clean water and slurry and the pore pressures are measured over time.

Three column tests were performed on pure Kaolinite clay, with initial bulk densities between 11 and 12.5kN/m³. In Figure 1 the soilwater interface (m), the bulk density (kN/m³) and the excess pore pressure (%) measured at 4 heights are shown over time (hours).

2.2 Rate-dependence in CRS tests on soft soil

To understand the loading and unloading response of soft soil at higher stress, tests in large CRS tests were by Vergote (2020). Figure 2 shows such a CRS test with variations in strain rate during compression. From the test the strain rate effect is much stronger at high void ratio and low stress compared to higher stresses. This suggests that the isotaches at high void ratio do not run parallel, in line with Xia et al. (2023) and observations in column settling tests. As part of the current work, additional CRS tests will be conducted to corroborate this hypothesis.

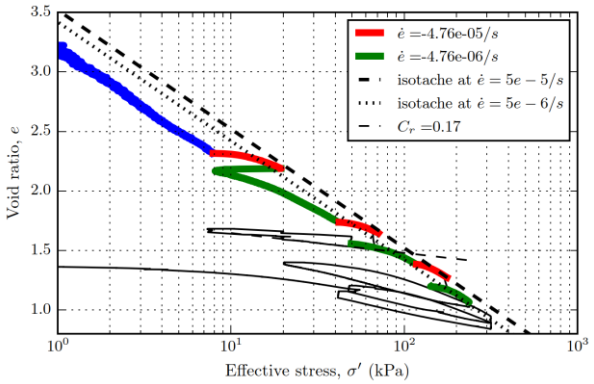

Figure 2. CRS test on soft soil with strain rate changes, from Vergote (2020).

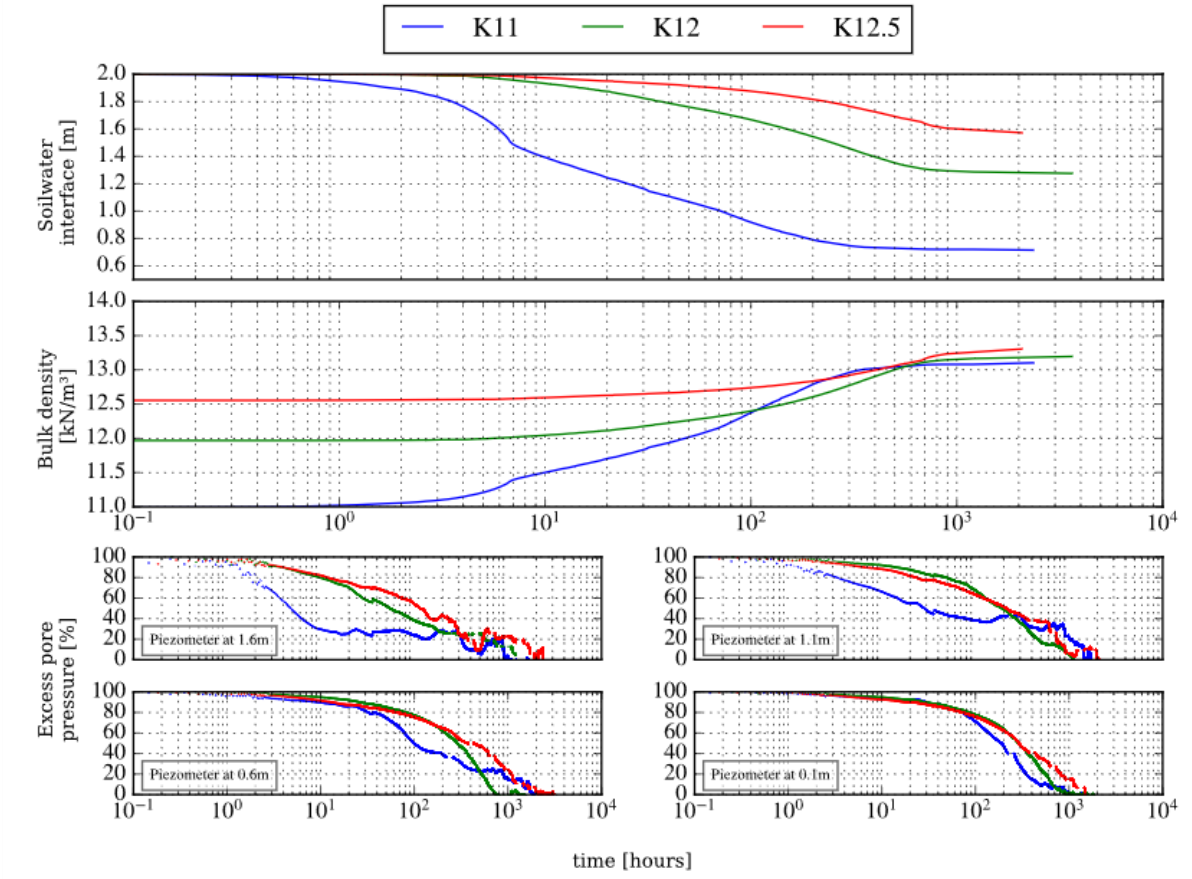

Figure 1. Column test results on Kaolinite samples with initial bulk densities: 11, 12 and 12.5kN/m³.

3 LARGE STRAIN CONVERGING ISOTACHE MODEL

3.1 Model features

The large strain isotache model as presented in Vergote et al. (2021) is extended to handle converging isotaches. The basis of the model is a set of isotaches constructed from a flexible reference isotache. This is the compression line corresponding to a fixed void ratio rate $\dot{e}_{ref}$. The reference isotache can be expressed in multiple ways:

$$e = e_{ref} - C_c \cdot log_{10}\,\sigma' \tag{1}$$

$$ln\left(\frac{e}{e_{ref}}\right) = -\rho_c \cdot ln(\sigma') \tag{2}$$

where e_{ref} is the reference void ratio at $\sigma' = 1kPa$, C_c the compression index, in case reference isotache of the shape (1) is used and ρ_c the compressibility parameter for a log-log response as eq. (2).

The isotaches are constructed relative to this reference isotache with the reference over-consolidation ratio $OCR_{ref} = \sigma'_{p,ref}/\sigma'$ with $\sigma'_{p,ref}$ the preconsolidation pressure calculated relativelly to the reference isotache.

A non-linear isotache system is adopted, where the spacing $\hat{C}_\alpha$ depends is expressed as proposed by Yuan (2016):

$$\frac{\hat{C}_\alpha}{C_{\alpha,ref}} = \frac{2}{\left(\dot{e}_{vp,c}/\dot{e}_{vp,c,ref}\right)^{-\beta_2/\beta_3}+1} \tag{3}$$

where the parameters β_2 controls the non-linearity of the isotache spacing, $\beta_3 = (C_c - C_r)/C_{\alpha,ref}$ and $C_{\alpha,ref}$ is the secondary compression index at the reference isotache. This implies that the spacing $\hat{C}_\alpha$ of the isotaches gets smaller at higher OCR_{ref} if $\beta_2 > 0$.

This flexible expression of isotaches enable further extensions to the model, if the constructed set of isotaches does not fully describe the observed behaviour. For example, distortion of isotaches is observed during unloading as an effect of swelling, which is expressed and validated in Vergote et al. (2021). For very soft soil, converging isotaches can be expressed similarly by adjusting the expression of $\hat{C}_\alpha$ as:

$$\frac{\hat{C}_\alpha}{C_{\alpha,ref}} = \frac{2 \cdot max\,(e^\eta, 1)}{\left(\dot{e}_{vp,c}/\dot{e}_{vp,c,ref}\right)^{-\beta_2/\beta_3}+1} \tag{4}$$

where a new convergence parameter η is introduced to express the non-parallel nature of isotaches at high void ratio. The effect is illustrated by comparing linear (Figure 3) with converging isotaches (Figure 4).

The model assumes that the isotaches get a larger spacing in function of the void ratio based on the empirical results to date. Additional lab test data is needed to confirm this relation. In this paper a validation is done based on column tests with kaolinite clay.

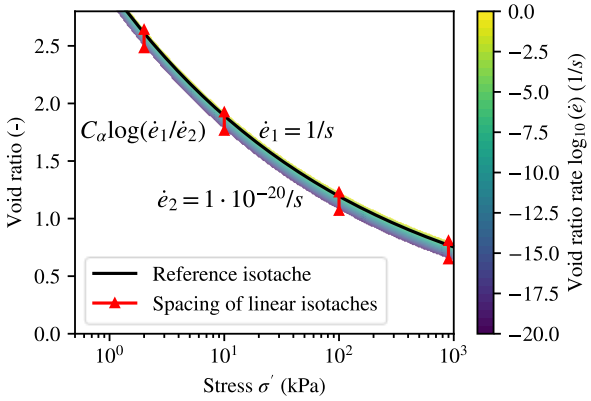

Figure 3. Isotaches for a linear system, $\beta_2 = 0$ and reference isotache expressed with eq. (2).

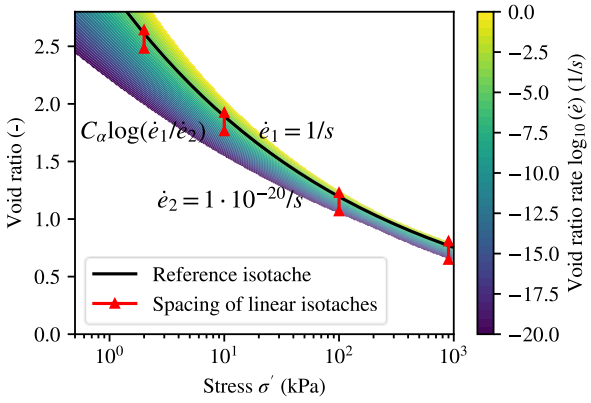

Figure 4. Converging isotaches, $\beta_2 = 0$ and $\eta = 2$.

3.2 Numerical implementation of large strain hydro-mechanical coupling with flexible isotaches

To validate the converging isotache model, simulate lab tests and create field predictions, a numerical model is implemented using the finite difference method. The process works in two steps: first the isotache relations are calculated in a fine grid $(e, \sigma, \dot{e}_{vp,c})$ for a set of parameters. Then the consolidation simulation is done with an implicit finite difference solution of the partial differential equation:

$$\frac{\dot{e}}{1+e} = -\left(\frac{k}{\gamma_w}\frac{\partial^2 u}{\partial z^2} + \frac{1}{\gamma_w}\frac{\partial k}{\partial z}\frac{\partial u}{\partial z}\right) \tag{5}$$

with a variable permeability $k(e)$, the weight of water γ_w and pore pressure u. The void ratio rate is the sum of the elastic and viscoplastic rate: $\dot{e} = \dot{e}_e + \dot{e}_{vp,c}$. The viscoplastic void ratio rate is defined by the isotache system, for every position e, σ', the viscoplastic rate is known. The elastic rate is defined by:

$$\dot{e}_e = \frac{C_r}{ln(10)} \cdot \frac{\dot{\sigma}}{\sigma} \qquad (6)$$

with the recompression index C_r. The solution is capable of handling large strains thanks to a piecewise updating of the grid at every depth Δz. Validation of the solver was done in Vergote (2020). Figure 5 shows the response of the current model with ($C_\alpha > 0$) and without viscosity ($C_\alpha \approx 0$).

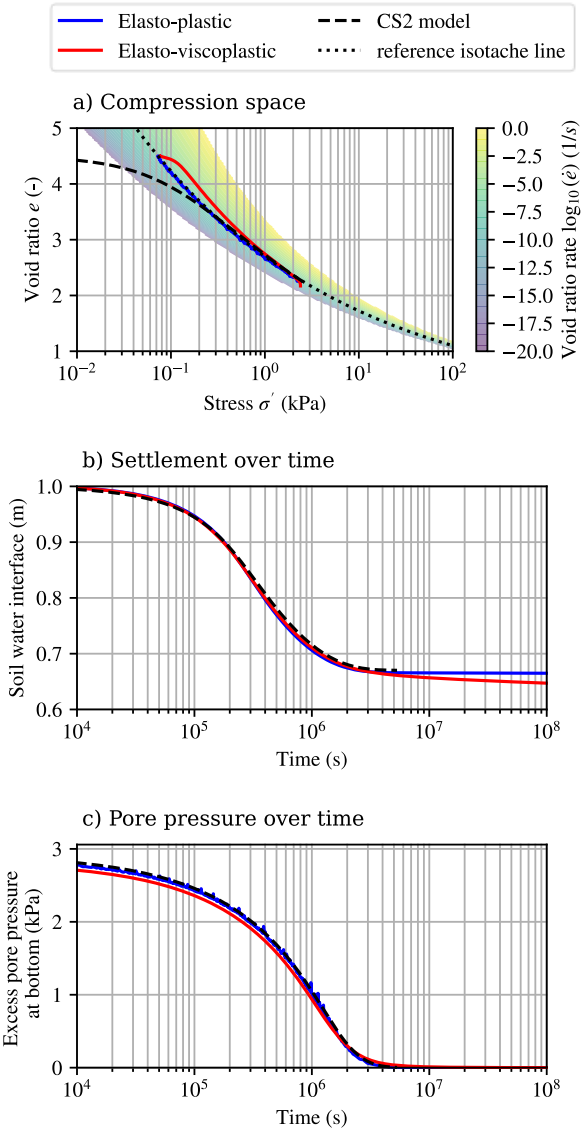

Figure 5. Model response for an elasto-plastic and elasto-viscoplastic model variant.

4 MODEL PERFORMANCE TO LAB TESTS

4.1 Large strain elastoplastic model

The elastoplastic large strain model as presented in Vergote and Mengé (2015) and based on the theory by Fox & Berles (1997), is not able to accurately predict both settlement and pore pressures as observed in the three column tests using any combination of material parameters in constitutive relations; permeability k(e) and compressibility e(σ'). Moreover, calibration of three homogeneous Kaolinite samples, with different initial bulk densities, leads to three different material parameter sets.

These findings are illustrated with a calibration and validation example, shown in Figure 6. First, the column test results of sample K12, with initial bulk density 12kN/m³, were used for model calibration. Afterwards, the calibrated model was validated with results of column tests K11 and K12.5 with bulk densities 11kN/m³ and 12.5kN/m³.

In Figure the soilwater interface and excess pore pressure of the lowest piezometer (0.08m height) are shown for the three column tests. After calibration, the elastoplastic large strain model (CS2), does not predict both settlements and pore pressures of sample K12 with high accuracy. When modelling the behavior of samples K11 and K12.5 with the calibrated model, shown in red in Figure 6, predictions are (slightly) inaccurate. For sample K11 the modelled settlements occur too slow and pore pressure dissipation is slightly overestimated. For sample K12.5 the modelled settlements occur too fast. Prediction of column tests with other boundary conditions (f.e. initial bulk density) lead with the elastoplastic large strain model (CS2) to less accurate results. One of the main reasons is the model assuming unique constitutive relations (k(e) and e(σ')) for the material. However, in soft soils these relations can change significantly over time and particularly at lower void ratios or higher effective stresses. In the column tests very large deformations are observed at low stresses. Depending on the initial bulk density of the sample the observed deformation at low stresses changes significantly between the tests, leading to 3 different material parameter sets for the same homogenous material. This effect (visco-plasticity) is not incorporated in the elastoplastic large strain model (CS2) due to time and strain independent constitutive relations. The elasto-viscoplastic effects should therefore be considered for more accurate predictions of large strain behavior of soft soils.

4.2 Large strain converging isotache model

After extending the large strain model with converging isotaches, the calibration, using a linear reference isotache (eq. (1)), leads to a better prediction of both settlement and pore pressure of individual column tests compared to the large strain elastoplastic model (CS2). However, inconsistencies between pore pressure and settlement predictions remain when modelling the behaviour of samples with different bulk densities.

Using the large strain converging isotache model with calibration based on column test K12 using a log-log reference isotache (eq. (2)), leads to an even better prediction of both settlement and pore pressure of individual column tests, as shown in blue (LSI (1)) in Figure 6. When using the log-log reference isotache (LSI(1)) both settlements and pore pressures are predicted with reasonable accuracy for all three column tests with one unique set of material parameters. After model calibration on sample K12 the settlements of sample K11 are predicted accurately but the pore pressure dissipation is slightly overestimated. For sample K12.5 both settlements and pore pressures are predicted with reasonable accuracy.

In the previous calibration and validation example calibration was performed solely on the results of column test K12. When using all three column tests for calibration a slightly better fit is obtained for both soil water interface and pore pressures, as shown in green (LSI (2)) in Figure 6.

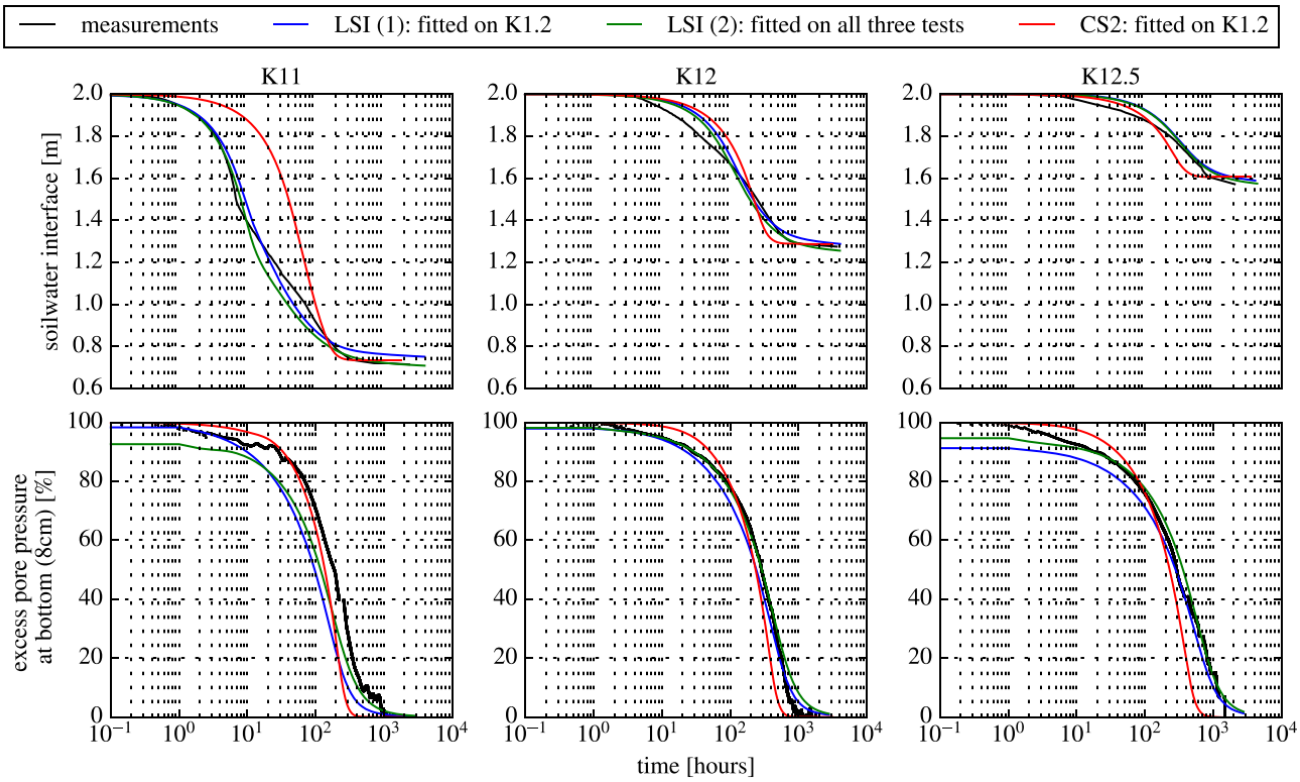

Figure 6. Column test results in black, elastoplastic large strain model (CS2) calibrated on K12 in red, large strain converging isotache model calibrated on K12 in blue (LSI (1)) and large strain converging isotache model calibrated on all three column tests in green (LSI (2)).

5 FUTURE WORK

The large strain converging isotache model improves the prediction of settlements and pore pressures in soft soils. More research would be required to explain the converging isotaches from a microstructural point of view. Additional experimental work on the strain rate effect during loading and unloading of soft soils will lead to a better understanding of the observations and can be used to further improve the converging isotache model. The experimental work can be extended with future long-term column tests on low plasticity clay, low plasticity silt and clay-silt mixtures. Additional CRS tests can be performed to obtain a better understanding of the strain rate effect.

The existing numerical model can be further improved to improve speed and numerical stability and can be further extended to increase the applicability of the model with additional features such as: the transition of sedimentation to consolidation, unloading, reloading, simulation of hydraulic filling, implementation of an axisymmetric model, prefabricated vertical drains and multi-layer soils.

6 CONCLUSIONS

Integrating the isotache theory in large strain consolidation models allow for more accurate consolidation predictions. Thanks to consideration of viscoplasticity, a more unified method for settlement predictions can be done, across time scales and strain levels.

Especially for very soft soils, experimental results suggest that the isotaches do not run parallel, but instead converge towards larger stress levels. In this paper, an extension to the large strain isotache model is proposed to align the isotaches closer to the experimental data with the introduction of a convergence factor η. The model is validated with three columns at varying density, indicating the convergence factor is needed to fit the data accurately.

ACKNOWLEDGEMENTS

The tests were carried out in the laboratory of the DEME Group. The authors are grateful for the help provided by Xavier Lepère and Iso Audenaert in designing and building the instrumented column set-up.

REFERENCES

Fox, P. J., and Berles, J. D. 1997. "CS2: A piecewise-linear model for large strain consolidation." *Int J Numer Anal Methods Geomech*, 21 (7): 453–475. https://doi.org/10.1002/(SICI)1096-9853(199707)21:7.

Gheisari, N., Qi, S. and Simms, P. 2023. "Incorporation of three different creep models into large-strain consolidation analysis of a clayey tailings deposit." *Comput Geotech*, 161. Elsevier Ltd. https://doi.org/10.1016/j.compgeo.2023.105533.

Gibson, R. E., England, G. L. and Hussey, M. J. L. 1967. "The theory of one-dimensional consolidation of saturated clays. I. Finite non-linear consolidation of thin homogeneous layers." *Géotechnique*, 17 (3): 261–273. https://doi.org/10.1680/geot.1967.17.3.261.

Li, P., Yin, J. H. Yin, Z. Y. and Chen, Z. 2023. "One–dimensional nonlinear finite strain analysis of self–weight consolidation of soft clay considering creep." *Comput Geotech*, 153. Elsevier Ltd. https://doi.org/10.1016/j.compgeo.2022.105081.

Vergote, T. A. 2020. "Deformation of soils: time and strain effects after unloading." National University of Singapore: Ph.D Thesis.

Vergote, T. A., Leung, C. F. and Chian, S. C. 2021. "Elastoviscoplastic modelling with distorted isotaches and swelling for constant strain rate and incremental loading." *Int J Numer Anal Methods Geomech*, 45 (13): 1920–1933. https://doi.org/10.1002/nag.3248.

Vergote, T., and Mengé, P. 2015. "Application of large strain consolidation theory in soft soil reclamation." *Advances in Soft Ground Engineering*, C. F. Leung, T. Ku, and S. C. Chian, eds., 978–981. Singapore: Research Publishing.

Xia, C., Zhu, M. Chen, W. Wang, X. and Chen, X. 2023. "Rheological consolidation solutions for multi-layered natural structured soft clays based on a nonparallel isotache model." *Acta Geotech*, 1–18. Springer Science and Business Media Deutschland GmbH. https://doi.org/10.1007/S11440-023-01951-Z/METRICS.

Yuan, Y. 2016. "A new elasto-viscoplastic model for rate-dependent behavior of clays." Massachusetts Institute of Technology: Ph.D Thesis.

Proceedings of the XVIII ECSMGE 2024
GEOTECHNICAL ENGINEERING CHALLENGES
TO MEET CURRENT AND EMERGING NEEDS OF SOCIETY
© 2024 the Authors
ISBN 978-1-032-54816-6
DOI 10.1201/9781003431749-675
Open Access: www.taylorfrancis.com, CC BY-NC-ND 4.0 license

ECSMGE 24
XVIII EUROPEAN CONFERENCE ON SOIL MECHANICS AND GEOTECHNICAL ENGINEERING

Effects of sustained loads on geogrid pullout behaviour embedded in a recycled construction and demolition waste

Effets de charges soutenues sur le comportement d'arrachement des géogrille intégrée dans des déchets de construction et de démolition recyclés

C.S. Vieira*, P.M. Pereira
CONSTRUCT, Faculty of Engineering, University of Porto, Porto, Portugal
**cvieira@fe.up.pt*

ABSTRACT: A suitable behaviour of backfill/geosynthetic interfaces is one of the key points to achieve a good performance of any geosynthetic reinforced structure. Previous researches have been showing that the interfaces between recycled construction and demolition (C&D) wastes and some geosynthetics have coefficients of interaction in the range of usual values for soil/geosynthetic interfaces. However, most of these studies only evaluated the geosynthetics pullout resistance under monotonic loading conditions (constant displacement or load rates during pullout) and do not consider their long-term behaviour. This paper presents a preliminary laboratory study conducted to investigate the effects of multistage loading on a geogrid pullout behaviour. After reaching a predefined value (40% or 70% of the geogrid pullout resistance) under load-controlled conditions, the pullout force was kept constant for 30 or 120 minutes and then increased until the geogrid pullout failure. The results obtained to date show that sustained loads periods did not reduced the geogrid pullout resistance and thus the usual pullout tests are on the safety side. The duration of the sustained load stage affected mainly the cumulative deformations on the geogrid, which are more significant when the constant load level is closer to the geogrid's pullout resistance.

RÉSUMÉ: Un comportement approprié des interfaces remblai/géosynthétique est un des points essentiels pour assurer une bonne performance de toute les structures renforcée par géosynthétique. Des recherches antérieures ont montré que les interfaces entre les déchets de construction et de démolition recyclés (C&D) et divers géosynthétiques ont des coefficients d'interaction qui se situent dans la gamme des valeurs habituelles pour les interfaces sol/géosynthétique. Cependant, la plupart de ces études n'ont évalué la résistance à l'arrachement des géosynthétiques que dans des conditions de charge monotone (déplacement constant ou taux de charge constant pendant l'arrachement) et n'ont pas considéré leur comportement à long terme. Cet article présente une étude préliminaire conduite en laboratoire pour étudier les effets d'un chargement en plusieurs étapes sur le comportement à l'arrachement d'une géogrille. Après avoir atteint une valeur prédéfinie (40 % ou 70 % de la résistance à l'arrachement de la géogrille) dans des conditions de charge contrôlée, la force d'arrachement a été maintenue constante pendant 30 ou 120 minutes, puis augmentée jusqu'à la rupture de la géogrille. Les résultats obtenus à cette date montrent que les périodes de charges soutenues n'ont pas réduit la résistance à l'arrachement de la géogrille et que les tests d'arrachement habituels sont donc du côté de la sécurité. La duration de la phase de charge soutenue affecte principalement les déformations cumulées sur la géogrille, qui sont plus importantes lorsque le niveau de charge constante est plus proche de la résistance à l'arrachement de la géogrille.

Keywords: Geosynthetics; recycled C&D wastes; pullout behaviour; sustained loads; long-term behaviour.

1 INTRODUCTION

In recent years several studies and applications of recycled Construction and Demolition (C&D) wastes have been carried mainly focused on their use in base and sub-base layers of transportation infrastructures or in concrete production. The valorisation of C&D waste in geosynthetic reinforced structures, such as steep slopes or retaining walls, is also a topic of recent interest (Vieira and Pereira 2018; Santos et al. 2013).

A suitable behaviour of backfill/geosynthetic interfaces is one of the key points to achieve a good performance of any geosynthetic reinforced structure (steep slopes and retaining walls). Previous researches have been showing that C&D waste/geosynthetic interfaces have coefficients of interaction in the range of usual values for soil/geosynthetic interfaces (Santos and Vilar 2008, Arulrajah et al. 2013, Vieira and Pereira 2016, Vieira and Pereira 2022). However, these studies, as most of those found in the literature for soil/geosynthetic interfaces, do not account for the long-term behaviour.

In typical pullout tests, an increasing force is applied to one end of the geosynthetic at a constant

displacement rate (displacement-controlled tests) until the geosynthetic failure (pullout). As will be mentioned below, pullout tests can also be carried out with a constant load rate (load-controlled tests). In this paper the effect of applying a constant pullout force (sustained load) at a pre-defined load level and time period before leading the geosynthetic to failure is studied. The influence of this different approach on a geogrid's pullout resistance and on the displacement for which it is mobilised is presented and discussed.

2 MATERIALS AND METHODS

2.1 Materials

The study was carried out with a fine-grained recycled construction and demolition (C&D) material, coming from the recycling process of non-selected C&D wastes (Figure 1a). Thus, it has a very heterogeneous composition (soil, stones, concrete and mortars, ceramics, …).

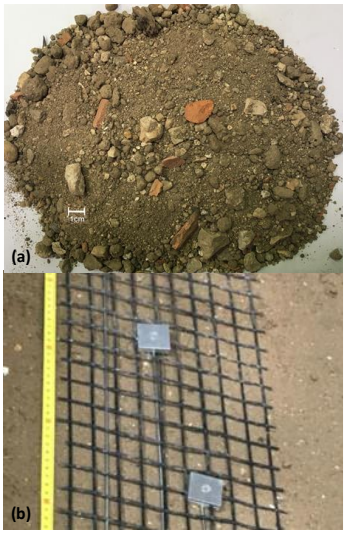

Figure 1. Materials: (a) recycled C&D waste; (b) geogrid.

Their constituents were evaluated following the European Standard EN 933-11:2009 for coarse aggregates. As the particles are sorted by hand, it is not humanly possible to classify particles smaller than 4 mm, so the test specimen according to the standard only includes particles with a higher dimension. Figure 2 shows the relative proportion of the constituents of recycled C&D material, where R_c refers to concrete, concrete products, mortar, concrete masonry units; R_u corresponds to unbound aggregate, natural stone, hydraulically bound aggregate; R_b refers to clay masonry units, calcium silicate masonry units, aerated non-floating concrete; R_a and R_g correspond to bituminous materials and glass, respectively and X is for other materials.

Table 1 summarises some grain size and compaction properties of the recycled C&D waste. Further details can be found in Carneiro et al. 2023).

A polyester geogrid (Figure 1b) with nominal tensile strength of 35 kN/m and corresponding elongation of 10.5% (values provided by the manufacturer) was used in this study.

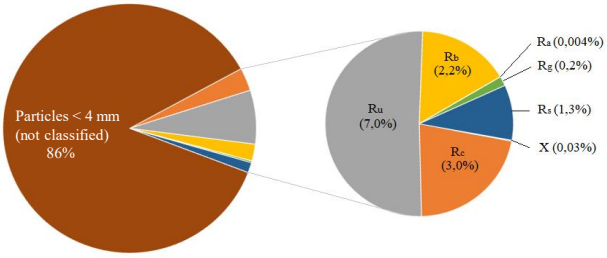

Figure 2. Constituents of the recycled C&D waste.

Table 1. Some properties of the recycled C&D waste.

D_{10} (mm)	D_{50} (mm)	D_{max} (mm)	Proctor compaction test	
			γ_{dmax} (kN/m³)	w_{opt} (%)
0.008	0.39	10	18.8	12

2.2 Laboratory study

The laboratory study comprises benchmark monotonic pullout tests and multistage pullout tests (Figure 3).

Geosynthetics pullout tests (monotonic tests) are usually carried out under displacement-controlled conditions, i.e. imposing a constant frontal displacement rate equal to 2 mm/min (± 10%) - EN 13738: 2004. According to this standard, constant stress loading methods, where the pullout force is applied to the geosynthetic under a uniform loading rate not exceeding 2 kN/m/min can also be used. In this study, benchmark monotonic load-controlled tests under a constant load increment rate of 0.55 kN/m/min were also carried out, since multistage pullout tests must be performed under load-controlled conditions in order to ensure that the pullout force remains constant during a predefined period of time (Figure 3).

Multistage pullout tests consist of an initial monotonic loading (load increment rate equal to 0.55 kN/m/min) to a predefined value of the pullout force (40% or 70% of the pullout resistance, P_{max}), followed by a sustained load stage (during 30 or 120 minutes), and after that, a constant load rate of 0.55 kN/m/min is applied again untile the geogrid pullout failure (Figure 3).

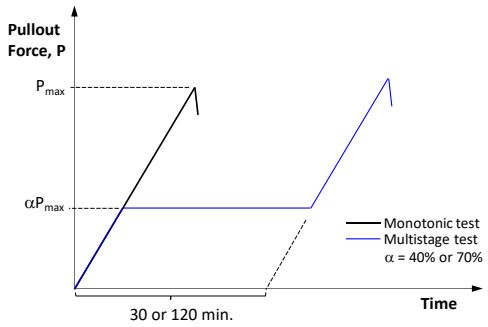

Figure 3. Schematic representation of the different setups of pullout tests carried out.

In all these tests the recycled C&D material was compacted to 90% of its maximum dry density and at the optimum moisture content (standard Proctor test) and the normal stress at the interface level was around 10 kPa. The material was compacted to 90% of its maximum dry density (although higher values are usually used on construction sites), because laboratory compaction above this value, using manual means, revealed to be very difficult.

The geogrid specimens were tested with initial dimensions of 250 mm wide × 750 mm long (inside the pullout box).

3 RESULTS AND DISCUSSION

3.1 Monotonic pullout tests

The displacements throughout the geosynthetic length are usually monitored, during pullout tests, using inextensible wires connected to the geosynthetic specimen (Figure 1b) and to linear potentiometers placed outside the pullout box (Vieira and Pereira 2022). However, the presence of the fixing elements affects the interface conditions and may even have influence on the pull-out resistance, depending on the geosynthetic type and strength (Lopes and Ladeira 1996; Ferreira et al. 2016). Figure 4 illustrates the effects of the displacement recording system (fixing elements, inextensible wires and linear potentiometers) on the geogrid's pulllout behaviour.

Figure 4 shows that the presence of this system leads to an overestimation of around 13% of the geogrid pullout resistance, meaning that the presence of the inextensible wires and corresponding fixing system (Figure 1b) somehow restricts the geogrid from being pulled out. In view of this evidence, the remaining pullout tests were carried out without monitoring of the displacements along the geogrid's length.

As mentioned in 2.2, monotonic pullout tests were carried out under displacement-controlled and load-controlled conditions. Figure 5 compares the geogrid´s pullout behaviour under both scenarios.

The geogrid's pullout resistance was 10 % higher when it was pulled out under a constant load increment rate when compared to its resistance under at a constant displacement increment. Although the load increment rate was selected such that the duration of both tests was similar, it was found that the geogrid was pulled out slightly more slowly under displacement-controlled conditions.

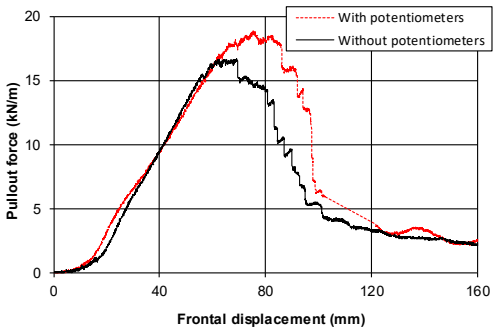

Figure 4. Influence of the presence of displacement recording system.

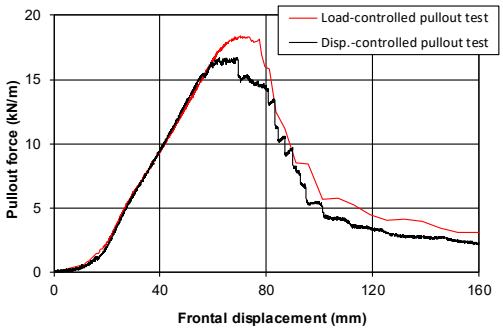

Figure 5. Geogrid pullout behaviour under displacement-controlled and load-controlled conditions.

Previous researches (Lopes and Ladeira 1996; Vieira et al. 2020) have shown that, due to intrinsic viscous response of polymeric geosynthetics, the geosynthetics pullout resistance is affected by the rate of loading and generally increases with an increase of the displacement rate. Thus, the conclusion drawn by the analysis of Figure 5 is consistent with what was expected.

3.2 Multistage pullout tests

3.2.1 Effect of sustained load level

Figure 6 presents the influence of the sustained load on the geogrid's pullout behaviour. It can be inferred from the analysis of Figure 6 that multistage loading led to a slight increase (lower than 10%) in the pullout resistance.

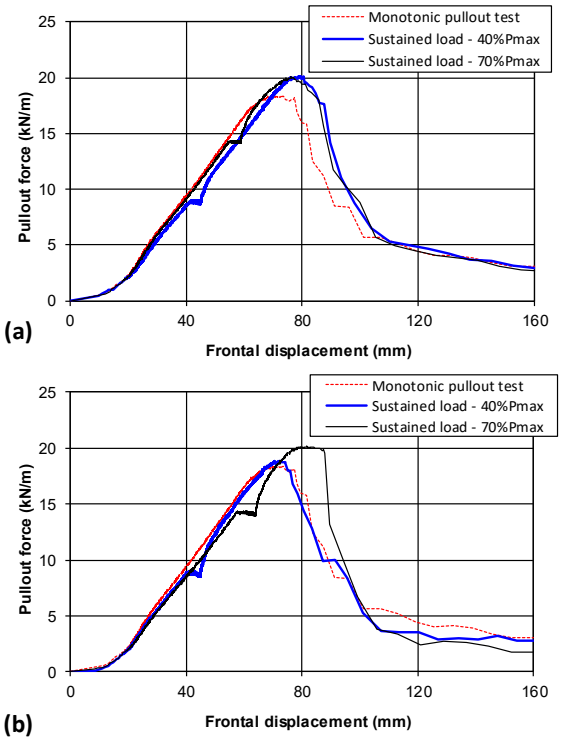

Figure 6. Influence of the sustained load (at 40%Pmax and 70% Pmax) on the geogrid's pullout behaviour: (a) for t = 30 minutes; (a) for t = 120 minutes.

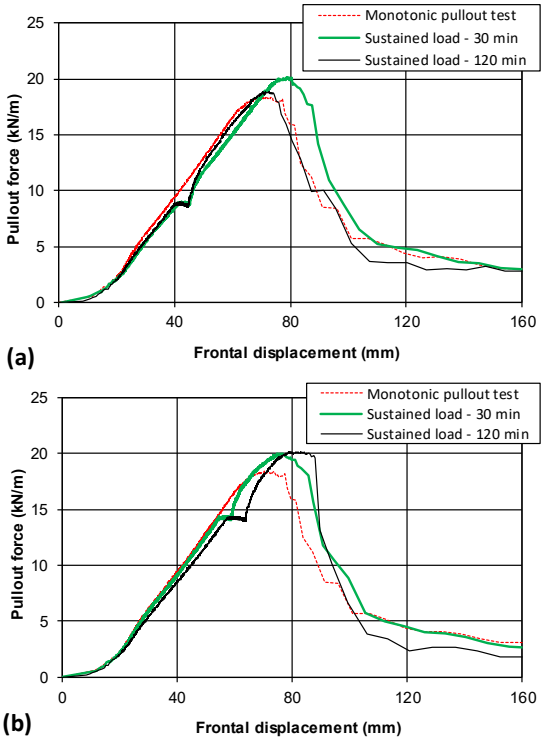

Figure 7. Influence of the time period of the sustained load: (a) at 40%Pmax; (b) at 70%Pmax.

For a sustained load stage of 30 minutes, the behaviour of the geogrid tested with sustained loading at 40%P_{max} and 70%P_{max} was very similar, both in terms of pullout resistance and of the displacement at which the peak resistance was reached. For the higher sustained load period (120 minutes), the behaviour of the geogrid at 40%P_{max} was very similar to that of the monotonic test (an increase in the pullout resistance of only 2.7%), while at 70%P_{max} there was an increase in the peak pullout resistance of around 10% (Figure 6b). The influence of the duration of the sustained load stage will be presented in the next section.

3.2.2 Influence of the duration of sustained load

The effects of the duration of the sustained load stage is shown in Figure 7. For the pullout tests with sustained load at 70%P_{max}, as expected, the longer period of constant load (120 minutes) led to the cumulative deformation on the geogrid and therefore the peak resistance tended to be mobilised for greater deformations. This evidence was not observed in the sustained load tests at 40%P_{max} (Figure 7a). This may be explained by the fact that geogrid´s deformation under constant load is more significant for higher loads, but this point needs to be further explored in future research.

Figure 8 presents the development of geogrid´s frontal displacements during the constant load period. The dashed vertical line marks the beginning of the constant load stage. While the cumulative displacements for 40%P_{max} were 3.8 mm and 4.6 mm, for t = 30 minutes and t = 120 minutes, respectively, the increase is more significant when the sustained load stage occurs at 70%P_{max} (from 4.2 mm to 6.6 mm, for t = 30 minutes and t = 120 minutes, respectively). It is also visible that for 40%P_{max} the displacements tend to stabilise, i.e. small variations after some time (Figure 8a), this is not the case for 70%P_{max} (Figure 8b).

4 CONCLUSIONS

This paper presented a laboratory study to characterize the pullout behaviour of a polyester geogrid embedded in a recycled C&D waste, with emphasis on the effects of sustained loads applied to the geogrid before its pullout failure.

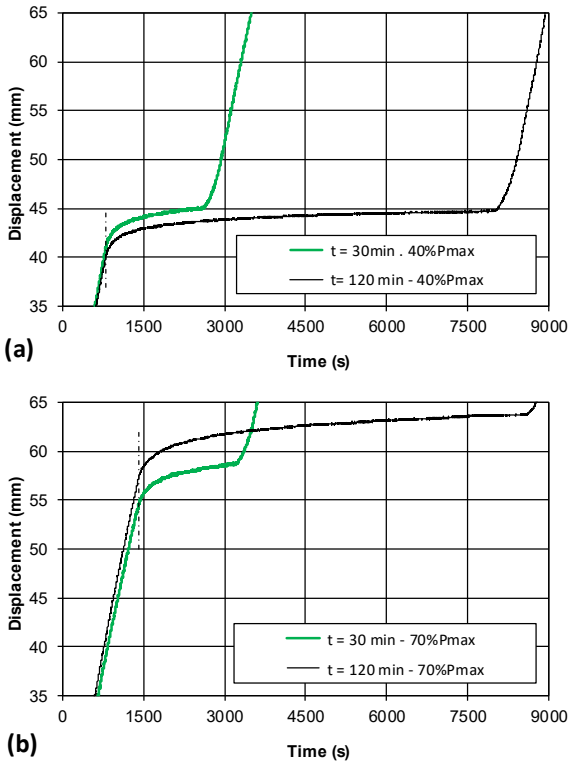

Figure 8. Development of geogrid pullout displacement during the sustained load periods: (a) for 40%Pmax; (b) for 70%Pmax.

The main conclusions of this study are summarized as follows:

- The geogrid's pullout resistance tended to be slightly higher when it was pulled out under a constant load increment rate when compared to its resistance under a constant displacement rate.
- Multistage pullout tests with a constant load stage did not significantly affect the geogrid´s pullout resistance. A slight increase in the pullout resistance was observed.
- The effect of the duration of the sustained load on the geogrid pullout behaviour is mostly seen in the cumulative deformations, which are more significant when the constant load is higher, i.e., is closer to the geogrid's pullout resistance.

It should be highlighted that this is a preliminary study that requires a more comprehensive research programme with other materials, other sustained load levels and longer durations.

ACKNOWLEDGEMENTS

This work was financially supported by: Project PTDC/ECI-EGC/30452/2017-POCI-01-0145-FEDER-030452—funded by FEDER funds through COMPETE2020—Programa Operacional Competitividade e Internacionalização (POCI) and by national funds (PIDDAC) through FCT/MCTES; Base Funding—UIDB/04708/2020 of the CONSTRUCT—Instituto de I&D em Estruturas e Construções—funded by national funds through the FCT/MCTES (PIDDAC).

REFERENCES

Arulrajah, A., Rahman, M. A., Piratheepan, J., Bo, M. W. and Imteaz, M. A. (2013). Interface shear strength testing of geogrid-reinforced construction and demolition materials. *Advances in Civil Engineering Materials* 2, 189-200.

Carneiro, J. R., Gomes, M. and Vieira, C.S. (2023). Inclined Plane Shear Behaviour of a Recycled Construction and Demolition Material–Geocomposite Interface. *Int. J. of Geosynth. and Ground Eng.* 9(88), https://doi.org/10.1007/s40891-023-00507-1.

EN 933-11:2009 Tests for geometrical properties of aggregates – Part 11: Classification test for the constituents of coarse recycled aggregate. CEN.

EN 13738: 2004 Geotextiles and geotextile-related products - Determination of pullout resistance in soil. European Committee for Standardization, Brussels, Belgium.

Ferreira, F. B., Vieira, C. S., Lopes, M. L. and Carlos, D. M. (2016). Experimental investigation on the pullout behaviour of geosynthetics embedded in a granite residual soil. *European Journal of Environmental and Civil Engineering* 20(9), 1147-1180, 10.1080/19648189.2015.1090927.

Lopes, M. L. and Ladeira, M. (1996). Influence of the confinement, soil density and displacement rate on soil-geogrid interaction. *Geotextiles and Geomembranes* 14(10), 543-554, 10.1016/S0266-1144(97)83184-6.

Santos, E. C. G., Palmeira, E. M. and Bathurst, R. J. (2013). Behaviour of a geogrid reinforced wall built with recycled construction and demolition waste backfill on a collapsible foundation. *Geotextiles and Geomembranes* 39, 9-19.

Santos, E. C. G. and Vilar, O. M. (2008). Use of Recycled Construction and Demolition Wastes (RCDW) as Backfill of Reinforced Soil Structures Proceedings of the 4th European Geosynthetics Conference, EUROGEO 4. Edimburg, 7-10 September 2008, Paper N.º 199.

Vieira, C. S., Pereira, P., Ferreira, F. and Lopes, M. L. (2020). Pullout Behaviour of Geogrids Embedded in a Recycled Construction and Demolition Material. Effects of Specimen Size and Displacement Rate. *Sustainability* 12(9):3825, https://doi.org/10.3390/su12093825.

Vieira, C. S. and Pereira, P. M. (2016). Interface shear properties of geosynthetics and construction and demolition waste from large-scale direct shear tests. *Geosynthetics International* 23(1), 62–70, http://dx.doi.org/10.1680/gein.15.00030.

Vieira, C. S. and Pereira, P. M. (2018). Use of mixed construction and demolition recycled materials in geosynthetic reinforced embankments. *Indian*

Geotechnical Journal 48(2), 279-292, 10.1007/s40098-017-0254-6.

Vieira, C. S. and Pereira, P. M. (2022). Influence of the Geosynthetic Type and Compaction Conditions on the Pullout Behaviour of Geosynthetics Embedded in Recycled Construction and Demolition Materials. *Sustainability* 14(3), 1207, https://doi.org/10.3390/su14031207.

Proceedings of the XVIII ECSMGE 2024
GEOTECHNICAL ENGINEERING CHALLENGES
TO MEET CURRENT AND EMERGING NEEDS OF SOCIETY
© 2024 the Authors
ISBN 978-1-032-54816-6
DOI 10.1201/9781003431749-676
Open Access: www.taylorfrancis.com, CC BY-NC-ND 4.0 license

ECSMGE 24
XVIII EUROPEAN CONFERENCE ON SOIL MECHANICS AND GEOTECHNICAL ENGINEERING

Effect of cyclic loading stress level and amplitude on the behaviour of a soft soil chemically stabilized unreinforced and fibre-reinforced

Effet du niveau et de l'amplitude des contraintes de chargement cycliques sur le comportement d'un sol meuble chimiquement stabilisé, non renforcé et renforcé de fibres

J. Villarroel-Ortega*
Depto. de Ingeniería en Construcción/Universidad de Magallanes, Punta Arenas, Chile
A.A.S. Correia
CIEPQPF/Department of Civil Engineering/University of Coimbra, Coimbra, Portugal
P.J. Venda Oliveira
ISISE/Department of Civil Engineering/University of Coimbra, Coimbra, Portugal
L. Leal Lemos
CGEO/Department of Civil Engineering/University of Coimbra, Coimbra, Portugal
**jorge.villarroel@umag.cl*

ABSTRACT: This works aims to characterise the effect ofin cyclic loading stress level and amplitude, on the behaviour of a soft soil chemically stabilized and reinforced with polypropylene fibres by comparing the results of unconfined compressive strength (UCS) and split tensile strength (STS) tests (STS) carried out before and after a cyclic loading stage. The laboratory work is based on the following tests: i) monotonic UCS and STS test (reference values); (ii) cyclic UCS and STS tests and (iii) monotonic UCS and STS tests performed after the cyclic loading stage (UCSpc and STSpc). From the results it is observed that the permanent deformations show a sharp increase at the beginning of the cyclic stage followed by a decrease in the strain rate for unreinforced and fibre-reinforced samples. In terms of cyclic loading stress level and amplitude, Ffor levels of stress and amplitudes of up to 50% of the maximum strength/load, the samples exhibit lower permanent strains but become stronger and stiffer than the reference values (monotonic tests). These observations are valid for both stabilised materials (unreinforced and fibre-reinforced).

RÉSUMÉ: Ce travail vise à caractériser l'effet du niveau de contrainte et de l'amplitude de la charge cyclique sur le comportement d'un sol meuble chimiquement stabilisé et renforcé avec des fibres de polypropylène en comparant les résultats des essais de résistance à la compression non confinée (UCS) et de résistance à la traction par flexion (STS) réalisés avant et après une étape de chargement cyclique. Le travail en laboratoire est basé sur les tests suivants: i) essai monotone de l'UCS et de la STS (valeurs de référence); ii) essais cycliques de l'UCS et de la STS; et iii) essais monotones de l'UCS et de la STS réalisés après l'étape de chargement cyclique (UCSpc et STSpc). Les résultats montrent que les déformations permanentes augmentent brusquement au début de la phase cyclique, suivies d'une diminution du taux de déformation pour les échantillons non renforcés et renforcés de fibres. En ce qui concerne le niveau de contrainte et l'amplitude de la charge cyclique, pour des niveaux de contrainte et d'amplitudes allant jusqu'à 50% de la résistance/charge maximale, les échantillons présentent des déformations permanentes plus faibles mais deviennent plus résistants et plus rigides que les valeurs de référence (essais monotones). Ces observations sont valables pour les matériaux stabilisés, qu'ils soient renforcés de fibres ou non.

Keywords: Ground improvement; unconfined compressive strength; split tensile strength; monotonic and cyclic loading; stabilisation of soft soils.

1 INTRODUCTION

When infrastructures such as bridge foundations or embankments are built on soft soil deposits, these soils tend to exhibit deformation over long periods due to consolidation and creep phenomena. Such behaviour of soft soils is a consequence of their weak geotechnical characteristics (low strength and

excessive deformability) fundamentally due to the high-water content, high specific surface of the particles (clays, silts) and high organic matter (OM) content. Therefore, it is essential to ensure stability and to control/minimise the deformations during the construction stage and structure life (Kitazume and Terashi, 2013). It is important to mention that in the past construction on soft soil deposits was avoided (Venda Oliveira et al., 2018) due to the above-mentioned stability and deformation problems. However, due to the population growth, development of societies and expansion of urban and industrial areas, the pressure to build on these soft soils has increased, which poses challenges in terms of geotechnical engineering. There are two main geotechnical solutions to solve these types of problems: add reinforcement elements to the ground, or improve the soil's properties by mechanical, physical or chemical methods (Kitazume & Terashi, 2013). The presence of the fibres attenuates the brittle behaviour of the composite material, and improves its tensile strength (Sukontasukkul and Jamsawang, 2012; Correia et al., 2015). The field of application of this technique is vast, for example: embankments on soft soils, stabilisation of slopes, stabilisation of contaminated soils, mitigation of vibrations induced by high-speed trains, retaining walls, etc. (Correia, 2011; Kitazume and Terashi, 2013). Some geotechnical structures are often subjected to cyclical loadings induced by different types of actions, such as wind, earthquakes, traffic loads, heavy machinery, sea waves on offshore structures and even vibrations due to explosives. It is very important to assess the repercussions of cyclical loadings on the mechanical behaviour of chemically stabilised, fibre-reinforced soft soils (Venda Oliveira et al., 2018). Despite the research to date, the impact of the cyclic loading stress level and the amplitude on the compressive strength and tensile behaviour of a stabilized soft soil reinforced with fibres has not been properly studied.

The main goal of this research is to analyze the effect of the cyclic loading in stress level and amplitude on the compressive and tensile and post-cyclic behaviour of a stabilized soft soil, unreinforced and reinforced with polypropylene fibres. The permanents strains or displacement developed during the cyclic stage and the stress-strain, and the load-displacement curves will be used to assess the effect of the parameters studies on the cyclic loading in both materials. To achieve such goals, the following experimental testing program was designed: (i) monotonic unconfined compressive strength (UCS) splitting tensile strength (STS) tests performed with samples not subjected to cyclic loading; (ii) cyclic (Cyc) UCS - STS tests; (iii) and post-cyclic UCS and STS tests (UCSpc - STSpc). Table 1 summarizes the experimental testing plan.

Table 1. Summarize test.

Mix	**Qty**	**M[a]**	**Cyclic Stage Loading Stress[b] (%)**			**Cyclic Stage Amplitude (%)**		
			10	50	70	5	10	20
U	2	2	1	2	1	2	2	1
R	2	2	2	2	1	1	2	1

U= Unreinforced; R=Reinforced samples

[a)] Monotonic Test; [b)] Stress level = q_u/q_{uref}; [b)] amplitude = q_u/q_{uref} =50% varying amplitude

2 MATERIALS

This study was carried out using a Portuguese soft soil, from the "Baixo Mondego" area, located in the centre of Portugal near the Mondego river, which has been characterised by many researchers (Coelho, 2000; Correia, 2011; Teles et al., 2014). The soil deposit was formed more than 20.000 years ago in a fluviomarine depositional environment and shows a thickness higher than 20 metres. On this work it was used a sample that was collected at a depth of 2.5 meters. Table 2 summarizes the main physical and chemical properties. It may be seen that the soil has a largely silty grain size distribution (71%) a low unit weight (14.6 kN/m^3), a high void ratio (> 2.0), a high natural water content (80.6%) and a higher organic matter (OM) content (9.3%). Also, those results have a high influence in the mechanical behaviour, inducing a low undrained shear strength ($c_u \approx 25$ kPa) and a high compressibility (Coelho, 2000). This clayey-silt organic soil with high plasticity was classified as OH (ASTM D2487). The chemical composition of the soil shows a high silica content (SiO_2=62%) and an alumina (Al_2O_3) content of 16%, which conferred pozzolanic properties to the soil.

The soft soil was stabilised with a Portuguese Portland cement binder (Portland cement Type I 42.5 R, produced by CIMPOR), which main chemical characteristics are presented in Table 3. Portland cement reacts immediately with water producing a high quantity of reaction products in the short terms; with time, the physico-chemical reactions (pozzolanic reactions) develop at a lower rate, helping the production of more cementitious products responsible for the enhancement of the mechanical properties of the stabilised soil.

Table 2. Coimbra soft soil main characteristics (average values) (Coelho, 2000 and Correia, 2011).

Physical Properties		Chemical composition	
w_{nat} (%)	80.67	pH (BS1377-	3.5
G_s	2.55	SiO_2 (%)	62
e_{nat}	2.03	Al_2O_3 (%)	16
γ (kN/m^3)	14.6	Fe_2O_3 (%)	48
OM (%)	9.3	CaO (%)	0.74
Grain size		MgO (%)	1.1
Clay (%)	10	Na_2O (%)	0.9
Silt (%)	71	K_2O (%)	3
Sand (%)	19	TiO_2 (%)	0.69
w_L (%)	71	MnO (%)	< 0.3
w_p (%)	43	P_2O_5 (%)	< 0.5
PI (%)	28	TOC (%)	2.79
LI (%)	1.35	CTC	11
USCS (ASTM D2487)	OH		

Table 3. Chemical characterisation of the Portland cement (average values; data from manufacturer).

Nomenclature	Value
SiO_2 (%)	19.30
Al_2O_3 (%)	5.09
Fe_2O_3 (%)	3.15
CaO Total (%)	63.87
MgO (%)	1.91
SO_3 (%)	3.15
K_2O (%)	1.13
Na_2O (%)	0.10
CaO Free (%)	2.19
Loss on ignition (%)	1.26

The polypropylene fibres used in this study are 12 mm in length, 32 mm in diameter and exhibit a great flexibility, a high specific surface (134 m^2/kg), a density of 905 kg/m^3, a tensile strength of 250 N/mm^2 and a Young's modulus of 3500 - 3900 N/mm^2 (in accordance with the product datasheet supplied by the manufacturer BEKAERT).

3 SAMPLE PREPARATION AND TESTING

The procedures and methodologies described below are based on the recommendations from EuroSoilStab (2001) and Correia (2011), though with slight differences. First, the soil was manually mixed to obtain a uniform paste. Then, a specified amount of cement (250 kg/m^3) was mixed with the required volume of water to increase the natural soil's water content from 80.67% to 115%. This paste was then mixed with the natural soil using a mechanical mixer at 142 rpm for 4 minutes. The soil-cement-water mixture was layered into cylindrical PVC molds (37 mm in diameter and 78 mm in height). After introducing each layer, the mold was lightly tapped by hand (20 times), and then it was lightly scarified before the next layer was added (each sample was divided into three equal layers). The samples were cured for 28 days in a controlled environment with a temperature of 20 ± 2 °C and humidity of 95 ± 5%. Subsequently, the samples were carefully removed from the PVC molds. Both surfaces were accurately ground to maintain parallelism, resulting in specimens measuring 37 mm in diameter and 76 mm in height. The remaining material was used to determine the moisture content of each sample. The specimens were then placed in the compression machine, and electronic devices (load cell and displacement transducer) were configured and adjusted. Unconfined compression strength (UCS) tests were conducted at a constant strain rate of 1% per minute (BS 1377-7, 1990). Cyclic loading tests were performed at 5.000 cycles, varying deviatoric stress level from 10%, 25%, and 70% ($0.50\times q_{u\text{-}max}$), with sinusoidal excitation at 0.5 Hz and an varying amplitude of ±5, ±10, ±20 ($\pm\ 0.10\times q_{u\text{-}max}$). After the cyclic stage, a monotonic UCS test (UCSpc) was carried out. To ensure the reliability of the procedure used, the tests were repeated at least twice.

4 ANALYSIS OF THE RESULTS

4.1 Effect of cyclic loading stress level

In Table 4, will be show the results of permanent strain resulted from the cyclic loading stress and the postcyclic test, strength parameters ($q_{u\ max}$, and strain). Is observed that concerning a higher stress level the strength starting to lose and the sample became fragile. On the case of the reinforced with fibres samples, the results show an improve of the behaviour on 50% of $q_{u\ max}$ of the level of stress. On the other side, is affected to higher stress level, taking the samples more brittle and losing strength.

In contrast, the split tensile test, STS and post cyclic stage and (STSpc), the higher forces applied, the sample became fragile however with less strength. In the case of reinforced occurs similarity effects (Table 5).

Table 4. STS test – effect of level of cyclic loading stress level.

Type	Stress level (%)	Test N°	Cyclic stage $\varepsilon_{ax\text{-}perm}$ (%)	UCS_{pc} $\varepsilon_{ax\text{-}failure}$ (%)	UCS_{pc} $q_{u\ max}$ (kPa)
without Fiber	10	T1	0.16	3.53	506.6
		T2	-	-	-
	50	T1	0.22	1.73	543.2
		T2	0.24	1.89	581.3
	70	T1	0.25	1.84	462.3
		T2	0.55	1.42	237.9
reinforced	10	T1	0.07	2.82	425.5
	50	T1	0.16	1.98	571.5
		T2	0.16	2.7	504.7
	70	T1	0.75	8.34	448.4
		T2	1.00	10.36	465.0

Table 5. STS test – effect of level of cyclic loading stress level.

Type	Stress level (%)	Test N°	Cyclic stage $\delta_{v\text{-}perm}$ (mm)	STS_{pc} $\delta_{v\text{-}failure}$ (mm)	STS_{pc} F_{max} (N)
unreinforced	10	T1	0.17	0.76	1877.9
		T2	-	-	-
	50	T1	0.22	0.89	1862.9
		T2	0.21	1	1755.3
	70	T1	0.23	0.59	1400.5
		T2	-	-	-
reinforced	10	T1	0.07	3.92	2030.8
		T2	0.19	2.78	2093.9
	50	T1	0.2	4.53	2123.4
		T2	0.2	2.43	2022.2
	70	T1	0.75	5.33	1841.7

In Figure 1 and 2 shown a pronounced increase in permanent axial strain on samples but is more showed in samples reinforced with PP fibres. This shown that the structural matrix of the soft soil became more affected by the cyclic loading when they have more force/strength applied due the mobilization of fibres inside of the solid skeleton of the sample.

The results suggest that applying different levels of stress leads to an increase in the strength and load-bearing capacity of the fiber-reinforced material when compared to the standard monotonic tests. However, it's worth noting that for higher stress levels, there is a decrease in strength and load-bearing capacity.

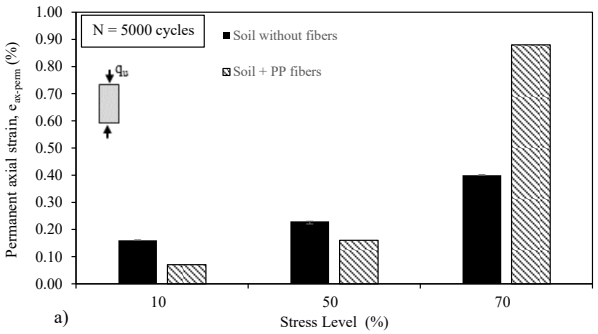

Figure 1. Effect of cyclic loading stress level on UCS_{pc} tests.

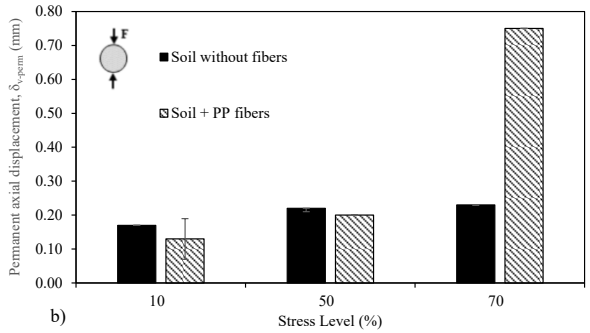

Figure 2. Evolution of permanent axial strain during the cyclic stage with cyclic loading stress level for STS_{pc} test.

These results seem to imply that, during the cyclic stage, the tensile strength of the fibres couldn't fully compensate for the deterioration of the cementitious matrix caused by the cyclic stage. Additionally, the presence of fibres impedes the development of certain cementitious bonds, leading to a loss in unconfined compressive strength and stiffness. Comparing unreinforced and reinforced samples, it becomes evident that permanent deformation is similar in both cases for stress amplitudes ranging from 5% to 10%. However, for a 20% stress amplitude, the reinforced samples subjected to UCS tests exhibit lower permanent deformation. This suggests that as material deformation increases, the fibres progressively engage, helping to reduce permanent axial strain (UCScyc tests) compared to their unreinforced counterparts.

4.2 Effect of cyclic loading amplitude

In case of the effect of cyclic loading amplitude, the results shown similar behaviour in contrast with stress level. Comparing unreinforced and reinforced samples, it becomes evident that permanent deformation is similar in both cases for stress amplitudes ranging from 5% to 10%. However, for a 20% stress amplitude, the reinforced samples subjected to UCS tests exhibit lower permanent

deformation. This suggests that as material deformation increases, the fibres progressively engage, helping to reduce permanent axial strain (UCScyc tests) compared to their unreinforced counterparts. Tables 6 and 7, as well as Figures 3 and 4, provide a summary of the results obtained during post-cyclic UCS and STS tests immediately after altering the cyclic stage's stress amplitude for the stabilized samples reinforced with polypropylene fibres. These results demonstrate an increase in the strength and load-bearing capacity of the stabilized fiber-reinforced material in comparison to the reference monotonic tests, albeit with a reduction as stress amplitude increases, which is linked to greater degradation of the cementitious matrix during the cyclic stage.

Table 6. UCS test – effect of cyclic loading amplitude.

Type	Amp (%)	Test N°	Cyclic stage	UCS_{pc}		
			$\varepsilon_{ax\text{-}perm}$ (%)	$\varepsilon_{ax\text{-}failure}$ (%)	$q_{u\ max}$ (kPa)	E_{u50} (MPa)
unreinforced	5	T1	0.13	1.79	473.3	92.1
		T2	0.08	1.77	608.6	48.3
	10	T1	0.22	1.73	543.2	71.2
		T2	0.24	1.89	581.3	72.7
	20	T1	0.3	1.21	321.8	80.5
reinforced	5	T1	0.15	3.1	631.7	38.9
	10	T1	0.16	1.98	571.5	69.2
		T2	0.16	2.7	504.7	52.8
	20	T1	0.38	1.62	371.1	82.7

Table 7. STS test – effect of cyclic loading amplitude.

Type	Amp (%)	Test N°	Cyclic stage	STS_{pc}	
			$\delta_{v\text{-}perm}$ (mm)	$\delta_{v\text{-}failure}$ (mm)	F_{max} (N)
unreinforced	5	T1	0.18	0.48	1120.4
		T2	0.21	1.45	2422.6
	10	T1	0.22	0.87	1862.9
		T2	0.22	1.00	1755.3
	20	T1	0.37	0.60	1052.9
reinforced	5	T1	0.19	2.47	2082.0
	10	T1	0.20	4.53	2123.4
		T2	0.20	2.43	2022.2
	20	T1	0.38	2.39	1816.9

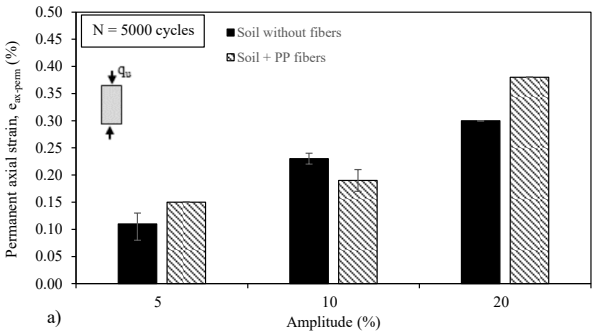

Figure 3. Effect of amplitude for UCS_{pc} tests.

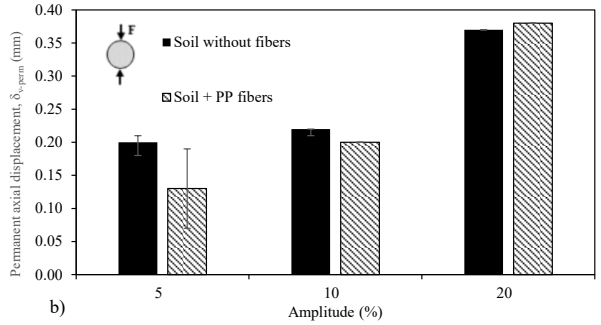

Figure 4. Effect of amplitude for STS_{pc} tests.

5 CONCLUSIONS

From the monotonic UCS and STS tests performed before cyclic loading (references values) and after cyclic loading stage (UCSpc and STSpc) for the stabilized soil reinforced with fibres and not reinforced are drawn:

a. As other works shown that could be observed that the permanent strains show a sharp increase at the beginning of the cyclic stage followed by a decrease in the strain rate for unreinforced and fibre-reinforced samples. In this work results are not shown, mainly for the highly effect on the detriment of the cementitios matrix due the load/stress applied above 50% of the $q_{u\text{-}max}$.

b. Addition of fibres promotes a reduction in the permanent axial strains for the UCS cyclic tests, the opposite effect could be observed for the STS cyclic tests, explained by the different failure mechanisms associated with each test.

c. Up to stress levels and amplitudes of 50% of the maximum strength/load, the samples display reduced permanent deformations and also demonstrate increased strength and stiffness when compared to the reference values from the monotonic tests. These findings hold true for both stabilized materials, whether they are unreinforced or fiber reinforced.

ACKNOWLEDGEMENTS

The authors appreciate the support of CIMPOR and to BEKAERT for supplying the binder and the fibres, and to the institutions that financially supported the research: CIEPQPF (UIDB/00102/2020), ISISE (UIDB/04029/2020), and ARISE (LA/P/0112/2020), FCT (POCI-01-0145-FEDER-028382), ACIV, Universidad de Magallanes, Punta Arenas, Chile and CONICYT PAI/INDUSTRIA 79090016.

REFERENCES

Coelho, P. (2000). Caracterização geotécnica de solos moles: estudo do local experimental da Quinta do Foja (Baixo Mondego) (Master's thesis). Available at: https://hdl.handle.net/10316/9845. accessed: 30/03/2024.

Correia, A.A.S. (2011), Applicability of deep mixing technique to the soft soil of Baixo Mondego, PhD Thesis, Univ. of Coimbra, Coimbra, Portugal. Available at: https://hdl.handle.net/10316/15688. accessed: 30/03/2024.

Correia, A. A., Oliveira, P. J. V. and Custódio, D. G. (2015). Effect of polypropylene fibres on the compressive and tensile strength of a soft soil, artificially stabilised with binders. Geotextiles and Geomembranes, 43 (2), pp. 97-106. DOI: https://doi.org/10.1016/j.geotexmem.2021.06.001.

EuroSoilStab (2002). Development of design and construction methods to stabilise soft organic soils: Design guide soft soil stabilisation. Industrial and Materials Technologies Programme (Brite-EuRam III), European Commission, p. 94.

Kitazume, M., & Terashi, M. (2013). The deep mixing method. CRC press, London, UK, https://doi.org/10.1201/b13873.

Sukontasukkul, P. & Jamsawang, P. (2012), Use of steel and polypropylene fibres to improve flexural performance of deep soil–cement column, Construction and Building Materials, 29, 201-05. DOI:10.1016/j.conbuildmat.2011.10.040.

Teles, J. M. (2013). Comportamento Mecânico do Solo Mole do Baixo Mondego Quimicamente Estabilizado Com Adição de Fibras Metálicas. MSc. Dissertation. Universidade de Coimbra. DOI: 10.14195/2184-8394_152_16.

Venda Oliveira, P.J., Correia, A.A.S., & Cajada, J.C.A. (2018), Effect of the type of soil on the cyclic behaviour of chemically stabilised soils unreinforced and reinforced with polypropylene fibres, Soil Dynamics and Earthquake Engineering, 115, 336-43. DOI: https://doi.org/10.1016/j.soildyn.2018.09.005.

Villarroel-Ortega, J. A., Correia, A. A., Venda Oliveira, P. J., & Lemos, L. J. (2022). Influencia de parámetros claves de cargas cíclicas sobre el comportamiento de un suelo estabilizado químicamente no reforzado y reforzado con fibras. Obras y proyectos, (31), 29-34. DOI: http://dx.doi.org/10.4067/s0718-28132022000100029.

Villarroel-Ortega. (2022), Characterisation of stress-strain behaviour of a chemically stabilised soft soil reinforced with fibres under monotonic and cyclic loadings, PhD Thesis, Univ. of Coimbra, Coimbra, Portugal. Available at: https://hdl.handle.net/10316/101696. accessed: 30/03/2024.

Proceedings of the XVIII ECSMGE 2024
GEOTECHNICAL ENGINEERING CHALLENGES
TO MEET CURRENT AND EMERGING NEEDS OF SOCIETY
© 2024 the Authors
ISBN 978-1-032-54816-6
DOI 10.1201/9781003431749-677
Open Access: www.taylorfrancis.com, CC BY-NC-ND 4.0 license

ECSMGE 24
XVIII EUROPEAN CONFERENCE ON SOIL MECHANICS AND GEOTECHNICAL ENGINEERING

Parametric study of stability in landfills due to changes in waste composition

Etude paramétriqueet de la stabilité dans les décharges dues aux changements dans la composition des déchets

H. Vučenović*, K. Herceg, D. Domitrović, Ž. Veinović
University of Zagreb Faculty of Mining, Geology and Petroleum Engineering, Zagreb, Croatia
**helena.vucenovic@rgn.unizg.hr*

ABSTRACT: The modern trend in waste management in most developed countries in Europe and the world is based on waste reduction, reuse and recycling, while landfilling is considered the least desirable method in the waste management process. Despite this trend, landfilling is still the leading method of waste disposal in most countries. Considering the increasing amount of waste, even if all methods to reduce the amount of waste are used, there will still be a need to build a landfill. Waste is a heterogeneous material whose physical, mechanical and chemical properties are highly dependent on the composition of the waste, so even minor changes in composition can affect the change in these properties. In Croatia, in the process of approaching European Union standards, the composition of disposed waste has changed significantly, primarily due to the fact that biowaste, plastic waste and paper are increasingly separated from total municipal waste. The separation of these constituents significantly affects the density, moisture and granulometric composition of the deposited waste, which in turn affects the stability and deformations of the landfill body itself, as well as the stability of the protective layer system. In this work, the effects of changes in the physical and mechanical parameters of the landfilled municipal waste on the stability of the landfill body were analyzed.

RÉSUMÉ: La tendance moderne en matière de gestion des déchets dans la plupart des pays développés d'Europe et du monde est basée sur la réduction, la réutilisation et le recyclage des déchets, tandis que la mise en décharge est considérée comme la méthode la moins souhaitable dans le processus de gestion des déchets. Malgré cette tendance, la mise en décharge reste la principale méthode d'élimination des déchets dans la plupart des pays. Compte tenu de la quantité croissante de déchets, même si toutes les méthodes visant à réduire la quantité de déchets sont utilisées, il sera toujours nécessaire de construire une décharge. Les déchets sont des matériaux hétérogènes dont les propriétés physiques, mécaniques et chimiques dépendent fortement de leur composition, de sorte que même des changements mineurs dans leur composition peuvent affecter l'évolution de ces propriétés. En Croatie, en voie de se rapprocher des normes de l'Union européenne, la composition des déchets éliminés a considérablement changé, principalement en raison du fait que les biodéchets, les déchets plastiques et le papier sont de plus en plus séparés des déchets municipaux totaux. La séparation de ces constituants affecte de manière significative la densité, l'humidité et la composition granulométrique des déchets déposés, ce qui à son tour affecte la stabilité et les déformations du corps de décharge lui-même, ainsi que la stabilité du système de couches protectrices. Dans ce travail, les effets des changements dans les paramètres physiques et mécaniques des déchets municipaux mis en décharge sur la stabilité du corps de la décharge ont été analysés.

Keywords: Landfill; MSW; kitchen waste; stability.

1 INTRODUCTION

Municipal solid waste (MSW) landfills are still a necessary part of the MSW management system although the current, modern waste management, requires minimization of the amount of mixed waste which is to be disposed at landfills (Puntarić et al., 2023). The 3R principle (*reduce, reuse, recycle*), and especially the intensive separate collection of waste, will certainly reduce the quantities of waste ending up at the landfill thus affecting the characteristics and properties of the disposed waste which will in turn affect the stability of landfill (Gomes et al., 2013; Singh & Uchimura, 2023). There is an open question: if the large, old landfill which is being filled for a couple of decades with the mixed MSW, starts receiving different waste material, with less glass, plastics, metals, and biodegradables, what will change considering geomechanical properties of the disposed material and the stability of the landfill? To answer that question, it is necessary to quantify the reduction of certain waste components and either measure or assess changes in the properties of waste.

Construction of Prudinec, the MSW landfill for the city of Zagreb, Croatia, begun in 1995 with the preparation of the new disposal surface and the construction of the bottom protective layer system (BPLS), on which a part of the old waste was transferred from an insanitary dumpsite in the immediate vicinity, as well as the newly collected waste (Budiša et al., 2014). A mixture of old and fresh waste was disposed of on the new prepared location, until 2003 when the disposal of only fresh MSW begun (Budiša et al., 2014). Separate waste collection in the city of Zagreb begun in 2002 (Fundurulja, 2009) and in the period 2002-2018 there was gradual increase of the separate waste collection of plastics, metals, glass, paper, and textile. According to the Companies Act (City of Zagreb, 2018) from the January 30th 2018, separate collection of the mixed plastic and metal waste. On September 23rd 2022 a decision was made by the Zagreb Holding, company which was incorporated in 2007 in line with the Companies Act and is 100% owned by the City of Zagreb, according to which mixed MSW must be collected in "blue bags" whose purchase price is 1,06€/40 l (Zagreb Holding, 2022). Therefore, since the September of 2022 collected and landfilled mixed MSW has a reduced amount of paper, metal, plastics, and compostable waste.

Changes in the composition of waste by removing compostable materials (unused cooked food is still being collected as a part if the mixed waste), plastic and metal, paper and cardboard, are reflected by changes in cohesion, angle of the internal friction, density, water content and other parameters (Gomes et al., 2013; Singh & Uchimura, 2023). Taking into consideration these changes it can be concluded that the stability of the Prudinec landfill might be changed, and the possible changes and effects are addressed in this paper.

2 THE MSW LANDFILL SITE PRUDINEC

Modern landfills are designed to protect human health and the integrity of the environment by controlling water and air emissions. The engineered protective systems incorporate advanced design features, including multi-layered liner construction, gas extraction and leachate removal systems.

The landfill site Prudinec is located on the southern bank of the Sava River, today, in the City of Zagreb. The decision to open dumpsite was made back in 1964.

The current Prudinec landfill is divided into cells 1 to 6, the area of each cell varies between 6 and 9 ha. The landfill has an almost rectangular shape with a length of approx. 1400 m and a width of approx. 450 m.

2.1 Landfill protective layers

An approx. 8 m high berm construction were erected at the foot of the deposited waste. The BPLS consists of 1 m thick clay layer and a 2.5 mm thick geomembrane as a barrier layers, above which a protective geotextile, a 0.5 m thick drainage layer for leachate collection and a filter geotextile are placed. The clay protective layer consists of highly plastic clay (Vukelic et al. 2004).

The final protective layer system of the landfill consists of gas drain composite, GCL and geomembrane, water drainage composite for the drainage of precipitation water, 0.85 m thick protective soil layer and 0.15 m thick humus layer. The membrane is only used in the upper part of the landfill, on the slopes only GCL is used as a barrier layer.

2.2 Historical instabilities of landfill site Prudinec

Slope stability analyses of municipal solid waste landfills are important to determine a safe landfill height and slopes inclination.

In August 2002, a localised landslide of the mentioned landfill was observed on the south side of landfill at the contact between the cover protection layer and the berm. The estimated affected area of the landslide was approximately 50 m long and 140 m wide. It had spread an estimated 100,000 m^3 of waste.

The field investigations carried out showed that the waste deposited in the area of the landslide did not differ in content and characteristics from the waste deposited elsewhere in the landfill. These were large quantities of old inert waste consisting of deposited municipal waste, soil and construction waste. As part of a field investigation, the leachate height was measured at the top of the bottom barrier layer in wells. The height of the leachate varied from 0.7 m to 11.5 m (Vukelic et al. 2004). In determining the cause of the landslide, other factors were also taken into account, such as the composition and properties of the protective layers and waste, the contacts of the layers and the performance and construction control of the landfill design.

The planning of a MSW landfill requires an appropriate characterization of the mechanical properties of the waste it contains. This is often very difficult due to the heterogeneity and highly variable composition of the waste. However, this is necessary to accurately assess the slope stability of the landfill and the interaction of the waste with other landfill

structures such as liners and gas and leachate collection systems (Gomes et al. 2013).

2.3 The impact of waste composition on landfill stability

In addition to the geometry, parameters such as compaction effort, pore pressure, protective layers, etc., the stability of the landfill is significantly influenced by the composition of the waste. Therefore, knowledge of the waste composition is generally one of the most valuable factors for estimating the properties of municipal waste (Cho et al. 2011; Jahanfar et al. 2017).

The changes that have occurred in recent years because of the introduction of a new waste separation and disposal policy can be seen, among other indicators, primarily in changes in waste parameters, unit weight, cohesion, and the friction angle. These changes certainly have an impact on the stability of the landfill slope. Based on these assumptions, an analysis of the effects of the change in strength parameters on the stability of the landfill slope and the safety factor was carried out.

The quantity of individual components such as paper, glass, plastic and biowaste previously made up a large proportion of municipal waste. Between 2002 and 2018, this composition gradually changed and is now significantly different. According to this trend, it is assumed that since the end of 2022 the proportion of plastic, paper, glass and metal has largely decreased and therefore the largest proportion of the total composition of municipal waste is kitchen waste. For this reason, it is assumed that the geotechnical parameters of the waste have also changed as a result of this change, which has an impact on the stability of the landfill.

For the numerical analysis of stability, it was necessary to collect data for the protective soil layers and the waste at the landfill. Certain materials in MSW are continuously degraded over time by various chemical and biological processes, while the properties of some materials do not change (Štefanák and Chalmovský 2022; Machado et al., 2002). For this reason, it was necessary to use parameters corresponding to a specific composition of the waste.

3 NUMERICAL MODEL

For the slope stability analysis of the landfill, a model with dimensions of 306 m width and 77 m height was created. The geometry of the landfill is simplified and consists of a subsoil, protective layer, drainage layer, dyke on the edge of the waste layer and the waste layer. The slope stability analysis of the model was carried out using Plaxis and soil and waste material were modelled using the Mohr-Coulomb model. The analysis was carried out for three proportions of kitchen waste in municipal waste, in percentages of 10%, 30% and 60%. The input parameters for waste were obtained from previous experimental studies (Cho et al. 2011; Ivšić et al. 2004). The material properties of the soil layers were taken from studies describing the Prudinec landfill (Kovačević Zelic et al. 2002, Vukelic et al. 2004). Geotechnical parameters are presented in Table 1.

Table 1. Geotechnical parameters.

Parameter	Unit weight (kN/m^3)	Friction angle (°)	Cohesion (kN/m^2)
Subsoil	18	32	10
Drainage layer	18	30	0,3
Sealing layer	19	21	24
Dyke	19	24	15
Kitchen waste 10%	8	33	5
Kitchen waste 30%	9	26	6
Kitchen waste 60%	10	17	7

3.1 Results of numerical analysis

The numerical analysis was performed for different percentages of kitchen waste in the waste composition. Three cases were modelled with 10%, 30% and 60% of kitchen waste in the composition of municipal waste (Figure 1).

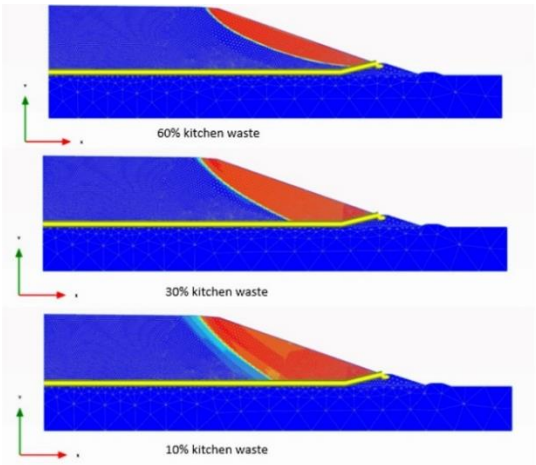

Figure 1. Failure planes for different amount of kitchen waste – 10%, 30% and 60%.

The results of the numerical analysis show that as the proportion of kitchen waste increases, the safety factor decreases and the slip surface is shallower (Figure 2).

For waste with a low proportion of kitchen waste, the contact layers in the lower sealing layer have the greater influence and the sliding surface runs largely

through the contact of these layers. For waste with a low proportion of kitchen waste, the contact layers in the lower sealing layer have the greater influence and the sliding surface runs largely through the contact of these layers. For waste with a higher proportion of kitchen waste, the probability of a sliding surface forming in the landfill body itself is higher.

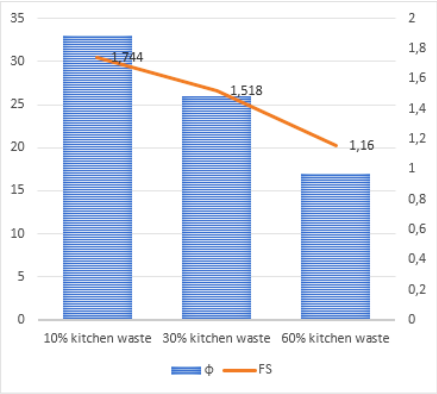

Figure 2. Change of the factor of safety with the change in the proportion of kitchen waste and friction angle of waste.

4 CONCLUSIONS

The stability of the landfill depends largely on the mechanical properties of the waste and the protective layer system. In contrast to the material parameters of the protective layers, the waste parameters change considerably over the years, not only due to the aging of the waste, but also due to changes in the composition of the deposited waste. Due to frequent changes in the waste management policy, the composition of the waste has changed significantly during the operational life of the Prudinec landfill. The composition of waste with the largest proportion of paper and plastics has now been replaced by waste with the largest proportion of kitchen waste. These changes mainly affected the reduction of the friction angle and, to a lesser extent, the reduction of cohesion. The results of the numerical analysis show that such a change has a significant effect on the reduction of the safety factor and the stability of the landfill. It can be concluded that the selection of relevant waste parameters and protective layer system is very important when assessing the overall safety of a landfill.

During the writing of this article, two landslides occurred at the Prudinec landfill. The first smaller one occurred in mid-November 2023 after a short but very intense period of rainfall. According to initial estimates, the area affected by this landslide was around 100 metres wide and 30 metres high. The second occurred in early December 2023 in the early morning when the air temperature was around -5 °C.

This landslide affected a significant part of the eastern side of landfill.

REFERENCES

City of Zagreb (2018). Act on the method of providing the public service of collecting mixed municipal waste and biodegradable municipal waste and services related to public service in the City of Zagreb, 2/2018, Official Act by the City Assembly of the City of Zagreb, Croatia.

Zagreb Holding (2022). Decision on the collection of municipal waste in the center of the city of Zagreb Zagreb holding, Zagreb, Croatia.

Cho, Y. M., Ko, J. H., Chi, L., and Townsend, T. G. (2011a). "Food waste impact on municipal solid waste angle of internal friction." Waste Manage., 31(1), 26–32.

Budiša, M., Burela, S., Šeparović, M., Končurat, L. (2014). Technical – technological solution of the existing waste disposal facility Prudinec/Jakuševec ECOINA, Zagreb, Croatia, Rep. 1.

Fundurulja, D. (2009). A combination of tradition and interesting solutions (original title: *Spoj tradicije i zanimljivih rješenja*, in Croatian). FONDEKO svijet – Naučno popularna revija o prirodi, čovjeku i ekologiji, 29, pp. 23-25.

Gomes, C, Lurdes Lopes, M. Venda Oliveira, P. J. (2013). Municipal solid waste shear strength parameters defined through laboratorial and in situ tests, *Journal of the Air & Waste Management Association*, 63(11), 1352-1368, http://doi.org/10.1080/10962247.2013.813876.

Ivšić, T., Petrović, I. i Verić, F. (2004). Overview of parameters for stability analysis on waste disposal sites, Građevinar, 56 (11.).

Jahanfar, A.; Gharabaghi, B.; McBean, E.; Dubey, B. (2017). Municipal Solid Waste Slope Stability Modeling: A Probabilistic Approach. Journal of Geotechnical and Geoenvironmental Engineering. 143. http://doi.org/10.1061/(ASCE)GT.1943-5606.0001704.

Kovačević-Zelić, B.; Kvasnička, P.; Domitrović, D.: Stability Analysis for the Landfill Jakusevec, Proceedings of the 12TH; Danube-European Conference, Passau, 27-28 May 2002., pp. 503-506.

Puntarić, E., Požgaj, Đ., Korica, Ž., Gumhalter Malić, L., Kušević-Vukšić, M., Bulat, V., Vešligaj, G., Krivanek, G. (2023). Report on municipal waste for 2022, Croatian Ministry of Economy and Sustainable Development, Zagreb, Croatia, Rep. 1.

Singh. V., Uchimura, T. (2023). Effect of Material Composition on Geotechnical Properties—Study on Synthetic Municipal Solid Waste, *Geotechnics*, 3, 397-415, https://doi.org/10.3390/geotechnics3020023.

Zagreb Holding (2014). Waste disposal plan on the cell 5d and 6 Zagreb holding, Zagreb, Croatia.

Vukelić, A, Kovačević Zelić, B. and Drnjević, B. (2004). "Landslide at the Jakusevec landfill." Geotechnical Engineering with Geosynthetics, eds. Floss, R., Brau, G., Nussbaumer, M. and Laackmann, K.. München, DGGT, 2004. 87-9.

Proceedings of the XVIII ECSMGE 2024
GEOTECHNICAL ENGINEERING CHALLENGES
TO MEET CURRENT AND EMERGING NEEDS OF SOCIETY
© 2024 the Authors
ISBN 978-1-032-54816-6
DOI 10.1201/9781003431749-678
Open Access: www.taylorfrancis.com, CC BY-NC-ND 4.0 license

ECSMGE 24
XVIII EUROPEAN CONFERENCE ON SOIL MECHANICS AND GEOTECHNICAL ENGINEERING

Critical state behaviour of anthropogenic clay in a direct simple shear test

Comportement à l'état critique d'argile anthropogénique dans un essai de cisaillement simple direct

N.S. Walrave*
Department of Geo-Engineering, TU Delft, The Netherlands
Fugro, Utrecht, The Netherlands

C. Zwanenburg
Department of Geo-Engineering, TU Delft, The Netherlands
Unit Geo-Engineering, Deltares, Delft, The Netherlands

I.E. van Gelder
SOCOTEC Geotechnics, Son, The Netherlands

n.walrave@fugro.com

ABSTRACT: In practical engineering the direct simple shear, DSS, tests are a valuable tool for parameter assessment, despite its known shortcomings. The shear stress mobilised at the end of the test is often used as a proxy for critical state strength. Several aspects complicate conducting reliable tests at large strain, in specific for clay samples. One of these effects is slippage between the sample and the platens. When slippage occurs, the measured resistance follows from the interface properties rather than soil behaviour. To better understand the critical state behaviour of clays during a DSS tests a test series is conducted on an anthropogenic stiff silty clay. The test series not only demonstrates that critical state conditions are reached before the end of the tests, but also that slippage tends to occur after reaching critical state conditions. Complimentary series of direct shear, DS, tests were conducted to further confirm critical state conditions are obtained. This confirms the applicability of DSS tests to obtain a soil specific proxy for critical state conditions without the influence of slippage. Hence, the presented method to derive critical state strengths from DSS tests, for anthropogenic clay, and thereby discarding the influence of slippage provides useful and reliable strength parameters for design.

RÉSUMÉ: En ingénierie pratique, les essais de cisaillement simple direct (DSS) sont un outil précieux pour l'évaluation des paramètres, malgré leurs limitations connues. La contrainte de cisaillement mobilisée à la fin de l'essai est souvent utilisée comme un indicateur de la résistance à l'état critique. Plusieurs aspects compliquent la réalisation de tests fiables à grande déformation. L'un de ces effets est le glissement entre l'échantillon et les plateaux. Lorsque le glissement se produit, la résistance mesurée dépend des propriétés de l'interface plutôt que du comportement du sol. Afin de mieux comprendre le comportement à grande déformation des argiles dans des conditions de DSS, une série de tests est réalisée sur une argile limoneuse anthropogénique rigide. Cette série de tests montre non seulement que les conditions d'état critique sont atteintes avant la fin des tests, mais aussi que le glissement a tendance à se produire après avoir atteint les conditions d'état critique. Une série complémentaire de tests de cisaillement direct (DS) est réalisée pour confirmer davantage l'obtention des conditions d'état critique. Cela confirme l'applicabilité des essais OC DSS sur les argiles anthropogéniques dans la conception des digues, à condition qu'un indicateur spécifique au sol pour les conditions d'état critique ait été déterminé à partir de tests en laboratoire, plutôt que la résistance à la fin de l'essai.

Keywords: Direct simple shear testing; anthropogenic clay; shear strength; slippage; laboratory testing.

1 INTRODUCTION

Parameter assessment using DSS testing is hampered by the unclear stress state of the sample (DeGroot et al., 1992). However, it is considered the best method to represent shearing conditions along a potential failure surface (Grimstad et al., 2012) especially in soft clays with anisotropic stress-strain-strength behaviour. DSS tests involve the rotation of principal stresses during the test making it suitable to study the rotation of principal stress directions beneath an embankment which leads to varying shear strength at different locations. This study explores the derivation of critical state behaviour during DSS testing, which is crucial for obtaining a reliable parameter assesment.

Critical state conditions are typically reached at large deformations, and the mobilized strength at the end of the test is often used as a proxy for critical state strength (Leroueil et al., 1990). However, large strains in DSS tests can induce anomalies like slip planes and slip between the sample and plates, making it challenging to determine model parameters for constitutive models in practical engineering applications.

In a typical DSS test the stack of rings is sheared uniformly. Figure 1 shows an example where slip between the sample and bottom plate has occurred. Three separate zones can be distinguished: i) at the top platen, ii) in the middle, and iii) at the bottom platen. The negative influence of the boundaries on the sample in DSS testing is well acknowledged. However, it is assumed that the centre of the sample is sheared in simple shear and governs the overall behaviour (i.e. DeGroot et al., 1992, Den Haan and Grognet, 2014). The deformation pattern depicted in Figure 1 indicates that, at least at the end of the test, the mobilized resistance is influenced by friction between the sample and the bottom plate, which raises questions regarding the validity and application of the test results.

The series of DSS tests that were perfomed to study the critical state behaviour focuses in particular on determining useful critical state strength parameters before slip occurrence, which we hypothesize to be in response to a significant amount of applied strain with critical state behaviour occur before slippage occures.

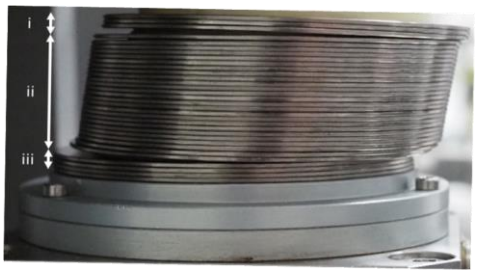

Figure 1. A result at the end of an OC DSS test with slippage.

2 SAMPLE CHARACTERISTICS

The research is performed on undisturbed anthropogenic samples from Ravenstein-Lith along the Meuse river in the Netherlands. The samples were retrieved above the phreatic line and tested at natural water content, γ_n, 22.2 to 42.4%. The dry density of the samples is 1.21-1.60 g/cm^3 with a void ratio of 0.65-1.15. The medium plasticity samples are characterized by a clay (< 2μm) content of 24.3%, a silt (2 < x < 63μm) content of 56.3%, a 17.5% sand (63 < x < 2000μm) content and 1.9% of organic content.

3 APPROACH AND METHODOLOGY

This study used a GDS instruments DSS apparatus with a 2 kPa loadcell with internal and external displacement sensors. Intact clay specimens were trimmed and fitted in between porous stones with distributed conical pins enclosed by a rubber membrane and a stack of low-friction rigid rings providing the lateral confinement but also allowing simple shear to occur. Bjerrum's (1973) recompression technique was used to reconsolidate the samples to the estimated in-situ vertical stress. During the stage of simple shearing a strain rate of 2%/hr was applied. Constant volume tests were conducted under undrained conditions per ASTM D6528-17 (2017) where the change in normal stress was assumed to be equivalent to the change in pore pressure (Dyvik et al., 1987). Corrections for membrane and slide table friction were applied to the horizontal load readings (Greeuw et al., 2016). In addition to DSS tests, DS tests were performed to verify at which strain level critical state conditions are reached using a Wille Geotechnik apparatus under water, following ISO 17892-10 (2018) guidelines, together with an area correction per Bareither et al. (2008).

4 RESULTS

During a DSS test, slippage was observed at the end of the test, occurring after applying some strain to the sample. This slippage along the upper and lower surfaces of the specimen leads to partial transfer of shear force from the platens to the sample, exceeding the mobilized friction at the soil-platen interface. Previous studies by e.g. Le Meil et al. (2016) have shown that using porous platens with protruding pins on cohesive soils can prevent slippage, allowing continued deformation of the specimen even after slippage has initiated. However, Le Meil et al. (2016) suggested that the embedment of protruding pins may create uneven stress concentrations in the boundary zone, as the shear strength undergoes changes when the pins cut through the soil. Consequently, the boundary zone surrounding the central region of the sample, where a simple shear stress state exists, exhibits interrelated slippage and shear. If the protruding pins cut through the soil in the boundary zone, localized softening occurs, and uniform simple shear conditions cannot be maintained due to strain localization.

The tests reveal that observed slip often corresponds to the formation of a distinct sliding plane (Figure 2). A schematic representation of this hypothesized stage is depicted in Figure 3b, where the initiation of a rupture plane occurs after a standard test

onset (Figure 3a). Additionally, Figure 3c illustrates the impact of excluding rings and a membrane during testing, while Figure 3d demonstrates the strain localization that occurs along the bottom and top platens in response to ongoing slippage along the shear plane.

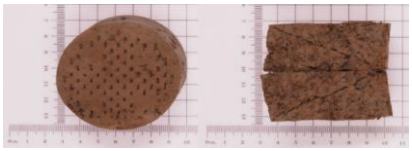

Figure 2. An OC DSS sample which experiences slip and shows a clear internal shear plane.

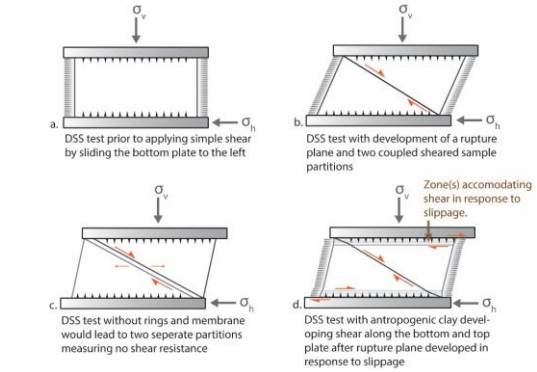

Figure 3. Schematic overview of the different stages of a DSS test result.

4.1 Tests under OC conditions

A total of seven DSS tests were conducted under overconsolidated (OC) conditions at natural water content. The corresponding stress – strain curves and normalised stress paths are shown in Figure 4 and 5 (i). The test results demonstrate unconventional behaviour with certain stress-strain curves exhibiting dips between 5 and 15% shear strain, and some normalised stress paths displaying odd behaviour in the form of a loop. Moreover, upon removing the sample from its set-up, a diagonal shear plane has formed within the sample, and it exhibits signs of slippage (see Figure 2).

In addition to tests at γ_n, five fully saturated tests were conducted (for test results see Figure 4 and 5 (ii)) and these showed, albeit less, still signs of slippage, but not a sign of the formation of shear bands or loop in the normalised stress paths.

4.2 Tests under NC conditions

Three additional normally consolidated (NC) DSS tests were conducted, and the test results align with those typically observed for NC clay (Figure 4 and 5 (iii)). In these tests, no slippage was observed, possibly due to the NC conditions where the vertical stress level surpasses the yield stress (> 100 kPa), resulting in adequate soil-platen interface grip. Moreover, no visual indications of diagonal shear zones were observed.

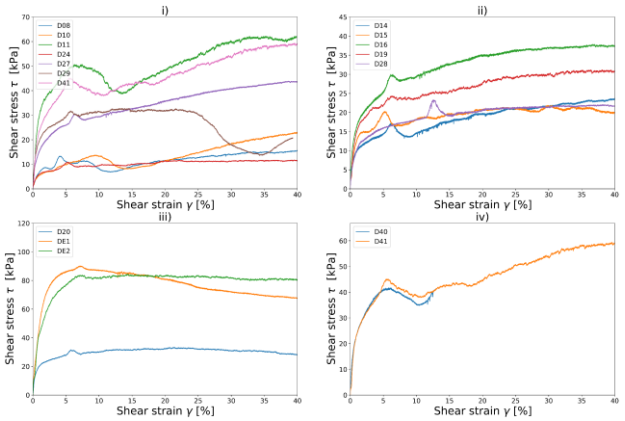

Figure 4. Shear stress - shear strain graphs of DSS tests under OC conditions at γ_n (i) OC conditions fully saturated (ii), NC conditions (iii) and fully developed and pre-maturely stopped DSS test (iv).

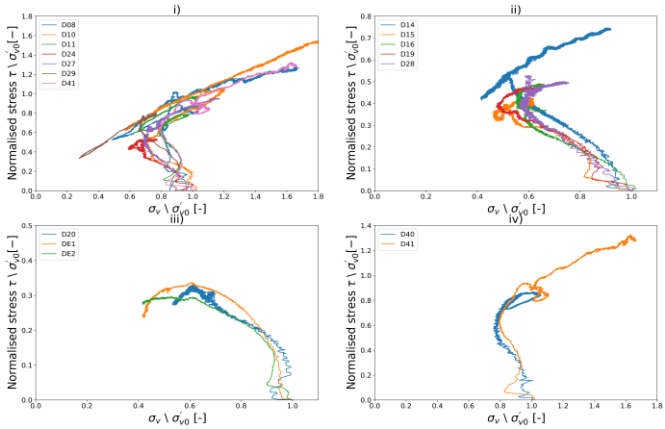

Figure 5. Stress paths of DSS tests under OC conditions at γ_n (i) OC conditions fully saturated (ii), NC conditions (iii) and fully developed and pre-maturely stopped DSS test (iv).

4.3 Direct shear tests

Although DS and DSS test are different, both in terms of failure mechanism and imposed boundary conditions, generally similar results are to be expected if these effects are accounted for (Hanzawa et al., 2007). Eight DS tests were performed which showed a constant mobilised shear stress when reaching 15% shear strain, indicating that critical state conditions have been reached and that critical state strength parameters in DSS tests can be determined earlier than the current proxy for shear strain, γ, of 40%.

4.4 Formation of the diagonal failure plane

During eight DSS tests a time-lapse video has been recorded. Test results showed both signs of slippage and development of a diagonal rupture surface. It is hypothesized that the sample has reached critical state

before slip occurs. To validate this hypothesis, two DSS tests were performed on samples from the same boring with sequential depth and in-situ water content (see Figure 4 and 5 (iv)). The first test (D40) was stopped at $\gamma = 13\%$ strain and the subsequent test (D41) was performed until reaching the prescribed $\gamma = 40\%$.

In sample D40, no signs of slip were observed at $\gamma = 13\%$, but an initiation of a diagonal rupture plane was evident. Sample D41 exhibited both slippage and a fully developed rupture plane, confirming the hypothesis. This suggests that a reliable practical indication of critical state strength can be obtained using DSS tests on an OC sample, provided a soil-specific proxy for critical state conditions is determined. The findings support the hypothesis depicted in Figure 4, showing the reliability of DSS tests until the development of the sliding plane and slightly beyond, offering an indication of critical state strength just prior to slip between the sample and plates. However, test results beyond these strain levels are considered unreliable as they do not reflect the true strength characteristics of the tested soil, but rather include other factors such as membrane strength.

5 CONCLUSIONS

A series of 17 DSS tests was conducted on both NC and OC samples of an anthropogenic clay. Under NC conditions, the tests exhibited textbook behaviour without slippage, as the clay behaved plastically without the formation of discrete failure surfaces. However, under OC field stress conditions, the tests displayed a noticeable dip in the stress-strain curve, corresponding to the development of a diagonal rupture plane. Continued testing revealed slippage between the sample and platens. It was observed that the stresses measured after the formation of the rupture plane no longer represented soil behaviour but were influenced by the membrane and ring stack that forced the parts to move according to the applied displacements from the device. Consequently, in DSS tests on anthropogenic clay, the strength at large strains cannot serve as a proxy for critical state strength, as is typically assumed for NC conditions. However, this research demonstrated that if a soil-specific proxy for critical state conditions is utilized, the results of OC DSS tests can be applied to determine strength parameters for geotechnical design.

ACKNOWLEDGEMENTS

This research was conducted as part of an MSc thesis at TU Delft in collaboration with Arcadis and SOCOTEC Geotechnics.

REFERENCES

ASTM D6528-17. 2017. Standard test method for consolidated undrained direct simple shear testing of fine grain soils. ASTM International: West Conshohocken, PA, USA.

Bareither, C. A., Benson, C. H., Edil, T. B. 2008. Comparison of shear strength of sand backfills measured in small-scale and large-scale direct shear tests. Canadian Geotechnical Journal, 45(9), 1224-1236. https://doi.org/10.1139/T08-058.

Bjerrum, L. 1973. Problems of soil mechanics and construction on soft clays and structurally unstable soils (collapsible, expansive and others). Proc. 8th Int. Conf. on Soil Mech. and Found. Eng., Moscow, 3: 111-159.

DeGroot, D.J., Ladd, C.C., Germaine, J.T. 1992. Direct simple shear testing of cohesive soils. Constructed Facilities Division, Department of Civil Engineering, Massachusetts Institute of Technology.

Den Haan, E.J., Grognet, M. 2014. A large direct simple shear device for the testing of peat at low stresses, Géotechnique letters, 4(4), 283-288. https://doi.org/10.1680/geolett.14.00033.

Dyvik, R., Berre, T., Lacasse, S., Raadim, B. 1987. Comparison of truly undrained and constant volume direct simple shear tests. Géotechnique, 37 (1), 3–10. https://doi.org/10.1680/geot.1987.37.1.3.

Greeuw, G., Essen, H. M., van, Van Duinen, T. A. 2016. Protocol laboratoriumproeven voor grondonderzoek aan waterkeringen. Deltares report 1230090-0190GEO-0002, The Netherlands.

Grimstad, G., Andresen, L., Jostad, H. P. 2012. Ngi-adp: Anisotropic shear strength model for clay. International journal for numerical and analytical methods in geomechanics, 36(4), 483–497. https://doi.org/10.1002/nag.1016.

Hanzawa, H., Nutt, N., Lunne, T., Tang, Y. X., Long, M. 2007. A comparative study between the NGI direct simple shear apparatus and the Mikasa direct shear apparatus. Soils and foundations, 47(1), 47-58. https://doi.org/10.3208/sandf.47.47.

Le Meil, G., Hendry, M., Martin, D. 2016. Direct simple shear (dss) testing of a very stiff glaciolacustrine clay. GeoVancouver 2016.

Leroueil S., Magnan J.P., Tavenas F. 1990. Embankments on soft soil, Translated by D.M. Wood, Ellis Horwood, New York.

ISO. 2018. ISO 17892-10:2018 geotechnical investigation and testing – laboratory testing of soil – part 10: Direct shear test.

Proceedings of the XVIII ECSMGE 2024
GEOTECHNICAL ENGINEERING CHALLENGES
TO MEET CURRENT AND EMERGING NEEDS OF SOCIETY
© 2024 the Authors
ISBN 978-1-032-54816-6
DOI 10.1201/9781003431749-679
Open Access: www.taylorfrancis.com, CC BY-NC-ND 4.0 license

ECSMGE 24
XVIII EUROPEAN CONFERENCE ON SOIL MECHANICS AND GEOTECHNICAL ENGINEERING

Numerical investigation on induced liquefaction during monopile installation by vibratory driving in a 1G scale test

Etude numérique de la liquéfaction induite lors de l'installation d'un monopile par battage vibratoire dans un essai à l'échelle 1G

T. Wehbe*
KU Leuven, Department of Civil Engineering, Leuven, Belgium
UCLouvain, Department of Civil Engineering, Louvain-la-neuve, Belgium

G. Anoyatis
KU Leuven, Department of Civil Engineering, Bruges, Belgium

H. Rattez
UCLouvain, Department of Civil Engineering, Louvain-la-neuve, Belgium

S. François
KU Leuven, Department of Civil Engineering, Leuven, Belgium

**tamara.wehbe@kuleuven.be*

ABSTRACT: The successful deployment of Offshore Wind Turbines (OWTs) requires fast, low- cost, reliable and environmentally friendly foundation installation methods. Vibratory driving, which is an attractive alternative to impact driving, has recently showed great potential in real-world applications. However, the knowledge about its effects on soil properties, and thus on the response of OWTs during the installation of monopiles is still limited. This study focuses on investigating the soil liquefaction which occurs in the vicinity of the foundation during vibratory monopile driving, in a 1G scale test. The combined approach of a vibratory driven pile in the laboratory, by introducing pertinent scaling laws, and the use of a numerical model to simulate the scale model in the laboratory is adopted. The findings from the numerical model provide insight into liquefaction initiation and progression and highlight the potential and limitations of linear models.

RÉSUMÉ: Le déploiement réussi d'éoliennes offshore (OWT) nécessite des méthodes d'installation de fondations rapides, peu coûteuses, fiables et respectueuses de l'environnement. La conduite vibratoire, qui constitue une alternative intéressante à la conduite par impact, a récemment démontré un grand potentiel dans les applications réelles. Cependant, les connaissances sur ses effets sur les propriétés des sols, et donc sur la réponse des OWT lors de la pose des monopieux, restent limitées. Cette étude se concentre sur l'étude de la liquéfaction du sol qui se produit à proximité de la fondation lors du battage vibratoire d'un monopieu, dans le cadre d'un essai à l'échelle 1G. L'approche combinée d'un pieu battu vibratoire en laboratoire, en introduisant des lois d'échelle pertinentes, et l'utilisation d'un modèle numérique pour simuler le modèle réduit en laboratoire est adoptée. Les résultats du modèle numérique donnent un aperçu de l'initiation et de la progression de la liquéfaction et mettent en évidence le potentiel et les limites des modèles linéaires.

Keywords: Monopile foundation; soil liquefaction; vibratory driving.

1 INTRODUCTION

Offshore wind power is a key component in the transition towards a more sustainable energy future. Despite the effectiveness of the predominantly used impact hammering for monopile installation, it poses challenges like noise pollution and concerns over pile durability, which makes vibratory driving an interesting alternative. Vibratory driving uses a high-frequency vibrator that transmits vertical vibrations to the monopile. These vibrations can increase the pore pressures in the vicinity of the driven foundation, resulting in reduction in the inter-particle soil friction, and thus, a decrease in effective stresses, which can lead to liquefaction. While vibratory driving offers a fast, environmentally friendly alternative, there is insufficient knowledge regarding its effects on the evolution of the mechanical properties of the soil, which control the (long-term) response of the OWT systems. In this regard, there has been an increasing interest in studying the development of liquefaction

during the installation process (Chrisopoulos et al. 2019; Esfeh and Kaynia 2019). Most efforts use non-linear models, while the application of simpler linear model is limited (Zhang et al. 2012).

This study is structured to present first a scaled 1g test in the laboratory followed by the linear numerical model used to calculate the force imposed on the pile and hence the soil-pile response to the applied force. Then, the model's ability to simulate pore water pressure development corresponding to liquefaction is assessed. Finally, conclusions from the study are presented.

2 PHYSICAL MODELING

The laboratory setup employed is based on the system initially developed by Holeyman et al. (Holeyman 2017; Jafari 2020) and is modified to meet our research needs. The current set up consists of a drop weight (ram) which is attached to a rope and a pulley system, and an anvil. The pile is kept in position using a centring rod and lateral supports. The pile is a hollow steel cylinder of external diameter D = 6 cm, length L = 50 cm and wall thickness t = 6 mm. The pile is driven in a saturated homogeneous sand of unit weight γsat =1920 kg/m^3, and relative density Dr = 68% that is representative of the densities of the soils met in the North Sea. The sand is placed in a steel container of inner diameter D_{box} = 110 cm, inner height H_{box} = 125 cm and thickness t_{box} = 2 mm. The relative density of sand is controlled using a sand pluviation system which allowed relatively homogeneous sand samples to be generated. The acceleration and hence the force imposed on the pile is measured using a 10000g accelerometer. Scaling laws required for down-scaling the applied force by a vibrohammer are adopted as explained byMazutti et al (Hein Mazutti et al. 2022) which designed a mini-vibro hammer for centrifuge testing. However, since we are considering a 1g test,the forces are scaled by a factor of 1/N^2.

3 VIBRATORY DRIVING MODEL

Herein a sub-structure approach is adopted: (i) the pile-soil system (pile and sandbox) is modeled using an axisymmetric finite element (FE) model to provide the pile head stiffness; and (ii) the calculated pile head stiffness is implemented in the Hybervib analytical model (Holeyman and Whenham 2017) to obtain the dynamic force imposed by the vibratory hammer. The force is then applied on the pile head using the FE model to conduct the drivability analysis. Within the framework of the analytical model, the harmonic force exerted by a vibro-hammer F_r working at frequency ω is defined as the mass of the eccentric masses *me*, multiplied by their corresponding acceleration.

$$F_r = me\omega^2 \sin(\omega t) \quad (1)$$

However, this model is extended to account for the displacement of the vibratory block m_b that constantly moves during the driving process. This is achieved by defining the total displacement of the system u_m as the relative displacement of the rotating masses u_r and the displacement of the block u_b:

$$u = u_r + u_b = e \sin \omega t + u_b \quad (2)$$

The different elements of the model are shown in Figure 1 in which the rigid pile is represented by its dynamic stiffness k^*.

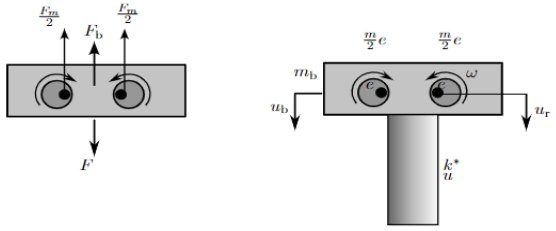

Figure 1. Schematic representation of the different elements of the vibratory driving model.

Hence, the total force exerted by a vibrohammer F is the summation of the force F_r and the force by the block F_b, which is defined as the product of the mass m_b and its acceleration $\ddot{u}_b$.

$$F = F_r + F_b \quad (3)$$

And in the frequency domain is,

$$k^*\hat{u} = me\omega^2 + m_b\omega^2 \quad (4)$$

where $\hat{u}$ is the pile head displacement at in the frequency domain, which is function of the dynamic stiffness of the rigid pile. Hence, this is computed initially and then followed by solving the system of equations of motion of the rigid system to compute the displacement.

The numerical implementation is done in MATLAB using the toolbox Stabil (François et al. 2021). The pile and the soil, which reflect on the setup, have been discretized using 2-noded line elements and 4-noded quadrilateral elements, respectively. The mesh size has been determined based on a 10-elements-per-wavelength rule.

Figure 2 shows the wave propagation in the sand box for a selected amplitude of the applied force at a

frequency equal to 1000 Hz which is representative of real scale driving at 25 Hz, using the proposed FE model. As shown in the figure, Rayleigh waves at the surface lose energy and attenuate with distance. Surface waves (C_s = 140 m/s) along the depth of the pile continue to propagate horizontally with a wavelength big enough to be fully captured in the system. P-waves, which travel at a faster speed (C_p = 280 m/s), are seen as a standing wave in the pile and propagate in radial direction below the pile. In order to mitigate reflections at the edge of the box, a 2 cm thick damping layer from rubber material is proposed whose effect is shown in figure 2.

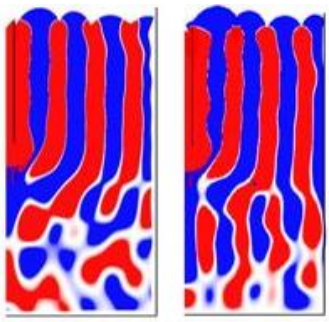

Figure 2. Animated representation of the wave propagation in the axisymmetric sand box model with a damping layer (left) and without a damping layer (right) at 1000 Hz.

4 LIQUEFACTION POTENTIAL

To evaluate the potential for liquefaction, the scheme described in (Seed 1971 and Towhata et al. 2008) is adopted. The strains within the soil are determined from the nodal displacements, leveraging the use of finely discretised transfinite mesh elements. The stress-strain relationship of the soil adheres to Hooke's law allowing us to employ a material stiffness matrix **D** that relates stresses **σ** to strains **ε** in the axisymmetric finite element model using the soil's modulus of elasticity E, and Poisson's ratio, ν:

$$\begin{Bmatrix} \hat{\sigma}_{rr} \\ \hat{\sigma}_{\theta\theta} \\ \hat{\sigma}_{zz} \\ \hat{\tau}_{rz} \end{Bmatrix} = \begin{bmatrix} 1-\nu & \nu & 0 & 0 \\ \nu & 1-\nu & 0 & 0 \\ 0 & 0 & 1-\nu & 0 \\ 0 & 0 & 0 & 0.5-\nu \end{bmatrix} \frac{E}{(1+\nu)(1-2\nu)} \begin{Bmatrix} \epsilon_{rr} \\ \hat{\epsilon}_{\theta\theta} \\ \hat{\epsilon}_{zz} \\ \hat{\epsilon}_{rz} \end{Bmatrix} \quad (5)$$

The stresses (all in kPa) obtained in the radial $\hat{\sigma}_{rr}$, circumferential $\hat{\sigma}_{\theta\theta}$ and the longitudinal directions $\hat{\sigma}_{zz}$ are used to calculate the maximum cyclic deviatoric stress exerted on the soil element, $\hat{q}$ where:

$$\hat{q} = \tau_{cyc} = \sqrt{3\hat{J}_2} \quad (6)$$

and

$$\hat{J}_2 = \frac{1}{6}[(\sigma_{rr} - \sigma_{\theta\theta})^2 + (\sigma_{\theta\theta} - \sigma_{zz})^2 + (\sigma_{zz} - \sigma_{rr})^2 + \sigma_{rz}^2] \quad (7)$$

This shear stress is then utilized to compute the Cyclic Stress Ratio (CSR), which is defined as the ratio between the shear stress and the effective vertical stress σ'$_v$:

$$CSR = \frac{\tau_{cyc}}{\sigma_v'} \quad (8)$$

Subsequently, the relative excess pore pressure r_u, which is equal to the ratio between excess pore pressure Δu and initial effective vertical stress σ_v' is employed as described by (Seed and Rahman 1978, Meijers 2007).

$$r_u = \frac{\Delta u}{\sigma_v'} = \frac{2}{\pi} \arcsin\left(\frac{N}{N_{liq}}\right)^{\frac{1}{2\theta}} \quad (9)$$

In which N is the applied number of cycles, equivalent to the frequency, N_{liq} is the required number of cycles to cause liquefaction and the empiral parameter θ = 0.7 is chosen (Seed and Rahman 1978, Meijers 2007). N_{liq} is calculated from the relationship proposed by (Rahman and Jaber 1986).

$$CSR = 0.44aN_{liq}^{-b} \quad (10)$$

in which b = 0.2 and a=0.44.

Figure 3 illustrates the results obtained employing an in terms of deviatoric stress q, critical stress ratio (CSR), and relative excess pore pressure, the latter being essential for computing the excess pore water pressure induced during the pile driving process. An eccentric moment of $1.2\text{x}10^{-3}$ kg.m is employed which demonstrates both the impact and the necessity for a minimal mass. These findings show stress concentration beneath the pile while driving in addition to stress generation due to surface waves. The results also underscore the potential for soil around the pile, rather than within it, to experience liquefaction.

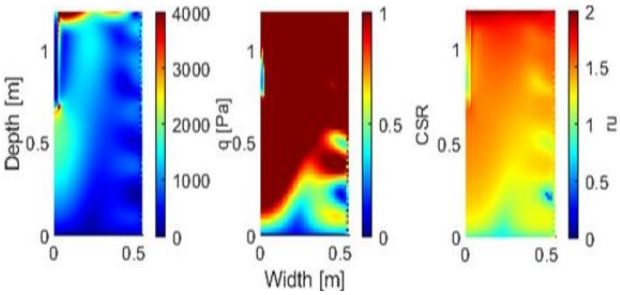

Figure 3. Variation of cyclic deviatoric stress q (left), the critical stress ratio CSR (middle) and the relative excess pore pressure r_u (right) along the sand box depth.

5 CONCLUSIONS

This paper presents an attempt to study induced liquefaction during vibratory pile driving with a focus on offshore applications. For this purpose, a a linear numerical model reflecting on an existing laboratory-scale experimental setup is employed. This is achieved by adopting scaling laws to obtain a vibratory hammer force. The results provide an overview of the wave propagation in the sand box, highlighting the need for adding a damping layer. Results in terms of cyclic shear stress development accounting for liquefaction phenomenon during driving, indicate the need to further investigate such mechanism using an equivalent linear approach.

ACKNOWLEDGEMENTS

Results presented in this paper were obtained within the frame of the project 3E220488 “Novel Installation and Extraction methods for Foundations. of Offshore Wind Turbines” funded by the Global PhD partnerships (between KU Leuven and UCLouvain). The financial support is gratefully acknowledged.

REFERENCES

Chrisopoulos, S. and Vogelsang, J. (2019). "A finite element benchmark study based on experimental modelling of vibratory pile driving in saturated sand." Soil Dynamics and Earthquake Engineering, 122, 248-260, https://doi.org/10.1016/j.soildyn.2019.01.001.

Esfeh, P. K. and Kaynia, A. M. (2019). "Numerical modeling of liquefaction and its impact on anchor piles for floating offshore structures." Soil Dynamics and Earthquake Engineering, 127, 105839. https://doi.org/10.1016/j.soildyn.2019.105839.

François, S., Schevenels, M., Dooms, D., Jansen, M., Wambacq, J., Lombaert, G., Degrande, G., and De Roeck, G. "Stabil: An educational matlab toolbox for static and dynamic structural analysis." Computer Applications in Engineering Education, 29(5), 1372-1389. https://doi.org/10.1002/cae.22391.

Hein Mazutti, J., Bienen, B., Bransby, F., Randolph, M., & Wager, G. (2022). Investigating vibro-driven monopile installation into sand in a geotechnical centrifuge. In 11th International Conference on Stress Wave Theory and Design and Testing Methods for Deep Foundations. https://doi.org/10.5281/zenodo.7151565.

Holeyman, A. (2017). "Battage de pieux métalliques dans la roche." Revue Française de Géotechnique, 1-21. https://doi.org/10.1051/geotech/2017014.

Holeyman, A. and Whenham, V. (2017). "Critical review of the hypervib1 model to assess pile vibro-drivability." Geotechnical and Geological Engineering, 35. https://doi.org/10.1007/s10706-017-0218-8.

Jafari, M. (2020). "Numerical and experimental investigation of monopile driving resistance in carbonate rocks." Ph.D. thesis, Universitie Catholic de Louvain.

Kramer, S.L. (1996) Geotechnical Earthquake Engineering. Prentice-Hall, New Jersey.

Meijers, P., "Settlement during Vibratory Sheet Piling." PhD Thesis, TU Delft, 2007.

Rahman, M. S.; Jaber, W. Y., "A Simplified Drained Analysis for Wave-Induced Liquefaction in Ocean Floor Sands" (1986). Soils and Foundations, 26(3), 57-68. https://doi.org/10.3208/sandf1972.26.3_57.

Seed, H. B. & Rahman, M.S. (1978) Wave - induced pore pressure in relation to ocean floor stability of cohesionless soils, Marine Geotechnology, 123-150. https://doi.org/10.1080/10641197809379798.

Towhata, I & Wu, W. & Borja, R.I. (2008). Geotechnical Earthquake Engineering. 1. 10.1007/978-3-540-35783-4. https://doi.org/10.1007/978-3-540-35783-4.

Zhang, J., Zhang, L., and Huang, H. (2012). "Evaluation of generalized linear models for soil liquefaction probability prediction." Environmental Earth Sciences, 68. https://doi.org/10.1007/s12665-012-1880-z.

Proceedings of the XVIII ECSMGE 2024
GEOTECHNICAL ENGINEERING CHALLENGES
TO MEET CURRENT AND EMERGING NEEDS OF SOCIETY
© 2024 the Authors
ISBN 978-1-032-54816-6
DOI 10.1201/9781003431749-680
Open Access: www.taylorfrancis.com, CC BY-NC-ND 4.0 license

ECSMGE 24
XVIII EUROPEAN CONFERENCE ON SOIL MECHANICS AND GEOTECHNICAL ENGINEERING

Seabed and sub-seabed boulders as an engineering hazard in the marine environment; methods of detection and quantification

Les risques techniques liés aux blocs rocheux de surface et enfouis dans l'environnement marin; une stratégie d'atténuation des risques pour les câbles sous-marins

M.J. Wetton*, D.P. Vaughan, N. Dyer
Cathie Associates, Newcastle upon Tyne, United Kingdom

**matthew.wetton@cathiegroup.com*

Abstract: Seabed and sub-seabed boulders are a significant design constraint, and financial risk to the design and installation of foundations for offshore Wind Turbine Generators, the trenching and installation of export and intra-array cables, and project design. Many windfarms under development in northern Europe and USA are built on geological formations which are either a direct product of, or subsequently influenced by, glaciation. These formations often contain high numbers of seabed and sub-seabed boulders; for example, the Marr Bank Formation of the North Sea. A primary objective for pre-construction geophysical surveys is to provide data to support a boulder mitigation strategy. This is required prior to installation to allow for an optimised construction methodology to be selected. The detection and quantification of boulders is the first step in a proposed five-step mitigation strategy. In this paper, we present an overview of the geophysical methods utilised for the detection of seabed and sub-seabed boulders, including the key considerations for the boulder detection requirements and subsequent survey specifications to meet these requirements. We present the technical and practical limitations to detection, as well as state-of-the-art solutions. The detection of boulders is followed by a detailed quantification of boulders, in order to understand the risks posed to engineering activities. The overall objective is to reduce engineering risk by better informing the location, design, and installation associated with emplacing infrastructure at and below the seabed.

Résumé: Les blocs rocheux présents sur le fond marin ou enfouis sous sa surface constituent une contrainte de conception importante et un risque financier non négligeable pour la conception et l'installation des fondations des générateurs d'éoliennes en mer, l'ensouillage et l'installation des câbles d'exportation et des câbles inter-éoliennes, ainsi que la conception du projet. De nombreux parcs éoliens en développement en Europe du Nord et aux États-Unis sont construits sur des formations géologiques qui sont soit le produit direct de la glaciation, soit qui ont été influencées ultérieurement par celle-ci. Ces formations contiennent souvent un grand nombre de blocs rocheux en surface et sous la surface; par exemple, la formation Marr Bank de la mer du Nord. L'un des principaux objectifs des études géophysiques préalables à la construction est de fournir des données permettant d'étayer une stratégie d'atténuation des risques liés aux blocs rocheux. Il est nécessaire de disposer de ces données avant l'installation, afin de permettre la sélection d'une méthodologie de construction optimale. La détection et la quantification des blocs rocheux constituent la première des cinq étapes d'une stratégie d'atténuation des risques. Dans cet article, nous présentons une vue d'ensemble des méthodes géophysiques utilisées pour la détection des blocs rocheux de surface et enfouis, incluant les considérations clés pour les exigences de détection des blocs rocheux et les spécifications des levés associés pour répondre à ces exigences. Nous présentons les limites techniques et pratiques de la détection, ainsi que les solutions les plus récentes. La détection des blocs rocheux est suivie d'une quantification détaillée de ceux-ci, afin de comprendre les risques posés aux activités d'ingénierie. L'objectif global consiste à réduire les risques techniques en informant mieux sur leur emplacement et fournir des données pour la conception et l'installation associés à la mise en place d'infrastructures sur et sous le fond marin.

Keywords: Geophysics; geophysical survey; boulders; hazard mitigation; risk analysis.

1 INTRODUCTION

Licenses for new offshore windfarm developments are being awarded with increasing frequency, with a trend towards larger lease areas as the size of turbines increases to meet power generation demand. Across some of the most active offshore wind regions (North Sea, Baltic Sea, and northeast USA), the geology at these sites is shaped or influenced by glaciation. Glacial sediments, typically till, consisting of a heterogenous mixture of clay, sand, gravel, and boulders varying widely in size and shape (McMillan & Powell, 1999) is often a source of seabed and sub-seabed boulders, in these environments.

The presence of boulders can have significant impact on the engineering works associated with development of a windfarm. They represent a significant constraint to a wide range of activities including: the installation of foundations; cable routing; trenching; design operations; installation operations for export and inter-array cables; and jack up operations. Failure to sufficiently identify and quantify the magnitude of the constraint can lead to considerable financial risk to a project. This may lead to problems where developers exceed project budgets, with increased installation timescales, encounter unexpected delays, and have to mitigate for wear or damage to installation equipment.

Where boulders are potentially present, a clear strategy is required to successfully manage the potential constraint using a risk-based approach. A five-step mitigation strategy is presented, the objective of which is to reduce the risk boulders may present to a practical and commercially viable level (Figure 1). This strategy can be employed at any stage of the project life cycle prior to construction, from desktop study to final engineering corridor planning. However, the greatest benefits result from implementation at the earliest stages of planning.

This paper focuses on the first stage of the strategy: the identification of the hazard and quantification of the risk, to allow for further mitigation to take place. The detection of boulders followed by a detailed quantification, allows for an improved understanding of the risks to engineering activities. Resulting in improved design, and installation of engineering infrastructure at and below the seabed.

2 DETECTION

The detection of boulders on and below the seabed is generally achieved through acoustic geophysical survey techniques. Geophysical surveys are often performed to inform a range of development activities concurrently, for example, cable thermal design, seabed mobility, UXO risk mitigation, and other constraints like anthropogenic material and infrastructure. Knowledge of the requirements for each constraint may allow for a single integrated survey to capture all the required data, with minimal risk of unanticipated re-survey requirements.

Geophysical techniques for this purpose are used throughout the world as a matter of routine. However, the regulations governing data acquisition, processing, and interpretation, vary significantly. In the USA and Germany, regulatory bodies publish exacting minimum standards of survey data accuracy and detectability (BOEM, 2017; BSH, 2014), whereas in other territories, less specific guidelines are available (BSI, 2015). Some of these guidelines are derived from oil and gas pipeline and rig site survey, standard industry practice, updated to meet the requirements of the renewables industry. Others originate from bodies such as the Carbon Trust (Carbon Trust, 2020) and offer a recommended practice when planning a marine geophysical survey.

Beyond aligning with regulatory requirements, successful detection, and quantification of boulder hazards at a given site first requires understanding the minimum object detection size and the sequence of site-characterisation operations (e.g., route selection and corridor alignment). Smaller objects are more challenging to detect so require a more highly specified survey to enable identification. The minimum object detection size would ideally be established at an early stage of planning the survey, as it defines a key objective of the data collection. Collaboration with engineers and designers to inform strategy and specification requirements is key to ensuring surveys are planned to meet the requirements for designing a mitigation strategy, (Burley et al., 2023; Carbon Trust, 2020).

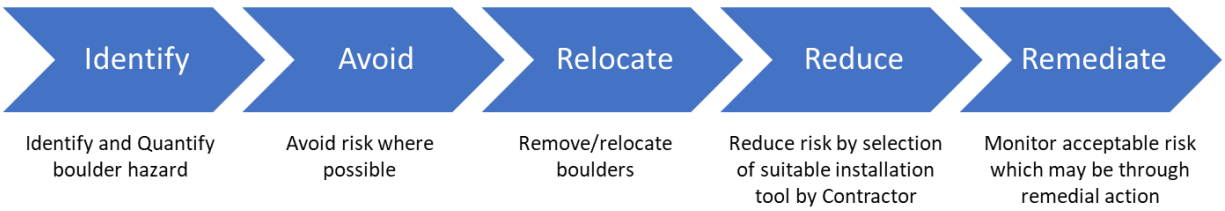

Figure 1. A five-step mitigation strategy, beginning with the identification of boulders followed by each mitigation option.

2.1 Seabed boulder detection techniques

For detection of seabed boulders, a combination of sidescan sonar (SSS), and multibeam echosounder (MBES) data, would typically be acquired, with new methods such as synthetic aperture sonar also becoming more common. A SSS system is a deep-towed sensor, flying a few meters above the seabed, scanning the seabed at a low angle of incidence. This setup allows a minimised distance between sensor and target, resulting in reduced travel time of the acoustic energy and typically giving a high resolution. The low angle of incidence produces the 'shadow', allowing for the measurement of object height. However, the accuracy is limited by underwater acoustic positioning which typically has an accuracy of +/- 2 m. The sensor operates a port and starboard channel (both sides of the sensor), but cannot look vertically down, resulting in a stripe of null coverage known as the "nadir" along the track of each survey line. Surveys specifications usually require a 200% coverage of SSS data. The overlapping adjacent swathes of data provides coverage of the nadir and can create multiple ensonifications of seabed objects from different directions, improving detection potential. The need to achieve this overlap contributes to the line spacing requirements of the survey and the swathe range of the SSS.

The MBES system is typically a hull mounted sensor, which then benefits from accurate Global Navigation Satellite System (GNSS) positioning and delivers a quantitative depth of objects, where SSS does not. MBES images a swath centred on the survey track. MBES systems can be mounted on subsea remotely operated vehicles (ROVs) and autonomous underwater vehicle (AUVs), that can overcome these shortcomings and provide solutions for challenging deep-water environments.

The key factor limiting object detectability for both systems, is the number of acoustic signal beams which might be expected to hit or illuminate a target of a given size. The higher the density of 'hits', the greater the potential to image smaller targets.

To reliably detect seabed boulders, a certain number of hits is required. For MBES a minimum of 9 hits is recommend for resolving an object from its surroundings (IHO, 2011) Objects can theoretically be interpreted from a one pixel footprint hit, however, to increase interpretation certainty, a 2-3 pixel footprint is preferred (IHO, 2011). If a survey is required to detect small objects, there will be an upper limit on the detection range (swathe) of each sensor. By definition wider swathes cover a larger footprint, but suffer from lower ping rates, and increased signal attenuation at higher frequencies, limiting resolution.

Once the engineering requirement is known, the survey specification to support detection of the minimum object size can be calculated. An indicative set of smallest resolvable sizes are provided for a range of typical equipment settings for SSS (Table 1), and MBES data (Table 2). These values are indicative and must be confirmed for survey planning, as specific equipment and survey conditions will cause variability in performance. Note that these values are specified to achieve a one-pixel footprint only.

Table 1. The maximum SSS range and suggested survey specification to detect various sizes of item.

Smallest resolvable item [m]	Maximum Range [m]	Line spacing (200% coverage) [m]	Suggested Frequency [kHz]
0.30	45	30	540
0.40	60	45	540
0.50	85	70	410
0.60	100	80	410

Table 2. The maximum MBES range and suggested survey specification to detect various sizes of item, for a 400 kHz sensor and water depth of 50 m.

Smallest resolvable item [m]	Required Ping density [/0.5 m^2]	Maximum Range [m]	Line spacing [m]
0.30	53	30	25
0.40	31	45	40
0.50	20	60	55
0.60	15.5	70	65

In this case, note that SSS data is higher resolution for any given range. This is fairly representative, although may not always be the case if a particularly high specification MBES system is deployed.

2.2 Sub-seabed boulder detection techniques

The detection of sub-seabed boulders is more challenging than seabed boulders. Industry standard practice is to utilise 2D sub bottom profiler (SBP) or 2D ultra-high resolution seismic reflection (2D UHRS) data. As with seabed methods, an appropriate survey plan and equipment specification is critical to ensure the detection of the required minimum size object.

SBP data is typified by high frequency content, which provides high vertical resolutions at the expense of a limited penetration of approximately 5 – 10 m below seabed depending on geological conditions. SBP systems often have a short firing interval (5Hz), providing high lateral resolution. SBP data is normally acquired for structural mapping of very shallow geological units but can be used to identify boulders in the sub-seabed through the interpretation of diffraction hyperbolae of the buried boulders.

2D UHRS data generates a more powerful signal at lower frequencies. Achieving deeper penetration of 50 – 100 m, depending on geological conditions, but with reduced vertical resolution. 2D UHRS data is useful for structural mapping of geological units, which can present a valuable input into boulder risk analysis, tracing the depth and extent of boulder-bearing units such as glacial till. A indicative set of parameters with the same limitations as Table 1 and Table 2 is provided in Table 3.

2D sub-seabed seismic techniques are limited by profiling in a narrow volume vertically below the sensor track, cannot reliably return precise locations of boulders below a survey-defined size limit, and boulder sizes are not precisely determined. However, 2D methods are useful to discover boulder-bearing strata, particularly in conjunction with geological interpretive ground models. As such, these techniques can only provide estimations for the spatial distribution of geological units and boulder density.

Table 3. Table outlining how expected vertical resolution and penetration of seismic data vary with frequency.

Data Type	Frequency (Hz)	Estimated Penetration* (m)	Approx. Vertical Resolution (m)*
SBP	5,000	10	0.10
	10,000	5	0.05
UHRS (Sparker)	500	100	0.40
	1000	50	0.20

* Based on typical glacial geology, with an assumed seismic velocity 1600 m/s

To reduce uncertainty, and increase the boulder detection potential, 3D seismic data may offer an alternative approach. The use of 3D data for offshore wind is currently limited but increasing. As demand to further understand the sub-seabed grows, new technologies and methods applicable to boulder detection are becoming available. 3D is available at all scales including: SBP-like, Sparker source UHRS, and airgun site survey and exploration data. In the very near seabed methods such as 3D high resolution imaging may provide an alternative to 2D profile data for the detection of boulders. Although costs for 3D seismic are higher than 2D, the increased information for sub-seabed boulder positioning, burial depth, and size estimates provides advantages not available with 2D methods.

3 QUANTIFICATION

Quantification begins, after the completion of acquisition and processing, with a full interpretation of all the available datasets. The interpretation should identify and measure the dimensions of each individual contact that poses a constraint to the engineering requirements. For seabed boulders this task is usually carried out on high frequency SSS data, utilising MBES data to verify positioning. The result is a contact list, with interpreted objects given a unique ID, X and Y coordinate, and dimensions (length, width, and height). For sub-seabed boulders, this typically requires interpretive mapping of the extent of boulder bearing units, ground modelling, and the identification of diffraction hyperbolae. Here emerging technologies such as automated or machine learning interpretation are becoming increasingly available.

Quantification of boulders does not always require interpretation of each ensonified object. Interpretation specifications should be proportional to the risk, engineering requirements, and mitigation strategy. For example, in areas of high-density boulders (boulder fields), knowledge of the exact dimensions and position of each boulder is not required, should an appropriate mitigation strategy be available (Burley et al., 2023).

The presence of boulders can then be assigned a risk rating across the site. Risk is typically calculated by assessing the impact, the consequence that encountering the hazard would have, and the likelihood of encountering the hazard. Hazards may be split into subcategories. In this example the risk level associated with boulders of different sizes is presented (Table 4). As the risk level impacts individual engineering methods differently, a method specific strategy is then required to mitigate the risk (Burley et al., 2023).

Table 4. Example of a typical risk register.

Boulder size [m]	Impact	Likelihood	Risk
0.2 – 0.5	Very Low	High	Low
0.5 – 1.5	Low	High	Medium
1.5 – 2.0	High	Low	Medium
> 2.0	Very High	Low	High

This simplistic risk register can be expanded further by considering size (dimensions) alongside density (distribution) and location (seabed or buried).

These three attributes are relevant to most engineering activities associated with wind farm development, and the constraints on each activity. By considering the contribution of each attribute to the risk register allows for a more thorough analysis and more specific mitigation.

As the impact of the boulder attributes are different for each engineering activity, the quantification of boulder risk should be tailored to the specific task.

Knowledge of the constraints for each task can then directly link to the risk value. Using an example of cable installation constraints (Table 5), the risk register can be expanded and tailored to the given engineering task (Table 6). This quantified risk can then be assessed with assigned risk values within the five-step mitigation strategy (Figure 1) for the most appropriate action (Burley et al., 2023).

Table 5. Relating boulder hazard to cable design constraint.

Individual Boulders	Boulder Fields	Constraint Level	
Size [m]	Density		
< 0.5	Low	Soft Constraint	Low
0.5 - 1.5	Medium		Medium
1.5 - 2	High		High
> 2	-	Hard Constraint	

Table 6. Example of an expanded risk register, for the installation of subsea cables.

Boulder Attribute		Impact	Likelihood	Risk
Size [m]	< 0.5	Low	High	Low
	0.5 – 1.5	Medium	High	High
	1.5 – 2.0	High	Low	Medium
	> 2.0	V. High	Low	High
Density	Low	Low	Medium	Low
	Medium	Medium	High	High
	High	High	Medium	High
Location	Seabed	High	Medium	High
	Sub-seabed	Medium	Low	Low

This type of analysis is well suited to risk-mapping. As the boulder attributes are spatially variable, so too is their risk. Risk-mapping can delineate and present the lateral variability of each attribute, allowing the complexity of the risk to be properly captured, and representing the geological conditions across the site. This method is particularly useful to delineate areas of boulder field, which are commonly encountered in previously glaciated terrains.

Illustrative maps presenting the risks of boulder size, density, and location, for the installation of subsea cables across a site, are presented as a series of figures below. Boulder size risk and its constraint on installation tools is presented in Figure 2 as a series of colour coded exclusion zones. Boulder density risk is presented in Figure 3, and boulder location risk as a function of the depth below seabed of interpreted boulder bearing units is presented in Figure 4.

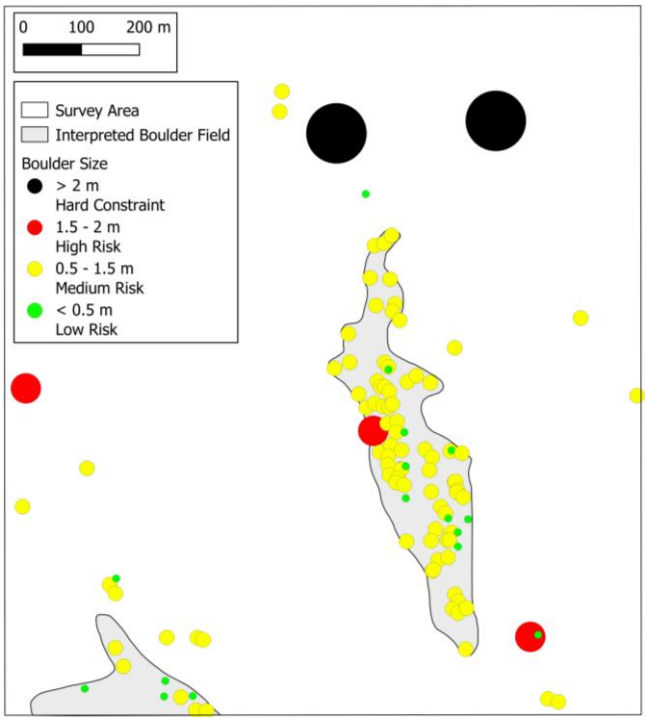

Figure 2. Lateral distribution of boulders and size dependant risk.

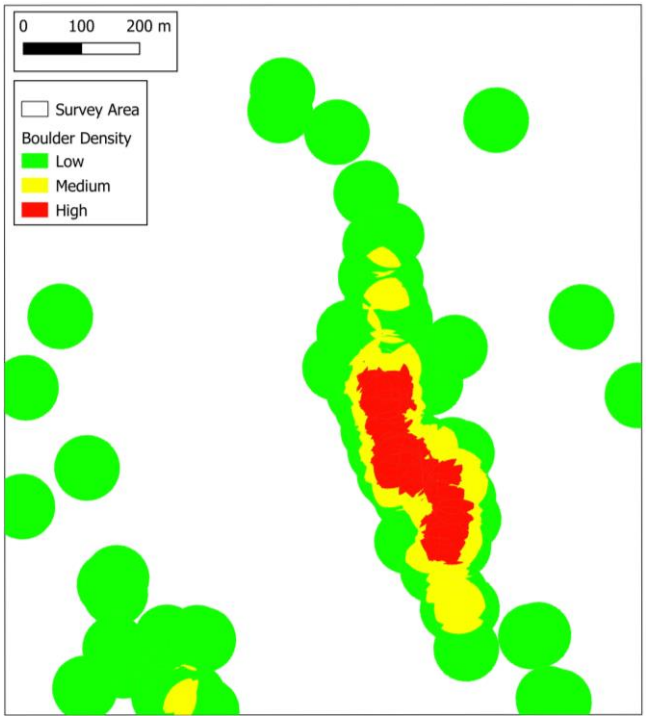

Figure 3. Density of interpreted boulders for a specified area.

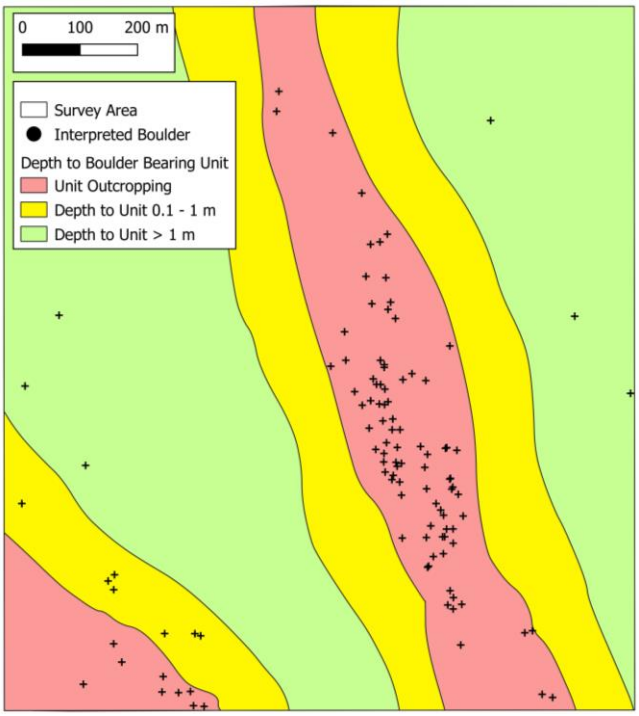

Figure 4. Risk of boulders as a function of location, through mapped boulder bearing geological units.

4 CONCLUSIONS AND OPPORTUNITIES

Boulder risk mitigation is not a new process, however this paper seeks to describe a systematic and best practice approach to the first stage of the risk mitigation process, by highlighting areas of potential optimisation and improvement.

By beginning the risk analysis process early in a development's schedule, survey campaigns can be designed and specified to identify the hazards that constrain engineering activities. This risk-based approach then defines the success of a campaign as achieving the level of understanding needed to mitigate against the risks. Engagement in risk-based thinking at an early stage may also provide additional efficiencies throughout the development cycle. Data acquired at an early stage of a project can be specified to meet the requirements of risk considerations that may not become relevant until later stages of a project. Conversely, this approach can also ensure surveys are not over specified, preventing time and resource from being spent on acquiring information that will never be used.

By increasing our understanding of the risks from boulders and how they can vary across a site, the mitigation strategies proposed can be more effectively planned. Identification of high risk or hard constraint areas can reduce the risk to engineering activities and increase the efficiency of installation.

Emerging technologies such as automated boulder interpretation, and synthetic aperture sonar may be influential in facilitating this growth of understanding, but are not a substitute for careful planning, detailed quality assurance, and well understood survey requirements. Which can be packaged into a bespoke, precise survey, detection, and quantification workflow, which can ultimately save a client time, resources, and money over the lifetime of a development.

REFERENCES

BOEM, 2017. *Geophysical and Geotechnical Investigation Methodology Assessment for Siting Renewable Energy Facilities on the Atlantic OCS, Vols. 1-6.,* s.l.: Bureau of Ocean Energy Management.

BSH, 2014. *Minimum requirements for geotechnical surveys and investigations into offshore wind energy structures, offshore stations and power cables, Second Update.,* s.l.: Bundesamt fur Seeschifffahrt und Hydrographie.

BSI, 2015. *BS5930:2015, Code of practice for ground investigatons ,* s.l.: The British Standards Institution.

Burley, L. et al., 2023. Surface and sub-surface boulders as an engineering hazard in the marine environment; a risk mitigation strategy for subsea cables. *European Conference on Soil Mechanics and Geotechnical Engineering.*

Carbon Trust, 2020. *Guidance for Geophysical Surveying for UXO and Boulders Supporting Cable Installation,* s.l.: The Carbon Trust.

IHO, 2011. Seafloor Classification an Feature Detection. In: *Manual on Hydrography.* Monaco: International Hydrographic Bureau, pp. 199-252.

ISO, 2017. *Geotechncial investigation and test - Identification and classification of soil - Part 1: Identification and description (14688-1),* Geneva: International Organization for Standardization.

McMillan, A. A. & Powell, J. H., 1999. *The classification of artificial (man made) ground and natural superficial deposits.,* s.l.: British Geological Survey Research Report.

Proceedings of the XVIII ECSMGE 2024
GEOTECHNICAL ENGINEERING CHALLENGES
TO MEET CURRENT AND EMERGING NEEDS OF SOCIETY
© 2024 the Authors
ISBN 978-1-032-54816-6
DOI 10.1201/9781003431749-681
Open Access: www.taylorfrancis.com, CC BY-NC-ND 4.0 license

ECSMGE 24
XVIII EUROPEAN CONFERENCE ON SOIL MECHANICS AND GEOTECHNICAL ENGINEERING

The potential of energy micropiles as energy geostructures

Le potentiel des micropieux énergétiques comme geostructures énergétiques

M.F. Yozy Kepdib, J.A. Facciorusso, C. Madiai
University of Florence, Florence, Italy

R.M. Singh*
Norwegian University of Science and Technology, Trondheim, Norway

**rao.m.singh@ntnu.no*

ABSTRACT: The energy crisis presently faced in the world and particularly in Europe, is raising alarm for the transition from fossil fuels to sustainable and renewable energy resources. It is in this light that low enthalpy geothermal energy is increasingly getting attention, in the heating and cooling sectors. With diversified technologies of geothermal extraction, it is important to choose the right technology for every situation considering both the economic and technical aspects. In the context of structural rehabilitation of buildings, micropiles stand as the optimum choice for retrofitting and underpinning of existing foundations. This technology could also be advantageously extended in the sector of energy rehabilitation, as the thermal performance of micropiles suitably equipped to allow heat exchange between the ground and the building has proven promising for use in heating, ventilation, and air conditioning systems. Although very similar to energy piles, the behavior of energy micropiles is expected to be different mainly due to the difference in sizes and spacing. As such, a comprehensive understanding of the thermo-mechanical behavior of energy micropiles is important in view of their application. To date, however, little research has been conducted on the subject. The paper introduces energy micropiles, discusses their thermal performance and thermo-mechanical behaviour, and describes a real case of energy micropiles application.

RÉSUMÉ: La crise énergétique à laquelle le monde est actuellement confronté, et particulièrement l'Europe, sonne l'alarme quant à la transition des combustibles fossiles vers des ressources énergétiques durables et renouvelables. C'est dans cette optique que l'énergie géothermique à basse enthalpie retient de plus en plus l'attention, dans les secteurs du chauffage et du refroidissement. Avec des technologies diversifiées d'extraction géothermique, il est important de choisir la technologie adaptée à chaque situation, en tenant compte à la fois des aspects économiques et techniques. Dans le contexte de la réhabilitation structurelle des bâtiments, les micropieux constituent le choix optimal pour la rénovation et la reprise en sous-œuvre des fondations existantes. Cette technologie pourrait également être avantageusement étendue au secteur de la réhabilitation énergétique, car les performances thermiques des micropieux convenablement équipés pour permettre l'échange thermique entre le sol et le bâtiment se sont révélées prometteuses pour une utilisation dans les systèmes de chauffage, de ventilation et de climatisation. Bien que très similaire aux pieux énergétiques, le comportement des micropieux énergétiques devrait être différent principalement en raison de la différence de dimension et d'espacement. Alors, une compréhension complète du comportement thermomécanique des micropieux énergétiques est importante en vue de leur application. Mais à ce jour, peu de recherches ont été menées sur le sujet. Cet article présente les micropieux énergétiques, discute de leur performance thermique et de leur comportement thermomécanique, et décrit une étude de cas réel d'utilisation des micropieux énergétiques.

Keywords: Energy micropiles; rehabilitation of buildings; thermal performance.

1 INTRODUCTION

In response to the 2022 energy crisis in Europe, the European Commission announced the joint action plan REPowerEU, aiming to reduce Russian gas consumption in the EU by 2/3 by the end of 2022 and phase it out by 2027. One of its focuses is "clean energy transition" with the goal of increasing the EU's 2030 renewable energy target from 40% to 45%. This crisis has boosted interest of geothermal energy across Europe.

Wells were the only methods used to harness geothermal energy until energy geostructures were introduced in the 1980s. Energy geostructures interact with the soil combining the conventional structural role with the energy one. They include foundations (piles, slabs), retaining walls (diaphragm walls, sheet walls), tunnels. Energy foundations with a specific heat flux typical between 20W/m and 80W/m (Brandl, 2006), are widely used today (Loveridge et al., 2020). Successful implementation of these foundations has been recorded (Sani et al., 2019). Diaphragm walls,

typically used as retention systems, offer a long-term exchanged power per square meter of about 15-20W/m2 (Bourne-Webb et al., 2016; Di Donna et al., 2017). Tunnels provide a larger volume of ground and surface for heat exchange. The heat exchanged can be directly utilized by adjacent buildings and integrated into district heating and cooling systems (Barla and Di Donna, 2018). The specific heat exchange power obtained from energy tunnels can range from 10 – 20 W/m2 in the absence of groundwater flow and 50-60 W/m2 in the case of relevant groundwater flow (Barla and Insana, 2023).

Heat transfer between the ground and the structure occurs through plastic pipes within the geostructure, where a heat exchanger fluid, like water, water + glycol, or a saline solution, circulates. Energy geostructures are cost effective and eco-friendly, and require no new infrastructure compared to energy wells, with a comparable thermal performance. Among them, micropiles, commonly used for structural retrofitting and rehabilitation of buildings, could be an appropriate solution for heating and cooling existing buildings with minimal available space.

This paper introduces the concept of micropiles, followed by the energy micropiles. The thermal performance and the thermo-mechanical behaviour of energy micropiles are discussed. Finally, a real case study involving the utilization of energy micropiles is presented.

2 ENERGY MICROPILES

Micropiles are smaller – diameter (usually less than 30 cm), drilled and grouted non-displacement piles that are usually reinforced. Micropile installation involves drilling a hole, placing reinforcement, and grouting the hole. In addition to this conventional type, steel micropiles and self-drilling micropiles are available today. These smaller piles may be feasible under the following constraints (Sabatini et al., 2005):

- Limited access or location in remote areas.
- Need for a support system in close proximity to existing structures.
- Difficult ground and drilling conditions (such as karstic areas, uncontrolled fills, boulders, etc).
- Requirements for minimizing noise and vibration.

Micropiles can be used for both in-situ reinforcement and structural support. Extending their application to provide heating and cooling to buildings could be very useful in many cases.

2.1 Thermal performance of energy micropiles

Ronchi et al., (2018) carried out numerical simulations for a conventional grouted micropile in summer conditions. Results of the numerical study show that a thermal power of about 30W/m was obtained after a 6-month period. In wet sediments, up to 111W/m of thermal power was obtained from the self-drilling grouted TITAN 73/53 energy micropile (Ischebeck, 2015). These values are comparable to those of energy piles, signifying the promise of energy micropiles as a technology for heating, ventilation, and air-conditioning systems.

Pipe length, concrete thermal conductivity and pipe diameter are the most important parameters in maximising the thermal efficiency of energy micropiles (Cecinato and Salciarini, 2022). However, the small section of micropiles poses a challenge when considering the pipe arrangements commonly employed in larger piles such as the W, spiral, partly W and the double-U shape. In literature, two primary pipe configurations stand out for energy micropiles, the single-U and the coaxial. Due to the greater possibility of interference in small sizes micropiles with U-pipes, it is predicted that the coaxial pipe configuration should be the most suitable for energy micropiles. Moreover, with the large volume of water in the annular space of the coaxial pipe arrangement, the micropile can serve as a storage tank, as water has a high specific heat capacity. However, the intrusion of grout in the annular space could reduce the thermal potential of the micropiles in the long term and should therefore be investigated.

In addition, increasing the number of micropiles in a group will increase the overall heat exchange rate of the system, although it reduces the average heat exchange rate of individual micropiles (Kong et al., 2021). The spatial arrangement of energy micropiles within a group exhibits minimal or negligible influence on the average heat exchange rate of each micropile (Kong et al., 2021). However, closely spaced thermally activated micropiles should be avoided as thermal interference can result in a significant loss of function (Lupattelli et al., 2023) with time. When the fluid inlet velocity and/or the inlet temperature of the heat exchange fluid are increased, the pile temperature also increases (Kong et al., 2021). Consequently, meticulous design considerations are imperative to ensure the structural integrity of the energy micropile system remains uncompromised.

2.2 Review of the thermo-mechanical behavior of energy micropiles

Although the energy micropile system and the energy pile system are quite similar, their behavior cannot be assumed to be similar both mechanically and

thermally, as the former has negligible end bearing capacity and smaller dimensions (Ronchi et al., 2018). Unlike energy piles, very little research has been done on energy micropiles. It is important to note that due to poor cleanout at the toe of micropiles, the side shear resistance largely controls the restraint for thermal expansion and contraction of energy micropiles (Casagrande et al., 2022).

For micropiles installed in granular soils and subjected to cyclic thermal loading, (Lupattelli et al., 2023) observed the development of irreversible settlement during the initial cooling cycles. However, these settlement values were deemed negligible and could be disregarded during the design process. When installed in stratified soil, the behavior of energy micropiles becomes a little more complex and needs more attention. (Casagrande et al., 2022) carried out TRT tests to understand the impact of different soil layers on the thermomechanical response of EMPs. An interesting finding was the development of plastic strains which occurred only in the organic clay layer after a certain amount of heating, while all the other layers (silty sand and sand soil) kept the thermo-elastic behavior. Furthermore, it was observed that the mobilized coefficient of thermal expansion decreased following each successive heating cycle. This reduction was associated with an increase in side shear resistance, thereby increasing restraint along the pile's length induced by heating. Additionally, variations in the coefficient of thermal expansion were noted across different soil layers, with the lowest value recorded in the organic clay soil layer.

Just like energy piles, thermal axial stresses are induced by thermal loading in energy micropiles. These stresses increase both with the inlet fluid temperature (Kong et al., 2021) and the number of loading cycles (Casagrande et al., 2022). Significant compression stresses were observed for long, slender micropiles (Lupattelli et al., 2023). Therefore, thermal stresses should also be considered during the structural design process. These observations highlight the complexity of the thermo-mechanical behavior of energy micropiles. The observations discussed in this section pertain to micropiles with a U-pipe configuration. However, to the best of the authors' knowledge, no study on the thermo-mechanical behavior of coaxial energy micropiles has been conducted. Thus, further research is essential for an appropriate design of these small piles.

3 REAL CASE OF ENERGY MICROPILES APPLICATION

Europe's first zero energy parking, Toriparkki, is situated underneath the Turku market square in Finland (Figure 1). The 30.000 m^2 parking produces 100% of the heat energy used by combining solar energy, district heating, geothermal energy and underground thermal storage. The geothermal system comprises of 561 steel energy small diameter piles amongst the 2000 piles installed. The micropiles lengths range from 15 to 45 m, with diameters of 14 cm and 17 cm (Lautkankare et al., 2020). Inside the 40 mm U-tube polyethylene pipes, water circulates. The ground being constituted of clay is appropriate for thermal energy storage.

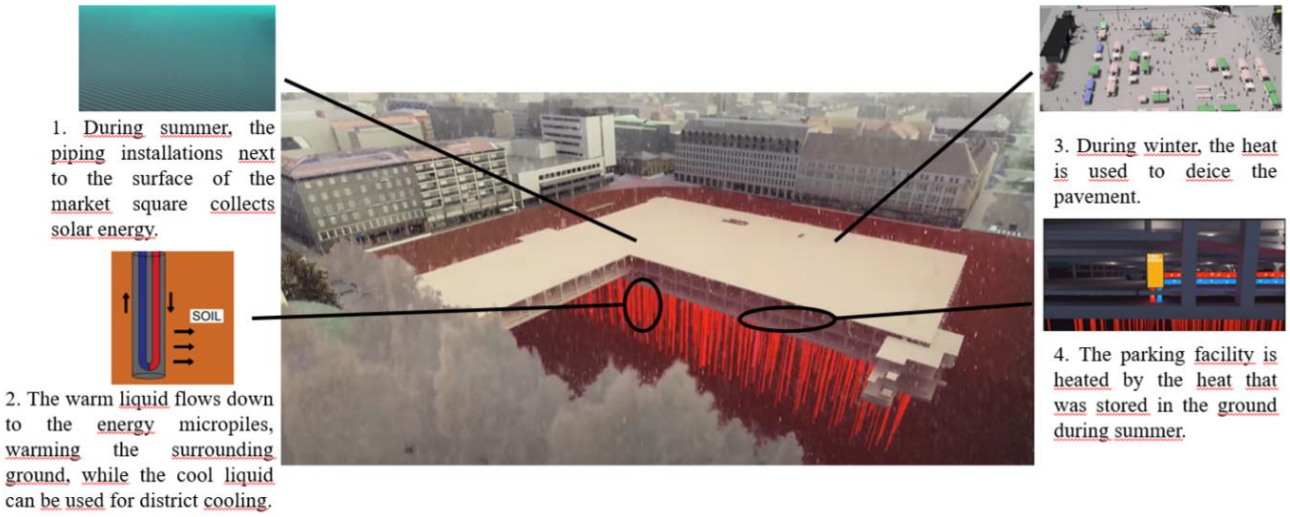

Figure 1. Illustration of the Toriparkki parking facility during winter. Adapted from (NollaE, 2019).

In summer, the surface of the market square is heated by the sun and the warm liquid flows underground through the piping system to the energy piles, warming the surrounding ground to a maximum depth of 50 m. The storage capacity and the heating power of the heat storage system are about 11.2 GWh and 6.6 M respectively. As autumn arrives, the thermal energy storage reaches its peak warmth, and the heated ground starts to release heat to the liquid in the energy piles. This warmed liquid then flows back up to the surface piping. Throughout winter, the heat stored underground is utilized to deice the pavement and heat the parking facility. As time progresses, the stored heat gradually diminishes, allowing the cool liquid in the system to be utilized for district cooling during spring. This heating system reduces CO2 emissions annually by about 950 tons compared to a heat pump facility.

4 CONCLUSIONS

Energy geostructures such as energy piles, slabs, walls, and tunnels, are efficient in providing renewable and clean energy for heating and cooling of buildings. However, their widespread adoption faces a common challenge in densely populated cities, where space constraints make it difficult, if not impossible, to implement individual geothermal systems. Micropiles, mostly used in structural retrofitting and rehabilitation, hold promise for providing sustainable energy for heating, ventilation, and air conditioning of existing buildings. Recent research has shown that the thermal performance of energy micropiles is comparable to that of energy piles. However, the small section of micropiles poses some challenges both in the thermal efficiency and thermo-mechanical behaviour. Nevertheless, it is predicted that the coaxial pipe configuration could be the most suitable pipe configuration for energy micropiles. In conclusion, more research should be carried out on energy micropiles for an appropriate thermal and thermo-hydro-mechanical design.

ACKNOWLEDGEMENT

The authors would like to express their gratitude to FRIEDR. ISCHEBECK GMBH for providing information and data on Titan micropiles and for organizing site visits.

REFERENCES

Casagrande, B., Saboya, F., McCartney, J. S., & Tibana, S. (2022). Investigation of a field-scale energy micropile in stratified soil under cyclic temperature changes. *Geomechanics for Energy and the Environment*, *29*. https://doi.org/10.1016/j.gete.2021.100263.

Cecinato, F., & Salciarini, D. (2022). Energy performance assessment of thermo-active micro-piles via numerical modeling and statistical analysis. *Geomechanics for Energy and the Environment*, *29*. https://doi.org/10.1016/j.gete.2021.100268.

Ischebeck. (2015). *TITAN Geothermal Energy*.

Kong, G. qiang, Cao, T., Hao, Y. hu, Zhou, Y., & Ren, L. wei. (2021). Thermomechanical properties of an energy micro pile-raft foundation in silty clay. *Underground Space (China)*, *6*(1), 76–84. https://doi.org/10.1016/j.undsp.2019.09.005.

Lautkankare, R., Salomaa, N., Martinkauppi, B., & Slobodenyuk, A. (2020). Underground parking lot at Turku market square-Zero energy parking hall and the biggest solar energy storage in the world. *Proceedings of the 12th Nordic Symposium on Building Physics (NSB 2020)*. https://doi.org/https://doi.org/10.1051/e3sconf/202017216008.

Loveridge, F., McCartney, J. S., Narsilio, G. A., & Sanchez, M. (2020). Energy geostructures: A review of analysis approaches, in situ testing and model scale experiments. *Geomechanics for Energy and the Environment*, *22*. https://doi.org/10.1016/j.gete.2019.100173.

Lupattelli, A., Bourne-Webb, P. J., Bodas Freitas, T. M., & Salciarini, D. (2023). A Numerical study of the behavior of micropile foundations under cyclic thermal loading. *Applied Sciences (Switzerland)*, *13*(17). https://doi.org/10.3390/app13179791.

NollaE. (2019, October 21). *Toriparkki energy system and world's largest solar thermal energy storage*.https://www.youtube.com/watch?v=EtJ9sFUG1kg.

Ronchi, F., Salciarini, D., Cavalagli, N., & Tamagnini, C. (2018). Thermal response prediction of a prototype Energy Micro-Pile. *Geomechanics for Energy and the Environment*, *16*,64–82. https://doi.org/10.1016/j.gete.2018.07.001.

Sabatini, P. J., Tanyu, B., Armour, T., Groneck, P., & Keeley, J. (2005). *Micropile design and construction reference manual*.

Sani, A. K., Singh, R. M., Amis, T., & Cavarretta, I. (2019). A review on the performance of geothermal energy pile foundation, its design process and applications. In *Renewable and Sustainable Energy Reviews* (Vol. 106, pp. 54–78). ElsevierLtd.https://doi.org/10.1016/j.rser.2019.02.008.

Proceedings of the XVIII ECSMGE 2024
GEOTECHNICAL ENGINEERING CHALLENGES
TO MEET CURRENT AND EMERGING NEEDS OF SOCIETY
© 2024 the Authors
ISBN 978-1-032-54816-6
DOI 10.1201/9781003431749-682
Open Access: www.taylorfrancis.com, CC BY-NC-ND 4.0 license

ECSMGE 24
XVIII EUROPEAN CONFERENCE ON SOIL MECHANICS AND GEOTECHNICAL ENGINEERING

Effect of the acetylation on the water resistance of biopolymer stabilised soil

Effet de l'acétylation sur la résistance à l'eau des sols stabilisés par des biopolymères

X. Yu*
University of Sheffield, Sheffield, UK

S.J. Armistead
University of Colorado, Boulder, USA

J. McGregor, N. Martsinovich, C.C. Smith
University of Sheffield, Sheffield, UK

**xinyuan.yu@sheffield.ac.uk*

ABSTRACT: The global soil stabilisation market is forecast to grow to $35 billion by 2027 driven primarily by infrastructure and construction activities and exacerbated by the increasingly urgent need to adapt to climate change. Naturally sourced biopolymers are a promising low carbon 'green' stabilising agent, achieving higher strength in stabilised soils than cement and at similar cost. However, widespread uptake of biopolymers is impeded by the fact that they typically suffer from (a) poor water resistance and (b) poor resistance to biodegradation over time. This paper presents interim results from a research study into novel biopolymer treatment processes which are applied at or subsequent to the soil/biopolymer mixing stage with the aim of enhancing resistance to water and biodegradation while involving the addition of only small volumes of natural materials. The specific approach described in this paper aims to minimize the interaction of vulnerable hydrophilic functional groups in the biopolymers with water through acetylation, whereby the hydrophilic groups are replaced by natural hydrophobic acetyl groups. Three mixing protocols are proposed and this paper examines the first protocol where the acetylation agents are added at the same time as the biopolymer is added to the soil. While this is the simplest process procedurally, results demonstrate that the strength on wetting is lower than non-acetylated chitosan treated soil. Improved performance is anticipated for the other protocols.

RÉSUMÉ: Le marché mondial de la stabilisation des sols devrait atteindre 35 milliards de dollars d'ici 2027, principalement en raison des activités d'infrastructure et de construction, et exacerbé par le besoin de plus en plus urgent de s'adapter au changement climatique. Les biopolymères d'origine naturelle constituent un agent stabilisateur "vert" prometteur, à faible teneur en carbone, qui confère aux sols stabilisés une résistance supérieure à celle du ciment, pour un coût similaire. Cependant, l'adoption généralisée des biopolymères est entravée par le fait qu'ils souffrent généralement (a) d'une faible résistance à l'eau et (b) d'une faible résistance à la biodégradation au fil du temps. Cet article présente les résultats provisoires d'une étude portant sur de nouveaux procédés de traitement des biopolymères appliqués au stade du mélange sol/biopolymère ou ultérieurement, dans le but d'améliorer la résistance à l'eau et à la biodégradation tout en n'impliquant l'ajout que de faibles volumes de matériaux naturels. L'approche spécifique décrite dans cet article vise à minimiser l'interaction des groupes fonctionnels hydrophiles vulnérables des biopolymères avec l'eau par acétylation, les groupes hydrophiles étant remplacés par des groupes acétyles hydrophobes naturels. Trois protocoles de mélange sont proposés et cet article examine le premier protocole dans lequel les agents d'acétylation sont ajoutés en même temps que le biopolymère est ajouté au sol. Bien qu'il s'agisse du processus le plus simple d'un point de vue procédural, les résultats montrent que la force de mouillage est inférieure à celle d'un sol traité au chitosane non acétylé. Des performances améliorées sont attendues pour les autres protocoles.

Keywords: Biopolymer; soil stabilisation; chitosan; water resistance.

1 INTRODUCTION

The global soil stabilisation market is expected to experience substantial growth, increasing from $25 billion in 2019 to an estimated $35 billion by 2027 (Emergen Research, 2020) with soil-chemical stabilisation, anticipated to be the fastest-growing sector. This growth is primarily attributed to heightened infrastructure and construction activities,

further fueled by the urgent imperative to address climate change, flood risk, and rising sea levels.

Despite this growth, there are environmental concerns associated with conventional commonly used chemical additives such as cement and lime. Biopolymers have been advocated as an alternative low-carbon sustainable stabilisation agent (Chang et al., 2020). Existing research has demonstrated that biopolymers can acheive considerable soil strength improvements with low additive dosage compared to traditional stabilisers such as cement or lime, while at similar cost. The potential for biopolymers to naturally degrade over time may also be seen as beneficial for temporary and semi-permanent works (lifetimes of decades), however there is a need to develop robust controls on the degradation process.

Key to this is to address the issues of biodegradation and strength reduction on exposure to water. This paper describes a systematic approach for improving the water/biodegradation resistance of biopolymer stabilised soils and reports intial results from an 18-month UK EPSRC funded research project.

2 BIOPOLYMER SOIL STABILISATION AND INFLUENCE OF WATER

Typically, biopolymers are dissolved in water, forming a viscous fluid, before thorough mixing with soil. On drying, the functional groups on the long chain structure can bind with other biopolymer molecules or soil particles giving rise to a significantly improved strength and stiffness after drying. Additions of 1-3% biopolymer by weight have been shown to give rise to strengths exceeding those achieved by e.g. addition of 8-10% of cement (Chang et al., 2015 and Muguda et al., 2017).

Biopolymer stabilisation will significantly depend on the mineralogy of the soil and the properties of the biopolymer involving either direct biopolymer-soil binding or physical coating of soil particles by biopolymer and biopolymer-biopolymer binding.

However some of these binding mechanisms can be weakened/outcompeted by water molecules. Experimental measurements on xanthan gum stabilised soils have previously demonstrated a loss of compressive strength upon exposure to water (Chang et al., 2015, 2020). Biopolymer tensile strength and stiffness can diminish significantly with increased water content (Yakimets et al., 2007). Elsewhere the addition of de-acetylated chitin has been shown to improve the mechanical properties of clay-based soils, however this effect is significantly reduced in the presence of water (Hataf et al., 2018).

3 DESIGN APPROACH

The approach described in this paper has been previously described in Smith et al. (2023) and is briefly summarized here. It is hypothesised that the biopolymer functional groups within a stabilised soil which may otherwise preferentially bind to water, can be treated post mixing to negate their vulnerability to water and biodegradation without affecting the soil-biopolymer binding. In this paper the conversion of 'vulnerable' functional groups utilising acetylation is examined.

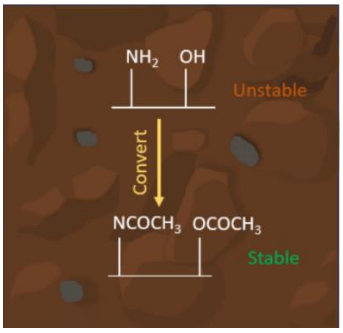

Figure 1. Enhancing biopolymer resistance to water and biodegradation through acetylation (after Smith et al., 2023).

Acetylation is a chemical process that has seen success as a non-toxic and environmentally friendly timber treatment technology (Mantanis, 2017). It involves replacing vulnerable hydrophilic functional groups with natural hydrophobic acetyl groups (shown in Figure 1). Re-acetylation can typically be carried out through the addition of acetic anhydride.

While this paper reports interim results based primarily on macro-geotechnical results from unconfined compression tests, and initial FTIR studies, additional studies will be carried out using XRD, GPC, zeta potential, TGA, and SEM to identify and characterize the binding and chemical reactions that occur.

Treatments agents will include various acetylation agents. In the wider project, three treatment protocols will be investigated:

1. Acetylation of the dissolved biopolymer immediately prior to soil mixing.
2. Mixing of the dissolved biopolymer with the soil followed by acetylation but prior to sample curing.
3. Mixing of the dissolved biopolymer with the soil followed by acetylation after sample curing.

It is anticpated that better performance will be seen in Protocols 2 and 3, however these will be more complex to apply in the field. This paper reports results from the evaluation of Protocol 1.

4 EXPERIMENTAL STUDY

4.1 Materials

Silica sand sourced from Cheshire, UK was puchased from Minerals Marketing Ltd, and was chosen for its local abundance. The particle sizes ranged between 0.06-0.5mm and the chemcial composition is listed in Table 1.

Table 1. Chemical composition of soils.

Chemical composition	Typical (%)
SiO2	94.68
Fe2O3	0.28
Al2O3	2.52
K2O	1.47
LOI	0.24

Chitosan biopolymer was utilised for the current study. Chitosan was selected due to its significant strengthening potential in soil stabilisation (Hataf et al., 2018; Adamczuk and Jozefaciuk, 2022), and its production route via de-acetylation of chitin, a material used by insects and crustaceans for exoskeletons and which has inherent water resistant properties. Chitin itself is a significant bi-product of the food industry. It is hypothesised that re-acetylation of chitosan, post soil treatment, will revert chemical bonds unused for soil binding to the chitin form and benefit from its associated properties such as high stability. The chitosan used in the study was purchased from Acros Organics, having a molecular weight ranging from 100000-300000 Da.

4.2 Sample preparation

The sample preparation process was divided into four stages: 1) preparation of the chitosan solution; 2) addition of the acetylation agent; 3) mixing with soils; 4) compaction into cylindrical specimen for testing.

Chitosan itself is insoluble in water, therefore the chitosan solution was prepared by dissolving chitosan powder in a 0.1M aqueous acetic acid solution. Following this, the acetylation agents were mixed in after a period of 5 minutes followed by mixing with the soils. 50 grams of final soil-biopolymer mixture was compacted into 38 mm diameter cylindrical hollow mould by a tamper to produce final specimens of 38 mm diameter and 25 mm height for testing. The samples were then cured by air drying in the laboratory over a 24 hour period at an average relative humidity of 50% and average temperature of 20°C.

Initial test sets utilised 25 mm height specimens to permit greater throughput of samples for parametric studies while providing semi-quantitative data. Verification of identified optimal treatment processes will be undertaken with 76 mm height samples in the future.

The chitosan to soils ratio was set at 1% by mass. The control test involved 1% chtiosan treated soils without any acetylation agent (`1%CS‘). Two different aceytlation approaches were involved in the study: (a) `1%CS-MeOH-Ac2O`: the addition of methanol (MeOH) with acetic anhydride (Ac2O), allowing acetyl groups to replace only the amino groups on the chitosan chain (Lavertu et al., 2012). This method is a common way to transform the structure of chitosan into chitin; (b) `1%CS-Ac2O`: the addition of Ac2O alone for uncontrolled acetylation.

4.3 Test program

The test programme was designed to assess the mechanical behaviour, water resistance and mechanical recovery after wetting of chitosan treated specimens following different treatments.

The mechanical behaviour of specimens was primarily evaluated through unconfined compression testing using a loading rate of 0.2 mm/min.

Water resistance was gauged through a simple water immersion test. The initial tests reported here utilised a two-hour immersion as an initial indicator of behaviours following water exposure. Specimens then underwent unconfined compression testing directly after the 2-hour immersion. Additionally, specimens subjected to a 2-hour wetting immersion followed by curing were tested to further assess their ability to recover mechanical properties post-wetting.

5 INITIAL RESULTS

5.1 Mechanical behaviours under dry condition

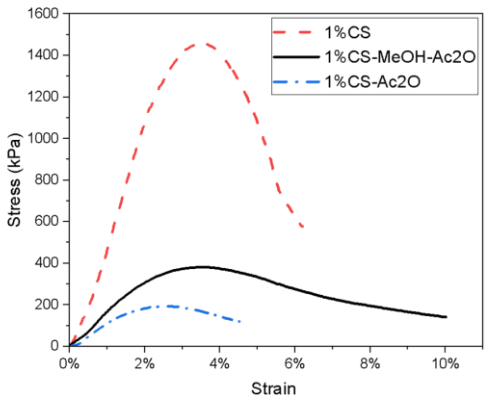

Figure 2. Stress-strain curves of 1% chitosan treated soil following 24 hours curing.

Figure 2 illustrates the stress-strain curves for specimens treated using the two reacetylation approaches following curing. The current reacetylation processes appear to reduce the strength of chitosan-treated soils, but this reduction is partly mitigated by approach (a) with the inclusion of methanol. This phenomenon could be attributed to the introduction of inactive acetyl groups, which may weaken the interactions between the biopolymer and the soil particles.

5.2 Water resistance

To assess water resistance, samples were immersed in water for 2 hours, and the results are shown in Figure 3. Both the 1%CS and 1%CS-MeOH-Ac2O specimens retained their shape in water, while the 1%CS-Ac2O specimen disintegrated. The resilience of 1%CS in water within the initial 2 hours can be attributed to the low solubility of chitosan, which only dissolves under acidic conditions. In contrast, the 1%CS-MeOH-Ac2O specimen absorbed a significant amount of water, behaving like a soft clay. While this reacetylation approach for this specimen should revert chitosan back to chitin, it may lead to randomly distributed acetyl groups (Gatto et al., 2019) that could lead to different characteristics compared to the original chitin, such as water absorbancy.

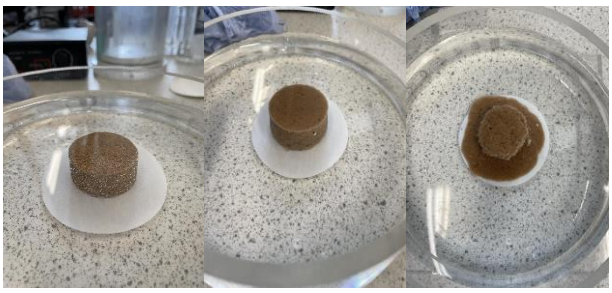

Figure 3. Specimens after two-hour water immersion test (a) 1%CS; (b) 1%CS-MeOH-Ac2O; (c) 1%CS-Ac2O.

Figure 4 presents a comparison of the unconfined compressive stress-strain responses of specimens after curing, wetting for 2 hours by immersion in a water bath, or wetting for 2 hours followed by a further curing stage. Both 1%CS and 1%CS-MeOH-Ac2O exhibit the ability to closely recover their stress-strain response after a single wetting and drying cycle. However, the failure modes of 1%CS and 1%CS-MeOH-Ac2O differ significantly as illustrated in Figure 5. While 1%CS experiences a compressive shear failure indicative of a peak material strength, 1%CS-MeOH-Ac2O displays a bulging response similar to a soft clay.

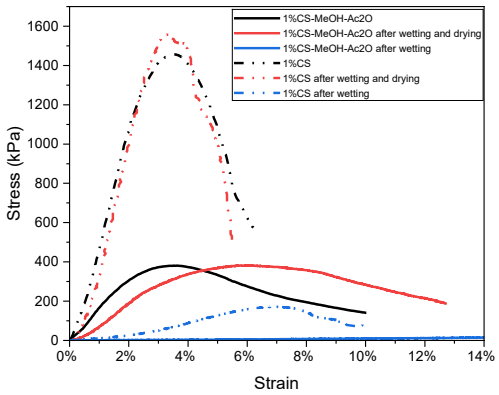

Figure 4. Stress-strain curve of specimen after drying, 2h wetting, 2h wetting and drying.



Figure 5. Failure mode of specimen after wetting (a)1%CS; (b)1%CS-MeOH-Ac2O.

6 DISCUSSION

FTIR results on pure re-acetylated chitosan samples have indicated the introduction of acetyl groups within the chitosan structure, and thus that the process appears to be able to regenerate the chitin structure (though with possible defects, Siripanich, 2023); however, the current mechanical testing indicates that it falls short of replicating certain anticpated properties. Notably, the water absorption ability increases, and the texture becomes softer upon exposure to water.

The initial re-acetylation methodology (Protocol 1) reported in this paper, while simple in operation suffers from the disadvantage that all agents are mixed together and that the reacetylation process may occur more rapidly than soil/biopolymer or biopolymer/biopolymer binding thus reducing strength gains. Further work will focus on the other staged protcols that provide more time for binding to develop before acetylation treatment.

7 CONCLUSIONS

The transformation of 'vulnerable' hydrophilic functional groups within a biopolymer through acetylation is hypothesised to hold significant promise in augmenting the biopolymer's resistance to both biodegradation and water. Three protocols are proposed:

1. Acetylation of the dissolved biopolymer immediately prior to soil mixing.
2. Mixing of the dissolved biopolymer with the soil followed by acetylation prior to sample curing.
3. Mixing of the dissolved biopolymer with the soil followed by acetylation after sample curing.

Results from initial studies on chitosan treated sandy soils reported in this paper focused on Protocol 1. While this is the simplest protocol operationally, the results were negative and indicated that while samples can retain their integrity on wetting they do not maintain their strength. On drying the strength characteristics are recovered. It is hypothesised that reacetylation process may occur more rapidly than soil/biopolymer or biopolymer/biopolymer binding thus reducing strength gains. Further studies will investigate Protocols 1 and 2 which are anticipated to provide improved performance.

ACKNOWLEDGEMENTS

This research was supported by the UK Engineering and Physical Sciences Research Council (EPSRC), under grant reference EP/X016943/1.

REFERENCES

Adamczuk, A., Jozefaciuk, G. (2022), Impact of Chitosan on the Mechanical Stability of Soils (2022), *Molecules*, 27, 2273, http://doi.org/10.3390/molecules27072273.

Armistead, S.J., Rawlings, A.E., Smith, C.C. and Staniland S.S. (2020). Biopolymer Stabilization/ Solidification of Soils: A Rapid, Micro-Macro, Cross-Disciplinary Approach. *Environmental Science & Technology,* 54(21):13963-13972.https://doi.org/10.1021/acs.est.0c02001.

ASTM. (2007). Standard test method for erodibility determination of soil in the field or in the laboratory by the jet index method. Annual Book of ASTM Standard: Section 4, Construction, 4, 252-256. https://www.astm.org/d5852-95.html.

Barber, A., Brandes, J., Leri, A., Lalonde, K., Balind, K., Wirick, S., Wang, J.,Gélinas, Y. (2017). Preservation of Organic Matter in Marine Sediments by Inner-Sphere Interactions with Reactive Iron. Scientific Reports, 7(1), 366. http://doi.org/10.1038/s41598-017-00494-0.

Chang, I., Im, J., Prasidhi, A. K., Cho, G. C. (2015). Effects of Xanthan gum biopolymer on soil strengthening. Construction and Building Materials, 74, 65-72. https://doi.org/10.1016/j.conbuildmat.2014.10.06.

Chang, I., Lee, M., Tran, A. T. P., Lee, S., Kwon, Y. M., Im, J., Cho, G. C. (2020). Review on biopolymer-based soil treatment (BPST) technology in geotechnical engineering practices. Transportation Geotechnics, 24, 100385. https://doi.org/10.1016/j.trgeo.2020.100385.

Emergen Research (2023), Soil Stabilization Market By Application (Agriculture, Industrial, Non-Agriculture), By Method (Chemical, Mechanical), By Additive (Mineral & Stabilizing agents, Polymers), Forecasts to 2027, https://www.emergenresearch.com/industry-report/soil-stabilization-market.

Gatto, M., Ochi, D., Yoshida, C. M. P., & da Silva, C. F. (2019). Study of chitosan with different degrees of acetylation as cardboard paper coating. Carbohydrate polymers, 210, 56-63. https://doi.org/10.1016/j.carbpol.2019.01.053.

Hataf, N., Ghadir, P., Ranjbar, N. (2018). Investigation of soil stabilization using chitosan biopolymer. Journal of cleaner production, 170, 1493-1500. https://doi.org/10.1016/j.jclepro.2017.09.256.

ISO 17556 (2019). Plastics – Determination of the ultimate aerobic biodegradability of plastic materials in soil by measuring the oxygen demand in a respirometer or the amount of carbon dioxide evolved, https://www.iso.org/standard/74993.html.

Lavertu, M., Darras, V., Buschmann, M. D. (2012). Kinetics and efficiency of chitosan reacetylation. Carbohydrate polymers, 87(2), 1192-1198. https://doi.org/10.1016/j.carbpol.2011.08.096.

Mantanis, G. I. (2017). "Chemical modification of wood by acetylation or furfurylation: A review of the present scaled-up technologies," BioRes. 12(2), 4478-4489.

Muguda, S., Booth, S. J., Hughes, P. N., Augarde, C. E., Perlot, C., Bruno, A. W., Gallipoli, D. (2017) Mechanical Properties of Biopolymer-Stabilised Soil-Based Construction Materials. Géotechnique Lett., 7 (4), 309– 314, http://doi.org/10.1680/jgele.17.00081.

Siripanich, N. (2023). Application Of Chitin As A Sustainable Material For Soil Stabilization Process). MSc Thesis. University of Sheffield.

Smith, C.C., McGregor, J., Martsinovich, N., Armistead, S., Yu, X., Siripanich, N. (2023). Enhancing the Water and Biodegradation Resistance of Biopolymer Stabilised Soils – Design Concepts. *International Conference on Bio-Based Building Materials, S.* Amziane, I. Merta, and J. Page (eds) RILEM Bookseries, vol 45. Springer, Cham. https://doi.org/10.1007/978-3-031-33465-8_23.

Yakimets, I., Paes, S.S., Wellner, N., Smith, A.C., Wilson, R.H., and Mitchell, J.R. (2007). Effect of Water Content on the Structural Reorganization and Elastic Properties of Biopolymer Films: A Comparative Study. *Biomacromolecules*, *8*, 1710–1722. https://doi.org/10.1021/bm070050x.

Proceedings of the XVIII ECSMGE 2024
GEOTECHNICAL ENGINEERING CHALLENGES
TO MEET CURRENT AND EMERGING NEEDS OF SOCIETY
© 2024 the Authors
ISBN 978-1-032-54816-6
DOI 10.1201/9781003431749-683
Open Access: www.taylorfrancis.com, CC BY-NC-ND 4.0 license

ECSMGE 24
XVIII EUROPEAN CONFERENCE ON SOIL MECHANICS AND GEOTECHNICAL ENGINEERING

Mechanical characteristics of non-cohesive soil improved by fibre and cement addition

Caractéristiques mécaniques des sols non cohésifs améliorées par l'ajout de fibres et de ciment

K. Zabielska-Adamska*, P. Dobrzycki**, M. Wasil
Bialystok University of Technology, Bialystok, Poland
**kadamska@pb.edu.pl; **patryk.dobrzycki@pb.edu.pl*

ABSTRACT: The work aimed to show changes in the mechanical characteristics of gravelly sand characterized by a lack of fines after adding dispersed reinforcement. Tests were conducted on natural non-cohesive soil or improved with a 1.5% cement additive. 18 mm long fibres were used, which were added in amounts of 0.1%, 0.2%, and 0.3% to the dry mass of compacted soil. The gravelly sand was compacted at the optimum water content to the maximum dry density by the Standard Proctor energy. The soil was sheared in triaxial conditions. The addition of fibres changed the sample behaviour on more plastic. The fibre content increases the maximum shear strength but it is obtained at greater relative strain. The cement lightly bound soil failure mode is diagonal through the failure plane, as in the case of semi-brittle material. Whereas the plane of destruction in the soil sample improved with cement and fibre addition is close to horizontal, which signifies that fibre-reinforced material entered its plastic zone.

RÉSUMÉ: Les travaux visaient à montrer l'évolution des caractéristiques mécaniques des sables graveleux caractérisés par un manque de fines après ajout de renforts dispersés. Les essais ont été réalisés sur sol naturel non cohésif ou amélioré avec un additif cimentaire à 1,5%. Des fibres de 18 mm de long ont été utilisées, qui ont été ajoutées en quantités de 0,1%, 0,2% et 0,3% à la masse sèche de sol compacté. Le sable graveleux a été compacté à la teneur en eau optimale jusqu'à la densité sèche maximale par l'énergie Standard Proctor. Le sol a été cisaillé en conditions triaxiales. L'ajout de fibres a modifié le comportement de l'échantillon sur davantage de plastique. La teneur en fibres augmente la résistance maximale au cisaillement mais elle est obtenue avec une déformation relative plus élevée. Le mode de rupture du sol légèrement lié du ciment est diagonal par rapport au plan de rupture, comme dans le cas d'un matériau semi-fragile. Alors que le plan de destruction dans l'échantillon de sol amélioré par l'ajout de ciment et de fibres est proche de l'horizontal, ce qui signifie que le matériau renforcé de fibres est entré dans sa zone plastique.

Keywords: Compacted soil; polypropylene fibre reinforcement; cement addition; shear strength; triaxial tests.

1 INTRODUCTION

Stabilization with hydraulic binders is an effective way to increase the stiffness of base and subbase layers and to improve the rutting of the subgrade. Another way to improve the soil properties is to use fibre-reinforcement. Scientists agree that fibre content is a recognized method for improving the shear strength and ductility of the stress-strain response of natural (Correia et al., 2021) or hydraulically bonded cohesive soils (Yang et al., 2022) but also natural (Michalowski and Čermák, 2003) and cemented non-cohesive soils (Consoli et al, 1998; Asghari et al., 2004; Haeri et al., 2005). The most used content of fibres to the dry mass of soil is 0.1−0.5%. Binder additives are used in various proportions, and the most common content of lime or cement is 2-10%. Cohesive soils are reinforced with fibres due to their brittleness after cementing or the possibility of cracking when drying. In the case of non-cohesive soils, silty sands are most often reinforced to improve mechanical properties. However, in recent years, research has also been carried out on gravelly sands with poor grain size characteristics, which require improvement due to low compaction possibilities.

The study aimed to investigate the influence of the addition of minimum cement content and polypropylene fibres on the compactibility and mechanical characteristics of post-glacial gravelly sand.

2 MATERIALS AND METHODS

The tested material is a Pleistocene glaciofluvial soil consisting of well-rounded quartz crumbles, as well as angular grains, with a considerable addition of lytic

particles and feldspars (Zabielska-Adamska et al. 2021). According to EN ISO 14688-1 standard, the tested soil is gravelly sand (grSa) with a median particle diameter D_{50} of 1.0 mm and the absence of fines (f_c = 0%). The soil is a poorly graded material with uniformity and curvature coefficients equalled 5.27 and 0.91, respectively. The unit weight, γ_s, is 26.0 kN/m^3.

Laboratory tests were conducted on samples of gravelly sand and gravelly sand with 1.5% 42.5R Portland cement addition to the dry mass of soil, and their mixtures with 0.1, 0.2 and 0.3% of the polyamide fibres with a length of 18 mm. The soil and polypropylene fibres are shown in Figure 1.



Figure 1. The polypropylene fibres with 18 mm longest and soil mixed with 0.3% of the fibres.

Compaction parameters, maximum dry density, $\rho_{d\,max}$, and optimum water content, w_{opt}, were found by the Standard Proctor method. The soil or soil and cement were mixed with polypropylene fibres using a laboratory mechanical stirrer, which is of great importance for the homogeneity of the tested samples (Zabielska-Adamska et al., 2023a).

Mechanical characteristics were performed in the triaxial test apparatus with a pneumatic way of applying the confining pressure and axial load. The cylindrical reconstituted samples were prepared in a bipartite mould by dynamic tamping of the material at w_{opt} into three layers to obtain $\rho_{d\,max}$ value from the Standard Proctor method. The diameters of the samples were about 70 mm, and the height was about 140 mm. The samples were tested directly after compaction (unstabilized hydraulically), and after 28 days of curing in constant temperature and humidity, wrapped in foil to avoid drying. All samples were tested with the ratio of shearing 0.1 mm/min by the CD method recommended for non-cohesive (ASTM D7181-20). Samples were not saturated to recreate the conditions prevailing in the pavement subgrade material but their degrees of saturation were about 0.80. After isotropic consolidation samples were sheared under confining pressure $\sigma_3' = 50$, 100 and 150 kPa.

3 TEST RESULTS AND ANALYSIS

3.1 Compaction results

The fibre addition results in an optimum water content decrease and a maximum dry density increase in both uncemented and cemented samples (Figure 2). Increasing fibre content from 0.2% to 0.3% practically does not influence the compaction parameters of gravelly sand and its mix with cement.

The cement addition to the gravelly sand increases the $\rho_{d\,max}$ value while decreasing the w_{opt}.

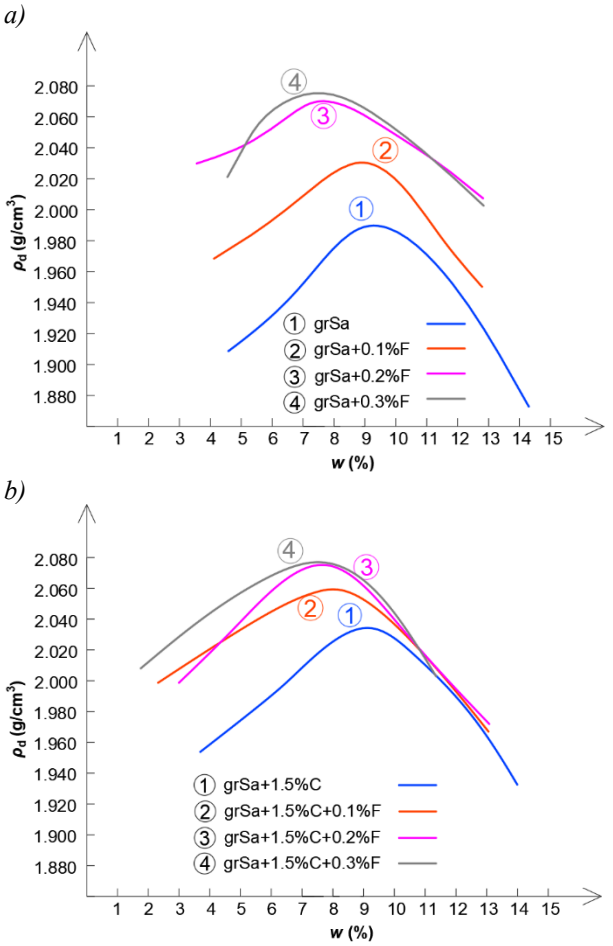

Figure 2. Compaction curves of tested materials with fibres: a) gravelly sand, b) sand and 1.5% of cement.

3.2 Triaxial test results

Test results for uncemented (Figure 3a) and lightly bound samples (Figure 3b) show that 1.5% cement addition increases twice the strength of tested samples that rises with the increase in confining pressure for each soil. The samples exhibit a gentle peak behaviour. The test results, presented in Figs. 3c-d, show the behaviour of the uncemented and cemented gravelly sand is changed by fibre addition. The peak strength and ultimate strength have increased whereas the initial strength is unchanged. The addition of fibres

proportionally changed the sample behaviour on more plastic and the maximum shear strength was obtained at greater relative strains.

Stiffness assessed by the E_{50} module decreases with fibre content (Tab. 1), both for uncemented and cemented samples. The addition of 1.5% cement practically does not improve it, which was also stated for greater cement addition (Du et al., 2020).

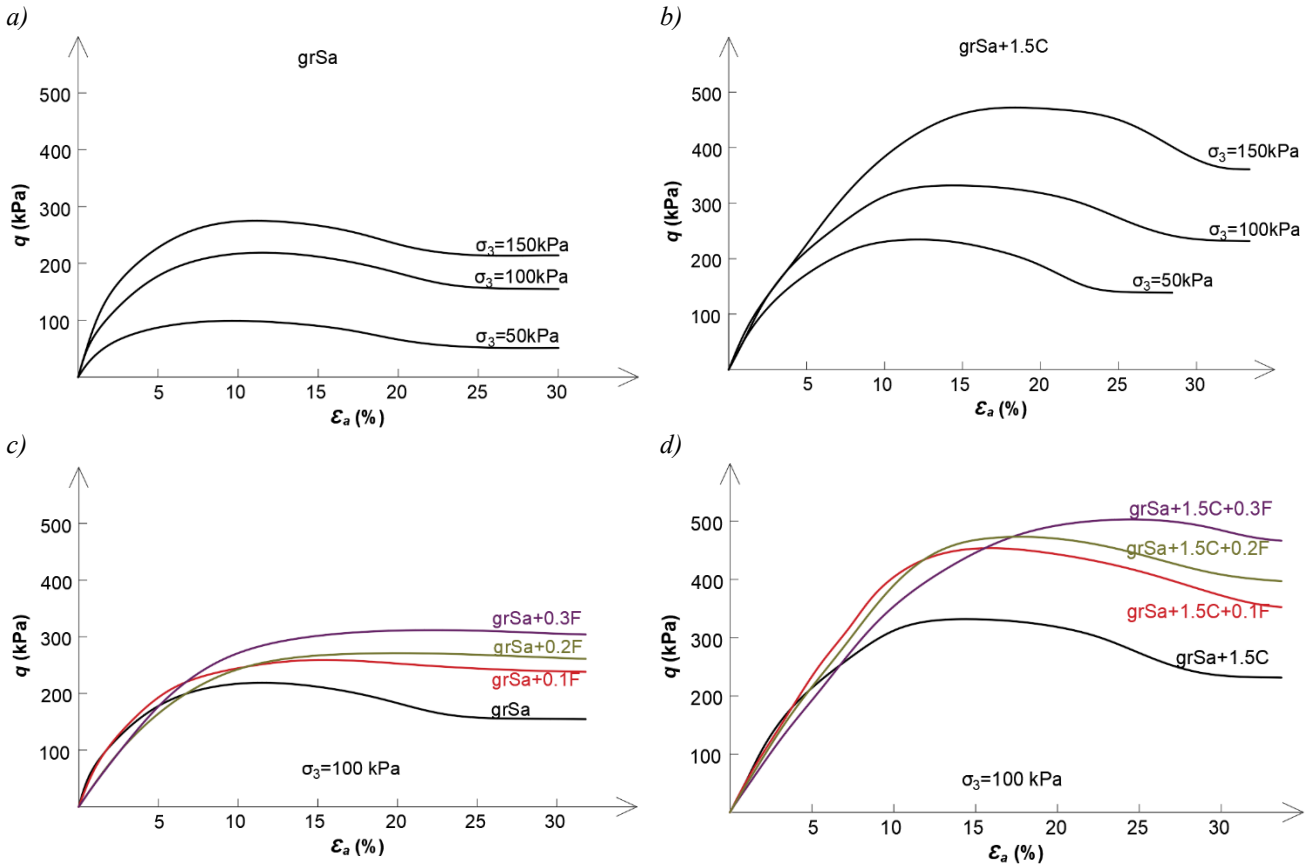

Figure 3. Results of CD triaxial tests shown as half of the deviator stress-strain curves for $\sigma_3' = 50$, 100 and 150 kPa for gravelly sand (a) and sand with 1.5% of cement addition (b), and 100 kPa for sand mix (c) and sand/cement with 0.1, 0.2 and 0.3% of fibres.

Table 1. Mechanical parameters of materials, where C – cement, and F – fibre content.

C	F	E_{50}	Shear strength parameters			
			Peak		Residual	
			ϕ'	c'	ϕ'	c'
%	%	MPa	°	kPa	°	kPa
0	0	10.39	40.3	1.3	38.5	0
	0.1	10.08	42.3	6.8	41.7	0
	0.2	7.84	43.5	8.8	43.2	5.1
	0.3	7.23	44.5	12.9	44.4	6.2
1.5	0	10.73	44.7	49.3	43.3	13.1
	0.1	9.33	45.0	82.6	45.7	45.9
	0.2	8.43	45.6	87.2	45.9	50.2
	0.3	7.51	45.8	88.2	46.5	60.6

The addition of cement and fibre improves shear strength parameters, both peak and residual (Tab. 1). Fibre content (0.1−0.3%) influences an increase of the effective angle of internal friction of natural grSa from 40.3° to 44.5°. In the case of stabilized soil, this increase is not so large and equals only 1.1°. Cohesion resistance grows significantly with the addition of fibres, both for natural and bounded materials. 1.5% of cement improves values of the angle of internal friction, but first of all – cohesion resistance.

Figure 4 shows various failure modes of samples damaged during the compression triaxial test. The sheared gravelly sand sample is characterized by the barrelling mode with a diagonal failure plane. The cement-bound soil failure mode is a typical single failure plane, obtained for semi-brittle material, whereas the plane of destruction in the uncemented and cemented samples improved with cement and fibre addition is close to horizontal. The horizontal failure plane signifies that fibre-reinforced material entered its plastic zone. In earlier research (Zabielska-Adamska et al., 2023b) carried out on grSa+1.5C with larger density (compacted by modified method) the

failure mode was vertical through failure plane as in the case of brittle material.

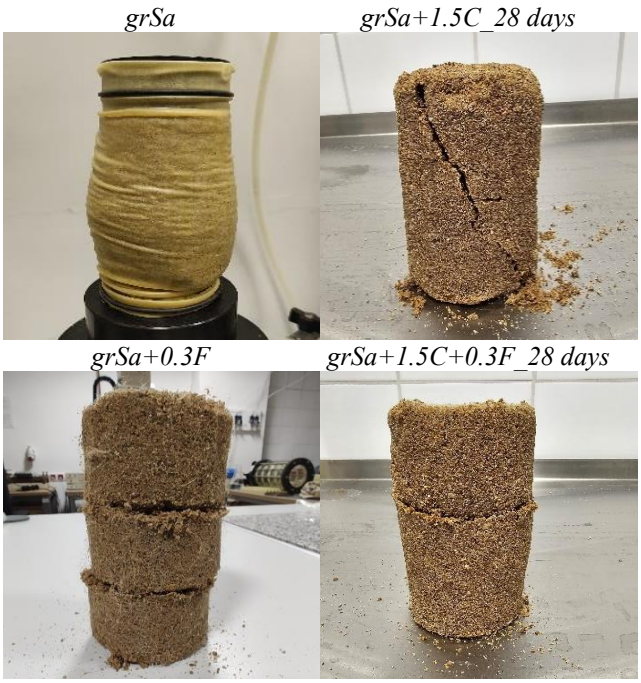

Figure 4. Views of sheared samples under $\sigma_3' = 100$ kPa.

4 CONCLUSIONS

1. The addition of 1.5% cement to gravelly sand increases peak and residual shear strength parameters, but practically does not impact on stiffness estimated by the E_{50} module.
2. Fibre reinforcement changes the behaviour of uncemented and slightly cemented gravelly sand. The peak and ultimate shear strength increased while the initial strength was the same. The peak and residual parameters increase, but the E_{50} module decreases.
3. The addition of 0−0.3% fibres regularly changed the behaviour of gravelly sand and its mix with cement on more plastic and where the peak strength was obtained at greater relative strain.

ACKNOWLEDGEMENTS

The investigations were conducted at Bialystok University of Technology in Poland under grant No.: WZ/WB-IIL/8/2023 and WI/WB-IIL/10/2023.

REFERENCES

Asghari, E., Toll, D.G. and Haeri, S.M. (2004). Effect of cementation on the shear strength of Tehran gravelly sand using triaxial tests. *Journal of Sciences*, 15 (1), 65-71.

ASTM D7181-20 Standard Test Method for Consolidated Drained Triaxial Compression Test for Soils.

Consoli, N.C., Prietto, P.D.M. and Uibrich, L.A. (1998). Influence of fiber and cement addition on behavior of sandy soil. *Journal of Geotechnical and Geoenvironmental Engineering*, 124 (12), 1211-1214. https://doi.org/10.1061/(ASCE)1090-0241(1998)124:12(1211).

Correia, N.S., Rocha, S.A., Lodi, P.C. and McCartney, J.S. (2021). Shear strength behavior of clayey soil reinforced with polypropylene fibers under drained and undrained conditions. *Geotextiles and Geomembranes*, 49, 1419-1426. https://doi.org/ 10.1016/j.geotexmem.2021.05.005.

Du, J., Zheng, G., Liu, B., Jiang, N.J. and Hu, J. (2020). Triaxial behavior of cement stabilized organic matter-disseminated sand. *Acta Geotechnica*, 16, 211-220. https://doi.org/ 10.1007/s11440-020-00992-y.

EN ISO 14688-1:2018. (2018). *Geotechnical Investigation and Testing. Identification and Classification of Soil. Identification and Description*, ISO, Geneva, Switzerland.

Haeri, S.M., Hosseini, S.M., Toll, D.G. and Yasrebi, S.S. (2005). The behaviour of an artificially cemented sandy gravel. *Geotechnical and Geological Engineering*, 23, 537-560. https://doi.org/10.1007/s10706-004-5110-7.

Michalowski, R.L.; Čermák, J. (2003). Triaxial compression of sand reinforced with fibers. Journal of Geotechnical and Geoenvironmental Engineering, 129, 125−136; https://doi.org/ 10.1061/(ASCE)10900241(2003)129:2(125).

Yang, X., Liang, S., Hou, Z., Feng, D., Xiao, Y. and Zhou, S. (2022). Experimental study on strength of polypropylene fiber reinforced cemented silt soil. *Applied Sciences*, 12, 8318. https://doi.org/ 10.3390/app12168318.

Zabielska-Adamska, K., Dobrzycki, P. and Wasil, M. (2023a). Compaction characteristics of coarse post-glacial soil improved by fiber-reinforcement and cement addition, In: *Smart Geotechnics for Smart Societies*. CRC Press, Astana, Kazakhstan, pp. 2606-26011.

Zabielska-Adamska, K., Dobrzycki, P. and Wasil, M. (2023b). Estimation of stiffness of non-cohesive soil in natural state and improved by fiber and/or cement addition in different load conditions. *Materials*, 16 (1), 417. https://doi.org/10.3390/ma 16010417.

Zabielska-Adamska, K., Wasil, M. and Dobrzycki, P. (2021). Resilient response of cement-treated coarse post-glacial soil to cyclic load. *Materials*, 14 (21), 6495. https://doi.org/10.3390/ma14216495.

Proceedings of the XVIII ECSMGE 2024
GEOTECHNICAL ENGINEERING CHALLENGES
TO MEET CURRENT AND EMERGING NEEDS OF SOCIETY
© 2024 the Authors
ISBN 978-1-032-54816-6
DOI 10.1201/9781003431749-684
Open Access: www.taylorfrancis.com, CC BY-NC-ND 4.0 license

ECSMGE 24
XVIII EUROPEAN CONFERENCE ON SOIL MECHANICS AND GEOTECHNICAL ENGINEERING

Evaluation of PFOS contamination in aquifers under single lined landfills

Evaluation de contamination d'aquifères par PFOS sous dépotoirs à revêtement composite singulier

L. Zhao*
University of Sydney, Sydney, NSW, Australia

R.K. Rowe
Queen's University, Kingston, ON, Canada

A. El-Zein
University of Sydney, Sydney, NSW, Australia

**linxue.zhao@sydney.edu.au*

ABSTRACT: Perfluorooctane sulfonic acid (PFOS) is among the most concerning types of a large group of compounds called per- and polyfluoroalkyl substances (PFAS). PFOS has captured significant attention due to its persistence in the environment and negative effects on human health. Landfills are a major source of PFOS to the surrounding aquifer and usually require composite liner systems for hydraulic and chemical containment. However, knowledge of the transport of PFOS through liner systems remains limited, and relevant numerical simulations are scarce. The paper reports an evaluation of PFOS contamination in the aquifer under a standard, single-liner, barrier system in a landfill, conducted using a 2D finite-element model of advective-diffusive PFOS transport. Three different levels of construction quality assurance (CQA) for the liner system are investigated. It's concluded that the advection process dominates PFOS transport through the liner system over molecular diffusion and mechanical dispersion. A considerable level of contamination for a scenario with excellent CQA indicates that a single composite liner may not be adequate to mitigate PFOS impact on an aquifer below or close to a municipal solid waste landfill.

RÉSUMÉ: Le perfluorooctane sulfonique (PFOS) est l'un des polluants les plus graves parmi le groupe des substances per- et polyfluoroalkyl (PFAS). Le PFOS a suscité l'intérêt en raison de sa persistance dans l'environnement et de ses effets néfastes sur la santé humaine. Les centres de décharge de déchets (dépotoirs) constituent une source majeure de PFOS pour les aquifères voisins et nécessitent un système de revêtement pour l'isolement hydraulique et chimique. Cependant, la connaissance de la migration du PFOS à travers les systèmes de revêtement des dépotoirs est limitée, et les simulations numériques du problème sont rares. Cette publication présente les résultats préliminaires d'une série de simulations en éléments finis en 2D du transport par diffusion-advection du PFOS à travers le dessous d'un dépotoir pourvu d'un revêtement composite singulier. Trois niveaux de qualité de construction de revêtement sont considérés. Les simulations tiennent compte des meilleures estimations de la distribution de probabilité des propriétés des matériaux, des variables environnementales et des taux de contaminants dans les déchets, afin de calculer des distributions de probabilité de la concentration maximale de PFOS dans l'aquifère. Les résultats des simulations révèlent que le processus d'advection est dominant par rapport à la diffusion moléculaire et à la dispersion mécanique. Le risque de contamination reste élevé, même dans un scénario de qualité de construction excellente, ce qui indique qu'un revêtement composite singulier n'est probablement pas suffisant pour protéger les aquifères situés sous les dépotoirs de déchets municipaux.

Keywords: PFOS; liner system; landfill; finite element method; construction quality assurance.

1 INTRODUCTION

Per- and polyfluoroalkyl substances (PFAS) are a diverse group of synthetic organic compounds with thermal stability, chemical inertness, and significant surfactant properties. They have been widely used since the 1950s in both consumer products and industrial applications (Renner, 2001), leading to their extensive detection in the environment, wildlife, and humans. Perfluorooctane sulfonic acid (PFOS, C_8F_{17}-SO_3H) is one of the most problematic PFAS compounds. Although the production of PFOS and its precursors ceased in the United States in 2002 (USEPA, 2000), PFOS remains notable in the environment due to its historical use (Paul et al., 2009),

continued precursor presence (Rhoads et al., 2008), and identification as an end product in PFAS environmental transformations (Bouazza, 2021). As the destination for most consumer products and industrial wastes containing PFAS, landfills are a major source of PFAS, including PFOS, to the environment. PFOS is widely detected in landfill leachates at ng/L to µg/L levels (Zhang et al. 2023). Meanwhile, the health advisory standard for PFOS in drinking water varies by jurisdiction, such as 70 ng/L for Australia (NHMRC, 2022), 600 ng/L set by Health Canada (2018), 4 ng/L set by the US Environmental Protection Agency (USEPA, 2023), and 100 ng/L for Europe (EurEau, 2018).

Geosynthetic composite liner systems are widely used in landfills to mitigate contamination and protect surrounding groundwater (Giroud and Bonaparte, 1989; Rowe, 1998, 2005, 2012; Rowe et al., 2004; Bouazza, 2002). A single composite liner system typically comprises a geomembrane (GMB), a geosynthetic clay liner (GCL) or a compacted clay liner (CCL), and an underlying attenuation layer. Hence investigating PFOS interactions with liner components to determine relevant material properties is necessary for evaluating PFOS's environmental impact in landfills equipped with liner systems.

While some studies have estimated key transport properties of PFOS in lining systems (Di Battista et al., 2020; Rowe et al., 2023; Rowe and Jabin, 2021; Bouazza, 2021; Schaefer et al., 2019), there have been very few attempts to numerically simulate the migration of PFOS in a liner system, partly because of limited data.

Rowe and Barakat (2021) examined the transport of PFOS in a municipal solid waste landfill lined by a single composite liner, which was numerically analysed using a 1½-D model finite-layer method (Rowe and Booker, 1984, 1985; Rowe et al., 1997; Rowe and Booker, 2004; Rowe and Abdelrazak, 2019) which considered the downward advective-diffusive-dispersive migration through periodically spaced wrinkles to an aquifer that was modelled as a boundary condition with horizontal flow. It was concluded that the no-leakage, pure-diffusion case can in principle maintain acceptable concentrations in the aquifer. However, with leakage through a reasonable number of holes in the geomembrane for landfills with a single liner system containing significant concentrations of PFOS in the leachate, there was likely to be a significant impact on a shallow underlying aquifer.

The present study uses a 2D finite element method (FEM) model to simulate the leakage of leachate and the migration of PFOS through a typical single-liner system while considering the full 2D effects of a series of leaks in the lining system.

The primary advantage of a 2D model over the 1½-D model used by Rowe and Barakat (2021) is the ability of the 2D model to examine migration downgradient of the landfill and the impact of monitoring points away from the landfill.

2 METHOD

2.1 Problem description

The 2D model of a municipal solid waste (MSW) landfill simulated in the study is shown in Figure 1, where PFOS transport involving both advection and diffusion occurs. The landfill is 400 m long in the direction of flow in the underlying aquifer and 100 m wide in the direction normal to the plane of the diagram. The landfill base is equipped with a single composite liner which is comprised of a 1.5 mm-thick HDPE GMB, a 7 mm-thick GCL, above a 3.743 m-thick attenuation layer (AL) and a 3 m-thick aquifer (AQ). The combined thickness of the clay liner and attenuation layers is selected according to MoE (1998). If the unlikely condition of no defects on GMB is assumed, the advective PFOS transport is eliminated and the leakage rate q_a is nil, giving a pure-diffusion problem. Selected input variables related to material properties, dimensions, and boundary conditions have been estimated, and are shown in Table 1.

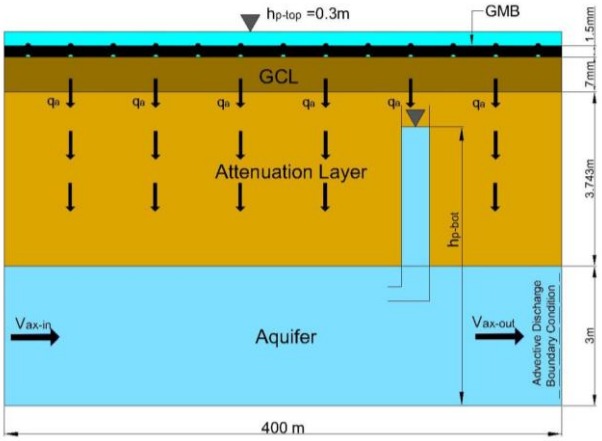

Figure 1. Schematic of the liner-subsoil system for "good CQA and with ELLS": holed wrinkles of 325 m/ha, corresponding to 13 leaks per 400 m. Not to scale.

Input parameters used in the simulations have been obtained based on an extensive review of the literature, data study and expert judgement. In addition, calibration on data from landfill cells where there is good construction quality assurance (CQA) and a dipole method electrical leak location survey (ELLS) gave an estimation of 325 m/ha for the holed wrinkle length per hectare (Rowe and Zhao, 2023). Two other levels of CQA are also investigated in this study, i.e.,

"good CQA and no ELLS" corresponding to 475 m/ha and "excellent CQA" corresponding to 75 m/ha.

Table 1. Input parameters.

Parameters	Symbols	GM estimations
Total hydraulic head drop across the model	ΔH	1.05 m
Length of holed wrinkle per hectare for "good CQA & no ELLS", "good CQA & with ELLS", and "excellent CQA"	L_w	475 m/ha, 325 m/ha, and 75 m/ha
Wrinkle width	$2b$	0.2 m
PFOS concentration in landfill leachate	C_0	900 ng/L
PFOS mass per unit waste mass	p_0	1800 ng/kg
Inward horizontal groundwater Darcy velocity in the aquifer	$V_{ax\text{-}in}$	0.95 m/a
Transmissivity	θ	1.0315×10^{-3} m^2/a
Hydraulic conductivity of GCL in contact with GMB	k_a	9.4×10^{-4} m/a
Hydraulic conductivity of GCL below holed wrinkles	k_b	7.52×10^{-3} m/a
Hydraulic conductivity of AL	K(AL)	1×10^{-7} m/s
Dispersivity of AL	α(AL)	0.052 m
Transverse dispersivity of AQ	α_T(AQ)	0.1 m
Longitudinal dispersivity of AQ	α_L(AQ)	2 m

2.2 Analysis method

The migration of PFOS within the investigated landfill model occurs in tandem with the flow of leachate, which is governed by the semi-coupled steady-state saturated water flow equation and time-dependent reactive diffusion-advection equation (RDAE) representing the transport of solutes. A specified mass of PFOS is applied at the top of the model's domain hence allowing for decline of PFOS concentration in the waste as is removed through leachate drainage and/or migration into the subsurface. The numerical simulations are conducted using the Soil Pollution Analysis System (SPAS), a multi-purpose finite-element method simulation software specifically tailored to lining systems (El-Zein, 2008; El-Zein and Balaam, 2012). Maximum concentration of PFOS anywhere in the aquifer, at any time, C_{max}, is computed by SPAS and used to characterise the level of contamination. The point in space and time at which maximum concentration is found is given by x_{max} and t_{max} (low transverse dispersivity in the aquifer leads to low dispersion of contaminants in the vertical direction and hence contaminants reaching the aquifer largely remain at the upper aquifer and reach their maximum concentrations at the top).

3 RESULTS AND DISCUSSION

Table 2 summarizes results of the simulations. C_{max} for the pure-diffusion case is 0.55 ng/L (occurring at 580 years), which is around two to three orders of magnitude lower than those of the advection-diffusion cases and occurs at much later time (Table 2). Such a contrast suggests that advection is the dominant process in PFOS transport through the liner system and causes the vast majority of its impact in the aquifer, while diffusion has a much smaller effect. Meanwhile, comparing the C_{max} value of 0.55 ng/L to four drinking water standards, namely 4 ng/L (USEPA), 70 ng/L (Australia), 100 ng/L (Europe), and 600 ng/L (Canada), indicates that a single-liner system with an intact GMB may serve as an effective barrier to PFOS.

Table 2. Summary of leakage rate and PFOS contamination.

Case	L_w (m/ha)	q_a (Lphd)	C_{max} (ng/L)	t_{max} (yr)	x_{max} (m)
Pure diffusion	0	0	0.55	580	400
Good CQA and no ELLS	475	300	508	145	391
Good CQA and with ELLS	325	197	403	155	386
Excellent CQA	75	46	176	145	335

However, even with high-quality ELLS and an excellent CQA, holed wrinkles in the GMB are inevitable, hence generating both advection and diffusion. Some landfills are designed with the leachate level below the potentiometric surface in the underlying aquifer which induces a "hydraulic trap" (Rowe, 1988; Rowe et al., 2000, 2004). In these cases, the flow through the holes in the geomembrane will be inward. However, when the leachate level is above the potentiometric surface in the underlying aquifer, leakage through holes will be downward. It is this latter case that is examined in this paper.

Figure 2 shows the horizontal variation in concentration at the top of the aquifer at 150 years. The overall rising trend of concentration is mainly attributed to the PFOS transport caused by the horizontal groundwater flow. Meanwhile, the "waves" in curves reflect the effect of leakage spikes under GMB defects.

Figure 3 shows PFOS concentration versus time at the point of highest concentration in the aquifer below the landfill. Contamination levels in the aquifer first increase to a peak before gradually declining. Under

the premise of good CQA, applying ELLS reduces the density of defects on the GMB, the leakage rate (q_a, reducing from 300 Lphd to 197 Lphd), and the peak PFOS concentration in the aquifer (C_{max}, declining from 508 ng/L to 403 ng/L). Under an excellent CQA, q_a and C_{max} will be reduced to 46 Lphd and 176 ng/L, respectively. This indicates that, as expected, a higher level of CQA can contribute to limiting PFOS contamination in the aquifer.

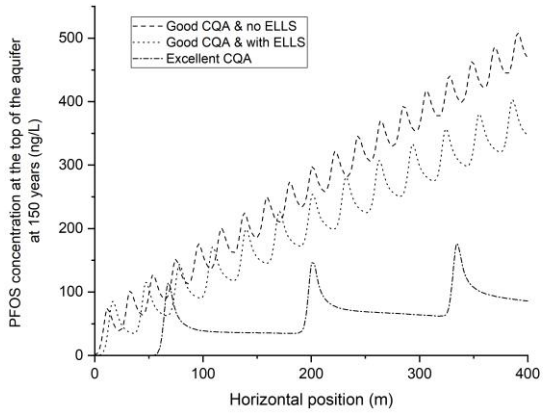

Figure 2. Change in PFOS concentration at the top of the horizontal direction in the aquifer at 150 years.

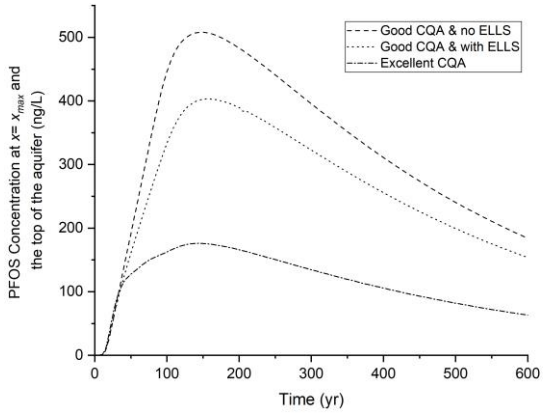

Figure 3. PFOS concentration over time at x= x_{max} and the top of the aquifer.

However, in all 3 cases considered, C_{max} remains higher than some of less stringent standards (i.e., 70 ng/L for Australia and 100 ng/L for Europe), and significantly higher than the strictest ones (4 ng/L for USEPA). Even the most lenient standard (600 ng/L for Canada), is approached by C_{max} under a good CQA. This is consistent with and adds support to the findings of Rowe and Barakat (2021) and suggests that single lining systems, even under high quality construction, may not be sufficient to protect groundwater from PFOS contamination under landfills unless the PFOS concentration in the landfill is substantially lower than that assumed or there is a substantially higher level of natural attenuation than that considered in this study. However, the simulations presented here are based on deterministic analyses for a single representative case under various assumptions of construction quality. In reality, there is significant uncertainty in input data and a more thorough assessment of the adequacy of different lining systems needs to take these uncertainties into account.

4 CONCLUSIONS

This study is the first to conduct a 2D finite element simulation of PFOS migration through landfills with a single composite lining system into underlying aquifers. The study's findings must be qualified by a number of limitations. These include the assumption of steady-state flow and full saturation, no adsorption or biodegradation of PFOS, and input parameters obtained based on limited information.

Despite these limitations, the study's key finding is noteworthy, indicating that, while high construction quality reduces the contamination level, single lining systems in MSW landfills may not be sufficient to prevent PFOS contamination in aquifers. Further investigations are required to assess the necessity of double composite lining systems to mitigate PFOS contamination in similar contexts. In addition, it is important to take into account data uncertainty in future analyses by estimating probability distributions of key input variables and conducting probabilistic simulations of PFOS contamination.

ACKNOWLEDGEMENTS

The project was funded by an Australian Research Council (ARC) Linkage Grant LP180101178.

REFERENCES

Bouazza, A. (2002). Geosynthetic clay liners. *Geotextiles and Geomembranes*, 20(1), pp. 3-17. https://doi.org/10.1016/S0266-1144(01)00025-5.Bouazza, A. (2021). Interaction between PFASs and geosynthetic liners: current status and the way forward. *Geosynthetics International*, 28(2), pp. 214-223. https://doi.org/10.1680/jgein.20.00033.

Di Battista, V., Rowe, R. K., Patch, D., and Weber, K. (2020). PFOA and PFOS diffusion through LLDPE and LLDPE coextruded with EVOH at 22 °C, 35 °C, and 50 °C. *Waste Management (Elmsford)*, 117, pp. 93-103. https://doi.org/10.1016/j.wasman.2020.07.036.

El-Zein, A. (2008). A general approach to the modelling of contaminant transport through composite landfill liners with intact or leaking geomembranes. *International Journal for Numerical and Analytical Methods in*

Geomechanics, 32(3), pp. 265-287. https://doi.org/10.1002/nag.626.

El-Zein, A. and Balaam, N. (2012). Saturated-unsaturated flow and solute transport in engineered liner systems: A new special-purpose finite element analysis software. *Australian Geomechanics Journal,* 47, pp. 11-26.

EurEau. (2018). Drinking Water Directive Plenary Vote. Available at: https://www.eureau.org/resources/briefing-notes/3011-drinking-water-directive-plenary-vote-eureau-explanatory-memorandum/file.

Giroud, J. P. and Bonaparte, R. (1989). Leakage through liners constructed with geomembranes - Part II: Composite liners. *Geotextiles and Geomembranes*, 8, pp. 71-111. https://doi.org/10.1016/0266-1144(89)90022-8.

Health Canada. (2018). Guidelines for Canadian Drinking Water Quality: Guideline Technical Document – Perfluorooctane Sulfonate (PFOS). Available at: https://www.canada.ca/content/dam/canada/health-canada/migration/healthy-canadians/publications/healthy-living-vie-saine/guidelines-canadian-drinking-water-quality-guideline-technical-document-perfluorooctane-sulfonate/PFOS%202018-1130%20ENG.pdf.

MoE. (2011). Ontario Regulation 232/98: Landfilling Sites, Environmental protection act, R.S.O. 1990, Amendment of October 2011. Government of Ontario. Available at: https://www.ontario.ca/laws/regulation/980232.

NHMRC. (2022). Australian Drinking Water Guidelines Version 3.8. Available at: https://www.nhmrc.gov.au/sites/default/files/documents/attachments/publications/Australian_Drinking_Water_Guidelines_ADWG_V3-8_Sep2022.pdf.

Paul, A. G., Jones, K. C., and Sweetman, A. J. (2009). A First Global Production, Emission, And Environmental Inventory For Perfluorooctane Sulfonate. *Environmental Science & Technology*, 43(2), pp. 386-392. https://doi.org/10.1021/es802216n.

Renner, R. (2001). Growing Concern Over Perfluorinated Chemicals. *Environmental Science & Technology*, 35(7), pp. 154A-160A. https://doi.org/10.1021/es012317k.

Rhoads, K. R., Janssen, E. M.-L., Luthy, R. G., and Criddle, C. S. (2008). Aerobic Biotransformation and Fate of N-Ethyl Perfluorooctane Sulfonamidoethanol (N-EtFOSE) in Activated Sludge. *Environmental Science & Technology*, 42(8), pp. 2873-2878. https://doi.org/10.1021/es702866c.

Rowe, R. K. (1988). Contaminant migration through groundwater: The role of modelling in the design of barriers. *Canadian Geotechnical Journal*, 25(4), pp. 778-798. https://doi.org/10.1139/t88-087.

Rowe, R. K. (1998). Geosynthetics and the minimization of contaminant migration through barrier systems beneath solid waste. *Proc. 6th Int. Conf. Geosynth.*, Atlanta, IFAI, St. Paul, Minn. 1, pp. 27-103.

Rowe, R. K. (2005). Long-term performance of contaminant barrier systems. 45th Rankine Lecture. *Geotechnique*, 55(9), pp. 631-678. https://doi.org/10.1680/geot.2005.55.9.631.

Rowe, R. K. (2012). Short and long-term leakage through composite liners, The 7th Arthur Casagrande Lecture. *Canadian Geotechnical Journal*, 49(2), pp. 141-169. https://doi.org/10.1139/t11-092.

Rowe, R. K. and Abdelrazek, A. Y. (2019). Effect of Interface Transmissivity and Hydraulic Conductivity on Contaminant Migration through Composite Liners with Wrinkles or Failed Seams. *Canadian Geotechnical Journal*, 56(11), pp. 1650–1667. https://doi.org/10.1139/cgj-2018-0660.

Rowe, R. K. and Barakat, F. B. (2021). Modelling the transport of PFOS from single lined municipal solid waste landfill. *Computers and Geotechnics*, 137, pp. 104280. https://doi.org/10.1016/j.compgeo.2021.104280.

Rowe, R. K. and Booker, J. R. (1984). The analysis of pollutant migration in a non-homogeneous soil. *Geotechnique*, 34(4), pp. 601-612. https://doi.org/10.1680/geot.1984.34.4.601.

Rowe, R. K. and Booker, J. R. (1985). "1-D pollutant migration in soils of finite depth". *Journal of Geotechnical Engineering*, ASCE, 111(4), pp. 479-499. https://doi.org/10.1061/(ASCE)0733-9410(1985)111:4(479).

Rowe, R. K. and Booker, J. R. (2004). POLLUTE Version 7 –1½ D Pollutant Migration through a Non-homogenous Soil. GAEA Technologies Ltd. https://gaea.ca/products.php.

Rowe, R. K. and Jabin, F. (2021). Effect of prehydration, permeant, and desiccation on GCL/Geomembrane interface transmissivity. *Geotextiles and Geomembranes*, 49(6), pp. 1451-1469. https://doi.org/10.1016/j.geotexmem.2021.04.006.

Rowe, R. K. and Zhao, L. (2023). Implications of double composite liner behaviour for PFAS containment. In: *9th International Congress on Environmental Geotechnics*, Chania, Greece, pp. 241-251. https://doi.org/10.53243/ICEG2023-64.

Rowe, R. K., Barakat, F. B., Patch, D., and Weber, K. (2023). Diffusion and partitioning of different PFAS compounds through thermoplastic polyurethane and three different PVC-EIA liners. *The Science of the Total Environment*, 892, pp. 164229-164229. https://doi.org/10.1016/j.scitotenv.2023.164229.

Rowe, R. K., Booker, J. R., and Fraser, J. (1997). POLLUTE Version 6.3 –1D Pollutant Migration through a Non-homogenous Soil. GAEA Technologies Ltd. https://gaea.ca/products.php.

Rowe, R. K., Caers, C. J., Reynolds, G., and Chan, C. (2000). Design and construction of barrier system for the Halton Landfill. *Canadian Geotechnical Journal*, 37(3), pp. 662-675. https://doi.org/10.1139/t99-131.

Rowe, R. K., Quigley, R. M., Brachman, R. W. I., and Booker, J. R. (2004) *Barrier Systems for Waste Disposal Facilities*, E & FN Spon, Taylor & Francis Books Ltd, London, pp. 587. https://doi.org/10.1201/9781482271935.

Schaefer, C. E., Drennan, D. M., Tran, D. N., Garcia, R., Christie, E., Higgins, C. P., and Field, J. A. (2019). Measurement of Aqueous Diffusivities for

Perfluoroalkyl Acids. *Journal of Environmental Engineering*, 145(11), pp. 6019006. https://doi.org/10.1061/(ASCE)EE.1943-7870.0001585.

USEPA. (2000). EPA and 3M announce phase out of PFOS. Available at: https://www.epa.gov/archive/epapages/newsroom_archive/newsreleases/33aa946e6cb11f35852568e1005246b4.html.

USEPA. (2023). Proposed PFAS National Primary Drinking Water Regulation. Available at: https://www.epa.gov/sdwa/and-polyfluoroalkyl-substances-pfas.

Zhang, M., Zhao, X., Zhao, D., Soong, T.-Y., and Tian, S. (2023). Poly- and Perfluoroalkyl Substances (PFAS) in Landfills: Occurrence, Transformation and Treatment. *Waste Management (Elmsford)*, 155, pp. 162-178. https://doi.org/10.1016/j.wasman.2022.10.028.

Proceedings of the XVIII ECSMGE 2024
GEOTECHNICAL ENGINEERING CHALLENGES
TO MEET CURRENT AND EMERGING NEEDS OF SOCIETY
© 2024 the Authors
ISBN 978-1-032-54816-6
DOI 10.1201/9781003431749-685
Open Access: www.taylorfrancis.com, CC BY-NC-ND 4.0 license

ECSMGE 24
XVIII EUROPEAN CONFERENCE ON SOIL MECHANICS AND GEOTECHNICAL ENGINEERING

Effect of saturation conditions on thermal properties of sands

Effet des conditions de saturation sur les propriétés thermiques des sables

Z. Zhou*, A. Diambra, T. Liu
University of Bristol, Bristol, United Kingdom
*zhixin.zhou@bristol.ac.uk

ABSTRACT: Soil thermal conductivity, diffusivity and heat capacity are critical parameters that govern the design of specific geotechnical infrastructure including energy piles, high-voltage cables and pipelines. The presence and flow of water are of particular importance as it dominates the conduction and convection hear transferring mechanisms, leading to a global increase in heat conduction ability by replacing air within the multi-phased soil system. This paper presents preliminary results from an experimental programme that aims to characterise the effects of saturation conditions on the thermal properties of a siliceous sand. Thermal conductivities were investigated for samples prepared to varied relative densities and degrees of saturation by two methods: (I) sand-water mixed at specific water contents and moist-tamped in moulds to the target densities; (II) cycles of wetting-draining applied to initially dry specimens through a customised test set-up. Thermal needles were employed that trigger transient heat source and monitor temperature variations. Significant differences were observed in the thermal conductivities between the Method I specimens and the Method II specimens in the first saturation stage. However, the differences diminished in the subsequent infiltration cycles. Overall, the results confirmed strong dependency of sand's thermal conductivity on saturation conditions as the presence of water envelopes and bridges sand particles in heat conduction.

RÉSUMÉ: La conductivité thermique, la diffusivité et la capacité thermique du sol sont des paramètres critiques qui régissent la conception d'infrastructures géotechniques spécifiques, notamment des pieux énergétiques, des câbles haute tension et des pipelines. La présence et le flux d'eau revêtent une importance particulière car ils dominent les mécanismes de transfert de chaleur par conduction et convection, entraînant une augmentation globale de la capacité de conduction de la chaleur en remplaçant l'air au sein du système de sol multi-phasique. Cet article présente les résultats d'un programme expérimental visant à caractériser les effets du degré de saturation sur les propriétés thermiques du sable siliceux. La conductivité thermique a été étudiée sur des échantillons préparés à des densités relatives et des degrés de saturation variés selon deux méthodes: (I) mélange de sable et d'eau à des teneurs en eau spécifiques, tassé humide dans des moules jusqu'aux densités cibles; (II) cycles d'humidification-drainage appliqués à l'aide d'un dispositif d'essai personnalisé. Les conductivités thermiques des échantillons ont été mesurées par des aiguilles thermiques déclenchant une source de chaleur transitoire et surveillant les variations de température. Des différences significatives ont été observées dans les conductivités thermiques des échantillons de la Méthode I par rapport à ceux de la Méthode II lors de la première étape de saturation. Cependant, ces différences se sont atténuées au cours des cycles d'infiltration ultérieurs. Dans l'ensemble, les résultats du programme d'essais préliminaires confirment une forte dépendance de la conductivité thermique du sable aux conditions de saturation et à la présence du film d'eau qui enveloppe et relie les particules de sable dans la conduction de chaleur.

Keywords: Thermal conductivity; saturation condition; high-voltage cables; porous media.

1 INTRODUCTION

Soil thermal properties dictate the storage and movement of heat in soils (De Vries, 1963) and govern heat transfer processes in various applications, including oil and gas pipelines, buried high-voltage (HV) electrical cables, agriculture, shallow geothermal system, thermal energy storage and nuclear waste disposal facilities (Gera et al., 1996; Malek et al., 2021; Nixon et al., 1991; Zhang and Wang, 2017). Thermal conductivity of soils is affected by a range of variables, for examples mineralogy, density, stress level and saturation conditions. The degree of saturation is a also crucial factor as it affects the transition of heat transfer from the solid phase to the liquid phase and the coupled process of heat conduction and moisture movement under various temperature gradients (Farouki, 1981).

Characterising thermal properties of partially saturated soil is crucial for onshore HV cables (Salata et al., 2015) and the landing parts of offshore HV cables, especially in regions where water tables may fluctuate daily or seasonally. Systematic investigation of soil's thermal conductivities in these application scenarios is required. This paper reports preliminary findings from an experimental programme that

investigates the impact of sample formation and saturation methods, wetting-draining cycles, and water level fluctuation on the thermal conductivity of granular soils.

2 MATERIAL AND METHODS

2.1 Soil tested

Leighton buzzard fraction B sand was used for this testing programme. It features a mean grain size d_{50} = 0.88 mm, coefficient of curvature C_c = 1, coefficient of soil uniformity C_u = 1.88, specific gravity G_s = 2.65, maximum and minimum void ratios e_{max} = 0.84 and e_{min} = 0.53, respectively (de Leeuw et al., 2021).

2.2 Sample preparation Method I

Method I for sample preparation was based on the conventional moist tamping method. Sand and water were mixed thoroughly at target water contents and filled in five layers into a cylindrical mould with an internal diameter of 50 mm and height of 130 mm. Each layer was tamped to achieve target void ratio and relative density. The adopted sample size followed the recommendation by ASTM (2022) and was compatible with the size of the thermal needle (2.4 mm diameter and 100 mm length) employed in the study (details see Section 2.4).

2.3 Sample preparation/saturation Method II

This method employed moulds of the same size as used in Method I. The specimen was initially prepared by pluviating dry sand to a target void ratio (relative density). Subsequently, water was percolated from the specimen base, and multiple saturation-desaturation cycles were applied through the inflow and outflow reservoirs, as shown in Figure 1. Specimen mass and its variations were measured by a digital balance placed beneath the sample, enabling continuous monitoring of the specimen's global water content and degree of saturation. In contrast to Method I, Method II enabled the application of wetting-draining cycles and simultaneous thermal conductivity measurements.

2.4 Equipment and test programme

The conventional transient thermal needle method was adopted in this study. The thermal unit was consisted of a single thermal needle (TR-3) and the TEMPOS thermal analyser supplied by the METER Group. The equipment allows thermal conductivity measurements in the range of 0.1-4 $W \cdot m^{-1} \cdot K^{-1}$ with an accuracy of ±10%. A 3-D printed top cap was designed to guide the needle's penetration from the centre of the specimen's top surface. Silicon grease was applied to the needle surface to enhance its contact with soil particles and improve the needle's sensitivity in capturing temperature variations (ASTM, 2022). Thermal tests were performed directly on the specimens prepared by Method I. Combinations of four relative densities (0%, 25.8%, 51.6%, 77.4%) and five degrees of saturation (0, 10%, 20%, 50%, 100%) were explored. The specimens prepared by Method II covered the same relative densities as those in Method I but with finer considerations of the degree of saturation.

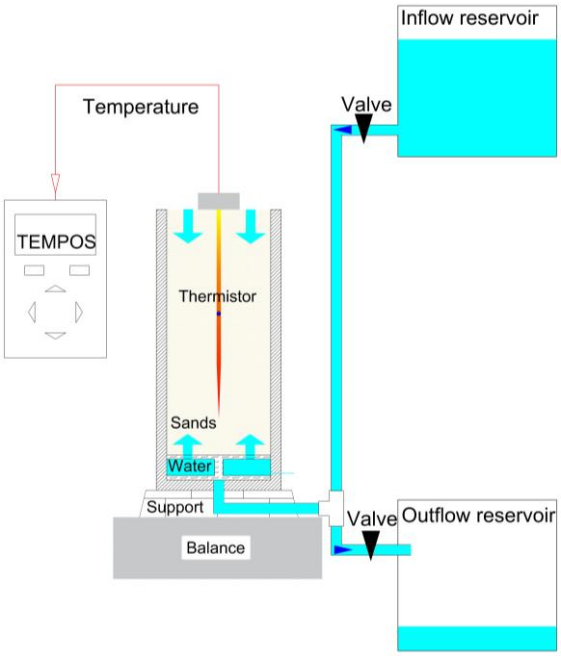

Figure 1. Schematic representation of the Method II set-up.

3 RESULTS AND DISCUSSION

3.1 Results from Method I

Figure 2 shows the variations of thermal conductivity against the degree of saturation (S_r) for the sand specimens prepared with Method I. Nominal trends are indicated with dashed straight lines. Under identical saturation level, specimens prepared at the lowest relative density, D_r = 0% ($e = e_{max}$) manifested lowest thermal conductivities. Higher-density specimens develop greater particle contact areas and therefore greater heat conduction capacity (Abu-Hamdeh, 2003). Sharp increases in thermal conductivity can be observed over the low S_r (<10%) range, followed by gradually increasing trends as S_r increased further.

The observed trends corroborate previous findings by Smits et al. (2010). Water surrounding sand particles enhances heat conduction through connected water channels, which act as a conduit for heat

exchange, noting the thermal conductivity of water (≈0.598 $W \cdot m^{-1} \cdot K^{-1}$) is significantly greater than that of air (≈0.02 $W \cdot m^{-1} \cdot K^{-1}$) (Aljundi et al., 2024). As the degree of saturation increased further, thermal conductivities rose only modestly as the main substitution processes of air by infilling water were largely completed at this stage.

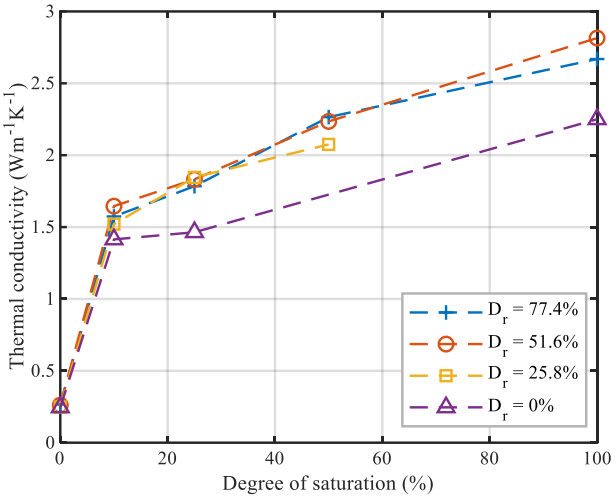

Figure 2. Measured thermal conductivities against degrees of saturation for specimens prepared by Method I.

3.2 Results from Method II

Figure 3 plots thermal conductivities against apparent degrees of saturation (S_r^*) for specimens prepared with Method II. Noting the progressive change in water level during the wetting-draining cycles and the non-uniform nature of the saturation process (especially in the 1st injection stage), apparent degrees of saturation (S_r^*) were computed based on the mass variations measured by the scale to represent the specimens' global saturation states.

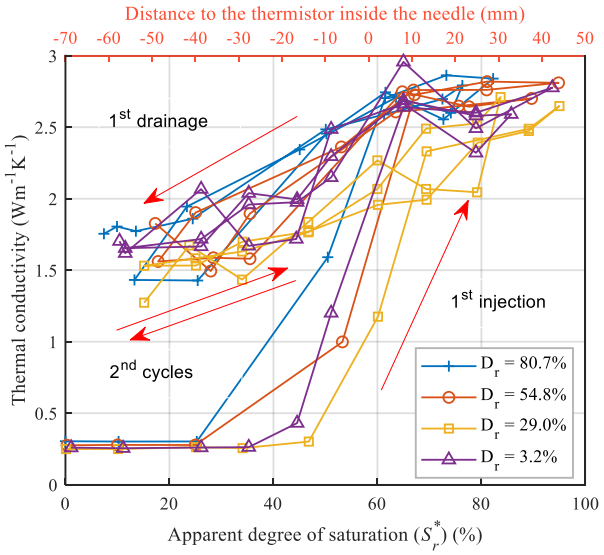

Figure 3. Measured thermal conductivities in two wetting-draining cycles for specimens prepared by Method II.

Figure 3 also plots on the upper x-axis distances between the estimated water levels and the thermistor positioned in the middle of the needle (see Figure 1) during the wetting-draining cycles. Water levels were approximated by assuming full saturation in the wetted zones, neglecting any capillary rise for the relatively coarse-grained uniform (d_{50} = 0.88 mm and C_u = 1.88) sand tested. Much more uniform distributions of water were expected in the subsequent draining-re-wetting cycles.

The measured thermal conductivities in the 1st percolation stage primarily relied on the water level relative to the thermistor. As water percolated into the lower part of the initially dry specimen, the water level remained below the thermistor level. The apparent degree of saturation (S_r^*) remained relatively low (< 30%) and the measured thermal conductivities largely represented those of dry specimens. Marked increases in thermal conductivities occurred as the water level ascended and S_r^* increased further to ≈70%.

Consistent and broadly linear trends can be observed in the subsequent desaturation and re-saturation cycles over the S_r^* range of 10-70%. Thermal conductivities appear to reach plateaux as S_r^* exceeded 70%. It is noted that natural gravity cannot de-saturate the specimens further to S_r^* <10% due to the presence of residual water.

An advanced multi-needle system is being developed at the University of Bristol that captures the distribution and evolution of thermal conductivity in unsaturated sands accurately.

3.3 Comparative analysis

Trends of thermal conductivity for the specimens prepared with Methods I and II are compared in Figure 4 for the first saturation stage and Figure 5 for the subsequent draining-wetting stages. Markedly different patterns are evident under relatively low S_r (or S_r^*) conditions of <60%. The results become more consistent under higher and more uniform saturation conditions in which the needle sensor was sufficiently immersed. Further increases in S_r^* resulted in relatively minimal increases in thermal conductivities, regardless of the specimen preparation method used.

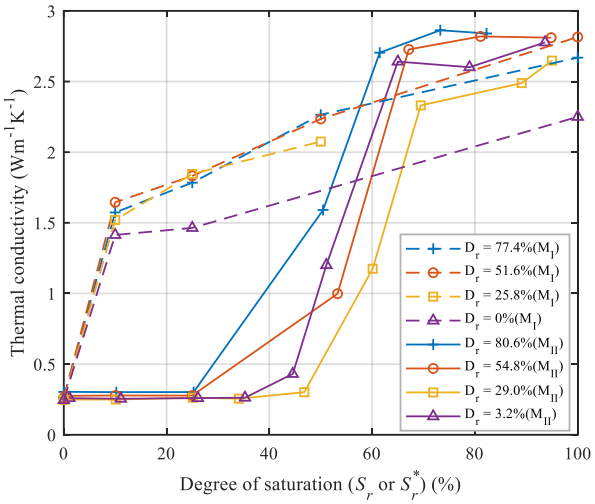

Figure 4. Comparison of measured thermal conductivities in the first saturation stage.

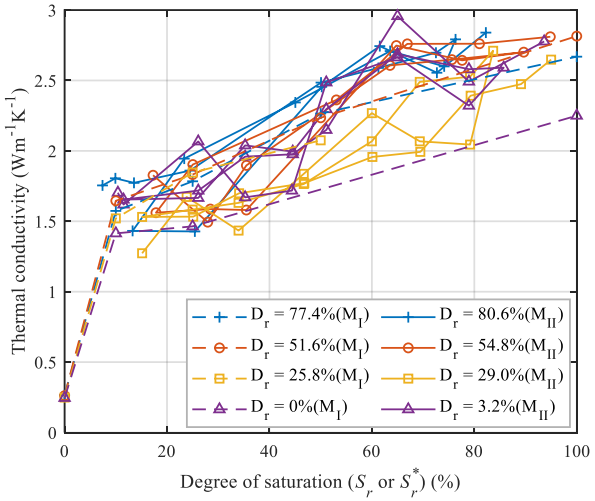

Figure 5. Comparison of measured thermal conductivities in the subsequent wetting-drying stages.

Compatible trends were observed in the subsequent wetting-drying cycles, despite the different specimen formation and saturation procedures employed (Figure 5). Saturating histories appear to yield only minor effects. Sand's thermal conductivity is primarily affected by its degree of saturation, although the water percolation process and any thermal coupling effects may also result in variations in the thermal conductivities of specimens prepared by Method II.

4 SUMMARY AND CONCLUSIONS

This paper presents preliminary results from an experimental programme designed to investigate the effects of saturation conditions on the thermal conductivity of silica sands. Two specimen preparation and saturation methods were employed: (a) a conventional method mixing sand and water at specified water content and tamping to target relative density; and (b) a customised experimental set-up that applied wetting-draining cycles and monitored water inflow and outflow. The measured thermal conductivities for the two methods exhibited significant disparities in the first saturation stage but became much more compatible in the subsequent de-saturation and re-saturation cycles. Further experimental study using an advanced multi-needle system is underway to investigate the potential effects of large number of wetting-draining cycles as well as coupled conduction-convection heat transfer process.

ACKNOWLEDGEMENTS

The authors thank the financial support by the University of Bristol and China Scholarship Council, and the technical support by Geoquip Marine, ScottishPower Renewables and Professor Justin Dix (University of Southampton). We thank Geoquip Marine for offering the use of the needle equipment.

REFERENCES

Abu-Hamdeh, N. H. (2003). Thermal properties of soils as affected by density and water content. *Biosystems engineering*, *86*(1), 97-102. https://doi.org/10.1016/S1537-5110(03)00112-0.

Aljundi, K., Pereira, C., Vieira, A., Maranha, J. R., Lapa, J., & Cardoso, R. (2024). Test conditions influence on thermal conductivity and contact conductance of sand at transient state. *Soils and Foundations*, *64*(1). https://doi.org/10.1016/j.sandf.2023.101405.

ASTM. (2022). Standard Test Method for Determination of Thermal Conductivity of Soil and Rock by Thermal Needle Probe Procedure. In (Vol. D5334 − 22a): ASTM Committee.

de Leeuw, L. W., Dietz, M. S., Milewski, H., Mylonakis, G., & Diambra, A. (2021). Relationship between texture of polypropylene coatings and interface friction for sand at low stress levels. *Can. Geotech. J. 58*(12), 1884-1897. https://doi.org/10.1139/cgj-2020-0321.

De Vries, D. A. (1963). Thermal properties of soils. *Physics of plant environment.*, 210-235.

Farouki, O. T. (1981). The Thermal-Properties of Soils in Cold Regions. *Cold Regions Science and Technology*, *5*(1), 67-75. https://doi.org/10.1016/0165-232x(81)90041-0.

Gera, F., Hueckel, T., & Peano, A. (1996). Critical issues in modelling the long-term hydro-thermomechanical performance of natural clay barriers. *Engineering Geology*, *41*(1-4), 17-33. https://doi.org/10.1016/0013-7952(95)00047-X.

Malek, K., Malek, K., & Khanmohammadi, F. (2021). Response of soil thermal conductivity to various soil properties. *International Communications in Heat and Mass Transfer*, *127*, 105516.

https://doi.org/10.1016/j.icheatmasstransfer.2021.105516.

Nixon, J. F. D., Saunders, R., & Smith, J. (1991). Permafrost and thermal interfaces from Normal Wells pipeline ditchwall logs. *Canadian Geotechnical Journal*, *28*(5), 738-745. https://doi.org/10.1139/t91-088.

Salata, F., Nardecchia, F., de Lieto Vollaro, A., & Gugliermetti, F. (2015). Underground electric cables a correct evaluation of the soil thermal resistance. *Applied Thermal Engineering*, *78*, 268-277. https://doi.org/10.1016/j.applthermaleng.2014.12.059.

Smits, K. M., Sakaki, T., Limsuwat, A., & Illangasekare, T. H. (2010). Thermal conductivity of sands under varying moisture and porosity in drainage–wetting cycles. *Vadose Zone Journal*, *9*(1), 172-180. https://doi.org/10.2136/vzj2009.0095.

Zhang, N., & Wang, Z. Y. (2017). Review of soil thermal conductivity and predictive models. *International Journal of Thermal Sciences*, *117*, 172-183. https://doi.org/10.1016/j.ijthermalsci.2017.03.013.

Proceedings of the XVIII ECSMGE 2024
GEOTECHNICAL ENGINEERING CHALLENGES
TO MEET CURRENT AND EMERGING NEEDS OF SOCIETY
© 2024 the Authors
ISBN 978-1-032-54816-6
DOI 10.1201/9781003431749-686
Open Access: www.taylorfrancis.com, CC BY-NC-ND 4.0 license

ECSMGE 24
XVIII EUROPEAN CONFERENCE ON SOIL MECHANICS AND GEOTECHNICAL ENGINEERING

Validation of a sulfide soil landfill numerical model

Validation d'un modèle numérique de décharge pour sols sulfurés

A. Ziagharib*, C. Maurice, Q. Jia, J. Laue
Department of Civil, Environmental and Natural Resources Engineering, Luleå University of Technology, Luleå, Sweden

J. Macsik
Ecoloop, Stockholm, Sweden

**Alaleh.Ziagharib@ltu.se*

ABSTRACT: Due to their silty texture and high organic content, sulfide soils are typically unsuitable for use as a foundation for construction projects. In most cases, excavation and replacement with other construction materials are needed to ensure the structural integrity of building or infrastructure. Landfills are commonly used for the disposal of excavated sulfide soil. Because of the chemical properties of these soils and the risk of acidification, these landfills need to be kept saturated to limit oxygen diffusion. However, the long-term behaviour of these landfills is not yet fully understood, highlighting the need for further research to investigate the fluctuation of the degree of saturation in the soil, under different conditions. This study examined the effect of seasons on the degree of saturation in sulfide soil landfills and its effect on oxygen transport. The objective of the current study was to validate a numerical model of a sulfide soil embankment, done using SEEP/W software, with data from the monitoring of a sulfide soil landfill, in Northern Sweden. A one-dimensional numerical model of the landfill was created using laboratory measurements of hydraulic conductivity and water retention capacity. This model was then validated by comparing it with data from installed sensors. The numerical model accurately predicted the degree of saturation changes over time in the landfilled soil. These findings allow engineers to optimize design and predict long-term performance under different environmental conditions. The study highlights the importance of numerical modelling in predicting long-term hydrological behaviour and offers valuable insights into sulfide soil landfill behaviour.

RÉSUMÉ: En raison de leur texture limoneuse et de leur forte teneur en matière organique, les sols sulfurés sont généralement inadaptés dans les fondations des projets de construction. Dans la plupart des cas, il est nécessaire de les remplacer par d'autres matériaux de construction pour garantir l'intégrité structurelle des bâtiments ou des infrastructures. Les sols sulfurés excavés sont couramment mis en décharges. En raison de leur propriétés chimiques et du risque d'acidification, il est nécessaire de maintenir ces décharges saturées pour limiter la diffusion de l'oxygène. Cependant, le comportement à long terme de ces décharges n'est pas encore pleinement compris, soulignant la nécessité de recherches supplémentaires pour étudier leurs fluctuations du degré de saturation dans différentes conditions. Cette étude a examiné l'effet de la consolidation et des saisons sur le degré de saturation des décharges de sol sulfuré, avec un accent particulier sur le transport de l'oxygène. L'objectif de cette étude était de valider numériquement un modèle de digue en sol sulfuré en utilisant le logiciel SEEP/W, avec des données provenant d'une installation de capteurs dans une décharge de sol sulfuré, dans le nord de la Suède.Un modèle numérique unidimensionnel de la décharge de sols a été créé en utilisant des mesures de laboratoire de la conductivité hydraulique et de la capacité de rétention d'eau. Ce modèle a ensuite été validé en le comparant aux données des capteurs installés.L'étude a montré que le modèle numérique prédisait avec précision les variations du degré de saturation au fil du temps dans le sol. Ces résultats permettent aux ingénieurs d'optimiser la conception des digues et d'en prédire les performances à long terme dans différentes conditions environnementales. L'étude met en évidence l'importance de la modélisation numérique pour prédire le comportement hydrologique à long terme et offre des informations précieuses sur le comportement des décharges de sol sulfuré.

Keywords: Sulfide soil landfill; numerical modelling; SEEP/W; saturation degree; oxygen transport.

1 INTRODUCTION

Sulfide soil contains high concentrations of mainly iron sulfides (e.g., pyrite). These minerals naturally occur in certain geological formations found worldwide, including tropical regions, Australia, and coastal areas of Sweden and Finland. Disturbing these soils through excavation or construction exposes the sulfide minerals to oxygen, leading to oxidation. This can create acidic conditions, lowering soil pH which leads to dissolved sulfate and metals released into water bodies, impacting aquatic life and infrastructure.

Sulfide soils are often silty and water-rich, and pose risks of settlement, soil failure, and frost heave in cold

regions. Therefore, they are often excavated and replaced with more construction-suitable soil types. The urbanization and construction of infrastructure in sulfide soil regions in sweden have heightened the demand for soil management alternatives e.g. disposal. Due to the soil's chemical properties, its disposal is complex, requiring measures to prevent oxidation and acidification. Hence, these soils must be deposited while remaining saturated to prevent environmental hazards.

Creating optimal conditions for sulfide soil is expensive and restricts landfill capacity. To expand landfill capacity and prevent oxidation, it is vital to understand the hydrological properties of sulfide and silty soils in unsaturated conditions. Some software, including one-dimensional (1-D) and two-dimensional (2-D) flow models, have been employed to help in the design and evaluation of soil covers such as VADOSE/W and SEEP/W(Song & Yanful, 2008). SEEP/W has been commonly used to simulate water infiltration in unsaturated systems e.g. (Aubertin et al., 2009; Bréard Lanoix, Pabst, & Aubertin, 2017; Bussière, Aubertin, & Chapuis, 2003; Cifuentes, Aubertin, Chapuis, Bussière, & Molson, 2006; Fala, 2003; Gwendoline, Bruno, Pabst, Émilie, & Roy, 2020; Martin, 2003).

This study aims to predict the behaviour of sulfide soil landfills under various conditions and identify short and long-term influencing parameters by validating a numerical model using SEEPW with on-site measurement data.

2 MATERIAL AND METHODS

2.1 Description of test plots

The test area is a sulfide soil landfill where fresh soil was recently deposited. A 60 cm layer of till covers the entire site, while the depth of the sulfide soil deposition exceeds 3 metres (Figure 1).

2.2 Field measurements

The installation of sensors for measuring temperature, water matric potential (WP), and volumetric water content (VWC), was carried out in the sulfide soil layer and cover in May 2022. Table 1 lists the depth of installation of instrumentation. It is important to note that additional sensors were installed in this case study; however, the data from these additional sensors has not been presented in this paper.

2.3 Finite element modelling

Hydrogeological numerical simulation was conducted using SEEP/W 2021. The sulfide soil landfill analyzed in this study is composed of two primary layers (cover and sulfide soil) based on the test plot. Specifically, the cover layer surface is represented as a distinct 60 cm layer with a finer mesh to reduce convergence challenges when modelling infiltration events into the arid ground, and to incorporate the impact of surface drying and desiccation.

In this study, the measured data from sensors were employed to verify the numerical model. The initial case was the same as the test plot case to verify the performance of the numerical model.

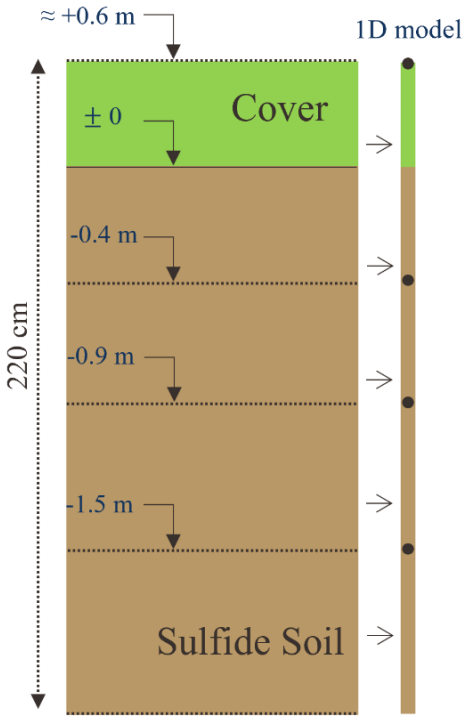

Figure 1. Soil layers and 1D model.

Table 1. Sensor installation position.

Layer	Depth (m)	Monitoring points	Sensors
Cover	≈ +0.6	Point 1	VWC & WP
	+0.1	-	
Sulfide soil	-0.1	-	
	-0.4	Point 2	VWC
	-0.9	Point 3	VWC
	-1.5	Point 4	WP

2.4 Input data

When conducting simulations of soil layers using SEEP/W software, it is essential to ensure that all necessary input data is included in the model. These input data including material properties, boundary conditions, and initial conditions are critical to the accuracy and reliability of the simulation results.

2.5 Material properties

The material properties of the soil layers must be accurately defined, including soil water characteristics curve (SWCC), and hydraulic conductivity. These parameters will play a significant role in determining the flow of water within the sulfide soil layers. The SWCs of material including air entry value (AEV) were derived from a pressure plate test conducted in the laboratory for the material used for the test plot. The SWCCs were fitted with theoretical curves using Van Genutchen model.

The saturated hydraulic conductivity (HC) was measured using permeability tests. The results then were used to predict unsaturated hydraulic conductivity using SEEP/w. The unsaturated hydraulic conductivity function is challenging to measure directly, and prediction methods are commonly used instead. In this study, Van Genutchen model was used to estimate unsaturated hydraulic conductivity of soil as a function of matric suction. The material properties used in the numerical modelling are summarized in Table 2.

Table 2. material properties.

Soil	Porosity	AEV (kPa)	HC (m/s)
Cover	0.3	50	10^{-7}
Sulfide soil	0.4	20	$5e10^{-7}$

2.6 Boundary and initial condition

The boundary and initial conditions must be properly defined to provide a comprehensive understanding of the water flow into and out of the soil layers. A Land Climate Interaction (LCI) boundary condition was applied to the top of the domain. The LCI boundary condition requires weather information, including air temperature, relative humidity, wind speed, and precipitation, which is essential for calculating infiltration and flux in the system caused by rainfall, snowmelt, evaporation, etc. This data was obtained from the Swedish Meteorological Institute website using a weather station at Umeå airport from May 2022 to September 2023. The bottom boundary was considered an open boundary condition, representing both inflow and outflow of water, depending on the local hydraulic gradients and other boundary conditions. The initial water table level was set at the cover surface level, and all soil layers were considered fully saturated at the first step of the simulation. This assumption was based on the water level measured at the site and measurements from samples taken from the site. The saturation water content was determined based on the maximum and minimum density of the soil at the site.

3 RESULTS

The study presents data collected between May 2022 and September 2023, which were used to evaluate the validation of a numerical model simulation for a sulfide soil landfill. The data consist of soil layer temperature, volumetric water content, and water flux in the soil layers. To compare the simulation results with measured data, three sensors were selected at points 1, 2 and 3 for volumetric water content and temperature and two sensors (point 1 and 4) for water flux to compare results from the numerical model and landfill case study, as indicated in *Table 1*.

In Figure 2, a comparison is made between temperatures in different soil layers and the air temperature. Notably, the temperature in the soil layers did not drop below freezing, despite sub-zero air temperatures during the winter. This phenomenon is attributed to the insulating effect of snow covering the soil surface, which prevents the soil layers from freezing. This observation is crucial when considering the potential impact of frost depth on the hydraulic conductivity of the soil layers and water flow. Figure 3 presents a comparison between measured and numerically calculated volumetric water content. Initially, differences in the results were observed due to sensor placement in disturbed soil following the excavation of a ditch in the soil layers to be able to install sensors. This led to significant fluctuations in soil volumetric water content.

Over time, the system reestablished equilibrium, and the results of the numerical model began to align with the observed trend. It is shown that during winter when the soil surface was covered by snow the soil layers, including sulfide soil remained saturated.

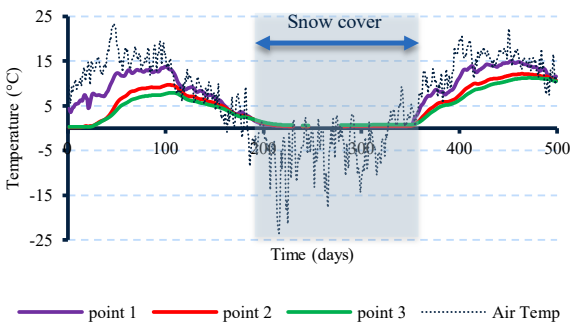

Figure 2. Comparing soil layer temperatures to air temperature.

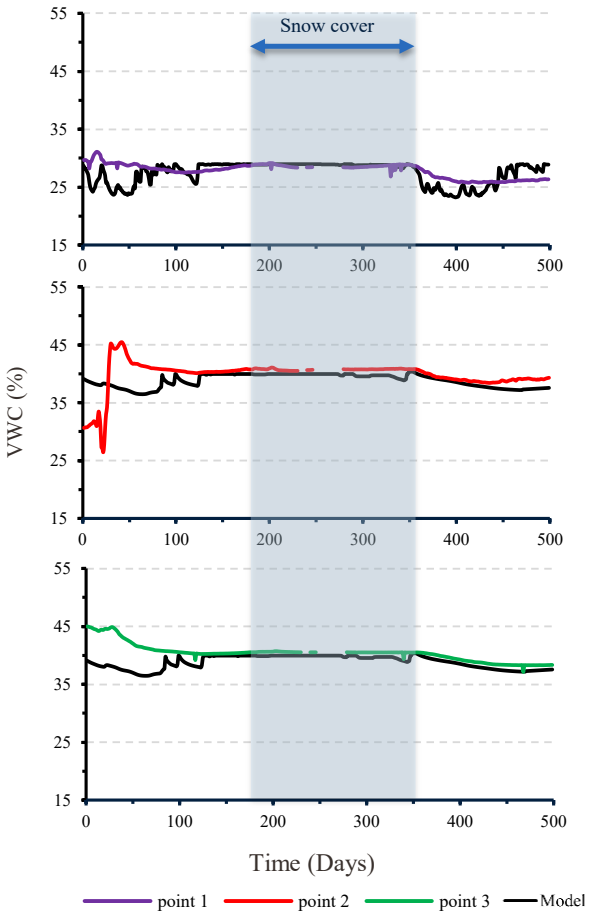

Figure 3. comparison measured and predicted VWC.

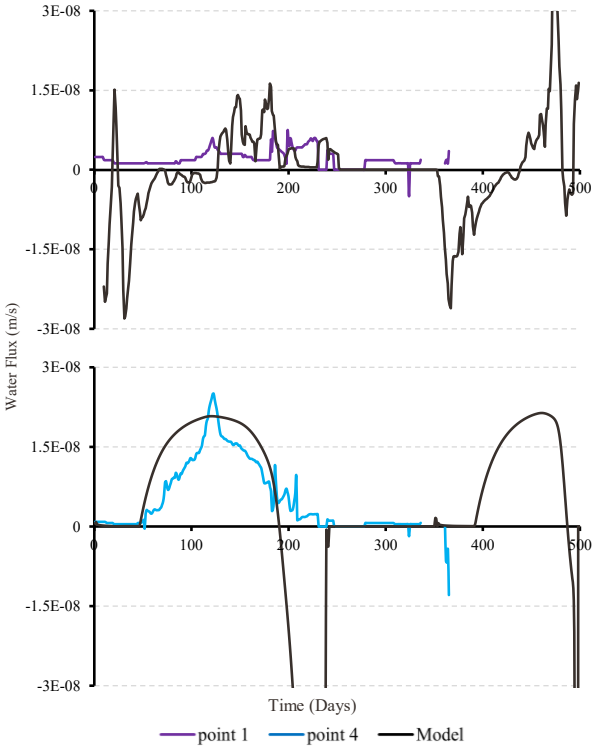

Figure 4. comparison measured and predicted water flux.

Figure 4 provides a depiction of water flux at specific points within the soil layers. These graphs are based on data recorded by water potential sensors. Unfortunately, these sensors only collected data for approximately 400 days, and not for the entire monitoring period until September 2023. Fluctuations in water potential reflect the dynamic movement of water into and out of a system. An increase in water potential signifies water entering or becoming more available within the system, often due to factors like rainfall, irrigation, or root water uptake. Latter is not the case in this specific case. Conversely, a decrease in water potential indicates water leaving the system, through processes such as evaporation, transpiration, or drainage. Water flux based on water potential can be calculated using Darcy's Law, where the flux equals the product of hydraulic conductivity and the negative gradient of water potential, providing a straightforward method for comparison between software outputs and calculated water flux values.

Water movement direction is indicated by positive or negative flux values in this paper. Positive flux signifies water moving towards the surface, such as during summer from days 0 to 200 due to higher temperatures and evaporation. With lower temperatures and autumn precipitation starting from day 120 to 200, the positive flux decreases, indicating slower water flow towards the surface and less water exiting the system. Negative flux denotes water moving away from the surface, potentially due to precipitation and snow melting in the springtime beginning from day 400. During the snow season, roughly between days 250 to 350, the flux is zero, likely due to snow covering the soil surface and preventing water from entering or leaving the system. Initial discrepancies between measured and predicted data may result from soil disturbance during sensor installation, but consistency improves over time, particularly between days 50 and 200.

At Point 4, there is a negative flux predicted just before the snow season, which is not reflected in the measured data. Similarly, there is negative flux occurring between approximately after snow season, which is also not found in the predicted data. In summary, differences exist between the measured data and the results of the numerical modelling.

These differences can be explained by the position of the water table and its fluctuations. However, it's important to note that the available data on water table fluctuation at the site is limited and hasn't been integrated into the model. Additionally, the properties of the soil are closely related to its density and water retention capacity. For this specific soil, further tests are necessary to measure its water retention capacity and hydraulic conductivity at various densities. The

changes in density over the monitoring period are also unknown. To enhance the accuracy of the model's predictions, it is beneficial to determine the consolidation properties of this soil and assess potential changes over the monitoring period.

Finally, it's crucial to acknowledge that the climate data used in this model is not specific to the site. Differences in temperature, precipitation, and other climate variables may introduce variations that impact the modelling results.

4 CONCLUSION

This study aimed to validate a numerical model for a sulfide soil landfill, with the objective of enhancing understanding of water movement and seepage in sulfide soil layers. The goal was to predict the behavior of these soil layers over an extended period. The numerical model successfully predicted the volumetric water content in various layers of the sulfide soil landfill. Additionally, the study compared the results of water flux from both measured and predicted data.

This comparison revealed that, although the prediction results came close to estimating the flux in the soil layers, disparities between the measured and improved data were evident. These differences may be attributed to inaccuracies in material properties, climate data, and the fluctuations of the water table under real conditions. To enhance prediction accuracy, it is essential to define more precise boundary and initial conditions for the model.

Continuing this research requires obtaining more comprehensive data on the material properties of sulfide soils in general, including their consolidation properties. Furthermore, accurate data on the density of soil layers at the specific landfill site is necessary, which can be acquired through borehole sampling. In addition, identifying the parameters that influence the saturation degree of sulfide soil landfills and quantifying the impact of each parameter through numerical analysis is crucial for further advancements in this field.

ACKNOWLEDGEMENTS

This project received funding from the European Regional Development Fund through the Interreg Botnia-Atlantica program. Gratitude is extended to the staff at the Dåva D.A.C waste centrefor their support in setting up and conducting the field installation.

REFERENCES

Aubertin, M., Cifuentes, E., Apithy, S., Bussière, B., Molson, J., & Chapuis, R. (2009). Analyses of water diversion along inclined covers with capillary barrier effects. *Canadian Geotechnical Journal, 46*(10), 1146-1164, https://doi.org/10.1139/T09-050.

Bréard Lanoix, M., Pabst, T., & Aubertin, M. (2017). Characterization of the hydrogeological properties of a sand layer placed on an experimental waste rock pile, In: *70th Canadian Geotechnical Conference (GeoOttawa 2017)*, Ottawa, Canada,.

Bussière, B., Aubertin, M., & Chapuis, R. P. (2003). The behavior of inclined covers used as oxygen barriers. *Canadian Geotechnical Journal, 40*(3), 512-535, https://doi.org/10.1139/t03-001.

Cifuentes, E., Aubertin, M., Chapuis, R., Bussière, B., & Molson, J. (2006). Analyses of water diversion length of inclined, layered soil covers.

Fala, O. (2003). *Étude des écoulements non saturés dans les haldes à stériles à l'aide de simulations numériques*: National Library of Canada= Bibliothèque nationale du Canada, Ottawa.

Gwendoline, H., Bruno, B., Pabst, T., Émilie, B., & Roy, P. (2020). Influence of climate change on the ability of a cover with capillary barrier effects to control acid generation. *Hydrogeology Journal, 28*(2), 763-779, https://doi.org/10.1007/s10040-019-02084-y.

Martin, V. (2003). *Étude des propriétés non saturées des stériles miniers*: École polytechnique de Montréal.

Song, Q., & Yanful, E. K. (2008). Monitoring and modeling of sand-bentonite cover for ARD mitigation. *Water, air, and soil pollution, 190*(1-4), 65-85, https://doi.org/10.1007/s11270-007-9581-z.

F - Future city world vision
F - Vision mondiale de la ville du futur

Proceedings of the XVIII ECSMGE 2024
GEOTECHNICAL ENGINEERING CHALLENGES
TO MEET CURRENT AND EMERGING NEEDS OF SOCIETY
© 2024 the Authors
ISBN 978-1-032-54816-6
DOI 10.1201/9781003431749-687
Open Access: www.taylorfrancis.com, CC BY-NC-ND 4.0 license

ECSMGE 24
XVIII EUROPEAN CONFERENCE ON SOIL MECHANICS AND GEOTECHNICAL ENGINEERING

Reinforcement of a coarse granular aggregate with microgrids: Influence on packing

Renforcement d'un agrégat granulaire grossier à l'aide de micro-grilles: Influence sur le paquetage

R. Anjos*, M. Pinho-Lopes
RISCO, Department of Civil Engineering, University of Aveiro, Aveiro, Portugal
W. Powrie
School of Engineering, University of Southampton, Southampton, United Kingdom
**rafaelanjos@ua.pt*

ABSTRACT: Micro-reinforcement using engineered fibres or particulate inclusions, such as strip fibres, has potential for improving the performance of coarse granular aggregates, such as materials for road bases or railway ballast. During loading, the aggregate particles move, and the soil skeleton is rearranged. Recent studies have shown the effectiveness of fibre reinforcement of soils and coarse granular aggregates. Usually, the fibres are mixed randomly within the soil skeleton, with consequences on packing. Fibres can be considered micro-reinforcements, as these are inclusions at the particle scale. Alternatively, other forms of micro-reinforcements can be used. Small elements of geogrids, herein designated microgrids, are alternative forms of micro-reinforcement. Their inclusion may also affect the packing of the particles of aggregate, as the presence of the reinforcement my affect the displacement and rotation of the adjacent particles. In this paper, the influence of microgrids on the packing of a coarse aggregate is analysed. For that, a container with two transparent faces was used. The aggregate and the micro-reinforcement elements were mixed at a predetermined volumetric ratio, placed in the container, and submitted to compaction. The addition of microgrids disrupted the natural grain packing, and corresponding increases in e_{max} and e_{min} were observed. For the microgrid with higher anchorage length, non-natural void formation was observed due to microgrid-microgrid interaction rather than microgrid-grain interlocking.

RÉSUMÉ: Le micro-renforcement à l'aide de fibres artificielles ou d'inclusions particulaires, telles que les fibres en bandes, peut améliorer les performances des agrégats granulaires grossiers, tels que les matériaux pour les bases routières ou le ballast des voies ferrées. Pendant le chargement, les particules d'agrégats se déplacent et le squelette du sol est réorganisé. Des études récentes ont montré l'efficacité du renforcement des sols et des agrégats granulaires grossiers par des fibres. En général, les fibres sont mélangées de manière aléatoire dans le squelette du sol, ce qui a des conséquences sur le paquetage. Les fibres peuvent être considérées comme des micro-renforts, car il s'agit d'inclusions à l'échelle des particules. D'autres formes de micro-renforts peuvent également être utilisées. Les petits éléments des géogrilles, appelés ici micro-grilles, sont d'autres formes de micro-renforcement. Leur inclusion peut également affecter le paquetage des particules de l'agrégat, car la présence du renforcement peut affecter le déplacement et la rotation des particules adjacentes. Dans cet article, l'influence des micro-grilles sur le paquetage d'un agrégat grossier est analysée. Pour ce faire, un conteneur à deux faces transparentes a été utilisé. L'agrégat et les micro-éléments de renforcement ont été mélangés selon un rapport volumétrique prédéterminé, placés dans le conteneur et soumis au compactage. L'ajout de micro-grilles a perturbé l'empilement naturel des grains, et des augmentations correspondantes d'e_{max} et d'e_{min} ont été observées. Pour la micro-grille ayant une longueur d'ancrage plus élevée, on a observé une formation de vides non naturels due à l'interaction micro-grille-micro-grille plutôt qu'à l'imbrication micro-grille-grain.

Keywords: Micro-reinforcement; packing; coarse aggregates; scaled-ballast.

1 INTRODUCTION

For the past two decades, researchers (Lirer et al. 2011; Michalowski & Čermák, 2003; Soriano et al. 2017) have tried to reinforce soils, mostly sands, with random micro-reinforcements, such as discrete fibres. The shear strength of the resulting composite material is governed by the micro and the macromechanical characteristics of both fibres and soil particles (Lirer et al. 2011). Discrete fibres play a significant role in increasing the overall shear strength and ductility of sands (Michalowski & Čermák, 2003). Because of the effectiveness of fibre reinforcement, the approach has been extended to coarse granular aggregates such as railway ballast.

Railway ballast is a coarse granular aggregate, generally obtained by quarrying high quality rock, used as a load bearing layer. The ballast layer supports the track superstructure and transfers the load generated at wheel-rail interface to the sub-base and the underlying soil. Laboratory testing of full-size ballast is difficult, expensive, and time-consuming. Thus, testing scaled-down ballast is an attractive solution for understanding the mechanics of full-size ballast (Sevi, 2008).

Ajayi et al. (2017a) studied the behaviour of 1/3 and 1/5 scaled ballast reinforced with randomly distributed strip fibres and analysed the influence of the fibre dimensions and fibre content. Ajayi et al. (2017a) observed that, in monotonic triaxial tests, fibre-reinforced gravels exhibited decreased dilation, increased ductility and increased peak deviator stress. Within the framework of classic soil mechanics principles, reduced dilatancy is consistent with higher ductility, but neither is consistent with an increased deviator stress. Thus Ajayi et al. (2017a) proposed a three-phase model for the grains, fibres and voids, with the fibres considered explicitly as a separate phase:

$$\upsilon = \frac{V_s+V_f+V_v}{V_s} = 1 + e + V_{fr} \qquad (1)$$

where υ is the specific volume of fibre-reinforced soil, V_s is the volume of solids, V_f is the volume of fibres, V_v is the volume of voids, e is the void ratio of the soil (considering soil particles only) and V_{fr} is the volumetric fibre ratio (V_f/V_s). This framework has the advantage of considering the fibres independently of the natural soil matrix (solids particles and voids).

Ajayi et al. (2017a) expressed the fibre dimensions normalised with respect to the effective diameter corresponding to 50% of soil particles, D50. LN is the normalised fibre length (= Lf/D50) and WN the normalised fibre width (= Wf/D50), where Lf is the fibre length and Wf is the fibre width.

For the case of 1/3 scale ballast reinforced with strip fibres, the minimum normalised fibre dimensions giving an effective improvement of the monotonic response were: LN = 7.1 and WN = 2.5 (Ajayi et al. 2017a). The volumetric fibre ratio, Vfr, is the ratio in Eq.1 that accounts for the presence of fibres in the soil matrix. For a given Vfr, as the grain size increases, the number of fibres required to develop similar grains–fibre interactions decreases. Thus for scaling purposes, Vfr is not a sufficient measure for representing the fibre content. When considering the mechanical behaviour of fibre reinforced granular materials across different grain size ranges, the number of fibres available for fibre-grain interaction is also important and can be defined by the fibre-grain ratio Nfg. For a given fibre length and width, Nfg is the ratio between Nf, the number of individual fibres in a fibre reinforced specimen and Ng the number of grains in a fibre reinforced specimen. Ng can be estimated using two different approaches: Approach 1, which assumes that all grains are approximately spherical with a diameter equal to D50 (Ajayi et al. 2017b); Approach 2, which divides the weight of the ballast specimen by the average weight of a single grain (Ferro et al. 2023).

Ferro et al. (2022) studied the ability of randomly distributed fibres to reinforce full-size ballast using packing tests and full-scale cyclic laboratory tests (single sleeper bay section of railway under plane strain conditions). From the full-scale tests, the authors concluded that the effectiveness of fibres in reducing the settlement of traditional railway track depends not only on their ability to increase the material shear resistance, but also on how little they influence the packing of ballast grains. To assess the effect of fibre reinforcement on the long-term settlement of ballast after cyclic load, Ferro et al. (2022) proposed an alternative measure of the propensity to pack of the fibre-reinforced composite, IDr:u which is the ratio of the range of reinforced void ratios (emax and emin, maximum and minimum void ratio of unreinforced ballast) to the corresponding range the unreinforced material (e^U_{max} and e^U_{min}, maximum and minimum void ratio of unreinforced ballast, respectively). For full-size ballast IDr:u should be smaller than 1.05 (Ferro et al. 2022).

The form of the reinforcement will result in different mobilisation mechanisms. Discrete fibres oriented horizontally can sustain tensile forces generated at the grains level (Soriano et al. 2017), while microgrids will tend to generate additional interaction mechanisms such as local interlocking. Indraratna et al. (2018) analysed geogrid reinforcement of railway ballast and defined a range for the geogrid aperture size, A, that maximise bearing capacity of the ballast layer, while reducing track settlement. The aperture size should not be smaller than 0.9D50 and larger than 1.2D50.

In this paper, two forms of microgrid were studied, particularly their effect on the packing of a coarse granular aggregate. Unreinforced and reinforced specimens were compacted using a shaking table and the effect of compaction on the grain packing was analysed.

2 MATERIALS AND METHODS

2.1 Materials

Freshly quarried gneiss granular aggregate was obtained from *Irmãos Cavaco* quarry (Aveiro, Portugal). This coarse material corresponds to a 1/3 scale representation of the full-size ballast used on Portuguese railways (BS EN 13450: Aggregates for Railway Ballast, 2013). The particle size distribution of the aggregate is shown in Figure 1. G_s is the aggregate specific gravity, C_u is the uniformity coefficient and *FI* the flakiness index. *FI* informs about the percentage by weight of an aggregate with an aspect ratio less than 0.6 times their mean size. The natural effective angle of shearing resistance (effective angle of friction), ϕ', of the coarse granular aggregate is 39°.

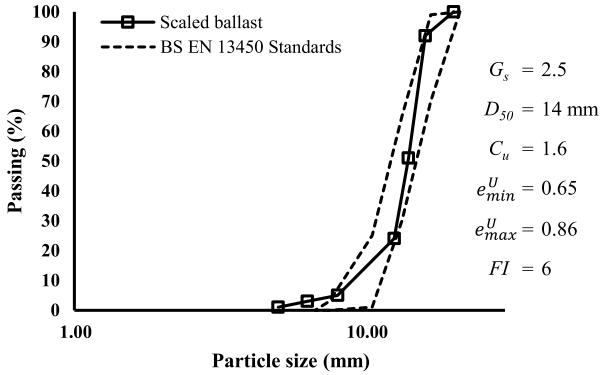

Figure 1. Aggregate particle size distribution and additional properties.

The microgrids were obtained from a commercially available geogrid by cutting pieces to a predefined geometry. Two different microgrid shapes were considered (Figure 2). The normalised dimensions of the microgrids are given in Table 1.

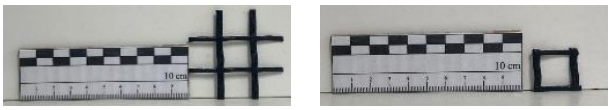

a) *b)*

Figure 2. Microgrids studied: a) MG1, b) MG2.

Table 1. Microgrids volume and normalised geometry: length, width, and aperture size.

Normalised dimensions	MG1	MG2
Volume of a single element (cm^3)	0.554	0.238
L_N (-)	3.9	1.8
W_N (-)	3.7	1.6
A/D_{50} (-)	1.1	1.1

The central element of MG1 and MG2 is the same (an opening of 16 mm × 16 mm). The difference between MG1 and MG2 is that the former includes additional elements beyond the central element (Figure 2). Thus, the normalised length and width of MG1 are nearly double of MG2. The normalised aperture size (A/D_{50}) of the microgrids is within the range proposed by Indraratna et al. (2018). However, the normalised length (L_N) and width (W_N) of the microgrids do not meet the optimum dimensions proposed by Ajayi et al. (2017a), for strip fibres.

2.2 Packing test

To assess the effect of the microgrids on the packing of the 1/3 scale ballast grains, packing tests were carried out. Two different plywood boxes were used: Box 1, cubic box with internal edges of 300 mm (all faces made 16 mm thick plywood); Box 2, cubic box with two 8 mm thick plexiglass faces, which allow for visual inspection of the particle movement during compaction, with longitudinal internal edges (268 and 300 mm). The boxes were stiff enough to ensure plane strain conditions. The packing tests were carried out in Box 1, and visual observation of the packing using Box 2.

For each packing test, Box 1 was filled manually and weighed. Loose conditions were obtained by placing the aggregate gently into the box. Dense conditions were obtained using a shaking table, with a frequency of 50 Hz and amplitude of 0.8 mm. Three episodes of shaking (approximately 300 seconds each) were applied after placing each layer of material (100 mm high) into the box, with a total of 3 layers. The box was slightly overfilled and the final top surface levelled by adding and removing individual grains. For the dense condition, the final level was obtained by hand-pressing the lid against the aggregates while vibrating. This process, described by Ferro et al. (2022), allows the maximum density to be achieved without grain breakage. Once the specimen had been levelled, the lid was placed on top of it and the actual height of aggregate was measured.

The packing tests (Box 1) were carried out for a predetermined volumetric fibre ratio of 3.2%, identified by Ajayi et al. (2017a) as the optimum Vfr for a coarse granular aggregate with grain dimensions similar to that used herein. The volume of microgrid reinforcement was calculated from the volume of solid particles and the bulk density of the specimen. Mineral particles were hand-mixed with microgrids on a specimen by specimen basis to ensure a random distribution of the microgrids within the grains.

For each condition (unreinforced, U; reinforced with microgrid 1, R MG1, and with microgrid 2, R MG2), 6 packing tests were carried out; 3 for the loosest (emax) and 3 for the densest (emin) condition,

resulting in a total of 18 tests. One additional packing test per condition was carried out in Box 2 (3 tests in total).

3 RESULTS AND DISCUSSION

3.1 Fibre-grain ratio

To assess the fibre-grain ratio, N_{fg}, it is necessary to estimate the number of grains per specimen. Table 2 summarises the estimates of the number of grains average value for 3 specimens per condition tested, N_g, using Approaches 1 (Ajayi et al. 2017b) and 2 (Ferro et al. 2023), described in section 1.

Table 2. Number of grains, N_g, and fibre-grain ratio, N_{fg}, for the specimens tested, using Approaches 1 (Ajayi et al. 2017b) and 2 (Ferro et al. 2023).

Nomenclature	U	R MG1	R MG2
V_{fr} (%)	-	3.2	3.2
N_g (-) Ajayi et al. (2017b)	11675	9914	10422
N_g (-) Ferro et al. (2023)	12175	10339	10867
N_{fg} (%) Ajayi et al. (2017b)	-	9.8	21.7
N_{fg} (%) Ferro et al. (2023)	-	9.4	20.8

Approach 2, proposed by Ferro et al. (2023), leads to higher number of grains per specimen (by ~4%) than the method proposed by Ajayi et al. (2017b). The different estimates of N_g influence the fibre-grain ratio, which are related to the volume of a single fibre. To better understand those relations, Figure 3 shows the influence of the volume of a single fibre on the fibre-grain ratio, N_{fg}. (for a constant volume of solids, V_s = 0.017 m^3, and volumetric fibre ratio, V_{fr}). As the volume of a single fibre increases, the number of grains that potentially can be engaged by each fibre decreases. The average volume of a single fibre MG1 and MG2 is, respectively 0.554 cm^3 and 0.238 cm^3. The differences in N_{fg} between the two approaches are small (Table 2, Figure 3). This is related to the shape of the aggregate particles studied: a reduce flakiness index, $FI \leq 15\%$, indicates that most grains have a reasonably spherical shape. For materials with higher FI, the approach proposed by Ferro et al. (2023) will tend to be more realistic.

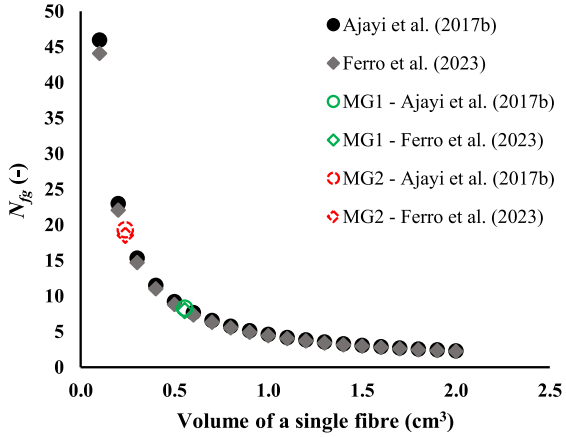

Figure 3. Variation of the fibre-grain ratio with the volume of a single fibre.

3.2 Packing

Table 3 summarises the packing test results (average for three specimens per condition); the maximum and minimum void ratio (e_{max} and e_{min}) and the ratio of the range of reinforced void ratios to that of the unreinforced material ($I_{Dr:u}$).

Table 3. Packing test results (average for 3 specimens per condition), maximum (e_{max}) and minimum (e_{min}) void ratio, standard deviation (σ), and grains packing disruption analysis ($I_{Dr:u}$).

Nomenclature	e_{max} (-)	σ (-)	e_{min} (-)	σ (-)	$I_{Dr:u}$ (-)
U	0.86	0.01	0.65	0.01	-
R MG1	1.42	0.02	0.93	0.02	2.25
R MG2	1.12	0.01	0.86	0.01	1.20

The addition of microgrids at V_{fr} = 3.2% led to an increase in both the maximum and the minimum void ratio of the mix relative to the unreinforced aggregate. For MG1, e_{max} increased by 64% and e_{min} by 33%; for MG2, this effect was less pronounced, with increases of 29% for e_{max} and 24% for e_{min}. Both microgrids interfered significantly with the natural packing of the aggregate grains, as $I_{Dr:u} > 1.05$. MG1, owing to its form and greater length than MG2, caused greater disruption to the natural packing with $I_{Dr:u}$ = 2.25.

The packing tests carried out in Box 2 allowed observation of the relative positions of the microgrids and grains, and changes during loading. Figure 4 shows cross sections of specimens, unreinforced and reinforced with MG1 and MG2, at different stages of the test: initial state, t = 0 s; half way through compaction, t = 150 s; and after compaction, t = 300 s. The distribution and arrangement of the microgrids on horizontal cross sections was also observed on

disassembling the boxes following the end of each test (plan view, Figure 4g and k).

The inclusion of microgrids MG1 and MG2 influenced the packing of the aggregate (Figure 3a, d and h). Particularly for MG1, the number and dimension of the voids in the vicinity of MG1 is important. Although the specimen R MG1 (as indicated by the values of emax and emin, Table 3) densified during compaction, the process did not eliminate such voids. Thus MG1 clearly disrupted the natural packing of the aggregate. For MG2, this was less evident, indicating that the form of MG2 is more easily accommodated by the aggregate particles than that of MG1.

Microgrid segregation was observed in both cases, and was more pronounced for MG1 than MG2. Again, this can be explained by the different forms of the microgrid reinforcements.

The results (Table 3) and the observations of the disrupted packing (Figure 4, with fibre overlapping) indicate that V_{fr} = 3.2 % is not optimum for this type of micro-reinforcement. However, this value was proposed by Ajayi et al. (2017a) for strip fibres not for microgrids. Thus further studies to optimise the form and the corresponding content of microgrids are needed.

During filling of Box 2 and at the start of the packing tests, it was evident that some microgrids were vertically oriented along the plexiglass. For this reason, at the end of the test the box was emptied carefully, in layers, to check if this was a boundary effect. The microgrid elements were found at both horizontal and vertical positions in all plan sections of the specimens (Figure 4). This is likely a consequence of the stabilisation effect that microgrids have, as they tend to lock-in aggregate particles in their vicinity and rotate along with grains.

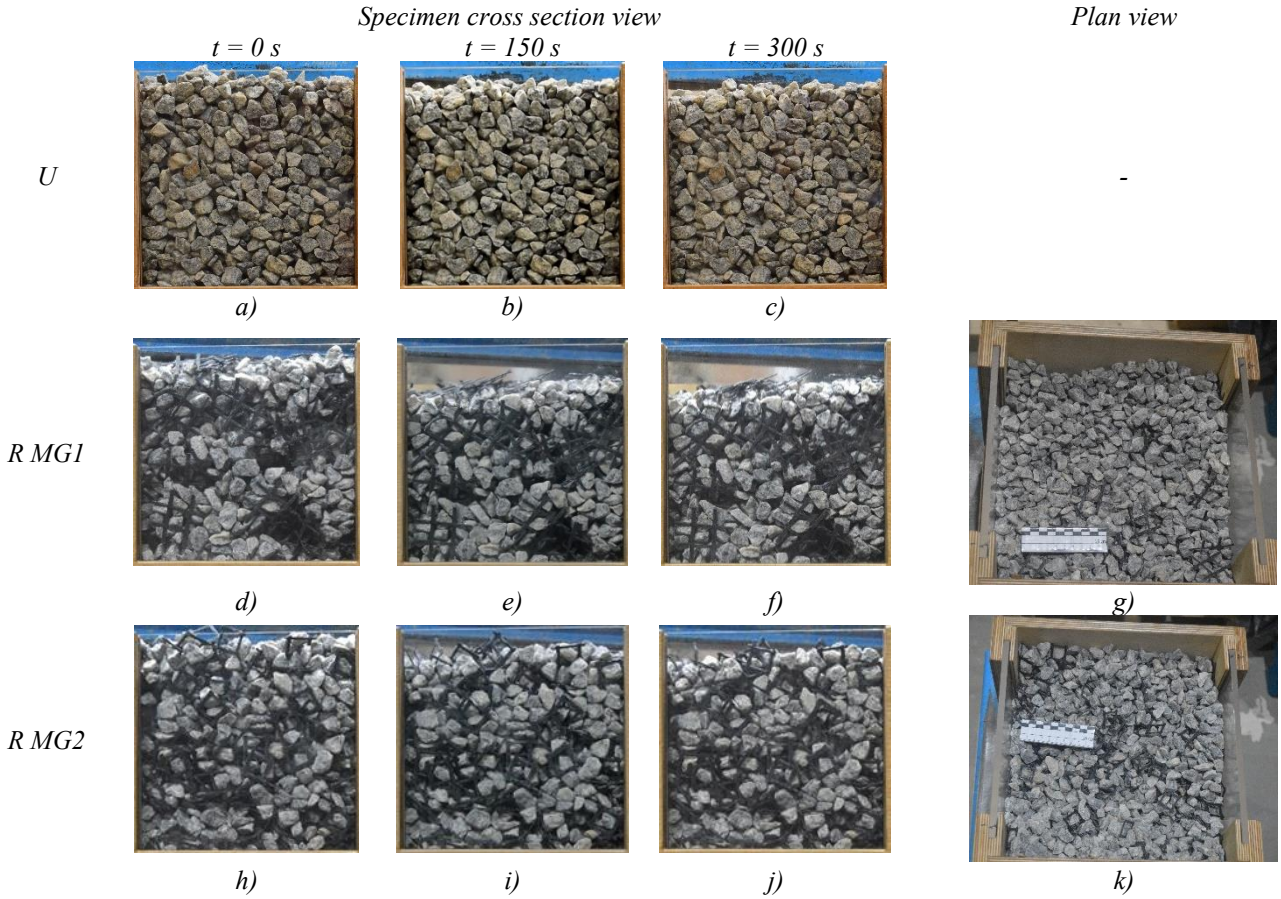

Figure 4. Cross section view of the packing tests (Box 2) at different moments: initial state (t = 0 s) a) U, d) MG1, h) MG2; after half way through compaction (t = 150 s) b) U, e) MG1, i) MG2; after compaction (t = 300 s) h) U, i) MG1, j) MG2, Plan view of specimens after compaction (Box 2) showing microgrid orientation: g) MG1, k) MG2.

4 CONCLUSIONS

In this paper, the reinforcement of a coarse aggregate (1/3 scale railway ballast) with two different types of microgrid was investigated using packing tests. The fibre-grain ratio was estimated using two different approaches from the literature. Images taken during the packing tests were analysed, to better understand

how the microgrids influence packing of aggregate particles. The main conclusions from the study are:

1. The inclusion of the microgrids influenced the aggregate packing and increased the maximum and minimum void ratios of the mix relative to the unreinforced aggregate.
2. The form of the microgrids affected the degree of disruption; the smaller microgrid, with only a central square element, was less disruptive.
3. The approaches used to estimate the number of grains per specimen gave similar results (4% difference).
4. The optimum volumetric fibre ratio V_{fr}= 3.2% for strip fibre reinforcement of similar aggregates is not appropriate for the microgrid reinforcements studied.
5. In contrast to strip fibre reinforcement, which adopt a generally horizontal orientation, microgrids orientate both vertically and horizontally within the aggregate particles.

Additional studies are needed to determine the optimum volumetric fibre ratio for microgrids and to give a better understanding of the micro mechanical interaction between microgrids and grains. Optimisation of the form of micro-reinforcement seems possible and needs further investigation.

ACKNOWLEDGEMENTS

The financial support of FCT ("Fundação para a Ciência e Tecnologia" – Portugal) is gratefully acknowledged through the project UIDB/04450/2020 (RISCO).

This research was supported by the doctoral Grant PRT / BD / 154385 / 2022 financed by Portuguese Foundation for Science and Technology (FCT), and with funds from The State Budget, from the European Social Fund (ESF) made available under Reginal Operational Program of the Center (Centro 2020), under MIT Portugal Program.

REFERENCES

Ajayi, O., Le Pen, L., Zervos, A., & Powrie, W. (2017a). A behavioural framework for fibre-reinforced gravel. *Géotechnique*, *67*(1), 56–68. https://doi.org/10.1680/JGEOT.16.P.023.

Ajayi, O., Le Pen, L., Zervos, A., & Powrie, W. (2017b). Scaling relationships for strip fibre reinforced aggregates. *Canadian Geotechnical Journal*, *54*. https://doi.org/10.1139/cgj-2016-0346.

BS EN 13450: (2013) Aggregates for railway ballast, Pub. L. No. 13450, BSI Standards Publication.

Ferro, E., Le Pen, L., Zervos, A., & Powrie, W. (2022). Fibre-reinforcement of railway ballast to reduce track settlement. *Géotechnique*, *0*(0),1-13 https://doi.org/10.1680/jgeot.21.00421.

Ferro, E., Le Pen, L., Zervos, A., & Powrie, W. (2023). Reducing the settlement of railway ballast by random fibre reinforcement. In *Geosynthetics: Leading the Way to a Resilient Planet* (pp. 1366–1371). CRC Press. https://doi.org/10.1201/9781003386889-175.

Indraratna, B., Ferreira, F. B., Qi, Y., & Ngo, T. N. (2018). Application of geoinclusions for sustainable rail infrastructure under increased axle loads and higher speeds. *Innovative Infrastructure Solutions*, *3*(1). https://doi.org/10.1007/s41062-018-0174-z.

Lirer, S., Flora, A., & Consoli, N. C. (2011). On the strength of fibre-reinforced soils. *Soils and Foundations*, *51*(4), 601–609. https://doi.org/10.3208/sandf.51.601.

Michalowski, R. L., & Čermák, J. (2003). Triaxial Compression of Sand Reinforced with Fibers. *Journal of Geotechnical and Geoenvironmental Engineering*, *129*(2), 125–136. https://doi.org/10.1061/(asce)1090-0241(2003)129:2(125).

Sevi, A. F. (2008). *Physical modeling of railroad ballast using the parallel gradation scaling technique within the cyclical triaxial framework*. University of Missouri.

Soriano, I., Ibraim, E., Andò, E., Diambra, A., Laurencin, T., Moro, P., & Viggiani, G. (2017). 3D fibre architecture of fibre-reinforced sand. *Granular Matter*, *19*(4). https://doi.org/10.1007/s10035-017-0760-3.

Proceedings of the XVIII ECSMGE 2024
GEOTECHNICAL ENGINEERING CHALLENGES
TO MEET CURRENT AND EMERGING NEEDS OF SOCIETY
© 2024 the Authors
ISBN 978-1-032-54816-6
DOI 10.1201/9781003431749-688
Open Access: www.taylorfrancis.com, CC BY-NC-ND 4.0 license

ECSMGE 24
XVIII EUROPEAN CONFERENCE ON SOIL MECHANICS AND GEOTECHNICAL ENGINEERING

State of the art on the recovery of mechanical energy in the city. The role of seismic metamaterials

État de l'Art sur la conversion de l'énergie mécanique en ville. Le rôle des métamatériaux sismiques

S. Brûlé*
CNRS, Aix-Marseille Université, Centrale Marseille, Institut Fresnel, Marseille, France

S. Guenneau
The Blackett Laboratory, Imperial College, SW7 2AZ, London, United Kingdom

S. Enoch
CNRS, Aix-Marseille Université, Centrale Marseille, Institut Fresnel, Marseille, France

**stephan.brule@yahoo.com*

ABSTRACT: Studies on structured soils, including seismic metamaterials, have shown the existence of complex wave phenomena within and around the structured zone. The aim is to assess areas where seismic or vibratory energy is concentrated, and to decide whether it would be worthwhile to exploit them by judiciously placing piezoelectric energy sensors. The article presents what is already being done with vibration sensors implanted in civil engineering structures and shows the potential interest of seismic metamaterials in this context. The modification of the surface signal by both structured soil and surface resonators meets the challenges of Civil Engineering through the effects of soil-structure interaction. Seismic metamaterials can therefore not only be considered for building protection, lensing and minimizing the effects of potentially deleterious Rayleigh waves, but also have potential applications in energy harvesting using ambient seismic noise.

RÉSUMÉ: Les études sur les sols structurés, dont les métamatériaux sismiques, ont montré l'existence de phénomènes d'onde complexe à l'intérieur et autour du sol transformé. Il s'agit d'évaluer les zones de concentration d'énergie sismique ou vibratile et de décider de l'intérêt de les valoriser en plaçant judicieusement des capteurs d'énergie piézoélectriques. L'article présente ce qui se fait déjà avec des capteurs de vibrations implantés dans des structures de génie civil et montre le potentiel intérêt des métamatériaux sismiques dans ce contexte. La modification du signal en surface à la fois par le sol structuré et les résonateurs de surface rejoignent les enjeux du génie civil par les effets de l'interaction sol-structure. Les métamatériaux sismiques peuvent donc non seulement être envisagés pour la protection des bâtiments, les effets de lentille et la minimisation des effets des ondes de Rayleigh potentiellement délétères, mais ils ont également des applications potentielles dans la collecte d'énergie en utilisant le bruit sismique ambiant.

Keywords: Energy harvesting device; seismic noise; seismic metamaterials; structured soils; smart city.

1 INTRODUCTION

In recent years, there has been growing interest in finding new ways to produce clean, sustainable energy. A new type of devices has emerged. They are called Energy Harvesting Devices - EHDs (Khaligh et al., 2010). One of the most innovative and promising methods is to harvest energy from pedestrian or road traffic, for example.

2 REVIEW OF SOME TYPES OF ENERGY HARVESTING DEVICES

When people walk, run or climb stairs, they generate kinetic energy that can be converted into electricity using various energy harvesting technologies.

Among all the energy related human activities we can consider in urban environment, traffic is one of the most energy-expensive ones, and, furthermore, it is characterized by great waste. Only 30% of the fuel potential is used to transfer kinetic energy to the vehicle and the largest part of this energy is dissipated in decelerating phases by brakes and gases (Ye et al., 2010).

The use of speed bumps is basically to slow the vehicle in certain areas such as school, residential streets, dangerous corner, and near car park area such as a bus station and hypermarket. “Powerbumps” are innovative energy harvesting devices that reduce the speed of vehicles by converting the kinetic energy otherwise wasted by brakes into electricity (Pirisi et al., 2012).

The amount of energy that can be gained from pedestrians depends on several factors, such as the number of people walking, their weight, and the frequency and intensity of their footsteps.

Piezoelectric tiles are one of the most common technologies used to harness energy from pedestrian traffic. These tiles are embedded in the ground and generate electricity when they are compressed by the weight of people walking on them. They can be installed in public spaces such as parks, plazas, and sidewalks to generate electricity that can be used to power lights, sensors, and other low-power devices.

Kinetic pavements are similar to piezoelectric tiles but designed to generate more energy. They use a more advanced technology that allows them to generate energy not only when compressed, but also when flexed. Kinetic pavements are typically made of a composite material that contains piezoelectric fibers.

The stairs generate electricity through the kinetic energy produced by people walking up and down them. The energy is then stored in batteries and used to power the station’s lighting system.

An energy harvester can be constructed by combining a mechanical structure with an energy transducer. The former commits itself to capture the mechanical energies and regularizing them into internal strain energy or kinetic energy of relevant components. Then, the transducer converts regularized energies into electricity to power low-consumption devices (Yin et al., 2023). The harvester system (figure 1), by means of the piezoelectric effect, converts the mechanical energy of the human being walking, running or jumping, in exploitable electric energy.

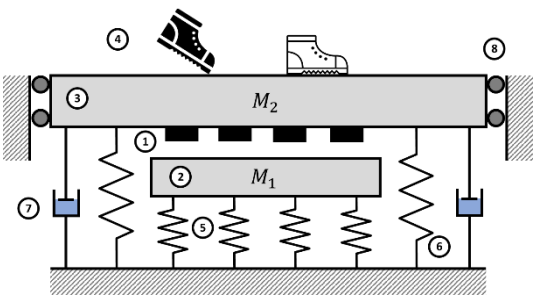

Figure 1. Schema of the harvester system (adapted from Malki et al., 2020). Legend: 1– piezoelectric patches, 2 – mass M_1, 3 – plate (mass M_2), 4 – pedestrian steps, 5 – substrate springs, 6 – centered springs, 7 – dashpot, 8 – sliding device.

3 HUGE OSCILLATORS IN THE CITY AND METACITY

Metacity was a concept first put forward in the late 1980s on the basis of experimental observations of soil response and its devastating effects. It has been known since the 1950s that the natural frequencies of any man-made structure are influenced by soil-structure interaction, particularly on soft soils, and that the presence of structures on the surface of a homogeneous half-space can significantly modify ground motion (Clouteau and Aubry, 2011; Guéguen et al., 2000; Trifunac, 1972; Wong et al., 1977). Most of the time, the problem of ground response is disconnected from that of the resonant response of buildings or group of buildings (figure 2a).

On the basis of studies carried out on the interaction of cities with the seismic signal (what could be viewed as a form of multiple scattering similar to that in Phononic Crystals PCs), some authors propose further extensions of this concept (Wirgin and Bard, 1996) based on analogies with electromagnetic and seismic metamaterials (Kadic et al., 2013; Merrit and Housner, 1954). This theoretical approach is consistent with studies of several authors on the influence of the trees of a forest on the surface waves (Maurel et al., 2018).

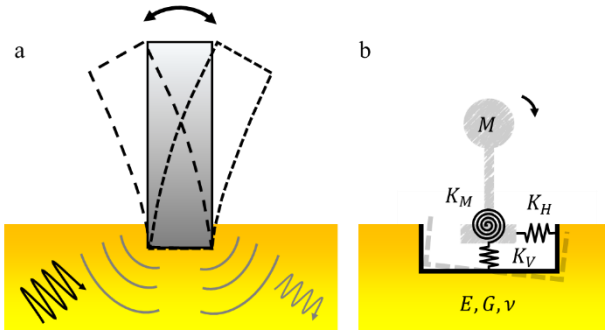

Figure 2. (a) The building vibrates as a result of seismic waves, then through inertial effects, becomes a secondary source of vibration itself. (b) Soil-foundation interface is modelled here in the case of three degree of freedom with analogic Maxwell models (K_H, K_V, respectively horizontal and vertical stiffnesses, K_M is the rotational stiffness of the model).

The concept here is to position sensors in areas where vibratory motion is amplified by surface resonators (Brûlé et al., 2019; Brûlé et al., 2020). Seismic metamaterials come into play by virtue of their ability to concentrate the mechanical energies of seismic waves and seismic ambient noise. It should be noted that seismic metamaterials were first studied in the case of earthquakes (Brûlé et al., 2014). City vibrations are also of interest to researchers, who are using the fiber optics (D.A.S. – Distributed Acoustic Sensing) already installed in cities as a gigantic

network of seismic sensors (Rodet et al., 2022). Distributed Acoustic Sensing is a technology that enables continuous, real-time measurements along the entire length of a fiber optic cable. For example, each building can be modeled as an oscillator with soil-foundation interface conditions. These interfaces can be represented by rheological models with several degrees of freedom (figure 2b).

4 ROLE OF SEISMIC METAMATERIAL

The main paradigm shift lies in the search for the specific modal signatures of all these objects (structured soils, foundations, etc.), which requires the implementation of specific material means in the field (seismic sensors, sensor density, etc.) and also analysis tools to extract the data of interest (Brûlé et al., 2024).

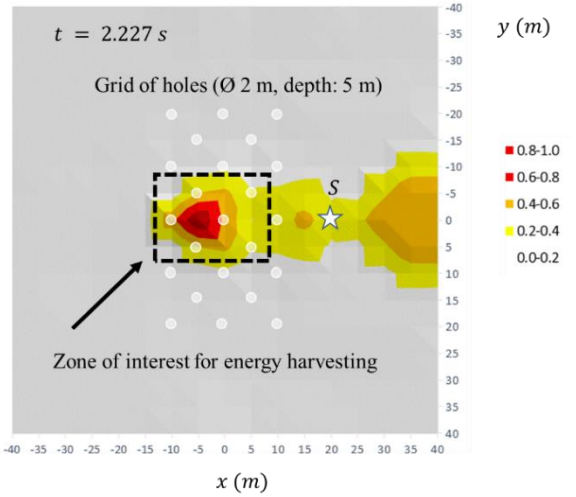

Figure 3. Example of a staggered hole pattern (20 – 40 m). The impact source (S) is located at 10 m from the long side. The energy scale is arbitrary and normalized. The figure shows energy concentrations at locations of interest for positioning vibration sensors (Brûlé et al., 2020).

The transposition of the principles of periodic media to materials as specific as terrestrial materials requires rigorous definition of the validity conditions. In particular, these conditions are the strain range of the soil making possible the justification of an elastic behavior and a thick and homogeneous sedimentary site to limit the reflection effects of the underlying geological layers of contrasted impedance.

The interpretation of the measurements is carried out from the perspective of the physical phenomena expected in periodic media. The seismic lenses tested (Brûlé et al., 2024) are explored as phononic crystals and metamaterials. By the effects observed, we point out the diffraction including Bragg reflection and double image of the source as a result of the negative refraction of a flat lens.

However, a metamaterial is defined as an artificial composite material made from the assembly of resonators of smaller dimensions, whose wavelength at resonance is much larger than their physical dimension. These possibilities of local resonances are verified for Helmholtz resonators or very soft soils with rigid inclusions. On a macroscopic scale, a metamaterial is likely to exhibit properties that are not found in nature, such as negative refractive index. In addition to these early interpretations, there is an analysis of the modification of the polarization of surface waves. This new reading of the data opens the discussion on other descriptions of phenomena such as the existence of local resonances of rigid elements placed in a soil, and no longer of empty cylinders, as well as on static or dynamic homogenization approaches, dynamic anisotropy, transformational optics, surface resonators, etc.

The modification of the signal by the fact of a structured soil and surface resonators are the link with Civil Engineering and the soil-structure interaction practiced in Earthquake Engineering (figure 3). Research subjects converge in seismology and on the effects of secondary sources generated by surface buildings.

5 SEISMIC AMBIENT NOISE

In urban areas and for the frequency range of interest for civil engineering structures (0.1 Hz to 30 Hz), the orders of magnitude for particle velocities at ground level are 10^{-6} to 10^{-5} m/s. For accelerations, values are of the order of 10^{-5} to10^{-3} m/s^2.

The rapid development of sensor sensitivity, miniaturization, falling costs and energy storage capacities will make it possible to exploit seismic ambient noise excacerbated by structured materials (in the ground or in buildings).

6 DISCUSSION AND CONCLUSIONS

The development of building construction is steadily moving towards smart buildings and cities. All free energies will be exploited: solar, geothermal, wind energy, seismic ambient noise, etc. A decisive turning point in the evolution of seismic metamaterials is their ability to create energy channels - rather chaotic, but potentially profitable for installing sensing devices.

REFERENCES

Brûlé, S., Enoch, S., Guenneau, S. (2024). The importance of full-scale experiments for the study of seismic metamaterials. Editor(s): Tapash Chakraborty,

Encyclopedia of Condensed Matter Physics (Second Edition), Academic Press, 2024, Pages 519-528.

Brûlé, S., Guenneau, S. (2020). Past, present and future of seismic metamaterials: experiments on soil dynamics, cloaking, large scale analogue computer and space–time modulations. *C. R. Phys.* 21, n°7-8, pp. 767-785. DOI: 10.5802/crphys.39. https://comptes-rendus.academie-sciences.fr/physique/articles/10.5802/crphys.39/.

Brûlé, S., Enoch, S., Guenneau, S. (2019). Role of nanophotonics in the birth of seismic megastructures. *Nanophotonics*. 8 (10): 1591–1605. https://doi.org/10.1515/nanoph-2019-0106.

Brûlé, S., Enoch, S., Guenneau, S. (2017). Sols structurés sous sollicitation dynamique : des métamatériaux en géotechnique, *Rev. Fr. Geotech.*, 151, 4. DOI: 10.1051/geotech/2017010.

Brûlé, S., Javelaud, E.H., Enoch, S., Guenneau, S. (2014). Experiments on Seismic Metamaterials: Molding Surface Waves. *Phys. Rev. Lett.*, n°112, 133901. DOI: https://doi.org/10.1103/PhysRevLett.112.133901.

Clouteau, D., Aubry, D. (2011). Modification of the ground motion in dense urban areas. *J. Comput. Acoust.* 9(4):1659–1675. https://doi.org/10.1142/S0218396X01001509.

Guéguen, P., Bard, P.Y., Semblat, J.F. (2000). From soil-structure interaction to site-city interaction, in *12th World Conference on Earthquake Engineering*, Auckland, New-Zealand.

Merritt, R.G., Housner, G.W. (1954). Effect of foundation compliance on earthquake stresses in multistory buildings. *Bull. Seismol. Soc. Am.* 44:551–569 25 (1954). https://doi.org/10.1785/BSSA0440040551.

Kadic, M., Bückmann, T., Schittny, R., Wegener, M. (2013). Metamaterials beyond electromagnetism. *Rep. Prog. Phys.* 76:26501. DOI: 10.1088/0034-4885/76/12/126501.

Khaligh, A., Chapman, P.L., Ghodssi, R. (2010). Special Section on Energy Harvesting. *IEEE Trans. Ind. Electron.* 2010, 57, 810–876.

Malki, Z., Ennawaoui, C., Hajjaji, A., Najihi, I., El Jouad, M., Boughaleb, Y. (2020). Pedestrian crossing system for the mechanical energy harvesting using piezoelectric materials. In *International Conference on Advances in Energy Technologies, Environment*. IOP Conf. Series: Materials Science and Engineering 948 (2020) 012030. DOI: 10.1088/1757-899X/948/1/012030.

Maurel, A., Marigo, J-J., Pham, K., Guenneau S. (2018). Conversion of Love waves in a forest of trees. *Phys. Rev. B* 98, 134311. https://doi.org/10.1103/PhysRevB.98.134311.

Pirisi, A., Grimaccia, F., Mussetta, M., Zich, R.E. (2012). Novel Speed Bumps Design and Optimization for Vehicles' Energy Recovery in Smart Cities. *Energies*, 5, 4624-4642. https://doi.org/10.3390/en5114624.

Rodet, J., Brûlé, S., Gueguen, Ph., Tauzin, B., Coutant, O., Lanticq, V., Rollet, R., Granger, J., Depret, O. (2022). Fibres optiques, sismologie et géotechnique pour ville intelligente : le projet DASARA à Lyon. In *11ème JNGG 2022*, 28-30 juin 2022, Lyon, France. p. 917-925.

Trifunac, M.D. (1972). Interaction of a shear wall with the soil for incident plane SH waves. *Bull. Seismol. Soc. Am.* 62:63–83. DOI: 10.1785/BSSA0620010063.

Wirgin, A., Bard, P-Y. (1996). Effects of buildings on the duration and amplitude of ground motion in Mexico City. *Bull. Seismol. Soc. Am.* 86(3):914–920.

Wong, H.L., Trifunac, M.D., Westermo, B. (1977). Effects of surface and subsurface irregularities on the amplitude of monochromatic waves. *Bull. Seismol. Soc. Am.* 67:353–368.

Ye, M., Jiao, S.J., Cao, B.G. (2010). Energy Recovery for the Main and Auxiliary Sources of Electric Vehicles. *Energies* 2010, 3, 1673–1690. https://doi.org/10.3390/en3101673.

Yin, B., Wei, J., Jiang, X., Liu, Y. (2023). A Pavement Piezoelectric Energy Harvester for Small Input Displacements. *Micromachines* 2023, 14, 292. https://doi.org/10.3390/mi14020292.

Proceedings of the XVIII ECSMGE 2024
GEOTECHNICAL ENGINEERING CHALLENGES
TO MEET CURRENT AND EMERGING NEEDS OF SOCIETY
© 2024 the Authors
ISBN 978-1-032-54816-6
DOI 10.1201/9781003431749-689
Open Access: www.taylorfrancis.com, CC BY-NC-ND 4.0 license

ECSMGE 24
XVIII EUROPEAN CONFERENCE ON SOIL MECHANICS AND GEOTECHNICAL ENGINEERING

Data analysis in geotechnics – an approach to the construction of an urban tunnel

Analyse de données en géotechnique - une approche dans la construction d'un tunnel urbain

A. de Vilhena Costa*
TPF, Consultores de Engenharia e Arquitetura, S.A.

I. Coelho
Metro do Porto, SA, Departamento de Infraestruturas

A. Gomes Correia
ISISE, Department of Civil Engineering, University of Minho

**andre.costa-lcmp@tpf.pt*

ABSTRACT: In contexts where empirical methods support decision-making, the need for organized information, often in a 'Just in Time' manner, is crucial. In such situations, machine learning (ML) and artificial intelligence (AI) based methods can play a significant role in offering meaningful solutions. Data must fulfil predefined criteria and be stored in structured databases. Quality of information and its organization are essential factors for predictive and decision-making algorithms. This paper will introduce essential database criteria and provide an example of data analysis for a case study to offer effective decision-making support for an underground construction project in an urban environment. In NATM (New Austrian Tunnelling Method) works, there is a heavy reliance on continuous monitoring and observation. Particularly in linear excavations, work cycles follow each other rapidly, often operating 24/7. The constant decision-making required for the progress of each daily cycle demands continually updated information that is readily available and presented in a clear and precise format for quick and rigorous interpretation.

RÉSUMÉ: Dans les contextes où les méthodes empiriques soutiennent la prise de décision, le besoin d'informations organisées, souvent en mode 'juste à temps', est crucial. Dans de telles situations, les méthodes basées sur l'apprentissage automatique (ML) et l'intelligence artificielle (IA) peuvent jouer un rôle significatif en offrant des solutions significatives. Les données doivent respecter des critères prédéfinis et être stockées dans des bases de données structurées. La qualité de l'information et son organisation sont des facteurs essentiels pour les algorithmes de prévision et de prise de décision. Cette communication introduira des critères essentiels pour les bases de données et fournira des exemples d'études de cas d'analyse de données afin d'offrir un soutien efficace à la prise de décision pour un projet de construction souterraine en milieu urbain. Les travaux réalisés selon NATM (New Austrian Tunneling Method) reposent largement sur la surveillance et l'observation continues. Particulièrement dans les excavations linéaires, les cycles de travail se succèdent rapidement, souvent en fonctionnement 24/7. La prise de décision constante nécessaire à l'avancement de chaque cycle quotidien exige des informations continuellement mises à jour, disponibles rapidement et présentées dans un format clair et précis pour une interprétation rapide et rigoureuse.

Keywords: Business intelligence; advanced data analysis; machine learning; Python; NATM; tunnels.

1 INTRODUCTION

The organization of data enables the search for predictive models, supports decision-making through algorithms, which can be established by AI, with the ultimate goal of automating processes.

Relational database technology has been adopted since the late 1970s (Vaisman and Zimániy, 2017). However, despite not being a new tool, some industries have not fully embraced the advantages it offers. Organized and structured information simplifies data analysis process.

Construction sector data management will improve with software like Building Information Modelling (BIM).

Efforts need to be made to evolve Big Data and AI strategies to achieve predictive algorithms.

This paper deals with underground excavation information from Circular Line construction contract of Metro do Porto (MdP) in progress, and some

hypothesis to data organization, management and analysis. It is an approach by construction site engineers, looking for decision-making tools.

2 BACKGROUND

Briefly, significant research and applications exist related specifically to data analysis through advanced algorithms to infer characteristics, predict trends, support decision making, etc., related to geotechnics in general (Gomes Correia et al., 2023; Gomes Correia, et al., 2020).

The interest of the subject it is clearly shown among academics and professional bodies like Federation of International Geo-engineering Societies (FedIGS), through the organization of regular event International Conference in Information Technology in Geo – Engineering (ICITG), launched by Joint Technical Committee 2 (JTC2) dedicated to Representation of Geo-engineering Data in Electronic Format (Gomes Correia et al, 2020). Also, TC309–Machine Learning and Big Data in ISSMGE, represents the same interest, in: 1) benchmark datasets, 2) Big Data acquisition, 3) site investigations and geo-materials behaviour; 4) Design; 5) Construction and maintenance; 6) industry interaction, standards and guidelines, points out to ML supported in geo-data, learning and making previsions, supported in AI algorithms (Zili Li et al, 2023). More recently, The International Society for Intelligent Construction (ISIC) is also working in the same line to provide source of knowledge and information on intelligent construction technologies for public agencies, contractors, consultants, academia, etc. (Gomes Correia, et al., 2020).

When I&D turns to concepts like *distributed ledger technologies* (DLT) or *blockchain* and *data lakes* (e.g. Mourão, 2022), or when internet of things (IoT) bring us the idea to access Data directly from devices, equipment's and machines, it is difficult to accept that old relational data bases or data base management systems are still not fully implemented.

3 INFORMATION TECHNOLOGY IN MdP CIRCULAR LINE CONSTRUCTION CONTRACT

Construction sector has already implemented commercial software platforms to communicate and manage documentation, between different stakeholders, in many cases as a contractual obligation established by the owner and NP EN ISO9001, Quality System Management System, documents normalization and control, related to the operationalization process and quality.

More recently, BIM, promise to bring the expected digital revolution to the sector, together with proper and long expected Data management. However, this technology it is not fully implemented in Portugal, regulation by "Portaria n.º 255/2023", recognizes that BIM importance justifies its use in public works project design. MdP Circular Line it is supported in BIM as a constructor contractual obligation. Implemented under its full capacity it enables daily analysis of solutions compatibility.

In construction operations, processes are established by Quality systems of Contractor, and approved by Supervisor. This includes executing, measuring and monitoring, safety and health procedures, like normalizes documents in use. The information collected along the way, it is frequently compiled in datasheets obeying to established formats and organized in a set of digital directories like a hierarchical db. This manual compilation of information it is done, independently, by different stakeholders (Contractor, Supervisor and Owner).

The overall system works and data it is available and accessible, but some work it is redundant (different player's repeat data compilation with same data), in a manual, arduous and repetitive labour. This system assures access to information (Python routines have already successfully tested), but it is not optimized, neither in data management, nor in the quality data analysis that enables.

4 PROCESSES WORKFLOW, INFORMATION AND RELATIONAL DATABASE

Evaluate processes workflow it is a need to plan activities during construction. Through an entity relationship diagram, can be identified the information produced and necessary along the process (Figure 1). Include in such diagram, all the dimensions (quality, environment, health and safety,…) of a construction contract in public works, can be a complex and extensive task. Along the process, routines supported in different code languages can be used, like SQL and Python.

Frequently, digital information acquired automatically it is transformed in pdf files or even paper support data, and loaded by different stakeholders, in a redundant, monotonous, laborious and joyless task. Sometimes, to approach specific questions, some organizations, reload information to a new shape or format, wasting time and resources.

When the process it is well known and all the variables are identified, the structure of a relational database can arise. The model of a data base, through

an entity-relation diagram can establish the architecture constructed with SQL code. At that stage, data loading may begin. This phase, however unavoidable, at least to some extent, can be minimized through: 1) automatic data acquisition; 2) shared database (Contractor, Supervisor and Owner).

5 RAW DATA TO A DATABASE

The ideal or traditional formula for planning and architecting an appropriate database for a specific project is not always achievable, be it due to limited project resources or lack of long-term perspective in project, life-cycle, or asset management.

When there is not a proper database, but instead exists dispersed data, more or less organized, but without pre-established formats or key links, it is still possible to organize the information to allow data analysis, through successive stages: extract, transform and modelling data. Lower quality initial data, enhance data edition challenge.

Considering that data sources are adequate, exists commercial software to enable all the phases of the process: 1) extract; 2) transform; 3) modelling; 4) calculations; 5) visualization; 6) publishing. In different moments of the process, AI algorithms enables simplification and automatic decisions.

Power BI, supporting DAX and M languages, enables to extract and transform data, as a interactive business intelligence and data visualization tool with visually appealing reports, dashboards, data insights, and a user-friendly interface.

During construction works on the Circular Line of MdP, attempts were made to data analysis: 1) Python code enables data analysis relative to excavation with explosives, stored it in an external server, and presenting the results graphically and periodically reports; 2) data is stored in an external server and fed into a business intelligence report using Power BI.

As an example, Figure 2 shows a detail of a Power BI report related to the vibrations monitoring due to the use of explosives in an area classified by UNESCO, adjacent to the iconic Torre dos Clérigos, where this project imposed a Vmax<2,5mm/s, strincter than the regulations set by standard (NP2074, 2015), that establishes 3mm/s as the maximum value for sensitive buildings.

6 FINAL REMARKS

NATM relies on continuous monitoring and observation. Together with settlements, groundwater levels, convergences data, all the information on design and operations represents a large amount of data, which is not always easy to navigate through and interpret in order to support decisions just in time (JIT), if it is not properly stored and managed.

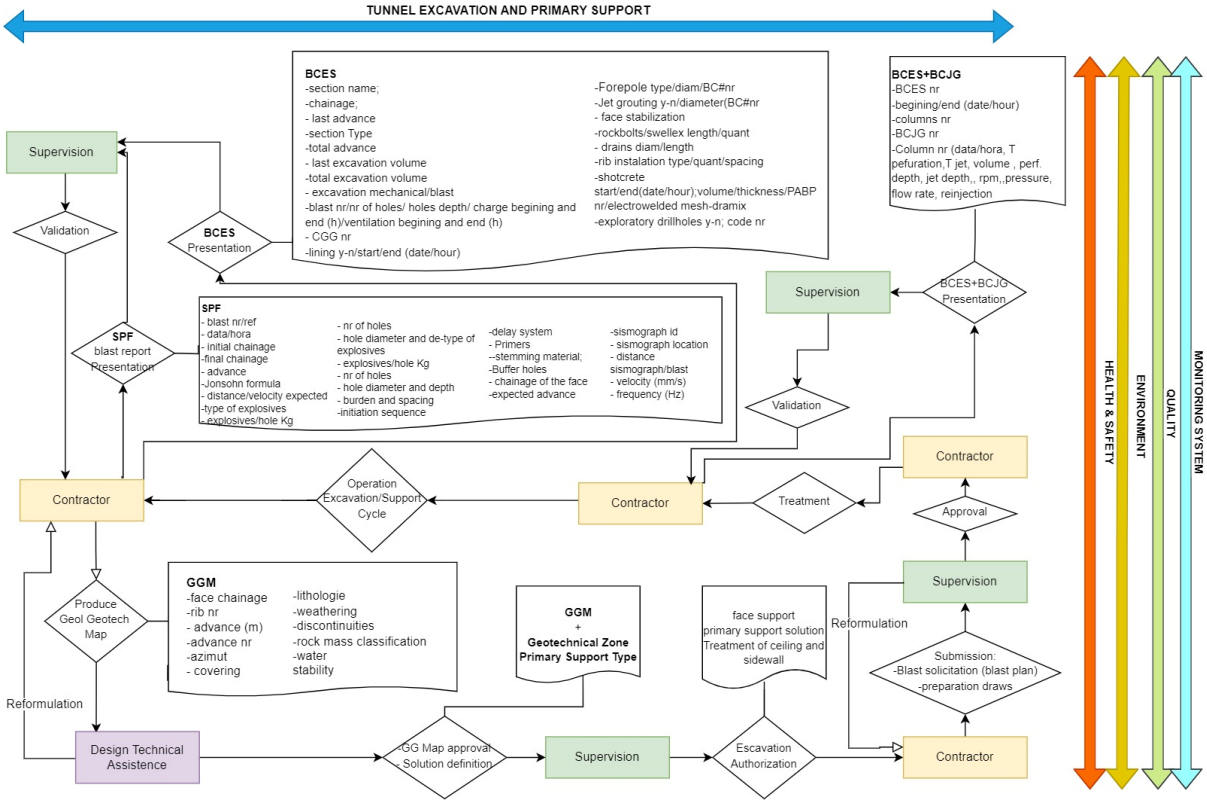

Figure 1. Tunnel excavation and primary supports processes workflow entity-relation diagram.

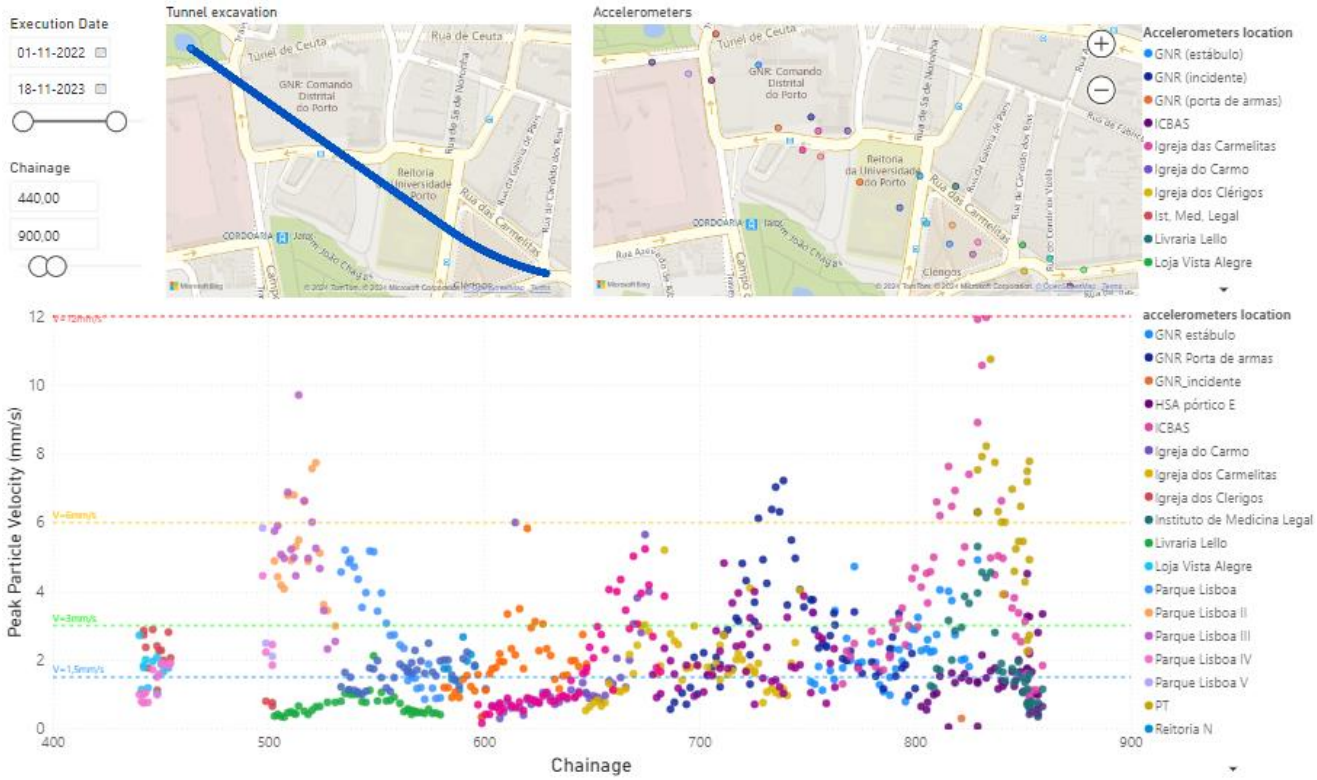

Figure 2. Blasting monitoring results data analysis.

In such environment, an attempt it being made to define a conceptual SQL database and to carry out data analyses on the real and existent hierarquical folders database, with Python code and Power BI.

Data and its management are critical for NATM construction operations, but must also remain available for the life-cycle and asset management.

This theme is in progress, as it addresses a subject still under study and which we hope to develop further in the future. Initially, this will involve data acquisition and storage methods, followed by the implementation of data analysis. At a more ambitious level, it encompasses the establishment of automated data analysis routines and decision support, involving artificial intelligence and machine learning algorithms.

ACKNOWLEDGEMENTS

The authors acknowledges MdP for data access.

REFERENCES

Gomes Correia, A. et al. (2023). *Trends on Construction in the Digital Era*, Proc. of ISIC 2022, Lecture Notes in Civil Engineering (LNCE, volume 306), Springer Nature Switzerland AG, https://doi.org/10.1007/978-3-031-20241-4.

Gomes Correia, A. et al. (2020). *Information Technology in Geo-Engineering*, Proc. of the 3rd ICITG 2019, Springer Series in Geomechanics and Geoengineering, Springer Nature Switzerland AG, https://doi.org/10.1007/978-3-030-32029-4.

Metro do Porto (2019). *Linha Circular-Troço Liberdade/S. Bento – Boavista/Casa da Música*. Projeto de Execução, Sener, CJC, NSE, Portugal.

Mourão, J. (2022) *Blockchain technology - potential application in the portuguese construction industry*. Master thesis. Faculdade de Engenharia da Universidade do Porto, Portugal.

NP EN ISO 9001 (2015). *Sistemas de Gestão da Qualidade – Requisitos; Quality Management Systems - Requirements*. Instituto Português da Qualidade (IPQ) (in Portuguese).

NP EN 2074 (2015): *Avaliação da influência de vibrações impulsivas em estruturas; Evaluating the influence of impulsive vibrations on structures*. Instituto Português da Qualidade (IPQ) (in Portuguese).

Portaria nº255/2023, de 7 de Agosto. DR 152/2023 Série I. Ministério da Habitação. Lisboa, Portugal.

Vaisman, A. and Zimányi, E. (2017). *Data Warehouse Systems - Design and implementation*. 2nd ed., Springer.

Zili Li et al. (2023). *Machine Learning and Big Data Acquisition in Underground Infrastructure*, Special Issue of *Tunnelling and Underground Space Technology*, Guest Eds., Elsevier Ltd.

Proceedings of the XVIII ECSMGE 2024
GEOTECHNICAL ENGINEERING CHALLENGES
TO MEET CURRENT AND EMERGING NEEDS OF SOCIETY
© 2024 the Authors
ISBN 978-1-032-54816-6
DOI 10.1201/9781003431749-690
Open Access: www.taylorfrancis.com, CC BY-NC-ND 4.0 license

ECSMGE 24
XVIII EUROPEAN CONFERENCE ON SOIL MECHANICS AND GEOTECHNICAL ENGINEERING

Geotechnical works impacting existing railway infrastructure – French practice in railway safety measures

Travaux géotechniques en interface avec l'infrastructure ferroviaire existante – Pratique française des mesures de sécurité ferroviaire

A. Guimond-Barrett*, R. English-Martin
SYSTRA, Paris, France

C. Czabanski, F. Chille
SNCF RESEAU, La Plaine Saint Denis, France

T. Kaira
UIC, Paris, France

**aguimond-barrett@systra.com*

ABSTRACT: The railway network in Europe spans approximately 200,000 km of track. Since 2012, a single interoperable European railway area facilitates the transportation of both passengers and goods across the continent. The needs for higher efficiency transportation modes are rapidly growing, and the shift towards rail in the EU is expected to accelerate because of its high environmental performance, sustainability, and safety. Meanwhile, the existing infrastructure is aging, with many assets being over a century old (earthworks, bridges, and tunnels). To meet these new challenges, modernization of the existing network is imperative. The regeneration of railway structures generally involves significant geotechnical engineering works due to the lack of available space or assets that are at the limit in terms of stability. These works are becoming increasingly complex and must be carried out with minimal traffic disruptions. In many countries, national guidelines have been published to assist engineers in the design and execution of geotechnical works near existing railway infrastructure. However, there are no European recommendations or standards. In order to discuss these national recommendations at the European level, this paper gives an overview of design, execution and control rules applied in France for geotechnical works on existing railway infrastructure. First, the characteristics of the French railway network are presented. Then, the main risks associated with geotechnical works close to railway traffic are identified. Finally, the implications of incorporating railway safety in the design and execution of works are highlighted.

RÉSUMÉ: Le réseau ferroviaire européen s'étend sur environ 200,000 km de voies. Depuis 2012, un espace ferroviaire européen unique et interopérable facilite le transport de passagers et de marchandises à travers le continent. Les besoins en modes de transport plus efficaces dans l'UE augmentent rapidement, et la transition ferroviaire devrait s'accélérer davantage en raison de ses performances environnementales, de durabilité et de sécurité élevées. Dans le même temps, l'infrastructure ferroviaire existante est vieillissante, de nombreux ouvrages ayant été construits il y plus d'un siècle (ouvrages en terre, ponts et tunnels). Pour répondre à ces nouveaux défis, la modernisation du réseau existant est impérative. La régénération des ouvrages ferroviaires implique généralement des travaux géotechniques importants en raison du manque d'espace disponible ou d'ouvrages à la limite en termes de stabilité. Ces travaux deviennent de plus en plus complexes et doivent être réalisés avec un minimum de perturbations pour les circulations. Dans de nombreux pays, des référentiels nationaux ont été publiés pour aider les ingénieurs à concevoir et à exécuter des travaux géotechniques à proximité des infrastructures ferroviaires existantes. Il n'existe cependant aucune recommandation ou norme européenne. Afin de présenter ces recommandations nationales au niveau européen, cet article donne un aperçu des règles de conception, d'exécution et de contrôle appliquées en France pour les travaux géotechniques sur les infrastructures ferroviaires existantes. Dans un premier temps, les caractéristiques du réseau ferroviaire français sont présentées. Ensuite, les principaux risques liés aux travaux géotechniques proches du trafic ferroviaire sont identifiés. Enfin, les implications de l'intégration de la sécurité ferroviaire dans la conception et l'exécution des travaux sont soulignées.

Keywords: Railway; safety; infrastructure.

1 INTRODUCTION

In Europe, the needs for higher efficiency transportation modes of passengers and goods across the continent are rapidly increasing. Transport by rail is viewed by many as a promising solution because of its high environmental performance, sustainability,

and safety. Growth of the railway industry is expected to accelerate in the future.

The rail network in Europe spans approximately 200 000 km of track. Since 2012, a single interoperable European railway area is established (Directives 2012/34, 2016/2370 and 2016/797 of the European Parliament). Infrastructure managers are required to grant non-discriminatory open access to railway infrastructure for domestic and international rail services. Meanwhile, the existing infrastructure in Europe is aging, with many assets being over a century old (earthworks, bridges, and tunnels).

To meet this future challenge of higher traffic and increased capacity, modernization of the existing European railway network is imperative. The regeneration of railway structures generally involves significant geotechnical engineering works due to the lack of available space or assets that are at the limit in terms of stability. These works are becoming increasingly complex and must be carried out with minimal traffic disruptions (Renard, 2011).

In many countries, national guidelines have been published to assist engineers in the design and execution of geotechnical works near existing railway infrastructure. However, there are no European recommendations or standards. The current technical specifications for interoperability (STI; EU regulation n°1299/2014) do not cover geotechnical works.

To discuss these national recommendations at the European level, this paper gives an overview of some design, execution and control rules applied in France for geotechnical works on existing railway infrastructure. First, the characteristics of the French railway network are presented. Then, the main risks associated with geotechnical works close to railway traffic are identified. Finally, the implications of incorporating railway safety in the design and execution of works are discussed.

2 OVERVIEW OF FRENCH RAIL INFRASTRUCTURE

The French railway network consists of 30 000 km of line, including 2 600 km of high-speed line, on which travel 15 000 trains per day. The map of the national rail network highlights the density of the tightly knit network in France (Figure 1).

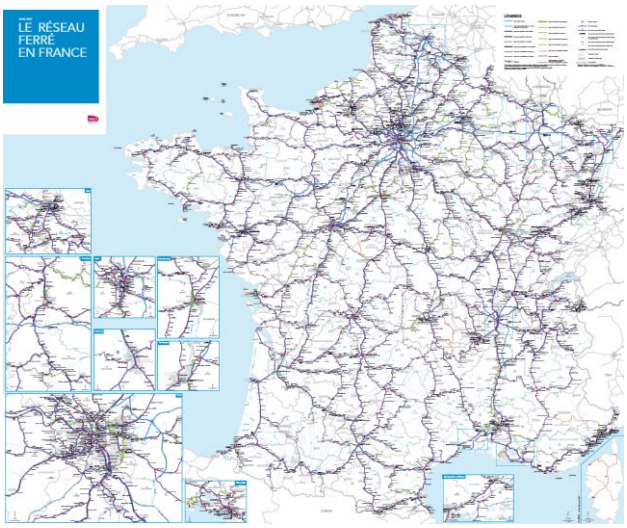

Figure 1. Map of the national rail network (from SNCF Réseau website).

Most main lines are standard UIC 1.435 m gauge, with only a few exceptions. A maximum permissible load of 22.5 tonnes per axle or 8 tonnes per linear metre is generally permitted.

The French railway network is composed of individual assets. The total number of earthworks is estimated at around 100 000 units, with a wide variety of structures (constitution, geometry, etc.) in many different environments (floodplains, rocky slopes, etc.). Over 32 000 rail bridges with a span greater than 2 meters were counted in a survey from 2018, with roughly 5 000 steel deck structures, 7 500 filler beams, 5 700 reinforced concrete or prestressed concrete bridges, 14 000 masonry bridges. There are approximately 20 000 retaining walls and 300 km of masonry covered slopes along the tracks in France. Lines pass through 1550 tunnels over a total length of 638 km, with an average tunnel span of 400 m (UIC, 2018).

Most of the assets were constructed 100 to 150 years ago during the industrial development of the second half of the 19th century. Structures are likely to deteriorate over time due to internal or external factors (Talfumière, 2011). These are mainly increase in traffic and loads and exposure to attacks from their environment (aggressive chemical conditons, erosion, submerssion, etc...). Degradations can lead to irreversible deformations with alterations of track geometry and/or more or less sudden failures in certain cases. A general lack of investment in maintenance and renewal projects over the years has resulted in poor track conditions in certain areas. Elsewhere, many assets have been reinforced at least once since their construction but these reinforcements are also aging and can become less efficient.

Geotechnical works carried out in operated railway environments are strongly impacted by the constraints

and risks brought about by train traffic. These specific risks are discussed in the following paragraph.

3 MAIN RISKS FOR GEOTECHNICAL WORKS NEAR OPERATED RAILWAYS

In addition to geotechnical hazards encountered in any ground engineering project, there are specific risks associated with works carried out near operated railway infrastructure. These are mainly related to:

- exposure of workers/equipment to moving trains / airflow effect
- exposure of workers/equipment to high voltage electrical installations
- potential damages to rail infrastructure with impact on traffic safety (disturbing signaling equipment, instability, and track geometry modifications)

In general, the closer the works are to the tracks, the greater the risks and the higher the costs of construction. Malfunction of signaling equipment can cause accidents such as train collisions. Damage to rail infrastructure caused by geotechnical works can have serious impacts on traffic safety. Overall stability must obviously always be guaranteed (equilibrium of the ground and of the structure at the Ultimate Limit State). Allowable displacements at the Serviceability Limit State (SLS) are often a major concern for projects near existing railway infrastructure. Indeed, unrestrained alterations of track geometry can ultimately lead to train derailment. Therefore, displacements are often a critical issue for projects.

The main risk treatment measures applied for the design and execution of geotechnical works in France to guarantee railway safety are presented in the following paragraph.

4 RAILWAY SAFETY IN DESIGN AND EXECUTION OF GEOTECHNICAL WORKS IN FRANCE

4.1 Standards and reference guides

Eurocodes are preferably applied for the design of geotechnical works on existing railway structures. However, there are instances where recent standards are difficult to apply, for example to justify the stability of old existing structures or for financial reasons. A risk tolerability principle known in France as GAME (*Globalement Au Moins Equivalent* meaning “globally at least as good”) is used as an alternative in some cases.

In addition, a complete collection of reference guides published by SNCF give further design prescriptions and most importantly guidance on execution of works near operated railway systems. Some important documents are in the reference list (IG90032; IG90033; MT40200; IN1226). The rules described in SNCF guidelines are applicable to works on the French railway network presented in paragraph 2. The purpose is to guarantee safe rail operations without unexpected traffic disruptions or accidents.

4.2 General risk treatment measures

4.2.1 Use of construction machinery near operated tracks

To mitigate the risks related to moving trains and electricity, safety perimeters for the use of construction machinery and equipment near the tracks are defined in IG90033 as protective measures. These perimeters apply to most machines used for geotechnical works such as mechanical excavators, piling and drilling rigs. When railway traffic is maintained while works are carried out, machines must under no circumstances enter the “Prohibited Zone” limited by a vertical plane 3 m from the track centreline or from any electrical installation (Figure 2). If there is a risk of accidental overturning of a piece of equipment, the limit of the prohibited zone is placed at 3 m from the nearest rail. Cranes and other lifting equipment can only operate outside a “Protection Zone” defined by a vertical plane 5 to 6 m from the axis of the track (included expected load sway). These limits also apply to boring rigs used for ground investigations.

Vibrations generated by powerful mechanical equipment (rotary hammer drills, hydraulic rock breakers, compactors, etc.) have the potential to cause significant disturbances to existing railway infrastructures. Continuous vibration monitoring is compulsory for works within 30 m of existing tracks. Allowable thresholds are set in SNCF standard IN1226 (2009).

Contractors are required to obtain specific qualifications from SNCF to be authorized to carry out works near operated tracks.

Various technologies exist to warn workers of approaching trains.

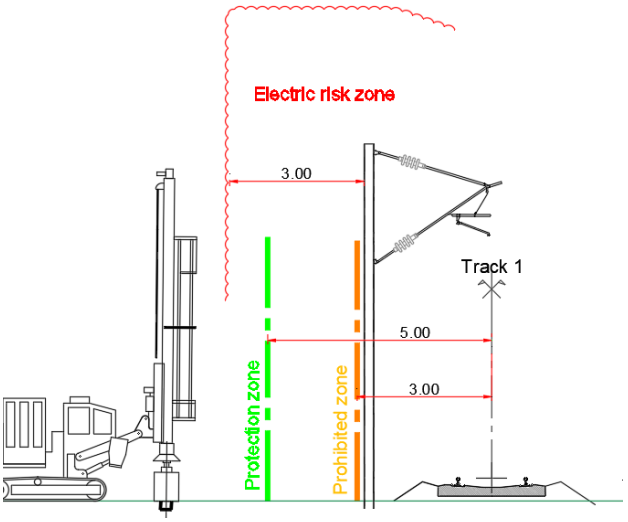

Figure 2. Zones for the use of construction machinery near the tracks following IG90033 (SNCF, 2018)

4.2.2 Track geometry quality

Settlements and displacements caused by geotechnical works are assessed in terms of track geometry. The main parameters used are (Figure 3):

1. Alignment
2. Track gauge
3. Cross level
4. Twist
5. Longitudinal level

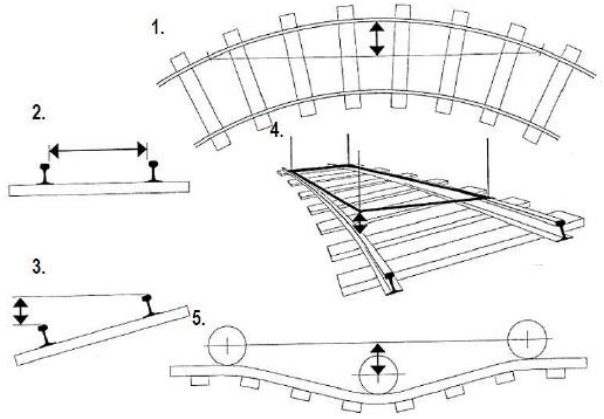

Figure 3. Schematic representation of principal track geometric parameters (Calon, 2016).

Maintaining the safety and regularity of railway operations requires that the characteristics of the traffic be considered (type, speed and frequency of traffic, importance of the line, etc.). For design, allowable track displacements depend on local conditions and vary depending on traffic speed: the faster the trains, the lower the allowable displacements. Limit values for tracks, switches and crossings in France are defined by reference guide MT40200. For each geometry parameter, the following thresholds are specified:

- Immediate Action Limit (IAL): Value which, if reached or exceeded, requires immediate measures to be taken to maintain track performance and guarantee traffic safety.
- Intervention Value (IV): threshold beyond which it is necessary to plan a short-term corrective intervention in order to avoid reaching the IAL.
- Alert value (AV): Alteration threshold beyond which specific monitoring should be carried out.

Examples of allowable longitudinal and cross levels against maximum train speed taken from MT40200 are presented in Figure 4 and Figure 5. Allowable longitudinal levels decrease linearly with traffic speed. Variations in allowable cross levels are less pronounced between 60 and 220 km/h, illustrating the higher risks for traffic safety in case of transverse default, even at moderate speed. Twist faults are of particular concern as they may cause the wheels to lose contact with the rail and derail the vehicle.

Integrating track geometry in design of geotechnical works often has important implications for projects. During initial design phases, it is recommended to limit anticipated track displacements below alert values (AV). When this is unachievable, different options are possible depending on local context:

- Reduce train speeds temporarily during works to maintain expected displacements below acceptable values,
- Perform frequent track geometry corrections by ballast maintenance to always guarantee satisfactory geometry during works,
- Carry out works during traffic interruptions (generally nights or weekends).

Such impacts on railway traffic must be anticipated. In France, traffic is planned 3 years in advance. Sufficient time must therefore be allowed between design and execution to allow for potential impacts on traffic to be incorporated in the transportation timetables. Selecting the most appropriate design option requires a global analysis balancing the potential benefits against costs and disadvantages (including operating losses for speed limitations and traffic interruptions).

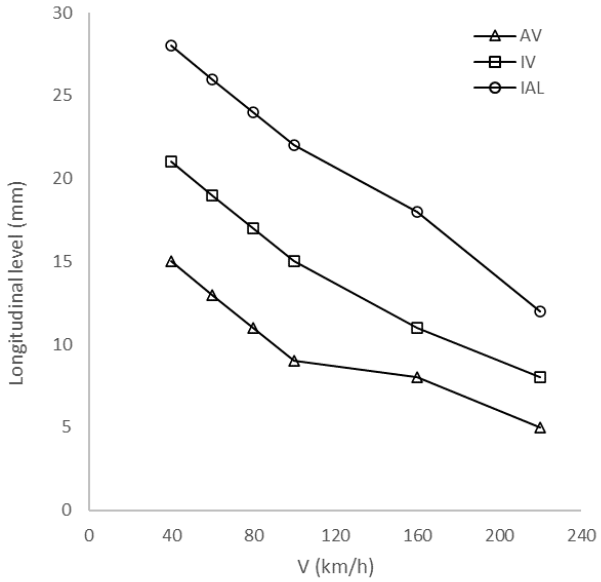

Figure 4. Examples of allowable longitudinal levels versus maximum train speed V (from MT40200 SNCF, 2021; measured over a wavelength of 15m)

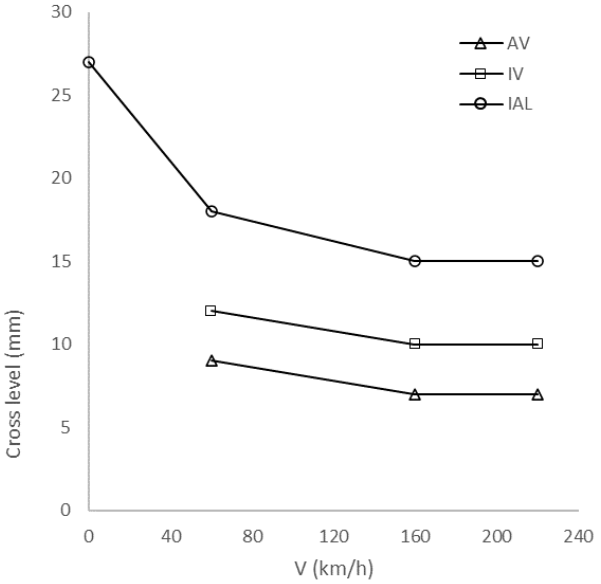

Figure 5. Examples of allowable cross levels versus maximum train speed V (from MT40200; SNCF, 2021)

It is important to note that the magnitude of allowable tracks displacements discussed above is millimetric whereas the commonly acknowledged precision for geotechnical settlement calculations is centimetric. Eurocode 7 asserts that understanding of the ground conditions depends on the extent and quality of the geotechnical investigations. Nevertheless, settlement calculations remain inaccurate and only give an approximate value. It is important that the uncertainties underlying settlement estimates be fully understood by all parties involved in such geotechnical projects (consultants, contractors, and infrastructure managers). In all projects with risks of track geometry modifications, it is appropriate to apply the approach known as "the observational method". The possibility for design adjustments during construction based on track geometry monitoring data must always be anticipated.

4.3 Excavations / retaining structures near operated tracks

According to reference guide IG90033, the effects of excavations near operated tracks must be considered when they are executed below a theoretical plane P0 inclined at 2 (horizontal direction) for 1 (vertical direction) and passing through a point located 3 meters from the axis of the track (Figure 6). Supports (i.e. retaining walls) are compulsory for excavations penetrating the theoretical plane P1 inclined at 3 (horizontal direction) for 2 (direction vertical) from the crest of the ballast.

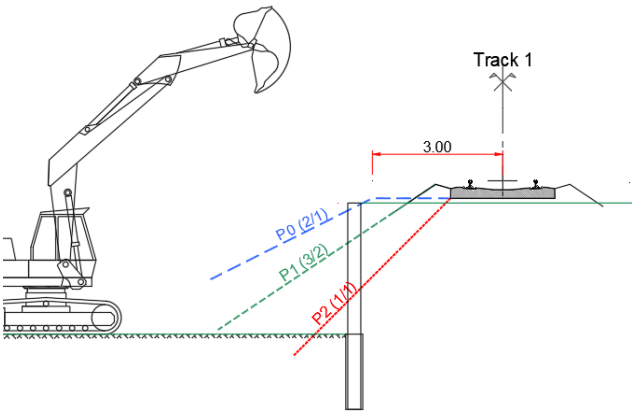

Figure 6. Excavation geometry near operated tracks from IG90033(SNCF, 2018)

Maximum allowable wall displacements are imposed in IG90033 based on the distance to the track and the depth of excavation. The displacements are also a function of the type of support and train speed, but do not depend on the surrounding ground conditions. The values were derived by SNCF from parametric studies on finite element models.

Figure 7 and Figure 8 present the theoretical example of an excavation located 5 m from an operated track. For both types of wall, allowable displacements decrease with traffic speed. Higher displacements are permitted for propped walls (Figure 8). Below 3 to 4 m, the allowable displacements decrease. This is asssumed to account for the greater risks associated with deep excavations.

Experience gained from imposing these thresholds for over 20 years in France has proven the

effectiveness of the method applied to maintain the geometry of tracks near open cuts.

In certain cases, it may be required to reduce traffic speed as a safety measure to increase admissible displacements for the design of retaining walls.

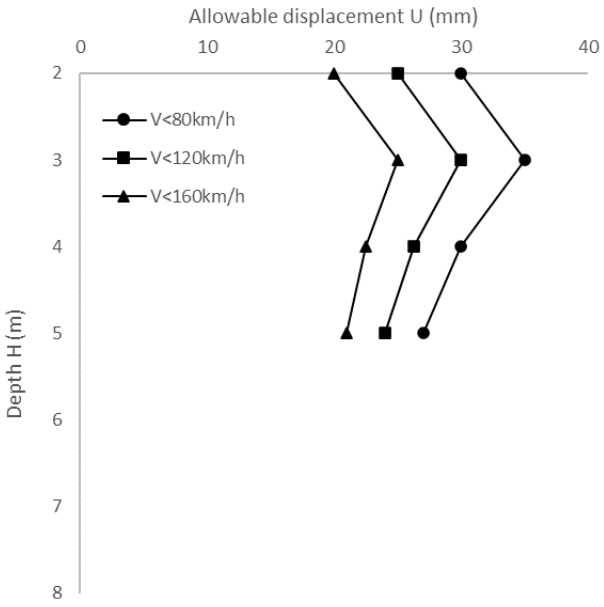

Figure 7. Example of allowable displacements for cantilever walls located 5 m from an operated track (IG 90033, Hécran=3m)

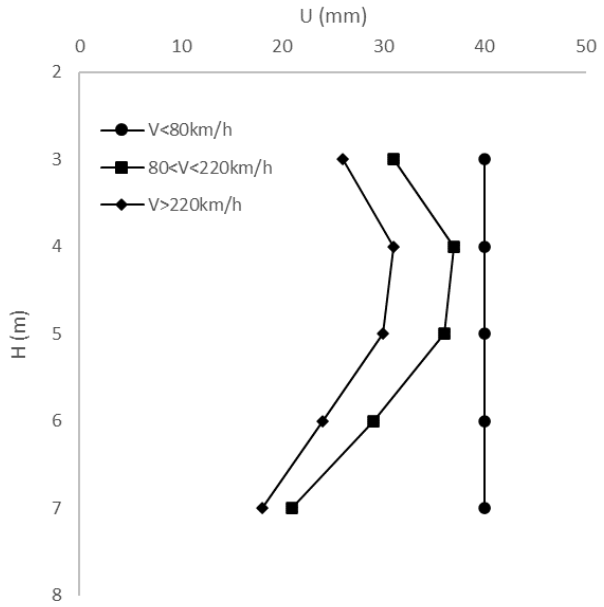

Figure 8. Allowable displacements of anchored/propped walls located 5 m from an operated track (IG90033; SNCF, 2018)

5 CONCLUSIONS

In this paper, specific risks for geotechnical works near operated railways are highlighted. In France, practice of railway safety measures is based on national reference guides validated by years of experience. Railway safety in projects can be achieved in part by takin into account traffic characteristics (especially speed) as design parameters. Geotechnical works will inevitably become more and more frequent within the interoperable European railway area. Hence, all infrastructure managers and operators would benefit from sharing local experiences and combining best-practices to guarantee a uniform level of safety everywhere in Europe.

REFERENCES

Calon, N. (2016). *Rôle de la couche intermédiaire dans le potentiel de la voie ferrée*. Thèse Doctorale en Géotechnique. Université Paris-Est, France.

SNCF (2022). IG90032 Conception et calcul des ouvrages d'art du Réseau Ferré National (in French).

SNCF (2018). IG90033 Règles de conception, réalisation et contrôle concernant les ouvrages provisoires et les opérations de construction (in French).

SNCF (2021). MT40200 Normes de géométrie en voie courante et en appareils de voie pour la pose neuve et la maintenance (in French).

SNCF (2009). IN1226 Protection des infrastructures ferroviaires lors de travaux à l'explosif ou avecengins mécaniques puissants.

Renard, C. (2011). La géotechnique ferroviaire à la SNCF, *Revue française de géotechnique*, n°134-135, pp. 5-6. https://doi.org/10.1051/geotech/2011134005.

Talfumière, V. (2011). Maintenance des ouvrages en terre sur le réseau ferré national, *Revue française de géotechniqu*e, n°134-135, pp. 7-14. https://doi.org/10.1051/geotech/2011134007.

UIC (2018). Repair works in tunnel. Union internationale des chemins de fer. Paris, France.

Proceedings of the XVIII ECSMGE 2024
GEOTECHNICAL ENGINEERING CHALLENGES
TO MEET CURRENT AND EMERGING NEEDS OF SOCIETY
© 2024 the Authors
ISBN 978-1-032-54816-6
DOI 10.1201/9781003431749-691
Open Access: www.taylorfrancis.com, CC BY-NC-ND 4.0 license

ECSMGE 24
XVIII EUROPEAN CONFERENCE ON SOIL MECHANICS AND GEOTECHNICAL ENGINEERING

Towards an open geotechnical data platform in France

Vers une plateforme de données géotechniques ouvertes en France

I. Halfon*, M. Beaufils
BRGM, F-45060 Orléans, France
i.halfon@brgm.fr

ABSTRACT: An important quantity of geotechnical data is constantly collected for all the new projects of civil engineering. This data includes generally core and destructive boreholes, in which samples are taken for laboratory testing and in situ geotechnical tests are performed. The density of geotechnical data is particularly high in urban areas. The data is collected by geotechnical engineering or drilling Companies for public or private owners. Data is essential to define the geotechnical conditions of a project and are obviously necessary for the geotechnical design of foundations or underground structures. However, most of the time, data is not accessible in a numerical format, and at the end of the project, is often forgotten, while it could be reused for neighbouring projects. It is a great loss of information and knowledge to the technical and scientific geosciences community, and it represents a significant cost for the country economy. In France, the BRGM (French geological survey office) is currently developing a new open access platform dedicated to the capitalization and accessibility of geotechnical data, compliant with the FAIR principles (Findable, Accessible, Interoperable and Reusable). This paper describes the challenges to overcome and the possible solutions, considering the high diversity of geotechnical tests, explains the need of keeping the exhaustive data set for each test, and describes the next stages of development.

RÉSUMÉ: Une quantité importante de données géotechniques est constamment collectée pour tous les nouveaux projets de génie civil. Ces données comprennent généralement des sondages carottés et destructifs, dans lesquels des échantillons sont prélevés pour des essais en laboratoire et des essais géotechniques in situ sont réalisés. La densité des données géotechniques est particulièrement élevée dans les zones urbaines. Les données sont collectées par des sociétés d'ingénierie géotechnique ou de forage pour le compte de maitres d'ouvrage publics ou privés. Les données sont essentielles pour définir les conditions géotechniques d'un projet et sont évidemment nécessaires pour la conception géotechnique des fondations ou des infrastructures. Mais la plupart du temps, les données ne sont pas accessibles sous format numérique, et à la fin du projet, elles sont souvent oubliées, alors qu'elles pourraient être réutilisées pour des projets voisins. C'est une grande perte d'informations pour la communauté technique et scientifique des géosciences, et cela représente un coût important pour l'économie du pays. En France, le BRGM (Bureau de Recherches Géologiques et Minières) développe actuellement une nouvelle plateforme de science ouverte dédiée à la capitalisation et à l'accessibilité des données géotechniques, conforme aux principes FAIR (Findable, Accessible, Interoperable and Reusable). Cet article décrit les difficultés techniques et solutions proposées, compte tenu de la grande diversité des essais géotechniques, explique la nécessité de conserver l'ensemble des données brutes pour chaque essai, détaille les différentes étapes du développement.

Keywords: Geotechnical data; open access; FAIR principles; standardization; data structuration.

1 INTRODUCTION

Geotechnical engineering encompasses the study of the mechanical properties of soils and rocks and their interaction with the structure or development to be built. The vast majority of geotechnical studies require the acquisition of a certain amount of data, including in particular the stratigraphic succession, the lithological description of the soils, the measurement of their identification parameters, the measurement of their mechanical behaviour parameters (resistance, deformability, consolidation, etc.). The density of geotechnical data is particularly high in urban areas.

The data includes generally core and destructive boreholes, with eventually samples for laboratory testing and in situ geotechnical tests.

For each project, one or more drilling contractors, laboratories and geotechnical engineers, acquire this data in one or more investigation stages as part of an order placed by the project owner.

The data is then analysed and interpreted by a geotechnical engineer. They produce a report, which presents the geotechnical model of the project derived from the investigations carried out, the geotechnical parameters interpreted and the various justifications for the geotechnical structure under investigation. The raw data is generally provided as an appendix to this report, in the form of borehole logs, photographs of

samples or cores, graphs, test reports, results tables, etc. This report and its appendices are attached to the tender documents for the works companies, who can also supplement them and make their own interpretations.

Once the work has been completed, the geotechnical reports and the data they contain are archived by the various parties involved. More often than not, if the structure does not behave abnormally, this data is never reused, or even forgotten altogether.

The advent of digital tools (databases, GIS, etc.) now makes it possible to capitalise on this data, and opens up the possibility of re-using it for neighbouring projects, for example, or quite simply to improve knowledge of the subsoil, facilitate and rationalise its development (Kokkala and Marinos, 2022), (Pando et al., 2022).

In France, the BRGM (French geological survey office) is currently developing a new open access platform dedicated to the capitalization and accessibility of geotechnical data, compliant with the FAIR principles (Findable, Accessible, Interoperable and Reusable).

2 ABOUT GEOTECHNICAL DATA

2.1 Nature, heterogeneity, provenance and reusability

Geotechnical data is both numerous and diverse in nature. It may be textual data (e.g. lithological descriptions or geotechnical classification symbols), single physical quantities (e.g. water content or density), pairs or groups of linked physical quantities (e.g. shear strength, which is made up of cohesion and friction angle), or temporal data (e.g. piezometric records).

It is also important to note the existence in geotechnics, as in other scientific disciplines, of a rich and sometimes ambiguous vocabulary to designate the different properties of soils and rocks, with terms of close physical meanings. For example, we speak of undrained cohesion, or undrained shear strength, or sometimes apparent cohesion, or even short-term cohesion. It is therefore essential to define a precise lexical reference system as part of a geotechnical data bank.

In addition, some geotechnical parameters are measured directly (e.g. the cone resistance of the static penetrometer). Others (most of them in fact) are the result of an in situ or laboratory test, involving raw measurements, parameters linked to the test or to the measuring device, intermediate calculations and interpretation by the engineer, leading in the end to interpreted parameters. For instance, in the Ménard pressuremeter test, the contextual data are the depth, the groundwater level, the probe characteristics and the calibration parameters. The raw data are the probe volume measurements at each step of pressure, and at different times. The intermediate parameters are the corrected pressure-volume measurements and the p_1 and p_2 pressures of the beginning and the end of the pseudo-elastic phase. And the final interpreted data are the net limit pressure (Pl*), the net creep pressure (Pf*) and the pressuremeter modulus (E_M).

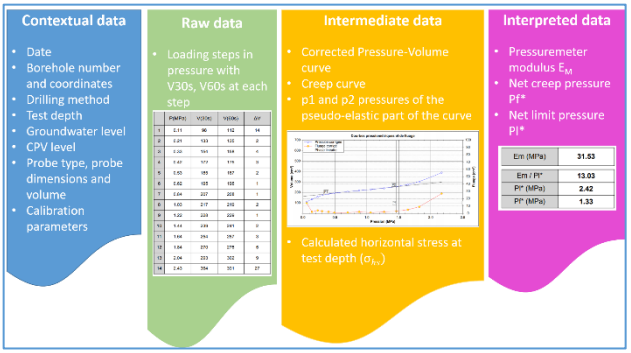

Figure 1. Different classes of data, example of the Ménard pressuremeter test (©BRGM).

The capitalisation of geotechnical parameters in a database therefore raises the question of what data do we want to store? One option would be to store only the final, interpreted data from a geotechnical test (e.g. Pl*, Pf* and E_M in the case of the previous example). However, this would appear to be a very restrictive choice: in fact, these parameters are of little use to the geotechnical engineer if he does not have all the contextual elements of the test (drilling method and diameter, probe dimensions and characteristics, volume-pressure raw data and curves, creep curve, etc.).

It is therefore essential to know and control the source of geotechnical data and, to do this, to be able to store in the database all the data from a geotechnical test: contextual data, raw measurements, curves, intermediate calculations and, of course, the interpreted values. This choice of exhaustiveness gives the engineer who re-uses the data the opportunity to assess the quality of the test and to make his own interpretation. On the other hand, this choice implies a number of constraints and requirements: the management of a large quantity of data, the use of a harmonised vocabulary for all geotechnical data, and the need of using structured and standardized data, i.e. data that obeys precise classification rules, and finally.

2.2 Data standardization and interoperability

Data structuration is a prerequisite for setting up a database. This essential step requires the use of an unambiguous vocabulary for the various physical properties that are stored. To ensure that this vocabulary is understood and shared by all geotechnical engineers, the logical choice is to draw on geotechnical standards (testing standards and Eurocode 7). Each term used for a physical quantity must be accompanied by a clear definition. Any synonyms must be listed and associated with this property.

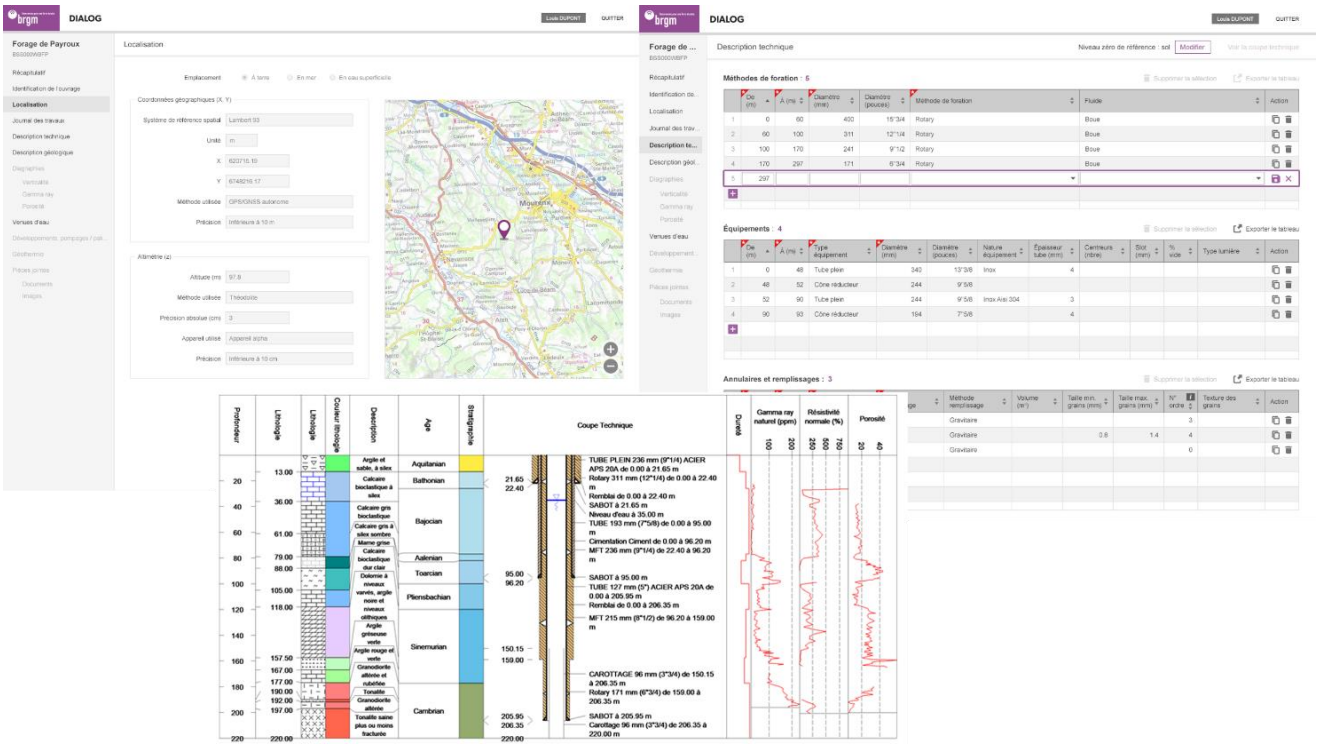

Figure 2. DIALOG web application screenshots (©BRGM).

In order to facilitate data description and to harmonise semantic, BRGM has established registers and acting as a reference point for geoscience vocabularies (https://data.geoscience.fr/ncl/). The registers published cover a wide range of earth sciences topics, including lithology, chronostratigraphy, fossils, minerals, as well as methods, observed properties and units of measurement. They include many entries relating to Geotechnics (in-situ tests, laboratory tests, geomechanical properties and associated units). Each register includes additional information such as synonyms, semantic relationships (hierarchies, equivalences, genealogies, etc.), as well as other useful information for subject specialists such as symmetrical relationships and replacements for obsolete terms.

For Geotechnics, the BRGM registry provides a list of ObservedProperties, Procedure. They have been drawn up as part of an open and collaborative science approach, so that any user can propose modifications or additions to the proposed definitions.

Interoperability is "the ability of a product or system, whose interfaces are fully known, to work with other existing or future products or systems without restrictions on access or implementation" (Wikipedia). Interoperability is also essential if data is to be easily exchanged, either to feed the database or to export data. It requires the development of data standards for all kind of geotechnical data, which is still not the case at present time.

2.3 Digital transition: BIM, Digital Twin, Geomodeling

Since 2018, BRGM has been looking to the issue of standardising geotechnical data. The opportunity to tackle this topic was offered by the national project MINnD, which main aim was to extend the capacities of OpenBIM standards, in particular the Industry Foundation Class (IFC) format from bSI, for describing infrastructures in their environment (Beaufils & al, 2020), (Rives & al, 2020).

For geotechnical engineering, the work was carried out in collaboration with several professional bodies in France, including ANDRA, CAN, CETU, EDF, EGIS, GEOLITHE, GEOS, SETEC, SYSTRA, TERRASOL and VINCI CONCESSIONS. There was a consensus to build the extension for geotechnics on existing

standards (e.g. NF P 94-500) or existing recommendations (e.g. AFTES GT32).

Having as a target the definition of a data exchange format with common semantics between GIS and BIM tools, the group focused on identifying the data exchanged, describing it and organising it.

The openGIS standards promoted by the Open Geospatial Consortium (OGC), used in particular for geology and hydrogeology, served as the basis for this work. Also the group was aware of the existence of the AGS/AGSi (Chadwick & al, 2019) and DIGGS (Bachus & al, 2020) standards and in February 2022 a project called the Geotech Interoperability Experiment was launched (Beaufils & al, 2022).

Again lead by BRGM, the project proposed to federate the geotech community around standards for BIM and GIS.

3 STATUS OF GEOTECHNICAL DATA MANAGEMENT IN FRANCE

3.1 Rules and laws

In France, geotechnical data is the property of the organisation that commissions and pays for it. French law, set out in the Mining Code, requires the declaration to the Authorities of any drilling deeper than 10 m, whatever its purpose (geological, hydrogeological, geotechnical, geothermal investigation, water pumping, etc.).

This declaration is made using a web application (DUPLOS) developed by BRGM. It must be made before the drilling is carried out. An identification number is then created by BRGM and sent to the organisation that made the declaration. The Mining Code also stipulates that all documents relating to the drilling can then be sent to BRGM. To this end, DIALOG, a web application has been developed to enable the lithological and stratigraphic description of the borehole, previously declared, to be entered. To date, this application cannot receive geotechnical properties, except a pdf file attachment.

3.2 BRGM Survey about a national geotechnical data base

Before starting to develop an open access national platform for geotechnical data, BRGM launched a survey to the French geotechnical community. The objectives of this survey were to: find out about the practices of French geotechnical engineers with regard to archiving and exchanging geotechnical data, assess the opinion of geotechnical engineers for data sharing, collect the expectations and needs of future users of the platform, and also their criticisms or warnings.

The survey took place in mid-2023. It was relayed by various geotechnical associations and more than 200 answers were collected A slight majority (53%) are representatives of geotechnical engineering companies, 20% are civil works or foundation contractors, 14% are engineers from public organisations, 6% are public owners. This high level of participation demonstrates the interest of French geotechnical community in this subject.

It appears that a large majority of respondents (85%) consult regularly or occasionally the BSS (subsoil database, which at date is a borehole database, with litho-stratigraphic data only).

With regard to archiving practices, digital archiving of geotechnical reports and data is widely used (92% for reports and 81% for geotechnical data). In the case of data, pdf format is used in the majority (53%). Re-usable formats (such as text, excel or csv) are used by 31% of respondents, and more structured formats (such as AGS, BIM or others) accounting for only 13%.

Support for the project from the geotechnical community is relatively good, as shown by the scores between 1 and 5 given to different proposals, presented in Figure 3. There is also a strong demand for all the raw values in order to be able to make full use of this database.

About a national openaccess geotechnical database, on a score from 1 (disagree) to 5 (agree), you would say	Score
This would make it easy to retrieve old data	4,6 / 5
This would make it possible to avoid carrying out (or repeating) investigations in areas where data is already available	3,6 / 5
This would help to better define new or future geotechnical investigations	4,6 / 5
This would be useful, provided that the raw data from the trials is accessible.	4,2 / 5
This is of limited use, as geotechnical investigation is always necessary anyway.	2,7 / 5
The benefits are limited, as we have no control over the quality or reliability of the tests carried out by others.	3,0 / 5
The benefits are limited, as it takes a lot of time to archive or consult data.	2,1 / 5
This is likely to reduce the market for geotechnical surveys.	2,5 / 5

Figure 3. Results of the BRGM survey about geotechnical database.

However, some concerns were expressed. For example the question of the reliability/quality of the data made available on the platform, and the risks of reducing the market for geotechnical surveys in France.

4 NATIONAL GEOTECHNICAL DATA PLATFORM – TECHNICAL ASPECTS

4.1 User profiles

Users of the platform will of course be geotechnical professionals (engineers, civil works contractors), but

also infrastructure project owners, teachers, students or simply individuals looking for information about the subsoil.

The data suppliers will be the public or private project owners who order for geotechnical investigations. They may delegate the supply of data files to their project managers or geotechnical sub-contractors.

4.2 Structured and unstructured data

The geotechnical data that will be collected can be classified into two categories: structured data and unstructured data.

Structured data is data that has already been organised in a digital format, which may be a proprietary format (for example the files used for acquisition equipment), a format specific to geotechnics (such as AGS or DIGGS), a format associated to the further application (ifc for BIM, or RESQML for geological modelling applications) or a csv or excel format with predefined fields. In order to be able to collect and store this structured data, it is necessary to make a mapping that provides the link between a given parameter in the database and the same parameter in the original file.

The unstructured data are the geotechnical test sheets only available in paper or pdf format. For these data, several possibilities will be provided: downloading the scanned document or pdf file, or manual entry of the test. Further developments based on AI are explored to extract key data in a pdf file.

4.3 Functionalities to develop

Data input interfaces will be developed, on the principle of the DIALOG application currently used to enter lithostratigraphic descriptions of boreholes. Ultimately, the goal is to welcome the largest possible variety of geotechnical tests. However, the tables for each type of test will be developed progressively so as to quickly have an operational tool for the most common tests (e.g. pressuremeter tests, which are very common in France), which will gradually be enhanced with the other types of test. As mentioned above, the content of these tables should include all the fields corresponding to contextual, raw, intermediate and interpreted data.

For users, the data will be accessible via a cartographic interface, with borehole points displayed, as in situ or laboratory tests are always attached to an investigation location. Data will be able to be exported in a variety of formats. Queries by geographical sector, by type of test or by geological unit will be developed.

Finally, connections with geotechnical tools and software are also envisaged: for example, with 2D or 3D geomodelling tools.

4.4 OpenGeotech: the project and its architecture

A pilot project, called OpenGeotech, is currently under development at BRGM. Aimed at giving substance to the standardisation work undertaken previously, it proposes to:

- extend the DIALOG application to the collection and description of geotechnical tests,
- have those data made available through an a standardized protocol called OGC SensorThings API, as recommended and promoted in the Geotech Interoperability Experiment.

In addition to illustrating and validating the standard activity previously mentionned, these two combined actions are done in order to facilitate the process of geotechnical data collection and also offer a „reward“ or „money back“ to the declarant by offering him the capacity to acess and reuse the declared data in other softwares (geomodeling, soil structure calculus or BIM tool) thanks to the interoperable API.

At the current stage of development, drilling parameters (instantaneous logs) and three types of test have been targeted: the Menard Pressuremeter test, the Standard Penetration Test (SPT) and the Cone Penetration Test (CPT).

The description of more tests is planned to be offered in the future, including Laboratory Tests and Samples / Specimen description. These actions will be carried on as part of a larger project in BRGM, currently known as the Geotech Information System project.

5 CONCLUSION AND PERSPECTIVES

Until now, in France, geotechnical data acquired during investigations is not usually reused. Although digital archiving is increasingly used by geotechnical engineers, the data is very rarely organised in a structured way.

The creation of a structured database enabling geotechnical data to be banked and shared with the public is a task that has been entrusted to BRGM by the authorities. It aims to enhance the value of the data acquired, to reduce the need to carry out new surveys unnecessarily, to better target the investigations to be carried out and to improve knowledge of the French subsoil.

A survey of French geotechnical professionals was launched in mid-2023. Most of them were in favour of the project, although they did express some concerns about the quality, reliability and confidentiality of the data.

From a technical point of view, the wealth and complexity of geotechnical data raises a number of questions about the choice of data to be banked, as well as the methods for feeding and consuming the data, and the exchange formats. BRGM has chosen to provide for the possibility of storing all the raw test data, so that future users can assess the quality of the data and re-analyse the tests.

A demonstrator called OpenGeotech is currently being developed in-house at BRGM. A first public version will be available by the end of 2024.

REFERENCES

Bachus, R., Machairas, N., Cadden, A. (2020). Standardizing Geodata Transfer and Storage. Deep Foundations, May/June 2020 Issue. https://dfi.dcatalog.com/v/May-June-2020/?page=97.

Beaufils, M., Halfon, I., Hassan,N., Galandrin, C., Miraillet, P., Le Hello, B. (2022). FAIR Geotechnical data to support BIM for Underground Infrastructure. *World Tunnel Congress 2022*, Sep 2022, Copenhague, Denmark. ⟨hal-03644840⟩.

Beaufils M., Le Hello B., Lorentz J., Castro-Moreno J., Beaudouin M., Grellet S. (2020) Proposition of Sustainable and Long-Term Geotechnical Data Management to Support Building Information Modeling. In: Correia A., Tinoco J., Cortez P., Lamas L. (eds) Information Technology in Geo-Engineering. ICITG 2019. Springer Series in Geomechanics and Geoengineering. Springer, Cham. https://doi.org/10.1007/978-3-030-32029-4_44.

Chadwick, N., Farmer, D., Chamfray, J. & Miles, S. (2019). Extension of the AGS Format to Incorporate Ground Model and Interpreted Data. 10.1007/978-3-030-32029-4_20.

Kokkala A., Marinos V. (2022). An engineering geological database for managing, planning and protecting intelligent cities: The case of Thessaloniki city in Northern Greece, Engineering Geology 301, 106617, https://doi.org/10.1016/j.enggeo.2022.106617.

Pando L., Flor-Blanco G., Llana-Funez S. (2022). Urban Geology from a GIS based Geotechnical system: a cas study in a medium-sized city (Oviedo, Spain), Environmental Earth Science 81:193, https://doi.org/10.1007/s12665-022-10287-y.

Rives, M., Borrmann, A. (2020) IFC-Tunnel Project. Report WP2: Requirements analysis report (RAR). Status: v1.0 – 2020-07-31. https://app.box.com/s/3p28520cgser0sa1bvunhc99bt4qhuza/file/711362091723. Retrieved August 16, 2021.

Proceedings of the XVIII ECSMGE 2024
GEOTECHNICAL ENGINEERING CHALLENGES
TO MEET CURRENT AND EMERGING NEEDS OF SOCIETY
© 2024 the Authors
ISBN 978-1-032-54816-6
DOI 10.1201/9781003431749-692
Open Access: www.taylorfrancis.com, CC BY-NC-ND 4.0 license

ECSMGE 24
XVIII EUROPEAN CONFERENCE ON SOIL MECHANICS AND GEOTECHNICAL ENGINEERING

The application of Digital Twins and the Internet of Things to assess the metro dynamic effects on historical buildings

L'application des jumeaux numériques et de l'Internet des objets pour évaluer les effets dynamiques du métro sur les bâtiments historiques

I. Kaliukh*, O. Trofymchuk, Y. Berchun, V. Berchun, Y. Melashenko, Y. Pavliuk
Institute of Telecommunication and Global Information Space, Kyiv, Ukraine

Y. Slyusarenko, V. Shokarev, V. Tytarenko, N. Kosheleva, Y. Ischenko, A. Shokarev, V. Shuminskiy
The State Research Institute of Building Constructions, Kyiv, Ukraine

V. Siedin, V. Kovba
State Enterprise "Pridniprovsk State Academy of Civil Engineering and Architecture", Dnipro, Ukraine

**kalyukh2002@gmail.com*

ABSTRACT: The Hostynnyi Dvir two-storey building erected in Kyiv at the beginning of the 19th century is complicated in plan and consists of two U-shaped parts. Under the building the metro tunnels pass with trains running on a normal (non-vibration-isolated) track every 2 minutes. The nature of the foundation structures damage indicates that the main cause of its occurrence is an uneven deformation of the foundations base due to the additional soil compaction under dynamic effects. The damage analysis shows that in fact the building is divided into several blocks and has experienced the spatial rigidity reduction. According to the results of the vibrodynamic tests carried out with the use of the Internet of Things during the metro trains movement, the additional vertical dynamic loads on the building foundations up to 1%, on the soil near the building up to 7%, and on the building floor up to 5% from the object own weight were determined. Modelling of the stress-strain state of the "base – foundation – metro" system is performed using the Midas GTS NX software package. The constructed Digital Twin is a three-dimensional model reflecting the actual soils layering and including the subway tunnels structures, foundations and superstructure parts. The building superstructure parts are included in the model for obtaining a more accurate initial stress-strain state for the base taking into account the building spatial rigidity. The obtained calculated acceleration values coincide with the results of vibrodynamic studies at the IoT sensors installation points.

RÉSUMÉ: Le bâtiment à deux étages Hostynnyi Dvir érigé à Kiev au début du XIXe siècle est de plan compliqué et se compose de deux parties en forme de U. Les tunnels du métro passent sous le bâtiment avec des trains circulant sur une voie normale (non isolée des vibrations) toutes les 2 minutes. La nature des dommages aux structures de fondation indique que la principale cause de leur apparition est une déformation inégale de la base des fondations due au compactage supplémentaire du sol sous les effets dynamiques. L'analyse des dommages montre que le bâtiment est en fait divisé en plusieurs blocs et a subi une réduction de la rigidité spatiale. Selon les résultats des tests vibrodynamiques effectués sur la base de l'Internet des objets, les charges dynamiques verticales supplémentaires sur les fondations du bâtiment jusqu'à 1%, sur le sol à proximité du bâtiment jusqu'à 7% et sur le sol du bâtiment jusqu'à à 5% du poids propre de l'objet ont été déterminés lors du mouvement des rames de métro. La modélisation de l'état contrainte-déformation du système "socle – fondation – métro" est réalisée à l'aide du progiciel Midas GTS NX. Le Digital Twin construit est un modèle tridimensionnel reflétant la stratification réelle des sols et comprenant les structures, les fondations et les parties de superstructure des tunnels de métro. Les valeurs d'accélération de conception obtenues coïncident avec les résultats des études vibrodynamiques aux points d'installation des capteurs IoT.

Keywords: Dynamic loading; metro; compacted urban development; finite element method; experiment.

1 INTRODUCTION

Hostynnyi Dvir is the main and central element of 'The Buildings Complex on Kontraktova Ploshcha (Contract Square), the 10th – the end of the 19th centuries' Architecture and Urban Planning Monument of Local Importance, which comprises a monumental trading store on Kontraktova Ploshcha in the historical neighborhood of Podil. It had partially been constructed in 1809–1813 under the project of Luigi Rusca and was then rebuilt in 1828–1833 according to the project of Andrii Melenskyi. The Hostynnyi Dvir two-storey building (HDB) with a

basement has a complicated plan as it consists of two U-shaped parts forming a closed internal area with the axial dimensions 122.2 m x 65.5 m (Figure 1).



Figure 1. Hostynnyi Dvir, photo of 1930s.

High traffic volumes are observed on the motor vehicle and tram routes located nearby. The metro tunnels pass under the HDB, and the metro trains run on the normal (non-vibration-isolated) tracks every two minutes (Figure 2).

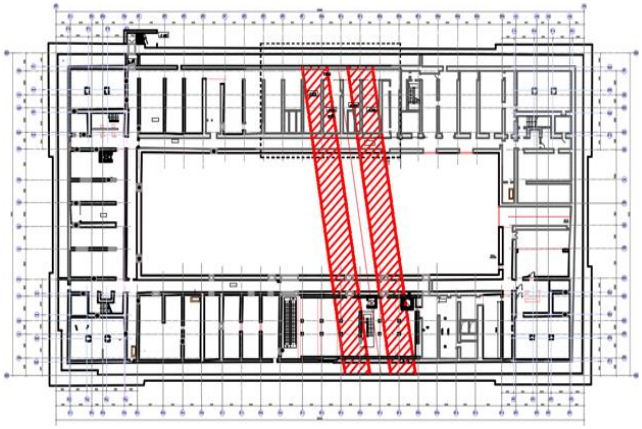

Figure 2. The layout of the Hostynnyi Dvir building. Two red stripes are the subway lines.

International concerns over cultural and natural heritage were reflected in the World Heritage Convention which was adopted by UNESCO in 1972 (World Heritage Convention, 2023). It aims at encouraging national governments to give greater protection to the sites of importance for nature conservation, to conduct research that allows gaining a deeper understanding of their cultural and natural heritage sites and the existing threats to them. The State Parties to this Convention are called on to integrate the protection of their cultural and natural heritage into regional planning programmes, to set up special services with an appropriate staff within their territories, to undertake scientific and technical conservation research, and to take measures giving their heritage a function in the day-to-day life of the community. The issues of dynamic effects on buildings and structures; transport vibration influence on the stress-strain state (SSS) of existing buildings, further deformations of their bases and foundations, their uneven settlements and other negative phenomena were considered in numerous works of such national and foreign researchers as Huston, 2011; Kaliukh et al., 2018; Lollino et al., 2006; Sedin et al., 2019.

2 METHODS FOR ASSESSING THE HDB BASE SSS CHANGES UNDER THE DYNAMIC EFFECTS

Assessment of the „base – structure“ system SSS change is generally made via comparing its specific technical parameters. The number and types of controlled parameters shall be determined according to the preliminary survey results, the regulatory and project documents requirements, and the conditions for maintaining the object operational characteristics throughout its lifecycle. The SSS technical parameters shall be identified pursuant to the results of the object technical conditions complex study including the following activities: visual inspection (defects, damage, assessment of compliance with the project etc.); instrumental studies of the materials strength; geodetic measurements of deformations (settlements, deflections, structures positions etc.); engineering geological and hydrogeological surveys; dynamic vibration tests of soils and structures; numerical 2llowance of the „base – foundation“ system SSS with an2llowancee for the parameters obtained from the investigations mentioned above. Reactions to changes in the structural components technical state are recorded by the monitoring system sensors, which allow receiving data on the object responses to the external and internal effects including the object and its individual components spatial displacements taking place in the form of deflections, settlements, rolls etc.; deformations in building structures; changes in dynamic characteristics of the building structures and building as a whole; and changes in the environment surrounding the object. The above information analysis and numerous examples of new construction activities under conditions of urban density in the city of Kyiv show an urgent need to elaborate a hybrid theoretical and methodological approach using the Internet of Things (IoT) as the logical continuation and development of the scientific and technical construction objects support for avoiding and preventing soil accidents in the future. The IoT sensors allow to carry out the tensometric measurements and the following physical quantities measurements: angles of buildings and structures inclination; levels of

crack opening (closure), object components shifts and expansion joints; vibrations; temperature; humidity; pressure etc. (Figure 3). The IoT basic elements in the sphere of geotechnics are as follows: procedures of sequential analysis when choosing the diagnostic criteria; means of technical diagnostics and methods for processing the obtained information; reference approximation models for the monitoring system testing by the in real time (online) comparison method; multilevel functions and means for monitoring research; diagnostic information concentration in the form of an appropriate database.

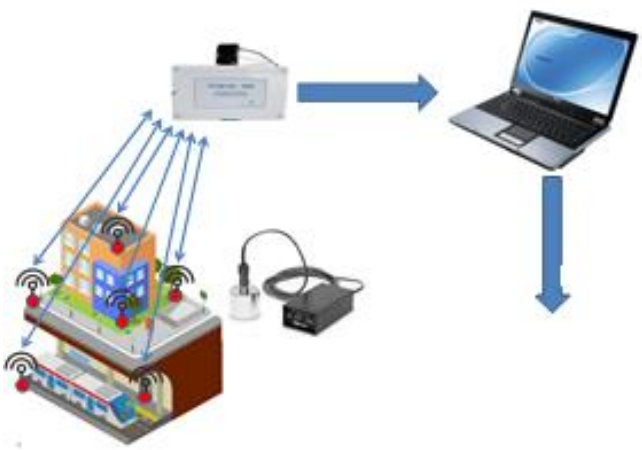

Figure 3. System for on-line monitoring of the object vibration characteristics using the IoT.

Numerical modelling of the HDB SSS under static and dynamic loads was carried out considering the results of checking the HDB mathematical model for its relevance to the real object. That allowed to take decisions on the possibility of using the data obtained after conducting computer experiments on the object mathematical model for setting up and clarifying the composition and placement of sensitive elements of the monitoring system determining the HDB load-bearing structures state. In this case, the relevance of the HDB computer model means that the HDB civil structures integral characteristics obtained from measurements during the field surveys and by means of modelling are almost identical; the discrepancy is within the acceptable range of permissible error.

3 EXPERIMENTAL STUDIES OF THE HDB USING THE IOT TECHNOLOGIES

The above-mentioned studies included the following elements: the visual inspection and instrumental studies of the structures materials strength; checking calculations to assess the "base – foundation – structure" system SSS for HDB; the vibrodynamic tests of soil, foundation and load-bearing structures under the effects of the metro trains, trams and motor vehicles traffic and construction equipment operation. The damage nature indicates that the building structures destruction is mainly caused by the uneven deformation of the HDB foundation bases due to the additional soil compaction under the dynamic effects. The damage analysis shows that in fact the building is divided into several blocks and has experienced the spatial stiffness reduction. According to the results of HDB vibrodynamic tests, the dominant frequencies of soil vibrations were determined as 15 Hz during the land transport movement and 55 Hz during the metro trains movement. The maximum vibration acceleration amplitudes determined with the values of 64 cm/s² in the horizontal direction and 42 cm/s² in the vertical direction under the simultaneous action of all possible dynamic effects were recorded for the soil near the building above the metro tunnels. During the metro trains movement, the HDB own weight caused additional vertical dynamic loads up to 1% on the building foundation, up to 7% on the soil near the building, and up to 5% on the building floor structures. The obtained calculation accelerograms serve as the initial conditions for the SSS modeling of HDB "base – construction – metro" system using the direct dynamic method.

4 SSS NUMERICAL MODELING FOR THE HDB BASE UNDER DYNAMIC EFFECTS USING THE DOUBLE TWINS METHOD

The existing methods do not allow to comprehensively solve the complicated task of forecasting the SSS changes in the "base – structure" system under the dynamic influences including the metro trains effects. The difficulty lies in the necessity of taking into account such important factors as urban density, which is often combined with a developed underground component, and complex engineering and geological conditions of the site with various soils layers. The modern software packages that implement the finite element method (FEM) allow taking into account all the above-mentioned features of real objects with sufficient accuracy. The Midas GTS NX is one of such software packages (Midas, 2018). To perform the numerical modeling, in this paper the Linear Time History is applied. In the GTS NX an implicit integration method for the direct time integration for the linear assignments is used. The GTS NX uses the HHT-α method proposed by Hilber, Hughes, and Taylor for the implicit direct integration. The proposed Digital Twins is a three-dimensional model presenting the actual soil layering, metro tunnel structure, and HDB foundations and

superstructure components. The superstructures are included in the model for obtaining a more accurate initial base SSS taking into account the building spatial rigidity. When solving FEM problems, the calculation area is considered as a collection of a finite number of elements. The main advantage of the SSS numerical calculations is that all components of stresses σ_{ij} (x, y, z), of deformations ε_{ij} (x, y, z) and of displacements u (x, y, z), v (x, y, z), and w (x, y, z) necessary for the SSS assessment and analysis for the entire soil massif are obtained at the output. As a result of the calculations, both the qualitative and quantitative pictures of the SSS parameters changes in the HDB foundations base under the dynamic impacts were obtained. The calculated values of the accelerations coincide with the results of vibrodynamic studies at the sensors installation points. Figure 4 present the assessment of the maximum zone of the dynamic impact during the movement of two trains.

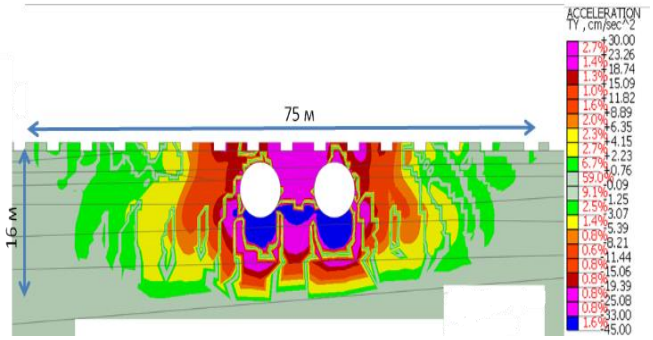

Figure 4. The maximum zone of the dynamic impact during two trains movement (acceleration). During the passage of metro trains, the maximum values of accelerations in the HDB foundation soil base reach 45 cm/s^2 (dark blue color) in the space between the tunnels and under the tunnels, more than 30 cm/s^2 is observed directly under the tunnels (pink and dark red colors), and approximately 20 cm/s^2 is recorded at a distance of 4 m from the nearest tunnel (pink color).

The influence zone of the metro is determined based on the analysis of changes in the parameters of the SSS system during static and dynamic calculations at characteristic points at a certain distance from the source of influence (metro tunnel). According to numerical calculations, it was found that vertical stresses at the base directly under the tunnel increase up to 35.8%. At a distance of 2 to 4 meters, the increase is in the range of [8.2; 11.3]%, at a distance of 8.5 meters, it is up to 2.5%, and at a distance of 13 meters, it is less than 1%. Horizontal stresses at the base directly under the tunnel increase up to 50.6%. At a distance of 2 to 4 meters, the increase is in the range of [8.1; 33.2]%, at a distance of 8.5 meters, it is up to 2.3%, and at a distance of 13 meters, it is less than 1%.

5 CONCLUSIONS

1. Based on the results of the SSS parameters analysis for the "base – foundation – building" system under static and dynamic influences, the qualitative and quantitative pictures of the HDB SSS parameters changes, as well as an idea of the actual vibrations distribution in the soil massif taking into account the real layering of soils, hydrological conditions, underground structures etc. were obtained.
2. The soil vibrations predominant frequencies of 15 Hz during the land transport movement and 55 Hz during the metro trains movement were experimentally determined. Considering the simultaneous action of all types of dynamic influence, the maximum values of vibration acceleration amplitudes of 64 cm/s^2 in the horizontal direction and 42 cm/s^2 in the vertical direction were recorded for the soil near the building above the metro lines.
3. In certain zones of the HDB soil base the excessive pore pressure occurs. The additional soil compaction is possible due to the vibrocompression.

REFERENCES

Huston D. (2011). Structural Sensing, Health Monitoring, and Performance Evaluation. CRC Press.

Kaliukh, I., Fareniuk, G., Fareniuk, I. (2018). Geotechnical Issues of Landslides in Ukraine: Simulation, Monitoring and Protection. In: Wu W., Yu HS. (eds) *Proceedings of China-Europe Conference on Geotechnical Engineering. Springer Series in Geomechanics and Geoengineering*. Springer, Cham, DOI: https://doi.org/10.1007/978-3-319-97115-5_124.

Lollino, G., Chiara, A. (2006). UNESCO World Heritage sites in Italy affected by geo-logical problems, specifically landslide and flood hazard. *Landslides*, 3(4), pp.311-321. https://doi.org/10.1007/s10346-006-0059-7.

Midas (2018) Civil On-line Manual - Civil structure design system. Available at : http://manual.midasuser.com/EN_Common/Civil/890/On-line_Manual.htm.

Samorodov, A.V., Sedin, V.L., Krotov, O.V. (2019). Procedure for Assigning a Soil Deformation Modulus of Large-Sized Slab and Slab-Pile Foundations Bases. *Soil Mech Found Eng.*, 56, pp.340–345. https://doi.org/10.1007/s11204-019-09612-8.

World Heritage Convention. (2023). Available at: https://www.iucn.org/our-work/informing-policy/international-policy/world-heritage-convention

Proceedings of the XVIII ECSMGE 2024
GEOTECHNICAL ENGINEERING CHALLENGES
TO MEET CURRENT AND EMERGING NEEDS OF SOCIETY
© 2024 the Authors
ISBN 978-1-032-54816-6
DOI 10.1201/9781003431749-693
Open Access: www.taylorfrancis.com, CC BY-NC-ND 4.0 license

ECSMGE 24
XVIII EUROPEAN CONFERENCE ON SOIL MECHANICS AND GEOTECHNICAL ENGINEERING

Digital transformation in geotechnical engineering

Digitalisation en ingénierie géotechnique

A. Măgureanu*, L. Sata
SBR Soletanche Bachy Fundații SRL, Bucharest, Romania
**magureanu@sbr.ro*

ABSTRACT: Dealing with a huge amount of information, and being constrained by deadlines it is very important, nowadays, to add efficiency in managing design and execution processes. The first step was to create a transparent framework in all the company's departments, where everyone can access, share and review information, then to create and deliver automated and inter-connected workflows. Site visits simulated site organization or safety trainings are now made using virtual reality. To implement a digital model, it is necessary to know the tools, software suite that can create models, through which automated processes can be realized, interactive communication systems or for arranging and browsing information. Further, in the design department, many models of geotechnical structural solutions can be generated, studied, verified, adapted, and optimized in a very short time, due to automated generative design processes. All information is then stored in a cloud-based network and can be shared automatically through routine-based processes. Virtual reality helps also to understand site constraints, visualize design model applied on site, or to check built geotechnical structures on the site or in the office. Digital transformation in geotechnical engineering, is, in fact a complex and very exciting process for us, it is a strategic element of the company, which generates innovation processes and thus results in better services delivered to our partners.

RÉSUMÉ: Traitant une énorme quantité d'informations tout en étant contraint par les délais, il est très important, de nos jours, d'ajouter de l'efficacité dans la gestion des processus de conception et d'exécution. La première étape a été de créer un cadre transparent dans tous les départements de l'entreprise, où tout le monde peut accéder et ensuite créer et fournir des flux de travail automatisés et interconnectés. Les visites de chantier, les simulations de planification ou encore les formations à la sécurité au travail se font désormais grâce à la réalité virtuelle. Afin de mettre en œuvre un modèle numérique, il est nécessaire de connaître les instruments et la suite logicielle qui permettent de créer des modèles à travers desquels des processus automatisés et des systèmes de communication interactifs peuvent être réalisés. De plus, dans le bureau d'études, de nombreux modèles de solutions structurelles géotechniques peuvent être générés, étudiés, vérifiés, adaptés et optimisés en très peu de temps, grâce à des processus de conception générative automatisés. Toutes les informations sont ensuite conservées sur Cloud et peuvent être partagées à l'aide de différents processus automatisés. La réalité virtuelle permet également de comprendre les contraintes du site, de visualiser le modèle de structure appliqué sur le site, ou encore de vérifier les structures géotechniques réellement construites sur le site. La digitalisation en ingénierie géotechnique est, en fait, une méthode complexe, un élément stratégique de l'entreprise qui génère des pistes d'innovation et se traduit ainsi par de meilleurs services fournis à nos partenaires.

Keywords: Digitalisation; transformation; virtual reality; generative; automation.

1 INTRODUCTION

The latest impact on all aspects of society and business involves a fusion of technologies that blur the boundaries between the physical, digital, and biological spheres. It is a force for change, the reason why companies must combine technology solutions for continuous innovation, which leads to rethink the way they operate.

Digitalization means progress, after all, and it has become increasingly discussed since the beginning of the pandemic. In the context in which construction sites are spread all over the country, the mobility of a person to go through all the construction sites, to assimilate all the information and to physically see their progress became more difficult.

Therefore, the current needs to create a transparent framework, a place where each person in the company can access the desired information at a click away, to visit a construction site virtually or to collect technical information in real time, have led to the creation of a virtual environment, an interactive storage space, a suite of intuitive programs and the individual transposition into a special foundation site through virtual reality.

In other words, by embracing digital technology, construction companies can improve their way of work

by increasing efficiency, bring solid communication to another level and be much more sustainable.



Figure 1. Digital customization of a construction site.

2 THE NECESSARY STEPS FOR DIGITALISATION

To implement a digital model, it is necessary to know the tools, the suites of programs that can create models, through which automated processes can be realized, interactive communication systems or for arranging and browsing information.

The next step is to share within the network (cloud based) the information and processes that require the input of the users. This ensures a clear and transparent communication of the entire process.

By a simple notification, each user is informed and becomes aware of the appearance of an information, of the taking over of a certain task or of the status of a project or construction site.

The most important stage is the horizontal integration (within the company) – that is, a real-time interconnection between the company's employees and the intra- and inter-departmental cooperation. After establishing the internal routine and processes, vertical integration completes the process by involving business partners in the digital interconnection process (e.g., creating an automated flow of orders, notices, invoices, notifications, etc.).

Digital transformation is having a great impact on the construction industry, making its mark on the organizational concept and Soletanche Bachy subsidiaries.

3 DIGITAL TRANSFORMATION IN GEOTECHNICS

At the group level, within Soletanche Bachy, we believe that digitalisation contributes to improving productivity and profitability, reduction of "downtime", increasing the interest of our clients and colleagues (interactive environment), capitalizing on the information and experiences gathered from our projects.

While every piece of information is filtered specifically and is stored altogether, having feedback from previous built projects is very important, whether it is technical, financial, or operational.

As such many breakdowns, high material consumptions can be avoided while the greenhouse gases emissions are reduced.



Figure 2. Digital site organization layout.

3.1 Design digitalisation

Design processes require comprehensive documentation, use of correct instruments and software and a continuous iteration regarding different structural models.

Therefore, it is very important to have routines which will allow automatic search for similar site conditions experienced on previous construction sites, for which, different design solutions were chosen. Of course, those preliminary trials, investigations, and tests (on piles, or on different materials, for example) will help significantly in choosing the right solution perfectly suited for project's purpose.

Nevertheless, return of experience for different solutions in various site conditions can have a great impact for the first step of project development.

The integration of all digital tools makes the design process smoother and with high level of precision.

For example, within a commercial centre foundation piles project, there are many iterations which can be done, to find the perfect balance between pile diameter, pile lengths, pile distribution and reinforced concrete footings.

Our tools make possible the integration of ground conditions, from current or past projects, architectural and structural detailing (columns dimensions, geometry of the building), loads and design and conformation local regulations to offer in a matter of seconds the most convenient piles diameter, distribution and even reinforced concrete footings.

Basically, what we call generative design is a design process that uses algorithms and artificial intelligence (AI) to generate a large number of design solutions that meet a set of constraints.

The user can then choose between the proposed alternatives and detail the project further, considering a lot of restraints as local conditions, site dimensions, materials efficiency, available machinery, and cost optimization.

Putting all the information altogether to have a unified model constantly adapted to real site conditions and updated by all the people which are working together for a specific project is a critical condition for improving the way all the information is shared, the processes used and the way that things are managed.

3.2 Construction site digitalisation

One of the biggest game changers in site management digitalisation is augmented reality (AR) which is bringing a sustainable support in project management, quality assurance and cost control. The software used, allows the user to envision different site layouts by superimposing 3D models into real life environments.

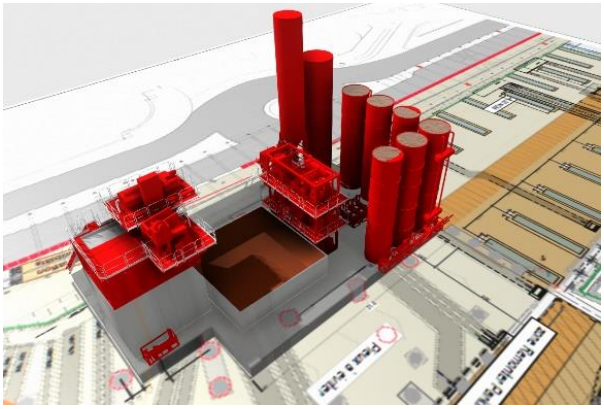

Figure 3. 3D projection of bentonite slurry plant.

This allows workers to see the planned layout of the project and to identify any potential problems early on. AR can also be used to provide workers with real-time instructions and feedback.

Augmented reality is used also to improve safety on construction sites, to highlight potential unsafe situations and to provide workers with instructions on how to avoid them. AR is also a great tool to improve collaboration between construction teams, engineers, architect and the final client.

Zetta-Lyze® is an interactive database platform, created by Soletanche Bachy, multi-application, multi-profile / profession, with multiple sources, easily accessible from anywhere, that offers real-time production information.

More than a working tool, it is a system for the automatic collection of design and production data of a project.

This data can be accessed, organized, and analysed, for an improved monitoring of the project in execution, simplifying our processes, and can be used for a response to a request for quotation, a discussion with a client.

Zetta-Lyze® allow engineers to prepare construction sites, store data, access all maps, display and analyse site data and edit reports.

Currently, there are over 1,150 connected construction sites and over 100 machines equipped throughout Europe, including Romania.

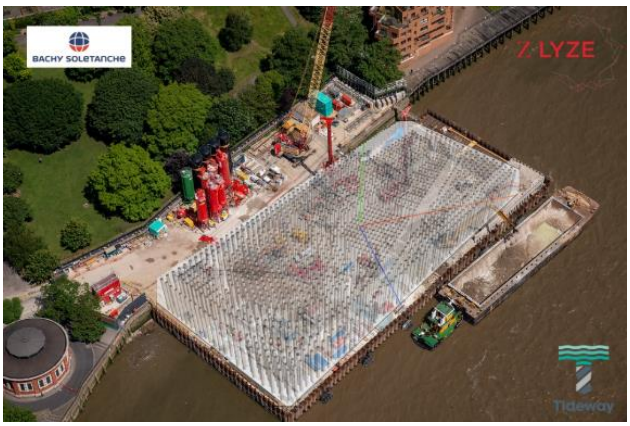

Figure 4. Site view on Z-Lyze.

3.3 Virtual reality

Research on the learning process shows that we acquire knowledge more effectively if we have the chance to test it in practice. Surviving a dangerous situation is therefore the best way to remember what should not be done and what should be done in the face of a real threat.

Virtual reality is used to enrich the introductory training in the field of health and safety, and after the completion of the theoretical part, the user enters our site through the VR kit.

The software allows the user to have a realistic experience on what to expect on a special foundation construction site.

This does not mean, however, that the user is automatically safe.

He can experience what it's like to fall into a trench or what can happen if he's within the working range of the machines. In this way, he is faced with potential threats, thanks to which in the real world there is a greater chance of remembering what can happen if he does not take the appropriate precautions.



Figure 5. Virtual reality safety training session – screenshot.

3.4 Integration of digital tools

Finally, at company level, we have decided that the best way to collaborate effectively is to reassemble all the tools we have created for our daily business.

There are a lot of processes, which when connected give a whole new meaning of the big picture.

From receiving the input for a design and build project, for example, all requirement data is cloud stored giving all workers access to initial data and alert everyone engaged in that project of any update or modification.

Because ground conditions data is essential for our engineering activity, all important information is uploaded in an internal ground database which extract and compare ground parameters from current conditions with the ones from previous built projects. In this manner, we are aware about possible difficulties which we may encounter on site.

Based on the ground report, digital tools can draw lithological profiles and propose deep foundation elements geometry.

After different restraints and criteria selection, design goes further with calculations integrated with finite element method (FEM) design software, offering results which automatically lead to a structural detailing of a special foundation element in an integrated drawing software.

At any moment, if any design input modifies, reiteration can be easily made and finally all the elements can change accordingly (geometry, material properties, capacities, structural detailing and drawings for example).

From that point on, project is being shared with other departments within the company and can be used on site for different purposes, including augmented reality and virtual reality.

Actual progress of working, productivity, materials usage, as-built updates, quality issues, optimization proposals, as well as cost control activity can be accessed and monitored by the team, ensuring a better response time for any action required.

4 CONCLUSIONS

Digital transformation is a complex and very exciting process for us, it is a strategic element of the company, which generates innovation processes and thus results in better services delivered to our partners.

Overall, digital transformation brings the wind of change for construction companies, which nowadays must keep up with the required fast pace and to be one step ahead of any challenges may appear.

REFERENCES

Soletanche Bachy (2021). *Digital Transformation.*
Soletanche Bachy (2019). *Zeta-Lyze.*
Soletanche Bachy (2020). *TiPS.*

Proceedings of the XVIII ECSMGE 2024
GEOTECHNICAL ENGINEERING CHALLENGES
TO MEET CURRENT AND EMERGING NEEDS OF SOCIETY
© 2024 the Authors
ISBN 978-1-032-54816-6
DOI 10.1201/9781003431749-694
Open Access: www.taylorfrancis.com, CC BY-NC-ND 4.0 license

ECSMGE 24
XVIII EUROPEAN CONFERENCE ON SOIL MECHANICS AND GEOTECHNICAL ENGINEERING

The integration of the underground space in the planning policies for Lisbon in the future

L'intégration de l'espace souterrain dans les politiques d'aménagement de Lisbonne à l'avenir

C. Pinto*, P. Leonardo, M. Inácio, A. Frias
Câmara Municipal de Lisboa, Lisbon, Portugal

I.M. Almeida
FCUL, Lisbon, Portugal

**claudia.pinto@cm-lisboa.pt*

ABSTRACT: In the last decades, Lisbon Municipality has implemented a database – GeoSIG to collect, analyse and produce specific outputs suitable for planning and management, using geological and geotechnical data obtained through several work field campaigns. This information allows the identification of the main constraints to occupation, such as a high thickness of coverage deposits or low depth of the water level. In addition, the same information can be used as an input to promote sustainability actions, such as better underground water management or a more responsible underground occupation. Besides the geological and geotechnical setting, Lisbon has also been doing a 3D underground structures and infrastructures representation, considering the impact that these objects can have on natural resources, specific the water flow. To achieve this, the geological and underground information was joined to promote the development and implementation of policies regarding the underground occupation, considering the impact mitigation and the possibility of exploring underground resources, allowing better decision-making.

RÉSUMÉ: Au cours des dernières décennies, la Municipalité de Lisbonne a mis en place une base de données - GeoSIG pour collecter, analyser et produire des résultats spécifiques adaptés à la planification et à la gestion, en utilisant des données géologiques et géotechniques obtenues au cours de plusieurs campagnes sur le terrain. Ces informations permettent d'identifier les principales contraintes à l'occupation, telles qu'une grande épaisseur des dépôts de couverture ou une faible profondeur du niveau de l'eau. De plus, ces mêmes informations peuvent être utilisées pour promouvoir des actions en faveur de la durabilité, telles qu'une meilleure gestion des eaux souterraines ou une occupation souterraine plus responsable. En plus du contexte géologique et géotechnique, Lisbonne a également réalisé une représentation en 3D des structures et infrastructures souterraines, en tenant compte de l'impact que ces objets peuvent avoir sur les ressources naturelles. Pour ce faire, les informations géologiques et souterraines ont été combinées pour favoriser le développement et la mise en œuvre de politiques relatives à l'occupation souterraine, en tenant compte de la réduction de l'impact et de la possibilité d'exploiter les ressources souterraines, ce qui permet de prendre de meilleures décisions.

Keywords: GeoSIG; geotechnical database; three-dimensional modelling; underground water; thematic cartography.

1 INTRODUCTION

Lisbon Municipality has a significant amount of geological and geotechnical characterization data obtained through numerous prospecting campaigns conducted within the city over the past decades.

These data constitute a valuable resource and, when properly organized, can generate highly applicable information in several areas of urban planning and management. Given the potential of this information, Lisbon Municipality (CML) has been working to optimize it so that it can be integrated into its Territorial Management Instruments (IGT), including the Lisbon Master Plan.

The continuous growth of available information resulting from geological-geotechnical studies, raises some issues, regarding data organization, standardization, validation, and integration into a three-dimensional model. This is aimed at transforming the data into dynamic tools for urban planning.

Two fundamental steps were identified: 1) the creation of a database that would gather, in a standardized and georeferenced manner, the information contained in the existing geological-geotechnical reports, resulting in the GeoSIG Platform (CML, 2016); and 2) the integration of this geological-geotechnical information with existing data related to

the underground occupation (basements and foundations).

Given the current occupation of the consolidated area of Lisbon, urban expansion will preferably occur through in the underground. This occupation will not be only through parking structures but also to railway and road infrastructures, part of the city's mobility system. The volume occupied by these structures and infrastructures is not yet available, and when such data exists, it is not properly organized and systematized, which in a certain way constrains the management of Lisbon subsurface.

To enhance subsurface management, Lisbon Municipality has initiated a project called the Three-Dimensional Underground Occupation Model - MODSUB 3D (CML, 2021).

The project aims to use the information available in construction projects stored in Lisbon archives, including the geometry and attributes of buried structures and foundation elements. Through a specialized data loading tool developed for this purpose, this information will be used to maintain an integrated database and a geographical layer within the GeoSIG application.

This information will serve as a base for the development of a three-dimensional subsurface model. When combined with the ongoing development of hydrogeological suitability mapping within the CML, it will enable a more effective assessment of the impact of subsurface occupation on the local hydrogeological flow.

Once integrated into the planning instruments, this information becomes a crucial support and decision-making tool in the context of urban management.

2 GEOTECHNICAL DATABASE – GEOSIG

Lisbon Municipality has been working in the development of a database supported by a management system with the aim of updating the processes of data input and updating. This effort also enables logical data storage, effective data management, optimization of editing and querying processes, and the provision of results for the necessary outputs. This action was developed under the framework of the LISBOA-01-0527-FEDER-000894 - Geotechnical Mapping in Urban Areas - Application to Lisbon, a project financed by the European Regional Development Fund (FEDER).

GeoSIG – Geologic, Geotechnical, and Hydrogeological Data Management for the Municipality of Lisbon is a web application designed for managing geological, geotechnical, and hydrogeological data within the Lisbon municipality. The primary goal is to integrate and apply this data in urban planning and simultaneously seeks to manage a sparse and often incomplete asset that was predominantly in paper format, with limited accessibility and processing capabilities.

This application was designed based on specific functional requirements allowing data management, several users interaction, access control and the definition of specific outputs to decision support purposes.

Currently, access to GeoSIG is limited to internal use by the Lisbon City Council due to copyright restrictions on existing data in geological and geotechnical reports. However, the spatial distribution of the information can be accessed in Lisboa Aberta platform of Lisbon Municipality (CML, 2018).

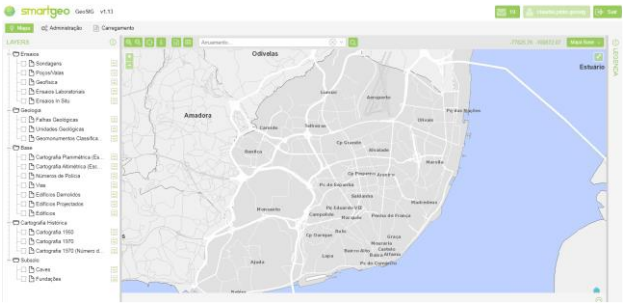

Figure 1. GeoSIG application main screen (Source: GeoSIG).

Until now, this platform integrates more than 13,000 boreholes, corresponding to 2,400 geological-geotechnical reports (Figure 2). The information from the geotechnical boreholes is added to the GeoSIG database by the municipality's technicians. This data comes from the geotechnical reports that are submitted by developers during licensing procedures, along with the excavation and peripheral containment projects.

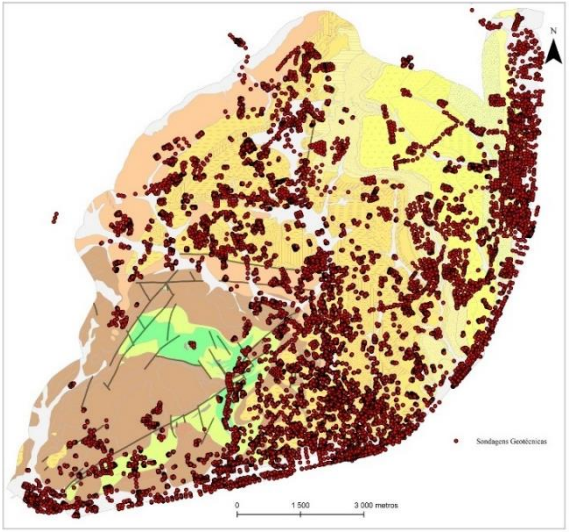

Figure 2. Distribution of geotechnical surveys available in the GeoSIG application (Source: GeoSIG).

Associated with each borehole are data related to the lithology, the water level, SPT test values, recovery rates, and other relevant information.

In addition, sample classifications submitted to laboratory analyses may be added, to record some physical properties of the samples, namely lithology, AASHTO, unified and RTR classes, as well as the granulometric index. It should be noted, however, that the vast majority of geological-geotechnical reports available do not include this type of information, so it will be incorporated into the platform at a later stage

The GeoSIG works in a georeferenced table format, where the depth value is associated with a parameters mentioned above. Currently this data are introduced into geosig by municipal technicians.

It should be noted that the GeoSIG database is intended to provide a macro-scale approach, which does not invalidate local studies. Thus, GeoSIG provides data for modeling more generic geotechnical characteristics, particularly lithology, lithostratigraphy, resistance (through SPT tests) and water levels. The information in the database is a fundamental tool for urban planning (Pinto et al., 2023) and can also be used to perform more specific studies (e.g., Oliveira et al., 2019)

3 THEMATIC MAPPING

To produce thematic mapping, it was necessary to implement a Geoscientific Information System which involve creating specific queries to the GeoSIG database to select the most relevant data for each purpose.

The thickness of coverage deposits and the water level are not limitations to urban development, but they can influence it due to problems related to land suitability and consequently construction costs. Therefore, modelling these factors can optimize projects and reduce costs, making it an essential tool in planning and management.

To achieve this, data obtained from geological-geotechnical boreholes were interpolated, specifically the depth of surficial fills and alluvial deposits, as well as the position of the water table. The operation was conducted using the IDW (inverse distance weight) interpolator.

The water table level was represented by points of different shades according to depth, and in the area, allowing the definition of depth classes. This knowledge facilitates the optimization of groundwater use and management.

From the analysis of Figure 3, it is clear that in the riverside area, the water table position is closer to the surface. Given that this area borders the Tagus River, this result was expected. In general, the water table is located between 3-6m, with exceptions in hilly areas where the water table is deeper. This is also related to the geological formation's permeability.

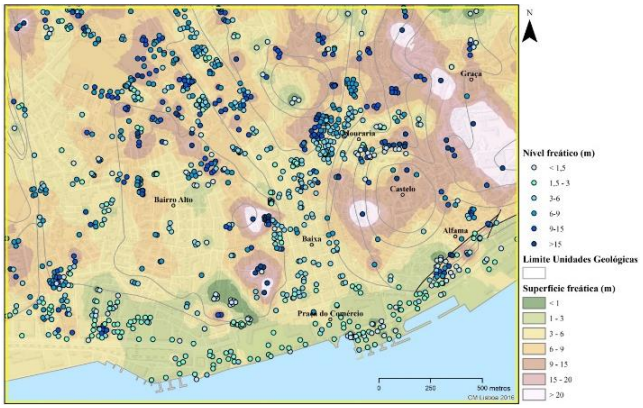

Figure 3. Factor map: Water level position (Source: GeoSIG).

4 MODSUB 3D

To support decision-making Lisbon Municipality has developed a tool that allows the input of the geometry and attributes of the structures and infrastructures existing in Lisbon subsurface – MODSUB 3D. These data will allow the development of three-dimensional models for the subsurface occupation in the city. This information combined with hydrogeological mapping, will enable the assessment of the impact of this occupation on the local hydrogeological flow. As part of the project implemented in pilot areas, data related to basements and foundations of 8,900 buildings were loaded.

The MODSUB 3D application is built upon a tool that allows the user to search for the building in question, make a spatial selection, and subsequently load the data obtained from the construction volume.

This tool allows the registration of the location, geometry, and alphanumeric attributes that define each of the information layers within the application, namely basements, tunnels, and foundations. It's important to note that basement and foundation objects must be associated with a building, while tunnel objects have geometries separate from the building stock.

The information loaded can be visualized through the GeoSIG application, as the geographic layers developed within the scope of MODSUB 3D have been integrated here (Figure 4).



Figure 4. Visualization of geographic information - GeoSIG application (Source: GeoSIG).

In addition to the thematic information presented here, the data included in MODSUB 3D also allows the generation of three-dimensional models. The example in Figure 5 demonstrates how it is possible to obtain a three-dimensional representation of an area (Parque das Nações), using information of the superficial and subsurface occupation.



Figure 5. Representation of the three-dimension model.

5 CONCLUSIONS

The GeoSIG application provides the bases to develop thematic maps and three-dimensional models for several purposes in a quick and efficient manner, making it an essential decision support tool. With this information, we identify the most critical areas of the city where it becomes mandatory to conduct geological-geotechnical and hydrogeological studies before construction works.

The developed working methodology can be easily generalized and replicated for other areas, as long as the basic information is available in a representative quantity for the territory and the data quality is adequate.

These tools can be used by several stakeholders, including designers, planning professionals, and others, to assess constraints and estimate costs related with with specific geotechnical projects. This, in turn, allows for project optimization and cost reduction from the early stages. Lastly, it's worth noting that the construction of underground infrastructure creates a physical barrier to the natural water flow. With these tools Lisbon services can perform a better management of this resources.

ACKNOWLEDGEMENTS

The authors are grateful for the financial support provided through the project LISBOA-01-0527-FEDER-000894 - Geotechnical Mapping in Urban Areas - Application to Lisbon, financed by the European Regional Development Fund (FEDER).

REFERENCES

CML (2016). GeoSIG – Informações e Serviços. Câmara Municipal de Lisboa. Available at: https://informacoeseservicos.lisboa.pt/prevencao/resiliencia-urbana/projetos/geosig, accessed: 11/03/2024. (GeoSIG – Information and Services in Portuguese).

CML (2018). Lisboa Aberta. Câmara Municipal de Lisboa. Available at: https://lisboaaberta.cm-lisboa.pt/index.php/pt/, accessed: 11/03/2024. (Open Lisbon in Portuguese).

CML (2021). ModSub 3D – Informações e Serviços. Câmara Municipal de Lisboa. https://informacoeseservicos.lisboa.pt/prevencao/resiliencia-urbana/projetos/modsub-3d, accesse: 11/03/2024. (ModSub 3D – Information and Services in Portuguese).

Oliveira, L., Teves-Costa, P., Pinto, C., Gomes, R.C., Almeida, I.M., Ferreira, C., Pereira, T. and Sotto-Mayor, M. (2019). Microzonagem sísmica baseada em dados de sondagens geotécnicas: aplicação a Lisboa. 11.º Congresso Nacional de Sismologia e Engenharia Sísmica. Lisbon, Portugal. (Seismic microzonation based on geotechnical data: application to Lisbon in Portuguese).

Pinto, C., Inácio, M., Almeida, I.M., Taborda, R., Leonardo, P. and Frias, A. (2023). O sistema de informação geocientífica GeoSIG e a sua aplicação no planeamento urbano da cidade de Lisboa, In: Atas do 18º Congresso Nacional de Geotecnia (18CNG), Évora, Portugal, pp 291-300 (The GeoSIG geoscientific information system and its application to urban planning in the city of Lisbon in Portuguese).

Proceedings of the XVIII ECSMGE 2024
GEOTECHNICAL ENGINEERING CHALLENGES
TO MEET CURRENT AND EMERGING NEEDS OF SOCIETY
© 2024 the Authors
ISBN 978-1-032-54816-6
DOI 10.1201/9781003431749-695
Open Access: www.taylorfrancis.com, CC BY-NC-ND 4.0 license

ECSMGE 24
XVIII EUROPEAN CONFERENCE ON SOIL MECHANICS AND GEOTECHNICAL ENGINEERING

Challenges in assessing the hydrogeological impact of underground structures in urban renewal projects

Défis liés à l'évaluation de l'impact hydrogéologique des structures souterraines dans les projets de rénovation urbaine

R. Ramos*, F.T. Jeremias, L. Caldeira
Laboratório Nacional de Engenharia Civil, Lisbon, Portugal

**rramos@lnec.pt*

ABSTRACT: Lisbon's urban renewal projects have led to an increase in the construction of underground structures such as basements and tunnels. As riverfront areas are prone to flooding, since 2010 the City Council has made it mandatory to carry out hydrogeological impact studies for urban developments involving underground works in alluvial areas. The Laboratório Nacional de Engenharia Civil (LNEC) has been carrying out these studies for twelve years, facing increasing model complexity due to the spread of underground structures. This paper provides some guidelines for conducting hydrogeological impact studies, highlighting the difficulties and challenges met in developing these studies and the strategies used to overcome them.

RÉSUMÉ: Les projets de rénovation urbaine de Lisbonne ont entraîné une augmentation de la construction de structures souterraines telles que les sous-sols et les tunnels. Les zones riveraines étant sujettes aux inondations, le conseil municipal a rendu obligatoire, depuis 2010, la réalisation d'études d'impact hydrogéologique pour les aménagements urbains impliquant des travaux souterrains dans les zones alluviales. Le Laboratório Nacional de Engenharia Civil (LNEC) réalise ces études depuis douze ans et doit faire face à une complexité croissante des modèles en raison de l'extension des structures souterraines. Ce document fournit quelques lignes directrices pour la réalisation d'études d'impact hydrogéologique, en soulignant les difficultés et les défis rencontrés lors de l'élaboration de ces études, ainsi que les stratégies utilisées pour les surmonter.

Keywords: Hydrogeological impact; urban area; underground constructions; groundwater; numerical modelling.

1 INTRODUCTION

Urban renewal projects in the city of Lisbon (Portugal) have led to an increase in the construction of impervious underground structures such as basements and tunnels. These structures affect groundwater, mostly in terms of water level, water quality, flow direction and flow rate, due to the barrier effect caused by their presence.

Coastal urban areas as Lisbon are prone to flooding. Consequently, since at least 2010, Lisbon City Council has required specific studies for projects involving underground works in alluvial zones. These studies include the characterisation of hydrogeological conditions and the assessment of hydrogeological impacts, with the aim of predicting whether the design works will increase the risk of flooding.

An impermeable underground structure that crosses the direction of flow can raise water levels upstream and lower them downstream, increasing the risk of flooding around the structure (Ricci *et al*., 2007).

LNEC has been carrying out hydrogeological impact studies in the Lisbon riverfront area for the last twelve years. Experience has shown that the development of this type of study is becoming increasingly complex, given the number of underground structures already built, under construction and planned.

Accordingly, based on LNEC's practice, some guidelines are given for carrying out hydrogeological impact studies, highlighting the difficulties and challenges identified during the development of these studies and the strategies to overcome them.

2 HYDROGEOLOGICAL IMPACT ASSESSMENT

In order to assess the hydrogeological impact of an underground structure, it is often necessary to simulate groundwater conditions by means of numerical modelling (Bonomi and Bellini, 2003; Ricci et al.,

2007; Yang et al., 2009; Paris et al., 2010; Pujades et al., 2012).

Since 2012, LNEC has carried out around twenty hydrogeological impact studies related to the construction of buildings (with one to seven underground levels) in the Lisbon riverfront area, mainly located in the lower part of the Alcântara valley.

The studies were performed using Aquaveo's Groundwater Modelling System (GMS), which includes the computer code for solving the groundwater flow equation (Modflow) developed by McDonald and Harbaugh (1988).

The methodology defined and applied by LNEC in these studies over the last twelve years comprises the following steps:

a) 3D simulation of the reference phase, representative of the situation before the construction of the underground structure, duly calibrated with the results of a hydrogeological monitoring campaign;
b) 3D simulation of the final construction phase, representative of the situation after construction of the underground structure (predictive model number 1);
c) Impact assessment based on a comparison of the results of the two previous simulations;
d) Evaluation of potential remedial measures to minimise the hydrogeological impact (predictive model number 2 also in 3D);
e) Validation of the prediction model(s) based on the results of the hydrogeological monitoring to be carried out after the construction of the underground structure.

Figure 1 shows an example of a hydrogeological impact assessment for the construction of a four-level basement near a hospital, with a gravity drainage and pumping systems installed at the bottom of the building. In this case, although the water level upstream of the underground structure was expected to rise by up to 1m, the impact was considered small as the water levels were expected to remain negative.

3 DIFFICULTIES AND CHALLENGES IDENTIFIED

During the development of the hydrogeological impact studies, several difficulties and challenges had to be overcome in order to obtain reliable results. The following sections introduce and describe them.

3.1 Data type

The geological/lithological model is the basis for the assembly of the hydrogeological model. Firstly, the geological solid model is developed based on borehole data, and then the numerical model is created and fitted to the previous model, as shown in Figure 2.

In order to develop a hydrogeological model that accurately represents the conditions at the future construction site, it is therefore essential to have a set of information on the characteristics of the ground and the aquifers that will be intersected by the structures.

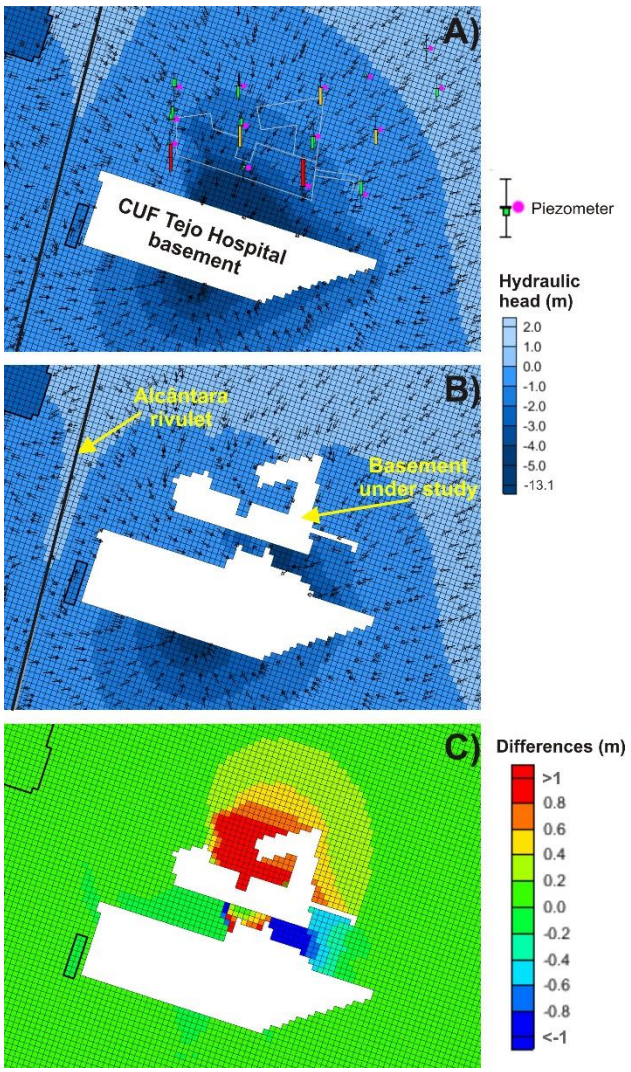

Figure 1. Example of hydrogeological impact assessment. A) Simulation of the reference phase (calibrated); B) Simulation of the final construction phase of the structure under study; C) Impact assessment.

As the design of underground works in alluvial areas generally involves the construction of diaphragm walls down to the bedrock, regardless of the number of basement levels to be constructed, both the alluvial deposits and the bedrock formations should be characterised

Therefore, prior to modelling, a site investigation and monitoring programme must be designed and carried out to provide the following data:

- Geological characteristics of the alluvial deposits (composition, thickness and spatial distribution) and the bedrock formations (nature, structure and stratigraphic sequence) based on borehole data and sampling. Boreholes should preferably be located outside and on all sides of the building area. The lithological information is also of paramount importance in the analysis of the solution obtained in the numerical groundwater flow model during the calibration process. It can often justify hydraulic potentials that may appear erroneous at first sight.
- Hydraulic conductivity of alluvial deposits and rock formations determined by water permeability tests in boreholes and/or pumping tests. It should be emphasised that in these studies the use of high-water pressures on the bedrock chambers does not add any value to the determination of hydraulic conductivity, since the works to be carried out do not impose any additional hydraulic loads;
- Water pressure distribution and flow direction in the aquifers crossed by the works, through monitoring campaigns carried out in at least three non-collinear piezometers installed in each aquifer;
- Evaluation of the influence of tides (in coastal areas) based on the interpretation of a continuous monitoring campaign of the water levels during at least one tidal cycle (one high and one low tide) under spring tide conditions. The behaviour of the records (water level variation curves) can also be used as a check on the consistency of the permeability test results.

By analysing the water levels measured in piezometers with more than one water pressure chamber installed in different formations, it is possible to understand whether there are water levels under pressure, *i.e.* confined aquifers. It is also possible to determine if water levels are affected by anthropogenic activities such as water extractions (permanent or temporary).

3.2 Reliable data

Site investigation programmes designed by non-geotechnical professionals usually fail to provide reliable hydrogeological data because piezometers are installed with a single water pressure chamber across multiple and different aquifer formations. This makes it impossible to determine the water levels and flow direction in each aquifer affected by the works. To avoid this situation, it is important to check the specifications already drawn up and propose the appropriate number of water pressure chambers depending on the number of aquifer formations to be intersected by the structures. If there is more than one aquifer formation, the water pressure chambers should be properly isolated so that they are independent.

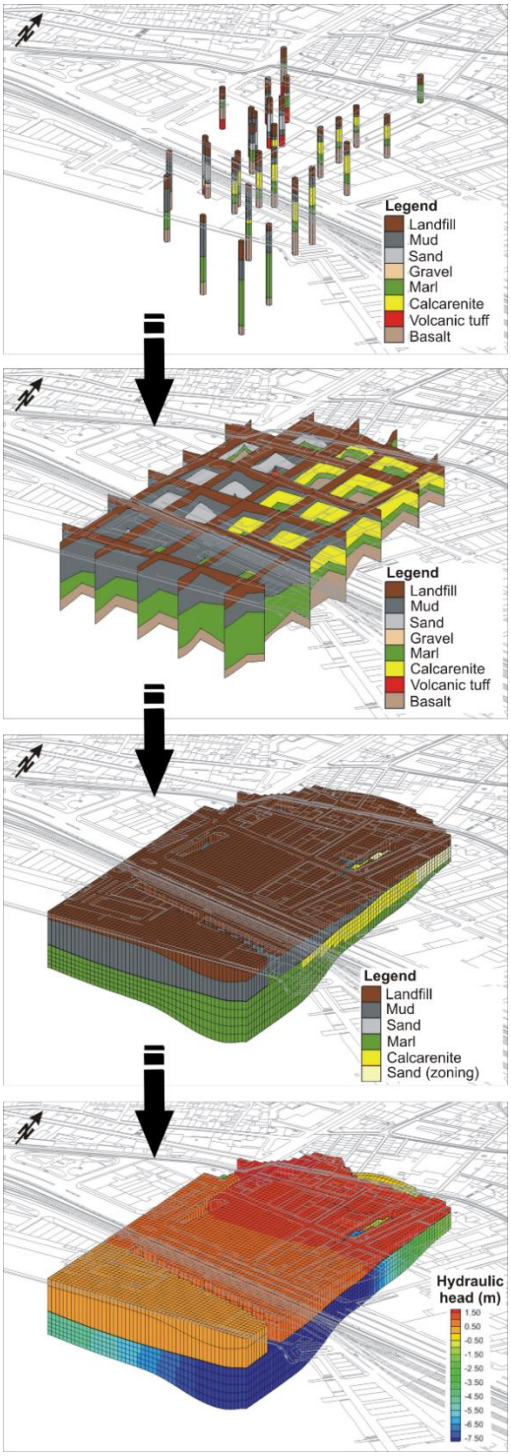

Figure 2. General stages in the creation of groundwater flow models.

Figure 3 shows the distribution of the borehole locations selected for the installation of piezometers where the construction of buildings with basements

was planned. After analysis of the existing information in the study area, it was determined that the data from previous site investigations works did not provided all the data needed to perform the study. Therefore, given the constraints identified in the study area, namely the density of buildings and the occurrence of infrastructures, a set of 7 borehole locations, shown in Figure 3, were defined for the installation of piezometers. Piezometers with double and triple water pressure chambers have been defined, depending on the number of aquifer formations that will be crossed by the building structure at each site.

During the drilling works, it is also necessary to check whether products that may affect the permeability of materials (such as bentonite) are used mainly in alluvial sands. The use of this type of product compromises the data obtained and prevents water permeability tests as well as the installation of piezometers.

As groundwater flows preferentially through permeable zones, it is important to determine the permeability of these layers associated with specific lithologies, such as sands and fractured rocks. These lithologies should therefore be selected for testing during or after drilling.

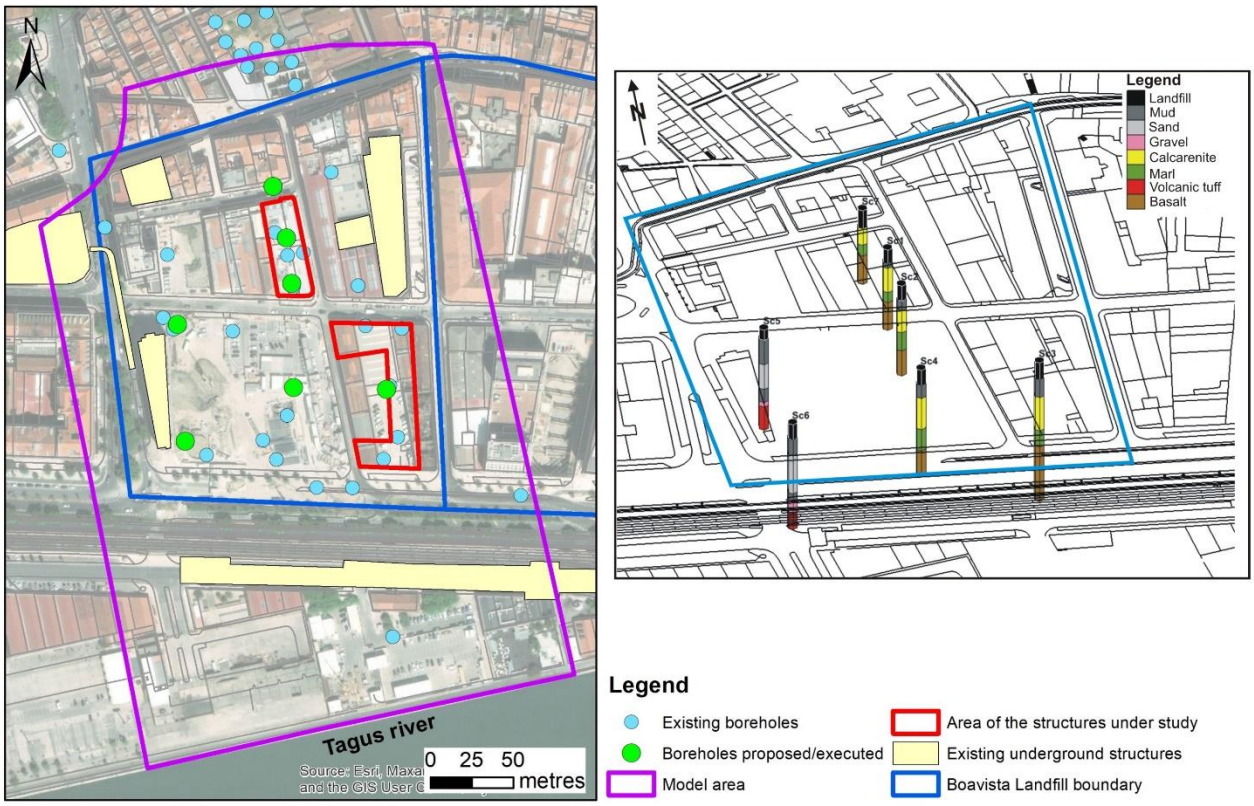

Figure 3. Distribution of the sites selected for the installation of piezometers in the Boavista landfill (Lisbon).

3.3 Model scale (dimensions)

However, such a study requires information on a very large area in order for the model to be representative of existing conditions and to take into account physical hydraulic boundaries and existing underground structures.

Hydrogeological impact studies are usually requested/contracted to consider only the construction area. However, such a study requires information on a wider area in order for the model to be representative of current conditions and to take into account physical geological and hydraulic boundaries and existing underground structures. Therefore, the geological and hydrogeological data should cover as much of the model area as possible.

3.4 Model complexity and calibration

The main challenge of the hydrogeological impact studies was undoubtedly the creation of highly complex numerical models and the respective calibration. The dimensions of the model to represent the physical geological and hydraulic boundaries the characteristics of the underground structures, as well as the interventions in the ground during the studies, all contributed in different ways to the complexity of the model.

The studies carried out in Lisbon's riverfront area focus on two important sites: the Alcântara valley and the Boavista landfill. Both areas are under constant development, with numerous building and tunnel projects in planning and construction phase.

An example of a model created for the Alcântara valley is shown in Figure 4. It is a very complex and extended model, covering an area of 1.3 km^2. This model includes several buildings with one to four basement levels, some of which have drainage and pumping systems installed at the bottom.

In areas affected by tides, the model should be run in a transient state, which increases the complexity of the modelling, especially during the calibration process.

In addition, in some cases water level behaviour can only be explained by water withdrawals whose location and characteristics are unknown.

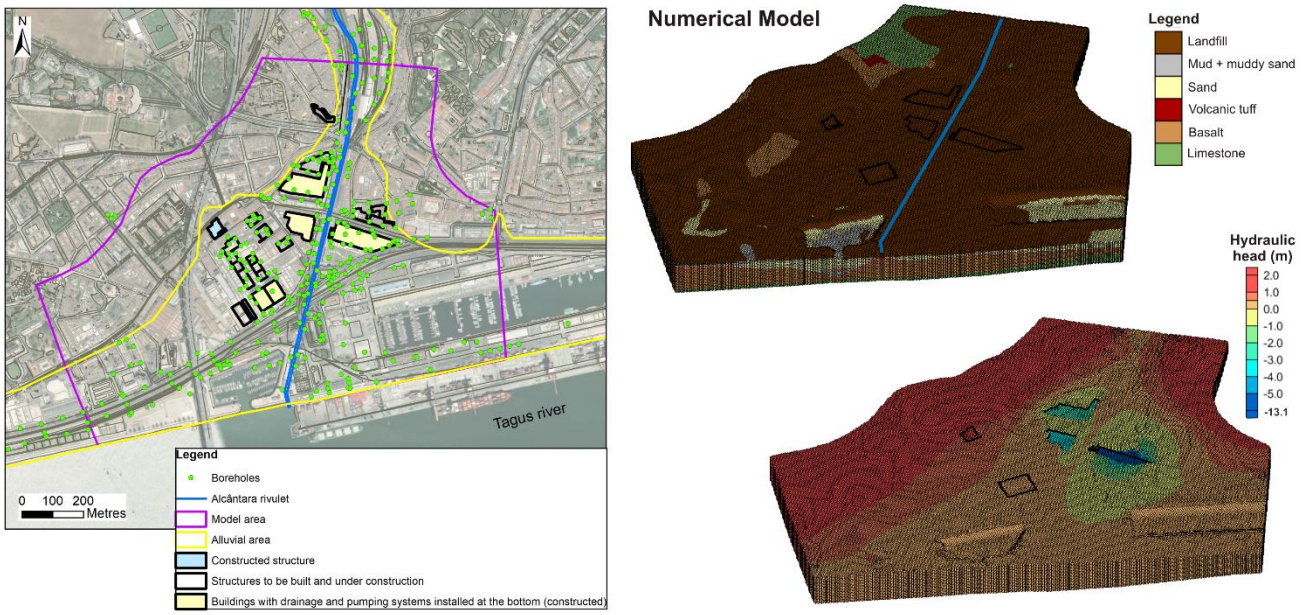

Figure 4. Dimensions, underground structures and characteristics of a numerical model developed for the Alcântara valley (Lisbon)

3.5 Study submission phase

According to the Lisbon City Council's administrative regulations, hydrogeological impact studies must be submitted at the earliest stage of the process, i.e. when the architectural project is being analysed.

This poses a problem because for the impact analysis it is necessary to include the geotechnical solutions in the model, namely the elevation of the bottom of the excavation and the base of the retaining walls, for which there is usually no concept or design at this stage.

As it is not possible to conduct the study without this information, part of the geotechnical concept and design must be developed before the architectural project is approved or alternatively, the worst-case scenario can be analysed, i.e. retaining walls that extend down to the bedrock. However, the best solution would be to require the study to be submitted with the geotechnical design.

3.6 Model validation

Numerical modelling is a representation of reality. It is then important to validate the results of the hydrogeological impact prediction models with field observations collected in piezometers during and after the construction of an underground structure. With this in mind, the data for the model must come from an area larger than the construction site, and the water levels must be monitored during the various phases of the work by means of piezometers installed outside the perimeter of the retaining walls.

3.7 Model reuse

Each study requires the creation of a groundwater flow model in sufficient detail to take into account the geological information of the site and the existing underground structures.

Since the studies and works are not carried out simultaneously and each new study provides data to update the knowledge of the geological and hydrogeological conditions, a new model must always be developed.

4 CONCLUSIONS

This paper provides a comprehensive overview of hydrogeological impact studies in the context of urban redevelopment projects involving the construction of

underground structures. These studies aim to support sustainable urban development by mitigating flood risks.

It also outlines a methodology for the studies, which involves numerical modelling to simulate groundwater conditions before and after construction. These simulations are used to assess the impact of the construction of underground structures on groundwater flow and to evaluate potential mitigation measures.

Based on LNEC's experience, several difficulties and challenges have been identified in the development of hydrogeological impact studies over the past twelve years, including obtaining reliable data, modelling at an appropriate scale, managing model complexity and validating model results.

Accurate groundwater modelling depends on comprehensive data on geological and hydrogeological characteristics obtained through site investigation and monitoring programmes. However, the main challenge is the development and calibration of complex numerical models that have to represent both the geological conditions and the underground structures. Finally, it should be emphasised that validation of the models with water levels measured in piezometers is a crucial task to ensure the accuracy of the predictions.

REFERENCES

Bonomi, T. and Bellini, R. (2003). The tunnel impact on the underground level in an urban area: a modelling approach to forecast it. *RMZ - Materials and Geoenvironment*, 50, (1), pp. 45-48.

Mcdonald, M.G. and Harbaugh, A.W. (1988). A modular three-dimensional finite-difference ground-water flow model. Techniques of Water-Resources Investigations. *Book 6 - Modeling Techniques*, Chapter A1, U.S. Geological Survey, United States Government Printing Office, Washington, 586 p. https://doi.org/10.3133/twri06A1.

Paris, A., Teatini, P., Venturini, S., Gambolati, G. and Brnstein, A.G., 2010. Hydrological effects of bounding the Venice (Italy) industrial harbour by a protection cut-off wall: a modeling study. *Journal of Hydrologic Engineering*, 15, (11), pp. 882-891. https://doi.org/10.1061/(ASCE)HE.1943-5584.00002.

Pujades, E., López, A., Carrera, J., Vázquez-Suñé and Jurado, A. (2012). Barrier effect of underground structures on aquifers. *Engineering Geology*, 145-146, pp. 41-49. https://doi.org/10.1016/j.enggeo.2012.07.004.

Ricci, G., Enrione, R. and Eusebio, A. (2007). Numerical modelling of the interference between underground structures and aquifers in urban environment. The Turin subway – line 1. In: Barták, Hrdine, Romancov and Zlámal (Eds.), Underground Space – the 4th Dimension of Metropolises, Taylor and Francis Group, London, United Kingdom, pp. 1323 1329.

Yang, F.R., Lee, C.H., Kung, W.J. and Yeh, H.F. (2009). The impact of tunneling construction on the hydrogeological environment of "Tseng-Wen Reservoir Transbasin Diversion Project" in Taiwan. *Engineering Geology*, 103, (1-2), pp. 39-58. https://doi.org/10.1016/j.enggeo.2008.07.012.

Proceedings of the XVIII ECSMGE 2024
GEOTECHNICAL ENGINEERING CHALLENGES
TO MEET CURRENT AND EMERGING NEEDS OF SOCIETY
© 2024 the Authors
ISBN 978-1-032-54816-6
DOI 10.1201/9781003431749-696
Open Access: www.taylorfrancis.com, CC BY-NC-ND 4.0 license

ECSMGE 24
XVIII EUROPEAN CONFERENCE ON SOIL MECHANICS AND GEOTECHNICAL ENGINEERING

Experiences with using parametric 3D modelling in geotechnical engineering

Expériences d'utilisation de la modélisation 3D paramétrique en géotechnique

M. Rømoen*, M. Kahlström, D. Ryghseter
Norwegian Geotechnical Institute, Oslo, Norway

N.B. Hansen
Geovita AS, Oslo, Norway

**magnus.romoen@ngi.no*

ABSTRACT: In recent years, geotechnical engineers at NGI and Geovita AS have adopted new ways of creating and using parametric 3D/BIM models in their engineering design. The models are used through the life cycle of the project, from idea to construction to as-built documentation. This new way of working has successfully been adopted on several ongoing, major infrastructure projects in Norway. All models for underground structural design, such as retaining walls, soil improvement, rock support etc., are developed through parametric modelling. The models mature throughout the project and adding information in the models makes them fully functioning BIM-models which can be used directly by the contractors. The use of parametric design greatly improves communication and multi-disciplinary design, reduces risk of collision and errors, and can lead to significant time and cost savings in projects compared to a manual geotechnical design. This article shows the possibilities of parametric modelling in geotechnical engineering and will hopefully inspire more geotechnical engineers to open this digital toolbox.

RÉSUMÉ: Ces dernières années, les ingénieurs en géotechnique du NGI et de Geovita AS ont adopté de nouvelles approches pour créer et utiliser des modèles paramétriques 3D/BIM dans leur processus de design d'ingénierie. Ces modèles sont utilisés tout au long du cycle de vie des projets, de l'idée à la construction, jusqu'à la documentation finale. Cette nouvelle manière de travailler a été intégrée avec succès à plusieurs projets d'infrastructures majeurs en Norvège, pour lesquels tous les modèles de design des infrastructures souterraines, comme les murs de soutènement, l'amélioration des sols, le support rocheux, sont développés à l'aide de la modélisation paramétrique. Les modèles évoluent tout au long du projet, et l'ajout d'informations dans les modèles BIM les rend entièrement fonctionnels et permet leur utilisation directe par les entrepreneurs. L'utilisation de la conception paramétrique améliore considérablement la communication et la conception multidisciplinaire, réduit les risques de collisions et d'erreurs, et peut entraîner des économies de temps et de coûts significatives dans les projets, comparativement à une conception géotechnique manuelle. Cet article présente les possibilités de la modélisation paramétrique en géotechnique et vise à encourager davantage d'ingénieurs en géotechnique à ouvrir cette boîte à outils numérique.

Keywords: Parametric modelling; BIM; automation.

1 INTRODUCTION

Focusing on infrastructure projects and geotechnical engineering, the subsurface in urban areas is becoming more congested, increasing complexity for new developments. BIM (Building Information Modelling) is increasingly being used in subsurface engineering (Gondar et al., 2019; Satyanaga el al., 2023), also for specific applications such as soil nailing (Nappa et al., 2019). In general, underground construction is moving towards more digitized workflows (Huang et al., 2021).

Geotechnical engineers should be prepared for the drawing-free projects that are coming and adopt to a more model-based design workflow following the principles of BIM.

A few years ago, NGI and Geovita AS began improving our design workflows largely enabled using parametric 3D-modelling tools and the development of scripts to automate the 3D modelling tasks.

2 3D MODELLING WORKFLOWS

2.1 The past workflow

Both companies have been 3D-modelling for several years. This was often static 3D-modelling in AutoCAD, which often gave very large and hence slow models. Since there often is late changes in the projects, these models were established at the end of the design phase to avoid too much re-work in the projects. And even if these models were only produced once, production of these models was very time consuming.

Late modelling also resulted in the lack of possibility for interdisciplinary class detection, which again could result in undetected conflicts and reasons for higher costs. The modelling was also mainly done for the geotechnical-structures, and not for the soil layering except for the bed rock surface.

2.2 Present workflow

Basis for the change in workflow was to find more suitable software, which would enable more dynamic models. Both companies ended up with using Leapfrog Works (Seequent) for modelling geology/soil/soil layering and the combination of Rhino and Grasshopper (Robert McNeel & Associates) for modelling geo-structures.

These software gives the possibility to establish the geotechnical models early in the projects, and the models will then evolve with the projects. The level of the model is of course always communicated with a given LOD- or MMI-value. The establishment of these models has several advantages:

- They are improving the communication about uncertainties (more about this later).
- They are basis for the calculations of the geotechnical engineer, which saves time in the calculation process.
- The early establishing of these models ensures better interdisciplinary clash control.
- They will early give a picture of both cost and carbon footprint.
- They are basis for execution for the contractors, both as models and as geodata.

Since we are using dynamic modelling, the always present changes in the projects will only result in a minimum of extra work, will cut the cost dramatically and makes new, updated models extremely quick.

3 PARAMETRIC MODELLING

Parametric design is something that has been in use for quite some time within other fields such as e.g., architecture and construction industry, but is still relatively new in the geotechnical world.

In short, parametric design is a new way of defining work tasks and planning throughout the entire construction process. In the CAD software Rhino there is a built-in framework for visual programming called Grasshopper. This works in such a way that you create a work process by "visually" connecting different components (or parameters) with nodes.

As an example: the work process can be "set out piles along an axis" and the components in this case will be e.g., "create a reference point", "set diameter of piles", "set pile length", "set centre distance between piles", "set number of piles further along the axis" and "construct cylinder object". Connecting these components then creates a kind of network, or a script, which together performs the desired work process. Updating a single component, e.g., "moving the reference point for the cylinder", will automatically cause all piles along the axis to move to the new reference point. This is what is called parametric modelling – that a dynamic network of interconnected components enables a complex work routine that is updated seamlessly with each update of a single component. As a bonus, you can reuse the same work routine over and over on project after project. This saves a lot of time and requires increased quality of each modelling task and delivery.

3.1 Sheet pile wall with tie-back anchors

As an example, for use in the geotechnical design, we take a closer look at a construction pit. We are in an early planning phase and the only thing we have received from the project is a line of proposals for the placement of the basement wall. In addition, we have a terrain model and a rock model. With these input parameters and a pre-defined script that creates sheet pile walls, see Figure 1, we get a 3D model of the construction pit within a few seconds.

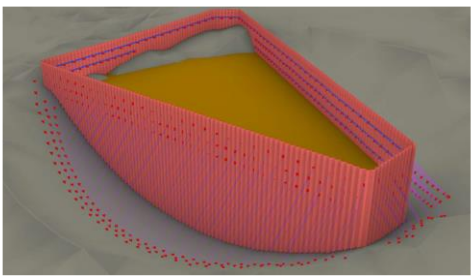

Figure 1. Sheet pile wall with tie-back anchors.

In addition to a script for generating sheet pile walls, we have developed scripts for different types of retaining structures (such as diaphragm walls, Berliner wand etc.), struts, tie-back-anchors, beams, lime-cement columns, jet grouting etc. All these scripts are

re-used, which gives a huge time-saving on new projects.

Back to the example above, if we now want to add tie-back-anchors in the model of our construction pit, we simply add it by serially connect the sheet piling script with a new script that generates anchor braces. The model with the anchors and the bed rock surface is given in the figure below. What is very important to point out here and which is essential for the models to be dynamic, is that these scripts must be connected. The reason for this is that if you move or change the original line, defining the basement, then both the sheet pile walls and the anchors are moved according to the new position.

3.2 Settlement analysis

The software is also used for performing an analytical settlement calculation over a larger area to assess the impact on the surroundings because of our planned construction pit.

The procedure involves creating a grid that covers the area you want to assess. A direction vector is then calculated and the distance from each cell in the grid to the construction pit. At the intersection between vector line and cell, three points are taken out (far, middle and nearest). In each of these three points, in each cell, the depth to rock and the depth is divided into segments with e.g. 0.5 m thickness. Soil parameters are calculated in the same way for each depth segment with Python code components in Grasshopper. Based on this, one can then perform a 1D settlement calculation (Janbu, 1970) in each individual point with a time component through approximation of the degree of consolidation from Terzaghi and Fröhlich (1936).

With this script it is possible to visualize the effect on the surrounding area because of the construction site. In Figure 2, one can see that the calculations indicate an influenced area up to 340 m from the construction pit.

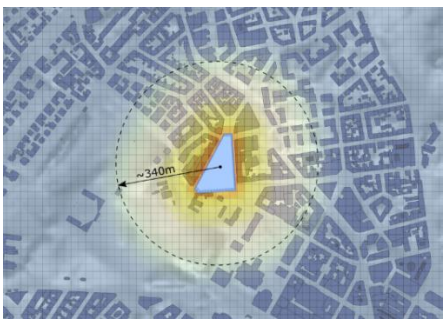

Figure 2. Calculation of influence area.

The effect of the construction work can also be calculated for points on each building object around the pit, see Figure 3. Resulting potential for damage to surrounding buildings can be visualized as damage classes.

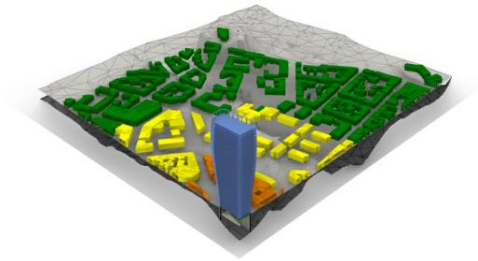

Figure 3. Visualization of potential damage on buildings.

3.3 Ground improvement with deep soil mixing

Parametric modelling is also used for establishing models for ground improvement with deep soil mixing.

There are several methods to improve the strength and stiffness of the ground, using vibration, impact, or by mixing a binder material into the soil. In this modelling example, we will focus on deep soil mixing, known in Norway as lime-cement-columns. With this method a binder, typically lime and cement, is mixed into the soil using air pressure and a rotational tool. These columns can be approx. 20 to 30 m long and commonly have a diameter of 600 to 800 mm. Columns are installed in various patterns such as grids, ribs, panels or single column, depending on the purpose and structural function of the ground improvement.

Large construction projects in soft-clay areas may have several tens of thousands of these columns installed to improve constructability and reduce ground risk. The modelling of the deep soil mixing with parametric modelling gives not only dynamic models, but the models are also basis for the execution by the contractor.

In our given example we connect another script, producing the lime-cement-columns to our construction pit, and we will then quickly get the result shown in Figure 4. Of course, we could now easily change parameters in the model.

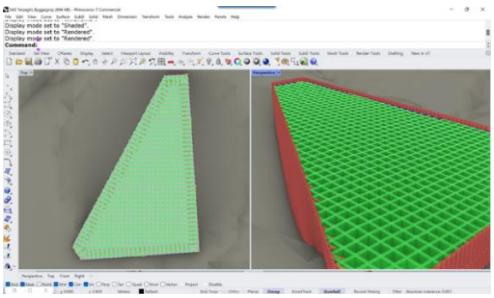

Figure 4. Excavation pit with lime-cement-columns.

3.4 Quantity take-off and sustainability

In all the scripts producing the models, we have also implemented a system for defining the properties of the objects which are summed up in geotechnical Psets, easily readable in the IFC-files we make in Rhino/Grasshopper. This is not only details about the structural element, but can also be details about tolerances, material properties, execution etc.

As the models develops through the project, this also means that we easily can see how the cost, emissions, etc. develops with changes in the models.

3.5 Visualization of uncertainty

Geotechnical engineering has a lot of uncertainties. The geotechnical engineer has often information about the soil conditions in points, but between these points the knowledge is uncertain.

One way to communicate to project stakeholders in the BIM model that geotechnical point information is interpolated and extrapolated to create continuous surfaces, such as the bedrock model, is to visualize on the surface mesh the closest distance from the mesh cell centre to the nearest borehole. Applying a colour map where green is “close” and “red” is further away yields a triangulated bedrock rendering as shown in Figure 5. This method does not quantify the uncertainty, e.g. a standard deviation, but is merely used as a simple visual communication tool in the BIM model.

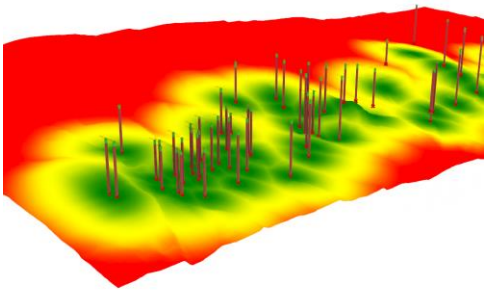

Figure 5. Visualization of pseudo-uncertainty based the distance of each mesh cell to the nearest borehole.

These models can further be part in a collaboration software which then easily can communicate the uncertainty to other participants in the project. Are your planned new building placed in the middle of a red area, then you have acquired a project with a high level of uncertainty, geotechnically speaking.

4 CONCLUSIONS

This paper describes how NGI and Geovita have adopted parametric 3D modelling to deliver examples of geotechnical analysis, BIM models and how to effectively communicate geotechnical uncertainty to projects stakeholders in the BIM model. The use of parametric design has greatly improved our engineering and project workflow, especially for larger infrastructure projects such as road and railway developments. The dynamic 3D models are updated continuously throughout the project and yields significant timesaving when the 3D geometry generation is automated using Grasshopper-scripts. Parametric modelling can be applied a wide range of geotechnical problems, including analysis of settlement and generating quantity take-offs for construction works. The authors highly recommend design and engineering firms within the geotechnical domain to adopt this way of working.

ACKNOWLEDGEMENTS

The authors are grateful to our clients for letting us develop the codes for the parametric design over several of our projects over the recent years.

REFERENCES

Gondar, J., Pinto, A. and Fartaria, C. (2019). The use of BIM technology in geotechnical engineering. *Proceedings of the XVII European Conference on Soil Mechanics and Geotechnical Engineering*.

Huang, M., Ninic, J., & Zhang, Q. (2021). BIM, machine learning and computer vision techniques in underground construction: Current status and future perspectives. Tunnelling and Underground Space Technology 108 https://doi.org/10.1016/j.tust.2020.103677.

Janbu, N. (1970). Method of settlement computation for various types of soils. *Soil Mech Found Eng* 7, 201–206 https://doi.org/10.1007/BF01704632.

Nappa, V., et.al. (2019). A new frontier of BIM process: Geotechnical BIM. *Proceedings of the XVII European Conference on Soil Mechanics and Geotechnical Engineering*.

Robert McNeel & Associates. Rhino 7, available at: https://www.rhino3d.com.

Satyanaga, A., Aventian, G., Makenova, Y., Zhakiyeva, A., Kamaliyeva, Z., Moon, S. and Kim, J. (2023). Building Information Modelling for Application in Geotechnical Engineering. *Infrastructures* 8(6).

Seequent. Leapfrog Works, available at: www.seequent.com/products-solutions/leapfrog-works/

Terzaghi, K. and Fröhlich, O. K. (1936). Theorie der Setzung von Tonschichte. Franz Deuticke, Leipzig/Wien.

Proceedings of the XVIII ECSMGE 2024
GEOTECHNICAL ENGINEERING CHALLENGES
TO MEET CURRENT AND EMERGING NEEDS OF SOCIETY
© 2024 the Authors
ISBN 978-1-032-54816-6
DOI 10.1201/9781003431749-697
Open Access: www.taylorfrancis.com, CC BY-NC-ND 4.0 license

ECSMGE 24
XVIII EUROPEAN CONFERENCE ON SOIL MECHANICS AND GEOTECHNICAL ENGINEERING

Insights on drop mass systems to predict pile compressive resistance from dynamic load test energy measurements

Perspectives sur les systèmes de masse tombante pour prédire la résistance à la compression des pieux à partir des mesures d'énergie des essais de chargement dynamique

J.A. Santos*
Instituto Superior Técnico – Universidade de Lisboa / TPF Consultores de Engenharia e Arquitetura S.A., Lisbon, Portugal

J. Viegas
TPF Consultores de Engenharia e Arquitetura S.A., Lisbon, Portugal

**jaime.santos@tecnico.ulisboa.pt*

ABSTRACT: We are currently immersed in the era of big data, where large volumes of data is generated and stored daily. However, the true challenge lies in transforming this data into meaningful and actionable information. To extract insights from these vast datasets, there is a growing dependence on machine learning techniques, which essentially build upon the foundation of traditional statistical methods. These techniques enable the creation of models that enhance our understanding of diverse subjects and facilitate informed decision-making. This study focuses on the establishment and exploration of a database derived from dynamic load tests on piles (DLT). In DLT on piles, impact hammers are employed, characterized by their potential energy or kinetic energy just before impact. Testing on high-capacity drilled deep foundations presents several challenges, including the need for sufficient energy to mobilize compressive static resistance of the pile. The investigation delves into understanding the correlation among various DLT test variables and uncovering potential relationships using supervised models, such as linear and non-linear regressions. The findings from this exploration have unveiled crucial insights, such as the influence of diameter on resistance and the existence of a non-linear relationship between resistance and the maximum energy transferred to the pile.

RÉSUMÉ: Nous sommes actuellement plongés dans l'ère du big data, où un volume immense de données est généré et stocké quotidiennement. Cependant, le véritable défi réside dans la transformation de ces données en informations significatives et exploitables. Pour extraire des insights de ces vastes ensembles de données, il existe une dépendance croissante aux techniques d'apprentissage automatique, qui s'appuient essentiellement sur les méthodes statistiques traditionnelles. Ces techniques permettent la création de modèles qui améliorent notre compréhension de sujets divers et facilitent la prise de décision éclairée. Cette étude se concentre sur l'établissement et l'exploration d'une base de données dérivée de essais de chargement dynamique de pieux (DLT). Dans le DLT sur les pieux, des marteaux d'impact sont utilisés, caractérisés par leur énergie potentielle ou leur énergie cinétique juste avant l'impact. Les essais sur des fondations profondes forées à haute capacité présentent plusieurs défis, notamment la nécessité d'une énergie suffisante pour mobiliser la résistance statique en compression du pieu. L'enquête vise à comprendre la corrélation entre diverses variables de test DLT et à découvrir des relations potentielles en utilisant des modèles supervisés, tels que des régressions linéaires et non linéaires. Les résultats de cette exploration ont révélé des informations cruciales, telles que l'influence du diamètre sur la résistance et l'existence d'une relation non linéaire entre la résistance et l'énergie maximale transférée au pieu.

Keywords: Dynamic load testing; exploratory data analysis; supervised models; pile foundation.

1 INTRODUCTION

Dynamic load testing systems use a mass to apply load to the head of the pile. This can be achieved either through a pile driving hammer, known as an impact driving system, or by dropping a mass, referred to as a drop mass system. Dynamic load testing can be conducted during the pile installation of precast concrete piles or steel piles (displacement piles) when driving with a hammer. Drop mass systems are employed to test cast-in-situ piles (bored piles, continuous flight auger, or other cast-in-situ piles) or testing associated with re-driving. These drop mass systems are characterized by their mass and maximum stroke (drop height), or the respective potential energy

(mass × acceleration × stroke) or kinetic energy immediately just before impact.

Testing high capacity drilled deep foundations poses several challenges, one of which is determining the required energy level to mobilize the compressive static resistance of the pile. Hussein et al. (1996) conducted a wave equation analytical study for the selection of a hammer for DLT of cast-in-place shafts. The studied shafts have ranges of diameters from 750mm to 1500mm and lengths from 10 to 30 diameters. Analysis results suggest as a general guideline that the hammer weight should be about 1.5% of the pile resistance.

According to EN ISO 22477-4:2018, the mass of the drop mass should be chosen to be greater than 2% of the design compressive static resistance of the pile (where the mass of the drop mass is expressed as a weight). In very hard soils, piles resting on hard bedrock, or where a pile is installed with a rock socket, drop mass weights of 1 % of the required design compressive static resistance can be sufficient to mobilize pile resistance.

Ideally, the applied energy or the stroke of the drop mass should be adjusted to achieve full mobilization of the pile skin friction and tip resistance. This study focuses on the establishment and exploration of a database derived from dynamic load tests on cast-in-place foundation piles of the Tagus River Lezíria Bridge River.

2 CASE STUDY

The Tagus River Lezíria Bridge comprises the north viaduct, the main bridge and the south viaduct with a total length of about 12 km. The viaducts are supported by piles with a diameter of 1500mm, and their lengths vary between 25 and 55 meters.

The construction methodology defined to install the piles is the following (Caputo, 2009):

i. Placement of a guide-steel tube with 6.00m of length.
ii. Driving a temporary casing with the use of vibrator down to the design depth.
iii. Internal cleaning of the casing up to the design depth with a hydraulic rig.
iv. Placement of the steel reinforcement cage.
v. Cleaning of the pile tip by “air-lift”.
vi. Pouring of the pile concrete simultaneously with the removal of the steel casing.

To validate the construction methodology and the pile design, a series of static and dynamic load tests were conducted (Santos, 2005).

Dynamic load tests were performed on 9 trial piles (6ϕ800mm and 3ϕ1500 mm) using specific equipment called SIPEX — Impact System for Trial Piles.

This system utilizes the free fall of two 100kN weights with a maximum drop height of 3m, capable of acting together or separately. The setup includes a guide tube and an attached steel cap block placed over the pile. The cap block ensures the centred and vertically applied impact and serves as protection against potential damage to the pile head (Figure 1). While this equipment is designed for testing ϕ1500 mm piles, it can also accommodate lower diameter piles using a reducer.

Multi-blow dynamic testing technique was employed, with applied energy varying between 40 and 600 kJ (or kNm) (Paraíso and Santos, 2020).



Figure 1. SIPEX: Drop mass system 100+100 kN.

The load tests were carried out in 3 locations along the route of the viaducts, and a supplementary ground investigation campaign was defined, consisting of boreholes accompanied by SPT tests and SCPT tests. There are alluvial deposits (soft silty clay, sands) overlying gravels, boulders and the Miocene bedrock (Figure 2).

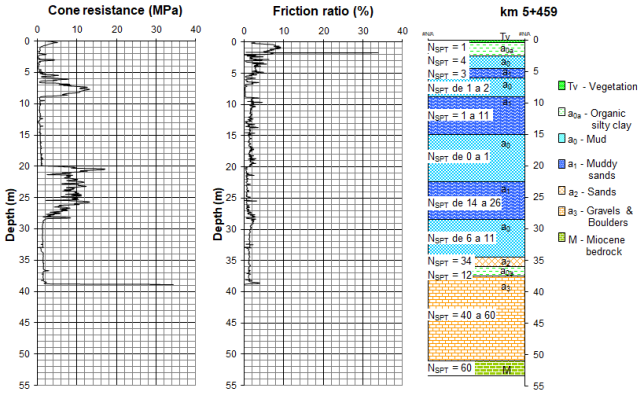

Figure 2. Typical Geological and Geotechnical Profile.

3 METHODOLOGY AND RESULTS

In the current investigation, we have at our disposal four variables derived from the DLT test: the diameter of the pile (D), the maximum potential energy of the hammer or rated energy (EP), the maximum energy transferred from the hammer to the pile (EMX), the mobilized resistance (R), and the ratio between the mobilized resistance and the service load $\left(\frac{R}{Qs}\right)$. To gain a deeper understanding of our data and the interplay among these variables, we initiated an exploratory data analysis (EDA). This type of analysis enables us to discern the strengths of relationships between variables and to further elucidate these connections. The data underwent processing utilizing the Python open-source language, leveraging prominent libraries including Pandas, Scipy, NumPy, Seaborn, and Matplotlib.

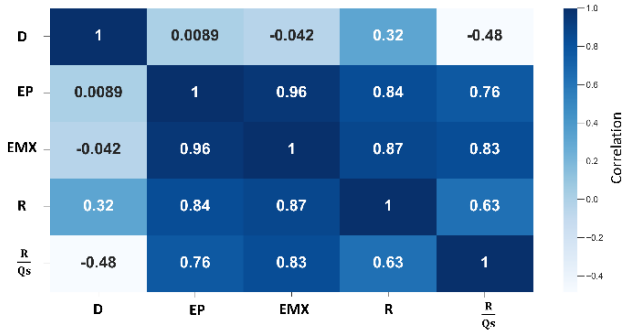

Figure 3. Correlation matrix for input variables.

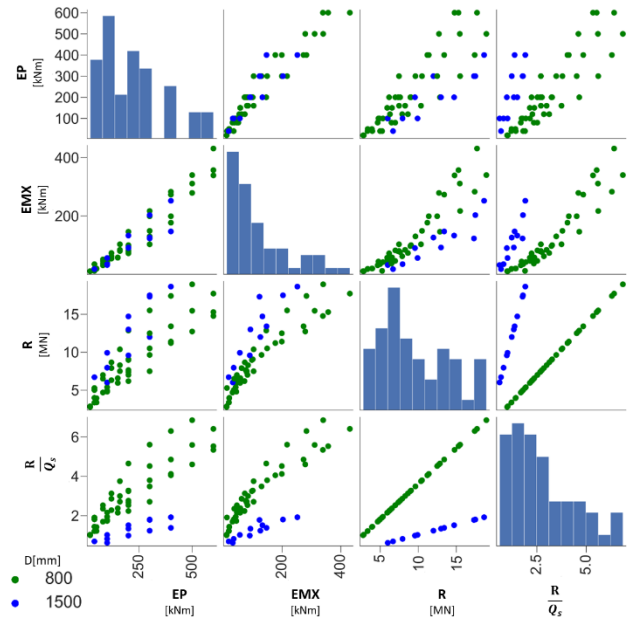

Figure 4. Scatterplot matrix depicting the relationships among the investigated variables. The green color represents the piles with 800 mm diameter and the blue the ones with 1500 mm.

Figure 3 showcases the correlation matrix for the aforementioned variables, while Figure 4 illustrates scatter plots for variable pairs. In this plot, piles with a diameter of 1500 mm are depicted in red, and those with an 800 mm diameter are represented in blue, complemented by variable histograms. A careful examination of these visualizations reveals that the diameter (D) demonstrates linear independence from rated energy (EP) but shows a weak correlation with the mobilized resistance (R). As anticipated, a larger diameter would correspondingly increase resistance. Additionally, it is apparent that there exists a non-linear relationship between mobilized resistance (R) and maximum energy transferred from the hammer to the pile (EMX), with a correlation coefficient of 0.87. The influence of pile diameter is also evident, separating the data into two groups, easily discernible by colour in the scatter plot.

Efficiency of the hammer is commonly assessed by calculating the ratio between the rated energy (EP) and the maximum energy transferred from the hammer to the pile (EMX). The maximum hammer height of drop is 3m leading to a 600 kNm rated energy, displayed in Figure 5 as EP, we can see that the survey was carried out for several heights (multi-blow testing technique), since the weight of the hammer was kept constant and equal to 200 kN. As depicted in Figure 5, it is evident that EMX is approximately 0.7 times EP, indicating a 30% energy loss.

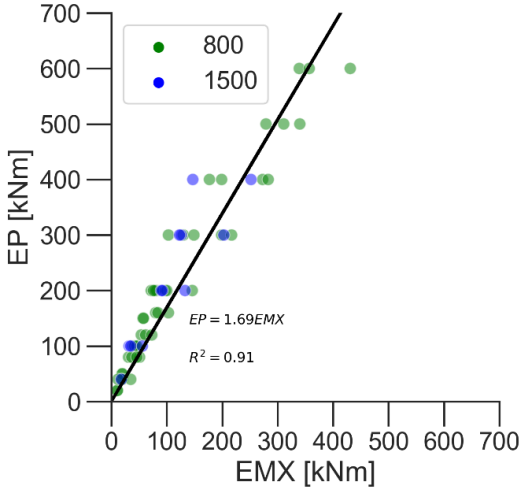

Figure 5. Relationship between the rated energy (EP) and the maximum energy transferred from the hammer to the pile (EMX), for both diameters 800mm (green) and 1500 mm (blue).

In this study, we determined the equivalent η coefficient to be 0.024m, as depicted in Figure 6 (η=EP/R). This value aligns with existing literature; for instance, Paraíso and Costa (2006) reported a value of 0.033m, while Paikowsky (2004) presented a value

of 0.025m. The dataset in our study displays lower dispersion, and the regression analysis yields a coefficient of determination (R^2) of 0.89, indicating a strong fit to the observed data.

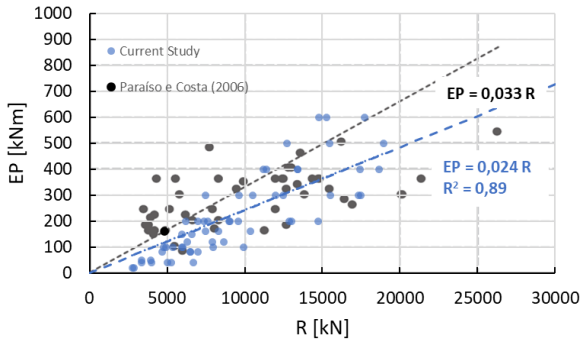

Figure 6. Comparison between the dataset of the current study (in blue) and the one presented in Paraíso e Costa (2006) (in black).

It is well-known that not all energy can be transferred from the hammer to the pile. If this were possible, the coefficient η would represent the displacement associated with the plastic deformation occurring at the lateral interface of the soil-pile and at the tip (Paraíso & Santos, 2020).

As indicated by EN ISO 22477-4:2018, Rausche et al. (2008) and Hussein et al. (1996), recommends that the weight of the hammer should be 1% - 2% of the desired resistance. Figure 7 elucidates this reasoning, where the ratio between the maximum energy transferred from the hammer to the pile (EMX) and the rated energy (EP) is plotted against the ratio between the hammer weight (W) and the resistance (R).

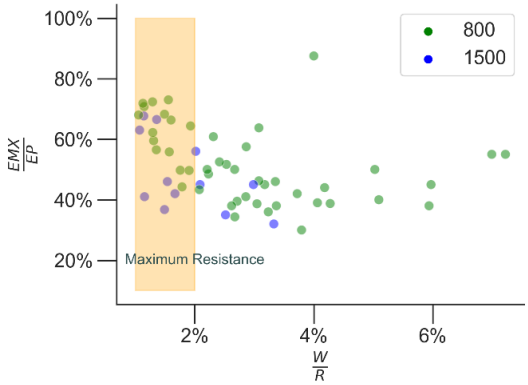

Figure 7. Relationship between the ratio of maximum energy transferred from the hammer to the pile (EMX) to rated energy (EP) and the ratio of hammer weight (W) to resistance (R).

It is evident that for the 800 mm diameter, the loss of energy is minimized when the weight/resistance ratio falls between 1% - 2% (shaded area in Figure 7), more precisely between 1% – 1.3%, in this study, for the blows which mobilized the maximum resistance. However, for the 1500 mm diameter, three points deviate from the trend, and within this interval, they still exhibit a lower energy ratio, approximately 40%. The efficiency of the hammer range from 30% to 87.5 %, with a mean of 50.9%.

If we look closer to the distribution of EMX for both diameters, depicted in Figure 8, we observe that both exhibit similar means. However, the 1500 mm diameter piles display higher dispersion due to the limited number of samples, which could justify this misalignment with the trend in Figure 7.

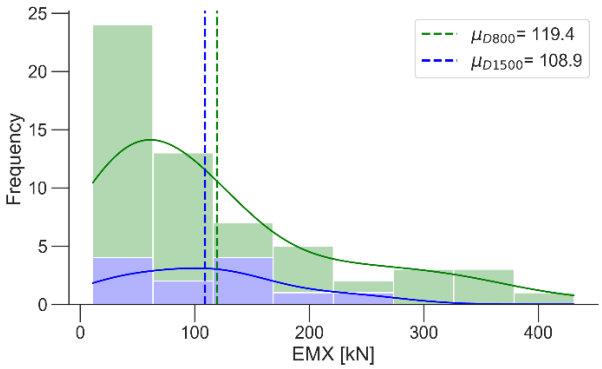

Figure 8. Distribution of the maximum energy transferred from the hammer to the pile (EMX) for both diameters. The green color represents the 800 mm diameter while the blue represents the 1500mm. The dashed lines are the mean of each distribution.

While the presented results are intriguing, the ultimate aim is to offer practical insights beneficial for designers. A key interest lies in determining the hammer parameters required to attain a specific resistance. To address this, we conducted a non-linear fitting between EMX and R, as depicted in Figure 9. Various functions underwent testing, and the one presented yielded the lowest Root Mean Square Error (RMSE).

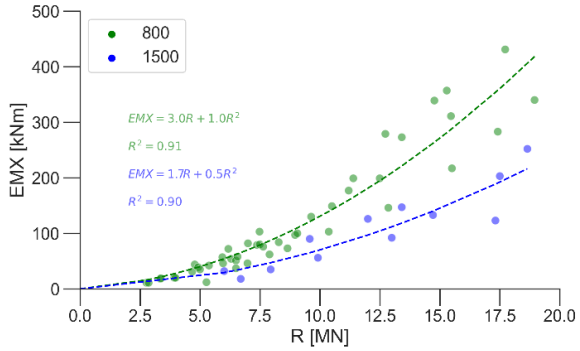

Figure 9. Non-linear relationship between the maximum energy transferred from the hammer to the pile (EMX) and the mobilized resistance (R). The green color represents piles with a 800 mm diameter while the blue represents those with a 1500mm diameter.

Notably, the equation for the 800 mm diameter is approximately double that of the equation for the 1500 mm diameter, revealing the influence of the diameter at the equation. It's essential to highlight that we constrained the regression to pass through the origin, underlining our expectation of zero energy applied for zero resistance. This graphical representation underscores that the requisite energy for achieving a given resistance is consistently lower for the larger diameter, thereby justifying an increased cost in pile designs with a corresponding reduction in associated equipment, or where the applied energy should be limited due to displacement issues.

4 CONCLUSIONS

In this comprehensive investigation, we examined variables derived from the Dynamic Load Test (DLT) such as the maximum potential energy of the hammer or rated energy (EP), the maximum energy transferred from the hammer to the pile (EMX), the mobilized resistance (R) and delved into their interrelationships. Practical implications to predict pile compressive resistance from dynamic load tests energy measurements are underscored and materialized by means of regressions equations. The results obtained not only align with current literature but also pave the way for valuable insights. Specifically, the formulated equations for predicting pile compressive resistance demonstrate excellent agreement with the dataset, boasting a coefficient of determination (R^2) around 0.9 (Figure 6 and Figure 9). This high level of correlation underscores the robustness and reliability of the equations in capturing the dynamics of the system.

As we strive for a more comprehensive understanding, future investigations should extend beyond the scope of this study. Exploring relationships with other variables tied to in situ characteristics, such as soil parameters, the lateral resistance, and tip resistance separately, holds the potential to enhance the accuracy and applicability of the derived equations. This broader inquiry would not only augment our confidence in employing these equations but also contribute to a more nuanced comprehension of the dynamic interactions at play during pile driving operations.

This study stands as a significant contribution to the field, providing practical tools for engineers and designers involved in pile-related projects.

REFERENCES

Caputo, A. (2009). Instrumented large diameter bored piles. *Deep Foundations on Bored and Auger Piles*, Van Impe (eds), pp. 213-227. Taylor and Francis Group, London, ISBN 978-0-415-47556-3.

EN ISO 22477-4 (2018). Geotechnical investigation and testing - testing of geotechnical structures. Testing of piles: dynamic load testing.

Hussein, M.; Rauche, F.; Linkins, G. (1996). Selection of a hammer for high strain dynamic testing of cast in place shafts. *Proceedings, 5th International Conference on the Application of Stress-Wave Theory to Piles*, pp. 759-772, Florida, USA.

Paikowsky, S. G. (2004). Drop weight dynamic testing of drilled deep foundations. Special Lecture, Proceedings, *7th International Conference on the Application of Stress-Wave Theory to Piles*, pp. 13-81, Kuala Lumpur, Malaysia.

Paraíso, S. C.; Costa, C. M. C. (2006). Análise do desempenho de martelo hidráulico autopropulsor testando estacas de alta capacidade de carga. *COBRAMSEG*, Curitiba, Paraná, Brasil, pp. 1079-1084.

Paraíso S.C. and Santos, J.A. (2020). Dynamic load testing with increasing energy for high bearing capacity piles. *Geotecnia* 150, 07-25. http://doi.org/10.24849/j.geot.2020.150.02

Rausche, F.; Richardson, B.; Likins G (1996). Multiple blow Capwap analysis of pile dynamic records. Proceedings, *5th International Conference on the Application of Stress-Wave Theory to Piles*, pp. 435 – 446, Florida, USA.

Santos, J.A. (2005). A10-Bucelas/Carregado/IC3 Highway, Carregado Subsection (A1) Benavente. Tagus River Crossing in Carregado. Load Tests on Trial Piles. *Analysis Report*. ICIST, Instituto Superior Técnico, Lisboa.

Proceedings of the XVIII ECSMGE 2024
GEOTECHNICAL ENGINEERING CHALLENGES
TO MEET CURRENT AND EMERGING NEEDS OF SOCIETY
© 2024 the Authors
ISBN 978-1-032-54816-6
DOI 10.1201/9781003431749-698
Open Access: www.taylorfrancis.com, CC BY-NC-ND 4.0 license

ECSMGE 24
XVIII EUROPEAN CONFERENCE ON SOIL MECHANICS AND GEOTECHNICAL ENGINEERING

A geotechnologist network

Un réseau de géotechnologues

S.D. Thomas*, K.G. Higgins
British Geotechnical Association, UK

**stephen.thomas@ogi.co.uk*

ABSTRACT: A Geotechnologist Network provides a platform and community to recognise and promote the valuable contribution to the Ground Engineering Industry delivered by skilled, knowledgeable and practical individuals that are critical to the delivery of a project. Whilst these individuals may not have the traditional education and qualifications as attained by chartered geotechnical engineers, their project contribution and responsibility, certainly equals and often exceeds those with more theoretical knowledge but lacking in practical experience. Network activity, including regular online webinars, serves to share the experiences of practitioners in the industry. These practical webinars are interlaced with other learning events, aimed to encourage practitioners to increase theoretical knowledge. This encourages progression to achieve qualifications, enabling individuals to aspire to advance within the industry. Webinars shared and delivered between practitioners, are growing exponentially, with this growth anticipated to continue in Europe and Worldwide.

RÉSUMÉ: Un réseau de géotechnologues fournit une plate-forme et une communauté pour reconnaître et promouvoir la précieuse contribution à l'industrie de l'ingénierie des sols fournie par des personnes compétentes, compétentes et pratiques qui sont essentielles à la réalisation d'un projet. Bien que ces personnes n'aient peut-être pas l'éducation et les qualifications traditionnelles acquises par les ingénieurs géotechniciens agréés, leur contribution au projet et leur responsabilité sont certainement égales et souvent supérieures à celles qui ont des connaissances plus théoriques mais qui manquent d'expérience pratique. L'activité de réseautage, y compris les webinaires en ligne réguliers, sert à partager les expériences des praticiens de l'industrie. Ces webinaires pratiques sont entrelacés avec d'autres événements d'apprentissage, visant à encourager les praticiens à accroître leurs connaissances théoriques. Cela encourage la progression vers l'obtention de qualifications, ce qui permet aux individus d'aspirer à progresser dans l'industrie. Les webinaires partagés et dispensés entre praticiens connaissent une croissance exponentielle, et cette croissance devrait se poursuivre en Europe et dans le monde entier.

Keywords: Geotechnologist; network; skilled; knowledgeable; practical.

1 INTRODUCTION

It has long been recognised that there are many talented skilled, knowledgeable and practical individuals (Figure 1), working in the Ground Engineering Industry; these individuals have a wealth of knowledge, that could be shared with others, but they rarely get the opportunity to speak at public society events. To promote the interaction between individuals with such attributes, the British Geotechnical Association (BGA) has initiated a Geotechnologist Network, as it is considered that the term Geotechnologist is appropriate to describe any skilled, knowledgeable and practical individual, with experience working in the Ground Engineering Industry. A geotechnologist is unlikely to be qualified in the professional sense, nor following a traditional route towards qualification. With a "Technologist" defined as an individual with a high level of skill and ability, who applies their scientific knowledge to the practical aims and purposes of human life, and "Geo"



Figure 1. A geotechnologist monitoring on site.

originating from the Greek word meaning "earth", it follows that a geotechnologist can be defined as:

An individual with a high level of skill and ability, who applies their scientific knowledge to achieve the practical aims and purposes of human life relating to the earth.

This definition could apply to individuals carrying out activities including, but not limited to, site investigation, laboratory and field testing, field monitoring, geospatial mapping, dewatering, piling, grouting, numerical modelling, drafters of drawings etc. The field is wide open, and we do not pretend to know all the possibilities.

The purpose of this Geotechnologist Network is to assemble skilled and practical individuals together as a knowledge-sharing community. Exactly how skilled and knowledgeable individual practitioners could assemble as a community of Geotechnologists was not known at the beginning of our journey.

Nevertheless, with the outcome to include and involve skilled and practical individuals within the Ground Engineering Industry, we chose to start our journey without knowing every step ahead of time, but reflecting on progress and then pivoting our guidance as feedback was received.

2 THE CONCEPT

The BGA is the United Kingdom Chapter of the International Society of Soil Mechanics and Geotechnical Engineering (ISSMGE). The ISSMGE is a Learned Society, with one of the objectives being:
"the promotion of international co-operation amongst engineers and scientists for the advancement and dissemination of knowledge in the field of geotechnics, and its engineering and environmental applications."

The object of the BGA, along with other national learned scientific societies, share the mission of:
"*the advancement of public education in the subject of soil & rock mechanics, and engineering geology, and their application"*
with these learned societies existing to promote:

(i) an academic discipline,
(ii) a profession, or
(iii) a group of related disciplines.

The authors recognised that whilst our Geotechnical Societies are very good at items (i) and (ii), by promoting those in the academic and professional world; through presenting lectures in grand theatres, with statues and names of famous engineers carved in stone around the walls, we have not recognised in the same way the individuals with skill and practical knowledge within item (iii) on whose shoulders much of the weight of the industry is supported.

With this accepted as an inherent weakness in our lack of recognition of skilled and practical individuals working within the Ground Engineering Industry, the BGA committed to initiating the development of a programme to incorporate those in the Ground Engineering Industry, who did not always enter our industry from the traditional qualification route, but nevertheless provide a hugely valuable contribution to the industry.

As published in Ground Engineering, in 2019 (EMAP, 2019a) Prof. Kelvin Higgins (author), as newly appointed Chair of the BGA, presented his wish to develop a technician community within the BGA. This followed a round table discussion, at which the need for advances to be made in the education of a Geotechnologist community through increased learning opportunities, and for continual professional development (EMAP, 2019b). A meeting was held with several employers to develop ideas. All were extremely supportive, but with the outbreak of the COVID-19 pandemic, the initiative stalled.

In 2022, BGA Executive member Dr Stephen Thomas (author) accepted the challenge set, and took the lead in developing this initiative in practice. Before the launch of this initiative in 2023, Dr Thomas undertook a year of research to provide guidance and focus on where this initiative could best deliver results.

This paper presents the key findings of the research, and whilst not a fully comprehensive research study, can nevertheless be used to advance this initiative and apply it to other societies in Europe and Worldwide.

3 THE JOURNEY

In the early days of the development of the initiative, the focus started with recognising those individuals who were, we thought initially to be at the periphery of the Ground Engineering Industry, but did not have an association of their own with which to belong.

The BGA Executive Committee considered initially the action of forming a sub-group within the BGA to which we could invite those who consider themselves not recognised to be openly acknowledged as valued individuals who provide a central and major contribution to the ground engineering community.

Our initial focus, we later learned, was centred too much on ourselves, i.e. the academics and professionals; inviting skilled and practical individuals to become one of us. However, after speaking to many of these skilled practitioners on a personal level, it became clear at an early stage, that without question, backgrounds were immensely varied, and much more multi-dimensional than the classical monoculture of School and University, Graduate-Engineer, and

ultimately a Professional, and that is just speaking about the authors. With this new focus in mind, based on our experience of working with skilled practitioners in the industry, enhanced by one year of speaking and learning from numerous practitioners explaining our vision to organise a society, we received an interesting clarity of response.

3.1 Opinion of professionals and academics

Whilst not a vast survey, there were some striking similarities in comments. The first was their perception of professional engineers, most of whom had studied and received higher degrees at university. It was as if we were Greek Gods, looking down at them from afar above the clouds. However, as authors, we are acutely aware that those working daily with geotechnology, are far more knowledgeable in essential practicalities to ensure solutions are implemented correctly in action.

3.2 Self-opinion of practitioners

Many practitioners consulted, described themselves as lacking in confidence with regard to their theoretical knowledge. They often referred to themselves as "*just me*", or "*it is only my view*", as well as having the opinion of their own knowledge compared to us in more fruitful and less confident language.

The lack of confidence in their own knowledge was despite the fact that many of the individuals conferred with, had extraordinary major project responsibility. For example, some held the responsibility for sinking shafts in loose saturated ground, whilst their workers were digging and launching a tunnel, describing their minute-by-minute decisions of ground strength, again in more fruitful language than in a standard textbook.

This practical experiential knowledge is gained from repeated observation, and in the authors' view, is no less valuable to a project. In fact, this is possibly more valuable than theoretical knowledge, because during construction processes, especially underground construction, the ground encountered is rarely as expected, and real-time decisions are often made from observations by skilled and practical individuals, rather than by those with more theoretical knowledge (Figure 2).

The individuals we spoke to were generally unaware of the much bigger picture with regard to the design and construction process, and particularly how this process depends to a high degree on their skill and knowledge. Our initiative is aimed at helping and guiding these individuals to understand where the meticulous work they accomplish contributes to the overall process. This dissemination of information has been achieved by providing speakers who have focussed on their role within a project (the importance of investigations, testing, monitoring etc.) or by interaction between the Geotechnologists themselves exchanging ideas.

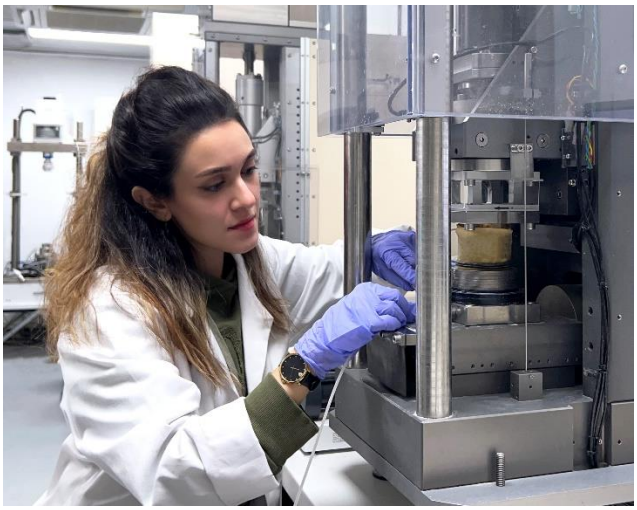

Figure 2. Geolabs laboratory technician.

As previously noted, the initial feedback from employers was very positive and they were willing to provide tangible support for this initiative. They were keen that their workforce became more engaged and understood the importance of their work.

4 REDEFINING A LEARNED SOCIETY

The essence of the authors' passion is that as a society we need to recognise all aspects of learning within our field, including academic, professional and practical.

Whilst the initial thoughts of the BGA were indeed to assemble a community of skilled practitioners, the initiative has now developed into one in which Geotechnologists are very much encouraged to lead and develop each other. As a consequence, the BGA plan is now to incorporate the Geotechnologist Network as a sub-group of the BGA, so having its own identity (similar to the highly successful Early Career Group), but at the same time being able to benefit from the established BGA administrative structure.

The fact is that many substantial developments and innovations arise from situations that are observed in practice. Here skilled and knowledgeable individuals, of the focus of this initiative, pull together to develop solutions in practice, that rarely require the modelling of second-order differential equations!

Learning resulting from developing solutions in practice, is known as experiential, or kinaesthetic learning, as opposed to theoretical learning.

We often treat these types of learning as either-or. Either we are academic, learned, theoretical thinkers, or we are practical, hands-on, technicians.

Whilst we all know that the most balanced and rounded knowledge is a blend of both theoretical and practical understanding, our learned societies do not necessarily recognise and reward the practical end of the knowledge spectrum.

In 1984, David Kolb (Kolb, 1984) published his groundbreaking Kolb Learning Cycle as depicted in Figure 3. This learning cycle is a pedagogical approach to human learning. He developed this model to teach his students at Stanford University. His goal was to help them learn better through self-directed study.

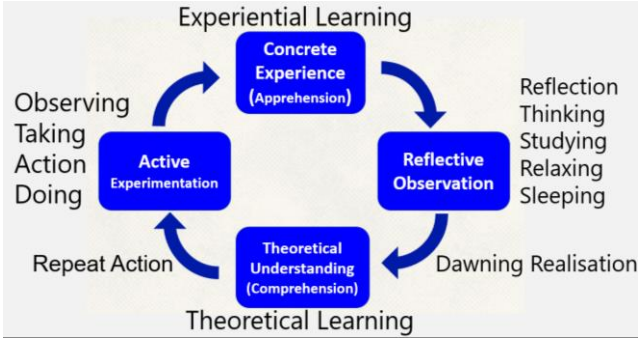

Figure 3. Kolb's four stages of learning (Kolb, 1984).

This theory of learning demonstrates how the practical knowledge gained by Geotechnologists can be very valuable to the Ground Engineering Industry.

Whilst a generalisation, those steeped in academic thinking can often focus around the bottom right area of the Kolb cycle i.e. reflecting & comprehending, with less focus on taking action in practice, so missing out on observation and apprehension.

Conversely, practical, skilled and knowledgeable individuals can spend their lives taking action, experiencing, observing and understanding behaviour through apprehension. This style of kinaesthetic learning, whilst gaining experience, can result in not fully comprehending the reasons behind the behaviour observed, and can miss out on a deeper understanding.

It is clear from this Kolb cycle, that when there is a full cycle of action and observation, with reflection and study, this results in both apprehension and comprehension, so leading to a deeper learning.

To this end, it is one of the aims of the Geotechnologist Network that individuals share their experiences, and then provide encouragement and guidance towards organisations that can provide tuition, learning and qualifications. This is being achieved initially by running webinars, delivered every two months, by the practical and skilled Geotechnologists themselves. Figure 4 presents the initial webinars presented and scheduled.

Date	Name & Organisation	Webinar Title
2023 Sep	Stephen Thomas, BGA	A Geotechnologist Network
2023 Nov	Christopher Wallace, Geolabs	Things that affect soil strength
2024 Jan	Christopher Swainston, Consultant	Environmental Sampling: What can go wrong
2024 Mar	Brian Sharkey, One Bore Tunnelling	Lab coats: white, Brown or Hi-Viz. Research & Innovation in the Workplace
2024 May	Jim Sheilds, RoGEP	Routes to becoming a Ground Engineering Professional
2024 July	Julian Lovell, Equipe Group	Diplomas in Field and Laboratory Geotechnical Activities

Figure 4. Webinars by the Geotechnologist Network.

The development of the webinars, delivered by the growing network of geotechnologists, has proved most successful on a number of counts.

(i) The network interest is growing exponentially.
(ii) A Geotechnologist sees their skills being shared.
(iii) A Geotechnologist sees their skills as recognised.
(iv) A Geotechnologist is directed towards learning.
(v) Theoreticians see more practical examples.

COMMENT

This initiative of a Geotechnologist Network is fully consistent with the aims of a learned society. It is not the intention of this network to provide a qualification or certification. However, this network can provide a catalyst for encouraging and guiding individuals towards organisations that provide further education to provide advancement to practitioners in our industry.

Much is to be gained by all working in our industry from the interaction with individuals with such practical skills, knowledge and experiences. The aim is that this initiative will promote these interactions and help develop and advance the pool of skills and knowledge within the entire geotechnical community.

ACKNOWLEDGEMENTS

We are most grateful to Andrew Ridley, David Toll, Peter Reading and others on the BGA committee, who provided advice and guidance throughout our collective journey.

A particular thanks also go to the numerous practitioners, each an early Geotechnologist, who have spoken to us in much-needed plain language of their industry experiences.

REFERENCES

Ground Engineering Magazine (2019a) Remaining Relevant. Interview with the new chair of the BGA. E-map. July 2019.

Ground Engineering Magazine (2019b). Stronger Together: A roundtable discussion. E-map. May 2019.

Kolb, D. A. (1984). Experiential learning: Experience as the source of learning and development. Englewood Cliffs, N.J: Prentice-Hall.

Proceedings of the XVIII ECSMGE 2024
GEOTECHNICAL ENGINEERING CHALLENGES
TO MEET CURRENT AND EMERGING NEEDS OF SOCIETY
© 2024 the Authors
ISBN 978-1-032-54816-6
Open Access: www.taylorfrancis.com, CC BY-NC-ND 4.0 license

ECSMGE 24
XVIII EUROPEAN CONFERENCE
ON SOIL MECHANICS AND
GEOTECHNICAL ENGINEERING

Author Index

Abate, G. 1421
Abdallah, A. 931
Abrantes, D. 2832
Abu-Farsakh, M.Y. 273, 278
Abushama, K.A. 2751
Acar, C. 2063
Adam, D. 1685, 2555
Adatepe, S. 2304
Agaiby, S.S. 723, 1080
Aguiar, M.F.P. 2486
Ahangar Asr, A. 1013
Ahmad, A. 1970, 2207
Aiche, O. 2059
Aires, A. 1881
Akçakal, Ö. 2063
Akdag, C.T. 2755
Al-Azazmeh, A. 282
Albino, U. 1430
Albuquerque, A. 3129, 3335
Albuquerque, P.J.R. 2486
Alekhin, A.A. 286
Alelvan, G.M. 689
Alencar, A. 291
Alesiani, P. 789
Alexander, J.S. 2760
Alhama Manteca, I. 3182
Al-Hashemi, H.M.B. 2895
Allard, J. 3123
Allievi, L. 2727, 2764
Almasraf, M. 295
Almeida e Sousa, J. 2573
Almeida, C. 1277, 1665
Almeida, F. 2067
Almeida, I.M. 3511
Almeida, S. 1017
Almukashfi, A. 301
Alqawasmeh, Q.I. 2768, 2772
Alvarado, M. 137
Alvarez, G.C. 2695
Alzate, A.M. 305
Amaral, P. 1214, 1232
Ambrosi, C. 1463
Amdal, Å.M.W. 1150
Amendola, C. 1425
Amorim, D.G. 1430
Amorosi, A. 1311
Amoroso, S. 679, 1255, 1946
Anastasiadis, A. 1188
Andrade Pais, L. 3129, 3335
Andrade, J.C. 2581, 2585
Andreasen, D.K. 311, 315
Andrieş, G. 2093
Andries, J. 3400
Anjos, B. 2148
Anjos, R. 3477
Ånes, E.W. 2777, 2783, 3030
Anning, P. 1023
Anoyatis, G. 438, 3088, 3194, 3400, 3436
Antão, A.N. 805, 1935
António, F.M. 1027
Antoinet, E. 3284
Antunes, P. 2274
Araújo Santos, L. 1860
Araújo, P. 2581, 2585
Arbanas, Ž. 554,1377
Arcos Álvarez, A.A. 2456
Arcos, J.L. 2071, 2218
Argyroudis, S. 1350
Argyroulis, K. 2076
Armistead, S.J. 3450
Arnold, A. 1890
Arroyo, M. 301, 610, 2292, 2821
Artoni, R. 2262
Arvind 3007
Asaka, Y. 705, 3066
Asanza-Izquierdo, E. 893, 1718
Askarinejad, A. 1890
Aslan, Y. 346, 1434
Åsli, G.W. 3030
Athanasiu, C. 320
Attari, Y. 1440
Aubram, D. 2735
Audrain, Ph. 2681
Aulestia, S. 1444
Aung, A.Y. 1485
Avelar, M.G. 2081
Avinash, L.S. 2788
Avramenko, M. 2085
Aye, Z.Z. 1485
Ayhan, B.U. 25
Azeiteiro, R.J N. 1712
Azeredo, T. 2534
Azevedo, G.F. 2793
Azevedo, N.M. 1600
Aziz, O.Q. 528
Azizi, A. 761

Bálint, Á. 2987
Bødker, L. 711
Büyüklü, M. 2960
Bačić, M. 1448
Bałachowski, L. 330
Babiy, S. 2797
Badinier, T. 326, 3171
Bahar, R. 2059, 2978
Baille, W. 2987
Balachowski, L. 2515
Baldwin, M. 1636
Bandini, P. 2589
Barbieri, P. 334
Bardanis, M. 727
Barker, C.A. 2089
Barreto, D. 1194, 2987
Barros, J. 1452
Barros, P. 2852
Barzan, M. 2801
Bassi, A. 1356
Batali, L. 2093
Bateman, A.H. 2880
Bates, L. 542
Bathurst, R.J. 3149
Batilas, A.B. 2925
Batilliot, L. 1100, 2538
Batocchioni, L. 2097
Bauduin, C. 2235

Bazarov, B. 995
Beal, X. 2071
Beaufils, M. 3497
Becci, B. 1319
Beck, J. 338
Beckett, C.T.S. 3316
Beckhaus, K. 178
Bednarek, R. 342
Bednarski, Ł. 1457
Bella, G. 1463
Bellezza, I. 2884
Belokas, G. 1795
Belton, J. 2895
Bendea, D. 301
Benta, A.A.R.C.A. 1027
Bento, J. 2101
Benz-Navarrete, M. 637
Berchun, V. 3503
Berchun, Y. 3503
Berenguer Todo Bom, L.A. 2805, 3078
Bernardo, F. 907, 1469
Berthoz, N. 346, 1434
Bertola, F. 2810
Bertolini, I. 1033, 1209, 1356
Bessason, B. 1249, 3190
Beuße, M. 2816
Bezuijen, A. 588, 2709
Bilotta, E. 113, 262, 444
Biondi, G. 1846
Black, M. 1291
Blackmore, R. 2895
Blanc, M. 330, 2681, 3171
Blanckaert, M. 352
Blanco Blanco, F.J. 2364
Bloss, B.R. 1527
Bodamer, R. 2245
Bodas Freitas, T.M. 356, 2827, 2832
Bogdanovic, A. 1038
Bogusz, W. 1475, 1481
Bohn, C. 881, 1566
Boiero, A. 2821
Bojadjieva, J. 1038
Boldini, D. 2025
Boley, C. 2964
Bonassisa, P. 1199
Bond, A.J. 1958
Bonić, Z. 2445
Bonito, F.A.B. 1027
Boonyarak, T. 1485
Borana, L. 390, 2195
Borgström, K. 1555
Bosch, J. 84
Boscov, M.E.G. 3335
Bottaro, L. 1491
Boumendjel-Game, O. 2107, 2331
Boureanu, A. 2113, 2559
Bourgeois, E. 967, 1905, 2266
Bourguignon, E. 1100
Bourne-Webb, P.J. 356, 2827, 2832
Boutillon, L. 2496
Bowen-Bravery, J. 2249
Boyko, I. 361
Bräu, G. 1497
Brûlé, S. 3483
Brček, M. 365, 478
Brčeková, J. 478
Bračko, T. 197, 1996
Branque, D. 346, 1434
Brasile, S. 1712
Braz, I. 2117, 2123, 2642
Briançon, L. 305, 881, 2440
Bridges, C.A. 1503, 2838
Brinkgreve, R.B.J. 861, 1712
Brito, A. 1507, 1622
Brosz, F. 369
Brouwer, J.W.R. 2127
Brown, M. 3316
Brown, M.J. 3270
Bruchental, C. 1245
Bruens, J.N. 750
Bruni, L. 204
Bryan, H.J.B. 2842
Buckley, R.M. 2760, 3104, 3321
Buggy, F.J. 2388
Bui, T. 1712
Bulolo, S. 1659
Burd, H.J. 3042, 3046
Burgraeve, A. 2172
Burley, L. 3329
Burley, L.J. 1042, 2842
Burlon, S. 1513, 1840, 1974, 2138
Burtin, P. 2132
Burtscher, S.L. 1301
Butcher, D. 1048
Butler, S. 2331
Buykx, S. 2921
Buyuklu, M. 84
Buzilă, I. 2563
Byrne, B.W. 3104
Cabral, R. 1269
Cabrera, M.A. 1052
Cahn, M. 2138
Caicedo, B. 1228
Cakir, E. 25
Calçada, R. 755
Caldas, P. 2144
Caldeira, L. 1622, 3243, 3515
Calissano, H. 1100, 2538
Callisto, L. 1950
Camões Lourenço, J. 3357
Camacho, D.L.D. 1770
Canetta, G. 1319
Cano, M. 2950
Capobianco, V. 1090
Cardoso, A. 2848
Cardoso, C. 3278
Cardoso, R. 1618, 2148, 2671, 3392
Carlos, D.M. 2152
Carlsson, C. 197
Carneiro, J.R. 2067
Carpinteiro, L. 881
Carrasco Díaz, D. 1606
Carreto, J. 1507, 1829
Carrilho Gomes, R. 1283
Carvajal Díaz, E. 2158, 2164, 2852
Carvalheira, A. 2534, 2551
Casagrande, M.D.T. 689
Casal, B. 2675, 3375
Cascante, G. 674
Cascone, E. 1846
Casini, F. 2313
Casselgren, J. 3165
Castaneda-Lopez, M.A. 375
Castellanza, R. 301
Castelli, F. 1730
Castro, C.D. 849
Castro, J. 1517, 2158, 2168, 3145
Cathie, D. 2172
Cavaleiro, V. 3129, 3335
Caxias, C. 2117, 2547
Cazacliu, B. 2262
Celot, A. 2313
Cengiz, C. 618, 1052, 1920
Cerek, K. 380
Cerfontaine, B. 154
Cerfontaine, B.P.J. 2880
Cernoch, P. 3050
Cerqueira, F. 3243
Cesaro, R. 384
Cetin, K.O. 25

Ceylan, Y.C. 3353
Chabrat, N. 2178
Chalak, C. 2440
Chambers, J.E. 1179
Chami, D. 2858
Chammas, R. 1543
Chammas, S.C. 1547
Chan, S.L. 1402
Chang, I. 3074
Chang, J.Q. 2183
Chang, M. 1113
Chao, C. 3176
Chapron, G. 1915
Chaquisse, C. 414
Chatzigogos, C. 1434
Che, S.P.C. 2189
Chen, C.Y. 1056
Chen, H.-W. 1056
Chen, J. 2862
Chen, X.W. 3293
Chen, Y.-H. 1521
Cheng, W.C. 2866
Chițu, O. 2563
Chiaradonna, A. 679
Chiarelli, A. 606
Chihi, F. 1062, 2870
Chille, F. 3491
Cho, G.C. 3074
Choudhary, S. 390, 2195
Choudhury, A. 1066
Chow, S. 3194
Chow, S.H. 3400
Chrisopoulos, S. 815
Christ, F. 395
Christensen, A.N. 1224
Christensen, C.W. 1527
Christensen, J.D. 2235
Christiansen, T.L. 197
Chu, M.-C. 1072
Chung, A.P. 2478
Chung, C. 262
Ciantia, M.O. 610, 2876, 3270
Cinicioglu, O. 2945, 3247
Cinicioglu, S. F. 295
Cininioglu, O. 295
Ciocaniu, I. 1584
Ciocaniu, I.A. 2199
Ciortan, R. 452
Ciumeică, D. 2113, 2203, 2559
Ciurleo, M. 1790
Claes, H. 3088
Closset, L. 1707
Coelho, I. 2507, 2534, 3487
Coelho, M.J. 1305
Coelho, P. 1860
Coelho, P.A.L.F. 1770
Cohn, A.G. 2296
Colaço, A. 400
Collico, S. 404
Collin, F. 3088
Collins, Ph.E.F. 3303
Collins, S. 1224
Comber, G. 2970
Conceição, M. 3329
Conn, A.T. 2880
Conrado-Palafox, A. 2207
Conti, R. 1425
Cordeiro Silva, R.A. 739
Cordoni, V.I. 410
Cornaro, A. 231
Corrêa, M.D. de O. 2288
Correia dos Santos, R. 2212
Correia, A.A.S. 2464, 3422
Cortés, M. 3123
Costa, A.C. 917
Costa, G.C.L.R. 2695
Costa, J. 1531
Coutinho, R.Q. 849
Creasey, J. 2880
Crispin, J.J. 1535
Cristelo, N. 1786
Cruz, J. 414, 2101
Cruz, M. 1452, 2148
Cruz, N. 2101, 414
Csetenyi, L. 3270
Cuccurullo, A. 2858
Cuceoglu, F. 25
Cudmani, R. 815
Cueto, N. 418
Cuinet, J.M. 2935
Cuira, F. 1974
Cuisinier, O. 931, 2178
Cunha, L. 1214
Cunha, R.P. 2486, 2793, 3297
Cvetković, D. 2445
Czabanski, C. 3491
Czerski, D. 1463

Đurić, M. 3224
Díaz, J.M. 1531
Díez, J.A. 1875
Düzceer, R. 2304
da Costa, C.H. 2218
da Silva, M.C.C.S. 424
Dahl, M. 618
Daktera, T. 1539
Dale, M.P. 3375
Dalwadi, M. 2895
Damgaard, J. 3218
Damians, I.P. 647, 3149
Danilov, P. 2563
Dano, C. 3137
Das, B.M. 633
Das, G. 2223
Das, S.K. 428
Dashwood, B. 1179
Datcheva, M. 2987
Davidson, C. 3316
Davies, M.C.R. 2249
Daxer, H.-P. 1301
de Bruijn, H.T.J. 2052
de Carvalho, M. 2227
de la Rosa Domínguez, L.M. 2368
de Lacerda, B.M. 1543, 1547
de Lima, D.R. 739
De Luca, F. 1131
De Luca, M. 1551
de Melo, D. 204
de Oliveira Souza, G. 3274
de Paiva, A.B.S.P. 2288
De Risi, R. 1131
de Rocquigny, E. 474
de Sanctis, L. 548
de Santos, C. 410
de Sauvage, J. 433, 532, 3171
de Silva, F. 1425
de Sousa, L.L.C.G. 572
de Vilhena Costa, A. 3487
Debaize, A. 2231
Deckner, F. 1555
Dedecker, K. 2231
Degago, S. 1241
Degu, Y. 1560
Della Corte, A. 438
Della Ragione, G. 444
Demir, B. 2235
Denies, N. 1497, 1566
Denis, A. 1707
Denk, O. 809
Depinois, S. 352
Dermenonville, F. 2538
Dervishaj, A. 1869
Desideri, A. 1311, 1594
Dete, H. 2241
Detert, O. 2317
Detlefsen, A.E. 448
Dettenborn, T. 3228
Devrani, R. 1076
Devriendt, C. 3024
Devrieze, Y. 3410

Dhakal, O.P. 1325
Di Buò, B. 723, 1080, 2884
Di Buccio, F. 1946
Di Costanzo, L. 1425
Di Laora, R. 384, 548
Di Luigi, G. 2884
Di Mariano, A. 1086, 1368, 1412
Di Mariano 444
Di Sante, M. 2884
Diakonov, I.P. 1801
Diambra, A. 2880, 3465
Dias, D. 2440
Dias, J. 2327, 2905
DiBiagio, A. 1090
Dijkstra, J.W. 2245, 2309
Diliberto, C. 931
Dimas, J.M. 2071
Dinc, A. 2304
Ding, R. 979
Dinis, A. 1273, 1881
Dinis, C.M. 1094
Dinis, J. 1119
Disantantonio, A. 1100
Divall, S. 2249, 2599, 3288
Divilly, M. 2346
Do, N.A. 1852
Dobrzycki, P. 3455
Dodaro, E. 2889
Dogaru, I. 1346
Dogaru, P. 452
Dominijanni, A. 2939
Domitrović, D. 3428
Dong, Y.P. 456
Donohue, S. 1179, 2223
Donovan, J. 1224
Dornecker, E. 2519
dos Santos, T.B. 1543
Dossey, M. 1444
Doubrovsky, M. 462
Doulala-Rigby, C. 2895
Dragomir, G. 1825
Drefke, C. 2964
Droniuc, N. 1170
Dubravina, V. 462
Dubreucq, T. 326, 330, 3171
Dudfield, J. 2331
Duffy, A.R. 1224
Duffy-Turner, M. 2254, 2731, 2895
Dufour, N. 346, 1100, 2538
Duro, J. 1606
Duy, M.N. 1104
Dyer, N. 1042, 3440
Dyson, A.P. 2974
Dytiuk, O. 799
Dzięcioł, J. 1572

Ebener, A. 1578
Edip, K. 1038
Effenberger, M.J.P. 45
Eguchi, M. 2352
Ehrlich, M. 1909
Eikebrokk, A. 1109
Eiksund, G.R. 1440
El Sawwaf, M. 2434
Eleftheriou, E. 2258
Elmaloglou, A. 84
Elsaid, A. 25
El-Zein, A. 497, 3459
Emeriault, F. 3137
Enbom, V. 1555
Ene, A. 1584
England, M. 3325
English-Martin, R. 3491
Enoch, S. 3483
Erginag, U.C. 2945, 3247
Erlingsson, S. 468, 1249, 3190
Ermoshina, L.Yu. 889
Escudero-Merino, D. 1718
Esnault-Fillet, A. 2148
Esposito, I. 1551
Estaire, J. 1588, 1724, 1958, 2405, 2613, 3159
Esteves, L. 2468
Euzen, G. 3001
Everton, J.H.C. 468
Ezzeddine, A. 2262

Förschler, Ph. 1640
Förster, U. 2052
Fărcaş, V.-S. 1245
F.Gabrieli 2889
Facciorusso, J.A. 3446
Fagundes, L. 414
Falcão, A.P. 1864
Fanelli, S. 875, 2266
Fansuri, M.H. 1113
Fantera, L. 1594
Faramarzi, A. 1644, 2031
Fargier, Y. 532
Farhadi, M.S. 745
Farhat, H. 2440
Farinha, M.L.B. 1600
Fartaria, C. 1119, 2270, 2451, 2460
Fasano, A. 945
Fattahi Masrour, F. 2388
Fei, W. 3261
Feng, S. 2901, 2987
Ferlisi, S. 697
Fernández Eusebio, A. 1606, 1612
Fernández Rodríguez, R. 1618
Fernández-Ruiz, J. 2168
Fernandes, E. 1273, 1881, 2274
Fernandes, L. 2278
Fernandes, M. 2218, 2827
Fernandez, C. 3137
Ferrari, A. 1756
Ferraz, R.W.M. 1527
Ferreira, A. 1277, 2905
Ferreira, C. 674, 1228
Ferreira, C.S. 1277
Ferreira, M. 1283, 2935
Ferreira, M.A. 1277
Ferreira, S. 907, 1469, 2101
Ficzek, K. 939
Fiddes, G. 1398
Fielder, S. 1048
Fierenkothen, C. 2519
Figueira, J.S. 1622
Figueiredo, A. 3278
Figueroa Palacios, G. 2282
Filho, F.C.S. 2793
Finiasz, A. 474
Fioravante, V. 1136, 2889
Fischer, S. 2637
Fleetwood, M. 2107
Flink, J. 3218
Flint, S. 3316
Flora, A. 1199
Fonseca, T.C.O. 1543
Fontes, M.M.M. 1929, 2288
Foresta, V. 697, 1160
Fornelli, D. 1335
Forsberg, T. 1555
Forsman, J. 3228
Forte, G. 1287
Fortunato, E. 400
Foti, S. 1950
Fraccica, A. 404, 2292
Fradj, N. 2909
François, B. 2810
François, S. 438, 3088, 3194, 3400, 3436
Francone, L. 1154
Francos, R. 3329
Frankovská, J. 478
Frankovska, J. 971

Fransen, M. 1052
Franza, A. 448, 1626, 2667, 3094
Fratalocchi, E. 2884
Frauenfelder, R. 1150
Freire, O. 1807
Freitas, D. 1123
Freitas, D.C. 670
French, G. 2675
French, G.R. 482, 3369, 3375
Freund, R. 3082
Frias, A. 1283, 3511
Friberg, O. 871
Fruzzetti, V.M.E. 789
Fu, L. 2296
Fujikawa, T. 3311
Fukatsu, S. 2380
Fung, H.K. 1630

Głuchowski, A. 511
Gabryś, K. 2915
Galindo, R. 291
Gallagher, E. 2921
Gallardo, A. 917
Gandolfi, S. 1650
Gans-Or, T. 492
Gao, H.D. 1205
Gao, Y. 497
Garantini, S. 2970
García Alberti, M. 2456
García, D. 670, 1123
Garcia, L.M. 137
Garcia, M. 1764
Garcia, N. 2300
Gardete, D. 3118
Garin, H. 1636
Garnier, P. 881
Gaspar, T.A.V. 503, 1127
Gastine, E. 72
Gaudicheau, P. 2681
Gaudio, D. 2925
Gavin, K. 2076
Ge, L. 955
Geanguş, R. 2563
Gehring, S. 1640
Gelonch, L. 410
Gens, A. 444, 777, 885, 1086
Georgiadis, K. 3345
Gerard, P. 2810, 2858
Gerressen, F.-W. 210
Gharsallaoui, H. 2995
Ghezzi, S. 1463
Ghosh, P. 831, 1066
Giani, M. 1463
Gil, R. 2071
Gilbert, Z. 2496
Gilder, C.E.L. 1131, 1535
Giretti, D. 1136, 2889
Gjelsvik, V. 507
Gjorgjeska, I. 1038
Godinho, A. 1881
Godinho, E. 356, 2827
Gokalp, A. 2304
Gomes Correia, A. 72, 301, 755, 3487
Gomes, F. 3243
Gomes, M.S. 1527
Gomes, P. 2528
Gomes, R. 400
Gomes, R.C. 1255, 1864
Gomes, T. 2117
Gonçalves, A.L. 2417, 2543, 2793
González, J. 660
González-Gallego, J. 1875
Gonzalez, I. 1452, 2148
Gonzalez-Ollauri, A. 3020
Goodarzi, M. 3078
Goss, C. 1224
Gottardi, G. 1033, 1209, 2889
Gourvenec, S.M. 154, 2880
Grégoire, C. 2093
Grabe, J. 1954, 380
Gragnano, C.G. 2889
Grandclerc, A. 2931
Grange, S. 1142, 2440
Graterol, E.P. 515
Greif, V. 3202
Gress, J.C. 2935
Guanche, R. 3145
Guarena, N. 2939
Guayacan-Carrillo, L.-M. 1915
Guenneau, S. 3483
Guerra, N.M.C. 805, 1935
Guglielmelli, C. 2309
Guida, G. 2313
Guimond-Barrett, A. 3491
Guirado, F. 875, 913
Guner, M. 2945, 3247
Gunn, M.J. 2502
Gunnvard, P. 2300
Gupta, R. 204
Gustavsson, H. 2341
Gutiérrez-Ch, J.G. 515
Gutierrez, E. 2950
Håård, A. 520
Hödlmoser, N. 656
Habert, J. 622, 875
Hadjiloo, E. 380
Hafstad, E. 2955
Hager, M. 2555
Hai, L. 1644
Haikola, M. 745
Haine, G. 2172
Hajjar, A.E. 2880
Halfon, I. 1707, 3497
Hamidi, A. 524
Hangen, H. 2317
Hansen, N.B. 3521
Hardy, S. 795
Harran, R. 84, 2960
Harrison, E.J. 1527
Harrison, J.P. 1724
Hasan, A.M. 528
Hashemi, A. 2945
Hassan, M. 1964
Hassaoui, J. 474
Haugen, M.K. 2323
Hawkins, W. 2751
Hawwa, G. 532
He, J.-W. 1402
Hededal, O. 572, 783, 865
Heitor, A. 927, 1650
Hell, M. 2625, 2703
Hendler, K. 2964
Hen-Jones, R. 1146
Hen-Jones, R.M. 2970
Henke, S. 338
Henriques, A. 538, 2270, 2327
Henriques, D. 2123
Herceg, K. 3428
Hernández-Aguirre, V.M. 1655
Heron, C.M. 2667
Herten, M. 2519
Heyerdahl, H. 1150
Heymann, G. 503
Higgins, K.G. 3530
Hino, T. 2950
Hinxman, D. 2842
Ho, C.F. 2974
Hoang, M. T. 352
Hocini, Y. 2978
Holcombe, E.A. 1131, 1146
Holeyman, A. 2995
Holloway, S. 1335
Holt, S. 1048
Hong, H. P. 334
Hope, A. 2331
Hou, B.J. 1394

Houng, D.Q. 2987
Houston, S. 727
Hov, S. 1924, 2777
Hovland, K. 2783
Howald, E.P. 1154
Howiacki, T. 1457
Hu, C.Y. 1389
Hu, Y.T. 1394
Huang, H.W. 2183, 2296
Huang, W. 1659
Huang, X. 2019
Hunt, H. 2337
Hunt, T. 1048
Hurtado, G. 1929
Huvaj, N. 2654, 3353

Ibell, T. 2751
Ibraim, E. 2880, 2901
Ibsen, L.B. 311, 315
Iervolino, L. 1160
Iglesias, R. 1606
Igoe, D. 2801, 2880, 2921, 3015, 3070, 961
Ikodinovic, I.B. 1901
Ikonen, L.A. 1992
Illés, Zs. 2982, 2987, 3206
Imre, E. 542, 2987
Inácio, M. 1277, 1283, 1665, 2991, 3511
Indraratna, B. 2337
Infante, D. 1166
Insana, A. 197
Iodice, C. 384, 548
Iovino, M. 548
Iravanian, A. 2341
Irvine, J. 2346
Ischenko, Y. 2352, 2358, 3503
Isobe, Y. 3311
Ito, R. 1703
Ivanovski, D. 1038
Izadifar, M. 278

Jürgens, H. 338
Jabbarzadeh, M. 1362
Jacobsz, S.W. 503
Jacquard, C. 474, 3274
Jafari, M. 2995, 3078
Jagodnik, V. 554, 1377
Jagu, A. 2681
Jahanshahinowkandeh, M. 3145
Jaksic, L. 560
Janevski, B. 564
Janga, J.K. 1669, 3060, 3265
Janodet, L. 1539
Jaoude, G.A. 1236
Jardine, R.J. 3104
Jaroszek, A. 342
Jassionnesse, C. 3001
Javadi, A.A. 1013
Jefferis, S.A. 2189
Jelušič, P. 1996
Jenck, O. 3137
Jeng, S.Y. 1394
Jeremias, F.T. 3515
Jerman, J. 1104
Ji, C. 2047
Jia, Q. 2300, 3470
Jiménez Ontiveros, E. 2364, 2368
Jiménez, E. 1146
Jiménez-Valera, J.A. 3182
Jimenez, M. 670
Joffrin, P. 532
Johansson, J.A.T. 520
Johari, A. 1013
Johnsen, K.E.L. 320
Johnson-Watts, T. 2249
Jommi, C. 1679, 3176
Joseph, T. 2925
Joshi, A.C. 3007
Joshi, S. 2223
Josifovski, J. 1675
Jostad, H.P. 1241, 1440
Jottier, T. 750
Jou, C.-Y. 1072
Joussellin, T. 2931
Judge, M. 2223
Jurko, J. 1170
Justiniano, R. 2278, 2372, 2376
Justo, J. 1517

Kádár, I. 2909
Kabeta, W.F. 330
Kadlíček, T. 3011
Kahlström, M. 3521
Kahrs, K. 507
Kaira, T. 3491
Kaliukh, I. 3503
Kamchoom, V. 3293
Kamei, S. 1740
Kamenar, N. 1377
Kaneda, K. 568
Kania, J.G. 572
Kao, Y.-C. 1072
Karlsrud, K. 2511
Kasyap, S. 2801
Kasyap, S.S. 2880, 3015
Katalinić, D. 554
Kato, T. 2739, 2862
Katsigiannis, G. 127, 1291, 2037, 2107, 2331, 2895
Katsumi, T. 2739, 2862
Katzenbach, R. 2637
Kawai, K. 2380
Kawalec, J. 2577
Kawasaki, S. 2085
Kaynia, A.M. 1109
Kegyes-Brassai, O. 1174
Kelek, B.E. 295
Kelly, L.C. 3020
Keykha, H.A. 2384
Khalili, R. 1679
Khan, Q. 1179
Kheffache, A. 3024
Khiatine, M. 2059
Kichaieva, O. 1685
Kiełczewski, T. 903
Kim, T. 3030
Kinslev, E.M. 3034
Kirichek, Y. 576, 799
Kiriyama, T. 983
Kissane, P. 2388
Kitano, Y. 2358
Kitanovski, T. 1038
Kjærstad, K.M. 2323
Klar, A. 3094
Kleiber, S. 2964
Klopčič, J. 596
Klotz, F. 2810
Knabe, B. 582
Knappett, J.A. 2876
Knutsson, R. 1444
Knutsson, S. 3165, 3396
Košir, M. 3224
Koch, E. 1689, 1852
Koelewijn, A.R. 2052
Koga, C. 3311
Koirala, A. 1183
Kollár, Cs. 2987
Konishi, C. 1703
Kono, T. 3038
Konstadinou, M. 560, 588, 1005
Konstantinidis, D. 3042, 3046
Konstantinou, M. 618
Kontoe, S. 1188, 3104, 3349
Kopecký, M. 365
Kopecskó, K. 2909
Kopf, F. 2555
Korkiala-Tanttu, L. 2341
Koronides, M. 1188
Korzec, A.P. 1693

Kosheleva, N. 3503
Kostal, J. 3050
Koteras, A. K. 311, 315
Kovács, A. 2982
Kovačević, M.S. 1448
Kovacs, G. 1174
Kovba, V. 3503
Krabbe, J.Z. 592
Krasiński, A. 2394
Kreitmair, M.J. 2768
Kriege, A. 1555
Krishnan, S. 1224
Krotov, O. 799
Kucova, E. 1699
Kuder, S. 596
Kudou-Wada, R. 1703
Kugler, T. 3054
Kumar, A. 761
Kumar, G. 3060
Kumar, M. 2195
Kumawat, A. 390
Kuparadze, D. 1408
Kurimoto, Y. 3066
Kushwaha, A. 1023
Kusumawardani, R. 1113
Kuttah, D. 600
Kuvik, M. 1699
Kuznetsova, A. 2400
Kuznetsova, D.P. 1330
Kwon, Y.M. 3074

Länsivaara, T. 2884
Länsivaara, T.T. 745
López, L. 2987
López-Querol, S. 3133
Löfman, M.S. 3228
Løyland, M. 683, 1463
L'Heureux, J.-S. 679, 897
Labar, B. 1174
Lacasse, S. 1752
Lachérade, L. 1707
Laera, A. 1712
Lafreme, N. 2496
Laina-Gómez, C. 1718
Laloui, L. 84, 1315, 1756, 2797, 2960, 3361
Lamas, A.N.P. 235
Lamas, L. 1724
Lambert, S. 881
Lambrughi, A. 606
Lande, E.J. 683, 2511
Lando, T. 1100
Lanquette, F. 1915
Lapa, J. 3381
Lapastoure, L.M. 2925
Lapastoure, L.-M. 3070
Lapcevic, R. 1901
Laranjo, M.L. 2144
Larsson, S. 520, 2955
Laskowski, C. 3198
Laskowski, C.B. 2405, 3123
Lau, J.W.C. 1402
Laue, J. 1444, 1811, 2300, 3165, 3396, 3470
Lavado Rodríguez, J. 2368
Lavasan, A.A. 395
Le Lan, P.S.F. 750
Le, T. 949
Le, T.M.H. 679, 1856
Leak, J. 1194, 2987
Leal Lemos, L. 3422
Lebrun, A. 3137
Ledesma, A. 410
Lee, J. 2925
Lee, M. 3074
Lee, S. 3074
Lei, J. 610
Leite, D. 1807
Leme, R.F. 2793
Lemnitzer, A. 2282
Lemos, L.J. 2464
Lengkeek, H.J. 837
Lenoir, T. 375, 2440
Lentini, V. 1730
Lenz, P. 2631
Leon Bal, A.R. 3078
Leonardo, P. 1283, 1665, 3511
Leplat, J. 2848
Leppla, S. 1964, 3082
Lerat, S. 2681
Lesny, K. 1578, 1734
Letizia, N. 3088
Leung, A.K. 3293
Lev Yehudi, O. 3094
Levesque, C. 1335, 1988
Leviäkangas, P. 2699
Li, L. 3100
Li, W. 2047
Li, Z.L. 2745
Liao, K.-W. 1521
Libardi, L.G. 3198
Librić, L. 1448
Liew, P. 2254, 2731
Lin, H.J. 1113
Lin, S. 1740, 1795
Lipiński, M.J. 1746
Lirer, S. 1199, 1594
Liu, J. 614
Liu, T. 3104, 3465
Liu, X.Y. 1205, 2043
Liu, Y.-X. 1072
Liu, Y.Y. 1056
Liu, Z.Q. 1373, 1752, 2296
Llabjani, Q. 1756
Lloret, A. 137
Lloret-Cabot, M. 761, 1760
Lo, K.C. 1389
Loche, M. 1325
Lodahl, M.R. 592
Logar, J. 596, 2409
Lohrasb, F. 1265
Lohrmann, T. 1640
Long, M. 618, 2223
Look, B.G. 2413
Lopes dos Santos, A. 622
Lopes, C. 693
Lopes, H. 3357
Lopes, I. 1764
Lopes, M. 538, 2417, 2524, 2543
Lopes, M.L. 2067
Lopez, F. 2421, 3109
Losacco, N. 2426
Loshelder, J.I. 2777
Loukas, A. 2925
Loukili, A. 2538
Lourenço, J.C. 628, 1770
Lukic, D. 1901
Lundberg, A.B. 2955
Lundvig, K.H. 827
Luo, Z. 633
Luong, T.A. 637
Lupattelli, A. 3113
Luukkonen, T. 2699
Luzia, R. 3118
Ly, J. 2089
Lysdahl, A.O.K. 1150
Lytvyn, O. 361

Márquez, A. 2168
Măgureanu, A. 2113, 3507
M.Kahlström 2323
Mašín, D. 3011, 3237
Ma, X. 2047
Maca, N. 1724, 1774
Macedo, J. 641, 2152
Machaček, J. 369
Machacek, H. 1780
Machacek, J. 197
MacRae, C. 1650
MacRobert, C.J. 262

Macsik, J. 3470
Macuh, B. 1996
Madhusudhan, B.R. 2430
Madiai, C. 3446
Maeda, K. 2380
Magdy, A. 2434
Mahler, A. 282, 3206
Mahmutovic, D. 809
Mahony, J. 2249
Maia, P.C. de A. 424
Majava, J. 2699
Makasis, N. 2772
Makki, L. 875, 2266
Makowska, K. 2625, 2703
Makrypidi, T. 1434
Malancu, T. 715
Malekmohammadi, K. 647
Malheiro, A.M. 1214, 1232
Manassero, M. 2939
Manaviparast, H.R. 1786
Mancuso, C. 2889, 3406
Mandaglio, M.C. 1790
Mandal, K. 1795
Mandolini, A. 384, 548, 606
Manea, S. 2199, 2203, 2621
Mangushev, R.A. 1801
Mannah, J. 2440
Manso, J. 1807
Manzanal, D. 3123, 3198
Marache, A. 1707
Marcelino, J. 1622, 1807, 2212
Marchadour, L.-A. 1992
Marchetti, D. 542, 679
Marchi, M. 1033, 1209, 1356
Marchiori, L. 3129, 3335
Marcu, D. 1584
Marin, A. 197
Marinaro, R. 917
Marinelli, M. 1425
Marinković, N. 2445
Markussen, L.M. 3218
Marques, F. 1214, 1232
Marques, N.C. 1807
Marques, O. 2581, 2585
Marques, P. 356, 2451, 2543
Marschall, P. 1756
Marshall, A.M. 2667
Martínez García, E. 2456
Martínez Sánchez, D. 2368
Martínez-Bacas, A.B. 651
Marte, R. 1218, 1301
Martin, C.M. 3042, 3046
Martin, G. 2880
Martinelli, D. 1154
Martins, C. 1988, 2270, 2451, 2460, 2648
Martins, L.A. 2464
Martsinovich, N. 3450
Marušić, D. 554, 1377
Marull, E. 3159
Marzouk, I. 656
Masaki, Y. 2862
Masrouri, F. 2178
Massimino, M.R. 1142, 1421
Mata, C. 1622
Matei, T. 2563
Mateus de Brito, J. 247
Mateus, S. 2507
Matias Ramos, P. 2468
Matos Fernandes, M. 1935
Matos, J. 1265, 1269
Matos, P. 2852
Matsumoto, T. 1383, 1740, 1795
Matthiesen, U. 2474, 3233
Mattsson, H. 3165
Mauko Pranjić, A. 3224
Maurice, C. 3470
Mavroulidou, M. 2384, 2502
Mayne, P.W. 723, 1080
Mazzieri, F. 2884
McAdam, R.A. 3104
McCabe, B.A. 2388
McCartney, J. 727
McDermott, F. 2223
McGregor, J. 3450
McLean, M.A. 1224
McNamara, A.M. 2599, 3288
Mechling, J.-M. 931
Medicus, G. 1786
Mediero, L. 515
Medjnoun, A. 2059, 2978
Meena, K. 2195
Meena, P.K. 390
Meier, C. 2964
Meireles, L.T.P. 3034
Meland, H.J. 1924
Melashenko, Y. 3503
Mele, L. 1199
Melentijevic, S. 2168
Menéndez-Vicente, C. 3133
Mendizabal, A. 1606
Mendonça, A. 2478
Mengé, P. 773
Meng, J. 1811
Menkiti, C.O. 2189
Merino, C. 660, 1815
Merino, S. 2613
Mertz, A. 3137
Meshkati, E. 560
Metje, N. 1644, 2031
Meza, R. 418
Miao, Y. 1205
Mickovski, S.B. 3020, 3141
Midão, C. 1821
Mihailescu, D. 1825
Milagres, A.N. 1929
Miliziano, S. 2097
Millen, M. 1297
Milosevic, J. 2482
Milutinovici, E. 1825
Minardi, V. 1319
Minatchy, C. 765, 875, 913
Miranda, L. 1829
Miranda, M. 1517, 2158, 2168, 3145
Miranda, T. 1452, 1786
Miranda, V.H. 1712
Mircea, I. 1341
Mirnyy, A. Yu. 1835
Mishra, A. 2788
Mishra, S.K. 1066
Mitlmeier, F. 664
Miyanohara, T. 2352
Miyata, Y. 935
Mladenovič, A. 3224
Mohamadzadeh Romiani, H. 2384
Mohammed, M.B. 3015
Moine, P. 2496
Moitinho de Almeida, I. 2991
Molano, L. 670, 1123
Moldovan, D.-V. 1245
Moldovan, I. D. 301
Moldovan, L.-E. 1245
Molina-Gómez, F. 674, 1228
Monaco, P. 679
Moncada, A. 647, 3149
Monells, D. 1606
Moniz, L. 1232
Monsås, E. 683
Montalti, L. 3153
Monteiro, B. 2274
Monteiro, D. 3118
Monteiro, F.F. 2486
Montero-Cubillo, N.S. 3159
Moormann, Ch. 45, 664, 821, 1840, 3054
Mora Cejudo, D. 1606, 1612
Moraci, N. 1790
Morais, M. 1665
Morais, M.V. 3129
Morais, P. 2478

Moreno Robles, J. 1606, 1612
Moreno, F. 3153
Moreno, J. 1886, 2417, 2543, 2543
Moretti, S. 1166
Mori, A. 2352
Morozov, V.S. 1330
Mortensen, P.A. 2323
Mortensen, P.-A. 2492
Motamedi, Z. 3165
Motta, L.M.G. 849
Moura, A.S. 739, 1984, 2793
Moura, T.K. 689
Mourtada, D. 1236
Mroueh, H. 967, 3171
Muñiz-Menéndez, M. 291, 773
Mugele, L. 1001
Mukhanov, D. 995
Mulligan, R. 2249
Muniyasamy, S. 1291
Munoz-Castelblanco, J. 2496
Muntau, B.S. 2607
Muraro, S. 3176
Murison, R.A. 503
Mussakhanova, S. 995, 3303
Mustafa, W.S. 3339
Mwandira, W. 2502
Mwinken, D.K. 2987
Mylonakis, G. 2880

Németh, A. 2909
Năstase, C. 2563
Nader, T. 622
Nagula, S.S. 1241, 1752
Nagy, A.-Cs. 1245
Nagy, G. 2982
Nagy, L. 2982
Nakai, K. 3307
Nakashima, K. 2085, 2380
Nancey, A. 2709
Nardo, A. 1846
Narsilio, G. 1896, 3261
Narsilio, G.A. 2768, 2772
Nascimento, D.A. 739
Nascimento, V. 2507
Nasr, A. 2434
Navarro Carrasco, S. 3182
Neel, A. 2681
Nehme, S.G. 3206
Nelsen, C. 204
Nettleton, I.M. 2254, 2731
Neves, A. 2905
Neves, J. 693
Newson, T. 334, 2207
Nguyen, L.T. 949
Nguyen, M.V. 1852
Nguyen, N.H. 2138
Nguyen, T.Q. 1852
Nguyen, V.T. 913
Nicodemo, G. 697
Nicoli, T.A. 1430
Nicotera, M.V. 1551
Nikolic, A. 945
Nilsen, E. 2511
Nilsen, N.G. 2783
Niroumand, H. 2515
Nishiie, S. 3038
Nishimura, T. 701, 3186, 3307
Nissen, H. 2519
Nogue Sanchez, C. 809
Nogueira, N. 2551
Norberto, B. 1335
Norkus, A. 1964
Nosenko, V. 361
Novais, B.C. 1929
Nuber, T. 1886
Nunes, P. 1119
Nyambayo, V. 1630

Oštir, K. 2409
O'Meara, J.A. 3375
Oberhollenzer, S. 683
Ocak, S. 25
Odagiri, M. 705
Odenwald, B. 1780
Oen, A. 1090
Oguz, E.A. 1856
Ohtsuka, S. 568
Okada, K. 2352, 2358
Okkels, N. 711, 827
Okkenhaug, G. 2783
Olafsdottir, E.A. 1249, 3190
Oldecop, L. 3198
Oliveira, A. 1909
Oliveira, A.S. 2486
Oliveira, C.S. 1283
Oliveira, J.P. 1860
Oliveira, L. 1255
Oliveira, M. 1491, 2148
Oliveira, S. 1600, 3357, 3149
Olivera Luis, V.H. 2364
Olson, M.H. 1517
Olteanu, A.C. 715
Omarov, A. 995
Onescu, A.C. 2199
Oprčkal, P. 3224
Orakci, O. 438, 3194
Orlandi, S. 3198
Orlandini, M. 606
Ormeche, M. 1864
Orr, T. 1588, 1734
Ortiz-Hernández, R. 1259
Ortuta, J. 3202
Osinski, P. 1852
Osman, A. 3353
Osman, A.S. 503, 1127
Osokin, A.I. 1801
Othman, M.M. 1131
Ottaviani, A. 204
Ouechten, N. 326
Owusu-Ansah, D. 1265, 1269
Ozelim, L.C.S.M. 689

Pérez-Herreros, J. 1974
Pöyry, E. 745
Paçi, E. 1869
Paşca, D.M. 1245
Pabst, T. 2783
Pacheco, P. 1277
Pagliaroli, A. 1255, 1946
Palaiologou, M. 2235
Palanisamy, S. 1224
Paludeto, T.M.L. 2524
Pan, Y. 2323
Panagiotis, E. 719
Panchal, J.P. 3288
Panchal, P.H. 1224
Pandrea, P. 1566, 2625, 2703
Paniagua, P. 618, 723, 1080, 1924, 2777
Paninski, J.C. 3082
Pantazidou, M. 727
Pantelidis, L. 733
Panuška, J. 365
Pap, M. 3206
Papathanassiou, G. 1350
Papić, J.Br. 564
Pardo de Santayana, F. 1606, 1612, 1875
Pariota, L. 1425
Parrilla Alcaide, A. 1606, 1612
Pastor, J.L. 2950
Pataridze, D. 1408
Pathak, D.R. 3212
Pathmanandavel, S. 262
Paulatto, E. 3218
Paulino, F. 1273, 1881
Pavšič, P. 3224
Pavliuk, Y. 3503
Pedro, A.M.G. 795, 2573
Peduto, D. 1160
Peixoto, A. 2528

Pelecanos, L. 2751
Pelletier, B. 352
Peranić, J. 554, 1377
Pereira, A. 2534
Pereira, A.M. 1094
Pereira, G. 187
Pereira, J.M. 913, 1915
Pereira, J.-M. 3171
Pereira, M. 1017
Pereira, M.L. 418
Pereira, P.M. 3416
Perez, A. 2543
Perneta, J.P.S. 418
Perttu, O.J. 3228
Petrella, F. 3218
Petronilho, M.R. 1929
Pfeiffer, W.T. 3233
Picarelli, L. 1287
Piciullo, L. 1752
Pico, M. 3237
Pigeot, L. 2538
Pille, T. 2231
Pina, R. 907, 1469, 2101
Pinargote, K. 1730
Pinheiro, M. 1452
Pinho-Lopes, M. 641, 2152, 3477
Pinkert, S. 492
Pinto, A. 855, 1119, 2117, 2123, 2270, 2372, 2376, 2417, 2451, 2460, 2524, 2543, 2547, 2642, 2648, 3243
Pinto, C. 96, 1277, 1283, 1665, 1724, 2991, 3381, 3511
Pinto, S. 2551
Pinyol, N.M. 137
Pirone, M. 1287, 2889, 3406
Pisco, G. 2551
Pistone, R. 907, 1469, 2101
Pistrol, J. 2555
Pitanga, H.N. 2081
Pitilakis, D. 1188
Pizzi, A. 1946
Plasencia, N. 3243
Plomteux, C. 1566
Pohl, M. 1886, 2474, 3233
Polat, S. 2945, 3247
Polemis Júnior, K. 739
Polo, M. 3137
Popa, A-E. 2203
Popa, H. 1584
Popa, M. 2563
Portmann, G. 1890
Post, M. 2052
Potts, D.M. 1188
Pouragha, M. 1896
Poursalimi, N. 697
Pousada, C. 1277
Powrie, W. 3477
Prada-Sarmiento, L.F. 955
Pradhan, S. 1127
Prados, A. 660
Previtali, M. 2876, 3270
Profittlich, M. 3325
Pryce, S. 1291
Pucker, T. 3251
Pujević, V. 3255
Pulko, B. 596, 2409
Purchase, D. 2502
Puspitaningrum, I. 1746
Putteman, J. 750, 2076

Qi, J. 1896, 2337, 3261
Quadros, C. 2241
Quesnel, F. 1707
Quintavalle, S. 2249
Quintero, J. 1297

Répássy, L. 2987
Rødvand, L. 1241
Rømoen, M. 3521
Rørvik, E.S. 1924
Racinais, J. 2132
Rackwitz, F. 2735, 2755
Radu, C. 2559, 2563
Rahman, M.H. 273
Rahman, M.M. 2866
Rajot, J.P 532
Rakic, D. 1901
Rallu, A. 1434, 346
Ramalho, F. 2327
Ramalho, J. 2274
Ramos, A. 755
Ramos, A.V.F.S. 2567
Ramos, R. 3515
Ramoser, H. 1218
Rampello, S. 1594
Rana, A. 761
Rattez, H. 3088, 3436
Ravera, E. 3361
Raviteja, K.V.N.S. 3265
Ray, R.P. 1689, 2101
Rayhansyah, R.R. 907, 1113
Raymackers, S. 2172, 2848
Reale, C. 641, 1301, 2921, 3477
Reddy, K.R. 1669, 3060
Reiffsteck, P. 637, 765, 1636, 2266, 3274
Remaud, D. 1905
Renault, P. 2002, 2008
Repsold, L.M. 2547, 2642, 2648, 3243
Reul, O. 1560
Rezende, F.F. 1430
Rezende, L. 1909
Rezende, V. 1547
Ria Zamara, K.A. 2577
Ribeiro, L. 1920
Ribeiro, V. 2581, 2585
Riccio, T. 3270
Richa, T. 1915
Richard, P. 2262
Rieman, L.P. 3321
Rijal, M. 3212
Rios, S. 1821, 1920
Rismanchian, A. 769
Rispal, M. 618, 1924, 2777, 2783, 3030, 3274
Rivera, L. 719, 2589, 3034
Roces, E. 2405
Rocha, F. 3001
Rocha, J. 773
Rodrìguez González, V. 2097
Rodríguez, C.E. 777
Rodrigues, A. 1491, 2547
Rodrigues, A.T. 2148, 2218
Rodrigues, C. 414
Rodrigues, N. 3357
Rodrigues, P.C. 2081
Rodrigues, R.F. 1929
Roed, M. 783
Rogério, F.P.S. 1935
Rogbeck, Y. 197
Rogoff, I. 1100
Rohac, J. 1941
Rohmer, J. 1707
Rojas-González, E. 1259
Roka, R.B. 3278
Rola, J. 2593
Roldan, L. 2593
Romero, E. 404, 2292, 2821
Romić, N. 2445
Rong, C.X. 2721
Roque, A.J. 1305
Rosa, N. 2689
Rosa, T.D. 689
Rosenberg, M. 582
Rossi, N. 1448
Rosso, A. 1356
Rotisciani, G.M. 1311
Roubos, A.A. 750, 837, 2076

Rowe, R.K. 497, 3459
Ruggeri, P. 789
Ruiz López, A. 614, 795
Ruiz, R. 893
Ruiz-Terán, P. 2158
Rupakhety, R. 1655
Russo, G. 1551, 2178
Ryghseter, D. 3521

Sánchez-Barberán, C. 291
Sørensen, K.K. 448, 572, 592
Sørlie, E. 1440
Sørlie, E.R. 320
Saadé, M. 3284
Sabaliauskaite, G. 2599, 3288
Sadeghi, H. 1362, 2603
Sahlab, Z.N. 1315, 84
Sakolpanya, T. 3293
Sakurai, K. 1703
Salciarini, D. 3113
Salehi, B. 2607
Saliba, F. 1430
Salimnezhad, A. 295
Salvatore, N. 1946
Sammito, M.S.V. 1142
Samorodov, O. 799
Sanagawa, T. 765
Sanchez, J.C. 1531
Sandane, T. 2492
Sandoval, B. 3297
Sanfratello, J.-P. 375
Santana, M. 2613
Santana, T. 805, 2482
Santo, A. 1287
Santos, A. 1214, 1232, 2950, 3329
Santos, A.M. 2288
Santos, J. 2617
Santos, J.A. 628, 3525
Santos, P. 2547
Santos, R. 2123
Sapin, L. 2148
Saraiva, J. 2172
Sarao Mannelli, I. 1319
Sarkar, D. 955
Sarkar, S. 3365
Sarmiento, J. 3145
Saroglou, H. 1291, 2107, 2331
Sarsembayeva, A. 995, 3303,
Sas, W. 511, 1572, 2915,
Sastre Jurado, C. 3024
Sata, L. 2113, 2203, 2559, 2621, 3507
Sato, K. 3311
Sato, S. 3307
Savatier, V. 809
Sawant, V.A. 3007
Scaringi, G. 1325
Scarpelli, G. 1950
Schauber, P. 2703
Schiewe, H. 821
Schindler, U. 815
Schlager, T. 821
Schneider, M. 2625, 2631, 2703
Schröder, M. 1954
Schuch, M. 1301
Schulenberg, J. 1669
Schweckendiek, T. 167, 1958
Schweiger, H.F. 656
Scotto di Santolo, A. 1166
Scutti, F. 1224
Segovia, M. 2071
Seikel, R. 1224
Seip, M. 1964, 2637
Semblat, J-F. 1974
Senent, S. 515
Senigagliesi, M. 789
Seršen, S. 3224
Serna-Garcia, J. 1086
Sevim, O. 2063
Sfriso, A.O. 2593
Shah, S.U.U.S. 1970
Shahien, M. 2434
Shapoval, V. 799
Sharafutdinov, R.F. 1330
Sharma, S. 989, 1076
Shen, Y. 1974
Shepherd, C.J. 3316
Sheshov, V. 1038
Shinde, N.S. 3321
Shirasb, A. 524
Shkodrani, N. 1740, 1795, 1869
Shokarev, A. 3503
Shokarev, V. 3503
Shuminskiy, V. 3503
Shwan, B.J. 528, 1980
Siderius, K. 861
Sieńko, R. 1457, 2625, 2703
Siedin, V. 3503
Silva Filho, F.C. 739
Silva, A. 1335, 1988, 3325
Silva, A.A. 1527
Silva, C. 693
Silva, C.M. 2486
Silva, D.F. 1984
Silva, J. 2642, 2648
Silva, L.F. 1430
Silva, M. 1119
Silva, N. 538, 855
Silva, P.R. 241
Silva, R.C. 1430
Silva, W. 1547
Silvano, R. 3329
Simões, C. 2117
Simões, F.M.F. 2671
Simões, G.K.S. 2567
Simões, J. 2585
Simões, J.E. 2581
Simões, J.P. 2274
Simon, B. 305
Simon, C. 1100
Simon, N. 2138
Simonin, L. 3088
Simsek, M.C. 2654
Singh, A. 831
Singh, R.M. 2603, 3392, 3446
Skejić, A. 564
Skouboe, E. 827
Sluis, J.J.M. 837
Slyusarenko, Y. 3503
Smaavik, T.R. 197
Smith, C.C. 1513, 3450
Smolar, J. 2409
Sołowski, W.T. 1679, 1992
Soares, C.C. 2695
Soares, F.L. 2567
Sobhan, K. 633
Soccodato, F.M. 2658
Soe, K. 843
Soete, J. 3088
Soive, A. 2538
Solà, B. 410
Soralump, S. 1183
Sorgatz, J. 1588
Sottile, M. 2593
Sousa, A. 855
Sousa, J. 2905
Sousa, M. 3118
Sousa, M.A.S. 849
Soylemez, B. 25
Spagnoli, G. 404, 2292, 2685
Stănciucu, M. 1341, 1346
Stahlhut, O. 2631
Stajszczak, P. 903
Stallebrass, S.E. 2249, 2599, 3288
Stals, M.T. 861
Stanković, B. 2445
Steenfelt, J.S. 783, 865
Steensen-Bach, J.O. 865
Stegner, J. 2964
Steinlechner, E. 2421, 3109

Sterpi, D. 2827
Štiberc, D. 1377
Stolyarov, Y.I. 1330
Stridal, A.C. 2783
Strozberg. I. 3335
Studart, A. 3335
Stutz, H.H. 1001, 1640
Stuyts, B. 3024
Su, L. 3176
Subervie, J. 2138
Sugimoto, M. 3038
Surapreddi, S. 831
Susinov, B. 1675
Sutman, M. 2945, 3247
Suzuki, Y. 3030
Svensson, M. 871
Sverdrup-Thygeson, K. 1150
Swamynaidu, M. 843, 2662
Świdziński, W. 1693
Szendefy, J. 3339
Szilvágyi, Zs. 939
Szymkiewicz, F. 637, 765, 875, 881, 913, 2266, 3171

Tabachnikov, S. 799
Taborda, D.M.G. 614, 795, 2258, 3345, 3349
Tafili, M. 955
Taftsoglou, M. 1350
Takahashi, K. 1703
Takai, A. 2739, 2862
Takano, C. 2085
Takatoshi, T. 705
Takeuchi, K. 1383
Tallaksen, L.M. 1090
Talmon, A. 560
Talut, E. 2138
Tang, A.-M. 3171
Tang, A.M. 913
Tang, B. 2721
Tang, C. 2667
Tantivangphaisal, P. 3349
Tarantino, A. 727
Tarragó, D. 885
Tasbasi, A.D. 3353
Tataki, E. 1042
Tavallali, A. 769
Tavares, A. 907, 1469, 2101
Tavares, G. 1491, 1622, 1764, 3357
Taylor, H.M. 1042
Taylor, R.N. 2599, 3288
Teittinen, T. 3228
Teles Fortes, D. 2101
Ten Bosch, S. 84, 3361
Terente, V. 1042, 3153, 3329
Terente, V.A. 2842
Ter-Martirosyan, A.Z. 889
Terqueux, C. 305
Terra, V.S. 2671
Terzis, D. 84, 1315, 2960
Teves-Costa, P. 1255
Thakur, Y. 3365
Thewes, M. 2183
Thillainadarajah, J.K. 1023
Thomas, S.D. 482, 2675, 3369, 3375, 3381, 3387, 3530
Thomassen, V.A. 3392
Thorel, L. 326, 330, 375, 2262, 2681
Thorsen, T. 711
Thusyanthan, I. 2925
Tian, Y. 3194, 3400
Tijera, A. 893
Tinat, C. 582
Tinoco, J. 1265, 1269
Tintelnot, G. 2685
Toda, Y. 2358
Toll, D. 1760
Toll, D.G. 761, 1127
Tolooiyan, A. 2974
Tomás, L. 2617
Tomásio, R. 1988, 2270, 2327, 2451, 2460, 2689
Tomac, S.K. 2235
Tommik, K. 3396
Tomono, Y. 1383
Tomsa, C. 715
Tonni, L. 1033, 1356
Topolnicki, M. 3, 1566, 2625, 2703
Torres, G. 1123
Torres, G.M. 670
Torres, I. 2346
Torres, J.M. 1815
Toth, T. 1174
Tourchi, S. 524, 1362
Towey, F. 2388
Toyoshima, A.H.P. 2695
Trafford, A. 1179
Tregub, O. 576
Trofymchuk, O. 3503
Tropeano, G. 2658
Trybocka, K. 1566
Tsai, C.-C. 1072
Tschuchnigg, F. 656, 1560
Tsegaye, A.B. 320, 897
Tsiampousi, A. 614, 795, 3345
Tsikas, A. 438
Tuomela, A. 2699
Turalić, A. 564
Tuttolomondo, A. 2797
Tyagi, A. 843, 2662, 3365
Tymiński, W. 903
Tytarenko, V. 3503

Ullah, N. 3400
Unas, M. 907
Upomo, T.C. 1113
Urciuoli, G. 1287
Uta, P. 2199

Valkaniotis, S. 1350
Valtucci, F. 1199
Van Damme, N. 2848
van der Kolk, B.J. 2052
van der Made, K-J. 1636
van der Pol, M. 750
van Duijnen, P.G. 167
van Eekelen, S.J.M. 167, 1920, 2625, 2703, 2709
van Gelder, I.E. 3432
van Kessel, T. 560
van Laerhoven, C.R. 2127
van Marrewijk, C.J.F. 750
Van, D.B. 1852
Vangla, P. 1076
Varain, K. 2440
Vardanega, P.J. 1131, 1146, 1535, 2901, 2970
Varela, E. 3145
Varga, G. 1062, 2870
Varga, R. 1996
Vargas-Alzate, Y.F. 1086, 1368, 1412
Vasconcelos, R. 777
Vasilescu, R. 913, 3171
Vaughan, D.P. 3440
Vaunat, J. 777, 1368, 1412
Vaz, N. 2581, 2585
Veinović, Ž. 3428
Velioğlu, M.N. 2063
Veloso, F. 2689
Venda Oliveira, P.J. 2464, 2478, 2715, 3422
Ventini, R. 2889, 3406
Vergote, T. 2172
Vergote, T.A. 3410
Verissimo, C.U.V. 739
Vernhes, J.D. 2002, 2008

Viana da Fonseca, A. 291, 674, 805, 1228, 1297, 1821, 1920, 1935
Vicente, S.H. 3228
Vidal, P. 3123
Viegas, J. 917, 3525
Vieira de Sousa, J.F. 418
Vieira, A. 218, 2991, 3278, 3381
Vieira, C.S. 3416
Vieira, G.M. de D. 2288
Viking, K. 520
Villard, P. 305, 923
Villarroel-Ortega, J. 3422
Vinck, K. 3104
Vitale, E. 2178
Vitale, P. 1373
Vitorino, S. 2013
Vivoda Prodan, M. 554, 1377
Vo-Cong, H. 1383
Vogt, S. 815
Vollmert, L. 2816
von der Tann, L. 618
von Solms, N. 3094
Vowles, M. 2107
Vratsikidis, A. 1188
Vučenović, H. 3428
Vynnykov, Y. 799

Waaser, T. 1398
Waldheim, G. 2955
Walker, C. 927
Walrave, N.S. 3432
Walter, H. 1513, 1724
Wang, C.H. 1389, 1394
Wang, G. 1205, 2043
Wang, L. 2866
Wang, P.H. 1389
Wang, W. 975
Wang, X.J. 2721
Wang, X.S. 2721
Ward, G. 2388
Wasil, M. 3455
Wassermann, A. 931
Watabe, Y. 935
Watanabe, K. 1740
Waterston, H.K. 2842
Watson, J. 2675, 3369
Wayne, M. 2577
Wayu, A. 2341
Wdowska, M. 1746
Webster, C. 1224
Wehbe, T. 3436
Weitjens, W. 3024
Wen, K. 2880
Wetton, M.J. 3440
White, D.J. 154, 2880
Whyte, S.A. 2760
Wichtmann, T. 955
Wiklund, V. 1444
Willoner, A. 2727, 2764
Winslow, P. 1650
Winter, M.G. 1398, 2254, 2731
Witt, K.J. 1780
Wittekoek, B. 1005, 1052, 2625, 2703, 2709
Wolf, Á. 939
Wolf, A. 1174
Wong, E.K.L. 1402
Wood, H. 2331
Woodcock, J. 945
Wopereis, L. 1052
Worku, A. 1560
Worthington, P. 2970
Wotzlaw, M. 2735
Wudtke, R. 1636

Xiao, M.Y. 334
Xie, J.C. 2019
Xu, J. 2667
Xue, Z.F. 2866

Yamamoto, I. 1740
Yang, M. 2047
Yang, N. 949
Yang, W. 2025
Yao, Z.S. 2721
Yding, S. 2235
Yeh, F.H. 955
Yenne, E. 1650
Yensri, P. 1644, 2031
Yeow, H. 2013
Yeow, H.C. 2037
Yildiz, T. 1408
Yokoyama, D. 765
Yousefpour, N. 1896
Yozy Kepdib, M.F. 3446
Yu, G.-M. 975
Yu, R. 2739
Yu, X. 3450
Zabielska-Adamska, K. 3455
Zachert, H. 369, 2625, 2703
Zahedi, P. 961
Zaiter, H. 967
Zalar Serjun, V. 3224
Zania, V. 719
Zapata, C. 1131, 1146
Zapata-Franco, A.M. 1368, 1412
Zarattini, F. 2889
Zarazvand, B. 971
Zdanowicz, K. 2703
Zdravković, L. 1188, 3255
Zhairbaeva, G.A. 286
Zhang, D. 2025
Zhang, D.M. 2183, 2296
Zhang, K. 1760, 2745
Zhang, M. 1659
Zhang, N. 610
Zhang, Q. 979
Zhang, S.Q. 2745
Zhang, W. 1659, 1760
Zhang, X. 2047
Zhang, X.-D. 975
Zhang, X.W. 1205, 2043
Zhang, Y. 1890, 2047
Zhang, Z. 975
Zhang, Z.-Q. 975
Zhang, Z.-T. 975
Zhao, B. 3100
Zhao, L. 3459
Zheng, J. 2876
Zhou, H. 989
Zhou, M. 979
Zhou, Y. 983
Zhou, Z. 3465
Zhou, Z.-H. 1402
Zhussupbekov, A. 995
Zhussupbekov, A.Zh. 286
Ziagharib, A. 3470
Zimbardo, M. 1166
Zimmaro, P. 1425
Zivaljevic, S. 2482
Zlatanović, E. 2445
Žlender, B. 197, 1996
Zotna, Y. 2002, 2008
Zürn, J. 1001
Zuretti, C. 301
Zuziak, K. 1457
Zwaan, R.A. 2709
Zwanenburg, C. 1005, 1052, 2052, 3432